JANUARY 2009
Volume 20, Number 1

© *Copyright 2009 by the American Chemical Society*

Bioconjugate Chemistry

Editorial: The Twentieth Year of *Bioconjugate Chemistry*

As we complete the second decade of the journal during this milestone year, we will occasionally look back to see how the subject has advanced. The science and technology of bioconjugate chemistry concern the joining of two or more molecular functions, using chemistry, biology, or combinations of the two, to make products with useful biological properties. While today the molecules involved may be almost anything, twenty years ago this was most highly developed with proteins. Appropriately, the first article in the first issue of *Bioconjugate Chemistry* was a review of protein chemistry by Means and Feeney (*1*), which begins, "With roots in ancient formulations, methods for the chemical derivatization of proteins continue to expand and develop. The creation of this new journal dealing exclusively with bioconjugate chemistry was barely conceivable just a few years ago. An explosion of interest in the subject during the last decade is, however, easily seen". The authors go on to explain that those ancient formulations were based on empirical observations, without any real understanding of the underlying chemistry. One of the cardinal reasons for the American Chemical Society to found the journal was to help bring order to this sometimes-unruly subject. However, the empirical roots are still very much the basis for progress; without that "What will happen if I do this?" curiosity, bioconjugate chemistry would lose its essential spirit. Over the years, innovations such as intein-mediated labeling, native ligation, enzyme-catalyzed conjugation, and the ubiquitous click reaction have added surprising new dimensions to the preparation of proteins tagged with synthetic molecules. This suggests that even more unexpected developments lie ahead. As someone remarked at a recent meeting, the best of today's bioconjugate chemistry is so remarkable, it is as if the dreams of a science fiction writer have become reality. Let us see what the new year brings.

Thanks to Our Reviewers

It is a pleasure to acknowledge the contributions of the reviewers of manuscripts submitted in 2008 for publication in *Bioconjugate Chemistry*. Their unselfish service has been essential in the shaping of the nineteenth volume of the journal. The scientific community is fortunate that its members are willing to share their time and specialized knowledge in this way. The reviewers are listed on the following pages.

Claude F. Meares
Editor-in-Chief

LITERATURE CITED

(1) Means, G. E., and Feeney, R. E. (1990) Chemical modifications of proteins: history and applications. *Bioconjugate Chem. 1*, 2–12.

10.1021/bc800546x CCC: $40.75 © 2009 American Chemical Society
Published on Web 01/21/2009

Reviewers for 2008

Seetharama Acharya
Samuel Achilefu
Michael Adam
Roger Adami
Greg Adams
Toshihiro Akaike
Mitsuru Akashi
Kazunari Akiyoshi
Fernando Albericio
Hugette Albrecht
Cameron Alexander
Christine Allen
Stephen Alley
Paulo Almeida
Silvia del Valle Alonso
Julio Alvarez
Simon Ametamey
Mansoor Amiji
Carolyn Anderson
Daniel Anderson
David Andreu
Kristi Anseth
Yasushi Arano
Bruce Armitage
Luis Arnaut
Shoichiro Asayama
Ulysse Asseline
You Han Bae
Clive Bagshaw
Sandor Bajusz
Rumiana Bakalova
James Baker
Alexandru Balaban
Rolf Barth
Jacqueline Barton
Amit Basu
Annette Beck-Sickinger
Christian Becker
Craig Beeson
Martin Behe
Ettore Benedetti
Dennis Benjamin
David Benson
Donald Bergstrom
Michael Bienert
Gary Bignami
Jozsef Bodi
Otto Boerman
Alexei Bogdanov
Elijah Bolotin
Elizabeth Boon
Geert-Jan Boons
Darryl Bornhop
A. Borsodi
Ross Boyle
Mark Bradley
Martin Brechbiel
Rui Brito
Steve Brocchini
Roland Brock
Lyudmila Bronstein
Natalia Broude
Tom Brown
Donald Buchsbaum
Jean-Claude Bunzli
Jason Burdick
Patrick Burke
Cynthia Burrows
Jean Cadet
Paolo Caliceti
Julio Camarero
Jacek Capala
Massimo Capobianco
Peter Caravan
Frank Carroll
Hyung Cha
Elliot Chaikof
Ken Chang
Kai Chen
Xi Chen
Xiaoyuan Chen
Kun Cheng
Dae Yoon Chi
Sun Hang Cho
Yearn Seong Choe
Insung Choi
Joon Sig Choi
Bong Hyun Chung
Seth Cohen
Paul Cordopatis
Patrick Couvreur
James Cowan
Gabriella Csik
Wenjin Cui
Alan Cuthbertson
Ekaterina Dadachova
Hongjie Dai
Mark Davis
Robert DeLong
Gerald DeNardo
Attila Demeter
Mahendra Deonarain
Michael Detty
Gilles Divita
Kalliopi Dodou
Svetlana Doronina
Steven Douglas
Allen Ebens
Eva Egelseer
Joachim Engels
Alan Epstein
Ramon Eritja
Dominique Erni
Neil Fairweather
Andreas Faust
Jan Feijen
Min Feng
Paolo Ferruti
Gregg Fields
David Filpula
M. G. Finn
Karen Forsberg-Nilson
Keith Fox
Ronald Frank
Stefan Franzen
Andreas Frey
Peter Fugedi
Nobutaka Fujii
T. Fujii
Kazuhisa Fujimoto
Koichi Fukase
Shiroh Futaki
Marcel Garcia
Franz Gabor
Laurie Gahan
Michael Gait
Jinming Gao
Xiaohu Gao
Elisa Garcia-Garayoa
Jean Gariepy
Martin Garnett
Corrada Geraci
Carlos Geraldes
Hanspeter Gerber
Hamid Ghandehari
Giovanna Ghirlanda
Indraneel Ghosh
Jeff Gildersleeve
Todd Giorgio
Christian Girard
Maurice Goeldner
Edie Goldsmith
Jonathan Gordon
Vicente Gotor
Michael Gozin
Ken Grabstein
Duncan Graham
Anna Grandas
Scott Grayson
Mark Green
Ernest Groman
Hermann Gruber
Zhongwu Guo
Rainer Haag
Itaru Hamachi
Philip Hamann
Kevin Hamblett
Justin Hanes
Atsushi Harada
Isabel Haro
Eva Harth
David Harvey
Frederick Haselton
Kenichi Hatanaka
Huixin He
Kevin Healy
Mary Hefford
Karl-Erik Hellstrom
Wim Hennink
Piet Herdewijn
Greg Hermanson
Tomasz Heyduk
Koji Higai
Donald Hnatowich
Robert Hoffman
Miklos Hollosi
Sarah Hook
Daniel Horak
Jari Hovinen
John Howl
Hideki Ichikawa
Toshihiro Ihara
Barbara Imperiali
Marcos Intaglietta
Joseph Irudayaraj
Miya Ishihara
Osamu Ito
Yoshihiro Ito
Bela Ivan
Yasuhiko Iwasaki
Hiroo Iwata
Hieronim Jakubowski
Scott Jeffrey
Raz Jelinek
J. Jimenez-Barbero
Kai Johnsson
Sangyong Jon
Arwyn Jones
Lee Josephson
Jingyue Ju
Rudolph Juliano
Hans Junginger
Ravi Kane
Achillefs Kapanidis
Kazunori Kataoka
John Katzenellenbogen
Hiroyoshi Kawakami
Brian Kay
David Kessel
Michael Kilbourn
Jong-Man Kim
Sung Wan Kim
William Alvin Kinney
Yoshiaki Kiso
Thomas Kissel
Trevor Kitson
Ronald Kluger
Linda Knight
Hisataka Kobayashi
Laszlo Kohidai
Robert Kok

Makoto Komiyama
Akihiko Kondo
Kenji Kono
Jindrich Kopecek
Pavla Kopeckova
Felix Kratz
Murali Krishna
James Kronauge
Eugenia Kumacheva
Hank Kung
Jun Kunisawa
Yutaka Kuroda
Ester Kwon
Young Kwon
Vinod Labhasetwar
Norbert Lange
Robert Langer
Kim Larsen
Benedict Law
Christopher Leamon
Bernard Lebleu
Doo Sung Lee
Kang Choon Lee
Robert Lee
Raphael Levy
Frederick Lewis
Jason Lewis
Michael Lewis
Chun Li
Jun Li
Pei Li
Shyh-Dar Li
Xiangyang Liang
Mi Hee Lim
Michael Lindberg
Karen E. Linder
Jun-qiu Liu
Shuang Liu
Ye Liu
Harri Lonnberg
Zheng-Rong Lu
Giovanni Lucignani
Robert Mach
Helmut Maecke
Mizuo Maeda
Bruno Maggio
Edmond Magner
Theodosia Maina
Yoshie Maitani
D. Majumdar
Noah Malmstadt
Marilena Manea
Charles Manning
Angel Maquieira
Wojciech Markiewicz
Jean Martinez
Atsushi Maruyama
Andreas Marx
Stephen Mather
Stefan Matile
Takehisa Matsuda
Koji Matsuoka
Mattias Hallbrink
Heather Maynard
Jason McCarthy
Thomas Meade
Igor Medintz
Rajendra Mehta
Oleg Melnyk
Bernard Meunier
Damon Meyer
Gabor Mezo
Yubin Miao
Chad Mirkin
Henning Mootz
Amram Mor
Catherine Murphy
Niren Murthy
Manfred Mutter
Helmut Maecke
K. Muller
Yves Muhly
Teruyuki Nagamune
Takeshi Nagasaki
Yukio Nagasaki
Matthias Nahrendorf
Hiroyuki Nakamura
Masanori Nakamura
Jun Nakanishi
Ikuhiko Nakase
Masamichi Nakayama
Ravin Narain
Ajit Narang
Arutselvan Natarajan
Hans Nauwynck
Michal Neeman
K. Neoh
Dario Neri
Edward Neuwelt
Peter Nielsen
Christof Niemeyer
Takuro Niidome
Makiya Nishikawa
Yuji Nishiuchi
Nobuhiro Nishiyama
Berthold Nock
Johannes Oehlke
Yu-Kyoung Oh
Yoshihiro Ohmiya
Yuichi Ohya
Nicole Okeley
Naoto Oku
Laszlo Otvos
David Oupicky
Takeaki Ozawa
Daniel Pack
Alan Packard
Marty Pagel
Emil Palecek
Francesco Pampaloni
Ravindra Pandey
Roberto Paolesse
Anna Papini
William Pardridge
Jong-sang Park
Ki-Dong Park
Kinam Park
Tae Gwan Park
Gianfranco Pasut
M. Patankar
Laszlo Patthy
John Patton
James Paulson
Thomas Perrier
Cecile Perrio
Thomas Peters
Blake Peterson
H. Pietzsch
David Piwnica-Worms
Michael Ploug
Nicola Pohl
Richard Pon
Margus Pooga
Vince Pozsgay
Jozsef Prechl
Glenn Prestwich
Michael Przybylski
Suzie Pun
Roberto Purrello
David Putnam
Jozsef Rabai
Michael Raghunath
Tariq Rana
Satya Reddy
Prakash Reddy
Manfred Reetz
Vytas Reipa
Rebecca Richards-Kortum
Matthew Robinson
Steve Roffler
Buck Rogers
Vincent Rotello
Hirohide Saito
Hideo Saji
Maria Sakarellos-Daitsiotis
Kazuo Sakurai
Aliasger Salem
Michele Samaja
John Sanderson
Kim Sapsford
Toshinori Sato
Nagichettiar Satyamurthy
David Schaffer
David Scheinberg
Eyk Schellenberger
Roger Schibli
August Schubiger
Benjamin Schuler
David Schwartz
Paolo Scrimin
Frank Seela
Paul Selvin
Takeshi Serizawa
Norbert Sewald
Robert Sharkey
Min-da Shau
Wei-Chiang Shen
Dean Sherry
Linda Shimizu
John Shively
Giovanni Sindona
Dorothy Sipkins
Masahiko Sisido
Uwe Sleytr
Stephen Sligar
Krzysztof Slowinski
Bradley Smith
Charles Smith
David Smith
David Smithrud
Claudia Sperling
Caroline Springer
Robert Stahelin
Patrick Stayton
Michael Strano
Yasuo Suda
H. Suli-Vargha
Brent Sumerlin
Guoming Sun
Shouheng Sun
Hsing-Wen Sung
Avadhesha Surolia
May Sutherland
Sonke Svenson
Mark Swihart
Rita Szabo
Francis Szoka
Maryam Tabrizian
Shigeori Takenaka
Kazuhito Tanabe
Akito Tanaka
Fujie Tanaka
Bertrand Tavitian
Sankaran Thayumanavan
Jim Thomas
David Thompson
Louis Tiefenauer
Richard Tilley
Jose Toca-Herrera
Brian Toki
Thomas Tolbert
Don Tomalia
Kenneth Tomer
Vladimir Torchilin
Eva Toth
Gabor Toth
Geza Toth
Dirk Tourwe
Alexander Trubetskoy
Yiider Tseng

Vassilios Tsikaris
Andrew Tsourkas
Eishun Tsuchida
Ching-Hsuan Tung
John Turchi
Karel Ulbrich
Hiroshi Uyama
Eric Vives
Ganesan Vaidyanathan
Henry VanBrocklin
Katalin Varnagy
A. Varvarigou
Graca Vicente
Pierre Vierling
Carlos Villa
Frederick Villamena
Borbala Vincze
Takehiko Wada
John Wade
Ernst Wagner
Dong-An Wang
J. Wang
Lai-Xi Wang
Qian Wang
Xiang Wang
Xueding Wang
Cezary Watala
Yoshihito Watanabe
Ross Weatherman
Ralf Weberskirch
Alexander Wei
Michael Welch
Paul Wentworth
Lars Wesemann
Andrew Whittaker
Eric Wickstrom
Chris Wiethoff
Scott Wilbur
Meir Wilchek
Christopher Wilds
Nicholas Williams
Natalie Winblade
Francoise Winnik
Karen Wooley
Dieter Worhrle
Bing Xu
Han-Mei Xu
Kenji Yamamoto
Hidenori Yamada
Tetsuji Yamaoka
Motoo Yamasaki
Kevin Yarema
Herman Yee
Venkata Yenugonda
Yoon Yeo
Makoto Yoshimoto
Shigehiro Yoshimura
Samuel Zalipsky
Li-He Zhang
Mingzhen Zhang
Subiao Zhang
Bingsuo Zou
Andrew Zydney

BC800546X

REVIEWS

siRNA Conjugate Delivery Systems

Ji Hoon Jeong,[†] Hyejung Mok,[‡] Yu-Kyoung Oh,[§] and Tae Gwan Park*[,‡]

College of Pharmacy, Sungkyunkwan University, Suwon 440-746, South Korea, Department of Biological Sciences, Korea Advanced Institute of Science and Technology, Daejeon 305-701, South Korea, and School of Life Sciences and Biotechnology, Korea University, Anam-dong, Seungbuk-gu, Seoul, South Korea. Received July 4, 2008; Revised Manuscript Received August 18, 2008

Small interfering RNA (siRNA) has been chemically conjugated to a variety of bioactive molecules, lipids, polymers, peptides, and inorganic nanostructured materials to enhance their pharmacokinetic behavior, cellular uptake, target specificity, and safety. To efficiently deliver siRNAs to the target cells and tissues, many different siRNA bioconjugates were synthesized and characterized, and their gene silencing efficiencies were tested in vitro and in vivo. In this review, recent developments of siRNA bioconjugates are summarized.

I. INTRODUCTION

Synthetic siRNAs have been considered a new class of nucleic acid therapeutics for treatment of various infectious and genetic diseases including cancer (*1*). RNA interference (RNAi), a cellular post-transcriptional gene silencing mechanism, can be induced by double-stranded siRNA consisting of 21−25 nucleotides that degrades a target mRNA in a highly sequence specific manner (*2*–*4*). Despite the high therapeutic potential of siRNA, its application in clinical settings is still limited mainly due to the lack of efficient delivery systems (*5*). Clinically acceptable siRNA delivery systems should be carefully designed to improve the stability of siRNA after administration into the body, to deliver siRNA specifically to the desired tissue site, and to facilitate the cellular uptake of siRNA within target cells (*6*)

A number of nonviral delivery carriers, including liposomes (*7, 8*), lipids (*9, 10*), polymers (*11, 12*), peptides (*13*), virus-based vectors (*14*), and pressurized hydrodynamic injection (*15*), have been suggested for improved intracellular delivery of siRNA. Various kinds of cationic species can form nanosized polyelectrolyte complexes with negatively charged siRNA by ionic interactions. The resulting complexes can provide excellent protection of siRNA from attack by extracellular nucleases and allow facile cellular uptake via an endocytic pathway. Among the carriers, a wide array of cationic polymers with different architectures and functionalities can also be molecularly engineered for further modifications to provide the carriers with targeted delivery, biodegradability, and prolonged circulation properties (*16*). However, many cationic agents used for condensing siRNAs have often exhibited severe cytotoxicity, limiting clinical applications.

Recently, it has been reported that direct conjugation of small drug molecules, aptamers, lipids, peptides, proteins, or polymers to siRNA could improve in vivo pharmacokinetic behavior of siRNA (*17*). Such siRNA bioconjugates, either with or without forming nanocomplexes with cationic carriers, could significantly enhance biological half-life with a concomitant increase of delivery efficiency to the target tissue while maintaining sufficient gene silencing activity. This short review focuses on the recent development of various siRNA conjugate delivery systems for in vitro and in vivo applications.

II. PREPARATION OF siRNA CONJUGATES

A. Site of Conjugation and Chemical Modification. Since siRNA is a hybridized product of two complementary strands (sense and antisense), there are four terminal ends for potential conjugation sites. After cellular uptake, an antisense strand of siRNA, a strand having a complementary sequence to a target mRNA, is incorporated into the RISC to initiate the RNAi mechanism. This characteristic strand bias could be greatly influenced by chemical modification or conjugation of siRNA. Previous observations showed that the integrity of the 5′-terminus of the antisense strand, rather than that of the 3′-terminus, is important for the initiation of an RNAi mechanism (*18*–*20*). Therefore, the 3′- and 5′-terminus of the sense strand and the 3′-terminus of the antisense strand are primarily considered as potential sites for conjugation with minimal influence on RNAi activity. Conjugation strategies of several siRNA conjugates in the literature are summarized in Table 1. Either the 3′- or 5′-terminus of the sense strand is generally used for conjugation. Also, most of the conjugates employ cleavable linkages including acid-labile and reducible bonds between siRNA and the conjugation partner for facilitating the release of intact siRNA inside cells. The acid-labile and disulfide linkages are expected to be cleaved in the acidic endosome compartments and the reductive cytosolic space, respectively. Some siRNA conjugates use the action of the endogenous Dicer, which can process a premature double-stranded RNA to generate an active siRNA (*17, 21*)

To improve the nuclease resistance of siRNA and enhance its stability in biological fluids, siRNA itself is chemically modified. Chemical modification of the phosphorothioate linkage (backbone phosphate group O → S) or the boranophosphate linkage (backbone phosphate group O → BH_3) has been popularly used, since it is considered a simple and effective

* Corresponding author. Tae Gwan Park, Ph.D. Tel: +82-42-869-2621; fax: +82-42-869-2610; E-mail: tgpark@kaist.ac.kr.
[†] Sungkyunkwan University.
[‡] Korea Advanced Institute of Science and Technology.
[§] Korea University.

10.1021/bc800278e CCC: $40.75 © 2009 American Chemical Society
Published on Web 11/17/2008

Table 1. Strategies for Synthesis of siRNA Conjugates

siRNA conjugate	site of conjugation (I)	site of conjugation (II)	linkage	conjugate chemistry	target siRNA
Cholesterol-siRNA	3′-end of sense strand (*33*)[a]	Cholesterol-aminocaproic acid-pyrrolidine linker	Noncleavable (pyrrolidone)	Solid-phase synthesis (phosphoramidite)	Apo-B-1 siRNA
	5′-end of sense strand (*49*)	Cholesterol phosphoramidite coupled to (CH2)−S-S-(CH2)6 linker	Reducible (disulfide)	Solid-phase synthesis (phosphoramidite)	p38 MAP kinase siRNA
α-tocopherol-siRNA	5′-end of antisense strand (*17*)[a]	α-tocopherol phosphoramidite	Cleavable (phosphodiester, cleavage site of Dicer)	Solid-phase synthesis (phosphoramidite)	Apo-B-1 siRNA
Lipid-siRNA	3′-end of sense strand (*34*)[a]	Hydroyprolinol-lipophile moiety	Noncleavable (trans-4-hydroxyprolinol)	Solid-phase synthesis (phosphoramidite)	Apo-B-1 siRNA
TAT-siRNA	3′-end amine of antisense strand (*46*)[b]	N-terminal Cys containing TAT	Noncleavable (amide bond)	Cross-linker (sulfo-succimidyl 4-(*p*-maleimidophenyl)-butyrate)	GFP siRNA/CDK9 siRNA
	5′-end thiol of sense strand (*49*)	C-terminal Cys containing TAT	Reducible (disulfide)	Disulfide exchange	p38 MAP kinase siRNA
Penetratin-siRNA	5′-end thiol of sense strand (*47*)[b]	N-terminal Cys containing penetratin	Cleavable (disulfide)	Oxidation	Luciferase siRNA
	5′-end thiol of sense strand (*49*)	C-terminal Cys containing penetratin	Cleavable (disulfide)	Disulfide exchange	p38 MAP kinase siRNA
Transportan-siRNA	5′-end thiol of sense strand (*47*)[b]	N-terminal Cys containing transportan	Cleavable (disulfide)	Oxidation	Luciferase siRNA
PEG-siRNA	3′-end amine of sense strand (*50, 55, 56, 81*)[b]	Thiol modified PEG	Cleavable (disulfide)	Disulfide exchange (SPDP)	VEGF siRNA
	5′-end thiol of sense strand (*65, 66*)	Acrylate modified PEG	Cleavable (*β*-thiopropionate)	Michael addition	Luciferase siRNA/RecQL1 siRNA
Peptide analogue of insulin-like growth factor 1-siRNA	5′-end amine of sense strand (*60*)	C-terminal carboxyl group of IGF1 analogue	Noncleavable (amide bond)	Carbodiimide chemistry (DCC/NHS)	Insulin receptor substrate 1 siRNA
Antibody-siRNA	3′-end biotin of sense strand (*63*)	Streptavidin-conjugated antibody	Noncleavable (tetra-ethyleneglycol)	Biotin-streptavidin	Luciferase siRNA
Aptamer-siRNA	5′-end of sense strand (*64*)	In vitro transcription	Cleavable (disulfide) or noncleavable	Biotin-streptavidin	Lamini A/C siRNA
	5′-end of sense strand (*21*)		Cleavable (phosphodiester)	RNA aptamer-siRNA chimera	Bcl-2 siRNA/PLK1 siRNA
Quantum dot-siRNA	5′-end thiol of sense strand (*69*)	Amine-modified quantum dot nanoparticle	Cleavable (disulfide) or noncleavable (thioether)	Disulfide exchange (SPDP) or Micheal addition	GFP siRNA
Iron oxide nanoparticle-siRNA	5′-end thiol of antisense strand (*70*)	MBS-activated iron oxide nanoparticle	Noncleavable (thioether)	Michael addition	GFP siRNA/survivin siRNA
Carbon nanotube-siRNA	5′-end thiol of sense strand (*71*)	Amine modified carbon nanotube	Cleavable (disulfide)	Disulfide exchange (SPDP)	Luciferase siRNA

[a] Chemical modification of backbone nucleotide: partial 2′-*O*-methyl sugar modification, phosphorothioate linkage. [b] Reaction with duplex siRNA -Cys: cysteine; rxn: reaction.

method to increase the nuclease resistance of siRNA (*22*–*25*). Modification of the 2′-hydroxyl group of the pentone sugar, such as 2′-*O*-methyl (*22*, *26*), 2′-*O*-(2-methoxyethyl) (*26*), 2′-deoxy-2′floro (*27*), 2′-deoxy-2′floro-*β*-D-arabinonucleic acid (FANA) (*28*), and a methylene linkage between the 2′ and 4′ positions of the ribose (locked nucleic acid, LNA) (*29*), has also been employed for the enhanced nuclease resistance of siRNA, since the 2′ modifications apparently did not interfere with the action of the intracellular RNAi machinery (*18*). The replacement of oxygen linked to the 4′ carbon of the ribose with sulfur and the modification of terminal nucleotides of siRNA have also been attempted to enhance resistance to enzymatic degradation (*30*, *31*). However, it should be noted that, in order to fully maintain its silencing activity of siRNA, extensive chemical modifications of siRNA are not desirable (*32*)

B. Lipophile−siRNA Conjugates. Cholesterol was covalently conjugated to siRNA for systemic delivery (*33*). Cholesterol was conjugated to the 3′-terminus of the sense strand of siRNA via a pyrrolidone linkage. The cholesterol−siRNA conjugate (chol-siRNA) could induce intracellular RNAi without the significant loss of gene silencing activity. In addition, the conjugate exhibited significantly higher cellular transfer efficiency in cultured cells without the aid of transfection agents. In animal experiments, the significant silencing of apoliporotein B (apoB) gene, which encodes a protein essential for cholesterol metabolism, was observed in the liver and the jejunum after intravenous administration of the chol-siRNA conjugate. The silencing of the apoB gene resulted in a decreased plasma apoB protein level and consequently a reduction in the total levels of cholesterol. The conjugation of cholesterol to siRNA improved in vivo pharmacokinetic behaviors of siRNA as well. Intravenously administered chol-siRNA was distributed to various tissues including the liver, heart, lungs, kidneys, and fat tissues and was detected in the tissues even 24 h after injection (*33*). In contrast, no detectable naked siRNA could be observed in the tissues 24 h after intravenous injection. In addition to the chol-siRNA conjugate, a series of lipophilic siRNA conjugates, including siRNA conjugates with bile acids and lipids, were synthesized (Figure 1) (*34*, *35*). They interacted with lipoproteins in the blood serum, such as high-density lipoprotein (HDL) and low-density lipoprotein (LDL), lipoprotein receptors, and transmembrane proteins, influencing tissue distribution and uptake behaviors of the siRNA conjugates (*34*). The degree of hydrophobicity, which directly relates to the length of the alkyl chain, seemed to be a major determinant for the affinity of siRNA−fatty acid conjugates to lipoproteins. The siRNA conjugates with higher affinity to lipoproteins, i.e., the ones with longer fatty acid chains, showed enhanced gene silencing capabilities, suggesting that lipoproteins may facilitate the cellular uptake of the conjugates. When systemically administered, chol-siRNA bound to HDL demonstrated ca. five times higher cleavage of the target RNA transcript (apoB) in mouse, compared to unbound chol-siRNA at the same concentration. This suggests that the association of lipoproteins may further improve the pharmacokinetic properties of lipophilic siRNA conjugates. The association of lipoprotein also changed tissue distribution profiles of the conjugates. The lipophilic siRNA conjugates bound to LDL were mainly distributed to the liver by the action of LDL receptors, while the conjugates bound to HDL were taken up by various tissues, including the liver, gut, kidneys, and steroidogenic organs. The high affinity of HDL to the scavenger receptor SR-BI plays an important role in the uptake of HDL-bound siRNA conjugates. Further optimization may be possible by modifying strategies for the formation of preassembly between the lipophilic siRNA conjugates and lipoproteins or by identifying new lipophilic conjugate partners that lead to more favorable interaction with serum lipoproteins.

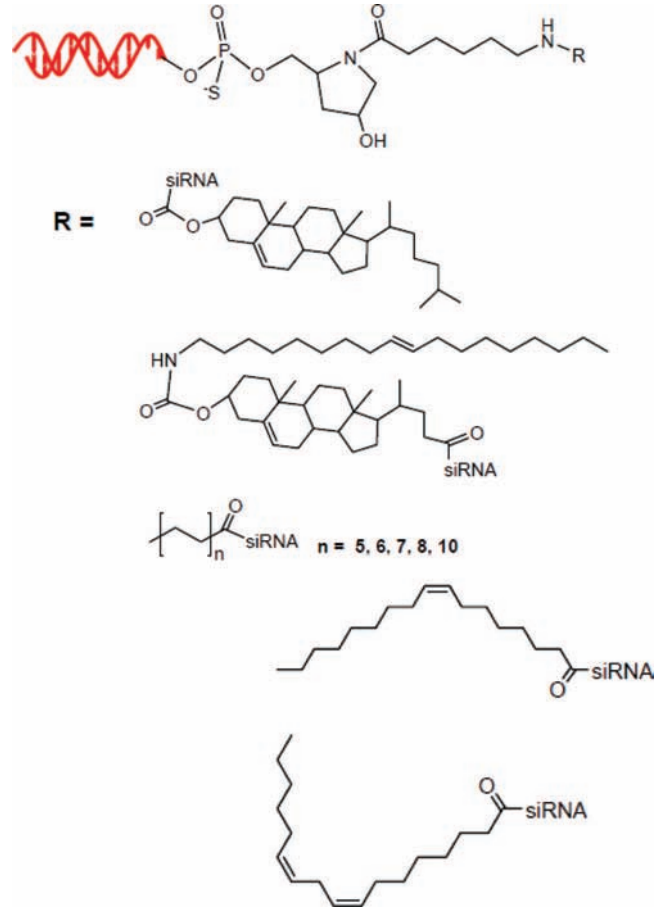

Figure 1. Structure of lipophile−siRNA conjugates. Various lipophiles (R), including cholesterol, bile acid, and a series of lipids with different chain lengths, were covalently conjugated to siRNA.

Although the animal results are encouraging, since the study showed the feasibility of using siRNAs as therapeutics, the requirement of a relatively high siRNA dose (50 mg/kg) remains to be solved for clinical applications.

Another lipophile−siRNA conjugate, α-tocopherol (vitamin E)-siRNA, was introduced for systemic siRNA delivery to the liver (*17*). Lipophilic vitamin E was covalently conjugated to the 5′-terminus of the antisense strand of 27/29-mer siRNA, which was partially modified with 2′-*O*-methylated ribose and phosphorothioate linkage. After intracellular delivery, the 27/29-mer siRNA was to be processed by the action of Dicer (*36*) to generate 21/21-mer siRNA, which caused the simultaneous release of the vitamin E moiety. The intravenous administration of the conjugate achieved a significant reduction of the target protein (apoB) in the liver without any induction of inflammatory interferons, such as interferon-α and interferon-*β* (*17*).

C. Peptide−siRNA Conjugates. A wide range of cell-penetrating peptides (CPPs), also called protein transduction domain (PTD), have been identified and employed as a vehicle for intracellular delivery of macromolecules such as proteins (*37*, *38*). Well-known examples of CPPs are TAT trans-activator protein (48−60) from human immunodeficiency virus type-1 (HIV-1) (*39*), Penetratin from the homeodomain protein of *Antennapaedia* (*40*), and Transportan, a hybrid amino acid sequence from glanin and mastoparan (*41*). The intracellular delivery efficiency of antisense oligonucleotides (*42*, *43*) and peptide nucleic acid (PNA) (*44*, *45*) could be improved by direct conjugation of CPPs. The same strategies were applied for the enhanced intracellular delivery of siRNA (Figure 2). TAT (47−57) was conjugated to the 3′-terminus of the antisense strand of an siRNA using a heterobifunctional cross-linker (HBFC), sulfo-

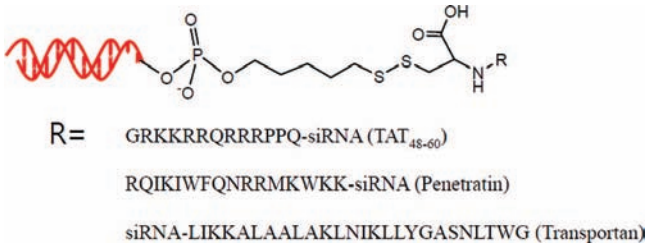

Figure 2. Structure of peptide−siRNA conjugates. Cell-penetrating peptides (TAT_{48-60}, penetratin, and transportan) were conjugated to siRNA through a terminal cysteine residue derivatized at either the N- or C-terminus of each peptide.

succinimidyl 4-(*p*-maleimidophenyl)butyrate (*46*). The TAT−siRNA conjugate demonstrated a dramatic improvement in the intracellular delivery of siRNA. The extent of cellular uptake showed a direct relationship with the amount of conjugate used for the transfection and the time elapsed after transfection. Cellular uptake of siRNA by the conjugate was as highly efficient as the commercial Lipofectamine formulation. The TAT−siRNA conjugate also successfully elicited the effective silencing of the target gene. Although TAT was conjugated to the antisense strand of siRNA via a noncleavable thioether linkage, the presence of the peptide did not seem to seriously interfere with the downstream process for the induction of RNAi, including the incorporation of TAT−siRNA into the RNA-induced silencing complex (RISC). The 5′-terminus of the antisense strand of siRNA was considered crucial for induction of the RNAi mechanism (*19, 20*). Many research groups used a cleavable linkage, such as the disulfide linkage, between CPP and siRNA to minimize potential reduction of RNAi activity by the presence of highly charged peptides. The disulfide linkage was employed for the conjugation of CPPs, including Penetratin and Transportan, to the 5′-terminus of the sense strand of siRNA. This delivery system was designed to improve the intracellular delivery of siRNA by the action of CPP and to release intact siRNA by reductive cleavage of the disulfide linkage between the CPP and the siRNA in the reductive cytoplasmic environment. The reductive release of intact siRNA from the conjugate may further facilitate the incorporation of siRNA into RISC by eliminating the potential interference of CPP. The CPP−siRNA conjugates, in which the disulfide linkage between the CPP and siRNA was formed by oxidation of thiol groups in the presence of oxidant, diamide, exhibited efficient suppression of the target reporter gene expression, such as luciferase or green fluorescence protein (GFP), in a variety of cell lines (*47*). The gene silencing efficacy of the conjugates was comparable to those of a cationic lipid-based formulation. Similar conjugates of Penetratin 1 peptide to siRNA, which also contain a disulfide linkage between the two components, were used for the delivery of siRNA to primary mammalian neuronal cells (*48*). The conjugate showed efficient down-regulation of the target genes, including superoxide dismutase (SOD) variants and caspases, in the neuronal cells without apparent cytotoxicity. However, the conjugation of CPP to siRNA did not appear to improve siRNA stability. The conjugates of CPP and siRNA showed similar degradation profiles to those of naked siRNA after exposure to mouse bronchoalveolar lavage (BAL) fluid (*49*). Besides, some peptide−siRNA conjugates elicited undesirable immune responses. Although intratracheal delivery of siRNA using CPP−siRNA conjugates successfully suppressed the expression of a target gene, p38 MAP kinase, the siRNA conjugate of Penetratin but not TAT(48−60) caused elevated secretion of inflammatory cytokines, such as interferon-α, tumor necrosis factor-α, and interleukin-12, after intratracheal distillation, suggesting the induction of innate immunity (*49*)

D. PEG−siRNA Conjugates. Poly(ethylene glycol) (PEG), a biocompatible, hydrophilic, and nonionic polymer, was conjugated to siRNA via a reducible disulfide linkage (Figure 3A) (*50*). The PEG−siRNA conjugate could be further complexed with cationic polymers or peptides as core condensing agents to form colloidal nanoparticles, so-called polyelectrolyte complex micelles (PEC micelles) (Figure 3B). The formation of PEC micelles and their use as a delivery vehicle for oligonucleic acid therapeutics has also been studied using PEG conjugated antisense oligonucleotides and siRNA in our previous studies (*50–54*). The negatively charged siRNA part was completely buried inside the polyelectrolyte core by the addition of the core-forming polycation due to charge neutralization, while the hydrophilic PEG segment surrounded the charge-neutralized core, improving the solubility of the insoluble polyelectrolyte core in an aqueous environment. The micelle-like core−shell structure, which is thermodynamically favored, provides additional stability to the PEC micelles when they are administered into the bloodstream, leading to prolonged circulation. The surrounding PEG shell also effectively prevented interparticular aggregation and shielded the surface charges of the core to make the PEC micelles neutral nanoparticles with a hydrophilic surface, resulting in acceptable blood compatibility. The PEG−siRNA conjugate itself showed much higher levels of siRNA stability than the naked siRNA in the presence of 50% serum. The conjugate lasted up to 16 h without a significant loss of integrity (*50*). The integrity of siRNA was fully maintained even after 48 h in 50% serum, when the PEG−siRNA formed PEC micelles via interactions with polyethylenimine (PEI). The PEC micelles achieved significantly enhanced transfection efficiency. A fusogenic cationic peptide, KALA, which is known to destabilize the endosomal membrane, was also used as a core forming agent to facilitate the endosomal escape process (*55*). The PEG−siRNA/PEI PEC micelles were used for local and systemic treatments for tumors in an animal model (*56*). An siRNA targeting vascular endothelial growth factor (VEGF) was chosen for antiangiogenic cancer therapy. The local and intravenous administration of the PEC micelles achieved significant retardation of tumor growth in tumor-bearing mice. In situ fluorescence imaging directly showed enhanced accumulation of the PEC micelles in a solid tumor region after intravenous injection through a mouse tail vein, suggesting the possibility of passive tumor targeting of siRNA therapeutics using the PEC micelles. This property of PEC micelles may be due to the passive diffusion of nanoparticles through the loosened endothelial vascular structure in the vicinity of highly proliferative tumors, which is called the enhanced permeation and retention (EPR) effect (*57*)

III. siRNA CONJUGATES FOR TARGETED DELIVERY

The lack of tissue- or cell-type specificity of siRNA is one of the most challenging problems in the development of therapeutic siRNAs. Targeted delivery of siRNA to the desired cells and tissues has been considered as an attractive way to bring siRNA drugs to clinical settings. The targeted siRNA delivery strategy not only minimizes the chance of potential adverse effects, but also reduces the amount of dose required to achieve a desired therapeutic effect. Cell-specific ligands, including aptamers, antibodies, sugar molecules, vitamins, and hormones, have been popularly employed to confer cell specificity on siRNA delivery systems (*58, 59*). Specific interaction between a specific ligand and its cellular membrane receptor generally enhances the cellular uptake by the aid of a mechanism called receptor-mediated endocytosis. Therefore,

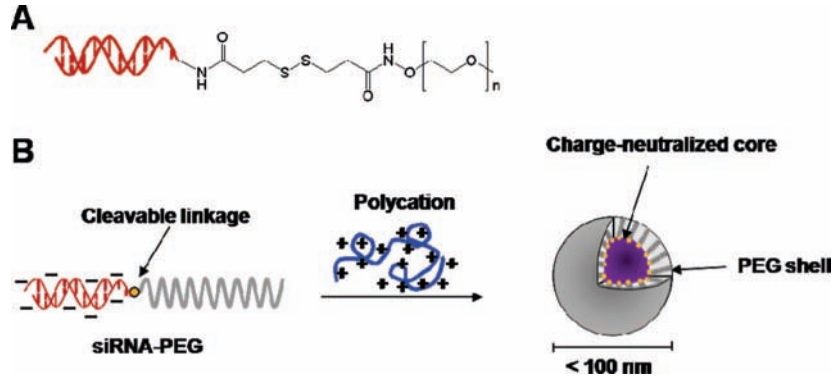

Figure 3. (A) Structure of PEG−siRNA conjugate. (B) Formation of PEC micelles from the interactions between PEG−siRNA conjugate and a polycation.

increasing specific cellular uptake by targeted delivery can significantly improve therapeutic efficacy with a much lower dose.

A. Ligand Peptide−siRNA Conjugates. For the receptor−ligand mediated delivery of siRNA, a ligand peptide for the targeted receptor was conjugated to siRNA. A carboxylic acid group of peptide mimetic of IGF1, D-(Cys-Ser-Lys-Cys) was activated and conjugated to an amine group of the 5′-sense strand of siRNA (*60*). After the annealing reaction, the gene silencing effect by an IGF1−siRNA conjugate was analyzed without the use of a transfection reagent. About 60% of the target IRS1 (insulin receptor substrate 1) gene expression was inhibited by the IGF1−siRNA conjugate, which was similar to that from the chol−siRNA conjugate.

B. Antibody−siRNA Conjugates. Antibody-mediated targeted drug delivery systems have attracted much attention due to their superior stability during systemic circulation and high selectiveness toward a target protein on the cell surface. A PEGylated immunoliposome-based brain targeting system was previously introduced, in which two antibodies were immobilized on the surface of liposomes (*61*). One monoclonal antibody was to target a transferring receptor expressed in the blood brain barrier (BBB), and the other antibody was to target insulin receptors expressed in brain cancer. The binding of transferrin receptor antibody may induce the transcytosis of the immunoliposome across the BBB. Similarly, the monoclonal antibody targeting the transferrin receptor at the BBB was directly conjugated to siRNA via a biotin−streptavidin linkage (*62*). The siRNA biotinylated at either terminus (3′ or 5′) of the sense strand was coupled to the streptavidin-conjugated antibody (Figure 5). The intravenous administration of the antibody−siRNA conjugate led to the efficient suppression of a reporter gene expression in a rat model bearing intracranially transplanted brain tumor.

C. Aptamer−siRNA Conjugates. Aptamers, modified oligonucleotides having selective affinities toward target proteins, are characterized by their globular structure, like the shape of tRNA. Generally, aptamers have intermediate molecular weights between small peptides (∼1 kDa) and single chain antibody fragments (∼25 kDa) (*63*). An aptamer targeting prostate-specific membrane antigen (PSMA), a cellular receptor abundantly expressed in prostate cancer cells, was directly conjugated to siRNA for prostate cell-specific delivery. Chu et al. used the biotin−streptavidin interaction for the conjugation of siRNA to the aptamer (Figure 4A) (*64*). Biotinylated siRNA and aptamer were joined together by using streptavidin via streptavidin−biotin interactions. The resulting conjugate was readily taken up by PSMA overexpressing cells without using transfection agents and successfully mediated specific RNAi, comparable to silencing activities by conventional lipoplexes. Another group proposed similar but more sophisticated targeting

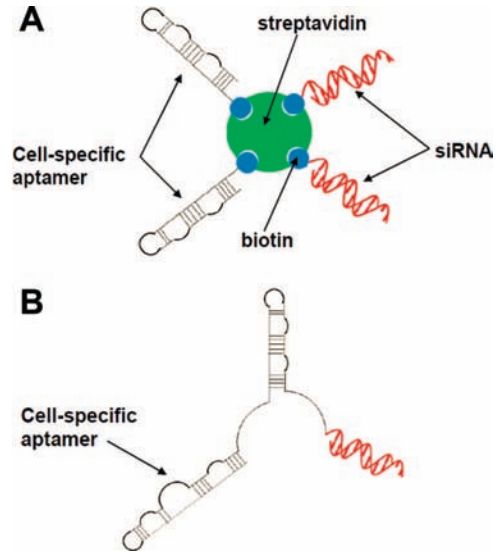

Figure 4. Schematic diagrams of aptamer−siRNA conjugates. (A) Conjugation of siRNA to a PSMA-targeting aptamer. The end group of the aptamer and siRNA was derivatized with biotin. Streptavidin was used as a core for the association of the biotinylated aptamer and siRNA. (B) Structure of chimeric conjugate of RNA aptamer and double-stranded siRNA. After intracellular delivery, the conjugate can be further processed by Dicer to induce RNAi.

system using a chimeric double-stranded RNA−aptamer hybrid (Figure 4B) (*21*). The chimera was synthesized by the in vitro runoff transcription method from a double-stranded DNA template containing a T7 RNA polymerase promoter. The dsRNA−aptamer hybrid was selectively bound to the cells overexpressing the target receptor, PSMA, and was taken up by the cells via receptor-mediated endocytosis. After the cellular uptake, the hybrid molecule could be further processed by endogenous Dicer, producing siRNA which target survival genes, such as polo-like kinase 1 (PLK1) and Bcl-2. Cell-type specific inhibition of tumor growth and tumor regression were achieved in a mouse tumor xenograft model by intratumoral administration of the chimeric siRNA delivery system. Although both proof-of-concept studies suggested the potential use of aptamers for the targeted delivery of siRNA drugs, nuclease susceptibility of aptamer ligands may limit their application in systemic treatments and the possibility of premature degradation of siRNA in the endolysosomal compartment due to the lack of endosomal escape machinery may require additional functionality.

D. Targetable Polyelectrolyte Complex Micelles. Polyelectrolyte complex (PEC) micelles consisting of PEG-conjugated siRNA and a polycation as a core forming agent can be formed by electrostatic interactions between negatively

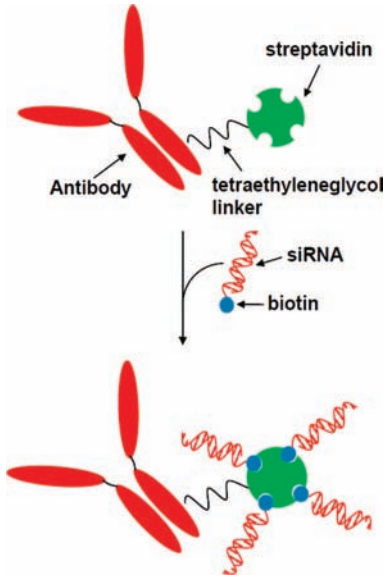

Figure 5. A schematic representation of antibody−siRNA conjugate. Biotinylated siRNA was coupled to streptavidin-conjugated antibody.

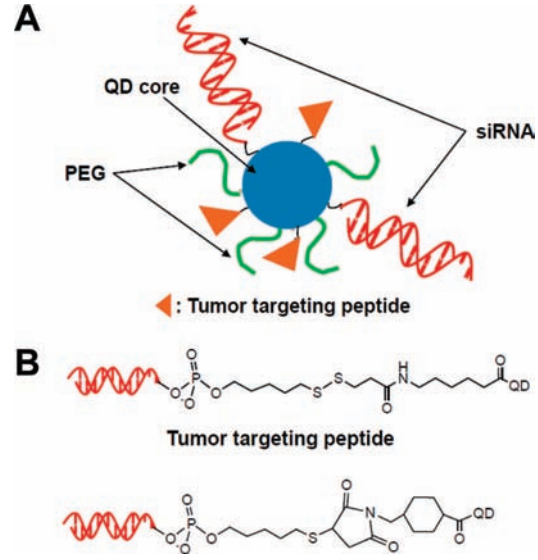

Figure 6. Quantum dot (QD)−siRNA conjugate. (A) A schematic diagram of a targetable QD−siRNA conjugate. Quantum dot modified with PEG and primary amine was used for further conjugation of siRNA and tumor targeting peptide. (B) The conjugate of QD−siRNA was synthesized through a reducible disulfide linkage or a nondegradable thioether linkage.

charged siRNA and polycation. The PEG segment acts as a hydrophilic shell protecting the charge-neutralized PEC core. In previous studies, PEC micelles could be passively targeted to a solid tumor region through the loosened endothelial junctions via the EPR effect (*56*). Because of the lack of cell specificity of the PEC micelles, the main route of cellular entry is expected to be adsorptive endocytosis. However, the cellular contact of PEC micelles may be hampered by the PEG shell that prevents nonspecific adsorption of blood components owing to the steric-hindrance effect of flexible PEG chains. Therefore, decoration of cell-specific ligands on the micelle surface would not only facilitate the cellular uptake via receptor-mediated endocytosis, but also reduce it by nontargeted cells. The lactose moiety was coupled to the distal end of the PEG−siRNA conjugate and used as a targeting ligand for the asialoglycoprotein receptors on hepatoma cells (*65, 66*). An siRNA was conjugated to the PEG segment via an acid-cleavable β-thiopropionate linkage and expected to be cleaved in the acidic environment of the endosomal compartment. The lactosylated-PEG−siRNA conjugate was used for the formation of PEC micelles by interacting with poly(L-lysine). The ligand installed PEC micelles containing siRNA targeting RecQL5 helicase demonstrated significant growth inhibition of the spheroids formed from human hepatocarcinoma cells (*66*). In our recent study, a luteinizing hormone-releasing hormone (LHRH) peptide analogue was attached to the end of PEG segment of the PEG−siRNA conjugate for the targeted siRNA delivery to ovarian cancer cells (Figure 7A) The system was designed to release siRNA in the cytoplasm by the reductive cleavage of the disulfide linkage between PEG and siRNA. The PEC micelles formed from the interaction between LHRH-PEG-siRNA and PEI (Figure 7B) showed selectiveness toward the ovarian cancer cells expressing LHRH receptors, leading to enhanced cellular uptake and suppression of the target gene expression. Surface installment of cell-specific targeting moieties onto the carriers gives selectivity toward target cells, which may increase the therapeutic effect in a target tissue with minimal risk of potential adverse effect by reducing the amount of the dose.

IV. siRNA−NANOPARTICLE CONJUGATES

Recently, various nanosized imaging agents (quantum dot nanoparticles, iron oxide nanoparticles, gold nanoparticles, carbon nanotubes, etc.) have been utilized for the development of multifunctional nanoparticles for dual therapeutic and diagnostic purposes (*67, 68*). QDs are fluorescent semiconductor nanocrystals with tunable emission properties in a wide range of colors (*69*). PEGylated QDs with surface amine groups were used for the conjugation of a tumor targeting peptide (F3), which binds to cell-surface nucleolin, and siRNA targeting a reporter gene encoding green fluorescence protein (GFP) (Figure 6) (*67*). The peptide and siRNA was attached to the QD using sulfo-LC-SPDP (sulfosuccinimidyl 6-(3′-[2-pyridyldithio]-propionamido) hexanoate) and sulfo-SMCC (sulfosuccinimidyl 4-(*N*-maleimidomethyl) cyclohexane-1-carboxylate) as heterofunctional cross-linkers. Sulfo-LC-SPDP generates a disulfide linkage that can be cleaved in the reductive cytoplasm, while sulfo-SMCC generates a stable thioether linkage. The QD−siRNA/F3 conjugate successfully delivered to HeLa cells without transfection agents presumably by receptor-mediated endocytosis. However, the gene silencing effect could not be observed due to the lack of an endosomal escape function (*67*). The addition of cationic liposomes after transfection of the QD conjugate led to significant reduction of the target gene expression in HeLa cells. Significantly higher silencing efficiency was observed with the conjugate containing a disulfide linkage between QD and siRNA, suggesting that the release of siRNA is required for the induction of RNAi due to the potential hindrance of large QD in the incorporation of siRNA into RISC.

Magnetic nanoparticles have been intensively investigated for their potential biomedical applications, such as magnetic resonance imaging (MRI), hyperthermia, magnetofection, and drug delivery (*70*). For siRNA delivery with concomitant visualization of its localization in vivo, siRNA was immobilized onto the surface of magnetic nanoparticles (*68*). Primary amine groups on the iron oxide nanoparticles were activated with a heterofunctional cross-linker, *m*-maleimidobenzoyl-*N*-hydroxysuccinimide ester (MBS), and then conjugated to the thiol group of the antisense strand of siRNA. Near-infrared Cy5.5 dye (NIRF) and membrane translocation peptides were also coated onto magnetic nanoparticles. Tumor tissues were successfully visualized by MRI and NIRF image due to the accumulation of the resultant magnetic nanoparticle−siRNA conjugate at the tumor tissue after intravenous injection. The

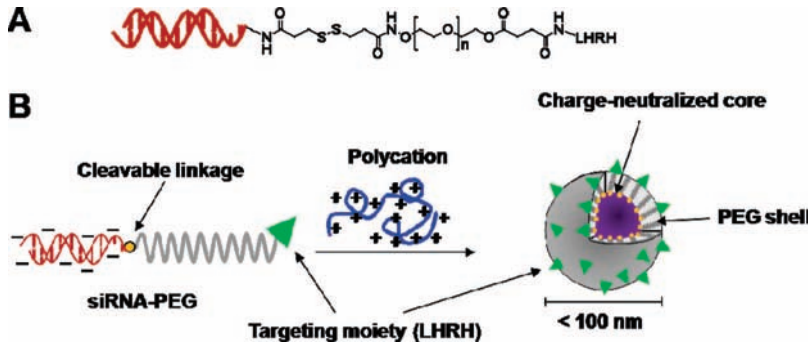

Figure 7. (A) Structure of an LHRH-tethered PEG−siRNA for targeting ovarian cancer cells. (B) The formation of PEC micelles from the interaction between LHRH-PEG-siRNA conjugate and a polycation (*81*).

mRNA level of target genes (green fluorescence protein and human survivin) was suppressed to below 15% by systemic injection of the magnetic nanoparticle−siRNA conjugate, compared to saline-treated controls. Although siRNA was conjugated onto magnetic nanoparticles via a noncleavable bond (thioether) in this experiment, surprisingly significant RNAi activity was achieved in vivo. The carbon nanotube−siRNA conjugates was also reported (*71*). The gene silencing effect by cleavable nanotube−siRNA conjugates was more enhanced about 20%, compared to that by lipofectamine/siRNA complexes and noncleavable nanotube−siRNA conjugates in vitro.

V. REDUCING OFF-TARGET EFFECTS BY siRNA CONJUGATES

Several recent papers have suggested that false-positive gene silencing could also be generated by siRNA due to its unexpected off-target effects. Recent evidence demonstrated that the off-target effects are mainly mediated by host innate immune response against the administered double-stranded RNA (siRNA) and the hybridization of siRNA-loaded RISC to undesirable mRNAs.

Synthetic siRNA can be recognized by cytoplasmic proteins, including RNA-dependent protein kinase, retinoid-acid-inducible gene 1 (RIG-1), and melanoma differentiation-associated gene 5 (MDA-5), to trigger downstream signal transduction required to elicit inflammatory responses (*72*, *73*). In addition, a series of transmembrane toll-like receptors (TLRs) are also known to play a crucial role in the recognition of synthetic siRNAs, which trigger innate immune responses (*74*). The siRNA-directed immune responses may be modulated by varying the sequence and backbone chemistry of siRNA and the type of delivery vehicle (*74*, *75*) The siRNA-dependent immune stimulation could be reduced by a certain degree of chemical modification in the backbone, including 2′-fluoro, 2′-*O*-methyl substitution and *N*-benzyl-2′-deoxyguanosine modification (*76*, *77*). However, the effect of siRNA conjugates on the inflammatory responses remains to be investigated. Previous reports suggest that the inflammatory responses can be induced depending on the property of a conjugation partner of siRNA. Intratracheal administration of Penetratin−siRNA conjugate could induce the expression of IFN-α and TNF-α, while TAT−siRNA and cholesterol−siRNA conjugate did not show any detectable immune responses (*49*). In the case of PEG−siRNA conjugate, the conjugation of PEG to siRNA seems not to further induce the expression of an inflammatory cytokine, interferon alpha (IFN-α) both in vitro and in vivo (*56*). It may be possible to reduce immune responses by conjugating appropriate materials to siRNA, which can hinder the interaction of siRNA with cellular proteins involved in the inflammatory signaling process.

Sometimes, silencing of unwanted genes by siRNA can occur. These false positive hits can be frequently observed in transcripts with ∼7 nucleotides of sequence complementarity at the 5′ end of the siRNA antisense strand (*78*, *79*). In addition, due to structural symmetry of siRNA strands, the incorporation of siRNA sense strand to RISC could lead to the off-target silencing of genes with sequence complementarity of the siRNA sense strand (*78*). Although improved selection of siRNA sequence may reduce the chance of off-target silencing, such a method cannot completely remove the off-target phenomenon, due to the lack of an efficient algorithm for the selection process (*79*). Recent study demonstrated that 5′-*O*-methylation at 5′ end of the siRNA sense strand could enhance biased incorporation of siRNA antisense into RISC, leading to reduction of the sense strand-directed off-target effect (*80*). This result suggests that the conjugation of proper materials to the 5′ terminus of the siRNA sense strand may further facilitate the biased strand selection process to reduce undesirable off-target effects. Reducing the off-target effect of siRNA is one of the challenging barriers that should be addressed before clinical applications of siRNA therapeutics. The conjugation of foreign materials to siRNA may be a double-edged sword, the benefit and risk, in terms of off-target effect. However, it is worth further investigation to determine whether the critical problem of siRNA can be avoided with siRNA bioconjugates.

VI. CONCLUSIONS

Therapeutic use of RNAi has gained a lot of attention because of its high specificity and broad therapeutic potential to target proteins that are not easily accessed and modulated by conventional small molecular weight or protein drugs. Synthetic siRNA is considered a major player in the induction of RNAi. Development of an efficient delivery system is one of the most challenging hurdles to turn siRNAs into clinically acceptable therapeutic drugs. A wide variety of siRNA conjugate delivery systems have been proposed, and some of them have demonstrated very promising preclinical results. Direct cleavable and noncleavable conjugation of various functional and nonfunctional molecules to siRNAs could not only improve their pharmacokinetic behaviors and cellular uptake efficiencies, but also promote cell specificities. To maximize delivery efficiency of siRNA bioconjugates, several crucial conjugation parameters, such as the conjugation site of siRNA, cleavability, the length of spacer, and the nature of molecules to be conjugated (charge, molecular weight, and hydrophobicity), should be carefully considered. A new class of siRNA bioconjugates integrating multiple functions in a single conjugate delivery system would be further required to solve various challenging barriers such as stability, prolonged circulation, target-specific cellular uptake, endosomal escape, and off-target property of siRNA.

ACKNOWLEDGMENT

This work was supported by the Ministry of Health and Welfare, and the National Research Laboratory program from the Ministry of Education, and Science and Technology, Republic of Korea.

LITERATURE CITED

(1) Elbashir, S. M., Harborth, J., Lendeckel, W., Yalcin, A., Weber, K., and Tuschl, T. (2001) Duplexes of 21-nucleotide RNAs mediate RNA interference in cultured mammalian cells. *Nature 411*, 494–8.

(2) McManus, M. T., and Sharp, P. A. (2002) Gene silencing in mammals by small interfering RNAs. *Nat. Rev. Genet. 3*, 737–47.

(3) Hannon, G. J., and Rossi, J. J. (2004) Unlocking the potential of the human genome with RNA interference. *Nature 431*, 371–8.

(4) Caplen, N. J., Parrish, S., Imani, F., Fire, A., and Morgan, R. A. (2001) Specific inhibition of gene expression by small double-stranded RNAs in invertebrate and vertebrate systems. *Proc. Natl. Acad. Sci. U.S.A. 98*, 9742–7.

(5) Jeong, J. H., Kim, S. W., and Park, T. G. (2007) Molecular design of functional polymers for gene therapy. *Prog. Polym. Sci. 32*, 1239–1274.

(6) Dorsett, Y., and Tuschl, T. (2004) siRNAs: applications in functional genomics and potential as therapeutics. *Nat. Rev. Drug Discovery 3*, 318–29.

(7) Landen, C. N., Jr., Chavez-Reyes, A., Bucana, C., Schmandt, R., Deavers, M. T., Lopez-Berestein, G., and Sood, A. K. (2005) Therapeutic EphA2 gene targeting in vivo using neutral liposomal small interfering RNA delivery. *Cancer Res. 65*, 6910–8.

(8) Zimmermann, T. S., Lee, A. C., Akinc, A., Bramlage, B., Bumcrot, D., Fedoruk, M. N., Harborth, J., Heyes, J. A., Jeffs, L. B., John, M., Judge, A. D., Lam, K., McClintock, K., Nechev, L. V., Palmer, L. R., Racie, T., Rohl, I., Seiffert, S., Shanmugam, S., Sood, V., Soutschek, J., Toudjarska, I., Wheat, A. J., Yaworski, E., Zedalis, W., Koteliansky, V., Manoharan, M., Vornlocher, H. P., and MacLachlan, I. (2006) RNAi-mediated gene silencing in non-human primates. *Nature 441*, 111–4.

(9) Santel, A., Aleku, M., Keil, O., Endruschat, J., Esche, V., Durieux, B., Loffler, K., Fechtner, M., Rohl, T., Fisch, G., Dames, S., Arnold, W., Giese, K., Klippel, A., and Kaufmann, J. (2006) RNA interference in the mouse vascular endothelium by systemic administration of siRNA-lipoplexes for cancer therapy. *Gene Ther. 13*, 1360–70.

(10) Yano, J., Hirabayashi, K., Nakagawa, S., Yamaguchi, T., Nogawa, M., Kashimori, I., Naito, H., Kitagawa, H., Ishiyama, K., Ohgi, T., and Irimura, T. (2004) Antitumor activity of small interfering RNA/cationic liposome complex in mouse models of cancer. *Clin. Cancer Res. 10*, 7721–6.

(11) Kim, S. H., Mok, H., Jeong, J. H., Kim, S. W., and Park, T. G. (2006) Comparative evaluation of target-specific GFP gene silencing efficiencies for antisense ODN, synthetic siRNA, and siRNA plasmid complexed with PEI-PEG-FOL conjugate. *Bioconjugate Chem. 17*, 241–4.

(12) Urban-Klein, B., Werth, S., Abuharbeid, S., Czubayko, F., and Aigner, A. (2005) RNAi-mediated gene-targeting through systemic application of polyethylenimine (PEI)-complexed siRNA in vivo. *Gene Ther. 12*, 461–6.

(13) Mok, H., and Park, T. G. (2008) Self-crosslinked and reducible fusogenic peptides for intracellular delivery of siRNA, *Biopolymers*.

(14) Grimm, D., Streetz, K. L., Jopling, C. L., Storm, T. A., Pandey, K., Davis, C. R., Marion, P., Salazar, F., and Kay, M. A. (2006) Fatality in mice due to oversaturation of cellular microRNA/short hairpin RNA pathways. *Nature 441*, 537–41.

(15) Song, E., Lee, S. K., Wang, J., Ince, N., Ouyang, N., Min, J., Chen, J., Shankar, P., and Lieberman, J. (2003) RNA interference targeting Fas protects mice from fulminant hepatitis. *Nat. Med. 9*, 347–51.

(16) Park, T. G., Jeong, J. H., and Kim, S. W. (2006) Current status of polymeric gene delivery systems. *Adv. Drug Delivery Rev. 58*, 467–86.

(17) Nishina, K., Unno, T., Uno, Y., Kubodera, T., Kanouchi, T., Mizusawa, H., and Yokota, T. (2008) Efficient in vivo delivery of siRNA to the liver by conjugation of alpha-tocopherol. *Mol. Ther. 16*, 734–40.

(18) Chiu, Y. L., and Rana, T. M. (2003) siRNA function in RNAi: a chemical modification analysis. *RNA 9*, 1034–48.

(19) Khvorova, A., Reynolds, A., and Jayasena, S. D. (2003) Functional siRNAs and miRNAs exhibit strand bias. *Cell 115*, 209–16.

(20) Schwarz, D. S., Hutvagner, G., Du, T., Xu, Z., Aronin, N., and Zamore, P. D. (2003) Asymmetry in the assembly of the RNAi enzyme complex. *Cell 115*, 199–208.

(21) McNamara, J. O., II, Andrechek, E. R., Wang, Y., Viles, K. D., Rempel, R. E., Gilboa, E., Sullenger, B. A., and Giangrande, P. H. (2006) Cell type-specific delivery of siRNAs with aptamer-siRNA chimeras. *Nat. Biotechnol. 24*, 1005–15.

(22) Amarzguioui, M., Holen, T., Babaie, E., and Prydz, H. (2003) Tolerance for mutations and chemical modifications in a siRNA. *Nucleic Acids Res. 31*, 589–95.

(23) Braasch, D. A., Jensen, S., Liu, Y., Kaur, K., Arar, K., White, M. A., and Corey, D. R. (2003) RNA interference in mammalian cells by chemically-modified RNA. *Biochemistry 42*, 7967–75.

(24) Braasch, D. A., Paroo, Z., Constantinescu, A., Ren, G., Oz, O. K., Mason, R. P., and Corey, D. R. (2004) Biodistribution of phosphodiester and phosphorothioate siRNA. *Bioorg. Med. Chem. Lett. 14*, 1139–43.

(25) Hall, A. H., Wan, J., Shaughnessy, E. E., Ramsay Shaw, B., and Alexander, K. A. (2004) RNA interference using boranophosphate siRNAs: structure-activity relationships. *Nucleic Acids Res. 32*, 5991–6000.

(26) Prakash, T. P., Allerson, C. R., Dande, P., Vickers, T. A., Sioufi, N., Jarres, R., Baker, B. F., Swayze, E. E., Griffey, R. H., and Bhat, B. (2005) Positional effect of chemical modifications on short interference RNA activity in mammalian cells. *J. Med. Chem. 48*, 4247–53.

(27) Blidner, R. A., Hammer, R. P., Lopez, M. J., Robinson, S. O., and Monroe, W. T. (2007) Fully 2′-deoxy-2′-fluoro substituted nucleic acids induce RNA interference in mammalian cell culture. *Chem. Biol. Drug Des. 70*, 113–22.

(28) Dowler, T., Bergeron, D., Tedeschi, A. L., Paquet, L., Ferrari, N., and Damha, M. J. (2006) Improvements in siRNA properties mediated by 2′-deoxy-2′-fluoro-beta-D-arabinonucleic acid (FANA). *Nucleic Acids Res. 34*, 1669–75.

(29) Elmen, J., Thonberg, H., Ljungberg, K., Frieden, M., Westergaard, M., Xu, Y., Wahren, B., Liang, Z., Orum, H., Koch, T., and Wahlestedt, C. (2005) Locked nucleic acid (LNA) mediated improvements in siRNA stability and functionality. *Nucleic Acids Res. 33*, 439–47.

(30) Hoshika, S., Minakawa, N., Kamiya, H., Harashima, H., and Matsuda, A. (2005) RNA interference induced by siRNAs modified with 4′-thioribonucleosides in cultured mammalian cells. *FEBS Lett. 579*, 3115–8.

(31) Czauderna, F., Fechtner, M., Dames, S., Aygun, H., Klippel, A., Pronk, G. J., Giese, K., and Kaufmann, J. (2003) Structural variations and stabilising modifications of synthetic siRNAs in mammalian cells. *Nucleic Acids Res. 31*, 2705–16.

(32) Rossi, J. J. (2004) Medicine: a cholesterol connection in RNAi. *Nature 432*, 155–6.

(33) Soutschek, J., Akinc, A., Bramlage, B., Charisse, K., Constien, R., Donoghue, M., Elbashir, S., Geick, A., Hadwiger, P., Harborth, J., John, M., Kesavan, V., Lavine, G., Pandey, R. K., Racie, T., Rajeev, K. G., Rohl, I., Toudjarska, I., Wang, G., Wuschko, S., Bumcrot, D., Koteliansky, V., Limmer, S., Manoharan, M., and Vornlocher, H. P. (2004) Therapeutic silencing of an endogenous gene by systemic administration of modified siRNAs. *Nature 432*, 173–8.

(34) Wolfrum, C., Shi, S., Jayaprakash, K. N., Jayaraman, M., Wang, G., Pandey, R. K., Rajeev, K. G., Nakayama, T., Charrise, K., Ndungo, E. M., Zimmermann, T., Koteliansky, V., Manoharan, M., and Stoffel, M. (2007) Mechanisms and optimization of in vivo delivery of lipophilic siRNAs. *Nat. Biotechnol. 25*, 1149–57.

(35) Lorenz, C., Hadwiger, P., John, M., Vornlocher, H. P., and Unverzagt, C. (2004) Steroid and lipid conjugates of siRNAs to enhance cellular uptake and gene silencing in liver cells. *Bioorg. Med. Chem. Lett. 14*, 4975–7.

(36) Kim, D. H., Behlke, M. A., Rose, S. D., Chang, M. S., Choi, S., and Rossi, J. J. (2005) Synthetic dsRNA Dicer substrates enhance RNAi potency and efficacy. *Nat. Biotechnol. 23*, 222–6.

(37) Lindgren, M., Hallbrink, M., Prochiantz, A., and Langel, U. (2000) Cell-penetrating peptides. *Trends Pharmacol. Sci. 21*, 99–103.

(38) Prochiantz, A. (2000) Messenger proteins: homeoproteins, TAT and others. *Curr. Opin. Cell Biol. 12*, 400–6.

(39) Vives, E., Brodin, P., and Lebleu, B. (1997) A truncated HIV-1 Tat protein basic domain rapidly translocates through the plasma membrane and accumulates in the cell nucleus. *J. Biol. Chem. 272*, 16010–7.

(40) Prochiantz, A. (1996) Getting hydrophilic compounds into cells: lessons from homeopeptides. *Curr. Opin. Neurobiol. 6*, 629–34.

(41) Pooga, M., Hallbrink, M., Zorko, M., and Langel, U. (1998) Cell penetration by transportan. *Faseb J. 12*, 67–77.

(42) Astriab-Fisher, A., Sergueev, D., Fisher, M., Shaw, B. R., and Juliano, R. L. (2002) Conjugates of antisense oligonucleotides with the Tat and antennapedia cell-penetrating peptides: effects on cellular uptake, binding to target sequences, and biologic actions. *Pharm. Res. 19*, 744–54.

(43) Turner, J. J., Arzumanov, A. A., and Gait, M. J. (2005) Synthesis, cellular uptake and HIV-1 Tat-dependent trans-activation inhibition activity of oligonucleotide analogues disulphide-conjugated to cell-penetrating peptides. *Nucleic Acids Res. 33*, 27–42.

(44) Turner, J. J., Ivanova, G. D., Verbeure, B., Williams, D., Arzumanov, A. A., Abes, S., Lebleu, B., and Gait, M. J. (2005) Cell-penetrating peptide conjugates of peptide nucleic acids (PNA) as inhibitors of HIV-1 Tat-dependent trans-activation in cells. *Nucleic Acids Res. 33*, 6837–49.

(45) Tripathi, S., Chaubey, B., Ganguly, S., Harris, D., Casale, R. A., and Pandey, V. N. (2005) Anti-HIV-1 activity of anti-TAR polyamide nucleic acid conjugated with various membrane transducing peptides. *Nucleic Acids Res. 33*, 4345–56.

(46) Chiu, Y. L., Ali, A., Chu, C. Y., Cao, H., and Rana, T. M. (2004) Visualizing a correlation between siRNA localization, cellular uptake, and RNAi in living cells. *Chem. Biol. 11*, 1165–75.

(47) Muratovska, A., and Eccles, M. R. (2004) Conjugate for efficient delivery of short interfering RNA (siRNA) into mammalian cells. *FEBS Lett. 558*, 63–8.

(48) Davidson, T. J., Harel, S., Arboleda, V. A., Prunell, G. F., Shelanski, M. L., Greene, L. A., and Troy, C. M. (2004) Highly efficient small interfering RNA delivery to primary mammalian neurons induces MicroRNA-like effects before mRNA degradation. *J. Neurosci. 24*, 10040–6.

(49) Moschos, S. A., Jones, S. W., Perry, M. M., Williams, A. E., Erjefalt, J. S., Turner, J. J., Barnes, P. J., Sproat, B. S., Gait, M. J., and Lindsay, M. A. (2007) Lung delivery studies using siRNA conjugated to TAT(48−60) and penetratin reveal peptide induced reduction in gene expression and induction of innate immunity. *Bioconjugate Chem. 18*, 1450–9.

(50) Kim, S. H., Jeong, J. H., Lee, S. H., Kim, S. W., and Park, T. G. (2006) PEG conjugated VEGF siRNA for anti-angiogenic gene therapy. *J. Controlled Release 116*, 123–9.

(51) Jeong, J. H., Kim, S. H., Kim, S. W., and Park, T. G. (2005) Polyelectrolyte complex micelles composed of c-raf antisense oligodeoxynucleotide-poly(ethylene glycol) conjugate and poly-(ethylenimine): effect of systemic administration on tumor growth. *Bioconjugate Chem. 16*, 1034–7.

(52) Jeong, J. H., Kim, S. W., and Park, T. G. (2003) A new antisense oligonucleotide delivery system based on self-assembled ODN-PEG hybrid conjugate micelles. *J. Controlled Release 93*, 183–91.

(53) Jeong, J. H., Kim, S. W., and Park, T. G. (2003) Novel intracellular delivery system of antisense oligonucleotide by self-assembled hybrid micelles composed of DNA/PEG conjugate and cationic fusogenic peptide. *Bioconjugate Chem. 14*, 473–9.

(54) Oishi, M., Nagatsugi, F., Sasaki, S., Nagasaki, Y., and Kataoka, K. (2005) Smart polyion complex micelles for targeted intracellular delivery of PEGylated antisense oligonucleotides containing acid-labile linkages. *ChemBioChem 6*, 718–25.

(55) Lee, S. H., Kim, S. H., and Park, T. G. (2007) Intracellular siRNA delivery system using polyelectrolyte complex micelles prepared from VEGF siRNA-PEG conjugate and cationic fusogenic peptide. *Biochem. Biophys. Res. Commun. 357*, 511–6.

(56) Kim, S. H., Jeong, J. H., Lee, S. H., Kim, S. W., and Park, T. G. (2008) Local and systemic delivery of VEGF siRNA using polyelectrolyte complex micelles for effective treatment of cancer. *J. Controlled Release 129*, 107–16.

(57) Maeda, H., Wu, J., Sawa, T., Matsumura, Y., and Hori, K. (2000) Tumor vascular permeability and the EPR effect in macromolecular therapeutics: a review. *J. Controlled Release 65*, 271–84.

(58) Wu, G., Yang, W., Barth, R. F., Kawabata, S., Swindall, M., Bandyopadhyaya, A. K., Tjarks, W., Khorsandi, B., Blue, T. E., Ferketich, A. K., Yang, M., Christoforidis, G. A., Sferra, T. J., Binns, P. J., Riley, K. J., Ciesielski, M. J., and Fenstermaker, R. A. (2007) Molecular targeting and treatment of an epidermal growth factor receptor-positive glioma using boronated cetuximab. *Clin. Cancer Res. 13*, 1260–8.

(59) Ikeda, Y., and Taira, K. (2006) Ligand-targeted delivery of therapeutic siRNA. *Pharm. Res. 23*, 1631–40.

(60) Cesarone, G., Edupuganti, O. P., Chen, C. P., and Wickstrom, E. (2007) Insulin receptor substrate 1 knockdown in human MCF7 ER+ breast cancer cells by nuclease-resistant IRS1 siRNA conjugated to a disulfide-bridged D-peptide analogue of insulin-like growth factor 1. *Bioconjugate Chem. 18*, 1831–40.

(61) Zhang, Y., Zhang, Y. F., Bryant, J., Charles, A., Boado, R. J., and Pardridge, W. M. (2004) Intravenous RNA interference gene therapy targeting the human epidermal growth factor receptor prolongs survival in intracranial brain cancer. *Clin. Cancer Res. 10*, 3667–77.

(62) Xia, C. F., Zhang, Y., Zhang, Y., Boado, R. J., and Pardridge, W. M. (2007) Intravenous siRNA of brain cancer with receptor targeting and avidin-biotin technology. *Pharm. Res. 24*, 2309–16.

(63) Hicke, B. J., and Stephens, A. W. (2000) Escort aptamers: a delivery service for diagnosis and therapy. *J. Clin. Invest. 106*, 923–8.

(64) Chu, T. C., Twu, K. Y., Ellington, A. D., and Levy, M. (2006) Aptamer mediated siRNA delivery. *Nucleic Acids Res. 34*, e73.

(65) Oishi, M., Nagasaki, Y., Itaka, K., Nishiyama, N., and Kataoka, K. (2005) Lactosylated poly(ethylene glycol)-siRNA conjugate through acid-labile beta-thiopropionate linkage to construct pH-sensitive polyion complex micelles achieving enhanced gene silencing in hepatoma cells. *J. Am. Chem. Soc. 127*, 1624–5.

(66) Oishi, M., Nagasaki, Y., Nishiyama, N., Itaka, K., Takagi, M., Shimamoto, A., Furuichi, Y., and Kataoka, K. (2007) Enhanced growth inhibition of hepatic multicellular tumor spheroids by lactosylated poly(ethylene glycol)-siRNA conjugate formulated in PEGylated polyplexes. *ChemMedChem 2*, 1290–1297.

(67) Derfus, A. M., Chen, A. A., Min, D. H., Ruoslahti, E., and Bhatia, S. N. (2007) Targeted quantum dot conjugates for siRNA delivery. *Bioconjugate Chem. 18*, 1391–6.

(68) Medarova, Z., Pham, W., Farrar, C., Petkova, V., and Moore, A. (2007) In vivo imaging of siRNA delivery and silencing in tumors. *Nat. Med. 13*, 372–7.

(69) Akerman, M. E., Chan, W. C., Laakkonen, P., Bhatia, S. N., and Ruoslahti, E. (2002) Nanocrystal targeting in vivo. *Proc. Natl. Acad. Sci. U.S.A. 99*, 12617–21.

(70) Gupta, A. K., and Gupta, M. (2005) Synthesis and surface engineering of iron oxide nanoparticles for biomedical applications. *Biomaterials 26*, 3995–4021.

(71) Kam, N. W., Liu, Z., and Dai, H. (2005) Functionalization of carbon nanotubes via cleavable disulfide bonds for efficient intracellular delivery of siRNA and potent gene silencing. *J. Am. Chem. Soc. 127*, 12492–3.

(72) Sioud, M. (2007) RNA interference and innate immunity. *Adv. Drug Delivery Rev. 59*, 153–63.

(73) Kato, H., Takeuchi, O., Sato, S., Yoneyama, M., Yamamoto, M., Matsui, K., Uematsu, S., Jung, A., Kawai, T., Ishii, K. J., Yamaguchi, O., Otsu, K., Tsujimura, T., Koh, C. S., Reis e Sousa, C., Matsuura, Y., Fujita, T., and Akira, S. (2006) Differential roles of MDA5 and RIG-I helicases in the recognition of RNA viruses. *Nature 441*, 101–5.

(74) Judge, A. D., Sood, V., Shaw, J. R., Fang, D., McClintock, K., and MacLachlan, I. (2005) Sequence-dependent stimulation of the mammalian innate immune response by synthetic siRNA. *Nat. Biotechnol. 23*, 457–62.

(75) Judge, A., and MacLachlan, I. (2008) Overcoming the innate immune response to small interfering RNA. *Hum. Gene Ther. 19*, 111–24.

(76) Judge, A. D., Bola, G., Lee, A. C., and MacLachlan, I. (2006) Design of noninflammatory synthetic siRNA mediating potent gene silencing in vivo. *Mol. Ther. 13*, 494–505.

(77) Puthenveetil, S., Whitby, L., Ren, J., Kelnar, K., Krebs, J. F., and Beal, P. A. (2006) Controlling activation of the RNA-dependent protein kinase by siRNAs using site-specific chemical modification. *Nucleic Acids Res. 34*, 4900–11.

(78) Jackson, A. L., Bartz, S. R., Schelter, J., Kobayashi, S. V., Burchard, J., Mao, M., Li, B., Cavet, G., and Linsley, P. S. (2003) Expression profiling reveals off-target gene regulation by RNAi. *Nat. Biotechnol. 21*, 635–7.

(79) Jackson, A. L., Burchard, J., Schelter, J., Chau, B. N., Cleary, M., Lim, L., and Linsley, P. S. (2006) Widespread siRNA "off-target" transcript silencing mediated by seed region sequence complementarity. *RNA 12*, 1179–87.

(80) Chen, P. Y., Weinmann, L., Gaidatzis, D., Pei, Y., Zavolan, M., Tuschl, T., and Meister, G. (2008) Strand-specific 5′-O-methylation of siRNA duplexes controls guide strand selection and targeting specificity. *RNA 14*, 263–74.

(81) Kim, S. H., Jeong, J. H., Lee, S. H., Kim, S. W., and Park, T. G. (2008) LHRH receptor-mediated delivery of siRNA using polyelectrolyte complex micelles self-assembled from siRNA-PEG-LHRH conjugate and PEI. *Bioconjugate Chem. 19*, 2156–2162.

BC800278E

Supporting Information for:

Reassembly of a Bioluminescent Protein *Renilla* luciferase Directed Through DNA Hybridization

Kyle A. Cissell, Yasmeen Rahimi, Suresh Shrestha, and Sapna K. Deo*,

Department of Chemistry & Chemical Biology

Indiana University Purdue University Indianapolis

Indianapolis, IN 46202

Materials and Methods.

Reagents: The plasmid containing the gene for Rluc (phRl-CMV) was purchased from Promega (Madison, WI). Chemically synthesized oligonucleotide probes (Probe 1, 5'-Thiol-TAGCTTATCAGACTGATGTTGA-3', Probe 2, 5'-TCAACATCAGTCTGATAAGCTA-Thiol-3', and free Probe 1, 5'-TAGCTTATCAGACTGATGTTGA-3') were obtained from Operon Biotechnologies (Huntsville, AL). Luria Bertani (LB) broth and agar were purchased from DIFCO Laboratories (Detroit, MI). The Hi-Trap copper chelating columns (1 mL) were purchased from GE Healthcare (Piscataway, NJ). Ampicillin, bovine serum albumin (BSA), and Coomasie Brilliant Blue R250 stain were obtained from Sigma Laboratories (St. Louis, MO). Protein molecular weight marker was purchased from Fisher Scientific. Coelenterazine (ctz) was purchased from Prolume (Pinetop, AZ). 96-well Neutravidin coated white microtiter plates and 1,8-bis-Maleimidotriethylene glycol ($BM(PEO)_2$) were purchased from Pierce Technology (Rockford, IL).

Apparatus

Bacterial cell cultures were grown in a Fisher Scientific orbital shaker, and centrifuged using a Beckman J2-MI centrifuge (Palo Alto, CA). Luminescence emission scans were obtained using the Varian Cary Eclipse Fluorescence Spectrophotometer (Palo Alto, CA). Luminescence intensity measurements were recorded using a Genios workstation luminometer (Tecan, NC). All luminescence intensities reported are the average of three replicates, and have been background corrected.

Construction of Rluc split fragments. The gene for *Rluc* from the plasmid phRl-CMV was employed as the initial template. Before constructing fragments of Rluc, we introduced a non-cleavable N-terminal 6x histidine tag on the Rluc gene to aid in protein purification, as well as a recognition site for *EcoRI* restriction enzyme cleavage. The 6-His tag and *EcoRI* site were introduced using site-directed mutagenesis with the following primers: RlucHisTagFor-5'CTAGCCACCATGCATCACCATCACCATCAC*GAATTC*GCTTCCAAGGTGTAC-3' and RlucHisTagRev-5'GTACACCTTGGAAGC*GAATTC*GTGATGGTGATGGTGATGCATGGTGGCTAG-3'. The bases coding for the histidine tag are underlined and the *EcoRI* site are italicized. In order to perform site-directed mutagenesis, primers were added to the template phRL-CMV, along with DNA polymerase and deoxynucleotide triphosphates (dNTPs). Next, polymerase chain reaction (PCR) was performed for 25 cycles to copy the new plasmid. Following PCR, the sample was digested with DpnI enzyme to digest plasmids that did not contain the added DNA. The mutated plasmid (pRluc-HisTag) was transformed into *E. coli* cells strain ER 2566, plated on LB agar supplemented with 100 μg/mL ampicillin, and DNA was isolated from the colonies via mini-preparation to perform gene sequencing and restriction analysis.

In order to genetically engineer the plasmid to code for the N-terminal Rluc fragment (amino acids 1-229), two stop codons were added between the codons for amino acids Gly229 and Lys230, using the plasmid pRluc-HisTag as the template DNA. Along with the stop codons, the DNA coding for a flexible linker (Ser Gly Gly Gly Gly Ser) and for a cysteine residue was added via site-directed mutagenesis as described above (Figure S1a). The primers which coded for the stop codons, flexible linker, and cysteine to construct the N-terminal fragment are the following:

BigLuxFor-

5'GTTAAGGGAGGC*AGTGGAGGTGGAGGTAGTTGT*TAGTAAAAGCCCGACGTC3' and

BigLuxRev-

5'GACGTCGGGCTTTTACTA*ACAACTACCTCCACCTCCACT*GCCTCCCTTAAC-3'. The bases coding for the stop codons are underlined, and the flexible linker and cysteine codons are italicized. After site-directed mutagenesis, the mutated plasmid (pSKD3) was transformed into ER 2566 competent cells, followed by minipreparation, restriction analysis, and gene sequencing to confirm the presence of the stop codons, flexible linker, and cysteine codons. The purpose of the flexible linker was to allow the oligo-Rluc fragments to come into close proximity, while decreasing the amount of strain on the Rluc fragments caused by the oligonucleotide hybridization. The cysteine residue is present to provide an accessible thiol moiety through which conjugation to thiol-modified oligonucleotide probes can occur.

In order to genetically engineer the plasmid coding for the C-terminal fragment (amino acids 230-311), a recognition site for *EcoRI* cleavage was added via site-directed mutagenesis between the codons coding for amino acids Gly229 and Lys230, using plasmid pRlucHisTag as the template. Also, a flexible linker and cysteine residue were added adjacent to the *EcoRI* cleavage site, on the N-terminal side of the C-terminal fragment (Figure S1b). The following primers were used for the addition of the *EcoRI* cleavage site, linker, and cysteine: SmallLuxFor-

5'GTTAAGGGAGGCGAATTC*TGTAGTGGAGGTGGAGGTAGT*AAGCCCGACGTC-3'

SmallLuxRev-

5'GACGTCGGGCTT*ACTACCTCCACCTCCACTACA*GAATTCGCCTCCCTTAAC-3'. The bases coding for the *EcoRI* site are underlined, and the linker and cysteine-coding DNA is

italicized. After site-directed mutagenesis was performed, followed by Dpn1 digestion, the new plasmid was transformed into ER 2566 cells. Minipreparation was performed to isolate the plasmid, followed by restriction analysis with *EcoRI*, and gene sequencing in order to confirm the addition of the *EcoRI* site, the linker, and the cysteine residue. Upon verification of the mutated plasmid, digestion with *EcoRI* was performed to cut the plasmid, resulting in two DNA fragments, one fragment representing the N-terminal fragment, and the other representing the linker, cysteine, and C-terminal fragment. After gel extraction, the C-terminal fragment was ligated to form the plasmid pSKD4 (Figure S1b). Gene sequencing and restriction analysis with *EcoRI* were performed again to verify that the C-terminal fragment plasmid did not contain the N-terminal fragment gene. Once verified, the plasmid pSKD4 was transformed into ER 2566 competent cells for protein expression.

Expression of Rluc Fragments.

Cells containing plasmids pSKD3 and pSKD4 coding for the Rluc N-and C-terminal fragments, respectively, were grown in Luria Bertani (LB)-broth containing ampicillin (100 μg/mL) at 37 °C to an optical density of 0.5 measured at 600 nm. Protein expression was induced using IPTG (1 mM final concentration) and the cells were grown for 24 h at room temperature. The cells were harvested by centrifugation at 16 °C, 8600 x g for 15 min, resuspended in PBS buffer (50 mM sodium phosphate buffer, pH 8.0 containing 300 mM NaCl), and were sonicated for 3 min with a 20 s on and 15 s off cycle. The crude protein was obtained by centrifugation at room temperature, 3000 x g, for 15 min.

Purification of Rluc Fragments.

The Hi-Trap copper chelating column precharged with $CuSO_4$ was prepared by washing with 5 mL of distilled water to remove the 20% ethanol storage solution. The column was equilibrated with 5 mL of binding buffer (50 mM sodium phosphate, pH 8.0 buffer containing 300 mM NaCl) before adding the samples of crude Rluc fragments. The column was then washed with 20 mL of binding buffer followed by a 10 mL of wash buffer (50 mM sodium phosphate, pH 8.0 containing 300 mM NaCl and 5 mM imidazole). The purified Rluc fragments were eluted with 2 mL of elution buffer (50 mM sodium phosphate, pH 8.0 containing 300 mM NaCl and 100 mM imidazole). The purity of eluted fractions was determined by SDS-PAGE. Protein concentration was determined via Bradford assay.

Control Study:

A 1 nanomole of Rluc N-terminal fragment and Rluc-C-terminal fragments were prepared in PBS buffer (100 mM sodium phosphate buffer containing 250 mM NaCl, 1 mM EDTA, and 0.1 % BSA, pH 7.4). To 1 nanomole of both fragments in a white, flat-bottom microtiter plate, 0.5 μL of coelenterazine (ctz) (1 mg/mL)was added and luminescence measurement was performed with a 100 ms integration time. Next, 1 nanomole of both fragments were mixed together and incubated at 37 °C for 30 min. At the end of 30 min, 0.5 μL of ctz was added to the plate and luminescence measurement was performed with a 100 ms integration time.

Labeling of Rluc fragments

The conjugations for both the C-terminal fragment and N-terminal fragment consisted of a two step process. First, the crosslinker $BM(PEO)_2$ and the Rluc fragments were linked through the cysteine thiol moiety which is adjacent to the SGGGGS flexible linker present on the fragments, followed by addition of the thiol-modified oligonucleotide probes (Figure S2). In order to

conjugate the Rluc fragments to $BM(PEO)_2$, the fragments' disulfide bonds formed from the exposed cysteine residues were reduced by adding 10-fold mole excess of TCEP to the Rluc fragments, while stirring for 30 min at room temperature. Next, the $BM(PEO)_2$ was added to the Rluc fragments in a two-fold mole excess, while stirring for 2 h at room temp. Before adding the thiol-modified oligonucleotide probes, the disulfide bonds between the probes were reduced with 40 mM TCEP for 30 min at 37°C. After reducing, the oligonucleotide probes were added dropwise to the stirring Rluc fragment-$BM(PEO)_2$ solution. The final mole ratio of Rluc fragment: crosslinker: oligonucleotide probe was 1:2:5. Upon linking the oligonucleotide probe to the Rluc fragment, extensive dialysis against PBS buffer (50 mM $NaHPO_4$, 300 mM NaCl, pH 7.2) was performed to remove unconjugated linker and probe. Unreacted Rluc fragments were not separated from labeled fragment since removal using dialysis will be a challenging task due to large size of Rluc fragments. However, the fragments are inactive in isolation and cannot form functional Rluc by self-reassembly therefore non-conjugated Rluc fragments would not cause any interference or yield any background signal. Further the complete conjugation of Rluc fragments with probes was verified by running an SDS-PAGE gel.

Hybridization Study:

A 5×10^{-6} M concentration of Rluc N-terminal fragment probe 2 conjugate and Rluc C-terminal fragment probe 1 conjugate was prepared in PBS buffer (100 mM sodium phosphate buffer containing 250 mM NaCl, 1 mM EDTA, and 0.1 % BSA, pH 7.4). A volume of 100 μL of both fragment probe conjugates were mixed together and incubated at 37 °C for 30 min. At the end of 30 min, the probe mixture was placed in a white, flat-bottom microtiter plate and 0.5 μL of coelenterazine (ctz) was added to the plate and luminescence measurement was performed with a

100 ms integration time. Control studies were performed using (1) buffer + ctz, (2) buffer + Rluc-N terminal fragment probe 1 conjugate + ctz, (3) buffer + Rluc-C terminal fragment probe 2 conjugate + ctz. Next, different concentrations of two Rluc fragment probe conjugates were mixed together in equimole amounts and incubated at 37 °C for 30 min. Coelenterazine was added at the end of the incubation period and the luminescence intensity was measured.

Effect of free probe 1:

A mixture of Rluc-N-terminal fragment probe 2 conjugate (50 μL, 1 x 10^{-6} M) and Rluc-C-terminal fragment probe 1 conjugate (50 μL, 1 x 10^{-6} M) was incubated at 37 °C for 30 min followed by the addition of 100 μL of two different concentrations (17 μM, 66 μM) of free probe and further incubation at 37 °C for 30 min in a microtiter plate. Next, 0.5 μL of ctz was added to the wells and luminescence measurement was performed. A one nucleotide mismatched probe (5'-TAGCTTATCCGACTGATGTTGA-3') was similarly added to hybridized probe-fragment complex and was followed by luminescence measurement.

Reassembly in cellular extract

The ER2566 cell extract was prepared by growing the strain in LB media up to an optical density of 0.9 measured at 600 nm. The cells were sonicated with a 20 s on and 20 s off cycle for 5 min in 50 mM sodium phosphate buffer, pH 7.4, containing 150 mM NaCl. The resulting mixture was directly used as an extract. Nanomole amounts of probe2-N-terimnal Rluc fragment and Probe1-C-terminal Rluc fragment were mixed with the cell extract and hybridized at 37 °C for 30 min. A luminescence measurement was performed after the addition of ctz.

(a)

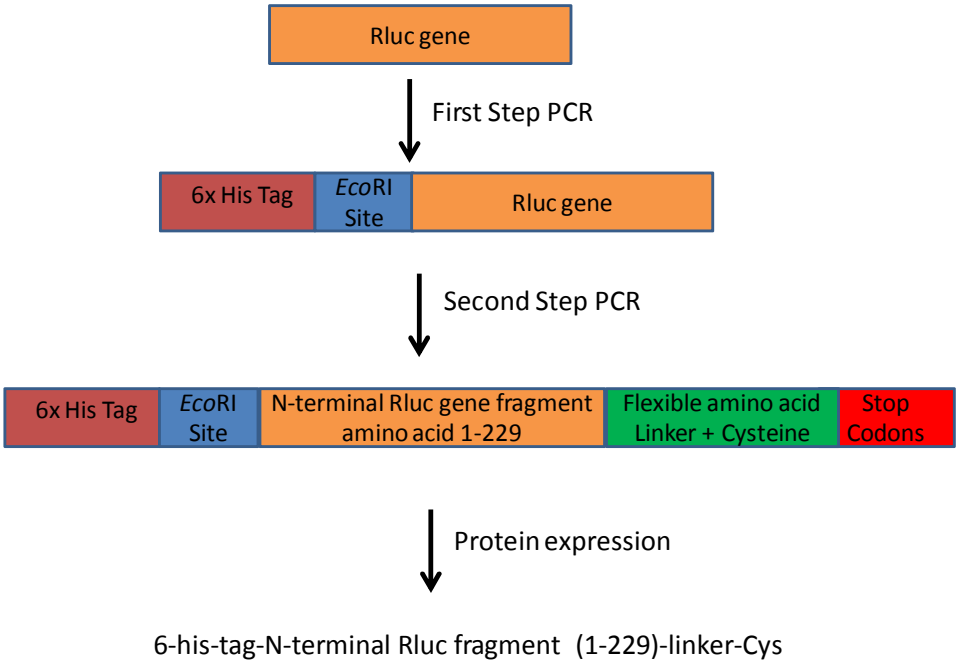

(b)

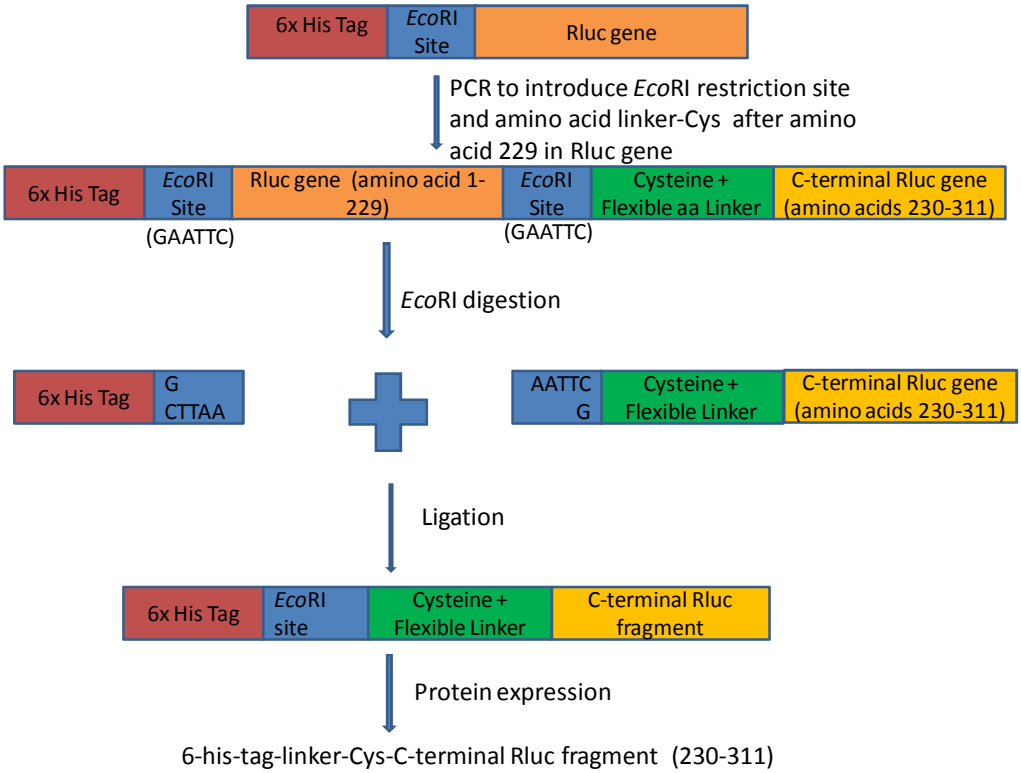

Figure S1. (a) The construction of N-terminal split Rluc fragment using genetic engineering. (b) The construction scheme for the C-terminal split Rluc fragment.

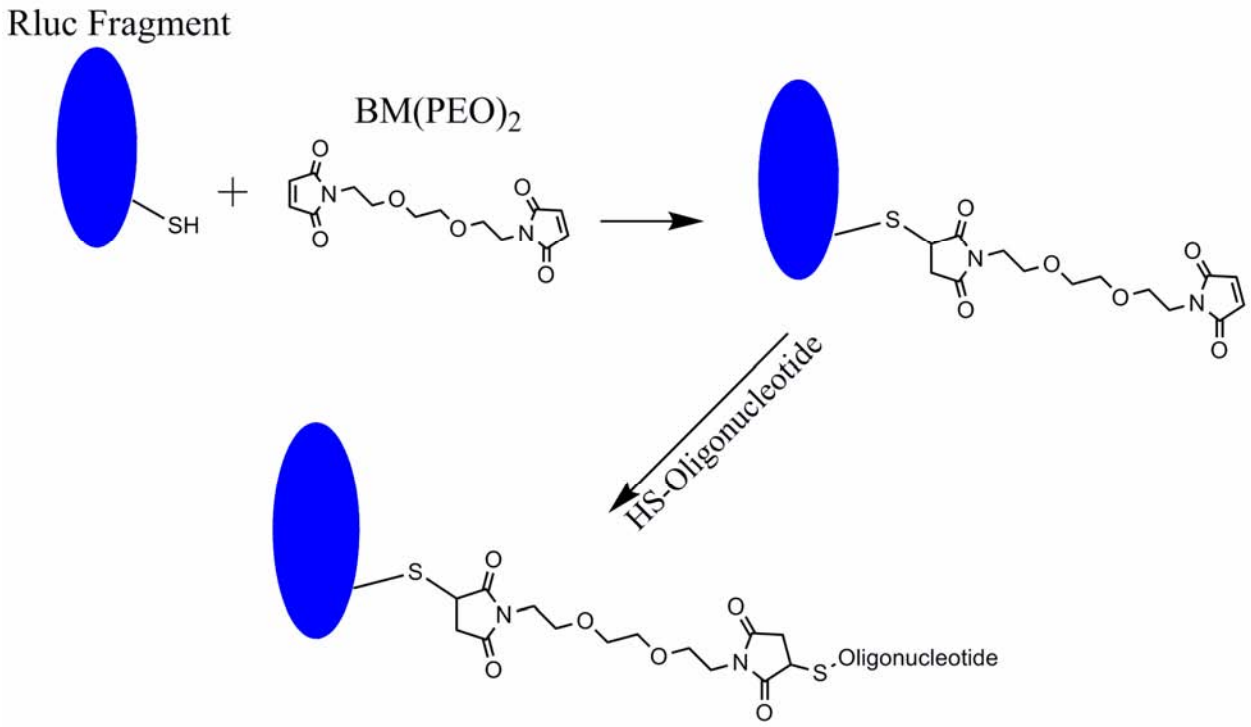

Figure S2. A schematic representing the two-step Rluc fragment conjugation to the oligonucleotide probe in the presence of the crosslinker $BM(PEO)_2$. The fragment is first conjugated to the crosslinker, and next the reduced oligonucleotide probe is added to allow conjugation through the free maleimide group.

COMMUNICATIONS

Reassembly of a Bioluminescent Protein *Renilla* Luciferase Directed through DNA Hybridization

Kyle A. Cissell, Yasmeen Rahimi, Suresh Shrestha, and Sapna K. Deo*

Department of Chemistry and Chemical Biology, Indiana University−Purdue University Indianapolis, Indiana 46202. Received July 18, 2008; Revised Manuscript Received November 10, 2008

Reassembly of split reporter proteins, also referred to as protein complementation, is utilized in the detection of protein−protein or protein−nucleic acid interactions. In this strategy, a reporter protein is fragmented into two inactive polypeptides to which interacting/binding partners are fused. The interaction between fused partners leads to the formation of a reassembled, active reporter. In this Communication, we have presented a proof-of-concept for the detection of a target nucleic acid sequence based on the reassembly of the bioluminescent reporter *Renilla* luciferase (Rluc), which is driven by DNA hybridization. Although, reassembly of Rluc though protein interactions has been demonstrated by others, the Rluc reassembly through DNA hybridization has not been shown yet, which is the novelty of this work. It is well established that bioluminescence detection offers significant advantages due to the absence of any background signal. In our study, two rationally designed fragments of Rluc were conjugated to complementary oligonucleotide probes. Hybridization of the two probes with fused Rluc fragments resulted in the reassembly of the fragments, generating active Rluc, measurable by the intensity of light given off upon addition of coelenterazine. Our study also shows that the reassembly of Rluc can be inhibited by an oligonucleotide probe that competes to bind to the hybridized probe−Rluc fragment complex, indicating a potential strategy for the quantitative detection of target nucleic acid. We were able to achieve the reassembly of Rluc fused to oligonucleotide probes using femtomole amounts of the probe−fragment protein conjugate. This concentration is approximately 4 orders of magnitude less than that reported using green fluorescent protein (GFP) as the reporter. A DNA-driven Rluc reassembly study performed in a cellular matrix did not show any interference from the matrix.

The split protein reassembly method has found applications as a biochemical tool to detect specific protein−protein and protein−nucleic acid interactions (*1*−*8*). In this method, two rationally designed fragments of a reporter protein are fused to proteins that are capable of interacting when close to one another. The fragments in isolation are inactive; however, biomolecular interactions between fused proteins leads to the formation of an active reporter, allowing for the detection of protein−protein interactions. This strategy has been successfully used in the reassembly of reporter proteins, specifically, dihydrofolate reductase, β-lactamase, ubiquitin, aminoglycoside kinase, *Renilla* luciferase, firefly luciferase, red fluorescent protein, and green fluorescent protein (GFP) driven by interacting proteins (*4, 5, 9*−*11*). There is only one report on reporter protein reassembly achieved through nucleic acid hybridization using split GFP as the reporter (*12*). In this study, the reassembly of split GFP upon formation of a hybrid between two complementary oligonucleotides at a 200 nM concentration was accomplished. Design and development of fluorescent proteins such as GFP have revolutionized the biochemical field. However, these proteins have some limitations because of the requirement of high energy excitation and high background signal, reducing the sensitivity of the signal measurement. In that respect, bioluminescent proteins that emit light by a biochemical reaction do not require a high energy excitation source and do not suffer from background noise in signal measurement (*13*−*17*). In a recent paper by Porter et al., these advantages of the bioluminescent enzyme firefly luciferase (Fluc) were utilized to detect proteins, small molecules, RNA, and double stranded DNA, both methylated and nonmethylated (*18*). This was accomplished through the expression of the Fluc fragments flanked by expressed protein domains, which bound to the specific target, bringing split Fluc fragments within close proximity. This allows for protein reassembly to occur, resulting in a luminescent signal upon the addition of luciferin, the substrate for Fluc. However, this method is not a hybridization-based assay that works for any target nucleic acid. This method will work only for targets for which peptide domains that bind to the target can be engineered. Taking this into consideration, here we evaluated in a proof-of-concept study of whether a bioluminescent protein, specifically *Renilla* luciferase (Rluc), is amenable to protein reassembly driven by DNA hybridization (Figure 1) similar to reassembly that can be achieved through protein complementation. We have also demonstrated the usefulness of this method in the detection of target nucleic acid. The reporter, Rluc, is a monomeric ∼38 kDa protein that catalyzes the oxidative decarboxylation of coelenterazine, the substrate that binds to Rluc, to coelenteramide, resulting in the production of light (*19*−*21*). One of the rationales for using Rluc in this study is that it is a small monomeric bioluminescent enzyme that is amenable to cellular imaging (*16, 22*−*26*). It

* To whom correspondence should be addressed. Phone: 317-278-7532. E-mail: sdeo@iupui.edu.

10.1021/bc8003099 CCC: $40.75 © 2009 American Chemical Society
Published on Web 12/09/2008

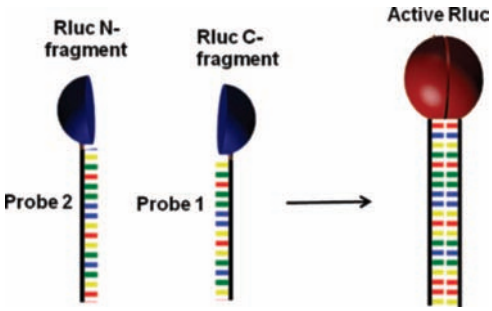

Figure 1. Schematic representation of the Rluc fragment reassembly driven through oligonucleotide probe hybridization.

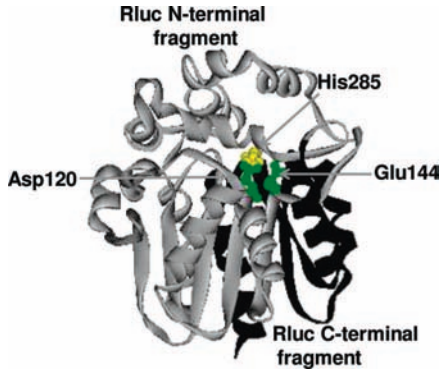

Figure 2. X-ray crystal structure of Rluc8, a mutant of Rluc showing the catalytic triad. The N-terminal Rluc fragment region is shown in gray, and the C-terminal Rluc fragment region is shown in black.

can be detected at very low levels over a broad dynamic range using inexpensive luminometers. Rluc also does not require post-translational modification for its activity. Several analogues of its substrate coelenterazine have been synthesized with different properties in terms of emission wavelength, quantum efficiency, and cell permeability, thus enhancing the applications of Rluc. Unlike fluorescence, there is no need for external excitation, and thus, problems with light scattering and source instability are avoided.

The most critical issue in the success of protein reassembly from its split fragments is the selection of a cleavage site in the protein. Availability of the three-dimensional structure can aid in the design of the protein fragments. Other considerations in the design of successful protein reassembly include small protein size, monomeric structure, and simplicity of the assay system. Reassembly of split *Renilla* luciferase from its fragments, driven by the interactions between the proteins myoD and Id in vivo, has been demonstrated (*27*), although the fragments were not isolated or purified. On the basis of this work a cleavage site of Gly229-Lys230 (Figure 2) was chosen to dissect Rluc in our study. The X-ray crystal structure of a mutant of Rluc (RL8) was solved recently (Figure 2) (*28*); however, we decided to select the cleavage site on the basis of prior complementation work performed in detecting protein−protein interactions using the native Rluc. The X-ray crystal structure of RL8 mutant shows that it has a classic α/β-hydrolase fold at its core and contains a catalytic triad made from Asp120-Glu144-His285. The cleavage site selected in our study, Gly229-Lys230, would be such that the residue Asp120 and Glu144 of the catalytic triad will be in the N-terminal fragment, whereas His285 will be in the C-terminal fragment. This suggests that although the substrate binding may occur in the N-terminal fragment, the catalytic triad is not completed until the two fragments come close for the generation of the bioluminescence signal. In the future, other cleavage sites will be evaluated on the basis of the X-ray crystal structure of the Rluc mutant. It would be

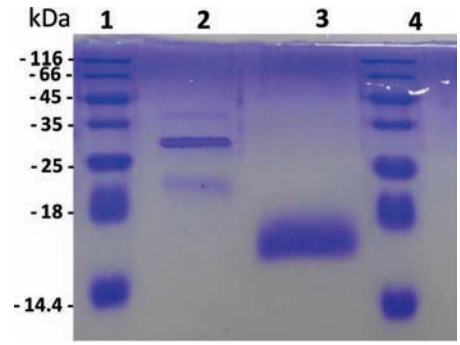

Figure 3. Picture of 12.5% SDS−PAGE gel of purified Rluc fragments stained with Coomassie Blue. Lane 1: molecular weight protein marker. Lane 2: purified N-terminal Rluc fragment. Lane 3: purified C-terminal Rluc fragment. Lane 4: molecular weight protein marker.

interesting to cleave Rluc such that the triad is kept intact in one of the fragments while the substrate binding is disturbed in the absence of assembly of the two fragments. This type of fragmentation where the active site is maintained may reduce the overall time needed for the reassembly of protein as observed in the case of split GFP work (*12*).

Using the gene for native *Rluc* from the plasmid phRL-CMV as the template, primers were designed to introduce a noncleavable 6-histidine tag to allow purification of the Rluc fragments as well as codons for a flexible amino acid linker and a cysteine residue for oligonucleotide probe conjugation (Supporting Information). The Rluc N-terminal fragment was constructed by introducing two stop codons after the amino acid Gly229 using site-directed mutagenesis (Supporting Information). Similarly, primers were designed to obtain the gene sequence of the C-terminal fragment of Rluc (amino acid 230−311) with a unique cysteine near its N-terminus (Supporting Information). Rluc fragments were expressed in *E. coli* cells and purified using a copper-immobilized Hi-Trap column (Supporting Information). The purity of the two fragments was verified using SDS−PAGE and Coomassie staining (Figure 3). The SDS−PAGE shows that the two fragments, the N-terminal fragment (∼30 kDa) and the C-terminal fragment (∼16 kDa), were purified efficiently. The concentrations of purified Rluc fragments were determined using a Bradford assay. The luminescence activity of the individual Rluc fragments (1 nmol) was monitored by adding the substrate coelenterazine (0.5 μL, 1 mg/mL). As expected, no luminescence signal was observed in the presence of substrate, indicating the inability of fragments to process the substrate (Figure 4). Next, the two fragments (1 nmol each) without the probe attached were mixed together followed by the addition of coelenterazine to check for any nonspecific binding between the fragments in the absence of oligonucleotide probes. The mixing of the two fragments did not result in the generation of any bioluminescence signal indicating that spontaneous reassembly between Rluc fragments does not occur (Figure 4).

Thiol-modified oligonucleotide probes were conjugated to the split Rluc fragments using maleimide-sulfhydryl chemistry through the homobifunctional cross-linker $BM(PEO)_2$ (1,8-bis-maleimidotriethylene glycol). The Rluc N-terminal fragment contains three cysteine residues buried within the protein structure. Therefore, we hypothesize that a cysteine introduced at the C-terminus during the construction of the fragment will be the major target site for oligonucleotide conjuation through the thiol moiety. The Rluc C-terminal fragment does not contain a cysteine residue; therefore, the cysteine introduced near the N-terminus of the C-terminal fragment via site-directed mutagenesis was targeted for the oligonucleotide conjugation. In order to perform the conjugation, Rluc fragments were first reduced using tricholroethyl phospine (TCEP). Rluc fragments

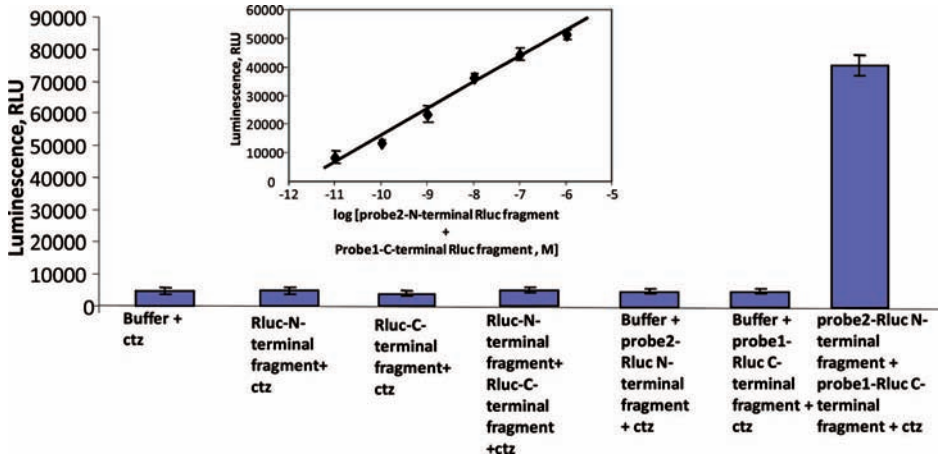

Figure 4. Bar graph showing the luminescence activity obtained in control and samples. The data are based on an average response of three samples ± the standard deviation. The inset shows a plot of luminescence activity obtained after mixing different moles of the probe1−Rluc N-terminal fragment conjugate and probe2−Rluc C-terminal fragment conjugates and adding coelenterazine. The data are based on an average response of three samples ± the standard deviation.

were then reacted with $BM(PEO)_2$ using the manufacturer's protocol in a 1:2 ratio of fragments to linker (Supporting Information). Both oligonucleotide probes (probe 2, 5′TCA-ACATCAGTCTGATAAGCTA3′-thiol and probe 1, thiol-5′TAGCTTATCAGACTGATGTTGA3′) were reduced using 40 mM TCEP at 37 °C and were added at a 5 times mole excess to the Rluc-$BM(PEO)_2$ conjugate. Probe 2 was conjugated to the N-terminal fragment, and probe 1 was fused to the C-terminal fragment. Since there is a unique cysteine introduced via site-directed mutagenesis in the C-terminal fragment, only one probe is conjugated to each fragment. Even though the N-terminal fragment contains three cysteine residues, the cysteine introduced via site-directed mutagenesis is more accessible for conjugation than the other three cysteine thiols. Unreacted probes and cross-linker were then separated using dialysis in sodium phosphate buffer (50 mM sodium phosphate, pH 7.2, containing 300 mM NaCl). In general, chemical conjugation techniques are not highly reproducible. However, in our studies we found about 70−80% conjugation efficiency monitored using SDS−PAGE analysis. This conjugation efficiency was found to be independent of the amount of mole excess of oligonucleotide probes used in the conjugation reaction. Furthermore, these conjugates were observed to be either mono-or bioligonucleotide conjugated as monitored using SDS−PAGE. Unreacted split fragments were not separated from the fragment−probe conjugates since the fragments alone are not active and thus will not contribute to any background signal.

Initially, a control study was performed to determine any background signal from fragment−probe conjugates. The bioluminescence measurements were performed by adding coelenterazine to Rluc-N-terminal fragment−probe 2 and to Rluc-C-terminal fragment−probe 1 separately. The luminescence signal obtained using probe−fragment conjugates was comparable to that obtained using buffer mixed with coelenterazine. Next, 5 nmol of each of the two probe−fragment conjugates were mixed together at 37 °C for 30 min, and bioluminescence intensity was measured after the addition of coelenterazine. Figure 4 depicts a bar graph of luminescence intensity obtained upon mixing the two complementary probe−fragments and the intensity obtained in the control study. The control resulted in a minimal background luminescence representative of the luminescence of coelenterazine alone. In comparison, a strong bioluminescence signal was observed upon the reassembly of Rluc fragments driven through probe hybridization. In another study, we mixed various concentrations of probe−Rluc fragment conjugates and measured bioluminescence signal after incubation (Figure 4 inset). A linear increase in luminescence with increasing concentrations of the two probe−fragment conjugates was obtained. We were able to detect Rluc with a detection limit of 5 fmoles (2.5×10^{-11} M) of probe−Rluc fragment conjugates. This detection limit was calculated corresponding to the signal obtained using the formula signal of the blank + 3 standard deviation of the blank. In a study performed using GFP as the reporter for fragment reassembly driven through DNA hybridization, the concentrations of probe−GFP fragment conjugates employed were 200 nM (*12*). Our results indicate that we were able to detect oligonucleotide probe hybridization using Rluc reassembly approximately 4 orders of magnitude lower than that with split GFP. A bioluminescence emission profile of the reassembled Rluc compared to the native Rluc (Figure 5) was obtained using a cuvette on a Cary Eclipse spectrophotometer (Varian, CA). The reassembled protein showed an emission maximum of 495 nm, while the native Rluc showed a 485 nm emission peak. This red shift of reassembled protein versus native protein has been observed previously with GFP (*12*). It is thought that the shift in emission wavelength may be explained by the change in proximity of the amino acids around the chromophore compared to the native Rluc, as well as the presence of the negatively charged DNA molecules driving the reassembly.

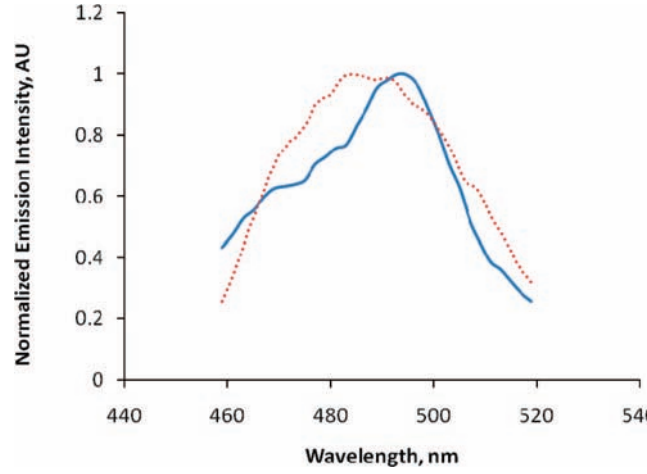

Figure 5. Luminescence emission profile obtained using a Cary Eclipse fluorometer of reassembled Rluc (solid line) and intact Rluc (dotted line) after adding coelenterazine.

Next, we studied the possibility of the potential application of reassembly of Rluc for the target nucleic acid detection. This was evaluated by examining whether the fragment reassembly driven through oligonucleotide hybridization can be competitively inhibited by a free complementary probe. When a 13.2 nmol of free oligonucleotide probe (5′-TAGCTTATCAGACTGATGTTGA-3′) was added to the reassembled Rluc fragment−probe complex (1 nmol each), we observed a reduction in the bioluminescence signal. Approximately 45% reduction in bioluminescence intensity in the presence of free probe compared to that in the control without the free probe was observed. Although we have used excess free probe, complete quenching of the bioluminescence was not observed. We believe that the possible reason for this is when the free probe is added to the fragment−probe hybridized complex, a higher temperature than 37 °C may be needed to separate hybridized strands, which may be due to a tight assembly between the probe−fragment hybridized complex. A similar phenomenon was observed in the study performed using GFP split fragments in oligonucleotide hybridization (*12*). To further validate this result, when we added 3.4 nmol of the free probe to the probe-directed reassembled Rluc (1 nmol each), a 25% reduction in the bioluminescence intensity was observed. This result indicates that the free probe can prevent DNA-directed reassembly of Rluc in a concentration-dependent manner. Ideally, a competitive assay can be performed such that the free probe is allowed to hybridize with the complementary probe−Rluc fragment followed by the addition of the second probe−Rluc fragment. An alternative method would be to simultaneously mix probe−fragment conjugates and the free probe. Another strategy to perform target nucleic acid quantitation can be based on designing the probes such that they bind adjacently to the target. Here, the Rluc fragments can be conjugated to the probes and directly added to the target to be detected. This would allow reassembly of fragments and the generation of active Rluc in the presence of the target, yielding an increase in the signal rather than a decrease and hence a higher sensitivity of detection. All of these strategies and application of Rluc reassembly in nucleic acid quantitation are under evaluation in our laboratory.

Finally, we performed the reassembly of probe−Rluc fragments in a cellular extract. This study was performed to evaluate whether the Rluc reassembly strategy will work in a more complex matrix. Another objective that was fulfilled by this experiment was to evaluate whether any nonspecific nucleic acid present in the sample will interfere with the hybridization of probes and hence the subsequent reassembly of Rluc fragments. For this study, we used the extract of *E. coli* strain ER 2566. We employed the sonication method to obtain the extract, which is also a method to get the genomic DNA (*29*). After sonicating *E.coli* strain ER 2566 cells in 50 mM sodium phosphate buffer, pH 7.2, containing 300 mM NaCl, 1 nmol of the probe 2-N-terminal Rluc fragment and probe 1-C-terminal Rluc fragment were mixed with the cell extract and hybridized. Bioluminescence emission intensity was measured after adding coelenterazine. The luminescence intensity obtained was comparable to that obtained in the in vitro study (Figure 6). A comparison of the light intensity in the buffer matrix and in the *E. coli* cell matrix showed an approximately 4.1% decrease from buffer matrix to cell matrix, which is within the allowed 10% limit. Therefore, reassembly of Rluc driven through DNA hybridization is not significantly affected by the sample matrix.

In summary, our work demonstrates that Rluc reassembly can be performed in vitro driven through oligonucleotide hybridization. The detection limit for Rluc reassembly was 5 fmoles (2.5×10^{-11} M) of probe−Rluc fragment conjugates, which is approximately 4 orders of magnitude lower than that reported using probe−GFP fragment conjugates. Our study also shows that the reassembly can be inhibited in the presence of a complementary oligonucleotide indicating that this strategy can be useful in the quantitative detection of target nucleic acid. The bioluminescence emission, small size, and monomeric structure make Rluc an efficient label for the development of complementation assays. Furthermore, the method developed offers the advantage of parallel analysis in a 96-well microtiter plate and makes it suitable for high throughput nucleic acid quantitation applications.

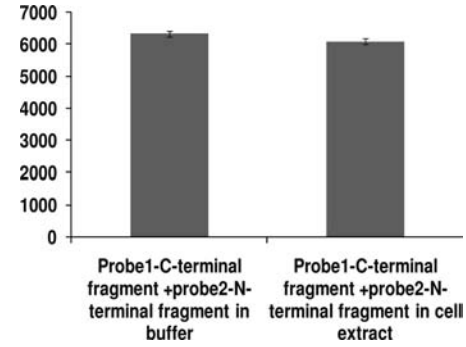

Figure 6. Bar graph showing the luminescence intensity obtained after adding coelenterazine to the samples containing probe−fragment conjugates in buffer and in *E. coli* cellular extract. The data are based on an average response of three samples ± the standard deviation.

ACKNOWLEDGMENT

This work was supported by a grant from the National Institutes of Health (EB008231-01).

Supporting Information Available: Methods for Rluc fragment genetic construction, expression and purification of protein fragments, conjugation of probe to Rluc fragments, and all hybridization studies, along with relevant figures. This material is available free of charge via the Internet at http://pubs.acs.org.

LITERATURE CITED

(1) Paulmurugan, R., and Gambhir, S. S. (2005) Firefly luciferase enzyme fragment complementation for imaging in cells and living animals. *Anal. Chem. 77*, 1295–1302.

(2) Paulmurugan, R., and Gambhir, S. S. (2007) Combinatorial library screening for developing an improved split-firefly luciferase fragment-assisted complementation system for studying protein-protein interactions. *Anal. Chem. 79*, 2346–2353.

(3) Paulmurugan, R., Umezawa, Y., and Gambhir, S. S. (2002) Noninvasive imaging of protein-protein interactions in living subjects by using reporter protein complementation and reconstitution strategies. *Proc. Natl. Acad. Sci. U.S.A. 99*, 15608–15613.

(4) Ooi, A. T., Stains, C. I., Ghosh, I., and Segal, D. J. (2006) Sequence-enabled reassembly of beta-lactamase (SEER-LAC): A sensitive method for the detection of double-stranded DNA. *Biochemistry 45*, 3620–3625.

(5) Magliery, T. J., Wilson, C. G., Pan, W., Mishler, D., Ghosh, I., Hamilton, A. D., and Regan, L. (2005) Detecting protein-protein interactions with a green fluorescent protein fragment reassembly trap: scope and mechanism. *J. Am. Chem. Soc. 127*, 146–157.

(6) Stains, C. I., Porter, J. R., Ooi, A. T., Segal, D. J., and Ghosh, I. (2005) DNA sequence-enabled reassembly of the green fluorescent protein. *J. Am. Chem. Soc. 127*, 10782–10783.

(7) Kim, S. B., Otani, Y., Umezawa, Y., and Tao, H. (2007) Bioluminescent indicator for determining protein-protein interactions using intramolecular complementation of split click beetle luciferase. *Anal. Chem. 79*, 4820–4826.

(8) Deo, S. K. (2004) Exploring bioanalytical applications of assisted protein reassembly. *Anal Bioanal Chem 379*, 383–390.
(9) Ozawa, T., Kaihara, A., Sato, M., Tachihara, K., and Umezawa, Y. (2001) Split luciferase as an optical probe for detecting protein-protein interactions in mammalian cells based on protein splicing. *Anal. Chem. 73*, 2516–2521.
(10) Gangopadhyay, J. P., Jiang, S. Q., and Paulus, H. (2003) An in vitro screening system for protein splicing inhibitors based on green fluorescent protein as an indicator. *Anal. Chem. 75*, 2456–2462.
(11) Galarneau, A., Primeau, M., Trudeau, L. E., and Michnick, S. W. (2002) Beta-lactamase protein fragment complementation assays as in vivo and in vitro sensors of protein protein interactions. *Nat. Biotechnol. 20*, 619–622.
(12) Demidov, V. V., Dokholyan, N. V., Witte-Hoffmann, C., Chalasani, P., Yiu, H. W., Ding, F., Yu, Y., Cantor, C. R., and Broude, N. E. (2006) Fast complementation of split fluorescent protein triggered by DNA hybridization. *Proc. Natl. Acad. Sci. U.S.A. 103*, 2052–2056.
(13) Whitehead, T. P., Kricka, L. J., Carter, T. J., and Thorpe, G. H. (1979) Analytical luminescence: its potential in the clinical laboratory. *Clin. Chem. 25*, 1531–1546.
(14) Thore, A. (1979) Luminescence in clinical analysis. *Ann. Clin. Biochem. 16*, 359–369.
(15) Shrestha, S., Paeng, I. R., Deo, S. K., and Daunert, S. (2002) Cysteine-free mutant of aequorin as a photolabel in immunoassay development. *Bioconjugate Chem. 13*, 269–275.
(16) Contag, C. H., and Bachmann, M. H. (2002) Advances in in vivo bioluminescence imaging of gene expression. *Annu. Rev. Biomed. Eng. 4*, 235–260.
(17) Kricka, L. J. (1991) Chemiluminescent and bioluminescent techniques. *Clin. Chem. 37*, 1472–1481.
(18) Porter, J. R., Stains, C. I., Jester, B. W., and Ghosh, I. (2008) A general and rapid cell-free approach for the interrogation of protein-protein, protein-DNA, and protein-RNA interactions and their antagonists utilizing split-protein reporters. *J. Am. Chem. Soc. 130*, 6488–6497.
(19) Matthews, J. C., Hori, K., and Cormier, M. J. (1977) Substrate and substrate analogue binding properties of *Renilla* luciferase. *Biochemistry 16*, 5217–5220.
(20) Matthews, J. C., Hori, K., and Cormier, M. J. (1977) Purification and properties of *Renilla reniformis* luciferase. *Biochemistry 16*, 85–91.
(21) Hart, R. C., Matthews, J. C., Hori, K., and Cormier, M. J. (1979) Renilla reniformis bioluminescence: luciferase-catalyzed production of nonradiating excited states from luciferin analogues and elucidation of the excited state species involved in energy transfer to *Renilla* green fluorescent protein. *Biochemistry 18*, 2204–2210.
(22) Mirasoli, M., Deo, S. K., Lewis, J. C., Roda, A., and Daunert, S. (2002) Bioluminescence immunoassay for cortisol using recombinant aequorin as a label. *Anal. Biochem. 306*, 204–211.
(23) Greer, L. F., III., and Szalay, A. A. (2002) Imaging of light emission from the expression of luciferases in living cells and organisms: a review. *Luminescence 17*, 43–74.
(24) Gould, S. J., and Subramani, S. (1988) Firefly luciferase as a tool in molecular and cell biology. *Anal. Biochem. 175*, 5–13.
(25) Desai, U. A., Deo, S. K., Hyland, K. V., Poon, M., and Daunert, S. (2002) Determination of prostacyclin in plasma through a bioluminescent immunoassay for 6-keto-prostaglandin F1alpha: implication of dosage in patients with primary pulmonary hypertension. *Anal. Chem. 74*, 3892–3898.
(26) Deo, S. K., and Daunert, S. (2001) Luminescent proteins from Aequorea victoria: applications in drug discovery and in high throughput analysis. *Fresenius' J. Anal. Chem. 369*, 258–266.
(27) Paulmurugan, R., and Gambhir, S. S. (2003) Monitoring protein-protein interactions using split synthetic renilla luciferase protein-fragment-assisted complementation. *Anal. Chem. 75*, 1584–1589.
(28) Loening, A. M., Fenn, T. D., and Gambhir, S. S. (2007) Crystal structures of the luciferase and green fluorescent protein from *Renilla reniformis*. *J. Mol. Biol. 374*, 1017–1028.
(29) Zhang, L., Foxman, B., Gilsdorf, J. R., and Marrs, C. F. (2005) Bacterial genomic DNA isolation using sonication for microarray analysis. *Biotechniques 39*, 640–644.

BC8003099

Single-Step Azide Introduction in Proteins via an Aqueous Diazo Transfer

Stijn F. M. van Dongen, Rosalie L. M. Teeuwen, Madhavan Nallani,† Sander S. van Berkel, Jeroen J. L. M. Cornelissen, Roeland J. M. Nolte, and Jan C. M. van Hest*

Institute for Molecules and Materials, Radboud University Nijmegen, Heyendaalseweg 135, 6525 AJ, Nijmegen, The Netherlands. Received October 9, 2008; Revised Manuscript Received November 19, 2008

The controlled introduction of azides in proteins provides targetable handles for selective protein manipulation. We present here an efficient diazo transfer protocol that can be applied in an aqueous solution, leading to the facile introduction of azides in the side chains of lysine residues and at the *N*-terminus of enzymes, e.g. horseradish peroxidase (HRP) and the red fluorescent protein DsRed. The effective introduction of azides was verified by mass spectrometry, after which the azido-proteins were used in Cu(I)-catalyzed [3 + 2] cycloaddition reactions. Azido-HRP retained its catalytic activity after conjugation of a small molecule. This modified protein could also be successfully immobilized on the surface of an acetylene-covered polymersome. Azido-DsRed was coupled to an acetylene-bearing protein allowing it to act as a fluorescent label, demonstrating the wide applicability of the diazo transfer procedure.

In recent years, with the advent of chemical biology the need to manipulate and modify proteins has increased considerably. One of the important limitations in selective chemical modification of proteins is the overabundance of functional groups present in these biomacromolecules. In order to introduce, site specifically, bioorthogonal reactive groups, multiple strategies have been developed. In many cases, the free thiol groups of cysteine residues are specifically targeted for conjugation because these functionalities are reactive and relatively rarely present in proteins (*1*−*4*). Unfortunately, electrophiles that readily react with thiols are, to a lesser extent, also susceptible to attack by amines or even alcohols, leading to loss of specificity. Furthermore, cysteines are often essential for the structural integrity and function of proteins and therefore cannot always be modified.

To overcome these shortcomings, some strategies make use of functional groups that do not naturally occur and are deliberately introduced, enabling individual targeting of these groups without inadvertent cross-linking or other reactions (*5*−*8*). An example of this approach is the [3 + 2] transition metal-catalyzed Huisgen cycloaddition between an azide and an acetylene function (*1, 9*−*11*). Since "click" chemistry has been shown to work well for protein modification, efficient methods for the controlled introduction of azides or acetylenes into biomolecules have become of great interest (*12*−*14*).

Although azido-modified amino acids can be introduced by single-site or multisite protein engineering replacement strategies (*7, 13, 15*), the degree of site specificity provided by these laborious methods is not always needed. This led us to investigate the possibility of applying the relatively mild and facile diazo transfer reaction to amines, in order to directly introduce azides at the lysine positions of proteins. Traditionally, however, the diazo transfer reaction is carried out on small organic molecules in organic solvents such as CH_2Cl_2, with trifluoromethanesulfonyl azide (TfN_3) as reagent and catalyzed by Cu(II) (*16*−*18*). These conditions make this type of reaction unsuitable for protein modification. Recently, this method was improved by Goddard-Borger and Stick (*19*), who introduced imidazole-1-sulfonyl azide hydrochloride (**1**, see Figure 1) as a nonexplosive and shelf-stable alternative to TfN_3. Particularly interesting is the fact that **1** can be applied in protic solvents. We therefore envisaged the use of compound **1** to perform the diazo transfer reaction on proteins and enzymes in aqueous solutions, residue-specifically introducing azido-moieties at their lysine residues or *N*-terminus.

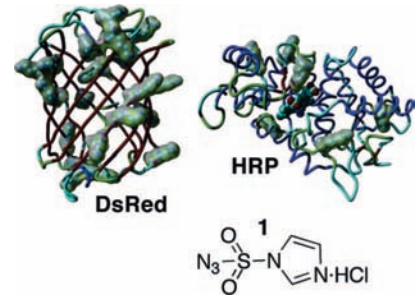

Figure 1. Structures of DsRed, horseradish peroxidase (HRP), and imidazole-1-sulfonyl azide hydrochloride (*1*). The molecular surfaces of all lysine residues in the proteins are shown. The structure of DsRed was derived from the PDB file 2VAD and contains 22 lysine residues. The structure of HRP was derived from PDB file 7ATJ and contains 6 lysine residues.

To study the applicability of this relatively simple method, we initially used the enzyme horseradish peroxidase (HRP, see Figure 1) as a model protein (*20, 21*). To functionalize HRP, it was dissolved in milliQ (MQ) pure water (200 μL, 2.5 mg/mL) and an aqueous solution of K_2CO_3 (100 μL, 2 mg/mL) was added, along with 25 μL of Cu(II)$SO_4 \cdot 5H_2O$ in MQ (1 mg/mL). After mixing, transfer agent **1** in MQ was added (1.75 equiv relative to the amines in HRP) and the reaction was left stirring overnight, after which the enzyme was purified using centrifugal filter devices. ESI-TOF analysis of the thus treated enzyme showed that, under the applied experimental conditions, an average of four amines were transformed into azides (see Figure 2). A small amount of HRP possessed three or five azides (out of a total of seven), which implies a statistical mixture of functionalized compounds.

The influence of the diazo transfer treatment and subsequent conjugation of a small molecule (butynol; see Supporting

* E-mail: j.vanhest@science.ru.nl.
† Current address: Institute of Materials Research & Engineering (IMRE), Research Link 3, Singapore 117602.

10.1021/bc8004304 CCC: $40.75 © 2009 American Chemical Society
Published on Web 12/19/2008

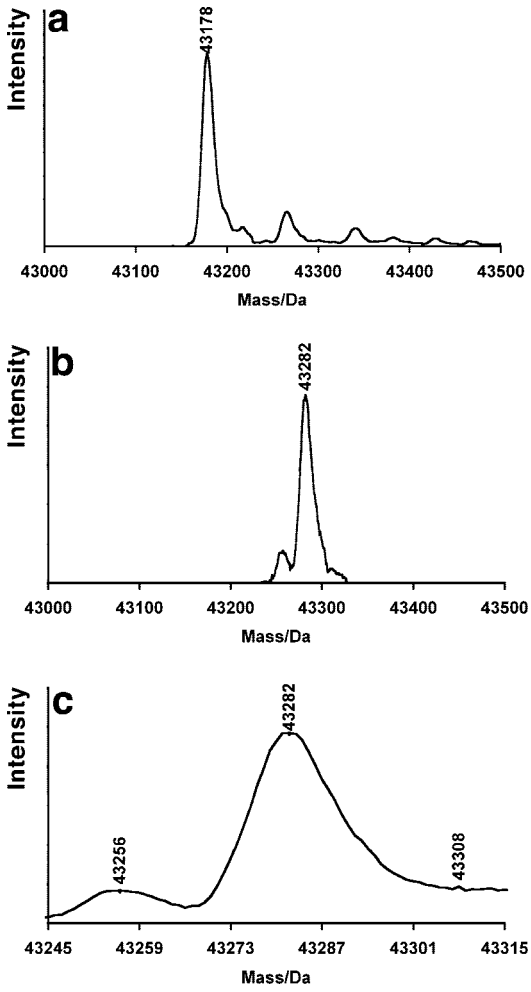

Figure 2. Mass spectrometry results (ESI-TOF): (a) unreacted HRP; (b) azido-HRP; (c) enlargement of (b). The mass difference between (a) and (b) is four times 26, corresponding to four diazo transfers. A closer inspection of (b), as shown in (c), reveals that tri- and penta-azido-substituted HRP molecules are also present, indicating that azido-HRP is a statistical mixture of transfer products.

Information) on the catalytic activity of HRP was assayed using 2,2′-azinobis(3-ethyl-benzothiazoline-6-sulfonic acid) (ABTS) as substrate, which is converted by HRP into the strongly absorbing product $ABTS^{\cdot+}$ using H_2O_2. A comparison was made with the catalytic activity of the untreated enzyme. The results are shown in Figure 3. It can be concluded that the activity of the enzyme is only slightly reduced by the introduction of the azido functions and the subsequent conjugation.

To test whether azido-HRP can be used for bioconjugation studies, experiments were performed to link this modified enzyme to the surface of polymersomes (*22*−*24*). Polymersomes are robust spherical vesicles with an average diameter of ca. 200 nm, created via the self-assembly of amphiphilic block copolymers (*25*, *26*). For our experiments, polymersomes derived from polystyrene$_{40}$-*b*-poly(L-isocyanoalanine(2-thiophen-3-yl-ethyl)amide)$_{50}$ (PS-PIAT) admixed with 10 wt % PS$_{40}$-poly(ethylene glycol)$_{67}$-acetylene were used (*24*), designed for exterior modification via the acetylene moieties presented on their surfaces. The compounds were incubated in a phosphate buffer (20 mM, pH 7.4) with azido-HRP for 60 h in the presence of a Cu(I) catalyst. Hereafter, they were washed using centrifugal filter devices until no residual HRP activity could be detected in the flowthrough. To test the resulting aggregates for HRP activity, they were incubated with ABTS in the presence of H_2O_2. The progress curves shown in Figure 4 indicate that azido-HRP can be successfully immobilized on the polymeric surfaces

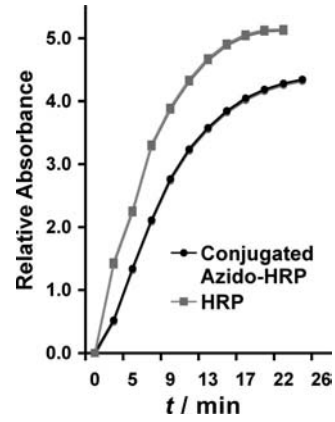

Figure 3. Catalytic activities of HRP and butynol-conjugated azido-HRP. Equal amounts of both enzymes were incubated with ABTS and H_2O_2, and the formation of $ABTS^{\cdot+}$ was measured over time. Comparison of the initial slopes suggests that the "clicked" HRP has retained 75% of its catalytic activity (see Supporting Information).

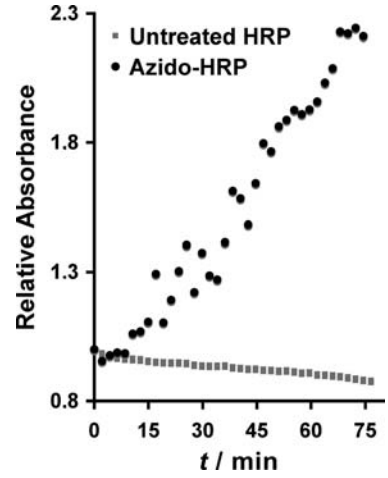

Figure 4. Progress curve for polymersomes with and without surface-conjugated HRP. The polymersomes were incubated with ABTS in the presence of H_2O_2, and the formation of $ABTS^{\cdot+}$ was measured as a function of time. After a short initial incubation period (i.e., 8 min), azido-HRP-conjugated polymersomes produced increasing amounts of $ABTS^{\cdot+}$ (black dots). Polymersomes that were incubated with untreated HRP did not show any activity (gray dots).

using "click" chemistry. Electron micrographs of the (clicked) polymersomes are shown in Figure 5.

To further evaluate the scope of our method, we also investigated the diazo transfer reaction on DsRed (see Figure 1), an engineered red fluorescent protein from *Discosoma striata* (*27*). To this end, DsRed was treated with transfer agent **1** in the presence of K_2CO_3 and $Cu(II)SO_4 \cdot 5H_2O$ in MQ (0.5 equiv of **1** was used relative to the amines in DsRed). Analysis by ESI-TOF revealed that under these experimental conditions an average of 4 amines were converted to the corresponding azides, as shown in Figure 6. The fluorescent azido-DsRed was subsequently reacted with a biochemically engineered elastin-like protein (ELP, MW 39.8 kDa) fitted with an acetylene moiety at its *N*-terminus. The Cu(I)-catalyzed conjugation successfully labeled the ELP with the fluorescent protein marker, as was demonstrated by SDS-PAGE analysis (Figure 7). As an additional demonstration, azido-DsRed was "clicked" to propargylic poly(ethylene glycol)$_{45}$ and analyzed in the same fashion (Figure 7) (*28*).

In summary, we may conclude that the diazo-compound **1** is a robust and facile transfer reagent for the introduction of azides in proteins. It was demonstrated that the catalytic activity of

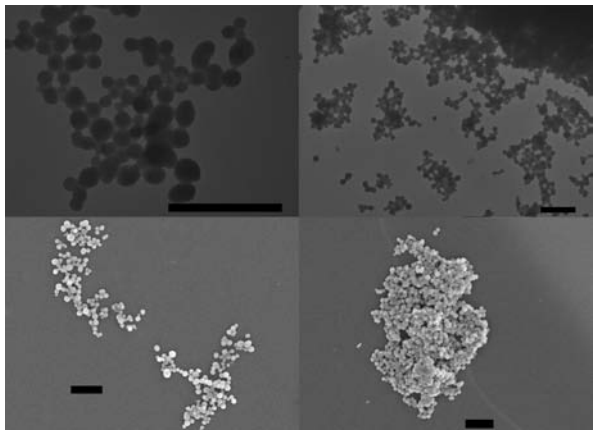

Figure 5. TEM and SEM images of polymersomes containing GOx (top row) and of vesicles containing GOx that have azido-HRP immobilized on their surfaces (bottom row). The black scale bars represent 1 μm.

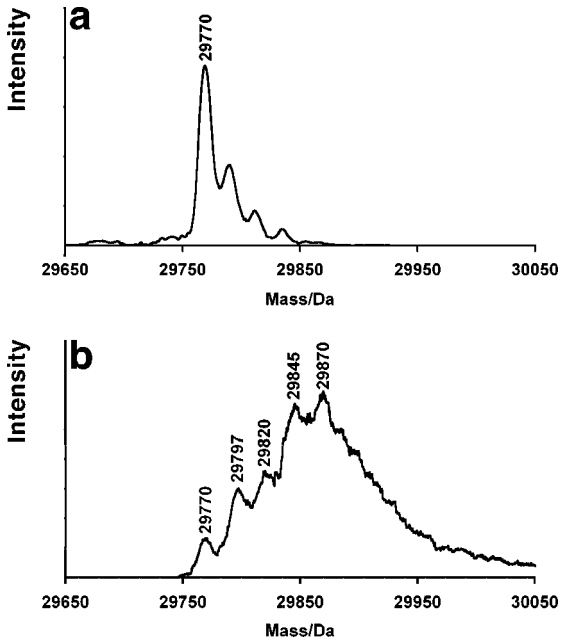

Figure 6. Mass spectrometry results (ESI-TOF) for (un)functionalized DsRed: (a) unreacted DsRed; (b) azido-DsRed. The broad signal shown in b contains approximate masses for mono-, di-, tri-, and tetra-azido-DsRed, along with a small signal for the unfunctionalised protein. This statistical mixture of transfer products, caused by the 22 lysine residues present in DsRed, slightly compromises the accuracy of the deconvolution results. The symmetry of the signal suggests that penta and higher degrees of azido-DsRed are also present.

enzymes, such as HRP, after the diazo transfer reaction and subsequent coupling to a small molecule was not substantially reduced. This was further verified by the immobilization of the azido-HRP on the surface of a polymersome, after which the catalytic activity of the enzyme was also retained. To further demonstrate the versatility of the diazo transfer reaction, the fluorescent protein DsRed was equipped with azides and subsequently conjugated to an acetylene-bearing elastin-like protein via Cu(I)-catalyzed triazole formation. These examples show that the diazo-transfer reaction is a suitable technique for the selective modification of proteins under ambient conditions. It should be noted, however, that the present method may not be suitable for proteins containing lysines that are essential to their biological activity.

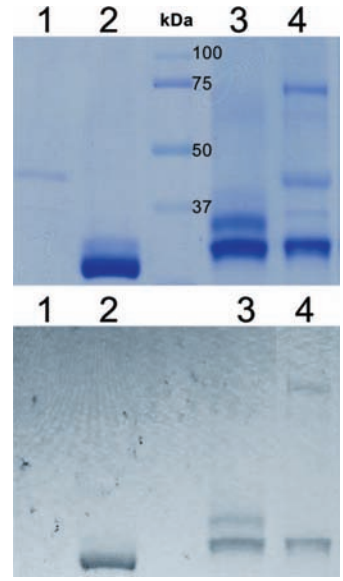

Figure 7. SDS-PAGE analysis of DsRed conjugation reactions. Proteins were visualized with Coomassie staining (top) or *via* fluorescence of DsRed (bottom): (1) acetylene-ELP; (2) azido-DsRed; (3) PEGylation of azido-DsRed. A signal with an increase in mass of ~2 kDa can be seen, corresponding to one PEG addition; (4) reaction of azido-DsRed with acetylene-ELP. A signal with a mass difference of ~40 kDa can be seen, corresponding to ELP-conjugated DsRed.

ACKNOWLEDGMENT

This work was funded in part by the Dutch National Research School Combination - Catalysis (NRSC-C) and NWO-ACTS. We thank RJRW Peters for the synthesis of α-Me, ω-dipropargylic poly(ethylene glycol)$_{45}$.

Supporting Information Available: Materials, equipment and protocols, synthesis of imidazole-sulfonylazide, diazo transfer conditions, preparation of polymersomes, 1,3-dipolar cycloaddition reaction conditions, enzyme activity assays, and ESI-TOF analysis. This material is available free of charge via the Internet at http://pubs.acs.org.

LITERATURE CITED

(1) Dirks, A. J. T., van Berkel, S. S., Hatzakis, N. S., Opsteen, J. A., van Delft, F. L., Cornelissen, J. J. L. M., Rowan, A. E., van Hest, J. C. M., Rutjes, F. P. J. T., and Nolte, R. J. M. (2005) Preparation of biohybrid amphiphiles via the copper catalysed Huisgen [3 + 2] dipolar cycloaddition reaction. *Chem. Commun. 33*, 4172−4174.

(2) Reulen, S. W. A., Brusselaars, W. W. T., Langereis, S., Mulder, W. J. M., Breurken, M., and Merkx, M. (2007) Protein-liposome conjugates using cysteine-lipids and native chemical ligation. *Bioconjugate Chem. 18*, 590–596.

(3) Heredia, K. L., Bontempo, D., Ly, T., Byers, J. T., Halstenberg, S., and Maynard, H. D. (2005) In situ preparation of protein - "Smart" polymer conjugates with retention of bioactivity. *J. Am. Chem. Soc. 127*, 16955–16960.

(4) Thordarson, P., Le Droumaguet, B., and Velonia, K. (2006) Well-defined protein-polymer conjugates-synthesis and potential applications. *Appl. Microbiol. Biotechnol. 73*, 243–254.

(5) Tilley, S. D., and Francis, M. B. (2006) Tyrosine-selective protein alkylation using π-allylpalladium complexes. *J. Am. Chem. Soc. 128*, 1080–1081.

(6) Van Hest, J. C. M., Kiick, K. L., and Tirrell, D. A. (2000) Efficient incorporation of unsaturated methionine analogues into proteins in vivo. *J. Am. Chem. Soc. 122*, 1282–1288.

(7) Wang, L., and Schultz, P. G. (2005) Expanding the genetic code. *Angew. Chem., Int. Ed. 44*, 34–66.

(8) Hahn, M. E., and Muir, T. W. (2005) Manipulating proteins with chemistry: a cross-section of chemical biology. *Trends Biochem. Sci. 30*, 26–34.
(9) Huisgen, R. (1963) 1,3-Dipolare Cycloadditionen - Ruckschau und Ausblick. *Angew. Chem., Int. Ed. 75*, 60460+.
(10) Lutz, J. F. (2007) 1,3-Dipolar cycloadditions of azides and alkynes: A universal ligation tool in polymer and materials science. *Angew. Chem., Int. Ed. 46*, 1018–1025.
(11) Wang, Q., Chan, T. R., Hilgraf, R., Fokin, V. V., Sharpless, K. B., and Finn, M. G. (2003) Bioconjugation by copper(I)-catalyzed azide-alkyne [3 + 2] cycloaddition. *J. Am. Chem. Soc. 125*, 3192–3193.
(12) Strable, E., Prasuhn, D. E., Udit, A. K., Brown, S., Link, A. J., Ngo, J. T., Lander, G., Quispe, J., Potter, C. S., Carragher, B., Tirrell, D. A., and Finn, M. G. (2008) Unnatural amino acid incorporation into virus-like particles. *Bioconjugate Chem. 19*, 866–875.
(13) Schoffelen, S., Lambermon, M. H. L., van Eldijk, M. B., and van Hest, J. C. M. (2008) Site-specific modification of *Candida antarctica* lipase B via residue-specific incorporation of a non-canonical amino acid. *Bioconjugate Chem. 19*, 1127–1131.
(14) Van Kasteren, S. I., Kramer, H. B., Gamblin, D. P., and Davis, B. G. (2007) Site-selective glycosylation of proteins: creating synthetic glycoproteins. *Nat. Protocols 2*, 3185–3194.
(15) Kodama, K., Fukuzawa, S., Nakayama, H., Kigawa, T., Sakamoto, K., Yabuki, T., Matsuda, N., Shirouzu, M., Takio, K., Tachibana, K., and Yokoyama, S. (2006) Regioselective carbon-carbon bond formation in proteins with palladium catalysis; New protein chemistry by organometallic chemistry. *ChemBioChem 7*, 134–139.
(16) Vasella, A., Witzig, C., Chiara, J. L., and Martinlomas, M. (1991) Convenient synthesis of 2-azido-2-deoxy-aldoses by diazo transfer. *Helv. Chim. Acta 74*, 2073–2077.
(17) Beckmann, H. S. G., and Wittmann, V. (2007) One-pot procedure for diazo transfer and azide-alkyne cycloaddition: Triazole linkages from amines. *Org. Lett. 9*, 1–4.
(18) Pothukanuri, S., and Winssinger, N. (2007) A highly efficient azide-based protecting group for amines and alcohols. *Org. Lett. 9*, 2223–2225.
(19) Goddard-Borger, E. D., and Stick, R. V. (2007) An efficient, inexpensive, and shelf-stable diazotransfer reagent: Imidazole-1-sulfonyl azide hydrochloride. *Org. Lett. 9*, 3797–3800.
(20) Adams, J. C. (1977) Technical considerations on use of horseradish-peroxidase as a neuronal marker. *Neuroscience 2*, 141.
(21) Hanker, J. S., Yates, P. E., Metz, C. B., and Rustioni, A. (1977) New specific, sensitive and non-carcinogenic reagent for demonstration of horseradish-peroxidase. *Histochem. 9*, 789–792.
(22) Felici, M., Marzá-Pérez, M., Hatzakis, N. S., Nolte, R. J. M., and Feiters, M. C. (2008) β-Cyclodextrin-appended giant amphiphile: aggregation to vesicle polymersomes and immobilisation of enzymes. *Chem.-Eur. J. 14*, 9914–9920.
(23) Opsteen, J. A., Brinkhuis, R. P., Teeuwen, R. L. M., Löwik, D. W. P. M., and van Hest, J. C. M. (2007) "Clickable" polymersomes. *Chem. Commun. 30*, 3136–3138.
(24) Van Dongen, S. F. M., Nallani, M., Schoffelen, S., Cornelissen, J. J. L. M., Nolte, R. J. M., and van Hest, J. C. M. (2008) A block copolymer for functionalisation of polymersome surfaces. *Macromol. Rapid Commun. 29*, 321–325.
(25) Discher, D. E., and Eisenberg, A. (2002) Polymer vesicles. *Science 297*, 967–973.
(26) Vriezema, D. M., Hoogboom, J., Velonia, K., Takazawa, K., Christianen, P. C. M., Maan, J. C., Rowan, A. E., and Nolte, R. J. M. (2003) Vesicles and polymerized vesicles from thiophene-containing rod-coil block copolymers. *Angew. Chem., Int. Ed. 42*, 772–776.
(27) Campbell, R. E., Tour, O., Palmer, A. E., Steinbach, P. A., Baird, G. S., Zacharias, D. A., and Tsien, R. Y. (2002) A monomeric red fluorescent protein. *Proc. Natl. Acad. Sci. U.S.A. 99*, 7877–7882.
(28) The small mass difference between lanes for DsRed is presumably caused by the influence of either Cu(II) or the introduced diazo-moieties; further investigations did not satisfactorily elucidate this. The fluorescent image still indicates that both bands are indeed DsRed signals.

BC8004304

SUPPORTING INFORMATION for:

Single-step azide introduction in enzymes and proteins via an aqueous diazo transfer

*Stijn F. M. van Dongen, Madhavan Nallani†, Rosalie L. M. Teeuwen, Sander S. van Berkel, Jeroen J. L. M. Cornelissen, Roeland J. M. Nolte, Jan C. M. van Hest**

Institute for Molecules and Materials, Radboud University Nijmegen, Toernooiveld 1, 6525 ED, Nijmegen, The Netherlands

* E-mail: j.vanhest@science.ru.nl

† Current address: Institute of Materials Research & Engineering (IMRE), Research Link 3, Singapore 117602

Reagents	S2
Instrumentation	S2
Synthesis of imidazole-sulfonylazide	S4
Diazo transfer conditions	S4
Preparation of polymersomes	S5
1,3-dipolar cycloaddition reaction conditions	S5
Enzyme activity assays	S6
ESI-TOF raw data	S8

Reagents

Heavy water (D_2O, 99.9%) was purchased from Aldrich. $CuSO_4$ (Merck), sodium ascorbate (Fluka, >99%), 4,7-diphenyl-1,10-bathophenanthroline disulfonic acid disodium salt (ligand) (Sigma-Aldrich), anhydrous sodium sulphate (Fluka, 99%), K_2CO_3 (Fisher), magnesium sulfate dihydrate (Fluka, 99%), NaN_3 (Acros, 99%), acetonitrile (MeCN)(Baker), Na_2CO_3 and Na_2HPO_4 (Merck) imidazole (99%, Fluka), sulfonyl chloride (Acros, 98.5%), 3-butyn-1-ol (Aldrich, 99%) and 2,2'-azinobis(3-ethyl-benzothiazoline-6-sulfonic acid) diammonium salt (ABTS) (Fluka, 99%) and all other chemicals were all used as received. Ultrapure water was purified using a WaterPro PS polisher (Labconco, Kansas City, MO) set to 18.2 MΩ/cm.

Horseradish peroxidase (E.C. 1.11.1.7) type VI and glucose oxidase (E.C. 1.1.3.4) type X-S from *Aspergillus niger* were purchased from Sigma (BioChemika). PS_{40}-$PIAT_{50}$ was purchased from Encapson B.V. (Nijmegen, The Netherlands). PS_{40}-PEG_{65}-acetylene was prepared as previously described (*1*). Ligand **3** was prepared as described elsewhere (*2*).

DsRed was prepared according to standard microbiological procedures. Elastin-like protein (ELP) was prepared under auxotrophic conditions where methionine was replaced by homopropargylglycine for acetylene incorporation, in analogy to previous work (*3*). The ELP construct can be described using the notation ELP$[V_5L_2G_3\text{-}90]^5$, where the capitals between the brackets represent the single letter amino acid code replacing guest residue Xaa in the pentapeptide ValProGyXaaGly. The subscript stands for the number of guest residues in the monomer gene, and the ELP consists of 90 pentapeptide repeats. (MALDI-TOF analysis of ELP calc. 39758; found 39551).

Instrumentation

^{1}H NMR spectra were recorded on a Varian Inova 400 MHz instrument at 25°C. Infrared spectra were measured on an ATI Matson Genesis Series FTIR spectrophotometer fitted with an ATR cell. Transmission electron microscopy (TEM) images were obtained using a JEOL JEM 1010

microscope (60 kV) equipped with a CCD camera. Scanning electron microscopy (SEM) images were obtained using a JEOL JSM T300 Scanning microscope (30kv). Samples were prepared by placing 10 µL of a solution on a carbon-coated copper grid for 15 min., after which the liquid was removed. The grid was washed by placing 10 µL MQ on it, which was subsequently removed, after which the grid was dried in vacuo. For SEM, grids were coated in 1.5 nm Pt/Au using a BALZERS sputter machine. UV absorption was measured using a Wallac Multilabel Counter 1420 (Victor Wallac). ESI-TOF measurements were performed using an AccuTOF-CS (JEOL) with samples dialized towards MQ containing 0.5% formic acid. LCQ spectra were obtained using an LCQ advantage max (Thermo Finnigan, Thermo scientific). SDS-PAGE analysis was performed using standard methodology for 10% crosslinked gels.

Synthesis of Imidazole-1-sulfonyl azide hydrochloride (1).

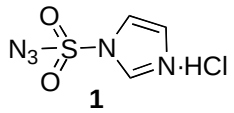

1

As described by Goddard-Borger *et al.*,(*4*) NaN_3, 3.26 g (50 mmol), was suspended in ice-cooled MeCN (50 mL) and 4.1 mL sulfuryl chloride (50 mmol, 1 eq.) was added dropwise, after which the mixture was stirred vigorously overnight allowing it to warm up to room temperature. The mixture was recooled to 0 °C, and 6.50 g imidazole (95 mmol, 1.9 eq.) was added in small portions, after which the reaction mixture was stirred over a period of 2.5 h allowing the temperature to rise to room temperature. The mixture was diluted with 100 mL EtOAc, washed twice with MilliQ water (MQ) and twice with a saturated $NaHCO_3$ solution, and dried over $MgSO_4$. Subsequently, 40 mL of HCl in EtOAc (4M) was added to the ice-cooled mixture, which was left to stand for 15 min. The resulting precipitate was isolated through filtration and washed with EtOAc (3 · 50mL). This produced 7.05 g (67.3%) of colorless (white) needles. LCQ: (Mass - Cl) calc. 174.01, found 173.93. FTIR: $\nu_{max.}$ 2362, 2169, 1436, 1196. ^{1}H NMR (D_2O): ∂ 7.44 (dd, 1H, *C*^{4}*H*), 7.85 (dd, 1H, *C*^{5}*H*), 9.17 (dd, 1H, *C*^{2}*H*).

Diazo-transfer to HRP. To a solution of HRP in MQ (200 µL, 2.5 mg/mL) an aqueous solution of K_2CO_3 (100 µL, 2 mg/mL) was added, along with 25 µL of a Cu(II)SO_4·5H_2O solution in MQ (1 mg/mL). After mixing, a solution of **1** in MQ was added (15 µL, 2 mg/mL, 1.75 equiv. relative to amines in HRP) and the reaction was left agitated overnight. The mixture was transferred to an Amicon UltraFree-MC centrifugal filter with a 3 kDa cutoff and centrifuged to dryness. The supernatant was redissolved in 600 µL MQ and centrifuged again. This procedure was repeated for a total of five washings. Finally, the product was redissolved in 200 µL MQ and analyzed by ESI-TOF (calc. for four transfers (based on 43178.00 found for unreacted HRP): 43281.96; found: 43282.00).

Diazo-transfer to DsRed. To 0.5 mL DsRed (2.6 mg/mL, 87 µM) was added 70 ⌈L K_2CO_3 (0.1 M in MilliQ water), 1 ⌈L $CuSO_4$ (40 mM in MilliQ water), ending with 20 ⌈L diazotransfer agent (24 mM in MilliQ water, 0.5 equiv. relative to amines in DsRed). The solution was incubated at room temperature overnight, and purified over a 5 mL Sephadex-G50 (Amersham Biosciences)

column equilibrated with MilliQ water. The solution was concentrated on a lyophilizer, yielding 2.5 mg/mL. The product was analyzed by ESI-TOF (calc. for three transfers + Na (based on 29768.95 found for unreacted DsRed): 29869.93; found: 29870.11).

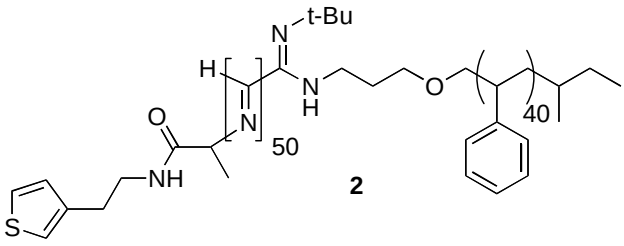

2

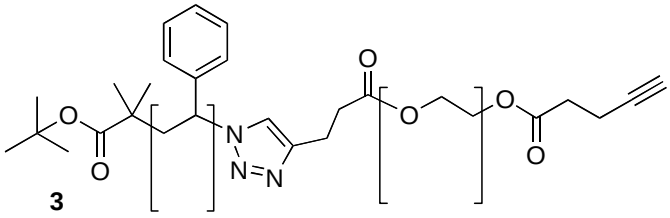

3

Preparation of polymersomes.

A solution of 0.5 mg PS-PIAT (**2**) in 0.5 mL tetrahydrofuran (THF) containing 10 wt.-% of anchor **3** was gently dripped into 2.25 mL of a phosphate buffer (20 mM, pH 7.4) with 250 µL of a GOx stock solution in the same buffer (2.5 mg/mL, 15.6 µM). and left to equilibrate for 30 min. The suspension was transferred to an Amicon Ultra Free-MC centrifugal filter with a 100 kDa cutoff and centrifuged to dryness. The polymersomes were redispersed in 600 µL of a phosphate buffer (20mM, pH 7.4) and centrifuged again. This step was repeated six times. The resulting vesicles were redispersed in 1mL phosphate buffer (20 mM, pH 7.4). Figure 5 (main text) gives representative electron micrographs of these polymersomes.

Conjugation of 3-butyn-1-ol to azido-HRP. 3-Butyn-1-ol (2.5 µL, $3.3 \cdot 10^{-2}$ mmol) was added to a solution of azido-HRP in MQ (100 µL, 2.5 mg/mL). Aqueous solutions of $Cu(II)SO_4 \cdot 5H_2O$ with sodium ascorbate (10 mM each, 10 µL) and 4,7-diphenyl-1,10-bathophenanthroline disulfonic acid disodium salt (ligand, 10 mM, 10 µL) were premixed, added to the enzyme solution and left for 14 hrs at room temperature. The mixture was then transferred to an Amicon UltraFree-MC centrifugal filter with a 3 kDa cutoff and centrifuged to dryness. The supernatant was redissolved in 600 µL MQ and centrifuged again. This procedure was repeated for a total of five washings. Finally, the product was redissolved in 100 µL MQ. The product was analyzed by ESI-TOF (calc. for one addition (based on 43178.00 for unreacted HRP): 43352.00; found: 43352.00), the result of which is shown in figure S3.

Conjugation of azido-HRP to polymersome surfaces. To a dispersion of GOx-containing polymersomes in 200 µL phosphate buffer (20 mM, pH 7.4) an aqueous solution of azido-functionalized HRP (33 µL, 75 µM, 2 equiv. relative to **3**) was added. Aqueous solutions of $Cu(II)SO_4 \cdot 5H_2O$ containing sodium ascorbate (10 mM each, 33 µL) and bathophenanthroline ligand (10 mM, 33 µL) were pre-mixed and then added to the dispersion, which was left at 4 °C for 60 hrs. The mixture was transferred to an Amicon UltraFree-MC centrifugal filter with a 100 kDa cutoff and centrifuged to dryness. The polymersomes were redispersed in 600 µL phosphate buffer (20 mM, pH 7.4) and centrifuged again. This step was repeated until no enzyme activity could be detected in the filtrate. The resulting biohybrid was redispersed in 200 µL phosphate buffer (20 mM, pH 7.4).

Conjugation of azido-DsRed to ELP.

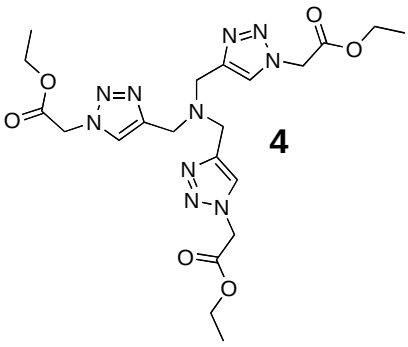

4

To a mixture of ELP (16 µL, 0.587 mg/mL in PBS buffer pH 6.5, MW 39.8 kDa) and azido-DsRed (2 µL, 3.3 mg/mL in MQ) was added 2 µL of CuBr/ligand mixture. The CuBr/Ligand mixture contained CuBr in MeCN (40 mM) and ligand **4** (80 mM) in a 1:1 v/v ratio. The reaction mixture was gently shaken at r.t. for 18 hours and used for gel electrophoresis without further purification.

Conjugation of α-Me, ω-propargylic PEG_{45} to azido-DsRed. To a mixture of PEG (5 µL, 2.3 mg/mL in MQ) and azido-DsRed (5 µL, 3.3 mg/mL in MQ) was added 2 µL of CuBr/ligand and 8 ⌈L MQ giving a total volume of 20 ⌈L. The CuBr/Ligand mixture contained CuBr in MeCN (40 mM) and ligand **4** (80 mM) in a 1:1 v/v ratio. The reaction mixture was gently shaken at r.t. for 18 hours and used for gel electrophoresis without further purification.

Activity assay for (azido-)HRP. An ABTS/H_2O_2 stock solution (4 mM in 20 mM phosphate buffer, pH 7.4, with 0.22% H_2O_2) was freshly prepared before each series of measurements. In a single well of a 96-well micro titer plate a solution of HRP or azido-HRP (2.5 µg/mL in 20 mM

phosphate buffer, pH 7.4, 100 µL) or an aliquot of control buffer (100 µL) was placed, followed by the ABTS/H_2O_2 stock solution (5 µL.) The monitoring of the formation of the radical cation of

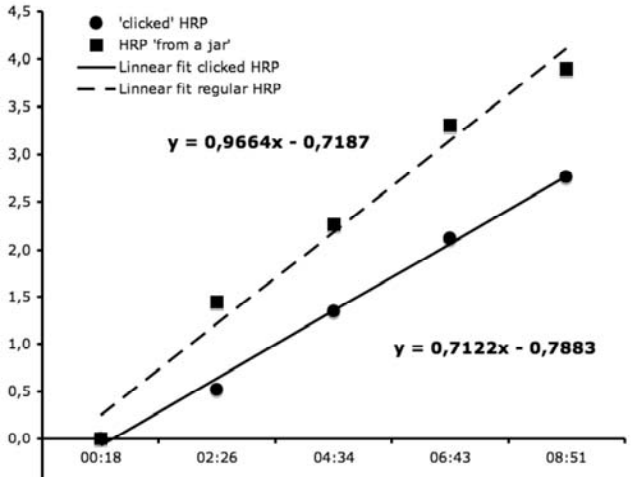

ABTS via its absorption at 405 nm was started immediately after mixing. A comparison of initial reaction rates is shown in figure S2.

Figure S2. Comparison of the linear parts of the progress curves for HRP and azido-HRP as shown in figure 3. The initial rates were compared *via* a linear fit on the first five data points, suggesting that azido-HRP retains 74% of untreated HRP's activity under these conditions. The inhibiting effect of azide moieties on HRP activity,could contribute to this result.

Activity assay for biohybrid polymersomes. A stock solution of glucose (1 M in 20 mM phosphate buffer, pH 7.4) was freshly prepared before each series of measurements, as was an ABTS stock solution (4 mM in 20 mM phosphate buffer, pH 7.4). In a single well of a 96-well micro titer plate a dispersion of polymersomes (100 µL) or an aliquot of control solution (100 µL) was placed, followed by the glucose (40 µL) and the ABTS (20 µL) stock solutions. The monitoring of the formation of the radical cation of ABTS via its absorption at 405 nm was started immediately after mixing.

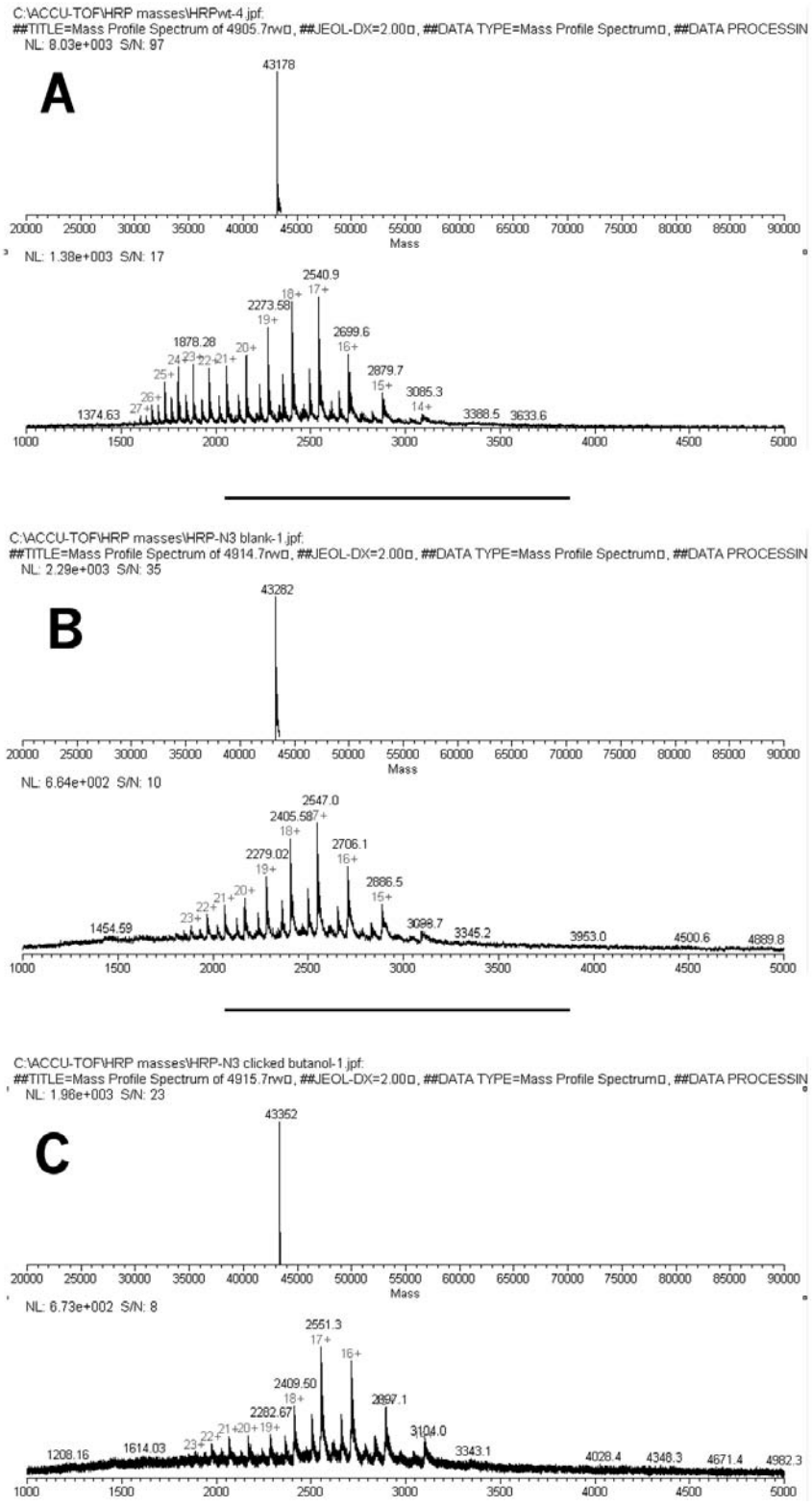

Figure S3. Mass spectra for HRP, azido-HRP and butynol-conjugated azido-HRP. Each panel shows both the experimental results and the deconvoluted peaks; **A.** Unreacted HRP; **B.** Azido-HRP; **C.** Azido-HRP reacted with 3-butyn-1-ol.

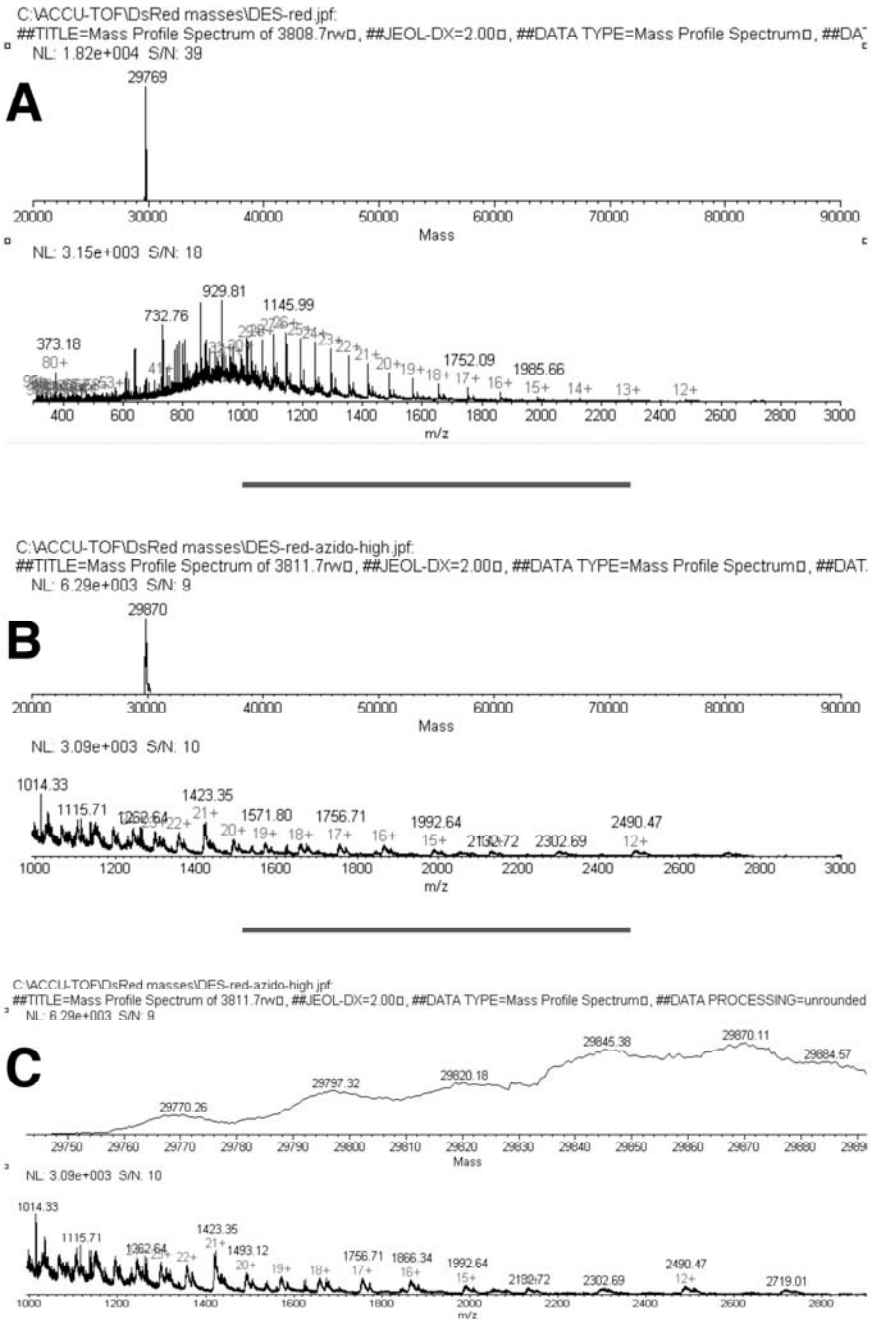

Figure S4. Mass spectra for DsRed and azido-DsRed. Each panel shows both the experimental results and the deconvoluted peaks; **A.** Unreacted DsRed; **B.** Azido-DsRed; **C.** Zoomed view of azido-DsRed.

(1) Van Dongen, S. F. M., Nallani, M., Schoffelen, S., Cornelissen, J. J. L. M., Nolte, R. J. M. and van Hest, J. C. M. (2008) A block copolymer for functionalisation of polymersome surfaces. *Macromol. Rapid Commun. 29*, 321-325.

(2) Van Kasteren, S. I., Kramer, H. B., Gamblin, D. P. and Davis, B. G. (2007) Site-selective glycosylation of proteins: creating synthetic glycoproteins. *Nat. Protocols 2*, 3185-3194.

(3) Schoffelen, S., Lambermon, M. H. L., van Eldijk, M. B. and van Hest, J. C. M. (2008) Site-specific modification of Candida Antarctica Lipase B via residue-specific incorporation of a non-canonical amino acid. *Bioconjugate Chem. 19*, 1127-1131.

(4) Goddard-Borger, E. D. and Stick, R. V. (2007) An efficient, inexpensive, and shelf-stable diazotransfer reagent: Imidazole-1-sulfonyl azide hydrochloride. *Org. Lett. 9*, 3797-3800.

ARTICLES

Conjugation of Latent Membrane Protein (LMP)-2 Epitope to Gold Nanoparticles as Highly Immunogenic Multiple Antigenic Peptides for Induction of Epstein−Barr Virus-Specific Cytotoxic T-Lymphocyte Responses in Vitro

Wai-Hung Cheung,[‡,§] Vera Sau-Fong Chan,[§,||] Heung-Wing Pang,[‡] Man-Kin Wong,[‡] Zhi-Hong Guo,[⊥] Paul Kwong-Hang Tam,[§] Chi-Ming Che,[‡] Chen-Lung Lin,*[,§,||] and Wing-Yiu Yu*[,†,‡]

Department of Applied Biology and Chemical Technology, The Hong Kong Polytechnic University, Hung Hom, Kowloon, Hong Kong, Department of Chemistry and Open Laboratory of Chemical Biology of the Institute of Molecular Technology for Drug Discovery and Synthesis, The University of Hong Kong, Pokfulam Road, Hong Kong, Department of Surgery, L9-30, Laboratory Block, 21 Sassoon Road, Faculty of Medicine Building, The University of Hong Kong, Hong Kong, Division of Surgery, Oncology, Reproductive Biology and Anaesthetic, Faculty of Medicine, Imperial College, U.K., and Department of Chemistry, Hong Kong University of Science and Technology, Clear Water Bay, New Territories, Hong Kong.
Received April 22, 2008; Revised Manuscript Received November 3, 2008

Nasopharyngeal carcinoma is a neoplasm with a high incidence in Southeast Asia, and it is strongly associated with Epstein−Barr virus (EBV) activation involving the expression of a weakly immunogenic protein, namely, latent membrane protein (LMP)-2. Previous immunological studies already identified the human leukocyte antigen (HLA)-A11 restricted peptide epitope (SSCSSCPLSK) in the LMP-2 antigen. In this work, we prepared gold nanoparticle (AuNP)−peptide conjugate **1** by treating the nanoparticles with the *N*-cysteinated LMP-2 epitope. The AuNP−peptide conjugates have been characterized by TEM (15−24 nm in diameter) and UV−vis spectroscopy (surface plasmon resonance absorption band at $\lambda_{max} = 520$ nm). In the presence of a CALNN capping peptide, the AuNP−peptide conjugates are stable in solution without aggregation at room temperature for at least 48 h. By ELIspot studies, AuNP−peptide conjugate **1** was found to elicit a significantly stronger INF-γ response [number of spot forming cells (SPC) = 727 ± 198] from peripheral blood mononuclear cells of healthy HLA-A11 donors when compared to that induced by the unconjugated LMP-2 peptides (SFC = 73 ± 28). Further studies showed that dendritic cells treated with conjugate **1** can effect CD8+ T-cell activation leading to epitope-specific cytotoxic T lymphocyte killing responses in vitro.

INTRODUCTION

Nasopharyngeal carcinoma (NPC) is a prevalent malignancy in Southeast Asia. Conventional treatment is ineffective for advanced NPC patients and is often accompanied with severe long-term side-effects. In this regard, immunotherapy is now attracting current interest in developing more effective cancer treatment. Epstein−Barr virus (EBV) is a γ-herpesvirus that resides in over 95% of the general population as a life-long asymptomatic harmless infection (*1*, *2*). However, poorly differentiated and undifferentiated NPC is strongly associated with EBV activation. The EBV latent membrane proteins (LMP-1 and -2) expressed in the tumor tissues have become the target antigens for cancer immunotherapy. A recent clinical study by Straathof and co-workers showed that the adoptive transfer of LMP- and LMP-2 specific cytotoxic T-lymphocytes (CTLs), which were generated by stimulating the peripheral blood mononuclear cells (PBMCs) with autologous EBV-transformed lymphoma cell lines (LCL), could induce antiviral response in vivo and conferred tumor regression in some advanced NPC patients (*3*). Apart from the LMP proteins, the LCLs are also known to produce six other nuclear antigens (EBNAs 1, 2, 3A, 3B and 3C, and EBNA-LP) (*4*) and some of which are oncogenic (*5*−*7*). Despite the encouraging clinical results, the use of EBV-transformed LCLs for CTL priming may jeopardize the safety of patients. Apparently, the development of synthetic peptide antigens that can induce EBV-specific CTL activation is clearly advantageous over whole-protein antigen mixtures in terms of safety and ease for production.

Dendritic cells (DC) are professional antigen-presenting cells for activation of antigen-specific CTL, which underlies effective cancer immunotherapy. Dendritic cells are responsible for processing and presenting human leukocyte antigen (HLA)-restricted peptide epitopes to CD8+ T cells through the major histocompatibility complex (MHC)-I pathway (*8*−*11*). Recently, one of us reported that intranodal injection of dendritic cells ex vivo pulsed with a HLA-A11 restricted LMP-2 epitope (SSC-

* (W.-Y.Y.) E-mail: bcwyyu@inet.ployu.edu.hk. (C.-L.L.) E-mail: steve.lin@imperial.ac.uk.
‡ Department of Chemistry and Open Laboratory of Chemical Biology of the Institute of Molecular Technology for Drug Discovery and Synthesis, The University of Hong Kong.
§ Department of Surgery, The University of Hong Kong.
|| Imperial College.
⊥ Hong Kong University of Science and Technology.
† The Hong Kong Polytechnic University.

10.1021/bc800167q CCC: $40.75 © 2009 American Chemical Society
Published on Web 12/22/2008

SSCPLSK) induced EBV specific CTL in vivo, and regression of metastatic tumor in selected NPC patients has been observed (*12*). Yet, the antitumor effect of this DC-based immunotherapy for NPC was not seen in all tested individuals, and the poor immunogenicity of the LMP-2 epitope is probably one of the reasons. Conventionally, keyhole limpet heamocycnin (KLH) and bovine serum albumin (BSA) have been used as carriers to conjugate with peptides for inducing antibody responses. Recently, KLH has been shown to have an adjuvant effect that primes dendritic cells for enhancing peptide specific CD8+ T cell responses (*13*−*15*); however, the potential side effects (*16*) from the use of this potent adjuvant have been a cause for concern in human settings. As a result, several alternative approaches have been exploited to enhance the immunogenicity of peptide antigens for human uses. A notable example is the multiple antigenic peptide (MAP) system based on the conjugation of multiple peptide epitopes onto a benign carrier such as liposomes and branched/dendrimeric poly lysine core (*17*−*22*). While arduous synthetic processes are often required, the purification and characterization of the MAP peptides are also technically demanding. In addition, the number of different epitopes incorporated into the construct is also limited, rendering development of a broad scope peptide vaccine difficult.

The use of nanoparticles as delivery vehicles for therapeutic agents is receiving current attention (*23*−*27*). For example, nanoparticle based biodegradable polymers such as poly(γ-glutamic acid) and poly(DL-lactic-coglycolic acid) have been used to deliver peptide/protein antigens to murine and human dendritic cells for effective induction of antigen-specific CTL responses (*28*). However, the nanoparticles were prepared by self-assembly of their polymers, and this process often operates in a small scale and at high dilution. By virtue of high surface area and chemical stability, biomolecule functionalized gold nanoparticles (AuNP) have found important applications in many areas, including catalysis, biosensing, and diagnostics (*29*−*36*). In search of highly immunogenic peptides for potential application to NPC immunotherapy, here we describe that bioconjugation of the LMP-2 epitope (SSCSSCPLSK) to gold nanoparticle (AuNP) is a simple and effective approach for assembling solution-stable immunogenic multivalent peptides. Immunoassay studies showed that the AuNP−peptide conjugate is a potent immunogen in inducing interferon (IFN)-γ production by peripheral blood mononuclear cells. Also, treatment of human dendritic cells with the nanoparticle−peptide conjugate resulted in EBV-specific CTL priming in vitro.

MATERIALS AND METHODS

The Fmoc-protected amino acids and the Wang resins were purchased from EMD Biosciences, Inc. (Novabiochem, 10394 Pacific Center Court, San Diego, CA 92121); the Wang resins precoated with amino acids were purchased from Advanced ChemTech Inc. (Louisville, KY), and the other chemicals were purchased from Aldrich Chemical Co. (P.O. Box 206, Milwaukee, WI 53201). All of the solvents were of HPLC or peptide synthetic grade and were used as received. The nanopure water was collected from a Barnsted water purification system (nanopure diamond).

Buffy coats were obtained from the Hong Kong Red Cross for research purposes; anti-HLA antibodies were purchased from US Biology Corp. (USA); antihuman CD8 and the isotype control antibodies were obtained from PharMingen (USA). The cytokines, GM-CSF (granulocyte macrophage colony stimulating factor) and Interleukin (IL)-4, were obtained from Peprotech Inc. (USA). MultiScreenHTS-IP PVDF filter Elispot plates (MSIPS4510) were purchased from Millipore Corp (USA); the ELIspot kit (SEL285) and ELIspot Blue Color Module (SEL002) were purchased from R&D System (USA). The ^{51}Cr-sodium chromate isotope for the chromium release assays was purchased from GE Healthcare Medical Co. Ltd., (CJS1−1mCi, USA). The peptides were prepared by a Chemspeed 500 parallel synthesizer. All of the samples were lyophilized by a Savant system (SC250DDA speedvac Plus). The peptides were analyzed and purified on a Waters HPLC system (Waters Alliance 2690 equipped with a 996 PDA UV−vis detector or Waters delta 500 preparative HPLC). The masses of the samples were determined by either matrix-assisted laser desorption ionization time-of-flight (MALDI-TOF, Amersham Biosciences, Voyager DE-STR MALDI TOF Mass spectrometry) or fast atom bombardment ionization (FAB, Finnigan MAT 95). The gold nanoparticles (AuNP) were analyzed by a transmission electron microscope [TEM, Philips (Techian 20)]. For the uptake of the AuNP−peptide conjugates by dendritic cells, a transmission electron microscope of Philips EM208s model was employed.

Solid Phase Peptide Synthesis. All of the peptides including the multiple antigenic peptides (MAP) were synthesized by solid phase peptide synthesis using the Fmoc-protected amino acid strategy (*37*). The crude peptides were purified by preparative HPLC, and >95% purity of the peptides were confirmed by analytical HPLC equipped with a UV−vis detector (monitoring wavelength $\lambda = 214$ nm). The purified peptides were lyophilized to give an amorphous white solid. The peptides were dissolved in 10 μL of DMSO and diluted with sterile phosphate buffered saline (PBS) to 2 mM. The solutions were kept at −70 °C for long-term storage (6 months) and −20 °C for temporary storage (2 weeks). The mass spectrometry data of the synthetic peptides are available in Supporting Information. The multiple antigenic peptide (MAP) **7** was synthesized from the Wang resin precoated with ([Fmoc-Lys(Fmoc)]$_2$-Lys-Cys(Acm)-β-Ala-resin (SM5105, Advanced ChemTech, Inc., Louisville, KY) using the Fmoc protected amino acid strategy as described earlier. The crude products were dialyzed with a dialysis tubing (1200 dalton cutoff; Sigma, D7884−10FT) in nanopure water containing urea (10%) and acetic acid (10%) for 48 h at room temperature. The purified products were lyophilized and analyzed by ESI-MS. The animo acid sequence of **7** was confirmed by the amino acid sequencing technique (Department of Zoology, The University of Hong Kong). MAP **8** was synthesized in a similar manner using the precoated Wang resin ([Fmoc-Lys(Fmoc)]$_4$-Lys$_2$-Lys-Cys(Acm)-β-Ala-Wang resin, SM5102).

Synthesis of Gold Nanoparticles (AuNPs) (*38*). A sodium citrate solution (0.5 g in 10 mL of water) was added to a boiling $KAuCl_4$ solution (36 mg in 90 mL of water). The color of the reaction mixture changed gradually from pale yellow to wine red over 30 min. The gold nanoparticles obtained in this manner were found to have particle sizes of 15−24 nm based on transmission electron microscopic analysis. The gold nanoparticle solution was used for the subsequent peptide conjugation without purification.

Synthesis of AuNP−Peptide Conjugate 1. To the gold nanoparticle solution prepared above (9 mL) was added the LMP-2′ peptide (C-SSCSSCPLSK; 0.1 mL of 2 mM in water) and the capping peptide CALNN (Cys-Ala-Leu-Asn-Asn) (0.9 mL of 2 mM in water). The reaction solution was stirred overnight at room temperature to afford AuNP−peptide conjugate **1** as a wine red solution. On the basis of HPLC analysis of the reaction mixture, unreacted/unbound LMP-2′ and CALNN peptides were not detected. The conjugate was purified by Sephadex column chromatography and lyophilized to obtain a red powder (3.0 mg). The red powder was resuspended in PBS for TEM, UV−vis spectroscopic analysis.

For the preparation of AuNP−peptide conjugates **2**−**6**, a similar protocol was employed by using different ratios of LMP-2′ and CALNN peptides (see Supporting Information).

HPLC Analysis of Peptides. Ten microliters of a sample was injected to a reverse phase column (Waters, Xterra column, 4.6 × 150 mm) using a gradient of solvent mixtures [solvent A (H_2O with 0.1% trifluoroacetic acid) and solvent B (acetonitrile with 0.1% trifluoroacetic acid); gradient program: 0−3 min A (100%), 20 min A (50%), 25 min A (100%), 25−30 min A (100%)] using an Alliance 2690 HPLC system with a photo diode array PDA (996) detector (monitoring wavelength λ = 214 nm). The % amount of the peptides was determined by comparing the authentic samples.

Peripheral Blood Mononuclear Cells (PBMCs) (*39*). The PBMCs were harvested from the buffy coats (Red Cross Hong Kong) by Ficoll-Hypaque (Pharmacia Biotech, Uppsala, Sweden) density gradient centrifugation. The PBMCs were washed with PBS three times and resuspended in culture medium for immediate use or frozen for later experiments by keeping in liquid nitrogen.

Human Leucocyte Antigen (HLA) Typing. The buffy coat (1 mL) was diluted with PBS (1 mL) and incubated with ACK buffer (2 mL; 150 mmol/L NH_4Cl, 61mmol/L $KHCO_3$, and 1 mmol/L Na_2EDTA; pH 7.4) for 5 min to lyse the red blood cells. The white blood cells were washed with PBS three times and resuspended in PBS (1 million cells/mL; 50 μL). To identify the HLA types of each PBMC, HLA-A2, HLA-A11, HLA-A2/A24, and HLA-A11/A24 antibodies (US Biology, H6098−28A and H6098−07A) were employed for immunostaining (at 4 °C for 20 min), followed by incubation with FITC-conjugated secondary antibody and subsequent flow cytometric analysis (BD, FACS Calibur). In this work, only the HLA-A11+/A2+ donors were used for the experiments. The HLA A2/A24 and HLA A11/A24 antibodies (US Biology, H6098−31, H6098−11) were also employed to discriminate any HLA A24+ donors.

ELIspot Assay. The ELIspot assay was performed using the ELIspot kit (SEL285) and ELIspot Blue Color Module (SEL002) by following the manufacturer's instruction. Briefly, 2 μL of the AuNP−peptides as prepared above was added to 1 mL of PBMCs (4×10^6 cell number) in complete medium (10 unit/mL of penicillin, 10 μg/mL of Streptomycin, and 10% fetal bovine serum in RPMI1640) and IL-2 (10 unit/mL) at 37 °C with 5% CO_2 for 18 h. The treated PBMCs were placed in triplicate onto the microtiter plate (96 wells) precoated with capture antibody. The ELIspot plate was kept at 37 °C with 5% CO_2 overnight and then washed with washing buffer (PBS with 0.05% of tween) three times. A detection antibody was added to the microtiter plate, and the mixture was kept at 2−8 °C for 16 h. The microtiter plate was then washed with washing buffer (three times) and the INFγ-releasing cells were revealed as color spots by adding a color developing agent. The blue spots were counted with a dissection microscope.

Generation of Dendritic Cells (*40*). PBMCs ($1 - 2 \times 10^7$ cells/well) were plated on a 6-well plate at 37 °C with humidified 5% CO_2 for 2 h in complete medium. The nonadherent cells were then removed, and fresh complete medium with GM-SCF (100 ng/mL) and IL-4 (100 ng/mL) was added to the semiadherent monocytes. The medium and the cytokines were changed every two to three days. On day 7, the immature dendritic cells were harvested. The purity of the harvested dendritic cells was about 80% as determined by immunostaining with antihuman CD11c antibody, followed by flow cytometry analysis.

Uptake of AuNP−Peptide Conjugate by Dendritic Cells (*31*). Briefly, 2 μL of **1** was added to 5×10^5 immature dendritic cells in 1 mL medium at 37 °C in humidified 5% CO_2 for 24 h. The treated cells were washed twice and fixed with 2.5% glutaraldehyde in cacodylate buffer at 4 °C for 16 h. Afterward, the dendritic cells were then washed and supported in agar gel. The agar gel was further dehydrated by shaking with stepwise increase in ethanol concentration from 50% to 100%. The dehydrated agar was embedded with epoxy resin by polymerization overnight at 60 °C. The resin was sliced for electron microscopic analysis. The dendritic cells were examined by a Philips EM208s transmission electron microscope (Electron Microscope Unit, Department of Pathology, Queen Mary Hospital).

Generation of Peptide-Specific Cytotoxic T-lymphocytes. The HLA A11+ CD8+ T cells were isolated from HLA-typed PBMCs by negative depletion (Dynal Biotech ASA, Dynabeads Goat antimouse IgG, 110.33) according to the manufacturer's instructions. The CD8+ T cells were obtained with about 80% purity based on flow cytometry analysis.

On day 7 (see Scheme 1), **1** (2 μL) was added to the immature dendritic cells (iDCs, 2×10^5 cells irradiated with 3000 rad) in 0.1 mL medium generated earlier, and the mixture was incubated for 1 h. The iDCs were then washed and mixed with CD8+ T cells (1×10^6 cells) in 1 mL of complete medium with β-mercapthanol (55 μM) and IL-2 (50 unit/mL). On day 10, 50 unit/mL of IL-2 was added to the medium. On day 14, CD8+ T cells were restimulated with the autologous dendritic cells pulsed with the peptide−AuNP conjugate as described above, and the restimulation procedure was repeated on day 21. The CD8+ T cells were harvested on day 28, and the specific killing efficiency of CTL was assessed by the chromium (^{51}Cr) release assay. In addition to **1**, MAP **7** (4 μL of 2 mM in water) and LMP-2 (native epitope = SSCSSCPLSK, 50 μL of 2 mM in water), **6** (2 μL of working solution), MAP-A24 (4 μL of 2 mM in water; see Figure 3 for structure) and HLA mismatched peptide (TYGPVFMSL, 50 μL of 2 mM in water) were used for comparison and as irrelevant controls.

Chromium (^{51}Cr) Release Assay (*41*). To prepare the target cells, autologous or HLA-matched PBMCs (4×10^6 cells) were cultured with phytohemagglutinin (PHA, 0.2 mg/mL) and IL-2 (400 unit/mL) in complete medium for 2 days to obtain PHA blast cells (*42*). The blast cells (*43*) (2×10^6) were washed three times and treated with 100 μL (0.1 mCi) of Na_2CrO_4 (1 mCi, Amersham, CJS1−1mci) for 1 h at 37 °C with 5% CO_2 to obtain chromium labeled target cells. The targets were split into two equal portions and pulsed with LMP-2 peptide (SSCSSCPLSK, 100 μM) and irrelevant peptide (YLSGANLNL, 100 μM) for 1 h. The peptide-pulsed PHA blasts were resuspended to 10^5 cell/mL and aliquot (100 μL, 10^4 cells/well) into the U-bottom 96-well plate in triplicate.

The specific CTLs (which were stimulated with **1**, **6**, **7**, MAP-A24, and HLA mismatched peptide) were harvested and used as effector cells for the cytotoxicity assay. Effector cells in triplicate (6.0×10^5, 2.0×10^5, 6×10^4, and 2×10^4 cells per well; cell number would vary according to donors) were placed on a 96 U bottom plate and cocultured with target cells (1×10^4 cells per well) for 4 h. The maximum release was obtained by lysing the target cells with 5% Triton X-100 in PBS. The spontaneous release was obtained from the supernatant of the target cells in medium only. The released chromium was counted by a scintillation counter (LKB Wallac, 1470 Wizard). % Cell lysis = (experimental release − spontaneous release)/(maximum release − spontaneous release) × 100%.

RESULTS AND DISCUSSION

Gold nanoparticles (AuNP) were prepared by reduction of $KAuCl_4$ (1 mmol) with sodium citrate according to a reported method (*38*). The nanoparticles showed a characteristic surface plasmon resonance absorption band at λ = 520 nm, and a TEM study revealed a size distribution of 15−24 nm (Figure 1). By standard solid phase peptide synthesis, the LMP-2 epitope (SSCSSCPLSK) (*44*, *45*) was prepared with purity >95% as confirmed by HPLC analysis. In this work, a cysteine residue

Scheme 1. Flow Chart Showing the Processes of the Cytotoxic T-Lymphocyte Generation and the ^{51}Cr Release Assay[a]

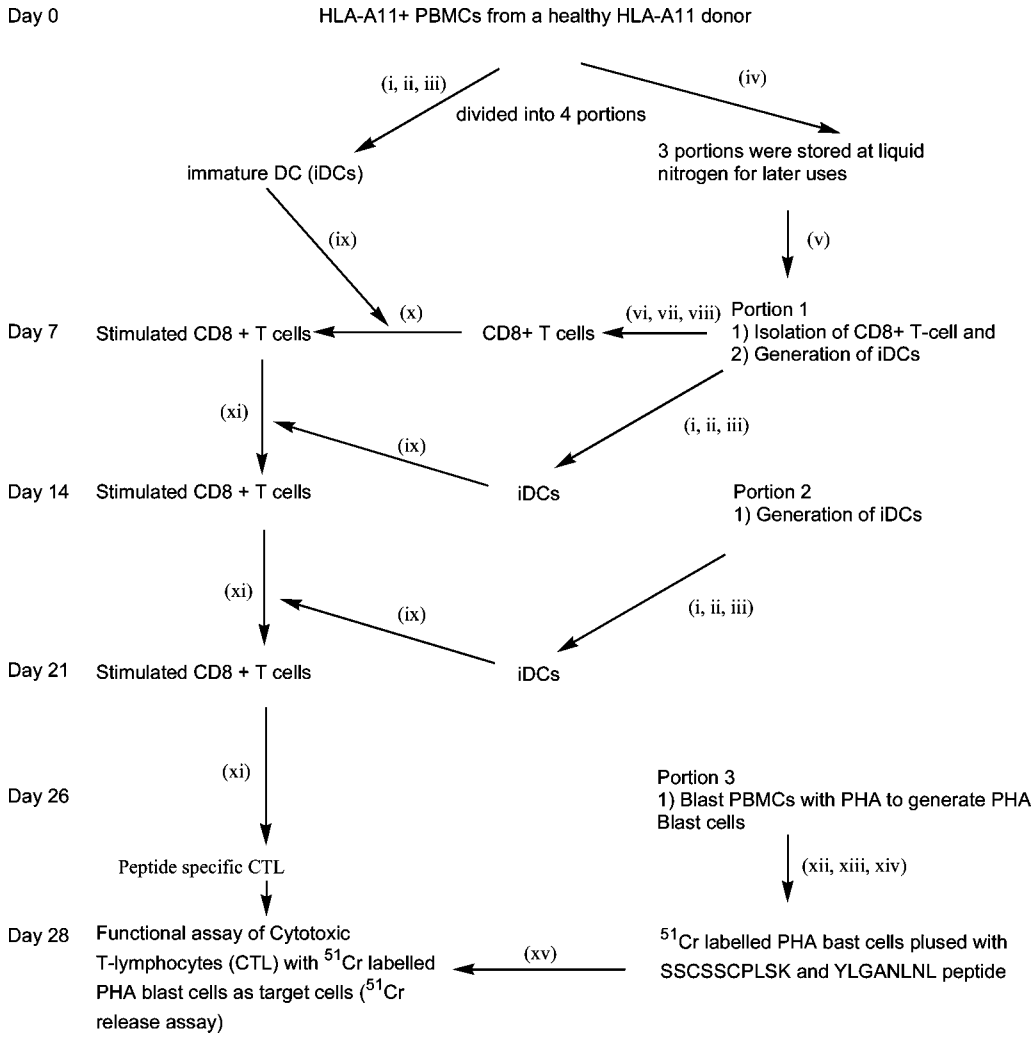

[a] Reagents and conditions: (i) PBMC (2×10^7 /well, 6 well), 37 °C, 5% CO_2, 2 h in complete medium (10 unit/mL of penicillin, 10 mg/mL of Streptomycin, 10% fetal bovine serum in RPMI 1640); (ii) removed non-adherent cells and washed semi-adherent monocytes by complete medium; (iii) replenished monocytes with complete medium containing GMCSF (100 ng/mL) and IL-4 (100 ng/mL) and changed medium every 3 days; (iv) 10% DMSO, 50% fetal bovine serum in RPMI 1640, in liquid nitrogen; (v) replenished with completed medium, 37 °C, 5% CO_2; (vi) mouse anti-human CD4, CD14, CD16, and CD56 (10 μg/mL/10^6 cell), 4 °C, 20 min, washed 3 times; (vii) Dynabeads (goat anti-mouse, IgG 110.33, 100 μL/mL), 4 °C, 30 min; (viii) magnetic beads depletion; (ix) immature DC (0.2×10^6, irradiated with 3000 rad), **1** (2 μL), 1 h; (x) CD8+ T (1×10^6, 1 mL) in complete medium with β-mercapthanol (55 μM) and IL-2 (50 unit/mL); (xi) replenish fresh medium with β-mercapthanol (55 μM) and IL-2 (50 unit/mL) every 3 days; (xii) PBMC (4×10^6), Phytohemagglutinin (PHA, 0.2 mg/mL) and IL-2 (400 unit/mL) in complete medium, in 2 days to become blast cells; (xiii) blast cells (2×10^6), Na_2CrO_4 (100 μL of 1 mCi/mL), 1 h, 37 °C, 5% CO_2, washed 3 times; (xiv) divided PHA blast cells into 2 equal parts and pulsed with LMP-2 peptide (SSCSSCPLSK, 50 μL of 2 mM) and irrelevant (YLSGANLNL, 50 μL of 2 mM), 37 °C, 5% CO_2, 1 h, washed 3 times; (xv) co-cultivated different E:T ratio of CTLs (100 μL) to PHA blast cells 10^4 cell/100 uL/well, 37 °C, 5% CO_2, 4 h. (Note: E:T ratio varied from donor to donor and depended on CTL harvested.)

was appended to the *N*-terminus of the LMP-2 epitope (i.e., C-SSCSSCPLSK = LMP-2′) to enable peptide ligation to the Au surface.

Conjugation of LMP-2 Peptide Epitope to Gold Nanoparticles. To the AuNP solutions was added the LMP-2′ peptide and the CALNN (Cys-Ala-Leu-Asn-Asn) peptide (mole ratio of LMP-2′/CALNN = 1:9), and a red solution of AuNP−peptide conjugate **1** was obtained. HPLC analysis of the red solution revealed that all of the LMP-2′ and the CALNN peptides were completely consumed for ligation to the nanoparticles. Conjugate **1** can be purified by Sephadex G-10 column chromatography and lyophilized to afford a red powder (3.0 mg). It is noteworthy that any species corresponding to the inter/intramolecular disulphide bond formation were not observed by LC-MS analysis (*46*). By employing different quantities of the LMP-2′ and CALNN peptides for the bioconjugation, AuNP−peptide conjugates **2**−**6** were prepared (see Supporting Information for details). In all cases, the LMP-2′ peptides were completely consumed for the bioconjugation, and thus, the equivalent peptide concentrations for the AuNP−peptide conjugates in solution should be 20 (**1**), 40 (**2**), 60 (**3**), 140 (**4**), and 200 μM (**5**). These solutions will be utilized as the working solutions for the biological assays. Treating the AuNPs with CALNN peptide alone (i.e., without LMP-2′ peptide) gave conjugate **6**, which will be used as the negative control in the immunoassays.

As noted earlier, conjugate **1** can be isolated as a red powder after Sephadex column purification followed by lyophilization. Conjugate **1** can be dissolved readily in PBS, and the UV−vis spectrum is characterized by a distinct UV−vis absorption band at λ_{max} = 520 nm. Similar spectral features were observed for **2**−**6** as well as the peptide-free gold nanoparticles (Figure 1b). For all of the AuNP−peptide conjugates, no significant changes in the particle diameters were observed after peptide conjugation according to TEM analyses.

As reported by Levy and co-workers (*47*), the CALNN sequence is important for maintaining solution stability of the

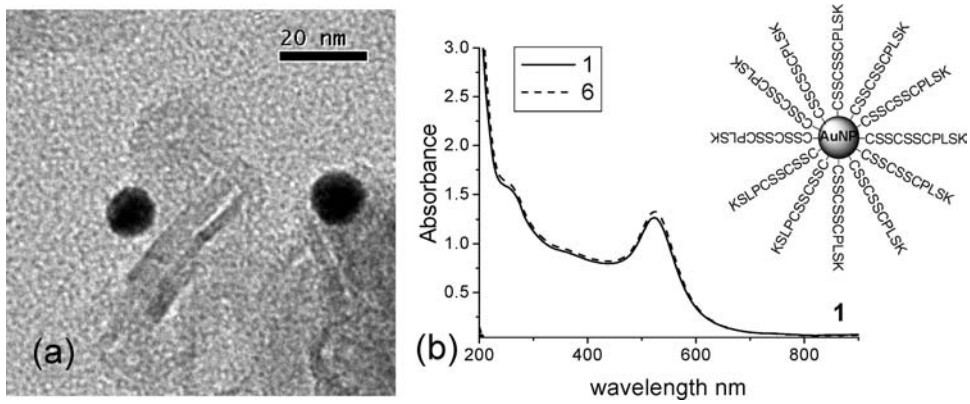

Figure 1. (a) TEM image of AuNP−peptide conjugate **1** (diameter = 15−24 nm) against PBS (shaded area); (b) UV−vis spectra of **1** (solid line) and **6** (dotted line) in PBS showing a characteristic surface plasmon band at 520 nm. Inset: schematic depiction of the AuNP−peptide conjugates.

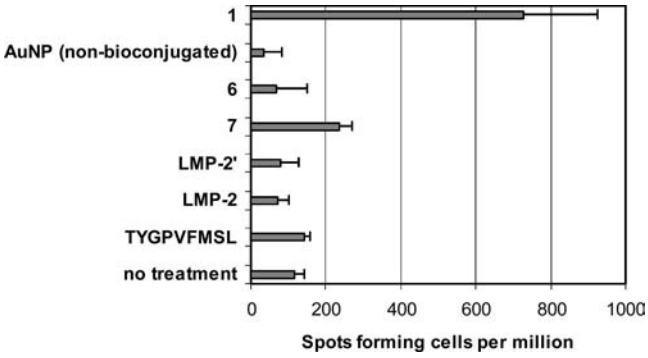

Figure 2. ELIspot results depicting the INF-γ release from the PBMCs of a HLA-A11 donor 1 upon stimulation by the peptides/conjugates; HLA mismatched A24 peptide = TYGPVFMSL.

AuNP−peptide conjugate without aggregation. By monitoring the surface plasmon resonance band (520 nm) of AuNP−peptide conjugates **1**−**4** (in PBS buffer) containing the CALNN sequence, no significant spectral changes were observed for those samples. The solutions of **1**−**4** were found to be stable at room temperature for at least 48 h without apparent precipitation. However, for the PBS solution of **5** that lacks the CALNN sequence, significant precipitation occurred over 48 h at room temperature. As expected, **6** containing only the CALNN peptide alone was stable in PBS solution under identical conditions.

INF-γ ELIspot Assay for the Peptide-Conjugated Gold Nanoparticles. Gamma interferon (INF-γ) is an important cytokine in provoking antiviral immunity (*48*). The immunogenicity of the AuNP−peptide conjugates **1**−**6** was evaluated by their activity to activate INF-γ producing cells in peripheral blood mononuclear cells (PBMCs) using the enzyme linked immunospot (ELIspot) assay. PBMCs from four healthy HLA-A11 donors were employed for this study. Briefly, PBMCs were treated with the AuNP−peptide conjugate **1** (equivalent epitope concentration in culture medium = 0.04 μM) in a 24-well plate for 16 h at 37 °C. The peptide-treated PBMCs (2×10^5 cells) were then incubated in triplicate wells for 24 h with INF-γ capture antibody precoated on a PVDF membrane. After washing, a color developing agent was added to the plate, and the INF-γ-releasing cells were identified as colored spots. The number of spot-forming cells (SFC) was counted with a dissection microscope.

Figure 2 shows the ELIspot results from donor 1. As expected, stimulation with nonpeptide conjugated AuNPs, conjugate **6** with CALNN peptide-alone, and the HLA-mismatched (TYGPVFMSL) peptides could not induce any significant IFN-γ response in the PBMCs. Interestingly, the unconjugated LMP-2 and LMP-2′ peptides (10 μM) also failed to induce a significant IFN-γ response [spot-forming cells (SFC) = 73 ± 28 vs 117 ± 24 of no peptide control) suggesting that this peptide per se was a poor immunogen and was unable to stimulate significant cytokine response from the PBMCs of healthy individuals by a simple single stimulation procedure. These results were in agreement with previous findings that this HLA-A11 restricted LMP-2 epitope (SSCSSCPLSK) is weakly immunogenic and that the CTL precursor frequency for this epitope in healthy individuals is very low (e.g., < 1/100,000 PBMCs) (*49*). However, when this weakly immunogenic epitope was administered in the form of gold nanoparticles, i.e., conjugate **1**, a strong and significant INFγ response was observed (SFC = 727 ± 198 vs 117 ± 24 in no peptide control, $P = 0.007$). It is noteworthy that in these experiments, the equivalent epitope concentration of conjugate **1** (0.04 μM) was much less than that of the unconjugated peptide (10 μM) under our experimental conditions, and yet, the observed INFγ response with conjugate **1** was 10-fold stronger than of the native peptide.

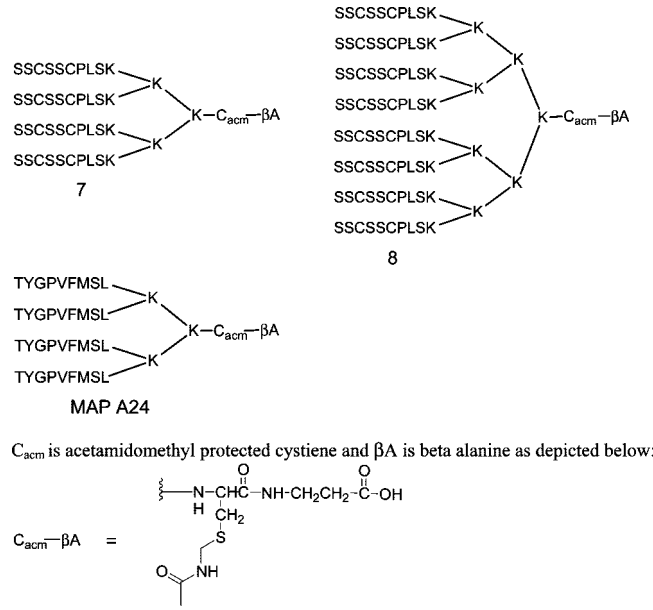

Figure 3. Schematic depiction of the multiple antigenic peptides 7, 8, and MAP A24.

Apart from the AuNP−peptide conjugates, the immunogenicity of the multiple antigenic peptides (MAP) derived from a branched lysine core was also examined in parallel by the ELIspot assays. In this work, antigen **7** conjugated with four LMP-2 epitopes (Figure 3) was also prepared by conventional

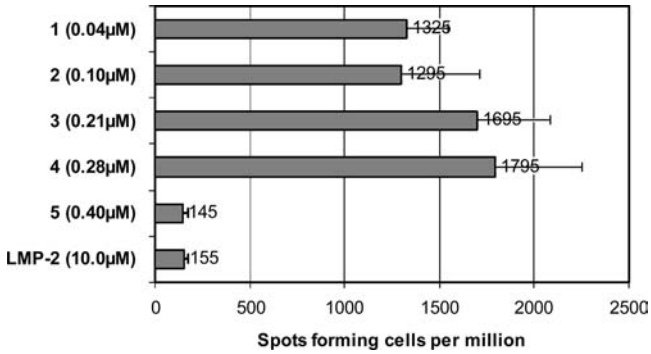

Figure 4. ELIspot results depicting the INF-γ release from the PBMCs of a HLA-A11 donor 4 upon stimulation by AuNP−peptide conjugates. Conjugates **1** with SFC of 1325 ± 218 ($P < 0.001$) when compared with the untreated group.

solid phase peptide synthesis. We found that stimulating the PBMCs of donor 1 by antigen **7** (8 μM) produced a sizable INF-γ response (SFC = 237 ± 33, $P = 0.008$ when compared with that of the no peptide control). Yet, this response was only about one-third of that induced by the AuNP−peptide **1** (SFC = 727 ± 198). However, an octavalent derivative **8** (i.e., eight LMP-2 epitopes covalently linked to a lysine core) failed to elicit a comparable INFγ response (SFC = 88 ± 4; data not shown).

The ELIspot results for two other HLA-A11 healthy donors-2 and -3 are given in Supporting Information. Irrespective of the variation among the donors, **1** induced the strongest INF-γ responses in the PBMCs of all the individuals versus other peptides tested herein.

Other AuNP−peptide conjugates with different LMP-2′ content were also tested for the INFγ release; the ELIspot assay was performed by employing a fixed quantity (2 μL) of the working solutions of **1**−**5**. As shown in Figure 4, stimulation of the PBMCs from a healthy A11 donor-4 with **1** (equivalent epitope concentration = 0.04 μM) induced a strong INFγ response (SFC = 1325 ± 218; $P = 0.0005$ compared with that of the no peptide control). Comparable responses were obtained for **2** (0.08 μM), **3** (0.12 μM), and **4** (0.28 μM; equivalent epitope concentrations in the culture medium given in brackets). However, conjugate **5** (equivalent epitope concentration = 0.4 μM *without the CALNN capping peptide*) induced a minimal INFγ response (SFC = 145 ± 27). It is noteworthy that this observed induction is only comparable to that induced by unconjugated LMP-2 peptide (10 μM; SFC = 155 ± 19). These results indicate that the stabilization effect offered by the CALNN capping peptide is essential for the optimal induction of immune response by these AuNP−peptide conjugates.

Dendritic cells (DC) are important for the efficient activation of antigen-specific CTL response, and we therefore examined the uptake of the AuNP−peptide conjugate by human dendritic cells. Immature DCs from a healthy HLA-A11 donor-5 were cocultured with **1** for 24 h. After washing, the stimulated DCs were processed for transmission electron microscopy (TEM) analysis. As shown in Figure 5, the gold nanoparticles can be identified as dark spots in the cell cytoplasm, suggesting that internalization of the antigen into the DCs may enable antigen processing by the MHC class I pathway for CD8+ T lymphocyte priming.

Next, we turned to test the ability of the AuNP−peptide conjugates to induce antigen specific CTL response. The immature dendritic cells derived from the PBMCs of three healthy HLA A11+ donor-6, -7, and -8 were stimulated with either conjugate **1** or other control peptides for 1 h, and were subsequently cocultured with autologous CD8+ T cells (80% purity) and restimulated weekly over 21 days (Scheme 1). The

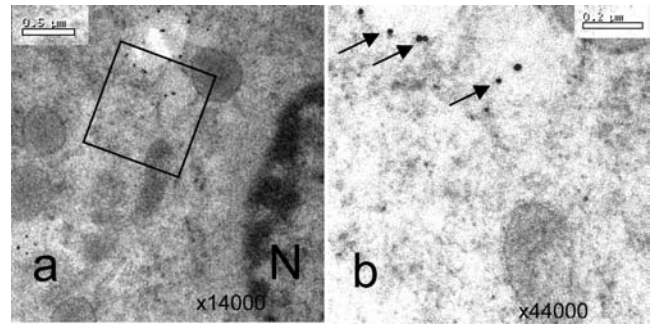

Figure 5. (a) TEM image of a dendritic cell showing the uptake of **1** into the cell (N denotes the nucleus); (b) magnification of the marked area shows **1** indicated by arrows.

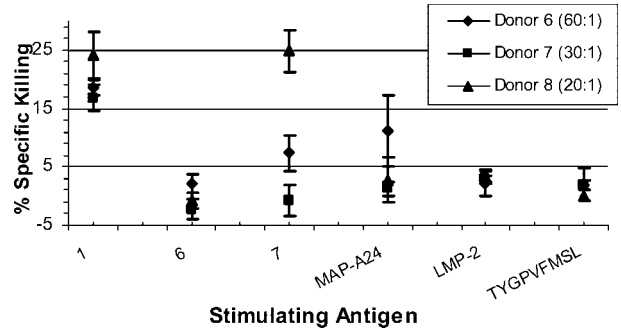

Figure 6. Results of % specific killings by CTLs reactivated from three HLA A11+ donors 6, 7, and 8 with various antigens, in response to autologous PHA blast cells pulsed with LMP-2 (SSCSSCPLSK). HLA mismatched peptide YLSGANLNL as irrelevant peptide. Inset indicates the effector-to-target (E:T) ratio.

cytotoxic CD8+ T-cells were subsequently harvested and tested for their ability to lyse autologous PHA blast cells presenting the EBV LMP-2 epitope SSCSSCPLSK by ^{51}Cr release assay (*41*). PHA blasts pulsed with an irrelevant peptide YLSGANLNL was also included as a nonspecific target for determining antigen-specific CTL killing. The antigen specific CTL killing was determined by the percent cell lysis observed with the LMP-2 target versus the one observed with an irrelevant target.

As depicted in Figure 6, stimulation of the DCs with **1** produced effective CTL responses for all three donor-6, -7, and -8 as manifested by the significant lysis of peptide-specific target cells of 15−25%. In contrast, <5% specific lysis was observed when **6** (the CALNN only-AuNP conjugate) was used as the DC stimulant.

The cytotoxic T-lymphocytes activated with the DCs that had been pulsed with the LMP-2 epitope alone and the HLA-mismatched A24 peptides induced only 2−4% CTL-mediated cell lysis. As noted earlier in the ELIspot assay, MAP **7** could induce some noticeable INFγ response. However, we found that significant CTL-mediated epitope specific cell lysis of 24% was only observed in donor-8; poor lysis results (0−7%) were found for donors-6 and -7.

To conclude, highly immunogenic multivalent EBV antigens can be prepared by conjugation of an EBV LMP-2 epitope onto Au nanoparticles. The AuNP−peptide conjugate is stable in solution and can elicit effective anti-LMP-2 immune response, at least in vitro. AuNP-LMP-2 peptide conjugate, therefore, may play a promising role in the future design of immunotherapy against NPC.

ACKNOWLEDGMENT

We acknowledge the financial support of the Innovation and Technology Fund (ITS/211/01) administered by the Innovation

and Technology Commission (HKSAR), The University of Hong Kong (University Development Fund and UGC matching grant No. 20600433), NSFC/RGC (N_HKU 721/04), RGC-CERG (HKU 7444/03M), and the Areas of Excellence Scheme (AoE/P-10/01) established under the University Grants Council, HKSAR.

Supporting Information Available: Synthesis and characterization of peptides and AuNP, isolation or generation of dendritic cells (DC) and cytotoxic T-lymphocyte (CTL), and results of immunological assays. This material is available free of charge via the Internet at http://pubs.acs.org.

LITERATURE CITED

(1) Young, L. S., and Rickinson, A. B. (2004) Epstein-Barr virus: 40 years on. *Nat. Rev. Cancer 4*, 757–768.

(2) Rickinson, A. B., and Moss, D. J. (1997) Human cytotoxic T lymphocyte responses to Epstein-Barr virus infection. *Annu. Rev. Immunol. 15*, 405–431.

(3) Straathof, K. C. M., Bollard, C. M., Popat, U., Huls, M. H., Lopez, T., Morriss, M. C., Gresik, M. V., Gee, A. P., Russell, H. V., Brenner, M. K., Rooney, C. M., and Heslop, H. E. (2005) Treatment of nasopharyngeal carcinoma with Epstein-Barr virus-specific T lymphocytes. *Blood 105*, 1898–1904.

(4) Rickinson, A. B. and Kieff, E. (1996) Epstein-Barr Virus, Fields Virology (Fields, B. N. and Knipe, D. M.) pp 2397−2446, Lippincott-Raven Publishers, Philadelphia.

(5) Tomkinson, B., Robertson, E., and Kieff, E. (1993) Epstein-Barr virus nuclear proteins EBNA-3A and EBNA-3C are essential for B-lymphocyte growth transformation. *J. Virol. 67*, 2014–2025.

(6) Petti, L., and Kieff, E. (1988) A sixth Epstein-Barr virus nuclear protein (EBNA3B) is expressed in latently infected growth-transformed lymphocytes. *J. Virol. 62*, 2173–2178.

(7) Humme, S., Reisbach, G., Feederle, R., Delecluse, H.-J., Bousset, K., Hammerschmidt, W., and Schepers, A. (2003) The EBV nuclear antigen 1 (EBNA1) enhances B cell immortalization several thousandfold. *Proc. Natl. Acad. Sci. U.S.A. 100*, 10989–10994.

(8) Hart, D. N. J., Jackson, D., and Nestle, F. (2002) Dendritic Cells and Cancer: Prospects for Cancer Vaccination, *Cancer Immune Therapy* (Walden, G. S. A. P., Ed.) pp 179−203, Wiley-VCH, Weinhem, Germany.

(9) Banchereau, J., and Palucka, A. K. (2005) Dendritic Cells as Therapeutic vaccines aganist cancer. *Nat. Rev. Immunology 296*, 296–306.

(10) Celluzzi, C. M., Mayordomo, J. I., Storkus, W. J., Lotze, M. T., and Falo, L. D., Jr. (1996) Peptide-pulsed dendritic cells induce antigen-specific CTL-mediated protective tumor immunity. *J. Exp. Med. 183*, 283–87.

(11) Mayordomo, J. I., Zorina, T., Storkus, W. J., Zitvogel, L., Celluzzi, C., Falo, L. D., Melief, C. J., Ildstad, S. T., Kast, W. M., and Deleo, A. B. (1995) Bone marrow-derived dendritic cells pulsed with synthesis tumor peptides elicit protective and therapeutic antitumour immunity. *Nat. Med. 1*, 1297–1302.

(12) Lin, C.-L., Lo, W.-F., Lee, T.-H., Ren, Y., Hwang, S.-L., Cheng, Y.-F., Chen, C.-L., Chang, Y.-S., Lee, S. P., Rickinson, A. B., and Tam, P. K. H. (2002) Immunization with Epstein-Barr virus (EBV) peptide-pulsed dendritic cells induces functional CD8+ T-cell immunity and may lead to tumor regrression in patients with EBV-positive nasopharyngeal carcinoma. *Cancer Res. 62*, 6952–6958.

(13) Millard, A. L., Ittelet, D., Schooneman, F., and Bernard, J. (2003) Dendritic cell KLH loading requirements for efficient CD4(+) T-cell priming and help to peptide-specific cytotoxic T-cell response, in view of potential use in cancer vaccines. *Vaccine 21*, 869–876.

(14) Shimizu, K., Thomas, E. K., Giedlin, M., and Mule, J. J. (2001) Enhancement of tumor lysate- and peptide-pulsed dendritic cell-based vaccines by the addition of foreign helper protein. *Cancer Res. 61*, 2618–2624.

(15) Schnurr, M., Galambos, P., Scholz, C., Then, F., Dauer, M., Endres, S., and Eigler, A. (2001) Tumor cell lysate-pulsed human dendritic cells induce a T-cell response against pancreatic carcinoma cells: an in vitro model for the assessment of tumor vaccines. *Cancer Res. 61*, 6445–6450.

(16) Na, I. K., Keilholz, U., Letsch, A., Bauer, S., Asemissen, A. M., Nagorsen, D., Thiel, E., and Scheibenbogen, C. (2007) Addition of GM-CSF to a peptide/KLH vaccine results in increased frequencies of CXCR3-expressing KLH-specific T cells. *Cancer Immunol. Immunother. 56*, 391–396.

(17) Guan, H. H., Budzynski, W., Koganty, R. R., Krantz, M. J., Reddish, M. A., Rogers, J. A., Longenecker, B. M., and Samuel, J. (1998) Liposomal formulations of synthetic MUC1 peptides: effects of encapsulation versus surface display of peptides on immune responses. *Bioconjugate Chem. 9*, 451–458.

(18) Nakano, Y., Mori, M., Nishinohara, S., Takita, Y., Naito, S., Kato, H., Taneichi, M., Komuro, K., and Uchida, T. (2001) Surface-linked liposomal antigen induces IgE-selective unresponsiveness regardless of the lipid components of liposomes. *Bioconjugate Chem. 12*, 391–395.

(19) Tanaka, Y., Kasai, M., Taneichi, M., Naito, S., Kato, H., Mori, M., Nishida, M., Maekawa, N., Yamamura, H., Komuro, K., and Uchida, T. (2004) Liposomes with differential lipid components exert differential adjuvanticity in antigen-liposome conjugates via differential recognition by macrophages. *Bioconjugate Chem. 15*, 35–40.

(20) McCormick, A. A., Corbo, T. A., Wykoff-Clary, S., Palmer, K. E., and Pogue, G. P. (2006) Chemical conjugate TMV-peptide bivalent fusion vaccines improve cellular immunity and tumor protection. *Bioconjugate Chem. 17*, 1330–1338.

(21) Defoort, J.-P., Nardelli, B., Huang, W., Ho, D. D., and Tam, J. P. (1992) Macromolecular assemblage in the design of a synthetic AIDS vaccines. *Proc. Natl. Acad. Sci. U.S.A. 89*, 3879–3883.

(22) Olive, C., Toth, I., and Jackson, D. (2001) Technological advances in antigen delivery and synthetic peptide vaccine development strategies. *Mini Rev. Med. Chem. 1*, 429–438.

(23) Chiellini, F., Piras, A. M., Errico, C., and Chiellini, E. (2008) Micro/nanostructured polymeric systems for biomedical and pharmaceutical applications. *Nanomedicine 3*, 367–393.

(24) Murakami, T., and Tsuchida, K. (2008) Recent advances in inorganic nanoparticle-based drug delivery systems. *Mini Rev. Med. Chem. 8*, 175–83.

(25) Thassu, D., Deleers, M., and Pathak, Y. (2007) *Nanoparticulate Drug Delivery Systems* (Thassu, D., Deleers, M., and Pathak, Y., Eds.) pp 1−32, Informa Healthcare, New York.

(26) Pridgen, E. M., Langer, R., and Farokhzad, O. C. (2007) Biodegradable, polymeric nanoparticle delivery systems for cancer therapy. *Nanomedicine 2*, 669–680.

(27) Amrite, A. C., and Kompella, U. B. (2006) *Nanoparticle Technology for Drug Delivery* (Gupta, R. P., and Kompella, U. B., Eds.) pp 319−360, Taylor & Francis, New York.

(28) Hong, S., Ackerman, A. L., Cody, V., Giodini, A., Hinson, E. R., Cresswell, P., Edelson, R. L., Saltzman, W. M., and Hanlon, D. J. (2006) Enhanced and prolonged cross-presentation following endosomal escape of exogenous antigens encapsulated in biodegradable nanoparticles. *Immunology 117*, 78–88.

(29) Bradley, J. S., and Schmid, G. (2004) Noble Metal Nanoparticle, *Nanoparticles: From Theory to Application* (Schmid, G., Ed.) pp 186−199, Wiley-VCH, Weinheim, Germany.

(30) Daniel, M. C., and Astruc, D. (2004) Gold nanoparticles: assembly, supramolecular chemistry, quantum-size-related properties, and applications toward biology, catalysis, and nanotechnology. *Chem. Rev. 104*, 293–346.

(31) de la Fuente, J. M., Berry, C. C., Riehle, M. O., and Curtis, A. S. G. (2006) Nanoparticle Targeting at Cells. *Langmuir 22*, 3286–3293.

(32) Yguerabide, J., and Yguerabide, E. E. (1998) Light-scattering submicroscopic particles as highly fluorescent analogs and their use as tracer labels in clinical and biological applications: I. Theory. *Anal. Biochem. 262*, 137–156.

(33) Yguerabide, J., and Yguerabide, E. E. (1998) Light-scattering submicroscopic particles as highly fluorescent analogs and their use as tracer labels in clinical and biological applications: II. Experimental characterization. *Anal. Biochem. 262*, 157–176.

(34) Thaxton, C. S., and Mirkin, C. A. (2004) DNA-Gold-Nanoparticle Conjugates, *Nanobiotechnology: Concepts, Applications and Perspectives* (Niemeyer, C. M., and Mirkin, C. A., Eds.) pp 288−207, Wiley-VCH, Weinheim, Germany.

(35) Schultz, S., Smith, D. R., Mock, J. J., and Schultz, D. A. (2000) Single-target molecule detection with nonbleaching multicolor optical immunolabels. *Proc. Natl. Acad. Sci. U.S.A. 97*, 996–1001.

(36) Taton, T. A., Mirkin, C. A., and Letsinger, R. L. (2000) Scanometric DNA array detection with nanoparticle probes. *Science 289*, 1757–1760.

(37) Chan, W. C., and White, P. D. (2000) Basic Procedures, *Fmoc Solid Phase Peptide Synthesis: A Practical Appraoch* (Chan, W. C., and White, P. D. , Eds.) pp 41−76, Oxford University Press, New York.

(38) Frens, G. (1973) Controlled nucleation for the regulation of the particle size in monodisperse gold suspensions. *Nat. Phys. Sci. 241*, 20–22.

(39) Plebanski, M. (2000) Preparation of Lymphocytes and Identification of Lymphocytes Subpopulations, *Lymphocytes: A Practical Approach* (Rowland-Jones, S. L., and McMichael, A. J., Eds.) pp10−12, Oxford University Press, New York.

(40) Gilliet, M. F., and Nestle, F. O. (2001) Generation of Blood-Derived Human Dendritic Cells for Antitumor Immunotherapy. *Sendritic Clee Protocols* (Robinson, S. P., and Stagg, A. J., Eds.) pp 297−306, Humana Press, Totowa, NJ.

(41) Schlager, S. I., and Adams, A. C. (1983) Uses of dyes and radioisotopic markers in cytotoxicity tests, in. *Methods Enzymol. 93*, 233–245.

(42) Geijtenbeek, T. B. H., Torensma, R., van Vliet, S. J., van Duijnhoven, G. C. F., Adema, G. J., van Kooyk, Y., and Figdor, C. G. (2000) Identification of DC-SIGN, a novel dendritic cell-specific ICAM-3 receptor that supports primary immune responses. *Cell 100*, 575–585.

(43) Redchenko, I. V., and Rickinson, A. B. (1999) Accessing Epstein-Barr virus-specific T-cell memory with peptide-loaded dendritic cells. *J. Virol. 73*, 334–342.

(44) Imanishi, T., Alaza, T., and Kimura, A. (1992) W15.1 Reference Tables, *HLA-1991* (Tsuji, K. , Aizawa, M., and Sasazuki, T., Eds.) pp 1066, Oxford University Press, Oxford.

(45) Lee, T. D., Zhao, T. M., Mickey, R., Sun, Y. P., Lee, G., Song, C. X., Cheng, D. Z., Zhou, S., Ding, S. Q., and Cheng, D. X. (1988) The polymorphism of HLA antigens in the Chinese. *Tissue Antigens 32*, 188–208.

(46) Chan, W. K., Ho, C. M., Wong, M. K., and Che, C. M. (2006) Oxidative amide synthesis and N-terminal α-amino group ligation of peptides in aqueous medium. *J. Am. Chem. Soc. 128*, 14796–14797.

(47) Levy, R., Thanh, N. T. K., Doty, R. C., Hussain, I., Nichols, R. J., Schiffrin, D. J., Brust, M., and Fernig, D. G. (2004) Rational and combinatorial design of peptide capping ligands for gold nanoparticles. *J. Am. Chem. Soc. 126*, 10076–10084.

(48) Gamero, A. M., Hodge, D. L., Reynolds, D. M., Rodriguez-Galan, M. C., Mohamadzadeh, M., and Young, H. A. (2006) The Interferon-[Gamma]: Gene and Protein Structure, Transcription Regulation, and Actions, *The Interferons: Characterizatoin and Application* (Meager, A., Ed.) pp 85−112, Wiley-VCH, Weinheim, Germany.

(49) Khanna, R., and Burrows, S. R. (2000) Role of cytotoxic T lymphocytes in Epstein-Barr virus-associated diseases. *Ann. Rev. Microbiol. 54*, 19–48.

BC800167Q

Supporting Information

Conjugation of Latent Membrane Protein (LMP)-2 Epitope to Gold Nanoparticles as Highly Immunogenic Multiple Antigenic Peptides for Induction of Epstein-Barr Virus Specific Cytotoxic T-Lymphocyte Responses *in vitro*

Wai-Hung Cheung, Vera Sau-Fong Chan, Heung-Wing Pang, Man-Kin Wong, Zhi-Hong Guo, Paul Kwong-Hang Tam, Chi-Ming Che, Chen-Lung Lin and Wing-Yiu Yu

Table of Content	Page
Table S1. Mass spectral data of the synthetic peptides	S2
Figure S1. A TEM image of citrate stabilized AuNP with 15 – 24 nm in diameter.	S3
Table S2 shows the formulation of various LMP-2' on gold nanoparticles conjugate	S4
Figure S2. ELIspot results of HLA A11+ restricted PBMCs from three healthy donors stimulated with various antigens	S5
Figure S3. Flow cytometry analysis of the HLA typing of donor 6, 7& 8	S6
Table S3. The % specific killing of CTLs stimulated from various antigens	S7

Peptides	Sequence	Overall Isolated % Yield	Experimental molecular mass value (m/z)[a]	Calculated molecular mass
LMP-2	SSCSSCPLSK	11	998.6709 (FAB)	997.4209
LMP-2'	CSSCSSCPLSK	11	1101.3355 (MALDI)	1100.4301
HLA mismatched A24 peptide	TYGPVFMSL	16	1014.8042 (FAB)	1013.4892
CA24	CTYGPVFMSL	18	1117.5565 (MALDI)	1116.4984
irrelevant peptide [(1)]	YLSGANLNL	14	964.3335 (MALDI)	963.5025
Capping peptide	CALNN	14	534.2601 (MALDI)	533.4268
Antigen **7**	$(SSCSSCPLSK)_4K_2KC_{acm}\beta A$	12	1097.9 [M^{4+}] (ESI)	4390.9738
Antigen **8**	$(SSCSSCPLSK)_8K_4K_2KC_{acm}\beta A$	10	1124.3 [M^{8+}]	8994.0571

[a] All experimental molecular mass values were reported as M^+ ion except otherwise noted.

Table S1. Mass spectral data of the synthetic peptides

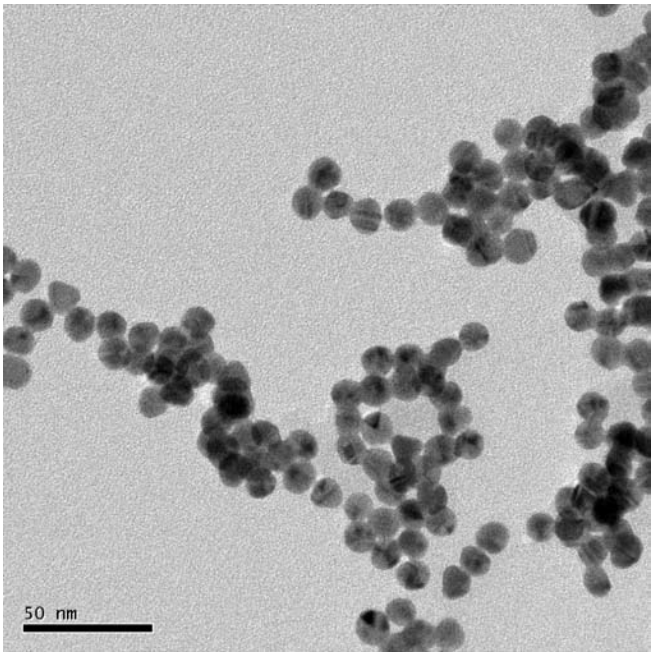

Figure S1. A TEM image of citrate stabilized AuNP with 15 – 24 nm in diameter.

Conjugate	Volume (mL) taken from the LMP-2′ stock solution	Volume (mL) taken from the CALNN stock solution	Volume (mL) taken from the AuNP solution	Mole ratio	
				LMP-2	CALNN
1	0.1	0.9	9.0	1	9
2	0.2	0.8	9.0	2	8
3	0.3	0.7	9.0	3	7
4	0.7	0.3	9.0	7	3
5	1.0	0.0	9.0	10	0
6	0.0	1.0	9.0	0	10

Concentrations of the LMP2′ and CALNN stock solutions = 2 mM

Table S2. shows the formulation of various LMP-2' on gold nanoparticles conjugates

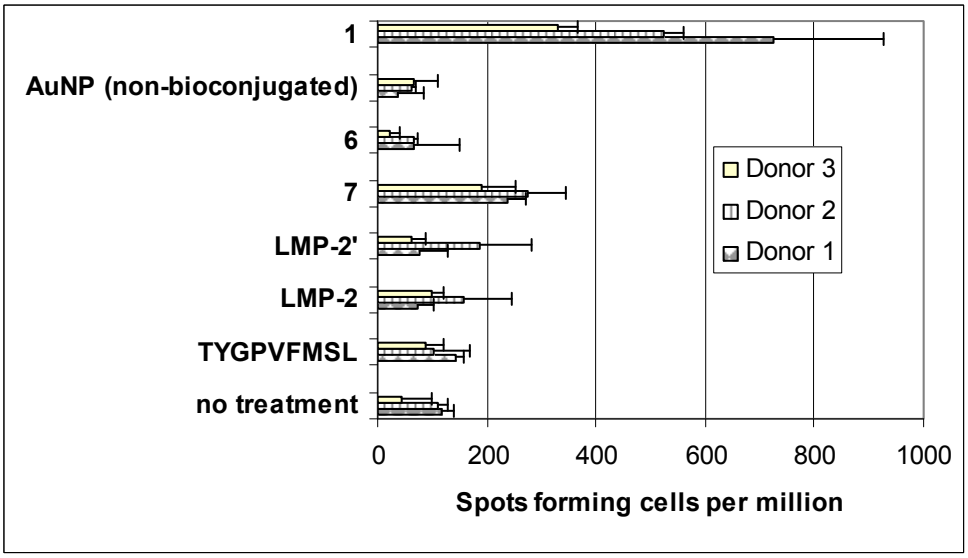

Figure S2. ELIspot results from three healthy HLA A11+ donors 1, 2 and 3 upon stimulation of their PBMCs with various peptide antigens

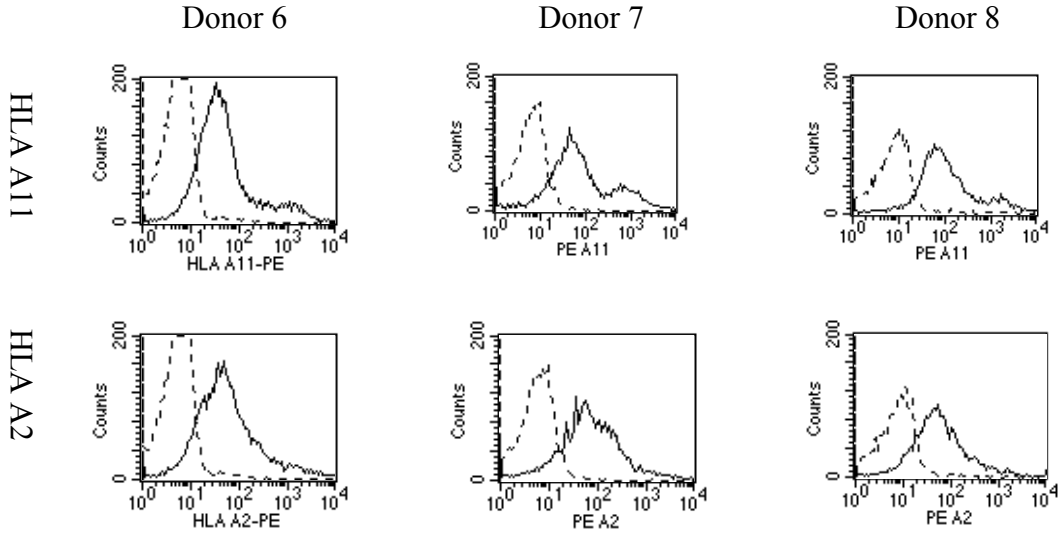

The histographs show immunostaining results for HLA- A11 and A2 with respective antibodies (solid lines); the results with isotype control are shown in dash lines.

Figure S3. Flow cytometry analysis of the HLA typing of donor 6, 7& 8

% Specific Killing (E:T ratio)	Antigen **1** Stimulated	Antigen **7** stimulated	LMP-2 stimulated
Donor 6 HLA A11+/A2+	**18 (60:1)**	7.3 (60:1)	1.5 (60:1)
Donor 7 HLA A11+/A2+	**16.9 (30:1)**	-0.7 (30:1)	3.3 (30:1)
Donor 8 HLA A11+/A2+	**24.0 (20:1)**	**24.8 (20:1)**	4.1 (20:1)

Table S3. The % specific killing of CTLs stimulated from various antigens

Literature Cited

(1) Liu, K.-J., Wang, C.-C., Chen, L.-T., Cheng, A.-L., Lin, D.-T., Wu, Y.-C., Yu, W.-L., Hung, Y.-M., Yang, H.-Y., Juang, S.-H., and Whang-Peng, J. (2004) Generation of Carcinoembryonic Antigen (CEA)-Specific T-Cell Responses in HLA-A*0201 and HLA-A*2402 Late-Stage Colorectal Cancer Patients after Vaccination with Dendritic Cells Loaded with CEA Peptides. *Clin. Cancer Res.* *10*, 2645-2651.

Targeting the Urokinase Plasminogen Activator Receptor with Synthetic Self-Assembly Nanoparticles

Ming Wang,[†] Dennis W. P. M. Löwik,[‡] Andrew D. Miller,[†,§] and Maya Thanou*[,†]

Imperial College Genetic Therapies Centre, Department of Chemistry, Flowers Building, Armstrong Road, Imperial College London, London SW7 2AZ, United Kingdom, Department of Organic Chemistry, Institute for Molecules and Materials, Radboud University Nijmegen, Toernooiveld 1- Huygens Building 03.016, 6525 ED Nijmegen, The Netherlands, and ImuThes Ltd, Flowers Building, Armstrong Road, London SW7 2AZ, United Kingdom. Received May 13, 2008; Revised Manuscript Received November 18, 2008

Targeting specific receptors is attracting growing interest in the fields of drug delivery and gene therapy for cancer treatment. The urokinase plasminogen activator receptor (uPAR) is overexpressed on many tumors, particularly that of prostate and breast cancers. The aim of this study is to design, prepare, and characterize a synthetic self-assembled nanoparticle that presents targeting ligands at a certain conformation and molar ratio on the surface of the particles. Here, we describe the synthesis of a novel uPAR targeting ligand consisting of an 11-amino-acid sequence named U11 peptide modified with an alkyl chain to form an U11 peptide−lipid amphiphile. This peptide−lipid is inserted into the outer layer of a parent stealth liposome by post-modification to derive a U11 peptide-targeted nanoparticle. We demonstrate that the peptide moieties become separated into more singular conformations as they are inserted into a liposome membrane, rendering them to be sufficiently biologically active to observe specific receptor-mediated endocytosis (RME) and delivery of plasmid DNA to uPAR positive cells (DU145 cells). The U11 peptide targeted nanoparticle transfection of DU145 cells is essentially 10-fold higher compared to transfection achieved by nanoparticles having a scrambled peptide sequence on their surface. U11 peptide targeted nanoparticles also proved to be uPAR-specific, as they did not improve transfection levels on the uPAR-negative cell line, HEK293.

INTRODUCTION

The urokinase plasminogen activator receptor (uPAR) is overexpressed on a variety of cancer cells, such as those of the prostate and the breast (*1*−*3*). As it is the receptor's natural ligand, the urokinase plasminogen activator (uPA) interacts with the cognate receptor, uPAR, to form a uPAR-uPA conjugate that enters cells by clathrin-coated, receptor-mediated endocytosis (*4*). The uPAR-uPA conjugate is subsequently involved in stimulating various cellular activities such as extracellular matrix invasion (*5*, *6*), plasminogen activation (*7*), cell adhesion, and metastasis (*8*, *9*). The uPA ligand is known to be a composite structure of three independent regions: an amino-terminal growth factor domain (termed ATF or GFD; growth factor domain), a kringle domain, and a carboxy-terminal domain, the region in which uPA exhibits catalytic properties (*10*, *11*). Crystallographic studies of the uPAR-uPA conjugate have revealed that the binding region of uPA for uPAR is localized at the tip of a β-hairpin loop within the GFD (*12*), representing amino acid residues 12−32 (*10*, *13*). Within this tip are two looped structures, one comprising seven amino acid residues (U7) and one of eleven amino acid residues (U11) (Table 1). The second loop, U11, appears to be the primary uPAR binding motif within the uPA binding tip (*14*, *15*). Previous studies from our laboratory have determined that the interaction of U11 peptide with uPAR is characterized by an equilibrium dissociation constant, K_d, of 1.3−1.4 μM (*16*).

Table 1. Amino Acid Sequences of Binding Epitopes within uPA with Specificity for uPAR[a]

	peptide sequence
residue 11−32 in EGF domain	CDCLNGGTC-VSNKYFSNIHWCNC
U7	DCLNGGT
U11	VSNKYFSNIHW
scrambled	ISKSVYNFWNH

[a] U7 and U11 indicate specific fragments within the binding region that exhibit high receptor affinity as synthetic peptides (*15*).

Considering the binding affinity along with and the RME properties of the uPAR-uPA complex, our expectation has been that the uPAR-uPA receptor−ligand system could hold potential for the targeting of synthetic nanoparticles, bearing therapeutic nucleic acids to either prostate or breast cancer.

Previously, uPAR-targeting has been used in gene delivery experiments making use of whole GDF fragments (*17*). In comparison with the use of antibodies, proteins, or protein fragments as receptor-targeting moieties, peptide-based ligands hold several advantages for receptor-mediated targeting such as increased organizational control plus the opportunity to exclude undesirable natural biological activities (*18*). A number of peptide-based ligands for targeted delivery are already described in the literature, the most prominent examples being the use of $\alpha_v\beta_{3/5}$ integrin receptor-targeting RGD family peptides (*19*, *20*). Other examples include $\alpha_9\beta_1$ integrin receptor-targeting peptide sequences (*21*) and the ApoE peptide that targets the LDL receptor (*22*). uPAR-specific peptides have also been used for viral vector retargeting and site-specific molecular imaging (*23*, *24*).

Here, we describe the synthesis of a simple U11 peptide−lipid amphiphile and the formulation of that peptide−lipid into nanoparticles using our laboratory's nomenclature and coding of each functional component. The "ABCD nanoparticle"

* To whom correspondence should be addressed. E-mail: maya.thanou@imperial.ac.uk; ming.wang05@imperial.ac.uk. Phone: +44 207 5943156. Fax: +44 207 594 5803.

[†] Imperial College London.

[‡] Radboud University Nijmegen.

[§] ImuThes Ltd.

10.1021/bc8001908 CCC: $40.75 © 2009 American Chemical Society
Published on Web 12/19/2008

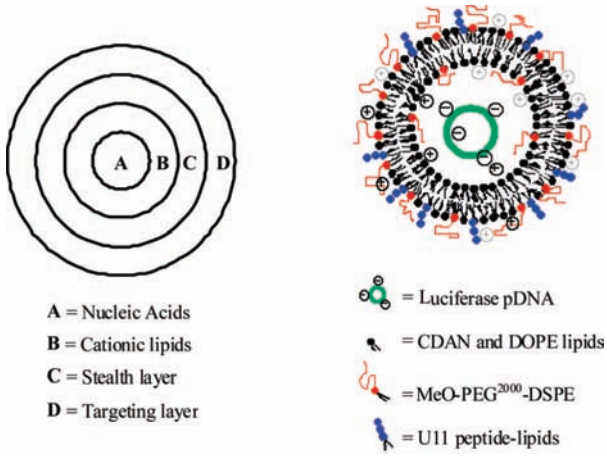

Figure 1. Structure of the synthetic self-assembly ABCD-type nanoparticle paradigm for nonviral vector mediated nucleic acid delivery. (Left) ABCD nanoparticles are assembled from tool kits of purpose-designed chemical components. They comprise the following concentric layers: A, nucleic acids (siRNA, miRNA, pDNA); B, lipid envelope layer; C, stealth/biocompatibility polymer layer; and D, biological recognition ligand layer. (Right) Representation of the actual pDNA-ABCD nanoparticle system formulated as part of the reported investigations here.

paradigm has been used to define multicomponent nanoparticles designed to substantially mediate nucleic acid delivery (Figure 1) (*25*). ABCD nanoparticles comprise a therapeutic nucleic acid such as pDNA (A-component) condensed into AB core particles by means of cationic and fusogenic lipids (B-component), which are then coated by post-modification or postcoupling procedures with variable amounts of a stealth polymer (such as poly-(ethylene glycol), lipid−PEG amphiphiles) (C-component) to provide stability in biological fluids. Ligands (D-component) may be similarly introduced sequentially for receptor targeting. Here, we prepare a number of nanoparticles based on ABCD systems, to identify and promote the targeting potential of such nanoparticles when decorated with U11 peptide−lipid amphiphile. The molar ratio of peptide−lipid in the nanoparticle is investigated with respect to their size and transfection efficiency. Nanoparticles are tested on uPAR overexpressing DU145 prostate cancer cells and on negative uPAR HEK293 (embryonic kidney) cell line as control.

MATERIAL AND METHODS

Chemical. 1,2-Dioleoyl-3-*sn*-phosphatidylethanolamine (DOPE), 1,2-dioleoyl-*sn*-glycero-3-phosphoethanolamine-*N*-(Lissamine Rhodamine B sulfonyl) (DOPE-Rho) and *N*-[methoxy(poly-(ethylene glycol)-2000)]-1,2-distearoyl-*sn*-glycero-3-phosphoethanolamine (MeO-PEG^{2000}-DSPE), and *N*-cholesteryloxycarbonyl-3,7-diazanonane-1,9-diamine (CDAN) were purchased from Avanti Polar Lipids (Alabaster, AL). 1,2-dioleoyl-*sn*-glycero-3-phosphocholine (DOPC), and cholesterol lipids were obtained from Sigma and Aldrich (UK). 4-(4-Formyl-3-methoxyphenoxy)butyryl AM (FMPB AM) resin, *O*-(benzotriazol-1-yl)-*N*,*N*,*N*',*N*'-tetramethyluronium (HBTU), hydroxybenzotriazole (HOBt), and all *N*-protected fluorenyl methyloxycarbonyl (Fmoc)-amino acids were purchased from Novabiochem (Nottingham, UK). *N*,*N*-Diisopropylethylamine (DIPEA), trifluoroacetic acid (TFA), triisopropylsilane (TIPS), and piperidine were obtained from Sigma-Aldrich (Poole, UK). Dimethylformamide (DMF) and acetonitrile were purchased from Rathburn (Walker-Burn, Scotland). Centrifugal filter device was obtained from Millipore UK.

Biological. DU145 and HEK293 cell lines were obtained from the ECACC (European Collection of Cell Culture, Wiltshire, UK). Dulbecco's Modified Eagle Media (DMEM), Optimem, fetal calf serum (FCS), penicillin and streptomycin, phosphate-buffered saline (PBS) and trypsin−EDTA were purchased from Gibco (Invitrogen, Netherlands). Luciferase reporter gene assay kit and reporter lysis buffer 5× were obtained from Promega (Southampton, UK), and BCA total protein content assay was purchased from Pierce (Rockford, USA). Urokinase plasminogen activator (uPA) was obtained from American Diagnostica (CT, USA). All plasticware, including falcon tubes and tissue culture flasks, was obtained from Falcon (Becton Dickinson, UK). 4′,6′-Diamidino-2-phenyindole, dilactate (DAPI) nuclear staining was purchased from Sigma-Aldrich (Poole, UK).

Synthesis of U11 Peptide−Lipids. FMPB AM resin (250 mg, 0.74 mmol/g loading) was combined with hexadecylamine (447 mg, 1.85 mmol, 10 equiv) and dissolved in DMF (50 mL). Acetic acid (105 μL, 1.85 mmol, 10 equiv) was then added to the flask followed by $NaCNBH_3$ (116 mg, 1.85 mmol, 10 equiv), and the reaction was stirred at 80 °C for 3 h under reflux. The resin was then transferred into a filtered reaction vessel and washed with CH_2Cl_2, MeOH, CH_2Cl_2, DMF, and CH_2Cl_2 three times in the respective order. Using a few beads from the reaction, the presence of a secondary amine was confirmed by the chloranil test (*26*). The U11 peptide sequence was extended by standard Fmoc-coupling strategy. All Fmoc-amino acids were activated with HOBt and HBTU (3 equiv) for 45 min per coupling and the Fmoc group removed at each step using 20% piperidine in DMF. The terminal amine was capped with Ac_2O and DIPEA (3 equiv) for 45 min before cleavage off the resin using 10 mL of 95:2.5:2.5 TFA/TIS/H_2O cocktail for 5 h. The solution was filtered, and the TFA mixture was precipitated in cold ether. The precipitate was collected by filtration, followed by resolvation in H_2O, and lyophilized overnight. Purification of peptide−lipids was carried out on a Gilson semipreparative HPLC system at a flow rate of 10 mL/min, using a Vydac C_4 protein column, with a gradient of 10% to 90% acetonitrile (20 min). ES mass spectroscopy of purified peptide−lipids was $[M + H]^+$, 1774.

Formulations of Nanoparticles. The following lipids CDAN, DOPE, and MeO-PEG^{2000}-DSPE were dissolved in chloroform at 5 mg mL^{-1}, 5 mg mL^{-1}, and 1 mg mL^{-1}, respectively. Appropriate aliquots were combined in a round-bottom flask (5 mL) and the solvent evaporated to dryness in vacuo to form a thin lipid film on the walls of the flask. For nonstealth, core AB nanoparticles, CDAN and DOPE lipids were combined in a 1:1 (m/m) ratio. For PEGylated nanoparticles (ABC), CDAN, DOPE, and MeO-PEG^{2000}-DSPE lipids were combined in a $(50 - x/50 - x/2x$ m/m/m ratio where x was between 0.25 and 2.5, as required). The flask was further purged with argon gas to remove final traces of organic solvent, then hydrated with double-distilled H_2O (ddH_2O) to give a lipid dispersion, which was then subjected to sonication for 30 min at 40 °C (final total lipid concentration, 1 mg mL^{-1}). After sonication, resulting cationic liposome solutions were further diluted to 0.5 mg mL^{-1} and pDNA (0.1 mg mL^{-1} in ddH_2O) was then added slowly by pipet under heavy vortex mixing conditions (final lipid/pDNA ratio, 12:1 w/w). To prepare targeted nanoparticles (ABCD), U11 peptide−lipid (or scrambled peptide−lipid) was dissolved (1 mg mL^{-1} in 20% EtOH in H_2O) and an appropriate aliquot (containing 1−5 mol % of peptide−lipid as required) was added to formulations of PEGylated (ABC) or non-PEGylated (AB) nanoparticle suspension (with different mol % of MeO-PEG^{2000}-DSPE), and the mixture was then incubated for 1 h at 37 °C. Excess peptide−lipids left uninserted into nanoparticles were removed by a centrifugal filtration (MWCO = 30 kDa) and centrifuged at 8000 *g* for 6 min before the redilution of the filtrate (containing nanoparticles) with ddH_2O, and the supernatant was analyzed. The amount of uninserted peptide−lipid

in the supernatant was determined by measuring the intrinsic amino acid fluorescence (excitation wavelength: I_{ex} 298 nm; emission maximum: I_{max} 349nm) and extrapolated against a concentration-dependent calibration curve. Components of all purified nanoparticles were characterized by the following methods: Analytical HPLC (0% to 100% acetonitrile in 20 mins, flow rate 1 mL/min) was used to determine the amount of CDAN lipids within the purified formulation, the Stewart assay for the determination of the amount of DOPE lipids (*27*) and UV−visible spectroscopy for the analysis of encapsulated DNA, using an $A^{0.1}{}_{260}$ value of 30.

Growth and Maintenance of Cells. DU145 and HEK293 cells were maintained in DMEM supplemented with 10% FCS (v/v) and 1% penicillin and streptomycin (DMEM +/+) in T-25 tissue culture flasks. On confluency, media was removed by aspiration and washed with 5 mL PBS. Cells were then detached from the flask by addition of 1.5 mL of trypsin−EDTA and incubated for 10 min at 37 °C and 10% CO_2. After detachment, cells were diluted with 5 mL DMEM +/+ and centrifuged to removed trypsin solution. Cells were resuspended in 5 mL DMEM +/+, diluted 1:10 with more DMEM +/+, of which 5 mL of diluted cells were placed in a new T-25 culture flask. DU145 cells were used up to a passage number of 30, after which they were discarded and a new batch defrosted.

In Vitro Transfections. uPAR-overexpressing human prostate cancer cell line (DU145) was cultured with DMEM +/+ at 37 °C and 5% CO_2. Cells were seeded at 4×10^4 cells/well in 24 well plates (0.5 mL volume per well) and incubated for 80 h (70% confluency) before experiments. For transfections, growth media was removed from wells by aspiration and replaced with 0.5 mL of Optimem-containing delivery systems that allowed 1 μg pDNA per well. Transfections were carried out for 3 h before transfection media was removed by aspiration and replaced with DMEM +/+ for further cell growth. After further incubation at 37 °C for 48 h, cells were lysed with 80 μL of 1× reporter lysis buffer per well. One cycle of freeze−thaw was carried out before cells were scraped from wells and centrifuged at 8000 *g* for 2 min to separate cellular debris. Supernatants were analyzed for luciferase transgene expression and normalized with the BCA total protein content kit.

Characterization of Nanoparticles. Nanoparticle sizes were measured by photon light scattering on a Coulter Delta N4 PCS plus 440SX photon correlation spectrometer (PCS). After assembly, all nanoparticles were diluted to 0.1 mg mL^{-1} in ddH_2O, a concentration allowing the count rate to stabilize between 4 and 6×10^4 counts per second. The calculated unimodal distribution was used as the determinant for average diameter size. For aggregation studies, the nanoparticles were diluted in the same volume of Optimem used in preparation of transfection cocktail. The diluted nanoparticles were then incubated at 37 °C and average particle diameter analyzed at the time points of 0, 30, 60, 90, and 120 min post-formulation. For aggregation studies in serum, nanoparticle solutions were diluted in fetal calf serum instead of Optimem. The diameter errors were taken as the standard deviations calculated by dynamic light scattering.

Secondary Structure Determination. Circular dichroism experiments were conducted using the Jasco J-715 spectropolarimeter equipped with Jasco PCT-348WI thermostat device. Targeted nanoparticles were prepared as before, by incubation of either 1 or 5 mol % U11 peptide−lipids with naked nanoparticles formulated with 0.5 mol % of MeO-PEG^{2000}-DSPE, at a lipid concentration of 1 mg/mL. A 0.1 mm path length cell was used to record spectra, values of ΔA were collected from 250 to 190 nm at an elevated temperature of 37 °C. A scan rate of 10 nm/min and a step resolution of 0.2 nm were used throughout.

Scheme 1. Structures of Main Lipids Used in Formulation: Cationic Lipid CDAN, Fusogenic Lipid DOPE, and Targeting Lipid U11 Peptide−Lipid

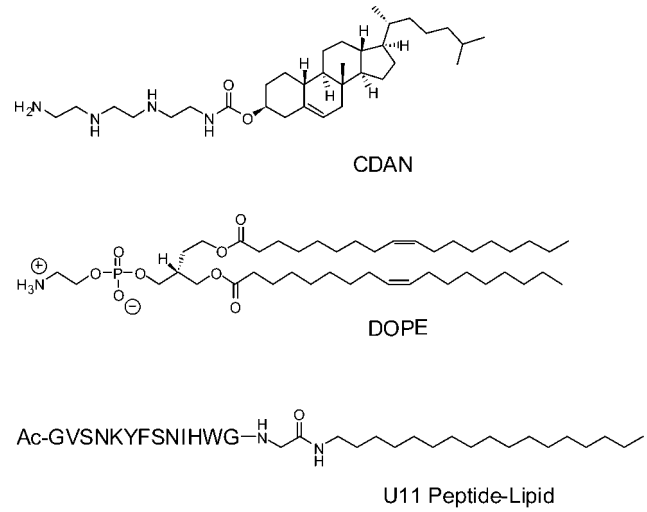

Fluorescence Imaging. Six-well plates were loaded with presterilized circular coverslips (thickness 1 mm) and cells seeded on top at a density of 6×10^4 cells/well. After incubation at 37 °C and 5% CO_2 for 80 h (70% confluency), growth media was removed from wells and replaced with an aliquot of nanoparticles (50 μg) in Optimem. Nanoparticles were incubated with cells for 1 or 2 h, before removal by aspiration; thereafter, coverslips were washed twice with PBS. Coverslips were then treated with paraformaldehyde per well (1 mL, 4%v/v) and incubated at 37 °C for 20 min, followed by another PBS wash (×2) and further incubation with 1 mL glycine solution (20 mg mL^{-1}). Cells were stained with 1 mL DAPI solution (100 nM) for 5 min at 37 °C, and after one last PBS wash, mounted face-down onto a microscopy slide with 1 drop of PBS/glycerol (1:1, v/v). Images were taken on an Olympus 251 scope.

Competitive Binding of Targeted Nanoparticles in the Presence of uPA. DU145 cells were seeded in 6-well plates and incubated for 80 h before 70% confluency was achieved. Cells were washed twice with cold PBS followed by incubation at 4 °C with glycine/NaCl (0.05 M/0.1 M, pH 3) for 5 min. After incubation, HEPES/NaCl (0.5 M/0.1 M, pH 7.5) was added to the wells before removal of all solution and washing with PBS. Optimem-containing 0 or 40 nM uPA was applied to the cells and incubated at 4 °C for 30 min. Rhodamine-labeled pDNA-encapsulated nanoparticles (ABCD; with U11- or scramble peptide) were then spiked into the cell medium to form concentrations of 25 μg lipids/well. The cells were then incubated for a further 30 min at 4 °C before removal of media and washing with PBS twice. After final washing, 1 mL of PBS (2% FCS) was added to each well, and the cells were detached from the wells. The cell-associated fluorescence per well was then analyzed by flow cytometry using a Becton Dickinson FACS 4 Color Caliber.

RESULTS

Synthesis of U11 and Control Peptide−Lipids. After synthesis on solid phase, the crude U11 peptide−lipid was then purified to homogeneity (>95%) by high-performance liquid chromatography (HPLC). The identity of the U11 peptide−lipid (Scheme 2, Table 1) was confirmed by electrospray mass spectrometry ($[M + H]^+$, 1774.0). The scrambled (control, Table 1) peptide-lipid was prepared in an equivalent manner, retaining the U11 amino acid residue composition, but with a reordered sequence.

Scheme 2. - Synthesis of U11 Peptide−Lipid on Solid Phase[a]

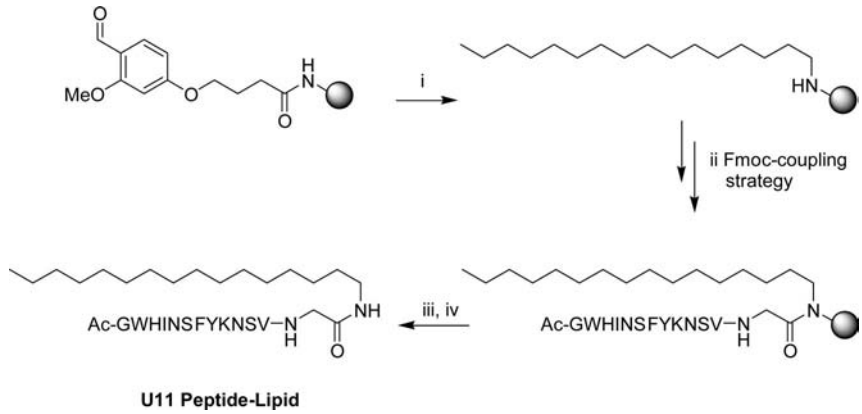

[a] (i) $C_{16}H_{33}-NH_2$, HOAc, $NaCNBH_3$, 80 °C, 3 h. (ii) (a) Extension of peptide chain using standard Fmoc-protocol with 3 equiv Fmoc-amino acid, HBTU (3 equiv), HOBt (3 equiv) in DMF, 1 h RT per coupling. (iii) Ac_2O, DiPEA in DMF, 1 h. (iv) 95/2.5/2.5 TFA/TIS/H_2O, 5 h RT.

Formulation of Nanoparticles. Nontargeted and targeted nanoparticles were prepared using the pDNA construct pEGFP-Luc (SV40 promoter) expressing the luciferase gene (*luc*). Cationic lipid (CDAN), neutral fusogenic lipid (DOPE), MeO-PEG^{2000}-DSPE, and synthetic U11 peptide−lipid (or control peptide−lipid) were added.

The CDAN/DOPE (1:1, m/m) cationic liposomes (Scheme 1) were chosen for their capacity to mediate high levels of transfections without cellular toxicity (*28*). Targeted, non-PEGylated nanoparticles were prepared by the method of post-modification, involving the incubation (at 37 °C, 1 h) of standard nanoparticles with an appropriate mol % (typically 1 or 5 mol %) of synthetic U11 peptide−lipid (or scrambled peptide−lipid as required). This procedure allowed the insertion of the lipid moieties of peptide−lipids into the outer leaflet membrane of the AB core nanoparticles in order to create targeted nanoparticles (*29*). Removal of excess, noninserted peptide−lipids was carried out by centrifugal filtration (MWCO = 30 kDa, Microcon Millipore), and gratifyingly, a very high level of peptide−lipid insertion (>90%) was observed using fluorescence analysis of the filtrate. Accordingly, no further nanoparticle purification steps were considered necessary. These purified particles were characterized by HPLC and Stewart assay to verify that CDAN and DOPE compositions, respectively, were unaltered (comparable to initial molar ratios) by the centrifugation process. Peptide−lipid content was confirmed by fluorescence spectroscopy (excitation wavelength, I_{ex} 298 nm; emission maximum, I_{max} 349 nm) and pDNA content was quantified by UV−visible spectroscopy (using $A^{0.1}{}_{260}$ value of 30).

PEGylated nanoparticles (ABC) were formulated along similar lines by the addition of pDNA to CDAN/DOPE/MeO-PEG^{2000}-DSPE ($50 - x/50 - x/2x$, m/m/m; x is 0.25 to 2.5) cationic liposomes (prepared as before) with rapid vortex mixing (final lipid/pDNA ratio 12:1, w/w, final pDNA concentration 0.1 mg mL^{-1}). Selected stealth nanoparticle systems were then incubated (at 37 °C, 1 h) with the appropriate mol % (typically 1 or 5 mol %) of synthetic U11 peptide−lipid (or scramble control peptide−lipid as required). Once again, this procedure allowed for the post-modification of these nanoparticle systems with peptide−lipids and the formation of ABCD-type nanoparticles (*25, 29*). Excess peptide−lipid was removed once again by centrifugal filtration and the composition of purified nanoparticles confirmed as described above.

Secondary Structure of U11 in Nanoparticles. Circular dichroism (CD) spectroscopy has been used widely to characterize protein or peptide secondary structures and their conformational changes (*30*). Ligand conformation on the surface of the nanoparticle is important as this affects the binding interactions.

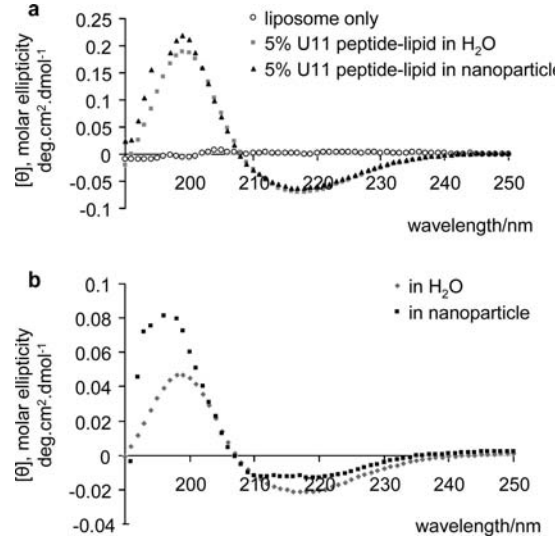

Figure 2. Circular dichroism spectra of U11 peptide−lipids alone and when incorporated on the surface of optimized nanoparticles (CDAN/DOPE/MeO-PEG^{2000}-DSPE 49.75:49.75:0.5, m/m/m) (BC system). (a) Peptide−lipids incorporated at 5 mol % on nanoparticles (▲) and in H_2O at equivalent concentration (grayscale ■); the spectra of liposomes without peptide−lipids are shown for comparison (○). (b) Peptide−lipids incorporated at 1 mol % on nanoparticles (■) and in H_2O at equivalent concentrations (♦). Negative maximum at ΔA_{216} indicates the presence of β-sheet aggregates.

Using CD spectroscopy, we report the change in organization of U11 peptide−lipids as they are inserted into CDAN/DOPE/MeO-PEG^{2000}-DSPE (49.75/49.75/0.5, m/m/m) PEGylated cationic liposomes (Figure 2a,b). CD spectra of the U11 peptide−lipids (1 or 5 mol %) were recorded before and immediately after incubation with nanoparticles (without pDNA) and compared with that recorded for U11 peptide−lipids incubated in H_2O only. Incubation of 1 and 5 mol % peptide−lipids in H_2O alone gave rise to spectra with significant negative maxima at ΔA_{216}, indicating the formation of β-sheet aggregates between the peptide bonds of the peptide−lipid molecules. The same spectral pattern was observed on the insertion of 5 mol % peptide−lipids into liposomal solutions, suggesting that incorporation of high concentrations of peptide−lipids into liposomes still results in β-sheet aggregation, this time most likely on the liposome surface (Figure 2a). Insertion of U11 peptide−lipid at a lower percentage, however, generated a spectrum with fewer characteristics of β-sheet formation, indicating the disruption of the β-sheet aggregates as the peptide−lipids are inserted into the liposomal layer (Figure 2b).

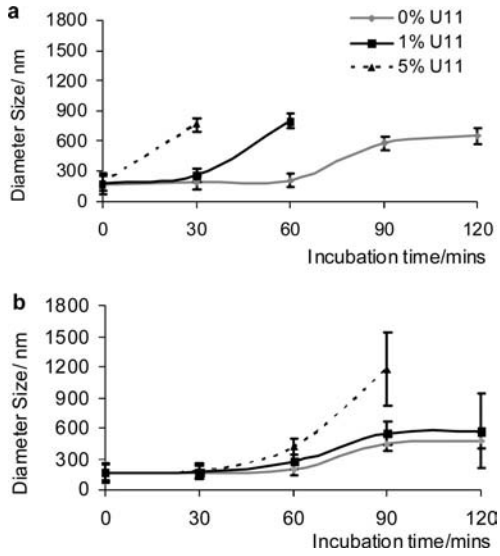

Figure 3. Effect of insertion of 0%, 1%, or 5% U11 peptide−lipid on the sizes of non-PEGylated nanoparticles (comprising CDAN/DOPE 1:1, m/m, and pDNA, lipid/pDNA ratio 12:1, w/w) incubated in (a) Optimem and in (b) 50% FCS over 120 min at 37 °C, as measured by PCS. Non-PEGylated nanoparticles with indicated mol % of U11 peptide−lipid have greater inclination for aggregation in transfection media, especially systems with high peptide−lipid loading. Diameter errors are plotted as the standard deviation calculated by PCS.

The reduction of β-sheet character on liposomal insertion could indicate the reorganization of the peptide−lipid aggregates into more separated chains when incorporated into the surface of the targeted nanoparticles.

Optimizing Mol % of U11 Peptide−Lipid. Core AB nanoparticles (non-PEGylated) and two targeted nanoparticle systems (comprising 1 or 5 mol % of U11 peptide−lipid) were incubated in transfection media or in 50% fetal calf serum (to mimic in vivo circulation conditions), and particle size was observed as a function of time. Nanoparticles with surface-inserted peptide−lipids were clearly less resistant to aggregation, although higher mole percentages of peptide−lipids lead to greater tendencies toward aggregation (Figure 3a,b). These data are consistent with a mechanism of aggregation promoted by hydrophobic and β-sheet-forming interactions between surface peptide ligands of U11-decorated nanoparticles. It appeared that colloidal stability of such systems was also poor for transfection and uPAR-mediated targeting studies. Using a plasmid-based reporter gene assay, transfection studies were performed with targeted nanoparticles, where U11-decorated nanoparticle transfections were found to be much less effective than corresponding lipid/pDNA nanoparticle transfections, thereby linking the detrimental effects of nanoparticle overaggregation with poor transfection efficiency (data not shown). Accordingly, we decided that non-PEGylated nanoparticles were not suitable for further transfection and that only stable nanoparticles should be used for uPAR-mediated targeting studies.

Optimizing Mol % of MeO-PEG^{2000}-DSPE in ABCD Nanoparticles. A general method for alleviating propensity toward aggregation of nanoparticles is by introducing poly(ethylene glycol) (PEG) units onto the surface of such nanoparticles. Nanoparticles were prepared with 1 mol % of U11 peptide−lipid in each case, plus 1−5 mol % of MeO-PEG^{2000}-DSPE. By increasing the percentage of MeO-PEG^{2000}-DSPE from 1 mol % to 5 mol %, nanoparticle stability was indeed observed in transfection media over time. However, transfection experiments on the DU145 cell (uPAR positive cell line) indicated no substantial difference in transfection levels achieved by PEGylated-targeted nanoparticles and corresponding nontargeted

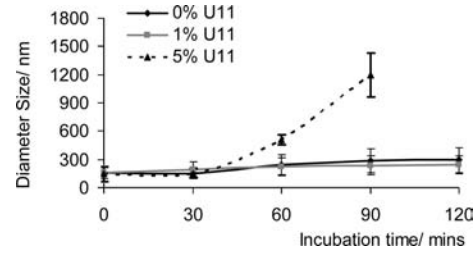

Figure 4. Effect of inclusion of U11 peptide−lipid (mol % as indicated) on PEGylated nanoparticle size with time. PEGylated, nontargeted nanoparticle (comprising CDAN/DOPE 1:1, m/m, and pDNA, lipid/pDNA ratio 12:1, w/w, MeO-PEG^{2000}-DSPE, 0.5 mol %; ABC) or targeted nanoparticles (1 or 5 mol % U11 peptide−lipid, ABCD). Nanoparticles were incubated in Optimem over 120 min at 37 °C, as measured by PCS. Both nontargeted and targeted (with 1 mol % U11 peptide−lipid) nanoparticles were both stable in transfection media, where the diameter was maintained under 250 nm throughout incubation time. However, higher loading with 5 mol % peptide−lipid was still prone to aggregation. Diameter errors are plotted as the standard deviation calculated by PCS.

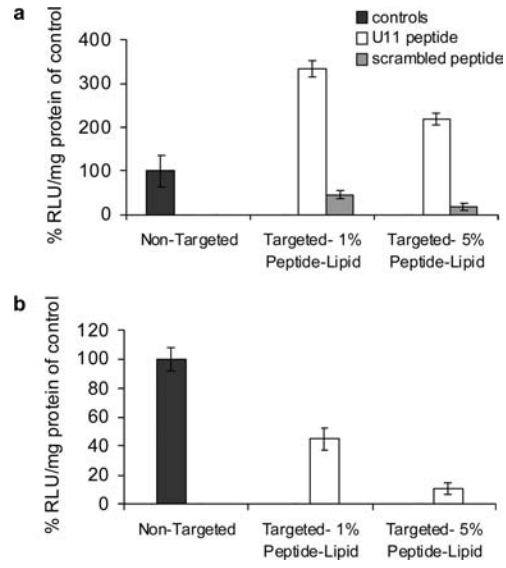

Figure 5. Luciferase transfection on uPAR-positive DU145 (a) and uPAR-negative HEK293 cell lines (b) with nanoparticles (nontargeted, comprising CDAN/DOPE 1:1, m/m, and pDNA, lipid/pDNA ratio 12:1, w/w, MeO-PEG^{2000}-DSPE, 0.5 mol %; ABC) or targeted nanoparticles (with 1 or 5 mol % of U11 peptide−lipid or nonspecific scrambled peptide−lipid; ABCD). Transfection data normalized on the value of nontargeted nanoparticle transfections. Transfection times for cells were 3 h in Optimem after which cells were incubated for 48 h before lysis and analysis for luciferase activity.

nanoparticles (data not shown). The inclusion of even only 1 mol % of MeO-PEG^{2000}-DSPE appeared to render nonfunctionality of targeted nanoparticles, presumably due to steric blocking of surface-attached U11 peptide−lipids by neighboring PEG chains. Nanoparticles stabilized with 0.5 mol % of MeO-PEG^{2000}-DSPE (ABCD), however, were shown to resist aggregation in transfection media (Figure 4), and their transfections were clearly enhanced over corresponding nontargeted nanoparticle-mediated transfections (Figure 5a) on DU145 cells.

U11 Peptide Enhanced Transfection. U11 decorated ABCD nanoparticles were formulated with 0.5 mol % of MeO-PEG^{2000}-DSPE and either 1 or 5 mol % of peptide−lipid (U11 sequence or scrambled control). uPAR is a common trait found in all cancers, where levels of its expression depend on the cell type (*31*). Transfections were performed in two cell lines, namely, uPAR positive cells (DU145) and uPAR negative cells (noncancerous HEK293 human embryonic kidney cell line) (*32*).

ABCD nanoparticles presenting 1 mol % U11 peptide ligand mediated the highest levels of DU145 transfection, nearly 3.5-fold higher than that by nontargeted nanoparticles (Figure 5a). Nanoparticles presenting 5 mol % U11 peptide−ligand mediated approximately half the levels of DU145 transfection compared to 1 mol % nanoparticles. In comparison, the highest level of HEK293 cell transfection was mediated by nontargeted nanoparticles. On these uPAR-negative cells, ABCD targeted nanoparticles presenting 1 mol % U11 peptide ligand mediated transfection levels that were about 50% of the control nanoparticle transfection level, while targeted nanoparticles presenting 5 mol % of U11 peptide−ligand mediated very poor transfection (Figure 5b). On uPAR-negative cell lines, the U11 peptide sequence becomes nonspecific for membrane receptors, hence functioning instead as a steric shield of the surface positive charges. In addition, as with the use of PEGylated lipids, inclusion of nonspecific polymer chains into the surface of nanoparticles results in their impaired cell uptake and transfection efficiency (*33*). There is a clear impression with reference to the nontargeted nanoparticle transfections that DU145 transfection mediated by nanoparticles presenting 1 mol % of U11 scrambled peptide is on par with HEK293 transfection mediated by nanoparticles presenting 1 mol % of U11 peptide ligand. Therefore, there appears to be a clear U11 peptide ligand mediated enhancement of approximately one log in ABCD-type nanoparticle transfection of uPAR positive cells (DU145) compared with key controls, namely, the transfection of uPAR positive cells by nanoparticles presenting 1 mol % of U11 scramble peptide, and the transfection of uPAR negative cells (HEK293) using nanoparticles presenting 1 mol % of U11 ligand.

For fluorescence microscopy, 1 mol % of the fluorescent probe lipid DOPE-Rhodamine (DOPE-Rho) was included into the optimized targeted and nontargeted nanoparticles. After introduction to DU145 cells, cell-associated rhodamine fluorescence was examined at 1 and 2 h post-administration (Figure 6). We observed that fluorescence intensity was much greater in cells treated with ABCD targeted nanoparticles as compared with control ABC nanoparticles, again another indication of receptor-targeted delivery by uPAR-U11 recognition. Although the images obtained do not allow us to attribute the increased fluorescence intensity solely to cell internalization, we can confidently conclude that the targeted ABCD nanoparticles are nevertheless binding more efficiently to the cell membrane than the nontargeted nanoparticles.

Competitive Binding of Targeted Nanoparticles in the Presence of uPA. Following analysis by fluorescence microscopy, flow cytometery was used to assess the uptake of rhodamine-labeled targeted nanoparticles by DU145 cells (Figure 6e). Cell-associated fluorescence generated by binding of scramble peptide−nanoparticles was 15% lower than that of U11-nanoparticles, indicating a decreased amount of binding due to the nonspecificity of the scrambled peptide sequence. The binding of such targeted nanoparticles was challenged by preincubation of the DU145 cells with a high concentration of uPA, to competitively block the uPAR receptors before administration of the nanoparticles. The binding study was performed at 4 °C to minimize receptor-mediated endocytosis. Using free uPA to block uPAR, the receptor to which U11 peptides are specific, binding of U11-nanoparticles was inhibited by 15%, whereas the binding by scramble peptide−nanoparticles was not affected. These data again emphasize the selectivity of U11-nanoparticles for uPAR, but also indicate the high level of background or nonspecific interactions between the nanoparticles and cell membranes.

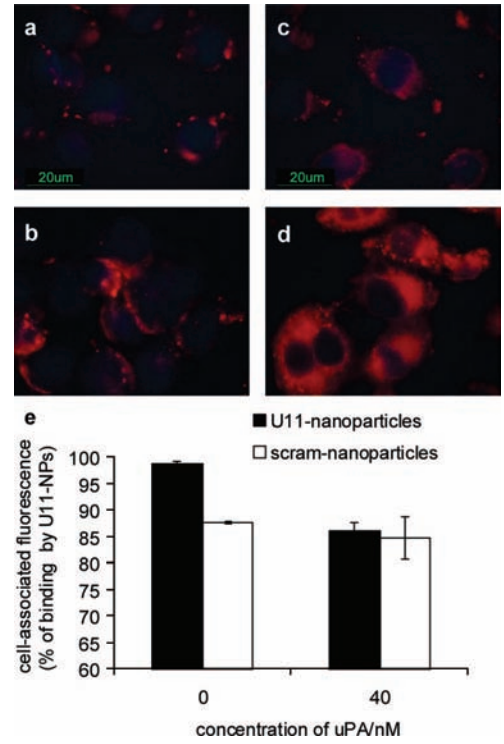

Figure 6. Uptake and binding of rhodamine-labeled optimized nanoparticles. For fluorescence microscopy, DU145 cells were incubated with nontargeted, ABC (a,b) and targeted ABCD nanoparticles (1 mol % U11) for 1 h (a,c) and 2 h (b,d) before fixing and visualizing. Images were overlaid with DAPI-nuclear staining. At 1 h, the cell-associated fluorescence appears similar in cells treated with targeted (c) and nontargeted nanoparticles (a). The difference in fluorescence is more apparent at 2 h, where cells treated with uPAR-targeted nanoparticles (d) show increased internal rhodamine intensity, compared to corresponding control nontargeted nanoparticles (b), an indication of either increased membrane binding or cellular internalization. Competitive binding of rhodamine-labeled nanoparticles with free uPA, assessed by flow cytometry (e), shows the lower cell binding by scramble peptide decorated nanoparticles, and demonstrates U11 specificity for uPAR by reduced cell binding of U11 nanoparticles after blocking of uPAR receptors with 40uM uPA.

DISCUSSION

The main objective of this study was to identify the potential of U11 grafting on the surface of nanoparticles for optimum uPAR binding and cell targeting. Here, the method of post-modification was chosen for the incorporation of peptide−lipids onto the surfaces of nanoparticles (*29*, *34*). In order to implement this strategy, a U11 peptide−lipid was prepared using an aldehyde-modified resin (FMPB resin) for the attachment of a hexadecylamine chain to the U11 peptide moiety by a reductive amination procedure (Scheme 2) (*35*, *36*). Initially, 1 or 5 mol % of the U11 peptide−lipid was inserted into nanoparticles lacking a stealth/biocompatibility polymer. The most striking aspect of the physicochemical behavior of these nanoparticles was their propensity to aggregate through nonspecific peptide−peptide interactions. (Figure 3a,b). Nanoparticles without PEGylation exhibited immediate aggregation in transfection media, where diameters of over >500 nm were recorded after 30−60 min incubation at 37 °C, a more than adequate demonstration of the need for a stealth polymer such as PEG. However, the overloading of such a sterically hindering polymer−lipid can have deleterious effects on the targeting ability of the nanoparticle, caused by shielding of the targeting peptides by the

polymer chains. The difficulty therefore lies within striking a balance between the molar percentages of the stealth lipid and the targeting peptide−lipid.

In this study, we also investigated the properties of the assembled nanoparticles and the organization of peptide targeting ligands on their surface. This poses as the first stage of development of nanoparticles for uPAR targeting and prostate cancer drug/gene therapies. For cancer targeting, nanoparticles require a diameter less than 200 nm to bypass the fenestration found in leaky tumor vasculature and between the tumor endothelium (*37, 38*). Accordingly, in the preparation of ABCD-type nanoparticles, the amount of stealth/biocompatible polymer (C-component) attached to the surface of AB core particles should be sufficient to prevent particle aggregation in all relevant biological fluids, but not so overburdening as to obscure the benefits of including a biological targeting ligand. Long chains of linear PEG units are intended to create a spherical, steric barrier around pDNA/lipid core nanoparticles, reducing the tendency for particle aggregation through the generation of steric repulsion (*39*). The steric effect provided by PEGylation also masks the lipophilic nature of the core AB nanoparticle and provides stealth properties against immune surveillance and serum aggregation, essential for in vivo applications. However, PEG at higher surface densities (>1 mol %) may interfere with the presentation of the ligand, reducing molecular recognition by the cognate receptor. This is in agreement with our transfection results using ABCD nanoparticles formulated with increasing percentages of MeO-PEG^{2000}-DSPE (data not shown). Much of our nanoparticle study described here was designed to find the most appropriate balance between incorporated components for the optimization of both stability and functional delivery of nucleic acids. In this event, this was achieved by including 0.5 mol % of MeO-PEG^{2000}-DSPE and 1 mol % of U11 peptide−lipid (Figures 4 and 5).

Nanoparticle integrity also depends on the balance of surface ligands. Similarly, as we observed, the inclusion of biological targeting ligands at higher surface densities (>1 mol %) can induce nanoparticle aggregation and interligand β-sheet aggregation (Figure 2a), without furnishing any benefits for transfection (Figure 3). Indeed, other reported studies on ligand loading have shown that lower loading rates of RGD peptide−lipid (<1 mol %) on DSPC vesicles did not reduce the binding effects of the ligand, nor was there reduction in the ability of RGD moieties to induce cell adhesions on HUVEC (human umbilicord endothelial) cells (*40*). Concurring with our data, it is believed that the physicochemical properties of the peptide (size, hydrophilicity) lead to particle aggregation on excessive loading.

The incorporation of peptide−lipids into lipid membranes for presentation of peptide ligands has been used widely in the literature (*41*−*45*), although few studies consider the effect of the anchoring procedure on the secondary structure of the ligand (*36, 46*). In our case, we investigated the effect of introducing peptide−lipids at high and lower molar percentages into the outer leaflet membrane of PEGylated cationic liposomes (Figure 2). The CD data clearly indicate that β-sheet, secondary structures are forming when the peptide−lipids are dissolved in aqueous solution (*47, 48*). However, when they are inserted at low concentrations (1 mol %), the same peptide−lipids appear to rearrange into more separated structures, as indicated by the reduction in ΔA_{216} in the CD spectrum. A targeted nanoparticle with surface ligands that are more separated into individual strands is more favorable for receptor binding. This phenomenon is only observed with peptide−lipids at low molar percentages, as the introduction of peptide−lipids into liposomes at 5 mol % showed β-sheet aggregation to the same extent as that observed in aqueous solution alone. This again highlights the advantages of incorporation of peptide−lipids at lower concentrations, where interparticle and intermolecular aggregation is prevented. Nanoparticle transfections using this formulation were clearly superior to all control transfections (including transfections with nanoparticles prepared from scramble control peptide−lipid) (Figure 5a), thereby suggesting that the U11 peptide−lipids were adopting appropriately active conformations to enable functional receptor mediated uptake of nanoparticles where uPAR were presented. Further evidence for receptor-mediated uptake in uPAR positive cells DU145 was obtained by fluorescence microscopy (Figure 6).

Previous work on ABCD nanoparticles in our laboratory had focused on the development of a $\alpha_9\beta_1$-integrin-targeting peptide−lipid for incorporation into nanoparticles in order to induce receptor-mediated uptake into appropriate cell lines followed by efficient transfection (*21*). Inclusion of the peptide−lipid into nanoparticles did indeed result in one log increase in nanoparticle-mediated transfection of a $\alpha_9\beta_1$-overexpressing cell line (in comparison with nanoparticle transfection without peptide−lipid). However, this enhanced transfection was found to be the result of nonspecific enhanced cellular uptake processes, as inclusion of the same ABCD nanoparticles gave the same increase in transfection of a cell line without $\alpha_9\beta_1$-integrin expression (in comparison with nontargeted nanoparticle transfection). Gratifyingly, the studies with U11-nanoparticle-mediated transfection and fluorescence microscopy data (Figures 5 and 6) do indicate the active involvement of receptor-mediated cell uptake processes and U11 ligand specificity for uPAR receptor. Uptake studies in DU145 cells further demonstrate the receptor specificity of the U11 peptide, where the binding of U11-targeted nanoparticles was shown to be reduced when the uPAR receptors are preblocked with high concentrations of free uPA ligand (Figure 6e). Flow cytometry showed that the binding of nanoparticles decorated with scramble peptides was 15% lower than that by U11-targeted nanoparticles, plus its uptake in uPAR-overexpressed cells was not affected by uPAR blocking. However, the maximum reduction in U11-nanoparticle binding by uPAR blocking was 15%, indicating the presence of strong nonspecific interactions that cause the binding of the nanoparticles to the cell membranes.

The challenge of nonspecific cell interactions is also emphasized by the relatively low transfection enhancement (3.5-fold) between transfections mediated by our leading U11-targeted ABCD nanoparticles and the corresponding control nanoparticles (Figure 5a). The reason for this may well lie in the high overall cationic charge of the nanoparticle systems. Zeta potentials were found to be on the order of +112 mV, a consequence of the high lipid/pDNA ratio of 12:1 (w/w) that corresponds to an N/P ratio of 4.25, assuming that each cytofectin CDAN presents a net charge of +1.7 at neutral pH (*49*). Cell membranes are typically anionic, owing in part to negatively charged cell surface proteoglycans, with which cationic nanoparticles may interact in a nonspecific manner to trigger cellular uptake by endocytosis without the requirement for receptor mediation (*50*). Therefore, the discrimination between ABCD and ABC-type nanoparticle mediated transfections should be improved by reducing the overall cationic charge of both nanoparticles. This could be feasible by engineering the lipid scaffold of these nanoparticles using alternative neutral lipids or cytofectins in order to reduce the lipid/pDNA ratio and overall mol % of cytofectin without impairing transfection efficiency and nanoparticle stability with respect to aggregation.

The design of therapeutic nanoparticles must consider both colloidal stability in biological fluids plus the ability to be tissue-specific. The targeting of such nanoparticles to tumor cells involves the use of surface ligands that are recognized and further internalized by the cancer-related receptors. The primary

sequence should already have intrinsic selectivity for its targeted receptor, but also important is the secondary conformation of the ligand, for maximizing receptor affinity. Here, in this study we show that, by tuning the mol % of each lipid component within the nanoparticle system, we can optimize the delivery efficacy of tumor-targeted nanoparticles.

CONCLUSION

In this study, we present for the first time uPAR-targeted nanoparticles for prostate cancer cells and we propose the example of tailormade solutions for different biological challenges. U11 is a peptide derived from the GFD in domain 1 of uPA and is responsible for binding to the receptor due to its epitopal folding. On the basis of this observation, we prepared U11 peptide−lipids that were inserted on the surface of the nanoparticles. It was shown that insertion of 0.5 mol % of PEG lipids induced particle stability and promoted receptor specificity for improved cell uptake and transfection. The U11-targeting strategy proved efficient and specific, where the U11 ABCD-type nanoparticles increased cell uptake and transfection levels in uPAR-expressing cell lines. It is expected that optimized U11-nanoparticles for in vivo administration will show the same specificity to uPAR expressing prostate cancers.

ACKNOWLEDGMENT

We thank The Royal Society and the EPSRC for providing the financial support for this project.

LITERATURE CITED

(1) Cantero, D., Friess, H., Deflorin, J., Zimmermann, A., Bründler, M. A., Riesle, E., Korc, M., and Büchler, M. W. (1997) Enhanced expression of urokinase plasminogen activator and its receptor in pancreatic carcinoma. *Br. J. Cancer 75*, 388–395.

(2) Costantini, V., Sidoni, A., Deveglia, R., Cazzato, O. A., Bellezza, G., Ferri, I., Bucciarelli, E., and Nenci, G. G. (1996) Combined overexpression of urokinase, urokinase receptor, and plasminogen activator inhibitor-1 is associated with breast cancer progression - An immunohistochemical comparison of normal, benign, and malignant breast tissues. *Cancer 77*, 1079–1088.

(3) Gavrilov, D., Kenzior, O., Evans, M., Calaluce, R., and Folk, W. R. (2001) Expression of urokinase plasminogen activator and receptor in conjunction with the ets family and AP-1 complex transcription factors in high grade prostate cancers. *Eur. J. Cancer 37*, 1033–1040.

(4) Andreasen, P. A., Sottrupjensen, L., Kjøller, L., Nykjaer, A., Moestrup, S. K., Petersen, C. M., and Gliemann, J. (1994) Receptor-mediated endocytosis of plasminogen activators and activator/inhibitor complexes. *FEBS Lett. 338*, 239–245.

(5) Danø, K., Behrendt, N., Høyer-Hansen, G., Johnsen, M., Lund, L. R., Ploug, M., and Romer, J. (2005) Plasminogen activation and cancer. *Thromb. Haemost. 93*, 676–681.

(6) Behrendt, N. (2004) The urokinase receptor (uPAR) and the uPAR-associated protein (uPARAP/Endo180): membrane proteins engaged in matrix turnover during tissue remodeling. *Biol. Chem. 385*, 103–136.

(7) Myöhänen, H., and Vaheri, A. (2004) Regulation and interactions in the activation of cell-associated plasminogen. *Cell. Mol. Life Sci. 61*, 2840–2858.

(8) Blasi, F., and Carmeliet, P. (2002) uPAR: a versatile signalling orchestrator. *Nat. Rev. Mol. Cell. Biol. 3*, 932–943.

(9) Andreasen, P. A., Egelund, R., and Petersen, H. H. (2000) The plasminogen activation system in tumor growth, invasion, and metastasis. *Cell. Mol. Life Sci. 57*, 25–40.

(10) Stoppelli, M. P., Corti, A., Soffientini, A., Cassani, G., Blasi, F., and Assoian, R. K. (1985) Differentiation-enhanced binding of the amino-terminal fragment of human urokinase plasminogen-activator to a specific receptor on U937 monocytes. *Proc. Natl. Acad. Sci. U.S.A. 82*, 4939–4943.

(11) Hansen, A. P., Petros, A. M., Meadows, R. P., Nettesheim, D. G., Mazar, A. P., Olejniczak, E. T., Xu, R. X., Pederson, T. M., Henkin, J., and Fesik, S. W. (1994) Solution structure of the amino-terminal fragment of urokinase-type plasminogen activator. *Biochemistry 33*, 4847–4864.

(12) Llinas, P., Le Du, M. H., Gårdsvoll, H., Danø, K., Ploug, M., Gilquin, B., Stura, E. A., and Ménez, A. (2005) Crystal structure of the human urokinase plasminogen activator receptor bound to an antagonist peptide. *EMBO J. 24*, 1655–1663.

(13) Appella, E., Robinson, E. A., Ullrich, S. J., Stoppelli, M. P., Corti, A., Cassani, G., and Blasi, F. (1987) The receptor-binding sequence of urokinase - a biological function for the growth-factor module of proteases. *J. Biol. Chem. 262*, 4437–4440.

(14) Fetrow, J. S. (1995) Omega loops: nonregular secondary structures significant in protein function and stability. *FASEB J. 9*, 708–717.

(15) Huai, Q., Mazar, A. P., Kuo, A., Parry, G. C., Shaw, D. E., Callahan, J., Li, Y., Yuan, C., Bian, C., Chen, L., Furie, B., Furie, B. C., Cines, D. B., and Huang, M. (2006) Structure of human urokinase plasminogen activator in complex with its receptor. *Science 311*, 656–659.

(16) Thanou, M., and Kean, T. (2006) *Proc. Int. Symp. Controlled Release Bioactive Mat. Controlled Release Soc. Vienna* 677.

(17) Sun, X. H., Tan, L., Li, C. Y., Tong, C., Fan, J., Li, P., and Zhu, Y. S. (2004) A novel gene delivery system targeting urokinase receptor. *Acta Biochim. Biophys. Sin. (Shanghai) 36*, 485–491.

(18) Stefanidakis, M., and Koivunen, E. (2004) Peptide-mediated delivery of therapeutic and imaging agents into mammalian cells. *Curr. Pharm. Des. 10*, 3033–3044.

(19) Colin, M., Harbottle, R. P., Knight, A., Kornprobst, M., Cooper, R. G., Miller, A. D., Trugnan, G., Capeau, J., Coutelle, C., and Brahimi-Horn, M. C. (1998) Liposomes enhance delivery and expression of an RGD-oligolysine gene transfer vector in human tracheal cells. *Gene Ther. 5*, 1488–1498.

(20) Schiffelers, R. M., Ansari, A., Xu, J., Zhou, Q., Tang, Q., Storm, G., Molema, G., Lu, P. Y., Scaria, P. V., and Woodle, M. C. (2004) Cancer siRNA therapy by tumor selective delivery with ligand-targeted sterically stabilized nanoparticle. *Nucleic Acids Res. 32*, e149.

(21) Waterhouse, J. E., Harbottle, R. P., Keller, M., Kostarelos, K., Coutelle, C., Jorgensen, M. R., and Miller, A. D. (2005) Synthesis and application of integrin targeting lipopeptides in targeted gene delivery. *ChemBioChem 6*, 1212–1223.

(22) Sauer, I., Dunay, I. R., Weisgraber, K., Bienert, M., and Dathe, M. (2005) An apolipoprotein E-derived peptide mediates uptake of sterically stabilized liposomes into brain capillary endothelial cells. *Biochemistry 44*, 2021–2029.

(23) Drapkin, P. T., O'Riordan, C. R., Yi, S. M., Chiorini, J. A., Cardella, J., Zabner, J., and Welsh, M. J. (2000) Targeting the urokinase plasminogen activator receptor enhances gene transfer to human airway epithelia. *J. Clin. Invest. 105*, 589–596.

(24) Knör, S., Sato, S., Huber, T., Morgenstern, A., Bruchertseifer, F., Schmitt, M., Kessler, H., Senekowitsch-Schmidtke, R., Magdolen, V., and Seidl, C. (2008) Development and evaluation of peptidic ligands targeting tumour-associated urokinase plasminogen activator receptor (uPAR) for use in alpha-emitter therapy for disseminated ovarian cancer. *Eur. J. Nucl. Med. Mol. Imaging 35*, 53–64.

(25) Kostarelos, K., and Miller, A. D. (2005) Synthetic, self-assembly ABCD nanoparticles; a structural paradigm for viable synthetic non-viral vectors. *Chem. Soc. Rev. 34*, 970–994.

(26) Vojkovsky, T. (1995) Detection of secondary-amines on solid-phase. *Pept. Res. 8*, 236–237.

(27) Stewart, J. C. (1980) Colorimetric determination of phospholipids with ammonium ferrothiocyanate. *Anal. Biochem. 104*, 10–14.

(28) Caussin, A., Spagnou, S., Keller, M., Jorgensen, M., Ulrich, K., Miller, A. D., and Perouzel, E. (2003) Trojene: A novel cationic liposome formulation with minimum handling features

and serum compatibility for non-viral gene delivery in vitro. *Mol. Ther. 7*, S220.
(29) Allen, T. M., Sapra, P., and Moase, E. (2002) Use of the post-insertion method for the formation of ligand-coupled liposomes. *Cell. Mol. Biol. Lett. 7*, 889–894.
(30) Berova N.; N. K.; Woody R. (2000) *Circular Dichroism: Principles and Applications*, Wiley-VCH, New York.
(31) Dass, K., Ahmad, A., Azmi, S. A., Sarkar, S. H., and Sarkar, F. H. (2008) Evolving role of uPA/uPAR system in human cancers. *Cancer Treat. Rev. 34*, 122–136.
(32) Resnati, M., Pallavicini, I., Wang, J. M., Oppenheim, J., Serhan, C. N., Romano, M., and Blasi, F. (2002) The fibrinolytic receptor for urokinase activates the G protein-coupled chemotactic receptor FPRL1/LXA4R. *Proc. Natl. Acad. Sci. U.S.A. 99*, 1359–1364.
(33) Romberg, B., Hennink, W. E., and Storm, G. (2008) Sheddable coatings for long-circulating nanoparticles. *Pharm. Res. 25*, 55–71.
(34) Uster, P. S., Allen, T. M., Daniel, B. E., Mendez, C. J., Newman, M. S., and Zhu, G. Z. (1996) Insertion of poly(ethylene glycol) derivatized phospholipid into pre-formed liposomes results in prolonged in vivo circulation time. *FEBS Lett. 386*, 243–246.
(35) Ten Brink, H. T., Meijer, J. T., Geel, R. V., Damen, M., Lowik, D. W., and van Hest, J. C. (2006) Solid-phase synthesis of C-terminally modified peptides. *J. Pept. Sci. 12*, 686–692.
(36) Lowik, D. W., Linhardt, J. G., Adams, P. J. H. M., and van Hest, J. C. (2003) Non-covalent stabilization of a beta-hairpin peptide into liposomes. *Org. Biomol. Chem. 1*, 1827–1829.
(37) Iyer, A. K., Khaled, G., Fang, J., and Maeda, H. (2006) Exploiting the enhanced permeability and retention effect for tumor targeting. *Drug Discovery Today 11*, 812–818.
(38) Yuan, F., Dellian, M., Fukumura, D., Leunig, M., Berk, D. A., Torchilin, V. P., and Jain, R. K. (1995) Vascular permeability in a human tumor xenograft: molecular size dependence and cutoff size. *Cancer Res. 55*, 3752–3756.
(39) Wheeler, J. J., Palmer, L., Ossanlou, M., MacLachlan, I., Graham, R. W., Zhang, Y. P., Hope, M. J., Scherrer, P., and Cullis, P. R. (1999) Stabilized plasmid-lipid particles: construction and characterization. *Gene Ther. 6*, 271–281.
(40) Jensen, T. W., Hu, B. H., Delatore, S. M., Garcia, A. S., Messersmith, P. B., and Miller, W. M. (2004) Lipopeptides incorporated into supported phospholipid monolayers have high specific activity at low incorporation levels. *J. Am. Chem. Soc. 126*, 15223–15230.
(41) Yagi, N., Ogawa, Y., Kodaka, M., Okada, T., Tomohiro, T., Konakahara, T., and Okuno, H. (2000) Preparation of functional liposomes with peptide ligands and their binding to cell membranes. *Lipids 35*, 673–680.
(42) Yagi, N., Yano, Y., Hatanaka, K., Yokoyama, Y., and Okuno, H. (2007) Synthesis and evaluation of a novel lipid-peptide conjugate for functionalized liposome. *Bioorg. Med. Chem. Lett. 17*, 2590–2593.
(43) Heurtault, B., Thomann, J. S., Jedrzejewska, J., Wels, W. S., Schuber, F., and Frisch, B. (2006) Liposome-based systems for anti-tumor vaccination: influence of lipopeptide adjuvants. *J. Liposome Res. 16*, 205–213.
(44) Liang, M. T., Davies, N. M., and Toth, I. (2005) Encapsulation of lipopeptides within liposomes: effect of number of lipid chains, chain length and method of liposome preparation. *Int. J. Pharm. 301*, 247–254.
(45) Espuelas, S., Roth, A., Thumann, C., Frisch, B., and Schuber, F. (2005) Effect of synthetic lipopeptides formulated in liposomes on the maturation of human dendritic cells. *Mol. Immunol. 42*, 721–729.
(46) Laczkó, I., Hollósi, M., Vass, E., and Tóth, G. K. (1998) Liposome-induced conformational changes of an epitopic peptide and its palmitoylated derivative of influenza virus hemagglutinin. *Biochem. Biophys. Res. Commun. 249*, 213–217.
(47) Stendahl, J. C., Rao, M. S., Guler, M. O., and Stupp, S. I. (2006) Intermolecular forces in the self-assembly of peptide amphiphile nanofibers. *Adv. Funct. Mater. 16*, 499–508.
(48) Guler, M. O., Hsu, L., Soukasene, S., Harrington, D. A., Hulvat, J. F., and Stupp, S. I. (2006) Presentation of RGDS epitopes on self-assembled nanofibers of branched peptide amphiphiles. *Biomacromolecule 7*, 1855–1863.
(49) Keller, M., Jorgensen, M. J., Perouzel, E., and Miller, A. D. (2003) Thermodynamic Aspects and Biological Profile of CDAN/DOPE and DC-Chol/DOPE Lipoplexes. *Biochemistry 42*, 6067–6077.
(50) Mounkes, L. C., Zhong, W., Cipres-Palacin, G., Heath, T. D., and Debs, R. J. (1998) Proteoglycans mediate cationic Liposome-DNA complex-based gene delivery in vitro and in vivo. *J. Biol. Chem. 273*, 26164–26170.

BC8001908

Probing Protein Conformations by in Situ Non-Covalent Fluorescence Labeling

Jennifer Julia Strunk, Ingo Gregor, Yvonne Becker, Peter Lamken, Suman Lata, Annett Reichel, Jörg Enderlein, and Jacob Piehler*

Institute of Biochemistry and Cluster of Excellence Macromolecular Complexes (CEF), Johann Wolfgang Goethe-University, Frankfurt/Main, Germany, Department of Molecular Neurosensorics, Caesar Research Centre, Bonn, Germany, and Institute of Physical and Theoretical Chemistry, Eberhard-Karls-University, Tübingen, Germany. Received May 20, 2008; Revised Manuscript Received November 11, 2008

The conformational dynamics of proteins plays a key role in their complex physiological functions. Fluorescence resonance energy transfer (FRET) is a particular powerful tool for studying protein conformational dynamics, but requires efficient site-specific labeling with fluorescent reporter probes. We have employed different tris-NTA/fluorophore conjugates, which bind histidine-tagged proteins with high affinity, for site-specific incorporation of FRET acceptors into proteins, which were covalently labeled with a donor fluorophore. We demonstrate versatile application of this approach for exploring the conformation of the type I interferon receptor ectodomains ifnar1-EC and ifnar2-EC. Substantial ligand-induced conformational changes of ifnar1-EC, but not ifnar2-EC, were observed by monitoring the fluorescence intensity and the fluorescence lifetime of the FRET donor. Time-resolved fluorescence correlation spectroscopy revealed a substantial conformational flexibility of ifnar1-EC and a ligand-induced tightening. Our results demonstrate that protein labeling with tris-NTA/fluorophores enables for efficient quantitative intramolecular FRET analysis.

INTRODUCTION

Protein−protein recognition frequently imposes conformational changes on the interaction partners. These conformational changes can modulate protein function, which plays a key role in many biological processes, in particular, in biological signaling cascades. Dissecting the conformational dynamics on the level of individual proteins proved particular promising for understanding the molecular basis of binding-induced structural changes (*1*−*4*). Single molecule fluorescence techniques are particularly capable of monitoring conformational dynamics in real time (*5*−*9*). One of the main challenges in this approach, however, is the need to incorporate appropriate fluorescence probes as reporter for conformational changes into the protein. For monitoring distance changes within macromolecules, typically fluorescence resonance energy transfer (FRET) is employed, which requires site-specific dual-color labeling. Covalent coupling of thiol-reactive fluorescence dyes to free cysteines is the most common approach toward site-specific labeling of proteins. For dual-color labeling, however, this approach is not suitable, requiring the separation of different species (*10*). Thus, alternative strategies for site-specific incorporation of a second fluorescence dye into proteins are required. Fusion with fluorescent proteins (*11, 12*) or with other proteins or peptide tags, which can be post-translationally labeled in a selective manner based on biomolecular recognition, is a powerful tool for labeling proteins (*13*−*17*). The size of the proteins involved in labeling and their flexible attachment to the target proteins, however, heavily reduce the distance resolution, which can be probed by intramolecular FRET. Thus, approaches for site-specific fluorescence with small recognition units are particularly promising for studying protein conformations (*17*−*21*).

Recently, we have described multivalent chelator heads (MCH) that recognize oligohistidines with subnanomolar affinity and high specificity (*22*). These chelators have been used for site-specific, quantitative labeling of His-tagged proteins in solution with several different fluorescence probes (*23*). Here, we have employed MCH conjugates (Figure 1a−c) for studying the conformational organization of the extracellular domain of a cytokine receptor and its changes upon ligand binding. The principle is depicted in Figure 1d,e: the proteins were site-specifically labeled with a fluorescence donor through covalent attachment through a free cysteine residue. Using MCH conjugates, a fluorescence acceptor is site-specifically incorporated in situ through a C-terminal decahistidine tag and the conformations can be probed by FRET (Figure 1d). The extracellular domains of the type I interferon receptor (*24*) subunits carrying a C-terminal decahistidine tag (ifnar1-H10 and ifnar2-H10) were employed as model systems for conformational analysis. While the high-affinity subunit ifnar2-H10 does not change its structure upon interferon binding (*25*), we have recently observed complex ligand-induced conformational changes of ifnar1-H10 (*26*). Ifnar1-H10 and ifnar2-H10 were site-specifically labeled through additional cysteines. For ifnar1-H10, the mutation N23C on the N-terminal Ig-like domain was incorporated by site-directed mutagenesis. The protein was labeled with the maleimide-functionalized green fluorescent dyes Oregon Green 488 (OG488) or Alexa Fluor 488 (AF488). In order to ensure quantitative ligand binding to ifnar1-H10, we used the interferon triple mutant H57A, E58A, and Q61A (IFNα2-HEQ), which binds ifnar1-H10 with ∼40-fold higher affinity (∼150 nM) than the wild-type (*27*). Ifnar2-EC, which binds both IFNα2 wt and HEQ with high affinity (∼5 nM), was employed as a reference protein, and three mutants with single cysteines in different positions were prepared for

* Corresponding author. Institute of Biochemistry, Biocenter N210, Max-von-Laue-Straβe 9, 60438 Frankfurt am Main, Phone +49 (0)69 79829468, Fax +49 (0)69 79829495. E-mail: j.piehler@em.uni-frankfurt.de.

10.1021/bc8002088 CCC: $40.75 © 2009 American Chemical Society
Published on Web 12/22/2008

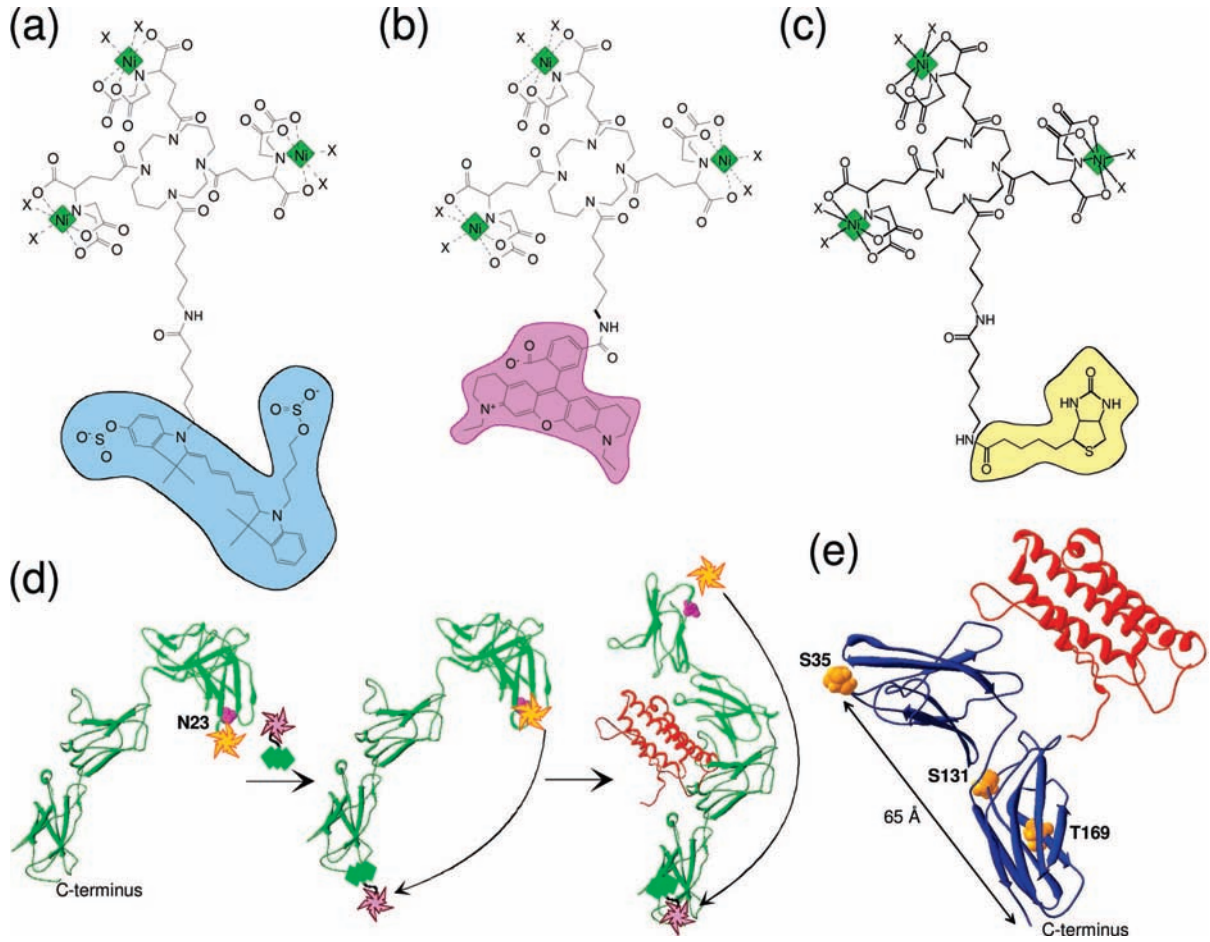

Figure 1. Principle of the fluorescence quenching assay. (a−c) MCH-based reporter probes used for monitoring conformational changes: (a) ^{FEW646}tris-NTA, (b)^{AT565}tris-NTA, and (c) ^{BT}tris-NTA. (d) By site-specific incorporation of the quencher dye through the His-tag, fluorophores attached to the protein are quenched in a distance-dependent manner. (e) NMR-based model of the ternary complex formed by ifnar2-EC (blue) with IFNα2-HEQ (red) (*34*). The position of residues mutated into cysteines for site-specific labeling (S35C, S131C, and T169C) are colored orange ifnar2.

experimentally calibrating the FRET efficiencies (indicated in Figure 1e).

EXPERIMENTAL PROCEDURES

Synthesis, Protein Expression, and Labeling. The tris-NTA/fluorophore conjugates with ATTO 565 (^{AT565}tris-NTA) and FEW Chemicals S0387 (^{FEW646}tris-NTA) were synthesized and loaded with Ni(II) ions as described previously (*23*, *28*). Ifnar1-EC with a C-terminal decahistidine-tag (ifnar1-H10) was expressed and purified as described before (*29*). Ifnar1 without His-tag (ifnar1-tl) was prepared from an ifnar1-H10 containing a factor Xa cleavage site upstream of the His-tag by proteolytic cleavage. Ifnar2-H10 was cloned into the same expression vector as ifnar1-H10 (pAcGP67B) and expressed in *Sf*9 insect cells as described for ifnar1-H10 (*29*). Single cysteine mutants of ifnar1-H10 (N23C) and ifnar2-H10 (S35C, S131C, and T169C, respectively) were generated by ligase chain reaction. The proteins were expressed and purified as wild-type ifnar1-H10. Thiol-specific labeling of these cysteine mutants required reduction of these additional cysteine residues without reducing the disulfide bonds in the proteins. Different conditions were found to be suitable for the different proteins: ifnar1 N23C was reduced by incubation with 3 mM tricarboxyethylphospine and 1 mM EDTA for 1 h; ifnar2-H10 mutants S35C, S131C, and T169C were reduced using 300 μM dithiothreitol for 1 h. After removing the reducing agent by SEC (Superdex 200 in 20 mM Tris pH 7.5, 50 mM sodium chloride), a 3-fold molar excess of the maleimide-functionalized fluorescence dye (OG488 and AF488 maleimide from Molecular Probes) was added and incubated overnight. The labeled proteins were further purified by ion exchange chromatography to separate unlabeled and multiply labeled species, followed by a final polish by SEC in 20 mM Hepes pH 7.5 and 150 mM NaCl (HBS).

Cuvette Fluorescence Assays. Fluorescence quenching experiments were carried out in HBS complemented with 1 mg/mL BSA. Fluorescence spectra were recorded with a Cary Eclipse (Varian, Germany) and fluorescence lifetime measurements were carried out in a FluoTime 200 instrument (Picoquant GmbH, Germany) using a 120 μL cuvette. A solution of 100 nM covalently labeled protein was filled into the cuvette, and the fluorescence measurement was carried out. Subsequently, 250 nM of ^{FEW646}tris-NTA, ^{AT565}tris-NTA, or ^{BT}tris-NTA was added to the protein solution in the cuvette, incubated for 15 min, and then the fluorescence spectra or fluorescence lifetime was recorded. Subsequently, 1 μM IFNα2-HEQ was added, and fluorescence spectra or fluorescence lifetime was recorded after 5 min. The stock solutions of the tris-NTA conjugates and IFNα2-HEQ were so concentrated that the change of volume was negligible. Fluorescence spectra were acquired with an excitation of OG488 and AF488 at 470 nm (5 nm slit-width). For ensemble fluorescence lifetime measurements, OG488 was excited at 493 nm by a pulsed LED (PLS500, Picoquant GmbH, Germany) with 500 ps pulse width and 20 MHz repetition rate. Fluorescence lifetimes were fitted by a double-

exponential decay. For evaluation of the FRET efficiency and the donor−acceptor distance, we treated each component independently.

Time-Resolved Fluorescence Correlation Spectroscopy. Time-resolved fluorescence correlation spectroscopy was carried out in a home-built confocal microscope that was described previously (*30*). The excitation laser used was a pulsed diode laser at 470 nm wavelength (PDL 470, PicoQuant GmbH, Germany) generating pulses with ca. 50 ps pulse width and 40 MHz repetition rate. Fast electronics (PicoHarp 300, PicoQuant GmbH, Germany) was used for recording the detected photons in time-correlated time-tagged recording mode. From these raw data, the autocorrelation curves $G(\tau)$ were calculated by cross-correlating photons from two different single-photon avalanche photodiodes. Binding experiments were carried out with 1 nM ^{OG488}ifnar1-H10 or ^{AF488}ifnar1-H10 mixed with 100 nM unlabeled ifnar1-H10 in HBS complemented with 1 mg/mL BSA. The mixture was incubated with 250 nM ^{AT565}tris-NTA for 15 min prior to the measurements, and with 1 μM IFNα2-HEQ for 5 min. For measurements with no addition of the tris-NTA conjugates, 1 mM EDTA was added in order to remove contaminating transition metal ions. Data were acquired over 30 min. The fitting of the normalized autocorrelation function data was done using the standard model introduced by Rigler et al. (*31*). To account for the complex photophysical processes, this model was extended using three exponential decay terms. Hence, the following model function was used to describe the data:

$$G(\tau) = G_D(\tau)G_F(\tau) + 1$$

with

$$G_D(\tau) = \frac{1}{N}\frac{1}{(1+\tau/\tau_{diff})\sqrt{1+\tau/(\gamma\tau_{diff})}}$$

and

$$G_F(\tau) = \frac{1}{1-\sum_3 A_j}\left[1-\sum_{j=1}^{3} A_j\left[1-\exp\left(\tau/\tau_j\right)\right]\right]$$

where τ is the lag time, τ_{diff} the diffusion time, τ_j the time constants of photophysical processes, and γ the aspect ratio of the confocal volume.

RESULTS AND DISCUSSION

Fluorescence quenching in solution was explored by using either ^{AT565}tris-NTA or ^{FEW646}tris-NTA binding to the decahistidine-tag of ^{OG488}ifnar1-H10. Typical assays using spectral fluorescence detection are shown in Figure 2. Upon addition of ^{AT565}tris-NTA, the fluorescence of ^{OG488}ifnar1-H10 was quenched by more than 50% (Figure 2a). The same fluorescence quenching was observed in the presence of a 10-fold excess of unlabeled, tagless ifnar1-EC (ifnar1-tl), confirming specific and exclusive binding of ^{AT565}tris-NTA to the His-tag of ifnar1-H10 (data not shown). Moreover, no change in fluorescence was observed after scavenging excess ^{AT565}tris-NTA by adding 200 nM His-tagged maltose binding protein (MBP-H10) to the ^{AT565}tris-NTA/^{OG488}ifnar1-H10 complex, excluding nonspecific interaction of excess ^{AT565}tris-NTA with other regions of ifnar1-H10. On the basis of the calculated Förster radius for this pair of fluorescence dyes (~58 Å), this extent of fluorescence quenching suggests a distance of less than 6 nm between dye attached to N23 and the C-terminal His-tag. Strikingly, a substantial increase in fluorescence was observed upon binding of the ligand IFNα2-HEQ (~70% of the signal before adding the quencher), suggesting a substantial spatial rearrangement of the Ig-like domains. Fluorescence dequenching by the ligand binding was fully reversed upon adding unlabeled, tagless ifnar1-EC (ifnar1-tl), corroborating that indeed ligand binding was responsible for this effect. No change in fluorescence intensity was observed upon ligand binding to ^{OG488}ifnar1-H10 without ^{AT565}tris-NTA (Figure 2c), confirming that fluorescence dequenching was not caused by interaction of the ligand with the fluorophore. Also, changes in the signal of the acceptor fluorescence were observed upon addition of the ligand. However, owing to the rather high excess of ^{AT565}tris-NTA (250 nM) compared to the fluorescence donor (100 nM), the background signal from direct excitation of AT565 was already rather high. Furthermore, the quantum yield of ^{AT565}tris-NTA is rather low due to strong quenching (by ~80%) of the fluorophore by the chelated Ni(II) ions (*23*).

Similar experiments were carried out with ^{FEW646}tris-NTA as a quencher (Figure 2b). As expected, substantially lower decrease of the fluorescence signal was observed upon binding of ^{FEW646}tris-NTA to ^{OG488}ifnar1-H10 (~25%, Figure 2b). Taking the theoretical Förster radius for this pair of dyes (~47 Å) into account, this effect confirmed an effective distance of less than 6 nm between N23 and the N-terminus. Again, the fluorescence recovered substantially upon addition of IFNα2-HEQ (~90% of the signal before adding the quencher), corroborating the spatial arrangement and the distance between the N-terminal Ig-like domain and the C-terminus. Dissociation of the ^{FEW646}tris-NTA from the His-tag by addition of 50 mM imidazole resulted into a full recovery of the fluorescence signal, confirming that the changes in fluorescence were due to interactions between ^{FEW646}tris-NTA and the His-tag.

The role of Ni(II) ions for the quenching of the covalently attached dye was explored by complex formation with ^{BT}tris-NTA instead of the fluorescent tris-NTA conjugates. Strikingly, no change in fluorescence of ^{OG488}ifnar1-H10 was observed upon complex formation (Figure 2d). Stable binding of ^{BT}tris-NTA and thus incorporation of Ni(II) ions was confirmed by subsequent addition of 250 nM ^{AT565}tris-NTA, which did not quench the fluorescence under these conditions, because the decahistidine tag was already blocked by ^{BT}tris-NTA. These experiments furthermore corroborated the high specificity of the fluorescence quenching by site-specific incorporation through the His-tag.

Ifnar1-H10 labeled with AF488 instead of OG488 as a fluorescence donor yielded similar results (Supporting Information), in agreement with the highly similar photophysical properties of AF488 and OG488. As a further control, as well as for calibrating the quenching signals, similar experiments were carried out with several single cysteine mutants of ifnar2-H10, which were used for site-specific labeling at different positions within the molecule (cf. Figure 1e). Upon addition of ^{FEW646}tris-NTA, the fluorescence decreased by ~20% (Figure 2). Importantly, however, no recovery of the fluorescence was observed after ligand binding. This is in line with the rigid structure of the protein observed in NMR, which remained essentially unchanged upon ligand binding (*32*). These results corroborate that the fluorescence changes observed for ifnar1-H10 were indeed due to conformational changes. Again, stronger quenching by ~35% was observed for binding of ^{AT565}tris-NTA (spectra not shown). On the basis of the distances between the C-terminus of ifnar2-EC and the mutated residue as determined from the NMR structure of ifnar2-EC, the quenching amplitudes obtained for different mutants were used for a distance calibration. The relative quenching amplitudes obtained for ^{FEW646}tris-NTA and ^{AT565}tris-NTA for different distances are compared in Figure 2f and fitted by the Förster function. From these calibration curves, Förster radii of 48 Å and 59 Å were estimated for ^{FEW646}tris-NTA and ^{AT565}tris-NTA, respectively, which were in excellent agreement with the Förster radii calculated from

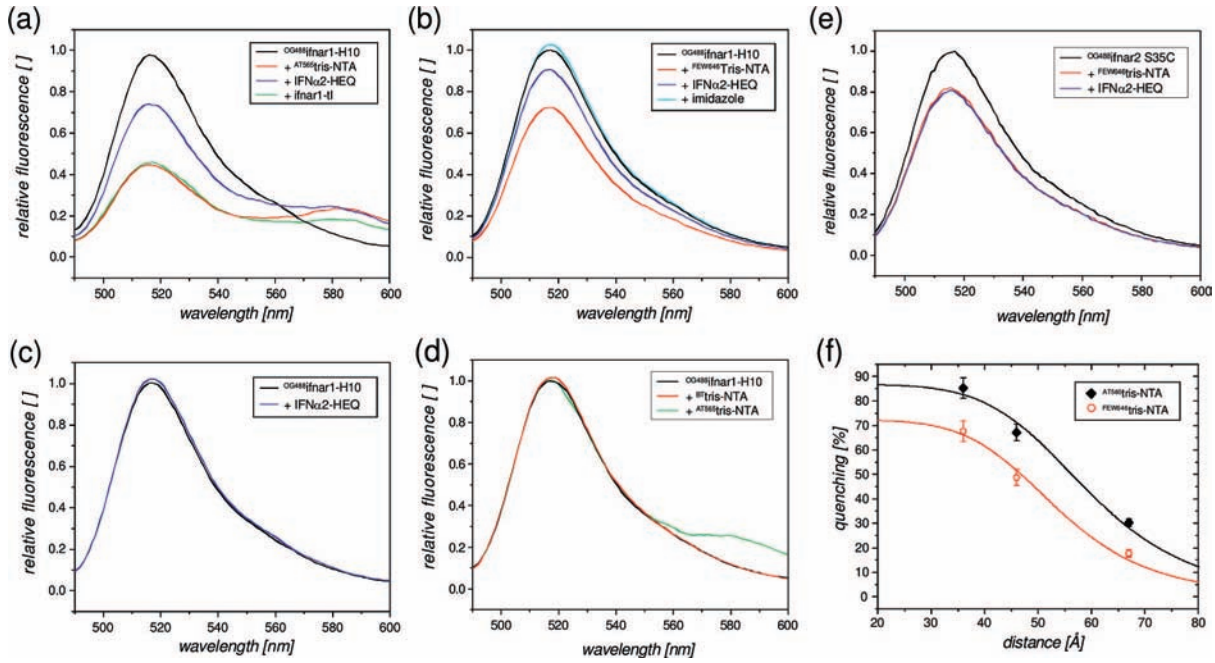

Figure 2. FRET experiments in solution. (a,b) Fluorescence spectrum of 100 nM ^{OG488}ifnar1-H10 before and after adding 250 nM ^{AT565}tris-NTA (a) or ^{FEW646}tris-NTA (b), and upon addition of the ligand IFNα2-HEQ (1 μM). In (a), IFNα2 HEQ was competed out of the complex by addition of 5 μM ifnar1-tl; in (b), ^{FEW646}tris-NTA was competed out of the complex by addition of 50 mM imidazole. (c) Fluorescence of 100 nM ^{OG488}ifnar1-H10 without tris-NTA conjugate before and after addition of 1 μM IFNα2-HEQ. (d) Fluorescence of 100 nM ^{OG488}ifnar1-H10 before and after addition of 250 nM ^{BT}tris-NTA, followed by the addition of 250 nM ^{AT565}tris-NTA. (e) Fluorescence spectrum of 100 nM ^{OG488}ifnar2-H10 S35C before and after adding 250 nM ^{FEW646}tris-NTA, and upon addition of the ligand (1 μM). (f) Comparison of relative quenching with ^{FEW646}tris-NTA and ^{AT565}tris-NTA for ifnar2-H10 labeled at three different positions and fit of the Förster equation.

Table 1. Relative Quenching and Estimated Mean Intramolecular Distances in ^{OG488}ifnar1-H10

	^{OG488}ifnar1-H10		^{OG488}ifnar1-H10/IFNα2-HEQ	
	Q [%][a]	r [Å][b]	Q [%][a]	r [Å][b]
^{AT565}tris-NTA	55 ± 2	56 ± 1	30 ± 2	67 ± 1
^{FEW646}tris-NTA	25 ± 2	56 ± 1	10 ± 2	68 ± 1

[a] Relative loss in fluorescence compared to ^{OG488}ifnar1-H10. [b] Distance between donor and quencher as estimated from the Förster radii (47 Å for ^{FEW646}tris-NTA and 58 Å for ^{AT565}tris-NTA).

absorbance and emission spectra assuming a quantum yield of 50% for the protein-bound OG488 (47 Å and 58 Å, respectively). On the basis of these Förster radii, the distances between N23 from the C-terminus before and after ligand binding were estimated (Table 1). Distances of ∼56 Å before and ∼67 Å (^{AT565}tris-NTA) as well as ∼68 Å (^{FEW646}tris-NTA) after ligand binding were obtained, highly consistent for both quencher. Thus, the N-terminal domain moves away from the C-terminal domain by ∼11−12 Å.

The multidomain architecture and the ligand-induced conformational change suggested that a flexible organization of the Ig-like domains of ifnar1 may contribute to the intramolecular FRET. We, therefore, further explored fluorescence quenching and ligand-induced dequenching by fluorescence lifetime measurements (Figure 3a,b). An overall decrease of the fluorescence lifetime was observed upon binding of ^{AT565}tris-NTA (Figure 3a) as well as ^{FEW646}tris-NTA (Figure 3b), which was followed by a recovery upon ligand binding. The differences in the decrease and recovery of the fluorescence lifetimes qualitatively matched well with the spectral data. The fluorescence lifetime curves obtained with ^{AT565}tris-NTA yielded substantially stronger changes in the fluorescence lifetime compared to ^{FEW646}tris-NTA and were therefore analyzed in more detail. All samples showed a biexponential decay indicating a rather complex scenario. We interpreted this as a two-state environment of the attached label, which might be either due to linker flexibility that allows the label to find two possible positions on the protein surface or due to conformational dynamics of the protein (see below). For ^{OG488}ifnar1-H10 alone, we observed two lifetimes of ∼2.5 ns and ∼4.4 ns (cf. Supporting Information). After binding of ^{AT565}tris-NTA, both lifetimes decreased (1.5 and 3.9 ns, respectively), but the effect was much more prominent in the case of the short-lifetime component. Upon addition of the ligand, both lifetimes increased (2.0 and 4.0 ns, respectively), and again the change in the short lifetime component was more pronounced. Using the previously estimated Förster radii, we could conclude that upon ligand binding the C-terminal His-tag moves by ∼12−14 Å away from the labeled position near the N-terminus (detailed in the Supporting Information), consistent with the conformational changes estimated from intensity changes.

We further explored the conformational dynamics of ifnar1-H10 by means of fluorescence correlation spectroscopy. FRET introduces an additional channel that de-excites the fluorescence of the fluorophore. For fluctuations of FRET efficiencies due to conformational dynamics, one expects to observe an additional decay term in the autocorrelation function. For this purpose, 1 nM ^{AF488}ifnar1-H10 mixed with 100 nM unlabeled ifnar1-H10 was incubated with 250 nM ^{AT565}tris-NTA, and fluorescence fluctuations in the confocal volume were followed by time-correlated single photon counting (TCSPC). Under these conditions, a similar excess of ^{AT565}tris-NTA was maintained as in the cuvette experiments, thus ensuring the same specificity and complete complex formation. Typical autocorrelation functions obtained for ^{AF488}ifnar1-H10 in different states are compared in Figure 3c and d. Normalization of the autocorrelation curves to individual fluorophores (data not shown) confirmed the intramolecular FRET signals obtained by ensemble measurements. A clear change in the shape of the correlation curve was observed upon binding of ^{AT565}tris-NTA (Figure 3c). Upon ligand binding, the autocorrelation curves

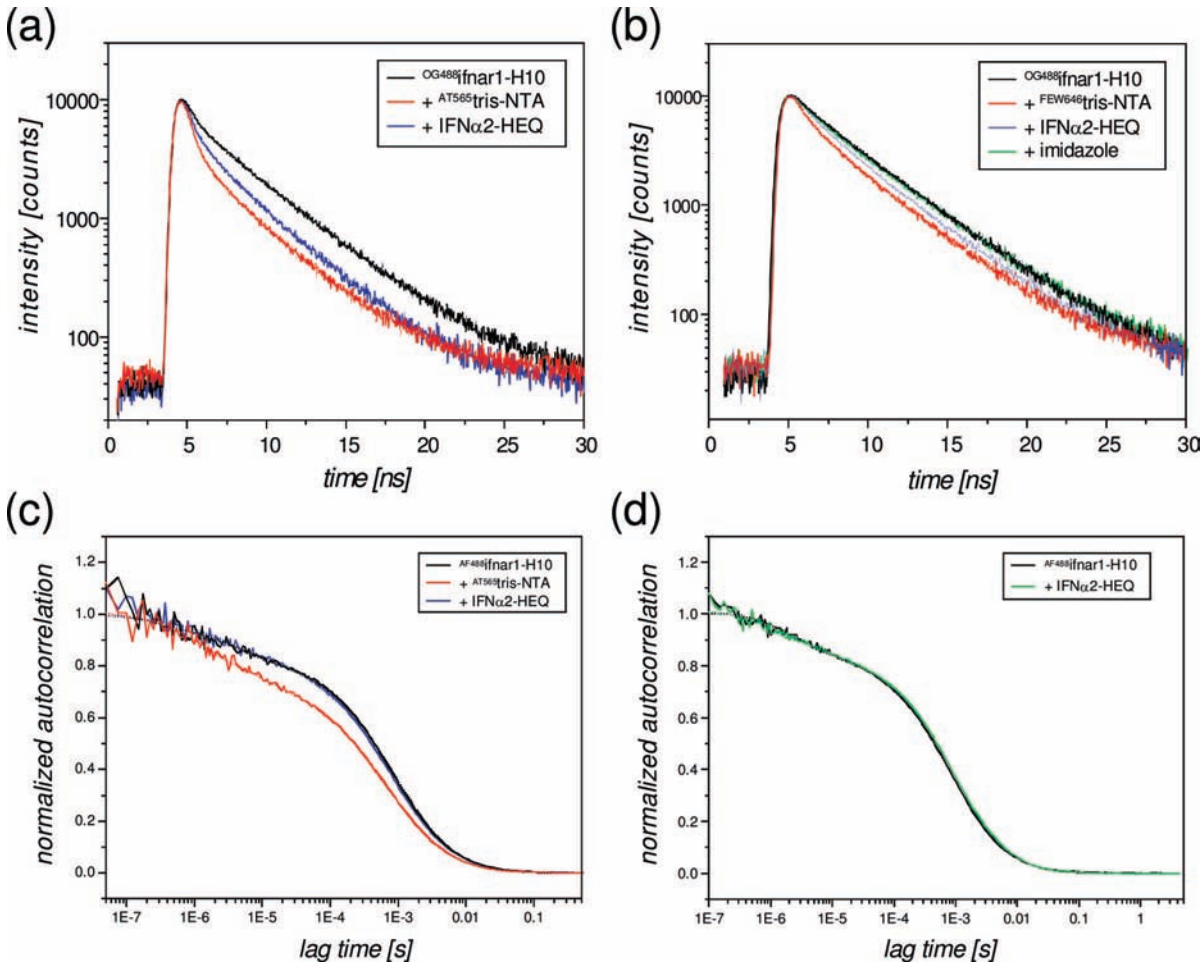

Figure 3. Probing conformational dynamics by time-resolved fluorescence experiments. (a) Fluorescence lifetime of ^{OG488}ifnar1-H10 before and after adding ^{AT565}tris-NTA, and upon addition of the ligand IFNα2-HEQ. (b) Fluorescence lifetime of ^{OG488}ifnar1-H10 before and after adding ^{FEW646}tris-NTA, after addition of the ligand IFNα2-HEQ, and after treatment with imidazole. (c) Autocorrelation curves for ^{AF488}ifnar1-H10, after binding of ^{AT565}tris-NTA, and after ligand binding (IFNα2-HEQ) to the ^{AF488}ifnar1-H10/^{AT565}tris-NTA complex. The fits of the curves are shown as dotted lines. (d) Autocorrelation curves for ^{AF488}ifnar1-H10 without ^{AT565}tris-NTA before and after ligand binding (IFNα2-HEQ). The fit of the curves are shown as dotted lines.

recovered to a very similar behavior as observed prior to the binding of ^{AT565}tris-NTA. These observations suggest that an additional mode of dynamic quenching takes place in the ^{AF488}ifnar1-H10/^{AT565}tris-NTA complex, which is lost upon complex formation with the ligand. In contrast, no changes in the shape of the autocorrelation curves were observed without ^{AT565}tris-NTA (Figure 3d). Fitting of the autocorrelation curves revealed a transition time of ∼200 μs, which we ascribe to conformational dynamics of ifnar1-H10 in the unliganded state. The amplitude of this photophysical decay term was 25% of the diffusional autocorrelation amplitude (Supporting Information Table 2). Very similar autocorrelation curves were obtained when the same experiments were carried out with ^{OG488}ifnar1-H10 (data not shown). These results clearly corroborate a conformational flexibility of ifnar1-H10, which is largely lost upon ligand binding. This observation is in line with the fact that the three N-terminal domains simultaneously interact with the ligand, thus reducing the potential flexibility of the molecule in the linker between SD2 and SD3.

CONCLUSIONS

These results demonstrate that noncovalent labeling by multivalent chelator heads efficiently complements cysteine-specific labeling for probing protein conformations. The key advantage of this approach is that an acceptor dye can be rapidly incorporated into the protein in situ in a quantitative fashion without the addition of other reagents being required. Thus, the fluorescence of the covalently attached fluorescence donor can be readily quantified before and after attachment of the acceptor dye, and the FRET efficiencies can be quantified reliably from the donor quenching even if the donor dye is coupled at a low degree of labeling. Compared to other noncovalent labeling techniques, the localization of the fluorophore is very well defined, though not as well as for a dye chemically coupled to a cysteine residue. The method is therefore particularly suited to explore the domain organization of multidomain proteins, which was applied to the ectodomain of ifnar1 (*26*). Binding of tris-NTA/fluorophore conjugates to the His-tag is fast, quantitative, and reversible under mild conditions, and suitable for labeling in live cells (*23, 33*). Our studies demonstrate the elegance and versatility of labeling through tris-NTA/fluorophore conjugates and its compatibility with different fluorescence detection techniques including TCSPC-based FCS.

ACKNOWLEDGMENT

We thank Thomas Gensch for help with the fluorescence lifetime instrument. This project was supported by grants to J.P. from the DFG (Emmy-Noether Program PI 405/1 and SFB 628), and from the Human Frontier Science Program (RGP60/2002). J.P. is a Heisenberg Professor funded by the DFG (PI 405/3) and was supported by the Cluster of Excellence "Macromo-

lecular Complexes" at the Goethe University Frankfurt (DFG Project EXC 115).

Supporting Information Available: Spectroscopic FRET experiments with ^{AF488}ifnar1-H10 and ^{AT565}tris-NTA and tabled fitting results for time-resolved fluorescence and FCS measurements. This material is available free of charge via the Internet at http://pubs.acs.org.

LITERATURE CITED

(1) Nevo, R., Stroh, C., Kienberger, F., Kaftan, D., Brumfeld, V., Elbaum, M., Reich, Z., and Hinterdorfer, P. (2003) A molecular switch between alternative conformational states in the complex of Ran and importin beta1. *Nat. Struct. Biol. 10*, 553–7.

(2) Slaughter, B. D., Unruh, J. R., Allen, M. W., Bieber Urbauer, R. J., and Johnson, C. K. (2005) Conformational substates of calmodulin revealed by single-pair fluorescence resonance energy transfer: influence of solution conditions and oxidative modification. *Biochemistry 44*, 3694–707.

(3) Majumdar, D. S., Smirnova, I., Kasho, V., Nir, E., Kong, X., Weiss, S., and Kaback, H. R. (2007) Single-molecule chemistry and biology special feature: single-molecule FRET reveals sugar-induced conformational dynamics in LacY. *Proc. Natl. Acad. Sci. U.S.A. 104*, 12640–5.

(4) Sacho, E. J., Kadyrov, F. A., Modrich, P., Kunkel, T. A., and Erie, D. A. (2008) Direct visualization of asymmetric adenine nucleotide-induced conformational changes in MutLα. *Mol. Cell 29*, 112–21.

(5) Ha, T., Ting, A. Y., Liang, J., Caldwell, W. B., Deniz, A. A., Chemla, D. S., Schultz, P. G., and Weiss, S. (1999) Single-molecule fluorescence spectroscopy of enzyme conformational dynamics and cleavage mechanism. *Proc. Natl. Acad. Sci. U.S.A. 96*, 893–8.

(6) Weiss, S. (2000) Measuring conformational dynamics of biomolecules by single molecule fluorescence spectroscopy. *Nat. Struct. Biol. 7*, 724–9.

(7) Heyduk, T. (2002) Measuring protein conformational changes by FRET/LRET. *Curr. Opin. Biotechnol. 13*, 292–6.

(8) Myong, S., Stevens, B. C., and Ha, T. (2006) Bridging conformational dynamics and function using single-molecule spectroscopy. *Structure 14*, 633–43.

(9) Michalet, X., Weiss, S., and Jager, M. (2006) Single-molecule fluorescence studies of protein folding and conformational dynamics. *Chem. Rev. 106*, 1785–813.

(10) Ratner, V., Kahana, E., Eichler, M., and Haas, E. (2002) A general strategy for site-specific double labeling of globular proteins for kinetic FRET studies. *Bioconjugate Chem. 13*, 1163–70.

(11) Tsien, R. Y. (1998) The green fluorescent protein. *Annu. Rev. Biochem. 67*, 509–44.

(12) Miyawaki, A., Sawano, A., and Kogure, T. (2003) Lighting up cells: labelling proteins with fluorophores. *Nat. Cell Biol. Suppl.* S1–7.

(13) Keppler, A., Gendreizig, S., Gronemeyer, T., Pick, H., Vogel, H., and Johnsson, K. (2003) A general method for the covalent labeling of fusion proteins with small molecules in vivo. *Nat. Biotechnol. 21*, 86–9.

(14) Chen, I., Howarth, M., Lin, W., and Ting, A. Y. (2005) Site-specific labeling of cell surface proteins with biophysical probes using biotin ligase. *Nat Methods 2*, 99–104.

(15) Miller, L. W., and Cornish, V. W. (2005) Selective chemical labeling of proteins in living cells. *Curr. Opin. Chem. Biol. 9*, 56–61.

(16) Miyawaki, A., and Tsien, R. Y. (2000) Monitoring protein conformations and interactions by fluorescence resonance energy transfer between mutants of green fluorescent protein. *Methods Enzymol. 327*, 472–500.

(17) Zhang, J., Campbell, R. E., Ting, A. Y., and Tsien, R. Y. (2002) Creating new fluorescent probes for cell biology. *Nat. Rev. Mol. Cell Biol. 3*, 906–18.

(18) Griffin, B. A., Adams, S. R., and Tsien, R. Y. (1998) Specific covalent labeling of recombinant protein molecules inside live cells. *Science 281*, 269–72.

(19) Yin, J., Straight, P. D., McLoughlin, S. M., Zhou, Z., Lin, A. J., Golan, D. E., Kelleher, N. L., Kolter, R., and Walsh, C. T. (2005) Genetically encoded short peptide tag for versatile protein labeling by Sfp phosphopantetheinyl transferase. *Proc. Natl. Acad. Sci. U.S.A. 102*, 15815–20.

(20) Jager, M., Nir, E., and Weiss, S. (2006) Site-specific labeling of proteins for single-molecule FRET by combining chemical and enzymatic modification. *Protein Sci. 15*, 640–6.

(21) Johnsson, N., and Johnsson, K. (2007) Chemical tools for biomolecular imaging. *ACS Chem. Biol. 2*, 31–8.

(22) Lata, S., Reichel, A., Brock, R., Tampé, R., and Piehler, J. (2005) High-affinity adaptors for switchable recognition of histidine-tagged proteins. *J. Am. Chem. Soc. 127*, 10205–15.

(23) Lata, S., Gavutis, M., Tampé, R., and Piehler, J. (2006) Specific and stable fluorescence labeling of histidine-tagged proteins for dissecting multi-protein complex formation. *J. Am. Chem. Soc. 128*, 2365–72.

(24) Uze, G., Schreiber, G., Piehler, J., and Pellegrini, S. (2007) The receptor of the type I interferon family. *Curr. Top. Microbiol. Immunol. 316*, 71–95.

(25) Chill, J. H., Nivasch, R., Levy, R., Albeck, S., Schreiber, G., and Anglister, J. (2002) The human interferon receptor: NMR-based modeling, mapping of the IFN-α 2 binding site, and observed ligand-induced tightening. *Biochemistry 41*, 3575–85.

(26) Strunk, J. J., Gregor, I., Becker, Y., Li, Z., Gavutis, M., Jaks, E., Lamken, P., Walz, T., Enderlein, J., and Piehler, J. (2008) Ligand binding induces a conformational change in ifnar1 that is propagated to its membrane-proximal domain. *J. Mol. Biol. 377*, 725–739.

(27) Jaitin, D. A., Roisman, L. C., Jaks, E., Gavutis, M., Piehler, J., Van der Heyden, J., Uze, G., and Schreiber, G. (2006) Inquiring into the differential action of interferons (IFNs): an IFN-{α}2 mutant with enhanced affinity to IFNAR1 is functionally similar to IFN-{β}. *Mol. Cell. Biol. 26*, 1888–97.

(28) Lata, S., Gavutis, M., Tampé, R., and Piehler, J. (2005)Specific and stable fluorescence labeling of histidine-tagged proteins for dissecting multi-protein complex formation. *J. Am. Chem. Soc*. in press.

(29) Lamken, P., Lata, S., Gavutis, M., and Piehler, J. (2004) Ligand-induced assembling of the type I interferon receptor on supported lipid bilayers. *J. Mol. Biol. 341*, 303–18.

(30) Böhmer, M., Pampaloni, F., Wahl, M., Rahn, H. J., Erdmann, R., and Enderlein, J. (2001) Time-resolved confocal scanning device for ultrasensitive fluorescence detection. *Rev. Sci. Instrum. 72*, 4145–4152.

(31) Rigler, R., Mets, Ü., Widengren, Ü., and Kask, P. (1993) Fluorescence correlation spectroscopy with high count rate and low background: analysis of translational diffusion. *Eur. Biophys. J. 22*, 169–175.

(32) Chill, J. H., Quadt, S. R., Levy, R., Schreiber, G., and Anglister, J. (2003) The human type I interferon receptor. NMR structure reveals the molecular basis of ligand binding. *Structure (Cambridge, U.K.) 11*, 791–802.

(33) Reichel, A., Schaible, D., Al Furoukh, N., Cohen, M., Schreiber, G., and Piehler, J. (2007) Noncovalent, site-specific biotinylation of histidine-tagged proteins. *Anal. Chem. 79*, 8590–600.

(34) Quadt-Akabayov, S. R., Chill, J. H., Levy, R., Kessler, N., and Anglister, J. (2006) Determination of the human type I interferon receptor binding site on human interferon-alpha2 by cross saturation and an NMR-based model of the complex. *Protein Sci. 15*, 2656–68.

BC8002088

Probing protein conformations by in *situ* non-covalent fluorescence labeling

Jennifer Julia Strunk[1], Ingo Gregor[2], Yvonne Becker[1], Peter Lamken[1], Suman Lata[1], Annett Reichel[1], Jörg Enderlein[3], Jacob Piehler[1*]

Supporting information

Supporting Figure 1 Fluorescence quenching assay with ^{AF488}ifnar1-H10 and ^{AT565}tris-NTA.

Supporting Table 1 Analysis of the fluorescence life time curves ^{OG488}ifnar1-H10 in different states.

Supporting Table 2 Autocorrelation times and amplitudes obtained from FCS measurements.

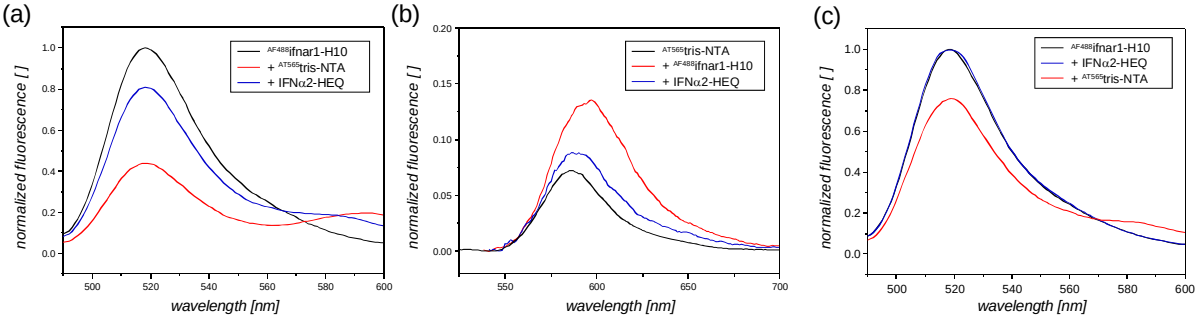

Supporting Figure 1 Fluorescence quenching assay with ^{AF488}ifnar1-H10 and ^{AT565}tris-NTA. (a) Quenching of ^{AF488}ifnar1-H10 with ^{AT565}tris-NTA, and recovery after addition of the ligand. (b) Fluorescence of ATTO 565 of the spectra shown in (a) as obtained by subtracting the fluorescence of AF488. (c) Fluorescence spectra of ^{AF488}ifnar1-H10 without and after addition of IFNa2-HEQ and after subsequent addition of the quencher ^{AT565}tris-NTA.

Supporting Table 1 Lifetimes t and amplitudes A obtained for a double-exponential decay of the fluorescence life time curves of fluorescence-labeled ifnar1-H10 in different states.

Ifnar1-H10 in complex with	t_1 [ns]	A_1 [%]	r_{DA} [R_0]	t_2 [ns]	A_2 [%]	r_{DA} [R_0]
– [a]	2.5	21		4.4	79	
^{AT565}tris-NTA [a]	1.5	27	1.0	3.9	73	1.4
^{AT565}tris-NTA/IFNα2-HEQ [a]	2.0	24	1.2	4.0	76	1.5
– [a]	2.2	14		4.2	86	
^{FEW646}tris-NTA [a]	1.6	20	1.0	4.0	80	1.6
^{FEW646}tris-NTA/IFNα2-HEQ [a]	2.0	21	1.3	4.0	79	1.7
– [b]	1.0	29		4.2	71	
^{AT565}tris-NTA [b]	1.0	50		3.8	50	
^{AT565}tris-NTA/IFNα2-HEQ [b]	1.2	42		3.8	58	
– [c]	1.3	35		4.3	65	
^{AT565}tris-NTA [c]	1.1	50		4.0	50	
^{AT565}tris-NTA/IFNα2-HEQ [c]	1.5	40		4.1	60	

[a] OG488-labeled, determined by ensemble measurements

[b] OG488-labeled, determined by TCSPC

[c] AF488-labeled, determined by TCSPC

By fitting the fluorescence decay curves we obtained the decay times and thus the quantum yields of the samples. A bi-exponential decay was fitted for all samples. We interpreted this as a two state environment of the attached label. This might be due to linker flexibility that allows the label to find two possible positions on the protein surface. For evaluation of the FRET efficiency and the donor-acceptor distance, we treated each component independently. The distance between fluorescence donor and acceptor (r_{DA}) were estimated separately for each of the two decay time constants according to:

$$\frac{R_0}{r_{DA}} = \frac{1}{k_{fl}}\left[\frac{1}{t_{fl}} - \frac{1}{t_{fl,0}}\right]$$

Where R_0 is the Förster radius of the FRET pair, k_{fl} is the fluorescence rate constant, t_{fl} and $t_{fl,0}$ are the fluorescence lifetimes with and without FRET, respectively. The fluorescence rate constant k_{fl} was estimated to be 0.218 ns^{-1} (assuming a quantum yield of 0.9 and a fluorescence lifetime of 4.1 ns). The r_{DA} obtained for different FRET pairs and the different fluorescence lifetimes are summarized in Supplementary Table 1. With the estimated values R_0 of 5.8 nm for ^{AT565}tris-NTA and of 4.7 nm for ^{FEW646}tris-NTA, a change in distance of 1.2 - 1.4 nm was obtained from the fluorescence lifetimes t_2.

Supporting Table 2 Autocorrelation times (t) and amplitudes (A) obtained from FCS measurements.

Ifnar1-H10 in complex with	τ_{diff} [ms]	A_{diff} [%]	τ_1 [µs]	A_1 [%][a]	τ_2 [µs]	A_2 [%][b]	τ_3 [µs]	A_3 [%][b]
–	5.2	70	21	7	3.4	7	0.2	14
IFNα2-HEQ	5.2	69	10	7	2	7	0.14	18
^{AT565}tris-NTA	5.2	62	224	11	10	13	1.2	14
^{AT565}tris-NTA/IFNα2-HEQ	5.2	69	39	9	3.2	8	0.2	14

[a] A_1 corresponds to the change in intramolecular FRET efficiency due to flexibility of the molecule.

[b] A_2 and A_3 are related to photophysical processes.

Cytoplasmic Delivery of Liposomal Contents Mediated by an Acid-Labile Cholesterol-Vinyl Ether-PEG Conjugate

Jeremy A. Boomer,[†] Marquita M. Qualls,[‡] H. Dorota Inerowicz, Robert H. Haynes, V. Srilakshmi Patri, Jong-Mok Kim, and David H. Thompson*

Department of Chemistry, Purdue University, 560 Oval Drive, West Lafayette, Indiana 47907-1393. Received June 13, 2008; Revised Manuscript Received October 30, 2008

An acid-cleavable PEG lipid, 1′-(4′-cholesteryloxy-3′-butenyl)-ω-methoxy-polyethylene[112] glycolate (CVEP), has been developed that produces stable liposomes when dispersed as a minor component (0.5−5 mol %) in 1,2-dioleoyl-*sn*-glycero-3-phosphoethanolamine (DOPE). Cleavage of CVEP at mildly acidic pHs results in dePEGylation of the latently fusogenic DOPE liposomes, thereby triggering the onset of content release. This paper describes the synthesis of CVEP via a six-step sequence starting from the readily available precursors 1,4-butanediol, cholesterol, and mPEG acid. The hydrolysis rates and release kinetics from CVEP/DOPE liposome dispersions as a function of CVEP loading, as well as the cryogenic transmission electron microscopy and pH-dependent monolayer properties of 9:91 CVEP/DOPE mixtures, also are reported. When folate receptor-positive KB cells were exposed to calcein-loaded 5:95 CVEP/DOPE liposomes containing 0.1 mol % folate-modified 1,2-distearoyl-*sn*-glycero-3-phosphoethanolamine-*N*-polyethylene[76] glycolamide (folate-PEG-DSPE), delivery of the calcein cargo to the cytoplasm of the cells was observed as determined by fluorescence microscopy and flow cytometry. Fluorescence resonance energy transfer analysis of lipid mixing in these cells was consistent with membrane−membrane fusion between the liposome and endosomal membranes.

INTRODUCTION

Liposomes are clinically important drug delivery vehicles that can encapsulate a wide variety of low molecular weight drugs (*1*) as well as biopharmaceutical agents such as peptides, oligonucleotides, and plasmids (*2*−*5*). Major advantages are often provided by this class of drug carrier system due to their ability to encapsulate cargo by exploiting transmembrane chemical gradients, so-called "remote loading" (*6, 7*), and passivate it toward biodegradation in vivo during its transport to the target tissue. The performance of these carriers in vivo can be further enhanced by passive targeting (*8, 9*) via the enhanced permeability and retention effect (*10*), typically achieved in liposome systems by incorporation of poly(ethylene glycol)−lipid conjugates (e.g., mPEG-DSPE)[1] within the bilayer membrane. The primary effect of the PEG layer is to reduce and/or mask opsinization (*11*), thereby improving blood circulation lifetimes by sterically stabilizing the liposomes against clearance by the reticuloendothelial system and promoting their deposition at sites of porous and poorly formed vasculature such as those found in tumor tissues and sites of inflammation (*12*−*14*). Once deposited at these sites, however, drug retention by PEGylated liposomes can limit the bioavailability of the active agent, even when they have been internalized via receptor-mediated endocytosis pathways using actively targeted liposomal constructs (*15*). These observations suggest that the development of triggerable liposome formulations bearing site-specific targeting ligands could produce greatly increased drug efficacy when exposed to the appropriate stimulus (*16*−*22*). Previous work from this laboratory (*23, 24*) suggests that this is indeed the case; however, the slow release kinetics in these systems provided the impetus to develop improved triggerable liposome systems.

Several groups have developed lipid-based carrier systems that employ triggering mechanisms activated by pH (*25*−*35*), disulfide exchange (*36*−*43*), enzymes (*44*−*46*), heat (*47*−*49*), and photochemical reactions (*50, 51*) for deploying the encapsulated contents in a site- and/or time-specific manner. The presence of low pH environments within ischemic tissues and endosomal compartments during receptor-mediated endocytosis and vesicle trafficking (Figure 1) suggests that acid-triggering approaches should be a widely applicable activation strategy, since they would not require an external stimulus to initiate liposomal content release. This has motivated the development of triggering strategies in which the latent fusogenicity of DOPE liposome formulations containing cleavable PEG−lipids is restored upon removal of the PEG corona via dePEGylation (Figure 2). Several fusogenic and/or targeted liposome constructs

* Corresponding author. FAX: 765-496-2592; Email: davethom@purdue.edu.

[†] Current address: Abbott Laboratories, Abbott Park IL.

[‡] Current address: Entropia Consulting Group.

[1] Abbreviations: BVEP, (*R*)-1,2-di-*O*-(1′*Z*,9′*Z*-octadecadienyl)-glyceryl-3-(ω-methoxy-poly(ethylene glycol[112])ate; CBS, citrate buffered saline; CVEP, 1′-(4′-cholesteryloxy-3′-butenyl)-ω-methoxy-polyethylene[112] glycolate; DCC, dicyclohexylcarbodiimide; DMAP, 4-*N*,*N*-dimethylaminopyridine; DOPE, 1,2-dioleoyl-*sn*-glycero-3-phosphoethanolamine; DPPC, 1,2-dipalmitoyl-*sn*-glycero-3-phosphocholine; DPPG, 1,2-dipalmitoyl-*sn*-glycero-3-phosphoglycerol; EDCI, 1-ethyl-3-(3-dimethylaminopropyl)carbodiimide; EPC, egg phosphatidylcholine; FD-DMEM, folate-deficient Dulbecco's modified Eagle's medium; folate-PEG-DSPE, 1,2-distearoyl-*sn*-glycero-3-phosphoethanolamine-*N*-(ω-1′-folate-poly(ethylene [76] glycol))amide; H_{II}, hexagonal II phase; HBS, HEPES buffered saline; HEPES, *N*-(2-hydroxyethyl)piperazine-*N*′-(2-ethanesulfonic acid); HMPA, hexamethylphosphoramide; HPLC-ELSD, HPLC with evaporative light scattering detection; L_α, lamellar phase; LDA, lithium diisopropylamide; KB, cells a carcinoma cell line of nasopharyngeal origin; mPEG5000, derivatives of ω-methoxy-poly(ethylene [112] glycol); OBS, oxalate buffered saline; mPEG-DSPE, 1,2-distearoyl-*sn*-glycero-3-phosphoethanolamine-*N*-(ω-methoxy poly(ethylene [112] glycol))amide; TBAF, tetrabutylammonium fluoride; TBAH, tetrabutylammonium hydroxide; THF, tetrahydrofuran; TOAB, tetraoctylammonium bromide; TRIS, tris(hydroxymethyl)aminomethane.

10.1021/bc800239b CCC: $40.75 © 2009 American Chemical Society
Published on Web 12/15/2008

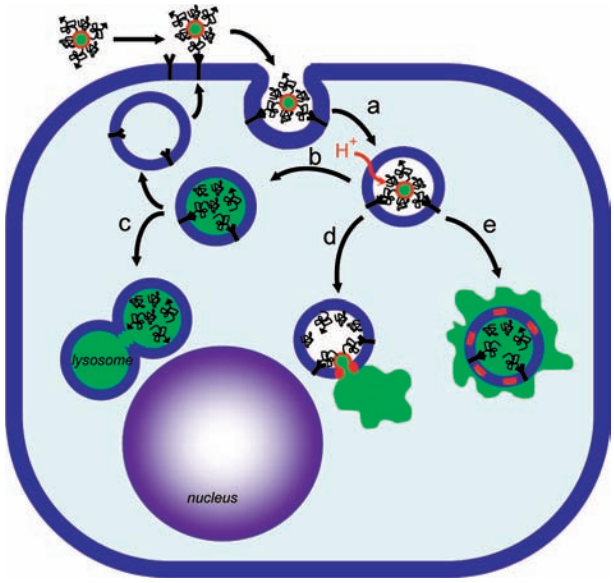

Figure 1. Conceptual diagram of receptor-mediated endocytosis pathway. Step a: Endosome formation. Step b: Endosome acidification and liposome degradation with endosomal trapping. Step c: Endosome−lysosome fusion. Step d: Liposome−endosome fusion. Step e: Lipid-mediated endosomolysis.

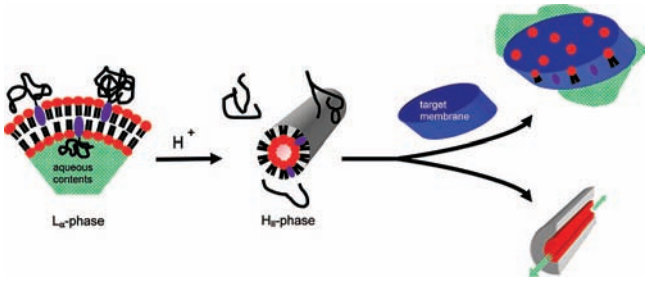

Figure 2. Schematic of lamellar → hexagonal II (L_α−H_{II}) phase transition driven by dePEGylation of cleavable PEG/DOPE liposomes (left and center). Detachment of PEG induces a change in the local membrane curvature leading to the formation of H_{II} domains within the bilayer. Contact of these sites with other lamellar phases can promote membrane−membrane fusion and transmembrane content transport (top right). Absence of membrane contact due to low membrane concentrations or steric repulsion results in L_α phase collapse and content release into the surrounding solution (bottom right).

stabilized by cleavable (*25*, *27*, *28*, *33*, *36*, *37*, *41*), exchangeable (*52*−*58*), or polymerizable (*59*) PEG conjugates have been designed and investigated; however, a broadly applicable system for in vivo application has yet to emerge.

Our laboratory previously reported a novel acid-labile PEG-lipid conjugate, (*R*)-1,2-di-*O*-(1′*Z*,9′*Z*-octadecadienyl)-glyceryl-3-(ω-methoxy-poly(ethylene glycol[112])ate (BVEP, Figure 3) that displays pH-dependent content release properties when dispersed as a minor component (i.e., 1−10 mol %) in BVEP/DOPE liposome formulations (*27*). The content release and membrane fusion kinetics of this system, however, are too slow for many envisioned in vivo applications. We anticipated that there were three possible reasons the observed release kinetics are slow: (1) the acid-labile vinyl ether linkages are buried too

[2]Since PEG is known to osmotically deplete waters of hydration at membrane and protein surfaces (*61*−*66*), it is also reasonable to expect that the local proton activity will be lower at this water-depleted interface—an effect that could impact either the first or second steps (or both) in the hydrolysis pathway (Figure 3). This would be especially problematic for BVEP since complete separation of PEG from the lipid anchor requires two sequential hydrolysis events.

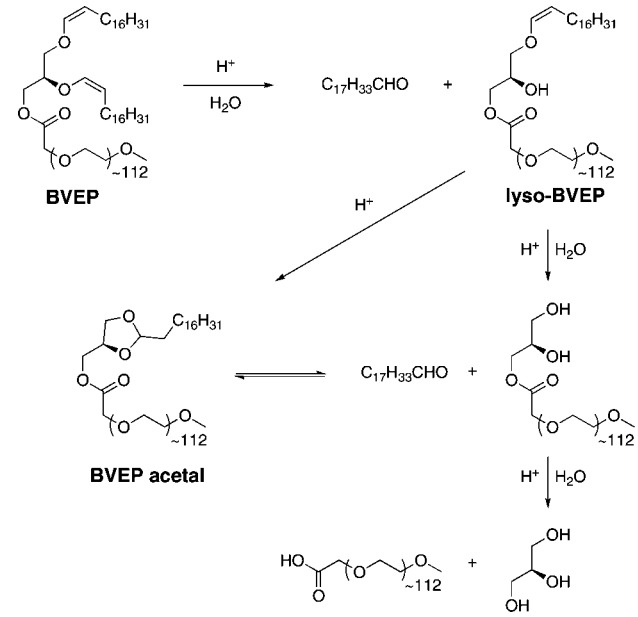

Figure 3. Acid-catalyzed hydrolysis pathway for BVEP. Mechanistic details of the rate-determining β-carbon protonation, oxonium ion hydration, and hemiacetal cleavage steps are not shown. The protonated intermediate of lyso-BVEP has two possible fates—trapping by water to give the desired products (bottom right) or intramolecular trapping to give the L_α-phase stabilizing species, BVEP acetal (bottom left).

deep in the membrane to permit rapid protonation of the vinyl ether β-carbon, the rate determining step in vinyl ether hydrolysis (*60*)[2]; (2) a side reaction of partially hydrolyzed BVEP produces BVEP acetal, a dioxolane-based PEG−lipid conjugate that could stabilize the DOPE membrane via binding of the single aliphatic chain; or (3) the PEG remains weakly adsorbed to the membrane even after it is fully hydrolyzed, thereby preventing the expected lamellar (L_α) to hexagonal (H_{II}) phase transition.

We have developed a cleavable PEG lipid, 1′-(4′-cholesteryloxy-3′-butenyl)-ω-methoxy-polyethylene[112] glycolate (CVEP, Figure 4), to circumvent these limitations. This lipopolymer target was designed because a single hydrolysis event would cleave the PEG headgroup from CVEP, thereby accelerating the rate of dePEGylation and the subsequent content release and/or fusion processes. Another integral part of this design was the relocation of the vinyl ether linkage closer to the aqueous region where the rate of hydrolysis could be enhanced by placing the acid-sensitive linkage within a region of higher proton activity. This paper describes the synthesis of CVEP, the physical characterization of CVEP/DOPE liposomes, and their performance with respect to intracellular delivery of liposomal cargo in folate receptor-positive KB cell culture using folate-targeted CVEP/DOPE formulations.

EXPERIMENTAL METHODS

Synthesis of CVEP. 2,2′-Dipyridylcarbonate was purchased from TCI-America. MPEG-acid was purchased from Shearwater Polymers. All other compounds were purchased from Aldrich and used without further purification unless otherwise stated. Triethylamine and diisopropylamine were distilled from CaH_2. All solvents used were spectrophotometric grade, dried over an appropriate desiccant, and distilled. Reactions were performed under an argon atmosphere. $Pd(PPh_3)_4$ was obtained from Strem. Column chromatography was typically performed with 230−400 mesh silica gel using high-grade solvents to elute the compounds. Thin layer chromatography was performed using Baker-flex IB-F plates and visualized using UV, I_2 adsorption, $KMnO_4$/

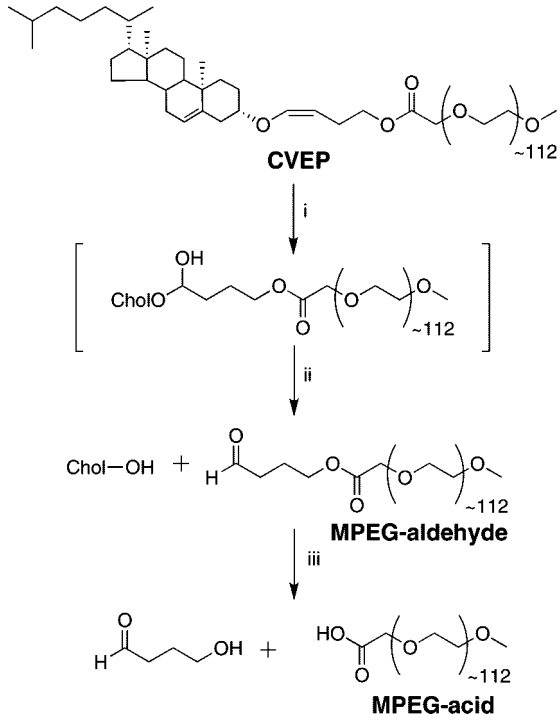

Figure 4. Acid-catalyzed hydrolysis pathway for CVEP. (i) Vinyl ether protonation and hydration; (ii) hemiacetal cleavage; (iii) subsequent hydrolysis of mPEG-aldehyde to produce mPEG-acid.

heat, and/or molybdic acid/heat. ^{1}H NMR and ^{13}C NMR spectra were recorded on a 4.7 T spectrometer. Chemical shifts are reported in ppm relative to the residual solvent peaks as the internal standard. Attached proton test (APT) results are reported as odd (O, one or three protons attached) or even (E, zero or two protons attached) after the corresponding ^{13}C chemical shifts.

*4-t-Butyldimethylsilyloxybutan-1-ol (**1**) (67).* *t*-Butyldimethylsilyl chloride (8.65 g, 57.4 mmol) in dry THF (25 mL) was added dropwise to a solution of 1,4-butanediol (22.0 g, 244 mmol; dried 2 h in vacuo) and imidazole (5.1 g, 70.5 mmol) in THF (100 mL) at 0 °C over a ~20 min period. The reaction, which turned cloudy after 10 min, was stirred for 1 h, warmed to room temperature, and ether (300 mL) added. The solution was then washed with saturated NH_4Cl (2 × 200 mL) and saturated NaCl (1 × 200 mL). The ether layer was dried over $MgSO_4$, filtered, evaporated, and dried in vacuo yielding a pale yellow oil (11.4 g, 97% yield). NMR analysis indicated that the product was sufficiently pure to utilize in the ensuing step without additional purification. TLC (4:1 hexane/ether, $KMnO_4$): $R_f = 0.35$. ^{1}H NMR ($CDCl_3$): 0.05 (s, 6H), 0.85 (s, 9H), 1.60 (m, 4H), 2.60 (bs, 1H), 3.65 (q, 4H). ^{13}C NMR/APT ($CDCl_3$): −5.54 (O), 18.15 (E), 25.76 (O), 29.60 (E), 29.79 (E), 62.33 (E), 63.18 (E).

*4-t-Butyldimethylsilyloxybutanoic acid (**2**) (68).* $KMnO_4$ (3.2 g, 20.2 mmol) was dissolved in water (50 mL), stirred vigorously for 10 min, then cooled to 0 °C. A solution of 4-*t*-butyldimethylsilyloxybutan-1-ol (**1**, 1.98 g, 9.7 mmol) and tetraoctylammonium bromide (TOAB, 812 mg, 1.5 mmol) in benzene (40 mL) was added dropwise via addition funnel over a ~20 min period. The solution was then warmed to room temperature and stirred for 3 h. The remaining $KMnO_4$ was quenched with $NaHSO_3$, producing a two-phase mixture with a colorless organic layer. Benzene (20 mL) and 50% CH_3CO_2H (50 mL) were added and the mixture extracted. The benzene layer was then washed with saturated NaCl (50 mL), dried over $MgSO_4$, filtered, evaporated, and dried in vacuo. The remaining TOAB was removed via elution through a small silica plug with 2:1 hexane/ether mobile phase. The solvent was evaporated and the sample dried in vacuo giving a colorless oil (1.65 g, 78% yield). TLC (1:1 hexane/ether, Bromphenol blue): $R_f = 0.65$. ^{1}H NMR ($CDCl_3$): 0.05 (s, 6H), 0.85 (s, 9H), 1.83 (p, $J = 7$ Hz, 2H), 2.44 (t, $J = 7$ Hz, 2H), 3.65 (t, $J = 7$ Hz, 2H), 11.09 (bs, 1H). ^{13}C NMR/APT ($CDCl_3$): −5.47 (O), 18.24 (E), 25.85 (O), 27.57 (E), 30.71 (E), 61.95 (E), 179.96 (E).

*Cholesteroyl-4-t-butyldimethylsilyloxybutanoate (**3**).* Cholesterol (609 mg, 1.58 mmol), 4-*t*-butyldimethylsilyloxy butanoic acid (**2**, 325 mg, 1.49 mmol), and DMAP (20 mg, 0.14 mmol) were dissolved in CH_2Cl_2 (15 mL) and the solution cooled to 0 °C. EDCI (284 mg, 1.49 mmol) was added, and the mixture was warmed to room temperature with stirring for 10 d. The reaction mixture was poured into H_2O (75 mL) and extracted with CH_2Cl_2 (3 × 75 mL). The combined CH_2Cl_2 layers were dried over $MgSO_4$, filtered, evaporated, dried in vacuo, and the crude product purified via chromatography (230−400 mesh silica, 9:1 hexane/ether, 1.5 cm diameter × 5 cm height) to give a white solid (780 mg, 90% yield). TLC (2:1 hexane/ether, acid char): $R_f = 0.52$. MP: 133−135 °C. ^{1}H NMR ($CDCl_3$): 0.05 (s, 6H), 0.65 (s, 3H), 0.8−2.05 (m, 49H), 2.25−2.4 (m, 4H), 3.65 (t, $J = 7$ Hz, 2H), 4.6 (m, 1H), 5.35 (d, $J = 5$ Hz, 1H). ^{13}C NMR ($CDCl_3$): −4.8, 12.4, 18.8, 19.1, 19.3, 19.7, 19.9, 21.5, 23.0, 23.1, 23.2, 23.3, 24.3, 24.8, 26.4, 26.5, 28.3, 28.5, 28.7, 31.5, 32.4, 36.3, 36.7, 37.1, 37.5, 38.6, 40.0, 40.2, 40.3, 42.8, 50.5, 56.6, 57.2, 62.5, 123.1, 140.2, 173.5. MS (CI): $m/z = 587$ (M + H).

*4-t-Butyldimethylsilyloxy-1-cholesteryloxy-1-diethylphosphoryloxy-1-butene (**4**).* *n*-Butyl lithium (795 μL, 1.94 mmol, 2.4 M in hexane) was added dropwise, via syringe, to diisopropylamine (453 μL, 3.23 mmol) in THF (250 μL) at −78 °C and the solution stirred for 30 min. Cholesteroyl-4-*t*-butyldimethylsilyloxy butanoate (**3**, 758 mg, 1.29 mmol) in THF (3 mL) was then slowly added dropwise, via syringe. The solution was stirred for an additional hour, followed by the addition of diethylchlorophosphate (373 μL, 2.58 mmol) in HMPA (4.9 mL) in three aliquots. The solution turned orange/brown and gelled. It was thawed enough to resume stirring, then returned to −78 °C for 10 min. The reaction was then warmed to room temperature and stirred for an additional hour. Ether (50 mL) was added and the reaction mixture filtered through a small silica plug. The solvent was evaporated, the oil redissolved in ether (75 mL), and the organic layer washed with 5% $NaHCO_3$ (3 × 75 mL). The ether layer was dried over $MgSO_4$, filtered, evaporated, and dried briefly in vacuo. The crude product was purified via flash chromatography (230−400 mesh silica, 6:1 hexane/ether, 2 cm diameter × 16 cm height) to give a white solid (750 mg, 81% yield). The product was used immediately without additional characterization. TLC (2:1 hexane: ether, I_2): $R_f = 0.35$.

*4-t-Butyldimethylsilyloxy-1-cholesteryloxy-1-butene (**5**).* Tetrakis(triphenylphosphine) palladium (15 mg, 12.4 μmol) and 4-*t*-butyldimethylsilyloxy-1-cholesteryloxy-1-diethylphosphoryloxy-1-butene (**4**, 270 mg, 373 μmol) were added to CH_2Cl_2 (8 mL) and cooled to 0 °C. Triethyl aluminum (653 μL, 653 μmol; 1.0 M in hexane) was then added dropwise via syringe. The solution was stirred at 0 °C for 1 h before warming to 23 °C and stirring for an additional 3 h. The crude mixture was purified via flash chromatography (230−400 mesh silica, 16:1 hexane/ether, 1.5 cm diameter × 20 cm height) to give a 90:10 cis/trans mixture as a white solid (66 mg, 31% yield). TLC (16:1 hexane/ether, *p*-anisaldehyde): $R_f = 0.75$ (cis), 0.71 (trans). ^{1}H NMR (C_6D_6, 90:10 cis/trans mixture): 0.13 (s, 6H), 0.68 (s, 3H), 0.8−2.75 (m, 51H), 3.4 (m, 1H), 3.75 (t, $J = 12$ Hz, 2H), 4.6 (dt, $J_1 = 8$ Hz, $J_2 = 7$ Hz, 0.9H), 5.15 (dt, $J_1 = 13$ Hz, $J_2 = 7$ Hz, 0.1H), 5.35 (m, 1H), 6.04 (dt, $J_1 = 7$ Hz, $J_2 = 2$ Hz, 0.9H), 6.15 (dt, $J_1 = 13$ Hz, $J_2 = 2$ Hz, 0.1H). ^{13}C NMR/APT (C_6D_6,

90:10 cis/trans mixture): −4.8 (O), 12.2 (O), 19.1 (O), 19.5 (O), 19.6 (O), 21.5 (E), 22.8 (O), 23.1 (O), 24.3 (E), 24.6 (E), 26.2 (O), 28.5 (O), 28.8 (E), 28.9 (E), 29.2 (E), 29.6 (E), 29.7 (E), 30.3 (E), 30.6 (E), 32.2 (O), 32.4 (E), 36.2 (O), 36.8 (E), 37.0 (E), 37.3 (E), 37.6 (E), 39.9 (E), 40.0 (E), 40.2 (E), 40.3 (E), 42.6 (E), 51.5 (O), 56.8 (O), 57.0 (O), 63.8 (E), 81.3 (O), 103.0 (O), 106.5 (O), 122.1 (O), 140.5 (E), 141 (O), 145.2 (O).

*4-Cholesteryloxy-3-buten-1-ol (**6**).* TBAF (210 μL, 210 μmol, 1.0 M in THF) and 1.0 mL 40% TBAH were added via syringe to 4-*t*-butyldimethylsilyloxy-1-cholesteryloxy-1-butene (**5**, 40 mg, 70 μmol) in THF (3 mL). The reaction was run for 12 h at 23 °C, then filtered through a small silica plug with ether and the solvent evaporated. The mixture was purified via flash chromatography (230−400 mesh silica, 8:1 hexane/ether, 1.5 cm diameter × 15 cm height) to give *cis*-4-cholesteryloxy-3-buten-1-ol (29 mg, 91% yield) and *trans*-4-cholesteryloxy-3-buten-1-ol (1.5 mg, 4% yield) as white solids (95% combined yield). TLC (2:1 hexane/ether, acid char): $R_f = 0.18$ (cis), 0.14 (trans). ^{1}H NMR (C_6D_6, cis): 0.65 (s, 3H), 0.8−2.05 (m, 39H), 2.3−2.53 (m, 4H), 3.35 (m, 1H), 3.58 (t, $J = 6$ Hz, 2H), 4.4 (dt, $J_1 = 7$ Hz, $J_2 = 7$ Hz, 1H), 5.35 (m, 1H), 5.98 (dt, $J_1 = 6$ Hz, $J_2 = 1$ Hz, 1H). ^{1}H NMR (C_6D_6, trans): 0.65 (s, 3H), 0.8−2.05 (m, 41H), 2.4−2.5 (m, 2H), 3.35 (t, $J = 7$ Hz, 2H), 3.5 (m, 1H), 4.95 (dt, $J_1 = 13$ Hz, $J_2 = 6$ Hz, 1H), 5.35 (m, 1H), 6.15 (dt, $J_1 = 12$ Hz, $J_2 = 1$ Hz, 1H). ^{13}C NMR/APT (C_6D_6, 70:30 cis/trans): 12.06 (O), 12.40 (O), 14.40 (O), 19.04 (O), 19.4 (O), 19.5 (O), 21.0 (E), 21.4 (E), 22.8 (O), 23.0 (O), 24.4 (E), 24.6 (E), 25.5 (E), 28.4 (O), 28.6 (E), 28.7 (E), 29.1 (E), 29.5 (E), 30.0 (E), 32.1 (O), 32.3 (E), 36.2 (O), 36.7 (E), 36.9 (E), 37.3 (E), 37.5 (E), 39.8 (E), 39.9 (E), 40.2 (E), 42.6 (E), 50.5 (O), 50.6 (O), 54.3 (E), 56.6 (O), 57.0 (O), 62.7 (E), 63.0 (E), 75.9 (O), 79.8 (O), 81.2 (O), 102.0 (O), 102.9 (O), 106.2 (O), 122.1 (O), 122.3 (O), 140.4 (E), 140.8 (E), 145.6 (O). MS (CI): $m/z = 457$ (M + H).

*1′-(4′-Cholesteryloxy-3′-butenyl)-ω-methoxy-poly(ethylene-[112]glycol)ate (CVEP, **7**).* 4-Cholesteryloxy-3-buten-1-ol (**6**, 44 mg, 96 μmol), mPEG5000-acid (435 mg, 87.0 μmol), DCC (21.6 mg, 104 μmol), and DMAP (10 mg, 81 μmol) were added to CH_2Cl_2 (7 mL) and stirred for 4 d. The reaction mixture was then cooled to 0 °C and the DCU removed via filtration (21 mg). The solvent was concentrated to 2 mL, dripped into cold ether (20 mL), and the ether solution centrifuged at 4000 rpm for 10 min. The ether was carefully decanted and the pellet triturated with fresh ether (20 mL). This process was repeated 5 times. The pellet was then dissolved in CH_2Cl_2, evaporated to a dry film, dissolved in 2 mL 18 MΩ Millipore H_2O, and lyophilized to give 420 mg PEG-containing product (86% yield based on recovered DCU). TLC (90:10:1 $CHCl_3$/MeOH/H_2O, I_2): $R_f = 0.75$. ^{1}H NMR ($CDCl_3$, cis): 0.65 (m, 3H), 0.75−2.5 (m, 50H + H_2O), 3.2−4.5 (m, >120H), 5.35 (m, 1H), 6.1 (m, 1H). ^{1}H NMR ($CDCl_3$, 65:35 cis/trans): 0.65 (m, 3H), 0.75−2.5 (m, 50H + H_2O), 3.2−4.5 (m, >120H), 5.35 (m, 1H), 6.08 (m, 0.65H), 6.15 (m, 0.35H).

Hydrolysis Kinetics. HPLC solvents were spectrophotometric grade and filtered through a 450 nm FP Vericel membrane (Gelman Sciences, Ann Arbor, MI) immediately prior to use. Reverse-phase HPLC analysis was performed with a Spherisorb C_{18} column (4.6 × 150 mm, 5 μm particles; Waters Corp., Milford, MA) protected with a C_{18} Guard-Pak prefilter (Waters). Peak detection was achieved with a Sedex 55 evaporative light scattering detector (Sedere, France). Pump control and data analysis were performed using *EZChrom* v. 6.8 (Scientific Software, Pleasanton, CA). The following gradient elution was performed with a flow rate of 1.5 mL/min: 0−29 min, 6:4 MeOH/H_2O; 30−50 min, MeOH; 51−65 min, 6:4 MeOH/H_2O. Chromatographic peaks assigned to mPEG-aldehyde ($R_T = 14$ min) and mPEG-acid ($R_T = 10$−11 min) were verified by comparison with retention times determined for standard samples. The identities of the peaks assigned to CVEP ($R_T = 35.2 \pm 0.2$ min) and cholesterol ($R_T = 36.3$ min) were confirmed by comparing the NMR and mass spectra of lyophilized HPLC fractions with reference spectra.

Preparation of Liposomes. DOPE and EPC were purchased from Avanti Polar Lipids (Alabaster, AL) as either lyophilized powders or chloroform stock solutions. Calcein was purchased from Sigma (St Louis, MO). A 50 mM calcein stock solution was prepared in 20 mM HEPES buffered saline (HBS, 150 mM NaCl, pH 8.0) or 20 mM TRIS (150 mM NaCl, pH 7.4). Low pH hydrolysis was performed in 20 mM citrate buffered saline (CBS, 150 mM NaCl, pH 4.5) or 20 mM oxalate buffered saline (OBS, 150 mM NaCl, pH 2.0).

Liposomes were prepared by the thin film method. A chloroform solution of the desired lipids (5 μmol) was carefully evaporated under nitrogen flow, producing an even, thin film. The film was placed under a 50 μm Hg vacuum for at least 3 h to remove trace solvent impurities. This film was then hydrated in 1 mL 50 mM calcein buffer stock buffer solution via 10 freeze−thaw−vortex cycles. The resulting multilamellar liposome solution was then extruded ten times through two stacked 100 nm polycarbonate filters at 50−60 °C with ∼200−300 psi nitrogen. After extrusion, the extraliposomal calcein buffer was exchanged with either 150 mM NaCl or 20 mM HBS buffer via a 0.5 × 25 cm Sephadex G-50 column. This exchange process typically resulted in a 2- to 2.5-fold dilution of the liposome solution. The liposomes were always used immediately, but appeared stable for ∼1 week when stored at 4 °C (as monitored by calcein leakage and light scattering).

EPC sink liposomes were prepared in the same manner as other liposomes at a 10-fold higher concentration (100 mg/mL) in 0.9% NaCl. These liposomes appeared to be stable for at least 3 weeks when stored at 4 °C.

Calcein Release Assay. All solutions were equilibrated at 37 °C for 10 min prior to mixing. An aliquot of liposome stock solution (100 μL) was added to 1.3 mL of HBS, CBS, OBS, TRIS, or 20 mM FD-DMEM containing 10% heat-inactivated fetal calf serum and 0.5% penicillin/streptomycin. Then, 100 μL 150 mM NaCl or 100 μL of EPC stock liposomes (sink experiments) were added. This solution was maintained at 37 °C for the duration of the experiment. At each time point, 100 μL aliquots were removed and diluted with 2 mL HBS. The fluorescence ($\lambda_{ex} = 490$ nm, $\lambda_{em} = 518$ nm) was then measured before and after the addition of two drops of 10% Triton X-100 (solution gently shaken to ensure complete liposome disruption). The percent release was then quantified using the ratio method: % release $= 100 \times [(T - T_o)/(1 - T_o)]$, where T = Triton ratio = (fluorescence before Trition/fluorescence after Triton) at time T and T_o = Triton ratio at $T = 0$ min (*26*).

Cytoplasmic Delivery of Calcein. Folate-deficient KB cells were plated at 100 000 cells/well in 33 mm dishes with 2.0 mL of FD-DMEM. Two hundred microliters of 5:95:0.5 CVEP/DOPE/folate-PEG-DSPE (targeted) or 5:95 CVEP/DOPE (non-targeted) liposomes (5 μM total lipid containing 50 mM entrapped calcein) were incubated at 37 °C for 2 h, followed by three thorough washes with PBS buffer (-Mg^{2+}, -Ca^{2+}) to remove any unbound liposomes. Fresh FD-DMEM (2 mL) was added and the cells incubated for an additional 2 h before qualitative fluorescence microscopy analysis of localization and total cellular fluorescence intensity. Fluorescence micrographs were taken approximately 6 h after introduction of liposomes. Endosomal pH inhibition was achieved by preincubating the cells in FD-DMEM containing 50 mM chloroquine 30 min prior to addition of liposomes.

Quantitative evaluation of endosomal release of calcein was determined by flow cytometry. Media from the cell culture

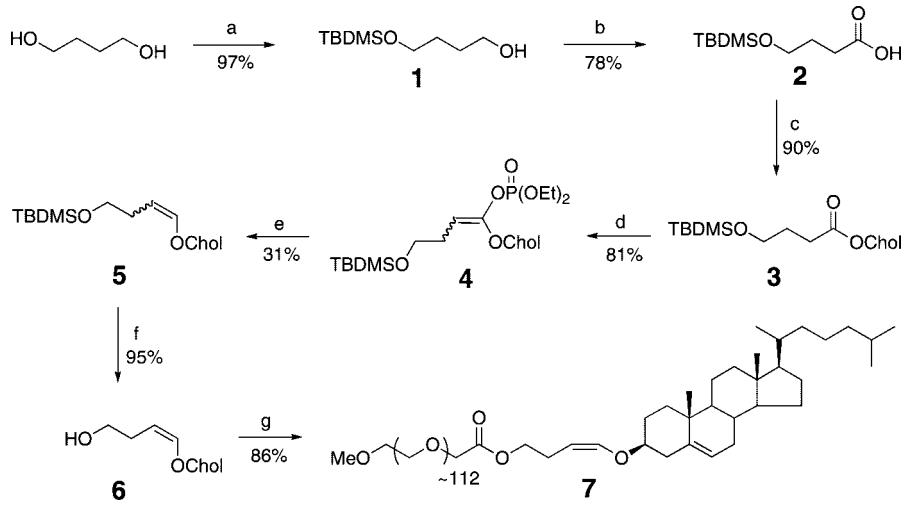

Figure 5. Synthesis pathway for CVEP. a: TBDMSCl, imidazole/THF, 0 °C, 1 h. b: $KMnO_4$, TOAB/C_6H_6/H_2O, 25 °C, 3 h. c: Cholesterol, DMAP, EDCI/CH_2Cl_2, 25 °C, 10 d. d: (1) LDA/HMPA, −78 °C, 1 h; (2) $(EtO)_2POCl$, −78 °C → 25 °C, 1 h. e: $Pd(PPh_3)_4$, Et_3Al/CH_2Cl_2, 0 °C → 25 °C, 1 h → 3 h. f: TBAF, TBAH/THF, 25 °C, 12 h. g: mPEG5000-acid, DCC, DMAP/CH_2Cl_2, 25 °C, 4 d.

dishes was removed and collected in 1.5 mL centrifuge tubes to ensure inclusion of all cells. Cell dissociation solution (100 μL) was added to the wells and incubated for 20 min. This fraction was then added to the collected media and centrifuged. An average of 5000 cells were then analyzed on a Coulter Epics XL flow cytometer using 488 nm excitation and 525 nm/620 nm emission filters.

Lipid Mixing Assay (*69*). NBD-PE (1%), Rh-PE (1%), and folate-PEG3350-DSPE (0.5%) were added to a benzene/methanol (95:5) solution of the CVEP/DOPE dispersion to be studied (5 μmol total lipid). The solution was vortexed thoroughly, frozen in liquid nitrogen, and then lyophilized overnight. The resulting lipid powder was hydrated with HEPES buffer, pH 7.4, and extruded as described above.

Cells were plated at 100 000 cells/well in Labtek 4-chambered coverslips that had been previously treated with fibronectin (4 μg/mL). KB cells were incubated for 2 h with 100 μL of the dual-labeled NBD-Rh liposome solution. Cells were then washed three times with liposome-free media, replenished with fresh media, and imaged at various intervals using a BioRad MRC 1024 laser confocal microscope (488 nm excitation). A 585 nm LP filter was used to collect the rhodamine fluorescence and a 535 nm filter was used to collect the NBD fluorescence.

Light Scattering. Liposome size was determined by quasi-elastic light scattering on a Coulter N4-Plus instrument and distributions calculated using the manufacturer's supplied software (version 1.1). Samples were prepared by diluting 25 μL liposome stock with 2 mL HBS. Experiments were run in triplicate and the size distributions averaged for these runs.

Transmission Electron Microscopy. Negatively stained EM samples were prepared with 1% $UO_2(OAc)_2$ using the post-staining method on Formvar-coated copper grids and analyzed using a Phillips TEM operating at 40 kV.

RESULTS AND DISCUSSION

Synthesis of CVEP (7). Initial attempts at the synthesis of CVEP via transformation of a cholesterol ester linkage to a vinyl ether linkage (*70*−*72*) in the presence of the PEG functionality proved unsuccessful. This outcome is likely due to the presence of water that is tightly bound by PEG (even after vacuum drying at 50 μm Hg in the presence of P_2O_5 for two days), which rapidly quenches the LDA reagent during the vinyl phosphate transformation. This approach was abandoned when it became clear that the same interference would occur during the subsequent $Et_3Al/Pd(PPh_3)_4$ reduction steps. Compounding this problem is the fact that the resulting product mixture would be too difficult to purify on a large scale because of the presence of the PEG moiety.

These problems prompted the development of a new synthetic route to CVEP (Figure 5) wherein the water-soluble polymer could be attached to the cholesterol membrane anchoring group during the final step, after installation of the vinyl ether functionality. In this strategy, the PEG headgroup and cholesterol lipid anchor are conjugated via a four-carbon, vinyl ether containing linker derived from 4-hydroxybutanoic acid. The three key advantages provided by this approach are as follows: (1) the PEG headgroup is added in the final step; (2) the Z-vinyl ether transformation step is easily accommodated; and (3) the route allows facile incorporation of a wide variety of alcohol-bearing lipid anchor substituents.

The CVEP synthesis sequence begins with the production of cholesteryl 4-*t*-butyldimethylsilyloxybutanate (*3*) from 1,4-butanediol in a three-step process. Monoprotection of 1,4-butanediol with *t*-butyldimethylsilyl chloride in THF afforded 4-*t*-butyldimethylsilyloxybutane-1-ol (*1*) in 97% yield after extraction of the excess 1,4-butanediol. The presence of the TBDMS ether necessitated the use of neutral oxidation conditions in the subsequent step. Initial attempts using pyridinium dichromate under neutral conditions were successful; however, yields were typically low and the purification difficult. Alternatively, alcohol **1** was readily converted in 78% yield to the corresponding carboxylic acid **2** via a two-phase potassium permanganate oxidation, mediated by tetraoctylammonium bromide as phase transfer catalyst. EDCI/DMAP-mediated coupling of acid **2** and cholesterol afforded **3** in 90% yield.[3]

The vinyl ether bond was then installed via a two-step ester reduction procedure. The kinetic enolate of ester **3** was *O*-trapped with diethylchlorophosphate in the presence of HMPA to afford a vinyl phosphate intermediate (*4*) in 81% yield after chromatographic purification. The normally facile $Et_3Al/Pd(PPh_3)_4$-mediated reduction of vinyl phosphates in hexane, however, failed to produce 4-*t*-butyldimethylsilyloxy-1-cholesteryloxy-1-butene (*5*); instead, a mixture of ester **3** and vinyl phosphate **4** was recovered. The use of CH_2Cl_2 as solvent provided vinyl ether **5** in 31% isolated yield, well below the 70+% yields typically observed for this transformation. Un-

[3]DCC/DMAP conditions were also employed to afford ester **3**; however, the use of EDCI is preferred since product isolation is easier when this dehydrating agent is employed.

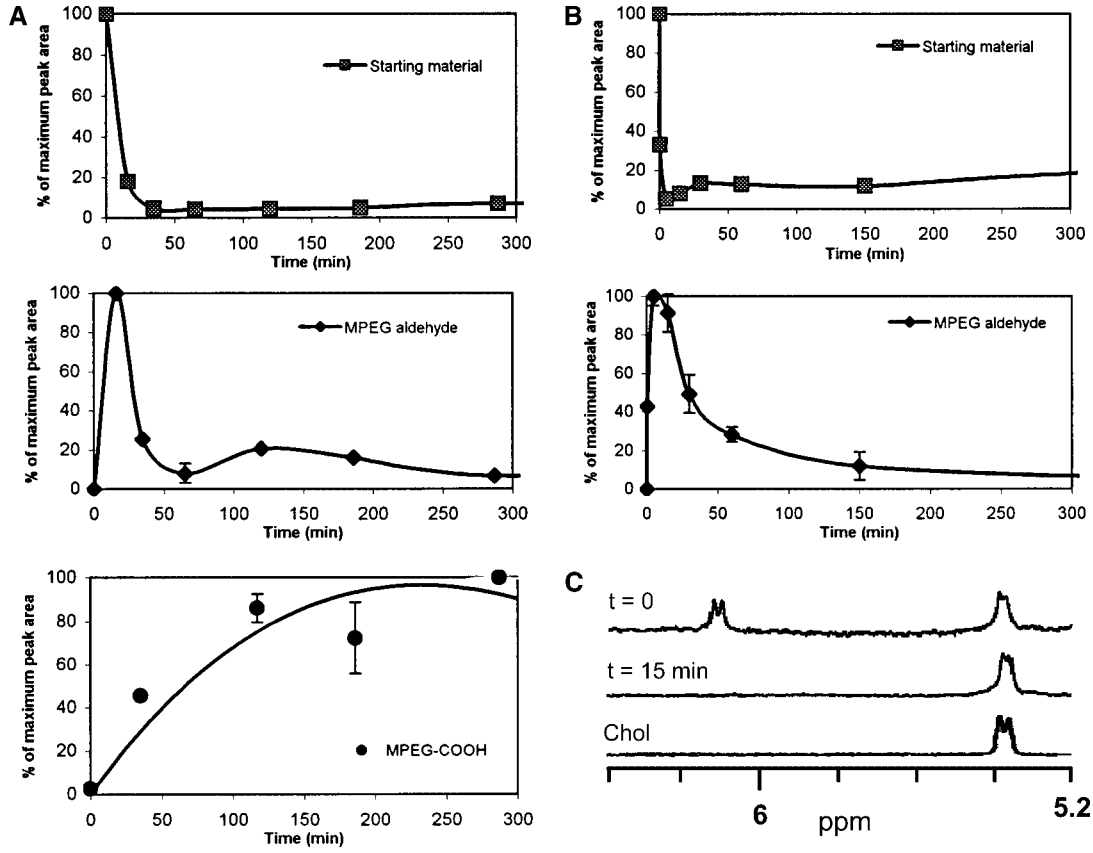

Figure 6. CVEP hydrolysis at 25 °C in acidic aqueous solution as detected by HPLC-ELSD (A,B) and ^{1}H NMR (C). A: CVEP hydrolysis kinetics at pH 1.0. Top: CVEP disappearance rate. Middle: mPEG-aldehyde appearance/disappearance rate. Bottom: mPEG-acid formation rate. B: CVEP hydrolysis kinetics at pH 3.0. Top: CVEP disappearance rate. Bottom: mPEG-aldehyde appearance/disappearance rate. C: NMR characterization of CVEP hydrolysis at pH 1.0. HPLC fractions eluting at $R_T = 32-37$ min were collected and lyophilized before NMR analysis. Top: CVEP before acid treatment, showing α-H vinyl ether signal (6.12 ppm) and cholesterol vinyl protons (5.38 ppm). Middle: Same CVEP sample after 15 min at pH 1.0. Bottom: Cholesterol standard.

fortunately, use of this more polar solvent produced scrambled vinyl ether stereochemistry (9:1 Z/E). Two other reduction methodologies, Li/NH_3/*t*-butanol and Bu_3SnH, were also attempted; however, these transformations either failed or regenerated ester **3**.

The final stages of CVEP synthesis involved deprotection of vinyl ether **5**, followed by esterification with ω-methoxy-poly(ethylene [112]glycol)-carboxymethyl (mPEG-acid). Desilylation of **5** with tetrabutylammonium fluoride afforded alcohol **6** in 95% overall yield. Addition of small amounts of tetrabutylammonium hydroxide (TBAH, 30% in water) significantly increased the reaction rate and ensured a basic solution, thereby preventing hydrolytic decomposition of the vinyl ether species (occasionally observed in its absence). Careful chromatographic separation of the E and Z stereoisomers of **6**, followed by a DCC/DMAP-mediated coupling reaction with mPEG-acid produced CVEP (*7*) in 86% yield.[4] The seven-step sequence in Figure 5 afforded the pure cis form of CVEP in 20% overall yield. All subsequent experiments utilized the pure Z CVEP isomer; however, no significant differences in release or hydrolysis rates were observed when 2:1 Z/E mixtures of CVEP were used.

CVEP Hydrolysis Kinetics. CVEP hydrolysis kinetics at 25 °C were determined via HPLC-ELSD by monitoring both the time-dependent disappearance of the CVEP peak ($R_T = 34-35$ min) at different pHs, as well as the appearance times of the degradation products mPEG-aldehyde, mPEG-acid, and cholesterol. Chromatographic peaks for CVEP and its hydrolysis products—cholesterol, mPEG-alcohol, and mPEG-acid—were verified by injection of known standards as well as by NMR and MS characterization of all collected fractions, except for mPEG-aldehyde (which used mPEG-alcohol as a retention time standard due to the rapid oxidation of this material to mPEG-acid). Under all conditions studied, decreasing CVEP peak areas were accompanied by proportional increases in the peak areas corresponding to mPEG-aldehyde, an intermediate product in the hydrolysis of CVEP (Figure 4). CVEP hydrolysis rates were very fast at pH 1 (Figure 6A), with less than 20% of CVEP remaining and maximal levels of mPEG-aldehyde and cholesterol existing after 15 min exposure. The disappearance rate for CVEP and the appearance rate for mPEG aldehyde were identical. As the reaction time increased, mPEG-acid slowly increased at the expense of both CVEP and mPEG-aldehyde, consistent with the reaction pathway shown in Figure 4. After 15 h reaction time, only two HPLC peaks were observed. ^{1}H NMR analysis of the material eluting between 32 and 37 min corresponded to cholesterol, whereas the lower R_T species ($R_T = 10-11$ min) was identified as mPEG-acid.

At pH 3 (Figure 6B), the rates for CVEP disappearance and mPEG-aldehyde appearance also occurred on similar time scales. Unlike the pH 1 experiments, however, the CVEP peak stopped decreasing in relative area after ~35 min and began to increase slightly with time. The peak for cholesterol also began decreasing at the same time as this apparent increase in CVEP concentration. We infer from these observations that a cholesterol−mPEG complex is formed at pH 3.0 (possibly the cholesterol−mPEG hemiacetal), which displays a similar reten-

[4]EDCI/DMAP coupling also provided CVEP, although the urea side product proved difficult to remove via the ether precipitation method.

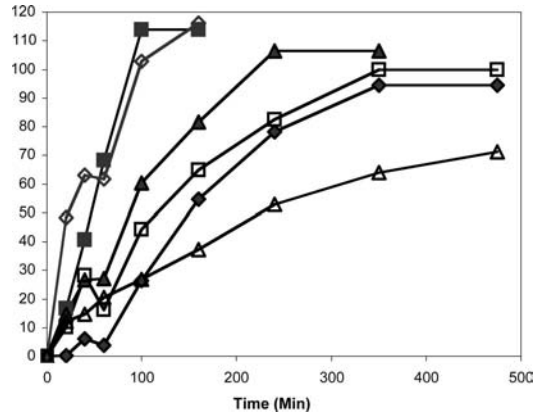

Figure 7. Calcein release kinetics at pH 2.0 as a function of CVEP molar ratio in extruded DOPE liposomes. CVEP/DOPE ratios: ■, 0.5:99.5; ◇, 1:99; ▲, 2:98; □, 3:97; ◆, 4:96; △, 5:95.

tion time to the CVEP starting material at 35.5 min. Physical mixtures of unmodified cholesterol and mPEG5000 at either pH 1 or 3 (control experiments) showed that only the CVEP sample treated at pH 3.0 produced a HPLC peak at this retention time. These observations support the hypothesis that mPEG−cholesterol complexation accounts for the peculiar increase in CVEP peak area at long reaction times at pH 3.0. The data in Figure 6C, showing loss of the vinyl ether α-proton resonance upon exposure to pH 1.0, provides further support of the reaction pathway proposed in Figure 4.

Acid-Triggered Content Release From CVEP/DOPE Liposomes. Liposomes were prepared via the thin film/extrusion method at CVEP/DOPE ratios ranging from 0.5:99.5 to 5:95. These liposomes were stable for approximately one week, except for the 0.5:99.5 dispersions where lipid aggregation was observed within 2 days. Liposomes prepared in this manner had diameters ranging between 150 and 220 nm as observed via light scattering analysis and electron microscopy.

Cargo release from CVEP/DOPE liposomes was examined using the calcein fluorescence dequenching assay. Calcein, encapsulated at self-quenching concentrations (50 mM), undergoes fluorescence dequenching as it leaks into the extraliposomal solution, producing an increase in calcein fluorescence at 520 nm. The calcein release percentage at each time point was then calculated using the ratio method (*26*). Figure 7 shows the calcein release rates from liposomes composed of different CVEP/DOPE ratios that were incubated at pH 2.0 and 37 °C. These data show that increased CVEP molar ratios in the CVEP/DOPE liposomal membrane caused a reduction in the observed acid-triggered calcein release rate. We conclude from these results that a critical concentration of CVEP is required to maintain a lamellar phase of DOPE, such that release rates are governed by the extent of displacement from that concentration. In other words, since the rate of CVEP hydrolysis is constant at a given temperature and pH, the rate of content release is controlled by the amount of CVEP present in the DOPE membrane above the minimal amount required to form a stable lamellar phase. Consequently, when the CVEP content is low, acid-catalyzed degradation of CVEP quickly reaches this critical concentration to produce a rapid release rate. As the CVEP concentration increases, however, more time is required for CVEP hydrolysis to reach this critical point such that slower content release rates are observed. Comparison of the $t_{50\%\ release}$ values for the 0.5−5% loadings revealed an approximately 15-fold decrease in leakage rates as the CVEP ratio increased, suggesting that content release rates scale in a roughly linear fashion with PEG loadings over this range. The small observed differences in release rates observed for 0.5:99.5 and 1:99 CVEP/DOPE formulations suggest that liposome formulations containing such low molar ratios may already be near the critical lamellar−hexagonal II ($L_\alpha-H_{II}$) phase boundary.

Content release rates from CVEP/DOPE liposomes were also examined at pH 4.5, a value that has been reported for late endosomal compartments within KB cells (*73*). The observed rates for 1%, 3%, and 5% CVEP loadings are shown in Figure 8A, B,C, respectively. The content release rates of pure CVEP/DOPE dispersions at pH 4.5 were surprisingly slow, typically only ∼5−10% higher than that observed at pH 7.4 and reaching a maximum of ≤25% after 24 h, regardless of the CVEP loading. We attempted to improve the acid-triggered release rates of these CVEP/DOPE dispersions by adding a second population of "sink" egg phosphatidylcholine (EPC) liposomes at a 25-fold molar excess, since Holland et al. have previously demonstrated that DOPE liposome dePEGylation could be enhanced by addition of a sink EPC liposome population into which their PEG−lipid conjugates could exchange from the host DOPE membrane (*53, 54*). Inclusion of sink liposomes in our CVEP/DOPE system was expected to increase the rate of content release at both pH 4.5 and 7.4 due to a similar PEG−lipid exchange process[5], however, substantial increases in release rate were only observed at pH 4.5 (i.e., sink liposome-induced increases were modest at pH 7.4—typically only 5−10% over a 24 h period). In the 1:99 CVEP/DOPE case (Figure 8A), the combination of pH 4.5 and sink liposomes produced 100% content release within 550 min, an ∼80% increase over the pH 4.5 alone and pH 7.4 + sink liposome cases. The overall magnitude of the sink liposome effect, however, was much less pronounced at the 3% and 5% loading levels, yet ≥70% release occurred over a 24 h period. Taken together, the pH 4.5 results are generally consistent with the observations made at pH 2.0—i.e., that increased CVEP loading leads to slower release kinetics from CVEP/DOPE dispersions. We can further infer from these results that contact between the CVEP/DOPE and sink EPC liposomal membranes promotes PEG adsorption to the polymer-free surface. If this occurs with EPC and hydrolyzed CVEP/DOPE liposomes, a net exchange of PEG onto the sink liposome surface can result, giving rise to an accelerated $L_\alpha-H_{II}$ transition and content leakage response. An alternative explanation is that PEG adsorption onto sink EPC during EPC-CVEP/DOPE contact simply improves the proton accessibility to the CVEP vinyl ether linkage, either by rehydrating the interface (due to a net reduction in the local oxoethylene monomer concentration at the CVEP/DOPE surface) or by physically displacing the cleavable site toward the bulk aqueous environment. Although additional experiments are necessary to clarify this issue, we favor the PEG desorption interpretation as the most likely pathway in this system.

Electron Microscopy of CVEP/DOPE Liposomes Before and After Acidification. Negatively stained electron microscopy images collected before and after treatment of a 8:92 CVEP/DOPE dispersion at pH 4.5 for 24 h revealed a transformation from vesicular structures with average diameters of ∼150 nm (Figure 9A) to electron-dense lipidic material indicative of hexagonal II phase lipid with periodic features of 3.6 nm repeat distances (Figure 9B). Transformation of vesicular structures at pH 8 into aggregated and electron opaque objects after acidification to pH 4 was observed for 8:92 CVEP/DOPE dispersions. The collapsed vesicle structures were similar to the

[5]DePEGylation induced by sink liposomes is believed to proceed via collision-mediated surfactant exchange of PEG−lipid conjugate from the host DOPE liposome membrane to the sink membrane pool. PEG−lipid exchange via the bulk aqueous phase, however, may also occur when the PEG substituents are large such that they tip the hydrophilic−lipophilic balance toward increased water solubility.

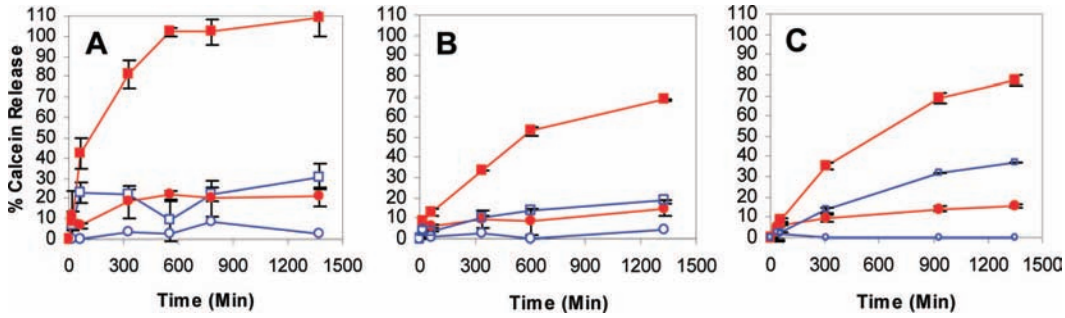

Figure 8. Calcein release kinetics at pH 4.5 as a function of CVEP loading and sink EPC liposomes. red ●, pH 4.5; red ■, pH 4.5 with sink EPC; ○, pH 7.4; □, with sink EPC. A, 1:99 CVEP/DOPE; B, 3:97 CVEP/DOPE; C, 5:95 CVEP/DOPE.

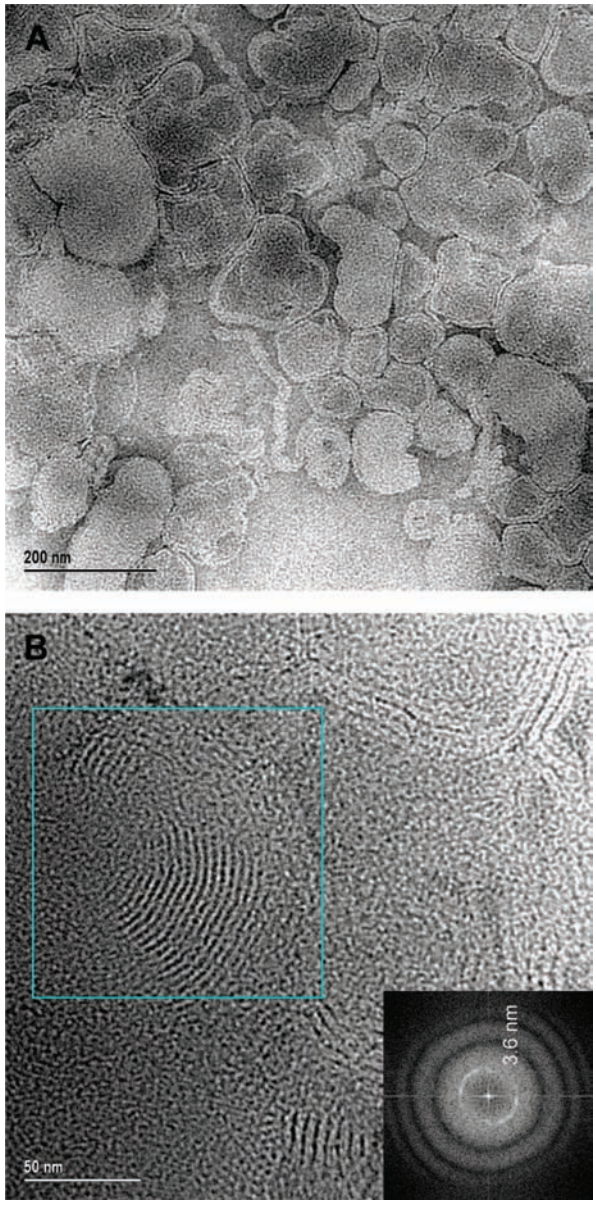

Figure 9. Negatively stained electron micrographs of CVEP/DOPE dispersions before (left) and after (right) 12 h exposure at pH 4.5. Samples were imaged with a FEI Tecnai F20 TEM operating at 4.5 kV using energy filtered detection for bright-field and selected area diffraction analysis.

hexagonal-phase structures previously observed in acidified BVEP/DOPE (*27*) and DHCVEP/DOPE (*28*) phases. These observations support the involvement of the acid-triggered $L_\alpha-H_{II}$ phase transition in this system.

Behavior of 1:9 CVEP/DOPE Monolayers Before and After Acidification. Langmuir monolayer hysteresis experiments were performed at pH 7 and 3.5 on 1:9 CVEP/DOPE monolayers to gain further insight into the adsorption behavior of PEG onto DOPE interfaces. As the pH 7 data in Figure 10A show, the presence of PEG introduces a weakly positive surface pressure at large molecular areas relative to 1:9 chol/DOPE (used as a model of a fully hydrolyzed 1:9 CVEP/DOPE monolayer) as has been shown for PEG adsorbed to DPPC monolayers (*74*). Upon further compression of the monolayers, the CVEP/DOPE isotherm is displaced by the same increment in molecular area at any given surface pressure due to the presence of the PEG headgroups at the interface. When the surface pressure is relaxed, the monolayer films re-expand with no apparent hysteresis. We infer from these findings that the neighboring PEG units in CVEP/DOPE monolayers interact with one another in the so-called mushroom regime (*75*) to produce a modest increase in surface pressure. The absence of hysteresis during surface pressure relaxation suggests, however, that there is little interaction between the PEG chains at low areal densities and the DOPE monolayer under these conditions.

CVEP/DOPE monolayers display substantially different behavior at pH 3.7 (Figure 10B). At large molecular areas, the CVEP/DOPE monolayers display low surface pressure as they did at pH 7, but unlike the pH 7 case, the isotherm is gradually displaced toward the chol/DOPE isotherm at small molecular areas. Most significantly, however, is the hysteretic behavior of the film upon re-expansion—essentially retracing the chol/DOPE film out to large molecular areas. Furthermore, the initially low surface pressure upon re-expansion to 150 $Å^2$/molecule was found to gradually increase to ~10 mN/m over a 10 min period. Since PEG hydrolysis occurs rapidly at this pH, we conclude from these observations that the hydrolyzed PEG remains adsorbed to the chol/DOPE surface until high surface pressures are applied (Figure 10C), when it is then "squeezed" out of the interface as has been reported for Poloxamers in DPPC and DPPG monolayers (*76*). Although the surface pressure in CVEP/DOPE liposomes is not known, the implications of these observations are that PEG adsorption to the hydrolyzed CVEP/DOPE liposome interface is the primary inhibition toward rapid cargo release and membrane fusion via inhibition of membrane−membrane contact. It also suggests a reason that sink liposomes are needed to exchange the adsorbed PEG from the hydrolyzed CVEP/DOPE liposome surface to another (sink) membrane surface so that $L_\alpha-H_{II}$ phase transition and membrane−membrane contact can occur for content leakage and membrane fusion, respectively.

Cytoplasmic Delivery of Calcein to Folate-Deficient KB Cells. We next explored whether KB cells produced endosomes that were sufficiently acidic for triggering the $L_\alpha-H_{II}$ phase transition of internalized CVEP/DOPE liposomes. Our hypothesis was that folate-targeted CVEP/DOPE liposomes could exploit the receptor-mediated endocytosis pathway to deliver

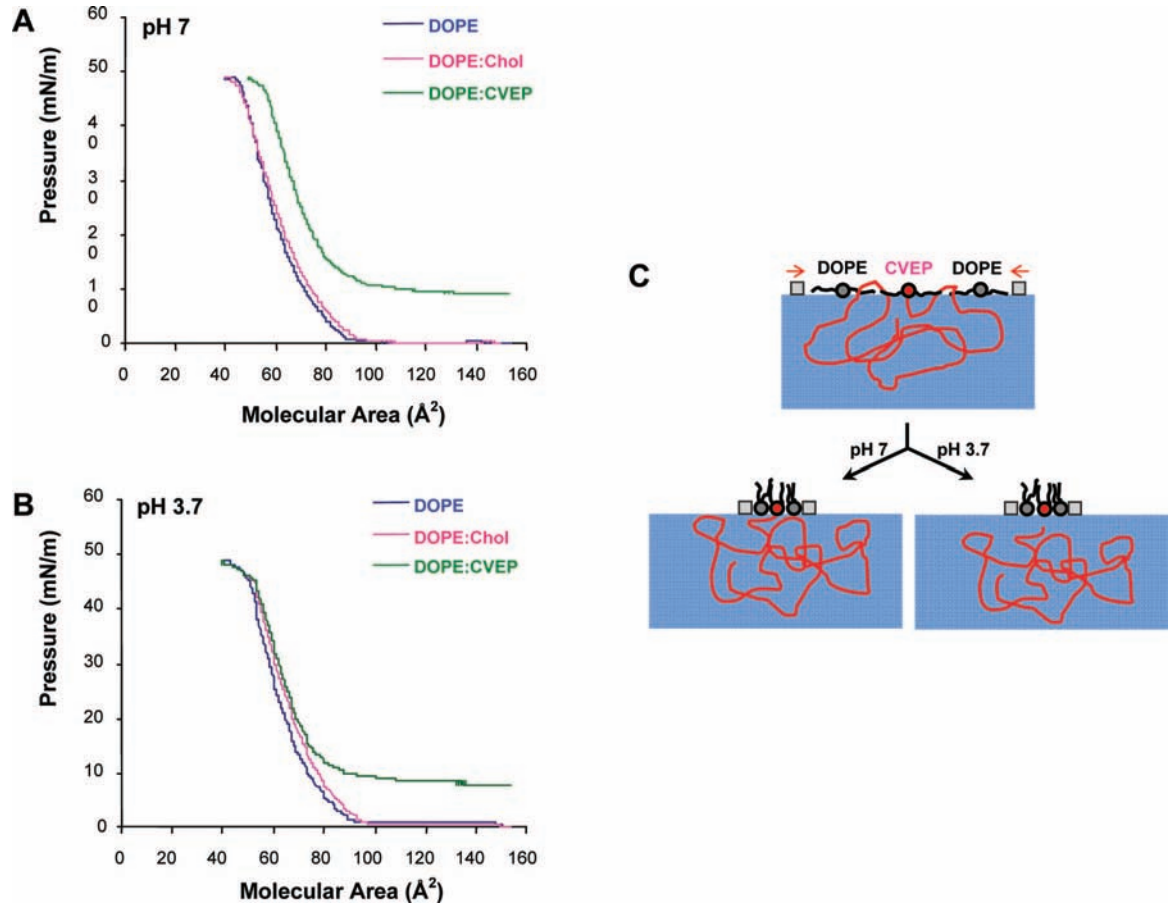

Figure 10. Compression cycles of DOPE, 1:9 chol/DOPE, and 1:9 CVEP/DOPE monolayers. A, pH 7.0; B, pH 3.7; C, Conceptual model showing that PEG is displaced from the chol/DOPE surface at high surface pressure in pH 3.7 solution (where CVEP is rapidly hydrolyzed), but remains adsorbed at low surface pressure and/or when CVEP is intact (pH 7.0). See text for experimental details.

their cargo directly to the cytoplasm via acid-triggered dePEGylation and liposome−endosomal membrane fusion (i.e., Figure 1, steps a, d, and e). It was first necessary to probe the stability of CVEP/DOPE liposomes in KB cell growth media by incubating them at 37 °C in either FD-DMEM (folate-deficient Dublecco's modified Eagle media) or pH 7.4 TRIS buffer (control). Even though the release kinetics of 0.5:99.5 CVEP/DOPE formulations were the most favorable in cell free suspensions, these low CVEP loadings produced liposomes that were too unstable in serum for in vitro experimentation. We found that 5:95 CVEP/DOPE liposomes were stable in serum, releasing less than 20% of their calcein payload over 24 h, most of which occurred within the first hour. This formulation was used for all subsequent cell culture experiments.

The cytoplasmic distribution of calcein within KB cells under various conditions is shown in Figure 11. In these experiments, the cells were incubated for 2 h with media containing liposomes, washed thoroughly to remove all extracellular liposomes, then incubated for an additional 2 h in liposome free media prior to examination via fluorescence microscopy. Bright field images are shown on the left and the corresponding fluorescence images on the right. Without folate targeting (Figure 11A,D), very low levels of fluorescence were visible. Since KB cells are known to accumulate materials via nonspecific pathways, the low levels of fluorescence observed in these experiments were likely the result of either autofluorescence or nonselective uptake of calcein-loaded liposomes from the media. Incorporation of 0.5 mol % folate−PEG−DSPE conjugate as a targeting agent within the 5:95 CVEP/DOPE formulation, however, produced a large increase in cellular fluorescence that appeared diffuse, indicative of cytoplasmic calcein delivery of calcein (Figure 11B,E). KB cells pretreated for 30 min with chloroquine, an inhibitor of endosomal acidification, exhibited strong punctate fluorescence and significantly reduced cytoplasmic staining, indicative of endosomal trapping (Figure 11C,F). This suggests that inhibition of acidification reduces the capacity for endosomal escape by blocking the acid-catalyzed dePEGylation reaction. Flow cytometric analysis of these cultures showed a nearly 40-fold increase in average calcein fluorescence when KB cells were incubated with 0.5:5:95 folate−PEG−DSPE/CVEP/DOPE//calcein compared to 5:95 CVEP/DOPE//calcein (nontargeted) controls, indicating that the calcein cargo is efficiently released from CVEP/DOPE liposomes that have been targeted to acidic endosomes (Supporting Information). Coincubation of KB cells with 0.5:5:95 folate−PEG−DSPE/CVEP/DOPE//calcein and excess folic acid (i.e., folate blockade with 2 μM folic acid) reduced the cell-associated calcein fluorescence by more than an order of magnitude. These observations are generally consistent with the findings of Baba et al. (*77*) who have reported that clathrin-dependent and clathrin-independent endocytosis are not appreciably affected by the presence of $<10\%$ surface coverage of nondegradable cholesterol-PEG2200, although internalization is affected at higher ($>20\%$) chol-PEG concentrations in the plasma membrane.

Attempts to identify the mechanism of cytoplasmic delivery via FRET dequenching experiments were inconclusive. Incubation of KB cells with folate-targeted 5:95 CVEP/DOPE liposomes containing 1% each Rh-PE and NBD-PE produced cells that exhibited signs of both Rh and NBD fluorescence, suggesting that some liposomes had undergone significant

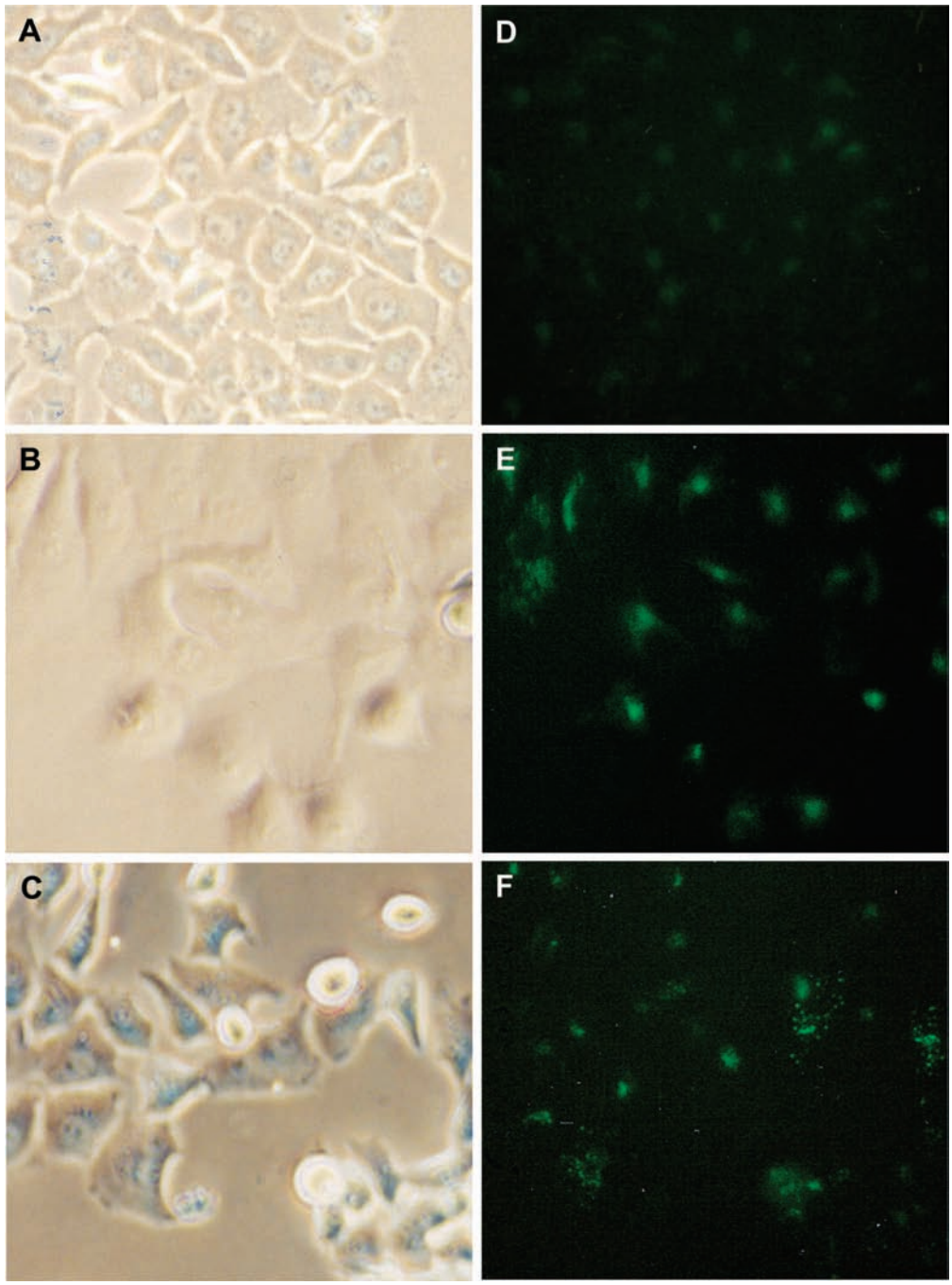

Figure 11. Phase contrast (A,B,C) and fluorescence (D,E,F) micrographs of KB cells treated for 2 h at 37 °C with 5:95 CVEP/DOPE (A,D), 0.5:5:95 folate−PEG−DSPE/CVEP/DOPE (B,E), and 0.5:5:95 folate−PEG−DSPE/CVEP/DOPE with chloroquine inhibition (C,F), rinsed, and incubated with liposome-free media for 2 h prior to imaging. The fluorescence apparent in panel D is due to nonselective uptake of calcein-loaded liposomes from the media.

demixing of the FRET probes, presumably via liposome−endosome membrane fusion, while Rh fluorescence was still observed in other regions, suggesting that the probes were still intimately mixed and engaged in FRET. Whether the latter case is the result of fusion inhibition by adsorbed PEG on hydrolyzed CVEP/DOPE liposomes or their incomplete hydrolysis/dePEGylation due to the presence of modestly acidic and/or early endosomes is not clear at this time. No obvious signs of cellular toxicity were observed in these experiments. Taken together, these results suggest that the combination of endosomal-targeting and acid-triggered content release represents a viable route for the cytoplasmic delivery of liposomal contents to KB cells, with the possible involvement of liposome−endosome membrane fusion as the mode of delivery to the cytosol.

CONCLUSIONS

An acid-labile lipid for triggering fusogenic liposome deP-EGylation has been synthesized and tested in solution and cell culture assays. The synthetic route developed for CVEP is readily amenable to a wide variety of alcohol-containing lipid anchor modifications as well as to varied PEG chain lengths and architectures. This cleavable PEG lipid was designed to increase the rate of contents release by requiring only a single vinyl ether cleavage event. The observed release kinetics in solution-phase experiments, however, were significantly slower

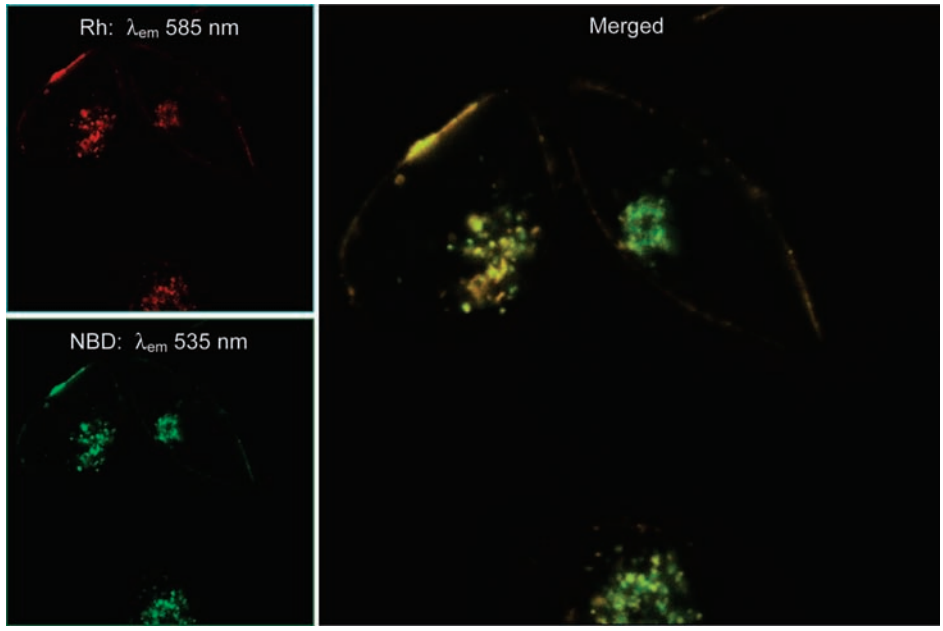

Figure 12. Confocal microscope images of KB cells treated as in Figure 11 with 0.5:5:95 folate−PEG−DSPE/CVEP/DOPE liposomes containing 1% Rh-PE and 1% NBD-PE. λ_{ex} = 488 nm; λ_{em}(Rh) = 585 nm; λ_{em}(NBD) = 535 nm. The areas of yellow fluorescence in the merged image to the right indicate cellular regions where both Rh and NBD fluorescence are apparent.

than those of the previously reported PEG lipid, BVEP. This suggests the possibility that the liposome structure and interactions between DOPE and CVEP (or its hydrolysis products) are such that the lamellar phase of DOPE is stabilized relative to BVEP/DOPE.

The inclusion of a second population of "sink" liposomes was found to substantially increase release from CVEP/DOPE liposomes at pH 4.5 without inducing significant leakage at pH 7.4. On the basis of monolayer experiments, we propose that the role of the sink liposomes is to provide a polymer-free interface which facilitates PEG desorption from the DOPE liposome surface via exchange. Since the endosomal membrane may be conceptually viewed as a large sink liposome, the necessity for sink liposomes in vitro was not expected to diminish the ability of these liposomes to elicit cytoplasmic delivery. In fact, CVEP/DOPE liposomes targeted to KB cells exhibited significant cytoplasmic delivery of calcein as evidenced by diffuse cellular fluorescence. Neutralization of the endosomal pH with chloroquine also produced strong, punctate fluorescence, indicative of endosomal trapping of the calcein that is retained by unhydrolyzed CVEP/DOPE liposomes. This result also suggests that exchange of unhydrolyzed CVEP into endosomal membranes must be kinetically slower than the rate of CVEP hydrolysis and PEG desorption. Without targeting, only small amounts of diffuse cellular fluorescence were observed due to nonspecific cellular uptake processes. In summary, the dePEGylative triggering strategy appears to be a promising route for the site-specific cytoplasmic delivery of liposomal contents.

ACKNOWLEDGMENT

J. A. Boomer synthesized CVEP and characterized the release properties of CVEP/DOPE liposomes. R. H. Haynes assisted with the CVEP synthesis and release experiments. M. M. Qualls characterized the CVEP/DOPE release properties in cell culture and performed the lipid mixing experiments. D. H. Inerowicz monitored the CVEP hydrolysis kinetics by HPLC, NMR, and MS. V. Srilakshmi Patri performed the flow cytometry experiments. J.-M. Kim performed the negative stain electron microscopy and the monolayer film balance experiments. The authors wish to acknowledge Dr. Oleg Gerasimov for his scientific contributions to the design of this system. The authors also thank Prof. J. Paul Robinson for his guidance with the confocal microscopy and flow cytometry experiments and the Purdue Cancer Center Analytical Cytology, NMR and MS Core Facilities for their support. This work was supported by NIH GM55266.

Supporting Information Available: Characterization data for the compounds described. This material is available free of charge via the Internet at http://pubs.acs.org.

LITERATURE CITED

(1) Drummond, D. C., Meyer, O., Hong, K. L., Kirpotin, D. B., and Papahadjopoulos, D. (1999) Optimizing liposomes for delivery of chemotherapeutic agents to solid tumors. *Pharmacol. Rev. 51*, 691–743.

(2) Allen, T. M., and Cullis, P. R. (2004) Drug delivery systems: Entering the mainstream. *Science 303*, 1818–1822.

(3) Hashida, M., Kawakami, S., and Yamashita, F. (2005) Lipid carrier systems for targeted drug and gene delivery. *Chem. Pharm. Bull. 53*, 871–880.

(4) Torchilin, V. P. (2005) Recent advances with liposomes as pharmaceutical carriers. *Nat. Drug Discovery 4*, 145–160.

(5) Peer, D., Karp, J. M., Hong, S., Farokhzad, O. C., Margalit, R., and Langer, R. (2007) Nanocarriers as an emerging platform for cancer therapy. *Nat. Nanotechnol. 2*, 751–760.

(6) Harrigan, P. R., Wong, K. F., Redelmeier, T. E., Wheeler, J. J., and Cullis, P. R. (1993) Accumulation of Doxorubicin and other lipophilic amines into large unilameller vesicles in response to transmembrane pH gradients. *Biochim. Biophys. Acta 1149*, 329–338.

(7) Haran, G., Cohen, R., Bar, L. K., and Barenholz, Y. (1993) Transmembrane ammonium sulfate gradients in liposomes produce efficient and stable entrapment of amphipathic weak bases. *Biochim. Biophys. Acta 1151*, 201–215.

(8) Klibanov, A. L., Maruyama, K., Beckerleg, A. M., Torchilin, V. P., and Huang, L. (1991) Activity of amphipathic poly(ethylene glycol) 5000 to prolong the circulation time of liposomes depends on the liposome size and is unfavorable for immuno-

liposome binding to target. *Biochim. Biophys. Acta 1062*, 142–148.
(9) Allen, T. M., Hansen, C., Martin, F., Redemann, C., and Yau-Young, A. (1991) Liposomes containing synthetic lipid derivatives of poly(ethylene glycol) show prolonged circulation half-lives in vivo. *Biochim. Biophys. Acta 1066*, 29–36.
(10) Iyer, A. K., Khaled, G., Fang, J., and Maeda, H. (2006) Exploiting the enhanced permeability and retention effect for tumor targeting. *Drug Discovery Today 11*, 812–818.
(11) Moghimi, S. M., and Szebeni, J. (2003) Stealth liposomes and long circulating nanoparticles: critical issues in pharmacokinetics, opsonization and protein-binding properties. *Prog. Lipid Res. 42*, 463–478.
(12) Kong, G., Anyarambhatla, G., Petros, W. P., Braun, R. D., Colvin, O. M., Needham, D., and Dewhirst, M. W. (2000) Efficacy of liposomes and hyperthermia in a human tumor xenograft model: Importance of triggered drug release. *Cancer Res. 60*, 6950–6957.
(13) Jain, R. K. (2001) Delivery of molecular medicine to solid tumors: lessons from in vivo imaging of gene expression and function. *J. Controlled Release* 7–25.
(14) Alexandrakis, G., Brown, E. B., Tong, R. T., McKee, T. D., Campbell, R. B., Boucher, Y., and Jain, R. K. (2004) Two-photon fluorescence correlation microscopy reveals the two-phase nature of transport in tumors. *Nat. Med. 10*, 203–207.
(15) Park, J. W., Kirpotin, D. B., Hong, K., Shalaby, R., Shao, Y., Nielsen, U. B., Marks, J. D., Papadadjopoulus, D., and Benz, C. C. (2001) Tumour targeting using anti-her2 immunoliposomes. *J. Liposome Res. 74*, 95–113.
(16) Ishida, T., Kirchmeier, M. J., Moase, E. H., Zalipsky, S., and Allen, T. M. (2001) Targeted delivery and triggered release of liposomal doxorubicin enhances cytotoxicity against human B lymphoma cells. *Biochim. Biophys. Acta 1515*, 144–158.
(17) Park, J. W., Hong, K. L., Kirpotin, D. B., Colbern, G., Shalaby, R., Baselga, J., Shao, Y., Nielsen, U. B., Marks, J. D., Moore, D., Papahadjopoulos, D., and Benz, C. C. (2002) Anti-HER2 immunoliposomes: enhanced efficacy attributable to targeted delivery. *Clin. Cancer Res. 8*, 1172–1181.
(18) Kirpotin, D. B., Drummond, D. C., Shao, Y., Shalaby, M. R., Hong, K., Nielsen, U. B., Marks, J. D., Benz, C. C., and Park, J. W. (2006) Antibody targeting of long-circulating lipidic nanoparticles does not increase tumor localization but does increase internalization in animal models. *Cancer Res. 66*, 6732–6740.
(19) Li, W. J., Huang, Z. H., MacKay, J. A., Grube, S., and Szoka, F. C. (2005) Low pH-sensitive poly(ethylene glycol) (PEG)-stabilized plasmid nanolipoparticles: effects of PEG chain length, lipid composition and assembly conditions on gene delivery. *J. Gene Med. 7*, 67–79.
(20) Walker, G. F., Fella, C., Pelisek, J., Fahrmeir, J., Boeckle, S., Ogris, M., and Wagner, E. (2005) Toward synthetic viruses: endosomal pH-triggered deshielding of targeted polyplexes greatly enhances gene transfer in vitro and in vivo. *Mol. Ther. 11*, 418–425.
(21) Chen, H. G., Zhang, H. Z., McCallum, C. M., Szoka, F. C., and Guo, X. (2007) Unsaturated cationic ortho esters for endosome permeation in gene delivery. *J. Med. Chem. 50*, 4269–4278.
(22) Kale, A. A., and Torchilin, V. P. (2007) Enhanced transfection of tumor cells in vivo using "smart" pH-sensitive TAT-modified PEGylated liposomes. *J. Drug Targeting 15*, 538–545.
(23) Rui, Y., Wang, S., Low, P. S., and Thompson, D. H. (1998) Diplasmenylcholine-folate liposomes: An efficient vehicle for intracellular drug delivery. *J. Am. Chem. Soc. 120*, 11213–11218.
(24) Qualls, M. M., and Thompson, D. H. (2001) Chloroaluminum phthalocyanine tetrasulfonate delivered via acid-labile diplasmenylcholine-folate liposomes: Intracellular localization and synergistic phototoxicity. *Int. J. Cancer 93*, 384–392.
(25) Guo, X., and Szoka, F. C. (2003) Chemical approaches to triggerable lipid vesicles for drug and gene delivery. *Acc. Chem. Res. 36*, 335–341.
(26) Gerasimov, O. V., Schwan, A., and Thompson, D. H. (1997) Acid-catalyzed plasmenylcholine hydrolysis and its effect on bilayer permeability: A quantitative study. *Biochim. Biophys. Acta 1324*, 200–214.
(27) Boomer, J. A., Inerowicz, H. D., Zhang, Z.-Y., Bergstrand, N., Edwards, K., Kim, J.-M., and Thompson, D. H. (2003) Acid-triggered release from sterically-stabilized fusogenic vesicles via a hydrolytic dePEGylation strategy. *Langmuir 19*, 6408–6415.
(28) Bergstrand, N., Arfvidsson, M. C., Kim, J.-M., Thompson, D. H., and Edwards, K. (2003) Interactions between pH-sensitive liposomes and model membranes. *Biophys. Chem. 104*, 361–379.
(29) Chen, F.-J., Asokan, A., and Cho, M. J. (2003) Cytosolic delivery of macromolecules: I. Synthesis and characterization of pH-sensitive acyloxyalkylimidazoles. *Biochim. Biophys. Acta 1611*, 140–150.
(30) Asokan, A., and Cho, M. J. (2003) Cytosolic delivery of macromolecules. II. Mechanistic studies with pH-sensitive morpholine lipids. *Biochim. Biophys. Acta 1611*, 151–160.
(31) Slepushkin, V., Simoes, S., De Lima, M. C. P., and Duzgunes, N. (2004) Sterically stabilized pH-sensitive liposomes. *Methods Enzymol. 387*, 134–147.
(32) Aissaoui, A., Martin, B., Kan, E., Oudrhiri, N., Hauchecorne, M., Vigneron, J. P., Lehn, J.-M., and Lehn, P. (2004) Novel cationic lipids incorporating an acid-sensitive acylhydrazone linker: synthesis and transfection properties. *J. Med. Chem. 47*, 5210–5223.
(33) Kale, A. A., and Torchilin, V. P. (2007) Design, synthesis, and characterization of pH-sensitive PEG-PE conjugates for stimuli-sensitive pharmaceutical nanocarriers: the effect of substitutes at the hydrazone linkage on the pH stability of PEG-PE conjugates. *Bioconjugate Chem. 18*, 363–370.
(34) Van Thienen, T. G., Demeester, J., and De Smedt, S. C. (2008) Screening poly(ethyleneglycol) micro- and nanogels for drug delivery purposes. *Int. J. Pharm. 351*, 174–185.
(35) Dufresne, M. H., Meier, C., Petereit, H. U., and Leroux, J. C. (2007) Proton-actuated membrane-destabilizing polyion complex micelles. *Bioconjugate Chem. 18*, 1010–1014.
(36) Kirpotin, D., Hong, K., Mullah, N., Papahadjopoulos, D., and Zalipsky, S. (1996) Liposomes with detachable polymer coating: destabilization and fusion of dioleoylphosphatidylethanolamine vesicles triggered by cleavage of surface-grafted poly(ethylene glycol). *FEBS Lett. 388*, 115–118.
(37) Zalipsky, S., Qazen, M., Walker, J. A., Mullah, N., Quinn, Y. P., and Huang, S. K. (1999) New detachable poly(ethylene glycol) conjugates: cysteine-cleavable lipopolymers regenerating natural phospholipid, diacyl phosphatidylethanolamine. *Bioconjugate Chem. 10*, 703–707.
(38) Ouyang, M., Remy, J. S., and Szoka, F. C. (2000) Controlled template-assisted assembly of plasmid DNA into nanometric particles with high DNA concentration. *Bioconjugate Chem. 11*, 104–112.
(39) Wetzer, B., Byk, G., Frederic, M., Airiau, M., Blanche, F., Pitard, B., and Scherman, D. (2001) Reducible cationic lipids for gene transfer. *Biochem. J. 356*, 747–756.
(40) Dauty, E., Remy, J. S., Zuber, G., and Behr, J.-P. (2002) Intracellular delivery of nanometric DNA particles via the folate receptor. *Bioconjugate Chem. 13*, 831–839.
(41) Guo, X., MacKay, J. A., and Szoka, F. C. (2003) Mechanism of pH-triggered collapse of phosphatidylethanolamine liposomes stabilized by an ortho ester polyethyleneglycol lipid. *Biophys. J. 84*, 1784–1795.
(42) Fuchs, S., Buethe, D., Khanna, A., Yadava, P., and Hughes, J. (2004) Sulfhydryl based cationic surfactants and the impact of polyanions on disulfide bond formation: Implications for gene transfer vectors. *J. Drug Targeting 12*, 347–353.
(43) Huang, Z. H., Li, W. J., MacKay, J. A., and Szoka, F. C. (2005) Thiocholesterol-based lipids for ordered assembly of bioresponsive gene carriers. *Mol. Ther. 11*, 409–417.

(44) Andresen, T. L., and Jorgensen, K. (2005) Synthesis and membrane behavior of a new class of unnatural phospholipid analogs useful as phospholipase A2 degradable liposomal drug carriers. *Biochim. Biophys. Acta 1669*, 1–7.

(45) Sarkar, N., Banerjee, J., Hanson, A. J., Elegbede, A. I., Rosendahl, T., Krueger, A. B., Banerjee, A. L., Tobwala, S., Wang, R. Y., Lu, X. N., Mallik, S., and Srivastava, D. K. (2008) Matrix metalloproteinase-assisted triggered release of liposomal contents. *Bioconjugate Chem. 19*, 57–64.

(46) Romberg, B., Hennink, W. E., and Storm, G. (2008) Enzyme-induced shedding of a poly(amino acid)-coating triggers contents release from dioleoyl phosphatidylethanolamine liposomes. *Int. J. Pharm. 355*, 108–113.

(47) Kono, K. (2001) Thermosensitive polymer-modified liposomes. *Adv. Drug Delivery Rev. 53*, 307–319.

(48) Paasonen, L., Romberg, B., Storm, G., Yliperttula, M., Urtti, A., and Hennink, W. E. (2007) Temperature-sensitive poly(N-(2-hydroxypropyl)methacrylamide mono/dilactate)-coated liposomes for triggered contents release. *Bioconjugate Chem. 18*, 2131–2136.

(49) Tashjian, J. A., Dewhirst, M. W., Needham, D., and Viglianti, B. L. (2008) Rationale for and measurement of liposomal drug delivery with hyperthermia using non-invasive imaging techniques. *Int. J. Hypothermia 24*, 79–90.

(50) Shum, P., Kim, J.-M., and Thompson, D. H. (2001) Phototriggering of liposomal drug delivery systems. *Adv. Drug Delivery Rev. 53*, 273–284.

(51) Zhang, Y.-Z., Shum, P., Yates, M., Messersmith, P. B., and Thompson, D. H. (2002) Formation of fibrinogen-based hydrogels using phototriggerable diplasmalogen liposomes. *Bioconjugate Chem. 13*, 640–646.

(52) Silvius, J. R., and Zuckermann, M. J. (1993) Interbilayer transfer of phospholipid-anchored macromolecules via monomer diffusion. *Biochemistry 32*, 3153–3161.

(53) Holland, J. W., Cullis, P. R., and Madden, T. D. (1996) Poly(ethylene glycol)-lipid conjugates promote bilayer formation in mixtures of non-bilayer-forming lipids. *Biochemistry 35*, 2610–2617.

(54) Holland, J. W., Hui, C., Cullis, P. R., and Madden, T. D. (1996) Poly(ethylene glycol)-lipid conjugates regulate the calcium-induced fusion of liposomes composed of phosphatidylethanolamine and phosphatidylserine. *Biochemistry 35*, 2618–2624.

(55) Mori, A., Chonn, A., Choi, L. S., Israels, A., Monck, M. A., and Cullis, P. R. (1998) Stabilization and regulated fusion of liposomes containing a cationic lipid using amphipathic polyethyleneglycol derivatives. *J. Liposome Res. 8*, 195–211.

(56) Adlakha-Hutcheon, G., Bally, M. B., Shew, C. R., and Madden, T. D. (1999) Controlled destabilization of a liposomal drug delivery system enhances mitoxantrone antitumor activity. *Nat. Biotechnol. 17*, 755–779.

(57) Li, W. M., Xue, L., Mayer, L. D., and Bally, M. B. (2001) Intermembrane transfer of polyethylene glycol-modified phosphatidylethanolamine as a means to reveal surface-associated binding ligands on liposomes. *Biochim. Biophys. Acta 1513*, 193–206.

(58) Auguste, D. T., Prud'homme, R. K., Ahl, P. L., Meers, P., and Kohn, J. (2003) Association of hydrophobically-modified poly(ethylene glycol) with fusogenic liposomes. *Biochim. Biophys. Acta 1616*, 184–195.

(59) Bondurant, B., and O'Brien, D. F. (1998) Photoinduced destabilization of sterically stabilized liposomes. *J. Am. Chem. Soc. 120*, 13541–13542.

(60) Keeffe, J. R., and Kresge, A. J. (1990) *The Chemistry of Enols* (Rappoport, E., Ed.) pp 399−483, Wiley, New York.

(61) Kenworthy, A. K., Simon, S. A., and McIntosh, T. J. (1995) Structure and phase behavior of lipid suspensions containing phospholipids with covalently attached poly(ethylene glycol). *Biophys. J. 68*, 1903–1920.

(62) Kuhl, T., Guo, Y. Q., Alderfer, J. L., Berman, A. D., Leckband, D., Israelachvili, J., and Hui, S. W. (1996) Direct measurement of polyethylene glycol induced depletion attraction between lipid bilayers. *Langmuir 12*, 3003–3014.

(63) Reid, C., and Rand, R. P. (1997) Probing protein hydration and conformational states in solution. *Biophys. J. 72*, 1022–1030.

(64) Kuhl, T. L., Majewski, J., Wong, J. Y., Steinberg, S., Leckband, D. E., Israelachvili, J. N., and Smith, G. S. (1998) A neutron reflectivity study of polymer-modified phospholipid monolayers at the solid-solution interface: Polyethylene glycol-lipids on silane-modified substrates. *Biophys. J. 75*, 2352–2362.

(65) Malinin, V. S., Frederik, P., and Lentz, B. R. (2002) Osmotic and curvature stress affect PEG-induced fusion of lipid vesicles but not mixing of their lipids. *Biophys. J. 82*, 2090–2100.

(66) Hansen, P. L., Cohen, J. A., Podgornik, R., and Parsegian, V. A. (2003) Osmotic properties of poly(ethylene glycols): Quantitative features of brush and bulk scaling laws. *Biophys. J. 84*, 350–355.

(67) Chang, Y.-C., Herath, J., Wang, T. H.-H., and Chow, C. S. (2008) Synthesis and solution conformation studies of 3-substituted uridine and pseudo-uridine derivatives. *Bioorg. Med. Chem. 16*, 2676–2686.

(68) Le Quement, S. T., Nielsen, T. E., and Meldal, M. (2007) Scaffold diversity through intramolecular cascade reactions of solid-supported cyclic N-acyliminium intermediates. *J. Comb. Chem. 9*, 1060–1072.

(69) Wolf, D. E., Winiski, A. P., Ting, A. E., Bocian, K. M., and Pagano, R. E. (1992) Determination of the transbilayer distribution of fluorescent lipid analogues by nonradiative fluorescence resonance energy transfer. *Biochemistry 31*, 2865–2873.

(70) Rui, Y., and Thompson, D. H. (1996) Efficient stereoselective synthesis of plasmenylcholines. *Chem.-Eur. J. 2*, 1505–1508.

(71) Boomer, J. A., and Thompson, D. H. (1999) Synthesis of acid-labile diplasmenyl lipids for drug and gene delivery applications. *Chem. Phys. Lipids 99*, 145–153.

(72) Thompson, D. H., Shin, J., Boomer, J. A., and Kim, J.-M. (2004) Preparation of plasmenylcholine lipids and plasmenyl-type liposome dispersions. *Methods Enzymol. 387*, 153–168.

(73) Lee, R. J., Wang, S., and Low, P. S. (1996) Measurement of endosome pH following folate receptor-mediated endocytosis. *Biochim. Biophys. Acta 1312*, 237–242.

(74) Winterhalter, M., Burner, H., Marzinka, S., Benz, R., and Kasianowicz, J. J. (1995) Interaction of poly(ethylene-glycols) with air-water interfaces and lipid monolayers: investigations on surface pressure and surface potential. *Biophys. J. 69*, 1372–1381.

(75) Efremova, N. V., Bondurant, B., O'Brien, D. F., and Leckband, D. E. (2000) Measurements of interbilayer forces and protein adsorption on uncharged lipid bilayers displaying poly(ethylene glycol) chains. *Biochemistry 39*, 3441–3451.

(76) Wu, G., Majewski, J., Ege, C., Kjaer, K., Weygand, M. J., and Lee, K. Y. C. (2005) Interaction between lipid monolayers and Poloxamer 188: an x-ray reflectivity and diffraction study. *Biophys. J. 89*, 3159–3173.

(77) Baba, T., Rauch, C., Xue, M., Terada, N., Fujii, Y., Ueda, H., Takayama, I., Ohno, S., Farge, E., and Sato, S. B. (2001) Clathrin-dependent and clathrin-independent endocytosis are differentially sensitive to insertion of poly(ethylene glycol)-derivatived cholesterol in the plasma membrane. *Traffic 2*, 501–512.

BC800239B

SUPPLEMENTARY INFORMATION

CYTOPLASMIC DELIVERY OF LIPOSOMAL CONTENTS MEDIATED BY AN ACID-LABILE CHOLESTEROL-VINYL ETHER-PEG CONJUGATE

Jeremy A. Boomer[#], Marquita M. Qualls[†], H. Dorota Inerowicz,
Robert H. Haynes, G.V. Srilaksmi Patri, Jong-Mok Kim,
David H. Thompson*

SYNTHESIS OFCVEP (7).

4-*t*-BUTYLDIMETHYLSILYLOXYBUTAN-1-OL (1). *t*-Butyldimethylsilyl chloride (8.65 g, 57.4 mmol) in dry THF (25 mL) was added dropwise to a solution of 1, 4-butanediol (22.0 g, 244 mmol; dried 2 h *in vacuo*) and imidazole (5.1 g, 70.5 mmol) in THF (100 mL) at 0 °C over a ~20 min period (turned cloudy after 10 min). The reaction was stirred for 1 h, warmed to room temperature, and ether (300 mL) added. The solution was then washed with saturated NH_4Cl (2 x 200 mL) and saturated NaCl (1 x 200 mL). The ether layer was dried over $MgSO_4$, filtered, evaporated and dried *in vacuo* yielding a pale yellow oil (11.4 g, 97% yield). NMR analysis indicated that the product was sufficiently pure to utilize in the ensuing step without additional purification. TLC (4:1 hexane:ether, $KMnO_4$): R_f = 0.35. ^{1}H-NMR ($CDCl_3$): 0.05 (s, 6H), 0.85 (s, 9H), 1.60 (m, 4H), 2.60 (bs, 1H), 3.65 (q, 4H). ^{13}C-NMR/APT ($CDCl_3$): -5.54 (O), 18.15 (E), 25.76 (O), 29.60 (E), 29.79 (E), 62.33 (E), 63.18 (E).

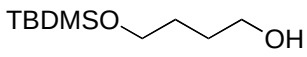

1

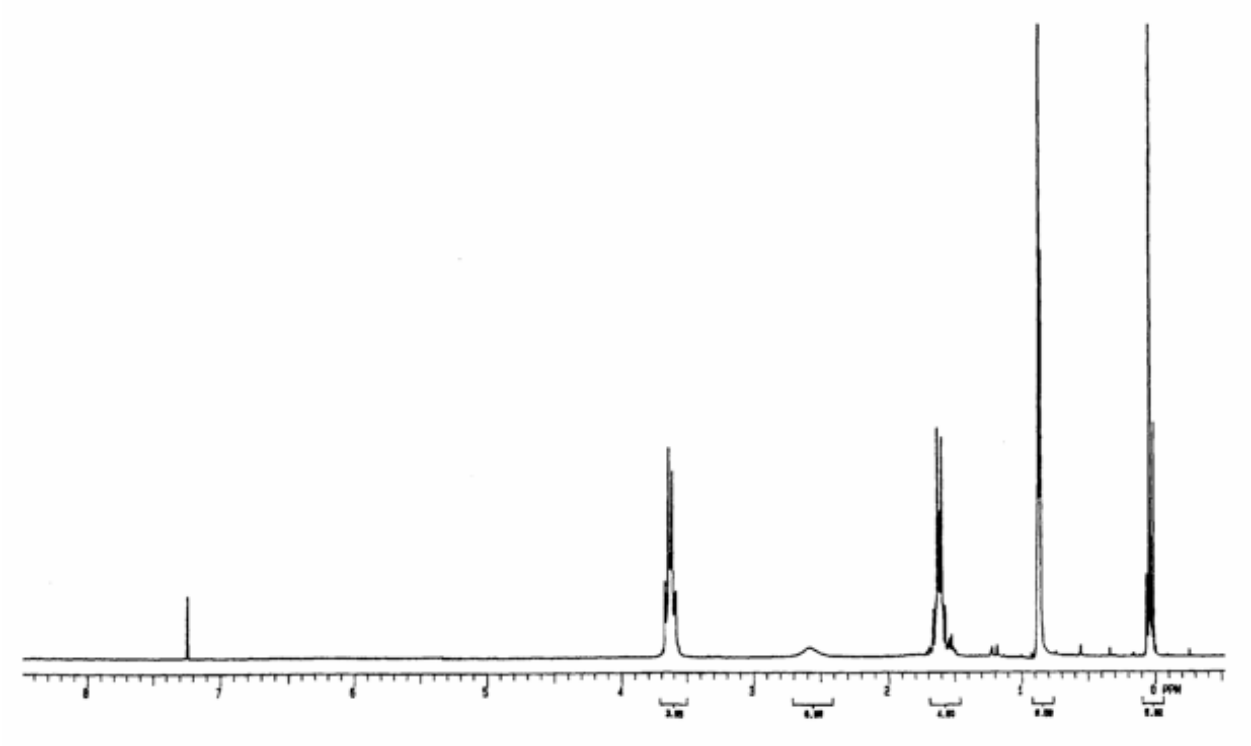

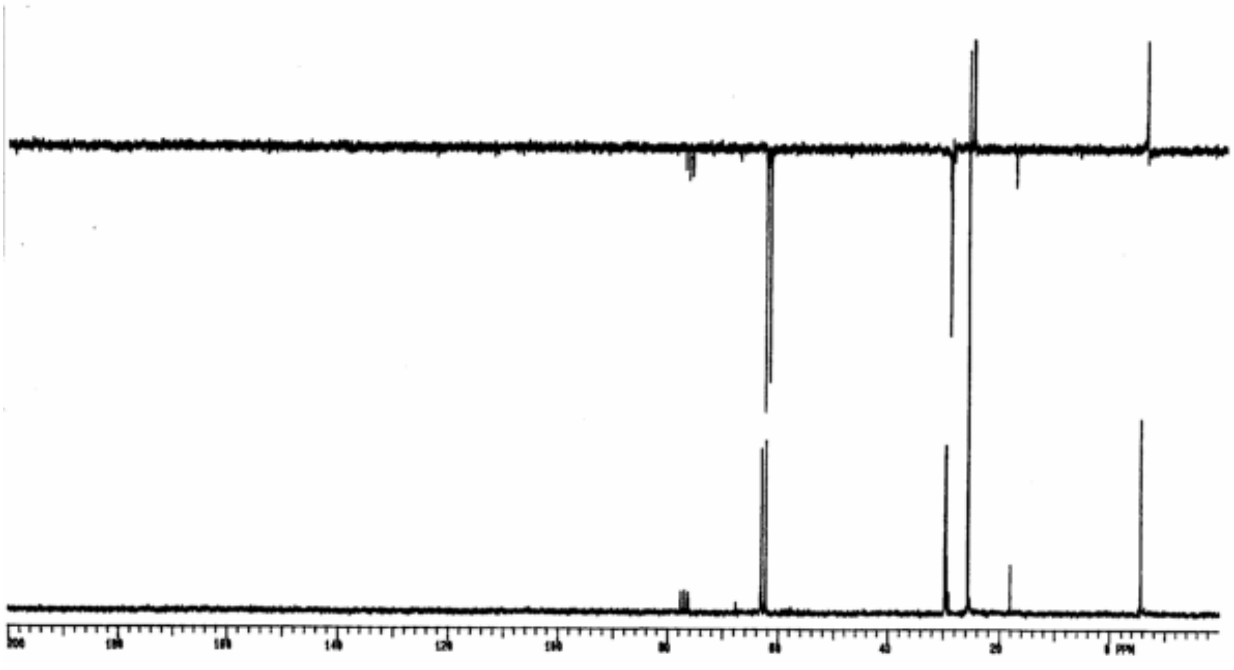

4-*t*-BUTYLDIMETHYLSILYLOXYBUTANOIC ACID (2). $KMnO_4$ (3.2 g, 20.0 mmol) was dissolved in water (50 mL), stirred vigorously for 10 min, then cooled to 0 °C. A solution of 4-*t*-butyldimethylsilyloxybutan-1-ol (**1**, 1.98 g, 9.7 mmol) and tetraoctylammonium bromide (TOAB, 812 mg, 1.5 mmol) in benzene (40 mL) was added dropwise via addition funnel over a ~20 min period. The solution was then warmed to room temperature and stirred for 3 h. The remaining $KMnO_4$ was quenched with $NaHSO_3$, producing a two-phase mixture with a colorless organic layer. Benzene (20 mL) and 50% CH_3CO_2H (50 mL) were added and the mixture extracted. The benzene layer was then washed with saturated NaCl (50 mL), dried over $MgSO_4$, filtered, evaporated, and dried *in vacuo*. The remaining TOAB was removed via elution through a small silica plug using 2:1 hexane:ether as the mobile phase. The solvent was evaporated and the sample dried *in vacuo* giving a colorless oil (1.65 g, 78% yield). TLC (1:1 hexane:ether, Bromphenol blue): R_f = 0.65. ^{1}H-NMR ($CDCl_3$): 0.05 (s, 6H), 0.85 (s, 9H), 1.83 (p, *J* = 7 Hz, 2H), 2.44 (t, *J* = 7 Hz, 2H), 3.65 (t, *J* = 7 Hz, 2H), 11.09 (bs, 1H). ^{13}C-NMR/APT ($CDCl_3$): -5.47 (O), 18.24 (E), 25.85 (O), 27.57 (E), 30.71 (E), 61.95 (E), 179.96 (E).

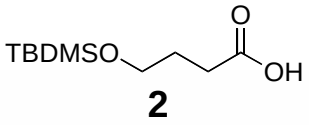

2

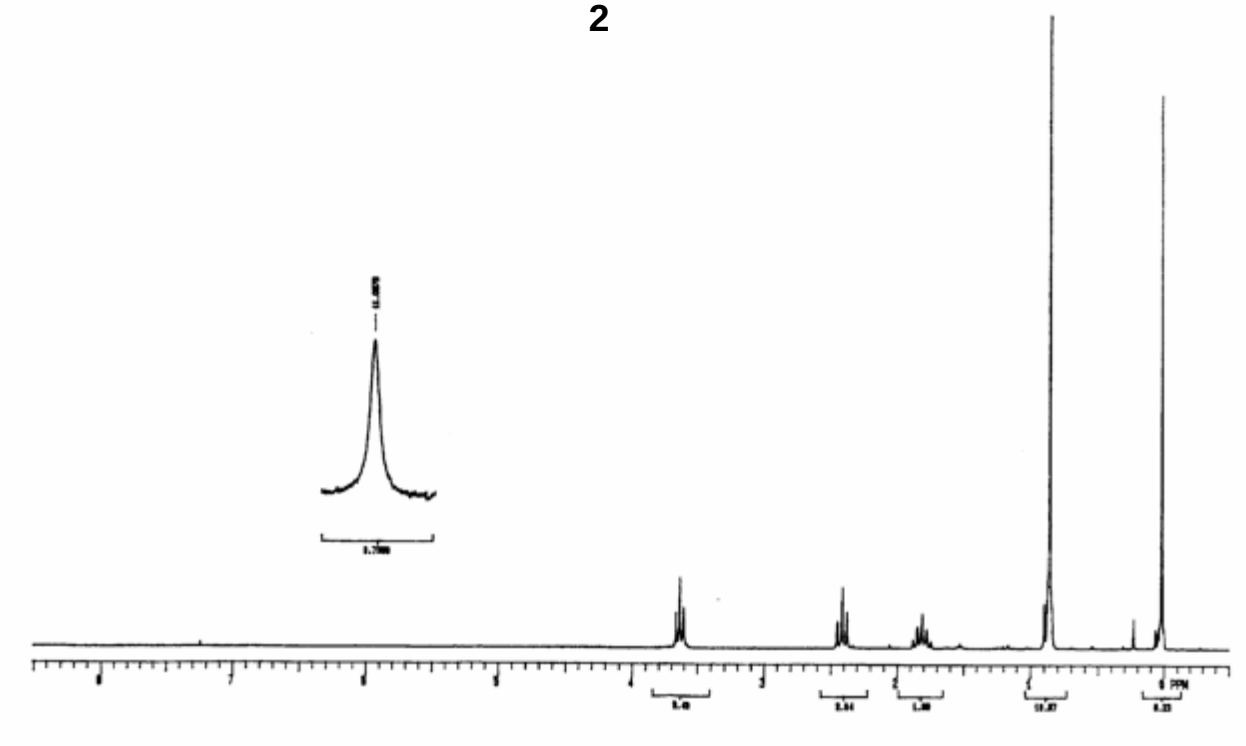

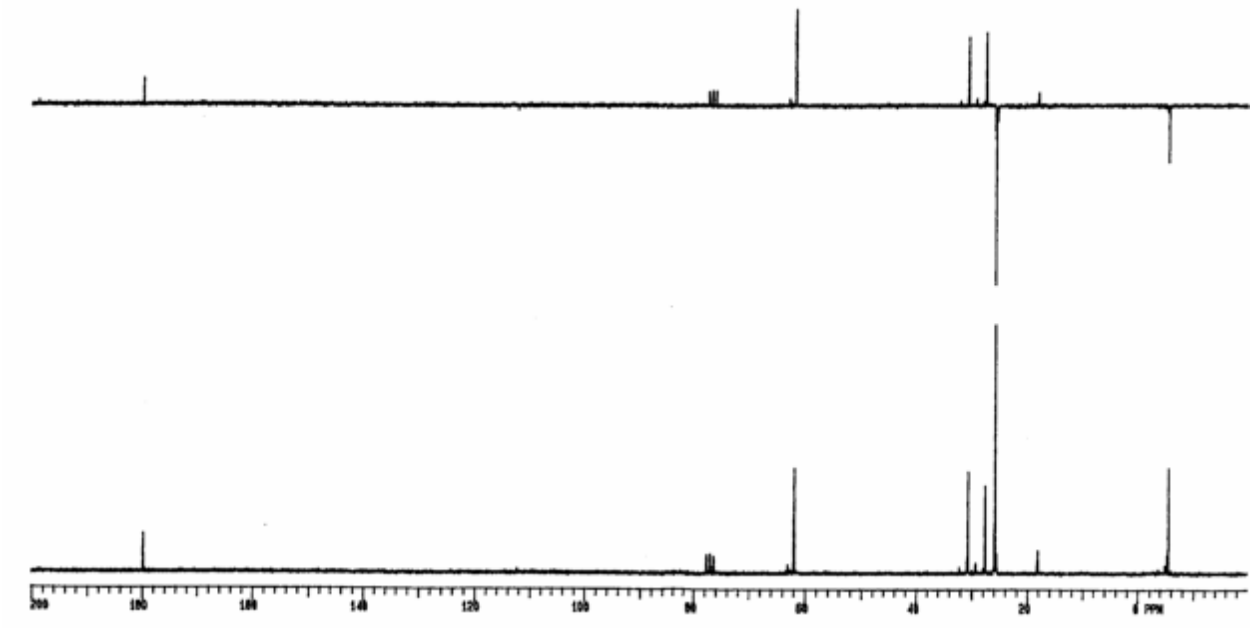

CHOLESTEROL 4-*t*-BUTYLDIMETHYLSILYLOXYBUTANOATE (3). Cholesterol (609 mg, 1.58 mmol), 4-*t*-butyldimethylsilyloxy butanoic acid (**2**, 325 mg, 1.49 mmol), and DMAP (20 mg, 0.14 mmol) were dissolved in CH_2Cl_2 (15 mL) and the solution cooled to 0 °C. Ethyldimethylaminopropylcarbodiimide (EDCI, 284 mg, 1.49 mmol) was added, the mixture warmed to room temperature, and stirred for 10 d. The reaction mixture was poured into H_2O (75 mL) and extracted with CH_2Cl_2 (3 x 75 mL). The combined CH_2Cl_2 layers were dried over $MgSO_4$, filtered, evaporated, and dried *in vacuo.* The crude product was purified via chromatography (230-400 mesh silica, 9:1 hexane:ether, 1.5 cm diameter x 5 cm height). A white solid (780 mg, 90% yield) was recovered. TLC (2:1 hexane:ether, acid char): R_f = 0.52. MP: 133-135 °C. ^{1}H-NMR ($CDCl_3$): 0.05 (s, 6H), 0.65 (s, 3H), 0.8-2.05 (m, 49H), 2.25-2.4 (m, 4H), 3.65 (t, *J* = 7 Hz, 2H), 4.6 (m, 1H), 5.35 (d, *J* = 5 Hz, 1H). ^{13}C-NMR ($CDCl_3$): -4.8, 12.4, 18.8, 19.1, 19.3, 19.7, 19.9, 21.5, 23.0, 23.1, 23.2, 23.3, 24.3, 24.8, 26.4, 26.5, 28.3, 28.5, 28.7, 31.5, 32.4, 36.3, 36.7, 37.1, 37.5, 38.6, 40.0, 40.2, 40.3, 42.8, 50.5, 56.6, 57.2, 62.5, 123.1, 140.2, 173.5. MS (CI): m/z = 587 (M+H).

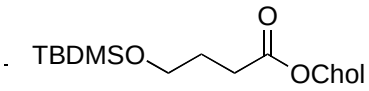

3

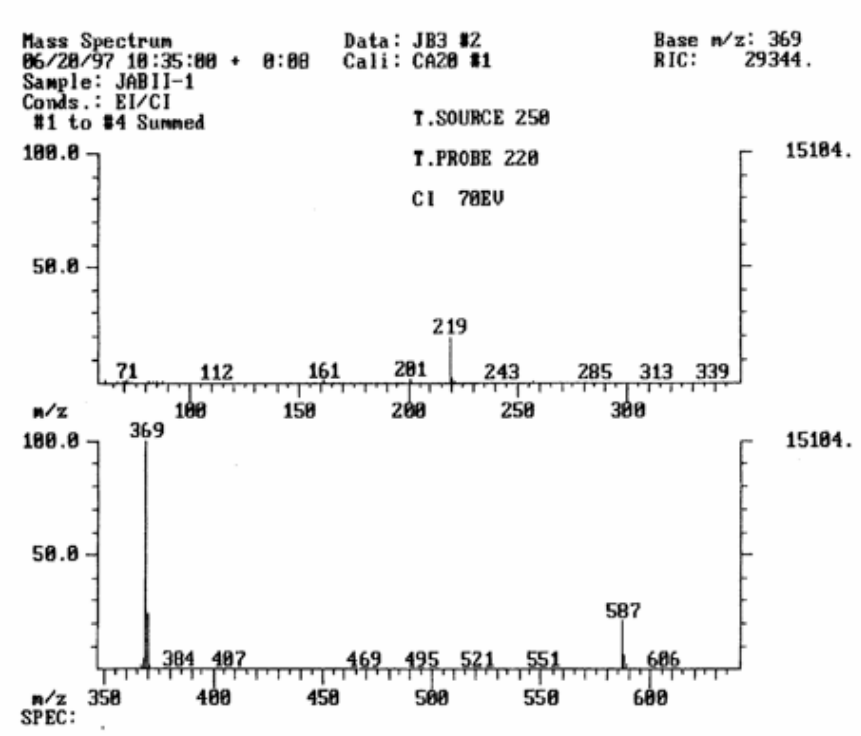

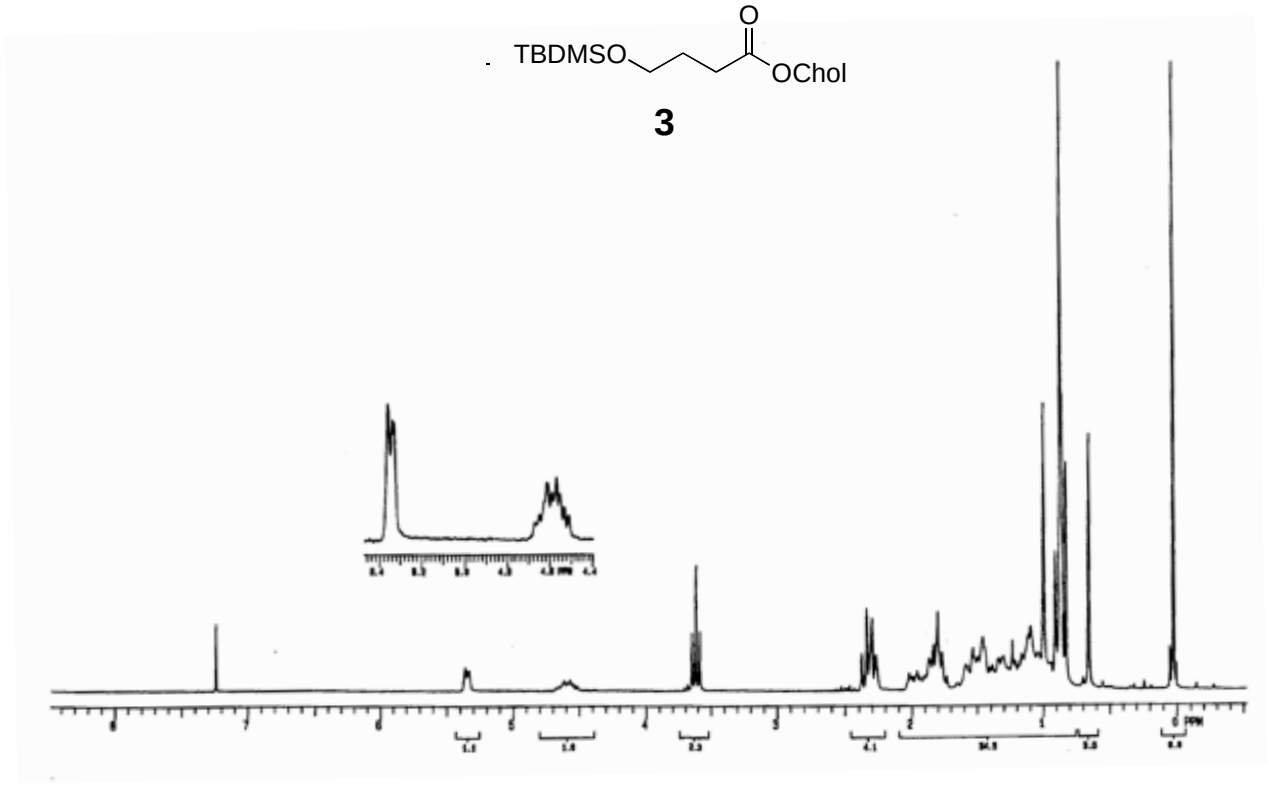

3

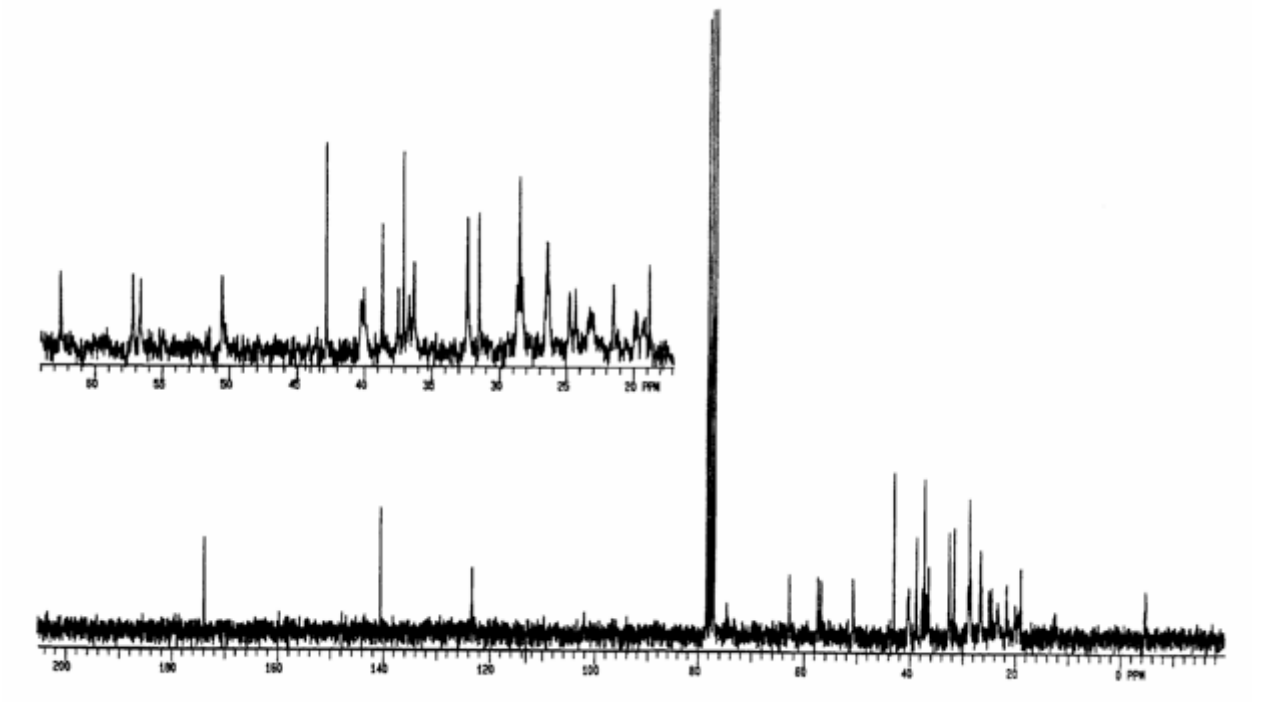

4-*t*-BUTYLDIMETHYLSILYLOXY-1-CHOLESTERYLOXY-1-DIETHYLPHOSPHORYLOXY-1-BUTENE (4). n-Butyl lithium (795 µL, 1.94 mmol, 2.4M in hexane) was added dropwise, via syringe, to diisopropylamine (453 µL, 3.23 mmol) in THF (250 µL) at -78 °C and the solution stirred for 30 min. Cholesteroyl-4-*t*-butyldimethylsilyloxy butanoate (**3**, 758 mg, 1.29 mmol) in THF (3mL) was then slowly added dropwise, via syringe. The solution was stirred for an additional hour, followed by the addition of diethylchlorophosphate (373 µL, 2.58 mmol) in HMPA (4.9 mL) in 3 aliquots. The solution turned orange/brown and gellated. It was thawed enough to stir, then returned to -78 °C for 10 min. The reaction was then warmed to room temperature and stirred for an additional hour. Ether (50 mL) was added and the reaction mixture filtered through a small silica plug. The solvent was evaporated, the oil redissolved in ether (75 mL), and the organic layer washed with 5% $NaHCO_3$ (3 x 75 mL). The ether layer was dried over $MgSO_4$, filtered, evaporated, and dried briefly *in vacuo*. The crude product was purified via flash chromatography (230-400 mesh silica, 6:1 hexane:ether, 2 cm diameter x 16 cm height). A white solid (750 mg, 81% yield) was recovered after evaporation. The product was used immediately without additional characterization. TLC (2:1 hexane:ether, I_2): R_f = 0.35.

4-*t*-BUTYLDIMETHYLSILYLOXY-1-CHOLESTERYLOXY-1-BUTENE (5).

Tetrakis(triphenylphosphine) palladium (15 mg, 12.4 µmol) and 4-*t*-butyldimethylsilyloxy-1-cholesteryloxy-1-diethylphosphoryloxy-1-butene (**4**, 270 mg, 373 µmol) were added to CH_2Cl_2 (8 mL) and cooled to 0 °C. Triethyl aluminum (653 µL 653 µmol; 1.0 M in hexane) was then added dropwise via syringe. The solution was stirred at 0 °C for 1 h before warming to room temperature and stirring for an additional 3 h. The crude mixture was purified via flash chromatography (230-400 mesh silica, 16:1 hexane:ether, 1.5 cm diameter x 20 cm height). A white solid (66 mg, 31% yield) was recovered as a 90:10 cis:trans mixture. TLC (16:1 hexane:ether, p-anisaldehyde): R_f = 0.75 (cis), 0.71 (trans). ^{1}H-NMR (C_6D_6, 90:10 cis:trans mixture): 0.13 (s, 6H), 0.68 (s, 3H), 0.8-2.75 (m, 51H), 3.4 (m, 1H), 3.75 (t, J = 12 Hz, 2H), 4.6 (dt, J_1 = 8 Hz, J_2 = 7 Hz, 0.9H), 5.15 (dt, J_1 = 13 Hz, J_2 = 7 Hz, 0.1H), 5.35 (m, 1H), 6.04 (dt, J_1 = 7 Hz, J_2 = 2 Hz, 0.9H), 6.15 (dt, J_1 = 13 Hz, J_2 = 2 Hz, 0.1H). ^{13}C-NMR/APT (C_6D_6, 90:10 cis:trans mixture): -4.8 (O), 12.2 (O), 19.1 (O), 19.5 (O), 19.6 (O), 21.5 (E), 22.8 (O), 23.1 (O), 24.3 (E), 24.6 (E), 26.2 (O), 28.5 (O), 28.8 (E), 28.9 (E), 29.2 (E), 29.6 (E), 29.7 (E), 30.3 (E), 30.6 (E), 32.2 (O), 32.4 (E), 36.2 (O), 36.8 (E), 37.0 (E), 37.3 (E), 37.6 (E), 39.9 (E), 40.0 (E), 40.2 (E), 40.3 (E), 42.6 (E), 51.5 (O), 56.8 (O), 57.0 (O), 63.8 (E), 81.3 (O), 103.0 (O), 106.5 (O), 122.1 (O), 140.5 (E), 141 (O), 145.2 (O).

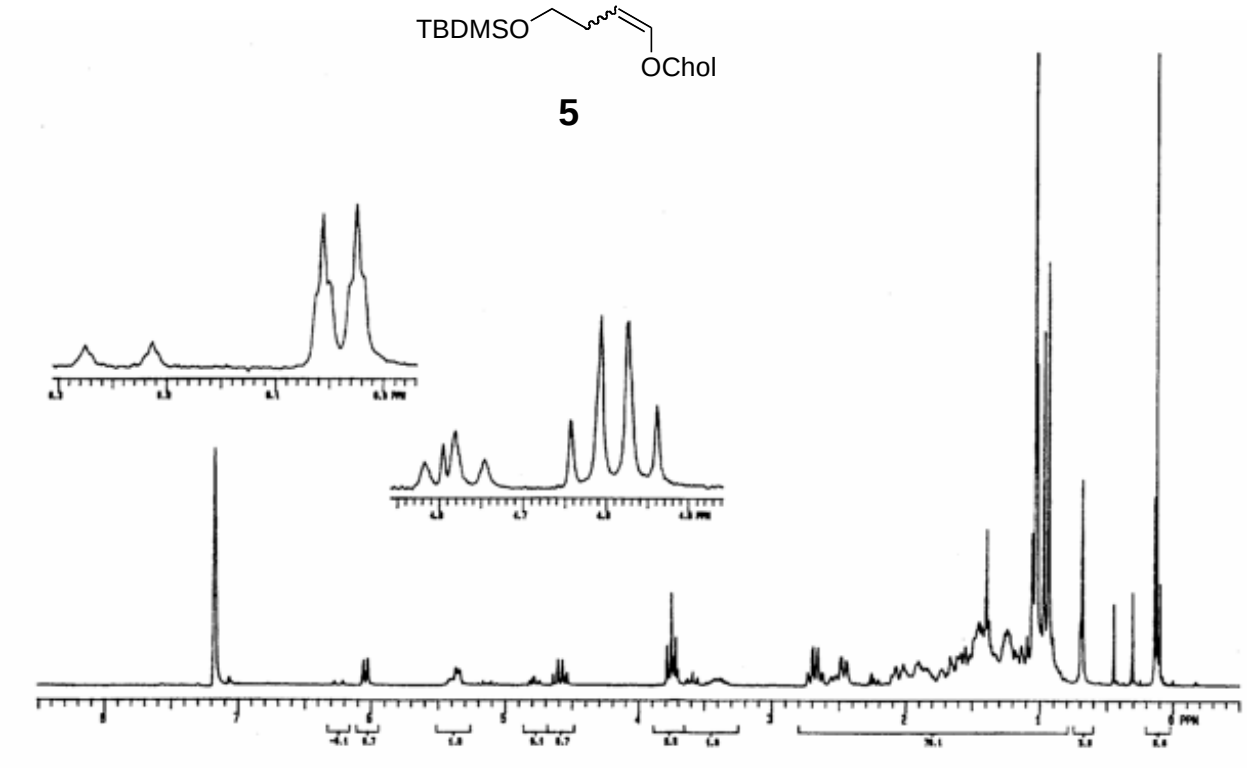

5

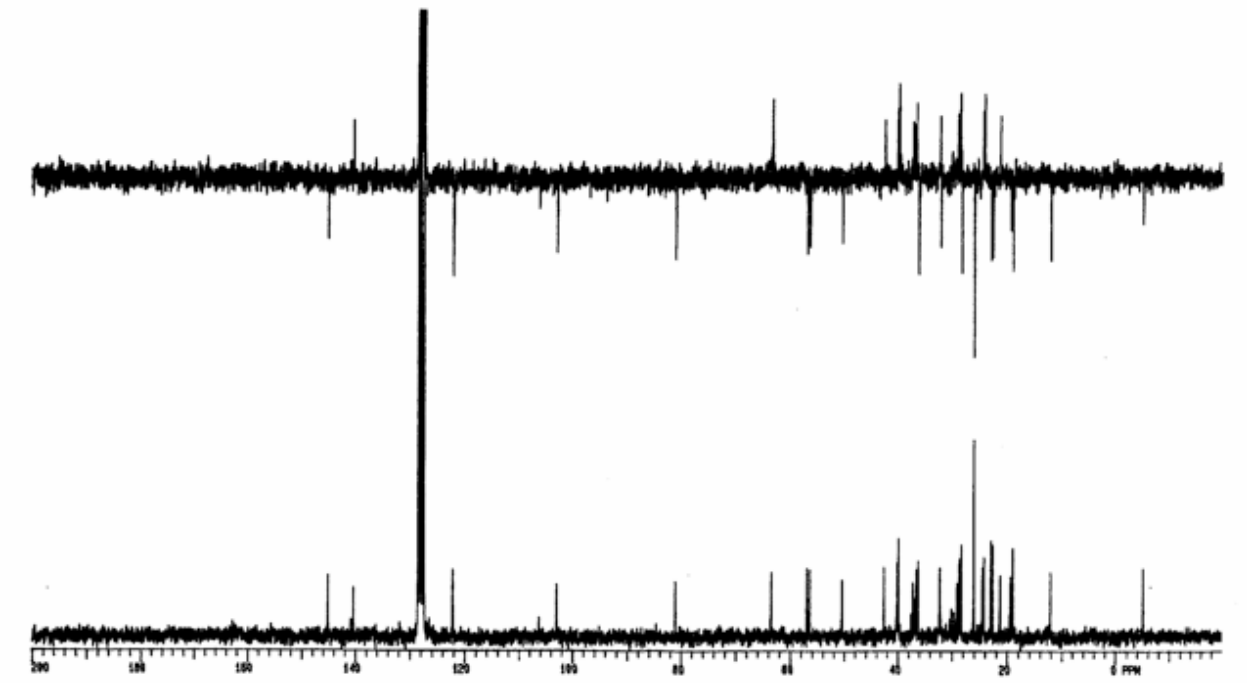

4-CHOLESTERYLOXY-3-BUTEN-1-OL (6). Tetrabutylammonium fluoride (TBAF, 210 µl, 210 µmol, 1.0 M in THF) and 1.0 mL 40% tetrabutylammonium hydroxide were added via syringe to 4-*t*-butyldimethylsilyloxy-1-cholesteryloxy-1-butene (**5**, 40 mg, 70 µmol) in THF (3 mL). The reaction was run for 12 h, then filtered through a small silica plug with ether and the solvent evaporated. The mixture was purified via flash chromatography (230-400 mesh silica, 8:1 hexane:ether, 1.5 cm diameter x 15 cm height) to give *cis*-4-cholesteryloxy-3-buten-1-ol (29 mg, 91% yield) and *trans*-4-cholesteryloxy-3-buten-1-ol (1.5 mg, 4% yield) as white solids (95% combined yield). TLC (2:1 hexane:ether, acid char): R_f = 0.18 (cis), 0.14 (trans). ^{1}H-NMR (C_6D_6, cis): 0.65 (s, 3H), 0.8-2.05 (m, 39H), 2.3-2.53 (m, 4H), 3.35 (m, 1H), 3.58 (t, J = 6 Hx, 2H), 4.4 (dt, J_1 = 7 Hz, J_2 = 7 Hz, 1H), 5.35 (m, 1H), 5.98 (dt, J_1 = 6 Hz, J_2 = 1 Hz, 1H). ^{1}H-NMR (C_6D_6, trans): 0.65 (s, 3H), 0.8-2.05 (m, 41H), 2.4-2.5 (m, 2H), 3.35 (t, J = 7 Hz, 2H), 3.5 (m, 1H), 4.95 (dt, J_1 = 13 Hz, J_2 = 6 Hz, 1H), 5.35 (m, 1H), 6.15 (dt, J_1 = 12 Hz), J_2 = 1 Hz, 1H). ^{13}C-NMR/APT (C_6D_6, 70:30 cis:trans): 12.06 (O), 12.40 (O), 14.40 (O), 19.04 (O), 19.4 (O), 19.5 (O), 21.0 (E), 21.4 (E), 22.8 (O), 23.0 (O), 24.4 (E), 24.6 (E), 25.5 (E), 28.4 (O), 28.6 (E), 28.7 (E), 29.1 (E), 29.5 (E), 30.0 (E), 32.1 (O), 32.3 (E), 36.2 (O), 36.7 (E), 36.9 (E), 37.3 (E), 37.5 (E), 39.8 (E), 39.9 (E), 40. 2 (E), 42.6 (E), 50.5 (O), 50.6 (O) 54.3 (E), 56.6 (O), 57.0 (O), 62.7 (E), 63.0 (E), 75.9 (O), 79.8 (O), 81.2 (O), 102.0 (O), 102.9 (O), 106.2 (O), 122.1 (O), 122.3 (O), 140.4 (E), 140.8 (E), 145.6 (O). MS (CI): m/z = 457 (M+H).

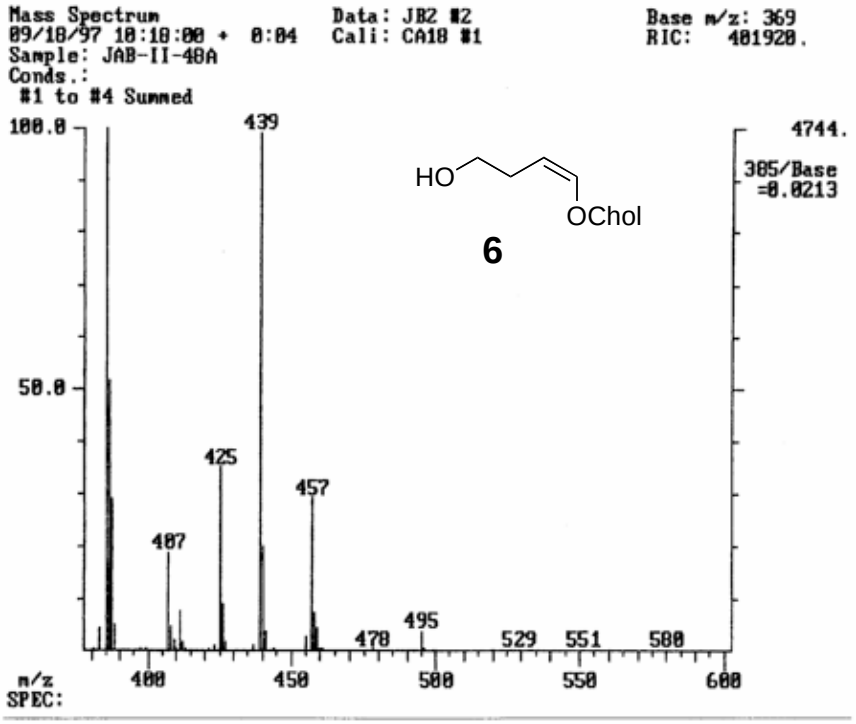

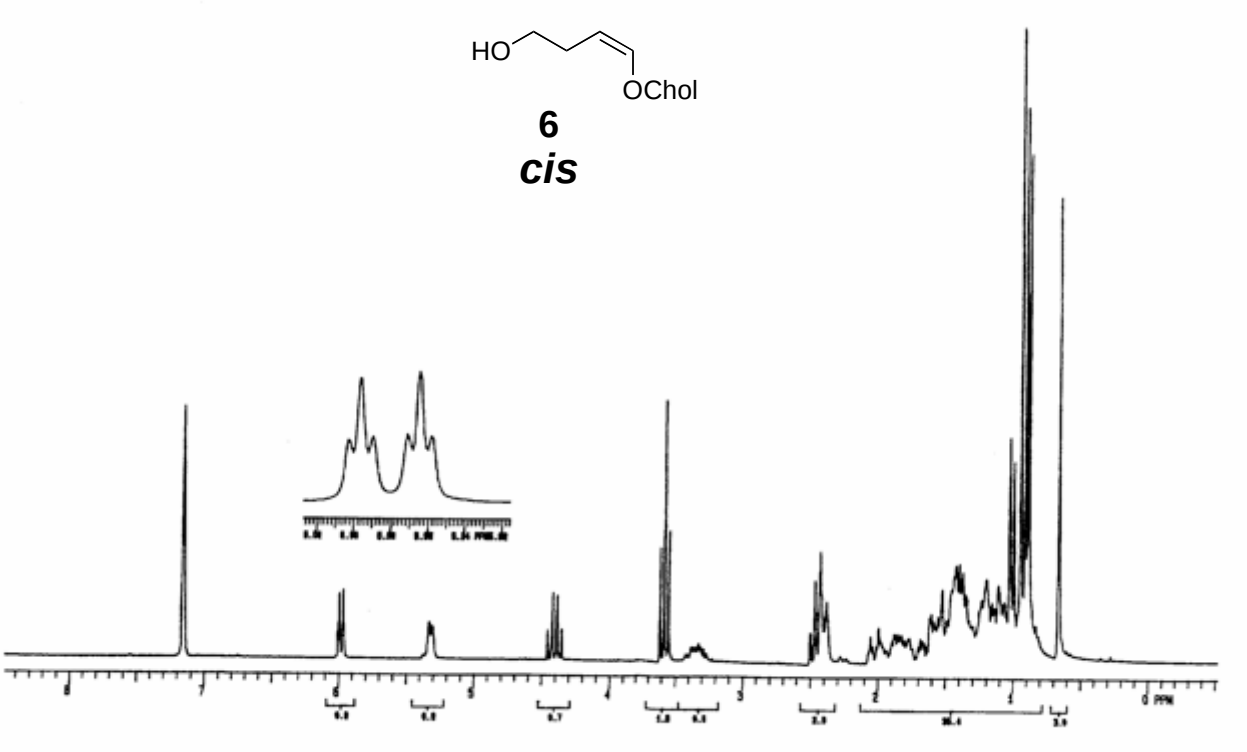
HO
OChol
6
cis

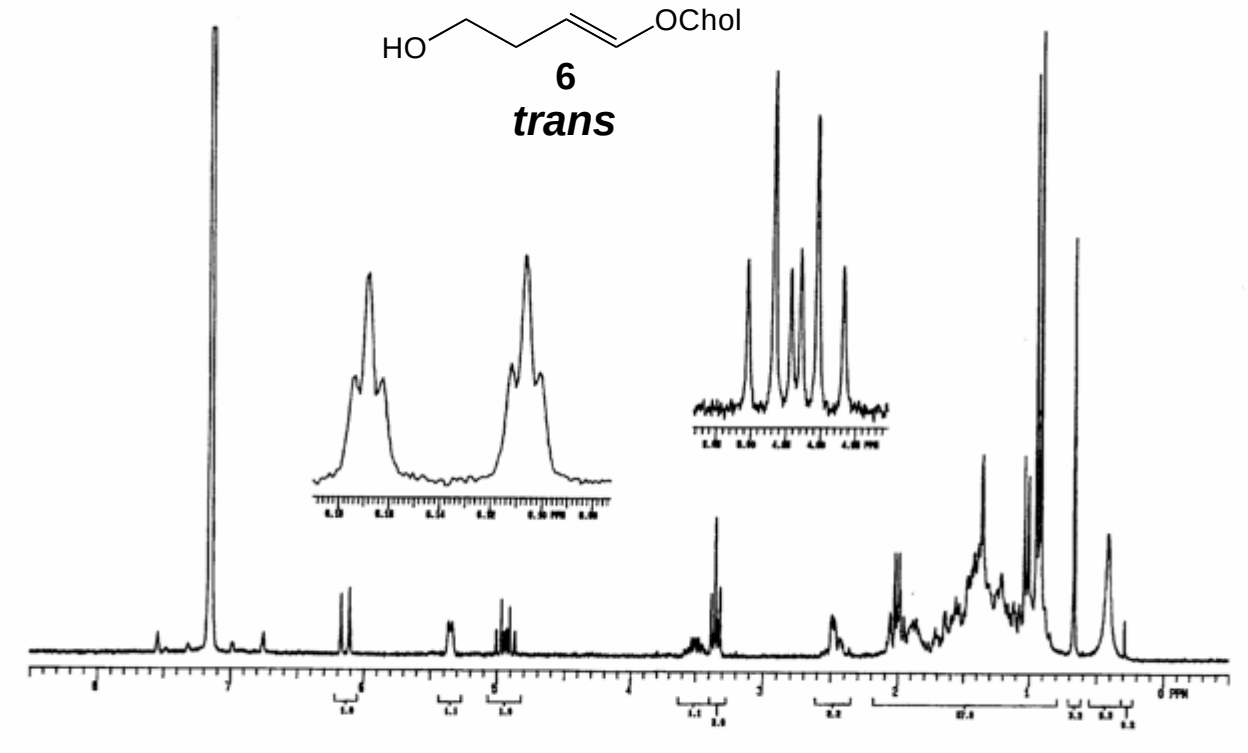
HO
OChol
6
trans

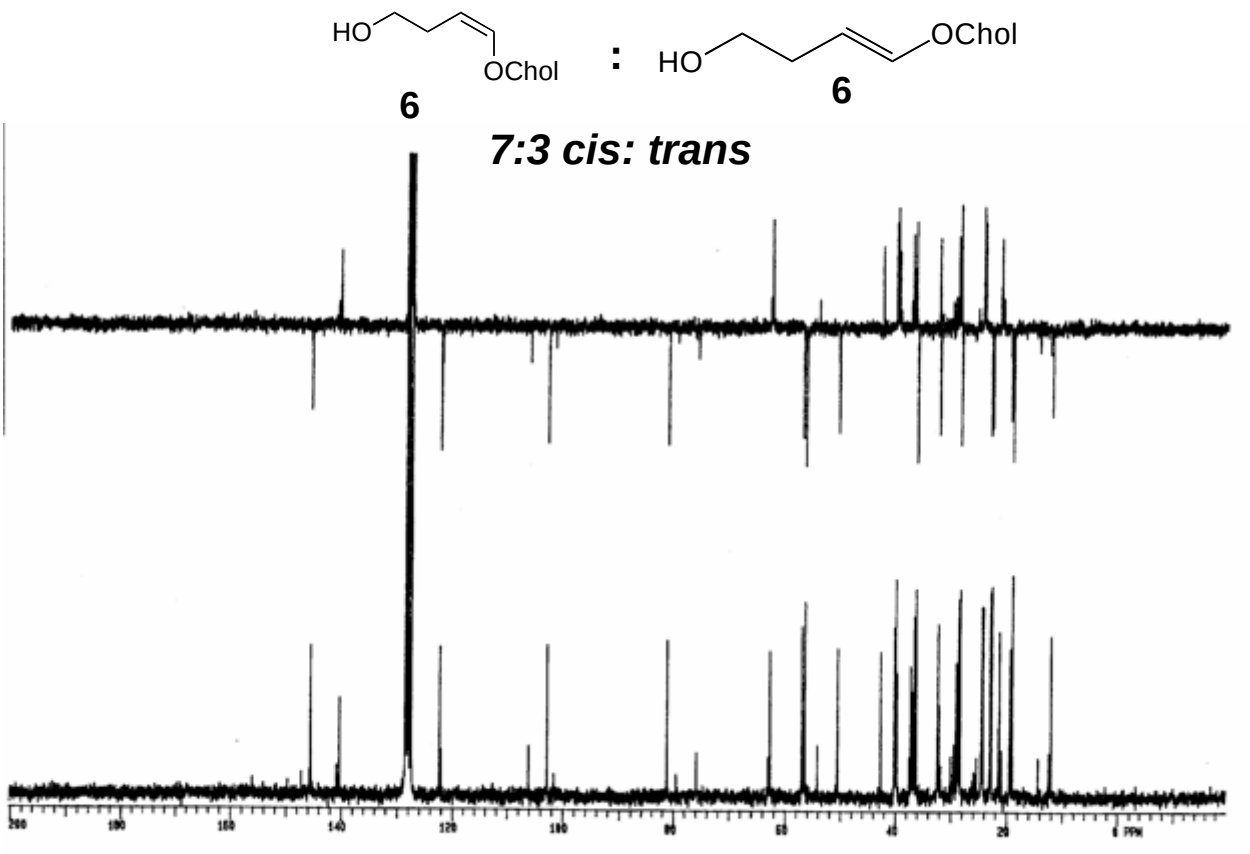
HO
OChol
6
:
HO
OChol
6
7:3 cis: trans

1´(4´-CHOLESTERYLOXY-3´-BUTENYL)-ω-METHOXY-POLYETHYLENE[112] GLYCOLATE (CVEP, 7). 4-Cholesteryloxy-3-buten-1-ol (**6**, 44 mg, 96 µmol), methoxy-poly(ethylene glycol)-carboxymethyl, MW 5000 (435 mg, 87.0 µmol), dicyclohexylcarbodiimide (DCC, 21.6 mg, 104 µmol), and 4-*N,N*-dimethylaminopyridine (DMAP, 10 mg, 81 µmol) were added to CH_2Cl_2 (7 mL) and stirred for 4 d. The reaction mixture was then cooled to 0 °C and the dicyclohexylurea crystals removed via filtration (21 mg). The solvent was concentrated to 2 mL, dripped into cold ether (20 mL), and the ether solution centrifuged at 4000 rpm for 10 min. The ether was carefully decanted and the pellet triturated with fresh ether (20 mL). This process was repeated 5 times. The pellet was then dissolved in CH_2Cl_2, evaporated to a dry film, dissolved in 2 mL 18 MΩ Millipore H_2O, and lyophilized to give 420 mg PEG containing product (86% yield based on recovered dicyclohexylurea). TLC (90:10:1 $CHCl_3$:MeOH:H_2O, I_2): R_f = 0.75. ^{1}H-NMR ($CDCl_3$, cis): 0.65 (m, 3H), 0.75-2.5 (m, 50H + H_2O), 3.2-4.5 (m, >120H), 5.35 (m, 1H), 6.1 (m, 1H). ^{1}H-NMR ($CDCl_3$, 65:35 cis:trans): 0.65 (m, 3H), 0.75-2.5 (m, 50H + H_2O), 3.2-4.5 (m, >120H), 5.35 (m, 1H), 6.08 M, 0.65H), 6.15 (m, 0.35H).

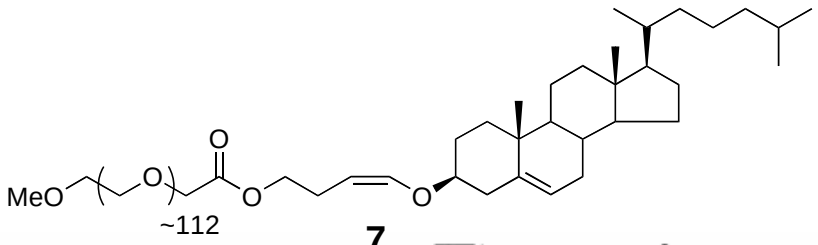

7

cis

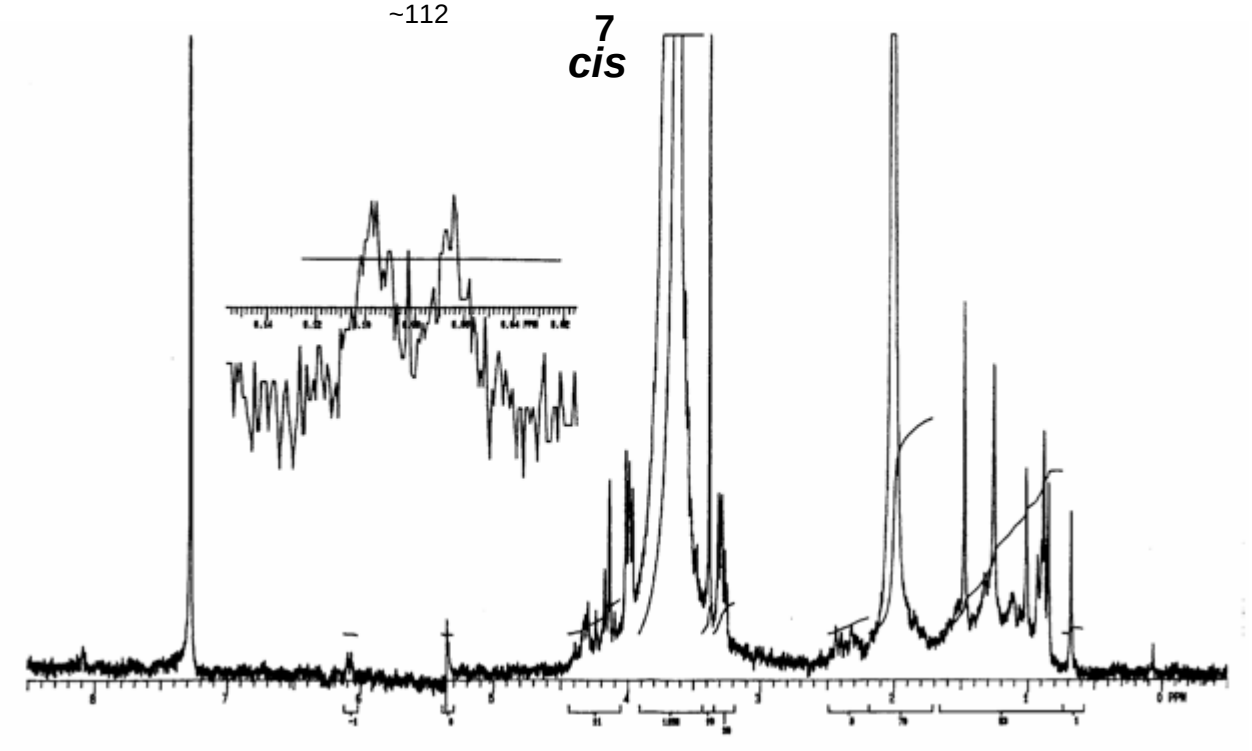

65:35 cis:trans

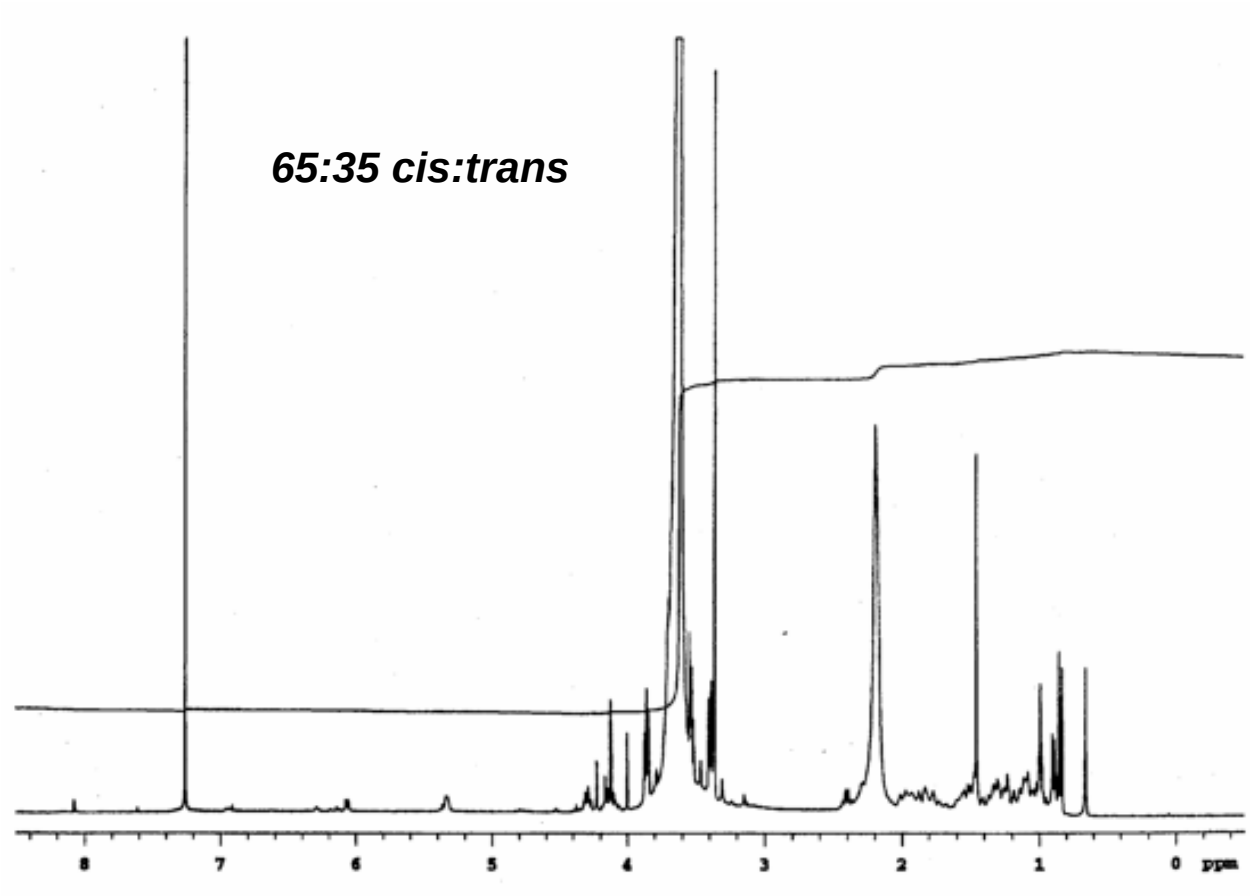

Flow Cytometry of KB cells treated with liposomes containing calcein as cytosolic marker prior to analysis (see Experimental Methods for details)

5:95 CVEP:DOPE (NON-TARGETED CONTROL)

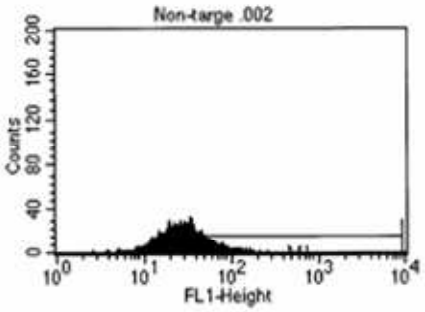

File: Non-targe .002 Sample ID: Non-targe
Gate: G1 Gated Events: 2907
Total Events: 5000 X Parameter: FL1-H FL1-Height (Log)

Marker	Left, Right	Events	% Gated	% Total	Mean	Geo Mean
All	1, 9910	2907	100.00	58.14	31.77	27.10
M1	20, 9390	2050	70.52	41.00	38.82	35.25

0.5:5:95 FOLATE-PEG-DSPE:CVEP:DOPE (TARGETED)

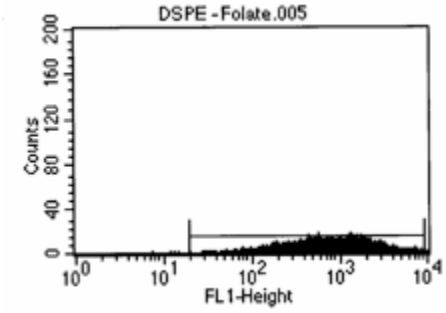

File: DSPE - Folate.005 Sample ID: DSPE - Folate
Gate: G1 Gated Events: 2798
Total Events: 5000 X Parameter: FL1-H FL1-Height (Log)

Marker	Left, Right	Events	% Gated	% Total	Mean	Geo Mean
All	1, 9910	2798	100.00	55.96	1181.17	743.72
M1	20, 9390	2789	99.68	55.78	1177.84	749.87

Systematic Research of Peptide Spacers Controlling Drug Release from Macromolecular Prodrug System, Carboxymethyldextran Polyalcohol−Peptide−Drug Conjugates

Yoshinobu Shiose,*,§ Hiroshi Kuga,† Hitoshi Ohki,‡ Masahiro Ikeda,‡ Fumiyoshi Yamashita,|| and Mitsuru Hashida||

Biological Research Laboratories IV and Medicinal Chemistry Research Laboratories II, Daiichi Sankyo Co. Ltd., Kasai R&D Center, Kita-Kasai 1-16-13, Edogawa-Ku, Tokyo 134-8630, Japan and Department of Drug Delivery Research, Graduate School of Pharmaceutical Sciences, Kyoto University, Kyoto 606-8501, Japan. Received June 13, 2008; Revised Manuscript Received October 9, 2008

The primary purpose of this study was to comprehensively delineate specificity of the peptide spacer sequence to tumor-expressed proteases for the design of macromolecular carrier−peptide spacer−drug conjugate system. 225 conjugates of carboxymethyldextran polyalcohol (CM-Dex-PA) as water-soluble carrier and a dansyl derivative (*N*-(4-aminobutyl)-5-(dimethylamino)-1-naphthalenesulfonamide, DNS) as the model drug linked with different tetrapeptide spacers (Gly-Gly-P_2−P_1, P_2, P_1: Ala, Asn, Gly, Cit, Gln, Ile, Leu, Met, Phe, Pro, Ser, Thr, Trp, Tyr, and Val) were combinatorially synthesized. First, the drug release assay of all of the fluorogenic model conjugates was performed in murine Meth A solid tumor homogenates. The drug release rate was higher with conjugates having hydrophobic amino acids at P_2. It was also found that conjugates with Asn release the drug rapidly and, in contrast, those with Pro does not. Second, we selected three peptide spacers (Gly-Gly-Phe-Gly, Gly-Gly-Ile-Gly, Gly-Gly-Pro-Leu), which release only DNS at different rates, and applied them to doxorubicin (DXR) conjugates. These three DXR conjugates were used for investigating relationships with drug release, pharmacokinetics, and antitumor activity against Meth A bearing mice of these conjugates. The release of DXR from the conjugates corresponded well with that of DNS conjugates in tumor homogenates. CM-Dex-PA-Gly-Gly-Phe-Gly-DXR and CM-Dex-PA-Gly-Gly-Ile-Gly-DXR indicated strong antitumor activity, with the comparable pharmacokinetic profile of released DXR in tumor. Taken with the fact that the drug release rate in tumor homogenates was ∼10-fold different between these two DXR conjugates, it is likely that cellular uptake of the conjugate would be rate-limiting, rather than the drug release process under the in vivo situation. However, much weaker antitumor activity was observed with CM-Dex-PA-Gly-Gly-Pro-Leu-DXR, of which the drug release was extremely slow.

INTRODUCTION

Development of macromolecular prodrugs, which alter the pharmacokinetic profile of an aimed drug through conjugation with macromolecules, is a promising approach to increasing therapeutic efficacy and reducing adverse effect of the drug. Coupling of low-molecular-weight drugs to water-soluble macromolecular carrier can involve the following: (1) the improvement of drug movement in the body, prolonging its residence time in the blood circulation; (2) sustained release of the drug from the carrier by chemical or enzymatic hydrolysis; (3) site-specific delivery of drug due to moieties recognizing target cells (*1*). In solid tumors, macromolecules are known to accumulate preferentially, due to the "enhanced permeability and retention (EPR)" effect, i.e., leakiness of tumor angiogenic blood vessels and lack of effective lymphatic drainage (*2*). Exploitation of such mechanisms for tumor targeting has been successfully proven with various anticancer drugs, including doxorubicin, paclitaxel, camptothecin, and their analogues (*3*−*6*).

In addition to the efficiency of delivery to target tissue, the stability of the drug−polymer linkage is an important factor in determining therapeutic potentials. Prodrugs intended for tumorotropic delivery are required to release the drug using proteolytic cleavage of the polymer−drug linker by overexpressed enzymes in the tumor tissue, including thiol protease cathepsin B, metalloproteases such as collagenases and stromelysins, and serine proteases like plasminogen activator and plasmin. Acid-activated cleavage of the polymer−drug bond can also be used since the polymeric drug encounters endosomal/lysosomal acidification in tumor cells. The works of Duncan et al. on poly-*N*-(2-hydroxypropyl)methacrylamide (HPMA)-*p*-nitroaniline conjugates linked with peptidyl spacers have suggested that of all the lysosomal proteases the thiol protease cathepsin B was primarily responsible for the cleavage of the drug−polymer linkage (*7*−*9*). In addition, the rate of release of the *p*-nitroaniline was found to be dependent on the specificity of the peptide spacer sequence to cathepsin B, with the fastest rates of hydrolysis being observed for Gly-Phe-Leu-Gly among nine tetrapeptide spacers tested (*10*).

Being aware that there have been a limited number of studies (*10*−*13*) on sequence specificity of peptide spacers in tumorotropic macromolecular prodrugs, we initiated this study to comprehensively delineate specificity of the peptide spacer sequence to tumor-expressed proteases in a similar manner to that reported by Schmid et al. (*14*). 225 conjugates of carboxylmethyl dextran polyalcohol (CM-Dex-PA) and a dansyl derivative (*N*-(4-aminobutyl)-5-(dimethylamino)-1-naphthalenesulfona-

* To whom correspondence should be addressed. Phone: +81-3-5696-3915. Fax: +81-3-5696-4264. E-mail:shiose.yoshinobu.gn@daiichisankyo.co.jp.

§ Biological Research Laboratories IV.

|| Kyoto University.

† Present address: Development Research Department, Daiichi Sankyo Inc., 389 Thornall Street, Edison, NJ 08837, USA.

‡ Medicinal Chemistry Research Laboratories II.

10.1021/bc800238f CCC: $40.75 © 2009 American Chemical Society
Published on Web 12/18/2008

Scheme 1. Synthesis of the CM-Dex-PA-Tetrapeptide-DNS Conjugates

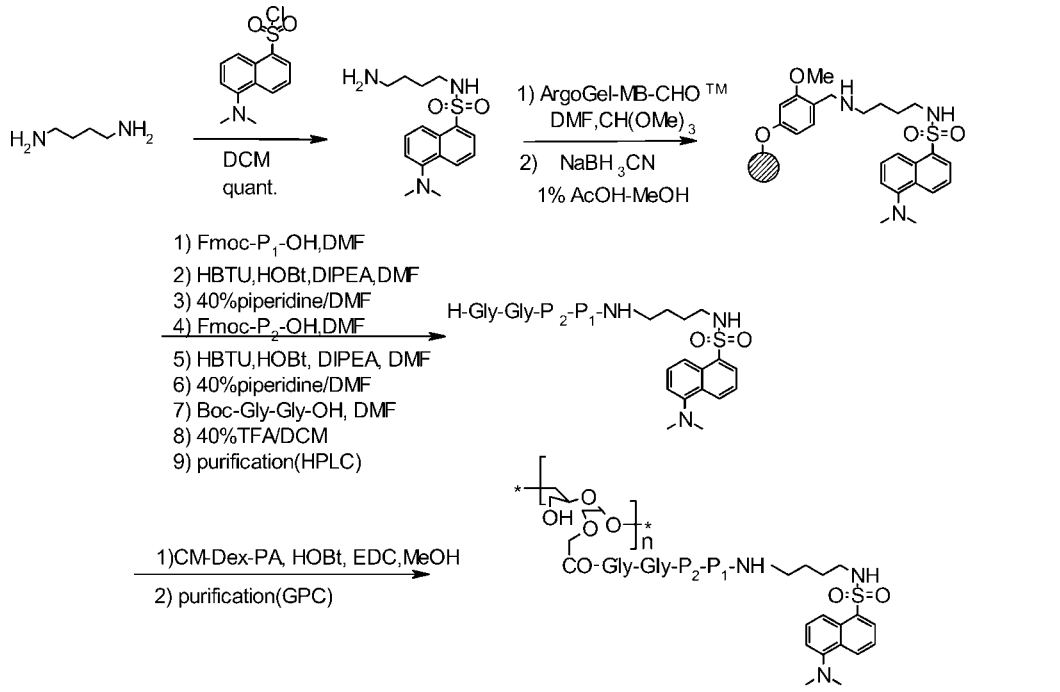

P_1,P_2 = Ala, Asn, Cit, Gln, Gly ,Ile, Leu, Met, Phe, Pro, Ser, Thr, Trp, Tyr ,Val

mide, DNS) linked with different tetrapeptide spacers were combinatorially synthesized, and the rate of release of DNS from the conjugates was measured using murine Meth A solid tumor homogenates. Effectiveness of CM-Dex-PA as a backbone of tumorotropic macromolecular prodrugs has been demonstrated in our previous studies (*6*). On the basis of the in vitro studies, conjugates of CM-Dex-PA and DXR[1]linked with different peptide spacers (Gly-Gly-Phe-Gly, Gly-Gly-Ile-Gly, and Gly-Gly-Pro-Leu) were designed. The in vitro drug release, pharmacokinetics, and in vivo antitumor activity of the carboxymethyldextran polyalcohol−doxorubicin conjugates were investigated to demonstrate the importance of peptide spacers in the design of macromolecular prodrugs.

EXPERIMENTAL PROCEDURES

Reagents. Fifteen fluoren-9-ylmethyloxycarbonyl (Fmoc)-protected amino acids were purchased from Bachem America Inc. (Torrance, CA). Doxorubicin (DXR) was obtained from Kyowa Hakko Co., Ltd. (Tokyo, Japan). Other chemicals were of reagent grade and used without further purification.

Synthesis of *N*-(4-Aminobutyl)-5-(dimethylamino)-1-naphthalenesulfonamide (DNS). After 1,4-butanediamine (33.0 g, 371 mmol) was dissolved in dichloromethane (100 mL), dansyl chloride (5.0 g, 18.5 mmol) in dichloromethane (100 mL) was added dropwise to the solution for 30 min on ice. The reaction mixture was stirred at room temperature for 20 h. After the solvent was evaporated, the residue was dissolved in ethyl acetate, washed with saturated sodium bicarbonate and NaCl, and then dried with sodium sulfate. After the solvent was evaporated, DNS (5.99 g) was yielded as oil. ^{1}H NMR ($CDCl_3$) δ: 1.28−1.37 (m, 2 H, CH_2), 1.43−1.49 (m, 2 H, CH_2), 2.57 (t, 2 H, J = 6.4 Hz, CH_2), 2.84−2.89 (m, 8 H, Me_2, CH_2), 7.18 (d, 1 H, J = 7.6 Hz, H-6 of Dansyl), 7.51, 7.55 (2d, 2 H, J = 8.3 Hz, 8.8 Hz, H-3, H-7 of Dansyl), 8.25 (d, 1 H, J = 7.0 Hz, H-2 of Dansyl), 8.33 (d, 1 H, J = 8.8 Hz, H-8 of Dansyl), 8.53 (d, 1 H, J = 8.3 Hz, H-6 of Dansyl).

Succinic acid (66 mg) was added to the solution of DNS (90 mg) in methanol (20 mL). The solvent was evaporated, and diethyl ether was added to the residue for solidification. The residue was washed with diethylether and dried to yield 130 mg of DNS salt (0.5 succinic acid 0.7 hydrate). Anal. Calcd for $C_{16}H_{23}N_3O_2S \cdot 0.5$ succinic acid $\cdot 0.7$ H_2O: C, 55.00; H, 7.03; N, 10.69; S, 8.16. Found: C, 55.10; H, 6.80; N, 10.46; S, 8.16. DNS was dissolved in 50% acetonitrile solution and prepared to 3.57 mg/mL. Furthermore, the solution was diluted to adequate concentration as HPLC standard sample.

Combinatorial Synthesis of CM-Dex-PA-Tetrapeptide-DNS Conjugates (Scheme 1). *a. Transduction to MB-CHO Resin of DNS.* DNS succinic salt (5.96 g, 18.54 mmol) in *N*,*N*-dimethylformamide (DMF, 30 mL) was added to trimethyl ester (30 mL) suspended with ArgoGelTM-MB CHO resin (6.9 g, 0.40 mmol/g). After shaking for 16 h, the solvent was removed, and the resin was washed with methanol and dried. To the resin, 1% acetic acid in methanol (100 mL) and 1 N $NaBH_3CN$ in tetrahydrofuran (THF, 20 mL) were added, and the solution was shaken for 2 days. The resin was isolated, washed with methanol and chloroform, and dried overnight to yield DNS-resin (19.7 g).

b. Synthesis of H-Gly-Gly-P_2-P_1-DNS by ACT496. Using DNS-resin (25 mg, 0.01 mmol), 225 kinds of crude H-Gly-Gly-P_2-P_1-DNS (15 × 15 amino acids) were synthesized by

[1]Abbreviations: Ala, L-alanine; Asn, L-asparagine; Cit, L-citrulline; DCC, *N*,*N*′-dicyclohexylcarbodiimide; DIPEA, diisopropylethylamine; DMF, *N*,*N*-dimethylformamide; DNS, *N*-(4-aminobutyl)-5-(dimethylamino)-1-naphthalenesulfonamide; DXR, Doxorubicin; EDC, 1-ethyl-3-(3-dimethylaminopropyl)carbodiimide; EDTA, ethylenediaminetetraacetic acid; Fmoc, fluoren-9-ylmethyloxycarbonyl; Gln, L-glutamine; Gly, L-glycine; GPC, gel permeation chromatography; HBTU, 2-(1*H*-benzotriazole-1-yl)-1,1,3,3-tetramethyluronium hexafluorophosphate; HOBt, 1-hydroxybenzotriazole; HPLC, high-performance liquid chromatography; Ile, L-isoleucine; LC/MS, liquid chromatography−mass spectrometry; Leu, L-leucine; MMPs, matrix metalloproteases; MES, 2-(*N*-morpholino)ethanesulfonic acid; Met, L-methionine; Phe, L-phenylalanine; Pro, L-Proline; Ser, L-serine; THF, tetrahydrofuran; Thr, L-Threonine; Tos, toluenesulfonyl; Trp, L-tryptophan; Trt, triphenylmethyl; Tyr, L-Tyrosine; Val, L-valine.

ACT496 (Advanced Chem. Tech., KY). P_2 and P_1 amino acids were Ala, Asn, Cit, Gln, Gly, Ile, Leu, Met, Phe, Pro, Ser, Thr, Trp, Tyr, and Val. The DNS resin was placed in the reaction vessel of the synthesizer and washed with DMF. The DMF was removed by filtration. To bond P_1 amino acid to DNS, a 0.1 M solution of Fmoc-protected amino acids in DMF (0.5 mL) was added, followed by 1-hydroxybenzotriazole (HOBt, 0.1 mL of 0.5 M solution in DMF), diisopropylethylamine (DIPEA, 0.2 mL of 0.5 M solution in DMF), and 2-(1*H*-benzotriazole-1-yl)-1,1,3,3-tetramethyluronium hexafluorophosphate (HBTU, 0.2 mL of 0.25 M solution in DMF). The mixture was shaken for 2 h at room temperature. Then, DMF was removed by filtration. The procedure was performed once again. The resin was washed three times with 1 mL DMF. To remove the Fmoc group, piperidine in DMF was added and the mixture shaken for 1 min. The resin was washed with DMF (3 times). The bonding of P_2 amino acid to P_1-DNS, the removal of Fmoc, and the bonding of Boc-Gly-Gly to P_2-P_1-DNS were performed following the same protocol as that for P_1 amino acid. After the reaction was completed, the resin was washed twice with 1 mL DMF, twice with 1 mL THF, once with 1 mL MeOH, and three times with 1 mL CH_2Cl_2. To remove the Boc group and isolate H-Gly-Gly-P_2-P_1-DNS from the resin, CH_2Cl_2 solution including 50% trifluoroacetic acid (1 mL) was added and incubated for 2 h. The crude H-Gly-Gly-P_2-P_1-DNS was collected by filtration and dried.

c. HPLC Purification of Crude H-Gly-Gly-P_2-P_1-DNS. The crude H-Gly-Gly-P_2-P_1-DNS, which was synthesized by the solid phase method, was dissolved in methanol (500 μL), transferred to Eppendorf tube, and evaporated. Then, these were dissolved in 10% methanol (100−200 μL) and purified by HPLC. The HPLC separation was performed on a 15 × 250 mm reversed-phase column packed with Capcell Pak C18 UG 120 (Shiseido, Tokyo, Japan) with 8 mL/min flow rate. The detector was set at 260 nm (UV-8020, Tosoh, Tokyo, Japan). The mobile phase consisted of methanol/acetonitrile (1:2) and 0.1 M trifluoroacetic acid, of which the proportion ranged from 20% to 45% according to the elution property of H-Gly-Gly-P_2-P_1-DNS. All samples were confirmed by LC/MS and HPLC purity (260 nm) >95%.

d. Synthesis of CM-Dex-PA. Carboxymethyl dextran polyalcohol (CM-Dex-PA) was synthesized from dextran (molecular weight 500 kDa, Pharmacia). Dextran (50 g) was dissolved in 0.1 M acetic acid buffer (pH 5.5, 5 L). A sodium periodic acid (165.0 g) was dissolved in distilled water (5 L) and added to the solution of dextran. The mixture was stirred under shade at 4 °C for ten days. Then, ethylene glycol (35 mL) was added and the mixture stirred overnight. The reaction mixture was adjusted to pH 7.5 using 8 M sodium hydroxide solution. Then, sodium borohydride (70 g) was added, and the mixture was stirred overnight. The solution was adjusted to pH 5.5 with acetic acid on ice, and ultrafiltration was performed using a Biomax 50 (size exclusion 50 kDa, Millipore). The filtration was freeze−dried to yield dextran polyalcohol (Dex-PA, 27.1 g). Dex-PA was dissolved in 14% sodium hydroxide solution (150 mL), and monochloroacetic acid (30 g) was added under cooling with ice and stirred at room temperature overnight. The reaction mixture was treated by ultrafiltration using Biomax 50 after having adjusted to pH 8 with acetic acid. A macromolecular fraction was freeze−dried, and Na salt (5.6 g) of CM-Dex-PA was obtained. The molecular weight of CM-Dex-PA was approximately 263 000 using pullulan standard by GPC and has a polydispersity index of 1.6 (M_w/M_n). The decrease in molecular weight of dextran following periodic acid oxidation has also been observed by Ahmad et al. (*15*), presumably due to structural changes associated with C2−C3 bond cleavage and increased molecular flexibility. The carrier was shelf-stable for over three months. On the other hand, the degrees of substitution of the CM groups in the carrier were determined by titration (ca. 0.0027 mol CM equiv per gram of CM-Dex-PA).

e. Synthesis of CM-Dex-PA-Gly-Gly-P_2-P_1-DNS. CM-Dex-PA was dissolved in collidine buffer (pH 7.0) containing 50% methanol to yield a concentration of 15 mg/mL. A 36 μL aliquot of 10 mg/mL 1-ethyl-3-(3-dimethylaminopropyl)carbodiimide (EDC) and 10 μL of 10 mg/mL HOBt in methanol was added to 200 μL of the CM-Dex-PA solution. H-Gly-Gly-P_2-P_1-DNS was dissolved in 42 μL of methanol, added to the reaction mixture, and then stirred for 3 h. 36 μL of the 10 mg/mL EDC solution was added and the mixture stirred for another 3 h, to yield CM-Dex-PA-Gly-Gly-P_2-P_1-DNS.

f. Purification of CM-Dex-PA-Gly-Gly-P_2-P_1-DNS. The reaction mixture of CM-Dex-PA-Gly-Gly-P_2-P_1-DNS was diluted with 600 μL of distilled water and subjected to GPC for purification. The conjugates were eluted with 0.1 M sodium acetate buffer (pH 5.0) containing 20% of acetonitrile using TSK GEL PW-6000XL column (Tosoh, Tokyo, Japan). The flow rate was 1 mL/min and detected at 254 nm (SPD-10A, Shimazu, Tokyo, Japan). The fraction eluting between 8.5 and 11.5 min, which corresponded to the molecular weight of 100 to 400 kDa, was collected.

g. Determination of DNS Contents in CM-Dex-PA-Gly-Gly-P_2-P_1-DNS. The eluate fraction was diluted 10 times with distilled water. The content of DNS associated with CM-Dex-PA-Gly-Gly-P_2-P_1-DNS was determined by the GPC system equipped with a fluorescence detector (RF-10A, Shimazu, Tokyo, Japan) set at excitation and emission wavelength of 335 and 530 nm, respectively. Other conditions were the same as mentioned above. The DNS content was calculated by the calibration curve of DNS. The DNS content of the conjugates ranged from 3% to 6% (w/w).

Synthesis of CM-Dex-PA-tetrapeptide-DXR Conjugates. CM-Dex-PA-Gly-Gly-Phe-Gly-DXR, CM-Dex-PA-Gly-Gly-Ile-Gly-DXR, and CM-Dex-PA-Gly-Gly-Pro-Leu-DXR were synthesized by Research Laboratory of Daiichi Pharmaceutical Co., Ltd. (Tokyo, Japan).

a. Synthesis of H-Gly-Gly-Phe-Gly-DXR. A mixture of H-Phe-Gly-OH (10 g, 44.0 mmol) and toluenesulfonyl (Tos) OH (8.36 g, 44.0 mmol) and benzylalcohol (10 mL) was suspended and refluxed through a Dean−Stark system for 16 h. A reaction mixture was concentrated, and ether was added to give Tos OH·H-Phe-Gly-OBzl (20 g, 94%). Triphenylmethyl (Trt) -Gly-Gly-OH·Et_3N (1.40 g, 3.0 mmol) and TosOH·H-Phe-Gly-OBzl (1.46 g, 3.0 mmol) and HOBT (490 mg, 3.6 mmol) and (*N*,*N*′-dicyclohexylcarbodiimide DCC, 740 mg, 3.6 mmol) were dissolved in DMF (10 mL) and the mixture stirred overnight. The mixture was concentrated, diluted with ethyl acetate, and washed with 5% aqueous citric acid, a saturated sodium bicarbonate solution, saturation solution of salt, and distilled water in this order. Then, it was dried with $MgSO_4$ and filtered, and the filtrate was concentrated. Trt-Gly-Gly-Phe-Gly-OBzl was obtained by column chromatography (CH_2Cl_2/MeOH = 50:1) to yield 1.5 g. Trt-Gly-Gly-Phe-Gly-OBzl (500 mg) and $HCOONH_4$ (150 mg) were dissolved in DMF (5 mL), followed by the addition of 5% Pd−C (500 mg) and agitation for 2 h. Pd−C was removed by filtration, and the filtrate was purified by column chromatography (CH_2Cl_2/MeOH = 50:1) to give Trt-Gly-Gly-Phe-Gly-OH (330 mg, 78%). ^{1}H NMR (CD_3OD): δ 7.18−7.45 (m, 20H), 4.64 (dd, 1H, J = 8.8, 5.6 Hz), 3.94 (d, 1H, J = 16.5 Hz), 3.80 (d, 1H, J = 16.5 Hz), 3.78 (d, 1H, J = 17.5 Hz), 3.64 (d, 1H, J = 17.5 Hz), 3.23 (dd, 1H, J = 14.2, 5.6 Hz), 2.90 (dd, 1H, J = 14.2, 8.8 Hz), 2.90 (s, 1H).

Trt-Gly-Gly-Phe-Gly-OH (330 mg, 0.57 mmol), DCC (141 mg, 0.68 mmol), and HOBt (92 mg, 0.68 mmol) were dissolved in DMF (120 mL), and DMF solution containing of HCl/DXR

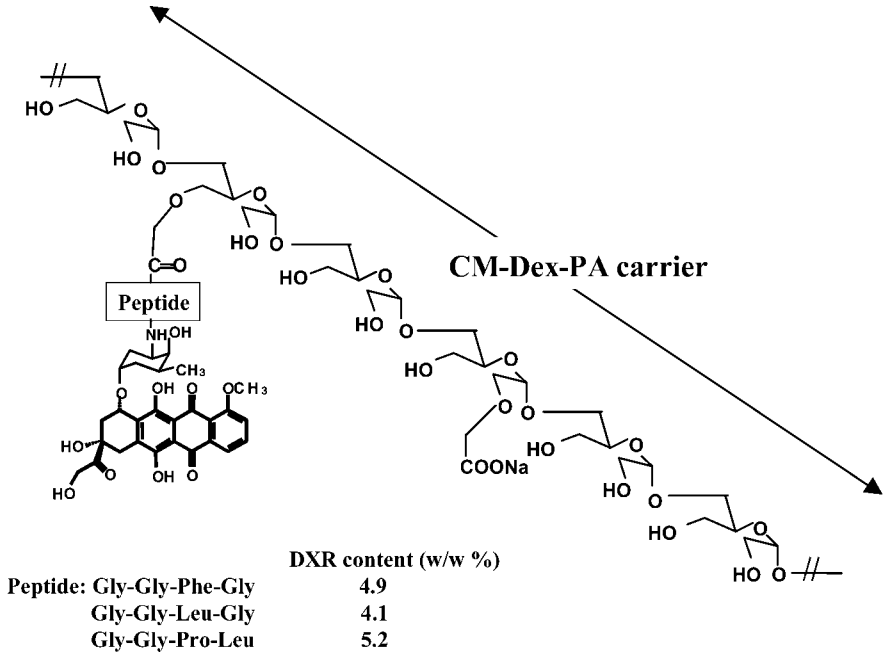

Figure 1. Partial structure of DXR conjugates.

(331 mg, 0.57 mmol) and triethylamine (0.063 mL, 0.57 mmol) were added and the mixture stirred for 16 h. Then, Trt-Gly-Gly-Phe-Gly-DXR was purified by column chromatogrphy (CH_2Cl_2/MeOH = 10/1) to yield 400 mg. ^{1}H NMR (CD_3OD): δ 7.91 (d, 1H, J = 7.6 Hz), 7.80 (t, 1H), 7.54 (d, 1H, J = 8.3 Hz), 7.16−7.26 (m, 5H), 5.43 (d, 1H, J = 3.9 Hz), 5.13 (br, 1H), 4.73 (s, 2H), 4.43 (dd, 1H, J = 8.4, 6.6 Hz), 4.30 (q, 1H, J = 6.6 Hz), 4.16 (m, 1H), 4.03 (d, 1H, J = 17.0 Hz), 4.02 (s, 3H), 3.86 (d, 1H, J = 16.9 Hz), 3.83 (d, 1H, J = 17.0 Hz), 3.77 (d, 1H, J = 15.9 Hz), 3.73 (d, 1H, J = 15.9 Hz), 3.62 (d, 1H, J = 1.5 Hz), 3.59 (d, 1H, J = 16.9 Hz), 3.13 (dd, 1H, J = 13.9, 6.6 Hz), 3.10 (d, 1H, J = 18.6 Hz), 3.00 (d, 1H, J = 18.6 Hz), 2.94 (dd, 1H, J = 13.9, 8.4 Hz), 2.38 (d, 1H, J = 14.7 Hz), 2.19 (dd, 1H, J = 14.7, 5.1 Hz), 1.98 (ddd, 1H, J = 12.7, 12.7, 3.9 Hz), 1.71 (dd, 1H, J = 12.7, 4.6 Hz), 1.28 (d, 3H, J = 6.6 Hz).

Trt-Gly-Gly-Phe-Gly-DXR (350 mg, 0.32 mmol) was dissolved in 75% AcOH (2 mL) and stirred for 1 h. Distilled water (10 mL) was added, and the solution was filtered and dried in vacuo. The resulting red solid product was collected by treatment of Dowex 1 × 8 ion-exchange resin (CL-form) and dried in vacuo to give HCl·H-Gly-Gly-Phe-Gly-DXR (180 mg).

b. Synthesis of CM-Dex-PA-Gly-Gly-Phe-Gly-DXR. CM-Dex-PA (750 mg) was dissolved in 50% MeOH/0.02 M Tris-maleate buffer (pH 7.0) (50 mL). HCl·H-Gly-Gly-Phe-Gly-DXR (100 mg) in MeOH (10 mL) and EDC·HCl (80 mg) in MeOH (4 mL) were added and the mixture stirred for 4.5 h. A solution of EDC·HCl (40 mg) in MeOH (4 mL) was added twice at 1.5 and 3 h. To stop the reaction, 3 M NaCl (50 mL) was added, and the mixture was filtered using a MW 50 kDa cutoff membrane. The product was dried in vacuo, redissolved in 3 M NaCl, and precipitated by dropping into EtOH (40 mL). The precipitate was collected, treated by ultrafiltration, and purified through a 0.22 μM filter, to give the product (740 mg). CM-Dex-PA-Gly-Gly-Ile-Gly-DXR and CM-Dex-PA-Gly-Gly-Pro-Leu-DXR were synthesized by the same method. The contents of DXR in the DXR conjugates ranged from 4% to 6% w/w, and contamination of free DXR was less than 0.01% DXR equiv. The partial structure of these conjugates was indicated in Figure 1.

Inoculation of Tumor Cells. Meth A (murine fibrosarcoma) was kindly obtained from Dr. Ichiro Azuma (Institute of Immunological Science, School of Medicine, Hokkaido University, Japan). Meth A tumors were propagated in vivo by subcutaneous inoculation of cells (1×10^6 cells/0.1 mL) into the left flank of syngenic male BALB/c mice (6 weeks of age). Murine histiocytoma M5076 cells were obtained from Japanese Foundation for Cancer Research (Tokyo, Japan). The cells were cultured in RPMI 1640 medium supplemented with 17% horse serum (Hyclone Laboratories, Logan, UT). M5076 solid tumors were propagated in vivo by subcutaneous inoculation of cells (1×10^6 cells/0.1 mL) into the left flank of syngenic male C57BL/6 mice (6 weeks of age).

Preparation of Tumor Homogenate from Meth A Solid Tumor in Mice. Meth A solid tumor homogenates were prepared according to the method of Rozhin et al. (*16*). On 21 days post-subcutaneous inoculation of Meth A tumor cells, the mice were sacrificed under anesthesia to excise the tumor tissue. A pool of the tumor tissues with a total weight of 27 g was washed three times with 20 mL of ice−cold MES buffer (250 mM sucrose, 25 mM MES, 1 mM EDTA, pH 6.5), and then placed in 35 mL of the fresh MES buffer. The tumor homogenization was performed at 4 °C for 5 min. The homogenate was centrifuged at 500 × g for 11 min, and the supernatant was collected and centrifuged again at the same condition. Furthermore, the supernatant was centrifuged at 15 000 × g for 19 min to yield a mitochondrial lysosomal pellet. The pellet was resuspended in citrate buffer (pH 5.5), quickly frozen, and stored at −80 °C. M5076 tumor homogenates were prepared by the same method.

Drug Release Assay of DNS Conjugates and DXR Conjugates in Tumor Homogenate. The enzyme reaction mixture consisted of 80 μL of Britton Robinson buffer (pH 4.5), 5 μL of 200 mM cysteine, 5 μL of 0.1% Brij 35, and 5 μL of the tumor homogenate. Five microliter of the DNS conjugate or DXR conjugate solution was added to the mixture and incubated at 40 °C for given time period (DNS conjugates, 2 or 20 h; DXR conjugates, 4, 8, 24 h). Then, acetonitrile (100 μL) was added to stop the reaction. Following centrifugation of the solution at 15 000 × g for 10 min, the amount of the liberated drug contained in the supernatant was determined by HPLC.

Release of DXR from the Conjugates in M5076 Cell Culture. Two milliliters of M5076 cell suspension (5×10^6 cells/mL) was seeded onto a 60 mm dish, and cultured in RPMI 1640 medium supplemented with 17% horse serum medium for 2 h. 100 μL of DXR conjugate solution (2 mg DXR equiv/mL) was added to the cell culture dish, and incubated at 37 °C in a humidified atmosphere of 5% CO_2 (v/v) in air. 24 h later, 1 M HCl containing 90% acetonitrile (2 mL) was added, and the lysate was taken and centrifuged for 10 min at 10 000 $\times$ *g*. The amount of DXR released from the conjugates was determined by HPLC.

Antitumor Activity of DXR Conjugates against Meth A Bearing Mice. After inoculation of Meth A cells (day 0), DXR conjugate (5, 20, or 40 mg DXR equiv/kg) or DXR (5, 10, or 20 mg/kg) were intravenously administered on day 9. On day 14, mice were sacrificed to excise and weigh tumor masses. The growth inhibition rate (IR) on the basis of tumor weight was calculated using the following formula: IR = (1 − TWt/TWc) × 100 (%), where TWt and TWc represent the mean tumor weight for treated and nontreated groups, respectively. The statistical significance of differences between the nontreated and treated groups was evaluated using Dunnett's test. The body weight of mice (BWt) was measured every day and compared to that on day 0 (BWc). The rate of body weight loss (BWL) was calculated on the basis of the following formula: BWL (%) = (1 − BWt/BWc) × 100. BWLmax indicates the maximum value of BWL.

Distribution of DXR in Tumor, Liver, and Serum after Administration of DXR Conjugates. Meth A bearing mice were intravenously administered with DXR conjugates or DXR at 20 mg DXR equiv/kg. In order to examine the release of DXR from macromolecular conjugates in detail, distribution of DXR following injection of the conjugates was measured on the same time scale as the case of DXR, which is rapidly distributed to and eliminated from tissues. That is, at 2, 4, 8, 24, and 48 h after injection, mice were anesthetized with dimethyl ether, and blood, liver, and tumor were collected. The blood were left to clot for 10 min and then centrifuged (10 000 $\times$ *g*, 10 min at 4 °C) to collect serum. The samples (serum, liver, and tumor) were stored at −30 °C until analysis. 100 μL of the serum was mixed with 100 μL of 1 M HCl containing 90% acetonitrile (v/v) and then centrifuged at 10 000 $\times$ *g* for 10 min at 4 °C. The supernatant was injected into the HPLC system. To liver and tumor 0.5 M HCl containing 50% acetonitrile (v/v) were added (1 mL solvent per 0.25 g tissue), homogenized on ice by the handy micro-homogenizer NS-310F (Microtec Co., LTD, Chiba, Japan), and centrifuged at 10 000 $\times$ *g* for 10 min at 4 °C. The supernatant was injected into the HPLC system. A preliminary experiment indicated that the procedure provided more than 95% recovery of DXR from tissues.

HPLC Condition. LC/MS was performed with an HP 1100 HPLC system with API 150Ex mass spectrometer on a Develosil Combi-RP-5 column (4.6 × 50 mm, Nomura Chemical Co., Ltd. Aichi, Japan). The mobile phase consisted of A, 0.1% HCOOH/H_2O (v/v), and B, 0.1% HCOOH/acetonitrile (v/v), with a linear gradient from 0% to 100% of B for 3.6 min (flow rate 2.5 mL/min). Determination of DNS and its peptide conjugates released was performed with a HPLC system on a Symmetry Shield RP18 column (4.6 × 100 mm, Waters Co., Milford, MA) and a fluorimetric detector (excitation 335 nm, emission 530 nm); the mobile phase consisted of acetonitrile and methanol (2:1) and 0.1 M sodium acetic acid, with a linear gradient from 30% to 90% for 15 min (flow rate 1 mL/min). Determination of DXR was performed on a Symmetry Shield RP18 column (4.6 × 100 mm) and a fluorimetric detector (excitation 480 nm, emission 590 nm); the mobile phase consisted of acetonitrile, methanol, and 0.1 M sodium acetic acid buffer (23.4/11.6/65.0, v/v/v, flow rate 1 mL/min).

RESULTS

Drug Release Assay of DNS Conjugates by Meth A Homogenate. Considering the pH dependence on the cathepsin activities associated with Meth A tumor homogenate (*17*), the drug release assay of the conjugates was performed at pH 4.5. When CM-Dex-PA-Gly-Gly-P_2-P_1-DNS was incubated, not only DNS but its peptide conjugate (P_1-DNS and P_2-P_1-DNS) were detected by HPLC. Figure 2 is a $P_2 \times P_1$ combination of pie charts, of which the diameter represents the total release rate. The red, blue, and yellow colors indicate DNS, P_1-DNS, and P_2-P_1-DNS. In the case of Pro at P_1, the release of DNS and its peptide conjugates was very slow (small chart) for any amino acids at P_2, while in the case of Asn at P_1, DNS (red color) was rapidly released. On the other hand, when P_2 was Val, Tyr, Trp, Phe, Met, Leu, or Ile, DNS was rapidly released. By contrast, Thr, Ser, Pro, Gly, Gln, Cit, and Ala at P_2 retarded the release of DNS and its peptide conjugates. Interestingly, when Asn was at P_2, P_1-DNS (blue color) was largely released. Taken together with the result of Asn at P_1, peptidases associated with Meth A tumor homogenates preferentially cleaved the carboxy side of Asn. In the case of Pro at P_1 and P_2, P_2-P_1-DNS (yellow color) and DNS tended to be mainly released, respectively, indicating that both the amino and carboxy sides of Pro are extremely resistant against the peptidases.

With regard to the conjugates which released DNS completely within 20 h, drug release for the shorter time (2 h) was also measured (Figure 3). When P_2 was Tyr, Phe, or Leu, and P_1 was Met, Leu, Gln, or Cit, the release of DNS were extremely high.

As well as Meth A homogenates, M5076 tumor homogenates were subjected to DNS release assays of the conjugates. When drug release in M5076 tumor homogenate was investigated with nine voluntarily selected conjugates (peptide: Gly-Gly-Leu-Met, Gly-Gly-Met-Asn, Gly-Gly-Gly-Asn, Gly-Gly-Phe-Gly, Gly-Gly-Ile-Cit, Gly-Gly-Ile-Leu, Gly-Gly-Pro-Gln, Gly-Gly-Pro-Ala, Gly-Gly-Met-Pro), it was highly correlated with that of Meth A tumor homogenate (Figure 4).

Comparison of Drug Release between DNS Conjugates and DXR Conjugates in Meth A Homogenates. As well as the DNS-bearing model conjugates, the release of DXR from DXR conjugates was investigated in Meth A homogenates. The conjugates, which have three typical peptide spacers (i.e., Gly-Gly-Phe-Gly, Gly-Gly-Ile-Gly, or Gly-Gly-Pro-Leu), were selected. Although the amount of DXR released within 20 h was less than that of DNS, the rank order of three types of conjugates was the same in both DXR- and DNS conjugates: that is, the release of the drugs was highest with conjugates having Gly-Gly-Phe-Gly, followed by Gly-Gly-Ile-Gly and Gly-Gly-Pro-Leu (Table 1).

Drug Release Assay of DXR Conjugates in M5076 Tumor Homogenates and in Vitro Cultured M5076 Cells. As well as Meth A homogenates, the M5076 tumor homogenates were subjected to drug release assays of DXR conjugates. DXR conjugates, for which the spacer varied in the rate of hydrolysis (Gly-Gly-Phe-Gly, Gly-Gly-Ile-Gly, Gly-Gly-Pro-Leu), were selected. The release rate constants of DXR from CM-Dex-PA-Gly-Gly-Phe-Gly-DXR, CM-Dex-PA-Gly-Gly-Ile-Gly-DXR, and CM-Dex-PA-Gly-Gly-Pro-Leu-DXR were 0.064 h^{-1}, 0.0066 h^{-1}, and 0.00013 h^{-1}, respectively (see Supporting Information). It indicated that, as well as in the case of DNS conjugates, the rank order of the DXR conjugates was the same in both Meth A and M5076 tumor homogenates.

In addition, the release of DXR from the conjugates was also evaluated in the in vitro cultured M5076 cells. Figure 5

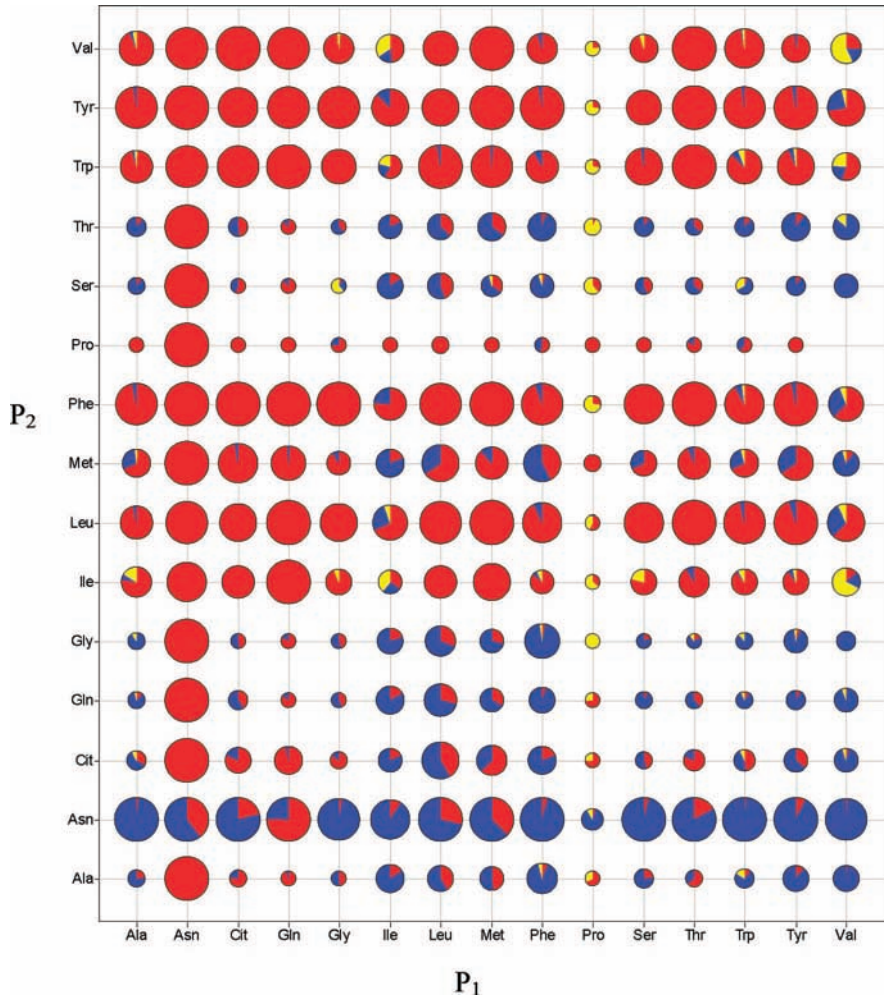

Figure 2. Characterization of DNS and its derivatives released from DNS conjugates in Meth A homogenate at 37 °C for 20 h. The vertical axis indicates the P_2 residure, and the horizontal axis indicates the P_1 residure. The total amounts of drug release are indicated by the size of circle, and the ratio of DNS, P_1-DNS, and P_2-P_1-DNS are indicated as red, blue, and yellow, respectively.

represents a plot of the amount released within 24 h in the cultured M5076 cells against the release rate constant evaluated in the homogenates. Although the rank order of drug release was the same in both cultured cells and tumor homogenates, the difference between CM-Dex-PA-Gly-Gly-Phe-Gly-DXR and CM-Dex-PA-Gly-Gly-Ile-Gly-DXR was not so remarkable in the cultured cells (ca. 1% for both) as expected from the tumor homogenates (~10-fold difference). It is likely that cellular uptake of the DXR conjugates is the rate-limiting step, and therefore the difference in the intracellular hydrolysis rate minimally affects the appearance of DXR from the conjugates.

Antitumor Activity of DXR Conjugates against Meth A Bearing Mice. Antitumor activity of CM-Dex-PA-Gly-Gly-Phe-Gly-DXR, CM-Dex-PA-Gly-Gly-Ile-Gly-DXR, and CM-Dex-PA-Gly-Gly-Pro-Leu-DXR was investigated in Meth A bearing mice. As shown in Table 2, intravenous injection of 5−40 mg/kg CM-Dex-PA-Gly-Gly-Phe-Gly-DXR remarkably decreased the tumor weight, although the loss of body weight (>20%) was observed at the highest dose. CM-Dex-PA-Gly-Gly-Ile-Gly-DXR, in spite of giving slower in vitro drug release than CM-Dex-PA-Gly-Gly-Phe-Gly-DXR, exhibited comparable antitumor activity to CM-Dex-PA-Gly-Gly-Phe-Gly-DXR, although two mice died at 40 mg/kg. On the other hand, antitumor effect of CM-Dex-PA-Gly-Gly-Pro-Leu-DXR was much less than the other two DXR conjugates. It clearly indicated that the rate of drug release is important in the antitumor activity. When DXR itself was administered at 20 mg/kg, four of six mice died, and antitumor activity was moderate. At 10 mg/kg, on the other hand, the antitumor activity and body weight loss were not observed. Thus, macromolecular prodrugs exhibiting a fast drug release due to tumor proteases, e.g., CM-Dex-PA-Gly-Gly-Phe-Gly-DXR and CM-Dex-PA-Gly-Gly-Ile-Gly-DXR, greatly improved therapeutic potential of DXR.

Distribution of DXR in Tumor and Liver after Administration of DXR Conjugates. The serum, hepatic, and tumoral levels of free DXR after intravenous injection of DXR conjugates were determined. When DXR was administered, the serum level of DXR was decreased rapidly in the early phase and gradually in the late phase. When the conjugates were injected intravenously, the serum level of free DXR was extremely low (Figure 6A).

As for administration of DXR, its tumoral level reached a maximum at 4 h and gradually decayed thereafter. In contrast, when CM-Dex-PA-Gly-Gly-Phe-Gly-DXR or CM-Dex-PA-Gly-Gly-Ile-Gly-DXR was administered, the tumoral level of free DXR released from the conjugates was gradually increased and remained high for a long time. The tumoral level of free DXR from the conjugates at 48 h was about 3-fold higher than the level following administration of DXR itself. In the case of CM-Dex-PA-Gly-Gly-Pro-Leu-DXR, the level of free DXR was minimally detected (Figure 6B).

DXR was highly distributed into the liver immediately after intravenous injection. In the case of CM-Dex-PA-Gly-Gly-Phe-Gly-DXR or CM-Dex-PA-Gly-Gly-Ile-Gly-DXR, the hepatic level of free DXR was kept low. The Cmax values for the conjugates were 5-fold lower than that for DXR. In the case of

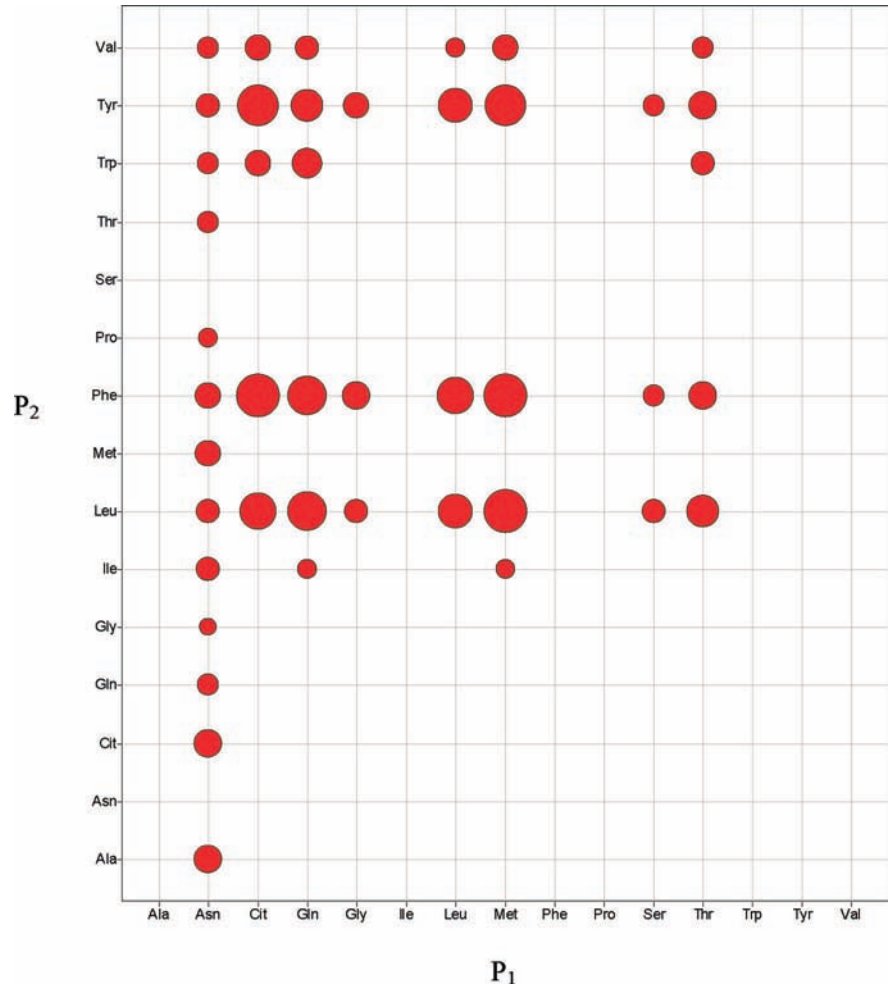

Figure 3. Released DNS for 2 h from DNS conjugates, which released DNS to 70% for 20 h. The vertical axis indicates the P_2 residure, and the horizontal axis indicates the P_1 residure. The amounts of drug released are indicated by the size of circle.

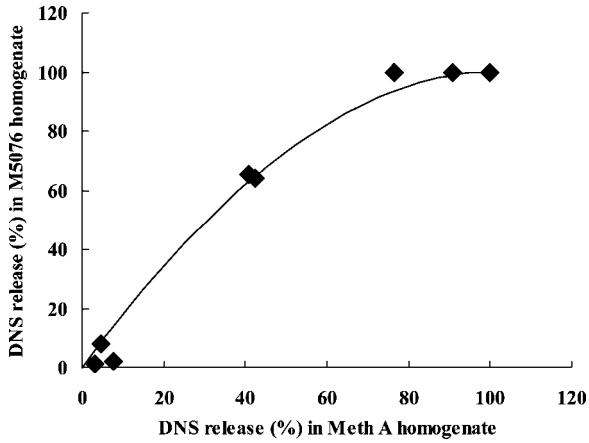

Figure 4. The relationship of released DNS from DNS conjugates between Meth A and M5076 homogenate. Several kinds of DNS conjugates were incubated in Meth A or M5076 homogenate for 20 h, and released DNS were determined by HPLC.

CM-Dex-PA-Gly-Gly-Pro-Leu-DXR, DXR was hardly detected in the liver as well as the tumor (Figure 6C).

DISCUSSION

Tumorotropic macromolecular prodrugs with peptide spacers promise to improve the efficacy and reduce the toxicity of the cancer chemotherapy. It is generally believed that the prodrugs

Table 1. Drug Release from DNS Conjugates and DXR Conjugates in 20 h Incubation with Meth A Homogenates

	drug release (%)	
peptide	DNS conjugate	DXR conjugate
Gly-Gly-Phe-Gly	100	100
Gly-Gly-Ile-Gly	41	8
Gly-Gly-Pro-Leu	15	0.3

that reached tumor tissues are taken up by tumor cells and release drug by lysosomal cysteine protease, cathepsins (*9*, *10*, *18*). Substrate specificity of cathepsins has been investigated over a few decades (*19*−*21*), including high-throughput profiling of serine and cysteine proteases using a microarray technique (*22*−*24*). However, taking into account that a polymer backbone sterically limits acceess of proteases to the peptide bond (*11*, *25*−*27*), systematic studies specialized to macromolecular prodrugs have been required. In this context, we combinatorially synthesized 225 fluorogenic macromolecular prodrugs with a CM-Dex-PA backbone and evaluated sequence dependence of amino acid spacers on the rate of drug release by tumor-associated proteases. We intended to evaluate structure−activity relationship of drug release under rather physiologically relevant conditions (i.e., tumor cell homogenates) than by individual cathepsins, since it was obvious that multiple proteases including cathepsins B and L are responsible for hydrolysis of the same type of macromolecular prodrugs (*17*).

Several investigations have already found that dipeptide having hydrophobic amino acid at P_2, such as Phe, Val, Leu, Ile, and Trp, and basic amino acid as Lys, or hydrogen bond

Table 2. Antitumor Activity of DXR Conjugates against Meth A Bearing Mice[a]

compound	schedule	dose[b] (mg/kg)	tumor weight mean ± SE (g)	tumor weight IR (%)	BWLmax[c]	D/U[d]
control			1.823 ± 0.446	0	<0	0/6
CM-Dex-PA-Gly-Gly-Phe-Gly-DXR	qdx1	40	0.207 ± 0.061***	89	21.6	0/6
	qdx1	20	0.260 ± 0.051***	86	6.7	0/6
	qdx1	10	0.389 ± 0.091***	79	2.5	0/6
	qdx1	5	0.759 ± 0.136**	58	1.7	0/6
CM-Dex-PA-Gly-Gly-Ile-Gly-DXR	qdx1	40	0.291 ± 0.115**	84	23.9	2/6
	qdx1	20	0.286 ± 0.089***	84	3.4	0/6
	qdx1	10	0.444 ± 0.038**	76	1.5	0/6
	qdx1	5	0.753 ± 0.167*	59	0.5	0/6
CM-Dex-PA-Gly-Gly-Pro-Leu-DXR	qdx1	40	1.094 ± 0.213	40	6.1	0/6
	qdx1	20	1.296 ± 0.166	29	<0	0/6
	qdx1	10	1.092 ± 0.300	40	<0	0/6
	qdx1	5	1.196 ± 0.185	34	<0	0/6
DXR	qdx1	20	0.738 ± 0.500	60	13	4/6
	qdx1	10	1.360 ± 0.282	25	3.7	0/6
	qdx1	5	1.571 ± 0.415	14	1.1	0/6

[a] Meth A cells were inoculated s.c. into BALB/c mice (Day 0). After 9 days, mice received a single (qd×1) administration of DXR conjugates and DXR (Day 9). Tumor weight was assessed on day 21. Asterisks indicate significant differences from the untreated control by Dunnett*s test. [b] Dose levels of compounds were expressed as those of DXR. [c] Maximum rate (%) of body weight loss, with numbers in parentheses denoting the day. <0 indicates no body weight loss. [d] Number of mice that died of toxicity/number of mice used. Death days were as follows. CM-Dex-PA-GGIG-DXR 40 mg/kg: day 16 and 17. DXR 20 mg/kg: days 17, 20, 20, and 20. *** $P < 0.001$. ** $P < 0.01$. * $P < 0.05$.

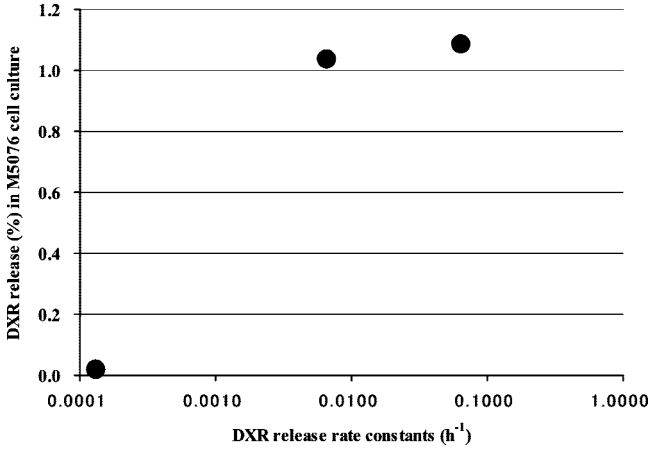

Figure 5. Relationship of released DXR from DXR conjugates between tumor homogenate and M5076 cell culture. CM-Dex-PA-Gly-Gly-Phe-Gly-DXR, CM-Dex-PA-Gly-Gly-Ile-Gly-DXR, and CM-Dex-PA-Gly-Gly-Pro-Leu-DXR were incubated with M5076 homogenate or M5076 cells for 24 h; released DXR were determined by HPLC (see Supporting Information).

amino acid as Cit at P_1, is able to be the substrate to cathepsin B (*28*). As shown in Figure 2, the release of DNS from prodrugs was rapid in the case of Val, Tyr, Trp, Phe, Met, Leu, and Ile at the P_2 position but slow in the case of Thr, Ser, Pro, Gly, Gln, Cit, and Ala. Thus, hydrophobicity of amino acids at P_2 would undoubtedly be important. When the P_1 position was a hydrophobic amino acid (Ile, Leu, Met, Phe, Tyr, Val), the cleavage appeared to occur even for spacers showing some resistance due to hydrophilic characters at P_2. It suggests that the proteases might simply recognize hydrophobic moieties and have a moderate sequence specificity. In addition, it should be noted that the P_1-DNS form tended to be released. From the viewpoint of molecular design, such hydrophobic amino acids should not be selected for P_1 to avoid the undesirable release of amino acid-conjugated drug.

In addition, when Asn was at P_1 or P_2, DNS and P_1-DNS, respectively, was released. It suggested that proteases associated with Meth A homogenate preferentially cleave the peptide bond at the C-terminal of Asn. On the other hand, the drug release rate became extremely low, when Pro was at P_1 or P_2. Pro, due to its distinctive cyclic structure in the side chain, exhibits steric hindrance and electrostatic repulsion and protects biologically active peptides against enzymatic degradation (*29*). Proteases associated with tumor cells would not be exceptional.

As mentioned above, it is desirable to design a macromolecular conjugate that does not release any conjugates with amino acids or peptides but only a native drug. On the basis of the examinations using fluorogenic macromolecular prodrugs, we selected three peptide spacers (Gly-Gly-Phe-Gly, Gly-Gly-Ile-Gly, Gly-Gly-Pro-Leu) that release only DNS at different rates and applied the spacers to the design of DXR conjugates. The rank order of the release of DXR from the conjugates was the same as that of DNS conjugates in both Meth A and M5076 tumor homogenates. Thus, examinations using fluorogenic macromolecular prodrugs undoubtedly gave useful information on the design of DXR conjugates. When CM-Dex-PA-Gly-Gly-Pro-Leu-DXR was administered to Meth A tumor-bearing mice, the tissue concentration of free DXR and antitumor activity was observed only minimally. This was quite reasonable, since the release of DXR from CM-Dex-PA-Gly-Gly-Pro-Leu-DXR was extremely slow in tumor homogenates. On the other hand, CM-Dex-PA-Gly-Gly-Phe-Gly-DXR and CM-Dex-PA-Gly-Gly-Ile-Gly-DXR, in spite of the fact that the release rate was ~10-fold different in tumor homogenates, exhibited similar pharmacokinetics and antitumor activity. The release of DXR from the conjugates would be determined not only by enzymatic activity but also by cellular uptake. It should be reiterated that water-soluble macromolecules hardly permeate plasma membranes. In the in vitro experiments using M5076 cells, the release of DXR was similar between CM-Dex-PA-Gly-Gly-Phe-Gly-DXR and CM-Dex-PA-Gly-Gly-Ile-Gly-DXR, being as slow as 1% of DXR per 24 h. Along with the fact that more than 15% of DXR could be released from these conjugates within 24 h, it is most likely that cellular uptake of the DXR conjugates is the rate-limiting step in vitro. As for DXR conjugates with the carboxymethyl−pullulan (CMPul) backbone (*12, 30, 31*), it has been reported that CMPul-Gly-Gly-Phe-Gly-DXR, which releases DXR rapidly in tumor homogenates, showed the highest antitumor activity, while CMPul-Gly-Gly-Gly-Gly-DXR, which releases DXR slowly, showed weaker activity than DXR in walker-256 and Yoshida sarcoma-bearing rat models. Our present investigation also revealed that the Gly-Gly-Gly-Gly spacer gave much slower release of DXR as compared to Gly-Gly-Phe-Gly and Gly-Gly-Ile-Gly spacers. Although the past (*12, 30, 31*) and present studies were different in terms of tumor models and polymer backbones, they presented an

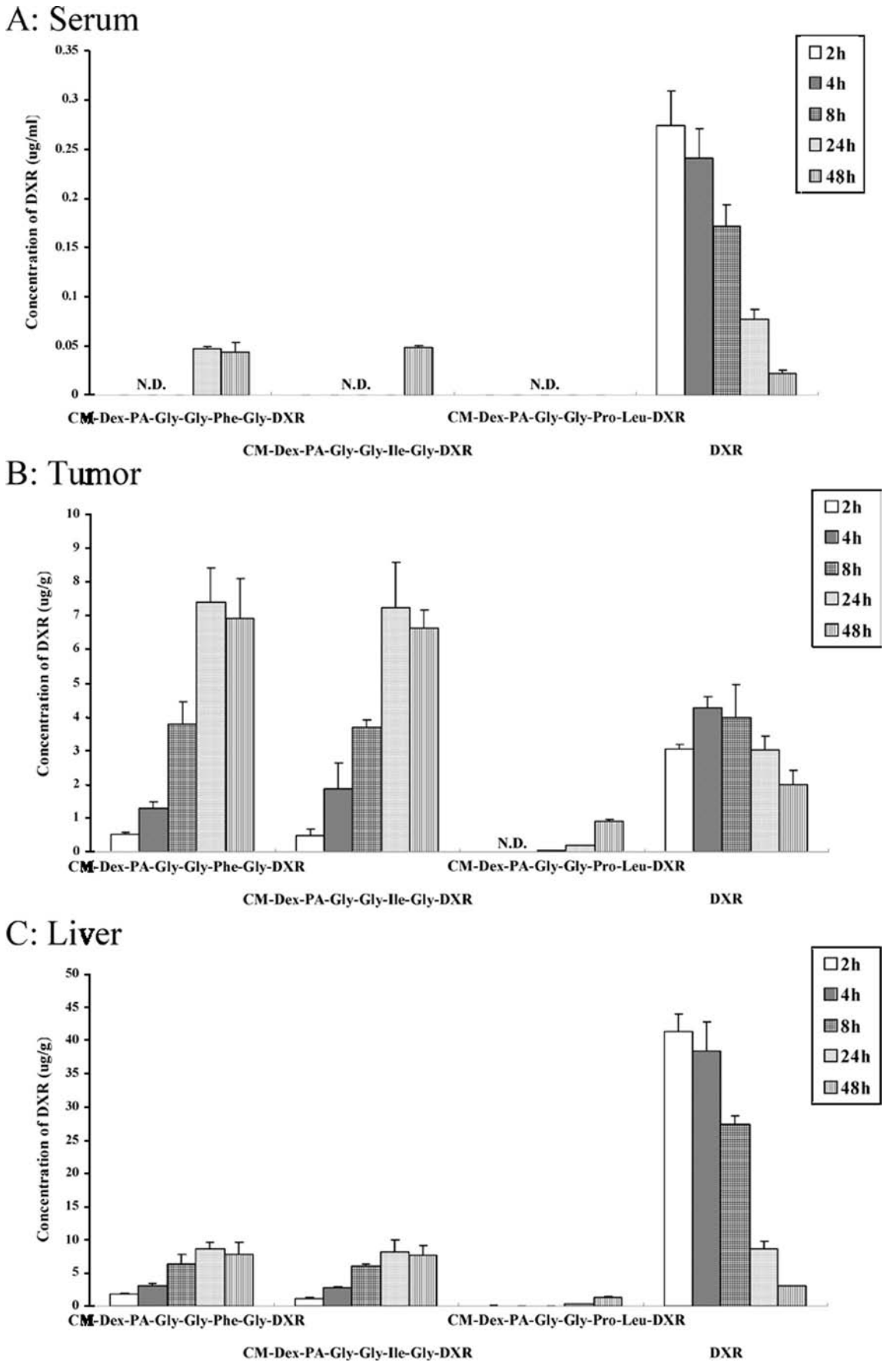

Figure 6. Pharmacokinetic profiles of free DXR after i.v. administration of DXR-conjugates or DXR to Meth A bearing mice at a dose equivalent to 20 mg/kg. Each point represents the mean for three mice; bars, SD. Parts A, B, and C indicate DXR concentration of serum, tumor, and liver, respectively. N.D.: Not detected.

essentially similar tendency. It might be concluded that the faster release of DXR provides greater antitumor activity, but the trend is saturated since cellular uptake of conjugates is smaller than the release of DXR based on the in vitro observations.

It is well-known that matrix metalloproteases (MMPs) are highly expressed in the tumor tissues. Macromolecular drug conjugates releasing active ingredients with MMPs have also been developed (*32*, *33*). These conjugates were designed on the basis of earlier studies on substrate specificity of MMPs demonstrating a consensus motif of Pro-X-X-X_{Hy} where X_{Hy} is a hydrophobic amino acid residue (*34*−*36*). It is also known that peptides having Leu and Ile instead of Pro in the sequence can be substrates for MMP-2 (*34*). Since our macromolecular prodrugs have quite different amino acid sequences, i.e., Gly-Gly-X-X, from MMP substrates and showed a fairly good in vitro/in vivo correlation of drug release, it is unlikely that MMPs are responsible for the release of DXR from the conjugates. At this moment, however, involvement of MMPs has yet to be ruled out.

In summary, we systematically investigated the properties of peptide spacers controlling the drug release from conjugates and found representative peptide spacers, which release only parent drug with different rates. With regard to DXR conjugates, the conjugates showing a faster drug release rate provided greater antitumor activity in tumor-bearing mice. Considering that antitumor drugs are classified into time−concentration product (AUC)-dependent and time-dependent drugs (*37*, *38*), however, the release rate of drugs needed to be controlled properly. We believe the present study provides useful information on the design of macromolecular prodrugs intended for antitumor chemotherapy.

ACKNOWLEDGMENT

The support of Dr. Kazuhiro Inoue is gratefully acknowledged. We thank Satoru Ohsuki for supporting the synthesis of the conjugates, and Setsuko Fukutake for carrying out the antitumor activity experiments.

Supporting Information Available: Additional table. This material is available free of charge via the Internet at http://pubs.acs.org.

LITERATURE CITED

(1) Kopecek, J., Kopeckova, P., Minko, T., Lu, Z.-R., and Peterson, C. M. (2001) Water soluble polymers in tumor targeted delivery. *J. Controlled Release 74*, 147–158.

(2) Maeda, H. (2001) The enhanced permeability and retention (EPR) effect in tumor vasculature: the key role of tumor-selective macromolecular drug targeting. *Adv. Enzyme Regul. 41*, 189–207.

(3) Vasey, P. A., Kaye, S. B., Morrison, R., Twelves, C., Wilson, P., Duncan, R., Thomson, A. H., Murray, L. S., Hilditch, T. E., Murray, T., Burtles, S., Fraier, D., Frigerio, E., and Cassidy, J. (1999) Phase I clinical and pharmacokinetic study of PK1 [N-(2-hydroxypropyl)methacrylamide copolymer doxorubicin]: first member of a new class of chemotherapeutic agents-drug-polymer conjugates. *Clin. Cancer Res. 5*, 83–94.

(4) Singer, J. W. (2005) Paclitaxel poliglumex (XYOTAX, CT-2103): a macromolecular taxane. *J. Controlled Release 109*, 120–126.

(5) Posey, J. A. III, Saif, M. W., Carlisle, R., Goetz, A., Rizzo, J., Stevenson, S., Rudoltz, M. S., Kwiatek, J., Simmons, P., Rowinsky, E. K., Takimoto, C. H., and Tolcher, A. W. (2005) Phase 1 study of weekly polyethylene glycol-camptothecin in patients with advanced solid tumors and lymphomas. *Clin. Cancer Res. 11*, 7866–7871.

(6) Inoue, K., Kumazawa, E., Kuga, H., Susaki, H., Masubuchi, N., and Kajimura, T. (2003) CM-dextran-polyalcohol-camptothecin conjugate: DE-310 with a novel carrier system and its preclinical data. *Adv. Exp. Med. Biol. 519*, 145–153.

(7) Duncan, R., Rejmanova, P., Kopecek, J., and Lloyd, J. B. (1981) Pinocytic uptake and intracellular degradation of N-(2-hydroxypropyl)methacrylamide copolymers. A potential drug delivery system. *Biochim. Biophys. Acta 678*, 143–150.

(8) Duncan, R., Lloyd, J. B., and Kopecek, J. (1980) Degradation of side chains of N-(2-hydroxypropyl) methacrylamide copolymers by lysosomal enzymes. *Biochem. Biophys. Res. Commun. 94*, 284–290.

(9) Duncan, R., Cable, H. C., Lloyd, J. B., Rejmanova, P., and Kopecek, J. (1982) Degradation of side-chains of N-(2-hydroxypropyl)methcrylamide copolymers by lysosomal thiol-proteinases. *Biosci. Rep. 12*, 1041–1046.

(10) Duncan, R., Cable, H. C., Lloyd, J. B., Rejmanova, P., and Kopecek, J. (1983) Polymers containing enzymatically degradable bond, 7. Design of oligopeptide side chains in poly N-(2-hydroxypropyl)methacrylamide copolymers to promote degradation by lysosomal enzymes. *Makromol. Chem. 184*, 1997–2008.

(11) Trouet, A., Masquelier, M., Baurain, R., and Deprez-De Campeneere, D. (1982) A covalent linkage between daunorubicin and proteins that is stable in serum and reversible by lysosomal hydrolases, as required for a lysosomotropic drug-carrier conjugate: in vitro and in vivo studies. *Proc. Natl. Acad. Sci. U.S.A. 79*, 626–629.

(12) Nogusa, H., Yano, T., Kashima, N., Yamamoto, K., Okuno, S., and Hamana, H. (2000) Structure-activity relationships of carboxymethylpullulan-peptide-doxorubicin conjugates-systematic modification of peptide spacers. *Bioorg. Med. Chem. Lett. 10*, 227–230.

(13) Veronese, F. M., Schiavon, O., Pasut, G., Mendichi, R., Andersson, L., Tsirk, A., Ford, J., Wu, G., Kneller, S., Davies, J., and Duncan, R. (2005) PEG-doxorubicin conjugates: influence of polymer structure on drug release, in vitro cytotoxicity, biodistribution, and antitumor activity. *Bioconjugate Chem. 16*, 775–784.

(14) Schmid, B., Warnecke, A., Fichtner, I., Jung, M., and Kratz, F. (2007) Development of albumin-binding camptothecin prodrugs using a peptide positional scanning library. *Bioconjugate Chem. 18*, 1786–1799.

(15) Ahmad, S., Tester, R. F., Corbett, A., and Karkalas, J. (2006) Dextran and 5-aminosalicylic acid (5-ASA) conjugates: synthesis, characterization and enzymic hydrolysis. *Carbohydr. Res. 341*, 2694–2701.

(16) Rozhin, J., Robinson, D., Stevens, M. A., Lah, T. T., Honn, K. V., Ryan, R. E., and Sloan, B. F. (1987) Properties of plasma membrane-associated cathepsin B-like cysteinase in metastatic B16 melanoma variants. *Cancer Res. 47*, 6620–6628.

(17) Shiose, Y., Ochi, Y., Kuga, H., Yamashita, F., and Hashida, M. (2007) Relationship between drug release of DE-310, macromolecular prodrug of DX-8951f, and cathepsins activity in several tumors. *Biol. Pharm. Bull. 30*, 2365–2370.

(18) Rejmanova, P., Pohl, J., Baudys, M., Kostka, V., and Kopecek, J. (1983) Polymers containing enzymatically degradable bond, 8. Degradation of oligopeptide sequences in N-(2-hydroxypropyl)methacrylamide copolymers by bovine spleen cathepsin B. *Makromol. Chem. 184*, 2009–2020.

(19) Barrett, A. J. (1980) Fluorimetric assays for cathepsin B and cathepsin H with methylcoumarylamide substrates. *Biochem. J. 187*, 909–912.

(20) Maciewicz, R. A., and Etherington, D. J. (1988) A comparison of four cathepsins (B, L, N and S) with collagenolytic activity from rabbit spleen. *Biochem. J. 256*, 433–440.

(21) Hasnain, D., Hirama, T., Huber, C. P., Mason, P., and Mort, J. S. (1993) Characterization of cathepsin B specificity by site-directed mutagenesis. Importance of Glu^{245} in the S2-P2 specificity for arginine and its role in transition state stabilization. *J. Biol. Chem. 268*, 235–240.

(22) Gosalia, D. N., and Diamond, S. L. (2003) Printing chemical libraries on microarray for fluid phase nanoliter reactions. *Proc. Natl. Acad. Sci. U.S.A. 100*, 8721–8726.

(23) Gosalia, D. N., Salisbury, C. M., Maly, D. J., Ellman, J. A., and Diamond, S. L. (2005) Profiling serine protease substrate specificity with solution phase fluorogenic peptide microarrays. *Proteomics 5*, 1292–1298.

(24) Gosalia, D. N., Salisbury, C. M., Maly, D. J., Ellman, J. A., and Diamond, S. L. (2005) High throughput substrate specificity profiling of serine and cysteine proteases using solution-phase fluorogenic peptide microarrays. *Mol. Cell. Proteomics 4*, 626–636.

(25) D'Souza, A. J. M., Topp, E. M. (2004) Release from polymeric prodrugs: linkages and their degradation. *J. Pharm. Sci. 93*, 1962−1979.

(26) Conover, C. D., Greenwald, R. B., Pendri, A., and Shum, K. L. (1999) Camptothecin delivery systems: the utility of amino acid spacers for the conjugation of camptothecin with polyethylene glycol to create prodrugs. *Anti-Cancer Drug Des. 14*, 499–506.

(27) Etrych, T., Jelinkova, M., Rihova, B., and Ulbrich, K. (2001) New HPMA copolymers containing doxorubicin bound via pH-sensitive linkage: synthesis and preliminary in vitro and in vivo biological properties. *J. Controlled Release 73*, 89–102.

(28) Dubowchik, G. M., Firestone, R. A., Padilla, L., Willner, D., Hofstead, S. J., Mosure, K., Knipe, J. O., Lasch, S. J., and Trail, P. A. (2002) Cathepsin B-labile dipeptide linkers for lysosomal release of doxorubicin from internalizing immunoconjugates: model studies of enzymatic drug release and antigen-specific in vitro antitumor activity. *Bioconjugate Chem. 13*, 858–869.

(29) Cunningham, D. F., and O'Connor, B. (1997) Proline specific peptidases. *Biochim. Biophs. Acta 1343*, 160–186.

(30) Nogusa, H., Yano, T., Kajiki, M., Gonsho, A., Hamana, H., and Okuno, S. (1997) Antitumor effects and toxicities of carboxymethylpullulan-peptide-doxorubicin conjugates. *Biol. Pharm. Bull. 20*, 1061–1065.

(31) Nogusa, H., Yano, T., Kajiki, M., Gonsho, A., Hamana, H., and Okuno, S. (2000) Distribution characteristics of carboxymethylpullulan-peptide-doxorubicin conjugates in tumor-bearing rats: different sequence of peptide spacers and DXR contents. *Biol. Pharm. Bull. 23*, 621–626.

(32) Lee, G. Y., Park, K., Kim, S. Y., and Byun, Y. (2007) MMPs-specific PEGylated peptide-DOX conjugate micelles that can contain free doxorubicin. *Eur. J. Pharm. Biopharm. 67*, 646–654.

(33) Chau, Y., Dang, N. M., Tan, F. E., and Langer, R. (2006) Investigation of targeting mechanism of new dextran-peptide-methotrexate conjugates using biodistribution study in matrix-metalloproteinase-overexpressing tumor xenograft model. *J. Pharm. Sci. 95*, 542–551.

(34) Chen, E. I., Kridel, S. J., Howard, E. W., Li, W., Godzik, A., and Smith, J. W. (2002) A unique substrate recognition profile for matrix metalloproteinase-2. *J. Biol. Chem. 277*, 4485–4491.

(35) Netzel-Artnett, S., Sang, Q. X., Moore, W. G., Navre, M., Birkedal-Hansen, H., and Van Wart, H. E. (1993) Comparative sequence specificities of human 72- and 92-kDa gelatinase (type IV collagenases) and PUMP (matrilysin). *Biochemistry 32*, 6427–6432.

(36) Seltzer, J. L., Akers, K. T., Weingarten, H., Grant, G. A., McCourt, D. W., and Eisen, A. Z. (1990) Cleavage specificity of human skin type IV collagenase (gelatinase). Identification of cleavage sites in type I gelatin, with confirmation using synthetic peptides. *J. Biol. Chem. 265*, 20409–20413.

(37) Shimoyama, M. (1975) The quantitative measurement of cytocidal actions of alkylating agents and anticancer antibiotics against in vitro cultured yoshida ascites sarcoma. *J. Jpn. Soc. Cancer Ther. 10*, 63–72.

(38) Shimoyama, M. (1975) The quantitative measurement of cytocidal actions of antimetabolites, vinca alkaloids and L-asparaginase against in vitro cultured yoshida ascites sarcoma. *J. Jpn. Soc. Cancer Ther. 10*, 195–201.

BC800238F

Supporting Information

Systematic research of peptide spacers controlling drug release from macromolecular prodrug system, Carboxymethyldextran polyalcohol-Peptide-Drug Conjugates

Yoshinobu Shiose,* Hiroshi Kuga,[†] Hitoshi Ohki,[‡] Masahiro Ikeda,[‡] Fumiyoshi Yamashita,[§] and Mitsuru Hashida[§]

*Biological Research Laboratories IV, Daiichi Sankyo Co. Ltd., Kasai R&D Center, Kita-Kasai 1-16-13, Edogawa-Ku, Tokyo 134-8630, Japan. [§]Department of Drug Delivery Research, Graduate School of Pharmaceutical Sciences, Kyoto University, Kyoto 606-8501, Japan.

[†]Present address: Development Research Department, Daiichi Sankyo Inc., 389 Thornall Street, Edison, NJ08837, U.S.A.

[‡]Present address: Medicinal Chemistry Research Laboratories II, Daiichi Sankyo Co. Ltd., Kasai R&D Center, Kita-Kasai 1-16-13, Edogawa-Ku, Tokyo 134-8630, Japan.

**Corresponding Author e-mail address*:shiose.yoshinobu.gn@daiichisankyo.co.jp.

CONTENTS:

Table 1. Time courses of the amount of DXR liberated from different DXR-conjugates in M5076 tumor homogenates. p.3.

Table 1. Time courses of the amount of DXR liberated from different DXR-conjugates in M5076 tumor homogenates.

Time (hr)	CM-Dex-PA-Gly-Gly-Phe-Gly-DXR DXR release (%)	CM-Dex-PA-Gly-Gly-Ile-Gly-DXR DXR release (%)	CM-Dex-PA-Gly-Gly-Pro-Leu-DXR DXR release (%)
4	20.98 ± 0.35	2.26 ± 0.11	BLQ
8	42.38 ± 1.54	4.7 ± 0.27	0.14 ± 0.12
24	100.49 ± 3.77	15.52 ± 0.24	0.29 ± 0.25
Release rate constants (h^{-1})	0.064	0.0066	0.00013

BLQ: Below limit of quantification

Antibacterial and Antifouling Polymer Brushes Incorporating Antimicrobial Peptide

Karine Glinel,*[,†,‡] Alain M. Jonas,[†,§] Thierry Jouenne,[‡] Jérôme Leprince,[||] Ludovic Galas,[||] and Wilhelm T. S. Huck*[,†]

Melville Laboratory for Polymer Synthesis, Department of Chemistry, University of Cambridge, Lensfield Road, Cambridge CB2 1EW, United Kingdom, Laboratoire Polymères, Biopolymères, Surfaces, FRE 3101, Université de Rouen, CNRS, Bd Maurice de Broglie, F-76821 Mont Saint Aignan, France, Research Center in Micro and Nanoscopic Materials and Devices (CeRMiN), Université catholique de Louvain, B-1348 Louvain-la-Neuve, Belgium, and INSERM U-413, Université de Rouen, INSERM, F-76821 Mont-Saint-Aignan, France. Received July 7, 2008; Revised Manuscript Received November 20, 2008

Surface-initiated atom transfer radical polymerization (ATRP) has been used to prepare antifouling copolymer brushes based on 2-(2-methoxyethoxy)ethyl methacrylate (MEO_2MA) and hydroxyl-terminated oligo(ethylene glycol) methacrylate (HOEGMA). The amount of hydroxyl reactive groups incorporated into the brushes was varied by changing the composition of the monomer mixture. These coatings were subsequently functionalized by a natural antibacterial peptide, magainin I, via an oriented chemical grafting on hydroxyl groups, which maintains the activity of the peptide. The antibacterial activity of the functionalized brushes was successfully tested against two different strains of gram-positive bacteria.

INTRODUCTION

The adhesion of bacteria on the surfaces of materials is of crucial importance in diverse fields such as ship hull fouling, contamination of medical devices, industrial cooling water systems, and food processing equipment (*1*−*3*). Once adhered on a solid surface, bacteria form colonies and subsequently biofilms that serve as reservoirs for the development of pathogenic infections (*4*−*6*). In this context, many studies were performed to generate thin coatings that reduce bacterial adhesion onto solid surfaces. The developed methods are mainly based on two different strategies: (i) the immobilization of biocidal substances and (ii) the deposition of an antifouling coating that prevents proteins and subsequently cell adhesion on the surface. The techniques employed to immobilize antibacterial substances onto solid surfaces involve chemical grafting, surface impregnation, or physical entrapment (*7*−*11*). As for the nonadhesive coatings, they are mainly self-assembled monolayers (SAMs) (*12*−*24*) or polymer brushes based on poly(ethylene glycol) (PEG) or its derivatives (*15*−*17*). However, even though the antifouling properties of PEG-based layers have been widely reported in the literature, these layers do not completely prevent the adhesion of bacteria (*18*−*21*). Therefore, it is desirable to combine both approaches in effective antibacterial coatings: nonadhesive properties to reduce initial cell adhesion and the simultaneous presence of a biocidal substance to kill bacteria adhering onto the surface.

Recently, polymer brushes have attracted considerable attention as a way to engineer the surface properties of materials (*22*). By comparison with other surface modification methods (e.g., SAMs), they offer a higher mechanical and chemical robustness, which results in a higher long-term stability. A broad range of chemical functionalities can be obtained from an adequate choice of the monomers, as we demonstrated by testing the antibacterial properties of sulfonate brushes loaded with silver ions (*23*). Among techniques used to prepare polymer brushes, the "grafting from" approach based on surface-initiated atom transfer radical polymerization (ATRP) offers an experimentally straightforward route to dense brushes with a narrow polydispersity, a controlled architecture, and a well-defined thickness and composition (*24*). We have reported previously on the preparation of copolymer brushes based on 2-(2-methoxyethoxy)ethyl methacrylate (MEO_2MA) and oligo(ethylene glycol) methacrylate (OEGMA) (*25*−*27*). These PEG-based brushes are expected to be nontoxic, non-immunogenic, non-antigenic, and nonadhesive toward cells (*28, 29*). Here, similar copolymer brushes incorporating a hydroxyl-terminated oligo(ethylene glycol) methacrylate (HOEGMA) monomer were used as a platform to immobilize a natural antimicrobial peptide.

Among the substances used to inhibit the growth of bacteria, the natural defense peptides that are secreted by living organisms such as plants, microorganisms, and various mammalians, insects, and amphibians have recently emerged as a particularly promising class of biocidal drugs (*30*−*32*). Indeed, compared to conventional antibacterial substances such as antibiotics, quaternary ammonium compounds, or heavy metal derivatives, defense peptides have been shown to act at a much lower concentration, which considerably limits the potential problems related to toxicity (*33*−*35*). Moreover, these natural peptides have a broad spectrum of antimicrobial or even antifungal activity, and they rarely promote bacterial resistance. Recently, a few studies have reported on the immobilization of antibacterial peptides coupled to SAMs (*7*) or polyelectrolyte multilayers (*10, 11*) to prepare antibacterial thin films.

In this paper, we describe the oriented end-grafting of an antimicrobial peptide on poly(MEO_2MA-*co*-HOEGMA) brushes. Beside their nonadhesive behavior, these copolymer brushes offer reactive hydroxyl groups which allow controlled loading of the brushes with antimicrobial peptide grafted on the brushes and consequently the activity of the resulting coatings. Magainin

* Corresponding authors. karine.glinel@univ-rouen.fr, phone+33(0)2 35 14 65 86, fax+33(0)2 35 14 67 04; wtsh2@cam.ac.uk, phone +44(0) 12 23 33 43 70, fax +44 (0)12 23 33 48 66.

† University of Cambridge.

‡ Université de Rouen, CNRS.

§ Research Center in Micro and Nanoscopic Materials and Devices (CeRMiN), Université catholique de Louvain.

|| Université de Rouen, INSERM.

10.1021/bc800280u CCC: $40.75 © 2009 American Chemical Society
Published on Web 12/29/2008

I, a 23-residue defense peptide initially isolated from the skin of the African clawed frog *Xenopus laevis* (*36, 37*), was selected for its broad biocidal activity against Gram-positive and Gram-negative bacteria and its non-hemolytic properties at its effective antimicrobial concentration. Magainin-functionalized copolymer brushes of various compositions were tested against two different gram-positive bacteria.

EXPERIMENTAL SECTION

Materials. Di(ethylene glycol) methyl ether methacrylate (MEO_2MA) (95%), and hydroxyl-terminated oligo(ethylene glycol) ether methacrylate (HOEGMA) of molar mass ~360 g/mol were obtained from Aldrich and were used without purification. FITC-labeled streptavidin (streptavidin^{FITC}) and *N*-(*p*-maleimidophenyl)isocyanate (PMPI) were purchased from AbD Serotec and Appolo Scientific, respectively. Copper(I) chloride (99.995+%) (Cu^ICl), copper(II) chloride (99.999+%) ($Cu^{II}Cl_2$), and 2,2′-dipyridyl (99+%) (bipy), tris(hydroxymethyl)aminomethane (tris) were from Aldrich. All solvents were distilled before use except methanol, which was analytical reagent grade. Milli-Q water (resistivity higher than 18.2 MΩ.cm) was obtained from a Millipore Simplicity 185 system. Silicon wafers (⟨100⟩ orientation) were obtained from Compact Technology Ltd.; they were cleaned for 10 min in an air plasma asher (100 W, Emitech K1050X) before use. Magainin I derivatives with an additional C-terminal cysteine residue and tagged with an N-terminal biotin moiety (Biotinyl-MAG-Cys) or untagged (MAG-Cys) were synthesized by the solid-phase methodology on Fmoc-Cys(Trt)-HMP resin by using a 433A Applied Biosystems peptide synthesizer and the standard Fmoc manufacturer's procedure. The synthetic peptides were purified by reversed-phase preparative HPLC on a Vydac 218TP1022 C_{18} column by using a linear gradient (10−60% over 60 min) of acetonitrile/trifluoroacetic acid (99.9:0.1; v/v) at a flow rate of 10 mL.min^{-1}. Analytical HPLC, performed on a Vydac 218TP54 C_{18} column, showed that the purity of the peptides was higher than 99.8%. The purified peptides were characterized by MALDI-ToF mass spectroscopy on a Voyager DEPRO in the reflecton mode with α-cyano-4-hydroxycinnamic acid as a matrix. LIVE/DEAD BacLight Bacterial Viability Kit L7007 containing SYTO 9 and propidium iodide dyes was purchased from Molecular Probes.

Preparation of the Antibacterial Brushes. *Initiator-Grafted Silicon Wafers.* The synthesis of the 2-bromo-2-methyl propionic acid 3-trichlorosilanylpropyl ester was adapted from a previously published procedures (*38*), and the formation of the initiator monolayer was performed as described previously (*39*). An ellipsometric thickness of 0.6−0.9 nm was found for the initiator monolayer (*25*).

Copolymer Brushes. The synthesis of the copolymer brushes by surface-initiated ATRP was adapted from a procedure recently published (*25*). Briefly, the monomers (95 mmol) were dissolved in a mixture of water (30 mL) and methanol (15 mL) (e.g., for a MEO_2MA/HOEGMA molar ratio of 67:33, 12 g of MEO_2MA (63.7 mmol) and 11.3 g of HOEGMA (31.3 mmol) were used) in a round-bottom flask sealed with a rubber septum. Bipy (5 mmol, 782 mg) and $Cu^{II}Cl_2$ (0.16 mmol, 21.5 mg) were added to this solution, which was stirred and degassed with a stream of nitrogen for 1 h. Cu^ICl (1.6 mmol, 158.5 mg) was then added quickly to the solution. The solution was stirred and degassed for 45 further min. Meanwhile, the initiator-grafted Si wafers (1 × 1 cm^2) were sealed into Schlenk tubes and were degassed (4 vacuum/nitrogen filling cycles). The polymerization solution was then syringed and quickly transferred to the Schlenk tubes. The Schlenk tubes containing the samples were kept at room temperature under an overpressure of nitrogen in the absence of stirring, for a given polymerization time that depends on the monomer ratio (from 3 h to 9 h). Then, the samples were removed, washed with water then methanol, dried with a stream of nitrogen, and stored under nitrogen before use. The polymerization times used for each monomer ratio were adapted to get copolymer brushes with an average thickness of about 110 nm (Table 1). Four different MEO_2MA/HOEGMA monomer ratios were tested to prepare the copolymer brushes: 100:0; 83:17, 67:33, and 33:67.

Table 1. Characteristics of the Poly(MOE_2MA-*co*-HOEGMA) Brushes

composition of the monomer mixture [MOE_2MA/HOEGMA]	reaction time (min)	brush thickness[a] (nm)
100:0	150	106
83:17	210	110
67:33	245	110
33:67	527	111

[a] Measured by ellipsometry.

Oriented Grafting of Magainin I Derivatives on Copolymer Brushes. Two milliliters of 6 mM PMPI solution prepared in distilled dry THF were transferred to a Schlenk tube containing the silicon wafer functionalized by the poly(MEO_2MA-*co*-HOEGMA) brush in a nitrogen-purged glovebox. After a reaction time of 6 h at room temperature, the silicon wafer was sonicated in distilled THF for 5 min, and the surface was thoroughly washed 3 times with distilled THF before finally being dried in a stream of nitrogen. Next, the PMPI-grafted brush was reacted with MAG-Cys or biotinyl-MAG-Cys derivative. For this, the silicon wafer was treated with a 280 μM solution of the peptide prepared in 100 mM tris buffer (pH 7.04). After a reaction time of 2 h 30 min at room temperature, the silicon wafer was sonicated 5 min in Tris buffer, thoroughly washed 3 times with Milli-Q water, and finally dried in a stream of nitrogen before use in bacterial assays.

Analytical Techniques. *Ellipsometry.* Ellipsometric measurements were carried out with a spectroscopic ellipsometer (α-SE from J. A. Woollam Co., Inc.). The data were fit using a Cauchy model for the index of refraction of the organic layer, using tabulated values for the index of refraction of silicon. The 1.5-nm-thick layer of native silicon oxide was included in the organic layer, since they have close indices of refraction. Five measurements were taken and averaged for each sample. In most cases, the standard deviation of the thickness about its average value was lower than 3 nm.

Optical Microscopy. Optical and fluorescence images were taken with a Nikon Eclipse ME600L microscope equipped with a FITC filter set and an Epi-Fluorescence module, and connected to a DN100 image-capture system. Images were processed using *IGOR Pro* software (Wavemetrics, Inc.).

Confocal Laser Scanning Fluorescence Microscopy (CLSM). CLSM imaging was carried out with a Leica SP2 upright confocal laser scanning microscope (DM RXA2) equipped with an Acousto-Optical Beam Splitter (AOBS) system and using a 63× oil immersion objective with numerical aperture 1.32 (Leica Microsystems, Rueil-Malmaison, France). SYTO 9 was excited at 476 nm and observed from 485 to 540 nm, and propidium iodide was excited at 514 nm and observed from 580 to 670 nm. The laser power, the gain, and the offset for each photomultiplier have been adjusted to optimize the bacteria detection.

Images of the CLSM observations (1024 × 1024 pixels) have been acquired through the sequential mode to avoid fluorescence emission spectrum overlap, and the signal/noise ratio has been increased through line (×2) and frame (×4) averaging. Overlay images have been built with post-acquisition Leica Confocal software (LCS).

Scheme 1. Oriented Grafting of MAG-Cys Derivative on Poly(MOE_2MA-*co*-HOEGMA) Brushes via a PMPI Heterolinker

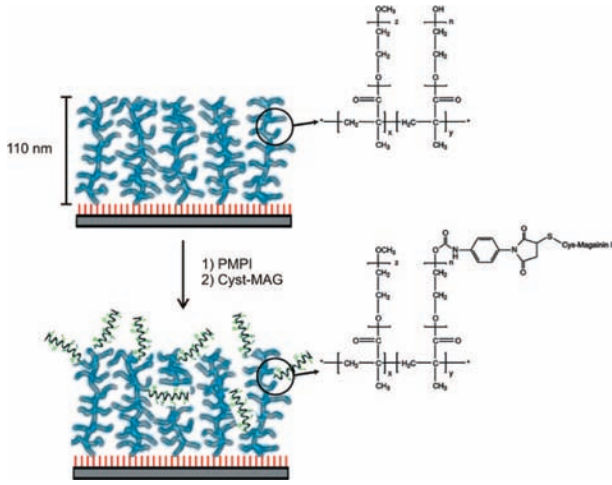

Fourier Transform Infrared Spectroscopy (FTIR). FTIR spectra were acquired between 1000 and 4000 cm^{-1} with a BioRad FTS-6000 spectrometer. The measurement were performed in transmission through the silicon wafers. The sample compartment was thoroughly purged with dry nitrogen before measurement.

X-ray Photoelectron Spectroscopy (XPS). XPS measurements were performed using a Kratos Axis Ultra spectrometer (Kratos Analytical) with a monochromatic Al Kα X-ray source ($h\nu$ 1486.6 eV). The pass energy was set at 40 eV for the detailed scans. In these conditions, the energy resolution gives a full width at half-maximum of the Ag $3d_{5/2}$ peak of about 0.1 eV. All binding energies were referenced to the *C*-(C,H) component of the C 1s peak fixed at 284.8 eV. The base pressure in the spectrometer was in the low 10^{-8} Torr range. Quantitative information was obtained by the photoemission peak areas of each element normalized according to acquisition parameters and sensitivity factors provided by the manufacturer. Peak decomposition was achieved with the Casa *XPS* software (Casa Software Ltd., UK), after subtraction of a linear baseline.

Bacterial Inhibition Assays. Magainin-functionalized brushes were tested against two Gram-positive bacteria: *Listeria ivanovii* (strain kindly provided by the UMR CNRS 6008 of University of Poitiers, France) and *Bacillus cereus* (strain kindly provided by the UMR CNRS 6143 of University of Rouen, France). Both bacteria strains were precultured in Mueller-Hinton broth for 18 h, then harvested by centrifugation (2000 × *g* for 15 min) and resuspended in distilled water. A functionalized silicon wafer was immersed in 10 mL of diluted bacteria suspension freshly prepared in distilled water (10^7 colony forming units (CFU).mL^{-1}). After 3 h incubation at room temperature, the silicon wafer was taken out and briefly rinsed with distilled water. To test the viability of bacteria adhering on the functionalized copolymer brush, the cells were immediately stained with the LIVE/DEAD BacLight Bacterial Viability Kit. For this, the wet silicon wafer was immersed in 2 mL of diluted viability kit solution. After an incubation time of 30 min, the silicon wafer was briefly rinsed with distilled water, and the surface was visualized by microscopy. The viability of the cells suspended in the distilled water was also controlled by counting the number of bacteria colonies grown on a seeded Mueller-Hinton agar medium (Difco). This control experiment confirmed that the viability of the bacteria was absolutely not affected after an incubation time of 3 h in water.

Culturability of sessile *L. ivanovvi* cells was also investigated. 1 × 1 cm^2 functionalized silicon wafers were deposited on 15 g/L κ-carrageenan plates (on which no bacterial growth occurs) and covered with a bacterial suspension (10^7 CFU.mL^{-1}). After incubation for 3 h at room temperature, wafers were picked up and rinsed with sterile distilled water. Adherent cells were recovered by sonication (two steps of 1 min at 50 W) of the material in 5 mL of sterile distilled water (Deltasonic bath, Meaux, France). The resulting cell population was enumerated by plating out decimal dilutions of the suspension on Plate Count Agar. After incubation for 24 h at 37 °C, the number of bacteria was expressed as CFU.cm^{-2} material.

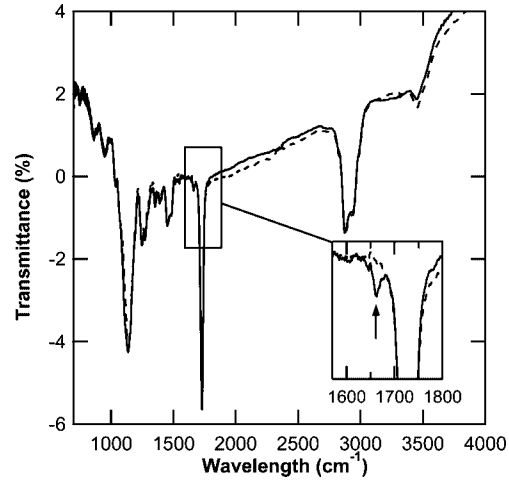

Figure 1. FTIR spectra of nonfunctionalized (dashed line) and MAG-Cys-functionalized (continuous line) poly(MOE_2MA-*co*-HOEGMA) [33:67] brushes. The arrow indicates the amide I absorption band.

RESULTS AND DISCUSSION

To prepare antibacterial coatings combining both biocidal and nonadhesive properties, we explored the tethering of a natural defense peptide, magainin I, on poly(MEO_2MA-*co*-HOEGMA) brush platforms. Because magainin I exerts its toxicity against bacteria by permeabilizing the cell membranes through pore forming or structural defects in membranes (*40*, *41*), it is important to maintain its mobility and its accessibility after attachment on the copolymer brushes (*7*). To maintain the solution properties of magainin I upon attachment to the brushes, the peptide derivatives were tethered on the hydroxyl extremities of the relatively long water-soluble and flexible oligo(ethylene glycol) side chains of the poly(MOE_2MA-*co*-HOEGMA) brushes (Scheme 1). Furthermore, to orient the peptide on the surface and allow it to easily access bacterial membranes, a cysteine residue was attached to the C-terminal side of magainin I. Because magainin I does not contain cysteine residue, the magainin I derivative MAG-Cys could be exclusively attached to the brushes by its C-terminal part, via a PMPI heterolinker (Scheme 1): the isocyanate moiety of the linker reacts with the hydroxyl group of the copolymer brushes; the maleimide reacts with the thiol function of the MAG-Cys or Biotinyl-MAG-Cys derivative (*42*, *43*). An interesting feature of the poly(MOE_2MA-*co*-HOEGMA) brushes is the possibility to vary their functionality in hydroxyl-reactive groups and subsequently the amount of immobilized magainin I, simply by changing the composition of the monomer mixture used. Various copolymer brushes of increasing content in reactive HOEGMA were thus prepared and subsequently functionalized by magainin I derivatives (Table 1). The reaction times used for the surface-initiated ATRP were adjusted to get ∼110-nm-thick brushes. The grafting of the MAG-Cys peptide on the copolymer brushes was confirmed by FTIR, which showed the occurrence of a new amide I absorption band centered at 1661 cm^{-1} after grafting (Figure 1). However, the poor signal/noise ratio obtained from these measurements does not allow us to quantify the real amount of peptide grafted

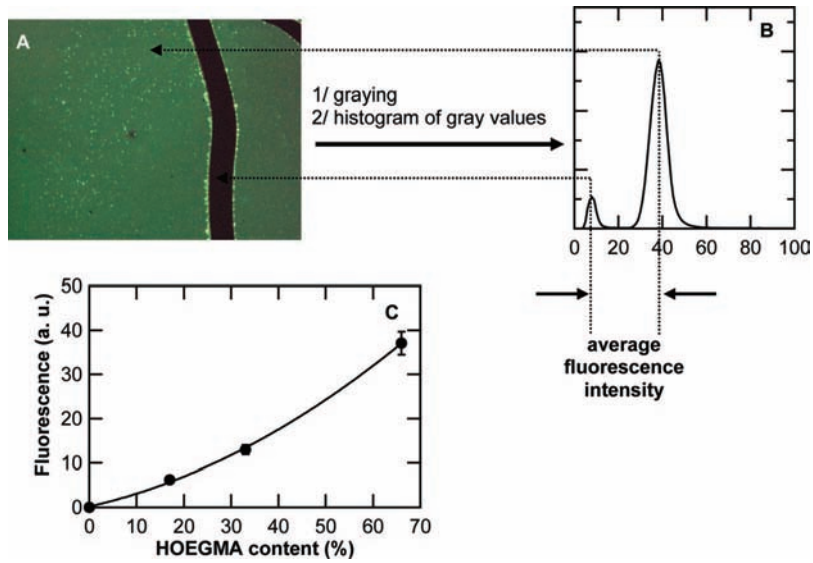

Figure 2. Image analysis of Biotinyl-MAG-Cys-grafted poly(MEO_2MA-*co*-HOEGMA) brushes incubated in a streptavidin^{FITC} solution: (A) Fluorescence image of a Biotinyl-MAG-Cys-grafted poly(MEO_2MA-*co*-HOEGMA) [33:67] brush; a deliberate scratch was made on the sample surface to determine the fluorescence background; (B) fluorescence intensity histogram computed from image (A) after graying; (C) fluorescence intensity of Biotinyl-MAG-Cys-grafted poly(MEO_2MA-*co*-HOEGMA) brushes vs their composition.

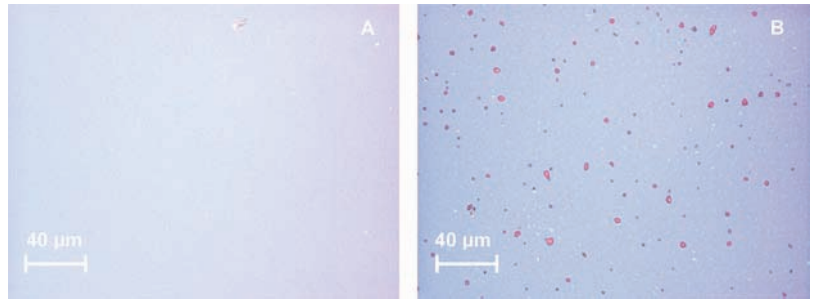

Figure 3. Optical micrographs of the brush surface after 3 h incubation in *L. ivanovii* suspension: (A) nonfunctionalized and (B) MAG-Cys-functionalized poly(MEO_2MA-*co*-HOEGMA) [33:67] brushes.

on the copolymer brushes. The percentage of monomer unit grafted by magainin was quantitatively estimated by XPS to be about 5% for a poly(MOE_2MA-*co*-HOEGMA) brush [67:33]. This percentage is significantly lower than the content of the brush in hydroxyl grafting moieties, which strongly supports the notion that the grafting reaction essentially occurs on the brush surface. To estimate qualitatively the influence of the composition of the copolymer brush on the amount of magainin I grafted on the brush surface, the brushes were functionalized with a biotin-tagged derivative (Biotinyl-MAG-Cys) and were subsequently incubated with streptavidin^{FITC}. Then, the surface-immobilized streptavidin^{FITC} was detected by fluorescence microscopy. For all Biotinyl-MAG-Cys-functionalized brushes tested, the surfaces were uniformly fluorescent on a micrometer scale, which indicates the uniform immobilization of the biotin-tagged magainin I molecules on the surface (Figure 2). In contrast, the absence of fluorescence of brushes not functionalized by magainin I (result not shown) testified to their inertness toward protein adsorption. Therefore, the fluorescence detected on functional brushes arises from the streptavidin binding to the biotin-tagged brushes, not from unspecific adsorption. The amount of grafted peptide was indirectly estimated as a function of the composition of the copolymer brush (e.g., HOEGMA content) by extracting the average fluorescence intensity by image analysis (Figure 2). For this, a deliberate scratch was made on the sample surface to determine the fluorescence signal-to-background (Figure 2). After graying the recorded image and computing the histogram of gray values, the fluorescence intensity was extracted as shown in Figure 2. The results displayed in Figure 2 show that the amount of streptavidin^{FITC} bound to the Biotinyl-MAG-Cys-functionalized brushes increases with the amount of HOEGMA in copolymer brush. As a consequence, the higher the content in hydroxyl reactive group in the brush, the higher the amount of magainin derivative grafted. This result confirms that the amount of tethered magainin I can be tuned by simply varying the composition of the copolymer brush used as a platform. Such a design is of a particular interest to optimize the biocidal properties of the surface.

The antibacterial properties of the MAG-Cys-modified brushes were tested toward two strains of Gram-positive bacteria: *L. ivanovii*, which causes serious food intoxications (*44*), and *B. cereus*, which is also involved in food-borne diseases and exhibits a high ability to adhere and to form biofilms on stainless steel (*45*) and glass (*46*). Experimentally, the functionalized silicon substrates were incubated for 3 h in bacteria suspension and immediately observed by optical microscopy. For the sake of comparison, a control adhesion test with unmodified copolymer brushes was also performed. The inspection of recorded micrographs (Figure 3) revealed the absence of bacteria on the unmodified poly(MOE_2MA-*co*-HOEGMA) [33:67] brush for both strains tested (results shown only for *L. ivanii*), which testifies to the inertness of this brush platform. A similar result was obtained for unmodified copolymer brushes of varying composition. In contrast, some bacteria were observed on magainin-functionalized brushes, but the cell coverage did not exceed 1% of the surface, independent of the copolymer brush composition. This result indicates that the bacterial attachment

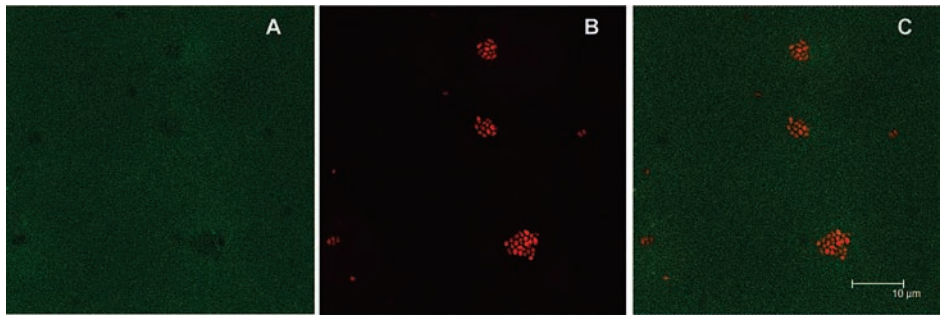

Figure 4. CLSM images of MAG-Cys-functionalized poly(MEO_2MA-*co*-HOEGMA) [33:67] brush incubated in the presence of *L. ivanovii* and subsequently stained with the LIVE/DEAD viability kit: (A) green channel image corresponding to alive stained bacteria; (B) red channel image corresponding to dead bacteria; (C) overlay image built from (A) and (B).

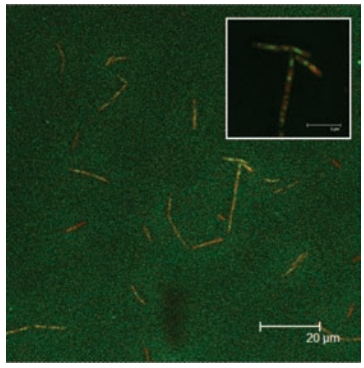

Figure 5. CLSM overlay image of MAG-Cys-functionalized poly(MEO_2MA-*co*-HOEGMA) [33:67] brush incubated in presence of *B. cereus* and subsequently stained with the LIVE/DEAD viability kit. The overlay image was built from both red channel and green channel images. Inset: An enlarged image of stained bacterial cells.

onto the brushes is exclusively due to the presence of the magainin I peptide, which interacts with cell membranes. To check the viability of the bacteria observed on the magainin-functionalized brushes, the adhering cells were stained with the fluorescent LIVE/DEAD viability kit before CLSM observation (*47*). The inspection of the green and red channels of the CLSM images obtained on magainin-functionalized brushes exposed to *L. ivanovii* (Figure 4) revealed only the presence of red-stained cells corresponding to dead bacteria. This observation was made even for the sample of lower grafting ratio (results not shown). Similar assays were performed on *B. cereus*. CLSM observations showed that every single *B. cereus* cell adhering to the surface of the functionalized brushes is partially red-stained (Figure 5), which testifies to the presence of damages to its membrane. The fact that *B. cereus* cells were not seen to be completely red-stained is most probably due to the staining process, which depends on the conditions and on the bacteria used, as was previously noted (*48, 49*). Bacterial cell counts performed with *L. ivanovii* after 3 h of contact, confirmed the antimicrobial properties of the magainin-grafted brushes. Indeed, a colonization of 700−800 $CFU.cm^{-2}$ was measured, independent of the composition of the copolymer brush. Sessile bacteria represents less than 0.0001% of the planktonic population, a ratio close to those reported by Kebir et al. (*50*) with *Pseudomonas aeruginosa* on antibacterial cross ionic copolyurethanes, and much lower than those generally obtained in same experimental conditions with raw materials (*50, 51*). Thus, the assays performed on both tested bacterial species demonstrate the high efficiency of the magainin-functionalized copolymer brushes to kill all the bacterial cells adhering on their surface. The biocidal activity was detected even for the lower grafting ratio in magainin I peptide tested.

One might wonder about how the grafted peptide molecules exert their antimicrobial effect. The detailed mode of antibacterial action of magainin is still unclear. However, it seems obvious that the membrane barrier properties are reduced by the presence of magainin molecules in the membrane, even though experimental data do not support the formation by magainin of well-defined membrane channels (*52*). As a consequence, the accumulation of magainin at the surface of the brushes combined with the flexibility of the HOEGMA side chains is probably sufficient to allow an antimicrobial effect, which is compatible with current models of magainin action, such as transmembrane helical bundles, toroidal model, carpet model, and the detergent-like peptide model (*52*). It has to be noted that biocidal activity of an antimicrobial peptide immobilized onto a solid surface via an oriented chemical grafting was also previously reported (*7*). Therefore, the magainin-functionalized brushes provide an efficient protection against bacterial spreading by killing cells in contact with them. The presence of the antimicrobial peptide combined with the intrinsic antifouling properties of the brushes should result in a strong delay of Biofilm formation, which is of interest for many applications in the medicine and food industries.

CONCLUSION

Bacterial biofilms cause infections as well as bacterial and chemical contaminations in many domains, from food and water industries to the biomedical field. On biomaterials, in particular, they often lead to removal of infected implants, because biofilms protect bacteria against antibacterial treatments and store bacteria for further infections. Among the possible methods of action against Biofilm formation, prevention by the control of the first stage of its formation (primary colonization of bacterial adhesion) is considered to be the most efficient strategy. Here, we described an original approach combining the antiadhesive property of poly(MEO2MA-*co*-HOEGMA) brushes and the antibacterial activity of an immobilized natural peptide to prepare efficient antibacterial coatings. Surface-initiated ATRP was used to synthesize nonadhesive poly(MEO2MA-*co*-HOEGMA) brushes that were subsequently used as platforms to covalently immobilize a natural antibacterial peptide. We demonstrated that the peptide can be tethered in various densities by changing the composition of the copolymer brushes, which allows variation of the biocidal activity of the coatings. The highly biocidal activity of the peptide-functionalized brushes was in evidence even for low levels of grafted peptide. The strategy developed here should be easily adaptable to coat various materials or items used in the medicine and food industries. Moreover, this approach could be generalized to other natural peptides to prepare thin coatings with a broad spectrum of activity against bacteria, fungi, and protozoa.

ACKNOWLEDGMENT

Dr. J. Gautrot (Melville Laboratory, Cambridge) and X. Laloyaux (CeRMiN, UCL, Louvain-la-Neuve) are thanked for FTIR and XPS measurements, respectively. The authors are thankful to the CIFA laboratory (UCL) for providing access to the XPS apparatus. This research was financially supported by the French National Research Agency (ANR) (project ANR-06-BLAN-0196-01).

LITERATURE CITED

(1) *Handbook of bacterial adhesion: principles, methods, and applications* (An, Y. H., Friedman, R. J., Eds.) Humana Press, Totowa, NJ, 2000.
(2) Costerton, J. W. (1999) Introduction to biofilm. *Int. J. Antimicrob. Agents 11*, 217–221.
(3) Gristina, A. G. (1987) Biomaterial-centered infection: microbial adhesion versus tissue integration. *Science 237*, 1588–1595.
(4) Costerton, J. W., Cheng, K. J., Geesey, G. G., Ladd, T. I., Nickel, J., Curtis, D. M., and Marrie, T. J. (1987) Bacterial Biofilm in nature and disease. *Annu. Rev. Microbiol. 41*, 435–464.
(5) Donlan, R. M., and Costerton, J. W. (2002) Biofilms: survival mechanisms of clinically relevant microorganisms. *Clin. Microbiol. Rev. 15*, 167–193.
(6) Costerton, J. W., Stewart, P. S., and Greenberg, E. P. (1999) Bacterial biofilms: a common cause of persistent infections. *Science 284*, 1318–1322.
(7) Gabriel, M., Nazmi, K., Veerman, E. C., Niew Amerongen, A. V., Zentner, A., Gabriel, M., Nazmi, K., and Veerman, E. C. (2006) Preparation of, LL-37-grafted titanium surfaces with bactericidal activity. *Bioconjugate Chem. 17*, 548–550.
(8) Samuel, U., and Guggenbichler, J. P. (2004) Prevention of catheter-related infections: the potential of a new nano-silver impregnated catheter. *Int. J. Antimicrob. Agents 23*, 75–78.
(9) Francolini, I., Norris, P., Piozzi, A., Donelli, G., and Stoodley, P. (2004) Usnic acid, a natural antimicrobial agent able to inhibit bacterial biofilm formation on polymer surfaces. *Antimicrob. Agents Chemother. 48*, 4360–4365.
(10) Etienne, O., Picart, C., Taddei, C., Haikel, Y., Dimarcq, J. L., Schaaf, P., Voegel, J.-C., Ogier, J. A., and Egles, C. (2004) Multilayer polyelectrolyte films functionalized by insertion of defensin: a new approach to protection of implants from bacterial colonization. *Antimicrob. Agents Chemother. 48*, 3662.
(11) Guyomard, A., Dé, E., Jouenne, T., Malandain, J.-J., Muller, G., and Glinel, K. (2008) Incorporation of a hydrophobic antibacterial peptide into amphiphilic polyelectrolyte multilayers: a bioinspired approach to prepare biocidal thin coatings. *Adv. Funct. Mater. 18*, 758.
(12) Prime, K. L., and Whitesides, G. M. (1991) Self-assembled organic monolayers: model systems for studying adsorption of proteins. *Science 252*, 1164–1167.
(13) Harder, P., Grunze, M., Dahint, R., Whitesides, G. M., and Laibinis, P. E. (1998) Molecular conformation in oligo(ethylene glycol)-terminated self-assembled monolayers on gold and silver surfaces determines their ability to resist protein adsorption. *J. Phys. Chem. B 102*, 426–436.
(14) Chapman, R. G., Ostuni, E., Liang, M. N., Meluleni, G., Kim, E., Yan, L., Pier, G., Warren, H. S., and Whitesides, G. M. (2001) Polymeric thin films that resist the adsorption of proteins and the adhesion of bacteria. *Langmuir 17*, 1225–1233.
(15) Senaratne, W., Andruzzi, L., and Ober, C. K. (2005) Self-assembled monolayers and polymer brushes in biotechnology: current applications and future perspectives. *Biomacromolecules 6*, 2427–2448.
(16) Heyes, C. D., Groll, J., Muller, M., and Nienhaus, G. U. (2007) Synthesis, patterning and applications of star-shaped poly(ethylene glycol) biofunctionalized surfaces. *Mol. Biosyst. 3*, 419–430.
(17) Fan, X., Lin, L., and Messersmith, P. B. (2006) Cell fouling resistance of polymer brushes grafted from Ti substrates by surface-initiated polymerization: effect of ethylene glycol side chain length. *Biomacromolecules 7*, 2443–2448.
(18) Ostuni, E., Chapman, R. G., Liang, M. N., Meluleni, G., Pier, G., Ingber, D. E., and Whitesides, G. M. (2001) Self-assembled monolayers that resist the adsorption of proteins and the adhesion of bacterial and mammalian cells. *Langmuir 17*, 6336–6343.
(19) Wei, J., Ravn, D. B., Gram, L., and Kingshott, P. (2003) Stainless steel modified with poly(ethylene glycol) can prevent protein adsorption but not bacterial adhesion. *Colloid Surf., B 32*, 275–291.
(20) Roosjen, A., Boks, N. P., van der Mei, H. C., Busscher, H. J., and Norde, W. (2005) Influence of shear on microbial adhesion to PEO-brushes and glass by convective-diffusion and sedimentation in a parallel plate flow chamber. *Colloid Surf., B 46*, 1–6.
(21) Roosjen, A., Kaper, H. J., van der Mei, H. C., Norde, W., and Busscher, H. J. (2003) Inhibition of adhesion of yeasts and bacteria by poly(ethylene oxide)-brushes on glass in a parallel plate flow chamber. *Microbiology 149*, 3239–3246.
(22) *Polymer Brushes: Synthesis, Characterization, Applications* (Advincula, R. C., Brittain, W. J., Baster, K. C., Ruhe, J., Eds.) Wiley-VCH Verlag GmbH, Weinheim, 2004.
(23) Ramstedt, M., Cheng, N., Azzaroni, O., Mossialos, D., Mathieu, H. J., and Huck, W. T. S. (2007) Synthesis and characterization of poly(3 sulfopropylmethacrylate) brushes for potential antibacterial applications. *Langmuir 23*, 3314–3321.
(24) Edmondson, S., Osborne, V. L., and Huck, W. T. S. (2004) Polymer brushes *via* surface-initiated polymerizations. *Chem. Soc. Rev. 33*, 14–22.
(25) Jonas, A. M., Glinel, K., Oren, R., Nysten, B., and Huck, W. T. S. (2007) Thermo-responsive polymer brushes with tunable collapse temperature in the physiological range. *Macromolecules 40*, 4403–4405.
(26) Jonas, A. M., Glinel, K., Oren, R., Nysten, B., and Huck, W. T. S. (2008) Effect of nanoconfinement on the collapse transition of responsive polymer brushes. *Nano Lett.* 40 ASAP article.
(27) Jonas, A. M., Hu, Z., Glinel, K., and Huck, W. T. S. (2008) Chain entropy and wetting energy control the shape of nano-patterned polymer brushes. *Macromolecules 41*, 6859–6853.
(28) Lutz, J.-F., Andrieu, J., Uezguen, S., Carsten, R., and Agarwal, S. (2007) Biocompatible, thermoresponsive, and biodegradable: simple preparation of "all-in-one" biorelevant polymers. *Macromolecules 40*, 8540–8543.
(29) Wischerhoff, E., Uhlig, K., Lankenau, A., Börner, H. G., Laschewsky, A., Duschl, C., and Lutz, J.-F. (2008) Controlled cell adhesion on PEG-based switchable surfaces. *Angew. Chem., Int. Ed. 47*, 5666–5698.
(30) Zasloff, M. (2002) Antimicrobial peptides of multicellular organisms. *Nature 415*, 389–395.
(31) Bowie, J. H., Wegener, K. L., Chia, B. C. S., Wabnitz, P. A., Carver, J. A., Tyler, M. J., and Wallace, J. C. (1999) Host defence antibacterial peptides from skin secretions of Australian amphibians. The relationship between structure and activity. *Protein Pept. Lett. 6*, 259–269.
(32) Bechinger, B., and Lohner, K. (2006) Detergent-like actions of linear amphipathic cationic antimicrobial peptides. *Biochim. Biophys. Acta 1758*, 1529–1539.
(33) Nicolas, P., and Mor, A. (1995) Peptides as weapons against microorganisms in the chemical defense system of vertebrates. *Annu. Rev. Microbiol. 49*, 277–304.
(34) Brogden, K. A. (2005) Pore formers or metabolic inhibitors in bacteria? *Nature 3*, 238–250.
(35) Bulet, P., Stöcklin, R., and Menin, L. (2004) Anti-microbial peptides: from invertebrates to vertebrates. *Immunol. Rev. 198*, 169–184.
(36) Zasloff, M. (1987) Magainins, a class of antimicrobial peptides from *Xenopus* skin: isolation, characterization of two active forms, and partial cDNA sequence of a precursor. *Proc. Natl. Acad. Sci. U.S.A. 84*, 5449–5453.

(37) Berkowitz, B. A., Bevins, C. L., and Zasloff, M. A. (1990) Magainins: a new family of membrane-active host defense peptides. *Biochem. Pharmacol. 39*, 625–629.

(38) Husseman, M., Malmstrom, E. E., McNamara, M., Mate, M., Mecerreyes, D., Benoit, D. G., Hedrick, J. L., Mansky, P., Huang, E., Russell, T. P., and Hawker, C. J. (1999) Controlled synthesis of polymer brushes by "living" free radical polymerization techniques. *Macromolecules 32*, 1424–1431.

(39) Brown, A. A., Khan, N. S., Steinbock, L., and Huck, W. T. S. (2005) Synthesis of oligo(ethylene glycol) methacrylate polymer brushes. *Eur. Polym. J. 41*, 1757–1765.

(40) Duchlohier, H., Molle, G., and Spach, G. (1989) Antimicrobial peptide magainin I from *Xenopus* skin forms anion- permeable channels in planar lipid bilayers. *Biophys. J. 56*, 1017–1021.

(41) Matsuzaki, K. (1998) Magainins as paradigm for the mode of action of pore forming polypeptides. *Biochim. Biophys. Acta 1376*, 391–400.

(42) Cha, T.-W., Boiadjiev, V., Lozano, J., Yang, H., and Zhu, X.-Y. (2002) Immobilization of oligonucleotides on poly(ethylene glycol) brush-coated Si surfaces. *Anal. Biochem. 311*, 27–32.

(43) Shen, G., Anand, M. F. G., and Levisky, R. (2004) X-ray photoelectron spectroscopy and infrared spectroscopy study of maleimide-activated supports for immobilization of oligodeoxyribonucleotides. *Nucleic Acids Res. 32*, 5973–5980.

(44) Roberts, A. J., and Wiedmann, M. (2003) Pathogen, host and environmental factors contributing to the pathogenesis of listeriosis. *Cell. Mol. Life Sci. 60*, 904–918.

(45) Peng, J. S., Tsai, W. C., and Chou, C. C. (2001) Surface characteristics of *Bacillus cereus* and its adhesion to stainless steel. *Int. J. Food Microbiol. 65*, 105–111.

(46) Lyndsay, D., Oosthuizen, M. C., Brözel, V. S., and von Holy, A. (2002) Adaptation of a neutrophilic dairy-associated *Bacillus cereus* isolate to alkaline pH. *J. Appl. Microbiol. 192*, 81–89.

(47) Boulos, L., Prévost, M., Barbeau, B., Coallier, J., and Desjardins, R. (1999) LIVE/DEAD BacLight: application of a new rapid staining method for direct enumeration of viable and total bacteria in drinking water. *J. Microbiol. Methods 37*, 77–86.

(48) Leuko, S., Legat, A., Fendrihan, S., and Stan-Lotter, H. (2004) Evaluation of the LIVE/DEAD *Bac*Light Kit for the detection of extremophilic archaea and visualization of microorganisms in environmental hypersaline samples. *Appl. Environ. Microbiol. 70*, 6884–6886.

(49) Wattanaphansak, S., Gebhart, C., Olin, M., and Deen, J. (2005) Measurement of the viability of Lawsonia intracellularis. *Can. J. Vet. 69*, 265–271.

(50) Kébir, N., Campistron, I., Laguerre, A., Pilard, J.-F., Bunel, C., and Jouenne, T. (2007) Use of new telechelic cis-1,4-polyisoprene cationomers in the synthesis of ionic polyurethanes and copolyurethanes bearing ammonium groups. Study of their thermo-mechanical, surface and antibacterial properties. *Biomaterials 28*, 4200–4208.

(51) Coquet, L., Cosette, P., Junter, G.-A., Beucher, E., Saiter, J.-M., and Jouenne, T. (2002) Adhesion of *Yersinia ruckeri* to fish farm materials: Influence of cell and material surface properties. *Colloids Surf., B: Biointerf. 26*, 373–378.

(52) Bouvrais, H., Méléard, P., Pott, T., Jensen, K. J., Brask, J., and Ipsen, J. H. (2008) Softening of POPC membranes by magainin. *Biophys. Chem. 137*, 7–12.

BC800280U

Synthesis and Characterization of Nonsteroidal-Linked $M(CO)_3^+$ (M = ^{99m}Tc, Re) Compounds Based on the Androgen Receptor Targeting Molecule Flutamide

Haiyang He,[†] Jennifer E. Morely,[†] Elsa Silva-Lopez,[†] Brienne Bottenus,[†] Maribel Montajano,[†] Glenn A. Fugate,[†] Brendan Twamley,[‡] and Paul D. Benny*[,†]

Department of Chemistry, Washington State University, P.O. Box 644630, Pullman, Washington 99164, and University Research Office, University of Idaho, Moscow, Idaho 83844. Received July 24, 2008; Revised Manuscript Received October 2, 2008

Androgen receptors are overexpressed in most primary and metastatic prostate cancers. A series of single photon emission computed tomography imaging agents (SPECT) utilizing the organometallic radioactive imaging species, *fac*-^{99m}Tc$(OH_2)_3(CO)_3^+$, were prepared on the basis of the structure of Flutamide, a potent nonsteroidal antiandrogen prostate cancer drug. Novel bifunctional chelate-linked Flutamide analogues were prepared using a newly developed universal alkylating reagent, 2-bromo-*N*-[4-nitro-3-(trifluoromethyl)phenyl]-acetamide, **1**. From compound **1**, several ligands (i.e., cysteine **2**, histidine **5**, imidazole **3**) were conjugated to the flutamide derivative to yield targeting ligands capable of either tridentate or monodentate coordination in a "2 + 1" complex. *fac*-$Re(CO)_3^+$ complexes were prepared and characterized with the functionalized conjugates to yield *fac*-$Re(CO)_3$(2-amino-3-(1-(2-(4-nitro-3-(trifluoromethyl)phenylamino)-2-oxoethyl)-1*H*-imidazol-4-yl) propanoate), **4**, *fac*-Re $(CO)_3$(2-(*S*-cysteinyl)-*N*-[4-nitro-3-(trifluoromethyl) phenyl]-acetamide), **6**, and *fac*-$Re(CO)_3$(picolinate)(2-(1*H*-imidazol-1-yl)-*N*-[4-nitro-3-(trifluoromethyl)phenyl]-acetamide), **7**. The corresponding radioactive ^{99m}Tc analogues were prepared and stability studies of the radioactive compounds were also conducted.

INTRODUCTION

Prostate cancer is the second leading cancer affecting men in the United States (*1*). Current screening methods utilized in medicine for prostate cancer involve a digital rectal exam, prostate specific antigen (PSA), and/or prostate core biopsies (*2, 3*). Each of these methods has their own limitations in specificity and accuracy in diagnosing prostate cancer. Major limitations of current diagnostic methods are caused by the inability to noninvasively image and spatially resolve cancerous tissues amidst normal prostate tissue without perturbation of the organ. Prostate cancer cells have been found to overexpress the androgen receptor (AR) during the cancer development (*4*). The AR provides an excellent biological target for discriminating from normal prostate cells due to the increased up-regulation of the AR. The overexpression of AR is most likely due to the increased transportation of testosterone into the cancerous cells, which has been attributed to a role in DNA transcription and cell proliferation (*5*).

Current treatment of prostate cancer involves single or combination treatment strategies from hormone treatment, radiation implants, surgical removal of the prostate, and/or chemical castration for eliminating testosterone production. Major side effects of the treatment methods involve decrease or elimination of normal sexual function and loss of urinary function. Hormone therapy, targeting the androgen receptor, is typically regarded as the first round of treatment for prostate cancer to control the prostate size and tumor growth. Several nonsteroidal antiandrogens, such as nilutamide, bicalutamide, flutamide, and the corresponding metabolite hydroxyflutamide, have been utilized as hormonal therapeutic agents in a clinic setting for a number of years (Figure 1) (*6*−*11*). Although hormone therapy may have some initial success, recurrent or hormone refractory prostate cancers may occur 1−3 years after hormone treatment as an advanced form of metastatic cancer that is resistant to chemotherapy and is believed to be androgen-independent due to a mutation of the AR (*12*).

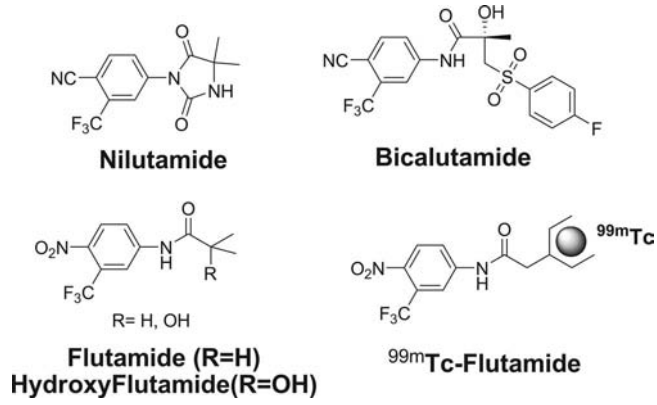

Figure 1. Examples of nonsteriodal antiandrogens clinically utilized in hormone therapy for prostate cancer and the ^{99m}Tc complex-linked flutamide reported within.

The presence or absence of AR in prostate cancer could be identified by a noninvasive imaging probe and would provide a key indicator in early screening as well as disease progression. Several positron emission tomography (PET) AR targeting analogues (i.e., flutamide, testosterone, dihydrotestosterone) have been previously reported for imaging. However, limitations in the half-life of positron (β^+) emitting isotopes, production, and PET imaging instrumentation required may have restricted clinical applications (*13*−*17*). Albeit with decreased resolution compared to PET, the development of a clinically routine single photon emission computed tomography (SPECT) imaging agent

* bennyp@wsu.edu.
[†] Washington State University.
[‡] University of Idaho.

10.1021/bc8003183 CCC: $40.75 © 2009 American Chemical Society
Published on Web 12/31/2008

Scheme 1. Preparation of 2-Bromo-*N*-[4-nitro-3-(trifluoromethyl)phenyl]acetamide, 1, and the Corresponding Ligand-Linked Flutamide Compounds by Conjugation of 1 with Cysteine and Imidazole to Generate the Respective Compounds 2 and 3

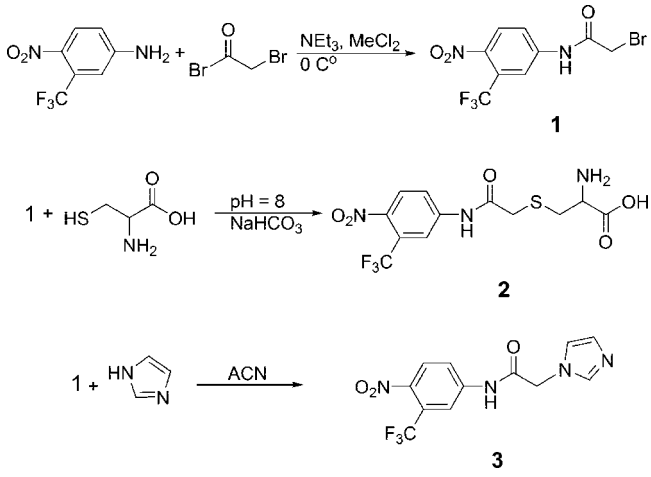

utilizing ^{99m}Tc (E_γ = 140 keV, I_γ = 89%, $t_{1/2}$ = 6.02 h) would provide an alternative for hospitals already equipped with a SPECT camera. A number of small-molecule-linked ^{99m}Tc(V) oxo complexes with steroids, such as testosterone, have been reported in the literature for prostate imaging (*18, 19*). The recent development of the organometallic precursor, *fac*-^{99m}Tc-$(OH_2)_3(CO)_3^+$, has several important advantages over Tc(V) oxo complexes for biological targeting of prostate cancer (*20*−*24*). The *fac*-^{99m}Tc$(OH_2)_3(CO)_3^+$ species can be conveniently prepared in aqueous conditions from pertechnetate isolated from a ^{99}Mo/^{99m}Tc generator with an Isolink kit produced by Tyco (*25*). The ^{99m}Tc organometallic complexes have a reduced molecular weight, molecular volume, polarity, and ligand size compared the ^{99m}Tc(V) oxo complexes. The stable CO ligands also help increase the lipophilicity of the compounds, which may assist in hepatic clearance rather than renal clearance. The chemical and structural differences of the two types of Tc compounds can have important implications in biological interactions of complexes. This is of particular importance, as bladder collection of more polar ^{99m}Tc agents would significantly impact the clarity of the images by increasing the background or completely obstructing the prostate.

Our investigation reported herein was designed to develop a model system to explore the feasibility of ^{99m}Tc-linked flutamide derivatives that utilized the *fac*-^{99m}Tc$(OH_2)_3(CO)_3^+$ precursor. We developed a central strategy that would generate a library of flutamide analogues capable of complexing the technetium species. The universal flutamide derivative was prepared and conditions determined to use general alkylation methods to covalently link a number of ligand systems to the flutamide derivative (Scheme 1). The flutamide-linked ligands were examined with both the nonradioactive rhenium for chemical and structural characterization followed by the radioactive ^{99m}Tc analogues to determine labeling effectiveness and radiochemical stability.

EXPERIMENTAL SECTION

All reagents and organic solvents were purchased from Aldrich, Acros, or Fluka in reagent grade or better and were used without further purification. Rhenium starting materials $Re(CO)_5OTf$, and *fac*-$[Re(CO)_3(H_2O)_3]OTf$, were prepared by literature methods from $Re_2(CO)_{10}$ purchased from Strem (*24, 26*). Rhenium complexes *fac*-$Re(CO)_3$(Histidine) and *fac*-$Re(OH_2)(CO)_3$(picolinate) were prepared by reacting the rhenium starting materials with the appropriate ligand according to reported methods (*27, 28*). Normal mouse serum (L10410) with 0.1% sodium azide was purchased from Caltag Laboratories and was centrifuged to remove particulate matter prior to use. Elemental analyses were performed by Quantitative Technologies, Inc., New Jersey. Separation and identification of compounds were conducted on a Perkin-Elmer Series 200 high pressure liquid chromatograph (HPLC) equipped with a UV/vis series 200 detector and a Perkin-Elmer Radiomatic 610TR detector utilizing a 30 cm 5 μm Agilent Zorbex SB-C18 column. The compounds were separated with a reverse-phase gradient system beginning with 0.1% trifluoroacetic acid (TFA) aqueous eluent gradually shifting to methanol according to the following method, 0−3.0 min (100% TFA), 3.0−9.0 min (75% TFA, 25% MeOH), 9.0−20.0 min (25% to 100% MeOH linear gradient), 20.0−25.0 min (100% MeOH) at a flow rate of 1.0 mL/min or 5.0 mL/min for separation. ^{1}H NMR spectra were recorded on a Varian 300 MHz spectrometer, and chemical shifts were referenced to the internal standard sodium 3-(trimethylsilyl) propionate-d_4 (TSP, 0.00 ppm) in D_2O or the residual solvent signal and/or tetramethylsilane (TMS) in organic solvents. Spectra were processed using Varian VNWR 6.1 software. IR spectra were collected with a Thermo Nicolet 6700 FT-IR with an ATR cell and analyzed with OMNIC 7.1a software. Mass measurements were performed as Q3 scans on an API4000 triple quadrupole (Applied Biosystems). Sample concentrations of ~0.1 μg/μL in methanol were infused at 10 μL/min, with orifice heating on, declustering potential 20 V, and entrance potential 10 V.

2-Bromo-*N*-[4-nitro-3-(trifluoromethyl)phenyl]acetamide, 1. Et_3N (5.9 mL, 42 mmol) was added slowly to a solution of bromoacetyl bromide (8.1 g, 40 mmol) and 5-amino-2-nitrobenzotrifluroride (7.0 g, 34 mmol) in CH_2Cl_2 (200 mL) at 0 °C. The solution was stirred for 2 h at 0 °C, which resulted in a clear solution. The solution was continuously stirred and allowed to reach rt overnight. The solution was washed with 0.6 M of HCl three times (200 mL × 3), followed by water. The organic phase was dried over Na_2SO_4, filtered, and evaporated to dryness to give a pure slight yellow product (9.9 g, 89%). Anal. Calcd for $C_9H_6BrF_3N_2O_3$: C, 33.05; H, 1.85; N, 8.57. Found: C, 33.00; H, 1.62; N, 8.33. ^{1}H NMR [δ (ppm), $CDCl_3$] 8.53 (s, 1H), 8.02 (m, 3H), 4.08 (s, 2H). ^{13}C NMR [δ (ppm), $CDCl_3$] 164.5, 141.3, 127.4, 125.6 (q), 123.6, 122.7, 120.0, 118.7 (q), 29.1. MS [$M^+ - Na^+$] 349.0, 351.1.

2-(*S*-Cysteinyl)-*N*-[4-nitro-3-(trifluoromethyl)phenyl]acetamide, 2. To a solution of excess cysteine (1.21 g, 10 mmol) in water (50 mL) was added $NaHCO_3$ (10 mL, 1 M), followed by **1** (1.0 g, 3.0 mmol) in CH_2Cl_2 (50 mL). The biphasic mixture was vigorously stirred overnight at rt. A small amount off-white solid product was observed in the reaction mixture and additional material was formed after selective evaporation of CH_2Cl_2 from the mixture. The off-white solid was filtered and dried under vacuum (0.75 g, 67%). Anal. Calcd for $C_{12}H_{12}F_3N_2O_5S \cdot 0.6H_2O$: C, 38.12; H, 3.52; N, 11.11. Found: C, 37.89; H, 3.28; N, 11.38. ^{1}H NMR [δ (ppm), DCl/D_2O, 0.25 M] 7.98 (d, J = 2.1 hz, 1H), 7.95 (d, J = 9.0 hz, 1H), 7.82 (dd, J = 2.1 and 9.0 hz, 1H), 4.48 (dd, J = 4 and 8 hz, 1H), 3.70 (s, 2H), 3.46 (dd, J = 4 and 15 hz, 1H), 3.29 (dd, J = 8 and 15 hz, 1H). ^{13}C NMR [δ (ppm), DCl/D_2O, 0.25 M] 173.4, 173.1, 145.2, 145.0, 130.3, 126.6, 125.9, 121.6, 55.4, 39.2, 35.0, 29.1. MS [M^+] 367.9, [$M^+ - Na^+$] 389.9.

2-(1*H*-Imidazol-1-yl)-*N*-[4-nitro-3-(trifluoromethyl)phenyl]acetamide, 3. To an acetonitrile solution (10 mL) containing imidazole (1.57 g, 5 mmol) was added **1** (0.33 g, 1 mmol). The solution was stirred overnight at rt, then evaporated to dryness under vacuum to yield a faint yellow solid. Water (10 mL) was added to the solid and the solution filtered. HCl (0.5 M, 10

mL) was added to the collected solid, and the corresponding mixture was centrifugated, and the solution collected, and the solid discarded. The slow addition of $NaHCO_3$ (1 M, 4 mL) to the centrifuged solution caused the formation of a yellow precipitate, which was filtered and dried to yield the desired faint yellow product **3** (0.26 g, 82%). Anal. Calcd for $C_{12}H_9F_3N_4O_3$: C, 45.87; H, 2.89; F, 18.14; N, 17.83; O, 15.28. Found: C, 44.60; H, 2.84; N, 17.07. ^{1}HNMR [δ (ppm), methanol-d_4] 9.04 (t, 1H), 8.23 (d, 1H), 8.03 (m, 2H), 7.69 (t, 1H), 7.27 (t, 1H), 5.36 (s, 2H). ^{13}CNMR [δ (ppm), methanol-d_4] 166.8, 142.9, 138.3, 127.0, 126.9, 124.5, 124.0, 122.5, 121.1, 117.9, 117.8, 49.5. MS [M^+] 315.0, [$M^+ - Na^+$] 337.0.

***fac*-Re(CO)$_3$(2-amino-3-(1-(2-(4-nitro-3-(trifluoromethyl)phenylamino)-2-oxoethyl)-1*H*-imidazol-4-yl)propanoate), 4.** To a room temperature acetonitrile solution (80 mL) of *fac*-Re(CO)$_3$(Histidine) (0.84 g, 2 mmol) and **1** (0.72 g, 2.2 mmol) was added Cs_2CO_3 (0.60 g, 2.2 mmol) and stirring continued overnight. The solution was filtered to remove the residual Cs_2CO_3 and salt byproducts, and the filtrate was collected and evaporated to dryness. The solid residue obtained from the filtrate was washed with a minimal amount of ethanol and water and dried under vacuum to yield the desired faint yellow product **4** (1.2 g, 90%). Anal. Calcd for $C_{18}H_{13}F_3N_5O_8Re$: C, 32.24; H, 1.95; N, 10.44. Found: C, 31.81; H, 2.17; N, 9.96. ^{1}H NMR [δ (ppm), acetone-d_6] 11.90 (s, 1H), 8.26 (d, 1H, J = 1.8 Hz), 8.12 (m, 3H), 7.18 (s, 1H), 5.75 (dd, J = 11.4 and 6.0 Hz, 1H, 1H), 5.4 (d, J = 17.1 Hz, 1H), 4.35 (overlapped, 1H), 4.34(overlapped, 1H), 3.51 (dd, J = 13.5 and 3 Hz, 1H), 3.37 (dd, J = 13 and 3 Hz, 1H). ^{13}C NMR [δ (ppm), acetone-d_6] 197.9, 196.5, 183.9, 165.8, 143.9, 142.9, 142.5, 134.9, 127.6, 124.4, 124.2, 123.9, 122.3,120.8,117.5, 52.4, 49.1. IR [cm^{-1}] 2018, 1879, 1604, 1525, 1342, 1147. MS [M^+] 672.3, [$M^+ - Na^+$] 694.2.

2-Amino-3-(1-(2-(4-nitro-3-(trifluoromethyl)phenylamino)-2-oxoethyl)-1*H*-imidazol-4-yl)propanoic Acid, 5. To an acetone solution (15 mL) containing compound **4** (0.34 g, 0.5 mmol) was added HCl solution (15 mL, 1 M), followed by H_2O_2 (0.6 mL) at rt. The mixture was continuously stirred and monitored by HPLC to determine reaction progress. After 3 d, the starting material **4** was no longer observed in the chromatogram, indicating the complete conversion of the Re starting material to the ligand **5**. The reaction mixture was neutralized by Na_2CO_3 (1 M), and the solution was directly purified by preparative HPLC to yield the yellow product **5** as a semisolid. (0.169 g, 83%). Anal. Calcd for $C_{19}H_{18}F_9N_5O_{10}$: C, 35.25; H, 2.80; F, 26.41; N, 10.82; O, 24.71. 35.29, H, 2.70 N, 9.35. ^{1}H NMR [δ (ppm), methanol-d_4] 9.14 (s, 1H), 8.30 (s, 1H), 8.06 (m, 2H), 7.74 (s, 1H), 5.43 (s, 2H), 4.47 (dd, J = 6 and 7 Hz, 1H), 3.56 (dd, J = 6 and 16 Hz, 1H), 3.46 (dd, J = 7 and 16.0 Hz, 1H). ^{13}C NMR [δ (ppm), methanol-d_4] 168.9, 165.3, 143.1, 142.6, 137.5, 127.6, 127.1, 124.5, 124.0, 122.8, 120.4, 118.0, 51.7, 51.5, 25.5. MS [M^+] 402.2.

***fac*-Re(CO)$_3$(2-(S-cysteinyl)-*N*-[4-nitro-3-(trifluoromethyl)phenyl]acetamide), 6.** To a solution of **2** (0.18 g, 0.5 mmol) and [Re(CO)$_5$OTf] (0.25 g, 0.52 mmol) in methanol (30 mL) was added Et_3N (75 μL, 0.54 mmol). The mixture was refluxed for 2 h, concentrated to 5 mL by rotary evaporation, and purified by preparative HPLC to yield the product **6** as a pale yellow solid (0.22 g, 69%). Anal. Calcd for $C_{15}H_{11}F_3N_3O_8ReS$: C, 28.30; H, 1.74; N, 6.60. Found: C, 27.99; H, 1.81; N, 6.47. ^{1}H NMR [δ (ppm), methanol-d_4, −14 °C] 8.25 (d, J = 2.1 hz, 1H), 7.98−8.09 (m, 2H), 6.24 (d, J = 10 hz, 1H), 5.02 (d, J = 10 hz, 1H), 4.36 (s, 1H), 4.24 (m, 1H), 3.92 (d, J = 15.3 Hz, 1H), 3.80 (d, J = 15.3 Hz, 1H), 3.04 (m, 2H). ^{13}C NMR [δ (ppm), methanol-d_4] 195.4, 193.3, 181.4, 167.4, 144.3, 143.9, 128.2, 125.5 (q),123.9, 121.6, 119.2 (q), 59.4, 41.7, 33.1. IR [cm^{-1}] 3000, 2029, 1903, 1530, 1267, 1146, 755. MS [M^+] 638.1, [$M^+ - Na^+$] 660.2.

Table 1. X-ray crystal data and structure refinement for compound 7

empirical formula	$C_{24}H_{19}F_3N_5O_9Re$	
formula weight	764.64	
temperature	90(2) K	
wavelength	0.71073 Å	
crystal system	monoclinic	
space group	*C*2/*c*	
unit cell dimensions	a = 19.0902(11) Å	α = 90°.
	b = 14.6852(8) Å	β = 100.5910(10)°.
	c = 20.6888(12) Å	γ = 90°.
volume	5701.2(6) Å^3	
Z	8	
density (calculated)	1.782 mg/m^3	
absorption coefficient	4.341 mm^{-1}	
F(000)	2976	
crystal size	0.34 × 0.25 × 0.23 mm^3	
crystal color and habit	yellow block	
diffractometer	Bruker/Siemens SMART APEX	
θ range for data collection	1.76° to 27.50°.	
index ranges	$-24 \le h \le 24$, $-19 \le k \le 19$, $-26 \le l \le 26$	
reflections collected	42 304	
independent reflections	6552 [R(int) = 0.0260]	
completeness to θ = 27.50°	100.0%	
absorption correction	semiempirical from equivalents	
max. and min. transmission	0.367 and 0.290	
solution method	XS, SHELXTL v. 6.14 (Bruker, 2003)	
refinement method	full-matrix least-squares on F^2	
data/restraints/parameters	6552/0/384	
goodness-of-fit on F^2	1.040	
final R indices [$I > 2\sigma(I)$]	$R1$ = 0.0201, w$R2$ = 0.0478	
R indices (all data)	$R1$ = 0.0233, w$R2$ = 0.0495	
largest diff. peak and hole	1.817 and −0.533 e.Å^{-3}	

***fac*-Re(CO)$_3$(picolinate)(2-(1*H*-imidazol-1-yl)-*N*-[4-nitro-3-(trifluoromethyl)phenyl]acetamide), 7.** To a methanol solution (5 mL) of *fac*-Re(OH$_2$)(CO)$_3$(picolinate) (0.033 g, 0.081 mmol) was added **3** (0.028 g, 0.089 mmol), and the solution was stirred at 50 °C for 3 h. The reaction solution was evaporated to dryness, then purified by preparative HPLC to yield the product **7** as a yellow solid. (0.040 g, 70%). X-ray quality single crystals of compound **7** were isolated as faint yellow rectangular blocks by slow evaporation of the compound in a 1:1 mixture of hexane/acetone. Anal. Calcd for $C_{21}H_{13}F_3N_5O_8Re$: C, 35.70; H, 1.85; N, 9.91. Found: C, 36.15; H, 1.97; N, 9.56. ^{1}H NMR [δ (ppm), methanol-d_4] 8.97 (dt, 1H), 8.05 (m, 6H), 7.76 (m, 1H), 7.14 (t, 1H), 6.96 (t, 1H), 4.90 (s, 2H). ^{13}C NMR [δ (ppm), methanol-d_4] 196.6, 174.2, 165.9, 152.2, 149.5, 141.2, 140.5, 129.2, 128.5, 124.2, 127.1, 124.5, 124.1, 122.5, 117.8, 117.7, 49.9. IR [cm^{-1}] 2021, 1912, 1653, 1537, 1345, 1167. MS [M^+] 708.4, [$M^+ - Na^+$] 730.5.

X-ray Crystallography. Crystals of compound **7** were removed from the flask; a suitable crystal was selected, attached to a glass fiber, and data were collected at 90(2) K using a Bruker/Siemens SMART APEX instrument (Mo Kα radiation, λ = 0.71073 Å) equipped with a Cryocool NeverIce low-temperature device. Data were measured using omega scans 0.3° per frame for 5 s, and a full sphere of data were collected. A total of 2400 frames were collected with a final resolution of 0.77 Å. Cell parameters were retrieved using SMART software (*29*) and refined using SAINTPlus (*30*) on all observed reflections. Data reduction and correction for Lp and decay were performed using the SAINTPlus software. Absorption corrections were applied using SADABS (*31*). The structure was solved by direct methods and refined by least-squares method on F^2 using the SHELXTL program package (*32*). The structure was solved in the space group *C*2/*c* by analysis of systematic absences. No decomposition was observed during data collection. Details of the data collection and refinement are given in Table 1. Further details are provided in the Supporting Information.

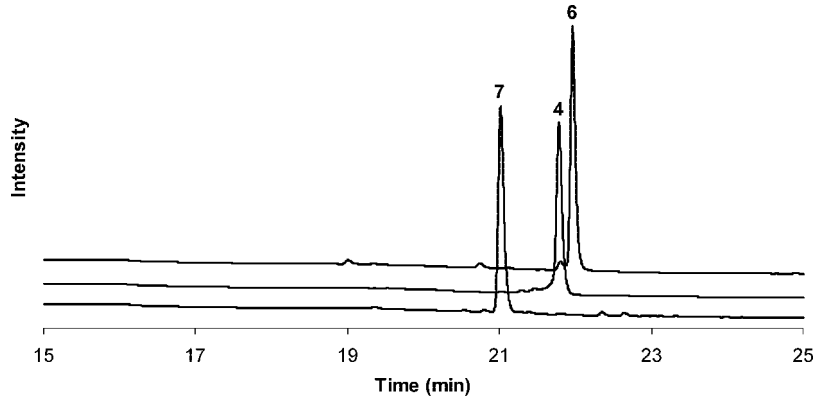

Figure 2. UV/vis HPLC (220 nm) chromatograph of Flutamide-linked rhenium tricarbonyl complexes of **4**, **6**, and **7**.

Radiochemistry. ^{99m}Tc-pertechnetate ($^{99m}TcO_4^-$) was purchased from Cardinal Health in Spokane, WA. IsoLink kits to prepare the $^{99m}Tc(H_2O)_3(CO)_3^+$ precursor were obtained as a gift from Tyco, Inc. The radiolabeled products were characterized by Perkin-Elmer Series 200 HPLC under the same mobile-phase conditions previously mentioned, except the γ emissions were detected with a Perkin-Elmer Radiomatic 610TR detector equipped with a Gamma B cell (80 μL loop). The *fac*-$^{99m}Tc(H_2O)_3(CO)_3^+$ precursor was prepared according to the manufacture's procedure, the addition via syringe of 10−20 mCi of $Na^{99m}TcO_4$ in 1 mL saline to the Isolink kit followed by heating at 95 °C for 20 min. The resulting solution was cooled in an ice bath, neutralized with HCl (∼100 μL, 1 M) and checked on the γ-HPLC system to ensure complete formation of the precursor.

General $^{99m}Tc(H_2O)_3(CO)_3^+$ Radiolabeling Procedure. The ligand **2** or **5** (100 μL, 10^{-4} or 10^{-5} M) and phosphate buffer (800 μL, 0.1 M) at pH 7.4 was added to a sealable labeling vial (5.0 mL). The vial was sealed and degassed with nitrogen for ∼10 min. The $^{99m}Tc(H_2O)_3(CO)_3^+$ precursor solution (100 μL) was added to the degassed vial and the vial heated for 30 min at 70 °C. The reaction mixture was then allowed to cool on an ice bath prior to injection and analysis by radio-HPLC.

2 + 1 Radiolabeling Procedure. *Method 1: One-Pot Preparation.* Ligand **3** (100 μL, 10^{-2} M), picolinic acid (100 μL, 10^{-4} M), and phosphate buffer (700 μL, 0.1 M) at pH 7.4 were added in order to a sealable labeling vial (5.0 mL). The vial was sealed and degassed with N_2 for ∼10 min. The $^{99m}Tc(H_2O)_3(CO)_3^+$ precursor solution (100 μL) was added to the degassed vial and heated for 30 min at 80 °C. The reaction mixture was allowed to cool on an ice bath prior to analysis by radio-HPLC.

Method 2: Stepwise Formation. Picolinic acid (100 μL, 10^{-4} M) and phosphate buffer (700 μL, 0.1 M) at pH 7.4 were added to a sealable vial (5.0 mL). The vial was purged with nitrogen for ∼10 min. The $^{99m}Tc(H_2O)_3(CO)_3^+$ precursor solution (100 μL) was added to the degassed vial and heated for 30 min at 80 °C. After the formation of *fac*-$^{99m}Tc(H_2O)(CO)_3$(picolinate) was confirmed by radio-HPLC, ligand **3** (100 μL, 10^{-2} M) was added to the vial and the sample heated for an additional 30 min at 80 °C.

Biological pH Stability Studies. The respective ^{99m}Tc labeled compound (100 μL) prepared with ligands **2**, **3**, or **5** as directed above was added to phosphate buffer (900 μL, 0.1 M) at pH 7.4. The vial was sealed and incubated at 37.0 °C for the duration of the study. The solution was examined by radio-HPLC at 1, 2, and 4 h during the incubation to determine the effective stability of the compounds.

Mouse Serum Stability Studies. The respective ^{99m}Tc complexes (100 μL) prepared from ligands **2**, **3**, or **5** as directed above was added to an Eppendorf 1.5 mL flextube containing 400 μL of normal mouse serum with 0.1% sodium azide that had been previously clarified by centrifugation. The tube was sealed and constantly heated at 37.0 °C for the duration of the study. The serum was examined by radio-HPLC at 1, 2, and 4 h of incubation to observe decomposition or loss of the radiolabeled complex due to a shift in the retention time or decrease in the product peak intensity.

Cell Studies. *In vitro* analysis of the ^{99m}Tc complexes were conducted with DU-145 according to established methods prepared from ligand **2** or **5** as directed above was added. Aliquots of compounds (4, 6, 8 μL of a 0.1 mCi/100 μL) were incubated in triplicate with androgen receptor positive DU-145 prostate cancer cell line for 2 h in a CO_2 incubator at 37 °C. The cells were washed twice with cold PBS to remove nonspecific bound ^{99m}Tc complex; the cells were collected and counted with a Cobra II γ counter for 1 min.

RESULTS AND DISCUSSION

Nonsteroidal antiandrogen drugs, i.e., flutamide, bicalutamide, nilutamide, have been found to effectively mitigate early-stage prostate cancer growth (Figure 1) (*10*). We report within this paper the first analogues of flutamide that incorporate technetium-99m complexes into the structure. Flutamide was modified to incorporate a number of ligand systems capable of coordinating the ^{99m}Tc species, *fac*-$^{99m}Tc(OH_2)_3(CO)_3^+$ (Figure 2). We report within the synthetic methods used to prepare the bifunctional flutamide compounds, characterization of rhenium complexes formed, and radiochemical preparation and stability studies of the technetium-99m complexes formed.

The focus of this work was to develop a flutamide analogue that could be conveniently functionalized with a variety of ligand systems quite readily. The designs of such analogues were restricted to modifications along the carbonyl axis of flutamide's amide bond as the dominent binding motif for the compound to the androgen receptor is understood to be the functionalized aromatic ring (*6, 7, 10, 34, 35*). Transforming the alkyl backbone into an alkyl halide provided an accessible group that could function as a synthetic handle for nucleophilic substitution by a number of reactive species (i.e., amines, thiols, alcohols) (*13,15,36,37*). The brominated flutamide compound, 2-bromo-*N*-[4-nitro-3-(trifluoromethyl)phenyl]-acetamide, **1**, was chosen as the congener of fluatamide in order for later incorporation of chelators. Compound **1** was prepared in high yield by the reaction of bromoacetyl bromide and 5-amino-2-nitrobenzotrifluroride in CH_2Cl_2 in the presence of triethylamine (Scheme 1). The crude product **1** isolated from the reaction mixture after acid washing the reaction mixture was clean enough to use for the subsequent experiments without further purification based on ^{1}H and ^{13}C NMR spectroscopy. Compound **1** could also be further purified by silica gel chromatography (ethyl acetate/hexane 1:5) or

Scheme 2. Preparation of Histidine-Linked Flutamide Ligand (5) by Alkylation with 1 of the Rhenium Histidine to Yield the Rhenium Histidine-Linked Flutamide Complex (4) and Followed by Demetallation to Generate the Free Ligand (5)

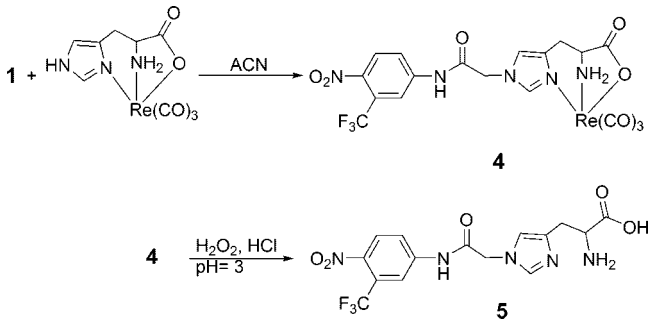

recrystallized from ethyl acetate. Compound **1** was found to be a strong irritant as a dry powder, and care was utilized when handling the material.

The reactivity of the acetyl bromide in compound **1** provided an excellent synthetic handle to functionalize with corresponding ligand systems. Introduction of compound **1** afforded a series of molecules **2**, **3**, and **5** that incorporate flutamide and ligands (cysteine, imidazole, histidine, respectively). These ligands had been previously identified for coordination with a $M(CO)_3$ ($M = Re$, ^{99m}Tc) species due to high-efficiency labeling methods (*27, 28, 38*). The synthetic routes to **2**, **3**, and **5** are divided into two categories, direct organic synthesis and metal-coordinated synthesis. Direct synthesis involved a standard alkylation synthesis route to couple **1** with the ligand. The ligands cysteine and imidizole were attached to **1** via the direct synthesis route in a one-step substitution reaction to yield the flutamide-coupled ligands, compounds **2** and **3**, respectively (Scheme 1). The metal-coordinated synthesis of compound **5** involves the use of a rhenium as a protecting group on the histidine (Scheme 2).

Direct synthetic methods allowed the preparation of the compounds directly from compound **1** (Scheme 1). The cysteine-linked flutamide analogue, **2**, was successfully prepared in high yield after a number of synthetic attempts. The reported method has an important synthetic advantage by utilizing the reactive differences between thiol and amine groups to yield the desired product without the use of protecting groups. Early attempts utilizing protecting groups on cysteine on the amine and the carboxylic acid with Boc-Cys-OMe did yield the corresponding alkylation product with **1**. However, deprotection with base of the methyl ester was found to also cleave the amide bond as indicated by the presence of 5-amino-2-nitrobenzotrifluroride in the reaction mixture. Potential amide cleavage was anticipated at high pH due to the strong electron-withdrawing groups (NO_2, CF_3) on the aromatic ring weakening the amide bond. By treatment of **1** with excess cysteine in aqueous conditions at slightly basic pH, alkylation selectivity of the thiol over the amine in cysteine and the avoidance of protecting groups that require basic deprotection methods yielded the desired product, **2**. Initially, the reaction was conducted in aqueous solution only, but it proceeded slowly with low yields (<25%) due to the limited solubility of compound **1**. Attempts to improve reactivity and solubility with increased base and/or heat yielded undesired cleavage products. It is noteworthy to mention that, when the reaction was carried out in biphasic reaction conditions (aqueous/methylene chloride), compound **1** readily dissolved in the methylene chloride and the reaction proceed smoothly without the need of a phase transfer catalyst at room temperature with a significant improvement in yield. Careful control of the solution pH in the reaction was critical to yield the desired product, **2**. The cystine dimer was observed as the major product instead of **2** when the reaction was carried out in acidic conditions (pH < 5). Other water-miscible solvents (i.e., DMF, methanol) did dissolve **1**; however, the reaction did not afford compound **2** in any appreciable yield. The conditions reported here are mild for alkylation of a thiol compared to refluxing 1 M NaOH that can lead to racemic mixtures or utilizing carcinogenic solvents. Ligand **2** was characterized by elemental analysis and ^1H and ^{13}C NMR spectroscopy.

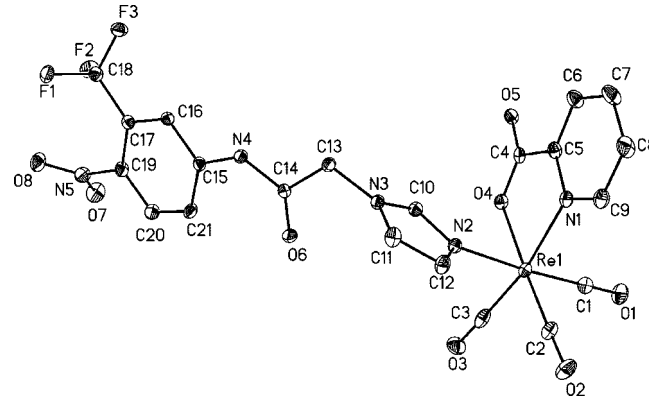

Figure 3. A modeled X-ray structure of *fac*-$Re(CO)_3$(Picolinate)(**3**), **7**, with 30% thermal ellipsoids. Hydrogen atoms are excluded for clarity.

An imidazole-linked flutamide analogue was prepared by treatment of **1** with excess imidazole in acetontrile gave **3** in high yield (Scheme 1). Under the reported reaction conditions, only the monosubstituted product was isolated, where the imidazole ligand was functioning as both the reactant and the proton scavenger. However, when the imidazole was added in stoichiometric concentrations and in the presence of an additional base (i.e., Cs_2CO_3) in acetonitrile, a mixture of the mono- and disubstituted products were observed. The mixed species were also observed when the reaction was conducted in a biphasic solvent system ($H_2O/MeCl_2$) similar to compound **2**. ^1H and ^{13}C NMR reported for **3** were consistent with the proposed compound.

Preparation of a N^{ϵ} histidine-linked flutamide compound ligand with **1** was originally attempted utilizing protecting groups similarly to previous reports (*28*, *39*, *40*). However, deprotection methods yielded cleavage products at the amide bond as noted previously in the synthesis of **2**. Therefore, utilizing a metal-coordinated synthetic route for the preparation of the ligand was a more appropriate method. In this procedure, $Re(CO)_3$ was coordinated in a tridentate fashion to the histidine ligand in place of more traditional organic protecting group (*28*). Alkylation of $Re(CO)_3$(histidine) with compound **1** in the presence of solid Cs_2CO_3 in an acetonitrile solution yielded compound **4** in near quantitative yields (Scheme 2). The reaction proceeds smoothly with no unwanted side products as indicated by HPLC, as the metal coordination bonds sufficiently protect the bound amine, carboxylate, and imidizole functional groups from substitution reactions (Figure 3). The coordinated imidazolyl ligand was of particular importance to maintain the coordination mode and strength for the subsequent ^{99m}Tc labeling. Dissociation of the nitrogen ligands from the rhenium center could lead to substitution at the NH_2 terminus or N^{τ} or disubstitution of the ring, similar to what was observed as a side product in the formation of compound **3**. The complexes were characterized by NMR, and comparison of **4** to the $Re(CO)_3$(Histidine) starting material illustrated similar splitting and slight downfield shifts for the protons associated with the coordinated histidine, indicating no change in the coordination mode of the ligand on the metal center. ^1H NMR of **4** in acetone showed two peaks associated with the imidazolyl group at 8.26

Scheme 3. Complexation of Flutamide-Linked Ligand Analogues with *fac*-M(CO)$_3$ (M = Re, ^{99m}Tc (a)) with Tridentate Ligands 2 and 5 to Generate *fac*-M(CO)$_3$(2) (6, 6a) and *fac*-M(CO)$_3$(5) (4, 4a) Complexes

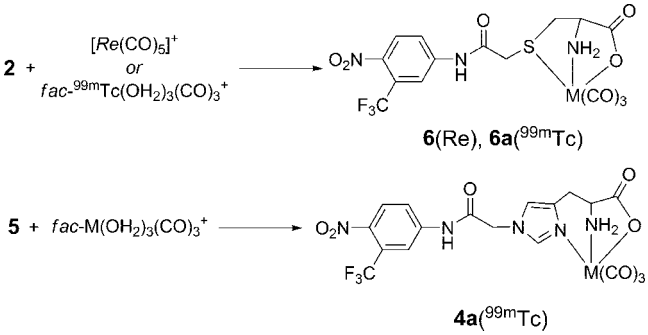

and 7.18 ppm, slightly shifted downfield from the Re(CO)$_3$(Histidine) starting material at 7.06 and 8.08 ppm. The aromatic protons of the molecule were overlapped in the spectrum to yield a multiplet at 8.12 ppm of 3H. The metal coordinated amine protons are observed as diastereotopic protons of equal integration of one proton as a doublet at 5.4 and mulitplet at 5.75 ppm. The chiral Hα was also observed as a multiplet at 4.35 ppm, and the beta protons Hβ were also diastereotopic, exhibiting a dd pattern at 3.51 and 3.37 ppm.

Removal of the coordinated rhenium tricarbonyl complex in **4** to generate the free ligand compound **5** was achieved under acidic oxidative conditions (Scheme 2). The selective oxidation and decomplexation of the rhenium center of **4** occurs by the addition of a 10-fold quantity of H_2O_2 under acidic conditions at room temperature. The reaction was monitored by HPLC and was completed after 3 days. Although a lower pH and increased H_2O_2 concentration would potentially decrease the reaction time, minimal amide cleavage products of the ligand were observed under the conditions reported. The free ligand **5** was isolated by preparatory HPLC from the reaction mixture in reasonable yields. Characterization of **5** by ^{1}H and ^{13}C NMR was consistent with the proposed structure and simplified in comparison to the corresponding rhenium complex, **4**.

Complexes were prepared from the ligands prepared above with rhenium and technetium-99m carbonyl precursors to yield M(CO)$_3$(Ligand/s) complexes. The preparation and characterization of the rhenium complexes provides a stable compound for characterization by standard methods and a reference for comparison to the radioactive ^{99m}Tc complexes in HPLC (Figure 2). The rhenium complexes of the flutamide-linked ligands were prepared by reacting the ligand with a rhenium carbonyl starting material as indicated in Scheme 3, except for complex **4a**, which was prepared directly from the Re(CO)$_3$(Histidine) complex as mentioned above. Ligands **2** and **3** utilized slightly different Re starting materials according to the solubility of the ligand system. Ligand **2** was reacted with the organic soluble [Re(CO)$_5$OTf] in methanol, due to the limited solubility of macroscopic amounts of **2** in water. The reaction involves the displacement of two CO molecules from the rhenium center upon complexation of **2** to generate the neutral complex Re(CO)$_3$(**2**), **6**, in high yield and isolated as a pale yellow solid. HPLC analysis of the product showed a single sharp peak with retention time of 22.1 min (Figure 2). Elemental analysis of **6** confirmed the existence of 1:1 ratio of rhenium to ligand. ^{13}C NMR profile of **6** is in consistent with the proposed structure. Relatively broad signals were observed in the ^{1}H NMR spectrum of **6** in CD_3OD at room temperature. At low temperature (−14 °C), sharp signals were observed, showing two sets of signals indicative of two coordination isomers in solution. The coordinated ligand **2** has a chiral carbon and prochiral sulfur resulting in the formation of diastereoisomers upon metal coordination. Two isomers can equilibrate fast by inversion of the sulfur configuration at room temperature. However, the minor species was observed at approximately 10% in the solution, indicating a preference for one coordination species with the Re(CO)$_3$ most likely due to interactions of functionalized thioether moiety driven by steric factors. Similar observations were reported for other thioether derivatives of cysteine Re(CO)$_3$ complexes (*26*, *38*).

Mundwiler et al. (*41*) reported a "2 + 1" mixed-ligand complex approach consisting of a bidentate and a monodentate ligand coordinated to the M(CO)$_3$ (M = Re, ^{99m}Tc) core provides an alternative method to single ligand coordination. This methodology was adopted to prepare a "2 + 1" flutamide derivative with the M(CO)$_3$ M = Re, ^{99m}Tc core. The rhenium complex, Re(CO)$_3$(pic)(**3**), **7**, prepared within this paper consisted of a bidentate picolinate and a monodentate flutamide fuctionalized imidazole, **3**. Two synthetic approaches, one-pot and stepwise synthesis, were attempted to prepare complex **7** (Scheme 4). The one-pot reaction yielded some of the product **7**; however, several other species were observed in the reaction mixture attributing multiple coordinating ligands of **3**. The stepwise synthesis provided a more clearly defined product in high yields. The compound *fac*-Re(OH$_2$)(CO)$_3$(picolinate) was prepared and isolated according to previous methods (*27*) and reacted with **3** in methanol to yield compound **7** as the only product in the HPLC chromatogram (Figure 2). Elemental analysis, ^{1}H and ^{13}C NMR as well as X-ray crystallography confirm the formation of complex **7**. ^{1}H NMR spectrum of **7** had increased overlapping signals at ∼8 ppm of the aromatic protons from the four protons of the coordinated picolinate and the three protons **3**. The methylene protons of **3** displayed a singlet signal, in contrast to doublet signals observed in **4**, suggesting that the monodentate ligand **3** is more flexible than the analogous tridentate ligand **5** in rhenium complexes. Crystals suitable for X-ray crystallography were obtained by diffusion of hexane into acetone solution of **7** (Figure 3). The structural parameters are listed in Table 1 and selected bond angles (°) and distances (Å) in Table 2. The rhenium center in complex **7** is a distorted octahedron with three CO ligands occupying the facial geometric sites in near-equivalent Re−C distances (1.89−1.92 Å) and C−Re−C angles (88.4−90.2°) with respect to each other. The other coordination sites are occupied by the coordinated "2 + 1" ligands, picolinate (pic) and **3**. Pic functions as a planar bidentate ligand (N, O) with distances and angles comparable to other reported structures (*27*, *41*, *42*). The monodentate ligand **3** is coordinated to the rhenium center through an imidazole nitrogen at N(2)−Re(1) 2.186 Å. The imidazole ligand itself is slightly tilted toward the plane of the pic ligand (∼83°) yielding an acutely distorted octahedron along the pic and **3** coordination sites. Compound **7** also exhibits interesting intermolecular NH−O (2.79 Å) hydrogen bonding between two molecules through the amide proton donor and the noncoordinated oxygen of the picolinate as a proton acceptor, yielding two hydrogen bond interactions per set of molecules in the unit cell.

Investigation of the radioactive ^{99m}Tc complexes were conducted by reacting ligands (**2**, **3**, and **5**) with the *fac*-[^{99m}Tc(CO)$_3$(H$_2$O)$_3$]$^+$ generated from a Tyco Isolink kit in aqueous conditions. The general labeling procedure for tridentate ligands **2** and **5** involved mixing the ligand with the *fac*-[^{99m}Tc(CO)$_3$(H$_2$O)$_3$]$^+$ at pH 7.4 and heating at 70 °C for 30 min (Scheme 3). Concentrations (10^{-4}, 10^{-5}, 10^{-6} M) were investigated at these conditions to determine effective labeling of the ligand. Both ligands **2** and **5** demonstrated good labeling of >90% at 10^{-4} and 10^{-5} M to yield *fac*-[^{99m}Tc(CO)$_3$(**2**)] **4a** and *fac*-[^{99m}Tc(CO)$_3$(**5**)] **6a** complexes (Figure 4). Labeling yields for both ligands **2** and **5** at 10^{-6} M were slightly diminished, 28% and 20% respectively, compared to the

Scheme 4. 2 + 1 Labeling Strategy for Reacting Ligand 3 with *fac*-M(OH$_2$)$_3$(CO)$_3$ (M = Re, ^{99m}Tc (a)) to Yield Complexes *fac*-M(CO)$_3$(pic)(3), (7, 7a)[a]

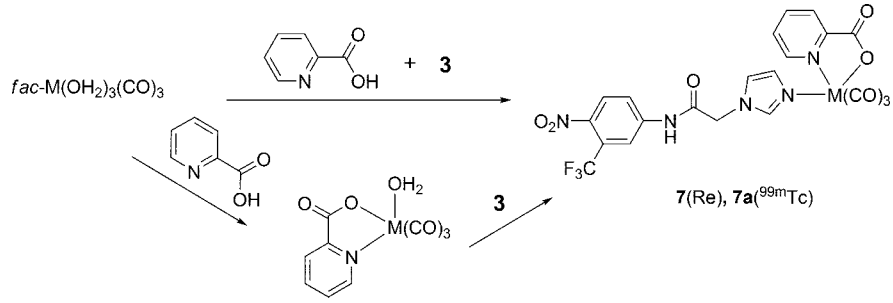

[a] Two strategies are reported: (1) single pot reaction; (2) stepwise addition of ligands.

Table 2. Selective Bond Angles (°) and Distance (Å) of *fac*-Re(CO)$_3$(Picolinate)(3), 7

bond lengths [Å]		angles [°]	
C(1)−Re(1)	1.920(3)	C(2)−Re(1)−C(3)	89.79(11)
C(2)−Re(1)	1.898(3)	C(2)−Re(1)−C(1)	88.41(11)
C(3)−Re(1)	1.902(3)	C(3)−Re(1)−C(1)	90.24(10)
N(1)−Re(1)	2.185(2)	C(2)−Re(1)−O(4)	175.05(9)
N(2)−Re(1)	2.186(2)	C(3)−Re(1)−O(4)	94.71(9)
O(4)−Re(1)	2.1424(17)	C(1)−Re(1)−O(4)	93.60(9)
		C(2)−Re(1)−N(1)	100.09(10)
		C(3)−Re(1)−N(1)	169.25(9)
		C(1)−Re(1)−N(1)	94.20(9)
		O(4)−Re(1)−N(1)	75.26(7)
		C(2)−Re(1)−N(2)	93.93(9)
		C(3)−Re(1)−N(2)	92.73(9)
		C(1)−Re(1)−N(2)	176.23(9)
		O(4)−Re(1)−N(2)	83.84(7)
		N(1)−Re(1)−N(2)	82.48(7)

Table 3. *fac*-^{99m}Tc(OH$_2$)$_3$(CO)$_3^+$ Labeling Yields Prepared at 30 min at 70 °C with pH 7.4 at Various Concentrations with Ligands (2, 3, and 5)

ligand (M)	10^{-4}	10^{-5}	10^{-6}
^{99m}Tc(CO)$_3$(**5**), (**4a**)	>99%	95%	20%
^{99m}Tc(CO)$_3$(**2**), (**6a**)	>99%	90%	28%
	10^{-2}		
Single Pot[a]			
^{99m}Tc(CO)$_3$(pic)(**3**), (**7a**)	71		
Stepwise Addition[b]			
^{99m}Tc(CO)$_3$(pic)(**3**), (**7a**)	70		

[a] The picolinate (pic) at 10^{-5} M and **3** were added to directly to the same vial. [b] ^{99m}Tc(CO)$_3$ was added to a picolinate (10^{-5} M) solution and heated for 30 min, then followed by the addition of **3** and 30 min additional heating.

Table 4. Stability Studies of ^{99m}Tc Complexes (4a, 6a, and 7a) Formed with Ligands (2, 3, and 5) at Biological pH (7.4) at 37 °C and in Normal Mouse Serum at 37 °C

	1 h	2 h	4 h
pH = 7.4 at 37 °C			
^{99m}Tc(CO)$_3$(**5**), (**4a**)	>95	>95	>95
^{99m}Tc(CO)$_3$(**2**), (**6a**)	88	88	88
Normal Mouse Serum at 37 °C			
^{99m}Tc(CO)$_3$(**5**), (**4a**)	85	82	80
^{99m}Tc(CO)$_3$(**2**), (**6a**)	95	95	95
^{99m}Tc(CO)$_3$(pic)(**3**), (**7a**)	81	77	70

previously reported ^{99m}Tc labeling with similar ligands at higher temperatures (95 °C) (*28*, *38*, *43*). When the reaction of *fac*-[^{99m}Tc(CO)$_3$(H$_2$O)$_3$]$^+$ with **2** or **5** was carried out at 95 °C, decreased labeling yields of **4a** and **6a** and the corresponding amide cleavage product as a ^{99m}Tc(CO)$_3$ free carboxylate ligand complex were observed in the radiochromatograms. The pH of

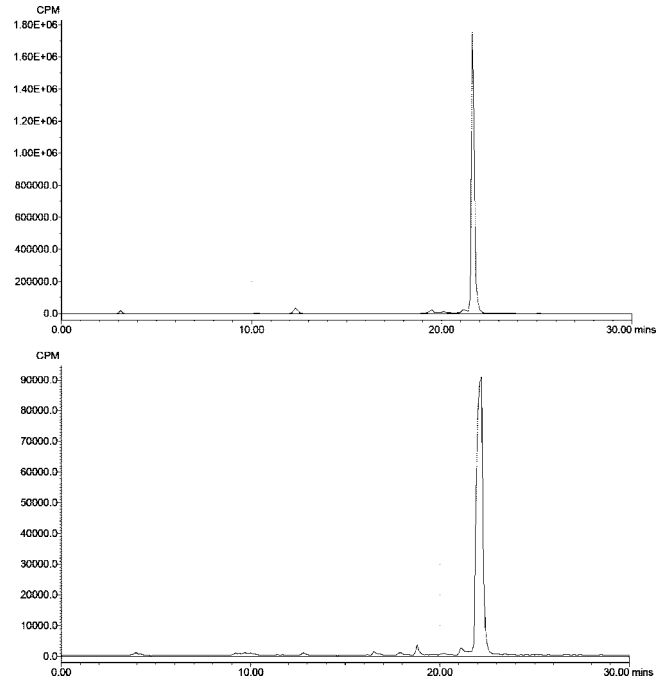

Figure 4. Radio HPLC of the ^{99m}Tc(CO)$_3$ complexes **4a** (top) and **6a** (bottom) formed with ligands **5** and **3**, respectively.

the labeling solution was also found to significantly impact the labeling yields observed. Reactions conducted in slightly acidic conditions between pH 6.5 and 7.4 would yield the desired product, **4a** and **6a**, without the appearance of cleavage products. Attempts to prepare **4a** and **6a** by direct addition of Isolink kit to the reaction mixture in 0.1 M phosphate buffer partially yielded the products and cleavage products. However, neutralization of the Isolink kit with hydrochloric acid to pH ~7.0 prior to addition to the ligand solution was found to be the imperative step in the labeling procedure as the kit solution is quite basic (pH ~11) during the production of *fac*-[^{99m}Tc(CO)$_3$(H$_2$O)$_3$]$^+$. Despite the combination of heating and pH effects impacting the labeling yields, carefully control of the reaction conditions afforded the desired compounds in good yield. The complexes **4a** and **6a** were further studied to determine the stability of the compound in solution at 37 °C in phosphate buffer (pH 7.4) and in mouse serum at 1, 2, and 4 h (Table 4). Both compounds, **4a** and **6a**, were found to be stable for up to four hours in the pH stability and the serum studies with minimal decomposition of complex or cleavage products observed in the radio-HPLC.

The "2 + 1" ^{99m}Tc complex, **7a**, with ligand **3** was prepared by similar methods to the rhenium analogues: one-pot and stepwise (Scheme 4). The preparation of **7a** by either method at 70 °C and pH 7.4 yielded a peak with a similar retention

time to the analogous rhenium complex (Table 3). Each of these methods had comparable labeling results of ~70%. The formation of the "2 + 1" complex **7a** required much higher concentrations (10^{-2} M) of **3** compared to the tridentate ligands **2** and **5**. HPLC purified complex **7a** was incubated in phosphate buffer (0.1 M, pH 7.4) and 37 °C to determine stability of the complex at 1, 2, and 4 h (Table 4). During this study, ligand **3** was observed to partially dissociate during incubation from complex **7a** to yield the intermediate species *fac*-^{99m}Tc(CO)$_3$(H$_2$O)(pic) as identified by retention time. Mouse serum studies further confirmed the instability of the "2 + 1" complex as multiple species in addition to the dissociation of **3** were observed in the radio-HPLC. Despite the previously reported and successful synthesis with the rhenium analogue (*41*), the "2 + 1" complex **7a** containing functionalized imidazole **3** may have limited application due to stability of the complex.

In vitro analysis were conducted with the ^{99m}Tc complexes (**4a**, **6a**) to determine cellular uptake with an androgen-positive DU-145 prostate cancer cell line. Incubation of the ^{99m}Tc complexes with the prostate cancer cells displayed a modest ~2% binding relative to control experiments. Although the uptake was much lower than expected, the decrease binding of these particular model compounds was anticipated. The changes in the chemical nature (i.e., polarity, steric bulk) of the native flutamide compound by introduction of the ^{99m}Tc complexes may have impacted the internalization of the modified compounds. Additionally, the functionalized flutamide complexes may also have decreased AR affinity due to poor metabolic conversion. The native flutamide compound is metabolized to the more potent α-hydroxyl antagonist, hydroxyflutamide, by the AR. Although it is uncertain the potential affect of the ^{99m}Tc complexes will have on the AR with limited internalization of the compounds, additional studies will be required.

CONCLUSION

The study presented here demonstrates the first $M(CO)_3$-linked flutamide compounds (M = Re, ^{99m}Tc) prepared for prostate cancer imaging. Although the amide bond of the flutamide was considered to be unstable due to hydrolytic cleavage, conditions were found to prepare the compounds in high yield. Reactions involving *fac*-^{99m}Tc(CO)$_3$(H$_2$O)$_3$ with tridentate ligands, cysteine and histidine, offered higher labeling yields and greater stability than the "2 + 1" approach utilizing a functionalized imidazole analogue. The tridentate ligands exhibited excellent radiochemical stability at 37 °C at physiological pH and in mouse serum. *In vitro* assays did show limited uptake in DU-145 prostate cancer cells. However, further investigations are required to conclusively determine internalization mechanism and androgen inhibition. Further studies involving metabolic activation of ^{99m}Tc(CO)$_3$ linked flutamide complexes to the hydroxyflutamide analogue and *in vivo* tumor model experiments are currently underway.

ACKNOWLEDGMENT

The authors wish to thank Mary Dyszlewski of Tyco Inc. for the Isolink kits and experimental protocols. The work was funded in part by the Department of Defense New Investigator Award Prostate Cancer (Grant # W81XWH0510556), the Department of Energy Radiochemistry Education Award Program (Grant # DEFG20705ID14-692IDNE006), and the Washington State University Start up fund. Funding for the X-ray facility at UI was provided by the M. J. Murdock Charitable Trust and NSF-EPSCoR.

Supporting Information Available: X-ray structural information for **7** (cif). This material is available free of charge via the Internet at http://pubs.acs.org.

LITERATURE CITED

(1) Jemal, A., Siegel, R., Ward, E., Murray, T., Xu, J. Q., and Thun, M. J. (2007) Cancer statistics, 2007. *Ca-a Cancer Journal for Clinicians 57*, 43–66.

(2) http://www.cancer.gov/cancertopics/pdq/treatment/prostate/patient.

(3) http://www.prostate-cancer.com/.

(4) Culig, Z. R., Klocker, H., Bartsch, G., Steiner, H., and Hobisch, A. (2003) Androgen receptors in prostate cancer. *J. Urol. 170*, 1363–1369.

(5) DeMarzo, A. M., Nelson, W. G., Isaacs, W. B., and Epstein, J. I. (2003) Pathological and molecular aspects of prostate cancer. *Lancet 361*, 955–964.

(6) Singh, S. M., Gauthier, S., and Labrie, F. (2000) Androgen receptor antagonists (antiandrogens): Structure-activity relationships. *Curr. Med. Chem. 7*, 211–247.

(7) Gao, W. Q., Kearbey, J. D., Nair, V. A., Chung, K. W., Parlow, A. F., Miller, D. D., and Dalton, J. T. (2004) Comparison of the pharmacological effects of a novel selective androgen receptor modulator, the 5 alpha-reductase inhibitor finasteride, and the antiandrogen hydroxyflutamide in intact rats: New approach for benign prostate hyperplasia. *Endocrinology 145*, 5420–5428.

(8) Urushibara, M., Ishioka, J., Hyochi, N., Kihara, K., Hara, S., Singh, P., Isaacs, J. T., and Kageyama, Y. (2007) Effects of steroidal and non-steroidal antiandrogens on wild-type and mutant androgen receptors. *Prostate 67*, 799–807.

(9) Yin, D. H., He, Y. L., Perera, M. A., Hong, S. S., Marhefka, C., Stourman, N., Krikovsky, L., Miller, D. D., and Dalton, J. T. (2003) Key structural features of nonsteroidal ligands for binding and activation of the androgen receptor. *Mol. Pharmacol. 63*, 211–223.

(10) Bohl, C. E., Chang, C., Mohler, M. L., Chen, J. Y., Miller, D. D., Swaan, P. W., and Dalton, J. T. (2004) A ligand-based approach to identify quantitative structure-activity relationships for the androgen receptor. *J. Med. Chem. 47*, 3765–3776.

(11) Miller, D. D., He, Y. L., Marhefka, C. A., Rakov, I. M., Hong, S. S., Hwang, D. J., Mohler, M. L., Kirichenko, S. N., Mustafa, S. M., Nair, V. A., Patil, R., Chung, K. W., Veverka, K. A., Steiner, M. S., Barnette, K. G., Yin, D. H., Gao, W. Q., Kearbey, J. D., Xu, H. P., Kim, J., Chen, J. Y., Bohl, C., and Dalton, J. T. (2003) Novel selective androgen receptor modulators (SARMs). *Abstr. Pap. Am. Chem. Soc. 226*, U1-U1.

(12) Isaacs, J. T., and Isaacs, W. B. (2004) Androgen receptor outwits prostate cancer drugs. *Nat. Med. 10*, 26–27.

(13) Parent, E. E., Dence, C. S., Jenks, C., Sharp, T. L., Welch, M. J., and Katzenellenbogen, J. A. (2007) Synthesis and biological evaluation of [F-18]bicalutamide, 4-[Br-76]bromobicalutamide, and 4-[Br-76]bromo-thiobicalutamide as nonsteroidal androgens for prostate cancer imaging. *J. Med. Chem. 50*, 1028–1040.

(14) Payen, O., Top, S., Vessieres, A., Brule, E., Plamont, M. A., McGlinchey, M. J., Muller-Bunz, H., and Jaouen, G. (2008) Synthesis and structure-activity relationships of the first ferrocenyl-aryl-hydantoin derivatives of the nonsteroidal antiandrogen nilutamide. *J. Med. Chem. 51*, 1791–1799.

(15) Nair, V. A., Mustafa, S. M., Mohler, M. L., Yang, J., Kirkovsky, L. I., Dalton, J. T., and Miller, D. D. (2005) Synthesis of irreversibly binding bicalutamide analogs for imaging studies. *Tetrahedron Lett. 46*, 4821–4823.

(16) Nair, V. A., Mustafa, S. M., Mohler, M. L., Fisher, S. J., Dalton, J. T., and Miller, D. D. (2004) Synthesis of novel iodo derived bicalutamide analogs. *Tetrahedron Lett. 45*, 9475–9477.

(17) Choe, Y. S., Lidstrom, P. J., Chi, D. Y., Bonasera, T. A., Welch, M. J., and Katzenellenbogen, J. A. (1995) Synthesis of 11-β-[F-18]fluoro-5-α-dihydrotestosterone and 11-β-[F-18]fluoro-19-nor-5-α-Dihydrotestosterone - preparation via halofluorination-reduction, receptor-binding, and tissue distribution. *J. Med. Chem. 38*, 816–825.

(18) Jurisson, S. S., and Lydon, J. D. (1999) Potential technetium small molecule radiopharmaceuticals. *Chem. Rev. 99*, 2205–2218.

(19) Das, T., Banerjee, S., Samuel, G., Bapat, K., Subramanian, S., Pillai, M. R. A., and Venkatesh, M. (2006) A novel ^{99m}Tc-labeled testosterone derivative as a potential agent for targeting androgen receptors. *Bioorg. Med. Chem. Lett. 16*, 5788–5792.

(20) Aebischer, N., Schibli, R., Alberto, R., and Merbach, A. E. (2000) Complete carbonylation of *fac*-$[Tc(H_2O)_3(CO)_3]^+$ under CO pressure in aqueous media: A single sample story. *Angew. Chem.-Int. Ed. 39*, 254.

(21) Alberto, R., Pak, J. K., van Staveren, D., Mundwiler, S., and Benny, P. (2004) Mono-, bi-, or tridentate ligands? The labeling of peptides with ^{99m}Tc-carbonyls. *Biopolymers 76*, 324–333.

(22) Alberto, R., Schibli, R., Egli, A., Schubiger, A. P., Abram, U., and Kaden, T. A. (1998) A novel organometallic aqua complex of technetium for the labeling of biomolecules: Synthesis of $[^{99m}Tc(OH_2)_3(CO)_3]^+$ from $[^{99m}TcO_4]^-$ in aqueous solution and its reaction with a bifunctional ligand. *J. Am. Chem. Soc. 120*, 7987–7988.

(23) Alberto, R., Schibli, R., Schubiger, A. P., Abram, U., Pietzsch, H. J., and Johannsen, B. (1999) First application of *fac*-$[^{99m}Tc(OH_2)_3(CO)_3]^+$ in bioorganometallic chemistry: Design, structure, and in vitro affinity of a 5-HT1A receptor ligand labeled with ^{99m}Tc. *J. Am. Chem. Soc. 121*, 6076–6077.

(24) Alberto, R., Schibli, R., Waibel, R., Abram, U., and Schubiger, A. P. (1999) Basic aqueous chemistry of $[M(OH_2)_3(CO)_3]^+$ (M = Re, Tc) directed towards radiopharmaceutical application. *Coord. Chem. Rev. 192*, 901–919.

(25) Alberto, R., Ortner, K., Wheatley, N., Schibli, R., and Schubiger, A. P. (2001) Synthesis and properties of boranocarbonate: A convenient in situ CO source for the aqueous preparation of $[^{99m}Tc(OH_2)_3(CO)_3]^+$. *J. Am. Chem. Soc. 123*, 3135–3136.

(26) He, H. Y., Lipowska, M., Xu, X. L., Taylor, A. T., Carlone, M., and Marzilli, L. G. (2005) $Re(CO)_3$ complexes synthesized via an improved preparation of aqueous *fac*-$[Re(CO)_3(H_2O)_3]^+$ as an aid in assessing ^{99m}Tc imaging agents. Structural characterization and solution behavior of complexes with thioether-bearing amino acids as tridentate ligands. *Inorg. Chem. 44*, 5437–5446.

(27) Schibli, R., La Bella, R., Alberto, R., Garcia-Garayoa, E., Ortner, K., Abram, U., and Schubiger, P. A. (2000) Influence of the denticity of ligand systems on the in vitro and in vivo behavior of ^{99m}Tc(I)-tricarbonyl complexes: A hint for the future functionalization of biomolecules. *Bioconjugate Chem. 11*, 345–351.

(28) Pak, J. K., Benny, P., Spingler, B., Ortner, K., and Alberto, R. (2003) N^{ε} functionalization of metal and organic protected L-histidine for a highly efficient, direct labeling of iomolecules with $[Tc(OH_2)_3(CO)_3]^+$. *Chem. Eur. J. 9*, 2053–2061.

(29) Hope, H. (1994) X-ray crystallography - a fast, first-resort analytical tool. *Prog. Inorg. Chem. 41*, 41–119.

(30) *SAINTPlus: v. 6.45a and v.7.23a, Data Reduction and Correction Program* (2003/2004) Bruker AXS, Madison, WI.

(31) *SADABS: v.2.01, v. 2004/1 an empirical absorption correction program* (2004) Bruker AXS Inc., Madison, WI.

(32) *SHELXTL: v. 6.14, Structure Determination Software Suite* (2004) Sheldrick, G. M.,Bruker AXS Inc., Madison, WI.

(33) Alves, S., Correia, J. D. G., Gano, L., Rold, T. L., Prasanphanich, A., Haubner, R., Rupprich, M., Alberto, R., Decristoforo, C., Santos, I., and Smith, C. J. (2007) In vitro and in vivo evaluation of a novel $^{99m}Tc(CO)_3$-pyrazolyl conjugate of cyclo-(Arg-Gly-Asp-D-Tyr-Lys). *Bioconjugate Chem. 18*, 530–537.

(34) Soderholm, A. A., Lehtovuori, P. T., and Nyronen, T. H. (2005) Three-dimensional structure-activity relationships of nonsteroidal ligands in complex with androgen receptor ligand-binding domain. *J. Med. Chem. 48*, 917–925.

(35) Van Dort, M. E., and Jung, Y. W. (2001) Synthesis and structure-activity studies of side-chain derivatized arylhydantoins for investigation as androgen receptor radioligands. *Bioorg. Med. Chem. Lett. 11*, 1045–1047.

(36) Jacobson, O., Bechor, Y., Icar, A., Novak, N., Birman, A., Marom, H., Fadeeva, L., Golan, E., Leibovitch, I., Gutman, M., Even-Sapir, E., Chisin, R., Gozin, M., and Mishani, E. (2005) Prostate cancer PET bioprobes: Synthesis of [F-18]-radiolabeled hydroxyflutamide derivatives. *Bioorg. Med. Chem. 13*, 6195–6205.

(37) Van Dort, M. E., and Jung, Y. W. (2004) Synthesis and structure-activity investigation of iodinated arylhydantoins and arylthiohydantoins for development as androgen receptor radioligands. *Bioorg. Med. Chem. Lett. 14*, 5285–5288.

(38) van Staveren, D. R., Benny, P. D., Waibel, R., Kurz, P., Pak, J. K., and Alberto, R. (2005) S-functionalized cysteine: Powerful ligands for the labelling of bioactive molecules with triaquatricarbonyltechnetium-99m(1+) $[^{99m}Tc(OH_2)_3(CO)_3]^+$. *Helv. Chim. Acta 88*, 447–460.

(39) Narayanan, S., Vangapandu, S., and Jain, R. (2001) Regiospecific synthesis of 2,3-disubstituted-L-histidines and histamines. *Bioorg. Med. Chem. Lett. 11*, 1133–1136.

(40) Kovalainen, J. T., Christiaans, J. A. M., Kotisaari, S., Laitinen, J. T., Mannisto, P. T., Tuomisto, L., and Gynther, J. (1999) Synthesis and in vitro pharmacology of a series of new chiral histamine H-3-receptor ligands: 2-(R and S)-amino-3-(1H-imidazol-4(5)-yl)propyl ether derivatives. *J. Med. Chem. 42*, 1193–1202.

(41) Mundwiler, S., Kundig, M., Ortner, K., and Alberto, R. (2004) A new [2 + 1] mixed ligand concept based on $[^{99(m)}Tc(OH_2)_3(CO)_3]^+$: a basic study. *Dalton Trans.* 1320–1328.

(42) Benny, P. D., Fugate, G. A., Morley, J. E., Twamley, B., and Trabue, S. (2008) Synthesis and characterization of 2,5-bis(benzylthio)-1,3,4-thiadiazole complexes with *fac*-$ReBr_3(CO)_3^{2-}$. *Inorg. Chim. Acta*. in press.

(43) van Staveren, D. R., Mundwiler, S., Hoffmanns, U., Pak, J. K., Spingler, B., Metzler-Nolte, N., and Alberto, R. (2004) Conjugation of a novel histidine derivative to biomolecules and labelling with $[^{99m}Tc(OH_2)_3(CO)_3]^+$. *Org. Biomol. Chem. 2*, 2593–2603.

BC8003183

Click Chemistry Functionalized Polymeric Nanoparticles Target Corneal Epithelial Cells through RGD-Cell Surface Receptors

Jiao Lu,[†] Meng Shi,[‡,§] and Molly S. Shoichet*[,†,‡,§]

Department of Chemistry, Department of Chemical Engineering and Applied Chemistry, and Institute for Biomaterials and Biomedical Engineering, Terrence Donnelly Center for Cellular and Biomolecular Research, University of Toronto, 160 College Street, Room 514, Toronto, Ontario M5S 3E1. Received July 24, 2008; Revised Manuscript Received November 17, 2008

Self-assembled polymeric nanoparticles modified with targeting ligands on the surface provide a means for localized cell delivery. To gain greater insight into the possibility of derivatizing poly(2-methyl-2-carboxytrimethylene carbonate-*co*-D,L-lactide) (poly(TMCC-*co*-LA)) nanoparticles using the Huisgen's 1,3 dipolar cycloaddition reaction, we synthesized amphiphilic copolymers comprising a hydrophobic poly(TMCC-*co*-LA) backbone and a hydrophilic poly(ethylene glycol) (PEG) pendant chain. By coupling amine-terminated PEG-azide to the carboxylic acid group of the poly(TMCC-*co*-LA) via EDC chemistry, an amphiphilic copolymer was formed. The poly(TMCC-*co*-LA)-*g*-PEG-N_3 self-assembled in aqueous solution and presented azide groups on the surface of the nanoparticles. Alkyne-modified KGRGDS peptides were synthesized and coupled to the azide-functionalized nanoparticles via Huisgen's 1,3 dipolar cycloaddition, which was catalyzed by copper sulfate and sodium ascorbate in aqueous solution. Using coumarin-modified lysine (K) of the KGRGDS peptide, fluorescence was used to determine that there were approximately 400 peptides bound to each nanoparticle. The bioactivity of the GRGDS nanoparticle was confirmed with a competitive cell attachment assay using rabbit corneal epithelial cells. This GRGDS-nanoparticle system may be suitable for targeted drug delivery.

INTRODUCTION

Peptides have attracted significant attention because of their diverse biological functionalities. For example, the Arg-Gly-Asp (RGD) containing motif is known to be vital for integrin-receptor mediated cell attachment, which influences cell migration, growth, and differentiation (*1*). The specific binding between RGD-containing peptides and their integrin receptors also plays an important role in cell targeting. The application of RGD-modified nanoparticles (NP) for endothelium targeting has been broadly studied (*2, 3*), specifically in the context of tumor vasculature, which undergoes continuous angiogenesis. RGD peptides can be used to prevent integrins from binding to their respective ligands, thereby causing apoptosis of endothelial cells of newly formed blood vessels (*4*).

Few studies have explored the use of RGD-containing nanoparticles for targeted delivery to the eye, yet fibronectin accumulates in the corneal epithelium after injury (*5*). In wound healing, the binding between RGD motifs on fibronectin and the $\alpha_v\beta_1$ integrin on the surface of corneal epithelial cells plays an important role in cell spreading and migration upon stimulation by epidermal growth factor (EGF) (*6*). Several features of the cornea profoundly reduce the efficiency of gene transfer or drug absorbance (*7, 8*) including the low permeability of the intact epithelial layer and the rapid secretion of tears. However, the delivery of ophthalmic drugs using polymeric nanoparticles engineered with targeting molecules, such as RGD-containing peptides, is promising for the treatment of a wide range of corneal epithelial defects such as corneal neovascularization, dystrophies, neurotrophic keratopathy, recurrent erosion, and dry eye syndrome, among others (*9*). Thus, coupling RGD-containing peptides to nanoparticles may provide a method for targeted drug delivery to the eye after injury.

Building on our previous experience with self-assembling polymers (*10*), we investigated the use of "click chemistry" to surface-functionalize novel nanoparticles with RGD peptides. The term "click chemistry" was first introduced by Sharpless et al. in 2001 to included those reactions that are broad in scope, have high yields, and are simple in product isolation, stereospecific, and compatible with both organic and aqueous reaction conditions (*11*). While "click chemistry" has come to include Diels−Alder among other coupling chemistries, Sharpless defined it as two small units being joined together with heteroatom links and fulfilling the above requirements. Among all the carbon−heteroatom bond formation reactions, the copper-catalyzed Huisgen 1,3-dipolar cycloaddition is the premier example of click chemistry and is known for its high degree of selectivity and stability (*11*). Moreover, the resulting triazole ring itself has been shown to possess a variety of biological functions including anti-HIV, antibacterial, and potent antihistamine activity (*12*−*14*). To take advantage of this click chemistry, we synthesized alkyne-KGRGDS and azide polymeric nanoparticles and reacted them together.

On the basis of the previous development of a novel copolymer backbone of poly(2-methyl-2-carboxytrimethylene carbonate-*co*-D,L-lactide) (poly(TMCC-*co*-LA)) (*15*), we coupled amine-terminated PEG-azide via EDC chemistry to the carboxylic acid groups of TMCC. The known properties of PEG, including water solubility, hydophilicity, and resistance to protein adsorption, make the polymer-*graft*-PEG structure highly desirable for biomaterial and drug delivery applications (*16*). This poly(TMCC-*co*-LA)-*g*-PEG-N_3 copolymer self-assembled to nanoparticles in aqueous solution and presented azide groups on the surface for further modification with alkyne-KGRGDS peptides by click chemistry (Scheme 1). The bioactivity of the peptide-modified nanoparticles was tested with rabbit corneal

* To whom correspondence should be addressed. 160 College, Room 514 Toronto, Ontario, M5S 3E1. Phone: 416-978-1460. Fax: 416-978-4317. E-mail: molly.shoichet@utoronto.ca.

[†] Department of Chemistry.

[‡] Department of Chemical Engineering and Applied Chemistry.

[§] Institute for Biomaterials and Biomedical Engineering.

10.1021/bc8003167 CCC: $40.75 © 2009 American Chemical Society
Published on Web 12/18/2008

Scheme 1. Immobilization of Alkyne-KGRGDS Peptides on Nanoparticles by the Aqueous Huisgen'S 1,3 Dipolar Cycloaddition Reaction, Catalyzed by Copper Sulfate and Sodium Ascorbate (Room Temperature, 5 h)

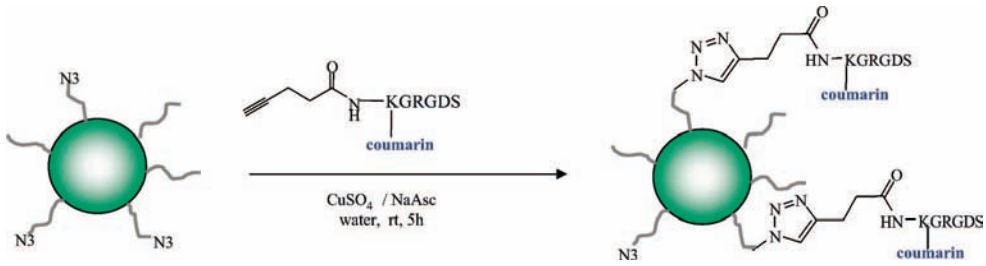

epithelial cells using a competitive cell attachment assay. To the best of our understanding, this is the first time that peptide-modified nanoparticles have been designed for targeted delivery to corneal epithelial cells.

EXPERIMENTAL PROCEDURES

Materials and Methods. The ^{1}H NMR spectra were recorded at 400 MHz at room temperature using a Varian Auto X8308−400 spectrometer. All the chemical shifts are in ppm. Molecular weights and polydispersity indices were measured by gel permeation chromatography (GPC) in THF relative to polystyrene standards on a system equipped with two-column sets (Viscotck GMHHR-M and Viscoteck GMHHR-H) and a triple detector array (TDA302) at room temperature with a flow rate of 0.6 mL/min THF eluent. Dynamic light scattering (DLS) measurements were performed using the Brookhaven 90Plus Particle Size Analyzer (Brookhaven Instruments, USA), which was operated at 647 nm at a scattering angle of 90°. Nanoparticle samples were suspended at 0.5 mg/mL in distilled water before the measurement. Cumulant analysis of light scattering data was used to estimate the hydrodynamic diameter and polydispersity of the nanoparticles. When the polydispersity equals zero, the sample is monodisperse, and as polydispersity increases so does the width of the distribution. As a general rule, nanoparticles are considered to have narrow size distributions when polydispersity is less than 0.025, and cumulant analysis works best when polydispersity is $\leq$0.3. (Additional information is available from Brookhaven.) The dry nanoparticle size was estimated by measuring the average diameter of 50 nanoparticles from images taken in the scanning transmission electron microscope (STEM) mode of the Hitachi S-5200 scanning electron microscope system operating at 30 kV. Samples were prepared by placing one drop of self-assembled nanoparticle solution (0.5 mg/mL in distilled water) on a carbon support film (Electron Microscopy Sciences, PA, USA). Excess solution was drained, and the sample was allowed to air-dry. The presence of an azide functional group was characterized by Nicolet Avatar 370 FTIR (Thermo Instruments Canada Inc.). The RGD-containing peptides were synthesized by solid-phase synthesis using a Pioneer Peptide Synthesis System (Foster City, CA, USA) using standard Fmoc/ HATU chemistry. The synthesized peptides were purified by HPLC (Jupiter 5 μ, C 18, 300 Å, 250 × 21.2 mm) using a gradient mixture of acetonitrile with 0.1% TFA and water. The gradient of acetonitrile with 0.1% TFA increased from 10% (10 min) to 30% (30 min) and finally to 90% (10 min). The Sephadex G-25 column was prepared according to the following procedures: Sephadex G-25 beads was soaked in 0.01 M PBS buffer at pH 7.4 overnight prior to packing the column (2.5 × 10 cm). The column was washed with the same PBS buffer for 1 h before use. The flow rate is determined by gravity. The Sepharose C4B column (5 × 15 cm) was prepared in the same manner as Sephades G-25 column, except distilled water was used instead of PBS buffer. Fluorescence intensity of coumarin was measured by a fluorescent microplate reader (SpectraMax GeminiEM, Molecular Device, USA) at excitation and emission wavelengths of 340 and 405 nm, respectively. The concentration of nanoparticles was measured by their absorbance in Bradford reagent (*10*) at 595 nm using a microplate reader (VersaMax, Molecular Devices, USA). Triplicate samples of equal volumes of NP solution and Bradford reagent were mixed in a clear 96-well plate at room temperature. After incubating for 30 s, a reading was taken.

All solvents and reagents were purchased from Sigma-Aldrich and were used as received, unless otherwise noted. Amino acids including Fmoc-Lys(MCA)-OH were purchased from Novabiochem (CA, USA). Activators and resins were obtained from Applied Biosystems (CA, USA). The peptides for cell attachment assays, GRGDS (97.8% pure, 490.48 g/mol), were acquired from Genscript Corp (New Jersey, USA). The SIRC-rabbit corneal epithelial cell line, CCL-60, was obtained from American type Culture Collection (ATCC, USA). Difunctional *tert*-butoxycarbonyl-protected amine-PEG-activated acid was purchased from Nektar Theraputics (Birmingham, AL, USA). All regenerated cellulose (RC) membranes were purchased from Spectrum Laboratories Rancho Dominguex (CA, USA). All the dialysis procedures used 4 L of distilled water as the exchange solvent. The water was replaced every 2 h for the first 8 h. 96-well reacti-bind amine-binding, maleic anhydride activated plates and the blocking buffer were purchased from Pierce. The Quant iT Picogreen dsDNA assay kit and the protocol are available from Invitrogen (Burlington, ON). The protocol document number is MP 07581, revised December 20th, 2005.

Synthesis of PEG-Azide (PEG-N_3). As shown in Scheme 2, difunctional *tert*-butoxycarbonyl-protected amine-PEG-activated acid (BocNH-PEG-NHS; **1**; 3446 Da, 1.00 g) and azido-octaethyleneglycol-amine (438.52 Da, 0.50 g) were dissolved in 10 mL of DMF and stirred for 24 h at room temperature. The reaction mixture was purified by dialysis against distilled water at room temperature for 24 h using a regenerated cellulose (RC) membrane with a molecular weight cutoff (MWCO) of 1 kDa. The dialyzed solution was freeze−dried to yield BocNH-PEG-N_3 **2** (0.92 g, 82% yield) as a white solid, which was then deprotected in 6 mL of 70% TFA aqueous solution. After 2 h, the reaction mixture was diluted with 18 mL of water and purified again by dialysis, as described above. After freeze−drying, a white solid product **3** (0.59 g, 64%) was recovered. The presence of the terminal azide group and the C−O bond were characterized by a stretching frequencies at 2103 cm^{-1} and 1012 cm^{-1}, respectively, in the FTIR spectrum. MALDI-TOF-MS: 3727.2 (calc. 3727.52). ^{1}H NMR (D_2O): δ 3.68 (s). For ^{1}H NMR and FTIR spectra, see Supporting Information Figure S1 for compound **2** and Figures S2 and S11 for compound **3**.

Synthesis of Poly(TMCC-*co*-LA)-*g*-PEG-N_3. The synthesis of PEG-grafted copolymer was carried out as illustrated in Scheme 3. The poly(TMCC-*co*-LA) **4** was synthesized by bulk copolymerization as previously reported (*10*). Copolymer **4** (100 mg) was dissolved in DMF (5 mL) and 10 mM MES buffer

Scheme 2. Synthesis of H_2N-PEG-N_3 by Reacting NHS-Activated PEG Chains with Amine-Terminated Octaethylene Glycol-Azide Followed by BOC Deprotection

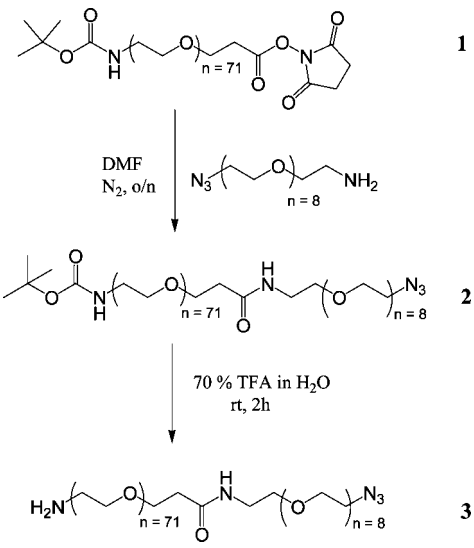

(0.5 mL, pH 5.5). *N*-ethyl-*N*′-(3-dimethylaminopropyl)carbodiimide hydrochloride (EDC, 10 wt %) and *N*-hydroxysulfosuccinimide (sulfo-NHS, 10 wt%) were then added, and the reaction solution was stirred at room temperature for 30 min. The PEG azide **3** (50 mg), dissolved in 0.5 M borate buffer (1 mL, pH 9.0), was slowly added to the activated copolymer solution under stirring. The reaction mixture was incubated at room temperature for 24 h, after which it was dialyzed against distilled water using an RC membrane at a MWCO of 12−14 kDa. The excess PEG was removed using a Sepharose C4B column equilibrated with distilled water. The collected fractions containing polymers were freeze−dried to give a white solid (55 mg, 50% yield). ^{1}H NMR (DMSO): δ 0.99 (br s, CH_3 from TMCC), 1.42−1.46 (m, CH_3 from LA), 3.49 (s, PEG), 4.19 (br s, methylene from TMCC), and 5.17−5.19 (m, CH from LA). ^{1}H NMR spectra of poly(TMCC-*co*-LA) **4** and poly(TMCC-*co*-LA)-*g*-PEG-azide **5** are shown in Supporting Information Figures S3 and S4.

Self-Assembly of Polymers to Nanoparticles by Dialysis. The nanoparticles **6** were prepared by self-assembly of poly(TMCC-*co*-LA)-*g*-PEG-azide by memberane dialysis, as previously reported (*15*). Briefly, copolymer **5** (15 mg) was dissolved in 1.5 mL of DMF/borate buffer (0.5 M, pH 9.0) at a volume ratio of 1.425 to 0.075. The solution was dialyzed against distilled water using a dialysis membrane with a MWCO of 12−14 kDa at room temperature for 8 h.

Synthesis of Alkyne-Modified KGRGDS. The synthesis of alkyne-modified KGRGDS peptide is shown in Scheme 4. The alkyne-modified KGRGDS was synthesized by solid-phase synthesis 4-pentynoic acid (0.20 g, 2 mmol) was activated by *N*,*N*′-diisopropyl carbodiimide (DIC, 1.24 mL, 8 mmol) in 10 mL of CH_2Cl_2 under N_2 for 30 min. Alkyne-KGRGDS was added, and the mixture was stirred at room temperature for another 2 h. The resin was filtered and washed with 20 mL each of dichloromethane, methanol, and isopropyl alcohol (IPA).

The resin recovered from the previous step was dissolved in TFA/water (9.5 mL/0.5 mL, v/v) and stirred for 2 h. The peptide dissolved in solution was separated from the resin by vacuum filtration and concentrated by rotary evaporation. The crude oily product was precipitated in 100 mL of cold ether and stored in a −80 °C freezer overnight. The precipitated white peptide (65 mg, 65% yield) was recovered by centrifugation and dried under N_2.

The product was further purified by HPLC to yield 50 mg of the final product as a white solid (yield 76%). The final product was confirmed by ^{1}H NMR and mass spectrometry (MS). ^{1}H NMR (D_2O, 400 MHz): δ 1.28−1.83 (m, 10H), 2.31 (s, 1H), 2.44 (m, 4H), 2.77−2.95 (m, 2H), 3.10−3.16 (t, 2H, J = 6 Hz), 3.18−3.22 (t, 2H, J = 6 Hz), 3.82−3.97 (m, 11H), 4.10−4.16 (dd, 1H, J_1 = 5 Hz, J_2 = 8 Hz), 4.26−4.32 (dd, 1H, J_1 = 5 Hz, J_2 = 8 Hz), 4.48−4.51 (dd, 1H, J_1 = 4 Hz, J_2 = 5 Hz), 4.79−4.81 (m, 1H) 6.30 (s, 1H), 6.99−7.02 (m, 2H), 7.62−7.64 (m, 1H). ESI-MS (MNa^+): 936.4 (calc. 937.38). (The same syntheses and characterization methods were used for the following additional peptides studied and are described in the Supporting InformationFigures S1−S8: alkyne-KGRGDS, scrambled alkyne-KGRDGS, alkyne-GRGDS, and scrambled alkyne-GRDGS.)

Immobilization of KGRGDS on Nanoparticles by Click Chemistry. Alkyne-modified KGRGDS, at concentrations of 25, 50, and 100 μg/mL, was reacted with poly(TMCC-*co*-LA)-*g*-PEG-azide nanoparticles (1.875 mg/mL) at room temperature in distilled water under catalysis with copper sulfate (0.6 μmol/mL) and sodium ascorbate (3.0 μmol/mL). The reaction mixture was stirred at room temperature for 1, 3, and 5 h (see Results and Discussion). It was then purified through a Sephadex G-25 column equilibrated with 0.01 M PBS buffer at pH 7.4.

Cell Attachment Assay. *GRGDS-Modified Cell Culture Plates.* The peptide sequence GRGDS in borate buffer (pH 9.0, 0.5 M) was placed in a 96-well reacti-bind amine-binding, maleic anhydride activated plates (100 μL/well) at a concentration of 100 μg/mL. The plate was incubated on a shaker at room temperature overnight, and the peptide solution was then removed. Protein blocking buffer (200 μL/well) was added and incubated for 1 h at room temperature to quench any remaining reactive maleic anhydride groups and block remaining open sites on the plate surface.

Preparation of Cells. SIRC-rabbit corneal epithelial cells were cultured in tissue culture plates with minimum essential medium α (α-MEM) containing 10% FBS, 1% penicillin/streptomycin, and 1% glutamine in an incubator (37 °C, 5% CO_2, 100% humidity). Before harvesting, cells were incubated with fresh cell culture medium containing with 10 ng/mL of epidermal growth factor (EGF) overnight.

Competitive Cell Attachment Assay. To test the binding affinity of the GRGDS-modified nanoparticles, the attachment of cells to GRGDS-modified cell culture wells was tested after preincubation with either GRGDS-nanoparticles or scrambled GRDGS-nanoparticles and compared to the cell attachment observed when cells were preincubated in soluble GRGDS. Specifically, a cell suspension of cultured rabbit corneal epithelial cells with an equal volume of 1 or 10 μg/mL of GRGDS or 2.0 mg/mL of peptide-modified nanoparticles with peptide concentration of 5.5 μg/mL in PBS buffer (0.01 M, pH 7.4) was preincubated at 37 °C for 30 min before plating into wells (1×10^4 cells/well, 100 μL). The cells were incubated at 37 °C for another 4 h after plating. The wells were then washed three times with fresh cell culture medium before quantifying the number of attached cells using the PicoGreen assay. It was assumed that every cell contained 7.7 pg of DNA.

RESULTS AND DISCUSSION

Synthesis of Poly(TMCC-*co*-LA)-*g*-PEG. The amphiphilic copolymer, poly(TMCC-*co*-LA)-*g*-PEG-azide, was designed specifically for the creation of RGD-nanoparticles by combining strategies of polymeric self-assembly and click chemistry of bioconjugation in one process. The copolymer is biodegradable and biocompatible for in vivo applications, amphiphilic with the ability to self-assemble into ordered structures, and capable

Scheme 3. Synthesis of Poly(TMCC-*co*-LA)-*g*-PEG-Azide[a]

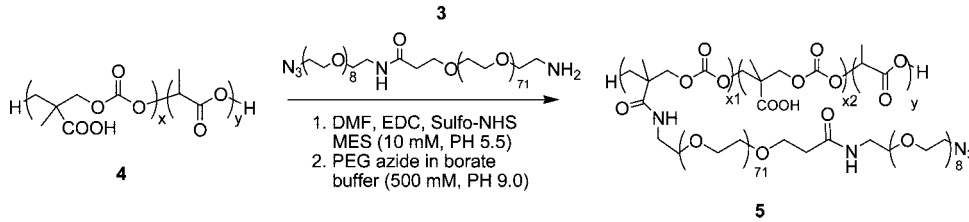

[a] The carboxylic acid groups on the copolymer backbone were first activated with *N*-(3-dimethylaminopropyl)-*N*′-ethylcarbodiimide hydrochloride (EDC) and *N*-hydroxysulfosuccinimide (Sulfo-NHS) for 30 min. Then, amine-terminated PEG azide was covalently bound under basic conditions overnight.

Scheme 4. Synthesis of the Alkyne-Modified KGRGDS Peptides[a]

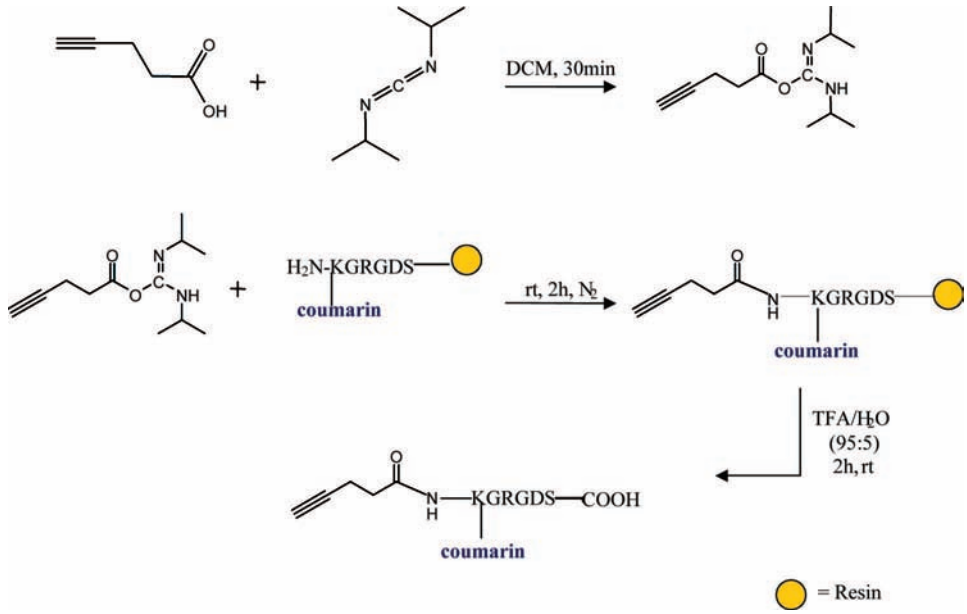

[a] 4-Pentynoic acid was activated by *N*,*N*′-diisopropylcarbodiimide (DIC) for 30 min and reacted with amine-terminated peptides. The peptide was cleaved from the resin using a 95% TFA aqueous solution for 2 h at room temperature.

of click chemistry chemistry due to the presence of azide groups at the PEG terminus.

The number average molecular weight and polydispersity of poly(TMCC-*co*-LA) were determined by GPC (see Supporting Information Figure S10), relative to polystyrene standards in THF, to be 30.4 kDa and 2.7, respectively. The molar percentage of TMCC in the copolymer was determined from ^{1}H NMR data to be 9.3% by comparing the integrated peak of TMCC methylene (4.18 ppm) with that of the LA methine (5.13−5.19 ppm). This number is slightly lower than the feed ratio (TMCC/D,L-lactide 10/45), where each D,L-lactide monomer contains two repeat units. This is probably because LA is more reactive than TMCC in the copolymerization, leading to an enrichment of LA in the copolymer (*17*). The random copolymer composition was estimated from ^{1}H NMR and GPC data to be poly(TMCC)$_{32}$-*co*-(LA)$_{310}$.

After copolymerization, the carboxylic acid groups along the copolymer chain were deprotected, allowing for further functionalization with PEG-N_3 using EDC chemistry. This resulted in amphiphilic copolymers of poly(TMCC-*co*-LA)-*g*-PEG-azide with well-defined hydrophobic and hydrophilic segments. The ratio of PEG grafted to poly(TMCC)$_{32}$-*co*-(LA)$_{310}$ was estimated by comparing the integrated peak areas from the ^{1}H NMR spectrum of PEG methylene (3.49 ppm) to that of the TMCC methylene (4.18 ppm). On average, there was approximately one PEG chain grafted to every poly(TMCC)$_{32}$-*co*-(LA)$_{310}$ backbone. The number average molar mass of poly(TMCC)$_{32}$-*co*-(LA)$_{310}$-*g*-PEG was calculated according to

$$M_{\text{n (poly(TMCC}-co-\text{LA)}-g-\text{PEG)}} = M_{\text{n (backbone)}} + (M_{\text{n (PEG)}} \times \#\text{ of PEG per copolymer backbone}) \quad (1)$$

Given that $M_{\text{n(backbone)}}$ is 30.4 kDa, $M_{\text{n(PEG)}}$ is 3.40 kDa and there is one PEG chain per copolymer backbone; the $M_{\text{n (poly(TMCC-}co\text{-LA)-}g\text{-PEG)}}$ is estimated at 33.8 kDa.

Estimation of the Molecular Weight of Nanoparticles (M_{NP}) and the Number of Chains Aggregated in a Nanoparticle (N_{agg}). When poly(TMCC-*co*-LA)-*g*-PEG was dissolved in DMF with 5% borate buffer and dialyzed against water (see Experimental Procedures), the hydrophobic poly(TMCC-*co*-LA) backbone self-assembled to form the nanoparticle core, while the hydrophilic PEG chains interacted with the surrounding water to form the nanoparticle shell. As observed by dynamic light scattering (DLS), the resulting self-assembled nanoparticles had an average diameter of 130.8 nm and a polydispersity index (PDI) of 0.2897, which indicates that the nanoparticles are polydisperse. By scanning transmission electron microscopy, the average diameter of the nanoparticles was 87.4 ± 12.5 nm (n = 50 nanoparticles, mean ± s.d.). The STEM image has been previously reported (*10*). The diameter measured by STEM is smaller than that measured by DLS, because STEM imaged the dry nanoparticles, whereas DLS detected the hydrated nanoparticles in aqueous solution. While the DLS data

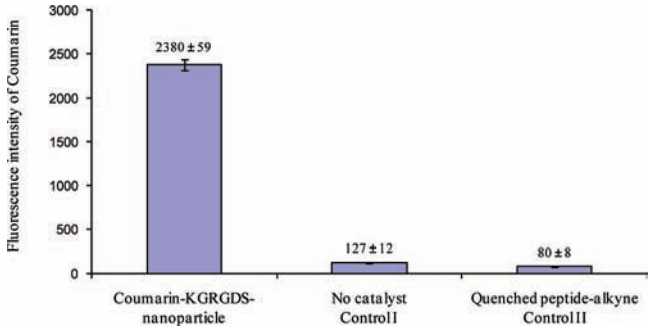

Figure 1. The fluorescence intensity of coumarin was readily detected on azide-functionalized nanoparticles that had reacted with alkyne-peptide in the presence of copper sulfate and sodium ascorbate. In control I, the identical incubation between peptides and nanoparticles was repeated in the absence of copper sulfate and sodium ascorbate, demonstrating the importance of the catalyst for successful peptide modification. In control II, peptides were preincubated with 4-azidoaniline for 3 h before incubating with nanoparticles and catalyst, demonstrating that alkyne groups were quenched and unavailable for reaction with nanoparticle-azide.

are a better measure of the hydrated nanoparticle diameter, the standard deviation of the mean calculated from the STEM data is likely a better indication of the polydispersity of the nanoparticles (*10*). Assuming that the dried nanoparticle is a hard sphere with negligible porosity, the molar mass of the nanoparticle M_{NP} can be calculated from

$$M_{NP} = \frac{4\pi R^2 N_A}{3\upsilon_2} \quad (2)$$

where R is the radius of the nanoparticle (43.7 ± 6.3 nm from STEM); υ_2 is the partial specific volume of the polymer, which is estimated at 0.95 mL/g, and N_A is Avogadro's constant (6.02×10^{23}) (*18*). The average nanoparticle aggregation number, N_{aggs}, can be estimated as

$$N_{agg} = M_{NP}/M_{n(\text{poly(TMCC-}co\text{-LA)-}g\text{-PEG})} \quad (3)$$

using the value of M_{NP} calculated from eq 2.

Thus, one nanoparticle comprises approximately (6.5 ± 0.4) $\times 10^3$ polymer chains.

Immobilization of Alkyne-KGRGDS on Azido-Nanoparticles by Click Chemistry. In the self-assembled nanoparticle system, the azide-alkyne Huisgen's cycloaddition reaction was designed to occur at the interface between the azide-PEG corona of the nanoparticles and the aqueous phase in which alkyne-peptides were dissolved. After the amphiphilic copolymer self-assembled into nanoparticles, the hydrophilic segments oriented outward to the water phase. The terminal azide groups are accessible to alkyne-functionalized molecules in the aqueous solution, enabling click chemistry at the PEG terminus of the self-assembled nanoparticles. Coumarin-modified alkyne-KGRGDS was reacted with azide-nanoparticles at room temperature for 5 h in the presence of copper sulfate and sodium ascorbate. To confirm the Huisgen's 1,3 dipolar cycloaddition reaction, two controls were carried out: (1) the reaction was carried out in the absence of catalyst; and (2) the reaction was carried out after quenching the alkyne groups on KGRGDS with a large excess of 4-azidoaniline.

The fluorescence of the coumarin-modified alkyne-KGRGDS was used to measure the success of the reaction between peptide-alkyne and azido-nanoparticle. As shown in Figure 1, nanoparticles incubated with an excess of alkyne-KGRGDS showed a strong fluorescent signal at (2380 ± 59) indicating that the fluorescent peptide was coupled to the nanoparticles. Neither the control group lacking the copper sulfate/ascorbic acid (127 ± 12) nor that with quenched peptide-alkyne (80 ± 8) showed significant fluorescence. Together, these data confirmed the successful Huisgen's 1,3 dipolar cycloaddition reaction between peptide-alkyne and azido-nanoparticle. The hydrodynamic diameter of the nanoparticles (130.8 nm), determined by DLS, did not change significantly after peptide modification (126.2 nm) where the PDI was 0.2879. This suggests that the nanoparticles do not aggregate as a result of peptide modification.

Estimation of the Amount of Peptides Per Nanoparticle. To estimate the amount of peptide coupled per nanoparticle, the concentrations of both peptide and nanoparticle were independently determined, relative to standard curves with known concentrations of peptides and nanoparticles. The concentration of peptide was measured by the fluorescence intensity associated with coumarin. The concentration of nanoparticles was measured by their absorbance in Bradford reagent (*10*) at 595 nm using a microplate reader. The number of peptides per nanoparticle (n) was estimated according to eq 4

$$n = \frac{\text{peptide[M]}}{\text{nanoparticle[M]}} \quad (4)$$

To determine the optimum reaction time and the maximum number of peptides that can be conjugated per nanoparticle, both the click chemistry reaction time and the alkyne-KGRGDS concentration were varied. In Figure 2a, azido-nanoparticles reacted with 7-fold molar excess of alkyne-KGRGDS catalyzed by copper sulfate and sodium ascorbate at room temperature for 1, 3, and 5 h. The amount of peptide per nanoparticle increased between 1 and 3 h, after which a plateau of 439 ± 11 (mean ± standard deviation) peptides per nanoparticle was achieved, demonstrating that the reaction was complete after 3 h. In Figure 2b, azido-nanoparticles reacted for 5 h with various concentrations of alkyne-KGRGDS, where the peptide to copolymer molar ratio increased from 2:1 to 7:1. As the peptide to polymer ratio increased, the amount of peptide bound per nanoparticle increased from 229 ± 2 to 406 ± 21. According to our calculation, each NP has approximately 6500 PEG groups, but only ~440 peptides immobilized. This low reaction yield may be explained by not all PEG chains having azido groups and some of the azido groups not being available for reaction due to steric interactions. For example, some of the azido groups may have been buried within the PEG corona. Although the yield for azide-alkyne Huisgen's cycloaddition reaction of small molecules is normally above 80% (*19*−*21*), the kinetics of this reaction are very different between small molecules and polymers. As reported, the yield of this reaction dropped below 50% when the cycloaddition reaction was performed between two polymers (*22*). The yield is expected to drop further with polymeric nanoparticles, where accessibility of the azido groups is limited by entangled polymer chains and steric hindrance associated with solid particles. The number of immobilized peptides per nanoparticle is comparable to literature values (*23*). While many of the PEG-azido groups are left unreacted, they are largely inert in cell culture, as has been previously shown with azido-sugars on the cell surface that were used for bioorthogonal chemistry (*28*). However, the click chemistry in this nanoparticle system is advantageous over other coupling methods described in the literature because of the specificity, speed, and relative ease of the reaction. While the Huisgen 1,3 dipolar cycloaddition reaction requires the introduction of alkyne and azide groups, the common thiol-maleimide Michael-type addition chemistry also requires the introduction of free thiol and maleimide groups. However, the ligation reaction of the thiol-maleimide occurs in the narrow pH range 6.5−7.5. If the pH is too high, hydrolysis of the maleimide will occur; if the pH is too low, the reaction will occur very slowly or not at all. Thiol groups are very reactive toward various electrophiles and rapidly deteriorate when in solution. A protecting group is usually introduced, followed by a deprotection step (*24*−*26*).

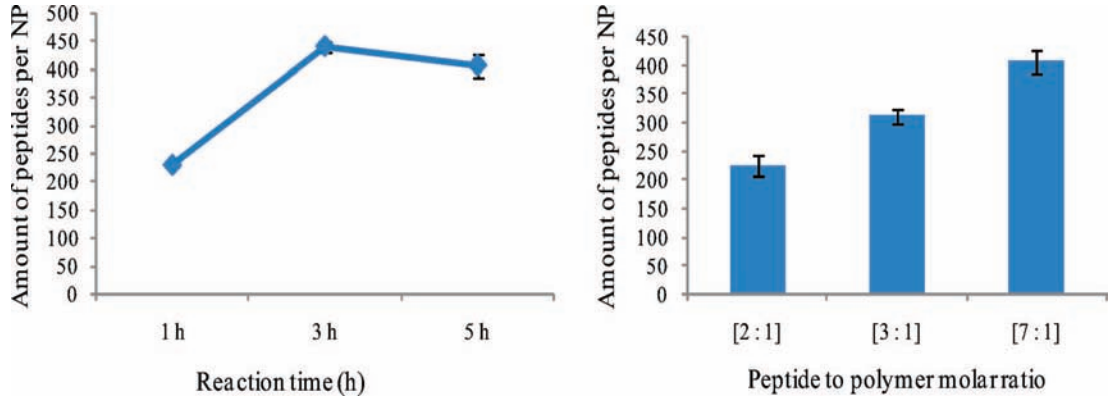

Figure 2. (a) Nanoparticles reacted with 7-fold molar excess of alkyne-KGRGDS catalyzed by copper sulfate and sodium ascorbate at room temperature for 1 h (229 ± 2), 3 h (439 ± 11), and 5 h (406 ± 21). (b) Nanoparticles reacted for 5 h with various concentrations of alkyne-KGRGDS where the peptide to copolymer molar ratio increased from 2:1 (224 ± 18) to 3:1 (311 ± 13) to 7:1 (406 ± 21). The numbers in parentheses are the means ± standard deviations for the number of peptides per nanoparticle.

Unlike the 3 h required for the click chemistry described herein, alternative coupling mechanisms, such as amine−aldehyde conjugation in the presence of the reducing agent, $NaBH_3CN$, has the disadvantage of requiring four days of reaction time (*27*) and the use of the highly toxic $NaBH_3CN$ reducing agent. Short reaction time, broad pH range, mild reaction conditions, and a simple purification process demonstrate the broad utility of click chemistry. Importantly, the click chemistry also allows us to couple the bioactive molecules (in this case, GRGDS peptides) in water after nanoparticle formation, thereby avoiding exposure of peptides (or proteins) to potentially denaturing organic solvents.

A clinically useful nanoparticle carrier for drug delivery, in addition to allowing surface modification, also has to be nontoxic, amenable to sterile filtration, and stable over a long period of time (*15*). Our nanoparticle system fulfills these criteria.

Cell Attachment Assay. Maleic anhydride functionalized 96-well plates were coated with amine-terminated GRGDS-containing peptides, and then, any unreacted sites were blocked with blocking buffer to ensure that GRGDS peptides were the only binding sites for corneal epithelial cells. To test the bioactivity of immobilized NP-GRGDS and the binding affinity between NP-GRGDS and corneal epithelial cells, a competitive cell attachment assay was performed, as shown quantitatively in Figure 3 and qualitatively in Supporting Information Figure S9. The number of corneal epithelial cells that adhered to the GRGDS-modified culture wells was quantified, comprising the positive control, as shown in Figure 3. The negative control, where the 96-well plate lacked the GRGDS peptide, showed very little cell adhesion. To better understand the binding affinity of this interaction, the epithelial cells were preincubated with soluble GRGDS peptides prior to plating on GRGDS-modified surfaces. As shown, cell attachment reduced from 70% to 40% compared to the positive control as the concentration of soluble GRGDS increased from 1 μg/mL to 10 μg/mL, indicating that the RGD integrin receptors on the cells were at least partially responsible for cell attachment. To determine the binding affinity of GRGDS bound to the nanoparticles, we repeated the preincubation study, replacing soluble GRGDS with NP-GRGDS.

When preincubated with NP-GRGDS prior to plating, fewer cells attached to the GRGDS-modified plate, similar to that observed when cells were preincubated with soluble GRGDS. The cell attachment was both significantly less than the positive control and similar to the negative control (where the cell plates lacked GRGDS). Importantly, the cell surface integrin−RGD interaction was confirmed with two controls: scrambled NP-GRDGS and NPs with blocked azido groups (i.e., no peptides). When the epithelial cells were preincubated with either scrambled NP-GRDGS or blocked NP-azido groups, the NPs did not sufficiently block the epithelial cell-surface integrin receptors, and thus, there were significantly more cells attached to the GRGDS-modified cell culture surfaces than had been observed when cells were preincubated with NP-GRGDS samples. However, there were fewer adherent cells after preincubation with either scrambled NP-GRDGS (1446 ± 377) or NP-blocked azido groups (1305 ± 215) relative to the positive control (1958 ± 214), which suggests some nonspecific binding of nanoparticles to cells.

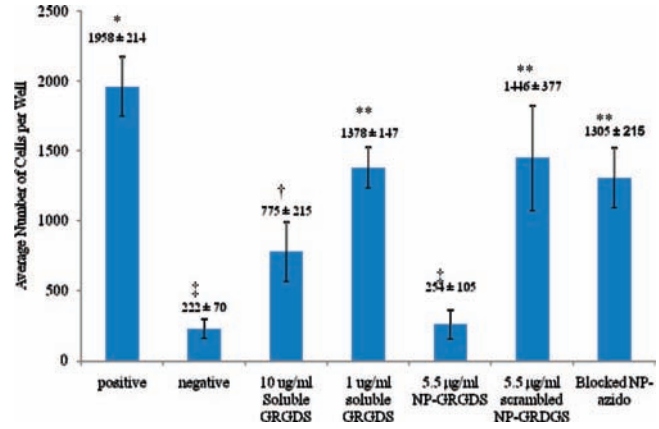

Figure 3. Competitive assay of rabbit corneal epithelial cell surface receptors to RGD. The positive control demonstrates a large number of cells bind to GRGDS-coated well-plate surfaces after a 4 h incubation. The negative control shows that few epithelial cells bind to unmodified well surfaces, demonstrating an RGD-mediated cell attachment. Competitive inhibition of cell attachment was demonstrated with soluble GRGDS (at concentrations of 10 and 1 μg/mL) where the number of adherent cells to the well plates decreased with increased GRGDS concentration. The bioactivity of the click chemistry bound NP-GRGDS (5.4 μg/mL) was confirmed by the similar competitive inhibition of cell attachment. The binding affinity of this interaction was verified with the scrambled NP-GRDGS (5.4 μg/mL) and nanoparticles with blocked azido groups where cell attachment was not inhibited. Shown are the mean ± standard deviation for $n = 3$ independent tests of triplicate assays; ANOVA was used for statistical analysis. The Posthoc analysis showed that there is a statistical difference ($p < 0.05$) between the different symbols.

Interestingly, NP-GRGDS samples seemed to be more effective at inhibiting epithelial attachment to the GRGDS-modified plates than soluble GRGDS, as demonstrated in Figure 3. While there is some nonspecific cell adhesion to the nanoparticles, as was observed with the NP controls, the NP-

GRGDS sample significantly reduced cell adhesion relative to the NP controls and the soluble GRGDS, indicating that additional mechanisms are required to explain the results. It is unlikely that there was any cytotoxicity associated with the remaining copper sulfate due to the small amount used, with our thorough purification methodology and literature demonstrating cell viability at 100−1000× greater copper concentrations (*29*). Thus, there are at least two possible explanations. The presence of multiple peptides on a given nanoparticle suggests multivalent interactions with the cells or avidity, as has been suggested by others (*23*). Alternatively, some of the soluble GRGDS peptides may have been internalized by the cells via an integrin-independent pathway, or even if by an integrin-dependent pathway, the integrin may have been recycled on the cell surface and available to interact with substrate-bound GRGDS-cell culture plates. A similar mechanism was observed by Castel et al. who showed that, at a concentration of 10 μg/mL, the RGD peptide targeted for $\alpha_v\beta_3$ was internalized in both α_v-integrin expressing and nonexpressing melanoma cells by an integrin-independent fluid-phase endocytosis pathway that did not alter the number of functional integrin receptors at the cell surface (*30*). This internalization occurred within 30 min at 37 °C. In our studies, relative to the soluble GRGDS, the NP-GRGDS effectively limited cell adhesion to the GRGDS coated well plates likely because it could not be internalized in the time frame studied due to the large particle size. Using confocal microscopy and fluorescent GRGDS-nanoparticles, we had no evidence for internalization (data not shown).

In order to improve the specificity and binding affinity of these GRGDS- nanopaticles, the synergistic proline-histidine-serine-arginine-asparagine (PHSRN) sequence can be similarly coupled to our nanoparticles, with the appropriate spacer between the two peptides (*31*)for optimal specificity with $\alpha_v\beta_1$ intergrins (*32*). Importantly, the platform conjugation technology described is applicable to a variety of peptides.

CONCLUSIONS

GRGDS peptides were successfully immobilized on self-assembled, polymeric nanoparticles using the azide-alkyne Huisgen 1,3 cycloaddition reaction. This chemistry is efficient and broadly applicable to a diversity of molecules. The azide-alkyne reaction was complete within 3 h and resulted in approximately 400 conjugated peptides per nanoparticle, allowing for interactions with cells that have $\alpha_v\beta_1$-integrin receptors up-regulated. The size of the nanoparticles detected by DLS was unchanged after peptide modification. The covalently bound NP-GRGDS peptides maintained their bioactivity and binding affinity with rabbit corneal epithelial cells relative to scrambled NP-GRDGS controls. These NP-GRGDS samples are small enough for sterile filtration and may be useful for targeted delivery to the injured eye.

ACKNOWLEDGMENT

We thank Professor Mitchell Winnik and Daniel Majonis for the use of their GPC, Dr. Neil Coombs for STEM imaging, and Ryan Wylie for helpful discussions. We are grateful to NSERC and CIHR for funding through the Collaborative Health Research Program.

Supporting Information Available: ^{1}H NMR data for compounds **2**−**5** and all the peptides, the cell images taken by inverted microscope, the GPC data for poly(TMCC-*co*-LA), and the IR spectrum for compound **3**. This material is available free of charge via the Internet at http://pubs.acs.org.

LITERATURE CITED

(1) Ruoslahti, E. (1996) RGD and other recognition sequences for integrins. *Annu. Rev. Cell Dev. Biol. 12*, 697–715.

(2) Kim, J. H., Kim, Y. S., Park, K., Kang, E., Lee, S., Nam, H. Y., Kim, K., Park, J. H., Chi, D. Y., Park, R. W., Kim, I. S., Choi, K., and Kwon, I. C. (2008) Self-assembled glycol chitosan nanoparticles for the sustained and prolonged delivery of antiangiogenic small peptide drugs in cancer therapy. *Biomaterials 29*, 1920–1930.

(3) Zhang, N., Chittasupho, C., Duangrat, C., Siahaan, T. J., and Berkland, C. (2007) PLGA nanoparticle-peptide conjugate effectively targets intercellular cell-adhesion molecule-1. *Bioconjugate Chem. 19*, 145–152.

(4) Pasqualini, R., Koivunen, E., and Ruoslahti, E. (1997) α_v Integrins as receptors for tumor targeting by circulating ligands. *Nat. Biotechnol. 15*, 542–546.

(5) Fujikawa, L. S., Foster, C. S., Harrist, T. J., Lanigan, J. M., and Colvin, R. B. (1981) Fibronectin in healing rabbit corneal wounds. *Lab Invest. 45*, 120–129.

(6) Nishida, T., Nakamura, M., Murakami, J., Mishima, H., and Otori, T. (1992) Epidermal growth factor stimulates corneal epithelial cell attachment to fibronectin through a fibronectin receptor system. *Invest. Ophthalmol. Vis. Sci. 33*, 2464–2469.

(7) Rosenblatt, M. I., and Azar, D. T. (2004) Gene therapy of the corneal epithelium. *Int. Ophthalmol. Clin. 44*, 81–90.

(8) Carlson, E. R., Liu, C. Y., Yang, X., Gregory, M., Ksander, B., Drazba, J., and Perez, V. L. (2004) In vivo gene delivery and visualization of corneal stromal cells using an adenoviral vector and keratocyte-specific promoter. *Invest, Ophthalmol. Vis. Sci. 45*, 2194–2200.

(9) Tong, Y. C., Chang, S. F., Liu, C. Y., Kao, W., Huang, C. H., and Liaw, J. (2007) Eye drop delivery of nano-polymeric micelle formulated genes with cornea-specific promoters. *J. Gene Med. 9*, 956–966.

(10) Shi, M., Wosnick, J. H., Ho, K., Keating, A., and Shoichet, M. S. (2007) Immuno-polymeric nanoparticles by Diels-Alder chemistry. *Angew. Chem., Int. Ed. 46*, 6126–6131.

(11) Kolb, H. C., Finn, M. G., and Sharpless, K. B. (2001) Click chemistry: diverse chemical function from a few good reactions. *Angew. Chem. Int. Ed. 40*, 2004–2021.

(12) Alvarez, R., VelAzquez, S., San-Felix, A., Aquaro, S., De Clercq, E., Perno, C. F., Karlsson, A., Balzarini, J., and Camarasa, M. J. (1994) 1,2,3-Triazole-[2′,5′-bis-O(-tert-butyldimethylsilyl)-β-D-ribofuranosyl]-3′-spiro-5″-(4′-amino-l″,2″-oxathiole 2″, 2″-dioxide)(TSAO) analogues: synthesis and anti-HIV-1 activity. *J. Med. Chem. 37*, 4185–4194.

(13) Alagarsamy, V., Meena, S., Ramaseshu, K. V., Solomon, V. R., and Kumar, T. (2007) 4-Cyclohexyl-1-substituted-4*H*-[1,2,4]triazolo [4,3-*a*] quinazolin-5-ones: novel class of mH1-antihistaminic agents. *Chem. Biol. Drug Des. 70*, 158–163.

(14) Aufort, M., Herscovici, J., Bouhours, P., Moreau, N., and Girard, C. (2008) Synthesis and antibiotic activity of a small molecules libraryof 1,2,3-triazole derivatives. *Bioorg. Med. Chem. Lett. 18*, 1195–1198.

(15) Shi, M., and Shoichet, M. S. (2008) Furan-functionalized copolymers for targeted drug delivery: characterization, self-assembly and drug encapsulation. *J. Biomater. Sci.: Polym. Edit. 15*, 1143–1157.

(16) Vlerken, L., Vyas, T., and Amiji, M. (2007) Poly(ethylene glycol)-modified nanocarriers for tumor-targeted and intracellular delivery. *Pharm. Res. 24*, 1405–1414.

(17) Chen, X., McCarthy, S. P., and Gross, R. A. (1998) Synthesis, modification, and characterization of L-lactide/2,2-[2-pentene-1,5-diyl]trimethylene carbonate copolymers. *Macromolecules 31*, 662–668.

(18) Jeong, B., Kibbey, M. R., Birnbaum, J. C., Won, Y. Y., and Gutowska, A. (2000) Thermogelling biodegradable polymers with hydrophilic backbones: PEG-*g*-PLGA. *Macromolecules 33*, 8317–8322.

(19) Lee, L. A., Mitchell, M. L., Huang, S. J., Fokin, V. V. K., Sharpless, B., and Wong, C. H. (2003) A potent and highly selective inhibitor of human-1,3-fucosyltransferase via click chemistry. *J. Am. Chem. Soc. 125*, 9588–9589.

(20) Perez-Balderas, F., Ortega-Munoz, M., Morales-Sanfrutos, J., Hernandez-Mateo, F., Calvo-Flores, F. G., Calvo-Asin, J. A., Isac-Garcia, J., and Santoyo-Gonzalez, F. (2003) Multivalent neoglycoconjugates by regiospecific cycloaddition of alkynes and azides using organic-soluble copper catalysts. *Org. Lett. 5*, 1951–1954.

(21) Seo, T. S., Li, Z., Ruparel, H., and Ju, J. (2002) Click chemistry to construct fluorescent oligonucleotides for DNA sequence. *J. Org. Chem. 68*, 609–612.

(22) Parrish, B., Breitenkamp, R. B., and Emrick, T. (2005) PEG- and peptide-grafted aliphatic polyesters by click chemistry. *J. Am. Chem. Soc. 127*, 7404–7410.

(23) Montet, X., Funovics, M., Montet-Abou, K., Weissleder, R., and Josephson, L. (2006) Multivalent effects of RGD peptides obtained by nanoparticle display. *J. Med. Chem. 49*, 6087–6093.

(24) Herron, J. N., Gentry, C. A., Davies, S. S., Wei, A., and Lin, J. (1994) Antibodies as targeting moieties: affinity measurements, conjugation chemistry and applications in immunoliposomes. *J. Controlled Release 28*, 155–166.

(25) Mercadal, M., Domingo, J. C., Petriz, J., Garcia, J., and De Madariaga, M. A. (1999) A novel strategy affords high-yield coupling of antibody to extremities of liposomal surface-grafted PEG Chains. *Biochim. Biophys. Acta 1418*, 232–238.

(26) Koning, G. A., Morselt, H. W., Velinova, M. J., Donga, J., Gorter, A., Allen, T. M., Zalipsky, S., Kamps, J. A., and Scherphof, G. L. (1999) Selective transfer of a lipophilic prodrug of 5-fluorodeoxyuridine from immunoliposomes to colon cancer cells. *Biochim. Biophys. Acta. 1420*, 153–167.

(27) Xiong, X. B., Mahmud, A., Uludag, H., and Lavasanifar, A. (2007) Conjugation of arginine-glycine-aspartic acid peptides to poly(ethylene oxide)-b-poly(ε-caprolactone) micelles for enhanced intracellular drug delivery to metastatic tumor cells. *Biomacromolecules 8*, 874–884.

(28) Saxon, E., and Bertozzi, C. R. (2000) Cell surface engineering by a modified Staudinger reaction. *Science 430*, 873–877.

(29) Chaderjian, W. B., Chin, E. T., Harris, R. J., and Etcheverry, T. M. (2005) Effect of copper sulfate on performance of a serum-free CHO cell culture process and the level of free thiol in the recombinant antibody expressed. *Biotechnol. Prog. 21*, 550–553.

(30) Castel, S., Pagan, R., Mitjans, J., Piulats, J., Goodman, S., Jonczyk, A., Huber, H., Vilaró, S., and Reina, M. (2001) RGD peptides and monoclonal antibodies, antagonists of αv-Integrin, enter the cells by independent endocytic pathways. *Lab. Invest. 81*, 1615–1626.

(31) Aota, S., Nomizu, M., and Yamada, K. M. (1994) The short amino acid sequence Pro-His-Ser-Arg-Asnin human fibronectin enhances cell-adhesive function. *J. Biol. Chem. 269*, 24756–24761.

(32) Craig, J. A., Rexeisen, E. L., Mardilovich, A., Shroff, K., and Kokkoli, E. (2008) Effect of linker and spacer on the design of a fibronectin-mimitic peptide evluated via cell studies and AFM adhesion forces. *Langmuir 24*, 10282–10292.

BC8003167

SUPPORTING INFORMATION FOR

Click Chemistry Funtionalized Polymeric Nanoparticles Target Corneal Epithelial Cells through RGD-cell Surface Receptors

Jiao Lu[1], Meng Shi[2,3] and Molly S. Shoichet* [1,2,3]

Department of Chemistry[1], Department of Chemical Engineering and Applied Chemistry[2],

Institute for Biomaterials and Biomedical Engineering[3]

Terrence Donnelly Center for Cellular and Biomolecular Research

University of Toronto

160 College Street Room 514, Toronto, ON M5S 3E1

Key words: Click chemistry, Nanoparticles, RGD peptides, functional biodegradable polymers, poly(trimethylene carbonate), poly(lactide), Rabbit corneal epithelial cell

*To whom correspondence should be addressed: 160 College, Room 514 Toronto, Ontario M5S 3E1. Phone: 416-978-1460 Fax: 416-978-4317 E-mail: molly.shoichet@utoronto.ca

S1. BOCNH-PEG-N_3

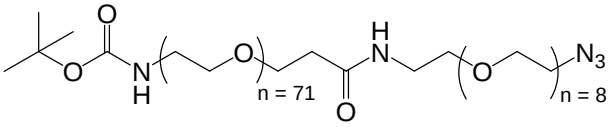

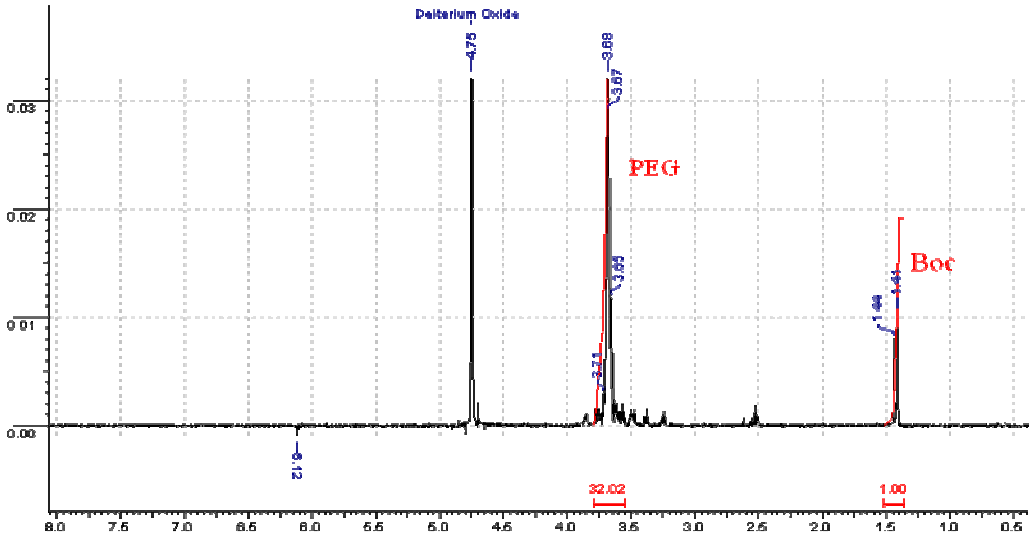

S2. H_2N-PEG-N_3

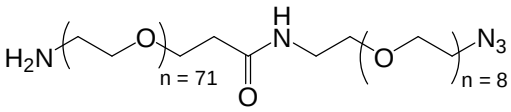

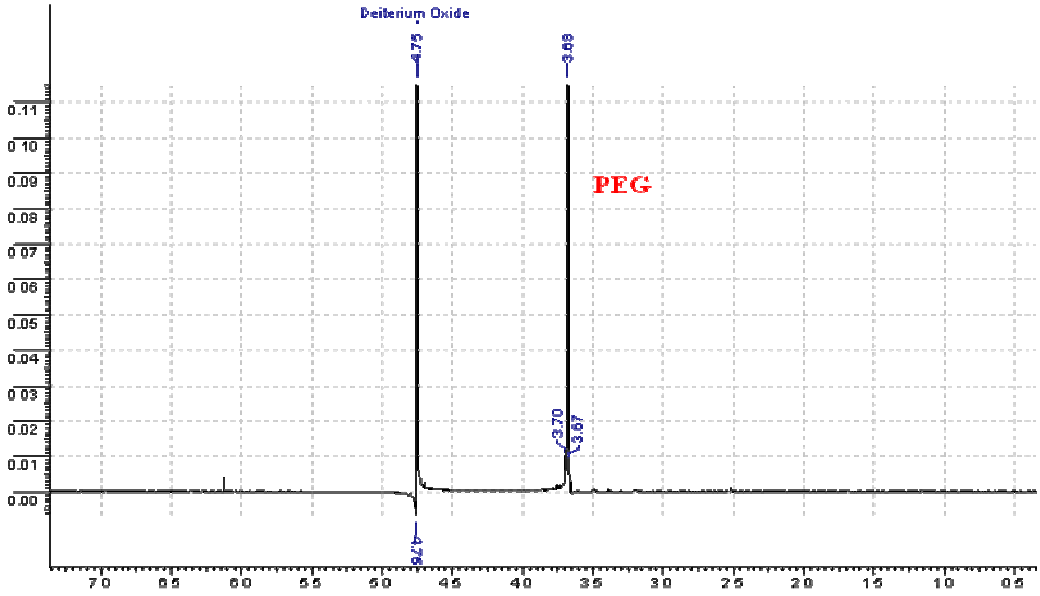

S3. POLY(TMCC*co*-LA)

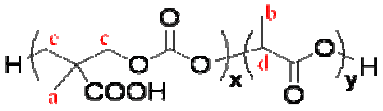

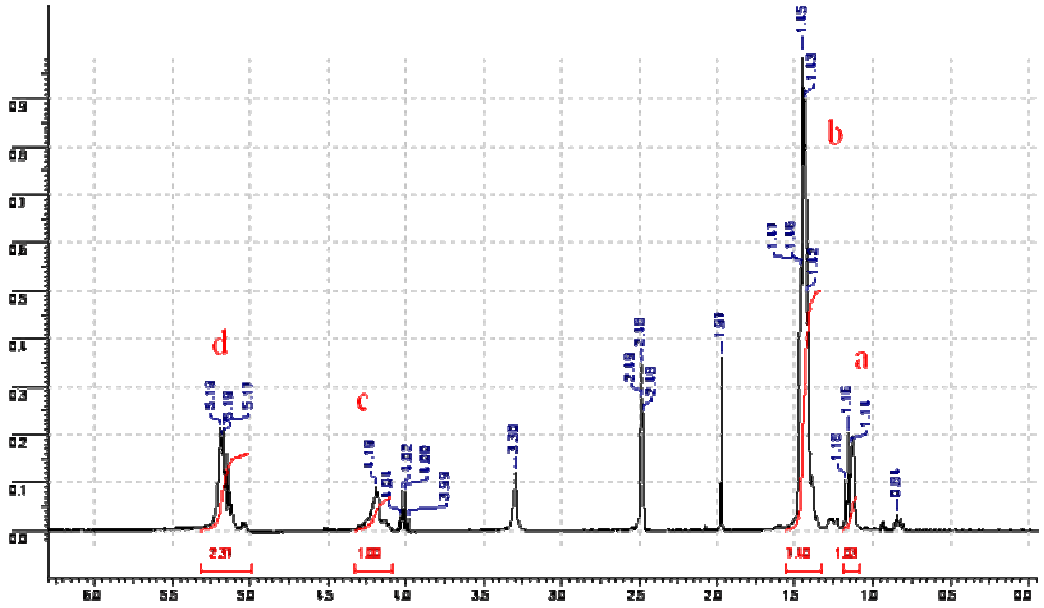

^{1}H (DMSO) δ 1.14-1.18 (br s, CH_3 from TMCC), 1.42-1.47 (m, CH_3 from LA), 4.19 (br s, methylene from TMCC) and 5.17-5.19 (m, CH from LA)

S4. POLY(TMCC*co*-LA)-G PEG-N_3

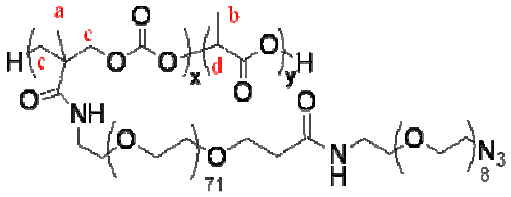

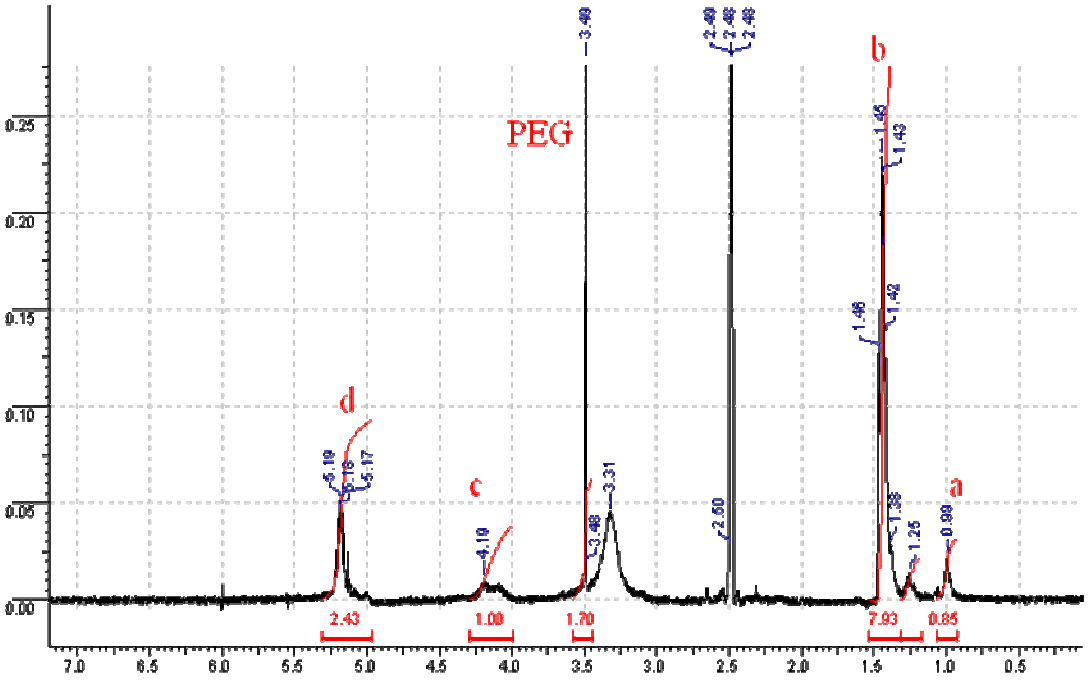

S5. ALKYNE-KGRGDS

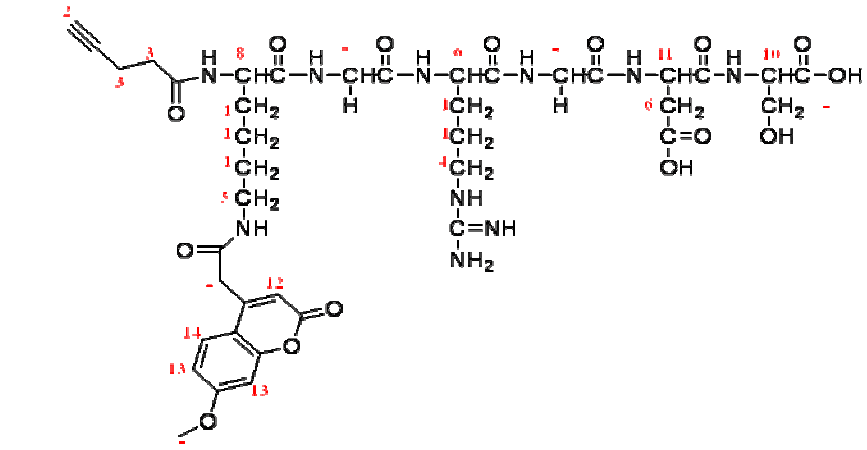

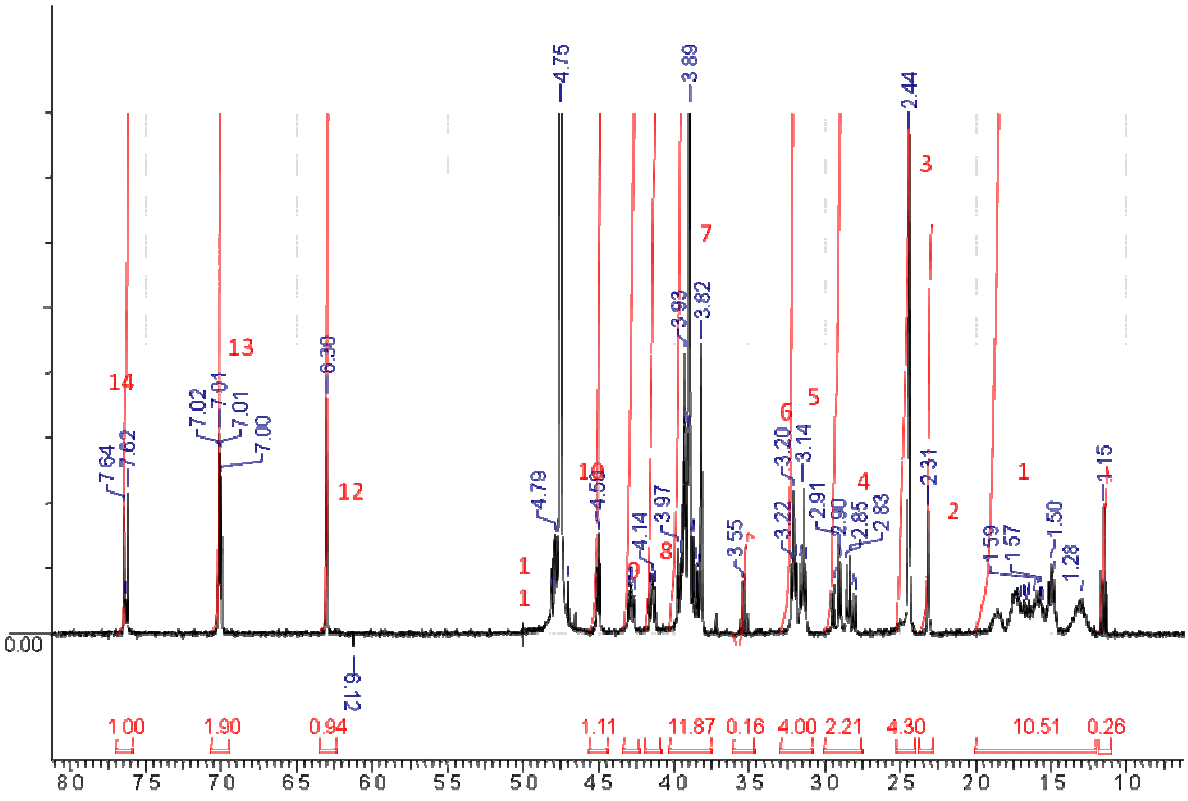

^{1}H NMR (D_2O, 400 MHz): δ 1.28-1.83 (m, 10H), 2.31 (s, 1 H), 2.44 (m, 4 H), 2.75-2.95 (m, 2 H), 3.10-3.16 (t, 2 H, J = 6 Hz), 3.18-3.22 (t, 2 H, J = 6 Hz), 3.82-3.97 (m, 11 H), 4.10-4.16 (dd, 1 H, J_1 = 5 Hz, J_2 = 8 Hz), 4.26-4.32 (dd, 1 H, J_1 = 5 Hz, J_2 = 8 Hz), 4.48-4.51 (dd, 1 H, J_1 = 4 Hz, J_2 = 5 Hz), 4.79 (m, 1H) 6.30 (s, 1H), 7.00-7.02 (m, 2 H), 7.62-7.64 (m, 1H). ESI-MS (MNa^+): 936.4 (calc. 937.38).

S6. SCRAMBLED ALLKYNE-KGRG

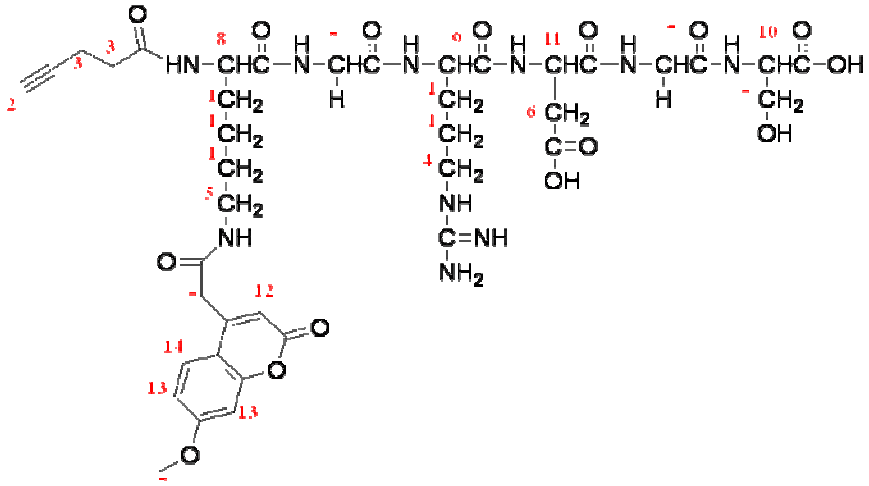

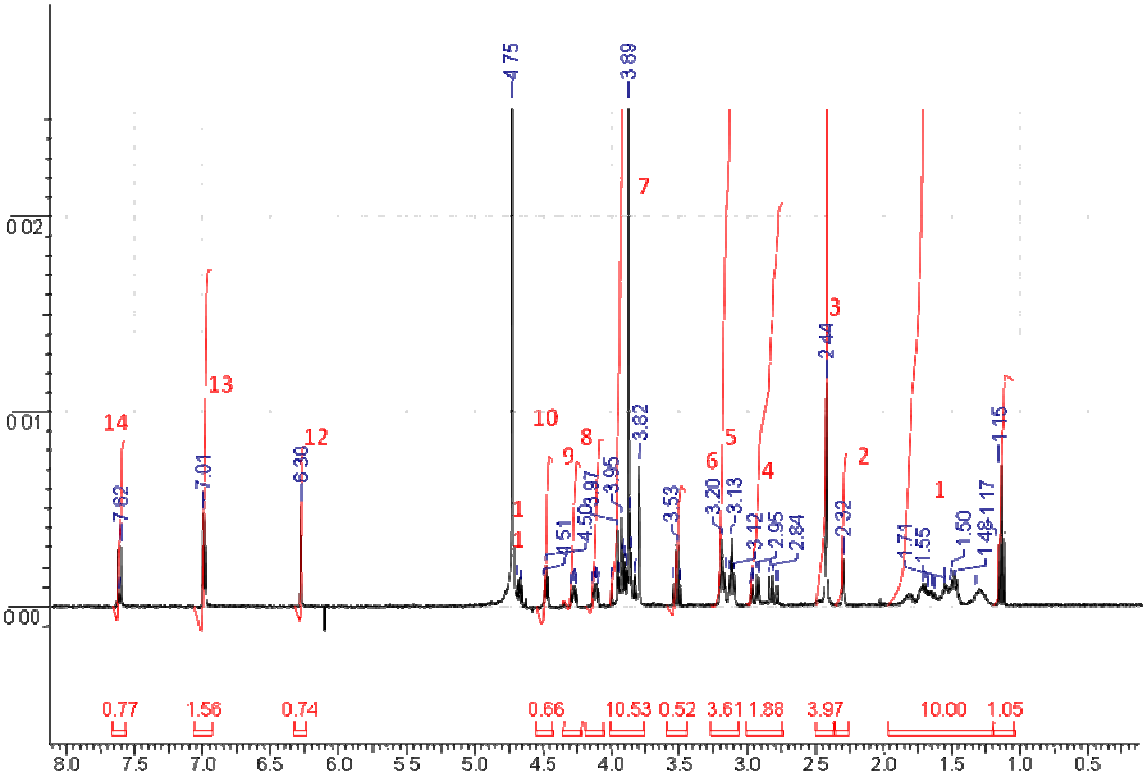

^{1}H NMR (D_2O, 400 MHz): δ 1.48-1.83 (m, 10H), 2.32 (s, 1 H), 2.44 (m, 4 H), 2.77-2.95 (m, 2 H), 3.10-3.16 (t, 2 H, J = 6 Hz), 3.18-3.22 (t, 2 H, J = 6 Hz), 3.82-3.97 (m, 11 H), 4.10-4.16 (dd, 1 H, J_1 = 5 Hz, J_2 = 8 Hz), 4.26-4.32 (dd, 1 H, J_1 = 5 Hz, J_2 = 8 Hz), 4.48-4.51 (dd, 1 H, J_1 = 4 Hz, J_2 = 5 Hz), 4.70-4.74 (m, 1H) 6.30 (s, 1H), 6.99-7.02 (m, 2 H), 7.62-7.64 (m, 1H). ESI-MS (MNa^+): 936.4 (calc. 937.38).

S7. ALKYNE-GRGDS

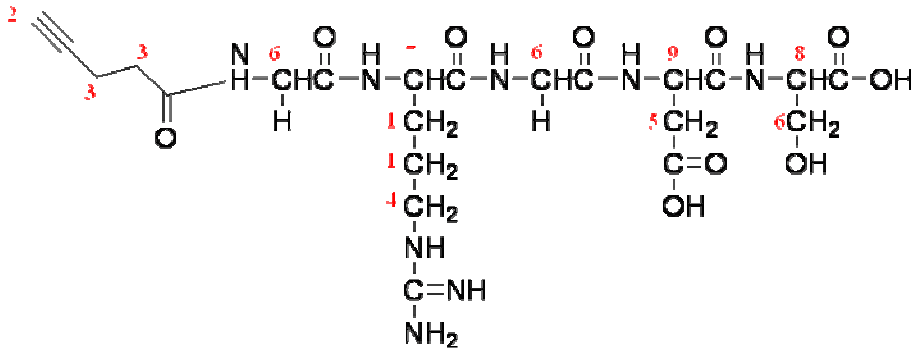

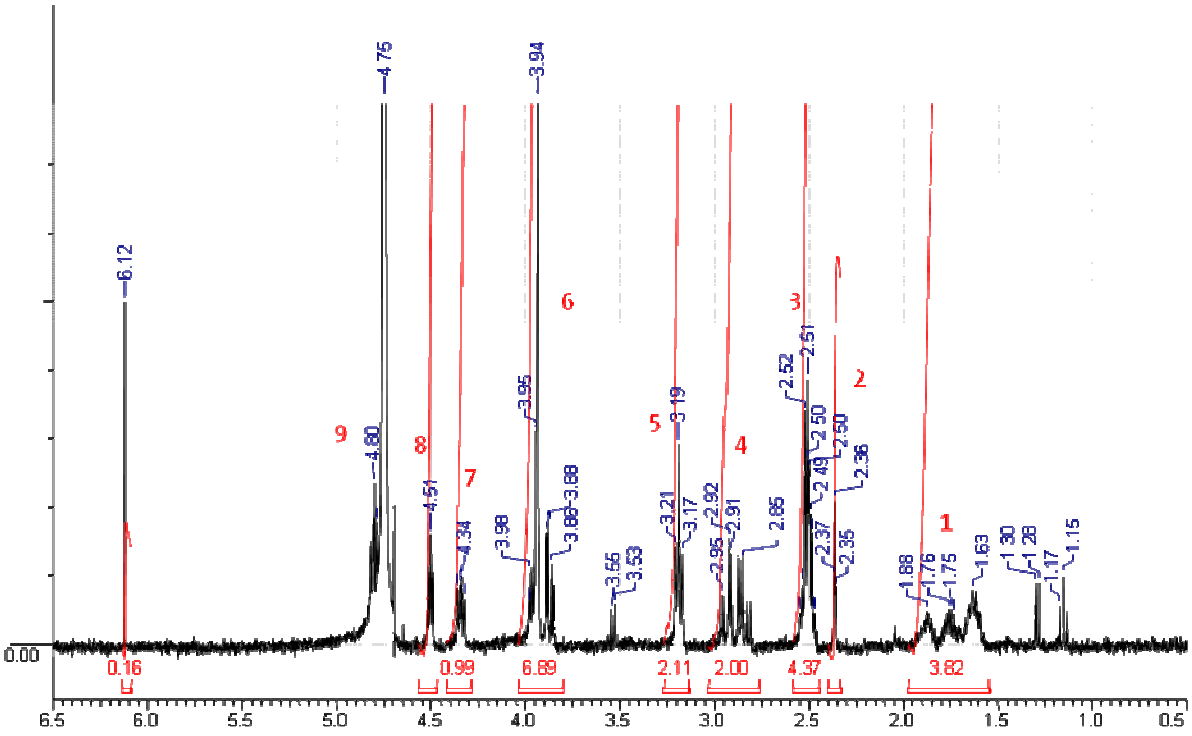

^{1}H NMR (D_2O, 400 MHz): δ 1.63-1.88 (m, 4H), 2.37 (s, 1 H), 2.49-2.52 (m, 4 H), 2.81-2.97 (m, 2 H), 3.17-3.21 (t, 2 H, *J* = 8 Hz), 3.85-3.99 (m, 6 H), 4.34 (m, 1 H), 4.49-4.52 (m, 1 H), 4.80-4.82 (m, 1 H). ESI-MS (MNa^+): 571.2 (calc. 570.6).

S8. SCRAMBLED-

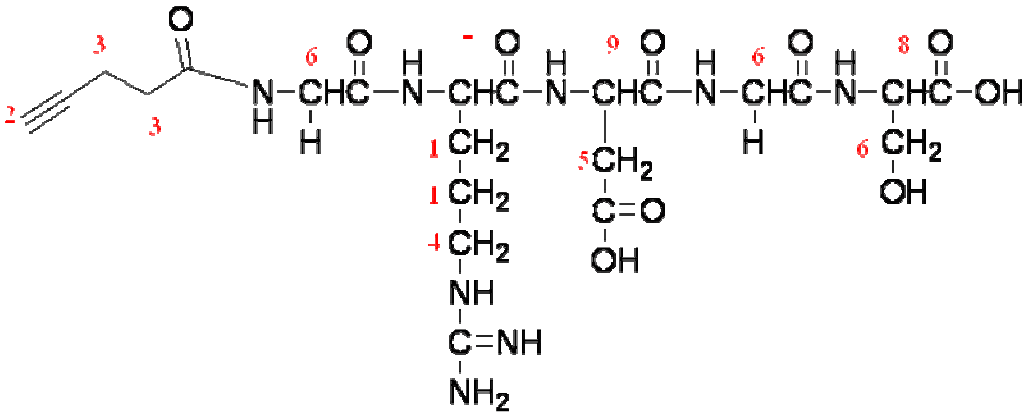

GRGDS

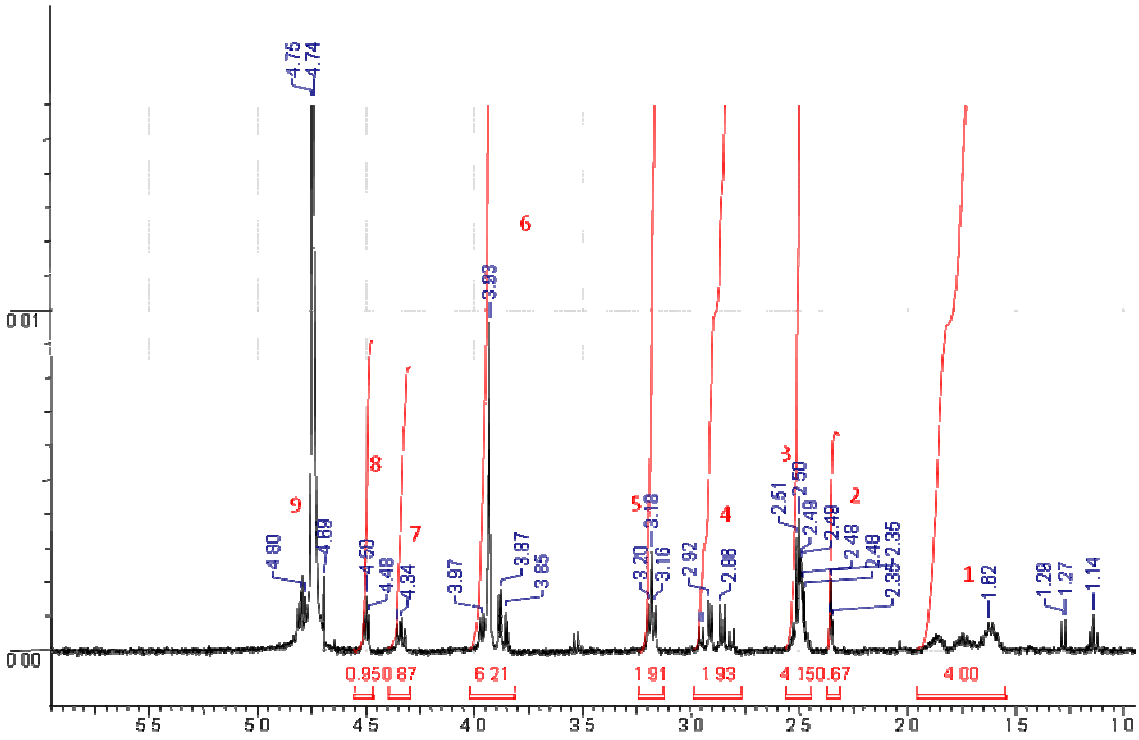

^{1}H NMR (D_2O, 400 MHz): δ 1.61-1.88 (m, 4H), 2.35 (s, 1 H), 2.48-2.53 (m, 4 H), 2.84-2.92 (m, 2 H), 3.16-3.20 (t, 2 H, *J* = 8 Hz), 3.84-3.97 (m, 6 H), 4.33-4.34 (m, 1 H), 4.48-4.51 (m, 1 H), 4.79-4.81 (m, 1 H). ESI-MS (MNa^+): 571.8 (calc. 570.6).

S9. CELL COMPETITIVE ASSAY

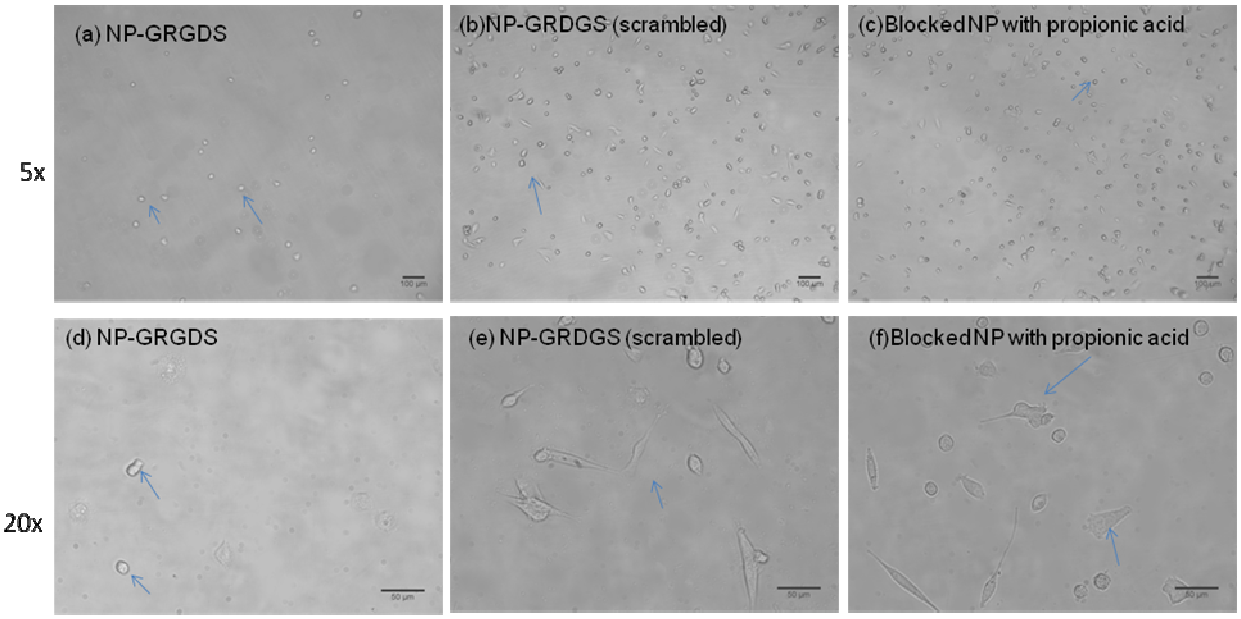

Rabbit corneal epithelial cell attachment assay to GRGDS-modified tissue culture plates. Competitive inhibition of cell attachment was tested with both the controls of soluble GRGDS and NP-GRGDS, scrambled NP-GRDGS and NP with blocked azido groups. 96-well plates were coated with GRGDS at a concentration of 100 μg/ml, and then epithelial cells were plated in the presence of the indicated concentrations of GRGDS. (a, d) pre-incubated with 5.4 μg/ml of NP-GRGDS prior to plating; (b, e) pre-incubated with 5.4 μg/ml scrambled NP-GRDGS and (c, f) nanoparticles where azido groups were blocked with 4-propionic acid. (0 μg/ml GRGDS) prior to plating. Cell images were acquired using a Zeiss Axiover S100 inverted microscope under 5× and 20× magnification. Arrows indicated attached corneal epithelial cells.

S10. GPC FOR POLY(TMCC-*co*-LA)

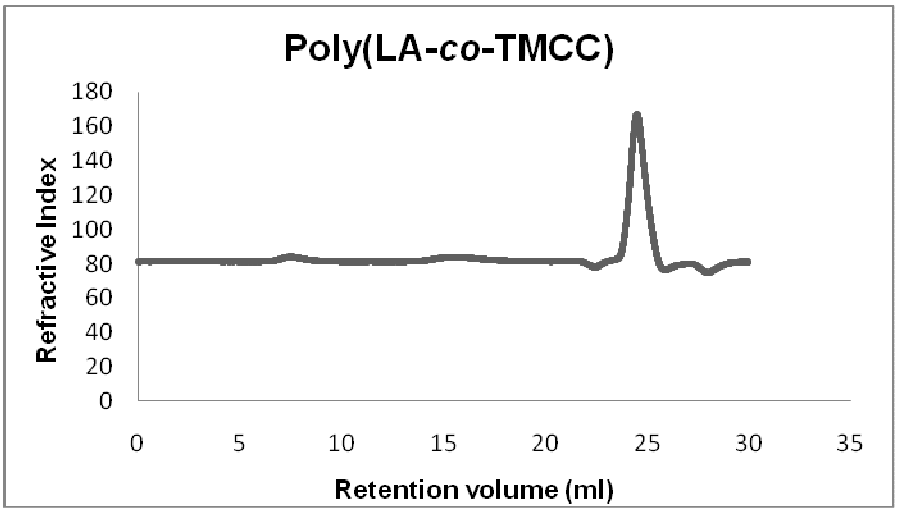

Evolution of organic size exclusion chromatogram for poly (TMCC-*co*-LA) sample obtained from bulk polymerization and THF was used as eluting solvent. The molar mass was determined relative to the polystyrene stardard. (Mn = 30.4 kDa, Mw = 83.2 kDa and PDI = 2.7).

S 11. FTIR SPECTRUM FOR NH_2-PEG-N_3

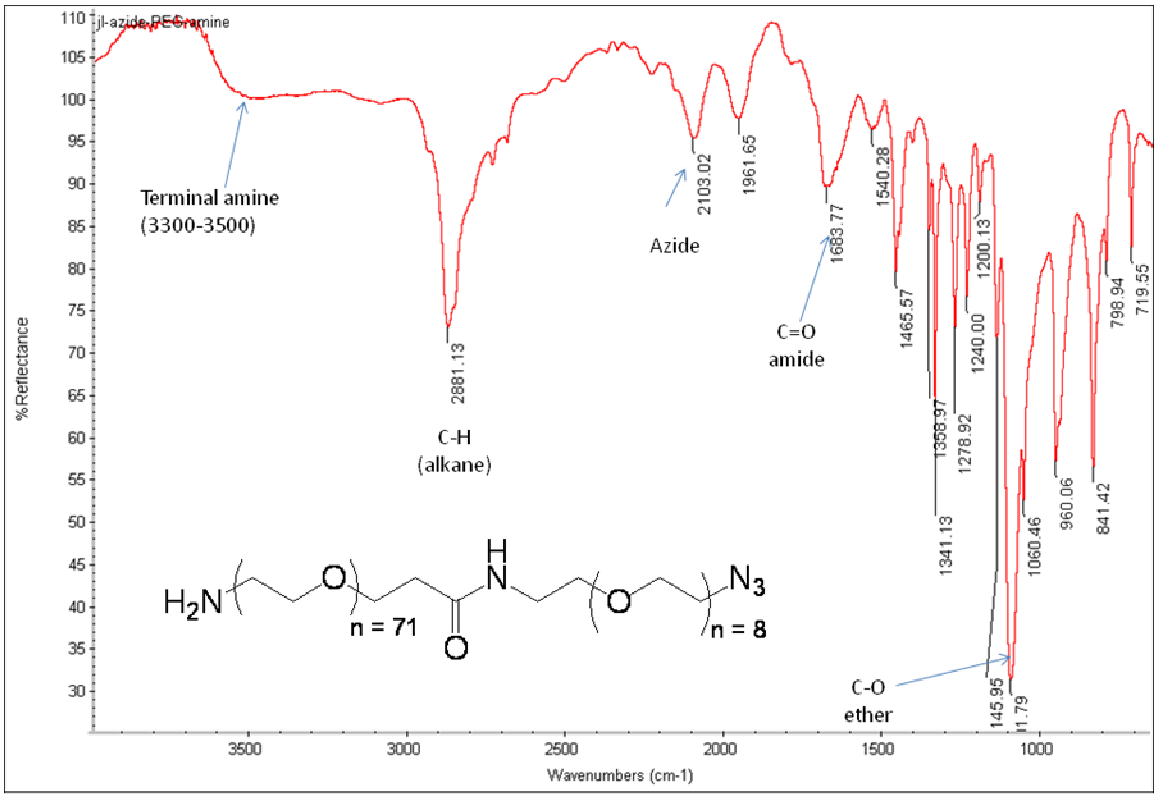

Bioconjugate Chemistry 20th Anniversary

Subscriber access provided by SHEMYAKIN-OVCHINNIKOV INST

Article

Novel Radioiodinated Aurones as Probes for SPECT Imaging of #-Amyloid Plaques in the Brain

Yoshifumi Maya, Masahiro Ono, Hiroyuki Watanabe, Mamoru Haratake, Hideo Saji, and Morio Nakayama

Bioconjugate Chem., **2009**, 20 (1), 95-101• DOI: 10.1021/bc8003292 • Publication Date (Web): 11 December 2008

Downloaded from http://pubs.acs.org on May 8, 2009

More About This Article

Additional resources and features associated with this article are available within the HTML version:

- Supporting Information
- Access to high resolution figures
- Links to articles and content related to this article
- Copyright permission to reproduce figures and/or text from this article

View the Full Text HTML

ACS Publications
High quality. High impact.

Bioconjugate Chemistry is published by the American Chemical Society. 1155 Sixteenth Street N.W., Washington, DC 20036

Novel Radioiodinated Aurones as Probes for SPECT Imaging of β-Amyloid Plaques in the Brain

Yoshifumi Maya,[†] Masahiro Ono,*[,†,‡] Hiroyuki Watanabe,[†] Mamoru Haratake,[†] Hideo Saji,[‡] and Morio Nakayama*[,†]

Department of Hygienic Chemistry, Graduate School of Biomedical Sciences, Nagasaki University, 1-14 Bunkyo-machi, Nagasaki 852-8521, and Department of Patho-Functional Bioanalysis, Graduate School of Pharmaceutical Sciences, Kyoto University, 46−29 Yoshida Shimoadachi-cho, Sakyo-ku, Kyoto 606-8501, Japan. Received July 29, 2008; Revised Manuscript Received November 10, 2008

We report a novel series of radioiodinated aurone derivatives as probes for imaging Aβ plaques in the brains of patients with Alzheimer's disease (AD) using single photon emission computed tomography (SPECT). In binding experiments in vitro, aurone derivatives showed very good affinity for Aβ aggregates (K_i = 1.1 to 3.4 nM). No-carrier-added radioiodinated aurones were successfully prepared through an iododestannylation reaction from the corresponding tributyltin derivatives. In biodistribution experiments using normal mice, aurone derivatives displayed high brain uptake (1.7−4.5% ID/g at 2 min) and rapid clearance from the brain (0.1−0.4% ID/g at 30 min), especially [^{125}I]**15**. Furthermore, a specific plaque labeling signal was observed in in vitro autoradiography of postmortem AD brain sections using [^{125}I]**15**. [^{125}I]**15** may be a useful SPECT imaging agent for detecting Aβ plaques in the brain of AD.

INTRODUCTION

Alzheimer's disease (AD) is a progressive neurodegenerative disorder characterized by cognitive decline, irreversible memory loss, disorientation, and language impairment. Senile plaques containing β-amyloid (Aβ) peptides and neurofibrillary tangles in the postmortem brain are two pathological hallmarks of AD (*1, 2*). Excessive production of Aβ via various normal or abnormal mechanisms is considered to be the initial neurodegenerative event in AD. Currently, it is difficult for clinicians to differentiate between the cognitive decline associated with normal aging and the cognitive decline associated with AD. There is no simple and definitive diagnostic method to detect Aβ plaques in the brain without postmortem pathological staining of brain tissue. Thus, the development of imaging agents for positron emission tomography (PET) or single photon emission computed tomography (SPECT), which can detect Aβ plaques in vivo, may assist with the early diagnosis of AD (*3*−*5*).

In the past few years, several groups have reported potential amyloid-imaging probes for the detection of Aβ plaques in vivo. Tracers such as [^{11}C]PIB (*6, 7*), [^{11}C]SB-13 (*8, 9*), [^{18}F]BAY94-9172 (*10*), [^{11}C]BF-227 (*11*), [^{18}F]FDDNP (*12*−*14*), and [^{123}I]IMPY (*15*−*18*) have been tested clinically and demonstrated utility (Figure 1). [^{123}I]IMPY is the only tracer for SPECT; the other five tracers are amyloid imaging probes for PET. Since SPECT is more valuable than PET in terms of routine diagnostic use, the development of more useful β-amyloid-imaging agents for SPECT has been a critical issue.

Recently, we have reported that radioiodinated aurones possessing a nucleophilic group (NH_2, NHMe, and NMe_2) function as a new backbone structure in the development of amyloid-imaging probes for SPECT (*19*). These compounds showed strong binding to Aβ aggregates (K_i = 1.2−6.8 nM), good penetration of the brain (1.9−4.6% ID/g at 2 min), and a fast washout from the brain (0.3−0.5% ID/g at 30 min). However, the aurone derivatives appeared inferior to IMPY in pharmacokinetics, although their high affinity for β-amyloid plaques is sufficient for imaging in vivo. Therefore, additional structural changes are essential to further improve the properties of aurone derivatives to make them suitable for the imaging of β-amyloid plaques in the brain.

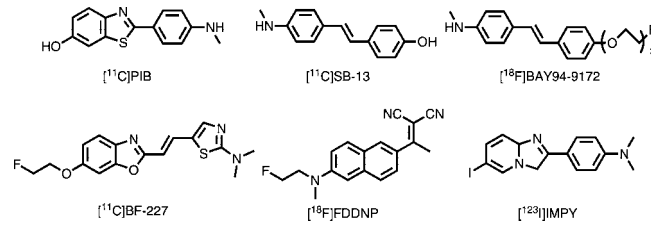

Figure 1. Chemical structure of Aβ imaging probes clinically tested.

To develop more promising aurones for SPECT-based imaging of β-amyloid plaques, we designed a novel series of radioiodinated derivatives with poly(ethylene glycol) (PEG). PEG is nontoxic, nonimmunogenic, highly soluble in water, and FDA-approved, and PEGylation has been used to change the pharmacokinetics of various biologically interesting proteins or peptides, leading to better therapeutics (*20, 21*). Therefore, PEGylated aurone derivatives are worthy of further evaluation as novel β-amyloid-imaging probes for SPECT.

In the present study, we designed and synthesized a novel series of radioiodinated aurone derivatives with not only 1 to 3 units of ethylene glycol at the 4′ position, but also other nucleophilic groups (-OCH_3 and -OH), and evaluated their biological potential as probes for imaging β-amyloid by testing their affinity for Aβ aggregates in vitro and their uptake by and

* To whom correspondence should be addressed. Phone +81-75-753-4608, Fax +81-75-753-4568, e-mail ono@pharm.kyoto-u.ac.jp for M. Ono. Phone +81-95-819-2441, Fax +81-95-819-2441, e-mail morio@nagasaki-u.ac.jp for M. Nakayama.

[†] Nagasaki University.

[‡] Kyoto University.

10.1021/bc8003292 CCC: $40.75 © 2009 American Chemical Society
Published on Web 12/11/2008

clearance from the brain in biodistribution experiments using normal mice.

MATERIALS AND METHODS

All reagents were commercial products and used without further purification unless otherwise indicated. ^{1}H NMR spectra were obtained on a Varian Gemini 300 spectrometer with TMS as an internal standard. Coupling constants are reported in hertz. Multiplicity was defined by s (singlet), d (doublet), t (triplet), and m (multiplet). Mass spectra were obtained on a JEOL IMS-DX instrument.

Chemistry. *Methyl 2-((Ethoxycarbonyl)methoxy)-5-bromobenzoate (**1**).* To a solution of 2-hydroxy-5-bromobenzoic acid methyl ester (1.5 g, 6.49 mmol) in acetone (10 mL) was added K_2CO_3 (2.7 g, 19.5 mmol) and ethylbromoacetate (1.3 mL, 7.78 mmol). The mixture was stirred for 3 h under reflux. After the solvent was evaporated, the residue was dissolved in water (100 mL) and extracted with ethyl acetate (100 mL). The organic layer was dried over Na_2SO_4, and evaporation of the solvent gave 1.60 g of **1** (77.7%). ^{1}H NMR NMR (300 MHz, $CDCl_3$) δ 1.29 (t, J = 7.2 Hz, 3H), 3.91 (s, 3H), 4.24 (q, J = 7.2 Hz, 2H), 4.69 (s, 2H), 6.78 (d, J = 9.0 Hz, 1H), 7.54 (d, J = 6.3 Hz, 1H), 7.96 (s, 1H).

*2-(Carboxymethoxy)-5-bromobenzoic Acid (**2**).* To a solution of **1** (1.6 g, 5.04 mmol) in methanol (10 mL) was added 10% aqueous KOH (3.0 mL). The mixture was stirred for 2 h at room temperature. The product formed by adding 1 N HCl was filtered to give 1.10 g of **2** (79.4%). ^{1}H NMR (300 MHz, CD_3OD) δ 4.81 (s, 2H), 7.02 (d, J = 8.7 Hz, 1H), 7.63 (dd, J = 2.4, 2.7 Hz, 1H), 7.93 (d, J = 2.4 Hz, 1H).

*5-Bromo-3-acetoxybenzofuran (**3**).* A mixture of acetic anhydride (20 mL), acetic acid (4 mL), anhydrous sodium acetate (1.0 g, 12.0 mmol), and **2** (100 mg, 0.36 mmol) was heated to reflux for 5 h. Water (100 mL) was then added, and the mixture was extracted with chloroform (100 mL). After drying of the organic layer on Na_2SO_4, evaporation gave 78 mg of **3** (86.5%). ^{1}H NMR (300 MHz, $CDCl_3$) δ 2.37 (s, 3H), 7.33 (d, J = 9.0 Hz, 1H), 7.43 (dd, J = 3.6, 2.1 Hz, 1H), 7.71 (s, 1H), 8.02 (s, 1H).

*5-Bromobenzofuran-3(2H)-one (**4**).* A mixture of **3** (78 mg, 0.31 mmol), methanol (3 mL), water (1 mL), and 1 N HCl (2 mL) was heated to reflux for 3 h. The precipitate formed was collected by filtration, washed with water, and dried under vacuum to obtain 15 mg of **4** (22.5%). ^{1}H NMR (300 MHz, $CDCl_3$) δ 4.67 (s, 2H), 7.06 (d, J = 9.0 Hz, 1H), 7.69 (dd, J = 2.1, 2.1 Hz, 1H), 7.79 (d, J = 2.1 Hz, 1H).

*(Z)-2-(4-Methoxybenzylidene)-5-bromobenzofuran-3(2H)-one (**5**).* To a solution of **4** (300 mg, 1.41 mmol) and 4-methoxybenzaldehyde (192 mg, 1.41 mmol) in chloroform (5 mL) was added Al_2O_3 (2.7 g, 26.0 mmol). The mixture was stirred for 20 min at room temperature. After filtration of the reaction mixture, the solvent of the filtrate was removed, and drying under vacuum yielded 410 mg of **5** (85.7%). ^{1}H NMR (300 MHz, $CDCl_3$) δ 3.88 (s, 3H), 6.91 (s, 1H), 6.99 (d, J = 9.0 Hz, 2H), 7.24 (d, J = 8.4 Hz, 1H), 7.73 (dd, J = 2.1, 2.1 Hz, 1H), 7.88 (d, J = 8.7 Hz, 2H), 7.92 (d, J = 1.8 Hz, 1H).

*(Z)-2-(4-Hydroxybenzylidene)-5-bromobenzofuran-3(2H)-one (**6**).* BBr_3 (3 mL, 1 M solution in CH_2Cl_2) was added to a solution of **5** (300 mg, 0.91 mmol) in CH_2Cl_2 (25 mL) dropwise in an ice bath. The mixture was allowed to warm to room temperature and stirred for 15 h. Water (50 mL) was added while the reaction mixture was cooled in an ice bath. The mixture was extracted with chloroform (2 × 30 mL), and the organic phase was dried over Na_2SO_4 and filtered. The filtrate was concentrated and the residue was purified by silica gel chromatography (hexane/ethyl acetate = 2:3) to give 15 mg of **6** (5.2%). ^{1}H NMR (300 MHz, DMSO-d_6) δ 1.23 (s, 1H), 6.92 (d, J = 8.4 Hz, 2H), 6.96 (s, 1H), 7.56 (d, J = 9.3 Hz, 1H), 7.88−7.92 (m, 3H), 7.95 (s, 1H). MS (EI) m/z 316 [M^+].

*(Z)-2-(4-Methoxybenzylidene)-5-(tributylstannyl)benzofuran-3(2H)-one (**7**).* A mixture of **5** (200 mg, 0.60 mmol), $(Bu_3Sn)_2$ (0.4 mL), and $(Ph_3P)_4Pd$ (50 mg, 0.043 mmol) in a mixed solvent (15 mL, 1:1 dioxane/Et_3N) was stirred under reflux for 24 h. The solvent was removed, and the resulting residue was purified by silica gel chromatography using chloroform to give 50 mg of **7** (15.3%). ^{1}H NMR (300 MHz, $CDCl_3$) δ 0.89−1.64 (m, 27H), 3.87 (s, 3H), 6.89 (s, 1H), 6.99 (d, J = 8.7 Hz, 2H), 7.31 (d, J = 8.1 Hz, 1H), 7.71 (dd, J = 0.9, 0.9 Hz, 1H), 7.86 (d, J = 9.0 Hz, 2H), 7.90 (d, J = 8.7 Hz 1H). MS (EI) m/z 528 [M^+].

*(Z)-2-(4-Hydroxybenzylidene)-5-(tributylstannyl)benzofuran-3(2H)-one (**8**).* The same reaction as described above to prepare **7** was used, and 10 mg of **8** was obtained in a 12.0% yield from **6**. ^{1}H NMR (300 MHz, $CDCl_3$) δ 0.86−1.60 (m, 27H), 6.74 (d, J = 9.0 Hz, 2H), 6.90 (s, 1H), 7.30 (d, J = 8.1 Hz, 1H), 7.69 (d, J = 8.1 Hz, 1H), 7.80 (d, J = 8.4 Hz, 2H), 7.89 (s, 1H). MS (EI) m/z 542 [M^+].

*(Z)-2-(4-Methoxybenzylidene)-5-iodobenzofuran-3(2H)-one (**9**).* To a solution of **7** (10 mg, 0.03 mmol) in $CHCl_3$ (3 mL) was added a solution of iodine in $CHCl_3$ (1 mL, 0.25 M) at room temperature. The mixture was stirred at room temperature for 5 min, and saturated $NaHSO_3$ solution (15 mL) was added. The organic phase was separated, dried over Na_2SO_4, and filtered. The solvent was removed, and the residue was purified by preparative TLC (2:3 hexane/ethyl acetate) to give 6 mg of **9** (84.0%). ^{1}H NMR (300 MHz, $CDCl_3$) δ 3.88 (s, 3H), 6.91 (s, 1H), 6.98 (d, J = 6.9 Hz, 2H), 7.14 (d, J = 8.4 Hz, 1H), 7.87−7.91 (m, 3H), 8.12 (d, J = 2.1 Hz, 1H). HRMS (EI) m/z calcd for $C_{16}H_{11}O_3I$ (M^+) 377.9753, found 377.9753.

*Methyl 2-((Ethoxycarbonyl)methoxy)-5-iodobenzoate (**10**).* The same reaction as described above to prepare **1** was used, and 2.62 g of **10** was obtained in a 99.0% yield from 2-hydroxy-5-iodobenzoic acid methyl ester. ^{1}H NMR (300 MHz, $CDCl_3$) δ 1.29 (t, J = 7.2 Hz, 3H), 3.90 (s, 3H), 4.25 (q, J = 6.0 Hz, 2H), 4.69 (s, 2H), 6.66 (d, J = 8.7 Hz, 1H), 7.71 (dd, J = 2.4, 2.4 Hz, 1H), 8.12 (d, J = 2.1 Hz, 1H).

*2-(Carboxymethoxy)-5-iodobenzoic Acid (**11**).* The same reaction as described above to prepare **2** was used, and 2.02 g of **11** was obtained in a 87.2% yield from **10**. ^{1}H NMR (300 MHz, CD_3OD) δ 4.81 (s, 2H), 6.89 (d, J = 9.0 Hz, 1H), 7.80 (dd, J = 2.7, 2.4 Hz, 1H), 8.10 (d, J = 2.4 Hz, 1H).

*5-Iodo-3-acetoxybenzofuran (**12**).* The same reaction as described above to prepare **3** was used, and 1.45 g of **12** was obtained in a 76.6% yield from **11**. ^{1}H NMR (300 MHz, $CDCl_3$) δ 2.37 (s, 3H), 7.23 (d, J = 8.1 Hz, 1H), 7.59 (dd, J = 1.5, 1.8 Hz, 1H), 7.90 (d, J = 1.5 Hz, 1H), 7.98 (s, 1H).

*5-Iodobenzofuran-3(2H)-one (**13**).* The same reaction as described above to prepare **4** was used, and 1.17 g of **13** was obtained in a 93.8% yield from **12**. ^{1}H NMR (300 MHz, $CDCl_3$) δ 4.65 (s, 2H), 6.96 (d, J = 9.0 Hz, 1H), 7.85 (dd, J = 1.8, 1.8 Hz, 1H), 7.99 (d, J = 1.8 Hz, 1H).

*(Z)-2-(4-Hydroxybenzylidene)-5-iodobenzofuran-3(2H)-one (**14**).* The same reaction as described above to prepare **5** was used, and 78 mg of **14** was obtained in a 87.0% yield from **13** and 4-hydroxybenzaldehyde. ^{1}H NMR (300 MHz, $CDCl_3$) δ 1.28 (s, 1H), 6.87 (s, 1H), 6.91 (d, J = 5.4 Hz, 2H), 7.29 (d, J = 8.7 Hz, 1H), 7.85 (d, J = 6.9 Hz, 2H), 8.12 (d, J = 6.9 Hz, 1H), 8.08 (d, J = 1.8 Hz, 1H). HRMS (EI) m/z calcd for $C_{15}H_9O_3I$ (M^+) 363.9596, found 363.9571.

*(Z)-2-(4-(2-Hydroxyethoxy)benzylidene)-5-iodobenzofuran-3(2H)-one (**15**).* A mixture of potassium carbonate (3.7 g, 26.8 mmol), **14** (194 mg, 0.53 mmol), and ethylene chlorohydrin (0.1 mL, 1.43 mmol) in anhydrous DMF (7 mL) was heated at 120 °C for 15 h. After cooling to room temperature, water was added,

and the reaction mixture was extracted with ethyl acetate. The organic layer was separated, dried over Na_2SO_4, and evaporated. The resulting residue was purified by silica gel chromatography using ethyl acetate to give 123 mg of **15** (56.5%). ^{1}H NMR (300 MHz, $CDCl_3$) δ 2.01 (s, 1H), 4.02 (s, 2H), 4.18 (t, J = 3.9 Hz, 2H), 6.89 (s, 1H), 7.00 (d, J = 7.5 Hz, 2H), 7.14 (d, J = 8.4 Hz, 1H), 7.80−7.92 (m, 3H), 8.12 (d, J = 1.8 Hz, 1H). HRMS (EI) *m*/*z* calcd for $C_{17}H_{13}O_4I$ (M^+) 407.9859, found 407.9879.

*(Z)-2-(4-(2-(2-Hydroxyethoxy)ethoxy)benzylidene)-5-iodobenzofuran-3(2H)-one (***16***).* The same reaction as described above to prepare **15** was used, and 56 mg of **16** was obtained in a 30.2% yield from **14** and ethylene glycol mono-2-chloroethyl ether. ^{1}H NMR (300 MHz, $CDCl_3$) δ 2.17 (s, 1H), 3.70 (d, J = 4.8 Hz, 2H), 3.78 (d, J = 4.8 Hz, 2H), 3.92 (t, J = 4.8 Hz, 2H), 4.21 (t, J = 4.5 Hz, 2H), 6.89 (s, 1H), 7.00 (d, J = 11.4 Hz, 2H), 7.13 (d, J = 8.7 Hz, 1H), 7.84−7.91 (m, 3H), 8.11 (d, J = 2.1 Hz, 1H). HRMS (EI) *m*/*z* calcd for $C_{19}H_{17}O_5I$ (M^+) 452.0121, found 452.0131.

*(Z)-2-(4-(2-(2-(2-Hydroxyethoxy)ethoxy)ethoxy)benzylidene)-5-iodobenzofuran-3(2H)-one (***17***).* The same reaction as described above to prepare **15** was used, and 140 mg of **17** was obtained in a 67.9% yield from **14** and 2-[2-(2-chloroethoxy)ethoxy] ethanol. ^{1}H NMR (300 MHz, $CDCl_3$) δ 1.96 (s, 1H), 3.74−3.80 (m, 6H), 3.92 (t, J = 4.8 Hz, 2H), 4.24 (t, J = 4.8 Hz, 2H), 4.45 (t, J = 4.5 Hz, 1H), 4.65 (t, J = 4.5 Hz, 1H), 6.91 (s, 1H), 6.98 (d, J = 9.0 Hz, 2H), 7.15 (d, J = 8.7 Hz, 1H), 7.85−7.92 (m, 3H), 8.15 (d, J = 2.1 Hz, 1H). HRMS (EI) *m*/*z* calcd for $C_{21}H_{21}O_6I$ (M^+) 496.0383, found 496.0381.

*(Z)-2-(4-(2-Hydroxyethoxy)benzylidene)-5-(tributylstannyl)benzofuran-3(2H)-one (***18***).* The same reaction as described above to prepare **7** was used, and 7 mg of **18** was obtained in a 25.0% yield from **15**. ^{1}H NMR (300 MHz, $CDCl_3$) δ 0.86−1.61 (m, 27H), 2.06 (s, 1H), 4.02 (s, 2H), 4.16 (t, J = 3.6 Hz, 2H), 6.88 (s, 1H), 6.99 (d, J = 9.0 Hz, 2H), 7.30 (d, J = 12.3 Hz, 1H), 7.73 (d, J = 9.0 Hz, 1H), 7.90−7.92 (m, 3H). MS (EI) *m*/*z* 572 [M^+].

*(Z)-2-(4-(2-(2-Hydroxyethoxy)ethoxy)benzylidene)-5-(tributylstannyl)benzofuran-3(2H)-one (***19***).* The same reaction as described above to prepare **7** was used, and 17 mg of **19** was obtained in a 31.4% yield from **16**. ^{1}H NMR (300 MHz, $CDCl_3$) δ 0.86−1.32 (m, 27H), 2.11 (s, 1H), 3.70 (t, J = 4.8 Hz, 2H), 3.78 (t, J = 4.8 Hz, 2H), 3.91 (t, J = 4.5 Hz, 2H), 4.22 (t, J = 5.1 Hz, 2H), 6.89 (s, 1H), 7.00 (d, J = 7.2 Hz, 2H), 7.31 (d, J = 8.1 Hz, 1H), 7.71 (d, J = 9.0 Hz, 1H), 7.88−7.91 (m, 3H). MS (EI) *m*/*z* 616 [M^+].

*(Z)-2-(4-(2-(2-(2-Hydroxyethoxy)ethoxy)ethoxy)benzylidene)-5-(tributylstannyl)benzofuran-3(2H)-one (***20***).* The same reaction as described above to prepare **7** was used, and 4 mg of **20** was obtained in a 30.3% yield from **17**. ^{1}H NMR (300 MHz, $CDCl_3$) δ 0.86−1.59 (m, 27H), 2.11 (s, 1H), 3.63 (t, J = 3.3 Hz, 2H), 3.73−3.75 (m, 4H), 3.90 (t, J = 4.2 Hz, 2H), 4.21 (t, J = 4.2 Hz, 2H), 6.88 (s, 1H), 7.10 (d, J = 8.7 Hz, 2H), 7.31 (d, J = 8.1 Hz, 1H), 7.64−7.70 (m, 3H), 7.90 (d, J = 4.8 Hz, 1H). MS (EI) *m*/*z* 659 [M^+].

Iododestannylation Reaction. The radioiodinated forms of compounds **9**, **14**, **15**, **16**, and **17** were prepared from the corresponding tributyltin derivatives by iododestannylation. Briefly, to initiate the reaction, the tributyltin derivative (50 μg/50 μL EtOH) was added to a mixture of a [^{125}I]NaI (3.7−7.4 MBq, specific activity 2200 Ci/mmol), 50 μL of H_2O_2 (3%), and 50 μL of 1 N HCl in a sealed vial. The reaction was allowed to proceed at room temperature for 2 min and was terminated by addition of $NaHSO_3$. The reaction, after neutralization with sodium bicarbonate, was extracted with ethyl acetate. The extract was dried by passing through an anhydrous Na_2SO_4 column and was then blown dry with a stream of nitrogen gas. The radioiodinated ligand was purified by HPLC on a Cosmosil C_{18} column with an isocratic solvent of H_2O/acetonitrile (3:7) at a flow rate of 1.0 mL/min.

Binding Assays Using the Aggregated Aβ Peptide in Solution. A solid form of Aβ(1−42) was purchased from Peptide Institute (Osaka, Japan). Aggregation was carried out by gently dissolving the peptide (0.25 mg/mL) in a buffer solution (pH 7.4) containing 10 mM sodium phosphate and 1 mM EDTA. The solution was incubated at 37 °C for 42 h with gentle and constant shaking. (*Z*)-2-(4-Aminobenzylidene)-5-iodobenzofuran-3(2*H*)-one ([^{125}I]AAU) was synthesized and used as the radioligand for the competition binding experiments (K_d value of [^{125}I]AAU is 4.2 nM) (*19*). The binding experiments were carried out in 12 × 75 mm borosilicate glass tubes according to a procedure described previously (*19*). A mixture containing 50 μL of test compound (0.8 nM−12.5 μM in 10% ethanol), 50 μL of 0.02 nM [^{125}I]AAU, 50 μL of Aβ(1−42) aggregate, and 850 μL of 10% ethanol was incubated at room temperature for 3 h. The mixture was then filtered through Whatman GF/B filters using a Brandel M-24 cell harvester, and the filters containing the bound ^{125}I ligand were placed in a gamma counter. Values for the half-maximal inhibitory concentration (IC_{50}) were determined from displacement curves of three independent experiments using GraphPad *Prism* 4.0, and those for the inhibition constant (K_i) were calculated using the Cheng-Prusoff equation (*22*): $K_i = IC_{50}/(1 + [L]/K_d)$, where [L] is the concentration of [^{125}I]AAU used in the assay, and K_d is the dissociation constant of AAU (4.2 nM) (*19*).

Staining of Amyloid Plaques in Transgenic Mouse Brain Sections. Tg2576 transgenic mice (20 month of age) were used as an Alzheimer's model. The brain was removed and sliced into serial sections 10 μm thick. Each slide was incubated with a 50% ethanol solution of compound **9**, **14**, **15**, **16**, and **17** (100 μM). Finally, the sections were washed in 50% EtOH for 3 min two times. Fluorescent observation was performed with the Nikon system (Excitation filter, 450−490 nm; Dichroic mirror, DM505; Barrier filter, BA520). Thereafter, the serial sections were also stained with thioflavin S, a pathological dye commonly used for staining Aβ plaques in the brain.

In Vivo Biodistribution in Normal Mice. Animal studies were conducted in accordance with our institutional guidelines and were approved by Nagasaki University Animal Care Committee. A saline solution (100 μL) containing radiolabeled agents (4.2−6.3 kBq) and 10% ethanol was intravenously injected directly into the tail vein of ddY mice (5 weeks old, average weight 20−25 g). The mice were sacrificed at various time points postinjection. The organs of interest were removed and weighed, and the radioactivity was measured with an automatic gamma counter (Aloka, ARC-380). Percent dose per gram of samples was calculated by comparing the sample counts with the counts of the initial dose.

In Vitro Autoradiography. Postmortem brain tissues from an autopsy-confirmed case of AD (73-year-old male) and a control subject (36-year-old male) were obtained from BioChain Institute Inc. The presence and localization of plaques on the sections were confirmed with immunohistochemical staining using a monoclonal Aβ antibody BC05 (Wako) as reported (*23*). The sections were incubated with [^{125}I]**15** (120000 cpm/100 μL) for 1 h at room temperature. They were then dipped in saturated lithium carbonate in 40% EtOH (two 2-min washes) and washed with 40% EtOH (one 2-min wash), before being rinsed with water for 30 s. After drying, the ^{125}I-labeled sections were exposed to a Fuji Film imaging plate overnight.

RESULTS AND DISCUSSION

Chemistry. The target aurone derivatives (**9**, **14**, **15**, **16**, and **17**) were prepared as shown in Schemes 1−3. The synthesis of

Scheme 1

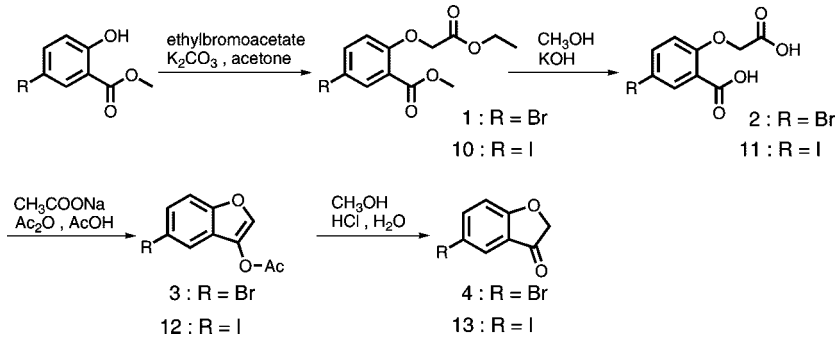

Scheme 2

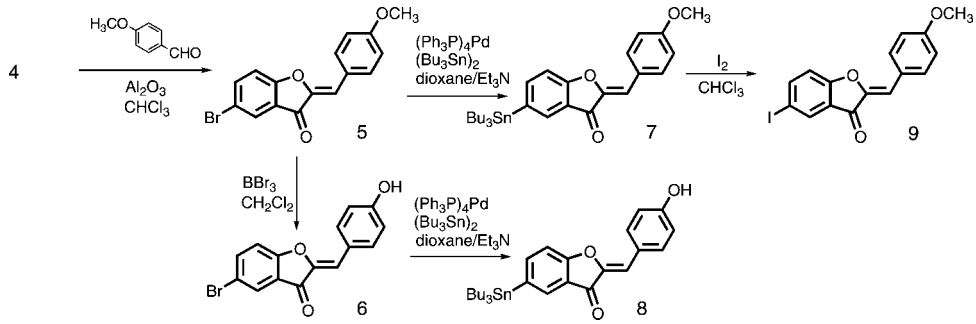

Scheme 3

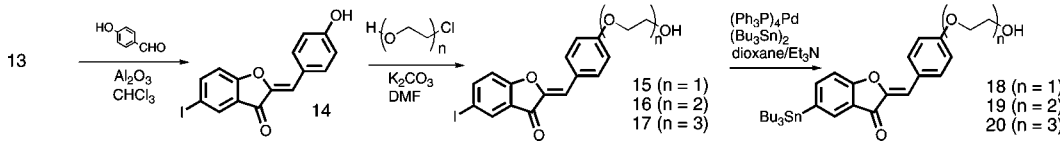

the aurone backbone was achieved by an Aldol reaction of benzofuranones with benzaldehydes using Al_2O_3 (*23*). In this process, benzofuranones were reacted with methoxy benzaldehyde or hydroxy benzaldehyde in the presence of Al_2O_3 in chloroform at room temperature to form compounds **5** and **14** in yields of 85.7% and 87.0%, respectively. Compound **5** was converted to **6** by demethylation with BBr_3 in CH_2Cl_2 (5.2% yields). Direct alkylation of **14** with ethylene chlorohydrin, ethylene glycol mono-2-chloroethyl ether, or 2-[2-(2-chloroethoxy)ethoxy]ethanol with potassium carbonate in DMF resulted in **15**, **16**, and **17**, respectively. The tributyltin derivatives (**7**, **8**, **18**, **19**, and **20**) were prepared from the corresponding compounds (**5**, **6**, **15**, **16**, and **17**) using a halogen to tributyltin exchange reaction catalyzed by Pd(0) for yields of 15.3%, 12.0%, 25.0%, 31.4%, and 30.3%, respectively. The tributyltin derivatives were used as the starting materials for radioiodination in the preparation of [^{125}I]**9**, [^{125}I]**14**, [^{125}I]**15**, [^{125}I]**16**, and [^{125}I]**17**. Novel radioiodinated aurones were achieved by an iododestannylation reaction using hydrogen peroxide as the oxidant, which produced the desired radioiodinated ligands (Scheme 4). It was anticipated that the no-carrier-added preparation would result in a final product bearing a theoretical specific activity similar to that of ^{125}I (2200 Ci/mmol). The radiochemical identities of the radioiodinated ligands were verified by coinjection with nonradioactive compounds by their HPLC profiles (Supporting Information). Five radioiodinated products were obtained in 25−57% radiochemical yields with radiochemical purities of >95% after purification by HPLC.

Binding Experiments Using Aβ Aggregates in Vitro. Our initial screening of the affinity of aurone derivatives (**9**, **14**, **15**, **16**, and **17**) was carried out with Aβ(1−42) aggregates, using

Scheme 4

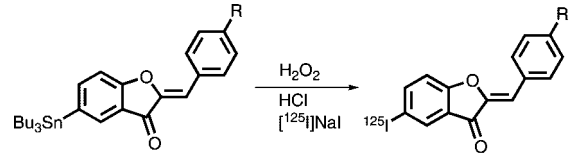

[^{125}I]AAU as the competing radioligand (Table 1). The K_i values estimated for **9**, **14**, **15**, **16**, and **17** were 2.9, 1.3, 1.1, 3.4, and 2.6 nM, respectively. These values suggested that the new series of aurone derivatives had binding affinity for Aβ(1−42) aggregates despite their substituted groups. The binding affinity is in the same range as that of aurone derivatives possessing a nucleophilic group (NH_2, NHMe, NMe_2), reported previously

Table 1. Inhibition Constants (K_i) of Newly Synthesized Aurone Derivatives for the Binding of Ligands to Aβ (1−42) Aggregates

compound	K_i (nM)[a]
9	2.89 ± 0.42
14	1.28 ± 0.29
15	1.05 ± 0.06
16	3.36 ± 0.29
17	2.56 ± 0.31

[a] Data are the mean ± SEM for two independent measurements done in triplicate.

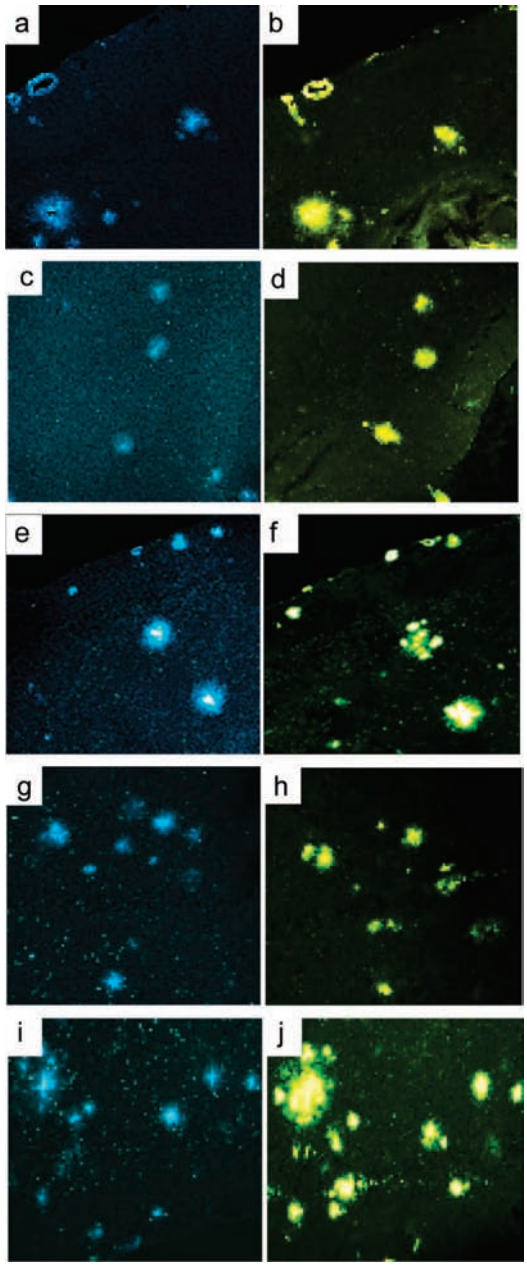

Figure 2. Neuropathological staining of **9**, **14**, **15**, **16**, and **17** (a, c, e, g, and i) in 10 μm sections from a mouse model of AD. Labeled plaques were confirmed by staining of the adjacent sections with thioflavin S (b, d, f, h, and j).

(*19*). These results clearly indicated that there exists considerable tolerance for structural modifications of aurone derivatives. The binding affinity of aurone derivatives is very close to that of known β-amyloid-imaging agents such as SB-13 ($K_i = 1.2$ nM) (*24*), PIB ($K_i = 2.8$ nM) (*25*), and IMPY ($K_i = 1.4$ nM) (*24*), indicating that they have strong enough affinity to test clinically.

Neuropathological Staining of Mouse Brain Sections. To confirm the affinity of aurone derivatives for β-amyloid plaques in the mouse brain, neuropathological fluorescent staining with **9**, **14**, **15**, **16**, and **17** was carried out using double transgenic Alzheimer's mouse brain sections (Figure 2). Many amyloid plaques were clearly stained with the derivatives, as reflected by the high binding affinity for Aβ aggregates in in vitro competition assays. The labeling pattern was consistent with that observed with thioflavin S. These results suggest that novel aurone derivatives show affinity for β-amyloid plaques in the mouse brain in addition to having binding affinity for synthetic Aβ42 aggregates.

Table 2. Biodistribution of Radioactivity after Injection of Aurone Derivatives in Normal Mice[a]

	time after injection (min)			
tissue	2	10	30	60
		[^{125}I]**9**		
blood	3.16 (0.82)	1.51 (0.23)	0.95 (0.19)	0.70 (0.60)
liver	6.87 (2.18)	5.16 (0.73)	2.76 (0.40)	1.86 (0.83)
kidney	7.26 (2.18)	7.00 (1.49)	4.93 (1.52)	2.43 (1.17)
intestine	1.59 (0.51)	4.70 (1.46)	11.67 (3.56)	9.02 (3.14)
spleen	1.45 (0.56)	0.74 (0.10)	0.48 (0.10)	0.43 (0.14)
pancreas	2.83 (0.75)	0.77 (0.17)	0.62 (0.75)	0.16 (0.05)
heart	3.84 (1.04)	1.06 (0.10)	0.37 (0.09)	0.25 (0.12)
stomach[b]	0.39 (0.20)	0.89 (0.48)	0.42 (0.13)	0.82 (0.46)
brain	1.69 (0.43)	0.54 (0.12)	0.11 (0.05)	0.03 (0.02)
		[^{125}I]**14**		
blood	3.14 (0.39)	2.77 (0.28)	1.75 (0.38)	0.87 (0.28)
liver	6.05 (1.49)	6.63 (1.08)	4.23 (0.63)	4.45 (3.14)
kidney	11.08 (2.96)	11.22 (2.26)	5.82 (1.11)	2.43 (1.04)
intestine	2.11 (0.75)	6.12 (0.83)	12.67 (2.13)	14.87 (5.42)
spleen	2.18 (0.48)	1.36 (0.83)	0.69 (0.14)	0.42 (0.02)
pancreas	5.28 (0.99)	2.65 (0.64)	0.92 (0.19)	0.36 (0.09)
heart	6.23 (0.63)	2.57 (0.41)	0.98 (0.14)	0.42 (0.14)
stomach[b]	0.93 (0.28)	1.46 (0.23)	1.22 (0.72)	1.89 (1.01)
brain	3.07 (0.39)	1.48 (0.19)	0.37 (0.07)	0.14 (0.12)
		[^{125}I]**15**		
blood	4.97 (0.96)	3.88 (1.09)	2.38 (0.85)	1.24 (0.35)
liver	13.4 (3.20)	13.3 (2.59)	7.60 (1.95)	5.27 (0.64)
kidney	11.3 (1.23)	10.8 (2.58)	6.09 (2.43)	2.50 (1.30)
intestine	2.78 (0.42)	7.83 (2.22)	17.82 (3.58)	20.93 (4.46)
spleen	2.72 (0.28)	1.02 (0.22)	0.50 (0.13)	0.21 (0.09)
pancreas	6.38 (0.63)	1.61 (0.61)	0.59 (0.21)	0.29(0.15)
heart	6.30 (0.65)	2.30 (0.46)	0.83 (0.15)	0.72 (0.58)
stomach[b]	1.88 (0.41)	3.23 (2.58)	5.15 (4.43)	1.45 (0.78)
brain	4.51 (0.25)	1.48 (0.28)	0.24 (0.03)	0.09 (0.04)
		[^{125}I]**16**		
blood	3.61 (0.74)	5.18 (2.54)	1.11 (0.73)	0.68 (0.45)
liver	12.5 (3.21)	11.6 (1.75)	9.31 (2.66)	7.12 (4.05)
kidney	12.0 (0.99)	10.3 (1.17)	5.75 (1.53)	2.55 (1.12)
intestine	2.35 (1.33)	8.18 (2.32)	19.7 (7.86)	26.38 (5.95)
spleen	2.26 (0.53)	1.56 (0.45)	0.78 (0.26)	0.45 (0.21)
pancreas	5.67(2.72)	2.24 (0.68)	1.40 (0.44)	0.39 (0.29)
heart	6.04 (0.38)	2.77 (0.94)	1.21 (0.66)	0.66 (0.57)
stomach[b]	1.71 (0.38)	5.65 (6.63)	5.00 (2.83)	6.58 (4.59)
brain	3.69 (0.22)	1.53 (0.31)	0.38 (0.05)	0.16 (0.03)
		[^{125}I]**17**		
blood	2.98 (0.64)	4.62 (2.17)	0.83 (0.64)	0.51 (0.31)
liver	12.95 (3.43)	11.20 (1.51)	8.34 (1.98)	7.70 (3.93)
kidney	11.58 (1.13)	9.66 (2.28)	5.84 (1.79)	2.41 (1.22)
intestine	2.52 (0.39)	7.50 (4.85)	17.95 (7.53)	22.64 (5.89)
spleen	2.26 (0.65)	1.40 (0.23)	0.84 (0.23)	0.56 (0.24)
pancreas	5.51 (0.59)	1.84 (0.44)	0.87 (0.37)	0.79 (0.70)
heart	5.67 (1.02)	2.24 (0.56)	1.40 (0.49)	0.39 (0.68)
stomach[b]	3.29 (1.47)	4.73 (5.14)	7.45 (4.62)	7.61 (5.20)
brain	2.81 (0.19)	2.32 (0.21)	0.18 (0.06)	0.08 (0.04)

[a] Expressed as % injected dose per gram. Each value represents the mean (SD) for 4−5 animals. [b] Expressed as % injected dose per organ.

Biodistribution Experiments. To evaluate brain uptake of the aurone derivatives, biodistribution experiments were performed in normal mice with five radioiodinated aurones ([^{125}I]**9**, [^{125}I]**14**, [^{125}I]**15**, [^{125}I]**16**, and [^{125}I]**17**) (Table 2). Radioactivity after injection of the aurone derivatives penetrated the blood−brain barrier showing excellent uptake ranging from 1.7% to 4.5% ID/g brain at 2 min postinjection, a level sufficient for imaging β-amyloid plaques in the brain. In addition, it displayed good clearance from the normal brain with 0.1−0.4% ID/g at 30 min postinjection. Since normal mice were used for the biodistribution experiments, no Aβ plaques were expected in the young mice; therefore, the washout of probes from the brain should be rapid to obtain a higher signal-to-noise ratio earlier in the AD brain. One way to select a ligand with

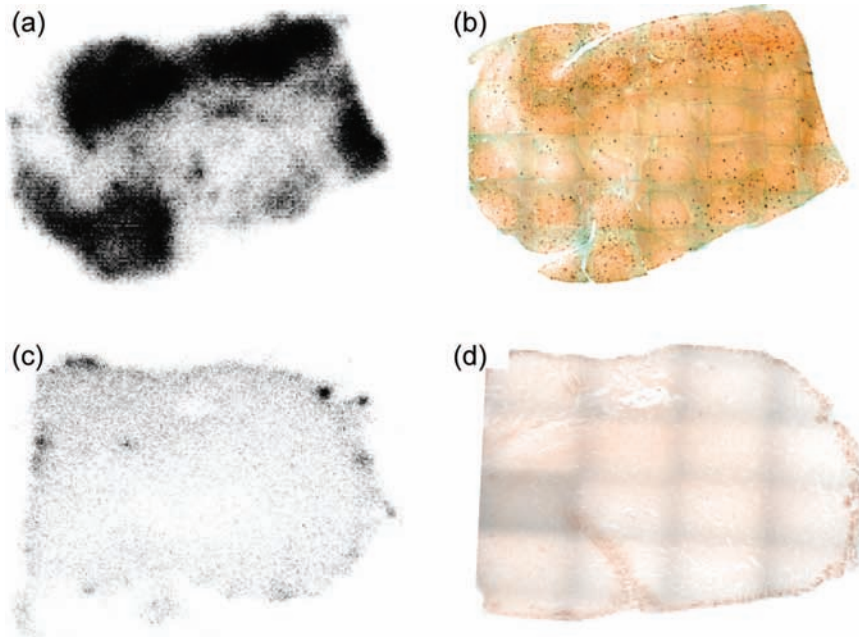

Figure 3. In vitro ARG of [^{125}I]**15** reveals a distinct labeling of amyloid plaques in AD brain sections (a). Under similar conditions, there is very little labeling of [^{125}I]**15** in control brain section (c). The presence and localization of plaques in the sections were confirmed with immunohistochemical staining using a monoclonal Aβ antibody (b, d).

appropriate in vivo kinetics is to use brain$_{2min}$/brain$_{30min}$ as an index to compare the washout rate. The five radioiodinated aurone derivatives [^{125}I]**9**, [^{125}I]**14**, [^{125}I]**15**, [^{125}I]**16**, and [^{125}I]**17** showed brain$_{2min}$/brain$_{30min}$ ratios of 15.4, 8.3, 18.8, 9.7, and 15.6, respectively. [^{125}I]**15** had the best washout index. Previously reported radioiodinated aurones showed high uptake (1.9−4.6% ID/g at 2 min postinjection) and good clearance from the brain (0.3−0.5% ID/g at 30 min postinjection) (*19*). However, the brain$_{2min}$/brain$_{30min}$ ratios of these compounds were 7.3−9.9, lower than that of [^{125}I]**15**, indicating that [^{125}I]**15** could clear more rapidly from the normal mouse brain than aurones with amino groups. It has been reported that [^{123}I]IMPY entered the brain rapidly (2.88% ID at 2 min postinjection) and was cleared from normal brain (0.26% ID at 30 min postinjection), indicating the brain$_{2min}$/brain$_{30min}$ ratio to be 11.1 (*16*). The aurone derivatives reported in this study appear superior to IMPY in pharmacokinetics, in addition to showing similar binding affinities sufficient for the imaging of β-amyloid plaques in vivo. The pharmacokinetics demonstrated by [^{125}I]**15** is critical to the detection of β-amyloid plaques in the AD brain.

In Vitro Autoradiography. Next, [^{125}I]**15** was investigated for its binding affinity for β-amyloid plaques by in vitro autoradiography in human AD brain sections as shown in Figure 3. Autoradiographic images of [^{125}I]**15** showed high levels of radioactivity in the brain sections (Figure 3a). Furthermore, we confirmed that the hot spots of [^{125}I]**15** corresponded with those of in vitro immunohistochemical staining in the same brain sections (Figure 3b). In contrast, normal human brain displayed no remarkable accumulation of [^{125}I]**15** (Figure 3c), correlating well with the absence of β-amyloid plaques (Figure 3d). These results demonstrate the feasibility of using [^{125}I]**15** as a probe for detecting β-amyloid plaques in the brains of AD patients with SPECT.

CONCLUSION

In conclusion, we successfully designed and synthesized a new series of aurone derivatives as amyloid-imaging agents with high affinity for Aβ(1−42) aggregates in vitro. The derivatives clearly stained amyloid plaques in an animal model of AD, reflecting strong binding to Aβ aggregates in vitro. In biodistribution experiments using normal mice, they displayed good penetration of and fast washout from the brain, especially [^{125}I]**15**. A specific plaque-labeling signal was clearly depicted by [^{125}I]**15** in postmortem AD brain sections. Taken together, the present results suggest [^{125}I]**15** to be a potentially useful probe for the SPECT-based imaging of β-amyloid plaques.

ACKNOWLEDGMENT

This work was supported in part by the Industrial Technology Research Grant Program in 2005 from the New Energy and Industrial Technology Development Organization (NEDO) of Japan and the Program for Promotion of Fundamental Studies in Health Sciences of the National Institute of Biomedical Innovation (NIBIO).

Supporting Information Available: HPLC data of compounds **9**, **14**, **15**, **16**, and **17**. This material is available free of charge via the Internet at http://pubs.acs.org.

LITERATURE CITED

(1) Klunk, W. E. (1998) Biological markers of Alzheimer's disease. *Neurobiol. Aging 19*, 145–7.
(2) Selkoe, D. J. (2001) Alzheimer's disease: genes, proteins, and therapy. *Physiol. Rev. 81*, 741–66.
(3) Selkoe, D. J. (2000) Imaging Alzheimer's amyloid. *Nat. Biotechnol. 18*, 823–4.
(4) Mathis, C. A., Wang, Y., and Klunk, W. E. (2004) Imaging β-amyloid plaques and neurofibrillary tangles in the aging human brain. *Curr. Pharm. Des. 10*, 1469–92.
(5) Nordberg, A. (2004) PET imaging of amyloid in Alzheimer's disease. *Lancet Neurol. 3*, 519–27.
(6) Mathis, C. A., Wang, Y., Holt, D. P., Huang, G. F., Debnath, M. L., and Klunk, W. E. (2003) Synthesis and evaluation of ^{11}C-labeled 6-substituted 2-arylbenzothiazoles as amyloid imaging agents. *J. Med. Chem. 46*, 2740–54.
(7) Klunk, W. E., Engler, H., Nordberg, A., Wang, Y., Blomqvist, G., Holt, D. P., Bergstrom, M., Savitcheva, I., Huang, G. F., Estrada, S., Ausen, B., Debnath, M. L., Barletta, J., Price, J. C., Sandell, J., Lopresti, B. J., Wall, A., Koivisto, P., Antoni, G., Mathis, C. A., and Langstrom, B. (2004) Imaging brain amyloid

in Alzheimer's disease with Pittsburgh compound-B. *Ann. Neurol. 55*, 306–19.

(8) Ono, M., Wilson, A., Nobrega, J., Westaway, D., Verhoeff, P., Zhuang, Z. P., Kung, M. P., and Kung, H. F. (2003) ^{11}C-labeled stilbene derivatives as Aβ-aggregate-specific PET imaging agents for Alzheimer's disease. *Nucl. Med. Biol. 30*, 565–71.

(9) Verhoeff, N. P., Wilson, A. A., Takeshita, S., Trop, L., Hussey, D., Singh, K., Kung, H. F., Kung, M. P., and Houle, S. (2004) In-vivo imaging of Alzheimer disease β-amyloid with [^{11}C]SB-13 PET. *Am. J. Geriatr. Psychiatry 12*, 584–95.

(10) Rowe, C. C., Ackerman, U., Browne, W., Mulligan, R., Pike, K. L., O'Keefe, G., Tochon-Danguy, H., Chan, G., Berlangieri, S. U., Jones, G., Dickinson-Rowe, K. L., Kung, H. P., Zhang, W., Kung, M. P., Skovronsky, D., Dyrks, T., Holl, G., Krause, S., Friebe, M., Lehman, L., Lindemann, S., Dinkelborg, L. M., Masters, C. L., and Villemagne, V. L. (2008) Imaging of amyloid beta in Alzheimer's disease with ^{18}F-BAY94-9172, a novel PET tracer: proof of mechanism. *Lancet Neurol. 7*, 129–35.

(11) Kudo, Y., Okamura, N., Furumoto, S., Tashiro, M., Furukawa, K., Maruyama, M., Itoh, M., Iwata, R., Yanai, K., and Arai, H. (2007) 2-(2-[2-Dimethylaminothiazol-5-yl]ethenyl)-6-(2-[fluoro]ethoxy)benzoxazole: A novel PET agent for in vivo detection of dense amyloid plaques in Alzheimer's disease patients. *J. Nucl. Med. 48*, 553–561.

(12) Agdeppa, E. D., Kepe, V., Liu, J., Flores-Torres, S., Satyamurthy, N., Petric, A., Cole, G. M., Small, G. W., Huang, S. C., and Barrio, J. R. (2001) Binding characteristics of radiofluorinated 6-dialkylamino-2-naphthylethylidene derivatives as positron emission tomography imaging probes for β-amyloid plaques in Alzheimer's disease. *J. Neurosci. 21*, RC189.

(13) Shoghi-Jadid, K., Small, G. W., Agdeppa, E. D., Kepe, V., Ercoli, L. M., Siddarth, P., Read, S., Satyamurthy, N., Petric, A., Huang, S. C., and Barrio, J. R. (2002) Localization of neurofibrillary tangles and β-amyloid plaques in the brains of living patients with Alzheimer disease. *Am. J. Geriatr. Psychiatry 10*, 24–35.

(14) Small, G. W., Kepe, V., Ercoli, L. M., Siddarth, P., Bookheimer, S. Y., Miller, K. J., Lavretsky, H., Burggren, A. C., Cole, G. M., Vinters, H. V., Thompson, P. M., Huang, S. C., Satyamurthy, N., Phelps, M. E., and Barrio, J. R. (2006) PET of brain amyloid and tau in mild cognitive impairment. *N. Engl. J. Med. 355*, 2652–63.

(15) Kung, M. P., Hou, C., Zhuang, Z. P., Zhang, B., Skovronsky, D., Trojanowski, J. Q., Lee, V. M., and Kung, H. F. (2002) IMPY: an improved thioflavin-T derivative for in vivo labeling of beta-amyloid plaques. *Brain Res. 956*, 202–10.

(16) Zhuang, Z. P., Kung, M. P., Wilson, A., Lee, C. W., Plossl, K., Hou, C., Holtzman, D. M., and Kung, H. F. (2003) Structure-activity relationship of imidazo[1,2-a]pyridines as ligands for detecting β-amyloid plaques in the brain. *J. Med. Chem. 46*, 237–43.

(17) Newberg, A. B., Wintering, N. A., Plossl, K., Hochold, J., Stabin, M. G., Watson, M., Skovronsky, D., Clark, C. M., Kung, M. P., and Kung, H. F. (2006) Safety, biodistribution, and dosimetry of ^{123}I-IMPY: a novel amyloid plaque-imaging agent for the diagnosis of Alzheimer's disease. *J. Nucl. Med. 47*, 748–54.

(18) Newberg, A. B., Wintering, N. A., Clark, C. M., Plossl, K., Skovronsky, D., Seibyl, J. P., Kung, M. P., and Kung, H. F. (2006) Use of ^{123}I IMPY SPECT to differentiate Alzheimer's disease from controls. *J. Nucl. Med. 47*, 78P.

(19) Ono, M., Maya, Y., Haratake, M., Ito, K., Mori, H., and Nakayama, M. (2007) Aurones serve as probes of β-amyloid plaques in Alzheimer's disease. *Biochem. Biophys. Res. Commun. 361*, 116–21.

(20) Roberts, M., Bentley, M., and Harris, J. (2002) Chemistry for peptide and protein PEGylation. *Adv. Drug Delivery Rev. 54*, 459–76.

(21) Harris, J., and Chess, R. (2003) Effect of pegylation on pharmaceuticals. *Nat. Rev. Drug Discovery 2*, 214–21.

(22) Cheng, Y., and Prusoff, W. (1973) Relationship between the inhibition constant (K1) and the concentration of inhibitor which causes 50% inhibition (I50) of an enzymatic reaction. *Biochem. Pharmacol.* 3099–3108.

(23) Bryant, W., and Huhn, G. (1995) A practical preparation of 7-methoxy-3(2H)-benzofuranone. *Synth. Commun. 25*, 915–20.

(24) Kung, M. P., Hou, C., Zhuang, Z. P., Skovronsky, D., and Kung, H. F. (2004) Binding of two potential imaging agents targeting amyloid plaques in postmortem brain tissues of patients with Alzheimer's disease. *Brain Res. 1025*, 98–105.

(25) Zhang, W., Oya, S., Kung, M. P., Hou, C., Maier, D. L., and Kung, H. F. (2005) F-18 stilbenes as PET imaging agents for detecting β-amyloid plaques in the brain. *J. Med. Chem. 48*, 5980–8.

BC8003292

Supporting Information for

Novel radioiodinated aurones as probes for SPECT imaging of β-amyloid plaques in the brain

Yoshifumi Maya,[†] Masahiro Ono,*[,†,‡] Hiroyuki Watanabe,[†] Mamoru Haratake,[†] Hideo Saji,[‡] Morio Nakayama,*[,†]

[†]Department of Hygienic Chemistry, Graduate School of Biomedical Sciences, Nagasaki University, 1-14 Bunkyo-machi, Nagasaki 852-8521, [‡]Department of Patho-Functional Bioanalysis, Graduate School of Pharmaceutical Sciences, Kyoto University, 46-29 Yoshida Shimoadachi-cho, Sakyo-ku, Kyoto 606-8501, Japan.

Reversed-phase HPLC analysis for compound 9, 14, 15, 16 and 17.

Compound	Retention time
9	11.9
14	5.23
15	12.6
16	12.2
17	11.8

UV (254 nm) trace of aurone derivatives by reversed-phase HPLC analysis using a mixture of H_2O/acetonitrile 3/7 for 9 and 17 or 1/1 for 15, 16 and 17 as a mobile phase.

Reversed-phase HPL C analysis for compound 9, 14, 15, 16 and 17.

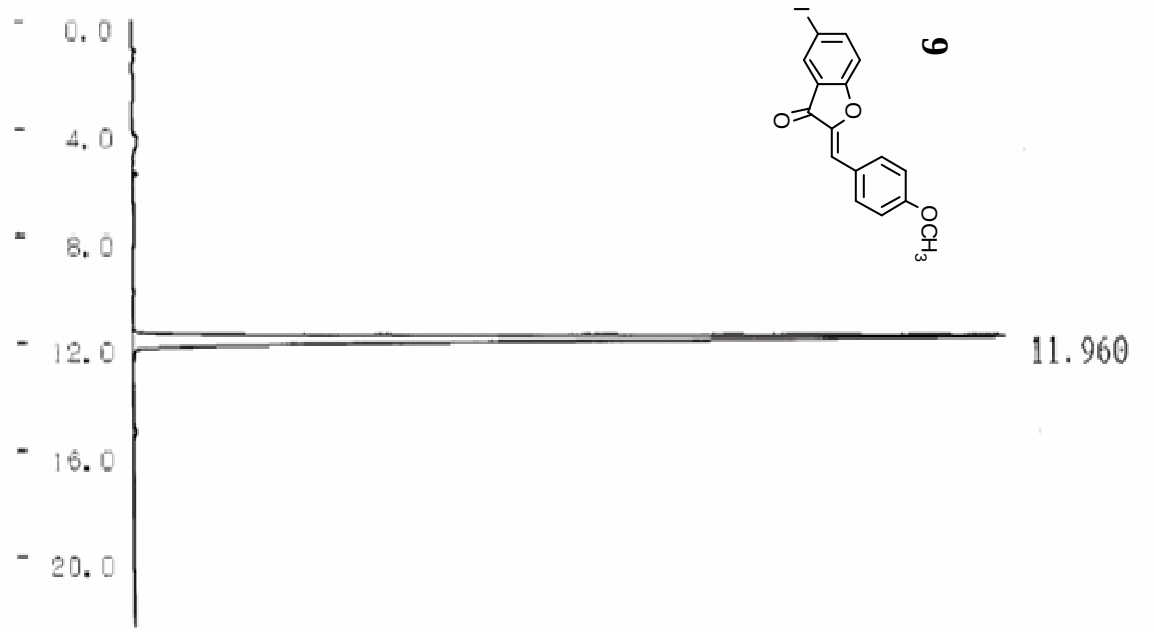

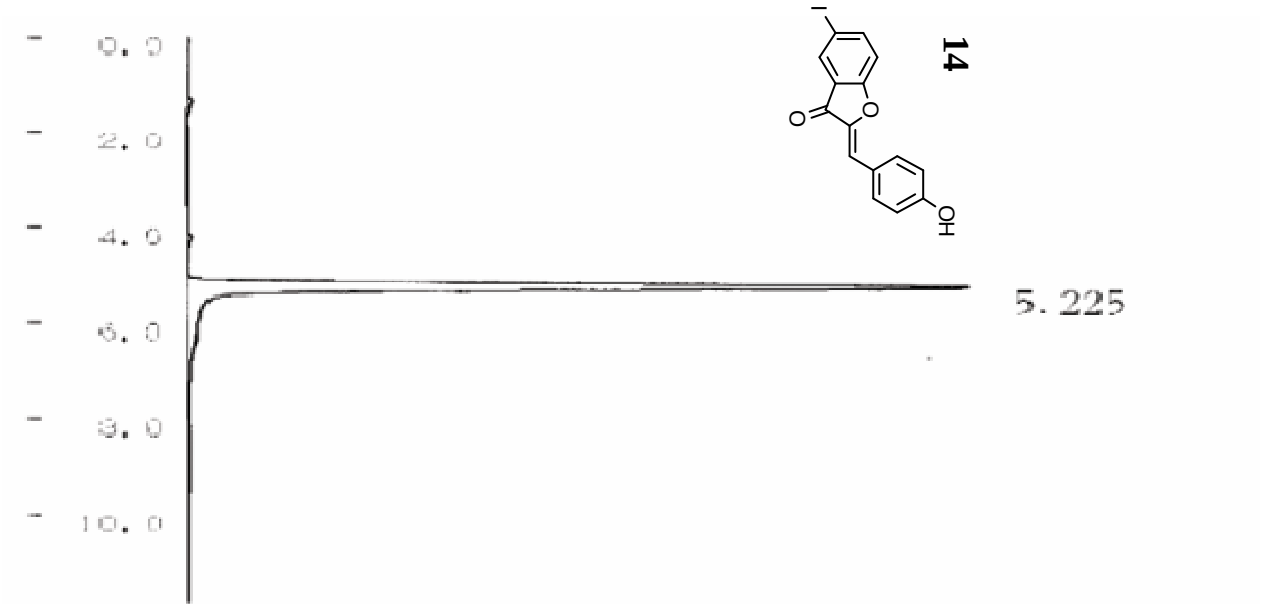
0.0
2.0
4.0
6.0
8.0
10.0
14
5.225

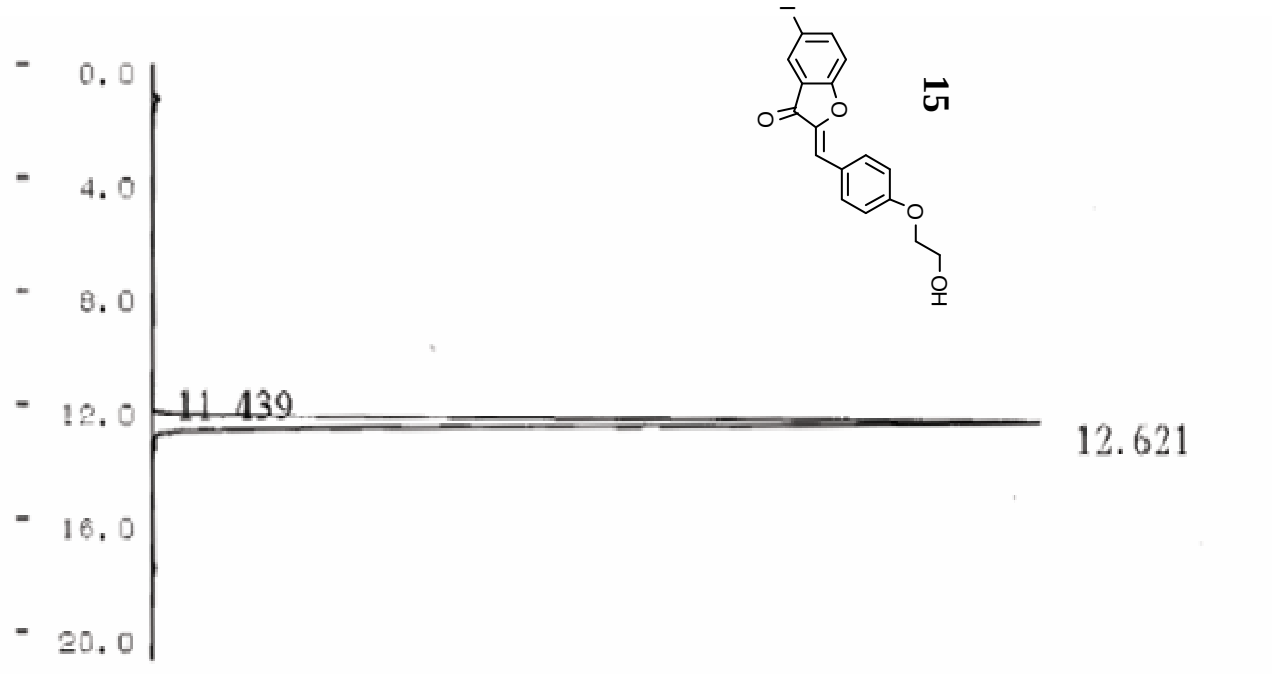
0.0
4.0
8.0
12.0
16.0
20.0
11.439
15
12.621

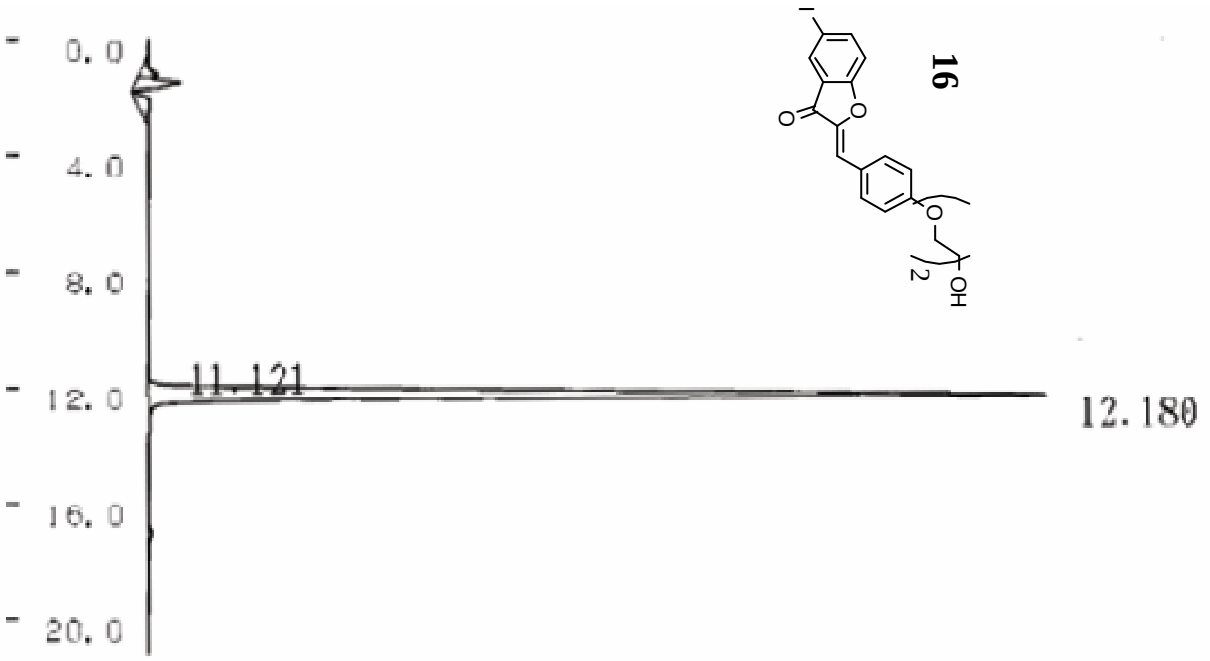
0.0
4.0
8.0
12.0
16.0
20.0
11.121
12.180
16
OH
2

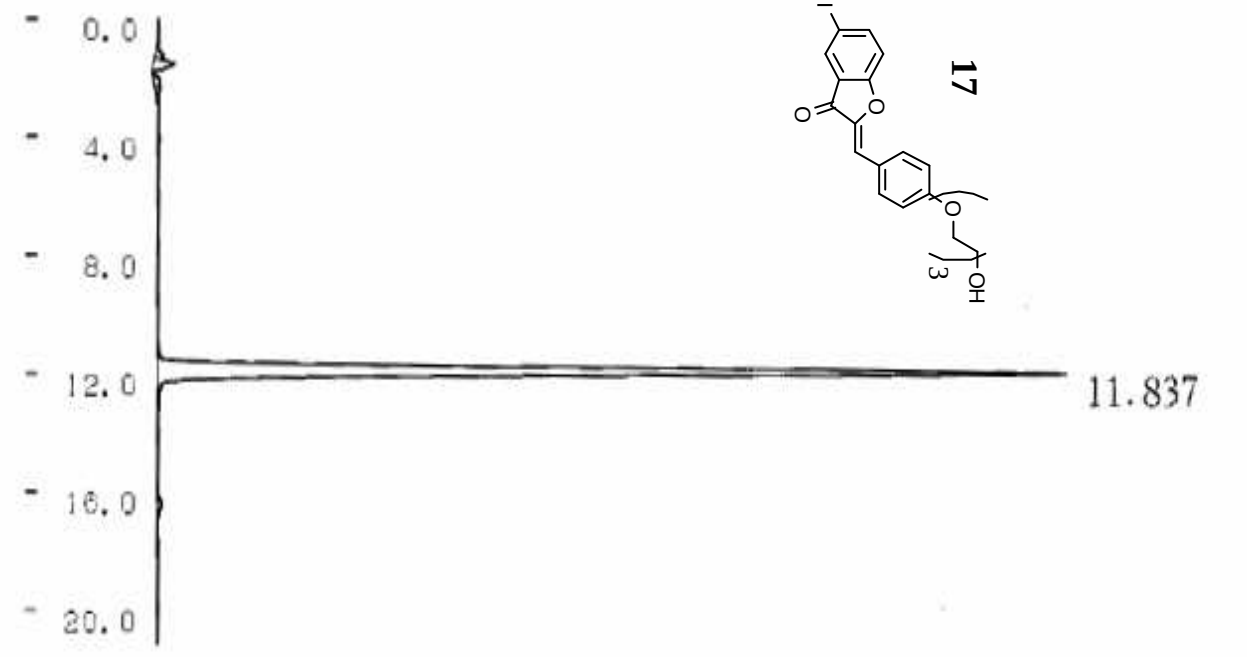
0.0
4.0
8.0
12.0
16.0
20.0
11.837
17
OH
3

Bioconjugate Chemistry 20th Anniversary

Subscriber access provided by SHEMYAKIN-OVCHINNIKOV INST

Article

Surface-Anchoring of Spontaneously Dimerized Epidermal Growth Factor for Highly Selective Expansion of Neural Stem Cells

Tadashi Nakaji-Hirabayashi, Koichi Kato, and Hiroo Iwata

Bioconjugate Chem., **2009**, 20 (1), 102-110• DOI: 10.1021/bc800331t • Publication Date (Web): 30 December 2008

Downloaded from http://pubs.acs.org on May 8, 2009

More About This Article

Additional resources and features associated with this article are available within the HTML version:

- Supporting Information
- Access to high resolution figures
- Links to articles and content related to this article
- Copyright permission to reproduce figures and/or text from this article

View the Full Text HTML

ACS Publications
High quality. High impact.

Bioconjugate Chemistry is published by the American Chemical Society. 1155 Sixteenth Street N.W., Washington, DC 20036

Surface-Anchoring of Spontaneously Dimerized Epidermal Growth Factor for Highly Selective Expansion of Neural Stem Cells

Tadashi Nakaji-Hirabayashi, Koichi Kato, and Hiroo Iwata*

Institute for Frontier Medical Sciences, Kyoto University, 53 Kawahara-cho, Shogoin, Sakyo-ku, Kyoto 606-8507, Japan.
Received July 31, 2008; Revised Manuscript Received November 21, 2008

To develop culture substrates for use in selective expansion of neural stem cells (NSCs), epidermal growth factor (EGF)-containing chimeric proteins were designed and synthesized by means of recombinant DNA technology. The chimeric proteins consisted of three components including an EGF domain, an α-helical oligopeptide, and a hexahistidine sequence. Two different α-helical oligopeptides were separately incorporated into chimeric proteins. Structural analyses by native gel electrophoresis and circular dichroism spectroscopy revealed that the heterodimer of these proteins was spontaneously formed through coiled-coil association of the α-helical oligopeptides. The monomeric and dimeric forms of these chimeric proteins were immobilized to the glass-based substrate via coordinate bonding between the hexahistidine and Ni(II) ions fixed on a substrate. The results of cell culture assays with NSCs showed that cells proliferated most rapidly and selectively on a substrate with the surface-anchored EGF dimer. The rate of cell proliferation on the surface with dimeric EGF was 1.3−2.0 times higher on the surfaces with monomeric EGF. In addition, the content of stem cells, determined 96 h after cell seeding, was highest on the surface with dimeric EGF (98%) among the surfaces studied (90−97% on surfaces with monomeric EGF). The observed growth rate and the stem cell content on the surface with EGF dimer were far beyond those in the standard neurosphere culture. The effect of surface-anchored dimeric EGF may be attributed to the enhanced dimerization of EGF-EGF receptor complexes leading to efficient signaling for mitogenic activity. We conclude that surface-anchoring of the EGF dimer provides an excellent substrate that allows the highly efficient expansion of NSCs.

INTRODUCTION

Large-scale production of neural stem cells (NSCs) with high purity is crucial for their clinical application in cell transplantation therapy for neurodegenerative diseases such as Parkinson's disease (*1, 2*). The culture substrate previously developed by our group (*3*) has the potential to provide the culture method that allows to selective expansion of NSCs from heterogeneous cell populations. The substrate was designed to display epidermal growth factor (EGF), a strong activator for the proliferation of NSCs (*4*), on the surface of a glass-based substrate. The key feature of substrate preparation was to terminally anchor EGF molecules to the surface through the hexahistidine sequence that was fused with EGF via recombinant DNA technology (*5*). The surface-anchoring of engineered growth factors was also reported by Ogiwara et al. (*6, 7*) and Nagaoka et al. (*8*).

The EGF-anchored substrate facilitates production of a cell population rich in NSCs (purity >92%). The selectivity of stem cell expansion is much higher than the neurosphere culture (*9, 10*) that has been used as the most standard method to obtain NSCs. However, a population expanded by our culture method still contains approximately 7% differentiated cells. For this reason, the present study was undertaken to improve much more the efficiency of NSC production. Our strategy adopted here was to promote the interaction of surface-anchored EGF with EGF receptors (EGFR) by designing spontaneously dimerizing EGF.

Numerous studies have shown that EGF binding to EGFR triggers receptor dimerization that is considered to be a critical step for the subsequent transduction of intracellular signaling (*11*). Inspired by this mechanism, we designed EGF-containing chimeric proteins that spontaneously form a dimerized form of EGF. The dimer was terminally anchored onto the substrate. Our expectation is that the preformed dimeric structure of EGF facilitates the formation of EGF-EGFR dimer complexes more efficiently than the monomeric form of EGF as presented on our previous substrate.

Our strategy for the spontaneous dimerization of EGF is to incorporate an α-helical oligopeptide that has the ability to participate in the formation of a coiled-coil structure. To avoid aggregation of proteins in expression host cells due to spontaneous homodimerization, we implemented here a heterodimerization system in which $(EKLASVK)_5$ (K5) and $(KELASVE)_5$ (E5) peptides form a stable coiled-coil structure. These peptides were designed according to previous reports (*12, 13*). The coiled-coil structure formed by the intermolecular association of α-helical peptides is an abundant motif found in various proteins (*14*) and has also been utilized for creating engineered biomaterials such as hydrogels (*15*−*17*), nanostructured molecular machines (*18*), and scaffolds for tissue engineering (*19*).

In this study, we synthesized two chimeric proteins containing an EGF domain and the K5 or E5 oligopeptide. As we previously reported, a hexahistidine sequence was further added to the C-terminus of both chimeric proteins, so as to anchor the chimeric proteins through coordination to the substrate on which Ni(II) ions were fixed. The heterodimerization of chimeric proteins was examined by native polyacrylamide gel electrophoresis (native PAGE) and circular dichroism (CD) spectroscopy. The effect of surface-anchored EGF dimer was studied by analyzing the adhesion and proliferation of cultured NSCs and the phosphorylation of EGFR. These assays revealed that NSCs proliferate much

* To whom correspondence should be addressed. Prof. Hiroo Iwata, E-mail: iwata@frontier.kyoto-u.ac.jp, Tel & Fax: +81-75-751-4119.

10.1021/bc800331t CCC: $40.75 © 2009 American Chemical Society
Published on Web 12/30/2008

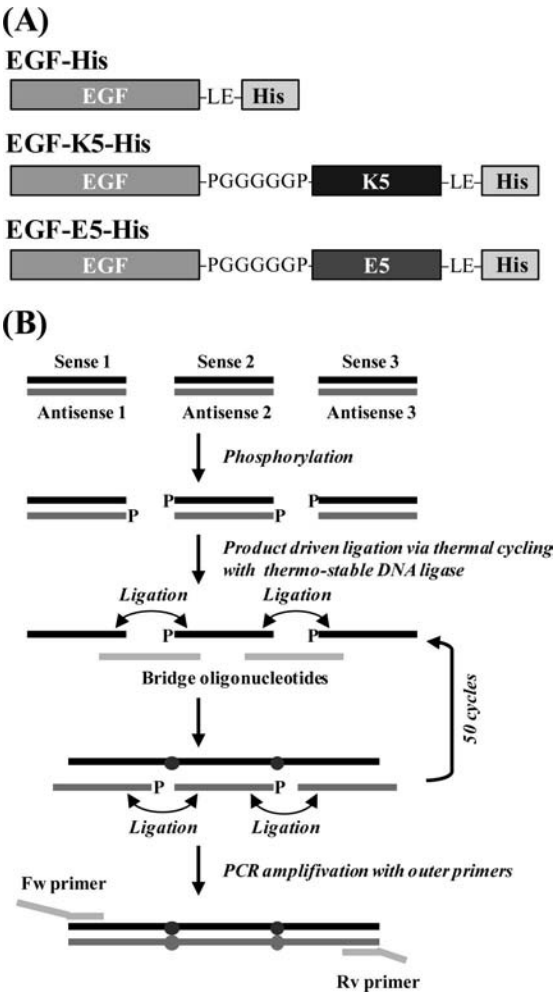

Figure 1. (A) Structure of EGF-containing chimeric proteins synthesized. (B) Schematic representation for the preparation of chimeric genes.

rapidly on the substrate with dimeric EGF than that with the monomeric one.

EXPERIMENTAL PROCEDURES

Plasmids. Synthetic DNA fragments (ca. 50 mer) corresponding to 5′-terminal, middle, and 3′-terminal parts of DNA encoding $(EKLASVK)_5$ (K5) and $(KELASVE)_5$ (E5) were purchased from Invitrogen (Carlsbad, CA). The 5′-terminal fragment contained 21-mer oligonucleotides for heptapeptides (PGGGGGP) to be inserted between EGF and the K5 or E5 sequence as a flexible linker (*20*, *21*) (Figure 1A). These fragments were ligated with each other in a proper order using the method by Pachuk et al. (*22*) to obtain DNAs encoding full-length K5 or E5 flanked with PGGGGGP at the N-terminus. The sequence of all oligonucleotides was shown in Table 1. All steps for ligation are schematically represented in Figure 1B. The 5′-end of the DNA fragments including sense 2 and 3 and antisense 2 and 3 were phosphorylated using T4 polynucleotide kinase. Then, the phosphorylated oligonucleotides were mixed with sense 1 and antisense 1 (each 1 μM) in a 50 μL reaction buffer (20 mM Tris-HCl, 25 mM KCl, 10 mM magnesium chloride, 0.5 mM NAD, and 0.01% Triton X-100, pH 8.3) containing 0.3 U/μL thermostable DNA ligase (Ampligase, Epicenter Technologies, Madison, WI) and 1 μM bridge oligonucleotides (Table 1). Chain reaction cloning was allowed to proceed by thermal cycling using GeneAmp 9600 (Applied Biosystems, Foster City, CA) under the following conditions: 50 cycles, denaturation at 94 °C for 30 s, annealing at 58 °C for 30 s, and ligation at 66 °C for 1 min. Finally, the ligated DNA was amplified by polymerase chain reaction (PCR) using outer primers (Table 1). The forward primers contained 20-mer oligonucleotides that overlapped with the 3′-region of EGF gene. Reverse primers contained an Xho I restriction site. On the other hand, the EGF gene was amplified by PCR from pET-22b-EGF (*4*) using specific primers (Table 1). The forward primers contained an Nde I site at the 5′-end. The reverse primers were flanked with 20-mer oligonucleotides that overlapped with the 5′-region of DNA for PGGGGGP-K5 or PGGGGGP-E5. The DNAs for EGF and PGGGGGP-K5 or PGGGGGP-E5 were annealed, extended by overlap extension (*23*), and amplified by PCR to obtain EGF-PGGGGGP-K5 and EGF-PGGGGGP-E5 chimeric genes. The chimeric genes were digested with Nde I and Xho I and inserted into the Nde I-Xho I site of pET-22b (Novagen, Darmstadt, Germany). The plasmids (pET-22b-EGF-K5, pET-22b-EGF-E5) were cloned in *Escherichia coli* (*E. coli*) DH5α. The correctness of the plasmids was confirmed by sequencing.

Protein Expression, Purification, and Refolding. The EGF chimeric proteins, EGF-K5-His and EGF-E5-His, were expressed in *E. coli* strain BL21-codonplus (Stratagene, La Jolla, CA) using overnight express autoinduction system (Novagen). The preparation of a control protein, EGF-His, was reported previously (*4*). These proteins obtained as inclusion bodies were extracted with 8 M urea solution containing 5 mM 2-mercaptoethanol and then purified using a Prime AKTA chromatography system (GE Healthcare Bio-Science Corp., Piscataway, NJ) equipped with a His Trap HP column (GE Healthcare). These proteins were refolded by dialyzing against a solution of reduced and oxidized forms of glutathione. The detailed conditions of the refolding procedure were provided in Supporting Information Table S3. Protein concentration was determined using a microBCA kit (Pierce Biotechnology, Rockford, IL). The yields of EGF-K5-His and EGF-E5-His were determined to be, respectively, 210 mg and 275 mg per liter of medium. The purity and molecular size of proteins were analyzed by sodium dodecylsulfate-polyacrylamide gel electrophoresis (SDS-PAGE). The biological activity of EGF contained in these proteins was assessed from the mitogenic activity in neurosphere culture (*9*).

Heterodimerization. EGF-K5-His and EGF-E5-His were mixed in PBS at various compositions, and the coiled-coil association between E5 and K5 peptide segments was allowed to proceed at room temperature for 30 min to obtain their heterodimer (dEGF-His). Heterodimerization was assessed by native PAGE in which 3 μg of total proteins were electrophoresced in 16% polyacrylamide gel with 50 mM Tris-HCl running buffer (pH 8.3) containing 192 mM glycine followed by staining with Coomassie brilliant blue.

CD Spectroscopy. Chimeric proteins were dissolved in PBS (pH 7.4) to a mean residue concentration of 4.2 mM (EGF-His) or 4.4 mM (EGF-K5-His, EGF-E5-His, and dEGF-His). dEGF-His solution was prepared by mixing 0.5 mg/mL EGF-E5-His (250 μL) with 0.5 mg/mL EGF-K5-His (250 μL). CD spectra were recorded with JASCO J-805 spectropolarimeter and a 1-mm path length cell at a response time of 0.5 s, a bandwidth of 1 nm, a scan speed of 100 nm/min, and 20 °C with an accumulation of 8 scans.

Substrate Preparation. As reported previously (*3*), EGF-containing chimeric proteins were anchored through the His sequence onto a glass-based substrate bearing a thin gold layer and a carboxylic acid-terminated alkanethiol monolayer on the surface. In brief, the mixed self-assembled monolayer consisting of 10% 16-mercapto-1-hexadecanoic acid (Aldrich, Munich, Germany) and 90% (1-mercaptoundec-11-yl)triethylene glycol

Table 1. Sequences of Primers and Oligonucleotides Used for the Synthesis of EGF-K5-His and EGF-E5-His

(A) EGF-K5-His

primer or oligonucleotide	sequence (5′ → 3′)
K5-sense 1	ctgaagtggtgggaactgcgcccaggcggtggaggtgggccggagaaattagcttct
K5-sense 2	gttaaggaaaagttggcctcagtcaaagagaagctcgcaagtgtgaaagaa
K5-sense 3	aaactggcgtccgtaaaggaaaaactcgctagcgtaaagctcgagcatgatg
K5-antisense 1	agaagctaatttctccggcccacctccaccgcctgggcgcagttcccaccacttcag
K5-antisense 2	ttctttcacacttgcgagcttctctttgactgaggccaacttttccttaac
K5-antisense 3	catcatgctcgagctttacgctagcgagtttttccttacggacgccagttt
bridge oligonucleotide I	gaggccaacttttccttaacagaagctaatttctccggcc
bridge oligonucleotide II	tcctttacggacgccagtttttctttcacacttgcgagct
forward primer	ctgaagtggtgggaactgcgcc
reverse primer	catcatgctcgagctttacgc
forward primer for EGF	ggccggcatatgaatagtgactctgaatgtcccc
reverse primer for EGF	tctccggcccaccgcctgggcgcagttcccaccacttcag

(B) EGF-E5-His

primer or oligonucleotide	sequence(5′→3′)
E5-sense 1	ctgaagtggtgggaactgcgcccaggcggtggaggtgggccgaaggagttagcttct
E5-sense 2	gttgaaaaggaattggcctcagtcgagaaagaactcgcatccgtagagaag
E5-sense 3	gagctagcgagtgtggaaaaggagcttgctagcgttgaactcgaggatctag
E5-antisense 1	agaagctaactccttcggcccacctccaccgcctgggcgcagttcccaccacttcag
E5-antisense 2	cttctctacggatgcgagttctttctcgactgaggccaattccttttcaac
E5-antisense 3	ctagatcctcgagttcaacgctagcaagctcctttccacactcgctagctc
bridge oligonucleotide I	gaggccaattcctttcaacagaagctaactccttcggcc
bridge oligonucleotide II	cttttccacactcgctagctccttctctacggatgcgagttc
forward primer	ctgaagtggtgggaactgcgcc
reverse primer	ctagatcctcgagttcaacgc
forward primer for EGF	ggccggcatatgaatagtgactctgaatgtcccc
reverse primer for EGF	ccttcggcccaccgcctgggcgcagttcccaccacttcag

(TEG-thiol, SensoPath Technologies, Bozeman, MT) was formed on a gold-evaporated surface. The triethylene glycol-terminated alkanethiol was used to prevent nonspecific protein adsorption and to control the surface density of EGF chimeric proteins (*3*). Then, the terminal carboxylic acid of 16-mercapto-1-hexadecanoic acid was activated by immersing the plate in an aqueous solution containing 50 mM *N*,*N*′-dicyclohexyl carbodiimide and 25 mM *N*-hydroxysuccinimide at room temperature for 30 min. Then, the plate was exposed to an aqueous solution containing 10 mM *N*-(5-amino-1-carboxypentyl) iminodiacetic acid (NTA; Dojindo Laboratories, Kumamoto, Japan) to couple with the activated carboxylic acid followed by exposure to 40 mM $NiSO_4$ solution to chelate Ni(II) ions. The His sequence in the chimeric proteins was coordinated to the fixed Ni(II) ions to anchor the proteins onto the surface. For the immobilization of dEGF-His, a solution containing 0.5 mg/mL EGF-E5-His and 0.5 mg/mL EGF-K5-His was prepared, and then the Ni(II)-chelated surface was exposed to the mixted solution. Prior to cell culture assays, the glass plates were washed with PBS and culture medium to remove weakly adsorbed chimeric proteins.

Surface Plasmon Resonance (SPR) Analysis. SPR analysis was carried out as before (*3*, *24*) using an in-house SPR apparatus. The light reflectance was continuously monitored at an incident angle 0.5° smaller than the resonance angle during the following procedures: After equilibrating with PBS, the surface of a Ni(II)-chelated gold plate was exposed to 20 mM sodium phosphate buffer (pH 7.4) containing 20 mM imidazole (binding buffer) in a flow cell for 5 min followed by circulation of binding buffer containing 50 μg/mL chimeric protein for 65 min. Subsequently, pure binding buffer was circulated for 50 min. The reflectance was converted to the resonance angular shift. The angular shift observed before and after the binding of chimeric protein was converted to the amount of EGF chimeric protein, assuming that unit angular shift corresponds to a protein density of 0.5 μg/cm^2 (*25*).

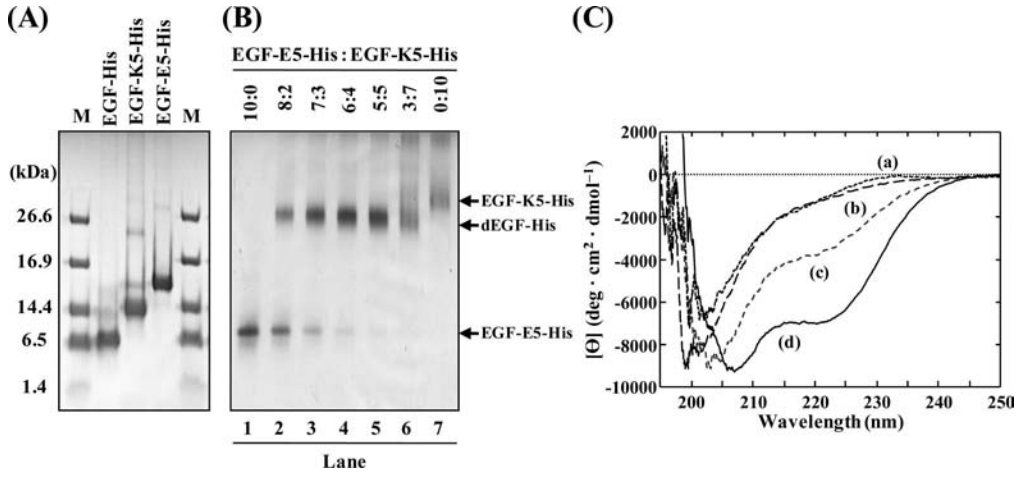

Figure 2. (A) The result of SDS-PAGE analysis for EGF-His, EGF-K5-His, and EGF-E5-His. M represents molecular weight standard. (B) The result of native-PAGE analysis performed for the mixture of EGF-K5-His and EGF-E5-His at various compositions. Compositions are indicated above the image of the gel. (C) Circular dichroism spectra of (a) EGF-His, (b) EGF-E5-His, (c) EGF-K5-His, and (d) dEGF-His.

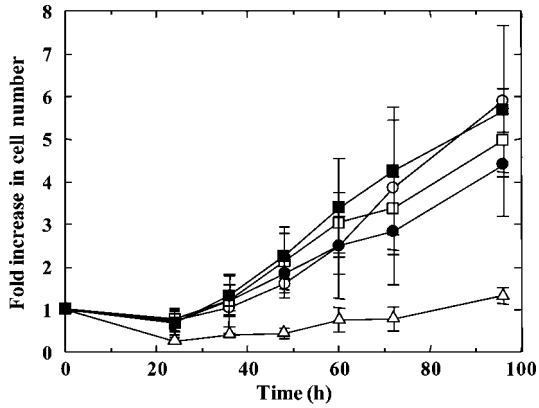

Figure 3. The growth curve of neurosphere-forming cells cultured in suspension in base medium containing 2% B27 with 20 ng/mL (○) EGF-His, (●) EGF-E5-His, (□) EGF-K5-His, and (■) dEGF-His or (Δ) without growth factor (control). Initial cell number: 2.1×10^4 cells/mL.

Table 2. Percentages of Cells Expressing Nestin and βIII after 4-Day Suspension Culture in the Presence of Chimeric Proteins or 4-Day Adherent Culture on the Substrate with Surface-Anchored Chimeric Proteins[a]

Chimeric protein	Nestin$^+$ βIII$^-$		Nestin$^+$	Nestin$^-$ βIII$^+$	Nestin$^-$ βIII$^-$
Dissolved in medium					
EGF-His	51.8 ± 10.9		61.2 ± 11.2	12.0 ± 4.4	26.8 ± 13.1
EGF-K5-His	45.1 ± 13.1		54.3 ± 08.3	11.7 ± 5.2	34.0 ± 10.3
EGF-E5-His	54.9 ± 14.3		64.5 ± 14.9	12.4 ± 7.1	23.1 ± 12.8
dEGF-His	52.6 ± 12.6		60.2 ± 14.0	9.8 ± 4.7	30.0 ± 16.7
Immobilized on substrate					
EGF-His	90.1 ± 3.5		4.4 ± 1.2	4.3 ± 1.6	0.7 ± 0.1
EGF-K5-His	96.7 ± 1.0	*	2.4 ± 0.6	0.5 ± 0.3	0.4 ± 0.2
EGF-E5-His	96.7 ± 1.8	*	1.0 ± 0.8	0.5 ± 0.4	0.2 ± 0.1
dEGF-His	98.3 ± 0.6		1.0 ± 0.4	0.5 ± 0.4	0.4 ± 0.3

[a] Data are expressed as mean ± standard deviation ($n = 3$, dissolved in medium; $n = 5$, immobilized on substrate). *Statistically significant (Tukey's HSD test, $p < 0.05$).

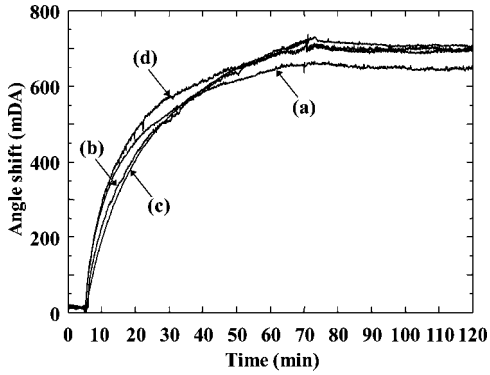

Figure 4. SPR sensorgrams obtained during the binding and dissociation of (a) EGF-His, (b) EGF-K5-His, (c) EGF-E5-His, and (d) dEGF-His to the Ni-chelated surfaces.

Cell Isolation and Culture. Cell isolation from the striatum of rat fetus (E16) and neurosphere culture were performed as reported previously (*3*−*5*). All the procedures were conducted according to the guidelines of the Animal Welfare Committee of the institute. Neurosphere forming cells at passage 2 were dissociated into single cells by treatment with 0.05% trypsin-EDTA solution. The single cells were suspended in a base medium [DMEM/F12 (1:1), 3 mM glutaMAX, 100 units/mL penicillin, 100 μg/mL streptomycin, and 5 μg/mL heparin] supplemented with 2% B27, and then seeded at 3×10^4 cells/cm^2 onto the substrates prepared as described earlier. Cells were cultured for 4 days at 37 °C under 5% CO_2 atmosphere. Finally, cells were washed gently with base medium to remove weakly adhering cells and observed with a phase-contrast optical microscope (BX51 TRF, Olympus Optical Co., Ltd., Tokyo, Japan).

Cell Proliferation Assay. Cell proliferation assays were carried out with neurosphere-forming cells cultured in suspension under base medium supplemented with 2% B27 containing 20 ng/mL EGF-His, EGF chimeric proteins, or recombinant human EGF (rhEGF, Invitogen Corp., Carlsbad, CA). Cells were cultured for 4 days, and then cell number was determined by the modified MTT assay (*3*). Cells were incubated in the base medium containing 10% cell counting reagent SF (Nacali Tesque, Kyoto, Japan) for 3 h, and then absorbance at 450 nm was determined for the medium using a microplate reader (model 5500, Bio-Rad, Hercules, CA). The number of cells proliferated on the substrates was also determined by the modified MTT assay. After the substrate was washed with DMEM/F12 (1:1) to remove nonadhering cells, cell number was determined as described above. The absorbance was converted to cell number using a calibration curve. The assays were carried out at 24, 36, 48, 60, 72, and 96 h after cell seeding.

Immunocytochemistry. After fixation and permeabilization, cells were immunofluorescently stained using antibodies against a neural stem cell marker (nestin, 1:200, mouse monoclonal Rat 401, BD pharmingen, Franklin Lakes, NJ) and a neuronal marker (class III β-tubulin; βIII, 1:600, rabbit polyclonal, Covance, Princeton, NJ), as reported previously (*3*, *5*, *23*). The localization of fluorescently labeled secondary antibodies was analyzed with an epifluorescent microscope (DP70, Olympus). Cells expressing these markers were counted on microphotographs for the area of 340×460 μm^2, which contained at most approximately 800 total cells, using *Image J* software (National Institutes of Health, Bethesda, MD). Cell numbers were determined on five different microphotographs for each sample, and the data are shown as the mean plus/minus standard deviation for five independent samples. In addition, neurosphere cells were dissociated and immunocytochemically stained. The conditions for fixation, permeabilization, blocking, reaction with antibodies, and counterstaining were the same as described above, but these procedures were performed in suspension by separating cells from each solution by centrifugation. The total cells and nestin- and βIII-positive cells were counted in the same manner as described above.

Western Blotting. Cells cultured for 2 days on the substrate were harvested using a cell scraper and dissolved in a lysis buffer (20 mM Tris-HCl, 150 mM NaCl, 1 mM EDTA, 1 mM EGTA, 1% Triton X-100, 1 mM Na_3VO_4, 10 mM $Na_4P_2O_7$, and 25 mM β-glycerolphosphate; pH 7.5) containing a cocktail of protease inhibitors (Complete Mini, Roche Diagnostics, Mannheim, Germany). The lysate was separated by SDS-PAGE and electrically blotted to a poly(vinylidene fluoride) membrane. After blocking with Blocking One-P (Nacalai Tesque, Kyoto, Japan), the membrane was immersed in a solution containing antibody against the phosphorylated form of EGFR (1:1000, #2236, Cell Signaling Technology, Danvers, MA) or total EGFR (1:1000, #2232, Cell Signaling Technology). The antibodies bound to the membrane were reacted with HRP-linked secondary antibody (1:5000, GE Healthcare) and visualized by the chemiluminescence reagent

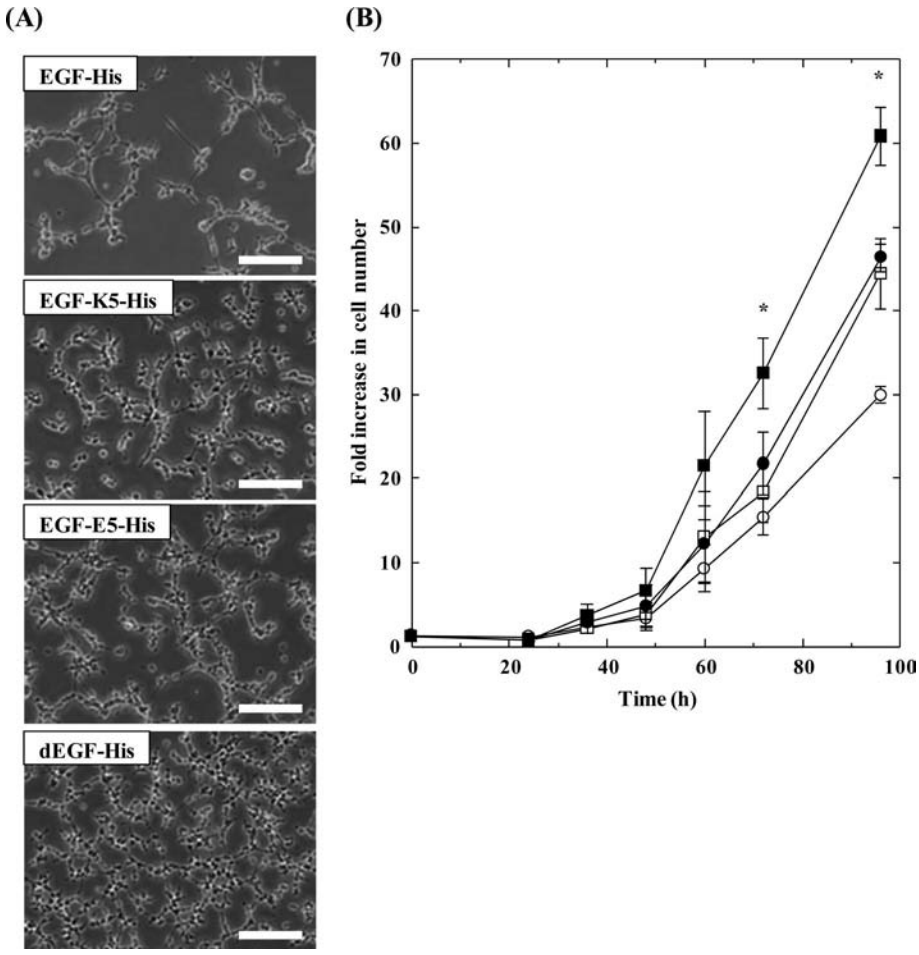

Figure 5. (A) Phase-contrast images of cells cultured for 48 h on the substrates with surface-anchored chimeric proteins. The identity of surface-anchored chimeric proteins is shown in the images. Bars: 100 μm. (B) Growth curves of cells cultured on the substrate with surface-anchored (○) EGF-His, (●) EGF-E5-His, (□) EGF-K5-His, and (■) dEGF-His. Data are expressed as mean ± standard deviation ($n = 3$). Cell seeding density: 3.0×10^4 cells/cm^2. *Cell growth on the substrates with dEGF-His was significantly large compared with that on each of the other substrates (Tukey's HSD test, $p < 0.05$). Apparent doubling time was 14.6 ± 2.3 h (EGF-His), 10.0 ± 1.0 h (EGF-K5-His), 8.7 ± 1.2 (EGF-E5-His), and 7.1 ± 1.3 h (dEGF-His), when determined from growth curves for 24−60 h.

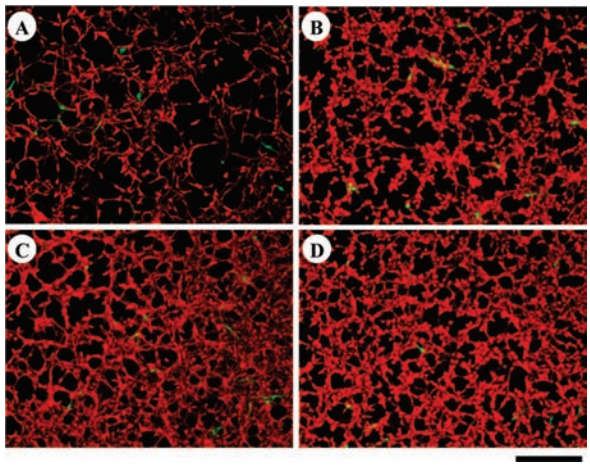

Figure 6. Immunofluorescent staining of nestin (red) and βIII (green) expressed in cells cultured for 4 days on the substrate with surface-anchored (A) EGF-His, (B) EGF-E5-His, (C) EGF-K5-His, and (D) dEGF-His. Bars: 100 μm.

(ECL plus, GE Healthcare). The intensity of protein bands was determined using *Image J* software. The data are shown as mean plus/minus standard deviation for three independent experiments.

Statistical Analysis. The results of cell proliferation, immunostaining of nestin and βIII, and Western blotting were statistically analyzed using software (JMP5.0.1a, SAS Institute Inc., Cary, NC). One-way analysis of variance (ANOVA) was performed for assessing significant differences. Tukey's honestly significant difference (HSD) test was performed for multiple comparisons at a significance level set of $p < 0.05$.

RESULTS

Characterization of Chimeric Proteins. As shown in Figure 2A, purified EGF-K5-His, EGF-E5-His, and EGF-His gave single bands in SDS-PAGE analysis. The molecular weights estimated from the mobility of protein bands are 7.1 kDa for EGF-His, 14.8 kDa for EGF-K5-His, and 15.6 kDa for EGF-E5-His. These molecular weights are nearly in agreement with those estimated from their amino acid compositions. However, a slight difference is seen between EGF-E5-His and EGF-K5-His, though these proteins are expected to have similar molecular weights. This is probably due to the acidic nature of EGF-E5-His that has the low capacity of SDS binding and hence exhibits reduced mobility in SDS-PAGE.

Figure 2B shows the result of native PAGE analysis carried out for the mixture of EGF-K5-His and EGF-E5-His at various compositions. Lanes 1 and 7 represent results for pure EGF-K5-His and EGF-E5-His, respectively. When the mixtures of these proteins were analyzed (Figure 2B, lanes 2−6), new bands appeared at the position between the bands of EGF-K5-His and EGF-E5-His, associated with a decrease in band intensity for both EGF-K5-His and EGF-E5-His. This result suggests the

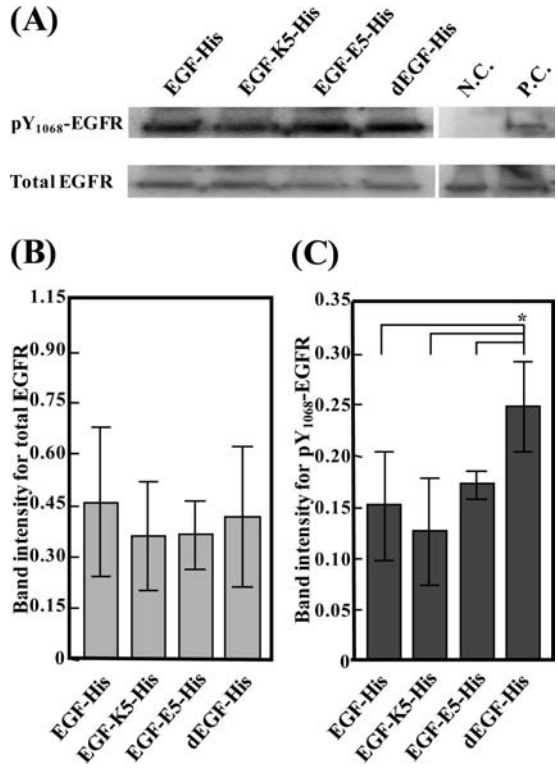

Figure 7. (A) The result of Western blot analysis for the phosphorylated EGFR and total EGFR. Lysates were prepared from cells cultured for 2 days on the substrate with surface-anchored chimeric proteins. N.C.: Negative control. Cells were cultured for 1 day in serum-free base medium without EGF-His. P.C.: Positive control. Cells were cultured for 1 day in serum-free base medium in the absence of EGF-His and then stimulated for 15 min with 1 μg/mL EGF-His. Data shown are representative of three independent experiments. (B,C) Quantative evaluation for the band intensity of (B) total EGFR and (C) pY_{1068}-EGFR. The data are expressed as mean $\pm$ standard deviation ($n = 3$). The asterisk indicated the statistical significance (Tukey's HSD test, $p < 0.05$) compared to other EGF-containing chimeric proteins.

formation of heterodimer, dEGF-His. A single, most intense band was visualized in lane 5 where the equimolar mixture of these proteins was electrophoresced. This result indicates the spontaneous and stoichiometric heterodimerization of EGF-K5-His and EGF-E5-His. However, the intensity of the dEGF-His bands appear to be higher than that expected from the mixing ratios and the band intensities of single components, EGF-K5-His and EGF-E5-His. This is probably due to enhancement of band intensity by dimer formation as shown in Supporting Information Figures S1 and S2.

Dimerization of Chimeric Proteins. Figure 2C shows the CD spectra recorded for EGF-containing chimeric proteins. The CD spectrum of EGF-His exhibited a small negative cotton effect around 216 nm, indicating the existence of β-strands (*26*). This is explained well from the fact that native EGF consists of 41% β-strands other than loops and random coils (no α-helical segments) (*27*). The spectrum of EGF-His is similar to that of native EGF (Supporting Information Figure S4) (*27*). In the spectrum of EGF-E5-His, a negative Cotton effect is additionally observed at 198 nm. This is indicative of random coil structure present in EGF-E5-His. Our observation that, as described earlier, this protein exhibited EGF bioactivity (Figure 3) suggested the proper secondary structure of the EGF domain. Thus, the random coil structure is presumably attributed to the E5 peptide. On the other hand, EGF-K5-His obviously exhibited a negative Cotton effect at 222 nm, representing α-helical structure due to the K5 peptide. The mixture of EGF-E5-His with EGF-K5-His displayed stronger dichroism at 208 and 222 nm and reduced absorption at 198 nm. This result suggests that heterodimerization, as detected by native PAGE (Figure 2B), is ascribed to the coiled-coil association between E5 and K5 peptides.

CD analysis was additionally carried out for α-helical segments alone and in a mixture with wild-type EGF, EGF-E5-His, or EGF-K5-His. These analyses were carried out with the tandem form of E5 [$(KELASVE)_{10}$, E10], because we failed to prepare E5 and K5 peptides in sufficient quantities for CD analysis, probably due to degradation of the short peptides during their expression in and purification from *E. coli*. The tandem form of K5 [$(EKLASVK)_{10}$] was also prepared but could not be used because of its poor solubility. As shown in Supporting Information Figures S4−S7, no detectable intermolecular and intramolecular interactions of the helical peptide operated with the EGF and His segments. The data further suggested self-associations of the helical peptides, associated with strong negative Cotton effect at 222 nm.

Biological Activity of Chimeric Proteins. Figure 3 shows the results of proliferation assays for the chimeric proteins. Cells proliferated approximately 5-fold during 96 h in the presence of chimeric proteins with no significant differences between conditions. The observed growth rates were similar to that for neurosphere-forming cells cultured in base medium containing rhEGF. This result suggests that the EGF domain contained in chimeric proteins holds biological activity without any perturbation of the His peptide. As shown in Table 2, when chimeric proteins were dissolved in a medium, their molecular architectures had minor effects on the differentiation of neurosphere-forming cells.

Surface Immobilization of Chimeric Proteins. The monomeric and dimeric forms of the chimeric proteins were coordinated to the Ni(II)-fixed surfaces. These processes were monitored by surface plasmon resonance analysis (*3*). As shown in Figure 4, all the chimeric proteins gave a similar angular sift corresponding to the surface density of ca. 0.32−0.35 μg/cm^2. This result implies that, on a molar basis, the surface density of an EGF domain on the EGF-His-immobilized substrate is approximately 1.5-fold higher than that on the substrates with immobilized EGF-K5-His, EGF-E5-His, and dEGF-His.

Adhesion, Extension, and Proliferation of NSCs. Supporting Information Figure S8 shows the phase-contrast microphotographs of cells cultured on the substrates with different chimeric proteins. The morphology of cells on the surface with EGF-His is similar to that observed in our previous studies (*3*−*5*). On this surface, cells proliferated and extended neurites. In comparison with the substrate with EGF-His, a slightly increased number of cells initially adhered on the substrates with EGF-K5-His and EGF-E5-His, and the larger number of cells are seen at the same time points. These trends are much more notable on the substrate with surface-anchored dEGF-His. In particular, cell confluency on the substrate with dEGF-His at 48 h (Figure 5A) is similar to that on the EGF-His-anchored substrate at 96 h.

Figure 5B shows the growth curves for cells cultured on the substrates with different chimeric proteins. The cell number increased 30-fold on the substrate with EGF-His during the initial 96 h, being in good accordance with our previous results (*4*). On the other hand, cells on the substrates with EGF-K5-His, EGF-E5-His, and dEGF-His were expanded, respectively, 42-, 45-, and 60-fold for 96 h. As shown in Figure 5B, the apparent doubling time is shorter in the case of EGF-E5-His and EGF-K5-His than EGF-His, and much more shortened in the case of dEGF-His (approximately half of the case with EGF-His).

Selective Expansion of NSCs. Figure 6 shows the result of immunofluorescent staining of cells cultured for 4 days on the substrates with surface-anchored chimeric proteins.

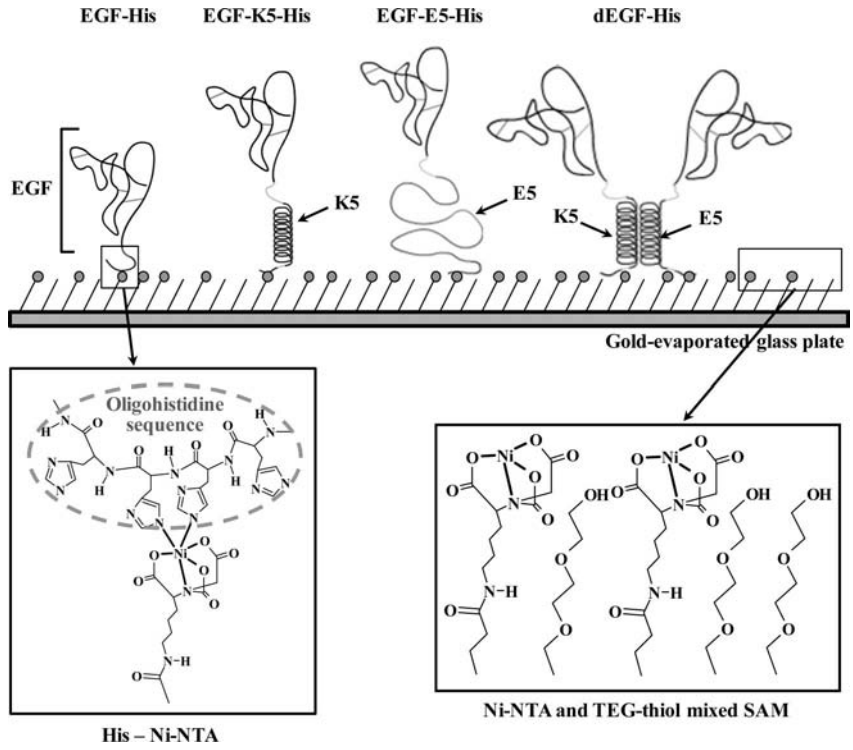

Figure 8. Schematic representation for EGF-containing chimeric proteins anchored to the Ni-chelated surface through coordination. Bold lines in the molecular formula represent chelate bonding. TEG-thiol: triethylene glycol-containing alkanethiol.

On all of the substrates studied here, the majority of cells expressed a neural stem cell marker, nestin (visualized in red), while few cells expressed a neuronal marker, βIII (visualized in green). These results indicate that neural stem cells were selectively proliferated on the substrates with surface-anchored chimeric proteins. However, as shown in Table 2, the fraction of nestin-expressing stem cells is varied depending on the type of chimeric proteins: The fraction of stem cells is significantly higher on the substrate with EGF-E5-His and EGF-K5-His than EGF-His. The highest fraction is seen on the substrate with dEGF-His among the substrates studied, although there was no statistical difference between the substrates with dEGF-His and EGF-E5-His.

EGFR Signaling. EGFR is a member of tyrosine kinase receptors and phosphorylated upon ligand binding to activate an intracellular signaling cascade (*11*). To analyze the phosphorylation of EGFR by Western blotting, we used antibodies against the phosphorylated form of EGFR (specific for pY_{1068}-EGFR) and total EGFR (specific for both phosphorylated and nonphosphorylated forms). The results are shown in Figure 7A. Neurosphere-forming cells were starved for 24 h in growth factor free base medium and then treated with 1 μg/mL EGF for 15 min before lysis as a positive control. Cells just starved in the absence of EGF were used as a negative control. Total EGFR was detected to a similar extent in negative and positive control cells, whereas pY_{1068}-EGFR was detected exclusively for the cells treated with EGF. In the case of cells cultured for 2 days on the substrates with surface-anchored chimeric proteins, strong bands of pY_{1068}-EGFR are seen for all of the substrates, indicating the occurrence of receptor phosphorylation. The band intensities determined for total EGFR and pY_{1068}-EGFR are shown in Figure 7B and C. As can be seen in Figure 7B, the level of EGFR expression was almost similar between substrates. In contrast, EGFR was most efficiently phosphorylated on the substrate with anchored dEGF-His (Figure 7C). The differences in the level of phosphorylation are statistically insignificant among the substrates with EGF-His, EGF-E5-His, and EGF-K5-His.

DISCUSSION

The E5 and K5 peptides were designed to create an α-helical coiled-coil structure stable under the physiological conditions. The coiled-coil structure is stabilized by hydrophobic effects operated between L and V at the core region of the associating chains (*12, 13*). We incorporated these peptides separately into EGF-His. Analyses by native PAGE (Figure 2B) and CD spectroscopy (Figure 2C) revealed that spontaneous coiled-coil association takes place to form a heterodimer consisting of EGF-E5-His and EGF-K5-His. In CD spectroscopic analysis (Figure 2C), disordered structure was suggested for the E5 peptide contained in monomeric EGF-His. α-Helical structure is induced in the E5 peptide when associated with EGF-K5-His (Figure 2C). According to these findings, the structure of the chimeric proteins at the surface may be schematically represented as in Figure 8.

On the surface with fixed Ni(II) ions, the His-containing EGF chimeric proteins are expected to be anchored through coordinate bonding, exposing the EGF domain toward outer environment. Our previous study using the monomeric form of EGF-His (*3*−*5*) demonstrated the structural integrity of surface-anchored EGF-His. In addition, it was shown that stable anchoring is necessary to establish adherent culture of NSCs (*5*). These effects are important for both the selective capture of EGFR-expressing NSCs on the surface and the efficient EGFR signaling leading to the active proliferation of captured cells (*6*−*8*).

In spite of the lower surface density of an EGF domain with dEGF-His, EGF-K5-His, and EGF-E5-His compared with EGF-His, the adhesion and proliferation of cells were most prominent on the surface with anchored dEGF-His. It is likely that, on the substrate with dEGF-His, the dimerized form of EGF efficiently facilitates dimerization of EGFR, transducing intracellular

signaling for mitogenic activity (Figure 7), associated with reduced doubling time (Figure 5B). Therefore, it appears that the highest purity of NSCs obtained on the substrate with surface-anchored dEGF-His is attributed to both efficient signaling in and rapid growth of NSCs. Moreover, the adhesion and proliferation of cells were also promoted on the surfaces with anchored EGF-K5-His and EGF-E5-His (Figure 5A,B) compared to the surface with EGF-His. These results suggest that the E5 and K5 peptides inserted between the EGF domain and the His sequence function as a flexible linker. Interestingly, the molecular architecture of chimeric proteins has an effect on the proliferation and differentiation of neurosphere-forming cells only when the chimeric proteins are anchored at the surface, but not when dissolved in solution (Figures 3 and 5B, and Table 2).

It is considered that EGFR signaling is activated by dimerization of EGF-EGFR complexes (*11*). In the case of surface-anchored monomeric EGF-His, the probability of receptor dimerization seems to be limited because of the reduced mobility of surface-anchored EGF. In the case of EGF anchored to the surface as a dimer, such a constraint may not affect receptor dimerization because two EGF domains are always located in close proximity to each other. Conceivably, this is the reason for the most efficient proliferation of NSCs observed on the surface with dEGF-His (Figure 6). Our estimation suggests that the distance between two EGF domains in the dimer form is approximately comparable to the span of two binding sites in dimerized EGFR (*28*). The results in which both EGF-E5-His and EGF-K5-His were surface-anchored as a single component also provided more efficient substrates than EGF-His does (Figures 5A,B and 6). This can also be explained from the mobility of the EGF domain enhanced by E5 and K5 peptides inserted between the EGF domain and the His sequence. Interestingly, the effects of these peptides are not noticeable when chimeric proteins are used as diffusible factors (Figures 3 and 5B).

Accordingly, the selective expansion of NSCs can be most efficiently achieved on the substrate with surface-anchored dEGF-His. On this substrate, cells are expanded 60-fold during 96 h of culture. It is important to note that more than 98% of the expanded cells express a stem cell marker, nestin, with no expression of a neuronal marker, βIII. These specifications are in large contrast to those with the standard neurosphere culture by which cells proliferate 6-fold for 96 h (Figure 3) to produce a heterogeneous population containing 60% of nestin-expressing cells (*3*).

CONCLUSION

By means of recombinant DNA technology, EGF was engineered to carry an α-helical peptide and a hexahistidine sequence. The chimeric proteins, EGF-E5-His and EGF-K5-His, spontaneously form a heterodimer, dEGF-His. NSCs proliferate most rapidly and selectively on the substrate with surface-anchored dEGF-His, compared to the other substrates with monomeric EGF. This effect may be attributed to the enhanced dimerization of EGF-EGFR complexes at the cell−substrate interface. The rate of cell proliferation on this surface is far beyond those on our conventional substrate with monomeric EGF-His, as well as those in the standard neurosphere culture. In conjunction with the capability of highly selective expansion of NSCs, it follows that the dEGF-His-immobilized substrate allows the most efficient preparation of NSCs. For the clinical application of our technology, further feasibility study is needed with human NSCs.

ACKNOWLEDGMENT

The part of this study was supported by Grant-in-Aid for Scientific Research (19300171,19·6117), MEXT, and a grant of Long-Range Research Initiative from the Japan Chemical Industry Association. T. N.-H. acknowledges JSPS for a research fellowship.

Supporting Information Available: Conditions of dialysis, the results of native PAGE, CD spectra and the related experimental procedures, and phase-contrast images of cells. This material is available free of charge via the Internet at http://pubs.acs.org.

LITERATURE CITED

(1) Kim, S. U. (2004) Human neural stem cells genetically modified for brain repair in neurological disorder. *Neuropathology 24*, 159–171.

(2) Goldman, S. (2005) Stem and progenitor cell-based therapy of the human central nervous system. *Nat. Biotechnol. 23*, 862–871.

(3) Nakaji-Hirabayashi, T., Kato, K., Arima, Y., and Iwata, H. (2007) Oriented immobilization of epidermal growth factor onto culture substrates for the selective expansion of neural stem cells. *Biomaterials 28*, 3517–3529.

(4) Kato, K., Sato, H., and Iwata, H. (2005) Immobilization of histidine-tagged recombinant proteins onto micropatterned surfaces for cell-based functional assays. *Langmuir 21*, 7071–7075.

(5) Nakaji-Hirabayashi, T., Kato, K., and Iwata, H. (2008) Essential role of structural integrity and firm attachment of surface-anchored epidermal growth factor in adherent culture of neural stem cells. *Biomaterials 29*, 4403–4408.

(6) Ogiwara, K., Nagaoka, M., Cho, C. S., and Akaike, T. (2005) Construction of a novel extracellular matrix using a new genetically engineered epidermal growth factor fused to IgG-Fc. *Biotechnol. Lett. 27*, 1633–1637.

(7) Ogiwara, K., Nagaoka, M., Cho, C. S., and Akaike, T. (2006) Effect of photo-immobilization of epidermal growth factor on the cellular behaviors. *Biochem. Biophys. Res. Commun. 345*, 255–259.

(8) Nagaoka, M., Ise, H., Harada, I., Koshimizu, U., Maruyama, A., and Akaike, T. (2008) Embryonic undifferentiated cells show scattering activity on a surface coated with immobilized E-cadherin. *J. Cell. Biochem. 103*, 296–310.

(9) Reynolds, B. A., Tetzlaff, W., and Weiss, S. A. (1992) A multipotent EGF-responsive striatal embryonic progenitor cell produces neurons and astrocytes. *J. Neurosci. 12*, 4565–4574.

(10) Caldwell, M. A., He, X., Wilkie, N., Pollack, S., Marshall, G., Wafford, K. A., and Svendsen, C. N. (2001) Growth factors regurate the survival and fate of cells derived from human neurospheres. *Nat. Biotechnol. 19*, 475–479.

(11) Ullrich, A., and Schlessinger, J. (1990) Signal transduction by receptors with tyrosine kinase activity. *Cell 61*, 203–212.

(12) McLachlan, A. D., and Stewart, M. (1975) Tropomyosin coiled-coil interactions: Evidence for an unstaggered structure. *J. Mol. Biol. 98*, 293–304.

(13) Tripet, B., Wagschal, K., Lavigne, P., Mant, C. T., and Hodges, R. S. (2000) Effects of side-chain characteristics on stability and oligomerization state of a *de novo*-designed model coiled-coil: 20 Amino acid substitutions in position "d". *J. Mol. Biol. 300*, 377–402.

(14) Meyers, M. A., Chen, P.-Y., Lin, A. Y.-M., and Seki, Y. (2008) Biological materials: Structure and mechanical properties. *Prog. Mater. Sci. 53*, 1–206.

(15) Wang, C., Stewart, R. J., and Kopeček, J. (1999) Hybrid hydrogels assembled from synthetic polymers and coiled-coil protein domains. *Nature 397*, 417–420.

(16) Petka, W. A., Harden, J. L., McGrath, K. P., Wirtz, D., and Tirrell, D. A. (1998) Reversible hydrogels from self-assembling artificial proteins. *Science 281*, 389–392.

(17) Mi, L., Fischer, S., Chung, B., Sundelacruz, S., and Harden, J. L. (2006) Self-assembling protein hydrogels with modular integrin binding domains. *Biomacromolecules 7*, 38–47.

(18) Fujita, Y., Funabashi, H., Mie, M., and Kobatake, E. (2007) Design of a thermocontrollable protein complex. *Bioconjugate Chem. 18*, 1619–1624.
(19) Nakaji-Hirabayashi, T., Kato, K., and Iwata, H. (2008) Self-assembling chimeric protein for the construction of biodegradable hydrogels capable of interaction with integrins expressed on neural stem/progenitor cells. *Biomacromolecules 9*, 1411–1416.
(20) Rose, G. D., Gierasch, L. M., and Smith, J. A. (1985) Turns in peptides and proteins. *Adv. Protein Chem. 37*, 1–109.
(21) Leszczynsky, J. F., and Rose, G. D. (1986) Loops in globular proteins: a novel category of secondary structure. *Science 234*, 849–855.
(22) Pachuk, C. J., Samuel, M., Zurawski, J. A., Snyder, L., Phillips, P., and Satishchandran, C. (2000) Chain reaction cloning: a one-step method for directional ligation of multiple DNA fragments. *Gene 243*, 19–25.
(23) Nakaji-Hirabayashi, T., Kato, K., Arima, Y., and Iwata, H. (2008) Multifunctional chimeric proteins for the sequential regulation of neural stem cell differentiation. *Bioconjugate Chem. 19*, 516–524.
(24) Hirata, I., Morimoto, Y., Murakami, Y., Iwata, H., Kitano, E., Kitamura, H., and Ikada, Y. (2000) Study of complement activation on well-defined surface using surface plasmon resonance. *Colloids Surf., B: Biointerfaces 18*, 285–292.
(25) Knoll, W. (1991) Polymer thin films and interfaces characterized with evanescent light. *Makromol. Chem. 192*, 2827–2856.
(26) Kelly, S. M., Jess, T. J., and Price, N. C. (2005) How to study proteins by circular dichroism. *Biochem. Biophys. Acta 1751*, 119–139.
(27) Prestrelski, S. J., Arakawa, T., Wu, C.-S. C., O'Neal, K. D., Westcott, K. R., and Narhi, L. O. (1992) Solution structure and dynamics of epidermal growth factor and transforming growth factor α. *J. Biol. Chem. 267*, 319–322.
(28) Ogiso, H., Ishitani, R., Nureki, O., Fukai, S., Yamanaka, M., Kim, J.-H., Saito, K., Sakamoto, A., Inoue, M., Shirouzu, M., and Yokoyama, S. (2002) Crystal structure of the complex of human epidermal growth factor and receptor extracellular domains. *Cell 110*, 775–787.

BC800331T

Supporting Information

Surface-anchoring of spontaneously dimerized epidermal growth factor for highly selective expansion of neural stem cells

Tadashi Nakaji-Hirabayashi, Koichi Kato, and Hiroo Iwata*

Institute for Frontier Medical Sciences, Kyoto University, 53 Kawahara-cho, Shogoin, Sakyo-ku, Kyoto 606-8507, Japan

*Corresponding author: Tel & Fax: +81-75-751-4119, E-mail: iwata@frontier.kyoto-u.ac.jp.

1. Refolding of chimeric proteins

Table S1. Conditions of dialysis performed for the refolding of EGF-K5-His and EGF-E5-His

Order	Composition	pH		Time (h)	T (^{o}C)
		EGF-K5-His	EGF-E5-His		
1	50 mM Tris-HCl, 10 mM NaCl, 0.2 M L-arginine, 8 M urea, 0.2 mM dithiothreitol	9.0	8.5	4	20
2	50 mM Tris-HCl, 10 mM NaCl, 0.2 M L-arginine, 8 M urea	9.0	8.5	8	20
3	50 mM Tris-HCl, 10 mM NaCl, 0.2 M L-arginine, 8 M urea, 1 mM reduced glutathione, 0.1 mM oxidized glutathione	9.0	8.5	12	4
4	50 mM Tris-HCl, 10 mM NaCl, 0.2 M L-arginine, 4 M urea, 3.75 mM reduced glutathione, 0.375 mM oxidized glutathione	9.0	8.5	12	4
5	50 mM Tris-HCl, 10 mM NaCl, 0.2 M L-arginine, 2 M urea, 3.75 mM reduced glutathione, 0.375 mM oxidized glutathione	9.0	8.5	12	4
6	50 mM Tris-HCl, 10 mM NaCl, 0.2 M L-arginine, 1 M urea, 3.75 mM reduced glutathione, 0.375 mM oxidized glutathione	9.0	8.5	12	4
7	50 mM Tris-HCl, 10 mM NaCl, 0.2 M L-arginine, 3.75 mM reduced glutathione, 0.375 mM oxidized glutathione	9.0	8.5	12	4
8	50 mM Tris-HCl, 10 mM NaCl, 0.2 M L-arginine, 0.5 mM reduced glutathione, 0.05 mM oxidized glutathione	9.0	8.5	12	4
9	50 mM Tris-HCl, 10 mM NaCl, 0.2 M L-arginine	8.5	8.0	12	4
10	50 mM Tris-HCl, 10 mM NaCl	8.0	8.0	12	4
11	Phosphate buffer saline (3 times)	7.4	7.4	12	4

2. Native PAGE analysis

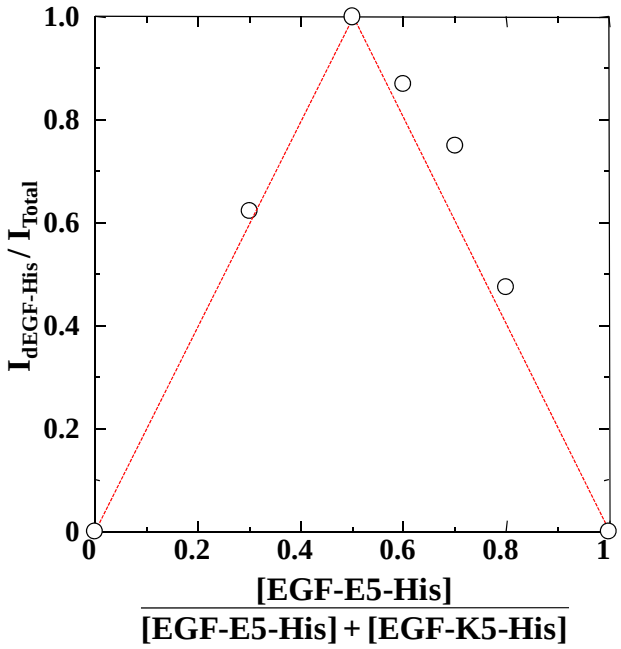

Figure S1. Band intensity ratio determined from the result of native PAGE shown in Figure 2B (see the main body of the article) using an Image J software. Data are plotted as a function of the molar fraction of EGF-E5-His in the mixed solution. Open circle: experimental results, red broken line: a curve predicted by assuming the stoichiometric interaction between EGF-E5-His and EGF-K5-His. $I_{dEGF-His}$: the band intensity for dEGF-His, I_{Total}: a sum of the band intensity for dEGF-His, EGF-E5-His, and EGF-K5-His. Note that the $I_{dEGF-His}$ / I_{Total} for the mixing ratio of 0.6, 0.7, and 0.8 is higher than the prediction.

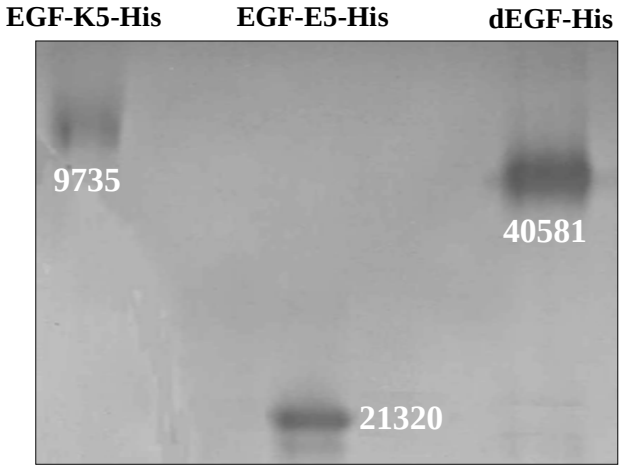

Figure S2. The result of native PAGE analysis performed for EGF-K5-His (0.2 mM), EGF-E5-His (0.2 mM), and dEGF-His (a mixture of 0.2 mM EGF-K5-His and 0.2 mM EGF-E5-His). Band intensities determined using an Image J software were shown in the image. Note that the band intensity for dEGF-His (ca. 40000) is enhanced compared with the sum of the band intensity for EGF-K5-EGF and EGF-E5-His (ca. 31000). At this moment, we have no clear explanation for the enhanced staining, but this is probably related to the alteration of ionic and hydrophobic nature of the monomers upon dimerization (*1*).

3. Interactions of α-helical peptide

CD spectroscopic analyses were performed for investigating the intramolecular and intermolecular interactions of an α-helical peptide with an EGF domain and the self-assembly of the peptides. First, we prepared the tandem forms of K5 [$(EKLASVK)_{10}$, K10] and E5 [$(KELASVE)_{10}$, E10] using recombinant DNA technology. This is because we failed to prepare E5 and K5 peptides in sufficient quantities for CD analysis, probably due to degradation of the short peptides during their expression in and purification from *E. coli*. The K10, however, had strong propensity to form insoluble substances probably because of coiled-coil formation and therefore could not be subjected to CD analysis. In contrast, E10 was successfully obtained in the soluble form and used for CD analysis alone or together with His-deficient EGF, EGF-E5-His, or EGF-K5-His.

Preparation of E10 peptide. cDNA encoding E10 (70 amino acids) was synthesized using chain reaction cloning method (*2)*. Synthetic DNA fragments (ca. 70 mer) corresponding to 5'-terminal, first middle, second middle, 3'-terminal parts of DNA encoding E10 were purchased from Invitrogen (Table S2). The 5'-terminal fragment contained 24-mer oligonucleotide for octapeptides (HHHHHHGG) to fuse His to the N-terminus. Four synthetic DNA fragments were ligated each other using three bridge primers (Table S2) to obtain DNA encoding full length E10 fused with HHHHHHGG at the N-terminus. All steps for ligation of DNA fragments were carried out at the same procedure in previous report (*2*). The ligated DNA was amplified by PCR using outer primers (Table S2). Forward primer contained an Nde I restriction site. Reverse primer contained an Xho I restriction site. The His-E10 gene was digested with Nde I and Xho I and inserted into the pET-22b (Novagen, Darmstadt, Germany) previously digested by the same restriction enzymes. This plasmid was cloned in *Escherichia coli* (*E. coli*) stain, DH5α, to obtain pET22–His-E10. The correctness of the plasmids, pET22–His-E10, was confirmed by sequencing.

E10 (Figure S3A) was expressed in *E. coli* stain, BL21-codonplus (Stratagene, La Jolla, CA) using Overnight Express Autoinduction System (Novagen). E10 obtained as inclusion bodies were extracted with phosphate buffer saline containing 8 M urea, and then purified using a Prime ÄKTA chromatography system (GE Healthcare Bio-Science Corp., Piscataway, NJ) equipped with a His Trap HP column (GE Healthcare). These proteins were refolded by step-wise dialyzing against the series of buffers (Table S3). The yields of E10 were determined to be 37 mg per liter of medium. The purity and molecular size of proteins were analyzed by sodium dodecylsulfate–polyacrylamide gel electrophoresis (SDS–PAGE) (Figure S3B). The result of SDS–PAGE analysis for E10 shows a single bund at 11 kDa, suggesting the dimerized form of the peptide even under the denatured condition with SDS.

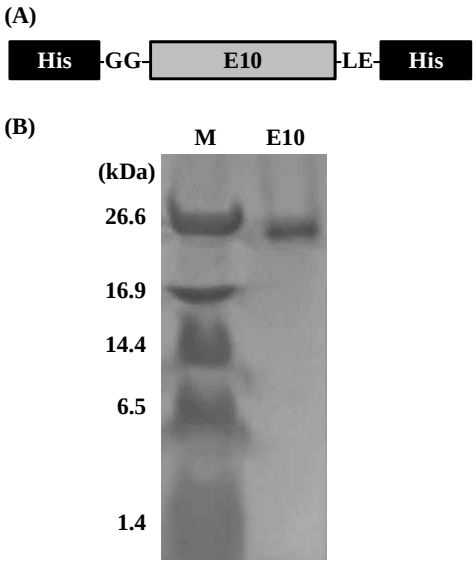

Figure S3. (A) Structures of E10 synthesized. His: hexahistidine sequence, E10: $(KELASVE)_{10}$ sequence (70 amino acids). (B) The result of SDS-PAGE analysis for E10. M represents molecular weight standard.

Table S2. Sequences of primers and oligonucleotides used for the synthesis of E10 peptide.

Primer or oligonucleotide	Sequence (5' → 3')[a]
Oligo 1	gcatcgcatatgcaccatcatcaccatcacgagctagccggcccaaaagagttggcgagcgttgaaaag
Oligo 2	gaactggcctctgtagagaaagagctcgcatccgtcgagaaggaactagcttcagtggaaaaggagctt
Oligo 3	gcgtcggtcgagaaagagttagcttctgttgaaaaggaattggcctcagtcgagaaagaactcgcatcc
Oligo 4	gtagagaaggagctagcgagtgtggaaaaggagcttgctagcgttgaacctgcgggtctcgagcaccac
Oligo 5	cttttcaacgctcgccaactcttttgggccggctagctcgtgatggtgatgatggtgcatatgcgatgc
Oligo 6	aagctccttttccactgaagctagttccttctcgacggatgcgagctctttctctacagaggccagttc
Oligo 7	ggatgcgagttctttctcgactgaggccaattccttttcaacagaagctaactctttctcgaccgacgc
Oligo 8	gtggtgctcgagacccgcaggttcaacgctagcaagctccttttccacactcgctagctccttctctac
Bridge oligo I	ttctctacagaggccagttccttttcaacgctcgccaact
Bridge oligo II	cgaccgacgcaagctccttttccactgaagctagttcctt
Bridge oligo III	ctcgctagctccttctctacggatgcgagttctttctcga
Forward primer	gcatcatatgcaccatcatcaccatcacgagctag
Reverse primer	ggtgctcgagacccgcaggttcaacgctagcaagctcctt

[a] Restriction sites are underlined.

Table S3. Dialysis conditions for the refolding of E10.

Order	Composition	pH	Time (h)	Temperature (^{o}C)
1	50 mM Tris-HCl, 10 mM NaCl, 0.2 M L-arginine, 8 M urea	8.5	6	4
2	50 mM Tris-HCl, 10 mM NaCl, 0.2 M L-arginine, 4 M urea	8.5	8	
3	50 mM Tris-HCl, 10 mM NaCl, 0.2 M L-arginine, 2 M urea	8.5	12	
4	50 mM Tris-HCl, 10 mM NaCl, 0.2 M L-arginine, 1 M urea	8.5	12	
5	50 mM Tris-HCl, 10 mM NaCl, 0.2 M L-arginine	8.5	12	
6	50 mM Tris-HCl, 10 mM NaCl	8.0	12	
7	Phosphate buffer saline (3 times)	7.4	12	

CD spectroscopy. Sample proteins were dissolved in PBS (pH 7.4) to a mean residue concentration of 0.855 mM (rhEGF) or 2.75 mM (E10, EGF-His, EGF-K5-His, and EGF-E5-His). In addition, the solution of E10 was mixed with a solution containing an equimolar concentration of EGF-His, EGF-K5-His, or EGF-E5-His to a total protein concentration of 5.50 mM.

As shown in Figure S4, CD spectrum for EGF-His was in good agreement with that for rhEGF, indicating that EGF-His had secondary structure to a similar extent to rhEGF. This result demonstrates that EGF-His is correctly refolded and that the His sequence has insignificant effect on the structure of the EGF domain.

Figure S5 shows the CD spectra for EGF-His, E10, and the their equimolar mixture. The spectrum for E10 exhibits a negative cotton effect at 222 nm, indicating the presence of α-helical structure. The spectrum for the mixture of EGF-His and E10 has similar shape and intensity to the theoretical spectrum obtained by numerical summation of the individual spectra. This provides the evidence for the undetectable interactions between E10 and EGF-His. Similar results were obtained from the CD spectroscopic analysis for the mixture of E10 with EGF-E5-His (Figure S6), indicating the undetectable interactions of E10 with any regions of EGF-E5-His polypeptide. Accordingly, the data presented in Figures S4–S6 demonstrate that no detectable intermolecular and intramolecular interactions of the model helical peptide (E10) are operated with EGF, E5, and His sequences.

In contrast to the results described above, the mixiging of E10 with EGF-K5-His gave rise to peculiar alterations in CD spectrum (Figure S7). Negative cotton effects were considerably intensified at 208 and 222 nm, making the spectrum quite different from the theoretical curve. This is plausibly due to the heterodimer formation between E10 and the K5 segment in EGF-K5-His through coiled-coil association. Although E10 spontaneously dimerizes by self-association (see also Figure S3), mixing of E10 with a K5 containing

protein might induce the formation of E10–K5 heterodimer with higher stability than the E10 homodimer. As we used E10 as a model peptide of E5, the results shown in Figure S5 support the coiled-coil association between E5 and K5 segments in EGF-E5-His and EGF-K5-His to form dEGF-His.

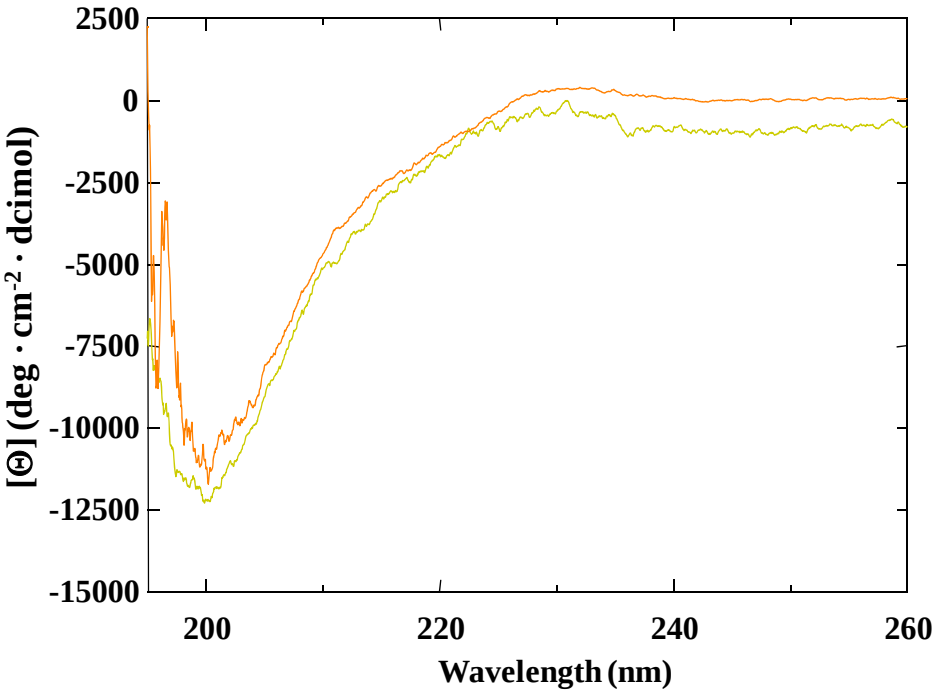

Figure S4. CD spectra for EGF-His (orange) and rhEGF (yellow). The spectrum for EGF-His is also presented in the main body of this paper (Figure 2C).

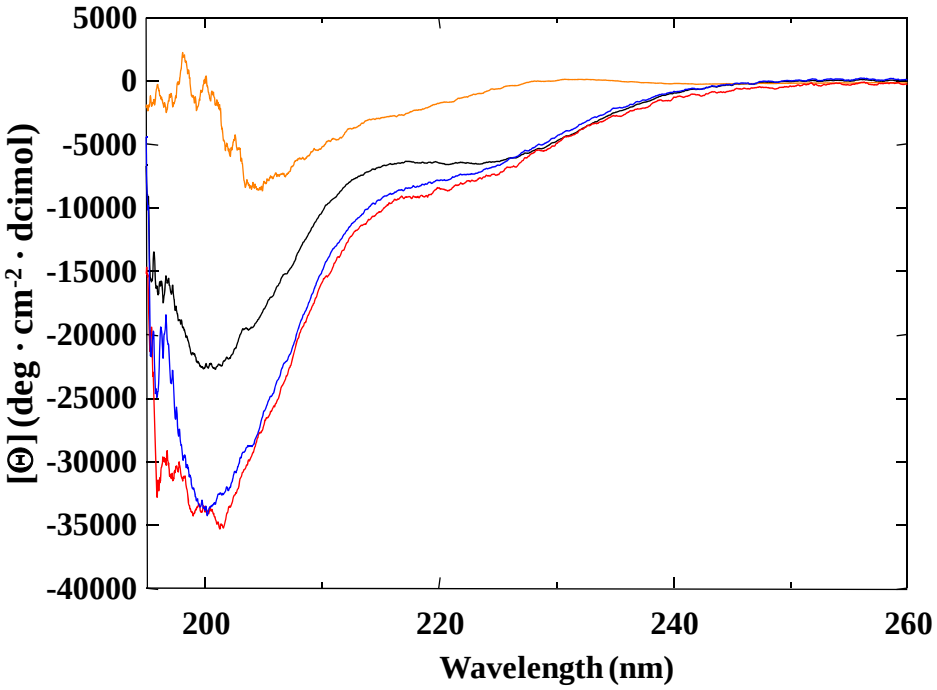

Figure S5. CD spectra for EGF-His (orange), E10 (black), and the equimolar mixture of EGF-His and E10 (red). The spectrum in blue represents the theoretical curve obtained by numerical summation of individual spectra (orange + black). The spectrum for EGF-His is also presented in the main body of this paper (Figure 2C).

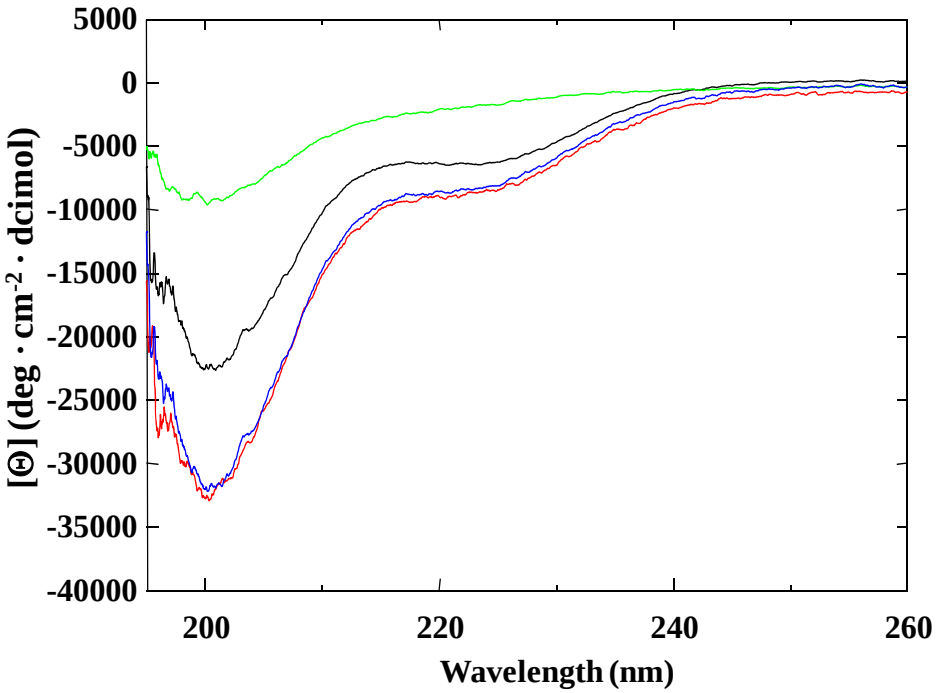

Figure S6. CD spectra for EGF-E5-His (right green), E10 (black), and the equimolar mixture of EGF-E5-His and E10 (red). The spectrum in blue represents the theoretical curve obtained by numerical summation of individual spectra (right green + black). The spectrum for EGF-E5-His is also presented in the main body of this paper (Figure 2C).

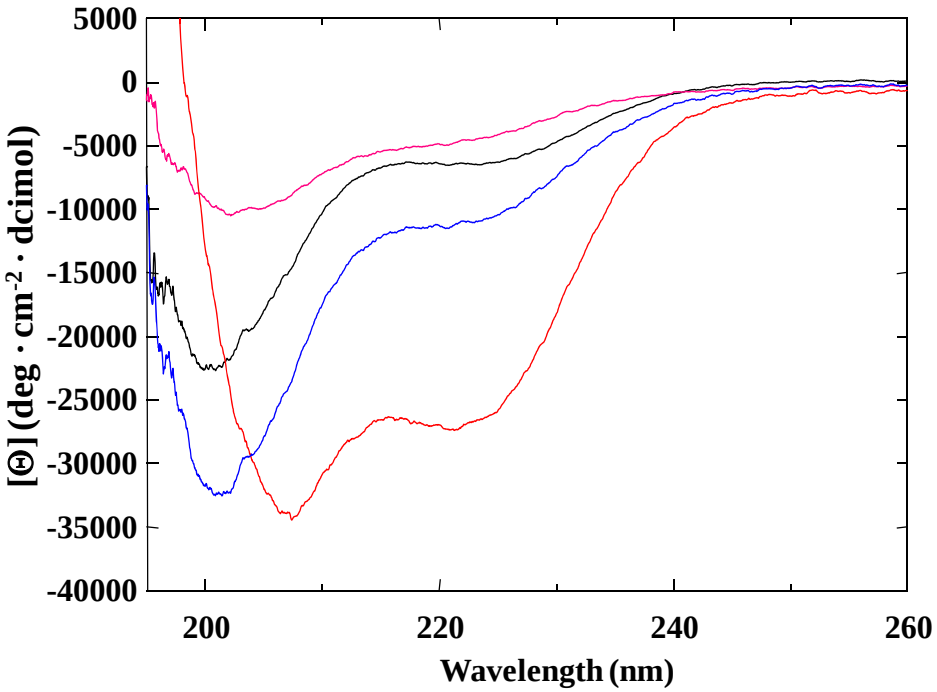

Figure S7. CD spectra for EGF-K5-His (pink), E10 (black), and the equimolar mixture of EGF-K5-His and E10 (red). The spectrum in blue represents the theoretical curve obtained by numerical summation of individual spectra (pink + black). The spectrum for EGF-K5-His is also presented in the main body of this paper (Figure 2C).

4. Cell growth on the substrate with surface-anchored EGF chimeric proteins

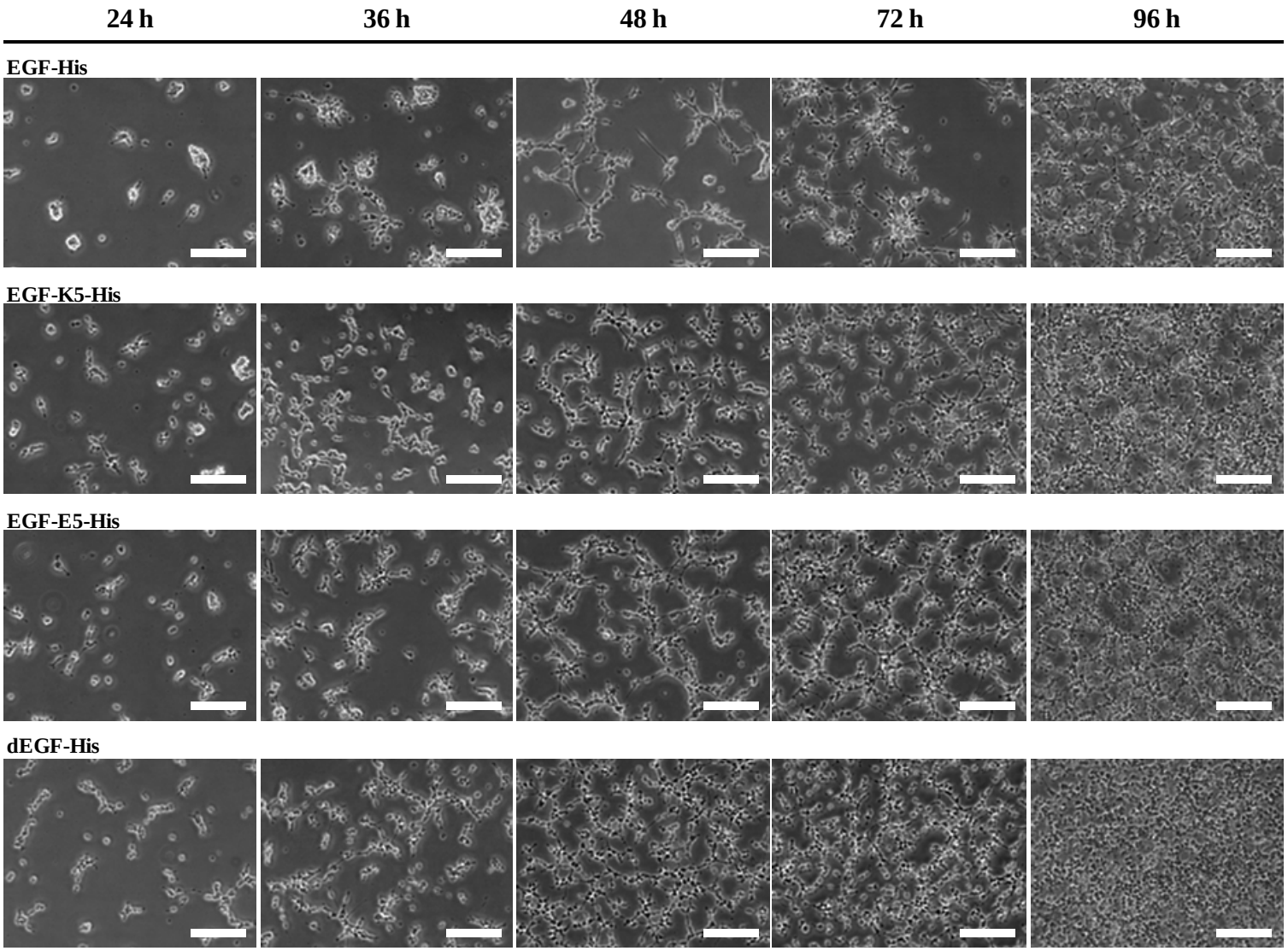

Figure S8. Phase-contrast images of cells cultured on the substrates with surface-anchored chimeric proteins. Images were acquired at 24, 36, 48, 72, and 96 h after seeding. The identity of surface-anchored chimeric proteins is shown on the left side of the images. Images for 48 h culture are the same as those in Figure 5A in the main body of this paper. Bars: 100 μm.

References

(1) Compton, S. J., and Jones, C. G. (1985) Mechanism of dye response and interference in the bradford protein assay. *Anal. Biochem. 151*, 369–374.

(2) Pachuk, C. J., Samuel, M., Zurawski, J. A., Snyder, L., Phillips, P., and Satishchandran, C. (2000) Chain reaction cloning: a one-step method for directional ligation of multiple DNA fragments. *Gene 243*, 19–25.

Bioconjugate Chemistry 20th Anniversary

Subscriber access provided by SHEMYAKIN-OVCHINNIKOV INST

Article

T-Cell Activation by Antigen-Loaded pH-Sensitive Hydrogel Particles *in Vivo*: The Effect of Particle Size

Joel A. Cohen, Tristan T. Beaudette, William W. Tseng, Eric M. Bachelder, Ines Mende, Edgar G. Engleman, and Jean M. J. Fre#chet

Bioconjugate Chem., **2009**, 20 (1), 111-119• DOI: 10.1021/bc800338n • Publication Date (Web): 22 December 2008

Downloaded from http://pubs.acs.org on May 8, 2009

More About This Article

Additional resources and features associated with this article are available within the HTML version:

- Supporting Information
- Access to high resolution figures
- Links to articles and content related to this article
- Copyright permission to reproduce figures and/or text from this article

View the Full Text HTML

ACS Publications
High quality. High impact.

Bioconjugate Chemistry is published by the American Chemical Society. 1155 Sixteenth Street N.W., Washington, DC 20036

T-Cell Activation by Antigen-Loaded pH-Sensitive Hydrogel Particles *in Vivo*: The Effect of Particle Size

Joel A. Cohen,[†] Tristan T. Beaudette,[†] William W. Tseng,[‡] Eric M. Bachelder,[†] Ines Mende,[‡] Edgar G. Engleman,[‡] and Jean M. J. Fréchet[†,*]

College of Chemistry, University of California, Berkeley, California, 94720-1460, and Department of Pathology, Stanford University School of Medicine, Palo Alto, California. Received August 6, 2008; Revised Manuscript Received October 9, 2008

Polymeric carriers designed to encapsulate protein antigens have great potential for improving the efficacy of vaccines and immunotherapeutics for diseases such as cancer. We recently developed a carrier system based on polyacrylamide hydrogel microparticles cross-linked with acid-labile moieties. After being phagocytosed by antigen-presenting cells, the protein encapsulated within the carrier is released and processed for subsequent presentation of antigenic epitopes. To understand the impact of particle size on the activation of T-cells following uptake by antigen-presenting cells, particles with mean diameters of 3.5 μm and 35 nm encapsulating a model protein antigen were synthesized by emulsion and microemulsion based polymerization techniques, respectively. *In vivo* tests demonstrated that both sizes of particles were effective at stimulating the proliferation of T-cells and were capable of generating an antigen-specific cytotoxic T-cell response when coadministered with immunostimulatory DNA. Contrary to previous reports in the literature, our results suggest that there is no significant difference in the magnitude of T-cell activation for the two sizes of particles used in these experiments. This disparity in findings may be related to fundamental differences in material properties of the carriers used in these studies, such as the hydrophilicity of the polyacrylamide particles described here versus the hydrophobic nature of carriers investigated by other groups.

INTRODUCTION

The physical dimensions of a biomaterial are key parameters that may dictate the interaction of the material with its surrounding biological environment, particularly when those dimensions are on the micro- or the nanoscale. For example, while many cell types are capable of ingesting small-sized particulate matter (typically <200 nm in diameter) by mechanisms such as pinocytosis, and receptor- and clathrin-mediated endocytosis (*1*), the uptake of particles with diameters up to several micrometers is generally restricted to the phagocytic antigen-presenting cells of the immune system such as macrophages and dendritic cells. This difference in uptake has been exploited in the development of protein antigen carrier systems, which often increase the efficacy of protein-based vaccines (*2*−*4*). Tuning the size of particulate antigen delivery systems can enable passive targeting of exogenous proteins to antigen-presenting cells for presentation of derived peptide fragments on major histocompatibility class I (MHC I) molecules, which can subsequently enhance the activation of cytotoxic T-lymphocyte (CTL) immune responses (*5*).

Several reports have highlighted the impact that particle size may have on interactions with antigen-presenting cells and the immune system in general. For example, while dendritic cells are capable of ingesting polystyrene particles ranging in size from tens of nanometers to micrometers in diameter, it appears that these cells may demonstrate preferential uptake for particles with diameters less than 300 nm *in vitro* (*6*). Early studies on the functional application of particulate antigen carriers indicated that, for proteins bound to the surface of polystyrene beads with diameters between 500 nm and 10 μm, carriers with diameters between 2 and 3 μm were most effective at inducing cross-presentation of antigenic peptides in macrophages in an ovalbumin-based model system *in vitro* (*7*). However, *in vivo* studies using a similar polystyrene-based system with diameters ranging from 20 nm to 2 μm suggested that particles less than 200 nm (*8*) or 100 nm (*9*) in diameter were most effective at generating CTL responses. Additional work showed that, among those particles with diameters less than 100 nm, 40−50 nm particles were potentially more effective at biasing the activation of the adaptive immune system toward a CTL-dominated response (*10*).

Carrier size has also been shown to influence *in vivo* behavior at the systemic level. Poly(propylene sulfide) particles with 20 and 45 nm diameters were shown to traffic to draining lymph nodes via convective transport through the lymphatic capillaries after subcutaneous injection, with the potential for targeting lymph-node-resident dendritic cells. In contrast, 100 nm particles were not observed to drain to the lymph nodes to any significant extent (*11, 12*). These observations are in agreement with an earlier report demonstrating that 0.5−1 μm polystyrene particles were generally found to reside at the site of injection after several days where they were capable of targeting peripheral antigen-presenting cells (*13*).

With these studies in mind, we aimed to investigate the effect of particle size on T-cell activation in a microparticulate carrier system we recently developed based on polyacrylamide networks containing pH-sensitive cross-links. This system has been shown to be effective at delivering protein antigens to cells of the immune system both *in vitro* and *in vivo* using particles typically greater than 1 μm in diameter (*14*−*17*). Compared to the particles used in the studies described above, which primarily utilized polystyrene or other hydrophobic-core carriers, this polyacrylamide-based system is inherently hydrophilic and mechanically compliant, and the protein payload is physically encapsulated, which should offer protection from proteolytic

* Corresponding author. Phone: (510) 643-3077. Fax (510) 643-3079; E-mail: frechet@berkeley.edu.

[†] College of Chemistry, University of California.

[‡] Stanford University School of Medicine.

10.1021/bc800338n CCC: $40.75 © 2009 American Chemical Society
Published on Web 12/22/2008

degradation prior to reaching the target antigen-presenting cells. The particles are relatively stable at physiological pH but degrade rapidly when they encounter the lower pH environment present in the lysosomes of cells. When ingested by antigen-presenting cells, the particles rapidly break down into smaller fragments, releasing their contents in a manner that enhances MHC I presentation of antigen-derived peptides (*14, 15, 17*).

To investigate the effect of particle size on T-cell activation using our polyacrylamide-based system, we first had to synthesize submicrometer-sized particles. To this end, we optimized the inverse emulsion conditions of free-radical polymerization to generate acid-labile polyacrylamide nanogels. After characterizing these nanoparticles, we investigated their ability to induce T-cell proliferation and an antigen-specific cytotoxic T-cell response *in vivo* in a direct comparison with the performance of analogous but larger acid-degradable particles.

EXPERIMENTAL PROCEDURES

General Procedures and Materials. Unless otherwise noted, all chemicals were purchased from Sigma-Aldrich (St. Louis, MO) and used without additional purification. Acrylamide, *N*,*N*′-methylene-bis-acrylamide, ammonium persulfate, and *N*,*N*,*N*′,*N*′-tetramethylethylenediamine (TMEDA) were purchased from Bio-Rad (Hercules, CA). Hexane (OmniSolv grade) was purchased from EMD (Gibbstown, NJ). UltraPure 0.1 μm filtered water and phosphate buffered saline (pH 7.4, PBS) were purchased from Invitrogen-Gibco (Carlsbad, CA). The pH of PBS solutions was adjusted using either HCl or NaOH. Unless otherwise noted, dried particles were suspended in buffer by alternately vortexing the solution and sonicating in a VWR model 75 water bath for 1−3 min until particle aggregates were no longer visible.

Cross-Linker Synthesis. Synthesis of the benzylidene acetal cross-linker **1** (Scheme 1) was performed as previously reported (*17*).

Preparation of 35 nm Diameter Particles. To prepare the organic continuous phase, AOT (sodium bis(2-ethylhexyl) sulfosuccinate) (178 mg, 0.40 mmol) and Brij 30 (poly(ethylene glycol) dodecyl ether with $M_n \sim 362$) (344 mg, 0.95 mmol) were added to a 20 mL borosilicate glass vial to which a stir bar was added. The vial was sealed with a Teflon-lined septum cap and purged with dry nitrogen for 10 min. Hexane (5 mL) was deoxygenated by bubbling dry nitrogen through the solvent for 10 min and was added to the vial. The vial was placed in an oil bath with the temperature set to 23.5 °C, and stirring was started at 600 rpm to dissolve the surfactants. For the aqueous phase, ovalbumin (7.0 mg) was dissolved in PBS (pH 9, 203 μL), to which acrylamide (48.0 mg, 0.68 mmol) and cross-linker **1** (39.0 mg, 0.07 mmol) were added and dissolved. A 20% (w/v) solution of ammonium persulfate in PBS (pH 9, 30 μL) was added to the monomer/protein solution. The mixture was sonicated for 30 s in a Branson 1210 water bath and added to the organic continuous phase dropwise via syringe over approximately 3 min. After 10 min, polymerization was initiated by the addition of TMEDA (20 μL) via syringe over the course of 2 min, and the mixture was stirred for 2 h. Solvent was removed by rotary evaporation, and absolute ethanol (5 mL) was added, resulting in a milky-white suspension. The particles were isolated by centrifugation for 10 min at 4000 × *g* at rt, and washed with absolute ethanol (4 × 5 mL), centrifuging as before. The particles were suspended with absolute ethanol (2 mL) and sonicated for 30 s in a Branson 1210 water bath. The ethanol was removed under vacuum and the particles dried overnight to yield a fine white powder (54.0 mg).

Nondegradable 35 nm Diameter Particles. Nondegradable particles used in light scattering studies were prepared as described above with the exception that *N*,*N*′-methylene-bis-acrylamide (10.8 mg, 0.07 mmol) was substituted for cross-linker **1** in the monomer mixture.

Scheme 1[a]

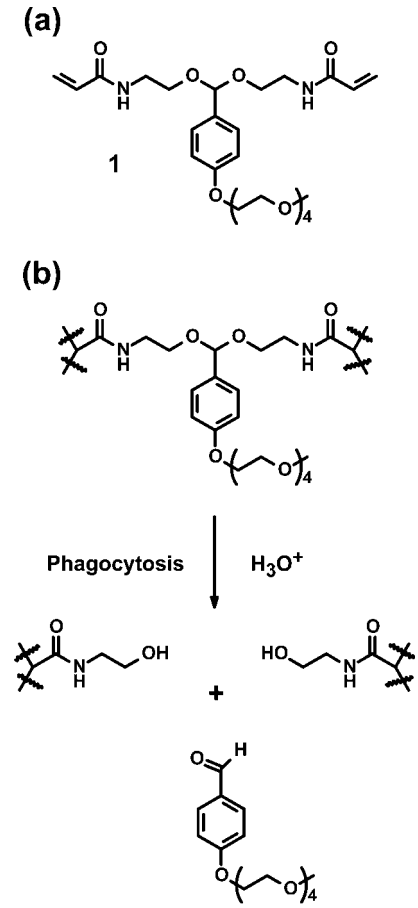

[a] (a) Acid-labile benzylidene acetal cross-linking monomer (**1**) used to prepare nanoparticles. (b) Hydrolysis of cross-linker in polymerized particles generates linear polyacrylamide chains with pendant alcohols along with the release of the corresponding benzaldehyde.

Fluorescently Labeled 35 nm Diameter Particles. Particles encapsulating an ovalbumin−AlexaFluor 488 conjugate (OVA-AF488, Invitrogen-Molecular Probes, Carlsbad, CA) were prepared as described above with the exception that the monomers were dissolved in a PBS solution containing 2 mg/mL of OVA-AF488 in lieu of using unlabeled ovalbumin.

Preparation of 3.5 μm Diameter Particles. The 3.5 μm diameter particles were synthesized according to a previously reported procedure (*16*). Briefly, ovalbumin (7.0 mg) was dissolved in 300 mM phosphate buffer (pH 8, 250 μL), to which acrylamide (63.0 mg, 0.89 mmol) and cross-linker **1** (63.0 mg, 0.12 mmol) were then added and dissolved. Ammonium persulfate (7.0 mg, 0.03 mmol) was added to the monomer/protein solution, and the mixture was added to the organic continuous phase (2.5 mL), consisting of a 3 wt % surfactant solution in hexane, using a 3:1 weight ratio of Span 80 (sorbitan monooleate) to Tween 80 (poly(ethylene glycol)−sorbitan monooleate). The two phases were emulsified by sonicating for 30 s using a Branson Sonifier 450 with a 0.5 in flat tip, an output setting of 2, and a duty cycle of 40%. Polymerization was initiated by the addition of TMEDA (25 μL), and the mixture was stirred at rt for 10 min. The particles were isolated by centrifugation for 10 min at 1380 × *g* at rt, and washed with hexanes (3 × 2 mL) and acetone (4 × 2 mL), centrifuging as before. The solvent was decanted and the particles dried overnight under vacuum to yield a fine white powder (53.7 mg).

Fluorescently Labeled 3.5 μm Diameter Particles. Particles encapsulating OVA-AF488 were prepared as described above with the exception that the monomers were dissolved in a PBS solution containing 10 mg/mL of OVA-AF488 in lieu of using unlabeled ovalbumin.

Ovalbumin-Free Particles. As background controls for determining protein loading, particles of each size were prepared as described above with the exception that no ovalbumin was included in the aqueous phase.

Scanning Electron Microscopy (SEM). A sample of 35 nm particles was suspended at 20 mg/mL in 1 mM NH_4OH (in UltraPure water) and deposited onto a silicon wafer. After 5 min, the residual solution was wicked away using filter paper, and the residue was dried overnight under vacuum. The sample was sputter-coated with a 1 nm film of gold/palladium and visualized using a Hitachi S-5000 SEM at 10 kV.

Particle Size Measurements. The size distribution of the 35 nm particles was determined by dynamic light scattering using a Zetasizer Nano-ZS instrument (Malvern Instruments, Malvern, UK) after suspending the particles at 2 mg/mL in PBS (pH 10). Particle samples were maintained at 25 °C and the instrument settings were determined automatically. The reported results represent the average particle size ± half-peak width at half-maximal height of 15 sequential measurements (to ensure measurement stability) from a multimodal data fit using the manufacturer's software package.

The size distribution of the 3.5 μm particles was determined using a Horiba Partica LA-950 laser scattering particle size distribution analyzer after suspending the particles at 5 mg/mL in PBS. The reported results represent the geometric mean ± standard deviation of the size distribution.

The refractive indices of PBS and polyacrylamide used in the size distribution calculations were 1.33 and 1.47, respectively (*18*), and the viscosity of PBS used was 0.888 cP. Particle size distributions for both measurement techniques were volume-weighted.

Determination of Particle Loading. Particles containing ovalbumin were suspended at a concentration of 5 mg/mL in PBS (pH 5). The solutions were incubated overnight at room temperature while vortexing at 1000 rpm to completely degrade the particles. The amount of protein released from the particles was quantified using a bicinchoninic acid (BCA) assay kit according to the manufacturer's instructions (Micro BCA Protein Assay Kit, Pierce, Rockford, IL). Dilutions of free ovalbumin were used as a standard. Absorbances were recorded using a SpectraMax 190 microplate reader (Molecular Devices, Sunnyvale, CA). Particle loading was corrected for background absorbance from ovalbumin-free particles degraded in the same manner.

^{1}H NMR. NMR samples were prepared in deuterated phosphate-buffered saline consisting of potassium phosphate monobasic (0.144 mg/mL), sodium phosphate dibasic heptahydrate (0.795 mg/mL), and sodium chloride (9 mg/mL) in D_2O. As necessary, this buffer was adjusted to pH 5 using 0.5 M DCl in D_2O. Particles were suspended at 3 mg/mL. Spectra were acquired using a 400 MHz Bruker spectrometer. Chemical shifts are reported relative to 3-(trimethylsilyl)propionic-2,2,3,3-d_4 acid (sodium salt) as a standard.

To monitor cross-link hydrolysis at pH 7.4, a 35 nm particle sample was maintained at 37 °C and spectra were acquired at the indicated time points. To monitor cross-link hydrolysis at pH 5, a particle suspension was maintained at 37 °C; and at the indicated time points, 0.6 mL aliquots were removed, hydrolysis was quenched by adding 2.4 μL of 1 M NaOD in D_2O, and the samples were transferred to sealed NMR tubes. Spectra were acquired within 1 h after samples were quenched.

To determine the cross-linker hydrolysis rate, the ratio of the integration of the benzaldehyde proton signal (δ 9.8 ppm) to the integration of the standard signal was calculated. The ratios were normalized to the ratio obtained from a completely hydrolyzed particle spectrum. To obtain the half-life with respect to hydrolysis, the normalized ratio was plotted versus time and initial data points were fit with an exponential function. All peak areas were determined by numerical integration after background subtraction using *Mathematica 5.0* (Wolfram Research).

Particle Degradation Measurements. To monitor degradation of the 35 nm particles by light scattering (*19*), samples were suspended at a concentration of 2 mg/mL in PBS at the indicated pH values. Samples (1 mL) were added to a cuvette sealed with parafilm to prevent evaporation and vortexed at 600 rpm at 37 °C between readings. Scattering intensity was measured using a Zetasizer Nano-ZS instrument with the temperature set to 37 °C, with the instrument settings held constant from run to run. Reported values represent the mean unadjusted scattering count rate.

Cell Lines and Culture. RAW 309 Cr.1 macrophages (#TIB-69) and HeLa cells (CCL-2), were purchased from ATCC (Manassas, VA) and were cultured in Dulbecco's Modified Eagle Medium containing 4.5 g/L D-glucose and supplemented with 10% fetal bovine serum, 100 units/mL of penicillin, 100 μg/mL streptomycin, and 2 mM GlutaMAX (DMEM). All culture media components were from Invitrogen-Gibco with the exception of the serum, which was from Hyclone (Logan, UT). Cell incubations were performed in a water-jacketed 37 °C/5% CO_2 incubator.

Nanoparticle Cytotoxicity. RAW 309 and HeLa cells were added to the wells of a 96-well tissue culture plate at 5×10^3 cells/well (100 μL/well in DMEM). After overnight incubation, the medium was exchanged for dilutions of ovalbumin-loaded 35 nm particles prepared in DMEM at the indicated concentrations in triplicate (100 μL/well). After 7 h, the wells were washed 3 × 150 μL with DMEM, and 100 μL of DMEM was added to each well. After 24 h, the medium was exchanged for 120 μL of a 0.83 mg/mL solution of MTT (3-(4,5-dimethyl-2-thiazolyl)-2,5-diphenyl-2*H*-tetrazolium bromide) in DMEM. After 3 h, the medium was exchanged for 200 μL of DMSO, and the plates were vortexed to dissolve the purple formazan crystals present. On a separate plate, 100 μL from each well was mixed with 100 μL of DMSO and 25 μL of a glycine buffer (0.1 M glycine, 0.1 M NaCl, pH 10.5), and the absorbance of each well was read at 570 nm using a SpectraMax 190 microplate reader. After background subtraction, each well was normalized to the average absorbance of wells containing cells not treated with particles.

Particle Uptake. RAW 309 and HeLa cells were added to the wells of a 12-well tissue culture plate at 1.5×10^5 cells/well (2 mL/well in DMEM). After overnight incubation, the medium was exchanged for particles encapsulating OVA-AF488 suspended at 0.25 mg/mL in DMEM (1 mL/well). At the indicated time points, cells were washed 3 × 1 mL with PBS, harvested by trypsinization, and centrifuged for 10 s at 13 000 × *g* at rt. The cells were then washed with 1 mL of PBS and centrifuged as before. The cell pellet was resuspended in 300 μL of a 4% paraformaldehyde solution (Electron Microscopy Sciences, Hatfield, PA) in PBS. Cells were analyzed for particle uptake using a Becton-Dickinson Biosciences FACSCalibur flow cytometer (San Jose, CA) with 488 nm excitation.

Confocal Microscopy. RAW 309 cells were seeded in the wells of a four-chambered glass Lab-Tek chamber slide (Nunc, Rochester, NY) at 2×10^4 cells/well (0.75 mL/well) in DMEM. After overnight incubation, the medium was aspirated from each well and 35 nm particles (suspended at 0.25 mg/mL in DMEM) encapsulating OVA-AF488 were added to the wells (0.5 mL/well). After 8 h, the wells were washed 3 × 0.75 mL with

DMEM, and 0.5 mL of DMEM was added to each well. After 16 h, the wells were washed 3 × 0.75 mL with PBS and incubated in a 4% paraformaldehyde solution in PBS for 15 min at rt. The cells were then washed 3 × 0.75 mL with PBS and incubated with 410 μL of a 1:40 dilution of phalloidin−AlexaFluor 546 (Invitrogen-Molecular Probes) in PBS for 30 min in the dark. After washing 3 × 0.75 mL with PBS and 1 × 0.75 mL with distilled water, mounting medium containing DAPI (4′,6 diamidino-2-phenylindole) (Vectashield, Vector Laboratories, Burlingame, CA) was added, and the slide was coverslipped and sealed with Cytoseal 60 (Richard-Allan Scientific, Kalamazoo, MI). Imaging was performed using a Zeiss LSM 510 Meta confocal microscope with a 63× objective (Carl Zeiss, Germany) using excitation wavelengths of 361 nm for DAPI, 488 nm for OVA-AF488, and 543 nm for phalloidin−AlexaFluor 546.

Animals. Male C57BL/6 mice and CD45.1 congenic C57BL/6 mice, 6 to 8 weeks of age, were purchased from the Jackson Laboratory (Bar Harbor, ME). The 1100Mjb mice (OT-I mice) express an H-2K^b restricted T-cell receptor specific for the octapeptide SIINFEKL ($OVA_{258-265}$) (*20*). All mice were housed in the Stanford Animal Facility in accordance with NIH guidelines, and all procedures were approved by the Stanford Institution for Animal Care and Use (IACUC).

***In Vivo* T-Cell Proliferation Assay.** Vaccinations with each particle type were normalized to 5 μg of ovalbumin per mouse. C57BL/6 mice ($n = 3$) received subcutaneous flank injections of particles in 200 μL of PBS, followed by intravenous adoptive transfer of 7.5 × 10^6 congenic OT-I T-cells 24 h later. The OT-I T-cells were labeled with 10 μM 5-(and-6)-carboxyfluorescein diacetate succinimidyl ester (CFSE, Invitrogen) prior to adoptive transfer in order to follow their proliferation by CFSE dilution. Mice vaccinated with 5 μg of free ovalbumin or PBS alone served as controls. Three days after adoptive transfer, draining inguinal lymph nodes were harvested from vaccinated mice, and single cell suspensions were stained with fluorochrome-conjugated antibodies against CD3 (BD Biosciences, San Jose, CA) and CD8 (BioLegend, San Diego, CA). The CFSE proliferation profile of gated CD3+ CD8+ T-cells was determined by flow cytometry.

***In Vivo* Cytotoxicity Assay.** C57BL/6 mice ($n = 4$, minimum) were vaccinated with each particle type normalized to 50 μg ovalbumin, with or without 10 μg CpG ssDNA (TCCATGACGTTCCTGACGTT, phosphorothioate backbone, Oligos, Etc., Wilsonville, OR), in a final volume of 200 μL PBS. At day 7 after vaccination, mice were injected intravenously with 1 × 10^7 CFSE-labeled target cells consisting of 50% SIINFEKL-pulsed splenocytes labeled with 5 μM CFSE and 50% unpulsed splenocytes labeled with 0.5 μM CFSE. Mice were tail-vein bled 18 h after adoptive transfer, and the CFSE profile of transferred cells was determined by flow cytometry for analysis of ovalbumin-specific cytotoxicity.

Endotoxin Testing. Particles were suspended at 5 mg/mL in PBS (pH 5) and degraded overnight at 37 °C while vortexing at 1200 rpm. The degraded samples were diluted to 1 mg/mL and 0.5 mg/mL in PBS (pH 7.4). The presence of endotoxin was quantified using an FDA-licensed colorimetric limulus amebocyte lysate assay cartridge with an Endosafe-PTS test system (Charles River Laboratories, Charleston, SC) with a detection range of 0.05−5 endotoxin units per mL (EU/mL). Endotoxin levels were measured at 0.14 EU/mg and less than 0.05 EU/mg (below the detection range of the assay) for the 3.5 μm and 35 nm particles, respectively. The presence of these levels of endotoxin has been found to result in minimal stimulation of immune cells (*21, 22*).

Statistical Data Analysis. In experiments where replicate samples were analyzed, the results are presented as the mean ± standard deviation unless otherwise noted. Comparisons of statistical significance were made using one-way analysis of variance combined with paired Student's *t* tests at a significance level of $p < 0.05$ after confirming equal variances with the Bartlett test.

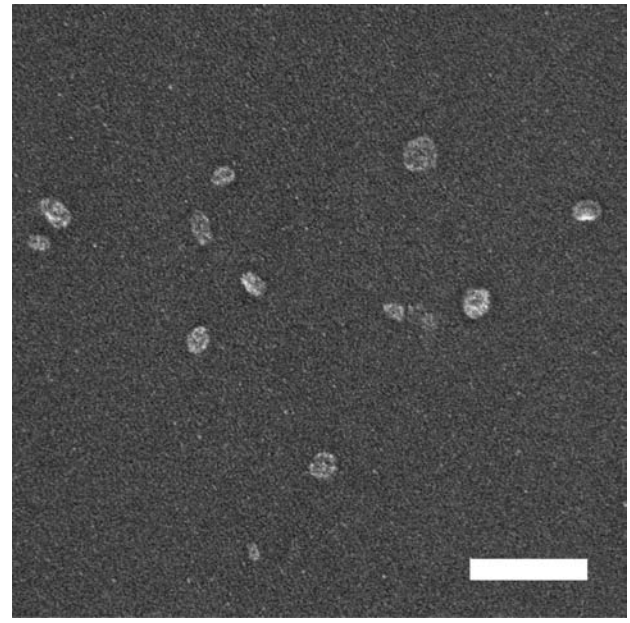

Figure 1. Representative SEM image of dried (unswollen), ovalbumin-loaded, 35 nm particles. The scale bar is equal to 200 nm.

RESULTS AND DISCUSSION

Nanoparticle Synthesis and Characterization. Reports in the literature have suggested that the size of particulate antigen carriers may influence vaccine efficacy *in vivo*; however, to the best of our knowledge there are no studies investigating this phenomenon in hydrogel systems. To this end, we sought to produce acid-labile polyacrylamide particles with diameters smaller than 100 nm. To achieve this goal, we investigated the possibility of polymerizing aqueous monomer-containing droplets formed in inverse microemulsions. The stable droplets formed under these conditions are typically less than 50 nm in diameter and upon polymerization yield swollen hydrogels less than 100 nm in diameter with relatively narrow size distributions. The synthesis of cross-linked polyacrylamide and polyacrylate hydrogel particles in this size range utilizing inverse microemulsions has been reported in the literature (*23, 24*), and the encapsulation of enzymes (*25*−*27*) in particles prepared by this technique has been demonstrated. However, in most cases the encapsulated species was intended to be retained within the particle structure, thus nondegradable cross-linking monomers such as *N*,*N*′-methylene-bis-acrylamide were generally used. In this report, we synthesized particles incorporating an acid-labile acetal cross-linker (**1**, Scheme 1) to afford release of the encapsulated protein at pH values encountered in the endolysosomal vesicles of antigen-presenting cells (∼pH 5) (*17*).

In the present study, we utilized this polymerization method to afford a good yield (ca. 60%) of particles approximately 20 nm in diameter in the dry state (Figure 1) and showing a size distribution of 32.6 ± 6.8 nm as measured by dynamic light scattering when suspended in PBS. Throughout the remainder of this report, these will be referred to as 35 nm particles. A small population of particles (approximately 10%) was also observed with a size centered around 310 nm, likely due to the formation of aggregates. To determine the amount of the model protein (ovalbumin) loaded in the particles, samples were

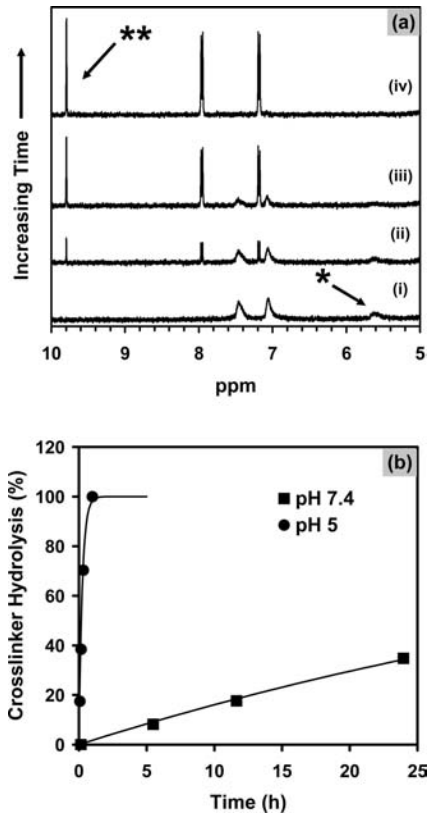

Figure 2. (a) ^{1}H NMR spectra demonstrating the time-dependent hydrolysis of benzylidene acetal cross-linker (*) and release of the resultant aldehyde (**) from ovalbumin-loaded nanoparticles at pH 5 at (i) 0, (ii) 5, (iii) 20, and (iv) 60 min. (b) Cross-linker hydrolysis kinetics for particles hydrolyzed at pH 7.4 and pH 5. Solid lines represent pseudo-first-order hydrolysis models fit using the initial data points at each pH value.

degraded in PBS (pH 5) overnight, and the released protein was quantified using a bicinchoninic acid assay (*28*). The particles were found to contain 5.4 ± 0.1% of ovalbumin by weight.

Cross-Linker Hydrolysis and Particle Degradation. To characterize the rate of cross-linker hydrolysis in the carrier particles, samples of 35 nm particles were suspended in deuterated phosphate buffers at pH 7.4 and pH 5, and ^{1}H NMR spectra were acquired after various times. Figure 2a illustrates the general behavior of the particles upon exposure to acidic conditions. The resonance attributed to the benzylidene acetal proton of the cross-linker within the particles appeared as a broad peak at 5.6 ppm. As the incubation time increased, the intensity of this peak diminished along with the concomitant appearance of a sharp peak at 9.8 ppm corresponding to the proton of the benzaldehyde liberated during hydrolysis. The growth rate of the latter peak can be modeled using pseudo-first-order kinetics with respect to the cross-linker concentration (*29*) to yield a half-life of particle cross-link hydrolysis of 40 h at pH 7.4, compared to 10 min at pH 5 (Figure 2b). These values are roughly equivalent to hydrolysis rates reported for a similar cross-linker in monomeric form (*30*). Within 1 h, hydrolysis was essentially complete at pH 5, while at pH 7.4, hydrolysis progressed slowly over the course of 10 days (data not shown).

A complementary view of particle stability as a function of pH was obtained using measurements of light scattering intensity for suspensions of the particles (Figure 3). The time required for the particles to fragment into linear polyacrylamide chains following cross-linker hydrolysis at pH 5 was approximately 3 h, as determined by a 90% decrease in scattering intensity. On the other hand, over the course of 8 h, no observable decrease in scattering intensity occurred at pH 7.4, and it took

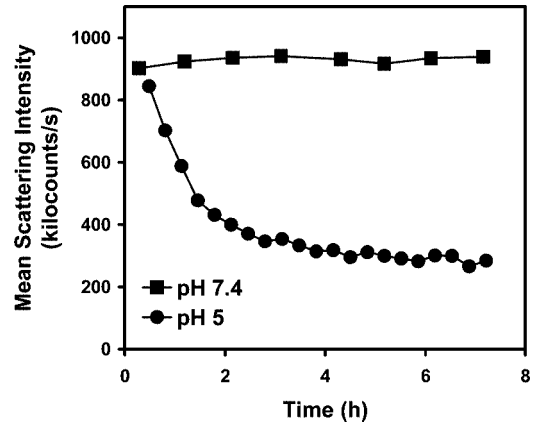

Figure 3. Fragmentation of ovalbumin-loaded nanoparticles as a function of time at pH 7.4 and pH 5 as observed by scattered light intensity measurements.

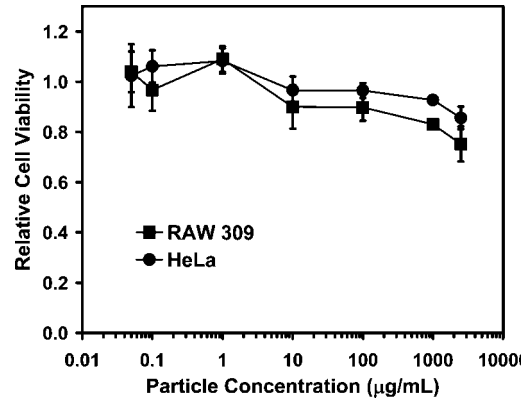

Figure 4. Evaluation of the cytotoxicity of ovalbumin-loaded 35 nm particles in phagocytic RAW 309 macrophages and non-phagocytic HeLa cells using an MTT-based assay.

over 9 days for the scattering intensity to decrease 90% from its original value (data not shown). We confirmed that the decrease in scattering intensity observed in the protein-loaded particles at acidic pH was dependent on the presence of acid-labile cross-links, as the scattering intensity of particles cross-linked with *N,N′*-methylene-bis-acrylamide showed no change in intensity at pH 5 over the same length of time (data not shown). Together, the NMR and light scattering data suggest that, while the particle cross-links hydrolyze relatively rapidly, overall particle degradation appears to be limited by disentanglement of the linear polymers that are formed as the result of cross-linker hydrolysis.

***In Vitro* Cytotoxicity and Uptake of 35 nm Diameter Particles.** In order to assess the cellular toxicity of the 35 nm particles, MTT-based assays were performed using cell lines with both phagocytic (RAW 309 macrophages) and non-phagocytic (HeLa) phenotypes. Cells incubated with 35 nm particles demonstrated very low particle-associated toxicity (Figure 4), with approximately 75% and 85% viability retained at doses up to 2.5 mg/mL in RAW 309 and HeLa cells, respectively.

As many non-antigen-presenting cells are capable of ingesting particulate material less than 200 nm in diameter, we compared the relative uptake of the 35 nm particles for both phagocytic (i.e., antigen-presenting cells) and non-phagocytic cells. The kinetics of particle uptake in RAW 309 macrophages was monitored *in vitro* by flow cytometry using acid-labile, fluorescently labeled 35 nm particles. A rapid increase in fluorescence intensity was initially observed indicating cellular uptake

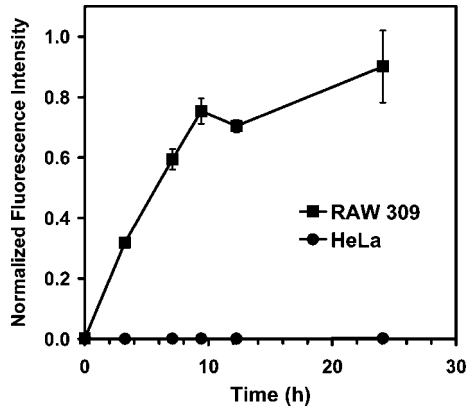

Figure 5. Comparison of the time-dependent *in vitro* cellular uptake of 35 nm particles encapsulating OVA-AF488 by phagocytic RAW 309 macrophages and non-phagocytic HeLa cells as measured by flow cytometry. Mean fluorescence channel values were averaged and normalized to the maximum observed value.

of nanoparticles, with a plateau occurring at approximately 9 h (Figure 5). In contrast, non-phagocytic HeLa cells showed minimal uptake of the 35 nm particles during the same time frame with a 200-fold difference observed between the maximum uptake values for each cell type. The neutral, hydrophilic nature of the polyacrylamide-based particles may limit uptake of the particles by non-phagocytic mechanisms.

Particle uptake was also confirmed by confocal microscopy. After 8 h of incubation with 35 nm particles containing fluorescently labeled ovalbumin, RAW 309 macrophages were fixed, stained, and imaged. As shown in Figure 6, fluorescence was observed throughout their cytoplasm. To ensure that the fluorescence was coming from within the cells, the focal plane was varied throughout the thickness of the cells. Fluorescence was observed as both punctate and diffuse signal. Although a definitive conclusion regarding protein release could not be reached from these data alone, the images may provide an indication that the diffuse signal may result from protein released from particles, while the punctate signal may result from protein entrapped in particles in the early stages of endocytosis prior to degradation (*31*). No fluorescence from within HeLa cells was observed when using the same microscope settings (data not shown), which is complementary to the minimal uptake observed by flow cytometry.

Effect of Particle Size on T-Cell Proliferation and Generation of Antigen-Specific Effector T-Cells. To assess the effect of particle size on the activation of T-cells *in vivo*, we prepared larger analogous acid-labile hydrogel particles by an inverse suspension polymerization method (*14*−*17*). Particles synthesized in this manner had a mean diameter of 3.67 ± 1.18 μm when suspended in PBS and are referred to as 3.5 μm particles in this report. These particles incorporated approximately the same mole percent of cross-linker (10%) and loading of ovalbumin (7.3 +/− 0.2% by weight) and were produced in ca. 40% yield. The 3.5 μm particles were comparable to the 35 nm particles in terms of their morphology as seen by SEM (Supporting Information Figure S1), their degradation characteristics, and their *in vitro* cytotoxicity (*14*). Additional experiments performed using particles containing fluorescently labeled ovalbumin showed similar *in vitro* uptake of both sizes of particles in RAW 309 macrophages as confirmed by flow cytometry (Supporting Information Figure S2). Using confocal microscopy, we found that the intracellular appearance and distribution of both types of particles in macrophages were also similar (Supporting Information Figure S3). We therefore expected that differences in T-cell activation induced by these

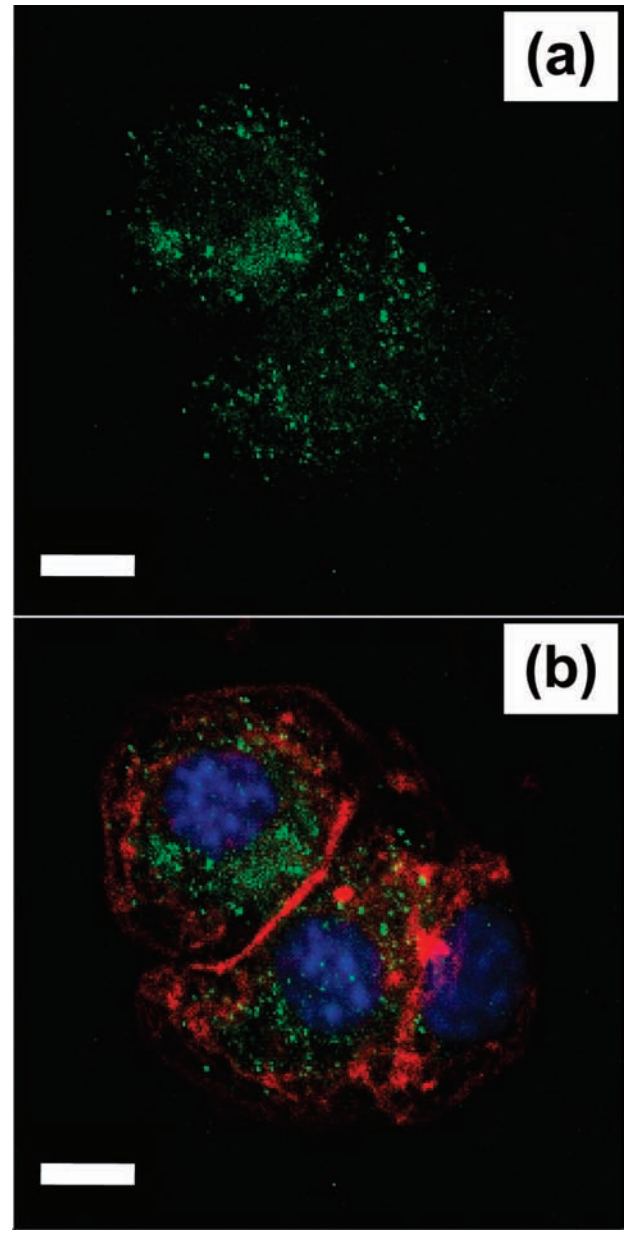

Figure 6. Confocal microscopy images of RAW 309 macrophages incubated with OVA-AF488-loaded 35 nm particles for 8 h followed by fresh medium for 16 h. (a) OVA-AF488 emission (green) and (b) merged with emission from actin stained with phalloidin−Alexa Fluor 546 (red) and nuclear DNA stained with DAPI (blue). The scale bar is equal to 10 μm.

two types of particles would primarily be due to the effect of particle size.

The purpose of encapsulating ovalbumin within the particles was to exploit existing *in vivo* experimental models that rely on the presentation of the immunodominant, ovalbumin-derived, SIINFEKL peptide ($OVAC_{258-265}$) in the context of MHC I molecules ($H\text{-}2K^b$) on the surface of antigen-presenting cells. The first experiment we used to assess the activation of T-cells by the two sizes of particles examined the ability of each type of particle to induce T-cell proliferation. We have previously shown that ovalbumin-loaded pH-sensitive particles are capable of stimulating the proliferation of T-cells *in vivo*, even at relatively low ovalbumin concentrations (*16*). In the present study, C57BL/6 mice were injected with either 3.5 μm or 35 nm particles in quantities normalized to deliver 5 μg of ovalbumin. After 24 h, CFSE-labeled naïve OT-I T-cells, capable of specifically recognizing SIINFEKL/MHC I com-

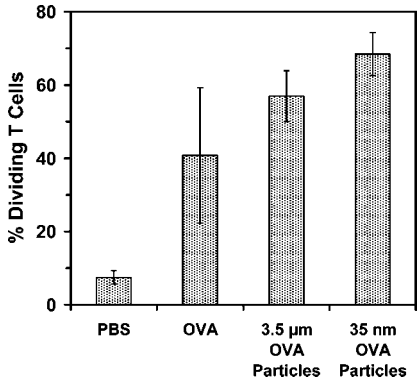

Figure 7. *In vivo* proliferation of SIINFEKL ($OVA_{258-265}$)/H-$2K^b$ specific CD8 T-cells in mice immunized with 3.5 μm and 35 nm ovalbumin-loaded particles. Data derived from CFSE profiles of gated CD3+ CD8+ T-cells isolated from lymph nodes of vaccinated mice 3 d after adoptive transfer.

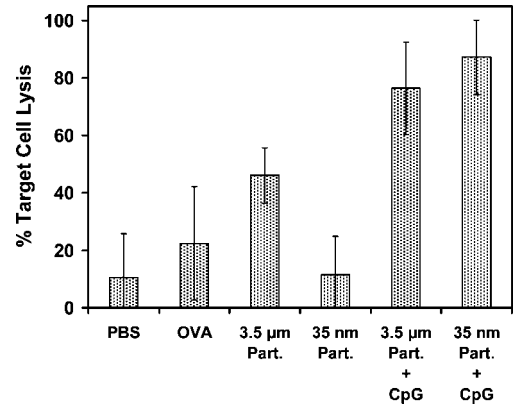

Figure 8. *In vivo* induction of T-cells capable of specific lysis of adoptively transferred SIINFEKL-pulsed splenocytes by 3.5 μm and 35 nm ovalbumin-loaded particles, both without and with coadministration of CpG oligonucleotide. The percentage of specific target cell lysis was determined by comparing remaining numbers of CFSE-labeled splenocytes pulsed with either SIINFEKL peptide or no peptide after adoptive transfer. Average and standard deviation of replicates ($n = 4$ for PBS, $n = 5$ for all others) is presented.

plexes, were adoptively transferred to each mouse. Three days later, draining lymph nodes were assessed for the fraction of OT-I cells that had undergone division in the interim as seen by a dilution of the CFSE signal present in the initially labeled OT-I cells. Figure 7 shows that both the 3.5 μm and the 35 nm particles were capable of stimulating OT-I cell proliferation with 57% and 68% of T-cells undergoing division, respectively, compared to mice injected with free ovalbumin, where only 41% of T-cells were found to be dividing. The level of T-cell division stimulated by 35 nm particles was greater than that of ovalbumin ($p < 0.018$), while 3.5 μm particles were not found to be more stimulatory than ovalbumin alone ($p < 0.12$). While the 35 nm particles appeared to be slightly more stimulatory than the 3.5 μm particles, the difference was not found to be statistically significant.

The proliferation of T-cells stimulated by these acid-labile carriers, however, only provides a general perspective on the activation capacity of this particle system. More importantly, we wanted to determine if antigen-specific effector T-cells were being generated *in vivo*, as this would indicate whether or not the particle formulations would be capable of stimulating an effective CTL response necessary for vaccine-related applications. For this experiment, C57BL/6 mice were injected with either 3.5 μm or 35 nm particles in quantities normalized to deliver 50 μg of ovalbumin. After 7 days, a population of cells consisting of equal amounts of C57BL/6 mouse splenocytes either pulsed or not pulsed with SIINFEKL were injected into the mice. Prior to injection, the two cell types were labeled with either high (SIINFEKL-pulsed) or low (non-SIINFEKL-pulsed) concentrations of CFSE to enable tracking of each set of cells. After 18 h, the quantities of circulating CFSE-labeled cells were analyzed by flow cytometry (Figure 8). A decrease in the fraction of SIINFEKL-pulsed cells relative to the fraction of nonpulsed cells was taken to indicate the presence of antigen-specific effector T-cell cytotoxicity. Without coadministration of additional immunostimulatory compounds, mice injected with 3.5 μm particles alone were found to generate a greater cytotoxic response (46% specific target cell lysis) than ovalbumin alone (22% specific target cell lysis). On the other hand, the 35 nm particles alone did not seem to generate a significant cytotoxic response, with specific cell lysis roughly equivalent to both ovalbumin and PBS controls. It may be possible that the decreased response generated by the 35 nm particles relative to that of the 3.5 μm particles may be associated with a dilution of the injected dose that could occur if the 35 nm particles are indeed small enough to be convectively transported through the lymphatic capillaries draining the injection site. In contrast, due to their larger size, the 3.5 μm particles likely reside at relatively high concentration at the injection site. Elucidating the actual reason for this disparity between the cytotoxicity stimulated by the 3.5 μm and 35 nm particles requires additional study.

We have previously demonstrated that incorporating short, single-stranded oligonucleotide sequences containing unmethylated CpG dinucleotides into the structure of our polyacrylamide-based hydrogel system greatly enhances the activation of antigen-presenting cells and improves the overall immune response (*16*). In addition, it was demonstrated that a similar effect could be observed if the CpG-containing oligonucleotide was simply coadministered along with ovalbumin-loaded particles. As a result, these types of particle formulations represent a more relevant context for antigen delivery than using particles that encapsulate antigen alone. Thus, we sought to investigate the impact of particle size on T-cell activation in formulations where particles were combined with immunostimulatory DNA. For ease of manipulating the experimental conditions such that particle size was the only factor varied, this latter method of coadministering the CpG oligonucleotide was chosen, and additional mice were administered with 10 μg of CpG DNA along with the 50 μg ovalbumin-equivalent of particles. Under these conditions, we found that both 3.5 μm and 35 nm particles were significantly more effective at generating antigen-specific cytotoxic T-cells compared to 3.5 μm particles administered without CpG ($p < 0.0036$ and $p < 0.0002$, respectively), with 76% and 87% specific target cell lysis, respectively (Figure 8). The small difference in target cell lysis between these two treatments was not found to be statistically significant.

Overall, the results of the *in vivo* tests of T-cell activation suggest that, for our acid-labile polyacrylamide-based hydrogel carrier system, particle size does not appear to play a significant role in the generation of CTL responses. Both sizes of particles tested in this study demonstrated a high capacity for stimulating populations of antigen-specific cytotoxic T-cells. Why the behavior we observed differs from reports in the literature for hydrophobic carriers suggesting that smaller particles are more effective in this application requires additional study. In all of the experiments described in this study, we were unable to ascribe the immunostimulatory activity observed using either of the particle types to the presence of particle-associated endotoxin. It is possible that these differences in behavior compared to previously studied polystyrene and poly(propylene sulfide) systems may be related to the overall hydrophilicity of the carrier system or the site of immobilization of the protein antigen being delivered (i.e., encapsulated within the bulk of

the carrier, or bound to the carrier surface), which may influence interactions of the particle system with phagosomal receptors in antigen-presenting cells. To this end, we plan to compare our polyacrylamide-based particle system side-by-side with polystyrene-based carriers to determine their relative stimulatory capacities.

CONCLUSION

In this study, we successfully synthesized and characterized acid-labile and protein-loaded polyacrylamide particles with sub-100 nm diameters by utilizing a microemulsion-based polymerization technique. These nanoparticles were analyzed to determine their degradation characteristics and were found to be readily taken up by antigen-presenting cells of the immune system. We were able to investigate the effect of particle size on T-cell activation *in vivo* using this hydrogel system in comparison to larger analogous particles. In comparison to 3.5 μm diameter particles, 35 nm particles were found to be equivalent at inducing T-cell proliferation and antigen-specific cytotoxicity *in vivo* when coadministered with immunostimulatory DNA. These results suggest that, for hydrophilic carrier systems, size may not be as critical of a factor in stimulatory capacity as in hydrophobic, surface-conjugated systems currently under evaluation. While the present work focused on the use of microemulsion-based hydrogels in immunological applications, we anticipate that these pH-sensitive particles with diameters less than 100 nm may also find use in other *in vivo* applications where their small size and inherently hydrophilic character could be advantageous. For example, we are currently evaluating these nanoparticles as targeted carriers of imaging and therapeutic agents for intravenous or pulmonary administration.

ACKNOWLEDGMENT

We thank the National Institutes of Health (R01 EB005824) for funding of this research; additional NIH support (PEN grant 1 U01 HL080729-01) led to the development of the 35 nm particles used in this study. We thank Ann Fischer and Michelle Yasukawa for help with cell culture studies and Paul Hudson for assistance with analysis of NMR spectra.

Supporting Information Available: Comparison of particle morphology by SEM and comparison of *in vitro* particle uptake by flow cytometry and confocal microscopy. This material is available free of charge via the Internet at http://pubs.acs.org.

LITERATURE CITED

(1) Rejman, J., Oberle, V., Zuhorn, I. S., and Hoekstra, D. (2004) Size-dependent internalization of particles via the pathways of clathrin-and caveolae-mediated endocytosis. *Biochem. J. 377*, 159–169.

(2) Bramwell, V. W., and Perrie, Y. (2005) Particulate delivery systems for vaccines. *Crit. Rev. Ther. Drug Carrier Syst. 22*, 151–214.

(3) Jiang, W., Gupta, R. K., Deshpande, M. C., and Schwendeman, S. P. (2005) Biodegradable poly(lactic-co-glycolic acid) microparticles for injectable delivery of vaccine antigens. *Adv. Drug Delivery Rev. 57*, 391–410.

(4) Reddy, S. T., Swartz, M. A., and Hubbell, J. A. (2006) Targeting dendritic cells with biomaterials: developing the next generation of vaccines. *Trends Immunol. 27*, 573–579.

(5) Heath, W. R., Belz, G. T., Behrens, G. M. N., Smith, C. M., Forehan, S. P., Parish, I. A., Davey, G. M., Wilson, N. S., Carbone, F. R., and Villadangos, J. A. (2004) Cross-presentation, dendritic cell subsets, and the generation of immunity to cellular antigens. *Immunol. Rev. 199*, 9–26.

(6) Reece, J. C., Vardaxis, N. J., Marshall, J. A., Crowe, S. M., and Cameron, P. U. (2001) Uptake of HIV and latex particles by fresh and cultured dendritic cells and monocytes. *Immunol. Cell Biol. 79*, 255–263.

(7) Kovacsovics-Bankowski, M., Clark, K., Benacerraf, B., and Rock, K. L. (1993) Efficient major histocompatibility complex class I presentation of exogenous antigen upon phagocytosis by macrophages. *Proc. Natl. Acad. Sci. U.S.A. 90*, 4942–4946.

(8) Harding, C. V., and Song, R. (1994) Phagocytic processing of exogenous particulate antigens by macrophages for presentation by class I MHC molecules. *J. Immunol. 153*, 4925–4933.

(9) Fifis, T., Gamvrellis, A., Crimeen-Irwin, B., Pietersz, G. A., Li, J., Mottram, P. L., McKenzie, I. F. C., and Plebanski, M. (2004) Size-dependent immunogenicity: therapeutic and protective properties of nano-vaccines against tumors. *J. Immunol. 173*, 3148–3154.

(10) Mottram, P. L., Leong, D., Crimeen-Irwin, B., Gloster, S., Xiang, S. D., Meanger, J., Ghildyal, R., Vardaxis, N., and Plebanski, M. (2007) Type 1 and 2 immunity following vaccination is influenced by nanoparticle size: formulation of a model vaccine for respiratory syncytial virus. *Mol. Pharmaceutics 4*, 73–84.

(11) Reddy, S. T., Rehor, A., Schmoekel, H. G., Hubbell, J. A., and Swartz, M. A. (2006) *In vivo* targeting of dendritic cells in lymph nodes with poly(propylene sulfide) nanoparticles. *J. Controlled Release 112*, 26–34.

(12) Reddy, S. T., van der Vlies, A. J., Simeoni, E., Angeli, V., Randolph, G. J., O'Neil, C. P., Lee, L. K., Swartz, M. A., and Hubbell, J. A. (2007) Exploiting lymphatic transport and complement activation in nanoparticle vaccines. *Nat. Biotechnol. 25*, 1159–1164.

(13) Randolph, G. J., Inaba, K., Robbiani, D. F., Steinman, R. M., and Muller, W. A. (1999) Differentiation of phagocytic monocytes into lymph node dendritic cells *in vivo*. *Immunity 11*, 753–761.

(14) Murthy, N., Xu, M., Schuck, S., Kunisawa, J., Shastri, N., and Frechet, J. M. J. (2003) A macromolecular delivery vehicle for protein-based vaccines: Acid-degradable protein-loaded microgels. *Proc. Natl. Acad. Sci. U.S.A. 100*, 4995–5000.

(15) Kwon, Y. J., Standley, S. M., Goodwin, A. P., Gillies, E. R., and Frechet, J. M. J. (2005) Directed antigen presentation using polymeric microparticulate carriers degradable at lysosomal pH for controlled immune responses. *Mol. Pharmaceutics 2*, 83–91.

(16) Standley, S. M., Mende, I., Goh, S. L., Kwon, Y. J., Beaudette, T. T., Engleman, E. G., and Frechet, J. M. J. (2007) Incorporation of CpG oligonucleotide ligand into protein-loaded particle vaccines promotes antigen-specific CD8 T-cell immunity. *Bioconjugate Chem. 18*, 77–83.

(17) Standley, S. M., Kwon, Y. J., Murthy, N., Kunisawa, J., Shastri, N., Guillaudeu, S. J., Lau, L., and Frechet, J. M. J. (2004) Acid-degradable particles for protein-based vaccines: enhanced survival rate for tumor-challenged mice using ovalbumin model. *Bioconjugate Chem. 15*, 1281–1288.

(18) Franklin, J., and Wang, Z. Y. (2002) Refractive index matching: A general method for enhancing the optical clarity of a hydrogel matrix. *Chem. Mater. 14*, 4487–4489.

(19) Hrubý, M., Koňák, Č., and Ulbrich, K. (2007) Poly(ethylene oxide)-coated polyamide nanoparticles degradable by glutathione. *Colloid Polym. Sci. 285*, 569–574.

(20) Hogquist, K. A., Jameson, S. C., Heath, W. R., Howard, J. L., Bevan, M. J., and Carbone, F. R. (1994) T-Cell receptor antagonist peptides induce positive selection. *Cell 76*, 17–27.

(21) Hoshino, K., Takeuchi, O., Kawai, T., Sanjo, H., Ogawa, T., Takeda, Y., Takeda, K., and Akira, S. (1999) Cutting edge: toll-like receptor 4 (TLR4)-deficient mice are hyporesponsive to lipopolysaccharide: evidence for TLR4 as the Lps gene product. *J. Immunol. 162*, 3749–3752.

(22) Napolitani, G., Rinaldi, A., Bertoni, F., Sallusto, F., and Lanzavecchia, A. (2005) Selected toll-like receptor agonist combinations synergistically trigger a T helper type 1-polarizing program in dendritic cells. *Nat. Immunol. 6*, 769–776.

(23) Vaskova, V., Stillhammerova, M., and Barton, J. (1994) Inverse microemulsion polymerization of acrylamide in the

presence of bi-unsaturated vinyl monomers. *Chem. Pap. 48*, 355–361.

(24) McAllister, K., Sazani, P., Adam, M., Cho, M. J., Rubinstein, M., Samulski, R. J., and DeSimone, J. M. (2002) Polymeric nanogels produced via inverse microemulsion polymerization as potential gene and antisense delivery agents. *J. Am. Chem. Soc. 124*, 15198–15207.

(25) Birrenbach, G., and Speiser, P. P. (1976) Polymerized micelles and their use as adjuvants in immunology. *J. Pharm. Sci. 65*, 1763–1766.

(26) Daubresse, C., Grandfils, C., Jerome, R., and Teyssie, P. (1994) Enzyme immobilization in nanoparticles produced by inverse microemulsion polymerization. *J. Colloid Interface Sci. 168*, 222–229.

(27) Munshi, N., Chakarvorty, K., De, T. K., and Maitra, A. N. (1995) Activity and stability studies of Ultrafine nanoencapsulated catalase and penicillinase. *Colloid Polym. Sci. 273*, 464–472.

(28) Smith, P. K., Krohn, R. I., Hermanson, G. T., Mallia, A. K., Gartner, F. H., Provenzano, M. D., Fujimoto, E. K., Goeke, N. M., Olson, B. J., and Klenk, D. C. (1985) Measurement of protein using bicinchoninic acid. *Anal. Biochem. 150*, 76–85.

(29) Kreevoy, M. M., and Taft, R. W. (1955) The evaluation of inductive and resonance effects on reactivity. I. Hydrolysis rates of acetals of non-conjugated aldehydes and ketones. *J. Am. Chem. Soc. 77*, 5590–5595.

(30) Murthy, N., Thng, Y. X., Schuck, S., Xu, M. C., and Frechet, J. M. J. (2002) A novel strategy for encapsulation and release of proteins: hydrogels and microgels with acid-labile acetal cross-linkers. *J. Am. Chem. Soc. 124*, 12398–12399.

(31) Cohen, J. L., Almutairi, A., Cohen, J. A., Bernstein, M., Brody, S. L., Schuster, D. P., and Fréchet, J. M. J. (2008) Enhanced cell penetration of acid-degradable particles functionalized with cell-penetrating peptides. *Bioconjugate Chem. 19*, 876–881.

BC800338N

T-cell Activation by Antigen-loaded pH-sensitive Hydrogel Particles *In Vivo*: The Effect of Particle Size

Joel A. Cohen[†], Tristan T. Beaudette[†], William W. Tseng[‡], Eric M. Bachelder[†],

Ines Mende[‡], Edgar G. Engleman[‡], and Jean M. J. Fréchet[†,*]

College of Chemistry, University of California, Berkeley, California, 94720-1460, and Department of Pathology, Stanford University School of Medicine, Palo Alto, California

*Corresponding Author: (phone) (510) 643-3077; (fax) (510) 643-3079; (email) frechet@berkeley.edu

Supporting Information

General Procedures and Materials S1
Experimental Methods S2

General Procedures and Materials

RAW 309 Cr.1 macrophages (#TIB-69) were purchased from ATCC (Manassas, VA) and were cultured in Dulbecco's Modified Eagle Medium containing 4.5 g/L D-glucose, and supplemented with 10% fetal bovine serum, 100 units/mL of penicillin, 100 μg/mL streptomycin, and 2 mM GlutaMAX (DMEM). All culture media components were from Invitrogen-Gibco with the exception of the serum, which was from Hyclone (Logan, UT). Cell incubations were performed in a water-jacketed 37 ºC/5% CO_2 incubator.

Experimental Methods

Scanning electron microscopy (SEM). A sample of the dried 3.5 μm particle powder was sputter coated with a 20 nm film of gold and visualized using a Hitachi S-4300SE/N SEM at 5 kV.

A sample of the dried 35 nm particle powder was sputter coated with 1 nm film of gold/palladium and visualized using a Hitachi S-5000 SEM at 10 kV.

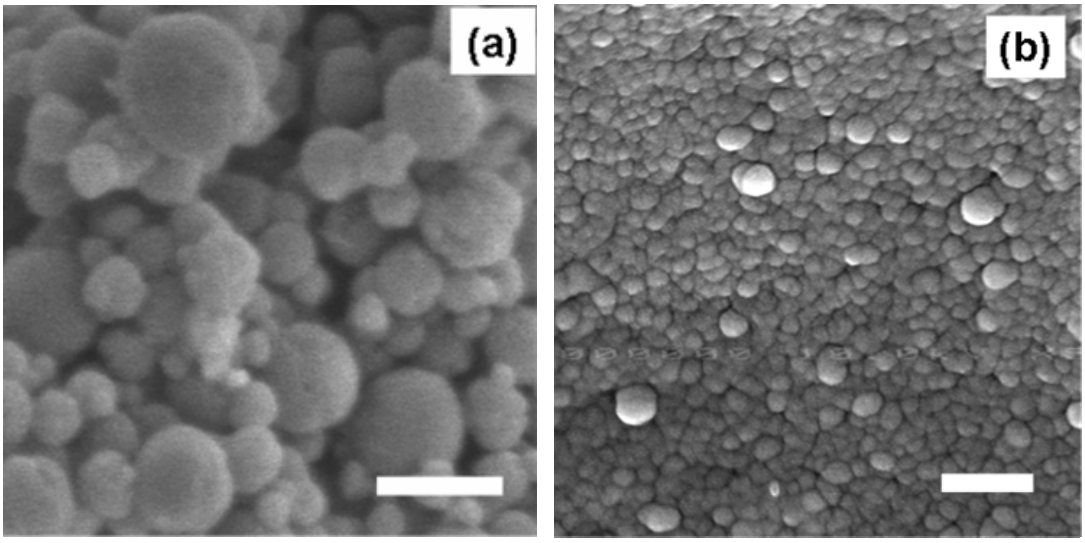

Figure S1. Representative SEM images of dry (unswollen) (a) 3.5 μm particles (scale bar equal to 1 μm), and (b) 35 nm particles (scale bar equal to 100 nm).

Particle Uptake. RAW 309 cells were added to the wells of a 12-well tissue culture plate at 1.5 x 10^5 cells/well (2 mL/well in DMEM). After overnight incubation, the medium was exchanged for a suspension of 3.5 μm particles or 35 nm particles (0.25 mg/mL in DMEM, 1 mL/well) encapsulating OVA-AF488. At the indicated time points cells were washed 3 x 1 mL with PBS, harvested by trypsinization, and centrifuged for 10 seconds at 13,000 x *g* at rt. The cells were then washed with 1 mL of PBS and centrifuged as before. The cell pellet was resuspended in 300 μL of a 4% paraformaldehyde solution (Electron Microscopy Sciences, Hatfield, PA) in PBS. Cells

were analyzed for particle uptake using a Becton-Dickinson Biosciences FACSCalibur flow cytometer (San Jose, CA) with 488 nm excitation.

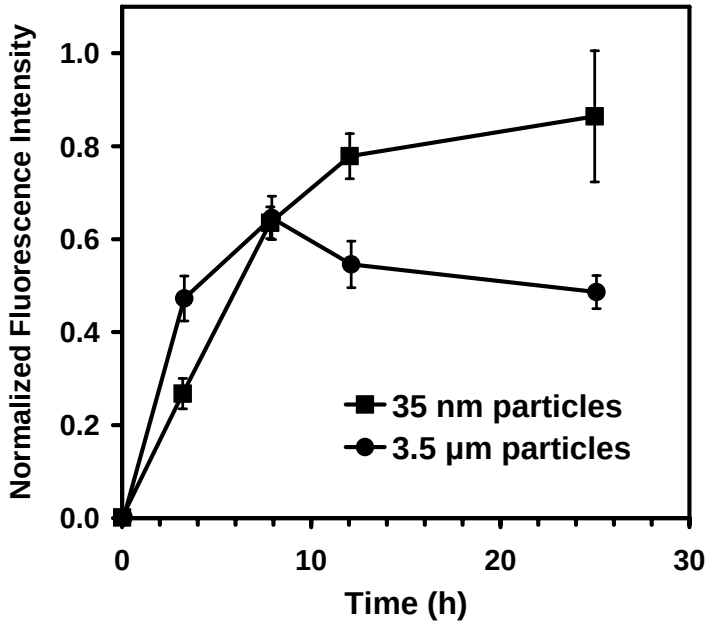

Figure S2. Comparison of the time-dependent *in vitro* cellular uptake of 35 nm particles (■) and 3.5 μm particles (●) encapsulating OVA-AF488 by phagocytic RAW 309 macrophages as measured by flow cytometry. Mean fluorescence channel values were averaged and normalized to the maximum observed value.

Confocal Microscopy. RAW 309 cells were seeded in the wells of a four-chamber Permanox Lab-Tek chamber slide (Nunc, Rochester, NY) at 2 x 10^4 cells/well (0.75 mL/well) in DMEM. After overnight incubation, the medium was aspirated from each well and either 3.5 μm particles or 35 nm particles (suspended at 0.25 mg/mL in DMEM) encapsulating OVA-AF488 were added to the wells (0.5 mL/well). After 8 h, the wells were washed 3 x 0.75 mL with DMEM, and 0.5 mL of DMEM was added to each well. After 19 h, the wells were washed 3 x 0.75 mL with PBS, and incubated in a 4% paraformaldehyde solution in PBS for 15 min at rt. The cells were then washed 3 x 0.75 mL with PBS, and incubated with 410 μL of a 1:40 dilution of phalloidin – AlexaFluor

546 (Invitrogen-Molecular Probes, Carlsbad, CA) in PBS for 30 min in the dark. After washing 3 x 0.75 mL with PBS and 1 x 0.75 mL with distilled water, mounting medium containing DAPI (4',6 diamidino-2-phenylindole) (Vectashield, Vector Labs, Burlingame, CA) was added and the slide was coverslipped and sealed with Cytoseal 60 (Richard-Allan Scientific, Kalamazoo, MI). Imaging was performed using a Zeiss LSM 510 Meta confocal microscope with a 40x objective (Carl Zeiss, Germany) using excitation wavelengths of 361 nm for DAPI, 488 nm for OVA-AF488, and 543 nm for phalloidin – AlexaFluor 546.

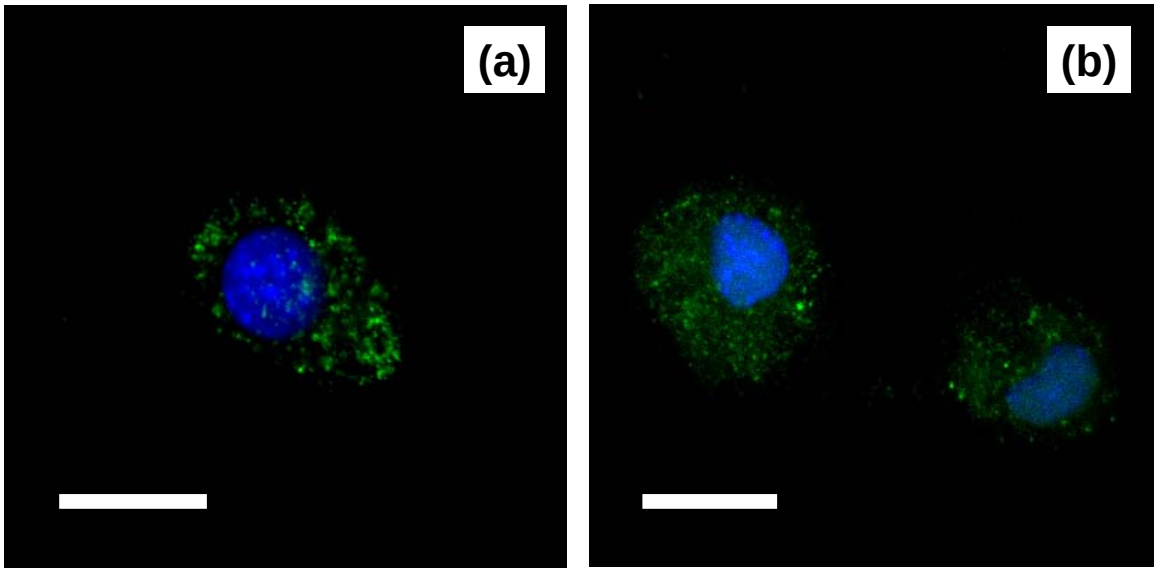

Figure S3. Representative confocal microscopy images of RAW 309 macrophages incubated with OVA-AF488-loaded 35 nm particles (a), or 3.5 μm particles (b), for 8 h followed by fresh medium for 19 h. OVA-AF488 emission (green) and merged with nuclear DNA stained with DAPI (blue). The scale bar is equal to 20 μm. Phalloidin stain omitted for clarity. The focal plane was varied throughout the thickness of the cells to ensure that the fluorescence was coming from within the cells.

Bioconjugate Chemistry 20th Anniversary

Subscriber access provided by SHEMYAKIN-OVCHINNIKOV INST

Article

Efficient Transfection of Blood#Brain Barrier Endothelial Cells by Lipoplexes and Polyplexes in the Presence of Nuclear Targeting NLS-PEG-Acridine Conjugates

Hongwei Zhang, Anton Mitin, and Serguei V. Vinogradov

Bioconjugate Chem., **2009**, 20 (1), 120-128• DOI: 10.1021/bc8003414 • Publication Date (Web): 09 December 2008

Downloaded from http://pubs.acs.org on May 8, 2009

More About This Article

Additional resources and features associated with this article are available within the HTML version:

- Supporting Information
- Access to high resolution figures
- Links to articles and content related to this article
- Copyright permission to reproduce figures and/or text from this article

View the Full Text HTML

ACS Publications
High quality. High impact.

Bioconjugate Chemistry is published by the American Chemical Society. 1155 Sixteenth Street N.W., Washington, DC 20036

Efficient Transfection of Blood−Brain Barrier Endothelial Cells by Lipoplexes and Polyplexes in the Presence of Nuclear Targeting NLS-PEG-Acridine Conjugates

Hongwei Zhang, Anton Mitin, and Serguei V. Vinogradov*

Department of Pharmaceutical Sciences and Center for Drug Delivery and Nanomedicine, College of Pharmacy, University of Nebraska Medical Center, Omaha, Nebraska. Received August 7, 2008; Revised Manuscript Received November 13, 2008

Brain capillary endothelial cells of the blood−brain barrier (BBB) are difficult targets for nonviral transfection even for the most potent transfection agents. Efficient protection and nuclear delivery of plasmid DNA are the key requirements for enhancing the transfection. We designed novel DNA intercalating conjugates of PEG−tris(acridine) with a short nuclear localization signal (NLS) peptide and investigated the effect of their complexes with luciferase-encoded plasmid DNA on lipoplex- and polyplex-mediated transfection of murine brain capillary endothelial bEnd.3 cells. These intercalation complexes protected DNA from nucleolytic degradation forming a protective PEG layer around plasmid DNA and could be efficiently condensed by Lipofectamine2000 or Exgen500 into nanosized particles. Complexation of plasmid DNA with a PEG-acridine/NLS-PEG-acridine mixture (9:1 w/w), taken in an amount equal to 5−6 NLS peptides per DNA molecule, significantly enhanced both lipo- and polyplex transfection efficacies and increased the number of transfected bEnd.3 endothelial cells in the presence of serum. Comparative transgene expression efficiency was significantly higher at longer PEG linker and optimal conjugate-to-DNA weight ratio, especially, at lower N/P ratio for both transfection agents, reaching 15−16-fold for lipoplexes and 10−11-fold for polyplexes. In addition, the NLS-PEG-acridine conjugates did not increase cytotoxicity of lipoplexes and polyplexes to bEnd.3 cells. These conjugates can serve as promising components for development of systemic nonviral transfecting approach to the transfection of the BBB and temporary modulation of its drug permeability.

INTRODUCTION

Many chemotherapeutic agents have limited penetration into the brain through the BBB because brain capillary endothelial cells (BCEC), forming the BBB, express various drug efflux transporter (DET) membrane proteins that actively remove drugs from the brain (*1*). Transient inhibition of the selective DET expression using RNA interference or other therapeutic approaches can potentially increase drug efficacy in the treatment of CNS-related diseases (*2*). It is known that successful application of nonviral vectors is largely limited by their relatively low transfection efficiency in spite of some attractive features like safety and low cost. Even more challenges remain for systemic nonviral gene delivery to the BCEC that have a high intrinsic resistance to the transfection compared to other cell lines (*3*). Nuclear accumulation of plasmid DNA is among the major barriers of nonviral gene delivery, especially in postmitotic, slow-dividing, and quiescent cells (*4, 5*). Actively dividing cells display a regular nuclear envelope disassembly and offer more opportunity for DNA to reach the nuclei. In addition, DNA is sensitive to degradation by nucleases in the cytoplasm.

Nuclear proteins are transferred from the cytoplasm into the nuclei through active transport across nuclear pores mediated by importins recognizing a nuclear localization signal (NLS) sequence (*6*). Various applications of short NLS peptides to increase the nuclear entry of plasmid DNA have been investigated, including covalent or non-covalent attachment of NLS peptides to DNA (*7*−*10*). Zanta et al. demonstrated that only one NLS peptide covalently linked to DNA could increase the transfection efficacy following an intracellular injection of the plasmid (*11*). Jeon et al. conjugated an NLS peptide to PLGA copolymer and demonstrated that slowly degradable PLGA nanospheres could increase the nuclear localization and transfection efficiency of foreign DNA (*12*). Covalent conjugation of NLS peptides to DNA appeared to be a straightforward method, but the modification could result in the loss of biological activity (*13*). Peptide nucleic acids (PNA) were also employed to attach NLS peptide to DNA via sequence-specific noncovalent binding in order to avoid a decrease in transcription activity (*14*). However, this method required individual PNA synthesis for each targeted DNA.

A nonspecific intercalation strategy is looking promising for application to the nonviral transfection. Acridine is a well-known molecule with high affinity to the DNA duplex. However, previous attempts to apply acridine conjugates of NLS peptide resulted in controversial data about their structural requirements for efficient transfection (*15, 16*). In the present study, we investigated effects of direct modification of plasmid DNA with NLS-PEG-acridine conjugates having various PEG linker lengths on the transfection of murine brain capillary endothelial bEnd.3 cells, an in vitro model of the BBB (*17*), by lipoplexes and polyplexes.

EXPERIMENTAL PROCEDURES

Materials. All solvents and reagents, except specially mentioned, were purchased from Sigma-Aldrich (St. Louis, MO) at the highest available quality grade and used without purification. Maleimide (MAL)-PEG_{5000}-*N*-hydroxysuccinimide (NHS), MAL-PEG_{3400}-NHS, and PEG_{5000}-NHS linkers were from JenKem Technology USA (Allen, TX) and MAL-PEG_{900}-NHS linker from Pierce (Rockford, IL). The cystein-containing NLS pep-

* Corresponding author. 986025 Nebraska Medical Center, Omaha, NE 68198-6025. Phone: 1-402-559-9362; email: vinograd@unmc.edu.

10.1021/bc8003414 CCC: $40.75 © 2009 American Chemical Society
Published on Web 12/09/2008

tides CAPKKKRKVA-$CONH_2$ and mutant peptide CAPKT-KRKVA-$CONH_2$ were synthesized by Biomer Technology (Pleasanton, CA) and purified by reverse-phase HPLC. Acridine 9-isothiocyanate was purchased from Acros Organic and purified by chromatography on silicagel before use.

Both gWIZ-Luc (6.7 kb) and gWIZ-GFP (5.7 kb) plasmids were originally purchased from Gene Therapy System (San Diego, CA), propagated in *E. coli* (DH5-α), and isolated using a Qiagen Giga plasmid purification kit (Valencia, CA). The plasmid DNA integrity and topology was analyzed by agarose gel electrophoresis.

Synthesis and Characterization of NLS-PEG-Acridine Conjugates. *Modification of the G1.0 PA-Dendrimer with PEG-Linkers.* MAL-PEG_{5000} (PEG_{3400} or PEG_{900})-NHS linkers or PEG_{5000}-NHS linker (10 μmol) were dissolved in 0.5 mL of water and slowly added to G1.0 PA-dendrimer (9 mg) dissolved in 0.5 mL of water and adjusted to pH 8.0 by 1 N HCl. The reaction continued under stirring for 30 min at 20 °C. The high-MW fraction of the PEGylated products was isolated by gel filtration on the Sephadex G-25 column (G-10 for the PEG_{900} derivative), concentrated in vacuo, and immediately used in the next step.

Reaction with Acridine 9-Isothiocyanate. Acridine 9-isothiocyanate (13 mg) was dissolved in 3 mL of methanol containing 4 μL of triethylamine and mixed with the previously obtained aqueous solution of a PEG−dendrimer conjugate. The reaction mixture was stirred for 1 h at 20 °C, and methanol was removed in vacuo.

The high-MW yellow fraction of the MAL-PEG-acridine product was isolated by gel filtration as previously described, concentrated in vacuo, and immediately used in the last step.

Reaction with Cystein-Containing NLS Peptides. A purified NLS peptide (9 mg) was dissolved in 0.5 mL of DMF and mixed with degassed aqueous solution of the MAL-PEG-acridine conjugate obtained in the previous step. The reaction mixture was left overnight at 4 °C. The final product was concentrated in vacuo, isolated by gel filtration as previously described, purified on the semipreparative reverse-phase HPLC column (C18, 5 μm, 1 × 25 cm), using gradient elution by acetonitrile in 0.1% trifluoroacetic acid (v/v), and lyophilized.

Analysis of NLS−Conjugates. Isolated compounds were analyzed by analytical reverse-phase HPLC. UV absorbance of these conjugates at 420 nm was measured to calculate the acridine content (ε_{420} 5500). MALDI-TOF mass spectrometry in positive mode and sinapinic acid as a matrix were used to determine an average MW of these conjugates. Amino acid analysis was conducted on the ABI Protein Analyzer following acid hydrolysis (UNMC Protein Structure Core Facility).

Preparation of Lipoplexes and Polyplexes Containing NLS−Conjugates. 7.5 μg of pDNA was initially incubated with different amounts of NLS-PEG-acridine conjugates or PEG−acridine conjugate (10 mg/mL) in 1 mL of 5% dextran (w/v) for 30 min. To prepare lipoplexes, 15 or 10 μL of Lipofectamine2000 in 5% dextran (w/v) was added to these complexes or pDNA. To prepare polyplexes, 20 or 14 μL of Exgen500 in 5% dextran (w/v) was added to these complexes or pDNA. Final formulations were incubated for 30 min at 20 °C with continuous shaking.

Particle Size and Surface Charge. The particle size and ζ-potential of the transfection complexes were measured using Zetasizer Nano ZS equipped with 50 mV laser (Malvern Instruments, Worcestershire, UK) in PBS at 25 °C (in triplicate).

Agarose Gel Mobility Shift Assay. Samples were loaded on 0.8% (w/v) UltraPure agarose (Invitrogen, Carlsbad, CA) and analyzed by electrophoresis at 120 V for 35 min in 1× TAE buffer. After electrophoresis, the gel was stained by ethidium bromide and subjected to image analysis.

Cell Line Culture. Murine brain capillary endothelial cell line bEnd.3 was purchased from American type Culture Collection (ATCC, Manassas, VA) and cultivated in Dulbecco's Modified Eagle's Medium (DMEM, Invitrogen, Carlsbad, CA) supplemented with 10% fetal bovine serum (FBS) and 2% penicillin−streptomycin in a humidified incubator containing 5% CO_2 at 37 °C.

In Vitro Transfection. All transfection studies were performed in the presence of 10% FBS. Unless specific indicated, bEnd.3 cells were seeded in 96-well plate with an initial density of 7×10^3 cells per well 24 h prior to transfection. The transfection complexes containing 0.5 μg of pDNA were added to each well and incubated for 4 h at 37 °C. The medium was then replaced by fresh medium, and cells were incubated for additional 40 h. Luciferase expression level was determined in the Bio-Tek FLx800 microplate fluorescence reader using a firefly luciferase assay kit (Biotium, Hayward, CA). Protein content was measured by the BCA assay (Pierce Biotechnology, Rockford, IL). All experiments were performed in 5 parallels, and the results were expressed as nanograms of luciferase per milligram of protein.

DNA Resistance to Degradation by DNase I. Both NLS−lipoplexes and NLS−polyplexes (pDNA/NLS-conjugate = 4:1, w/w) were incubated at 37 °C with DNase I (1 U/μg pDNA) in DNase reaction buffer (Promega/Fisher Scientific, Pittsburgh, PA). After incubation, the samples were placed on ice and treated with 10 μL of stop buffer (Promega) and 30 μL of heparin sodium (5000 USP U/mL, American Pharmaceutics Partners, Schaumburg, IL). The samples were then analyzed by 0.8% agarose gel electrophoresis as described above.

In the functional test of DNA protection, 4.5 μg of pDNA was incubated with 1.1 μg of PEG_{5000}-acridine for 30 min at room temperature. This complex was incubated with DNase I (0.005 U/μg DNA) at 37 °C for 15, 30, or 60 min. The reaction was stopped by adding 1 μL of stop buffer and cooling on ice. The solution was then incubated with 12 μL of Exgen500 for 15 min at 25 °C. Naked pDNA was used as control and treated by DNase I under identical conditions. The bEnd.3 cells were transfected by these complexes in the presence of serum as indicated above.

Evaluation of Gene Expression by Flow Cytometry. bEnd.3 cells were seeded in 6-well plates with an initial density of 4×10^5 cells per well 24 h prior to transfection. Three micrograms of the green fluorescent protein (GFP)-encoded pDNA was pretreated with NLS-PEG_{5000}-acridine, encapsulated in lipo- or polyplexes, and added to the cells in the medium containing 10% FBS. Following incubation for 4 h at 37 °C, the medium was replaced by a fresh one, and cells were incubated for additional 40 h. The transfected cells were rinsed with PBS, trypsinized with 0.3 mL trypsin-EDTA solution, and resuspended in 0.5 mL PBS with 0.1% FBS. The percentage of cells displaying GFP-associated fluorescence was quantified by flow cytometry (FACSCalibur, BD Biosciences, San Jose, CA). The experiments were performed in triplicate.

Confocal Microscopy Analysis. pDNA was labeled with CX-Rhodamine by the Label IT Tracker intracellular nucleic acid localization kit (Mirus Bio Corporation, Madison, WI) according to the manufacturer's instructions. bEnd.3 cells were seeded in 8-chamber culture slides (BD Biosciences, Bedford, MA) with an initial cell density of 1.5×10^4 per chamber 24 h prior to transfection. The transfection complexes containing 0.7 μg of the rhodamine-labeled pDNA were added to the cells as described above. After transfection, cells were washed by PBS and fixed by 4% (w/v) paraformaldehyde for 15 min on ice. Then, the SlowFade gold with DAPI solution (Invitrogen) was applied to the cells. The

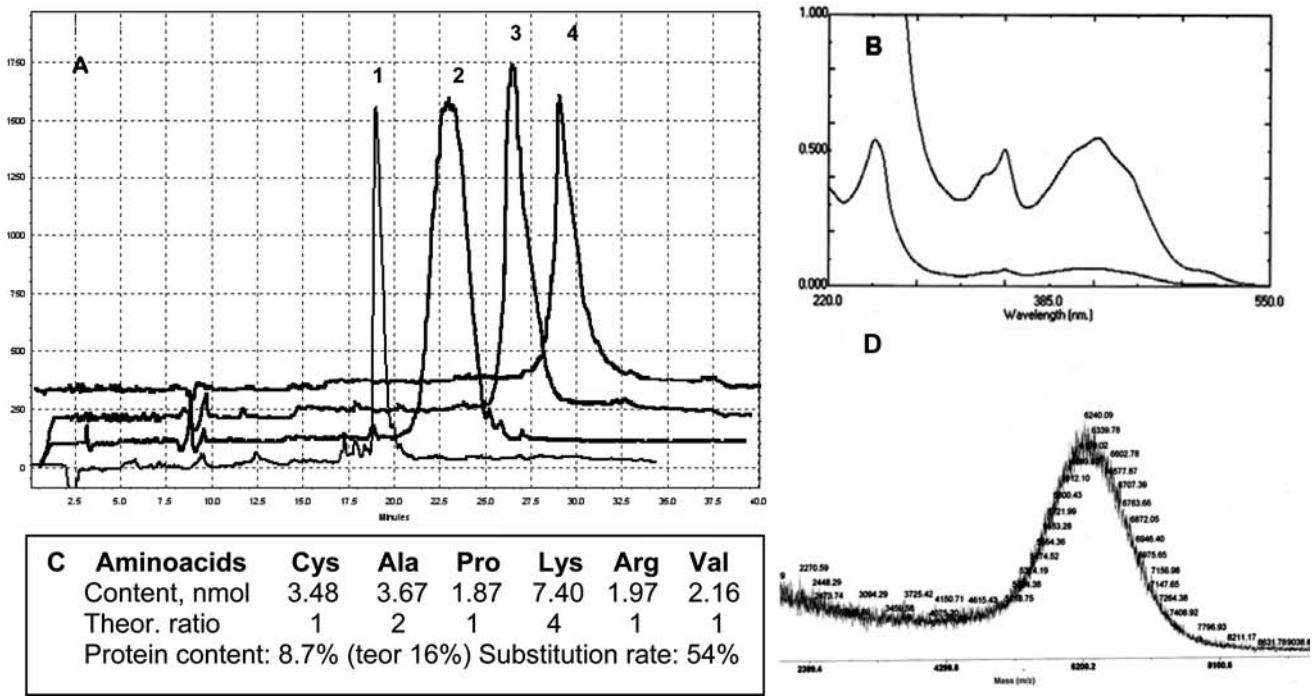

Figure 1. (A) Analytical reverse-phase HPLC (UV detector: 220 nm) of isolated NLS peptide (*1*) and NLS-PEG-acridine conjugates (**2**, PEG_{900}; **3**, PEG_{3400}; **4**, PEG_{5000}). (B) UV spectrum of the NLS-PEG_{5000}-acridine. Acridine absorbance: 420 nm (50% acetonitrile−water, ε 5500). (C) Amino acid analysis of the NLS-PEG_{5000}-acridine conjugate. Expected amino acid ratio in the NLS peptide is shown in the third row. (D) MALDI-TOF spectrum of the NLS-PEG_{5000}-acridine. The average Mw of 5900 belongs to PEG_{5000}−tris(acridine) conjugate, and the average Mw of 7000 corresponds to NLS-PEG_{5000}-tris(acridine) conjugate; superposition of two nearly equal fractions of both conjugates results in the observed average Mw of 6300.

Scheme 1. Synthesis of NLS-PEG-Acridine Conjugates MAL-PEG-NHS: Bifunctional Maleimide-PEG-*N*-Hydroxysuccinimide Derivatives

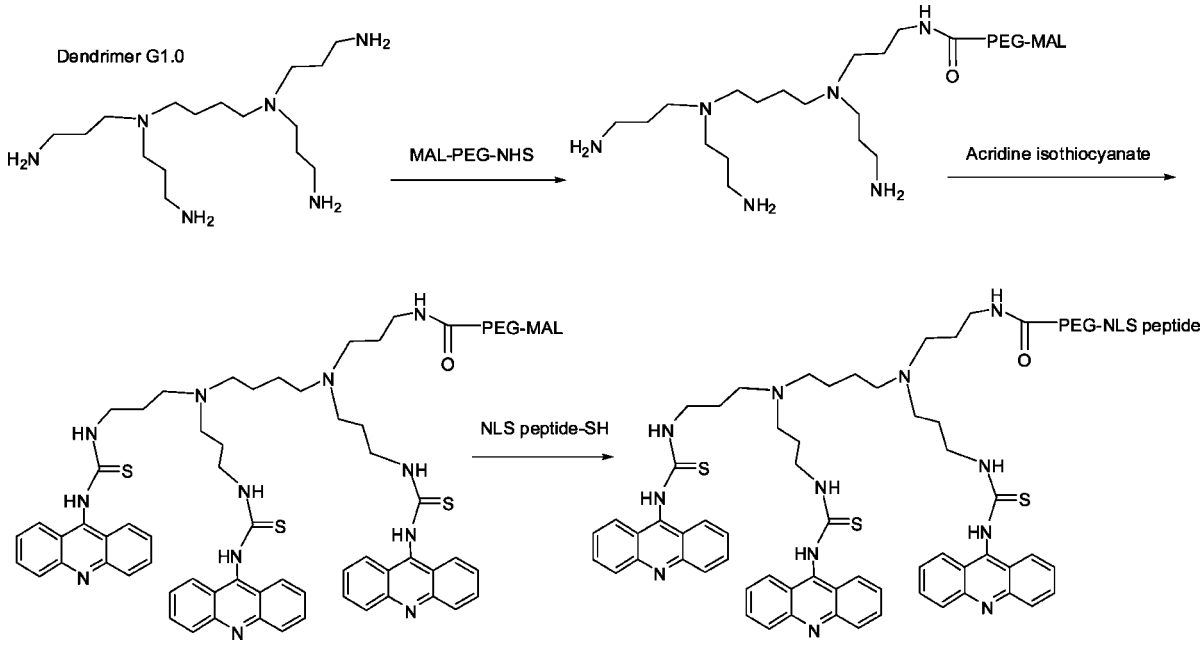

slides were carefully sealed and observed under an LSM 510 confocal laser scanning microscope (Carl Zeiss, Germany).

Nuclear Accumulation of pDNA. To directly measure nuclear accumulation of fluorescent DNA, bEnd.3 cells were seeded in 6-well plates with an initial density of 2×10^5 cells per well 24 h prior to transfection. CX-Rhodamine labeled pDNA was used to prepare NLS-polyplexes at 4:1 (w/w) ratio as mentioned above. Cells were transfected for 4 h in the presence of 10% FBS at 37 °C, then washed by PBS 3 times, and allowed to grow in complete medium for 24 h. The transfected cells were rinsed with PBS, trypsinized with 0.3 mL trypsin−EDTA solution, and resuspended in 0.5 mL PBS/0.1% FBS. For each sample, cells were counted and 4×10^5 cells were collected by centrifugation at 600 *g* for 5 min at 4 °C. The genomic DNA was extracted from nuclei using the Genomic DNA Isolation Kit (Biovision Inc.,

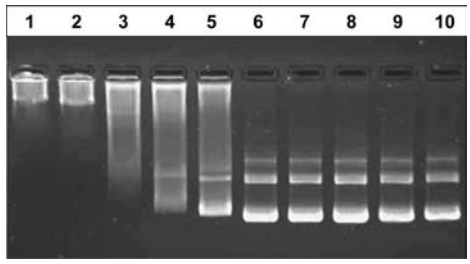

Figure 2. Agarose electrophoresis mobility assay following the pDNA binding with NLS-PEG_{5000}-acridine. 0.5 μg of pDNA was incubated with the NLS conjugate for 30 min at 25 °C at different weight ratios and analyzed by 0.8% (w/v) agarose gel electrophoresis. Lanes 1−5, pDNA with NLS-PEG_{5000}-acridine at weight ratios of 1:6, 1:4, 1:2, 1:1, and 2:1; lane 6, pDNA with NLS−peptide alone; lane 7, pDNA with PEG_{5000} alone; lane 8, pDNA with acridine alone; lane 9, pDNA with the mixture of NLS peptide, PEG_{5000}, and acridine; lane 10, pDNA alone as control.

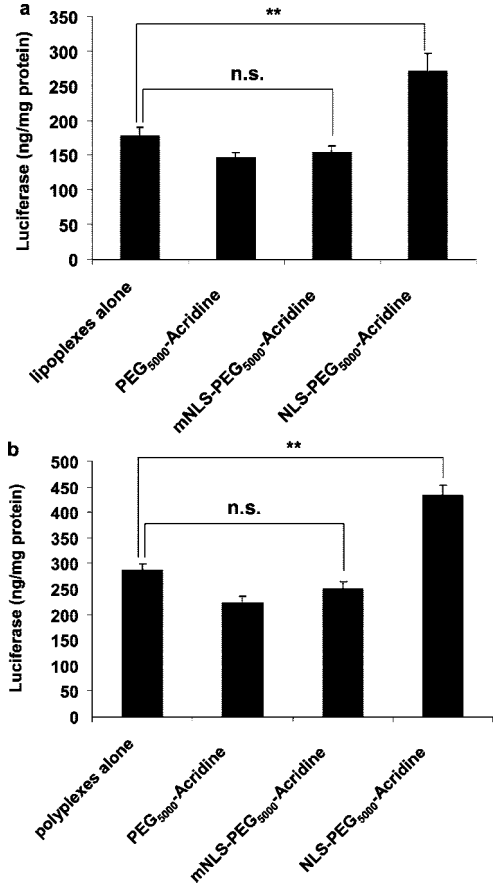

Figure 3. Sequence-specific enhancement of luciferase expression levels in bEnd.3 cells transfected by NLS−lipo- and polyplexes. bEnd.3 cells were transfected with different complexes containing 0.5 μg pDNA/well at pDNA/conjugate ratio 6:1 for 4 h at 37 °C in the presence of 10% FBS. The luciferase expression level and protein content were determined 40 h post-transfection. Results are presented as mean ± SEM ($n = 5$). **, $P < 0.01$; n.s., no significant difference.

Mountain View, CA) (*18*). Extracted DNA was resuspended in 1 mL of TE buffer and analyzed by fluorescence at λ_{ex} 576 nm/λ_{em} 597 nm. The experiment was performed in triplicate.

Cytotoxicity Assay. Cytotoxicity of NLS−conjugates and transfection complexes in bEnd.3 cell culture was evaluated by the thiazolyl blue tetrazolium bromide (MTT) assay as described previously (*19*). Briefly, bEnd.3 cells were seeded in a 96-well plate at initial density of 7×10^3 per well 24 h prior the assay. NLS−conjugates and transfection complexes were incubated with cells using transfection conditions. Then, 20 μL of the MTT solution (5 mg/mL) was added to each well, and formazan crystals were allowed to form for 4 h. The medium was carefully removed, and 200 μL of dimethylsulfoxide (DMSO) was added to each well. The plate was then incubated for 15 min at 37 °C, and the absorbance of formazan was measured at 570 nm using a model 680 microplate reader (Bio-Rad Laboratories, Hercules, CA). The experiments were performed in 5 parallels, and cell viability was calculated relative to that of untreated cells.

Table 1. Properties of NLS−Lipo- and Polyplexes

DNA/conjugate ratio (w/w)		diameter (nm)	ζ-potential (mV)
lipoplexes		180.6 ± 1.3	37.8 ± 1.1
+NLS-PEG_{5000}-acridine-	1:1	204.7 ± 1.3	32.4 ± 0.9
	4:1	176.2 ± 0.9	35.9 ± 0.8
	16:1	177.9 ± 0.7	37.1 ± 1.2
+NLS-PEG_{3400}-acridine-	1:1	189.2 ± 1.2	31.8 ± 0.9
	4:1	168.1 ± 1.1	35.2 ± 1.4
	16:1	177.8 ± 0.9	36.6 ± 1.2
+NLS-PEG_{900}-acridine-	1:1	178.2 ± 0.8	33.1 ± 1.2
	4:1	176.4 ± 1.3	33.5 ± 1.3
	16:1	177.4 ± 1.2	34.8 ± 0.9
polyplexes		68.4 ± 1.1	35.6 ± 0.9
+NLS-PEG_{5000}-Acridine-	1:1	71.9 ± 1.1	30.1 ± 0.8
	4:1	70.6 ± 0.8	33.4 ± 1.2
	16:1	70.4 ± 0.8	35.1 ± 1.1
+NLS-PEG_{3400}-Acridine-	1:1	75.1 ± 1.1	29.8 ± 1.2
	4:1	71.4 ± 0.8	35.7 ± 1.1
	16:1	71.5 ± 1.2	35.2 ± 0.9
+NLS-PEG_{900}-Acridine-	1:1	76.2 ± 1.2	29.5 ± 1.2
	4:1	71.2 ± 1.1	33.9 ± 1.2
	16:1	72.8 ± 0.9	34.6 ± 1.1

Statistical Analysis. Experiment results are presented as means ± SEM. Statistical significance was determined by the paired sample's *t*-test using SPSS 13.0 software (SPSS Inc., Chicago, IL). In all cases, $P < 0.05$ was considered statistically significant.

RESULTS

Synthesis and Characterization of NLS−Conjugates. Preliminary molecular modeling showed that conjugates of acridine 9-isothiocyanate with the generation 1.0 PA-dendrimer have proper dimensions and good fitting for intercalation in the double helix of DNA. To prepare NLS-PEG-acridine conjugates, we used heterofunctional maleimide-PEG-*N*-hydroxysuccinimide linkers of MW 900, 3400, and 5000 Da (Scheme 1). Initially, these linkers were modified with a large excess of generation 1.0 PA dendrimer. For fast product isolation, we used a significant difference between PEGylated products and reactants. All MAL-PEG-dendrimer conjugates were isolated by gel filtration, and then all three remaining primary amino groups were immediately modified with acridine 9-isothiocyanate. The MAL-PEG-acridine product was also purified by gel filtration and immediately introduced into reaction with the thiolated NLS peptide. Final NLS-PEG-acridine conjugates were isolated by reverse-phase HPLC using a C18 semipreparative column and extended gradient of the acetonitrile concentration. However, it was difficult to completely separate the NLS-PEG-acridine conjugates from corresponding PEG−acridine conjugates. On the basis of the amino acid analysis, an average yield at the last step was ca. 50%. The NLS-PEG-acridine and PEG−acridine conjugates eluted in one peak by analytical HPLC and could be easily separated from the free NLS peptide (peak 1, Figure 1A). A stronger retention of NLS−PEG conjugates of higher Mw was also observed. The characteristic mass distribution in the MALDI-TOF mass spectra confirmed the presence of overlapping PEG-acridine and NLS-PEG-acridine molecules in near-equimolar ratio. As an example, NLS-PEG_{5000}-acridine sample showed overlaying of two PEG-containing peaks with

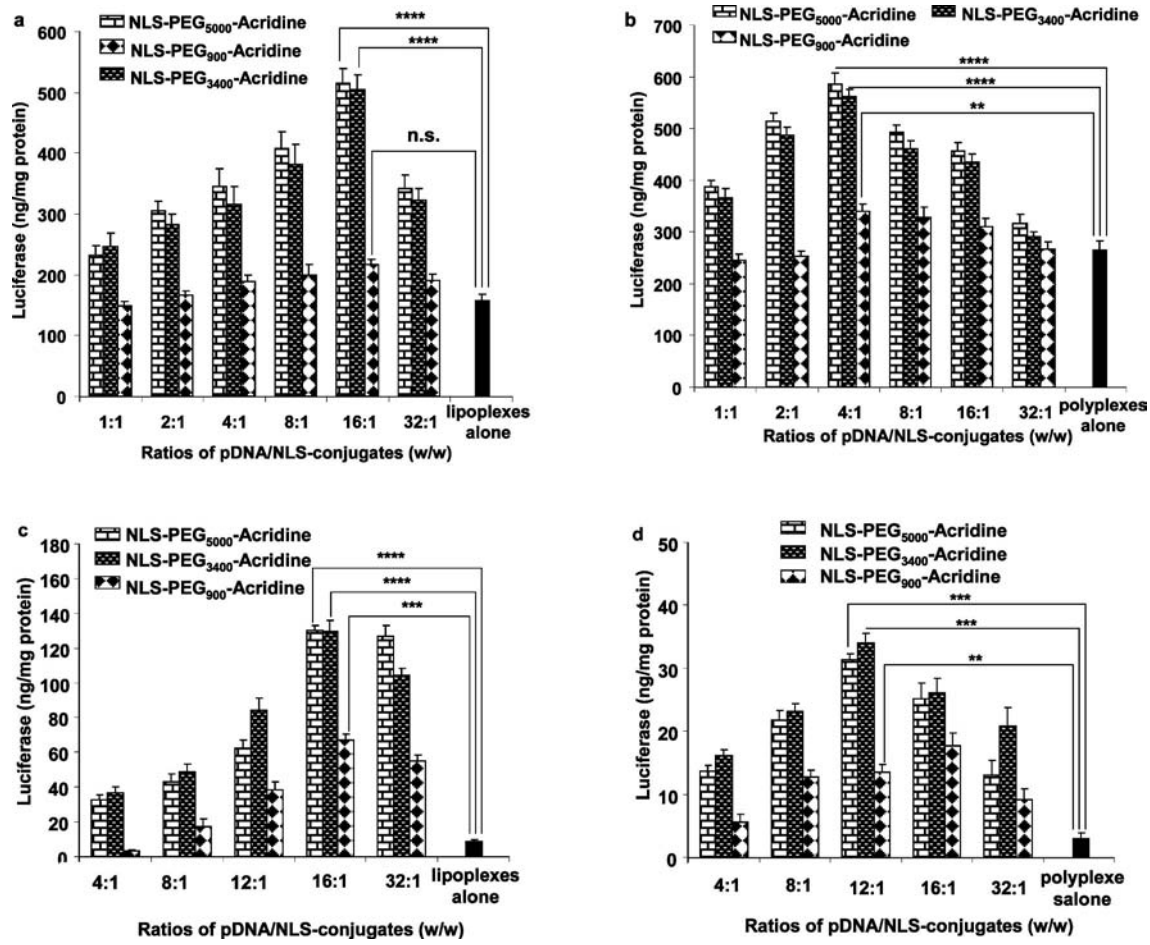

Figure 4. Optimization of the effect of NLS−conjugates on the luciferase expression in bEnd.3 cells transfected by lipo- and polyplexes. NLS−lipo- and polyplexes were prepared at optimized (a and b) and 1/3 lower (c and d) ratios of transfection reagents to pDNA. bEnd.3 cells were incubated with complexes containing 0.5 μg pDNA/well for 4 h at 37 °C in the presence of 10% FBS. The luciferase expression level and protein content were determined 40 h post-transfection. Results are presented as mean ± SEM ($n = 5$). **, $P < 0.01$; ***, $P < 0.005$; ****, $P < 0.0001$.

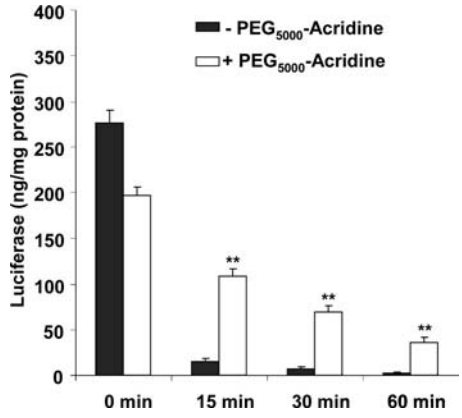

Figure 5. Protective effect of PEG molecules on the luciferase pDNA activity. Naked pDNA or pDNA complexed with PEG_{5000}−acridine conjugate at the ratio 6:1 was treated by DNase I (0.005 U/μg DNA) at 37 °C for different time periods. Exgen500 was then added to both mixtures, and they were used to transfect bEnd.3 cells for 4 h at 37 °C in the presence of 10% FBS. Results are presented as mean ± SEM ($n = 5$). (**, $P < 0.01$).

an average MW between 5900 and 7000 Da, corresponding to PEG_{5000}-acridine and NLS-PEG_{5000}-acridine conjugates, respectively, presented in the final product in nearly equal amounts (Figure 1D). By UV-spectrophotometric data, NLS-PEG-acridine conjugates contained the molar amounts of acridine that were close to values calculated for the corresponding tris(acridine) conjugates (Figure 1B). Finally, amino acid microanalysis after the total acidic hydrolysis of NLS-PEG-acridine conjugates demonstrated the presence of peptide with the correct amino acid content and provided the protein content that was used to calculate the NLS peptide derivatization degree. On the basis of these data, the total peptide content in the obtained NLS−conjugates was equal to 8−13% and equivalent to the NLS peptide derivatization degree of 40−54% (Figure 1C).

Binding of NLS−Conjugates to pDNA. The binding of NLS−conjugates with plasmid DNA was analyzed by the band shift assay using agarose electrophoresis. As shown in Figure 2, pDNA showed the first signs of retardation at pDNA to NLS-PEG_{5000}-acridine ratio 2:1 (wt) and, then, was efficiently retained in the wells at lower ratios. By contrast, individual NLS peptide, PEG, or acridine showed no influence on the pDNA mobility. These results suggest that only the binding of NLS-PEG_{5000}-acridine conjugate with pDNA resulted in the increase of total MW and steric hindrance of the intercalation complex and was observed as band retardation during electrophoresis. Similar results were obtained with NLS-PEG_{3400}-acridine and NLS-PEG_{900}-acridine, although at various weight ratios for all conjugates (data not shown).

Properties of NLS−Lipoplexes and NLS−Polyplexes. Intercalation complexes have been prepared by premixing of NLS−conjugates with pDNA, and following the short incubation, these complexes were mixed with Lipofectamine2000 or Exgen500 at optimized ratios recommended by manufacturers. Compared to plain lipo- and polyplexes, NLS−lipo- and NLS−polyplexes demonstrated slightly increased particle size and decreased surface charge (Table 1). Introduction of

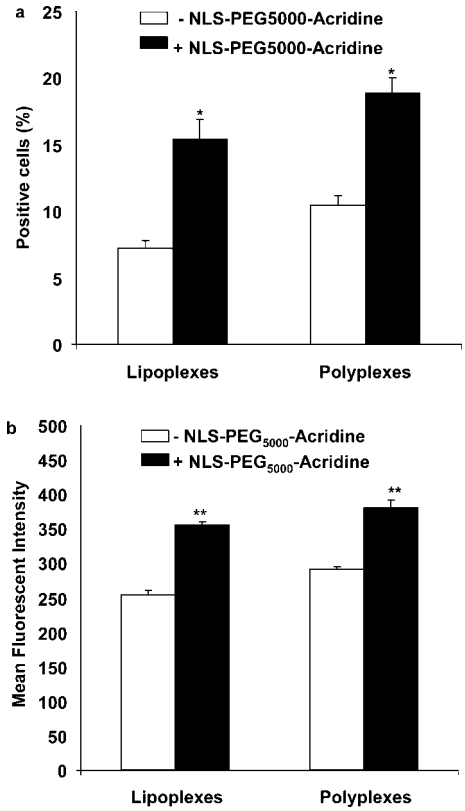

Figure 6. Enhancement of transfection efficiency and GFP expression levels in bEnd.3 cells in the presence of NLS-PEG_{5000}-acridine conjugate. Cells were treated in 6-well plates with NLS−lipo- and polyplexes containing 3 μg of the green fluorescent protein pDNA for 4 h at 37 °C. 40 h later, cells were trypsinized and analyzed by flow cytometry. Results are presented as mean ± SEM ($n = 3$). *, $P < 0.05$; **, $P < 0.01$.

NLS−conjugates in lipo- and polyplexes practically did not affect protection of encapsulated pDNA against enzymatic degradation at conditions when free pDNA was completely digested (Figure S1, Supporting Information).

The intrinsic cytotoxicity of NLS−conjugates was very low ($IC_{50} = 5-7$ mg/mL at 24 h incubation) and did not enhance the cytotoxicity of lipoplexes and polyplexes incubated with bEnd.3 cells. As shown in Figure S2 (Supporting Information), the cytotoxicity of plain lipoplexes at the optimized ratio of transfection reagent to DNA was generally higher than that of polyplexes; NLS−lipoplexes and polyplexes followed the same trend.

In Vitro Transfection. bEnd.3 cells were transfected by lipoplexes or polyplexes in the presence of 10% serum. First, the capability of NLS−conjugate to improve the transgene expression was investigated. NLS-PEG_{5000}-acridine significantly enhanced luciferase expression by lipoplex (Figure 3a) and polyplex transfection (Figure 3b) ($P < 0.01$). On the contrary, no or a slight decrease in transfection was observed when pDNA was coupled with PEG_{5000}−acridine or mNLS-PEG_{5000}-acridine before complexation with transfection reagents. The influence of various NLS−conjugates and different pDNA/conjugate ratios on lipoplex and polyplex-mediated luciferase transgene expression is illustrated in Figure 4. At the optimized ratio of Lipofectamine2000 to pDNA, the highest luciferase expression level was observed at the ratio of pDNA to NLS-PEG_{5000}-acridine of 16:1 (w/w) (Figure 4a). The NLS-PEG_{3400}-acridine conjugate showed a very similar enhancing effect. However, further reduction of the PEG length resulted in lower or no enhancement as indicated for NLS-PEG_{900}-acridine conjugate. At a 33% lower ratio of Lipofectamine2000 to pDNA, the observed comparative transfection increase for NLS−lipoplexes over plain lipoplexes was even more significant ($P < 0.0001$) (Figure 4c). The addition of NLS-PEG_{5000}-acridine, NLS-PEG_{3400}-acridine, and NLS-PEG_{900}-acridine to lipoplexes resulted in 15-, 15-, and 8-fold increases of the luciferase expression, respectively. In terms of polyplexes, NLS−conjugates also displayed a very strong effect on transfection (Figure 4b,d). At the optimized ratio of Exgen500 to pDNA, the highest luciferase expression level was observed at the pDNA to NLS-PEG_{5000}-acridine ratio 4:1 (w/w) (Figure 4b). At the 33% lower ratio, the improving effect of NLS-PEG-acridine conjugates also becomes more evident (Figure 4d). Application of NLS-PEG_{5000}-acridine, NLS-PEG_{3400}-acridine, and NLS-PEG_{900}-acridine resulted in 11-, 11-, and 6- fold increase of the luciferase expression, respectively. The pDNA dose dependence was determined at fixed optimal ratios for both NLS−lipoplexes and polyplexes (Figure S3, Supporting Information). Our results demonstrated that the highest transfection level could be achieved at pDNA doses used in the study, and the transgene expression began to drop at higher doses, evidently, because of the toxicity of transfection agents.

The protective role of bulk PEG chains on the resistance of the pDNA/PEG_{5000}−acridine complex to enzymatic hydrolysis was illustrated by the luciferase expression functional test. The complexed luciferase-encoded pDNA was primarily treated with DNase I and then mixed with Exgen500. Comparative results of the bEnd.3 cell transfection by the protected and naked DNA treated with DNase I are shown in Figure 5. Tremendous loss of transfection activity of the naked pDNA was observed after the enzymatic digestion, resulting in the complete disappearance 30 min post-treatment. By contrast, the pDNA/PEG−acridine complex was much more stable, and 20% luciferase activity still remained after 60 min of incubation.

Flow Cytometry Assay. Since NLS-PEG_{5000}-acridine demonstrated the strongest enhancing effect, we quantitatively studied transfection efficiency and GFP expression levels for NLS−lipoplexes and polyplexes by flow cytometry. Our flow cytometry results showed that NLS-PEG_{5000}-acridine could enhance both GFP transfection efficiency and GFP expression. Specifically, we observed a stronger effect on transfection efficiency (2.13- and 1.81-fold enhancement) than on the GFP expression level (1.40- and 1.31-fold enhancement) for lipoplexes and polyplexes, respectively ($P < 0.01$; Figure 6a,b).

Subcellular Localization of pDNA. Effect of NLS-PEG_{5000}-acridine on the nuclear accumulation of rhodamine-labeled pDNA in bEnd.3 cells was studied 24 h post-transfection (Figure 7). Using confocal microscopy, we observed only a limited amount of rhodamine-labeled pDNA in the nuclei and perinuclear area following the transfection by lipoplexes or polyplexes (Figure 7A,D). In contrast, cells transfected by NLS−lipoplexes or polyplexes showed much more pDNA delivered inside the nuclei and in the perinuclear area (Figure 7B,E). Similar results were obtained with NLS-PEG_{3400}-acridine and NLS-PEG_{900}-acridine conjugates for both types of transfection complexes (data not shown). The lateral confocal images clearly demonstrate efficient penetration of the rhodamine-labeled DNA into the nuclei (Figure 7C,F).

For direct evaluation of nuclear accumulation of rhodamine-labeled pDNA following the polyfection, total nuclear DNA was extracted from the isolated nuclei of transfected cells and its fluorescence intensity was determined. As shown in Figure 7G, NLS-PEG_{5000}-acridine polyplex enhanced nuclear accumulation of pDNA by almost 2-fold compared with plain

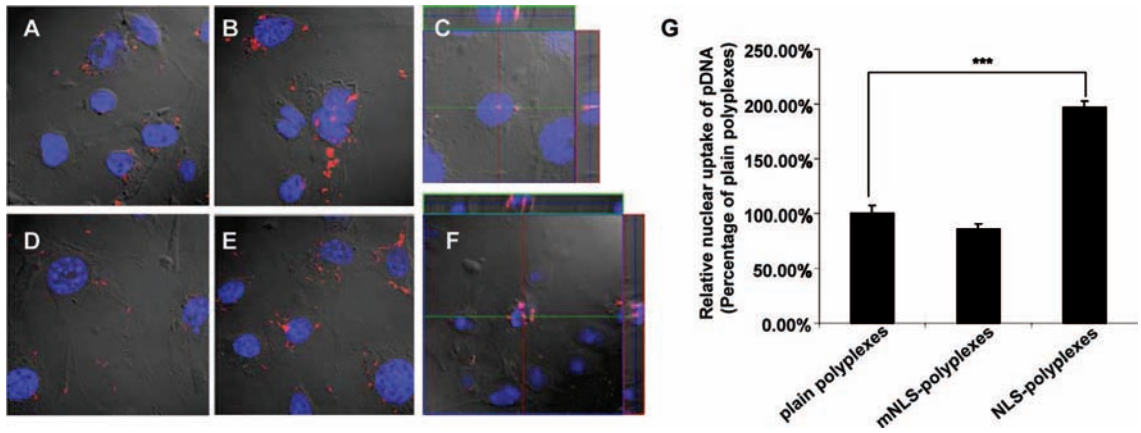

Figure 7. Enhanced intracellular and nuclear accumulation of rhodamine-labeled pDNA following the transfection of bEnd.3 cells with NLS−lipo- and polyplexes. Confocal microscopy images of bEnd.3 cells 24 h post-transfection by pDNA complexed with NLS-PEG_{5000}-acridine conjugate (6:1) at optimal transfection agent ratios in the presence of 10% FBS. After fixation, the cells were imaged using laser scanning confocal microscope. Panes A,D show lipo- and polyplexes without NLS−conjugates, respectively. NLS−poly- and lipoplexes are shown in panes B,E in regular mode, respectively, and in lateral mode in panes C,F, respectively. (G) Accumulation of rhodamine-labeled pDNA in nuclei 24 h following transfection of bEnd.3 cells by plain or NLS−polyplexes. The fluorescence of isolated nuclear DNA following transfection with plain polyplex was taken for 100%. ***, $P < 0.005$.

polyplexes ($P < 0.05$), while the corresponding mutant mNLS−polyplex showed no enhancement effect.

DISCUSSION

Efficient nuclear delivery of plasmid DNA is one of major requirements for successful nonviral transfection. Different approaches have been explored to increase nuclear accumulation including association of DNA with hydrophobic molecules (*20*), engineered histone H2B (*21*), and adenovirus hexon protein (*22*), but without a notable success. Application of NLS peptides and cellular machinery for transporting nuclear proteins was shown to be a very promising approach, although many experiments resulted in only limited success. The major problem is the size of the nuclear pores, which is restrictive to molecules larger than 23 nm in diameter. Only direct attachment of NLS peptide to pDNA, not affecting its expression activity, demonstrated positive effects, while condensing the DNA with NLS-modified carriers usually had no effect on transfection (*11*). The second decisive factor is stability of pDNA in cytoplasm. Fast degradation of pDNA by cytosolic nucleases, following its release from lipo- or polyplex, and lower mobility of free pDNA in cytoplasm can be additional reasons for the rapid loss of transfection activity. In addition, finally, in slowly dividing cells pDNA has a lower chance to internalize in the nuclei during mitosis, which is probably the major way for the carrier-associated DNA to efficiently penetrate nuclei.

In this study, we demonstrated that noncovalent modification of pDNA by PEG−tris(acridine) conjugates of NLS peptide could significantly enhance nuclear accumulation and transgene expression in slowly dividing cells following the lipoplex or polyplex-mediated transfection. Acridine-based intercalating agents tightly bind double-stranded DNA ($K_d < 10^{-9}$ M), and no sequence specificity is required for this process (*23, 24*). Previously, we demonstrated that modification of oligonucleotides with acridine 9-isothiocyanate strongly enhanced their antisense activity (*25*). Recent data on NLS-polypeptide-acridine constructs confirmed that acridines as anchor molecules for noncovalent, strong, and reversible binding of NLS peptide to pDNA could be an inexpensive alternative to PNA clamps (*16*). Here, we constructed novel intercalating conjugates based on the generation 1.0 PA dendrimer linked to three acridine molecules and one NLS peptide via a PEG linker. This scheme allowed us to find an appropriate distance between the peptide and tris(acridine) anchor to achieve an efficient pDNA protection and in vitro transfection by lipo- and polyplexes. Previously, Boulanger et al. reported that, when the distance between NLS peptide and anchor molecule was shorter than 20 methylene groups, NLS−conjugates showed no enhancing effect on transfection ability of lipo- and polyplexes in vitro (*15*). Our results demonstrated that the NLS-PEG-acridine conjugates with longer PEG linkers (PEG_{5000} and PEG_{3400}) showed rather similar high transfection enhancement, while the effect of shorter PEG linker with 40 methylene groups was much lower. Our data showed that the optimal MW requirement for the PEG linker is close to 3000 Da. Evidently, a sufficiently long PEG linker can facilitate the NLS peptide recognition by nuclear transport proteins, such as importins.

Since high PEG density may potentially affect the cellular binding of transfection complexes, reducing transfection efficiency, the amount of NLS conjugates used in transfection was optimized at two constant weight ratios of transfection agent to pDNA. A significant increase was observed at the higher optimized weight ratios recommended for both agents by manufacturers (Figure 4a,b), although the highest differences could be observed at the 33% lower weight ratios ($P < 0.0001$, Figure 4c,d). The strong positive charge of transfection complexes is the major factor that determines cellular uptake and endosomal escape of pDNA in vitro. In our conditions, at the optimized ratios of transfection agents to pDNA, cellular capacity to internalize and express large amounts of exogenous DNA can already be at saturation. The effect of nuclear targeting on the transgene expression may be hidden in these conditions. This conclusion is partially confirmed by the transfection dose dependence results, where both lipoplexes and polyplexes at fixed ratios of NLS−conjugate to pDNA and transfection agents to pDNA demonstrated a bell-shaped dependence on the pDNA dose, and maximum luciferase expression was observed at the dose 0.5 μg per well used in transfection experiments (Supporting Information Figure S3). Thus, our results at the higher ratio are obtained at nearly maximum transfection level for the used number of bEnd.3 cells. By contrast, at the 33% lower weight ratio, the number of internalized pDNA molecules was reduced and the effect of NLS-promoted nuclear accumulation became more evident. Very low amounts of NLS conjugates were required to obtain a significant accumulation of pDNA, 1/16 and 1/4 of the pDNA weight for lipoplexes and polyplexes, respectively. Calculations of the optimal number of peptide molecules per pDNA molecule give us 4−5 NLS peptides for

lipoplexes and 16−20 NLS peptides for polyplexes. It is interesting to note that, at the lower amount of Exgen500 in polyplexes, optimal pDNA to NLS conjugates weight ratio also dropped to 12:1, corresponding to 5−7 NLS peptides per pDNA. Evidently, an average minimal amount of 5−6 NLS peptides is generally sufficient for efficient delivery of pDNA molecule into the nuclei. On the contrary, equal amounts of the PEG_{5000}−acridine conjugate did not result in any enhancement and even suppressed the transfection. In control experiments with the PEG_{5000}−acridine conjugate, containing a mutant NLS peptide with point mutation (Lys→Thr), the luciferase expression level was even slightly lower compared to plain polyplexes (Figure 3). These results indicated that observed improvements of transgene expression were caused by sequence-specific active nuclear transport rather than by beneficial effect of the cationic peptide sequence.

Under transfection efficiency is usually mentioned the ability to transfect a certain number of cells, while transgene expression level typically shows how efficient the pDNA expression is within the cell. Successful nuclear entry and subsequent expression of only one copy of pDNA may result in the GFP-derived fluorescence and change the cell count from negative to positive. Efficient degradation of internalized exogenous pDNA can be a cause of the observed differences. At equally effective cellular uptake of transfection complexes, pDNA protected by the PEG coating has a better chance to remain intact in the cytoplasm and eventually be delivered to the nuclei. Previously, nucleolytic degradation of pDNA in the cytoplasm was recognized as another barrier to efficient nonviral transfection (*26*). PEGylation is one of the successful approaches to protect protein therapeutics from enzymatic degradation and hydrolysis (*27*). Here, we investigated the protective effect of PEG coating of pDNA against DNase digestion. Evidently, a sufficient amount of attached PEG molecules along with the optimal number of NLS peptide-modified PEG molecules via intercalation strategy can form a protective PEG layer that should considerably shield pDNA from interaction with cytosolic nucleases following its release from lipo- and polyplexes. Our results demonstrated a longer persistence of functional pDNA following the treatment with DNase I for NLS-PEG-acridine conjugate-modified pDNA vs naked pDNA (Figure 5).

Our confocal microscopy results qualitatively demonstrated better cellular persistence and nuclear incorporation of NLS-PEG-acridine conjugate-modified fluorescent pDNA; a significant pDNA accumulation was observed also in perinuclear regions after lipo- or polyplex-mediated transfection (Figure 7B,E). In the nuclear incorporation studies, fluorescent pDNA was observed in the form of red dots rather than in the form of diffuse staining. This is consistent with previous reports, which showed the similar punctuated signals for nuclear-imported pDNA (*28, 29*). The diffuse fluorescent signals observed in earlier experiments could be caused by degraded DNA (*30*). However, the confocal pictures are insufficient for quantitative evaluation of nuclear accumulation of pDNA and explanation of all these observed improvements in the expression of luciferase-encoded pDNA. The direct isolation and quantitation of fluorescent pDNA from the nuclei of transfected cells strongly suggested that NLS−conjugate could significantly ($P < 0.005$) improve nuclear transport of exogenous pDNA in comparative polyplex transfection experiments, while mutant NLS-modified and nonmodified conjugates did not affect the nuclear accumulation compared to naked DNA (Figure 7G).

Safety is another important issue in the development of gene delivery systems. The NLS-PEG-acridine conjugates showed very low cytotoxicity and at the concentrations used had no effect on the summary cytotoxicity of lipoplexes and polyplexes (Supporting Information Figure S3). Additionally, application of the lower amount of transfection agent together with enhancing NLS−conjugates potentially can significantly reduce toxicity of lipo- and polyplexes without compromising high levels of the achieved nonviral transfection.

In conclusion, the present study demonstrated that the novel NLS-PEG-acridine conjugates could effectively increase nuclear accumulation of pDNA and transgene expression levels at the lipoplex- or polyplex-mediated transfection of slowly dividing cells such as BCEC in the presence of serum. Therefore, these conjugates can be used as potential components for development of nonviral gene delivery systems for systemic applications. This general approach can also be applied to the attachment of other modifying or targeting peptides to further enhance gene delivery to specific cells in vivo and penetration across cellular barriers hampering application of nonviral transfection strategies.

ACKNOWLEDGMENT

The financial support from National Institute of Neurodegenerative Diseases and Stroke (R01 NS050660 for S.V.V.) is gratefully acknowledged. The authors thank Janice Taylor and James Talaska of the Confocal Laser Scanning Microscope Core Facility (University of Nebraska Medical Center) supported by the Nebraska Research Initiative and the Eppley Cancer Center for providing assistance with confocal microscopy. The authors also thank Victoria B. Smith and Linda M. Vilkie of the Cell Analysis Core Facility at UNMC for their help in flow cytometry assay.

Supporting Information Available: Figures S1−S3 as described in the text. This material is available free of charge via the Internet at http://pubs.acs.org.

LITERATURE CITED

(1) Ohtsuki, S., and Terasaki, T. (2007) Contribution of carrier-mediated transport systems to the blood-brain barrier as a supporting and protecting interface for the brain: importance for CNS drug discovery and development. *Pharm. Res. 24*, 1745–1758.

(2) Calcagno, A. M., Kim, I. W., Wu, C. P., Shukla, S., and Ambudkar, S. V. (2007) ABC drug transporters as molecular targets for the prevention of multidrug resistance and drug-drug interactions. *Curr. Drug Delivery 4*, 324–33.

(3) Suh, W., Han, S. O., Yu, L., and Kim, S. W. (2002) An angiogenic, endothelial-cell-targeted polymeric gene carrier. *Mol. Ther. 6*, 664–672.

(4) Zabner, J., Fasbender, A. J., Moninger, T., Poellinger, K. A., and Welsh, M. J. (1995) Cellular and molecular barriers to gene transfer by a cationic lipid. *J. Biol. Chem. 270*, 18997–19007.

(5) Brunner, S., Sauer, T., Carotta, S., Cotton, M., Saltik, M., and Wagner, E. (2000) Cell cycle dependence of gene transfer by lipoplex, polyplex and recombinant adenovirus. *Gene Ther. 7*, 401–407.

(6) Paschal, B. M. (2002) Translocation through the nuclear pore complex. *Trends Biochem. Sci. 27*, 593–596.

(7) Ciolina, C., Byk, G., Blanche, F., Thuillier, V., Scherman, D., and Wils, P. (1999) Coupling of nuclear localization signals to plasmid DNA and specific interaction of the conjugates with importin alpha. *Bioconjugate Chem. 10*, 49–55.

(8) Nagasaki, T., Myohoji, T., Tachibana, T., Futaki, S., and Tamagaki, S. (2003) Can nuclear localization signals enhance nuclear localization of plasmid DNA? *Bioconjugate Chem. 14*, 282–286.

(9) Bremner, K. H., Seymour, L. W., Logan, A., and Read, M. L. (2004) Factors influencing the ability of nuclear localization

sequence peptides to enhance nonviral gene delivery. *Bioconjugate Chem. 15*, 152–161.
(10) Pouton, C. W., Wagstaff, K. M., Roth, D. M., Moseley, G.,W., and Jans, D. A. (2007) Targeted delivery to the nucleus. *Adv. Drug Delivery Rev. 59*, 698–717.
(11) Zanta, M. A., Belguise-Valladier, P., and Behr, J. P. (1999) Gene delivery: a single nuclear localization signal peptide is sufficient to carry DNA to the cell nucleus. *Proc. Natl. Acad. Sci. U.S.A. 96*, 91–96.
(12) Jeon, O., Lim, H. W., Lee, M., Song, S. J., and Kim, B. S. (2007) Poly(L-lactide-co-glycolide) nanospheres conjugated with a nuclear localization signal for delivery of plasmid DNA. *J. Drug Targeting 15*, 190–198.
(13) Sebestyen, M. G., Ludtke, J. J., Bassik, M. C., Zhang, G., Budker, V., Lukhtanov, E. A., Hagstrom, J. E., and Wolff, J. A. (1998) DNA vector chemistry: the covalent attachment of signal peptides to plasmid DNA. *Nat. Biotechnol. 16*, 80–85.
(14) Branden, L. J., Mohamed, A. J., and Smith, C. I. (1999) A peptide nucleic acid nuclear localization signal fusion that mediates nuclear transport of DNA. *Nat. Biotechnol. 17*, 784–787.
(15) Boulanger, C., Giorgio, C. D., and Vierling, P. (2005) Synthesis of acridine-nuclear localization signal (NLS) conjugates and evaluation of their impact on lipoplex and polyplex-based transfection. *Eur. J. Med. Chem. 40*, 1295–1306.
(16) Shiraishi, T., Hamzavi, R., and Nielsen, P. E. (2005) Targeted delivery of plasmid DNA into the nucleus of cells via nuclear localization signal peptide conjugated to DNA intercalating bis- and trisacridines. *Bioconjugate Chem. 16*, 1112–1116.
(17) Omidi, Y., Campbell, L., Barar, J., Connell, D., Akhtar, S., and Gumbleton, M. (2003) Evaluation of the immortalized mouse brain capillary endothelial cell line, b.End3, as an in vitro blood-brain barrier model for drug uptake and transport studies. *Brain Res. 990*, 95–112.
(18) Kim, Y., Yoon, J. W., Xiao, X., Dean, N. M., Monia, B. P., and Marcusson, E. G. (2007) Selective down-regulation of glioma-associated oncogene 2 inhibits the proliferation of hepatocellular carcinoma cells. *Cancer Res. 67*, 3583–593.
(19) Zhang, H. W., Zhang, L., Sun, X., and Zhang, Z. R. (2007) Successful transfection of hepotoma cells after encapsulation of plasmid DNA into negatively charged liposomes. *Biotechnol. Bioeng. 96*, 118–124.
(20) Vandenbroucke, R. E., Lucas, B., Demeester, J., De Smedt, S. C., and Sanders, N. N. (2007) Nuclear accumulation of plasmid DNA can be enhanced by non-selective gating of the nuclear pore. *Nucleic Acids Res. 35*, e86.
(21) Wagstaff, K. M., Glover, D. J., Tremethick, D. J., and Jans, D. A. (2007) Histone-mediated transduction as an efficient means for gene delivery. *Mol. Ther. 15*, 721–731.
(22) Carlisle, R. C., Bettinger, T., Ogris, M., Hale, S., Mautner, V., and Seymour, L. W. (2001) Adenovirus hexon protein enhances nuclear delivery and increases transgene expression of polyethylenimine/plasmid DNA vectors. *Mol. Ther. 4*, 473–483.
(23) Wirth, M., Buchardt, O., Koch, T., Nielsen, P. E., and Norden, B. (1988) Interactions between DNA and mono-, bis-, tris-, tetrakis-, and hexakis(aminoacridines). A linear and circular dichroism, electric orientation relaxation, viscometry, and equilibrium study. *J. Am. Chem. Soc. 110*, 932–939.
(24) Nielsen, P. E., Zhen, W. P., Henriksen, U., and Buchardt, O. (1988) Sequence-influenced interactions of oligoacridines with DNA detected by retarded gel electrophoretic migrations. *Biochemistry 27*, 67–73.
(25) Cho-Chung, Y. S., Nesterova, M. V., Severin, E. S., and Vinogradov, S. V. (1991) Chemical modification enhances the inhibitory effect of regulatory subunit antisense oligodeoxynucleotide of cAMP-dependent protein kinase type I on cell proliferation. *Biochem. Int. 25*, 767–773.
(26) Wagstaff, K. M., and Jans, D. A. (2007) Nucleocytoplasmic transport of DNA: enhancing non-viral gene transfer. *Biochem. J. 406*, 185–202.
(27) Harris, J. M., and Chess, R. B. (2003) Effect of pegylation on pharmaceuticals. *Nat. Rev. Drug Discovery 2*, 214–21.
(28) Rebuffat, A., Bernasconi, A., Ceppi, M., Wehrli, H., Verca, S. B., Ibrahim, M., Frey, B. M., Frey, F. J., and Rusconi, S. (2001) Selective enhancement of gene transfer by steroid-mediated gene delivery. *Nat. Biotechnol. 19*, 1155–1161.
(29) Hama, S., Akita, H., Iida, S., Mizuguchi, H., and Harashima, H. (2007) Quantitative and mechanism-based investigation of post-nuclear delivery events between adenovirus and lipoplex. *Nucleic Acids Res. 35*, 1533–1543.
(30) Zelphati, O., Liang, X., Hobart, P., and Felgner, P. L. (1999) Gene chemistry: functionally and conformationally intact fluorescent plasmid DNA. *Hum. Gene Ther. 10*, 15–24.

BC8003414

Supporting Information to the manuscript:

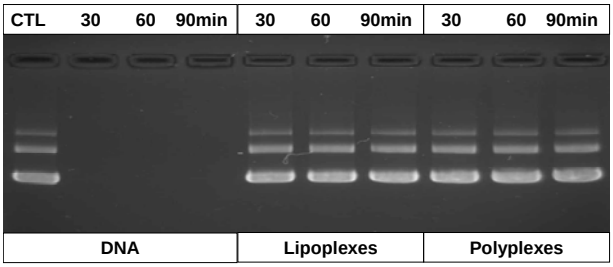

Figure S1. Protective ability of lipo- and polyplexes was not affected in the presence of NLS-PEG-acridine conjugates. NLS-lipo- and polyplexes were prepared at the 6:1 ratio (w/w) of pDNA to NLS-PEG_{5000}-acridine and tested for their ability to protect DNA against degradation by DNase I at 37 ^{o}C. 10 µL aliquots containing 0.5 µg of pDNA were taken at each time point.

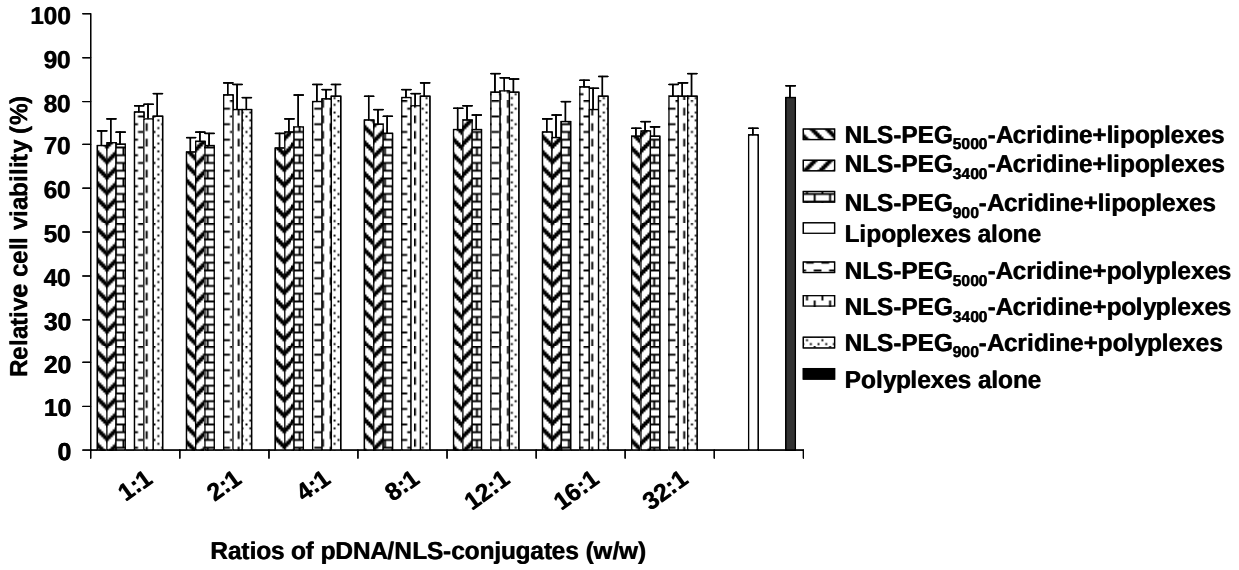

Figure S2. Cytotoxicity of NLS-lipo- and polyplexes in bEnd.3 cells. Relative cell viability was measured by a MTT assay following 4 h incubation at 37^{o}C and calculated by comparing with untreated cellular control. Results are presented as means ±SEM (n=5).

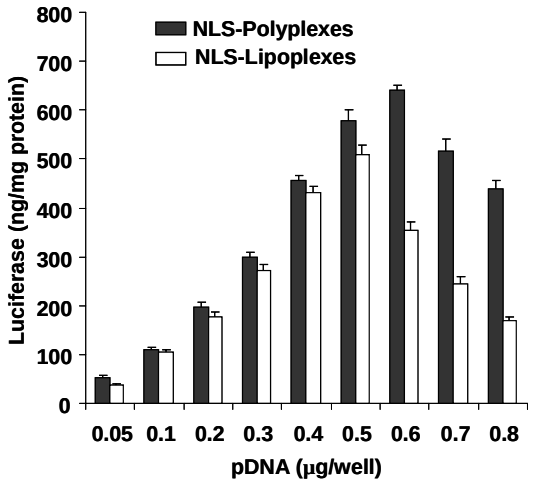

Figure S3. Relationship between the dose of NLS-lipoplexes (open bars) and NLS-polyplexes (black bars) and luciferase expression level in bEnd.3 cells. NLS-lipo- and polyplexes have been prepared at the pDNA/conjugate ratio 6:1 and optimal ratios of transfection agents to DNA. Cells were transfected for 4 h at 37^{o}C in the presence of 10% FBS. Results are presented as mean ±SEM (n=5).

Bioconjugate Chemistry 20th Anniversary

Subscriber access provided by SHEMYAKIN-OVCHINNIKOV INST

Article

Synthesis and Evaluation of Multivalent Branched HPMA Copolymer#Fab# Conjugates Targeted to the B-Cell Antigen CD20

Russell N. Johnson, Pavla Kopec#kova#, and Jindr#ich Kopec#ek

Bioconjugate Chem., **2009**, 20 (1), 129-137• DOI: 10.1021/bc800351m • Publication Date (Web): 22 December 2008

Downloaded from http://pubs.acs.org on May 8, 2009

More About This Article

Additional resources and features associated with this article are available within the HTML version:

- Supporting Information
- Access to high resolution figures
- Links to articles and content related to this article
- Copyright permission to reproduce figures and/or text from this article

View the Full Text HTML

ACS Publications
High quality. High impact.

Bioconjugate Chemistry is published by the American Chemical Society. 1155 Sixteenth Street N.W., Washington, DC 20036

Synthesis and Evaluation of Multivalent Branched HPMA Copolymer−Fab′ Conjugates Targeted to the B-Cell Antigen CD20

Russell N. Johnson,[†] Pavla Kopečková,[‡] and Jindřich Kopeček*[,†,‡]

Departments of Bioengineering, and Pharmaceutics and Pharmaceutical Chemistry, University of Utah, Salt Lake City, Utah 84112. Received August 15, 2008; Revised Manuscript Received September 26, 2008

Several drug delivery designs combine synthetic drug carriers with covalently conjugated targeting moieties. Such modifications of monoclonal antibodies (mAb), or their Fab′ fragments, inevitably result in diminished affinity for their targeted tissue. In an attempt to overcome this limitation, high molecular weight, branched *N*-(2-hydroxypropyl)methacrylamide (HPMA) copolymers were synthesized and conjugated with Fab′ fragments of the anti-CD20 antibody, 1F5. This produced multivalent conjugates with varying valency (amount of Fab′ per macromolecule) targeted to the B-cell antigen CD20. Evaluation of a multivalent effect was done by determining the apparent K_D at low concentrations of conjugates, the Sips heterogeneity factor, *a*, and the binding enhancement factors of each construct. The results clearly indicated that multivalency could improve the affinity of the HPMA copolymer−Fab′ conjugates to that of unconjugated mAb.

INTRODUCTION

A central tenet of modern drug delivery is to increase the concentration of drug in diseased tissues, while limiting its systemic exposure (*1, 2*). This translates to increased therapeutic efficiency and reduced side effects. Increasing concentrations in diseased tissues can be challenging and has been addressed through both synthetic (*3*−*5*) and biological approaches (*6, 7*). Several studies have combined high-affinity targeting moieties and high molecular weight drug carriers to confer tissue specificity and enhanced bioactivity to polymer−drug conjugates (*8*−*12*). However, covalent modification of targeting moieties resulted in diminished affinity (*13*). Multivalent conjugate designs were one approach that improved the specificity of the construct (*14*). Successful studies have demonstrated that multivalent carbohydrates (*15*), peptides (*16*), or other small molecules (*17*) can enhance binding affinity to targeted tissue. Other larger and more specific molecules such as monoclonal antibodies and Fab′ have only been rarely used in such approaches. In this study, we synthesized a high molecular weight soluble polymer that is able to accommodate multiple Fab′ fragments to produce a multivalent drug carrier. Furthermore, we demonstrated the effects of multivalent and multimeric binding of our constructs to the B-cell antigen CD20 in experiments using whole cells.

The soluble polymer poly[*N*-(2-hydroxypropyl)methacrylamide] (pHPMA) is inert and biocompatible (*18, 19*). It has been used extensively as an anticancer drug delivery platform that is able to improve the physicochemical and pharmacokinetic properties of the polymer−drug conjugates by increasing circulating half-life, increasing the solubility of hydrophobic drugs, affecting passive accumulation in solid tumors, and providing the potential to evade multidrug resistance mediated by efflux pumps (*18, 20*). A number of studies have developed methods of HPMA copolymer synthesis that create high molecular weight, branched copolymers that are soluble in water (*21, 22*). Similar HPMA copolymers were used to create multivalent conjugates using anti-CD20 Fab′ antibody fragments.

As with any well-designed drug delivery system, the biological target is of critical importance. CD20 is a reliable B-cell marker that is highly expressed on normal and malignant B-cell populations (*23, 24*) and has been successfully used as a target with the first FDA-approved monoclonal antibody, Rituximab (*25, 26*). CD20 is a 33−37 kDa, integral membrane receptor that forms dimers and tetramers in the cell membrane (*27, 28*). In the absence of a known ligand, there is remarkable diversity of epitopes among anti-CD20 mAb clones. The most studied and best characterized clones include Rituximab, B1, 2H7, and 1F5 (*29*). Our study utilized 1F5, which has a dissociation constant (K_D) between 20 and 30 nM (*30*), while the K_D for Rituximab is around 4 nM (*31*). Rituximab and 1F5 bind distinct epitopes on CD20 (*32, 33*). Notably, cross-linking certain CD20-ligated mAb, including 1F5, with secondary antibodies (generally goat-antimouse Ab) can induce apoptosis (*34, 35*). This fact has clinical relevance for Rituximab. Its activity is partially attributed to ligated Rituximab becoming cross-linked by effector cells. Cross-linking, in turn, induces antibody-dependent cell-mediated cytotoxicity (ADCC). However, a full response to Rituximab requires a high-affinity allele of an Fc receptor on effector cells (FcγRIIIa). Patients that are not homozygous for the allele have diminished responses (*36*). Recent studies have shown that multivalent Rituximab constructs are able to effectively induce apoptosis independent of effector cells (*37, 38*).

A construct that is able to elicit apoptosis without the need to be internalized by a cell has clinical relevance. Such a construct could be used in a therapeutic regimen such as those used in either Bexxar (*39*) or Zevalin (*40*), where anti-CD20 constructs and radioimmunotherapeutics could be given in combination to treat refractory disease. The multivalent construct would induce apoptosis independent of effector cells, and the radioimmunotherapeutic could synergistically eliminate neighboring malignant cell populations which may not express CD20 via a bystander effect.

In this study, several multivalent HPMA copolymer−(anti-CD20) Fab′ conjugates were designed and synthesized. The conjugates varied in the amount of Fab′ per polymer chain to allow studies that could determine the effect of a conjugate's

* To whom correspondence should be addressed. Phone: (801) 581-7211. Fax: (801) 581-7848. E-mail: Jindrich.Kopecek@utah.edu.
[†] Department of Bioengineering.
[‡] Department of Pharmaceutics and Pharmaceutical Chemistry.

10.1021/bc800351m CCC: $40.75 © 2009 American Chemical Society
Published on Web 12/22/2008

valence on binding to B-cell antigen CD20. The apparent K_D at low concentrations of conjugates, the Sips heterogeneity factor, and the affinity enhancement factors of each construct were determined.

EXPERIMENTAL PROCEDURES

Materials. Chemicals and solvents used were of reagent grade or better unless otherwise stated. *N*-(2-Hydroxypropyl)methacrylamide (HPMA) was prepared as previously described (*41*). *N*-(3-Aminopropyl)methacrylamide hydrochloride (AMA) was purchased from Polysciences (Warrington, PA). Succinimidyl-4-(*N*-maleimidomethyl)cyclohexane-1-carboxylate (SMCC) was purchased from Soltec Ventures (Beverly, MA). Tris(2-carboxyethyl) phosphine hydrochloride (TCEP) and Iodogen tubes were purchased form Thermo Scientific (Waltham, MA). Tetraethylene glycol dimethacrylate (TGD), phthalic dicarboxaldehyde (OPA), and 3-mercaptopropionic acid (MPA) were purchased from Sigma Aldrich (St. Louis, MO). Carrier free radionuclide sodium iodide-125 was purchased from Perkin-Elmer (Waltham, MA).

Cell Lines, Hybridomas, Fab′ Fragment Preparation. Human Burkitt's B-cell non-Hodgkin's lymphoma Raji cells (ATCC, Bethesda, MD) were cultured in RPMI-1640 medium (Sigma, St. Louis, MO) supplemented with 10% fetal bovine serum (Hyclone, Logan, UT). Cells were grown at 37 °C in a humidified atmosphere of 5% CO_2 (v/v). All experiments were performed using cells in exponential growth. The anti-CD20 hybridoma clone 1F5 (ATCC, Bethesda, MD) was initially cultured and recloned through limiting dilution in RPMI 1640 supplemented with 10% FBS in a humidified environment with 5% CO_2 in air (*42*). The selected clone was adapted to chemically defined, serum-free media (Invitrogen, Carlsbad, CA). Adapted cells were used to seed a CellMax bioreactor (Spectrum Laboratories, Rancho Dominguez, CA) according to the manufacturer's instructions. Anti-CD20 mAb was purified on a Protein G Sepharose 4 Fast Flow column (GE Healthcare, Piscataway, NJ) from bioreactor harvest supernatant. Whole IgG_{2a} was digested into $F(ab')_2$ with lysyl endopeptidase (Wako Chemicals USA, Richmond, VA) following the protocol of Fowers et al. (*43*). Purity of harvested IgG_{2a} and digested $F(ab')_2$ were shown to be >95% by SDS-PAGE and SEC (size exclusion chromatography). Immediately prior to using, 5 mg/mL of $F(ab')_2$ was reduced to Fab′ with 4 mM TCEP in 0.1 M phosphate buffer (pH 6.5) at room temperature for 30 min.

Preparation of Multivalent Conjugates. The synthesis of copolymers, their fractionation, polymeranalogous modification with SMCC, Fab′ binding, and fractionation of the conjugates are depicted in Scheme 1. The HPMA copolymer containing side chains terminated in NH_2 groups (*P-NH₂*) was prepared by radical polymerization using AIBN as the initiator. Briefly, HPMA (658.7 mg, 93 mol %), AMA (53.6 mg, 6 mol %), TGD (16.5 mg, 1 mol %), and AIBN (3.4 mg) were dissolved in 2.9 g of DMSO. After mixing, the polymerization solution was bubbled with argon, sealed in a glass ampule, and then incubated at 50 °C for 24 h. After polymerization, the HPMA copolymer was precipitated and washed in acetone, and then washed with diethyl ether. The precipitate was dried, dissolved in H_2O, and dialyzed against distilled water using dialysis tubing with a molecular weight cutoff of 12−14 kDa (Spectrum Laboratories, Rancho Dominguez, CA) to remove any unreacted monomers. The polymer was then lyophilized, dissolved in PBS, and fractionated on a Sephacryl S-500 preparative column (GE Healthcare, Piscataway, NJ) to produce two fractions. The fraction with the very high molecular weight was discarded; the fraction with an upper limit of Mw ∼500 kDa was fractionated a second time on a Superose 6 HR16/60 preparative column (GE Healthcare, Piscataway, NJ) to produce a molecular weight "ladder" of ten fractions. Two fractions (*P-7NH₂*: 34 kDa, 5.5 mol % NH_2, yield 2.7 wt %; and *P-3NH₂*: 193 kDa, 5.5 mol % NH_2, yield 18 wt %) were selected for the synthesis of conjugates. The fractions *P-3NH₂* and *P-7NH₂* were dialyzed against water and then lyophilized. The molecular weight averages were estimated using size-exclusion chromatography on an analytical Superose 6 column (GE Healthcare, Piscataway, NJ). All SEC was done using an ÄKTA FPLC system (GE Healthcare, Piscataway, NJ).

Scheme 1. Synthesis of Multivalent HPMA Copolymer−Fab′ Conjugates Targeted to the B-Cell Antigen CD20

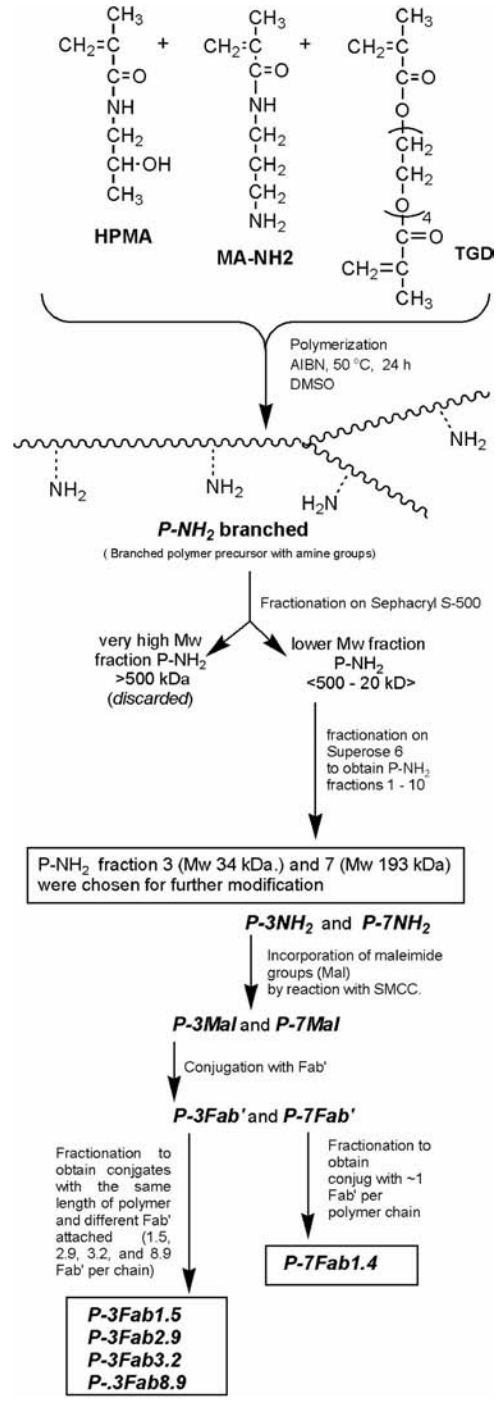

Polymeranalogous Conversion of Pendant Amine Groups into Maleimide Groups. The fractions *P-3NH₂* and *P-7NH₂* (*P-3NH₂*: 37 mg, 22.5 μmol $-NH_2$; *P-7NH₂*: 6 mg, 3.6 μmol $-NH_2$) were reacted with excess SMCC (14.4 mg, 45.6 μmol; 2.4 mg, 7.2 μmol, respectively) in dry DMF under basic

conditions (DIPEA: 26 μL, 72 μmol; 2.1 μL, 12 μmol, respectively) to generate pendant maleimide groups. The activated precursor was precipitated into an excess of acetone, filtered, and washed with ether to remove free SMCC. The conversion of amine groups into maleimide on the polymer proceeded with ~72% to 75% conversion, as determined by modified Ellman's assay. The products *P-3Mal* and *P-7Mal* were then conjugated with reduced 1F5 Fab′ fragments as previously described (*13*). Briefly, approximately 5 mg of either *P-3Mal* or *P-7Mal* (~2.3 μmol maleimide) was dissolved in 50 μL of DMF. Then, 10 mg of Fab′ (0.2 μmol) in 2 mL of PBS (pH 6.5) was added to the reaction, and the solution was mixed overnight at room temperature. The products were fractionated (and unbound Fab′ removed) on a size-exclusion S6 preparative column HR 16/60. HPMA copolymer−Fab′ conjugates containing different amounts of Fab′ per macromolecule, *P-3Fab1.5*, *P-3Fab2.9*, *P-3Fab3.2*, *P-3Fab8.9*, and *P-7Fab1.4*, were isolated and characterized. In these abbreviations, the number following Fab′ indicated the amount of Fab′ fragments per macromolecule.

Effective Diameter of HPMA Copolymer−Fab′ Conjugates. The effective diameter for fractions of HPMA copolymer−Fab′ conjugates was evaluated by dynamic light scattering (Brookhaven Scientific Instruments, Holtsville) in PBS at a concentration of at least 1 mg/mL. Prior to analysis, the solution containing conjugates were filtered through a 0.45 μm filter. In addition to the effective diameter, dynamic light scattering (DLS) also calculated the distribution of size, referred to as the polydispersity index (PDI), which differs from molecular weight polydispersity (M_w/M_n). DLS PDI values greater than 0.2 are considered to be heterogeneous, and those below 0.2 are considered homogeneous. The effective diameter of whole Ab served as a positive control with both effective diameters (measured 13.6 nM, literature 14.3) and PDI values (0.06 measured, literature 0.05) compared well with published values (*44*).

Determination of Fab′ Content per Polymer Chain. The composition of the conjugates, the ratio of protein to polymer, was determined in one step by amino acid analysis. This method enabled measurement of, after acid hydrolysis, both individual amino acids from Fab′ as well as 1-amino-2-propanol released from HPMA monomer units. Calibration was done using free 1F5 Fab′ and HPMA homopolymer. A small amount (>3 mg) of Fab′, homopolymer, or conjugate was dissolved in 6 N HCl in a small ampule, bubbled with nitrogen for 5 min, and then the ampule was sealed. The solution was incubated at 125 °C for 24 h, the ampule was opened, and the hydrolyzed product was dried in vacuo. Hydrolyzed products were dissolved in dH_2O, and then derivatized with OPA and MPA prior to being analyzed on a HPLC with an eclipse XDB-C8 column (Agilent, Santa Clara, CA). Fab′ concentration was calibrated with a peak produced by hydrolyzed glutamate, which had an elution time of 9.4 min. Poly(HPMA) concentration was calibrated with a peak produced by 1-amino-2-propanol, which had a retention time of 23.9 min.

Iodination of Fab′ and Multivalent Fab′ Constructs. Reduced anti-CD20 Fab′, anti-CD20 HPMA copolymer−Fab′ conjugates, and whole antiCD20 IgG molecules were labeled with $Na^{125}I$ using Iodo-Gen tubes as previously described (*13*). Approximately 300 μg of Fab′ or IgG in 0.3 mL PBS was added to a glass vial coated with 4 μg of Iodo-Gen, followed by 0.5 mCi of $Na^{125}I$. After the solution was incubated (and shaken) at room temperature for 7 min, ^{125}I-labeled protein was separated from free ^{125}I by passing the reaction mixture over a PD-10 desalting column (GE Healthcare, Piscataway, NJ). The labeled molecules were stored at 4 °C in PBS. The specific radioactivity of each conjugate was between 0.7 and 1.5 μCi/μg.

Binding Experiments. Raji cells grown in RPMI containing 10% FBS were washed twice with HBSS. The cells were adjusted to 4×10^6 cells/mL and split into two volumes. To one of the volumes of Raji cells, unlabeled anti-CD20 IgG was added to a final concentration of 500 nM to block CD20 for a negative control. Serial dilutions of ^{125}I-labeled anti-CD20 IgG, Fab′, and multivalent Fab′ conjugates were made from 2000 nM to 1 nM of Fab′ fragment concentration. Millipore 96-well filter plates, coated with a 1% solution of nonfat dry milk in distilled water and incubated at 4 °C overnight, were washed with HBSS. For each of the serial dilutions, 25 μL of negative control cells were added to a single well, and 25 μL of unblocked cells were added to three different wells; then, 25 μL of the respective dilutions were added to each well. The filter-well plates were incubated for 90 min at 120 rpm on a shaker at 25 °C. Following incubation, the Raji cells were washed twice with 200 μL of cold HBSS with 10% FBS, and then collected on filters. The filters were allowed to air-dry, removed from the plate, and counted. Negative control wells were used to correct for nonspecific binding.

The equilibrium binding was evaluated using either single-site binding parameters (eq 1) or the Sips equation (eq 2) using *Sigma Plot* (Systat Software, San Jose, CA). Data was also drafted in Scatchard plots.

$$B = \frac{B_{max} F}{K_D + F} \tag{1}$$

$$B = \frac{B_{max}\left(\frac{1}{K_D} F\right)^a}{1 + \left(\frac{1}{K_D} F\right)^a} \tag{2}$$

where B is the concentration of bound ligand, F is the concentration of free ligand, B_{max} is the theoretical limit of bound ligand, K_D is the dissociation constant, and a is the Sips heterogeneity factor. When a is equal to 1, the Sips equation simplifies to the single-site binding equation.

RESULTS

Synthesis of Multivalent Conjugates. Copolymerization of HPMA with a small amount of the cross-linker TGD, at conditions below the gel point, yielded an HPMA copolymer with broadly distributed molecular weight that ranged from 20 kDa to greater than 1000 kDa (Scheme 1). The yield of this polymerization reaction was 69%, with a reproducible molecular weight profile after three separate polymerization experiments. Macromolecules with a molecular weight higher than 500 kDa were removed by fractionation on a SEC column. The fraction containing macromolecules with M < 500 kDa (45% by weight of original copolymer) was used to build a molecular weight "ladder" with narrowly disperse molecular weights by a second fractionation. The amine content of these fractions was 5.5 mol %. Two of the fractions, *P-3NH*$_2$ (Mw =193 kDa) and *P-7NH*$_2$ (Mw = 34 kDa), were selected for the use in conjugate synthesis and were activated by a reaction with SMCC. The maleimide content in polymer precursors *P-3Mal* and *P-7Mal* was 4.1 mol %.

Reduced Fab′ fragments of the anti-CD20 mAb were conjugated to polymer precursors *P-3Mal* and *P-7Mal* via thioether bonds in an overnight reaction. The *P-3Fab′* conjugate was fractionated on a SEC column to provide fractions with different amounts of bound Fab′ fragments per macromolecule. The free (unbound) Fab′ could be easily separated from the conjugate fractions (Figure 1). However, only a single fraction was isolated from the *P-7Fab′* conjugate (data not shown). The fractions are referred to by the fraction number (e.g. *P-3* or *P-7*) and by the

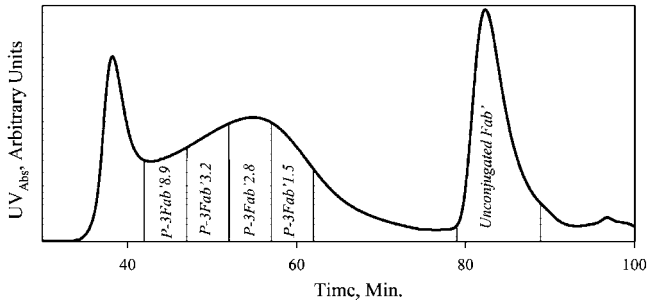

Figure 1. Fractionation of the *P-3Fab′* conjugate by size exclusion chromatography. Elution profile of reaction mixture on a Superose S6 preparative column (HR 10/30, FPLC system); buffer PBS pH 6.5; flow rate 1 mL/min; amount of sample applied 10 mg in 2 mL; detection absorbance at 280 nm. The numerical suffix at the fraction designation is the average valence as determined by amino acid analysis.

Table 1. Chemical and Physical Analysis of Polymeric Precursors and Conjugates

conjugate	Mw[a]	Pd[b]	valence[c]	effective diameter[d]	PDI[e]
P-7Fab′1.4	34	1.16	1.4	10.8	0.070
P-3Fab′1.5	193	1.25	1.5	17.8	0.203
P-3Fab′2.9	193	1.25	2.9	21.3	0.19
P-3Fab′3.2	193	1.25	3.2	30.2	0.168
P-3Fab′8.9	193	1.25	8.6	38.7	0.174

[a] Molecular weight average of polymeric precursor as determined by size exclusion chromatography. [b] Polydiversity, ratio of molecular weight averages given by weight average over number average. [c] Valence of conjugate or Fab′ per polymer chain as determined by modified amino acid analysis (see Experimental Procedures). [d] Effective diameter of conjugates as determined by dynamic light scattering (DLS). [e] Value of polydispersity index of the diameter of the conjugate determined by DLS.

number of Fab′ fragments per polymer chain as determined by modified amino acid analysis (e.g., *P-3Fab′8.9*).

Determination of Valence. A modified amino acid analysis protocol was used to determine the Fab′ per polymer chain or valence of each fraction. The method cleaved 1-amino-2-propanol from the HPMA monomer units. Following derivatization with OPA and MPA, the 1-amino-2-propanol related peak was well-separated from Fab′-associated amino acid peaks. It is important to note that the analysis determined the average valence, which is dependent on the polydispersity of the conjugate fraction. The polydispersity within each conjugate fraction was not determined in this study, but the elution volumes for each fraction were sufficiently small to guarantee a low polydispersity (1.2−1.3).

Amino acid analysis demonstrated that Fab′ "loading" was responsible for the broadened FPLC profile of the conjugates as seen in Figure 1. The fractions of *P-3* conjugate with the highest valence of 8.9 Fab′/chain eluted first. The *P-3* fraction with the lowest valence *P-3Fab1.5* eluted last. Determination of valence also confirmed that Fab′ loading was directly related to the size of the polymeric precursor. After conjugation, the larger polymer fraction *P-3* had a broad distribution of Fab′ per chain with a median valence of ∼3 Fab′/chain, while the fraction *P*-7 (Mw 34 kDa) had an average valence of 1.4 Fab′ per polymer chain (Table 1).

Analysis of the effective diameters of HPMA copolymer−Fab′ conjugates by DLS demonstrated that Fab′ loading directly corresponded with the size of the conjugate. Loading of Fab′ extended HPMA copolymers from their native random coil structure. As the valence of the polymeric precursor increased, the effective diameter also increased (Figure 2). In the case of *P-3* fractions, the fraction with the most Fab′ per chain, *P-3fab8.9*, had an effective diameter of 38.7 nm, while the

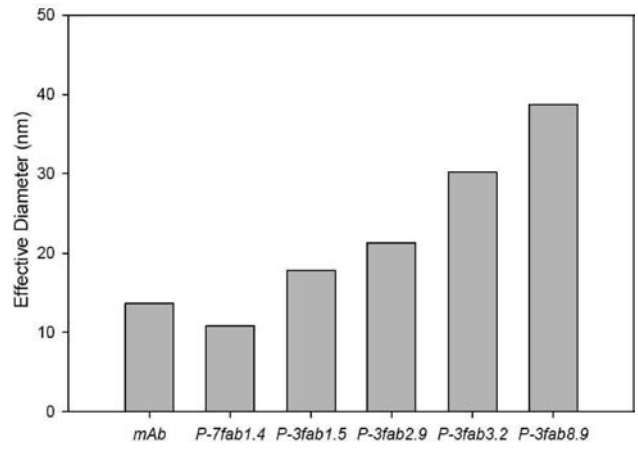

Figure 2. Effective diameters of the multivalent HPMA copolymer−Fab′ conjugates as determined by dynamic light scattering (DLS). The effective diameter corresponded to the valence of each conjugate.

fraction with the least Fab′ per chain, *P-3fab1.5*, had an effective diameter of 17.8 nm. Also, fractionation of the conjugate produced low polydispersity index values near or below 0.2 as shown in Table 1. To ensure that the fractions were not aggregates, a Zimm plot was also used to calculate the molecular weight of the conjugate *P-3fab′8.9*. The calculated molecular weight was 611 ± 43 kDa, a value that corresponded well with the molecular weight estimates made by adding the molecular weight of polymer and the total molecular mass of Fab′ attached to the conjugate.

Binding Isotherms and Scatchard Plots. The single-site binding equation produced a good fit to experimental data for the analysis of CD20 binding with whole Ab or with Fab′. The binding constants (K_D) were 19 nM and 58 nM, respectively. The average number of CD20 receptors per cells was 217 000 ± 27 000 and 217 000 ± 39 000 as calculated from binding experiments with whole Ab and Fab′ fragments, respectively. Both K_D and receptors/cell were close to other published values (*30, 31*). However, the single-site binding equation failed to adequately model the binding of multivalent conjugates to the CD20 receptor, with the most significant deviation occurring at low concentrations of Fab′. A better fit was produced by the Sips equation; typical data for conjugate *P-3Fab′3.2* are shown on Figure 3c,d. The Sips equation uses the same K_D and B_{max} fitting parameters as the single-site binding equation and adds a heterogeneity constant, *a*, as a fitting parameter (eq 1) (*45*). If the heterogeneity constant is set to 1, the Sips equation simplifies to the single-site binding equation. For that reason, K_D and B_{max} values listed in Table 1 for mAb and Fab′ are listed as $K_{D,Sips}$ and $B_{max,Sips}$. Figure 3 provides a representative example of how the Sips equation was used to fit the binding isotherm data and of the curved Scatchard plot. For the conjugates evaluated, the Sips heterogeneity constant was within the interval ⟨0.78; 0.99⟩ (Table 2). The isotherms for conjugates *P-3Fab′1.5, P-3Fab′2.9, P-3Fab′8.9,* and *P-7Fab′1.4* are presented in Supporting Information.

The Scatchard plots of the multivalent conjugates were concave curves, whereas the Scatchard plots for whole Ab and Fab′ were linear. The curvature of the Scatchard plots was relevant in describing the multimeric nature of binding; the latter was also described by the heterogeneity constant, *a*, of the Sips equation. Curvature of Scatchard plots may suggest a number of phenomena, including heterogeneity of binding sites, and nonspecific binding. In the analysis of experimental data, nonspecific binding was subtracted from total binding. Also, the heterogeneity of binding sites was considered to be minimal, since the thioether bond would be distant from the binding site

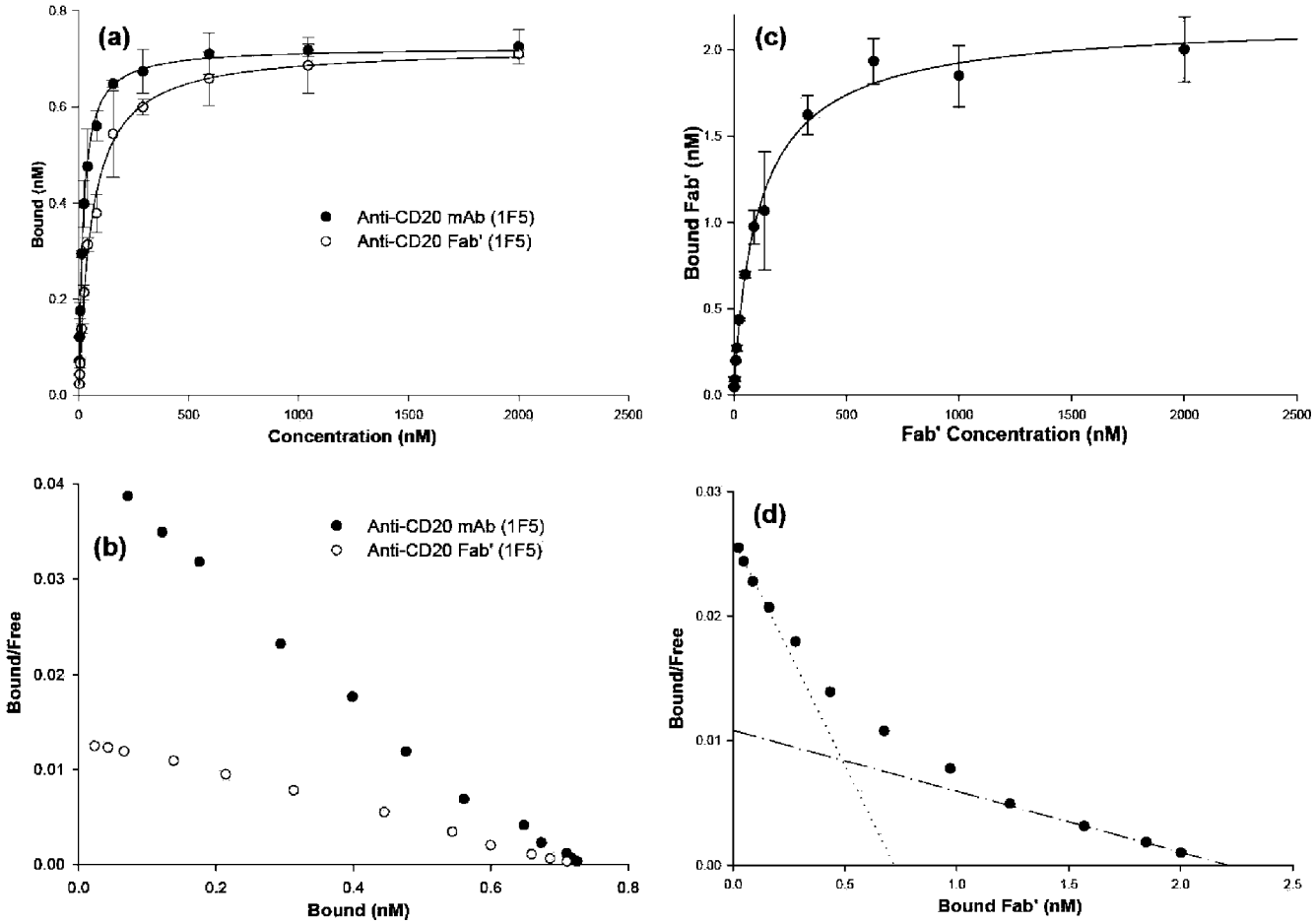

Figure 3. Representative examples of binding of ^{125}I-labeled anti-CD20 mAb (1F5), Fab′, and multivalent conjugate *P-3Fab′3.2* to CD20(+) Raji cells. (a) Isotherms of mAb or Fab′ fit with the single-site binding equation using a least-squares method. (b) The Scatchard plot for the binding of mAb and Fab′. (c) Binding isotherm of *P-3Fab′3.2* fitted with the Sips equation. (d) Binding data for *P-3Fab′3.2* evaluated using a Scatchard plot. The slope of the dotted line in is equal to $1/K_{D,low[Fab']}$, while the slope of the dash−dot line is equal to $1/K_{D,sat[Fab']}$. Other multivalent conjugates had similar isotherms and Scatchard plots as *P-3Fab′3.2* (see Supporting Information). Each concentration was corrected for nonspecific binding as described in the Experimental Procedures.

Table 2. Results of Binding Analysis

targeting molecule	$K_{D,Sips}$ (nM) [a]	$K_{D,low[Fab']}$ (nM) [b]	$K_{D,Sat[Fab']}$ (nM) [c]	$B_{max,Sips}$ (nM) [d]	$B_{max,scat}$ (nM) [e]	a [f]	valence [g]	valence [h]
mAb	19 ± 1	NA	NA	0.72 ± 0.13	0.72	1	-	-
Fab′	58 ± 4	NA	NA	0.72 ± 0.09	0.72	1	-	-
P-7Fab′1.4	85 ± 11	47	109	0.98 ± 0.04	1.01	0.99 ± 0.08	1.4	1.4
P-3Fab′1.5	86 ± 14	32	190	1.09 ± 0.05	1.14	0.78 ± 0.06	1.6	1.5
P-3Fab′2.9	182 ± 35	34	226	2.04 ± 0.01	2.01	0.81 ± 0.07	2.8	2.9
P-3Fab′3.2	115 ± 25	27	204	2.18 ± 0.10	2.21	0.93 ± 0.09	3.1	3.2
P-3Fab′8.9	439 ± 165	15	257	7.5 ± 1.10	6	0.78 ± 0.16	8.2	8.9

[a] Affinity binding constant determined by a least-squares fit of binding isotherm data. [b] Affinity binding constant derived from the inverse slope of Scatchard curves at low concentrations of Fab′. [c] Affinity binding constant derived from the inverse slope of Scatchard curves at saturating concentrations of Fab′. [d] Theoretical limit of bound ligand determined by a least-squares fit of the single-site binding equation. [e] Theoretical limit of bound ligand determined by graphical extrapolation of Scatchard plots to the *x*-axis. [f] Heterogeneity factor determined by the Sips equation. [g] Valence of conjugates determined with modified amino acid analysis. [h] Valence of conjugates determined by the ratio of B_{max} of the conjugate over B_{max} of the Fab′

of the Fab′ (*13*). In this instance, a concave Scatchard plot suggests negative cooperativity. Consequently, the strongest binding will occur at the lowest concentration of multivalent conjugate. At low concentrations, a multivalent conjugate can bind multiple receptors. As the concentration of the conjugate increases, the probability of a single multivalent conjugate binding multiple receptors is reduced to the point that each multivalent molecule only binds a single receptor (all of the receptors are occupied by different molecules). As a result, the ratio of the conjugate's B_{max} divided by the B_{max} of the Fab′ is indicative of the total valence of the conjugate or Fab′ per polymer chain. The valence of conjugates (Fab′ per macromolecule) determined with binding isotherms was in good agreement with the values determined by chemical analysis (Table 2).

The multivalent or multimeric binding effect may be quantified by the enhancement factor, the ratio of the apparent binding constant, $K_{D,Sat[Fab']}$, at saturating concentrations of Fab′ and the apparent binding constant, $K_{D,low[Fab']}$, at low concentrations of Fab′ (*46*). The apparent binding constants were extrapolated from relevant sections of Scatchard plots. The $K_{D,low[Fab']}$ are shown in Figure 4, and the enhancement factors in Figure 5. The largest enhancement factor, 17.7, of the investigated conjugates was found for *P-3Fab′8.9*. The $K_{D,low[Fab']}$ for

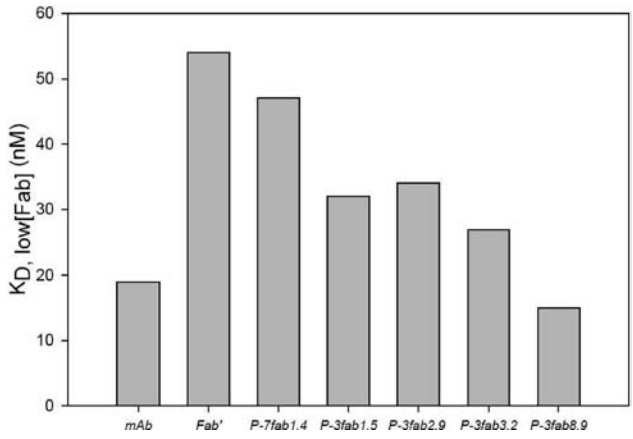

Figure 4. Apparent binding constants, $K_{D,low[Fab']}$, for anti-CD20 Ab, Fab′ fragment, and HPMA copolymer−Fab′ conjugates. The $K_{D,low[Fab']}$ is indicative of the slope of the Scatchard plot at low concentrations of Fab′ (see Figure 3d). Generally, the $K_{D,low[Fab']}$ decreased (affinity increased) as the valence of the construct increased.

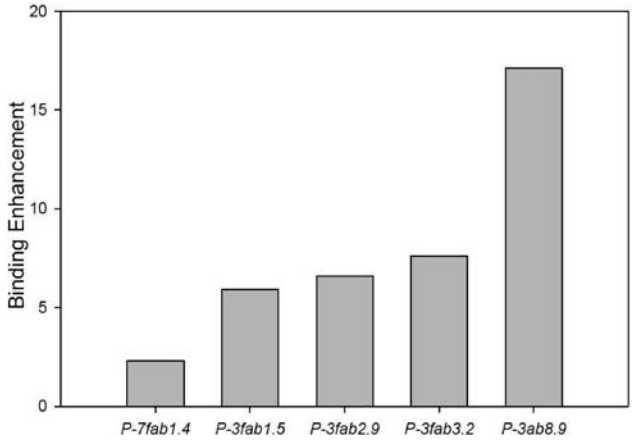

Figure 5. Binding enhancement for anti-CD20 Ab, Fab′ fragment, and HPMA copolymer−Fab′ conjugates. Enhancement is derived from increase in affinity due to multiple binding sites per construct. It was calculated by dividing the $K_{D,sat[Fab']}$ by $K_{D,low[Fab']}$.

P-3Fab′8.9 was 15 nM; the $K_{D,Sat[Fab']}$ was 256.5 nM. The smallest enhancement factor was for conjugate *P-7Fab′1.4*, which had a $K_{D,low[Fab']}$ of 47 nM, a $K_{D,Sat[Fab']}$ of 108.1 nM, and an enhancement factor of 2.3.

The $K_{D,low[Fab']}$ values provide good evidence of a multivalent, multimeric binding enhancement as shown in Figure 4. The value observed for *P-3Fab′8.9* (15 nM) was better than those for free Ab (19 nM) and free Fab′ (58nM).

DISCUSSION

The aim of this study was to demonstrate that water-soluble polymers have potential as multivalent drug carriers. To this end, high molecular weight branched HPMA copolymers were prepared by copolymerization of HPMA with a cross-linking agent (TGD) at conditions below the gel point. Fractions of different molecular weight were used in the synthesis of multivalent HPMA copolymer−Fab′ conjugates. The Fab′ fragment (of anti-CD20 1F5 antibodies) was attached to the copolymers via a thioether bond. The maximum enhancement of binding affinity for the target Raji cells achieved here (17.7 times) bodes well for the development of novel, more effective long-circulating polymer−drug conjugates. To ensure biocompatibility, degradable sequences have to be incorporated into the HPMA copolymer carrier structure, using primary chains with molecular weight below the renal threshold. This can be achieved by connecting primary HPMA copolymer chains via enzymatically degradable cross-links (bridges). Previously, two approaches have been used for the synthesis of degradable, water-soluble, cross-linked (branched) copolymers short of gel point. The first approach consisted of cross-linking reactive HPMA copolymer precursors, containing side chains terminated in reactive ester groups, with degradable α,ω-diaminooligopeptides (*47*−*49*). The second approach was to use biodegradable cross-linkers and prepare the conjugates by copolymerization. One cross-linker, N^2,N^5-bis(*N*-methacryloylglycylphenylanaylleucylglycyl)ornithine methyl ester, has been used to reproducibly synthesize high molecular weight branched HPMA copolymers that can be lysosomally degraded to primary chains to facilitate elimination from the organism by renal filtration (*21*). It is interesting to note that the efficacy of doxorubicin conjugates with branched HPMA copolymers, in an ovarian carcinoma xenograft model, increased with increasing molecular weight of the conjugate (*22*).

The enlargement of the effective diameter of HPMA copolymer with conjugation Fab′ was demonstrated qualitatively by SEC and quantitatively with DLS. This result is not unexpected. HPMA copolymers, in an aqueous environment, have a dynamic, random coil conformation. Dispersive forces would exist between intrachain Fab′ that would result in stretching out the polymer chain. This report demonstrated that enlargement of the HPMA copolymer was directly related to the amount of Fab′ that had been loaded onto the polymer. Due to the nature of HPMA copolymers, the conjugates would maintain a dynamic and flexible structure, a property that may increase the effective valence of the conjugates, and the ability of intrachain Fab′ to gain access and bind to CD20.

The valence of the conjugates was analyzed chemically with a modified amino acid analysis method (*50*). The valence was confirmed by comparing the B_{max} of each conjugate with the B_{max} of unconjugated Fab′ (Table 2). The two determinations corresponded well and infer that the polydispersity among the fractions was narrow (1.2−1.3). However, the effective valence, or the maximum amount of Fab′ per conjugate that could bind CD20, was not determined. It can be hypothesized that most intrachain Fab′ could bind with CD20 simultaneously at low concentrations of conjugate. The formation of dynamic oligomers of CD20 in lipid rafts (*29, 51*) would create several local binding sites for the targeted conjugate. After the first Fab′ of a conjugate bound to a CD20 molecule, the dynamic and flexible nature of the HPMA copolymer backbone (*52*) would allow a conformational response within the polymer, so that intrachain Fab′ could bind proximal CD20 molecules. Also, the size of the conjugates appears to favor multivalent interactions, since conjugates with higher orders of valency had effective diameters in a saline solution greater than whole mAb, 14.3 nm (*44*), and in the theoretical range of cross-linked Abs.

Multivalency is important for the clinical efficacy of Rituximab. Ghetie and co-workers demonstrated enhanced efficacy of tetravalent homodimers prepared by cross-linking of Rituximab with heterobifunctional reagents (*37*). Homodimers and trimers possessed similar binding affinity to lymphoma B cells in vitro but a slower rate of dissociation when compared to the monomer. Zhang et al. (*38*) cross-linked Rituximab with oxidized dextran (M_w = 6000) into high molecular weight conjugates (no data on molecular weight provided) possessing similar binding avidity as Rituximab monomer. In both cases (*37, 38*), multivalent conjugates induced apoptosis in CD20(+) cells.

It is notable that the single-site binding equation accurately modeled isotherms for both mAb and unconjugated Fab′ bound to CD20, but failed with multivalent constructs. In this case, the Sips equation provided a good model. This is likely due to

the thermodynamic assumptions of the single-site binding equation. It assumes that there is a single energy of adsorption, regardless of ligand concentration (*53, 54*). This assumption is not valid for a multivalent conjugate that can bind multimerically to a cell surface (*55*). In the case of a multivalent Fab′ conjugate such as *P-3Fab′8.9*, a single conjugate molecule could bind multiple CD20 receptors at low concentrations. As the concentration of *P-3Fab′8.9* is increased, it would become less likely that the conjugate could bind multiple receptors to the point that each multivalent conjugate could only bind to a single receptor (*56*). Just as the probability of a conjugate binding multiple receptors is reduced, so is the energy of adsorption reduced with an increase of conjugate concentration. This is reflected in a concave Scatchard plot and a heterogeneity factor, *a*, that is less than 1. In this context, the factor, *a*, represents the distribution of adsorption energies at all concentrations of conjugate and the binding constant K_D represents the average affinity of binding (*45, 57*). However, in an in vivo setting, the concentration of the conjugate at the target site is expected to be low. Consequently, the binding enhancement for the multivalent conjugates (Figure 5) should be fully operative.

Evidence of multivalent interactions involving the conjugates and CD20 include a general increase of affinity of the conjugates toward CD20 (Figure 4) and an increase of the enhancement factor (Figure 5) with increase of a conjugate's valence. The theoretical basis of a multivalent interaction is that the first univalent interaction creates a complex in which the remaining free binding sites on both species are at greatly enhanced local concentrations. Such "cooperative" interactions are also responsible for two strands of DNA annealing, viruses binding to cells, and the folding of proteins into stable structures. Several studies have demonstrated that multivalent enhancement can improve the binding affinity of low-affinity targeting moieties, such as saccharides binding to concavanalin A, by several orders of magnitude (*58−60*). Depending on the adsorption kinetics, these studies have displayed similar binding isotherms (*61*). However, the multivalent effect dramatically increased the average binding constant K_D of the multivalent ligand, rather then merely recovering the binding constant associated with the monomeric ligand, as we were able to demonstrate. The best explanation for this is the increased effective diameter of the construct, which would not be observed in studies that involve small, low-affinity multivalent molecules. The increased diameter of the multivalent construct directly impacts the K_{on} rate of the construct by limiting the construct diffusivity (*62*).

Several studies have evaluated the stability of the thioether bond made by maleimide and cysteine under saline and serum conditions. Studies of HPMA copolymer−Fab′ conjugates have demonstrated stability under saline conditions (*13*). In another study that measured the half-life of antibody−drug conjugates, it was shown that the thioether bond has a half-life of seven days in serum (*63*). Interestingly, this did not affect the overall effectivity of drug, and the half-life could be extend by substituting the thioether bond with a bromoacetamide linker, a strategy that could also be utilized in a future design. Other HPMA copolymer constructs conjugated to Fab′ fragments by thioether bonds have shown stability in vivo (*64*).

In summary, methods to produce multivalent HPMA copolymer−anti-CD20 Fab′ conjugates and to analyze their multivalent binding to the B-cell antigen CD20 were examined. Binding of the multivalent constructs was characterized by the binding constant, K_D, the Sips heterogeneity factor, *a*, and the binding enhancement factor. The multivalent constructs bound the B-cell antigen CD20 in a manner that was consistent with negative cooperative models. It was revealed that using Fab′ conjugated to soluble branched HPMA copolymer can result in binding enhancement that can surpass binding affinities of whole mAb. Furthermore, the multivalent binding of these conjugates may be useful in exploring cell-surface dynamics involved with induction of apoptosis, initiated by cross-linking the B-cell antigen CD20.

ACKNOWLEDGMENT

The research was supported in part by the NIH grant CA51578 from the National Cancer Institute.

Supporting Information Available: Binding isotherms and Scatchard plots for *P-3Fab1.5*, *P-3Fab2.9*, *P-3Fab8.9*, and *P-7Fab1.4*. This material is available free of charge via the Internet at http://pubs.acs.org.

LITERATURE CITED

(1) Allen, T. M. (2002) Ligand-targeted therapeutics in anticancer therapy. *Nat. Rev. Cancer 2*, 750–763.

(2) Couvreur, P., and Vauthier, C. (2006) Nanotechnology: intelligent design to treat complex disease. *Pharm. Res. 23*, 1417–1450.

(3) Duncan, R., Kopečková-Rejmanová, P., Strohalm, J., Hume, I., Cable, H. C., Pohl, J., Lloyd, J. B., and Kopeček, J. (1987) Anticancer agents coupled to *N*-(2-hydroxypropyl)methacrylamide copolymers. I. Evaluation of daunomycin and puromycin conjugates in vitro. *Br. J. Cancer 55*, 165–174.

(4) Duncan, R., and Spreafico, F. (1994) Polymer conjugates. Pharmacokinetic considerations for design and development. *Clin. Pharmacokinet. 27*, 290–306.

(5) Putnam, D., and Kopeček, J. (1995) Polymer conjugates with anticancer activity. *Adv. Polym. Sci. 122*, 55–123.

(6) Schuster, J. M., and Bigner, D. D. (1992) Immunotherapy and monoclonal antibody therapies. *Curr. Opin. Oncol. 4*, 547–552.

(7) von Mehren, M., Adams, G. P., and Weiner, L. M. (2003) Monoclonal antibody therapy for cancer. *Annu. Rev. Med. 54*, 343–369.

(8) Hongrapipat, J., Kopečková, P., Liu, J., Prakongpan, S., and Kopeček, J. (2008) Combination chemotherapy and photodynamic therapy with Fab′ fragment targeted HPMA copolymer conjugates in human ovarian carcinoma cells. *Mol. Pharmaceutics 5*, 696−709.

(9) Duncan, R. (2006) Polymer conjugates for drug targeting. From inspired to inspiration. *J. Drug Targeting 14*, 333–335.

(10) Merdan, T., Callahan, J., Petersen, H., Kunath, K., Bakowsky, U., Kopečková, P., Kissel, T., and Kopeček, J. (2003) Pegylated polyethylenimine-Fab′ antibody fragment conjugates for targeted gene delivery to human ovarian carcinoma cells. *Bioconjugate Chem. 14*, 989–996.

(11) Říhová, B., Jelínková, M., Strohalm, J., Šťastný, M., Hovorka, O., Plocová, D., Kovář, M., Dráberová, L., and Ulbrich, K. (2000) Antiproliferative effect of a lectin- and anti-Thy-1.2 antibody-targeted HPMA copolymer-bound doxorubicin on primary and metastatic human colorectal carcinoma and on human colorectal carcinoma transfected with the mouse Thy-1.2 gene. *Bioconjugate Chem. 11*, 664–673.

(12) Říhová, B., Kopečková, P., Strohalm, J., Rossmann, P., Větvička, V., and Kopeček, J. (1988) Antibody-directed affinity therapy applied to the immune system: in vivo effectiveness and limited toxicity of daunomycin conjugated to HPMA copolymers and targeting antibody. *Clin. Immunol. Immunopathol. 46*, 100–114.

(13) Omelyanenko, V., Kopečková, P., Gentry, C., Shiah, J. G., and Kopeček, J. (1996) HPMA copolymer-anticancer drug-OV-TL16 antibody conjugates. 1. Influence of the method of synthesis on the binding affinity to OVCAR-3 ovarian carcinoma cells in vitro. *J. Drug Targeting 3*, 357–373.

(14) Mammen, M., Choi, S., and Whitesides, G. M. (1998) Polyvalent interaction in biological systems: implications for design and use of multivalent ligands and inhibitors. *Angew. Chem., Int. Ed. 37*, 2754–2794.

(15) Gestwicki, J. E., Cairo, C. W., Strong, L. E., Oetjen, K. A., and Kiessling, L. L. (2002) Influencing receptor-ligand binding mechanisms with multivalent ligand architecture. *J. Am. Chem. Soc. 124*, 14922–14933.

(16) Ding, H., Prodinger, W. M., and Kopeček, J. (2006) Identification of CD21-binding peptides with phage display and investigation of binding properties of HPMA copolymer-peptide conjugates. *Bioconjugate Chem. 17*, 514–523.

(17) Hong, S., Leroueil, P. R., Majoros, I. J., Orr, B. G., Baker, J. R., Jr., and Banaszak Holl, M. M. (2007) The binding avidity of a nanoparticle-based multivalent targeted drug delivery platform. *Chem. Biol. 14*, 107–115.

(18) Kopeček, J., Kopečková, P., Minko, T., and Lu, Z. (2000) HPMA copolymer-anticancer drug conjugates: design, activity, and mechanism of action. *Eur. J. Pharm. Biopharm. 50*, 61–81.

(19) Říhová, B., Bilej, M., Větvička, V., Ulbrich, K., Strohalm, J., Kopeček, J., and Duncan, R. (1989) Biocompatibility of *N*-(2-hydroxypropyl) methacrylamide copolymers containing adriamycin. Immunogenicity, and effect on haematopoietic stem cells in bone marrow in vivo and mouse splenocytes and human peripheral blood lymphocytes in vitro. *Biomaterials 10*, 335–342.

(20) Minko, T., Kopečková, P., and Kopeček, J. (2000) Efficacy of chemotherapeutic action of HPMA copolymer-bound doxorubicin in a solid tumor model of ovarian carcinoma. *Int. J. Cancer 86*, 108–117.

(21) Dvořák, M., Kopečková, P., and Kopeček, J. (1999) High-molecular weight HPMA copolymer-adriamycin conjugates. *J. Controlled Release 60*, 321–332.

(22) Shiah, J. G., Dvořák, M., Kopečková, P., Sun, Y., Peterson, C. M., and Kopeček, J. (2001) Biodistribution and antitumour efficacy of long-circulating *N*-(2-hydroxypropyl)methacrylamide copolymer-doxorubicin conjugates in nude mice. *Eur. J. Cancer 37*, 131–139.

(23) Anderson, K. C., Bates, M. P., Slaughenhoupt, B. L., Pinkus, G. S., Schlossman, S. F., and Nadler, L. M. (1984) Expression of human B cell-associated antigens on leukemias and lymphomas: a model of human B cell differentiation. *Blood 63*, 1424–1433.

(24) Stashenko, P., Nadler, L. M., Hardy, R., and Schlossman, S. F. (1981) Expression of cell surface markers after human B lymphocyte activation. *Proc. Natl. Acad. Sci. U.S.A. 78*, 3848–3852.

(25) Boye, J., Elter, T., and Engert, A. (2003) An overview of the current clinical use of the anti-CD20 monoclonal antibody rituximab. *Ann. Oncol. 14*, 520–535.

(26) Reff, M. E., Carner, K., Chambers, K. S., Chinn, P. C., Leonard, J. E., Raab, R., Newman, R. A., Hanna, N., and Anderson, D. R. (1994) Depletion of B cells in vivo by a chimeric mouse human monoclonal antibody to CD20. *Blood 83*, 435–445.

(27) Tedder, T. F., McIntyre, G., and Schlossman, S. F. (1988) Heterogeneity in the B1 (CD20) cell surface molecule expressed by human B-lymphocytes. *Mol. Immunol. 25*, 1321–1330.

(28) Tedder, T. F., and Schlossman, S. F. (1988) Phosphorylation of the B1 (CD20) molecule by normal and malignant human B lymphocytes. *J. Biol. Chem. 263*, 10009–10015.

(29) Deans, J. P., Li, H., and Polyak, M. J. (2002) CD20-mediated apoptosis: signalling through lipid rafts. *Immunology 107*, 176–182.

(30) Michel, R. B., and Mattes, M. J. (2002) Intracellular accumulation of the anti-CD20 antibody 1F5 in B-lymphoma cells. *Clin. Cancer Res. 8*, 2701–2713.

(31) Cardarelli, P. M., Quinn, M., Buckman, D., Fang, Y., Colcher, D., King, D. J., Bebbington, C., and Yarranton, G. (2002) Binding to CD20 by anti-B1 antibody or $F(ab')_2$ is sufficient for induction of apoptosis in B-cell lines. *Cancer Immunol. Immunother. 51*, 15–24.

(32) Polyak, M. J., and Deans, J. P. (2002) Alanine-170 and proline-172 are critical determinants for extracellular CD20 epitopes; heterogeneity in the fine specificity of CD20 monoclonal antibodies is defined by additional requirements imposed by both amino acid sequence and quaternary structure. *Blood 99*, 3256–3262.

(33) Binder, M., Otto, F., Mertelsmann, R., Veelken, H., and Trepel, M. (2006) The epitope recognized by rituximab. *Blood 108*, 1975–1978.

(34) Hofmeister, J. K., Cooney, D., and Coggeshall, K. M. (2000) Clustered CD20 induced apoptosis: src-family kinase, the proximal regulator of tyrosine phosphorylation, calcium influx, and caspase 3-dependent apoptosis. *Blood Cells Mol. Dis. 26*, 133–143.

(35) Shan, D., Ledbetter, J. A., and Press, O. W. (1998) Apoptosis of malignant human B cells by ligation of CD20 with monoclonal antibodies. *Blood 91*, 1644–1652.

(36) Cartron, G., Dacheux, L., Salles, G., Solal-Celigny, P., Bardos, P., Colombat, P., and Watier, H. (2002) Therapeutic activity of humanized anti-CD20 monoclonal antibody and polymorphism in IgG Fc receptor FcγRIIIa gene. *Blood 99*, 754–758.

(37) Ghetie, M. A., Bright, H., and Vitetta, E. S. (2001) Homodimers but not monomers of Rituxan (chimeric anti-CD20) induce apoptosis in human B-lymphoma cells and synergize with a chemotherapeutic agent and an immunotoxin. *Blood 97*, 1392–1398.

(38) Zhang, N., Khawli, L. A., Hu, P., and Epstein, A. L. (2005) Generation of rituximab polymer may cause hyper-cross-linking-induced apoptosis in non-Hodgkin's lymphomas. *Clin. Cancer Res. 11*, 5971–5980.

(39) Horning, S. J., Younes, A., Jain, V., Kroll, S., Lucas, J., Podoloff, D., and Goris, M. (2005) Efficacy and safety of tositumomab and iodine-131 tositumomab (Bexxar) in B-cell lymphoma, progressive after rituximab. *J. Clin. Oncol. 23*, 712–719.

(40) Wiseman, G. A., White, C. A., Witzig, T. E., Gordon, L. I., Emmanouilides, C., Raubitschek, A., Janakiraman, N., Gutheil, J., Schilder, R. J., Spies, S., Silverman, D. H., and Grillo-Lopez, A. J. (1999) Radioimmunotherapy of relapsed non-Hodgkin's lymphoma with zevalin, a ^{90}Y-labeled anti-CD20 monoclonal antibody. *Clin. Cancer Res. 5*, 3281s–3286s.

(41) Kopeček, J., and Bažilová, H. (1973) Poly[*N*-(2-hydroxypropyl)methacrylamide]: 1. Radical polymerization and copolymerization. *Eur. Polym. J. 9*, 7–14.

(42) Ong, G. L., Elsamra, S. E., Goldenberg, D. M., and Mattes, M. J. (2001) Single-cell cytotoxicity with radiolabeled antibodies. *Clin. Cancer Res. 7*, 192–201.

(43) Fowers, K. D., Callahan, J., Byron, P., and Kopeček, J. (2001) Preparation of Fab′ from murine IgG2a for thiol reactive conjugation. *J. Drug Targeting 9*, 281–294.

(44) Allen, T. M., Brandeis, E., Hansen, C. B., Kao, G. Y., and Zalipsky, S. (1995) A new strategy for attachment of antibodies to sterically stabilized liposomes resulting in efficient targeting to cancer cells. *Biochim. Biophys. Acta 1237*, 99–108.

(45) Nisonoff, A., and Pressman, D. (1958) Heterogeneity and average combining constants of antibodies from individual rabbits. *J. Immunol. 80*, 417–428.

(46) Crespo-Biel, O., Lim, C. W., Ravoo, B. J., Reinhoudt, D. N., and Huskens, J. (2006) Expression of a supramolecular complex at a multivalent interface. *J. Am. Chem. Soc. 128*, 17024–17032.

(47) Cartlidge, S. A., Duncan, R., Lloyd, J. B., Kopečková-Rejmanová, P., and Kopeček, J. (1987) Soluble, crosslinked *N*-(2-hydroxypropyl)methacrylamide copolymers as potential drug carriers: 3. Targeting by incorporation of galactosamine residues. Effect of route of administration. *J. Controlled Release 4*, 265–278.

(48) Cartlidge, S. A., Duncan, R., Lloyd, J. B., Kopečková-Rejmanová, P., and Kopeček, J. (1987) Soluble crosslinked *N*-(2-hydroxypropyl)methacrylamide copolymers as potential drug carriers: 2. Effect of molecular weight on blood clearance and body distribution in the rat after intravenous administration. Distribution of unfractionated copolymer after intraperitoneal,

subcutaneous or oral administration. *J. Controlled Release 4*, 253–264.
(49) Cartlidge, S. A., Duncan, R., Lloyd, J. B., Rejmanová, P., and Kopeček, J. (1986) Soluble crosslinked *N*-(2-hydroxypropyl)methacrylamide copolymers as potential drug carriers: 1. Pinocytosis by rat visceral yolk sacs and rat intestine cultured in vitro. Effect of molecular weight on uptake and intracellular degradation. *J. Controlled Release 3*, 55–56.
(50) Irvine, G. B. (1997) Amino acid analysis. Precolumn derivatization methods. *Methods Mol. Biol. 64*, 131–138.
(51) DeLisi, C. (1981) The effect of cell size and receptor density on ligand--receptor reaction rate constants. *Mol. Immunol. 18*, 507–511.
(52) Bohdanecký, M., Bažilová, H., and Kopeček, J. (1974) Poly[*N*-(2-hydroxypropyl)methacrylamide] - II Hydrodynamic properties of dilute solutions. *Eur. Polym. J. 10*, 405–410.
(53) Frankel, M. E., and Gerhard, W. (1979) The rapid determination of binding constants for antiviral antibodies by a radioimmunoassay. An analysis of the interaction between hybridoma proteins and influenza virus. *Mol. Immunol. 16*, 101–106.
(54) Scatchard, G. (1942) Equilibrium thermodynamics and biological chemistry. *Science 95*, 27–32.
(55) Dam, T. K., Roy, R., Das, S. K., Oscarson, S., and Brewer, C. F. (2000) Binding of multivalent carbohydrates to concanavalin A and Dioclea grandiflora lectin. Thermodynamic analysis of the "multivalency effect". *J. Biol. Chem. 275*, 14223–14230.
(56) Dower, S. K., Titus, J. A., and Segal, D. M. (1984) Cell surface dynamics: concepts and models, In *Receptors and ligands in intercellular communication; 3* (Perelson, A. S., DeLisi, C., and Wiegel, F. W., Eds.) p xvii, Dekker, New York.
(57) Sips, R. (1948) On the structure of a catalyst surface. *J. Chem. Phys. 16*, 490–495.
(58) Cairo, C. W., Gestwicki, J. E., Kanai, M., and Kiessling, L. L. (2002) Control of multivalent interactions by binding epitope density. *J. Am. Chem. Soc. 124*, 1615–1619.
(59) Mammen, M., Dahmann, G., and Whitesides, G. M. (1995) Effective inhibitors of hemagglutination by influenza virus synthesized from polymers having active ester groups. Insight into mechanism of inhibition. *J. Med. Chem. 38*, 4179–4190.
(60) Roy, R., Page, D., Perez, S. F., and Bencomo, V. V. (1998) Effect of shape, size, and valency of multivalent mannosides on their binding properties to phytohemagglutinins. *Glycoconj. J. 15*, 251–263.
(61) Dam, T. K., Roy, R., Page, D., and Brewer, C. F. (2002) Negative cooperativity associated with binding of multivalent carbohydrates to lectins. Thermodynamic analysis of the "multivalency effect". *Biochemistry 41*, 1351–1358.
(62) Shoup, D., and Szabo, A. (1982) Role of diffusion in ligand binding to macromolecules and cell-bound receptors. *Biophys. J. 40*, 33–39.
(63) Alley, S. C., Benjamin, D. R., Jeffrey, S. C., Okeley, N. M., Meyer, D. L., Sanderson, R. J., and Senter, P. D. (2008) Contribution of linker stability to the activities of anticancer immunoconjugates. *Bioconjugate Chem. 19*, 759–765.
(64) Lu, Z. R., Shiah, J. G., Kopečková, P., and Kopeček, J. (2003) Polymerizable Fab' antibody fragment targeted photodynamic cancer therapy in nude mice. *STP Pharma Sci. 13*, 69–75.

BC800351M

Synthesis and evaluation of multivalent branched HPMA copolymer-Fab' conjugates targeted to the B-cell antigen CD20

R. Johnson, P. Kopečková, and J. Kopeček

Supporting Information

Binding analysis of each multivalent conjugate was performed as described in the Experimental Procedures section. Briefly, Raji cells grown in RPMI medium containing 10% fetal bovine serum (FBS) were washed twice with Hank's balanced salt solution (HBSS). The cells were adjusted to $4x10^6$ cells/ml and split into two volumes. To one of the volumes of Raji cells, unlabeled anti-CD20 IgG was added to a final concentration of 500 nM to block CD20 for a negative control. Serial dilutions of ^{125}I-labeled anti-CD20 IgG, Fab', and multivalent Fab' conjugates were made from 2000 nM to 1 nM of Fab' fragment concentration. Millipore 96-well filter plates, coated with a 1% solution of nonfat dry milk in distilled water and incubated at 4 °C overnight, were washed with HBSS. For each of the serial dilutions, 25 µL of negative control cells were added to a single well, and 25 µL of unblocked cells were added to 3 different wells; then 25 µL of the respective dilutions were added to each well. The filter-well plates were incubated for 90 min at 120 rpm on a shaker at 25 °C. Following incubation, the Raji cells were washed twice with 200 µL of cold HBSS with 10% FBS, and then collected on filters. The filters were allowed to air-dry, removed from the plate and counted. Negative control wells were used to correct for non-specific binding. Isotherms were evaluated with the Sips equation using SigmaPlot software (Systat Software, San Jose, CA).

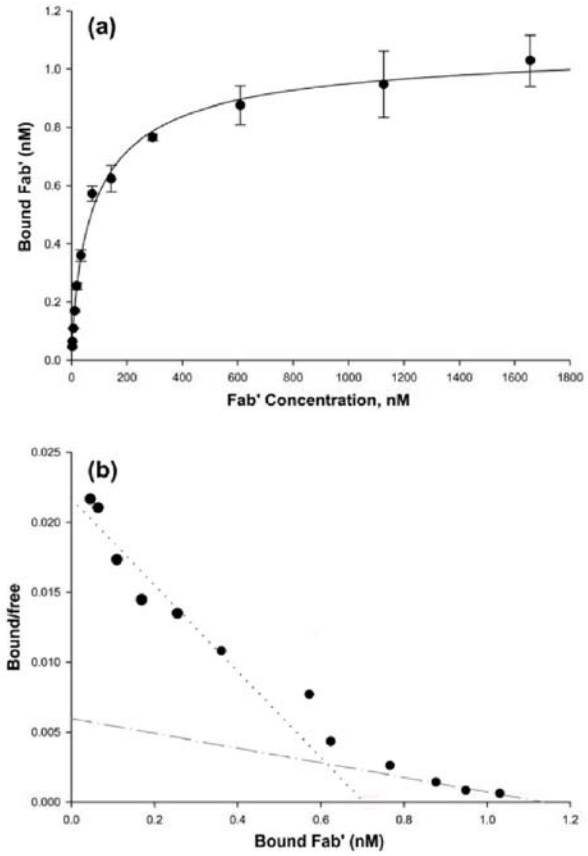

Suporting Information Figure 1. Binding analysis of conjugate *P-3Fab1.5*. (a) The isotherm for conjugate *P-3Fab1.5* was fitted with the Sips equation using the least squares method. (b) Scatchard plot of the binding data.

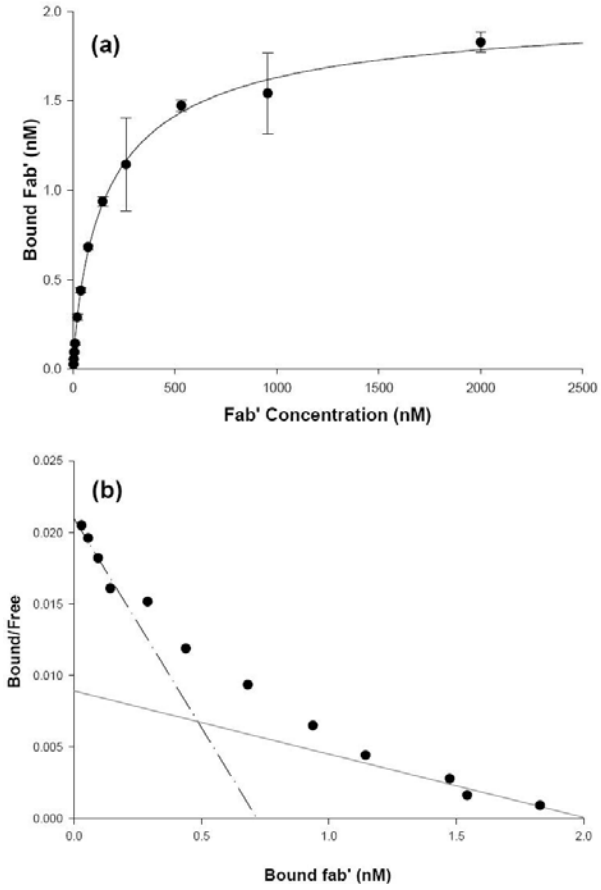

Suporting Information Figure 2. Binding analysis of conjugate *P-3Fab2.9*. (a) The isotherm for conjugate *P-3Fab2.9* was fitted with the Sips equation using the least squares method. (b) Scatchard plot of the binding data.

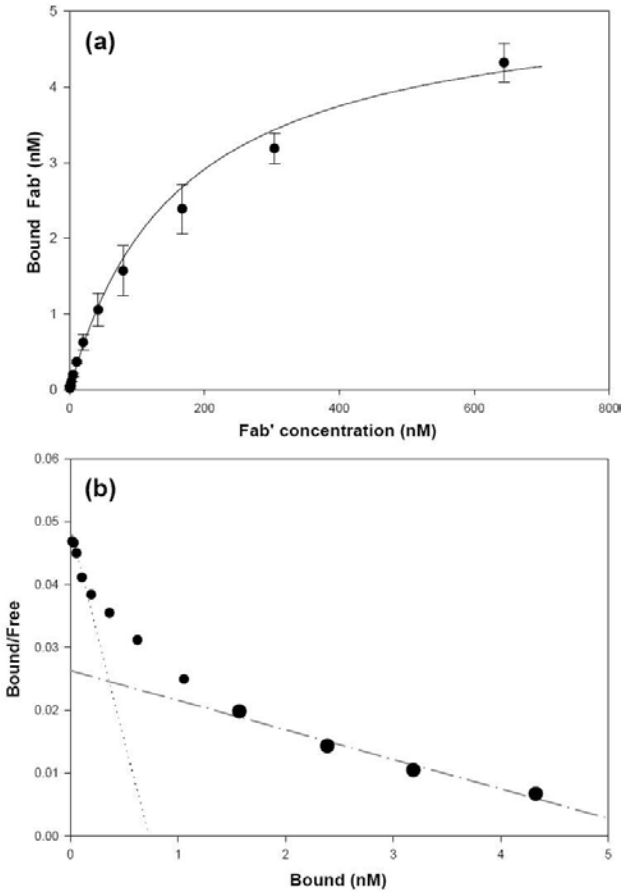

Suporting Information Figure 3. Binding analysis of conjugate *P-3Fab8.9*. (a) The isotherm for conjugate *P-3Fab2.9* was fitted with the Sips equation using the least squares method. (b) Scatchard plot of the binding data.

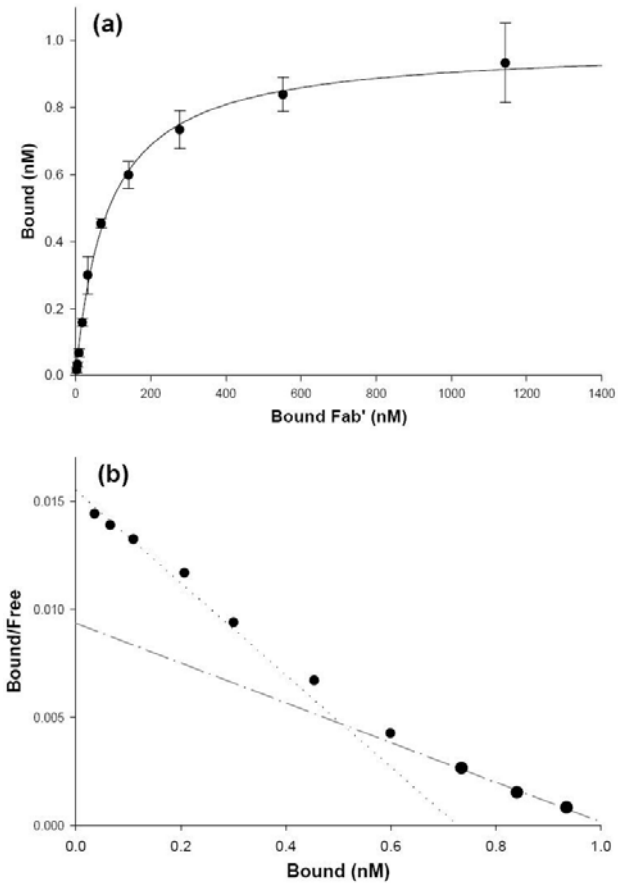

Suporting Information Figure 4. Binding analysis of conjugate *P-7Fab1.4*. (a) The isotherm for conjugate *P-3Fab2.9* was fitted with the Sips equation using the least squares method. (b) Scatchard plot of the binding data.

Subscriber access provided by SHEMYAKIN-OVCHINNIKOV INST

Article

Conjugation of Kahalalide F with Gold Nanoparticles to Enhance in Vitro Antitumoral Activity

Leticia Hosta, Mateu Pla-Roca, Jordi Arbiol, Carmen Lo#pez-Iglesias, Josep Samitier, Luis J. Cruz, Marcelo J. Kogan, and Fernando Albericio

Bioconjugate Chem., **2009**, 20 (1), 138-146• DOI: 10.1021/bc800362j • Publication Date (Web): 12 December 2008

Downloaded from http://pubs.acs.org on May 8, 2009

More About This Article

Additional resources and features associated with this article are available within the HTML version:

- Supporting Information
- Access to high resolution figures
- Links to articles and content related to this article
- Copyright permission to reproduce figures and/or text from this article

View the Full Text HTML

ACS Publications
High quality. High impact.

Bioconjugate Chemistry is published by the American Chemical Society. 1155 Sixteenth Street N.W., Washington, DC 20036

Conjugation of Kahalalide F with Gold Nanoparticles to Enhance in Vitro Antitumoral Activity

Leticia Hosta,[†,‡] Mateu Pla-Roca,[‡,§] Jordi Arbiol,[||] Carmen López-Iglesias,[⊥] Josep Samitier,[‡,§] Luis J. Cruz,[†] Marcelo J. Kogan,*[,#,▽] and Fernando Albericio*[,†,‡,○]

Institute for Research in Biomedicine; CIBER-BBN, Networking Centre on Bioengineering, Biomaterials and Nanomedicine; Institute for Bioengineering of Catalonia; and Scientific and Technical Services, Barcelona Science Park, University of Barcelona, Baldiri Reixac 10, 08028-Barcelona, Spain, Scientific and Technical Services, University of Barcelona, Lluis Solé i Sabaris 3-5, 08028 Barcelona, Spain, Department of Pharmacological and Toxicological Chemistry, Faculty of Chemistry and Pharmacy, Casilla 233, University of Chile, Olivos 1007, Independencia, Santiago, Chile, Centre for Advanced Interdisciplinary Research in Material Sciences, Av. Blanco Encalada 2008 Santiago, Chile, and Department of Organic Chemistry, University of Barcelona, Martí i Franqués 1, 08028 Barcelona, Spain. Received August 24, 2008; Revised Manuscript Received November 8, 2008

Two Cys-containing analogues of the anticancer drug Kahalalide F are synthesized and conjugated to 20 and 40 nm gold nanoparticles (GNPs). The resulting complexes are characterized by different analytical techniques to confirm the attachment of peptide to the GNPs. The self-assembly capacity of a peptide dramatically influences the final ratio number of molecules per nanoparticle, saturating the nanoparticle surface and prompting multilayered capping on the surface. In such way, the nanoparticle could act as a concentrator for the delivery of drugs, thereby increasing bioactivity. The GNP sizes and the conjugation have influence on the biological activities. Kahalalide F analogues conjugated with GNPs are located subcellularly at lysosome-like bodies, which may be related to the action mechanism of Kahalalide F. The results suggest that the selective delivery and activity of Kahalalide F analogues can be improved by conjugating the peptides to GNPs.

INTRODUCTION

Nanotechnology offers tremendous potential for medical diagnosis and therapy. Various types of nanoparticles have been explored for biomedical applications (*1*−*3*), having been widely employed in biological systems (*4*−*6*). Nanoparticles have been suggested for imaging (*7*−*13*), screening (*14*), and biosensing (*15*−*17*), not using only gold nanoparticle optical properties but also electrical (*18*−*23*), and furthermore are known to carry higher payloads of drugs than other vehicles and are currently used in gene and drug delivery (*24*−*26*), as well as in cancer diagnostics and therapeutic applications (*27*−*29*). Gold NPs (GNPs) display several features that make them well-suited for biomedical applications, including straightforward synthesis, stability (*30*), and the facile ability to incorporate secondary tags such as peptides targeted to specific cell types to afford selectivity (*31, 32*). On the other hand, GNPs have been used in photothermal therapy for the destruction of cancer cells or tumors. When irradiated with a focused laser in the near-infrared region (NIR) of suitable wavelength, targeted aggregates of GNPs, nanorods, or nanoshells can kill bacteria (*33*) and cancer cells (*34*).

* To whom correspondence should be addressed. Phone: +5629782897, email: mkogan@ciq.uchile.cl. Phone: +34934037088, Fax: 0034 934037126, e-mail: albericio@pcb.ub.cat.

[†] Institute for Research in Biomedicine, Barcelona Science Park.

[‡] CIBER-BBN, Networking Centre on Bioengineering, Biomaterials and Nanomedicine, Barcelona Science Park.

[§] Institute for Bioengineering of Catalonia, Barcelona Science Park.

[||] Scientific and Technical Services, University of Barcelona.

[⊥] Scientific and Technical Services, Barcelona Science Park.

[#] University of Chile.

[▽] Centre for Advanced Interdisciplinary Research in Material Sciences.

[○] Department of Organic Chemistry, University of Barcelona.

The conjugation of GNPs to an antitumoral drug could play two parallel roles: to enhance the delivery of a drug to the cell by presenting numerous peptide copies anchored to the nanoparticle surface and to help in the delivery of the nanoparticle to the pathological cell favoring the local aggregation of nanoparticles in tumor cells by increasing absorption in the NIR where tissues present low NIR region radiation absorption, after irradiation.

Nanobiotechnology is expected to widen the therapeutic index of current cancer therapies. For example, tumor-targeting drug delivery vectors are now approaching "true" nanometer size, which allows them to arrive in close proximity to several biological targets (*35*). Cellular delivery involving the transfer of various drugs and bioactive molecules (e.g., peptides, proteins, and DNA) through the cell membrane into the cytoplasm has generated great interest because the general administration of drugs and biomolecules suffers from inefficiency and enzymatic degradation, among other problems. Hence, there is a pressing need to develop safe and efficient transport vehicles to deliver drugs into cells (*36*). Taking into account the advantages of GNPs for drug delivery, in this work we have conjugated a Kahalalide F analogue, an antitumoral drug candidate, with GNPs to enhance the delivery of Kahalalide F to tumoral cells by increasing its cytotoxic effect. Kahalalide F is a marine cyclodepsipeptide isolated from a mollusk, *Elysia rubefescens*, with antitumoral activity (*37*). Two synthetic diasteromeric analogues of the Kahalalide F (Figure 1) were synthesized and conjugated with GNPs. Kahalalide F is the most bioactive member of the Kahalalide family of peptides. The presence of the compound appears to cause alterations in cell lysosomes, meaning that lysosomes become a target for Kahalalide F action (*38, 39*). Kahalalide F exerts a potent in vitro cytotoxic activity toward several tumor cell lines and specimens derived from various human solid tumors. In contrast, nontumor cell lines are 5 to 40 times less sensitive to Kahalalide F (*40*).

10.1021/bc800362j CCC: $40.75 © 2009 American Chemical Society
Published on Web 12/12/2008

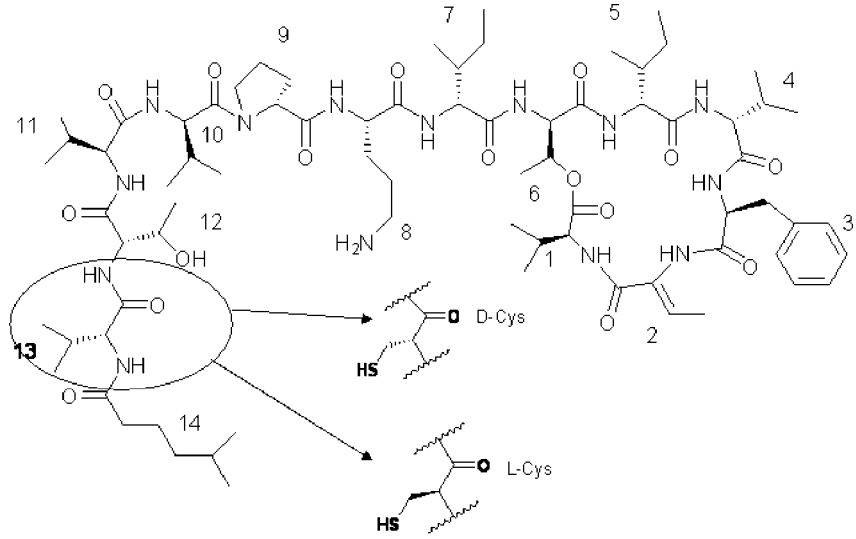

Kahalalide F: 5-MeHex[14]-**DVal[13]**-Thr[12]-Val[11]-DVal[10]-DPro[9]-Orn[8]-DalloIle[7]-DalloThr[6](&)-DalloIle[5]-DVal[4]-Phe[3]-(Z)Dhb[2]-Val[1]&

P1: D-Val[13] is replaced by D-Cys; **P2:** D-Val[13] is replaced by L-Cys

Figure 1. Structures of Kahalalide F, **P1**, and **P2**; amino acid sequences and linear cyclopeptides are represented in a one-line text formula using the protocol of Spengler et al. (*43*).

Kahalalide F shows in vitro activity against prostate and colon cancer cells, and to a lesser extent, antiviral, antifungal, and bactericide activity (*41*). Two clinical phase I trials in adult patients with advanced prostate cancer and pretreated solid tumors have established the recommended dose for two distinct treatment regimes (once a week and five consecutive days every 3 weeks) (*40, 42*). Kahalalide F phase II clinical trials in hepatocellular carcinoma, non-small cell lung cancer (NSCLC), and melanoma finished in 2006. Moreover, Kahalalide F is being tested in phase II clinical trials in patients with severe psoriasis.

Herein, we report on the ability of Kahalalide F analogue−GNP complexes to enter HeLa cells. The penetration, localization, and in vitro cytotoxicity of the conjugates in HeLa cells were evaluated.

MATERIALS AND METHODS

Materials. Cl-TrtCl-resin (100 mg, 1.56 mmol/g), protected Fmoc-L-amino acids and Fmoc-D-amino acids derivatives, were purchased from Iris Biotech GmbH (Marktredwitz, Germany), Luxembourg Industries (Tel-Aviv, Israel), Neosystem (Strasbourg, France), Calbiochem-Novabiochem AG (Laüfelfingen, Switzerland), and Bachem AG (Bubendorf, Switzerland). Diisopropylcarbodiimide (DIC) was obtained from Fluka Chemika (Buchs, Switzerland); HOAt, from GL Biochem (Shanghai, China); PyBOP, from Calbiochem−Novabiochem AG; and *N*,*N*-diisopropylethylamine (DIEA), from Merck (Darmstadt, Germany). Solvents for peptide synthesis and RP-HPLC were obtained from Scharlau (Barcelona, Spain). Trifluoroacetic (TFA) acid was supplied by KaliChemie (Bad Wimpfen, Germany). Other chemicals used were obtained from Aldrich (Milwaukee, WI) and were of the highest purity commercially available.

Peptide Synthesis and Purification. Both peptides were synthesized on solid phase using a method previously reported by our group (*44*). HPLC was performed using a Waters Alliance 2695 (Waters, MA) chromatography system with a PDA 995 detector, a reverse-phase Symmetry C_{18} (4.6 × 150 mm) 5 μm column, and a linear gradient of MeCN with 0.036% TFA into H_2O with 0.045% TFA. The system was run at a flow rate of 1.0 mL/min. HPLC-MS was performed using a Waters Alliance 2796 with a UV/vis detector 2487, ESI-MS Micromass ZQ (Waters) chromatography system, a reverse-phase Symmetry 300 C_{18} (3.9 × 150 mm) 5 μm column, and H_2O with 0.1% formic acid, and MeCN with 0.07% formic acid, as mobile phases. Mass spectra were recorded on a MALDI Voyager DE RP time-of-flight (TOF) spectrometer (PE Biosystems, Foster City, CA).

Synthesis of GNPs. GNPs were produced by reduction of hydrogen tetrachloroaurate ($HAuCl_4 \times H_20$) obtained from Aldrich (Milwaukee, WI).

20 nm Nanoparticles. $HAuCl_4 \times H_2O$ (8.7 mg) was added to a sodium citrate solution (100 mL, 2.2 mM) at 150 °C reflux. The reducing agent was added rapidly, and the reaction was allowed to continue under uniform and vigorous stirring until a red wine color was observed (*45*).

40 nm Nanoparticles. Same procedure as above except that a lower concentration of reducing agent was used (100 mL of a 1.22 mM solution of sodium citrate).

Conjugation of Peptides with GNPs. An excess of peptide was used for the conjugation (*6*). Peptide solutions (1 mg/mL in MilliQ water) were added dropwise to 10 mL of GNPs solution at room temperature with magnetic stirring, and agitation was then maintained for 15 min. The conjugates were then purified by dialysis over three days in a Spectra/Por MWCO membrane: 6−8000 against 2.2 mM sodium citrate. The solution was refreshed six times to eliminate the excess peptide (**P1** or **P2**).

UV−visible. UV−vis absorption spectra were recorded at room temperature with a 2501PC UV−vis recording spectrophotometer (Shimadzu Corporation, Kyoto, Japan).

High-Resolution Transmission Electron Microscopy (HR-TEM). Drops of GNPs conjugated to both Kahalalide F analogues under uranyl acetate staining were deposited over carbon-coated Formvar films on copper grids. To obtain the transmission electron microscopy (HRTEM) results, a field emission gun microscope JEOL 2010F was used, working at 200 kV and with a point-to-point resolution of 0.19 nm.

Electron Energy Loss Spectroscopy (EELS). Electron energy loss spectra (EELS) were obtained in a Gatan Image

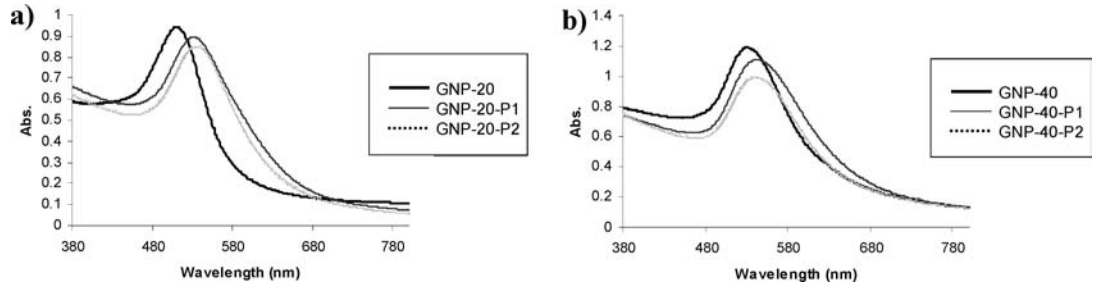

Figure 2. UV−vis spectra of GNPs and their respective conjugates; a shift in the maximum is representative of the conjugation. (a) GNP-20, GNP-20-P1, and GNP-20-P2; and (b) GNP-40, GNP-40-P1, and GNP-40-P2.

Filter (GIF 2000) coupled to the JEOL 2010F microscope, with an energy resolution of 1.2 eV.

X-ray Photoelectron Spectroscopy (XPS). Gold surfaces were purchased from Arrandee (Germany), and PMMA surfaces, from GoodFellow (Huntingdon, United Kingdom). XPS studies were performed by depositing a drop of GNPs or the conjugates over PMMA surfaces, and then drying the samples under reduced pressure before analysis. Gold surfaces functionalized with **P1** were obtained by immersion of **P1** (0.1 mg) in a $CHCl_3$ (1 mL) solution for 24 h.

Cell Culture and Incubation with the Conjugates. HeLa cell line was obtained from ATTC no CCL-2 (Manasas, VA) and maintained in DMEM low-glucose medium (Biological Industries) containing 10% fetal calf serum (FCS), 2 mM glutamine, 50 U/mL penicillin, and 0.05 g/mL streptomycin. For experiments, exponentially growing HeLa cells were detached from the culture flasks using a trypsin−0.25% ethylenediaminetetraacetic acid (EDTA) solution, and the cell suspension was seeded at a concentration of 3.5×10^3 cells/cm^2 onto glass coverslips (Nalge Nunc International, Rochester, NY). Experiments were carried out 24 h later, when the confluence was approximately 70−80%. Non-adherent cells were washed away and attached cells were incubated at 37 °C in 5% CO_2 in DMEM with a known concentration of GNPs.

WST-1 Assay. HeLa viability in the presence of unconjugated or conjugated nanoparticles was tested using a WST-1 assay, including a control with no nanoparticles added. For each assay, 3.5×10^3 cells/cm^2 were seeded onto a 96 well plate (Nalge Nunc) and cultured for 24 h. The conjugates were added in a 1:4 (conjugate/DMEM) ratio. Cells were incubated for 24 h at 37 °C under a 5% CO_2 atmosphere. After 20 h, 10 μL of WST 1 were added. The cells with the conjugate solutions were incubated for another 4 h. Cell viability is expressed as a percentage ratio of cells treated with the different compounds against untreated cells.

Confocal Laser Scanning Microscopy (CLSM). For the cellular localization of GNP conjugates, HeLa cells were plated on glass coverslips, grown to 60% confluence, and then incubated (at 37 °C under a 5% CO_2 atmosphere) with either **P1**− and **P2**−nanoparticle conjugates for 24 h. At indicated time points, the coverslips were rinsed extensively with phosphate-buffered saline (PBS), and the cells were fixed with 4% paraformaldehyde in PBS for 20 min at room temperature and then rehydrated in PBS.

Once the cells were fixed, the coverslips with cells were mounted onto glass slides with Mowiol mounting media (Calbiochem, CA), and then allowed to dry overnight prior to microscopy analysis. The samples were examined using an Olympus Fluoview 500 confocal microscope with a 60×/1.4 NA objective.

Nanoparticle Localization by Transmission Electron Microscopy (TEM). HeLa cells were incubated with conjugated or unconjugated gold nanoparticles for 24 h. Cells were fixed with 2.5% glutaraldehyde in phosphate buffer, and then kept in the fixative at 4 °C for 24 h. The cells were then washed with the same buffer, and postfixed with 1% osmium tetraoxide in the same buffer containing 0.8% potassium ferricyanide at 4 °C. The samples were then dehydrated in acetone, infiltrated with Epon resin for 2 days, embedded in the resin, and polymerized at 60 °C for 48 h. Ultrathin sections were obtained using a Leica Ultracut UCT ultramicrotome, and then mounted on Formvar-coated copper grids. The sections were stained with 2% uranyl acetate in water and lead citrate, and then observed under a JEM-1010 electron microscope (Jeol, Japan).

RESULTS AND DISCUSSION

Modification of Kahalalide F for Conjugation with GNPs. Two Kahalalide F analogues **P1** and **P2** (Figure 1) were synthesized and conjugated to NPs. For conjugation with GNPs, a free thiol containing Cys that facilitates the attachment to the gold surface was introduced in the peptide sequence. In **P1**, the D-^{13}Val was replaced by a D-Cys residue that does not seem to be crucial for biological activity. To determine whether the Cys configuration affects toxicity, **P2** was obtained from where the D-Val had been replaced by a L-Cys instead a D-Cys, as in **P1**.The change of chirality from D-Cys (**P1**) to L-Cys (**P2**) should induce a decrease in antitumoral activity from **P1** to **P2**. These results are in agreement with Jimenez et al., who reported that when the chirality of a residue of the Kahalalide F tail changes, the activity decreases (*46*).

P1 and **P2** were synthesized using a Fmoc/tBu solid-phase synthesis strategy (Supporting Information) (*44*).

Conjugation of P1 and P2 with GNPs. GNP cellular uptake is heavily dependent on nanoparticle size (*47*). In this work, **P1** and **P2** were conjugated to two different GNP sizes, i.e., 20 and 40 nm (GNP-20 and GNP-40, respectively) obtaining conjugates GNP-20-P1, GNP-20-P2, GNP-40-P1, and GNP-40-P2 in order to determine the influence of nanoparticle size on the penetration and cytotoxicity of the conjugates.

GNPs were obtained via the sodium citrate reduction method (*48*−*52*), which allows the synthesis of clusters between 6 and 60 nm by adding varying amounts of the reducing agent. The GNPs were characterized by UV−vis and TEM (Supporting Information). The peptide-capped GNPs were prepared by mixing a colloidal gold solution with an excess of peptide to obtain functionalized gold surfaces. The conjugates were exhaustively characterized by using UV−vis spectroscopy, amino acid analysis (AAA), transmission electron microscopy (TEM), electron energy loss spectroscopy (EELS), and X-ray spectroscopy (XPS).

Characterization of Conjugates. *UV*−*visible Spectroscopy.* UV−vis spectra of GNPs were taken (Figure 2). The characteristic correlation between surface plasmon resonance band and nanoparticle size (*53*) (520 nm for the 20 nm size, and 530 nm for the 40 nm size) was observed. In peptide−GNP conjugates, the wavelength of maximum absorption was shifted to longer

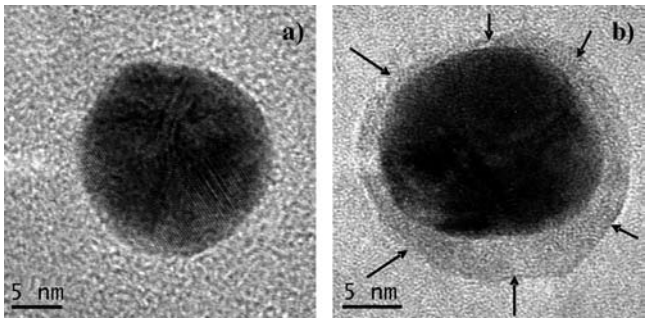

Figure 3. (a) bare GNP-20 and (b) GNP-20-P1.

wavelengths (Figure 2), which could be explained by the capping of the nanoparticle surface with the peptide molecules.

High-Resolution Transmission Electron Microscopy (HR-TEM). Figure 3 shows high-resolution TEM micrographs (HRTEM) of GNP-20 (Figure 3a) and GNP-20-P1 (Figure 3b). The presence of a layer around the nanoparticle core (Figure 3b) corresponding to the peptide was observed following uranyl acetate staining. As observed, the peptide covered the whole surface of the nanoparticle and increased the hydrodynamic size of the peptide-capped nanoparticle by 6 nm (the GNP metallic core as 20 nm in diameter, while the GNP-20-P1 was approximately 25 nm). The capping of GNPs by the adsorption of proteins was observed by TEM by other authors (*54*). However, in our case, although the nanoparticle was capped with a short peptide (approximately 1 nm long in an extended form), the formation of a wide layer (5 nm) was observed. This result led us to conclude that the nanoparticle was capped by a peptide multilayer.

Further characterization of the conjugates was carried out as described next. EELS (electron energy loss spectroscopy) and XPS (X-ray photoelectron spectroscopy) were used to confirm the presence of S−Au bonds on the surface, and amino acid analysis was performed to determine the number of peptide molecules that were conjugated to the GNPs.

Electron Energy Loss Spectroscopy (EELS). An accurate analysis of the electron energy loss near edge spectra (ELNES) at the Au $O_{2,3}$ edge (54 eV), showed that the shape of the edge changed slightly when the spectrum was obtained on the unconjugated GNPs with regard to the **P1**-conjugates (Figure 4b,e, respectively). The change of the ELNES shape at the Au $O_{2,3}$ edge can be directly attributed to a bonding variation on some of the Au surface atoms. To determine the cause of this bonding variation, we also analyzed the S $L_{2,3}$ edge placed at around 165 eV. In this case, energy-filtered spectra obtained on the Au conjugated nanoparticle surfaces showed a clear signal around 165 eV (Figure 4f), indicating the presence of S atoms on the Au nanoparticle surface as detailed by Olmedo et al. (*55*).

The same energy region analyzed on the unconjugated nanoparticle surfaces showed a noise signal only, as indicated in Figure 4c. Given that the unconjugated sample was assumed to have a low quantity of S atoms, it was used to evaluate the signal-to-noise ratio at the S $L_{2,3}$ energy region. The average ratio between the maximum on the Au $O_{2,3}$ peak and the maximum noise signal after background subtraction found at the S $L_{2,3}$ energy region was 4×10^{-3} for the unconjugated nanoparticles. However, values of up to 8×10^{-3} were found for the functionalized nanoparticles, indicating that the increase in the signal-to-noise ratio may be due to bound S atoms. This last result corroborates the presence of S atoms on the Au surface, which would be responsible for the slight change in the Au $O_{2,3}$ ELNES spectra due to their bonding. Consequently, the presence of bound S atoms would indicate the functionalization of the GNPs with P1.

X-ray Photoelectron Spectroscopy (XPS). The gold colloids were further characterized by X-ray photoelectron spectroscopy (XPS). XPS studies were carried out on **P1**-conjugate and unconjugated gold nanoparticles deposited on polymethylmethacrylate surfaces (PMMA). This polymeric surface was used to minimize interference coming from the substrate, a problem commonly observed when sulfur-containing compounds are analyzed on silicon surfaces (*56*).

The S_{2p} spectrum gave a weak signal due to the presence of only one sulfur atom per attached peptide (Figure 5). The signal consists of a broad band with a maximum at 163.2 eV that corresponds to sulfur grafted onto gold, indicating the presence

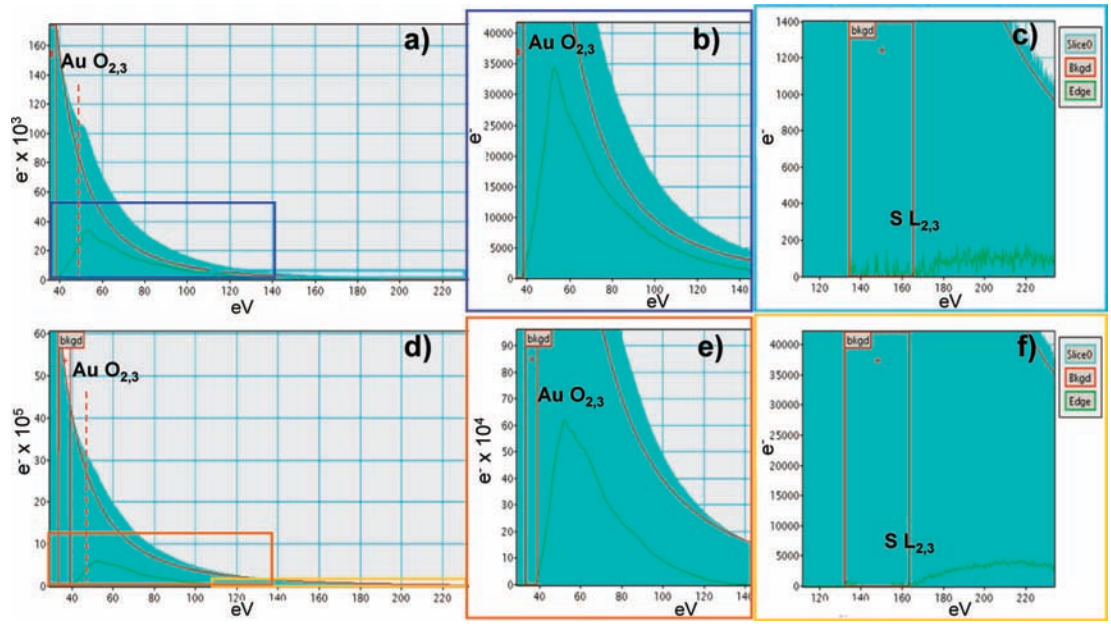

Figure 4. (a) EELS spectrum obtained on the surface of a non-functionalized GNP-20. (b) Detail of the Au $O_{2,3}$ ELNES spectrum bound by the blue rectangle in (a). (c) Detail of the S $L_{2,3}$ edge bound by the cyan rectangle in (a). (d) EELS spectrum obtained on the surface of GNP-20-P1. (e) Detail of the Au $O_{2,3}$ ELNES spectrum bound by the dark orange rectangle in (d). (f) Detail of the S $L_{2,3}$ edge bound by the pale orange rectangle in (d).

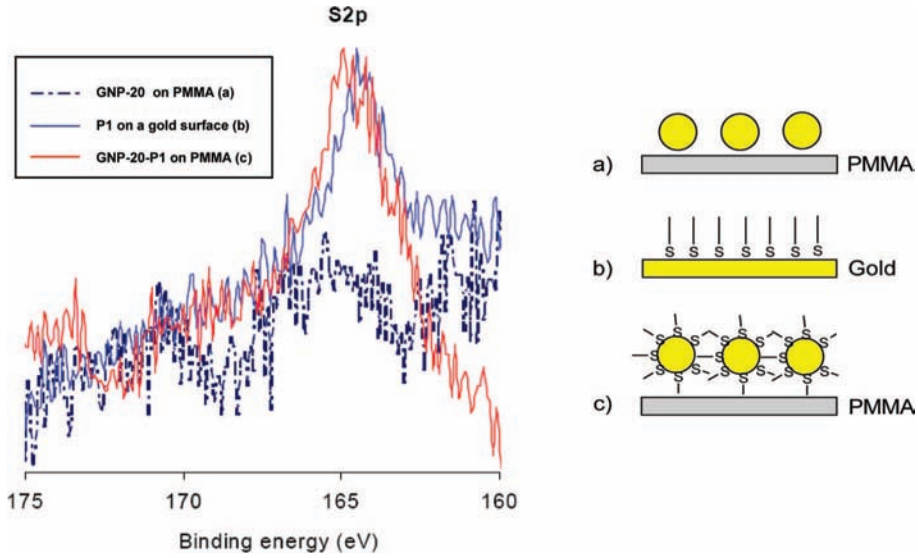

Figure 5. XPS S_{2p} region spectra of (a) GNP-20 on PMMA, (b) **P1**-functionalized gold surfaces, and (c) GNP-20-**P1** on a PMMA surface. The spectra have been normalized.

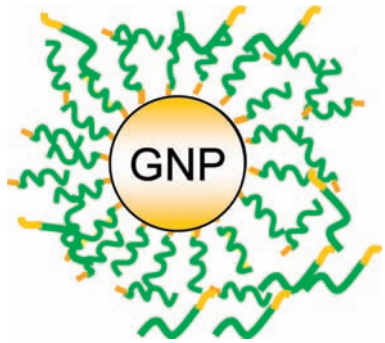

Figure 6. Representation of the functionalization of GNPs with the Kahalalide F analogues and the formation of adlayers. The peptide chain is depicted in green; the thiols belonging to the cysteins are depicted in orange.

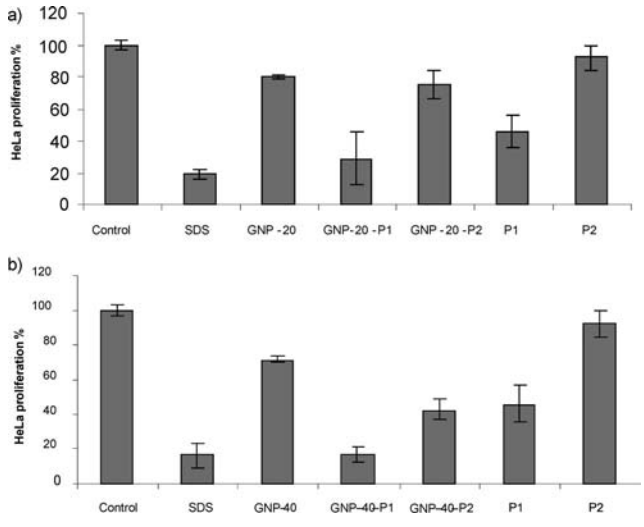

Figure 7. Antiproliferation results of the incubation of **P1**- and **P2**-conjugated 20 nm (a) and 40 nm (b) gold nanoparticles with HeLa cells for 24 h. Cell culture media and SDS were used as negative and positive controls, respectively. The conjugated and nonconjugated peptides were screened against the HeLa cells at a concentration of 1×10^{-5} M. The GNP concentration is the same in all samples.

of Au−S bonds. Although $S_{2p3/2}$ and $S_{2p1/2}$ signals can usually be observed separately, we observed a single broad band, presumably due to shielding of the electron emission by the large peptide. A similar S_{2p} signal was obtained when the peptide was on a non-functionalized gold surface (*57*).

Determination of the Number of Peptide Molecules per GNP. To determine the number of peptide molecules per nanoparticle, nondialyzed aliquots of the conjugated solutions (2.5 mL) were centrifuged at 13 500 rpm for 30 min. The supernatant was lyophilized and then analyzed by HPLC to determine the amount of unconjugated peptide. Approximately 85% of the peptide used in the conjugation was attached to the GNPs. The number of peptides per particle was calculated by dividing the concentration of grafted peptide by the amount of GNPs in solution, which was determined spectrophotometrically considering the molar extinction coefficients detailed in ref *58*. Despite the GNP's size (GPN-20 or GPN-40), the conjugates showed ratios of 60 000 ± 5000 peptide molecules per nanoparticle. However, assuming that the surface of a GNP-20 is 1256 nm^2 or 5024 nm^2 for a GNP-40 and that the surface of a single peptide molecule in an extended conformation is 0.6 nm^2 (data obtained from molecular modeling calculation using the *Insight II* software package), the theoretical number of molecules that would completely cover a GNP-20 surface is only 2090 and 8373 for a GNP-40. This indicated to us that not all peptide molecules were chemisorbed to the nanoparticle surface through the sulfur bond, with the excess of peptide being attached to the nanoparticle by another sort of interaction (Figure 6). One option is the formation of peptide adlayers due to the hydrophobic character of KF, which prompts the assembly of the peptide on the GNP surface in aquous media. Kahalalide F spontaneously self-assembles in aqueous solution, forming spherical supramolecular structures as has been observed by TEM (Supporting Information). This formation of peptide adlayers is a relevant issue to consider when the conjugation of a peptide to a GNP is considered and dramatically influences the final ratio of molecules per nanoparticle, saturating the nanoparticle surface and prompting multilayered capping on the surface. In such a way, the nanoparticles are acting as a concentrator for the delivery of drugs, thereby increasing bioactivity. The influence of the conjugation of **P1** and **P2** on cytotoxic activity was examined as follows.

Cytotoxicity Studies. The degree of cytotoxicity of single peptides (**P1** and **P2**), single GNP solutions (GNP-20 and GNP-40), and their respective conjugates was determined by the WST-1 assay in HeLa tumor cells following 24 h of incubation.

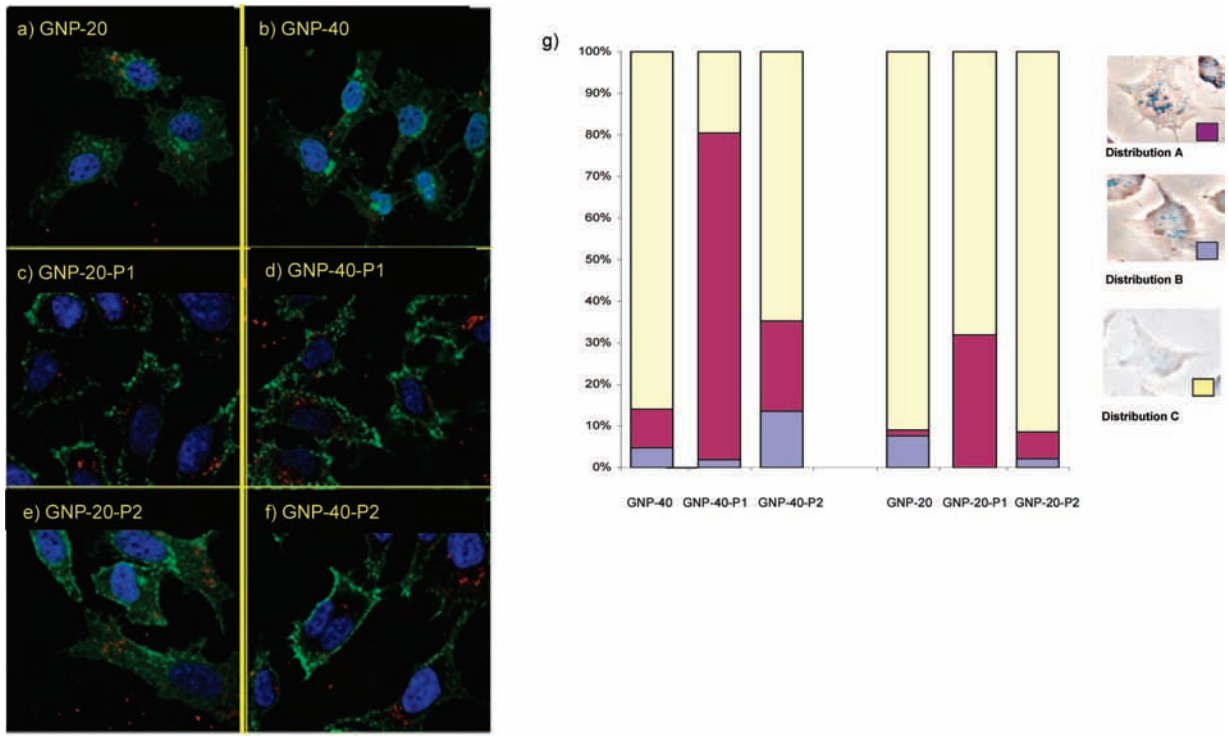

Figure 8. Localization of GNPs and their conjugates in HeLa cells incubated for 24 h (a−f); the red dots represent reflections of groups of nanoparticles. Membranes (green) were stained with a fluorescence marker (WGA), and nuclei (blue) by a DNA marker (Hoechst). Left column: GNP-20. Right column: GNP-40. (g) Percentage of accumulation of GNPs in HeLa cells. The proportion of cells that contain 10 or more reflecting spots (nanoparticules) is represented in burgundy (distribution A). The proportion of cells that contain more than 3 and less than 10 reflecting spots is represented in blue (distribution B). The proportion of cells that contain less than 3 reflecting spots is depicted in yellow (distribution C). The total number of cells taken into account was 100 for each nanoparticle sample.

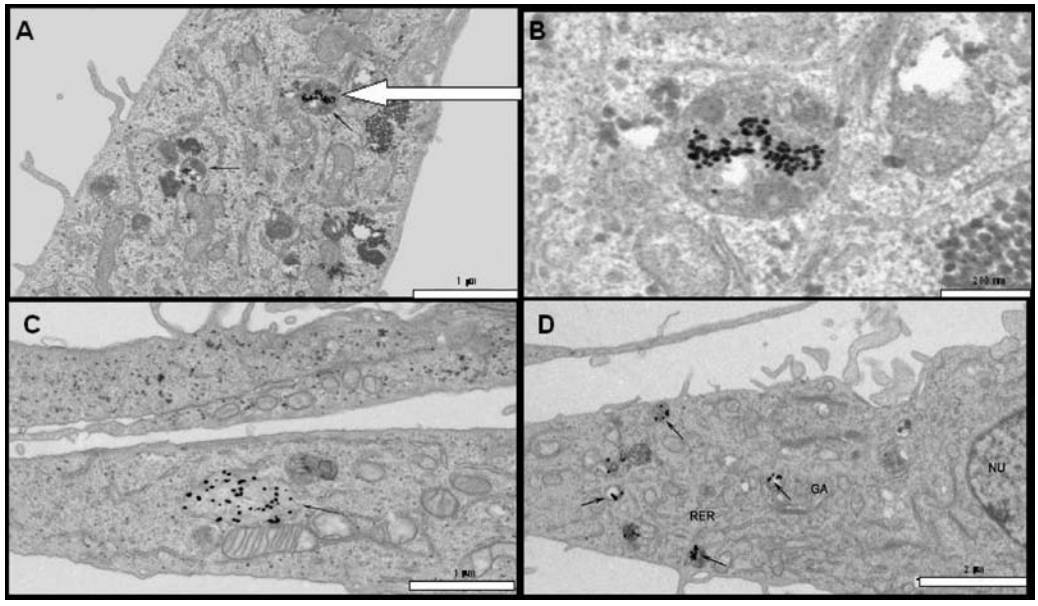

Figure 9. TEM images of HeLa cells incubated with (A) GNP-20-P1. The arrows indicate the presence of the GNPs inside lysosome-like structures. (B) Higher magnification of the accumulated GNP-20-**P1** inside lysosome-like structures. (C) GNP-40-**P1** and (D) bare GNP-20. NU (nucleus), RER (rough endoplasmic reticulum), GA (Golgi apparatus).

Cell culture medium and SDS were considered as negative and positive controls (0% and 80% of inhibition, respectively). The results showed that GNPs displayed residual cytotoxicity against HeLa cells, determined in approximately 22% inhibition for GNP-20 and GNP-40 (Figure 7 and Supporting Information). Regarding the cytotoxicity of single peptides, **P2** was found to be less cytotoxic than **P1** (10% vs 50% inhibition, respectively). The cytotoxicity of conjugates **P1** and **P2** with GNP-20 did not change with respect to the free peptides (Figure 7 and Supporting Information). In contrast, for **P1** and **P2** conjugated with GNP-40 the cytotoxicity is higher with respect to the free peptides (Figure 7). This enhancement could be the result of better cell uptake of the former conjugate, which would be consistent with the findings of Chithrani et al. (*47*). The authors reported that, among nanoparticles of different sizes, those of 50 nm demonstrated the highest level of uptake by HeLa cells. In agreement with these results, Osaki et al. (*59*) qualitatively showed that 50 nm nanoparticles entered the cells via receptor-mediated

endocytosis more efficiently than smaller ones. We attributed the enhanced toxicity of GNP-40-P1 and GNP-40-P2 with respect to **P1** and **P2** to a synergic effect between the peptide and the GNP-40 that favored the penetration and targeting to the lysosome (the putative target of Kahalalide F) (*38*). Confocal and TEM observations to evaluate the accumulation and localization of the conjugates in the cells were carried out.

Cellular Localization of Conjugates. *Accumulation of the Peptide−GNP Conjugates by Confocal Laser Scanning Microscopy (CLSM).* To study the influence of the peptide conjugation on the penetration and distribution of GNPs in cells, both conjugated and unconjugated nanoparticles were observed under confocal microscopy for detection of their reflections. It is important to mention that, in this technique, single GNPs could not be observed; however, if the nanoparticles had been localized together in a cell region, then their detection would have been possible. The cells were fixed with paraformaldehyde and the membranes and nuclei stained. Figure 8 shows how GNPs and peptide−GNP accumulate in cells. Bare GNPs accumulate in cells in low proportion with respect to the conjugates. As expected, the accumulation of GNP-40 is higher than GNP-20, which is in accordance with the results Chitriani et al. (*47*), who hypothesized that GNP uptake is mediated by nonspecific adsorption of serum proteins onto the gold surface; these proteins induce the nanoparticles to enter into cells via the mechanism of receptor-mediated endocytosis. On the other hand, functionalized nanoparticles with peptides presented a higher degree of accumulation in HeLa cells with respect to bare GNPs, with the GNP-40-P1 conjugate showing the highest accumulation. The functionalization of GNPs with **P1** and **P2** introduces a positive charge into the nanoparticle. This charge is achieved by Orn (see Figure 1), which is charged positively at pH = 7.4. This positive charge favors interaction with the membrane (charged negatively) and consequently enhances penetration into the cell. There are several examples in the literature describing the addition of Lys or Arg residues for transfecting molecules into cells (*60*, *61*). The lower accumulation of GNPs that are capped with citrate ions in comparison to functionalized nanoparticles could be explained by the fact that the charge of the GNPs is negative (due to the citrate stabilizing ligand). Anionic molecules and structures bind less efficiently to cell surfaces than neutral or cationic molecules, since electrostatic repulsion between the negatively charged surface membrane and cellular environment will repel nanoparticles. Thus, to gain entry, these GNPs must be capped with serum proteins.

Localization of the Conjugates by Transmission Electron Microscopy (TEM). Localization of the peptide−GNP conjugates in the cells was investigated with by TEM. HeLa cells were incubated for 24 h with either conjugated or unconjugated GNPs. TEM images (Figure 9) showed that the penetration of GNP was lower than that of peptide−GNP. Both GNPs and peptide−GNPs were localized in lysosome-like structures. This behavior was not surprising due to lysosomal compartmentalization and was certainly the expected result in most cell uptake processes.

CONCLUSIONS

In summary, conjugating Kahalalide F analogues to GNPs improves the ability of the peptide to target tumoral cell lysosomes (the putative target for Kahalalide F) by using GNPs with high capacity to enter into the cell, thus allowing higher concentrations of peptide molecules which in turn enhances cytotoxicity, as observed for peptides conjugated to GNP-40. The conjugation of bioactive peptides such as Kahalalide F to GNP could be used to direct the drug to the desired pharmacological target, thereby widening the therapeutic index of current cancer therapies. In addition, the peptides conjugated to GNP-40 could find application in treatments based on the destruction of tumoral cells by applying NIR radiation to cells that contain accumulated nanoparticles.

ACKNOWLEDGMENT

This study was partially supported by Chile, FONDAP 11980002 (17070002), FONDECYT 1061142, FONDECYT 7060219; Spain, CICYT (CTQ2006-03794/BQU), ISCIII (CIBER, nanomedicine), MEyC (CENIT, nanopharma), PharmaMar, the Generalitat de Catalunya (2005SGR 00662), the Institute for Research in Biomedicine, and the Barcelona Science Park. M.K. and F.A. give special thanks to AECI for providing a Chile−Spain collaboration grant.

Supporting Information Available: Experimental details. This material is available free of charge via the Internet at http://pubs.acs.org.

LITERATURE CITED

(1) Alivisatos, P. (2004) The use of nanocrystals in biological detection. *Nat. Biotechnol. 22*, 47–52.
(2) Kim, J., Park, S., Lee, J. E., Jin, S. M., Lee, J. H., Lee, I. S., Yang, I., Kim, J. S., Kim, S. K., Cho, M. H., and Hyeon, T. (2006) Designed fabrication of multifunctional magnetic gold nanoshells and their application to magnetic resonance imaging and photothermal therapy. *Angew. Chem., Int. Ed. 45*, 7754–7758.
(3) Katz, E., and Willner, I. (2004) Integrated nanoparticle-biomolecule hybrid systems: Synthesis, properties, and applications. *Angew. Chem., Int. Ed. 43*, 6042–6108.
(4) Krpetic, Z., Porta, F., and Scari, G. (2006) Selective entrance of gold nanoparticles into cancer cells. *Gold Bull. 39*, 66–68.
(5) Panyam, J., Zhou, W. Z., Prabha, S., Sahoo, S. K., and Labhasetwar, V. (2002) Rapid endo-lysosomal escape of poly(D,L-lactide-co-glycolide) nanoparticles: implications for drug and gene delivery. *Faseb J. 16*.
(6) Kogan, M. J., Bastus, N. G., Amigo, R., Grillo-Bosch, D., Araya, E., Turiel, A., Labarta, A., Giralt, E., and Puntes, V. F. (2006) Nanoparticle-mediated local and remote manipulation of protein aggregation. *Nano Lett. 6*, 110–115.
(7) Veiseh, O., Sun, C., Gunn, J., Kohler, N., Gabikian, P., Lee, D., Bhattarai, N., Ellenbogen, R., Sze, R., Hallahan, A., Olson, J., and Zhang, M. Q. (2005) Optical and MRI multifunctional nanoprobe for targeting gliomas. *Nano Lett. 5*, 1003–1008.
(8) El-Sayed, I. H., Huang, X. H., and El-Sayed, M. A. (2005) Surface plasmon resonance scattering and absorption of anti-EGFR antibody conjugated gold nanoparticles in cancer diagnostics: Applications in oral cancer. *Nano Lett. 5*, 829–834.
(9) Jiang, W., Papa, E., Fischer, H., Mardyani, S., and Chan, W. C. W. (2004) Semiconductor quantum dots as contrast agents for whole animal imaging. *Trends Biotechnol. 22*, 607–609.
(10) Berciaud, S., Cognet, L., Blab, G. A., and Lounis, B. (2004) Photothermal heterodyne imaging of individual nonfluorescent nanoclusters and nanocrystals. *Phys. Rev. Lett. 93*, 257402/1–257402/4.
(11) Boyer, D., Tamarat, P., Maali, A., Lounis, B., and Orrit, M. (2002) Photothermal imaging of nanometer-sized metal particles among scatterers. *Science 297*, 1160–1163.
(12) Sonnichsen, C., Franzl, T., Wilk, T., von Plessen, G., Feldmann, J., Wilson, O., and Mulvaney, P. (2002) Drastic reduction of plasmon damping in gold nanorods. *Phys. Rev. Lett. 88*, 077402/1–077402/4.
(13) Yguerabide, J., and Yguerabide, E. E. (2001) Resonance light scattering particles as ultrasensitive labels for detection of analytes in a wide range of applications. *J. Cell. Biochem.* 71–81.
(14) Englebienne, P., Van Hoonacker, A., and Verhas, M. (2001) High-throughput screening using the surface plasmon resonance effect of colloidal gold nanoparticles. *Analyst 126*, 1645–1651.

(15) Karhanek, M., Kemp, J. T., Pourmand, N., Davis, R. W., and Webb, C. D. (2005) Single DNA molecule detection using nanopipettes and nanoparticles. *Nano Lett. 5*, 403–407.
(16) Medintz, I. L., Clapp, A. R., Melinger, J. S., Deschamps, J. R., and Mattoussi, H. (2005) A reagentless biosensing assembly based on quantum dot-donor Forster resonance energy transfer. *Adv. Mater. 17*, 2450–2455.
(17) Taton, T. A., Lu, G., and Mirkin, C. A. (2001) Two-color labeling of oligonucleotide arrays via size-selective scattering of nanoparticle probes. *J. Am. Chem. Soc. 123*, 5164–5165.
(18) Haguet, V., Martin, D., Marcon, L., Heim, T., Stievenard, D., Olivier, C., El-Mahdi, O., and Melnyk, O. (2004) Combined nanogap nanoparticles nanosensor for electrical detection of biomolecular interactions between polypeptides. *Appl. Phys. Lett. 84*, 1213–1215.
(19) Marcon, L., Stievenard, D., and Melnyk, O. (2008) Characterization of nanogap chemical reactivity using peptide-capped gold nanoparticles and electrical detection. *Bioconjugate Chem. 19*, 802–805.
(20) Moller, R., Csaki, A., Kohler, J. M., and Fritzsche, W. (2001) Electrical classification of the concentration of bioconjugated metal colloids after surface adsorption and silver enhancement. *Langmuir 17*, 5426–5430.
(21) Park, S. J., Lazarides, A. A., Mirkin, C. A., Brazis, P. W., Kannewurf, C. R., and Letsinger, R. L. (2000) The electrical properties of gold nanoparticle assemblies linked by DNA. *Angew. Chem., Int. Ed. 39*, 3845.
(22) Park, S. J., Taton, T. A., and Mirkin, C. A. (2002) Array-based electrical detection of DNA with nanoparticle probes. *Science 295*, 1503–1506.
(23) Velev, O. D., and Kaler, E. W. (1999) In situ assembly of colloidal particles into miniaturized biosensors. *Langmuir 15*, 3693–3698.
(24) Kohler, N., Sun, C., Wang, J., and Zhang, M. Q. (2005) Methotrexate-modified superparamagnetic nanoparticles and their intracellular uptake into human cancer cells. *Langmuir 21*, 8858–8864.
(25) Panyam, J., and Labhasetwar, V. (2003) Biodegradable nanoparticles for drug and gene delivery to cells and tissue. *Adv. Drug Delivery Rev. 55*, 329–347.
(26) Yang, P. H., Sun, X. S., Chiu, J. F., Sun, H. Z., and He, Q. Y. (2005) Transferrin-mediated gold nanoparticle cellular uptake. *Bioconjugate Chem. 16*, 494–496.
(27) Chen, J. Y., Wiley, B., Li, Z. Y., Campbell, D., Saeki, F., Cang, H., Au, L., Lee, J., Li, X. D., and Xia, Y. N. (2005) Gold nanocages: Engineering their structure for biomedical applications. *Adv. Mater. 17*, 2255–2261.
(28) Hirsch, L. R., Stafford, R. J., Bankson, J. A., Sershen, S. R., Rivera, B., Price, R. E., Hazle, J. D., Halas, N. J., and West, J. L. (2003) Nanoshell-mediated near-infrared thermal therapy of tumors under magnetic resonance guidance. *Proc. Natl. Acad. Sci. U.S.A. 100*, 13549–13554.
(29) Loo, C., Lin, A., Hirsch, L., Lee, M. H., Barton, J., Halas, N., West, J., and Drezek, R. (2004) Nanoshell-enabled photonics-based imaging and therapy of cancer. *Technol. Cancer Res. Treat. 3*, 33–40.
(30) Daniel, M. C., and Astruc, D. (2004) Gold nanoparticles: Assembly, supramolecular chemistry, quantum-size-related properties, and applications toward biology, catalysis, and nanotechnology. *Chem. Rev. 104*, 293–346.
(31) Wang, Z., Levy, R., Fernig, D. G., and Brust, M. (2005) The peptide route to multifunctional gold nanoparticles. *Bioconjugate Chem. 16*, 497–500.
(32) Levy, R., Thanh, N. T. K., Doty, R. C., Hussain, I., Nichols, R. J., Schiffrin, D. J., Brust, M., and Fernig, D. G. (2004) Rational and combinatorial design of peptide capping Ligands for gold nanoparticles. *J. Am. Chem. Soc. 126*, 10076–10084.
(33) Zharov, V. P., Mercer, K. E., Galitovskaya, E. N., and Smeltzer, M. S. (2006) Photothermal nanotherapeutics and nanodiagnostics for selective killing of bacteria targeted with gold nanoparticles. *Biophys. J. 90*, 619–627.
(34) Zharov, V. P., Galitovskaya, E. N., Johnson, C., and Kelly, T. (2005) Synergistic enhancement of selective nanophotothermolysis with gold nanoclusters: Potential for cancer therapy (vol 37, pg 219, 2005). *Lasers Surg. Med. 37*, 329–329.
(35) Paciotti, G. F., Kingston, D. G. I., and Tamarkin, L. (2006) Colloidal gold nanoparticles: A novel nanoparticle platform for developing multifunctional tumor-targeted drug delivery vectors. *Drug Dev. Res. 67*, 47–54.
(36) Xu, Z. P., Zeng, Q. H., Lu, G. Q., and Yu, A. B. (2006) Inorganic nanoparticles as carriers for efficient cellular delivery. *Chem. Eng. Sci. 61*, 1027–1040.
(37) Janmaat, M. L., Rodriguez, J. A., Jimeno, J., Kruyt, F. A. E., and Giaccone, G. (2005) Kahalalide F induces necrosis-like cell death that involves depletion of ErbB3 and inhibition of Akt signaling. *Mol. Pharmacol. 68*, 502–510.
(38) GarciaRocha, M., Bonay, P., and Avila, J. (1996) The antitumoral compound Kahalalide F acts on cell lysosomes. *Cancer Lett. 99*, 43–50.
(39) Sewell, J. M., Mayer, I., Langdon, S. P., Smyth, J. F., Jodrell, D. I., and Guichard, S. M. (2005) The mechanism of action of Kahalalide F: Variable cell permeability in human hepatoma cell lines. *Eur. J. Cancer 41*, 1637–1644.
(40) Rademaker-Lakhai, J. M., Horenblas, S., Meinhardt, W., Stokvis, E., de Reijke, T. M., Jimeno, J. M., Lopez-Lazaro, L., Martin, J. A. L., Beijnen, J. H., and Schellens, J. H. M. (2005) Phase I clinical and pharmacokinetic study of Kahalalide F in patients with advanced androgen refractory prostate cancer. *Clin. Cancer Res. 11*, 1854–1862.
(41) Hamann, M. T., Otto, C. S., Scheuer, P. J., and Dunbar, D. C. (1996) Kahalalides: Bioactive peptide from a marine mollusk *Elysia rufescens* and its algal diet *Bryopsis* sp. *J. Org. Chem. 61*, 6594–6600.
(42) Pardo, B., Paz-Ares, L., Tabernero, J., Ciruelos, E., Garcia, M., Salazar, R., Lopez, A., Blanco, M., Nieto, A., Jimeno, J., Izquierdo, M. A., and Trigo, J. M. (2008) Phase I clinical and pharmacokinetic study of kahalalide F administered weekly as a 1-h infusion to patients with advanced solid tumors. *Clin. Cancer Res. 14*, 1116–1123.
(43) Spengler, J., Jimenez, J. C., Burger, K., Giralt, E., and Albericio, F. (2005) Abbreviated nomenclature for cyclic and branched homo- and hetero-detic peptides. *J. Pept. Res. 65*, 550–555.
(44) Lopez-Macia, A., Jimenez, J. C., Royo, M., Giralt, E., and Albericio, F. (2001) Synthesis and structure determination of kahalalide F. *J. Am. Chem. Soc. 123*, 11398–11401.
(45) Sagara, T., Kato, N., and Kakashima, N. (2002) Electroreflectance study of gold nanoparticles immobilized on an aminoalkanethiol monolayer coated on a polycrystalline gold electrode surface. *J. Phys. Chem. B 106*, 1205–1212.
(46) Jimenez, J. C., Lopez-Macia, A., Gracia, C., Varon, S., Carrascal, M., Caba, J. M., Royo, M., Francesch, A. M., Cuevas, C., Giralt, E., and Albericio, F. (2008) Structure-activity relationship of kahalalide F synthetic analogues. *J. Med. Chem. 51*, 4920–4931.
(47) Chithrani, B. D., Ghazani, A. A., and Chan, W. C. W. (2006) Determining the size and shape dependence of gold nanoparticle uptake into mammalian cells. *Nano Lett. 6*, 662–668.
(48) Bauer, G., Hassmann, J., Walter, H., Haglmuller, J., Mayer, C., and Schalkhammer, T. (2003) Resonant nanocluster technology - from optical coding and high quality security features to biochips. *Nanotechnology 14*, 1289–1311.
(49) Hogemann, D., Ntziachristos, V., Josephson, L., and Weissleder, R. (2002) High throughput magnetic resonance imaging for evaluating targeted nanoparticle probes. *Bioconjugate Chem. 13*, 116–121.
(50) Liu, J. Q., Zhang, Q., Remsen, E. E., and Wooley, K. L. (2001) Nanostructured materials designed for cell binding and transduction. *Biomacromolecules 2*, 362–368.

(51) Marinakos, S. M., Anderson, M. F., Ryan, J. A., Martin, L. D., and Feldheim, D. L. (2001) Encapsulation, permeability, and cellular uptake characteristics of hollow nanometer-sized conductive polymer capsules. *J. Phys. Chem. B 105*, 8872–8876.

(52) West, J. L., and Halas, N. J. (2000) Applications of nanotechnology to biotechnology - Commentary. *Curr. Opin. Biotechnol. 11*, 215–217.

(53) Link, S., and El-Sayed, M. A. (1999) Size and temperature dependence of the plasmon absorption of colloidal gold nanoparticles. *J. Phys. Chem. B 103*, 4212–4217.

(54) Tkachenko, A. G., Xie, H., Liu, Y. L., Coleman, D., Ryan, J., Glomm, W. R., Shipton, M. K., Franzen, S., and Feldheim, D. L. (2004) Cellular trajectories of peptide-modified gold particle complexes: Comparison of nuclear localization signals and peptide transduction domains. *Bioconjugate Chem. 15*, 482–490.

(55) Olmedo, I., Araya, E., Sanz, F., Medina, E., Arbiol, J., Toledo, P., Alvarez-Lueje, A., Giralt, E., and Kogan, M. J. (2008) How changes in the sequence of the peptide CLPFFD-NH2 can modify the conjugation and stability of gold nanoparticles and their affinity for beta-amyloid fibrils. *Bioconjugate Chem. 19*, 1154–1163.

(56) Usually XPS characterizations are performed on silicon oxide surfaces. Silicon surfaces present two signals corresponding to Si2s and Si2p at 165 and 167 eV, respectively. The Si2s and S2 signals overlapped. The use of PMMA instead of a silicon surface is proposed in the present work in order to avoid interference. XPS characterization of the polymer was performed to discard sulphur impurities.

(57) Barr, T. L. (1994) *Modern ESCA: the principles and practice of X-ray photoelectron Spectroscopy*, CRC Press, Boca Raton, FL.

(58) Jain, P. K., Lee, K. S., El-Sayed, I. H., and El-Sayed, M. A. (2006) Calculated absorption and scattering properties of gold nanoparticles of different size, shape, and composition: Applications in biological imaging and biomedicine. *J. Phys. Chem. B 110*, 7238–7248.

(59) Osaki, F., Kanamori, T., Sando, S., Sera, T., and Aoyama, Y. (2004) A quantum dot conjugated sugar ball and its cellular uptake on the size effects of endocytosis in the subviral region. *J. Am. Chem. Soc. 126*, 6520–6521.

(60) Fernandez-Carneado, J., Kogan, M. J., Pujals, S., and Giralt, E. (2004) Amphipathic peptides and drug delivery. *Biopolymers 76*, 196–203.

(61) Lee, K. D., Nir, S., and Papahadjopoulos, D. (1993) quantitative-analysis of liposome-cell interactions invitro-rate constants of binding and endocytosis with suspension and adherent J774-cells and human monocytes. *Biochemistry 32*, 889–899.

BC800362J

Supporting Information

Conjugation of Kahalalide F with gold nanoparticles to enhance *in vitro* antitumoral activity

Leticia Hosta, Mateu Pla-Roca, Jordi Arbiol, Carmen López-Iglesias, Josep Samitier, Luis J. Cruz, Marcelo J. Kogan, and Fernando Albericio

Solid-Phase Synthesis …….. 2

Characterization of P1 and P2 ……... 3

RP-HPLC chromatograms……..…… 3

MALDI-TOF spectras……...…… 4

TEM of unconjugated gold nanoparticles …….. 5

XPS spectra ……...……8

Quantification of gold nanoparticles loading…… 9

HRTEM conjugated GNPs……. 9

Amino acid analysis ……..……..……. 10

Anti-proliferation assay……. 11

Solid-Phase Synthesis

Two epimer peptides were synthesized using the Fmoc solid-phase strategy in polypropylene syringes fitted with polyethylene porous disks. Side chains of Fmoc aminoacids were protected as follows: Thr was protected with the *tert*-butyl group (tBu) and Cys with the trityl group (Trt). Solvents and soluble reagents were removed by suction. Washings between deprotection, couplings and subsequent deprotection steps were carried out with DMF and DCM using 10 mL of solvent/g of resin each time. The Fmoc group was removed by treatment with piperidine: DMF (1:4) for 20 min. All syntheses were performed on Cl-TrtCl resin (100 mg each peptide). Couplings of all Fmoc-aa-OH (4 equiv) except with the dipeptide Alloc-Phe-(Z)Dhb-OH were performed with DIC (4 equiv) and HOAt (4 equiv) in DMF for 1.5 h at room temperature. Recouplings were done with PyBOP (4 equiv), HOAt (4 equiv) and DIEA (12 equiv) for 1.5 h at room temperature. The coupling of dipeptide Alloc-Phe-(Z)Dhb-OH (1 equiv) was performed with DIEA (1 equiv) for 5 min , DIEA (2 equiv) for 1 h. The resin was washed with DMF and DCM after each coupling. After each coupling, the capping steps were performed with Ac_2O: DIEA: DMF (4:2:94) but with the dipeptide Alloc-Phe-(Z)Dhb-OH the capping step was done with Methanol (300 μL).

Alloc group was removed with $Pd(PPh_3)_4$ (0.1 equiv) in the presence of $PhSiH_3$ (10 equiv) during 15 min and it was repeated three times.

To cleave the peptide from the solid support, the resin was washed with DCM (3 x 1 min), dried, and then washed again with a mixture TFA: DCM (1:99) (6 x 1 min) and washed with DCM and the filtered was collected in a round-bottom flask which contained 100 μL H_2O and 50 μL DIEA. TFA was then removed by evaporation under reduced pressure, and peptides were precipitated with cold anhydrous TBME, dissolved in H_2O: MeCN (1:1) and then lyophilized. The two peptides were cycled upon dissolution in a PyAOP (4 equiv) and DIEA (8 equiv) solution. It was then stirred at room temperature for 24 h. Cyclization was monitored RP-HPLC. The solution was then evaporated with N_2 , dissolved in

H_2O: MeCN(1:1) and then lyophilized. The crude peptides were purified by semi-preparative HPLC.

Characterization of P1 and P2

Code	t_r (HPLC-RP) *min	% Purity (HPLC-RP)	Mass Calc.	Mass Exp. (*m/z*) $[M+1]^+$, $[M+Na]^+$ and $[M+K]^+$
P1	10,57	95,69	1480,89	1481,89/ 1503,89/ 1519,89
P2	10,39	97,67	1480,89	1481,89/ 1503,89/ 1519,89

* using a gradient H_2O: MeCN 0: 30 to 30: 70 in 15 min.

Table 1: Characterization of P1 and P2

RP-HPLC chromatograms

P1

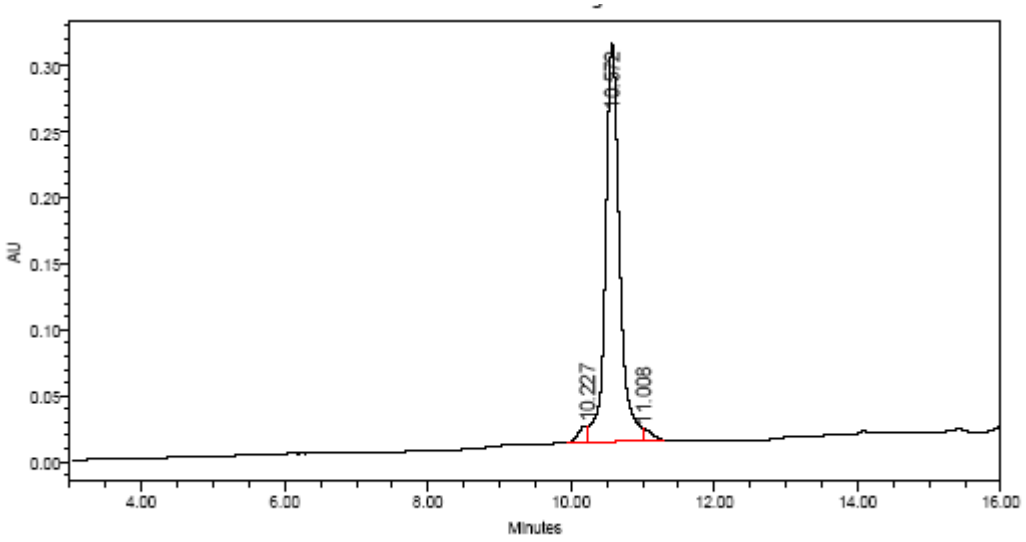

P2

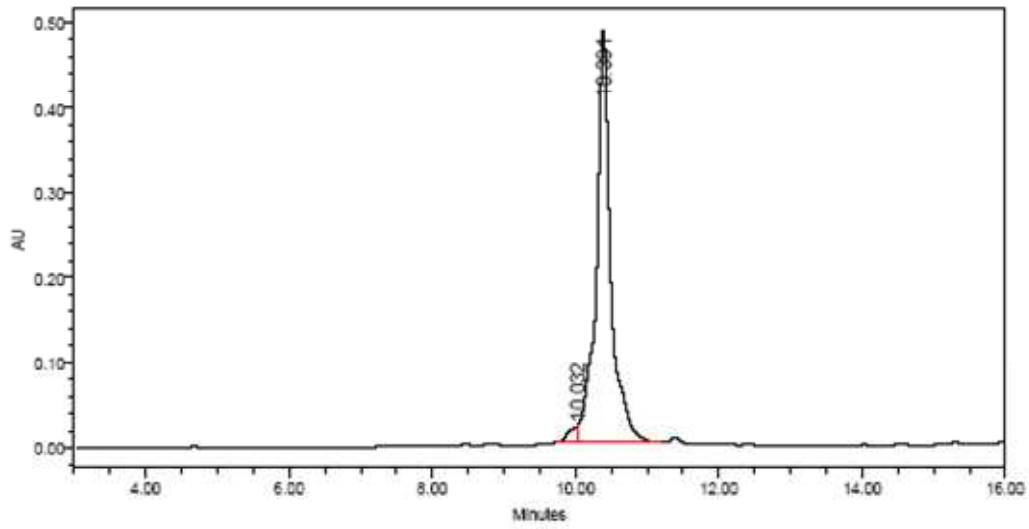

MALDI-TOF spectra

P1

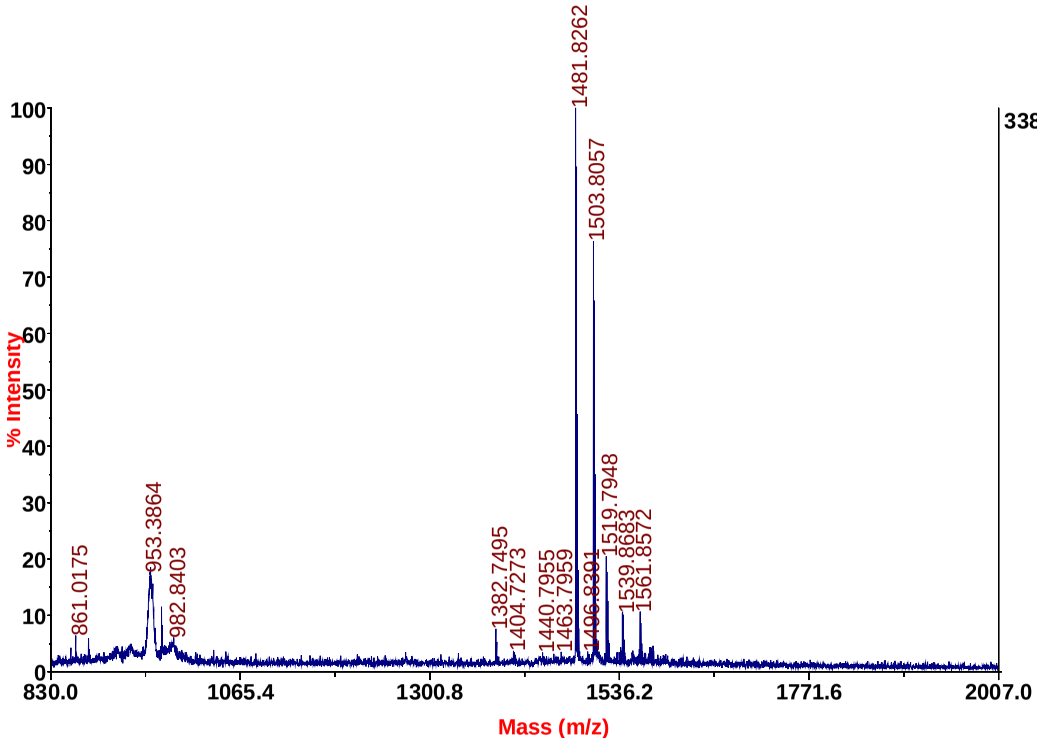

P2

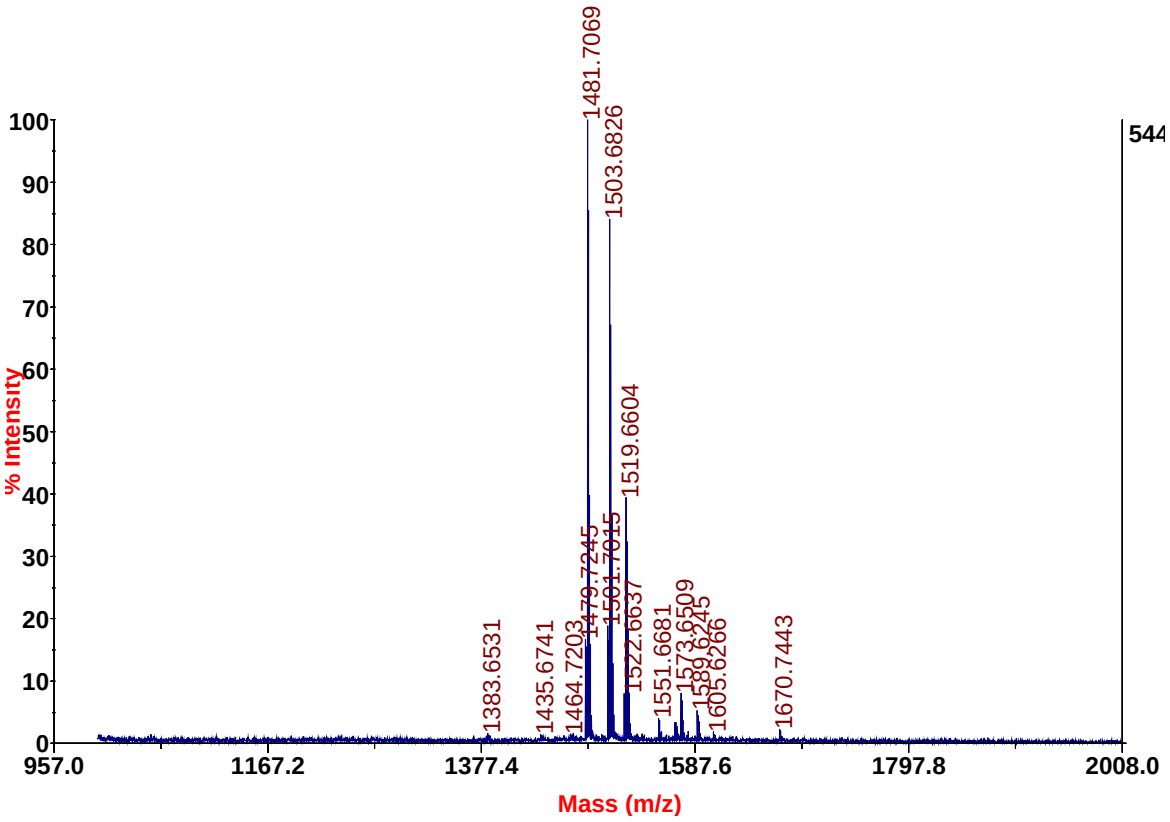

TEM of unconjugated gold nanoparticles

Drops of bare gold nanoparticles were deposited over carbon-coated Formvar films on copper grids. The samples were viewed with a transmission electron microscope (JEOL JEM 1010 (Japan)) at an accelerating voltage of 80 kV. The images were obtained with a CCD Megaview III (SIS) camera (Münster, Germany).

The gold nanoparticles were free from aggregation, and had a size variation of either 7% (for the 20 nm nanoparticles) or 10% (for the 40 nm nanoparticles).

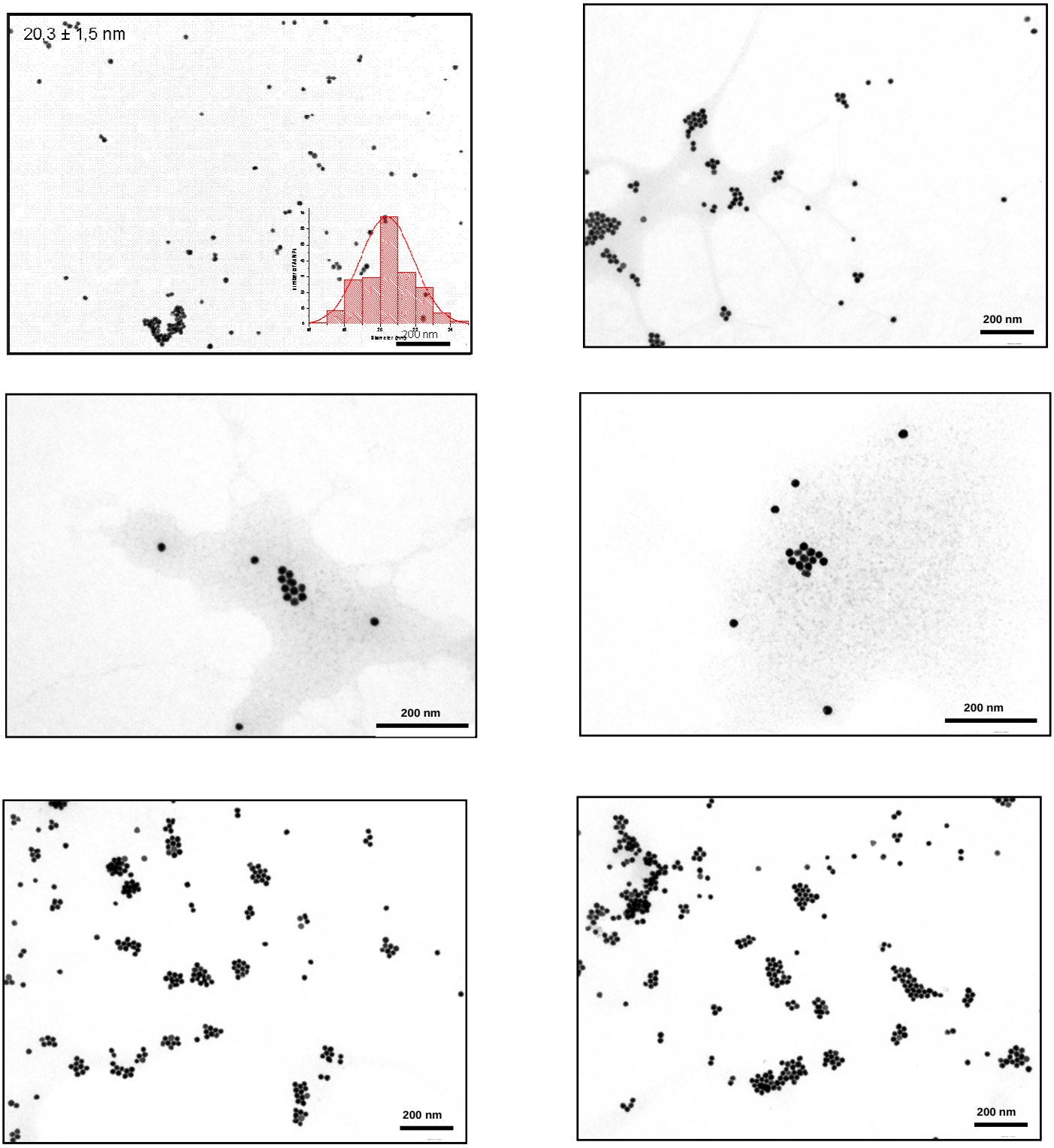

Figure S1. TEM images of 20 nm gold nanoparticle solution.

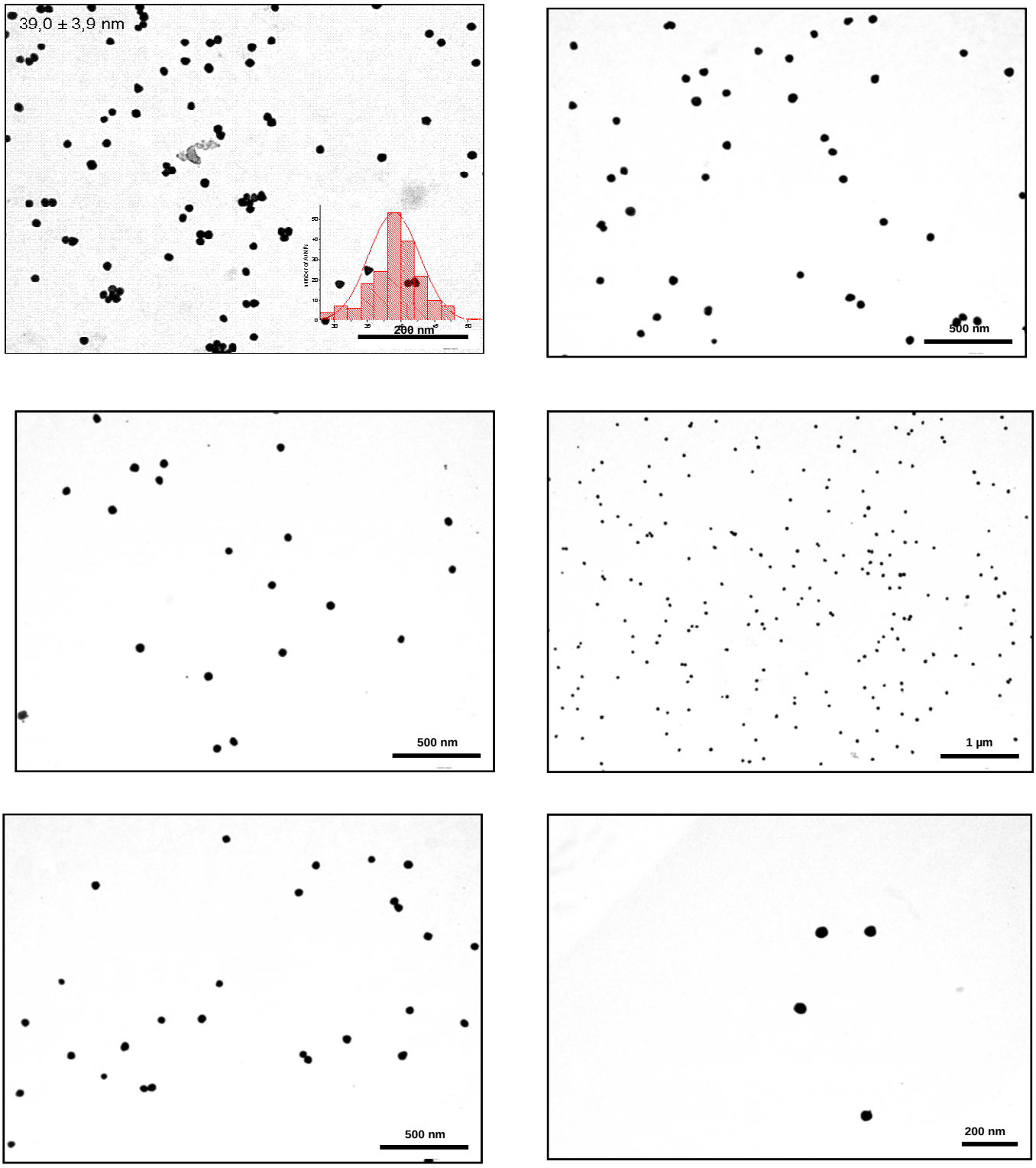

Figure S2. TEM images of 40 nm gold nanoparticle solution

XPS

The XPS spectra were centred at 163.2 eV. Based on the various chemical environments of the sulphur atom, two different groups of chemical states can be differentiated. One group corresponds to the sulphur present in the unreacted peptide and the second group corresponds to the chemisorbed sulphur. Subgroups, such as the difference in chemical shift induced by various metal absorbing sites[1], can be identified.

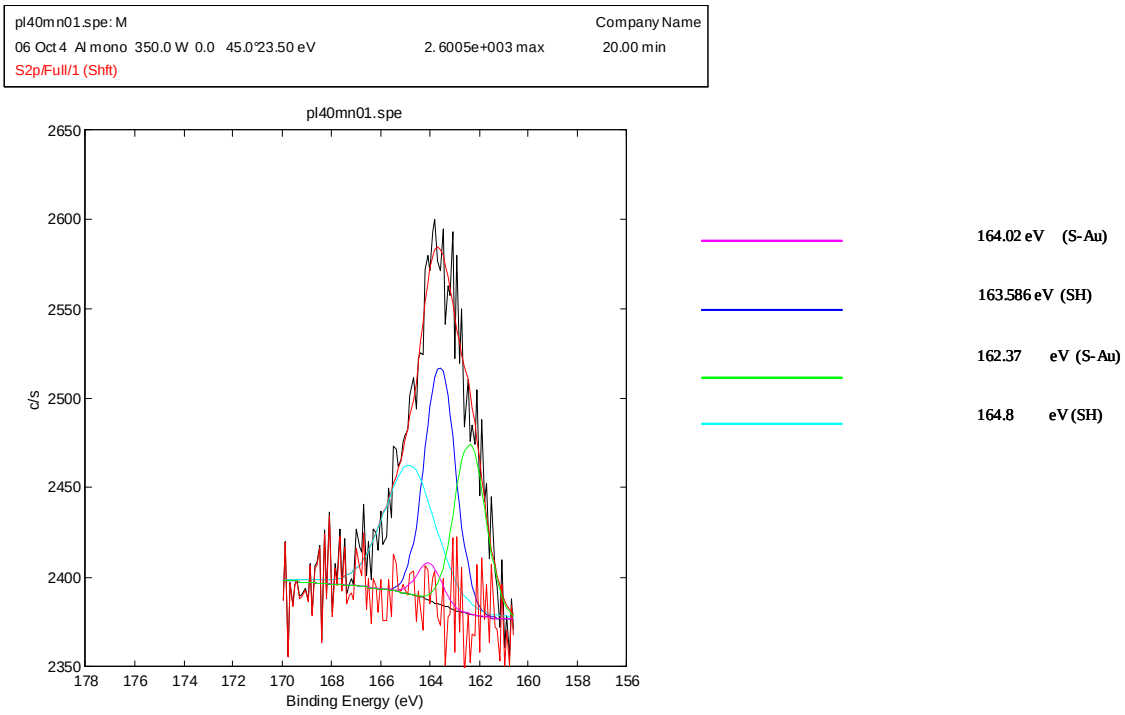

Figure S3. High-resolution XPS spectra of S 2p photoelectrons of P1-20 nm gold conjugates.

Quantification of gold nanoparticle loading

Aliquots (3 mL) of both conjugated solutions were centrifuged at 13,500 rpm for 30 min (AuNP-peptide sediments). The supernatant was lyophilised, and then analysed by HPLC. The resulting chromatogram was interpolated into the calibration curve. The percentage of unconjugated peptide was thus determined to be ca. 15 %.

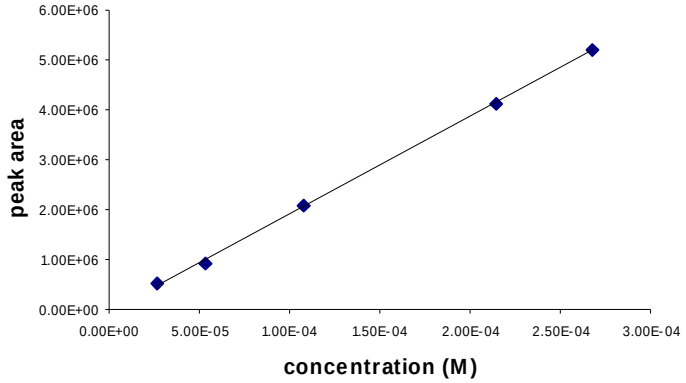

Figure S4. Calibration curve of P1: concentration of P1 is plotted against the area of the HPLC peak.

HRTEM

P1-20-GNP

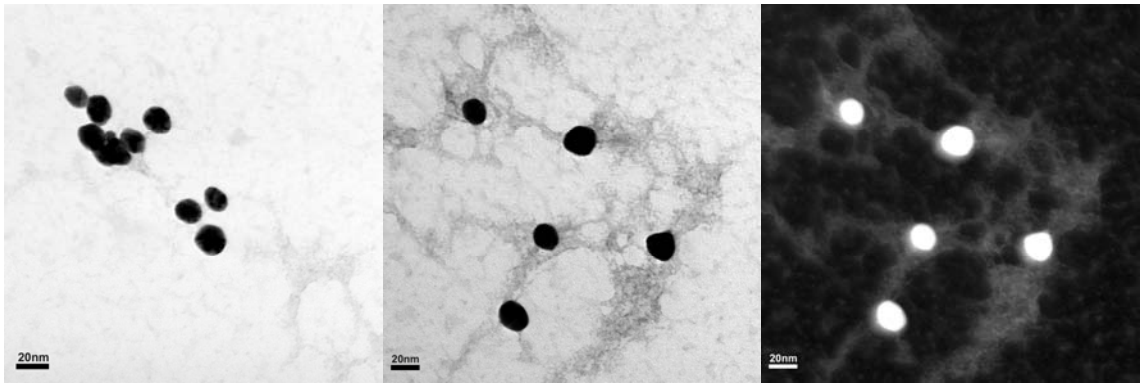

Figure S4. **HRTEM image of** P1-20-GNP.

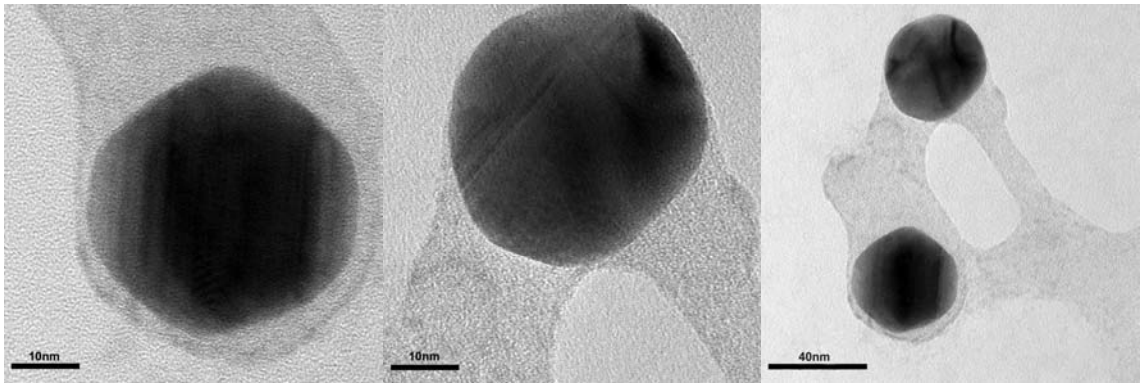

Figure S5. **HRTEM image of** P1-40-GNP.

Amino acid analysis

The relationship among the concentrations of the amino acids valine, isoleucine and proline is 4: 2: 1 in P1 and P2. The same relationship was observed on the gold conjugates by means of amino acid analysis, showing that no disruption of the peptides occurs, proving that the peptides maintain their integrity during the conjugation and dialysis process.

Amino acid analysis was carried out by the AccQ.Tag method after acid hydrolysis with HCl (6N) for 24 hours at 110°C. The analysis was performed in a Waters Delta 600 RP-LC system with UV detection at 254 nm. Each peptide was thus determined to contain four Val, two Ile and one Pro.

	Val (mM) (4)	Ile (mM) (2)	Pro (mM) (1)
P1 20 nm gold nanoparticle	0.2486	0.1279	0.0663
P2 20 nm gold nanoparticle	0.9465	0.4717	0.2925
P1 40 nm gold nanoparticle	0.4512	0.2299	0.1326
P2 40 nm gold nanoparticle	1.1504	0.7323	0.4902

Anti-proliferation assay

HeLa viability in the presence of unconjugated or conjugated nanoparticles was tested using a WST 1 assay, including a control with no nanoparticles added. For each assay 3.5 x 10^3 cells/cm^2 were seeded on a 96-well plate (Nalge Nunc) and cultured for 24 h. The conjugates were added in a 1:4 (conjugate/DMEM) ratio. Cells were incubated for 24 h at 37º C under a 5% CO_2 atmosphere. After 20 h, WST 1 was added. The cells with the conjugate solutions were incubated for a further 4 h. Cell viability is expressed as a percentage ratio of cells treated with the different compounds against untreated cells. All determinations were carried out in sextuplicate and Tukey's multiple comparison test after one-way ANOVA statistics was also performed.

Tukey's Multiple Comparison Test	**P value**
control vs SDS	P < 0.001
control vs AuNP-20nm	P < 0.001
control vs AuNP-20-P1	P < 0.001

control vs AuNP-P2	P < 0.001
control vs P1	P < 0.001
control vs P2	P > 0.05
SDS vs AuNP-20nm	P < 0.001
SDS vs AuNP-20-P1	P > 0.05
SDS vs AuNP-P2	P < 0.001
SDS vs P1	P < 0.001
SDS vs P2	P < 0.001
AuNP-20nm vs AuNP-20-P1	P < 0.001
AuNP-20nm vs AuNP-P2	P > 0.05
AuNP-20nm vs P1	P < 0.001
AuNP-20nm vs P2	P < 0.01
AuNP-20-P1 vs AuNP-P2	P < 0.001
AuNP-20-P1 vs P1	P < 0.001
AuNP-20-P1 vs P2	P < 0.001
AuNP-P2 vs P1	P < 0.001
AuNP-P2 vs P2	P < 0.001
P1 vs P2	P < 0.001

Tukey's Multiple Comparison Test	P value
control vs SDS	P < 0.001

control vs AuNP-40nm	P < 0.001
control vs AuNP-P1	P < 0.001
control vs AuNP-P2	P < 0.001
control vs P1	P < 0.001
control vs P2	P < 0.001
SDS vs AuNP-40nm	P < 0.001
SDS vs AuNP-P1	P > 0.05
SDS vs AuNP-P2	P < 0.001
SDS vs P1	P < 0.001
SDS vs P2	P < 0.001
AuNP-40nm vs AuNP-P1	P < 0.001
AuNP-40nm vs AuNP-P2	P < 0.001
AuNP-40nm vs P1	P < 0.001
AuNP-40nm vs P2	P < 0.05
AuNP-P1 vs AuNP-P2	P < 0.001
AuNP-P1 vs P1	P < 0.001
AuNP-P1 vs P2	P < 0.001
AuNP-P2 vs P1	P > 0.05
AuNP-P2 vs P2	P < 0.001
P1 vs P2	P < 0.001

[1] Bensebaa, F.; Zhou, Y. ; Deslandes, Y. ; Kruus, E. ; Ellis, T. H. XPS study of metal-sulphur bonds in metal alkanethiolate materials. *Surface Science* **1998**, *405*, L472-L476.

Subscriber access provided by SHEMYAKIN-OVCHINNIKOV INST

Article

Tumor-Specific Detection of an Optically Targeted Antibody Combined with a Quencher-Conjugated Neutravidin "Quencher-Chaser": A Dual "Quench and Chase" Strategy to Improve Target to Nontarget Ratios for Molecular Imaging of Cancer

Mikako Ogawa, Nobuyuki Kosaka, Peter L. Choyke, and Hisataka Kobayashi

Bioconjugate Chem., **2009**, 20 (1), 147-154• DOI: 10.1021/bc8003765 • Publication Date (Web): 12 December 2008

Downloaded from http://pubs.acs.org on May 8, 2009

More About This Article

Additional resources and features associated with this article are available within the HTML version:

- Supporting Information
- Access to high resolution figures
- Links to articles and content related to this article
- Copyright permission to reproduce figures and/or text from this article

View the Full Text HTML

ACS Publications
High quality. High impact.

Bioconjugate Chemistry is published by the American Chemical Society. 1155 Sixteenth Street N.W., Washington, DC 20036

Tumor-Specific Detection of an Optically Targeted Antibody Combined with a Quencher-Conjugated Neutravidin "Quencher-Chaser": A Dual "Quench and Chase" Strategy to Improve Target to Nontarget Ratios for Molecular Imaging of Cancer

Mikako Ogawa, Nobuyuki Kosaka, Peter L. Choyke, and Hisataka Kobayashi*

Molecular Imaging Program, Center for Cancer Research, National Cancer Institute, National Institute of Health. Received September 4, 2008; Revised Manuscript Received November 1, 2008

In vivo molecular cancer imaging with monoclonal antibodies has great potential not only for cancer detection, but also for cancer characterization. However, the prolonged retention of intravenously injected antibody in the blood causes low target tumor-to-background ratio (TBR). Avidin has been used as a "chase" to clear the unbound, circulating biotinylated antibody and decrease the background signal. Here, we utilize a combined approach of a fluorescence resonance energy transfer (FRET) quenched antibody with an "avidin chase" to increase TBR. Trastuzumab, a humanized monoclonal antibody against human epidermal growth factor receptor type 2 (HER2), was biotinylated and conjugated with the near-infrared (NIR) fluorophore Alexa680 to synthesize Tra-Alexa680-biotin. Next, the FRET quencher, QSY-21, was conjugated to avidin, neutravidin (nAv), or streptavidin (sAv), thus creating Av-QSY21, nAv-QSY21, or sAv-QSY21 as "chasers". The fluorescence was quenched in vitro by binding Tra-Alexa680-biotin to Av-QSY21, nAv-QSY21, or sAv-QSY21. To evaluate if the injection of quencher-conjugated avidin derivatives can improve target TBR by using a dual "quench and chase" strategy, both target (3T3/HER2+) and nontarget (Balb3T3/ZsGreen) tumor-bearing mice were employed. The "FRET quench" effect induced by all the QSY21 avidin-based conjugates reduced but did not totally eliminate background signal from the blood pool. The addition of nAv-QSY21 administration increased target TBR mainly because of the "chase" effect where unbound conjugated antibody was preferentially cleared to the liver. The relatively slow clearance of unbound nAv-QSY21 leads to further reductions in background signal by leaking out of the vascular space and binding to unbound antibodies in the extravascular space of tumors, resulting in decreased nontarget tumor-to-background ratios but increased target TBR due to the "FRET quench" effect, because target-bound antibodies were internalized and could not bind to nAv-QSY21. In conclusion, the proposed "quench-and-chase" system combines two strategies, fluorescent quenching and avidin chasing, to improve target TBR and reduce nontarget TBR, which should result in both improved tumor sensitivity and improved specificity.

INTRODUCTION

In vivo molecular cancer imaging with monoclonal antibodies has great potential for cancer detection and characterization. However, a high target tumor signal is required to overcome the high background signal arising from the slow blood clearance of antibodies. "Avidin chase" is a classic method to increase TBR in immunoscintigraphy by reducing background signal arising from circulating unbound antibodies by accelerating hepatic clearance (*1*−*5*). In this method, radiolabeled biotinylated antibodies circulating in the blood are "chased" from the circulation after avidin injection, since the avidin−biotin antibody complex is rapidly removed from circulation in the liver. This "chase" paradigm has recently been applied to dendrimer- and albumin-based MRI contrast agents and optical imaging agents (*6*−*8*).

Activation of optical probes at the target can further increase TBR. The fluorescence signal from optical imaging probes can be deactivated and activated (or "quenched and dequenched") by changing the surrounding environment. FRET is one mechanism of quenching whereby fluorescence energy is transferred from an electronically excited donor molecule to a ground-state acceptor molecule (*9*). Activation can also be achieved with other modalities. For instance, MRI signal from contrast agents can be deactivated and activated (*10,11*). However, the percentage change in signal between the activated and deactivated state is substantially higher for optical imaging. If the acceptor molecule is a quencher, which does not emit light when it returns to the ground state, the fluorescence from the donor molecule is absorbed and the molecular probe is quenched. FRET is observed only when the distance between the donor and the acceptor is less than 100 Å, the so-called Förster radius (*9*). The avidin−biotin linkage allows a FRET interaction to occur between the fluorophore and its quencher, a phenomenon that has been exploited in in vitro assays for many years (*12*−*14*). Thus, when the appropriate pair of fluorophore-quencher molecules is linked via avidin−biotin binding to a carrier molecule, such as an antibody, the fluorescent signal from the donor fluorophore is quenched by the acceptor quencher molecule.

* Correspondence to Hisataka Kobayashi, M.D., Ph.D., Molecular Imaging Program, Center for Cancer Research, National Cancer Institute, NIH, Building 10, Room 1B40, MSC1088, Bethesda, MD 20892-1088. Phone: 301-451-4220; Fax: 301-402-3191; E-mail: kobayash@mail.nih.gov.

10.1021/bc8003765 This article not subject to U.S. Copyright. Published 2009 by the American Chemical Society
Published on Web 12/12/2008

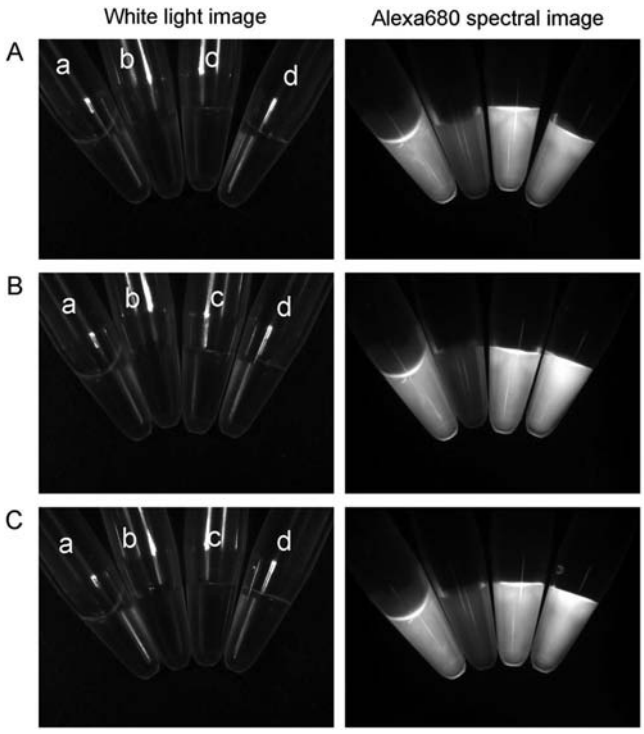

Figure 1. FRET quench by forming Tra-Alexa680-biotin and Av-QSY21 (A), nAv-QSY21 (B), or sAv- QSY21 (C) complexes in vitro. a, Tra-Alexa680-biotin + PBS; b, Tra-Alexa680-biotin + QSY21 conjugated avidin or derivatives; c, Tra-Alexa680 + PBS; d, Tra-Alexa680 + QSY21 conjugated avidin or derivatives. The fluorescence was quenched by forming Tra-Alexa680-biotin and Av- QSY21, nAv-QSY21, or sAv-QSY21 complexes.

In this study, we combined two strategies to improve target TBR: "FRET quenching" and an avidin "chase". Trastuzumab, a humanized monoclonal IgG_1 antibody to human epidermal growth factor receptor type 2 (HER2), was biotinylated and conjugated with a near-infrared (NIR) fluorophore, AlexaFluor680 (Alexa680). To implement this dual "quench and chase" strategy, QSY-21 (quencher) was conjugated to avidin or to one its derivatives, neutravidin or streptavidin, resulting in simultaneous tumor-specific activation (or dequenching) and improved background clearance. This "quench-and-chase" system was evaluated in vivo, using both HER2 positive and negative tumor bearing mice to demonstrate improved target TBR and reduced nontarget TBR.

EXPERIMENTAL PROCEDURES

Reagents. Trastuzumab (Tra), an FDA-approved humanized anti-HER-2 antibody, was purchased from Genentech Inc. (South San Francisco, CA). Alexa680-NHS ester and QSY21-NHS ester were purchased from Invitrogen Corporation (Carlsbad, CA). Amine-reactive biotin, sulfosuccinimidyl-6-(biotin-amido)hexanoate (Sulfo-NHS-LC-Biotin) was purchased from Pierce Chemical Co. (Rockford, IL). ZsGreen plasmid was purchased from Clontech Laboratories, Inc. (Mountain View, CA). All other chemicals used were of reagent grade.

Synthesis of Alexa680 Conjugated Biotinylated Antibody (Tra-Alexa680-biotin). Trastuzumab (6.8 nmol) was incubated with Alexa680-NHS (55 nmol, 5 mM in DMSO) in 0.1 M Na_2HPO_4 (pH 8.5) at room temperature for 30 min. The mixture was purified with a Sephadex G50 column (PD-10; GE Healthcare, Piscataway, NJ). The protein concentration was determined with the Coomassie Plus protein assay kit (Pierce Biotechnology, Rockford, IL) by measuring the absorption at 595 nm with a UV−vis system (8453 Value UV−visible Value System; Agilent Technologies, Santa Clara, CA). The concentration of Alexa680 was measured by absorption with the UV−vis system to confirm the number of fluorophore molecules conjugated to each trastuzumab molecule. The number of Alexa680 per antibody was ∼4−5. The resulting conjugate (Tra-Alexa680) was concentrated using a centrifugal filter device (Centricon YM-30, Millipore, Bedford, MA) to 37 μM. Then, NHS-LC-biotin (195 nmol, 5 mM in DMSO) was added to this solution and reacted in 0.1 M Na_2HPO_4 (pH 8.5) at room temperature for 30 min. Unreacted biotin was separated from antibody by Sephadex G50 column and the Tra-Alexa680-biotin was purified. The biotin labeling ratio was determined by the HABA method (*15*). The number of biotin molecules conjugated to trastuzumab was ∼11.

Synthesis of QSY21 Conjugated Avidin, Neutravidin, and Streptavidin (Av-QSY21, nAv-QSY21, sAv-QSY21). Avidin, neutravidin, or streptavidin (14 nmol) were incubated with

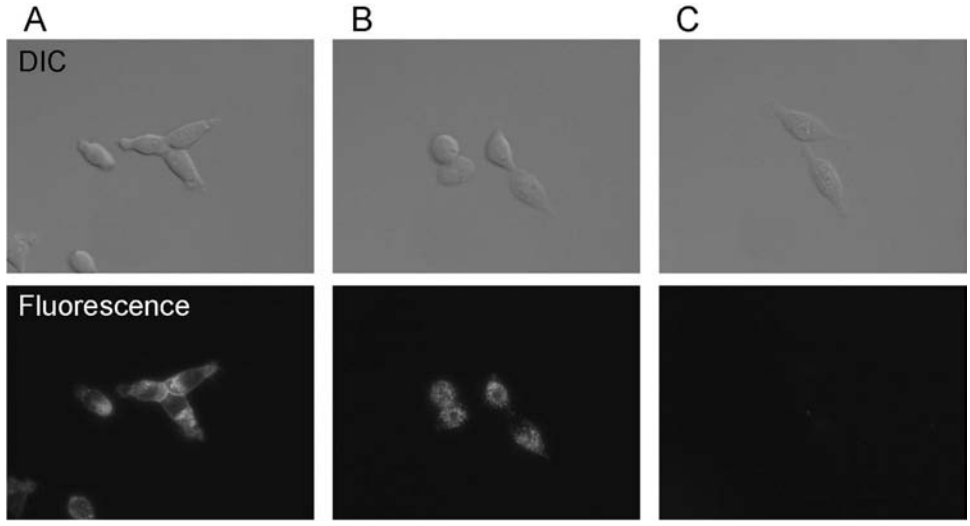

Figure 2. 3T3/HER2+ cell images of (A) 6.5 h after incubation with Tra-Alexa680-biotin, (B) 6 h after incubation with Tra-Alexa680-biotin then added nAv-QSY21 30 min before observation, and (C) 6.5 h after incubation with both Tra-Alexa680-biotin and nAv-QSY21. The bright fluorescence signal was detected on the surface as well as inside the cells with Tra-Alexa680-biotin incubation (A). In contrast, nAv-QSY21 only quenched the fluorescence on the cell surface (B) but not the fluorescence yielded from the internalized antibodies.

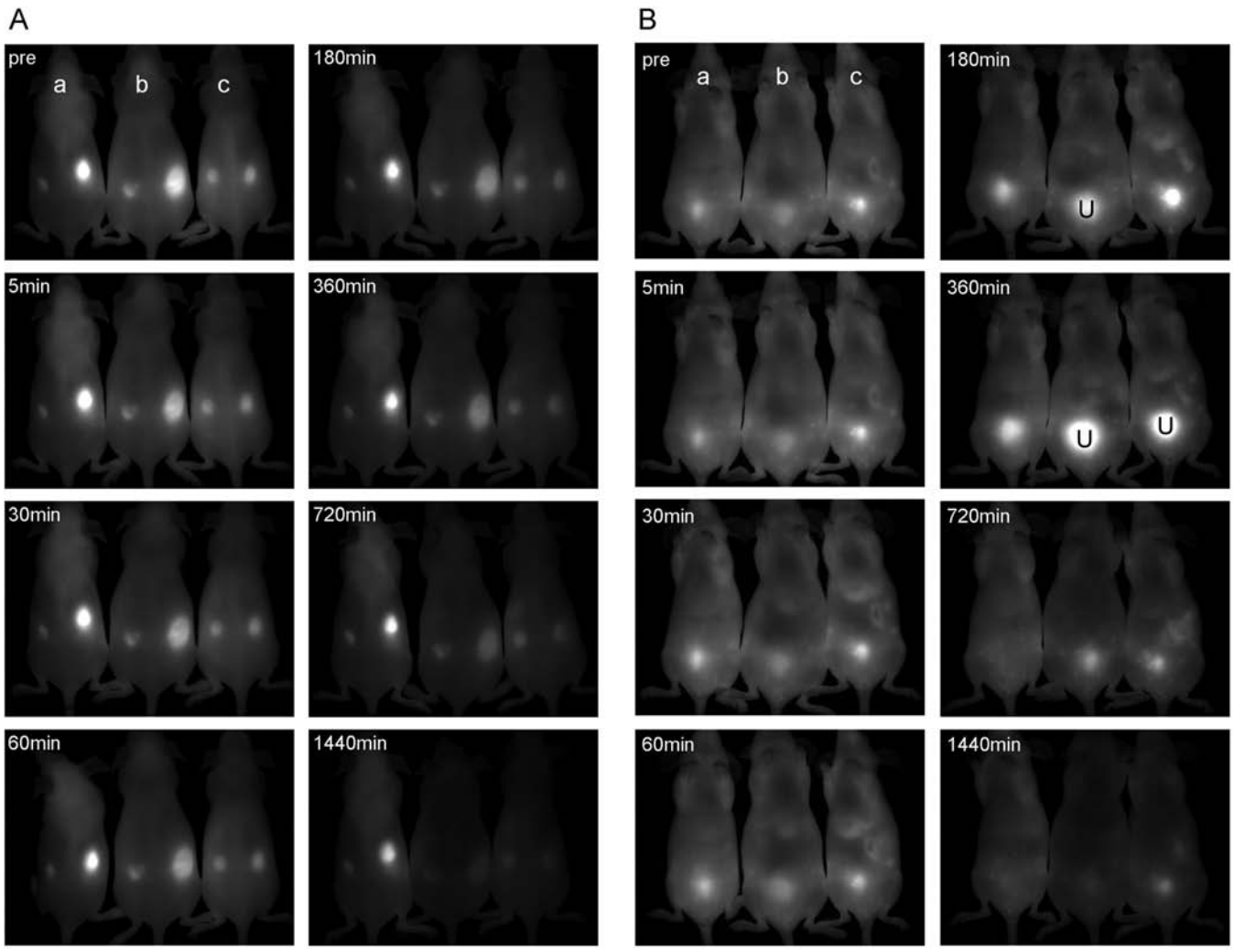

Figure 3. Comparison of Alexa680 spectral images after (b) Av-QSY21 (250 μg, iv) or (c) avidin (250 μg, iv) injection into Tra-Alexa680-biotin treated mice at each time point. (a) nontreated control. A, prone; and B, supine images. Tra-Alexa680-biotin (50 μg, iv) was injected into tumor-bearing mice (left dorsal, 3T3/HER2+; right dorsal, Balb/3T3/ZsGreen HER2− shown in A) one day before avidin treatments. The accumulation in the lower abdomen shown in B is the urine (U) in the bladder.

QSY21-NHS (42 nmol, 12 mM in DMSO) in 0.1 M Na_2HPO_4 (pH 8.5) at room temperature for 30 min. Each mixture was purified with a Sephadex G50 column. The concentrations of protein and QSY21 were measured as described above. The number of QSY21 per avidin or avidin derivative was approximately 1.

Determination of FRET Quench Effect with Complexes of Tra-Alexa680-biotin and Av-QSY21, nAv-QSY21, or sAv-QSY21 in Vitro. Tra-Alexa680-biotin (0.034 nmol in 100 μL PBS) was mixed with Av-QSY21, nAv-QSY21, or sAv-QSY21 (0.171 nmol in 100 μL PBS). For control, Av-QSY21, nAv-QSY21, or sAv-QSY21 was mixed with Tra-Alexa680. The change in fluorescence intensity was investigated with the Maestro In Vivo Imaging System (CRi Inc., Woburn, MA) using 671 to 705 nm excitation and 750 nm long-pass emission filters.

Determination of FRET Quench Effect before and after Cell Binding of Tra-Alexa680-biotin. 3T3/HER2+ (1×10^4) were plated on a cover glass-bottomed culture well and incubated for 16 h. Then, Tra-Alexa680-biotin was added to the medium (10 μg/mL), and the cells were incubated for 6 h. Then, to check the quench effect, nAv-QSY21 was added to the medium (50 μg/mL) and the cells were incubated for an additional 30 min. As a control, the cells were incubated with Tra-Alexa680-biotin for 6.5 h without nAv-QSY21 or incubated for 6.5 h with both Tra-Alexa680-biotin and nAv-QSY21. Cells were washed once with PBS, and fluorescence microscopy was performed using an Olympus BX51 microscope (Olympus America, Inc., Melville, NY) equipped with the following filters: excitation wavelength 590 to 650nm, emission wavelength 662.5 to 747.5 nm. Transmitted light differential interference contrast (DIC) images were also acquired.

Mouse Tumor Model. All procedures were carried out in compliance with the Guide for the Care and Use of Laboratory Animal Resources (1996), National Research Council, and approved by the local Animal Care and Use Committee.

The *HER2* gene transfected NIH3T3 (3T3/HER2+) cell line was the positive control, and green fluorescence protein transfected Balb/3T3 cell line (Balb/3T3/ZsGreen) was used as a negative control, since the Balb/3T3/ZsGreen cell line does not express HER2 receptor. The cell lines were grown in RPMI 1640 (Life Technologies, Gaithersburg, MD) containing 10% fetal bovine serum (Life Technologies), 0.03% L-glutamine, 100 units/mL penicillin, and 100 μg/mL streptomycin in 5% CO_2 at 37 °C.

Both receptor-positive and -negative tumor cell lines were implanted in the same mice. 3T3/HER2+ cells (2×10^6 cells in PBS) were injected subcutaneously in the left dorsum, and Balb/3T3/ZsGreen cells (2×10^6 cells in PBS) were injected

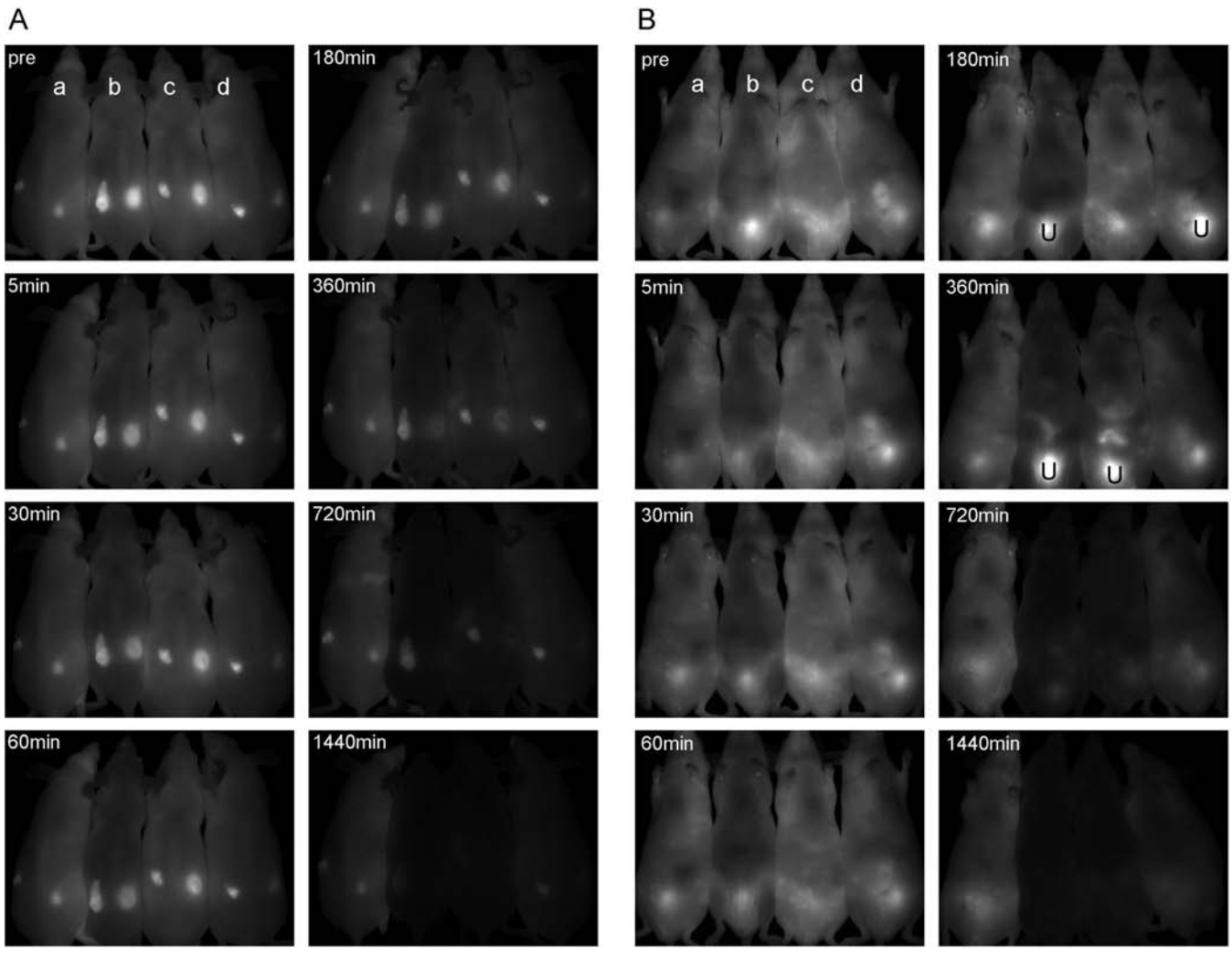

Figure 4. Comparison of Alexa680 spectral images after (b) nAv-QSY21 (250 μg, iv), (c) neutravidin (250 μg, iv), or (d) Av-QSY21 (250 μg, iv) injection into Tra-Alexa680-biotin treated mice at each time point. (a) nontreated control. A, prone; and B, supine images. Tra-Alexa680-biotin (50 μg, iv) was injected into tumor-bearing mice (left dorsal, 3T3/HER2+; right dorsal, Balb/3T3/ZsGreen HER2− shown in A) one day before neutravidin treatments. The accumulation in the lower abdomen shown in B is the urine (U) in the bladder.

subcutaneously into the right dorsum. The experiments were performed at 5−8 days after cell injection.

In Vivo Spectral Imaging Studies. Tra-Alexa680-biotin (50 μg) was injected via the tail vein into tumor-bearing (3T3/HER2+ and Balb/3T3/ZsGreen HER2-) mice ($n = 4$ in each group). One day after the Tra-Alexa680-biotin injection, the mice were anesthetized with intraperitoneally administered 10% sodium pentobarbital with 0.1% scopolamine butyl bromide, then spectral fluorescence images were obtained using the Maestro In Vivo Imaging System (CRi Inc., Woburn, MA) using two filter sets. The deep red filter sets were used to image Alexa680 fluorescence, and the blue filter sets were used for ZsGreen fluorescence. The deep red filter sets use a band-pass filter from 642 to 680 nm (excitation) and a long-pass filter over 702 nm (emission); the blue filter sets use a band-pass filter from 437 to 476 nm (excitation) and a long-pass filter over 493 nm (emission). The tunable emission filter was automatically stepped in 10 nm increments from 650 to 950 nm for the deep red filter sets and from 500 to 800 nm for the blue filter sets, while the camera captured images at each wavelength interval with constant exposure.

After taking the images, Av-QSY21, nAv-QSY21, or sAv-QSY21 (250 μg) were injected via tail vein into mice already injected with Tra-Alexa680-biotin. Then, fluorescence images were obtained in the same manner as described above at 5, 30, 60, 180, 360, 720, and 1440 min after the Av-QSY21, nAv-QSY21, or sAv-QSY21 injection. The spectral fluorescence images were then unmixed on the basis of their spectral patterns using commercial software (*Nuance* software, CRi, Inc., Woburn, MA). Prone images were used for fluorescence intensity measurement. Regions of interest measurements were placed on the Alexa680 spectrum images with reference to the white light and ZsGreen spectrum images to measure the fluorescence intensities of the 3T3/HER2+ and Balb/3T3/ZsGreen HER2- tumor. For the background signal, regions of interest were placed between the tumors. Data are presented as the mean ± SD. Statistical analysis was carried out using the Mann−Whitney *U*-test.

RESULTS

Complexes of Tra-Alexa680-biotin and Av-QSY21, nAv-QSY21, or sAv-QSY21 Are Quenched. As shown in Figure 1, the fluorescence was quenched by adding Av-QSY21, nAv-QSY21, or sAv-QSY21 to the Tra-Alexa680-biotin solution. The quenching capacities were 2.4-, 4.4-, and 3.2-fold for Av-QSY21, nAv-QSY21, or sAv-QSY21, respectively. On the other hand, there was no effect on non-biotinylated probe, Tra-Alexa680.

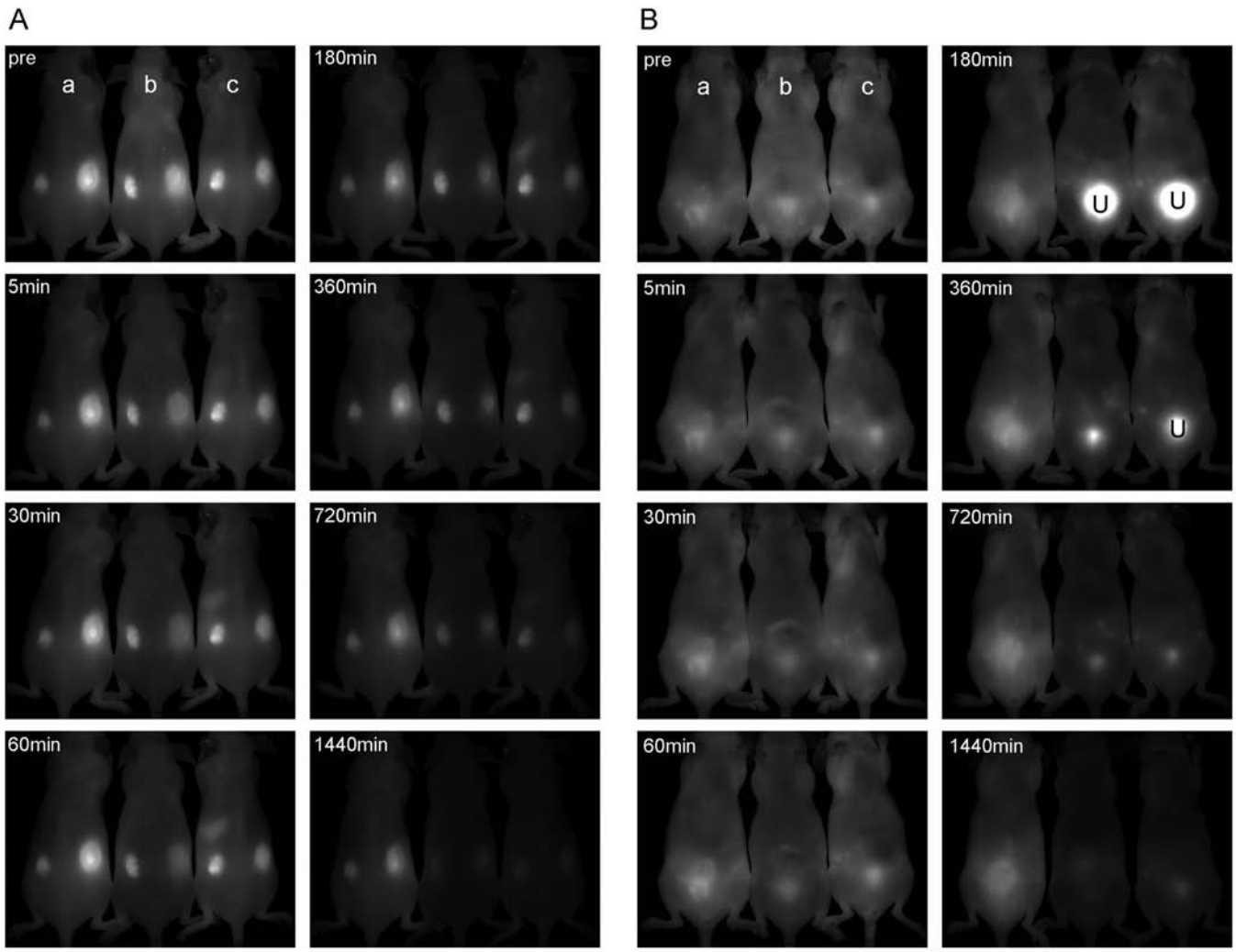

Figure 5. Comparison of Alexa680 spectral images after (b) sAv-QSY21 (250 μg, iv) or (c) streptavidin (250 μg, iv) injection into Tra-Alexa680-biotin treated mice at each time point. (a) nontreated control. A, prone; and B, supine images. Tra-Alexa680-biotin (50 μg, iv) was injected into tumor-bearing mice (left dorsal, 3T3/HER2+; right dorsal, Balb/3T3/ZsGreen HER2− shown in A) one day before streptavidin treatments. The accumulation in the lower abdomen shown in B is the urine (U) in the bladder.

nAv-QSY21 Quenched Tra-Alexa680-biotin on the Cell Surface but Not Internalized Conjugates. To investigate FRET quenching effects in vitro, fluorescence microscopy studies were carried out. High fluorescence signal was detected on the surface as well as inside of the cells with Tra-Alexa680-biotin incubation alone (Figure 2A). In contrast, after nAv-QSY21 was added quenching was observed at the cell surface (Figure 2B) but not from previously internalized Tra-Alexa680-biotin. When both Tra-Alexa680biotin and nAv-QSY21 were added at the same time, fluorescence signal could not be detected either on the surface or inside the cells even 6.5 h after incubation (Figure 2C).

Pharmacokinetic Effect of Adding Av-QSY21, nAv-QSY21, or sAv-QSY21 to Tra-Alexa680-biotin in Vivo. Figures 3 to 6 show the prone and supine images of tumor-bearing mice with time, respectively. The measured fluorescence values are represented by changes in TBR (=(TBR at each time point)/(TBR at 0 min)) and summarized in Figure 7. The changes in background fluorescence intensity from the body are shown in Figure 8.

The background fluorescence was immediately decreased by all QSY21 conjugated molecules, Av-QSY21, nAv-QSY21, and sAv-QSY21. The largest decrease was observed for nAv-QSY21 treatment. The background fluorescence was decreased only at 180 min postinjection of non-QSY21 conjugated neutravidin or later time points. The decreased level was not significant for avidin-treated mice compared to nontreated controls except for the 1440 min time point. For streptavidin-treated mice, the background level was even higher than the control group at 30 min after the injection, and it was decreased at 180 min and later time points.

After nAv-QSY21 injection, fluorescence from the HER2 negative tumor decreased while the TBR in HER2 positive tumor increased with time. As a result, at 720+ min after injection of the nAv-QSY21 only the HER2 positive tumor was visualized. The unconjugated neutravidin resulted in decreased nontarget tumor-to-background ratio; however, the effect was much weaker than with QSY21-conjugated neutravidin, indicating the combined effects of the "quench and chase" strategy. The sAv-QSY21 complex resulted in decreased fluorescence in the HER2 negative tumor, but the tumor was still barely visible. In addition, since streptavidin does not have a substantial "chase effect", the TBR for HER2 positive tumors did not increase with streptavidin without QSY21 conjugation. The Av-QSY21 and avidin treatment did not result in a difference between targeted and nontargeted tumors, indicating that the avidin or Av-QSY21 primarily affected the unbound antibodies in the circulation.

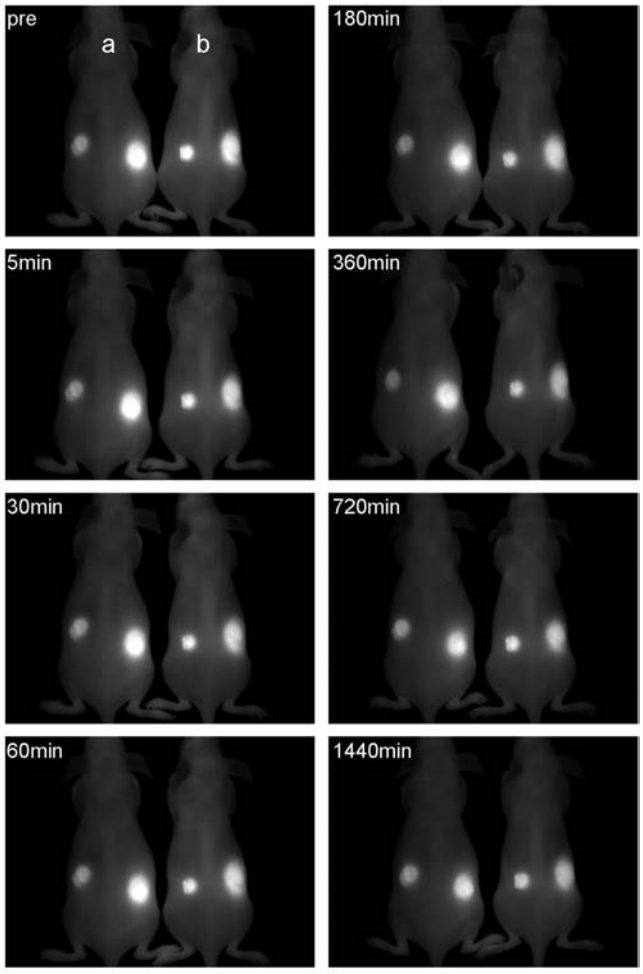

Figure 6. Alexa680 spectral images of non-biotinylated antibody, Tra-Alexa680 treated mice. a, nontreated control; b, nAv-QSY21 (250 μg, iv). No effect was observed by nAv-QSY21 treatment.

The liver fluorescence due to the chase effect was observed at 30 min+ postinjection with avidin and 360 min+ postinjection of neutravidin, but this liver signal was not observed for QSY21-conjugated avidin or neutravidin due to FRET quench effects.

DISCUSSION

To achieve target specific imaging with high tumor TBR, we combined "avidin chase" and "FRET quenching" methods, which reduce background signal by a combination of rapidly clearing unbound conjugate through the liver as well as photochemically quenching non-internalized labeled and biotinylated antibody. As expected, the FRET quencher, QSY21 conjugated to avidin, and its derivatives quenched the fluorescence of extracellular Tra-Alexa680-biotin in vitro (Figure 1). Among the three avidin derivatives, the quenching efficiency was strongest for nAv-QSY21, although the number of biotin binding sites and affinities for biotin are the same for avidin, neutravidin, and streptavidin. Some structural differences including isoelectric points or hydrophilicity in each derivative might affect the steric distance between Alexa680 and QSY21 leading to differences in quenching efficiency. Quenching was only observed when the QSY21−avidin (or derivative) complex was mixed with biotinylated antibody, but not with non-biotinylated antibody. Therefore, quenching is due to the FRET effect between Alexa680 and QSY21 after forming the avidin−biotin bond.

To investigate this phenomenon in vivo, both targeted (3T3/HER2+) and nontargeted (Balb3T3/ZsGreen) tumor-bearing mice were employed. The "FRET quench" effect induced by all QSY21−avidin (and derivatives) reduced background signal from the blood pool just after the injection (Figures 3, 4, 5, and 8). This rapid decline in signal represents the "FRET quench" effect in vivo; non-QSY21 conjugated avidin derivatives, with the exception of avidin, did not decrease background at the initial time point. The injected QSY21−avidin (and derivatives) conjugates rapidly distributed in the circulation and bound to circulating Tra-Alexa680-biotin in the blood forming an avidin−biotin bond, leading to "FRET quenching". The background signal quenching effect was stronger for nAv-QSY21 and sAv-QSY21 than for Av-QSY21. This is likely because the blood clearance of avidin is much faster than for streptavidin (*16, 17*) or neutravidin, which are deglycosylated and neutralized avidins (*18, 19*). The prolonged relative retention of nAv-QSY21 and sAv-QSY21 in circulation increased the likelihood of binding with Tra-Alexa680-biotin, which was distributed in both the vascular and extravascular spaces.

In contrast, unconjugated avidin reduced the background signal as a result of the "chase" effect. The "chase" effect of avidin is quicker than the other avidin derivatives (*20*). A consequence of this faster clearance was that avidin was less effective in "chasing" Tra-Alexa680-biotin that had entered the extravascular space due to the EPR effect, leading to a reduced target-to-nontarget tumor ratio.

In comparison to avidin complexes, the complexes formed by neutravidin and streptavidin and the biotinylated antibody in circulation are more slowly formed and cleared (*20*).

At the initial points, the background signal was increased by nonconjugated streptavidin compared to controls as shown in Figures 4 and 7. We hypothesize that streptavidin, which has minimal "chase" effects, leads to retention of the biotinylated antibody in the circulation by forming streptavidin−biotin antibody complex that leads to a redistribution of Tra-Alexa680-biotin from the extravascular space to the circulation, thus increasing the fluorescence signal of the background. This increase was not observed with sAv-QSY21, because the fluorescence from the circulating streptavidin−biotin antibody complex was quenched by the "FRET effect".

With nAv-QSY21, the slower clearance of neutravidin compared to avidin and the faster clearance of neutravidin−biotin antibody complex compared to streptavidin−biotin antibody complex increased the target TBR because of the "chase" effect, where unbound conjugate was preferentially cleared by the liver. Relatively slow clearance of nAv-QSY21 allows leaking out and binding to the unbound antibodies in the extravascular space, resulting in decreased nontarget TBR but increased target TBR due to the "FRET quench" effect, because target-bound antibodies were internalized and could not bind to nAv-QSY21. In this model, nAv-QSY21 remained in the circulation long enough to leak out and bind nonspecifically to Tra-Alexa680-biotin, which had nonspecifically entered the extravascular space of the nontarget Balb3T3 (HER2−) tumor due to the enhanced permeability and retention (EPR) effect. These nAv-QSY21-biotin antibody complexes were quenched and gradually cleared to the liver. Therefore, the background level was continuously decreased after nAv-QSY21 administration due to the combined effects of "FRET quenching" and background "chasing". On the other hand, neither "quench" nor "chase" effects were observed when non-biotinylated Tra-Alexa680 was used (Figure 6). These results support the dual functionality of nAv-QSY21 as both a "quencher" and a "chaser".

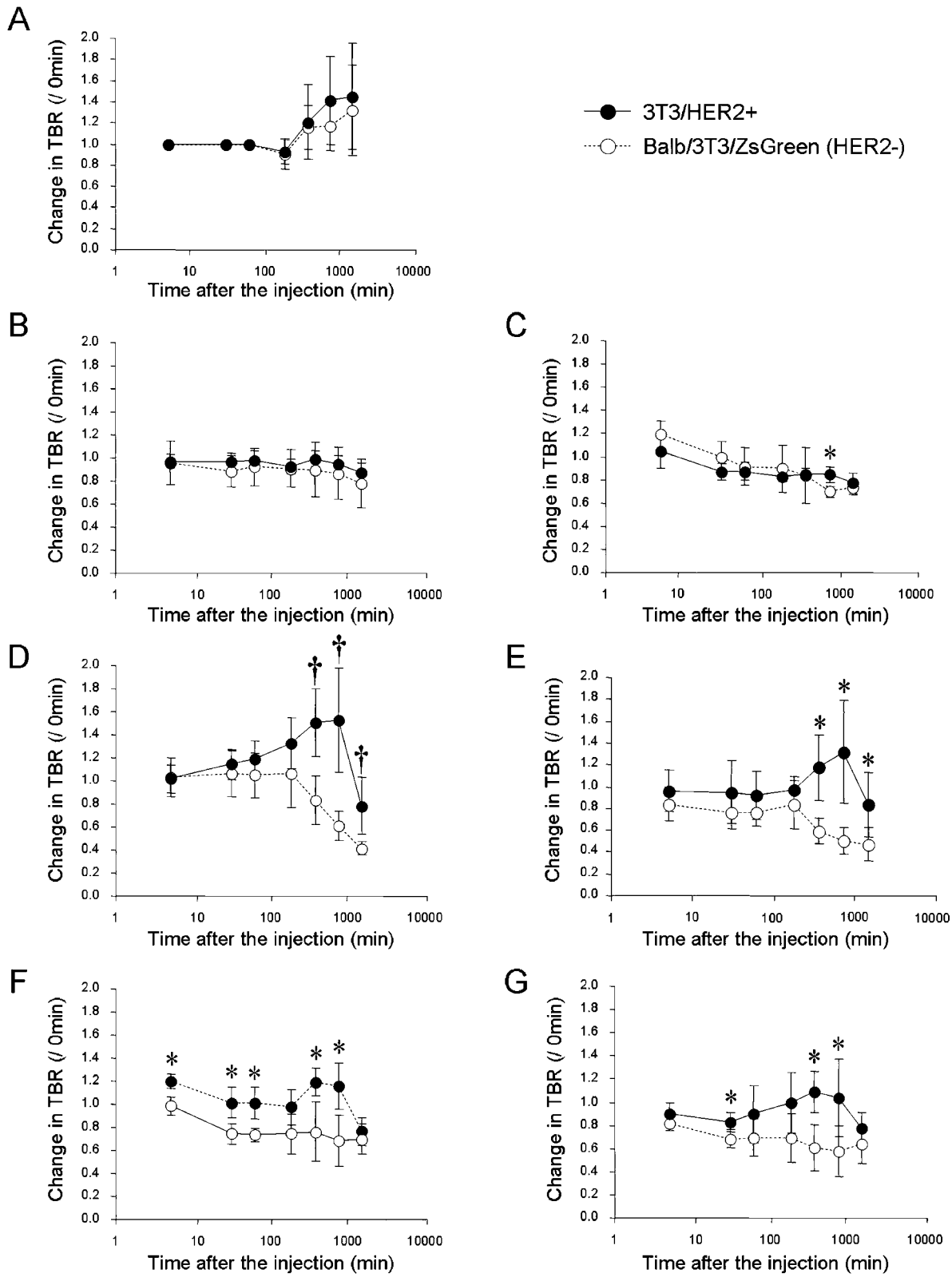

Figure 7. Time courses of changes in fluorescence TBR (TBR in each time point/TBR at 0 min) in HER2 positive and HER2 negative tumors. A, nontreatment; B, Av-QSY21; C, avidin; D, nAv-QSY21; E, neutravidin; F, sAv-QSY21; G, streptavidin. *$P < 0.05$, †$P < 0.005$ (Mann−Whitney U-test) vs HER2 negative tumor in each treated condition.

In conclusion, the proposed "quench and chase" strategy using nAv-QSY21 allowed high TBR in target tumor and reduced TBR in the nontarget tumor, resulting in successful imaging with a fluorescently labeled antibody. This "quench and chase" system can distinguish the tumor-specific targeted antibody fraction from the nonspecific accumulation of the antibody in the tumor due to EPR effects. Recently, multiple pairs of fluorophore−quencher have been developed, and these pairs could be readily adapted for the "quench and chase" strategy. Furthermore, the principle of "quench and chase" can be applied to other carrier molecules, such as peptides, dendrimers, and liposomes, to achieve high TBR during in vivo molecular imaging. Thus, "quench and chase" is a

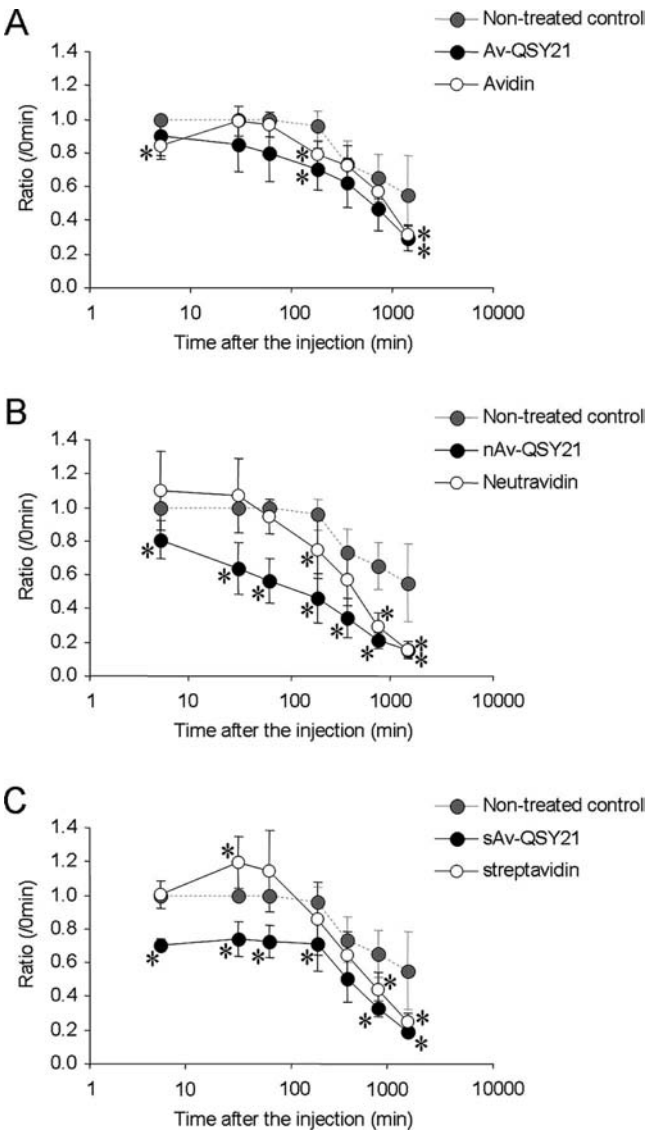

Figure 8. Change in background fluorescence intensities after (A) avidin or Av-QSY21, (B) neutravidin or nAv-QSY21, or (C) streptavidin or sAv-QSY21 treatments. *P < 0.05 (Mann−Whitney U-test) vs non-treated control.

generalizable dual strategy to improve the target TBR of molecular optical probes.

ACKNOWLEDGMENT

This research was supported by the Intramural Research Program of the NIH, National Cancer Institute, Center for Cancer Research.

Supporting Information Available: Change in fluorescence signal in HER2 positive and HER2 negative tumors. This material is available free of charge via the Internet at http://pubs.acs.org.

LITERATURE CITED

(1) Klibanov, A. L., Martynov, A. V., Slinkin, M. A., Sakharov, I., Smirnov, M. D., Muzykantov, V. R., Danilov, S. M., and Torchilin, V. P. (1988) Blood clearance of radiolabeled antibody: enhancement by lactosamination and treatment with biotin-avidin or anti-mouse IgG antibodies. *J. Nucl. Med. 29*, 1951–6.

(2) Sinitsyn, V. V., Mamontova, A. G., Checkneva, Y. Y., Shnyra, A. A., and Domogatsky, S. P. (1989) Rapid blood clearance of biotinylated IgG after infusion of avidin. *J. Nucl. Med. 30*, 66–9.

(3) Kobayashi, H., Sakahara, H., Hosono, M., Yao, Z. S., Toyama, S., Endo, K., and Konishi, J. (1994) Improved clearance of radiolabeled biotinylated monoclonal antibody following the infusion of avidin as a "chase" without decreased accumulation in the target tumor. *J. Nucl. Med. 35*, 1677–84.

(4) Kobayashi, H., Sakahara, H., Endo, K., Yao, Z. S., and Konishi, J. (1996) Inflammation-seeking scintigraphy with radiolabeled biotinylated polyclonal IgG followed by the injection of avidin chase. *Nucl. Med. Biol. 23*, 29–32.

(5) Sato, N., Saga, T., Sakahara, H., Nakamoto, Y., Zhao, S., Kuroki, M., Iida, Y., Endo, K., and Konishi, J. (2000) Avidin chase can reduce myelotoxicity associated with radioimmunotherapy of experimental liver micrometastases in mice. *Jpn. J. Cancer Res. 91*, 622–8.

(6) Dafni, H., Gilead, A., Nevo, N., Eilam, R., Harmelin, A., and Neeman, M. (2003) Modulation of the pharmacokinetics of macromolecular contrast material by avidin chase: MRI, optical, and inductively coupled plasma mass spectrometry tracking of triply labeled albumin. *Magn. Reson. Med. 50*, 904–14.

(7) Kobayashi, H., Kawamoto, S., Star, R. A., Waldmann, T. A., Brechbiel, M. W., and Choyke, P. L. (2003) Activated clearance of a biotinylated macromolecular MRI contrast agent from the blood pool using an avidin chase. *Bioconjugate Chem. 14*, 1044–7.

(8) Hama, Y., Koyama, Y., Choyke, P. L., and Kobayashi, H. (2007) Two-color in vivo dynamic contrast-enhanced pharmacokinetic imaging. *J. Biomed. Opt. 12*, 034016.

(9) Vogel, S. S., Thaler, C., and Koushik, S. V. (2006) Fanciful FRET. *Sci STKE*. re 2.

(10) Querol, M., and Bogdanov, A., Jr. (2006) Amplification strategies in MR imaging: activation and accumulation of sensing contrast agents (SCAs). *J. Magn. Reson. Imaging 24*, 971−82.

(11) Urbanczyk-Pearson, L. M., Femia, F. J., Smith, J., Parigi, G., Duimstra, J. A., Eckermann, A. L., Luchinat, C., and Meade, T. J. (2008) Mechanistic investigation of beta-galactosidase-activated MR contrast agents. *Inorg. Chem. 47*, 56–68.

(12) Grant, S. A., Xu, J., Bergeron, E. J., and Mroz, J. (2001) Development of dual receptor biosensors: an analysis of FRET pairs. *Biosens. Bioelectron. 16*, 231–7.

(13) Oh, E., Hong, M. Y., Lee, D., Nam, S. H., Yoon, H. C., and Kim, H. S. (2005) Inhibition assay of biomolecules based on fluorescence resonance energy transfer (FRET) between quantum dots and gold nanoparticles. *J. Am. Chem. Soc. 127*, 3270–1.

(14) Liu, L., Wei, G., Liu, Z., He, Z., Xiao, S., and Wang, Q. (2008) Two-photon excitation fluorescence resonance energy transfer with small organic molecule as energy donor for bioassay. *Bioconjugate Chem. 19*, 574–9.

(15) Green, N. M. (1965) A spectrophotometric assay for avidin and biotin based on binding of dyes by avidin. *Biochem. J. 94*, 23C–24C.

(16) Schechter, B., Silberman, R., Arnon, R., and Wilchek, M. (1990) Tissue distribution of avidin and streptavidin injected to mice. Effect of avidin carbohydrate, streptavidin truncation and exogenous biotin. *Eur. J. Biochem. 189*, 327–31.

(17) Rosebrough, S. F. (1993) Pharmacokinetics and biodistribution of radiolabeled avidin, streptavidin and biotin. *Nucl. Med. Biol. 20*, 663–8.

(18) Rosebrough, S. F., and Hartley, D. F. (1996) Biochemical modification of streptavidin and avidin: in vitro and in vivo analysis. *J. Nucl. Med. 37*, 1380–4.

(19) Yao, Z., Zhang, M., Sakahara, H., Nakamoto, Y., Higashi, T., Zhao, S., Sato, N., Arano, Y., and Konishi, J. (1999) The relationship of glycosylation and isoelectric point with tumor accumulation of avidin. *J. Nucl. Med. 40*, 479–83.

(20) Kobayashi, H., Sakahara, H., Endo, K., Hosono, M., Yao, Z. S., Toyama, S., and Konishi, J. (1995) Comparison of the chase effects of avidin, streptavidin, neutravidin, and avidin-ferritin on a radiolabeled biotinylated anti-tumor monoclonal antibody. *Jpn. J. Cancer Res. 86*, 310–4.

BC8003765

Supplemental figure 1.

Change in fluorescence signal in HER2 positive and HER2 negative tumors. One day after the Tra-Alexa680-biotin (50 μg, iv) injection, avidin (250 μg, iv) was injected to each mouse. Fluorescence images were obtained in the same manner as described above at 5, 30, 60, 180, 360, 720 and 1440 min after the avidin injection (A). The additional nAv-QSY21 injection (250 μg, iv) was performed 30min after the avidin injection to investigate the quenching effect, and images were obtained in the same manner at 5, 30, 60, 180, 360, 720 and 1440 min after the nAv-QSY21 injection (B). The additionally injected nAv-QSY21 decreased the fluorescence only from HER2 negative tumor. Because the chase effect is mostly performed by previous avidin treatment, these results show the quenching effect of nAv-QSY21.

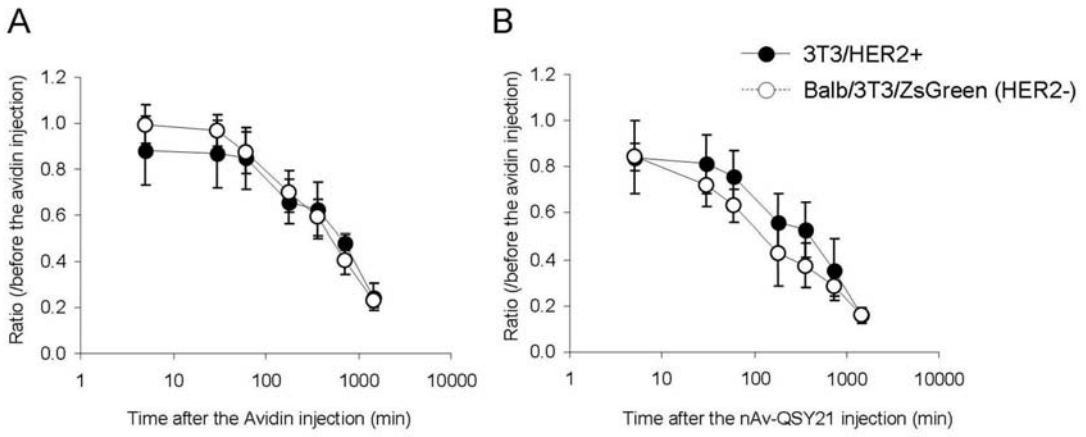

Bioconjugate Chemistry 20th Anniversary

Subscriber access provided by SHEMYAKIN-OVCHINNIKOV INST

Article

Construction of Carbohydrate Microarrays by Using One-Step, Direct Immobilizations of Diverse Unmodified Glycans on Solid Surfaces

Sungjin Park, Myung-Ryul Lee, and Injae Shin

Bioconjugate Chem., **2009**, 20 (1), 155-162• DOI: 10.1021/bc800442z • Publication Date (Web): 05 January 2009

Downloaded from http://pubs.acs.org on May 8, 2009

More About This Article

Additional resources and features associated with this article are available within the HTML version:

- Supporting Information
- Access to high resolution figures
- Links to articles and content related to this article
- Copyright permission to reproduce figures and/or text from this article

View the Full Text HTML

ACS Publications
High quality. High impact.

Bioconjugate Chemistry is published by the American Chemical Society. 1155 Sixteenth Street N.W., Washington, DC 20036

Construction of Carbohydrate Microarrays by Using One-Step, Direct Immobilizations of Diverse Unmodified Glycans on Solid Surfaces

Sungjin Park, Myung-Ryul Lee, and Injae Shin*

Department of Chemistry, Yonsei University, Seoul 120-749, Korea. Received October 15, 2008; Revised Manuscript Received December 3, 2008

Carbohydrate microarrays have received great attention as high-throughput analytic tools in studies of carbohydrate-mediated biological processes. Most of the methods employed to fabricate glycan microarrays rely on the immobilization of modified glycans on the properly derivatized surfaces. This immobilization strategy requires the availability of modified glycans whose syntheses in many cases are time-consuming and difficult. We have developed a simple and direct immobilization technique that involves a one-step, site-specific attachment of diverse unmodified glycans to the hydrazide-derivatized glass surface. To demonstrate the generality of this direct immobilization method, we examined its use for the construction of carbohydrate microarrays containing a variety of glycans. The results of protein and cell-binding experiments indicate that the glycan microarrays, prepared by using this methodology, are applicable to the rapid evaluation of glycan-mediated biomolecular interactions and the determination of quantitative binding affinities between carbohydrates and proteins.

INTRODUCTION

Carbohydrates are vital components of living systems and a large group of biomolecules that are present mainly in the form of glycoconjugates inside or on the surfaces of cells. Through their interactions with proteins, the glycoconjugates are involved in a wide variety of important biological processes, such as cell differentiation, cell adhesion, signaling, trafficking, and immune response (for some recent reviews, see *refs 1*−*3*). Carbohydrate−protein recognition events also play key roles in many pathological processes, including infection by pathogens, cancer cell metastasis, and inflammation processes (*4, 5*). Consequently, the understanding of glycan−protein interactions at the molecular level provides deep insight into glycan-mediated biological processes and enables the development of more effective therapeutic agents and diagnostic tools in the postgenomics era.

Since 2002, carbohydrate microarrays, which are composed of diverse glycans orderly and densely attached to a single chip substrate, have been extensively developed as reliable and efficient tools for the rapid analysis of carbohydrate-based biomolecular interactions (*6*−*9*). The microarray technology has notable advantages over the use of conventional methods, such as the hemagglutination inhibition assay, enzyme-linked lectin assay, surface plasmon resonance (SPR), and isothermal titration calorimetry (ITC). The most significant advantage is that glycan microarrays enable fast, quantitative, and simultaneous analyses of a number of glycan−protein interactions with small amounts of carbohydrate samples. Another notable feature is that glycans immobilized on microarrays strongly interact with proteins, even in cases where the proteins have low binding affinities to the monovalent carbohydrates in solution. This is due to the fact that immobilized glycans display multivalent binding to proteins caused by a cluster effect. Owing to these advantageous characteristics, carbohydrate microarray-based technologies are applicable to high-throughput analyses of glycan−protein interactions.

A variety of carbohydrate microarray formats that use different surfaces and immobilization methods have emerged over the past few years (for some reviews, see *refs 10*−*16*). The most general method for construction of these microarrays involves site-specific and covalent immobilization of chemically modified carbohydrates to properly derivatized surfaces. For example, we have shown that carbohydrate microarrays can be fabricated by attaching maleimide- or hydrazide-conjugated glycans on respective thiol- or epoxide-coated glass surfaces (*6, 17*−*20*). This immobilization strategy requires the use of properly functionalized sugars, which are typically prepared by multistep synthetic sequences. To circumvent the need for synthetically intensive methods, one-step procedures for the preparation of functionally conjugated sugars have been developed and used for the fabrication of glycan microarrays. For example, amine appended sugars have been prepared by reacting free carbohydrates with 2,6-diaminopyridine in the presence of sodium cyanoborohydride or with *N*-methylaminooxy-containing bifunctional linkers (*21, 22*). The modified sugars, generated in these ways, are then covalently immobilized on the NHS ester-coated surfaces.

However, the requirement for derivatization of glycans by either one-step or multistep sequences remains a significant hurdle for the construction of microarrays containing diverse sugars. In order to avoid the need for functionalized glycans, immobilization strategies that employ unmodified sugars have been developed. One approach involves the attachment of ploysaccharides to the nitrocellulose-coated or the black polystyrene-coated surfaces (*8, 9*). This immobilization strategy is limited by a size dependence and nonspecific adsorption of glycans. An alternative approach that does not require modified sugars involves photoinduced covalent attachment of unmodified sugars to surfaces that are coated with photolabile groups (*23*). A major drawback of this technique is associated with nonspecific attachment of glycans to the surfaces.

An ideal method for the construction of carbohydrate microarrays would rely on site-specific, size-independent covalent attachment of unmodified sugars to proper surfaces. In recent investigations directed at this goal, we have developed a novel, direct, site-specific technique for immobilization of unmodified carbohydrates, including simple carbohydrates, oligosaccharides and polysaccharides, on hydrazide- and aminooxy-derivatized

* Corresponding author. (phone) +82-2-2123-2631; (fax) +82-2-364-7050; (e-mail): injae@yonsei.ac.kr.

10.1021/bc800442z CCC: $40.75 © 2009 American Chemical Society
Published on Web 01/05/2009

surfaces (*24*). This method eliminates the need for laborious and tedious glycan derivatization. To demonstrate the scope and applicability of this approach, carbohydrate microarrays containing a variety of glycans (58 glycans) have been constructed by using one-step, direct attachment of free carbohydrates to a hydrazide-coated surface. These microarrays have been employed for analysis of sugar binding specifities of lectins, antibodies, and bacterial cells. In addition, this microarray format has been applied to the determininations of binding affinities between proteins and glycans. The results of these studies, which have led to the development of facile methods to prepare carbohydrate microarrays and their application to investigations of glycan-mediated biomolecular interactions, are described below.

MATERIALS AND METHODS

General. All chemical and biochemical products were of analytical grade and purchased from commercial suppliers: lectins from Vector Laboratories (Peterborough, UK) and Sigma-Aldrich (St. Louis, MO, USA); Cy3 and Cy5 *N*-hydroxysuccinimide from Amersham Pharmacia biotech (Piscataway, NJ, USA); carbohydrates from Sigma-Aldrich, Calbiochem (Gibbstown, NJ, USA), TCI Corporation (Tokyo, Japan), Acros (Morris Plains, NJ, USA), Senn Chemicals (Dielsdorf, Switzerland), Carbohydrate Synthesis (Oxford, UK), Dextra Laboratories (Reading, UK), and GlycoTech Corporation (Gaithersburg, MD, USA); antidextran antibody from Stemcell Technologies Inc. (Vancouver, BC, Canada) and monoclonal antichondroitin 6-sulfate antibody from MP Biochemicals Inc. (Solon, OH, USA); amine-coated glass slide from Nuricell (Seoul, Korea); SYTO 83 from Molecular Probes (Carlsbad, CA, USA). The solutions of carbohydrates were printed on the surface with a MicroSys 5100 from Cartesian Technologies Inc. (Irvine, CA, USA). Carbohydrate microarrays probed with fluorescent dye labeled-lectins were scanned with an ArrayWoRx Biochip Reader from Applied Precision (Northwest Issaquah, WA, USA).

Preparation of Aminooxy- And Hydrazide-Functionalized Glass Slides Tethered by Oligo(ethylene glycol). Commercially available amine-coated glass slides were kept in a staining jar containing a solution of succinic anhydride (3%) in DMF with gentle shaking for 3 h. The slides were washed with DMF and a solution of diisopropylcarbodiimide (DIC, 3%) and *N*-hydroxysuccinimide (NHS, 3%) in DMF was poured into a staining jar. After gentle shaking for 3 h, the slides were washed with DMF. The slides were immersed into a solution of 4,7,10-trioxa-1,13-tridecanediamine (3%) in DMF with gentle shaking for 3 h. After washing with DMF, the slides were dried by purging with argon gas.

To prepare hydrazide-coated slides, a solution of succinic anhydride (3%) in DMF was poured into a staining jar that contained the slides treated with 4,7,10-trioxa-1,13-tridecanediamine. After gentle shaking for 3 h, the slides were washed with DMF. A solution of DIC (3%) and NHS (3%) in DMF was poured into a staining jar and the slides were gently shaken for 3 h. After washing with DMF, the slides were immersed into a solution of hydrazine monohydrate (3%) in DMF with gentle shaking for 3 h. After washing with DMF, the slides were dried by purging with argon gas. The derivatized slides can be stored at room temperature in a desiccator for several weeks.

To prepare aminooxy-coated slides, a solution of *N*-(2-bromoethoxy)phthalimide (3%) and TEA (3%) in DMF was poured into a staining jar that contained the slides treated with 4,7,10-trioxa-1,13-tridecanediamine. After gentle shaking for 6 h, the slides were washed with DMF. The slides were immersed into a solution of hydrazine monohydrate (3%) in DMF with gentle shaking for 3 h. After washing with DMF, the slides were dried by purging with argon gas. The derivatized slides can be stored at room temperature in a desiccator for several weeks.

Preparation of Hydrazide-Functionalized Glass Slides Tethered by Poly(ethylene glycol). Commercially available amine-coated glass slides were kept in a staining jar containing a solution of poly(ethylene glycol) diglycidyl ether (3%, average $M_n \sim 526$) in 10 mM $NaHCO_3$ with gentle shaking for 1 h. After washing with water, the slides were immersed into a solution of 4,7,10-trioxa-1,13-tridecanediamine (3%) in 10 mM $NaHCO_3$ with gentle shaking for 1 h. They were washed with water and soaked into a solution of succinic anhydride (3%) in DMF with gentle shaking for 3 h. After washing with DMF, the slides were treated with a solution of DIC (3%) and NHS (3%) in DMF with gentle shaking for 3 h. They were washed with DMF and immersed into a solution of hydrazine monohydrate (3%) in DMF with gentle shaking for 3 h. The slides were washed with water and dried by purging with argon gas. The derivatized slides can be stored at room temperature in a desiccator for several weeks.

Printing of Carbohydrates on the Surface. Carbohydrates were dissolved in sodium phosphate buffer (pH 5.0) containing 30% glycerol. A solution of carbohydrates (1 nL, 30 mM) from a 384-well plate was printed in predetermined places on a hydrazide or aminooxy-coated glass slide with a distance of 250 μm between the centers of adjacent spots. After completion of printing, the slide was placed into a humidity chamber at 50 °C for 12 h, and then, a compartmentalized plastic film that was coated by adhesive on one side (thickness: 0.1−0.2 mm) was attached to the glass slide (*17*). The slide was washed with PBS (pH 7.4) containing 0.1% Tween 20 and a solution of 0.1% Tween 20 possessing 1% BSA was dropped in the blocks. After incubation for 0.5 h, the slide was washed with the same buffer without BSA.

Detection of Carbohydrate−Protein Interactions. The printed slides were probed with fluorescent dye-labeled lectins (1−10 μg/mL) or unlabeled antibodies in PBS (pH 7.4) containing 0.1% Tween 20 for 1 h at room temperature. For ConA binding, $MnCl_2$ and $CaCl_2$ were added at final concentrations of 1 mM. The unbound lectins or antibodies were then removed by washing with the same buffer and rinsed with water. After drying by purging with argon gas, the slide treated with fluorescent dye-labeled lectins was scanned by using an ArrayWoRx scanner. The slide probed with unlabeled antibodies was further treated with FITC-secondary IgG antibody and then scanned by using a microarray scanner. Fluorescence intensity was analyzed using *ImaGene 6.1* software from BioDiscovery.

Detection of Glycan−Pathogen Interactions. *E. coli* ORN 178 and 208 strains were grown in LB media at 37 °C for 12 h and then harvested by centrifugation. The collected cells were suspended with PBS buffer containing $CaCl_2$ (1 mM) and $MnCl_2$ (1 mM). SYTO 83 (50 μM) was added to the suspension of bacterial cells, and then, the mixture was poured onto the carbohydrate microarray. After 30 min, unbound cells were removed by gentle washing with PBS buffer and water. The slide was scanned by using a microarray scanner. Fluorescence intensity was analyzed using *ImaGene 6.1* software from BioDiscovery.

Determination of Dissociation Constants for Protein−Glycan Interactions Using Carbohydrate Microarrays. The carbohydrate microarray containing fucose, Fucα1,2Gal, Fucα1,3GlcNAc, Fucα1,4GlcNAc, and GalNAcα1,3(Fucα1,2)Gal was treated with a solution of 0.1% Tween 20 possessing 1% BSA at room temperature for 30 min. The microarray was washed with PBS (pH 7.4) containing 0.1% Tween 20 and then probed with various concentrations (0.1 nM−4 μM)

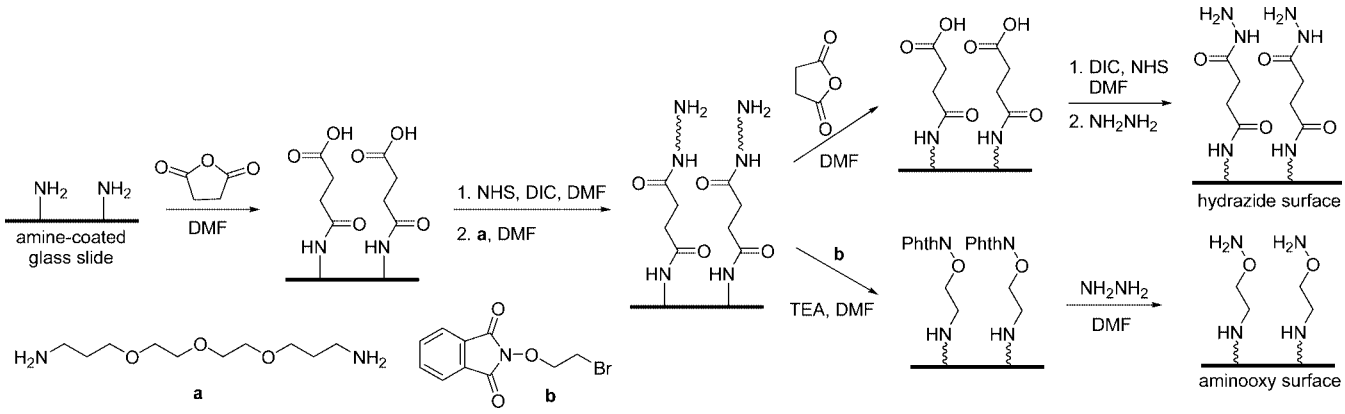

Figure 1. Preparation of hydrazide- and aminooxy-derivatized glass slides from amine-coated glass slides.

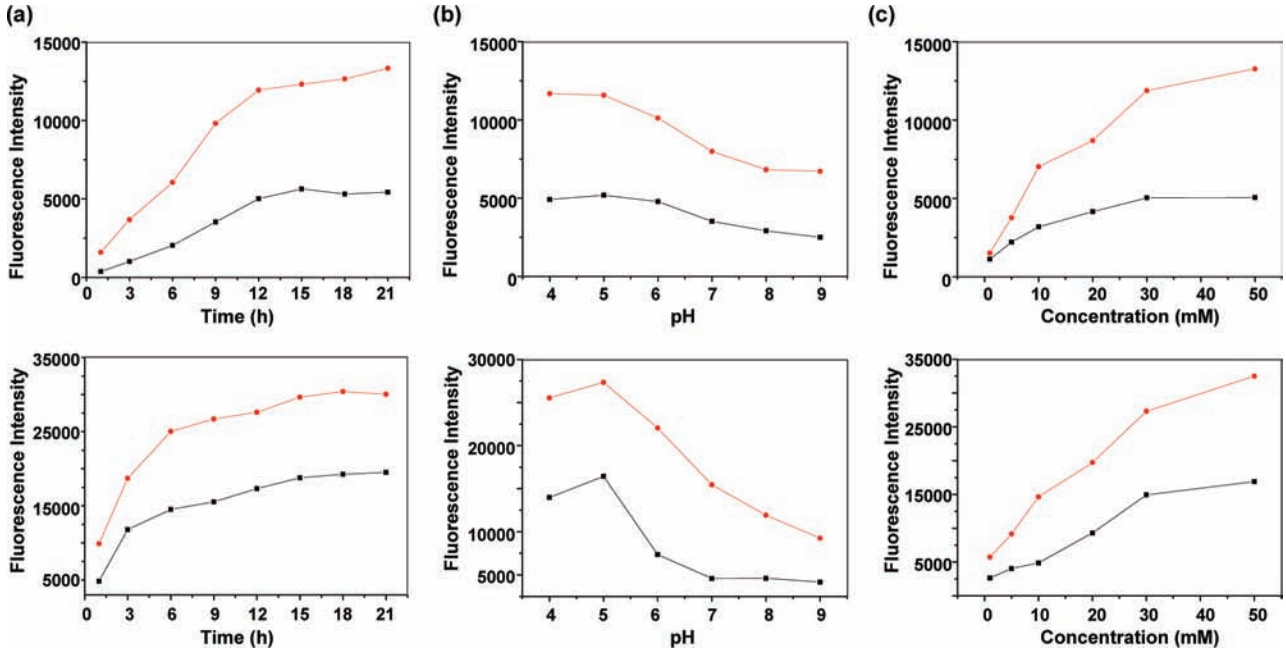

Figure 2. Immobilization of fucose (top) and *N,N′*-diacetylchitobiose (bottom) on the hydrazide (red line) and aminooxy (black line) functionalized glass surfaces as a function of (a) incubation time, (b) pH, and (c) concentration. Fluorescence intensities were measured after probing immobilized sugars with Cy5-AA and Cy3-WGA, respectively.

of Cy5-AA in PBS buffer containing 0.1% Tween 20 for 1 h at room temperature. The unbound proteins were removed by washing with PBS containing 0.1% Tween 20 by gentle shaking. After drying by purging with argon gas, the slide was scanned by using a microarray scanner. The fluorescence intensity of spots was measured and used for data processing. The means for replicate spots for each glycan was calculated, and then the mean and standard deviations for the three replicate experiments were determined and used for subsequent K_d measurement.

Apparent dissociation constants were obtained by the commercial nonlinear regression program *Origin 8.0*. Fluorescence intensity of replicate spots was plotted as a function of AA concentration. Nonlinear line-fitting to the equation was carried out,

$$Fl = Fl_{max}[P]_o/(K_d+[P]_o)$$

where Fl is the fluorescence intensity of spots for AA binding at a given concentration, Fl_{max} is the maximum fluorescence intensity, $[P]_o$ is the initial concentrations of the lectin, and K_d is the equilibrium dissociation constant for AA-surface-linked glycan interactions (*20*).

RESULTS AND DISCUSSION

The identification of suitable functional groups that efficiently react with free glycans is a prerequisite for the development of direct immobilization processes for the construction of carbohydrate microarrays. Reactions of aminooxy or hydrazide groups with unmodified carbohydrates, known to take place chemoselectively, have been widely employed for the synthesis of various glycoconjugates (*25*, *26*). We have used this technique, involving covalent immobilization of unmodified glycans on the aminooxy- or hydrazide-derivatized surfaces, for the facile fabrication of carbohydrate microarrays.

Glass slides, functionalized by aminooxy and hydrazide groups, are prepared from the commercially available amine-modified glass slides by the route shown in Figure 1. The surface amino groups are reacted with succinic anhydride in order to produce carboxylic acid groups, which are then reacted with *N*-hydroxysuccinimide (NHS) and diisopropylcarbodiimide (DIC) to generate activated NHS ester. Reaction with 4,7,10-trioxa-1,13-tridecanediamine (**a**) results in insertion of oligo-

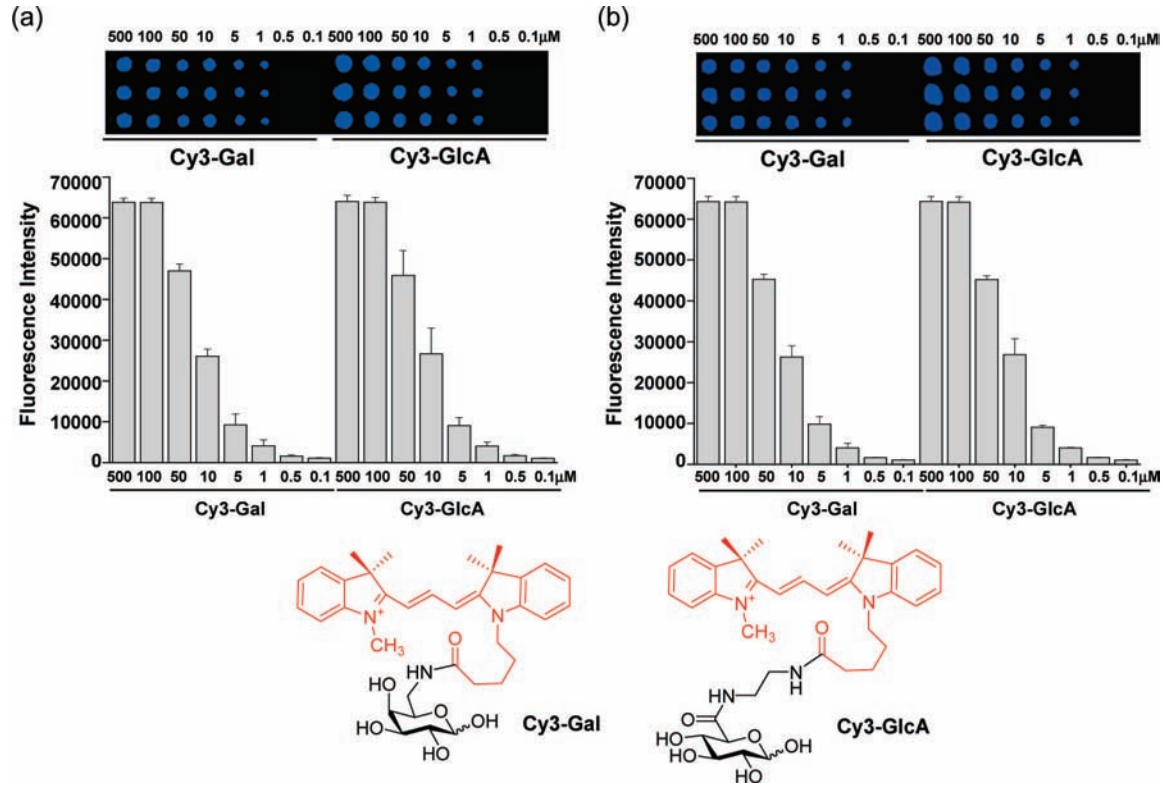

Figure 3. Immobilization of various concentrations (0.1−500 μM) of Cy3-Gal and Cy3-GlcA on (a) hydrazide and (b) aminooxy-coated glass slides.

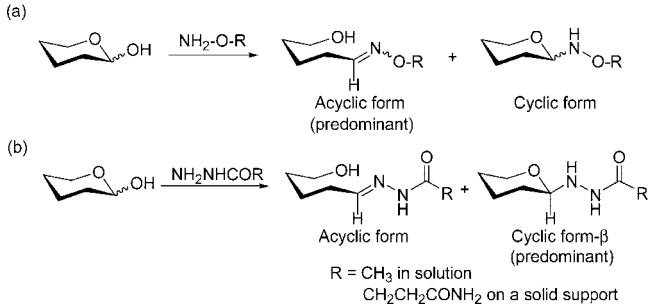

Figure 4. Products obtained from reactions of glycans with (a) aminooxy and (b) hydrazide groups.

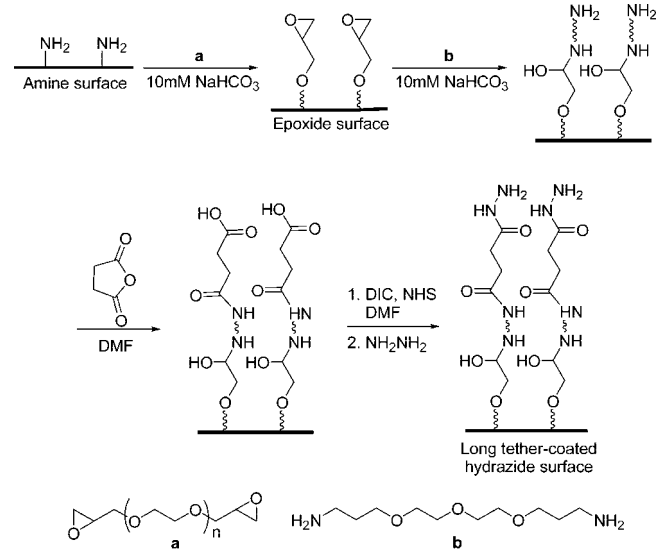

Figure 5. Preparation of hydrazide-coated glass slides containing a PEG linker.

(ethylene glycol) tether, which will serve to increase the accessibility of proteins to glycan ligands and to reduce nonspecific adsorption of proteins to the substrate during protein binding. The resulting amine-derivatized surfaces are sequentially treated with succinic anhydride, DIC-NHS, and hydrazine to prepare the target hydrazide-coated glass slide. The aminooxy-coated slide is obtained by treatment of the amine-derivatized slide with *N*-(2-bromoethoxy)phthalimide (**b**) followed by hydrazine-induced removal of phthaloyl group. Although the surface modification processes described above require synthetic procedures, they simply and reproducibly generate derivatized glass slides that can be stored in a desiccator for months.

Optimized conditions (temperature, time, pH, and concentration) have been probed for glycan immobilization on the hydrazide- and aminooxy-derivatized glass slides. To determine the optimized immobilization temperature and time, fucose and *N,N′*-diacetylchitobiose (30 mM in sodium phosphate buffer containing 30% glycerol, pH 5.0) were printed on both derivatized substrates by using a robotic pin-type microarrayer. Since ligation reactions are generally performed at relatively high temperature (*25*), the resulting slides were kept in a humid chamber for 1−21 h at temperatures of 22, 37, or 50 °C. To measure the extent of glycan immobilization, the slides were incubated with Cy5-*Aleuria aurantia* (Cy5-AA) and Cy3-wheat germ agglutinin (Cy3-WGA) for 0.5−1 h. The carbohydrate microarrays prepared at 50 °C show the highest fluorescence intensities after probing with proteins (data not shown). It has been reported previously that unmodified glycans are immobilized on a hydrazide-coated gold surface and an aminooxy-acetyl-coated glass surface at 18 °C and room temperature, respectively (*27, 28*). However, our results show that the glycans are not efficiently attached to hydrazide- and aminooxy-coated glass surfaces at low temperature. Finally, microarrays obtained using incubation time greater than 12 h incubation at 50 °C display similarly high fluorescence intensities (Figure 2a). The results of these experiments indicate that unmodified glycans

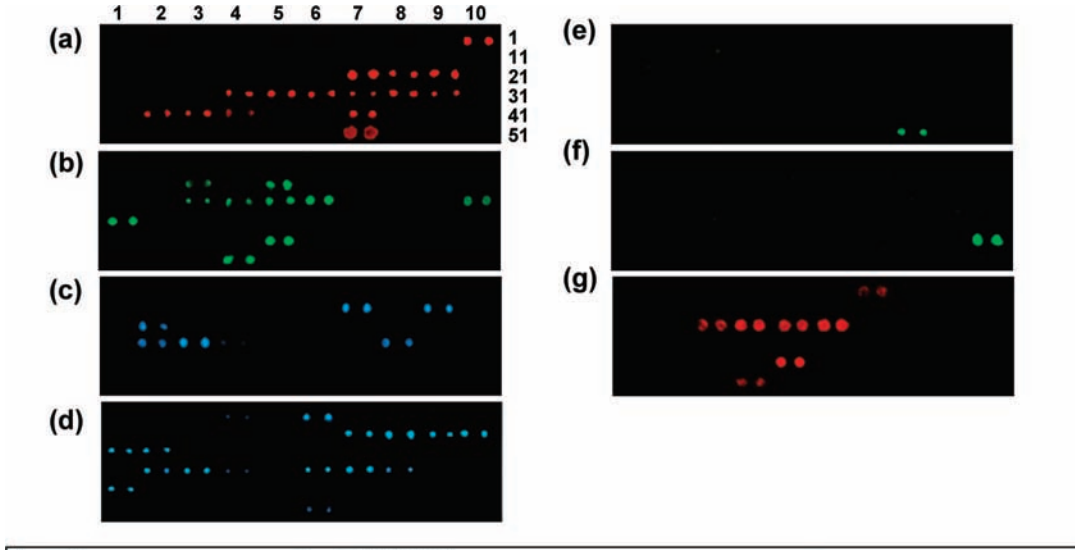

1	Glc	21	Galβ1,3GalNAc	41	NeuNAcα2,6Galβ1,4GlcNAc
2	GlcNAc	22	GalNAcβ1,4Gal	42	Fucα1,2Galβ1,3(Fucα1,4)GlcNAc (Le^b)
3	GlcA	23	Manα1,2Man	43	Fucα1,2Galβ1,4(Fucα1,3)GlcNAc
4	Gal	24	Manα1,3Man	44	NeuNAcα2,3Galβ1,4(Fucα1,3)GlcNAc (sialyl Le^x)
5	GalA	25	Manα1,4Man	45	Manα1,3(Manα1,6)Manα1,6(Manα1,3)Man
6	GalNAc	26	Manα1,6Man	46	NeuNAcα2,3Galβ1,4(NeuNAcα2,6)GlcNAc-β1,3Galβ1,4Glc
7	Man	27	Fucα1,2Gal		
8	Man-6-PO_3^{2-}	28	Fucα1,3GlcNAc	47	Fucα1,2Galβ1,3(Fucα1,4)GlcNAcβ1,3Galβ1,4Glc
9	ManNAc	29	Fucα1,4GlcNAc	48	chondroitin sulfate A
10	Fuc	30	Glcα1,4Glcα1,4Glc	49	dermatan sulfate
11	Rham	31	Glcα1,6Glcα1,6Glc	50	chondroitin sulfate C
12	Xyl	32	Galα1,3Galβ1,4GlcNAc	51	chondroitin sulfate D
13	maltose	33	Galα1,4Galβ1,4Glc	52	colominic acid
14	cellobiose	34	Galα1,3(Fucα1,2)Gal	53	heparin
15	isomaltose	35	Galβ1,3(Fucα1,4)GlcNAc (Le^a)	54	mannan
16	*N,N′*-diacetylchitobiose	36	Galβ1,4 (Fucα1,3)Gal	55	hyaluronic acid
17	Galα1,4Gal	37	Galβ1,4 (Fucα1,3)GlcNAc (Le^x)	56	galactan
18	lactose	38	GalNAcα1,3(Fucα1,2)Gal	57	fucoidan
19	Galα1,6Gal	39	Fucα1,2Galβ1,4GlcNAc	58	dextran
20	Galβ1,4GlcNAc (LacNAc)	40	NeuNAcα2,3Galβ1,4GlcNAc		

Figure 6. Fluorescence images of glycan microarrays containing 58 glycans probed with (a) Cy5-AA, (b) FITC-ConA, (c) Cy3-BS-I, (d) Cy3-RCA_{120}, (e) antidextran antibody followed by incubation with FITC-labeled antiantibody, (f) antichondroitin 6-sulfate antibody followed by incubation with FITC-labeled antiantibody, and (g) *E. coli* ORN178 strain preincubated with SYTO 83 (see Supporting Information for quantitative fluorescence intensity data).

are efficiently immobilized after 12 h incubation at 50 °C. It is important to note that extensive washing of the slides with PBS buffer after immobilization of the carbohydrates does not affect lectin binding, demonstrating that the covalent linkages between carbohydrates and aminooxy or hydrazide groups on the surface are stable.

To investigate the effects of pH and concentration on immobilization efficiencies, fucose and *N,N′*-diacetylchitobiose were immobilized on both substrates at pHs between 4 and 9 and concentrations in the range 1−50 mM for a the fixed incubation time (12 h) and temperature (50 °C). Probing of the slides with proteins reveals that 20−30 mM concentration of carbohydrates and pH 4−5 are ideal for efficient immobilization (Figure 2b,c). Although glycans immobilized at lower concentrations (1−5 mM) can interact with proteins, higher concentrations (20−30 mM) of glycans are desired in order to obtain reproducible and reliable binding results, especially in the case of glycans that are only weakly bound to proteins. It is worthwhile mentioning that the immobilization concentrations used in this procedure are relatively high in comparison with those used in other methods. However, this immobilization technique leads to efficient construction of microarrays, since a little of underivatized glycans (spotting volume: 1 nL) are required.

An interesting observation made in these experiments is that carbohydrates immobilized on hydrazide-coated glass slides exhibit more intense fluorescence signals after lectin binding than those immobilized on aminooxy-coated slides. There are two possible explanations that account for this result. The first is that hydrazide groups on the surface react with free glycans more efficiently than do aminooxy groups. To examine this possibility, galactose (Gal) and glucuronic acid (GlcA), linked to a fluorescence probe (Cy3) at their C-6 positions, were immobilized on both types of substrate under the same conditions (0.1−500 μM concentrations for 12 h at 50 °C). As shown in Figure 3, the two glycans were attached to both substrates with similar efficiencies, indicating that two functional groups on the surface have a similar reactivity with glycans.

A second possible explanation focuses on differences in the nature of anomeric linkage involved in sugar attachment to the surfaces. It is known that reactions of unmodified glycans with aminooxy group-possessing substances produce acyclic adducts preferentially (Figure 4a) (*26*, *29*). However, it has been reported that cyclic products with β-configuration at the anomeric centers are produced predominantly in reactions of carbohydrates with substances containing hydrazide groups (Figure 4b) (*25*, *30*, *31*). Consequently, the nature of the linkage present in products obtained from reactions of carbohydrates with hydrazide groups was investigated. For this study, four carbohydrates (glucose, mannose, fucose, and maltose) were reacted with hydrazide derivatives in solution and on a solid support (pH 5, 50 °C, 12 h). NMR analyses of mixtures obtained from these reactions show that β-anomeric adducts are produced predominantly (more than 90%) in both cases (*24*). Therefore, it is likely that the stronger binding of proteins to carbohydrates attached to hydrazide-modified surface rather than aminooxy-coated sur-

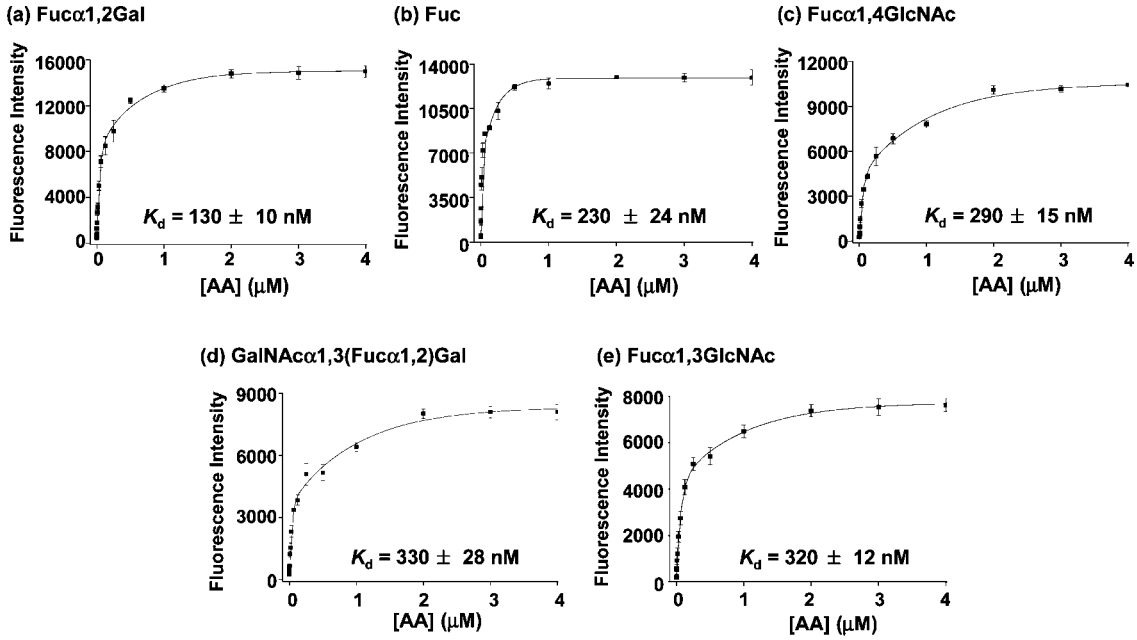

Figure 7. Determination of dissociation constants (K_d) for (a) AA-Fucα1,2Gal, (b) AA-fucose, (c) AA-Fucα1,4GlcNAc, (d) AA-GalNAcα1,3(Fucα1,2)Gal, and (e) AA-Fucα1,3GlcNAc interactions using carbohydrate microarrays.

faces results from a higher ratio of cyclic to acyclic linkages present in the former system.

The effect of insertion of a tether between hydrazide groups and the surface on protein binding was examined. For this purpose, hydrazide-coated glass slides containing poly(ethylene glycol) (PEG) were prepared by the procedure shown in Figure 5. A commercially available amine-coated glass slide is first treated with poly(ethylene glycol) diglycidyl ether (**a**) to place epoxide groups on the surface. The resulting substrate is then reacted with diamine **b** to introduce amino groups. The PEG-containing hydrazide-functionalized substrates are obtained by sequential reactions with succinic anhydride, DIC-NHS, and hydrazide. The results of protein binding experiments show that hydrazide substrates containing a long spacer arm give higher S/N ratios (around 1.5 times) than those arising from hydrazide substrates containing a shorter linkage. As a consequence, hydrazide-coated glass slides tethered by the long spacer arm were used throughout the remainder of this study. To our knowledge, these hydrazide-modified surfaces containing PEG were prepared for the first time for the construction of microarrays.

Prior to applications of carbohydrate microarrays, we measured the number of carbohydrates immobilized on the surface. To this end, various concentrations (500 μM−0.5 μM) of Cy3-Gal were printed on the hydrazide-coated slide, and the fluorescence intensity of the printed spots was measured before and after immobilization. The density of maximum carbohydrate immobilized on the surface was measured to be $10^{14}-10^{15}$ molecules/cm^2, a similar value to carbohydrates attached to the glass surface by other methods (see Supporting Information) (*32*).

To demonstrate the utility of this immobilization method and the application of the arrayed glycans to the rapid analysis of glycan−protein recognition events, 58 glycans (1 nL, 30 mM) shown in Figure 6 were printed in duplicate on a hydrazide-derivatized glass slide in a microarray format. The glycans comprise simple carbohydrates, oligosaccharides, and polysaccharides. The microspotted slide was kept at 50 °C for 12 h, washed with water, and dried. Since lectins serve as important models for studying glycan−protein interactions at the molecular level, the glycan microarrays were probed with the four fluorescent dye-labeled lectins, Cy5-AA, FITC-ConA, Cy3-*Bandeiraea simplicifolia* I (Cy3-BS-I), and Cy3-*Ricinus communis* agglutinin 120 (Cy3-RCA$_{120}$). Fluorescence data of carbohydrate microarrays obtained after probing with lectins are shown in Figure 6. The data demonstrate clearly that Cy5-AA interacts selectively with its cognate fucose-containing ligands and that it does not bind to the other sugars on the microarrays (Figure 6a). The carbohydrate microarrays treated with FITC-ConA exhibits binding to α-mannose and α-glucose containing ligands, a result that is consistent with the established specificity of this lectin (Figure 6b). However, this lectin does not recognize monomeric mannose and glucose that are attached to the surface with β-configurations.

Binding specificities of two galactose/*N*-acetylgalactosamine binding proteins, Cy3-labeled BS-I and RCA$_{120}$, were determined by using these microarrays. The results of microarray experiments indicate that BS-I recognizes terminal α-galactose and α-*N*-acetylgalactosamine residues preferentially. In contrast, BS-I rarely interacts with monomeric galactose and *N*-acetylgalactosamine owing to the fact that these glycans are immobilized to the surface with β-configuration (Figure 6c). However, RCA$_{120}$ was shown to bind to a broader range of galactose/*N*-acetylgalactosamine containing glycans than does BS-1 (Figure 6d). RCA$_{120}$ recognizes terminal galactose and *N*-acetylgalactosamine residues as well as galactan, but it rarely binds to Le^a (*33*). Subsequently, binding specificities of antibodies were analyzed by using carbohydrate microarrays. The results of experiments, in which carbohydrate microarrays were probed with antidextran and antichondroitin 6-sulfate antibodies followed by treatment with FITC-secondary IgG antibody, show that each antibody interacts with the corresponding antigen selectively (i.e., antidextran antibody binds to dextran and antichondroitin 6-sulfate antibody binds to chondroitin sulfate C) (Figure 6e,f). The observations made in this effort demonstrate that carbohydrate microarrays prepared by a direct immobilization method can be effectively employed to assess carbohydrate-binding properties of proteins.

Many bacteria, including pathogens, express specific lectins on pili. Pathogenic properties are caused by the initial binding of pathogens to host cells through specific glycan−protein interactions. In order to demonstrate that the fabricated glycan microarrays can be used to detect pathogens, microarrays containing 58 glycans were incubated with *E. coli* ORN178

strain, which was pretreated with SYTO 83. In accord with the fact that the ORN178 strain expresses a mannose-binding protein, a gene product of *fimH*, on pili, the microspots containing mannose epitopes were found to display fluorescence (Figure 6g) (*34*, *35*). In contrast, glycan microarrays treated with the ORN208 strain which lacks the *fimH* gene do not show fluorescence signals in the regions containing these glycans (data not shown).

Recently, we developed a procedure in which carbohydrate microarrays are used to determine binding affinities of glycans for protein (*20*). The microarrays, prepared through the one-step, direct immobilization method described above, were applied to measuring dissociation constants (K_d) associated with lectin surface-linked glycan interactions. For this study, the five fucose-containing glycans, fucose, Fucα1,2Gal, Fucα1,3GlcNAc, Fucα1,4GlcNAc, and GalNAcα1,3(Fucα1,2)Gal, were printed in replicates of five on a hydrazide-derivatized surface. The resulting microarrays were incubated with various concentrations (0.1 nM-4 μM) of Cy5-AA. After 1 h incubation, the microarrays were thoroughly washed with PBS buffer to remove unbound lectin. Fluorescence intensities of microspots were quantitated by using a microarray scanner. The K_d values of Fucα1,2Gal, fucose, Fucα1,4GlcNAc, GalNAcα1,3(Fucα1,2)Gal, and Fucα1,3GlcNAc are determined to be 1.3×10^{-7} M, 2.3×10^{-7} M, 2.9×10^{-7} M, 3.3×10^{-7} M, and 3.2×10^{-7} M, respectively (Figure 7). These studies demonstrate clearly that this immobilization technique is suitable for measuring quantitative binding affinities of glycans for protein.

CONCLUSIONS

The investigation described above has led to the development of a simple and efficient method for the construction of carbohydrate microarrays that relies on site-specific and covalent immobilization of unmodified carbohydrates on a hydrazide-coated surface. The insertion of a hydrophilic poly(ethylene glycol) linker between hydrazide groups and the surface leads to the desired orientational flexibility and increased accessibility of binding partners to the glycan ligands. Protein and cell-binding experiments show that, irrespective of their size, all types of carbohydrates undergo efficient covalent bonding to the hydrazide-coated surface. The glycan microarrays, generated in this way, are applicable to the rapid analysis of carbohydrate−protein recognition events, the detection of pathogens, and measurements of quantitative binding affinities of glycans for protein. This immobilization method can be readily modified to enable the identification and quantification of binding patterns of biologically relevant materials. As such, the technique should open new avenues for elucidating glycan−protein interactions. Of great significance is the fact that this free glycan based immobilization procedure can be used by scientists who lack organic synthesis experience.

ACKNOWLEDGMENT

This work was supported by grants from the NRL (R0A-2005-000-10027-0) and Protein Chip Technology programs of KOSEF/MEST. S.P. thanks the BK21 program (KRF).

Supporting Information Available: Synthesis of Cy3-labeled Gal and GlcA, measurement of the density of an immobilized carbohydrate, and quantitative analysis of fluorescence intensity of a carbohydrate microarray probed with proteins and cells. This material is available free of charge via Internet at http://pubs.acs.org.

LITERATURE CITED

(1) Seeberger, P. H., and Werz, D. B. (2007) Synthesis and medicinal applications of oligosaccharides. *Nature 446*, 1046–1051.

(2) Park, S., Lee, M.-R., and Shin, I. (2008) Chemical tools for functional studies of glycans. *Chem. Soc. Rev. 37*, 1579–1591.

(3) Raman, R., Raguram, S., Venkataraman, G., Paulson, J. C., and Sasisekharan, R. (2005) Glycomics: an integrated systems approach to structure-function relationships of glycans. *Nat. Methods 2*, 817–824.

(4) Smith, A. E., and Helenius, A. (2004) How viruses enter animal cells. *Science 304*, 237–242.

(5) Fuster, M. M., and Esko, J. D. (2005) The sweet and sour of cancer: glycans as novel therapeutic targets. *Nat. Rev. Cancer 5*, 526–542.

(6) Park, S., and Shin, I. (2002) Fabrication of carbohydrate chips for studying protein-carbohydrate interactions. *Angew. Chem., Int. Ed. 41*, 3180–3182.

(7) Fukui, S., Feizi, T., Galustian, C., Lawson, A. M., and Chai, W. (2002) Oligosaccharide microarrays for high-throughput detection and specificity assignments of carbohydrate-protein interactions. *Nat. Biotechnol. 20*, 1011–1017.

(8) Wang, D., Liu, S., Trummer, B. J., Deng, C., and Wang, A. (2002) Carbohydrate microarrays for the recognition of cross-reactive molecular markers of microbes and host cells. *Nat. Biotechnol. 20*, 275–280.

(9) Willats, W. G. T., Rasmussen, S. E., Kristensen, T., Mikkelsen, J. D., and Knox, J. P. (2002) Sugar-coated microarrays: a novel slide surface for the high-throughput analysis of glycans. *Proteomics 2*, 1666–1671.

(10) Park, S., Lee, M.-R., and Shin, I. (2008) Carbohydrate microarrays as powerful tools in studies of carbohydrate-mediated biological processes. *Chem. Commun.* 4389–4399.

(11) Horlacher, T., and Seeberger, P. H. (2008) Carbohydrate arrays as tools for research and diagnostics. *Chem. Soc. Rev. 37*, 1414–1422.

(12) Laurent, N., Voglmeir, J., and Flitsch, S. L. (2008) Glycoarrays-tools for determining protein-carbohydrate interactions and glycoenzyme specificity. *Chem. Commun.* 4400–4412.

(13) Paulson, J. C., Blixt, O., and Collins, B. E. (2006) Sweet spots in functional glycomics. *Nat. Chem. Biol. 2*, 238–248.

(14) Shin, I., Park, S., and Lee, M.-R. (2005) Carbohydrate microarrays: an advanced technology for functional studies of glycans. *Chem. Eur. J. 11*, 2894–2901.

(15) Feizi, T., and Chai, W. (2004) Oligosaccharide microarrays to decipher the glyco code. *Nat. Rev. Mol. Cell Biol. 5*, 582–588.

(16) Feizi, T., Fazio, F., Chai, W., and Wong, C.-H. (2003) Carbohydrate microarrays-a new set of technologies at the frontiers of glycomics. *Curr. Opin. Struct. Biol. 13*, 637–645.

(17) Park, S., Lee, M.-R., Pyo, S.-J., and Shin, I. (2004) Carbohydrate chips for studying high-throughput carbohydrate-protein interactions. *J. Am. Chem. Soc. 126*, 4812–4819.

(18) Lee, M.-R., and Shin, I. (2005) Fabrication of chemical microarrays by efficient immobilization of hydrazide-linked substances on epoxide-coated glass surfaces. *Angew. Chem., Int. Ed. 44*, 2991–2884.

(19) Park, S., Lee, M.-R., and Shin, I. (2007) Fabrication of carbohydrate chips and their use to probe protein-carbohydrate interactions. *Nat. Protocols 2*, 2747–2758.

(20) Park, S., and Shin, I. (2007) Carbohydrate microarrays for assaying galactosyltransferase activity. *Org. Lett. 9*, 1675–1678.

(21) Xia, B., Kawar, Z. S., Ju, T., Alvarez, R. A., Sachdev, G. P., and Cummings, R. D. (2005) Versatile fluorescent derivatization of glycans for glycomic analysis. *Nat. Methods 2*, 845–850.

(22) Bohorov, O., Andersson-Sand, H., Hoffmann, J., and Blixt, O. (2006) Arraying glycomics: a novel bi-functional spacer for one-step microscale derivatization of free reducing glycans. *Glycobiology 16*, 21C–27C.

(23) Angeloni, S., Ridet, J. L., Kusy, N., Gao, H., Crevoisier, F., Guinchard, S., Kochhar, S., Sigrist, H., and Sprenger, N. (2005) Glycoprofiling with micro-arrays of glycoconjugates and lectins. *Glycobiology 15*, 31–41.

(24) Lee, M.-R., and Shin, I. (2005) Facile preparation of carbohydrate microarrays by site-specific, covalent immobilization of unmodified carbohydrates on hydrazide-coated glass slides. *Org. Lett. 7*, 4269–4272.

(25) Leteux, C., Childs, R. A., Chai, W., Stoll, M. S., Kogelberg, H., and Feizi, T. (1998) Biotinyl-l-3-(2-naphthyl)-alanine hydrazide derivatives of N-glycans: versatile solid-phase probes for carbohydrate-recognition studies. *Glycobiology 8*, 227–236.

(26) Jiménez-Castells, C., de la Torre, B. G., Andreu, D., and Gutiérrez-Gallego, R. (2008) Neo-glycopeptides: the importance of sugar core conformation in oxime-linked glycoprobes for interaction studies. *Glycoconj. J. 25*, 879–887.

(27) Zhi, Z. L., Powell, A. K., and Turnbull, J. E. (2006) Fabrication of carbohydrate microarrays on gold surfaces: direct attachment of nonderivatized oligosaccharides to hydrazide-modified self-assembled monolayers. *Anal. Chem. 78*, 4786–4793.

(28) Zhou, X., and Zhou, J. (2006) Oligosaccharide microarrays fabricated on aminooxyacetyl functionalized glass surface for characterization of carbohydrate-protein interaction. *Biosens. Bioelectron. 21*, 1451–1458.

(29) Hatanaka, Y., Kempin, U., and Park, J.-J. (2000) One-step synthesis of biotinyl photoprobes from unprotected carbohydrates. *J. Org. Chem. 65*, 5639–5643.

(30) Shinohara, Y., Sota, H., Gotoh, M., Hasebe, M., Tosu, M., Nakao, J., and Hasegawa, Y. (1996) Bifunctional labeling reagent for oligosaccharides to incorporate both chromophore and biotin groups. *Anal. Chem. 68*, 2573–2579.

(31) Ojala, C. R., Ostman, J. M., and Ojala, W. H. (2002) The saccharide-hydrazide linkage: molecular and crystal structures of the semicarbazide derivatives of D-glucose, D-galactose, and D-xylose, including a 'forbidden' conformation of the galactose derivative. *Carbohydr. Res. 337*, 21–29.

(32) Liang, P.-H., Wang, S.-K., and Wong, C.-H. (2007) Quantitative analysis of carbohydrate-protein interactions using glycan microarrays: determination of surface and solution dissociation constants. *J. Am. Chem. Soc. 128*, 13668–13669.

(33) Manimala, J. C., Roach, T. A., Li, Z., and Gildersleeve, J. C. (2006) High-throughput carbohydrate microarray analysis of 24 lectins. *Angew. Chem., Int. Ed. 45*, 3607–3610.

(34) Connell, H., Agace, W., Klemm, P., Schembri, M., Marild, S., and Svanborg, C. (1996) Type 1 fimbrial expression enhances *Escherichia coli* virulence for the urinary tract. *Proc. Natl. Acad. Sci. U.S.A. 93*, 9827–9832.

(35) Nagahori, N., Lee, R. T., Nishimura, S.-I., Pagé, D., Roy, R., and Lee, Y. C. (2002) Inhibition of adhesion of type 1 fimbriated *Escherichia coli* to highly mannosylated ligands. *ChemBioChem 3*, 836–844.

BC800442Z

SUPPORTING INFORMATION

Construction of Carbohydrate Microarrays by Using One-step, Direct Immobilizations of Diverse Unmodified Glycans on Solid Surfaces

Sungjin Park, Myung-Ryul Lee, and Injae Shin*

Synthesis of Cy3-Gal conjugate 4

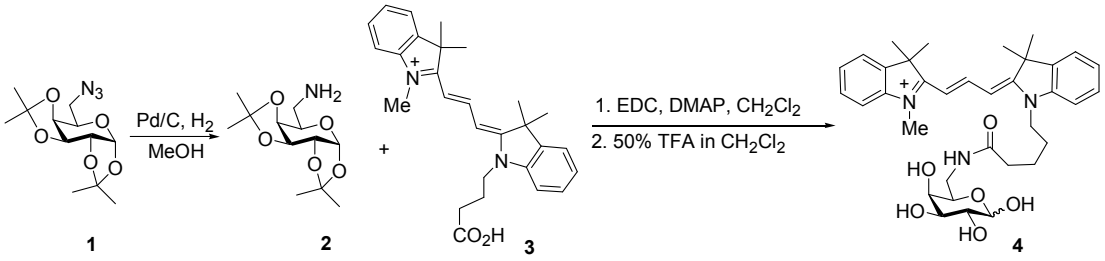

Compound **1** (5.3 mg, 18.5 μmol, 1 eq.), prepared by the known procedure (Yang, J. *et al. Org. Lett.* 2003.*5*, 2223), was reduced by reacting with H_2 and 10% Pd/C in MeOH (5 mL) for 30 min. The reaction mixture was filtered though a Celite pad and the filtrate was concentrated under the reduced pressure to give **2** as a quantitative yield. To a stirred solution of **2** (3.5 mg, 13.5 μmol, 1 equiv.) in CH_2Cl_2 (300 μL) was added EDC (3.9 mg, 20.3 μmol, 1.5 equiv.), DMAP (0.8 mg, 6.75 μmol, 0.5 equiv.) and **3** (5.8 mg, 13.5 μmol, 1 equiv.). The reaction mixture was stirred for 4 h at room temperature. The reaction mixture was diluted with CH_2Cl_2 and the organic layer was washed with water. The organic layer was dried over anhydrous $MgSO_4$, filtered, and then concentrated under the reduced pressure. The crude product was used for the next reaction without further purification. To a stirred solution of the above compound in CH_2Cl_2 (250 μL) was added TFA (250 μL). The reaction mixture was stirred for 1 h. The volatile solvent was removed under the reduced pressure. The crude product was purified by preparative reversed phase-HPLC (Vydac C_{18} column, 250 x 22 mm, pore size: 5 μm) with a gradient 2-100% CH_3CN in water over 90 min to give **4** in 80% yield: ^{1}H NMR (250 MHz, CD_3OD) δ 8.54 (t, 1 H, J = 13.4), 7.56-7.28 (m, 8 H), 6.43 (d, 1 H, J = 12.5), 4.48-4.39 (m, 1 H), 4.28-4.14 (m, 5 H), 3.99-3.94 (m, 2 H), 3.69 (s, 3 H), 2.71-2.52 (m, 4 H), 1.77 (m, 14 H); ^{13}C NMR (125 MHz, CD_3OD) δ 175.6, 175.0, 172.7, 151.1, 143.0, 142.4, 141.1, 141.0, 129.0,

128.9, 125.8, 125.7, 122.4, 122.3, 111.4, 111.2, 102.8, 102.7, 85.9, 81.9, 80.7, 80.3, 76.2, 76.1, 63.1, 49.6, 49.5, 43.9, 42.6, 32.7, 30.7, 27.3, 26.8, 22.3; MALDI-TOF-MS calcd for $C_{35}H_{46}N_3O_6$ $[M]^+$ 604.3387, found 604. 3284.

Synthesis of Cy3-GlcA conjugate 8

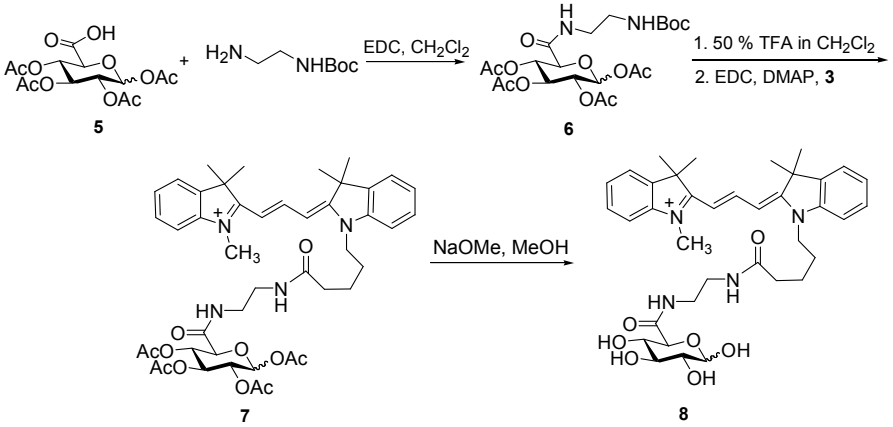

To a stirred solution of **5** (120 mg, 0.33 mmol, 1 equiv.), prepared by the known procedure (Wong, A. W. *et al*. *Can. J. Chem.* 2001*, 79*, 510), in CH_2Cl_2 (3 mL) was added EDC (95.0 mg, 0.50 mmol, 1.5 equiv.) and *t*-butyl *N*-(2-aminoethyl)carbamate (63.1 mg. 0.39 mmol, 1.2 equiv.). The reaction mixture was stirred for 3 h at room temperature. The reaction mixture was diluted with CH_2Cl_2 and the organic layer was washed with water. The organic layer was dried over anhydrous $MgSO_4$, filtered and then concentrated under the reduced pressure. The crude product was purified by flash column chromatography (1:1 to 1:3 hexane/EtOAc) to give **6** (121 mg, 0.24 mmol) in 74% yield: ^{1}H NMR (250 MHz, CD_3OD) δ 6.38 (d, 1 H, *J* = 3.6), 5.48 (t, 1 H, *J* = 10.1), 5.21 (t, 1 H, *J* = 10.1), 5.12 (dd, 1 H, *J* = 3.6, 10.1), 4.29 (d, 1 H, *J* = 10.1), 3.22 (t, 2 H, *J* = 5.36), 3.16-3.13 (m, 2 H), 2.19 (s, 3 H), 2.03 (s, 3 H), 2.02 (s, 3 H), 2.00 (s, 3 H), 1.43 (s, 9 H); ^{13}C NMR (62.5 MHz, CD_3OD) δ 171.6, 171.5, 171.4, 171.3, 171.2, 171.0, 170.5, 169.5, 169.2, 158.2, 92.7, 90.0, 80.3, 74.7, 73.4, 72.4, 71.6, 71.0, 70.9, 70.6, 70.5, 40.9, 29.1, 20.8, 20.7, 20.6, 20.4; MALDI-TOF-MS calcd for $C_{21}H_{32}N_2O_{12}$ $[M+Na]^+$ 527.1955, found 527.1928.

To a stirred solution of **6** (30 mg, 59.5 μmol, 1 equiv.) in CH_2Cl_2 (500 μL) was added TFA (500 μL). After 1 h, the volatile solvent was removed under the reduced pressure. The crude product was used for next reaction without further purification. A solution of the above compound (18.2 mg, 45 μmol, 1 equiv.), EDC (12.9 mg, 67.5 μmol, 1.5 equiv.), DMAP (2.7 mg, 22.5 μmol, 0.5 equiv.) and **3** (19.3 mg, 45 μmol, 1 equiv.) in CH_2Cl_2 (300 μL) was stirred for 4 h at room temperature. The reaction mixture was diluted with CH_2Cl_2 and the organic layer was washed with water. The

organic layer was dried over anhydrous $MgSO_4$, filtered, and then concentrated under the reduced pressure. The crude product was purified by flash column chromatography (15:1 to 5:1 EtOAc/MeOH) to give **7** (26.1 mg, 31.5 μmol) in 70 % yield: ^{1}H NMR (250 MHz, $CDCl_3$) δ 8.72 (bs, 1 H), 8.53 (bs, 1 H), 8.40 (t, 1 H, *J* = 13.1), 7.43-7.34 (m, 4 H), 7.29-7.23 (m, 2 H), 7.18-7.15 (m, 2 H), 7.04 (d, 1 H, *J* = 14.0), 6.95 (d, 1 H, *J* = 14.0), 6.38 (d, 1 H, *J* = 3.63), 5.52 (t, 1 H, *J* = 9.70), 5.38 (t, 1 H, *J* = 9.96), 5.19 (dd, 1 H, *J* = 3.63, 9.96), 4.48 (d, 1 H, *J* = 9.96), 4.21 (bs, 2 H), 3.75 (s, 3 H), 3.43 (m, 4 H), 2.52 (bs, 2 H), 2.08 (s, 3 H), 2.03 (s, 3 H), 2.00 (s, 3 H), 1.98 (s, 3 H), 1.87 (m, 4 H), 1.73 (s, 6 H), 1.72 (s, 6 H); ^{13}C NMR (100 MHz, $CDCl_3$) δ 174.4, 173.9, 173.7, 170.0, 169.5, 169.4, 169.1, 166.8, 150.8, 142.7, 141.8, 140.5, 140.4, 128.9, 128.8, 125.3, 122.0, 121.8, 111.1, 110.9, 104.4, 103.9, 88.7, 71.1, 69.6, 69.3, 69.2, 49.0, 48.9, 44.0, 39.9, 38.8, 35.2, 31.8, 29.6, 28.2, 28.1, 28.0, 26.3, 22.6, 21.0, 20.7, 20.6, 20.4; MALDI-TOF-MS calcd for $C_{45}H_{57}N_4O_{11}$ $[M]^+$ 829.4024, found 829.4041.

A solution of **7** (26.1 mg, 31.5 μmol) and 0.5 M NaOMe (63 μL) in MeOH (567 μL) was stirred for 2 h at room temperature. After neutralization with Dowex 50W-X8 ion exchange resin, the resin was filtered and washed with MeOH twice. The solvent was removed under the reduced pressure. The crude product was purified by preparative RP-HPLC (Vydac C_{18} column, 250 x 22 mm, pore size: 5 μm) with a gradient 2-100% CH_3CN in water over 90 min to give **8** (15.2 mg, 23.0 μmol) in 73 % yield: ^{1}H NMR (250 MHz, CD_3OD) δ 8.60 (t, 1 H, *J* = 13.8), 7.55-7.48 (m, 2 H), 7.45-7.42 (m, 2 H), 7.38-7.28 (m, 4 H), 6.46 (d, 2 H, *J* = 13.5), 4.27-4.08 (m, 4 H), 3.93-3.82 (m, 2 H), 3.69 (s, 3 H), 2.28 (bs, 2 H), 1.86 (s, 16 H); MALDI-TOF-MS calcd for $C_{37}H_{49}N_4O_7$ $[M]^+$ 661.3601, found 661.3453.

Measurement of the density of a carbohydrate immobilized on the surface. Various concentrations (500 μM–0.5 μM) of Cy3-Gal were printed on the hydrazide-coated slide in three replicates and their fluorescence intensities were read by a microarray scanner. After 12 h incubation at 50 ^{o}C, the slide was washed with PBST (0.1% Tween 20) buffer (5 min x 3). The fluorescence intensities were read by a microarray scanner.

The number of immobilized Cy3-Gal (*No*) is calculated by the following equation.

$No = CVN_AQ_{post}/Q_{pre}$

where C is the printing concentration (500 μM–0.5 μM), V is the printing volume (1 nL), N_A is Avogadro's Number, Q_{post} is the fluorescence intensity after immobilization of a carbohydrate, and Q_{pre} is the fluorescence intensity before immobilization of a carbohydrate.

When the surface is saturated (around 500 to 100 μM Cy3-Gal), the ratio from Q_{pre} and Q_{post} is 0.92. The density of maximum carbohydrate immobilized on the surface is between 2.2 x 10^{14} and 1.09 x 10^{15} molecules/cm^2. Each spot in the microarray is around 0.18 mm diameter.

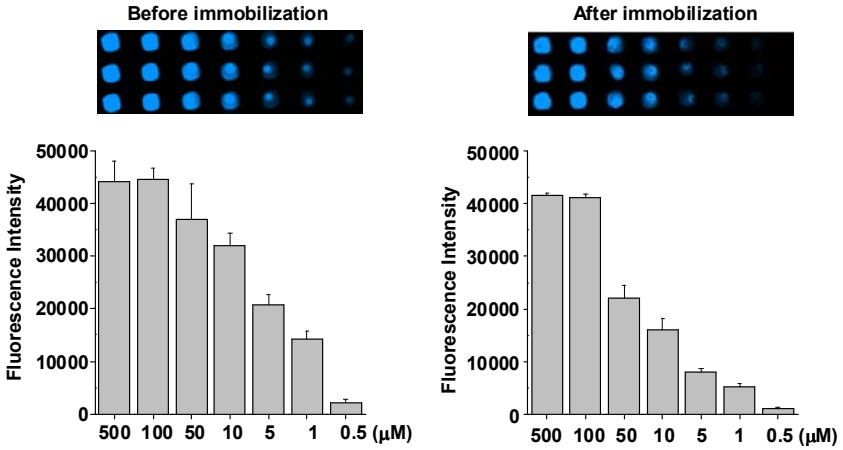

Quantitative analysis of fluorescence intensity of a carbohydrate microarray probed with proteins and cells.

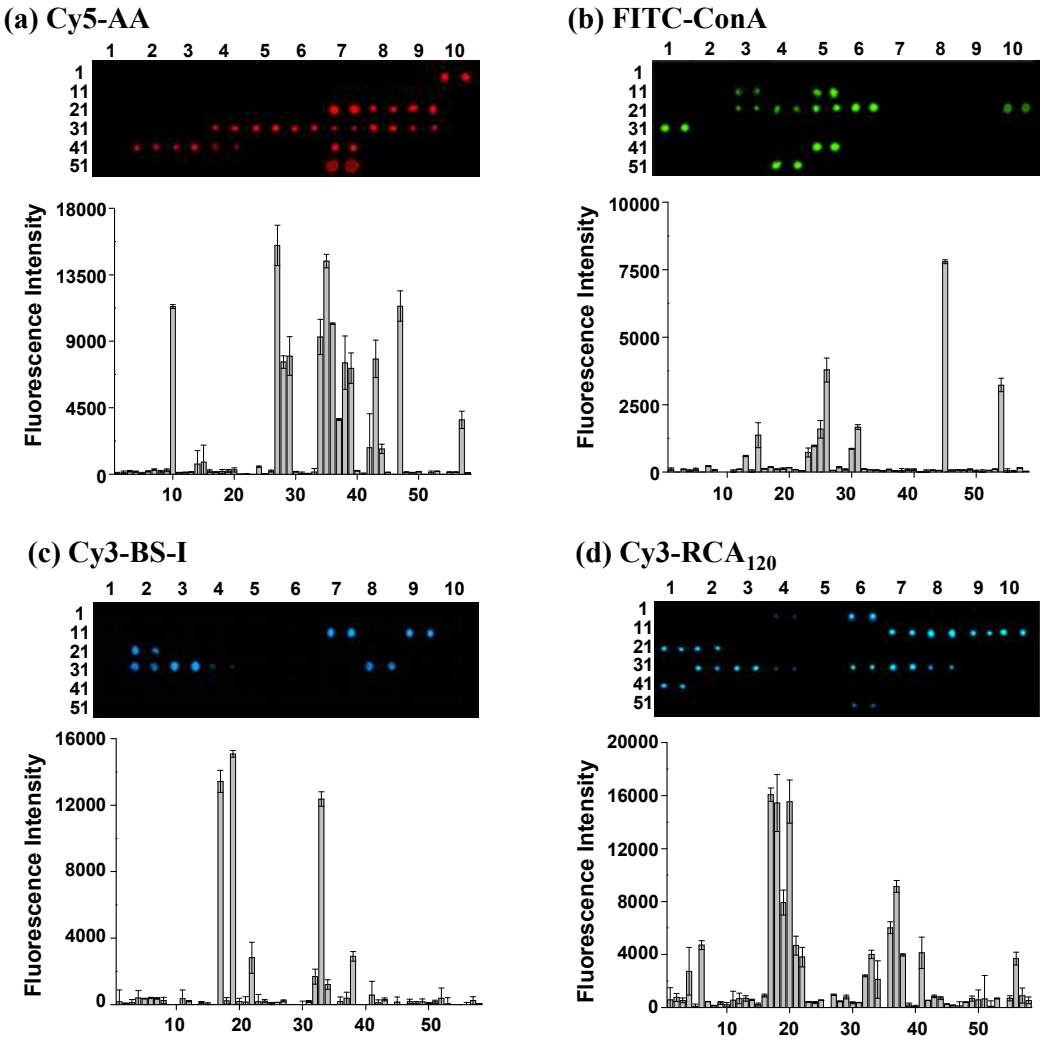

(e) anti-dextran antibody

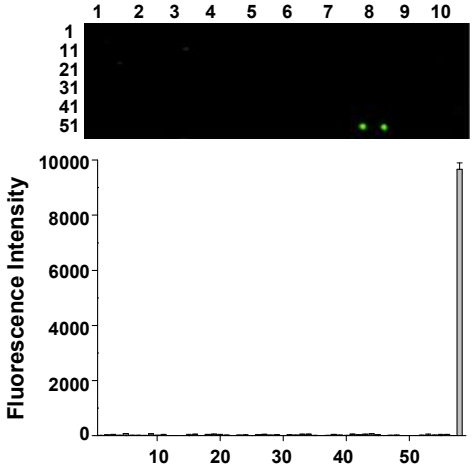

(f) anti-chondroitin 6-sulfate antibody

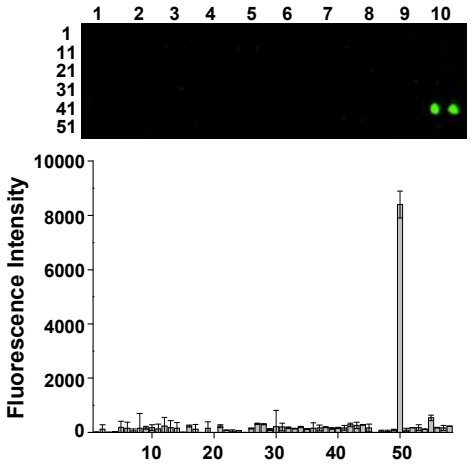

(g) *E. coli* ORN 178

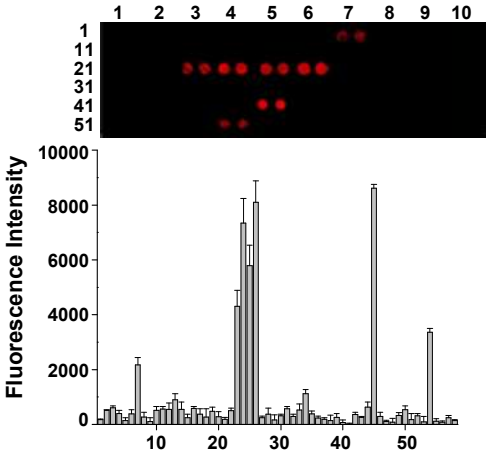

TECHNICAL NOTES

Dual Fluorescent Labeling Method to Visualize Plasmid DNA Degradation

Charudharshini Srinivasan,[⊥,†] Shafiuddin Siddiqui,[#,‡] Lawrence K. Silbart,[§] Fotios Papadimitrakopoulos,[||] and Diane J. Burgess*[,†]

Department of Pharmaceutical Sciences, University of Connecticut, 69 North Eagleville Road, Unit 3092; Department of Animal Science, Center of Excellence for Vaccine Research, University of Connecticut, 1390 Storrs Road, Unit 4163; Department of Allied Health Sciences, Center of Excellence for Vaccine Research, University of Connecticut, 358 Mansfield Road; and Nanomaterials Optoelectronics Laboratory, Polymer Program, Department of Chemistry, Institute of Materials Science, University of Connecticut, 97 North Eagleville Road, Unit 3136, Storrs, Connecticut 06269. Received May 8, 2008; Revised Manuscript Received November 11, 2008

The efficiency of nonviral vectors for gene delivery may be enhanced by understanding the key barriers that limit the translocation of the therapeutic DNA into the nucleus. One such barrier is the instability of DNA in the cytoplasm. In this work, we have developed a method to dual-label plasmid DNA to be utilized as a tool to elucidate DNA instability during its trafficking in the intracellular microenvironment. Plasmid DNA containing rhodamine and maleimide groups linked using peptide nucleic acid (PNA) linkers was utilized for conjugation. Covalent conjugation of the maleimide group with a second fluorophore, fluorescein, did not alter the electrophoretic mobility or the structural integrity of the DNA, as confirmed by gel electrophoresis. The intact DNA was visualized as a single color (yellow) due to the close proximity of the green and red fluorophores. DNA degradation was simulated using restriction endonucleases (*Bam*H1 and *Pfl*MI) to cut the DNA at two or more sites resulting in color separation. Confocal time-lapse imaging was utilized to follow DNA stability upon incubation of Lipofectamine2000/dual-labeled DNA complexes in CHO-K1 cells. Yellow fluorescent voxels were seen in the cell cytoplasm indicating the presence of intact DNA. Red and green fluorescent voxels were also seen in a few cells, suggesting separation of the fluorophores and probable DNA degradation. The methodology developed in this report provides a new tracking tool for investigators to explore DNA degradation at the molecular level inside single cell.

INTRODUCTION

Transfection of therapeutic DNA mediated by nonviral gene delivery has been investigated over the past three decades as a safer alternative to viral vectors for use in the treatment of genetic, infectious, and acquired diseases (*1*−*6*). However, the transfection efficiencies that can be achieved using nonviral vectors are relatively low when compared to viral-based delivery systems (*4*, *7*, *8*). Although several different approaches have been investigated to enhance transfection, success has been limited and low efficiency remains a concern (*9*−*12*). Consequently, only approximately 26% of all gene therapeutics in clinical trials utilize nonviral vectors, whereas approximately 68% utilize viral vectors (the remaining 6% utilize RNA transfer, yeast, bacterial, or unknown vectors) (http://www.wiley.co.uk/genmed/clinical) (*13*).

Gene trafficking is being investigated to understand the barriers that hinder the translocation of nonviral vectors and their payload from outside the cell into the nucleus (*11*, *14*−*19*). Such information could then be used to redesign nonviral vectors for improved transfection. Gene trafficking of nonviral vectors involves cellular binding and uptake, endosomal escape, safe transport through cytosol, and nuclear delivery. Several reviews have been recently published that describe gene trafficking in detail and the dependency of the trafficking process on the nature of the delivery vector (*5*, *11*, *20*−*22*). Depending on the vector used, one or more of these steps may limit transfection efficiency.

Cellular binding and uptake of gene delivery vectors is well-understood and depends on the interaction between the vector and the cell surface (*5*, *7*, *11*, *12*). Vectors are usually transported into the cell in endosomes. The environment within the endosomes (low pH and the presence of nucleases) is hostile to DNA. Much research has been conducted and vectors have been developed that promote rapid escape from endosomes (such as fusogenic lipids, peptides, and lysosomotropic agents *23*−*25*). Depending on the nature of the vector, the DNA may be released

* To whom correspondence and reprint requests should be addressed. Department of Pharmaceutical Sciences, University of Connecticut, 69 North Eagleville Road, Unit 3092, Storrs, CT 06269, USA. Phone: 860-486-3760. Fax: 860-486-0538. E-mail: d.burgess@uconn.edu.

† Department of Pharmaceutical Sciences.

‡ Department of Animal Science, Center of Excellence for Vaccine Research.

§ Department of Allied Health Sciences, Center of Excellence for Vaccine Research.

|| Institute of Materials Science.

⊥ Current address: Immune Disease Institute, Harvard Medical School, 3 Black Fan Circle, 3rd Floor, Rm 3024, Boston, MA 02115. E-mail: csrinivasan@idi.harvard.edu.

Current address: 77 Avenue Louis Pasteur, Room 720, Harvard Institute of Medicine, Center for Neurological Disease, Boston, MA 02115. Email: ssiddiqui1@bics.bwh.harvard.edu.

10.1021/bc800184j CCC: $40.75 © 2009 American Chemical Society
Published on Web 12/16/2008

into the cytoplasm together with the vector or as free DNA. Free DNA is subject to degradation by the many endo- and exonucleases that are present in the cell. Although the majority of these reside in the nucleus, some are located within the cytoplasm (*26, 27*). Degradation of free DNA by nucleases present in the cytoplasm may be considerable due to the significant time required for transport through the cytoskeletal network (*22*). Finally, the DNA must be translocated into the nucleus that may occur by passive entry during mitotic cell division and/or by active process through pores in the nuclear membrane. This is dependent on the DNA conformation as well as cellular characteristics (*28, 29*). Although much work has been conducted to understand these transport processes, the amount of DNA lost at these various steps is unknown. For example, although a vector may be designed to promote endosomal escape, some DNA may be degraded prior to escape. Consequently, it would be useful to have a method to track DNA degradation throughout the entire trafficking process.

To date, there are only a few reports that describe investigations into DNA degradation. These include studying nuclease activity on plasmid DNA with different cytosolic extracts using gel electrophoresis (*30, 31*); monitoring intracellular disappearance of DNA by fluorescence in situ hybridization (FISH); visualization of plasmid DNA fragmentation using terminal deoxynucleotidyl transferase-mediated dUTP nick end labeling (TUNEL) assay; and radiolabeled ^{32}P-release from end-labeled fragmented DNA (*30, 31*). These studies have provided important information on the effect of cytosolic nucleases on DNA, but are limited since they have been performed using microinjected materials in single cells and require isolated cell fractions or fixed cells, which may not represent events that occur in living cells (*30, 31*).

Investigations based on labeling techniques have involved monitoring gold-labeled DNA by transmission electron microscopy (TEM) (*32, 33*) and single dye labeled delivery vector/DNA (oligonucleotides or plasmid DNA) by confocal imaging (*34,35*). TEM only provides static images of cells, and the dye labeled DNA complexes have been imaged immediately following microinjection and therefore lack critical information about DNA stability once released from the complex.

On the basis of the above, there is a great need to develop a tool to monitor real-time degradation processes in live cells. Live cell tracking is commonly performed using fluorescent dyes to label biomolecules such as antibodies, peptides (*36*), and small oligonucleotides (*37, 38*). Labeling of plasmid DNA can be challenging, since chemical modification may render the DNA nonfunctional (*39*−*41*). However, we have previously demonstrated successful labeling of plasmid DNA with quantum dots using peptide nucleic acid (PNA) chemistry without loss of functionality for long-term single cell tracking studies (*19*).

In this study, we have demonstrated a novel approach to monitor plasmid DNA degradation that utilizes dual-labeled DNA as a probe. The DNA was labeled with two different fluorophores (rhodamine and fluorescein) via PNA linkers. The two dyes are expected to be seen as a single color in intact DNA due to colocalization, but when the DNA strands are broken and the segments move apart, color separation may be observed. This concept was demonstrated using restriction enzymes to cut the DNA. Confocal time-lapse imaging was used to follow cellular uptake of DNA as well as probable degradation, as demonstrated by color separation, occurring within the cytoplasm. The plasmid DNA was shown to have retained its structural integrity following dual labeling. This dual-labeling technique provides a novel approach to visualize plasmid DNA instability at a single cell level throughout the trafficking pathway.

Scheme 1. Schematic Illustration of pGeneGrip-gWIZ DNA Dual-Labeled with Fluorescein and Rhodamine Labels at Site-1 and and Site-2, Respectively[a]

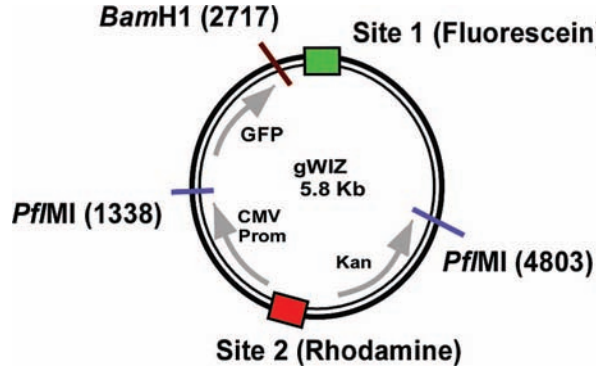

[a] The plasmid with restriction enzymes (*Bam*H1 and *Pfl*MI) used to digest at single and double recognition sites, respectively, on the dual-labeled plasmid DNA are shown.

MATERIALS AND METHODS

Plasmid DNA Preparation. Green fluorescent protein encoding pGeneGrip-gWIZ plasmid DNA (∼5.8 kb) with hCMV IE promoter−enhancer gene sequence was purchased from Genlantis (San Diego, CA). The pGeneGrip plasmid contains two PNA binding sites (sites −1 and −2) that are attached to maleimide and rhodamine (Rh) labels through PNA linkers, respectively (*19, 40*). The general method for chemical conjugation of plasmid DNA to PNA linkers has been reported in detail in our previously published work (*19*). The total concentration and purity of DNA in solution was determined spectroscopically at 260 and 280 nm using a Beckman DU 7400 spectrophotometer. Plasmid DNA structural integrity was analyzed using a 0.8% w/v DNA agarose gel.

Dual Labeling of Plasmid DNA with Fluorophores. pGeneGrip-gWIZ plasmid was dual-labeled by covalent conjugation of the maleimide group at site-1 with fluorescein (Schemes 1 and 2). For this reaction, 5-((2-(and-3)-*S*-(acetylmercapto)succinoyl)amino)fluorescein (SAMSA fluorescein, A-685) (**1**) (Molecular probes, Invitrogen Corp., Carlsbad, CA) was utilized as a fluorophore (Scheme 2). It was activated prior to the conjugation reaction to expose free thiol residues as described below (Scheme 2).

Activation of SAMSA Fluorescein. Activation of **1** was performed by incubating the stock solution (10 mg/mL) of SAMSA fluorescein prepared in 0.1 N sodium hydroxide for 15 min at room temperature. It was then neutralized with 6 N hydrochloric acid and buffered with 0.5 M sodium phosphate buffer, pH 7.0−7.2 to generate **2**; Scheme 2.

Reaction of Activated Fluorescein with Maleimide-PNA Labeled Plasmid DNA. The maleimide−PNA labeled plasmid (6.5 nanomol) was immediately reacted with approximately 12-fold excess of fluorescein (**2**) freshly prepared (80 nanomol) in 500 μL 0.5 M sodium phosphate buffer. The reaction mixture was incubated for 30 min at room temperature and the uncoupled **2** was removed by buffer exchange with five washes of 10 mM HEPES buffer (pH 7.4) using 100 kDa Centricon, ultrafiltration centrifugal filter units (YM-100, Millipore, Billerica, MA) and centrifuging at 2000 rpm, for 20 min. The filtrate was discarded and the supernatant consisting of the final conjugate mixture was stored in 10 mM HEPES buffer, pH 7.4, 4 °C, until further use.

Scheme 2. Schematic Illustration of Conjugation of Activated SAMSA Fluorescein to Rhodamine/Maleimide Labeled pGeneGrip-gWIZ Plasmid DNA[a]

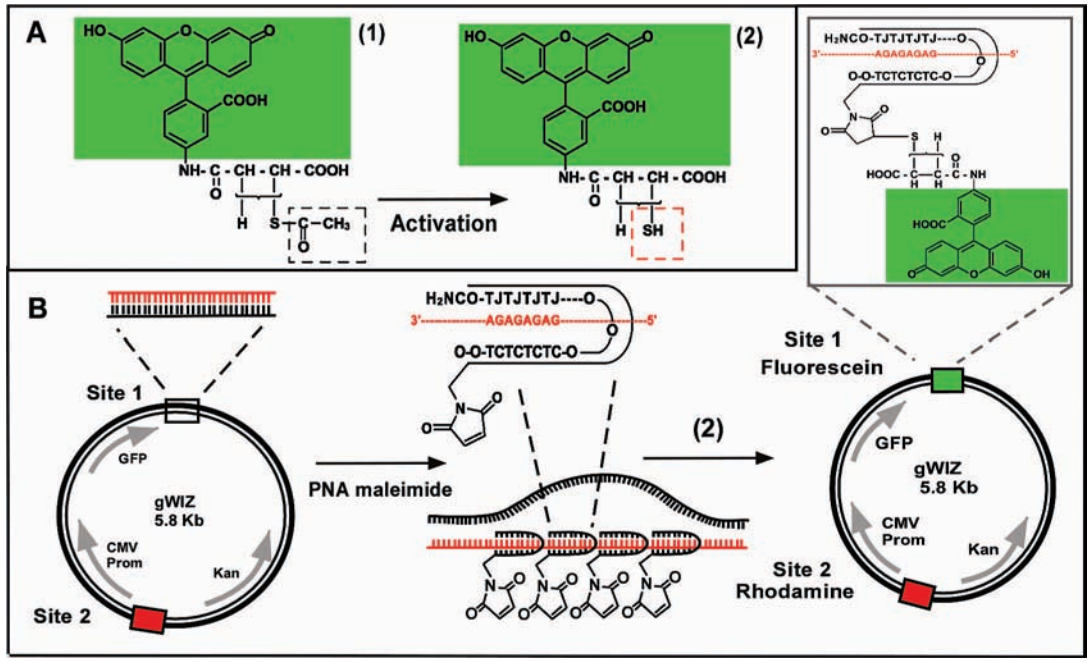

[a] (A) Activation of SAMSA fluorescein (**1**): 0.1 N sodium hydroxide, 15 min incubation; 6 N hydrochloric acid; and 0.5 M sodium phosphate buffer, pH 7.2. This removes the acetyl protecting group in SAMSA fluorescein and exposes the thiol groups (**2**). (B) The free thiol residue on activated SAMSA fluorescein (**2**) covalently reacts with the maleimide group on the plasmid DNA to generate the dual-labeled plasmid DNA.

Agarose Gel Electrophoresis. 0.8% w/v agarose gel electrophoresis was run at 67 V/cm, for 2 h. As a control, a 1 Kb (1 μg/μL) DNA ladder was run by mixing with loading dye (6× solution, 0.25% Bromophenol Blue, 50% glycerol in 1× TAE buffer) (Invitrogen Corp., Carlsbad, CA). Plasmid DNA labeled to rhodamine (Rh) and purified dual-labeled DNA (Rh and activated SAMSA fluorescein) were mixed with a drop of 100% glycerol and 1× TAE buffer prior to electrophoresis. Glycerol was used for sample preparation of the labeled DNA to avoid any interference in fluorophore imaging with the dyes present in the loading dye solution. A Bio-Rad Molecular Imager FX (Hercules, CA) equipped with the appropriate excitation and emission standard filters for Rh and SAMSA fluorescein was used (495/520 nm for fluorescein and 560/590 nm for Rh) to image the labeled DNA bands. The gel was then stained with ethidium bromide nucleic acid stain (final concentration, 0.5 μg/mL) for 30 min followed by three water washes to remove any excess stain and visualized using appropriate filters for ethidium bromide (Ex/Em, 518/605 nm). Bio-Rad Quantity One software was used for analysis of the gel images before and after ethidium bromide staining. The direction of the gel run is shown by (+) and (−) signs.

Restriction Digestion Reaction and Analysis by Gel Electrophoresis. Single and double restriction digestion sites on the dual-labeled pGeneGrip gWIZ-GFP plasmid were identified using New England Biolabs NEBcutter v 2.0 sequence software. The restriction endonucleases *Bam*H1 (20 000 units/mL) and *Pfl*MI (8000 units/mL) (New England BioLabs, Ipswich, MA) were used to digest single and double recognition sites in a non-encoding region of the gWIZ-GFP plasmid, respectively, as shown in the schematic (Scheme 1). The reactants were mixed according to the manufacturers' protocol and incubated for 2 h in a water bath maintained at 37 °C. Gel electrophoresis studies were performed to analyze the digestion reaction fragments (1% w/v agarose, run in 1× TAE buffer, at 67 V/cm, for 1 h). A 1 Kb DNA ladder (1 μg/μL) and purified dual-labeled DNA before digestion were used as controls. *Bam*H1 and *Pfl*MI digested fragments were fully loaded onto the wells in the presence of glycerol prior to gel electrophoresis. Bio-Rad Molecular Imager FX and Quantity One software were used as described above.

Cell Transfection. Transfection studies were conducted in CHO-K1 cells (ATCC, Manassas, VA) by plating 0.5 × 10^6 cells/dish in Bioptechs Delta T dishes (Bioptechs Inc., Butler, PA) one day before the experiment. When the cell population reached 70−80% confluency, they were washed with Hanks' Balanced Salt Solution (HBSS) media, and transfection was carried out in serum-free F12-K media (Invitrogen Corp., Carlsbad, CA). Lipofectamine2000 (Invitrogen Corp., Carlsbad, CA) transfection reagent was used following the manufacturer's protocol. The transfection complexes prepared by complexing dual-labeled DNA conjugates (pGeneGrip gWIZ) (2.76 μg) with Lipofectamine2000 (8.6 μg) at a DNA/lipid ratio of 0.8 μg /2.5 μg w/w were incubated for 15 min before addition to the cells.

Confocal Microscopy. Leica SP2 confocal laser scanning microscope equipped with Ar/Kr, Kr/Ne, and He/Ne lasers (Bannockburn, IL) was used for live cell imaging. Time-lapse imaging with sequential scanning for individual fluorophores was performed following addition of the dual-labeled DNA complexes to CHO-K1 cells. Z-Sectioning was conducted to assist in locating the dual-labeled DNA within the boundaries of the cell membrane. The temperature of the cells during observation was maintained at 37 °C, using a Bioptechs ΔT4 open dish system in a L-15 carbon dioxide free medium.

RESULTS

pGeneGrip gWIZ plasmid DNA containing maleimide/rhodamine groups was successfully dual-labeled via PNA/DNA hybridization using two different PNA linkers at site-1 and site-2 (Scheme 1). The green fluorophore (SAMSA fluorescein) (**1**) was covalently conjugated with the maleimide groups, which are present at site-1, a non-encoding site, as shown in Scheme 2. Prior to the conjugation reaction, (**1**) was activated with sodium hydroxide to remove the acetyl protecting group generating its thiol functionality (**2**). The free thiol moiety on

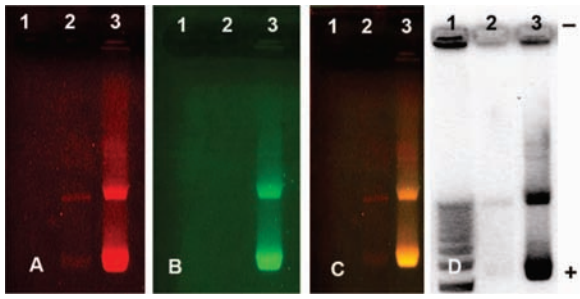

Figure 1. Agarose gel electrophoresis of dual-labeled DNA before and after staining with ethidium bromide DNA stain. Lane 1, DNA ladder; lane 2, DNA labeled with rhodamine (Rh) alone; and lane 3, purified dual-labeled DNA conjugate (Rh (red) and activated SAMSA fluorescein (green)). Panels A and B show exposure at wavelengths that excite the red and the green dyes, respectively. Panel C is the overlap of A and B. Panel D is the UV-excited photoluminescence emission of ethidium bromide (EtBr) stain.

the activated fluorescein was then reacted with the maleimide groups on the plasmid DNA to form a covalent sulfide linkage. pGeneGrip gWIZ plasmid DNA contains approximately 6−10 rhodamine groups and 6−10 PNA−maleimide sites for fluorescein attachment. To maximize conjugation with the plasmid DNA, a 12-fold excess of fluorescein, i.e., a ratio of fluorescein/DNA of 120:1, was used. Unbound fluorophores were removed by ultrafiltration using a 100 kDa membrane (see Materials and Methods section), and this was confirmed by gel electrophoresis. The conjugates remained stable over the 3 month study period.

Gel electrophoresis was used to confirm the dual labeling of plasmid DNA. Detection of the two fluorophores (Rh and fluorescein) conjugated to the DNA was based on direct laser excitation fluorescence imaging using Molecular Imager FX equipped with multichannel excitation and emission filters. The agarose gel revealed two different forms of DNA (lower and higher mobility bands corresponding to open circular forms and supercoiled DNA, respectively) with the majority of the DNA being in the supercoiled conformation (Figure 1). The absence of a band corresponding to rhodamine-labeled DNA upon excitation for fluorescein confirmed lack of any spectral overlap between the two fluorophores used (Figure 1A,B, lane 2). The overlap of panels A and B resulted in yellow bands in lane 3 due to the close proximity of the fluorophores (red and green) on the intact dual-labeled DNA (Figure 1C, lane 3). For comparison, ethidium bromide stained DNA bands are shown in Figure 1D.

To simulate DNA degradation, a model experiment was conducted using the restriction endonucleases *Bam*H1 and *Pfl*MI that cut the plasmid DNA in non-encoding regions at specific single and double recognition sites, respectively (Scheme 1). Gel electrophoresis confirmed the different DNA digestion fragments (Figure 2). Panels A and B in Figure 2 show the emission bands of rhodamine and fluorescein, respectively, after separate excitation using the appropriate filters. Prior to the addition of the restriction enzymes, the DNA bands (open circular and supercoiled forms) are yellow due to the close proximity of the red and green labels on the intact DNA (Figure 2C, lane 2). Upon digestion with the restriction enzyme (*Bam*H1) that cuts at a single site, the circular DNA is linearized, resulting in a single linear strand which has a lower mobility than the supercoiled DNA in lane 2. This linearized DNA is visualized as a yellow band due to the close proximity of the fluorophores (Figure 2C, lane 3). Upon addition of the restriction enzyme *Pfl*MI, which cuts the DNA into two fragments (dual site cutter), the DNA is seen as individual red and green bands, as the two fluorophores are now separated (Figure 2C, lane 4). The DNA fragment containing rhodamine has a lower molecular weight than the fragment containing fluorescein. This difference is observed on the gel electrophoresis with the rhodamine-containing DNA fragment possessing higher mobility than the fluorescein-containing fragment.

On the basis of these observations, dual-labeled DNA was used to explore intracellular trafficking of DNA following transfection in CHO-K1 cells with the cationic liposome, Lipofectamine2000. The lipoplexes containing DNA conjugates were observed using confocal imaging at both the red and green channels (Figure 3I). At the initial time point prior to cellular uptake, imaging was conducted at a focal plane above the cells (0 h, Figure 3I). The overlapped image is visualized as yellow fluorescent voxels due to colocalization of the red and green fluorophores on the intact DNA. Live cell time-lapse imaging at various time points over a 3 h period showed the uptake and intracellular distribution of the DNA conjugates (Figure 3). Optical Z-sectioning was performed to locate the labeled DNA within the boundaries of the cell. Time-lapse imaging at 1, 2, and 3 h revealed yellow as well as individual red and green fluorescent voxels (Figure 3II, A−C) shown by arrows and enlarged images (B1 and C1). The uptake of the DNA conjugates increased with time with only a few conjugates observed at 1 h. At the 1 h time point (Figure 3IIA), only 18% of cells showed uptake of labeled DNA. By 2 h (Figure 3IIB), ∼59% of cells showed uptake of labeled DNA, with ∼32% of cells showing color separation due to DNA degradation. At the 3 h time point (Figure 3IIC), ∼72% of the cells showed uptake of the labeled DNA, with 41% of cells showing DNA degradation.

DISCUSSION

The methodology reported here to dual-label plasmid DNA through PNA linkers shows promise as a bioimaging tool to efficiently elucidate intracellular DNA degradation. pGeneGrip plasmid DNA contains rhodamine fluorophores. SAMSA fluorescein (green) was chosen as a second fluorophore due to its efficient coupling to the pendant maleimide groups on the plasmid DNA. This dual-labeling method did not change the mobility or the supercoiled conformation of the plasmid DNA as confirmed by gel electrophoresis studies.

Gel electrophoresis studies following restriction enzyme digestion demonstrated the utility of dual-labeled plasmid DNA to visualize differences in the plasmid DNA when intact or degraded. This study confirmed visualization of the undigested intact plasmid DNA as a yellow color (due to the close proximity of the two fluorophore labels) with the majority being in the supercoiled form. On the other hand, fragmented DNA, cut at the *Pfl*MI sites (Scheme 1), was seen as two colors (red and green), due to separation of the two fluorophores. The DNA that had undergone only a single site cut (i.e., linearized plasmid DNA) at the *Bam*H1 site is visualized as a yellow color. This could lead to discrepancies in the discrimination of intracellular DNA degradation fragments during tracking studies, since degradation must be at an advanced stage (i.e., beyond at least a single cut) before it can be detected using this methodology. There is a good probability of two or more double strand breaks to occur in a single plasmid intracellularly, since at the onset of endonuclease activity, exonucleases will quickly start the degradation process at the free ends of linearized DNA. Although the possibility of a single cut in DNA is unlikely, a normalization factor can be developed to account for the nondiscernable single cut event. This normalization factor can be determined as a function of enzymatic digestion measured using gel electrophoresis. Single cut and intact DNA can be distinguished in gel electrophoresis, since the single cut DNA, which cannot be in the supercoiled form, has a different mobility (lane 3, Figure 2).

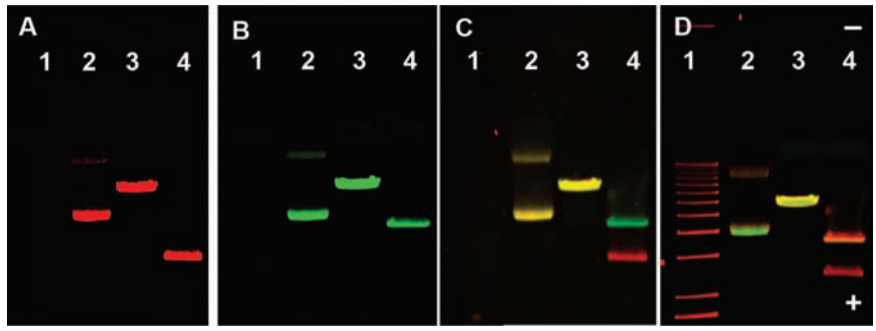

Figure 2. Agarose gel electrophoresis of dual-labeled DNA after treatment with *Bam*H1 and *Pfl*MI restriction enzymes. Lane 1, DNA ladder; lane 2, dual-labeled DNA (Rh (red) and activated SAMSA fluorescein (green)) before digestion; lane 3, *Bam*H1 treated (single site cutter); lane 4, *Pfl*MI treated (two site cutter). Panels A and B show exposure at wavelengths that excite the red and the green dyes, respectively. Panel C is the overlap of A and B. Panel D is the overlapped image after ethidium bromide (EtBr) staining. In panel C, the yellow bands in lanes 2 (DNA before digestion) and 3 (linearized DNA after *Bam*H1 digestion) are due to the close proximity of the red and green dyes on the DNA, whereas in lane 4, the red and green colors are separated after *Pfl*MI digestion at two sites. In panel D, EtBr staining compromises the dye colors in lanes 2−4.

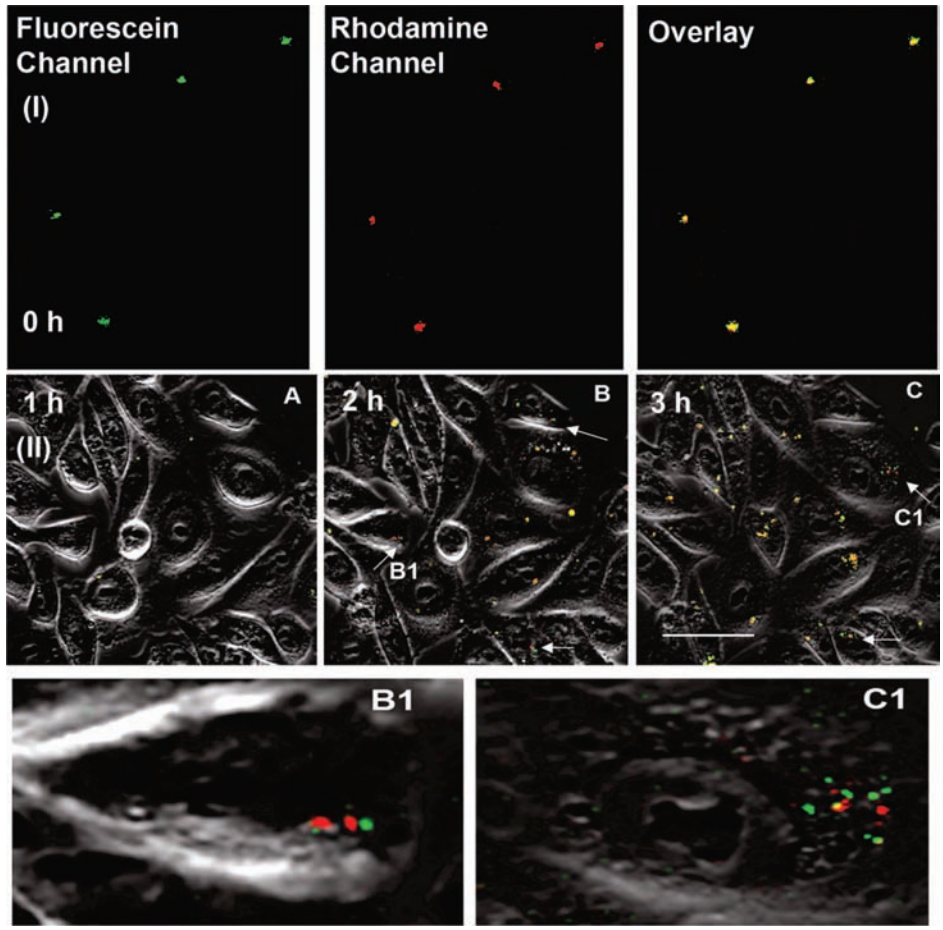

Figure 3. Confocal imaging for uptake of dual-labeled plasmid DNA (rhodamine and activated SAMSA fluorescein) incubated for 0−3 h in the presence of Lipofectamine2000 in CHO-K1 cells. (I) Sequential scanning at the initial time point (0 h). Panels are shown in the following order: green fluorescence (activated SAMSA fluorescein); red fluorescence (rhodamine); and overlap of red and green channels. (II) Time-lapse imaging with sequential scanning for 0−3 h post-transfection (bar 10 μm). Panels A−C overlapped images of all channels at 1, 2, and 3 h, respectively, and revealed yellow as well as individual red and green fluorescent voxels shown by arrows and enlarged images (B1 and C1). The yellow fluorescent voxels in the overlapped images are due to the close proximity of green and red fluorophores in intact dual-labeled DNA. The uptake of the DNA conjugates increased with time with only a few conjugates observed at 1 h. The amount of red and green separation also appears to increase with time (as shown in B1 and C1), indicating progressive DNA degradation.

The practical application of dual-labeled DNA to indicate DNA instability was verified following uptake in CHO-K1 cells using confocal microscopy. The combination of time-lapse imaging and dual-labeled DNA tracking revealed yellow fluorescent voxels in the cytosplasm (which likely represent intact plasmids), as well as color separation, which is indicative of DNA degradation. The yellow fluorescent voxels, evident in the cytoplasm at the 1, 2, and 3 h time points post-transfection, indicate that this DNA is probably in the supercoiled form and/or protected by the cationic liposome vector. Lechardeur et al. reported that lipid-encapsulated plasmid DNA enhanced the stability to degradation (∼25%) when compared to naked plasmid DNA (∼75%) within 4 h after microinjection into the cytosol (*31*). Supercoiled DNA is less susceptible to degradation by cytosolic nucleases, especially endoexonucleases when compared to linearized plasmid or open, circular forms of

plasmid DNA (*42*−*45*). In addition, the more compact nature of supercoiled DNA increases diffusion through the actin and mictrotubular network, thereby allowing a more rapid migration toward the perinuclear region when compared to linear DNA (*42*).

At the 1 h time point post-transfection, only a few yellow fluorescent voxels were seen and there was no red and green separation. The low number of yellow fluorescent voxels observed at the 1 h time point is due to incomplete uptake. This is in agreement with our previous studies, which revealed that maximum uptake of these complexes occurred at approximately 3 h in CHO-K 1 cells (*19*). The amount of red and green separation also appears to increase with time (as shown in Figure 3II), indicating progressive DNA degradation.

Since cationic lipoplexes are generally taken up via the endosomal route (*46*), it is possible that the degradation observed may be due to either entrapment of some complexes in the lysosomal compartment (*33, 46*) or degradation by cytosolic nucleases following release from the endosomes (*31, 46*−*48*). To further elucidate this, future experiments will require labeling of the various subcellular compartments. To address any complexity involved in detection of colocalization or fluorophore separation, we propose to label DNA using similar technology at more than two sites. Imaging of DNA conjugates longer than 3 h was not feasible due to photobleaching of the conjugated fluorophores. This is expected to be alleviated by the use of quantum dots as opposed to organic fluorophores (*19*). Nevertheless, this technique enabled observation of DNA degradation within cells by concurrent tracking using confocal time-lapse imaging. It is anticipated that the use of the dual-labeling technique described here, in combination with organelle stains and nuclease inhibitors (*30, 31, 34, 45, 49*), will be very valuable in elucidating inefficiencies at the different DNA cellular trafficking stages.

CONCLUSIONS

Plasmid DNA was successfully dual-labeled with rhodamine and fluorescein at two separate sites. Gel electrophoresis confirmed the mobility and structural integrity of the dual-labeled DNA. Cellular DNA degradation, simulated using restriction endonucleases, revealed intact DNA as a single color and degraded DNA as two separate colors. Confocal time-lapse imaging and intracellular tracking studies enabled simultaneous visualization of DNA distribution and degradation. A major limitation of this study was the photo-instability of the organic fluorophores used, which significantly limited the time over which DNA tracking at a single cell level could be conducted. More stable fluorophores, such as quantum dots (*19, 50*−*52*) as described in our previous work (*19*), could be used to perform long-term tracking studies.

ACKNOWLEDGMENT

We thank the UCONN Flow Cytometry/Confocal Microscopy core facility for use of instrumentation. This research was supported in part by the Parenteral Drug Association Foundation Schering-Plough Grant, NSF DMI 0303950, ONR N000LY0610016PR, and ARO DAAD-02-1-0381.

LITERATURE CITED

(1) Wolff, J. A., and Rozema, D. B. (2008) Breaking the bonds: non-viral vectors become chemically dynamic. *Mol. Ther. 16*, 8–15.
(2) Wasungu, L., and Hoekstra, D. (2006) Cationic lipids, lipoplexes and intracellular delivery of genes. *J. Controlled Release 116*, 255–64.
(3) Nabel, G. J. (2004) Genetic, cellular and immune approaches to disease therapy: past and future. *Nat. Med. 10*, 135–41.
(4) Luo, D., and Saltzman, W. M. (2000) Synthetic DNA delivery systems. *Nat. Biotechnol. 18*, 33–37.
(5) Patil, S. D., Rhodes, D. G., and Burgess, D. J. (2005) DNA-based therapeutics and DNA delivery systems: a comprehensive review. *AAPS J. 7*, E61−77.
(6) Rolland, A. (2005) Gene medicines: The end of the beginning? *Adv. Drug Delivery Rev. 57*, 669–673.
(7) Pouton, C. W., and Seymour, L. W. (1998) Key issues in non-viral gene delivery. *Adv. Drug Delivery Rev. 34*, 3–19.
(8) Wiethoff, C. M., and Middaugh, C. R. (2003) Barriers to nonviral gene delivery. *J. Pharm. Sci. 92*, 203–17.
(9) Joshee, N., Bastola, D. R., and Cheng, P. W. (2002) Transferrin-facilitated lipofection gene delivery strategy: characterization of the transfection complexes and intracellular trafficking. *Hum. Gene Ther. 13*, 1991–2004.
(10) Simoes, S., Slepushkin, V., Pires, P., Gaspar, R., de Lima, M. P., and Duzgunes, N. (1999) Mechanisms of gene transfer mediated by lipoplexes associated with targeting ligands or pH-sensitive peptides. *Gene Ther. 6*, 1798–807.
(11) Khalil, I. A., Kogure, K., Akita, H., and Harashima, H. (2006) Uptake pathways and subsequent intracellular trafficking in nonviral gene delivery. *Pharmacol. Rev. 58*, 32–45.
(12) El Ouahabi, A., and Ruysschaert, J.-M. (2005) Formation and intracellular trafficking of lipoplexes and polyplexes. *Mol. Ther. 11*, 336–347.
(13) Favaro, E., and Indraccolo, S. (2007) Gene therapy of cancer in the clinic: good news in sight from Asia? *Curr. Opin. Mol. Ther. 9*, 477−82.
(14) Rejman, J., Conese, M., and Hoekstra, D. (2006) Gene transfer by means of lipo- and polyplexes: role of clathrin and caveolae-mediated endocytosis. *J. Liposome Res. 16*, 237–47.
(15) Manunta, M., Nichols, B. J., Tan, P. H., Sagoo, P., Harper, J., and George, A. J. (2006) Gene delivery by dendrimers operates via different pathways in different cells, but is enhanced by the presence of caveolin. *J. Immunol. Meth. 314*, 134–46.
(16) Radler, J. O., Koltover, I., Salditt, T., and Safinya, C. R. (1997) Structure of DNA-cationic liposome complexes: DNA intercalation in multilamellar membranes in distinct interhelical packing regimes. *Science 275*, 810–4.
(17) Chesnoy, S., and Huang, L. (2000) Structure and function of lipid-DNA complexes for gene delivery. *Annu. Rev. Biophys. Biomol. Struct. 29*, 27–47.
(18) Goncalves, C., Mennesson, E., Fuchs, R., Gorvel, J. P., Midoux, P., and Pichon, C. (2004) Macropinocytosis of polyplexes and recycling of plasmid via the clathrin-dependent pathway impair the transfection efficiency of human hepatocarcinoma cells. *Mol. Ther. 10*, 373–85.
(19) Srinivasan, C., Lee, J., Papadimitrakopoulos, F., Silbart, L. K., Zhao, M., and Burgess, D. J. (2006) Labeling and intracellular tracking of functionally active plasmid DNA with semiconductor quantum dots. *Mol. Ther. 14*, 192–201.
(20) Panyam, J., and Labhasetwar, V. (2003) Biodegradable nanoparticles for drug and gene delivery to cells and tissue. *Adv. Drug Delivery Rev. 55*, 329–47.
(21) Bally, M. B., Harvie, P., Wong, F. M., Kong, S., Wasan, E. K., and Reimer, D. L. (1999) Biological barriers to cellular delivery of lipid-based DNA carriers. *Adv. Drug Delivery Rev. 38*, 291–315.
(22) Lechardeur, D., Verkman, A. S., and Lukacs, G. L. (2005) Intracellular routing of plasmid DNA during non-viral gene transfer. *Adv. Drug Delivery Rev. 57*, 755–767.
(23) Simoes, S., Slepushkin, V., Gaspar, R., Lima, M. C. d., and Duzgunes, N. (1998) Gene delivery by negatively charged ternary complexes of DNA, cationic liposomes and transferrin or fusigenic peptides. *Gene Ther. 5*, 955–64.
(24) Hope, M. J., Mui, B., Ansell, S., and Ahkong, Q. F. (1998) Cationic lipids, phosphatidylethanolamine and the intracellular delivery of polymeric, nucleic acid-based drugs. *Mol. Membr. Biol. 15*, 1–14.
(25) Godbey, W. T., Wu, K. K., and Mikos, A. G. (1999) Poly(ethylenimine) and its role in gene delivery. *J. Controlled*

Release 60, 149–160.
(26) Fraser, M. J., Tynan, S. J., Papaioannou, A., Ireland, C. M., and Pittman, S. M. (1996) Endo-exonuclease of human leukaemic cells: evidence for a role in apoptosis. *J. Cell Sci. 109*, 2343–60 (Pt 9).
(27) Lacks, S. A. (1981) Deoxyribonuclease I in mammalian tissues. Specificity of inhibition by actin. *J. Biol. Chem. 256*, 2644–8.
(28) Escriou, V., Carriere, M., Scherman, D., and Wils, P. (2003) NLS bioconjugates for targeting therapeutic genes to the nucleus. *Adv. Drug Delivery Rev. 55*, 295–306.
(29) Neves, C., Escriou, V., Byk, G., Scherman, D., and Wils, P. (1999) Intracellular fate and nuclear targeting of plasmid DNA. *Cell Biol. Toxicol. 15*, 193–202.
(30) Pollard, H., Toumaniantz, G., Amos, J. L., Avet-Loiseau, H., Guihard, G., Behr, J. P., and Escande, D. (2001) Ca^{2+}-sensitive cytosolic nucleases prevent efficient delivery to the nucleus of injected plasmids. *J. Gene Med. 3*, 153–64.
(31) Lechardeur, D., Sohn, K. J., Haardt, M., Joshi, P. B., Monck, M., Graham, R. W., Beatty, B., Squire, J., O'Brodovich, H., and Lukacs, G. L. (1999) Metabolic instability of plasmid DNA in the cytosol: a potential barrier to gene transfer. *Gene Ther. 6*, 482–97.
(32) Briane, D., Lesage, D., Cao, A., Coudert, R., Lievre, N., Salzmann, J. L., and Taillandier, E. (2002) Cellular pathway of plasmids vectorized by cholesterol-based cationic liposomes. *J. Histochem. Cytochem. 50*, 983–91.
(33) Zabner, J., Fasbender, A. J., Moninger, T., Poellinger, K. A., and Welsh, M. J. (1995) Cellular and molecular barriers to gene transfer by a cationic lipid. *J. Biol. Chem. 270*, 18997–9007.
(34) Cornelis, S., Vandenbranden, M., Ruysschaert, J. M., and Elouahabi, A. (2002) Role of intracellular cationic liposome-DNA complex dissociation in transfection mediated by cationic lipids. *DNA Cell Biol. 21*, 91–7.
(35) Jones, R. A., Cheung, C. Y., Black, F. E., Zia, J. K., Stayton, P. S., Hoffman, A. S., and Wilson, M. R. (2003) Poly(2-alkylacrylic acid) polymers deliver molecules to the cytosol by pH-sensitive disruption of endosomal vesicles. *Biochem. J. 372*, 65–75.
(36) Fernandez, B., Galvez, N., Sanchez, P., Cuesta, R., Bermejo, R., and Dominguez-Vera, J. M. (2007) Fluorescence resonance energy transfer in ferritin labeled with multiple fluorescent dyes. *J. Biol. Inorg. Chem.*
(37) Zelphati, O., and Szoka, F. C., Jr. (1996) Intracellular distribution and mechanism of delivery of oligonucleotides mediated by cationic lipids. *Pharm. Res. 13*, 1367–72.
(38) Noguchi, A., Furuno, T., Kawaura, C., and Nakanishi, M. (1998) Membrane fusion plays an important role in gene transfection mediated by cationic liposomes. *FEBS Lett. 433*, 169–73.
(39) Zelphati, O., Liang, X., Hobart, P., and Felgner, P. L. (1999) Gene chemistry: functionally and conformationally intact fluorescent plasmid DNA. *Hum. Gene Ther. 10*, 15–24.
(40) Zelphati, O., Liang, X., Nguyen, C., Barlow, S., Sheng, S., Shao, Z., and Felgner, P. L. (2000) PNA-dependent gene chemistry: stable coupling of peptides and oligonucleotides to plasmid DNA. *Biotechniques. 28*, 304–10, 312−4, 316.
(41) Tanimoto, M., Kamiya, H., Minakawa, N., Matsuda, A., and Harashima, H. (2003) No enhancement of nuclear entry by direct conjugation of a nuclear localization signal peptide to linearized DNA. *Bioconjugate Chem. 14*, 1197–202.
(42) Remaut, K., Sanders, N. N., Fayazpour, F., Demeester, J., and De Smedt, S. C. (2006) Influence of plasmid DNA topology on the transfection properties of DOTAP/DOPE lipoplexes. *J. Controlled Release 115*, 335–43.
(43) Cherng, J. Y., Schuurmans-Nieuwenbroek, N. M., Jiskoot, W., Talsma, H., Zuidam, N. J., Hennink, W. E., and Crommelin, D. J. (1999) Effect of DNA topology on the transfection efficiency of poly((2-dimethylamino)ethyl methacrylate)-plasmid complexes. *J. Controlled Release 60*, 343–53.
(44) Glasspool-Malone, J., and Malone, R. W. (1999) Marked enhancement of direct respiratory tissue transfection by aurintricarboxylic acid. *Hum. Gene Ther. 10*, 1703–13.
(45) Ross, G. F., Bruno, M. D., Uyeda, M., Suzuki, K., Nagao, K., Whitsett, J. A., and Korfhagen, T. R. (1998) Enhanced reporter gene expression in cells transfected in the presence of DMI-2, an acid nuclease inhibitor. *Gene Ther. 5*, 1244–50.
(46) Xu, Y., and Szoka, F. C., Jr. (1996) Mechanism of DNA release from cationic liposome/DNA complexes used in cell transfection. *Biochemistry 35*, 5616–23.
(47) Zabner, J. (1997) Cationic lipids used in gene transfer. *Adv. Drug Delivery Rev. 27*, 17–28.
(48) Zuhorn, I. S., Kalicharan, R., and Hoekstra, D. (2002) Lipoplex-mediated transfection of mammalian cells occurs through the cholesterol-dependent clathrin-mediated pathway of endocytosis. *J. Biol. Chem. 277*, 18021–8.
(49) Torriglia, A., Chaudun, E., Courtois, Y., and Counis, M. F. (1997) On the use of Zn2+ to discriminate endonucleases activated during apoptosis. *Biochimie 79*, 435–8.
(50) Gao, X., Yang, L., Petros, J. A., Marshall, F. F., Simons, J. W., and Nie, S. (2005) In vivo molecular and cellular imaging with quantum dots. *Curr. Opin. Biotechnol. 16*, 63–72.
(51) Watson, A., Wu, X., and Bruchez, M. (2003) Lighting up cells with quantum dots. *Biotechniques 34*, 296–300, 302−3.
(52) Alivisatos, A. P., Gu, W., and Larabell, C. (2005) Quantum dots as cellular probes. *Annu. Rev. Biomed. Eng. 7*, 55–76.

BC800184J

A Multifunctional Single-Attachment-Point Reagent for Controlled Protein Biotinylation

Elisabeth Garanger,[†] Ralph Weissleder,[†,‡] and Lee Josephson*[,†]

Center for Molecular Imaging Research, Massachusetts General Hospital and Harvard Medical School, Building 149, 13th Street, Boston, Massachusetts 02129, and Center for Systems Biology, Massachusetts General Hospital and Harvard Medical School, 185 Cambridge Street, Boston, Massachusetts 02114. Received September 15, 2008; Revised Manuscript Received November 4, 2008

The biotin/avidin system is one of the most widely used affinity detection and affinity capture systems in biology. However, the determination of the exact number of biotin tags attached onto a substrate is complicated by the fact that biotin does not present any light-absorbing or -emitting properties. Here, we describe a fluorescent biotinylation reagent designed from the general multifunctional single-attachment-point (MSAP) reagent concept. A Lys-Cys dipeptide scaffold was used to display a biotin functional group and a fluorescein functional group along with an *N*-hydroxysuccinimide ester reactive group. The resulting bifunctional MSAP reagent, Fl-Biotin-NHS, was used to prepare a monobiotinylated version of cetuximab, which was further reacted with avidin to obtain a soluble avidin-based cetuximab oligomer. The MSAP peptide-scaffold approach allows fluorophores, chromophores, or reactive groups to be combined with biotin and provides a broad approach to obtain multifunctional biotin-based reagents.

INTRODUCTION

The recognition of biotinylated molecules by avidin (or streptavidin) is one of the most widely exploited affinity capture systems in immunohistochemistry, biochemical purification, and a variety of assay systems (*1*). In many systems, where either avidin or biotin is immobilized, the capture is not highly sensitive to the number of biotins per mole of biotinylated protein. However, when the reaction between avidin and a biotinylated protein occurs in solution, the degree of biotinlylation of the protein is of considerable importance. The self-assembly of biotinylated proteins into avidin-mediated protein oligomers can produce profound changes in bioactivity, such as those that occur when biotinylated MHC molecules form streptavidin-based tetramers (*2*).

Reacting avidin with biotinylated proteins containing more than one biotin per mole can lead, not to tetramers, but to extended complexes of avidin and biotinylated proteins, which eventually precipitate (Figure 1A). Reacting avidin with biotinylated proteins containing an average of less than one biotin per mole leads to mixtures of avidin-mediated oligomers and non-biotinylated proteins (Figure 1B). Reacting avidin with proteins containing an average of one biotin per mole maximizes the formation of soluble avidin-mediated oligomers (Figure 1C). Thus, when synthesizing soluble avidin-mediated protein oligomers, there is a need to obtain proteins that have (on average) a single biotin per mole. This in turn requires a simple, sensitive, and accurate method for determining the numbers of biotins.

We describe here an *N*-hydroxysuccinimide (NHS) ester-activated version of biotin and fluorescein, which can be used to determine the degree of biotinylation of proteins based on fluorescein's absorbance or fluorescence. The reagent, termed

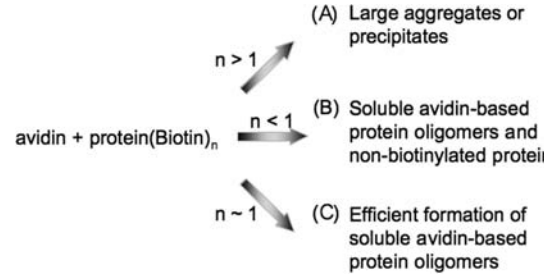

Figure 1. Reactions of biotinylated proteins with a tetrameric avidin. (A) When biotinylated proteins are over-biotinylated, with multiple biotins per mole ($n > 1$), large soluble aggregates or precipitates form, due to avidin tetravalency. (B) When biotinylated proteins are under-biotinylated, $n < 1$, non-biotinylated protein is present. (C) Mono-biotinylated proteins, $n \sim 1$, maximize the formation of soluble avidin-based protein oligomers.

"Fl-Biotin-NHS", employed our multifunctional single-attachment-point (MSAP) technology (*3*), where fluorescein, biotin, and the NHS ester are attached to a peptide scaffold. The Fl-Biotin-NHS reagent was used to obtain a mono-biotinylated cetuximab that was further reacted with avidin to prepare a soluble avidin-based cetuximab oligomer. To demonstrate the flexibility of the MSAP peptide scaffold approach to reagent design, a second fluorescent biotin reacting with thiol groups, "Fl-Biotin-MAL", is also presented.

EXPERIMENTAL PROCEDURE

Synthesis of Biotin-Lys(monosuccinimidylsuberate)-Cys(5-acetamidofluorescein)-NH_2, Fl-Biotin-NHS. The linear biotin-Lys(Boc)-Cys(Trt) sequence was elongated onto the Rink amide MBHA resin using standard Fmoc/*t*Bu solid-phase peptide synthesis procedures described earlier (*3*). Peptide full deprotection and cleavage from the resin with TFA/TIS/H_2O/EDT (95:2:2:1) afforded the biotin-Lys(H)-Cys(H)-NH_2 peptide as a white powder after lyophilization. ($C_{19}H_{34}N_6O_4S_2$) Calc. exact mass 474.2; found m/z $[M + H]^+ = 475.1$. Solutions of Biotin-

* Corresponding author. Center for Molecular Imaging Research, Massachusetts General Hospital and Harvard Medical School, Building 149, 13th Street, Boston, MA 02129 (USA). Phone: 617-726-6478, Fax: 617-726-5708, E-mail: ljosephson@mgh.harvard.edu.

[†] Center for Molecular Imaging Research.

[‡] Center for Systems Biology.

10.1021/bc800392t CCC: $40.75 © 2009 American Chemical Society
Published on Web 12/11/2008

Lys(H)-Cys(H)-NH_2 (12.1 mg, 25.5 μmol) in 510 mL anhydrous DMF, fluorescein-5-iodoacetamide (8 mg, 15.5 μmol, 0.6 equiv) in 155 μL anhydrous DMF and DIPEA (5 μL, 28.7 μmol, 1.1 equiv) were mixed together overnight at room temperature. The reaction mixture was purified by RP-HPLC, and the fraction collected was lyophilized. Biotin-Lys(H)-Cys(5-acetamidofluorescein)-NH_2 (8.4 mg, 9.7 μmol, 63% yield) was obtained as a yellow powder. ($C_{41}H_{47}N_7O_{10}S_2$) Calc. exact mass 861.3; found m/z $[M + H]^+ = 862.0$. A solution of biotin-Lys(H)-Cys(5-acetamidofluorescein)-NH_2 (5.9 mg, 6.8 μmol) in 274 μL anhydrous DMF containing DIPEA (1.3 μL, 7.5 μmol, 1.1 equiv) was added slowly to a solution of DSS (50 mg, 135.7 μmol, 19.8 equiv) in 1360 μL anhydrous DMF. The reaction mixture was stirred for 48 h at room temperature. The reaction mixture was purified by RP-HPLC and the fraction collected lyophilized. Biotin-Lys(monosuccinimidylsuberate)-Cys(5-acetamidofluorescein)-NH_2 (5.2 mg, 4.7 μmol, 68% yield) was obtained as a yellow powder. ($C_{53}H_{62}N_8O_{15}S_2$) Calc. exact mass 1114.4; found m/z $[M + H]^+ = 1115.0$, $[M + Na]^+ = 1137.0$.

Synthesis of Biotin-Lys(γ-maleimidobutyryloxy)-Cys(5-acetamidofluorescein)-NH_2, Fl-Biotin-MAL. A solution of Biotin-Lys(H)-Cys(5-acetamidofluorescein)-NH_2 (4.2 mg, 4.9 μmol) in 240 μL anhydrous DMF containing DIPEA (1.0 μL, 5.7 μmol, 1.2 equiv) was added to a solution of GMBS (6.9 mg, 24.6 μmol, 5.1 equiv) in 246 μL anhydrous DMF. The reaction mixture was stirred overnight at room temperature. The reaction mixture was purified by RP-HPLC and the fraction collected lyophilized. Biotin-Lys(γ-maleimidobutyryloxy)-Cys(5-acetamidofluorescein)-NH_2 (3.3 mg, 3.2 μmol, 66% yield) was obtained as a yellow powder. ($C_{49}H_{54}N_8O_{13}S_2$) Calc. exact mass:1026.3; found m/z $[M + H]^+ = 1027.0$, $[M + Na]^+ = 1149.9$.

Biotinylation of Cetuximab with Fl-Biotin-NHS. Various amounts of a solution of Fl-Biotin-NHS in DMSO (10 mM) were added to Erbitux (2 mg/mL). Typically, 1.35 equiv of reagent for a final degree of biotinylation of 1 were used. The reaction was left for 1 h at room temperature and purified by size-exclusion chromatography using a Sephadex PD-10 column. Immunoconjugates were prepared in phosphate buffer pH 8 at 0.8 mg mL^{-1}.

Absorbance Measurements. Absorption spectra were measured on a Varian Cary 50 Bio UV−visible sprectrophotometer. Solutions of increasing concentrations of Fl-Biotin-NHS in phosphate buffer pH 8 were used to obtain a standard curve of optical density versus Fl-Biotin concentration. The absorbance was measured at the 493 nm absorbance maximum of Fl-Biotin-NHS. Solutions of cetuximab-(Fl-Biotin)$_n$ immunoconjugates were diluted two times. Absorbance was measured at 496 nm, absorbance maximum of cetuximab-(Fl-Biotin)$_n$. Each measurement was repeated three times. The number of biotin tags for each immnunoconjugate was obtained from the standard curve.

Fluorescence Measurements. Fluorescence emission spectra were recorded on a Varian Cary Eclipse fluorescence spectrophometer. Solutions of increasing concentrations of Fl-Biotin-NHS in phosphate buffer pH 8 were used to obtain the standard curve of fluorescence intensity at 519 nm versus Fl-Biotin concentration. Solutions of cetuximab-(Fl-Biotin)$_n$ immunoconjugates were diluted two times. Each measurement was repeated three times. The number of biotin tags for each immnunoconjugate was obtained from the standard curve.

Preparation of the Cetuximab−Avidin Oligomer. A solution of Avidin-Cy3.5$_{1.4}$ (0.8 mg/mL; 800 μL, 10 nmol) in phosphate buffer pH 7.2 was added to a solution of cetuximab-Fl-Biotin$_{1.1}$ (3.1 mg/mL; 2.75 mL, 57 nmol). The mixture was stirred overnight at 4 °C and purified by size exclusion chromatography using a Sephacryl 300-HR column (volume = 59.2 mL). The high valency was eluted in 34−40 mL phosphate buffer pH 7.2.

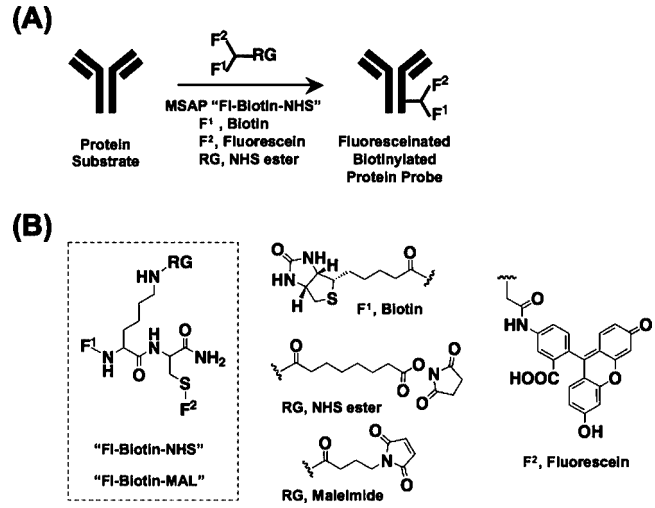

Figure 2. Multifunctional single-attachment-point (MSAP) reagents for the synthesis of biotinylated proteins. (A) A protein substrate, such as a monoclonal antibody, reacts with the MSAP reagent "Fl-Biotin-NHS" to yield a fluorescent (F^2), biotinylated (F^1) probe in one step. (B) Design of the "Fl-Biotin-NHS" and "Fl-Biotin-MAL" MSAP reagents. To the Lys-Cys dipeptide scaffold are attached the F^1 functional group biotin, the F^2 functional group fluorescein-acetamide, and either an *N*-hydroxysuccinimide (NHS) ester or a maleimide (MAL) reactive group RG.

Determination of the Number of Cetuximab in the Cetuximab−Avidin Oligomer by Absorbance. Absorption spectrum (200−800 nm) of the cetuximab−avidin oligomer was measured in phosphate buffer pH 7.2. Absorbance at 583 nm gave the concentration of Cy3.5 in the complex (150 000 M^{-1} cm^{-1}), without interference from fluorescein. Absorbance at 496 nm, corrected for the absorption of the Cy3.5 fluorochrome at this wavelength (18 000 M^{-1} cm^{-1}), gave the concentration of fluorescein in the complex (74 000 M^{-1} cm^{-1}). The ratio between fluorescein and Cy3.5 concentrations enabled an estimation of the number of cetuximab per avidin based on 1.1 Fl-Biotin per cetuximab and 1.4 Cy3.5 per avidin.

Photon Correlation Spectroscopy. Volume-weighted average diameters were obtained by light scattering using a Nano-2S Zetasizer (Malvern Instruments). Solutions of (a) ferritin (1 mg/mL), (b) cetuximab (1 mg/mL), (c) avidin (1 mg/mL), (d) avidin (1 mg/mL) + cetuximab (1 mg/mL), and (e) cetuximab−avidin oligomer, were measured.

"Native" Gel Electrophoresis. "Native" SDS-PAGE was performed using a Tris-HCl gel from 4% to 15% polyacrylamide. Samples were prepared by using 20 μL of protein solution and 5 μL of a buffer containing Tris (25 mM), glycine (192 mM), pH 8.3, 10% glycerol, and bromophenol. Electrophoresis was run (from the anode to the cathode) with a buffer containing SDS (3.5 mM), Tris (25 mM), and glycine (192 mM) at pH 8.3. No reducing agent (β-mercaptoethanol) was used.

RESULTS AND DISCUSSION

The principles behind the MSAP reagent concept are shown in Figure 2. As shown in Figure 2A, the MSAP reagent, "Fl-Biotin-NHS", had two functional groups (F^1 = biotin, F^2 = fluorescein) and a reactive group (RG) as an NHS ester. The chemical structure of Fl-Biotin-NHS is further clarified in Figure 2B. A Lys-Cys dipeptide scaffold was employed for the attachment of biotin (F^1), fluorescein (F^2), and a reactive *N*-hydroxysuccinimide ester reactive group (RG).

To demonstrate some of the flexibility possible with the peptide scaffold-based MSAP strategy, we prepared "Fl-Biotin-

Table 1. Fluorescent Biotin MSAPs

peptide scaffold	F^1	F^2	RG	MW (g mol^{-1})	designation
F^1-Lys(RG)-Cys(F^2)-NH_2	biotin	fluorescein-5-acetamide	*N*-hydroxysuccinimide ester	1115.2	Fl-biotin-NHS
F^1-Lys(RG)-Cys(F^2)-NH_2	biotin	fluorescein-5-acetamide	maleimide	1027.1	Fl-biotin-MAL

MAL", where a maleimide RG replaced the NHS ester. Fl-Biotin-MAL becomes a site-specific labeling reagent when reacted with bioengineered proteins containing a single thiol. The properties of Fl-Biotin-NHS and Fl-Biotin-MAL are given in Table 1. All subsequent experiments employed Fl-Biotin-NHS.

The Fl-Biotin-NHS MSAP, formally biotin-Lys(monosuccinimidylsuberate)-Cys(5-acetamidofluorescein)-NH_2, was synthesized as shown in Figure 3. Biotin was attached to the N-terminus of the protected Lys(Boc)-Cys(Trt) peptide on the solid phase. After deprotection and release from the resin, the thiol and amine groups were selectively reacted with fluorescein-5-iodoacetamide and with the cross-linker dissuccinimidyl suberate (DSS), respectively. Full characterization of Fl-Biotin-NHS is provided in the Supporting Information accompanying this manuscript. Fl-Biotin-MAL was prepared similarly by using an amine to thiol heterobifunctional cross-linker (*N*-[γ-maleimidobutyryloxy]succinimide, GMBS).

Fl-Biotin-NHS was employed to prepare biotinylated versions of the monoclonal antibody cetuximab where the number of biotins varied from 0.1 to 2.5 per mol of antibody. Absorbance and fluorescence standard curves acquired with Fl-Biotin-NHS were used to determine the number of Fl-Biotin moieties per antibody. A perfect fit between the absorbance of the immunoconjugates and the amount of Fl-Biotin-NHS reagent used per cetuximab was obtained. The fluorescein absorption signal (496 nm) enabled direct quantification of a wide range of biotinylation levels (Figure 4A and C). Samples containing from 0.5 up to 25 biotins per antibody could be measured from a single standard curve. Biotinylation levels obtained from fluorescence and absorbance signals were in very good concordance until the number of biotins reached a value of 15 (Figure 4C). Indeed, fluorescence quenching was noticed to occur when the conjugates contained more than 15 Fl-Biotin motifs. However, in the case of a low degree of biotinylation, the exact number of biotin per antibody can be more accurately determined by fluorescence than by absorbance (Figure 4B). Indeed, when the Fl-Biotin content of the immunoconjugate is low, the fluorescence peak can still be distinguished from the background conversely to the absorbance signal.

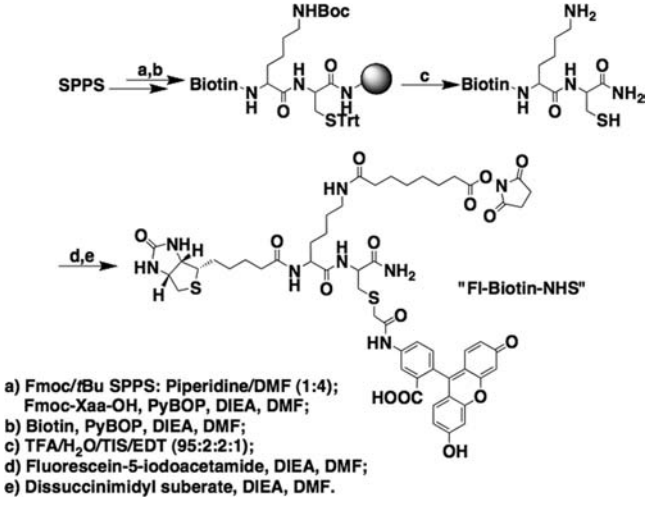

Figure 3. Synthesis of the "Fl-Biotin-NHS" MSAP or biotin-Lys-(monosuccinimidylsuberate)-Cys(5-acetamidofluorescein)-NH_2 ($C_{53}H_{62}N_8O_{15}S_2$; MW = 1115.23 g mol^{-1}). Biotin was attached to the N-terminus of the protected Lys-Cys peptide on the solid phase. After deprotection and release from the resin, the thiol and amine groups are selectively reacted with fluorescein-5-iodoacetamide and the cross-linker dissuccinimidyl suberate, respectively. The high flexibility of the synthetic strategy allows various substitutions of the Lys-Cys peptide scaffold and thus various MSAPs compositions.

In every case, we found both absorbance and fluorescence methods of Fl-Biotin more sensitive than the HABA method (Figure 4A and B). The commonly used method for estimating the extent of biotinylation of proteins, i.e., the molar ratio of biotin to protein, is based on the displacement of the HABA dye (4′-hydroxyazobenzene-2-carboxylic acid) from an HABA−Avidin complex absorbing visible light at 500 nm. Replacement of HABA by biotin in the complex translates into a decrease in the absorption intensity at 500 nm proportionally to the number of bound biotins. In the microplate assay format suggested in the EZ Biotin Quantitation Kit (Pierce), the decrease in absorbance for a regular antibody (MW 150 kDa, at 1 mg.mL^{-1}) containing an average of five biotins per protein is around 0.057, corresponding to a 10% decrease of the initial absorbance value. For the same antibody modified with only one biotin, the decrease is 0.011, corresponding to a 2% decrease of the initial absorbance value. This method lacks accuracy for low biotinylation levels.

We then considered the preparation of an avidin-based cetuximab oligomer from a monobiotinylated cetuximab and a tetrameric avidin. Fl-Biotin-NHS was thus used to modify cetuximab with 1.1 Fl-Biotin motifs per antibody. The latter was further incubated with avidin modified with the Cy3.5 fluorochrome. (Figure 5). Modification of the antibody and of the avidin with fluorescein and Cy3.5 fluorochromes, respec-

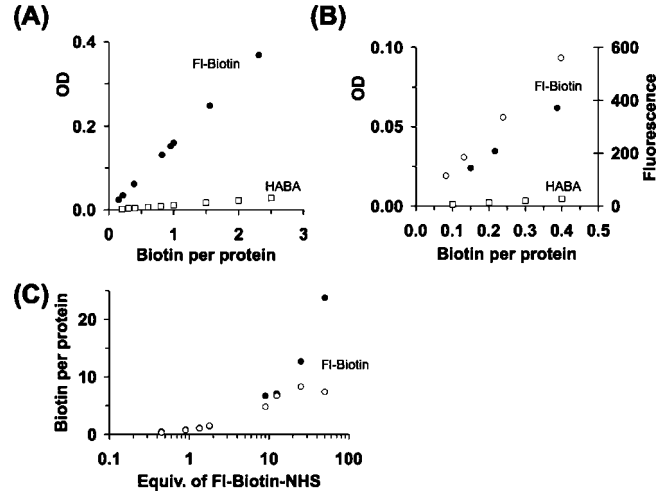

Figure 4. Comparison of the sensitivity of Fl-Biotin-NHS with the HABA dye displacement-based method for the determination of biotinylation of a monoclonal antibody (cetuximab). (A) Biotin per protein determined by Fl-Biotin's absorbance (496 nm, •) versus the HABA method (500 nm, □). Fl-Biotin is more sensitive than the HABA method, based on the displacement of the HABA dye from the HABA−Avidin complex by biotin (A_{500} = A_{500}HABA−Avidin − A_{500}HABA−Avidin−Biotin). (B) Biotin per protein at low biotinylation levels determined by Fl-Biotin absorbance (496 nm, •), the HABA method (500 nm, □), and Fl-Biotin fluorescence (519 nm, ○). (C) Quenching of Fl-Biotin fluorescence with high numbers of Fl-Biotin per mole of protein. At high levels of Fl-Biotin (n > 15), fluorescence quenching causes an underestimation of the number of Fl-Biotin per protein. Note that each measurement is the average of three replicates; error bars are included.

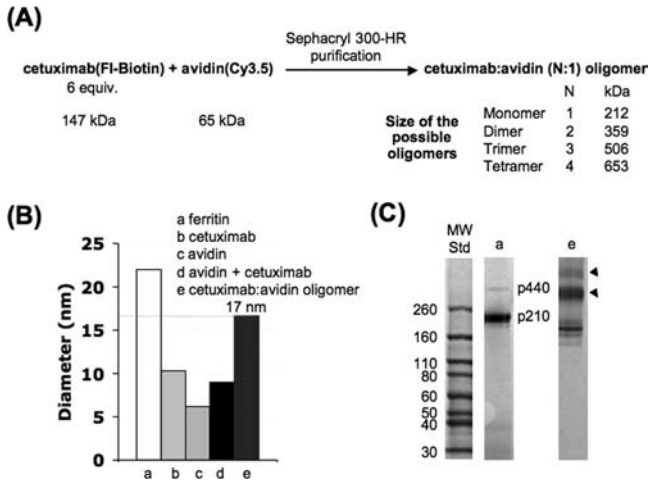

Figure 5. Synthesis and characterization of a cetuximab−avidin oligomer. (A) Synthesis of the oligomer. Six molar equivalents of a monobiotinylated cetuximab was reacted with avidin(Cy3.5). The reaction mixture was purified by gel filtration and the oligomer was isolated. (B) Characterization of the cetuximab oligoner by laser light scattering. The volume-weighted diameter was 17 nm. (C) Characterization of the cetuximab oligomer by SDS-PAGE (no mercaptoethanol). Lane "MW Std" shows various molecular weight standards. Lane "a" is a ferritin standard which gave species of 210 and 440 kDa. Lane "e" is the cetuximab−avidin oligomer. The most prominent species was slightly smaller than 440 kDa ferritin. The cetuximab−avidin oligomer contains a mixture of the dimer, 359 kDa, and of the trimer, 506 kDa.

tively, facilitated (i) the separation of the complex by gel filtration (Sephacryl 300-HR) and (ii) the determination of the ratio of cetuximab to avidin in the cetuximab−avidin oligomer. Absorbance measurements concluded 2.3 cetuximab per avidin (data not shown). The oligomer was characterized by dynamic laser light scattering and gel electrophoresis. The size of the oligomer was 17 nm (volume-weighted) as measured by light scattering (Figure 5B). The size of the oligomer was also assessed by "native" (no reducing agent) SDS-PAGE and compared to ferritin, a globular protein, presenting two major bands, p210 and p440, at 210 and 440 kDa, respectively. The oligomer presents two species. The most prominent species is slightly smaller than 440 kDa ferritin. Altogether, the results of the three characterization methods converge to the conclusion that the cetuximab oligomer obtained is a mixture of the dimer, 359 kDa, and of the trimer, 506 kDa.

An advantage of the MSAP synthetic strategy shown in Figure 3 is its ability to allow substitutions of the functional groups or reactive groups on the biotin-Lys-Cys dipeptide. Since the dipeptide is made by manual solid-phase synthesis, sufficient dipeptide was obtained to allow it to be split into portions for reactions with different functional groups. In particular, the single amine and single thiol of the dipeptide can be reacted in a chemoselective manner with a variety of reagents under mild conditions, to generate a variety of biotinylated molecules. Since fluorescein was not exposed to the harsh conditions of deprotection, any thiol-reactive fluorochrome can be substituted for fluorescein-5-iodoacetamide, including near-infrared fluorochromes, some of which do not survive the harsh conditions of deprotection. Thus, MSAP chemistry provides a broad new strategy for designing biotinylated reagents that can feature a variety of possible reporter groups (e.g., chromophores, fluorochromes, chelators) and, as we have shown, *N*-hydroxysuccinimide ester or maleimide reactive groups.

CONCLUSION

A peptide scaffold based, multifunctional, single-attachment-point reagent (MSAP) was used to obtain the fluorescent biotin, Fl-Biotin-NHS. Fl-Biotin-NHS was then used to attach 1.1 biotins per mole to cetuximab, and the biotinylated antibody reacted with avidin to obtain an avidin−cetuximab oligomer. The Fl-Biotin-NHS can be used to biotinylate protein substrates with the degree of biotinylation determined by absorbance or fluorescence. In addition, MSAP reagents provide a broad new approach to the design of multifunctional biotins.

ACKNOWLEDGMENT

This work was supported by R01 EB004472, R01 EB00662 and P50 CA86355.

Supporting Information Available: Full characterization of Fl-Biotin-NHS. This material is available free of charge via the Internet at http://pubs.acs.org.

LITERATURE CITED

(1) Savage, D., Mattson, G., Desai, S., Nielander, G., Morgensen, S., and Conklin, E. (1994) *Avidin-biotin chemistry: a handbook*, 2nd ed., PIERCE Chemical Company.

(2) Klenerman, P., Cerundolo, V., and Dunbar, P. R. (2002) Tracking T cells with tetramers: new tales from new tools. *Nat. Rev. Immunol. 2*, 263–72.

(3) Garanger, E., Weissleder, R., and Josephson, L. (2008) Simplified syntheses of complex multifunctional nanomaterials. *Chem. Commun.* (39), 4792–4.

BC800392T

SUPPORTING INFORMATION

A Multifunctional Single-Attachment-Point Reagent for Controlled Protein Biotinylation

Elisabeth Garanger, Ralph Weissleder and Lee Josephson*

Characterization of Fl-Biotin-NHS.

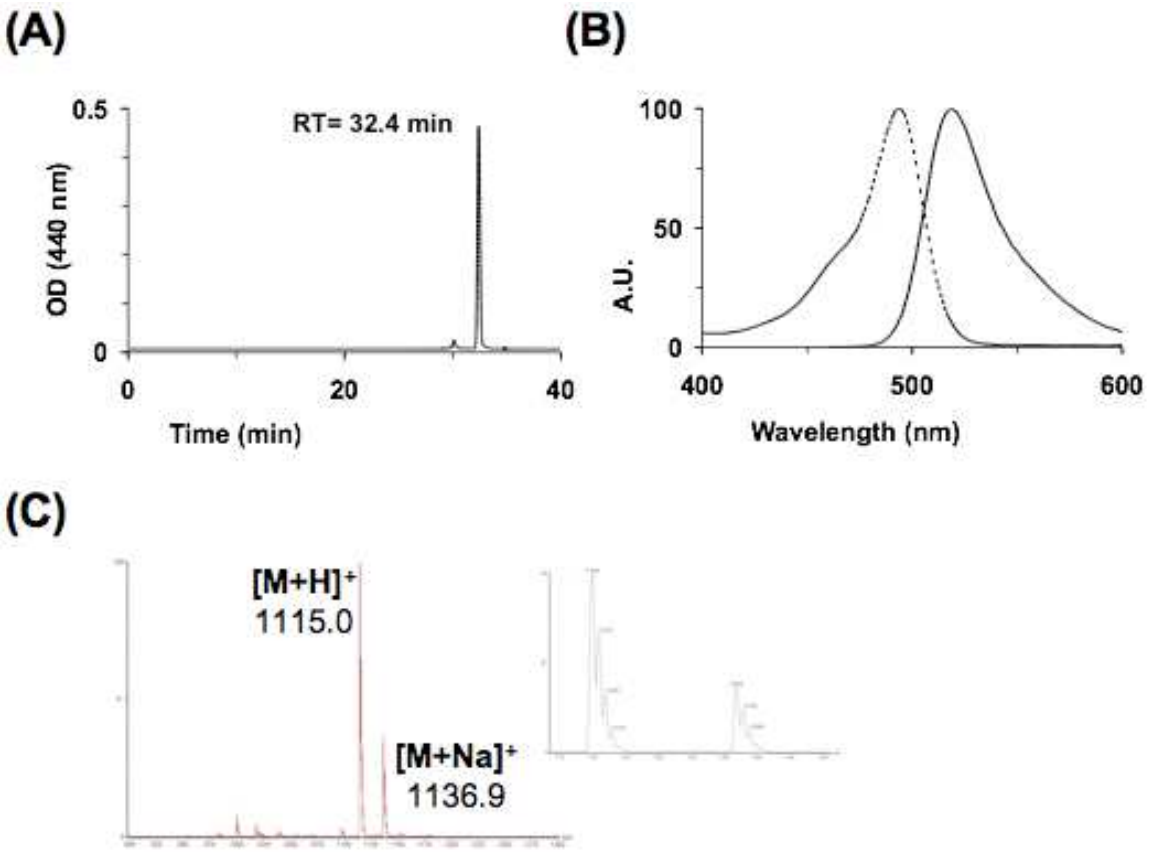

(A) Analytical RP-HPLC chromatogram of the purified compound (UV monitoring at 440 nm, linear gradient 5% acetonitrile/H_2O/TFA (90:9.9:0.1) for 5 min, 5-60% in 30 min): Retention Time=32.4 min.

(B) Absorbance and fluorescence spectra in phosphate buffer pH 7.2.

(C) MS-ESI spectrum (m/z [900-1300]) and zoom of the two monocharged peaks. Calc. exact mass: 1,114.4; found m/z: $[M+H]^+$=1,115.0, $[M+Na]^+$=1,136.9.

Subscriber access provided by SHEMYAKIN-OVCHINNIKOV INST

Technical Note

In Vivo SPECT and Real-Time Gamma Camera Imaging of Biodistribution and Pharmacokinetics of siRNA Delivery Using an Optimized Radiolabeling and Purification Procedure

Olivia M. Merkel, Damiano Librizzi, Andreas Pfestroff, Tino Schurrat, Martin Be#he#, and Thomas Kissel

Bioconjugate Chem., **2009**, 20 (1), 174-182• DOI: 10.1021/bc800408g • Publication Date (Web): 18 December 2008

Downloaded from http://pubs.acs.org on May 8, 2009

More About This Article

Additional resources and features associated with this article are available within the HTML version:

- Supporting Information
- Access to high resolution figures
- Links to articles and content related to this article
- Copyright permission to reproduce figures and/or text from this article

View the Full Text HTML

ACS Publications
High quality. High impact.

Bioconjugate Chemistry is published by the American Chemical Society. 1155 Sixteenth Street N.W., Washington, DC 20036

In Vivo SPECT and Real-Time Gamma Camera Imaging of Biodistribution and Pharmacokinetics of siRNA Delivery Using an Optimized Radiolabeling and Purification Procedure

Olivia M. Merkel,[†] Damiano Librizzi,[‡] Andreas Pfestroff,[‡] Tino Schurrat,[‡] Martin Béhé,[‡,§] and Thomas Kissel*[,†]

Department of Pharmaceutics and Biopharmacy, Philipps-Universität Marburg, Ketzerbach 63, 35037 Marburg, Germany, Department of Nuclear Medicine, University Hospital Giessen and Marburg GmbH, Baldingerstrasse, 35043 Marburg, Germany, and Department of Nuclear Medicine, University of Freiburg, Hugstetterstrasse 55, 79106 Freiburg, Germany. Received September 24, 2008; Revised Manuscript Received November 8, 2008

Single photon emission computed tomography (SPECT) imaging provides a three-dimensional method for exactly locating gamma emitters in a noninvasive procedure under in vivo conditions. For characterization of siRNA delivery systems, molecular imaging techniques are extremely helpful to follow biodistribution under in experimental animal studies. Quantification of biodistribution of siRNA and nonviral delivery systems using this technique requires efficient methods to stably label siRNA with a gamma emitter (e.g., ^{111}In or ^{99m}Tc) and to purify labeled material from excesses of radiolabel or linkers. In the following study, we have optimized labeling and purification of siRNA, which was then applied as free siRNA or after complexation with polyethylenimine (PEI) 25 kDa for in vivo real-time gamma camera and SPECT imaging. Quantification of scintillation counts in regions of interest (ROIs) was compared to conventional scintillation counting of dissected organs, and the data acquired by imaging was shown to corroborate that of scintillation counting. This optimization and proof of principle study demonstrates that biodistribution and pharmacokinetics of siRNA and the corresponding polyplexes can be determined using SPECT, leading to comparable results as conventional methodology.

INTRODUCTION

Single photon emission computed tomography (SPECT) imaging is an attractive method which allows three-dimensional localization of gamma emitters such as ^{111}In ($E\gamma = 171$ and 245 keV) or ^{99m}Tc ($E\gamma = 140$ keV) using a noninvasive procedure under in vivo conditions. Such techniques would be extremely helpful for assessing siRNA and their corresponding nonviral delivery systems with regard to biodistribution and targeting.

SPECT, compared to positron emission tomography (PET), is less elaborate and expensive and shows additionally a higher resolution in small animals. The disadvantage of SPECT and PET providing only functional but no morphological information can be alleviated by either combining SPECT or PET and computed axial tomography (CT), magnetic resonance imaging (MRI), or anatomical landmarking. For the latter, bones are visualized using radioactively ^{99m}Tc-labeled bisphosphonates. Dual-isotope SPECT recordings can then be recorded in separate channels for each energy window and superimposed to generate 3D images. This dual-isotope SPECT method has not been utilized to investigate siRNA delivery systems so far. Although it does not provide the same information as SPECT/CT or SPECT/MRI, it, of course, gives better insight than single-isotope SPECT.

The field of siRNA delivery has rapidly evolved in recent years; however, only few in vivo studies combining siRNA delivery with noninvasive molecular imaging techniques such as SPECT or PET have appeared in the literature (*1*, *2*). Several groups have labeled siRNA with ^{32}P (*3*, *4*), which is a beta emitter and can only be determined using scintillation counting or autoradiography in an end point study but not in in vivo imaging. Phosphodiester and phosphorothioate siRNA have been reported to be labeled with ^{123}I and ^{125}I (*5*), but radiometal labeling is usually preferred over radiohalogen labeling because of stability reasons (*6*, *7*). In an earlier report, siRNA had been labeled with ^{111}In, but biodistribution was only quantified invasively (*8*). A recent PET/bioluminescence study (*2*) using DOTA-chelated ^{64}Cu was the first report of assessing siRNA delivery by PET imaging. An earlier study (*9*) quantitated distribution of ^{99m}Tc-labeled single strands using a gamma camera, but unfortunately allowed only for an estimation of biodistribution of duplexes. SPECT, compared to PET, provides better spatial resolution in small animals and does not require synthesis of short-lived and high-energy emitters. Additionally, using high-resolution SPECT imaging based on multi-pinhole collimation, which is a prototype of the latest small animal scanners, allowed us to use a clinical camera (*10*).

Quantification of biodistribution of siRNA and their delivery systems using SPECT or two-dimensional gamma camera imaging requires efficient methods for stably labeling siRNA with a gamma-emitting isotope as well as fast and efficient purification of labeled materials from excesses of radiolabel or linkers.

The fate of pDNA after intravenous application of different nonviral vectors, such as polyethylenimine (PEI) or PEGylated PEI (PEG-PEI), has been reported previously (*11*, *12*), but it cannot be assumed that siRNA polyplexes would perform identically under in vivo conditions. In fact, several studies demonstrated differences between siRNA and DNA containing polyplexes (*13*, *14*). Hence, dual isotope SPECT would be of interest for in vivo live imaging the biodistribution of siRNA

* Address for correspondence. Philipps-Universität Marburg, Department of Pharmaceutics and Biopharmacy, Ketzerbach 63, D-35032 Marburg, Germany. TEL: +49-6421-282 5881. FAX: +49-6421-282 7016. E-mail kissel@staff.uni-marburg.de.

[†] Philipps-Universität Marburg.

[‡] University Hospital Giessen and Marburg GmbH.

[§] University of Freiburg.

10.1021/bc800408g CCC: $40.75 © 2009 American Chemical Society
Published on Web 12/18/2008

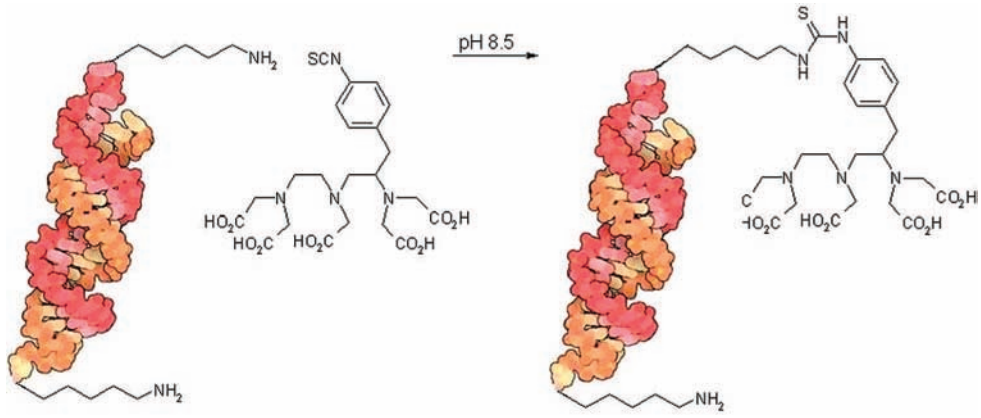

Figure 1. Reaction of amine-modified siRNA and p-SCN-Bn-DTPA in the formation of a thiourea derivative. Both strands bear a C6-NH_2 linker, but a coupling degree of 2 mol/mol could not be achieved.

polyplexes. As ^{111}In can be complexed with chelators such as p-SCN-Bn-DTPA, we have developed an optimized a method (*8*) for covalently labeling amine-modified siRNA and applied this labeled siRNA in real time live imaging of the distribution of our previously in vitro investigated PEI/siRNA polyplexes (*15*).

MATERIALS AND METHODS

Materials. Amine-modified luciferase GL3 siRNA with a C6-NH_2 linker at each 3′ of the double strand was purchased from Dharmacon (Lafayette, CO, USA). 2-(4-Isothiocyanatobenzyl)diethylenetriaminepentaacetic acid (p-SCN-Bn-DTPA) was purchased from Macrocyclics (Dallas, TX, USA), arsenazo(III), yttrium(III) chloride, and diethyl pyrocarbonate (DEPC) from Sigma-Aldrich Laborchemikalien GmbH (Seelze, Germany). The purification columns miRACLE were purchased from Stratagene (La Jolla, CA, USA), RNeasy Mini from Qiagen (Hilden, Germany), and PD-10 from Amersham Pharmacia Biotech (Freiburg, Germany). The radioactive substances $^{111}InCl_3$ and ^{99m}Tc-alendronate were purchased from Covidien Deutschland GmbH (Neustadt a.d. Donau, Germany), and balb/c mice from Charles River WIGA (Sulzfeld, Germany).

Polyethylenimine, PEI 25 kDa (Polymin, 25 kDa), was a gift from BASF (Ludwigshafen, Germany); all other chemicals used were of analytical grade. All buffers were treated with 0.1% diethyl pyrocarbonate (DEPC).

Methods. *p-SCN-Bn-DTPA Coupling.* Amine-modified luciferase GL3 siRNA was dissolved in siRNA buffer provided by the manufacturer. Coupling of p-SCN-Bn-DTPA was accomplished by a previously described method (*8*). Briefly, 20 nmol siRNA in 10 μL siRNA buffer, adjusted to pH 8.5 with an equal volume of 0.2 M $NaHCO_3$, was mixed with a 50-fold excess of the chelator dissolved in 36 μL DMSO. In our experiments, we used the amine-reactive variant of DTPA (p-SCN-Bn-DTPA) instead of DTPA-dianhydride (cDTPA). Incubation times were varied from 45 min as reported to 3 h. The coupling degree was determined after purification by quantification of DTPA in a nonradioactive assay described by Pippin et al. (*16*). Briefly, absorption of a complex of arsenazo(III) and yttrium(III) at 652 nm is measured, and sample DTPA content can be calculated or a calibration curve can be recorded due to decreasing absorption of the complex falling apart after addition of DTPA.

PD-10 Size Exclusion Chromatography (SEC). One method used for separation of labeled siRNA from p-SCN-Bn-DTPA or radiolabel was size exclusion chromatography SEC employing a PD-10 Sephadex G25 prepacked column. The column was equilibrated with 50 mL DEPC-treated PBS before the reaction mixture was applied to the column. Fractions of 13 droplets each were collected. RNA content was measured UV-metrically at 260 nm using a Pharmacia Ultrospec 2000 UV/vis, Pharmacia Biotech (Freiburg, Germany), and the radioactive signal in 10 μL of each fraction was determined using a Gamma Counter Packard 5005 (Packard Instruments, Meriden, CT, USA).

miRACLE and RNeasy Purification. Spin column purification was conducted as described for the miRACLE columns. Briefly, 1 or 100 μg siRNA for miRACLE or RNeasy columns, respectively, were diluted to 600 μL with 2 M sodium acetate, ethanol, and guanidinium salts containing "binding buffer" provided in the miRACLE kit and applied to a spin column. Columns were centrifuged for 2 min at 16 000 *g* and washed 3 times with 600 μL "low salt wash buffer" by centrifugation for 1 min at 16 000 *g*. The membranes were dried by a fifth centrifugation step without applying any solution. RNA was then eluted by incubating the membrane with 50 μL 60 °C warm DEPC-treated RNase free water for 2 min and following centrifugation for 1 min at 16 000 *g*. This step was repeated and followed by a third incubation where 25 μL DEPC-treated 0.5 M sodium acetate, pH 4.5, were applied instead of water to achieve a final concentration of 0.1 M sodium acetate in the siRNA solution.

Radiolabeling. Radiolabeling of the p-SCN-Bn-DTPA-coupled siRNA was accomplished in 0.1 M sodium acetate buffer, pH 4.5. For the validation of the method, small amounts of 10 nmol siRNA were incubated with 16.2 MBq $InCl_3$ for 30 min at room temperature. For in vivo experiments, 111 nmol siRNA were incubated with 28.9 MBq $InCl_3$ for 30 min at room temperature, followed by either PD-10 SEC or spin column binding, washing, and elution, or a combination of both methods. For in vivo experiments, siRNA was purified using a PD-10 column first. Fractions 5−9 (compare Figure 4A and B), which showed both a high radioactive signal and the strongest UV absorption at 260 nm and do not contain any free p-SCN-Bn-DTPA or indium, were combined and further purified as well as concentrated using RNeasy columns as described above.

Animal Studies. All animal experiments were carried out according to the German law of protection of animal life and approved by an external review committee for laboratory animal care.

For in vivo experiments in 4-week-old balb/c mice (∼20 g), 35 μg Bn-DTPA coupled thiourea derivative of siRNA, corresponding to 2.57 nmol and 0.255 MBq, were either administered as free siRNA or after complexation at an N/P ratio of 6 with 25 kDa branched PEI. Free siRNA or complexes were injected i.v. to the tail vein, and biodistribution was followed by perfusion live imaging and static imaging acquired with a Siemens e.cam gamma camera (Siemens AG, Erlangen, Germany). Biodistribution 2 h post-injection was investigated by

A

Purification method	Yield [%]	Coupling Degree [mol/mol]
PD-10 GPC	108.5 +/- 20.5	3.23 +/- 0.141
miRACLE spin columns	92.6 +/- 6.4	0.17 +/- 0.002
RNeasy spin columns	79.6 +/- 4.1	0.33 +/- 0.002

B

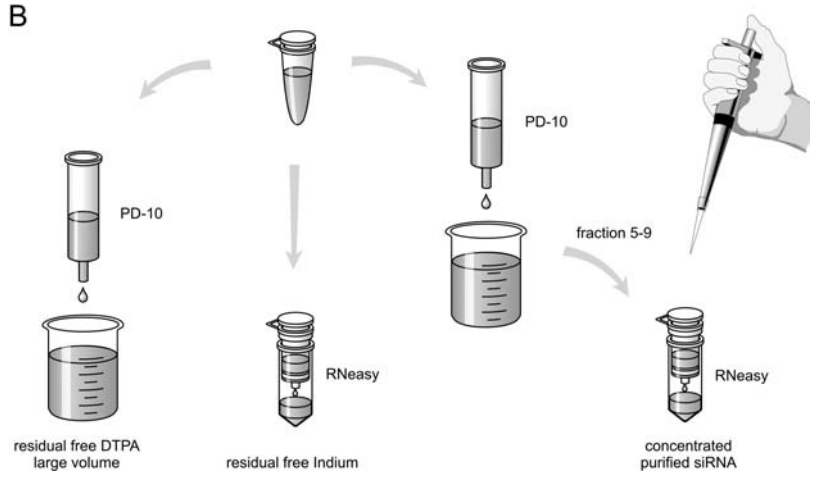

Figure 2. (A) Yields and p-SCN-Bn-DTPA coupling degrees analyzed after different methods of siRNA purification. (B) Purification with a PD-10 column did not effectively separate siRNA from an excess of unreacted p-SCN-Bn-DTPA. RNeasy columns did not desalt from $InCl_3$, and therefore, a combined purification after annealing was employed.

high-resolution SPECT imaging using a custom-built multiplexing multi-pinhole collimator, mounted on the Siemens e.cam gamma camera, quantified by analysis of regions of interest (ROIs) in the planar gamma camera images, and was eventually compared to conventional gamma counting of dissected organs.

For anatomical landmarking in the SPECT images, mice were additionally injected with 4 MBq ^{99m}Tc-labeled phosphonate 4 h before imaging.

Statistics. Analytical measurements were conducted in triplicate. Animal experiments include 5 animals per group; results are given as mean values. Two-way ANOVA and statistical evaluation was accomplished using GraphPad *Prism 4.03* (GraphPad Software, LaJolla, USA).

RESULTS AND DISCUSSION

While labeling of amine-modified siRNA with p-SCN-Bn-DTPA was accomplished differently from the method previously reported (*8*) and could not be improved by variation of incubation time, purification of the reaction mixture, on the other hand, was extensively optimized. For coupling the amine-modified siRNA, we preferred the use of p-SCN-Bn-DTPA over cyclic DTPA anhydride (cDTPA) (*8*), since in the coupling reaction with the latter, one of the chelating teeth is used for amide formation in a ring opening reaction. The advantage of formation of a thiourea derivative in a standard reaction of amines and the benzyl-isothiocyanate modified DTPA is the fact that each chelating tooth is available for complex formation after DTPA is unaffected by the reaction of the benzyl-spaced isothiocyanate, which is shown in Figure 1. In search of a faster purification method than extensive dialysis, which would yield a higher percentage of siRNA recovery and protect the siRNA from degradation, a method was employed that is known from RNA isolation from cells or tissues. First of all, spin columns specifically developed for miRNA isolation (miRACLE, Stratagene) were used to validate the method and to quantify the yield. The basic principle of this purification or isolation method is the binding of RNA in the presence of chaotropic salts to the silica membrane of the spin columns. Additionally, RNA is made insoluble by a high concentration of ethanol of at least 70% v/v in the presence of 10% v/v 2 M sodium acetate buffer, and therefore can be washed extensively but rapidly with low salt buffers containing 70% v/v ethanol. Finally, the RNA is eluted with water or TE buffer. Due to the chelating activity of EDTA in TE buffer, which could later complex parts of radioactive indium, all siRNA was eluted with DEPC-treated water.

The miRACLE spin columns proved to be applicable for siRNA, as the yield of eluted siRNA was 92.6 ± 6.4% and the coupling degree determined after purification was 16.9 ± 2.1% (compare Figure 2A). Because of their low binding capacity (1 μg RNA per column) and bigger reaction feeds needed for in vivo application, the use of RNeasy Mini columns (Qiagen) that hold 100 μg of RNA was validated in the next step. Since the buffer composition of the binding and washing buffers in the RNeasy kit is proprietary, buffers from the miRACLE kit, which were assured to be free of chelators, were used for all spin column purifications. The yield of the siRNA recovery could extensively be increased from 40%, which had been eluted with 25 °C warm DEPC−water to 79.6 ± 4.1% after incubating the siRNA on the membrane for 2 min with 60 °C warm DEPC−water.

The coupling degree of such purified siRNA was determined to be 32.9 ± 1.8% as shown in Figure 2A.

For purification after radiolabeling, in the first approach, PD-10 (Amersham) SEC was employed as described by Van de Water et al. (*8*). After analysis of the collected fractions for UV-metrically determined siRNA concentration and gamma-counted radioactivity, RNA peak fraction and peak fraction of the radioactivity seemed to be shifted, as shown in Figure 3A, and the radioactive signal slowly decreased before a second peak appeared. Due to the principle of SEC, big particles are eluted first, then smaller ones in later fractions. Since the siRNA had only been brought into contact with DEPC-treated buffers upon receipt, we precluded degradation. One possible explanation was that siRNA had not been fully annealed, and possibly only the single strands had been effectively labeled with p-SCN-Bn-

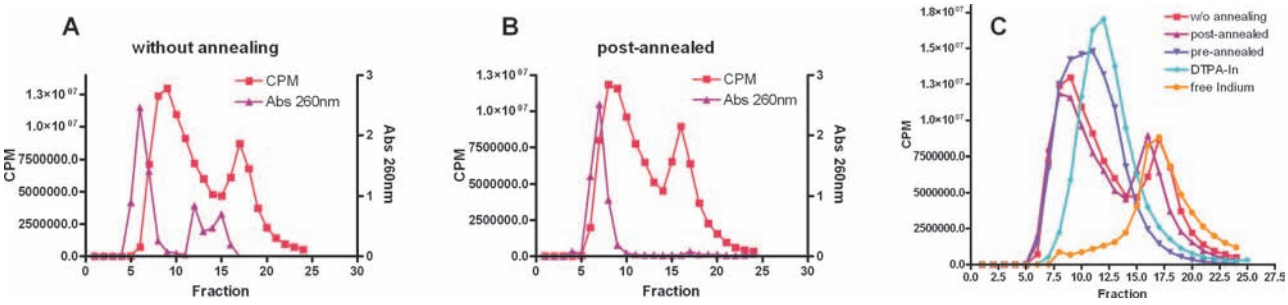

Figure 3. PD-10 size exclusion chromatographs of purified siRNA. (A) RNeasy purified siRNA without annealing. Radioactivity and RNA peaks are shifted. (B) RNeasy purified siRNA after postannealing. Peaks are concurrent, but radioactivity signal decreases slowly. (C) Overlay of radioactivity signals. p-SCN-Bn-DTPA-Indium appears after fraction 7 and is the reason for the slow decrease of signal in RNeasy purified siRNA and the broad peak in PD-10 purified preannealed siRNA (blue). Free indium peaks at fraction 17 and is not apparent in PD-10 purified preannealed siRNA due to excess of free p-SCN-Bn-DTPA.

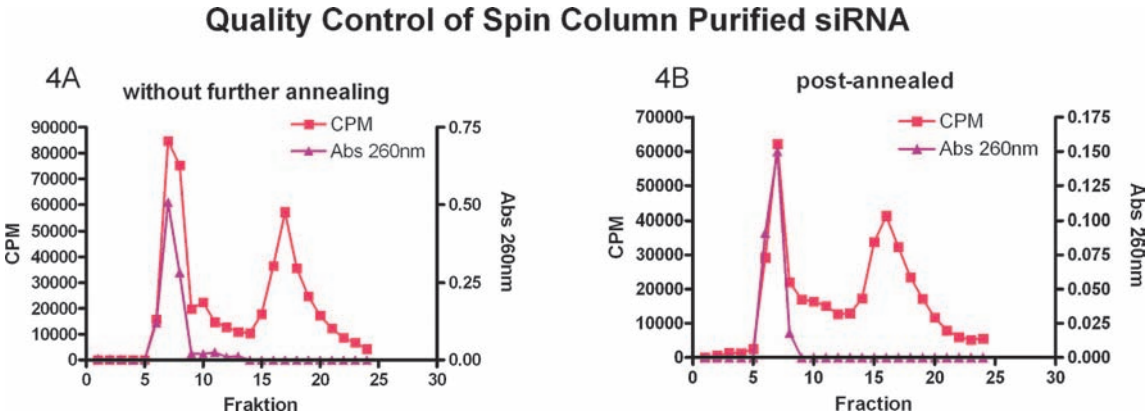

Figure 4. PD-10 size exclusion chromatographs of siRNA that was purified with RNeasy spin columns after coupling and after radiolabeling. RNA and radioactivity peaks are concurrent in climax and anticlimax, but a substantial amount of free indium is left in solution.

DTPA. To prove this, radiolabeling was repeated (a) without annealing and (b) with annealing of the siRNA strands by heating up to 94 °C for 2 min after p-SCN-Bn-DTPA-labeling, and with (c) preannealed siRNA. To make sure that the annealed double strands would not be separated on the membranes of the spin columns or under harsh conditions such as 16 000 *g* centrifugal force, this reaction mixture was purified on a PD-10 column. Here, a mathematically calculated coupling degree of theoretically 323% and therefore an excess of at least 123% of free p-SCN-Bn-DTPA was determined, as shown in Figure 2A.

The same amounts of free indium (orange line, Figure 3C) or free p-SCN-Bn-DTPA-chelated indium (green line, Figure 3C), which had been in the reaction mixtures, were each applied to a PD-10 column in separate experiments. This allowed us to detect when free indium and when indium chelated by residual free p-SCN-Bn-DTPA would be eluted from the PD-10 column and which peak in the chromatographs represented each of those two compounds. Free indium showed a peak at fraction 17, with p-SCN-Bn-DTPA-indium at fraction number 12. The overlay of each indium signal in Figure 3C allowed us to clearly identify the second, smaller peak in Figure 3A,B to be the free Indium.

Reannealing of the precoupled siRNA strands finally caused concurrence of the radioactivity and the siRNA peak, which is shown in Figure 3B. Without annealing, again a shift of both peaks was observed (compare Figure 3A). However, the decrease of the radioactivity signal of the reannealed sample (Figure 3B) fell less steeply than the RNA signal. In the preannealed sample (blue line in Figure 3C), which obviously contained a high amount of free p-SCN-Bn-DTPA (compare Figure 2A), the indium peak was even broader and did not show a free indium peak after fraction 15.

Since spin column purification after p-SCN-Bn-DTPA coupling had proven to be much more effective than SEC, it was next employed for purification after radiolabeling of another sample of which small aliquots were applied to a PD-10 column for quality control either without further treatment (Figure 4A) or after reannealing (Figure 4B). The chromatographs of those two aliquots did not show significant differences, but finally, the peaks of RNA concentration and radioactivity matched in both peak and valley. However, as a second, smaller peak appeared again after fraction 15, it must be admitted that the spin column purification is highly effective for separation of siRNA (approximately 13.6 kDa) from small molecules like p-SCN-Bn-DTPA (650 Da), but cannot fully separate siRNA from large excesses of salts like $InCl_3$. The best strategy therefore seemed to be a combination of SEC and spin column purification, as another benefit of a following spin column purification is the fact that the peak fractions from SEC can be combined and concentrated on the columns, as shown in Figure 2. Annealing of siRNA should be accomplished after p-SCN-Bn-DTPA coupling to achieve a high coupling degree.

The final yield after combined purification of 125 nmol siRNA of which 111 nmol siRNA was labeled with 28.8 MBq was 81.2% with a specific activity of 99 MBq/μmol.

Functionality of the labeled siRNA was investigated in vitro and found not to be significantly different from a nonlabeled duplex of the same sequence (data not shown).

In the in vivo experiments, labeled and purified siRNA was either administered as free siRNA, as reported earlier (*8*), or after complexation with 25 kDa branched PEI, which has already been characterized concerning in vivo biodistribution and pharmacokinetics after complexation of pDNA and ODNs (*11*, *17*, *18*) and has lately been used for in vivo siRNA delivery (*19*−*24*).

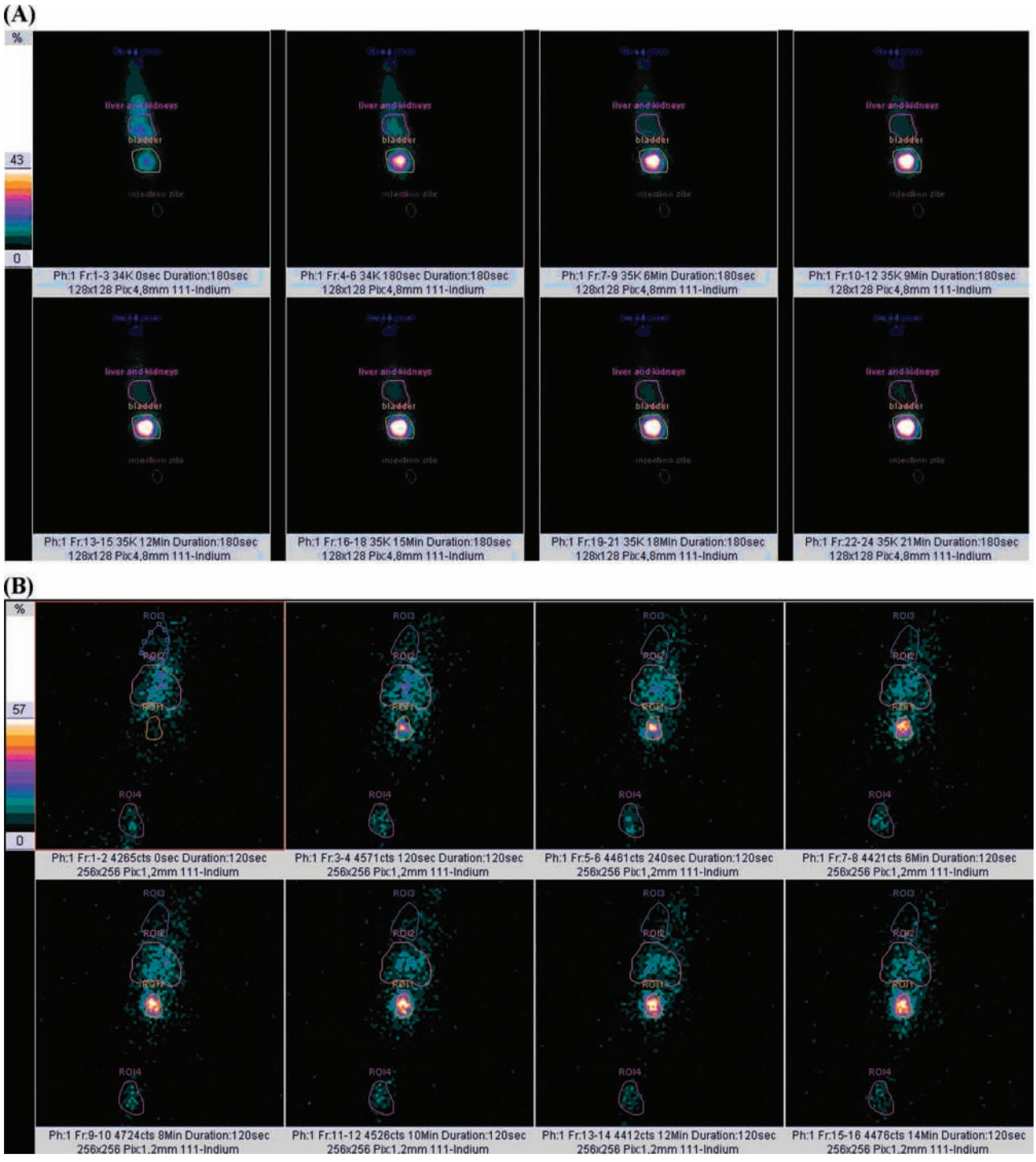

Figure 5. Planar gamma camera perfusion movie with regions of interest for lifetime quantification after injection of 35 μg siRNA, corresponding to 2.57 nmol and 0.255 MBq ^{111}In (A) as free siRNA and (B) complexed at N/P of 6 with 25 kDa bPEI.

In the real-time perfusion study, rapid accumulation of PEI-complexed siRNA in the liver and in the kidneys could be observed, as well as an increasing signal in the bladder, as shown in Figures 5B, 6B, and Movie 4 (Supporting Information). Quantification of scintillation counts in the ROIs as a function of time, as shown in Figure 6B, reveal that the half-life of PEI-complexed siRNA in the blood pool (blue line, Figure 6B and C) is only 168.5 s, which is in good agreement with published data (*25*). The signal in the liver and kidneys decreases to a plateau after initial accumulation (pink line, Figure 6B), and the signal of residual radioactive material in the injection site (purple line, Figure 6B) decreases as well to a certain extent. Free siRNA, on the other hand, showed initial uptake into the liver and kidneys, as shown in Figure 6A (pink line), but no accumulation. Our real time perfusion recording shows very rapid excretion into the bladder (Figure 5A and Movie 1, Supporting Information), which is visualized and quantified in Figure 6A. While activity in the liver and kidneys decreases (Figure 6A, pink line), it increases to the same extent in the bladder (Figure 6A, orange line).

SPECT images recorded 2 h post-injection corroborated the observation of accumulation of PEI-complexed siRNA in liver, kidneys, and bladder by providing more three-dimensional, regional information (compare Figure 7B and Movie 2, Supporting Information), and gamma scintillation counting of dissected organs confirmed that PEI 25 kDa complexed siRNA

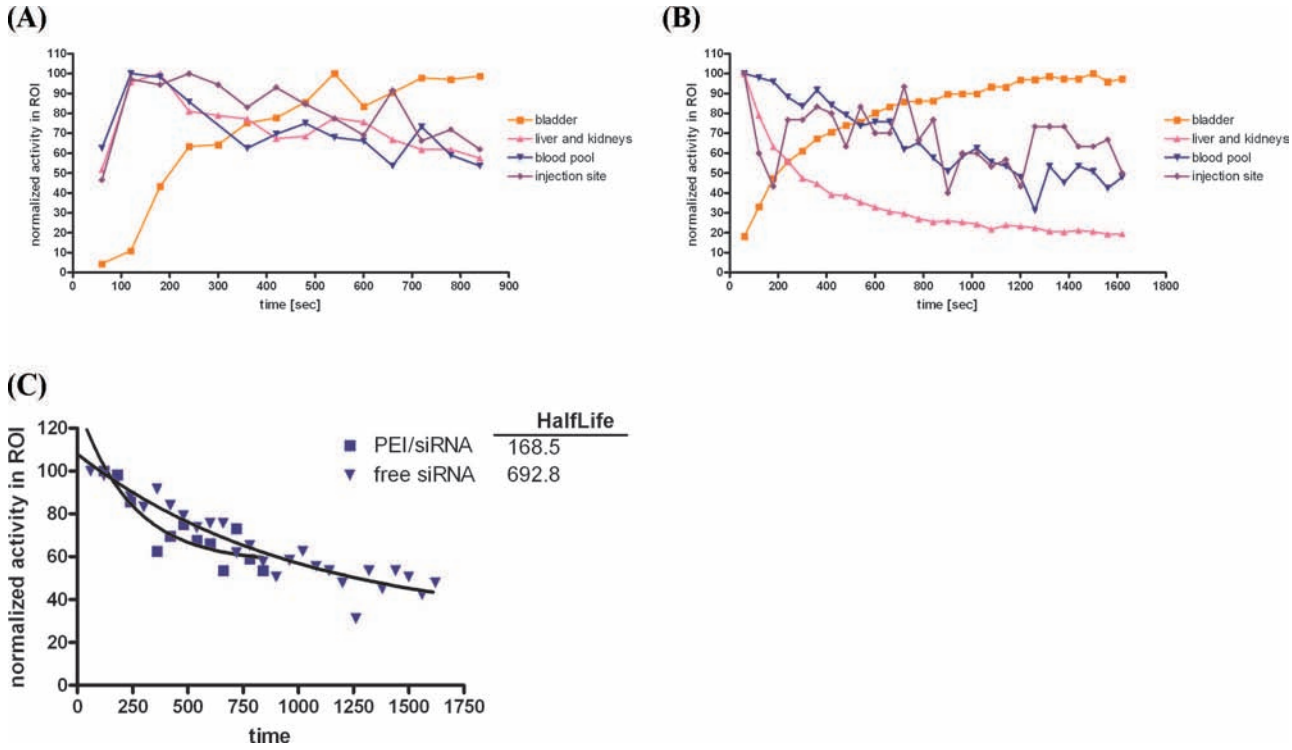

Figure 6. Normalized graphical analysis of activity in regions of interest in Figures 5A and 5B. 6A: Free siRNA, 6B: PEI-complexed siRNA, 6C: Pharmacokinetic analysis of siRNA in circulation. 273 × 162 mm (300 × 300 DPI).

accumulated in the liver and was renally excreted, as it was found to be in the urine and not in the bladder tissue (compare Figure 8A). Confirmation of noninvasive data by invasive data, which has been reported in drug delivery (*26*) and gene therapy (*27*) studies, was the critical part of this investigation and was successfully achieved.

Free siRNA could be measured in the kidneys, as reported earlier (*8*), and partly in the liver, but was also eliminated through the bowel. Due to their instability in serum, free siRNA duplexes are rapidly degraded upon injection. Therefore, small fragments bearing the label supposedly circulate in the blood pool and show a different behavior than macromolecules or nanoplexes.

Fast renal clearance and a high signal in the urine in biodistribution studies with PEI/pDNA polyplexes had so far been interpreted as degraded plasmid being excreted (*28*). In our study, on the other hand, we found higher signals in the urine for PEI-complexed siRNA compared to free siRNA, 2 h after injection. One reason could be that the free siRNA had been excreted to the bladder faster than PEI-complexed siRNA and got lost by urination before the animals were sacrificed. However, the signal in the urine cannot only be caused by degradation products, knowing that renal clearance might even be faster than siRNA degradation (*25*). In fact, free siRNA, which for sure had partly been degraded after injection, showed a different profile from complexed siRNA. In the case of free siRNA, no distinct deposition in any certain organ could be observed (Figure 8A), and the percentage of injected dose that was still in circulation after 2 h was 9% per mL blood compared to 1% for PEI 25 complexed siRNA (Figure 8). The half-life of free siRNA was 692.8 s (compare Figure 6A and C). SPECT images of mice treated with free siRNA (Figure 7A) showed no distinct deposition in any organ either, except for the bladder. One explanation for this could be long circulation and almost no deposition of small fragments of degraded siRNA or a binding of amine-modified siRNA to blood components. It is known that siRNA is degraded rapidly in vivo by serum nucleases and that this can be prevented or retarded by chemical modification of the nucleotides or by complexation with an appropriate delivery system (*29*−*31*). In our earlier publication, we showed that bPEI 25 kDa as well as PEGylated derivatives do have the potential to protect siRNA from RNase degradation (*15*). As formulation with the polymer seemed to drive kinetics and distribution, PEI-complexed siRNA showed a clear accumulation in the liver of 15% injected dose per organ (Figure 8A), although not as prominent as observed with pDNA, which had been reported to be up to 40% (*11*). Accumulation in the spleen could not be observed either, although more labeled polymer (2.9%, data not shown) than labeled siRNA (0.9%, Figure 8A) was found to be taken up—possibly by macrophages. This again supports the assumption by Merdan et al. (*11*) of polyplexes at least partly falling apart into free polymer, which is then especially taken up by the liver and spleen, and into siRNA, which is excreted or degraded upon release from the complex.

A primary deposition in the lungs and secondary redistribution, which had been assumed for PEI/pDNA complexes earlier (*11*, *32*), could not be observed in our perfusion studies. Nor did we observe acute or lethal toxicity, which had been described by several groups investigating biodistribution and kinetics of PEI/pDNA polyplexes (*33*). The fact that we did not observe any lethality or lung accumulation is in good agreement with former reports that explained death of laboratory animals after embolism to be caused by entrapment of aggregates of polyplexes and blood components in the lung capillaries (*34*).

The disadvantage of imaging techniques not differentiating between free label, degraded, or intact labeled compound can only be overcome by verification using autoradiography or after specific siRNA isolation and purification of intact 21-mers and photometric quantification. This aspect also stresses the importance of efficient purification after the labeling process.

A shortcoming of the imaging compared to gamma scintillation of dissected organs is the fact that planar pictures do not allow for differentiation among organs in the same plane of projection, such as liver and kidneys or urine and

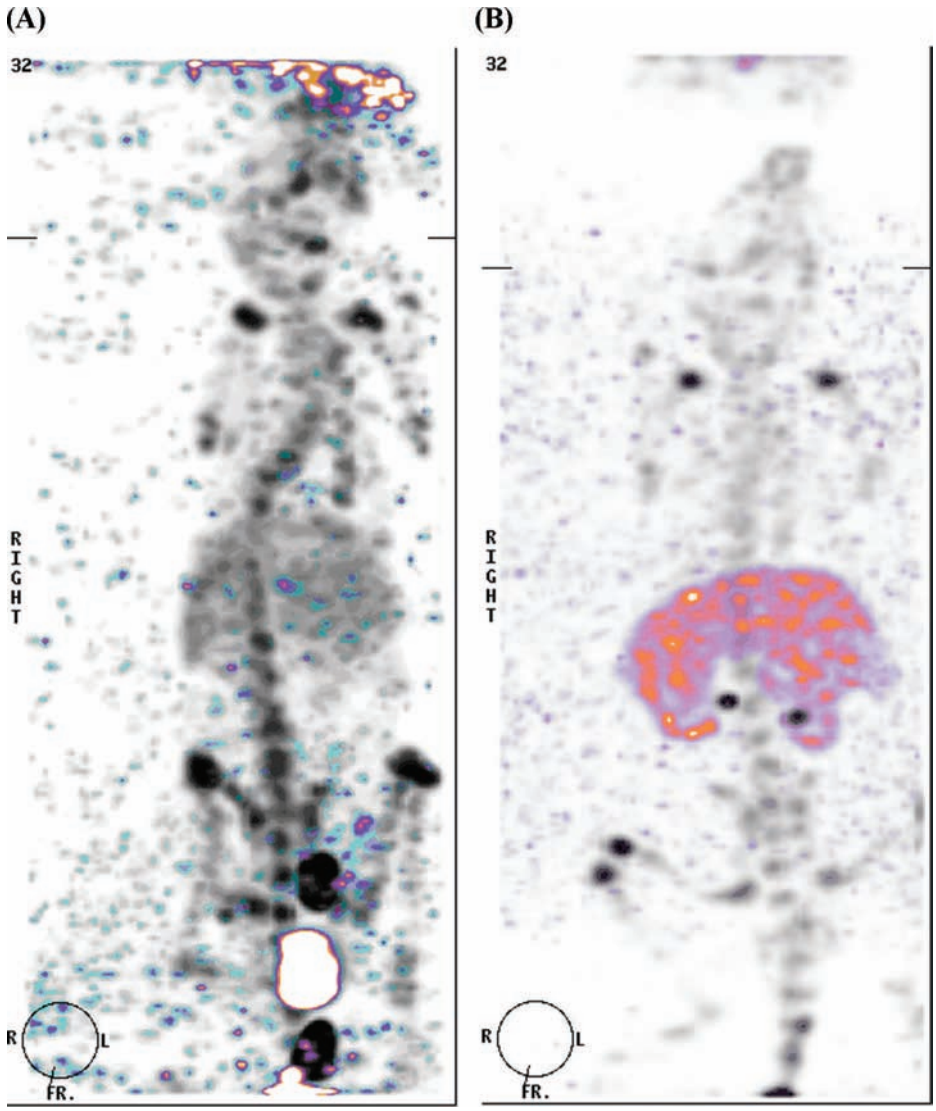

Figure 7. SPECT image of 4 week old male balb/c mouse injected with 35 μg siRNA, corresponding to 2.57 nmol and 0.255 MBq ^{111}In (purple, blue, and orange), and 8 MBq ^{99m}Tc-labeled phosphonate (grayscale) for anatomical landmarking. (A) free siRNA, (B) complexes at N/P 6 with 25 kDa bPEI.

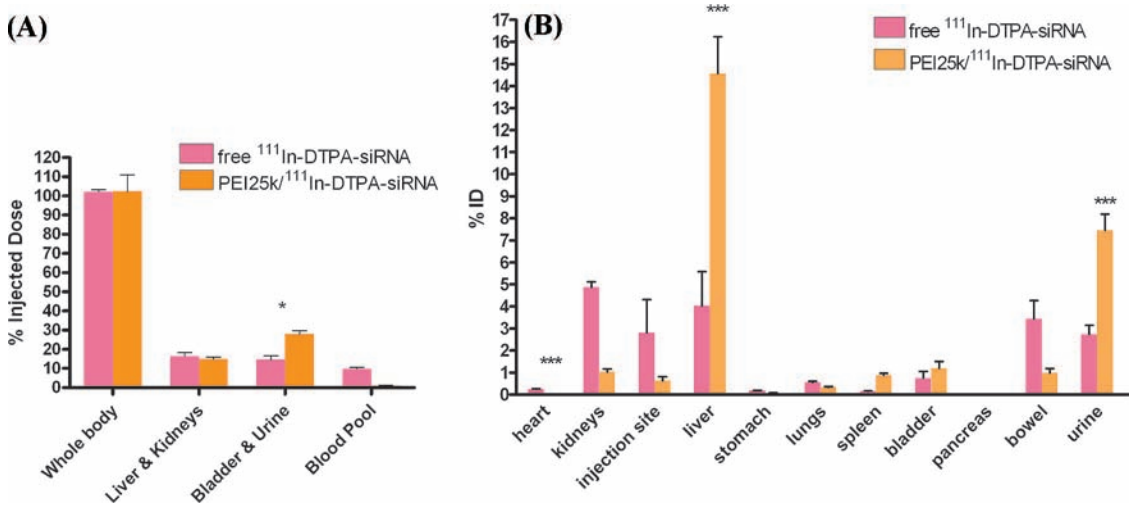

Figure 8. (A) Scintillation analysis of regions of interest 2 h after injection. (B) Scintillation analysis of dissected organs 2 h after injection expressed as % injected dose per organ.

bladder (Figure 8). Regions of interest always expressing the total scintillation counts of all organs in the plane of projection and organs, which do not show significant uptake, can hardly be analyzed. In our study, only the liver, kidneys, urine, and bladder showed strong signals and could easily be detected in planar images, but the significant difference

in uptake to the liver of free siRNA and PEI/siRNA polyplexes could only be shown after dissection of organs (Figure 8A).

CONCLUSION

In summary, we developed an optimized and simple method for coupling p-SCN-Bn-DTPA to siRNA and purification of those radiolabeled siRNA complexes with high yields of these expensive materials. Once the siRNA bears the radioactive label, it can be applied in noninvasive perfusion, kinetics, and biodistribution studies, which corroborate the results from end point scintillation counting methods but offer the advantage of live imaging and examination at various time points in the same animal, reducing the number of animals needed in comparison to conventional techniques. Dual isotope SPECT and gamma camera imaging are very useful methods to follow biodistribution of polyplexes especially with respect to the kinetics of distribution. For determination of exact scintillation counts in every single organ, the latter have to be dissected. However, imaging clearly is able to assess siRNA delivery, biodistribution, and even pharmacokinetics, if a ROI is placed in the blood pool, without sacrificing animals. This proof of principle allows us to investigate distribution and kinetics of a variety of our vectors by multiple methods, including double labeling of vector and load, in the future.

ACKNOWLEDGMENT

The authors are grateful to Ulla Cramer and Klaus Keim for excellent technical support, and to Helmut Höffken, MD, for expert medical advice. The financial support of Deutsche Forschungsgemeinschaft (DFG Forschergruppe 627) is gratefully acknowledged.

Supporting Information Available: Two animated gif files of SPECT images comparable to Figure 7A,B and two gif files of the perfusion studies shown in Figure 5A,B. This material is available free of charge via the Internet at http://pubs.acs.org.

LITERATURE CITED

(1) Bartlett, D. W., and Davis, M. E. (2008) Impact of tumor-specific targeting and dosing schedule on tumor growth inhibition after intravenous administration of siRNA-containing nanoparticles. *Biotechnol. Bioeng. 99*, 975–85.

(2) Bartlett, D. W., Su, H., Hildebrandt, I. J., Weber, W. A., and Davis, M. E. (2007) Impact of tumor-specific targeting on the biodistribution and efficacy of siRNA nanoparticles measured by multimodality in vivo imaging. *Proc. Natl. Acad. Sci. U.S.A. 104*, 15549–54.

(3) de Martimprey, H., Bertrand, J.-R., Fusco, A., Santoro, M., Couvreur, P., Vauthier, C., and Malvy, C. (2007) siRNA nanoformulation against the Ret/PTC1 junction oncogene is efficient in an in vivo model of papillary thyroid carcinoma. *Nucleic Acids Res. 36*, e2.

(4) Wolfrum, C., Shi, S., Jayaprakash, K. N., Jayaraman, M., Wang, G., Pandey, R. K., Rajeev, K. G., Nakayama, T., Charrise, K., Ndungo, E. M., Zimmermann, T., Koteliansky, V., Manoharan, M., and Stoffel, M. (2007) Mechanisms and optimization of in vivo delivery of lipophilic siRNAs. *Nat. Biotechnol. 25*, 1149–57.

(5) Braasch, D. A., Paroo, Z., Constantinescu, A., Ren, G., Oz, O. K., Mason, R. P., and Corey, D. R. (2004) Biodistribution of phosphodiester and phosphorothioate siRNA. *Bioorg. Med. Chem. Lett. 14*, 1139–43.

(6) Barendswaard, E. C., Scott, A. M., Divgi, C. R., Williams, C., Jr., Coplan, K., Riedel, E., Yao, T. J., Gansow, O. A., Finn, R. D., Larson, S. M., Old, L. J., and Welt, S. (1998) Rapid and specific targeting of monoclonal antibody A33 to a colon cancer xenograft in nude mice. *Int. J. Oncol. 12*, 45–53.

(7) Clarke, K., Lee, F.-T., Brechbiel, M. W., Smyth, F. E., Old, L. J., and Scott, A. M. (2000) In vivo biodistribution of a humanized anti-Lewis Y monoclonal antibody (hu3S193) in MCF-7 xenografted BALB/c nude mice. *Cancer Res. 60*, 4804–4811.

(8) Van de Water, F. M., Boerman, O. C., Wouterse, A. C., Peters, J. G., Russel, F. G., and Masereeuw, R. (2006) Intravenously administered siRNA accumulates in the kidney and selectively suppresses gene function in renal proximal tubules. *Drug Metab. Dispos. 34*, 1393–7.

(9) Liu, N., Ding, H., Vanderheyden, J. L., Zhu, Z., and Zhang, Y. (2007) Radiolabeling small RNA with technetium-99m for visualizing cellular delivery and mouse biodistribution. *Nucl. Med. Biol. 34*, 399–404.

(10) Schramm, N. U. E., G., Engeland, U., Schurrat, T., Behe, M., and Behr, T. M. (2003) High-resolution SPECT using multipinhole collimation. *IEEE Trans. Nucl. Sci. 50*, 315–320.

(11) Merdan, T., Kunath, K., Petersen, H., Bakowsky, U., Voigt, K. H., Kopecek, J., and Kissel, T. (2005) PEGylation of poly(ethylene imine) affects stability of complexes with plasmid DNA under in vivo conditions in a dose-dependent manner after intravenous injection into mice. *Bioconjugate Chem. 16*, 785–92.

(12) Kunath, K., von Harpe, A., Petersen, H., Fischer, D., Voigt, K., Kissel, T., and Bickel, U. (2002) The structure of PEG-modified poly(ethylene imines) influences biodistribution and pharmacokinetics of their complexes with NF-κB decoy in mice. *Pharm. Res. 19*, 810–7.

(13) Gary, D. J., Puri, N., and Won, Y. Y. (2007) Polymer-based siRNA delivery: perspectives on the fundamental and phenomenological distinctions from polymer-based DNA delivery. *J. Controlled Release 121*, 64–73.

(14) Tseng, S.-j., and Tang, S.-C. (2007) Development of poly(amino ester glycol urethane)/siRNA polyplexes for gene silencing. *Bioconjugate Chem. 18*, 1383–1390.

(15) Mao, S., Neu, M., Germershaus, O., Merkel, O., Sitterberg, J., Bakowsky, U., and Kissel, T. (2006) Influence of polyethylene glycol chain length on the physicochemical and biological properties of poly(ethylene imine)-graft-poly(ethylene glycol) block copolymer/SiRNA polyplexes. *Bioconjugate Chem. 17*, 1209–18.

(16) Pippin, C. G., Parker, T. A., McMurry, T. J., and Brechbiel, M. W. (1992) Spectrophotometric method for the determination of a bifunctional DTPA ligand in DTPA-monoclonal antibody conjugates. *Bioconjugate Chem. 3*, 342–5.

(17) Kunath, K., von Harpe, A., Fischer, D., Petersen, H., Bickel, U., Voigt, K., and Kissel, T. (2003) Low-molecular-weight polyethylenimine as a non-viral vector for DNA delivery: comparison of physicochemical properties, transfection efficiency and in vivo distribution with high-molecular-weight polyethylenimine. *J. Controlled Release 89*, 113–25.

(18) Fischer, D., Osburg, B., Petersen, H., Kissel, T., and Bickel, U. (2004) Effect of poly(ethylene imine) molecular weight and PEGylation on organ distribution and pharmacokinetics of polyplexes with oligodeoxynucleotides in mice. *Drug Metab. Dispos. 32*, 983–992.

(19) Urban-Klein, B., Werth, S., Abuharbeid, S., Czubayko, F., and Aigner, A. (2005) RNAi-mediated gene-targeting through systemic application of polyethylenimine (PEI)-complexed siRNA in vivo. *Gene Ther. 12*, 461–6.

(20) Schiffelers, R. M., and Storm, G. (2006) ICS-283: a system for targeted intravenous delivery of siRNA. *Expert Opin. Drug Delivery 3*, 445–54.

(21) Schiffelers, R. M., Ansari, A., Xu, J., Zhou, Q., Tang, Q., Storm, G., Molema, G., Lu, P. Y., Scaria, P. V., and Woodle, M. C. (2004) Cancer siRNA therapy by tumor selective delivery with ligand-targeted sterically stabilized nanoparticle. *Nucleic Acids Res. 32*, e149.

(22) Kim, S. H., Jeong, J. H., Lee, S. H., Kim, S. W., and Park, T. G. (2008) Local and systemic delivery of VEGF siRNA using polyelectrolyte complex micelles for effective treatment of cancer. *J. Controlled Release 129*, 107–16.
(23) Grzelinski, M., Urban-Klein, B., Martens, T., Lamszus, K., Bakowsky, U., Hobel, S., Czubayko, F., and Aigner, A. (2006) RNA interference-mediated gene silencing of pleiotrophin through polyethylenimine-complexed small interfering RNAs in vivo exerts antitumoral effects in glioblastoma xenografts. *Hum. Gene Ther. 17*, 751–66.
(24) Ge, Q., Filip, L., Bai, A., Nguyen, T., Eisen, H. N., and Chen, J. (2004) Inhibition of influenza virus production in virus-infected mice by RNA interference. *Proc. Natl. Acad. Sci. U.S.A. 101*, 8676–81.
(25) Dykxhoorn, D. M., Palliser, D., and Lieberman, J. (2006) The silent treatment: siRNAs as small molecule drugs. *Gene Ther. 13*, 541–52.
(26) Wang, D., Sima, M., Mosley, R. L., Davda, J. P., Tietze, N., Miller, S. C., Gwilt, P. R., Kopeckova, P., and Kopecek, J. (2006) Pharmacokinetic and biodistribution studies of a bone-targeting drug delivery system based on N-(2-hydroxypropyl)methacrylamide copolymers. *Mol. Pharm. 3*, 717–25.
(27) de Vries, E. F., Buursma, A. R., Hospers, G. A., Mulder, N. H., and Vaalburg, W. (2002) Scintigraphic imaging of HSVtk gene therapy. *Curr. Pharm. Des. 8*, 1435–50.
(28) Kawabata, K., Takakura, Y., and Hashida, M. (1995) The fate of plasmid DNA after intravenous injection in mice: involvement of scavenger receptors in its hepatic uptake. *Pharm. Res. 12*, 825–30.
(29) Bumcrot, D., Manoharan, M., Koteliansky, V., and Sah, D. W. (2006) RNAi therapeutics: a potential new class of pharmaceutical drugs. *Nat. Chem. Biol. 2*, 711–9.
(30) Behlke, M. A. (2006) Progress towards in vivo use of siRNAs. *Mol. Ther. 13*, 644–70.
(31) Morrissey, D. V., Lockridge, J. A., Shaw, L., Blanchard, K., Jensen, K., Breen, W., Hartsough, K., Machemer, L., Radka, S., Jadhav, V., Vaish, N., Zinnen, S., Vargeese, C., Bowman, K., Shaffer, C. S., Jeffs, L. B., Judge, A., MacLachlan, I., and Polisky, B. (2005) Potent and persistent in vivo anti-HBV activity of chemically modified siRNAs. *Nat. Biotechnol. 23*, 1002–7.
(32) Ishiwata, H., Suzuki, N., Ando, S., Kikuchi, H., and Kitagawa, T. (2000) Characteristics and biodistribution of cationic liposomes and their DNA complexes. *J. Controlled Release 69*, 139–48.
(33) Ogris, M., Brunner, S., Schuller, S., Kircheis, R., and Wagner, E. (1999) PEGylated DNA/transferrin-PEI complexes: reduced interaction with blood components, extended circulation in blood and potential for systemic gene delivery. *Gene Ther. 6*, 595–605.
(34) Chollet, P., Favrot, M. C., Hurbin, A., and Coll, J. L. (2002) Side-effects of a systemic injection of linear polyethylenimine-DNA complexes. *J. Gene Med. 4*, 84–91.

BC800408G

FEBRUARY 2009
Volume 20, Number 2

© *Copyright 2009 by the American Chemical Society*

Bioconjugate Chemistry

REVIEWS

Bioconjugate-Based Molecular Umbrellas

Vaclav Janout and Steven L. Regen*

Department of Chemistry, Lehigh University, Bethlehem, Pennsylvania 18015. Received July 14, 2008; Revised Manuscript Received September 23, 2008

Molecular umbrellas are "amphomorphic" compounds that can produce a hydrophobic or hydrophilic exterior when exposed to a hydrophobic or hydrophilic microenvironment, respectively. Such molecules are composed of two or more facial amphiphiles that are connected to a central scaffold. Molecular umbrellas that have been synthesized to date, using bile acids as umbrella "walls", polyamines such as spermidine and spermine as scaffold material, and L-lysine as "branches", have been found capable of transporting certain hydrophilic peptides, nucleotides, and oligonucleotides across liposomal membranes by passive diffusion. They have also have been shown to increase water solubility and hydrolytic stability of a hydrophobic drug, and to exhibit significant antiviral activity. The ability of a fluorescently labeled molecular umbrella to readily enter live HeLa cells suggests that such conjugates could find use as drug carriers.

INTRODUCTION

Membranes play a central role in the structure and function of cells by serving as barriers that permit the transport of only those ions and molecules that are necessary for maintaining the living state (*1*). Due to their strongly hydrophobic interior, delivering hydrophilic drugs across these naturally occurring lipid bilayers into the cytoplasm of cells has proven to be difficult (*2*−*20*). Finding ways to promote the transport of hydrophilic agents across lipid bilayers, in general, by passive diffusion represents a major challenge (Figure 1).

A common approach to this problem has been to synthesize drug analogues that are smaller in size and more lipophilic (i.e., lipid-soluble) based (*1*, *4*, *5*, *7*). Thus, according to the classic solution-diffusion model of bilayer transport, the permeability coefficient (*P*) of a permeant is directly proportional to its water-membrane partition coefficient (*K*) and its diffusion coefficient (*D*), but inversely proportional to the thickness (*x*) of the bilayer (*1*). Since $P = (K \times D)/x$, an increase in lipophilicity is expected to increase *P* by increasing *K*. Also, a decrease in the size of a permeant is expected to increase *P* by increasing *D*, due to a reduction in the resistance toward diffusion.

In this review, we describe a fundamentally different approach to this transport problem that is based on the concept of "molecular umbrellas". We also show how these unique amphiphilic molecules have potential as drug modifiers, and as drugs, themselves.

MOLECULAR UMBRELLA CONCEPT

To overcome the incompatibility that exists between a hydrophilic agent and the hydrophobic interior of a lipid bilayer, we conceived of a class of molecules that was intended to function like "molecular umbrellas" (*21*). Specifically, such molecules were expected to cover the attached agent and shield it from the hydrophobic environment as it crosses the membrane. Our approach to the synthesis of molecular umbrellas has been to couple two or more facial amphiphiles (molecules having a hydrophobic and a hydrophilic face) to a central scaffold. For

* E-mail: slr0@lehigh.edu.

10.1021/bc800296g CCC: $40.75 © 2009 American Chemical Society
Published on Web 11/20/2008

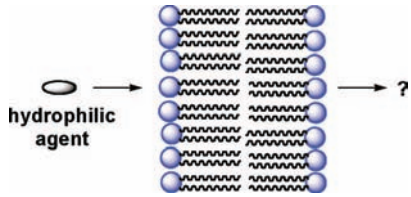

Figure 1. Stylized illustration of a hydrophilic agent trying to cross a phospholipid bilayer.

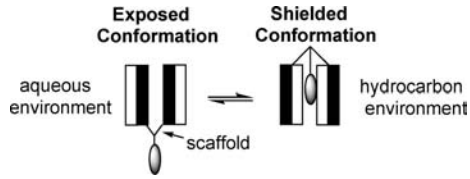

Figure 2. Stylized illustration of a di-walled molecular umbrella, bearing a hydrophilic agent, which is in an exposed and a shielded conformation in aqueous and hydrocarbon environments, respectively.

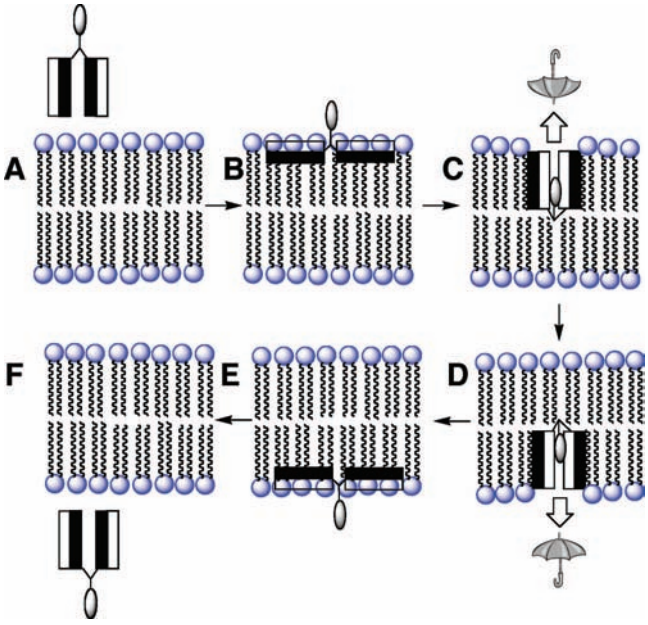

Figure 3. A hypothetical mechanism of bilayer transport for a diwalled molecular umbrella.

convenience, we refer to each such an amphiphilic unit as a "wall". When immersed in a hydrocarbon environment, a molecular umbrella is expected to adopt a shielded conformation in which the facially amphiphilic units mask not only their own hydrophilicity, but also that of the attached hydrophilic agent. When immersed in an aqueous environment, they are then expected to form an exposed conformation that allows each hydrophilic face and the attached agent to make direct contact with water. We have introduced the term "amphomorphic" to describe the ability of such molecules to produce a hydrophobic or hydrophilic exterior on demand.

A stylized illustration of a molecular umbrella in an exposed and in a shielded conformation is shown in Figure 2. Here, the shaded and unshaded rectangles represent the hydrophobic and hydrophilic faces of each amphiphilic unit, respectively, and the lightly shaded oval represents a covalently attached, hydrophilic agent.

How could a molecular umbrella cross a lipid bilayer? Our working hypothesis is illustrated in Figure 3. In brief, the molecular umbrella first approaches the lipid bilayer in a fully exposed conformation (structure A). Hydrophobic interactions with the membrane interior then lead to an adsorbed state in which the hydrophilic faces are in contact with the polar headgroup region and the hydrophobic faces are in intimate contact with the hydrocarbon region of the lipid bilayer (structure B). Subsequent absorption into the interior of the membrane, being driven by hydrophobic forces, then affords structure C. Translocation to the adjoining leaflet, 180° rotation, then produces D. Finally, reversal of the steps leading to B and A, affording E and F, respectively, then releases the conjugate from the other side of the membrane. In essence, the molecular umbrella functions by masking the hydrophilicity of the hydrophilic agent as it crosses the hydrocarbon interior of the membrane.

UMBRELLA FRAMEWORKS

Our work in this area has focused on the use of naturally occurring starting material for the synthesis of molecular umbrellas, based on the belief that they would be biodegradable and nontoxic. Thus, we have made extensive use of facially amphiphilic bile acids as umbrella "walls", polyamines such as spermidine and spermine as scaffold material, and L-lysine as "branches" (Figure 4). Representative di-walled and tetra-walled frameworks that we have employed are shown in Figure 5. Here, "X" represents the "handle" of the umbrella where a desired agent is attached. To date, the "R" groups that have been used include OCH_3, OH, $OCONH_2$, and OSO_3Na. For all of the studies that are described in the following sections, the molar ratio of molecular umbrella/lipid that has been used is typically $<1/100$. In all cases where molecular umbrella conjugates have been reacted with glutathione, the conversions have been found to be quantitative.

UMBRELLA TRANSPORT OF PEPTIDES, NUCLEOTIDES, AND OLIGONUCLEOTIDES ACROSS LIPOSOMAL MEMBRANES

Peptide Transport. Glutathione (Glu-Cys-Gly, GSH) is a simple tripeptide that exists in millimolar concentrations in the cytoplasm of mammalian cells. It is strongly hydrophilic and does not readily cross lipid bilayers by passive diffusion. Because of these properties, and also because its thiol moiety can be used for covalent attachment to a molecular umbrella, we have used GSH for feasibility studies.

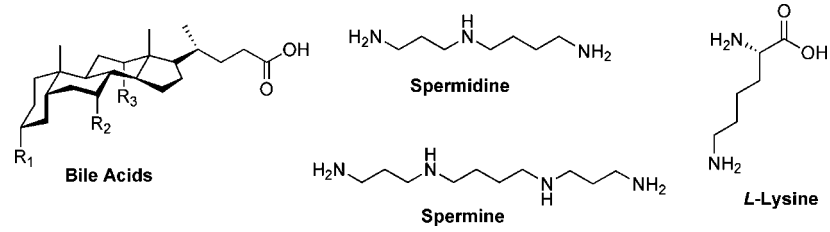

Figure 4. Representative building blocks for the synthesis of molecular umbrellas. Typical "R" groups that have been used to date include OCH_3, OH, $OCONH_2$, and OSO_3Na.

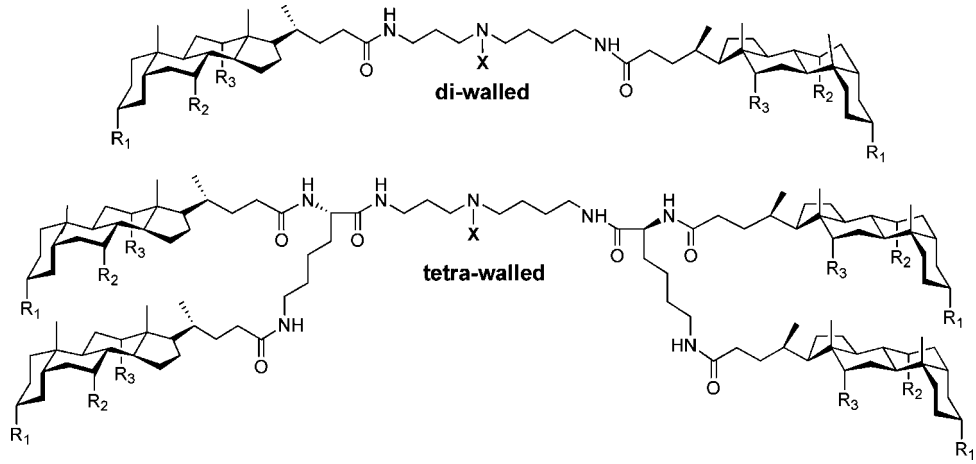

Figure 5. Common frameworks used in the synthesis of molecular umbrellas. Here, "X" represents the "handle" of the umbrella that can bind to a desired agent is attached. Typical "R" groups that have been used to date include OCH_3, OH, $OCONH_2$, and OSO_3Na.

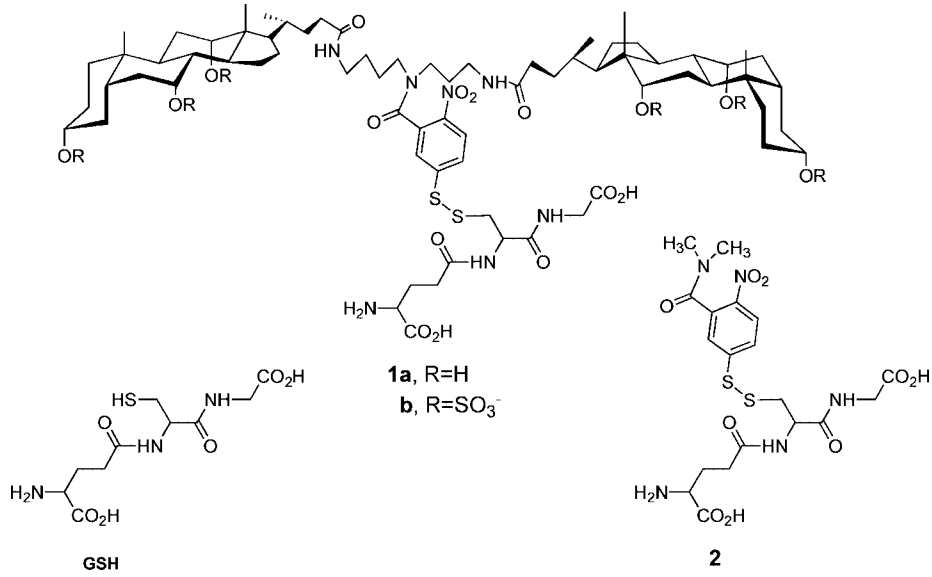

Figure 6. Structures of glutathione (**GSH**), di-walled molecular umbrellas that have been covalently attached to glutathione (**1a** and **1b**), and a control conjugate, **2**.

Two specific molecular umbrella−glutathione conjugates that were synthesized (i.e., **1a** and **1b**) are shown in Figure 6 (*22, 23*). In each case, a 5-thiol(2-nitrobenzoyl) group serves as the "handle". Also shown in Figure 6 is a non-umbrella analogue, **2**, which has been used as a control. The methods of synthesis for preparing **1a** and **1b** are outlined in Figures 7 and 8, respectively.

The ability of **1a** and **1b** to cross phospholipid bilayers by passive diffusion was demonstrated by adding a solution of each conjugate to liposomes made from 1-palmitoyl-2-oleoyl-*sn*-glycero-3-phosphocholine (POPC, 200 nm, extrusion), which contained GSH within their aqueous interior. Thus, the appearance of the 5-thiol(2-nitrobenzoyl) "handle" (i.e., the formation of USH via thiolate−disulfide interchange) provided evidence for liposomal entry (Figure 9). That this exchange reaction occurred within the interior of the liposomes was confirmed by quantifying the amount of cystine (GSSG) that had been produced and entrapped in the liposomes. In sharp contrast to **1a** and **1b**, addition of **2** to similar liposomal dispersions did not produce any detectable USH under similar experimental conditions.

A similar entry by **1a** has been found to occur with liposomes having thicker membranes made from 1,2-di(13-*cis*-docosenoyl)-*sn*-glycero-3-phosphocholine (C22:1) (*24*). However, in contrast to POPC membranes, where the formation of USH exhibited a first-order dependency on the molecular umbrella and the entrapped GSH, only a first-order dependency of the molecular umbrella was found when we used thicker membranes; that is, the rate of formation of USH was independent of the entrapped GSH. These results indicated that the rate-determining step for umbrella entry into POPC liposomes was the thiolate−disulfide interchange reaction, but it was membrane permeation for the (C22:1) liposomes. At the same time, they indicated the involvement of transport-active monomers for the latter system.

Related experiments that have been carried out using an analogue of **1a**, which contained only a single facial amphiphile (i.e., **6a**), showed that transport across the thicker liposomes was still possible (Figure 10) (*24*). In this case, however, the rate of appearance of USH showed a second-order dependency on the concentration of this "skimpy" molecular umbrella and independent of the concentration of entrapped GSH. Control experiments established that GSH did not leak out of the liposomes during the thiolate−disulfide exchange reaction and that GSSG was formed within the aqueous interior. Taken together, these results indicated that membrane permeation was rate-limiting for the skimpy molecular umbrella and that dimers are the transport-active species, most likely operating in a "face-to-face" orientation (Figure 10).

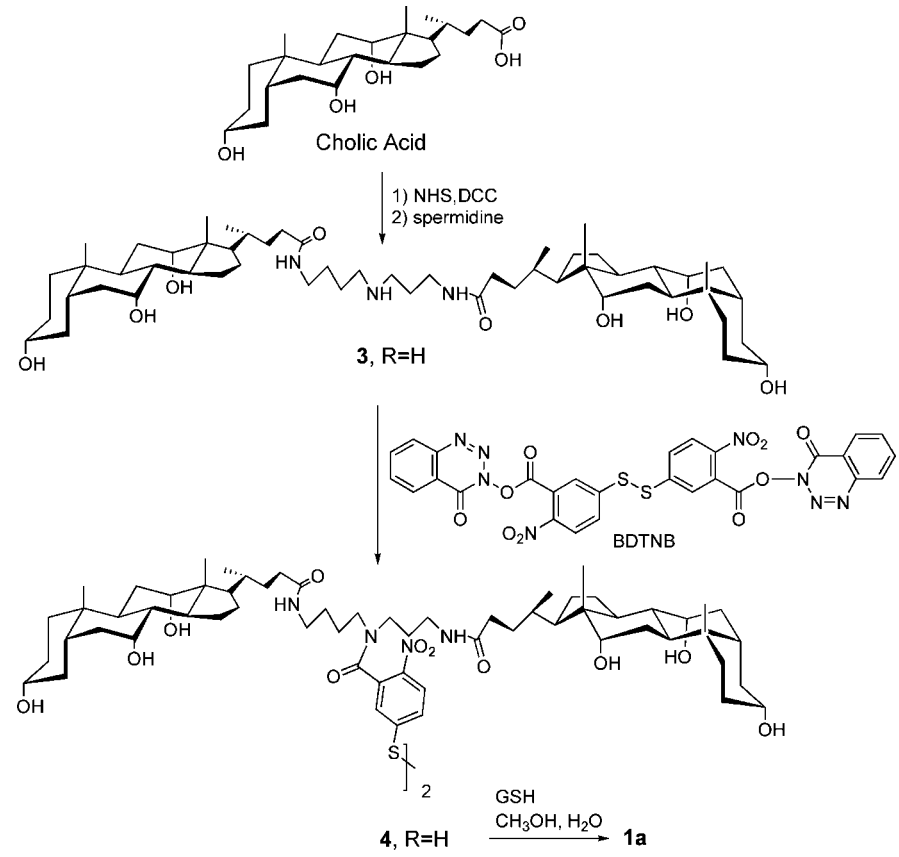

Figure 7. Synthetic scheme for the preparation of **1a**.

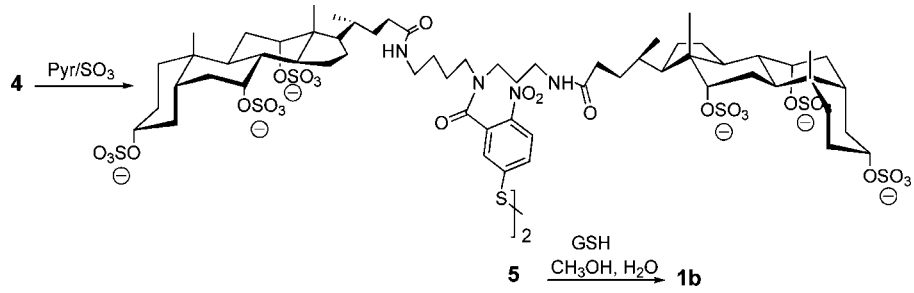

Figure 8. Synthetic scheme for the preparation of **1b**.

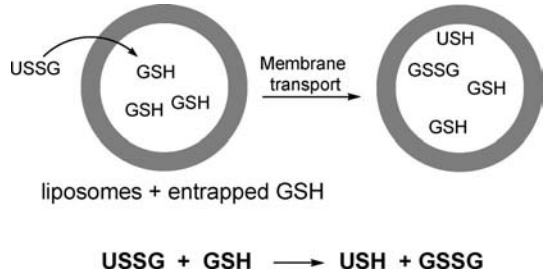

Figure 9. Stylized illlustration of a molecular umbrella-glutathione conjugate (USSG) crossing into a liposome loaded with glutathione (GSH), followed by thiolate−disulfide interchange to form oxidized glutathione (GSSG) and USH.

Similar experiments that were carried out with **6b**, which is devoid of facial hydrophilicity, showed no evidence of reaction (*24*). Control experiments that were carried out in which **6b** was first bound to both the inner and outer leaflets of the liposomes (double-sided addition), followed by treatment with external GSH, showed that 55% of the conjugate underwent rapid reaction. The fact that ca. one-half of **6b** was unreactive toward externally added GSH provided strong evidence that this conjugate crosses lipid bilayers very slowly, if at all. These results were significant because they ruled out the possibility that the ability of **6a** to cross lipid bilayers was simply due to an increase in the overall hydrophobicity of the peptide after attachment to the molecular umbrella. Thus, it provided strong evidence for an novel mechanism of transport, requiring the presence of facial amphiphilicity.

For all of the molecular umbrellas described thus far, a 2-nitrobenzoyl-5-dithio moiety was used as a detachable handle. Since the cytoplasm of cells is rich in glutathione, such a handle could be considered in the design of prodrugs. Two limitations of the use of this handle, however, are the following: (i) the presence of a cysteine residue is necessary for coupling the peptide to the umbrella, and (ii) the peptide is released in a non-native state; that is, it leaves as a glutathione conjugate (Figure 11).

As an alternative to the 2-nitrobenzoyl-5-dithio handle, we explored a prodrug strategy that was based on a thiol-induced reductive fragmentation of a *o*-dithiobenzyl carbamate (Figure 12) (*25*, *26*). For feasibility studies, a molecular umbrella

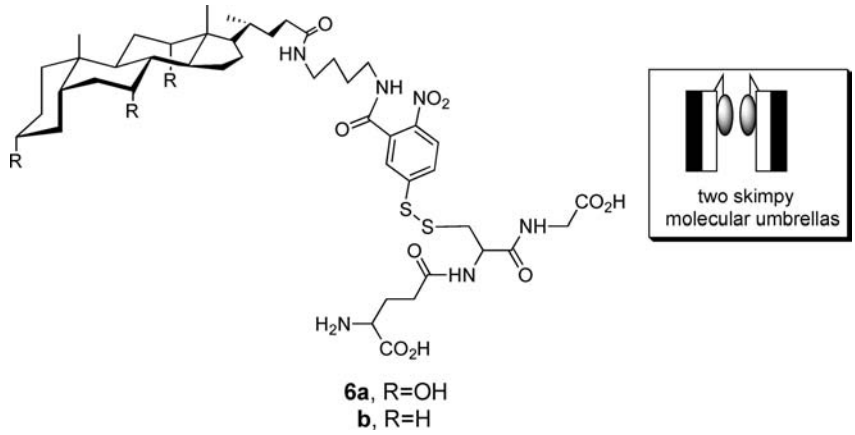

Figure 10. Structure of a single-walled ("skimpy") molecular umbrella bearing glutathione (**6a**), a non-umbrella analogue (**6b**), and a stylized illustration showing two skimpy molecuar umbrellas in a face-to-face orientation.

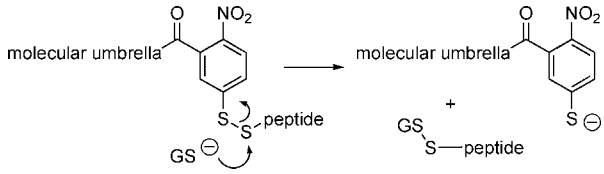

Figure 11. Cleavage of a molecular umbrella−glautathione conjugate by a glutathione molecule.

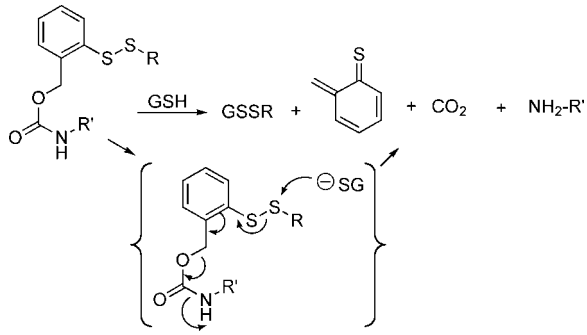

Figure 12. Thiol-induced reductive fragmentation of a *o*-dithiobenzyl carbamate liberating an organic amine.

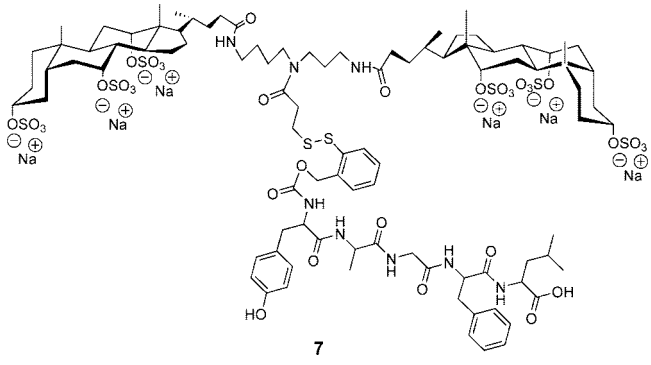

Figure 13. Structure of a di-walled molecular umbrella bearing DADLE with a fully detachable handle.

conjugate of an opioid peptide was synthesized; that is, **7**; DADLE, H-Tyr-D-Ala-Gly-Phe-D-Leu-OH (Figure 13) (*27*).

The fact that **7** was capable of releasing the native DADLE was confirmed by treating a solution of the conjugate with excess GSH. As expected, the solution became effervescent and the appearance of the *o*-thiobenzoquinone methide product was detected by UV (264 nm). At the end of the reaction, thin layer chromatography confirmed the complete disappearance of **7** and the appearance of the free form of DADLE, which could be isolated in 82% yield. Using liposomal targets loaded with excess GSH, it was then demonstrated that **7** could cross lipid bilayers and release DADLE to their aqueous compartment.

Nucleotide Transport. In an effort to expand the scope of molecular umbrellas as membrane transporters, we became keenly interested in antisense oligonucleotides. Currently, antisense oligonucleotides are believed to have considerable promise as therapeutic agents for the treatment of a wide range of diseases; e.g., non-small cell lung cancer, Crohn's disease, malignant melanoma, chronic lymphocytic leukemia, and multiple myeolma. To date, most, if not all, approaches that have been used to deliver antisense oligonucleotides into cells have taken advantage of endocytotic pathways. Release from resulting endosomal−lysosomal compartments by some unknown and inefficient mechanism then delivers a portion of the oligonucleotide to the cytoplasm where it can reach intended targets. In principle, the delivery of antisense oligonucleotides, directly into the cytoplasm via passive transport, could lead to greater overall efficacy.

Before exploring oligonucleotide transport, we sought to demonstrate the feasibility of transporting cleavable forms of adenosine 5′-monophosphate (AMP) and adenosine 5′-triphosphate (ATP) across phospholipid bilayers. Although several studies have been aimed at creating prodrugs of nucleoside 5′monophosphates, reports of membrane transporters of nucleoside 5′-triphosphates are rare.

Two conjugates that we prepared using 5-thiol(2-nitrobenzoyl) as an umbrella handle and thiol forms of AMP and ATP were **8a** and **8b** (Figure 14) (*28*). Synthetic methods that were used to prepare these conjugates were similar to those used for the molecular umbrella−glutathione conjugates.

In principle, attack by glutathione on the disulfide moiety could occur by two different pathways. In one pathway, attack on the sulfur atom of the 5-thiol(2-nitrobenzoyl) moiety by glutathione would result in the direct release of the free nucleotide (Figure 15). Subsequent attack by a second glutathione molecule would then liberate USH plus the oxidized form of glutathione (GSSG). An alternative pathway (not shown) is one in which glutathione initially attacks the sulfur atom of the nucleotide, thereby liberating USH, directly. Further attack by GSH on the glutathione−nucleotide conjugate would then afford the free nucleotides plus GSSG. By monitoring the reaction of **8a** and **8b** with GSH by UV, we were able to obtain strong evidence for a two-stage release that occurs by the first pathway, as shown in Figure 15. Subsequent transport experiments that were carried out with **8a** and **8b** and liposomes loaded with GSH resulted in the release of these nucleotides within the aqueous compartment of the liposomes.

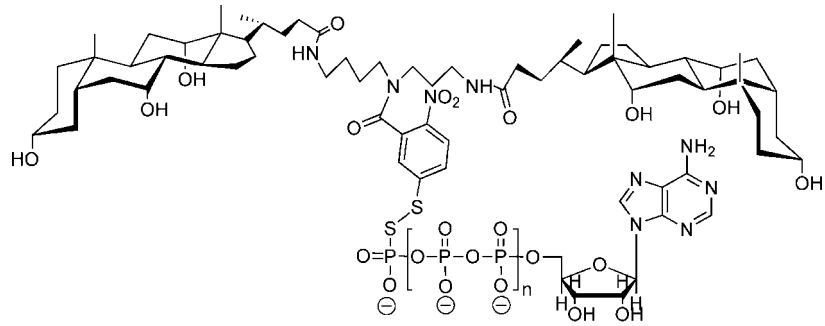

8a, n=0
b, n=1

Figure 14. Structures of diwalled molecular umbrellas bearing a thiolated form of AMP and ATP.

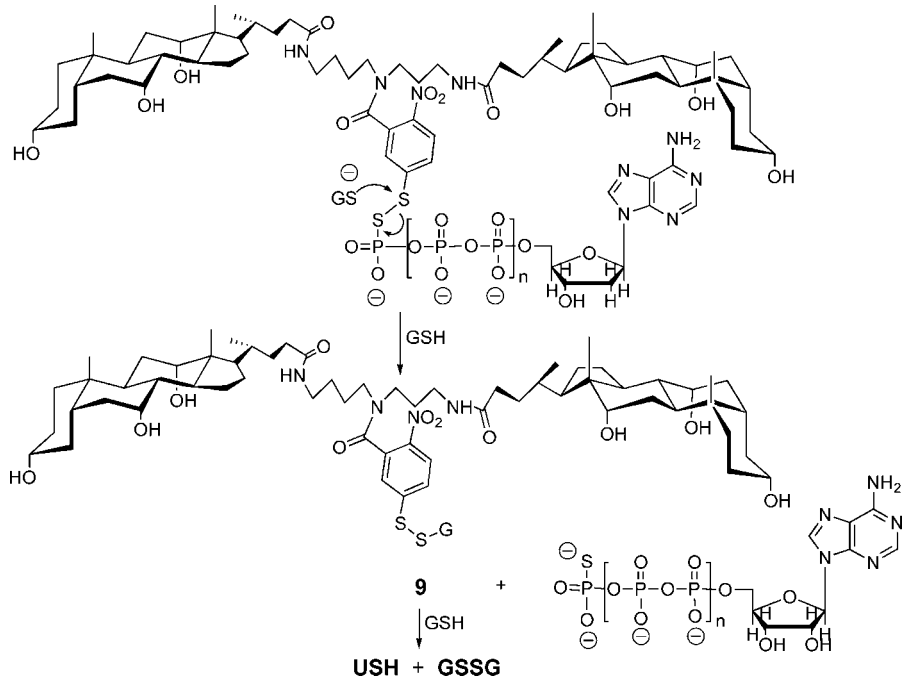

Figure 15. One possible pathway for the cleavage of a di-walled molecular umbrella by glutathione to liberate a nucleotide.

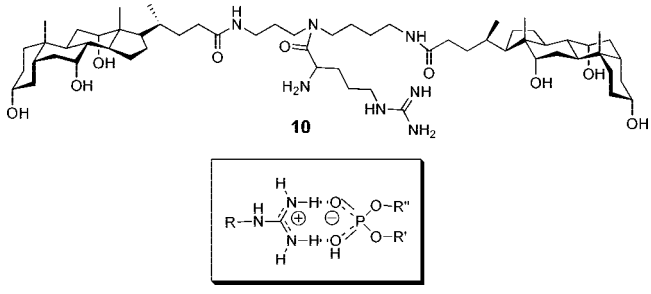

10

Figure 16. Structure of a di-walled molecular umbrella bearing a guanidinium handle, and a probable structure for the guanidinium moiety binding to a phosphate group.

In related studies, molecular umbrella **10** was found capable of transporting ATP across liposomal membranes in a catalytic manner (Figure 16) (*29*). In this case, a guanidinium moiety was chosen as an umbrella handle because of its ability to bind phosphate groups via hydrogen bonding and electrostatic association. Thus, incubation of liposomes containing co-entrapped ATP and GSH with **10** resulted in the selective release of ATP. The fact that GSH was retained by these liposomes showed that the integrity of the membrane was retained during this transport process.

Oligonucleotide Transport. The ability of molecular umbrellas to transport nucleotides across lipid bilayers encouraged us to consider similar transport of an oligonucleotide. An obvious concern, however, was the size of an oligonucleotide relative to that of the molecular umbrella. Specifically, di- and tetra-walled molecular umbrellas would not be capable of shielding an entire oligonucleotide. In Figure 17, we show a mechanism by which umbrella transport of an oligonucleotide across a lipid bilayer might be possible. Here, the conjugate first penetrates the membrane to produce a shielded conformation (A). Subsequent opening of the umbrella across the bilayer, and simultaneous folding of the oligonucleotide into a partial "U", then leaves most of the membrane-internalized phosphate groups pointing toward the hydrophilic faces of the umbrella (B), allowing for translocation and umbrella closure to form C.

To test the feasibility of umbrella-mediated oligonucleotide transport, conjugates **11a**, **11b**, **12a**, and **12b** were synthesized using a 16-mer oligonucleotide (S-dT_{16}) as a prototype (Figure 18) (*30*, *31*). Similar to our studies with umbrella−glutathione conjugates, liposomes were loaded with GSH and the release of USH monitored by UV. In all cases, oligonucleotide delivery to the interior of the liposomes was observed. Control experiments confirmed the absence of release of entrapped GSH throughout the course of these influx experiments. Comparison

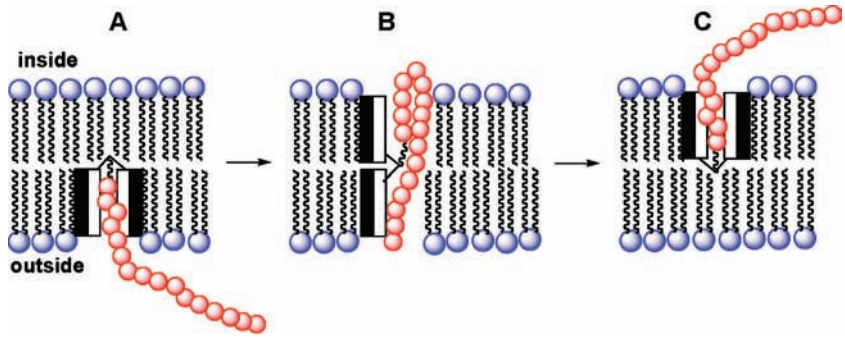

Figure 17. Stylized illustration of a di-walled molecular umbrella−oligonucleotide conjugate crossing a phospholipid bilayer.

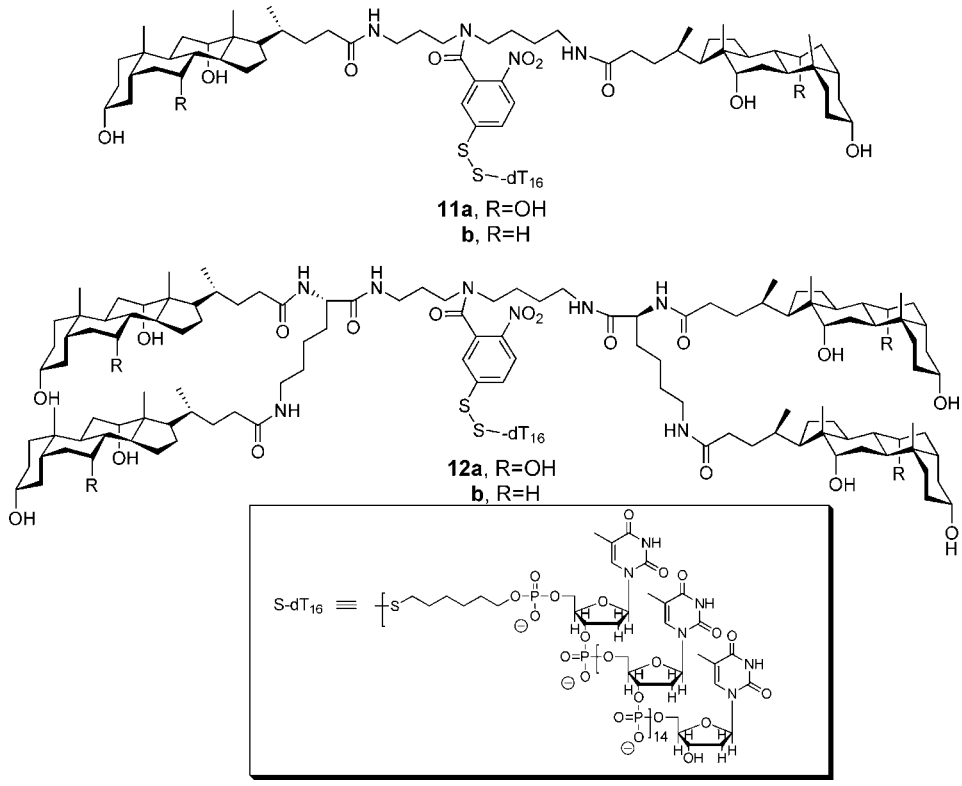

Figure 18. Structures of di-walled (**11a**, **11b**) and tetra-walled (**12a**, **12b**) molecular umbrellas bearing an oligonucleotide.

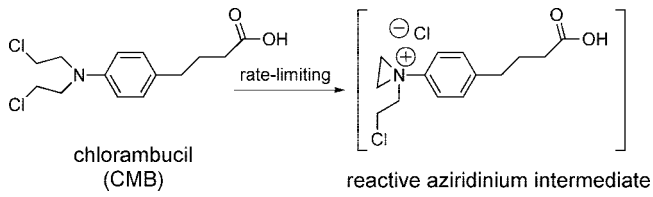

Figure 19. Chlorambucil undergoing a rate-limiting intramolecular displacement reaction.

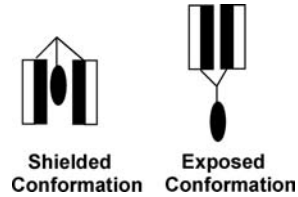

Figure 20. Stylized illustration of a di-walled molecular umbrella, bearing a hydrophobic agent, which is shown in a shielded and an exposed conformation.

of these molecular umbrella−oligonucleotide conjugates revealed greater transport rates with the tetra-walled umbrellas as compared with their di-walled analogues. The deoxycholic acid−based, di-walled molecular umbrella conjugate (**11b**) was found to be ca. 50% more active than the cholic acid−based analogue (**11a**), but the reverse was found to be the case for the tetra-walled molecular umbrella conjugates.

MOLECULAR UMBRELLAS AS DRUG MODIFIERS

While molecular umbrellas were originally designed to promote drug transport across hydrophobic barriers, they can also improve the water solubility and hydrolytic stability of certain hydrophobic drugs. A molecular umbrella conjugate of the anticancer agent, chlorambucil (CMB), illustrates both of these features.

Chlorambucil is an alkylating agent that undergoes a rate-limiting intramolecular displacement to form an aziridinium ion (Figure 19). Subsequent reaction with nucleophiles (e.g., DNA) or water then produces alkylated and hydrolyzed products, respectively. Because charge is developed in the transition state leading to the aziridinium ion, its rate of formation should be faster in a polar environment. Conversely, slower rates are expected in hydrophobic environments. Thus, if CBM were

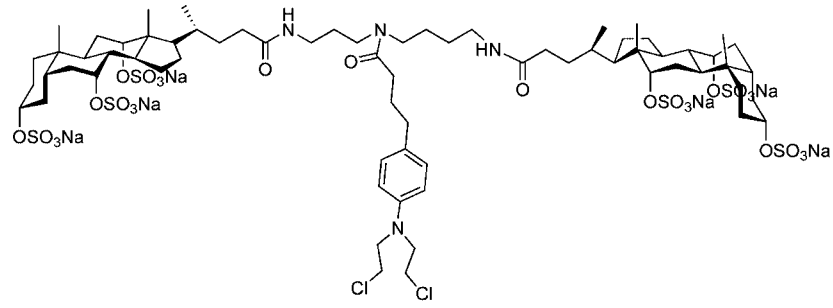

13

Figure 21. Structure of a di-walled molecular umbrella that has been conjugated to chlorambucil.

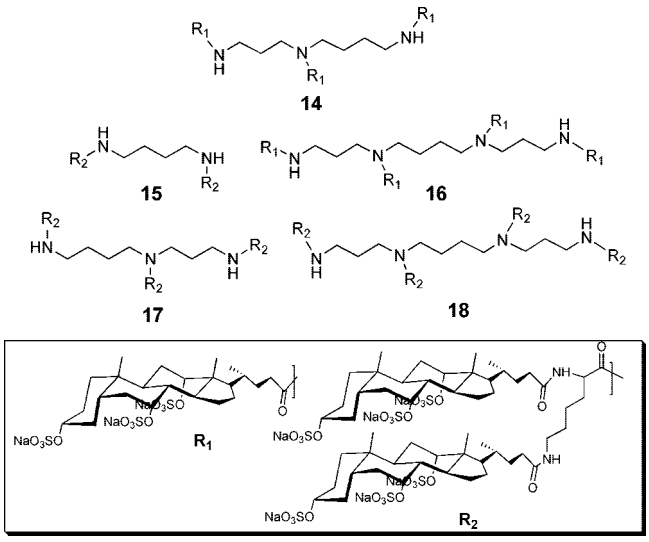

Figure 22. Structures of molecular umbrellas bearing three (**14**), four (**15**, **16**), six (**17**), and eight (**18**) persulfated choloyl groups.

attached to a molecular umbrella, and if the umbrella were to adopt a shielded conformation in water—where the CMB is covered by the hydrophobic faces of the umbrella—this could lead to enhanced stability. An illustration of such shielding is shown in Figure 20, where CMB is represented by a darkened oval, and the shaded and unshaded rectangles represent the hydrophobic and hydrophilic face of each amphiphilic unit, respectively. In addition, by exposing each hydrophilic face of the amphiphilic units to the aqueous phase, a significant increase in water solubility would also be expected.

Experimentally, chlorambucil was found to have a solubility in water that was less than 500 μg/mL. In sharp contrast, **13** showed a water solubility that was 1.20 g/mL (Figure 21) (*32*). Thus, attachment of CMB resulted in an increase in water solubility of more than 3 orders of magnitude! In addition, whereas CMB showed a half-life in phosphate buffer (pH 7.4) of 16 min, the molecular umbrella conjugate **13** had a half-life of ca. 40 min. Thus, covalent attachment of CMB to this di-walled molecular umbrella resulted in a dramatic increase in water solubility and a modest increase in hydrolytic stability. In preliminary studies, we compared the activity of chlorambucil with **13** in inhibiting the growth of human lymphoblastic leukemia (CCRF-CEM) cells, as well as human colon carcinoma (HCT-116) cells. For the leukemia cells, the activity of the molecular umbrella conjugate was substantially lower relative to CMB; that is, the concentrations needed to inhibit 50% growth were 173 and 2.15 μM for **13** and CMB, respectively. For the colon cancer cells, the difference was less pronounced. In this case, the concentrations needed to inhibit 50% growth were 53.7 and 11.4 μM, respectively.

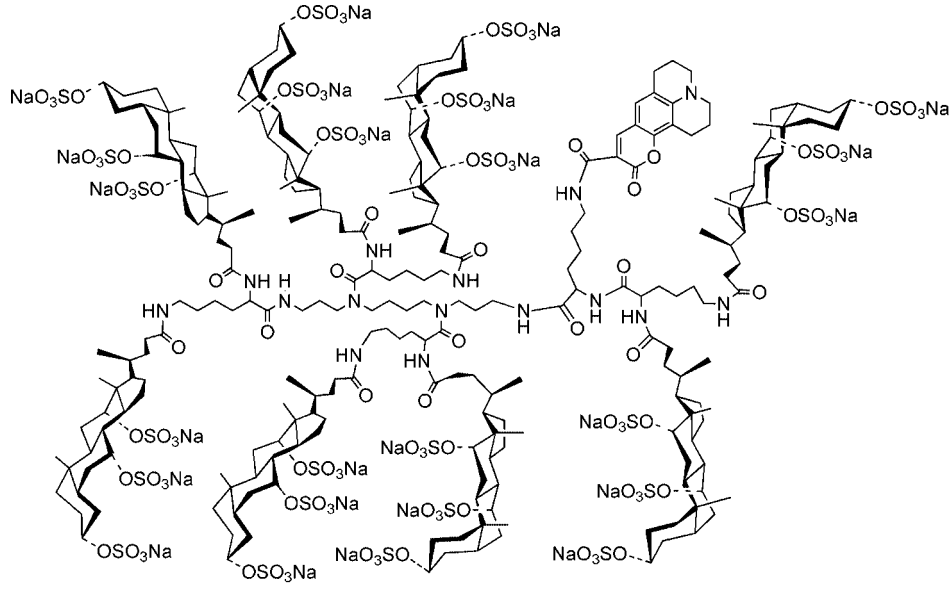

19

Figure 23. Structure of a fluorescently labeled, persulfated molecular umbrella, **19**.

MOLECULAR UMBRELLAS AS ANTIVIRAL AGENTS

Anionic polymers such as dextran sulfate and cellulose sulfate are known to inhibit cellular binding of HIV and HSV by competing for viral envelope glycoproteins. The possibility that persulfated molecular umbrellas might behave in a similar way, together with their potential for crossing hydrophobic barriers (e.g., the blood−brain barrier), suggests that such compounds could function as novel therapeutic agents as well as microbicides.

With this thought in mind, five persulfated molecular umbrellas (**14**, **15**, **16**, **17**, and **18**) were synthesized, and their anti-HIV activity measured using U87.CD4.CCR5 cells, replication defective HIV-1 virus, and a luciferase assay (Figure 22) (*33*). At a dosage of 1 μg/mL, **18** showed moderate activity; **15**, **16**, and **17** were less active, and **14** was inactive. At 100 μg/mL, all conjugates showed significant activity and inhibition was >95% with **18**. The anti-HSV activity of these conjugates was also compared by conducting plaque reduction assays with HSV-2(G) and human cervical epithelial cells (CaSki). At a concentration of 100 μg/mL, all of the conjugates completely inhibited HSV-2. At a concentration of 10 μg/mL, complete and very significant inhibition was found for **18** and **17**, respectively. In contrast, the activities of **14**, **15**, and **16** were only modest at this concentration.

Toxicity studies that have been carried out with **18** has shown that it is non-cytotoxic toward CaSki cells (*33, 34*). Thus, human cervical cells were exposed to serial dilutions of **18** (in the absence of virus) overnight (acute) or for 3 h each day for 4 consecutive days (chronic) to examine the effects on cell growth and viability using an MTS assay. No cytotoxicity was observed following chronic or acute exposure even at concentrations as high as 1000 μg/mL.

CELLULAR UPTAKE OF MOLECULAR UMBRELLAS

An important question that bears directly on the potential of molecular umbrellas as drug carriers is whether they are capable of crossing the plasma membrane of living cells. To address this question, we synthesized a fluorescently labeled molecular umbrella analogue of **18** (i.e., **19**) and investigated its interaction with live HeLa cells (Figure 23) (*35*).

In these experiments, confocal microscopy was used to section optically through the cellular volume to establish that the fluorescent label was dispersed within the cell and not bound to its outer surface. Cells were also labeled with Syto-59 to mark their nucleus and their cytoplasm. After a 10 min incubation period with 4 μM of **19**, this molecular umbrella could be readily detected inside the cells. Thus, **19** was found to be diffuse in the cytoplasm and punctate in the nucleus. The former is generally considered to be an indication of cellular entry via passive diffusion. In addition, the molecular umbrella within the nucleus was bound in spots that colocalize with nucleoli. In preliminary studies, treatment of HeLa cells with NaN_3 and 2-deoxyglucose (to deplete ATP production) only modestly inhibited the cellular uptake of **19**. This observation lends further support for passive diffusion playing a significant role in the cellular entry of this molecular umbrella. The fact that **19** is concentrated at the nucleus of these cells is intriguing, but the basis for this localization is not presently understood. It does raise the possibility, however, that molecular umbrellas of this type could be used for the nuclear targeting of drugs.

OTHER RIGID FACIAL AMPHIPHILES USED IN PROMOTING MEMBRANE TRANSPORT

Although this review has focused, sharply, on molecular umbrellas as membrane transporters, it should be noted other types of rigid facial amphiphiles have been devised that promote the transport of ions and small molecules. In a recent report, for example, it was shown that cholic acid could be transformed into cyclotrimeric and cyclotetrameric "toroidal amphiphiles" with inward-directed ammonium substitutents, and that the cyclotrimeric form was capable of transporting chloride anions across vesicle bilayers (*36*). In an earlier study, four Amphotericin B molecules were coupled to a calix[4]arene and found to promote the transport of K^+ across liposomal membranes (*37*). Finally, a variety of novel scaffolds (e.g., *p*-octaphenyl unit) have been used to construct a rich assortment of membrane-spanning pores having facial amphiphilicity (*38, 39*).

PROSPECTUS

The feasibility of synthesizing molecular umbrellas from bioconjugates, which are capable of transporting hydrophilic agents across lipid bilayers, has been established. Thus, it has been shown that molecular umbrellas derived from certain bile acids, polyamines, and amino acids (e.g., cholic acid, spermidine, and lysine) can transport hydrophilic peptides, nucleotides, and oligonucleotides across liposomal membranes. It has also been demonstrated that molecular umbrellas can enhance the water solubility and hydrolytic stability of a hydrophobic drug. Certain persulfated molecular umbrellas also show promise as antiviral agents for use as microbicides and as therapeutic agents.

To gain a deeper understanding of how molecular umbrellas cross lipid bilayers, additional studies are needed that provide fundamental insight into the interactions of these novel amphomorphic molecules with lipid bilayers. Further studies that show how transport rates and membrane binding are influenced by systematic changes in the structure and composition of (i) the molecular umbrella, (ii) the attached agent, and (iii) the lipid membrane should also prove valuable in clarifying probable mechanism(s) of membrane transport. The fact that **19** readily enters live HeLa cells, and that passive transport appears to play a significant role in this entry process, implies that fundamental insight gained from model studies should aid the rational design of molecular umbrellas as drug carriers.

ACKNOWLEDGMENT

This work was supported by the National Institues of Health (PHS Grants GM51814).

LITERATURE CITED

(1) Stein, W. D. (1986) *Transport and Diffusion Across Cell Membranes*, Academic Press, San Diego, CA.
(2) Langel, U. (2002) *Cell-Penetrating Peptides: Processes and Applications*, CRC Press, Boca Raton, FL.
(3) Curiel, D. T., and Douglas, J. T., Eds. (2002) *Vector Targeting for Therapeutic Gene Delivery*, John Wiley & Sons, Inc., New York.
(4) Lipinski, C. A., Lombardo, F., Dominy, B. W., and Feeney, P. J. (2001) Experimental and computational approaches to estimate solubility and permeability in drug discovery and development settings. *Adv. Drug Delivery Rev. 46*, 3–26.
(5) Pidgeon, C., Ong, S., Liu, H., Qiu, X., Pidgeon, M., Dantzig, A. H., Munroe, J., Homback, W. J., Kasher, J. S., Glunz, L., and Szczerba, T. (1995) IAM chromatography: an in vitro screen for predicting drug membrane permeability. *J. Med. Chem. 38*, 590–594.
(6) Juliano, R. L., Alahari, S., Yoo, H., Kole, R., and Cho, M. (1999) Antisense pharmacodynamics: critical issues in the transport & delivery of antisense oligonucleotides. *Pharm. Res. 16*, 494–502.

(7) Boguslavsky, V., Hruby, V. J., O'Brien, D. F., Misicka, A., and Lipkowski, A. (2003) Effect of peptide conformation on membrane permeability. *J. Peptide Res. 61*, 287–297.
(8) Dias, N., and Stein, C. A. (2002) Antisense oligonucleotides: basic concepts and mechanisms. *Mol. Cancer Ther. 1*, 347–355.
(9) Rothbard, J. B., Jessop, T. C., Lewis, R. S., Murray, B. A., and Wender, P. A. (2004) Role of membrane potential and hydrogen bonding in the mechanism of translocation of guanidinium-rich peptides into cells. *J. Am. Chem. Soc. 126*, 9506–9507.
(10) Wender, P. A., Rothbard, J. B., Jessop, T. C., Kreider, E. L., and Wylie, B. L. (2002) Oligocarbamate molecular transporters: design, synthesis, and biological evaluation of a new class of transporters for drug delivery. *J. Am. Chem. Soc. 124*, 13382–13383.
(11) Rothbard, J. B., Kreider, E., VanDeusen, C. L., Wright, L., Wylie, B. L., and Wender, P. A. (2002) Arginine-rich molecular transporters for drug delivery: role of backbone spacing in cellular uptake. *J. Med. Chem. 45*, 3612–3618.
(12) Suzuki, T., Futaki, S., Niwa, M., Tanaka, S., Ueda, K., and Sugiura, Y. (2002) Possible existence of common internalization mechanisms among arginine-rich peptides. *J. Biol. Chem. 277*, 2437–2443.
(13) Terrone, D., Leung, S., Sang, W., Roudaia, L., and Silvius, J. R. (2003) Penetratin and related cell-penetrating cationic peptides can translocate across lipid bilayers in the presence of a transbilayer potential. *Biochemistry 42*, 13787–13799.
(14) Sakai, N., Takeuchi, T., Futaki, S., and Matile, S. (2005) Direct observation of anion-mediated translocation of fluorescent oligoarginine carriers into and across bulk liquid and anionic bilayer membranes. *ChemBioChem 6*, 114–122.
(15) Sakai, N., Futaki, S., and Matile, S. (2006) Anion hopping of (and on) functional oligoarginines: from chloroform to cells. *Soft Matter 2*, 636–641.
(16) Takeuchi, T., Kosuge, M., Tadokoro, A., Sugiura, Y., Nishi, M., Kawata, M., Sakai, N., Matile, S., and Futaki, S. (2006) Direct and rapid cytosolic delivery using cell-penetrating peptides mediated by pyrenebutyrate. *ACS Chem. Biol. 1*, 299–303.
(17) Ziegler, A., Blatter, X. L., Seelig, A., and Seelig, J. (2003) Protein transduction domains of HIV-1 and SIV TAT interact with charged lipid vesicles: binding mechanism and thermodynamic analysis, *Biochemistry 42*, 9185–9194.
(18) Binder, H., and Lindblom, G.,. (2003) Charge-dependent translocation of the trojan peptide penetratin across lipid membranes. *Biophys. J. 85*, 982–995.
(19) Fuchs, S. M., and Raines, R. T. (2003) Pathway for polyarginine entry into mammalian cells. *Biochemistry 43*, 2438–2444.
(20) Potocky, T. B., Menon, A. K., and Gellman, S. H. (2003) Cytoplasmic and nuclear delivery of a TAT-derived peptide and a β-Peptide after endocytic u,ptake into HeLa Cells. *J. Biol. Chem. 278*, 50188–50194.
(21) Janout, V., Lanier, M., and Regen, S. L. (1996) Molecular umbrellas. *J. Am. Chem. Soc. 118*, 1573–1574.
(22) Janout, V., DiGiorgio, C., and Regen, S. L. (2000) Molecular umbrella-assisted transport of a hydrophilic peptide across a phospholipid membrane. *J. Am. Chem. Soc. 122*, 2671–2672.
(23) Janout, V., Zhang, L. H., Staina, I. V., DiGiorgio, C., and Regen, S. L. (2001) Molecular umbrella-assisted transport of glutathione across a phospholipid membrane. *J. Am. Chem. Soc. 123*, 5401–5406.
(24) Janout, V., Staina, V., Bandyopadhyay, P., and Regen, S. L. (2001) Evidence for an umbrella mechanism of bilayer transport. *J. Am. Chem. Soc. 123*, 9926–9927.
(25) Senter, P. D., Pearce, W. E., and Greenfield, R. S. (1990) Development of a drug-release strategy based on the reductive fragmentation of benzyl carbamate disulfides. *J. Org. Chem. 55*, 2975–2978.
(26) Zalipsky, S., Qazen, M., Walker, J. A., Mullah, N., Quinn, Y. P., and Huang, S. K. (1999) New detachable poly(ethylene glycol) conjugate: cysteine-cleavable lipopolymers regenerating natural phospholipid, diacyl phosphatidylethanolamine. *Bioconjugate Chem. 10*, 703–707.
(27) Jing, B., Janout, V., and Regen, S. L. (2003) Fully-detachable molecular umbrellas as peptide delivery agents. *Bioconjugate Chem. 14*, 1191–1196.
(28) Janout, V., Jing, B., and Regen, S. L. (2002) Molecular umbrella-assisted transport of thiolated AMP and ATP across phospholipid bilayers. *Bioconjugate Chem. 13*, 351–356.
(29) Janout, V., Jing, B., Staina, I. V., and Regen, S. L. (2003) Selective transport of ATP across a phospholipid bilayer by a molecular umbrella. *J. Am. Chem. Soc. 125*, 4436–4437.
(30) Janout, V., and Regen, S. L. (2005) A needle and thread approach towards bilayer transport: permeation of a molecular umbrella-oligonucleotide conjugate across a phospholipid membrane. *J. Am. Chem. Soc. 127*, 22–23.
(31) Janout, V., Jing, B., and Regen, S. L. (2005) Molecular umbrella-assisted transport of an oligonucleotide across cholesterol-rich phospholipid bilayers. *J. Am. Chem. Soc. 127*, 15862–15870.
(32) Vijayaraghavan, S., Jing, B., Vrablik, T., Chou, T. C., and Regen, S. L. (2003) Enhanced hydrolytic stability and water solubility of an aromatic nitrogen mustard by conjugation with molecular umbrellas. *Bioconjugate Chem. 14*, 667–671.
(33) Jing, B., Janout, V., Herold, B. C., Klotman, M. E., Heald, T., and Regen, S. L. (2004) Persulfated molecular umbrellas as anti-HIV and anti-HSV agents. *J. Am. Chem. Soc. 126*, 15930–15931.
(34) Madan, R. P., Mesquita, P. M. M., Cheshenko, N., Jing, B., Shende, V., Guzman, E., Healt, T., Keller, M. J., Regen, S. L., Shattock, R. J., and Herold, B. C. (2007) Molecular umbrellas: a novel class of candidate microbicides to prevent human immunodeficiency virus and herpes simplex virus infections. *J. Virol. 81*, 7636–7646.
(35) Mehiri, M., Jing, B., Ringhoff, D., Janout, V., Cassimeris, L., and Regen, S. L. (2008) Cellular entry and nuclear targeting by a highly anionic molecular umbrella. *Bioconjugate Chem. 19*, 1510–1513.
(36) Whitmarsh, S. D., Redmond, A. P., Sgarlata, V., and Davis, A. P. (2008) Cationic cyclocholamides; toroidal amphiphiles with potential for anion transport. *Chem. Commun.* 3669–3671.
(37) Paquet, V., Zumbuehl, A., and Carreira, E. M. (2006) Biologically active amphotericin B—calix[4]arene conjugates. *Bioconjugate Chem. 17*, 1460–1463.
(38) Matile, S., Som, A., and Sorde, N. (2004) Recent synthetic ion channels and pores. *Tetrahedron 60*, 6405–6435.
(39) Sakai, N., Mareda, J., and Matile, S. (2008) Artificial β-barrels, *Acc. Chem. Res.* Published Online: July 1, 2008.

BC800296G

COMMUNICATIONS

Cationic Nucleoside Lipids Based on a 3-Nitropyrrole Universal Base for siRNA Delivery

Claire Ceballos,[†] Carla A. H. Prata,[‡] Suzanne Giorgio,[†] Frédéric Garzino,[†] Dominique Payet,[§] Philippe Barthélémy,[||] Mark W. Grinstaff,*[,‡] and Michel Camplo*[,†,‡]

Centre Interdisciplinaire de Nanosciences de Marseille CINaM, UPR-CNRS 3118, Université Aix-Marseille II, Luminy, case 913, 13288 Marseille cedex 09, France, Departments of Chemistry and Biomedical Engineering, Metcalf Center for Science and Engineering, Boston University, Boston, Massachusetts 02215, Centre d'Immunologie de Marseille Luminy, Parc scientifique de Luminy, 13288 Marseille, Cedex 9, France, and Inserm U869, Université Victor Segalen Bordeaux 2, F-33076, Bordeaux, F-33076 France. Received October 10, 2008; Revised Manuscript Received December 12, 2008

Cationic nucleoside lipids based on a 3-nitropyrrole universal base were prepared from D-ribose using a straightforward chemical synthesis. Several studies including DLS, TEM, and ethidium bromide (EthBr) assay demonstrated that these amphiphilic molecules form supramolecular organizations of nanometer size in aqueous solutions and are able to bind nucleic acids. siRNA knockdown experiments were performed with these nucleolipids, and we observed protein knockdown activity similar to the siPORT *NeoFX* positive control. No significant cytotoxicity was found.

Nucleolipids—amphiphiles possessing both nucleic acid recognition and lipophilic alkyl chain components—are emerging as tools both for constructing supramolecular assemblies and for nucleic acid delivery (*1*−*13*). The area of nucleic acid delivery is particularly interesting, since gene delivery provides a mechanism to introduce new genes in cells for basic in vitro research experiments as well as to replace or supplement a defective or missing gene in a patient as part of a clinical therapy (*14*−*20*). Consequently, synthetic lipids, as well as other DNA carriers such as calcium phosphate particles, dendrimers, or surface-mediated assemblies (*21*), are highly sought after. Minimally toxic to cells, these lipids also afford high DNA or RNA transfection activity. Recently, we have reported the synthesis and transfection activity of a series of cationic and glycosylated nucleolipids which are both nontoxic and active DNA transfection agents (*11, 13*). In an ongoing effort to expand the scope and properties of this family of lipids, we are synthesizing analogues where the thymine nucleobase is replaced by the synthetic 3-nitropyrrole universal base and evaluating the potential of these nucleolipids for siRNA delivery. Herein, we report the synthesis, physicochemical properties, and siRNA transfection efficiency of a universal-base nucleolipid, the tosylate salt of 1-(2′,3′-dioleyl-5′-trimethylammonium-(α,*β*)-D-ribofuranosyl)-3-nitropyrrole.

The target nucleolipid, **7**, which is shown in Figure 1, possesses three key components: a quaternized amine at the 5′ position, two oleic acid chains linked at the 2′ and 3′ positions, and a 3-nitropyrrole attached at the anomeric position. The cationic charge is responsible for electrostatic binding to the nucleic acids and the oleyl chains contribute to stabilization of the resulting nucleic acid−nucleolipid assembly through hydrophobic chain−chain interactions. The 3-nitropyrrole, which is perhaps the best characterized universal base analogue, was introduced to circumvent the restrictive hydrogen bonding pattern controlling typical purine−pyrimidine hydrogen motifs by incorporating the weakly hydrogen bonding nitro substituent (*22*−*24*). It is known that the 3-nitropyrrole group can form complementary base pairs with all four natural bases without significantly destabilizing neighboring base pair interactions. As a result, it has been used for diverse applications including hybridization of DNA duplexes, oligonucleotide probes and primers, peptide nucleic acids, and sequencing by MALDI mass spectrometry (*25*).

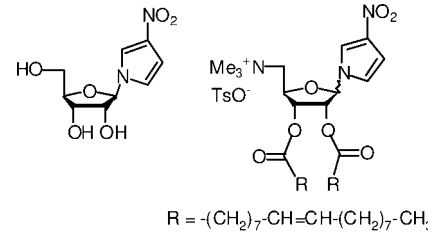

Figure 1. Chemical structure of the universal nucleobase and nucleolipid (tosylate salt of 1′-(2′,3′-dioleyl-5′-trimethylammonium-α,*β*-D-ribofuranosyl)-3-nitropyrrole).

The α and *β* anomers of 1′-(2′,3′-dioleyl-5′-trimethylammonium-D-ribofuranosyl)-3-nitropyrrole, **7a** and **7b**, respectively, were synthesized from D-ribose as shown in Scheme 1. Briefly stated, 5-*O*-*tert*-butyldimethylsilyl-2,3-*O*-isopropylidene-D-ribose, **2**, was prepared in two steps from D-ribose following a published procedure (*26*). Next, the stereoselective chlorination of the protected sugar, **2**, with CCl_4 and hexamethylphosphorus triamide (HMPT) (*27*) was followed by coupling with the anion

* Contact: mgrin@bu.edu or camplo@univmed.fr.
[†] Centre Interdisciplinaire de Nanosciences de Marseille CINaM, UPR-CNRS 3118.
[‡] Boston University.
[§] Centre d'Immunologie de Marseille Luminy.
[||] Inserm U869, Université Victor Segalen Bordeaux.

10.1021/bc800432n CCC: $40.75 © 2009 American Chemical Society
Published on Web 01/21/2009

Scheme 1[a]

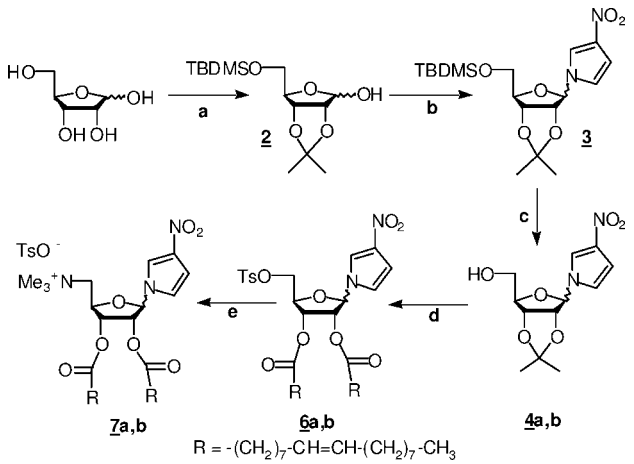

[a] Reaction conditions: (a) (i) acetone, $CuSO_4$, 94% yield, (ii) TBDMSCl, DMAP, TEA 35% yield; (b) (i) CCl_4, HMPT, (ii) 3-nitropyrrole, NaH, CH_3CN, 40% yield; (c) TBAF dry THF, 71% yield, α/β 3:1; (d) (i) TsCl, TEA, DCM **5a** (94% yield), **5b** (56% yield)), (ii) TFA/H_2O, quant., (iii) oleic acid, DCC/DMAP, **6a** (77% yield), **6b** (87% yield); (e) NMe_3, CH_3CN 60°C, 40 hrs, **7a** and **7b** quant. yields.

of 3-nitropyrrole formed from the commercially available 1-(triisopropylsilyl)pyrrole (*28*). Deprotection of the resulting derivative **3** afforded the mixture of (α) **4a** (53%) and (β) **4b** (18%) anomers with the (α) form as the major isolated polar isomer. The relative stereochemistry of these compounds was assigned by NOESY and COSY experiments (data not shown). Compounds **4a** and **4b** were then separately tosylated with TsCl/TEA to give **5a** and **5b** (structures not shown), deprotected with TFA/H_2O, and coupled with oleic acid using DCC/DMAP to afford the nucleolipids **6a** and **6b**. Finally, **6a** and **6b** were reacted with trimethylamine for two days in a sealed tube to afford the nucleolipids **7a** and **7b**. The complete characterization data, including ^{1}H NMR, ^{13}C NMR, and elemental analysis, can be found in the Supporting Information. A differential scanning calorimetry (DSC) trace of the hydrated nucleolipid **7a** or **7b** shows no phase-transition temperature from −40 to 80 °C.

Next, to determine whether the universal base nucleolipids **7a** and **7b** bind nucleic acids, we performed a standard ethidium bromide fluorescence displacement assay with calf thymus DNA as a model system (*29*). DNA binding was observed for **7a** and **7b** as the fluorescence intensity decreased rapidly (see Supporting Information for curves and details). The nucleolipids formed a 6:1 and 2:1 complex for **7a** and **7b** with a binding constant of $\sim 10^{-7}$ M,$^{-1}$ similar in magnitude to DOTAP (*30*). This universal base, 3-nitropyrrole, was expected to bind DNA or RNA based on the published data. Previous thermal denaturation studies with 1-(2′-deoxy-β-D-ribofuranosyl)-3-nitropyrrole showed that this base pairs with the four naturally occurring bases with little discrimination (*31, 32*). The nitro group of 3-nitropyrrole polarizes the π-aromatic system enhancing the π-stacking interactions, and yet as a poor hydrogen bond participator, it does not distinguish among the bases. Considering the minor differences between DNA and siRNA in terms of base composition and ability to hydrogen bond and from π-stacking arrangements, the 3-nitropyrrole base is likely to interact with the bases of siRNA as well as DNA.

As **7a** and **7b** are amphiphilic, the dispersion of these nucleolipids in water by sonication leads to vesicles in the presence and absence of DNA. Again, DNA was used as a model system. In the absence of DNA, vesicle size, as measured by DLS, was 84.7 and 458.4 nm for compounds **7a** and **7b**, respectively. For **7b**, we observed a broad

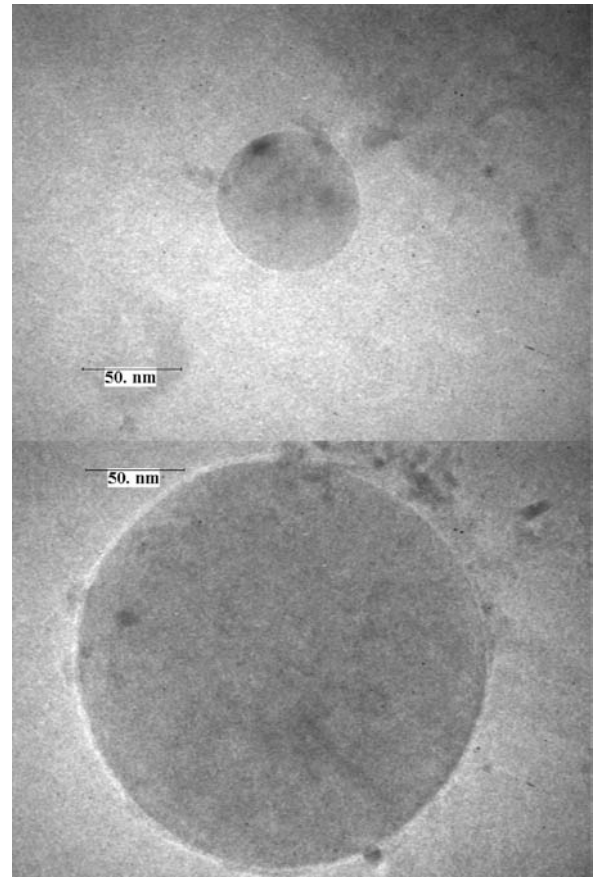

Figure 2. TEM image of single isolated vesicles obtained with **7a** (top) and **7b** (bottom).

distribution of vesicle sizes. In the presence of DNA, and at different compound/DNA charge ratios, lipoplexes were formed of 132.4 nm (**7a**/DNA 2:1), 179.3 nm (**7a**/DNA 5:1), and 469.8 nm (ratio **7b**/DNA 2:1), 516.1 nm (ratio **7b**/DNA 5:1). Transmission electron microscopy (TEM) experiments were performed on vesicle samples **7a** and **7b** using a Philips CM 10 (negative staining with ammonium molybdate 1% water, Cu/Pd carbon-coated grids). Both anomers (α and β) of the nucleolipids formed small vesicles. Representative images of vesicles formed by **7a** and **7b** with diameters of roughly 80 and 220 nm, respectively, are shown in Figure 2. Similar experiments performed with vesicles formed from nucleolipid−DNA solutions were inconclusive as to the location of the DNA within the structure.

The transfection of siRNA with **7a** and **7b** was next performed to evaluate the reduction in protein synthesis. Experiments were performed using glyceraldehyde-3-phosphate dehydrogenase (GAPDH) siRNA (Ambion). Complete details can be found in the Supporting Information, and the transfection experiments were performed in the presence of serum. Three distinct cell lines were used, including human liver (HepG2), mouse fibroblast (NIH 3T3), and Chinese hamster ovarian (CHO) cells. siRNA transfection results were accessed after 48 h as a function of both anomer and cation/anion (N/P) mole ratio. In each experiment, controls using GAPDH siRNA and negative control siRNA were used at 30 mM. siPORT *NeoFX* was used as the positive control. As shown in Figure 3, siRNA knockdown was observed for both nucleolipids in the three different cell lines, with values comparable, not significantly significant, to the positive control *NeoFX*. The transfection activity of **7a** was significant vs siRNA ($p < 0.05$) in NIH 3T3 and CHO cells with N/P ratios of 1, 5, 15, and 20 and 1 and 5, respectively. The transfection activity of **7b** was significant vs siRNA ($p <$

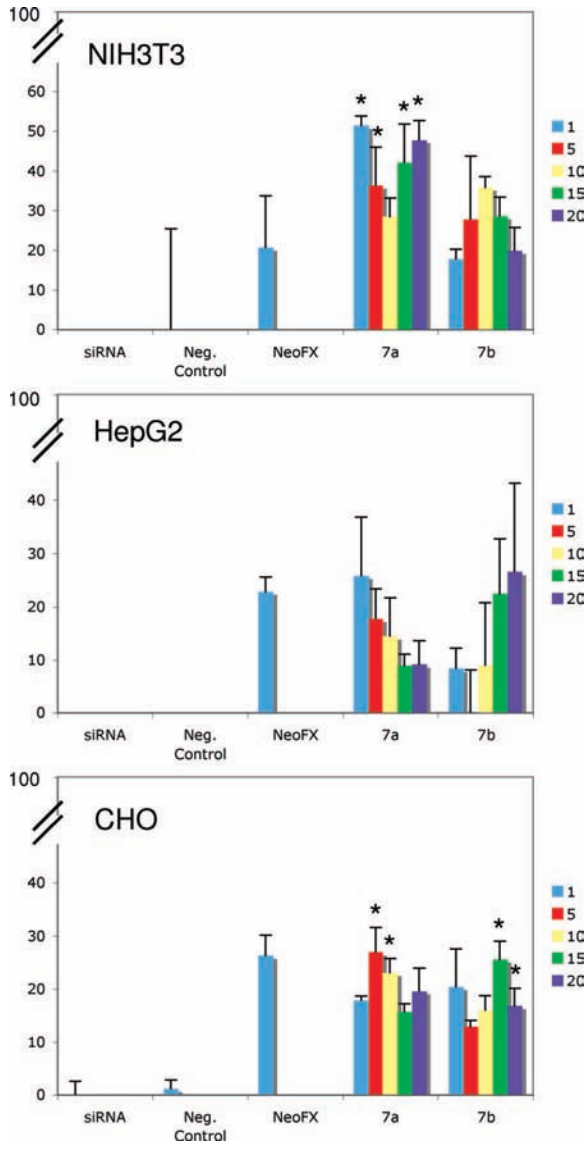

Figure 3. siRNA transfection results after 48 h in HepG2, NIH 3T3, and CHO cells as a function of nucleolipid (**7a** and **7b**) and N/P mole ratio. $N = 3$; $*p < 0.05$ vs siRNA control.

0.05) in CHO cells with N/P ratios of 15 and 20, respectively. The configuration of the anomeric position does not have a significant role in the transfection. In addition, none of the nucleolipids showed a significant cytotoxicity at this concentration using an MTS assay with CHO cells, as the viability was similar to the negative control (see SI).

In summary, we have synthesized and characterized a new universal base nucleolipid for siRNA delivery. The nucleolipids possess a cationic charge, a 3-nitropyrrole base, and two oleyl chains, and these lipids form vesicles in the presence and absence of nucleic acids. siRNA delivery and resulting protein knockdown were observed in three separate cell lines: hamster ovarian, mouse fibroblast, and human liver cells. This is the first report of such activity with a nucleolipid. Work is in progress to synthesize additional universal nucleolipids (including the nitroindole and nitroimidazole analogues for siRNA delivery), as well as to develop a structure−activity relationship. Nucleolipids are one of the newest types of synthetic lipid vectors being explored and, like others in the lipid family, offer the potential advantages of ease of synthesis, carriers of large and small nucleic acid payloads, and minimal toxicity (*11*, *14*−*17*, *33*−*42*). The synthesis and evaluation of new lipids that possess unique head groups, backbones, or hydrophobic chains for nucleic acid binding and/or self-assembly will facilitate the identification of optimal carriers for nucleic acids in vitro and in vivo; efforts in this area should be encouraged and promoted.

ACKNOWLEDGMENT

P.B. acknowledges financial support from the Army Research Office. M.W.G. acknowledges support from BU and the NIH. The authors also thank Pascal Raynal for technical assistance.

Supporting Information Available: Synthesis, characterization data, transfection studies, and cell cytotoxicity data. This material is available free of charge via the Internet at http://pubs.acs.org.

LITERATURE CITED

(1) Gissot, A., Camplo, M., Grinstaff, M. W., and Barthélémy, P. (2008) Nucleoside, nucleotide and oligonucleotide based amphiphiles: A successful marriage of nucleic acids with lipids. *Org. Biomol. Chem. 6*, 1324–1333.

(2) Milani, S., Baldelli Bombelli, F., Berti, D., and Baglioni, P. (2007) Nucleolipoplexes: A new paradigm for phospholipid bilayer-nucleic acid interactions. *J. Am. Chem. Soc. 129*, 11664–11665.

(3) Cuomo, F., Lopez, F., Ruggero, A., Colafemmina, G., and Ceglie, A. (2008) Nucleotides and nucleolipids derivatives interaction effects during multi-lamellar vesicles formation. *Colloids Surf., B: Biointerfaces 64*, 184–193.

(4) Moreau, L., Camplo, M., Wathier, M., Taib, N., Laguerre, M., Bestel, I., Grinstaff, M. W., and Barthélémy, P. (2008) Real time imaging of supramolecular assembly formation via programmed nucleolipid recognition. *J. Am. Chem. Soc. 130*, 14454–14455.

(5) Bestel, I., Campins, N., Marchenko, A., Fichou, D., Grinstaff, M. W., and Barthélémy, P. (2008) Two dimensional self-assembly and complementary base pairing between amphiphile nucleotides on graphite. *J. Colloid Interface Sci. 323*, 435−440.

(6) Moreau, L., Barthélémy, P., Maataoui, M. E., and Grinstaff, M. W. (2004) Supramolecular assemblies of nucleoside-based amphiphiles. *J. Am. Chem. Soc. 126*, 7533–7539.

(7) Moreau, L., Ziarelli, F., Grinstaff, M. W., and Barthélémy, P. (2006) Self-assembled microspheres from f-block elements and nucleoamphiphiles. *Chem. Commun. 15*, 1661–1663.

(8) Moreau, L., Campins, N., Grinstaff, M. W., and Barthélémy, P. (2006) A fluorocarbon nucleoamphiphile for the construction of actinide loaded microspheres. *Tetrahedron Lett. 47*, 7117–7120.

(9) Barthélémy, P., Prata, C. A. H., Filocamo, S. F., Immoos, C. E., Maynor, B. W., Hashmi, S. A. N., Lee, S. J., and Grinstaff, M. W. (2005) Supramolecular assemblies of DNA with neutral nucleoside amphiphiles. *Chem. Commun.* 1261–1263.

(10) Campins, N., Dieudonné, P., Grinstaff, M. W., and Barthélémy, P. (2007) Nanostructured assemblies from nucleotide based amphiphiles. *New J. Chem. 31*, 1928–1934.

(11) Chabaud, P., Camplo, M., Payet, D., Serin, G., Moreau, L., Barthélémy, P., and Grinstaff, M. W. (2006) Cationic nucleoside lipids for gene delivery. *Bioconjugate Chem. 17*, 466–472.

(12) Moreau, L., Barthélémy, P., Li, Y., Luo, D., Prata, C. A. H., and Grinstaff, M. W. (2005) Nucleoside phosphocholine amphiphile for in vitro DNA transfection. *Molecular BioSystems 1*, 260–264.

(13) Arigon, J., Prata, C. A. H., Grinstaff, M. W., and Barthélémy, P. (2005) Nucleic acid complexing glycosyl nucleoside-based amphiphile. *Bioconjugate Chem. 16*, 864–872.

(14) Luo, D., and Saltzman, W. M. (2000) Synthetic DNA delivery systems. *Nat. Biotechnol. 18*, 33–37.

(15) Davis, M. E. (2002) Non-viral gene delivery systems. *Curr. Opin. Biotechnol. 13*, 128–131.

(16) Kabanov, A. V., Felgner, P. L., and Seymour, L. W. (1998) *Self-assembling complexes for gene delivery: From laboratory to clinical trial*, John Wiley and Sons, New York.
(17) Felgner, P. L. (1990) Particulate systems and polymers for in vitro and in vivo delivery of polynucleotides. *Adv. Drug Delivery Rev. 5*, 163–187.
(18) Putnam, D. (2006) Polymers for gene delivery across length scales. *Nat. Mater. 5*, 439–451.
(19) Reineke, T. M., and Grinstaff, M. W. (2005) Designer materials for nucleic acid delivery. *Mat. Res. Soc. Bull. 30*, 635–639.
(20) Barthélémy, P., Lee, S. J., and Grinstaff, M. W. (2005) Supramolecular assemblies with DNA. *Pure Appl. Chem. 77*, 2133–2148.
(21) Pannier, A. K., and Shea, L. D. (2004) Controlled release systems for DNA delivery. *Mol. Ther. 10*, 19–26.
(22) Loakes, D. (2001) Survey and summary: The applications of universal DNA base analogues. *Nucleic Acid Res. 29*, 2437–2447.
(23) Loakes, D., and Brown, D. M. (1994) 5-Nitroindole as an universal base analogue. *Nucleic Acid Res. 29*, 4039–4034.
(24) Harki, D. A., Graci, J. D., Edathil, J. P., Castro, C., Cameron, C. E., and Peterson, B. R. (2007) Synthesis of a universal 5-nitroindole ribonucleotide and incorporation into RNA by a viral RNA-dependent RNA polymerase. *ChemBioChem 8*, 1359–1362.
(25) Harki, D. A., Graci, J. D., Korneeva, V. S., Ghosh, S. K. B., Hong, Z., Cameron, C. E., and Peterson, B. R. (2002) Synthesis and antiviral evaluation of a mutagenic and non-hydrogen bonding ribonucleoside analogue: 1-β-D-ribofuranosyl-3-nitropyrrole. *Biochemistry 41*, 9026–9033.
(26) Stewart, A. O., and Williams, R. M. (1985) C-glycosidation of pyridyl thioglycosides. *J. Am. Chem. Soc. 107*, 4289–4296.
(27) Harusawa, S., Imazu, T., Takashima, S., Araki, L., Ohishi, H., Kurihara, T., Sakamoto, Y., Yamamoto, Y., and Yamatodani, A. J. (1999) Synthesis of 4(5)-[5-(aminomethyl)tetrahydrofuran-2-yl- or 5-(aminomethyl)-2,5-dihydrofuran-2-yl]imidazoles by efficient use of a PHSe group: Application to novel histamine H3-ligands. *J. Org. Chem. 64*, 8608–8615.
(28) Bray, B. L., Mathies, P. H., Naef, R., Solas, D. R., Tidwell, T. T., Artis, D. R., and Muchowski, J. M. (1990) N-(Triisopropylsilyl)pyrrole. A progenitor "par excellence" of 3-substituted pyrroles. *J. Org. Chem. 55*, 6317–6328.
(29) Geall, A. J., and Blasgbrough, I. S. (2000) Rapid and sensitive ethidium bromide fluorescence quenching assay of polyamine conjugate-DNA interactions for the analysis of lipoplex formation in gene therapy. *J. Pharm. Biomed. Anal. 22*, 849–859.
(30) Cain, B. F., Baguley, B. C., and Demmy, M. W. (1978) Potential antitumor agents. 28. Deoxyribonucleic acid polyintercalating agents. *J. Med. Chem. 21*, 658–668.
(31) Bergstrom, D. E., Zhang, P., Toma, P. H., Andrews, P. C., and Nichols, R. (1995) Synthesis, structure, and deoxyribonucleic-acid sequencing with a universal nucleoside - 1-(2′-deoxy-β-D-ribofuranosyl)-3-nitropyrrole. *J. Am. Chem. Soc. 117*, 1201–1209.
(32) Nichols, R., Andrews, P. C., Zhang, P., and Bergstrom, D. E. (1994) A universal nucleoside for use at ambiguous sites in DNA primers. *Nature 369*, 492–493.
(33) Behr, J. P. (1993) Synthetic gene-transfer vectors. *Acc. Chem. Res. 26*, 274–278.
(34) Huang, L., Hung, M., and Wagner, E., Eds. (1999) *Nonviral vectors for gene therapy*, Academic Press, New York, p 442.
(35) Miller, A. D. (1998) Cationic liposomes for gene therapy. *Angew. Chem. Int. 37*, 1768–1785.
(36) Remy, J., Sirlin, C., Vierling, P., and Behr, J. (1994) Gene transfer with a series of lipophilic DNA-binding molecules. *Bioconjugate Chem. 5*, 647–654.
(37) Deshmukh, H. M., and Huang, L. (1997) Liposome and polylysine mediated gene transfer. *New J. Chem. 21*, 113–124.
(38) Legendre, J. Y., and Szoka, F. C. J. (1992) Delivery of plasmid DNA into mammalian cell lines using pH sensitive liposomes: Comparison with cationic liposomes. *Pharm. Res. 10*, 1235–1242.
(39) MacDonald, R. C., Ashley, G. W., Shida, M. M., Rakhmanova, V. A., Tarahovsky, Y. S., Kennedy, M. T., Pozharski, E. V., Baker, K. A., Jones, R. D., Rosenzweig, H. S., Choi, K. L., Qiu, R., and McIntosh, T. J. (1999) Physical and biological properties of cationic triesters of phosphatidylcholine. *Biophys. J. 77*, 2612–2629.
(40) Robbins, P. D., Tahara, H., and Ghivizzani, S. C. (1998) Viral vectors for gene therapy. *Trends Biotechnol. 16*, 35–40.
(41) Miller, A. D. (2003) The problem with cationic liposome/micelle-based non-viral vector systems for gene therapy. *Curr. Med. Chem. 10*, 1195–1211.
(42) Liu, Y. M., Wenning, L., Lynch, M., and Reineke, T. M. (2004) New poly(D-glucaramidoamine)s induce DNA nanoparticle formation and efficient gene delivery into mammalian cells. *J. Am. Chem. Soc. 126*, 7422–7423.

BC800432N

SUPPORTING INFORMATION

Cationic Nucleoside Lipids possessing a 3-Nitropyrrole Universal Base for siRNA Delivery

Claire Ceballos[†], Carla A.H. Prata[‡], Suzanne Giorgio[†], Frédéric Garzino[†], Dominique Payet[§], Philippe Barthélémy[#], Mark W. Grinstaff[‡,]* and Michel Camplo[†,‡,]*

[†] Centre Interdisciplinaire de Nanosciences de Marseille CINaM, UPR-CNRS 3118, Université Aix-Marseille II, Luminy, case 913, 13288 Marseille cedex 09, France. [‡] Departments of Chemistry and Biomedical Engineering, Metcalf Center for Science and Engineering, Boston University, Boston MA 02215,USA. [§] Centre d'Immunologie de Marseille Luminy, Parc scientifique de Luminy, 13288 Marseille, Cedex 9, France. [#] Inserm, U869, Université Victor Segalen Bordeaux 2, F-33076, Bordeaux, France.

Experimental Section

Material. Unless noted otherwise, all starting materiel were purchased from Sigma-Aldrich, Acros or Alfa Aesar and used as received. Some solvents were distilled under argon over appropriate drying agent: tetrahydrofuran and diethylether over sodium/benzophenone, dichloromethane over $CaCl_2$. Unless otherwise stated, the other solvents were used as commercially available. All compounds were characterized by ^{1}H NMR, ^{13}C NMR and mass spectroscopy. 250 MHz and 62.5 MHz 13C Nuclear Magnetic Resonance (NMR) spectra were recorded either on a Bruker AC 250. The spectra were taken at 20 °C and referenced against residual proton-solvent signals (^{1}H: $CDCl_3$: 7.26 ppm, and ^{13}C: 77 ppm). The ^{1}H NMR coupling constants (J) are reported in Hz. ESI-MS and elemental analyses were performed at the spectropole of the *Faculte des Sciences et Techniques de Saint Jerôme*, Marseille, France. Electrospray Ionisation Mass Spectra (ESI-MS) were recorded with an API///Plus sciex triple quadripole spectrophotometer in the positive mode. Elemental analyses were recorded with a Thermo Finnigan EA 1112 elemental analysis apparatus driven by the Eager 300 software. TEM

microscopy experiments were performed on a Philipps CM10 (negative staining with ammonium molybdate 1% in water, Cu/Pd carbon coated grids). Analytical thin layer chromatography (tlc) was performed on pre-coated glass plates with kieselgel 60F254 neutral with aluminium support plate (0.25mm layer thickness), SDS. The developed plates were air-dried and exposed to UV light and (or) sprayed with a solution of cerium sulphate (1%) and molybdic acid (1.5%) in 10% aqueous sulphuric acid and heated at 150°C. Preparative thin layer chromatography was performed on glass plates with Merck silica gel 60F-254 as the adsorbent (layer thickness 2mm or 1mm). Column chromatography was performed on Merck silica gel 60 (0.063-0.200mm). Melting point (mp) were measured with an Electrothermal 9100.

2,3-O-isopropylidene-D-ribose, 1 To a stirring solution of D-ribose (10g, 0.06 mol) in dry acetone (200 mL) was added a catalytic amount of H_2SO_4 at room temperature. Then $CuSO_4$ was added. After being stirred for 40h at 37 °C, the solution was filtered and washed with small quantities of acetone. The filtrate was neutralized with $Ca(OH)_2$ and stirred for 15 minutes. The mixture was filtered and the filtrate was evaporated under reduced pressure (T<40 °C) to give **1** (11.76g, 94%) as a yellow syrup.^{1}H NMR ($CDCl_3$): δ 5.39 (1H,m); 4.82 (1H, d, J=6.00Hz); 4.57 (1H, d, J=6.00Hz); 4.40 (1H,m); 4.22 (2H, m); 2.17 (2H,s); 1.48 (3H,s); 1.31 (3H,s). ^{13}C NMR (CDCl3): δ 102.31, 95.56, 82.36, 73.12, 72.01, 63.45, 29.03. FAB, MS m/z : 191(M+1)

5-O-*tert*-butyldimethylsilyl-2,3-O-isopropylidene-D-ribofuranose, 2

2,3-O-isopropylidene-D-ribose (6.27 g; 0.03 mol) was dissolved in dry dichloromethane (10ml) containing triethylamine (5.11 mL; 36.72 mmol) and 4-(dimethylamino)pyridine (DMAP) (450 mg; 3.69 mmol). The solution was cooled to 0°C and *tert*-butyldimethylsilylchloride (TBDMSCl) (5.40 g; 35.76 mmol) dissolved in dry dichloromethane (20 mL) was added

dropwise. The mixture was stirred at ambient temperature overnight. The mixture was then concentrated under reduced pressure, and the residue was triturated with THF. The organic phase was filtered andevaporated before the crude product was purified by flash column chromatography (90/10: pentane/Et_2O) to give **2** (3.46 g, 35%) as a yellow oil.

^{1}H NMR ($CDCl_3$): δ 5.33 (1H,d , J=11.37Hz); 4.70 (1H, d, J=6.00Hz); 4.57 (1H, d, J=6.00Hz); 4.36 (1H,m); 3.76 (2H, d, J=2.50Hz); 1.58 (1H,sl); 1.48 (3H,s); 1.32 (3H,s); 0.92(9H,s); 0.09 (3H,s) 0.06 (3H,s)^{13}C NMR ($CDCl_3$): δ 111.03, 102.44, 100.01, 88.64, 85.98, 80.73, 65.79, 27.36, 26.01, 24.93, 19.11, -6.01, -6.03. FAB, MS m/z : 305 (M+1)

1'-(5'-O-*tert* -butyldimethylsilyl-2',3'-O-isopropylidene-D-ribofuranosyl)-3-nitropyrrole, 3

First step : Carbon tetrachloride (433 µL, 4.49 mmol) was added to a stirring solution of **2** (1.22 g; 2.87 mmol) in anhydrous THF (10 mL). The solution was cooled to -70°C and hexamethylphosphorous triamide (700 µL, 3.82 mmol) was added dropwise for 5 minutes, and the mixture was allowed to stir at the same temperature for 5 minutes. The resulting compound was allowed to warm to room temperature and further stirred for 2 hours. The solvent was evaporated and the residue dissolved in diethyl ether. The resulting insoluble materiel was removed by decantation and the organic layer was evaporated to give the crude compound **3** as an orange oil.

Second step: To a cooled solution (0 °C) of 3-nitropyrrole (629 mg, 5.61 mmol) dissolved in anhydrous acetonitrile (9 mL) was added NaH (60%, 223 mg, 5.6 1mmol); the solution was stirred at room temperature for 30 minutes. To the resulting bright yellow solution, the chloro sugar obtained from the first step was dissolved in anhydrous acetonitrile and transferred via canula. The reaction mixture was then warmed to room temperature and stirred for 40 hours. The mixture was poured into H_2O (50 mL) and extracted with CH_2Cl_2 (3*50 mL). The organic layers

were combined and successively washed with saturated aqueous NH_4Cl and saturated aqueous NaCl. The organic layer was dried over $MgSO_4$ and concentrated in vacuo. The residue was purified by flash column chromatography (70/30: cyclohexane/EtOAc) to give **3** (579mg, 40%) as a yellow oil. ^{1}H NMR ($CDCl_3$): δ 7.71 (1H, m); 6.72 (2H, m); 5.93 (1H, d, J=4.26Hz); 4.87 (1H, dd, J=0.63Hz, J=6.00Hz); 4.42 (1H, dd, J=2.21Hz, J=2.00Hz);); 3.89 (1H, dd, J=2.21Hz, J=11.21Hz); 3.76 (1H, dd, J=2.00Hz, J=11.05Hz); 1.42 (3H,s); 1.32 (3H,s); 0.93 (9H, s); 0.10 (6H,s). ^{13}C NMR ($CDCl_3$): δ 137.40, 119.24, 118.76, 114.14, 105.88, 95.22, 86.21, 86.14, 81.04, 63.44, 27.20, 25.77, 25.19, 18.26, -5.61, -5.71. FAB, MS m/z : 398 (M+1)

1'-(2',3'-O-isopropylidene-D-ribofuranosyl)-3-nitropyrrole, 4a and 4b

To a solution of **3** (596 mg, 1.49 mmol) in dry THF (5 mL) was added TBAF (1M in THF) (3 mL, 2.98 mmol) at room temperature and the mixture was stirred for 30 minutes. The solution was evaporated under reduced pressure, diluted with CH_2Cl_2 and washed with brine. The organic layer was dried on $MgSO_4$ and evaporated under reduced pressure. The crude product was purified by flash column chromatography (cyclohexane/EtOAc : 70/30 to 50/50) to give the anomer α **4a** (227 mg, 53%) as a white solid and the anomer β **4b** (75 mg, 18%) as a yellow oil.

1'-(2',3'-O-isopropylidene-α-D-ribofuranosyl)-3-nitropyrrole, 4a

mp=107°C. ^{1}H NMR ($CDCl_3$): δ 7.73 (1H, t, J=2.05Hz); 6.73 (2H, d, J=2.05Hz); 5.94 (1H, d, J=4.42Hz); 4.92 (1H, dd, J=1.11Hz, J=6.00Hz); 4.85 (1H, dd, J=4.42Hz, J=6.16Hz);); 4.46 (1H, t, J=2.84Hz); 3.94 (1H, td, J=2.84Hz, J=11.34Hz); 3.81 (1H, td, J=3.16Hz, J=11.21Hz); 1.40 (3H,s); 1.32 (3H,s)

^{13}C NMR ($CDCl_3$): δ 140.23, 121.12, 120.20, 113.80, 104.99, 90.73, 83.30, 81.94, 80.60, 64.30, 22.51, 24.20. FAB-MS m/z : 285 (M+1), 302 (M+16), 307 (M+23), 323 (M+29)

1'-(2',3'-O-isopropylidene-β-D-ribofuranosyl)-3-nitropyrrole, 4b

^{1}H NMR ($CDCl_3$): δ 7.80 (1H, dd, J=2.21Hz, J=4.11Hz); 6.80 (1H, dd, J=2.37Hz, J=3.32Hz); 6.74 (1H, dd, J=1.90Hz, J=3.32Hz); 5.62 (1H, d, J=3.32Hz); 4.89 (1H, dd, J=2.84Hz, J=6.32Hz);); 4.76 (1H, dd, J=3.32Hz, J=6.48Hz); 4.35 (1H, q, J=3.16Hz); 3.96 (1H, dd, J=3.47Hz, J=11.85Hz); 1.59 (3H,s); 1.36 (3H,s). ^{13}C NMR ($CDCl_3$): δ 141.68, 119.69, 119.33, 114.73, 106.22, 94.79, 85.90, 82.27, 80.74, 62.56, 27.19, 25.22. FAB-MS m/z : 285 (M+1), 302 (M+16), 307 (M+23), 323 (M+29)

1'-(2',3'-O-isopropylidene-5-O-tosyl-α-D-ribofuranosyl)-3-nitropyrrole, 5a

Compound **4a** (100mg, 0.35mmol) was dissolved in dry dichloromethane (4 mL) and the solution was cooled to 0°C. NEt_3 (196 μL, 1.41 mmol) was added, as well as tosyl chloride (200 mg, 1.05 mmol), in small portions. The solution was then allowed to warm to room temperature and stirred overnight. Dichloromethane was added and the solution was successively washed with brine and aqueous $NaHCO_3$ 5% w/v. The organic layer was dried on $MgSO_4$, filtered and concentrated under reduced pressure. The residue was purified by preparative layer chromatography (cyclohexane/EtOAc:60/40) to give **5a** (145 mg, 94%) as a white solid. mp = 111-113°C. ^{1} H NMR ($CDCl_3$): δ 7.78 (2H, d, J=8.22Hz); 7.64 (1H,m); 7.37 (2H, d, J=8.10Hz); 6.69 (2H, m); xx (1H, d, J=3.63Hz); 4.82 (2H,m); 4.51 (1H, t, J=2.35Hz); 4.19 (2H, d, J=2.60Hz); 2.44 (3H,s); 1.37 (3H,s); 1.27 (3H,s). ^{13}C NMR ($CDCl_3$): δ 145.82, 137.01, 131.83, 130.26, 127.86, 120.93, 120.11, 114.29, 105.55, 90.72, 81.55, 80.53, 80.20, 71.06, 25.47, 24.17, 21.69. FAB-MS m/z : 439 (M+1)

1'-(2',3'-O-isopropylidene-5-O-tosyl-β-D-ribofuranosyl)-3-nitropyrrole, 5b

Compound **5b** was obtained in 56% yield from compound **4b** by the procedure described above. Purification by preparative layer chromatography (cyclohexane/ EtOAc : 70/30) gave a yellow oil. ^{1}H NMR ($CDCl_3$): δ 7.75 (2H, d, J=8.37Hz); 7.60 (1H,t, J=2.05Hz); 7.34 (2H, d, J=8.50Hz); 6.72(2H, t, J=1.9Hz); 5.56(1H, d, J=3.32Hz); 4.84 (1H,dd, J=3.32Hz, J=6.30Hz); 4.45 (1H, q, J=2.84Hz); 4.28 (1H, dd, J=3.00Hz, J=11.06Hz); 4.13 (1H, dd, J=3.00Hz, J=11.06Hz); 2.44 (3H,s); 1.57 (3H,s); 1.35 (3H,s). ^{13}C NMR ($CDCl_3$): δ 145.69, 137.81, 131.10, 127.88, 119.31, 118.93, 115.08, 106.35, 94.71, 85.13, 82.78, 80.55, 68.56, 27.06, 25.13, 26.67. FAB-MS m/z : 439 (M+1)

1'-(2',3'-dioleyl-5-O-tosyl-α-D-ribofuranosyl)-3-nitropyrrole, 6a

At 0°C, compound **5a** (145 mg, 0.33 mmol) was dissolved in 3.5 mL of an aqueous trifluoroacetic acid / H_2O (6/1) solution and stirred for 1 hour at 0°C. The solvents were co-evaporated with methanol under reduced pressure, and the residue was dried in vacuo. The crude product was dissolved in dry CH_2Cl_2 (7 mL) and the solution was cooled to 0°C. Dicyclohexylcarbodiimide (271 mg, 1.32 mmol), (dimethylamino)pyridine (161 mg, 1.32 mmol) and oleic acid (372 mg, 1.32 mmol) were added, and the mixture was stirred at room temperature overnight. DCU was then filtered, and the filtrate was successively washed with aqueous 2N HCl and aqueous saturated $NaHCO_3$ solutions. The organic layer was dried on $MgSO_4$, filtered and evaporated under reduced pressure. The crude product purified by flash column chromatography (cyclohexane/EtOAc : 95/5) gave **6a** (236mg, 77%) as a yellow oil. ^{1}H NMR ($CDCl_3$): δ 7.80 (1H, d, J=8.22Hz); 7.66 (1H,t, J=2.05Hz); 7.37 (2H, d, J=7.90Hz); 6.67 (1H, dd, J=1.90Hz, J=3.32Hz); 6.59(1H, dd, J=2.53Hz, J=3.32Hz); 5.88 (1H, d, J=5.53Hz); 5.44(2H,m); 5.33 (4H,m); 4.54 (1H, q, J=2.84Hz); 4.31 (1H, dd, J=3.00Hz, J=11.37 Hz), 4.18 (1H, dd, J=2.68Hz , J= 11.21Hz); 2.45 (3H,s);); 2.33 (2H, t, J=3.00Hz); 2.31 (4H, t, J=3.00Hz); 1.99 (8H,m); 1.25

(44H,m); 0.86 (6H, t, J=6.32Hz). ^{13}C NMR ($CDCl_3$): δ 172.15, 145.59, 137.44, 132.21, 130.10, 130.05, 130.82, 130.01, 129.63, 129.60, 120.82, 105.20, 88.21, 75.86, 73.26, 70.90, 70.54, 60.34, 31.88, 29.74, 29.67, 29.51, 29.10, 29.02, 27.20, 27.14, 22.67, 14.19. FAB-MS m/z : 927 (M+1), 944 (M+18), 949 (M+23), 965 (M+29)

1'-(2',3'-dioleyl-5-O-tosyl-β-D-ribofuranosyl)-3-nitropyrrole, 6b

Compound **6b** was obtained from **5b** with the same procedure described above. Purification by flash column chromatography (cyclohexane/EtOAc : 95/5) gave **6b** as a yellow oil in 87% yield. ^{1}H NMR ($CDCl_3$): δ 7.84 (2H, d, J=8.21Hz); 7.62 (1H,t, J=2.05Hz); 7.37 (2H, d, J=8.53Hz); 6.77 (2H,m); 5.61 (1H, d, J=5.05Hz); 5.34 (6H,m); 5.34 (6H,m); 5.23 (1H,m); 4.34 (2H, m); 2.45 (3H,s), 2.33 (4H,m); 2.00 (8H,m); 1.67 (4H, m); 1.26 (44H, m); 0.87 (6H,m). ^{13}C NMR ($CDCl_3$): δ 172.05, 143.64, 136.44, 131.94, 131.72, 130.75, 129.43, 129.22, 123.58, 122.75, 121.02, 105.85, 82.12, 76.93, 70.92, 69.54, 60.29, 33.94, 33.30, 32.52, 30.32, 30.10, 29.76, 25.42, 23.14, 14.12. FAB-MS m/z : 927 (M+1), 944 (M+18), 949 (M+23), 965 (M+29)

Tosylate salt of 1'-(2',3'-dioleyl-5'-trimethylammonium-α-D-ribofuranosyl)-3-nitropyrrole, 7a

Anhydrous triethylamine (1 mL) was transferred to a pressure tube cooled at -50°C via canula. Next, anhydrous acetonitrile (2 mL) and a solution of **6a** (118 mg, 0.13 mmol) in dry THF (2 mL) were added. The tube was sealed and heated in an oil bath at 50°C during 48h then cooled to -20°C and opened. The solvents were evaporated under reduced pressure to give **7a** (125mg, quantitative) as a brown oil. ^{1}H NMR ($CDCl_3$): δ 7.68 (2H, d, J=8.06Hz); 7.64 (1H,m); 7.12 (2H, d, J=8.06Hz); 6.62 (2H,m); 6.26 (1H, d, J=4.42Hz); 5.67 (1H, t, J=4.74Hz); 5.33 (44H,m); 4.79 (1H, m); 4.46 (1H, m); 4.20 (1H,m), 3.37 (9H,s); 2.32 (3H,s); 1.99 (8H, m); 1.60 (4H, m); 1.26 (44H,m); 0.87 (6H, t, J=6.48Hz). ^{13}C NMR ($CDCl_3$): δ 173.21, 142.25, 140.51, 131.94, 137.52,

132.53, 130.73, 125.25, 123.14, 121.56, 106.83, 82.48, 78.41, 73.46, 67.88, 64.48, 51.91, 33.92, 33.32, 32.56, 30.42, 30.32, 30.12, 29.78, 26.48, 24.12, 21.19, 14.12. FAB-MS m/z : 814 (M cation). Anal Calc C,66.97 ; H, 9.30 ; N ,4.26 ; Found calc C,66.98 ; H, 9.41; N, 4.30.

Tosylate salt of 1'-(2',3'-dioleyl-5'-trimethylammonium-β-D-ribofuranosyl)-3-nitropyrrole, 7b

This compound was prepared from **6b** with the same procedure described above to yield **7b** as a brown oil with quantitative yield. ^{1}H NMR ($CDCl_3$): δ 7.80 (1H,m); 7.70 (2H, d, J=8.06Hz); 7.12 (2H, d, J=8.22Hz); 7.03 (1H,m); 6.60 (1H, m); 5.68 (1H, d, J=6.00Hz); 5.32 (4H,m); 4.66 (1H, dd, J=4.11Hz, J=10.27Hz); 4.42 (1H, t, J=11.05Hz); 4.06 (1H,m), 3.33 (9H,s); 2.84 (2H, d, J=7.42Hz); 2.32 (3H, m); 1.98 (8H, m); 1.56 (4H,m); 1.25 (44H,m); 0.86 (6H, t, J=6.00Hz). ^{13}C NMR ($CDCl_3$): δ 173.21, 142.25, 140.51, 131.94, 137.52, 132.53, 130.73, 125.25, 123.14, 121.56, 106.83, 82.48, 78.41, 73.46, 67.88, 64.48, 51.91, 33.92, 33.32, 32.56, 30.42, 30.32, 30.12, 29.78, 26.48, 24.12, 21.19, 14.12. FAB-MS m/z : 814 (M cation). Anal Calc C,66.97 ; H, 9.30 ; N ,4.26 ; Found calc C,66.30 ; H, 9.46; N, 4.00.

Vesicles Preparation

1 mg/mL of compounds **7a** or **7b** was dissolved in chloroform or dichloromethane. The solution was evaporated and dried on vacuum for 2 hrs. 1mL of DI water was added, and the solution was hydrated overnight at 4°C. The resulting solution was sonicated for 20 min. prior to any measurements.

DNA – Cationic Amphiphile Displacement Assay

A competitive displacement fluorescence assay using ethidium bromide (EthBr) was used for the DNA binding studies. This assay involves the addition of aliquots of the compound to a 3 mL solution of EthBr (1.3 μM) and calf thymus DNA (3 μM) in buffer (100 mM NaCl, 100 mM Tris, pH 7.4) with the decrease of fluorescence (λ_{exc}=546 nm, λ_{em}=600 nm; 1 cm path length glass cuvette, slit width 3 nm) recorded after 5 minutes of equilibrium time following each addition. Calf thymus DNA was used instead of siRNA due to the high costs associated with required amount of siRNA for this experiment.

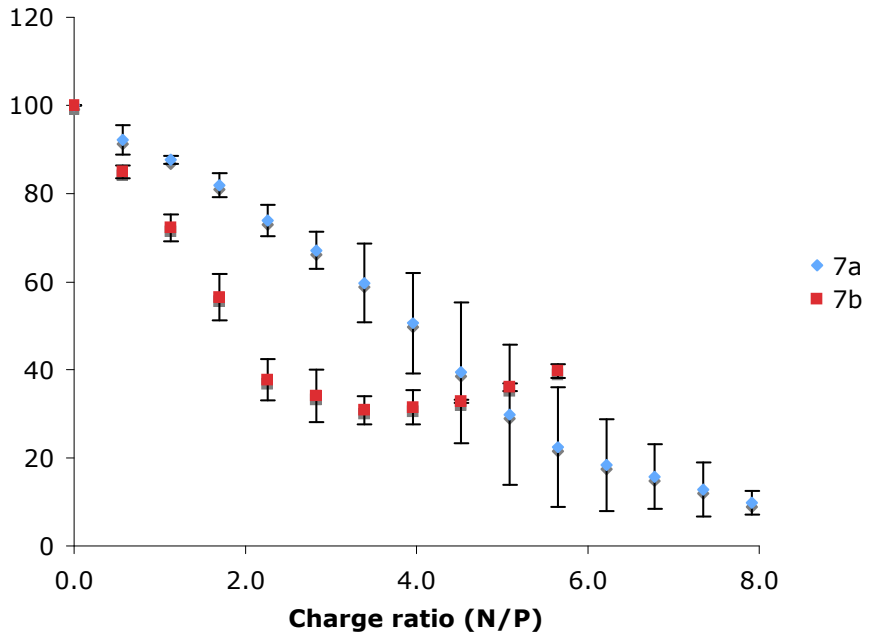

Dynamic light scattering

The diameter of the liposomes and lipid/DNA assemblies was measured at a 90° angle using 90 Plus particle size analyzer (Brookhaven Instruments Model 90 Plus). All solutions used in the study were filtered through a 0.02 μm membrane prior to use. The vesicles of lipid and

DNA were prepared as described above in the vesicle preparation section. The diameter reported corresponds to the average of three experiments in aqueous solution. The 90 Plus particle sizing software was used for data acquisition and analysis. Calf thymus DNA was used instead of siRNA due to the high costs associated with required amount of siRNA for this experiment

siRNA transfection

Trypsine adherent cells were diluted in normal growth medium to 1 x 10^5 cells per mL. The transfection reagent was diluted in serum free medium and incubated at room temperature for 10 min before use. Next siRNA (GAPDH siRNA or negative control siRNA, Ambion) was diluted in serum free medium. The siRNA and the tranfection reagent were mixed, incubated for 10 min at room temperature and dispensed into a culture plate with cells and serum containing medium. Depending on the experimental design, the ration of lipid, siRNA, and incubation time was varied. The cell suspension was then overlayed onto the transfection mixture. The sample was then incubated at 37 °C and 5% CO_2. Gene knockdown activity was assessed after 48 h.

The gene knockdown assay performed was KDalert™ GAPDH Assay (Ambion) following the manufacturer protocol. Briefly, 48 hr after siRNA transfection, the serum-containing culture medium was aspirated from the transfected cells. Next, 200 μL KDalert Lysis Buffer was added to each sample well. The cells were incubated at 4 °C for 20 min to lyse them. The cell lysate was pipeted up and down 4–5 times to homogenize the lysate. 10 μL of each lysate or GAPDH enzyme dilution (including the GAPDH Working Stock) was transfered to the wells of a clean 96 well plate. Finally, 90 μL of KDalert Master Mix was added to each sample using a multi-channel pipettor. The increase in fluorescence of the samples was measured at

room temp.

Cytotoxicity

Cytotoxicity was assessed using both a formazan-based proliferation assay (CellTiter 96 AQueous One Solution Cell Proliferation Assay kit, Promega) and a total protein-based assay (Pierce). Chinese hamster ovarian cells (CHO, ATCC, Manassas, VA) were cultured in complete F12K media (ATCC) containing 10% fetal calf serum (Sigma) and 1% penicillin and streptomycin (500 IU/mL and 5000 μg/ml, respectively, Mediatech, Herndon, VA) at 37 ^{o}C in 5% CO_2 with humidity. When the CHO cells reached about 90% confluency, the cells were split into 24-well plates with a 1:4 ratio using a standard trypsin-based technique. For these experiments, CHO cells were seeded onto a 24-well plate with an appropriate density of 1 x 10^6 cells per well. After 48h the MTS substrate was added to each well and the plate was incubated for 4 h at 37 ^{o}C in a humidified, 5% CO_2 incubator. The amount of soluble formazan produced by cellular reduction of the substrates MTS was recorded at 490 nm using a multi-well plate reader. For the total protein-based proliferation assay, cells were lysed at the same time when transfection efficiency was assayed. A 10 μL of lysates were transferred to a separate multi-well plate. Total protein contents were assessed using the Coomassie Blue protein kit (Pierce, Rockford, IL) following the manufacturer protocol. Negative and positive controls were non-treated cells and commercial lipids treated cells, respectively. The proliferation results were expressed as percentages of non-treated cells.

Protein C-Terminal Modification through Thioacid/Azide Amidation

Xiaohong Zhang, Fupeng Li, Xiao-Wei Lu, and Chuan-Fa Liu*

Division of Chemical Biology and Biotechnology, School of Biological Sciences, Nanyang Technological University, 60 Nanyang Drive, Singapore 637551. Received November 10, 2008; Revised Manuscript Received January 6, 2009

The preparation of protein bioconjugates has been largely dependent on the development of selective chemistries that are orthogonal to the diverse functionalities present in a protein. Here, we report a new method for C-terminus-directed modification of recombinant proteins. The method is based on the thioacid/azide amidation reaction. Essentially, hydrothiolytic cleavage of the thioester intermediate in protein splicing yields a recombinant protein with a unique thioacid group at the C-terminus, which is then chemoselectively amidated with an electron-poor organic azide carrying a biofunctional tag. The small ubiquitin protein was used as a model system to demonstrate the utility of this new bioconjugation method. C-terminal PEGylation or biotinylation of ubiquitin was readily achieved through amidation of ubiquitin thioacid with a sulfonazide-functionalized PEG or biotin derivative. Our data validate that thioacid/azide amidation is a mechanistically novel and practically useful method for site-selective protein modification.

Site-selective protein modification techniques are important tools for protein structure−function study and drug discovery (*1*−*3*). For instance, such techniques can be used to label proteins with a special biophysical probe for structural and biochemical studies (*4*) or with a biocompatible polymer for the development of protein-based therapeutic agents (*5*). They are also useful as immobilizing techniques to tether proteins to solid supports for the fabrication of protein chips (*6*).

Traditional methods for protein modification rely mainly on classic acylation or alkylation chemistries involving the side chain functional groups of Lys, Asp/Glu, and Cys residues (*1*). However, the use of these methods is often limited by the fact that proteins typically carry multiple copies of the targeted residue, making it difficult to control the degree and site of modification. This commonly results in product mixtures with considerable structural heterogeneity. Nontraditional methods have also been developed recently that target the electron-rich side chain aromatic rings of Trp or Tyr residues (*7*). Because these aromatic amino acids are found less frequently on the protein surface, it may be possible to achieve single-site modification if one such residue is solvent-exposed (*8*). However, these new techniques also have limitations because of the low likelihood of having a single solvent-exposed aromatic residue in most proteins. Molecular biology methods that make use of the cell's protein synthesis machinery offer powerful alternatives to chemically based techniques for protein modification. Recent excitement is seen with the methodology developed by Schultz's group and others (*9*). These methods rely on the use of an amber stop codon and a corresponding suppressor tRNA to incorporate into a protein a desired unnatural amino acid which may already carry the biophysical probe of interest in place or contain a unique chemical/photochemical reactivity for later use (*9*).

Compared to modifying the internal residues, protein C-terminal modification offers some distinct advantages. The C-terminal tail of a protein is usually flexible and solvent-exposed, which makes it easily accessible by the tagging reagent. Modifying the C-terminus is also less likely to adversely affect a protein's biological activity as the active spot of a protein is often distant from the terminal end. Moreover, since there is only one C-terminus in a protein, in principle it should be possible to distinguish it from the internal residues for single-site modification. There exist several enzymatic and biosynthetic methods to introduce a C-terminal modification onto a protein. For instance, C-terminal specific labeling has been carried out by catalytic transacylation reactions using carboxypeptidase Y (*10, 11*). Puromycin-based techniques have also been developed that allow the incorporation of various C-terminal tags (*12, 13*). Exploitation of intein-mediated protein splicing (*14*) has generated very useful approaches to protein C-terminal modification (*15*−*17*), which are mostly based on the thioester-mediated ligation chemistry (*18*).

In our efforts to develop new chemoselective methods for protein synthesis and modification, we have paid much attention to a unique functional group, the thioacid. For instance, we have made use of the soft and powerful nucleophilicity of thioacids in the development of a highly effective thioacid capture peptide ligation method (*19*). The synthetic utility of the thioacid group is also experiencing renewed interest in the thioacid/azide amidation reaction (*20*) for the preparation of complex amides (*21*). Thorough mechanistic studies by Williams et al. suggest that this reaction proceeds through the formation of a thiatriazoline intermediate which subsequently decomposes to yield the amide product (*21, 22*). The reaction is especially fast with electron-deficient azides such as sulfonazides, owing to a highly efficient prior capture mechanism (*22*). Although previous studies have only demonstrated thioacid/azide coupling with small thioacids such as thiobenzoic acid and N-protected amino thioacids (*21, 23*−*25*), its unique reaction features imply that it should have the required chemical orthogonality to work in a chemoselective manner with large and complex thioacid compounds such as peptides and proteins. In our recent work, clean and near-quantitative formation of the amidation products was shown between unprotected thioacid peptides and tosyl azide in highly dilute solutions (*26*). In the present study, we extend the application of thioacid/azide amidation to C-terminal modification of recombinant proteins (Figure 1).

* To whom correspondence should be addressed. Chuan-Fa Liu, Division of Chemical Biology and Biotechnology, School of Biological Sciences, Nanyang Technological University, 60 Nanyang Drive, Singapore 637551. E-mail: cfliu@ntu.edu.sg. Tel: +65-6316-2867. Fax: +65-6791-3856.

10.1021/bc800488n CCC: $40.75 © 2009 American Chemical Society
Published on Web 01/13/2009

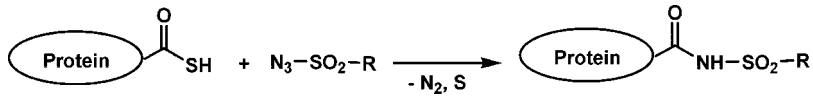

Figure 1. General scheme of protein C-terminal modification through thioacid/azide amidation.

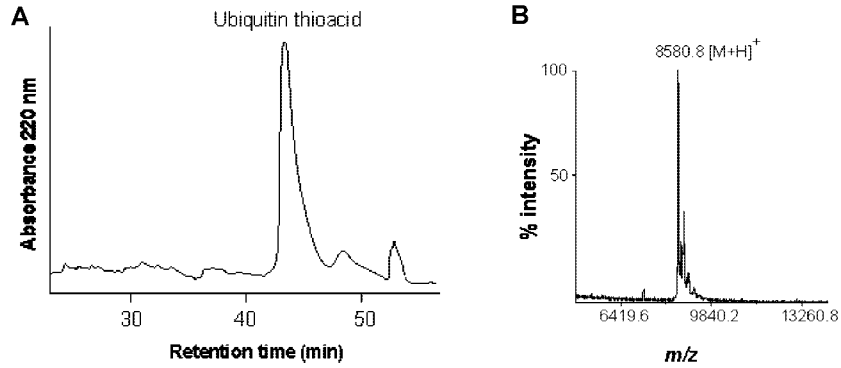

Figure 2. Purification and characterization of ubiquitin thioacid. (A) HPLC profile of C8 semiprep purification of the ubiquitin thioacid eluate from chitin beads after hydrothiolysis. The ubiquitin thioacid was eluted by a linear gradient of buffer B in buffer A from 0% to 60% in 60 min. (B) MALDI-TOF MS of purified ubiquitin thioacid. *m*/*z* $[M + H]^+$ found: 8580.8, MW calcd: 8580.9 (average)/8576.3 (isotopic). The higher MW species in the spectrum were due to adducts of the sinapic acid matrix.

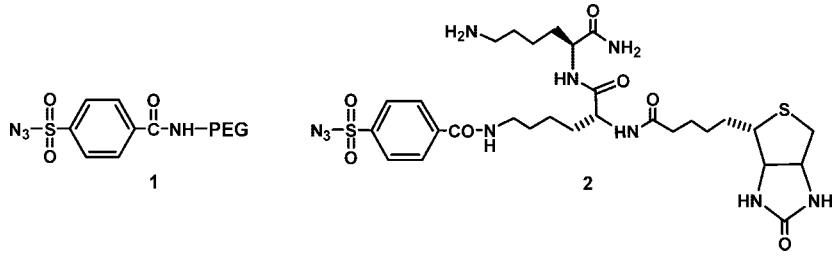

Figure 3. Sulfonazides useful for C-terminal PEGylation (**1**) or biotinylation (**2**) of recombinant thioacid proteins.

We chose the small ubiquitin protein as a model system to test this new protein C-terminal modification method. A crucial step is to obtain the thioacid protein in a sufficient amount. We referred to the method previously proposed by Begley et al. for the production of recombinant proteins with a C-terminal thioacid (*27*), which is based on the mechanism of capturing and cleaving the thioester intermediate of protein splicing with hydrosulfide ions. Although the potential utility of this method was discussed by the authors (*27*), no application examples have been reported since its publication. Therefore, in our work, we cloned the ubiquitin gene into the pTYB1 vector (New England Biolabs), which contains the VMA intein from *S. cerevisiae*. The ubiquitin-intein-CBD fusion protein was overexpressed in *E. coli* and affinity-purified by binding to chitin beads. The cleavage of ubiquitin from the fusion protein was performed by incubation at 37 °C of the bound fusion protein in the hydrothiolytic cleavage buffer (0.1 M Na_2S, 0.25 M HEPES, 0.5 M NaCl, 1 mM EDTA, pH 8.0) overnight. These conditions were similar to those used for hydrothiolysis of synthetic peptide thioesters (*26, 28*). In the previous work by Begley et al. of preparing a 66-residue protein thioacid ThiS-COSH, the cleavage was done with 30 mM ammonium sulfide at 4 °C (*27*). The cleaved ubiquitin thioacid was eluted from chitin beads and purified by RP-HPLC (Figure 2A). High-resolution MS analysis confirmed the presence of the thioacid group (Figure 2B). The yield of the ubiquitin thioacid was typically 4−5 mg per liter of cell culture.

Two benzenesulfonazide-functionalized tagging agents **1** and **2** (Figure 3) were prepared for introducing a PEG or biotin moiety, respectively, onto the C-terminus of the recombinant ubiquitin (see Supporting Information for the synthesis of these two compounds).

The PEGylation reagent or PEG-sulfonazide **1** (Figure 3) contains a PEG component with an average MW of ca. 5000 Da. It was synthesized to test thioacid amidation with large sulfonyl azides. The amidation reaction of the ubiquitin thioacid with the PEGylation reagent **1** was performed in an aqueous solution: 0.3 mM ubiquitin thioacid, 2 mM PEG sulfonazide **1** in 6 M Gdn-HCl containing 3 mM 2,6-lutidine. The reaction took about 10 h to complete at r.t. and was accompanied by some hydrolysis (Figure 4). 2,6-Lutidine is the recommended base catalyst from previous studies with small thioacids (*21, 22*). We observed that, if the reaction was conducted in a HEPES-buffered solution (pH 7 or 8) instead, more hydrolysis occurred and the hydrolyzed ubiquitin-COOH appeared immediately after the ubiquitin thioacid was mixed with the azide (data not shown). Therefore, the use of 2,6-lutidine helped minimize the hydrolysis of the ubiquitin thioacid. On the basis of HPLC analysis, the yield of the PEGylation reaction was about 65%. Despite an excess amount of PEGylation agent used, only the mono-PEGylation product (Figure 4A, peak 3 from trace b) was formed in the reaction, which was also confirmed by MS analysis (Figure 4B), indicating that tagging PEG to the protein was highly chemoselective and site-specific. The relatively lengthy reaction time and some degree of hydrolysis may be a result of the large molecular weight and steric hindrance of the PEGylation reagent **1** in which the relatively hydrophobic sulfonylazide may be made less accessible by a surrounding long and hydrophilic PEG chain. The small Gly residue at the C-terminus of ubiquitin may also have contributed to the hydrolysis of the thioacid.

The biotinylation reagent or biotinyl-Lys(N_3SO_2Bz)-Lys-NH_2 **2** (Figure 3) was prepared by solid-phase synthesis. In this compound, the biotin and sulfonyl azide moieties are linked to

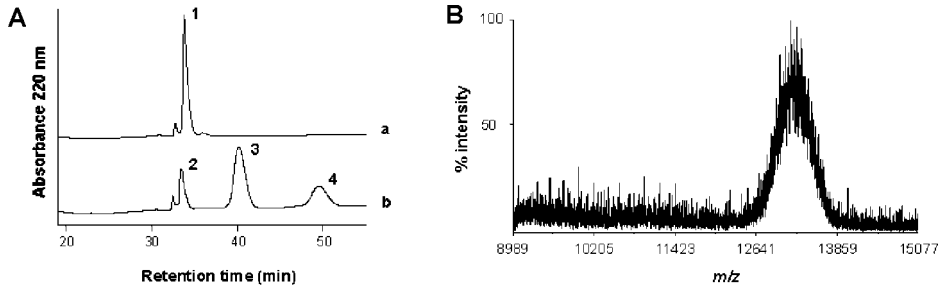

Figure 4. PEGylation of ubiquitin thioacid. (A) Analytical RP-HPLC (Vadyc C4 column) monitoring of the amidation of ubiquitin thioacid with the PEGylation reagent. Trace a, purified ubiquitin-COSH (peak 1). Trace b, reaction at 10 h. Peak 2, the hydrolyzed product ubiquitin-COOH; peak 3, the PEGylated ubiquitin; peak 4, excessive PEGylation reagent **1**. HPLC gradient: 0−60% of buffer B in buffer A for 60 min. (B) MALDI-TOF of the PEGylated product, average *m*/*z* $[M + H]^+$ found ∼13 350, average MW calcd ∼13 500).

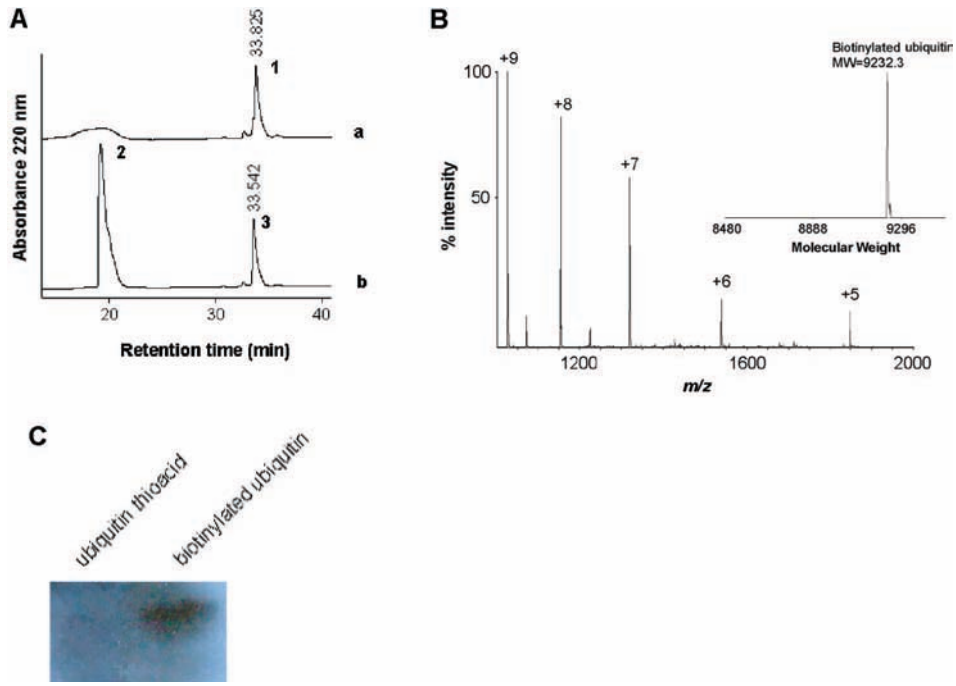

Figure 5. Reaction of ubiquitin-COSH with biotin-Lys(N_3SO_2Bz)-Lys-NH_2. (A) Analytical RP-HPLC monitoring of amidation of ubiquitin thioacid with biotinyl-Lys(N_3SO_2Bz)-Lys-NH_2 **2** on a Vadyc C4 column. HPLC gradient: 0−40% of buffer B in buffer A for 40 min. Trace a, peak 1: ubiquitin thioacid. Trace b, the reaction mixture at 4 h. Peak 2, biotinyl-Lys(N_3SO_2Bz)-Lys-NH_2 **2**; peak 3, the biotinylation product containing some minor amount of hydrolyzed ubiquitin in the front. (B) ESI-MS spectrum profile of the last three quarters of peak 3 which contained the biotinylated ubiquitin. MW found 9232.3, MW calcd 9228.5. (C) Western blot analysis of the biotinylated ubiquitin using an avidin-HRP conjugate (Bio-Rad Laboratories, USA).

the respective α- and ε-amino groups of a Lys residue. A second Lys residue is included to increase its water solubility. In the thioacid/azide coupling reaction, 0.3 mM ubiquitin thioacid in 6 M Gdn-HCl containing 3 mM 2,6-lutidine was reacted with ca. 10 equiv of biotinyl-Lys(N_3SO_2Bz)-Lys-NH_2 **2** at r.t. for about 4 h to give the biotinylated ubiquitin product (Figure 5). The ligation product eluted a little earlier than the thioacid and almost coeluted with (only slightly behind) the hydrolysis product. In fact, according to MS analysis, the first quarter of fractions of the product peak (peak 3 of trace b, Figure 5A) contained about 30% ubiquitin-COOH (see Supporting Information), and the last three quarters of the peak contained only the ligation product (Figure 5B). No remaining ubiquitin-COSH was detected. The desired amidation product had the expected molecular weight as analyzed by ESI-MS (Figure 5B). As it is much smaller than the PEGylation reagent, the biotinylation reagent reacted faster with the ubiquitin thioacid. Again, except for a minor amount of hydrolysis, no other side reactions were detected. The amidation yield was estimated to be at least 85% by HPLC analysis. The biotinylated ubiquitin was able to bind to avidin as shown by Western blot analysis (Figure 5**C**).

PEG has been used as a biofunctional group for protein modification since 1977 (*29*). Covalent attachment of PEG to therapeutic proteins has some desirable functions such as increasing their in vivo stability and solubility (*5*). It is also very common to covalently tag biotin to a biomolecule such as a protein for use in biochemical assays (http://en.wikipedia.org/wiki/Biotinylation). Traditional PEGylation and biotinylation methods are nonspecific and introduce PEG or biotin nonspecifically onto nucleophilic amino acids in proteins, giving a mixture of product isomers (*30*). Thioacid/azide amidation represents a novel method for bioconjugation with a distinctly different mechanism from the intermolecular acylation reactions of conventional amidation. The amidation of thioacids with electron-poor azides involves a prior capture step followed by efficient intramolecular addition to give a thiatriazoline intermediate which spontaneously collapses to form the amide bond (*22*). These unique features determine the highly chemoselective nature of this reaction, as demonstrated herein by the C-terminus-specific PEGylation or biotinylation of ubiquitin. The reaction can accommodate a broad range of solvents from organic to aqueous (*21*−*26*). Notably, in this study the amidation

of ubiquitin with both the PEG and biotin azide compounds was conducted in a denaturing solution containing 6 M GdnHCl, which will be useful for minimally soluble biomolecules such as membrane proteins. In conclusion, we have demonstrated herein that thioacid/azide amidation is a simple and efficient method for specific C-terminal modification of recombinant proteins. Amidation of ubiquitin thioacid with excess PEG and biotin sulfonazides shows that this reaction is highly specific despite the presence of a large number of functional groups in the protein and remains effective even with large azide compounds. Since protein and peptide thioacids can be easily prepared through hydrothiolysis of the corresponding thioesters (*26*−*28*), the thioacid/azide amidation reaction has the potential to become one of the most useful methods for C-terminal modification of bioactive peptides and proteins.

ACKNOWLEDGMENT

The authors thank the Ministry of Education (MOE) of Singapore for financial support, as well as Nanyang Technological University.

Supporting Information Available: Experimental procedures and supplementary data. This material is available free of charge via the Internet at http://pubs.acs.org.

LITERATURE CITED

(1) Hermanson, G. T. (1996) *Bioconjugate Techniques*. Academic Press, San Diego.
(2) Foley, T. L., and Burkart, M. D. (2007) Site-specific protein modification: advances and applications. *Curr. Opin. Chem. Biol. 11*, 12–19.
(3) Wang, L., and Schultz, P. G. (2005) Expanding the genetic code. *Angew. Chem., Int. Ed. 44*, 34–66.
(4) Deiters, A., Geierstanger, B. H., and Schultz, P. G. (2005) Site-specific in vivo labeling of proteins for NMR studies. *ChemBioChem 6*, 55–58.
(5) Harris, J. M., and Chess, R. B. (2003) Effects of PEGylation on pharmaceuticals. *Nat. Rev. Drug Discovery 2*, 214–221.
(6) Camarero, J. A. (2008) Recent developments in the site-specific immobilization of proteins onto solid supports. *Biopolymers (Pept. Sci.) 90*, 450–458.
(7) Antos, J. M., and Francis, M. B. (2006) Transition metal catalyzed methods for site-selective protein modification. *Curr. Opin. Chem. Biol. 10*, 253–262.
(8) Antos, J. M., and Francis, M. B. (2004) Selective tryptophan modification with rhodium carbenoids in aqueous solution. *J. Am. Chem. Soc. 126*, 10256–10257.
(9) Xie, J., and Schultz, P. G. (2006) A chemical tool kit for proteins−an expanded genetic code. *Nat. Rev. Mol. Cell. Biol. 7*, 775–782.
(10) Buckler, D. R., Haas, E., and Scheraga, H. A. (1993) C-terminal labeling of ribonuclease A with an extrinsic fluorescent probe by carboxypeptidase Y-catalyzed transpeptidation in the presence of urea. *Anal. Biochem. 209*, 20–31.
(11) Stennicke, H. R., Olesen, K., Sorensen, S. B., and Breddam, K. (1997) C-terminal incorporation of fluorogenic and affinity labels using wild-type and mutagenized carboxypeptidase Y. *Anal. Biochem. 248*, 141–8.
(12) Agafonov, D. E., Rabe, K. S., Grote, M., Voertler, C. S., and Sprinzl, M. (2006) C-terminal modifications of a protein by UAG-encoded incorporation of puromycin during in vitro protein synthesis in the absence of release factor 1. *ChemBioChem 7*, 330–6.
(13) Chattopadhaya, S., Tan, L. P., and Yao, S. Q. (2006) Strategies for site-specific protein biotinylation using in vitro, in vivo and cell-free systems: toward functional protein arrays. *Nat. Protoc. 1*, 2386–98.
(14) Xu, M. Q., and Perler, F. B. (1996) The mechanism of protein splicing and its modulation by mutation. *EMBO. J. 15*, 5146–53.
(15) Chong, S., Mersha, F. B., Comb, D. G., Scott, M. E., Landry, D., Vence, L. M., Perler, F. B., Benner, J., Kucera, R. B., Hirvonen, C. A., Pelletier, J. J., Paulus, H., and Xu, M.-Q. (1997) Single-column purification of free recombinant proteins using a self-cleavable affinity tag derived from a protein splicing element. *Gene 192*, 271–281.
(16) Muir, T. W., Sondhi, D., and Cole, P. A. (1998) Expressed protein ligation: A general method for protein engineering. *Proc. Natl. Acad. Sci. U.S.A. 95*, 6705–6710.
(17) Kalia, J., and Raines, R. T. (2006) Reactivity of intein thioesters: appending a functional group to a protein. *ChemBioChem 7*, 1375–83.
(18) Dawson, P. E., Muir, T. W., Clark-Lewis, I., and Kent, S. B. H. (1994) Synthesis of proteins by native chemical ligation. *Science 266*, 776–779.
(19) Liu, C.-F., Rao, C., and Tam, J. P. (1996) Acyl disulfide-mediated intramolecular acylation for orthogonal coupling between unprotected peptide segments. Mechanism and application. *Tetrahedron Lett. 37*, 933–936.
(20) Hakimelahi, G. H., and Just, G. (1980) A simple synthesis of 2,2-disubstituted tetrahydrothiophenes. *Tetrahedron Lett. 21*, 2119–2122.
(21) Shangguan, N., Katukojvala, S., Greenberg, R., and Williams, L. J. (2003) The reaction of thio acids with azides: A new mechanism and new synthetic applications. *J. Am. Chem. Soc. 125*, 7754–7755.
(22) Kolakowski, R. V., Shangguan, N., Sauers, R. R., and Williams, L. J. (2006) Mechanism of thio acid/azide amidation. *J. Am. Chem. Soc. 128*, 5695–702.
(23) Merkx, R., Brouwer, A. J., Rijkers, D. T. S., and Liskamp, R. M. J. (2005) Highly efficient coupling of β-substituted aminoethane sulfonylazides withthioacids, towards a new chemical ligation reaction. *Org. Lett. 7*, 1125–1128.
(24) Barlett, K. N., Kolakowski, R. V., Katukojvala, S., and Williams, L. J. (2006) Thio acid/azide amidation: An improved route to N-acyl sulfonamides. *Org. Lett. 8*, 823–826.
(25) Merkx, R., van Haren, M. J., Rijkers, D. T. S., and Liskamp, R. M. J. (2007) Resin-bound sulfonyl azides: efficient loading and activation strategy for the preparation of the N-acyl sulfonamide linker. *J. Org. Chem. 72*, 4574–4577.
(26) Zhang, X., Lu, X.-W., and Liu, C.-F. (2008) Solid-phase synthesis of peptide thioacids through hydrothiolysis of resin-bound peptide thioesters. *Tetrahedron Lett. 49*, 6122–6125.
(27) Kinsland, C., Taylor, S. V., Kelleher, N. L., McLafferty, F. W., and Begley, T. P. (1998) Overexpression of recombinant proteins with a C-terminal thiocarboxylate: implications for protein semisynthesis and thiamin biosynthesis. *Protein Sci. 7*, 1839–42.
(28) Tan, X. H., Zhang, X., Yang, R., and Liu, C.-F. (2008) A simple method for preparing peptide C-terminal thioacids and their application in sequential chemoenzymatic ligation. *ChemBioChem 9*, 1052–6.
(29) Abuchowski, A., McCoy, J. R., Palczuk, N. C., van Es, T., and Davis, F. F. (1977) Effect of covalent attachment of polyethylene glycol on immunogenicity and circulating life of bovine liver catalase. *J. Biol. Chem. 252*, 3582–6.
(30) Grace, M. J., Lee, S., Bradshaw, S., Chapman, J., Spond, J., Cox, S., Delorenzo, M., Brassard, D., Wylie, D., Cannon-Carlson, S., Cullen, C., Indelicato, S., Voloch, M., and Bordens, R. (2005) Site of pegylation and polyethylene glycol molecule size attenuate interferon-α antiviral and antiproliferative activities through the JAK/STAT signaling pathway. *J. Biol. Chem. 280*, 6327–36.

BC800488N

Protein C-terminal Modification through Thioacid/Azide Amidation

Xiaohong Zhang, Fupeng Li, Xiao-Wei Lu and Chuan-Fa Liu*

SUPPORTING INFORMATION

INSTRUMENTATION

Analytical and semi-prep HPLC were performed on a Shimadzu UFLC system equipped with a PDA-100 photodiode array detector. A C4 reverse phase column (Vydac, 250 x 4.6 mm) was used for analytical analysis. A C8 reverse phase column (Vydac, 250 x 10 mm) was used for semi-prep purification. The analytes were eluted using a gradient mixture of two solvents: buffer A was distilled deionized water containing 0.05% TFA and buffer B was 90% ACN in distilled deionized water containing 0.05% TFA. The flow rate was 1 mL/min for analytical analysis, 2.5 mL/min for semi-prep purification.

ESI mass spectra were recorded using a bench-top ion trap mass spectrometer (FINNIGAN LCQ Deca XP MAX). High resolution MALDI mass spectra were recorded using a 4800 MALDI TOF/TOF Analyzer (Applied Biosystems) and sinapic acid as the matrix. ^{1}H and ^{13}C NMR spectra were recorded on a Bruker DRX-400 (400 MHz) NMR spectrophotometer. ^{13}C spectra were recorded in broad band decoupled mode. ^{1}H and ^{13}C chemical shifts are quoted in ppm relative to the internal standard tetramethylsilane (TMS) or the residual solvent proton signals.

SYNTHESIS OF SULFONAZIDE COMPOUNDS

1. PEG sulfonazide **1**

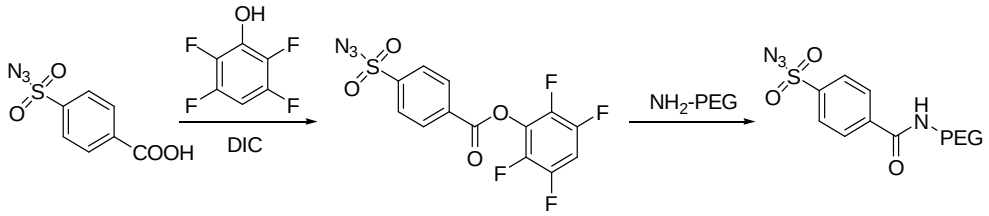

1

4-Carboxybenzensulphonylazide (113.6 mg, 0.5 mmol), 2,3,4,6-tetrafluorophenol (91.4 mg, 0.55 mmol) and N,N'-diisopropylcarbodiimide (DIC) (117 μL, 0.75 mmol) were dissolved in dry DCM (2 mL) at 0 ℃, and two drops of TEA was added. The reaction mixture was stirred at room temperature overnight. H_2O was added to quench the reaction. The mixture was extracted with DCM and the combined DCM layer was washed with brine, dried and concentrated to yield a light yellow solid (180 mg). 20 mg of this product without any further purification was dissolved in dry DCM (2 mL), followed by addition of aminopolyethylene glycol 5,000 monomethylether (266 mg, 1 eq.) and DIEA (27 μL) at 0 ℃. The mixture was allowed to stir at room temperature for 2 h. DCM was removed and the residue was washed with cold ether and centrifuged to get a white precipitate. The precipitate was washed two more times with cold ether. The crude product was purified by preparative HPLC. The functionized PEG product had good UV absorption at the wavelengths of 220 and 260 nm used for HPLC detection, which facilitated its purification. MALDI-TOF was used to determine the molecular weight of the product (Fig. S1).

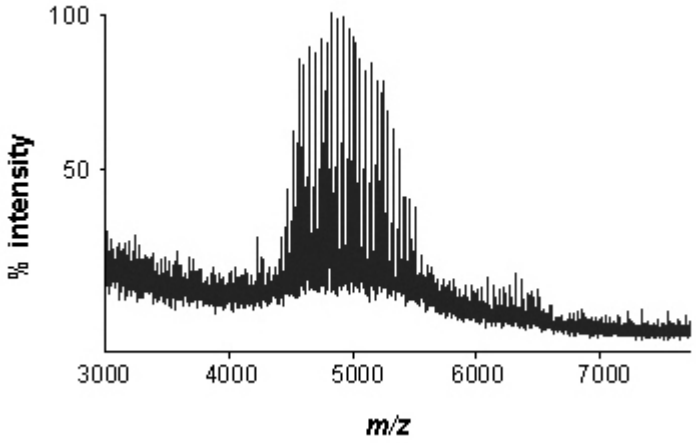

Figure S1. MALDI-TOF mass spectrum of purified PEG sulfonazide **1**.

2. Biotin-Lys(N_3SO_2Bz)-Lys-NH_2 **2**

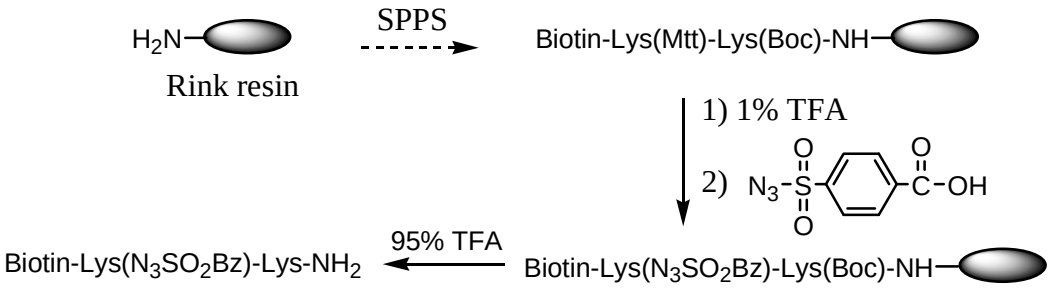

4 eq. of Fmoc-Lys(Boc)-OH was used to load to the Rink resin. The second Lys was coupled using Fmoc-Lys(Mtt)-OH. After Fmoc deprotection, 4 eq. of *D*-biotin was used to couple to the N-terminal amine. The protecting group Mtt was removed by 1% TFA in DCM (1×10min, 1×20min). Then 4 eq. of 4-carboxybenzensulphonylazide, 4 eq. of PyBOP and 10 eq. of DIEA were mixed and added to the resin. The reaction was done at room temperature for 2 h. This biotinyl-Lys(N_3SO_2Bz)-Lys-NH_2 **2** was cleaved from the resin with 95% TFA/ 5% H_2O, and purified by RP-HPLC. The molecular weight was determined by ESI-MS. *m/z* $[M+H]^+$ found: 709.3, MW calcd: 708.3.

PREPARATION OF UBIQUITIN THIOACID

The plasmid containing human ubiquitin gene obtained from Dr. Peter Chong's lab was the resource of ubiquitin. Ubiquitin gene was amplified by PCR using the primers:

Ubi_F: 5'-GGTGGTCATATGCAGATCTTTGTGAAG-3' and

Ubi_R:5'-GGTGGTTGCTCTTCCGCAGCCACCTCGCAGGCG-3'. The PCR condition was 95 ℃ for 3 min, 30 cycles of 95 ℃ 30 s, 54 ℃ 30 s, 72 ℃ 30s, and 72 ℃ 10 min for final extension. The PCR product was purified and ligated into the T-easy vector (Promega). The T-Ubi vector was transformed into E.Coli cell and amplified. The extracted and purified vector T-Ubi was digested with *Nde*I and *Sap*I restriction enzymes, the digested segment was purified and ligated into the identically digested pTYB1 vector (New England Biolabs). And the correct insert was then confirmed by DNA sequencing.

The plasmid pTYB1-Ubi was transformed into *E. Coli* BL21(DE3) $CaCl_2$ competent cells. The cells were grown in LB medium containing 100μg/ml Ampicillin at 37 ºC with shaking at 250 rpm to an OD_{600} of 0.6-0.8. The target protein was induced by 50 μM IPTG at 15 ºC for 18 h. After centrifuge at 6000 rpm for 10 min, cell pellets from 1 liter culture were suspended in 50 mL of lysis buffer (20 mM HEPES, 0.5 M NaCl, 1 mM EDTA, pH 7.0). Cells were broken by a microfluider (Microfluidics, Newton, USA, chamber press, 12K/50 psi), and cell debris was removed by centrifugation at 20,000 g for 30 min. SDS PAGE gel analysis showed the expression of the fusion protein in its soluble form (Fig. S2A). The obtained supernatant was mixed with 10

mL chitin beads (New England Biolabs) pre-equilibrated with the lysis buffer (20 mM HEPES, 0.5 M NaCl, 1 mM EDTA, pH 7.0) at 37 ºC for 2 h. And the beads were then poured into a column and washed with lysis buffer. The fusion protein was cleaved by adding 10 mL of cleavage buffer (100 mM Na_2S, 0.25 M HEPES, 0.5 M NaCl, 1 mM EDTA, pH 8.0) and incubating at 37 ºC overnight. The cleaved product was purified by semi-prep C8 RP-HPLC (Vydac C8 column, 250×10 mm) and analyzed by SDS-PAGE gel (Fig. S2B) and MALDI-MS (Fig. 2B).

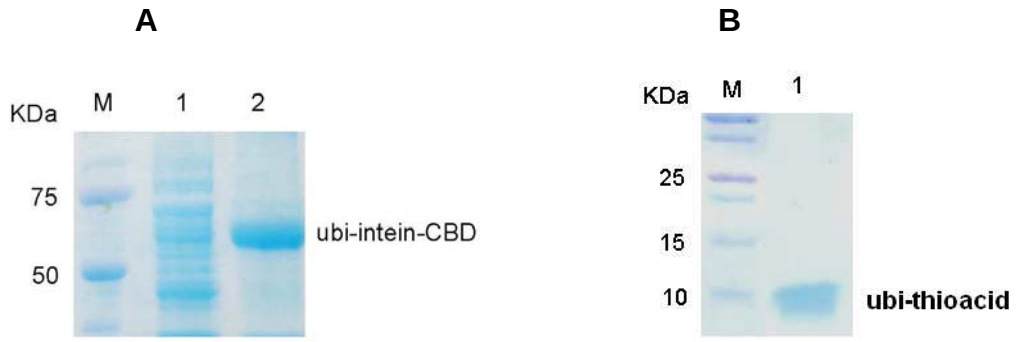

Figure S2. (**A**) 12 % SDS-PAGE gel analysis of ubiquitin-intein-CBD expressed in BL21(DE3) cell transformed with pTYB1-ubi. Lane M, protein markers; lane 1, uninduced cell culture; lane 2, IPTG-induced cell culture. (**B**) 18% SDS-PAGE gel analysis of ubiquitin thioacid. Lane M, protein markers; lane 1, the cleaved ubiquitin thioacid.

THIOACID/AZIDE AMIDATION FOR PROTEIN C-TERMINAL LABELING

For demonstrating the C-terminal labeling of proteins by a biophysical or other functional group, ubiquitin thioacid was subject to amidation reaction with either the PEG sulfonazide **1** or biotinyl-Lys(N_3SO_2Bz)-Lys-NH_2 **2**. In the reaction, 0.3 mM ubiquitin thioacid, 5-10 eq. of PEG azide **1** or biotin-Lys(N_3SO_2Bz)-Lys-NH_2 **2,** and 3 mM 2,6-lutidine were dissolved in 6 M Gdn-HCl. The reactions were conducted at room temperature. Analytical RP-HPLC (Vydac C4 column) was used to monitor the

reactions. For the biotinylation reaction, ESI-MS (Fig. S3) showed a minor amount of hydrolysis product (Fig. S3A) which eluted closely with the biotinylated product in HPLC (Fig. 5A).

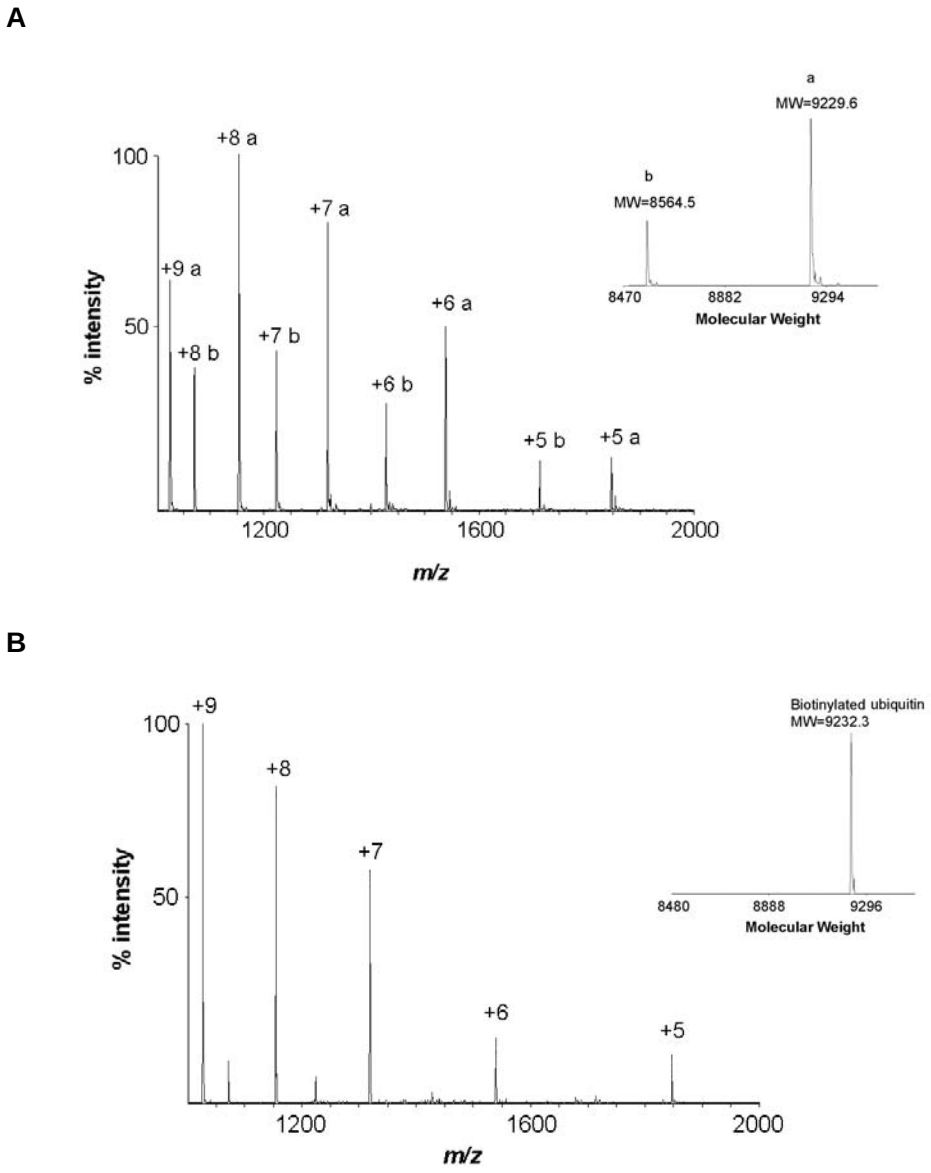

Figure S3. ESI-MS spectra of the amidation product between ubiquitin thioacid and biotinyl-Lys(N_3SO_2Bz)-Lys-NH_2 **2.** (**A**) The first quarter of peak 3 in Figure 5(A) contained the biotinylated ubiquitin (**a**, calcd. MW 9228.5) and hydrolyzed ubiquitin (**b**, calcd MW 8564.8). (**B**) Same as Fig. 5B. ESI-MS of the last 3 quarters of peak 3 in Figure 5A in which only the amidation product was detected. The inserts are the deconvoluted MW spectra.

WESTERN BLOT ANALYSIS OF BIOTINYLATED UBIQUITIN

After electrotransferring the samples from 18% SDS-PAGE gel to the PVDF (polyvinylidene difluoride) membrane (Pall Life Sciences, USA), the membrane was blocked by 5% (w/v) non-fat milk in TBS buffer (100 mM Tris-HCl, 150mM NaCl, pH 7.5) containing 0.1% Tween-20. A 1:10,000 diluted avidin-HRP conjugate (Bio-Rad, USA) was used to detect the biotinylated product as visualized by chemiluminescence (SuperSignal West Dura Trial Kit, Pierce, USA).

Dual Labeled Peptides as Tools to Study Receptors: Nanomolar Affinity Derivatives of TIPP (Tyr-Tic-Phe-Phe) Containing an Affinity Label and Biotin as Probes of δ Opioid Receptors

Jane V. Aldrich,* Vivek Kumar,[†,§] Thomas F. Murray,[‡] Wei Guang,[†] and Jia Bei Wang[†]

Department of Medicinal Chemistry, School of Pharmacy, 1251 Wescoe Hall Drive, University of Kansas, Lawrence, Kansas 66045, Department of Pharmaceutical Sciences, School of Pharmacy, University of Maryland, Baltimore, Maryland 21201, and Department of Pharmacology, College of Medicine, Creighton University, Omaha, Nebraska 68178.
Received October 1, 2008; Revised Manuscript Received December 10, 2008

A general strategy for the design of dual labeled peptides was developed, and derivatives of the δ opioid receptor (DOR) selective antagonist TIPP (Tyr-Tic-Phe-PheOH) containing both an affinity label and biotin were prepared by solid-phase synthesis. Tyr-Tic-Phe-Phe(*p*-X)-Asp-NH$(CH_2CH_2O)_2$-CH_2CH_2NH-biotin (where X = N═C═S or $NHCOCH_2Br$) exhibit nanomolar DOR affinity. The ability to detect receptors labeled with these peptides following solubilization and SDS-PAGE demonstrate the applicability of this design approach for dual labeled peptide derivatives.

Affinity labels, ligands that bind to their target in a nonequilibrium manner, are important pharmacological tools to study receptors and their biological effects. These irreversible ligands bind to their targets in a two-step process, first binding reversibly, followed by formation of a covalent bond with their target (*1*). These ligands are useful pharmacological tools to study receptors (*1*) and, by determining their point of attachment to their target, can be used to examine receptor−ligand interactions at the molecular level (*2, 3*).

While affinity labels without an additional functionality are useful pharmacological tools, a second label is required to detect the labeled receptors and take full advantage of this class of ligands. This typically has involved using radiolabeled derivatives of affinity labels (see, for example, *refs 2, 4, 5*), but the preparation of radiolabeled ligands requires specialized facilities and handling to incorporate the radioactive atom. Biotin or a fluorescent group are attractive alternatives to a radioactive label for incorporation into ligands (*6*). Ligands containing a biotin or a fluorescent group in addition to a reactive affinity label can have several advantages, both in ease of preparation and in application in various pharmacological assays. To date, the only such ligands described for opioid receptors are "reporter affinity labels" (see ref *7*) in which an *o*-phthalaldehyde group on the ligand functions as an affinity label that reacts with an amine and a thiol on the receptor and yields a fluorescent isoindole group. This approach to affinity labeling is very limited, however, because it requires that two nucleophilic receptor residues be in close proximity to one another and to the phthalaldehyde on the ligand.

Our research focuses on the synthesis of labeled derivatives of opioid peptides as tools to study opioid receptors. We have been particularly successful in identifying electrophilic affinity label derivatives of several peptides selective for δ opioid receptors (DOR) (*8*−*11*), including analogues of the potent and selective DOR antagonist TIPP (Tyr-Tic-Phe-PheOH, where Tic = 1,2,3,4-tetrahydroisoquinoline-3-carboxylic acid)[1] (*9, 10*). The [Phe(*p*-X)[4]]TIPP derivatives (where X is an isothiocyanate or bromoacetamide group) have high affinity for DOR (IC_{50} = 5 nM) and inhibit binding in a wash-resistant manner (*9, 10*).

We have also incorporated biotin into TIPP, attached to the C-terminus via a hydrophilic diamine linker to separate biotin from the small hydrophobic peptide (*12*). This maintains the basic N-terminal amine, which is important for the interaction of most opioid peptides with opioid receptors; Asp was also incorporated in the peptide to maintain an acidic C-terminal functionality, which is important for high DOR selectivity (*12, 13*). The resulting peptide TIPP-Asp-NH$(CH_2CH_2O)_2CH_2CH_2$NH-biotin (**1a**) exhibits high affinity (K_i = 12 nM) for DOR (*12*).

Combining an affinity label and second labeling functionality into the same molecule is a particularly appealing approach for peptide derivatives because of their polymeric nature. This approach has been applied to label neurokinin receptors with substance P derivatives containing both a photoaffinity label and a biotin derivative and to study peptide ligand−receptor interactions (see ref *14*). Here, we describe the synthesis and evaluation of the first dual labeled opioid peptide derivatives containing both an affinity label and a second nonradioactive labeling functionality as tools to study opioid receptors.

On the basis of our success with initial TIPP derivatives, we combined an affinity label and biotin in the same peptide to give the dual labeled peptides **1c** and **1d** (Figure 1). The corresponding amine-containing peptide **1b** was prepared as a

* Corresponding author. Department of Medicinal Chemistry, 1251 Wescoe Hall Dr., 4050 Malott Hall, University of Kansas, Lawrence, KS 66045-7582. Tel.: 785-864-2287. Fax: 785-864-5326. E-mail: jaldrich@ku.edu

[†] University of Maryland Baltimore.

[‡] Creighton University.

[§] Current address: BASF Corporation, 100 Campus Dr., Florham Park, NJ 07932

[1]Abbreviations: Alloc, allyloxycarbonyl; CHO, Chinese hamster ovary; DAMGO, [D-Ala[2],NMePhe[4],glyol[5]]enkephalin; DIC, *N,N*-diisopropylcarbodiimide; DIEA, *N,N*-diisopropylethylamine; DMA, *N,N*-dimethylacetamide; Dmt, 2′,6′-dimethyltyrosine; DPDPE, *cyclo*[D-Pen[2],D-Pen[5]]enkephalin; Fmoc, fluorenylmethoxycarbonyl; HOBt, hydroxybenzotriazole; HRP, horseradish peroxidase; PyBOP, benzotriazole-1-yl-oxy-tris-pyrrolidino-phosphonium hexafluorophosphate; SDS-PAGE, sodium dodecylsulfate polyacrylamide gel electrophoresis; TCDI, thiocarbonyl diimidazole; TFA, trifluoracetic acid; Tic, 1,2,3,4-tetrahydroisoquinoline-3-carboxylic acid; TIPP, Tyr-Tic-Phe-PheOH.

10.1021/bc800420t CCC: $40.75 © 2009 American Chemical Society
Published on Web 01/28/2009

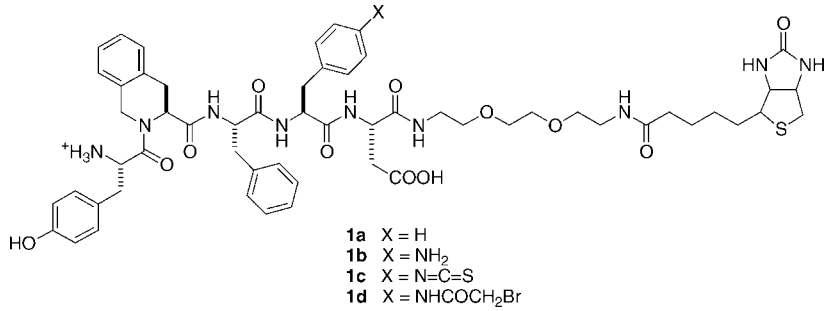

Figure 1. Dual labled TIPP derivatives.

Scheme 1

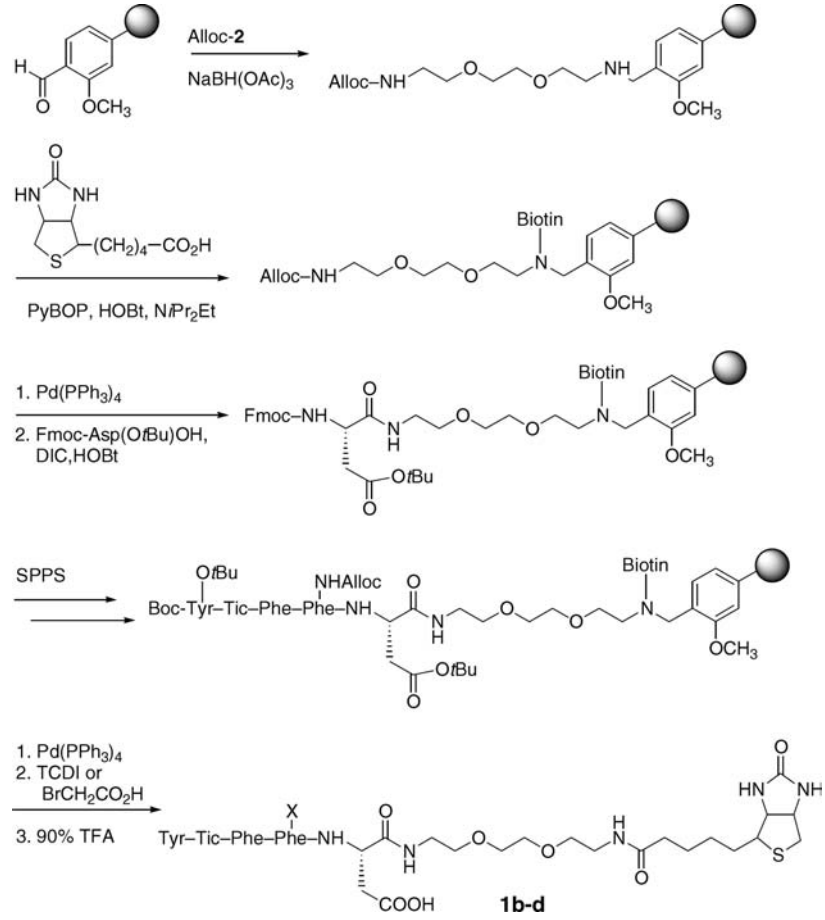

reversible control compound for the pharmacological assays. The dual labeled TIPP derivatives were prepared by solid-phase synthesis using a modification of the strategy developed in our laboratory to prepare the reversible biotinylated peptide **1a** (Scheme 1) (*12*). This strategy uses the Alloc (allyloxycarbonyl) group for orthogonal protection of the amine groups to which both the biotin and affinity label groups are attached. Following reductive amination of an an aldehyde-containing solid-phase resin with the monoprotected hydrophilic diamine linker Alloc-$NH(CH_2CH_2O)_2CH_2CH_2NH_2$ (Alloc-**2**) and introduction of the biotin, the peptide was assembled on the resin by standard procedures (see Supporting Information for detailed procedures). Following completion of the peptide chain, the Alloc group was removed from Phe(*p*-NHAlloc)[4] and the resin then treated with thiocarbonyl diimidazole (TCDI) or bromoacetic acid plus *N*,*N*-diisopropylcarbodiimide (DIC) to yield the isothiocyanate and bromoacetamide derivatives, respectively. The dual labeled peptides **1c** and **1d** plus the amine-containing peptide **1b** were cleaved from the resins and deprotected using 90% aqueous trifluoracetic acid (TFA). Mass spectrometric analysis verified the formation of the desired derivatives (see Supporting Information, Table S1).

Table 1. DOR Affinities of 1a-1d[a,b]

TIPP(*p*-X)-Asp-linker-Biotin[c]	IC_{50} (nM) ± S.E.M
X = H (**1a**)	24.8 ± 8.4
X = NH_2 (**1b**)	33.3 ± 8.4
X = N=C=S (**1c**)	40.5 ± 9.6
X = $NHCOCH_2Br$ (**1d**)	10.4 ± 2.0

[a] Using [^{3}H]DPDPE (*cyclo*[D-Pen^2,D-Pen^5]enkephalin) as the radioligand. Results are mean ± SEM of 3 independent experiments. [b] IC_{50} > 10 000 nM at MOR for all compounds. [c] Linker = $-NH(CH_2CH_2O)_2CH_2CH_2NH-$.

The purified peptides were initially evaluated for DOR and μ opioid receptor (MOR) affinities in radioligand binding assays under standard conditions (*15*) (Table 1). The dual labeled peptides **1c** and **1d** and the amine-containing analogue **1b** retain nanomolar DOR affinity, with comparable or, in the case of

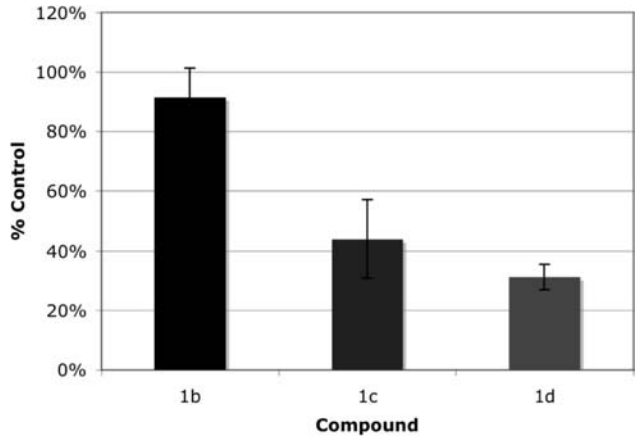

Figure 2. Wash-resistant inhibition of [^{3}H]DPDPE binding to DOR by TIPP derivatives **1b**−**1d** compared to untreated control membranes following preincubation at 33, 40, and 10 nM, respectively, for 90 min. The results are the average of 3 independent experiments.

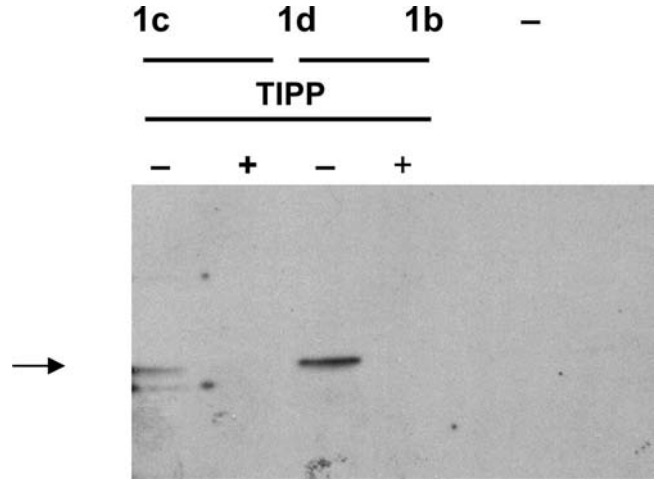

Figure 3. Detection of labeled DOR by streptavidin−HRP conjugate following solubilization and SDS-PAGE. Myc-mδ/hμ CHO cells were incubated with the test peptide for 20 min at 25 °C at the following concentrations: (1) 200 nM **1c**, (2) 200 nM **1c** + 20 μM TIPP, (3) 50 nM **1d**, (4) 50 nM **1d** + 20 μM TIPP, (5) 165 nM **1b**, and (6) no peptide; when TIPP was included, it was added 15 min prior to the test peptide. See the Supporting Information for the isolation procedure. The arrow points to the band for the labeled DOR.

1d, higher affinity to the parent biotinylated peptide **1a**. Thus, the combination of an affinity label on Phe^4 and a C-terminal biotin is well tolerated by DOR. These results parallel those found for the TIPP affinity label derivatives without the C-terminal extension (*9, 10*), although the DOR affinity of the dual labeled peptides containing biotin is somewhat lower (8- and 2-fold for **1c** and **1d**, respectively) than that of the corresponding affinity labeled tetrapeptides. Peptides **1a**−**1d** all exhibit negligible affinity for MOR.

The ability to combine the affinity label and biotin with retention of nanomolar affinity for DOR is dependent on the position of the affinity label. In contrast to the results described here, when the affinity label was incorporated in Phe^3, the DOR affinity of the resulting dual labeled derivatives decreased dramatically to micromolar concentrations (Aldrich, Kumar, and Murray, manuscript in preparation), even though incorporation of an affinity label on Phe^3 is well tolerated in the shorter tetrapeptide TIPP (*9*).

The ability of the affinity label derivatives **1c** and **1d** to inhibit DOR binding in a wash-resistant manner was then assessed as previously described (*8*), with the amine-containing peptide **1b** serving as a reversible control (Figure 2). Incubation with peptides **1c** and **1d** at concentrations equal to their IC_{50} values for 90 min at room temperature, followed by extensive washing of the membranes, resulted in recovery of only 44 ± 13% and 31 ± 4%, respectively, of the binding to control membranes. Thus, the C-terminal extension does not appear to alter the orientation of the reactive functionality on Phe^4 in the receptor site, so that, like the shorter TIPP derivatives (*9, 10*), both **1c** and **1d** exhibit wash-resistant inhibition of binding. These peptides are much more potent DOR affinity labels than the enkephalin affinity label derivative DALCE ([D-Ala^2,Leu^5, Cys^6]enkephalin), which requires a concentration of 3 μM to cause 50% loss of DOR binding sites (*16*). Peptide **1d** appears to be comparable to FIT (fentanyl isothiocyanate), SUPERFIT ((+)-*cis*-3-methylfentanyl isothiocyanate) and NTII (5′-naltrindole isothiocyanate), which cause approximately 50% loss of DOR at concentrations of 1−10 nM (*17*−*19*), although differences in experimental procedures make it difficult to directly compare the results from the different studies.

Membranes treated with the reversible amine-containing peptide **1b** exhibited >90% of the control membrane binding, indicating that the washing procedure effectively removed noncovalently bound peptide. These results for **1b** are in marked contrast to the very lipophilic fluorescent Dmt-Tic derivative Dmt-Tic-Glu-NH$(CH_2)_5$NH-fluorescein (Dmt = 2′,6′-dimethyltyrosine), which cannot be removed from the mouse vas deferens preparation by extensive washing (*20*). This marked difference illustrates the advantage of our design strategy in which a hydrophilic linker is incorporated to decrease the hydrophobicity of our peptides, thereby minimizing nonspecific interactions.

The utility of the dual labeled peptides **1c** and **1d** was demonstrated by solubilizing labeled DOR, followed by sodium dodecylsulfate polyacrylamide gel electrophoresis (SDS-PAGE, Figure 3). The cells were incubated with peptides **1b**−**1d** in the presence or absence of TIPP, and following solublization with RIPA+ buffer and immunoprecipitation according to procedures previously described (*21*), the proteins were subjected to SDS-PAGE. After Western blotting, proteins labeled with the biotinylated peptide were detected using a streptavidin−horseradish peroxidase (HRP) conjugate and a chemoluminescent substrate. Labeled proteins were detected when the cells were incubated with the affinity labels **1c** or **1d** alone, but not when the cells were incubated with peptides **1c** or **1d** in the presence of TIPP or with reversible peptide **1b** (Figure 3). These results clearly demonstrate that peptides **1c** and **1d** are binding covalently and specifically to DOR. To our knowledge, this represents the first report where an affinity labeled opioid receptor has been detected on a gel without using a radiolabeled ligand and demonstrates the utility of the dual labeled peptides to directly detect labeled receptors using the biotin functionality.

Thus, we have developed a strategy for the preparation of dual labeled peptides containing both an affinity label and a second label such as biotin. The applicability of the design and synthetic strategies was demonstrated by the preparation of dual labeled TIPP derivatives containing both functionalities. The results for these TIPP derivatives show that an affinity label and biotin can be combined in the same peptide with retention of both high opioid receptor affinity and covalent binding of the affinity labels to the receptor. The detection of the labeled receptors following solubilization illustrates the immense potential for application of these derivatives as pharmacological tools to study opioid receptors; these studies are currently underway in our laboratories. This strategy can be applied to other peptides, including ligands for other biological targets as well as for opioid receptors.

ACKNOWLEDGMENT

This research was supported by a grant from the National Institute on Drug Abuse (R01 DA10035). The authors thank Jennif Chandler and B. Marinda Thomas for performing the radioligand binding assays.

Supporting Information Available: Experimental procedures and analytical data (HPLC, capillary electrophoresis and mass spectral analysis) for peptides **1b**−**1d**. This material is available free of charge via the Internet at http://pubs.acs.org.

LITERATURE CITED

(1) Takemori, A. E., and Portoghese, P. S. (1985) Affinity labels for opioid receptors. *Annu. Rev. Pharmacol. Toxicol. 25*, 193–223.

(2) Chen, C., Yin, J., de Riel, J. K., DesJarlais, R. L., Raveglia, L. F., Zhu, J., and Liu-Chen, L.-Y. (1996) Determination of the amino acid residue involved in [^{3}H]β-funaltrexamine covalent binding in the cloned rat μ opioid receptor. *J. Biol. Chem. 271*, 21422–21429.

(3) Zhang, Y., McCurdy, C. R., Metzger, T. G., and Portoghese, P. S. (2005) Specific cross-linking of Lys233 and Cys235 in the mu opioid receptor by a reporter affinity label. *Biochemistry 44*, 2271–2275.

(4) Newman, E. L., Borsodi, A., Toth, G., Hepp, F., and Barnard, E. A. (1986) Mu-receptor specificity of the opioid peptide irreversible reagent, [^{3}H]DALECK. *Neuropeptides 8*, 305–315.

(5) Szücs, M., Belcheva, M., Simon, J., Benye, S., Tóth, G., Hepp, J., Wollemann, M., and Medzihradsky, K. (1987) Covalent labeling of opioid receptors with ^{3}H-D-Ala^2-Leu^5-enkephalin chloromethyl ketone. I. Binding characteristics in rat brain membranes. *Life Sci. 41*, 177–184.

(6) Middleton, R. J., and Kellam, B. (2005) Fluorophore-tagged GPCR ligands. *Curr. Opin. Chem. Biol. 9*, 517–525.

(7) Le Bourdonnec, B., El Kouhen, R., Lunzer, M. M., Law, P. Y., Loh, H. H., and Portoghese, P. S. (2000) Reporter affinity labels: an *o*-phthalaldehyde derivative of β-naltrexamine as a fluorogenic ligand for opioid receptors. *J. Med. Chem. 43*, 2489–2492.

(8) Maeda, D. Y., Ishmael, J. E., Murray, T. F., and Aldrich, J. V. (2000) Synthesis and evaluation of *N*,*N*-dialkyl enkephalin-based affinity labels for δ opioid receptors. *J. Med. Chem. 43*, 3941–3948.

(9) Maeda, D. Y., Berman, F., Murray, T. F., and Aldrich, J. V. (2000) Synthesis and evaluation of isothiocyanate derivatives of the δ-opioid receptor antagonist Tyr-Tic-Phe-Phe (TIPP) as potential affinity labels for δ-opioid receptors. *J. Med. Chem. 43*, 5044–5049.

(10) Kumar, V., Murray, T. F., and Aldrich, J. V. (2002) Solid phase synthesis and evaluation of Tyr-Tic-Phe-Phe(*p*-NHCO-CH_2Br) ([Phe(*p*-NHCOCH_2Br)^4]TIPP, a potent affinity label for the δ opioid receptors. *J. Med. Chem. 45*, 3820–3823.

(11) Aldrich, J. V., Choi, H., and Murray, T. F. (2004) An affinity label for δ opioid receptors derived from [D-Ala^2]deltorphin I. *J. Pept. Res. 63*, 108–115.

(12) Kumar, V., and Aldrich, J. V. (2003) A solid phase synthetic strategy for labeled peptides: synthesis of a biotinylated derivative of the δ opioid receptor antagonist TIPP (Tyr-Tic-Phe-PheOH). *Org. Lett. 5*, 613–616.

(13) Schiller, P. W., Nguyen, T. M.-D., Weltrowska, G., Wilkes, B. C., Marsden, B. J., Lemieux, C., and Chung, N. N. (1992) Differential stereochemical requirements of μ vs δ opioid receptors for ligand binding and signal transduction: development of a class of potent and highly δ-selective peptide antagonists. *Proc. Natl. Acad. Sci. U.S.A. 89*, 11871–11875.

(14) Sachon, E., Bolbach, G., Chassaing, G., Lavielle, S., and Sagan, S. (2002) $C_\gamma H_2$ of Met^{174} side chain is the site of covalent attachment of a substance P analog photoactivable in position 5. *J. Biol. Chem. 277*, 50409–50414.

(15) Arttamangkul, S., Ishmael, J. E., Murray, T. F., Grandy, D. K., DeLander, G. E., Kieffer, B. L., and Aldrich, J. V. (1997) Synthesis and opioid activity of conformationally constrained dynorphin A analogues. 2. Conformational constraint in the "address" sequence. *J. Med. Chem. 40*, 1211–1218.

(16) Bowen, W. D., Hellewell, S. B., Kelemen, M., Huey, R., and Stewart, D. (1987) Affinity labeling of δ-opiate receptors using [D-Ala^2,Leu^5,Cys^6]enkephalin. Covalent attachment via thiol-disulfide exchange. *J. Biol. Chem. 262*, 13434–13439.

(17) Burke, T. R., Jacobson, A. E., Rice, K. C., Silverton, J. V., Simonds, W. F., Streaty, R. A., and Klee, W. A. (1986) Probes for narcotic receptor mediated phenomena. 12. *cis*-(+)-3-Methylfentanyl isothiocyanate, a potent site-directed acylating agent for δ opioid receptors. Synthesis, absolute configuration, and receptor enantioselectivity. *J. Med. Chem. 29*, 1087–1093.

(18) Portoghese, P. S., Sultana, M., Nelson, W. L., Klein, P., and Takemori, A. E. (1992) δ Opioid antagonist activity and binding studies of regioisomeric isothiocyanate derivatives of naltrindole: evidence for δ receptor subtypes. *J. Med. Chem. 35*, 4086–4091.

(19) Zhu, J., Yin, J., Law, P.-Y., Claude, P. A., Rice, K. C., Evans, C. J., Chen, C., Yu, L., and Liu-Chen, L.-Y. (1996) Irreversible binding of *cis*-(+)-3-methylfentanyl isothiocyanate to the δ opioid receptor and determination of its binding domain. *J. Biol. Chem. 271*, 1430–1434.

(20) Balboni, G., Salvadori, S., Dal Piaz, A., Bortolotti, F., Argazzi, R., Negri, L., Lattanzi, R., Bryant, S. D., Jinsmaa, Y., and Lazarus, L. H. (2004) Highly selective fluorescent analogue of the potent δ-opioid receptor antagonist Dmt-Tic. *J. Med. Chem. 47*, 6541–6546.

(21) Deng, H. B., Yu, Y., Pak, Y., O'Dowd, B. F., George, S. R., Surratt, C. K., Uhl, G. R., and Wang, J. B. (2000) Role of the C-terminus in agonist-induced μ opioid receptor phosphorylation and desensitization. *Biochemistry 39*, 5492–5499.

BC800420T

Supporting Information

Dual Labeled Peptides as Tools to Study Receptors: Nanomolar Affinity Derivatives of TIPP (Tyr-Tic-Phe-Phe) Containing an Affinity Label and Biotin as Probes of δ Opioid Receptors

Jane V. Aldrich, Vivek Kumar, Thomas F. Murray, Jia Bei Wang, and Wei Guang

Contents:

Experimental procedures
Synthesis
Pharmacological evaluation
Table S1. Characterization of dual labeled peptides by HPLC, capillary electrophoresis (CE) and ESI-MS (electrospray ionization mass spectrometry).
References

EXPERIMENTAL PROCEDURES

Synthesis. Stepwise solid-phase peptide synthesis was carried out on a Biosearch 9500 automated peptide synthesizer using a modification of the procedure described previously (*1*). The monoprotected hydrophilic diamine linker Alloc-NH$(CH_2CH_2O)_2CH_2CH_2NH_2$ (Alloc = allyloxycarbonyl) (*2*) was prepared and attached to an aldehyde-containing solid phase resin (4-(4-formyl-3-methoxyphenoxy)butyryl AM resin, 0.85 mmol/g, Novabiochem, San Diego, CA) by reductive amination using triacetoxysodium borohydride in trimethylorthoformate / dichloromethane (1:2), as described previously (*1*). Following introduction of biotin using benzotriazole-1-yl-oxy-tris-pyrrolidino-phosphonium hexafluorophosphate (PyBOP), 1-hydroxybenzotriazole (HOBt) and *N*,*N*-diisopropylethylamine (DIEA) in dimethylsulfoxide/ *N*,*N*-dimethylformamide (1:1) for 6 h and removal of the Alloc group using $Pd(PPh_3)_4$ (*1*), Fmoc-Asp(OtBu) (Fmoc = fluorenylmethoxycarbonyl) was attached to the resulting primary amine using *N*,*N*-diisopropylcarbodiimide (DIC) and HOBt (4 equivalents each relative to the resin) in *N*,*N*-dimethylacetamide (DMA) (*1*). Following removal of the Fmoc protecting group with 20% piperidine in DMA, Fmoc-Phe(*p*-NHAlloc), prepared in our laboratory (*3*), was coupled to the resulting free amine using PyBOP, HOBt, and DIEA in DMA. The peptide chain was extended, using DIC and HOBt and a 4-fold excess of reagents to couple Fmoc-Phe and Fmoc-Tic. PyBOP plus HOBt and DIEA (4:4:8 equiv, respectively, relative to the resin) was used to couple Boc-Tyr(O*t*Bu) (4 equivalents) to the secondary amine of Tic^2. Following completion of the peptide chain, the Alloc group was removed from $Phe(p\text{-}NHAlloc)^4$ using $Pd(PPh_3)_4$. The resin was then treated with thiocarbonyl diimidazole or bromoacetic acid plus DIC in DMA to yield the isothiocyanate and bromoacetamide derivatives, respectively. The dual labeled peptides **1c** and **1d** plus the amine-containing peptide **1b** were cleaved from the resins and deprotected using 90% aqueous trifluoroacetic aicd (TFA).

The peptides were purified to >98% homogeneity by semipreparative HPLC on a Vydac column 218-TP column (22 x 250 mm) with a Vydac guard cartridge using a linear gradient of 20 to 50% aqueous acetonitrile containing 0.1% TFA over 30 min at a flow rate of 20 ml/min.

Purity was confirmed by analytical HPLC and capillary electrophoresis. Electrospray ionization mass spectrometric (ESI-MS) analysis verified the formation of the desired derivatives. Analytical data for peptides **1b-1d** are provided in Table S1.

Pharmacological evaluation. The peptides were initially evaluated for DOR and MOR affinities in radioligand binding assays under standard conditions (*4*) using cloned receptors stably expressed on Chinese hamster ovary (CHO) cells and [^{3}H]DPDPE (*cyclo*[D-Pen^2,D-Pen^5]enkephalin) and [^{3}H]DAMGO ([D-Ala^2,NMePhe^4,glyol^5-enkephalin), respectively, as the radioligands.

The ability of the peptides to inhibit DOR binding in a wash-resistant manner was then assessed according to the previously described procedure (*5*). Using concentrations equal to their IC_{50} values (33, 40 and 10 nM, respectively), the peptides **1b-1d** were preincubated with CHO cell membranes for 90 min at room temperature followed by washing the membranes (5 times) by dilution and centrifugation (*5*). The membranes were then evaluated for [^{3}H]DPDPE binding compared to untreated control membranes. The results are the average of 3 independent experiments.

Labeled DOR were detected with streptavidin-horse radish peroxidase (HRP) conjugate following solubilization and sodium dodecylsulfate polyacrylamide electrophoresis (SDS-PAGE). Myc-mouse DOR /human MOR expressing CHO cells were incubated with the test peptide as indicated in Figure 1 for 20 min at 25 ˚C; when TIPP was included it was added 15 min prior to the test peptide. The proteins were extracted with RIPA+ buffer containing protease inhibitors (1% NP-40, 0.5% sodium deoxycholate, 0.1% SDS, 5 mM EDTA, 10 mM NaF, 10 mM Na^2 pyrophosphate, 1 µM okadaic acid, 0.1 mM phenylmethanesulfonyl fluoride, 10 µg/mL leupeptin and 1 µg/mL pepstatin A in phosphate buffered saline) and subjected to immunoprecipitation with anti-Myc antibody (Sigma) (*6*). The proteins were then separated on 8% SDS-PAGE gels. Following Western blotting onto PVDF membranes, the membranes were treated with diluted streptavidin-HRP conjugate (Pierce, 1:1,000,000 dilution) and SuperSignal West Femto Maximum Sensitivity Chemoluminescent Substrate (Pierce). DOR (~65 kDa) were detected for all the samples on the same Western blot using the Myc antibody (data not shown).

Table S1. Characterization of dual labeled peptides by HPLC, capillary electrophoresis (CE) and ESI-MS.

			ESI-MS *m/z*	
Peptide	**HPLC t_r (min)** [a]	**CE t_m (min)** [b]	**Found**	**Calcd**
1b	9.41	10.26	1121.0	1121.5 $(M+H)^+$
1c	17.42	17.38	1163.0	1163.5 $(M+H)^+$
1d	13.00	15.93	1241.0, 1243.0[c]	1241.4 $(M+H)^+$

[a] HPLC conditions: Vydac 218-TP column (4.6 x 250 mm) with guard cartridge, solvent A = 0.1% TFA in water and solvent B = 0.1% TFA in MeCN, flow rate 1 mL/min, linear gradient of 20 to 50% over 20 min; peptide purity was >98%.

[b] CE conditions: 50 cm capillary, 50 mM phosphate buffer, pH 2.5, 15 kV; peptide purity was >98%.

[c] Two peaks were observed due to isotopes of bromine.

References

(1) Kumar, V., and Aldrich, J. V. (2003) A Solid Phase Synthetic Strategy for Labeled Peptides: Synthesis of a Biotinylated Derivative of the δ Opioid Receptor Antagonist TIPP (Tyr-Tic-Phe-PheOH). *Org. Lett. 5*, 613-616.

(2) Aldrich, J. V., and Kumar, K. (2006), Methods of synthesizing and using derivatives of [2-(2-aminoethoxy)ethoxy]acetic acid. US. patent 7,038078 B2.

(3) Leelasvatanakij, L., and Aldrich, J. V. (2000) Solid Phase Synthetic Strategy for the Preparation of Peptide-Based Affinity Labels: Synthesis of Dynorphin A Analogues. *J. Pept. Res. 56*, 80-87.

(4) Arttamangkul, S., Ishmael, J. E., Murray, T. F., Grandy, D. K., DeLander, G. E., Kieffer, B. L., and Aldrich, J. V. (1997) Synthesis and Opioid Activity of Conformationally Constrained Dynorphin A Analogues. 2. Conformational Constraint in the "Address" Sequence. *J. Med. Chem. 40*, 1211-1218.

(5) Maeda, D. Y., Ishmael, J. E., Murray, T. F., and Aldrich, J. V. (2000) Synthesis and Evaluation of *N,N*-Dialkyl Enkephalin-Based Affinity Labels for δ Opioid Receptors. *J. Med. Chem. 43*, 3941-3948.

(6) Deng, H. B., Yu, Y., Pak, Y., O'Dowd, B. F., George, S. R., Surratt, C. K., Uhl, G. R., and Wang, J. B. (2000) Role of the C-Terminus in Agonist-Induced μ Opioid Receptor Phosphorylation and Desensitization. *Biochemistry 39*, 5492-5499.

Subscriber access provided by SHEMYAKIN-OVCHINNIKOV INST

Communication

Self-Assembling DNA Quadruplex Conjugated to MRI Contrast Agents

Jianfeng Cai, Erik M. Shapiro, and Andrew D. Hamilton

Bioconjugate Chem., **2009**, 20 (2), 205-208• DOI: 10.1021/bc8004182 • Publication Date (Web): 06 January 2009

Downloaded from http://pubs.acs.org on May 8, 2009

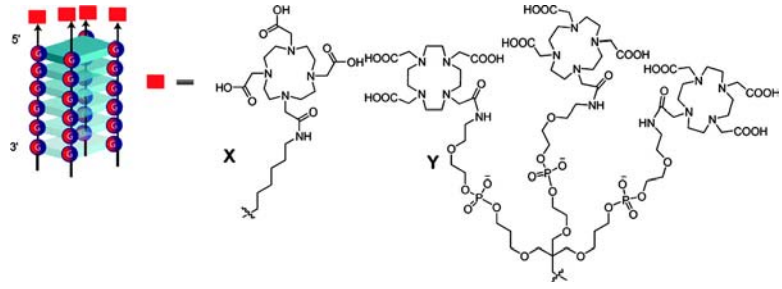

More About This Article

Additional resources and features associated with this article are available within the HTML version:

- Supporting Information
- Access to high resolution figures
- Links to articles and content related to this article
- Copyright permission to reproduce figures and/or text from this article

View the Full Text HTML

ACS Publications
High quality. High impact.

Bioconjugate Chemistry is published by the American Chemical Society. 1155 Sixteenth Street N.W., Washington, DC 20036

Self-Assembling DNA Quadruplex Conjugated to MRI Contrast Agents

Jianfeng Cai, Erik M. Shapiro,* and Andrew D. Hamilton*

Department of Chemistry, Yale University, 225 Prospect Street, New Haven, Connecticut 06511, and Department of Diagnostic Radiology, Yale University School of Medicine, 300 Cedar Street, New Haven, Connecticut 06520. Received October 1, 2008; Revised Manuscript Received November 12, 2008

We report the preparation and magnetic resonance (MR) characterization of new MRI contrast agents based on gadolinium complexes conjugated to a self-assembling DNA quadruplex scaffold. As a single gadolinium−DOTA chelated DNA strand, the r_1 molar relaxivity is 6.4 mM^{-1} s^{-1} per Gd and increases to 11.7 mM^{-1} s^{-1} per Gd upon formation of a DNA quadruplex. Similar results were obtained when a gadolinium−DOTA dendrimer was conjugated to DNA, with the r_1 molar relaxivity increasing to 12.9 mM^{-1} s^{-1} per Gd upon the formation of DNA quadruplex, compared to that of 6.0 mM^{-1} s^{-1} for a single strand of gadolinium−DOTA dendrimer chelate. This yields an r_1 molar relaxivity of 154.8 and 46.8 mM^{-1} s^{-1} per DNA quadruplex based on DOTA dendrimer or monomer, respectively. Importantly, the DNA quadruplex scaffold is approximately 2.5 nm^3 in size, potentially enabling this type of contrast agent to be used for targeted delivery in vivo to detect specific cells or tissues, even behind intact blood vessels.[1]

The targeted and non-invasive detection of specific pathologies in humans is a major research focus in the broad area of bioimaging sciences. To this end, magnetic resonance imaging (MRI) has emerged as an important and useful imaging strategy. As a noninvasive imaging technique, MRI provides three-dimensional images of anatomic structures of living organisms at high spatial resolution (~100 μm isotropic) at scan times of less than 30 min (*1*). Similar to other molecular imaging technologies, targeted MRI requires the delivery of specific probes to detect underlying biological abnormalities. Commonly used MR targeting constructs include paramagnetic liposomes (*2*), paramagnetic perfluorocarbon nanoparticles (*3*), superparamagnetic iron oxide nanoparticles (*4*), and small paramagnetic chelates (*5*). Almost always, the paramagnetic metal used is Gd^{3+} because of its ability to increase the longitudinal relaxation rate (R_1) of water protons and therefore to enhance the observable signal. Superparamagnetic iron oxide nanoparticles create local magnetic field distortions, which increases the transverse relaxation rate (R_2), effectively destroying signal and making dark contrast in images.

Targeted MRI has had a major impact on the detection and treatment of cancer (*6*) and atherosclerosis (*7*). This is largely due to the accessibility of blood vessels in these diseases, as most nanoparticle formulations are on the order of 30 to >100 nm in diameter and are too large to extravasate from undamaged blood vessels (*8*). Furthermore, even if they were to escape into the extracellular space, their large size limits their diffusion within the tissue (*9*). Diseases, such as small, nonaggressive tumors, Alzheimer's plaques, and ischemic tissues, which manifest themselves without leaky blood vessels or behind the intact blood−brain barrier, have been challenging to target. Thus, the large size of most nanoparticle constructs limits their general usage, and there is much interest in synthesizing ultrasmall nanoparticles for targeted MRI (*10*).

A significant barrier to the development of new generations of small Gd-based MR agents is the low molar relaxivity (r_1) of chelated gadolinium. Clinical contrast agents have molar r_1 values of 3−7 mM^{-1} s^{-1} (*8*), resulting in the need for high concentrations to enhance the MRI signal (*11*). Significant research has focused on increasing the rotational correlation time (τ_c) of the gadolinium-containing complex to increase molar relaxivity and, hence, to obtain more efficient contrast agents (*12*). For example, clinically used small molecule contrast agents have been conjugated to high-molecular-weight macromolecules including proteins (*11*), polymers (*13*), and self-assembled peptide amphiphile nanofibers (*14*). This has resulted in the increase of r_1 to 7.3, 19.3, and 22.8 mM^{-1} s^{-1}, respectively. Recently, several contrast agents with even higher relaxivities have been reported. For example, Aime et al. showed that a lipophilic Gd-AAZTA complex bound to albumin had a relaxivity of 84 mM^{-1} s^{-1} (*15*). Yang et al. also designed protein-based contrast agents and demonstrated relaxivities of 35−130 mM^{-1} s^{-1} (*16*). Caravan et al. reported dual-binding GdDTPA tetramers that showed relaxivities of 46−50.8 mM^{-1} s^{-1} when bound to albumin (*17*). Wilson et al. prepared gadolinium−carbon nanotube complexes with relaxivities of 159−179 mM^{-1} s^{-1} (*18*). However, MRI contrast agents designed for general use in targeting multiple epitopes are rare.

Here, we report the design, preparation, and characterization of new MR agents based on ordered and self-assembling DNA quadruplex scaffolds (*19*). The quadruplex-based DOTA (1,4,7,10-tetraazacyclododecane-1,4,7,10-tetraacetic acid) derivatives have almost 30-fold increased r_1 versus clinical Gd-chelate contrast agents and 2-fold increased r_1 compared to the single oligonucleotide (ODN)−DOTA conjugate. These constructs further allow integration of bioactive functions to the quadruplex scaffolds leading potentially to the design of targeted contrast agents. Thus, these new agents provide a general template with high r_1 molar relaxivity and ultrasmall size.

The ODN conjugated DOTAs were prepared by DNA solid-phase coupling on a 1 μmol scale. The 5′-ends of the quadruplex-forming oligonucleotides were tethered with DOTA (**1X** and **1Y**) (Figure 1). In **2X** and **2Y**, DOTA and DOTA

* andrew.hamilton@yale.edu and erik.shapiro@yale.edu.

[1]By assuming an average distance of 3.4 Å between base pairs, and a distance of 11 Å between adjacent guanines in each tetrad, the volume of the DNA quaduplex scaffold was calculated to be 1.1 × 1.1 × 2.04 = 2.5 nm^3.

10.1021/bc8004182 CCC: $40.75 © 2009 American Chemical Society
Published on Web 01/06/2009

(a)

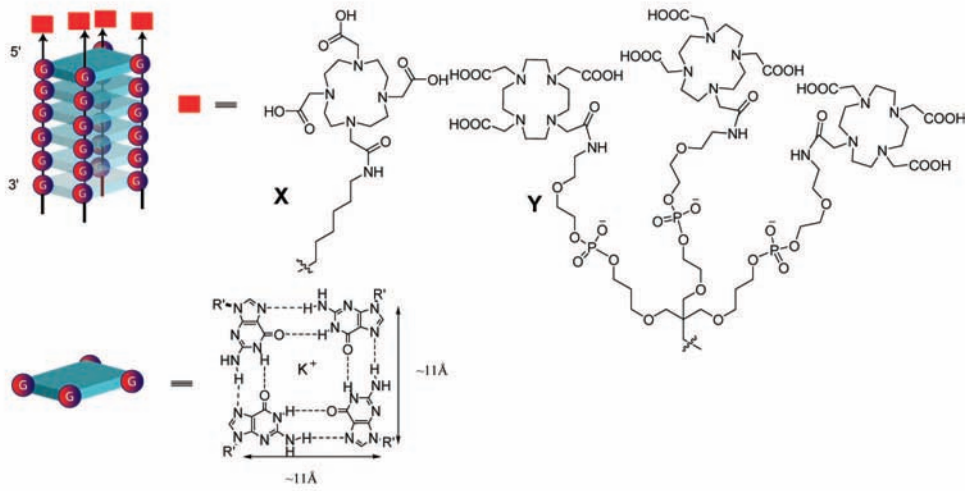

(b)

Oligonucleotide	Sequence
1X	[**X**-d(TGGGGGGTTTT)]4
2X	[**X**-d(CGTCATATCTTA)]
1Y	[**Y**-d(TGGGGGGTTTT)]4
2Y	[**Y**-d(TGTCATATCTTT)]

Figure 1. (a) Functionalized parallel G-quadruplex with DOTA appendages. (b) Sequences of the designed oligonucleotides where G-quadruplex **1X** and **2Y** are tethered to DOTA or DOTA dendrimer fragments, respectively. **2X** and **2Y** are DOTA or DOTA dendrimer appended single strands that cannot form quadruplex structure

dendrimers, respectively, were tethered to a single-strand sequence that is incapable of forming self-assembled structures (Figure 1).

The synthesis of the modified oligonucleotides and the incorporation of Gd(III) ions (*20*) are detailed in the Supporting Information. Briefly, ODNs on the solid support were tethered with modifiers [5′-amino- modifier C6 was used to prepare **1X** and **2X**, while tribler phosphoramidite and 5′-amino-modifier 5 (see Supporting Information) were used to prepared **1Y** and **2Y**], which were then coupled with DOTA using PyBOP and DIPEA in DMF overnight. The DOTA-conjugated ODNs were subjected to deprotection in concentrated aqueous ammonia at 55 °C for 16 h and incubated with gadolinium (III) citrate overnight at room temperature. The ODN conjugates were then purified by HPLC and confirmed by MALDI-TOF. Functionalized parallel quadruplexes were prepared in buffer (10 mM Tris-HCl, 80 mM KCl, pH 7.5) and incubated for 48 h (*21*). The secondary structures of the complexes were confirmed by circular dichroism (CD) spectroscopy (Figure 2). The designed functionalized quadruplexes **1X** and **1Y** showed a positive ellipticity at 263 nm and a negative peak at 241 nm, which is characteristic of a tetramolecular parallel quadruplex (*22*−*24*). In contrast, incubation of **2X** and **2Y** only showed a weak signal at 273 nm and a negative peak at 250 nm in the CD spectrum, indicating no quadruplex formation.

The r_1 of the contrast agents was measured by MRI with concentrations of samples confirmed by inductively coupled plasma (ICP)-MS measurements (see Supporting Information for methods). Compared to the single DNA−DOTA counterpart

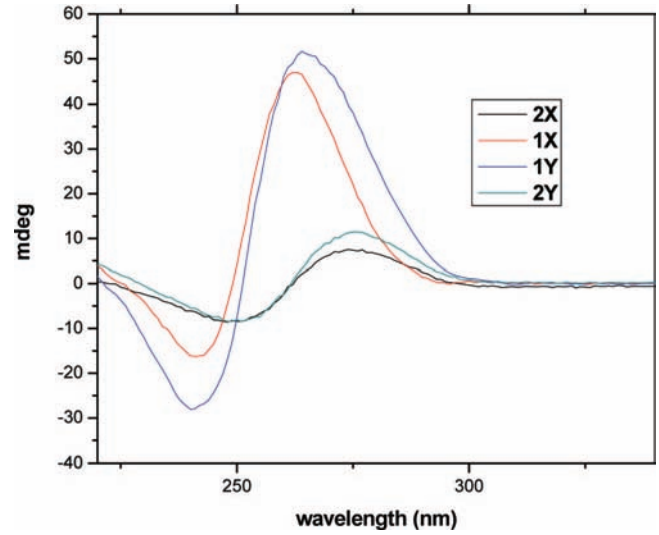

Figure 2. Circular dichroism spectra of ODNs after self-assembly. All measurements were done in 80 mM KCl, 10 mM Tris-HCl, pH 7.5 buffer. Concentrations of all ODNs were 60 μM for the single strand.

2X, the efficacy of the contrast agents has been greatly improved through formation of the quadruplex. **1X** displays a relaxivity of 11.7 mM^{-1} s^{-1} per Gd(III) ion and 46.8 mM^{-1} s^{-1} per DNA quadruplex, while **2X** has a relaxivity of 6.4 mM^{-1} s^{-1} per Gd(III) and per molecule (Supporting Information Figure S1).

Table 1. Gd(III) Ionic and Molecular Relaxivities of Standard MRI Contrast Agents and New Agents 1X, 2X, 1Y, and 2Y at 4.0 T and 20.5 °C

DNA	MW (g/mol) (based on DNA single strand)	Gd ionic r_1 (mM^{-1} s^{-1})	no. of Gd	molecular r_1 (mM^{-1} s^{-1})
1X	4150.1	11.7	4	46.8
2X	4315.0	6.4	1	6.4
1Y	5920.9	12.9	12	154.8
2Y	6088.0	6.0	3	18
Gd-DTPA (*8*)	743	4.5	1	4.5
Gd-DOTA (*25*)	561	3.5	1	3.5

The relaxivity of **2X** is in the normal range of currently used clinical contrast agents, yet **1X** shows a 2-fold increased relaxivity per Gd(III). This per complex r_1 is higher than that of contrast agents based on a previously reported genetically engineered protein (*11*) and synthetic dendrimer-based contrast agent ($\sim$35 mM^{-1} s^{-1}) (*26*). Importantly, this is the case even though our quadruplex-based agents have much lower molecular weight and the increase in r_1 is likely due to the more ordered features of the DNA aggregate. Of note, the r_1 of **1X** matches that of a recently reported, similarly sized (14 kDa) Gd-conjugated contrast agent (*5*). This agent is a Gd-conjugated to the C2A domain of synaptotagmin, which is specific for phosphatidylserine (PS), whereas **1X** is designed for general use in targeting multiple epitopes.

The hypothesis that quadruplex formation increases the relaxivity of DNA-linked contrast agents is further supported by studying a Gd-DOTA dendrimer conjugated DNA system. **1Y** displays a relaxivity of 12.9 $mM^{-1}s^{-1}$ per Gd(III) ion and 154.8 $mM^{-1}s^{-1}$ per DNA quadruplex complex, while **2Y** has a relaxivity of 6.0 $mM^{-1}s^{-1}$ per Gd(III) and per molecule (Supporting Information Figure S1). The relaxivities are comparable between **2X** to 2**Y**, probably due to the flexibility of the linkers within the DOTA dendrimers. But again, **1Y** shows a 2-fold increased relaxivity per Gd(III) compared to **2Y** and a much higher relaxivity per quadruplex than **1X**, since three Gd (III) ions are contained within each strand. We also observe an increase in relaxivity per Gd(III) ion from **1X** to **1Y**, which is probably because formation of the ordered DNA quadruplex offsets the flexibility of the linkers within the dendrimer.

Other contrast agents conjugated to viruses, various proteins, and synthetic polymers have been reported to display higher r_1 values per molecule (*27, 28*). However, the Gd-conjugated DNA quadruplex contrast agents reported here have several advantages including a low molecular weight and small size (2−3 nm), which could prove critical for targeted delivery and detection of specific cells or tissues, even behind intact blood vessels. Second, the DNA construct occurs naturally and is biodegradable, potentially mitigating toxic effects. Third, the size of the quadruplex contrast agents can be modified by varying the lengths of the DNA sequences. Fourth, it may be possible to obtain quadruplex CAs with higher relaxivity if DOTA dendrimers with more rigid and shorter linkers can be tethered on the end of the DNA quadruplex scaffold. Lastly, functionalized DNA quadruplexes have been shown to target specific proteins (*19, 29*), leaving open the possibility of functionalizing the quadruplex with fragments that target specific cells or tissues.

In conclusion, we have described the design and synthesis of high-relaxivity DNA quaduplexes that can serve as improved MRI contrast agents. The ordered structure of the quadruplex leads to an increase in the relaxivities of the new MRI contrast agents. Further improvements in gadolinium relaxivity and packaging can be expected by conjugating Gd-DOTA dendrimers with rigid and shorter linkers as well as tethering bioactive groups to the DNA for use in targeted diagnosis.

ACKNOWLEDGMENT

We thank the National Institute of Health (NIH) (P30 NS-052519) and the National Science Foundation (NSF) (CHE-0750357) for financial support of this work.

Supporting Information Available: Procedures for oligonucleotides synthesis, quadruplex formation, Gd(III) ion incorporation and measurements of the relaxivities of **1X**, **2X**, **1Y**, and **2Y**. This material is available free of charge via the Internet at http://pubs.acs.org.

LITERATURE CITED

(1) Shapiro, E. M., Sharer, K., Skrtic, S., and Koretsky, A. P. (2006) In vivo detection of single cells by MRI. *Magn. Reson. Med. 55*, 242–249.

(2) Mulder, W. J., Strijkers, G. J., van Tilborg, G. A., Griffioen, A. W., and Nicolay, K. (2006) Lipid-based nanoparticles for contrast-enhanced MRI and molecular imaging. *NMR Biomed. 19*, 142–164.

(3) Tran, T. D., Caruthers, S. D., Hughes, M., Marsh, J. N., Cyrus, T., Winter, P. M., Neubauer, A. M., Wickline, S. A., and Lanza, G. M. (2007) Clinical applications of perfluorocarbon nanoparticles for molecular imaging and targeted therapeutics. *Int. J. Nanomed. 2*, 515–526.

(4) Artemov, D. (2003) Molecular magnetic resonance imaging with targeted contrast agents. *J. Cell Biochem. 90*, 518–524.

(5) Krishnan, A. S., Neves, A. A., de Backer, M. M., Hu, D. E., Davletov, B., Kettunen, M. I., and Brindle, K. M. (2008) Detection of cell death in tumors by using MR imaging and a gadolinium-based targeted contrast agent. *Radiology 246*, 854–862.

(6) Artemov, D., Mori, N., Ravi, R., and Bhujwalla, Z. M. (2003) Magnetic resonance molecular imaging of the HER-2/neu receptor. *Cancer Res. 63*, 2723–2727.

(7) Briley-Saebo, K. C., Mulder, W. J., Mani, V., Hyafil, F., Amirbekian, V., Aguinaldo, J. G., Fisher, E. A., and Fayad, Z. A. (2007) Magnetic resonance imaging of vulnerable atherosclerotic plaques: current imaging strategies and molecular imaging probes. *J. Magn. Reson. Imaging 26*, 460–479.

(8) Artemov, D., Bhujwalla, Z. M., and Bulte, J. W. (2004) Magnetic resonance imaging of cell surface receptors using targeted contrast agents. *Curr. Pharm. Biotechnol. 5*, 485–494.

(9) Muldoon, L. L., Sandor, M., Pinkston, K. E., and Neuwelt, E. A. (2005) Imaging, distribution, and toxicity of superparamagnetic iron oxide magnetic resonance nanoparticles in the rat brain and intracerebral tumor. *Neurosurgery 57*, 785–796.

(10) Xie, J., Chen, K., Lee, H. Y., Xu, C., Hsu, A. R., Peng, S., Chen, X., and Sun, S. (2008) Ultrasmall c(RGDyK)-coated Fe3O4 nanoparticles and their specific targeting to integrin alpha(v)beta3-rich tumor cells. *J. Am. Chem. Soc. 130*, 7542–7543.

(11) Karfeld, L. S., Bull, S. R., Davis, N. E., Meade, T. J., and Barron, A. E. (2007) Use of a genetically engineered protein for the design of a multivalent MRI contrast agent. *Bioconjugate Chem. 18*, 1697–1700.

(12) Caravan, P., Ellison, J. J., McMurry, T. J., and Lauffer, R. B. (1999) Gadolinium(III) chelates as MRI contrast agents: structure, dynamics, and applications. *Chem. Rev. 99*, 2293–2352.

(13) Langereis, S., de Lussanet, Q. G., van Genderen, M. H., Meijer, E. W., Beets-Tan, R. G., Griffioen, A. W., van Engelshoven, J. M., and Backes, W. H. (2006) Evaluation of Gd(III)DTPA-terminated poly(propylene imine) dendrimers as contrast agents for MR imaging. *NMR Biomed. 19*, 133–141.

(14) Bull, S. R., Guler, M. O., Bras, R. E., Meade, T. J., and Stupp, S. I. (2005) Self-assembled peptide amphiphile nanofibers conjugated to MRI contrast agents. *Nano Lett. 5*, 1–4.

(15) Gianolio, E., Longo, D., Longo, I., Menegotto, I., and Aime, S. (2007) Relaxometric and modelling studies of the binding of a lipophilic Gd-AAZTA complex to fatted and defatted human serum albumin. *Chem.-Eur. J. 13*, 5785–5797.

(16) Yang, J. J., Yang, J., Wei, L., Zurkiya, O., Yang, W., Li, S., Zou, J., Zhou, Y., Maniccia, A. L. W., Mao, H., Zhao, F., Malchow, R., Zhao, S., Johnson, J., Hu, X., Krogstad, E., and Liu, Z.-R. (2008) Rational design of protein-based MRI contrast agents. *J. Am. Chem. Soc. 130*, 9260–9267.

(17) Zhang, Z., Spiller, M., McMurry, T. J., Lauffer, R. B., and Caravan, P. (2005) Multilocus binding increases the relaxivity of protein-bound MRI contrast agents. *Angew. Chem., Int. Ed. 44*, 6766–6769.

(18) Sitharaman, B., Kissell, K. R., Hartman, K. B., Tran, L. A., Baikalov, A., Rusakova, I., Sun, Y., Khant, H. A., Ludtke, S. J., Chiu, W., Laus, S., Toth, E., Helm, L., Merbach, A. E., and Wilson, L. J. (2005) Superparamagnetic gadonanotubes are high-performance MRI contrast agents. *Chem. Commun.* 3915–3917.

(19) Tagore, D. M., Sprinz, K. I., Fletcher, S., Jayawickramarajah, J., and Hamilton, A. D. (2007) Protein recognition and denaturation by self-assembling fragments on a DNA quadruplex scaffold. *Angew. Chem., Int. Ed. Engl. 46*, 223–225.

(20) Jaakkola, L., Ylikoski, A., and Hovinen, J. (2007) Solid-phase oligonucleotide labeling with DOTA. In *Current Protocols Nucleic Acid Chemistry* Chapter 14, Unit 4.31, Wiley, USA.

(21) Jayawickramarajah, J., Tagore, D. M., Tsou, L. K., and Hamilton, A. D. (2007) Allosteric control of self-assembly: modulating the formation of guanine quadruplexes through orthogonal aromatic interactions. *Angew. Chem., Int. Ed. Engl. 46*, 7583–7586.

(22) Dapic, V., Abdomerovic, V., Marrington, R., Peberdy, J., Rodger, A., Trent, J. O., and Bates, P. J. (2003) Biophysical and biological properties of quadruplex oligodeoxyribonucleotides. *Nucleic Acids Res. 31*, 2097–2107.

(23) Balagurumoorthy, P., and Brahmachari, S. K. (1994) Structure and stability of human telomeric sequence. *J. Biol. Chem. 269*, 21858–21869.

(24) Balagurumoorthy, P., Brahmachari, S. K., Mohanty, D., Bansal, M., and Sasisekharan, V. (1992) Hairpin and parallel quartet structures for telomeric sequences. *Nucleic Acids Res. 20*, 4061–4067.

(25) Caravan, P., Ellison, J. J., McMurry, T. J., and Lauffer, R. B. (1999) Gadolinium(III) chelates as MRI contrast agents: structure, dynamics, and applications. *Chem. Rev. 99*, 2293–2352.

(26) Kobayashi, H., and Brechbiel, M. W. (2004) Dendrimer-based nanosized MRI contrast agents. *Curr. Pharm. Biotechnol. 5*, 539–549.

(27) Aime, S., Frullano, L., and Crich, S. G. (2002) Compartmentalization of a gadolinium complex in the apoferritin cavity: a route to obtain high relaxivity contrast agents for magnetic resonance imaging. *Angew. Chem., Int. Ed. 41*, 1017–1019.

(28) Allen, M., Bulte, J. W., Liepold, L., Basu, G., Zywicke, H. A., Frank, J. A., Young, M., and Douglas, T. (2005) Paramagnetic viral nanoparticles as potential high-relaxivity magnetic resonance contrast agents. *Magn. Reson. Med. 54*, 807–812.

(29) Sprinz, K. I., Tagore, D. M., and Hamilton, A. D. (2005) Self-assembly of bivalent protein-binding agents based on oligonucleotide-linked organic fragments. *Bioorg. Med. Chem. Lett. 15*, 3908–3911.

BC8004182

Self-Assembling DNA Quadruplex Conjugated to MRI Contrast Agents

Jianfeng Cai,[†] *Erik M. Shapiro,*[*,‡] *and Andrew D. Hamilton*[*,†]

[†]Department of Chemistry, Yale University, 225 Prospect Street, New Haven, CT 06511

[‡]Department of Diagnostic Radiology, Yale University School of Medicine, 300 Cedar Street, New Haven, CT 06520

Experimental section

Materials and instruments

DOTA (1,4,7,10-tetraazacyclododecane-1,4,7,10-tetraacetic acid) was purchased from Sigma-Aldrich and used without further purification. The core oligonucleotides sequences were synthesized by W. M. Keck Foundation Biotechnology Resource Laboratory, Yale University using automated solid phase synthesis. The modified phosphoramidite 5'-amino-modifier C6 (6-(4-Monomethoxytritylamino)hexyl-(2-cyanoethyl)-(N,N-diisopropyl)-phosphoramidite), 5'-amino-modifier 5 (2-[2-(4-Monomethoxytrityl) -aminoethoxy]ethyl-(2-cyanoethyl)-N,N-diisopropyl)-phosphoramidite), and trebler phosphoramidite (Tris-2,2,2-[3-(4,4'-dimethoxytrityloxy)propyloxymethyl]ethyl-[(2-cyanoethyl)-(N,N-diisopropyl)]-phosphoramidite) were obtained from Glen Research. The oligonucleotides were first subjected to gel filtration using Microspin G-25 columns (GE health care), then purified by reverse-phase HPLC (Varian Prostar) equipped with a timberline TL-105 column heater. The concentrations of the purified oligonucleotides were determined based on their absorption at 260 nm using an Agilent A453 UV-vis spectrometer. The molecular weights of the purified oligonucleotides were obtained by MALDI-TOF (Matrix-Assistant Laser Desorption Ionization-Time of Flight) using an Applied Biosystems Voyager-DE PRO workstation. The Formation of DNA quadruplexes was confirmed by circular dichroism (CD) spectroscopy. ICP analysis was done by Bodycote testing group.

Standard preparation of oligonucleotides

To 4 mg of DOTA (12 mg for the preparation of dendrimers **1Y** and **2Y**) in a vial was added 4mg Pybop (12 mg for the preparation of dendrimers **1Y** and **2Y**), 1 ml of anhydrous DMF and 60 μl DIPEA and the mixture was stirred for 1 min. Then the solution was transferred into syringes and attached to the cartridge for solid-phase coupling. The cartridge contained the resin tethered with the activated amino modified oligonucleotide (1.0 μmol). The activated DOTA solution was pushed through the cartridge 3 times and agitated for 1 hr. This procedure was repeated three times and then the cartridge was allowed

to shake overnight. The solution was removed and the cartridge was washed two times with 2 ml DMF and 3 times with 2 ml acetonitrile. The resin was dried by blowing argon through the cartridge for 1 hr, and then the DNA was cleaved from the solid support with 30% NH_4OH for 2h at RT, followed by global deprotection with 30% NH_4OH (3 ml) at 55 ℃ for 16 h. The gadolinium (III) was introduced by adding 15 mol equiv of gadolinium (III) citrate and the mixture was stirred overnight at ambient temperature.

The GOTA tethered oligonucleotides were purified by an HPLC column maintained at 65 ℃. The molecular weights of the de-salted purified oligonucleotides were analyzed by MALDI-TOF using 9:1:1 mixture of 2,4,6-trihydroxyacetopheone (THAP) (10 mg/ml in 50% CH_3CN/water), ammonium citrate (50 mg/ml in water), and oligonucleotide solution, repectively.

Oligonucleotide **1X**. MALDI-TOF Calculated: 4153.0, found: 4150.1

Oligonucleotide **2X**. MALDI-TOF Calculated: 4315.01, found: 4311.4

Oligonucleotide **1Y**. MALDI-TOF Calculated: 5920.9, found: 5921.5

Oligonucleotide **2Y**. MALDI-TOF Calculated: 6088.0, found: 6085.7

Exposure to quadruplex self-assembly conditions

Typically, the purified aliquot of ODNs in an Eppendorf tube was diluted to the desired concentration by using the buffer (10 mM Tris-HCl, 80 mM KCl, pH 7.5). Then the tube was tightly capped and sealed with parafilm, and heated at 95 ℃ for 15 min. The solution was slowly cooled to room temperature and then incubated at 4 ℃ for 48 hr. The formation of quadruplexes was assessed by CD spectroscopy.

The measurements of relaxivity

Molar relaxivity was measured at the field strength of 4.0 Tesla at 20.5 ^{o}C on a Bruker Biospec MRI instrument. Four concentrations were used for both the single strand construct and the quadruplex, including a zero concentration control. A saturation recovery T_1 mapping protocol was used employing spin echo readouts, incorporating ten TRs ranging from 50 msec to 10 seconds. T_1s were calculated for each concentration and inversely plotted in seconds versus concentration in millimolar, the slope yielding molar relaxivity. All concentrations were verified by ICP emission spectroscopy.

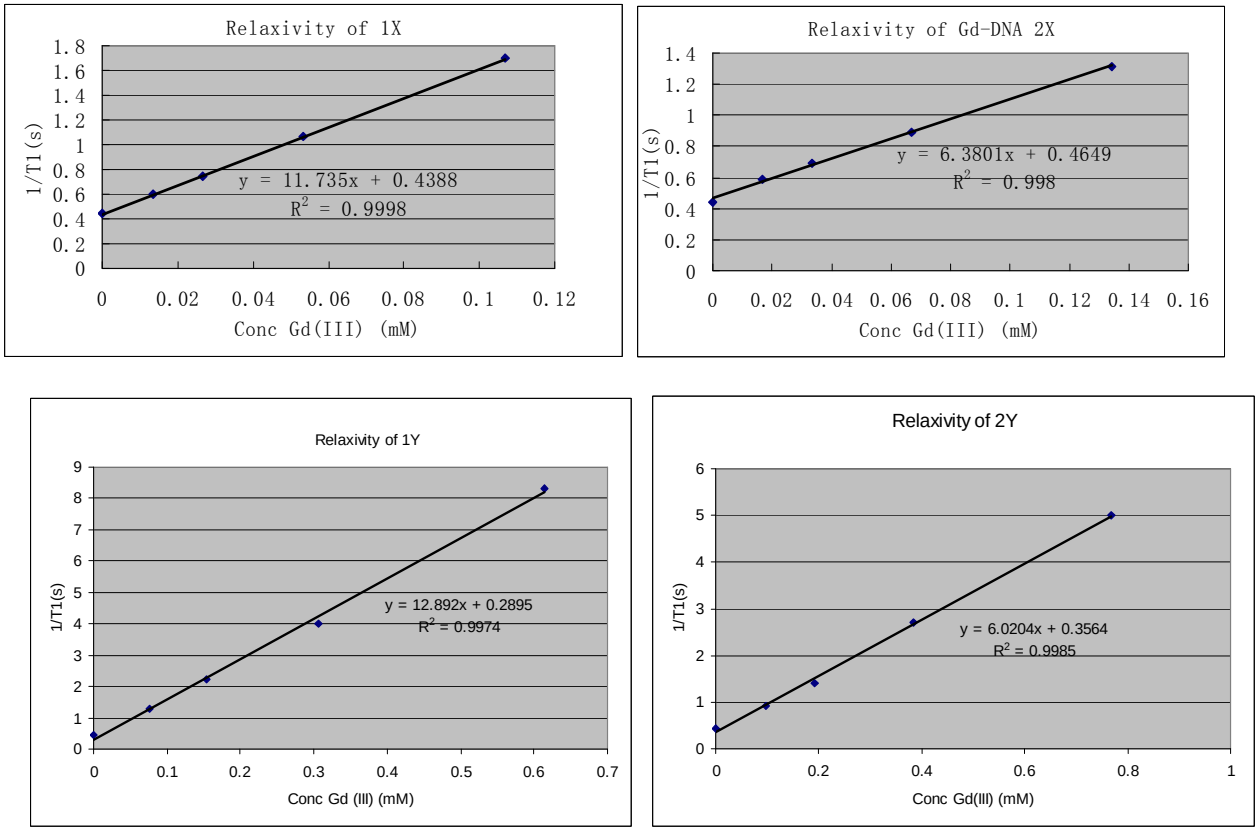

Figure S1. Relaxivity calculations for **1X, 2X, 1Y** and **2Y**.

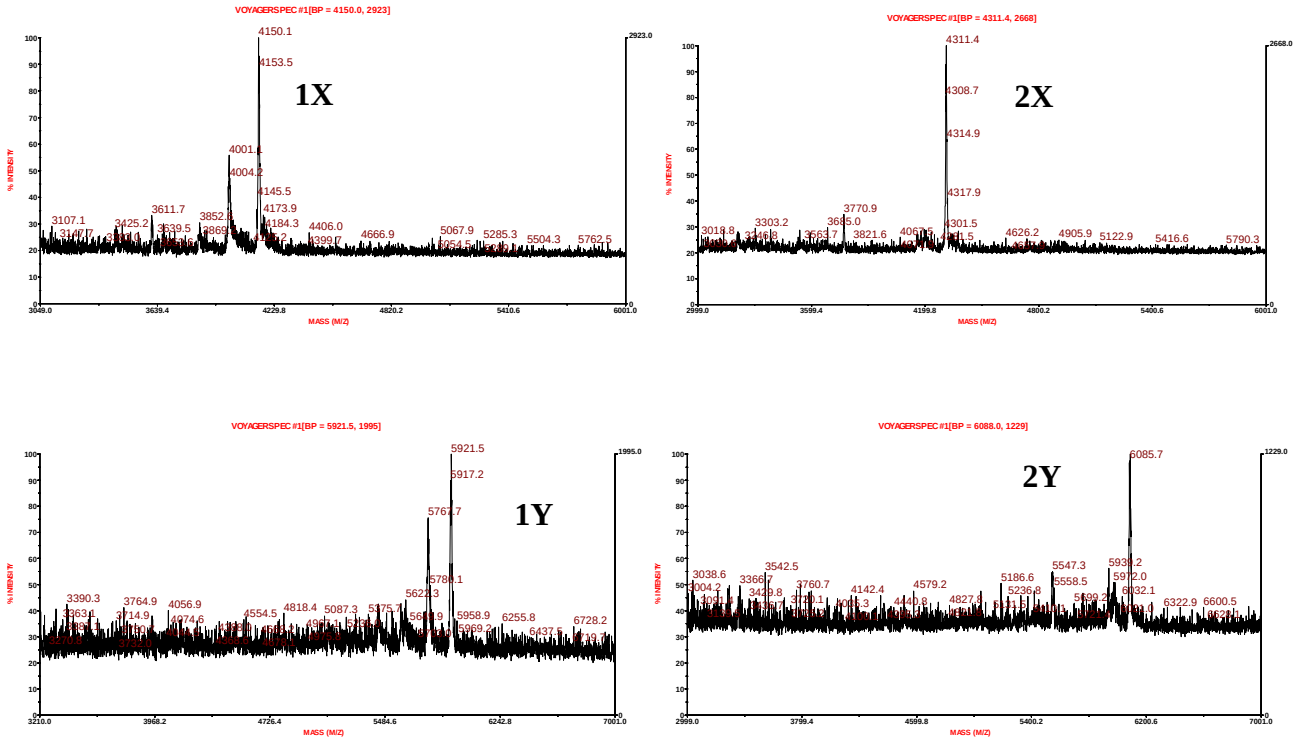

Figure S2. MALDI data of **1X**, **2X, 1Y** and **2Y**.

Subscriber access provided by SHEMYAKIN-OVCHINNIKOV INST

Communication

PNIPAM Gel-Coated Gold Nanorods for Targeted Delivery Responding to a Near-Infrared Laser

Takahito Kawano, Yasuro Niidome, Takeshi Mori, Yoshiki Katayama, and Takuro Niidome

Bioconjugate Chem., **2009**, 20 (2), 209-212• DOI: 10.1021/bc800480k • Publication Date (Web): 09 January 2009

Downloaded from http://pubs.acs.org on May 8, 2009

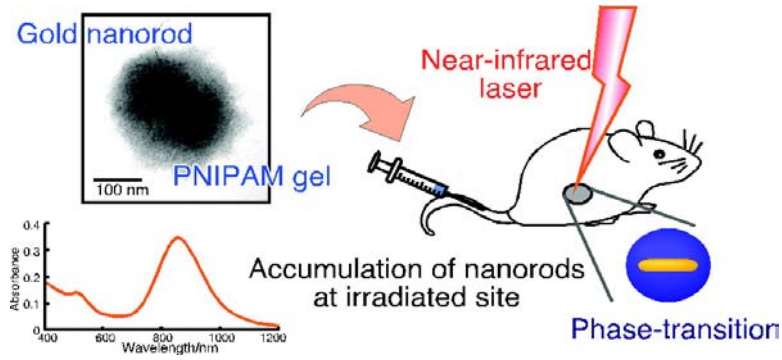

More About This Article

Additional resources and features associated with this article are available within the HTML version:

- Supporting Information
- Access to high resolution figures
- Links to articles and content related to this article
- Copyright permission to reproduce figures and/or text from this article

View the Full Text HTML

ACS Publications
High quality. High impact.

Bioconjugate Chemistry is published by the American Chemical Society. 1155 Sixteenth Street N.W., Washington, DC 20036

PNIPAM Gel-Coated Gold Nanorods for Targeted Delivery Responding to a Near-Infrared Laser

Takahito Kawano,[†] Yasuro Niidome,[†] Takeshi Mori,[†,‡] Yoshiki Katayama,[†,‡,§] and Takuro Niidome*[,†,‡,#]

Department of Applied Chemistry, Faculty of Engineering, and Center for Future Chemistry, Kyushu University, 744 Moto-oka, Nishi-ku, Fukuoka 819-0395, Japan, and CREST and PRESTO, Japan Science and Technology Corporation, Kawaguchi, 332-0012, Japan. Received November 6, 2008; Revised Manuscript Received December 22, 2008

Gold nanorods can be used as photothermal converters, permitting near-infrared (NIR) light to be transmitted deep into tissues without causing damage. We prepared hybrid nanorods with a core−shell structure, i.e., a single gold nanorod encapsulated in a poly (*N*-isopropylacrylamide) nanogel. Hybrid nanorods demonstrated remote, reversible, pulsatile phase transition and in vivo action after irradiation using a NIR laser.

The development of in vivo delivery of drugs using functional nanomaterials is a cornerstone of successful cancer therapy (*1*−*4*). Strategies for the accumulation and release of drugs with nanomaterials have been intensively developed, including those caused by external stimuli (e.g., temperature, light, magnetic field, ultrasound, specific molecules) (*5*−*9*). External stimuli trigger conversion of the physicochemical properties of the drug carrier, so the pharmacokinetics of the injected drug could be remotely controlled from outside the tissues in vivo. Among stimuli-responsive drug carriers, thermo-responsive polymers such as poly(*N*-isopropylacrylamide) (PNIPAM) induced phase transition at a lower critical solution temperature (LCST) and are widely used in biomaterial science (*10, 11*). Ultraviolet- and visible light-sensitive materials can be delivered and release drugs after responding to external stimuli (*12*). Current strategies have not enabled the accumulation and release of drugs to be controlled within a limited area without tissue damage.

In this study, as a new class of external stimuli, we focused on near-infrared (NIR) light (650−900 nm). This allowed maximal penetration of light of tissues due to minimal optical absorption by intrinsic components such as hemoglobin (<650 nm) and water (>900 nm) (*13*). NIR light can be transmitted deep into tissue without significant damage and could have biomedical applications. Rod-shaped gold nanoparticles ("gold nanorods") have an intense absorption band in the NIR region and show highly efficient photothermal conversion (*14*−*16*). The photothermal effect of gold nanorods actuated by irradiating NIR light induces phase transition of the thermo-responsive polymer. Using PNIPAM hydrogel-coated gold nanorods, NIR light can trigger conversion of the hydrophobic nanorod surface and formation of aggregates. In targeted delivery, PNIPAM-coated gold nanorods circulate freely after systemic injection; the NIR laser then irradiates to the targeted site, and nanorods form aggregates and accumulate at the irradiated site without tissue damage (*17, 18*).

Our research group has prepared capillary PNIPAM hydrogels containing gold nanorods; irradiation by an NIR laser induced rapid shrinkage of the gels and released the incorporated drug (*19*). Kumacheva et al. prepared hybrid PNIPAM microgels, which successfully absorbed cationic surfactant-stabilized gold nanorods on submicrometer-sized spheres of PNIPAM-*co*-acrylic acid hydrogels by electrostatic interaction (*20*). Recently, this group showed that electrostatic interaction alone was not the governing force driving the absorption gold nanorods into microgels (*21*). However, for in vivo delivery based on systemic injection, applying the hybrid microgels would be disadvantageous because the size was too large to circulate in blood flow. PNIPAM gels loaded with gold nanorods should be nanosized and well-dispersed within the blood to enable targeted drug delivery using hybrid PNIPAM nanogels after systemic injection.

Our strategy involved using hybrid nanogels with a well-defined core−shell structure, i.e., a single gold nanorod encapsulated in a PNIPAM nanogel. The core−shell structure of NIPAM gel-coated nanorods prevented aggregation and dissociation by nonspecific interaction with blood components. We developed a novel preparation of core−shell PNIPAM gel-coated gold nanorods by colloid−template polymerization. Hybrid nanogels were used to demonstrate photothermal phase transition by an NIR laser and remote actuation after systemic injection in vivo.

PNIPAM gel-coated gold nanorods were prepared by colloid−template polymerization and silica etching (Figure 1). Gold nanorods had a length of 54.8 nm and an aspect ratio of 5.7. They were stabilized by the cationic detergent cetyltrimethylammonium bromide (CTAB) in aqueous solution (Figure 2A) (*22*−*24*).

First, gold nanorods were modified with the amphiphilic polymer poly(ethylene glycol) (PEG) (*25*). PEG-modified gold nanorods were coated with a silica layer using the modified Stöber method, which is based on the hydrolysis of tetraethyl orthosilicate (TEOS) in ethanol/water mixture in the presence of nanorods, which act as "seeds" (*26, 27*). After coating with silica shells, nanorods were dispersed without aggregation. Silica shells with a thickness of 16.7 nm around the nanorods were observed by transmission electron microscopy (Figure 2B). Spectra of the silica-coated nanorods showed a red shift of the surface plasmon band corresponding to the longitudinal oscillation mode because of an increase in local refractive index around the nanorods produced by the silica shells (Figure 2G) (*28, 29*). The silane-coupling agent 3-(methacryloxy)propyl triethoxysilane (MPS) was used to modify the surface of the silica-coated nanorods, which led to the formation of methacryl groups on the surface.

* Corresponding author. E-mail: niidome-tcm@mbox.nc.kyushu-u.ac.jp; (+81) 92-802-2851.
[†] Department of Applied Chemistry.
[‡] Center for Future Chemistry.
[§] CREST.
[#] PRESTO.

10.1021/bc800480k CCC: $40.75 © 2009 American Chemical Society
Published on Web 01/09/2009

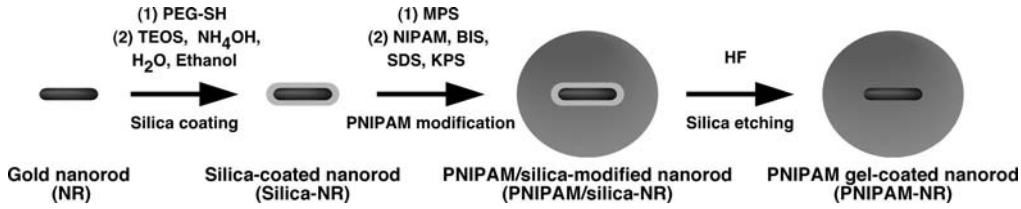

Figure 1. Preparation of PNIPAM-coated gold nanorods (schematic).

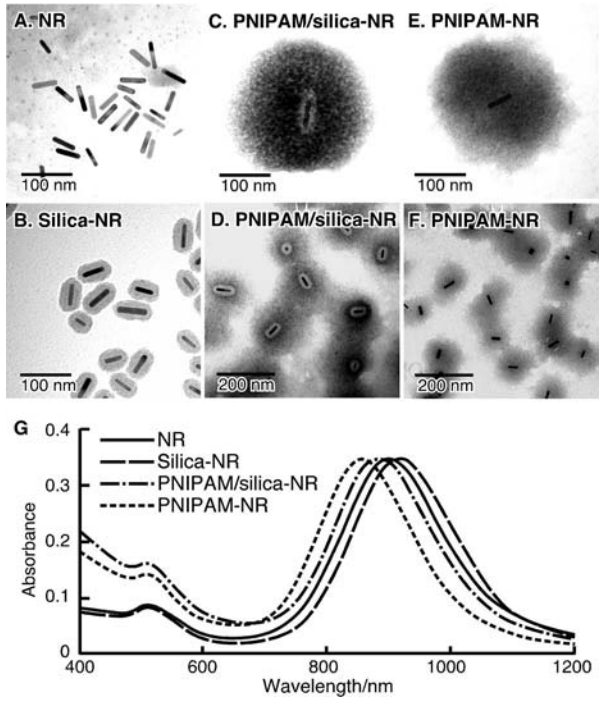

Figure 2. (A−F) Transmission electron microscopy (TEM) images of gold nanorods. (G) UV−visible-NIR spectra of gold nanorods.

Second, silica-coated nanorods were modified with PNIPAM shells by precipitation polymerization (*30, 31*). In the presence of MPS-modified silica nanorods, precipitation polymerization of NIPAM and *N*,*N*′-methylene bisacrylamide (MBA) as cross-linker was done using potassium persulfate (KPS) as an initiator, resulting in the formation of PNIPAM gel/silica-coated gold nanorods. Figure 2C,D shows the core of a single silica-coated gold nanorod modified with the shell of PNIPAM gel. Successful PNIPAM modification involved polymerization at a low concentration of gold nanorod solution (final gold atom concentration of 0.5 mM): this prevented aggregation between nanorods. Thickness of the PNIPAM shells could be adjusted by changing the amount of the NIPAM monomer and concentration of the silica-coated gold nanorods. A blue shift of the longitudinal surface plasmon band would be due to a change in the local refractive index produced by the PNIPAM shell. Silica templates were selectively etched using hydrofluoric acid. A hollow PNIPAM nanocapsule containing a single gold nanorod was observed (Figure 2E,F). Increase of absorption in the visible region (∼500 nm) was due to light scattering of PNIPAM nanogels (Figure 2G).

The temperature-induced change in size of the PNIPAM-coated gold nanorods with different cross-linking densities was measured by dynamic light scattering. All nanogels exhibited thermoresponse discontinuous phase-transition behavior (Figure 3A). Nanogels with lower cross-linking density (7.5%) showed a sharper phase transition curve than those with higher cross-linking densities (10% and 12.5%). Phase transition of all nanogels occurred at the same temperature (about 34 °C).

We investigated the photothermal phase transition of nanogels by irradiation using a focused NIR laser of wavelength 807 nm (Figure 3B). Here, to avoid aggregation, we employed a low concentration (50 μg/mL) of the nanogels. Small shrinkage of nanogels was observed after irradiation using an NIR laser for 10 min at low power (2.1 W/cm^2). Nanogels shrank considerably and rapidly when irradiated using a laser at high power (3.4 W/cm^2 and 4.2 W/cm^2). A cycle of shrinkage and swelling could be induced by switching the laser on and off. We roughly calculated input energy into a gold nanorod and required energy to increase the temperature of the NIPAM layer on the gold nanorod by 20 °C. The nanogel was assumed as a sphere (ϕ = 300 nm), the volume of the nanorod in the gel was insignificat, and the specific heat was the same as that of water. As a result of the calculation, the input energy into one gold nanorod (1.1×10^{-7} J) was 100-fold higher than the required energy to increase the temperature (1.2×10^{-9} J). It is enough to induce the phase transition of the PNIPAM layer, even the heat diffused into the silica layer and the surroundings. Gold nanorods did not exhibit a decrease or shift of the absorption peak due to irradiation by the NIR laser (data not shown). Dansylamide (which gives a fluorescent spectrum sensitive to hydrophobic environment) was mixed with nanogels, and then the mixture was irradiated by the NIR laser at various powers to investigate the nanogel environment. When the power of the NIR laser was raised, the fluorescence peak was blue-shifted and its intensity increased (Figure 3C). This indicated that the dye molecules

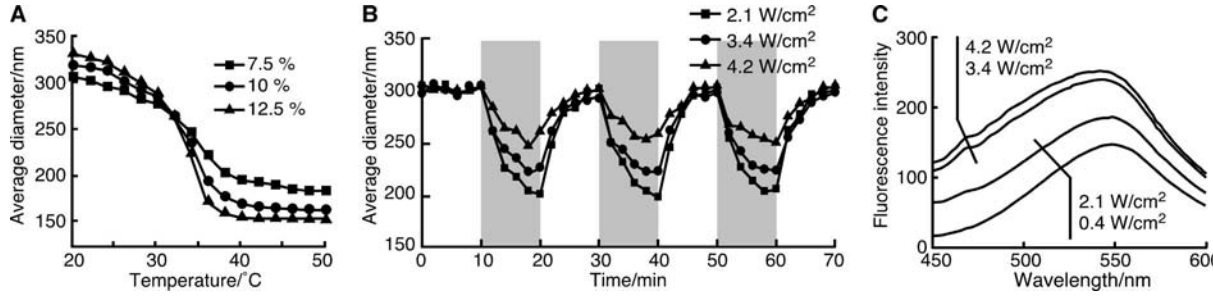

Figure 3. (A) Temperature dependence of hydrodynamic diameters of PNIPAM-coated gold nanorods with increasing cross-linking density. (B) Hydrodynamic diameters of PNIPAM-coated gold nanorods upon irradiation using a NIR laser with increasing power density. Periods of laser irradiation are indicated by the gray area. (C) Fluorescence spectra of dansylamide in the presence of PNIPAM-coated gold nanorods at several laser powers.

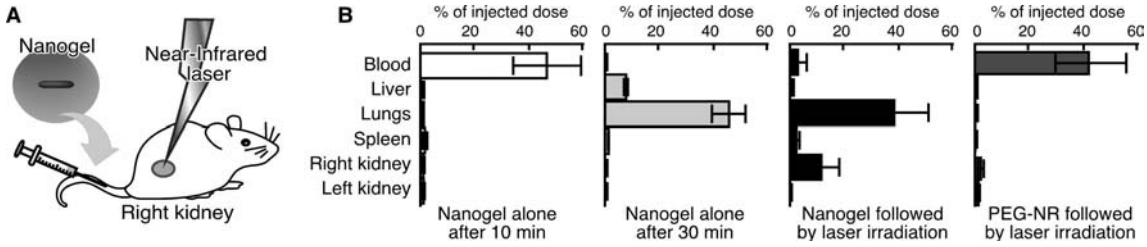

Figure 4. (A) Distributions of PNIPAM-coated gold nanorods after injection (i.v.) with or without irradiation using an NIR laser. (B) White and light-gray bars indicate injection of nanogels alone after 10 and 30 min, respectively. Black bars indicate injection of nanogels followed by laser irradiation. Dark-gray bars indicate injection of PEG-modified gold nanorods and laser irradiation.

were in a more hydrophobic environment than the original environment due to phase transition of the PNIPAM gel.

Next, we tried a feasible study on in vivo application, that is, accumulation of nanogels at laser-irradiated site in mice due to the hydrophobic surfaces induced by the photothermal effect. The hydrophobic surface could interact with cellular membrane or extracellular matrix. The nanogels with high concentration (2.5 mg/mL) were systemically injected into mice. The right kidney was immediately irradiated using the NIR laser (807 nm, 3.4 W/cm^2) (Figure 4A). Organs were subsequently collected, and the amounts of the gold nanorods in organs were evaluated by inductively coupled plasma mass spectrometry (ICP-MS; Figure 4B). When a solution of PNIPAM-coated gold nanorods was injected, nanogels were distributed primarily in the blood (47%) and lungs (46%) after 10 and 30 min, respectively. The LCST of the nanogels was 34 °C lower than body temperature, but they circulated in the blood within 10 min because of a slow phase transition response to a jump in environmental temperature (*19*). After 30 min, nanogels accumulated in the lungs. This was due to formation of a hydrophobic surface on the nanogel after full phase transition at body temperature. Significant accumulation of gold in the irradiated right kidney was observed after irradiation of the right kidney for 10 min immediately after injection of nanogels. Accumulation was not observed in the left kidney, and the amount of gold in the blood was lower than in the case without laser irradiation. PNIPAM-coated gold nanorods, which circulated in the blood after injection, accumulated due to induced rapid photothermal phase transition in the irradiated site. Gold nanorods were also detected in the lungs. Hydrophobic nanogels that could not accumulate in the irradiated site would be trapped in the capillary vessels in the lungs. In the case of injection of PEG-modified gold nanorods followed by laser irradiation, gold nanorods were primarily found in the blood, similar to the case of nanogels without laser irradiation. These results suggested that accumulation of nanogels in targeted sites was due to photothermal phase transition and aggregation of PNIPAM nanogels after irradiation using a NIR laser.

In summary, we prepared hybrid nanogels (a single gold nanorod encapsulated in a PNIPAM nanogel) by colloid−template polymerization and silica etching. PNIPAM-coated gold nanorods demonstrated photothermal phase transition and accumulation in local targeted sites which were irradiated. For in vivo application, hybrid nanogels should be optimized with respect to the LCST, size, and sensitivity by changing monomer composition and nanorod size to induce a sharp transition in the relevant physiologic range (38−42 °C). We used gold nanorods as a photothermal agent to absorb NIR light that can penetrate tissues. Gold nanorods are also used as probes for in vivo imaging techniques (two-photon luminescence, photoabsorption) (*32, 33*). NIPAM gel-coated nanorods may enable simultaneous application of targeted delivery of drugs, photothermal therapy, and bioimaging using a NIR laser.

ACKNOWLEDGMENT

This research was supported by the Precursory Research for Embryonic Science and Technology (PRESTO) and the Core Research Program for Evolution Science and Technology (CREST) from the Japan Science and Technology Agency.

Supporting Information Available: Experimental details. This material is available free of charge via the Internet at http://pubs.acs.org.

LITERATURE CITED

(1) Heath, J. R., and Davis, M. E. (2008) Nanotechnology and cancer. *Annu. Rev. Med. 59*, 251–265.
(2) Haag, R., and Kratz, F. (2006) Polymer therapeutics: concepts and applications. *Angwe. Chem., Int. Ed. 45*, 1198–1215.
(3) Peer, D., Karp, J. M., Hong, S., Farokhzad, O. C., Margalit, R., and Langer, R. (2007) Nanocarriers as an emerging platform for cancer therapy. *Nat. Biotechnol. 2*, 751–760.
(4) Ferrari, M. (2005) Cancer nanotechnology: opportunities and challenges. *Nat. Rev. Cancer 5*, 161–171.
(5) Bae, Y. H., Okano, T., and Kim, S. W. (1991) Replace "On-off" thermocontrol of solute transport. I. Temperature dependence of swelling of N-isopropylacrylamide networks modified with hydrophobic components in water. *Pharm. Res. 8*, 531–537.
(6) Nishiyama, N., Iriyama, A., Jang, W. D., Miyata, K., Itaka, K., Inoue, Y., Takahashi, H., Yanagi, Y., Tamaki, Y., Koyama, H., and Kataoka, K. (2005) A novel gene carrier enveloped with dendrimer-based photosensitizer for photochemical transfection *in vivo*. *Nat. Mater. 4*, 934–941.
(7) Derfus, A. M., Maltzahn, G., Harris, T. J., Duza, T., Vecchil, K. S., Ruoslahti, E., and Bhatia, S. N. (2007) Remotely triggered release from magnetic nanoparticles. *Adv. Mater. 19*, 3932–3936.
(8) Kost, J., Leong, K., and Langer, R. (1989) Ultrasound-enhanced polymer degradation and release of incorporated substances. *Proc. Natl. Acad. Sci. U.S.A. 86*, 7663–7666.
(9) Fischel-Ghodsian, F., Brown, L., Mathiowitz, E., Brandenburg, D., and Langer, R. (1988) Enzymatically controlled drug delivery. *Proc. Natl. Acad. Sci. U.S.A. 85*, 2403–2406.
(10) Yoshida, R., Sakai, K., Okano, T., and Sakurai, Y. (1994) Modulating the phase transition temperature and thermosensitivity in *N*-isopropylacrylamide copolymer gels. *J. Biomater. Sci. Sci. Polym. 6*, 585–598.
(11) Nayak, S., and Lyon, L. A. (2005) Soft Nanotechnology with Soft Nanoparticles. *Angew. Chem., Int. Ed. 44*, 7686–7708.
(12) Suzuki, A., and Tanaka, T. (1990) Phase transition in polymer gels induced by visible light. *Nature 346*, 345–347.
(13) Weissleder, R. (2001) A clearer vision for *in vivo* imaging. *Nat. Biotechnol. 19*, 316–317.
(14) Yu, Y.-Y., Chang, S.-S., Lee, C. -L., and Wang, C. R. C. (1997) Gold Nanorods: electrochemical synthesis and optical properties. *J. Phys. Chem. B 101*, 6661–6664.
(15) Link, S., Mohamed, M. B., and El-Sayed, M. A. (1999) Simulation of the optical absorption spectra of gold nanorods as a function of their aspect ratio and the effect of the medium dielectric constant. *J. Phys. Chem. B 103*, 3073–3077.

(16) Chou, C.-H., Chen, A.-D., and Wang, C. R. C. (2005) Highly efficient, wavelength-tunable, gold nanoparticle based optothermal nanoconvertors. *J. Phys. Chem. B 109*, 11135–11138.

(17) Dreher, M. R., Liu, W., Michelich, C. R., Dewhirst, M. W., and Chilkoti, A. (2007) Thermal cycling enhances the accumulation of a temperature-sensitive biopolymer in solid tumors. *Cancer Res. 67*, 4418–4424.

(18) Raucher, D., and Chilkoti, A. (2001) Enhanced uptake of a thermally responsive polypeptide by tumor cells in response to its hyperthermia-mediated phase transition. *Cancer Res. 61*, 7163–7170.

(19) Shiotani, A., Mori, T., Niidome, T., Niidome, Y., and Katayama, Y. (2007) Stable incorporation of gold nanorods into *N*-isopropylacrylamide hydrogels and their rapid shrinkage induced by near-IR laser irradiation. *Langmuir 23*, 4012–4018.

(20) Gorelikov, I., Field, L. M., and Kumacheva, E. (2004) Hybrid microgels photoresponsive in the near-infrared spectral range. *J. Am. Chem. Soc. 126*, 15938–15939.

(21) Das, M., Mordoukhovski, L., and Kumacheva, E. (2008) Sequestering gold nanorods by polymer microgels. *Adv. Mater. 20*, 2371–2375.

(22) Niidome, Y., Nishioka, K., Kawasaki, H., and Yamada, S. (2003) Rapid synthesis of gold nanorods by the combination of chemical reduction and photoirradiation processes; morphological changes depending on the growing processes. *Chem. Commun. 18*, 2376–2377.

(23) Nikoobakht, B., and El-sayed, M. A. (2001) Evidence for bilayer assembly of cationic surfactants on the surface of gold nanorods. *Langmuir 17*, 6368–6374.

(24) Gao, J., Bender, C. M., and Murphy, C. J. (2003) Dependence of the gold nanorod aspect ratio on the nature of the directing surfactant in aqueous solution. *Langmuir 19*, 9065–9070.

(25) Niidome, T., Yamagata, M., Okamoto, Y., Akiyama, Y., Takahashi, H., Kawano, T., Katayama, Y., and Niidome, Y. (2006) PEG-modified gold nanorods with a stealth character for *in vivo* applications. *J. Controlled Release 114*, 343–347.

(26) Pastoriza-Santos, I., Pérez-Juste, J., and Liz-Marzán, L. M. (2006) Silica-coating and hydrophobation of CTAB-stabilized gold nanorods. *Chem. Mater. 18*, 2465–2467.

(27) Stöber, W., Fink, A., and Bohn, E. J. (1968) Controlled growth of monodisperse silica spheres in the micron size. Range. *Colloid Interface Sci. 26*, 62–69.

(28) Link, S., and El-Sayed, M. A. (1999) Spectral properties and relaxation dynamics of surface plasmon electronic oscillations in gold and silver nanodots and nanorods. *J. Phys. Chem. B 103*, 8410–8426.

(29) Liz-Marzán, L. M., Giersig, M., and Mulvaney, P. (1996) Synthesis of nanosized gold-silica core-shell particles. *Langmuir 12*, 4329–4335.

(30) Deng, Y., Yang, W., Wang, C., and Fu, S. (2003) A novel approach for preparation of thermoresponsive polymer magnetic microspheres with core-shell structure. *Adv. Mater. 15*, 1729–1732.

(31) Singh, N., and Lyon, L. A. (2007) Au nanoparticle templated synthesis of pNIPAm nanogels. *Chem. Mater. 19*, 719–726.

(32) Wang, H., Huff, T. B., Zweifel, D. A., He, W., Low, P. S., Wei, A., and Cheng, J. X. (2005) In vitro and in vivo two-photon luminescence imaging of single gold nanorods. *Proc. Natl. Acad. Sci. U.S.A. 102*, 15752–15756.

(33) Niidome, T., Akiyama, Y., Shimoda, K., Kawano, T., Mori, T., Katayama, Y., and Niidome, Y. (2008) In vivo monitoring of intravenous injected gold nanorods using near-infrared light. *Small 4*, 1001–1007.

BC800480K

Supporting information

PNIPAM Gel-Coated Gold Nanorods for Targeted Delivery Responding to a Near-Infrared Laser

Takahito Kawano[†], Yasuro Niidome[†], Takeshi Mori[†‡], Yoshiki Katayama[†‡§],

Takuro Niidome[†‡#]*

[†]Department of Applied Chemistry, Faculty of Engineering, Kyushu University, 744 Moto-oka, Nishi-ku, Fukuoka 819-0395, Japan

[‡]Center for Future Chemistry, Kyushu University, 744 Moto-oka, Nishi-ku, Fukuoka 819-0395, Japan

[§]CREST, Japan Science and Technology Corporation, Kawaguchi, 332-0012, Japan

[#]PRESTO, Japan Science and Technology Corporation, Kawaguchi, 332-0012, Japan

* Corresponding author. E-mail: niidome-tcm@mbox.nc.kyushu-u.ac.jp

Fax: (+81) 92-802-2851.

Experimental

Preparation of gold nanorods

Gold nanorods were supplied by Mitsubishi Materials Corporation (Tokyo, Japan). Average length and width of prepared gold nanorods was 54.8 nm and 9.6 nm, respectively (aspect ratio: 5.7). PEG-modified gold nanorods were prepared as follows. A solution of gold nanorods containing cetyltrimethylammonium bromide (CTAB) was centrifuged at 14,000 × g for 10 min, decanted, and resuspended in water to remove excess CTAB. One milliliter of a solution of 1 mM gold nanorods (concentration of gold atom) was added to 200 μL of 1 mM $PEG_{20,000}$-SH. The mixture was stirred overnight, and was dialyzed.

Silica-coating of gold nanorods

A solution of the prepared PEG-modified gold nanorods was concentrated by centrifugation. One-hundred microliters of a solution of 10 mM PEG-modified gold nanorods was diluted with 780 μL of ethanol. The mixture was added to 20 μL of 5% ammonia solution, and 100 μL of 50 mM tetraethyl orthosilicate (TEOS). The reaction was allowed to proceed for 24 h at room temperature. The reaction mixture was added to 100 μL of 100 mM 3-(methacryloxy) propyl triethoxysilane (MPS) to graft methacryl groups on the surface. The mixture was stirred for 24 h and dialyzed against ethanol/water solution (9/1) to remove excess MPS.

PNIPAM-modification of gold nanorods

The resulting solution of silica-coated gold nanorods was centrifuged, decanted, and resuspended in water. In the polymerization procedure, silica-coated gold nanorods grafted with MPS were used as seeds for the precipitation polymerization of *N*-isopropylacrylamide (NIPAM) and *N*,*N*'-methylene bisacrylamide (MBA) using sodium dodecyl sulfate (SDS) as a stabilizer and potassium sulfate (KPS) as an initiator. The reaction was allowed to proceed for 4 h at 70°C. Typical components for modification of PNIPAM shells were: 1 mL of 2 mM silica-coated gold nanorods; 1.8 mL of 100 mM NIPAM solution; 0.4 mL of 50 mM MBA solution; 0.04 mL of 100 mM SDS solution; 0.4 mL of 10 mM KPS solution; and 0.36 mL of distilled water. The solution was bubbled through nitrogen for 5 min to remove residual oxygen.

Characterization and measurements

Absorption spectra of gold nanorods from the visible to near-infrared light region were measured with a spectrophotometer, JASCO V-570 (Tokyo, Japan). Morphologies of gold nanorods were observed with a transmission electron microscope JOEL JEM-2010 (Tokyo, Japan) after staining with 1% phosphotungstic acid. Sizes of PNIPAM-coated gold nanorods in water were evaluated with Malvern Zetasizer Nano ZS (Worcestershire, UK). Nanogels solutions were diluted to 50 μg/mL and allowed to equilibrate at appropriate temperatures for 5 min before data collection of scattered light from a He–Ne laser (633 nm).

Laser irradiation experiments

Photothermal-driven size change of nanogels was measured at 25°C with Zetasizer Nano ZS. The nanogels solutions in water (50 μg/mL, 1 mL) were irradiated using a NIR continuous-wave diode laser of wavelength at 807 nm with a beam diameter of 5.5 mm (Alfright Corporation, Madison, USA). The NIR laser irradiated from the top of the solution. The laser was turned-off during measurements of nanogel size due to the effects of scattered light produced by the laser. Fluorescence intensities of dansylamide (20 μM) mixed with nanogels (0.5 mg/mL) were measured with a spectrofluorophotometer Shimadzu RF-5300PC (Tokyo, Japan). Fluorescence spectra were measured at an excitation wavelength of 340 nm.

In-vivo experiments

After mice were anesthetized, an incision was made in the back and the right kidney exposed. PNIPAM-coated gold nanorods (2.5 mg/mL, 300 μL) were injected (*i.v.*) into mice. A NIR laser (wavelength, 807 nm; power, 3.4 W/cm^2; beam diameter, 5.5 mm) immediately irradiated light into the right kidney for 10 min. Blood and organs were isolated and completely lysed in aqua regia. Mixtures were evaporated and dissolved in water. Quantitative analysis of gold was done by inductively coupled plasma mass spectrometry using Agilent 7500c (Tokyo, Japan). Data were represented as percentage of injection dose.

Bioconjugate Chemistry 20th Anniversary

Subscriber access provided by SHEMYAKIN-OVCHINNIKOV INST

Article

HPMA Polymer-Based Site-Specific Delivery of Oligonucleotides to Hepatic Stellate Cells

Ningning Yang, Zhaoyang Ye, Feng Li, and Ram I. Mahato

Bioconjugate Chem., **2009**, 20 (2), 213-221• DOI: 10.1021/bc800237t • Publication Date (Web): 09 January 2009

Downloaded from http://pubs.acs.org on May 8, 2009

More About This Article

Additional resources and features associated with this article are available within the HTML version:

- Supporting Information
- Access to high resolution figures
- Links to articles and content related to this article
- Copyright permission to reproduce figures and/or text from this article

View the Full Text HTML

ACS Publications
High quality. High impact.

Bioconjugate Chemistry is published by the American Chemical Society. 1155 Sixteenth Street N.W., Washington, DC 20036

ARTICLES

HPMA Polymer-Based Site-Specific Delivery of Oligonucleotides to Hepatic Stellate Cells

Ningning Yang, Zhaoyang Ye, Feng Li, and Ram I. Mahato*

Department of Pharmaceutical Sciences, University of Tennessee, Health Science Center, Memphis, Tennessee 38103. Received June 12, 2008; Revised Manuscript Received December 4, 2008

The objective was to determine whether bioconjugation of type I collagen specific triplex forming oligonucleotide (TFO) to N-(2-hydroxypropyl) methacrylamide (HPMA) containing tetrapeptide Gly-Phe-Leu-Gly (GFLG) and mannose 6-phosphate (M6P) can provide their targeted delivery to hepatic stellate cells (HSCs). Following bioconjugation, M6P-GFLG-HPMA-GFLG-^{32}P-TFO was characterized by PAGE, HPLC, and GPC, and then its biodistribution was determined. TFO was dissociated from the conjugate when incubated with papain and formed triplex with the target DNA duplex. Type 1 collagen gene expression was significantly inhibited when HSC-T6 cells were transfected with this conjugate. Following tail vein injection into rats, M6P-GFLG-HPMA-GFLG-^{32}P-TFO was rapidly cleared from the circulation and accumulated mainly in the liver. The plasma concentration versus time profile was biphasic, with 12.37 min as $t_{1/2}$ of distribution and 2886.48 min as $t_{1/2}$ of elimination. A large proportion of the injected M6P-GFLG-HPMA-GFLG-^{32}P-TFO was taken up by the HSCs of both normal and fibrotic rats, which were isolated by liver perfusion at 30 min post-injection. Preinjection of M6P-GFLG-HPMA-GFLG-ONP into fibrotic rats decreased the liver uptake of the conjugates from 60% to 13%, suggesting M6P/TGFII receptor-mediated endocytosis of the conjugates by HSCs. Almost 80% of the total liver uptake in fibrotic rats was contributed by HSCs. In conclusion, conjugation with M6P-HPMA-GFLG significantly increased TFO delivery to the HSCs and could be potentially used for treating liver fibrosis.

INTRODUCTION

Chronic liver injury and inflammation of hepatocytes may lead to overproduction of type I collagen and other extracellular matrix (ECM) by hepatic stellate cells (HSCs), which are distributed throughout the hepatic lobule and serve as the principle fibrogenic cells (*1*). Activation of HSCs affects liver architecture and eventually liver function (*2*). Until now, no pharmaceutical intervention is available to treat this fibrotic disease (*3*). The application of most antifibrotic drugs has not been successful, partly because these drugs do not accumulate in the target liver cells or cause serious side effects elsewhere in the body. Alteration of the pharmacokinetic profiles of antifibrotic drugs by means of drug targeting represents a promising approach in the development of an effective antifibrotic drug (*4*).

Direct inhibition of type I collagen synthesis by HSCs is a potential target to prevent liver fibrosis. Earlier, we developed a triplex-forming oligonucleotide (TFO), which can form a triplex with the target sequence (C1) located in the rat α1(I) collagen gene promoter and inhibit the transcription of this gene (*5*). Mannose-6-phosphate/insulin-like growth factor II (M6P/IGFII) receptor is expressed on HSCs, and its expression is upregulated upon activation of these cells due to acute or chronic liver injury (*6*). Therefore, this TFO molecule is a potential candidate for treating liver fibrosis.

Following systemic administration, oligonucleotides (ODNs) widely distribute throughout the body with higher accumulation in the liver and kidney (*7*−*9*). We determined the in vivo distribution of the TFO molecules in normal and fibrotic rats (*10*). Almost 45% of the injected dose was accumulated in the liver at 30 min post-tail vein injection in normal rats, but only 35% of the injected dose in fibrotic rats. Since the intrahepatic distribution of the TFO was nonspecific, we synthesized mannose-6-phosphate−bovine serum albumin (M6P-BSA) and conjugated to TFO via a disulfide bond for its enhanced delivery to HSCs (*11*). Since the treatment of liver fibrosis may require repeated injections of TFO at high dose, high molecular weight globular BSA (66430 Da) may not be a suitable carrier for TFO delivery to the HSCs due to possible immune reaction. *N*-(2-Hydroxypropyl) methacrylamide (HPMA) copolymer has shown great potential for delivery of small molecular drugs (*12*−*14*). Although HPMA has also been used for oligonucleotide delivery, no targeting ligands were used for its site-specific delivery to target cells, and its biodistribution and uptake by different liver cell types was not determined after systemic administration. Even though biodistribution of oligonucleotides to the liver has been reported before (*15*−*17*), the authors did not determine oligonucleotides delivery to HSCs, which are the principal liver fibrotic cells.

In this study, we conjugated M6P to HPMA and then to TFO via GFLG linker, which is known to be cleaved by lysosomal enzymes (*15*). Following bioconjugation and purification, we determined (i) whether TFO can be released from the conjugate

* Address for correspondence: Ram I. Mahato, Ph.D., Department of Pharmaceutical Sciences, University of Tennessee Health Science Center, 19 South Manassas (Room 224), Memphis, TN 38103-3308, Tel: (901)448-6929, Fax: (901)448-2099, E-mail: rmahato@utmem.edu, http://cop.utmem.edu/rmahato.

10.1021/bc800237t CCC: $40.75 © 2009 American Chemical Society
Published on Web 01/09/2009

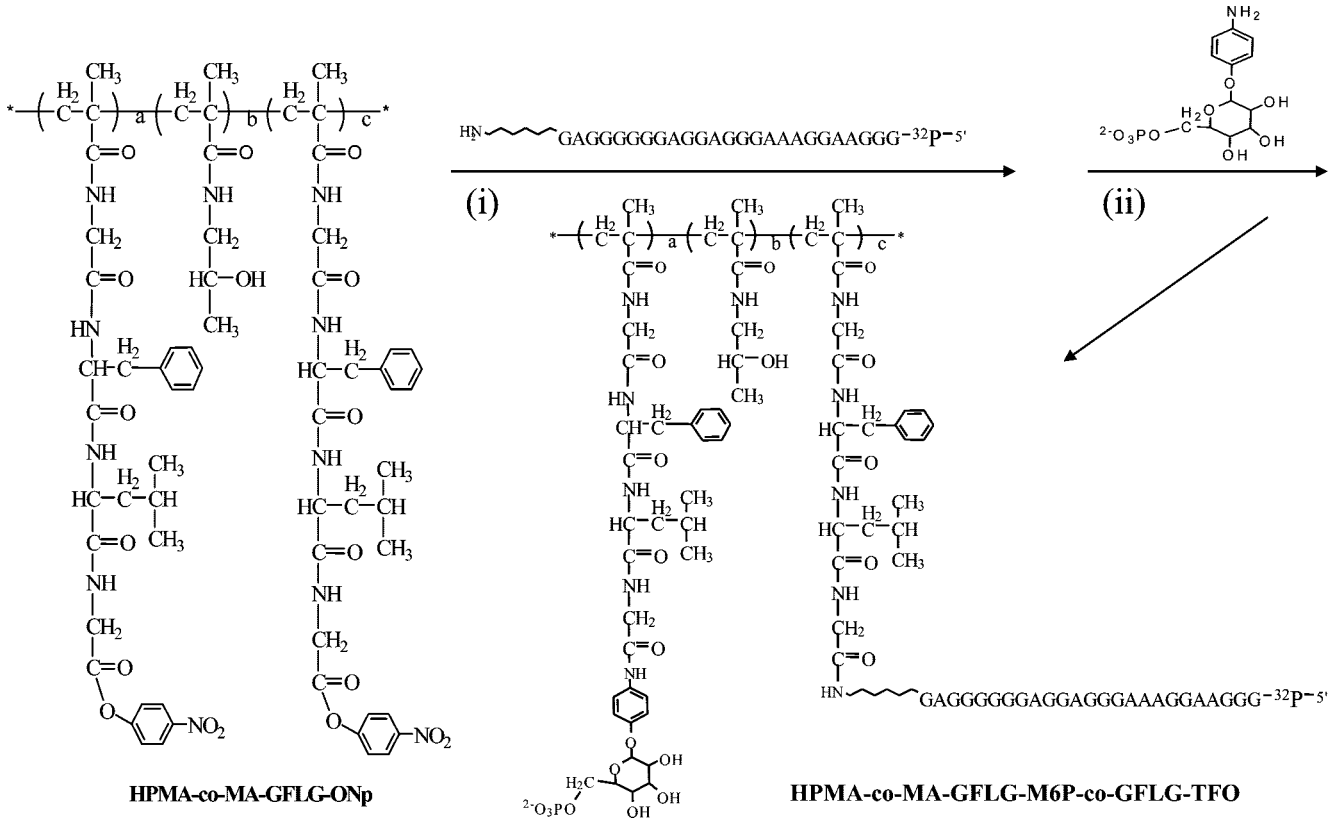

Figure 1. Synthesis scheme of M6P-GFLG-HPMA-GFLG-TFO.

after cellular uptake and (ii) biodistribution of M6P-GFLG-HPMA-GFLG-^{32}P-TFO at the whole body, organ (liver), and cellular (liver cells) levels after tail vein injection into rats.

EXPERIMENTAL PROCEDURES

Materials. Poly (HPMA-*co*-GFLG-ONP) was purchased from Varian Inc. (Amherst, MA). *p*-Nitrophenyl-α-D-mannopyranoside (pnpM), phosphorus oxide chloride, palladium (10 wt % on activated carbon), papain, methylene blue, *N*,*N*′-diisopropylethylamine, Histodenz (nycodenz), and pronase were purchased from Sigma-Aldrich (St. Louis, MO). Sephadex G75 (superfine) was procured from Pharmacia Fine Chemicals AB (Uppsala, Sweden). Dialysis tubing (molecular weight cutoff of 1000 Da) was purchased from Spectrum Laboratories, Inc. (Houston, TX). BioGel *P*6 DG Gel was from Bio-Rad Laboratories (Hercules, CA). [γ-^{32}P]-dATP was purchased from MP Biomedicals (Irvine, CA), and T4 polynucleotide kinase was from New England Biolabs (Beverly, MA). Soluene-350 (tissue solubilizer) and HionicFluor (scintillation fluid) were purchased from Perkin-Elmer (Boston, MA). Hydrogen peroxide (H_2O_2) was purchased from Fisher Chemical (Fair Lawn, NJ). Heparin was purchased from American Pharmaceutical Partners, Inc. (Los Angeles, CA). Ca^{2+}/Mg^{2+}-free Hank's balanced salt solution (Cellgro) was purchased from MediaTech (Washington, DC), and type IV collagenase was from Worthington Biochemical Corporation (Lakewood, NJ). Isoflurane was purchased from Baxter Pharmaceutical Products, Inc. (Deerfield, IL). TFO, which was a 25mer antiparallel fully phosphorothioate ODN (3′-GAGGGGGGAGGAGGGAAAGGAAGGG-5′) targeting rat α1 (I) collagen gene promoter, and TFO-3′-NH_2 were synthesized by Invitrogen (Carlsbad, CA). All solvents and chemicals used in this study were used as available without further purification.

Animals. Male Sprague−Dawley rats weighing 130−150 g were purchased from Harlan Co. (San Diego, CA) and were housed individually under the controlled light (12/12 h) and temperature conditions and had free access to food and water.

Synthesis of *p*-Isothiocyanatophenyl-6-phospho-α-D-mannopyranoside. *p*-Nitrophenyl-α-D-mannopyranoside (pnpM) (3 g, 10 mmol) was dissolved in pyridine (4 mL, 50 mmol), acetonitrile (10 mL, 190 mmol), and water (0.4 mL, 22 mmol). To this solution, phosphorus oxide chloride (4 mL, 44 mmol) was added, and the mixture was stirred for 1 h at 0 °C. The reaction mixture was poured onto 120 g of ice. pH was adjusted to 7.0 by slowly adding 2.5 M NaOH on ice, and the neutralized solution was evaporated to dryness. The solid material was dissolved in 150 mL water. The solution was concentrated under reduced pressure at 35 °C in a rotary evaporator to a final volume of 3−4 mL. The concentrated solution was kept at 4 °C overnight for crystallization and crystals was filtered and washed with 10 mL absolute ethanol. The compound was recrystallized from a 10 mL water/100 mL ethanol mixture, redissolved in water, and lyophilized to give *p*-nitrophenyl-6-phospho-α-D-mannopyranoside (pnpM6P). pnpM6P (1 mmol) was dissolved in 20 mL of a 4:1 (v/v) methanol−water mixture. To this solution, 30 mg of 10% palladium on activated carbon was added. The suspension was stirred under hydrogen (1 atm) at room temperature for 2 h. After filtration, the methanolic solution was evaporated under reduced pressure at 40 °C and lyophilized to give *p*-aminophenyl-6-phospho-α-D-mannopyranoside (papM6P).

Synthesis of M6P-GFLG-HPMA-GFLG-TFO Conjugate. The synthesis scheme of M6P-GFLG-HPMA-GFLG-TFO is shown in Figure 1. Poly(HPMA-*co*-MA-GFLG-ONP) (5 mg, 2.25 μmol of ONP) and TFO-NH_2 (0.8 mg, 0.1 μmol) were dissolved in anhydrous dimethyl sulfoxide (DMSO, 100 μL). Then, *N*,*N*′-diisopropylethylamine (DIPEA, 3 μL) was added and reacted overnight at room temperature. papM6P (3 mg, 10 μmol) was dissolved in H_2O (100 μL) and dimethyl sulfoxide (DMSO) (200 μL) mixture, and DIPEA (3 μL) was added.

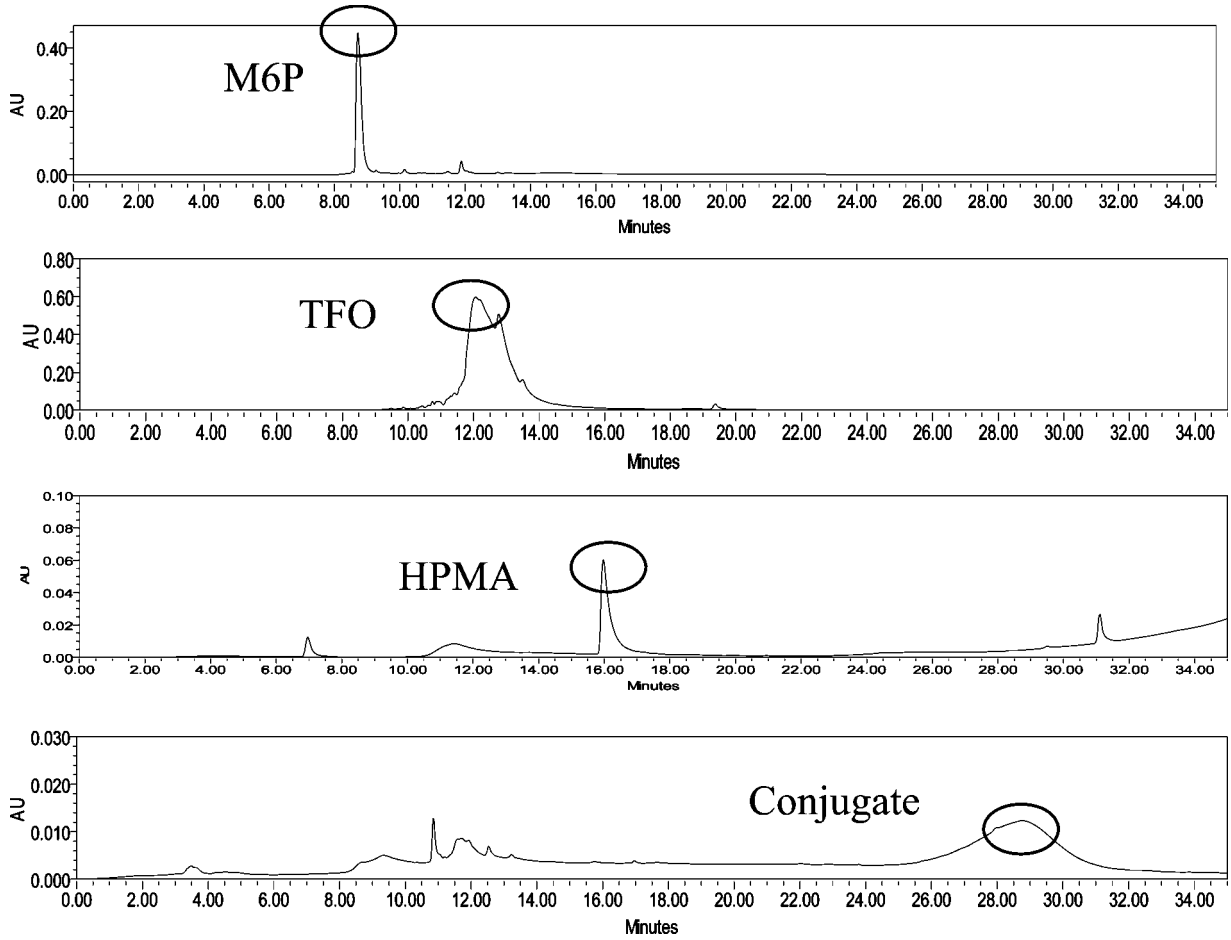

Figure 2. HPLC chromatography of M6P-GFLG-HPMA-GFLG-TFO conjugate. There is a new peak for conjugate different from the reactants, such as M6P, poly(HPMA-*co*-GFLG-ONP), and TFO.

Reaction was allowed to proceed for 24 h at room temperature. The reaction mixture was dialyzed against H_2O for a day, purified on a Sephadex G75 Gel column with pure water, freeze−dried, kept at −80 °C, and resuspended in 0.9% saline before use.

In Vitro Characterization. The purity of intermediate and final products was monitored by reverse phase-high performance liquid chromatography (RP-HPLC), which was carried on Altech Prosphere C18 column (250 mm × 4.6 mm × 5 μm) by Waters Breeze HPLC/GPC system (Waters, Milford, MA) with detection at 260 nm using a gradient of 40% to 100% acetonitrile in 0.1 M triethylammonium acetate (TEAA) at a flow rate of 1 mL/min at room temperature. M6P-GFLG-HPMA-GFLG-^{32}P-TFO was analyzed by 20% polyacrylamide gel electrophoresis (PAGE) at 80 V for 2 h. The gels were stained with methylene blue or autoradiographed.

The molecular weight of M6P-GFLG-HPMA-GFLG-TFO was also measured by gel permeation chromatography (GPC), which was carried on Waters Ultrahydrogel 250 column (7.8 × 300 mm) by Waters Breeze HPLC/GPC system (Waters, Milford, MA) with Waters 2414 Refractive Index detector and mobile phase containing 0.02% sodium azide (NaN_3) in HPLC water, at a flow rate of 0.5 mL/min. Polyethylene oxide (PEO) of different molecular weights (MW = 20 000, 31 380, 50 450, and 71 700 Da) was used as standard for calibration. HPMA-*co*-MA-ONP was used as a positive control and the molecular weight of M6P-GFLG-HPMA-GFLG-TFO was determined.

Determination of Sugar Content. Sugar content was determined by the resorcinol−sulfuric acid method (*18*). 200 μL of 6 mg/mL resorcinol and 1 mL of 75% sulfuric acid were added to M6P-GFLG-HPMA-GFLG-TFO solution containing 5−100 nmol of sugar in 200 μL. The mixtures were vortexed and heated at 90 °C for 30 min and subsequently placed in a cold-water bath for 30 min in the dark. The optical density of the solution was measured at 430 nm. PnpM was used to generate the standard curve to calculate the number of M6P per conjugate.

In Vitro Enzymatic Dissociation and Triplex Formation of M6P-GFLG-HPMA-GFLG-^{32}P-TFO. To determine whether TFO will be dissociated from M6P-GFLG-HPMA-GFLG-TFO conjugate after cellular uptake, papain (10 μM), glutathione (GSH, 250 mM), and M6P-GFLG-HPMA-GFLG-^{32}P-TFO (TFO concentration 100 μM) were incubated together at 37 °C in 0.1 M phosphate buffer containing 1 mM EDTA (PE buffer, total volume of 300 μL). At 1, 2, 8, and 24 h, 100 μL of the sample was collected and analyzed by 20% PAGE at 80 V for 2 h, followed by autoradiography.

To determine whether the TFO released from M6P-GFLG-HPMA-GFLG-TFO can still form triplex, the target duplex DNA was prepared by equal amounts of ODNs, T1: 5′-GAG GGG GGA GGA GGG AAA GGA AGG GAA AGG-3′ and T2: 5′-CCT TTC CCT TCC TTT CCC TCC TCC CCC CTC-3′, being heated at 80 °C for 5 min in 0.25 M NaCl, followed by slow cooling to room temperature. Triplex formation was initiated by the mixing of 3 μL of 3× buffer [135 mM Tris−acetate, pH 7.0, 30 mM $MgCl_2$], 3.5 μL of duplex DNA (∼3 μg), and 2.5 μL of the released ^{32}P-TFO (∼1 × 10^5 cpm). The reaction mixture was incubated at 37 °C for another 24 h. Two microliters of a 50% glycerol solution containing bromophenol blue was added, and samples were directly loaded

onto 15% native polyacrylamide gel, prepared in a buffer containing 50 mM Tris−acetate, pH 7.0, and 10 mM $MgCl_2$. Electrophoresis was performed at 8 V/cm at 4 °C in the buffer containing 89 mM Tris−Borate and 20 mM $MgCl_2$. The gel was autoradiographed at 4 °C overnight.

Transfection of TFO and M6P-GFLG-HPMA-GFLG-TFO. Immortalized rat hepatic stellate cells (HSC-T6) kindly provided by Dr. Scott Friedman of Mount Sinai School of Medicine, New York, were seeded in 6-well plates at a density of 11×10^5 cells for 12 h until 50% confluence in DMEM containing 10% of FBS. The growth medium was replaced with a prewarmed serum-free DMEM medium. TFO was mixed with pyridinium cationic liposome at 3/1 (±) charge ratio and then used for transfection at the dose of 5 μg TFO/well. For the conjugate, M6P-GFLG-HPMA-GFLG-TFO was dissolved in saline and applied to the cells at the dose of 5 μg TFO. Negative control wells were added the same amount M6P-GFLG-HPMA. Six hours later, 10% FBS was added to each well, and then the cells were cultured for additional 72 h. Following transfection, the cell culture medium was concentrated using Microcon YM-30 columns (Millipore) to retain proteins of >30 kDa. The concentrated medium was lysed using 2× Laemmli sodium dodecyl sulfate (SDS) sample buffer containing 100 mM Tris, pH 6.8, 200 mM dithiothreitol (DTT), 4% SDS, 20% glycerol, and 0.2% bromophenol blue. To detect β-actin, which was used as an intrinsic reference of sample loading, the cells were lysed directly with 1× Laemmli SDS sample buffer. The lysate samples were boiled at 100 °C for 5 min and subjected to 4% to 15% SDS-polyacrylamide (SDS-PAGE) gel electrophoresis and subsequently transferred to Immobilon polyvinylidene fluoride (PVDF) membrane (Millipore). After blocking with 5% nonfat dried milk in 1× PBST containing 0.05% Tween-20 in PBS for 1 h at room temperature, the membrane was incubated with goat antirat type I collagen and β-actin primary antibodies (Santa Cruz) for 16 h at 4 °C. The membranes were then incubated with horseradish peroxidase (HRP)-conjugated donkey antigoat secondary antibody (Santa Cruz) for 1 h at room temperature. Target proteins were detected by enhanced chemiluminescence (ECL, GE Healthcare).

Biodistribution of M6P-GFLG-HPMA-GFLG-^{32}P-TFO. The animal protocol was approved by the Animal Care and Use Committee (ACUC), Department of Comparative Medicine, University of Tennessee Health Science Center, Memphis, TN 38163. Male Sprague−Dawley rats weighing 130−150 g were used in this study, and three rats were used for each time point. Unlabeled and M6P-GFLG-HPMA-GFLG-^{32}P-TFO were mixed in saline to give a final concentration of 1 mg/mL and specific activity of 1×10^6 cpm/mL. Rats were anesthetized by inhalation of isoflurane, and M6P-GFLG-HPMA-GFLG-^{32}P-TFO was injected via tail vein at a dose of 0.2 mg/kg body weight. At 2.5, 5, 15, 30, 60, and 90 min postinjection, 0.5 mL blood was collected by cardiac puncture in heparinized tubes, and urine was collected directly from the bladder using a 0.26 gauge needle syringe. The animals were then sacrificed, and major tissues (liver, kidney, spleen, heart, and lung) were collected, washed, blotted dry, weighed, and stored at −80 °C. The radioactivity of the urine sample was counted directly after adding 10 mL of scintillation fluid. 150 μL of plasma and 150 mg of each tissue were incubated with 2 mL tissue solubilizer for 3 h at 55 °C and overnight at 37 °C in a shaker. 400 μL of H_2O_2 was added and incubated at 55 °C for another 30 min. Ten milliliters of scintillation fluid was added to each sample and the radioactivity was counted using a liquid scintillation counter.

Determination of Pharmacokinetic Profiles. Plasma data were analyzed using *WinNonlin Professional* (version 5.2, Pharsight Corporation, Mountain View, CA). M6P-GFLG-HPMA-GFLG-^{32}P-TFO plasma concentration data versus time were fitted into a two-compartment model, where

$$\frac{dx_1}{dt} = k_{21} \times X_2 - (k_{10} + k_{12})X_1 = \frac{d\,C_p}{d\,t} \times V_1 \quad (1)$$

$$\frac{d\,x_2}{d\,t} = k_{21} \times X_1 - k_{21} \times X_1 = \frac{d\,C_t}{d\,t} \times V_2 \quad (2)$$

where X_1 is amount of drug in the central compartment, and X_2 is the amount of the drug in the peripheral compartment. Since we assumed that elimination only occurred from the central compartment, k_{12} and k_{21} are the rate constants for efflux from the plasma to tissues and from tissues to the plasma, respectively. k_{10} is the elimination constant of the central compartment. The change in the amount of radioactivity of M6P-GFLG-HPMA-GFLG-^{32}P-TFO in the plasma with time can be described as a biexponential equation.

$$C_p(t) = A \times e^{-\alpha t} + B \times e^{-\beta t} \quad (3)$$

where α and β are the hybrid constants for distribution and elimination, respectively. C_p represents the plasma concentration at time t; A and B are the Y-axis intercepts, where

$$A = \frac{\text{dose} \times (\alpha - k_{21})}{V_1 \times (\alpha - \beta)} = \frac{\text{dose} \times (k_{21} - \beta)}{V_1 \times (\alpha - \beta)} \quad (4)$$

The change in the amount of radioactivity in a tissue with time can be described as follows:

$$Q(t) = \frac{\text{dose} \times k_{12}}{V_2 \times (\alpha - \beta)}(e^{-\alpha t} - e^{-\beta t}) \quad (5)$$

where $Q(t)$ (% of dose/g) represents the amount of radioactivity in 1 g of the tissue, and $C_p(t)$ (% of dose/mL) is the plasma concentration of radioactivity.

$$\frac{dQ(t)}{dt} = k_{12} \times C_p(t) - k_{21} \times C_t(t) \quad (6)$$

where k_{12} (h^{-1}) and k_{21} (h^{-1}), as mentioned above, are the rate constants for efflux from the plasma to the tissue and from the tissue to the plasma, respectively. In the present study, the efflux process can be considered negligible during the initial time points up to 90 min. Hence, eq 6 integrates to

$$k_{12} = \frac{Q(t_1)}{\int_0^{t_1} C(t)\,dt} = C_t(t_1)/\text{AUC}_{0-t_1} \quad (7)$$

From eq 7,

$$\text{CL}_{\text{in}} = \frac{Q(t_1)}{\int_0^{t_1} C(t)\,dt} = Q(t_1)/\text{AUC}_{0-t_1} \quad (8)$$

where t_1 (h) is the sampling time. $C(t)$ (μg TFO/mL plasma) is the plasma concentration of radioactivity, and CL_{in} ($mL \cdot h^{-1} \cdot g^{-1}$) is the tissue uptake rate index from the plasma to the tissue. According to eq 8, the tissue uptake rate index is calculated using the amount of radioactivity in the tissue and the area under the plasma concentration−time curve (AUC). Then, the organ clearance (CL_{org}) is expressed as follows:

$$\text{CL}_{\text{org}} = \text{CL}_{\text{in}} \times W \quad (9)$$

where W (g) is the total weight of the organ. When the tissue uptake process followed nonlinear kinetics, CL_{in} values would represent an average value for the overall experimental period. Total body clearance (CL_{total}) was calculated from AUC for infinite time (AUC_∞) by the following equation:

$$\text{CL}_{\text{total}} = \text{Dose}/\text{AUC}_\infty \quad (10)$$

The tissue uptake clearance and index were calculated using the values up to 90 min after injection, assuming that TFOs were fairly stable within this period.

Induction of Liver Fibrosis. Dimethylnitrosamine (DMN) induced liver fibrosis in rats has been shown to have a pathology closely resembling that of human cirrhosis. Male Sprague−Dawley rats weighing 130−150 g (Harlan Co., San Diego, CA) were housed individually under controlled light (12/12 h) and temperature conditions and had free access to food and water. To induce liver fibrosis, DMN was injected intraperitoneally into rats at a dose of 10 mg/kg of body weight in saline. Injections were given in the afternoons of the first 3 consecutive days of each week for 4 weeks.

Competition in Hepatic Uptake of M6P-BSA-^{32}P-TFO. Two minutes before the injection of M6P-GFLG-HPMA-GFLG-^{32}P-TFO at a TFO dose of 0.2 mg/kg (specific activity: 1×10^6 cpm/mL), liver fibrotic rats received 10 mg/kg of $(M6P)_{16}$-GFLG-HPMA. At 30 min postinjection, blood and other major organs were harvested as described above for radioactivity measurement.

Isolated Rat Liver Perfusion. To determine the effect of M6P on the hepatic uptake of TFOs by hepatocytes, HSCs, Kupffer, and endothelial cells, the livers of normal and fibrotic rats were perfused in situ after intravenous administration of M6P-GFLG-HPMA-GFLG-^{32}P-TFO, HPMA-GFLG-^{32}P-TFO, or ^{32}P-TFO at the dose of 0.2 mg of TFO/kg body weight. At 30 min postadministration, rats (200−250 g) were anesthetized by inhalation of isoflurane, 100 U heparin was injected via the tail vein, the abdomen was opened, and the portal vein was cannulated with a PE-60 polyethylene tube. The liver was first perfused with 2 mL of diluted heparin solution at 20 units/mL to avoid blood clots in the liver. The liver was preperfused in situ with 200 mL of Ca^{2+}/Mg^{2+}-free Hank's balanced salt solution at a flow rate of 15 mL/min and was then perfused with Hank's balanced salt solution containing 0.05% type IV collagenase and 0.1% Pronase for an additional 250 mL at a flow rate of 10 mL/min. All the perfusion solutions were incubated at 37 °C. After perfusion, different liver cell types were separated and radioactivity was measured as described by Cheng et al. (*10*). The contributions of various cell types to the total liver accumulation were calculated as the percentage of total hepatic uptake.

Statistical Analysis. Data were expressed as the mean ± standard deviation (SD). The difference between any two groups was determined by ANOVA. $p < 0.05$ was considered statistically significant.

RESULTS

Synthesis and in Vitro Characterization of M6P-GFLG-HPMA-GFLG-^{32}P-TFO. The synthesis scheme of M6P-GFLG-HPMA-GFLG-TFO is shown in Figure 1. *p*-Nitrophenyl-α-D-mannopyranoside (pnpM) was phosphorylated to give *p*-nitrophenyl 6-phospho-α-D-mannopyranoside (pnpM6P). This intermediate product was characterized by electron spray ionization−mass spectrum (ES-MS) as described before (*11*) (data not shown). RP-HPLC was used to monitor the purity of the intermediate and final products. From the RP-HPLC chromatograms of M6P, TFO, HPMA, and M6P-GFLG-HPMA-GFLG-TFO (Figure 2), almost all free M6P and TFOs were removed from the conjugate after purification. M6P-GFLG-HPMA-GFLG-TFO was separated from free TFO using a G75 column. As shown in Figure 2, M6P-GFLG-HPMA-GFLG-^{32}P-TFO conjugate was eluted earlier than ^{32}P-TFO. PAGE analysis of M6P-GFLG-HPMA-GFLG-^{32}P-TFO also confirmed successful conjugation and purity of the conjugate. As shown in Figure 3, unlike free TFO, there was no band shift for the conjugate. We also measured the molecular weight of M6P-GFLG-HPMA-GFLG-TFO by gel permeation chromatography (GPC) and determined that molecular weight was 51 418 Da, which matched well with the calculated molecular weight of 51 362 Da. Although poly(HPMA-*co*-GFLG-ONP) contains 8.33 mol % of ONP, the average number of M6P per conjugate was determined to be 14.67.

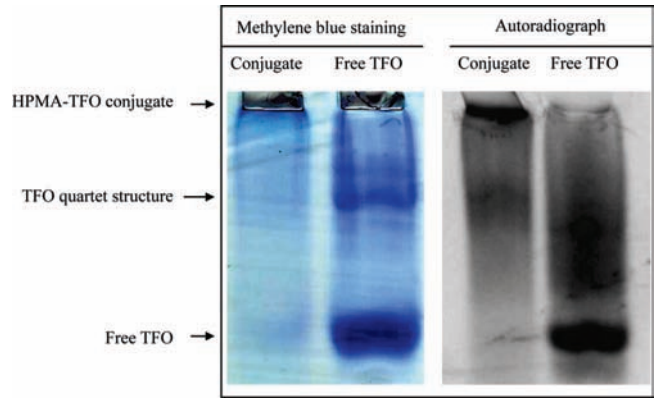

Figure 3. Polyacrylamide gel electrophoresis (PAGE) of M6P-GFLG-HPMA-GFLG-TFO. (A) Methylene blue staining. (B) Autoradiography. There was no band shift for the conjugate.

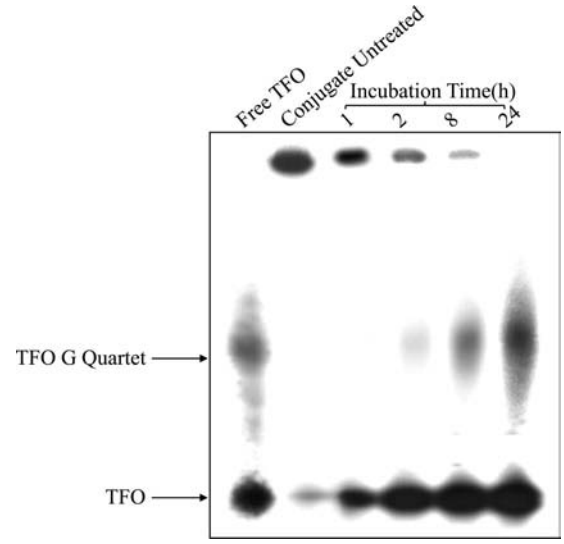

Figure 4. TFO dissociation from M6P-GFLG-HPMA-GFLG-TFO by papain. The conjugate was treated with papain for 1, 2, 8, and 24 h, followed by polyacrylamide gel electrophoresis (PAGE) and autoradiography. The conjugate not treated with papain was used as a control.

In Vitro Enzymatic Dissociation and Triplex Formation of M6P-GFLG-HPMA-GFLG-^{32}P-TFO. To determine whether TFO can be dissociated from M6P-GFLG-HPMA-GFLG-^{32}P-TFO endocytosis in the lysosome, the radioactivity was measured after polyacrylamide gel electrophoresis and autoradiography at 1, 2, 8, and 24 h post-incubation of the conjugate with papain at 37 °C (*19*). The band of the conjugate gradually disappeared along the incubation time (Figure 4). In contrast, this conjugate resulted in no band shift in the absence of papain.

GFLG linker is expected to be stable in the bloodstream but cleaved inside the cells by enzymatic dissociation by lysosomal enzymes (*20*). The release from the M6P-GFLG-HPMA-GFLG-TFO conjugate will enable TFO to traffic to the nucleus for triplex formation with genomic DNA. There should be no adverse effect on triplex formation due to this conjugation and cleavage. The M6P-GFLG-HPMA-GFLG-TFO conjugate was treated with papain and incubated with the target duplex DNA for another 24 h, and the sample was then applied on a 15%

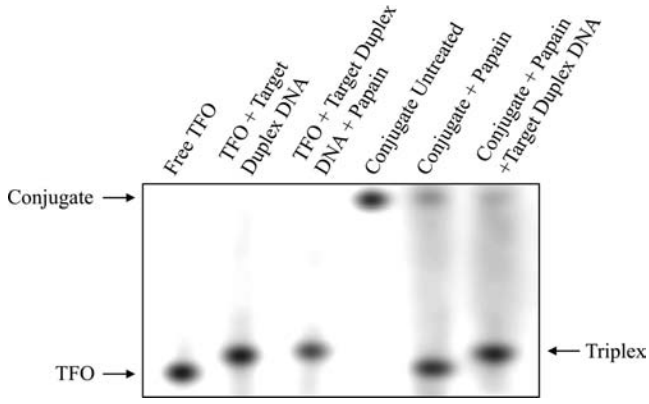

Figure 5. Triplex formation with target duplex DNA after release from M6P-GFLG-HPMA-GFLG-^{32}P-TFO conjugate. Samples were applied on 15% native PAGE at 4 °C in 89 mM Tris−borate buffer, containing $MgCl_2$ (20 mM) for 4 h. Lane 1: ^{32}P-TFO. Lane 2: duplex DNA/^{32}P-TFO (200:1) incubated for 24 h. Lane 3: Duplex DNA/^{32}P-TFO (200:1) and papain incubated for 24 h. Lane 4: M6P-GFLG-HPMA-GFLG-^{32}P-TFO. Lane 5: M6P-GFLG-HPMA-GFLG-^{32}P-TFO incubated with papain for 24 h at 37 °C. Lane 6: duplex DNA/M6P-GFLG-HPMA-GFLG-^{32}P-TFO (200:1) incubated for 24 h at 37 °C with papain.

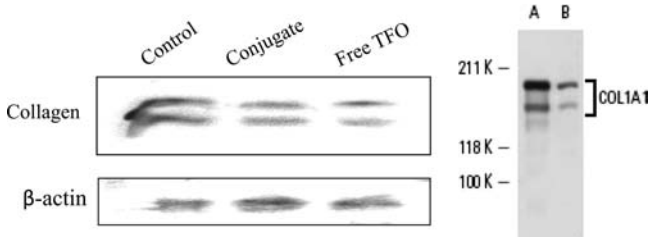

Figure 6. Inhibition of collagen gene expression. Transfection of HSC-T6 cells with TFO (lane 3) and M6P-GFLG-HPMA-GFLG-TFO (lane 2) inhibited collagen gene expression compared to the control group (lane 1). Western blot analysis of collagen primary antibody provided Santa Cruz is also shown in the right figure.

native polyacrylamide gel at 4 °C. Following electrophoresis, the gel was autoradiographed at 4 °C overnight. As shown in Figure 5, there was triplex formation observed with target duplex DNA not only for free TFO (lane 2) but also for released TFO (lane 6), which was at a molar ratio of 200 between duplex DNA and TFO.

Inhibition of Collagen type I Gene Expression by M6P-GFLG-HPMA-GFLG-TFO. To confirm that TFO conjugation to M6P-HPMA does not adversely affect its ability to inhibit the transcription of type I collagen, we transfected HSC-T6 cells with TFO and M6P-GFLG-HPMA-GFLG-TFO. Compared to the control cells treated with M6P-HPMA (lane 1), type I collagen gene expression by the cells treated with M6P-GFLG-HPMA-GFLG-TFO (lane 2) decreased as efficiently as that by the cells treated with the TFO (lane 3) (Figure 6). Since the molecular weight of collagen type 1 precursor is 130−140 kDa and that of mature collage type 1 is 70−90 Da, there were 2 bands for collagen, which is in good agreement with the supplier's Western blot analysis.

Biodistribution of M6P-GFLG-HPMA-GFLG-TFO. Following synthesis and purification of M6P-GFLG-HPMA-GFLG-^{32}P-TFO, we determined the biodistribution of this conjugate at 2.5, 5, 15, 30, 60, and 90 min post-injection into the rat tail vein. Figure 7 shows the time course of radioactivity in the plasma, urine, liver, kidney, lung, and heart. Conjugation with M6P-GFLG-HPMA-GFLG-ONP significantly increased the accumulation of ^{32}P-TFO in the liver, as compared to our previously reported biodistribution data of free ^{32}P-TFO (*10*). Almost 70% of the conjugate accumulated in the liver at 30

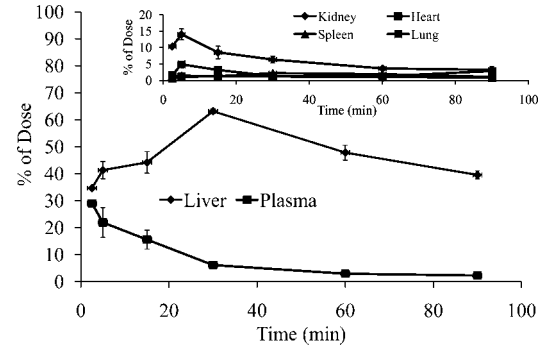

Figure 7. Biodistribution of M6P-GFLG-HPMA-GFLG-^{32}P-TFO and free ^{32}P-TFO after tail vein injection into rats at a dose of 0.2 mg TFO/kg of body weight.

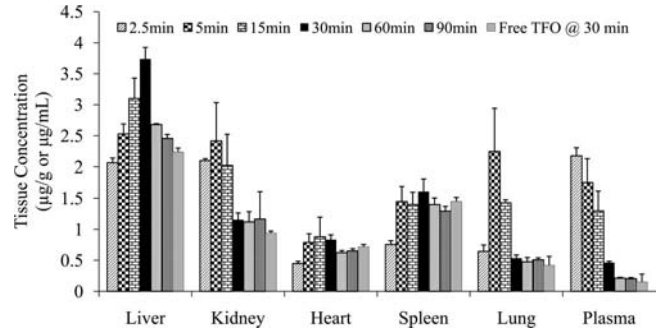

Figure 8. Concentration time profiles of radioactivity in different organs and the plasma after tail vein injection of M6P-GFLG-HPMA-GFLG-^{32}P-TFO and free ^{32}P-TFO into rats at a dose of 0.2 mg TFO/kg of body weight.

min post-injection and 60% at 60 min post-injection (Figure 7); however, only 40% of free ^{32}P-TFO was in the liver at 30 min (*10*). Figure 8 shows the tissue concentration of M6P-GFLG-HPMA-GFLG-^{32}P-TFO in the plasma (μg/mL) and tissues (μg/g) after tail vein injection into rats. The conjugation with M6P-GFLG-HPMA-GFLG-ONP significantly increased the accumulation of radioactivity in the liver and was highest at 30 min post-injection. The conjugate concentration was high not only in the liver, but also in the spleen and kidney. However, radioactivity in the kidney rapidly decreased with time. We also included the tissue accumulation data of ^{32}P-TFO at 30 min post-injection for comparison.

We also calculated the pharmacokinetic profiles using a two-compartment model by plotting plasma concentration versus time, analyzing data using *WinNonlin* professional software. As shown in Figure 9, there was good fit between observed and predicted results. Plasma elimination of M6P-GFLG-HPMA-GFLG-^{32}P-TFO was biphasic with a distribution half-life ($T_{1/2\alpha}$) of 12.37 min and elimination half-life ($T_{1/2\beta}$) of 2886.48 min. Figure 9 also summarizes the pharmacokinetic parameters such as AUC, V_d, and CL. Consistent with the rapid clearance (0.059 mL/min), M6P-GFLG-HPMA-GFLG-^{32}P-TFO had a large V_d of 231.33 mL; Table 1 summarizes the AUC, tissue uptake rate index, and organ clearance for representative organs at 90 min after systemic administration of ^{32}P-TFO and M6P-GFLG-HPMA-GFLG-^{32}P-TFO in rats. The liver uptake rate indices and clearance of the conjugate were significantly higher than those of ^{32}P-TFO: 2176 ± 58 vs 376 ± 38 μL h^{-1}g^{-1} and 11 531 ± 308 vs 2218 ± 206 μL/h, respectively. The tissue uptake rate indices and organ clearances of heart, kidney, and lung were significantly higher than those of ^{32}P-TFO, possibly due to an increase in the in vivo stability of TFO upon conjugation with M6P-GFLG-HPMA-GFLG-ONP.

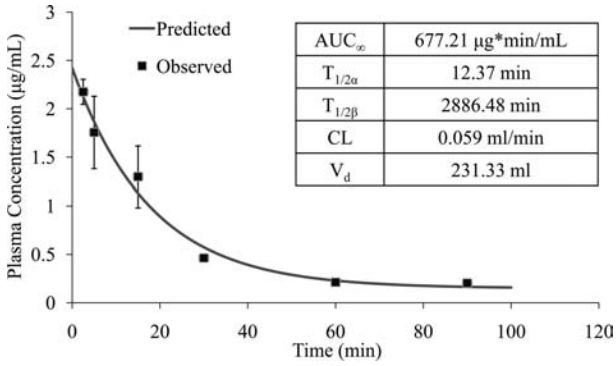

AUC_∞	677.21 μg*min/mL
$T_{1/2\alpha}$	12.37 min
$T_{1/2\beta}$	2886.48 min
CL	0.059 ml/min
V_d	231.33 ml

Figure 9. Pharmacokinetic profiles of M6P-GFLG-HPMA-GFLG-^{32}P-TFO at 30min after post vein injection. Plasma data was analyzed using a two-compartment model with *WinNonlin Enterprise* (v 5.2) software. AUC = area under the curve; CL = clearance; V_d = volume of distribution.

Effect of Fibrosis on Biodistribution. We recently reported significant decrease in the hepatic uptake of ^{32}P-TFO when injected into fibrotic rats (*10*). To make sure that there is no decrease in the hepatic uptake of M6P-GFLG-HPMA-GFLG-^{32}P-TFO, we determined the biodistribution of this conjugate at 30 min post-injection in fibrotic rats. To exclude the possibility that HPMA, the backbone, is not involved in the specific uptake of the TFO, we also determined the biodistribution of HPMA-GFLG-^{32}P-TFO at 30 min post-injection. There was no decrease in the hepatic uptake of M6P-GFLG-HPMA-GFLG-^{32}P-TFO in fibrotic rats (Figure 10). As expected, HPMA-GFLG-^{33}P-TFO accumulation in the liver was much lower than that of M6P-GFLG-HPMA-GFLG-^{32}P-TFO and decreased when fibrotic rats were used (Figure 10). This may be due to the fact that M6P/IGFII receptors are up-regulated during fibrosis (*21*), which should increase the uptake by HSCs via receptor-mediated endocytosis and cancel out any adverse effect created by a decrease in the sinusoidal gap.

Competition in Hepatic Uptake. To determine whether the hepatic uptake of M6P-GFLG-HPMA-GFLG-^{32}P-TFO is mediated by M6P/IGFII receptor-mediated endocytosis, we preinjected an excess amount of $(M6P)_{16}$-GFLG-HPMA followed by injection of the conjugate in fibrotic rats. This resulted in a significant decrease in the hepatic uptake of the conjugate in fibrotic rats (Figure 11), possibly due to M6P/IGFII receptor-mediated endocytosis of the conjugates.

Hepatic Cellular Localization. To determine the uptake of M6P-GFLG-HPMA-GFLG-^{32}P-TFO by different liver cell types, the livers of normal and fibrotic rats were perfused at 30 min post tail vein injection, and hepatocytes, HSCs, Kupffers, and endothelial cells were isolated for determination of the amount of radioactivity in these cells. As shown in Figure 12, HSCs were the major site for the uptake of this conjugate. Furthermore, the uptake of M6P-GFLG-HPMA-GFLG-^{32}P-TFO by HSCs was significantly higher compared to that of free ^{32}P-TFO. Although there was no significant decrease in the overall hepatic recovery of M6P-GFLG-HPMA-GFLG-^{32}P-TFO, uptake by the HSCs of DMN-induced liver fibrotic rats was much higher than that of normal rats (79.63 ± 2.56% vs 51.55 ± 2.02%) (Figure 12). We also perfused the livers of both normal and fibrotic rats at 30 min post-injection of HPMA-GFLG-^{32}P-TFO and determined the intrahepatic distribution of the TFO by different liver cells. As can be seen in Figure 12, the conjugation of ^{32}P-TFO with GFLG-HPMA did not significantly increase the TFO uptake by HSCs of both normal and fibrotic rats, suggesting that the HPMA backbone is not involved in the specific uptake of the TFO.

DISCUSSION

Excessive production of extracellular matrix (ECM), primarily type I collagen, by activated HSCs is known to be one of the major causes of liver fibrosis (*1*). The entire region spanning from −140 to −200 of α1(I) collagen gene promoter exists as a symmetric polypurine−polypyrimidine tract in which the polypyrimidine sequence at −141 to −170 is called the C1 region present on the noncoding strand, whereas the adjacent polypurine sequence from −171 to −200 is called the C2 region located on the coding strand. The cis-acting element is the C1 and C2 regions, playing an important role in collagen transcription (*22*). We have previously demonstrated that TFOs could form a triplex in this region and inhibit the activity of the α1(I) collagen promoter in vitro (*5, 23*). In addition, TFOs have been shown to partly reverse fibrosis in a dimethylnitrosamine (DMN) induced liver fibrosis rats, indicating the therapeutic potential of these TFOs (*10*).

M6P is a ligand for the M6P/IGF II receptor, which is up-regulated in activated HSCs during liver fibrosis, enabling selective accumulation of M6P-conjugated carrier or drug molecules (*24*). M6P conjugation to albumin increased the uptake of M6P-BSA by HSCs in liver fibrotic rats (*25*). Conjugation of M6P to virus recombinant interleukein-10 (*v*IL-10) significantly increased the hepatic uptake of *v*IL-10 by the liver.

To avoid the use of polycations, Rajur et al. conjugated ODNs to asialoorosomucoid via a disulfide bond (*26*). However, this strategy is not suitable for the TFO, since direct conjugation of molecules to the TFOs often disrupts the triplex-forming ability of the TFOs, which is essential for transcription inhibition. Furthermore, liver fibrosis results in the loss of sinusoidal fenestrae, suggesting that particulate delivery systems may not be good for TFO delivery to the HSCs.

To avoid any nonspecific ionic interaction and the large particle size, we recently conjugated TFO to M6P-BSA via a disulfide bond and demonstrated enhanced uptake by the HSCs after systemic administration of M6P-BSA-TFO into normal and fibrotic rats (*27*). However, repeated administration of this conjugate is likely to cause an immune reaction due to BSA, and thus, we synthesized M6P-GFLG-HPMA-GFLG-ONP and conjugated to TFO, where GFLG is a lysosomally degradable tetrapeptide and thus will facilitate lysosomal release of TFO and its escape to the cytoplasm after cellular uptake. Following synthesis and characterization using RP-HPLC and GPC, we determined whether TFO could be dissociated from the conjugate by incubating M6P-GFLG-HPMA-GFLG-TFO with papain, and TFO release was monitored. As shown in Figure 4, free TFO release concentration increased with incubation time with papain, which is consistent with the literature (*20*). Papain is a cysteine protease hydrolase enzyme and belongs to the same family as cathepsin B, which is the most important enzyme in the lysosomes to cleave GFLG spacer (*17, 19, 20*).

To make sure the TFO released from the conjugate can form a triplex to the target duplex DNA, we incubated M6P-GFLG-HPMA-GFLG-TFO with papain for 24 h and then used the released TFO to form a triplex with the target duplex DNA. As can be seen in Figure 5, the TFO released from the conjugate formed a triplex with duplex DNA.

To confirm that TFO conjugation to M6P-GFLG-HPMA does not adversely affect its ability to inhibit the transcription of type I collagen, we transfected HSC-T6 cells with M6P-GFLG-HPMA-GFLG-TFO. Compared to the control cells treated with M6P-HPMA, type I collagen gene expression by the cells treated with M6P-GFLG-HPMA-GFLG-TFO decreased as efficiently as that by the cells treated with the TFO (Figure 6).

Table 1. Tissue Uptake Rate Index and Clearance of ^{32}P-TFO and M6P-GFLG-HPMA-GFLG-^{32}P-TFO after Systemic Administration into Rats

		tissue uptake rate index (μL/h/g)					organ clearance (μL/h)				
sample	AUC_{90} (μg min/mL)	liver	kidney	heart	spleen	lung	liver	kidney	heart	spleen	lung
conjugate	67.11	2176 ± 58	1033 ± 391	578 ± 31	1146 ± 68	450 ± 112	11531 ± 308	1137 ± 430	318 ± 17	436 ± 26	383 ± 26
TFO	95.15	376 ± 38	235 ± 29	49 ± 3	205 ± 10	55 ± 9	2218 ± 206	241 ± 41	23 ± 2	83 ± 7	42 ± 8

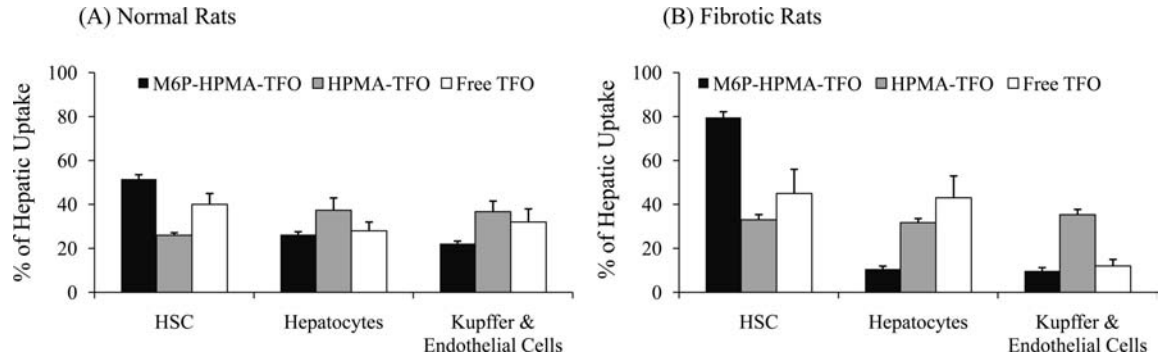

Figure 12. Intrahepatic distribution of M6P-GFLG-HPMA-GFLG-^{32}P-TFO in normal and fibrotic rats. The liver was perfused in situ by collagenase/Pronase digestion at 30 min post-injection of M6P-GFLG-HPMA-GFLG-^{32}P-TFO, HPMA-GFLG-^{32}P-TFO, or ^{32}P-TFO at dose of 0.2 mg TFO/kg of body weight. Hepatocytes, Kupffer and endothelial cells, and hepatic stellate cells (HSC) were separated, and the associated radioactivity was measured. The contribution of each liver cell type was exposed as percentage of total liver uptake. Results are expressed as the mean ± SD (n = 3).

Conjugation of TFO to M6P-GFLG-HPMA-GFLG-ONP significantly increased TFO delivery to the liver from 47% for ^{32}P-TFO to 70% for M6P-GFLG-HPMA-GFLG-^{32}P-TFO at 30 min post-injection. To determine whether the hepatic uptake of M6P-GFLG-HPMA-GFLG-^{32}P-TFO is mediated by M6P/IGF II receptor-mediated endocytosis, we preinjected rats with an excess amount of M6P-GFLG-HPMA-GFLG-ONP. This resulted in a significant decrease in the hepatic accumulation of this conjugate in fibrotic rats (Figure 11). This confirmed the receptor-mediated uptake of this conjugate, since the M6P/TGF II receptor is up-regulated in liver fibrotic rats; the hepatic accumulation was almost completely inhibiting by saturating this receptor. Rachmawati et al. also demonstrated almost 50% inhibition in the hepatic uptake of M6P-IL-10 conjugates in fibrotic rats (*28*).

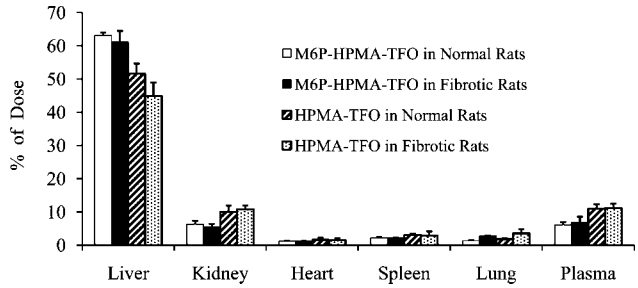

Figure 10. Effect of fibrosis on hepatic uptake of M6P-GFLG-HPMA-GFLG-^{32}P-TFO and HPMA-^{32}P-TFO after systemic administration into DMN-induced fibrotic rats. At 30 min post-injection of this conjugate (1×10^6 cpm) at a dose of 0.2 mg/kg, blood was collected by cardiac puncture. Rats were sacrificed; major organs were isolated, washed with saline, and subjected into scintillation counting. Values are the mean ± SD of 3 rats.

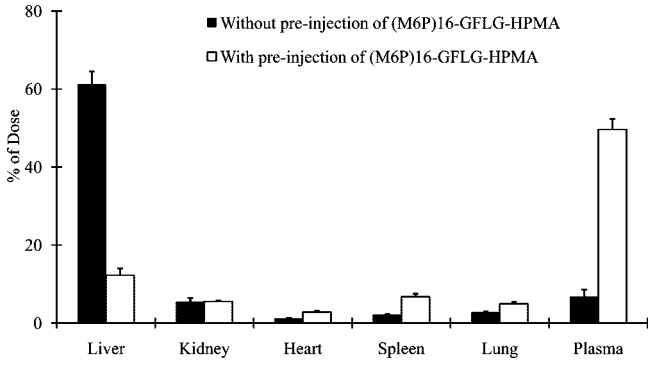

Figure 11. Effect of excess M6P-GFLG-HPMA on the biodistribution of M6P-GFLG-HPMA-GFLG-^{32}P-TFO in fibrotic rats.

To determine the hepatic cellular localization, the liver was perfused at 30 min post-injection of M6P-GFLG-HPMA-GFLG-^{32}P-TFO, HPMA-GFLG-^{32}P-TFO, or ^{32}P-TFO and different liver cells were separated by fractionation on the Histodenz gradient. As shown in Figure 12, almost 80% of the total liver uptake was contributed by HSCs cells of fibrotic rats, but only 55% by HSCs of normal rats. The percentage of uptake by hepatocytes was relatively low in both normal and fibrotic rats. However, the conjugation of TFO with GFLG-HPMA did not significantly increase the TFO uptake by HSCs of both normal and fibrotic rats (Figure 12); suggesting that the HPMA backbone is not involved in the specific uptake of the TFO.

In conclusion, conjugate with M6P-GFLG-HPMA-GFLG-ONP significantly enhanced the uptake of the TFO by HSCs, and thus, this conjugate may be suitable for inhibiting α1 (I) collagen gene expression by HSCs and may potentially treat liver fibrosis.

ACKNOWLEDGMENT

This work was supported by a grant EB003922 from the National Institutes of Health. The authors thank for Lin Zhu for help in animal experiments.

LITERATURE CITED

(1) Ye, Z., Houssein, H. S., and Mahato, R. I. (2007) Bioconjugation of oligonucleotides for treating liver fibrosis. *Oligonucleotides 17*, 349–404.

(2) Friedman, S. L. (2000) Molecular regulation of hepatic fibrosis, an integrated cellular response to tissue injury. *J. Biol. Chem. 275*, 2247–50.

(3) Pinzani, M., Rombouts, K., and Colagrande, S. (2005) Fibrosis in chronic liver diseases: diagnosis and management. *J. Hepatol. 42 Suppl*, S22–36.

(4) Hagens, W. I., Mattos, A., Greupink, R., de Jager-Krikken, A., Reker-Smit, C., van Loenen-Weemaes, A., Gouw, I. A., Poelstra, K., and Beljaars, L. (2007) Targeting 15d-prostaglandin J2 to hepatic stellate cells: two options evaluated. *Pharm. Res. 24*, 566–74.

(5) Ye, Z., Guntaka, R. V., and Mahato, R. I. (2007) Sequence-specific triple helix formation with genomic DNA. *Biochemistry 46*, 11240–52.

(6) Cheng, K., and Mahato, R. I. (2007) Gene modulation for treating liver fibrosis. *Crit. Rev. Ther. Drug Carrier Syst. 24*, 93–146.

(7) Sawai, K., Mahato, R. I., Oka, Y., Takakura, Y., and Hashida, M. (1996) Disposition of oligonucleotides in isolated perfused rat kidney: involvement of scavenger receptors in their renal uptake. *J. Pharmacol. Exp. Ther. 279*, 284–90.

(8) Agrawal, S., Temsamani, J., and Tang, J. Y. (1991) Pharmacokinetics, biodistribution, and stability of oligodeoxynucleotide phosphorothioates in mice. *Proc. Natl. Acad. Sci. U.S.A. 88*, 7595–9.

(9) Takakura, Y., Mahato, R. I., Yoshida, M., Kanamaru, T., and Hashida, M. (1996) Uptake characteristics of oligonucleotides in the isolated rat liver perfusion system. *Antisense Nucleic Acid Drug Dev. 6*, 177–83.

(10) Cheng, K., Ye, Z., Guntaka, R. V., and Mahato, R. I. (2005) Biodistribution and hepatic uptake of triplex-forming oligonucleotides against type alpha1(I) collagen gene promoter in normal and fibrotic rats. *Mol. Pharm. 2*, 206–17.

(11) Ye, Z., Cheng, K., Guntaka, R. V., and Mahato, R. I. (2005) Targeted delivery of a triplex-forming oligonucleotide to hepatic stellate cells. *Biochemistry 44*, 4466–76.

(12) Kopecek, J., Kopeckova, P., Minko, T., and Lu, Z. (2000) HPMA copolymer-anticancer drug conjugates: design, activity, and mechanism of action. *Eur. J. Pharm. Biopharm. 50*, 61–81.

(13) Gao, S. Q., Lu, Z. R., Petri, B., Kopeckova, P., and Kopecek, J. (2006) Colon-specific 9-aminocamptothecin-HPMA copolymer conjugates containing a 1,6-elimination spacer. *J. Controlled Release 110*, 323–31.

(14) Sirova, M., Strohalm, J., Subr, V., Plocova, D., Rossmann, P., Mrkvan, T., Ulbrich, K., and Rihova, B. (2007) Treatment with HPMA copolymer-based doxorubicin conjugate containing human immunoglobulin induces long-lasting systemic anti-tumour immunity in mice. *Cancer Immunol. Immunother. 56*, 35–47.

(15) Jensen, K. D., Kopeckova, P., and Kopecek, J. (2002) Antisense oligonucleotides delivered to the lysosome escape and actively inhibit the hepatitis B virus. *Bioconjugate Chem. 13*, 975–84.

(16) Jensen, K. D., Nori, A., Tijerina, M., Kopeckova, P., and Kopecek, J. (2003) Cytoplasmic delivery and nuclear targeting of synthetic macromolecules. *J. Controlled Release 87*, 89–105.

(17) Wang, L., Kristensen, J., and Ruffner, D. E. (1998) Delivery of antisense oligonucleotides using HPMA polymer: synthesis of A thiol polymer and its conjugation to water-soluble molecules. *Bioconjugate Chem. 9*, 749–57.

(18) Monsigny, M., Petit, C., and Roche, A. C. (1988) Colorimetric determination of neutral sugars by a resorcinol sulfuric acid micromethod. *Anal. Biochem. 175*, 525–30.

(19) Lu, Z. R., Gao, S. Q., Kopeckova, P., and Kopecek, J. (2001) Modification of cyclosporin A and conjugation of its derivative to HPMA copolymers. *Bioconjugate Chem. 12*, 129–33.

(20) Ding, H., Kopeckova, P., and Kopecek, J. (2007) Self-association properties of HPMA copolymers containing an amphipathic heptapeptide. *J. Drug Targeting 15*, 465–74.

(21) De Bleser, P. J., Scott, C. D., Niki, T., Xu, G., Wisse, E., and Geerts, A. (1996) Insulin-like growth factor II/mannose 6-phosphate-receptor expression in liver and serum during acute CCl4 intoxication in the rat. *Hepatology 23*, 1530–7.

(22) Joseph, J., Kandala, J. C., Veerapanane, D., Weber, K. T., and Guntaka, R. V. (1997) Antiparallel polypurine phosphorothioate oligonucleotides form stable triplexes with the rat alpha1(I) collagen gene promoter and inhibit transcription in cultured rat fibroblasts. *Nucleic Acids Res. 25*, 2182–8.

(23) Nakanishi, M., Weber, K. T., and Guntaka, R. V. (1998) Triple helix formation with the promoter of human alpha1(I) procollagen gene by an antiparallel triplex-forming oligodeoxyribonucleotide. *Nucleic Acids Res. 26*, 5218–22.

(24) Beljaars, L., Olinga, P., Molema, G., de Bleser, P., Geerts, A., Groothuis, G. M., Meijer, D. K., and Poelstra, K. (2001) Characteristics of the hepatic stellate cell-selective carrier mannose 6-phosphate modified albumin (M6P(28)-HSA). *Liver 21*, 320–8.

(25) Beljaars, L., Molema, G., Weert, B., Bonnema, H., Olinga, P., Groothuis, G. M., Meijer, D. K., and Poelstra, K. (1999) Albumin modified with mannose 6-phosphate: A potential carrier for selective delivery of antifibrotic drugs to rat and human hepatic stellate cells. *Hepatology 29*, 1486–93.

(26) Rajur, S. B., Roth, C. M., Morgan, J. R., and Yarmush, M. L. (1997) Covalent protein-oligonucleotide conjugates for efficient delivery of antisense molecules. *Bioconjugate Chem. 8*, 935–40.

(27) Ye, Z., Cheng, K., Guntaka, R. V., and Mahato, R. I. (2006) Receptor-mediated hepatic uptake of M6P-BSA-conjugated triplex-forming oligonucleotides in rats. *Bioconjugate Chem. 17*, 823–30.

(28) Rachmawati, H., Reker-Smit, C., Lub-de Hooge, M. N., van Loenen-Weemaes, A., Poelstra, K., and Beljaars, L. (2007) Chemical modification of interleukin-10 with mannose 6-phosphate groups yields a liver-selective cytokine. *Drug Metab. Dispos. 35*, 814–21.

BC800237T

Bioconjugate Chemistry 20th Anniversary

Subscriber access provided by SHEMYAKIN-OVCHINNIKOV INST

Article

Optimizing a Waveguide-Based Sandwich Immunoassay for Tumor Biomarkers: Evaluating Fluorescent Labels and Functional Surfaces

Harshini Mukundan, Hongzhi Xie, Aaron S. Anderson,
W. Kevin Grace, John E. Shively, and Basil I. Swanson

Bioconjugate Chem., **2009**, 20 (2), 222-230• DOI: 10.1021/bc800283e • Publication Date (Web): 27 January 2009

Downloaded from http://pubs.acs.org on May 8, 2009

More About This Article

Additional resources and features associated with this article are available within the HTML version:

- Supporting Information
- Access to high resolution figures
- Links to articles and content related to this article
- Copyright permission to reproduce figures and/or text from this article

View the Full Text HTML

ACS Publications
High quality. High impact.

Bioconjugate Chemistry is published by the American Chemical Society. 1155 Sixteenth Street N.W., Washington, DC 20036

Optimizing a Waveguide-Based Sandwich Immunoassay for Tumor Biomarkers: Evaluating Fluorescent Labels and Functional Surfaces

Harshini Mukundan,[†] Hongzhi Xie,[†] Aaron S. Anderson,[†] W. Kevin Grace,[†] John E. Shively,[‡] and Basil I. Swanson*[,†]

MS: J567, Physical Chemistry and Applied Spectroscopy, Los Alamos National Laboratory, Los Alamos, New Mexico 87545, and Beckman Research Institute, City of Hope, 1450 East Duarte Road, Duarte, California 91010. Received July 8, 2008; Revised Manuscript Received November 25, 2008

The sensor team at the Los Alamos National Laboratory has developed a waveguide-based optical biosensor for the detection of biomarkers associated with disease. We have previously demonstrated the application of this technology to the sensitive detection of carcinoembryonic antigen in serum and nipple aspirate fluid from breast cancer patients. In this publication, we report improvements to this technology that will facilitate transition to a point-of-care diagnostic system and/or robust research tool. The first improvement involved replacing phospholipid bilayers used for waveguide functionalization with self-assembled monolayers. These thin films are stable, specific, and robust silane-based surfaces that reduce nonspecific binding and enhance the signal to background ratio. Second, we have explored four different fluorescent labeling paradigms to determine the optimal procedure for use in the assay. Labeling the detector antibody with an organic dye (AlexaFluor 647) in the hinge region allows for unusual signal enhancement with repeat excitation (at 635 nm) in our assay format, thereby facilitating a better signal resolution at lower concentrations of the antigen. We have also labeled the detector antibody with photostable quantum dots through either the amine groups of lysine (Fc, NH) or using a histidine tag in the hinge region of the antibody (Hinge, H). Both labeling strategies allow for acceptable signal resolution, but quantum dots show much greater resistance to photobleaching than organic dyes.

INTRODUCTION

Breast cancer affects 200 000 women annually in the United States. The probability of survival is much higher with early diagnosis (95%) compared to metastatic disease (26%) (*1*). Current diagnostic techniques are, however, unsatisfactory when applied to early detection. For example, mammography can detect the tumor only when palpable, suffers from high false positive and negative rates, and requires confirmatory invasive biopsies as a consequence. In addition, it cannot be used on women less than 40 years of age because of intrinsically denser breasts in that population (*2*). Other methods are also either expensive (e.g., magnetic resonance imaging) or are associated with nonspecific results (standard immunoassays) (*3*). Thus, there is a need for a sensitive, specific, quantitative, rapid, and noninvasive diagnostic for breast cancer.

Certain "biomarkers" are differentially expressed in cancer, typically very early in disease onset, and can potentially be used for detection. Since no single biomarker can effectively predict all stages of cancer, detection of a suite of these molecules is a requisite of any diagnostic strategy that utilizes them. However, current immunoassay techniques cannot accomplish this in complex, small-volume patient samples. Therefore, the American Society for Clinical Oncology does not currently recommend these markers for the early detection of breast cancer (*4*).

The sensor team at the Los Alamos National Laboratory has developed a waveguide-based optical biosensor for the sensitive detection of such markers in a sandwich immunoassay format. The optical properties and assay procedures have been outlined elsewhere (*5*). Briefly, a sandwich immunoassay using a fluorescently labeled detector antibody is performed on the functionalized surface of single-mode planar optical waveguides. Only fluorescent molecules within the evanescent field of the waveguide (0−250 nm from the surface) are excited, facilitating optical separation of surface-bound entities from solution contaminants. This spatial filtering minimizes the background fluorescence associated with complex biological samples such as blood and sputum. We have previously demonstrated the application of this technology to the sensitive detection of breast cancer (unpublished data) (*6*), influenza viruses (*7*), and *Bacillus anthracis* protective antigen (*5*). We have successfully adapted the optical biosensor to the detection of carcinoembryonic antigen (CEA), a breast cancer biomarker in serum and nipple aspirate fluid from patients with abnormal mammograms (unpublished data) (*6*). CEA was detected in a small cohort of patient samples with excellent sensitivity (limit of detection = <0.5 pM), specificity (low nonspecific binding or false results), and speed (15 min). We have assessed the reproducibility of our assay by two different approaches. Repeat measurements were made with 25 pM human CEA on the same waveguide as a measure of intra-assay variability. The signal observed with each measurement was completely eliminated by photobleaching before subsequent measurements were made. The waveguide background was low (∼16 relative fluorescence units (RFU)) with a standard deviation of 3 between measurements. 25 pM CEA yielded, on average, 1046 RFU with a standard deviation of 119 between measurements. We have also assayed for interassay variability by measuring CEA concentrations in a human patient sample in 4 different waveguides in entirely different experiments. Although the raw values for background and signal differ among waveguides, the extrapolated CEA concentration (based on an internal human purified CEA

* To whom all correspondence is addressed. MS J567, C-PCS, C-Division, Los Alamos National Laboratory, Los Alamos, New Mexico 87545, basil@lanl.gov, (505)-667-5814(phone), (505)-667-0440 (Fax).

[†] Los Alamos National Laboratory.

[‡] City of Hope.

10.1021/bc800283e CCC: $40.75 © 2009 American Chemical Society
Published on Web 01/27/2009

standard) was 78 pM ($n = 4$ repeats) with a standard deviation of <1.5. These numbers establish both the inter- and intra-assay reproducibility of our waveguide-based assay for CEA (*5*). However, our waveguide assay still required optimization to make it more amenable for use in clinical or research setting. For instance, phospholipid bilayers (PLBs) used in the initial demonstration for waveguide surface functionalization, are neither robust nor stable, and allow nonspecific interactions in complex biological samples. Our team has developed alternative functional surfaces that overcome these disadvantages. Silane-based self-assembled monolayers (SAMs) are robust (can be washed with detergents) and stable (>300 days in air), effectively resist nonspecific interactions, and are potentially regenerable (*8*). The present manuscript demonstrates the superior performance of SAMs (in comparison with PLBs) when applied to the detection of CEA.

In our initial demonstration of the CEA assay, the detector antibody was labeled with an organic dye (AlexaFluor 647, AF647) in the Fc region (primary, NH labeling) using the NH groups on the lysine residues. The current study compares this strategy to one where the antibody is labeled with AF647 in the hinge region (H labeling) using a histidine tag. In addition to organic dyes, we have also analyzed the use of photostable quantum dots (QDs) as the fluorescent label. QDs have been extensively researched as fluorescence reporters or probes for several biological applications (*9*). They consist of nanometer-scale atom clusters with a semiconductor core and shell and an amphiphilic polymer coating (*10*) that provides a protective, water-soluble surface that can be differentially modified. QDs show a direct, predictable relationship between their physical size and the energy of the exciton (and, therefore, the wavelength of emitted fluorescence). This "tuneability" has allowed for the development of a series of QDs that have common excitation profiles but different fluorescent emission maxima. Exploiting this property, one can potentially envision a multiplex detection format using QDs that emit at different wavelengths. In addition, QDs exhibit excellent brightness and much greater photostability than traditional organic fluorophores (*9*). This makes long-term imaging/excitation possible under conditions that would lead to the photoinduced deterioration (photobleaching) of other types of fluorophores. These features have facilitated the use of QDs in several bioapplications such as immunofluorescence assays, live cell imaging, biotechnology detection, single molecule biophysics, and in vivo animal imaging (*11*−*13*). NH-and H-labeling with both QDs and organic dyes were evaluated in the current study. NH labeling has been shown to sometimes compromise antigen binding activity of the antibody. Therefore, we chose to evaluate two different labeling protocols and determine the one that offered the best sensitivity.

EXPERIMENTAL PROCEDURES

Materials. Purified CEA and antibodies (T84.1, capture and T84.66, detector) were obtained from our collaborators at the City of Hope. These antibodies were selected by epitope mapping and therefore form an effective sandwich by binding orthogonal epitopes of CEA (unpublished data) (*6*). Amino-functionalized QD (655 nm, QD655), Qdot655 ITK carboxyl quantum dots, and AF647-*N*-hydroxysuccinimide (NHS) ester labeling kits were purchased from Invitrogen. Biotinylation, protein estimation, and electrophoresis reagents were obtained from Pierce. Tri-*n*-octylphosphine oxide (TOPO) and tri-*n*-octylphosphorine (TOP) capped CdSe/ZnS core/shell QDs were a generous gift from Dr. S. Jeong (Los Alamos National Laboratory) (*14, 15*).

Gel filtration columns and spin filters were from Harvard Apparatus. Buffers, chemicals, immunoblot materials, and other components were purchased from Sigma Aldrich or Fisher Scientific unless otherwise specified. Waveguides were obtained from nGimat, Atlanta, GA. 1,2-Dioleoyl-*sn*-glycero-3-phosphocholine (DOPC) and 1,2-dioleoyl-*sn*-glycero-3-phosphoethanolamine-*N*-(cap biotinyl) (sodium salt) were purchased from Avanti Polar Lipids. Materials required for SAM preparation are listed in detail elsewhere (*8*).

Methods. *Biotinylation of the Capture Antibody.* The capture antibody (2 mg/ml, 500 μL) was incubated with Sulfo-NHS biotin (10 mM, 20 molar excess) for 1 h at room temperature (RT) on a rotator. Macro Spin gel filtration columns (molecular weight cutoff (MWCO) 100 kD, 150 μL capacity) were hydrated for 2 h with PBS, and the biotinylated antibody was separated from free-biotin by centrifugation in the hydrated columns for 5 min. The extent of biotinylation was determined using an EZ Biotin Quantitation Kit (Pierce) that measures the degree of biotinylation using 4′-hydroxyazobenzene-2-carboxylic acid. Protein concentration was determined by measuring absorbance of the conjugate at 280 nm using bovine serum albumin (BSA) as the standard.

Functionality of the biotinylated antibody (i.e., ability to bind antigen) was assessed by immunoblot analysis. For this, CEA (1 nM, 3 μL) was blotted on nitrocellulose filter paper and allowed to air-dry. The paper was subsequently blocked with fish gelatin (4.5% v/v solution in PBS) for 2 h at RT and probed overnight at 4 °C with the biotinylated antibody. Unbound antibody was removed by washing with PBS/Tween-20 (0.1% v/v, 3×, 1 min each) followed by PBS (4×, 1 min each). The blot was then incubated with a secondary antibody (goat−anti-mouse labeled with alkaline phosphatase, 0.001 mg/mL, 2 mL, 1 h at RT). Again, unbound antibody was removed by washing and specific staining detected with NBT-BCIP (one-step alkaline phosphatase substrate). Unlabeled antibody was used as the positive control and PBS-0.5% BSA as the negative. The same protocol was also used for the evaluation of the fluorescently labeled detector antibodies (see below).

Biotinylation of the capture antibody (i.e., incorporation of biotin on the antibody) was also assessed by immunoblot. One nanomolar antibody was blotted on nitrocellulose filter paper. Following blocking, the blot was probed using streptavidin labeled with alkaline phosphatase (0.001 mg/mL in PBS, 2 mL) for 1 h at RT. Unbound antibody was removed by washing, and the blot was developed as described earlier. Unlabeled antibody was used as the negative control and sulfo-NHS-biotin as the positive control.

Fluorescent Labeling of the Detector Antibody. Multiple strategies were used for generating fluorescent detector bioconjugates. In each case, protein concentration was measured by determining absorbance at 280 nm using bovine serum albumin (BSA) as standard. Functionality of the labeled antibody was evaluated by immunoblot analysis (as outlined earlier). Labeling was verified, where applicable, by gel electrophoresis. Both agarose and polyacrylamide (PAGE) gel electrophoresis techniques were employed.

Primary Labeling of Detector Antibody with AF647 (T84.66-NH-AF647). An AF647-NHS ester labeling kit (catalogue #A20173, Invitrogen) was used, and the reaction was carried out according to the manufacturer's recommendation. Briefly, the antibody (2 mg/mL, 500 μL) was reacted with AF647-NHS ester in the dark for 1 h at RT on a rotator. Labeled protein was separated from free dye by gel filtration (G-25, Sephadex). Degree of labeling was determined by UV/vis spectroscopy to be 4 mol of dye per mole of protein based on the corrected ratio of absorbance at 650 and 280 nm, respectively.

Hinge Labeling of Detector Antibody with AF647 (T84.66-H-AF647). Detector antibody (8 mg/mL, 500 μL) in PBS, pH 8.0, was reacted with 20 mM tris(2-carboxylethyl) phosphine (TCEP) (400 nmol, 30-fold molar excess) at 37 °C for 2 h under

argon. The mixture was purified by spin filtration (G-25, Sephadex) and then reacted with a 50 molar excess of AF647-maleimide in PBS at 37 °C for 2 h under argon on a rotator. The reaction mixture was again purified by G-25 spin filtration (MWCO 100 kD), and labeled protein was collected. Protein reduction was confirmed by nonreducing gel electrophoresis.

NH Labeling of Detector Antibody with QD (T84.66-NH-QD655). Carboxyl-coated QD655 stock solution (8 μM, 20 μL) was blended in borate buffer (25 mM, pH 7.3) and mixed with the antibody (47 μM, 10 μL). *N*-Ethyl-*N*′-dimethylaminopropylcarbodiimide hydrochloride (EDC, 100 mM, 2.4 μL) was added to this reaction mixture and gently stirred for 2 h at RT. The reaction was quenched by addition of borate buffer (50 mM, 100 μL, pH 9.0) and further incubated for 2 h at RT.

Free and conjugated QDs were visualized by sodium dodecyl sulfate (SDS)-PAGE followed by UV illumination at 366 nm. Proteins were stained with GelCode (blue) reagent. The conjugate was separated by spin filtration (membrane MWCO 100 kDa) followed by at least five exchanges with borate buffer (50 mM, pH 8.5). Absorbance of QD655 was measured to calculate its concentration ($\varepsilon_{638} = 8 \times 10^5\ M^{-1}\ cm^{-1}$). The molar ratio of antibody to QD in the conjugate was 3:1.

Hinge Labeling of Detector Antibody with QD625 (T84.66-H-QD625). [TOP/TOPO]-capped CdSe/ZnS core/shell quantum dots with an emission maximum at 625 nm were used to prepare dihydrolipoic acid (DHLA)-coated QDs (*16*). DHLA was freshly prepared from α-lipoic acid by sodium borohydride reduction (*17*). DHLA-QD625 (1 μM, 100 μL) was diluted with borate buffer (25 mM at pH 9.0, 78 μL), mixed with His_6-anti-CEA antibody (18 μM, 22 μL), and incubated overnight at 4 °C. Conjugation was verified by running the His_6-anti-CEA-DHLA-QD625 on native polyacrylamide (4−15% gradient) and agarose (1%) gels. This confirmed the absence of free QDs in the conjugate. Absorbance of the conjugate was used to determine QD625 concentration ($\varepsilon_{605} = 4.5 \times 10^5\ M^{-1}\ cm^{-1}$). Antibody concentration was determined by the Bicinchoninic acid assay (BCA) using BSA as standard. The average number of antibodies per QD was about 4.

Preparation of the Waveguides and Coating with Sensing Film(s). Single-mode planar optical waveguides consisting of a polished fused silica substrate (lower refractive index) coated with silicon oxy nitride (SiON*x*, high refractive index) with a 10 nm coating of SiO_2 (lower refractive index, which allows the functionalization of the waveguide surface) were used. Waveguides and glass coverslips were cleaned by sonication in chloroform and ethanol (5 min each), followed by exposure to UV-light and ozone (40 min). The cleaned surfaces were functionalized using either PLBs or SAMs.

The preparation of biotinylated (1%) unilamellar vesicles (PLBs) by sonication has been previously described (*5*). Briefly, thin films of DOPC (5 mM stock in $CHCl_3$, 50 μL) with 1% cap biotinyl (v/v, sodium salt, 5 mM stock in $CHCl_3$, 0.6 μL) were deposited on the walls of test tubes by evaporation of chloroform under argon. The films were rehydrated in PBS (1×, ∼0.01 M, 40 min) and subsequently subjected to eight freeze−thaw cycles (frozen in liquid nitrogen and thawed in warm tap water) and sonicated with a probe tip sonicator (Branson, 50% duty cycle for 5 min).

Waveguides and coverslips were assembled into a flow cell using a gasket to form a tight seal between them as has been outlined earlier (*5*−*7*). A supported bilayer was then formed on the cleaned flow cell surface by injecting the vesicle solution into the flow cell and allowing it to stabilize overnight. It is important to ensure that there are no air bubbles generated during the coating as they can damage the PLBs. The functionalized surface was subsequently blocked with PBS containing 2% BSA for 1 h before use for most experiments. These bilayer-coated waveguides remained stable for a maximum of 1 week under refrigeration.

Preparation of SAMs has also been described previously (*8*). Briefly, waveguide and coverslip surfaces were cleaned as described above. The substrates were submerged in water, blown dry, and placed in a vacuum desiccator with a small volume (∼50 μL) of 1-(3-aminopropyl)-1-methyldiethoxy silane (AP-MDES). The vacuum chamber was evacuated to ∼200 Torr and allowed to stand for 2 h. After coating, the substrates were baked at 110 °C for 30 min, allowed to cool in a drying desiccator, rinsed with ethanol, blown dry, and analyzed by contact angle. Poly(ethylene glycol) (PEG) reagents containing a carboxylic acid at one end and either a methoxy group (99−99.99% of the total PEG volume) or a protected amine (0.01−1% of the PEG volume) at the other were coupled to the amine surfaces overnight using standard peptide coupling conditions, again followed by contact angle analysis. The protecting groups were removed by immersion in a piperidine/NMP solution, and biotin was attached to the resulting free amine via its commercially available *N*-hydroxysuccinimide ester. All steps after aminosilanization were carried out in *N*-methylpyrrolidinone (NMP) as the solvent, and the slides were rinsed thoroughly between steps. After biotinylation, the slides were rinsed with NMP, acetone, and ethanol and were blown dry under a stream of argon. SAM-coated waveguides and coverslips were mounted into flow cells as described for the preparation and use of phospholipid bilayers, but the SAMs were not blocked and were therefore available for immediate use.

Waveguide-Based Sandwich Immunoassay for CEA. All experiments used the same batch of waveguides, functionalized and mounted in flow cells as described before. However, intrinsic waveguide background can vary, which accounts for some differences in the measured signal/background (S/B) (see Results).

A general schematic of the assay on the waveguide-based biosensor is shown in Figure 1 (unpublished data) (*6*). To provide a facile method of coupling light, diffraction gratings are etched on the surface of the waveguide. Excitation light is coupled into these gratings by positioning the laser beam at the appropriate angle of impingement. Two different excitation lasers were used: 532 nm (diode pumped Neodinium YAG laser, CrystaLaser, Reno, Nevada) for all QD experiments and 635 nm (Diode Laser, Coherent, Auburn, CA) for AF647 experiments. We selected waveguides that couple in approximately the same laser power (∼50% of the incident beam). A USB 2000 fiberoptic spectrometer (Ocean Optics, Dunedin) was used to collect isotropic emissions from the waveguide. Appropriate long-pass optical filters were used to filter out the excitation light. It is important to note that these filters do not affect the specific signal or alter the ratio of observed intensities.

All experiments used 100 nM each of the capture and detector antibodies and PBS-0.5% BSA as the wash buffer, with an injection volume of 200 μL. The flow cells were incubated for 5 min at room temperature and rinsed with approximately 20 flow cell volumes of buffer before measurement (3 s integration) unless otherwise specified. The following experimental groups were assessed: (1) SAMs vs PLBs as the functional surface for detection of CEA using T84.66-NH-AF647; (2) detection of CEA using T84.66-H-AF647 detector antibody; (3) detection of CEA using T84.66-NH-QD655 detector antibody; (4) detection of CEA using T84.66-H-QD655 detector antibody. All experiments were repeated at least twice using SAMs with 1% biotin except experiment 1.

The general experimental design is outlined in Figure 1. The first measurement acquired is the waveguide background, which quantifies a determination of the background fluorescence associated with intrinsic impurities in the waveguide surface.

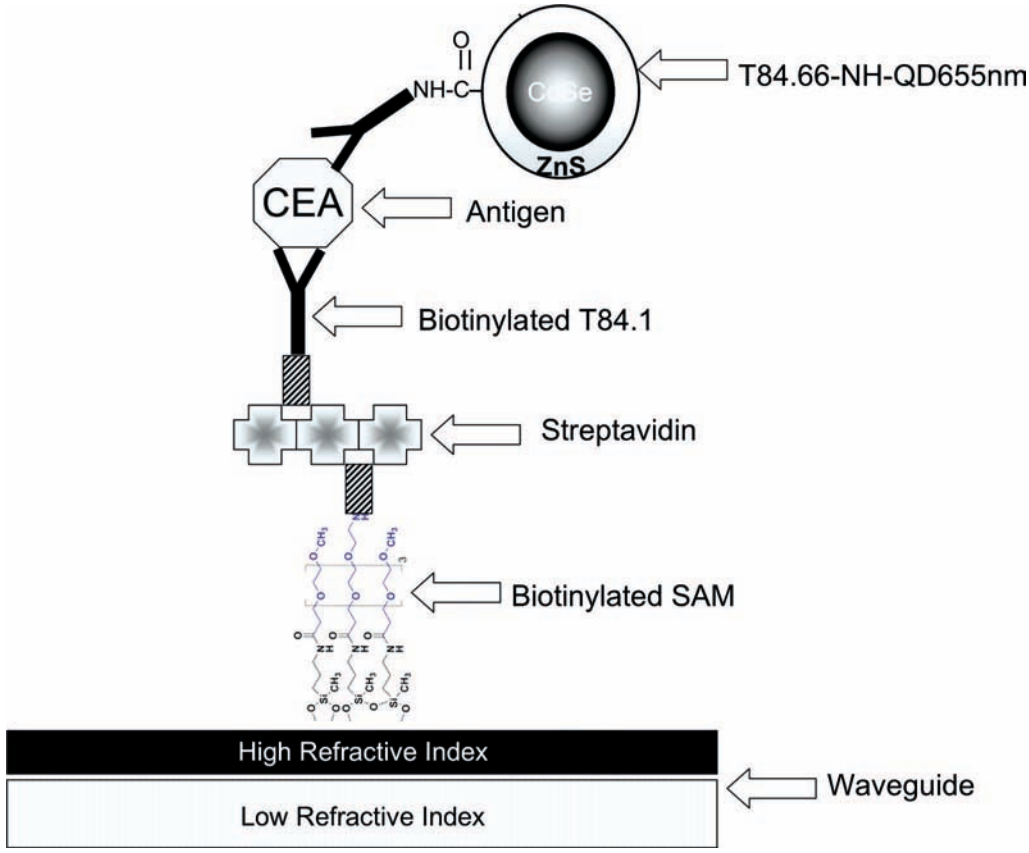

Figure 1. Schematic representation of the sandwich assay for CEA on a functionalized waveguide surface. Surface is functionalized with SAMs containing 1% biotin. Alternatively, PLBs can be used. This illustration depicts a detector antibody labeled with the QD in the NH domain. Both QDs and AF647 have been used for fluorescent labeling. Antibodies can be labeled in the NH domain or in the hinge region. See text for details. Diagram not to scale.

The assay utilizes the well-known biotin−avidin interaction to trap the biotinylated capture antibody to the waveguide surface. For this, the biotin on the PLB or SAM surface is entirely saturated with streptavidin (10 nM). A small concentration of streptavidin (1 pM) is fluorescently labeled with an organic dye (AF647 or 565 depending on the excitation wavelength used). The fluorescent signal (∼200−400 RFU) obtained from this is used as an indicator of system and surface functionality. Fluorescence measurements are relative to the instrument being used. The units reported in this manuscript are as measured on our waveguide-based optical biosensor using an Ocean Optics Spectrometer interface. Fluorescence measurements made using our biosensor will be reported as RFU in this manuscript. This signal is completely removed by repeat excitation with the laser (photobleaching, 15 s) before addition of the capture antibody to avoid skewing the results. Once the capture antibody is trapped, NSB associated with complex fluids is assessed by measuring the autofluorescence of a 50% solution of bovine serum in PBS. Next, the NSB of the fluorescent detector (the fluorescently labeled antibody used that particular experiment) is determined. This measurement is an indication of the nonspecific interaction of the fluorescent detector with the active surface in the absence of the antigen. The NSB signal is completely removed by photobleaching for the organic dyes before specific measurement is made. In the case of photostable QDs, the signal is subtracted from the final specific signal. In either case, repeat additions of the detector to the active surface are made (data not shown) to determine that there is no further increase in NSB.

Assessment of NSB is followed by antigen addition (CEA, 100 pM, 200 μL in PBS with 0.5% BSA). Following antigen incubation and wash, the detector antibody (100 nM, 200 μL in PBS) is added. Specific binding of the detector to CEA (effective sandwich) results in a positive signal, which is measured. Repeat excitations are performed to measure photostability.

RESULTS

CEA Detection Using T84.66-NH-AF647 Detector Antibody on a SAM vs PLBs. Figure 2A demonstrates detection of CEA (100 pM, 200 μL) on a SAM surface without any blocking. A signal of 3636 RFU over a waveguide background of 8 results in a S/B of 483. The NSB associated with 50% serum is 69 RFU, whereas that associated with the detector antibody is 193. In contrast, the S/B for the same assay using a PLB surface without blocking (Figure 2B) is only 44 (specific signal of 1143 over a background of 26 RFU). Some of the difference in measured S/B is attributed to the lower intrinsic background of some waveguides compared to the others. Yet, the NSB associated with serum (115 RFU) and the fluorescent detector (238 RFU) are also higher than that seen with SAMs, and the specific signal is greatly compromised with the use of PLBs. Assay performance on PLBs is dramatically improved when the defect sites in the bilayer that presumably give rise to NSB are preblocked with PBS containing 2% BSA for 2 h before use (Figure 2C). A S/B of 74 is realized (specific signal of 3030 RFU over a background of 41 RFU). When the PLBs are blocked, NSB associated with serum and detector antibody are both lower than seen in the absence of blocking, which is consistent with our previous results against other targets (*5*, *7*). However, the assay performance is still poorer than that achieved with the use of SAMs.

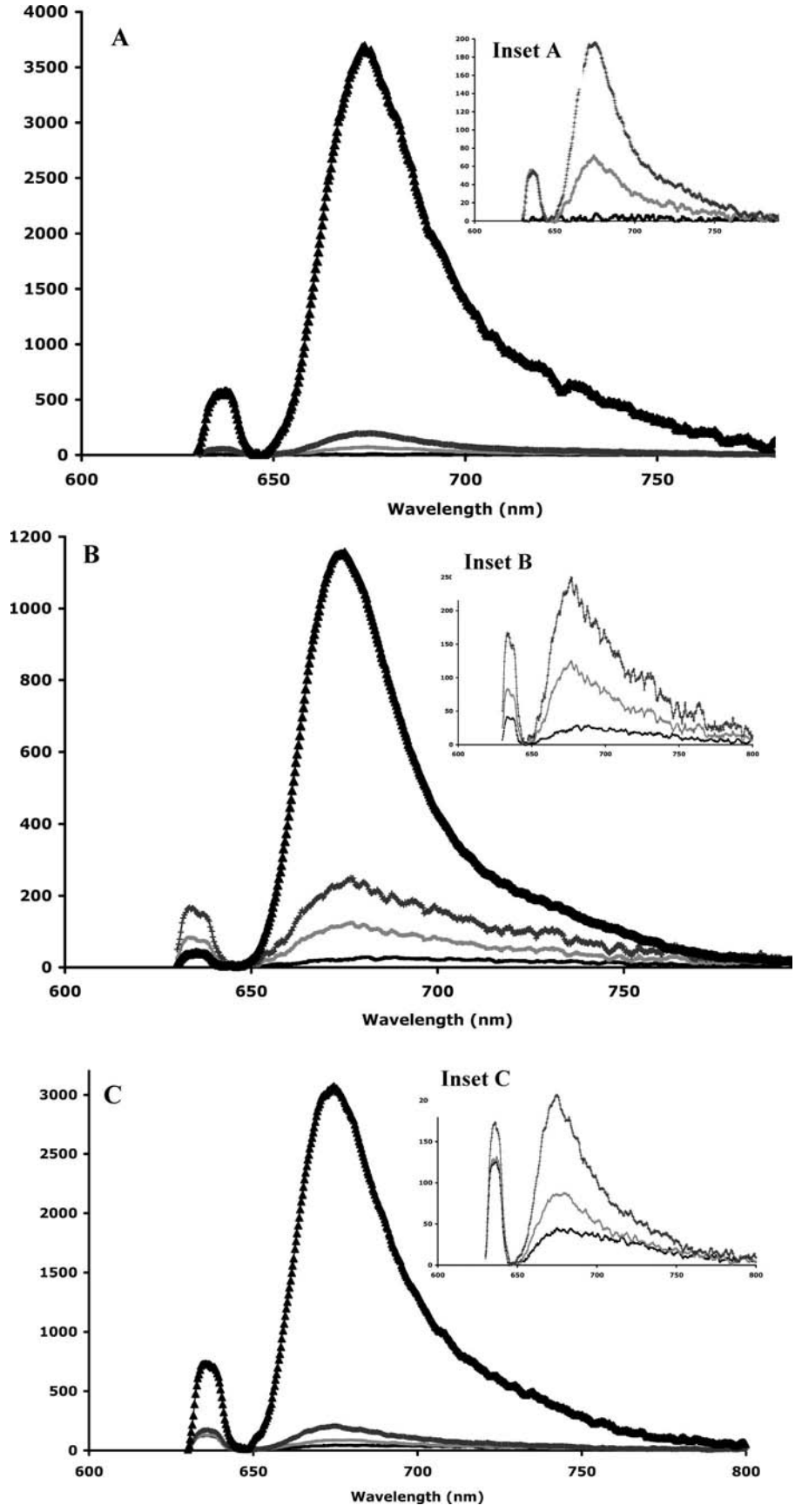

Figure 2. Determination of optimal surface for waveguide functionalization. CEA [100 pM] detection using T84.66-nH-AF647 detector antibody on a (A) SAM surface with 1% biotin, (B) PLB with 1% biotin without blocking, and (C) PLB with 1% biotin and blocking with PBS containing 2% BSA. Data are plotted as relative fluorescence units as a function of wavelength. Assay performance on a SAM surface (A) gives the maximal signal/background (483) and lowest NSB (69 RFU) for 100 pM CEA. Insets (in each graph) are an enlarged representation of the waveguide background and nonspecific binding curves redrawn for clarity. Key: Boxed squares (■) indicate waveguide background, gray circles (•) indicate nonspecific background associated with serum. + indicates detector associated nonspecific binding. Black triangles (▲) indicate specific signal with the addition of 100 pM CEA.

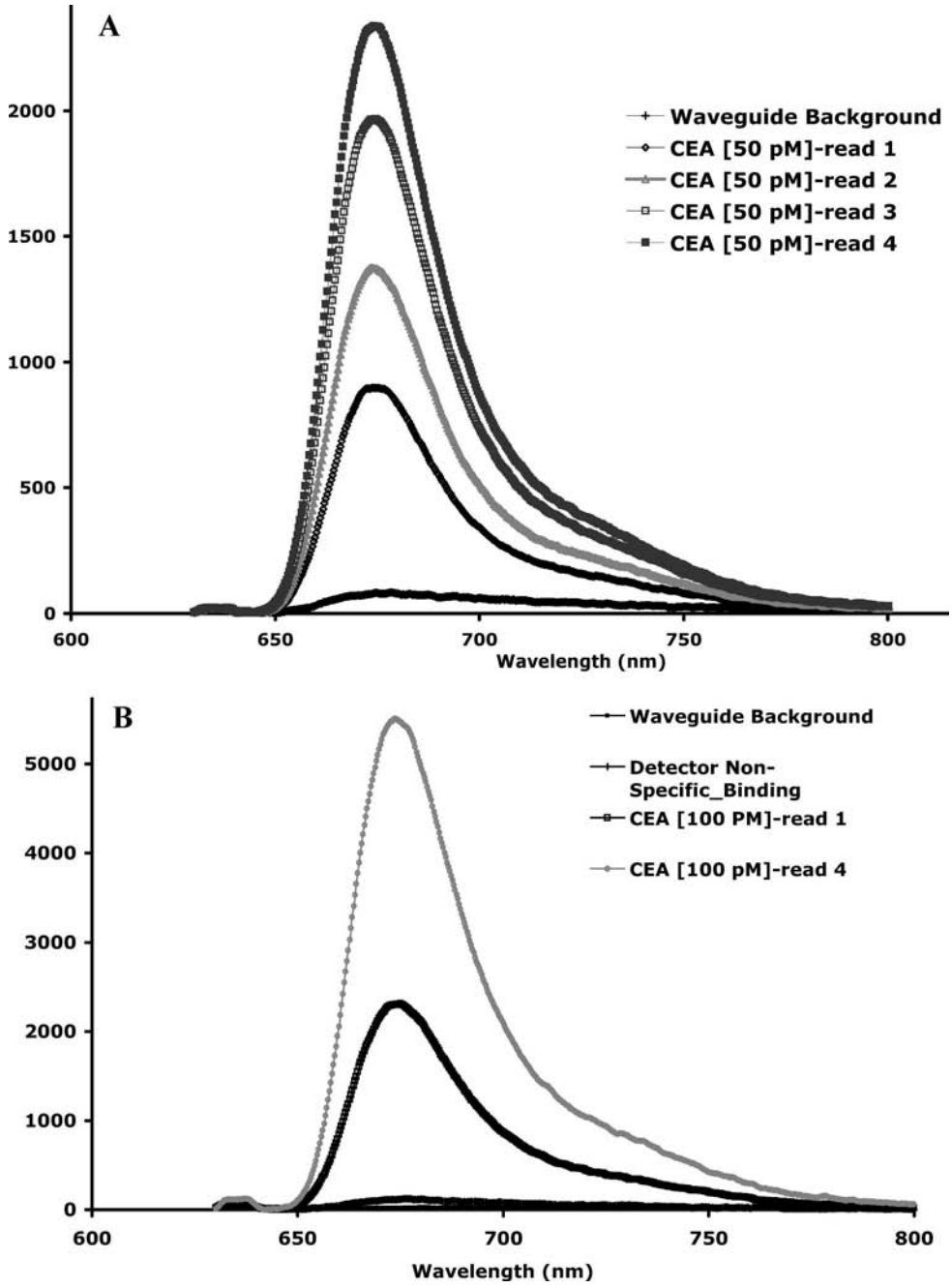

Figure 3. Unusual signal amplification using T84.66-H-AF647. Hinge labeling of the detector antibody with AF647 resulted in unusual signal amplification with repeat excitation (A). The amplitude of the measured signal almost doubled (over an unchanged background) after 4 repeat excitations. Figurer 3B demonstrates the initial (read 1, S/B of ~11) and final (read 4, S/B of 82) signals observed with [100 pM] CEA using this detector antibody.

Table 1. Summary of Measured Signal Intensity at Different Concentrations of CEA Using the Waveguide-Based Optical Biosensor[a]

[CEA] pM	signal (3 s) (RFU)	max signal (RFU)	integration time (s)	S/B (3 s)	S/B (12 s)
Bg	31.97 ± 8				
NSB	75 ± 14				
1	118.27	154.87	6	3.7	4.8
50	1212.6	2767.8	12	37.9	86.6
100	2302.72	5474.85	12	72.0	171.2
200	3033.08	6033.08	18	94.9	188.7

[a] T84.66-H-AF647 was used as the detector antibody.

Unusual Signal Amplification using T84.66-H-AF647 as the Detector. Hinge labeling of the detector antibody resulted in unusual signal amplification with repeat excitation (3 s integration each, Figure 3). Figure 3A demonstrates this increase in signal amplitude with repeat excitation in the detection of 50 pM CEA using T84.66-H-AF647. The initial signal (read 1) measured is 893 RFU over a waveguide background of 80 RFU, resulting in a S/B of 11.2. The amplitude of the measured signal increases to 1365 RFU (read 2) with repeat excitation corresponding to a S/B of 17 for the same concentration of CEA. The maximum signal measured for 50 pM CEA in this labeling format is 2320 RFU (read 4) resulting in a S/B of 29. Subsequent excitation results in photobleaching (data not shown). The exact reasons for this response are unclear but potential explanations are outlined in the Discussion. Figure 3B demonstrates signal obtained during the detection of CEA (100 pM) using this labeling strategy. An "initial" signal of 2303 RFU (read 1) over a waveguide background of 28 RFU corresponds to a S/B of

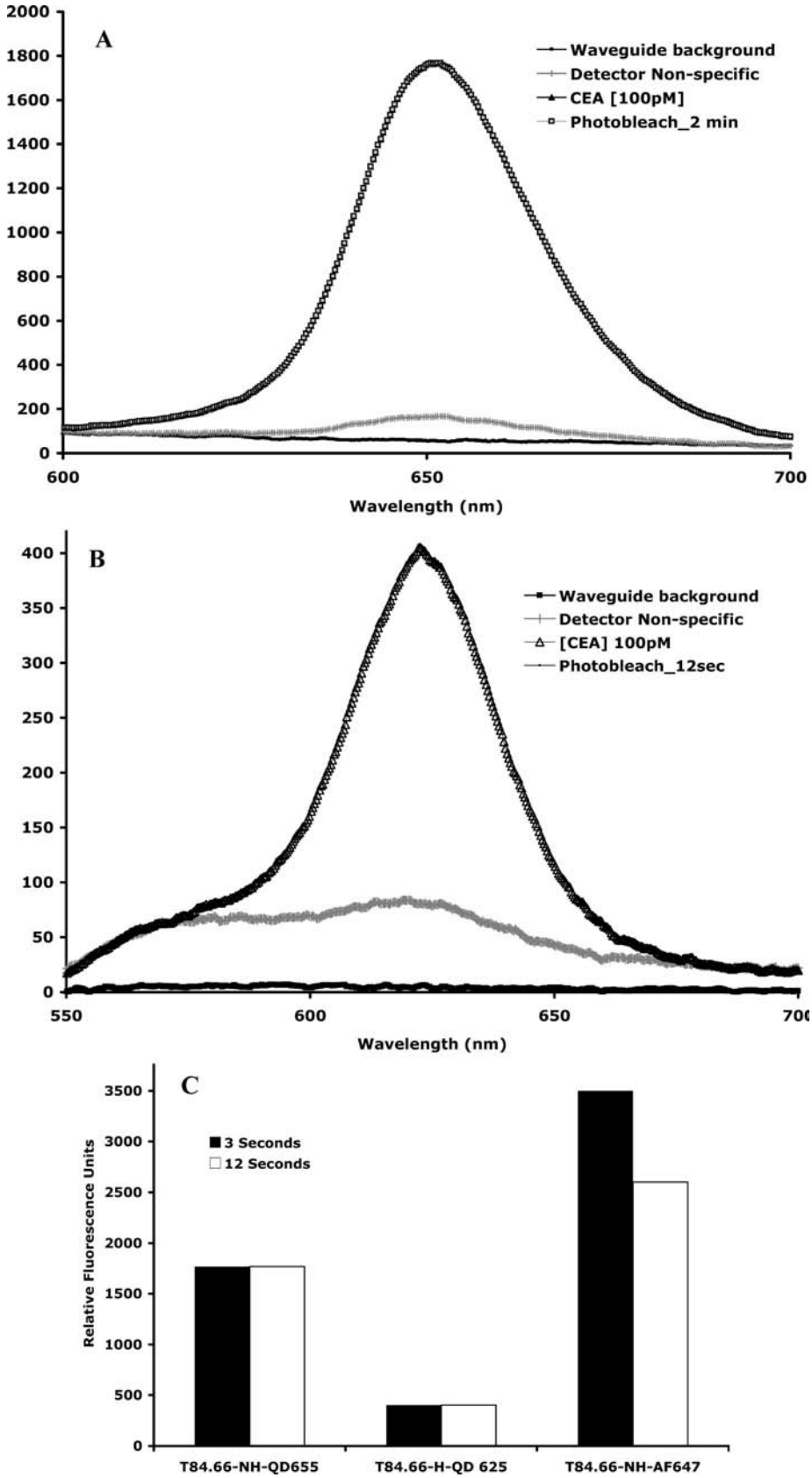

Figure 4. Detection of CEA using QD labeled antibodies. Both NH (QD655, A) and hinge (QD625, B) labeled antibodies were evaluated for the detection of 100 pM CEA. Whereas observed S/B is lower compared to that reported in Figure 2A, there is no photobleaching of the observed fluorescence after 2 min of excitation with the laser (C). As indicated in part C, the signal remains stable following 3 and 12 s of exposure to the laser when the antibody is labeled with QDs, whereas a significant decrease in intensity is seen when the antibody is labeled with AF647. Key: Boxed squares (■) indicate waveguide background, gray circles (•) indicate photobleaching after 12 s of exposure. + indicates detector associated nonspecific binding. Black triangles (▲) indicate specific signal with the addition of 100 pM CEA.

82, which is similar to that obtained with T84.66-NH-AF647 detector (Figure 2C, curve 1) for the same concentration of CEA. Repeat excitation resulted in increase in signal and a maximum signal intensity of 5498 RFU (read 4, S/B of 195), which is much higher than was observed with T84.66-NH-AF647 under similar experimental conditions. There is no increase in the detector antibody associated NSB with repeat excitation (6 repeats, 100 nM antibody in each addition, data not shown).

Table 1 summarizes signal amplification at different concentrations of CEA. The data was obtained from different waveguides, which explains the lack of absolute linearity in measured signals. The waveguide background and NSB values are averages of those obtained in the different experiments (all numbers were within the expected range). Repeat excitation of the fluorescent detector results in signal amplification in each case. Note that the excitation time required to achieve maximum signal is dependent on antigen concentration. Whereas the signal maximizes in 6 s with 1 pM CEA, it takes 18 s of excitation with 200 pM CEA. After the maximum signal is reached, photobleaching commences in each case. Thus, the maximum S/B obtained with any given concentration of CEA is significantly increased using this labeling strategy. Because the number of excitations required is dependent on the CEA concentration, it is difficult to use this approach for quantitative detection in unknown samples. However, this strategy could be advantageous in a purely qualitative test.

Detection of CEA Using QD Labeled Antibodies. Both NH (655 nm QD) and hinge (625 nm QD) labeling of T84.66 with QDs were evaluated. Figure 4A shows the signal obtained for the detection of 100 pM of CEA using 100 nM of T84.66-NH-QD655. A signal intensity of 1767 RFU is observed over a NSB (associated with detector antibody) of 167 RFU. Upon correction for NSB, a S/B of 3 is obtained. There is no apparent photobleaching observed despite 2 min excitation with the laser (532 nm) followed by a single reading at 3 s integration. We also evaluated hinge labeling of the detector antibody (Figure 4B). The observed signal intensity (402) was much lower than that seen with the other labeling paradigms, but the NSB and waveguide background were also lower. When corrected for NSB, a S/B of ~55 is evidenced for this labeling strategy. Again, the observed signal was extremely photostable, and there was no decrease in signal intensity following a 2 min excitation. A comparison of initial signals and the signal after 12 s exposure is shown in Figure 4C. Up to 10 μM of free QDs does not contribute to any measurable signal (data not shown).

DISCUSSION

This study addresses the surface and antibody labeling strategies to improve our current test for CEA. Generally, biodetection using the optical biosensor requires functionalization of the waveguide with a surface that allows for conjugation of antibodies or other recognition ligands. We have previously demonstrated the use of PLBs for waveguide functionalization and sensitive detection of CEA (*6*) (unpublished data). These surfaces are composed of lipid molecules, which make up all biological membranes. These structures are responsible for the selective permeability of cells, a factor that contributes to the low NSB associated with their use in most in vitro studies. In addition, bilayers are inexpensive, easy to prepare, and are well-suited for ligand attachment. However, lipid bilayers are unsuitable for a point-of-care diagnostic setting because they cannot endure prolonged storage (>1 week), harsh environments such as elevated temperatures, or passage through an air−water interface. Furthermore, high concentrations of lipids or urea in some biological samples (such as urine) results in elevated NSB, which limits the successful application of PLBs to biodiagnostic approaches. To overcome these disadvantages, we utilized PEG-modified, silane-based thin films. These coatings facilitate covalent attachment and chemical flexibility, and minimize NSB. We have previously demonstrated the application of these surfaces to the sensitive detection of the *Bacillus anthracis* protective antigen. Alkane SAMs terminated with PEG groups have been used for minimizing NSB (*8*). Concurrent with these results, use of SAMs as the functional surface in our assay abrogates the necessity for blocking. As shown in Figure 2A,B, lack of blocking diminishes the signal resolution obtained with PLBs as the functional surface, but it does not adversely affect functionality of the SAMs (data not shown).

Antibodies labeled with fluorescent dyes are inherently more stable. Of such dyes, long wavelength dyes (such as AF647) have lower background fluorescence (*18*−*20*). Alexa Fluor dyes are suited for bioapplications because of their brightness, photostability, water solubility, and pH compatibility. AF647, in particular, shows relatively small change in the fluorescence spectra and intensity when conjugated to antibodies in contrast with other dyes such as Cy5 (*20, 22*). Following this reasoning, we selected AF647 for our experimental setup. As indicated in Figure 2, use of T84.66-NH-AF647 as the labeled reporter antibody results in a significant S/B with 100 pM of CEA. There is a 15−20% decrease in signal with repeat excitation (photobleaching) as is typically expected from such dyes.

We also explored labeling T84.66 with AF647 in the hinge region. Labeling in this area is advantageous, since it directs the modification away from the antigen-binding region. This can be especially critical for larger reporters such as QDs. Mild reduction allowed for the generation of two half-antibody fragments containing free sulfhydryl groups in the hinge region. The fluorescent dye was then conjugated to the hinge region. When used as the detector for CEA, however, this material resulted in unusual signal enhancement (rather than photobleaching) with repeat excitation. It has been demonstrated that AF647 is more photostable and resistant to fluorescence quenching (at optimal degree of labeling) upon protein conjugation (*20, 22*). But the novel signal increase reported here is unprecedented. This antibody had 4 mol of AF647 per mole of protein, which is an optimal degree of labeling, according to the manufacturer. We have separated the labeled antibody from free AlexaFluor dye by gel filtration. In any case, we have also tested NSB associated with free AF647 in our assay and found no increase in fluorescence (data not shown). We speculate that, since multiple AF647 molecules are associated with a single antibody, some dye molecules are excited only after the fluorescence associated with others is quenched. This phenomenon, in combination to the relative photostability of AF647 dyes, could result in an increase in fluorescence. These hypotheses may explain why the increase in fluorescence is proportional to the concentration of the antigen, and hence the concentration of detector antibody in the system. Why this does not occur with T84.66-NH-AF647 (which also has ~4 mol of the dye/mol of protein) is, however, unclear. A possible explanation involves the conformation of the antibody when labeled in the hinge region, which allows for fluorescence quenching and subsequent photon release. It is apparent that the unusual signal amplification allows for a better S/B with lower concentrations of the antigen. This feature may be advantageous in attempting to develop a point-of-care diagnostic for breast cancer, especially in low volume samples such as NAF. However, since the degree of excitation and extent of amplification are dependent on the antigen concentration, quantitation of this phenomenon is not easy. This is a disadvantage for cancer detection, because most tumor biomarkers are normally expressed in the body at basal concentrations, even without cancer present. Therefore, a test for cancer should be quantitative for accurate diagnosis. This labeling strategy does

have potential for applications where a yes/no answer is adequate, e.g., infectious diseases like tuberculosis.

No single biomarker is an accurate indicator of cancer. Therefore, an efficient diagnostic strategy should be able to detect multiple biomarkers in a single sample. To achieve this eventuality, we explored the use of QD labeled antibodies as a fluorescence detector in our assay system.

In this manuscript, we evaluated both NH and SH labeling of antibodies. Both strategies allowed for the detection of CEA at a concentration of 100 pM, although the S/B was lower than that seen with T84.66-NH-AF647. The signal intensity measured with hinge labeling (Figure 4B) is lower than that seen with primary NH labeling (Figure 4A). However, the NSB is also lower. Therefore, the extrapolated S/B is comparable in both labeling strategies. Also, the observed signal is stable for over 2 min of excitation with the laser (Figure 4), a time over which signal from AF647 would be almost entirely photobleached. This photostability of core−shell quantum dots is a distinct advantage for multiplex detection as well, especially in attempting to engineer a multichannel sensor for simultaneous detection. It is also possible to envision an internal photostable standard (in lieu of streptavidin-AF647) that is used for both system functionality assessment and quantitation of antigen in unknown samples (unpublished data) (*6*).

To conclude, we have improved a sandwich assay for CEA on our waveguide-based OB by incorporating better surfaces and photostable detectors. These modifications will enable our biosensor to function as a robust research tool to probe biological interactions or as a point-of-care diagnostic method to detect a variety of disease targets.

ACKNOWLEDGMENT

The authors thank Karen Grace, Sohee Jeong, and Jennifer Martinez at the Los Alamos National Laboratory for help with waveguide instrumentation and helpful suggestions. This work was supported, in part, by a Los Alamos National Laboratory directed research (LDRD) grant.

LITERATURE CITED

(1) www.mayoclinic.com/health/breast_self_exam/WO00026.

(2) Berlin, L. (2001) The missed breast cancer redux: Time for educating the public about the limitations of mammography? *AJR 176*, 1131–1134.

(3) Hoisington, L. A., Scherer, D. L., and Berger, K. L. (2007) Breast MR imaging: applications and pitfalls. *Radiol. Technol. 78* (5), 367–377.

(4) Duff, M. J. (2006) Serum tumor markers in breast cancer: are they of clinical value? *Clin Chem. 52*, 345–351.

(5) Martinez, J. S., Grace, W. K., Grace, K. M., Hartman, N., and Swanson, B. I. (2005) Pathogen detection using single mode planar optical waveguides. *J. Mater. Chem. 15*, 4639–4647.

(6) Mukundan, H., Holt, A., Martinez, J. M., Kubicek, J., Shively, J. E., and Swanson, B. I. Planar optical waveguides for detection of tumor biomarkers, *Sens. Actuators*, in revision, 2008.

(7) Kale, R., Mukundan, H., Price, D., Foster-Harris, J., Lewallen, D. M., Swanson, B. I., Schmidt, J. G., and Iyer, S. S. (2008) Detection of intact influenza viruses using biotinylated biantennary S-sialosides. *J. Am. Chem. Soc. 130* (26), 8169–8171.

(8) Anderson, A. S., Dattelbaum, A. M., Montano, G. A., Price, D., Schmidt, J., Martinez, J. M., Grace, W. K., Grace, K., and Swanson, B. I. (2008) Functional PEG-modified thin-films for biological detection. *Langmuir 24* (5), 2240–2247.

(9) Pinaud, F., Michalet, X., Bentolila, L. A., Tsay, J. M., Doose, S., Li, J. J., Iyer, G., and Weiss, S. (2006) Advances in fluorescence imaging with quantum dot bio-probes. *Biomaterials 27* (9), 1679–87.

(10) Alivisatos, A. P. (1996) Semiconductor clusters, nano crystals and quantum dots. *Science 271* (5251), 933–937.

(11) Michalet, X., Pinaud, F., Bentolila, L. A., Tsay, J., Doose, S., Li, J., Sundaresan, G., Wu, A. M., Gambhir, S. S., and Weiss, S. (2005) Quantum dots for live cells and *in vivo* imaging, diagnostics and beyond. *Science 307* (5709), 538–544.

(12) Medintz, I. L., Uyeda, H. T., Goldman, E. R., and Matoussi, H. (2005) QD bioconjugates for imaging, labeling and sensing. *Nat. Mater. 4* (6), 435–446.

(13) Gao, X., Yang, L., Petros, J. A., Marshall, F. F., Simons, J. W., and Nie, S. (2005) In vivo molecular and cellular imaging with quantum dots. *Curr. Opin. Biotechnol. 16* (1), 63–72.

(14) Murray, C. B., Norris, D. J., and Bawendi, M. G. (1993) Synthesis and characterization of nearly monodisperse CdE (E = sulfur, selenium, tellurium) semiconductor nanocrystallites. *J. Am. Chem. Soc. 115*, 8706–8710.

(15) Hines, M. A., and Guyot-Sionnest, P. (1996) Synthesis and characterization of strongly luminescing ZnS-capped CdSe nanocrystals. *Phys. Chem. 100*, 468–471.

(16) Mattoussi, H., Mauro, J. M., Goldman, E. R., Anderson, G. P., Sundar, V. C., Mikulec, F. V., and Bavendi, M. G. (2000) Self assembly of CdSe-ZnS quantum dot bioconjugates using an engineered recombinant protein. *J. Am. Chem. Soc. 122*, 12142–12150.

(17) Gunsalus, C., Barton, L. S., and Gruber, W. (1956) Biosynthesis and structure of lipoic acid derivatives. *J. Am. Chem. Soc. 78*, 1763.

(18) Flanagan, J. H., Jr., Khan, S. H., Menchen, S., Soper, S. A., and Hammer, R. P. (1997) Functionalized tricarbocyanine dyes as near-infrared fluorescent probes for biomolecules. *Bioconjugate Chem. 8* (5), 751–756.

(19) Haugland, R. P. (2002) *Handbook of Fluorescent Probes and Research Products*, Molecular Probes Inc., Eugene, OR.

(20) Berlier, J. E., Rothe, A., Buller, G., Bradford, J., Gray, D. R., Filanoski, B. J., Telford, W. G., Yue, S., Liu, J., Cheung, C. Y., Chang, W., Hirsch, J. D., Beechem, J. M., and Haugland, R. P. (2003) Quantitative Comparison of Long-wavelength Alexa Fluor Dyes to Cy Dyes: Fluorescence of the Dyes and Their Bioconjugates. *J. Histochem. Cytochem. 51* (12), 1699–1712.

(21) Randolph, J. B., and Waggoner, A. S. (1997) Stability, specificity and fluorescence brightness of multiply-labeled fluorescent DNA probes. *Nucleic Acids Res. 25* (14), 2923–2929.

(22) Gruber, H. J., Hahn, C. D., Kada, G., Riener, C. K., Harms, G. S., Ahrer, W., and Dax, T. G. (2000) Anomalous fluorescence enhancement of Cy3 and Cy3.5 versus anomalous fluorescence loss of Cy5 and Cy7 upon covalent linking to IgG and noncovalent binding to avidin. *Bioconjugate Chem. 11*, 696–704.

BC800283E

Subscriber access provided by SHEMYAKIN-OVCHINNIKOV INST

Article

Versatile Cyclic Templates for Assembly of Axially Oriented Ligands

Neeraj Chopra, Wenxun Gan, Hans Schreiber, Josh W. Kurutz, and Stephen C. Meredith

Bioconjugate Chem., **2009**, 20 (2), 231-240• DOI: 10.1021/bc800312x • Publication Date (Web): 21 January 2009

Downloaded from http://pubs.acs.org on May 8, 2009

More About This Article

Additional resources and features associated with this article are available within the HTML version:

- Supporting Information
- Access to high resolution figures
- Links to articles and content related to this article
- Copyright permission to reproduce figures and/or text from this article

View the Full Text HTML

ACS Publications
High quality. High impact.

Bioconjugate Chemistry is published by the American Chemical Society. 1155 Sixteenth Street N.W., Washington, DC 20036

Versatile Cyclic Templates for Assembly of Axially Oriented Ligands

Neeraj Chopra,[§] Wenxun Gan,[‡] Hans Schreiber,[§] Josh W. Kurutz,[†] and Stephen C. Meredith*[,§,†]

Departments of Pathology, Chemistry, and Biochemistry and Molecular Biology, The University of Chicago, Chicago, Illinois.
Received July 21, 2008; Revised Manuscript Received November 12, 2008

In this paper, we describe two novel types of planar cyclic peptide templates for the facile addition of ligands that extend axially from the plane of the template ring. The first uses β-amino acids of alternating D- and L-chirality, since the insertion of the additional methylene group in the peptide backbone was predicted and subsequently shown by NMR and molecular modeling, to reorient ligands attached to amino acid side chain axially with respect to the template ring. A second contains alternating D- and L-amino acids with an achiral Gly residue interposed between each chiral amino acid. The inserted Gly residues also tend to reorient side chains axially rather than radially, as was demonstrated by NMR and molecular modeling. The axial orientation of attached ligands is intended to foster or allow interactions among attached ligands in situations in which this is desired. Two such situations that we consider are (1) development of immunological reagents with avidity effects and (2) modeling of oligomers in fibril-forming peptides. Toward the first of these goals, we demonstrated that these templates are suitable for attaching macromolecules, by incorporating two types of protein, neutravidin and trypsinogen. Toward the second goal, we demonstrate the attachment of two different fibril-forming peptides to the template. The templates described herein thus have many of the desirable traits of such molecules, i.e., (1) multivalency for the attachment of multiple ligands, (2) suitable chemical functions for facile attachment of ligands, (3) versatility as to the number and spacing of ligand attachment sites, (4) sufficient rigidity so that the attached ligands can be similarly oriented with respect to the template, and (5) sufficient flexibility to allow even large ligands, such as proteins, to attach and interact.

INTRODUCTION

Cyclic peptides and their peptidomimetic homologues are versatile molecules with distinctive self-assembly properties. The concept of template-assisted peptide synthesis (TASP) was introduced and first developed by Mutter and colleagues (*1*−*3*) (see also *refs 4*−*11* for review and more recent examples). Ghadiri and co-workers described planar, cyclic peptides containing alternating D- and L-amino acids that self-assemble into tubular structures with a β-sheet-like structure. The planarity of the rings derives from the cancellation of the innate twists of the β-strands by the alternation of D- and L-amino acids (*12, 13*). Some of these compounds have antibacterial activity because of their ability to stack into nanotubes that insert into bacterial membranes (*14*−*16*), while others self-assemble into artificial transmembrane ion channels (*17, 18*). In addition to these properties attributable to self-assembly, cyclic peptides and peptidomimetics can also serve as templates for attaching and assembling a wide variety of ligands (*10, 11, 19*−*27*).

In the templates designed by Ghadiri et al. (*12*−*17*), the amino acid side chains are oriented radially from the ring, which, depending on the nature of the side chains, can either promote or prevent lateral association of the rings. In addition, the rigidity and β-sheet-like structure render these molecules prone to self-association into tubular aggregates, unless measures are taken to prevent this, such as N-methylation (*28*). As schematized in Figure 1A, the radial orientation of side chains would also orient any ligands attached to these side chains radially, which therefore tends to prevent interactions among these ligands.

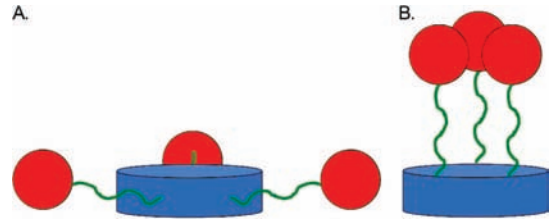

Figure 1. Schematic depiction of planar cyclic peptide templates. Peptides made of alternating D- and L-α-amino acids, such as those described by Ghadiri and colleagues (*12*−*17*) have been observed to project their side chains radially, as depicted in (A). The use of alternating D- and L-β-amino acids (chiral α-carbon atom) or the addition of an odd number of atoms between alternating D- and L-α-amino acids, is predicted to project the side chains axially, as depicted in (B).

There are situations, however, in which it would be desirable to promote interaction among ligands attached to a template. Two such instances are (1) attachment of high-affinity single-chain antibodies fragments (scFv molecules) and high-affinity single-chain T-cell receptors (scTCR) "payloads", in which avidity effects are desirable; and (2) controlled modeling of intermediates in the formation of amyloid fibrils. In both of these cases, it would be desirable to orient ligands attached to amino acid side chains oriented axially rather than radially, as demonstrated schematically in Figure 1B. The incorporation of amino acids with reactive side chains into the template could allow facile attachment of protein or other ligands to the ring.

For these reasons, we have developed two strategies for synthesizing cyclic planar templates with axially oriented side chains. In addition to allowing interactions among attached ligands, we also reasoned that such templates would also have a reduced tendency toward aggregation into tubular β-sheet-like structures than previously described structures. The two strategies are the following:

* To whom correspondence should be addressed: The University of Chicago, 5841 S. Maryland Ave., Chicago, IL 60637, U.S.A. Fax: (+1) 773-834-5251. E-mail: scmeredi@uchicago.edu. Phone: 773-702-1267.
[§] Department of Pathology.
[‡] Department of Chemistry.
[†] Department of Biochemistry and Molecular Biology.

10.1021/bc800312x CCC: $40.75 © 2009 American Chemical Society
Published on Web 01/21/2009

(1) We have synthesized cyclic peptides containing β-amino acids with alternating D- and L- chirality about the α-carbon atom, i.e., amino acids containing an "extra" methylene carbon atom in the backbone chain. Preliminary modeling studies suggested that the insertion of this additional odd-numbered atom into the backbone chain would have the effect of reorienting the side chains axially with respect to the template backbone, as opposed to radially. For brevity, these templates will be referred to as type 1 axial templates.

(2) We have also synthesized cyclic peptides that retain the alternation of D- and L-α-amino acids, but insert the nonchiral amino acid, glycine, between each of the chiral amino acids. Like the scheme above using β-amino acids, preliminary modeling studies suggested that the addition of glycine would have the effect of reorienting side chains axially. In addition, the insertion of glycines in this manner would also impart additional flexibility to the ring, in those cases in which such flexibility is needed to allow interactions between ligands attached to the side chains. For brevity, these templates will be referred to as type 2 axial templates.

In this paper, we describe the synthesis and structural characterization of these two types of templates and the facile attachment of protein ligands to reactive amino acid side chain groups. Ideally, such templates should have the following characteristics: (1) multivalency for the attachment of multiple ligands; (2) suitable chemical functions for facile attachment of ligands; (3) versatility as to the number and spacing of ligand attachment sites; (4) sufficient rigidity so that the attached ligands can be similarly oriented with respect to the template; and (5) sufficient flexibility to allow even large ligands, such as proteins, to attach and interact. Since these ligands could include scFv and scTCR molecules, the template should be flexible enough to allow avidity effects to occur and, in the case of fibril-forming peptide, to allow for conformational rearrangements to occur. We will show, below, that the templates significantly satisfy these criteria.

EXPERIMENTAL PROCEDURES

Materials. Boc-Leu-OCH_2-PAM resins, Boc-amino acids, *S*-trityl-β-mercaptopropionic acid and 2-(1*H*-benzotriazol-1-yl)-1,1,3,3-tetramethyluroniumhexafluorophosphate (HBTU) were from Peptides International. Benzotriazole-1-yl-oxy-tris-(dimethylamino)-phosphonium hexafluorophosphate) (BOP) and *N*-α-Fmoc-L-aspartic acid β-4-{*N*-[1-(4,4-dimethyl-2,6-dioxocyclohexylidene)-3-methylbutyl]-amino} benzyl ester (α-Fmoc-β-ODMAB-Asp) were from Novabiochem. 4-Dimethylaminopyridine (DMAP) was from Aldrich. *N*-α-Boc-*N*-β-Fmoc-D-2,3-diaminopropionic acid (α-Boc-β-Fmoc-D-DAP) was from ChemImpex, Inc. *N*-α-Fmoc-L-aspartic acid α-*t*-butyl ester (Fmoc-Asp-α-OtBu) was from Bachem International. All other amino acids were from Novabiochem, Applied Biosystems, Midwest Biotech, or Anaspec. *N*,*N*-Diisopropylethylamine (DIEA) was obtained from Applied Biosystems. *N*,*N*-Dimethylformamide (DMF), dichloromethane (DCM), diethyl ether, HPLC-grade acetonitrile, and guanidine hydrochloride were from Fisher Chemicals. Trifluoroacetic acid (TFA) was obtained from Halocarbon Products. HF was from Matheson.

Peptide Synthesis and Purification. Most peptides and peptide-α-thioesters were made manually by solid-phase peptide synthesis using tBoc chemistry with "in situ neutralization", essentially as described previously (*29, 30*). In general, after chain assembly was complete, peptides were simultaneously deprotected and cleaved from the resin by treatment with anhydrous HF containing *p*-cresol (90:10, v/v) for 1 h at 0 °C. After evaporation of the HF under reduced pressure, crude products were precipitated and triturated with chilled diethyl ether, and the peptide products were dissolved in 50% aqueous acetonitrile and purified, or lyophilized for storage.

For synthesis of peptides with β-peptide bonds, i.e., Peptides 1, C1, and C1-Mal and its derivatives, we used standard FMOC chemistry to form β-peptide bonds using the reagents described above. PAM resin was activated with 1 mmol of α-FMOC-β-ODmab-Asp and 10% (w/v) 4-(dimethylamino)pyridine (DMAP), essentially as described (*31*−*33*), so that this amino acid was immobilized to the resin through its α-carboxyl group. For the cyclization reaction, the DMAB group was removed by three 20 min incubations with 2% hydrazine (v/v), followed by three washes with 5% DIEA (v/v). The cyclization reaction was carried out using BOP at 22 °C for 36 h, followed by HOBt/DIC/DIEA for 48 h. Maleimide hexanoic acid (Sigma Chemicals) was added to the N-terminus or to DAP side chains of selected peptides (described below) by the usual coupling method, prior to HF cleavage.

Crude peptides were purified by RP-HPLC on a preparative C18 (Zorbax) column using gradients of water (0.1% TFA, v/v) and acetonitrile (0.1% TFA, v/v). In some cases, isocratic mixtures of water and acetonitrile (0.1% TFA, v/v) were needed instead of gradients for peptides that were difficult to purify. Peptide purity was typically greater than 97% by analytical RP-HPLC (Supporting Information, Figure S1). The molecular masses of the peptides were verified by ESI and MALDI-TOF mass spectrometry.

Electron Microscopy. Peptide solutions were adsorbed onto a glow-discharged, 400-mesh, carbon-coated support film and stained with 1% uranyl acetate. Micrographs were recorded using a FEI Tecnai F30st-STEM Microscope at magnifications of 15 000×, 39 000×, and 98 000×.

Circular Dichroism. Circular dichroic (CD) spectra were collected using an Aviv model 202 CD spectrophotometer (Lakewood, NJ) equipped with a temperature-controlled holder. Peptides were dissolved in 10 mM sodium phosphate, pH 7.40. A 1 or 10 mm path length was used for the measurements, which were collected at 0.2−0.5 nm intervals from 260 to 190 nm, with a 1 s averaging time and a 1 nm bandwidth. Five scans were collected, and the data were averaged and baseline-corrected.

NMR. NMR was performed at 14 °C using a 600 MHz Varian Unity Inova spectrometer equipped with a cryogenic probe. Peptide concentration was ∼3.1 mM in 100 mM sodium phosphate, pH 4.52. A 1.0 mM solution of sodium 2,2-dimethyl-2-silapentane-5-sulfonate (DSS, Cambridge Isotope Laboratories) was used for external chemical shift referencing. Two-dimensional experiments included TOCSY and NOESY for spin assignments, CT-COSY for measurement of $^3J_{NH\alpha}$.

Molecular Dynamics Simulations. The initial coordinates of cyclic peptides were modeled using the *Chem3D* program. Hydrogen atoms were built to the initial structure using the HBUILD module of the CHARMM molecular simulation program (*34*). The all-atom structure was then solvated in a $38.7 \times 38.7 \times 38.7$ Å^3 cubic solvent box with TIP3P (*35*) water so that water extended at least 10 Å away from the surface of the peptide. Four Na^+ ions and seven Cl^- ions were added to the system to neutralize the charge of the peptide. Periodical boundary conditions were applied with the images generated by the CRYSTAL module in CHARMM. Covalent bonds involving hydrogen atoms were constrained with SHAKE (*36*), and the particle mesh Ewald (PME (*37*)) was used to treat long-range electrostatic interactions. After an initial minimization of the system, MD simulations were performed for 1 ns at a constant temperature of 300 K using the CHARMM version 33a2 with the CHARMM27 force field (*38*).

RESULTS

Design and Synthesis of Cyclic Template Peptides. A list of the peptides synthesized for these studies is given in Table

Table 1. Peptides Synthesized for These Studies

name	sequence
Peptide 1	(α-Boc-^{D}DAP-α-tBu-Asp)$_2$-α-Boc-^{D}DAP-Asp(α-PAM Resin)
Peptide C1	Cyclo-(^{D}DAP-Asp)$_3$
Peptide C1-Mal	Cyclo-(^{D}DAP(β-hexanoylmaleimide)-Asp)$_3$
Peptide 2	NH_2-(^{D}CysGlyArgGly)$_3$-SCH_2CH_2C(O)-Leu-OH
Peptide C2	Cyclo-(^{D}CysGlyArgGly-)$_3$
Peptide 3	NH_2-(^{D}CysGlyCysGly)$_3$-SCH_2CH_2C(O)-Leu-OH
Peptide C3	Cyclo-(^{D}CysGlyCysGly)$_3$
Peptide 4	Mal-PEG-GNNQQNY-OH
Peptide 5	Mal-SDDYYYGFGSNKFGRPRDP-OH
Peptide 6	Mal-GEGEGEGK-OH
Peptide 6(Biotin)	Mal-GEGEGEGK(Biotin)-OH
Peptide 7	Cyclo-(^{D}Cys(S-Mal-GEGEGEGK-OH)-Gly-Arg-Gly)$_3$
Peptide 7(Biotin)	Cyclo-(^{D}Cys(S-Mal-GEGEGEGK(Biotin)-OH)-Gly-Arg-Gly)$_3$

1. Peptide 1, the linear precursor for Peptide C1 and Peptide C1-Mal, was synthesized as shown in Figure 2. In Peptides 1 and C1, all residues are linked by β-peptide bonds. Synthesis started by activating PAM resin (see Experimental Procedures) with 1 mmol of α-FMOC-β-ODmab-Asp and 10% (w/v) DMAP, so that this amino acid was immobilized to the resin through its α-carboxyl group. After removing the FMOC, the free α-amino group was coupled to α-Boc-β-FMOC-^{D}DAP by standard FMOC chemistry. Standard FMOC chemistry was then employed to extend the peptide, alternately with Fmoc-Asp-α-OtBu and α-Boc-β-FMOC-^{D}DAP, until the hexapeptide, Peptide 1, had been synthesized. Peptide C1 is derived from Peptide 1 (Figure 2) by coupling the free β-COOH group of the C-terminal Asp to the free β-NH_2 group of ^{D}DAP on the resin after the ODmab groups had been removed by three 20 min incubations with 2% (v/v) hydrazine, as described elsewhere (*39*−*41*). For this reaction, the free amino and carboxyl termini of the peptide were coupled by reaction for 36 h with BOP; followed by 48 h with HOBt/DIC/DIEA, at the end of which a ninhydrin test was negative. To produce Peptide C1-Mal, the α-tBOC protecting groups on the DAP residues were removed by TFA, after which maleimide hexanoic acid was coupled to the free α-amino groups. Finally, the derivatized, cyclized Peptide C1 or Peptide C1-Mal was removed from the resin using anhydrous HF.

Type 2 axial template peptides were synthesized from thioester-containing linear precursors, such as Peptides 2 and 3. The scheme for synthesizing Peptides C2 (or C3) is shown in Figure 3. Peptides 2 and 3 contain both of the groups needed for native chemical ligation, i.e., an N-terminal Cys and a C-terminal thioester (*44*, *43*). Briefly, the linear peptide was synthesized on a PAM resin loaded with Leu to which mercaptopropionic acid had been attached, producing a thioester upon extension of the peptide chain to produce Peptide 2 or 3 (*29*). Peptides were synthesized using optimized Boc solid phase peptide synthesis (*30*). The linear peptides were cyclized by native chemical ligation, as described elsewhere (*44*). Peptide 2C (Figure 3) is derived from Peptide 2 by native chemical ligation of the deprotected peptide. Peptides at ∼2 mg/mL were dissolved in 100 mM sodium phosphate, pH 7.20, containing 6 M guanidine HCl and 10 mM tris(2-carboxyethyl)phosphine (TCEP). To monitor the course of the reaction, small aliquots of the reaction mixture were examined by analytical RP-HPLC. Cyclization of the deprotected linear peptides was remarkably clean and rapid. Examples of reactions using this chemistry are shown in Supporting Information, Figures S2 and S3, for Peptide C1-Mal (m/z = 1184.2, expected = 1183.1); MALDI-TOF mass spectrometry of Peptide C2 showed m/z = 1120 as compared to its linear precursor, for which m/z = 1339, in both cases matching the expected masses. For Peptide C1-Mal, the reactions were performed on resin, while for Peptide C2, the reaction was carried out with the peptide in solution.

Electron Microscopy. The inclusion of charged amino acids, Arg, Asp, and α,β-diamino propionic acid (DAP), into the sequence, was sufficient to yield highly soluble products and prevent the formation of insoluble nanotube structures. For Peptides 1, C1, 2, and C2, no precipitate was visible after centrifugation (10 min, 16 000 × *g*), and electron microscopy revealed only a small amount of amorphous material that appeared to be protein dried on the grid (Figure 4B shows Peptide C2, which is typical of these peptides). In contrast to Peptides 1, C1, 2, and C2, Peptide C3, cyclo-(^{D}CysGlyCysGly)$_3$, made well-ordered, insoluble nanotubes in buffer (Figure 4A).

Circular Dichroic Spectroscopy. As anticipated for peptides containing residues of alternating chirality, Peptides 1, C1-Mal (Figure 5A), 2, and C2 (Figure 5B) showed little ellipticity. The spectrum could not be measured for Peptides 3 and C3 because of their poor solubility. The linear peptides 1 and 2 showed a small amount of negative ellipticity, increasingly so at wavelengths of <220 nm. The cyclic peptides, C1-Mal and C2, showed virtually no ellipticity, suggesting that they are roughly planar.

NMR Spectroscopy. The structure and state of aggregation of Peptide C1-Mal and C2 were examined further using one- and two-dimensional NMR spectra (Figures 6 and 7, respectively). 1D-^{1}H NMR spectra of Peptides C1-Mal and C2 (Figures 6B and 7B, respectively) showed sharp lines, indicating that these peptides were not highly aggregated (or necessarily aggregated at all). The TOCSY spectra (*45*), shown in Figures 6C and 7C, for Peptides C1-Mal and C2, respectively, were remarkable in showing only one set of cross peaks for each spin system, indicating a time-averaged symmetrical structure, and consistent with the predicted 3-fold axis of symmetry.

$^3J_{NH\alpha}$ coupling constants were calculated from CT-COSY (*46*) spectral data (Figures 6D and 7D, for Peptides C1-Mal and C2, respectively) using the Karplus equation (*47*) $^3J_{NH\alpha} = 6.4\cos^2(\phi - 60) - 1.4\cos(\phi - 60) + 1.9$. $^3J_{NH\alpha}$ coupling constants were 6.6 Hz for Cys and 6.3 Hz for Arg for Peptide C2, from which one calculates values for ϕ for Arg and ^{D}Cys that are consistent with an extended structure such as a β-sheet, i.e., −157° and −165°, respectively[1] (*47*−*50*). For Gly, the apparent $^3J_{NH\alpha}$ coupling constant was 11.4 Hz for Peptides C2. This anomalously high value likely arises from additional contributions from coupling between the two Hα atoms, as well as the individual NH-α couplings.

For the CT-COSY spectrum of Peptide C1-Mal, which contains amide bonds between β-amino acids, the following interpretations can be made. First, the $^3J_{2.HN-2.HB}$ coupling constant (see figure for nomenclature) was 8.3; this ^3J is analogous a $^3J_{NH\alpha}$ coupling constant for α peptides, and suggests an extended, β-strand-like conformation. Second, the $^3J_{1.HN1-1.HB}$ coupling constant was 12.3. Like the $^3J_{NH\alpha}$ coupling constants for the Gly residues of Peptide C2, this ^3J is anomalously high, and also likely arises from additional contributions from coupling between the two Hα atoms, as well as the individual NH-α couplings. Finally, the $^3J_{1.HN2-1.HA}$ coupling constant is 8.1 and also suggests an extended conformation around this amide bond.

NOESY (*51*, *52*) spectra (Figures 6E and 7E, for Peptides C1-Mal and C2, respectively) showed no medium- or long-range cross peaks, as is typical of β-sheet structures. Notably, for Peptide C1-Mal there is only one resonance for each type of spin system, consistent with the expected threefold axis of the peptide. For Peptide C2, there were two distinguishable

[1]Two important limitations pertain to this statement, however. First, other values for the parameters have been reported (*49*, *50*), which yield other values for ϕ. Second, because J coupling is a time-averaged observable, values of $^3J_{NH\alpha}$ in the range of 6−7 are difficult to interpret, since they may represent either β-sheet or random coil (*47*).

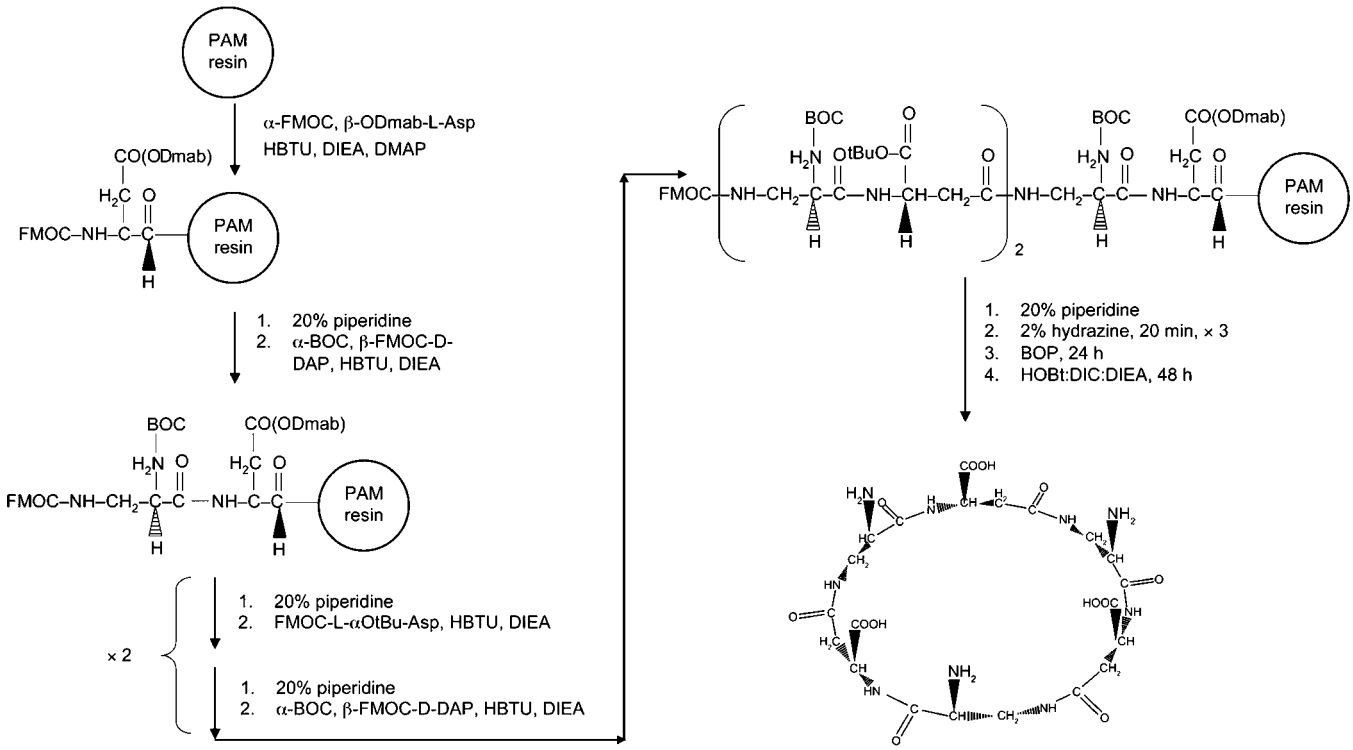

Figure 2. Synthetic schemes for Peptide C1, Cyclo-(^{D}DAP-Asp)$_3$.

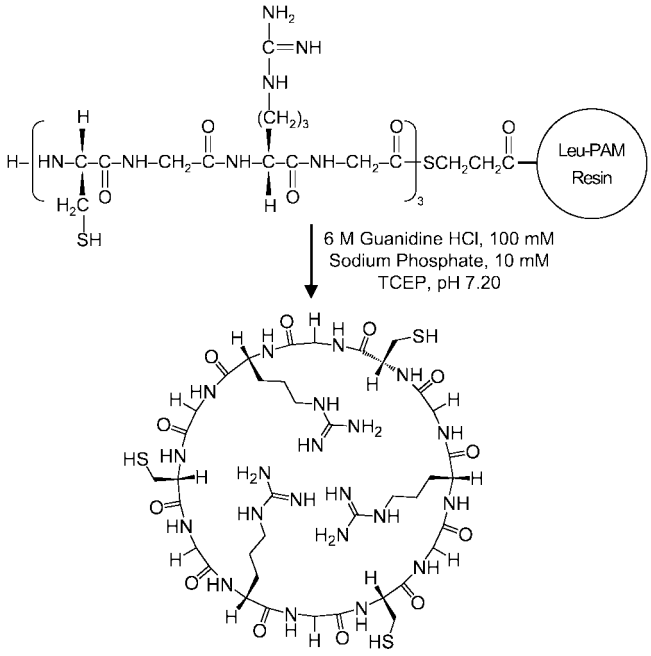

Figure 3. Synthetic scheme for Peptide C2, Cyclo-(^{D}CysGlyArgGly)$_3$.

resonance frequencies for the Gly HN and Hα atoms of Peptide C2, suggesting that, in the repeating sequence -^{D}CGRG-, the two Gly residues are in nonequivalent environments. The fact that there were *only* two cross peaks for Gly, however, is again consistent with the expected threefold symmetry axis of the peptide. Chemical shifts of the HN and Hα resonances were compared to random coil values to assess the prevalence of backbone torsion angles consistent with canonical secondary structures (*53*). None of the secondary chemical shifts was greater than 0.1 ppm, indicating no consistent difference from random coil conformation.

Molecular Modeling of Peptides C1 and C2. We performed explicit solvent molecular dynamics simulations of Peptides C1-Mal and C2 using the CHARMM program (*34*). The structures resulting from molecular dynamic simulations and energy minimization are illustrated in Figure 8A,B (for Peptides C1-Mal and C2, respectively), which again indicate that the amino acid side chains are oriented approximately axially, rather than radially with respect to the backbone of the cyclic peptide. This is especially true for Peptide C1-Mal, in which the hexanoyl-maleidimo group project above the plane of the ring. For Peptide C2, the axial orientation is more consistent for the Arg than Cys residues. Although one of the Cys residues projects axially, the others appear somewhat dispersed around the plane of the cyclic peptide, perhaps owing to the flexibility imparted to the peptide chain by the Gly residues.

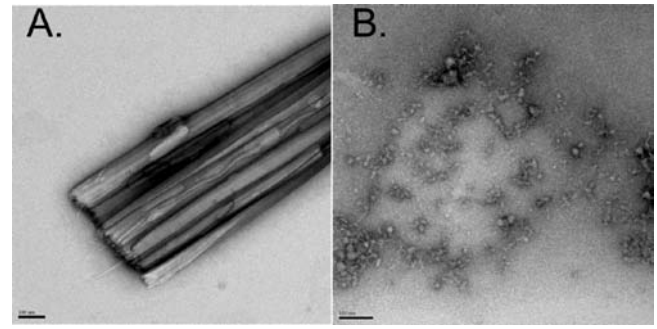

Figure 4. Electron micrographs of cyclized Peptide C3 (A, Cyclo-(^{D}CysGlyCysGly)$_3$) and Peptide C2 (B, Cyclo-(^{D}CysGlyArgGly)$_3$). Peptide C2 showed no fibrils or nanotubes; similarly, when Peptides 1, C1, and C2 were centrifuged (10′, 16 000 × *g*), no precipitate was visible, and electron microscopy revealed only a small amount of amorphous material that appeared to be protein dried on the grid. In contrast, Peptide C3 showed insoluble material that appeared to be nanotubes in electron micrographs. Magnifications shown are 39 000 X (A) and 49 000 X (B).

Attachment of Protein Ligands to Reactive Side Chains of Peptides C1-Mal and C2. The ultimate use of these templates will be to attach peptide and protein ligands, such as high-affinity scFv molecules and fibril-forming peptides. Toward

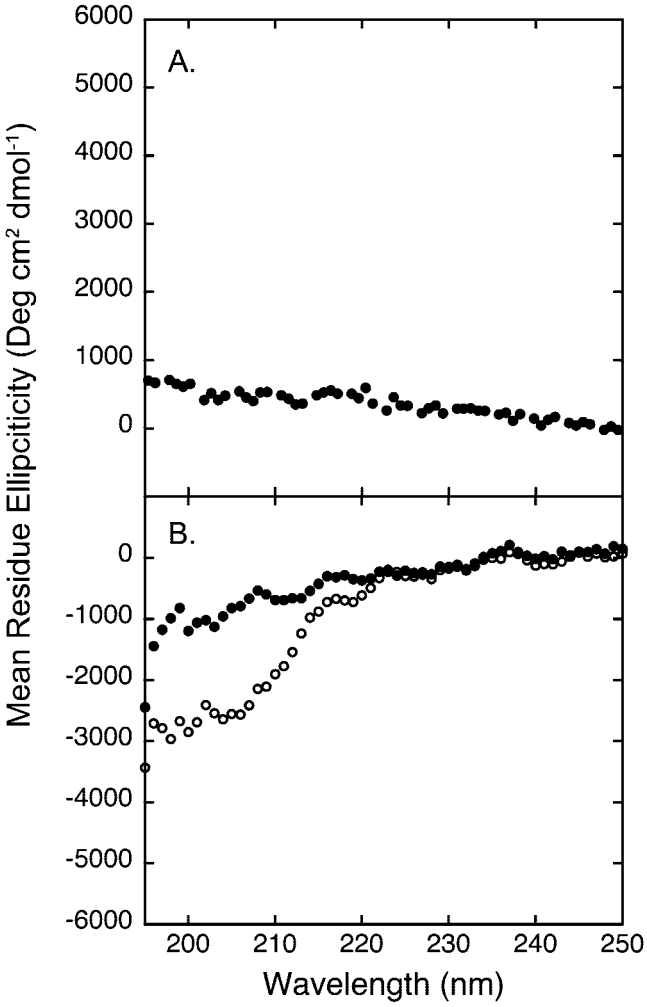

Figure 5. Circular dichroic spectrum of Peptide C1-Mal (A, ●), Cyclo-(^{D}DAP(β-hexanoylmaleimide)-Asp)$_3$), and Peptides 2 (B, ○), NH_2-(^{D}CysGlyArgGly)$_3$-SCH_2CH_2C(O)-Leu-OH and C2 (B, ●), Cyclo-(^{D}CysGlyArgGly-)$_3$). The spectra were taken with peptide concentrations of ∼100 μM, in 10 mM sodium phosphate, pH 7.40.

this end, we developed schemes for attaching such ligands to Peptides C1-Mal and C2. The ligands we tested included two proteins, trypsinogen (25 kD) and neutravidin (64 kD), and two fibril-forming peptides, Peptides 4 and 5. Figure 9A shows a generalizable scheme for attaching proteins and peptides with free α-amino groups to Peptide C1-Mal. The reagent SATA (*N*-succinimidyl-*S*-acetylthioacetate) contains an N-hydroxysuccinimidyl group that reacts with primary amines to yield a protected sulfhydryl (*54*). This sulfhydryl is later deprotected by a brief reaction with hydroxylamine, yielding an N-terminal thiolated protein, which is reactive toward a maleimide group. For this reaction, we used Peptide C1-Mal, in which hexanoylmaleimide had been attached to the α-amino groups of DAP.

We derivatized a sample protein, trypsinogen (Sigma), using SATA by a slightly modified version of the procedure described by Duncan et al. (*54*). Briefly, trypsinogen (∼2 mg/mL) was dissolved in 10 mM sodium phosphate, pH 7.50, also containing 1 mM EDTA. Twenty microliters of 100 μM SATA in DMSO was added to 2 mL of the protein solution, which was then allowed to react at 22 °C for 30 min. The acetyl group was then removed by allowing the protein to react with 50 mmol of hydroxylamine HCl and 2.5 mmol EDTA (added as solids), after readjustment of pH to 7.40. C1-Mal was dissolved in DMSO and added to derivatized trysinogen in a molar ratio of approximately 1:3. The derivatized trypsinogen was then allowed to react with Peptide C1-Mal at 22 °C for 16 h. As shown in Supporting Information, Figure S4A, the reaction leads to the disappearance of unreacted trypsinogen and template, and the appearance of three new peaks, with apparent molecular weights consistent with one, two, and three molecules of trypsinogen attached to the template, of which the largest peak is that containing three molecules of trypsinogen.

We developed an alternate strategy (Figure 9B) for attaching protein ligands to Peptide C2, for the purpose of assessing the ability of this cyclic template to accommodate macromolecule ligands. This strategy is for use primarily for proteins that bind with moderate or high affinity to a specific ligand (in this case, biotin) or are expressed as a fusion protein with a partner that binds a ligand. Accordingly, we synthesized Peptide 6, which consists of a short hydrophilic "spacer" peptide, with a biotinyl group on the ε-amino group of the C-terminal Lys residue and an N-terminal maleimide. Peptide 6 readily reacted with the Cys residues of Peptide C2, with essentially quantitative attachment to the three thiols, thus forming Peptide 7. Figure S5A (Supporting Information) shows the results of analytical RP-HPLC of the reaction mixture. One of the peaks (peak 4 in the chromatogram) contains the desired reaction product, as shown by MALDI-TOF mass spectrometry (Supporting Information, Figure S5B, m/z = 3987.7, expected = 3985.1). Peak 3 in the chromatogram is unreacted Peptide 6. Peaks 1 and 2 are the template with one and two copies of Peptide 6 attached. Similar results were also obtained with Peptide 6(Biotin), which contains an ε-NH_2-biotinylated Lys residue.

In order to attach neutravidin to Peptide 7(Biotin), the latter peptide was dissolved in 100 mM sodium phosphate, pH 7.20, also containing 2% (v/v) DMSO, after which neutravidin was added to the solution. The reaction was monitored by size exclusion chromatography using Superdex 200. After incubation of neutravidin with Peptide 7, the reaction product eluted from the column with an apparent molecular weight of ∼200 kD, i.e., consistent with a trimer, whereas the unreacted neutravidin eluted at a later time, with apparent molecular weights of ∼60 and 120 kD, i.e., monomer and dimer (Supporting Information, Figure S4B). These results show the potential of these cyclic peptide templates to accommodate macromolecules of the size of ∼64 kD, indicating that they could also be used as carriers of other molecules of similar size.

Attachment of Fibril-Forming Peptide Ligands to Reactive Side Chains of Peptide C2. Another goal of these studies is to produce templates that can be used to model soluble oligomeric intermediates of the fibrillogenesis pathyway. Two such peptides are Peptides 4 and 5. Peptide 4 is an N-terminal maleimidyl homologue of a short fibril-forming polyglutamine/asparagine peptide from the yeast prion protein Sup35 (*55*−*61*). Peptide 5 is an N-terminal maleimidyl homologue of a peptide described in an earlier paper (*62*), which was discovered fortuitously to form amyloid fibrils. For this ligation reaction, Peptide 4 or 5 was dissolved in a ligation buffer containing 7.5% (v/v) DMSO and 8 M urea; Peptide C2 was added to give a 3-fold molar excess of Peptide 4 or 5. The reaction was monitored by analytical RP-HPLC and mass spectrometry. Although this reaction was considerably slower than the reactions of Peptide 6 (∼48 h for completion of reaction), MALDI-TOF mass spectrometry demonstrated that peptide had added to all three thiol sites of Peptide C2. The reaction was not complete, and some of the template molecules contained only one or two copies of Peptide 4 or 5 (Supporting Information, Figures S6 and S7, respectively).

DISCUSSION

In this paper, we have described two schemes for synthesizing cyclic planar templates, to which ligands can be attached in an axial rather than radial orientation with respect to the ring of

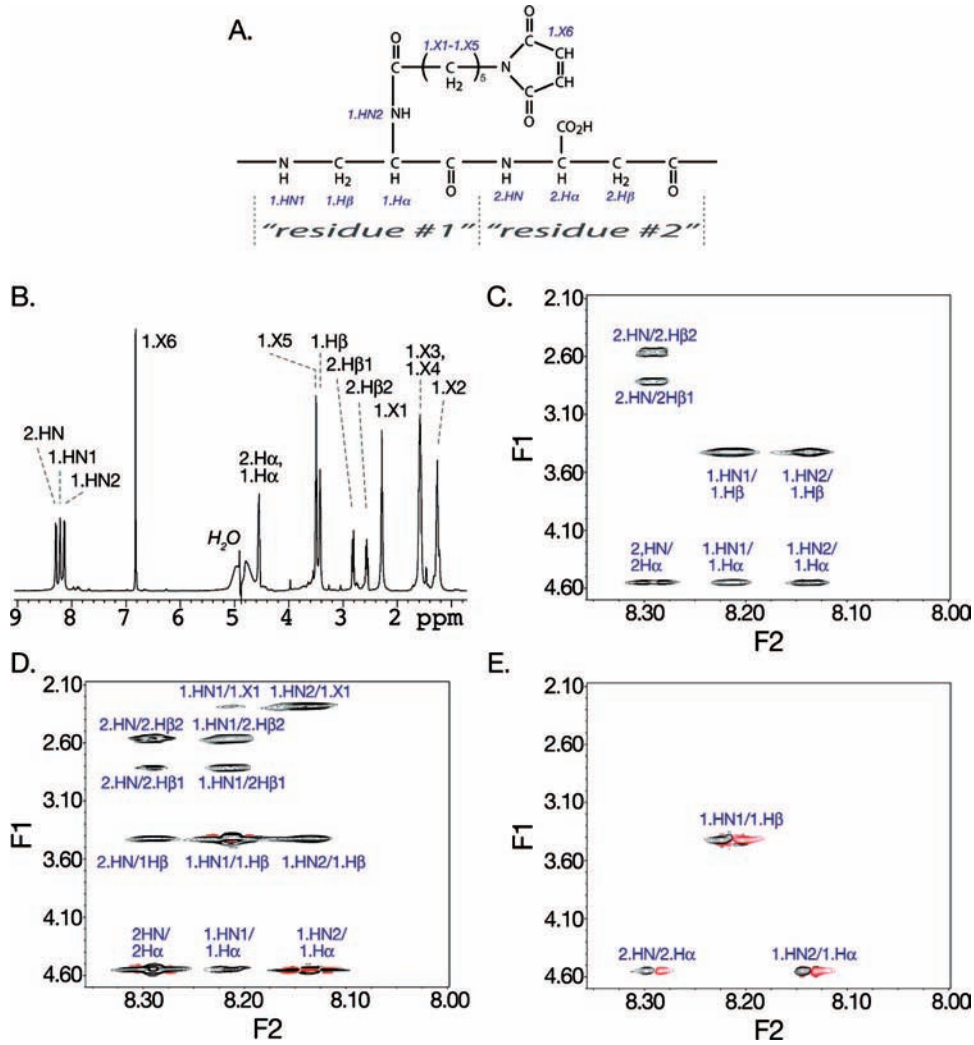

Figure 6. NMR spectra of Peptide C1-Mal. (A) Schematic for the sequence of Peptide C1-Mal, showing nomenclature for the relevant atoms. (B) 1D-^{1}H spectrum of this peptide showing narrow NMR lines, consistent with an ordered structure. (C) Amide to aliphatic region of the TOCSY spectrum of Peptide C1-Mal. (D) Amide to H_α region of the NOESY spectrum of this peptide. (E) CT-COSY spectrum of Peptide C1-Mal, showing only a single spin system for each type of amino acid.

the template. Previous templates, such as those described by Ghadiri and co-workers, used alternating D- and L-α-amino acids, which leave the side chains oriented approximately radially. As mentioned above, such peptides have served as a scaffold of a variety of ligands. These include α-helical bundles (*10, 19*), some of which model hemoproteins (*20*) or metalloproteins (*21*), a von Willebrand Factor domain (*22*), the peptide hormone, relaxin (*23*), and class I MHC molecules (*2*). Several templates also offer the advantage of regioselectivity (*11,24,25*). In addition to cyclic peptides, macrocyclic peptidomimetics have also served as templates for molecular assembly (*26, 27*). Finally, a novel strategy uses a set of plant cyclic peptides, the cyclotides, as a scaffold for a natural combinatorial peptide template (*63, 64*). The cyclotides are exceptionally stable and resistant to denaturation, making them excellent for engrafting biologically active peptides.

The cyclic planar templates described in this paper are highly versatile. The choice of three ligand-binding sites per peptide was arbitrary, and the choice of protein ligands was somewhat generic. There is no obvious reason that the peptide chain could not be extended to include additional ligand binding sites, since the cyclization reactions are, if anything, simpler for longer peptide chains than the relative short ones we have chosen. Similarly, trypsinogen was chosen as a rather generic, unremarkable ligand, and any protein containing a free amino terminus should be amenable to this approach. Neutravidin was chosen because of its high affinity for biotin, which is readily incorporated into the template through reaction with a short, hydrophilic, "spacer" peptide. Neutravidin was also chosen because the avidins are so widely used as tools in immunoenzymology and molecular biology (*65*−*74*).

The versatility of these approaches notwithstanding, we developed these molecules with two particular classes of ligands in mind, for two separate but complementary purposes. First, these templates, especially the type 1 axial template peptides containing β-amino acid (i.e., with β-peptide bonds), can be used to model the intermediates in the formation of amyloid fibrils. Amyloid fibrils form by a multistep process in which monomeric peptides first aggregate into soluble oligomers and then form partially ordered "protofibrils" and eventually form ordered β-sheet-rich fibrils. Protein aggregation underlies many neurodegenerative diseases, such as Alzheimer's Disease, Parkinson's Disease, Huntington's Disease, and amyotrophic lateral sclerosis. In addition, protein aggregation and "misfolding" are implicated in the pathogenesis of many diseases outside of the central nervous system, including diabetes mellitus, transthyretin-associated cardiomyopathies, several peripheral polyneuropathies, and pediatric cirrhosis associated with mutations in α1-antitrypsin. Although fibrillar aggregates are readily visualized, much recent attention has focused on soluble oligomeric

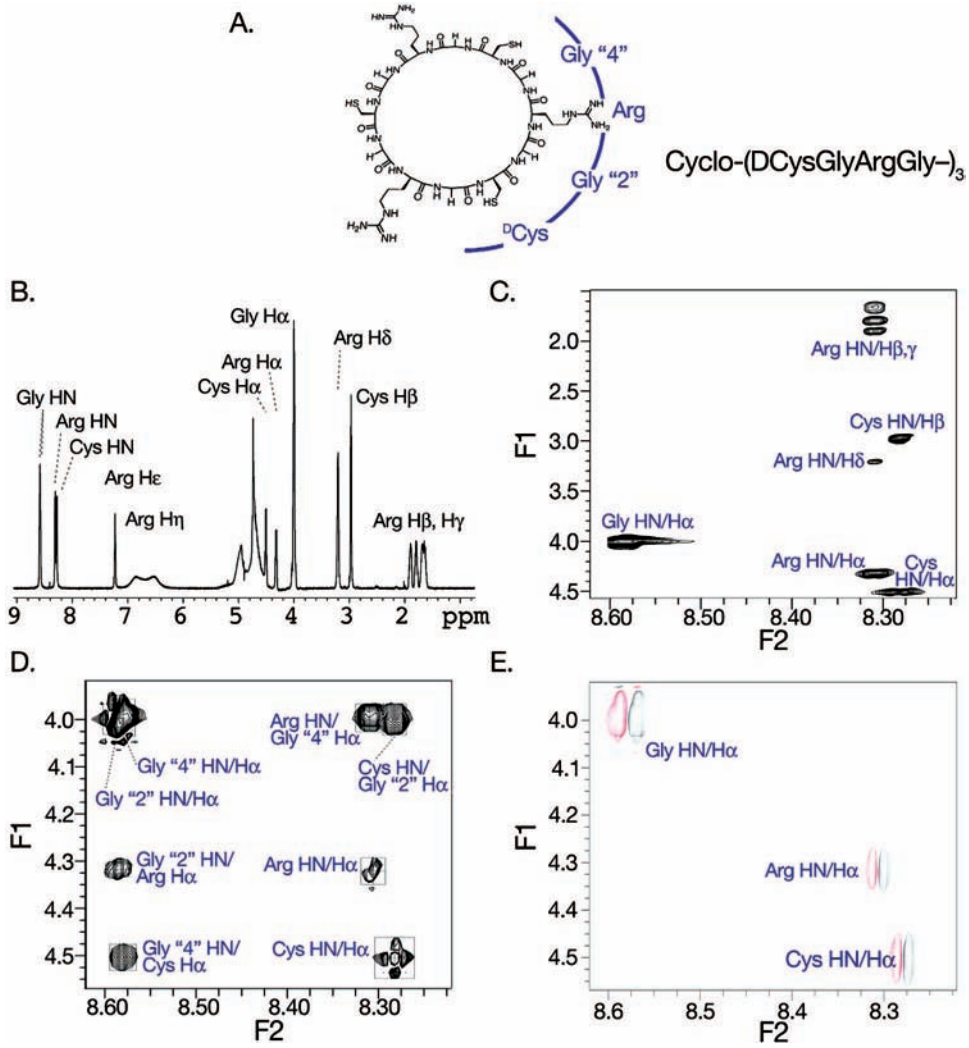

Figure 7. NMR spectra of Peptide C2. (A) Schematic for the sequence of Peptide C2, showing nomenclature for the relevant atoms. (B) 1D ^{1}H spectrum of this peptide showing narrow NMR lines, consistent with an ordered structure. (C) Amide to aliphatic region of the TOCSY spectrum of Peptide C2. (D) Amide to H_α region of the NOESY spectrum of this peptide. (E) CT-COSY spectrum of Peptide C2, showing a only single spin system for each type of amino acid, but separate spin systems for Gly "2" and Gly "4".

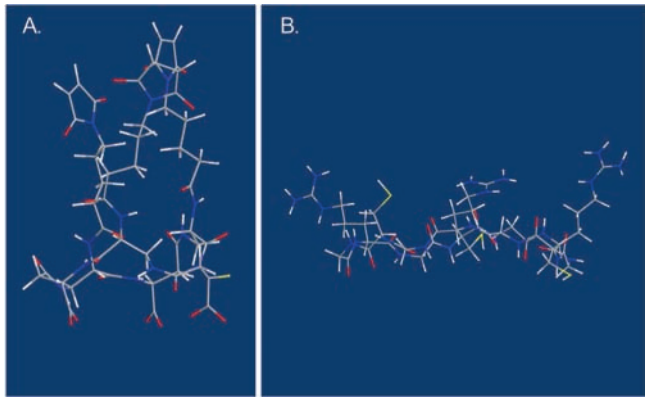

Figure 8. Molecular modeling of Peptides C1-Mal and C2 (A and B, respectively) using the CHARMM force field, with modified parameters for Cys residues. The peptides are approximately planar, and most side chains project axially with respect to the plane of the ring.

precursors of the fibrils as possibly important cytotoxic and neurotoxic species (*75*−*79*). Little is known about the structure of the oligomers, and there are several important unanswered questions about how such oligomers assemble. Structural studies have been impeded by the fact that oligomers are at low abundance and are inherently unstable and heterogeneous. Furthermore, while aggregation into fibrils is believed to proceed by a nucleation-growth mechanism, an unanswered question is whether formation of oligomers, protofibrils, and fibrils proceeds solely by the addition of monomers to nuclei and fibril growth sites. An alternate view holds that fibrils can grow through the addition of "quanta" of multiple peptides, as small oligomers, to the growing fibril. The cyclic templates described in this paper can be used to form stable oligomers of defined stoichiometry, and hence can be used for structural studies. In addition, such oligomers can be used to address the latter question of whether extension of nuclei and fibrils proceeds by addition of single molecules or oligomeric packets. Two recent papers have described the use of a similar approach, primarily with the goal of performing high-throughput screens of fibrillogenesis inhibitors. One study reports the comparison of monomeric and multimeric displays of quinacrine derivatives, as a design principal for a new class of inhibitors against β-amyloid fibril formation (*80*). These multimers exhibited a cluster of four quinacrine derivatives on a rigid cyclopeptidic scaffold. In a second paper, the same group performed high-throughput screening for compounds that block β-amyloid fibril formation (*81*). These studies used a covalent assembly of four β-amyloid fragments, $(A\beta_{16-37}Y_{20}K_{22}K_{24})_4$. Using this tool, they were able to perform screens of potential inhibitors with greatly improved

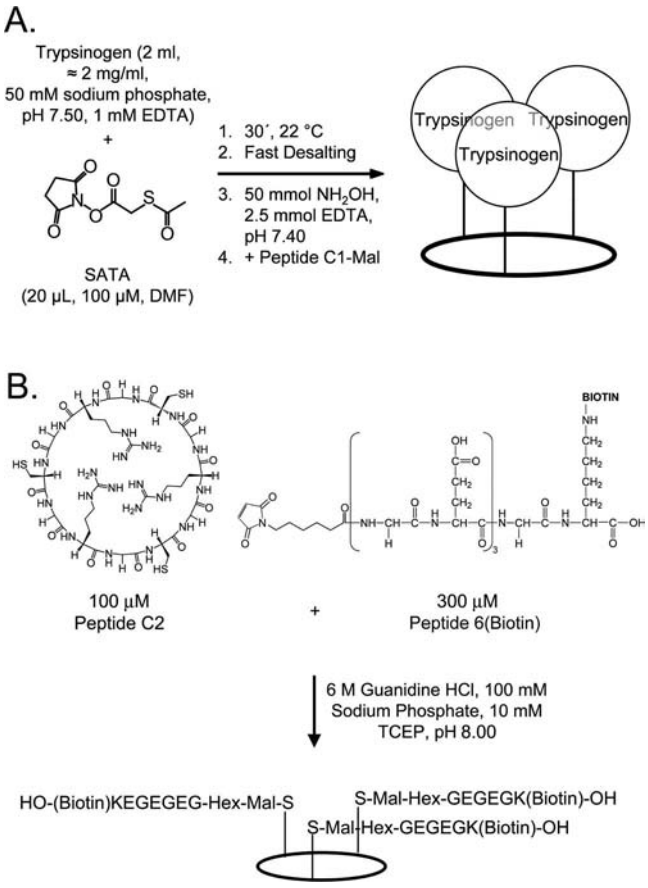

Figure 9. Strategies for attaching protein and peptide ligands to cyclic axial templates. (A) For attachment of protein or peptide ligands to Peptide C1-Mal, the ligand (in this case, trypsinogen) is allowed to react with the agent, SATA, under the conditions shown in the figure and described in the text. This yields an N-terminal thiol group after removal of the acetyl group using hydroxylamine. The thiolated protein then reacts readily with Peptide C1-Mal. (B) Attachment of a protein to Peptide C2 proceeds by first attaching a short, hydrophilic "spacer" sequence, Peptide 6(Biotin), which also contains the ligand for the protein in question, here a biotin moiety attached to the side chain of a Lys residue. Peptide 6(Biotin) is attached to the template Peptide C2 by thioether ligation, a reaction between the maleimido function of Peptide 6(Biotin) and the thiols of the Cys side chains in Peptide C2. Biotin then serves as a ligand for a protein, neutravidin. This approach could be extended to other proteins that bind with moderate or high affinity to a ligand, or to fusion proteins containing a ligand-binding partner.

speed compared to convential methods using thioflavin fluorescence assays of fibril formation.

Second, the cyclic templates described in this paper can be used to attach "payload" molecules, such as high-affinity single-chain antibodies fragments (scFv molecules) and high-affinity single-chain T cell receptors (scTCR) molecules for the eventual development of immunological reagents. The protein ligands that we attached to the templates have little to distinguish them from many others, suggesting that it should be straightforward to extend these approaches to many other protein ligands. As a "proof-of-principle", we described the attachment of trypsinogen and neutravidin to templates, demonstrating that proteins are not sterically hindered from binding to the template.

In conclusion, the templates described in this paper fulfill the criteria defined at the outset, namely, that they are multivalent for the attachment of multiple ligands; specifically and readily reactive for the facile attachment of ligands; versatile as to the number and spacing of ligand attachment sites; sufficiently rigid to define the orientation of ligands with respect to the template; and yet flexible enough to allow attachment of and interactions among macromolecular ligands. We believe that these templates will be useful for a variety of purposes that may extend well beyond those outlined above.

ACKNOWLEDGMENT

We thank Yimei Chen of the Electron Microscopy Facility, and Dr. Giridhir Reddy of the Peptide Facility at The University of Chicago. This work was supported by the NIH Cardiovascular Pathophysiology Training Grant (HL07237, NC), NIH (P01-CA97296 HS, SCM), NIH (NS042852 SCM), and Alzheimer's Association IIRG-06-27794 (SCM).

Supporting Information Available: Reverse-phase HPLC and MALDI-TOF mass spectrometry of Peptide 2, NH_2-(^{D}CysGlyArgGly)$_3$-$SCH_2CH_2C(O)$-Leu-OH; of Peptide C1-Mal, Cyclo-(^{D}DAP(β-hexanoylmaleimide)-Asp)$_3$; and of Peptide C2, Cyclo(-NH-(^{D}CysGlyArgGly)-CO-)$_3$. Reaction of Peptide C1-Mal with trypsinogen (after reaction of trypsinogen with SATA), and of Peptide 7, Cyclo-(^{D}Cys(S-Mal-GEGEGEGK(Biotin)-OH)-Gly-Arg-Gly)$_3$, with neutravidin, as monitored by size exclusion chromatography using Superdex 200. Reverse-phase HPLC and MALDI-TOF mass spectrometry of products of the reaction of Peptide 6, Mal-GEGEGEGK-OH (Mal = maleimidylhexanoyl), with cyclic template Peptide C2, Cyclo(-NH-(DCysGlyArgGly)-CO-). Reverse-phase HPLC and MALDI-TOF mass spectrometry of products of the reaction of the cyclic template Peptide C2, Cyclo(-NH-(DCysGlyArgGly)-CO-) with two fibril-forming peptides, Peptide 4, Mal-PEG-GNNQQNY-OH, and Peptide 5, Mal-SDDYYYGFGSNKFGRPRDP-OH. This material is available free of charge via the Internet at http://pubs.acs.org.

LITERATURE CITED

(1) Mutter, M., Hersperger, R., Gubernator, K., and Müller, K. (1989) The construction of new proteins: V. A template-assembled synthetic protein (TASP) containing both a 4-helix bundle and β-barrel-like structure. *Proteins 5*, 13–21.
(2) Tuchscherer, G., Servis, C., Corradin, G., Blum, U., Rivier, J., and Mutter, M. (1992) Total chemical synthesis, characterization, and immunological properties of an MHC class I model using the TASP concept for protein de novo design. *Protein Sci. 1*, 1377–1386.
(3) Floegel, R., and Mutter, M. (1992) Molecular dynamics conformational search of six cyclic peptides used in the template assembled synthetic protein approach for protein de novo design. *Biopolymers 32*, 1283–1310.
(4) Altmann, K. H., and Mutter, M. (1990) A general strategy for the de novo design of proteins--template assembled synthetic proteins. *Int. J. Biochem. 22*, 947–956.
(5) Tuchscherer, G., Steiner, V., Altmann, K. H., and Mutter, M. (1994) De novo design of proteins. Template-assembled synthetic proteins (TASP). *Methods Mol. Biol. 36*, 261–285.
(6) Tuchscherer, G., and Mutter, M. (1995) Templates in protein de novo design. *J. Biotechnol. 41*, 197–210.
(7) Tuchscherer, G., and Mutter, M. (1995) Protein design as a challenge for peptide chemists. *J. Pept. Sci. 1*, 3–10.
(8) Mutter, M., and Tuchscherer, G. (1997) Non-native architectures in protein design and mimicry. *Cell. Mol. Life Sci. 53*, 851–863.
(9) Tuchscherer, G., Grell, D., Mathieu, M., and Mutter, M. (1999) Extending the concept of template-assembled synthetic proteins. *J. Pept. Res. 54*, 185–194.
(10) Grell, D., Richardson, J. S., and Mutter, M. (2001) Protein design and folding: template trapping of self-assembled helical bundles. *J. Pept. Sci. 7*, 146–151.
(11) Peluso, S., Rückle, T., Lehmann, C., Mutter, M., Peggion, C., and Crisma, M. (2001) Crystal structure of a synthetic cyclodecapeptide for template-assembled synthetic protein design. *ChemBioChem 2*, 432–437.

(12) Ghadiri, M. R., Granja, J. R., Milligan, R. A., McRee, D. E., and Khazanovich, N. (1993) Self-assembling organic nanotubes based on a cyclic peptide architecture. *Nature 366*, 324–327.

(13) Bong, D. T., Clark, T. D., Granja, J. R., and Ghadiri, M. R. (2001) Self-assembling organic nanotubes. *Angew. Chem., Int. Ed. Engl. 40*, 988–1011.

(14) Dartois, V., Sanchez-Quesada, J., Cabezas, E., Chi, E., Dubbelde, C., Dunn, C., Granja, J., Gritzen, C., Weinberger, D., Ghadiri, M. R., and Parr, T. R., Jr. (2005) Systemic antibacterial activity of novel synthetic cyclic peptides. *Antimicrob. Agents Chemother. 49*, 3302–3310.

(15) Fernandez-Lopez, S., Kim, H. S., Choi, E. C., Delgado, M., Granja, J. R., Khasanov, A., Kraehenbuehl, K., Long, G., Weinberger, D. A., Wilcoxen, K. M., and Ghadiri, M. R. (2001) Antibacterial agents based on the cyclic D, L-α-peptide architecture. *Nature 412*, 452–456.

(16) Horne, W. S., Wiethoff, C. M., Cui, C., Wilcoxen, K. M., Amorin, M., Ghadiri, M. R., and Nemerow, G. R. (2005) Antiviral cyclic D,L-α-peptides: targeting a general biochemical pathway in virus infections. *Bioorg. Med. Chem. 13*, 5145–5153.

(17) Ghadiri, M. R., Granja, J. R., and Buehler, K. L. (1994) Artificial transmembrane ion channels from self-assembling peptide nanotubes. *Nature 369*, 301–304.

(18) Chaloin, L., Méry, J., Van Mau, N., Divita, G., and Heitz, F. J. (1999) Synthesis of a template-associated peptide designed as a transmembrane ion channel former. *Peptide Sci. 5*, 381–391.

(19) Causton, A. S., and Sherman, J. C. (2002) A comparison of three- and four-helix bundle TASP molecules. *J. Peptide Sci. 8*, 275–282.

(20) Rau, H. K., DeJonge, N., and Haehnel, W. (2000) Combinatorial synthesis of four-helix bundle hemoproteins for tuning of cofactor properties. *Angew. Chem., Int. Ed. Engl. 39*, 250–253.

(21) Schnepf, R., Hörth, P., Bill, E., Wieghardt, K., Hildebrandt, P., and Haehnel, W. (2001) De novo design and characterization of copper centers in synthetic four-helix-bundle proteins. *J. Am. Chem. Soc. 123*, 2186–2195.

(22) Hauert, J., Fernandez-Carneado, J., Michielin, O., Mathieu, S., Grell, D., Schapira, M., Spertini, O., Mutter, M., Tuchscherer, G., and Kovacsovics, T. (2004) A template-assembled synthetic protein surface mimetic of the von Willebrand factor A1 domain inhibits botrocetin-induced platelet aggregation. *ChemBioChem 5*, 856–864.

(23) Mathieu, M. N., Wade, J. D., Tan, Y. Y., Summers, R. J., and Tregear, G. W. (2000) Novel strategy for the synthesis of template-assembled analogues of rat relaxin. *J. Peptide Sci. 6*, 235–242.

(24) Dumy, P., Eggleston, I. M., Esposito, G., Nicula, S., and Mutter, M. (1996) Solution structure of regioselectively addressable functionalized templates: an NMR and restrained molecular dynamics investigation. *Biopolymers 39*, 297–308.

(25) Peng, Z. H. (1999) Solid phase synthesis and NMR conformational studies on cyclic decapeptide template molecule. *Biopolymers 49*, 565–574.

(26) Glenn, M. P., Pattenden, L. K., Reid, R. C., Tyssen, D. P., Tyndall, J. D., Birch, C. J., and Fairlie, D. P. (2002) β-strand mimicking macrocyclic amino acids: templates for protease inhibitors with antiviral activity. *J. Med. Chem. 45*, 371–381.

(27) Barrett, A. G., Hennessy, A. J., Le Vézouët, R., Procopiou, P. A., Seale, P. W., Stefaniak, S., Upton, R. J., White, A. J., and Williams, D. J. (2004) Synthesis of diverse macrocyclic peptidomimetics utilizing ring-closing metathesis and solid-phase synthesis. *J. Org. Chem. 69*, 1028–1037.

(28) Horne, W. S., Ashkenasy, N., and Ghadiri, M. R. (2005) Modulating charge transfer through cyclic D,L-α-peptide self-assembly. *Chemistry 11*, 1137–1144.

(29) Hackeng, T. M., Griffin, J. H., and Dawson, P. E. (1999) Protein synthesis by native chemical ligation: expanded scope by using straightforward methodology. *Proc. Natl. Acad. Sci. U.S.A. 96*, 10068–10073.

(30) Schnölzer, M., Alewood, P., Jones, A., Alewood, D., and Kent, S. B. (2002) In situ neutralization in Boc-chemistry solid phase peptide synthesis. Rapid, high yield assembly of difficult sequences. *Int. J. Pept. Protein Res. 40*, 180–193.

(31) Wang, S. S., Tam, J. P., Wang, B. S., and Merrifield, R. B. (1981) Enhancement of peptide coupling reactions by 4-dimethylaminopyridine. *Int. J. Pept. Protein Res. 18*, 459–467.

(32) Gamet, J.- P., Jacquier, R., and Verducci, J. (1984) Étude de la racemisation induite par la dmap dans les reactions de couplage peptidique. *Tetrahedron 40*, 1995–2001.

(33) Takeda, K., Ayabe, A., Suzuki, M., Konda, Y., and Harigaya, Y. (1991) An Improved method for the synthesis of active esters of n-protected amino acids and subsequent synthesis of dipeptides. *Synthesis 1991*, 689–690.

(34) Brooks, B. R., Bruccoleri, R. E., Olafson, B. D., States, D. J., Swaminathan, S., and Karplus, M. (1983) CHARMM: A program for macromolecular energy, minimization, and dynamics calculations. *J. Comput. Chem. 4*, 187–217.

(35) Jorgensen, W. L., Chandrasekhar, J., Madura, J. D., Impey, R. W., and Klein, M. L. (1983) Comparison of simple potential functions for simulating liquid water. *J. Chem. Phys. 79*, 926–935.

(36) Ryckaert, J. P., Ciccotti, G., and Berendsen, H. J. C. (1977) Numerical integration of the cartesian equations of motion of a system with constraints: molecular dynamics of n-alkanes. *J. Comput. Phys. 23*, 327–341.

(37) Darden, T., York, D., and Pedersen, L. (1993) Particle mesh Ewald: An N·log(N) method for Ewald sums in large systems. *J. Chem. Phys. 98*, 10089–10092.

(38) MacKerell, A. D., Jr., Bashford, D., Bellott, M., Dunbrack, R. L., Jr., Evanseck, J. D., Field, M. J., Fischer, S., Gao, J., Guo, H., Ha, S., Joseph-McCarthy, D., Kuchnir, L., Kuczera, K., Lau, F. T. K., Mattos, C., Michnick, S., Ngo, T., Nguyen, D. T., Prodhom, B., Reiher, W. E., III, Roux, B., Schlenkrich, M., Smith, J. C., Stote, R., Straub, J., Watanabe, M., Wiórkiewicz-Kuczera, J., Yin, D., and Karplus, M. (1998) All-atom empirical potential for molecular modeling and dynamics studies of proteins. *J. Phys. Chem. B 102*, 3586–3616.

(39) Chan, W. C., Bycroft, B. W., Evans, D. J., and White, P. D. (1995) A novel 4-aminobenzyl ester-based carboxy-protecting group for synthesis of atypical peptides by Fmoc-Bu^t solid-phase chemistry. *J. Chem. Soc., Chem. Commun. 1995*, 2209–2210.

(40) Cudic, M., John, D., Wade, J. D., and Otvos, L, Jr. (2000) Convenient synthesis of a head-to-tail cyclic peptide containing an expanded ring. *Tetrahedron Lett. 41*, 4527–4531.

(41) Malkinson, J. P., Zloh, M., Kadom, M., Errington, R., Smith, P. J., and Searcey, M. (2003) Solid-phase synthesis of the cyclic peptide portion of chlorofusin, an inhibitor of p53-MDM2 interactions. *Org. Lett. 5*, 5051–5054.

(42) Dawson, P. E., Muir, T. W., Clark-Lewis, I., and Kent, S. B. (1994) Synthesis of proteins by native chemical ligation. *Science 266*, 776–779.

(43) Dawson, P. E., and Kent, S. B. (2000) Synthesis of native proteins by chemical ligation. *Annu. Rev. Biochem. 69*, 923–960.

(44) Bang, D., Chopra, N., and Kent, S. B. (2004) Total chemical synthesis of crambin. *J. Am. Chem. Soc. 126*, 1377–1383.

(45) Davis, D. G., and Bax, A. (1985) Assignment of complex proton NMR spectra via two-dimensional homonuclear Hartmann-Hahn spectroscopy. *J. Am. Chem. Soc. 107*, 2820–2821.

(46) Girvin, M. E. (1994) Increased sensitivity of COSY spectra by use of constant-time t_1 periods (CT COSY). *J. Magn. Reson., Ser. A 108*, 99–104.

(47) Pardi, A., Billeter, M., and Wüthrich., K. (1984) Calibration of the angular dependence of the amide proton-C^α proton coupling constants, $^3J_{HN\alpha}$, in a globular protein. Use of $^3J_{HN\alpha}$ for identification of helical secondary structure. *J. Mol. Biol. 180*, 741–751.

(48) Wagner, G., Braunl, W., Havel, T. F., Schaumann, T., Go, N., and Wüthrich, K. (1987) Protein structures in solution by

nuclear magnetic resonance and distance geometry. The polypeptide fold of the basic pancreatic trypsin inhibitor determined using two different algorithms, DISGEO and DISMAN. *J. Mol. Biol. 196*, 611–639.

(49) Bax, A., Kontaxis, G., and Tjandra, N. (2001) Dipolar couplings in macromolecular structure determination. *Methods Enzymol. 339*, 128–174.

(50) Hudson, B. P., Martinez-Yamout, M. A., Dyson, H. J., and Wright, P. E. (2004) Recognition of the mRNA AU-rich element by the zinc finger domain of TIS11d. *Nat. Struct. Mol. Biol. 11*, 257–264.

(51) Macura, S., and Ernst, R. R. (1980) Elucidation of cross relaxation in liquids by two-dimensional N.M.R. spectroscopy. *Mol. Phys. 41*, 95–107.

(52) Jeener, J., Meier, B. H., Bachmann, P., and Ernst, R. R. (1979) Investigation of exchange processes by two-dimensional NMR spectroscopy. *J. Chem. Phys. 71*, 4546–4553.

(53) Wishart, D. S., and Case, D. A. (2001) Use of chemical shifts in macromolecular structure determination. *Methods Enzymol. 338*, 3–34.

(54) Duncan, R. J. S., Weston, P. D., and Wrigglesworth, R. (1983) A new reagent which may be used to introduce sulfhydryl groups into proteins, and its use in the preparation of conjugates for immunoassay. *Anal. Biochem. 132*, 68–73.

(55) Wickner, R. B. (1994) [URE3] as an altered URE2 protein: evidence for a prion analog in *Saccharomyces cerevisiae*. *Science 264*, 566–569.

(56) Paushkin, S. V., Kushnirov, V. V., Smirnov, V. N., and Ter-Avanesyan, M. D. (1996) Propagation of the yeast prion-like [psi+] determinant is mediated by oligomerization of the SUP35-encoded polypeptide chain release factor. *EMBO J. 15*, 3127–3134.

(57) King, C. Y., Tittmann, P., Gross, H., Gebert, R., Aebi, M., and Wuthrich, K. (1997) Prion-inducing domain 2−114 of yeast Sup35 protein transforms in vitro into amyloid-like filaments. *Proc. Natl. Acad. Sci. U.S.A. 94*, 6618–6622.

(58) Glover, J. R., Kowal, A. S., Schirmer, E. C., Patino, M. M., Liu, J. J., and Lindquist, S. (1997) Self-seeded fibers formed by Sup35, the protein determinant of [PSI+], a heritable prion-like factor of *S. cerevisiae*. *Cell 89*, 811–819.

(59) Nelson, R., Sawaya, M. R., Balbirnie, M., Madsen, A. Ø., Riekel, C., Grothe, R., and Eisenberg, D. (2005) Structure of the cross-β spine of amyloid-like fibrils. *Nature 435*, 773–778.

(60) Tanaka, M., Chien, P., Yonekura, K., and Weissman, J. S. (2005) Mechanism of cross-species prion transmission: an infectious conformation compatible with two highly divergent yeast prion proteins. *Cell 121*, 49–62.

(61) Shewmaker, F., Wickner, R. B., and R Tycko, R. (2006) Amyloid of the prion domain of Sup35p has an in-register parallel β-sheet structure. *Proc. Natl. Acad. Sci. U.S.A. 103*, 19753–19759.

(62) Lazar, K. L., Kurutz, J. W., Tycko, R., and Meredith, S. C. (2006) Encapsulation and NMR on an aggregating peptide before fibrillogenesis. *J. Am. Chem. Soc. 128*, 16460–16461.

(63) Craik, D. J., Cemazar, M., Wang, C. K. L., and Daly, N. L. (2006) The cyclotide family of circular miniproteins: Nature's combinatorial peptide template. *Biopolymers 84*, 250–266.

(64) Clark, R. J., Daly, N. L., and Craik, D. J. (2006) Structural plasticity of the cyclic-cystine-knot framework: implications for biological activity and drug design. *Biochem. J. 394*, 85–93.

(65) Green, N. M. (1975) Avidin. *Adv. Protein Chem. 29*, 85–133.

(66) Guesdon, J. L., Ternynck, T., and Avrameas, S. (1979) The use of avidin-biotin interaction in immunoenzymatic techniques. *J. Histochem. Cytochem. 27*, 1131–1139.

(67) Bayer, E. A., and Wilchek, M. (1980) The use of the avidin-biotin complex as a tool in molecular biology. *Methods Biochem. Anal. 26*, 1–45.

(68) Hsu, S. M., Raine, L., and Fanger, H. (1981) The use of antiavidin antibody and avidin-biotin-peroxidase complex in immunoperoxidase technics. *Am. J. Clin. Pathol. 75*, 816–821.

(69) Green, N. M. (1990) Avidin and streptavidin. *Methods Enzymol. 184*, 51–67.

(70) Airenne, K. J., Marjomäki, V. S., and Kulomaa, M. S. (1999) Recombinant avidin and avidin-fusion proteins. *Biomol. Eng. 16*, 87–92.

(71) Schetters, H. (1999) Avidin and streptavidin in clinical diagnostics. *Biomol. Eng. 16*, 73–78.

(72) Laitinen, O. H., Hytönen, V. P., Nordlund, H. R., and Kulomaa, M. S. (2006) Genetically engineered avidins and streptavidins. *Cell. Mol. Life Sci. 63*, 2992–3017.

(73) Wilchek, M., Bayer, E. A., and Livnah, O. (2006) Essentials of biorecognition: the (strept)avidin-biotin system as a model for protein-protein and protein-ligand interaction. *Immunol. Lett. 103*, 27–32.

(74) Laitinen, O. H., Nordlund, H. R., Hytönen, V. P., and Kulomaa, M. S. (2007) Brave new (strept)avidins in biotechnology. *Trends Biotechnol. 25*, 269–277.

(75) Bitan, G., Kirkitadze, M. D., Lomakin, A., Vollers, S. S., Benedek, G. B., and Teplow, D. B. (2003) Amyloid β-protein (Aβ) assembly: Aβ 40 and Aβ 42 oligomerize through distinct pathways. *Proc. Natl. Acad. Sci. U.S.A. 100*, 330–335.

(76) Caughey, B., and Lansbury, P. T. (2003) Protofibrils, pores, fibrils, and neurodegeneration: separating the responsible protein aggregates from the innocent bystanders. *Annu. Rev. Neurosci. 26*, 267–298.

(77) Lesne, S., Koh, M. T., Kotilinek, L., Kayed, R., Glabe, C. G., Yang, A., Gallagher, M., and Ashe, K. H. (2006) A specific amyloid-β protein assembly in the brain impairs memory. *Nature 440*, 352–357.

(78) Goldsbury, C., Frey, P., Olivieri, V., Aebi, U., and Muller, S. A. (2005) Multiple assembly pathways underlie amyloid-beta fibril polymorphisms. *J. Mol. Biol. 352*, 282–298.

(79) Stefani, M. (2007) Generic cell dysfunction in neurodegenerative disorders: role of surfaces in early protein misfolding, aggregation, and aggregate cytotoxicity. *Neuroscientist 13*, 519–531.

(80) Dolphin, G. T., Ouberai, M., Dumy, P., and Garcia, J. (2007) Designed amyloid β peptide fibril - a tool for high-throughput screening of fibril inhibitors. *ChemMedChem 2*, 1613–1623.

(81) Dolphin, G. T., Chierici, S., Ouberai, M., Dumy, P., and Garcia, J. (2008) A multimeric quinacrine conjugate as a potential inhibitor of Alzheimer's β-amyloid fibril formation. *ChemBioChem 9*, 952–963.

BC800312X

Supporting Material for:

Neeraj Chopra, Wenxun Gan, Hans Schreiber, Josh W. Kurutz, and Stephen C. Meredith

Versatile Cyclic Templates for Assembly of Axially Oriented Ligands.

List of Supporting Figures:

1. Reverse phase HPLC and MALDI-TOF mass spectrometry of Peptide 2, NH2–(^{D}CysGlyArgGly)$_3$–$SCH_2CH_2C(O)$–Leu-OH.

2. Reverse phase HPLC (A) and MALDI-TOF mass spectrometry (B) of Peptide C1-Mal, Cyclo-(^{D}DAP(β-hexanoylmaleimide)-Asp)$_3$.

3. Reverse phase HPLC (A) and MALDI-TOF mass spectrometry (B) of Peptide C2, cyclo(–NH–(^{D}CysGlyArgGly)–CO–)$_3$.

4. (A) Reaction of Peptide C1-Mal with trypsinogen, after reaction of trypsinogen with SATA, as monitored by size exclusion chromatography using Superdex 200. (B) Reaction of Peptide 7, Cyclo-(^{D}Cys(S-Mal-GEGEGEGK(Biotin)-OH)-Gly-Arg-Gly)$_3$, with neutravidin, as monitored by size exclusion chromatography using Superdex 200.

5. Reverse phase HPLC (A) and MALDI-TOF mass spectrometry (B) of products of the reaction of Peptide 6, Mal-GEGEGEGK–OH (Mal = maleimidylhexanoyl), with cyclic template Peptide C2, cyclo(–NH–(DCysGlyArgGly)–CO–).

6. Reverse phase HPLC (A) and MALDI-TOF mass spectrometry (B) of products of the reaction of the fibril-forming Peptide 4, Mal-PEG-GNNQQNY–OH, with the cyclic template Peptide C2, cyclo(–NH–(DCysGlyArgGly)–CO–).

7. Reverse phase HPLC (A) and MALDI-TOF mass spectrometry (B) of products of the reaction of the fibril-forming Peptide 5, Mal-SDDYYYGFGSNKFGRPRDP–OH with Peptide C2, cyclo(–NH–(^{D}CysGlyArgGly)–CO–).

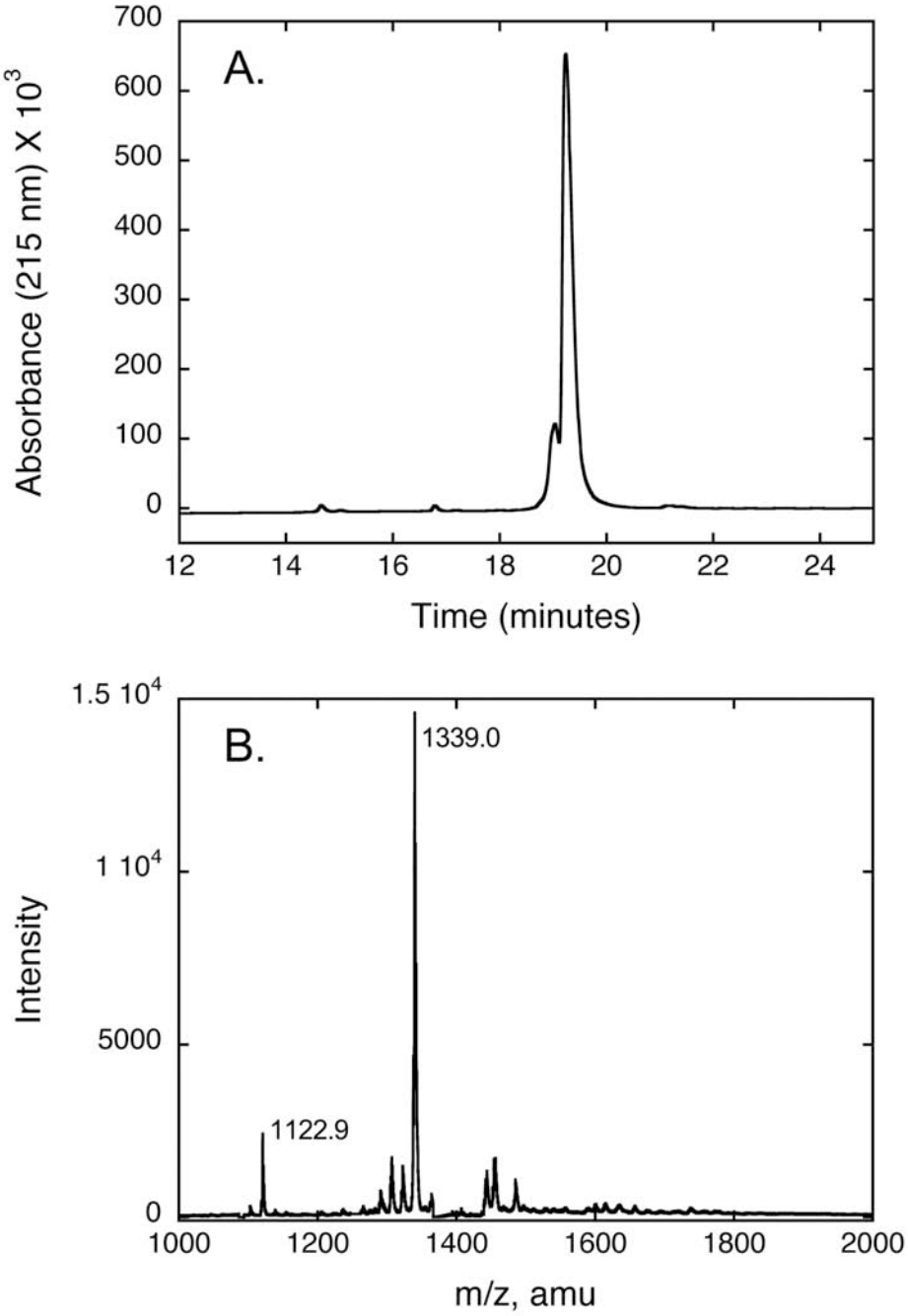

Figure S1. Reverse phase HPLC (A) and MALDI-TOF mass spectrometry (B) of Peptide 2, NH2–(^{D}CysGlyArgGly)$_3$–$SCH_2CH_2C(O)$–Leu-OH. The mass spectrometry was performed on the peptide eluting as the largest peak. The peak was collected and used for further reactions.

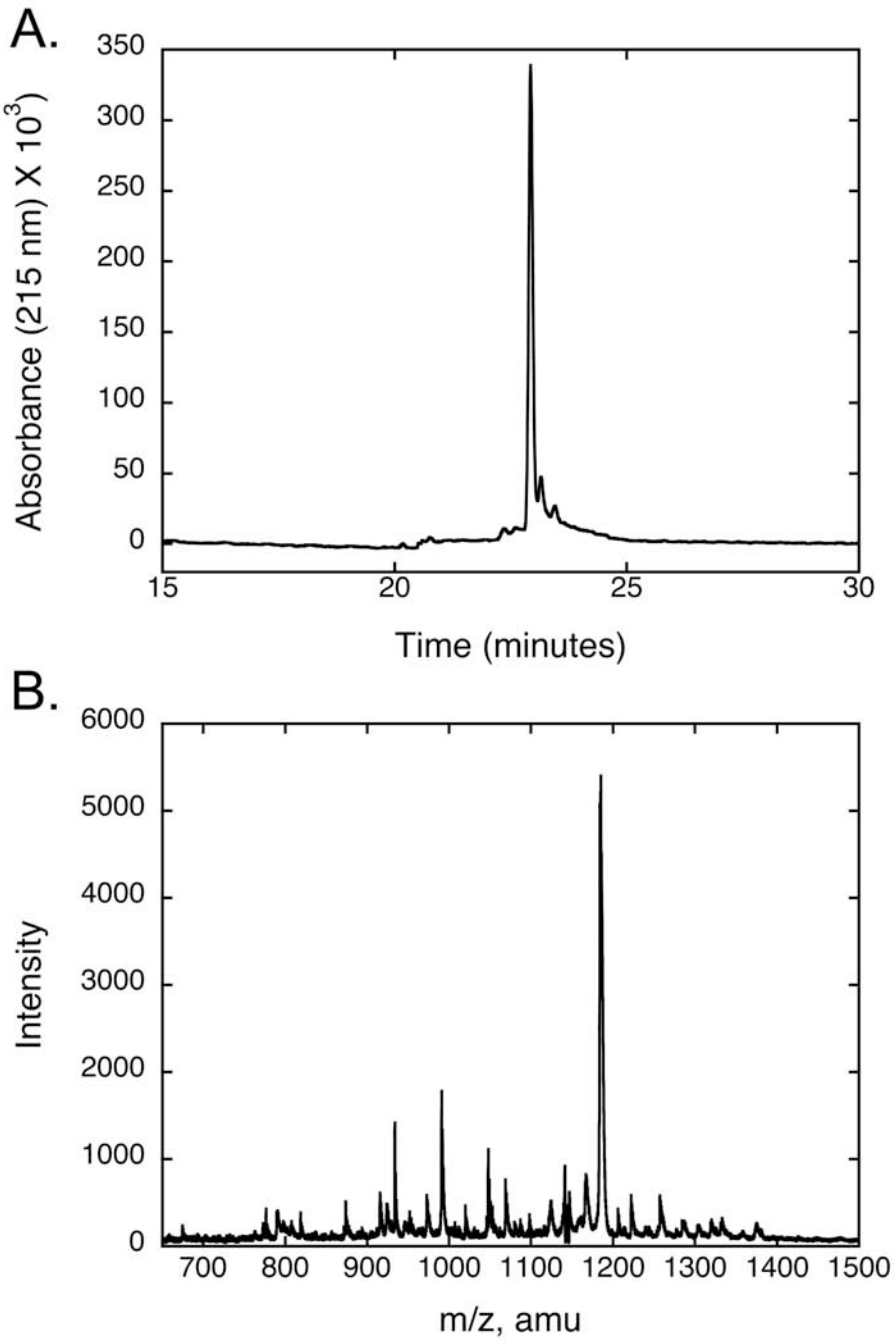

S2. Reverse phase HPLC (A) and MALDI-TOF mass spectrometry (B) of Peptide C1-Mal, Cyclo-(^{D}DAP(β-hexanoylmaleimide)-Asp)$_3$. The gradient was water to acetonitrile (both containing 0.1 % TFA, v:v), 0 to 60% over 30 minutes.

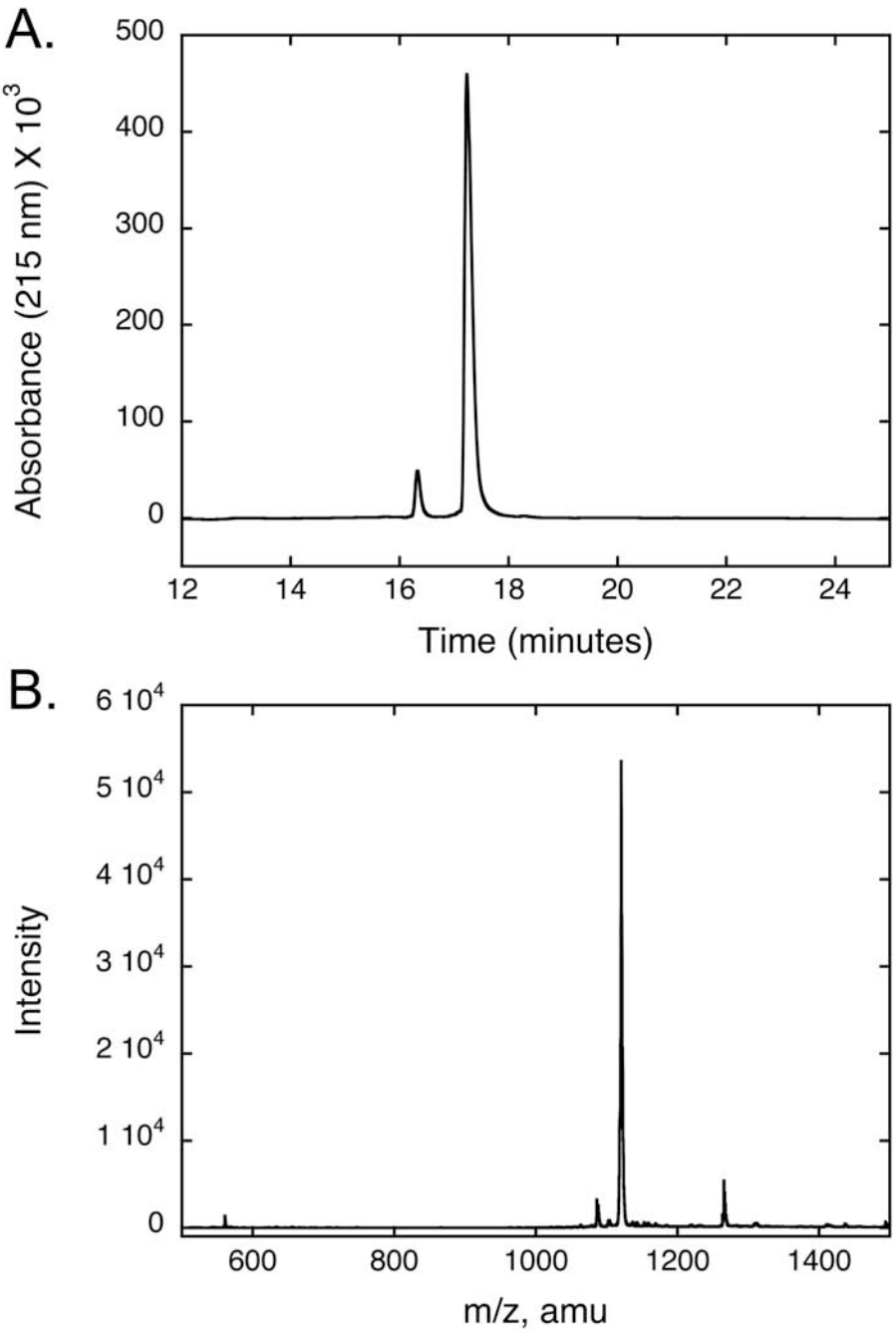

S3. Reverse phase HPLC (A) and MALDI-TOF mass spectrometry (B) of Peptide C2, cyclo(–NH–(^{D}CysGlyArgGly)–CO–)$_3$. Conditions are as described in the paper in for Figure S2. The peak is well separated from the other reaction products.

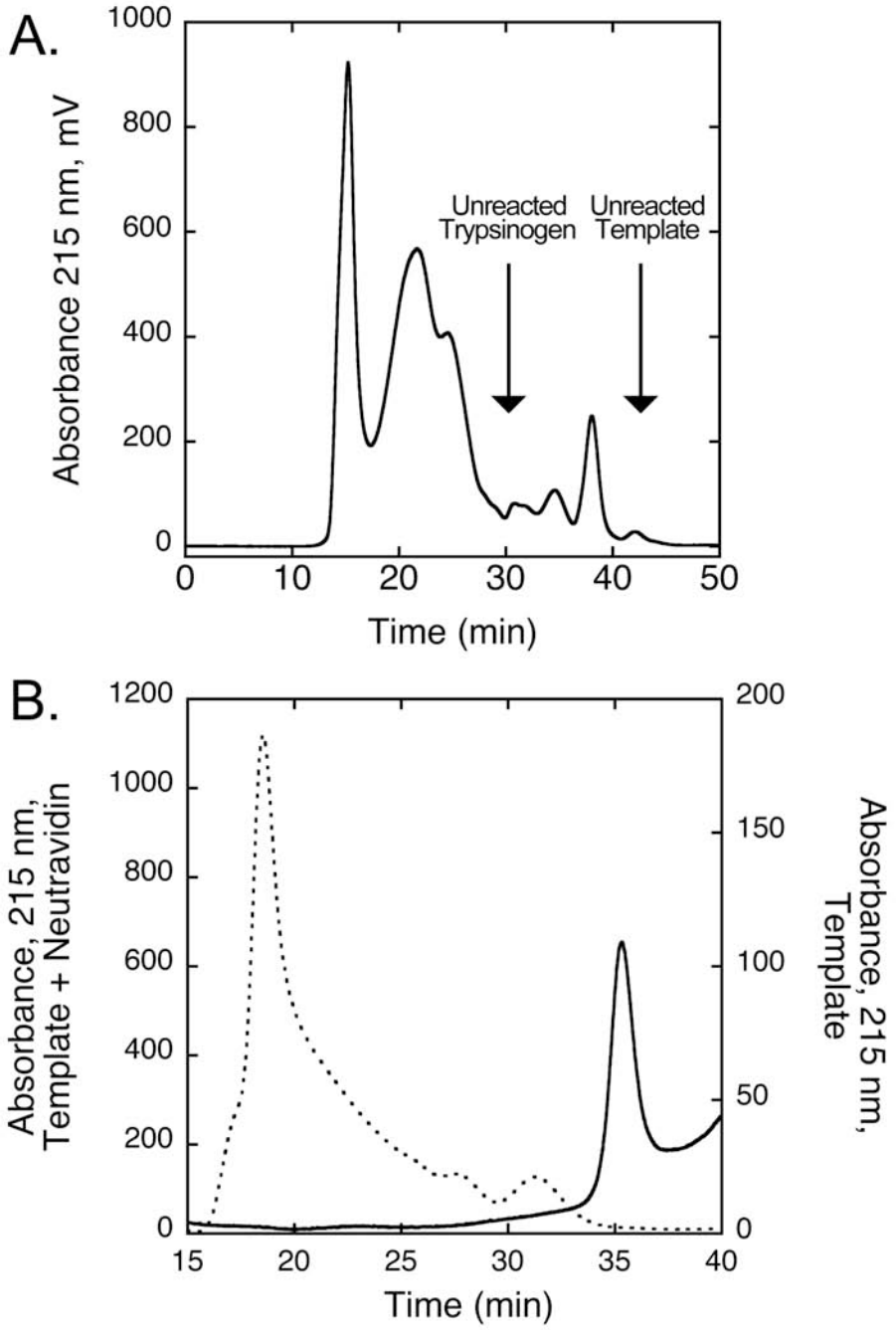

S4 (A) Reaction of Peptide C1-MaI with trypsinogen, after reaction of trypsinogen with SATA. The course of the reaction was monitored by size exclusion chromatography using Superdex 200. The figure shows a large peak consisting of the template peptide with three molecules of trypsinogen attached, and two smaller peaks containing one or

two molecules of trypsinogen. The elution positions of unreacted trypsinogen and unreacted template are marked by arrows. (B) Reaction of Peptide 7, Cyclo-(^{D}Cys(S-Mal-GEGEGEGK(Biotin)-OH)-Gly-Arg-Gly)$_3$, with neutravidin, as monitored by size exclusion chromatography using Superdex 200. Effluent is monitored at 215 nm. A large total volume peak, attributable to DMSO, is not shown. Elution of Peptide 7 alone is shown with a solid line; the product of reaction of neutravidin and Peptide 7 is shown with the dotted line.

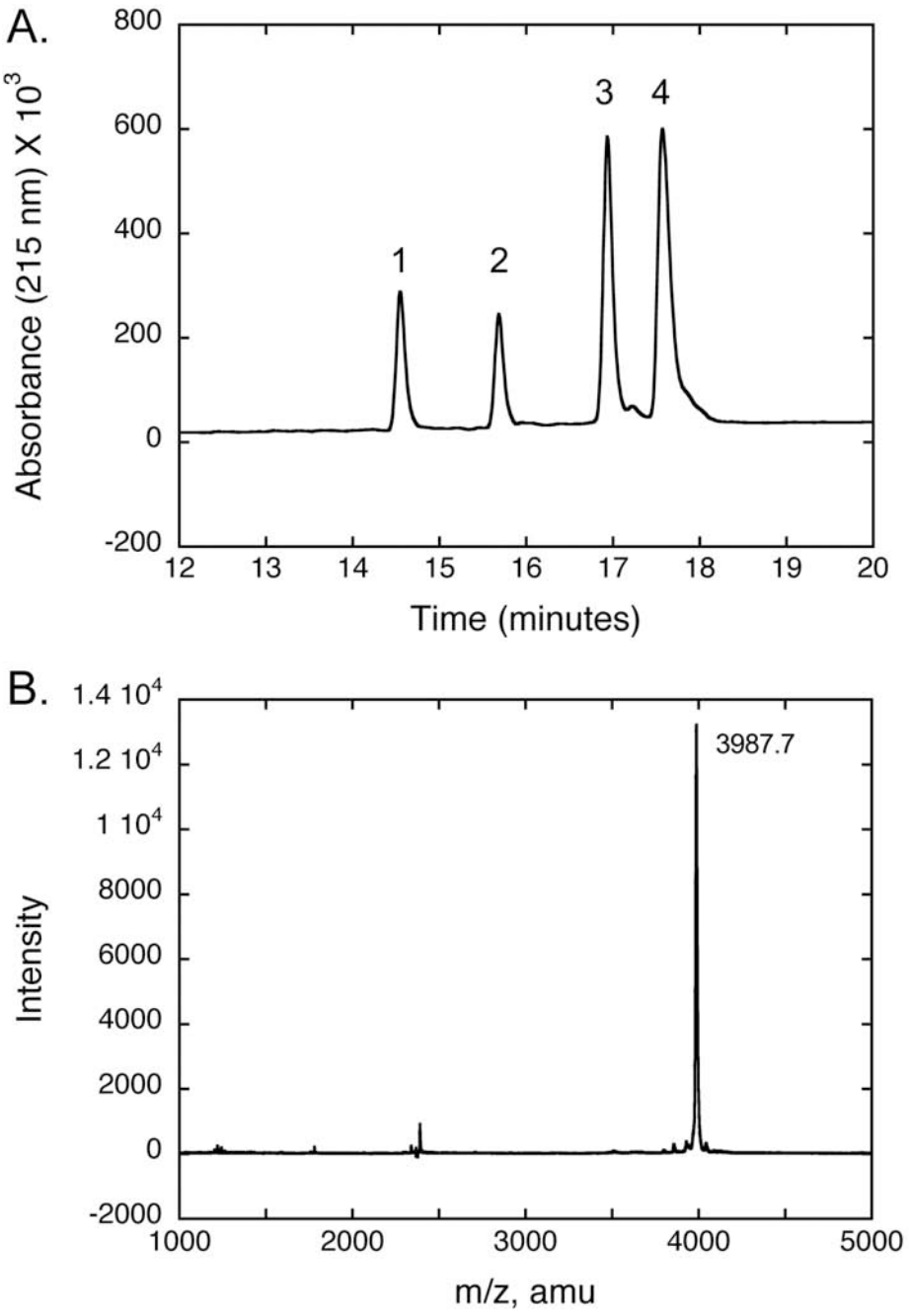

S5. Reverse phase HPLC (A) and MALDI-TOF mass spectrometry (B) of products of the reaction of Peptide 6, Mal-GEGEGEGK–OH (Mal = maleimidylhexanoyl), with cyclic template Peptide C2, cyclo(–NH–(DCysGlyArgGly)–CO–). MALDI-TOF mass spectrometry identifies peak 4 in the preparative RP-HPLC chromatogram as the

template with three attached molecules of Peptide 6. The purified product has m/z = 3987.7 (expected = 3985.1). Peak 3 in the chromatogram is unreacted Peptide 6; peaks 1 and 2 are the template with one and two molecules of Peptide 6 attached.

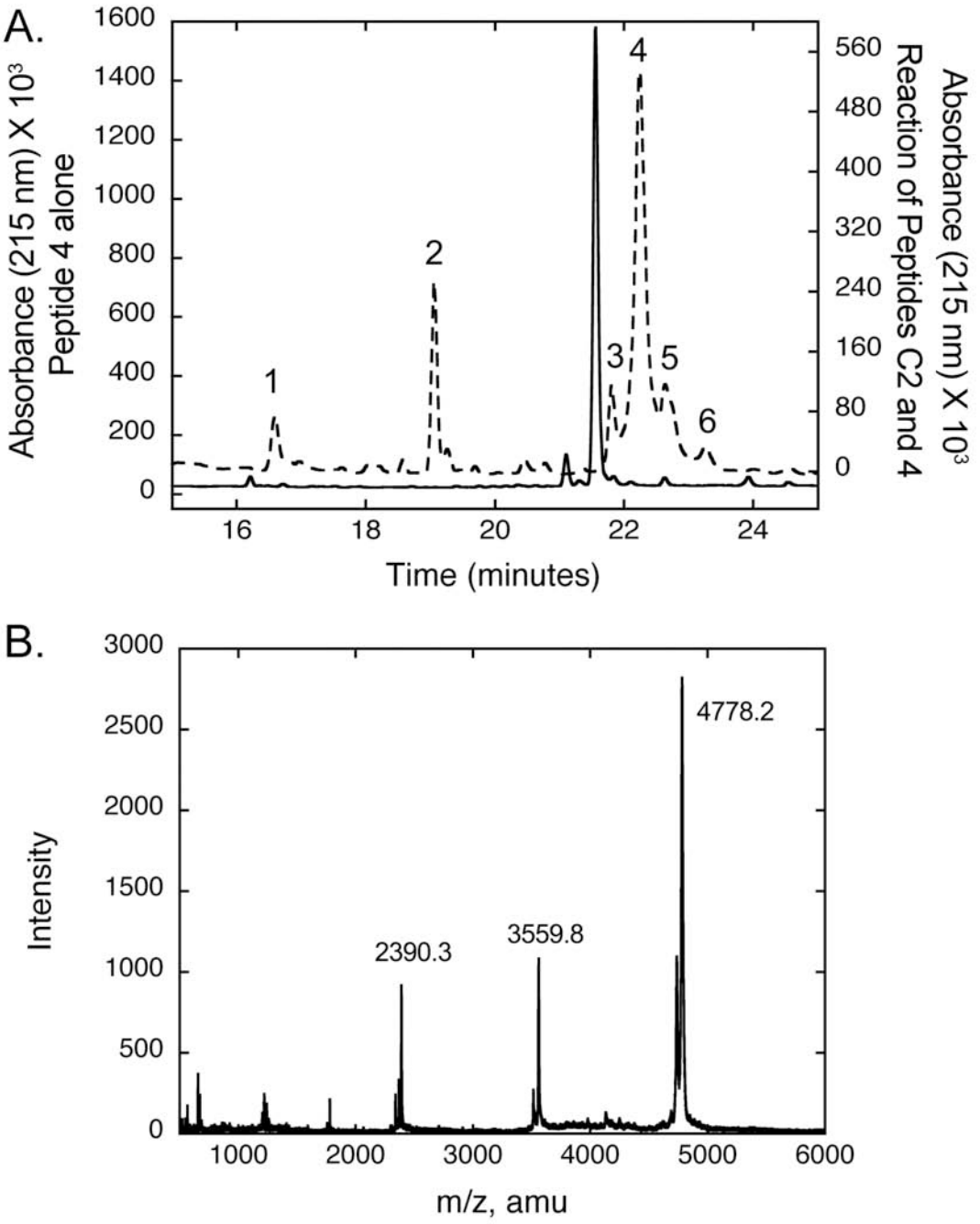

S6. Reverse phase HPLC (A) and MALDI-TOF mass spectrometry (B) of products of the reaction of the fibril-forming Peptide 4, Mal-PEG-GNNQQNY–OH, with the cyclic template Peptide C2, cyclo(–NH–(DCysGlyArgGly)–CO–). The tracing shows Peptide C2 alone (solid line) and the products of the reaction (dashed line). MALDI-TOF mass

spectrometry shows a mixture of products. The predominant product, labelled peak 4, is the cyclic Peptide C2 with three ligated copies of Peptide 4 (m/z = 4778.2); the peak also contains Peptide C2 with one or two ligated copies of Peptide 4 (m.z = 3559.8 and 2390.3, respectively). No attempt was made to separate the products of this reaction.

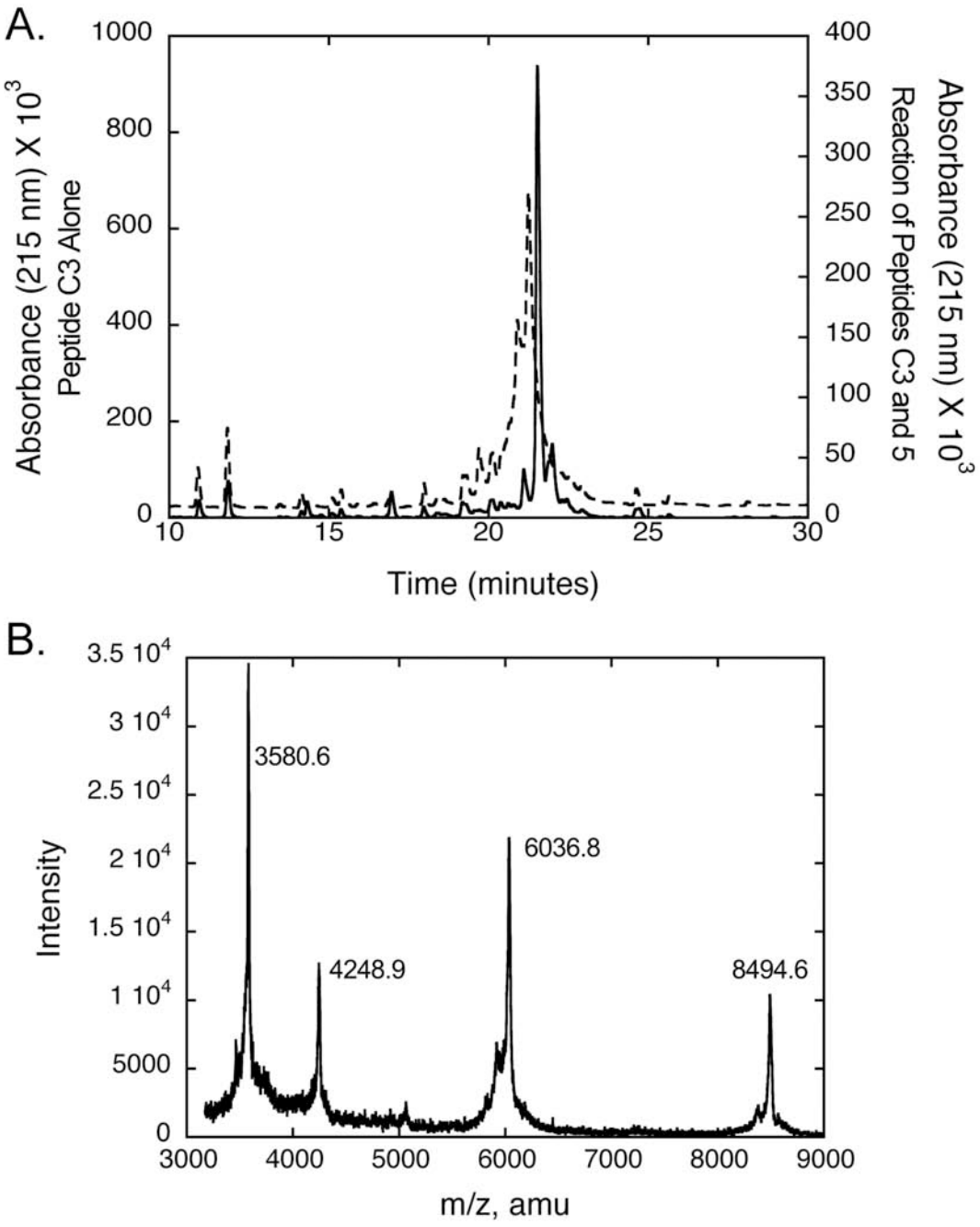

S7. Reverse phase HPLC (A) and MALDI-TOF mass spectrometry (B) of products of the reaction of the fibril-forming Peptide 5, Mal-SDDYYYGFGSNKFGRPRDP–OH with Peptide C2, cyclo(–NH–(^{D}CysGlyArgGly)–CO–). The products (dotted line) elute from the column slightly earlier than unreacted Peptide 5 (solid line), indicating an increase in

the apparent molecular weight. MALDI-TOF mass spectrometry shows that the products are a mixture of compounds, i.e. the Peptide C2 containing one, two or three ligated copies of Peptide 5. No attempt was made to isolate the individual species.

Bioconjugate Chemistry 20th Anniversary

Subscriber access provided by SHEMYAKIN-OVCHINNIKOV INST

Article

Antigen Delivery with Poly(Propylacrylic Acid) Conjugation Enhances MHC-1 Presentation and T-Cell Activation

Suzanne Flanary, Allan S. Hoffman, and Patrick S. Stayton

Bioconjugate Chem., **2009**, 20 (2), 241-248• DOI: 10.1021/bc800317a • Publication Date (Web): 06 January 2009

Downloaded from http://pubs.acs.org on May 8, 2009

More About This Article

Additional resources and features associated with this article are available within the HTML version:

- Supporting Information
- Access to high resolution figures
- Links to articles and content related to this article
- Copyright permission to reproduce figures and/or text from this article

View the Full Text HTML

ACS Publications
High quality. High impact.

Bioconjugate Chemistry is published by the American Chemical Society. 1155 Sixteenth Street N.W., Washington, DC 20036

Antigen Delivery with Poly(Propylacrylic Acid) Conjugation Enhances MHC-1 Presentation and T-Cell Activation

Suzanne Flanary, Allan S. Hoffman, and Patrick S. Stayton*

Department of Bioengineering, University of Washington, Seattle, Washington 98195. Received July 24, 2008; Revised Manuscript Received October 3, 2008

While many infectious diseases are controlled by vaccine strategies, important limitations continue to motivate the development of better antigen delivery systems. This study focuses on the use of a pH-sensitive polymeric carrier based on poly(propylacrylic acid) (PPAA) to address the need for more potent CD8 cytotoxic T-cell (CTL) responses. An MHC-1/CD8 CTL cell model system with ovalbumin as the protein antigen was used to test whether PPAA could enhance the delivery of ovalbumin into the MHC-1 display pathway. Ovalbumin was conjugated to poly(propylacrylic acid-*co*-pyridyldisulfide acrylate) (PPAA-PDSA) by disulfide exchange to make reversible conjugates that could be reduced by the glutathione redox system in the cytosol of antigen presenting cells. The PPAA-PDSA ovalbumin conjugates displayed the pH-sensitive membrane disruptive properties of the parent polymer as determined by their hemolysis activities (sharply active at the endosomal pH values of 6−6.5). The polymer−ovalbumin conjugates exhibited strong 22-fold increases in the MHC-1 presentation and ovalbumin-specific CTL activation compared to free ovalbumin. No CTL activation was observed with control conjugates of ovalbumin and poly(methylacrylic acid) (PMAA) that do not display membrane disruptive activies, suggesting that it is the membrane destabilizing properties of the polymer that result in increased MHC-1 display and CTL activation. Further mechanistic studies quantitated the time course of stable intracellular localization of radiolabeled conjugates. 52% of initially internalized PPAA-conjugated ovalbumin remained in the cells after 4 h, compared to less than 10% of ovalbumin or PMAA−ovalbumin. These results showing enhanced cytosolic delivery and MHC-1 presentation for the PPAA−antigen conjugates suggest that they warrant future characterization as a CD8-enhancing vaccine delivery system.

INTRODUCTION

Vaccines currently play an important role in medicine, but many pathogens remain resistant to vaccine development, and therapeutic vaccines against cancer have faced considerable efficacy challenges. One of the most general challenges in the vaccine field is generating a robust and efficacious CD8 cytotoxic T-lymphocyte response, even though many potentially suitable antigens against tumors and infectious agents have been identified (*1*−*3*). $CD8^+$ cytotoxic T-lymphocytes (CTLs) are able to directly kill diseased cells and are critical to effective immunotherapy (*4, 5*), while $CD4^+$ helper T-lymphocytes also play an important role in a sustained immune response (*6, 7*). Helper T-lymphocytes are activated upon recognition of antigens presented by major histocompatibility complex class 2 (MHC-2) proteins. This pathway is accessed by exogenous antigens that are processed and combined with MHC-2 molecules within modified endosomal compartments of the APC. CTLs are activated by recognition of antigenic peptides displayed by MHC-1 proteins that are accessed primarily via the cytoplasm, although class I cross-presentation of antigens present in vesicular compartments can occur to some degree, especially in the case of larger particulate substances taken up by phagocytosis (*8*−*10*).

Exogenous proteins enter APCs through macropinocytosis and are often degraded, sequestered, or exocytosed in the endosomal−lysosomal pathway without gaining access to the cytoplasm (*11*−*13*). Enhancing the escape of therapeutic protein antigens from the compartments in which they are endocytosed could potentially increase the efficacy of protein vaccines through increased activation of CTLs (*14, 15*). Several groups have explored the use of pH-sensitive polymer-based delivery systems that take advantage of the decreased pH in the endosome. Carrier particles containing acid-degradable linkages, such as acetal (*14*−*16*), hydrozone (*17, 18*), or ketal (*19*) bonds, have been developed to degrade more rapidly in the acidic endosomal environment to trigger release of their cargo. Block ionmer complexes have been developed that increase in positive charge at endosomal pH, which could potentially result in endosomal membrane interaction (*20*). A popular approach has utilized cationic polymer systems, which enhance endosomal release via the "proton sponge effect" (*21*−*25*). Additionally, particles formed from poly(D,L-lactic-*co*-glycolic acid) (PLGA) have been widely investigated for antigen delivery and have resulted in increasing MHC-1 presentation of encapsulated antigens (*26*−*28*). While some endosomal escape is observed for this system (*27*), a mechanism for cytosolic delivery is not well established.

Our group has developed synthetic polymers based on alkyl(acrylic acid) monomers that display pH-sensitive, membrane-destabilizing activities (*29*−*36*). In the ionized state, the polymers are inactive at membrane destabilization, but at the decreased pH levels typical of the endosome (pH 5.5−6.5), the carboxyl groups become protonated and the polymers transition to a state that is membrane-destabilizing. This mechanism mimics the pH-dependent membrane disruptive activity of pathogenic proteins such as hemaglutinin (*37, 38*) and diphtheria toxin (*39, 40*), and of synthetic fusogenic peptides such as GALA (*41*). The mechanistic utility of pathogenic proteins has demonstrated the importance of endosomal release in MHC-1 presentation and CTL activation (*42*−*46*), but

* Corresponding author address: Patrick Stayton, UW Bioengineering, Box 355061, 1705 NE Pacific St., Seattle, WA 98195, stayton@u.washington.edu, 206-685-8148.

10.1021/bc800317a CCC: $40.75 © 2009 American Chemical Society
Published on Web 01/06/2009

corresponding biological responses to the pathogenic proteins has limited their clinical translation.

Here, we report the characterization of a pH-responsive, membrane-destabilizing polymeric carrier for cytosolic protein antigen delivery in a model MHC-1 presentation system. This model utilizes CD8+ T-cells that is activated upon T-cell receptor ligation to an MHC-1/ovalbumin peptide complex displayed from a model RAW macrophage cell (*14*, *47*). The poly(propylacrylic acid-*co*-pyridyldisulfide acrylate) (PPAA-PDSA) polymer was designed to conjugate ovalbumin by disulfide exchange between thiolated protein and the PDSA monomers. The resulting protein−polymer disulfide bond can be reduced by the cytosolic glutathione reduction system to leave the free antigen for subsequent proteolytic processing. Results showing a strong enhancement of CTL activation suggest that the intracellular pharmacokinetic step of vesicular release is a limiting barrier to subsequent protein processing and MHC-1 presentation.

MATERIALS AND METHODS

Polymer Synthesis. All chemicals and reagents were ACS grade purchased from Sigma-Aldrich, St. Louis, MO, and used without further purification unless otherwise noted. For the synthesis of the PPAA-PDSA polymer, 0.007 mol propylacrylic acid (PAA) (Gateway Chemical Technology, St. Louis, MO), 0.00011 mol PDSA (*33*), and 0.000056 mol free-radical initiator azobisisobutyronitrile (AIBN, purified by recrystallization from methanol) were combined in a 5 mL flask and degassed by 4 rounds of freeze−vacuum−thaw, then reacted at 60 °C for 24 h. The polymer was dissolved in 3 mL dimethyl formamide (DMF) and purified by 3 rounds of precipitation in 500 mL diethyl ether. Poly(methacrylic acid-*co*-PDSA) (PMAA-PDSA) was synthesized for use as a control polymer. It was formed by reversible addition fragmentation chain transfer polymerization (RAFT) by combining 0.016 mol methacrylic acid (MAA) (purified by distillation), 0.00022 mol PDSA, 0.000052 mol chain transfer agent 4-cyanopentanoic acid dithiobenzoate (CTP) (*48*), 0.000052 mol initiator 2,2′-azobis (2,4-dimethyl valeronitrile) (V-65, Wako Chemicals USA, Richmond VA), and 3 mL DMF in a 5 mL round-bottom flask. The reaction was degassed by purging with N_2 for 20 min, then polymerized at 40 °C for 24 h. Six milliliters DMF was added, and the polymer was purified by 3 rounds of precipitation in 1 L diethyl ether.

Polymer compositions were determined by ^{1}H NMR using a Bruker AVance 300 MHz instrument and deuterated dimethyl sulfoxide (DMSO-d_6, Fisher Chemical, Pittsburgh, PA). The characteristic ^{1}H NMR (DMSO-d_6) polymer peaks were as follows: 4.0 ppm (2H, O-CH_2-R, PDSA), 7.2 ppm (1H, aromatic, PDSA), 7.8 ppm (2H, aromatic, PDSA), 8.5 ppm (1H, aromatic, PDSA), 12.1 ppm (1H, -COOH, PAAc/MAAc). PDSA content was determined both by NMR and by the absorbance at 343 nm of pyridine-2-thione released from the polymer following reduction with excess of dithiothreitol (DTT). The polymer molecular weights were determined by GPC using a Viscotek VE2001 sample module and VE3580 refractive index detector (Viscotek, Houston, TX), and Tosoh TSK-GEL α-3000 and α-4000 columns (Tosoh Biosciences, Montgomeryville, PA). Polymer molecular weights were determined on the basis of poly(methacrylic acid) (PMMA) standards using HPLC-grade DMF with 0.1% lithium bromide as the mobile phase. The pK_a of the PPAA-PDSA was determined by acid/base titration of 50 mg polymer in distilled, deionized water, starting at pH 12.5 and titrating with 0.1 N HCl.

Polymer−Protein Conjugation and Characterization. Conjugation was performed via disulfide exchange between the PDSA component of the polymer and free thiols introduced onto ovalbumin by reaction with Traut's reagent (2-iminothiolane, Pierce Biotechnology, Rockford, IL). Ten milligrams ovalbumin was mixed with a 10× molar excess of Traut's reagent in conjugation buffer (0.1 M phosphate buffer, pH 7.8, 0.15 M NaCl, 5 mM EDTA) for 1 h at room temperature. The reaction mixture was purified using a PD-10 desalting column containing Sephadex G-25 (MWCO 5kD, GE Healthcare, Piscataway, NJ) and the degree of modification was estimated by Ellman's assay (Pierce Biotechnology, Rockford, IL). A 2.5× molar excess of polymer, either PPAA-PDSA or PMAA-PDSA, was immediately added to the modified protein and allowed to react 2 h at room temperature in conjugation buffer. The degree of conjugation was estimated by measuring the absorbance at 343 nm (A_{343}) of the pyridine-2-thione group released from PDSA upon disulfide exchange, and the conjugate was purified on a PD-10 column and lyophilized for storage.

Radioactively labeled PPAA-PDSA and PMAA-PDSA−ovalbumin conjugates were formed for use in the cellular uptake and exocytosis experiments. The procedure was identical to that listed above, with the following exceptions. Ovalbumin was mixed with a 20-fold molar excess of Traut's reagent. A 3× molar excess of ^{14}C-iodoacetamide (MP Biomedical, Solon, OH) was then added to react with some of the introduced thiol groups. After reacting for 1 h, the 2.5× molar excess of polymer was added to form the conjugate.

The molecular weight distribution was determined by GPC (Viscotek VE2001 sample module, VE3580 RI Detector, Waters Corp. Ultrahydrogel columns) in 0.1 M sodium phosphate buffer, pH 8, using poly(ethylene oxide) (PEO) standards (Polysciences, Inc., Warrington, PA). The final weight percent of ovalbumin in the conjugates was determined by the BCA protein assay (Pierce Biotechnology, Rockford, IL), using an ovalbumin standard curve. SDS-PAGE (polyacrylamide gel electrophoresis) was performed to detect any unreacted ovalbumin in the conjugate solution. Precast Tris-HCl polyacrylamide gels, 4−20% gradient, sample and running buffer, and protein standards were purchased from Bio-Rad, Hercules, CA. On the basis of the results of the BCA assay, conjugates were loaded onto the gels in the appropriate amounts to give 10 μg of ovalbumin per lane. Gels were run for 45 min at 100 mA, then visualized using Coomassie staining (Bio-Rad, Hercules, CA).

Red Blood Cell Hemolysis. The pH-dependent membrane-disruptive ability of the polymers and polymer−protein conjugates was estimated using a red blood cell hemolysis assay, described previously (*29*). Briefly, red blood cells were isolated and added to polymer and conjugate solutions (normalized to equivalent polymer amounts) of varying concentrations in 0.1 M phosphate buffer at pH values of 5.8, 6.6, and 7.4. The degree of RBC membrane disruption (% hemolysis) was quantified by measuring the absorbance at 541 nm of the hemoglobin released into the solution by lysed cells, in comparison with complete lysis by Triton X-100 detergent. Sample concentrations were all normalized to contain 5 μg/mL of polymer, and samples were performed in triplicate with error reported as ±1 standard deviation.

MHC- I Antigen Presentation and CTL Activation Assay. The ability of the polymer to increase cytoplasmic delivery and subsequent MHC class I antigen presentation was evaluated using the *lacZ* antigen presentation assay (*14*, *47*). This assay utilizes a specialized *LacZ* B3Z CTL hybridoma. These CTLs produce β-galactosidase upon recognition of the ovalbumin class I antigenic epitope SIINFEKL complexed with the MHC class I molecule H-2K^b, present on RAW 309.1 CR macrophages. Therefore, a measure of β-galactosidase activity can be used to determine the degree to which delivered ovalbumin is presented as a class I antigen. All tissue culture reagents were purchased from Invitrogen Corp., Carlsbad, CA, unless otherwise noted.

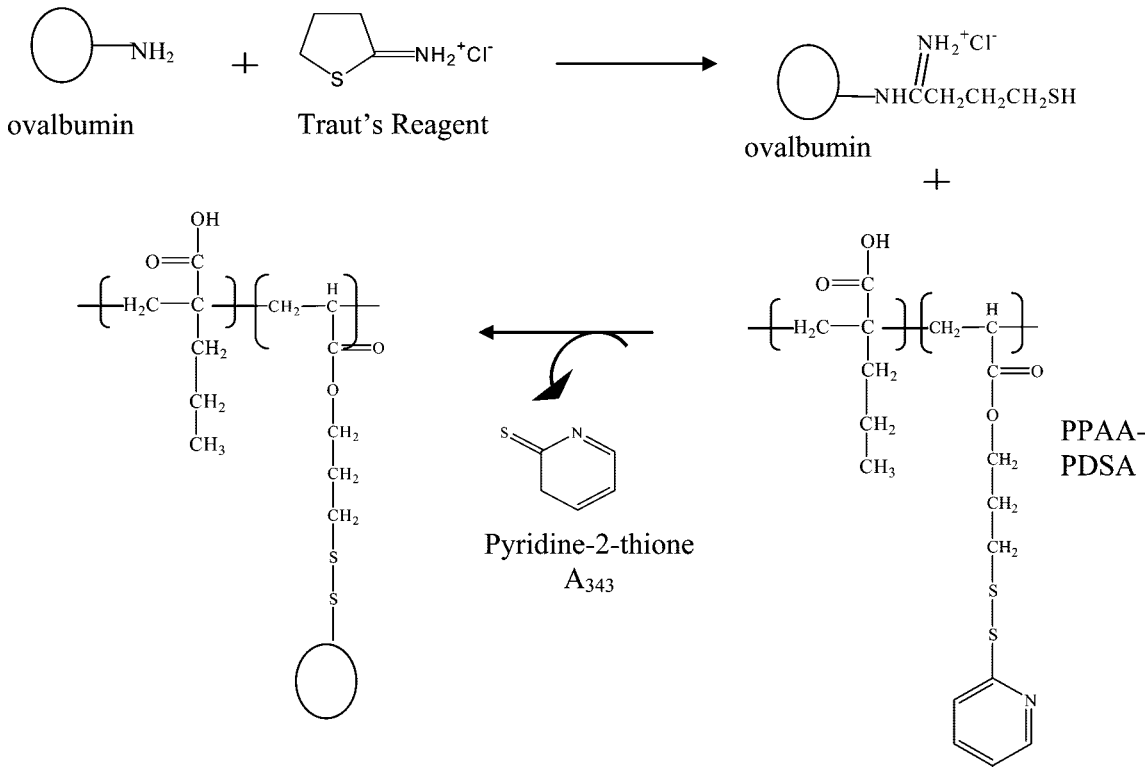

Figure 1. Schematic of chemistry for conjugation of ovalbumin to the PDSA moiety of the PPAA-PDSA polymer. The protein is first modified using Traut's reagent to convert primary amines to thiols, then the polymer is added and a disulfide exchange reaction occurs, releasing pyridine-2-thione. Reaction progress can be monitored by measuring A_{343} of released pyridine-2-thione. PPAA and PMAA conjugates consisting of 1.7 μg polymer per μg ovalbumin were formed.

RAW 309.1 CR macrophages (ATCC, Manassas, VA) were cultured in 90% DMEM with D-glucose and L-glutamine, 10% fetal bovine serum (FBS), supplemented with 100 U/mL penicillin/100 μg/mL streptomycin. B3Z CTLs were a gift from Dr. Nilabh Shastri, UC Berkeley. They were cultured in 90% RPMI medium with D-glucose and L-glutamine, 10% FBS, supplemented with 100 U/mL penicillin/100 μg/mL streptomycin, 50 μM 2-mercaptoethanol (Sigma-Aldrich, St. Louis, MO), and 1 mM sodium pyruvate. For the assay, RAW cells were plated at 5×10^4 cells per well in a 96-well plate and grown overnight. PPAA−ovalbumin conjugates and control samples were added to the cells and incubated 6 h in DMEM with 5% FBS. Three sample concentrations were tested: 50 μg/mL, 100 μg/mL, and 150 μg/mL (samples were normalized to represent equivalent ovalbumin concentrations). RAW cells were rinsed with DMEM; then, 1×10^5 B3Z cells per well were added and incubated 16 h. Cells were rinsed with phosphate buffered saline, then 100 μL lysis buffer [100 μM mercaptoethanol (Sigma-Aldrich, St. Louis, MO), 9 mM $MgCl_2$ (Sigma-Aldrich, St. Louis, MO), and 0.15 mM chlorophenol red β-D-galactoside (EMD Biosciences, San Diego, CA) in PBS] was added. After 4 h, the absorbance of released chlorophenol red was measured at 595 nm. All samples were evaluated in triplicate and errors are reported as ± 1 standard deviation. Maximum possible β-galactosidase production was determined by chemically stimulating the B3Z cells in media containing 3.15 μM ionomycin (Sigma-Aldrich, St. Louis, MO) and 10 ng/mL phorbol 12-myristate 13-acetate (Sigma-Aldrich, St. Louis, MO) for 4 h before rinsing and adding the lysis buffer.

Cellular Uptake and Exocytosis of ^{14}C-Ovalbumin and Ovalbumin−Polymer Conjugates. The cellular uptake and exocytosis of ^{14}C-labeled ovalbumin and the PPAA and PMAA−ovalbumin conjugates was studied in RAW 309.1 CR macrophages, using a procedure similar to that described by Besterman et al. (*49*). For measurement of the cellular accumulation of ^{14}C ovalbumin over time, RAW macrophages were plated in a 48-well plate at 75 000 cells/well and allowed to grow overnight. Ovalbumin, PPAA−ovalbumin conjugate, PMAA−ovalbumin conjugate, or a PPAA and ovalbumin physical mixture was added to the cells at a concentration of 50 μg/mL of ovalbumin. Samples were incubated for 15 min, 30 min, 1 h, or 2 h. The cells were then washed 2× with PBS and lysed using 1% Triton X-100 in water. Radioactivity in the cell media, PBS wash, and cell lysate was measured using a Beckman-Coulter LS 6500 liquid scintillation counter. EcoScint scintillation fluid was obtained from National Diagnostics, Atlanta, GA. Uptake of ^{14}C-ovalbumin is presented as the % radioactivity present in the cell lysate compared to the total radioactivity delivered. The experiment was performed with a minimum of $n = 3$.

To measure the exocytosis of ^{14}C-ovalbumin, RAW macrophages were again plated at 75 000 cells/well in a 48-well plate and allowed to grow overnight. Ovalbumin, PPAA−ovalbumin conjugate, PMAA−ovalbumin conjugate, or a PPAA and ovalbumin physical mixture was added to the cells at a concentration of 50 μg/mL of ovalbumin. Samples were incubated for either 1 or 15 min, then non-internalized conjugate was removed and cells were washed 2× with media. Fresh media was added to the cells at the following time points: 5 min, 10 min, 20 min, 30 min, 1 h, 2 h, and 4 h. The reappearance of ^{14}C-ovalbumin in the supernatant was measured at each time point. After 4 h, cells were lysed with 1% Triton X-100 and the radioactivity in the lysate was measured. The amount of ovalbumin internalized after the 1 or 15 min incubation time was determined as a percentage of the total delivered. The amount of ovalbumin exocytosed at each time point, as well as the amount remaining in the cells after 4 h, was then determined as a percentage of the total internalized. The experiments were performed with a minimum of $n = 3$.

In Vitro Cytotoxicity of Polymers and Conjugates. The cytotoxicity of the PPAA and PMAA polymers and conjugates was determined for both the RAW and B3Z cell lines used in the MHC-1 presentation assay. Cytotoxicity was evaluated using the LDH (lactate dehydrogenase) assay (Roche Applied Sciences, Indianapolis, IN). This assay allows colorimetric measurement of LDH activity in the supernatant, which correlates to the proportion of dead or damaged cells. Cells were plated at 5×10^4 cells/well in their normal culture media, and polymer and conjugate samples were added to concentrations up to 300 μg/mL, then incubated for 24 h. Cells were centrifuged at 250 *g* for 10 min, then 100 μL supernatant was removed and combined with 100 μL LDH reagent. The absorbance at 490 nm (reference 650 nm) was recorded every 5 min for 30 min, and cell survival was determined by comparing to untreated cells and cells lysed with 1% Triton X-100 in water. Each sample was evaluated in triplicate, and errors are reported as the standard error of the mean (SEM).

Statistical Anaylsis. Statistical testing was performed on all data using analysis of variance (ANOVA). The least significant difference (LSD) method was subsequently used for comparison of specific groups in the ANOVA analysis.

RESULTS AND DISCUSSION

Synthesis and Characterization of Polymers and Conjugates. The conjugation scheme for attaching ovalbumin to PPAA-PDSA is shown in Figure 1. The conjugates are formed through disulfide exchange of the ovalbumin thiol with the PDSA group in the polymer and are designed to be reduced by glutathione in the cell cytoplasm, freeing the protein for processing and MHC-1 presentation. The membrane-disruptive PPAA-PDSA polymer was synthesized by free-radical polymerization and resulted in a polymer with 3 mol % PDSA and $M_w = 26$ kD, $M_n = 10$ kD, and PDI = 2.6, based on GPC analysis using PMMA standards. The pK_a of this polymer was determined by acid/base titration to be 6.8, which is in the range of the early endosome. A non-membrane-disruptive polymer, PMAA-PDSA, of similar size ($M_w = 34$ kD, $M_n = 12$ kD, PDI = 2.8) containing 2 mol % PDSA was synthesized as a control. Methacrylic acid is less hydrophobic than propylacrylic acid in the protonated form and does not cause any membrane disruption in the RBC hemolysis assay.

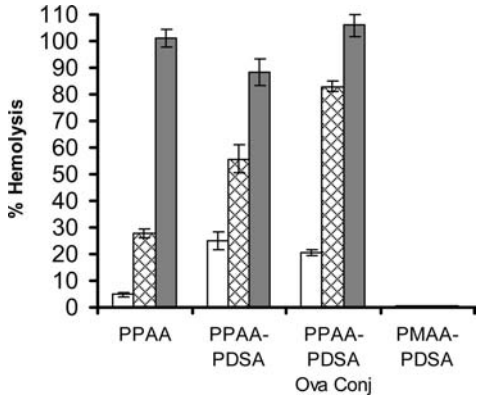

Figure 2. pH-dependent hemolysis properties of PPAA polymers and ovalbumin conjugates. Red blood cells were isolated and added to polymer and conjugate solutions (polymer concentrations = 5 μg/mL) in 0.1 M phosphate buffer at pH values of 7.4 (□), 6.6 (×), and 5.8 (■). Hemolysis is reported as a percentage of complete lysis by Triton X-100. PPAA-PDSA shows high membrane-disruptive activity at pH 5.8 but considerably lower membrane disruption at pH 7.4. The polymer retains its hemolysis capabilities after conjugation to the hydrophilic protein ovalbumin. PMAA-PDSA, however, does not lyse red blood cells at any pH due to the decreased hydrophobicity of its methyl side chain compared with the propyl side chain of PPAA.

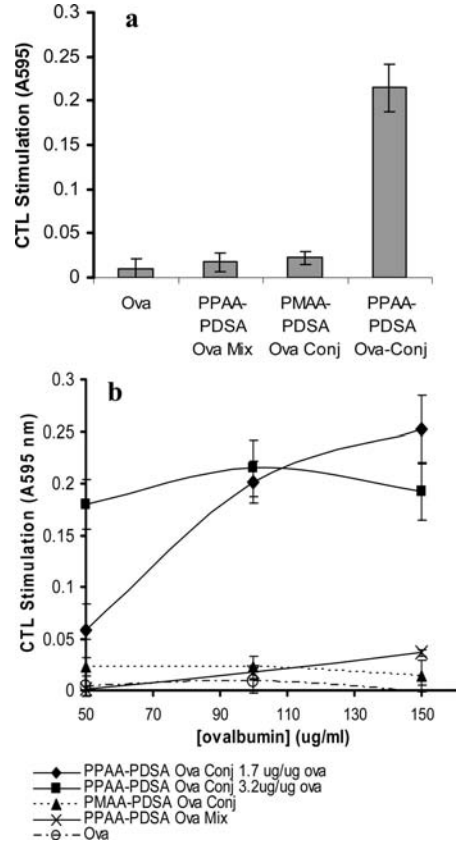

Figure 3. CTL activation/MHC-I presentation of PPAA−ovalbumin conjugates. Samples were incubated with RAW macrophages for 6 h then removed and B3Z T-cells were added for 16 h. Cells were rinsed and incubated 4 h with lysis buffer containing chlorophenol red β-D-galactoside, then absorbance of released chlorophenol red was measured at 595 nm. Samples were evaluated in triplicate and errors are reported as ±1 standard deviation. For reference, the maximum possible β-galactosidase production was determined by chemically stimulating the B3Z cells using PMA/ionomycin for 4 h, which gave an A_{595} of 0.56. (a) Ovalbumin concentration = 100 μg/mL. The PPAA−ovalbumin conjugate shows significantly greater CTL activation than do any of the control samples ($p < 0.0005$). This is likely due to the endosomal disruption provided by PPAA, which allows the protein to more efficiently access the MHC-I pathway in the cytoplasm. However, PMAA conjugation results in low CTL activation, similar to that for free ovalbumin or a PPAA ovalbumin physical mixture ($p = 0.2$). This suggests that the increase in MHC-1 presentation provided by PPAA is due to its endosomal disruptive properties rather than solely to increased uptake due to its larger size compared to free ovalbumin. (b) The PPAA−ovalbumin conjugates enhance CTL stimulation is a dose-dependent manner. When the polymer ratio is increased from 1.7 μg/μg ova to 3.2 μg/μg ova, maximal CTL activation is reached at a lower ovalbumin concentration.

The degree of thiolation of the ovalbumin used to form the polymer−ovalbumin conjugates was determined by Ellman's assay to be 15% of the total available lysines. The ovalbumin conjugates formed from both the PPAA-PDSA and PMAA-PDSA polymers were found by BCA assay to contain 37 weight % ovalbumin and 63 weight % polymer, or 1.7 μg polymer per μg protein, and GPC analysis gave $M_w = 200$ kD, $M_n = 45$ kD, PDI = 4.4 for the PPAA-PDSA−ovalbumin conjugate and $M_w = 130$ kD, $M_n = 57$ kD, PDI = 2.3 for the PMAA-PDSA−ovalbumin conjugate. The ^{14}C-labeled conjugates used for the cellular internalization studies were of similar sizes: $M_w = 140$ kD, $M_n = 40$ kD, PDI = 3.5 for the PPAA conjugate and $M_w = 120$ kD, $M_n = 50$ kD, PDI = 2.4 for the PMAA conjugate. The degree of thiolation of the ovalbumin used to form these conjugates was determined by Ellman's assay to be 30%. The radiolabeled PPAA and PMAA conjugates were found

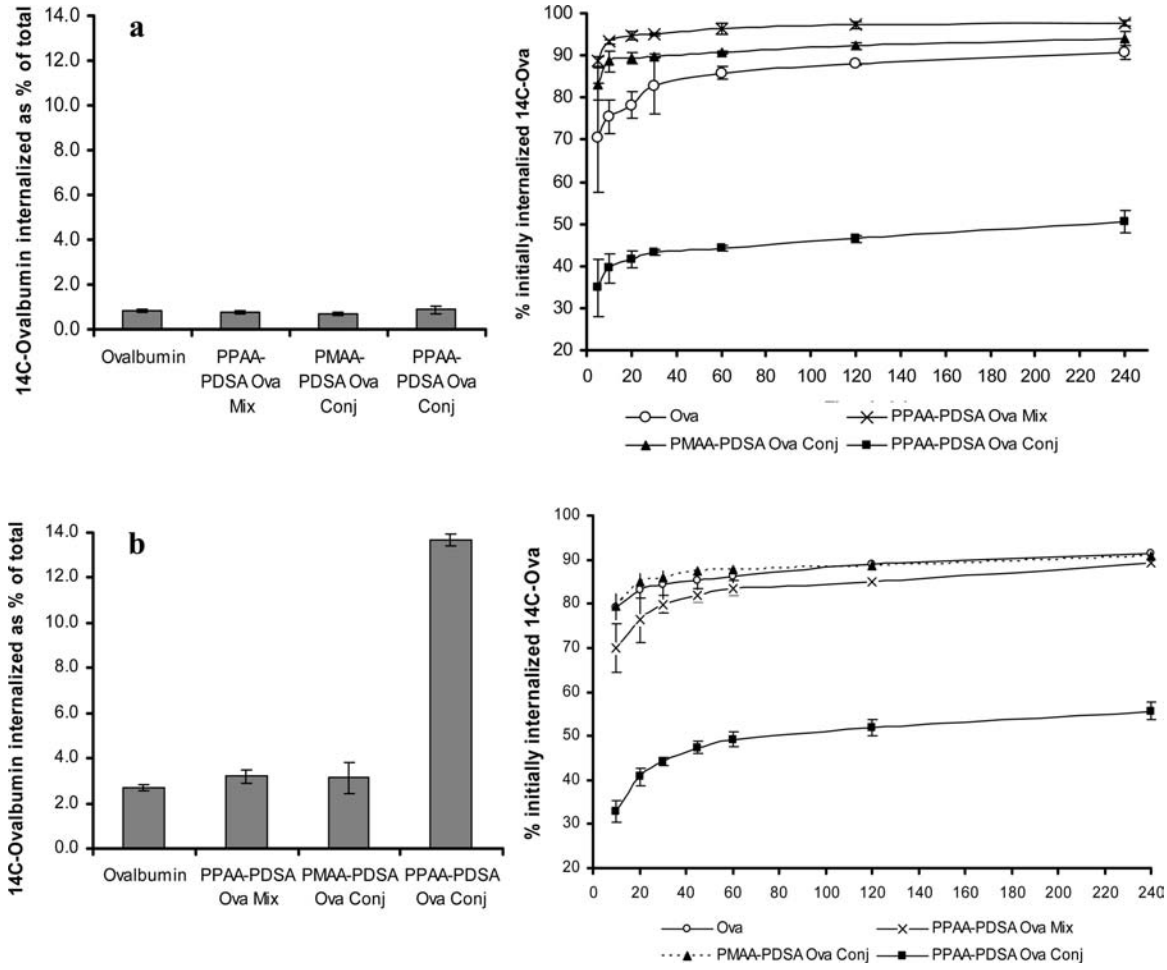

Figure 4. Exocytosis of ^{14}C-ovalbumin after (a) 1 min uptake time and (b) 15 min uptake time. Samples were incubated with RAW macrophages and non-internalized conjugate was removed. Fresh media was added to the cells at various time intervals and the reappearance of ^{14}C-ovalbumin in the supernatant was measured. After 4 h, cells were lysed with 1% Triton X-100 and the radioactivity in the lysate was measured. Samples were evaluated with a minimum of $n = 3$. The amount of ovalbumin initially internalized was determined as a percentage of the total delivered (left-side panels). It can be seen that the amount of ovalbumin taken into the cells in 1 min is similar for all samples ($p = 0.66$) giving a uniform starting point for the exocytosis measurements. However, the preferential accumulation of PPAA−ovalbumin is already noticeable at the 15 min uptake time. The amount of ovalbumin exocytosed at each time point was then calculated as a percentage of the amount initially internalized (right-side panels). Most exocytosis occurred in the first 30 min, and exocytosis rates were similar for all samples. However, the amount of ovalbumin that remained in the cells and was not exocytosed was greatly enhanced for PPAA conjugates. This effect is likely due to the ability of the polymer to disrupt the endosomal membrane and deliver the ovalbumin to the cytosol before exocytosis can occur.

to be 34 and 40 wt % ovalbumin, or 1.9 μg polymer per μg protein and 1.5 μg polymer per μg protein, respectively. SDS-PAGE was performed to ensure that free protein did not remain in the conjugate mixtures, as it could interfere with interpretation of the MHC-1 presentation assay results.

Red Blood Cell Hemolysis. Red blood cell hemolysis assays were performed to evaluate the pH-dependent membrane-disruptive activity of the polymers and polymer−protein conjugates (*50*). Hemolysis assays were conducted at three pH values (7.4, 6.6, and 5.8) in order to approximate physiological conditions and the conditions found in early and late endosomes. Conjugate concentrations were adjusted to contain 5 μg/mL of polymer. The results of this assay are detailed in Figure 2. As expected, the PPAA-PDSA polymer and conjugates were considerably more hemolytic at the lower pH characteristic of the endosome (pH 5.8). The PPAA-PDSA polymer shows slightly higher hemolyis at physiological pH than does a PPAA homopolymer of the same size, which consistently gives less than 10% hemolysis. This increased hemolyis at pH 7.4 is likely due to the hydrophobicity added by the PDSA monomer, especially the pyridyl group, which is removed upon conjugation. The increased hemolysis at pH 7.4 has not resulted in increased cytotoxicity at the concentrations and incubation times used. The PPAA−ovalbumin conjugates have similar hemolysis profiles to the PPAA-PDSA polymer alone, indicating that the polymer retains its hemolytic activity when attached to the 40 kD ovalbumin protein.

MHC-I Antigen Presentation and CTL Activation Assay. The ability of the polymer to enhance delivery of protein antigen into the MHC class I pathway was evaluated using the *LacZ* class I presentation assay (*14*, *47*). The PPAA-PDSA−ovalbumin conjugate resulted in a strong 22-fold increase in MHC-I presentation and CTL activation compared to free ovalbumin ($p = 0.0001$), as shown in Figure 3. The ovalbumin must be chemically attached to the PPAA in order to be effectively delivered into the MHC-1 pathway, as physical mixtures showed only background CTL activation levels ($p = 0.20$ compared to free ovalbumin). The PMAA−ovalbumin conjugates did not significantly enhance CTL activation over delivery of free ovalbumin ($p = 0.72$). These results correlate the membrane destabilizing activity of the polymer to the level of MHC-1 pathway and CTL activation, and suggest that the increase in presentation is not solely the result of increased cellular uptake due to the larger size of the conjugate compared to free ovalbumin. Furthermore, PPAA conjugation increases the CTL activation in a dose-dependent manner, whereas higher

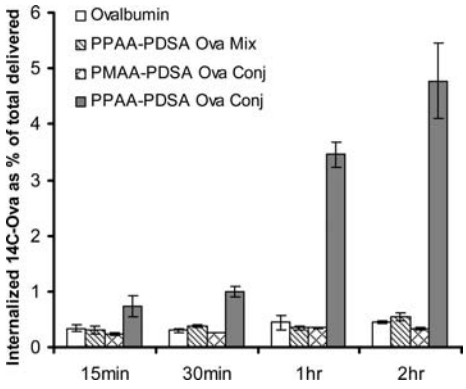

Figure 5. Uptake of ^{14}C-ovalbumin−PPAA increases over time. RAW macrophages were incubated with samples at a concentration of 50 μg/mL of ovalbumin. The cells were then washed with PBS and lysed using 1% Triton X-100. Radioactivity in the cell media, PBS wash, and cell lysate was measured; and uptake of ^{14}C-ovalbumin was calculated as the % radioactivity present in the cell lysate compared to the total radioactivity delivered. Experiments were performed in triplicate and error is expressed as ±1 standard deviation. It can be seen that PPAA-conjugated ovalbumin continually accumulates significantly in the cell, whereas the control sample levels remain fairly constant ($p > 0.09$). This is likely due to the ability of PPAA−ovalbumin to escape the endosome before being exocytosed.

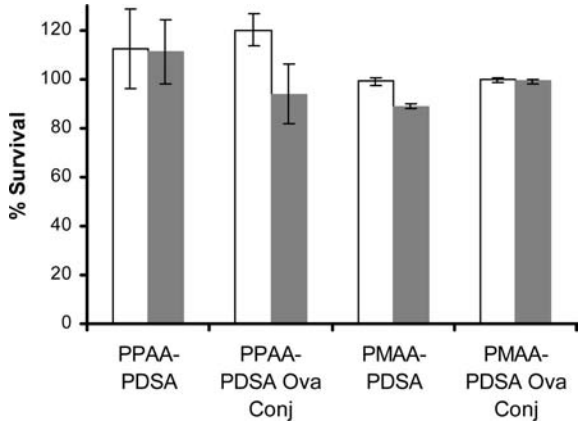

Figure 6. Cytotoxicity of PPAA and PMAA polymers and conjugates. Cytotoxicity was determined for both RAW and B3Z cells using the LDH assay. Samples were added to cells for 24 h at a concentration of 300 μg/mL polymer, twice the highest concentration used in the MHC-1 presentation assay. The cell supernatant was then combined with LDH reagent and the absorbance at 490 nm was recorded. Percent survival $= 1 - [(A_{490}$ of sample $- A_{490}$ of untreated cells control)/(A_{490} of TritonX control $- A_{490}$ of untreated cells control)] $\times$ 100%. Samples were evaluated in triplicate and error is expressed as ± SEM. It can be seen that excessive toxicity was not observed for any of the samples.

concentrations of control samples do not result in significant increases in CTL activation ($p < 0.2$) (Figure 3b). Increasing the amount of PPAA in the conjugate further exaggerates this effect: when the weight ratio of polymer/protein is doubled from 1.7 to 3.2 μg polymer per μg protein, CTL activation increases, becoming maximized at a lower ovalbumin concentration. While direct comparisons to other similar antigen delivery systems are not possible due to the different carrier architectures (soluble vs particulate) and differences in experimental conditions and data presentation, the PPAA conjugates perform similarly to those reported previously with the B3Z CTL activation assay. Acid-degradable particles used to deliver ovalbumin have resulted in maximal A_{595} values (the measure of CTL activation) in the range 0.25−0.4 (*14*, *16*), which is similar to that reported in our study, and PLGA particles have been shown to provide a 5-fold increase in CTL activation over delivery of ovalbumin alone (*26*).

Cellular Uptake and Exocytosis of ^{14}C-Ovalbumin and Ovalbumin−Polymer Conjugates. In order to further explore the mechanism of PPAA action, the cellular uptake and internalization of radiolabeled ovalbumin was studied in RAW macrophages. It was found that the major effect of PPAA was to reduce the amount of ovalbumin recycled back out of the cell after initial internalization. The samples were incubated with RAW macrophages for 1 min, and fresh media was applied after washing of the cells at regular time intervals from 5 min to 4 h. The amount of radioactivity that reappeared in the supernatant at each time interval was measured, as well as the radioactivity remaining in the cells. This method is similar to methods previously employed for the study of exocytosis of radiolabeled sucrose in guinea pig alveolar macrophages (*49*), hapten−protein conjugates in murine macrophages (*51*), and PLGA nanoparticles in vascular smooth muscle cells (*52*). The initial amount of ^{14}C-ovalbumin taken up by the cells was statistically similar for all the sample groups ($p = 0.66$) and was approximately 0.8% of the total amount delivered (Figure 4a, left panel). However, less PPAA-conjugated ovalbumin was exocytosed compared to the control groups, which is detailed in the exocytosis profiles shown in Figure 4a, right panel. This resulted in the greater and more stable accumulation of the PPAA−ovalbumin inside the cells, even after 4 h of exocytosis. 52% of the internalized PPAA−ovalbumin was found inside the cells at 4 h, whereas less than 10% of the ovalbumin remained for the free ovalbumin, the physical mixture, and the non-membrane-active PMAA conjugate.

Similar exocytosis trends are found when the initial incubation was extended to 15 min (Figure 4b). At this uptake time, the amount of PPAA-conjugated ovalbumin initially inside the cell was already considerably greater than the control groups (left panel). When normalized to the initial amount taken up, the exocytosis profiles were similar to those for the 1 min uptake (right panel). Furthermore, between 15 min and 2 h, the amount of intracellular PPAA−ovalbumin increased from 0.75% of the total amount delivered to 4.8%, whereas the control groups remain within experimental error of the initial values ($p > 0.09$) (Figure 5). These results support the hypothesis that PPAA−ovalbumin accumulates in the cell as a result of endosomal escape to the cytosol with an accompanying decrease in exocytosis. It can be noted that, for all samples, reappearance of the radiolabeled ovalbumin in the supernatant was observed as early as 5 min after the cells were washed, and the majority of exocytosis occurred in the first 30 min, a time scale which is in accordance with previous exocytosis studies (*49*, *51*, *52*).

In Vitro Cytotoxicity of Polymers and Polymer−Ovalbumin Conjugates. The cytotoxicity of the PPAA-PDSA and PMAA-PDSA polymers and conjugates was tested in both the RAW macrophages and B3Z T-cells. Concentrations up to 300 μg/mL, twice the concentration used in the MHC-I presentation assay, were tested using the LDH assay. Cell survival was calculated by comparing the polymer-treated cells with untreated cells and with cells lysed with 1% Triton X-100. It can be seen in Figure 6 that none of the PPAA-PDSA or PMAA-PDSA polymers or their ovablumin conjugates induce toxicity in either cell type at this concentration.

CONCLUSIONS

In this study, a pH-sensitive, membrane-disruptive polymer, poly(propylacrylic acid) (PPAA), was synthesized and used to enhance the cytoplasmic delivery and MHC-I presentation of a model protein antigen, ovalbumin. The protein was derivatized to have a thiol group, which was reacted with the pendant PDSA

disulfide bond on the polymer to yield a polymer−protein conjugate linked by a disulfide bond. This polymer−S-S-protein linkage was designed to allow release of the protein by glutathione reduction in the cytoplasm. The polymer exhibited low toxicity in vitro and retained its membrane-disruptive capabilities after attachment to the hydrophilic protein, as indicated by a red blood cell hemolysis assay. Conjugation to the PPAA polymer was shown to result in increased intracellular accumulation and decreased exocytosis of ovalbumin, which corresponded to significantly enhanced MHC-I presentation of ovalbumin and subsequent CTL activation. This effect is attributed to destabilization of the endosomal membrane by PPAA in the low pH environment of the endosome and is in accordance with previous studies investigating the destabilizing action of PPAA (*32*, *33*, *53*). This system shows promise for protein vaccine strategies against cancer and viruses and is also applicable to any technique requiring improved delivery of a protein cargo to the cytoplasm of a cell.

ACKNOWLEDGMENT

This project was supported by funding from the National Institutes of Health (grant R01EB2991-01) and the Whitaker Foundation. We also thank Nilabh Shastri (UC Berkeley) for the B3Z hybridoma cells, which were essential to this study.

LITERATURE CITED

(1) Moingeon, P. (2001) Cancer vaccines. *Vaccine 19*, 1305–1326.

(2) Scanlan, M. J., Simpson, A. J., and Old, L. J. (2004) The cancer/testis genes: Review, standardization, and commentary. *Cancer Immunity 4*, 1–15.

(3) Folgori, A., Capone, S., Ruggeri, L., Meola, A., Sporeno, E., Ercole, B. B., Pezzanera, M., Tafi, R., Arcuri, M., Fattori, E., Lahm, A., Luzzago, A., Vitelli, A., Colloca, S., Cortese, R., and Nicosia, A. (2006) A T-cell HCV vaccine eliciting effective immunity against heterologous virus challenge in chimpanzees. *Nature Med. 12*, 190–197.

(4) Boon, T., Cerottini, J. C., Eynde, B. V., Bruggen, P., and Pel, A. V. (1994) Tumor antigens recognized by T lymphocytes. *Annu. Rev. Immunol. 12*, 337–365.

(5) Engers, H., Lahaye, T., Sorenson, G., Glasebrook, A., Horvath, C., and Brunner, K. (1984) Functional activity in vivo of effector T cell populations. II. Anti- tumor activity exhibited by syngeneic anti-MoMULV-specific cytolytic T cell clones. *J. Immunol. 133*, 1664–1670.

(6) Knutson, K. L., and Disis, M. L. (2006) Tumor antigen-specific T helper cells in cancer immunity and immunotherapy. *Cancer Immunol. Immunother. 54*, 721–728.

(7) Gao, F. G., Khammanivong, V., Liu, W. J., Leggatt, G. R., Frazer, I. H., and Fernando, G. J. P. (2002) Antigen-specific CD4+ T-cell help is required to activate a memory CD8+ T cell to a fully functional tumor killer cell. *Cancer Res. 62*, 6438–6441.

(8) Tacken, P. J., Torensma, R., and Figdor, C. G. (2006) Targeting antigens to dendritic cells in vivo. *Immunobiology 211*, 599–608.

(9) Guermonprez, P., Valladeau, J., Zitvogel, L., Thery, C., and Amigorena, S. (2002) Antigen presentation and T cell stimulation by dendritic cells. *Annu. Rev. Immunol. 20*, 621–667.

(10) Rock, K. L., and Shen, L. (2005) Cross-presentation: underlying mechanisms and role in immune surveillance. *Immunol. Rev. 207*, 166–183.

(11) Moore, M. W., Carbone, F. R., and Bevan, M. J. (1988) Introduction of soluble protein into the class I pathway of antigen processing and presentation. *Cell 54*, 777–785.

(12) Wattiaux, R., Laurent, N., Wattiaux-De Coninck, S., and Jadot, M. (2000) Endosomes, lysosomes: their implication in gene transfer. *Adv. Drug Delivery Rev. 41*, 201–208.

(13) Mukherjee, S., Ghosh, R. N., and Maxfield, F. R. (1997) Endocytosis. *Physiol. Rev. 77*, 759–803.

(14) Murthy, N., Xu, M., Schuck, S., Kunisawa, J., Shastri, N., and Frechet, J. M. J. (2003) A macromolecular delivery vehicle for protein-based vaccines: Acid-degradable protein-loaded microgels. *Proc. Natl. Acad. Sci. U.S.A. 100*, 4995–5000.

(15) Kwon, Y. J., Standley, S. M., Goh, S. L., and Frechet, J. M. J. (2005) Enhanced antigen presentation and immunostimulation of dendritic cells using acid-degradable cationic nanoparticles. *J. Controlled Release 105*, 199–212.

(16) Standley, S. M., Kwon, Y. J., Murthy, N., Kunisawa, J., Shastri, N., Guillaudeu, S. J., Lau, L., and Frechet, J. M. J. (2004) Acid-degradable particles for protein-based vaccines: enhanced survival rate for tumor-challenged mice using ovalbumin model. *Bioconjugate Chem. 15*, 1281–1288.

(17) Bae, Y., Nishiyama, N., Fukushima, S., Koyama, H., Yasuhiro, M., and Kataoka, K. (2005) Preparation and biological characterization of polymeric micelle drug carriers with intracellular pH-triggered drug release property: Tumor permeability, controlled subcellular drug distribution, and Enhanced in vivo antitumor efficacy. *Bioconjugate Chem. 16*, 122–130.

(18) Kale, A., and Torchilin, V. P. (2007) Design, synthesis, and characterization of pH-sensitive PEG-PE conjugates for stimuli-sensitive pharmaceutical nanocarriers: The effect of substitutes at the hydrazone linkage on the pH stability of PEG-PE conjugates. *Bioconjugate Chem. 18*, 363–370.

(19) Heffernan, M. J., and Murthy, N. (2005) Polyketal nanoparticles: A new pH-sensitive biodegradable drug delivery vehicle. *Bioconjugate Chem. 16*, 1340–1342.

(20) Oh, K. T., Bronich, T. K., Bromberg, L., Hatton, T. A., and Kabanov, A. V. (2006) Block ionomer complexes as prospective nanocontainers for drug delivery. *J. Controlled Release 115*, 9–17.

(21) Boussif, O., Lezoualc'h, F., Zanta, M. A., Mergny, M. D., Scherman, D., Demeneix, B., and Behr, J. P. (1995) A versatile vector for gene and oligonucleotide transfer into cells in culture and in vivo: polyethylenimine. *Proc. Natl. Acad. Sci. U.S.A. 92*, 7297–7301.

(22) Akinc, A., Thomas, M., Klibanov, A. M., and Langer, R. (2005) Exploring polyethyleneimine-mediated DNA transfection and the proton sponge hypothesis. *J. Gene Med. 7*, 657–663.

(23) Lim, Y., Kim, S., Suh, H., and Park, J. (2002) Biodegradable, endosome disruptive and cationic network-type polymer as a highly efficient and nontoxic gene delivery carrier. *Bioconjugate Chem. 13*, 952–957.

(24) Lee, E. S., Na, K., and Bae, Y. H. (2005) Doxorubicin loaded pH-sensitive polymeric micelles for reversal of resistant MCF-7 tumor. *J. Controlled Release 103*, 405–418.

(25) Wang, J., Mongayt, D., and Torchilin, V. P. (2005) Polymeric micelles for delivery of poorly soluble drugs: preparation and anticancer activity In vitro of paclitaxel incorporated into mixed micelles based on poly(ethylene glycol)-lipid conjugate and positively charged lipids. *J. Drug Targeting 13*, 73–80.

(26) Shen, H., Ackerman, A. L., Cody, V., Giodini, A., Hinson, E. R., Cresswell, P., Edelson, R. L., Saltzman, W. M., and Hanlon, D. J. (2006) Enhanced and prolonged cross-presentation following endosomal escape of exogenous antigens encapsulated in biodegradable nanoparticles. *Immunology 117*, 78–88.

(27) Panyam, J., Zhou, W.-z., Prabha, S., Sahoo, S. K., and Labhasetwar, V. (2002) Rapid endo-lysosomal escape of poly(DL-lactide-co-glycolide) nanoparticles: implications for drug and gene delivery. *FASEB J. 16*, 1217–1226.

(28) Newman, K. D., Kwon, G. S., Miller, G. G., Chlumecky, V., and Samuel, J. (2000) Cytoplasmic delivery of a macromolecular fluorescent probe by poly(D,L-lactic-co-glycolic acid) microspheres. *J. Biomed. Mater. Res. 50*, 591–597.

(29) Murthy, N., Robichaud, J. R., Tirrell, D. S., Stayton, P. S., and Hoffman, A. S. (1999) The design and synthesis of polymers for eukaryotic membrane disruption. *J. Controlled Release 61*, 137–143.

(30) Murthy, N., Chang, I., Stayton, P. S., and Hoffman, A. S. (2001) pH-sensitive hemolysis by random copolymer of alkyl acrylates and acrylic acid. *Macromol. Symp. 172*, 49–55.

(31) Cheung, C. Y., Murthy, N., Stayton, P. S., and Hoffman, A. S. (2001) A pH-sensitive polymer that enhances cationic lipid-mediated gene transfer. *Bioconjugate Chem. 12*, 906–910.

(32) Lackey, C. A., Press, O. W., Hoffman, A. S., and Stayton, P. S. (2002) A biomimetic pH-responsive polymer directs endosomal release and intracellular delivery of an endocytosed antibody complex. *Bioconjugate Chem. 13*, 996–1001.

(33) Murthy, N., Campbell, J., Fausto, N., Hoffman, A. S., and Stayton, P. S. (2003) Bioinspired pH-responsive polymers for the intracellular delivery of biomolecular drugs. *Bioconjugate Chem. 14*, 412–419.

(34) Bulmus, V., Woodward, M., Lin, L., Murthy, N., Stayton, P., and Hoffman, A. (2003) A new pH-responsive and glutathione-reactive, endosomal membrane-disruptive polymeric carrier for intracellular delivery of biomolecular drugs. *J. Controlled Release 93*, 105–120.

(35) El-Sayed, M. E., Hoffman, A. S., and Stayton, P. S. (2005) Rational design of composition and activity correlations for pH-responsive and glutathione-reactive polymer therapeutics. *J. Controlled Release 104*, 417–427.

(36) Henry, S. M., El-Sayed, M. E. H., Pirie, C. M., Hoffman, A. S., and Stayton, P. S. (2006) pH-Responsive poly(styrene-alt-maleic anhydride) alkylamide copolymers for intracellular drug delivery. *Biomacromolecules 7*, 2407–2414.

(37) Wiley, D. C., and Skehel, J. J. (1987) The structure and function of the hemagglutinin membrane glycoprotein of influenza virus. *Annu. Rev. Biochem. 56*, 365–394.

(38) Skehel, J. J., and Wiley, D. C. (2000) Receptor binding and membrane fusion in virus entry: the influenza hemagglutinin. *Annu. Rev. Biochem. 69*, 531–569.

(39) Malenbaum, S. E., Collier, R. J., and London, E. (1999) Membrane topography of the T domain of diphtheria toxin probed with single tryptophan mutants. *Biochemistry 37*, 17915–17922.

(40) Wang, J., Rosconi, M. P., and London, E. (2006) Topography of the hydrophilic helices of membrane-inserted diphtheria toxin T domain: TH1-TH3 as a hydrophilic tether. *Biochemistry 45*, 8124–8134.

(41) Li, W., Nicol, F., and Szoka, F. C. J. (2004) GALA: a designed synthetic pH-responsive amphipathic peptide with applications in drug and gene delivery. *Adv. Drug Delivery Rev. 56*, 967–985.

(42) Cabiaux, V. (2004) pH-sensitive toxins: interactions with membrane bilayers and application to drug delivery. *Adv. Drug Delivery Rev. 56*, 987–997.

(43) Goletz, T. J., Klimpel, K. R., Leppla, S. H., Keith, J. M., and Berzofsky, J. A. (1997) Delivery of antigens to the MHC Class I pathway using bacterial toxins. *Hum. Immunol. 54*, 129–136.

(44) Goletz, T. J., Klimpel, K. R., Arora, N., Leppla, S. H., Keith, J. M., and Berzofsky, J. A. (1997) Targeting HIV proteins to the major histocompatibility complex class I processing pathway with a novel gp120-anthrax toxin fusion protein. *Proc. Natl. Acad. Sci. U.S.A. 94*, 12059–12064.

(45) Doling, A. M., Ballard, J. D., Shen, H., Krishna, K. M., Ahmed, R., Collier, R. J., and Starnbach, M. N. (1999) Cytotoxic T-lymphocyte epitopes fused to anthrax toxin induce protective antiviral immunity. *Infect. Immun. 67*, 3290–3296.

(46) De Haan, L., Hearn, A. R., Rivett, A. J., and Hirst, T. R. (2002) Enhanced delivery of exogenous peptides into the class I antigen processing and presentation pathway. *Infect. Immun. 70*, 3249–3258.

(47) Sanderson, S., and Shastri, N. (1993) LacZ inducible, antigen/MHC-specific T cell hybrids. *Int. Immunol. 6*, 369–376.

(48) Mitsukami, Y., Donovan, M. S., Lowe, A. B., and McCormick, C. L. (2001) Water-soluble polymers. 81. Direct synthesis of hydrophilic styrenic-based homopolymers and block copolymers in aqueous solution via RAFT. *Macromolecules 34*, 2248–2256.

(49) Besterman, J. M., Airhart, J. A., Woodworth, R. C., and Low, R. B. (1981) Exocytosis of pinocytosed fluid in cultured cells: Kinetic evidence for rapid turnover and compartmentation. *J. Cell Biol. 91*, 716–727.

(50) Plank, C., Oberhauser, B., Mechtler, K., Koch, C., and Wagner, E. (1994) The influence of endosome-disruptive peptides on gene transfer using synthetic virus-like transfer systems. *J. Biol. Chem. 269*, 12918–12924.

(51) Weaver, D. J., Jr., and Voss, E. W., Jr. (1998) Analysis of rates of receptor-mediated endocytosis and exocytosis of a fluorescent hapten-protein conjugate in murine macrophage: implications for antigen processing. *Biol. Cell 90*, 169–181.

(52) Panyam, J., and Labhasetwar, V. (2003) Dynamics of endocytosis and exocytosis of poly(D,L-lactide-co-glycolide) nanoparticles in vascular smooth muscle cells. *Pharm. Res. 20*, 212–220.

(53) Albarran, B., To, R., and Stayton, P. S. (2005) A TAT-streptavidin fusion protein directs uptake of biotinylated cargo into mammalian cells. *Protein Eng., Des. Sel. 18*, 147–152.

BC800317A

Bioconjugate Chemistry 20th Anniversary

Subscriber access provided by SHEMYAKIN-OVCHINNIKOV INST

Article

Novel System to Achieve One-Pot Modification of Cargo Molecules with Oligoarginine Vectors for Intracellular Delivery

Kentaro Takayama, Akiko Tadokoro, Si#lvia Pujals, Ikuhiko Nakase, Ernest Giralt, and Shiroh Futaki

Bioconjugate Chem., **2009**, 20 (2), 249-257• DOI: 10.1021/bc800327f • Publication Date (Web): 22 January 2009

Downloaded from http://pubs.acs.org on May 8, 2009

More About This Article

Additional resources and features associated with this article are available within the HTML version:

- Supporting Information
- Access to high resolution figures
- Links to articles and content related to this article
- Copyright permission to reproduce figures and/or text from this article

View the Full Text HTML

ACS Publications
High quality. High impact.

Bioconjugate Chemistry is published by the American Chemical Society. 1155 Sixteenth Street N.W., Washington, DC 20036

Novel System to Achieve One-Pot Modification of Cargo Molecules with Oligoarginine Vectors for Intracellular Delivery

Kentaro Takayama,[†] Akiko Tadokoro,[⊥,‡] Sílvia Pujals,[§] Ikuhiko Nakase,[†] Ernest Giralt,[§,||] and Shiroh Futaki*[,†,‡]

Institute for Chemical Research, Kyoto University, Uji, Kyoto 611-0011, Japan, SORST, JST, Kawaguchi, Saitama 332-0012, Japan, Institute for Research in Biomedicine, Barcelona Science Park, Baldiri Reixac 10, 08028 Barcelona, Spain, and Department of Organic Chemistry, University of Barcelona, Martí i Franquès 1-11, 08028 Barcelona, Spain. Received July 29, 2008; Revised Manuscript Received November 14, 2008

There are a growing number of reports showing the usefulness of cell-penetrating peptides (CPPs) including oligoarginines for intracellular delivery of macromolecules. Although the covalent attachment of the CPP segments to the cargo molecules is usually required to ensure effective delivery, conventional methods of conjugation need several manipulation steps that are often time-consuming and laborious. Here, we report a novel approach to allow easy modification of cargo molecules with oligoarginine CPPs. The key feature is the employment of oligoarginines (R8 and R12) equipped with a sulfosuccinimidylsuberyl moiety (BS^3-R8 and -R12). One-pot modification is achieved simply by mixing BS^3-R8 and -R12 with cargos in an aqueous buffer. The usefulness of this approach was exemplified through the conjugate formation with Fab fragments of immunoglobulin G, amino-functionalized poly(ethylene glycol)s (amino-PEGs), and amino quantum dots (amino-QDs), yielding an efficient cellular uptake.

INTRODUCTION

Cell penetrating peptides (CPPs) including oligoarginines have been reported as a potent tool for intracellular delivery. Conjugated with CPPs, various molecules with low membrane-permeability have successfully been delivered into cells simply by adding the conjugates to the cells without the need of special apparatus (*1*−*3*). These molecules include peptides and proteins (*4*), oligonucleotides and their derivatives (*5*), nanoparticles such as liposomes and quantum dots, synthetic polymers, and so on (*6*); easy and efficient delivery of these molecules was difficult with pre-existing methodologies (e.g., microinjection and electroporation). This technology has been opening new avenues not only for basic studies on cell functions but also for future therapies including drug delivery and cell manipulations. This also provides access by chemists to elucidate and control cell functions using synthetic agonists/antagonists, fluorescently labeled/caged molecules, and so on (*7*).

For the efficient introduction of the above bioactive cargo molecules into cells, modification of the cargo molecules with CPPs is inevitable. One of the popular methods for this is to prepare recombinant fusion proteins bearing CPP segments (*4, 8*). However, this approach is only applicable to proteins, and it takes some days for the preparation of the fusion proteins. In addition, the addition of the CPP segments sometimes results in a decrease in yields in production of the recombinant proteins in *E. coli* and in purification compared with the parent proteins (*9*). If the cargo is relatively small peptides (e.g., <20 amino acids), direct solid-phase synthesis of peptides having tandem alignment of CPP (∼10 amino acids) and cargo sequences can be employed. However, an increase in the total chain length should diminish the overall synthetic yields, and therefore, chemical conjugation of the CPP segments to the cargo becomes an alternative idea.

This approach is not limited to proteins but is applicable to various types of molecules and thus has wider applicability. Cargo molecules can be prepared so as to be equipped with CPP segments from the beginning as a part of their structures (*8, 10*). Alternatively, the CPP segments may be attached via disulfide cross-linking (*11, 12*) or via suitable cross-linkers to the pre-existing cargo molecules (*13, 14*). However, in the former cross-linking, the cargo molecules must have a free sulfhydryl moiety that has to be selectively cross-linked with CPPs. In the latter case, various types of hetero/homobifunctional cross-linkers are commercially available; typical ones are designed to have functional groups to form cross-links between amino moieties (e.g., succinimidyl esters) and/or thiol moieties (e.g., maleimides or alkyl halides). Amino moieties are more popularly found in proteins, as their N-terminus and the ε-position of lysine side chains rather than cysteines provide more feasibility in the design of cross-linking. However, conventional methods of cross-linking formation employ stepwise introduction of CPPs and cargos on cross-linkers (*13, 15*). This usually requires purification using gel filtration or dialysis in each step, which is laborious and time-consuming and may lead to inactivation of the cargo molecules. In addition, insoluble aggregate formation is often observed during these treatments. Therefore, development of easier methods of introducing CPPs to cargo moieties has been desired.

Here, we report a novel approach to allow easy modification of cargo molecules with oligoarginine CPPs equipped with a preactivated sulfosuccinimidylsuberyl moiety (BS^3-R8 and -R12) in one pot (Figure 1). Oligoarginines (R8 and R12) are known as representative and reliable CPPs to achieve efficient intracellular delivery. Functionalization of R8/R12 with the sulfosuccinimidyl-suberyl moiety then provides an activated system for simple mixing

* To whom correspondence should be addressed. Shiroh Futaki, Professor, Institute for Chemical Research, Kyoto University, Uji, Kyoto 611-0011, Japan. Tel: +81-774-38-3210. Fax: +81-774-32-3038. E-mail: futaki@scl.kyoto-u.ac.jp.

[†] Kyoto University.

[‡] SORST, JST.

[§] Institute for Research in Biomedicine.

[||] University of Barcelona.

[⊥] Present address: Faculty of Pharmacy, Osaka Ohtani University, Tondabayashi, Osaka 584-8540, Japan.

10.1021/bc800327f CCC: $40.75 © 2009 American Chemical Society
Published on Web 01/22/2009

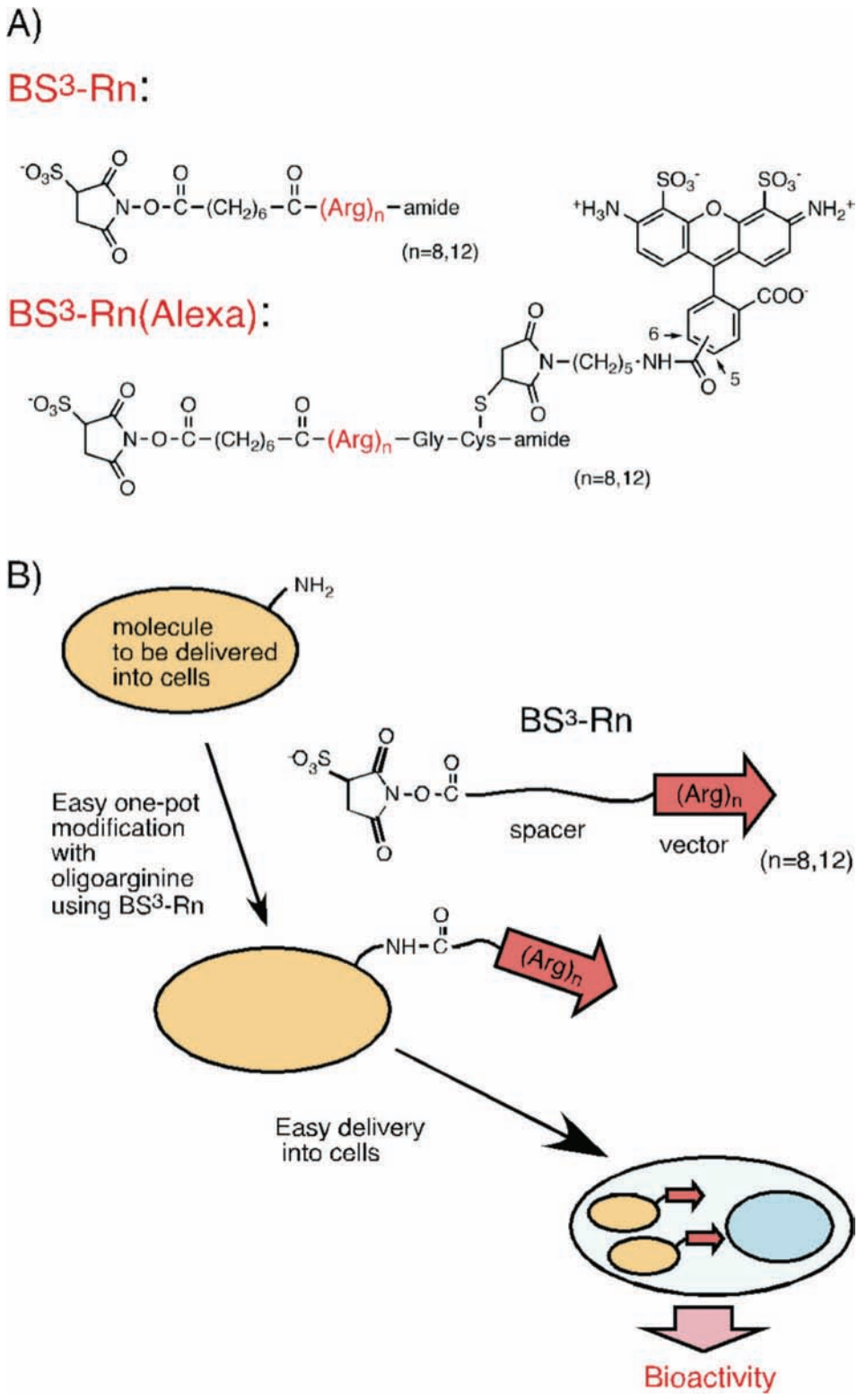

Figure 1. Structures of BS^3-oligoarginine agents for one-pot modification of cargo molecules (A) to achieve easy and efficient modification and eventual intracellular delivery (B).

and conjugating with amino moieties of different cargo molecules. The usefulness of this approach was exemplified through the conjugate formation with immunoglobulin Fab fragments, amino-functionalized poly(ethylene glycol)s (amino-PEGs) and amino quantum dots (amino-QDs).

EXPERIMENTAL PROCEDURES

Preparation of BS^3-R8 and BS^3-R12. *R8 and R12 Peptides.* Peptide segments of R8 [$(Arg)_8$-amide] and R12 [$(Arg)_{12}$-amide] were similarly prepared as reported using Fmoc (9-fluorenylmethyloxycarbonyl) solid-phase peptide synthesis and HPLC purification (*16*). Fluorescently labeled R8 and R12 [R8(Alexa): $(Arg)_8$-Gly-Cys(Alexa)-amide; R12(Alexa): $(Arg)_{12}$-Gly-Cys(Alexa)-amide] were also prepared by the treatment of $(Arg)_8$-Gly-Cys-amide and $(Arg)_{12}$-Gly-Cys-amide (similarly prepared as above) with Alexa Fluor 488 C_5 maleimide sodium salt (Invitrogen) as reported (*16*).

BS^3 Derivatization. The bis(sulfosuccinimidyl)suberate (BS^3) cross-linker (Pierce) (1.5 equiv to each peptide) in H_2O (400 μL) was added to an aqueous solution (600 μL) of R8 or R12 (0.5−0.7 μmol). After adjusting the pH of the solution to 7−8 with *N*-methylmorpholine (NMM), the mixture was gently stirred at 20 °C for 20 min. In the case of modification of R8(Alexa) and R12(Alexa), these peptides were similarly reacted with BS^3 in H_2O/CH_3CN (3:1) in 1 mL. Progress of the reaction was monitored by HPLC, and the product was directly purified by HPLC using a Chromolith Performance RP-18 column (4.6 × 100 mm) (Merck). Subsequent lyophilization yielded a fluffy powder of the respective products. The mass of the products was confirmed by matrix-assisted laser desorption ionization time-of-flight mass spectrometry (MALDI-TOFMS). Yield in the BS^3 derivatization: BS^3-R8, BS^3-R12, BS^3-R8(Alexa), BS^3-R12(Alexa) 67%, 61%, 79%, 74%, respectively. MALDI-TOF MS for BS^3-R8, BS^3-R12, BS^3-R8(Alexa), and BS^3-R12(Alexa): 1599.8 [expected for $(M + H)^+$ 1599.9]; 2225.6 [expected for $(M + H)^+$ 2224.6]; 2479.6 [expected for $(M + Na)^+$ 2479.7]; 3104.8 [expected for $(M + Na)^+$ 3104.5], respectively.

Conjugation of Alexa 488-Labeled Fab Fragment [Fab(Alexa)] with Oligoarginine Peptides. *Alexa 488-Labeled Fab Fragments [Fab(Alexa)].* The Fab fragments were prepared from a commercially available polyclonal antibody preparation (Venogloblin-IH, Mitsubishi Pharma) using the ImmunoPure Fab Preparation Kit (Pierce) as already reported (*15, 17, 18*). Alexa 488-labeling was then conducted by the treatment of Fab (36 mg/mL) in phosphate-buffered saline (PBS) (250 μL) with Alexa 488 carboxylic acid, succinimidyl ester (Invitrogen) (5 equiv to Fab) in DMF (5 μL), and 1 M $NaHCO_3$ (25 μL) at room temperature for 2 h with gentle stirring. The mixture was loaded on a Microcon YM-30 ultrafilter (molecular weight cutoff 30 000) (Millipore) and concentrated on the filter. Repetitive addition of PBS and filtration (×5) was conducted to remove the unreacted Alexa reagent.

One-Pot Modification of Fab(Alexa) Using BS^3-R8 and BS^3-R12. BS^3−R*n* (*n* = 8 and 12) [3 equiv to Fab(Alexa)] in H_2O (3 μL) were added to Fab(Alexa) in PBS (13.3 mg/mL, 100 μL), and the mixture was gently stirred at room temperature for 2 h. The mixture was then loaded on a Microcon YM-30 ultrafilter, concentrated, and washed with PBS (×5) to remove unreacted BS^3−R*n* peptides as described above to yield Fab(Alexa)-R8 and Fab(Alexa)-R12, respectively. The yields were calculated by comparing the absorbance (280 nm) of Fab before and after R*n* (*n* = 8 or 12) modification. The number of the respective R*n* peptides conjugated to Fab(Alexa) was estimated by sodium dodecyl sulfate−polyacrylamide gel electrophoresis (SDS-PAGE).

Conjugation of Fab(Alexa) with R8 and R12 Using Conventional Heterobifunctional Agent (EMCS). To a PBS solution of Fab(Alexa) (13.3 mg/mL, 100 μL), *N*-(6-maleimidocaproyloxy)succinimide (EMCS) (Dojindo) [3 equiv to Fab(Alexa)] in dimethylformamide (DMF) (1 μL) was added, and the mixture was gently stirred at room temperature for 2 h. Subsequently, the mixture was loaded on a Microcon YM-30 ultrafilter, concentrated, and washed with PBS (×3) to remove the unreacted EMCS reagent. R12GC [$(Arg)_{12}$-Gly-Cys-amide (*18*)] [3 equiv to Fab(Alexa)] in PBS (3 μL) was then added to the above Fab(Alexa) solution (100 μL), and the mixture was gently stirred at room temperature for 2 h. Subsequently, the mixture was filtered and washed with PBS (×5) using a Microcon YM-30 to remove unreacted R12GC to obtain Fab(Alexa)-EMCS-R12.

Conjugation of Oligoarginine Peptides with Poly(ethylene glycol)s (PEGs). Amino-PEGs (propylamine-functionalized poly(ethylene glycol)s, Sunbright PA series, NOF) (0.45−0.65 μmol) in H_2O (400 μL) were added to a solution of BS^3-R8(Alexa) or BS^3-R12(Alexa) (0.5−0.7 μmol, 1.1 equiv) in H_2O/CH_3CN (600 μL, 7:5) in the presence of NMM (0.2 μL), and the mixture was stirred at room temperature for 1−2 h, followed by RP-HPLC purification to yield the desired conjugates (53−87%) (Table 2). The mass of the conjugates was confirmed by MALDI-TOF MS (Supporting Information).

Table 1. Yield of Fab(Alexa)-R*n* Conjugates

conjugates	amount of Fab(Alexa) before conjugation	yield
Fab(Alexa)-R8	1.33 mg	0.84 mg (60%)
Fab(Alexa)-R12	1.33 mg	1.07 mg (75%)
Fab(Alexa)-EMCS-R12	1.33 mg	0.45 mg (31%)

Table 2. Yield of PEG-R*n*(Alexa) Conjugates

conjugates	amount of PEG before reaction	yield
PEG5000-R8(Alexa)	1.3 mg	1.2 mg (66%)
PEG12000-R8(Alexa)	1.3 mg	1.1 mg (72%)
PEG30000-R8(Alexa)	3.0 mg	2.8 mg (87%)
PEG5000-R12(Alexa)	1.2 mg	1.0 mg (53%)
PEG12000-R12(Alexa)	2.8 mg	2.2 mg (64%)
PEG30000-R12(Alexa)	7.0 mg	5.7 mg (75%)

Modification of Quantum Dots with R12 peptides. To a borate buffer (pH 8.3) solution of quantum dots (QDs) coated with amino-functionalized PEG (Q-dot 605 ITK, Invitrogen) (8 μM, 25 μL), BS^3-R12 (18 nmol, 1 equiv to amino groups of QDs) in H_2O (475 μL) was added, and the mixture was gently stirred at room temperature for 2 h, followed by dialysis for 36 h (molecular weight cutoff 7000) against H_2O (500 mL) at 4 °C. To obtain information on the number of the R12 molecules introduced on a particle of QDs, the QDs were similarly treated with BS^3-R12(Alexa) instead of BS^3-R12 for 2 h and then ultrafiltered. By measuring the absorbance (495 nm) of the filtrate, it was determined that approximately 60 molecules of R12 were conjugated on each particle.

Cell Culture. The human cervical cancer-derived HeLa cells were maintained in α-minimum essential medium (α-MEM) with 10% heat-inactivated calf serum. Cells were grown on 100 mm dishes and incubated at 37 °C under 5% CO_2 to approximately 70% confluence. A subculture was performed every 3−4 days.

Confocal Microscopy of Peptide Internalization. HeLa cells (2×10^5) were plated on 35 mm glass-bottomed dishes (Iwaki) and cultured in α-MEM with 10% heat-inactivated calf serum for 48 h. After complete adhesion, the culture medium was exchanged, and the cells were then incubated at 37 °C with fresh medium (200 μL) containing the peptide conjugates and washed with PBS (×3). The concentration of the respective conjugates is given in the figure legends. Distribution of the peptide conjugates was then analyzed using a confocal laser scanning microscope FV300 (Olympus) equipped with a 40× objective without fixing the cells to avoid artifactual localization of the internalized peptides (*19*). For detection of Alexa 488-labeled conjugates, the fluorescence signals were detected by excitation with the 488 nm Ar laser using an emission filter (510−530 nm). For detection of QD605, fluorescence signals were detected following excitation with the 543 nm He−Ne laser using a >565 nm emission filter.

Flow Cytometry. HeLa cells (7.0×10^4) in fresh culture medium (1 mL) were plated into 24-well microplates (Iwaki) and cultured for 48 h in α-MEM containing 10% heat-inactivated calf serum. After complete adhesion, the cells were incubated at 37 °C for 30 min with fresh medium (200 μL) containing peptide conjugates prior to washing with PBS (400 μL). The cells were then treated with 0.01% trypsin in PBS (200 μL) at 37 °C for 10 min prior to the addition of PBS (300 μL). The cells were centrifuged at 3000 rpm for 5 min. After

the supernatant was removed, the cells were washed with 400 μL of PBS and centrifuged at 3000 rpm for 5 min. After this washing cycle was repeated, the cells were suspended in PBS (400 μL) and subjected to fluorescence analysis on a FACS-calibur (BD Biosciences) flow cytometer using 488 nm laser excitation and a 515 to 545 nm emission filter.

RESULTS AND DISCUSSION

Design and Preparation of BS^3-Modified Oligoarginine Peptides. Chemical conjugation is one of the practical methods for attaching cargo molecules to be delivered into cells with CPPs. Various chemical cross-linkers have already been employed for the conjugation of cargo molecules with CPPs (*13, 20, 21*). However, as described in the introduction, stepwise attachment of CPPs and cargos on cross-linkers is often laborious and time-consuming due to the necessity of purification after the respective steps of attachment. The prolonged treatment and purification often is accompanied by insoluble aggregate formation that makes the handling of the conjugates difficult and diminishes the functions and biological activities of the cargo molecules (*9*). Therefore, development of simple and easy methods of CPP modification has been desired.

The succinimidyl ester is one of the most popularly employed and effective active esters for carboxylic acids, and this leads to prompt amide bond formation with amino moieties (*22*). Oligoarginines (R*n*, $n = 6-12$) are among the representative classes of CPP, and the internalization efficiencies are comparable to or not less than those of popularly employed Tat (*23*) and antennapedia (penetratin) (*24*) peptides. The guanidino moiety of arginine is a stronger base (pK_a 12.5) compared with the α-amino moiety of lysine (pK_a 9.0). However, the nucleophilicity of the guanidino moiety is much less than that of the amino group (*25*). Therefore, if we could prepare oligoarginine peptides bearing a carboxylic acid preactivated as a succinimidyl ester, a simple mixing of these peptides with the cargo molecules may lead to efficient cross-linking formation (Figure 1).

In this article, we have employed a commercially available homobifunctional cross-linker bis(sulfosuccinimidyl)suberate (BS^3), which has sulfonated succinimidyl esters on both carbonyl moieties of suberic acid (Figure 2). Treatment of oligoarginine peptides (R8 and R12) with an excess amount of this reagent would predominantly yield BS^3−oligoarginine conjugates (BS^3-R8 and BS^3-R12) resulting from the nucleophilic attack of the N-terminus amino moiety of the oligoarginines at one of the carbonyl moieties of BS^3.

For the preparation of the BS^3-R8 and BS^3-R12 conjugates, we took the approach of direct modification of the free oligoarginine peptides with BS^3 reagents. The R8 and R12 peptides [(Arg)$_n$-amide, $n = 8$ and 12] were prepared using Fmoc solid-phase peptide synthesis and purified by HPLC. The resulting peptides without protection groups were treated with 1.5 equiv of BS^3 cross-linking agent in H_2O at room temperature for 20 min, and the product was directly purified by HPLC (Figure 2A). The reaction proceeded very smoothly to produce the desired BS^3−oligoarginine conjugates in high yields (67% and 61% for BS^3-R8 and BS^3-R12, respectively). No significant byproducts were observed by HPLC including any suffering from hydrolysis of the succinimidyl ester of the BS^3-conjugates or the dimers of R8/R12 where two molecules of the peptides were introduced on both of the carbonyl moieties of the BS^3 agent (Figure 2C). The BS^3 conjugates of Alexa 488-labeled R8 and R12 [(Arg)$_n$-Gly-Cys(Alexa)-amide, $n = 8$ and 12] were similarly prepared without difficulty with a yield of 79% and 74%, respectively (Figure 2B). Preparation of other BS^3-activated CPPs [HIV-1 Rev(34−50), Thr-Arg-Gln-Ala-(Arg)$_2$-Asn-(Arg)$_4$-Trp-Arg-Glu-Arg-Gln-Arg (*13*); SAP, (Val-Arg-Leu-Pro-Pro-Pro)$_3$ (*26*); (Arg-Ahx-Arg)$_4$ (Ahx = 6-aminohexyl)

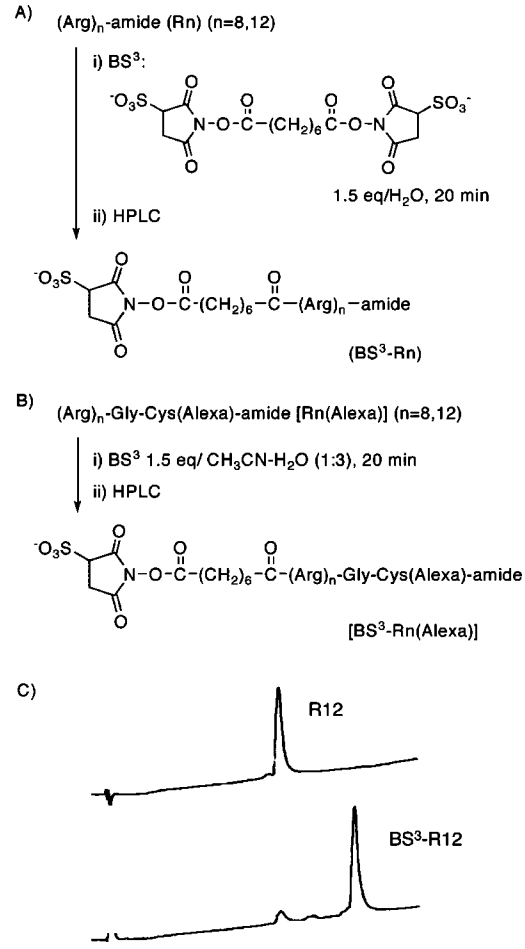

Figure 2. Preparation of BS^3-R*n* (A) and BS^3-R*n*(Alexa) (B) agents ($n = 8$, 12). Modification of the oligoarginine peptides with BS^3 reagent proceeds without difficulty as exemplified in the reaction monitored by HPLC in the preparation of BS^3-R12 (C) [column, Chromolith Performance RP-18; gradient, linear gradient of CH_3CN (4−20%) in 0.1% aqueous TFA over 8 min; flow, 4 mL/min; detection, 215 nm].

(*27*); (Arg-Ahx)$_6$-Arg (*28*)] was also performed without difficulty (details of their preparation and analysis of the cellular uptake of their conjugates with Fab (Alexa) is shown in the Supporting Information). The obtained powders of these BS^3-conjugates were fairly stable when stored in a −20 °C freezer, and no significant decomposition of the samples was observed by HPLC after one month.

Application of BS^3-Modified Oligoarginines to the Preparation of Fab-Oligoarginine Conjugates. To assess the usefulness of the above BS^3-modified oligoarginines for the conjugation of proteins with oligoarginines as intracellular delivery vectors, the Fab segment of immunoglobulin G (IgG) was employed as a model. Recently, antibodies have been regarded as promising and powerful molecular target drugs, and the intracellular delivery of antibodies is also a challenge in antibody therapy (*29−31*). The Fab fragments of the antibodies are regarded as functional low-molecular-weight components retaining the antibody specificities (*32, 33*). It has already been reported that conjugation of antibodies with CPPs greatly increases the internalization efficiency of antibodies into cells (*34*). We also reported that in vivo distribution of Fab segments was considerably affected by the conjugation with CPPs (*17, 18*).

The Fab segments prepared from human polyclonal IgG were labeled with Alexa 488 so that one or two molecules of Alexa 488 were attached to one Fab molecule. Conjugation of the above fluorescently labeled Fab segments [Fab(Alexa)] was

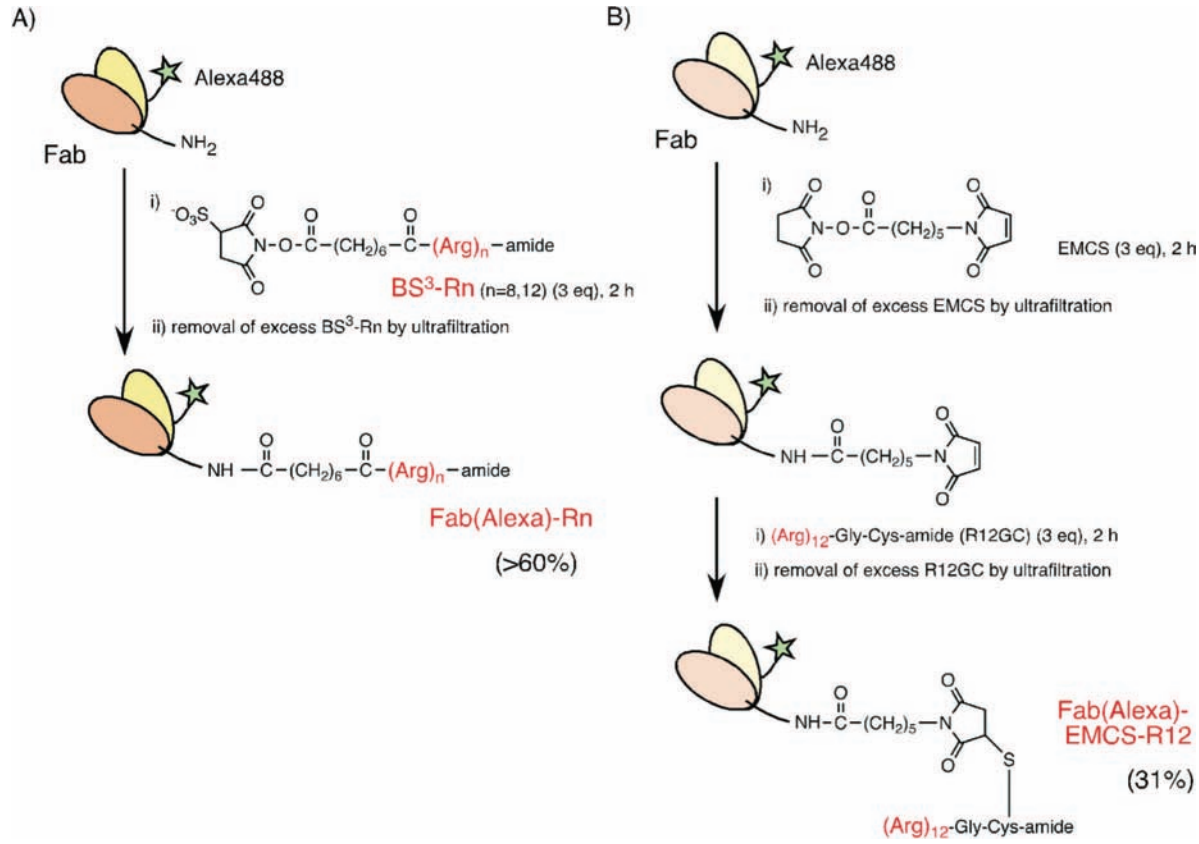

Figure 3. Simple one-pot modification of Fab(Alexa) with oligoarginines using BS^3-R*n* agents (A). A conventional modification method using heterobifunctional cross-linker *N*-(6-maleimidocaproyloxy)succinimide (EMCS) required extra steps for manipulation with a lower yield (B).

conducted using the BS^3−oligoarginine conjugates (Figure 3A). The Fab(Alexa) was treated with 3 equiv of BS^3−R*n* ($n = 8$ and 12) at 20 °C for 2 h. The procedure was very simple, and aqueous solutions of both Fab(Alexa) and BS^3−R*n* were just mixed and gently stirred. There was no obvious aggregation observed during the reaction. The mixture was then charged on an ultrafilter and washed with PBS repetitively to remove unreacted BS^3−R*n*. Through SDS-PAGE, it was confirmed that an average of one or two R*n* segments were introduced onto a Fab segment (Figure 4A). The yields of Fab(Alexa) following modification with R8 and R12 were 60% and 75%, respectively (Table 1).

As a control experiment of conjugation using a conventional heterobifunctional cross-linker, *N*-(6-maleimidocaproyloxy)succinimide (EMCS) was simultaneously conducted (Figure 3B). First, Fab(Alexa) was treated with EMCS [3 equiv to Fab(Alexa)] at room temperature for 2 h to form amide bonds between the amino groups of Fab(Alexa) and the activated carbonyl group of EMCS. The unreacted EMCS was removed by washing on an ultrafilter. R12GC [3 equiv to Fab(Alexa)] was then added to Fab(Alexa)-EMCS so that the thiol group of R12GC could attack the maleimide moiety of EMCS. Two hours later, the excess R12GC was removed by ultrafiltration. During the incubation of Fab(Alexa)-EMCS with R12GC, a certain amount of insoluble aggregates was formed, and this diminished the overall yield in the conjugate formation [31% from Fab(Alexa)].

To analyze this further, Fab(Alexa)-EMCS was similarly treated with the R12 peptide [$(Arg)_{12}$-amide] that lacks the Gly-Cys residue to interact with the maleimide moiety. Addition of the R12 peptide to the Fab(Alexa) solution resulted in spontaneous formation of precipitate, and approximately 60% of the protein was precipitated in the first 8 min, and 70% in 60 min. Similar results were obtained following addition of R12GC to Fab(Alexa)-EMCS. These results suggested that modification with EMCS hampered the hydrophilic and ionic balance of Fab(Alexa), and the addition of the R12 peptide then enhanced precipitate formation. Detailed optimization of the cross-linking condition using EMCS may reduce this effect and so increase yield, but this would be time-consuming, requiring larger amounts of starting material. However, the amount of formed precipitate is much smaller when using BS^3-R8/R12, presumably because it has a relatively lower effect on the solubility of the Fab protein, and thus gives higher conjugate yields.

SDS-PAGE of the obtained conjugate Fab(Alexa)-EMCS-R12 suggested that an average of one to two molecules of R12GC was conjugated with one Fab(Alexa) molecule (Figure 4A).

Internalization of Fab(Alexa)-R8 and Fab(Alexa)-R12 conjugates was then confirmed by incubating HeLa cells with the respective conjugates (1 μM) in serum containing α-MEM [α-MEM (+)] at 37 °C for 3 h. After washing with PBS, intracellular fluorescence was monitored by confocal microscopy (Figure 4B). Distinct signals of the Fab(Alexa)-R*n* conjugates were observed for both cells treated with Fab(Alexa)-R8 and Fab(Alexa)-R12, and the intensity of the signals was comparable to those of the cells similarly treated with Fab(Alexa)-EMCS-R12. In contrast, few signals were observed for the cells treated with Fab(Alexa) without bearing oligoarginine segments.

The above results strongly suggest the practicability of the BS^3−oligoariginine conjugates for introduction of the CPP segments to proteins. Simply by mixing the BS^3−oligoarginine conjugates with the proteins to be delivered into cells, efficient modification with the oligoarginine CPPs was achieved *in one pot*. The procedures are very easy while saving time for modification and ensuring high yields. If the conventional stepwise cross-link formation as was shown is compared with the use of EMCS, it is clear that skipping the steps of reaction and purification would diminish the loss of the products by aggregation and physical adsorption on the experimental ap-

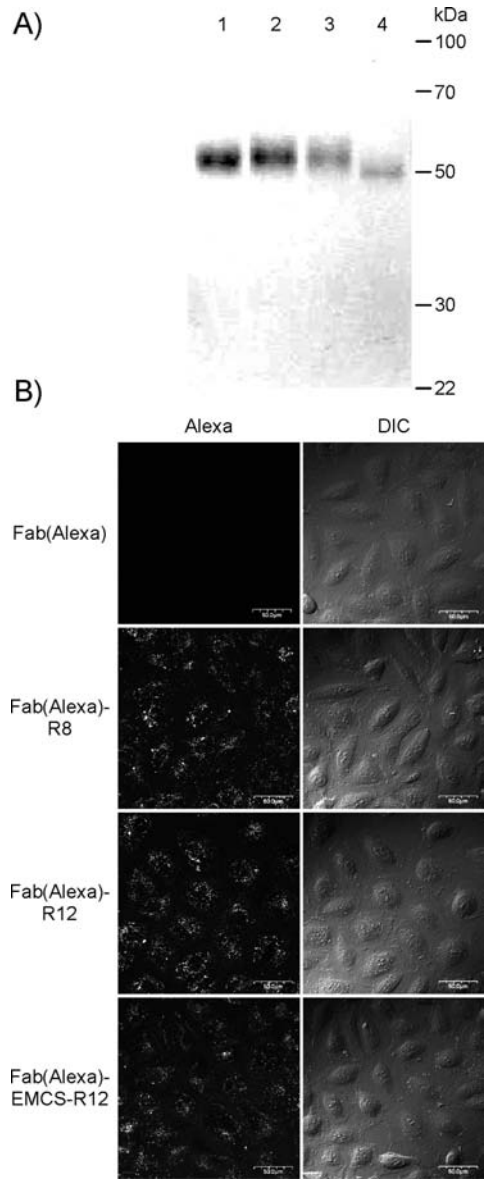

Figure 4. (A) SDS-PAGE of Fab(Alexa)-oligoarginine conjugates [10% acrylamide; Coomassie Brilliant Blue staining; Lanes 1−4, Fab(Alexa)-R8, Fab(Alexa)-R12, Fab(Alexa)-EMCS-R12, and Fab(Alexa), respectively (10 μg each)]. The sample buffer employed here did not contain reducing agents (e.g., 2-mercaptoethanol) to maintain disulfide bonds in Fab during electrophoresis. (B) Cellular uptake of Fab was considerably accelerated by conjugation with oligoarginine vectors [cells, HeLa; incubation, 1 μM in α-MEM (+) for 3 h at 37 °C; Scale bars, 50 μm]. Fluorescence images of the green layer (Alexa) and differential interference contrast (DIC) images are shown.

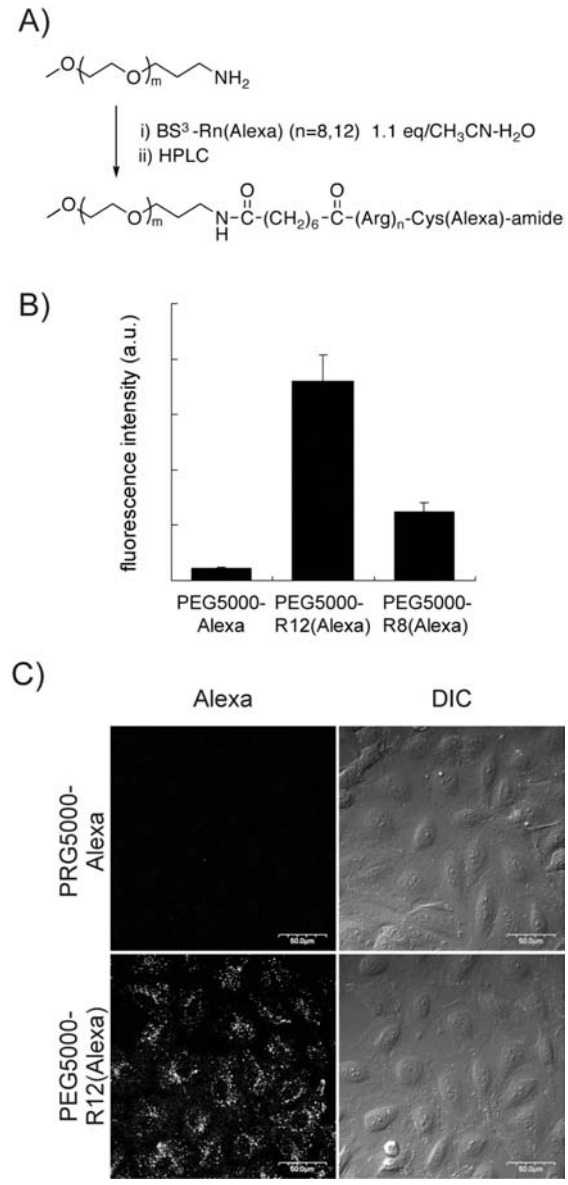

Figure 5. Application of BS^3-R*n* agents to the oligoarginine modification of synthetic polymers. (A) Conjugation of BS^3-R*n*(Alexa) (n = 8, 12) with amino-PEGs. (B) FACS analysis of cellular uptake of PEG5000-R*n*(Alexa) (n = 8 and 12). HeLa cells were treated with the conjugates (10 μM) in α-MEM(+) for 30 min at 37 °C. (C) Cellular uptake of PEG-R12(Alexa) (10 μM) by HeLa cells incubated in α-MEM(+) for 30 min at 37 °C. PEG5000 labeled with Alexa488 but lacking the R12 segment was prepared as a reference by the treatment of amino-PEG5000 with Alexa Fluor 488 carboxylic acid, succinimidyl ester (Invitrogen), followed by the HPLC purification. Scale bars, 50 μm. Fluorescence images of the green layer (Alexa) and the DIC images are shown.

paratus. This criterion is critical when precious proteins have to be conjugated with CPPs. In addition, an ultrafilter was employed here to minimize the loss of the samples by physical adsorption and deformation of the protein structures during manipulation. The use of gel filtration or dialysis for purification steps would further emphasize the advantages of this approach in yields and reduction of labor compared to the conventional methods.

It may be difficult to modify specific lysine residues in proteins with CPPs when the proteins contain multiple lysines, and biological activity might be affected in some cases where there are multiple cross-links or when cross-linking inactivates a critical residue. However, we believe that this simple conjugation approach has great impact for delivery of proteins or other compounds into cells, especially post-translationally modified proteins (e.g., with sugars) or other less-characterized macromolecules. This approach should also be useful for cellular assays investigating multiple numbers of proteins or compounds; optimization of the cross-linking methods would then be considered at later stages.

PEG−Oligoarginine Conjugates. To further assess the applicability of this approach to the modification of synthetic polymers, the conjugation of terminal amino-functionalized poly(ethylene glycol)s (amino-PEGs) with oligoarginine was conducted (Figure 5). PEGs have been widely utilized for elongation of drug retention time in the blood, especially for high molecular weight pharmaceuticals (*35*, *36*). Indeed, CPP-modified liposomes were targeted to tumor tissues with a decrease in nonspecific tissue distribution by the PEGylation (*6*, *37*).

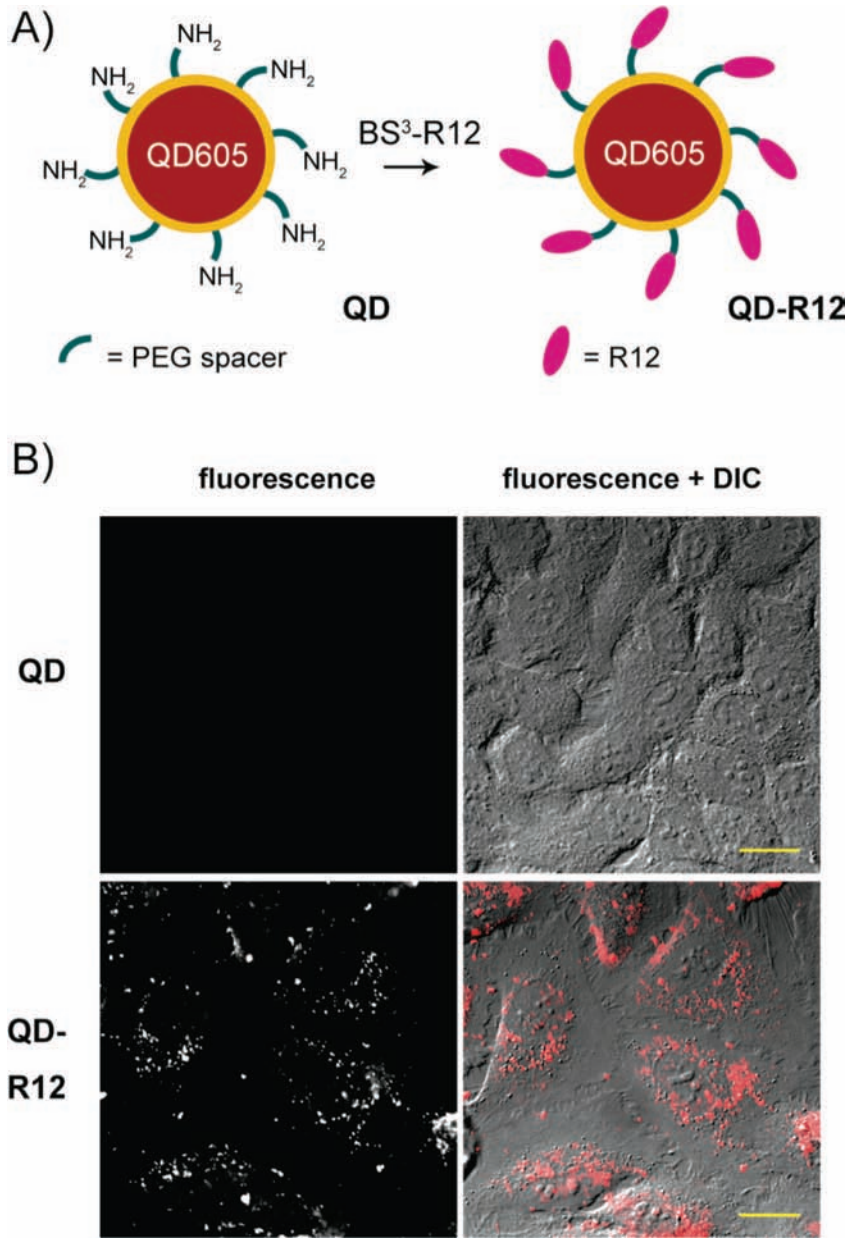

Figure 6. (A) A scheme of modification of QDs with oligoarginine using the BS^3-R12 agent. (B) R12 modification was highly effective in improving the cellular uptake of QDs. HeLa cells were treated with 30 nM QD and QD-R12 in α-MEM (+) for 2 h at 37 °C followed by removing those samples and incubation in fresh α-MEM (+) for 4 h at 37 °C. Scale bars, 20 μm. Fluorescence images of the red layer and the merged pictures of the fluorescence and the DIC images (fluorescence + DIC) are shown.

Here, amino-PEGs of different average molecular weights, namely, amino-PEG5000, amino-PEG12000, and amino-PEG30000, were subjected to modification with oligoarginines. Slight excess amounts of BS^3-R8(Alexa) and BS^3-R12(Alexa) were treated with amino-PEGs of different molecular weights for 1−2 h. All of the reactions proceeded smoothly without difficulty even in the cases of PEGs of high molecular weights. A single purification with HPLC gave the desired PEG−oligoarginine conjugates [PEG5000-R*n*(Alexa), PEG12000-R*n*(Alexa), and PEG30000-R*n*(Alexa) (n = 8 and 12), respectively] in satisfactory yields (53−87%) (Table 2). The mass of the products was confirmed by MALDI-TOFMS. Thus, the usefulness of BS^3−oligoarginine conjugates was also exemplified for the modification of synthetic polymers.

Additionally, the cellular uptake of PEG5000-R8(Alexa) and PEG5000-R12(Alexa) was examined (Figure 5B,C). The PEG5000 conjugates in α-MEM(+) were incubated with HeLa cells at 37 °C for 30 min, and the cellular uptake of the conjugates was monitored by confocal microscopy and assessed by flow cytometry. Conjugation with oligoarginine significantly reinforced the cellular uptake of PEG5000 even in the presence of serum. In contrast to the distinct signals of the internalized PEG5000-R12(Alexa), which were observed by microscopic observation, very few signals were observed for the cells treated with PEG without bearing the R12 peptide (Figure 5C). Elevenfold and 4-fold increases in the cellular uptake of PEG5000 were, respectively, observed when conjugated with R12 and R8 (Figure 5B). Increase in the molecular weight of PEG diminished the cellular uptake of the conjugates. However, the amount of cellar uptake of PEG30000-R12(Alexa) was still five times higher than that of free PEG5000-Alexa (Supporting Information Figure S4).

QD−R12 Conjugates. Finally, the applicability of BS^3-R12 peptides for the modification of quantum dots (QDs) was demonstrated (Figure 6). Quantum dots, colloidal semiconductor nanocrystals prepared in the size 1−20 nm, have unique optical

and spectroscopic properties that are tunable to a desired narrow emission spectrum, are relatively insensitive to the wavelength of excitation light, have a high quantum yield, and are photostable bright fluorophores (*38*, *39*). These properties should be beneficial as fluorescent probes for the analysis of intracellular functions.

Intracellular delivery of QDs by conjugation with CPPs (*40*) has already been reported. Usually, QDs are coated with synthetic polymers or proteins including streptavidins to improve water solubility and feasibility of surface modification. In previous reports, CPPs were conjugated with QDs via avidin−biotin interaction and heterofunctional (amine−thiol directed) cross-linkers. These methods also need multiple steps and had difficulties in workup. The molecular size of streptavidin-derivatized QDs is largely increased, and modification of the QDs with suitable cross-linkers before the introduction of thiol-functionalized CPPs is needed (*41*, *42*). These stepwise conjugation methods usually require purification using gel filtration (*43*, *44*) and dialysis in each step, which is laborious and time-consuming and may lead to loss of QDs. Therefore, our system may provide QDs by the easy and facile means of modification with CPPs. Here, we employed QDs (diameter, 16 nm) functionalized with PEGs bearing ∼90 free amino termini per particle (Figure 6A). The QDs were treated with equimolar amounts of BS^3-R12 to the amino termini of QDs for 2 h, similarly to the case of modification of amino-PEGs as described above. The reaction proceeded with the lowest amount of aggregate formation, and dialysis of the samples to remove unreacted BS^3-R12 yielded the R12-modified QDs (QD-R12) bearing approximately 60 molecules of the R12 peptide per particle.

Modification of R12 also resulted in an increase in internalization efficiency of the QDs (Figure 6B). The QD−R12 conjugate (30 nM) was treated with HeLa cells in α-MEM(−) at 37 °C for 2 h, and the cells were then incubated with fresh α-MEM(+) at 37 °C for 4 h. Bright fluorescent signals of QDs were intracellularly observed, whereas very few signals were obtained for the cells treated with QDs without conjugation with the R12 peptide. As previously reported (*45*), there was a significant influence of cargo size on the intracellular delivery using CPPs, and larger cargoes usually required longer incubation periods before showing evidence of being internalized.

CONCLUSIONS

We have synthesized oligoarginine peptides bearing succinimide-preactivated carboxylates using the homobifunctional BS^3 cross-linkers. Synthesized BS^3-modified oligoarginine peptides (BS^3−R*n*) were used for the conjugation with cargo molecules possessing amino groups such as Fab fragments of antibodies, amino-PEGs, and QDs. These oligoarginine−cargo conjugates were efficiently internalized into the cells. The procedure for oligoarginine modification was quite simple, involving simply mixing BS^3−R*n* with the cargos. Reactions proceeded very smoothly and in high yields with no significant aggregate formation. Therefore, the application of this novel one-pot system for intracellular delivery of various other substances containing reactive amino groups is widely expected in the future.

ACKNOWLEDGMENT

This work was supported in part by Grants-in-Aid for Scientific Research from the Ministry of Education, Culture, Sports, Science, and Technology of Japan. K. T. is grateful for JSPS Research Fellowship for Young Scientists and S. P. for a FPU fellowship and a temporary stay grant from the Ministerio de Ciencia e Innovación.

Supporting Information Available: HPLC retention times for the BS^3-modified oligoarginine peptides, preparation of BS^3−Rev, BS^3−SAP, BS^3-(R-Ahx-R)$_4$, and BS^3-(R-Ahx)$_6$-R, cellular uptake of their conjugates with Fab(Alexa), MALDI-TOFMS of PEG5000-R12(Alexa), and the cellular uptake of PEG-R12(Alexa) conjugates. This material is available free of charge via the Internet at http://pubs.acs.org.

LITERATURE CITED

(1) Futaki, S., Ed. Special theme issue on membrane permeable peptide vectors: chemistry and functional design for the therapeutic applications *Adv. Drug Deliv. Rev.* 2008, *60*, 447−614.
(2) Joliot, A., and Prochiantz, A. (2004) Transduction peptides: from technology to physiology. *Nat. Cell Biol. 6*, 189–196.
(3) Langel, Ü., Ed. (2006) *Handbook of Cell-Penetrating Peptides*, 2nd ed.; CRC Press: London.
(4) Wadia, J. S., and Dowdy, S. F. (2005) Transmembrane delivery of protein and peptide drugs by TAT-mediated transduction in the treatment of cancer. *Adv. Drug Delivery Rev. 57*, 579–596.
(5) Lebleu, B., Moulton, H. M., Abes, R., Ivanova, G. D., Abes, S., Stein, D. A., Iversen, P. L., Arzumanov, A. A., and Gait, M. J. (2008) Cell penetrating peptide conjugates of steric block oligonucleotides. *Adv. Drug Delivery Rev. 60*, 517–529.
(6) Torchilin, V. P. (2008) Tat peptide-mediated intracellular delivery of pharmaceutical nanocarriers. *Adv. Drug Delivery Rev. 60*, 548–558.
(7) Goun, E. A., Pillow, T. H., Jones, L. R., Rothbard, J. B., and Wender, P. A. (2006) Molecular transporters: synthesis of oligoguanidinium transporters and their application to drug delivery and real-time imaging. *ChemBioChem 7*, 1497–1515.
(8) Schwarze, S. R., Ho, A., Vocero-Akbani, A., and Dowdy, S. F. (1999) In vivo protein transduction: delivery of a biologically active protein into the mouse. *Science 285*, 1569–1572.
(9) Gadea, G., Boublik, Y., Delga, S., and Roux, P. (2005) Efficient production of Clostridium botulinum exotoxin C3 in bacteria: a screening method to optimize production yields. *Protein Expr. Purif. 40*, 164–168.
(10) Nakase, I., Niwa, M., Takeuchi, T., Sonomura, K., Kawabata, N., Koike, Y., Takehashi, M., Tanaka, S., Ueda, K., Simpson, J. C., Jones, A. T., Sugiura, Y., and Futaki, S. (2004) Cellular uptake of oligoarginine peptides: roles for macropinocytosis and actin rearrangement. *Mol. Ther. 10*, 1011–1022.
(11) Turner, J. J., Arzumanov, A. A., and Gait, M. J. (2005) Synthesis, cellular uptake and HIV-1 Tat-dependent trans-activation inhibition activity of oligonucleotide analogues disulphide-conjugated to cell-penetrating peptides. *Nucleic Acids Res. 33*, 27–42.
(12) Lewin, M., Carlesso, N., Tung, C. H., Tang, X. W., Cory, D., Scadden, D. T., and Weissleder, R. (2000) Tat peptide-derivatized magnetic nanoparticles allow in vivo tracking and recovery of progenitor cells. *Nat. Biotechnol. 18*, 410–414.
(13) Futaki, S., Suzuki, T., Ohashi, W., Yagami, T., Tanaka, S., Ueda, K., and Sugiura, Y. (2001) Arginine-rich peptides. An abundant source of membrane-permeable peptides having potential as carriers for intracellular protein delivery. *J. Biol. Chem. 276*, 5836–5840.
(14) Rothbard, J. B., Garlington, S., Lin, Q., Kirschberg, T., Kreider, E., McGrane, P. L., Wender, P. A., and Khavari, P. A. (2000) Conjugation of arginine oligomers to cyclosporin A facilitates topical delivery and inhibition of inflammation. *Nat. Med. 6*, 1253–1257.
(15) Kameyama, S., Horie, M., Kikuchi, T., Omura, T., Tadokoro, A., Takeuchi, T., Nakase, I., Sugiura, Y., and Futaki, S. (2007) Acid wash in determining cellular uptake of Fab/cell-permeating peptide conjugates. *Biopolymers 88*, 98–107.
(16) Nakase, I., Tadokoro, A., Kawabata, N., Takeuchi, T., Katoh, H., Hiramoto, K., Negishi, M., Nomizu, M., Sugiura, Y., and Futaki, S. (2007) Interaction of oligoarginine peptides with membrane-associated proteoglycans is crucial for induction of actin organization and macropinocytosis. *Biochemistry 46*, 492–501.

(17) Kameyama, S., Horie, M., Kikuchi, T., Omura, T., Takeuchi, T., Nakase, I., Sugiura, Y., and Futaki, S. (2006) Effects of cell-permeating peptide binding on the distribution of ^{125}I-labeled Fab fragment in rats. *Bioconjugate Chem. 17*, 597–602.

(18) Kameyama, S., Okada, R., Kikuchi, T., Omura, T., Nakase, I., Takeuchi, T., Sugiura, Y., and Futaki, S. (2006) Distribution of immunoglobulin Fab fragment conjugated with HIV-1 REV peptide following intravenous administration in rats. *Mol. Pharm. 3*, 174–180.

(19) Richard, J. P., Melikov, K., Vivès, E., Ramos, C., Verbeure, B., Gait, M. J., Chernomordik, L. V., and Lebleu, B. (2003) Cell penetrating peptides. A reevaluation of the mechanism of cellular uptake. *J. Biol. Chem. 278*, 585–590.

(20) Kang, H., DeLong, R., Fisher, M. H., and Juliano, R. L. (2005) Tat-conjugated PAMAM dendrimers as delivery agents for antisense and siRNA oligonucleotides. *Pharm. Res. 22*, 2099–2106.

(21) Torchilin, V. P., Rammohan, R., Weissig, V., and Levchenko, T. S. (2001) TAT peptide on the surface of liposomes affords their efficient intracellular delivery even at low temperature and in the presence of metabolic inhibitors. *Proc. Natl. Acad. Sci. U.S.A. 98*, 8786–8791.

(22) Anderson, G. W., Zimmerman, J. E., and Callahan, F. (1963) N-Hydroxysuccinimide esters in peptide synthesis. *J. Am. Chem. Soc. 85*, 3039–3039.

(23) Vivès, E., Brodin, P., and Lebleu, B. (1997) A truncated HIV-1 Tat protein basic domain rapidly translocates through the plasma membrane and accumulates in the cell nucleus. *J. Biol. Chem. 272*, 16010–16017.

(24) Derossi, D., Joliot, A. H., Chassaing, G., and Prochiantz, A. (1994) The third helix of the Antennapedia homeodomain translocates through biological membranes. *J. Biol. Chem. 269*, 10444–10450.

(25) Kiso, Y., Sakikawa, H., Fujiwara, Y., Kimura, T., and Akaji, K. (1990) A fluoride ion final deprotection method in solid phase peptide synthesis. *Peptide Chemistry 1989*, (Yanaihara, N., Ed.) pp 153−158, Protein Research Foundation: Minoh.

(26) Pujals, S., Fernández-Carneado, J., Ludevid, M. D., and Giralt, E. (2008) D-SAP: a new, noncytotoxic, and fully protease resistant cell-penetrating peptide. *ChemMedChem 3*, 296–301.

(27) Abes, S., Moulton, H. M., Clair, P., Prevot, P., Youngblood, D. S., Wu, R. P., Iversen, P. L., and Lebleu, B. (2006) Vectorization of morpholino oligomers by the (R-Ahx-R)$_4$ peptide allows efficient splicing correction in the absence of endosomolytic agents. *J. Controlled Release 116*, 304–313.

(28) Rothbard, J. B., Kreider, E., VanDeusen, C. L., Wright, L., Wylie, B. L., and Wender, P. A. (2002) Arginine-rich molecular transporters for drug delivery: role of backbone spacing in cellular uptake. *J. Med. Chem. 45*, 3612–3618.

(29) Mather, J. P. (2006) Special theme issue on Engineered antibody therapeutics. *Adv. Drug Delivery Rev. 58*, 631–765.

(30) Baker, M. (2005) Upping the ante on antibodies. *Nat. Biotechnol. 23*, 1065–1072.

(31) Reichert, J. M., Rosensweig, C. J., Faden, L. B., and Dewitz, M. C. (2005) Monoclonal antibody successes in the clinic. *Nat. Biotechnol. 23*, 1073–1078.

(32) Teillaud, J. L., Desaymard, C., Giusti, A. M., Haseltine, B., Pollock, R. R., Yelton, D. E., Zack, D. J., and Scharff, M. D. (1983) Monoclonal antibodies reveal the structural basis of antibody diversity. *Science 222*, 721–726.

(33) Mian, I. S., Bradwell, A. R., and Olson, A. J. (1993) Structure, function and properties of antibody binding sites. *J. Mol. Biol. 217*, 133–151.

(34) Anderson, D. C., Nichols, E., Manger, R., Woodle, D., Barry, M., and Fritzberg, A. R. (1993) Tumor cell retention of antibody Fab fragments is enhanced by an attached HIV TAT protein-derived peptide. *Biochem. Biophys. Res. Commun. 194*, 876–884.

(35) van Vlerken, L. E., Vyas, T. K., and Amiji, M. M. (2007) Poly(ethylene glycol)-modified nanocarriers for tumor-targeted and intracellular delivery. *Pharm. Res. 24*, 1405–1414.

(36) Caliceti, P., and Veronese, F. M. (2003) Pharmacokinetic and biodistribution properties of poly(ethylene glycol)-protein conjugates. *Adv. Drug Delivery Rev. 55*, 1261–1277.

(37) Kale, A. A., and Torchilin, V. P. (2007) "Smart" drug carriers: PEGylated TATp-modified pH-sensitive liposomes. *J. Liposome Res. 17*, 197–203.

(38) Murray, C. B., Norris, D. J., and Bawendi, M. G. (1993) Synthesis and characterization of nearly monodisperse CdE (*E* = sulfur, selenium, tellurium) semiconductor nanocrystallites. *J. Am. Chem. Soc. 115*, 8706–8715.

(39) Michalet, X., Pinaud, F. F., Bentolila, L. A., Tsay, J. M., Doose, S., Li, J. J., Sundaresan, G., Wu, A. M., Gambhir, S. S., and Weiss, S. (2005) Quantum dots for live cells, in vivo imaging, and diagnostics. *Science 307*, 538–544.

(40) Stroh, M., Zimmer, J. P., Duda, D. G., Levchenko, T. S., Cohen, K. S., Brown, E. B., Scadden, D. T., Torchilin, V. P., Bawendi, M. G., Fukumura, D., and Jain, R. K. (2005) Quantum dots spectrally distinguish multiple species within the tumor milieu in vivo. *Nat. Med. 11*, 678–682.

(41) Ruan, G., Agrawal, A., Marcus, A. I., and Nie, S. (2007) Imaging and tracking of tat peptide-conjugated quantum dots in living cells: new insights into nanoparticle uptake, intracellular transport, and vesicle shedding. *J. Am. Chem. Soc. 129*, 14759–14766.

(42) Zhou, M., and Ghosh, I. (2007) Quantum dots and peptides: a bright future together. *Biopolymers 88*, 325–339.

(43) Tsay, J. M., Trzoss, M., Shi, L., Kong, X., Selke, M., Jung, M. E., and Weiss, S. (2007) Singlet oxygen production by peptide-coated quantum dot-photosensitizer conjugates. *J. Am. Chem. Soc. 129*, 6865–6871.

(44) Zhou, M., Nakatani, E., Gronenberg, L. S., Tokimoto, T., Wirth, M. J., Hruby, V. J., Roberts, A., Lynch, R. M., and Ghosh, I. (2007) Peptide-labeled quantum dots for imaging GPCRs in whole cells and as single molecules. *Bioconjugate Chem. 18*, 323–332.

(45) Tünnemann, G., Martin, R. M., Haupt, S., Patsch, C., Edenhofer, F., and Cardoso, M. C. (2006) Cargo-dependent mode of uptake and bioavailability of TAT-containing proteins and peptides in living cells. *FASEB J. 20*, 1775–1784.

BC800327F

Supporting Information:

Novel System to Achieve One-Pot Modification of Cargoes with Oligoarginine Vector for Intracellular Delivery

Kentaro Takayama,[†] Akiko Tadokoro,[‡,#] Sílvia Pujals,[§] Ikuhiko Nakase,[†] Ernest Giralt,[§] and Shiroh Futaki[†, ‡,*]

[†]Institute for Chemical Research, Kyoto University, Uji, Kyoto 611-0011, Japan
[#]SORST, JST, Kawaguchi, Saitama 332-0012, Japan
[§]Institute for Research in Biomedicine, University of Barcelona, Barcelona Science, 08028 Barcelona, Spain

1. Retention times in HPLC for BS^3-R8, BS^3-R12, BS^3-R8(Alexa), and BS^3-R12(Alexa)

BS^3-R8: 8.96 min (gradient 5–85%, 30 min)
BS^3-R12: 9.38 min (gradient 5–85%, 30 min)
BS^3-R8(Alexa): 9.38 min (gradient 10–60%, 25 min)
BS^3-R12(Alexa): 9.26 min (gradient 10–60%, 25 min)

Condition:
Column: Cosmosil $5C_4$-AR-300, 4.6 × 150 mm
Solvent system: linear gradient of CH_3CN containing 0.1% trifluoroacetic acid (TFA) in 0.1% aqueous TFA
Flow rate: 1 mL/min
Detection: 215 nm.

2. Structures, yields, and characterization of BS^3-Rev, BS^3-SAP, BS^3-(R-Ahx-R)$_4$, and BS^3-(R-Ahx)$_6$-R

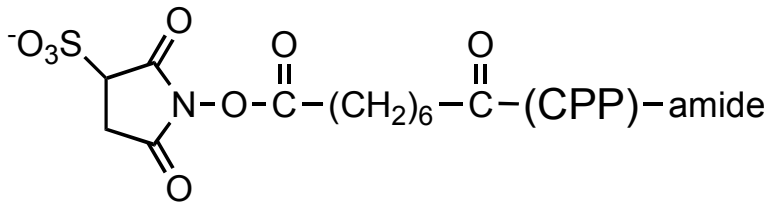

BS^3-Rev: (CPP) = Thr-Arg-Gln-Ala-$(Arg)_2$-Asn-$(Arg)_4$-Trp-Arg-Glu-Arg-Gln-Arg
Yield: 75%
MALDI-TOFMS: 2769.2 [expected for $(M+H)^+$ 2769.1]
Retention time in HPLC: 11.55 min (gradient 5–55%, 25 min) [Column: Cosmosil $5C_4$-AR-300, 4.6 × 150 mm: solvent system: linear gradient of CH_3CN containing 0.1% TFA in 0.1% aqueous TFA; flow rate: 1 mL/min; detection: 215 nm]

BS^3-SAP: (CPP) = $(Val-Arg-Leu-Pro-Pro-Pro)_3$
Yield: 70%
MALDI-TOFMS: 2329.5 [expected for $(M+H)^+$ 2328.8]
Retention time in HPLC: 17.83 min (gradient 5–55%, 25 min) [Column: Cosmosil $5C_4$-AR-300, 4.6 × 150 mm: solvent system: linear gradient of CH_3CN containing 0.1% TFA in 0.1% aqueous TFA; flow rate: 1 mL/min; detection: 215 nm]

BS^3-(R-Ahx-R)$_4$: (CPP) = $(Arg-Ahx-Arg)_4$
Yield: 58%
MALDI-TOFMS: 2052.4 [expected for $(M+H)^+$ 2051.5]
Retention time in HPLC: 10.42 min (gradient 5–55%, 25 min) [Column: Cosmosil $5C_4$-AR-300, 4.6 × 150 mm: solvent system: linear gradient of CH_3CN containing 0.1% TFA in 0.1% aqueous TFA; flow rate: 1 mL/min; detection: 215 nm]

BS^3-(R-Ahx)$_6$-R : (CPP) = $(Arg-Ahx)_6$-Arg
Yield: 50%
MALDI-TOFMS: 2122.0 [expected for $(M+H)^+$ 2121.6]
Retention time in HPLC: 11.27 min (gradient 5–55%, 25 min) [Column: Cosmosil $5C_4$-AR-300, 4.6 × 150 mm: solvent system: linear gradient of CH_3CN containing 0.1% TFA in 0.1% aqueous TFA; flow rate: 1 mL/min; detection: 215 nm]

3. Conjugation of Alexa 488-labeled Fab fragment [Fab(Alexa)] with Rev, SAP, $(R\text{-}Ahx\text{-}R)_4$, and $(R\text{-}Ahx)_6\text{-}R$

These conjugates were prepared as described for Fab(Alexa)-R8 and Fab(Alexa)-R12 using BS^3-Rev, BS^3-SAP, BS^3-$(R\text{-}Ahx\text{-}R)_4$, and BS^3-$(R\text{-}Ahx)_6$-R, respectively. Preparative yields for Fab(Alexa)-Rev, Fab(Alexa)-SAP, Fab(Alexa)-$(R\text{-}Ahx\text{-}R)_4$, and Fab(Alexa)-$(R\text{-}Ahx)_6$-R were 21%, 53%, 53%, and 52%, respectively.

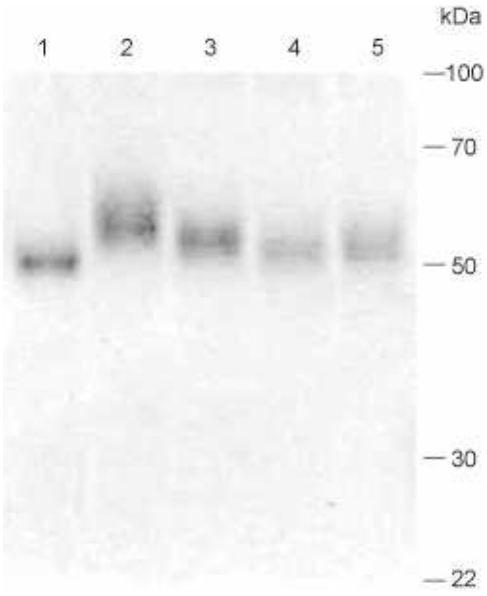

Figure S1. SDS-PAGE of Fab(Alexa)-Rev, Fab(Alexa)-SAP, Fab(Alexa)-$(R\text{-}Ahx\text{-}R)_4$, and Fab(Alexa)-$(R\text{-}Ahx)_6$-R. Lane 1-5: Fab, Fab(Alexa)-SAP, Fab(Alexa)-Rev, Fab(Alexa)-$(R\text{-}Ahx\text{-}R)_4$, and Fab(Alexa)-$(R\text{-}Ahx)_6$-R, respectively. On average 1-2 molecules of peptides were attached to Fab.

4. Cellular uptake of Fab(Alexa)-Rev, Fab(Alexa)-SAP, Fab(Alexa)-$(R\text{-}Ahx\text{-}R)_4$, and Fab(Alexa)-$(R\text{-}Ahx)_6$-R

The conjugates were incubated with HeLa cells and cellular uptake was monitored using confocal microscopy as shown in Figure 4B. In contrast to Fab(Alexa)-Rev Fab(Alexa)-R8 and Fab(Alexa)-R12, showing high efficiency of cellular uptake, the cellular uptake of Fab(Alexa)-SAP, Fab(Alexa)-$(R\text{-}Ahx\text{-}R)_4$, and Fab(Alexa)-$(R\text{-}Ahx)_6$-R was much lower. Although these CPPs have been reported as efficient intracellular delivery vectors, efficiency of these CPPs to internalize Fab (~50 kDa) was found to be lower than that of R12 and Rev peptides.

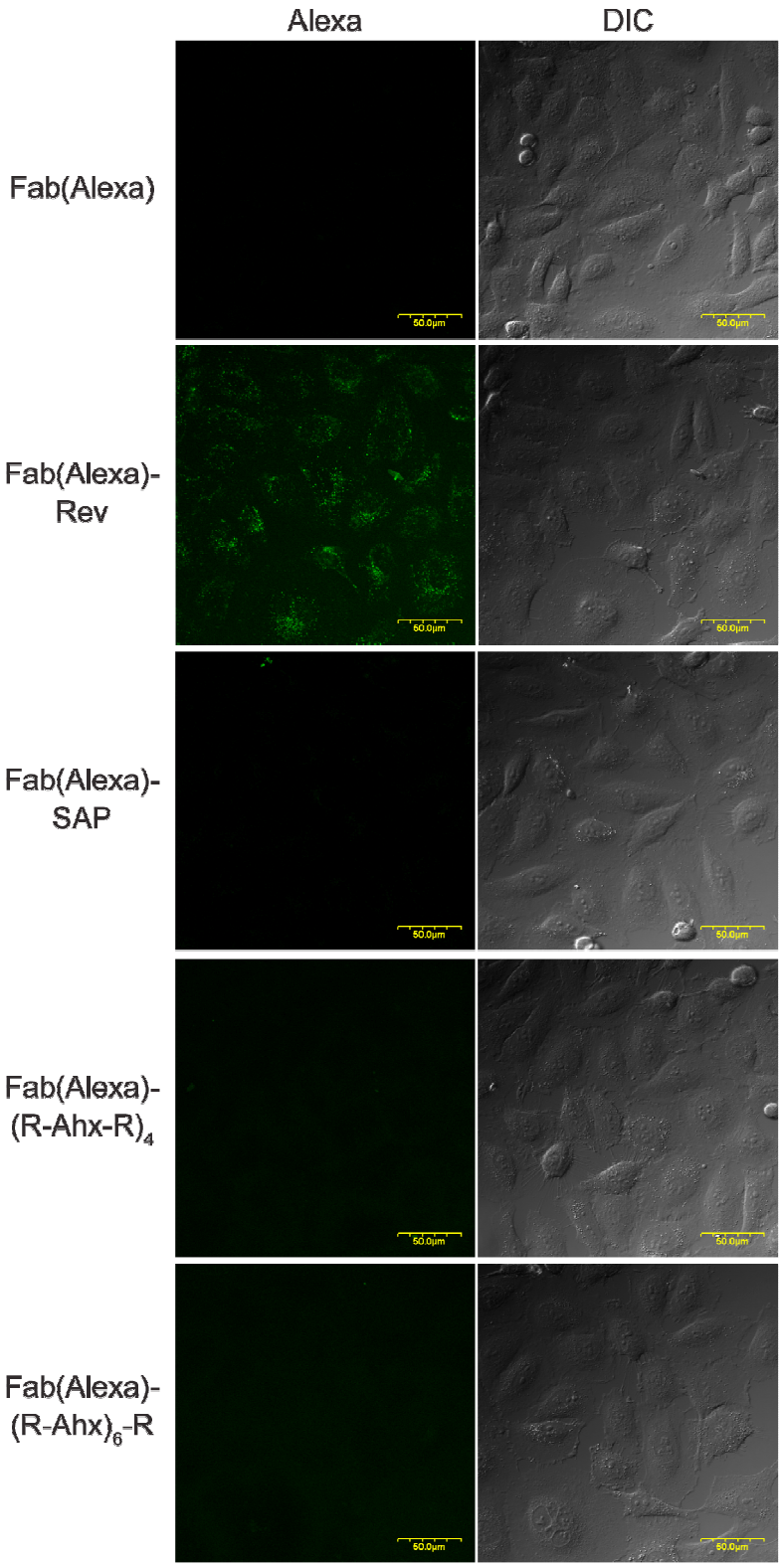

Figure S2. Cellular uptake of Fab(Alexa)-Rev, Fab(Alexa)-SAP, Fab(Alexa)-(R-Ahx-R)$_4$, and Fab(Alexa)-(R-Ahx)$_6$-R. Conjugates, 1 μM; incubation, 3 h.

5. MALDI-TOFMS of PEG5000-R12(Alexa)

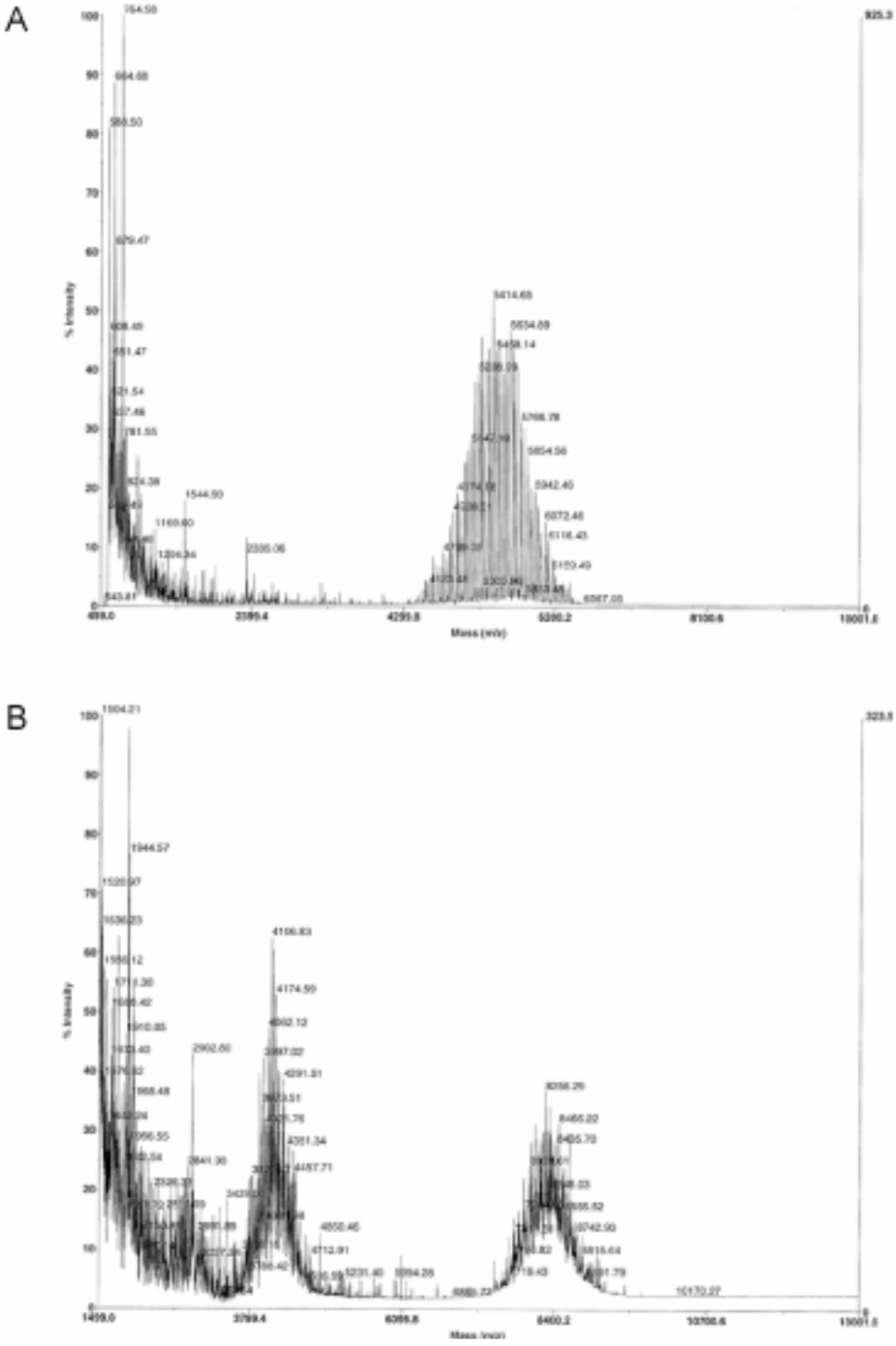

Figure S3. MALDI-TOFMS of amino-PEG5000(A) and PEG5000-R12(Alexa) (B)

6. Cellular uptake of PEG-R12(Alexa) conjugates

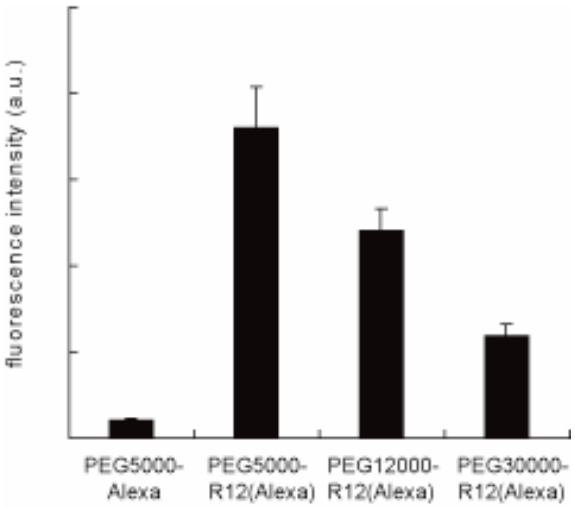

Figure S4. Cellular uptake of PEG-R12(Alexa) conjugates. These conjugates were incubated with HeLa cells and cellular uptake was analyzed as in Figure 5B.

Bioconjugate Chemistry 20th Anniversary

Subscriber access provided by SHEMYAKIN-OVCHINNIKOV INST

Article

Modulation of p*K* of Brooker's Merocyanine by DNA Hybridization

Hiromu Kashida, Kanae Sano, Yuichi Hara, and Hiroyuki Asanuma

Bioconjugate Chem., **2009**, 20 (2), 258-265• DOI: 10.1021/bc800335h • Publication Date (Web): 26 January 2009

Downloaded from http://pubs.acs.org on May 8, 2009

More About This Article

Additional resources and features associated with this article are available within the HTML version:

- Supporting Information
- Access to high resolution figures
- Links to articles and content related to this article
- Copyright permission to reproduce figures and/or text from this article

View the Full Text HTML

ACS Publications
High quality. High impact.

Bioconjugate Chemistry is published by the American Chemical Society. 1155 Sixteenth Street N.W., Washington, DC 20036

Modulation of pK_a of Brooker's Merocyanine by DNA Hybridization

Hiromu Kashida, Kanae Sano, Yuichi Hara, and Hiroyuki Asanuma*

Graduate School of Engineering, Nagoya University, Furocho, Chikusa, Nagoya 464-8603, Japan, and Core Research for Evolution Science and Technology (CREST), Japan Science and Technology Agency (JST), Kawaguchi, Saitama 332-0012, Japan. Received August 5, 2008; Revised Manuscript Received December 15, 2008

Brooker's merocyanine (BM), which changes its emission and absorption maxima upon protonation, was introduced into oligodeoxyribonucleotide (ODN) via D-threoninol by postsynthetic modification on a CPG (controlled-pore glass) support. The pK_a of BM in the modified ODN increased from 9.5 to 10.1 upon hybridization. As a result, absorption maxima shifted from 492 to 432 nm at pH 10.0 by the presence of its complementary strand. This spectral shift was sufficiently large so that DNA hybridization could easily be discriminated even by the naked eye; the color of the solution changed from orange to yellow upon hybridization. In addition, the fluorescence emission was strongly quenched upon hybridization, demonstrating that this probe can also detect the target DNA by the fluorescence change. Ratiometric detection of hybridization was also possible by simultaneous excitation of both protonated and deprotonated BMs. Furthermore, we could also modulate its pK_a by the antiparallel stacking of two BM molecules in the duplex; the pK_a of BM decreased from 10.1 to 9.7 by the stacking of two BMs in an antiparallel manner. Thus, control of the microenvironment around the BM molecule allowed modulation of its pK_a, which is applicable to the sequence-specific recognition of target DNA.

INTRODUCTION

Folding of biomacromolecules creates specific regions or internal spaces in which the microenvironment is different from the bulk solution due to the effective shielding from the solvent. Such shielded space is advantageous to modulate the properties of a specific amino residue, such as pK_a, for the effective recognition of a substrate or enzymatic reaction. For example, enzymes modulate the pK_a of the side chains (functional groups) of amino acid residues at their active sites, which are usually located in a cavity or cleft, to catalyze the reaction effectively (*1*). Since pK_a significantly affects proton transfer or proton-mediated charge relay that is closely related to the catalytic reaction, pK_a is strictly controlled by salt bridges, hydrogen bonding, hydrophobic interactions, and so on (*1*, *2*). Similarly, "folded" oligonucleotides modulate the pK_a of functional groups because they significantly affect the catalytic activity of ribozymes or triplex-forming efficiency (*3*−*5*). Since a duplexed oligonucleotide is composed of a hydrophobic core of base pairs that are surrounded by highly charged polyanions, its inside is considerably "negative". Such a negative microenvironment raises the pK_a of the nucleobases (*6*); an increase in pK_a of cytidine in a third strand facilitates triplex formation (note that N-3 of cytosine is protonated in a triplex) (*5*). Intercalated molecules are also affected by a negative microenvironment; 3,8-diamino-6-phenylphenanthridine (DAPP), which is known as a typical intercalator, changes its pK_a from 5.80 to 8.00 upon binding to DNA (*7*, *8*).

Previously, we utilized the pK_a change of a dye by tethering it to an oligodeoxyribonucleotide (ODN) for the detection of duplex formation (*9*). Naphthyl Red, which is one of the pH-responsive dyes and changes its λ_{max} by protonation, was incorporated into the middle of ODN on D-threoninol. In the single-stranded state, the pK_a of Naphthyl Red was 5.8, whereas it increased to 6.5 upon duplex formation. NMR analyses revealed that Naphthyl Red was intercalated in the duplex between adjacent base pairs, and the dimethylamino group of Naphthyl Red was located in the vicinity of phosphodiesters of the complementary strand. On the basis of these analyses, we confirmed that the increase in pK_a by duplex formation was attributed to the accumulated negative charge of phosphate anions around the intercalated Naphthyl Red. This pK_a change was advantageous to the sequence-specific probing of DNA simply by color change. Naphthyl Red in a single-stranded state was completely deprotonated at pH 7.0, whereas it was partially protonated by the presence of its complementary strand. Such protonation−deprotonation induced a significant change of λ_{max} (from 466 to 545 nm by hybridization), which allowed detection of DNA with the naked eye (Note: This large shift at pH 7.0 was induced not only by the pK_a change but also by the decrease in electron density on the dimethylamino group due to the negative microenvironment). To the best of our knowledge, it was the first example of a DNA probe based on a pK_a change by hybridization. However, since Naphthyl Red did not exhibit fluorescence, detection of DNA was possible only by the change of absorption maximum.

Scheme 1. Protonation and Deprotonation of Original Brooker's Merocyanine

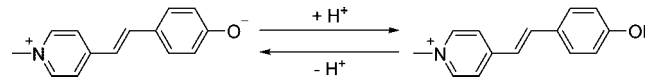

In the present study, we introduced Brooker's merocyanine (BM) instead of Naphthyl Red into ODN on D-threoninol. Brooker's merocyanine is known to exhibit large solvatochromism and is widely used as a probe to detect the polarity of the microenvironment (*10*−*13*). Unlike the previous Naphthyl Red, BM changes not only its absorption but also emission spectrum upon protonation (Scheme 1) (*14*, *15*). Hence, incorporation of BM into ODN is expected to change its pK_a by hybridization, which allows sequence-specific detection of DNA both by absorption and emission spectra.

EXPERIMENTAL PROCEDURES

Materials. All the conventional phosphoramidite monomers, CPG columns, reagents for DNA synthesis, and Poly-Pak II

* asanuma@mol.nagoya-u.ac.jp.

10.1021/bc800335h CCC: $40.75 © 2009 American Chemical Society
Published on Web 01/26/2009

Scheme 2. Synthesis of Modified ODN (BM1)[a]

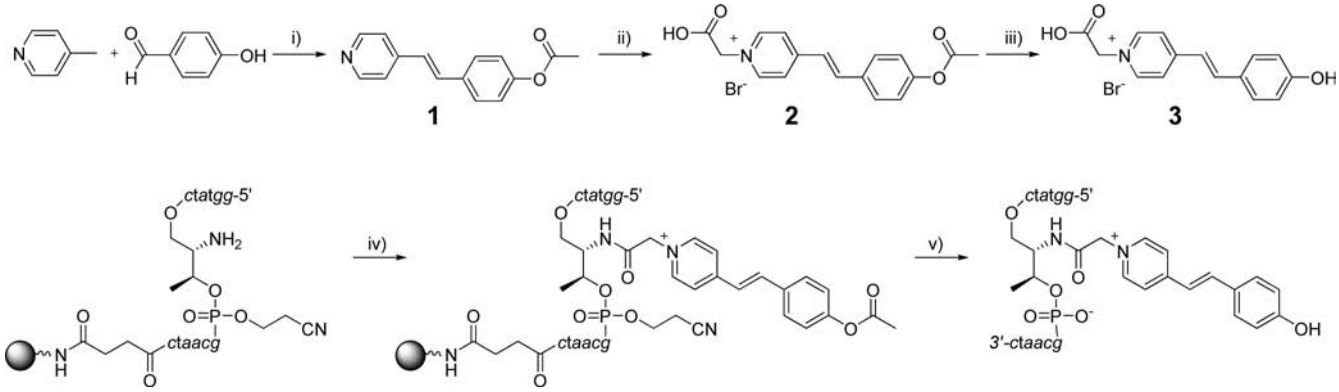

[a] (i) Acetic anhydride, reflux, 1 day, 32%; (ii) bromoacetic acid, CH_3CN, rt, 3 h, quant.; (iii) basic alumina, MeOH, 16%; (iv) **2**, PyBOP, PPTS, *N*-methylmorpholine, DMF, rt, 3 days; (v) 25% aqueous ammonia solution, 55 °C, 8 h.

cartridges were purchased from Glen Research. Other reagents for the synthesis of phosphoramidite monomers were purchased from Tokyo Kasei Co., Ltd., and Aldrich.

Synthesis of the Brooker's Merocyanine (compound 3). Compound **3** was synthesized as follows (*16*, *17*): 6.0 mL (62 mmol) of 4-picoline was added to a solution of 5.0 g (41 mmol) of 4-hydroxybenzaldehyde dissolved in acetic anhydride (20 mL). After the mixture was refluxed for 24 h, the solution was removed by evaporation. Then, the crude product was dissolved into CH_2Cl_2 and washed with an aqueous saturated solution of $NaHCO_3$ aq. (twice), and then dried over Na_2SO_4. Finally, the solvent was removed in vacuo, and the product was subjected to recrystallzation from EtOH/water to afford compound **1** (yield: 32%). ^{1}H NMR for **1** [DMSO-d_6 (TMS), 500 MHz] δ = 8.59 (d, 2H, J = 6.0 Hz), 7.71 (d, 2H, J = 6.5 Hz), 7.57 (m, 3H), 7.25 (d, 1H, J = 16.5 Hz), 7.19 (d, 2H, J = 8.5 Hz), 2.28 (s, 3H).

1.0 g (4.2 mmol) of **1** was dissolved in acetonitrile and reacted with 0.58 g (4.2 mmol) of bromoacetic acid for 3 h at room temperature. After the reaction was completed, the precipitate was filtered and dried in vacuo. The product (compound **2**) was used without purification (yield: quant.). ^{1}H NMR for **2** [DMSO-d_6 (TMS), 500 MHz] δ = 8.90 (d, 2H, J = 7.0 Hz), 8.29 (d, 2H, J = 7.5 Hz), 8.06 (d, 1H, J = 16.5 Hz), 7.82 (d, 2H, J = 8.5 Hz), 7.54 (d, 1H, J = 16.5 Hz), 7.29 (d, 2H, J = 8.5 Hz), 5.42 (s, 2H), 2.31 (s, 3H).

0.73 g (1.9 mmol) of **2** was subjected to column chromatography over basic alumina (methanol). The fraction of merocyanine was collected and recrystallized from ethanol to afford 0.10 g of compound **3** (yield: 16%). ^{1}H NMR for **3** [DMSO-d_6 (TMS), 500 MHz] δ = 8.11 (d, 2H, J = 6.5 Hz), 7.64 (d, 1H, J = 15.5 Hz), 7.53 (d, 2H, J = 6.5 Hz), 7.29 (d, 2H, J = 8.0 Hz), 6.54 (d, 1H, J = 15.0 Hz), 6.13 (d, 2H, J = 9.0 Hz), 4.49 (s, 2H).

Synthesis of the Modified DNA Tethering Brooker's Merocyanine. ODNs involving Alloc- (allyloxycarbonyl-) protected D-threoninol residues were synthesized on an automated DNA synthesizer (H-8-SE DNA synthesizer, NIHON TECHNO SERVICE Co., Ltd.) by using the corresponding phosphoramidite monomer according to a previous report (*18*) and other conventional methods. The postsynthetic procedure for introducing merocyanine on CPG anchoring ODN was as follows: The Alloc group was deprotected by treatment with $Pd(PPh_3)_4$ (10 equiv) and *N*-methylaniline (1000 equiv) as a scavenger in CH_2Cl_2. The amino group on D-threoninol was coupled with **2** (Scheme 2: 100 equiv) with PyBOP (250 equiv) as a coupling reagent in DMF. In addition, *N*-methylmorpholine (300 equiv) and pyridinium *p*-toluenesulfonate (100 equiv) were added to accelerate the reaction. After the Poly-Pak treatment,

Scheme 3. Sequences of ODNs Synthesized in This Study

they were purified by reversed-phase HPLC. The yield of amide coupling was 44% as estimated from HPLC analysis. The modified ODNs were characterized by MALDI-TOFMS (Autoflex II, Bruker Daltonics).

MALDI-TOFMS for **BM1**: Obsd. 4048.9 (Calcd. for [**BM1** + H^+]: 4049.8). **BM2**: Obsd. 4048.6 (Calcd. for [**BM2** + H^+]: 4048.8). **BM3**: Obsd. 4056.8 (Calcd. for [**BM3** + H^+]: 4056.8). **cBM1**: Obsd. 4048.5 (Calcd. for [**cBM1** + H^+]: 4049.8).

BM-modified ODNs did not decompose at −20 °C under dark conditions at either pH 7.0 or 10.0. However, when the ODNs were kept at room temperature in the presence of ambient light, about 20% was degraded after 1 week.

Spectroscopic Measurements. UV−vis and CD spectra were measured on a JASCO model V-550 and a JASCO model J-820, respectively, with a 10 mm quartz cell. Fluorescence spectra were measured on a JASCO model FP-6500 with a microcell. All of them were equipped with programmed temperature controllers. Conditions of the sample solutions were as follows: [NaCl] = 100 mM, [DNA] = 5 μM. For measurements at pH 7.0, 9.1, or 10.0, 10 mM phosphate, Tris, or CAPS (*N*-cyclohexyl-3-aminopropanesulfonic acid) buffer was used. All the samples were incubated at 60 °C for 5 min and then cooled at a rate of 4 °C min^{-1} before the measurement.

Titration Experiments. The pK_a was determined from the absorbance of the sample at 20 °C. The pH was adjusted by adding small amounts of conc. NaOH solution to the sample. Conditions of the sample solutions were as follows: [NaCl] = 100 mM, [Na_2HPO_4/NaH_2PO_4] = 10 mM. Since pH titration could not be conducted at pH higher than 10 due to the dissociation of the duplex, pK_a was determined by assuming a following equation with a curve-fitting program equipped with *KaleidaGraph 3.5* (Synergy Software):

$$A = A_{HA} + \frac{(A_A - A_{HA})}{10^{(pK_a - pH)} + 1} \quad (1)$$

where A_{HA} and A_A denote absorbance of fully protonated and deprotonated forms. Errors of pK_a's were estimated within 0.04.

Measurement of Melting Temperature. The melting curve of duplex DNA was obtained with the above apparatus by

Table 1. Effects of pH on the Melting Temperature (T_m) of BM1/N1 and Absorption Maxima of Single-Stranded BM1 and BM1/N1[a]

		λ_{max}/nm[b]	
pH	T_m/°C	**BM1**	**BM1/N1**
7.0	39.5	407	418
8.0	38.7	408	415
9.1	37.2	410	421
10.0	32.2	492	432
10.5	23.8	476	478

[a] Solution conditions: [ODN] = 5 μM, [NaCl] = 100 mM. [b] UV−vis spectrum was measured at 0 °C.

measuring the change of absorbance at 260 nm versus temperature. The melting temperature (T_m) was determined from the maximum in the first derivative of the melting curve. Both the heating and cooling curves were measured, and the T_m obtained from them coincided with each other within 2.0 °C. The temperature ramp was 1 °C min^{-1}.

RESULTS AND DISCUSSION

Synthesis of Modified ODN Tethering BM on D-Threoninol. For the incorporation of BM into ODN, we could not adopt conventional phosphoramidite chemistry because amide coupling of BM (compound **2** in Scheme 2) with D-threoninol did not proceed for some reason. We also tried conventional postsynthetic modification in aqueous solution (*19*, *20*): the *N*-hydroxysuccinimidyl ester of BM (compound **2** in Scheme 2) was reacted with the amino group of D-threoninol incorporated into ODN in aqueous solution under several reaction conditions according to the literature (*21*, *22*). However, decomposition of this activated ester proceeded much faster than the desired coupling reaction. In order to overcome this difficulty, we recently developed a new postsynthetic modification of DNA on a controlled-pore glass (CPG) column by the use of allylic protection (*18*). First, Alloc- (allyloxycarbonyl-) protected D-threoninol was incorporated into the desired position of ODN. Then, the Alloc group was selectively deprotected on CPG column after DNA synthesis by $Pd(PPh_3)_4$ with other protecting groups on nucleobases keeping intact, followed by the coupling of acetyl-protected BM (compound **2** in Scheme 2) with the deprotected amino group on D-threoninol for 3 days. Finally, ODNs were cleaved from CPG and deprotected by conventional treatment with ammonium hydroxide solution. Although the total yield was not high (about 40% or below), we successfully obtained the desired ODN. In Scheme 3, modified ODNs tethering BM synthesized in the present study are listed.

Effect of the Introduction of BM on Duplex Stability. Before evaluating the pK_a of BM, we first investigated the effect of the incorporation of BM on duplex stability. The melting temperature (T_m) of **BM1/N1** involving one **X** residue at the center of the sequence was determined as 39.5 °C at pH 7.0 from the change of absorbance at 260 nm (see Table 1). Since the T_m of native duplex without BM residue (**N0/N1**) was 47.7 °C, the introduction of BM significantly destabilized the duplex. The T_m did not change from pH 7 to 9, and slightly decreased at pH 10 as shown in Table 1. However, T_m significantly decreased to 23.8 °C at pH 10.5, due to the deprotonation of imino protons of guanine and thymine. Therefore, spectroscopic measurements were carried out below 20 °C where duplexes sufficiently formed even at pH 10.5.

Hybridization of BM-tethered ODN with its native complementary strand showed both bathochromicity and hypsochromicity at pH 7.0 where the BM residue was protonated (*vide infra*) (Note: UV−vis spectra of single-stranded **BM1** and **BM1/N1** are in Supporting Information). In addition, a very weak and slightly negative circular dichroism (CD) was induced at around 400 nm where BM had its characteristic absorption (compare dotted line with solid line in Figure 1). These spectroscopic behaviors are characteristic of intercalated chromophores (*23*−*25*). Previously, we reported the solution structure of modified ODN tethering an azobenzene moiety and found that azobenzene was completely intercalated in the DNA duplex (*26*). In that case, both bathochromicity and negatively induced weak CD were observed (*27*). Thus, we conclude that BM is intercalated between the neighboring base pairs. The instability of the duplex tethering BM is attributed to the nonplanar structure of the BM residue, because steric hindrance between the benzene ring and the C═O of the amide bond twists the methylene chain (see Supporting Information).

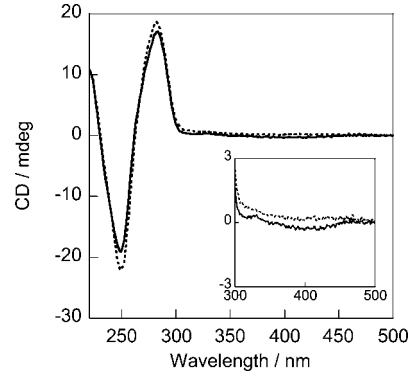

Figure 1. CD spectra of **BM1/N1** (solid line) and **N0/N1** (dotted line) at pH 7.0 (10 mM phosphate buffer), 0 °C. Induced CD at around 400 nm is magnified in inset.

Evaluation of the pK_a of BM. *Intrinsic pK_a of BM before Incorporation into DNA.* In order to evaluate the intrinsic spectroscopic properties of BM before incorporation of ODN, we first measured the absorption spectrum of compound **3** that involves a carboxylate group. An absorption maximum for **3** appeared at 381 nm at pH 7.0 (see Supporting Information), which was 6 nm longer than that for original BM without the carboxylate group (Scheme 1). When the pH was raised above 8, a new peak appeared at 451 nm as shown in Figure 2, demonstrating that compound **3** was deprotonated. From a titration curve monitored at 450 nm as shown in Figure 2b, the pK_a of **3** was determined to be 8.8 (Note: Addition of native duplex (**N0**/**N1**) to the buffer solution of compound **3** (pH 9.1, 0 °C) did not change the UV−vis spectra. See Supporting Information). Kuder et al. reported a relationship between temperature and pK_a of original BM (*14*). From their equation, the pK_a of original BM at 20 °C was estimated to be 8.6, which almost coincided with that of **3**. In addition, the absorption maximum of deprotonated **3** largely shifted depending on the polarity of the solvent as is observed for original BM (See Supporting Information) (*10*−*13*).

pK_a of BM in the Single-Strand and Duplex. To investigate whether protonation was enhanced upon hybridization, UV−vis spectra of **BM1** and **BM1/N1** were measured by changing the pH of the solution (Figures 3A and 4A). λ_{max} at each pH is listed in Table 1. At around pH 7, **BM1** in the single-stranded state gave λ_{max} at 407 nm, indicating that most of BM was protonated. An increase of pH diminished the peak at 407 nm and produced a new peak at around 490 nm due to the deprotonation of BM. From the titration curve monitored at 490 nm shown in Figure 3B (Note: As shown in Table 1, λ_{max} shifted to shorter wavelength above pH 10.2. Thus, pK_a of **BM1** was determined from the absorbance at pH 7.18–10.16), pK_a was determined to be 9.5 at 20 °C, which is 0.7 higher than that of 3. The pK_a difference between the compound **3** and single-stranded **BM1** might be attributed to the electrostatic interaction

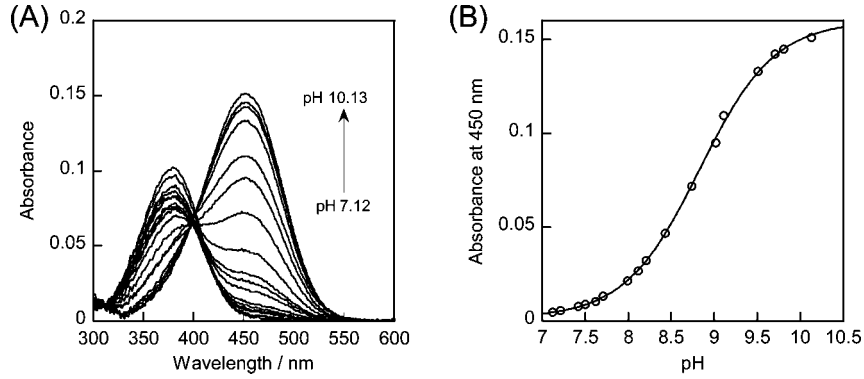

Figure 2. (A) UV−vis spectra of Brooker's merocyanine (compound **3**) at various pH (from 7.12 to 10.13) and (B) plots of the absorbance of **3** at 450 nm as a function of pH values at 20 °C. Solution conditions are as follows: [**3**] = 5 μM, [NaCl] = 100 mM, [NaH_2PO_4/Na_2HPO_4] = 10 mM.

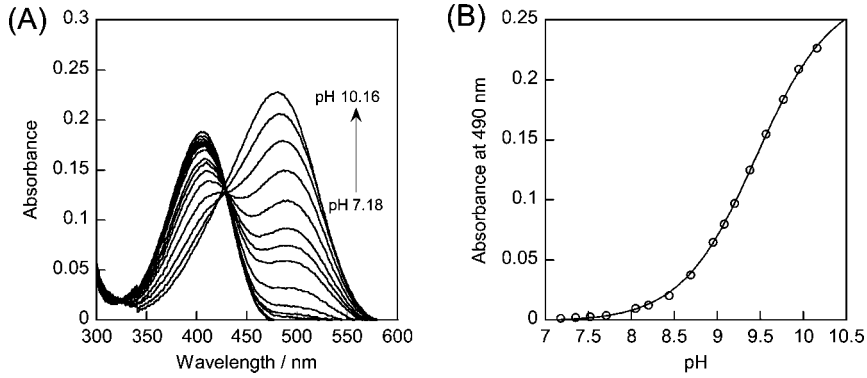

Figure 3. (A) UV−vis spectra of **BM1** at various pHs (from 7.18 to 10.16) and (B) plots of the absorbance of **BM1** at 490 nm as a function of pH values at 20 °C. Solution conditions are as follows: [ODN] = 5 μM, [NaCl] = 100 mM, [NaH_2PO_4/Na_2HPO_4] = 10 mM.

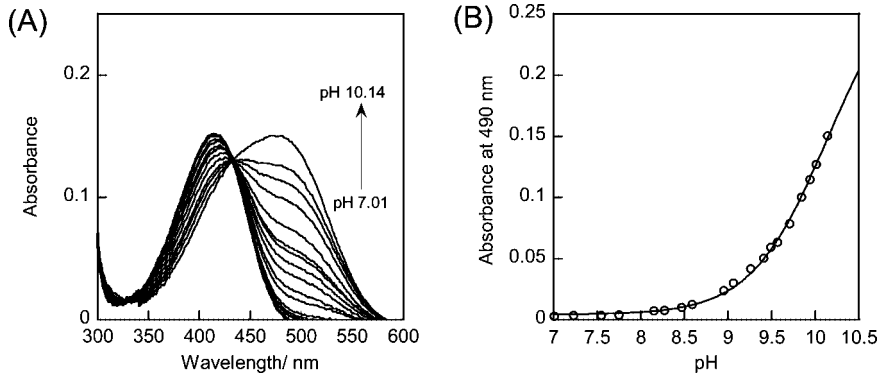

Figure 4. (A) UV−vis spectra of **BM1/N1** at various pHs (from 7.01 to 10.14) and (B) plots of the absorbance of **BM1/N1** at 490 nm as a function of pH values at 20 °C. Solution conditions are as follows: [ODN] = 5 μM, [NaCl] = 100 mM, [NaH_2PO_4/Na_2HPO_4] = 10 mM.

of phosphate anions and hydrophobic environment generated by natural bases.

The pK_a was further increased upon hybridization as shown in Figure 4. Protonated BM in **BM1/N1** gave λ_{max} at 414 nm, and a new peak appeared at a longer wavelength as pH increased. The pK_a of BM in **BM1/N1** was determined to be 10.1 from absorbance at 490 nm (Figure 4B), which is 0.6 higher than that of single-stranded **BM1**. Such an increase in pK_a by hybridization, namely, the suppression of deprotonation from BM, is attributed to the negative charges on phosphodiesters surrounding the intercalated BM.

Detection of DNA Hybridization by Use of pK_a Change. The change of pK_a is applicable to the detection of DNA hybridization. Figure 5 shows UV−vis spectra of **BM1/N1** and single-stranded **BM1** at pH 10.0. At this pH, BM in the single strand was almost deprotonated and λ_{max} appeared at 492 nm. On the other hand, hybridization with its complementary strand, **N1**, raised the pK_a from 9.5 to 10.1, and thus, about half of BM was deprotonated. Consequently, λ_{max} shifted from 492 to 432 nm by hybridization. A spectral shift between the single strand and the duplex was as large as 60 nm and hybridization could easily be discriminated by the naked eye as shown in Figure 6. The solution of single-stranded ODN was colored orange, whereas it changed to yellow by adding the complementary strand. Interestingly, the color change of BM is opposite to that of Naphthyl Red, which shows a red shift upon hybridization (*9*). DNA probes that provide both red and blue shifts upon hybridization were successfully prepared by selecting the appropriate dyes on D-threoninol.

Fluorescence Detection of DNA Hybridization. *Fluorescence Change by Hybridization.* Unlike Naphthyl Red that we previously reported (*9*), both protonated and deprotonated BMs

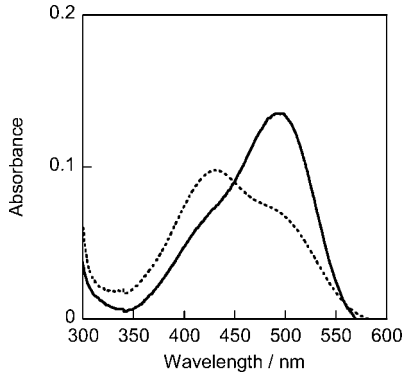

Figure 5. UV−vis spectra of single-stranded **BM1** (solid line) and **BM1/N1** (dotted line) at 0 °C. Solution conditions are as follows: [ODN] = 5 μM, [NaCl] = 100 mM, pH 10.0 (10 mM CAPS buffer).

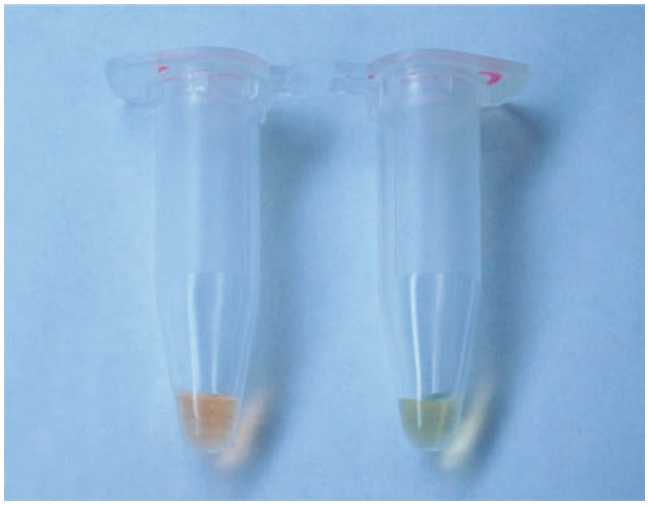

Figure 6. Color change upon hybridization at pH 10.0 (10 mM CAPS buffer). Single-stranded **BM1** (left) and **BM1/N1** (right).

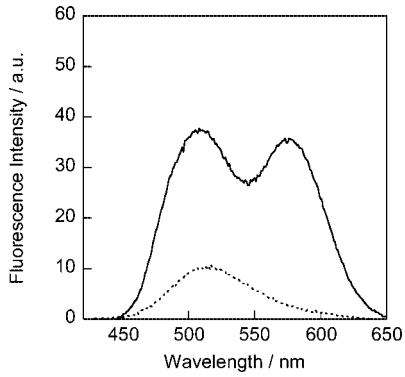

Figure 7. Fluorescence emission spectra (400 nm excitation) of **BM1** (solid line) and **BM1/N1** (dotted line). Solution conditions are as follows: [ODN] = 5 μM, [NaCl] = 100 mM, pH 7.0 (10 mM phosphate buffer), 0 °C.

are known to emit fluorescence by exciting them with a different wavelength. Figure 7 shows fluorescence emission spectra of single-stranded **BM1** and **BM1/N1** at pH 7.0 excited at 400 nm where protonated BM has its λ_{max}. Although the protonated form was dominant at pH 7.0, BM showed two peaks at 505 and 574 nm in the single-stranded state. We first assigned these two fluorescences as protonated (505 nm) and deprotonated (574 nm) BM, respectively. However, since the fluorescence at 574 nm was not observed in **BM2** and **BM3** (see Supporting

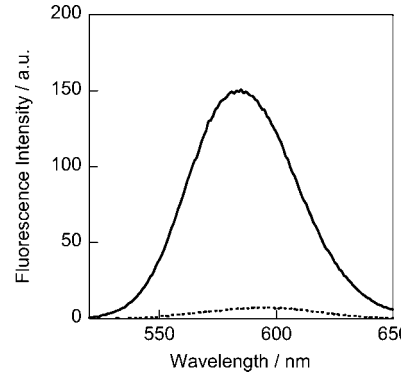

Figure 8. Fluorescence emission spectra (500 nm excitation) of **BM1** (solid line) and **BM1/N1** (dotted line). Solution conditions are as follows: [ODN] = 5 μM, [NaCl] = 100 mM, pH 9.1 (10 mM Tris buffer), 0 °C.

Information), this might be derived from exciplex formation of BM and a nucleobase (probably cytosine or guanine) (*28, 29*) (Note: Excitation spectra of single-stranded **BM1** monitored at 505 and 574 nm almost coincided. In both excitation spectra, two peaks at around 260 and 408 nm were observed. See Supporting Information for excitation spectra of single-stranded **BM1**). When the complementary strand (**N1)** was added to **BM1**, a peak at 574 nm disappeared, and emission at 510 nm assignable to the protonated BM fluorescence decreased.

Emission from deprotonated BM was observed at higher pH. Figure 8 shows fluorescence emission spectra from excitation at 500 nm of **BM1** and **BM1/N1** at pH 9.1. At this pH, BM was almost protonated in the duplex, whereas that in the single strand was partly deprotonated. Hence, fluorescence from deprotonated BM was relatively strong in the single-stranded state, whereas it was very weak in the duplex (compare the dotted with solid line in Figure 8). Since the intensity of the emission at 570 nm was 26 times higher than that of duplex, duplex formation was detectable even by fluorescence change as well as absorption spectra (Note: At a temperature below T_m, **BM1** showed similar behavior upon hybridization. At 20 °C, intensity of **BM1** at 570 nm was 14 times higher than that of **BM1/N1** (data not shown)). Addition of an excess amount of noncomplementary ODN (such as T_{11}) to either single-stranded **BM1** or **BM1/N1** solution did not affect the emission spectra (see Supporting Information). Furthermore, a one-base mismatch could be discriminated from a full-matched complementary strand by tuning the measurement temperature (Note: Incorporation of one-base mismatch greatly destabilized the duplex. Hence, a full-matched sequence could be discriminated from a mismatched one by measuring the spectra at the temperature between these T_ms. See Supporting Information for the actual data), demonstrating that sequence-specific recognition is possible with this probe. We also examined other sequences and found that fluorescence became smaller by hybridization with all the modified ODNs involving BM we synthesized (see Figure 9), although the degree of quenching depended on the sequence. It is assumed that a neighboring guanosine residue in **BM1** also contributed to the fluorescence quenching (Note: The following three factors contribute to the quenching of fluorescence from BM, although we cannot evaluate the contribution of each factor to the quenching quantitatively: protonation (or deprotonation), hybridization, and quenching by neighboring natural nucleobases).

Ratiometric Detection of Hybridization. The advantage of using BM as a chromophore is that ratiometric analysis is possible, since simultaneous excitation of both protonated and deprotonated forms gives two different emissions. As shown in Figure 9, the excitation of only the deprotonated form (at

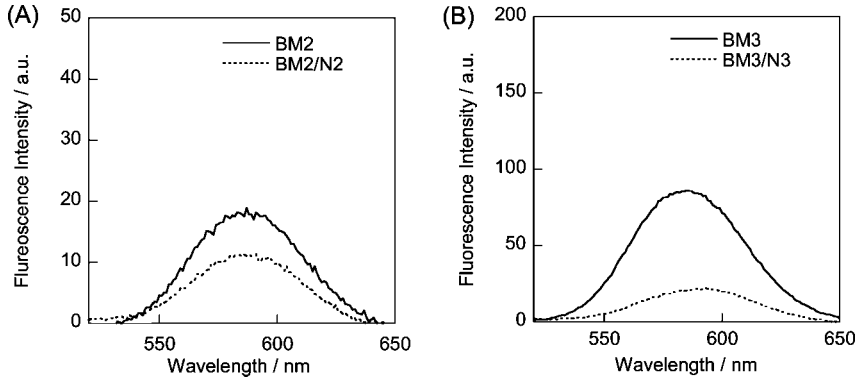

Figure 9. Fluorescence emission spectra (500 nm excitation) of single strands (solid lines) and duplexes (dotted lines) of (A) **BM2** and (B) **BM3**. Solution conditions are as follows: [ODN] = 5 μM, [NaCl] = 100 mM, pH 9.1 (10 mM Tris buffer), 0 °C.

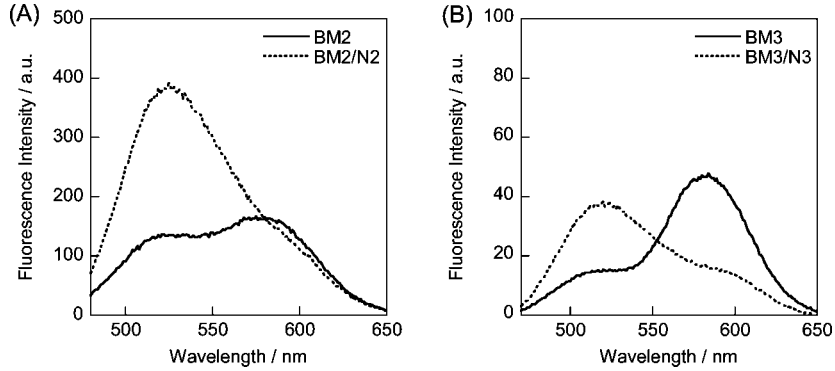

Figure 10. Fluorescence emission spectra (460 nm excitation) of single strands (solid lines) and duplexes (dotted lines) of (A) **BM2** and (B) **BM3**. Solution conditions are as follows: [ODN] = 5 μM, [NaCl] = 100 mM, pH 9.1 (10 mM Tris buffer), 0 °C. Note that the sensitivity of the spectrometer was high for **BM2** and **BM2**/**N2**, and it was medium for **BM3** and **BM3**/**N3**.

Scheme 4. Decrease in pK_a by Anti-Parallel Stacking between Two BMs

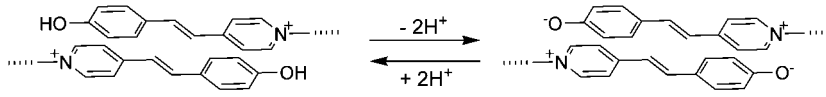

500 nm) did not sufficiently discriminate single-stranded **BM2**, **BM3**, and **BM2/N2**, **BM3/N3** duplexes due to the small change in fluorescence intensity. However, ratiometric analysis by simultaneous excitation (at 460 nm) fairly improved the discrimination efficiency. Figure 10B shows emission spectra of **BM3** and **BM3**/**N3** excited at 460 nm where both protonated and deprotonated BM have absorption. In the single-stranded state, emission at 584 nm from deprotonated BM was dominant. However, hybridization of its complementary strand made emission at 584 nm weak, and a new peak appeared at 520 nm (compare dotted with solid lines in Figure 10). Accordingly, hybridization was detectable from the change of the ratio of the emission intensities at 584 and 520 nm: I_{520}/I_{584} was 0.3 for **BM3**, whereas it was 2.4 for **BM3**/**N3**. Similarly, **BM2**, for which it was hard to probe cDNA by 500 nm excitation, induced a reasonable change of I_{520}/I_{584}; the I_{520}/I_{584} of **BM2** was 0.8 and that of **BM2**/**N2** was 2.5. Ratiometric detection of other sequences was further investigated (see Supporting Information).

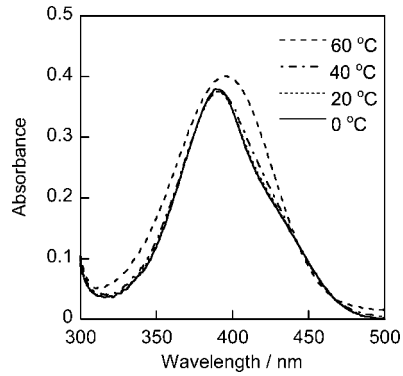

Figure 11. UV−vis spectra of **BM1/cBM1** at various temperatures. Solution conditions are as follows: [ODN] = 5 μM, [NaCl] = 100 mM, pH 7.0 (10 mM phosphate buffer).

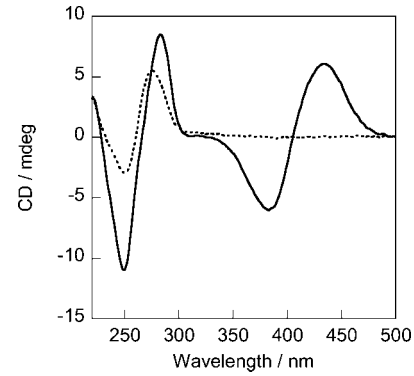

Figure 12. CD spectra of **BM1/cBM1** at 0 °C (solid line) and 70 °C (dotted line). Solution conditions are as follows: [ODN] = 2 μM, [NaCl] = 100 mM, pH 7.0 (10 mM phosphate buffer).

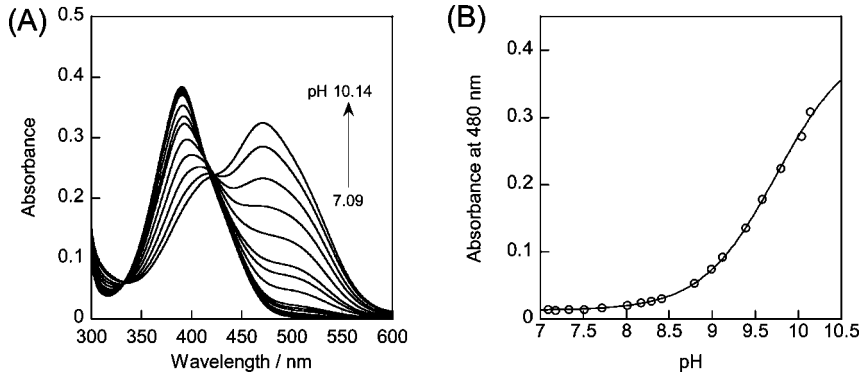

Figure 13. (A) UV−vis spectra of **BM1/cBM1** at various pH (from 7.09 to 10.14) and (B) plots of the absorbance of **BM1/cBM1** at 480 nm as a function of pH values at 20 °C. Solution conditions are as follows: [ODN] = 5 μM, [NaCl] = 100 mM, [NaH_2PO_4/Na_2HPO_4] = 10 mM.

Although the I_{520}/I_{584} value depended on the neighboring sequences, all the sequences we examined changed its value upon hybridization, demonstrating the wide availability of BM tethered ODN for the sequence-specific recognition of DNA. We also found that neighboring GC pairs quenched the fluorescence of protonated merocyanine much more strongly than that of the deprotonated form, which contributed to the sequence dependence of I_{520}/I_{584}. The detection limit of this probe was around 50 nM as estimated from the I_{520}/I_{584} value under the conditions employed here (see Supporting Information). Other dyes such as SNAFL (seminaphthofluoresceins) and SNARF (seminaphthorhodafluors) (*30*), which also change emission and absorption by protonation, might be utilized for ratiometric detection of hybridization by this method.

Modulation of pK_a by "Base-Pairing" between BMs. Recently, we reported that "threoninol-nucleotides" tethering functional molecules (such as dyes) on D-threoninols at the center of ODNs allowed interstrand "base-pairing" of the dyes by hybridization (*31*), such as a **BM1/cBM1** combination, both of which involve a BM as a "threoninol-nucleotide". In this duplex, "base-paired" BMs are stacked in an antiparallel manner as depicted in Scheme 4. Since a positive charge on the BM of one strand is located at close proximity to the hydroxyl group on that of its counter strand, the negatively charged microenvironment will be partially compensated for by this positive charge (left side of Scheme 4), and thus, the pK_a of BM is expected to decrease. In addition, the betaine structure of deprotonated BM possessing both positive and negative charges on an identical molecule will stabilize the stacked BMs due to electrostatic interactions (right side of Scheme 4). This effect might also contribute to the decrease of pK_a of BM.

We verified the "base-pairing" from the spectroscopic behavior of BM by the hybridization of **BM1/cBM1** at pH 7.0. At 60 °C, where the duplex was dissociated into two single strands (note that the T_m of **BM1/cBM1** is 49.9 °C), a broad peak was observed at 396 nm in UV−vis spectra (Figure 11). When the temperature was lowered below its T_m, however, the peak shifted to a shorter wavelength, and narrowing of the band was observed. The absorption maximum of **BM1/cBM1** at 0 °C appeared at 389 nm, which was 29 nm shorter than that of **BM1/N1**. Such a hypsochromic shift and narrowing of the band are characteristic of dye aggregation stacked in a face-to-face manner. The increase in the melting temperature of **BM1/cBM1** (49.9 °C) compared with that of **BM1/N1** (39.5 °C) also supports the antiparallel stacking of BM (Note: Insertion of one-base mismatch to **BM1/cBM1** destabilized duplex. Melting temperature of duplex containing C-T mismatch (5′-GGTATC**X**TCAATC-3′/3′-CCATAG**X**CGTTAG-5′) was 45.5 °C, which was 4.4 °C lower than that of **BM1/cBM1**. This result indicates that incorporation of tentative "base-pair" of two BMs did not disturb the recognition of its complementary strand). In addition, induced CD also supported the dimerization of BMs in **BM1/cBM1** (see Figure 12). At 70 °C, where **BM1** and **cBM1** were completely dissociated to single strands, there was no CD at 350−500 nm. However, a positive couplet was distinctly observed at around 400 nm when the temperature was lowered to 0 °C, far below the T_m. This result clearly shows that two BMs in **BM1/cBM1** were stacked and excitonically coupled (Note: **BM1/cBM1** did not exhibit excimer emission but showed quenching of fluorescence from BM fluorophore at pH 7.0. This self-quenching also supports the dimerization of BM in the duplex. See Supporting Information). On the basis of these results, we concluded that two BMs were stacked in an antiparallel manner as depicted in Scheme 4.

Figure 13 shows the pH dependence of the absorption spectrum of **BM1/cBM1**. Plots of absorbance at 480 nm vs pH (Figure 13B) determined the pK_a of BM to be 9.7. As we expected, this value was 0.4 lower than that of **BM1/N1**, demonstrating that the pK_a of BM was controllable by antiparallel stacking as depicted in Scheme 4. This pK_a shift is applicable to the detection of sequence-specific DNA by quencher-free molecular beacons that have two BMs on both sides (*32*). When the beacon is closed, two BMs are stacked in an antiparallel manner and deprotonated. An opened beacon by hybridization with the target promotes the protonation of BM and induces the spectral change (Note: T_m of **BM1/cBM1** was 10 °C higher than that of **BM1/N1**, indicating that introduction of "base-paired" BMs into molecular beacon stabilize closed state rather than open state. Accordingly, shorter stem and longer loop would be appropriate for designing BM-tethered molecular beacon).

CONCLUSIONS

Brooker's merocyanine was introduced into ODN and its pK_a was modulated by hybridization. The pK_a of BM in the single-stranded ODN increased by hybridization due to the "negative" microenvironment in the duplex. Concurrently, the color of the solution changed from orange to yellow so that duplex formation was easily detected even by the naked eye. Fluorescence emission spectra as well as absorption also changed upon hybridization. In addition, ratiometric detection of DNA hybridization was also possible. The pK_a of BM was also modulated by antiparallel stacking between two BMs. These ODNs involving BM whose pK_a is controllable by its microenvironment are applicable to the detection of mismatched DNA and quencher-free molecular beacons.

ACKNOWLEDGMENT

This work was supported by Core Research for Evolution Science and Technology (CREST), Japan Science and Technol-

ogy Agency (JST). Partial supports by a Grant-in-Aid for Scientific Research from the Ministry of Education, Culture, Sports, Science and Technology, Japan, and The Mitsubishi Foundation (for H.A.) are also acknowledged.

Supporting Information Available: Additional information as described in the text. This material is available free of charge via the Internet at http://pubs.acs.org.

LITERATURE CITED

(1) Harris, T. K., and Turner, G. J. (2002) Structural basis of perturbed pK_a values of catalytic groups in enzyme active sites. *IUBMB Life 53*, 85–98.

(2) Gunner, M. R., Mao, J., Song, Y., and Kim, J. (2006) Factors influencing the energetics of electron and proton transfers in proteins. What can be learned from calculations. *Biochim. Biophys. Acta 1757*, 942–968.

(3) Perrotta, A. T., Shih, I.-H., and Been, M. D. (1999) Imidazole rescue of a cytosine mutation in a self-cleaving ribozyme. *Science 286*, 123–126.

(4) Muth, G. W., Ortoleva-Donnelly, L., and Strobel, S. A. (2000) A single adenosine with a neutral pK_a in the ribosomal peptidyl transferase center. *Science 289*, 947–950.

(5) Wu, P., Kawamoto, Y., Hara, H., and Sugimoto, N. (2002) Effect of divalent cations and cytosine protonation on thermodynamic properties of intermolecular DNA double and triple helices. *J. Inorg. Biochem. 91*, 277–285.

(6) Acharya, P., Acharya, S., Cheruku, P., Amirkhanov, N. V., Földesi, A., and Chattopadhyaya, J. (2003) Cross-modulation of the pK_a of nucleobases in a single-stranded hexameric-RNA due to tandem electrostatic nearest-neighbor interactions. *J. Am. Chem. Soc. 125*, 9948–9961.

(7) Jones, R. L., and Wilson, W. D. (1981) Effect of ionic-strength on the pK_a of ligands bound to DNA. *Biopolymers 20*, 141–154.

(8) Misra, V. K., and Honig, B. (1995) On the magnitude of the electrostatic contribution to ligand-DNA interactions. *Proc. Natl. Acad. Sci. U.S.A. 92*, 4691–4695.

(9) Asanuma, H., Kashida, H., Liang, X. G., and Komiyama, M. (2003) DNA-Naphthyl Red conjugate as a visualizing probe of DNA hybridization. *Chem. Commun.* 1536–1537.

(10) Brooker, L. G. S., Keyes, G. H., and Heseltine, D. W. (1951) Color and constitution. XI.1 Anhydronium bases of p-hydroxystyryl dyes as solvent polarity indicators. *J. Am. Chem. Soc. 73*, 5350–5356.

(11) Jacques, P. (1986) On the relative contributions of nonspecific and specific interactions to the unusual solvatochromism of a typical merocyanine dye. *J. Phys. Chem. 90*, 5535–5539.

(12) Catalán, J., Pérez, P., Elguero, J., and Meutermans, W. (1993) Solvatochromism of sterically hindered stilbazolium betaines and its relationship to Reichardt's $E_T(30)$ scale: the problem of the measurement of the polarity vs the acidity of alcohols. *Chem. Ber. 126*, 2445–2448.

(13) Reichardt, C. (1994) Solvatochromic dyes as solvent polarity indicators. *Chem. Rev. 94*, 2319–2358.

(14) Kuder, J. E., and Wychick, D. (1974) Acid-based equilibria in the ground and excited states of a solvatochromic merocyanine dye. *Chem. Phys. Lett. 24*, 69–72.

(15) Burda, C., Abdel-Kader, M. H., Link, S., and El-Sayed, M. A. (2000) Femtosecond dynamics of a simple merocyanine dye: does deprotonation compete with isomerization? *J. Am. Chem. Soc. 122*, 6720–6726.

(16) Wyrzykiewicz, E., and Lapucha, A. (1982) Reactions of (e)-hydroxystilbazoles with halocarboxylic acids. *Pol. J. Chem. 56*, 815–817.

(17) Koopmans, C., and Ritter, H. (2007) Color change of *N*-isopropylacrylamide copolymer bearing Reichardts dye as optical sensor for lower critical solution temperature and for host-guest interaction with β-cyclodextrin. *J. Am. Chem. Soc. 129*, 3502–3503.

(18) Asanuma, H., Hara, Y., Noguchi, A., Sano, K., and Kashida, H. (2008) Postsynthetic modification of DNA via threoninol on a solid support by means of allylic protection. *Tetrahedron Lett. 49*, 5144–5146.

(19) Reynolds, M. A., Beck, T. A., Hogrefe, R. I., McCaffrey, A., Jr., and Vaghefi, M. M. (1992) A non-nucleotide-based linking method for the preparation of psoralen-derivatized methylphosphonate oligonucleotides. *Bioconjugate Chem. 3*, 366–374.

(20) Fukui, K., Morimoto, M., Segawa, H., Tanaka, K., and Shimidzu, T. (1996) Synthesis and properties of an oligonucleotide modified with an acridine derivative at the artificial abasic site. *Bioconjugate Chem. 7*, 349–355.

(21) Viladkar, S. M. (2002) Guanine rich oligonucleotide-amino acid/peptide conjugates: preparation and characterization. *Tetrahedron 58*, 495–502.

(22) Ami, T., and Fujimoto, K. (2006) Fluorescence labeling of DNA based on photochemical ligation. *Sci. Technol. Adv. Mater. 7*, 249–254.

(23) Müller, W., and Crothers, D. M. (1968) Studies of the binding of actinomycin and related compounds to DNA. *J. Mol. Biol. 35*, 251–290.

(24) Pradhan, P., Jernström, B., Seidel, A., Nordén, B., and Gräslund, A. (1998) Induced circular dichroism of benzo[a]pyrene-7,8-dihydrodiol 9,10-epoxide stereoisomers covalently bound to deoxyribooligonucleotides used to probe equilibrium distribution between groove binding and intercalative adduct conformations. *Biochemistry 37*, 4664–4673.

(25) Eriksson, B., and Nordén, B. (2001) Linear and circular dichroism of drug-nucleic acid complexes. *Methods Enzymol. 340*, 68–98.

(26) Liang, X. G., Asanuma, H., Kashida, H., Takasu, A., Sakamoto, T., Kawai, G., and Komiyama, M. (2003) NMR study on the photoresponsive DNA tethering an azobenzene. Assignment of the absolute configuration of two diastereomers and structure determination of their duplexes in the trans-form. *J. Am. Chem. Soc. 125*, 16408–16415.

(27) Asanuma, H., Liang, X. G., Yoshida, T., and Komiyama, M. (2001) Photocontrol of DNA duplex formation by using azobenzene-bearing oligonucleotides. *ChemBioChem 2*, 39–44.

(28) Yamana, K., Iwase, R., Furutani, S., Tsuchida, H., Zako, H., Yamaoka, T., and Murakami, A. (1999) 2′-Pyrene modified oligonucleotide provides a highly sensitive fluorescent probe of RNA. *Nucleic Acids Res. 27*, 2387–2392.

(29) Kawai, T., Ikegami, M., and Arai, T. (2004) Exciplex formation between pyrene and guanine in highly polar solvents. *Chem. Commun.* 824–825.

(30) Whitaker, J. E., Haugland, R. P., and Prendergast, F. G. (1991) Spectral and photophysical studies of benzo[c]xanthene dyes: Dual emission pH sensors. *Anal. Biochem. 194*, 330–344.

(31) Kashida, H., Fujii, T., and Asanuma, H. (2008) Threoninol as a scaffold of dyes (threoninol-nucleotide) and their stable interstrand clustering in duplexes. *Org. Biomol. Chem. 6*, 2892–2899.

(32) Venkatesan, N., Seo, Y. J., and Kim, B. H. (2008) Quencher-free molecular beacons: a new strategy in fluorescence based nucleic acid analysis. *Chem. Soc. Rev. 37*, 648–663.

BC800335H

Modulation of pK_a of Brooker's Merocyanine by DNA Hybridization

Hiromu Kashida, Kanae Sano, Yuichi Hara and Hiroyuki Asanuma*

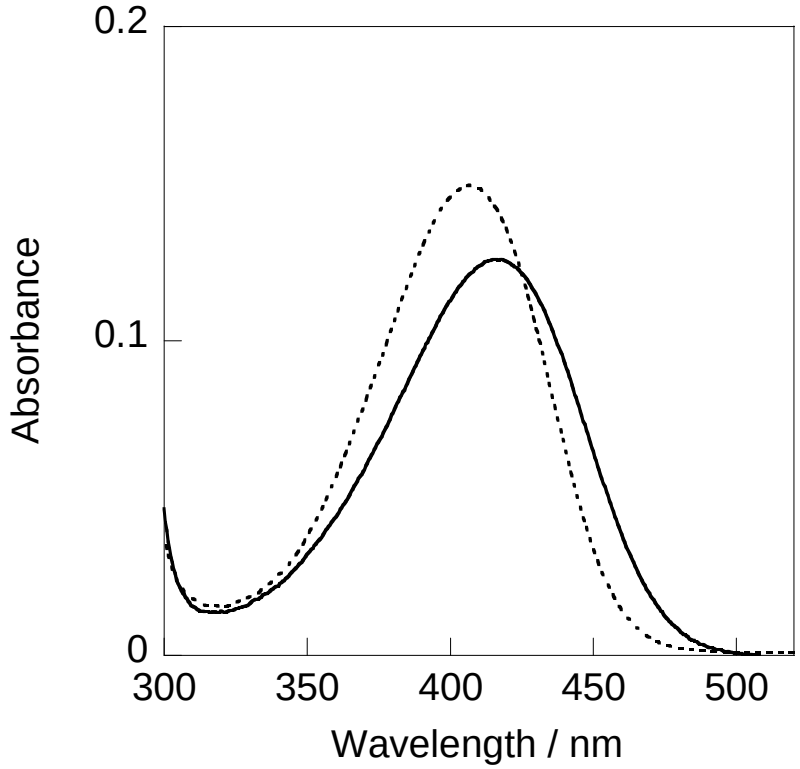

Figure S-1. UV-Vis spectra of **BM1**/**N1** (solid line) and single-stranded **BM1** (dotted line) at pH 7.0 (10 mM phosphate buffer), 0 ^{o}C, in the presence of 100 mM NaCl.

BM1 : 5'-GGTATC**X**GCAATC-3'
N1 : 3'-CCATAGCGTTAG-5'

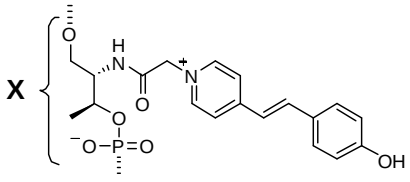

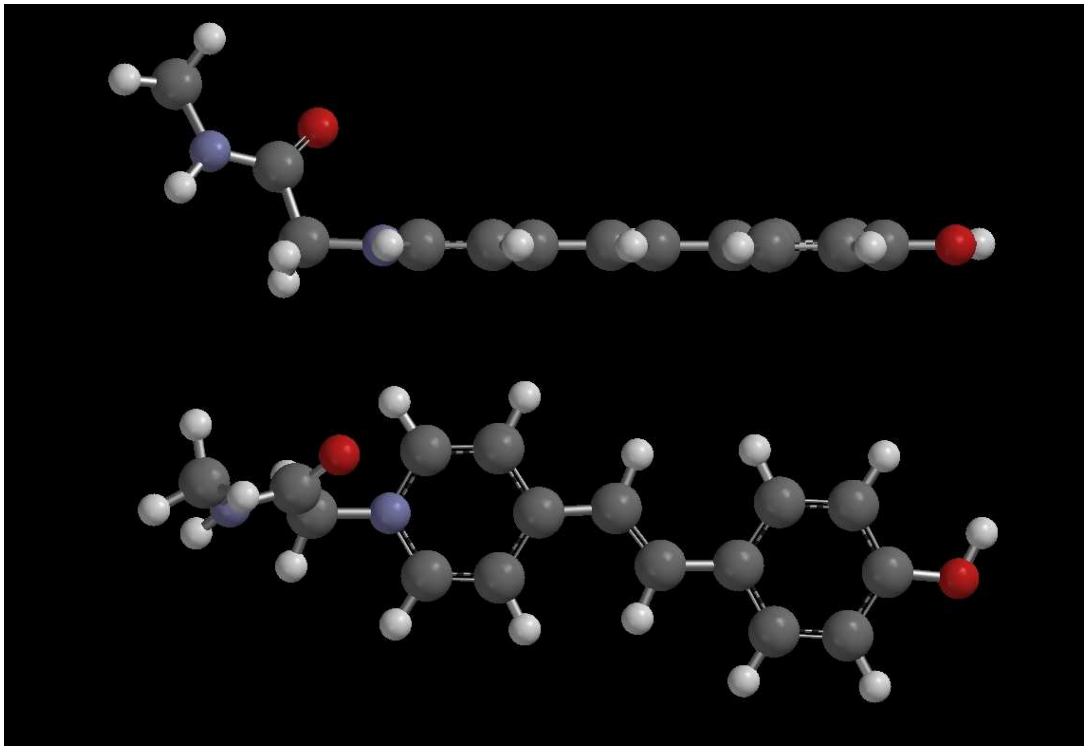

Figure S-2. Top and side views of energy-minimized structure of Brooker's merocyanine calculated by HF/6-31G*. The calculated structure is shown below.

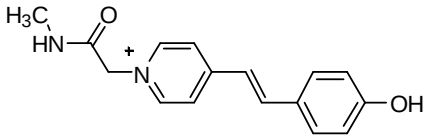

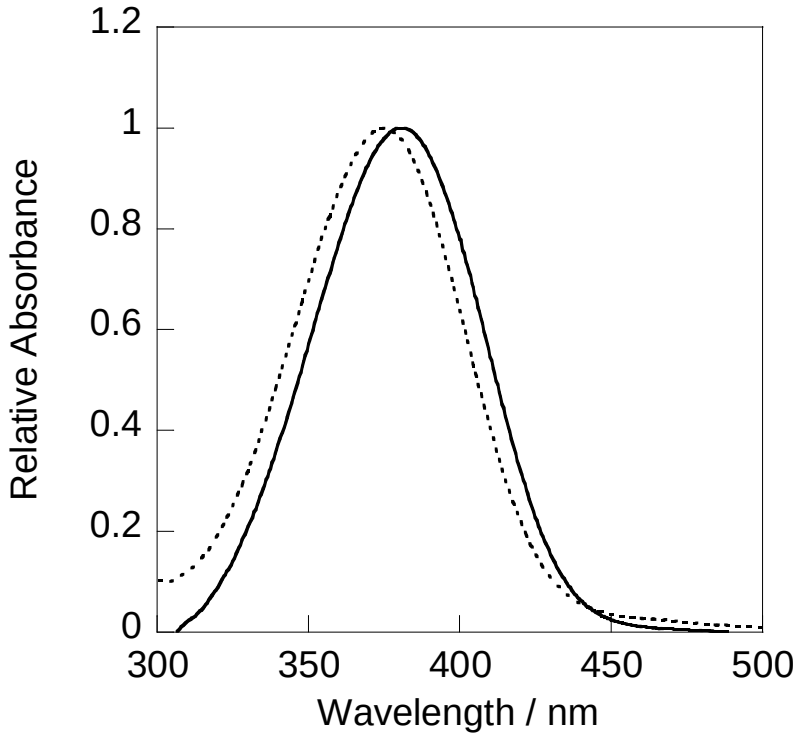

Figure S-3. UV-Vis spectra of **3** (solid line) and Brooker's merocyanine (BM: dotted line) at pH 7.0 (10 mM phosphate buffer), 0 ^{o}C, in the presence of 100 mM NaCl. Each spectrum was normalized at the absorption maximum. Chemical structures of **3** and BM were shown below.

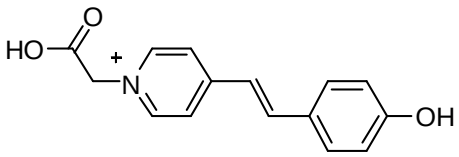

3

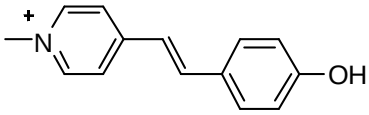

Brooker's merocyanine

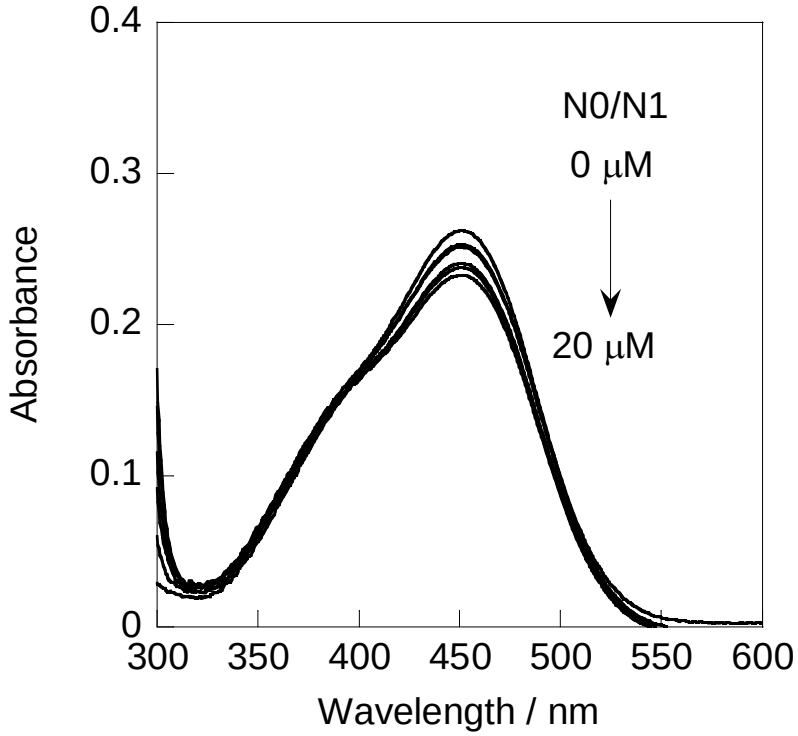

Figure S-4. UV-Vis spectra of **3** with various concentration of native DNA duplex (**N0**/**N1**).The concentration of **N0**/**N1** were 0, 4, 8, 12, 16 and 20 μM.
Solution conditions are as follows:
[**3**] = 10 μM, [NaCl] = 100 mM, pH 9.1 (10 mM Tris buffer), 20 ^{o}C.

N0 : 5'-GGTATCGCAATC-3'
N1 : 3'-CCATAGCGTTAG-5'

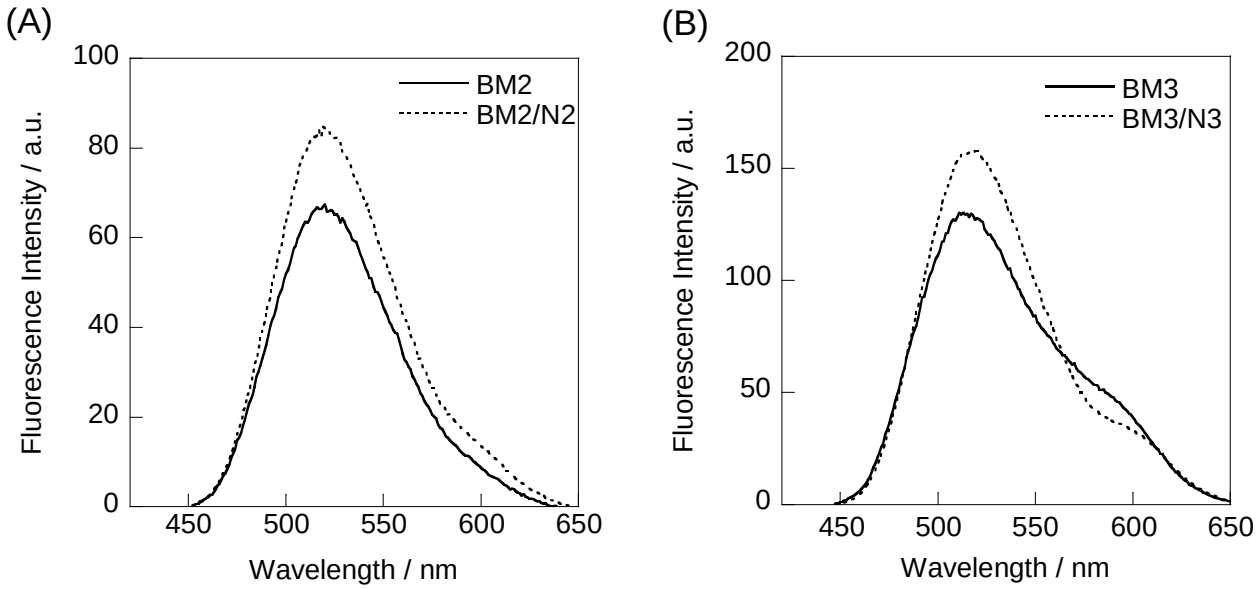

Figure S-5. Fluorescence emission spectra excited at 400 nm of single strands (solid lines) and duplexes (dotted lines) of (A) **BM2**, (B) **BM3**. Solution conditions are as follows:
[ODN] = 5 μM, [NaCl] = 100 mM, pH 7.0 (10 mM phosphate buffer), 0 ^{o}C.

BM2 : 5'-GGTATA**X**TCAATC-3'
N2 : 3'-CCATATAGTTAG-5'
BM3 : 5'-GGTATA**X**ACAATC-3'
N3 : 3'-CCATATTGTTAG-5'

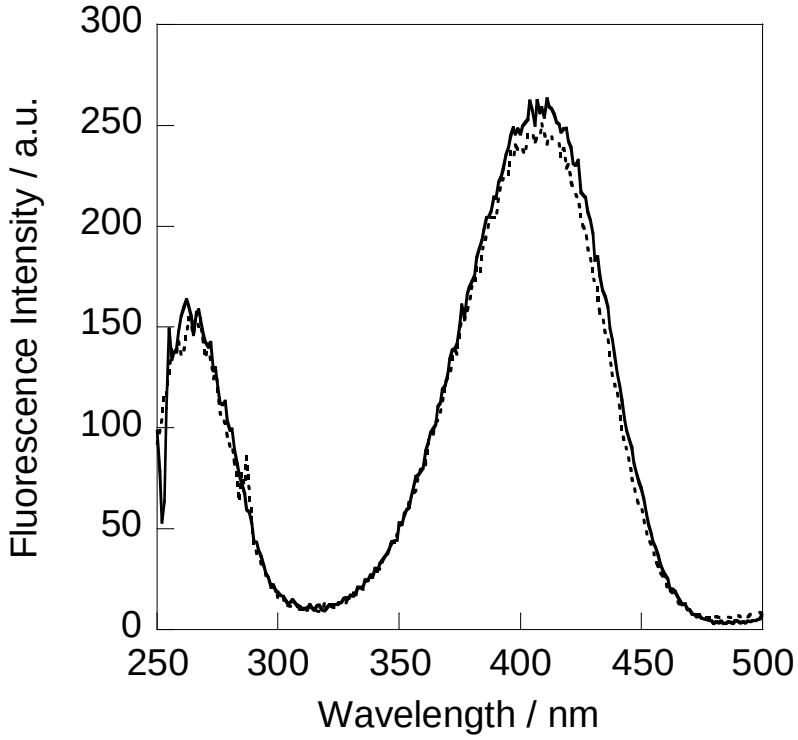

Figure S-6. Fluorescence excitation spectra of **BM1** monitored at 505 nm (solid line) and 574 nm (dotted line). Solution conditions are as follows:
[**BM1**] = 5 μM, [NaCl] = 100 mM, pH 7.0 (10 mM phosphate buffer), 0 ^{o}C.

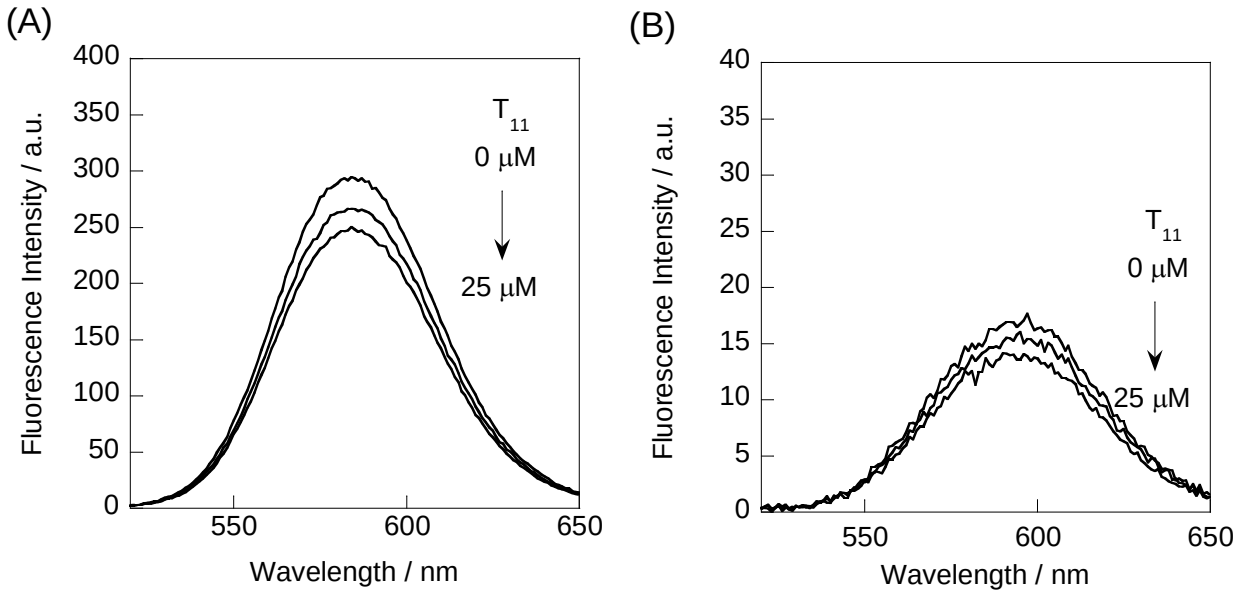

Figure S-7. Fluorescence emission spectra excited at 500 nm of (A) **BM1** and (B) **BM1**/**N1** with and without T_{11}. Concentrations of T_{11} were 0, 12.5 and 25 μM.
Solution conditions are as follows:
[**BM1**] = [**N1**] = 5 μM, [NaCl] = 100 mM, pH 9.1 (10 mM Tris buffer), 0 ^{o}C.

T_{11} : 5'-T_{11}-3'

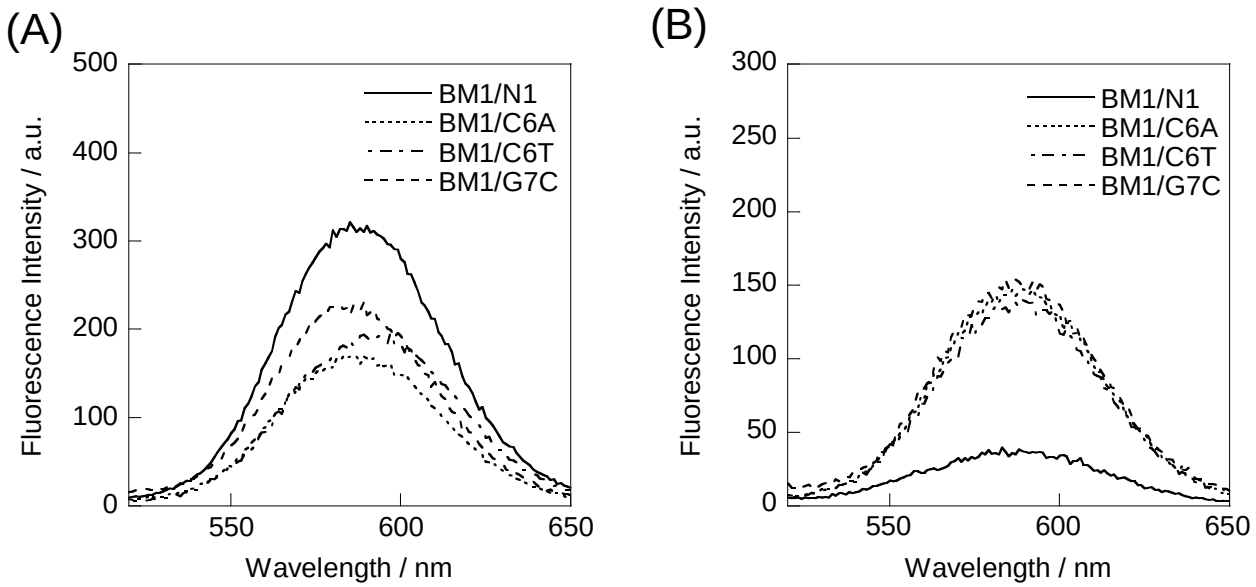

Figure S-8. Fluorescence emission spectra excited at 500 nm of full-matched (**BM1**/**N1**) and mismatched (**BM1**/**C6A**, **BM1**/**C6T** and **BM1**/**G7C**) duplexes at (A) 0 ^{o}C and (B) 30 ^{o}C. Melting temperatures of each duplex was 37.2 ^{o}C (**BM1**/**N1**), 24.8 ^{o}C (**BM1**/**C6A**), 26.8 ^{o}C (**BM1**/**C6T**) and 24.6 ^{o}C (**BM1**/**G7C**).
Solution conditions are as follows:
[ODN] = 5 μM, [NaCl] = 100 mM, pH 9.1(10 mM Tris buffer).
Note that the sensitivity of the spectrometer was high for these spectra while medium for spectra in Figure 8 of the main text.

BM1 : 5'-GGTATC**X**GCAATC-3'
N1 : 3'-CCATAGCGTTAG-5'
C6A : 3'-CCATAGAGTTAG-5'
C6T : 3'-CCATAGTGTTAG-5'
G7C : 3'-CCATACCGTTAG-5'

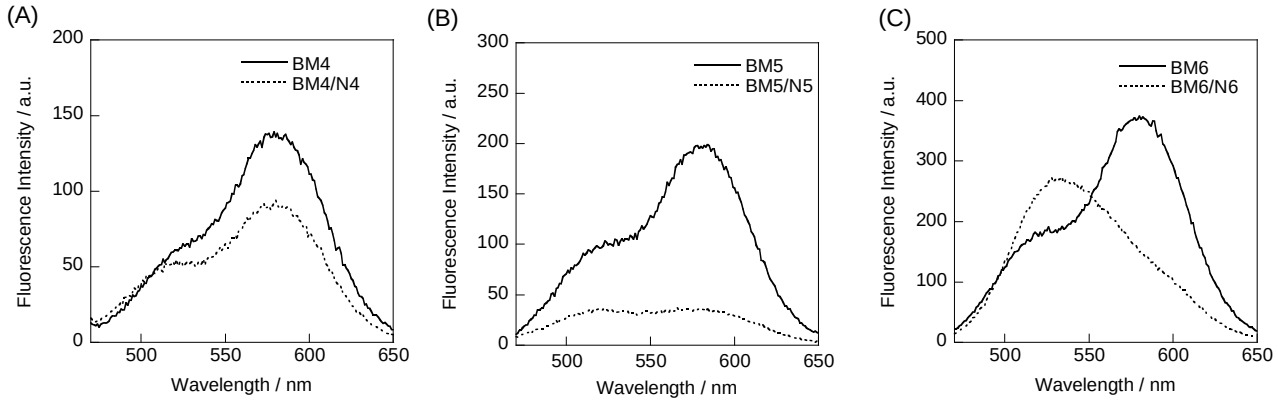

Figure S-9. Fluorescence emission spectra (460 nm excitation) of single strands (solid lines) and duplexes (dotted lines) of (A) **BM4**, (B) **BM5** and (C) **BM6**. The ratios of the emission intensities at 584 and 520 nm: I_{520}/I_{584} of single strands and duplexes were 0.45 (**BM4**), 0.56 (**BM4**/**N4**), 0.46(**BM5**), 0.96 (**BM5**/**N5**), 0.48 (**BM6**) and 1.72 (**BM6**/**N6**).

Solution conditions are as follows:
[ODN] = 5 μM, [NaCl] = 100 mM, pH 9.1 (10 mM Tris buffer), 0 ^{o}C.

BM4 : 5'-GGTATA**X**CCAATC-3'
N4 : 3'-CCATATGGTTAG-5'
BM5 : 5'-GGTATC**X**TCAATC-3'
N5 : 3'-CCATAGAGTTAG-5'
BM6 : 5'-GGTATT**X**TCAATC-3'
N6 : 3'-CCATAAAGTTAG-5'

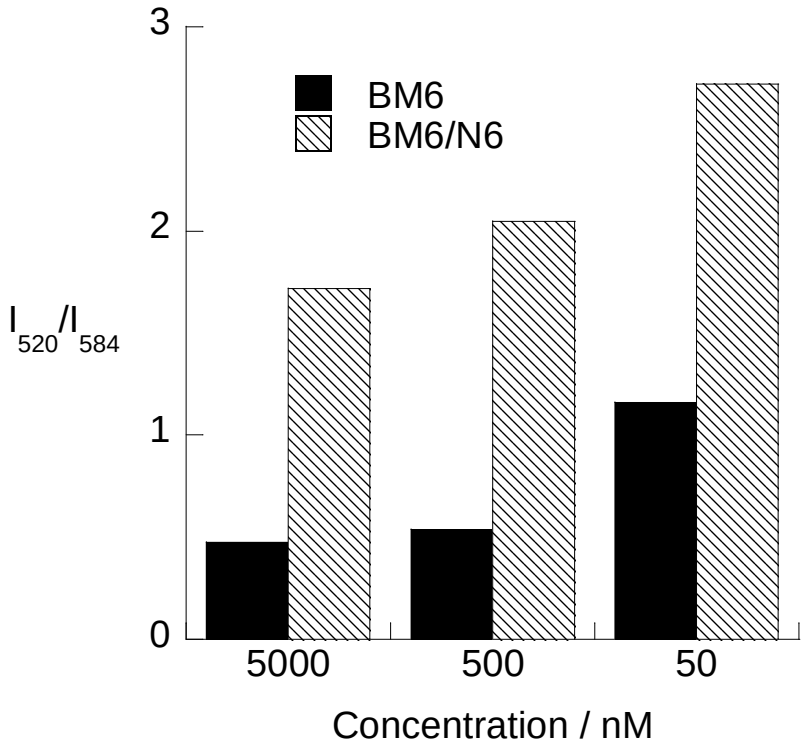

Figure S-10. Intensity ratios of the emission at 520 nm and 584 nm (I_{520}/I_{584}) of **BM6** and **BM6**/**N6** at various concentrations. Excitation wavelength was 460 nm.
Solution conditions are as follows:
[NaCl] = 100 mM, pH 9.1 (10 mM Tris buffer), 0 ^{o}C.

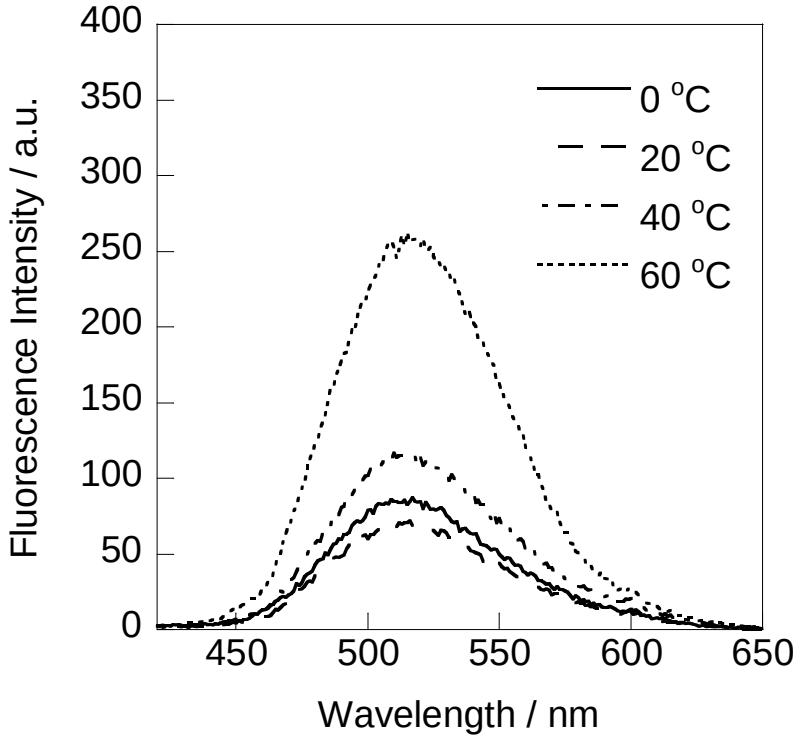

Figure S-11. Fluorescence emission spectra excited at 400 nm of **BM1/cBM1** at various temperatures. Solution conditions are as follows:
[ODN] = 5 μM, [NaCl] = 100 mM, pH 7.0 (10 mM phosphate buffer)

BM1 : 5'-GGTATC**X**GCAATC-3'
cBM1 : 3'-CCATAG**X**CGTTAG-5'

Table S-1. Absorption maxima of Brooker's merocyanine (BM) and **3** in various solvents.

solvent	ν_{max} / cm^{-1}	
	BM	**3**[a,b)]
water	22,624[c)]	22,148
MeOH	20,704[c)]	20,768
EtOH	19,471[d)]	20,000
DMSO	17,483[c)]	17,684
DMF	17,182[c)]	17,498

a) Small amount of sodium methoxide was added according to ref. c).
b) Determined at 20 °C.
c) P. Jacques, *J. Phys. Chem.*, **1986**, *90*, 5535.
d) J. Catalán *et al.*, *Chem. Ber.*, **1993**, *126*, 2445.

Subscriber access provided by SHEMYAKIN-OVCHINNIKOV INST

Article

The Use of 3-Aminophthalimide as a Pro-Chemiluminescent Label in Chemiluminescence and Fluorescence-Based Cellular Assays

Demetra Mavri-Damelin, Jonathan Wilden, Ali-Reza Mani, Clare Selden, Humphrey J. F. Hodgson, and Leonard H. Damelin

Bioconjugate Chem., **2009**, 20 (2), 266-273• DOI: 10.1021/bc800361r • Publication Date (Web): 13 January 2009

Downloaded from http://pubs.acs.org on May 8, 2009

More About This Article

Additional resources and features associated with this article are available within the HTML version:

- Supporting Information
- Access to high resolution figures
- Links to articles and content related to this article
- Copyright permission to reproduce figures and/or text from this article

View the Full Text HTML

ACS Publications
High quality. High impact.

Bioconjugate Chemistry is published by the American Chemical Society. 1155 Sixteenth Street N.W., Washington, DC 20036

The Use of 3-Aminophthalimide as a Pro-Chemiluminescent Label in Chemiluminescence and Fluorescence-Based Cellular Assays

Demetra Mavri-Damelin,[§,†] Jonathan Wilden,[‡] Ali-Reza Mani,[†] Clare Selden,[†] Humphrey J. F. Hodgson,[†] and Leonard H. Damelin*[,†]

Centre for Hepatology at the Royal Free-Hampstead Campus, Royal Free and University College Medical School, London NW3 2PF, and Department of Chemistry, University College London, 20 Gordon Street, London, WC1H 0AJ, United Kingdom.
Received August 23, 2008; Revised Manuscript Received December 17, 2008

We present a labeling system for direct chemiluminescence-based cellular bioassays using the stable pro-chemiluminescent, luminol precursor, 3-aminophthalimide (API). API-coupled reporter molecules are detected chemiluminometrically after treatment with hydrazine, which converts the API label to luminol. API derivatives containing a variety of functional groups are readily synthesized, allowing for ease of coupling via the imide nitrogen to a host of reporter molecules. The fluorescent nature of APIs further allows for dual fluorescence and chemiluminescence studies. To highlight the utility of this label, we show that API-labeled insulin can be successfully utilized in cellular binding and transport assays and that an API-coupled mitochondrial probe (API−triphenylphosphonium^{+}) can be used to both fluorescently and chemiluminometrically investigate mitochondrial function. We also assess the use of API as a polysaccharide and nucleic acid label, and we show that API-labeled palmitic acid undergoes cellular transport and lipid metabolism.

INTRODUCTION

Chemiluminescence-based bioassays are highly sensitive, quantitative, reproducible, less hazardous, and less costly than radio-isotope-based methodologies. Assays are often indirect; i.e., the chemiluminescent signal is generated when an enzyme label, coupled to a reporter molecule, catalyzes the oxidation of a chemiluminescent substrate. However, direct assays, where a reporter molecule is tagged with a compound that undergoes direct chemiluminescence upon induction, offers a number of potential advantages over indirect assays. These include increased simplicity, the attachment of multiple labels to the reporter, and the avoidance of large enzyme-coupled reporter molecules, which can exhibit significantly reduced affinity for the target and negates their use in cellular probe-based investigations (*1*). Luminol (3-aminophthalhydrazide) is one of the most widely used chemiluminescent substrates. Its oxidation by a variety of oxidizing agents at pH 10−11, catalyzed by metal ions (e.g., Cu^{2+}, Co^{2+}, Mn^{2+}, Fe^{2+}, and ferricyanide) to 3-aminophthalate, with the emission of light at 425 nm, was reported in 1928 (*2*−*4*). Commonly used luminol-based indirect bioassays, typically catalyzed by peroxidase coupled reporter molecules, are broadly linear and practically efficient (*5*). However, luminol is seldom used in direct assays due to label instability, and the finding that the coupling of this molecule (often via its amino function) to reporters leads to a significant reduction in quantum yield (*6*).

Here, we present direct chemiluminescent cellular bioassays using the luminol precursor, 3-aminophthalimide (API). Our rationale for doing so is founded on the fact that, although not directly chemiluminescent, 3-aminophthalimide can be considered a pro-chemiluminescent substrate since it reacts with hydrazine (the Ing-Manske procedure) to form a primary amine and "free" (noncovalently linked) luminol (*7*). Thus, assays involve the use of API-coupled reporter molecules, detected chemiluminometrically after treatment with hydrazine, which converts the API label to unconjugated luminol, circumventing the problems associated with covalently linked luminol (Figure 1). The use of the API system offers the additional advantages of ease of synthesis: 3-aminophthalimide derivatives containing a variety of functional groups can be readily synthesized, allowing for ease of coupling via the imide nitrogen to a host of reporter molecules. Fluorescence properties: 3-aminophthalimides are highly fluorescent molecules (*8*), allowing for dual fluorescence and chemiluminescence studies.

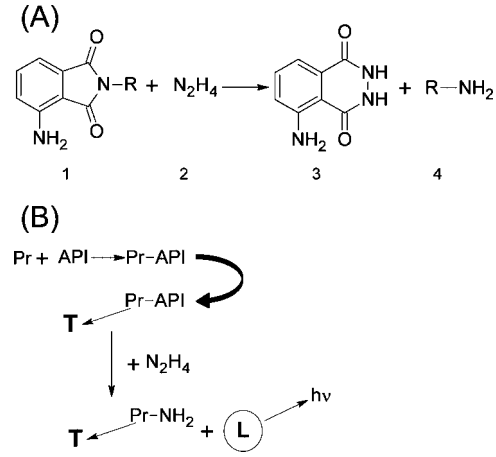

Figure 1. Assay principle. (A) 3-Aminophthalimide derivatives (API) (**1**) are converted by hydrazine (**2**) to luminol (**3**) and a primary amine (**4**). (B) Cellular probes (Pr) are labeled with API moieties. Labeled probes bind to or enter target (T). Hydrazine treatment converts the API-probe to unconjugated luminol (L), which is quantified chemiluminometrically.

* To whom correspondence should be addressed. Current address: AIDS Virus Research Unit, National Institute of Communicable Diseases, Sandringham, Johannesburg, Private Bag X4, 2131, South Africa. Tel: +27 11 386-6400. Fax: +27 11 386-6465. E-mail: leonardd@nicd.ac.za.

† Royal Free and University College Medical School.

‡ University College London.

§ Current address: School of Molecular & Cell Biology, University of the Witwatersrand, Private Bag 3, Wits, 2050, South Africa.

10.1021/bc800361r CCC: $40.75 © 2009 American Chemical Society
Published on Web 01/13/2009

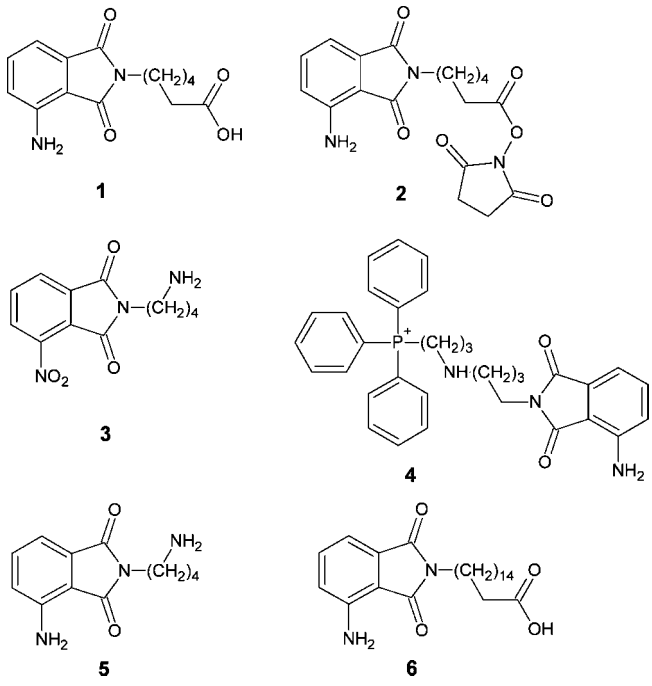

Figure 2. Structures of API derivatives and intermediates. (**1**) 4-Amino-2-(hexanoic acid)-isoindole-1,3-dione, (**2**) 4-Amino-2-(hexanoic acid-*N*-hydroxysuccinimido ester)-isoindole 1,3-dione, (**3**) 2-(4-Aminobutyl)-4-nitro-isoindole-1,3-dione, (**4**) 4-Amino-2-[4-(3-triphenylphosphonium-propylamino)-buytl]-isoindole-1,3-dione bromide, (**5**) 4-Amino-2-(4-aminobutyl)-isoindole-1,3-dione, (**6**) 4-Amino-2-(hexadecanoic acid)-isoindole-1,3-dione.

We show that API-labeled insulin can be successfully utilized in cellular binding and transport assays and that an API-coupled mitochondrial probe can be used to investigate mitochondrial function by chemiluminescence and fluorescence microscopy. We also assess the use of API as a polysaccharide and nucleic acid label, and we show that API-labeled palmitic acid can be readily synthesized and undergoes cellular transport and incorporation into complex lipid species. Our study illustrates that the use of API in dual fluorescence and chemiluminescence assays has potentially broad application in the biomedical sciences.

MATERIALS AND METHODS

Materials. Unless otherwise stated, all reagents were from Sigma-Aldrich, Dorset, U.K. Cell culture medium and supplements were from Gibco, Invitrogen, Paisley, U.K. The structures of API derivatives and intermediates are shown in Figure 2.

Cell Culture. HepG2 hepatoma cells (ECACC, Wiltshire, U.K.) were cultured in α-MEM or DMEM supplemented with 10% FBS, 100 units/mL penicillin, and 100 μg/mL streptomycin. Cells were maintained at 37 °C in 5%CO_2.

Time-Resolved Chemiluminescence Studies. A 24 μM NH_2-API aqueous solution (50 μL) was mixed with an equal quantity of 98% hydrazine hydrate and heated for 30 min at 60 °C. Thereafter, 50 μL of the hydrazine-treated sample was transferred to a well of a 96-well chemiluminescence plate, to which was added 15 μL of a 0.02 g/mL iodophenol solution (in 1 N NaOH). Time-resolved luminescence was then determined using a Tropix TR717 multiplate luminometer with injector, in kinetics mode, after luminescence induction by the injection of 100 μL 0.045% ferricyanide solution into the well.

Determination of API to Luminol Conversion Efficiency by GC-MS Analysis. HepG2 cell lysates (2 mg/mL total protein) or PBS samples (100 μL) were spiked with 56 nmol of API-palmitate in DMSO such that 100% conversion of API to luminol by hydrazine treatment would yield 56 nmol (10 μg) luminol. Samples were then incubated with an equal volume of 98% hydrazine hydrate for 30 min at 60 °C. Luminol was extracted from hydrazine-treated samples using ENV^+ reverse-phase extraction columns (Isolute SPE products). In brief, the samples were dissolved in 1 mL Tris-HCl buffer (20 mM, pH 8.0) and extracted on an ENV^+ column, which had already been prewashed with 1 mL methanol and 4 mL of Tris-HCl buffer (pH 8.0). The columns were washed with water and eluted with 2 mL of methanol. Purified samples were dried under vacuum and derivatized to the *tert*-butyl dimethylsilyl derivative by the addition of 20 μL of diisopropylethylamine, 30 μL dimethylformamide, and 30 μL of *N*-(*t*-butyl dimethylsilyl)-*N*-methyltrifluoroacetamide for 1 h at 60 °C. Derivatized samples were dried under nitrogen and redissolved in 20 μL of *n*-undecane. Samples were applied to a GC equipped with a 15 m DB-1701 (J&W Scientific, Folsom, CA) capillary column (0.25 mm internal diameter, 0.25 mm film thickness) interfaced with a mass spectrometer (Trio 1000; Fisons Instruments, Beverly, MA). The ion source and interface temperatures were set at 200 and 320 °C, respectively. Samples were analyzed in negative-ion chemical ionization mode with ammonia as the reagent gas, using 1 μL of each sample for injection. The initial column temperature was maintained at 150 °C for 1 min increasing to 300 at 20 °C/min. The mass spectrum obtained for silylated luminol is shown in Figure 3C. The major fragment ion for derivatized luminol has an *m*/*z* of 404, which corresponds to a deprotonated molecular ion for the silylated derivative. For quantitative measurement of luminol, ions were monitored by single ion monitoring at 404 *m*/*z* and their concentrations determined against known amounts of standards.

Preparation of NHS-API. 4-Amino-2-(hexanoic acid-*N*-hydroxysuccinimido ester)-isoindole-1,3-dione (NHS-API) (**2**) was synthesized by the esterification of 4-amino-2-(hexanoic acid)-isoindole-1,3-dione (**1**) with di(*N*-succinimidyl) carbonate. Initially, (**1**) was synthesized by fusing equal quantities (2.6 mmol) of 3-nitrophthalic anhydride and 6-amino-*n*-caproic acid at 153 °C for 10−15 min. The melt [crude 2-(hexanoic acid)-4-nitro-isoindole-1,3-dione] was washed with boiling water and resuspended in 10 mL 10% sodium dithionite. Reduction was carried out for at least 20 min with maintenance of the pH at 7−7.5, until most of the suspension had dissolved. After the removal of insoluble residue, the pH was adjusted to 3.0 with HCl and crude (**1**) precipitated with brine. The resultant oily yellow pellet was washed with water, lyophilized, and reacted with 2.6 mmol di(*N*-succinimidyl) carbonate in 2 mL pyridine/3 mL acetonitrile for 1 h at 60 °C, then dried at 60 °C for a further hour under nitrogen. The resultant crude (**2**) was purified on a silica gel 60 column using dichloromethane/acetone (40/80) as the mobile phase and/or recrystallized from ethyl acetate. Lyophilized aliquots were stored desiccated at −20 °C until use. ^{1}H NMR ($CDCl_3$, 500 MHz): 8.11−8.05 (2H, m, 2 × ArH), 7.92 (1H, t, j = 7.7 Hz, ArH), 5.21, (2H, br s, NH_2), 3.72 (2H, t, j = 7.2 Hz, CH_2), 2.83 (4H, br s, 2 × CH_2), 2.60 (2H, t, j = 7.2 Hz, CH_2CO), 1.82−1.61 (6H, m, 3 × CH_2) ppm.^{13}C NMR ($CDCl_3$, 125 MHz): 170.3 (s, C═O), 169.2 (s, 2 × C═O), 165.9 (s, C═O), 163.0 (s, C═O), 145.2 (s, C(Ar)), 135.2 (d, CH(Ar)), 128.5 (d, CH(Ar)), 127.0 (d, CH(Ar)), 38.4 (t, CH_2), 30.9 (t, CH_2), 27.9 (t, CH_2), 25.6 (t, 2 × CH_2), 24.1 (t, CH_2). FTIR (thin film, cm^{-1}): 3476 w, 3374 w, 2943 m, 1780 m, 1735 s, 1715 s, 1695 s, 1633 m, 1341 m. LRMS (CI + ve): 404 (55%), 374 ($[MH]^+$, 37%), 259 ($[M\text{-}ONSu]^+$, 100%). $C_{18}H_{19}N_3O_6$ requires 373.1274.

Preparation of API and Fluorescein-Labeled Insulin. Lyophilized human recombinant insulin (3.5 mg) (Novo Nordisk) was resolubilized in 1 mL of 50 mM borate buffer (pH 9.0) to which was added 0.3 μmol of NHS-API synthesized as

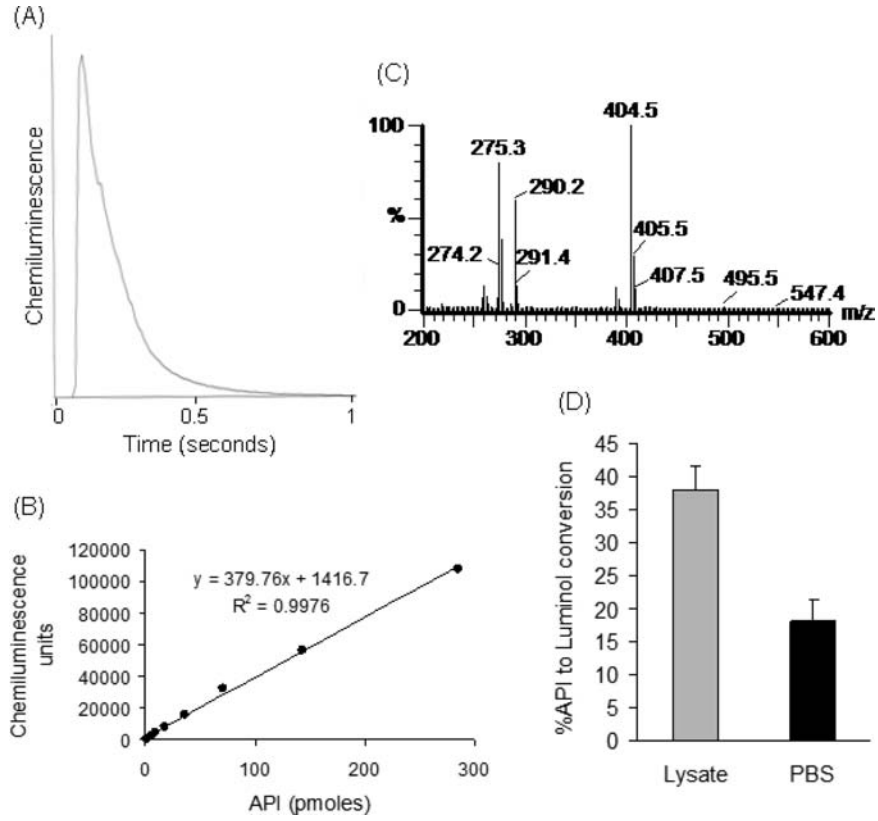

Figure 3. (A) Rate of light emission for 0.6 nmol of NH_2-API treated with hydrazine and induced by ferricyanide in the presence of the enhancer, iodophenol. (B) Typical standard curve for API. NHS-API stocks were doubly diluted in 1:1 DMSO/Tris-HCl (pH 8.5) solution. Triplicate dilutions were treated with an equal volume of hydrazine and chemiluminescence determined as for insulin studies. (C) Mass spectrum obtained for silylated luminol. The major fragment ion for derivatized luminol has an *m*/*z* of 404, which corresponds to a deprotonated molecular ion for the silylated derivative. (D) Conversion (%) of 56 nmol of API-palmitate in 100 μL cell lysate (gray bar) or PBS (black bar) to luminol after treatment with an equal volume of hydrazine as described for insulin studies. Complete (100%) conversion is assumed to yield 56 nmol (10 μg) of luminol. After hydrazine treatment, luminol was detected and quantified by GC-MS using a luminol standard curve, $n = 3$, $\pm$ SD. Assays were carried out in triplicate.

above, or 0.3 μmol of commercially available fluorescein-5(6)-carboxamidocaproic acid *N*-succinimidyl ester (NHS-Fluorescein) (Sigma, U.K.) in 200 μL DMSO. After 1 h at room temperature the API or fluorescein-labeled insulin was purified on PD-10 columns (GE Health Sciences, Amersham, U.K.) and the concentration of eluted, labeled insulin determined by the BCA assay (*9*). The concentration of insulin-bound API was determined by measuring the absorbance of the labeled insulin fractions at 395 nm (peak absorbance for API (395 nm) was determined for 5 mM NH_2-API in DMSO with a Unicam UV300 spectrophotometer). Insulin-bound fluorescein was determined by measuring the absorbance of labeled insulin fractions at 495 nm (*10*). Molar values were determined from API and fluorescein−albumin standard curves.

API-Insulin Binding Studies. HepG2 cells maintained in 12-well culture dishes until 80% confluence were used for insulin binding assays as previously described (*11*). After washing with HBSS, cells were exposed to 1 mL binding buffer (*11*), containing 5, 2.5, 1.25, and 0.625 μM API-insulin and incubated at 4 °C in the dark for 19 h. Thereafter, labeled binding buffer was removed from the cells, the cells were washed with 3 × 1 mL PBS, removed from the wells by scraping, pelleted, resuspended in 200 μL water, sonicated, and 10 μL of the lysate used for protein quantification by the BCA assay. For API measurement, cell lysates or labeled binding buffer (100 μL) were mixed with an equal volume of 98% hydrazine hydrate, heated at 60 °C for 30 min and 50 μL of the hydrazine treated sample mixed with 15 μL of a 0.02 g/mL iodophenol solution (in 1 N NaOH). Luminescence was then quantified for 10 s using a Tropix TR717 multiplate luminometer after luminescence induction by the injection of 100 μL 0.045% ferricyanide solution to each sample.

Insulin Transport Studies. For a comparison of API and fluorescein-labeled insulin uptake, HepG2 cells maintained in 6-well culture plates until 80% confluence were exposed to 2 mL binding buffer containing 10 μM API or fluorescein-labeled insulin. After 19 h, cells were washed with 2 × 2 mL unlabeled binding buffer and incubated for a further hour at 37 °C to induce insulin uptake. Thereafter, cells were washed with 2 × 2 mL PBS (pH 7.4), incubated with 2 mL PBS (pH 3.8) for 10 min, washed twice more with the latter buffer to remove remaining externally bound insulin, pelleted, and sonicated in 400 μL water. API chemiluminescence was determined as above, while for fluorescein−insulin, cell lysates (100 μL) were mixed with an equal volume of 1.5 M Tris buffer (pH 8.8) and fluorescence quantified using a cytofluor spectrofluorimeter at 485 nm excitation/530 nm emission.

Preparation of TPP-API. 4-Amino-2-[4-(3-triphenylphosphonium-propylamino)-butyl]-isoindole-1,3-dione bromide (TPP-API) (**4**) was synthesized by the coupling of 2-(4-aminobutyl)-4-nitro-isoindole-1,3-dione (**3**) with [2-(1,3dioxan-2yl)ethyl]-triphenylphosphonium bromide (DETP) (Aldrich, Dorset, U.K.) using reductive amination. Initially, crude (**3**) was prepared as follows: 6.2 mmol of putrescine dihydrochloride was combined with 0.012 mol of sodium hydroxide in 1 mL methanol and vortexed until dissolution of the hydroxide pellets. The suspension was centrifuged at 3500 *g* for 5 min and the supernatant (1 mL) placed in a thick walled 50 mL glass tube, to which was added 2.6 mmol 3-nitrophthalic anhydride. The mixture was rapidly heated at 180 °C until converted to a yellow melt.

The warm melt (crude (**3**)) was dissolved in 10 mL methanol and dried under nitrogen, yielding a yellow solid, which was coupled to DETP as follows: DETP (3.1 mmol) was stirred with 0.03 g *p*-toluene sulfonic acid (in 20 mL methanol) to allow for dioxan hydrolysis. After 1 h, crude (**3**) (dissolved in 10 mL water) was added to the above and the solution adjusted to pH 7. Reductive amination was initiated by the addition of 3.1 mmol sodium cyanoborohydride and the pH maintained at 6.8−7.0 for 1 h with HCl, yielding crude 4-nitro-2-[4-(3-triphenylphosphonium-propylamino)-butyl]-isoindole-1,3-dione bromide, which was reduced by the addition of 3 g (10%) sodium dithionite. The resultant yellow precipitate (crude (**4**)) was washed extensively with water. Crude product was lyophilized and stored desiccated at −20 °C until use or as frozen DMSO stocks.

Fluorescence Microscopy. HepG2 cells grown on Falcon Tissue culture-treated slides and stained with API-derivatives or JC-1 were viewed with a Nikon Eclipse TE 200 microscope using Nikon 1CH31010 Lucifer Yellow and 1CH31003 R & B Phycoerythrin (PE) filter sets, respectively, and *LuciaG* v 4.8 imaging software.

Preparation of NH_2-API. 4-Amino-2-(4-aminobutyl)-isoindole-1,3-dione (**5**) for heparin studies was prepared from mono-Boc-protected putrescine and 3-nitrophthalic anhydride (3NPA). Initially, equivalent amounts (0.023 mol) of putrescine and $(Boc)_2O$ were reacted in methanol in the presence of an iodine catalyst (0.0023 mol) according to the method of Varala et al. (*12*). The resultant precipitate (crude monoprotected diamine) was washed extensively with water, lyophilized, and 0.5 g fused with an equivalent amount of 3NPA at 153 °C for 10 min. The melt (crude 2-(4-Boc-aminobutyl)-4-nitro-isoindole-1,3-dione was dissolved in 10 mL THF and reduced to Boc protected (**5**) with 10% dithionite. Phase separation was achieved by the addition of excess sodium bicarbonate, and the organic phase collected and dried under nitrogen. Crude Boc-protected (**5**) was purified by silica gel chromatography, deprotected with trifluoroacetic acid for 10 min, dried under nitrogen, and redissolved in water. The resultant water-soluble, 4-amino-2-(4-aminobutyl)-isoindole-1,3-dione, trifluoroacetate salt was lyophilized and stored desiccated at −20 °C until use. FTIR (thin film, cm^{-1}): 2950 m, 1686 s, 1634 m, 1535 m. LRMS (CI + ve): 264 ($[M + MeOH]^+$, 20%), 234 ($[MH]^+$, 15%), 217 ($[M - NH_2]^+$, 15%), 148 (100%). HRMS (CI + ve): $[MH]^+$, $C_{12}H_{15}N_3O_2$ requires 234.12425. Found 234.12428.

Heparin Labeling. Porcine heparin (2 mg) was dissolved in 0.5 mL acetate buffer (100 mM, pH 5.5) to which was added 10 μL of a 0.5 M sodium periodate stock solution. After 5 min in the dark, 10 μL 0.5 M NaOH was added along with 0.5 mL 2% sodium tetraborate to give a final pH of 9.3. To this oxidized heparin solution, 2 mg of NH_2-API in 50 μL DMSO was then added, along with 100 μL of a 1 M sodium cyanoborohydride stock and coupling achieved by incubation at room temperature for 18 h. Labeled heparin was purified on PD-10 columns, and the concentration of eluted, labeled API-heparin determined by the carbazole assay (*13*). The concentration of heparin-bound API was determined by measuring the absorbance of the labeled heparin fractions at 395 nm.

Preparation of API-Palmitic Acid. Ω-Labeled API-palmitic acid (4-amino-2-(hexadecanoic acid)-isoindole-1,3-dione) (**6**) was synthesized as follows: 16-Bromopalmitic acid (1.5 mmol) (Aldrich) in 10 mL ethanol was added to excess (20 mL) 30% ammonia solution and heated in a boiling water bath for 1 h in a 50 mL capped tube with constant mixing. The resultant white precipitate (crude 16-aminopalmitic acid, ammonium salt) was converted to the potassium salt with potassium hydroxide, lyophilized, and 0.4 g fused with 0.5 g 3NPA at 180 °C until the formation of a light brown melt was evident. The cooled melt was washed with boiling water and reduced with 10% sodium dithionite solution as above, yielding a yellow solid (crude (**6**)), which was acidified and washed with water. Crude API-palmitic acid was purified by silica gel chromatography using ethyl acetate and/or recrystallized from dichoromethane and stored desiccated at −20 °C until use. ^1H NMR ($CDCl_3$, 500 MHz): 7.58 (1H, dd, j = 8.5, 7.2 Hz, ArH), 7.35 (1H, d, j = 7.2 Hz, ArH), 7.04 (1H, d, j = 8.5 Hz, ArH), 5.41 (2H, br s, NH_2), 3.92 (1H, t, j = 7.4 Hz, NCHH), 3.85 (1H, t, j = 7.2 Hz, NCHH), 2.56 (2H, t, j = 7.5 Hz, CH_2CO_2H), 1.94−1.79 (4H, m, 2 × CH_2), 1.61−1.42 (22H, m, 11 × CH_2). ^{13}C NMR ($CDCl_3$, 125 MHz): 179.8 (s, C═O), 167.5 (s, C═O), 166.0 (s, C═O), 145.2 (s, C(Ar)), 135.1 (d, CH(Ar)), 128.5 (d, CH(Ar)), 126.9 (s, C(Ar)), 121.0 (d, CH(Ar)), 112.7 (s, C(Ar)), 38.9 (t, CH_2), 37.7 (t, CH_2), 34.1 (t, CH_2), 29.7 (t, 2 × CH_2), 29.5 (t, 2 × CH_2), 29.3 (t, 2 × CH_2), 29.1 (t, 2 × CH_2), 28.8 (t, CH_2), 28.4 (t, CH_2), 26.9 (t, CH_2), 24.8 (t, CH_2). FTIR (thin film, cm^{-1}): 3394 w, 2918 s, 2847 s, 1753 m, 1718 s, 1697 s, 1634 m, 1541 m, 1467 m. LRMS (EI + ve): 416 (M^+, 32%), 175 ($[M - (CH_2)_{14}CO_2H]^+$, 100%). HRMS (EI + ve): M^+, $C_{24}H_{36}N_2O_4$ requires 416.26696. Found 416.26604.

Lipid Metabolism Studies. HepG2 cells grown to 80% confluence in 50 cm^2 flasks in DMEM were labeled with 5 mL of medium containing 240 μM API-palmitic acid for 24 h. Thereafter, labeled medium was collected and lyophilized, and cells washed with PBS, detached by scraping, and pelleted. Both cell pellets and lyophilized medium were lipid extracted by the Folch method (*14*). Lipid extracts were dried under nitrogen, resuspended in 20 μL Folch reagent, and spotted (6 μL) onto C18 silica TLC plates (Aldrich, UK) and lipid species separated using 95% methanol.

Lipase Treatment of Folch Extracts. Dried Folch extracts from cell pellets were resuspended in 300 μL 0.25 M Tris-HCl (pH 7.3) containing 0.4% sodium deoxycholate. Samples were warmed briefly to 80 °C and vortexed to emulsify lipids. Samples (100 μL) were treated with lipase (28 units) (4 μL of a 7 unit/μL stock in water) or water alone for 1 h at 30 °C. These were then lyophilized, Folch extracted, and separated on C18 TLC plates as above.

Chemiluminescent Quantification of Lipid Transport. HepG2 cells grown to 80% confluence in 25 cm^2 flasks in DMEM as above were washed with 2 × 5 mL PBS (pH 7.4) and to each flask was added, 5 mL fatty acid transport medium, with or without 5 μg/mL Filipin complex. After 30 min at 37 °C, 50 μL of an API-palmitic acid solution in DMSO (2.4 mM) was added to flasks (final concentration 24 μM). Cells were incubated for 30 min at 37 °C and washed with cold medium (2 × 5 mL), detached by scraping, pelleted, resuspended in 0.4 mL PBS, and sonicated. Lysates (200 μL) were chemiluminometrically quantified, as for insulin, while total protein was assayed using the BCA assay.

Labeling of DNA with API. Initially, to introduce allylamine dUTP into a DNA probe, which would allow for labeling with API, a 529bp AMPKα2 fragment was amplified by PCR from a pcDNA3 plasmid construct containing the full-length cDNA sequence. The following primers and conditions were used: Forward (F) 5′-tggctgagaagcagaagcac-3′ and reverse (R) 5′-ggcgatccacagctagttcg-3′. PCR mix: Buffer (Qiagen), 0.5 mM $MgCl_2$, 0.1 mM dATP, 0.1 mM dCTP, 0.1 mM dGTP, 0.05 mM dTTP, 0.05 mM allyl-amine dUTP, 5 ng DNA, 0.5 μM primer F, 0.5 μM primer R, 1 unit Taq DNA polymerase (Qiagen). Final volume 20 μL.

Cycling conditions: 94 °C 3 min; (94 °C 30 s, 57 °C 30 s, 72 °C 1 min) 30 cycles; 72 °C 10 min. PCR amplified product (11 × 20 μL samples) either having been synthesized using allylamine dUTP: dTTP in a 1:1 ratio or dUTP alone was pooled and concentrated using Qiaquick PCR purification kit (Qiagen). Samples were eluted with 50 μL 4 mM potassium phosphate

buffer (pH 8.5), to which was added 30 μL 0.3 M bicarbonate buffer (pH 9.1). To this, 20 μL of a NHS-API stock was added (17 mg/mL in a 1:11 pyridine/DMSO solution), the mixture mixed for 3 min and then incubated for a further 40 min at room temperature. Labeled DNA was purified again as above, with an additional 80% ethanol wash step, eluted with a final volume of 150 μL (50 μL 10 mM Tris-HCl (pH 8.5) and 2 $\times$ 50 μL H_2O) and quantified using a Nanodrop microspectrophotometer. Samples were lyophilized and stored at -80 °C until use.

Transfection Studies. API-DNA or unlabeled DNA (1.6 μg) in 100 μL αMEM was added to 4 μL Lipofectamine 2000 (Invitrogen) in 100 μL αMEM. After 20 min, the 200 μL DNA/Lipofectamine complex was added to 90% confluent HepG2 cells in 12 well plates. Control wells were exposed to 200 μL medium alone, medium with labeled or unlabeled DNA without Lipofectamine, and medium with only Lipofectamine. After 5 h, incubation at 37 °C, 1 mL αMEM supplemented with 10% FBS was added to the wells and cells cultured for a further 16 h as above. Thereafter, cells were washed with 2 $\times$ 2 mL PBS, harvested with a cell scraper, pelleted, resuspended in 300 μL PBS, sonicated and 100 μL lysates treated with an equal volume of hydrazine hydrate, and chemiluminometrically quantified as for insulin studies. Total protein was determined by the BCA assay. For fluorescence microscopy, half the volume of DNA/Lipofectamine mixture was added to HepG2 cells on tissue-culture treated Falcon slides. After 4.5 h, cells were washed with 2 $\times$ 0.5 mL PBS and viewed with a Lucifer yellow filter as above.

RESULTS

API derivatives treated with hydrazine and induced by ferricyanide in the presence of the enhancer iodophenol underwent rapid chemiluminescence with maximum light emission occurring within 0.25 s (Figure 3A). Assays were broadly linear (typically from 0.6 nmol to 1 pmol) with a detection limit of 0.3 pmol (Figure 3B). Furthermore, GC-MS analysis indicates that hydrazine treatment of API-spiked cell lysates results in an approximately 40% API to luminol conversion efficiency (Figure 3C,D).

We investigated the use of the API system in cellular binding studies. NHS-API, an amine-reactive *N*-hydroxysuccinimide ester coupled API derivative was synthesized and used to label human recombinant insulin. The resultant API-labeled insulin was used in insulin binding and uptake studies using HepG2 cells according to Calzi et al. (*11*): (a) Insulin receptor-dependent insulin binding was assessed by quantifying cell-bound label relative to unbound, or free, label still present in the binding buffer. (b) Insulin receptor mediated insulin endocytosis was assessed by quantifying internalized label by chemiluminometry, after treatment of cell pellets with hydrazine.

A Scatchard plot (bound ligand/free ligand vs bound ligand) revealed that API-insulin produced a typical curvilinear plot (Figure 4A), previously shown to be indicative of insulin binding using ^{125}I-labeled insulin (*15*). Endocytosis studies showed that insulin receptor mediated insulin uptake, for cells exposed to 10 μM API-insulin, was 24-fold greater than that for cells exposed to the same concentration of fluorescein-labeled insulin, which was prepared from commercially available NHS-fluorescein in an identical manner to that of API-insulin (Figure 4B).

We have also used the API system in dual fluorescence and chemiluminescence mitochondrial studies. API was coupled to triphenylphosphonium bromide (TPP), a well-established mitochondrial probe, which accumulates in mitochondria in a membrane potential-proportional manner (*16*). Cells stained with TPP-API and viewed by fluorescence microscopy exhibited

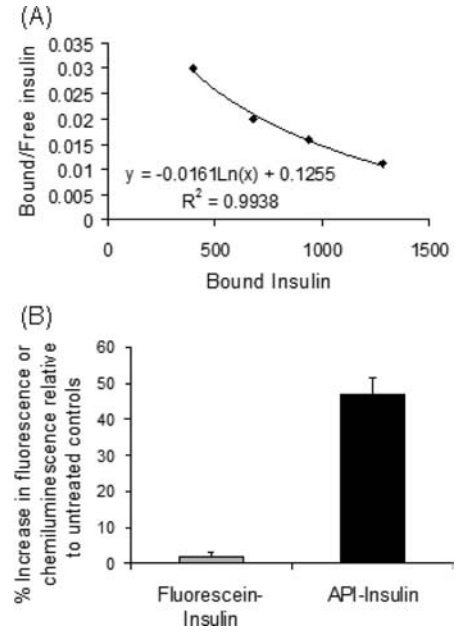

Figure 4. (A) Scatchard plot of cell bound, API-labeled insulin, normalized for total cellular protein (mg/mL), over unbound labeled insulin remaining in the binding buffer vs cell-bound, labeled insulin. (B) Comparison of API and fluorescein-labeled insulin uptake by HepG2 cells. HepG2 cells were exposed to 10 μM API or fluorescein-labeled insulin for 19 h and then for 1 h at 37 °C to induce insulin uptake. Fluorescein fluorescence (gray bar) and API-luminescence (black bar) in 100 μL cell lysate were determined and expressed as a % increase relative to untreated control lysates. Samples were normalized for total protein as above, $n = 3$, $\pm$ SE. Assays were carried out in triplicate.

green, brightly fluorescent foci (white arrow) indicating the accumulation of this compound within mitochondria (Figure 5A). In the presence of a mitochondrial respiration inhibitor cocktail, focal staining was abolished (Figure 5B), clearly indicating that TPP-API accumulated within mitochondria in a membrane potential-dependent manner. Cells stained with the mitochondrial dye JC-1 exhibited identical focal staining, which was significantly diminished, although not completely abolished by incubation of cells with the same mitochondrial respiration inhibitor cocktail (Figure 5C,D).

To quantify TPP-API mitochondrial accumulation, HepG2 cells were labeled with 65 μM TPP-API with or without mitochondrial respiration inhibitor cocktail for 45 min. Cells were then homogenized, the mitochondrial fraction obtained by centrifugation (*17*), and mitochondria assessed for internalized label by chemiluminometry, after treatment with hydrazine. Mitochondria from cells exposed to inhibitor cocktail exhibited a 25% reduction in TPP-API chemiluminescence in comparison to cells exposed to TPP-API alone (Figure 5E).

To illustrate the use of the API-system in polysaccharide labeling, an API molecule containing a terminal amine group was synthesized and coupled to heparin by periodate oxidation and reductive amination. API-labeled heparin was used in cellular uptake studies according to Dudás et al. (*18*). HepG2 cells incubated with 5 μg API-heparin for 18 h and viewed by fluorescence microscopy exhibited fluorescent cytosolic and nuclear staining, indicating cellular uptake of heparin in a manner similar to that observed using biotinylated heparin and fluorescein-labeled streptavidin detection (*18*) (Figure 6A,B). Heparin uptake could also be quantified chemiluminometrically after hydrazine treatment of cell lysates, as above (Figure 6C).

We also investigated the use of the API system in lipid studies; an API-labeled long chain fatty acid, API-palmitic acid, was synthesized and used to investigate cellular uptake and lipid

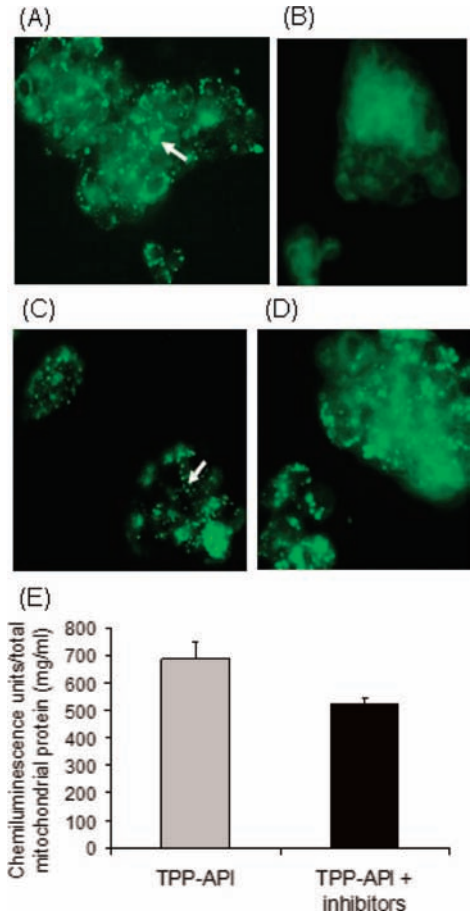

Figure 5. HepG2 cells on Falcon tissue culture-treated slides were incubated with 65 μM API-TPP for 45 min without (A) or with (B) respiration-inhibitor cocktail (13 μg/mL Oligomycin, 10 μg/mL Antimycin A, 5 μM Rotenone), washed with PBS and viewed by fluorescence microscopy (Lucifer yellow filter, 40× magnification). White arrow indicates fluorescent foci. (C) Fluorescence microscopy for HepG2 cells exposed to the mitochondrial probe JC-1. Cells cultured on tissue culture slides in 0.5 mL DMEM were stained with 6.5 μM JC-1 for 45 min and viewed by fluorescence microscopy using a PE filter at 40× magnification. (D) JC-1 stained HepG2 cells in the presence of inhibitor cocktail, as above. (E) Cells exposed to 65 μM API-labeled TPP for 45 min without (gray bar) or with respiration-inhibitor cocktail (black bar) were washed with PBS, harvested, and cell-mitochondrial fractions obtained as previously described (*17*). Mitochondrial pellets were sonicated in 200 μL water and 50 μL lysates, hydrazine treated, and assayed as for API-insulin. Chemiluminescence values are per total mitochondrial protein (mg/mL), $n = 3$, $\pm$ SE. Assays performed in triplicate.

metabolism. HepG2 cells incubated with 24 μM API-palmitic acid for 23 h and viewed by fluorescence microscopy exhibited both membrane staining and discrete cytosolic accumulation (Figure 7A). Total lipid extracts from cells incubated with API-palmitate and separated using C18/silica thin layer chromatography contained fluorescent API-labeled lipid species with increased hydrophobicity. This indicated the incorporation of API-palmitic acid into more complex lipid species, a proportion of which was exported into culture medium (Figure 7B). In addition, a significant proportion of these fluorescent API-labeled lipid species was degraded by lipase treatment, indicating the incorporation of API-palmitic acid into acyl-glycerides (Figure 7C). To quantify lipid transport using the API chemiluminescence system, HepG2 cells were incubated with 24 μM API-palmitate for 30 min with or without filipin complex, an inhibitor of caveolin-dependent fatty acid transport (*19*). Cell pellets were assessed for internalized fatty acid by chemiluminometry, following sonication, as above. HepG2 transport of API-palmitic

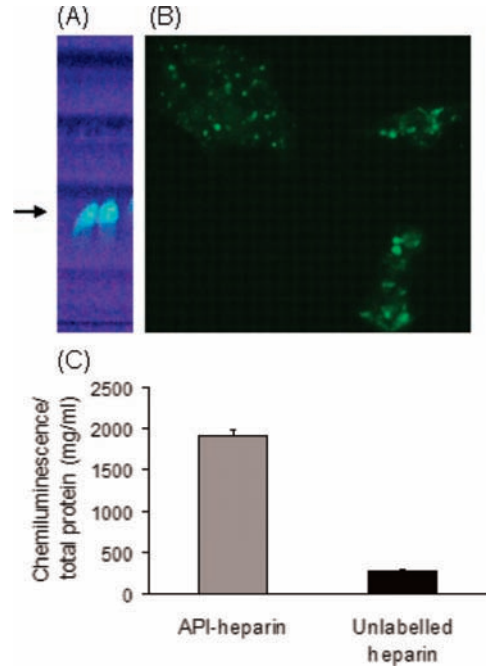

Figure 6. (A) API-heparin on a 4−20% TBE polyacrylamide gel, visualized using a transilluminator (arrow). (B) Fluorescence microscopy for HepG2 cells exposed to 5 μg API-labeled heparin for 18 h, indicating discrete cytosolic and nuclear staining (Lucifer yellow filter, 40× magnification). (C) API-heparin nuclear transport. Cells were exposed to 10 μg API-heparin (gray bar) or unlabeled heparin (black bar) for 18 h. Thereafter, cells were washed with PBS, lysed with 1% NP40, and nuclear pellets obtained by centrifugation at 900 *g*. Pellets were sonicated in 200 μL PBS, and 100 μL samples treated with hydrazine and assayed for chemiluminescence as for insulin studies. Samples are normalized for total protein (mg/mL), $n = 3$, $\pm$ SD. Assays performed in duplicate.

acid was reduced (20%) in the presence of filipin (Figure 7D), indicating that API-palmitic acid transport was partly caveolin-dependent. This is in agreement with a previous study which utilized NBD-labeled stearic acid (*19*).

To test the applicability of the API system as a nucleic acid label, a 529 base pair DNA fragment was amplified from a plasmid containing the AMP-activated kinase alpha subunit (AMPKα2) by PCR using allylamine-dUTP, a modified base containing an allylamine functional group. This allowed for the incorporation of terminal amine groups within the PCR product. The resultant allylamine PCR product was then labeled with the amine reactive NHS-API, yielding a fluorescent API-DNA conjugate. The API-labeled DNA was then used for transfection studies using HepG2 cells. HepG2 cells were transfected with 0.8 μg labeled DNA using Lipofectamine 2000 for 4.5 h and viewed by fluorescence microscopy. Discrete regions of fluorescent DNA/lipofectamine complex were visibly incorporated into membranes (Figure 8A). In addition, fluorescent DNA/lipofectamine complexes were also evident on the surfaces of cells and on the slide surface (Figure 8A).

To quantitatively assess DNA uptake using lipofectamine transfection, cells were transfected with 1.6 μg of labeled DNA or 1.6 μg of unlabeled control DNA with or without lipofectamine for 16 h. Cells were then sonicated and assayed for chemiluminescence after hydrazine treatment, as previously described. Cells exposed to API-DNA exhibited significant levels of chemiluminescence while all controls displayed only background levels (Figure 8B).

DISCUSSION

In this study, we investigated the use of the luminol precursor, 3-aminophthalimide in direct chemiluminescence cellular bio-

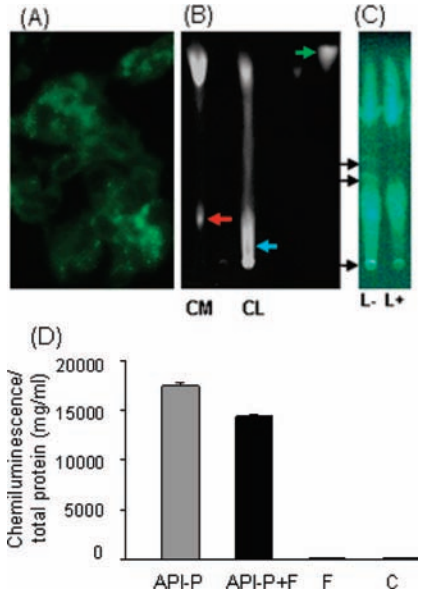

Figure 7. (A) HepG2 cells exposed to 24 μM API-palmitic acid (Lucifer yellow filter, 40× magnification). (B) Lipid profiles of HepG2 cells exposed to 240 μM API-palmitic acid. Total lipid extracts from culture medium (CM) and lysates (CL) were separated on C18/silica TLC plates. Mobility is inversely proportional to hydrophobicity. (green →) API-palmitic acid reference, (blue →) fluorescent API-lipid species in cell lysates, and (red →) lipid exports into cell culture medium. (C) Untreated (L−) or lipase-treated (L+) extracts. Arrows indicate fluorescent acyl-glyceride lipid species susceptible to lipase degradation. (D) Effect of filipin on API-palmitate transport in HepG2 cells exposed to 24 μM API-palmitic acid, without (API-P, gray bar) or with 5 μg/mL filipin complex (API-P+F, black bar). Chemiluminescence was also determined for cells exposed to fillipin (F) or medium (C) alone. Normalized for total protein (mg/mL), $n = 3$, ± SD. Assays performed in triplicate.

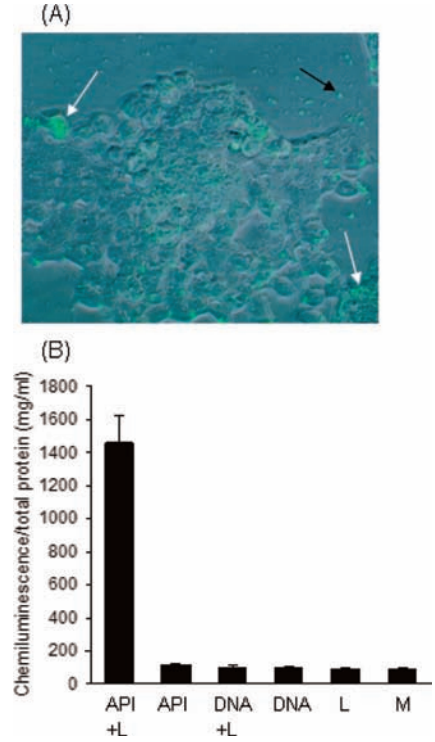

Figure 8. (A) HepG2 cells transfected with 0.8 μg API-labeled DNA using lipofectamine 2000 for 5 h and viewed by fluorescence microscopy (Lucifer yellow filter, 20× magnification). Fluorescent DNA/lipofectamine complexes were incorporated into membranes (white arrows), and fluorescent DNA/lipofectamine complexes were evident on the surfaces of both cells and slide (black arrow). (B) API-DNA uptake for cells exposed to αMEM with 1.6 μg API-DNA +Lipofectamine (API + L), API-DNA alone (API), 1.6 μg unlabeled DNA +Lipofectamine (DNA + L), unlabeled DNA (DNA), Lipofectamine alone (L), and medium alone (M) for 16 h. Cell lysates (100 μL) were treated with hydrazine and assayed as above. Normalized for total protein (mg/mL), $n = 4$, ± SD. Assays performed in triplicate.

assays. We established that API assays are rapid, sensitive, and broadly linear; and the ease of synthesis of API derivatives, with a variety of functional groups, makes this molecule applicable for a range of cellular applications. We clearly demonstrate its utility in (a) receptor-dependent binding and transport of API-labeled insulin, (b) the qualitative (fluorescence) and quantitative (chemiluminescence) assessment of mitochondrial function by API-TPP, (c) polysaccharide (heparin) transport, (d) lipid transport and metabolism using API-palmitate, and (e) assessment of DNA transfection efficiency using API-labeled DNA.

The API assay system would therefore serve as a sensitive and economical substitute for a variety of radio-isotope-based methodologies and, importantly, offers the advantage of fluorescence monitoring of probe or substrate entry and localization within live cells, prior to chemiluminescent quantification. Although concern may arise over the use of hydrazine hydrate as a developing agent, due to its toxicity and corrosive properties, the use of appropriate protective clothing and eyewear and the carrying out of assays in well-ventilated laboratories and fume hoods, when developing samples, significantly reduces the risk of harmful exposure. Furthermore, unlike radioactive waste, which is hazardous and burdensome to dispose of, dilute hydrazine solutions and hydrazine-contaminated waste are effectively neutralized by hypochlorite, allowing for safe and rapid disposal.

Additional advantages of this label are its neutrality and relatively small size in comparison to other bulky and/or charged fluorophores. The latter advantages making API particularly useful for metabolic studies, as illustrated using API-palmitic acid, which was clearly incorporated into more complex lipid species by HepG2 cells, a proportion of which was actively exported from the cell. The neutrality and smaller size of API in comparison to fluorescein are also the likely reasons for the observed increase in cellular transport of API-insulin in comparison to the fluorescein-labeled peptide. Although fluorescein−insulin has been previously used in insulin binding studies (*20*, *21*), we found that not only did labeling insulin with NHS-API yield a higher specific activity than commercially available NHS-fluorescein, but Scatchard analysis for fluorescein−insulin yielded an atypical negative cooperativity plot (data not shown). This suggested that fluorescein labeling altered the affinity of insulin for its receptor. Therefore, a combination of steric hindrance, charge, and lower specific activity all likely contributed to reduced receptor binding and transport for fluorescein−insulin in comparison API-insulin.

Another potential application for the API system lies in the finding that aminophthalimides display solvatofluorochromism (i.e., altered emission wavelength in response to polarity changes) (*22*). Although not explored in this study, it is envisaged that API-based investigations could yield valuable information regarding the total quantity of labels within cells (determined chemiluminometrically) and its distribution within distinct microenvironments (e.g., lipid bodies c/o cytosol), determined fluorometrically.

Finally, although we have focused on cellular-based bioassays in this study, the simplicity of the API system would allow for its potential utility in a variety of non-cell-based bioassays such as high-throughput competitive binding studies, kinase assays, and enzyme assays utilizing API-labeled substrates. Indeed,

preliminary studies have found that both gold nanoparticles and beta-eliminated kinase substrates could be labeled with terminal thiol-containing API derivatives, which further highlights the versatility and broad applicability of this labeling system.

ACKNOWLEDGMENT

We thank UCL Business PLC for providing proof of concept funding for this research. This work is funded by a private company and the author, L. H. Damelin, declares that he has a financial conflict of interest.

LITERATURE CITED

(1) Kessler, C. (1992) *Nonradioactive Labeling and Detection of Biomolecules* (Kessler, C., Ed.) Springer, New York.

(2) Albrecht, H. O. (1928) Uber die chemiluminescenz des aminophthalsaurehydrazids. *Z. Phys. Chem. 136*, 321.

(3) Whitehead, T. P., Kricka, L. J., Carter, T. J. N., and Thorpe, G. H. G. (1979) Analytical luminescence: Its potential in the clinical laboratory. *Clin. Chem. 25*, 1531–1546.

(4) Shulman, S. G. (1993) *Molecular Luminescence Spectroscopy. Volume 77.Part 3: Chemical Analysis Series* (Shulman, S. G., Ed.) John Wiley and Sons, New York.

(5) Waseem, A., Yaqoob, M., and Nabi, A. (2004) Determination of iron in blood serum using flow injection with luminol chemiluminescence detection. *Luminescence 19*, 333–338.

(6) Schroeder, H. R., and Yeager, F. M. (1978) Chemiluminescence yields and detection limits of some isoluminol derivatives in various oxidation systems. *Anal. Chem. 50*, 1114–1120.

(7) Khan, M. N. (1995) Kinetic evidence for the occurrence of a stepwise mechanism in hydrazinolysis of phthalimide. *J. Org. Chem. 60*, 4536–4541.

(8) Gulis, I. M., Komyak, A. I., Saechnikov, K. A., and Tsvirko, V. A. (1989) Fluorescent spectroscopy of 3-aminophthalimide molecules cooled in an ultrasonic jet. *J. Appl. Spectrosc. 50*, 257–262.

(9) Smith, P. K., Krohn, R. I., Hermanson, G. T., Mallia, A. K., Gartner, F. H., Provenzano, M. D., Fujimoto, E. K., Goeke, N. M., Olsom, B. J., and Klenk, D. C. (1985) Measurement of protein using bicinchoninic acid. *Anal. Biochem. 150*, 76–85.

(10) Hermanson, G. T. (2008) Fluorescent probes, In *Bioconjugate Techniques*, 2nd ed., pp 396−497, Chapter 9, Academic Press, New York.

(11) Calzi, S. L., Choice, C. V., and Najjar, S. M. (1997) Differential effect of pp120 on insulin endocytosis by two variant insulin receptor isoforms. *Am. J. Physiol. Endocrinol. Metab. 273*, 801–808.

(12) Varala, R., Nuvula, S., and Matile, S. R. (2006) Molecular iodine-catalyzed facile procedure for N-Boc protection of amines. *J. Org. Chem. 71*, 8282–8286.

(13) Cesaretti, M., Luppi, E., Maccari, F., and Volpi, N. (2003) A 96-well assay for uronic acid carbazole reaction. *Carbohydr. Polym. 54*, 59–61.

(14) Folch, J., Lees, M., and Sloane Stanley, G. H. (1957) A simple method for the isolation and purification of total lipides from animal tissues. *J. Biol. Chem. 226*, 497–509.

(15) Donner, D. B. (1980) Regulation of insulin binding to isolated hepatocytes: Correction for bound hormone fragments linearizes Scatchard plots. *Proc. Natl. Acad. Sci. U.S.A. 77*, 3176–3180.

(16) Ross, M. F., Kelso, G. F., Blaikie, F. H., James, A. M., Cocheme, H. M., Filipovska, A., Ros, T., Hurd, T. R., Smith, R. A. J., and Murphy, M. P. (2005) Lipophilic triphenylphosphonium cations as tools in mitochondrial bioenergetics and free radical biology. *Biochemistry (Moscow) 70*, 222–230.

(17) Pallotti, F., and Lenaz, G. (2001) Isolation and subfractionation of mitochondria from animal cells and tissue culture lines. *Methods in Cell Biology, Volume 65 Mitochondria.* (Pon, L. A., and Schon, E. A., Eds.) pp 2−31, Chapter 1, Academic Press, London.

(18) Dudás, J., Ramadori, G., Knittel, T., Neubauer, K., Raddatz, D., Egedy, K., and Kovalszky, I. (2000) Effect of heparin and liver heparan sulphate on interaction of HepG2-derived transcription factors and their cis-acting elements: altered potential of hepatocellular carcinoma heparan sulphate. *Biochem. J. 350*, 245–51.

(19) Pohl, J., Ring, A., and Stremmel, W. (2002) Uptake of long-chain fatty acids in HepG2 cells involves caveolae: analysis of a novel pathway. *J. Lipid. Res. 43*, 1390–1399, http://www.ncbi.nlm.nih.gov/sites/entrez?Db=pubmed&Cmd=Search&Term=%22Pohl%20J%22%5BAuthor%5D&itool=EntrezSystem2.PEntrez.Pubmed.Pubmed_ResultsPanel.Pubmed_RVAbstractPlus.

(20) Hentz, N. G., Richardson, J. M., Sportsman, J. R., Daijo, J., and Sittampalam, G. S. (1997) Synthesis and characterization of insulin-fluorescein derivatives for bioanalytical applications. *Anal. Chem. 69*, 4994–5000.

(21) Rajagopal, J., Anderson, W. J., Kume, S., Martinez, O. I., and Melton, D. A. (2003) Insulin staining of ES cell progeny from insulin uptake. *Science 299*, 363.

(22) Okamoto, H., Kohno, M., Satake, K., and Kimura, M. (2005) An azacrowned phthalimide as a metal-ion sensitive sovatofluorochromic fluorophore: fluorescence properties and a mimic integrated logic operation. *Bull. Chem. Soc. Jpn. 78*, 2180–2187.

BC800361R

Bioconjugate Chemistry 20th Anniversary

Subscriber access provided by SHEMYAKIN-OVCHINNIKOV INST

Article

Compared to Purpurinimides, the Pyropheophorbide Containing an Iodobenzyl Group Showed Enhanced PDT Efficacy and Tumor Imaging (I-PET) Ability

Suresh K. Pandey, Munawwar Sajjad, Yihui Chen, Anupam Pandey, Joseph R. Missert, Carrie Batt, Rutao Yao, Hani A. Nabi, Allan R. Oseroff, and Ravindra K. Pandey

Bioconjugate Chem., **2009**, 20 (2), 274-282• DOI: 10.1021/bc8003638 • Publication Date (Web): 03 February 2009

Downloaded from http://pubs.acs.org on May 8, 2009

More About This Article

Additional resources and features associated with this article are available within the HTML version:

- Supporting Information
- Access to high resolution figures
- Links to articles and content related to this article
- Copyright permission to reproduce figures and/or text from this article

View the Full Text HTML

ACS Publications
High quality. High impact.

Bioconjugate Chemistry is published by the American Chemical Society. 1155 Sixteenth Street N.W., Washington, DC 20036

Compared to Purpurinimides, the Pyropheophorbide Containing an Iodobenzyl Group Showed Enhanced PDT Efficacy and Tumor Imaging (^{124}I-PET) Ability

Suresh K. Pandey,[†] Munawwar Sajjad,*[,§] Yihui Chen,[†] Anupam Pandey,[†,||] Joseph R. Missert,[†] Carrie Batt,[†] Rutao Yao,[§] Hani A. Nabi,[§] Allan R. Oseroff,[‡] and Ravindra K. Pandey*[,†]

PDT Center, Cell Stress Biology and Department of Dermatology, Roswell Park Cancer Institute, Buffalo, New York 14263, and Department of Nuclear Medicine, State University of New York, Buffalo, New York 14214. Received August 25, 2008; Revised Manuscript Received December 15, 2008

Two positional isomers of purpurinimide, 3-[1′-(3-iodobenzyloxyethyl)] purpurin-18-*N*-hexylimide methyl ester **4**, in which the iodobenzyl group is present at the top half of the molecule (position-3), and a 3-(1′-hexyloxyethy)purpurin-18-*N*-(3-iodo-benzylimide)] methyl ester **5**, where the iodobenzyl group is introduced at the bottom half (N-substitued cyclicimide) of the molecule, were derived from chlorophyll-*a*. The tumor uptake and phototherapeutic abilities of these isomers were compared with the pyropheophorbide analogue **1** (lead compound). These compounds were then converted into the corresponding ^{124}I-labeled PET imaging agents with specific activity >1 Ci/μmol. Among the positional isomers **4** and **5**, purpurinimide **5** showed enhanced imaging and therapeutic potential. However, the lead compound **1** derived from pyropheophorbide-*a* exhibited the best PET imaging and PDT efficacy. For investigating the overall lipophilicity of the molecule, the 3-*O*-hexyl ether group presnt at position-3 of purpurinimide **5** was replaced with a methyl ether substituent, and the resulting product **10** showed improved tumor uptake, but due to its significantly higher uptake in the liver, spleen, and other organs, a poor tumor contrast in whole-body tumor imaging was observed.

INTRODUCTION

Positron emission tomography (PET) has wide appeal for research at the drug development stage as it allows studying the drug distribution noninvasively (*1*). Dedicated animal PET systems whose resolution could reach near 1 mm have intensified this field by enabling drug studies with murine disease models. In recent years, ^{18}F-fluorodeoxyglucose (^{18}F-FDG) has been the primary PET tracer. It is being used in the evaluation of several neoplasms, both before and after therapy, as well as the planning of the radiotherapy in various cancers. Its use in the assessment of cancer after therapy, including restaging tumors and monitoring tumor response has been of particular interest for oncologists. However, ^{18}F-FDG suffers from pitfalls in cases such as where tumors are not metabolically active enough. Additionally, a short half-life of ^{18}F-isotope (110 min) limits its use in studies involving antibodies and photosensitizers (PS) related to porphyrins for use in photodynamic therapy (PDT), which take considerably longer time to accumulate in a tumor in high concentrations (*2*). In this respect, ^{124}I is a better choice due to its half-life of 4.2 days (*3, 4*). The labeling technique for ^{124}I-nuclide is now well established, and this approach is continuously being followed to label a variety of biologically active molecules (*5*−*12*). In the past few years, various porphyrin-based photosensitizers have been labeled/chelated with ^{111}In, ^{113}Sn, and ^{99}mTc radionuclide for the purpose of scintigraphy (SPECT) (*13*−*21*). The metalation of the porphyrin core, however, alters the physicochemical characteristics of the molecule. The clinically effective PS have also been labeled with ^{131}I, ^{14}C, and ^{3}H mainly for the purpose of understanding their pharmacokinetic and phamacodynamic characteristics (*22*−*26*). There are a few reports in the field of PDT where various F-18 based radiotracers such as ^{18}F-FDG (*27*−*29*), ^{18}F-FHBG{9-(4-^{18}F-fluoro-3-hydroxymethyl-butyl)guanine} (*30*), ^{18}F-FLT (3′-deoxy-3′-18F-fluorothymidine) (*31*), and ^{99}mTc-Annexin V (*32*) have been used to monitor cellular events during and post-PDT in vivo.

One of the main reasons for using the porphyrin-based compounds in phototherapy is their ability to retain in tumor (*33*−*35*). The tumor localizing ability of certain porphyrins has also been explored in developing multifunctional agents, where these compounds were used as vehicles to deliver the desired imaging moieties (fluorescence, MRI, and PET) to tumors (*36*−*41*).

For quite some time, one of the objectives of our laboratory has been to develop photosensitizers with long absorption wavelengths >700. Irradiation of tumors with light in this range should allow deeper tissue penetration, which may help in treating the large and deeply seated tumors. To achieve our goal, we modified the in vivo unstable purpurin-18 and bacteriopurpurin systems, and synthesized a series of tumor-avid *N*- and *O*-alkyl- or the corresponding trifluoromethylbenzyl substituted purpurinimides (700 nm) and bacteriopurpurinimides (800 nm) with variable lipophilicity (*42, 43*). Some of the synthetic analogues showed promising in vivo activity. Interestingly, among the compounds with similar lipophilicity, the position of the substituents at various peripheral positions of the tetrapyrrolic system showed a significant difference in long-term tumor response.

* To whom correspondence should be addressed. (R.K.P.) PDT Center, Cell Stress Biology, Roswell Park Cancer Institute, Buffalo, NY 14263. Phone: 716-845-3203. Fax: 716-845-8920. E-mail: ravindra.pandey@roswellpark.org. (M.S.) Department of Nuclear Medicine, State University of New York, Buffalo, NY 14214. Phone: 716-838-5889ext. 118. Fax: 716-838-4918. E-mail: msajjad@buffalo.edu.

[†] PDT Center, Roswell Park Cancer Institute.

[‡] Department of Dermatology, Roswell Park Cancer Institute.

[§] State University of New York.

[||] Undergraduate summer student (2007), SUNY, Geneseo, NY.

10.1021/bc8003638 CCC: $40.75 © 2009 American Chemical Society
Published on Web 02/03/2009

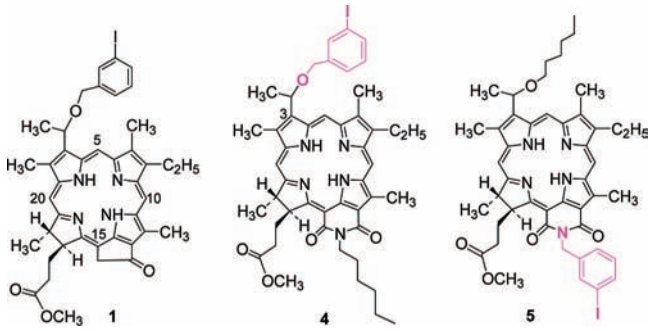

Figure 1. Structures of 3-(1′-*m*-iodobenzyloxy) pyropheophorbide **1** and the iodobenzyl purpurinimides **4** and **5** (isomers).

Herein, we report the synthesis of the iodobenzyl substituted purpurinimides **4** and **5** (positional isomers; Figure 1) and their significant difference in PDT efficacy. The comparative biodistribution properties of the corresponding ^{124}I-analogues as well as their tumor imaging (PET) abilities are also discussed.

EXPERIMENTAL PROCEEDURES

Chemistry. All chemicals were of reagent grade and used as such. Solvents were dried using standard methods. Reactions were carried out under nitrogen atmosphere and were monitored by precoated (0.20 mm) silica TLC plastic sheet (20 × 20 cm) strips (POLYGRAM SIL N-HR) and/or UV−visible spectroscopy. Silica gel 60 (70−230 mesh, Merck) was used for column chromatography. Melting points were determined on a Fisher−Johns melting point apparatus. UV−visible spectra were recorded on a Varian (Cary-50 Bio) spectrophotometer. ^{1}H NMR spectra were recorded on a Brucker AMX 400 MHz NMR spectrometer at 303 K. Proton chemical shifts (δ) are reported in parts per million (ppm) relative to $CDCl_3$ (7.26 ppm), pyridine-d_5 (7.22 ppm, most downfield), or TMS (0.00 ppm). Coupling constants (J) are reported in Hertz (Hz), and s, d, t, q, p, m, and br refer to singlet, doublet, triplet, quartet, pentet, multiplet, and broad, respectively. HRMS data were obtained from the Mass Spectroscopy facility of Michigan State University. Analytical HPLC was used to assess the purity of compounds. A Waters (Milford, MA) system including a Waters 600 Controller, a Delta 600 pump, and a 996 Photodiode Array Detector was used. A reverse phase, Symmetry C18, 5 μm, 4.6 × 150 mm column (Waters, Made in Ireland) was used under an isocratic setting of MeOH/H_2O for final compounds (**1**, **4**, **5**, and the corresponding trimethyl stannyl analogues). The solvent flow rate was kept constant at 1.00 mL/min, and the detector was set at 254, 410, 535, and 660 nm (for pyropheophorbides-*a* **1**, and its trimethyl stannyl derivative) and 254, 415, 545, and 700 nm (for purpurininimides **4**, **5**, and their trimethyl stannyl derivatives). All final products were found to be >95% pure, and their retention time is reported in the characterization section. Reactions were first carried out for nonradioactive iodine and analyzed in the above HPLC system. However, in the case of final I-124 radiolabeling HPLC data obtained from the above system were transferred to another system comprising a Chrom Tech Iso-2000 pump, Hitachi L-4000 UV detector, and a radiation detector. These detectors are connected to a computer with HP Chemstation software via an HP 35900E interface. A Bioscan system 200 imaging scanner was used for thin layer chromatography of the radiolabeled compounds.

Synthesis of 3-{1′-(3-Iodobenzyloxy)ethyl}pyropheophorbide-*a* Methyl Ester (1). It was synthesized by following our previously reported procedure (*40*). Yield: 77%. MP = 112−114 °C; analytical RP HPLC (95/5: MeOH/H_2O): t_R = 20.97min, >96%. UV−vis (MeOH): 662 (4.75 × 10^4), 536 (1.08 x10^4), 505 (1.18 × 10^4), 410 (1.45 × 10^5). ^{1}H NMR ($CDCl_3$; 400 MHz): δ 9.76, 9.55 and 8.56 (all s, 1H, meso-H); 7.76(s, 1H, ArH); 7.64 (d, J = 6.8, 1H, ArH); 7.30 (d, J = 8.0, 1H, ArH); 7.05 (t, J = 8.2, 1H, ArH); 6.00 (q, J = 6.9, 1H, 3^1-H); 5.28 (d, J = 19.8, 1H, 13^2-CH_2); 5.13 (d, J = 19.8, 1H, 13^2-CH_2); 4.70 (d, J = 12.0, 1H, OCH_2Ar); 4.56 (dd, J = 3.2,11.6, 1H, OCH_2Ar); 4.48−4.53 (m, 1H, 18-H); 4.30−4.33 (m, 1H, 17-H); 3.72 (q, J = 8.0, 2H, 8-C$\underline{H}_2$CH$_3$); 3.69, 3.61, 3.38 and 3.21 (all s, all 3H, for 17^3-CO_2CH_3 and 3 × ring CH_3); 2.66−2.74, 2.52−2.61 and 2.23−2.37 (m, 4H, 17^1-H and 17^2-H); 2.18 (dd, J = 2.8, 6.4, 3H, 3^1-CH_3); 1.83 (d, J = 8.0, 3H, 18-CH_3); 1.72 (t, J = 7.6, 3H, 8-CH$_2$C$\underline{H}_3$); 0.41 (brs, 1H, NH); −1.71 (brs, 1H, NH). HRMS for $C_{41}H_{43}N_4O_4I$: 783.2329 (calculated, M + 1); found, 783.2407. Anal. Calcd. for $C_{41}H_{43}N_4O_4I$: C, 62.91; H, 5.54; N, 7.16; I, 16.21. Found: C, 62.60; H, 5.59; N, 7.13; I16.45.

Synthesis of 3-{1′-(3-Iodobenzyloxy)ethyl}purpurin-18-*N*-hexylimide Methyl Ester (4). 30% Hydrobromic acid (HBr) in acetic acid (2 mL) was added to purpurin-18-*N*-hexylimide methyl ester (100 mg, 0.15mmol) (*23*), and the reaction was stirred at room temperature for 2 h. After evaporating the acids under high vacuum (0.1 mmHg), excess of 3-iodobenzyl alcohol (0.45 mL, 20-fold excess), dry dichloromethane (5 mL), and anhydrous potassium carbonate (40 mg) were added. The reaction mixture was stirred under nitrogen atmosphere for 45 min. It was then diluted with dichloromethane (200 mL), washed with aqueous sodium bicarbonate solution (100 mL), and then with water (2 × 200 mL). The dichloromethane layer was dried over anhydrous sodium sulfate, concentrated, and treated with diazomethane. Evaporation of the solvent gave a syrupy residue, which was chromatographed over a silica column using (1:4) ethyl acetate/hexane as eluant to remove excess 3-iodobenzylalcohol, followed by (1:1) ethyl acetate/hexane to yield 110 mg (81%) of the desired compound **4**, which is sticky in nature. Analytical HPLC (Symmetry C18; 99/1: MeOH/H_2O): t_R = 38.71 min, >96%. UV−vis (MeOH): 701(4.31 × 10^4), 545 (2.15 × 10^4), 508 (7.32 × 10^3), 414 (1.31 × 10^5). ^{1}H NMR ($CDCl_3$; 400 MHz): δ 9.72 (s, 1H, meso-H); 9.66 (s, 1H, meso-H); 8.58 (s, 1H, meso-H); 7.75 (s, 1H, ArH); 7.64 (d, J = 9.2, 1H, ArH); 7.29 (d, J = 7.2, 1H, ArH); 7.06 (dt, J = 2.4, 7.4, 1H, ArH); 5.88 (q, J = 6.2, 1H, 3^1-H); 5.41 (d, J = 8.8, 1H, 17-H); 4.68 (dd, J = 2.6,12.6, 1H, OCH_2Ar); 4.55 (dd, J = 3.2,12.0, 1H, OCH_2Ar); 4.45 (t, J = 6.8, 2H, NC$\underline{H}_2$(CH$_2$)$_4$CH$_3$); 4.37 (q, J = 7.2, 1H, 18-H); 3.84 (s, 3H, 12-CH_3); 3.68 (q, J = 7.6, 2H, 8-C$\underline{H}_2$CH$_3$); 3.56 (s, 3H, 17^2-CO_2CH_3); 3.31 (split s, 3H, 2-CH_3); 3.14 (s, 3H, 7-CH_3); 2.63−2.72 (m, 1H, 17^1-H); 2.38−2.48 (m, 1H, 17^2-H); 2.26−2.36 (m, 1H, 17^1-H); 2.12 (dd, J = 2.2, 6.6, 3H, 3^1-CH_3); 1.95−2.05 (m, 3H, 17^2-H, and NCH$_2$C$\underline{H}_2$(CH$_2$)$_3$CH$_3$); 1.77 (d, J = 7.2, 3H, 18-CH_3); 1.68 (t, J = 7.6, 3H, 8-CH$_2$C$\underline{H}_3$); 1.56−1.61 (m, 2H, N(CH$_2$)$_2$C$\underline{H}_2$(CH$_2$)$_2$-CH$_3$); 1.38−1.50 (m, 4H, N(CH$_2$)$_3$(C$\underline{H}_2$)$_2$CH$_3$); 0.95 (t, J = 7.0, 3H, N(CH$_2$)$_5$C$\underline{H}_3$); −0.14 (brs, 1H, NH); −0.19 (brs, 1H, NH). HRMS for $C_{47}H_{54}N_5O_5I$: 896.3171 (calculated, M + 1); found, 896.3241.

Synthesis of 3-{1′-(Hexyloxy)ethyl}purpurin-18-*N*-(3-iodo)-benzylimide Methyl Ester (5). Hydrobromic acid (HBr) (30%) in acetic acid (2 mL) was added to purpurin-18-*N*-(3-iodo)benzylimide methyl ester (100 mg, 0.125 mmol) (*23*), and the reaction was stirred at room temperature for 2 h. After evaporating the acids under high vacuum (0.1 mmHg), an excess of *n*-hexanol (0.5 mL, 30-fold excess), dry dichloromethane (5 mL), and anhydrous potassium carbonate (25 mg) were added to the residue. The reaction mixture was stirred under nitrogen atmosphere for 45 min. It was then diluted with dichloromethane (200 mL), washed with aqueous sodium bicarbonate solution (100 mL), and then with water (2 × 200 mL). The dichloromethane layer was dried over anhydrous sodium sulfate,

concentrated, and treated with diazomethane. Evaporation of the solvent gave a syrupy residue, which was chromatographed over a silica column using 1% acetone in dichloromethane as eluant to yield 95 mg (85%) of the desired compound **5**, which is sticky in nature. Analytical HPLC (Symmetry C18; 99/1: MeOH/H_2O): t_R = 48.97 min, >96%. UV−vis (MeOH): 700 (4.31×10^4), 545 (2.05×10^4), 508 (7.76×10^3), 414 (1.29×10^5). ^{1}H NMR ($CDCl_3$; 400 MHz): δ 9.75 (splits, 1H, meso-H); 9.62 (s, 1H, meso-H); 8.53 (s, 1H, meso-H); 8.09 (s, 1H, ArH); 7.70 (d, J = 7.6, 1H, ArH); 7.66 (d, J = 8.0, 1H, ArH); 7.60 (d, J = 7.6, 1H, ArH); 7.32 (d, J = 8.4, 1H, ArH); 7.10 (t, J = 7.8, 1H, ArH); 5.77 (q, J = 6.8, 1H, 3^1-H); 5.61 (s, 2H, NC$\underline{H}_2$Ar); 5.37(d, J = 8.4, 1H, 17-H); 4.35 (q, J = 7.2, 1H, 18-H); 3.81 (s, 3H, 12-CH_3); 3.65 (m, 4H, 8-C$\underline{H}_2CH_3$, OC$\underline{H}_2(CH_2)_4CH_3$); 3.56 (s, 3H, 17^2-$CO_2CH_3$); 3.30 (s, 3H, 2-$CH_3$); 3.18 (s, 3H, 7-$CH_3$); 2.62−2.72 (m, 3H, OCH_2-C$\underline{H}_2(CH_2)_3CH_3$ and 17^1-H); 2.30−2.45 (m, 2H, 17^2-H and 17^1-H); 2.05 (dd, J = 2.4, 6.8, 3H, 3^1-CH_3); 1.95−2.02 (m, 1H, 17^2-H); 1.70−1.80 (m, 5H, 18-CH_3 and $O(CH_2)_2C\underline{H}_2$-$(CH_2)_2CH_3$); 1.67 (t, J = 8.0, 3H, 8-$CH_2C\underline{H}_3$); 1.23 (m, 4H, $O(CH_2)_3(C\underline{H}_2)_2CH_3$); 0.78 (m, 3H, $O(CH_2)_5C\underline{H}_3$); 0.04 (brs, 1H, NH); −0.07 (brs, 1H, NH). HRMS for $C_{47}H_{54}N_5O_5I$: 896.3171 (calculated, M + 1); found, 896.3241.

Synthesis of 3-{1′-(3-Trimethylstannylbenzyloxy)ethyl}purpurin-18-*N*-hexylimide Methyl Ester (6). To a solution of 3-{1′-(3-iodobenzyloxy)ethyl}purpurin-18-*N*-hexylimide methyl ester (**4**) (15 mg, 0.017 mmol) in dry THF (10 mL) were added hexamethylditin (15 μL, 0.072 mmol) and bis-(triphenylphosphine)palladium (II) dichloride (5 mg), and the reaction mixture was stirred at 60 °C for 2 h. The reaction mixture was rotavapoed to dryness, and the crude product was purified over a silica gel column using CH_2Cl_2 as eluant to yield 12 mg (77%) of title compound **6**. Analytical HPLC (Symmetry C18; 99/1: MeOH/H_2O): t_R = 48.19 min, >95%. ^{1}H NMR ($CDCl_3$; 400 MHz): δ 9.73 (s, 1H, meso-H); 9.66 (s, 1H, meso-H); 8.56 (s, 1H, meso-H); 7.42 (m, 2H, ArH); 7.34 (m, 2H, ArH); 5.90 (m, 1H, 3^1-H); 5.41 (dd, J = 2.6, 9.0, 1H, 17-H); 4.76 (dd, J = 4.4,11.6, 1H, OCH_2Ar); 4.55 (dd, J = 1.2,12.0, 1H, OCH_2Ar); 4.45(m, 2H, NC$\underline{H}_2(CH_2)_4CH_3$); 4.36 (q, J = 7.3, 1H, 18-H); 3.85 (s, 3H, 12-CH_3); 3.68 (q, J = 7.6, 2H, 8-C$\underline{H}_2CH_3$); 3.55 (s, 3H, 17^2-CO_2CH_3); 3.31 (split s, 3H, 2-CH_3); 3.11 (s, 3H, 7-CH_3); 2.63−2.72 (m, 1H, 17^1-H); 2.38−2.48 (m, 1H, 17^2-H); 2.26−2.36 (m, 1H, 17^1-H); 2.12 (dd, J = 2.4, 6.8, 3H, 3^1-CH_3); 1.95−2.05 (m, 3H, 17^2-H and $NCH_2C\underline{H}_2(CH_2)_3CH_3$); 1.77 (d, J = 7.2, 3H, 18-CH_3); 1.68(t, J = 7.6, 3H, 8-$CH_2C\underline{H}_3$); 1.61(m, 2H, $N(CH_2)_2C\underline{H}_2(CH_2)_2CH_3$);1.38−1.50 (m, 4H, $N(CH_2)_3(C\underline{H}_2)_2CH_3$); 0.95 (t, J = 7.2, 3H, $N(CH_2)_5C\underline{H}_3$); 0.18 (s, 9H, $Sn(CH_3)_3$); −0.09 (brs, 1H, NH); −0.16 (brs, 1H, NH).

Synthesis of 3-{1′-(Hexyloxy)ethyl}purpurin-18-*N*-(3-trimethylstannyl)benzylimide Methyl Ester (7). It was synthesized following the procedure described above for **6** from the respective compound 3-{1′-(hexyloxy)ethyl}purpurin-18-*N*-(3-iodo)benzylimide methyl ester (**5**). Yield: 75%. Analytical HPLC (Symmetry C18; 99/1: MeOH/H_2O): t_R = 53.13 min, >95%. ^{1}H NMR($CDCl_3$; 400 MHz): δ 9.75 (splits, 1H, meso-H); 9.64 (s, 1H, meso-H); 8.53 (s, 1H, meso-H); 7.89 (s, 1H, ArH); 7.66 (d, J = 8.0, 1H, ArH); 7.39 (d, J = 7.2, 1H, ArH); 7.32 (m, H, ArH); 5.78 (q, J = 6.6, 1H, 3^1-H); 5.68 (q, J = 13.8, 2H, NCH_2Ar); 5.38 (d, J = 8.0, 1H, 17-H); 4.35 (m, 1H, 18-H); 3.83 (s, 3H, 12-CH_3); 3.57−3.68 (m, 4H, 8-C$\underline{H}_2CH_3$, OC$\underline{H}_2(CH_2)_4CH_3$); 3.54 (s, 3H, 17^2-$CO_2CH_3$); 3.30 (s, 3H, 2-$CH_3$); 3.18 (s, 3H, 7-$CH_3$); 2.62−2.72 (m, 3H, $OCH_2C\underline{H}_2$-$(CH_2)_3CH_3$ and 17^1-H); 2.30−2.45 (m, 2H, 17^2-H and 17^1-H); 2.05 (dd, J = 2.6, 6.6, 3H, 3^1-CH_3); 1.95−2.02 (m, 1H, 17^2-H); 1.73 (d,J=7.6,3H,18-CH_3); 1.67 (t, J = 7.6, 3H, 8-$CH_2C\underline{H}_3$); 1.25 (m, 6H, $O(CH_2)_2(C\underline{H}_2)_3CH_3$); 0.78 (m, 3H, $O(CH_2)_5C\underline{H}_3$); 0.27 (s, 9H, $Sn(CH_3)_3$); −0.01(brs, 1H, NH); −0.13 (brs, 1H, NH).

Synthesis of 3-{1′-(Methoxy)ethyl}purpurin-18-*N*-(3-iodo)-benzylimide Methyl Ester (10). It was prepared by following the method described for compound **5** except the intermediate bromo-derivative was reacted with methanol, instead of *n*-hexanol. Pure product was obtained by column chromatography over a silica column using 1% acetone in dichloromethane as eluant. Analytical HPLC (Symmetry C18; 99/1: MeOH/H_2O): t_R = 31.42 min, >98%. UV−vis (CH_2Cl_2): 700 (4.31×10^4), 545 (2.12×10^4), 414 (1.29×10^5). ^{1}H NMR ($CDCl_3$; 400 MHz): δ 9.66 (s, 1H, meso-H); 9.64 (s, 1H, meso-H); 8.54 (s, 1H, meso-H); 8.08 (s, 1H, ArH); 7.70 (d, J = 8.0, 1H, ArH); 7.60 (d, J = 8.0, 1H, ArH); 7.10 (t, J = 8.0, 1H, ArH); 5.73 (q, J = 6.9, 1H, 3^1-H); 5.63 (s, 2H, NC$\underline{H}_2$Ar); 5.38 (dd, J = 1.6, 8.4, 1H, 17-H); 4.35 (q, J = 7.2, 1H, 18-H); 3.84 (s, 3H, 12-CH_3); 3.67 (q, J = 7.4, 2H, 8-C$\underline{H}_2CH_3$); 3.56 (s, 3H, 17^2-CO_2CH_3); 3.54 (d, J = 2.8, 3H, OCH_3); 3.32 (s, 3H, 2-CH_3); 3.19 (s, 3H, 7-CH_3); 2.62−2.72 (m, 1H, 17^1-H); 2.30−2.45 (m, 2H, 17^2-H and 17^1-H); 2.06 (dd, J = 2.2, 6.6, 3H, 3^2-CH_3); 1.92−2.02 (m, 1H, 17^2-H); 1.76 (d, J = 6.0, 3H, 18-CH_3); 1.68 (t, J = 7.6, 3H, 8-$CH_2C\underline{H}_3$); 0.03 (brs, 1H, NH); −0.07 (brs, 1H, NH). HRMS for $C_{42}H_{44}N_5O_5I$: 826.2387 (calculated, M + 1); found, 826.2470.

Synthesis of 3-{1′-(Methoxy)ethyl}purpurin-18-*N*-(3-trimethylstannyl)benzylimide Methyl Ester (11). The title compound was synthesized following the procedure described above for compound **7** from the respective compound 3-{1′-(methoxy)ethyl}purpurin-18-*N*-(3-iodo)benzylimide methyl ester (**10**). Yield: 80%. Analytical HPLC (Symmetry C18; 99/1: MeOH/H_2O): t_R = 35.79 min, >98%. ^{1}H NMR ($CDCl_3$; 400 MHz): δ 9.68 (s, 1H, meso-H); 9.65 (s, 1H, meso-H); 8.56 (s, 1H, meso-H); 7.90 (s, 1H, ArH); 7.68 (d, J = 7.6, 1H, ArH); 7.40 (d, J = 6.8, 1H, ArH); 7.34 (t, J = 7.2, 1H, ArH); 5.60−5.80 (m, 3H, 3^1-H and NC$\underline{\mathbf{H}}_2$Ar); 5.38 (dd, J = 2.0, 6.8, 1H, 17-H); 4.36 (q, J = 7.2, 1H, 18-H); 3.84 (s, 3H, 12-CH_3); 3.67 (q, J = 7.4, 2H, 8-C$\underline{H}_2CH_3$); 3.56 (s, 3H, 17^2-CO_2CH_3); 3.55 (d, J = 2.8, 3H, OCH_3); 3.33 (s, 3H, 2-CH_3); 3.20(s, 3H, 7-CH_3); 2.62−2.72 (m, 1H, 17^1-H); 2.30−2.50 (m, 2H, 17^2-H and 17^1-H); 2.08 (dd, J = 2.2, 6.6, 3H, 3^2-CH_3); 1.92−2.02 (m, 1H, 17^2-H); 1.76 (d, J = 7.2, 3H, 18-CH_3); 1.68 (t, J = 7.8, 3H, 8-$CH_2C\underline{H}_3$); 0.28 (s, 9H, $Sn(CH_3)_3$); −0.03 (brs, 1H, NH); −0.12(brs, 1H, NH).

Radioactive Labeling. ^{124}I-analogues of **4**, **5**, and **10** were prepared from the corresponding trimethylstannyl analogues **6**, **7**, and **11**, respectively, by following the procedure as described below for the ^{124}I-analogue of compound **4**.

Synthesis of ^{124}I-Labeled Analogue of 3-{1′-(3-iodobenzyloxy)ethyl}purpurin-18-*N*-hexylimide Methyl Ester (4). The trimethyltin analogue **6** (50 μg) was dissolved in 50 μL of 5% acetic acid in methanol. Then, 100 μL of 5% acetic acid in methanol was added to $Na^{124}I$ in 10 μL of 0.1 N NaOH. The two solutions were mixed, and an IODOGEN bead (Pierce Biotechnology, Inc., Rockford, IL 61106) was added. The reaction mixture was incubated at room temperature for 15 min, the iodobead was removed, and the reaction mixture was injected on an HPLC column (Symmetry C18 5 μm, 150 × 4.6 mm), which was eluted with an isocratic 99/1 MeOH/H_2O at a flow rate of 1 mL/min. The UV detector was set at 254 nm wavelength. The labeled product (**4**) eluted at 46.7 min was collected, and the solvent was evaporated to dryness under a stream of N_2 at 60 °C. The product was formulated in saline containing 10% ethanol for in vivo experiments. RadioTLC confirmed the radiochemical purity (>95%) of the product. A standard curve was generated between peak area versus mass by injecting known mass of carrier **4** onto the column. The mass

associated with the labeled product was calculated by relating the peak area of the UV absorbance peak of **4** in the labeled product to the standard curve. The specific activity was obtained by dividing the activity of the labeled product collected by the calculated mass in micromoles. Specific activity of the radio labeled product was >1 Ci/μmol. The radiochemical yield was found to be 40%.

PET Imaging. Mice were imaged in the micropet FOCUS 120, a dedicated 3D small-animal PET scanner (Concorde Microsystems Incorporated) at State University of New York at Buffalo (south campus) under the Institutional Animal Care and Use Committee (IACUC) guidelines. The C3H mice were subcutaneously injected with 3×10^5 RIF cells in 30 μL complete α- MEM (into the axilla), and tumors were grown until they reached 4−5 mm in diameter (approximately 5 days). All tumored C_3H mice were injected via the tail vein 50−200 μCi of **1**, **8**, **9**, and **12**.

After 24, 48, 72, and 96 h postinjection, the mice were anesthetized by inhalation of isoflurane/oxygen, placed head first prone for imaging, and the acquisition time was set for 30 min. Radioiodine uptake by the thyroid or stomach was not blocked.

Biodistribution Studies. All studies were performed as per IACUC guidelines. The mice were injected with 50−200 μCi of **1**, **8**, **9**, and **12** via tail vein, and 3 or 4 mice each at 24, 48, 72, and 96 h time interval were sacrificed and body organs (tumor, heart, liver, spleen, kidney, lung, muscle, etc.) removed immediately. After weighing, the amount of radioactivity in the tumor (50−150 mg), body organs, and blood was measured by a gamma well counter. Radioactivity uptake was calculated as the percentage of the injected dose per gram of the tissue (%ID/g). Statistical analyses and data (%ID/g vs time point) were plotted using Microsoft Excel.

In Vitro Photosensitizing Efficacy. The photosensitizing activity of **4**, **5**, and **10** was determined in the RIF tumor cell line. The RIF tumor cells were grown in α-MEM with 10% fetal calf serum, L-glutamine, penicillin, streptomycin, and neomycin. Cells were maintained in 5% CO_2, 95% air, and 100% humidity. For determining the PDT efficacy, these cells were plated in 96-well plates at a density of 5×10^3 cells/well in complete media. After an overnight incubation at 37 °C, the photosensitizers were added at variable concentrations and incubated at 37 °C for 24 h in the dark. Prior to light treatment, the cells were replaced with drug-free complete media. Cells were then illuminated with an argon-pumped dye laser set at 700 nm at a dose rate of 3.2 mW/cm^2 for 0−6 J/cm^2. After PDT, the cells were incubated for 48 h at 37 °C in the dark. Following the 48 h incubation, 10 μL of 5.0 mg/mL solution of 3-[4,5-dimethylthiazol-2-yl]-2,5-diphenyltetra-zoliumbromide (MTT) dissolved in PBS (Sigma, St. Louis, MO) was added to each well. After a 4 h incubation at 37 °C, the MTT and media were removed, and 100 μL DMSO was added to solubilize the formazin crystals. The 96-well plate was read on a microtiter plate reader (Miles Inc. Titertek Multiscan Plus MK II) at an absorbance of 560 nm. The results were plotted as percent survival of the corresponding dark (drug no light) control for each compound tested, and each experiment was done with 4 replicate wells.

In Vivo Photosensitizing Efficacy. The in vivo PDT experiments were performed in C3H mice when tumors grew to 4−5 mm in diameter (approximately day 5 post inoculation). The day before laser light treatment, all hair was removed from the inoculation site, and the mice were injected intravenously with varying photosensitizer concentrations. At 24 h postinjection, the mice were restrained without anesthesia in Plexiglas holders and then treated with laser light from an argon-pumped dye laser tuned to emit drug-activating wavelengths as set by the monochromator (665 nm for **1**, 705 nm for **4**, **5**, and **10**). The compounds were treated with light under similar treatment parameters under the fluence rate of 75 mW/cm^2 with a light dose of 135 J/cm^2. The mice were observed daily for signs of weight loss, necrotic scabbing, or tumor regrowth. If tumor growth appeared, the tumors were measured using two orthogonal measurements L and W (perpendicular to L), and the volumes were calculated using the formula $V = (L \times W^2)/2$ and recorded. Mice were considered cured if there was no sign of tumor regrowth by day 60 post-PDT treatment.

RESULTS AND DISCUSSION

Chemistry. For the synthesis of desired compounds, methylpheophorbide-*a*, isolated from *Spirulina pacifica* was converted into purpurin-18 methyl ester by following the known methodology (*44*). For the preparation of 3-(1′-*m*-iodobenzyloxyethyl) analogue **4**, it was first reacted with *n*-hexylamine, the intermediate amide derivative (isomeric mixture) so obtained on intramolecular cyclization under basic reaction conditions, and gave **2** in excellent yield. Further reaction of purpurinimide **2** with HBr/AcOH at room temperature produced the intermediate bromo-analogue, which was dried under vacuum and immediately reacted with *m*-iodobenzyl alcohol to afford **4** as a mixture of methyl ester and the corresponding carboxylic acid, which on treating with diazomethane produced the methyl ester derivative **4** in >70% yield. For the synthesis of the related isomer **5**, the purpurin-18 methyl ester was first refluxed with *m*-iodobenzyl amine, and the intermediate **3** thus obtained on reacting with 1-hexanol by following the approach depicted in Scheme 1 gave the desired photosensitizer in modest yield. Compound **10** was synthesized from **3** following the methodology outlined for **5** and by replacing *n*-hexanol with methanol. For the preparation of the corresponding ^{124}I-analogues **8**, **9**, and **12**, the trimethylstannyl substituted analogues **6**, **7**, and **11** on electrophilic aromatic iodination with Na^{124}I in the presence of iodogen beads afforded the ^{124}I-labeled purpurinimides **8**, **9**, and **12** with >95% radioactive specificity. The purity of the final compounds (**4**, **5**, and **10**) was confirmed by NMR (experimental section) and HPLC analysis (see Supporting Information).

Biological Studies. *Comparative Imaging and Biodistribution of ^{124}I-Labeled Purpurinimide Isomers **8**, **9**, and **12**.* The PET imaging and biodistribution study of the radioactive purpurinimides **8** were performed in C3H mice bearing RIF tumors. In a typical experiment, 12 tumored mice were injected with each compound (50−200 μCi), and 3 mice/group were imaged at 24, 48, 72, and 96 h for 30 min with microPET (Siemens Preclinical Solutions, Knoxville, TN), and finally sacrificed after the 96 h time point. Mice used in longitudinal imaging received higher activity (150−200uCi) compared to the mice used in biodistribution alone (50−100 uCi).

For the biodistribution studies, selected organs [tumor, muscle, kidney, lungs, intestine (gut), stomach, spleen, heart, and lung] were removed, weighed, and measured in a gamma well counter. The tail was also taken into consideration in biodistribution studies to determine the accuracy of the injection. Interestingly, the two isomers showed a remarkable difference in imaging and biodistribution characteristics. The imaging and biodistribution data also correlated well with each other. Between the two isomers, isomer **8** (*O*-iodobenzyloxyethyl purpurinimide) had a higher background (liver and spleen), and the tumor was not visualized. Although the tumor was also not significantly visualized with isomer **9** (*N*-(3-iodobenzyl purpurinimide), compared to compound **8**, the background images were not as high (Figure 2). If compared with lead compound **1** (^{124}I-labeled), purpurinimide **9** also exhibited higher tumor uptake at 72 and 96 h PI, and unfortunately, higher background uptake negated tumor visualization (Figure 3). However, in

Scheme 1[a]

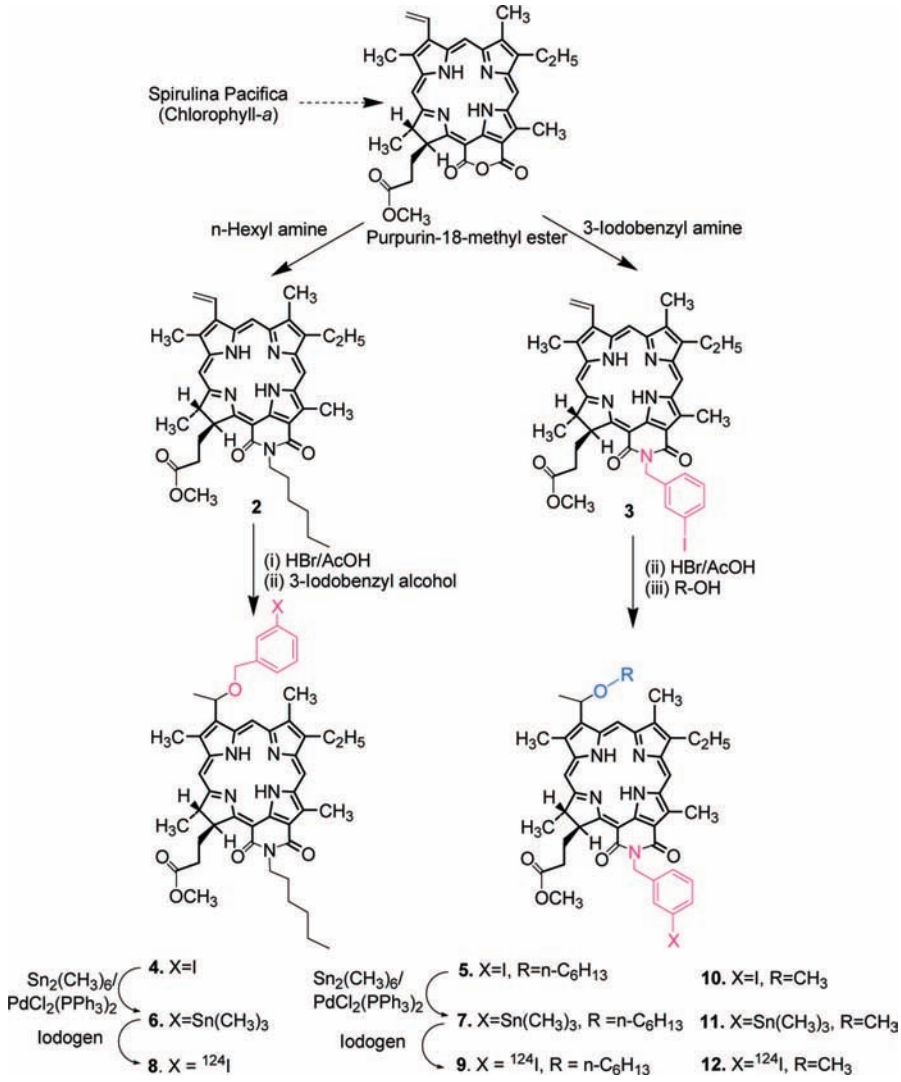

[a] Purpurinimides **4**, **5** (isomers), **10** and the corresponding ^{124}I-analogues **8**, **9**, and **12**, respectively.

comparison with the ^{124}I- analogue of pyropheophorbide **1**, both purpurinimide isomers **8** and **9** showed exceptionally high liver (32-fold and 8-fold, respectively) and spleen uptake (85-fold and 3-fold, respectively) at 24 h PI. The significantly high uptake of purpurinimides **8** and **9** in the liver and spleen resulted in nonvisualization of the tumor and thus produced a poor contrast in whole body PET-imaging. Among isomers **8** and **9**, isomer **9** was selected for further modifications. The 1′-hexyloxyethyl group present at the top half of the molecule (position-3) was replaced with a methyl substituent. The resulting product **10**, with a reduced overall lipophilicity, was labeled with ^{124}I (compound **12**) and the PET imaging biodistribution data were performed in C3H mice bearing RIF tumors. The results obtained from the biodistribution studies suggest that the reduction in the overall lipophilicity of the molecule substantially reduces the uptake of purpurinimide **12** in the spleen and liver and therefore enhances its tumor imaging capability at 96 h postinjection. The biodistribution and whole-body PET imaging results obtained from compounds **1**, **8**, **9**, and **12** suggest that for an efficient tumor imaging agent it is of utmost important to have a high uptake of the contrast agent in the tumor with a faster clearance profile from other organs. This characteristic possibly explains the improved imaging capability of lead compound **1** over that of the other agents studied so far.

Comparative in Vitro PDT Efficacy. The in vitro phototosensitizing ability of the structural isomers **4** and **5** was compared

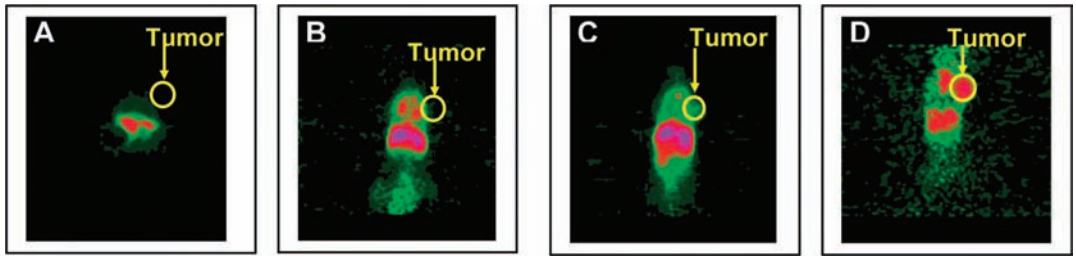

Figure 2. Comparative microPET emission images (coronal view) of C3H mice with RIF tumors at 48 h PI of ^{124}I-124 labeled purpurinimides **8** (A), **9** (B), **12** (C), and the lead compound **1** (D).

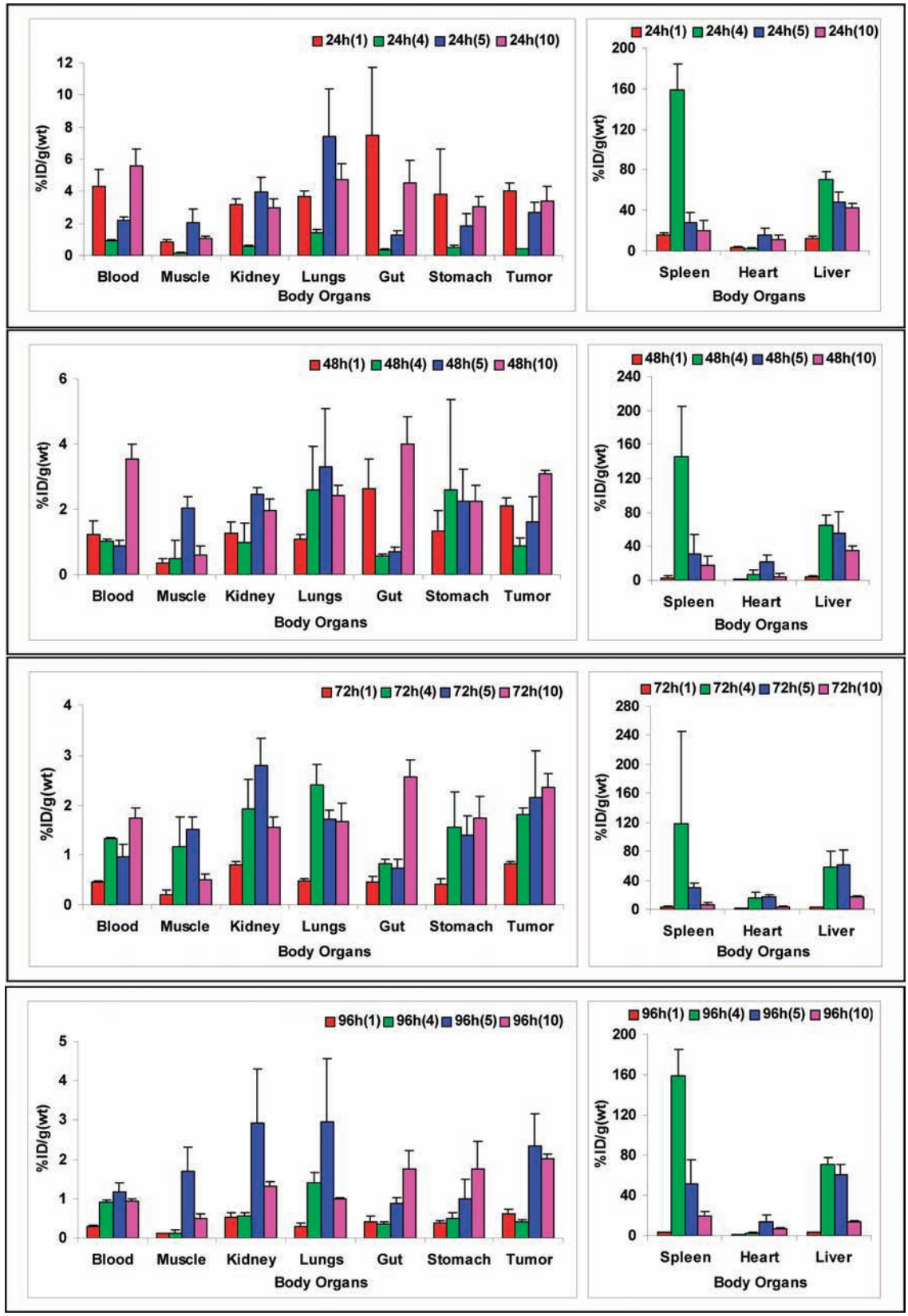

Figure 3. Comparative biodistribution of (^{124}I-labeled) pyropheophorbide-**1** and the purpurinimides-**8**, **9**, and **12** at 24, 48, 72, and 96 h PI in C3H mice bearing RIF tumors (4 mice/time point). Note: compounds **8**, **9**, and **12** are ^{124} L-labeled **4**, **5**, and **10**, respectively.

at variable experimental conditions (MTT assay; see Experimental Procedures) in RIF cells. Both isomers were ineffective in vitro at lower light and drug doses. However, as can be seen from Figure 4, at 24 h postincubation and higher light dose (6.0 J/cm^2, drug concentration (1.0 μM and higher), isomer **5** was more effective than the structural isomer **4**. Reducing the overall lipophilicity of **5**, by replacing the O-hexyl group at position-3 with an O-methyl group **10** produced enhanced efficacy over isomers **4** and **5**.

In Vivo PDT Efficiency of Pyropheophorbide-a **1** *and Purpurinimide Isomers 4 and 5.* The in vivo PDT efficacy of isomers **4** and **5** was determined at three doses (1.0, 2.0, and

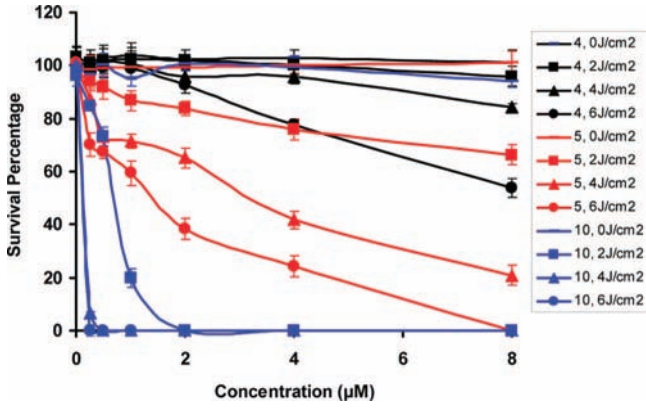

Figure 4. Comparative in vitro photosensitizing activity of **4**, **5**, and **10** at variable drug concentrations and light doses in RIF tumor cells at 24 h post incubation.

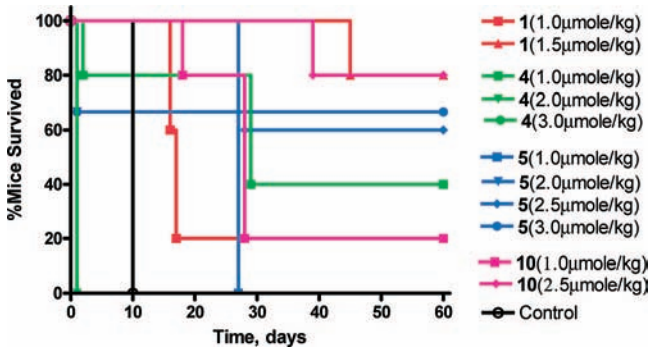

Figure 5. Kaplan−Meier plot for compounds **1**, **4**, **5**, and **10** at various doses. C3H mice bearing RIF tumor (5 mice/group) on the shoulder. Light dose: 135 J/cm^2, 75 mW/cm^2 mice/group.

3.0 μmol/kg) and was compared with lead compound **1** in C3H mice bearing RIF tumors (5 mice/group). The tumors were exposed to light (λ_{max} = 705 nm for **4** and **5**; 665 nm for **1**, 135 J/cm^2, 75 mW/cm^2) at 24 h postinjection. The tumor regrowth was measured daily. From the results summarized in Figure 5, it can be seen that compound **4**, having the iodobenzyl group at the top half of the molecule, at a dose of 1.0 μmol/kg gave a good response (2/5 mice were tumor free on day 60). At the same dose, the isomer **5** in which the iodobenzyl group is present at the lower half of the molecule did not gave any significant long-term tumor response. Under the same treatment parameters, compound **1** produced some tumor response; however, it was more effective at a dose of 1.5 μmol/kg, and 4/5 mice were tumor free on day 60. Among isomers **4** and **5**, at higher doses (e.g., 2 μmol/kg) compound **4** was toxic, and all mice died within 24 h PDT treatment (Figure 5), whereas compound **5** did not show any significant activity. However, at higher doses (2.5 and 3.0 μmol/kg) it was found to be quite effective.

To investigate the effect of the overall lipophilicity in PDT efficacy, the hexyl ether group present at position-3 in **5** was replaced with a methyl ether substituent **10**, and the biological efficacy of both the analogues was compared at doses of 1.0 and 2.5 mmol/kg. The tumors were treated with a laser light (λ_{max} = 705 nm, 135 J/cm^2, 75 mW/cm^2) at 24 h postinjection. From the results summarized in Figure 5, it can be seen that among the two analogues, methyl ether derivative **10** showed enhanced activity than the corresponding hexyl ether analogue **5**; however, it was at least 1.5-fold less effective over lead compound **1** derived from methyl pyropheophorbide-*a*. For an accurate reflection of the actual therapeutic response, further studies with a larger group of mice under variable treatment parameters are currently in progress.

CONCLUSIONS

Our results suggest that the nature and the position of the substituents in purpurinimides make a significant difference in tumor uptake, which also reflects their imaging and PDT potential. Between the two structural isomers **4** and **5**, compound **5** containing an N-iodobenzyl group introduced at the bottom half of the purpurinimide showed improved imaging and phototherapeutic abilities than **4** where the iodobenzyl group was present at position-3 of the molecule. Decreasing the overall lipophilicity of compound **5** by substituting the hexyl ether with a methyl ether group (compound **10**) further improved its PET imaging ability and PDT efficacy. However, for establishing a correlation between the overall lipophilicity and tumor imaging potential, it is necessary to investigate a series of compounds within a particular system, and these studies are currently in progress.

ACKNOWLEDGMENT

The financial support from the NIH (CA 114053, CA 127369, and CA 55791), the Oncologic Foundation of Buffalo, Roswell Park Alliance Foundation, and the shared resources of the RPCI support grant (P30CA16056) is highly appreciated.

Supporting Information Available: The ^{1}H NMR spectra of compounds **4**−**7**, **10**, **11**, and the HPLC chromatograms of compounds **1**, **4**, **5**, and **10**. This material is available free of charge via the Internet at http://pubs.acs.org.

LITERATURE CITED

(1) Massoud, T. F., and Gambhir, S. S. (2003) Molecular imaging in living subjects: seeing fundamental biological processes in a new light. *Gene Dev. 17*, 545–580.

(2) Verel, I., Vissser, G. W. M., and van Dongen, G. A. (2005) The promise of immuno-PET in radioimmunotherapy. *J. Nucl. Med. 46*, 164S–171S.

(3) Pentlow, K. S., Graham, M. C., Lambrecht, R. M., Daghighian, F., Bacharach, S. L., Bendriem, B., Finn, R. D., Jordan, K., Kalaigian, H., Karp, J. S., Robeson, W. R., and Larson, S. M. (1996) Quantitative imaging of iodine-124 with PET. *J. Nucl. Med. 37*, 1557–1562.

(4) González-Trotter, D. E., Manjeshwar, R. M., Doss, M., Shaller, C., Robinson, M. K., Tandon, R., Adams, G. P., and Adler, L. P. (2004) Quantitation of small-animal 124I activity distributions using a clinical PET/CT scanner. *J. Nucl. Med. 45*, 1237–1244.

(5) Sundaresan, G., Yazaki, P. J., Shively, J. E., Finn, R. D., Larson, S. M., Raubitschek, A. A., Williams, L. E., Chatziioannou, A. F., Gambhir, S. S., and Wu, A. M. (2003) 124I-Labeled engineered anti-CEA minibodies and diabodies allow high-contrast, antigen-specific small-animal PET imaging of xenografts in athymic mice. *J. Nucl. Med. 44*, 1962–1969.

(6) Zanzonico, P., O'Donoghue, J., Chapman, J. D., Schneider, R., Cai, S., Larson, S., Wen, B., Chen, Y., Finn, R., Ruan, S., Gerweck, L., Humm, J., and Ling, C. (2004) Iodine-124-labeled iodo-azomycin-galactoside imaging of tumor hypoxia in mice with serial microPET scanning. *Eur. J. Nucl. Med. Mol. Imag. 31*, 117–128.

(7) Soghomonyan, S. A., Doubrovin, M., Pike, J., Luo, X., Ittensohn, M., Runyan, J. D., Balatoni, J., Finn, R., Tjuvajev, J. G., Blasberg, R., and Bermudes, D. (2005) Positron emission tomography (PET) imaging of tumor-localized Salmonella expressing HSV1-TK. *Cancer Gene Ther. 12*, 101–108.

(8) Robinson, M. K., Doss, M., Shaller, C., Narayanan, D., Marks, J. D., Adler, L. P., González- Trotter, D. E., and Adams, G. P.

(2005) Quantitative immuno-positron emission tomography imaging of HER2-Positive tumor xenografts with an Iodine-124 labeled anti-HER2 diabody. *Cancer Res. 65*, 1471–1478.

(9) Dekker, B., Keen, H., Lyons, S., Disley, L., Hastings, D., Reader, A., Ottewell, P., Watson, A., and Zweit, J. (2005) MBP-annexin V radiolabeled directly with iodine-124 can be used to image apoptosis in vivo using PET. *Nucl. Med. Biol. 32*, 241–252.

(10) Pinchuk, A. N., Rampy, M. A., Longino, M. A., Skinner, R. W., Gross, M. D., Weichert, J. P., and Counsell, R. E. (2006) Synthesis and structure-activity relationship effects on the tumor avidity of aadioiodinated phospholipid ether analogues. *J. Med. Chem. 49*, 2155–2165.

(11) Veach, D. R., Namavari, M., Beresten, T., Balatoni, J., Minchenko, M., Djaballah, H., Finn, R. D., Clarkson, B., Gelovani, J. G., Bornmann, W. G., and Larson, S. M. (2005) Synthesis and in vitro examination of [^{124}I]-, [^{125}I]- and [^{131}I]-2-(4-iodophenylamino) pyrido[2,3-*d*]pyrimidin-7-one radiolabeled Abl kinase inhibitors. *Nucl. Med. Biol. 32*, 313–321.

(12) Shaul, M., Abourbeh, G., Jacobson, O., Rozen, Y., Laky, D., Levitzki, A., and Mishani, E. (2004) Synthesis and in vitro examination of [^{124}I]-, [^{125}I]- and [^{131}I]-2-(4-iodophenylamino) pyrido[2,3-*d*]pyrimidin-7-one radiolabeled Abl kinase inhibitors. *Bioorg. Med. Chem. 12*, 3421–3429.

(13) Schmidt, M. H., Reichert, K. W. II., Ozker, K., Meyer, G. A., Donohoe, D. L., Bajic, D. M., Whelan, N. T., and Whelan, H. T. (1999) Preclinical evaluation of benzoporphyrin derivative combined with a light-emitting diode array for photodynamic therapy of brain tumors. *Pediatr. Neurosurg. 30*, 225–231.

(14) Whelan, H. T., Kras, L. H., Ozker, K., Bajic, D., Schmidt, M. H., Liu, Y., Trembath, L. A., Uzum, F., Meyer, G. A., Segura, A. D., and Collier, B. D. (1994) Selective incorporation of In-111-labeled photofrin(tm) by glioma tissue in-vivo. *J. Neuro-Oncol. 22*, 7–13.

(15) Origitano, T. C., Karesh, S. M., Henkin, R. E., Halama, J. R., and Reichman, O. H. (1993) Photodynamic therapy for intracranial neoplasms - investigations of photosensitizer uptake and distribution using In-111 photofrin-II single photon-emission computed-tomography scans in humans with intracranial neoplasms. *Neurosurgery 32*, 357–364.

(16) Nakajima, S., Yamauchi, H., Sakata, I., Hayashi, H., Yamazaki, K., Maeda, T., Kubo, Y., Samejima, N., and Takemura, T. (1993) In-111 labeled mn-metalloporphyrin for tumor imaging. *Nucl. Med. Biol. 20*, 231–237.

(17) Subbarayan, M., Shetty, S. J., Srivastava, T. S., Noronha, O. P., Samuel, A. M., and Mukhtar, H. (2001) Water-soluble Tc-99m-labeled dendritic novel porphyrins tumor imaging and diagnosis. *Biochem. Biophys. Res. Commun. 281*, 32–36.

(18) Babbar, A. K., Singh, A. K., Goel, H. C., Chauhan, U. P., and Sharma, R. K. (2000) Evaluation of Tc-99m-labeled Photosan-3, a hematoporphyrin derivative, as a potential radiopharmaceutical for tumor scintigraphy. *Nucl. Med. Biol. 27*, 587–592.

(19) Schuitmaker, J. J., Feitsma, R. I., Journée-De Korver, J. G., Dubbelman, T. M., and Pauwels, E. K. 1993) Tissue distribution of bacteriochlorin-a labeled with Tc-99m-pertechnetate in hamster greene melanoma. *Int. J. Radiat. Biol. 64*, 451–458.

(20) Lu, X. M., Fischman, A. J., Stevens, E., Lee, T. T., Strong, L., Tompkins, R. G., and Yarmush, M. L. (1992) Sn-chlorin e6 antibacterial immunoconjugates - an in vitro and in vivo analysis. *J. Immunol. Methods 156*, 85–99.

(21) Ma, B., Li, G., Kanter, P., Lamonica, D., Grossman, Z., and Pandey, R. K. (2003) N_2S_2-Tc-99m conjugates as tumor imaging agents: synthesis and biodistribution studies. *J. Porphyrins Phthalocyanines 1*, 500–507.

(22) Westerman, P., Glanzmann, T., Andrejevic, S., Braichotte, D. R., Forrer, M., Wagnieres, G. A., Monnier, P., van den Bergh, H., Mach, J. P., and Folli, S. (1998) Long circulating half-life and high tumor selectivity of the photosensitizer meta-tetrahydroxyphenylchlorin conjugated to polyethylene glycol in nude mice grafted with a human colon carcinoma. *Int. J. Cancer 76*, 842–850.

(23) Vrouenraets, M. B., Visser, G. W., Stewart, F. A., Stigter, M., Oppelaar, H., Postmus, P. E., Snow, G. B., and van Dongen, G. A. (1999) Development of meta-tetrahydroxyphenylchlorin-monoclonal antibody conjugates for photoimmunotherapy. *Cancer Res. 59*, 1505–1513.

(24) Whelpton, R., Michael-Titus, A. T., Jamdar, R. P., Abdillahi, K., and Grahn, M. F. (1996) Distribution and excretion of radiolabeled temoporfin in a murine tumor model. *Photochem. Photobiol. 63*, 885–891.

(25) Lawrence, D. S., Gibson, S. L., Nguyen, M. L., Whittemore, K. R., Whitten, D. G., and Hilf, R. (1995) Photosensitization and tissue distribution studies of the picket fence porphyrin, 3,1-tpro, a candidate for photodynamic therapy. *Photochem. Photobiol. 61*, 90–98.

(26) Wilson, B. C., and VanLier, J. E. (1989) Radiolabeled photosensitizers for tumor imaging and photodynamic therapy. *J. Photochem. Photobiol. B 3*, 459–463.

(27) Moore, J. V., Waller, M. L., Zhao, S., Dodd, N. J., Acton, P. D., Jeavons, A. P., and Hastings, D. L. (1998) Feasibility of imaging photodynamic injury to tumours by high-resolution positron emission tomography. *Eur. J. Nucl. Med. 25*, 1248–1254.

(28) Lapointe, D., Brasseur, N., Cadorette, J., La Madeleine, C., Rodrigue, S., van Lier, J. E., and Lecomte, R. (1999) High-Resolution PET imaging for in vivo monitoring of tumor response after photodynamic therapy in mice. *J. Nucl. Med. 40*, 876–882.

(29) Berard, V., Rousseau, J. A., Cadorette, J., Hubert, L., Bentourkia, M., van Lier, J. E., and Lecomte, R. (2006) Dynamic imaging of transient metabolic processes by small-animal PET for the evaluation of photo sensitizers in photodynamic therapy of cancer. *J. Nucl. Med. 47*, 1119–1126.

(30) Dong, D., Dubeau, L., Bading, J., Nguyen, K., Luna, M., Yu, H., Gazit-Bornstein, G., Gordon, E. M., Gomer, C., Hall, F. L., Gambhir, S. S., and Lee, A. S. (2004) Spontaneous and controllable activation of suicide gene expression driven by the stress-inducible Grp78 promoter resulting in eradication of sizable human tumors. *Hum. Gene Ther. 15*, 553–561.

(31) Sugiyama, M., Sakahara, H., Sato, K., Harada, N., Fukumoto, D., Kakiuchi, T., Hirano, T., Kohno, E., and Tsukada, H. (2004) Evaluation of 3′-deoxy-3′-F-18-fluorothymidine for monitoring tumor response to radiotherapy and photodynamic therapy in mice. *J. Nucl. Med. 45*, 1754–1758.

(32) Subbarayan, M., Hafeli, U. O., Feyes, D. K., Unnithan, J., Emancipator, S. N., and Mukhtar, H. (2003) A simplified method for preparation of Tc-99m-annexin V and its biologic evaluation for in vivo imaging of apoptosis after photodynamic therapy. *J. Nucl. Med. 44*, 650–656.

(33) Henderson, B. W., and Dougherty, T. J. (1992) How does photodynamic therapy work. *Photochem. Photobiol. 55*, 145–157.

(34) Dougherty, T. J., Gomer, C. J., Henderson, B. W., Jori, G., Kessel, D., Korbelik, M., Moan, J., and Peng, Q. (1998) Photodynamic therapy. *J. Natl. Cancer Inst. 90*, 889–905.

(35) Dolmans, D. E., Fukumura, D., and Jain, R. K. (2003) Photodynamic therapy for cancer. *Nat. Rev. Cancer 3*, 380–387.

(36) Pandey, R. K., Goswami, L. N., Chen, Y., Gryshuk, A. L., Missert, J. R., Oseroff, A., and Dougherty, T. J. (2006) Nature: A rich source for developing multifunctional agents. Tumor-imaging and photodynamic therapy. *Lasers Surg. Med. 38*, 445–467.

(37) Pandey, S. K., Chen, Y., Zawada, R. H., Oseroff, A., and Pandey, R. K. (2006) Utility of tumor-avid photosensitizers in developing bifunctional agents for tumor imaging and/or phototherapy. Proceedings of SPIE, the International Society for Optical Engineering. *Proc SPIE 6139*, 6139051−613905−7.

(38) Chen, Y., Gryshuk, A. L., Achilefu, S., Ohulchansky, T., Potter, W., Zhong, T., Morgan, J., Chance, B., Prasad, P. N.,

Henderson, B. W., Oseroff, A., and Pandey, R. K. (2005) A novel approach to a bifunctional photosensitizer for tumor imaging and phototherapy. *Bioconjugate Chem. 16*, 1264.

(39) Li, G., Slansky, A., Dobhal, M. P., Goswami, L. N., Graham, A., Chen, Y., Kanter, P., Alberico, R. A., Spernyak, J., Morgan, J., Mazurchuk, R., Oseroff, A., Grossman, Z., and Pandey, R. K. (2005) Chlorophyll-a analogues conjugated with aminobenzyl-DTPA as potential bifunctional agents for magnetic resonance imaging and photodynamic therapy. *Bioconjugate Chem. 16*, 32–42.

(40) Pandey, S. K., Gryshuk, A. L., Sajjad, M., Zheng, X., Chen, Y., Abouzeid, M. M., Morgan, J., Charamisinau, I., Nabi, H. A., Oseroff, A., and Pandey, R. K. (2005) Multimodality agents for tumor imaging (PET, fluorescence) and photodynamic therapy. A possible "see and treat" approach. *J. Med. Chem. 48*, 6286–6295.

(41) Pandey, S. K., Sajjad, M., Chen, Y., Batt, C., Nabi, H. A., Oseroff, A., and Pandey, R. K. (2007) Potential of chlorophyll based photosensitizer for detecting matastasis and photodynamic therapy, 54th Society of Nuclear Medicine Annual Meeting, Washington, DC, June 2−6.

(42) Gryshuk, A. L., Chen, Y., Goswami, L. N., Pandey, S. K., Missert, J. R., Ohulchanskyy, T., Potter, W., Prasad, P. N., Oseroff, A., and Pandey, R. K. (2007) Structure-activity relationship among purpurinimides and bacteriopurpurinimides: Trifluoromethyl substituent enhanced the photosensitizing efficacy. *J. Med. Chem. 50*, 1754–1767.

(43) Gryshuk, A. L., Graham, A., Pandey, S. K., Potter, W. R., Missert, J. R., Oseroff, A., Dougherty, T. J., and Pandey, R. K. (2002) A first comparative study of purpurinimide-based fluorinated vs. nonfluorinated photosensitizers for photodynamic therapy. *Photochem. Photobiol. 76*, 555–559.

(44) Zheng, G., Potter, W. R., Camacho, S. H., Missert, J. R., Wang, G., Bellnier, D. A., Henderson, B. W., Rodgers, M. A., Dougherty, T. J., and Pandey, R. K. (2001) Synthesis, photophysical properties, tumor uptake, and preliminary in vivo photosensitizing efficacy of a homologous series of 3-(1′-alkyloxy)ethyl-3-devinylpurpurin-18-N-alkylimides with variable lipophilicity. *J. Med. Chem. 44*, 1540–1559.

BC8003638

SUPPORTING INFORMATION

Compared to Purpurinimides, the Pyropheophorbide Containing an Iodobenzyl Group showed Enhanced PDT Efficacy and Tumor Imaging (^{124}I-PET) Ability

Suresh K. Pandey[1], Munawwar Sajjad[3,*], Yihui Chen[1], Anupam Pandey[1,¶]
Joseph R. Missert[1], Carrie Batt[1], Rutao Yao[3], Hani A. Nabi[3],
Allan R. Oseroff[2] and Ravindra K. Pandey[1,*]

[1]PDT Center, Cell Stress Biology and [2]Department of Dermatology
Roswell Park Cancer Institute, Buffalo, NY 14263
[3]Department of Nuclear Medicine,
State University of New York, Buffalo, NY 14214

Contents:

S1: Title page
S2: NMR spectrum of compound **10**
S3: NMR spectrum of compound **11**
S4: NMR spectrum of compound **5**
S5: NMR spectrum of compound **7**
S6: NMR spectrum of compound **4**
S7: NMR spectrum of compound **6**
S8: HPLC chromatogram of compound **1**
S9: HPLC chromatogram of compound **4**
S10: HPLC chromatogram of compound **5**
S11: HPLC chromatogram of compound **10**
S12: HPLC chromatograms of I-124 labeled compounds **8, 9** and **12.**

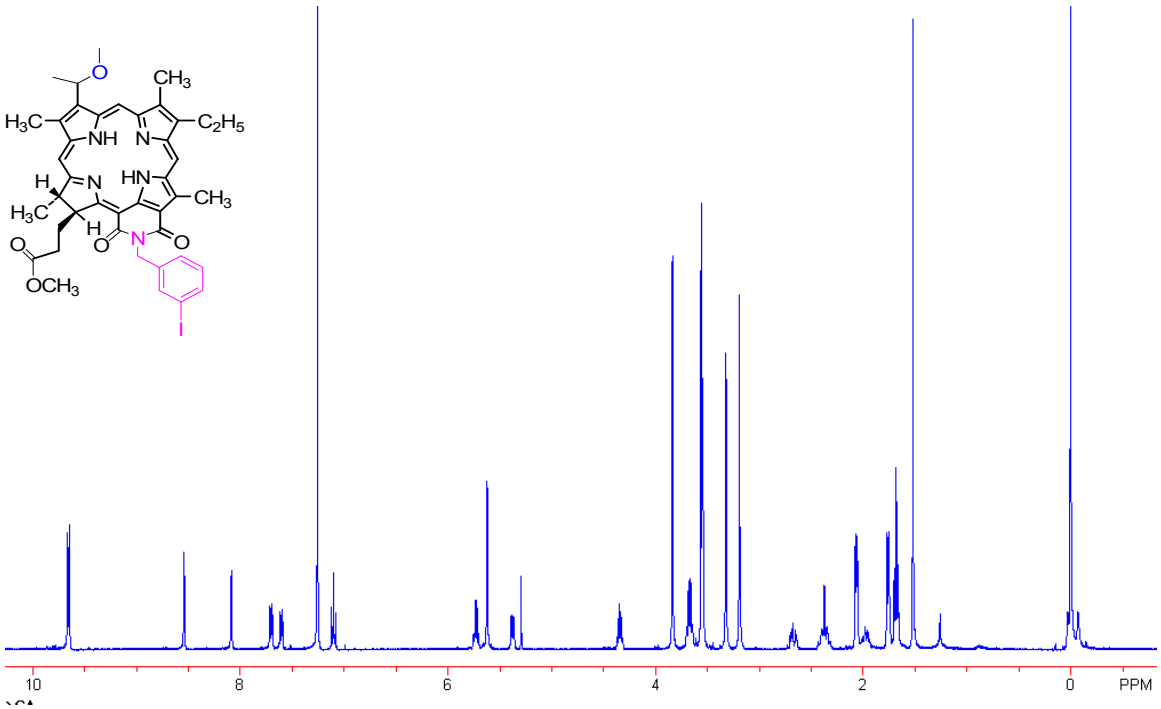
O
CH3
H3C
NH
N
C2H5
H
N
HN
CH3
H3C
H
O
N
O
O
OCH3
I
10
8
6
4
2
0
PPM

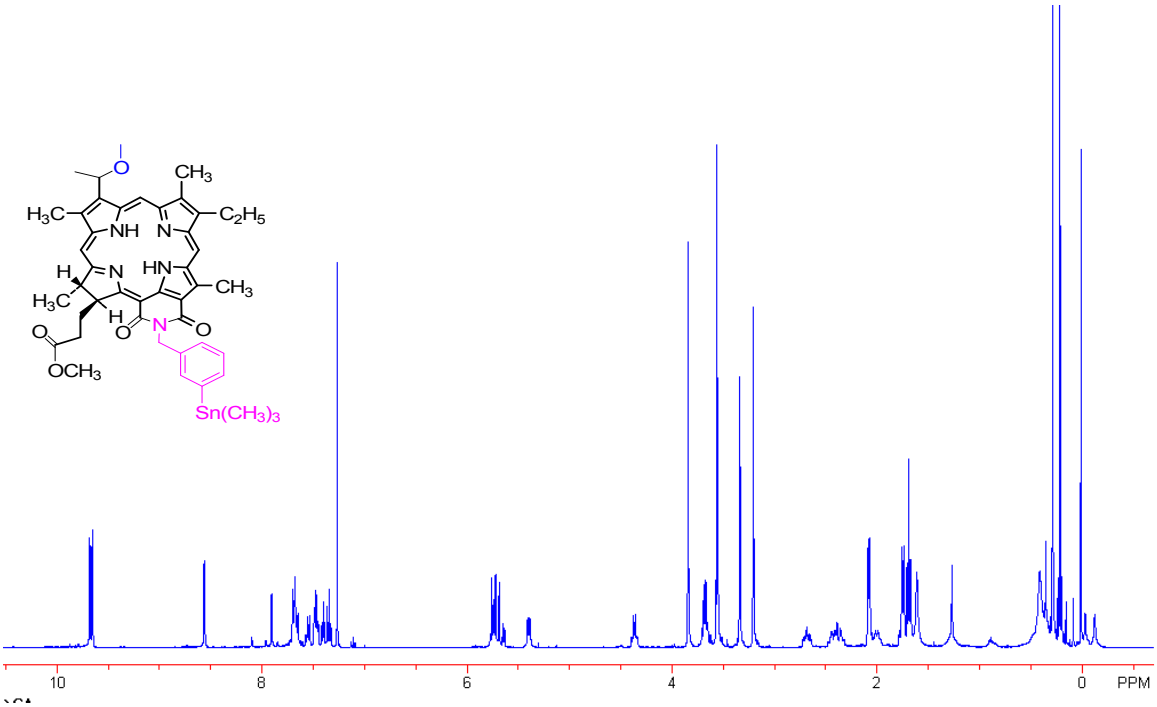
O
CH3
H3C
C2H5
NH
N
H
N
HN
CH3
H3C
H
O
N
O
O
OCH3
Sn(CH3)3
10
8
6
4
2
0
PPM

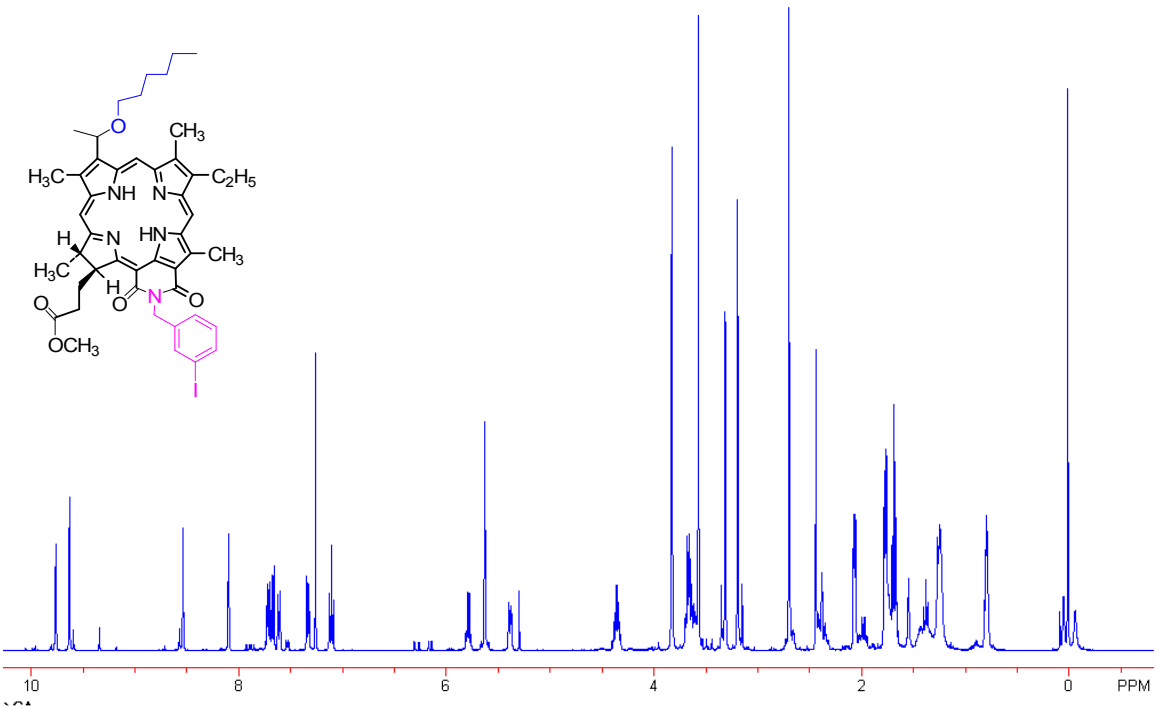
O
CH3
H3C
C2H5
NH
N
H
N
HN
CH3
H3C
H
O
O
N
O
O
OCH3
I
10
8
6
4
2
0
PPM

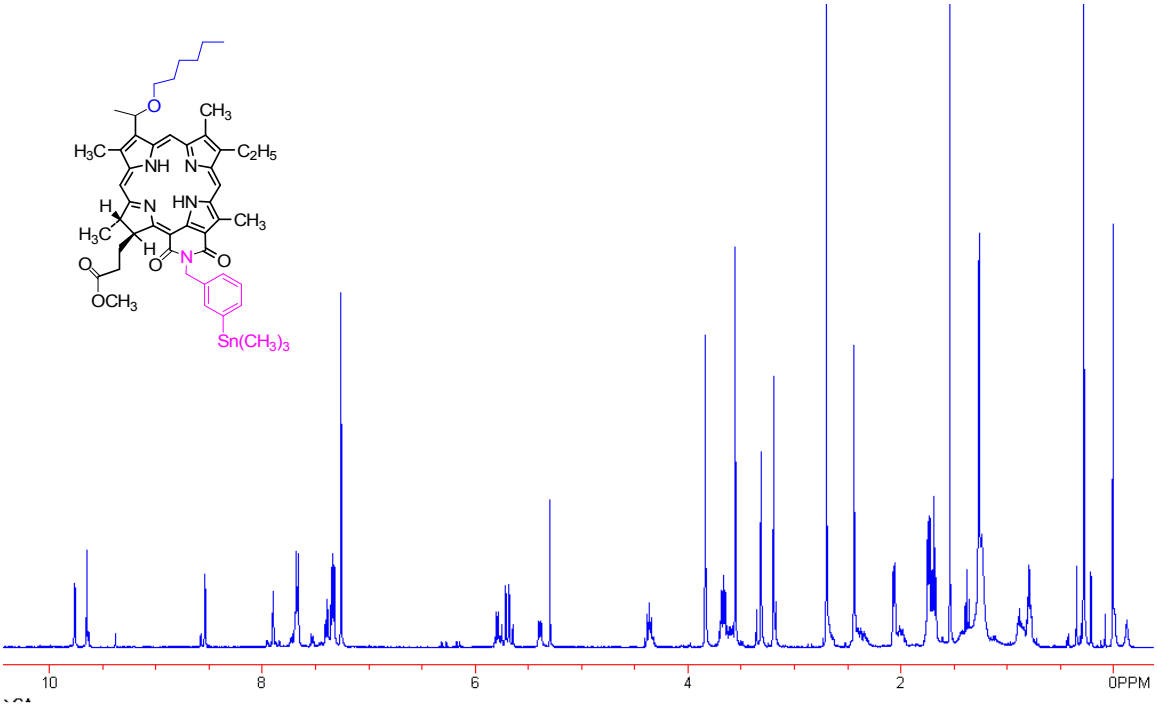
O
CH3
H3C
NH
N
C2H5
H
N
HN
CH3
H3C
H
O
N
O
O
OCH3
Sn(CH3)3
10
8
6
4
2
0PPM

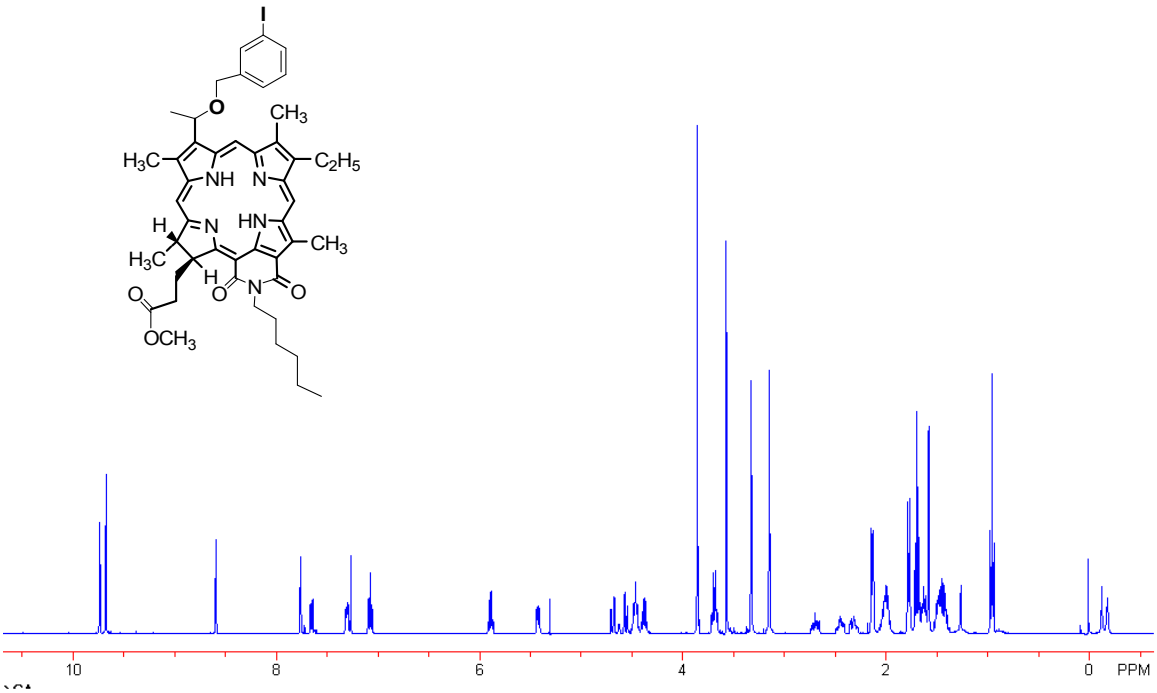
I
O
CH3
H3C
C2H5
NH
N
H
N
HN
CH3
H3C
H
O
N
O
O
OCH3
10
8
6
4
2
0
PPM

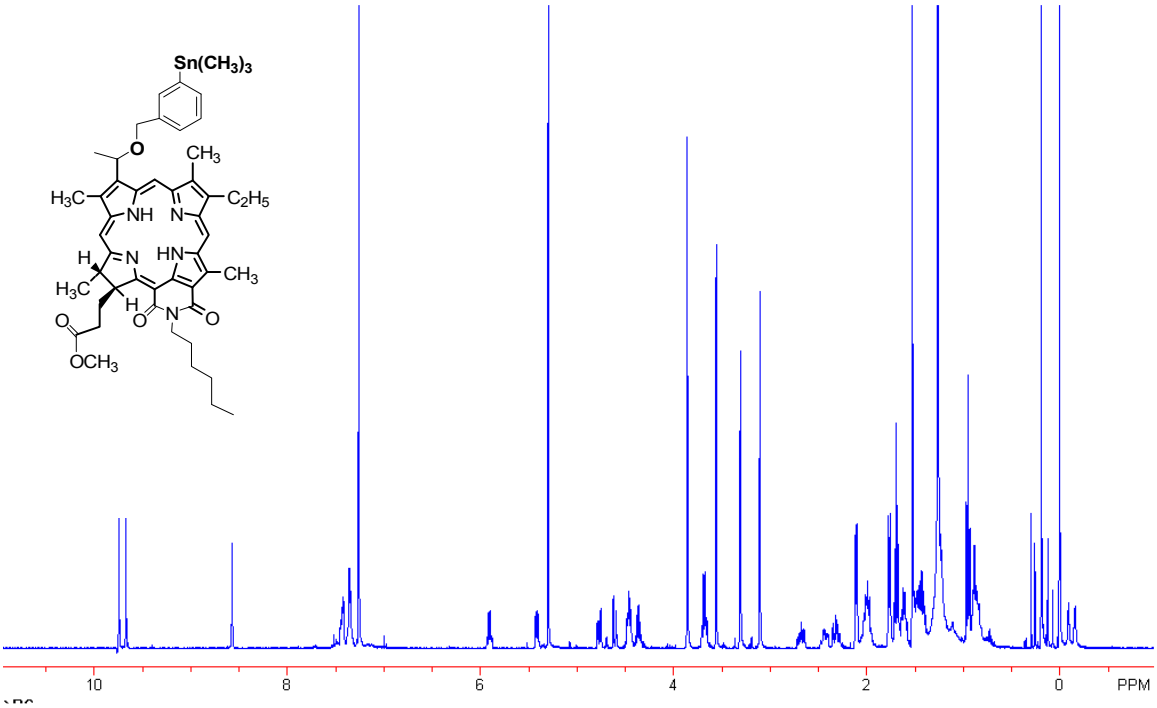
Sn(CH3)3
O
CH3
H3C
NH
N
C2H5
H
N
HN
CH3
H3C
H
O
N
O
O
OCH3
10
8
6
4
2
0
PPM

HPLC system: Waters (Milford, MA) system including waters 600 Controller, Delta 600 pump and 996 Photodiode Array Detector was used. Reverse phase, Symmetry® C18, 5 µm, 4.6 x 150 mm column was used under isocratic setting. The eluting solvent for all the compounds is pure MeOH.

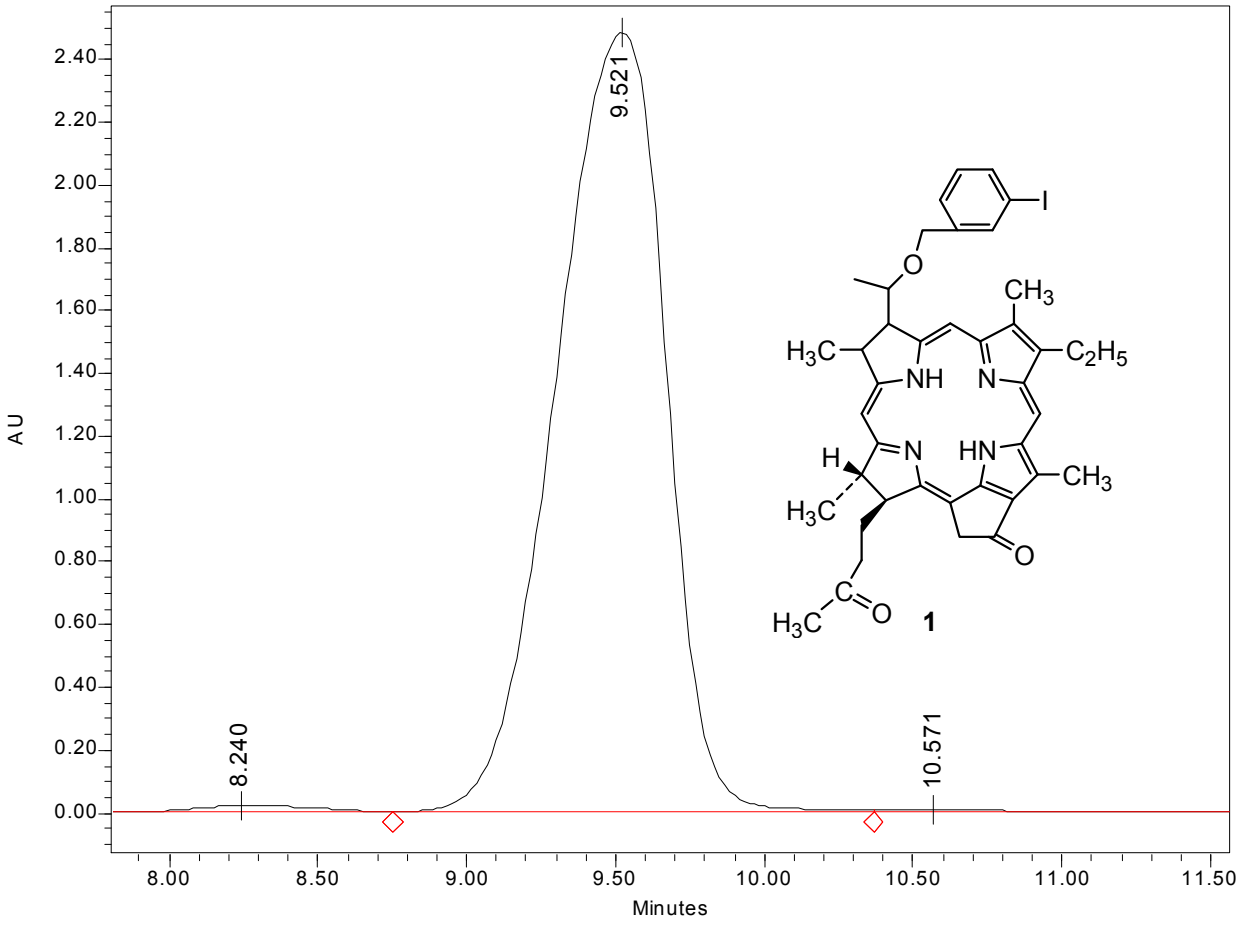

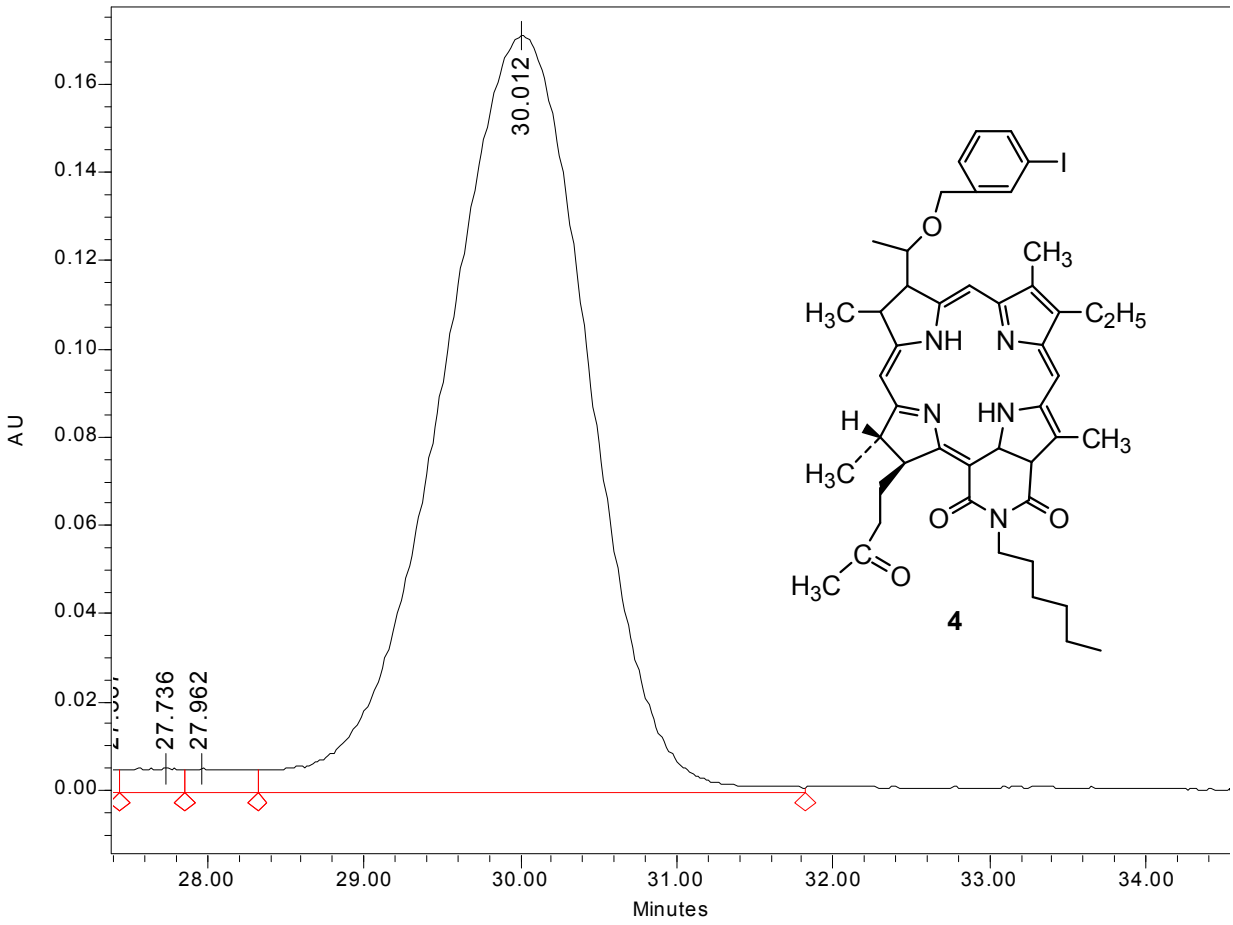
30.012
27.736
27.962
AU
0.16
0.14
0.12
0.10
0.08
0.06
0.04
0.02
0.00
28.00
29.00
30.00
31.00
32.00
33.00
34.00
Minutes
I
O
CH3
H3C
NH
N
C2H5
H
N
HN
CH3
H3C
O
N
O
C
O
H3C
4

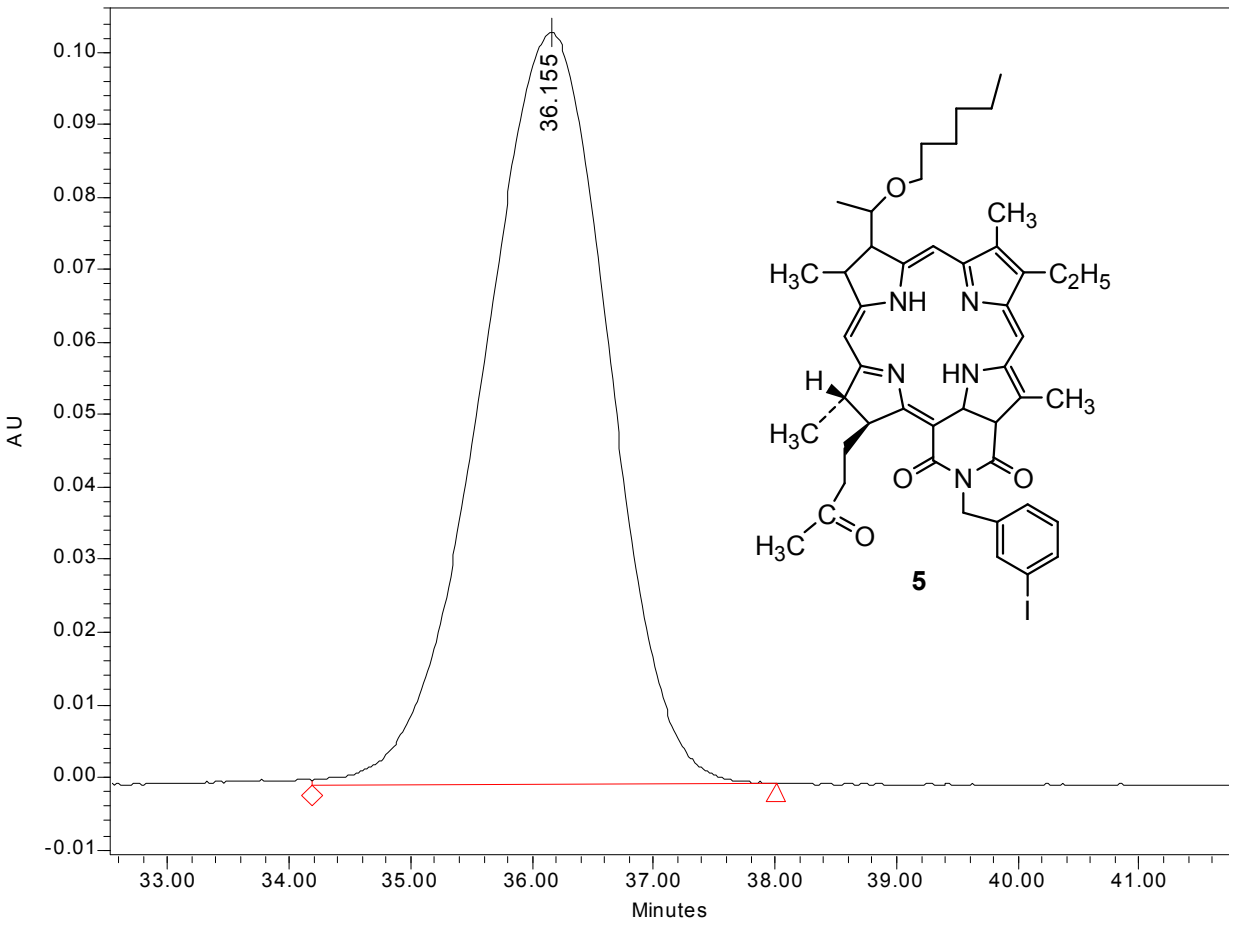
36.155
AU
0.10
0.09
0.08
0.07
0.06
0.05
0.04
0.03
0.02
0.01
0.00
-0.01
33.00
34.00
35.00
36.00
37.00
38.00
39.00
40.00
41.00
Minutes
O
CH3
H3C
C2H5
NH
N
H
N
HN
CH3
H3C
O
N
O
C
O
H3C
I

5

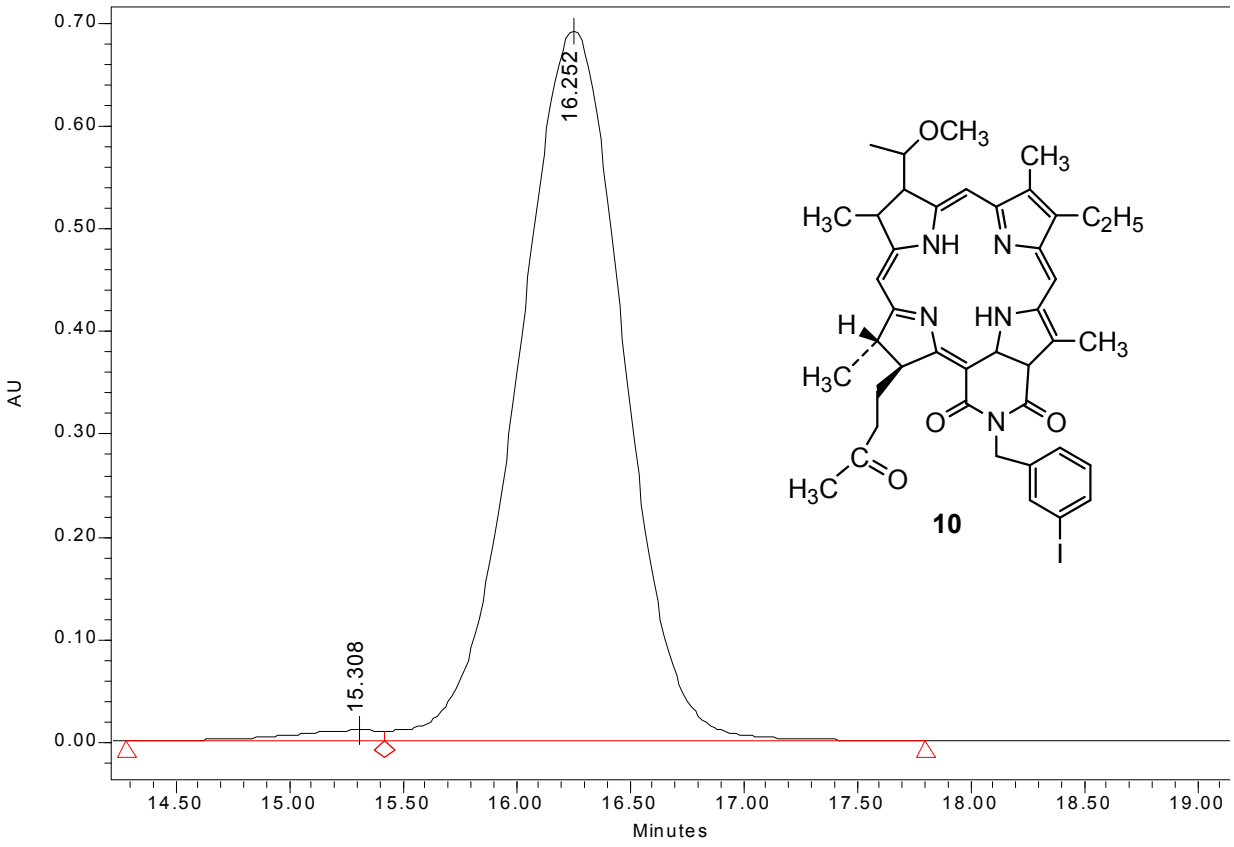
0.70
0.60
0.50
0.40
0.30
0.20
0.10
0.00
AU
16.252
15.308
14.50
15.00
15.50
16.00
16.50
17.00
17.50
18.00
18.50
19.00
Minutes
OCH3
CH3
H3C
C2H5
NH
N
H
N
HN
CH3
H3C
O
N
O
C
O
H3C
10
I

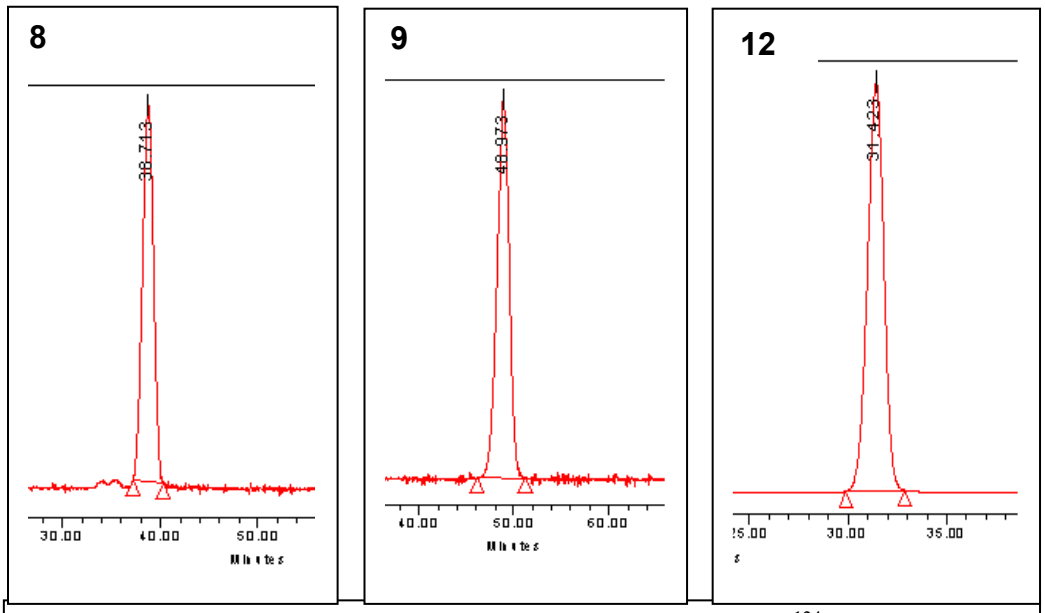

Figure : Radio- HPLC chromatograms showing the purity of the ^{124}I-labeled purpurinimides **8, 9** and **12.**

Note:

The difference in the retention times between the labeled and non-labeled compounds is due to the difference of the size of the HPLC column and the polarity of the eluting solvents.

Bioconjugate Chemistry 20th Anniversary

Subscriber access provided by SHEMYAKIN-OVCHINNIKOV INST

Article

Poly(*N*,*N*-dimethylacrylamide)-Coated Maghemite Nanoparticles for Stem Cell Labeling

Michal Babic#, Daniel Hora#k, Pavla Jendelova#, Kater#ina Glogarova#, Vi#t Herynek, Miroslava Trchova#, Katari#na Likavc#anova#, Petr Lesny#, Emil Pollert, Milan Ha#jek, and Eva Sykova#

Bioconjugate Chem., **2009**, 20 (2), 283-294• DOI: 10.1021/bc800373x • Publication Date (Web): 14 January 2009

Downloaded from http://pubs.acs.org on May 15, 2009

More About This Article

Additional resources and features associated with this article are available within the HTML version:

- Supporting Information
- Access to high resolution figures
- Links to articles and content related to this article
- Copyright permission to reproduce figures and/or text from this article

View the Full Text HTML

ACS Publications
High quality. High impact.

Bioconjugate Chemistry is published by the American Chemical Society. 1155 Sixteenth Street N.W., Washington, DC 20036

Poly(*N*,*N*-dimethylacrylamide)-Coated Maghemite Nanoparticles for Stem Cell Labeling

Michal Babič,[†,‡] Daniel Horák,*[,†,‡] Pavla Jendelová,[‡,§] Kateřina Glogarová,[§] Vít Herynek,[‡,||] Miroslava Trchová,[†] Katarína Likavčanová,[§] Petr Lesný,[‡,§] Emil Pollert,[⊥] Milan Hájek,[‡,||] and Eva Syková[‡,§]

Institute of Macromolecular Chemistry, Academy of Sciences of the Czech Republic, Heyrovský Sq. 2, 162 06 Prague 6, Czech Republic, Center for Cell Therapy and Tissue Repair, Charles University, V Úvalu 84, 150 06 Prague 5, Czech Republic, Institute of Experimental Medicine, Academy of Sciences of the Czech Republic, Vídeňská 1083, 142 20 Prague 4, Czech Republic, Institute for Clinical and Experimental Medicine, Vídeňská 1958/9, 140 21 Prague 4, Czech Republic, and Institute of Physics, Academy of Sciences of the Czech Republic, Cukrovarnická 10, 162 53 Prague 6, Czech Republic. Received September 3, 2008; Revised Manuscript Received November 13, 2008

Maghemite (γ-Fe_2O_3) nanoparticles were obtained by the coprecipitation of Fe(II) and Fe (III) salts with ammonium hydroxide followed by oxidation with sodium hypochlorite. Solution radical polymerization of *N*,*N*-dimethylacrylamide (DMAAm) in the presence of maghemite nanoparticles yielded poly(*N*,*N*-dimethylacrylamide) (PDMAAm)-coated maghemite nanoparticles. The presence of PDMAAm on the maghemite particle surface was confirmed by elemental analysis and ATR FTIR spectroscopy. Other methods of nanoparticle characterization involved scanning and transmission electron microscopy, atomic adsorption spectroscopy (AAS), and dynamic light scattering (DLS). The conversion of DMAAm during polymerization and the molecular weight of PDMAAm bound to maghemite were determined by using gas and size-exclusion chromatography, respectively. The effect of ionic 4,4′-azobis(4-cyanovaleric acid) (ACVA) initiator on nanoparticle morphology was elucidated. The nanoparticles exhibited long-term colloidal stability in water or physiological buffer. Rat and human bone marrow mesenchymal stem cells (MSCs) were labeled with uncoated and PDMAAm-coated maghemite nanoparticles and with Endorem as a control. Uptake of the nanoparticles was evaluated by Prussian Blue staining, transmission electron microscopy, T_2-MR relaxometry, and iron content analysis. Significant differences in labeling efficiency were found for human and rat cells. PDMAAm-modified nanoparticles demonstrated a higher efficiency of intracellular uptake into human cells in comparison with that of dextran-modified (Endorem) and unmodified nanoparticles. In gelatin, even a small number of labeled cells changed the contrast in MR images. PDMAAm-coated nanoparticles provided the highest T_2 relaxivity of all the investigated particles. In vivo MR imaging of PDMAAm-modified iron oxide-labeled rMSCs implanted in a rat brain confirmed their better resolution compared with Endorem-labeled cells.

INTRODUCTION

Recently, superparamagnetic iron oxide nanoparticles have found widespread application in medicine, in particular as contrast agents in magnetic resonance imaging (MRI) (*1*). Contrast agents in MRI improve the detection and characterization of lesions by changing the signal intensity of target tissues when compared with the surrounding tissue (*2*). Understanding the interactions between the nanoparticles and cells is crucial for improving their behavior in vivo and in vitro. The direct use of nanoparticles as in vivo MRI contrast agents results in their biofouling in the blood plasma and the formation of aggregates that are quickly sequestered by cells of the reticular endothelial system (RES) such as macrophages. Both small particle size and surface chemical structures are key parameters determining the blood half-life in the circulation, opsonization, biokinetics, and the biodistribution of magnetic nanoparticles (*3–5*). It is therefore essential to engineer the surface of the iron oxide to minimize biofouling and the aggregation of the particles under physicochemical conditions (i.e., high salt and protein concentrations) for long periods. Surface modifications of magnetic iron oxide nanoparticles with biocompatible polymers are potentially beneficial for preparing MR contrast agents for in vivo applications. Such particles can circulate in the plasma for long periods by escaping uptake by the RES. Iron oxide nanoparticles coated with dextran and its derivates, such as Feridex (Endorem) and Resovist, are commercially available. Iron oxide nanoparticles also show potential for in vitro cell labeling followed by in vivo MRI tracking, an approach that is being investigated for stem cell therapy (*6*, *7*). Dextran-coated agents are, however, insufficiently taken up by the cells during cultivation; consequently, modifications of the iron oxide surface are attempted in order to increase the internalization of the nanoparticles. One promising approach toward increasing the local concentration of the nanoparticles in cells is to conjugate them with targeting molecules that have a high affinity for tumor cells (*8–10*). Target-specific molecules, including monoclonal antibodies (*11*), proteins (*12*), peptides, and folic acid (*10*), have been investigated to increase the site-specific accumulation of MR contrast agents in tumor cells. Several transfection agents have been suggested to facilitate the effective magnetic labeling of cells by endocytosis into endosomes (*13*). These are mostly cationic, positively charged compounds (*14*). Superparamagnetic

* To whom correspondence should be addressed. E-mail: horak@imc.cas.cz.

[†] Institute of Macromolecular Chemistry, Academy of Sciences of the Czech Republic.

[‡] Charles University.

[§] Institute of Experimental Medicine, Academy of Sciences of the Czech Republic.

[||] Institute for Clinical and Experimental Medicine.

[⊥] Institute of Physics, Academy of Sciences of the Czech Republic.

10.1021/bc800373x CCC: $40.75 © 2009 American Chemical Society
Published on Web 01/14/2009

iron oxide nanoparticles have thus been incorporated into hemoglobin within red cells, short human immunodeficiency virus-transactivator transcription (TAT) proteins (*15*), polyamines (polycationic poly(L-lysine) (PLL) (*16*)), magnetodendrimers (*17*), and antigen-specific internalizing monoclonal antibodies (*18*). The complexing of PLL with iron oxide occurs through electrostatic interactions of the negatively charged iron oxide nanoparticles with the polycation, allowing for the efficient incorporation of iron oxide nanoparticles into endosomes for magnetic cell labeling. A disadvantage of PLL-modified iron oxides is, however, that they aggregate in the presence of some electrolytes.

In our previous reports, the efficiency of cellular uptake was investigated following D-mannose and PLL modification of the iron oxide surface (*19*, *20*). These systems were relatively stable in cell culture media; however, their further modification with antibodies, enzymes, or proteins, was difficult. In an attempt to design a novel coating of iron oxide nanoparticles that would not only ensure their very good colloidal stability but also enable the subsequent covalent attachment of highly specific biomolecules (antibodies, enzymes, peptides, etc.), PDMAAm was selected. Its advantage consists in the easy formation of homogeneous networks and copolymers with various functional monomers (*21*). Our preliminary biological experiments confirmed not only the nontoxicity of the PDMAAm coating but also its ability to enhance cellular uptake. In this study, PDMAAm coating of iron oxide particles was investigated in more detail utilizing in vitro cell labeling followed by MR cell tracking. As a model, rat and human mesenchymal stem cells (rMSCs and hMSCs) were labeled with PDMAAm-coated nanoparticles, and nanoparticle internalization into cells was visualized with light and TEM microscopy. In addition, the effect of PDMAAm-coated iron oxide nanoparticles on cell viability and labeling efficiency was quantified. Moreover, MR relaxometry of labeled cells was used to measure relaxation times, which are responsible for contrast enhancement in MR images.

EXPERIMENTAL SECTION

Materials. *N*,*N*-Dimethylacrylamide (DMAAm; Aldrich, Milwaukee, USA) was distilled (56 °C/266 Pa). 4,4′-Azobis(4-cyanovaleric acid) (ACVA), $FeCl_2 \cdot 4H_2O$, and $FeCl_3 \cdot 6H_2O$ were purchased from Fluka (Buchs, Switzerland) and used without further purification. All other chemicals were supplied by Aldrich and used as received. Endorem, a MRI contrast agent based on superparamagnetic dextran-coated iron oxide nanoparticles, was obtained from Guerbet (Roissy, France). Ultrapure Q water ultrafiltered on a Milli-Q Gradient A10 system (Millipore, Molsheim, France) was used for preparation of the solutions.

Preparation of Ferrofluid. Two procedures are generally used for the preparation of iron oxide nanoparticles: an in situ and a stepwise method. In this report, a two-step procedure was used. Colloidal $Fe(OH)_3$ was first precipitated from $FeCl_3 \cdot 6H_2O$ added to less than an equimolar amount of ammonia, followed by the addition of $FeCl_2 \cdot 4H_2O$ (molar ratio Fe(III)/Fe(II) = 2). Mixing was simply achieved by rapid sonication. The mixture was then poured into an excess of ammonia, and a magnetite (Fe_3O_4) coagulate was formed. The key step in the formation of a stable magnetite colloid after the synthesis consists in its careful purification from all impurities by washing and magnetic separation in water, a process called peptization. Briefly, 12 mL 0.2 M $FeCl_3 \cdot 6H_2O$ aqueous solution was mixed with 12 mL 0.5 M NH_4OH solution under sonication (Sonicator W-385; Heat Systems-Ultrasonics, Inc., Farmingdale, USA) for 2 min at laboratory temperature to form the $Fe(OH)_3$ colloid. Then, 6 mL of 0.2 M $FeCl_2 \cdot 4H_2O$ aqueous solution was added under sonication and the mixture poured into 36 mL of 0.5 M NH_4OH aqueous solution. The resulting magnetite coagulate was left to grow for 15 min, magnetically separated, and repeatedly (7−10×) washed with Q-water to remove all impurities (including NH_4Cl) remaining after the synthesis. The above-formed pure magnetite was sonicated for 3 min with 2 mL of 0.1 M sodium citrate solution and oxidized at room temperature with 1.5 mL of 5 wt % sodium hypochlorite to maghemite. The precipitate was again repeatedly (7×) washed with Q-water using magnetic separation/decantation to obtain a stable colloid.

Coating by Solution Radical Polymerization of DMAAm in the Presence of Maghemite Nanoparticles. In a typical experiment, 1 g of DMAAm and 0.01 g of ACVA initiator were dissolved in 30 mL of aqueous colloid containing 0.5 g of γ-Fe_2O_3, and the mixture was purged with nitrogen to remove oxygen for 10 min. PDMAAm was synthesized under stirring (400 rpm) at 70 °C for 8 h. The resulting colloid was washed 8 times with water by centrifugation/redispersion to remove excessive polymer, unreacted monomer, and initiator, and redispersed.

For comparison, iron oxide nanoparticles were also encapsulated in neat PDMAAm added to the particles, followed by a thorough purification by repetitive centrifugation/redispersion in water.

Characterization of the Particles. The particles were observed in a scanning electron microscope (SEM, JEOL JSM 6400). A drop of particle dispersion was smeared between glasses for microscopy to obtain a thin layer, dried, and surface-coated with a 4-nm platinum layer using a SCD 050 sputtering device (BalTech, Lichtenstein). Transmission electron microscopy (TEM) was performed on a JEOL JEM 200 CX to determine the particle size of the iron oxides. The average diameter and particle size distribution PDI (weight-number-average particle diameter ratio D_w/D_n) were obtained by statistical analysis of at least 500 particles using the Atlas program (Tescan Brno, Czech Republic). The X-ray diffraction measurement was carried out with a Bruker D8 diffractometer using Cu Kα radiation and a Sol-X energy dispersive detector. The amount of iron in the coated nanoparticles was found by AAS (Perkin-Elmer 3110) of an extract of the sample obtained with dilute HCl (1:1) at 80 °C for 1 h. The amount of PDMAAm bound to the particles after polymerization was determined after their lyophilization by elemental analysis (Perkin-Elmer 2400 Series II CHNS/O Analyzer, Shelton, CT, USA).

The coating of PDMAAm on the surface of magnetic nanoparticles was investigated using a Thermo Nicolet NEXUS 870 FTIR Spectrometer (Madison, WI, USA) in a water-purged environment with a DTGS detector in the wavenumber range from 400 to 4000 cm^{-1}. A Golden Gate Heated Diamond ATR Top-Plate (MKII Golden Gate single reflection ATR system) (Specac Ltd., Orpington, Great Britain) was used for measuring the spectra of powdered samples by ATR spectroscopy. Typical parameters used were 256 sample scans, 4 cm^{-1} resolution, Happ-Genzel apodization, and KBr beamsplitter.

The hydrodynamic diameter D_h and the zeta-potential of both the unwashed colloid (0.2 mL of original colloid diluted to 2 mL) and the colloid repeatedly (8×) washed with water through ultracentrifugation/redispersion were determined by dynamic light scattering (DLS) with an Autosizer Lo-C (Malvern Instruments Ltd., Malvern, UK). Colloidal stability was evaluated visually according to the presence of sediment on the bottom of the vial.

To determine the molecular weight (M_w) of PDMAAm bound to maghemite, maghemite was first dissolved in concentrated HCl. The resulting dark yellow solution was diluted with water and PDMAAm separated on a PD 10 desalting column (Amersham Biosciences, Buckinghamshire, UK). Finally, PD-

MAAm was lyophilized and dissolved in acetate buffer ($c \sim 3$ mg/mL). The M_w was determined by size-exclusion chromatography in an aqueous methanol solution on a Shimadzu HPLC system equipped with RI, UV, and multiangle light scattering DAWN EOS (Wyatt Co., USA) detectors using a mobile phase consisting of 20% 0.3 M acetate buffer (pH 6.5; 0.5 g/L NaN_3) and 80% methanol (flow rate 0.5 mL/min) with a GPC column TSKgel G6000PW (300 × 7.8 mm; 15 μm; Tosoh Bioscience, Japan).

The conversion versus DMAAm polymerization time was calculated from the concentration of monomers during polymerization monitored after the addition of hydrochinone (50 mg/mL) by a GC Perkin-Elmer (Norwalk, CT, USA) with FID detector using 30 m length, 0.32 mm inner diameter Rtx-624 column with 1.8 μm thick film (Restek, Bellefonte, PA, USA). Calibration was performed using an external standard.

Cell Cultures and Cell Labeling. In vitro cellular uptake experiments were performed using rat and human bone marrow mesenchymal stem cells. Rat bone marrow mesenchymal stem cells (rMSCs) were obtained from the tibia and femur of 4-week-old Wistar rats. The ends of the bones were cut, and the marrow was extruded with Dulbecco's modified Eagle's medium (DMEM, PAA Laboratories, Linz, Austria) by using a needle and a syringe (*22*). Marrow cells were plated in a 75-cm^2 tissue culture flask (TPP, Trasadingen, Switzerland) in DMEM medium containing 10% fetal bovine serum (FBS, PAA Laboratories, Linz, Austria), 100 units/mL penicillin (Gibco BRL, Paisley, Scotland), and 0.1 mg/mL streptomycin (Gibco BRL). After 24 h, the nonadherent cells were removed by replacing the medium.

Human bone marrow mesenchymal stem cells (hMSCs) were obtained from the bone marrow of healthy donors after obtaining informed consent. Bone marrow aspirates were diluted in phosphate-buffered saline (PBS) and centrifuged through a density gradient (Ficoll-Paque Plus, GE Healthcare Life Sciences, Vienna, Austria) for 30 min at 1000 *g* (*22*, *23*). Nucleated cells from the interface were plated in a 75-cm^2 tissue culture flask in α-modified Eagle's medium (α-MEM, Gibco BRL) containing 10% FBS, 100 units/mL penicillin, and 0.1 mg/mL streptomycin. After 48 h, the nonadherent cells were removed by replacing the medium.

Both types of cells were cultured in a humidified 5% CO_2 incubator. The medium was replaced every 3 days as the cells grew to confluence. The cells were labeled with iron oxide nanoparticles. For cell labeling, either uncoated γ-Fe_2O_3 nanoparticles, the contrast agent Endorem, or PDMAAm-coated γ-Fe_2O_3 nanoparticles were used at the same concentration −15 μg Fe_2O_3/mL of media. After 72 h, the contrast agent was washed out by replacing the culture medium.

Transmission Electron Microscopy (TEM). Nanoparticle localization inside the cells was observed by transmission electron microscopy. MSCs were incubated with the nanoparticles for 72 h, transferred onto polylysine-coated coverslips, fixed in 2.5% glutaraldehyde in 0.1 M Sörensen buffer for 48 h at 4 °C, and stained by 1% osmium tetraoxide in 0.1 M Sörensen buffer for 2 h. Cells were then dehydrated in ethanol, immersed in propylene oxide, and flat embedded in Epon 812 using gelatin capsules. After polymerization for 72 h at 60 °C, coverslips were removed by liquid nitrogen. Ultrathin sections of 60 nm were examined with a Philips Morgagni 268D transmission electron microscope (FEI Inc., Hillsboro, OR, USA).

Cell Viability. The viability of cells was analyzed using a colorimetric assay based on the cleavage of the tetrazolium salt WST-1 (4-[3-(4-iodophenyl)-2-(4-nitrophenyl)-2*H*-5-tetrazolio]-1,3-benzene disulfonate) (Roche Diagnostics, Mannheim, Germany) to a highly water-soluble formazan dye by mitochondrial dehydrogenases in viable cells (*24*). rMSCs or hMSCs (2nd and 5th passages) were plated on 96-well plates (TPP, Trasadingen, Switzerland) at a density of 5×10^3 cells/well. The cells were cultured and labeled with iron oxide nanoparticles as described above. Twelve wells of each cell type were labeled with Endorem and 12 wells with PDMAAm-coated maghemite nanoparticles, and 12 wells were not labeled and served as control samples. On the day that nanoparticles were withdrawn (day 3), 10 μL of the WST-1 solution was added to 100 μL of culture medium per well, and the cells were kept in the incubator (37 °C) for an additional 2 h. The absorbance was measured using an ELISA plate reader (Tecan Spectra, Tecan Trading, Switzerland) at a wavelength of 450 nm.

Labeling Efficiency and Staining Intensity. Labeling efficiency was determined by manually counting the number of Prussian Blue-stained and unstained cells in 96-well plates and measuring the staining intensity of Prussian Blue-stained cells colorimetrically. Twelve optical fields from each plate were scanned using an Axioplan Imaging II microscope at 100× magnification using a 10×/0.75 objective lens, an AxioCam digital camera, and AxioVision 4 software (microscope setup from Zeiss, Oberkochen, Germany). All of the cells in the scanned images were manually labeled as Prussian Blue-stained or unstained using Jasc Paint Shop Pro 8 (Corel Corporation, Ottawa, Canada). The scanned images with manually labeled cells were processed by the Image analysis toolbox of MATLAB software (The MathWorks, Inc., MA, USA). Before the analysis, we validated the colorimetric scale from the image colors corresponding to the increasing intensities of the Prussian Blue staining of the cells. Then we processed each Prussian Blue-stained cell in the image and determined the intensity of the cytoplasmic staining as the intensity of the color of the cytoplasm on the scale. As a result, two parameters were obtained: (i) the presence or absence of a label inside the cells expressed as the percentage of labeled cells and (ii) the amount of label inside the cells, which correlates with the intensity of the staining.

In Vitro MR Relaxometry and MR Imaging of Labeled Cells Suspended in Gelatin. MR relaxometry of the particles was performed using a Bruker MiniSpec 0.5 T relaxometer and a Bruker BioSpec 4.7 T imager (both Etlingen, Germany). The latter apparatus was also used for MR imaging. Two types of labeled cells, rat and human MSCs, were dispersed in gelatin in the following concentrations: 50, 100, 200, 400, and 800 cells/μL. Control samples containing suspensions of unlabeled cells and Endorem-labeled cells were measured at the same concentrations. For T_1 relaxometry, the standard saturation recovery sequence was used; T_2 relaxometry was performed with a CPMG multispin−echo sequence. Measured relaxation times were converted to relaxation rates and related to cell concentrations. MR imaging was performed with T_2-weighted turbo-spin echo (effective echo time TE = 35 ms, repetition time TR = 3 s) and T_2*-weighted gradient echo (TE = 5 ms, TR = 100 ms) sequences that are commonly used in in vivo measurements.

Iron Analysis. The amount of iron in the cells after mineralization was determined by spectrophotometry. Cell-containing samples were mineralized by the addition of 5 mL of HNO_3 and 1 mL of H_2O_2 in an ETHOS 900 microwave mineralizator (Millestone, Sydney, Australia). Deionized water was added to reach a total volume of 100 mL. The iron content was determined using a Spectroflame M120S apparatus (Spectro, Littleton, MA, USA) calibrated with a standard Astasol solution (Analytika, Prague, Czech Republic). The measurements were repeated four times, and the average mean value was determined.

Cell Grafting. The rats (n = 5) were anesthetized with isoflorane and mounted in a stereotactic frame. Using an aseptic technique, a burr hole (1 mm) was made in the skull to expose the dura overlying the cortex. PDMAAm-modified iron oxide-

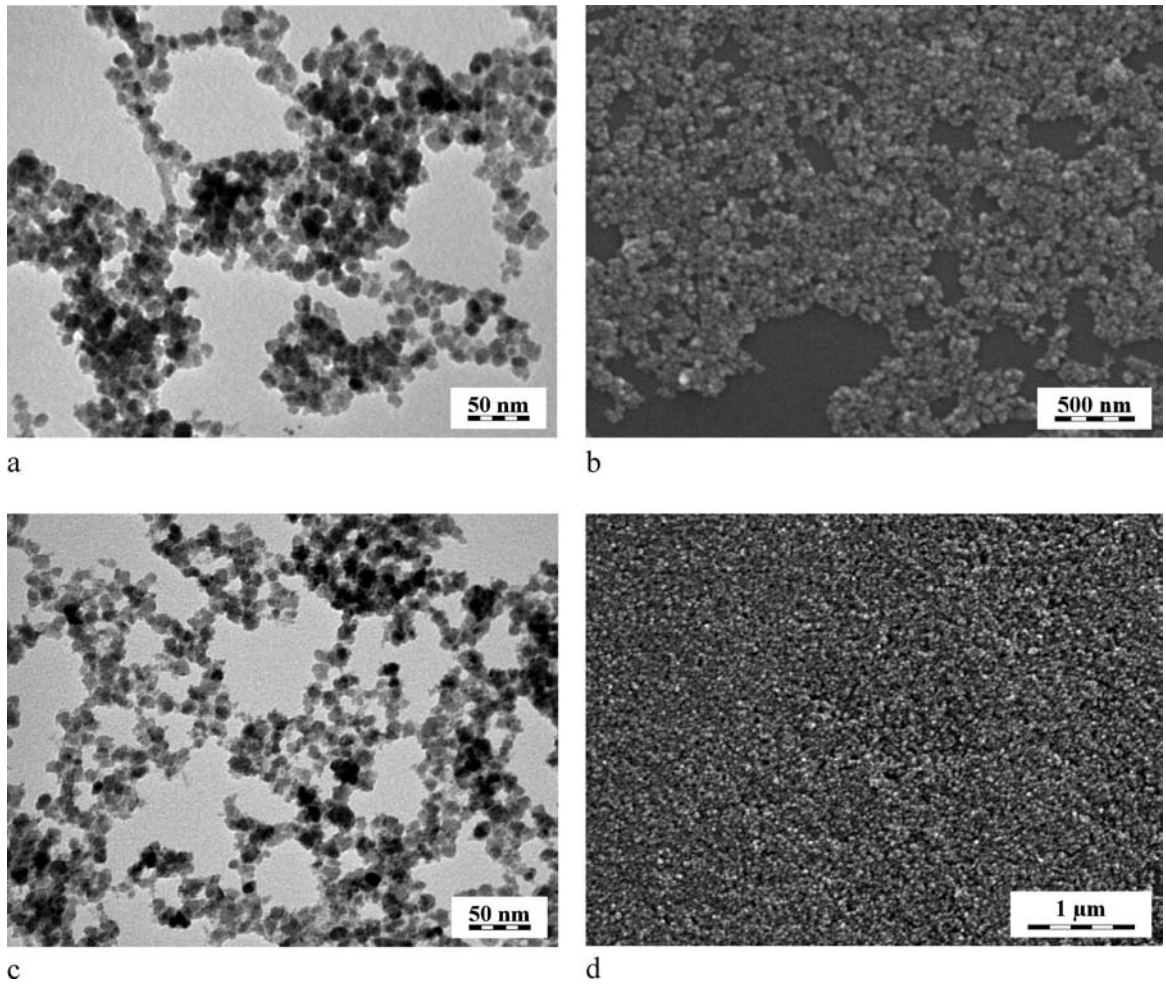

Figure 1. (a,c) TEM and (b,d) SEM micrographs of (a,b) primary uncoated γ-Fe_2O_3 particles No. 1 and (c,d) particles coated with PDMAAm by solution polymerization No. 5.

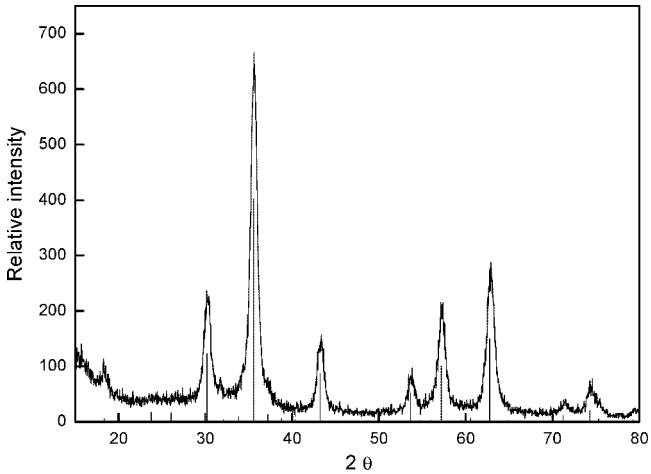

Figure 2. X-ray diagram of synthesized γ-Fe_2O_3 nanoparticles. Vertical bars, γ-Fe_2O_3 standard.

labeled cells or Endorem-labeled cells (5,000 cells suspended in 5 μL of PBS) were slowly injected intracerebrally into the brain over a 10-min period using a Hamilton syringe. Unlabeled cells were injected as a control. The opening was closed by bone wax, and the skin was sutured.

MR Imaging. The in vivo MR images were obtained on a 4.7 T Bruker imager equipped with a homemade surface coil. The rat was anesthetized by passive inhalation of 1.5−2% isoflorane in air. Breathing was monitored during the measurements. Single sagittal, coronal, and transversal images were obtained by a fast gradient echo sequence for localizing, then both T_2-weighted (turbospin echo sequence, TE = 35 ms, TR = 3 s, number of acquisitions AC = 8, matrix size 256 × 256, field of view FOV = 3.5 × 3.5 cm, slice thickness 0.75 mm) and T_2*-weighted (gradient echo sequence, TE = 12 ms, TR = 180 ms, number of acquisitions AC = 48, same geometry) axial images were acquired.

RESULTS AND DISCUSSION

Preparation of Maghemite. Maghemite (γ-Fe_2O_3) nanoparticles are one of the most commonly used ferric oxide particles because of their simple synthesis and chemical stability. Their advantage is that iron participates in human metabolism and is thus well tolerated by the living organism. First, magnetite was precipitated; its colloidal stability was achieved by charges induced by Fe^{3+} ions. However, because the above colloid is chemically unstable, undergoing uncontrolled oxidation upon contact with air, it was controllably chemically oxidized to maghemite, which shows long-term stability in either alkaline or acidic media. The ultimate advantage of the above procedure consists in the simplicity of purification by magnetic separation/decantation, which is much more convenient than the commonly used but more elaborate and time-consuming method of ultracentrifugation.

TEM and SEM images (Figure 1a,b) show agglomerated maghemite particles in a dry state. The agglomerates consist of primary particles with an average size D_n = 6.3 nm and a polydispersity index PDI = 1.33. X-ray diffraction measure-

Table 1. Modification of Maghemite Nanoparticles by the Solution Polymerization of DMAAm

sample	polymerization feed			colloidal stability[e]	D_h[c] (nm)	bound PDMAAm[d] (wt %)
	γ-Fe_2O_3 (g)	DMAAm (g)	ACVA (mg)			
1[a]	0.5	0	0	−	127 ± 3	0
2[b]	0.5	0.5	0	−	161 ± 3	0.21
3	0.5	0.375	3.8	aggr.	n.a.	
4	0.5	0.5	5	++	81.4 ± 0.6	0.7
5	0.5	1	10	++	56.9 ± 0.3	1.2
6	0.5	1.5	15	+	171 ± 5	1.95
7	0.5	1	5	++	77.8 ± 0.3	1.52
8	0.5	1	15	+	172 ± 22	1.7
9	0.5	1	20	aggr.	n.a.	2.74
10	0.5	1	30	aggr.	n.a.	4.95
11	0.5	0.375	10	++	55 ± 5	1.03
12	0.5	0.5	10	++	67 ± 3	1.1
13	0.5	1.5	10	aggr.	328 ± 4	1.06
14	0.5	2	10	aggr.	614 ± 12	1.6
15	1	1	10	++	76.6 ± 0.5	2.1
16	1.5	1	10	++	83.5 ± 0.2	0.88
17	2	1	10	++	75.1 ± 0.1	0.96
18	2.5	1	10	++	76 ± 0.5	0.74

[a] Primary uncoated γ-Fe_2O_3 (control). [b] PDMAAm solution was added to neat γ-Fe_2O_3 particles. [c] D_h, hydrodynamic diameter determined by dynamic light scattering. [d] From elemental analysis. [e] −, poor stability (aggregation within a week); +, high stability (no sediment after 3 months of storage); ++, very high stability (no sediment after 6 months of storage).

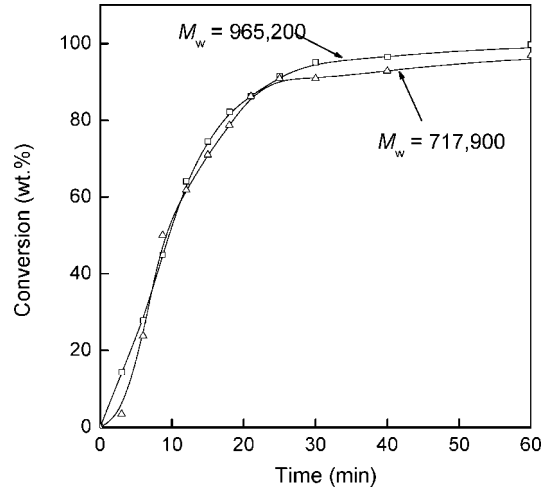

Figure 3. Conversion curves of DMAAm in solution polymerization in (Δ) the presence and (□) absence of γ-Fe_2O_3.

ments of the synthesized particles evidenced the typical spinel structure of γ-Fe_2O_3 (Figure 2). With respect to a small size of the crystallites, weak superstructural patterns indicated for the standard material were not detectable. Detailed Mössbauer spectra were published elsewhere (*25*).

Solution Radical Polymerization of DMAAm in the Presence of Maghemite Nanoparticles. The surface modification of nanoparticles is a general strategy for enhancing the permeability of nanoparticle-based therapeutics. To modify the iron oxide surface, the solution radical polymerization of DMAAm in aqueous ferrofluid was investigated. This could produce a dispersion of maghemite nanoparticles stable in a medium suitable for subsequent polymerization of DMAAm, thus facilitating their subsequent incorporation in the polymer microspheres. At the same time, it provides a model for investigating the effect of iron oxide nanoparticles on the polymerization process. In the system, ACVA was preferred over 2,2′-azobisisobutyronitrile (AIBN) as an initiator because its solubility in an aqueous monomer solution is much higher than that of AIBN. An additional advantage of ACVA consists in its carboxyl group's ability to interact with iron oxide. The polymerization conditions are summarized in Table 1. The effect of several polymerization parameters, such as the concentrations

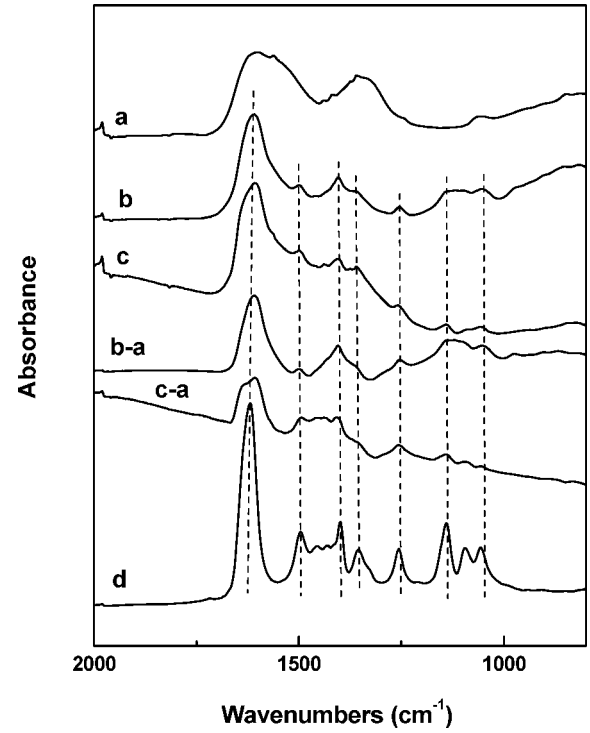

Figure 4. ATR FTIR spectra of γ-Fe_2O_3 nanoparticles before and after surface modification with PDMAAm. (a) Before modification, (b) coating by solution polymerization in the presence of γ-Fe_2O_3 nanoparticles No. 3, (c) coating by encapsulation of γ-Fe_2O_3 nanoparticles in the polymer No. 2, (b-a) and (c-a) the corresponding differential spectra of coated and uncoated γ-Fe_2O_3, and (d) pure PDMAAm.

of the monomer, the initiator, and the iron oxide in the feed, on particle size and the amount of PDMAAm bound to the particles was investigated. For the sake of comparison, the characteristics of neat (uncoated) maghemite nanoparticles and of nanoparticles coated with a solution of preprepared PDMAAm are also shown in Table 1.

Conversion Curves. Conversion curves were determined in order to estimate the effect of maghemite on the polymerization process. The presence of maghemite colloid in the feed affected the molecular weight of the resulting PDMAAm compared to solution radical polymerization without maghemite. The mo-

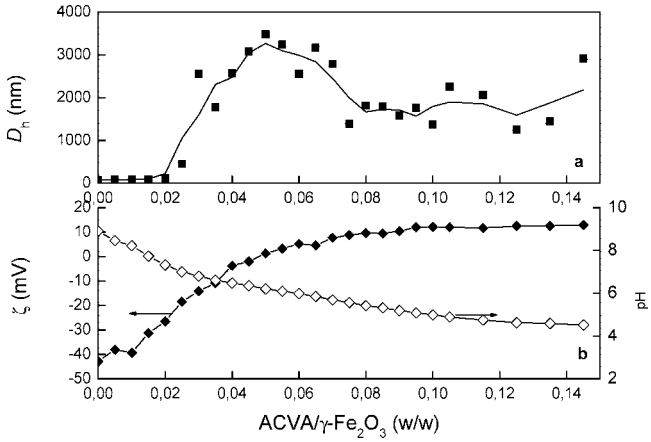

Figure 5. Dependence of the (■) hydrodynamic diameter D_h (a), (◆) ζ-potential, and (◇) pH (b) on the ACVA/γ-Fe_2O_3 ratio.

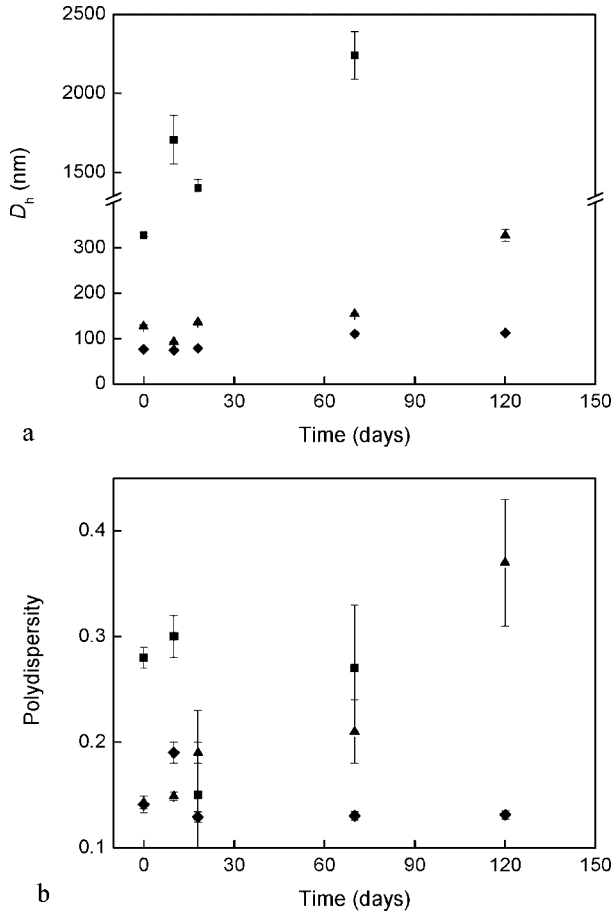

Figure 6. Dependence of the (a) hydrodynamic particle diameter D_h and (b) polydispersity, measured by dynamic light scattering, on storage time; (▲) uncoated γ-Fe_2O_3 No. 1, PDMAAm-coated γ-Fe_2O_3 (◆) No. 18, and (■) No. 13.

lecular weight of PDMAAm prepared in the presence of maghemite was 717,900, i.e., lower than that prepared in its absence (965,200). This can be attributed to the growing polymer chains probably terminating on the nanoparticle surface as documented by the slower consumption of monomers in the initial and final stages of the polymerization (Figure 3). Because of the termination, PDMAAm can be attached to the maghemite surface. The possible complexation of the ACVA initiator with maghemite Fe atoms can contribute to additional DMAAm initiation. At γ-Fe_2O_3/DMAAm ratios of 0.5/0.375 (w/w) and lower, free PDMAAm was present in the mixture after polymerization. The colloidal stability then decreased with an increasing γ-Fe_2O_3/DMAAm ratio.

FTIR Spectra. The structure of the surface and the efficiency of the coating of magnetic nanoparticles were analyzed by surface-sensitive ATR FTIR spectroscopy. FTIR spectra of iron oxide before modification, after coating by solution radical polymerization in the presence of γ-Fe_2O_3 nanoparticles, after coating by encapsulation of maghemite nanoparticles in the polymer, the corresponding differential spectra of coated and uncoated surfaces, and the spectrum of pure PDMAAm are shown in Figure 4. The spectrum of coating by encapsulation of maghemite γ-Fe_2O_3 nanoparticles (see corresponding differential spectrum) is relatively weak and is very close to the spectrum of pure PDMAAm. This signifies that some amount of polymer adheres to the surface of the nanoparticles. The spectrum of coating by solution radical polymerization in the presence of maghemite nanoparticles (see corresponding differential spectrum) is stronger and differs from the spectrum of pure PDMAAm in some aspects. The band of Amide I (*26*) observed at 1618 cm^{-1} is shifted to 1608 cm^{-1}, and the intensity of the band of Amide II observed at 1404 cm^{-1} increased after polymerization. The peaks of CH_3 deformation vibration at about 1495 and 1354 cm^{-1} decreased in their relative intensity. We hypothesize that these changes correspond to the interaction of the protonated NH^+ groups of PDMAAm with citrates complexed on the iron oxide surface. Citrate is adsorbed on the ferric oxide surface via one or two carboxylate moieties, allowing the use of one of the ungrafted carboxylic acid groups to bind a polycation. This confirms that the PDMAAm shell has effectively formed at the surface of the iron oxide particles.

DLS, TEM, and Elemental Analysis. Particle size and its distribution have a strong effect on the physical and biochemical properties of colloidal dispersions. Many methods have been described for the measurement of average particle size, such as electron microscopy, dynamic light scattering, and chromatographic methods; the former two techniques were used in this study.

ACVA-initiated solution polymerization of DMAAm in the presence of maghemite nanoparticles produced a very stable colloid, with the particles typically in the hydrodynamic size (D_h) range of 50−170 nm. Because DLS provides information on the hydrodynamic particle size of whole particle clusters, including polymer coating layers and the magnetic core, the size of the iron oxide core alone was examined by TEM. Figure 1c,d shows TEM and SEM images of the obtained DMAAm-coated nanoparticles with an average size $D_n = 7.5$ nm and a polydispersity index PDI = 1.20. A comparison of Figure 1a,b and Figure 1c,d reveals that both the shape and the size of the particles after the coating process effectively did not change from those of the uncoated particles. It is worth pointing out that the particle size determined by TEM was smaller compared with the particles size of the same latex obtained from DLS measurements (Table 1). These results confirm the presence of a hydrophilic polymer hairy layer on the particle surface, which increases the value of the average hydrodynamic diameter during the DLS measurements and which is collapsed onto the particle surface during the drying of the TEM sample. It should also be remembered that while TEM provides the number-average particle size, DLS gives the z-average, which is sensitive to large-size particles.

Effect of the Reaction Parameters. The effect of the amount of the monomer in the polymerization feed on colloidal stability, hydrodynamic particle size, and the percentage of PDMAAm bound to the particles (determined from elemental analysis) at a constant initiator concentration (1 wt % in the monomers) is documented in Table 1 for experiments Nos. 3−6. Particles aggregated at low amounts of bound PDMAAm. The percentage

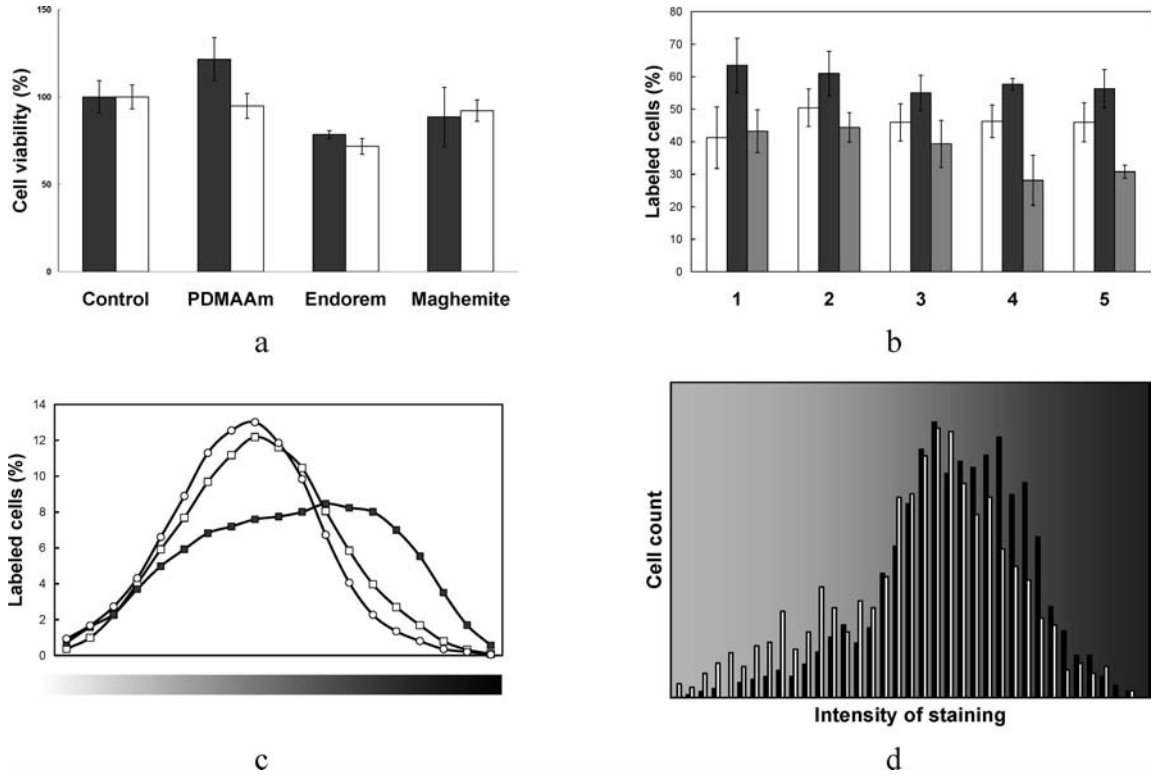

Figure 7. (a) Viability of rat (■) and human MSCs (□) labeled with several types of iron oxide nanoparticles. PDMAAm-coated nanoparticles No. 7 were used. (b) Labeling efficiency (expressed as the percentage of labeled cells) of rat MSCs from the 1st−5th passage (columns 1−5) labeled with uncoated γ-Fe_2O_3 (□), PDMAAm-coated γ-Fe_2O_3 No. 7 nanoparticles (■), and Endorem (gray square). (c) Distribution of the intensity of Prussian Blue staining (*x*-axis) of rMSCs labeled with uncoated γ-Fe_2O_3 (□), PDMAAm-coated γ-Fe_2O_3 nanoparticles (■), and Endorem (○). (d) Histograms of the intensity of staining of rat and human MSCs; note that hMSCs (■) are more intensively labeled than rMSCs (□).

Table 2. Cell Labeling Efficiency with Surface-Modified and Unmodified Iron Oxide Nanoparticles

	percentage of labeled cells	
	rMSC	hMSC
Endorem	39 ± 6	68 ± 5
uncoated γ-Fe_2O_3	46 ± 5	70 ± 5
PDMAAm-coated γ-Fe_2O_3	59 ± 5	82 ± 5

of bound PDMAAm generally reached up to ca. 2 wt %, while free PDMAAm was removed during washing. The more DMAAm in the polymerization feed, the more PDMAAm was bound to the particles.

The effect of the amount of initiator in the feed on colloidal stability, hydrodynamic particle diameter, and the percentage of bound PDMAAm is documented in Table 1 for experiments Nos. 5 and 7−10. At <10 mg of ACVA in the polymerization feed, the D_h of the resulting particles was smaller than that of the primary maghemite particles (Table 1). This can be explained by the steric repulsion of PDMAAm chains on their surface, which decreases the number of particle associates measured by DLS. At higher ACVA amounts, the stability of the colloidal system was lost, and the particles aggregated. Both the hydrodynamic particle size D_h and the percentage of bound PDMAAm determined from elemental analysis increased with increasing amounts of the initiator in the feed up to 15 mg of ACVA (Nos. 5, 7, and 8 in Table 1). The increasing percentage of bound PDMAAm at higher initiator concentrations can be ascribed to a larger number of carboxyl groups available to anchor more PDMAAm chains on the maghemite particle and/or a greater tendency toward particle aggregation. To explain why steric stabilization occurred only at concentrations lower than 15 mg of ACVA in the feed, ACVA was added to the maghemite colloid, and hydrodynamic diameter D_h, ζ-potential, and pH were monitored depending on the ACVA/γ-Fe_2O_3 ratio. With the ACVA/γ-Fe_2O_3 ratio increasing from ~0.02 (w/w), hydrodynamic diameter sharply increased (Figure 5a). This can be explained by the increase of ζ-potential from ca. −43 mV, reaching a critical value at −30 mV and accompanied by a steep decrease of pH till the ACVA/γ-Fe_2O_3 ratio reached 0.02 (Figure 5b). It should be noted that ± 30 mV is the limiting value for effective electrostatic stabilization. Further ACVA addition thus increased ζ-potential up to 13 mV, which was inadequate to stabilize the particles; consequently, they aggregated. The coating efficiency of PDMAAm was further deduced from a comparison of maghemite modified by solution radical polymerization of DMAAm with a sample obtained by the addition of separately prepared PDMAAm to the maghemite colloid. The data shown in Table 1 (Nos. 2 and 4) argue in favor of solution polymerization.

The effect of the amount of the monomer in the polymerization feed at constant amounts of initiator and maghemite is shown in Table 1 for experiments No. 5 and 11−14. Particle aggregation occurred with amounts of 1.5 g or more DMAAm in the feed, probably because of the undesirable physical cross-linking of PDMAAm chains and the increased viscosity of the reaction mixture. At a constant amount of initiator in the feed, the percentage of PDMAAm bound to the particles did not change with increasing amounts of DMAAm (with the exception of No. 14 in Table 1 because of the high viscosity of the mixture), thus documenting the key role of the amount of initiator on encapsulation efficiency.

The effect of the amount of γ-Fe_2O_3 added in the feed under otherwise identical conditions is documented by experiments No. 5 and 15−18 in Table 1. While the particle diameter was almost constant (within the experimental error), the amount of bound PDMAAm decreased with increasing amounts of γ-Fe_2O_3 in the feed, as expected.

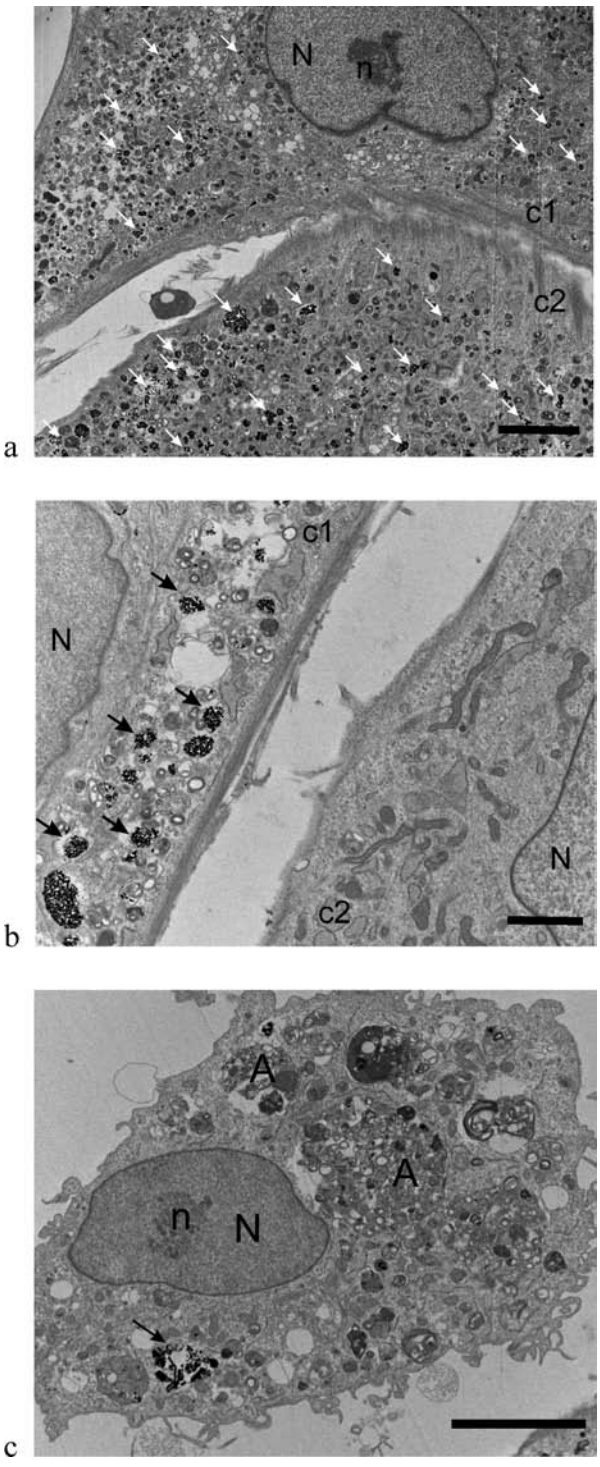

Figure 8. TEM micrographs of rMSCs labeled with (a) PDMAAm-coated γ-Fe_2O_3 nanoparticles, (b) Endorem, and (c) uncoated γ-Fe_2O_3. Arrows indicate nanoparticles inside the endosomes. A, autophagosome; N, nucleus; n, nucleolus; c1 and c2, cell 1 and cell 2, respectively. Scale bar: a,c, 500 nm; b, 200 nm.

Colloidal Stability. The long-term colloidal stability of PDMAAm-coated maghemite nanoparticles is of utmost importance for prospective biological applications. The stability of some dispersions over time was determined by DLS (Figure 6). Almost no increase in the hydrodynamic size and consistently low polydispersity over several months were observed in colloid No. 18, thus documenting its perfect stability in water due to the presence of the PDMAAm coating. The colloidal stability of such samples is denoted as very high in Table 1. The good colloidal stability suggests that the stabilization of the maghemite nanoparticles was primarily dependent on the steric repulsion of the attached hydrophilic PDMAAm chains. In comparison, uncoated nanoparticles No. 1 were unstable. Both the hydrodynamic diameter and polydispersity of these particles increased with time because of aggregation. Similarly, the stability of nanoparticles No. 13, prepared in the presence of large amounts of monomer, was poor. This can be explained by the high viscosity of the polymerization mixture, as a consequence of which the PDMAAm chains could entangle, resulting in particle aggregation. This is documented by the extremely large size and polydispersity determined by DLS in Figure 6a,b.

Viability of Cells. In order to examine the acute toxicity of PDMAAm-coated maghemite nanoparticles, both rMSCs and hMSCs were incubated for 72 h with sample No. 7, uncoated nanoparticles No. 1, and Endorem (control) at concentrations of 15 μg γ-Fe_2O_3/mL, and cell viability was assessed using the WST-1 assay. The viability of both rat and human MSCs labeled with PDMA nanoparticles did not markedly decrease compared to that of unlabeled MSCs (control). When mesenchymal stem cells were labeled with Endorem, their viability decreased by 32%, and uncoated nanoparticles decreased the viability by 15% (Figure 7a). However, the TEM images showed that the cells labeled with uncoated nanoparticles were undergoing programmed cell death (see below); therefore, in long-term follow up the viability would be affected.

Cell Labeling Efficiency. To investigate the role of the PDMAAm coating and its effect on the internalization of the maghemite nanoparticles by target cells, both hMSCs and rMSCs were incubated with PDMAAm-coated nanoparticles No. 7 or Endorem; uncoated maghemite nanoparticles served as controls. The uptake of nanoparticles into the cells (expressed as the percentage of labeled cells) was investigated using Prussian Blue staining. The cellular uptake of particles generally depends on the cell type and the particle size and surface properties, including surface charge and surface hydrophilicity (*27, 28*). It also depends on the number of passages of the cells, which is a characteristic physiological cell property. The lower the passage, the more efficient the cell labeling. The most intensive staining of any iron oxide nanoparticles was thus observed for cells from the first and second passages, while the intensity of the blue staining decreased in the fifth passage (only 30% of cells were labeled with Endorem). rMSCs cultured with PDMAAm-coated maghemite nanoparticles showed considerably higher nanoparticle uptake (59%) than those cultured with Endorem (39%; Table 2). This means that the number of rMSCs labeled by PDMAAm-coated γ-Fe_2O_3 was more than 50% higher than the number labeled by Endorem. Moreover, the labeling efficiency (percentage of labeled cells) was stable and was not dependent on the number of passages (Figure 7b). Even higher PDMAAm-nanoparticle uptake was observed in hMSCs (82%; Table 2), whereas Endorem uptake was 68%. The number of hMSCs labeled by PDMAAm-coated γ-Fe_2O_3 was thus more than 20% greater than the number labeled by Endorem. Histograms showing the intensity of Prussian Blue staining, which corresponds to the amount of label inside the cell, revealed that more cells were intensely stained with PDMAAm-coated nanoparticles than with Endorem or maghemite (Figure 7c). These results were even more apparent or amplified in hMSCs (Figure 7d). Although a relatively large number of cells were labeled with uncoated maghemite nanoparticles, the advantage of the PDMAAm coating consists in the possibility of its modification, thus introducing desired functional groups. An additional substantial advantage of PDMAAm-coated γ-Fe_2O_3 exists in the stability of the formed colloid, in contrast to uncoated γ-Fe_2O_3 nanoparticles that coagulate after the addition of the culture media. Coagulation of uncoated maghemite nanoparticles also leads to the attachment of the nanoparticles

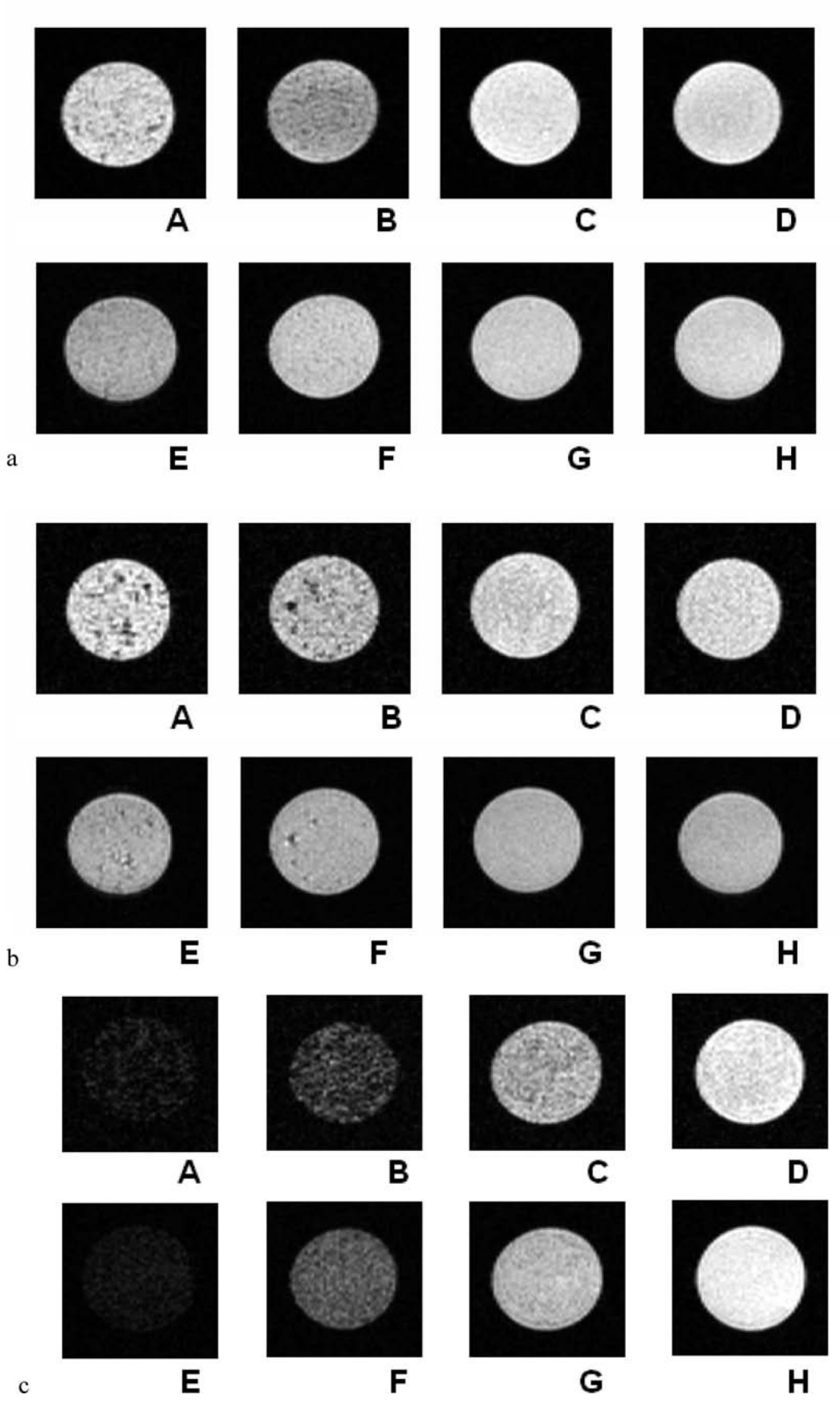

Figure 9. MRI of phantoms containing labeled (a) human and (b) rat mesenchymal stem cells suspended in gelatin measured by a T_2*-weighted gradient echo sequence (A−D) and by a T_2-weighted turbo-spin echo sequence (E−H). A,E, cells labeled by PDMAA-coated maghemite nanoparticles No. 7; B,F, cells labeled by uncoated maghemite nanoparticles No. 1; C,G, cells labeled by Endorem; D,H, unlabeled cells. Each sample (0.5 mL) contained 25,000 cells, yielding on average 1 cell per image voxel. For comparison, an MRI of phantoms containing a high number (400,000) of labeled human cells is shown in c; the phantoms are in the same order as in a.

Table 3. Relaxation Rates r_1 and r_2 (Related to Cell Concentration) of hMSCs and rMSCs Labeled with Endorem (Control), Uncoated (Control) No. 1, and PDMAAm-Coated Maghemite Nanoparticles No. 7, and the Amount of Iron Internalized Inside the Cells[a]

	hMSCs ($s^{-1}/10^6$) cells/mL)				rMSC ($s^{-1}/10^6$ cells/mL)			
	r_1 (0.5 T)	r_2 (0.5 T)	r_2 (4.7 T)	Fe (pg/cell)	r_1 (0.5 T)	r_2 (0.5 T)	r_2 (4.7 T)	Fe (pg/cell)
Endorem	undetectable	0.88 ± 0.34	1.7 ± 0.5	3.2 ± 0.5	0.21 ± 0.19	0.13 ± 0.14	0.72 ± 0.09	undetectable
uncoated γ-Fe_2O_3	0.52 ± 0.09	7.13 ± 0.77	9.8 ± 3.3	17.1 ± 0.3	0.55 ± 0.20	3.67 ± 0.62	4.95 ± 0.17	29.3 ± 4.9
PDMAAm-coated γ-Fe_2O_3	1.19 ± 0.04	27.26 ± 0.24	40.8 ± 1.6	36.9 ± 0.5	0.41 ± 0.13	2.91 ± 0.50	4.18 ± 0.40	23.2 ± 2.9

[a] Measured at 0.5 and 4.7 T.

Figure 10. T_2-weighed MR image of a rat brain with 5,000 rMSCs labeled with PDMAAm-coated nanoparticles No. 7 or Endorem, implanted in the left or right hemisphere, respectively. White and black arrows indicate the injection sites in the head and the nanoparticles in the brain, respectively.

to the cell surface. This effect is also responsible for the high labeling efficiency of uncoated maghemite nanoparticles. It was difficult to distinguish using light microscopy whether the nanoparticles were inside the cells or just attached to the cell surface. Cells with iron oxides attached to the surface are better targets for macrophages after transplantation, and iron oxides incorporated into macrophages can also give a false positive signal on MRI.

TEM Images. Intracellular uptake was also visualized with TEM as it provides higher resolution than does light microscopy. While these methods cannot provide a quantitative measurement of cellular uptake, they demonstrate the importance of visualization to determine the distribution of particles on a cellular and subcellular level. PDMAAm chains are thought to form a complex with surface charges on the cell surface or else have an affinity with the cell membrane that facilitates endocytosis. A TEM image (Figure 8) shows that the cells internalized the PDMAAm-coated maghemite nanoparticles in large numbers and accumulated them in endosomes. Organelles and cell structures were not affected by the presence of coated nanoparticles inside the cells. However, the majority of cells labeled with uncoated maghemite were undergoing programmed cell death, probably by autophagia. The cells contained large autophagosomes, recognized in micrographs as membrane bound organelles with other organelles clearly contained within them, together with uncoated nanoparticles (Figure 8b). MSCs stained with Endorem showed a heterogeneous distribution of the nanoparticles. Some of the cells contained numerous endosomes filled with nanoparticles, others only a few or none (Figure 8c). The results obtained from TEM images are in agreement with those of our colorimetric analysis of the intensity of Prussian Blue staining (Figure 7c) as well as with those obtained from MR relaxometry (see text below and Table 3).

NMR Relaxometry. The iron oxide concentration of labeled rat and human cells was assessed using MR relaxometry. Relaxation rates measured at 0.5 and 4.7 T are listed in Table 3. Relaxation rates r_1 and r_2 are related to the number of cells per mL after subtracting the contribution of unlabeled cells. At a higher field strength (4.7 T), the contribution of all the particles to total r_1 was negligible; the values are therefore not provided. PDMAAm-coated iron oxide-labeled human cells provided significantly higher r_1 and r_2 at both 0.5 and 4.7 T fields than Endorem- and uncoated-iron-oxide-labeled cells. Large differences were obtained in the relaxation rates of PDMAAm-labeled human and rat cells, with r_2 several times higher for human cells. PDMAAm-coated iron oxide-labeled rat cells provided higher relaxation rates than Endorem-labeled ones; however, they were quite comparable to data obtained from uncoated-iron-oxide-labeled cells. Iron analysis proved that the higher relaxation rates of PDMAAm-coated or uncoated iron-oxide-labeled cells compared with Endorem-labeled ones are caused mainly by higher iron internalization (Table 3). It is interesting to note that human cells prefer PDMAAm-coated nanoparticles to both Endorem and uncoated ones, whereas in the case of rat cells, uncoated iron particles are internalized slightly better than PDMAAm-coated ones (both nanoparticles are internalized at a markedly higher rate than Endorem). These results are in good agreement with the relaxometry results.

MR Imaging of Cells after Nanoparticle Internalization in Gelatin. Gelatin samples with suspended cells labeled by PDMAAm-coated iron oxide nanoparticles, Endorem, and bare particles were examined by MRI to evaluate the potential of PDMAAm-coated iron oxide nanoparticles as a targeted MR contrast agent. Figure 9 compares MR images of cell phantoms. The T_2-and T_2*-weighted MR images of phantoms containing cells incubated with PDMAAm-coated and uncoated iron oxide nanoparticles show a significant negative contrast enhancement (signal darkening) over those containing cells labeled with Endorem and unlabeled cells (Figure 9a,b). As the MR images are normalized during processing, it is not possible to decide (based on observation with the naked eye) which of the two types of nanoparticles provides better contrast. However, the MR image of phantoms containing a high number of cells (Figure 9c) unambiguously proves that cells labeled by PDMAAm-coated iron oxide nanoparticles show significantly higher negative contrast enhancement. The results thus confirm that there is a preferential uptake of PDMAAm-coated iron oxide nanoparicles, i.e., the amount of internalized iron is markedly higher (see also Table 3), especially in human cells.

In Vivo MR Imaging. Magnetic labeling and MRI were used to noninvasively monitor cells injected into rats. PDMAAm-coated iron-oxide- and Endorem-labeled rMSCs (5,000 cells in 5 μL of PBS) were injected into the left and right rat hemispheres, respectively. Only cells labeled with PDMAAm-coated iron-oxide nanoparicles (left hemisphere) were detected (Figure 10).

CONCLUSIONS

In this article, PDMAAm-coated γ-Fe_2O_3 nanoparticles were obtained by the solution radical polymerization of DMAAm in the presence of maghemite nanoparticles obtained by the

chemical coprecipitation of Fe(II) and Fe (III) salts with ammonium hydroxide and subsequent oxidation with sodium hypochlorite. The presence of the PDMAAm coating on the maghemite surface was confirmed by both elemental analysis and ATR FTIR spectroscopy. PDMAAm coating provided good dispersibility of the magnetic nanoparticles in an aqueous medium and substantially improved iron oxide colloidal stability in the culture medium compared with uncoated maghemite, which immediately precipitated or aggregated within 1 h. A key parameter determining the amount of PDMAAm bound on maghemite nanoparticles is the amount of initiator in the polymerization feed. The amount of the initiator also influences the stability of the colloid. A narrow range of reaction conditions (5−15 mg of ACVA in the feed) was found under which particle aggregation was avoided, and at the same time, PDMAAm coating of the particles was high. DLS data revealed that the particle sizes were not altered even after several months of incubation in water. The surface of the particles is the determining factor for the efficiency of cellular uptake. Magnetic cellular labeling was evaluated by Prussian Blue staining for iron content, T_2 relaxometry, and MR imaging of labeled cell suspensions. PDMAAm coating did not adversely affect the penetration of the iron oxide nanoparticles into cells. After 72 h of culture in media containing 15 μg of iron oxide per 1 mL, the morphology and viability of both rMSCs as well as hMSCs were close to those of unlabeled cells, suggesting the biocompatibility of the nanoparticles. PDMAAm-coated maghemite nanoparticles turned out to be particularly suitable for labeling rat and human MSCs for in vivo MR cell tracking. The PDMAAm-coated maghemite nanoparticles were shown to be taken up by the target cells at significantly higher levels than were Endorem nanoparticles coated with dextran, thus allowing a minimum amount of imaging agent to be used. In addition, the labeling was not dependent on cell passage number, which can be particularly useful for cell expansion. Significant contrast enhancement was demonstrated by cells labeled with PDMAAm-coated maghemite nanoparticles and implanted in a rat brain over cells labeled with Endorem.

The fact that PDMAAm coating of iron oxide nanoparticles improves cellular uptake is, to the best of our knowledge, a new observation yet to be published. In subsequent research, PDMAAm-coated maghemite nanoparticles can be further modified by covalent attachment of highly specific biomolecules (antibodies, peptides, etc.) to make labeling more specific. In potential applications, cells can be labeled in vitro with the nanoparticles prior to transplantation. After transplantation of the labeled cells, in vivo imaging monitors cell migration throughout the body. The ability to track the extent of migration following direct implantation or systemic injection in vivo using noninvasive MR imaging techniques is the greatest advantage of the described procedure. Cellular monitoring is particularly important for evaluating cell-based therapies.

ACKNOWLEDGMENT

The financial support of the Center for Cell Therapy and Tissue Repair No. 1M0538, the Grant Agency of AS CR (grants KAN201110651 and KAN200200651), the Grant Agency of the Czech Republic (203/09/1242) and the EC-FP6 project DiMI (LSHB-CT-2005-512146) is gratefully acknowledged.

LITERATURE CITED

(1) Lewin, M., Carlesso, N., Tung, C. H., Tang, X. W., Cory, D., Scadden, D. T., and Weissleder, R. (2000) Tat peptide-derivatized magnetic nanoparticles allow in vivo tracking and recovery of progenitor cells. *Nat. Biotechnol. 18*, 410–414.

(2) Modo, M., Hoehn, M., and Bulte, J. W. (2005) Cellular MR imaging. *Mol. Imaging 4*, 143–64.

(3) Wilhelm, C., Billotey, C., Roger, J., Pons, J. N., Bacri, J. C., and Gazeau, F. (2003) Intracellular uptake of anionic superparamagnetic nanoparticles as a function of their surface coating. *Biomaterials 24*, 1001–1011.

(4) Metz, S., Bonaterra, G., Rudelius, M., Settles, M., Rummeny, E. J., and Daldrup-Link, H. E. (2004) Capacity of human monocytes to phagocytose approved iron oxide MR contrast agents in vivo. *Eur. Radiol. 14*, 1851–1858.

(5) Muller, K., Skepper, J. N., Posfai, M., Trivedi, R., Horwath, S., Corot, C., Lancelot, E., Thompson, P. W., Brown, A. P., and Gillard, J. H. (2007) Effect of ultrasmall superparamagnetic iron oxide nanoparticles (Ferumoxtran-10) on human monocyte-macrophages in vitro. *Biomaterials 28*, 1629–1642.

(6) Hinds, K. A., Hill, J. M., Shapiro, E. M., Laukkanen, M. O., Silva, A. C., Combs, C. A., Varney, T. R., Balaban, R. S., Koretsky, A. P., and Dunbar, C. E. (2003) Highly efficient endosomal labeling of progenitor and stem cells with large magnetic particles allows magnetic resonance imaging of single cells. *Blood 102*, 867–872.

(7) Syková, E., and Jendelová, P. (2007) Migration, fate and in vivo imaging of adult stem cells in the CNS. *Cell Death Differ. 14*, 1336–1342.

(8) Veiseh, O., Sun, C., Gunn, J., Kohler, N., Gabikian, P., Lee, D., Bhattarai, N., Ellenbogen, R., Sze, R., Hallahan, A., Olson, J., and Zhang, M. (2005) Optical and MRI multifunctional nanoprobe for targeting glicomas. *Nano Lett. 5*, 1003–1008.

(9) Huh, Y. M., Jun, Y. W., Song, H. T., Kim, S., Choi, J. S., Lee, J. H., Yoon, S., Kim, K. S., Shin, J. S., Suh, J. S., and Cheon, J. (2005) In vivo magnetic resonance detection of cancer by using multifunctional magnetic nanocrystals. *J. Am. Chem. Soc. 127*, 12387–12391.

(10) Sun, C., Sze, R., and Zhang, M. (2006) Folic acid-PEG conjugated superparamagnetic nanoparticles for targeted cellular uptake and detection by MRI. *J. Biomed. Mater. Res. 78A*, 550–557.

(11) Tiefenauer, L. X., Kuhne, G., and Andres, R. Y. (1993) Antibody-magnetite nanoparticles: in vitro characterization of a potential tumor-specific contrast agent for magnetic resonance imaging. *Bioconjugate Chem. 4*, 347–352.

(12) Kresse, M., Wagner, S., Pfefferer, D., Lawaczek, R., Elste, V., and Semmler, W. (1998) Targeting of ultrasmall superparamagnetic iron oxide (USPIO) particles to tumor cells in vivo by using transferring receptor pathways. *Magn. Reson. Med. 40*, 236–242.

(13) Arbab, A. S., Bashaw, L. A., Miller, R. B., Jordan, E. K., Lewis, B. K., Kalish, H., and Frank, J. A. (2003) Characterization of biophysical and metabolic properties of cells labeled with superparamagnetic iron oxide nanoparticles and transfection agent for cellular MR imaging. *Radiology 229*, 838–846.

(14) Gershon, H., Ghirlando, R., Guttman, S. B., and Minsky, A. (1993) Mode of formation and structural features of DNA-cationic liposome complexes used for transfection. *Biochemistry 32*, 7143–7151.

(15) Jesephson, L., Tung, C. H., Moore, A., and Weissleder, R. (1999) Highly-efficient intracellular magnetic labeling with novel superparamagnetic-tat peptide conjugates. *Bioconjugate Chem. 10*, 186–171.

(16) Kostura, L., Kraitchman, D. L., Mackay, A. M., Pittenger, M. F., and Bulte, J. W. M. (2004) Feridex labeling of mesenchymal stem cells inhibits chondrogenesis but not adipogenesis or osteogenesis. *NMR Biomed. 17*, 513–517.

(17) Strable, E., Bulte, J. W. M., Moskowitz, B., Vivekanandan, K., and Douglas, T. (2001) Synthesis and characterization of soluble iron oxide-dendrimer composites. *Chem. Mater. 13*, 2201–2209.

(18) Bulte, J. W., Zhang, S., van Gelderen, P., Herynek, V., Jordan, E. K., Duncan, I. D., and Frank, J. A. (1999) Neurotransplantation of magnetically labeled oligodendrocyte progenitors: Magnetic resonance tracking of cell migration and myelination. *Proc. Natl. Acad. Sci. U.S.A. 96*, 15256–15261.

(19) Horák, D., Babič, M., Jendelová, P., Herynek, V., Trchová, M., Pientka, Z., Pollert, E., Hájek, M., and Syková, E. (2007) D-mannose-modified iron oxide nanoparticles for stem cell labeling. *Bioconjugate Chem. 18*, 635–644.

(20) Babič, M., Horák, D., Trchová, M., Jendelová, P., Glogarová, K., Lesný, P., Herynek, V., Hájek, M., and Syková, E. (2008) Poly(L-lysine)-modified iron oxide nanoparticles for stem cell labeling. *Bioconjugate Chem. 19*, 740–750.

(21) Orakdogen, N., and Okay, O. (2006) Reentrant conformation transition in poly(*N*,*N*-dimethylacrylamide) hydrogels in water-organic solvent mixtures. *Polymer 47*, 561–568.

(22) Azizi, S. A., Stokes, D., Augelli, B. J., DiGirolamo, C., and Prockop, D. J. (1998) Engraftment and migration of human bone marrow stromal cells implanted in the brains of albino rats: Similarities to astrocyte grafts. *Proc. Natl. Acad. Sci. U.S.A. 95*, 3908–3913.

(23) Pittenger, M. F., Mackay, A. M., Beck, S. C., Jaiswal, R. K., Douglas, R., Mosca, J. D., Moorman, M. A., Simonetti, D. W., Craig, S., and Marshak, D. R. (1999) Multilineage potential of adult human mesenchymal stem cells. *Science 284*, 143–147.

(24) Ishiyama, M., Shiga, M., Sasamoto, K., Mizoguchi, M., and He, P. (1993) A new sulfonated tetrazolium salt that produces a highly water-soluble formazan dye. *Chem. Pharm. Bull. 41*, 1118–1122.

(25) Závěta, K., Kančík, A., Maryško, M., Pollert, E., and Horák, D. (2006) Superparamagnetic properties of γ-Fe_2O_3 particles: Mössbauer spectroscopy and d.c. magnetic measurements. *Czech. J. Phys. 56* (Suppl. E), 83–91.

(26) Socrates, G. (2001) In *Infrared and Raman Characteristic Group Frequencies*, pp 143−145, Wiley, New York.

(27) Sun, R., Dittrich, J., Le-Huu, M., Mueller, M. M., Bedke, J., Kartenbeck, J., Lehman, J. K., Krueger, R., Bock, M., Huss, R., Seliger, C., Grone, H. J., Misselwitz, B., Semmler, W., and Kiessling, F. (2005) Physical and biological characterization of superparamagnetic iron oxide- and ultrasmall superparamagnetic iron oxide-labeled cells: A comparison. *Invest. Radiol. 40*, 504–513.

(28) Bentzen, E. L., Tomlinson, I. D., Mason, J., Gresch, P., Warnement, M. R., Wright, D., Sanders-Bush, E., Blakely, R., and Rosenthal, S. (2005) Surface modification to reduce non-specific binding of quantum dots in live cell assays. *Bioconjugate Chem. 16*, 1488–1494.

BC800373X

Bioconjugate Chemistry 20th Anniversary

Subscriber access provided by SHEMYAKIN-OVCHINNIKOV INST

Article

PEGylation of Anti-Sialoadhesin Monoclonal Antibodies Enhances Their Inhibitory Potencies without Impairing Endocytosis in Mouse Peritoneal Macrophages

Julie Ducreux, Donatienne Tyteca, Bernard Ucakar, Thierry Medts, Paul R. Crocker, Pierre J. Courtoy, and Rita Vanbever

Bioconjugate Chem., **2009**, 20 (2), 295-303• DOI: 10.1021/bc800390g • Publication Date (Web): 14 January 2009

Downloaded from http://pubs.acs.org on May 15, 2009

More About This Article

Additional resources and features associated with this article are available within the HTML version:

- Supporting Information
- Access to high resolution figures
- Links to articles and content related to this article
- Copyright permission to reproduce figures and/or text from this article

View the Full Text HTML

ACS Publications
High quality. High impact.

Bioconjugate Chemistry is published by the American Chemical Society. 1155 Sixteenth Street N.W., Washington, DC 20036

PEGylation of Anti-Sialoadhesin Monoclonal Antibodies Enhances Their Inhibitory Potencies without Impairing Endocytosis in Mouse Peritoneal Macrophages

Julie Ducreux,[†] Donatienne Tyteca,[‡] Bernard Ucakar,[†] Thierry Medts,[‡] Paul R. Crocker,[§] Pierre J. Courtoy,[‡] and Rita Vanbever*[,†]

Department of Pharmaceutical Technology, School of Pharmacy, and Cell Biology Unit, de Duve Institute, Université catholique de Louvain, 1200 Brussels, Belgium, and Wellcome Trust Biocentre, College of Life Sciences, University of Dundee, Dundee DD1 5EH, United Kingdom. Received September 12, 2008; Revised Manuscript Received December 4, 2008

Poly(ethylene glycol) (PEG) 5 kDa and 20 kDa have been previously conjugated to two anti-sialoadhesin (Sn) monoclonal antibodies (mAbs), SER-4 and 3D6, and shown to dramatically increase their inhibitory potency in solid-phase red blood cell binding assays. In the present study, we evaluated the effect of anti-Sn SER-4 and 3D6 mAbs PEGylation on their inhibition of cell adhesion in mouse peritoneal macrophages. We also examined whether Sn-mediated PEGylation could affect plasma membrane functions of macrophages as to prevent accessibility, binding, and endocytosis of macromolecules and particles. Conjugation of PEG to plasma membrane is known to cause immune tolerance by impairing protein−protein and cell−cell interactions. PEGylation of SER-4 and 3D6 mAbs increased by 4-fold their inhibition of Sn-mediated erythrocyte binding to macrophages. PEGylated SER-4 and 3D6 mAbs did not impair macrophage membrane integrity, cell metabolism, nor pinocytosis of macromolecules and phagocytosis of latex particles. Thus, PEGylation of antibodies directed to cell surface receptors could be potentially exploited in a therapeutic setting to increase inhibitory potency of antibodies without impairing vital functions of cells.

INTRODUCTION

The covalent coupling of poly(ethylene glycol) (PEG) to proteins is a well-established technique to enhance the therapeutic potential of peptides and proteins. Multiple benefits of PEGylation include prolongation of protein half-life in the body and elimination of its immunogenicity (for reviews, see *refs 1, 2*:). PEGylation has also been extended to cells and tissues. Red blood cells (RBC) were the first example of cell surface PEGylation to produce transfusable universal blood (*3*). The covalent coupling of PEG (molecular weight, MW, 5 kDa) to proteins exposed on RBC surfaces could attenuate the immunologic recognition of surface antigens without adversely affecting viability, morphology, deformability, and other membrane functions (*4, 3*). Interestingly, PEGylation of proteins exposed on the surface of rat pancreatic islets (PEG MW, 5 kDa) conferred immunotolerance of the islets without interfering with glucose homeostasis and islet viability in vitro (*5*). In vivo, the PEGylation of the islets extended their survival despite a reduced dose of immunosuppressive medication (*6*). The immunoprotective effect of PEG was mainly due to the large steric exclusion volume provided by the flexibility of PEG molecules.

In a recent study, we explored an additional benefit of PEGylation based on the concept of PEG-dependent steric hindrance. We showed that PEGylation of two monoclonal antibodies (mAbs), SER-4 and 3D6, directed to the macrophage adhesion molecule, sialoadhesin (Sn), dramatically increased their efficacy for blocking Sn-mediated interactions (*7*). Sn (Siglec-1, CD169) is a 185 kDa macrophage-restricted adhesion molecule and a member of the Siglec family of sialic acid binding immunoglobulin (Ig)-like lectins (*8*). Sn mediates sialic acid-dependent adhesion of macrophages to a range of cell types including lymphoid and myeloid cells (*9*). Sn was originally characterized in the mouse as a nonphagocytic sialic acid-dependent sheep erythrocyte receptor expressed on macrophage subsets (*10*), especially those in secondary lymphoid organs (*11*). Sn can be upregulated on monocytes and macrophages during inflammatory responses, including autoimmune diseases (*12, 13*), and on macrophages that infiltrate human breast tumors (*14*). The inhibitory potencies of PEGylated mAbs were evaluated using a well-defined solid-phase RBC binding assay in which recombinant Sn was coated on a plate and allowed to bind RBC in the presence and absence of anti-Sn mAbs. In this assay, neither unconjugated SER-4 nor 3D6 mAb was able to inhibit RBC binding to Sn when added alone, whereas both mAbs were originally identified as blocking antibodies for RBC binding to peritoneal macrophages (*15*). These contradictory results might be explained by the density of Sn coated on the microplate versus that expressed on macrophages. Considering that the interaction of Sn with sialoglycoconjugates is multivalent, the large amount of Sn coated on the plate generated a higher-order multivalency with sialoglycoconjugates on RBC surfaces (*16, 17*). Therefore, the high-density coating of Sn used in the solid-phase RBC binding assay led to higher avidity binding of RBC, which were less efficiently inhibited by SER-4 or 3D6.

The present study aimed to evaluate the inhibitory potency of PEGylated SER-4 and 3D6 in a cellular environment using peritoneal macrophages induced to express Sn (*18*). As PEGylation of cells, such as RBC, and pancreatic islets were shown to camouflage their surface and repel the binding of immune cells and proteins, we also tested the specificity of the inhibition, that is, we evaluated if Sn PEGylation, using PEGylated SER-4 and 3D6, only affected Sn-mediated macrophage interactions or led to Sn receptor-independent side effects, as to prevent the

* Author to whom correspondence should be addressed. Tel.: +32 2 764 73 25. Fax: +32 2 764 73 98. E-mail: rita.vanbever@uclouvain.be.

[†] School of Pharmacy, Université catholique de Louvain.

[‡] de Duve Institute, Université catholique de Louvain.

[§] Wellcome Trust Biocentre.

10.1021/bc800390g CCC: $40.75 © 2009 American Chemical Society
Published on Web 01/14/2009

Table 1. Assessment of Cell Integrity[a]

treatment (10 μg/mL)	cell viability tests: Trypan blue exclusion (% of viable cells)	LDH release (% of total)	MTT conversion (% of untreated cells)
untreated cells (control)	92.1 ± 7.3	13.3 ± 2.8	100 ± 11.6
SER-4 and 3D6	89.9 ± 4.2	13.0 ± 4.9	108.1 ± 19.4
SER-4−2PEG 20 kDa	84.5 ± 3.9	15.3 ± 4.0	90.0 ± 11.3
3D6−2PEG 5 kDa	88.0 ± 1.9	14.2 ± 3.6	89.3 ± 4.4
3D6−1PEG 20 kDa	87.6 ± 2.8	14.7 ± 4.2	93.5 ± 13.0
3D6−2PEG 20 kDa	90.0 ± 3.6	14.7 ± 2.6	87.0 ± 17.4
SER-4−2PEG 20 kDa and 3D6−2PEG 20 kDa	92.1 ± 3.6	13.7 ± 4.6	89.2 ± 14.7
Triton 1% (cell death by necrosis)	0.7 ± 1.3[b]	98.9 ± 3.3[b]	17.9 ± 2.2[b]

[a] Plasma membrane integrity and cell metabolism of Sn-expressing TPM were assessed by LDH release, Trypan blue exclusion, and MTT reduction. Data are the mean ± SD of 3 pooled independent experiments (carried out in duplicate). [b] Tukey test, $p < 0.0001$.

accessibility, binding, and endocytosis of macromolecules and particles by macrophages.

EXPERIMENTAL PROCEDURE

Animals. Female C57BL6 mice were bred at the Faculty of Medicine animal facilities of the Université catholique de Louvain (Belgium) and used between 7 and 11 weeks of age. Animals had free access to tap water and laboratory diet during the experimental period. All experimental protocols with mice were approved by the Institutional Animal Care and Use Committee of the Faculty of Medicine of the Université catholique de Louvain.

Preparation of Sn-Expressing Peritoneal Macrophages. Thioglycollate-elicited peritoneal macrophages (TPM) from female C57BL6 mice were obtained 4 days after intraperitoneal injection of 1 mL Brewer's modified thioglycollate broth. About 15 million cells per mouse were recovered by peritoneal lavage with 5 mL HBSS of which ~70% are macrophages (*19*). TPM were seeded at 1.25×10^6 macrophages/cm^2 on collagen I precoated multiwell tissue culture plate (Corning Life Sciences, Lowell, MA, USA) in RPMI 1640 supplemented with 2 mM L-glutamine and 10% fetal bovine serum. Nonadherent cells were removed by washing after 40 min of incubation in a humidified atmosphere at 37 °C in 5% CO_2. In order to induce sialoadhesin expression, TPM were incubated in fresh medium supplemented with 2 mM L-glutamine and 10% C57BL6 mouse serum during 3 days (*18*).

PEGylation of SER-4 and 3D6 mAbs. The most amine reactive groups of SER-4 and 3D6 mAbs were conjugated to 1 or 2 molecules of PEG 5 kDa or 20 kDa, as previously described (*7*). Modification of mAb with PEG molecules was abbreviated; for example, SER-4−2PEG 5 kDa and denotes a modification of SER-4 mAb with 2 linear PEG chains of 5 kDa.

Evaluation of Cell Membrane Integrity and Cell Metabolism. After 3 days in culture with mouse serum, Sn-expressing TPM were washed with RPMI + 0.1% BSA and precooled at 4 °C. Fcγ receptors on TPM surfaces were blocked using a rat monoclonal antibody against mouse CD16/32 receptors (clone 2.4G2, 1:150) at 4 °C for 20 min. Cells were then incubated with fresh serum-free medium containing 10 μg/mL of SER-4−2PEG 20 kDa, 3D6−2PEG 5 kDa, 3D6−1PEG 20 kDa, 3D6−2PEG 20 kDa, or a combination of SER-4−2PEG 20 kDa and 3D6−2PEG 20 kDa at 4 °C for 45 min. Cells were finally transferred in a humidified atmosphere at 37 °C in 5% CO_2 during 4 h. Plasma membrane integrity of cells after incubation with PEGylated mAbs was assessed by the release of lactate dehydrogenase (LDH) and the exclusion of Trypan blue. LDH activity was assessed by measuring the NADH consumption during the reduction of pyruvate into lactate (*20*). Results were expressed as the percentage of activity detected in the medium over the sum of the activities in the medium and in the cells. Trypan blue exclusion results were expressed as the percentage of viable cells. Cell metabolism was assessed by the reduction of 3-(4,5-dimethylthiazol-2-yl)-2,5-diphenyl tetrazolium bromide (MTT), a yellow water-soluble tetrazolium dye reduced by metabolically active cells to a water-insoluble purple formazan (*21*). Results were expressed as the percentage of metabolically active cells. In all assays, untreated cells and Triton-treated cells were used as controls.

Red Blood Cell Rosetting Assay. 5×10^4 TPM were added in wells of a collagen I precoated 48-well tissue culture plate and induced to express Sn by culture in 10% mouse serum for 3 days. Cells were washed with RPMI + 0.1% BSA and precooled at 4 °C. Fcγ receptors on TPM surface were blocked, as described above, at 4 °C for 20 min. Cells were then incubated with 300 μL of 3-fold serial dilutions of the different species of SER-4-PEG or 3D6-PEG alone or in combination at 4 °C for 45 min. Three hundred microliters of freshly prepared human RBC at 1% vol/vol was added directly to the wells and incubated at 37 °C for 30 min. Unbound RBC were removed by repeated washing with medium. The percentage of macrophage binding of >4 RBC, i.e., rosettes, was determined under optical microscopy (100 cells counted; Axiovert S100, Zeiss, Minneapolis, MN, USA) (*22*). The percentage of rosettes was normalized to the percentage of rosetting activity in the absence of mAbs (considered to be equal to 100%). As controls, TPM were incubated with an irrelevant rat IgG2a, to test the specificity of mAbs, or with nonfunctional PEG in RPMI + 0.1% BSA, to evaluate a possible nonspecific effect of the polymer on RBC binding. In the latter case, the concentration of PEG solution was adjusted to the number of PEG molecules found in a solution composed of a mixture of both PEGylated mAbs.

Characterization of Endocytosis Modes. *Nonspecific Adsorptive Endocytosis.* FITC-albumin was used as tracer of nonspecific adsorptive endocytosis (*23*). Sn-expressing TPM were first washed with warm medium without serum and incubated at 37 °C during 30 min. The uptake of FITC-albumin by Sn-expressing TPM was measured using increasing concentrations of FITC-albumin in serum-free medium at 37 °C for 2 h. After 6 washes for 30 s with PBS-Ca^{2+}-Mg^{2+} (removing 75−80% of tracers bound at 4 °C), intracellular uptake of FITC-albumin was measured in cell lysates prepared in 0.05% (vol/vol) Triton X-100 by fluorimetry (λ_{exc} 485 nm, λ_{em} 530 nm; Packard Fluorocount Microplate Fluorometer, Packard Instrument Company, Meriden, CT, USA). For competition studies, fresh serum-free medium containing 700 μM bovine albumin (A4378, Sigma-Aldrich, St Louis, MO, USA) was incubated with Sn-expressing TPM 1 h at 4 °C prior to a coincubation with 7 μM FITC-albumin at 37 °C for 2 h. Cells were then washed 6 times with PBS-Ca^{2+}-Mg^{2+} and digested with 0.05% (vol/vol) Triton X-100. Energy depletion of Sn-expressing TPM was performed by incubation with 5 mM sodium azide (NaN_3) and 60 mM 2-deoxy-D-glucose (2-DOG) in serum-free medium (ATP depletion medium). Cells were preincubated in ATP

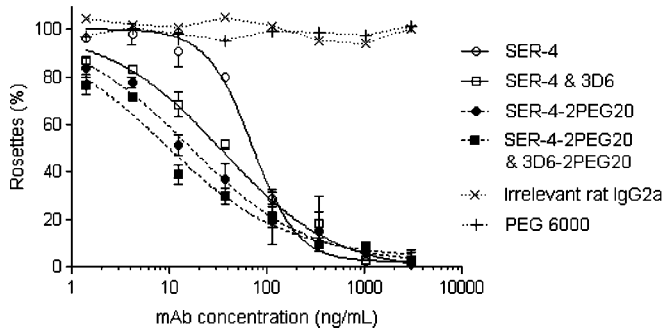

Inhibitor	IC_{50} (ng/mL)
SER-4	70.2 ± 3.5
3D6	71.2 ± 6.7
SER-4 & 3D6	36.7 ± 9.2
SER-4-2PEG20	16.0 ± 2.6
3D6-2PEG5	8.8 ± 1.0
3D6-1PEG20	9.1 ± 0.7
3D6-2PEG20	10.7 ± 2.3
SER-4-2PEG20 & 3D6-2PEG20	8.8 ± 2.2

Figure 1. Inhibition of RBC binding to Sn-expressing TPM by PEGylated SER-4 and 3D6 mAbs. Data are the mean ± SD of two pooled independent experiments (carried out in duplicate). Rosette formation is the % of macrophages that bound >4 RBC. IC_{50} are concentrations inhibiting 50% of rosette formation. Experiments with irrelevant IgG2a and PEG 6 kDa used in comparable concentrations did not show any inhibitory effect on rosette formation.

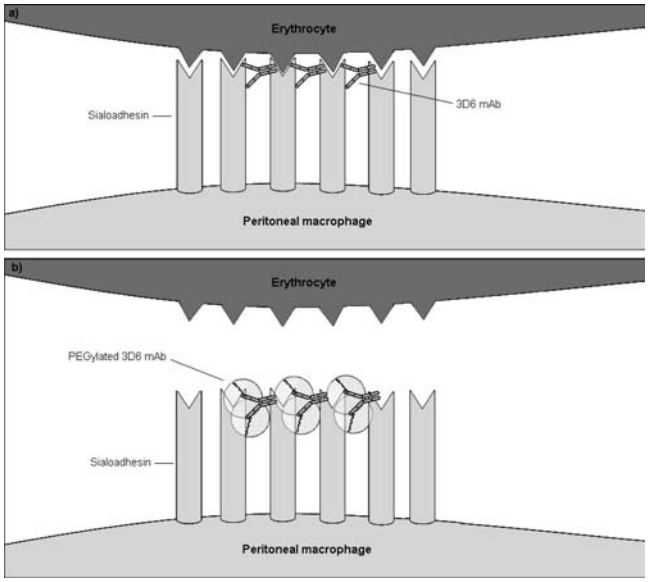

Figure 2. Creation of a sterical hindrance by PEG on Sn molecules. Interaction between an erythrocyte and a macrophage occurs when both sialic acids and Sn cluster, to create high-avidity binding. At the same concentration, unmodified 3D6 mAb did not inhibit erythrocyte binding to the macrophage (a), whereas PEGylated 3D6 mAb did (b). The higher potency of PEGylated mAbs to inhibit erythrocyte binding was likely due to a sterical effect created by PEG molecules around Sn.

depletion medium at 37 °C for 20 min and incubated with 7 μM FITC-albumin in ATP depletion medium for 2 additional hours. Cells were then washed 6 times with PBS-Ca^{2+}-Mg^{2+} and digested with 0.05% (vol/vol) Triton X-100.

Receptor-Mediated Endocytosis. Iron-saturated transferrin was labeled with ^{125}I using iodogen-precoated tubes to a specific radioactivity of 2600−3300 cpm/ng protein. Sn-expressing TPM surface binding of ^{125}I-transferrin was determined by incubating cells precooled at 4 °C with increasing concentrations of ^{125}I-transferrin in serum-free medium supplemented with 0.1% BSA for 1 h. Cells were then washed and radioactivity was measured in cell lysates prepared in 0.05% (vol/vol) Triton X-100 (Minaxiγ gamma counter, Packard Instrument Company, Meriden, CT, USA). For competition studies, human serum was incubated with Sn-expressing TPM 1 h at 4 °C prior to a coincubation with 50 nM ^{125}I-transferrin for one additional hour at 4 °C. Cells were then washed 6 times with PBS-Ca^{2+}-Mg^{2+} and surface-digested with 0.2% (wt/vol) Pronase in RPMI at 4 °C for 45 min to distinguish transferrin accessible on the plasma membrane (Pronase-sensitive) from sequestered transferrin (Pronase-resistant) (*24*). Pronase-resistant fraction (containing intracellular ^{125}I-transferrin) was pelleted by centrifugation at 250 × *g* at 4 °C for 5 min. The supernatant (containing surface-accessible transferrin) was kept, and the pellet was finally washed twice with PBS-Ca^{2+}-Mg^{2+} and lysed in 0.05% (vol/vol) Triton X-100. Radioactivity was measured in Pronase-resistant and Pronase-sensitive fractions. Energy depletion of Sn-expressing TPM was performed by incubation in ATP depletion medium at 37 °C for 20 min (see above). Cells were then precooled at 4 °C and incubated with 50 nM ^{125}I-transferrin in ATP depletion medium for 1 h. Cells were washed and reincubated at 37 °C in fresh prewarmed ATP depletion medium for 10 min. Cells were then rapidly cooled down to 4 °C, washed 6 times with PBS-Ca^{2+}-Mg^{2+}, surface digested, and radioactivity in Pronase-resistant and Pronase-sensitive fractions were measured.

Internalisation Assays. Sn-expressing TPM were first washed with warm medium without serum and incubated at 37 °C over 30 min. Cells were washed and precooled at 4 °C. Fcγ receptors on TPM surface were blocked as described above at 4 °C for 20 min. Cells were finally washed and incubated with a combination of SER-4−2PEG 20 kDa and 3D6−2PEG 20 kDa at 4 °C for 45 min prior to incubation with tracers of endocytosis.

FITC-Albumin Endocytosis. FITC-albumin was directly added to cells at a final concentration of 7 μM and incubated at 37 °C for the indicated intervals. Cells were washed 6 times with PBS-Ca^{2+}-Mg^{2+}, and intracellular uptake of FITC-albumin was measured on sonicated cell lysates prepared in 0.05% (vol/vol) Triton X-100 by fluorimetry.

^{125}I-Transferrin Endocytosis. ^{125}I-transferrin was directly added to cells at a final concentration of 50 nM and allowed to bind at 4 °C for 1 h. Cells were washed 6 times at 4 °C with PBS-Ca^{2+}-Mg^{2+} and reincubated at 37 °C in fresh prewarmed serum-free medium supplemented with 0.1% BSA for the indicated intervals. Cells were then rapidly cooled down to 4 °C, washed, and surface-digested with 0.2% (wt/vol) Pronase in RPMI at 4 °C for 45 min. Radioactivity was measured in Pronase-resistant and Pronase-sensitive fractions to distinguish intracellular from surface-accessible transferrin.

Phagocytosis. Red fluorescent carboxylate-modified latex beads of 2 μm were used as tracer of phagocytosis. Following the incubation with PEGylated mAbs, an equivalent volume of latex beads in serum-free medium was added directly to the wells at a final concentration of 270 beads/nL, mixed, and incubated at 37 °C for the indicated intervals. After 6 washes for 30 s with PBS-Ca^{2+}-Mg^{2+} (removing more than 80% of the beads bound at 4 °C), uptake of the beads was measured on sonicated cell lysates prepared in 0.05% (vol/vol) Triton X-100 by fluorimetry (λ_{exc} 485 nm, λ_{em} 610 nm). To inhibit phagocytosis (*25*), Sn-expressing TPM were first preincubated with 10 μM cytochalasin B in serum-free medium at 37 °C for 30 min

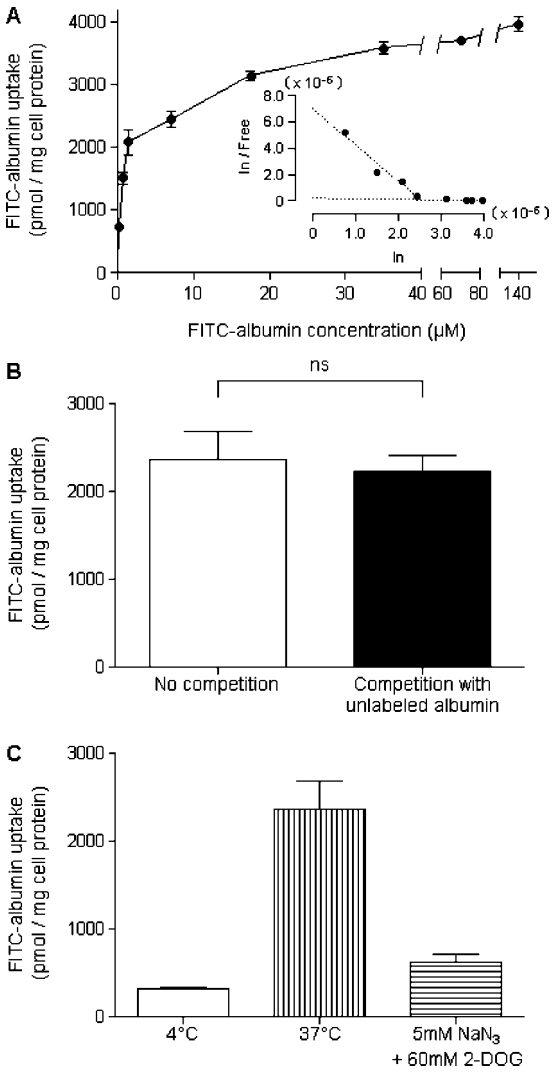

Figure 3. FITC-albumin is taken up by nonspecific adsorptive endocytosis in Sn-expressing TPM. (A) Adsorptive uptake of FITC-albumin. FITC-albumin uptake was measured as a function of substrate concentration in untreated cells at 37 °C for 2 h. Inset, scatchard analysis of the uptake (In values in abscissa are in μmol/μg cell protein; In/Free ratios in the ordinate are in L/μg cell protein). Two components of internalization were revealed with a high internalization constant ($K_{uptake} = 0.36\ \mu$M) for the first one and a low internalization constant for the second one ($K_{uptake} = 18.88\ \mu$M). (B) No competition for FITC-albumin uptake at 37 °C for 2 h. Cells were incubated with 7 μM FITC-albumin alone (open bar) or with a 100-fold excess of unlabeled albumin (filled bar); ns: no significant difference (*t* test, $p > 0.05$). (C) Endocytic uptake of FITC-albumin is evidenced by inhibition at low temperature and upon energy depletion. Cells were incubated with 7 μM FITC-albumin at 4 °C for 1 h (open bar) or at 37 °C for 2 h (vertically striped bar). Cellular ATP was depleted by incubating cells in ATP depletion medium at 37 °C for 20 min. Cells were then incubated with 7 μM FITC-albumin in ATP depletion medium at 37 °C for 2 h (horizontally striped bar).

and incubated with latex beads (270 particles/nL) in serum-free medium containing 10 μM cytochalasin B at 37 °C for the indicated intervals. Cells were then washed 6 times 30 s with PBS-Ca^{2+}-Mg^{2+} and digested with 0.05% (vol/vol) Triton X-100.

Localization of Fluorescent Latex Beads in Sn-Expressing TPM by Confocal Microscopy. Untreated and PEGylated cells, that is, pretreated with the combination of SER-4−2PEG 20 kDa and 3D6−2PEG 20 kDa, were incubated with 1 μm green-fluorescent latex beads or 2 μm red-fluorescent latex beads at 37 °C for 3 h, washed 6 times 30 s with PBS-Ca^{2+}-Mg^{2+}, and were fixed at room temperature in 4% paraformaldehyde for 30 min. Cells were then washed 5 times with PBS and aspecific sites were blocked by incubation in BSA/lysine solution at room temperature for 30 min. To label the surface membrane of Sn-expressing TPM, rat antimouse F4/80 mAb (1:200) was incubated in BSA/lysine solution at room temperature for 1 h. Cells were then washed 6 times 5 min with BSA/lysine and incubated with Alexafluor 647-conjugated goat antirat IgG antibody (1:200) at room temperature for 1 h. Cells were finally washed 6 times 5 min with PBS, postfixed in 4% paraformaldehyde, washed 3 times with PBS, and mounted on glass slides with mowiol. Cells were observed with a Zeiss confocal laser scanning microscope LSM510 Meta-multiphoton. Data were analyzed with Zeiss LSM software to obtain $x-y$, $x-z$, and $y-z$ views of cells.

Fate of Anti-Sn mAbs. 3D6 mAb was labeled with ^{125}I using iodogen-precoated tubes to a specific radioactivity of 2800−3500 cpm/ng of protein. Fcγ receptors on Sn-expressing TPM surface were blocked, and cells were then surface-labeled with 5 μg/mL ^{125}I-3D6 mAb in serum-free medium supplemented with 0.1% BSA at 4 °C for 45 min. Fresh prewarmed serum-free medium was then directly added to ^{125}I-3D6 solution in wells, and cells were incubated at 37 °C for the indicated intervals. Cells were then rapidly cooled down to 4 °C, washed 6 times with PBS-Ca^{2+}-Mg^{2+}, and surface-digested with 0.2% (wt/vol) Pronase in RPMI for 45 min as described above.

Analysis. All data were normalized to the cell protein content. Protein concentrations were measured by microBCA protein assay using BSA as the protein standard. Unless otherwise stated, results were expressed as mean ± standard deviation (SD) of 3 wells of 1 representative experiment. Statistical comparisons of experimental values (by unpaired *t* test or one-way analysis of variance (ANOVA) test and Tukey post-test) and other mathematical analyses were performed using the GraphPad *Prism* software for Windows (v 5.00, La Jolla, CA, USA). Differences were considered significant at $p < 0.05$.

RESULTS AND DISCUSSION

SER-4 and 3D6 are monoclonal rat IgG2a anti-Sn antibodies directed to two distinct epitopes of mouse Sn, domains 2 and/or 3 for SER-4, and domain 1 for 3D6 (*9*). We showed previously in solid-phase binding assays that PEGylation of SER-4 and 3D6 mAbs strongly promoted their inhibitory potencies against RBC binding (*7*). SER-4 carrying 2 molecules of PEG 20 kDa (SER-4−2PEG 20 kDa) or 3D6 carrying 2 molecules of PEG 5 kDa (3D6−2PEG 5 kDa) alone each resulted in about 75% inhibition, which was only reached by the combination of unmodified mAbs. Moreover, 3D6 carrying 1 or 2 molecules of PEG 20 kDa (3D6−1PEG 20 kDa or 3D6−2PEG 20 kDa) could totally inhibit RBC binding as shown by serial dilutions. When SER-4-PEG and 3D6-PEG were tested in combination, their inhibitory potency further increased in line with the degree of PEGylation.

In the present study, only these derivatized mAbs and the combination of SER-4 and 3D6 with 2 molecules of 20 kDa were tested. SER-4 and 3D6 mAbs with other extents of derivatization that did not inhibit RBC binding in solid-phase assays were not studied.

Effect of PEGylated Anti-Sn mAbs Binding on Sn-Expressing TPM Viability. PEG molecules larger than 400 Da are considered nontoxic, and PEG has been approved by the FDA for use in food and cosmetics (*26*). However, Murad et al. showed that, when surface of RBC was highly derivatized with PEG 5 kDa, PEGylation induced adverse structural and functional effects on cells (*4*). Therefore, in the present assay, we evaluated the effect of PEGylated SER-4 and 3D6 on Sn-expressing TPM viability and cell function using different cytotoxicity assays (Table 1): LDH release and Trypan blue

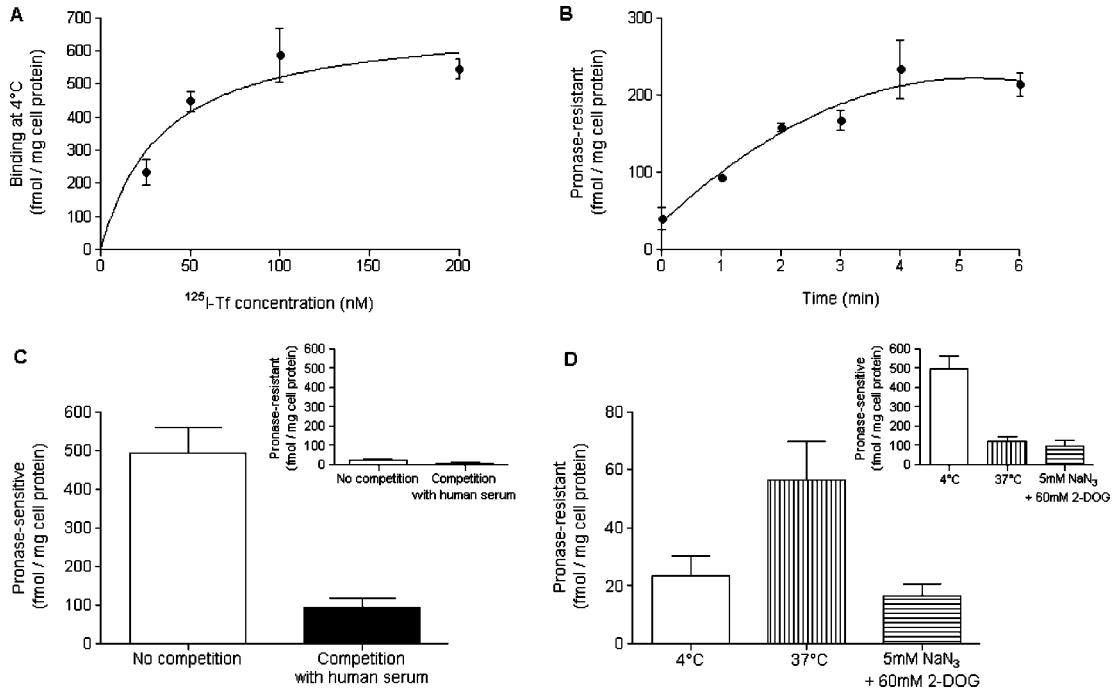

Figure 4. ^{125}I-transferrin endocytosis by Sn-expressing TPM. (A) Specific binding of ^{125}I-transferrin at increasing concentrations at 4 °C. (B) Kinetics of ^{125}I-transferrin internalization. Cells were surface-labeled with 50 nM ^{125}I-transferrin at 4 °C, washed, and reincubated at 37 °C in transferrin-free medium for the indicated intervals. Increase in Pronase-resistant counts indicate values of intracellular transferrin. (C) Competitive binding of ^{125}I-transferrin at 4 °C. Cells were incubated with ^{125}I-transferrin in serum-free medium for 1 h (open bar) or incubated with human serum for 1 h then with ^{125}I-transferrin in human serum for an additional hour (filled bar). Pronase-sensitive counts indicate values of surface-accessible transferrin. Inset, Pronase-resistant counts of the same cells. (D) Endocytosis of ^{125}I-transferrin is evidenced by incubation at low temperature and upon energy depletion. Cells were surface-labeled with 50 nM ^{125}I-transferrin at 4 °C and then washed (open bar) or further reincubated at 37 °C in transferrin-free medium for 10 min (vertically striped bar). ATP-depleted cells were surface-labeled at 4 °C with 50 nM ^{125}I-transferrin in ATP depletion medium for 1 h, washed, and reincubated at 37 °C in ATP depletion conditions for 10 min (horizontally striped bar). Inset, Pronase-sensitive counts of the same cells.

exclusion to assess plasma membrane integrity and MTT reduction to determine the metabolic activity. In these assays and in the subsequent ones, we tested the PEGylated mAbs concentration that inhibited with the highest efficacy the binding of RBC to Sn in solid-phase binding assay (*7*). Whatever the PEGylated mAbs, none of them showed any appreciable damage to the plasma membrane or alteration of metabolic activity of TPM.

Inhibition of RBC Binding to Sn-Expressing TPM by PEGylated Anti-Sn mAbs. In order to assess the inhibitory potency of PEGylated SER-4 and 3D6 mAbs on Sn-mediated interaction in a cellular environment, we used peritoneal macrophages induced to express Sn. As already shown (*22*), parent SER-4 and 3D6 mAbs inhibited RBC binding to macrophages with a high efficacy when used alone (Figure 1). However, PEGylated mAbs used alone were all better inhibitors than unconjugated SER-4 or 3D6 mAbs used alone or in combination. On the basis of IC_{50}, SER-4 containing 2 molecules of PEG 20 kDa was a 4-fold stronger inhibitor than unlabeled SER-4. The combination of SER-4 and 3D6, each carrying 2 molecules of PEG 20 kDa resulted in an IC_{50} of ~9 ng/mL, a 4-fold reduction IC_{50} as compared to the mixture of the non-PEGylated mAbs. This suggested that PEG molecules conferred an additional sterical hindrance around the antibody and, hence, around the receptor that prevented with higher efficacy the RBC approach (as illustrated in Figure 2). To verify that the decreased RBC binding was not the result of a nonspecific interaction of PEG molecules with macrophage surfaces, RBC binding to TPM was evaluated after incubation with PEG alone (Figure 1). PEG was not able to inhibit RBC binding by itself, indicating that the increased inhibitory potency provided by PEGylated mAbs was not due to a nonspecific binding of the polymer to the macrophage surface. Because it was the most efficient, further studies were carried out with the combination of SER-4 and 3D6 coupled with 2 molecules of PEG 20 kDa.

Effect of Sn-Mediated PEGylation of Macrophages on Albumin and Transferrin Endocytosis. Scott et al. have shown that, when erythrocytes are PEGylated, the rapid motility and molecular flexibility of the heavily hydrated PEG chains affect the global surface of cells and prevent protein−protein interactions as antibody-mediated RBC agglutination via blood group antigen (*27*). Therefore, PEGylation of Sn-expressing TPM with PEGylated SER-4 and 3D6 mAbs could affect the entire cell surface and thereby impair endocytosis mechanisms of macrophages, one of their key functions. This was examined by a series of endocytosis assays.

Nonspecific Adsorptive Endocytosis of Albumin by Sn-Expressing TPM. Nonspecific adsorptive endocytosis is a saturable process at high concentration involving, prior to internalization, interaction with nonspecific sites on the plasma membrane. In contrast to kidney proximal tubules or endothelial cells, albumin is internalized in macrophages by nonspecific interaction (*23*) and is accepted as a tracer of nonspecific adsorptive endocytosis in this cell type (*28*). To characterize the nonspecific adsorptive endocytosis of albumin in Sn-expressing TPM, its uptake was investigated in various conditions (Figure 3). FITC-albumin uptake was measured as a function of substrate concentration in untreated cells. Figure 3A shows saturation of uptake at a concentration of 17.5 μM indicating that FITC-albumin is internalized via a process saturable at high concentration, characteristic of adsorptive endocytosis. The efficiency of accumulation after 2 h was estimated at about 150×10^6 molecules per cell, i.e., 2 orders of magnitude higher than fluid-phase endocytosis. Subsequent studies were carried out at a nonsaturating albumin concentration (7 μM). To further clarify whether the binding of FITC-albumin

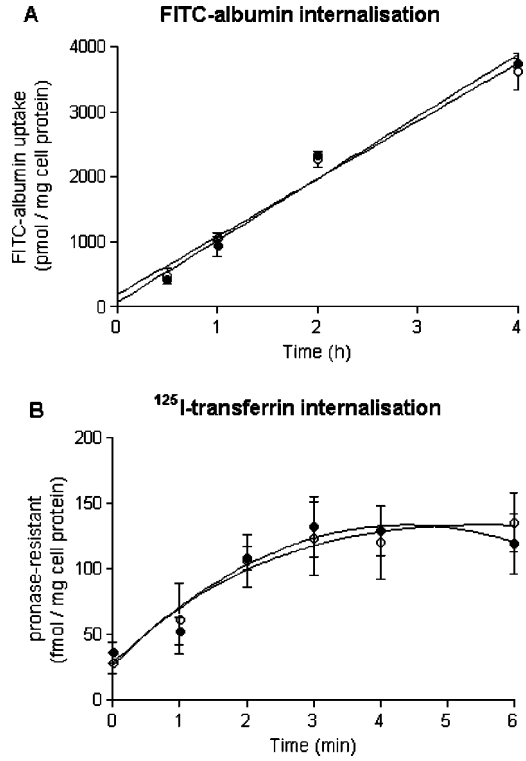

Figure 5. Effect of PEGylated anti-Sn mAbs on nonspecific adsorptive endocytosis of FITC-albumin (A) and on receptor-mediated endocytosis of ^{125}I-transferrin (B) in Sn-expressing TPM. Cells were either left untreated (open circles) or pretreated with a combination of SER-4−2PEG20 and 3D6−2PEG20 both at 10 μg/mL (filled circles) at 4 °C for 45 min. (A) FITC-albumin was added at a final concentration of 7 μM and cells were reincubated at 37 °C for the indicated intervals. Experiments were reproduced twice with similar results. (B) After incubation with 50 nM ^{125}I-transferrin at 4 °C for 1 h, cells were reincubated at 37 °C in transferrin-free medium for the indicated intervals. Increase of Pronase-resistant counts indicate the amounts of intracellular transferrin. Experiments were reproduced three times with similar results.

to Sn-expressing TPM was specific or not, a competition study was carried out using a 100-fold excess of unlabeled albumin (Figure 3B). Unlabeled albumin did not affect the uptake of FITC-albumin, indicating that this tracer binds nonspecifically to Sn-expressing TPM surface. To confirm that FITC-albumin was taken up by endocytosis, we looked at the effect of low temperature and energy depletion. Figure 3C shows that both treatments dramatically reduced the uptake of FITC-albumin in macrophages. Taken together, these results confirm that TPM induced to express Sn internalize albumin by nonspecific adsorptive endocytosis.

Receptor-Mediated Endocytosis of Transferrin by Sn-Expressing TPM. Receptor-mediated endocytosis is a specific adsorptive endocytosis mode characterized by the specific binding of a ligand to its cell surface receptor followed by internalization of ligand−receptor complexes. Transferrin is the most commonly used tracer of receptor-mediated endocytosis, and its internalization was at first studied in peritoneal macrophages induced to express Sn (Figure 4). As shown in Figure 4A, ^{125}I-transferrin binding at 4 °C to untreated TPM reached saturation at ∼600 fmol/mg cell protein, corresponding to ∼35 000 binding sites/cell, with an apparent K_d of 30 nM. Further studies were carried out with an initial concentration of 50 nM ^{125}I-transferrin (below saturation). Pronase-resistant or intracellular transferrin increased very rapidly (∼3500 molecules/cell/min) to level off after ∼6 min (Figure 4B), a time sufficient for apotransferrin−receptor complexes to be recycled on the cell surface (*29*). In a competition study, human serum (containing 35 μM transferrin) significantly decreased the binding of ^{125}I-transferrin to the cell surface, indicating that this tracer specifically binds to Sn-expressing TPM in a receptor-dependent manner (Figure 4C, Pronase-sensitive fraction). As expected for endocytosis, acquisition of intracellular ^{125}I-transferrin was largely inhibited at 4 °C (Figure 4D). Since formation of clathrin-coated pits and -vesicles supporting receptor internalization requires cellular ATP, receptor-mediated endocytosis is an energy-dependent process (*30*). Cellular ATP of Sn-expressing TPM was depleted, and ^{125}I-transferrin internalization was studied for 10 min. Figure 4D shows that ATP depletion significantly reduced the uptake of ^{125}I-transferrin in macrophages. Cellular ATP depletion also reduced the binding of ^{125}I-transferrin (Figure 4D, inset), as ATP is also needed for the recycling of transferrin receptors (*31*). These results indicate that TPM induced to express Sn internalize transferrin via receptor-mediated endocytosis.

Effect of PEGylated Anti-Sn Mabs on Nonspecific Adsorptive Endocytosis of Albumin and Receptor-Mediated Endocytosis of Transferrin. To assess the effect of PEGylated anti-Sn mAbs on FITC-albumin and ^{125}I-transferrin uptake in Sn-expressing TPM, the combination of SER-4−2PEG 20 kDa and 3D6−2PEG 20 kDa mAbs was incubated with cells at 4 °C prior to addition of 7 μM FITC-albumin or 50 nM^{125}I-transferrin. PEGylation of Sn-expressing TPM using PEGylated SER-4 and 3D6 impaired neither the binding nor the kinetics of internalization of either FITC-albumin or ^{125}I-transferrin at any time (Figure 5). Uptake of FITC-albumin (Figure 5A) and intracellular accumulation of ^{125}I-transferrin into cells (Figure 5B) were comparable in PEGylated and untreated TPM. PEGylation of Sn expressed on the TPM surface using PEGylated mAbs inhibited neither nonspecific adsorptive nor specific receptor-mediated protein interactions, and this might be explained in two ways. First, as Jang et al. showed that surface PEGylation of pancreatic islets could not completely prevent the infiltration of cytotoxic molecules into the islets (*32*), we suggest that PEG molecules coupled to antibodies directed to Sn on the TPM surface did not prevent the passage of macromolecules, such as albumin and transferrin, across the meshes of PEG. Second, it remains possible that the specific and local PEGylation of Sn expressed on TPM surface using PEGylated mAbs had no sterical impact on the whole cell surface and therefore did not prevent the approach, the binding and the internalization of albumin and transferrin (as illustrated in Figure 6). Indeed, the studies on pancreatic islets showed that an efficient immunocamouflage of cells by PEG is in part governed by the surface concentration of PEG (*33*): the higher the cell surface covered by PEG molecules, the higher the PEG hindrance.

Effect of Sn-Mediated PEGylation of Macrophages on Phagocytosis of Latex Beads. Phagocytosis is a receptor- and actin-dependent process utilized by mononuclear phagocytes and neutrophils to ingest and clear large particles (>0.5 μm) (*34*). This internalization process serves to remove foreign particles such as parasites or to remove host cells such as apoptotic bodies (*35*). Scott et al. showed that PEGylation of sheep erythrocytes could inhibit their phagocytosis without impairing protein interactions such as antibody-mediated agglutination via blood group antigen (*27*). Therefore, although PEGylation of Sn expressed on the TPM surface did not affect the internalization of macromolecules such as albumin and transferrin, it could negatively affect phagocytosis of particles. In comparison with macromolecules, particles of larger size could not easily escape the sterical effect created by PEG molecules on the cell surface.

Phagocytosis of Latex Beads by Sn-Expressing TPM. The effect of PEGylation of TPM surface on phagocytosis was investigated by studying the accumulation of red fluorescent

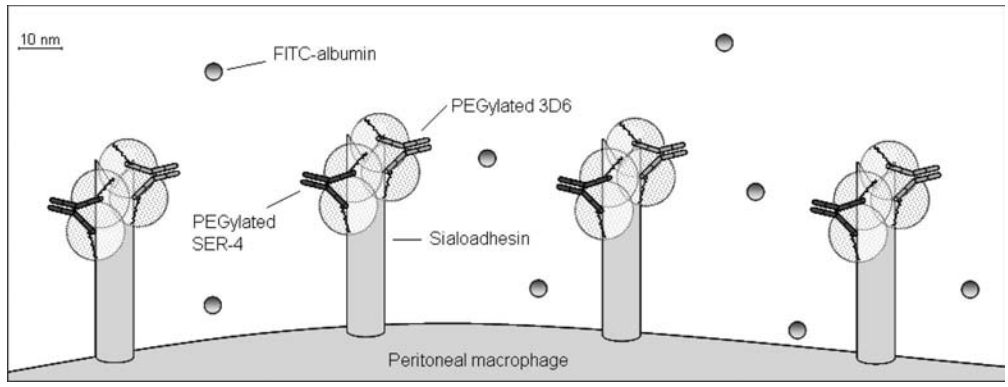

Figure 6. SER-4 and 3D6 mAbs modified with 2 molecules of PEG 20 kDa did not inhibit protein interactions with Sn expressing macrophages. The specific and local PEGylation of Sn expressed on macrophage surface using PEGylated SER-4 and 3D6 mAbs had no sterical impact on the whole cell surface and therefore did not prevent the approach, the binding and the internalization of albumin. The number of Sn molecules per cell was estimated from the number of ^{125}I-3D6 mAbs bound per cell (see Figure 10), and Sn molecules were homogenously distributed on the macrophage surface.

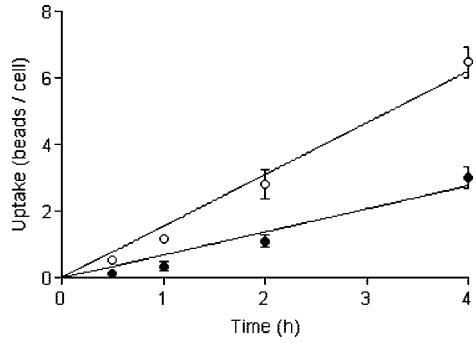

Figure 7. Inhibition of 2 μm red fluorescent latex beads phagocytosis in Sn-expressing TPM by 10 μM cytochalasin B. Sn-expressing TPM were either left untreated (open circles) or preincubated with 10 μM cytochalasin B at 37 °C for 30 min (filled circles). A final concentration of 270 beads/nL was added and cells were reincubated at 37 °C for the indicated intervals.

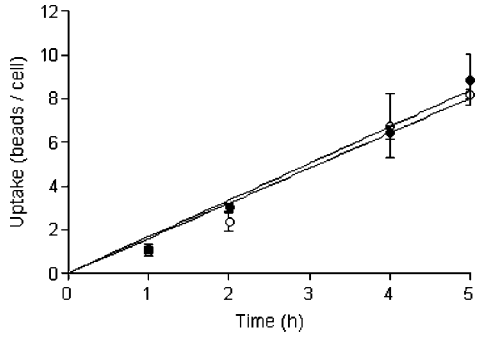

Figure 8. Effect of PEGylated anti-Sn mAbs on phagocytosis of 2 μm red fluorescent latex beads in Sn-expressing TPM. Cells were either left untreated (open circles) or pretreated with a combination of SER-4−2PEG20 and 3D6−2PEG20 both at 10 μg/mL (filled circles) at 4 °C for 45 min. A final concentration of 270 beads/nL was added, and cells were reincubated at 37 °C for the indicated intervals. Experiments were reproduced three times with similar results.

carboxylate-modified polystyrene latex beads of a large size (2 μm, 270 particles/nL). Latex beads can be taken up by both pinocytosis and phagocytosis, but the relative contribution of phagocytosis increases with the particle diameter (*25*). Figure 7 shows that 2-μm-diameter latex beads were largely internalized by phagocytosis, as suggested by a ∼50% inhibition by cytochalasin B, an inhibitor of microfilaments formation during phagocytosis (*36*).

Effect of PEGylated Anti-Sn Mabs on Phagocytosis of Latex Beads. To assess the effect of PEGylation of Sn-expressing TPM on phagocytosis, the combination of SER-4−2PEG 20 kDa and 3D6−2PEG 20 kDa mAbs was first incubated with cells at 4 °C prior to addition of latex beads at a final concentration of 270 particles/nL. Figure 8 shows that PEGylation of Sn on TPM did not detectably interfere with phagocytosis. The rate of accumulation of the beads was constant and identical in PEGylated cells as compared with untreated cells. Internalization of latex beads by both untreated and PEGylated cells was confirmed by confocal microscopy. Internalization of 1 μm latex beads was observed into both untreated (Figure 9A) and PEGylated cells (Figure 9B) by reference to the plasma membrane that was immunolabeled in blue using anti-F4/80 mAb. The same observations were made with 2 μm latex beads (data not shown).

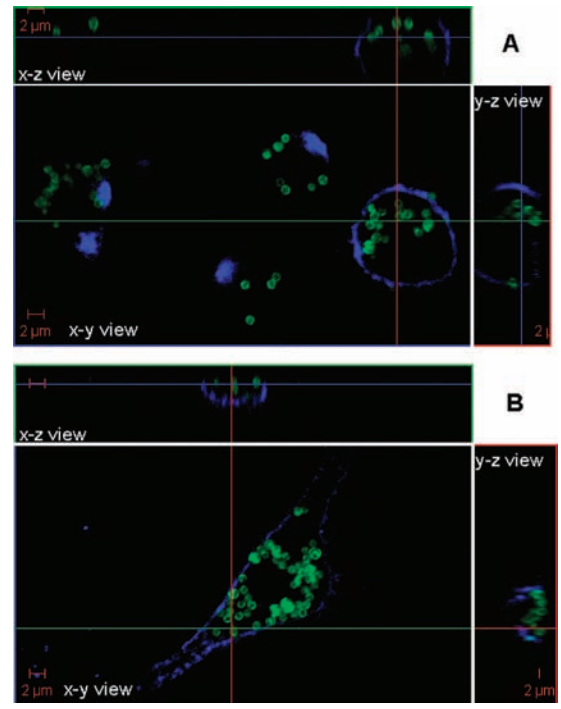

Figure 9. Effect of PEGylated anti-Sn mAbs on phagocytosis of latex beads in Sn-expressing TPM: localization of latex beads in untreated (A) and PEGylated (B) macrophages. After incubation with 1 μm latex beads (green; 270 beads/nL) for 3 h, cells were fixed and incubated wit rat antimouse F4/80 mAb, then with Alexafluor 647-conjugated goat antirat IgG antibody to identify the plasma membrane (blue).

These results suggest that PEGylation of Sn expressed on the TPM surface using PEGylated mAbs only hindered the

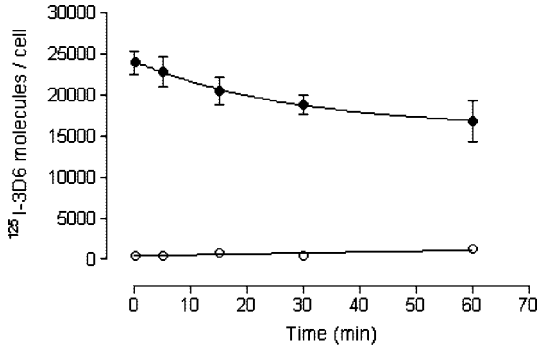

Figure 10. Fate of ^{125}I-3D6 mAb in Sn-expressing TPM. Cells were surface-labeled with 5 μg/mL ^{125}I-3D6 mAb at 4 °C for 45 min. Fresh, prewarmed serum-free medium was then directly added to ^{125}I-3D6 solution in wells, and cells were incubated at 37 °C for the indicated intervals. Intracellular 3D6 mAb molecules (open circles) were distinguished from surface-accessible 3D6 mAb molecules (filled circles) by digestion of cell surface with 0.2% (wt/vol) Pronase.

receptor and its environment. Consequently, the PEG hindrance did not affect the whole cell surface and did not impair the binding and uptake of particles.

Fate of ^{125}I-Anti-Sn mAb in Sn-Expressing TPM. Our present study shows that Sn-mediated PEGylation of macrophages improves the inhibition of cell adhesion activity of Sn without affecting pinocytosis of macromolecules and phagocytosis of particles. To verify that the absence of effect on endocytosis and phagocytosis was not due to a shedding of PEGylated mAbs from the cell surface, we studied the fate of ^{125}I-3D6 mAb in Sn-expressing cells (Figure 10). ^{125}I-3D6 mAb was not detectably internalized when cells were incubated at 37 °C (Figure 10, open circles, Pronase-resistant counts), and shedding of ^{125}I-3D6 mAb bound to the cell surface was moderate (Figure 10, Pronase-sensitive counts) over 1 h. Binding of ^{125}I-3D6 mAb at 4 °C to Sn-expressing TPM reached 400 fmol/mg cell protein, corresponding to ~24 000 molecules/cell. A slight release of ^{125}I-3D6 mAb was observed during the first 15 min at 37 °C (~230 molecules/cell/min), decreasing the number of binding sites to ~20 000 molecules/cell. Then, an equilibrium between bound mAbs and free mAbs in solution kept the binding of ^{125}I-3D6 mAb to Sn-expressing cell surface almost constant over 1 h. The release of mAbs from the cell surface slowed down to ~80 molecules/cell/min, and ~17 000 molecules of ^{125}I-3D6 mAb remained bound to the cell surface after 1 h at 37 °C (Figure 10, filled circles, Pronase-sensitive counts).

In conclusion, this study reports that PEGylation of SER-4 and 3D6 mAbs directed to the macrophage adhesion molecule, Sn, greatly increases their efficacy to inhibit RBC Sn-mediated binding to macrophages as compared with unmodified mAbs. Flexibility and motility of PEG molecules on SER-4 and 3D6 mAbs most likely create a steric hindrance around antibodies that increases the inhibition of RBC specific binding to Sn. Moreover, we show that a local Sn-mediated PEGylation of macrophages and the consequent steric effects of PEG are safe to cells, as PEGylated SER-4 and 3D6 mAbs did not impair membrane integrity, cell metabolism nor the pinocytosis of macromolecules and the phagocytosis of particles close to the size of bacteria. Thus, PEGylation of antibodies directed to cell surface receptors could be potentially exploited in a therapeutic setting, such as autoimmune or inflammatory diseases, to increase the inhibitory potency of antibodies without impairing vital cell functions.

ACKNOWLEDGMENT

This work was supported by a FIRST EUROPE EPH3310300R054F/415744 grant (Région Wallonne, Belgium, and European social fund). The authors would like to thank the Fonds de la Recherche Scientifique - Fonds National de la Recherche Scientifique (F.R.S-FNRS, Belgium) and the Région Bruxelloise (confocal microscopy). Rita Vanbever is a Chercheur Qualifié of the FNRS.

LITERATURE CITED

(1) Veronese, F. M., and Pasut, G. (2005) PEGylation, successful approach to drug delivery. *Drug Discovery Today 10*, 1451–1458.

(2) Chapman, A. P. (2002) PEGylated antibodies and antibody fragments for improved therapy: a review. *Adv. Drug Delivery Rev. 54*, 531–545.

(3) Tan, Y., Qiu, Y., Xu, H., Ji, S., Li, S., Gong, F., and Zhang, Y. (2006) Decreased immunorejection in unmatched blood transfusions by attachment of methoxypolyethylene glycol on human red blood cells and the effect on D antigen. *Transfusion 46*, 2122–2127.

(4) Murad, K. L., Mahany, K. L., Brugnara, C., Kuypers, F. A., Eaton, J. W., and Scott, M. D. (1999) Structural and functional consequences of antigenic modulation of red blood cells with methoxypoly(ethylene glycol). *Blood 93*, 2121–2127.

(5) Lee, D. Y., Yang, K., Lee, S., Chae, S. Y., Kim, K. W., Lee, M. K., Han, D. J., and Byun, Y. (2002) Optimization of monomethoxy-polyethylene glycol grafting on the pancreatic islet capsules. *J. Biomed. Mater. Res. 62*, 372–377.

(6) Lee, D. Y., Park, S. J., Nam, J. H., and Byun, Y. (2006) A combination therapy of PEGylation and immunosuppressive agent for successful islet transplantation. *J. Controlled Release 110*, 290–295.

(7) Ducreux, J., Vanbever, R., and Crocker, P. R. (2008) The inhibitory potencies of monoclonal antibodies to the macrophage adhesion molecule sialoadhesin are greatly increased following PEGylation. *Bioconjugate Chem. 19*, 2088–2094.

(8) Crocker, P. R., Mucklow, S., Bouckson, V., McWilliam, A., Willis, A. C., Gordon, S., Milon, G., Kelm, S., and Bradfield, P. (1994) Sialoadhesin, a macrophage sialic acid binding receptor for haemopoietic cells with 17 immunoglobulin-like domains. *EMBO J. 13*, 4490–4503.

(9) van den Berg, T. K., Breve, J. J., Damoiseaux, J. G., Dopp, E. A., Kelm, S., Crocker, P. R., Dijkstra, C. D., and Kraal, G. (1992) Sialoadhesin on macrophages: its identification as a lymphocyte adhesion molecule. *J. Exp. Med. 176*, 647–655.

(10) Crocker, P. R., and Gordon, S. (1986) Properties and distribution of a lectin-like hemagglutinin differentially expressed by murine stromal tissue macrophages. *J. Exp. Med. 164*, 1862–1875.

(11) Schadee-Eestermans, I. L., Hoefsmit, E. C., van de Ende, M., Crocker, P. R., van den Berg, T. K., and Dijkstra, C. D. (2000) Ultrastructural localisation of sialoadhesin (siglec-1) on macrophages in rodent lymphoid tissues. *Immunobiology 202*, 309–325.

(12) Hartnell, A., Steel, J., Turley, H., Jones, M., Jackson, D. G., and Crocker, P. R. (2001) Characterization of human sialoadhesin, a sialic acid binding receptor expressed by resident and inflammatory macrophage populations. *Blood 97*, 288–296.

(13) Jiang, H. R., Hwenda, L., Makinen, K., Oetke, C., Crocker, P. R., and Forrester, J. V. (2006) Sialoadhesin promotes the inflammatory response in experimental autoimmune uveoretinitis. *J. Immunol. 177*, 2258–2264.

(14) Nath, D., Hartnell, A., Happerfield, L., Miles, D. W., Burchell, J., Taylor-Papadimitriou, J., and Crocker, P. R. (1999) Macrophage-tumour cell interactions: identification of MUC1 on breast cancer cells as a potential counter-receptor for the macrophage-restricted receptor, sialoadhesin. *Immunology 98*, 213–219.

(15) Crocker, P. R., Kelm, S., Dubois, C., Martin, B., McWilliam, A. S., Shotton, D. M., Paulson, J. C., and Gordon, S. (1991) Purification and properties of sialoadhesin, a sialic acid-binding receptor of murine tissue macrophages. *EMBO J. 10*, 1661–1669.

(16) Crocker, P. R., Werb, Z., Gordon, S., and Bainton, D. F. (1990) Ultrastructural localization of a macrophage-restricted sialic acid binding hemagglutinin, SER, in macrophage-hematopoietic cell clusters. *Blood 76*, 1131–1138.

(17) Hashimoto, Y., Suzuki, M., Crocker, P. R., and Suzuki, A. (1998) A streptavidin-based neoglycoprotein carrying more than 140 GT1b oligosaccharides: Quantitative estimation of the binding specificity of murine sialoadhesin expressed on CHO cells. *J. Biochem. 123*, 468–478.

(18) Crocker, P. R., Hill, M., and Gordon, S. (1988) Regulation of a murine macrophage haemagglutinin (sheep erythrocyte receptor) by a species-restricted serum factor. *Immunology 65*, 515–522.

(19) Wu, Q., Feng, Y., Yang, Y., Jingliu, Zhou, W., He, P., Zhou, R., Li, X., and Zou, J. (2004) Kinetics of the phenotype and function of murine peritoneal macrophages following acute inflammation. *Cell Mol. Immunol. 1*, 57–62.

(20) Vassault, A. (1983) *Lactate Dehydrogenase. UV-method with pyruvate and NADH. Methods of enzymatic analysis*, pp 118−125, VCH, New York.

(21) Weyermann, J., Lochmann, D., and Zimmer, A. (2005) A practical note on the use of cytotoxicity assays. *Int. J. Pharm. 288*, 369–376.

(22) Crocker, P. R., and Gordon, S. (1989) Mouse macrophage hemagglutinin (sheep erythrocyte receptor) with specificity for sialylated glycoconjugates characterized by a monoclonal antibody. *J. Exp. Med. 169*, 1333–1346.

(23) Kooistra, T., Pratten, M. K., and Lloyd, J. B. (1981) Serum-dependence of fluid-phase pinocytosis and specificity in adsorptive pinocytosis of simple proteins in rat peritoneal macrophages. *Biosci. Rep. 1*, 587–594.

(24) Cupers, P., Veithen, A., Kiss, A., Baudhuin, P., and Courtoy, P. J. (1994) Clathrin polymerization is not required for bulk-phase endocytosis in rat fetal fibroblasts. *J. Cell Biol. 127*, 725–735.

(25) Pratten, M. K., and Lloyd, J. B. (1986) Pinocytosis and phagocytosis: the effect of size of a particulate substrate on its mode of capture by rat peritoneal macrophages cultured in vitro. *Biochim. Biophys. Acta 881*, 307–313.

(26) Fishburn, C. S. (2008) The pharmacology of PEGylation: Balancing PD with PK to generate novel therapeutics. *J. Pharm. Sci. 97*, 4167–4183.

(27) Scott, M. D., Murad, K. L., Koumpouras, F., Talbot, M., and Eaton, J. W. (1997) Chemical camouflage of antigenic determinants: Stealth erythrocytes. *Proc. Natl. Acad. Sci. U.S.A. 94*, 7566–7571.

(28) Faghihi, S. M., Aronson, N. N., Jr., and Dean, R. T. (1982) Temperature dependence of certain integrated membrane functions in macrophages. *J. Cell Sci. 57*, 115–127.

(29) Mukherjee, S., Ghosh, R. N., and Maxfield, F. R. (1997) Endocytosis. *Physiol. Rev. 77*, 759–803.

(30) Schmid, S. L., and Carter, L. L. (1990) ATP is required for receptor-mediated endocytosis in intact cells. *J. Cell Biol. 111*, 2307–2318.

(31) Podbilewicz, B., and Mellman, I. (1990) ATP and cytosol requirements for transferrin recycling in intact and disrupted MDCK cells. *EMBO J. 9*, 3477–3487.

(32) Jang, J. Y., Lee, D. Y., Park, S. J., and Byun, Y. (2004) Immune reactions of lymphocytes and macrophages against PEG-grafted pancreatic islets. *Biomaterials 25*, 3663–3669.

(33) Chen, A. M., and Scott, M. D. (2001) Current and future applications of immunological attenuation via pegylation of cells and tissue. *BioDrugs 15*, 833–847.

(34) Allen, L. A. H., and Aderem, A. (1996) Mechanisms of phagocytosis. *Curr. Opin. Immunol. 8*, 36–40.

(35) Conner, S. D., and Schmid, S. L. (2003) Regulated portals of entry into the cell. *Nature 422*, 37–44.

(36) Cooper, J. A. (1987) Effects of cytochalasin and phalloidin on Actin. *J. Cell Biol. 105*, 1473–1478.

BC800390G

Bioconjugate Chemistry 20th Anniversary

Subscriber access provided by SHEMYAKIN-OVCHINNIKOV INST

Article

Magnetic Separation of Melanoma-Specific Cytotoxic T Lymphocytes from a Vaccinated Melanoma Patient's Blood Using MHC/Peptide Complex-Conjugated Bacterial Magnetic Particles

Masayuki Takahashi, Yasuto Akiyama, Junpei Ikezumi, Takeshi Nagata, Tomoko Yoshino, Akira Iizuka, Ken Yamaguchi, and Tadashi Matsunaga

Bioconjugate Chem., **2009**, 20 (2), 304-309• DOI: 10.1021/bc800398d • Publication Date (Web): 14 January 2009

Downloaded from http://pubs.acs.org on May 15, 2009

More About This Article

Additional resources and features associated with this article are available within the HTML version:

- Supporting Information
- Access to high resolution figures
- Links to articles and content related to this article
- Copyright permission to reproduce figures and/or text from this article

View the Full Text HTML

ACS Publications
High quality. High impact.

Bioconjugate Chemistry is published by the American Chemical Society. 1155 Sixteenth Street N.W., Washington, DC 20036

Magnetic Separation of Melanoma-Specific Cytotoxic T Lymphocytes from a Vaccinated Melanoma Patient's Blood Using MHC/Peptide Complex-Conjugated Bacterial Magnetic Particles

Masayuki Takahashi, Yasuto Akiyama, Junpei Ikezumi, Takeshi Nagata, Tomoko Yoshino, Akira Iizuka, Ken Yamaguchi, and Tadashi Matsunaga*

Department of Biotechnology, Tokyo University of Agriculture and Technology, 2-24-16, Naka-cho, Koganei, Tokyo 184-8588, Japan, and Immunotherapy Division, Shizuoka Cancer Center Research Institute, 1007, Shimo-nagakubo, Nagaizumi-cho, Sunto-gun, Shizuoka, 411-8777, Japan. Received September 17, 2008; Revised Manuscript Received November 26, 2008

Target antigen-specific cytotoxic T lymphocytes (CTLs) play a key role in anticancer and antivirus immunity in the body, and purification of CTLs from heterogeneous immune cells is desired for an efficient cancer immunotherapy and fundamental research. Herein, a novel magnetic nanoparticle conjugated with major histocompatibility complex (MHC)/peptide complexes was developed for the magnetic separation of melanoma-specific CTLs. To conjugate biotinylated MHC/peptide complexes on nanosized bacterial magnetic particles (BacMPs), which were synthesized intracellularly by magnetotactic bacteria, phased modification of biotin and streptavidin onto BacMPs was investigated. When biotin was modified on BacMPs, a polyethylene oxide (PEO)-linker contributed to the maintenance of the high dispersion properties of BacMPs. Furthermore, nonspecific binding of BacMPs to cell surface was prevented by controlling the level of streptavidin bound on BacMPs and through PEO blocking of the empty streptavidin sites on BacMPs. Finally, single-step magnetic separation of melanoma-specific CTLs was demonstrated using developed MHC/MAGE-1 A24 peptide complex-conjugated BacMPs. Melanoma-reactive cells and melanoma-specific CTLs were successfully separated from stimulated peripheral blood mononuclear cells derived from a vaccinated melanoma patient with 93.1% and 87.7% purity, respectively, and specificity of antigen recognition and cytokine secretion from separated CTLs were confirmed. The potential of MHC/peptide complex-conjugated BacMPs was indicated for efficient separation of antigen-specific CTLs in cancer immunotherapy and fundamental research.

INTRODUCTION

Cytotoxic T lymphocytes (CTLs) become activated when, through T cell receptors (TCRs), they recognize major histocompatibility complex (MHC)/peptide complexes that are present on the surface of cancer cells and other infected cells. Once activated, they clonally expand and trigger a cytotoxic response against these cells. CTLs play a key role in anticancer and antivirus immunity. Single CTLs, which express individual TCRs, recognize a pair of antigenic peptides and polymorphic helices of MHC proteins with one-to-one correspondence (*1, 2*). For effective immunotherapy using CTLs, target antigen-specific CTLs must be purified from various cell mixtures, such as those in blood samples, and significant demand persists for the development of efficient CTL separation technology.

Separation of target cells from a heterogeneous cell mixture is used widely in biological and medical applications. Among current cell separation techniques, magnetic cell sorting is a popular tool for isolating cells such as monocytes, B-lymphocytes, and hematopoietic stem cells (CD14, CD19, and CD34 positive cells, respectively) from peripheral blood (*3*−*6*). The use of antibody-conjugated magnetic particles (immunomagnetic particles) is a proven, rapid, and simple technique relative to fluorescence-activated cell sorting (FACS) (*7*). Antibodies conjugated on magnetic particles usually recognize antigens on the surface of target cells (e.g., CD markers), and cells labeled with magnetic particles are successfully separated from unlabeled cells. However, for the separation of antigen-specific CTLs, immunomagnetic particles are not effective, and alternative magnetic particles are required. For the separation of antigen-specific CTLs from cell mixtures, tetrameric MHC/peptide complexes, which combine purified and biotinylated single MHC/peptide complexes with PE-labeled streptavidin (MHC/peptide tetramer), have been used to label target cells that are then separated by flow cytometric sorting (*8*−*10*). However, improvements in throughput and absolute sterility of the flow cytometer are required, and thus, a magnetic separation system that uses magnetic particles to recognize antigen-specific CTLs was considered suitable for the separation of CTLs.

The magnetotactic bacterium synthesizes intracellular nanosized bacterial magnetic particles (BacMPs) of 50 to 100 nm in diameter that are covered with a stable lipid bilayer. BacMPs, which have a single magnetic domain of magnetite and exhibit strong ferrimagnetisms, can be collected easily with commercially available permanent magnets. The lipid membrane provides BacMPs with a high surface area and good dispersion properties, creating various applications for BacMPs. Magnetic cell separation using BacMPs has been reported previously (*11*−*14*), and many cell types were separated with high purity from peripheral blood mononuclear cells (PBMCs) or whole blood directly using BacMPs displaying protein A or protein G, which are IgG binding proteins, conjugated to antibodies. Furthermore, this system is not only simple but also noninvasive to the separated cells, because BacMPs are collectable using available permanent magnets rather than the special magnetic columns needed for the collection of commercialized magnetic nanoparticles. Therefore, we hypothesized that the magnetic cell separation system using BacMPs will be suitable for efficient

* Direct fax: +81-42-385-7713; phone: +81-42-388-7020; e-mail: tmatsuna@cc.tuat.ac.jp.

10.1021/bc800398d CCC: $40.75 © 2009 American Chemical Society
Published on Web 01/14/2009

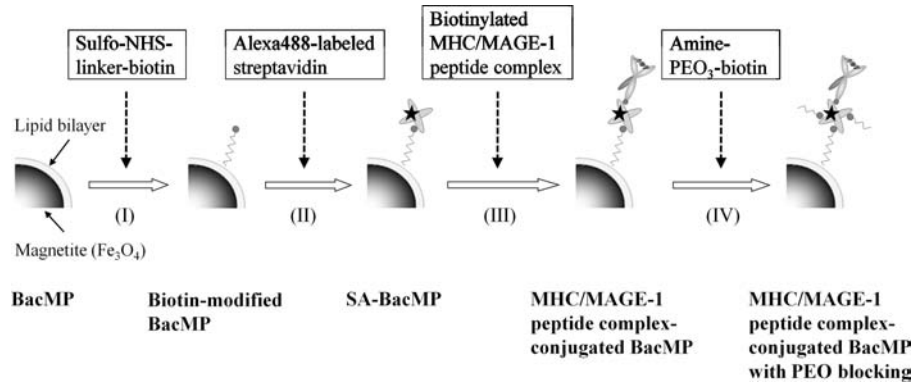

Figure 1. Schematic diagram for preparation of MHC/MAGE-1 peptide complex-conjugated BacMPs.

separation of antigen-specific CTLs, furthering the application of CTLs in immunotherapy.

In this report, novel magnetic particles were developed for the separation of melanoma-specific CTLs. First, MHC/MAGE-1 A24 peptide complexes that are presented on the surface of melanoma cells were conjugated on BacMPs by a chemical procedure. The prevention of nonspecific binding of BacMPs to the cell surface was considered critical in this process. Furthermore, antibody-independent magnetic separation of melanoma-specific CTLs from in vitro stimulated PBMCs derived from a vaccinated melanoma patient was performed using the MHC/MAGE-1 A24 peptide complex-conjugated BacMPs, and the function of separated CTLs was confirmed.

EXPERIMENTAL PROCEDURES

Cultivation of Magnetic Bacteria. *M. magneticum* AMB-1 was microaerobically cultured in magnetic spirillum growth medium at 28 °C as previously described (*15*). Microaerobic conditions were established by sparging the cultures with argon gas. Batch cultures were prepared in 10 L media bottles. AMB-1 transformants were cultured under these conditions in 5 μg/mL ampicillin.

Preparation of BacMPs. BacMPs were purified from AMB-1, according to the methods of Tanaka and Matsunaga (*16*). Cultured cells were collected by centrifugation, suspended in 40 mL of HEPES (10 mM) buffer (pH 7.4), and disrupted by three passes through a French press cell at 1500 kg/cm^2 (Ohtake Works Co. Ltd., Tokyo, Japan). BacMPs were collected from cell debris using a neodymium−iron−boron (Nd−Fe−B) magnet. Collected BacMPs were washed with HEPES buffer at least 10 times. During each wash, BacMPs were dispersed by ultrasonication and collected using the Nd−Fe−B magnet. The concentration of BacMPs in suspension was estimated by optical density at 660 nm (OD_{660}) using a spectrophotometer (UV-2200, Shimadzu, Kyoto, Japan). Purified BacMPs were stored at 4 °C in phosphate buffered saline (PBS) solution.

Immobilization of Streptavidin on BacMPs. BacMPs (5 mg) were incubated with 1 mM Sulfo-NHS-LC_2-Biotin (Pierce, Rockford, IL, USA) or 1 mM Sulfo-NHS-PEO_{12}-Biotin (Pierce) in 5 mL of borate buffer (pH 8.0) for 1 h at room temperature with pulsed sonication every 3 min (Figure 1-I). After incubation, biotin-modified BacMPs were magnetically separated from the reaction mixture using the Nd−Fe−B magnet and washed with PBS buffer containing 0.1% (v/v) Tween 20 (one time) and then PBS buffer (two times). BacMPs (3 mg) were then incubated with 0.125−1 μM Alexa488-labeled streptavidin (Invitrogen, Carlsbad, CA, USA) in 3 mL of PBS buffer for 1 h at room temperature with pulsed sonication (Figure 1-II). Streptavidin-immobilized BacMPs (SA-BacMPs) were washed three times with PBS buffer using the Nd−Fe−B magnet to remove excess non-immobilized streptavidin and suspended in PBS buffer containing 0.1% sodium azide before use. In the three washing steps, all supernatants were collected, and the fluorescence intensity of each solution was measured using a microplate reader at an excitation of 485 nm and an emission of 520 nm. The amount of Alexa488-labeled streptavidin that was not immobilized on biotin-modified BacMPs was calculated from the fluorescence intensity attained from a calibration curve, and streptavidin immobilized on biotin-modified BacMPs was then calculated by deducing the amount of non-immobilized streptavidin from initially added streptavidin. The number of streptavidin immobilized on a single BacMP was calculated from the amount of streptavidin immobilized on biotin-modified BacMPs (BacMP diameter = 75 nm and BacMP density = 5.2 g/cm^3).

Analysis of Size Distribution of SA-BacMPs. The size distributions of SA-BacMPs biotinylated with Sulfo-NHS-LC_2-Biotin or Sulfo-NHS-PEO_{12}-Biotin were analyzed using an electrophoretic light scattering spectrophotometer (ELS-8000, Otsuka Electronics, Osaka, Japan). SA-BacMPs were added to 3 mL of deionized distilled water to achieve a final concentration of 10 μg/mL. Solutions were sonicated prior to measurement.

Conjugation of MHC/Peptide Complexes to SA-BacMPs. SA-BacMPs (300 μg) were incubated with 0.75 μM biotinylated MHC/MAGE-1 A24 peptide (NYKHCFPEI) complexes (MBL, Nagano, Japan) or biotinylated MHC/HIV A24 peptide (RYLRDQQLL) complexes (MBL) in 600 μL of TNE buffer (10 mM Tris, 150 mM NaCl, 0.5 mM EDTA, and 0.1% sodium azide; pH 8.0) for 30 min at room temperature with pulsed sonication every 10 min (Figure 1-III). After three washes in PBS buffer, Amine-PEO_3-Biotin (10 mM, Pierce) in PBS buffer was added to MHC/peptide complex-conjugated BacMPs (500 μg/mL) to block empty streptavidin sites on BacMPs (Figure 1-IV). After incubation for 30 min at room temperature, MHC/peptide complex-conjugated BacMPs with PEO blocking were washed magnetically and preserved in PBS buffer containing 0.1% sodium azide until use.

The average number of MHC/peptide complexes conjugated on a single SA-BacMP was evaluated using alkaline phosphatase (ALP)-labeled antibodies. MHC/peptide complexes conjugated on SA-BacMPs (20 μg) were incubated with mouse IgG2a anti-β2 microglobulin monoclonal antibodies (40 μL sample, 30 μg/mL, Immunotech, Marseille, France) for 60 min at room temperature. After three washes, BacMPs were incubated with ALP-labeled antimouse IgG (20 μL sample, 10 μg/mL, Santa Cruz Biotechnology Inc., Santa Cruz, CA, USA) for 30 min at room temperature. After three washes, the resuspended complexes (20 μL sample, 100 μg of BacMPs/mL) were mixed with 80 mL of Lumi-Phos 530 including Lumigen PPD {4-methoxy-4[3-phosphatephenyl]spirio[1,2-dioxetane-3,2′-adamantane] disodium salt} (3.3×10^{-4} M) as a luminescence substrate for alkaline phosphatase, and the resulting luminescence intensity

was measured by a Lucy-2 luminescence reader (Aloka, Co. Ltd., Tokyo, Japan). The numbers of ALP-labeled IgG (molecular weight of $F(ab)_2$ IgG = 100 kDa) were calculated from the luminescence intensity attained from a calibration curve. The values for the number of ALP-labeled IgGs were used to attain the number of MHC/peptide complexes conjugated on a single SA-BacMP.

Evaluation of Nonspecific Binding of BacMPs to Cell Surfaces. Raji cells (2×10^5 cells) in 50 μL of separation buffer (PBS buffer containing 0.5% bovine serum albumin (BSA) and 2 mM EDTA) were mixed with 10 μg of SA-BacMPs, MHC/MAGE-1 A24 peptide complex-conjugated BacMPs, or MHC/MAGE-1 A24 peptide complex-conjugated BacMPs with PEO blocking for 10 min at 4 °C. After washing by centrifugation, the cell suspension (1 mL) was transferred to a test tube (10 mm × 75 mm) and magnetically collected using the Nd−Fe−B magnet for 5 min. The dimensions of magnets used for cell separation were $20 \times 12 \times 5$ mm^3. The surface magnetic flux density of the magnets was 400 mT. The number of cells that were nonspecifically separated during magnetic separation was determined by direct cell counting under a microscope.

Preparation of CTLs. All PBMCs were derived from a metastatic melanoma patient given dendritic cell (DC) vaccines. Clinical research using PBMCs from melanoma patients was approved by the Institutional Review Board of the Shizuoka Cancer Center, Shizuoka, Japan. All patients gave written informed consent. PBMCs were stimulated twice in vitro with MAGE-1 A24 peptide-pulsed autologous DCs at a ratio of 1:10 to 1:100 in GT-T507 medium (Kohjin Bio Co., Saitama, Japan) supplemented with 2 mM L-glutamine, 100 U/mL penicillin, 100 μg/mL streptomycin, 50 μg/mL gentamycin, 50 μM β-mercaptoethanol, 1 mM sodium pyruvate, and 5% AB human serum (Cambrex, Walkerville, MD, USA) (referred to as CTL medium). Additionally, cultured CTLs were boosted weekly with two rounds of stimulation at a ratio of 1:10 with MAGE-1 A24 peptide-pulsed T2-A24 cells, which are a human hybrid (B and T lymphoblast) cell line transfected with the HLA-A24 gene (*17*).

Magnetic Cell Separation using MHC/MAGE-1 A24 Peptide Complex-Conjugated BacMPs. Stimulated PBMCs (1.5×10^7 cells) in 120 μL of staining buffer (PBS containing 2% fetal bovine serum (FBS) and 0.1% sodium azide) were reacted with 120 μL of allophycocyanin (APC)-labeled anti-CD8 mAb (BD Biosciences, San Jose, CA, USA) for 30 min on ice. After removing excess antibody by centrifugation, cell aliquots (2×10^6 cells) in 80 μL of separation buffer were incubated with 20 μL of MHC/MAGE-1 or HIV A24 peptide complex-conjugated BacMPs for 10 min at 4 °C. After washing by centrifugation, cells suspended in 1 mL of separation buffer were transferred to a test tube, and cells labeled by BacMPs were separated magnetically as described above. The magnetic separation was performed three times at intervals of 5 min. Magnetically separated cells were resuspended in staining buffer as a positive fraction. To analyze the ratio of melanoma-specific CTLs to CTLs suspension, CTLs (2×10^6 cells) stained with APC-labeled anti-CD8 mAb were reacted further with PE-labeled MHC/MAGE-1 A24 peptide tetramer (MBL) for 30 min on ice and washed with excess tetramer by centrifugation. The purity of targeted cells in separated cells and CTL suspensions was analyzed using a BD FACS Canto flow cytometer (Becton Dickinson, Franklin Lakes, NJ, USA). A total of 50 000 events were analyzed for each sample.

Measurement of IFN-γ Secreted by Separated Melanoma-Specific CTLs. MHC/MAGE-1 A24 peptide complex-conjugated BacMPs were fabricated by immobilizing 1 μM streptavidin and conjugating 0.5 μM MHC/MAGE-1 A24 peptide complexes on the biotin-modified BacMPs, and melanoma-specific CTLs were separated using the MHC/MAGE-1 A24 peptide complex-conjugated BacMPs using the protocol described above. After an overnight incubation in CTL medium, separated CTLs (1×10^5 cells) and MAGE-1 A24 peptide-pulsed TISI cells (1×10^5 cells), a human B-lymphoblastoid cell line presenting HLA-A24, were coincubated in a round-bottom 96-well microculture plate for 24 h in RPMI-1640 medium containing 5% FBS. Finally, supernatants were collected, and the amount of IFN-γ in the supernatants was measured using an ELISA kit specific for human IFN-γ (Biosource, Camallilo, CA, USA).

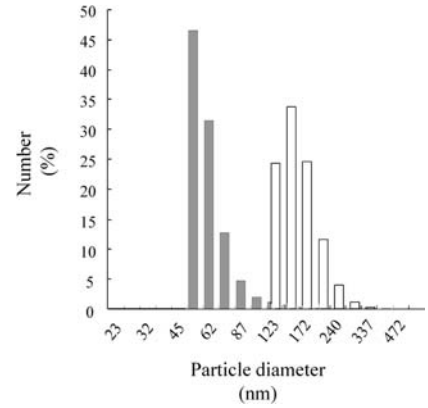

Figure 2. Particle size distribution of SA-BacMPs biotinylated with Sulfo-NHS-LC_2-biotin (empty bars) or Sulfo- NHS-PEO_{12}-biotin (solid bars).

RESULTS

Introduction of Biotin on BacMPs. To conjugate biotinylated MHC/peptide complexes on BacMPs, phased modifications of biotin and streptavidin onto BacMPs were studied. In the first step, biotin introduction onto BacMPs was performed by modifying the amine group on the surface of BacMPs. To modify biotin once on BacMPs, two amino-reactive cross-linkers, Sulfo-NHS-LC_2-Biotin (linker length: 30.5 Å) and Sulfo-NHS-PEO_{12}-Biotin (linker length: 56 Å), were individually reacted in the presence of BacMPs for covalent linkage between the amine group of BacMPs and the cross-linker. The dispersion of streptavidin-immobilized BacMPs (SA-BacMPs) that were biotinylated with LC_2-linker or PEO_{12}-linker was evaluated as the size distribution of the BacMPs in solution (Figure 2). The average diameter of SA-BacMPs biotinylated with the LC_2-linker was 159.4 ± 36.0 nm, and the average diameter of SA-BacMPs biotinylated with the PEO_{12}-linker was 63.3 ± 17.7 nm. SA-BacMPs biotinylated with the PEO_{12}-linker showed better dispersion due to the hydrophilic linker. Furthermore, as the diameter of BacMP is 50 to 100 nm, it was considered that multiple biotin-modified BacMPs did not bind to a streptavidin molecule.

Correlation Between the Number of Streptavidin Molecules Bound on BacMPs and Nonspecific Binding of BacMPs to Cell Surfaces. Streptavidin molecules were immobilized onto biotin-modified BacMPs with PEO_{12}-linker. Excessive immobilization of streptavidin, a highly hydrophobic molecule (*18*), on BacMPs was predicted to cause nonspecific binding of SA-BacMPs to cells. Therefore, the correlation between the number of streptavidin molecules bound on BacMPs and nonspecific binding of SA-BacMPs to cell surfaces was investigated. SA-BacMPs, which were prepared by reacting streptavidin with biotin-modified BacMPs at different concentrations, were incubated with Raji cells, and the number of cells, which were separated magnetically as a result of nonspecific binding of SA-BacMPs to cell surfaces, were counted directly

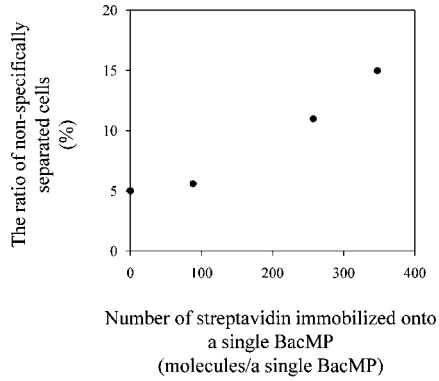

Figure 3. Correlation between the number of streptavidin molecules bound on a single BacMP and nonspecific binding of BacMPs to cell surface. The number of streptavidin molecules bound on a single biotin-modified BacMP was evaluated by measuring the fluorescence intensity of non-immobilized streptavidin in the supernatant. The numbers of Raji cells separated nonspecifically using each SA-BacMPs were counted, and then, the ratio of nonspecifically separated Raji cells was calculated

Table 1. Number of MHC/MAGE-1 Peptide Complexes Conjugated on a Single SA-BacMP on Which Different Number of Streptavidin Molecules Immobilized

Number of Streptavidin or MHC/MAGE-1 Peptide Complexes on a Single SA-BacMP (Molecules/a Single BacMP)	
streptavidin	MHC/MAGE-1 peptidecomplex
339 ± 10	16.0 ± 1.3
132 ± 21	17.9 ± 2.1

under a microscope. Then, the correlation between the number of streptavidin molecules immobilized on a single BacMP and nonspecific binding of SA-BacMPs to cell surfaces was estimated (Figure 3). The number of nonspecifically separated cells increased in proportion to the number of streptavidin molecules immobilized on BacMPs. Immobilization of approximately 100 streptavidin molecules on a single BacMP did not influence the nonspecific binding property of BacMPs. These results show that value of less than 100 streptavidin molecules per BacMP are suitable for efficient cell separation.

Fabrication of MHC/Peptide A24 Complex-Conjugated BacMPs with Little Nonspecific Binding to Cells. MHC/peptide complex-conjugated BacMPs were fabricated by reacting biotinylated MHC/peptide complexes with SA-BacMPs. The number of MHC/peptide complexes conjugated on a single SA-BacMP was evaluated using mouse anti-β2 microglobulin mAb and ALP- labeled antimouse IgG. Eighteen MHC/MAGE-1 A24 peptide complexes were conjugated per BacMP on which 100 streptavidin molecules were immobilized, and the number of MHC/MAGE-1 A24 peptide complexes per BacMP was almost equal to that of BacMPs on which over 300 streptavidin molecules were immobilized (16 MHC/MAGE-1 A24 peptide complexes, Table 1). From these results, we speculated that only 1 or 0 MHC/peptide complexes was bound to a single streptavidin molecule on BacMPs, and confirmed that many empty streptavidin sites remained immobilized on BacMPs. For blocking of these empty streptavidin sites and, therefore, suppression of nonspecific binding of BacMPs to cells, MHC/peptide complex-BacMPs were incubated with amine-PEO_3-biotin. The nonspecific binding of three different MHC/peptide complex-conjugated BacMPs to cells was evaluated (Figure 4), and nonspecific binding of BacMPs to cell surfaces was decreased markedly by PEO blocking on BacMP surfaces. The ratio of cells separated nonspecifically using MHC/MAGE-1 A24 peptide complex-conjugated BacMPs with PEO blocking was approximately one-sixth that observed using BacMPs without PEO blocking. These results suggest that PEO blocking

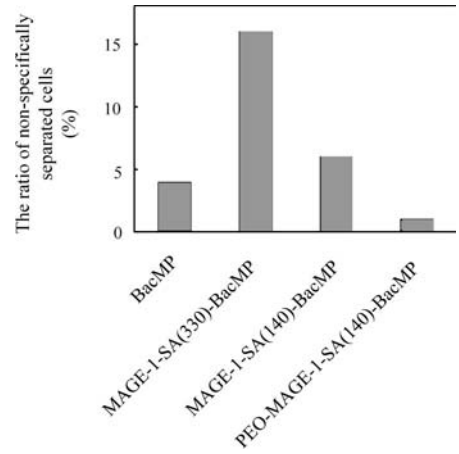

Figure 4. Nonspecific binding of BacMPs to the cell surface. The numbers of Raji cells separated nonspecifically using wild-type BacMPs (BacMP), MHC/MAGE-1 peptide complex-conjugated BacMPs on which 330 streptavidin molecules per BacMP (MAGE-1-SA(330)-BacMP), and 140 streptavidin molecules per BacMP (MAGE-1-SA(140)-BacMP) were immobilized, and MHC/MAGE-1 peptide complex-conjugated BacMPs with PEO blocking (PEO-MAGE-1-SA(140)-BacMP), on which 140 streptavidin molecules per BacMP were immobilized, were counted. Then, the ratio of nonspecifically separated Raji cells was calculated.

of MHC/MAGE-1 A24 peptide complex-conjugated BacMPs is necessary for the high-purity magnetic separation required for melanoma-specific CTLs. Therefore, we used PEO-blocked MHC/MAGE-1 A24 peptide complex-conjugated BacMPs for the following CTL separation experiments.

Magnetic Separation of Melanoma-Specific CTLs Using MHC/MAGE-1 A24 Peptide Complex-Conjugated BacMPs. Magnetic separation of melanoma-specific CTLs from in vitro stimulated PBMCs prepared from a vaccinated melanoma patient using MHC/MAGE-1 A24 peptide complex-conjugated BacMPs was performed and evaluated using a PE-labeled MHC/MAGE-1 A24 peptide tetramer and APC-labeled anti-CD8 mAb. The purity of melanoma-reactive cells (PE-MAGE-1 tetramer positive in Figure 5A) and melanoma-specific CTLs (PE-MAGE-1 tetramer positive and APC-anti-CD8 mAb positive in Figure 5A) in the stimulated PBMC from a melanoma patient were 31.2% and 30.1%, respectively. Most melanoma-reactive cells were melanoma-specific CTLs. MHC/MAGE-1 or HIV (negative control) A24 peptide complex-conjugated BacMPs were incubated in stimulated PBMCs, and the number of magnetically separated cells was counted. The number of cells separated nonspecifically using MHC/HIV A24 peptide complex-conjugated BacMPs was approximately one-sixth of the number of cells separated using MHC/MAGE-1 A24 peptide complex-conjugated BacMPs. Therefore, it was concluded that the target cells, which react to melanoma cells, were separated by the interaction with MHC/MAGE-1 A24 peptide complexes conjugated on BacMPs. Then, according to analysis of the separated cells using MHC/MAGE-1 A24 peptide complex-conjugated BacMPs, 93.1% of the separated cells were melanoma-reactive cells (Alexa-488-MAGE-1-BacMPs positive in Figure 5B), and 87.7% of those were melanoma-specific CTLs (Alexa-488-MAGE-1-BacMPs positive and APC-anti-CD8 mAb positive in Figure 5B). These results indicate that MHC/MAGE-1 A24 peptide complex-conjugated BacMPs bind to targeted melanoma-specific CTLs with high selectivity and that these cells were separated with high purity using this system.

Function of Separated Melanoma-Specific CTLs. The specificity of antigen recognition and cytokine secretion of CTLs following magnetic separation using MHC/MAGE-1 A24 peptide complex-conjugated BacMPs were evaluated. The amount

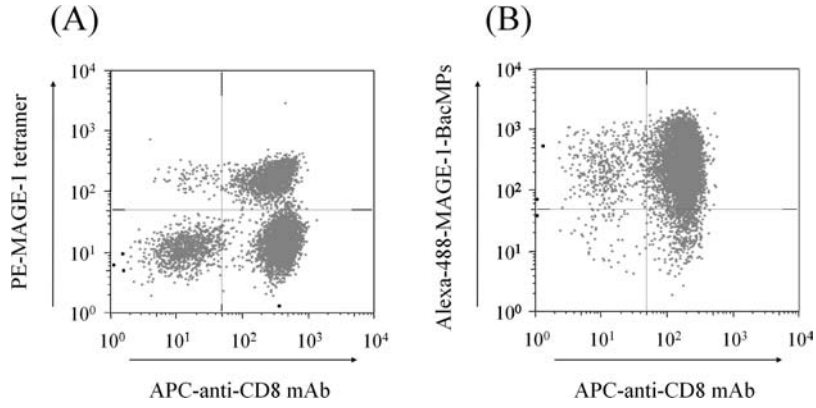

Figure 5. Magnetic separation of melanoma-specific CTLs using MHC/MAGE-1 peptide complex-conjugated BacMPs. Cells before (A) and after (B) magnetic separation were analyzed by flow cytometry and are shown accordingly. Prior to magnetic separation, the cells were stained with APC-labeled anti-CD8 mAb (APC-anti-CD8 mAb). For the analysis of cells before magnetic separation, PE-labeled MHC/MAGE-1 peptide tetramers (PE-MAGE-1 tetramer) were used. Upon magnetic separation, the cells were analyzed with reference to the fluorescence intensity of Alxa-488 labeled to the MHC/MAGE-1 peptide complex-conjugated BacMPs (Alexa-488-MAGE-1-BacMPs).

Table 2. Levels of IFN-γ Secreted by Separated Melanoma-Specific CTLs Incubated with TISI Cells or MGAE-1 Peptide-Pulsed TISI Cells

	Amount of Secreted IFN-γ (pg/mL)
MAGE-1 peptide-pulsed TISI cells	1049 ± 24.7
TISI cells	34 ± 4.4

of IFN-γ in the supernatants of CTLs cultured with MAGE-1 A24 peptide-pulsed TISI cells was measured (Table 2). The separated CTLs cultured with peptide nonpulsed TISI cells, which did not express MAGE-1 A24 peptide and MHC (HLA-A24) complexes on the cell surface, secreted little IFN-γ. It was indicated that the CTLs cultured with peptide nonpulsed TISI cells did not activate. Furthermore, it was suggested that BacMPs on CTLs were not a cytotoxin and did not activate the CTLs. On the other hand, the amount of IFN-γ secreted by the separated CTLs cultured with MAGE-1 A24 peptide-pulsed TISI cells was approximately 30 times more than that of the CTLs cultured with peptide nonpulsed TISI cells. These results indicate that the CTLs separated using MHC/MAGE-1 A24 peptide complex-conjugated BacMPs were stimulated specifically by MAGE-1 A24 peptide and MHC complexes expressed on TISI cells, and the stimulated CTLs were able to secrete IFN-γ, a normal function of melanoma-specific CTLs.

DISCUSSION

In preparing a population of target cells for applications such as cell translation or cell immunotherapy, techniques for separating these cells from a heterogeneous cell mixture must produce large numbers of highly pure target cells. For magnetic cell separation, the magnetic strength, size, and surface characteristics of magnetic particles influence the purity of separated cells. It is possible to reduce nonspecific binding to cells, which causes decreased purity, by controlling the particle surface characteristics. Specially, various surface modifications, such as the addition of poly(ethylene glycol) and polysaccharide to add hydrophilicity to the particles, have been demonstrated to reduce nonspecific interactions with the cell surface (*19*−*22*). In this report, BacMPs, which are known to elicit little nonspecific binding, were developed for the magnetic separation of melanoma-specific CTLs. First, the surfaces of BacMPs were coated with a PEO linker, and the hydrophilicity and steric barrier of the PEO contributed to the progress of distribution of BacMPs (*23*). Then, the number of streptavidin molecules immobilized on single BacMPs was controlled. This was performed, as it was speculated that excessive immobilization of streptavidin augments hydrophobicity and therefore accelerates nonspecific binding of BacMPs to nontarget cells (*18*). It has also been known that animal cells prefer to attach to particles as they increase in hydrophobicity (*20*). In the present study, nonspecific binding of BacMPs to nontarget cells was reduced markedly by controlling the number of immobilized streptavidin molecules per BacMP and via further modification of PEO on BacMPs. Finally, BacMPs that specifically target CTLs through the conjugation of MHC/peptide complexes on their surfaces allowed for the isolation of target CTLs with high purity.

In all previous reports, magnetic separation of antigen-specific CTLs has been demonstrated using both a PE-labeled MHC/peptide tetramer for targeting the cells and magnetic particles displaying anti-PE antibodies for magnet marking of the cells via the tetramer (*24*−*27*). This two-step separation lacks precision, is time-consuming, and is difficult to automate, and for these reasons, this technique is limited in its application toward immunotherapies. Therefore, we proposed the novel separation system in which antigen-specific CTLs are separated in a single-step process using BacMPs with directly conjugated MHC/peptide complexes as a more suitable process for use in immunotherapy. Conjugation of MHC/peptide complexes on magnetic nanoparticles for cell separation and single-step separation of antigen-specific CTLs was the first trial.

In this report, we demonstrated efficient melanoma-specific CTL separation using MHC/MAGE-1 A24 peptide complex-conjugated BacMPs. The BacMPs conjugated with MHC/MAGE-1 A24 peptide complexes bound to targeted melanoma-specific CTLs with little nonspecific binding to nontarget cells, and a single-step magnetic separation of the melanoma-specific CTLs from stimulated PBMCs derived from a vaccinated metastatic melanoma patient was achieved while maintaining CTL function. CTLs separated efficiently and with high purity will be useful in developing immunotherapies and in fundamental research.

ACKNOWLEDGMENT

This work was funded in part by a Grant-in-Aid for Scientific Research on Priority Areas “City Area Program” from the Ministry of Education, Culture, Sports, Science, and Technology of Japan.

LITERATURE CITED

(1) Anderson, B., Park, B. J., Verdaguer, J., Amrani, A., and Santamaria, P. (1999) Prevalent CD8(+) T cell response against

one peptide/MHC complex in autoimmune diabetes. *Proc. Natl. Acad. Sci. U.S.A. 96*, 9311–9316.
(2) Pinilla, C., Rubio-Godoy, V., Dutoit, V., Guillaume, P., Simon, R., Zhao, Y., Houghten, R. A., Cerottini, J. C., Romero, P., and Valmori, D. (2001) Combinatorial peptide libraries as an alternative approach to the identification of ligands for tumor-reactive cytolytic T lymphocytes. *Cancer Res. 61*, 5153 5160.
(3) Hermentin, P., Doenges, R., Franssen, U., Bieva, C., Vander Brugghen, F. J., Stryckmans, P., Friesen, H. J., Optaczy, B., Schneider, S., Ax, W., et al. (1990) Hinge-thiol coupling of monoclonal antibody to silanized iron oxide particles and evaluation of magnetic cell depletion. *Bioconjugate Chem. 1*, 411–418.
(4) Campbell, J. D., Piechaczek, C., Winkels, G., Schwamborn, E., Micheli, D., Hennemann, S., and Schmitz, J. (2005) Isolation and generation of clinical-grade dendritic cells using the CliniMACS system. *Methods Mol. Med. 109*, 55–70.
(5) Jing, Y., Moore, L. R., Williams, P. S., Chalmers, J. J., Farag, S. S., Bolwell, B., and Zborowski, M. (2007) Blood progenitor cell separation from clinical leukapheresis product by magnetic nanoparticle binding and magnetophoresis. *Biotechnol. Bioeng. 96*, 1139–1154.
(6) Leyendeckers, H., Voth, E., Schicha, H., Hunzelmann, N., Banga, P., and Schmitz, J. (2002) Frequent detection of thyroid peroxidase-specific IgG+ memory B cells in blood of patients with autoimmune thyroid disease. *Eur. J. Immunol. 32*, 3126–3132.
(7) Miltenyi, S., Muller, W., Weichel, W., and Radbruch, A. (1990) High gradient magnetic cell separation with MACS. *Cytometry 11*, 231–238.
(8) Altman, J. D., Moss, P. A., Goulder, P. J., Barouch, D. H., McHeyzer-Williams, M. G., Bell, J. I., McMichael, A. J., and Davis, M. M. (1996) Phenotypic analysis of antigen-specific T lymphocytes. *Science 274*, 94–96.
(9) Verginis, P., McLaughlin, K. A., Wucherpfennig, K. W., von Boehmer, H., and Apostolou, I. (2008) Induction of antigen-specific regulatory T cells in wild-type mice: visualization and targets of suppression. *Proc. Natl. Acad. Sci. U.S.A. 105*, 3479–3484.
(10) Vonderheide, R. H., Domchek, S. M., Schultze, J. L., George, D. J., Hoar, K. M., Chen, D. Y., Stephans, K. F., Masutomi, K., Loda, M., Xia, Z., Anderson, K. S., Hahn, W. C., and Nadler, L. M. (2004) Vaccination of cancer patients against telomerase induces functional antitumor CD8+ T lymphocytes. *Clin. Cancer. Res. 10*, 828–839.
(11) Yoshino, T., Hirabe, H., Takahashi, M., Kuhara, M., Takeyama, H., and Matsunaga, T. (2008) Magnetic cell separation using nano-sized bacterial magnetic particles with reconstructed magnetosome membrane. *Biotechnol. Bioeng. 101*, 470–477.
(12) Kuhara, M., Takeyama, H., Tanaka, T., and Matsunaga, T. (2004) Magnetic cell separation using antibody binding with protein a expressed on bacterial magnetic particles. *Anal. Chem. 76*, 6207–6213.
(13) Matsunaga, T., Takahashi, M., Yoshino, T., Kuhara, M., and Takeyama, H. (2006) Magnetic separation of CD14+ cells using antibody binding with protein A expressed on bacterial magnetic particles for generating dendritic cells. *Biochem. Biophys. Res. Commun. 350*, 1019–1025.
(14) Takahashi, M., Yoshino, T., Takeyama, H., and Matsunaga, T. (2008) Direct magnetic separation of immune cells from whole blood using bacterial magnetic particles displaying protein G, *Biotechnol. Prog.*, in press.
(15) Matsunaga, T., Sakaguchi, T., and Tadokoro, F. (1991) Magnetite formation by a magnetic bacterium capable of growing aerobically. *Appl. Microbiol. Biotechnol. 35*, 651–655.
(16) Tanaka, T., and Matsunaga, T. (2000) Fully automated chemiluminescence immunoassay of insulin using antibody-protein A-bacterial magnetic particle complexes. *Anal. Chem. 72*, 3518–3522.
(17) Akiyama, Y., Kuzushima, K., Tsurumi, T., and Yamaguchi, K. (2004) Analysis of HLA-A24-restricted CMVpp65 peptide-specific CTL with HLA-A*2402-CMVpp65 tetramer. *Immunol. Lett. 95*, 199–205.
(18) Schwidop, W. D., Klossek, P., Muller, R., and Claus, R. (1990) Procedure for the purification of streptavidin by hydrophobic interaction chromatography. *J. Chromatogr. 520*, 325–331.
(19) Horak, D., Babic, M., Jendelova, P., Herynek, V., Trchova, M., Pientka, Z., Pollert, E., Hajek, M., and Sykova, E. (2007) D-Mannose-modified iron oxide nanoparticles for stem cell labeling. *Bioconjugate Chem. 18*, 635–644.
(20) Hu, Y., Xie, J., Tong, Y. W., and Wang, C. H. (2007) Effect of PEG conformation and particle size on the cellular uptake efficiency of nanoparticles with the HepG2 cells. *J. Controlled Release 118*, 7–17.
(21) Lewin, M., Carlesso, N., Tung, C. H., Tang, X. W., Cory, D., Scadden, D. T., and Weissleder, R. (2000) Tat peptide-derivatized magnetic nanoparticles allow in vivo tracking and recovery of progenitor cells. *Nat. Biotechnol. 18*, 410–414.
(22) Natarajan, A., Gruettner, C., Ivkov, R., DeNardo, G. L., Mirick, G., Yuan, A., Foreman, A., and DeNardo, S. J. (2008) NanoFerrite particle based radioimmunonanoparticles: binding affinity and in vivo pharmacokinetics. *Bioconjugate Chem. 19*, 1211–1218.
(23) Sadzuka, Y., Nakade, A., Hirama, R., Miyagishima, A., Nozawa, Y., Hirota, S., and Sonobe, T. (2002) Effects of mixed polyethyleneglycol modification on fixed aqueous layer thickness and antitumor activity of doxorubicin containing liposome. *Int. J. Pharm. 238*, 171–180.
(24) Appel, H., Kuon, W., Kuhne, M., Wu, P., Kuhlmann, S., Kollnberger, S., Thiel, A., Bowness, P., and Sieper, J. (2004) Use of HLA-B27 tetramers to identify low-frequency antigen-specific T cells in Chlamydia-triggered reactive arthritis. *Arthritis Res. Ther. 6*, R521–534.
(25) Barnes, E., Ward, S. M., Kasprowicz, V. O., Dusheiko, G., Klenerman, P., and Lucas, M. (2004) Ultra-sensitive class I tetramer analysis reveals previously undetectable populations of antiviral CD8+ T cells. *Eur. J. Immunol. 34*, 1570–1577.
(26) Kim, S. K., Devine, L., Angevine, M., DeMars, R., and Kavathas, P. B. (2000) Direct detection and magnetic isolation of Chlamydia trachomatis major outer membrane protein-specific CD8+ CTLs with HLA class I tetramers. *J. Immunol. 165*, 7285–7292.
(27) McDermott, A. B., Spiegel, H. M., Irsch, J., Ogg, G. S., and Nixon, D. F. (2001) A simple and rapid magnetic bead separation technique for the isolation of tetramer-positive virus-specific CD8 T cells. *Aids 15*, 810–812.

BC800398D

Bioconjugate Chemistry 20th Anniversary

Subscriber access provided by SHEMYAKIN-OVCHINNIKOV INST

Article

Microplate-Based Characterization of Protein-Phosphoinositide Binding Interactions Using a Synthetic Biotinylated Headgroup Analogue

Denghuang Gong, Matthew D. Smith, Debasis Manna, Heidi E. Bostic, Wonhwa Cho, and Michael D. Best

Bioconjugate Chem., **2009**, 20 (2), 310-316• DOI: 10.1021/bc8004107 • Publication Date (Web): 30 January 2009

Downloaded from http://pubs.acs.org on May 15, 2009

More About This Article

Additional resources and features associated with this article are available within the HTML version:

- Supporting Information
- Access to high resolution figures
- Links to articles and content related to this article
- Copyright permission to reproduce figures and/or text from this article

View the Full Text HTML

ACS Publications
High quality. High impact.

Bioconjugate Chemistry is published by the American Chemical Society. 1155 Sixteenth Street N.W., Washington, DC 20036

Microplate-Based Characterization of Protein-Phosphoinositide Binding Interactions Using a Synthetic Biotinylated Headgroup Analogue

Denghuang Gong,[†] Matthew D. Smith,[†] Debasis Manna,[‡] Heidi E. Bostic,[†] Wonhwa Cho,[‡] and Michael D. Best*[,†]

Department of Chemistry, The University of Tennessee, Knoxville, Tennessee 37996, and Department of Chemistry, The University of Illinois at Chicago, Chicago, Illinois 60607. Received September 24, 2008; Revised Manuscript Received December 10, 2008

Membrane lipids act as important regulators of a litany of important physiological and pathophysiological events. Many of them act as site-specific ligands for cytosolic proteins in binding events that recruit receptors to the cell surface and control both protein function and subcellular localization. Phosphatidylinositol phosphates (PIP_ns) are a family of signaling lipids that regulate numerous cellular processes by interacting with a myriad of protein binding modules. Characterization of PIP_n-binding proteins has been hampered by the lack of a rapid and convenient quantitative assay. Herein, microplate-based detection is presented as an effective approach to characterizing protein-PIP_n binding interactions at the molecular level. With this assay, the binding of proteins to isolated PIP_n headgroups is detected with high sensitivity using a platform that is amenable to high-throughput screening. In the studies described herein, biotinylated PI-(4,5)-P_2 headgroup analogue **1** was designed, synthesized, and immobilized onto 96-well streptavidin-coated microplates to study receptor binding. This assay was used to characterize the binding of the PH domain of β-spectrin to this headgroup. The high affinity interaction that was detected for surface association ($K_{d,\ surf} = 6$ nM $\pm$ 3), demonstrates that receptor binding modules can form high affinity interactions with lipid headgroups outside of a membrane environment. The results also indicate the feasibility of the assay for rapid characterization of PIP_n-binding proteins as well as the promise for high-throughput analysis of protein-PIP_n binding interactions. Finally, this assay was also employed to characterize the inhibition of the binding of receptors to the PIP_n-derivatized microplates using solution phase competitors. This showcases the viability of this assay for rapid screening of inhibitors of PIP_n-binding proteins.

INTRODUCTION

Lipids present in cellular membranes act as key regulators of important biological processes. A primary role of these species is to act as site-specific ligands in molecular recognition events that result in the recruitment of cytosolic effector proteins to the membrane surface, a process that generally regulates both protein function and subcellular localization (*1*−*3*). Protein−lipid binding interactions lie at the heart of many of the most important cellular pathways, which is likely due to the ability to transmit information from the membrane into cellular signaling cascades.

One family of phospholipids involved in many crucial biological events consists of phosphate derivatives of phosphatidylinositol, collectively known as phosphoinositides (PIP_ns) (*3*−*7*). The study of PIP_ns is vital as these lipids have been heavily implicated in several high-profile pathophysiological events including the onset of cancer, leukemia, and diabetes (*8*). A prominent example involves the conversion of phosphatidylinositol-4,5-bisphosphate (PI-(4,5)-P_2) to phosphatidylinositol-3,4,5-trisphosphate, with the forward and reverse reactions catalyzed by phosphoinositide 3-kinase (PI-3K) (*9*) and the phosphatase PTEN (*10*), respectively. Both PI-3K (*11*) and the tumor suppressor PTEN (*12*) are among the most frequently mutated enzymes in tumorigenesis.

The PIP_n family consists of seven isomeric phosphodiester-linked *myo*-inositol headgroups containing every possible combination of phosphorylation at the 3-, 4-, and 5-positions. Because of the structural similarity and yet functional diversity of these compounds, their study generally requires a synthetic approach to obtain homogeneous samples of the natural lipid or analogues thereof. However, the synthesis of PIP_ns represents a significant barrier to these efforts. In addition to this synthetic difficulty, the study of PIP_n-effector protein binding events generally faces additional challenges. For example, the complexity of the membrane environment complicates binding characterization due to its inherent heterogeneity.

An important question pertaining to protein−PIP_n binding is what structural features are required for membrane binding to occur, as some proteins show strong binding to the lipid headgroup alone, while others require the full membrane environment for interaction (*4*, *6*). In particular, crystal structures of certain pleckstrin homology (PH) domains indicate a shallow binding pocket, which, combined with other evidence, indicates predominantly headgroup-driven association (*3*). However, instances of PH domain membrane-insertion are documented (*13*, *14*), and other domains (phox homology (PX) and Fab1, YOTB, Vac1, and EEA1 (FYVE)) require the membrane for lipid headgroup binding. This disparity makes it necessary to determine the headgroup-binding affinities of PIP_n-binding proteins to understand how PIP_ns drive the specific membrane recruitment of diverse effectors for cell regulation.

A rapidly growing number of cellular proteins are known to bind PIP_ns. Many of these proteins contain specialized PIP_n-binding modules, such as the PH, PX, FYVE, and the more recently discovered β-propellers that bind PIP_n (PROPPIN) domains (*3*). Among the large number of reported PIP_n-binding modules, PIP_n affinities and specificities are known to vary widely, requiring the careful investigation of each distinct receptor with each PIP_n isomer. Such studies are hampered by the diversity of domain families, exemplified by the PH domains, for which recent sequence homology searches have implicated

* To whom correspondence should be addressed. E-mail: mdbest@utk.edu.

[†] The University of Tennessee.

[‡] The University of Illinois at Chicago.

10.1021/bc8004107 CCC: $40.75 © 2009 American Chemical Society
Published on Web 01/30/2009

over 250 family members in humans (*3*), many of which remain uncharacterized. Finally, proteins exist that interact with PIP_ns but lack a well-defined PIP_n-binding site. Characterization of these important groups of proteins would be advanced by a rapid and reliable quantitative assay for determining the affinity and specificity for each PIP_n isomer. Herein, we present a new microplate-based quantitative assay for PIP_n binding, which can be applied to large scale high-throughput screening.

EXPERIMENTAL PROCEDURES

General Experimental Details. Dry solvents were obtained from a Pure Solv solvent delivery system purchased from Innovative Technology, Inc. Column chromatography was performed using 230−400 mesh silica gel purchased from Sorbent Technologies. NMR spectra were obtained using a Bruker AC250 spectrometer updated with a TecMag data collection system, a Varian Mercury 300 spectrometer, and a Bruker Avance 400 spectrometer. Mass spectra were obtained with JEOL DART-AccuTOF spectrometer with high resolution capabilities and an ABI Voyager DE Pro MALDI spectrometer. HPLC data was obtained using an HP series 1100 HPLC with an Alltech Lichrosphere SI 60 50U column with HPLC grade solvents purchased from Fisher. Optical rotation values were obtained using a Perkin-Elmer 241 polarimeter. Microplate-based chemiluminescence measurements were performed using a BioTek Synergy 2 multidetection microplate reader. White reacti-bind streptavidin high binding capacity (HBC) coated 96-well microplates for chemiluminescence studies were purchased from Pierce Biotechnology (Rockford, IL). Goat polyclonal anti-GST tag HRP-conjugate was purchased from Novus Biologicals (Littleton, CO). Supersignal ELISA femto maximum sensitivity substrate was purchased from Pierce Biotechnology (Rockford, IL). The GST-tagged PH domain of β-spectrin was expressed and purified as previously described (*15*).

1D-4,5-*O*-Bisbenzyl-1-*O*-(*tert*-butyldiphenylsilyl-2,3,6-*O*-tris-(benzyloxymethyl)-myo-inositol (3). To a solution of **2** (0.586 g, 0.96 mmol) in 1,2-dichloroethane (21 mL) were added diisopropylethylamine (1.7 mL, 9.83 mmol) and benzyloxychloromethyl ether (1.4 mL, 10.1 mmol). The reaction mixture was stirred at reflux for 24 h. Diisopropylethylamine (1.7 mL, 9.83 mmol) and benzyloxychloromethyl ether (1.4 mL, 10.1 mmol) were added to the solution, and the mixture was stirred at reflux for another 24 h. After the reaction was finished, water was added, and the crude reaction mixture was extracted with methylene chloride (2 × 50 mL). The organic phase was dried with magnesium sulfate, filtered, and then concentrated. The crude product was then purified by chromatography on silica gel (acetone/hexane 1:5) giving **3** (0.631 g, 68%) as a syrup.

$[\alpha]_D^{296K}$ 25.8 ($c = 0.95$, $CHCl_3$); ^{1}H NMR (400 MHz, $CDCl_3$) δ 7.88 (dd, J = 13.6, 7.3 Hz, 4H), 7.75 (t, J = 7.6 Hz, 4H), 7.42−7.14 (m, 23H), 6.94−6.89 (m, 4H), 5.92 (t, J = 10.1 Hz, 1H), 5.50 (t, J = 9.7 Hz, 1H), 5.05 (d, J = 6.8 Hz, 1H), 4.86−4.80 (m, 3H), 4.73 (d, J = 6.8 Hz, 1H), 4.55−4.45 (m, 2H), 4.33−4.02 (m, 7H), 3.67 (dd, J = 10.3, 2.0 Hz, 1H), 3.58 (m, 1H), 1.11 (s, 9H); ^{13}C NMR (100.5 MHz, $CDCl_3$) δ 166.0, 165.6, 138.2, 137.7, 137.4, 136.0, 135.9, 133.8, 132.8, 130.2, 130.0, 129.7, 129.6, 128.2, 128.1, 127.9, 127.7, 127.4, 127.3, 96.6, 95.5, 91.8, 77.7, 74.9, 74.5, 73.0, 72.8, 72.2, 69.9, 69.4, 68.9, 27.3, 27.2, 19.3. MALDI-HRMS $[M + Na]^+$ calcd for $C_{60}H_{62}O_{11}SiNa$, 1009.3959; found, 1009.3936.

1D-1-*O*-(*tert*-Butyldiphenylsilyl-2,3,6-*O*-tris-(benzyloxymethyl)-myo-inositol (4). A solution of **3** (0.631 g, 0.650 mmol) in methanol (40 mL) was treated with sodium methoxide (1.6 g, 29.6 mmol) at room temperature for 18 h. Then sodium methoxide (1.0 g, 18.5 mmol) was added to the reaction solution, and the mixture was stirred at room temperature for 3 h, after which the contents were filtered. The resulting residue was dissolved in water (50 mL), and the aqueous solution was extracted with methylene chloride (2 × 50 mL). In addition, the previous filtrate was concentrated in vacuum and then extracted with methylene chloride (2 × 50 mL) from water (50 mL). The combined organic layer was then dried with magnesium sulfate, filtered, concentrated, and purified by chromatography on silica gel (hexanes/acetone, 3:1) to provide pure diol **4** (0.393 g, 80%) as a syrup.

$[\alpha]_D^{296K}$ 86.1 ($c = 1.36$, $CHCl_3$); ^{1}H NMR (250 MHz, $CDCl_3$) δ 7.68 (t, J = 7.3 Hz, 4H), 7.41−7.19 (m, 21H), 5.02 (d, J = 6.8 Hz, 1H), 4.90−4.83 (m, 2H), 4.73−4.45 (m, 8H), 4.34−4.25 (m, 2H), 3.99−3.91 (m, 2H), 3.77−3.75 (m, 2H), 3.40 (dd, J = 9.6, 1.8 Hz, 1H), 3.13−3.10 (m, 1H), 2.78 (m, 1H), 1.03 (s, 9H);^{13}C NMR (62.9 MHz, $CDCl_3$) δ 138.2, 135.9, 135.6, 134.1, 133.4, 129.9, 129.5, 128.5, 128.4, 128.3, 128.02, 127.98, 127.72, 127.66, 127.5, 127.4, 95.5, 93.5, 85.2, 76.3, 75.7, 74.2, 73.2, 72.2, 70.3, 69.2, 27.0, 19.4. HRMS $[M + O_2]^-$ calcd for $C_{46}H_{54}O_{11}Si$, 810.34354; found, 810.34393.

1D-1-*O*-(*tert*-Butyldiphenylsilyl-2,3,6-*O*-tris-(benzyloxymethyl)-myo-inositol 4,5-bis-(dibenzyl phosphate) (5). To a solution of diol **4** (0.73 g, 0.958 mmol) and 1-*H*-tetrazole (17 mL, 7.67 mmol, 0.45 M in acetonitrile) in methylene chloride (30 mL) was added dibenzyl *N*,*N*-diisopropylphosphoramidite (1.93 mL, 5.75 mmol) under nitrogen gas, and the mixture was stirred at room temperature for 18 h. The reaction solution was cooled to − 60 °C, and *m*-CPBA (2.2 g, 57−86%) was added. The mixture was stirred at this temperature for 60 min and then slowly warmed to room temperature after the removal of the cooling bath. The solution was diluted to 180 mL with methylene chloride and washed with saturated aqueous sodium bicarbonate (2 × 100 mL), and the aqueous phase was extracted with methylene chloride (100 mL). The combined organic phase was dried with magnesium sulfate, filtered, and concentrated, and the residue was purified by chromatography on silica gel (hexanes/acetone, 3:1) giving bis-phosphodiester **5** (1.17 g, 81%) as a syrup.

$[\alpha]_D^{296K}$ −2.5 (c = 0.805, $CHCl_3$); ^{1}H NMR (400 MHz, $CDCl_3$) δ 7.68−7.78 (m, 4H), 7.03−7.35 (m, 41H), 4.93−5.22 (m, 12H), 4.77−4.80 (m, 3H), 4.59 (d, J = 12.0 Hz, 1H), 4.39−4.47 (m, 3H), 4.28−4.32 (m, 2H), 4.16 (d, J = 6.8 Hz, 1H), 4.05 (d, J = 12.4 Hz, 1H), 3.95 (d, J = 7.2 Hz, 1H), 3.49 (s, 1H), 3.39 (dd, J = 10.0, 1.6 Hz, 1H), 1.11 (s, 9H); ^{13}C NMR (100.5 MHz, $CDCl_3$) δ 133.7, 132.6, 130.1, 130.0, 128.5, 128.4, 128.3, 128.2, 128.2, 128.0, 128.0, 127.9, 127.8, 127.6, 127.5, 127.3, 96.6, 95.5, 93.2, 78.4, 77.8, 75.2, 75.1, 74.0, 73.7, 70.7, 69.5, 69.5, 69.4, 69.3, 69.1, 69.1, 27.3, 19.3; ^{31}P NMR (161.8 MHz, $CDCl_3$) δ −0.83 (s, 1P), −1.21 (m, 1P). MALDI-HRMS $[M + Na]^+$ calcd for $C_{74}H_{80}O_{15}P_2SiNa$, 1321.4634; found, 1321.4602.

1D-2,3,6-*O*-Tris-(benzyloxymethyl)-myo-inositol 4,5-bis-(dibenzyl phosphate) (6). A solution of fully protected inositol **5** (1.17 g, 0.90 mmol) in *N*,*N*-dimethylformamide (30 mL) was treated with tetrabutylammonium fluoride trihydrate (0.90 g, 2.85 mmol) at room temperature for 12 h. After the reaction was finished, the solution was partitioned between ethyl acetate (200 mL) and H_2O (150 mL). The aqueous layer was further extracted with ethyl acetate (100 mL), and the combined organic layer was washed with brine (150 mL), dried with magnesium sulfate, and filtered. Following concentration, the residue was purified by chromatography on silica gel (hexanes/acetone, 2:1) to give alcohol **6** (0.854 g, 88%) as a syrup.

$[\alpha]_D^{296K}$ −36.3 (c = 1.0, $CHCl_3$); ^{1}H NMR (300 MHz, $CDCl_3$) δ 7.14−7.35 (m, 35H), 4.92−5.19 (m, 11H), 4.61−4.79 (m, 6H), 4.39−4.54 (m, 4H), 4.29 (s, 1H), 4.24 (d, J = 2.1 Hz, 1H), 3.88 (t, J = 9.3 Hz, 1H), 3.72 (d, J = 10.2 Hz, 1H), 3.55 (d, J = 9.3 Hz, 1H); ^{13}C NMR (100.5 MHz, $CDCl_3$) δ 138.0, 137.7, 136.9, 136.3, 136.2, 136.2, 136.1, 136.0, 128.7, 128.6,

128.5, 128.5, 128.4, 128.4, 128.3, 128.2, 128.1, 128.1, 128.0, 128.0, 127.9, 127.8, 127.7, 127.7, 97.3, 95.8, 95.0, 83.5, 79.5, 79.5, 78.1, 78.0, 75.8, 75.3, 70.7, 70.6, 69.9, 69.7, 69.6, 69.6, 69.6, 69.4, 69.4, 69.3; ^{31}P NMR (161.8 MHz, $CDCl_3$) δ −1.13 (s, 1P), −1.50 (s, 1P). MALDI-HRMS $[M + Na]^+$ calcd for $C_{58}H_{62}O_{15}P_2Na$, 1083.3456; found, 1083.3410.

Benzyl (6-benzyloxycarbonylaminohexyl) 1D-2,3,6-*O*-tris-(benzyloxymethyl)-myo-inosit-1-yl phosphate 4,5-bis-(dibenzyl phosphate) (7). To a solution of cbz-aminohexanol (0.694 g, 2.76 mmol) in methylene chloride (30 mL) under nitrogen was added 1-*H* tetrazole (4.6 mL of a 0.45 M solution in acetonitrile, 2.07 mmol) and benzyloxy-bis(diisopropylamino)-phosphine (1.392 g, 4.11 mmol). This mixture was allowed to stir at room temperature for 2 h, at which point the solution was extracted with methylene chloride (3 × 80 mL) from saturated sodium bicaronate (80 mL). The combined organic phase was then dried with magnesium sulfate, filtered, concentrated and the residue was purified by chromatography on silica gel (eluant: hexane/ethyl acetate/triethylamine 100:10:1). The resulting colorless liquid (0.983 g, 2.0 mmol) was then added to a solution of alcohol **6** (0.854 g, 0.805 mmol) and 1-*H* tetrazole (5.3 mL of a 0.45 M solution in acetonitrile, 2.4 mmol) in methylene chloride (36 mL) under nitrogen, and the mixture was allowed to stir at room temperature for 18 h. The reaction solution was then cooled to −60 °C and *m*-CPBA (0.7 g, 57−86%) was added. Stirring was continued at this temperature for 60 min before the reaction was slowly warmed to room temperature. The solution was then extracted with methylene chloride (3 × 80 mL) from saturated sodium bicarbonate (60 mL). The combined organic phase was dried with magnesium sulfate, concentrated, and the residue was chromatographed on silica gel (hexanes/acetone, 3:1) to afford tris-phosphotriester **7** (0.53 g, 45%) as a syrup.

$[\alpha]_D^{296K}$ −22.9 (c = 1.0, $CHCl_3$); ^{1}H NMR (300 MHz, $CDCl_3$) δ 7.16−7.34 (m, 45H), 4.41−5.20 (m, 28H), 4.20−4.34 (m, 2H), 3.88−3.95 (m, 2H), 3.71 (d, J = 9.0 Hz, 1H), 3.07−3.14 (m, 2H), 1.20−1.48 (m, 8H); ^{13}C NMR (100.5 MHz, $CDCl_3$) δ 156.4, 138.2, 137.9, 137.5, 136.7, 136.2, 136.1, 136.0, 135.9, 135.8, 135.8, 128.6, 128.4, 128.4, 128.4, 128.3, 128.2, 128.2, 128.0, 128.0, 127.9, 127.8, 127.7, 127.7, 127.6, 127.5, 127.4, 96.6, 95.6, 94.6, 78.8, 76.4, 74.9, 74.7, 74.6, 74.5, 70.4, 70.4, 69.7, 69.7, 69.6, 69.5, 69.4, 69.3, 69.3, 68.1, 67.9, 66.5, 40.8, 30.0, 29.9, 29.7, 26.0, 24.9; ^{31}P NMR (161.8 MHz, $CDCl_3$) δ −1.19 (m, 3P). MALDI-HRMS $[M + Na]^+$ calcd for $C_{79}H_{88}NO_{20}P_3Na$, 1486.5005; found, 1486.5027.

1-(6-Aminohexyl sodium phosphate)-1D-myo-inositol-4,5-bis-(disodium phosphate) (8). To a solution of compound **7** (0.57 g, 0.389 mmol) in methanol (50 mL) was added 20% palladium hydroxide on charcoal (0.67 g). The mixture was then stirred for 3 days at room temperature with 1 atm of hydrogen (balloon). Next, the catalyst was removed by filtration, and the residue was with washed with methanol. The solvent was removed in vacuum, and the crude product was dissolved in water and stirred for 3 h with Chelex 100 resin (Sigma, Na^+ form). The resin was removed by filtration, and the filtrate was lyophilized to give amino-conjugate **8** (0.245 g, 100%) as a white solid.

$[\alpha]_D^{296K}$ −14.9 (c = 1.0, H_2O); ^{1}H NMR (300 MHz, D_2O) δ 4.19−4.24 (m, 2H), 3.88−4.00 (m, 5H), 3.69 (dd, J = 9.6, 2.7 Hz, 1H), 2.99 (d, J = 7.8 Hz, 2H), 1.63−1.70 (m, 4H), 1.40−1.43 (m, 4H); ^{13}C NMR (100.5 MHz, D_2O) δ 80.0, 78.6, 78.0, 74.2, 74.1, 73.3, 68.9, 42.1, 32.0, 29.2, 27.7, 27.0; ^{31}P NMR (121.5 MHz, D_2O) δ 5.20 (s, 1P), 4.78 (s, 1P), 0.92 (s, 1P). MALDI-HRMS (free acid, $[M + H]^+$) calcd for $C_{12}H_{28}NO_{15}P_3H$, 520.0745; found, 520.0729.

1-(6-(14-Biotinamido-3,6,9,12-tetraoxatetradecanamido)hexyl sodium phosphate)-1D-myo-inositol 4,5-bis-(disodium phosphate) (1). Succinimidyl ester **9** was dissolved in dimethylformamide (1 mL) and compound **8** (7 mg, 0.011 mmol), dissolved in TEAB (0.5 M, 1 mL), was added. The mixture was stirred at room temperature for 24 h. The solvent was removed under reduced pressure, and the residue was washed with acetone (4 × 2 mL) and then dried in vacuo. The resulting white solid was dissolved in water, and the solution was stirred for 3 h with Chelex 100 resin (Sigma, Na^+ form). The resin was removed by filtration, and the filtrate was lyophilized to give the product (13 mg, 100%) as a white solid.

^{1}H NMR (300 MHz, D_2O) δ 4.56−4.58 (m, 1H), 4.38−4.41 (m, 1H), 4.04−4.25 (m, 3H), 3.82−3.95 (m, 4H), 3.58−3.74 (m, 14H), 2.93−3.40 (m, 14H), 2.72−2.85 (m, 2H), 2.24 (d, J = 6.9 Hz, 2H), 1.33−1.79 (m, 16H); ^{31}P NMR (121.5 MHz, D_2O) δ 5.79 (s, 1P), 5.70 (s, 1P), 0.87 (s, 1P). MALDI-HRMS (free acid, $[M + H]^+$) calcd for $C_{32}H_{61}N_4O_{22}P_3SH$, 979.2784; found, 979.2775.

Microplate Analysis of PI-(4,5)-P_2 Headgroup-β-spectrin PH Domain Binding. Binding assays were performed using streptavidin-coated 96-well microplates. The wash buffer that was used was 20 mM Tris buffer at pH 8.0 with 0.05% tween as a blocking additive to avoid nonspecific surface adsorption. In general, the wells that were to be used for analysis were washed with 200 μL of wash buffer for 30 min. This was removed, followed by the addition of the appropriate solutions of biotin-TEG-PI-(4,5)-P_2 ligand **1** or control **8** or **13** in water, and incubation for 1 h. Next, these solutions were removed, and the wells were washed with 3 × 250 μL wash buffer. Following this, 200 μL of GST-tagged β-spectrin PH domain solutions in wash buffer were added to each well. After a 1 h incubation, the protein solution was removed, and the wells were washed with 3 × 250 μL wash buffer. Next, 200 μL of a solution of goat polyclonal anti-GST tag HRP-conjugate was added to each well and allowed to incubate for 1 h. This solution was then removed, and the wells were washed with 3 × 250 μL wash buffer. Chemiluminescence detection of bound antibody was next performed using supersignal ELISA femto maximum sensitivity substrate. Here, a 1:1 mixture of the substrate and peroxide solutions were mixed, 100 μL of which was added to each well. The microplate was then immediately placed in the microplate reader, and the chemiluminescence at 425 nm was repeatedly measured for ∼5 min. Several readings that provided optimal signal were then averaged, and the change in chemiluminescence was plotted verses the concentration of the varying component. The resulting curve was fit via the program SigmaPlot using the Langmuir isotherm: $C = C\text{max}*[P]/(K\text{d, surf} + [P])$ (C = chemiluminescence; P = protein) to calculate dissociation constants. For Figure 1A, solutions of **1** varied from 0−500 nM, β-spectrin PH domain added was fixed at 100 ng/mL, and anti-GST Ab was added at 10 ng/mL. For Figure 1B, [**1**] immobilized was fixed at 500 nM, β-spectrin PH domain solutions ranged from 0−15 nM, and the anti-GST Ab solution was 100 ng/mL. For Figure 2, [**1**] immobilized was fixed at 500 nM, solutions of fixed β-spectrin PH domain (200 ng/mL) and varying competitor **8** (0−4 μM) were used, and anti-GST Ab solution was 10 ng/mL.

RESULTS AND DISCUSSION

Because of the importance of the PIP_ns in cell regulation and the diversity of proteins that target these lipids in terms of structure and the details of recognition, it is imperative to develop efficient approaches for characterizing PIP_n recognition at the molecular level. Current assays for detecting interactions utilize lipid-functionalized nitrocellulose membranes (such as PIP strips, Echelon Biosciences, Salt Lake City, UT), vesicle pelleting, fluorescence, isothermal titration calorimetry (ITC), or SPR-based methods (*16*). However, these methods do not

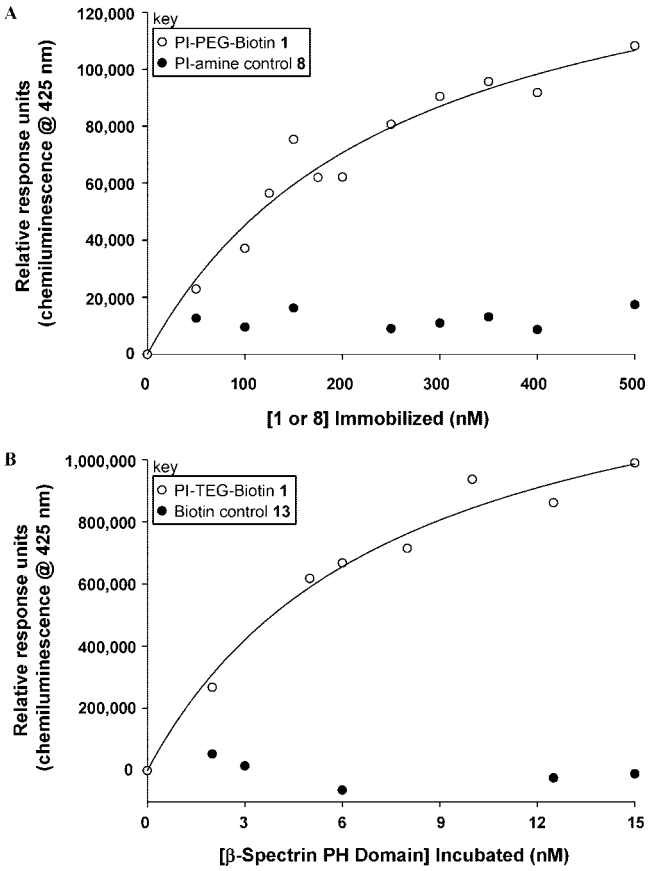

Figure 1. Microplate assay results obtained with (A) varying concentration of ligand **1** with fixed [receptor] and (B) fixed [**1**] with changing [receptor]. Both results indicate sensitive detection of headgroup binding.

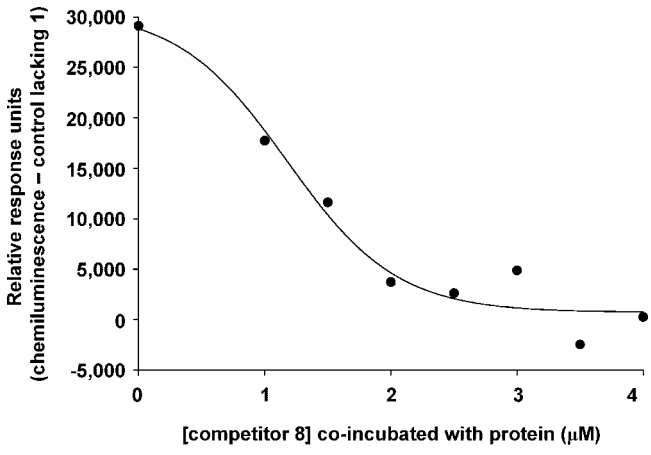

Figure 2. Inhibition of protein binding to the ligand-functionalized surface using solution-phase competitor **8**.

allow for high-throughput quantification, which is required to elucidate the grand scope of complexities associated with receptor-PIP_n binding.

Microarray analysis has proven highly effective for high-throughput quantification of protein−ligand binding, including cell surface receptor−ligand binding interactions. Generally, optical detection is utilized, which benefits from high sensitivity and easy access to studies. Another advantage is that the surface display of target ligands allows for the formation of multivalent binding interactions, which are common in membrane-based biological recognition events (*17, 18*), and are known to occur with certain PIP_n-targeting proteins (*3*). Detection in a multivalent context is important as ligand preferences of receptors can differ between solution-phase studies and those using a multivalent surface (*19, 20*). In microarray analysis, ligand density can be directly controlled via the amount of ligand that is deposited on the surface. In fact, binding affinities have been found to vary depending upon the concentration of ligand immobilized in microarray analysis, indicating the occurrence of multivalent interactions (*21, 22*). The described advantages have been exhibited in the development of DNA (*23, 24*), protein and peptide (*25*−*27*), and carbohydrate (*20, 22, 28*−*34*) microarray systems, while lipid microarrays have only recently emerged (*21, 35*).

Toward our goal of a high-throughput microarray platform for efficient characterization of PIP_n-binding, we have initially devised a microplate-based detection system. The first task in this pursuit was the development of a ligand-immobilization strategy, for which synthetic biotinylated PI-(4,5)-P_2 headgroup analogue **1** (Scheme 1) was designed. PI-(4,5)-P_2 was chosen for initial studies as it is the most abundant member of the PIP_n family. The isolated headgroup motif was employed to directly investigate the extent to which effector proteins interact with this moiety outside of the membrane environment. Ligand **1** also contains a biotin group for immobilization onto streptavidin surfaces, as this high affinity noncovalent interaction enforces quantitative immobilization while avoiding potential nonspecific surface attachment. Finally, a tetraethylene glycol (TEG) spacer was introduced between the headgroup and biotin to distance the ligand from the microplate surface.

The synthesis of PI-(4,5)-P_2-TEG-biotin conjugate **1** benefited from protocols previously developed for accessing inositol headgroups (*36*−*38*) and amino-functionalized tetherable analogues thereof (*39*−*42*). Specifically, the synthetic route to protected PI-(4,5)-P_2 headgroup **6** (Scheme 1) employed a procedure modified from that reported by Bruzik and co-workers (*38*). First, compound **2** was obtained in four steps from *myo*-inositol as previously described. This contains benzoyl groups at positions 4 and 5, the phosphorylation sites in the final compound, and a silyl group at the 1 position, where the phosphodiester linkage occurs in the natural lipid. At this point, we accessed compound **3** by installing benzyloxymethyl (BOM) groups at the 2, 3, and 6 positions to allow for convenient global deprotection via hydrogenolysis at the end of the synthesis. After benzoyl group removal to **4**, phosphoramidite chemistry was used to access fully protected headgroup analogue **5**. Following silyl deprotection to **6**, a protected amine group attached via a phosphodiester linkage was introduced to generate **7**. Global deprotection by hydrogenolysis then yielded conveniently functionalizable PI-(4,5)-P_2-amine **8**. Finally, coupling of **8** with biotin-TEG-NHS ester reagent **9** (synthesized in seven steps from TEG; see Supporting Information for details) provided PI-(4,5)-P_2-TEG-biotin conjugate **1**.

The experimental approach to PIP_n microplate analysis using ligand **1** employed a surface-based antibody assay as depicted in Scheme 2. First, PI-(4,5)-P_2 headgroup immobilization was achieved by incubating conjugate **1** in different wells of a streptavidin-coated 96 well microplate, followed by thorough buffer washes. Next, the ligand was incubated with the effector protein. For our initial study, we sought to characterize the PI-(4,5)-P_2 headgroup-binding of the PH domain of the protein β-spectrin. To do so, we expressed and purified this domain with an appended glutathione-*S*-transferase (GST) tag, used for detection and purification purposes, as previously described (*15*). Following buffer washes to remove unbound protein, a horseradish peroxidase (HRP)-conjugated anti-GST antibody was used, followed by further washing. Finally, chemiluminescence-

Scheme 1. Synthetic Route to PI-(4,5)-P_2-TEG-Biotin Conjugate 1

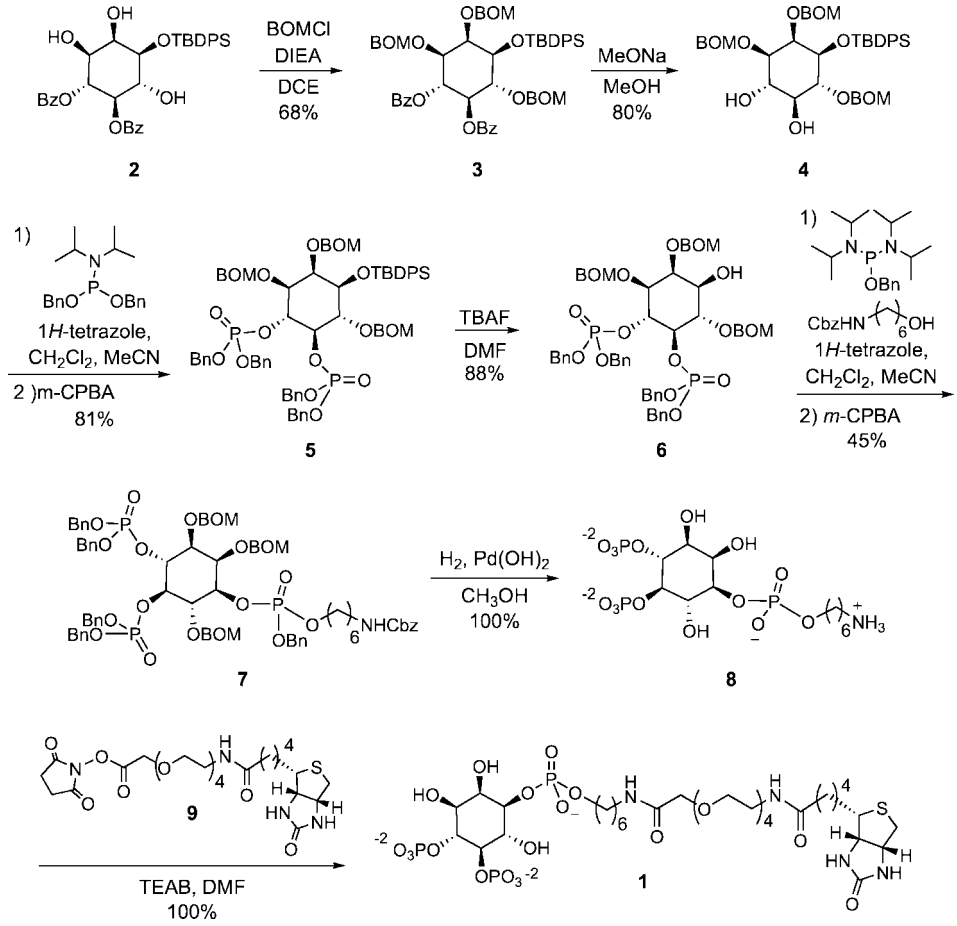

Scheme 2. Microplate-Based Assay for the Detection of Receptor-PIP_n Headgroup Binding Interactions

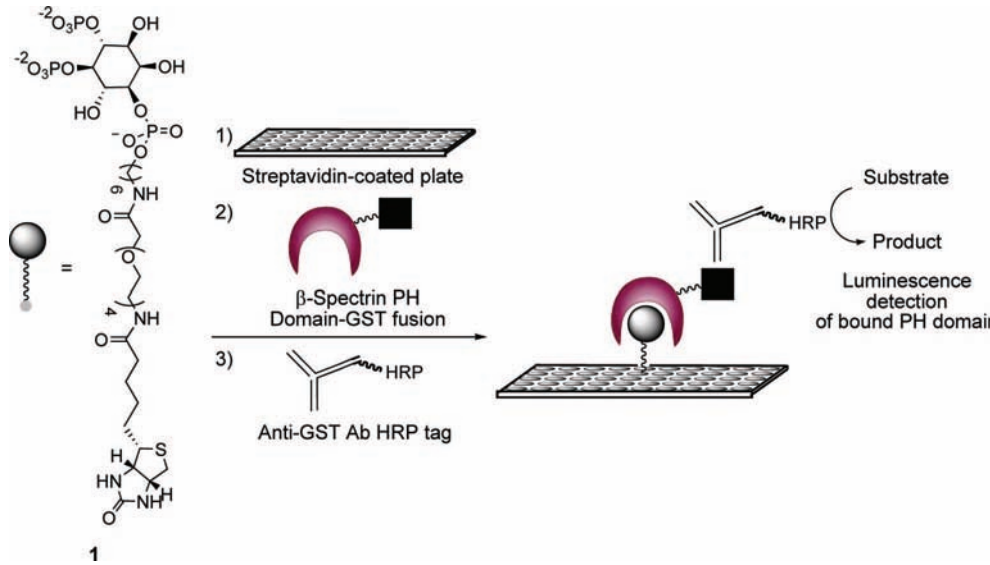

based detection of the secondary antibody using a microplate reader was performed to transduce the presence of bound protein.

The described microplate assay was successfully employed to probe PI-(4,5)-P_2 headgroup-β-spectrin PH domain association via multiple approaches. First, analysis was performed by introducing varying concentrations of ligand **1** into the plate and incubating with fixed protein and antibody concentrations. A representative binding curve indicating enhanced protein recruitment upon increasing immobilized ligand is shown in Figure 1A. The results show highly sensitive detection of binding, as the rise in the curve corresponds to less than 50 pmol of ligand immobilized in the plate. Also shown in Figure 1A is a control study in which PI-amine compound **8**, which lacks the biotin moiety, was incubated in place of **1**. This resulted in the background signal, which indicates that the biotin group of **1** is required for surface deposition and rules out potential nonspecific ligand and protein adsorption onto the plate.

The microplate binding assay was also carried out by depositing a fixed concentration of ligand **1** that correlates to strong protein recruitment from the previous study (500 nM) and varying the receptor concentration, for which results are shown in Figure 1B. Once again, sensitive detection of binding was obtained. Here, results were used to calculate a dissociation constant ($K_{d,\ surf}$) value by fitting the data to the Langmuir isotherm (*22*), with multiple readings yielding an average value of 6 nM ± 3. Figure 1B also includes a second control in which biotin-TEG compound **13** (see Supporting Information for structure), which lacks the PI-(4,5)-P_2 headgroup, was immobilized in place of ligand **1**, again resulting in no signal. The combined results for the controls in Figure 1A and B show that both the PI-(4,5)-P_2 headgroup and biotin moieties of compound **1** are necessary for protein binding.

The binding affinity of the GST-tagged PH domain of β-spectrin interacting with liposomes containing full PI-(4,5)-P_2 lipids was previously determined (K_d = 125 nM ± 18) using a surface plasmon resonance assay (*15*). While the value reported herein differs from this previous study, this is to be expected since the current assay was designed to detect binding in a different environment, that in which the interaction with the lipid headgroup is studied outside of the membrane. As a result, the two assays utilize different formats, and thus, each K_d value is specific to the model system employed for analysis. For example, the presentation and clustering of the PI-(4,5)-P_2 headgroup will vary between microplate surfaces that are directly derivatized with the biotinylated ligand (current assay) compared with studies employing the full lipid incorporated into immobilized liposomes (previous assay). For this reason, we have qualified the dissociation constant measured herein as $K_{d,\ surf}$, as has been indicated in similar approaches employing surface-based binding measurements (*22*).

The results from this assay indicate that receptor binding domains can form high affinity interactions with PIP_n headgroups outside of the membrane environment. The strong binding affinity that was observed using the isolated headgroup provides evidence that PI-(4,5)-P_2-binding is primarily driven by interactions with the headgroup in the case of this particular receptor. These results are in line with previous reports in which strong interactions (K_d = 27.3 nM) between other PH domains and solubilized PIP_n headgroup analogues were observed and the fact that these soluble headgroups effectively displaced receptor-full PIP_n lipid complexes (*43*). However, different PIP_n-binding receptors are known to require the membrane context for binding (*4*, *6*), indicating that the headgroup is not sufficient to enforce association. This diversity in receptor binding mode dictates that each protein must be analyzed independently to determine the molecular-level details of each particular receptor. Therefore, deconvolution of the complexities of receptor−PIP_n affinities, specificities, and binding modes requires a high-throughput assay such as the approach described herein.

In order to extend the described microplate-based strategy, we sought to perform competitive assays to detect the perturbation of protein-binding to the ligand-functionalized microplate surface. Here, microplate wells functionalized with PI-(4,5)-P_2-TEG-biotin conjugate **1** at a fixed concentration were simultaneously incubated with β-spectrin PH domain and a varying amount of soluble PI-(4,5)-P_2-amine headgroup analogue **8**. Figure 2 shows a resulting dose-dependent response curve, in which the extent of protein bound to the surface is diminished through incubation with increasing concentrations of competitive binding partner **8**. These results further confirm the strong association of receptors with the PI-(4,5)-P_2 headgroup outside of the membrane context and showcase the efficacy of our microplate assay for detecting the inhibition of receptor−PIP_n interactions.

The described microplate-based approach provides highly sensitive detection of PIP_n-binding as well as competitive inhibition of recognition. As such, this assay is applicable to a range of studies aimed at characterizing binding at the molecular level, including the determination of PIP_n-binding specificities of receptors, the extent to which headgroup binding drives association with different proteins, and the evaluation of compounds that inhibit binding. Currently, we are extending these studies toward our goal of a high-throughput microarray assay for systematic analysis of the headgroup-binding affinities and specificities of the diverse effector domains and proteins that interact with the PIP_ns. The eventual goal in this regard is the implementation of biotinylated headgroup analogues of all naturally occurring PIP_n isomers for simultaneous microarray analysis of receptors of interest.

ACKNOWLEDGMENT

M.D.B. acknowledges the University of Tennessee for support, and W.C. acknowledges funding from the National Institutes of Health (GM68849).

Note Added after ASAP Publication: This paper published ASAP on January 30, 2009 with an error in Scheme 1 and in the procedure for the synthesis of compound **7**. The revised version was published on February 3, 2009.

Supporting Information Available: Further synthetic procedures and characterizations. This material is available free of charge via the Internet at http://pubs.acs.org.

LITERATURE CITED

(1) Cho, W. H., and Stahelin, R. V. (2005) Membrane-protein interactions in cell signaling and membrane trafficking. *Annu. Rev. Biophys. Biomol. Struct. 34*, 119–151.
(2) Hurley, J. H. (2006) Membrane binding domains. *Biochim. Biophys. Acta 1761*, 805–811.
(3) Lemmon, M. A. (2008) Membrane recognition by phospholipid-binding domains. *Nature Rev. Mol. Cell Biol. 9*, 99–111.
(4) Lemmon, M. A. (2003) Phosphoinositide recognition domains. *Traffic 4*, 201–213.
(5) McLaughlin, S., Wang, J. Y., Gambhir, A., and Murray, D. (2002) PIP2 and proteins: Interactions, organization, and information flow. *Annu. Rev. Biophys. Biomol. Struct. 31*, 151–175.
(6) Prestwich, G. D. (2004) Phosphoinositide signaling: From affinity probes to pharmaceutical targets. *Chem. Biol. 11*, 619–637.
(7) Di Paolo, G., and De Camilli, P. (2006) Phosphoinositides in cell regulation and membrane dynamics. *Nature 443*, 651–657.
(8) Pendaries, C., Tronchere, H., Plantavid, M., and Payrastre, B. (2003) Phosphoinositide signaling disorders in human diseases. *FEBS Lett. 546*, 25–31.
(9) Katso, R., Okkenhaug, K., Ahmadi, K., White, S., Timms, J., and Waterfield, M. D. (2001) Cellular function of phosphoinositide 3-kinases: Implications for development, immunity, homeostasis, and cancer. *Annu. Rev. Cell Dev. Biol. 17*, 615–675.
(10) Maehama, T., and Dixon, J. E. (1998) The tumor suppressor, PTEN/MMAC1, dephosphorylates the lipid second messenger, phosphatidylinositol 3,4,5-trisphosphate. *J. Biol. Chem. 273*, 13375–13378.
(11) Samuels, Y., Wang, Z. H., Bardelli, A., Silliman, N., Ptak, J., Szabo, S., Yan, H., Gazdar, A., Powell, D. M., Riggins, G. J., Willson, J. K. V., Markowitz, S., Kinzler, K. W., Vogelstein, B., and Velculescu, V. E. (2004) High frequency of mutations of the PIK3CA gene in human cancers. *Science 304*, 554–554.
(12) Chow, L. M. L., and Baker, S. J. (2006) PTEN function in normal and neoplastic growth. *Cancer Lett. 241*, 184–196.

(13) Flesch, F. M., Yu, J. W., Lemmon, M. A., and Burger, K. N. (2005) Membrane activity of the phospholipase C-delta(1) pleckstrin homology (PH) domain. *Biochem. J. 389*, 435–441.
(14) Manna, D., Albanese, A., Park, W. S., and Cho, W. (2007) Mechanistic basis of differential cellular responses of phosphatidylinositol 3,4-bisphosphate- and phosphatidylinositol 3,4,5-trisphosphate-binding pleckstrin homology domains. *J. Biol. Chem. 282*, 32093–32105.
(15) Das, A., Base, C., Manna, D., Cho, W., and Dubreuil, R. R. (2008) Unexpected complexity in the mechanisms that target assembly of the spectrin cytoskeleton. *J. Biol. Chem. 283*, 12643–12653.
(16) Cho, W. W., Bittova, L., and Stahelin, R. V. (2001) Membrane binding assays for peripheral proteins. *Anal. Biochem. 296*, 153–161.
(17) Mammen, M., Choi, S. K., and Whitesides, G. M. (1998) Polyvalent interactions in biological systems: Implications for design and use of multivalent ligands and inhibitors. *Angew. Chem., Int. Ed. 37*, 2755–2794.
(18) Kiessling, L. L., Gestwicki, J. E., and Strong, L. E. (2006) Synthetic multivalent ligands as probes of signal transduction. *Angew. Chem., Int. Ed. 45*, 2348–2368.
(19) Horan, N., Yan, L., Isobe, H., Whitesides, G. M., and Kahne, D. (1999) Nonstatistical binding of a protein to clustered carbohydrates. *Proc. Natl. Acad. Sci. U.S.A. 96*, 11782–11786.
(20) Bryan, M. C., Fazio, F., Lee, H. K., Huang, C. Y., Chang, A., Best, M. D., Calarese, D. A., Blixt, C., Paulson, J. C., Burton, D., Wilson, I. A., and Wong, C. H. (2004) Covalent display of oligosaccharide arrays in microtiter plates. *J. Am. Chem. Soc. 126*, 8640–8641.
(21) Liang, P. H., Imamura, M., Li, X., Wu, D., Fujio, M., Guy, R. T., Wu, B.-C., Tsuji, M., and Wong, C. H. (2008) Quantitative microarray analysis of intact glycolipid-CD1d interaction and correlation with cell-based cytokine production. *J. Am. Chem. Soc. 130*, 12348–12354.
(22) Liang, P. H., Wang, S. K., and Wong, C. H. (2007) Quantitative analysis of carbohydrate-protein interactions using glycan microarrays: Determination of surface and solution dissociation constants. *J. Am. Chem. Soc. 129*, 11177–11184.
(23) Stoughton, R. B. (2005) Applications of DNA microarrays in biology. *Annu. Rev. Biochem. 74*, 53–82.
(24) Bulyk, M. L. (2006) DNA microarray technologies for measuring protein-DNA interactions. *Curr. Opin. Biotechnol. 17*, 422–430.
(25) Min, D. H., and Mrksich, M. (2004) Peptide arrays: towards routine implementation. *Curr. Opin. Chem. Biol. 8*, 554–558.
(26) Wilson, D. S., and Nock, S. (2003) Recent developments in protein microarray technology. *Angew. Chem., Int. Ed. 42*, 494–500.
(27) Kung, L. A., and Snyder, M. (2006) Proteome chips for whole-organism assays. *Nat. Rev. Mol. Cell Biol. 7*, 617–622.
(28) Feizi, T., Fazio, F., Chai, W., and Wong, C.-H. (2003) Carbohydrate microarrays: A new set of technologies at the frontiers of glycomics. *Curr. Opin. Struct. Biol. 13*, 637–645.
(29) Ratner, D. M., Adams, E. W., Disney, M. D., and Seeberger, P. H. (2004) Tools for glycomics: Mapping interactions of carbohydrates in biological systems. *ChemBioChem 5*, 1375–1383.
(30) Werz, D. B., and Seeberger, P. H. (2005) Carbohydrates as the next frontier in pharmaceutical research. *Chem.—Eur. J. 11*, 3194–3206.
(31) Calarese, D. A., Lee, H. K., Huang, C. Y., Best, M. D., Astronomo, R. D., Stanfield, R. L., Katinger, H., Burton, D. R., Wong, C. H., and Wilson, I. A. (2005) Dissection of the carbohydrate specificity of the broadly neutralizing-anti-HIV-1 antibody 2G12. *Proc. Natl. Acad. Sci. U.S.A. 102*, 13372–13377.
(32) Huang, C. Y., Thayer, D. A., Chang, A. Y., Best, M. D., Hoffmann, J., Head, S., and Wong, C. H. (2006) Carbohydrate microarray for profiling the antibodies interacting with Globo H tumor antigen. *Proc. Natl. Acad. Sci. U.S.A. 103*, 15–20.
(33) Pilobello, K. T., and Mahal, L. K. (2007) Deciphering the glycocode: the complexity and analytical challenge of glycomics. *Curr. Opin. Chem. Biol. 11*, 300–305.
(34) Pohl, N. L. (2008) Fluorous tags catching on microarrays. *Angew. Chem., Int. Ed. 47*, 3868–3870.
(35) Kanter, J. L., Narayana, S., Ho, P. P., Catz, I., Warren, K. G., Sobel, R. A., Steinman, L., and Robinson, W. H. (2006) Lipid microarrays identify key mediators of autoimmune brain inflammation. *Nature Med. 12*, 138–143.
(36) Prestwich, G. D. (1996) Touching all the bases: Synthesis of inositol polyphosphate and phosphoinositide affinity probes from glucose. *Acc. Chem. Res. 29*, 503–513.
(37) Painter, G. F., Grove, S. J. A., Gilbert, I. H., Holmes, A. B., Raithby, P. R., Hill, M. L., Hawkins, P. T., and Stephens, L. (1999) General synthesis of 3-phosphorylated myo-inositol phospholipids and derivatives. *J. Chem. Soc., Perkin Trans. 1*, 923–935.
(38) Kubiak, R. J., and Bruzik, K. S. (2003) Comprehensive and uniform synthesis of all naturally occurring phosphorylated phosphatidylinositols. *J. Org. Chem. 68*, 960–968.
(39) Schafer, R., Nehlssahabandu, M., Grabowsky, B., Dehlingerkremer, M., Schulz, I., and Mayr, G. W. (1990) Synthesis and application of photoaffinity analogs of inositol 1,4,5-trisphosphate selectively substituted at the 1-phosphate group. *Biochem. J. 272*, 817–825.
(40) Prestwich, G. D., Marecek, J. F., Mourey, R. J., Theibert, A. B., Ferris, C. D., Danoff, S. K., and Snyder, S. H. (1991) Tethered IP3: Synthesis and biochemical applications of the 1-*O*-(3-aminopropyl) ester of inositol 1,4,5-trisphosphate. *J. Am. Chem. Soc. 113*, 1822–1825.
(41) Marecek, J. F., Estevez, V. A., and Prestwich, G. D. (1992) New tetherable derivatives of *myo*-inositol 2,4,5-trisphosphates and 1,3,4-trisphosphates. *Carbohydr. Res. 234*, 65–73.
(42) Tegge, W., and Ballou, C. E. (1992) Syntheses of D-*myo*-Inositol 1,4,5-trisphosphate affinity ligands. *Carbohydr. Res. 230*, 63–77.
(43) Kavran, J. M., Klein, D. E., Lee, A., Falasca, M., Isakoff, S. J., Skolnik, E. Y., and Lemmon, M. A. (1998) Specificity and promiscuity in phosphoinositide binding by Pleckstrin homology domains. *J. Biol. Chem. 273*, 30497–30508.

BC8004107

Supporting Information

Synthesis of biotin-PEG linker 9: Biotinylated PEG linker **9** was synthesized from tetraethyleneglycol (Supporting Information Figure 1). First, literature procedures were used to access known compound **10** in four steps.[1, 2] The amine group of **10** was then deprotected, followed by direct biotinylation to **12**, ethyl ester hydrolysis to **13** and coupling of the resulting carboxyl group to *N*-hydroxysuccinimide to produce activated ester **9**.

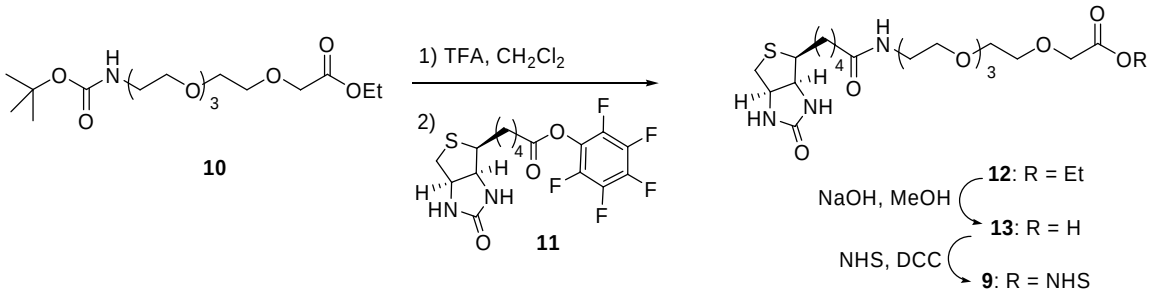

Supporting Information Figure 1. Synthesis of biotinylated PEG linker **9**.

Ethyl 14-biotinamido-3,6,9,12-tetraoxatetradecan-1-oate (12) PEG analog **10** (723 mg, 1.959 mmol) was dissolved in dry dichloromethane (3 mL) along with trifluoroacetic acid (3mL). The solution was stirred at room temperature for 3 hours and then the solvent was removed under reduced pressure and placed on a vacuum line for 3-4 hours. The crude deprotected amine was then directly biotinylated. This crude was dissolved in anhydrous N,N-dimethylformamide (15 mL) and triethylamine (3 mL) was added. With stirring was added biotin pentafluorophenyl ester **11** (804 mg, 1.959 mmol). The reaction was allowed to stir overnight at room temperature. The reaction solution was then concentrated under reduced pressure and purified by chromatography on silica gel with a gradient system of 0-20% methanol/chloroform to afford **12** as a white solid (704 mg, 71% over 2 steps).

^{1}H NMR (300MHz, $CDCl_3$) δ 7.04 (bs, 1H), 6.83 (bs, 1H), 6.03 (bs, 1H), 4.52 (bs, 1H), 4.32-4.15 (m, 5H), 3.90-3.43 (m, 16H), 3.22-3.14 (m, 1H), 2.92-2.74 (m, 2H), 2.24 (bs, 2H), 1.68-1.26 (m, 9H) HRMS $[M+H]^+$ cacld for $C_{22}H_{39}N_3O_8S$ 506.25361, found 506.25310. ^{13}C NMR (100.5 MHz, $CDCl_3$) δ 173.4, 170.4, 70.9, 70.5, 70.4, 70.1, 70.0, 68.6, 61.8, 60.8, 60.3, 55.8, 40.5, 39.1, 36.0, 28.3, 28.2, 25.7, 14.2; HRMS $[M+H]^+$ calcd for $C_{22}H_{39}N_3O_8S$ 506.25361, found 506.25310.

14-biotinamido-3,6,9,12-tetraoxatetradecanoic acid (13) Ester **12** (122mg, 0.242 mmol) was dissolved in methanol (2 mL). With vigorous stirring, 2M NaOH (2 mL) was added. After 45 minutes, TLC showed no starting material remaining. The reaction was neutralized with Dowex 50WX8-200 H+ resin to a pH of ~5. The resin was removed by filtration and the solvent was removed under reduced pressure to afford **13** as a tan solid (118 mg, quantative).

^{1}H NMR (300MHz, CD_3OD) δ 4.38-4.34 (m, 1H), 4.19-4.15 (m, 1H), 3.93-3.88 (m, 2H), 3.49-3.80 (m, 14H), 3.16 (t, J = 4.7 Hz, 2H), 3.08-3.00 (m, 1H), 2.75-2.69 (m, 1H), 2.52-2.48 (m, 1H), 2.00 (t, J = 7.2 Hz, 2H), 1.51-1.19 (m, 6H). ^{13}C NMR (100.5 MHz, CD_3OD) δ 176.13, 174.34, 165.95, 130.79, 127.10, 71.62, 71.44, 71.22, 70.60, 69.28, 63.37, 61.65, 56.96, 41.06, 40.32, 36.72, 29.73, 29.47, 26.84; HRMS $[M+H]^+$ calcd for $C_{20}H_{36}N_3O_8S$ 478.22231, found 478.22030.

14-biotinamido-3,6,9,12-tetraoxatetradecanoic acid *N*-hydroxysuccinimidyl ester(**9**) To a solution of biotin-PEG-carboxylic acid **13** (40 mg, 0.084 mmol) in dimethylformamide (2 mL) was added *N*-hydroxysuccinimide (12 mg, 0.10 mmol) and 1-Ethyl-3-(3-

dimethyllaminopropyl)carbodiimide hydrochloride (EDC•HCl, 20 mg, 0.10 mmol). The mixture was stirred at room temperature for 24 h. The reaction solution was concentrated under reduced pressure, and the residue was washed with ethyl ether (3 x 2 mL) and then dried in vacuum. The resulting light yellow gum was used directly in the next step without further purification.

(1) Shirude, P. S., Kumar, V. A., and Ganesh, K. N. (2005) BisPNA targeting to DNA: Effect of neutral loop on DNA duplex strand invasion by aepPNA-N7G/aepPNA-C substituted peptide nucleic acids. *Eur. J. Org. Chem.*, 5207-5215.
(2) Jullien, L., and Lehn, J. M. (1988) The Chundle Approach to Molecular Channels Synthesis of a Macrocycle Based Molecular Bundle. *Tetrahedron Lett. 29*, 3803-3806.

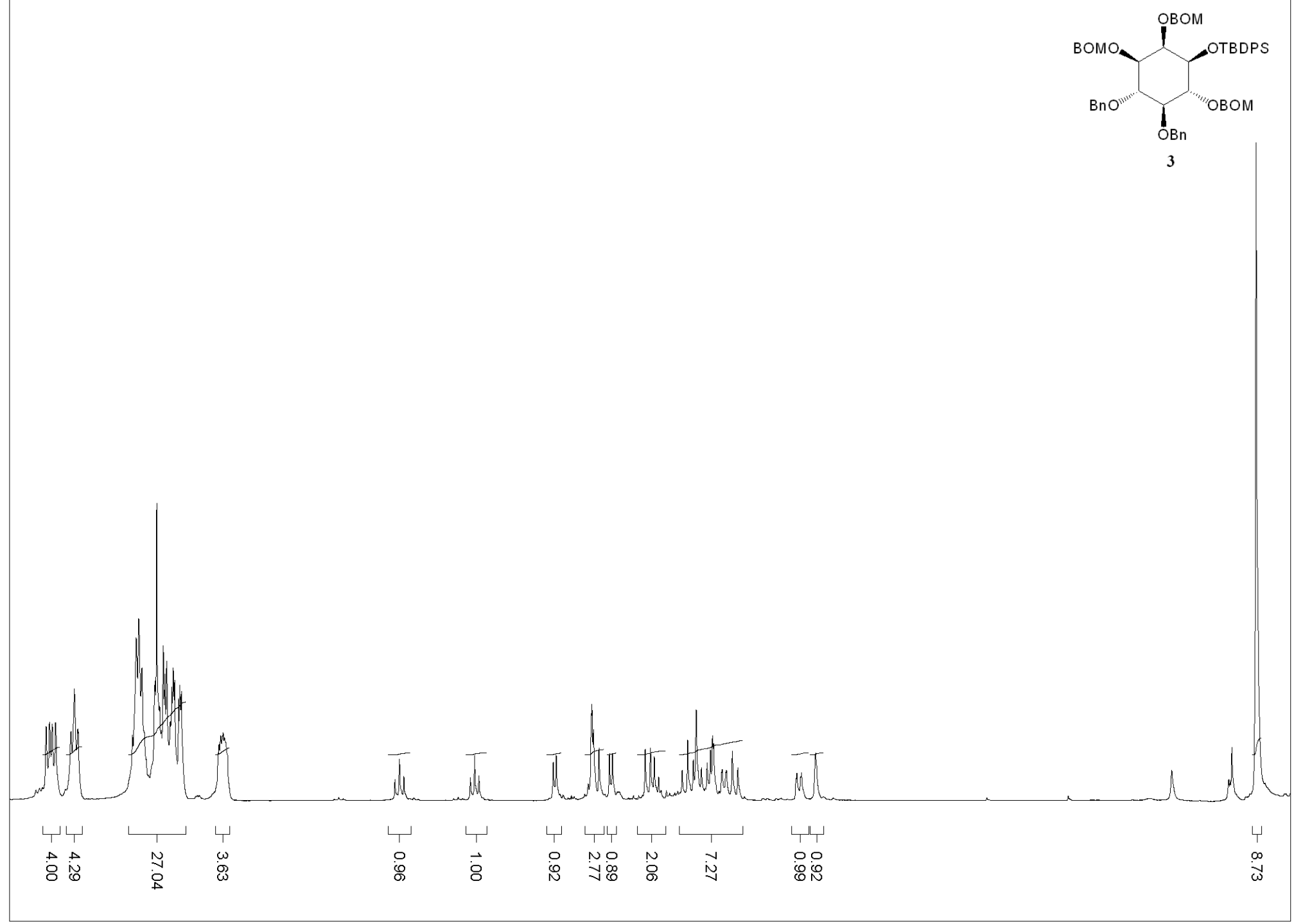
OBOM
BOMO
OTBDPS
BnO
OBOM
OBn
3
4.00
4.29
27.04
3.63
0.96
1.00
0.92
2.77
0.89
2.06
7.27
0.99
0.92
8.73
8.0
7.0
6.0
5.0
4.0
3.0
2.0
1.0
ppm (f1)

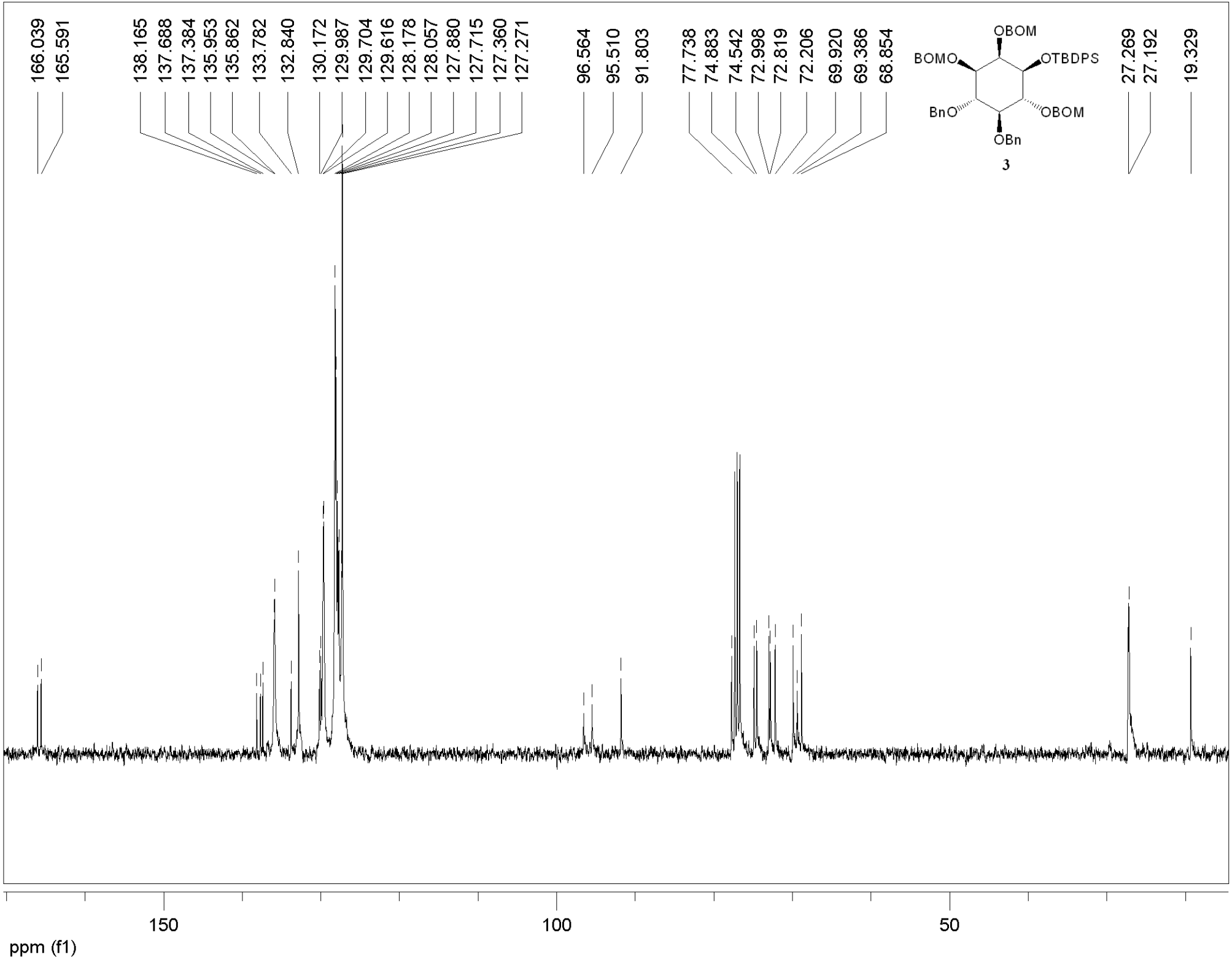
166.039
165.591
138.165
137.688
137.384
135.953
135.862
133.782
132.840
130.172
129.987
129.704
129.616
128.178
128.057
127.880
127.715
127.360
127.271
96.564
95.510
91.803
77.738
74.883
74.542
72.998
72.819
72.206
69.920
69.386
68.854
27.269
27.192
19.329
OBOM
BOMO
OTBDPS
BnO
OBOM
OBn
3
150
100
50
ppm (f1)

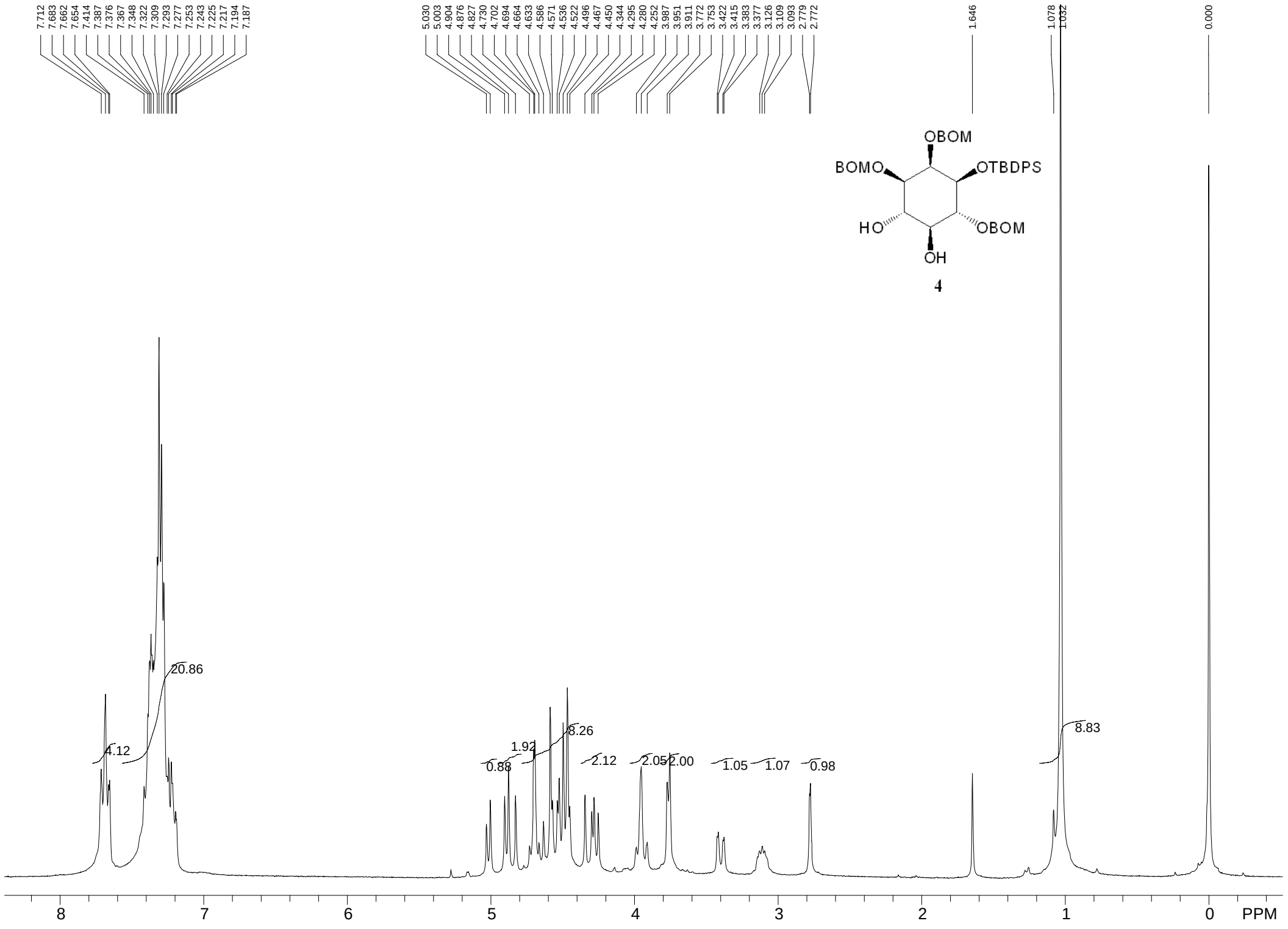
7.712
7.683
7.662
7.654
7.414
7.387
7.376
7.367
7.348
7.322
7.309
7.293
7.277
7.253
7.243
7.225
7.217
7.194
7.187
5.030
5.003
4.904
4.876
4.827
4.730
4.702
4.694
4.664
4.633
4.586
4.571
4.536
4.522
4.496
4.467
4.450
4.344
4.295
4.280
4.252
3.987
3.951
3.911
3.772
3.753
3.422
3.415
3.383
3.377
3.126
3.109
3.093
2.779
2.772
1.646
1.078
1.032
0.000
OBOM
BOMO
OTBDPS
HO
OBOM
OH
4
20.86
4.12
0.88
1.92
8.26
2.12
2.05
2.00
1.05
1.07
0.98
8.83
8
7
6
5
4
3
2
1
0
PPM

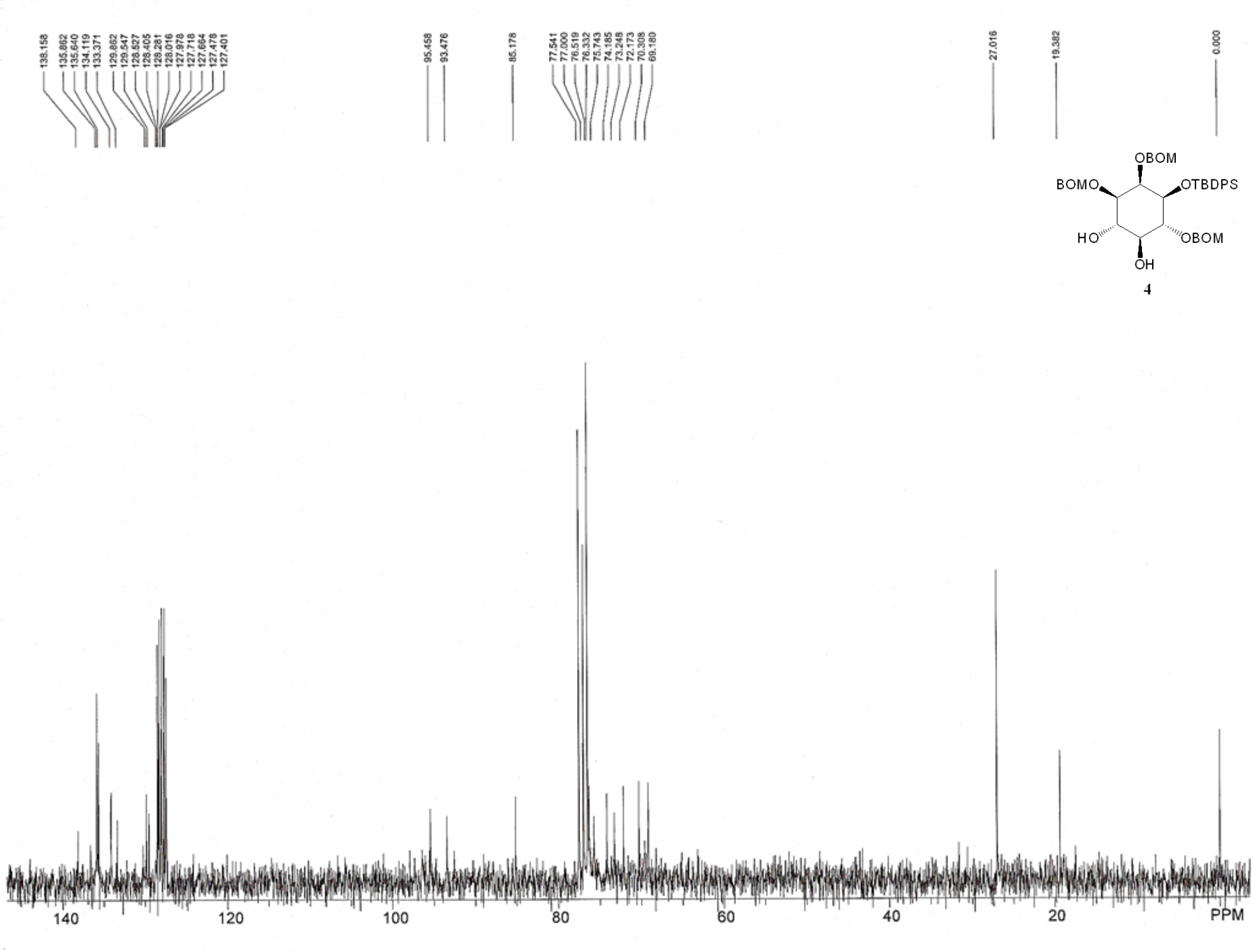
138.158
135.862
135.640
134.119
133.371
129.862
129.547
128.527
128.405
128.281
128.016
127.978
127.718
127.664
127.478
127.401
95.458
93.476
85.178
77.541
77.000
76.519
76.332
75.743
74.185
73.248
72.173
70.308
69.180
27.016
19.382
0.000
OBOM
BOMO
OTBDPS
HO
OBOM
OH
4
140
120
100
80
60
40
20
PPM

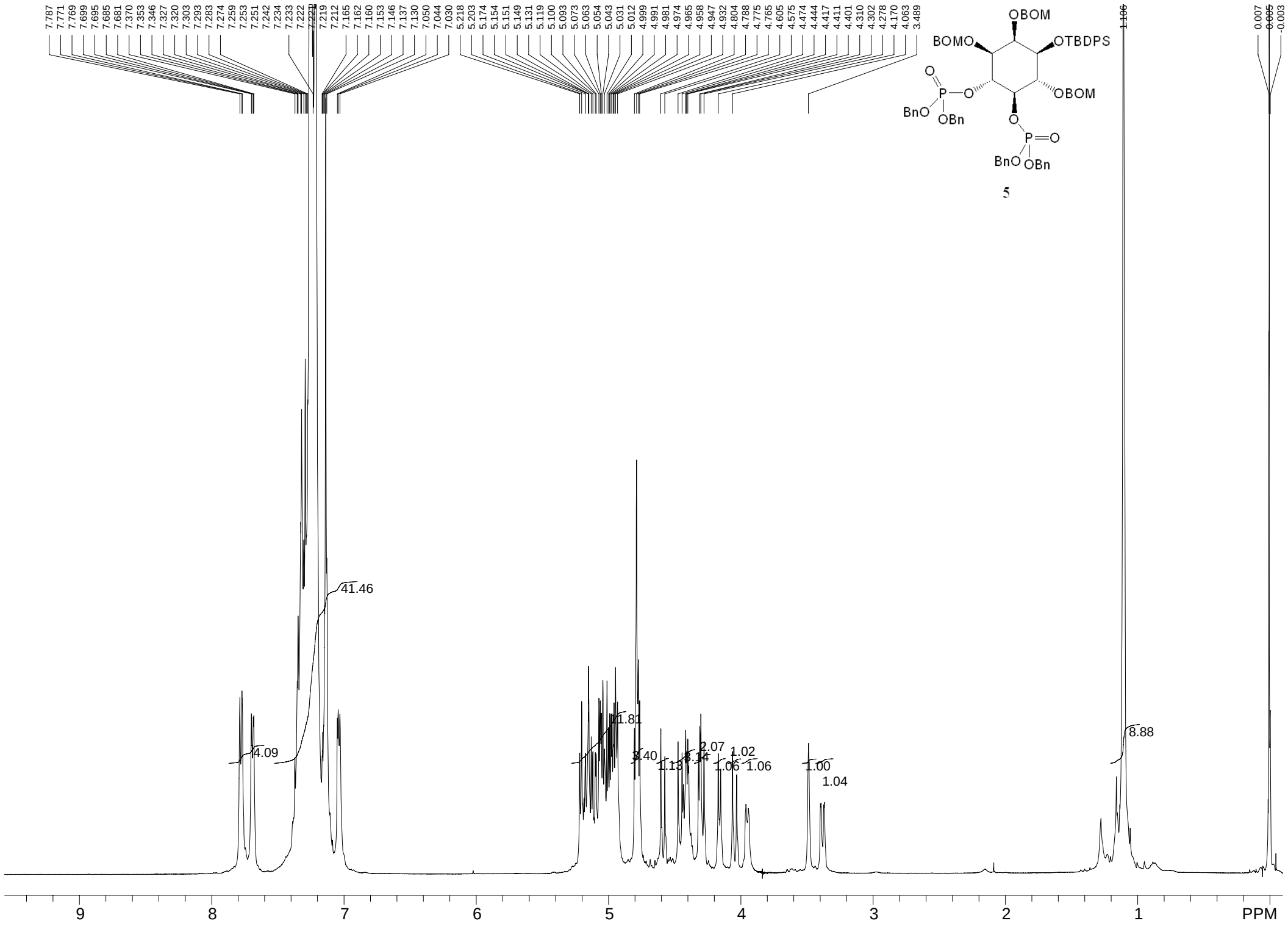
7.787 7.771 7.769 7.699 7.695 7.685 7.681 7.370 7.353 7.346 7.327 7.320 7.303 7.293 7.283 7.274 7.259 7.253 7.251 7.242 7.234 7.233 7.222 7.221 7.219 7.212 7.165 7.162 7.160 7.153 7.146 7.137 7.130 7.050 7.044 7.030 5.218 5.203 5.174 5.154 5.151 5.149 5.131 5.119 5.100 5.093 5.073 5.063 5.054 5.043 5.031 5.012 4.999 4.991 4.981 4.974 4.965 4.958 4.947 4.932 4.804 4.788 4.775 4.765 4.605 4.575 4.474 4.444 4.417 4.411 4.401 4.310 4.302 4.278 4.170 4.063 3.489
1.106
0.007 0.005 -0.003
OBOM
BOMO
OTBDPS
OBOM
BnO
OBn
BnO
OBn
41.46
4.09
11.81
3.40
1.13
3.14
2.07
1.02
1.06
1.06
1.00
1.04
8.88
9 8 7 6 5 4 3 2 1 PPM

5

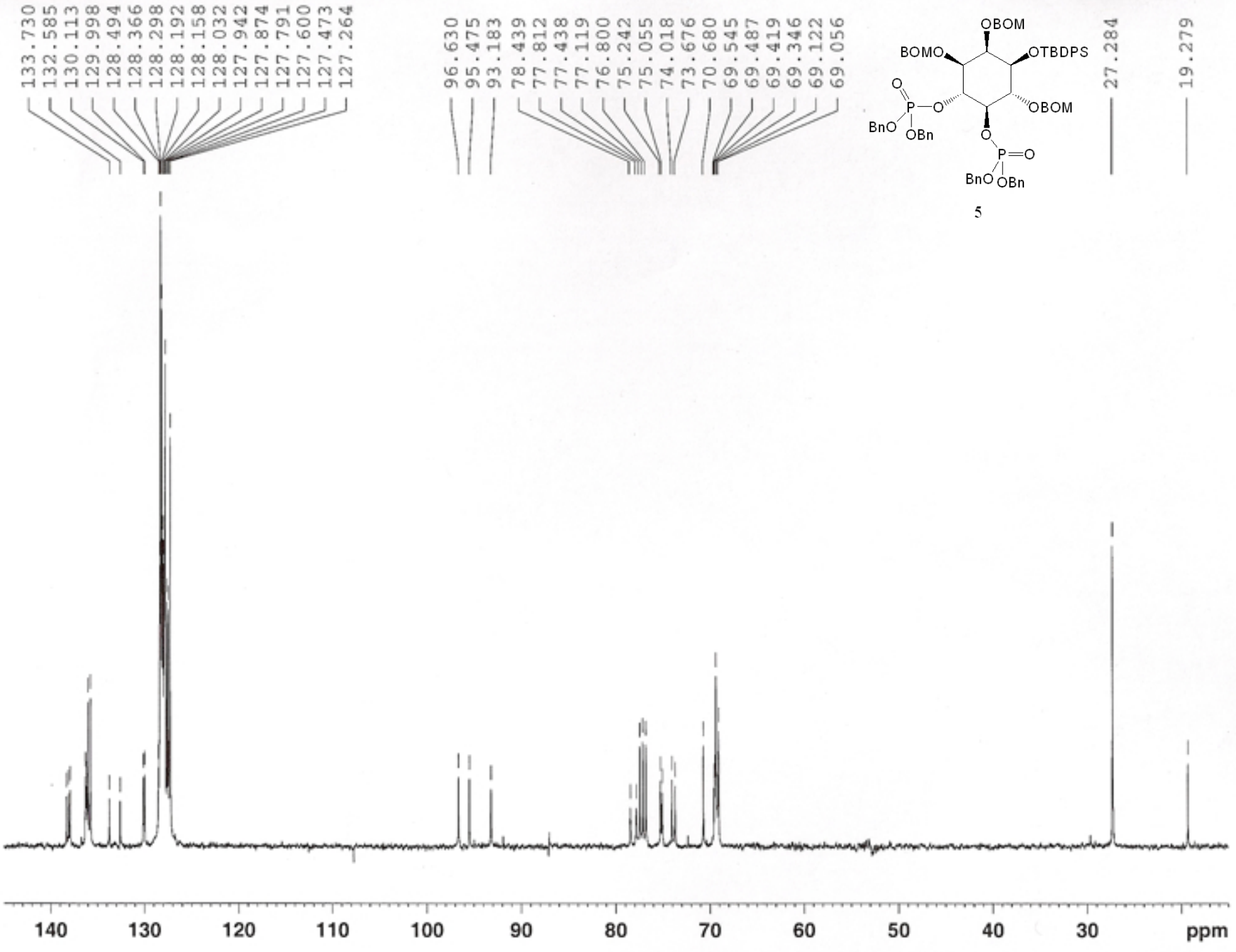
133.730
132.585
130.113
129.998
128.494
128.366
128.298
128.192
128.158
128.032
127.942
127.874
127.791
127.600
127.473
127.264
96.630
95.475
93.183
78.439
77.812
77.438
77.119
76.800
75.242
75.055
74.018
73.676
70.680
69.545
69.487
69.419
69.346
69.122
69.056
27.284
19.279
OBOM
BOMO
OTBDPS
OBOM
BnO
OBn
BnO
OBn
5
140
130
120
110
100
90
80
70
60
50
40
30
ppm

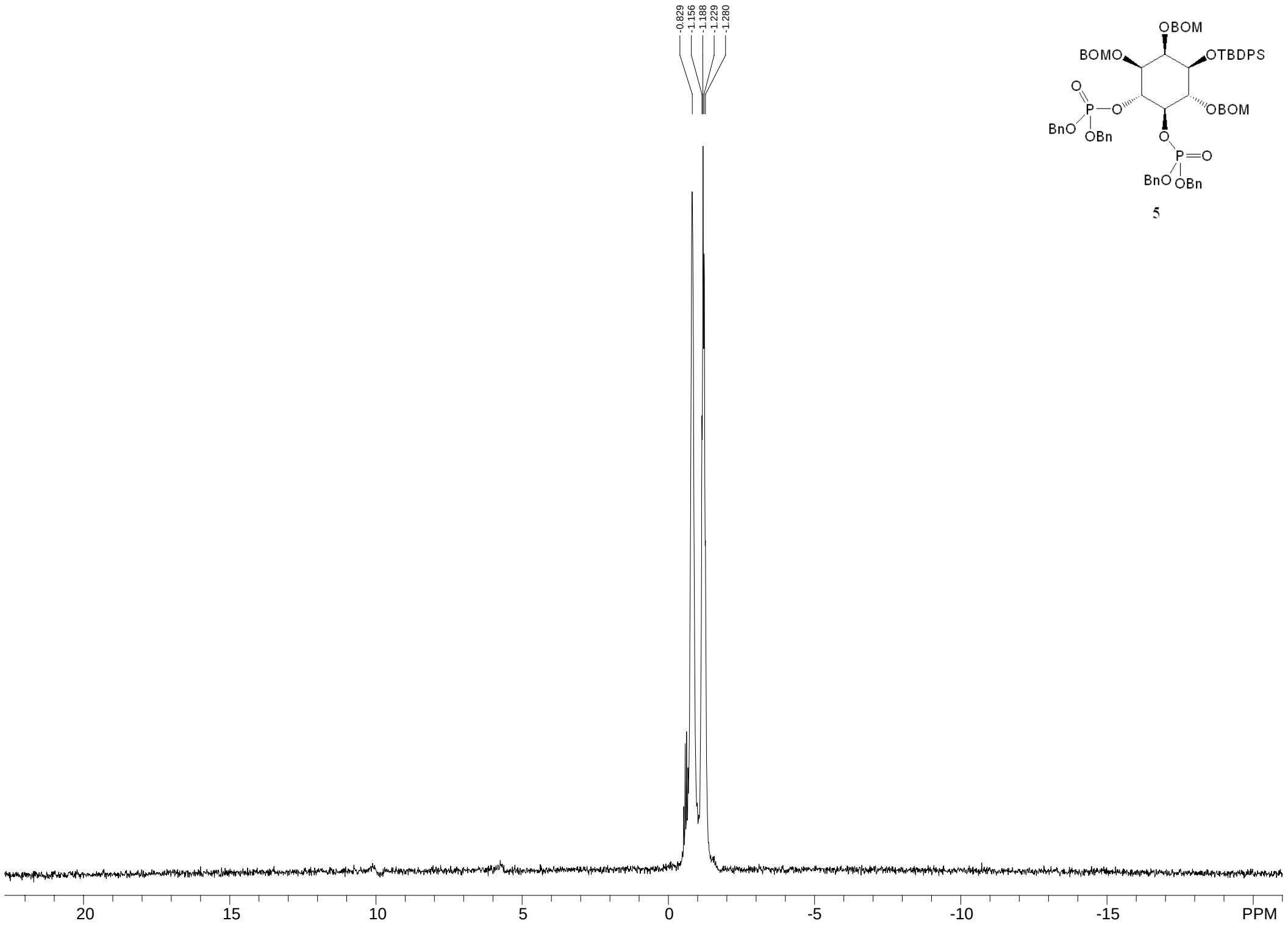
-0.829
-1.156
-1.188
-1.229
-1.280
OBOM
BOMO
OTBDPS
OBOM
BnO
OBn
P
O
BnO
OBn
5
20
15
10
5
0
-5
-10
-15
PPM

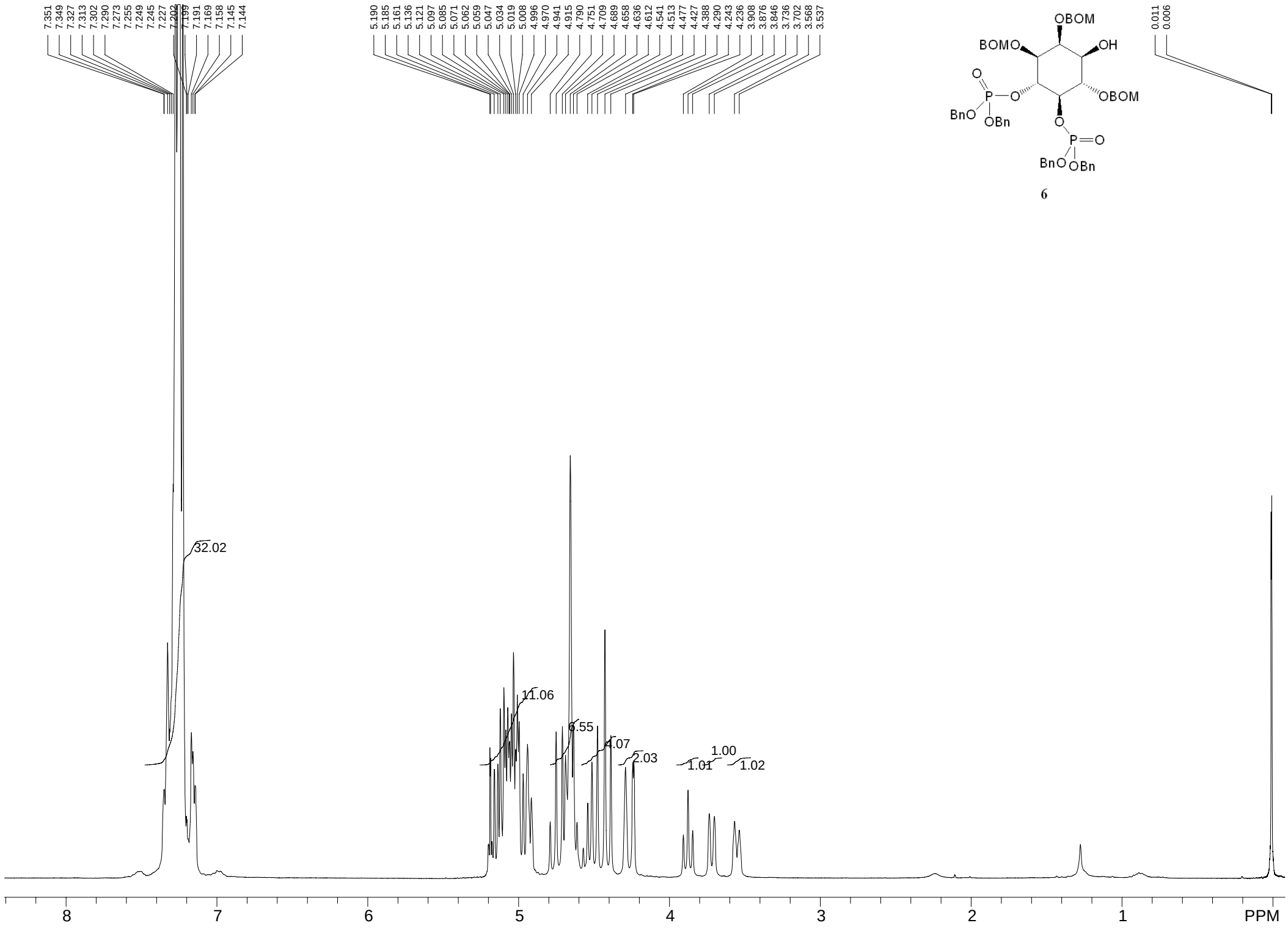
7.351
7.349
7.327
7.313
7.302
7.290
7.273
7.255
7.249
7.245
7.227
7.202
7.195
7.191
7.169
7.158
7.145
7.144
5.190
5.185
5.161
5.136
5.121
5.097
5.085
5.071
5.062
5.059
5.047
5.034
5.019
5.008
4.996
4.970
4.941
4.915
4.790
4.751
4.709
4.689
4.658
4.636
4.612
4.541
4.513
4.477
4.427
4.388
4.290
4.243
4.236
3.908
3.876
3.846
3.736
3.702
3.568
3.537
0.011
0.006
OBOM
BOMO
OH
O
P
O
OBOM
BnO
OBn
O
P=O
BnO
OBn
32.02
11.06
6.55
4.07
2.03
1.01
1.00
1.02
8
7
6
5
4
3
2
1
PPM

6

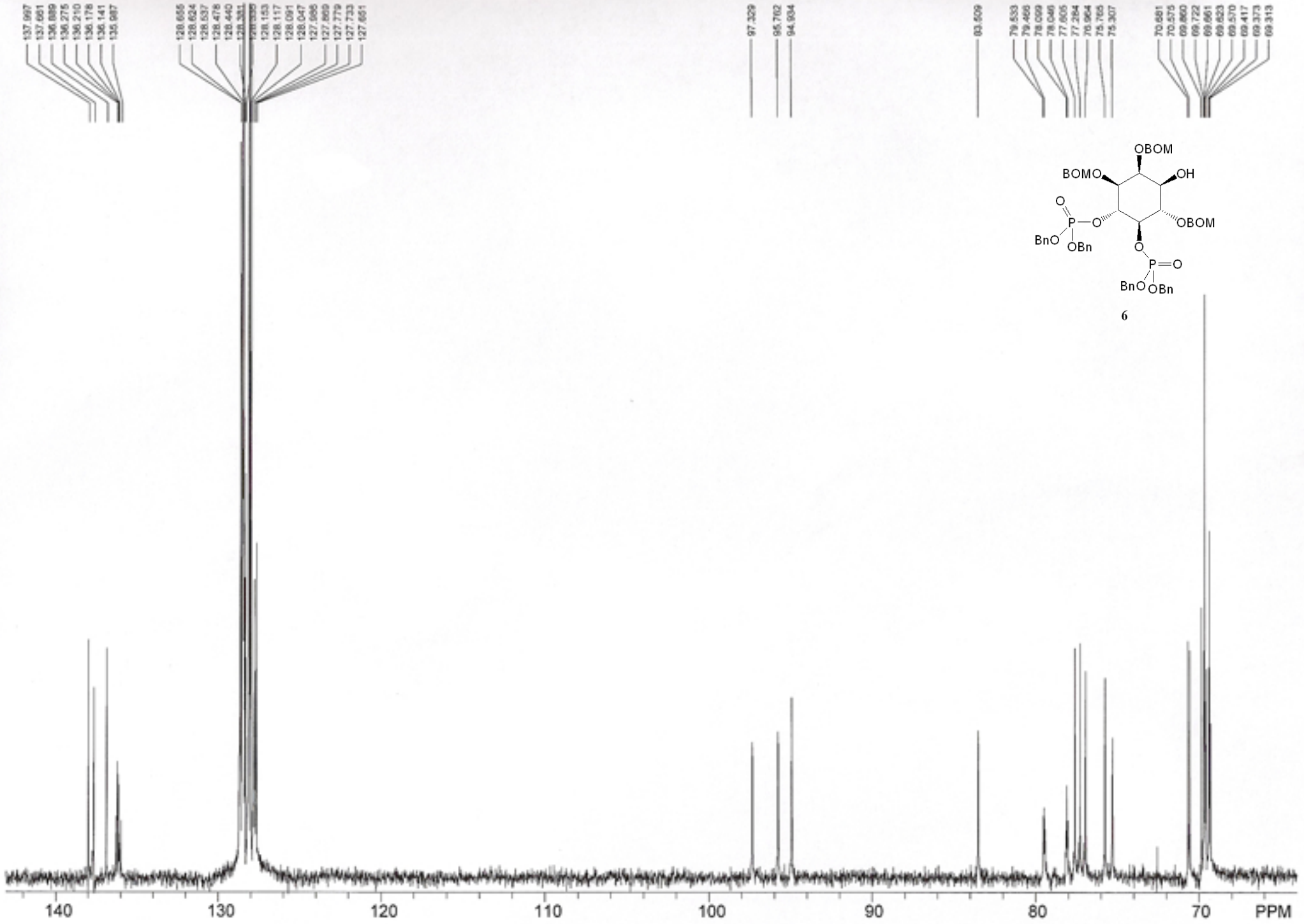
137.997
137.661
136.889
136.275
136.210
136.178
136.141
135.987
128.656
128.624
128.537
128.476
128.440
128.331
128.153
128.117
128.091
128.047
127.986
127.869
127.779
127.733
127.651
97.329
95.702
94.934
83.509
79.533
79.466
78.099
78.046
77.605
77.284
76.964
75.765
75.307
70.681
70.575
69.800
69.722
69.661
69.623
69.570
69.417
69.373
69.313
OBOM
BOMO
OH
O
P
O
OBOM
BnO
OBn
O
P=O
BnO
OBn
6
140
130
120
110
100
90
80
70
PPM

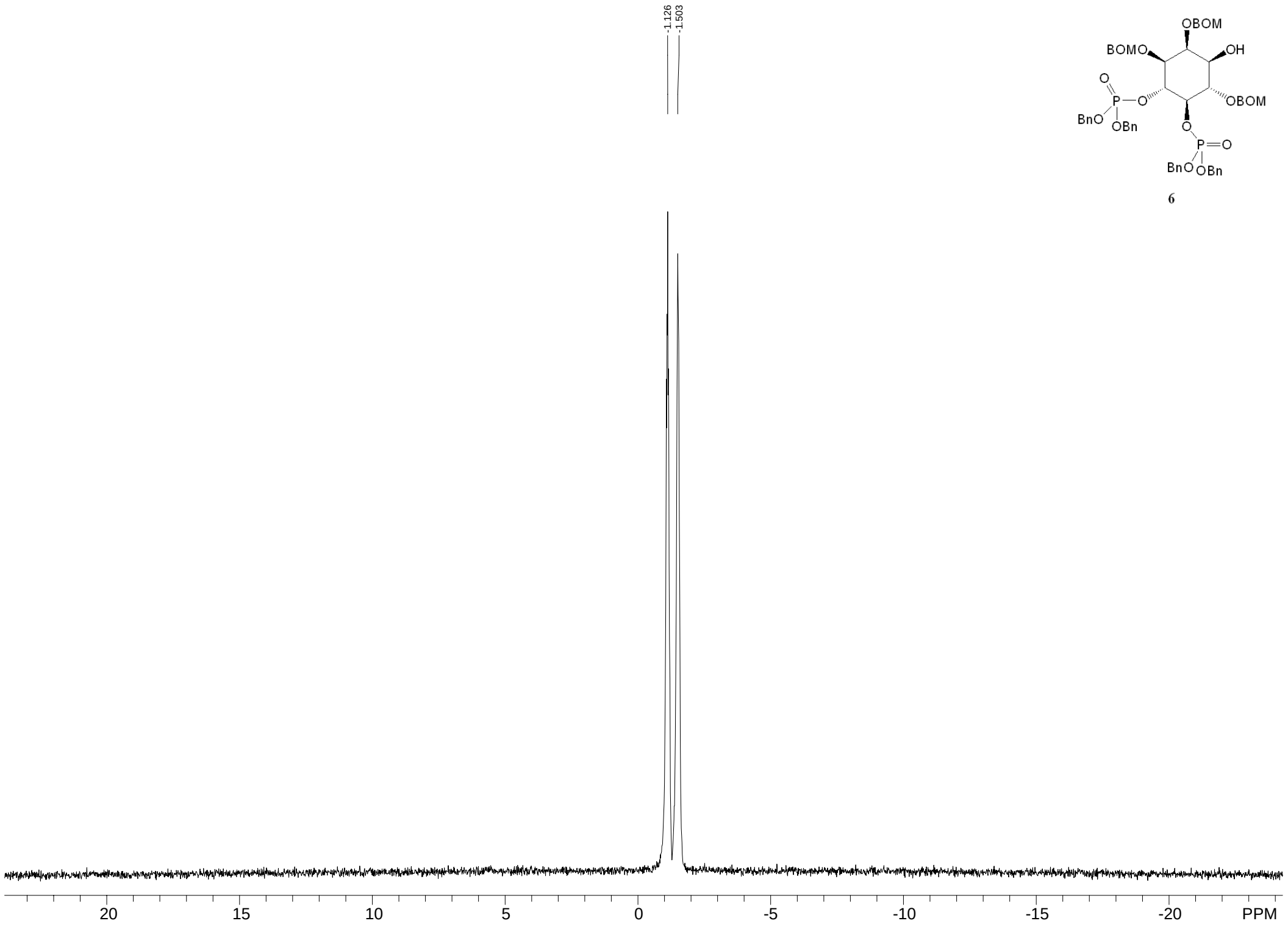
-1.126
-1.503
OBOM
BOMO
OH
OBOM
O
P
O
BnO
OBn
O
P=O
BnO
OBn
20
15
10
5
0
-5
-10
-15
-20
PPM

6

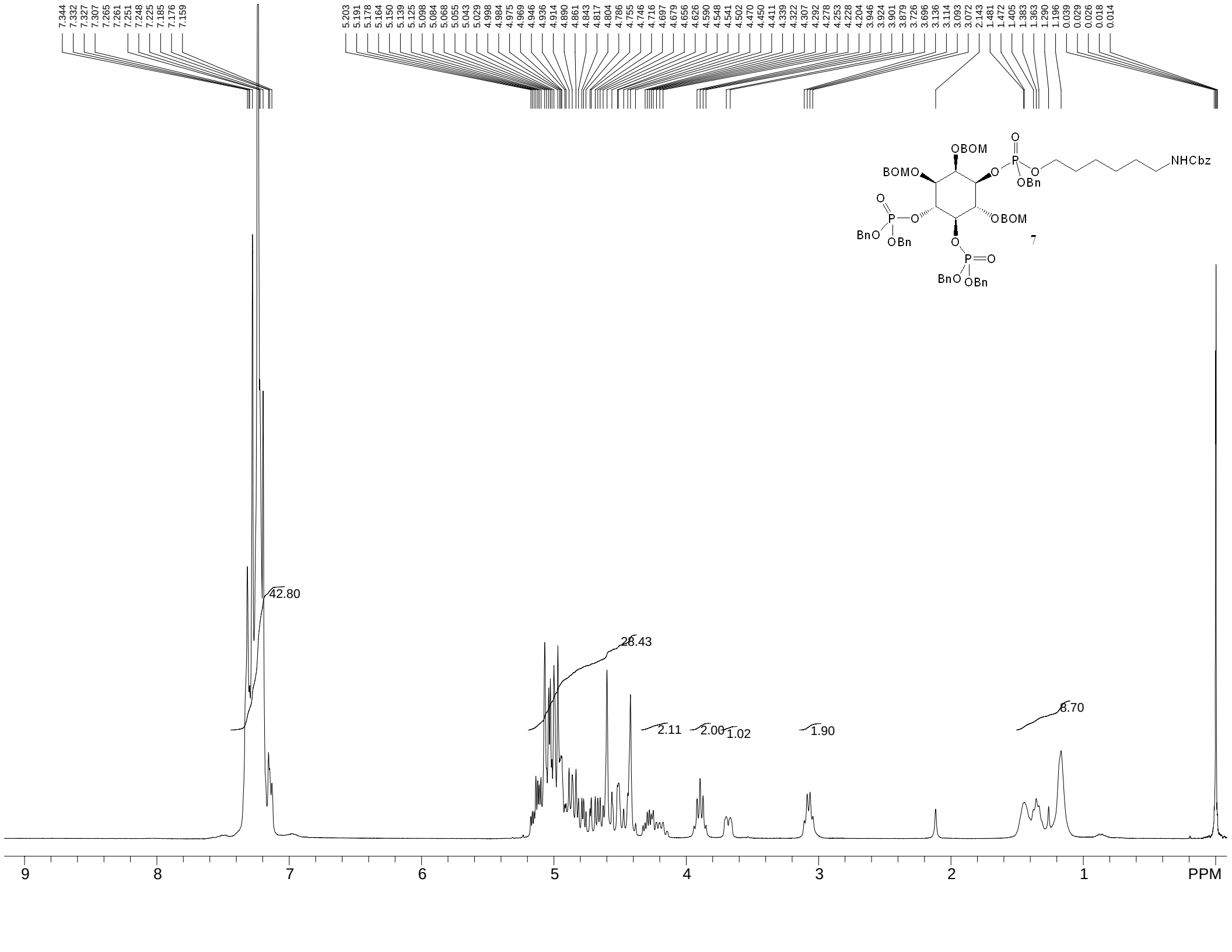
7.344
7.332
7.327
7.307
7.265
7.261
7.251
7.248
7.225
7.185
7.176
7.159
5.203
5.191
5.178
5.164
5.150
5.139
5.125
5.098
5.084
5.068
5.055
5.043
5.029
4.998
4.984
4.975
4.969
4.946
4.936
4.914
4.890
4.861
4.843
4.817
4.804
4.786
4.755
4.746
4.716
4.697
4.679
4.656
4.626
4.590
4.548
4.541
4.502
4.470
4.450
4.411
4.339
4.322
4.307
4.292
4.278
4.253
4.228
4.204
3.946
3.924
3.901
3.879
3.726
3.696
3.136
3.114
3.093
3.072
2.143
1.481
1.472
1.405
1.383
1.363
1.290
1.196
0.039
0.029
0.026
0.018
0.014
OBOM
BOMO
O
P
O
OBn
NHCbz
OBOM
BnO
OBn
O
P
O
BnO
OBn
7
42.80
28.43
2.11
2.00
1.02
1.90
6.70
9
8
7
6
5
4
3
2
1
PPM

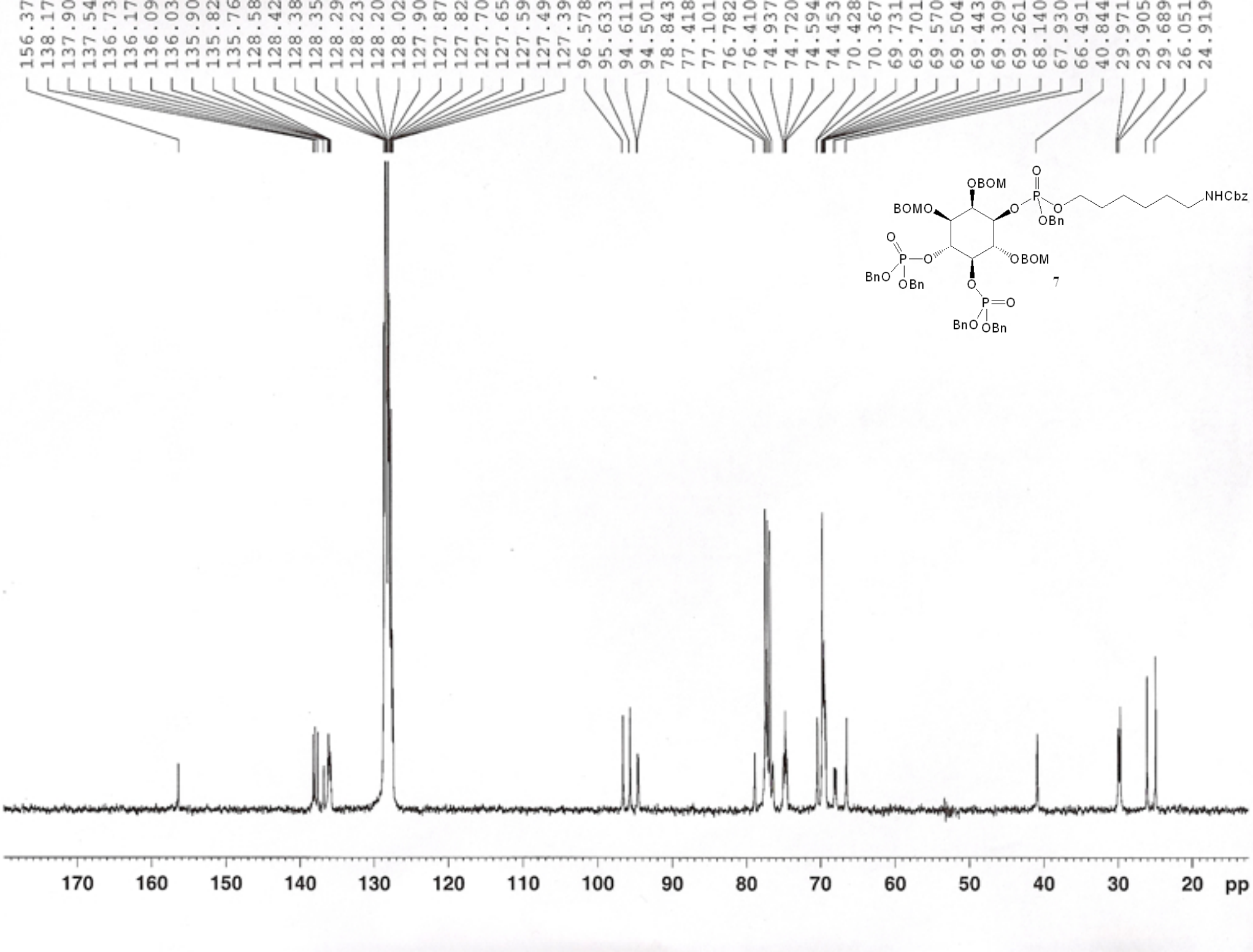
156.37
138.17
137.90
137.54
136.73
136.17
136.09
136.03
135.90
135.82
135.76
128.58
128.42
128.38
128.35
128.29
128.23
128.20
128.02
127.90
127.87
127.82
127.70
127.65
127.59
127.49
127.39
96.578
95.633
94.611
94.501
78.843
77.418
77.101
76.782
76.410
74.937
74.720
74.594
74.453
70.428
70.367
69.731
69.701
69.570
69.504
69.443
69.309
69.261
68.140
67.930
66.491
40.844
29.971
29.905
29.689
26.051
24.919
OBOM
BOMO
O
P
O
OBn
NHCbz
OBOM
BnO
OBn
O
P=O
BnO
OBn
7
170
160
150
140
130
120
110
100
90
80
70
60
50
40
30
20
pp

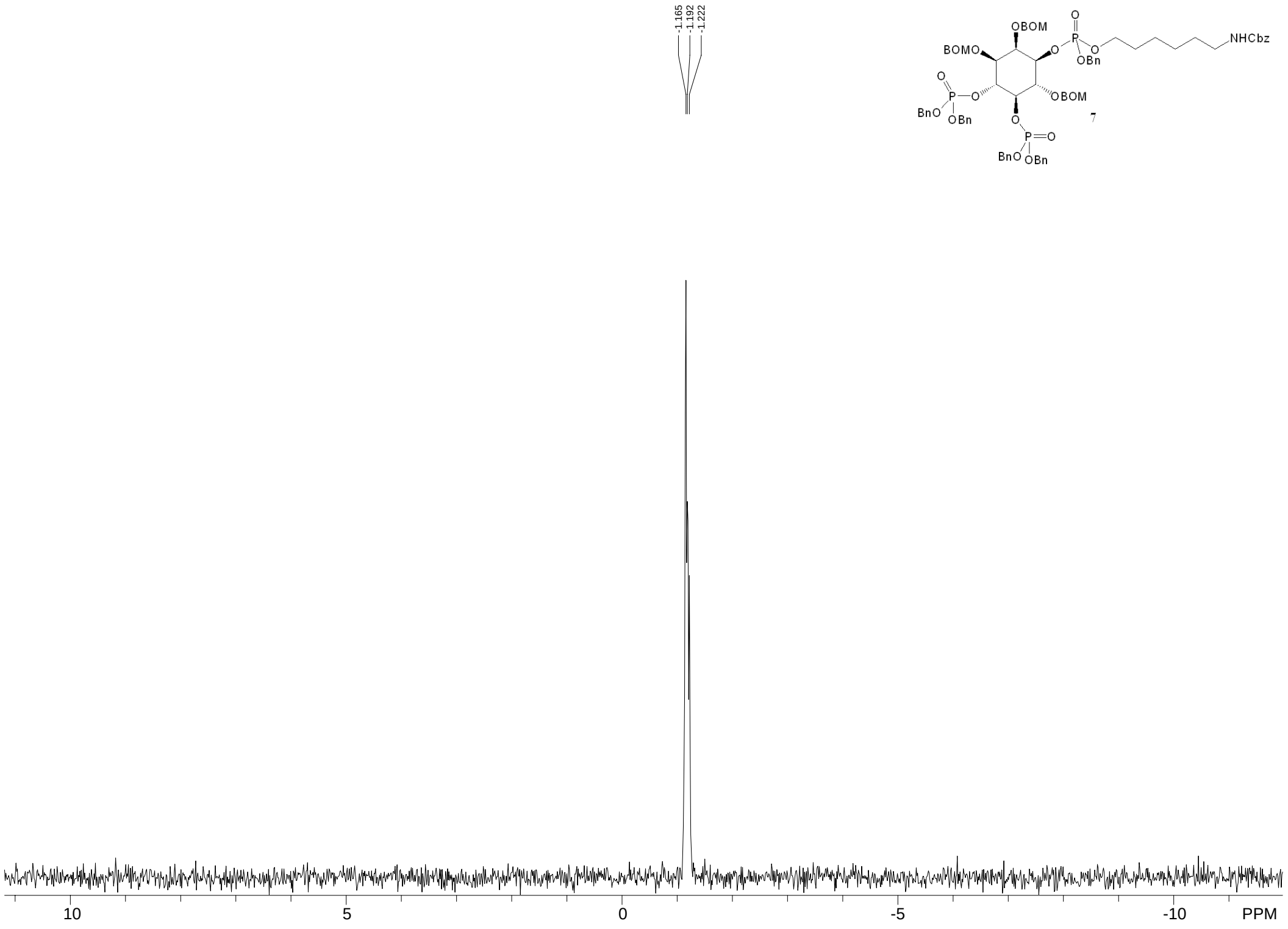
-1.165
-1.192
-1.222
OBOM
BOMO
O
P
O
OBn
NHCbz
OBOM
BnO
OBn
OBOM
O
P=O
BnO
OBn
7
10
5
0
-5
-10
PPM

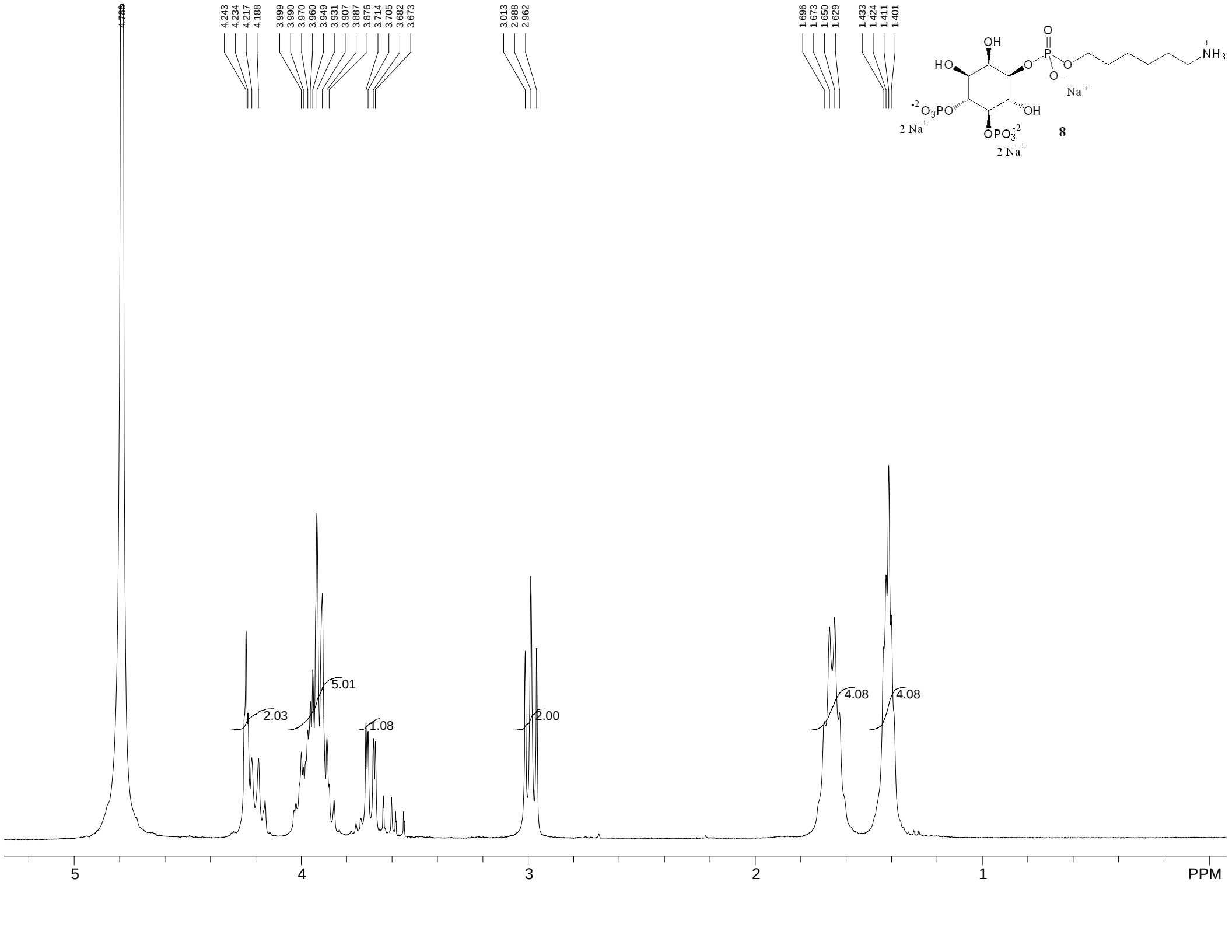
4.789
4.243
4.234
4.217
4.188
3.999
3.990
3.970
3.960
3.949
3.931
3.907
3.887
3.876
3.714
3.705
3.682
3.673
3.013
2.988
2.962
1.696
1.673
1.650
1.629
1.433
1.424
1.411
1.401
2.03
5.01
1.08
2.00
4.08
4.08
5
4
3
2
1
PPM
HO
OH
O
P
O
O
O
NH3
Na+
-2 O3PO
OH
OPO3-2
2 Na+
2 Na+
8

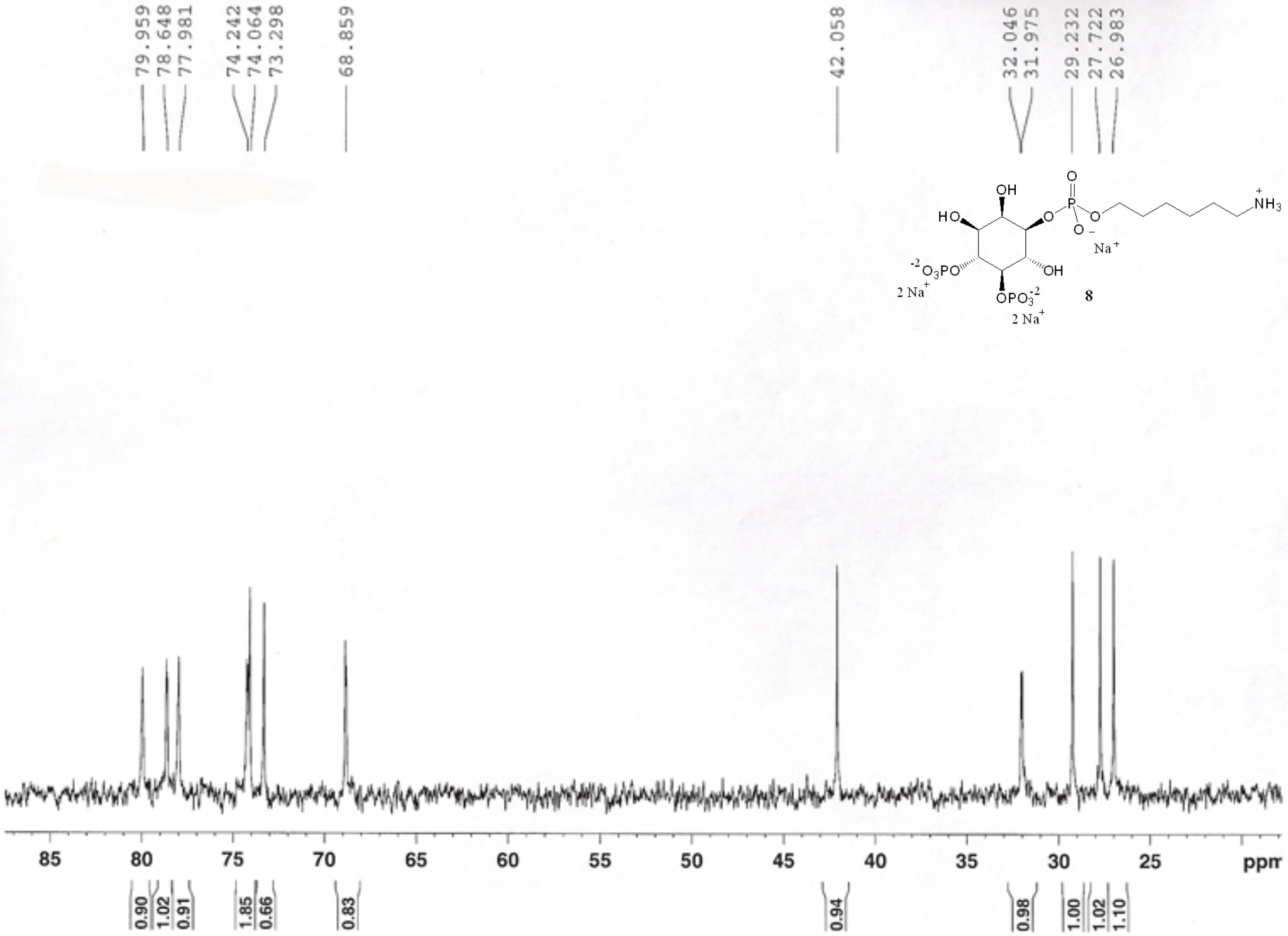
79.959
78.648
77.981
74.242
74.064
73.298
68.859
42.058
32.046
31.975
29.232
27.722
26.983
OH
HO
O
P
O
O
NH3
Na+
-2 O3PO
OH
2 Na+
OPO3-2
2 Na+
8
85
80
75
70
65
60
55
50
45
40
35
30
25
ppm
0.90
1.02
0.91
1.85
0.66
0.83
0.94
0.98
1.00
1.02
1.10

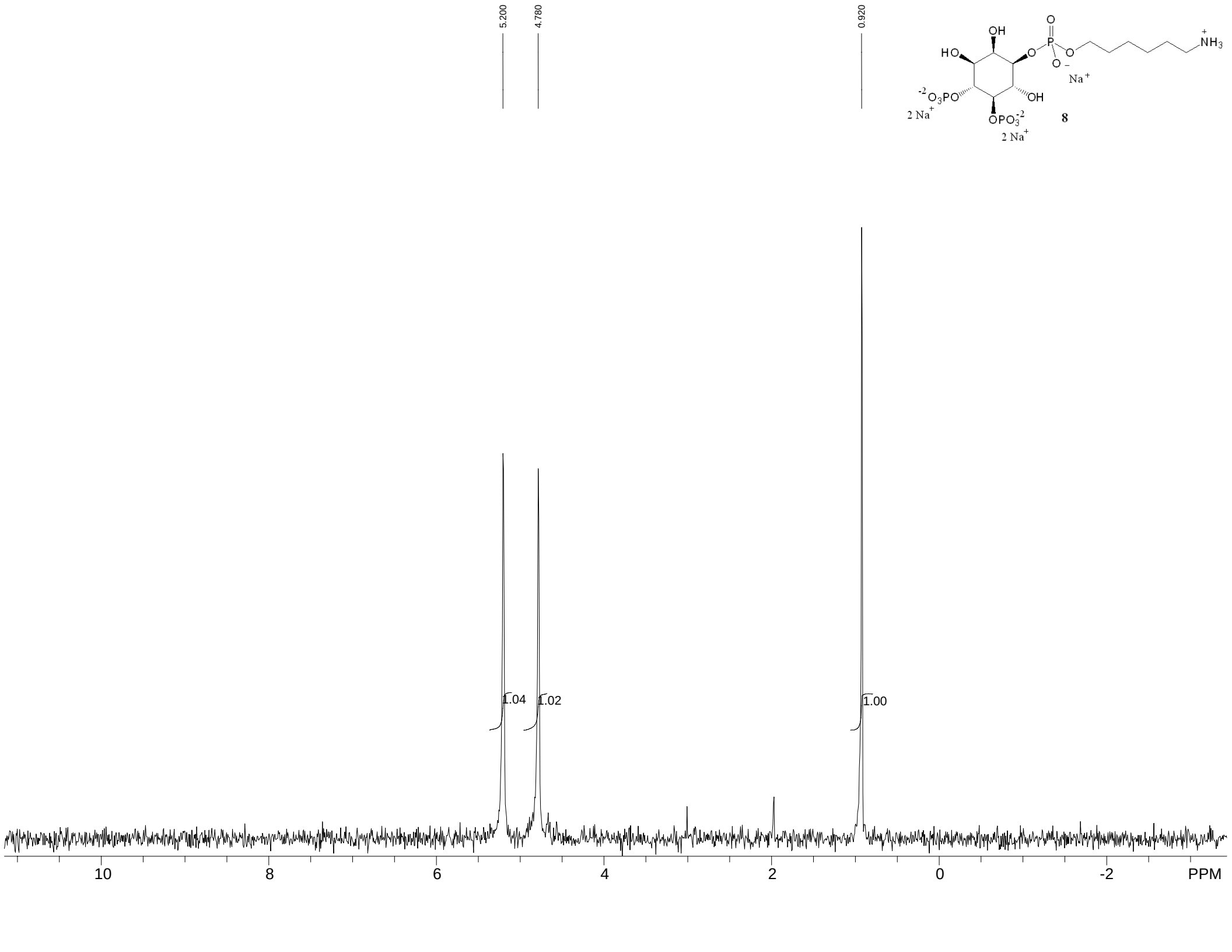
5.200
4.780
0.920
OH
HO
O
P
O
O
O
Na+
NH3
-2 O3PO
OH
2 Na+
OPO3-2
2 Na+
8
1.04
1.02
1.00
10
8
6
4
2
0
-2
PPM

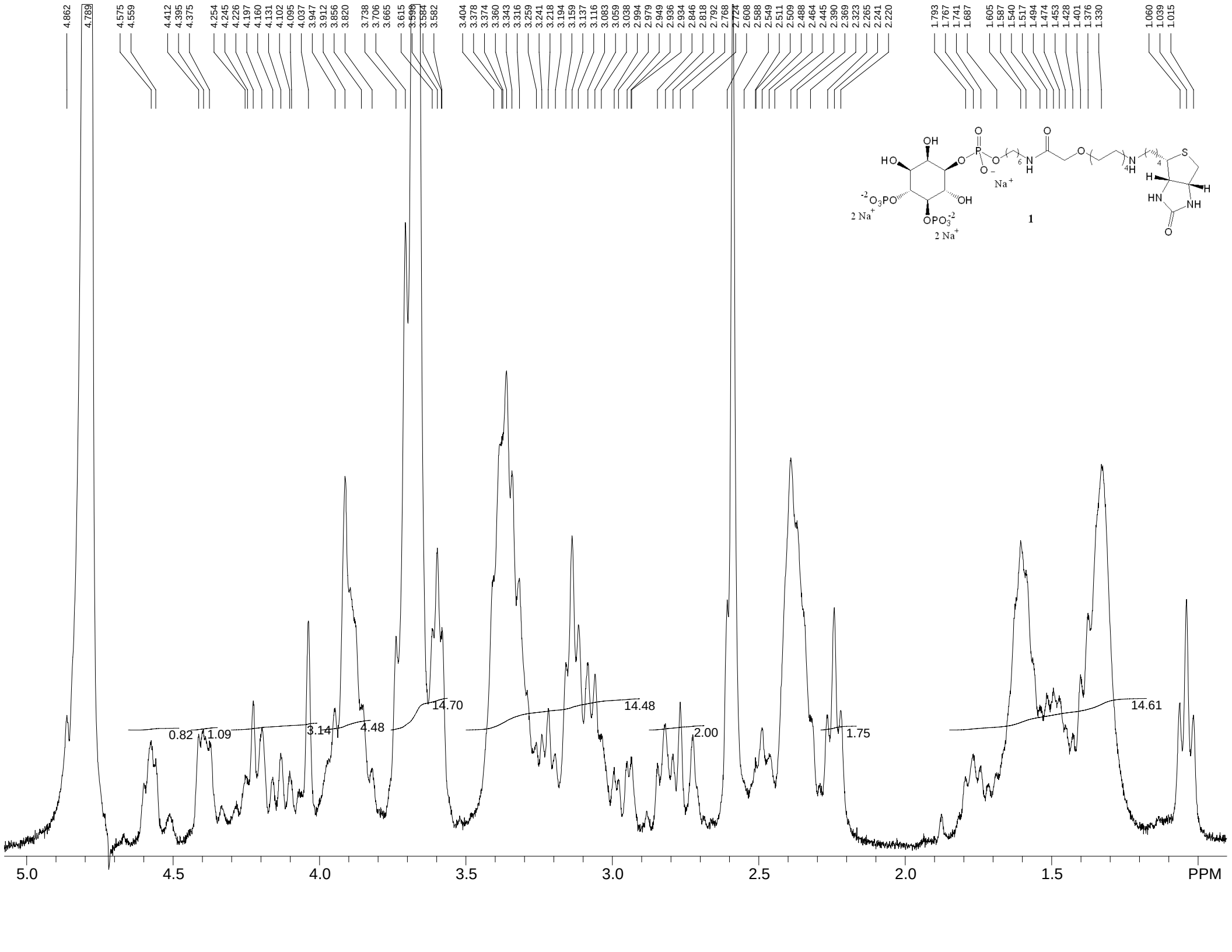
4.862
4.789
4.575
4.559
4.412
4.395
4.375
4.254
4.245
4.226
4.197
4.160
4.131
4.102
4.095
4.037
3.947
3.912
3.856
3.820
3.738
3.706
3.665
3.615
3.596
3.584
3.582
3.404
3.378
3.374
3.360
3.343
3.316
3.259
3.241
3.218
3.194
3.159
3.137
3.116
3.083
3.059
3.038
2.994
2.979
2.949
2.936
2.934
2.846
2.818
2.792
2.768
2.724
2.608
2.588
2.549
2.511
2.509
2.488
2.464
2.445
2.390
2.369
2.323
2.265
2.241
2.220
1.793
1.767
1.741
1.687
1.605
1.587
1.540
1.517
1.494
1.474
1.453
1.428
1.401
1.376
1.330
1.060
1.039
1.015
0.82
1.09
3.14
4.48
14.70
14.48
2.00
1.75
14.61
5.0
4.5
4.0
3.5
3.0
2.5
2.0
1.5
PPM

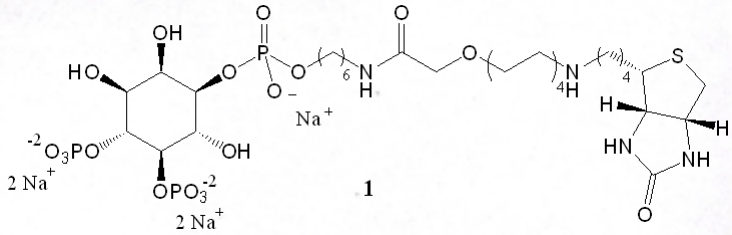
OH
HO
O
P
O
O⁻
Na⁺
6
N
H
O
O
O
4
N
H
S
H
H
HN
NH
O
-2 O3PO
2 Na+
OH
OPO3-2
2 Na+

1

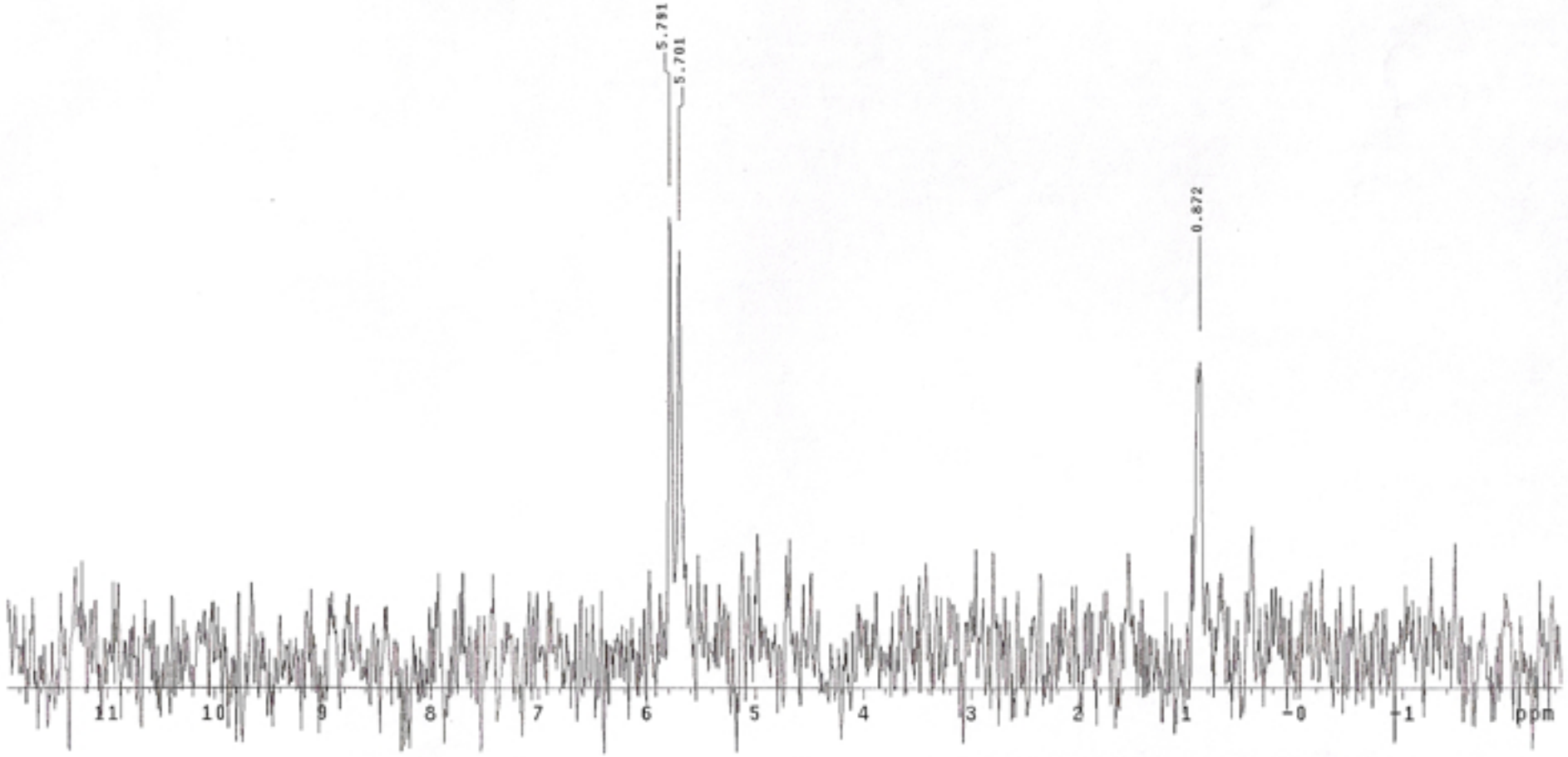
5.791
5.701
0.872
11
10
9
8
7
6
5
4
3
2
1
0
-1
ppm

Subscriber access provided by SHEMYAKIN-OVCHINNIKOV INST

Article

Kit-Like F-Labeling of Proteins: Synthesis of 4-(Di-*tert*-butyl[F]fluorosilyl)benzenethiol (Si[F]FA-SH) Labeled Rat Serum Albumin for Blood Pool Imaging with PET

Bjo#rn Wa#ngler, Gabriele Quandt, Ljuba Iovkova, Esther Schirrmacher, Carmen Wa#ngler, Guido Boening, Marcus Hacker, Michael Schmoeckel, Klaus Jurkschat, Peter Bartenstein, and Ralf Schirrmacher

Bioconjugate Chem., **2009**, 20 (2), 317-321• DOI: 10.1021/bc800413g • Publication Date (Web): 08 January 2009

Downloaded from http://pubs.acs.org on May 15, 2009

More About This Article

Additional resources and features associated with this article are available within the HTML version:

- Supporting Information
- Access to high resolution figures
- Links to articles and content related to this article
- Copyright permission to reproduce figures and/or text from this article

View the Full Text HTML

ACS Publications
High quality. High impact.

Bioconjugate Chemistry is published by the American Chemical Society. 1155 Sixteenth Street N.W., Washington, DC 20036

Kit-Like ^{18}F-Labeling of Proteins: Synthesis of 4-(Di-*tert*-butyl[^{18}F]fluorosilyl)benzenethiol (Si[^{18}F]FA-SH) Labeled Rat Serum Albumin for Blood Pool Imaging with PET

Björn Wängler,*[,†] Gabriele Quandt,[||,†] Ljuba Iovkova,[||,#] Esther Schirrmacher,[‡] Carmen Wängler,[§] Guido Boening,[†] Marcus Hacker,[†] Michael Schmoeckel,[⊥] Klaus Jurkschat,[#] Peter Bartenstein,[†] and Ralf Schirrmacher*[,§]

Department of Nuclear Medicine, Hospital of the Ludwig-Maximilians-University, Munich, Germany, Lady Davis Institute, Jewish General Hospital, and McConnell Brain Imaging Centre, Montreal Neurological Institute, McGill University, Montreal, Canada, Department of Cardiac Surgery, Ludwig-Maximilians-University, Munich, Germany, and Department of Inorganic Chemistry II, University of Dortmund, Dortmund, Germany. Received September 29, 2008; Revised Manuscript Received November 24, 2008

Radiosyntheses of ^{18}F-radiopharmaceuticals for positron emission tomography (PET) normally require an extraordinarily high effort of technical equipment and specially trained personnel. We recently reported a novel method for the introduction of fluorine-18 into peptides for PET-imaging based on silicon-^{18}F-chemistry (SiFA technique). We herewith introduce the first SiFA-based Kit-like radio-fluorination of a protein (rat serum albumin, RSA) and demonstrate its usefulness for in vivo imaging with μPET in normal rats as well as in a rat heterotropic transplanted heart model. As a labeling agent, we prepared 4-(di-*tert*-butyl[^{18}F]fluorosilyl)benzenethiol (Si[^{18}F]FA-SH) by simple isotopic exchange in 40−60% radiochemical yield (RCY) and coupled it directly to a Sulfo-SMCC derivatized RSA in an overall RCY of 12% within 20−30 min. The technically simple labeling procedure does not require any elaborated purification procedures and is a straightforward example of a successful application of Si−^{18}F chemistry for in vivo imaging with PET.

INTRODUCTION

Molecular imaging in life sciences has positioned itself as a driving force in understanding in vivo interactions of biologically active compounds within the human body (*1*−*5*). As a result of the rising medicinal interest in positron emission tomography (PET) (*6*)—an imaging modality noninvasively depicting the distribution of radiolabeled biomarkers in vivo—the syntheses of radiolabeled biomarkers with the positron-emitting radiohalide fluorine-18 have gained widespread interest in the life sciences (*7, 8*). Although its important role in life sciences has been validated, numerous PET tracers are still far from being considered a routine method for in vivo imaging in patients. This is mainly a result of the complicated syntheses of PET imaging agents. Up until now, only one PET imaging agent, namely, the glucose derivative [^{18}F]fluorodeoxyglucose (2-[^{18}F]FDG), has gained widespread application in nuclear medicine and can be prepared in a fully automated synthesis unit by technicians (*9*). 2-[^{18}F]FDG is a rather simple radiotracer in terms of radiochemistry, and the method of ^{18}F-fluorination (a simple one-step radiolabeling) cannot be transferred to the synthesis of more complex compounds such as peptides and proteins. Simple methods for the ^{18}F-labeling of these substances are highly sought after, because a great number of new compounds intended for PET imaging are based on peptides and antibodies. Most labeling methods for the introduction of ^{18}F into proteins so far described are cumbersome and problematic as a result of the high technical skill needed for preparation (*10*−*13*). Most recently, two chemoselective methods for the ^{18}F-labeling of peptides and proteins have been reported using [^{18}F]FDG-maleimidehexyloxime (*14*) and [^{18}F]-FBA (*15*) as prosthetic labeling agents. Our group and others have searched for novel pathways to introduce ^{18}F into peptides and small molecules based on the formation of Si−^{18}F bonds. The formation of Si−^{18}F bonds as a tool in radiochemistry was communicated in 1985 for the first time (*16*) and proposed again in 1999 (*17*). We recently introduced simple one- and two-step ^{18}F-fluorination methods for peptides (*18, 19*). The described procedures are based on the formation of silicon−^{18}F bonds (in contrast to conventional carbon−^{18}F chemistry) originating from the unexpectedly efficient isotopic nonradioactive ^{19}F for radioactive ^{18}F exchange, which we named the silicon−fluorine-acceptor (SiFA) method. It has been shown most recently that Si−^{18}F chemistry can also be applied under no-carrier-added conditions, giving rise to high specific activities (*20*), and this chemistry was used for the labeling of a bombesin analogue intended for tumor imaging (*21*). We therefore endeavored to (1) transfer the SiFA method to the labeling of proteins, (2) demonstrate in vivo stability of the introduced ^{18}F-label with μPET (small PET camera for animals), and (3) show successful in vivo imaging. As proof of feasibility, we chose rat serum albumin (RSA) as a suitable protein for demonstrating the Kit-like labeling by the SiFA method. The resulting compound, [^{18}F]SiFA-labeled RSA for blood pool imaging with μPET, was applied in healthy rats ($n = 3$) as well as in a heterotropic heart model rat, demonstrating its usefulness compared to [^{18}F]FDG as a viability marker in the latter case.

EXPERIMENTAL SECTION

Materials. Commercially available chemical compounds were purchased in highest purity and used without further purification.

* To whom correspondence should be addressed. Bjoern Waengler: Tel +49 (89) 7095 4657, fax +49 (89) 7095 4648, bjoern.waengler@med.uni-muenchen.de. Ralf Schirrmacher: Tel (514) 340 8222 5212, fax (514) 340 7502, E-mail: ralf.schirrmacher@mcgill.ca.

† Hospital of the Ludwig-Maximilians-University.

University of Dortmund.

‡ Jewish General Hospital, McGill University.

§ Montreal Neurological Institute, McGill University.

⊥ Ludwig-Maximilians-University.

|| Gabriele Quandt and Ljuba Iovkova contributed equally. Synthesis of SiFA-SH was performed by L. Iovkova and K. Jurkschat.

10.1021/bc800413g CCC: $40.75 © 2009 American Chemical Society
Published on Web 01/08/2009

Illustra Nap-5 and Nap-10-columns were obtained from GE Healthcare Europe GmbH (Freiburg, Germany).

Instruments. NMR experiments were carried out with Bruker DRX 400, Bruker DRX 300, and Varian Mercury 200 spectrometers. The chemical shifts δ are given in ppm and are referenced to the solvent peaks with the usual values calibrated against tetramethylsilane (^{1}H, ^{13}C, ^{29}Si) and $CFCl_3$ (^{19}F). The high-resolution mass spectra were obtained with LTQ Orbitrap mass spectrometer (Thermo Electron) using acetonitrile as the mobile phase. The acetonitrile solutions were injected via a TriPlus Autosampler onto a DFS system (Perfluorkerosene as reference), connected with a Trace GC Ultra 2000 system (column DB-5MS (25 m, 0.25 mm ID, film 0.1 mm). FT infrared spectra were recorded using a Bruker IFS28 spectroemeter. Elemental analyses were performed on a LECO-CHNS-932 analyzer.

For analysis of the reaction mixtures and quality control, an Agilent series 1200 HPLC was used with a multiwavelength UV detector and a Raytest (Straubenhardt, Germany) radioactivity detector. The columns used were a Chromolith Performance RP-18 (100 × 4.6 mm) (Merck, Darmstadt, Germany) and a Superdex 75 size exclusion column (GE Healthcare Europe Freiburg, Germany), eluted with 10 mM phosphate buffer at pH 7.2, for quality control. UV/vis spectra were recorded using a Ultrospec 1100 pro (Amersham Biosciences Europe GmBH, Freiburg, Germany) apparatus. The PET scan was performed using a Siemens Inveon 120 small animal PET system (Siemens Preclinical Imaging, Knoxville, TN).

1-(*tert*-Butyldimethylsilanylsulfanyl)-4-(di-*tert*-butylfluorosilanyl)benzene. At −78 °C and under magnetic stirring, a solution of *t*-butyllithium in pentane was added to a solution of 4-bromophenylsulfanyl-*tert*-butyldimethylsilane (*22*) (2.61 g, 8.60 mmol) in diethyl ether (30 mL). After the reaction mixture had been stirred for 30 min at −78 °C, the resulting suspension was added dropwise over a period of 20 min to a cooled solution (−78 °C) of di-*tert*-butydifluorosilane (*23*) (1.86 g, 10.32 mmol) in diethyl ether (30 mL). The reaction mixture was allowed to warm to room temperature over a period of 12 h. The reaction mixture was hydrolyzed with a saturated solution of NaCl. The organic layer was separated, and the aqueous layer was extracted three times with diethyl ether at 50 mL each. The combined organic layers were dried over magnesium sulfate. After the magnesium sulfate had been filtered, the filtrate was evaporated in vacuo to give a residue that contained 16% di-*tert*-butylfluorophenylsulfanylsilane and 84% 1-(*tert*-butyldimethylsilanylsulfanyl)-4-(di-*tert*-butylfluorosilanyl)benzene. The latter was purified by distillation under reduced pressure (bp 188−190 °C, 5×10^{-3} Torr) to provide 2.74 g (7.13 mmol, 83% yield) of 1-(*tert*-butyldimethylsilanylsulfanyl)-4-(di-*tert*-butylfluorosilanyl)benzene as a yellow oil.

^{1}H NMR (300.13 MHz, $CDCl_3$): δ 7.44 (m, 4H, H_{arom}), 1.03 (d, $^4J(^1H-^{19}F) = 1.1$ Hz, 18H, CH_3), 0.95 (s, 9H, CH_3), 0.17 (s, 6H, CH_3). ^{13}C{^{1}H} NMR (100.63 MHz, $CDCl_3$): δ 134.5 (s, C_i), 134.0 (d, $^3J(^{13}C-^{19}F) = 4$ Hz, C_m), 133.6 (s, C_o), 131.7 (d,$^2J(^{13}C-^{19}F) = 14$ Hz, C_p), 27.2 (s, CH_3), 26.3 (s, CCH_3), 20.1 (d,$^2J(^{13}C-^{19}F) = 12$ Hz, CCH_3), 18.9 (s, CH_3), −6.8 (s, SiCH_3). ^{19}F NMR (282.38 MHz, $CDCl_3$): δ −191.5 (s, $^1J(^{19}F-^{29}Si) = 298$ Hz). ^{29}Si{^{1}H } NMR (59.63 MHz, $CDCl_3$): δ 14.4 (d, $^1J(^{29}Si-^{19}F) = 298$ Hz). Elemental analysis calculated (%) for $C_{20}H_{37}FSSi_2$ (384.74 g/mol): C 62.4, H 9.7, found C 62.3, H 9.4. GC-EI-HRMS: Calculated for $C_{20}H_{37}F^{32}S^{28}Si_2$ 384.2133, found 384.2146.

4-(Di-*tert*-butylfluorosilanyl)benzenethiol (SiFA-SH). A solution of 1-(*tert*-butyldimethylsilanylsulfanyl)-4-(di-*tert*-butylfluorosilanyl)benzene (2.6 g, 6.75 mmol) in dichloromethane 10 mL to which had been added trifluoracetic acid (7.7 g, 5.2 mL, 67.5 mmol) was stirred for 24 h (*22*). The volatiles were evaporated in vacuo (up to 10^{-3} Torr) to afford 4-(di-*tert*-butylfluorosilanyl)benzenethiol as a yellowish oil in quantitative yield.

^{1}H NMR (300.13 MHz, C_6D_6): δ 7.47 (d, $^3J(^1H-^1H) = 8$ MHz, 2H, H_{arom}), 7.07 (d, $^3J(^1H-^1H) = 8$ MHz, 2H, H_{arom}), 3.12 (s, 1H, SH), 1.09 (d, $^4J(^1H-^{19}F) = 1$ Hz,18H, CH_3). ^{13}C{^{1}H} NMR (75.48 MHz, C_6D_6): δ 134.5 (d, $^3J(^{13}C-^{19}F) = 4$ Hz, C_m), 133.9 (s, C_i), 129.9 (d, $^2J(^{13}C-^{19}F) = 14$ Hz, C_p), 128.2 (s, C_o), 27.2 (s, CH_3), 20.2 (d,$^2J(^{13}C-^{19}F) = 12$ Hz, CCH_3). ^{19}F NMR (282.38 MHz, $CDCl_3$): δ −190.7 (s, $^1J(^{19}F-^{29}Si) = 298$ Hz). ^{29}Si{^{1}H } NMR (59.63 MHz, $CDCl_3$): δ 14.2 (d, $^1J(^{29}Si-^{19}F) = 298$ Hz). IR (KBr): ν (SH) 2571 cm^{-1}. Elemental analysis: calculated (%) for $C_{14}H_{23}FSSi$ (270.48 g/mol) C 62.2, H 8.6, found C 62.0, H 8.7. GC-EI-HRMS: Calculated for $C_{14}H_{23}F^{32}S^{29}Si$ 270.1268, found 270.1269.

Modification of RSA with Sulfosuccinimidyl-4-(*N*-maleimidomethyl)cyclohexane-1-carboxylate Sodium Salt (Sulfo-SMCC). RSA (5 mg, 75 nmol) was dissolved in 0.5 mL phosphate buffer (PB) (0.1 M, pH 7.2). 10 μL (2.1 mg, 4.81 μmol in 100 μL DMSO) of a freshly prepared 48 mM Sulfo-SMCC stock solution was added and reacted at room temperature for 1 h. The derivatized protein was purified by using a Nap-5 column (equilibration buffer: 0.1 M PB, pH 6.5) and obtained in quantitative yield. The degree of maleimide modification was determined using Ellman's assay (cf. Supporting Information) applying MESNA (sodium 2-mercaptoethanesulfonate) and revealed approximately 2.5 maleimide groups per albumin (*24*).

1st Kit (Labeling Agent): Radiosynthesis of [^{18}F]SiFA-SH. The azeotropically dried [^{18}F]F^-/tetrabutylammoniumbicarbonate complex (∼1−2 GBq, cf. Supporting Information) was dissolved in dry DMSO (100 μL). SiFA-SH (10 μg, 37 nmol, 10 μL of a 1 mg/mL stock solution in DMSO) was added and reacted at room temperature for 5 min without stirring. Reaction control via RP-HPLC (Chromolith RP-18 performance, 4 mL/min, linear gradient starting from 100% water + 0.1% TFA to 100% acetonitrile + 0.1% TFA in 5 min) revealed a radiochemical yield of 40−60% for this step (R_t = 5.5min). The [^{18}F]SiFA-SH/DMSO solution was used for protein labeling without further purification.

2nd Kit (Labeling of Protein); Reaction of [^{18}F]SiFA-SH with RSA. One milliliter of the maleimide-functionalized RSA 5 mg, 75 nmol, in buffer (0.1 M PB, pH 7.2), as obtained in the protein derivatization step, was added to [^{18}F]SiFA-SH (100 μL of the DMSO solution as obtained above) and reacted at room temperature for 10 min without stirring. The ^{18}F-labeled protein was purified using a Nap-10 column (equilibration buffer: 0.1 M PB, pH 7.2) where only the first milliliter of the eluent was collected to ensure high purity of the product. The decay-corrected radiochemical yield was approximately 12%, and quality control using size exclusion HPLC revealed a radiochemical purity of ≥97% (Superdex 75 size exclusion column, 1 mL /min 10 mM PB pH 7.2, R_t = 14.5 min).

In Vivo Biodistribution of [^{18}F]SiFA-RSA in Healthy Rats and in a Heterotropic Rat Heart Transplantation Model. CD rats were housed according to German animal protection laws and protocols of the local committee. Experiments were performed under inhalation anesthesia (oxygen 1.2 L/min, isofluran 1.5 vol %) and appropriate warming to prevent hypothermia. 20−60 MBq of [^{18}F]SiFA-RSA was intravenously administered via a lateral tail vein. List mode data were acquired over 30 min using a Siemens Inveon 120 small animal PET system (Siemens Preclinical Imaging, Knoxville, TN) and divided into temporal frames of increasing length varying from 20 s to 5 min for the assessment of temporal changes in regional tracer accumulation. Tomographic volumes were created using three iterations of 3D OSEM, followed by 16 iterations of 3D

Scheme 1[a]

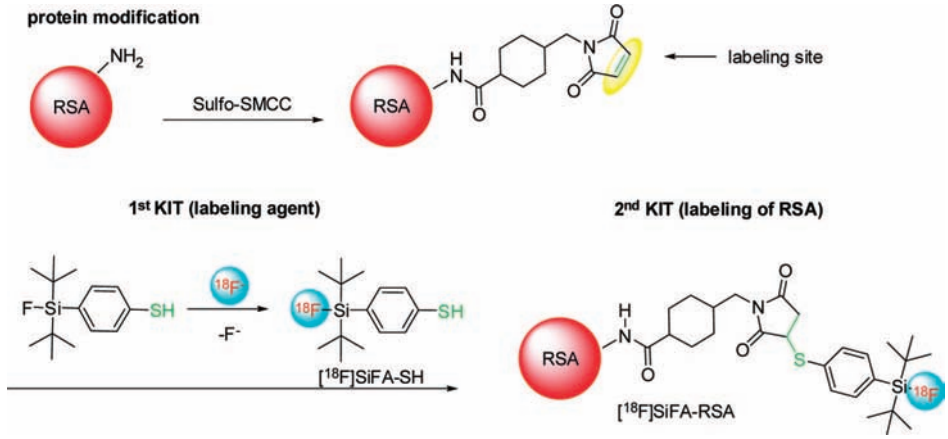

[a] Derivatization of rat serum albumin (RSA) applying sulfo-SMCC (protein modification step: RSA 5 mg, 75 nmol, was reacted with Sulfo SMCC (210 μg, 481 nmol) for 1 h at room temperature and subsequently purified by means of size exclusion gel cartridge filtration (illustra NAP-5), synthesis of [18]F]SiFA-SH (1st Kit, dried [18]F]F/tetrabutylammoniumbicarbonate complex 1−2 GBq in 100 μL DMSO were reacted 5 min at room temperature with SiFA-SH (10 μg, 37 nmol dissolved in 10 μL DMSO) and subsequent [18]F labeling of RSA (2nd Kit, the crude mixture obtained in the 1st Kit was added to derivatized RSA 5 mg, 75 nmol in PB (0.1 M, pH = 6.5) and reacted at ambient temperature for 10 min. Finally, the desired product was purified with an illustra Nap-10 cartridge).

OS-MAP iterative reconstruction, yielding a transaxial spatial resolution of approximately 1.4 mm (*25*). Additional experiments were performed using a heterotropic rat heart transplantation model, where the aorta of the transplanted heart was connected to the aorta abdominalis of the recipient rat. The aortic valve of the graft was occluded so that blood was circulating through the coronary arteries into the myocardium and was drained through coronary veins into the right atrium and ventricle. Arteria pulmonalis was connected with the inferior vena cava of the recipient rat.

RESULTS AND DISCUSSION

The SiFA labeling procedure of proteins with [18]F is based on the preceding synthesis of a small [18]F-labeled compound, which then reacts in good yields with the modified protein. In order to call it a true Kit labeling procedure, making it more applicable to a wide range of potential users, no step in the preparation of the labeled protein must use costly equipment such as HPLCs or sophisticated purification procedures. The SiFA labeling of RSA is based on the thiol-maleimide labeling concept and includes (1) derivatization of RSA with maleimido groups before the labeling of RSA to make it amenable to the SiFA labeling approach, (2) synthesis of the thiol-bearing [18]F]SiFA labeling agent from the nonradioactive SiFA compound by isotopic exchange—as a suitable SiFA compound for [18]F-labeling, we chose 4-(di-*tert*-butylfluorosilyl)benzenethiol (SiFA-SH), which was yielded quantitatively by treating the intermediate compound 1-(*tert*-butyldimethylsilanylsulfanyl)-4-(di-*tert*-butylfluorosilanyl)benzene with TFA (cf. Experimental Section), and (3) reaction of [18]F]SiFA-SH with RSA. The maleimido moieties could be easily introduced into the protein by reacting RSA with the heterobifunctional cross-linking reagent sulfosuccinimidyl-4-(*N*-maleimidomethyl)cyclohexane-1-carboxylate sodium salt (Sulfo-SMCC) in a simple procedure (Scheme 1, protein modification) and a gel cartridge purification step (*26*).

The first labeling step involved the introduction of [18]F]fluorine into the small, thiol moiety bearing prosthetic SiFA-SH compound by fast isotopic exchange for further labeling of the maleimido-modified RSA (Scheme 1, first Kit labeling agent). [18]F]SiFA-SH is supposed to selectively react with maleimido groups via a Michael Addition. Nonradioactive SiFA-SH (10 μg, 37 nmol) was labeled with up to 1−2 GBq of azeotropically dried $^{18}F^-$ in 100 μL dimethylsulfoxide (DMSO) at room temperature for 5 min. The incorporation of the radioactive $^{18}F^-$ into SiFA-SH was between 40% and 60% as determined by radio-HLPC. The calculated specific activity for [18]F]SiFA-SH was between 11 and 34 GBq/μmol (298 and 919 Ci/mmol) and is sufficient for protein labeling in general. The unexpected efficiency of the isotopic exchange has been elucidated by performing DFT calculations on some model fluorosilanes previously (*19*). Purification of [18]F]SiFA-SH thus formed was not necessary, as the unreacted $^{18}F^-$ does not compromise the subsequent conjugation reaction with RSA. The crude [18]F]SiFA-SH was mixed with 1 mL of the sulfo-SMCC derivatized RSA (5 mg, 75 nmol) in phosphate buffer (0.1 M, pH 7.2) originating from the protein modification step (Scheme 1, second Kit labeling of RSA). After gel cartridge (Illustra Nap-10) purification, the product [18]F]SiFA-RSA was isolated in 1 mL phosphate buffer and sterile-filtered for injection. The chemical and radiochemical purity was >97% according to size exclusion LC.

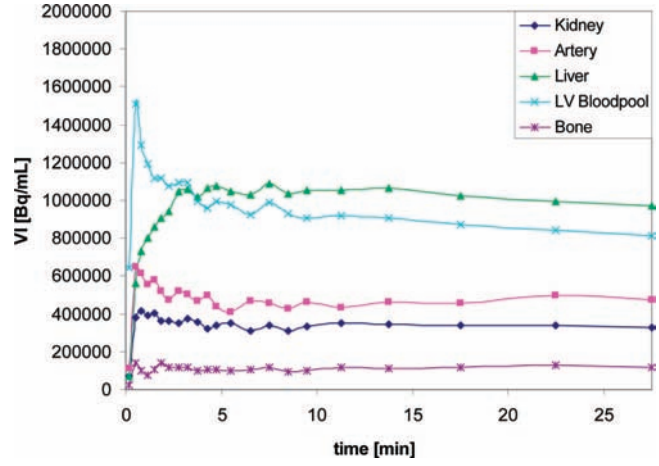

Figure 1. Time−activity curves of a CD rat after application of [18]F]SiFA-RSA, derived from the image data. Radioactivity was measured over 30 min in the liver, the kidney, the arteries, the bone, and the left ventricle (LV) using the volume of interest (VOI) technique. Curves are reflecting [18]F]SiFA-RSA blood pool activity.

To assess the in vivo applicability of the [18]F]SiFA-RSA, 25−60 MBq were injected in healthy rats (n = 3) and evaluated by means of μPET. Rat biodistribution data showed nearly constant whole blood radioactivity from minute 2 over the next

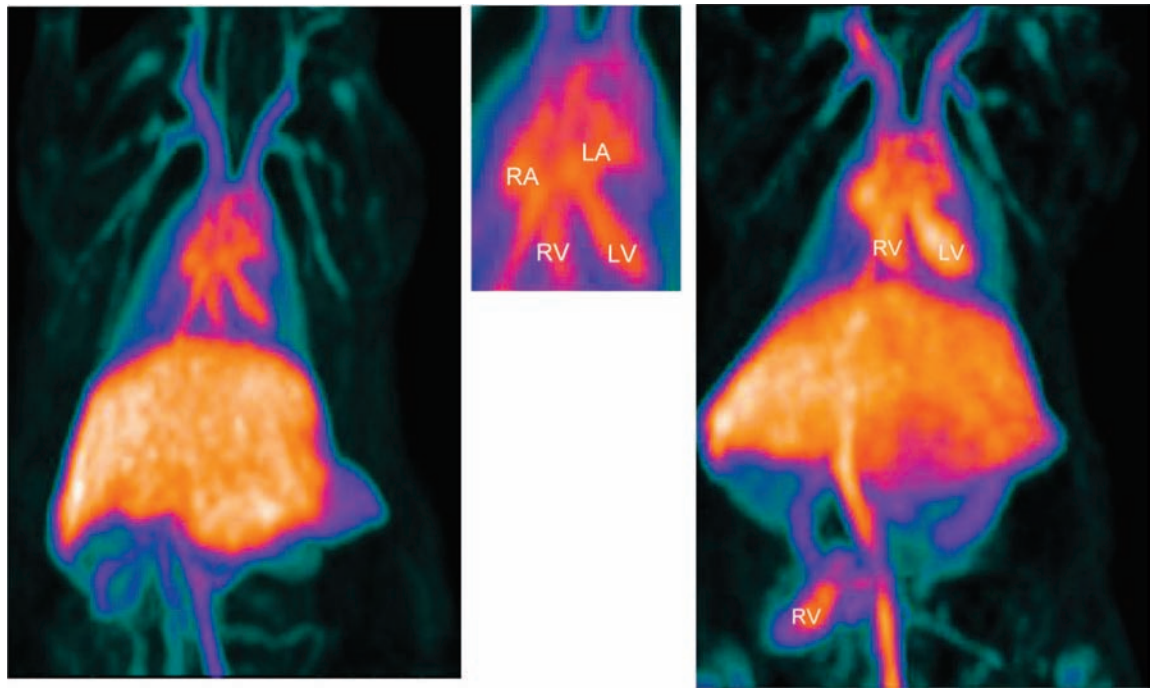

Figure 2. (left) Maximum intensity projection image ("best septal view") of an [^{18}F]SiFA-RSA blood pool scan of a healthy rat acquired over 30 min, showing radiotracer accumulation in the large arteries, the liver, and the heart. As indicated in the enlarged image cutout (middle), atria and ventricles can easily be identified. (right) Heterotopic rat heart transplantation model showing [^{18}F]SiFA-RSA blood pool in both the orthotopic and the heterotopic heart placed in the abdomen. Only right atrium and right ventricle are filled with blood in this model. RA, right atrium; LA, left atrium; RV, right ventricle; LV, left ventricle.

25 min after injection. While the liver as an organ with a large blood volume showed high uptake similar to the blood pool, kidney uptake was in the range of the arterial blood volume (Figure 1). Only slight radioactivity accumulation was registered in the bone, demonstrating minimal disposal of unbound [^{18}F]fluoride *in vivo*. Due to these characteristics, ^{18}F-labeled RSA represents a nearly ideal tracer for small animal PET blood pool studies. Blood pool imaging in planar or single photon emission computer tomography (SPECT) technique was shown to accurately estimate left and right ventricular volumes and ejection fractions in both humans (*27*) and mice (*28*) and, thus, can be used for monitoring different kinds of cardiac or cardiotoxic oncological therapies. Additionally, as demonstrated in Figure 2, PET blood pool imaging could serve for more advanced applications like monitoring blood pool in a heterotopic rat heart transplantation model. For this model, common [^{18}F]-FDG imaging glucose metabolism of the transplant was not feasible, as the heterotopic heart does not metabolize ^{18}F-FDG due a myocardial shift to fatty acid metabolism after denervation (cf. Supporting Information). Using [^{18}F]SiFA-RSA, the heterotopic heart blood pool and with it the endocardial borders could easily be visualized.

These examples proved applicability of this new labeling technique in nuclear medicinal imaging, and we intend to introduce SiFA-labeled human serum albumin as a blood pool tracer for human imaging studies. It is anticipated that for all proteins the same procedure can be applied. Step 1: SiFA-SH is incubated with dried $^{18}F^-$ at room temperature for 5 min. Step 2: The crude mixture is added to the sulfo-SMCC-derivatized protein in aqueous buffer and reacted at room temperature for the appropriate time. Step 3: The final purification is performed using a gel cartridge (Nap-10) to obtain the labeled protein in an injectable solution. The overall time for the synthesis of [^{18}F]SiFA-RSA takes 20−30 min only and is therefore one of the fastest ^{18}F-labeling procedures for proteins to date, which completely omits the use of costly technical equipment such as HPLC.

In anticipation of human applicability of this labeling Kit procedure, it is noteworthy to state that we entirely avoided toxic substances commonly applied in ^{18}F-chemistry such as harmful solvents like acetonitrile and kryptand (Kryptofix2.2.2.), which in turn also facilitates a clinical application of this new labeling method. Due to the high convenience of the radiochemistry presented here, we are currently investigating whether SiFA-SH labeled single-chain antibodies and other biologically active proteins might serve as valuable imaging agents for PET.

CONCLUSIONS

In conclusion, we demonstrated that the synthesis of a ^{18}F-labeled sulfo-SMCC derivatized protein (RSA) could be easily achieved using the novel silicon-based labeling synthon [^{18}F]SiFA-SH in sufficient overall RCYs of 12% after 20−30 min only. The entire procedure is independent of using complicated equipment such as HPLC and only needs two consecutive gel cartridge purification steps including protein modification. Injection of the purified [^{18}F]SiFA-RSA into healthy rats as well as into a rat bearing an abdominally transplanted second heart confirmed its usefulness as a new ^{18}F-labeled blood pool imaging agent with PET.

Supporting Information Available: Preparation of azeotropically dried [^{18}F]F^-/tetrabutylammoniumbicarbonate-complex, Ellman's assay to determine maleimide group derivatization of proteins, supplementary videos showing rotating maximum-intensity projections of healthy rats as (a) dynamic images, as summed images (b) with and (c) without ECG gating, as well as (d) a rat with a heterotopic (abdominally) transplanted heart, connected to the descending aorta and the inferior vena cava. This material is available free of charge via the Internet at http://pubs.acs.org.

LITERATURE CITED

(1) Willmann, J. K., van Bruggen, N., Dinkelborg, L. M., and Gambhir, S. S. (2008) Molecular imaging in drug development. *Nat. Rev. 7*, 591–697.

(2) Rudin, M., and Weissleder, R. (2003) Molecular imaging in drug discovery and development. *Nat. Rev. 2*, 123–131.

(3) Glaser, M., Luthra, S. K., and Brady, F. (2003) Applications of positron-emitting halogens in PET oncology. *Int. J. Oncol. 22*, 253–267.

(4) Snyder, S. E., and Kilbourn, M. (2003) Chemistry of Fluorine-18 Radiopharmaceuticals, In *Handbook of Radiopharmaceuticals, Radiochemistry and Applications* (Welch, M., and Redvanly, C. S., Eds.) pp 195−227, Chapter 6, Wiley, Chichester.

(5) Blower, P. (2006) Towards molecular imaging and treatment of disease with radionuclides: the role of inorganic chemistry. *Dalton Trans.* 1705–1711.

(6) Phelps, M. E. (2000) Inaugural article: positron emission tomography provides molecular imaging of biological processes. *Proc. Natl. Acad. Sci. U.S.A. 97*, 9226–9233.

(7) Ametamey, S. M., Honer, M., and Schubiger, P. A. (2008) Molecular imaging with PET. *Chem. Rev. 108*, 1501–1516.

(8) Schirrmacher, R., Wängler, C., and Schirrmacher, E. (2007) Recent developments and trends in ^{18}F-radiochemistry: syntheses and applications. *Mini-Rev. Org. Chem. 4*, 317–329.

(9) Hamacher, K., Coenen, H. H., and Stöcklin, G. (1986) Efficient stereospecific synthesis of no-carrier-added 2-[^{18}F]-fluoro-2-deoxy-D-glucose using aminopolyether supported nucleophilic substitution. *J. Nucl. Med. 27*, 235–238.

(10) Vaidyanathan, G., and Zalutsky, M. R. (1992) Labeling proteins with fluorine-18 using N-succinimidyl 4-[^{18}F]fluorobenzoate. *Int. J. Rad. Appl. Instrum. 19*, 275–81.

(11) Herman, L. W., Fischman, A. J., Tomkins, R. G., Hanson, R. N., Byon, C., Strauss, H. W., and Elmaleh, D. R. (1994) The use of pentafluorophenyl derivatives for the ^{18}F labelling of proteins. *Nucl. Med. Biol. 21*, 1005–1010.

(12) Chang, Y. S., Jeong, J. M., Lee, Y. S., Kim, H. W., Rai, G. B., Lee, S. J., Lee, D. S., Chung, J. K., and Lee, M. C. (2005) Preparation of ^{18}F-human serum albumin: a simple and efficient protein labeling method with ^{18}F using a hydrazone-formation method. *Bioconjugate Chem. 16*, 1329–1333.

(13) Berndt, M., Pietzsch, J., and Wuest, F. (2007) Labeling of low-density lipoproteins using the ^{18}F-labeled thiol-reactive reagent N-[6-(4-[^{18}F]fluorobenzylidene)aminooxyhexyl]maleimide. *Nucl. Med. Biol. 34*, 5–15.

(14) Wuest, F., Berndt, M., Bergmann, R., van den Hoff, J., and Pietzsch, J. (2008) Synthesis and application of [^{18}F]FDG-maleimidehexyloxime ([^{18}F]FDG-MHO): A [^{18}F]FDG-based prosthetic group for the chemoselective ^{18}F-labeling of peptides and proteins. *Bioconjugate Chem. 19*, 1202–1210.

(15) Flavell, R. R., Kothari, P., Bar-Dagan, M., Synan, M., Vallabhajosula, S., Friedman, J. M., Muir, T. W., and Ceccarini, G. (2008) Site-specific ^{18}F-labeling of the protein hormone leptin using a general two-step ligation procedure. *J. Am. Chem. Soc. 130*, 9106–9112.

(16) Rosenthal, M. S., Bosch, A. L., Nickles, R. J., and Gatley, S. J. (1985) Synthesis and some characteristics of no-carrier added [^{18}F]fluorotrimethylsilane. *Int. J. Appl. Radiat. Isot. 36*, 318–319.

(17) Walsh, J. C., Akhoon, K. M., Satyamurthy, N., Barrio, J. R., Phelps, M. E., Gambhir, S. S., and Toyokuni, T. (1999) Application of silicon-fluoride chemistry to fluorine-18 labeling agents for biomolecules: a preliminary note. *J. Labelled Compd. Radiopharm. 42*, S1.

(18) Schirrmacher, R., Bradtmoeller, G., Schirrmacher, E., Thews, O., Tillmanns, J., Siessmeier, T., Buchholz, H. G., Bartenstein, P., Wängler, B., Niemeyer, C. M., and Jurkschat, K. (2006) ^{18}F-Labeling of peptides by means of an organosilicon-based fluoride acceptor. *Angew. Chem., Int. Ed. 45*, 6047–6051.

(19) Schirrmacher, E., Wängler, B., Cypryk, M., Bradtmöller, G., Schäfer, M., Eisenhut, M., Jurkschat, K., and Schirrmacher, R. (2007) Synthesis of p-(di-tert-butyl[^{18}F]fluorosilyl)-benzaldehyde ([^{18}F]SiFA-A) with high specific activity by isotopic exchange: a convenient labeling synthon for the ^{18}F-labeling of N-aminooxy derivatized peptides. *Bioconjugate Chem. 18*, 2085–2089.

(20) Mu, L., Hoehne, A., Schubiger, P. A., Ametamey, S. M., Graham, K., Dinkelborg, L., Stellfeld, T., Srinivasan, A., Voigtmann, U., and Klar, U. (2008) Silicon-based building blocks for one-step ^{18}F-radiolabeling of peptides for PET imaging. *Angew. Chem., Int. Ed. 47*, 4922–4925.

(21) Hoehne, A., Mu, L., Honer, M., Schubiger, P. A., Ametamey, S. M., Graham, K., Stellfeld, T., Borowski, S., Berndorff, D., Klar, U., Voigtmann, U., Cyr, J. E., Friebe, M., Dinkelborg, L., and Srinivasan, A. (2008) Synthesis, ^{18}F-labeling, and in vitro and in vivo studies of bombesin peptides modified with silicon-based building blocks. *Bioconjugate Chem. 19*, 1871–1879.

(22) Brikh, A., and Morin, C. (1999) Boronated thiophenols: a preparation of 4-mercaptophenylboronic acid and derivatives. *J. Organomet. Chem. 581*, 82–86.

(23) Rempfer, B., Oberhammer, H., and Aunert, N. (1986) The (p-d) π bonding in fluorosilanes? Gas-phase structures of $(CH_3)_{4-n}SiF_n$ with $n = 1-3$ and of $(tert\text{-}Bu)_2SiF_2$. *J. Am. Chem. Soc. 108*, 3893–3897.

(24) Wängler, C., Moldenhauer, G., Eisenhut, M., Haberkorn, U., and Mier, W. (2008) Antibody-dendrimer conjugates: the number, not the size of the dendrimers, determines the immunoreactivity. *Bioconjugate Chem. 19*, 813–820.

(25) Mumcuoglu, E. U., Leahy, R., Cherry, S. R., and Zhou, Z. (1994) Fast gradient-based methods for Bayesian reconstruction of transmission and emission PET images. *IEEE Trans. Med. Imaging 13*, 687–701.

(26) Brinkley, M. A. (1992) A survey of methods for preparing protein conjugates with dyes, haptens and crosslinking reagents. *Bioconjugate Chem. 3*, 2–13.

(27) Hesse, B., Lindhardt, T. B., Acampa, W., Anagnostopoulos, C., Ballinger, C., Bax, J. J., Edenbrandt, L., Flotats, A., Germano, G., Stopar, T. G., Franken, P., Kelion, A., Kjaer, A., Le Guludec, D., Ljungberg, M., Maenhout, A. F., Marcassa, C., Marving, J., McKiddie, F., Schaefer, W. M., Stegger, L., and Underwood, R. (2008) EANM/ESC guidelines for radionuclide imaging of cardiac function. *Eur. J. Nucl. Med. Mol. Imaging 35*, 851–885.

(28) Chin, B. B., Metzler, S. D., Lemaire, A., Curcio, A., Vemulapalli, S., Greer, K. L., Petry, N. A., Turkington, T. G., Coleman, R. E., Rockman, H., and Jaszczak, R. J. (2007) Left ventricular functional assessment in mice: feasibility of high spatial and temporal resolution ECG-gated blood pool SPECT. *Radiology 245*, 440–448.

BC800413G

Kit-like ^{18}F-labeling of proteins: Synthesis of 4-(di-tert-butyl[^{18}F]fluoro-silyl)benzenethiol (Si[^{18}F]FA-SH) labeled rat serum albumin for blood pool imaging with PET

Björn Wängler, Gabriele Quandt, Ljuba Iovkova , Esther Schirrmacher, Carmen Wängler, Guido Boening, Marcus Hacker, Michael Schmoeckel, Klaus Jurkschat , Peter Bartenstein and Ralf Schirrmacher

Supporting Information:

Preparation of [N(*n*-Bu)$_4$]^{18}F using [N(*n*-Bu)$_4$]HCO$_3$ for SiFA labeling Aqueous [^{18}F]fluoride (5000-9000 MBq) that had been prepared by the ^{18}O(p,n)^{18}F nuclear reaction on an enriched [^{18}O]water (95 %) was loaded onto a Chromafix PS-HCO$_3$ (GE-Healthcare Europe) cartridge and eluted with a mixture of 800µL acetonitrile and 200µL aqueous tetrabutylammonium hydrogen carbonate solution (c = 0.075 mmol/mL, ABX, Radeberg, Germany) and azeotropically dried using acetonitrile (2 x 1 mL, stream of nitrogen, 80°C). The "dried" [N(*n*-Bu)$_4$]^{18}F complex was dissolved in DMSO (100 - 250 µL) and this stock solution was used for labeling.

Ellman's assay A 2 mM solution of MESNA (sodium 2-mercaptoethanesulfonate) in PB (0.1 M, pH 8) was diluted to obtain solutions of the following concentrations: 125 µM, 64 µM, 32 µM, 16 µM, 8 µM, 4 µM, and 2 µM. To 1 mL of each of these solutions, 200 µL of a solution of Ellman′s reagent (5,5′-dithio-bis-(2-nitrobenzoic acid), 4 mg/mL in PB (0.1 M, pH 8)) was added and the absorption of the obtained mixtures was measured at 412 nm in a UV/vis spectrometer to give the calibration curve. The thiol concentrations of the samples were determined analogously by adding 200 µL of the solution of Ellman′s reagent to 1 mL of sample in PB (0.1 M, pH 8) and by measuring the absorption at 412 nm. The number of maleimides per RSA was determined by reacting it with an access of MESNA (5 equiv) and subsequent titration of free thiol with Ellman′s assay.

Figure: Maximum intensity projection image of the heterotopic rat heart transplantation model showing [^{18}F]FDG uptake only in the orthotopic heart (OH).

Bioconjugate Chemistry 20th Anniversary

Subscriber access provided by SHEMYAKIN-OVCHINNIKOV INST

Article

A Biodegradable Low Molecular Weight Polyethylenimine Derivative as Low Toxicity and Efficient Gene Vector

Yuting Wen, Shirong Pan, Xin Luo, Xuan Zhang, Wei Zhang, and Min Feng

Bioconjugate Chem., **2009**, 20 (2), 322-332• DOI: 10.1021/bc800428y • Publication Date (Web): 16 January 2009

Downloaded from http://pubs.acs.org on May 15, 2009

More About This Article

Additional resources and features associated with this article are available within the HTML version:

- Supporting Information
- Access to high resolution figures
- Links to articles and content related to this article
- Copyright permission to reproduce figures and/or text from this article

View the Full Text HTML

ACS Publications
High quality. High impact.

Bioconjugate Chemistry is published by the American Chemical Society. 1155 Sixteenth Street N.W., Washington, DC 20036

A Biodegradable Low Molecular Weight Polyethylenimine Derivative as Low Toxicity and Efficient Gene Vector

Yuting Wen,[†,‡] Shirong Pan,[‡,*] Xin Luo,[†] Xuan Zhang,[‡] Wei Zhang,[‡] and Min Feng[†]

School of Pharmaceutical Sciences and the First Affiliated Hospital, Sun Yat-sen University, Guangzhou, 510080, China.
Received October 8, 2008; Revised Manuscript Received December 15, 2008

Polyethylenimine (PEI) is a class of cationic polymers proven to be effective for gene delivery. However, PEI is nondegradable and the molecular weight of PEI affects the cytotoxicity and gene transfer activity. Aiming to prepare a biodegradable gene vector with high transfection efficiency and low cytotoxicity, we conjugated low molecular weight (LMW) PEIs to the biodegradable backbone polyglutamic acids derivative (PEG-*b*-PBLG) by aminolysis to form PEIs combined PEG-*b*-PLG-*g*-PEIs (GGI). Two copolymers, GGI 30 and GGI 40, were synthesized. The chemistry of GGI was characterized using IR, ^{1}H NMR and ^{13}C NMR, GPC, and CD, respectively. The degradation behaviors of copolymer GGI in papain solution were investigated. GGIs showed good DNA condensation ability and high protection of DNA from nuclease degradation. The zeta potential of the GGI/pDNA polyplexes was ~15 mV, and the particle size was in the range 102−138 nm at N/P ratios between 10 and 30. The particle size and the morphology of the polyplex was further confirmed by transmission electron microscope (TEM). In cytotoxicity assay, GGIs were significantly less toxic than PEI 25k. The degradation product of GGI exhibited negligible effects on cells even at high copolymer concentration. The results of GFP flow cytometry and fluorescence imaging showed that the trasnfection efficiencies of GGIs were all markedly higher than PEI 25k in Hela, HepG2, Bel 7402, and 293 cell lines. Importantly, the presence of serum had a lower inhibitive effect on the transfection activity of GGI in comparison to PEI 25k and Lipofectamine 2000. Therefore, PEG-*b*-PLG-*g*-PEI copolymers may be attractive cationic polymers for nonviral gene therapy.

INTRODUCTION

In the past decade, cationic polymers have become the major type of nonviral gene delivery carriers, due to their advantages over viral vectors, including the ability to deliver larger DNA molecules, low immunogenicity, and relative safety (*1*−*4*).

Among the cationic polymers, polyethylenimine (PEI) is regarded to be one of the most successful and widely studied gene delivery polymers. PEI has been proven to be effective in gene delivery due to its condensation of DNA, which facilitates endocytosis, as well as its "proton sponge effect", which can prevent the DNA from endosomal disruption (*5*, *6*).

Many studies have shown that the molecular weight of PEI is the most effective parameter for the gene transfection efficiency and cytotoxicity (*7*−*11*). It was observed that PEI gene transfer activity increased with an increase in molecular weight, whereas the cytotoxicity appears to increase with increasing polymer size. For example, low molecular weight (LMW) PEI (<2 kDa) was proven to be nontoxic but could not effectively condense DNA and displayed very poor transfection activity. In contrast, high molecular weight (HMW) PEI (PEI 25k) showed high transfection efficiency but also significant cytotoxicity. In addition, HMW PEI, which is nonbiodegradable, probably would give rise to the accumulation of cytotoxicity in vivo, so the long-term safety of HMW PEI is further problematic.

To circumvent the problems described above, one rational way was suggested to enhance the gene delivery efficiency of polymer with low cytotoxicity, achieved by combining LMW PEIs together using degradable linkages to form combined PEI with suitable high molecular weights. A series of degradable cross-linked LMW PEIs were investigated, which were synthesized by linking several LMW PEIs to various cross-linking reagents, such as diacrylate (*10*), glutadialdehyde (*12*), oligo(L-lactic acid-*co*-succinic acid) (*13*), dithiobis(succinimidylpropionate), and dimethyl-3,3′-dithiobispropionimidate·2HCl (*14*). The results showed that the transfection efficiency of these cross-linked PEIs was comparable to that of PEI 25k or even higher, while the cytotoxicity was much lower than that of PEI 25k. Another strategy was to employ linear chains to link LMW PEIs together. Wong et al. synthesized PEI-*g*-chitosan by performing cationic polymerization of aziridine in the presence of oligochitosan. The results revealed that PEI-*g*-chitosan showed a higher transfection efficiency than that of PEI 25k both in vitro and in vivo (*15*). Tang et al. employed cyclodextrins to cross-link LMW branched PEI (MW 600) to form HMW cationic polymers (average MW 61 kDa), which displayed high gene transfection and low cytotoxicity in vitro (*16*). Jiang et al. designed the CHI-*g*-PEI copolymer by performing an imine reaction between periodate-oxidized chitosan and LMW PEI (800 Da). The results indicated that CHI-*g*-PEI had a lower cytotoxicity and showed higher transfection efficiency than PEI 25k (*17*).

Polyglutamic acid is a biodegradable polypeptide, which is susceptible to enzymatic digestion in the human body. It is reported that polyglutamic acids are biocompatible, do not elicit an immune response, and have low toxicities in vivo (*18*). Introduction of nonionic hydrophilic PEG to the cationic gene delivery polymer is actively pursued, because PEG facilitates the formation of polyplexes with improved solubility, reduced aggregation, lower cytotoxicity, and possibly decreases opsonization with serum proteins in the bloodstream (*19*, *20*).

Thus, our idea of polymer design was to create biodegradable backbone poly(amino acid) derivates (PEG-*b*-PBLG) first, and

* Corresponding author. E-mail: gzpshr@163.com, Tel.: +86-20-87755766-8147, Fax: +86-20-87750632.
† School of Pharmaceutical Sciences.
‡ First affiliated Hospital.

10.1021/bc800428y CCC: $40.75 © 2009 American Chemical Society
Published on Web 01/16/2009

Table 1. Feed Composition and Molecular Characteristics of Intermediated Copolymer PEG-*b*-PBLG

PEG-*b*-PBLG copolymer	amount in feed				Mn of each block[a]		
	BLG-NCA		PEG-NH_2		PEG	PBLG	Mn[a]
GE 1	4.0 g	15.1 mmol	1.5 g	0.3 mmol	5000	20600	25600
GE 2	4.0 g	15.1 mmol	0.75 g	0.15 mmol	5000	33000	38000

[a] As determined by ^{1}H NMR spectroscopy.

Table 2. Feed Composition and Molecular Characteristics of Final Product PEG-*b*-PLG-*g*-PEI

polymer	intermediate copolymer	amount in feed (g)			Mn of each block[a]				
		GE	PEI	2-HP	PEG	PLG	PEI	Mn[a]	Mn[b]
GGI 30	GE 1	1.0	15.6	1.8	5000	8500	26100	35100	39200
GGI 40	GE 2	1.0	16.8	1.9	5000	14600	40300	59900	56000

[a] As determined by ^{1}H NMR spectroscopy. [b] As determined by GPC.

then attach the LMW PEIs (MW 423 Da) to the side chains of poly(amino acid)s by the reaction of aminolysis. It is expected that the novel biodegradable copolymers PEG-*b*-PLG-*g*-PEIs (GGI) show the characteristics of high transfection efficiency, low cytotoxicity, and degradability. In the present study, we reported the synthesis and characterization of GGI. Their degradability, DNA condensation ability, DNA protection ability, and cytotoxicity were checked. The in vitro transfection efficiency was investigated in the absence and presence of serum, compared with PEI 25k and commercially available Lipofectamine 2000.

MATERIALS AND METHODS

Materials. Polyethylenimine with average molecular weight of 423 Da (PEI 423) and 25 kDa (PEI 25k) were purchased from Aldrich. Amine-terminated poly(ethylene glyol) monomethyl ether (mPEG-NH_2) with a molecular weight of 5 kDa was purchased from Kaizheng Biotech Development Co. Ltd., Beijing. 2-Hydroxypyridine (2-HP) was purchased from Fluka. Tetrahydrofuran (THF) was dried and distilled in the presence of sodium immediately before use. *N*,*N*-Dimethylformamide (DMF) was dried over calcium hydride and distilled prior to use. DNase I and 3-(4,5-dimethylthiazol-2-yl)-2,5-diphenyltetrazolium bromide (MTT) were purchased from Sigma. Lipofectamine 2000 was obtained from Invitrogen Corporation. The reporter plasmids, pEGFP-C1, was a gift from West China University of Medical Sciences (Chengdu China). The plasmid was propagated in *Escherichia coli* DH5-α and purified by the Qiagen endotoxin-free plasmid purification kit (Qiagen, CA, USA). The DNA concentration was checked by the measurement of UV absorbance at 260 nm using a biophotometer (Eppendorf 5840R, Germany). The other materials and solvents were used as received without further purification.

Synthesis of PEG-*b*-PBLG. First, γ-benzyl glutamate (BLG) was prepared according to the method reported in the literature (*21*). *N*-Carboxyanhydride of γ-benzyl L-glutamate (BLG-NCA) was synthesized by reaction of the ester with triphosgene in THF. Typically, γ-benzyl glutamate (3 g, 0.0127 mol) was suspended in dried THF (30 mL), and triphosgene (1.8 g, 0.0061 mol) was added. The suspension was stirred at 60 °C. After approximately 15 min reaction, the reaction solution turned clear. After reaction for 30 min, the reaction mixture was precipitated with an excess of cold petroleum ether. The mixture then was stored at 4 °C for 24 h to let the crystals grow. The white crystalline product was filtered off and washed with petroleum ether. The precipitate was dried in vacuo at room temperature for 4 h.

Typical synthesis procedure of poly(ethylene glycol)-*block*-poly(γ-benzyl L-glutamate) (PEG-*b*-PBLG) was as follows. BLG-NCA was dissolved in dried $CHCl_3$ (20 mL/1 g). mPEG-NH_2 was added as the macroinitiator at a monomer/initiator ratio of 50:1 for GE 1 and 100:1 for GE 2. The detailed feeding amount of material for PEG-*b*-PBLG synthesis was presented in Table 1. The mixture solution was stirred for 72 h at room temperature. The product mixture was precipitated with an excess of ethanol under vigorous stirring to obtain a white solid, while the unreacted PEG-NH_2 remained dissolved in the mixture solution. After filtration, diblock copolymer PEG-*b*-PBLG was obtained under vacuum at 40 °C for 24 h.

Synthesis of PEG-*b*-PLG-*g*-PEIs (GGI). PEG-*b*-PLG-*g*-PEIs was prepared by aminolysis of PEG-*b*-PBLG using LMW PEI. PEG-*b*-PBLG was dissolved in dried DMF (10 mL/1 g) and put on an oil bath at 40 °*C*. Polyethylenimine (PEI 423) (10× mol ratio to the ester groups of PEG-*b*-PBLG) and 2-hydroxypyridine (2-HP) (5× mol ratio to the ester groups of PEG-*b*-PBLG) were added, and the solution was stirred for 48 h. The detailed feeding amount of material for GGI synthesis was presented in Table 2. The product PEG-*b*-PLG-*g*-PEIs was obtained after precipitation in cold ether, followed by dialysis against water (2 days) using a dialysis bag with 3.5 kDa molecular weight cut off (MWCO), and finally freeze−dried.

Characterization of Polymers. The FTIR spectra of polymers were recorded in pressed KBr pellets on a Fourier transformation infrared spectrometer (Bruker, EQUINOX 55). ^{1}H NMR and ^{13}C NMR spectra in D_2O or $CDCl_3$ were recorded with a superconducing Fourier transform nuclear magnetic resonace spectrometer (Varian INOVA500NB 500 MHZ). Gel permeation chromatography (GPC) was performed using a Waters 515−410 chromatograph to detect the molecular weights and molecular weight distribution of the polymer. Circular dichroism spectra (CD) was recorded on a JASCO J-810 spectrometer on samples with concentrations at 0.5 mg/mL, using a scan rate of 20 nm/min and a cell path length of 1.0 mm.

Polymer Degradation Studies. The degradation profile of LMW PEIs combined copolymer GGI by papain was investigated using capillary viscosity measurements. In a typical experiment, GGI 40 was dissolved in PBS (pH = 7.4) and combined with a papain solution in PBS. The final concentrations of GGI 40 and papain were 2 mg/mL and 1 mg/mL, respectively. The total volume was 12 mL. The mixture was stirred at 37 °C, and 2 mL 20% trichloroacetic acid (TCA) was added as a function of time to prevent further degradation during the measurement of the viscosity. The samples were then freeze−dried for 24 h to get the degradation product. Capillary visosity measurements were carried out to determine the η_{inh} of the degradation product, at 25 °C in PBS. The concentration was 0.5 g/dL. Inherent viscosity (η_{inh}) was calculated by the following equation: $\eta_{inh} = \ln(t/t_0)/c$, where t was the flow time of the polymer solution, t_0 the flow time of the solvent, and c the degradation product concentration. The degree of the degradation was estimated by η_{inh} relative reduction (%). η_{inh} relative reduction (%) = $\eta_{inh\ (t)}/\eta_{inh(t0)}$, where $\eta_{inh(t)}$ was the η_{inh} of polymer solution at the function time of t, $\eta_{inh(t0)}$ was the η_{inh} of the initial polymer solution.

Preparation of Copolymer/pDNA Polyplexes. All polymer/pDNA polyplexes were freshly prepared before use. Polyplexes were prepared by adding polymer solutions to equal volumes of pEGFP-C1 with gentle vortexing and incubated at room temperature for 30 min. The concentration of polymer solution was based on the chosen N/P ratios of polymer/pDNA. The polyplexes were produced in 150 mM NaCl at pH 7.4 [transmission electron microscope (TEM) observation], in 10 mM NaCl at pH 7.4 (particle size and zeta potential measurements), or in PBS at pH 7.4 (other experiments).

Gel Retardation Assay. Agarose gel retardation assay was used to determine the DNA binding ability of copolymer GGI. Polymer/pDNA complexes were prepared at various N/P ratios ranging from 0.5 to 3 in PBS (pH=7.4). The complexes were mixed with appropriate amounts of 6× gel-loading buffer (Sigma), and then electrophoresced on a 0.9% (w/v) agarose gel containing ethidium bromide (0.5 μg/mL of the gel) in 0.5× Tris-boric acid-EDTA (TBE). The location of DNA in the gel was analyzed on a UV illuminator and photographed by a UVIpro gel image sytem (UVItec).

DNase I Protection Assay. Polymer/pDNA complexes were prepared at N/P ratio of 0.5/1 to 10/1 at a final pDNA concentration of 40 μg/mL and 10 μL total volumn. The complex solutions were incubated with 4 μL DNase I (100 μg/mL, in 50 mmol/L Tris-Cl, 10 mmol/L $MgCl_2$, pH = 7.4) at 37 °C for 30 min. The DNase I was inactivated by adding 4 μL of 25 mM ethylenediaminetetraacetic acid (EDTA), followed by incubating at room temperature for 10 min. The pDNA was then released from the polyplexes by adding 1% sodium dodecyl sulfate (SDS), and analyzed by 0.9% agarose gel electrophoresis.

Particle Size and Zeta Potential Measurements. Particle size and zeta potentials of the polymer/pDNA complexes were measured with Malvern Zetasizer Nano ZS90 (Malvern, UK) in a 10 mM NaCl aqueous solution. The morphologies of the complexes of polymer/pDNA were examined with a JEM-2010 HR transmission electron microsope (TEM). Polyplexes were prepared as described above in the preparation of copolymer/pDNA polyplexes procedure. To prepare the samples, a small drop of dilute particle dispersion was spread onto a carbon-coated grid. The dried specimens were then negatively stained with a drop of 2% phosphotungstic acid (PTA) for 30 min and dried at room temperature.

Cell Culture. Human cervix epithelial carcinoma cells (Hela), human hepatoblastoma cells (HepG2), human hepatoblastoma cells (Bel 7402), and human embryonic kidney cells (293) were cultured in Dulbecco's Modified Eagle Medium (DMEM) with 10% (v/v) fetal bovine serum (FBS) and 1% penicillin−streptomycin, at 37 °C under 5% CO_2. The cells were purchased from the Shanghai Cell Bank, Chinese Academy of Medical Sciences.

Cytotoxicity Determination. MTT assay was employed to measure the cytotoxicity of the polymers. Hela cells (1.2×10^4 cells/well) were seeded in 96 well plates in 200 μL DMEM medium containing 10% FBS. When the cells achieved 70−80% confluence (incubation for 20−24 h), the growth media were replaced by fresh serum-free media or media with serum containing various amount of polymers, respectively. The medium in each well was replaced with 200 μL of fresh complete medium 4 h later. After additional incubation for 48 h, 25 μL of stock solution of MTT (5 mg/mL in PBS) was added to each well. After 4 h of incubation, medium was changed with 150 μL DMSO to dissolve the fomazan crystal formed by live cells. Absorbance was measured at 570 nm using an ELISA microplate reader (Bio-Rad). The cell viability was expressed as a percentage of the absorbance to that of the control experiment without polymers.

Transfection Efficiency Measurements. The effectiveness of GGI 30 and GGI 40 as carriers in gene delivery were compared with PEI 25k and Lipofectamine 2000. The transfection efficiency was quantified by the percentage of cells expressing green fluorescent protein (GFP), analyzed by flow cytometry using a FACS Caliber System from Becton-Dickinson (San Joes, CA). The levels of GFP expression were characterized using fluorescence microscopy (Olympus, Japan).

Hela cells (15×10^4 cells/well), HepG2 cells (15×10^4 cells/well), Bel 7402 cells (12×10^4 cells/well), and 293 cells (10×10^4 cells/well) were seeded in 12-well plates, respectively, and incubated at 37 °C under 5% CO_2 for 24 h in 1 mL of DMEM medium containing 10% FBS. GGI/pDNA and PEI 25k/pDNA complexes of various N/P ratios were prepared as described above. At the time of transfection, the media in each well were replaced by 1 mL of DMEM without FBS. 200 μL of polymer/pDNA polyplex suspension, containing 4 μg of pEGFP-C1, was added to each well and incubated with cells for 4 h at 37 °C. After 4 h transfection time, the media were replaced by 1 mL of DMEM containing 10% FBS, and the cells were further incubated for 44−48 h. After being observed using a fluorescence microscope, cells were separately harvested from each well by the trypsin-EDTA treatment, and suspended in 200 μL of PBS (pH 7.4). The cells were transferred to flow cytometry cuvettes for analysis. The nontransfected cells were used as a negative control.

Scheme 1. Synthesis Procedure of GGI

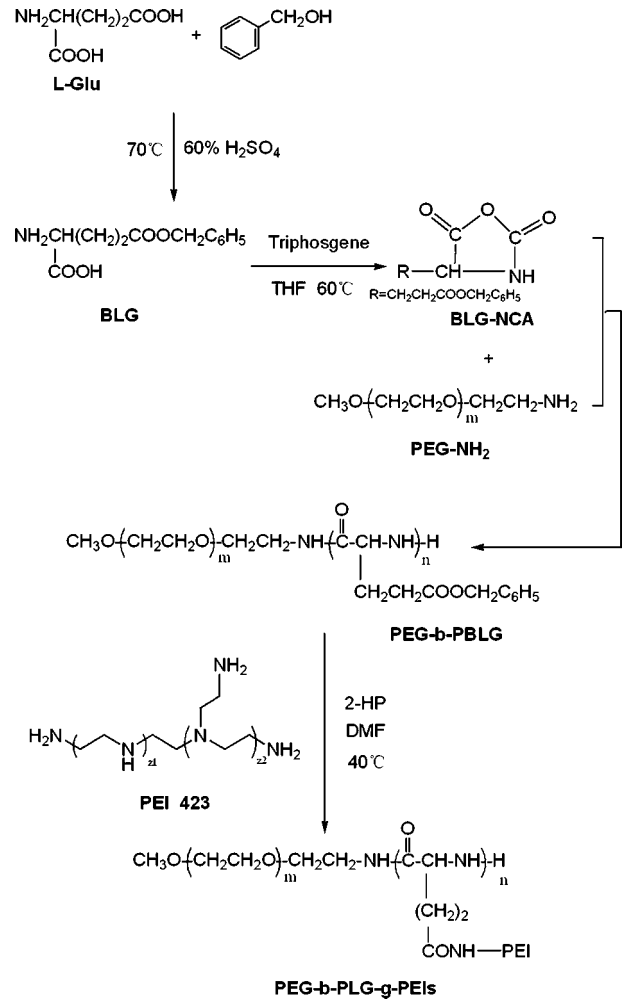

In Vitro Transfection Experiment in Serum. The process of transfection experiments was the same as described above, except that the medium at the time of transfection was replaced with DMEM containing 10% FBS.

Statistical Analysis. Where suggested, all results were summarized as means ± standard deviation, and statistical variations p value between the group means were analyzed by the Student's t-test.

RESULTS AND DISCUSSION

Design and Synthesis of PEG-*b*-PLG-*g*-PEIs (GGI). As described in the Introduction, we aimed to synthesize a low molecular weight (LMW) PEI combined biodegradable polymer GGI. The copolymer GGI was synthesized in two steps as shown in Scheme 1: (1) to prepare the backbone PEG-*b*-PBLG by ring

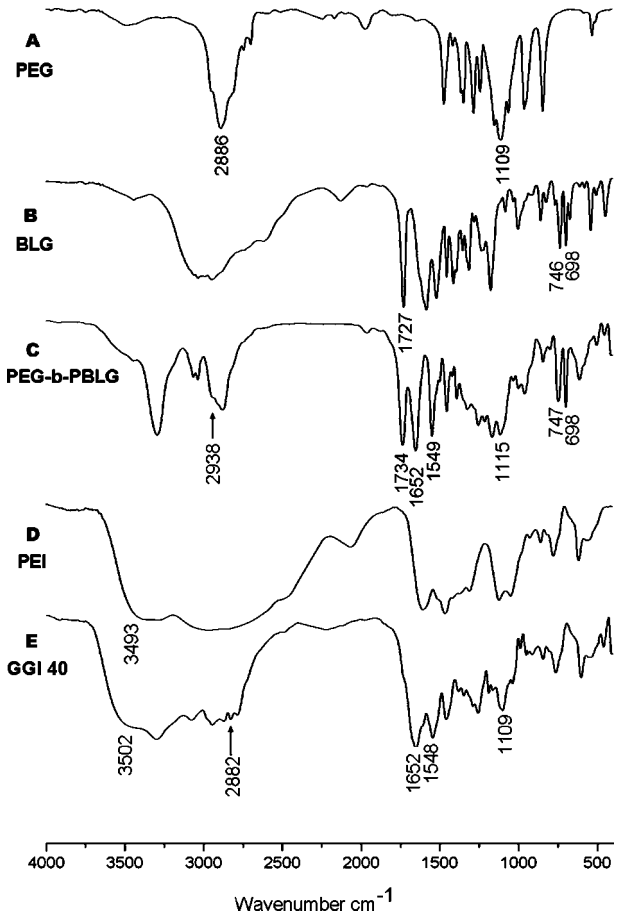

Figure 1. The IR spectra of (A) mPEG, (B) BLG, (C) PEG-*b*-PBLG, (D) PEI 423, and (E) GGI 40.

opening polymerization (ROP) of BLG-NCA in the presence of PEG-NH_2 as macroinitiator. (2) The triblock copolymer GGI was synthesized by aminolysis of PEG-*b*-PBLG using LMW PEI 423.

Aminolysis reaction was employed to form GGI by grafting LMW PEI to the backbone PEG-*b*-PBLG and debenzylation. It was known that chain scission of the backbone (amide linkages of polypeptide) would occur during the process of aminolysis (*22*). Thus, we used 2-hydroxypyridine (2-HP) as a bifunctional catalyst in the reaction to reduce the main chain cleavage according to the literature (*23*). In our pre-experiment, we optimized the reaction conditions for aminolysis to minimize the main chain cleavage, concerning to the reaction temperature, reaction time, and the additional amount of 2-HP. The results of the pre-experiment showed that the aminolysis reaction occurred at 40 °C and lasted for 48 h, with the amount of 2-HP equaling to the ratio of 2-HP to ester 5/1 could minimize the polypeptide degradation.

In addition, since PEI 423 has more than one functional reaction site (primary amine groups) with the ester group of PEG-*b*-PBLG, gelation might occur in the aminolysis reaction theoretically. In our experiment, the reaction mixtures were clear solutions during the whole aminolysis process, and the two products GGI 30 and GGI 40 were water-soluble, indicating that no or negligible gelation product was produced practically.

Characterization of GGI. Figure 1 showed the FTIR spectra of the diblock intermediate and the corresponding graft copolymer. The peak at 2886 cm^{-1} (C−H stretch vibration) and 1109 cm^{-1} (C−O stretch vibration) were characteristics of the PEG block (Figure 1A). Obviously, PEG blocks were present in the intermediate prepolymer PEG-*b*-PBLG (Figure 1C) and the final graft triblock copolymer GGI (Figure 1E). For PEG-*b*-PBLG (Figure 1C), the absorptions at 1652 cm^{-1} (*amide I*) and 1549 cm^{-1} (*amide II*) were attributed to the amide group, suggesting the formation of the polypeptide block. The peaks at 698 cm^{-1} and 747 cm^{-1} from the phenyl group and the peak at 1734 cm^{-1} from the ester carbonyl group were characteristics of PBLG block carrying protection groups. For triblock copolymer GGI (Figure 1E), it similarly owned the characterisitcs absorption at 1652 cm^{-1} (*amide I*) and 1548 cm^{-1} (*amide II*), indicating that the polypetide block PLG block existed. In comparison to diblock copolymer PEG-*b*-PBLG, the absorptions at 698 cm^{-1} and 747 cm^{-1} attributed to the phenyl protection group and the peak at 1734 cm^{-1} disappeared, and a new strong peak at 3502 cm^{-1} assigned to N−H stretch vibration of PEI appeared in the spectrum of GGI, indicating that the aminolysis reaction took place and PEI successfully grafted to the PLG block. These FTIR results were consistent with the expected structures of copolymer GGI.

The structure of the intermediate prepolymer PEG-*b*-PBLG and the graft copolymer GGI were also confirmed by ^{1}H NMR spectra (Figure 2). The peak **a** at 3.65 ppm (-CH_2CH_2-) was attributed to the protons of the PEG block Figure 2A. The characteristic absorption of PEG block was observed also in Figure 2B,D,E, indicating the existence of a PEG block in PEG-*b*-PBLG as well as in the copolymer GGI. For PEG-*b*-PBLG (Figure 2B), the peak **b** at 3.91 ppm (-CH-) and the peaks **c**,**d** at 1.89−2.21 ppm (-CH_2CH_2-) were assigned to the PBLG block. Furthermore, the peak **f** at 7.24 ppm (-C_6H_5) and the peak **e** at 5.02 ppm (-CH_2Ph) were attributed to the phenyl group of the protecting group of PBLG block. The degree of polymerization of PBLG (DP_{PBLG}) in the diblock copolymer PEG-*b*-PBLG was obtained from the integral ratio of -CH_2CH_2- (3.54 ppm, **a**) to -CH_2Ph (5.02 ppm **e**), as shown in the following formula, $DP_{PBLG} = (5000)/(44) \times (2e)/(a)$. Feed composition and molecular characteristics of diblock copolymer PEG-*b*-PBLG were summarized in Table 1. In the case of triblock copolymer GGI 30 (Figure 2D) and GGI 40 (Figure 2E), the peak shifts of them were similar, while the peak areas were inconsistent. The characteristic resonances **g**,**h** (2.12−2.96 ppm, -CH_2CH_2NH-) assigned to the PEI block were observed and the peaks at 7.24 ppm and 5.02 ppm attributed to the phenyl group were absent compared to the ^{1}H NMR spectra of PEG-*b*-PBLG, demonstrating that the protecting groups (phenyl groups) were removed by aminolysis with PEI 423. The results were in line with those described above obtained in the FTIR measurements and suggested the successful synthesis of diblock intermediate copolymer PEG-*b*-PBLG and the triblock graft copolymer GGI.

From the ^{1}H NMR spectra, the PLG length and PEI graft density of the GGI copolymer were calculated from the integral values of the characteristic peaks of PEG (-CH_2CH_2-, **a**, ∼3.65 ppm), PLG (-COCHNH-, **b**, ∼3.91 ppm), and PEI (-CH_2CH_2NH-, **g**−**h**, 2.12−2.96 ppm), using the known molecular weights of PEG and PEI. The detailed compositions and the molecular weights of GGI are summarized in Table 2.

Gel permeation chromatography (GPC) was performed to verify the successful synthesis of graft triblock copolymer GGI. GGI 30 and GGI 40, after purification, both exhibited unimodal molecular weight distributions in the GPC traces, indicating no or negligible homopolymer residue in the graft copolymer product, as illustrated in Figure 3. The molecular weights of GGI 30 and GGI 40 analyzed by GPC (Table 2) were close to those calculated from ^{1}H NMR spectra.

Figure 4 represented the ^{13}C NMR spectra of PEG-*b*-PLG-*g*-PEIs (GGI 40), the corresponding chemical shifts were as follows: the signals of PEG block, 57.4 ppm (CH_3O-, **g**), 68.4 ppm (-OCH_2CH_2O-, **f**); the signals of PLG block, 28.2 ppm (β-C, **a**), 32.3 ppm (γ-C, **b**), 56.5 ppm (α-C, **d**), 175.1 ppm

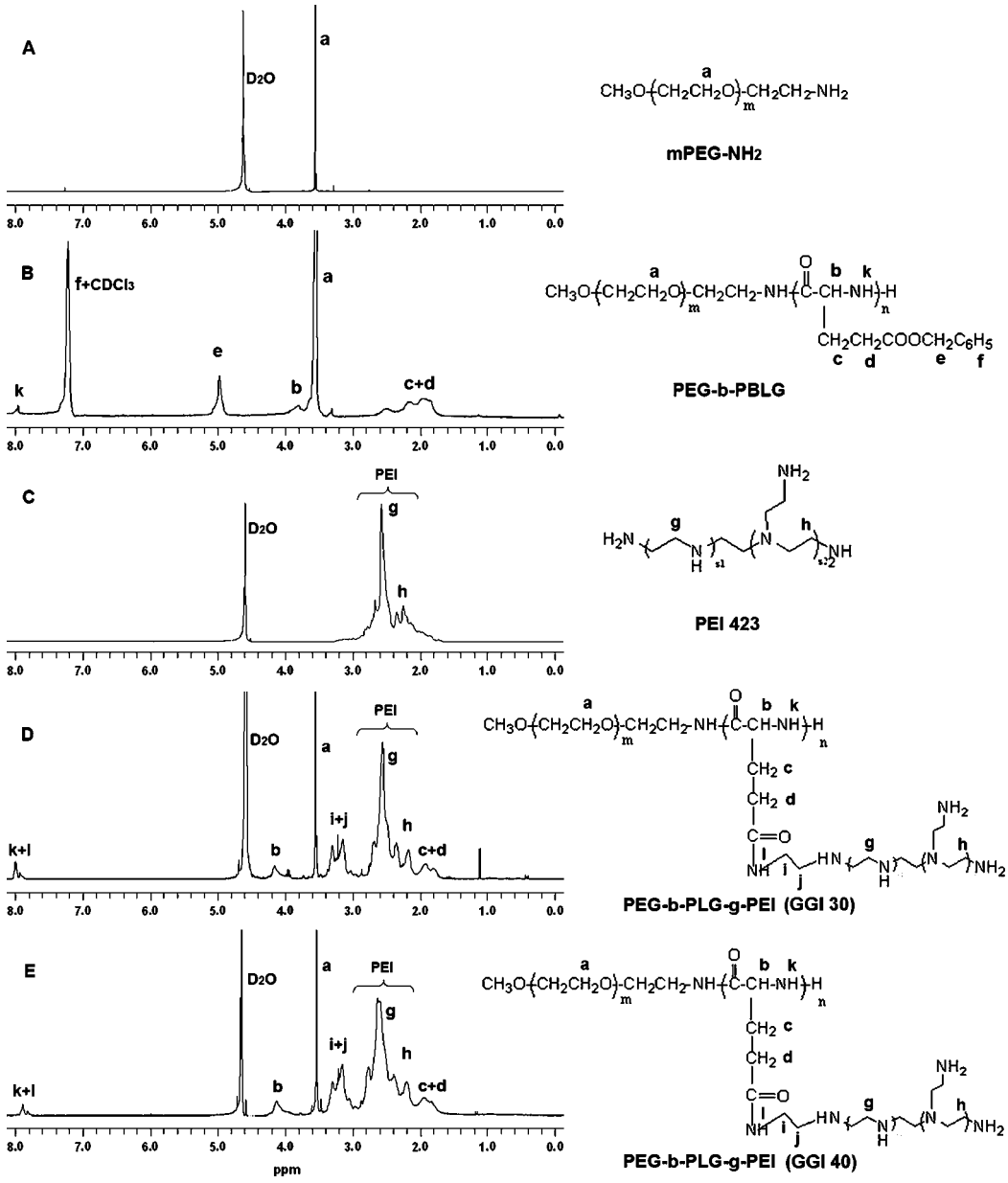

Figure 2. The ^{1}H NMR spectra (500 MHZ) and their assignments of (A) mPEG-NH_2 (D_2O), (B) PEG-*b*-PBLG ($CDCl_3$), (C) PEI 423 (D_2O), (D) GGI 30 (D_2O), and (E) GGI 40 (D_2O).

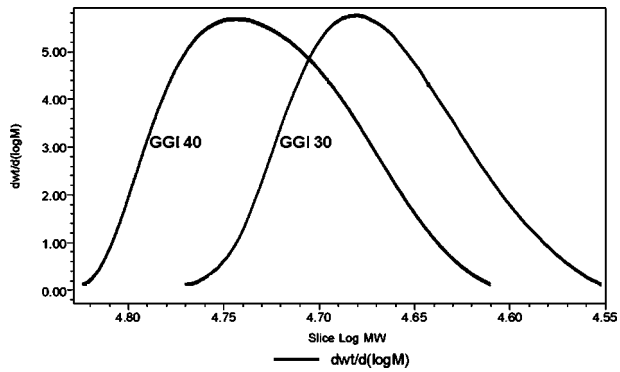

Figure 3. GPC traces of GGI 30 and GGI 40.

(-CONH-, **e**). The singals of PEI block were well-separated in the typical area between 35 and 58 ppm (-CH_2CH_2NH-, **c**); the seven signals of the corresponding methylene groups were assigned as indicated in Figure 4.

Since both intermediate copolymer PBLGs and final product GGIs were polypeptide derivatives, circular dichroism (CD) spectroscopy was employed to checked the secondary structure of the PBLG and GGI. First, we took dichloromethane ($CHCl_2$) as the solvent of the copolymers. As shown in Figure 5A, a strong positive $(\pi-\pi^*)_{perpendicular}$ band at ca. 195 nm, a negative $(\pi-\pi^*)_{parallel}$ band at ca. 208 nm, and a negative $n-\pi^*$ band at ca. 222 nm were observed in the spectra of all the four copolymers including PBLGs and GGIs, which suggested the α-helix-like structures of the copolymers. The results indicated that introduction of PEG block and PEI blocks as side chains of the polymer did not affect the α-helix conformation of the polymer. It is reported that the intensity of the peak (polarimetry strength) in the CD spectra is directly proportional to the content of the peptide bond of the polypeptide (*24, 25*), so we judged the content of PLG block of the polymer according to CD spectra. From the CD spectra (Figure 5A), GE 2 showed the highest PLG content, followed by GE 1, GGI 40, and GGI 30, which was in accordance with the results calculated from ^{1}H NMR. In addition, we took 10 mM NaCl (pH 7.4) as the solvent

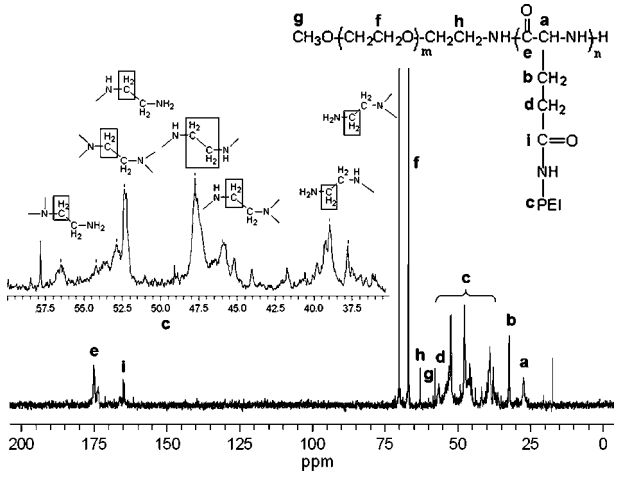

Figure 4. ^{13}C NMR spectrum of GGI 40 dissolved in D_2O.

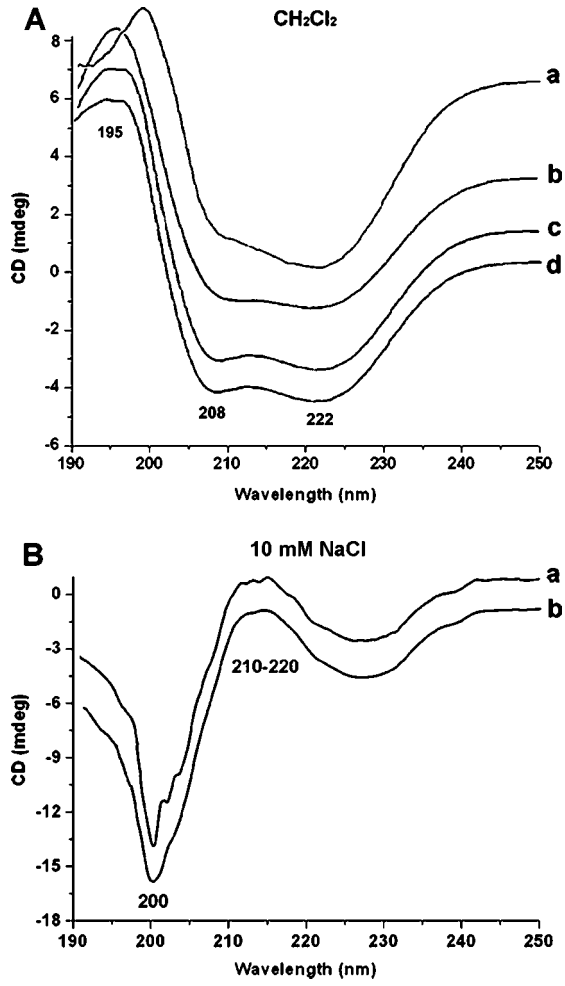

Figure 5. (A) Circular dichroism spectra of copolymers in $CHCl_2$ (a) GGI 30, (b) GGI 40, (c) GE 1, and (d) GE 2. (B) CD spectra of copolymers in 10 mM NaCl (a) GGI 30 and (b) GGI. CD spectra were collected at an ambient temperature.

of the copolymers to check the secondary structure of the copolymer. As PBLG copolymer was water-insoluble, we failed to take the CD spectra of GE 1 and GE 2 for comparison. As shown in Figure 5B, CD spectra of GGI 30 and GGI 40 showed a typical inflected curve with a gradual positive maximum at ca. 210−220 nm and a negative minimum at ca. 200 nm, which was characteristic of a random coil conformation. Due to electrostatic repulsion between the side groups, it is very difficult

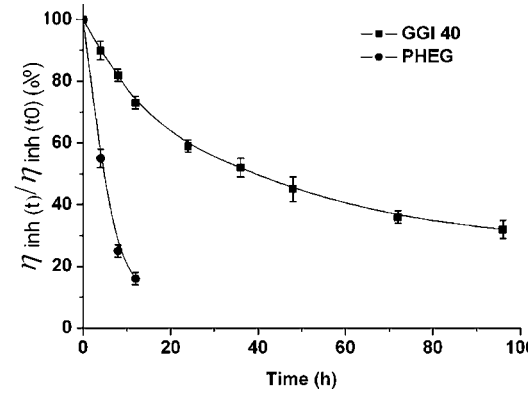

Figure 6. Relative reduction of the η_{inh} of copolymer GGI 40 in function of time after treatment with papain. PHEG was used as control. (n = 3, error bars represented standard deviation.)

to form helical or extended structures in a charged state (*24*). GGI 30 and GGI 40 formed random coil-like structure, not an α-helix conformation, in pH 7.4 solution due to the high charge repulsion between the ionized PEI side chains. From the CD spectra of GGIs, we further confirmed that PEI successfully grafted to the main backbone of PLG as the side chains.

Degradation Profile of GGI. Degradation of the gene carrier is crucial for safe and efficient gene delivery in vivo. The appropriate degradation of the polymer enables reduction of cytotoxicity due to small molecular weights by degradation in vivo and easy elimination by excretion pathway (*10*). The aim of our study is synthesis of biodegradable polymers for gene delivery. Thus, the degradation profile of GGI was investigated in a medium containing papain. Poly(hydroxyethyl L-glutamine) (PHEG) (Mn 52 kDa) was used as the control in the experiment, to study the effection of grafting PEI to the degradation characteristic of polymer. As shown in Figure 6, the result showed that copolymer GGI 40 was biodegradable. There was a rapid initial degradation in the first 24 h, followed by a gradual degradation thereafter. After 96 h, GGI 40 had retained 32% of its original η_{inh}. The control polymer PHEG, degraded much faster, retained only 21% of its initial η_{inh} after 12 h. There seems to be a relationship between the amount of positive charges of the polymer chain and the degradation speed (*23*). The side chains of GGI were PEI 423, which would be protonated in PBS (pH 7.4), while the side chains of PHEG, hydroxyethyl, bore no charges. In addition, the molecular weight and the size of the side chains of GGI were larger than that of PHEG. Probably, the effect of steric hindrance and electrostatic interaction induced by PEI hindered the enzyme papain approach to the degradation reaction site. Thus, grafting PEI to the side chain would lower the speed of degradation comparing to PHEG.

Characterization of GGI/pDNA Complexes. One prerequisite as a polymeric gene carrier is DNA condensation (*20*). Gel retardation assay was performed to investigate whether the synthesized GGIs were able to condense DNA, and the data were compared to that obtained using LMW PEI 423 and HMW PEI 25k. As shown in Figure 7A, PEI 423 used for the preparation of GGI could not retard the migration of pDNA even at an N/P ratio of 100, indicating that pure PEI 423 was incapable of forming complexes with pDNA. These results were consistent with the reported result that only PEI with a molecular weight higher than 2 kDa could form stable complexes with DNA (*12, 26*). In the case of PEI 25k (Figure 7A), an N/P ratio of 2 was sufficient to completely inhibit pDNA mobility. A drop in the total ethidium bromide (EtBr) staining at an N/P ratio of 3 and higher was observed, probably due to exclusion of the dye by plasmid condensation. Figure 7A demonstrated that both

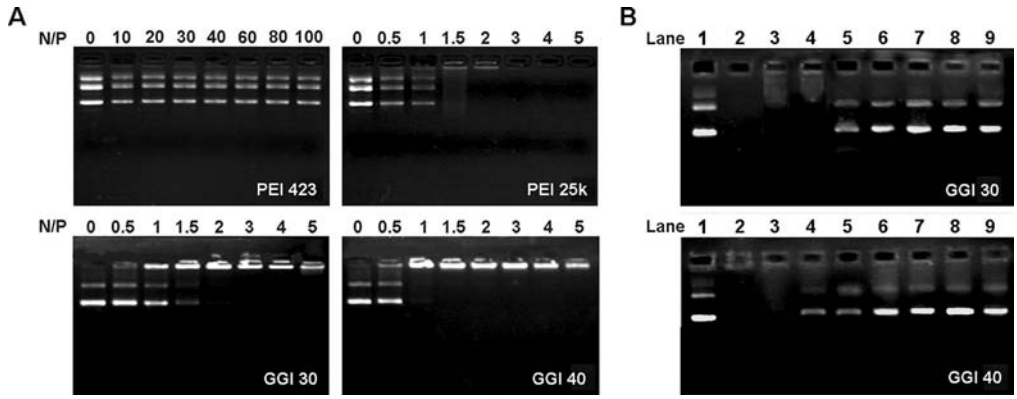

Figure 7. (A) Gel retardation assay. Agarose gel electrophoresis of GGI/DNA (pEGFP-C1) complexes at various N/P ratios. LMW PEI 423 and HMW PEI 25k were used as a control. (B) DNase I protection assay. DNA was released by adding 1% SDS to the GGI/DNA complexes at various N/P ratios after treatment with DNase I. Lane 1: naked plasmid DNA (pEGFP-C1), as negative control. Lane 2: naked DNA treated with DNase I as positive control. Lanes 3−9: GGI/DNA complexes at N/P ratio of 0.1, 1, 1.5, 2, 3, 5, 10.

GGI 30 and GGI 40 had a great capacity to condense DNA effectively where DNA was completely retarded at N/P ratio of 2.0 and 1.0, respectively, showing the similar DNA condensation capability to HMW PEI 25k. However, GGI/pDNA complexes did not lead to EtBr exclusion as PEI 25k did, even at high N/P ratio, suggesting that GGI did not condense DNA as tightly as PEI 25k did. It must be noted that the DNA compaction capabilities of GGIs were significantly enhanced in comparison to PEI 423, indicating that the modification of PEI of grafting LMW PEIs (PEI 423) to the main chain of PEG-PLG to form a LMW PEI combined copolymer GGI with suitable HMW could ameliorate the DNA condensation ability of the polymer. Probably, the extended conformation of GGI and the high molecular weight PEI block of GGI contributed to the good DNA condensation capability. In addition, GGI 40 showed an increasing pDNA condensation capability compared to GGI 30, possibly due to the increasing amino density upon increasing the PLG length as well as the increased PEI molecular weight of the polymer.

For a sufficient gene delivery system, the cationic vectors must be able to protect DNA from degradation by cellular nucleases in serum and extracellular matrix (*27*). In this study, DNase I protection assay was performed to confirm that GGI protected DNA from DNase I degradation. As shown in Figure 7B, after incubation with excess DNase I, both GGI 30 and GGI 40 effectively protected DNA from degradation by DNase I at N/P ratio of 2 and higher, while naked DNA was completely degraded by DNase I. The ability of GGI to protect DNA from enzymatic cleavage was close to that of PEI 25k, which could fully protect DNA from degradation by DNase I at N/P ratio of 1.8 (data not shown). That is to say, the conditions that GGIs bind DNA not as tightly as PEI 25k do not affect its DNA protection ability.

Figure 8A showed the particle sizes of GGI copolymer/DNA complexes prepared in 10 mM NaCl according to various N/P ratios, in comparison with PEI 423/DNA and PEI 25k/DNA complex. As shown in Figure 8A, LMW PEI 423 formed loose polyplexes with a size of approximately 600 nm, from N/P 1:1 to N/P 30:1. The trend of the sizes was in accordance with the results of gel retardation experiments, indicating that PEI 423 could not compact pDNA efficiently. In contrast, two synthesized LMW PEIs combining copolymer GGIs (GGI 30 and GGI 40) could effectively compact pDNA into small nanoparticles. Generally, the particle size decreased with an increase in N/P ratio until the N/P ratio was up to 10. The mean particle size of the complexes was in the range 102−138 nm and remained relatively constant over the range of 10:1 to 30:1 N/P ratios. As presented in Figure 8A, there was no remarkable difference in the diameters between GGI 30/DNA and GGI 40/DNA complexes at high N/P ratios, which were similar to those of complexes prepared with commercially available PEI 25k. However, at N/P ratio between 1 and 5, PEI 25k formed larger complexes with diameters of 320 nm compared with GGIs. This effect can be explained by instabilities of the PEI 25k/pDNA complexes and aggregate formation. In addition, we investigated the stability of the polyplexes in 10 mM NaCl (data shown in Supporting Information, Figure S1). It was found that the size of the GGI/pDNA polyplexes at N/P ratio of 20 remained constant and did not aggregate over a time period of 24 h. On the contrary, the size of PEI 25k/DNA complexes at N/P ratio of 20 changed from ∼200 nm to ∼800 nm, indicating that large aggregates were formed. Obviously, the presence of hydrophilic PEG block for GGI led to a successful colloidal stability of polyplexes even at low polymer concentration or high salt concentration. The great stability of the GGI/pDNA complex may be feasible for in vivo application (*12, 26*).

The formation of GGI/pDNA complexes (in 150 mM NaCl, pH 7.4) was further monitored by observation of the morphology examined with TEM. Both GGI 30 and GGI 40 formed well-defined spherical and compact complexes with plasmid DNA at a representative N/P ratio of 20 (Figure 8B). The micrographs clearly revealed that the sizes of the nanoparticles ranged 140−200 nm, which were suitable applications for endocytic cellular uptake (*28*). The results of the TEM experiments also could be confirmed by DLS measurements of the complexes. The corresponding size distributions of the complexes, measured by dynamic light scattering, were unimodal. The average particle size of GGI 30/pDNA complex was 190 ± 18 nm, and that of GGI 40/pDNA complex was 142 ± 11 nm (Figure 8B).

A positive surface charge of untargeted polyplexes is necessary for the attachment to anionic cell surface and endocytosis (*29*). To estimate the surface charge of the polymer/pDNA complexes, we measured the zeta potentials. The surface charge of copolymer polylexes was measured in 10 mM NaCl solutions, at N/P ratios of 1 to 30. As indicated in Figure 8C, even a large excess of LMW PEI 423 (N/P = 30) did not increase the zeta potential sufficiently, and the zeta potential was still negative. As expected, polyplexes of HMW PEI 25k with pDNA exhibited high zeta potential of 20 mV to 30 mV at the N/P ratio of 10 to 30. In the case of synthesized copolymers GGIs, GGI 30 and GGI 40 showed similar surface charge at various N/P ratios. Generally, at N/P ratio 1, zeta potentials of both GGI 30/pDNA and GGI 40/pDNA were negative, showing incomplete complexation. With increasing N/P ratio, zeta potentials of the GGI/pDNA complexes rapidly increased and reached plateaus about 15 mV at N/P ratios between 10 and 30. It must be noted that GGI/pDNA complexes showed significantly lower zeta potential values compared to PEI 25k/pDNA complexes ($p < 0.01$). This

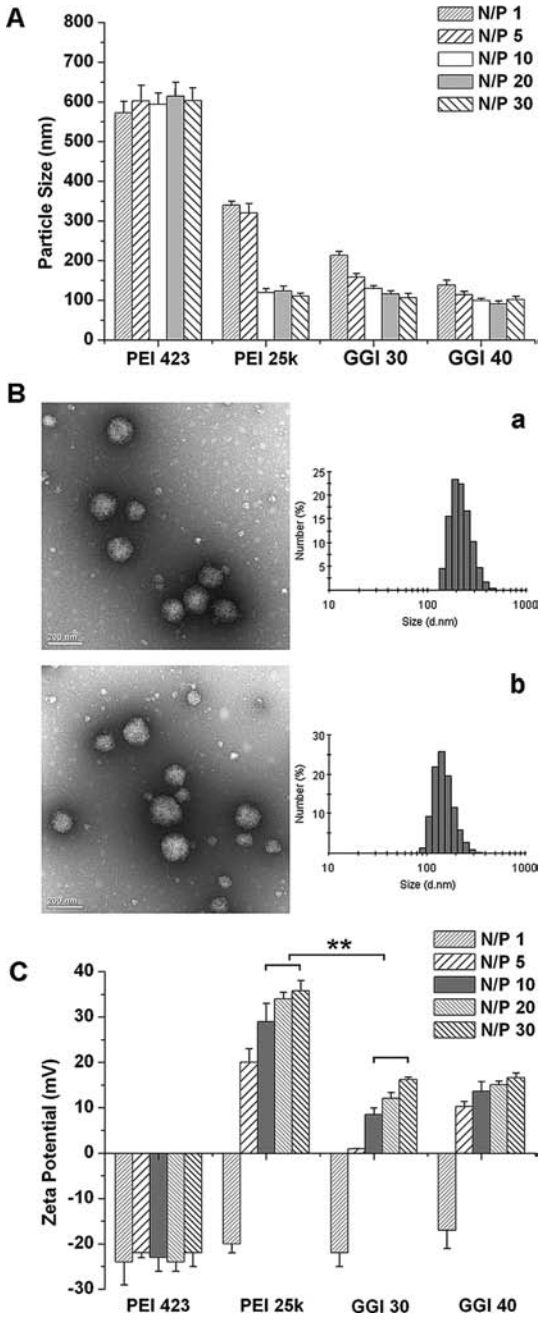

Figure 8. (A) Particle size of complexes formed with GGI copolymers and PEI homopolymers as determined by DLS at various N/P ratios in 10 mM NaCl. (B) TEM images of GGI/DNA complex at N/P ratio of 20 in 150 mM NaCl (scale bar = 200 nm) and the corresponding size distribution of the complexes detected by DLS. (a) GGI 30, (b) GGI 40. (C) Zeta potentials of complexes formed with GGI copolymers and PEI homopolymers as determined by DLS at various N/P ratio in 10 mM NaCl. Significant differences between copolymer and PEI 25k polyplexes are marked with an asterisk, $^{**}p < 0.01$.

could be explained by the structure of copolymer GGI. LMW PEIs combined with GGI did not condense DNA as tightly as PEI 25k did, and the charge shielding effect of PEG possibly led to the lower zeta potential of GGI, in comparison with PEI 25k. Since the positive surface charge of PEI polyplexes is related to cytotoxicity, we assumed that the moderate zeta potentials of GGI polyplexes might be a benefit for obtaining a better balance between cellular uptake and cytotoxicity.

Cytotoxicity of Copolymer GGI. To determine if the LMW PEI combined biodegradable copolymer GGI retained the low cytotoxicity of its starting material PEI 423, we investigated

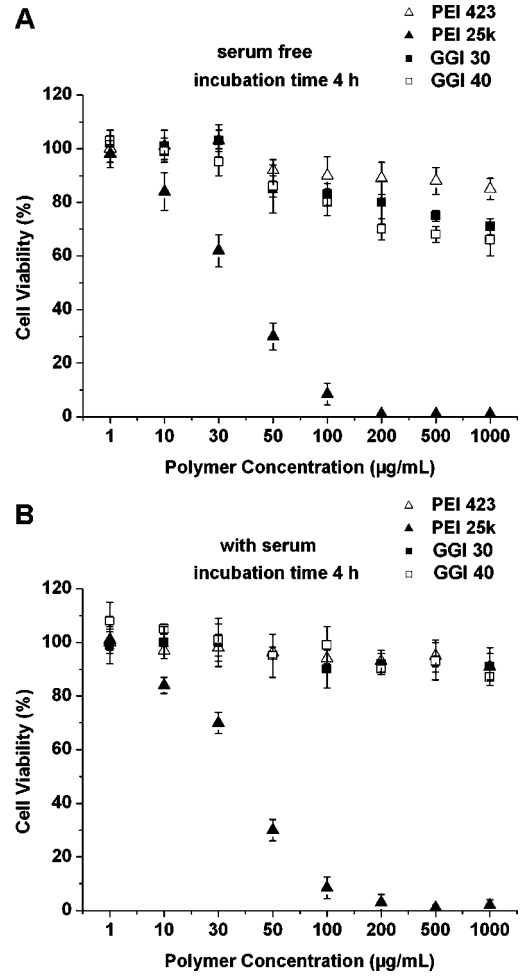

Figure 9. Cell viability of GGI copolymers and PEI homopolymers in the concentration range 1−1000 μg/mL in Hela cell line, determined by the MTT assay. (A) Cells were treated with polymers for 4 h in a serum-free medium. (B) Cells were treated with polymers for 4 h in a serum-containing medium. ($n = 4$, error bars represented standard deviation.)

the cytotoxicity of GGIs using a cell viability assay based on MTT. LMW PEI 423 and HMW PEI 25k were used as reference. Hela cells were exposed to various concentrations of polymers ranging from 1 μg/mL to 1000 μg/mL for 4 h, and cytotoxicity was assayed 48 h later. In agreement with the reported results (*7, 30*), LMW PEI 423 showed very low cytotoxicity. The cell viability was over 90% at the tested concentration (Figure 9A). The results showed that GGIs exhibited good cell viability below the concentration of 100 μg/mL (over 80%) and showed above 70% cell viability at concentration between 100 μg/mL and 1000 μg/mL. Our results also demonstrated that GGI 30 exhibited a slight reduction of cytotoxicity at high concentration compared with GGI 40, probably due to a shorter chain of the PLG block and lower amount of PEI grafted to the PLG block of GGI. On the contrary, the cell viability results showed that HMW PEI 25k, which is commonly used in gene delivery systems, exhibited significantly greater cytotoxicity than both GGI 30 and GGI 40 from the concentration of 10 μg/mL ($p < 0.01$). In addition, a very sharp drop in the number of viable cells was observed for PEI 25k with increasing concentration, while it was much more gradual for GGI. This fact indicated that the therapy window for GGIs was much wider than that of PEI 25k.

It should be noted that, in the presence of 10% serum, both GGI 30 and GGI 40 exhibited similar cell viability as LMW PEI 423, showing above 90% cell viability at the tested

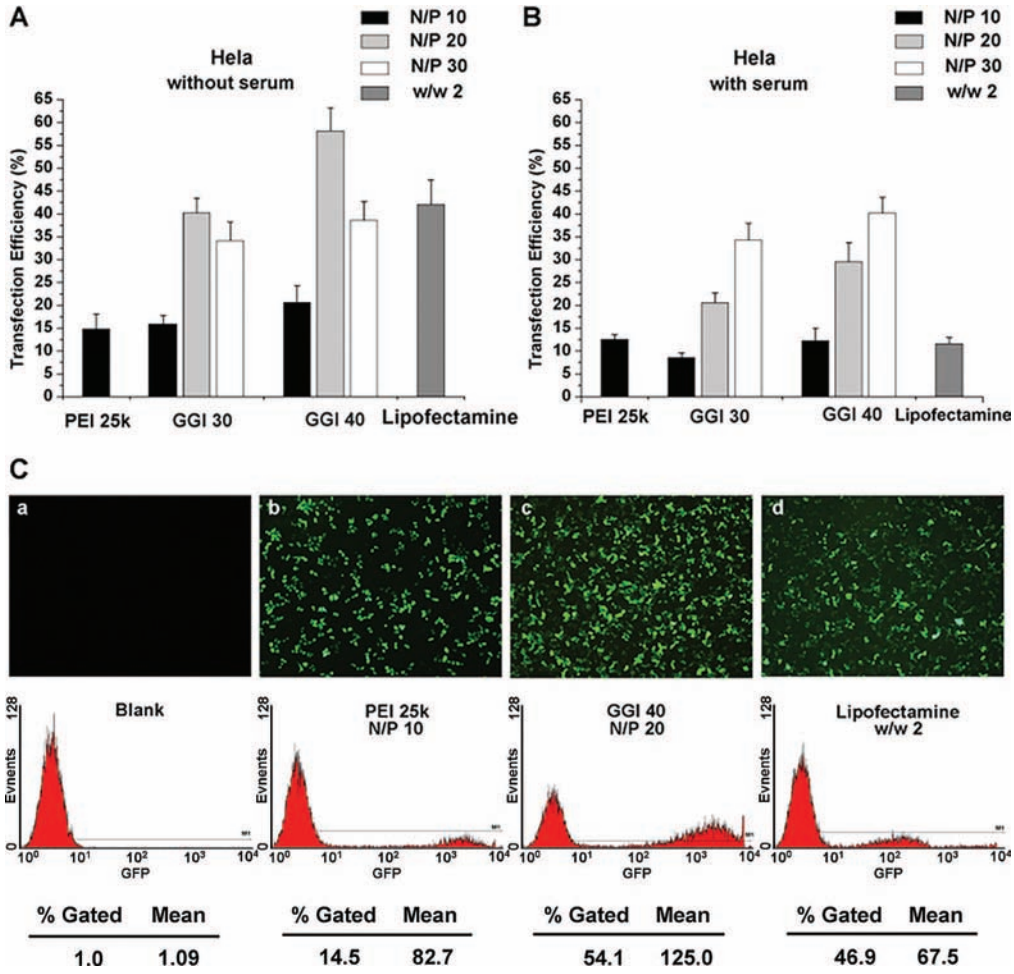

Figure 10. (A) In vitro gene transfection efficiency of the GGI/pEGFP-C1 complexes at various N/P ratios in serum-free medium in Hela cell line, in comparison with that of HMW PEI 25k (at its optimal N/P ratio of 10) and cationic lipid Lipofectamine 2000 (w/w 2). (B) In vitro gene transfection efficiency of the GGI/pEGFP-C1 complexes at various N/P ratios in serum-containing medium in Hela cell line, in comparison with that of PEI 25k and Lipofectamine 2000. ($n = 3$, error bars represented standard deviation.) (C) Fluorescence images (Row 1) and flow cytometry analyzed graphs of cell distribution expressing GFP (Row 2) of Hela cells transfected with (a) PBS (negative control), (b) PEI 25k/pEGFP-C1 (N/P 10), (c) GGI 40/pEGFP-C1 (N/P 20), (d) Lipofectamine 2000 (w/w 2) (magnification 200×).

concentration (Figure 9B). However, HMW PEI 25k still exhibited a remarkably higher cytotoxicity than those of GGI above the concentration of 10 μg/mL, although the serum was presence ($p < 0.01$).

Furthermore, GGIs, which are derived from poly(amino acid)s, are biodegradable copolymers confirmed by previous experiments. The copolymer GGIs may degrade in cells, producing a glutamine acid unit with LMW PEI and PEG. Thus, we investigated the cytotoxicity of the polymer degradation products. Copolymer GGI 30 and GGI 40 were incubated for 24 and 96 h at 37 °C in PBS with papain (the same procedure we used in the degradation assay). MTT was measured after the cell exposure to the lyophilized degraded polymer mixture. The results indicated that, at the observed concentration (1000 μg/mL and 2000 μg/mL), the degradation products exhibited no effect on cell viability (over 90%), suggesting that the degradation products of GGIs were essentially nontoxic (data shown in Supporting Information, Figure S2).

Therefore, the MTT results suggested that GGI retained the characteristics of LMW PEI in cytotoxicity, and the biocompatibility as well as the long-term safety of GGI were significantly improved in comparison to PEI 25k.

Transfection Efficiency in Vitro. The in vitro gene delivery efficiency of the LMW PEI combined copolymer GGI in Hela cells was evaluated using pEGFP-C1 as a marker gene, in the absence and presence of serum. The transfection efficiency of GGI 30 and GGI 40 were compared with HMW PEI 25k and commercially available cationic lipid Lipofectamine 2000.

The transfection efficiency of pEGFP-C1 in Hela was quantified using flow cytometry in terms of cell population expressing GFP. Figure 10A showed the percentage of the Hela cells expressing GFP at different N/P ratios using GGIs in the absence of serum. It revealed that, within the N/P ratios of 10, 20, and 30 we tested, both GGI 30/pEGFP-C1 and GGI 40/pEGFP-C1 polyplexes exhibited their maximum efficiency values at N/P ratio of 20. Up to 58% transfection was achieved by the GGI 40, which was statistically significantly higher than the 14% transfection obtained from the HMW PEI 25k ($p < 0.01$), at its optimal N/P ratio of 10. Also, the transfection efficiency of GGI 40 was very comparable to that of commercially available Lipofectamine (47%). No statistically significant differences existed between the data of GGI 40 at N/P ratio of 20−30 and the data of the Lipofectamine at its opitmal w/w ratio of 2/1.

Furthermore, in order to directly visualize the transfected cells expressing pEGFP, GFP expression in Hela cells was observed by an inverted fluorescent microscope. All the polymers were at their optimal transfection N/P ratio. In the microscopic images (Figure 10C), the cells transfected with GGI 40/pEGFP-C1 showed more bright green fluorescent spots than PEI 25k/pEGFP-C1. It appears that the amount of green cells transfected by GGI 40 and Lipofectamine 2000 were similar, but the

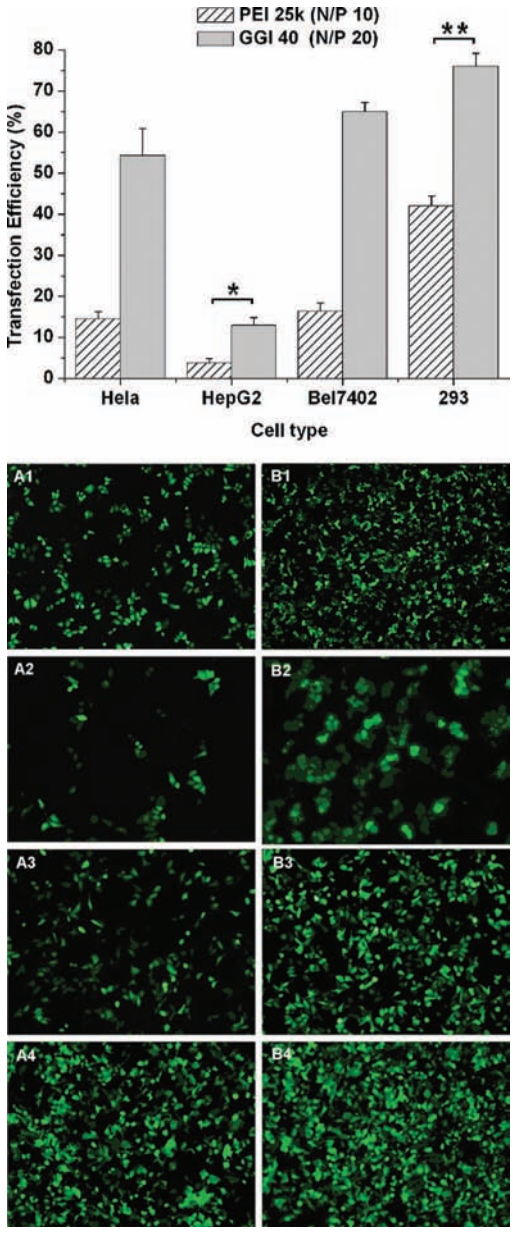

Figure 11. (A) Comparison of the in vitro gene transfection efficiency between GGI 40 and HMW PEI 25k at their optimal N/P ratios in Hela, HepG2, Bel 7402, and 293 cells. Significant differences between GGI and PEI 25k polyplexes are marked with an asterisk: $*p < 0.05$, $**p < 0.01$. ($n = 3$, error bars represented standard deviation.) (B) Comparison of the fluorescence images of (1) Hela, (2) HepG2, (3) Bel 7402, and (4) 293 cells transfected with (A) HMW PEI 25k at its optimal N/P ratio of 10 and (B) GGI 40 at its optimal N/P ratio of 20 (magnification 200×).

fluorescent spots of Lipofectamine 2000 were much dimmer than that of GGI 40, indicating that GGI 40 expressed more fluorescent proteins than those with Lipofectamine. The results were in accordance with the flow cytometry results, suggesting that LMW PEI combined copolymer GGI was more effective as a gene carrier, compared with HMW PEI 25k and Lipofectamine 2000.

In addition, we studied the effect of serum on the transfection efficiency of GGI/pDNA complexes. Since therapeutic gene transfection is in vivo, it is crucial to investigate the influence of serum on the transfection efficiency. As shown in Figure 10B, for GGI 30 and GGI 40 at N/P ratio of 10 and 20, the transfection efficiencies were both slightly decreased in the serum-supplemented medium. At N/P ratio of 30, no significant difference could be observed between the efficiencies in the presence and absence of serum. For PEI 25k and Lipofectamine 2000, however, the transfection efficiencies were decreased drastically with 10% FBS. These results implied that GGI might be more suitable for in vivo gene transfecion.

Since it was reported that the transfection efficiency of polyplexes might be dependent on cell lines (*17*, *31*), we further gave a direct comparison of the transfection efficiency of HMW PEI 25k and LMW PEIs combined copolymer GGI 40 at their optimal N/P ratio, in Hela, HepG2, Bel7402, and 293 cell lines. Both the results of flow cytometry (Figure 11A) and the image of the expression of GFP (Figure 11B) showed that, in four cell lines, the transfection efficiencies of GGI 40 were statistically significantly higher than PEI 25k. It also can be noticed that the transfection efficiencies of GGI 40 and PEI 25k were dependent on cell line. The sequential oreder was 293 > Bel7402 > Hela > HepG2.

CONCLUSION

In this study, we demonstrated that a novel degradable PEG-*b*-PLG-*g*-PEIs copolymer, a kind of combined LMW PEIs, was synthesized and evaluated as a new gene vector. The obtained polymers GGI 30 and GGI 40 showed degradability, a great ability to condense DNA and to protect pDNA against DNase I. The physicochemical properties, particle size, morphology, and zeta potential of GGI/pDNA polyplexes were suitable for gene delivery. The in vitro cell viability as well as gene transfection suggested that GGI had great potential as a gene carrier, especially GGI 40, which had significantly lower cytotoxicity and higher transfection efficiency, as compared to PEI 25k. In particular, the transfection efficiency of GGI was not markedly decreased in the presence of serum in comparison with PEI 25k and Lipofectamine 2000. Therefore, GGI can be a promising new nonviral gene delivery vector for future gene therapy applications, due to its degradability, low cytotoxicity, and high transfection efficiency.

ACKNOWLEDGMENT

The authors greatly acknowledge the financial support from the National Natural Science Foundation of the People's Republic of China (30570500).

Supporting Information Available: Figure S1. The aggregation tendency of GGI/DNA complexes prepared in 10 mM NaCl, in comparison with that of PEI 25k. Polyplexes were prepared at N/P ratio of 20. Figure S2. Cytotoxicity of GGI degradation products at the concentration of 1 mg/mL and 2 mg/mL. The GGI degradation products were prepared by inbubating GGI with papain for 24 and 96 h at 37 °C. This material is available free of charge via the Internet at http://pubs.acs.org.

LITERATURE CITED

(1) Varga, C. M., Tedford, N. C., Thomas, M., Klibanov, A. M., Griffith, L. G., and Lauffenburger, D. A. (2005) Quantitative comparison of polyethylenimine formulations and adenoviral vectors in terms of intracellular gene delivery processes. *Gene Ther. 12*, 1023–32.

(2) Mazda, O. (2002) Improvement of nonviral gene therapy by Epstein-Barr virus (EBV)-based plasmid vectors. *Curr. Gene Ther. 2*, 379–92.

(3) Douglas, K. L. (2008) Toward development of artificial viruses for gene therapy: a comparative evaluation of viral and nonviral transfection. Biotechnol. Prog.

(4) Park, T. G., Jeong, J. H., and Kim, S. W. (2006) Current status of polymeric gene delivery systems. *Adv. Drug Delivery Rev. 58*, 467–86.
(5) Demeneix, B., Behr, J., Boussif, O., Zanta, M. A., Abdallah, B., and Remy, J. (1998) Gene transfer with lipospermines and polyethylenimines. *Adv. Drug Delivery Rev. 30*, 85–95.
(6) Boussif, O., Lezoualc'h, F., Zanta, M. A., Mergny, M. D., Scherman, D., Demeneix, B., and Behr, J. P. (1995) A versatile vector for gene and oligonucleotide transfer into cells in culture and in vivo: polyethylenimine. *Proc. Natl. Acad. Sci. U.S.A. 92*, 7297–301.
(7) Godbey, W. T., Wu, K. K., and Mikos, A. G. (1999) Size matters: molecular weight affects the efficiency of poly(ethylenimine) as a gene delivery vehicle. *J. Biomed. Mater. Res. 45*, 268–75.
(8) Kunath, K., von Harpe, A., Fischer, D., Petersen, H., Bickel, U., Voigt, K., and Kissel, T. (2003) Low-molecular-weight polyethylenimine as a non-viral vector for DNA delivery: comparison of physicochemical properties, transfection efficiency and in vivo distribution with high-molecular-weight polyethylenimine. *J. Controlled Release 89*, 113–25.
(9) Peng, Q., Zhong, Z., and Zhuo, R. (2008) Disulfide cross-linked polyethylenimines (PEI) prepared via thiolation of low molecular weight PEI as highly efficient gene vectors. *Bioconjugate Chem. 19*, 499–506.
(10) Forrest, M. L., Koerber, J. T., and Pack, D. W. (2003) A degradable polyethylenimine derivative with low toxicity for highly efficient gene delivery. *Bioconjugate Chem. 14*, 934–40.
(11) Zhong, Z., Feijen, J., Lok, M. C., Hennink, W. E., Christensen, L. V., Yockman, J. W., Kim, Y. H., and Kim, S. W. (2005) Low molecular weight linear polyethylenimine-*b*-poly(ethylene glycol)-*b*-polyethylenimine triblock copolymers: synthesis, characterization, and in vitro gene transfer properties. *Biomacromolecules 6*, 3440–8.
(12) Kim, Y. H., Park, J. H., Lee, M., Kim, Y. H., Park, T. G., and Kim, S. W. (2005) Polyethylenimine with acid-labile linkages as a biodegradable gene carrier. *J. Controlled Release 103*, 209–19.
(13) Petersen, H., Merdan, T., Kunath, K., Fischer, D., and Kissel, T. (2002) Poly(ethylenimine-*co*-L-lactamide-*co*-succinamide): a biodegradable polyethylenimine derivative with an advantageous pH-dependent hydrolytic degradation for gene delivery. *Bioconjugate Chem. 13*, 812–21.
(14) Gosselin, M. A., Guo, W., and Lee, R. J. (2001) Efficient gene transfer using reversibly cross-linked low molecular weight polyethylenimine. *Bioconjugate Chem. 12*, 989–94.
(15) Wong, K., Sun, G., Zhang, X., Dai, H., Liu, Y., He, C., and Leong, K. W. (2006) PEI-*g*-chitosan, a novel gene delivery system with transfection efficiency comparable to polyethylenimine in vitro and after liver administration in vivo. *Bioconjugate Chem. 17*, 152–8.
(16) Tang, G. P., Guo, H. Y., Alexis, F., Wang, X., Zeng, S., Lim, T. M., Ding, J., Yang, Y. Y., and Wang, S. (2006) Low molecular weight polyethylenimines linked by beta-cyclodextrin for gene transfer into the nervous system. *J. Gene Med. 8*, 736–44.
(17) Jiang, H. L., Kim, Y. K., Arote, R., Nah, J. W., Cho, M. H., Choi, Y. J., Akaike, T., and Cho, C. S. (2007) Chitosan-graft-polyethylenimine as a gene carrier. *J. Controlled Release 117*, 273–80.
(18) Anderson, J. M. (1985) In vitro and in vivo studies of drug-releasing poly(amino acids). *Ann. N.Y. Acad. Sci. 446*, 67–75.
(19) Kunath, K., von Harpe, A., Petersen, H., Fischer, D., Voigt, K., Kissel, T., and Bickel, U. (2002) The structure of PEG-modified poly(ethylene imines) influences biodistribution and pharmacokinetics of their complexes with NF-κB decoy in mice. *Pharm. Res. 19*, 810–7.
(20) Neu, M., Fischer, D., and Kissel, T. (2005) Recent advances in rational gene transfer vector design based on poly(ethylene imine) and its derivatives. *J. Gene Med. 7*, 992–1009.
(21) Pan, S. R., Wang, Q. M., and Yi, W. (2007) Preparation of hydrophilic polyhydroxyalkyl glutamine crosslinked films and its biodegradability. *J. Biomater. Appl. 22*, 181–92.
(22) Pytela, J., Jakes, J., and Rypacek, F. (1994) A study of enzymic degradation of a macromolecular substrate, poly[N5-(2-hydroxyethyl)-L-glutamine], by gel permeation chromatography and kinetic modelling. *Int. J. Biol. Macromol. 16*, 15–20.
(23) Dekie, L., Toncheva, V., Dubruel, P., Schacht, E. H., Barrett, L., and Seymour, L. W. (2000) Poly-L-glutamic acid derivatives as vectors for gene therapy. *J. Controlled Release 65*, 187–202.
(24) Zhou, J., Wang, B., Tong, W., Maltseva, E., Zhang, G., Krastev, R., Gao, C., Mohwald, H., and Shen, J. (2008) Influence of assembling pH on the stability of poly(L-glutamic acid) and poly(L-lysine) multilayers against urea treatment. *Colloids Surf., B: Biointerfaces 62*, 250–7.
(25) Bruch, M. D., and Gierasch, L. M. (1990) Comparison of helix stability in wild-type and mutant LamB signal sequences. *J. Biol. Chem. 265*, 3851–8.
(26) Petersen, H., Kunath, K., Martin, A. L., Stolnik, S., Roberts, C. J., Davies, M. C., and Kissel, T. (2002) Star-shaped poly(ethylene glycol)-block-polyethylenimine copolymers enhance DNA condensation of low molecular weight polyethylenimines. *Biomacromolecules 3*, 926–36.
(27) Zhu, J., Tang, A., Law, L. P., Feng, M., Ho, K. M., Lee, D. K., Harris, F. W., and Li, P. (2005) Amphiphilic core-shell nanoparticles with poly(ethylenimine) shells as potential gene delivery carriers. *Bioconjugate Chem. 16*, 139–46.
(28) Tian, H. Y., Deng, C., Lin, H., Sun, J., Deng, M., Chen, X., and Jing, X. (2005) Biodegradable cationic PEG-PEI-PBLG hyperbranched block copolymer: synthesis and micelle characterization. *Biomaterials 26*, 4209–17.
(29) Je, J. Y., Cho, Y. S., and Kim, S. K. (2006) Characterization of (aminoethyl)chitin/DNA nanoparticle for gene delivery. *Biomacromolecules 7*, 3448–51.
(30) Sun, Y. X., Xiao, W., Cheng, S. X., Zhang, X. Z., and Zhuo, R. X. (2008) Synthesis of (Dex-HMDI)-g-PEIs as effective and low cytotoxic nonviral gene vectors. *J. Controlled Release 128*, 171–8.
(31) Arote, R., Kim, T. H., Kim, Y. K., Hwang, S. K., Jiang, H. L., Song, H. H., Nah, J. W., Cho, M. H., and Cho, C. S. (2007) A biodegradable poly(ester amine) based on polycaprolactone and polyethylenimine as a gene carrier. *Biomaterials 28*, 735–44.

BC800428Y

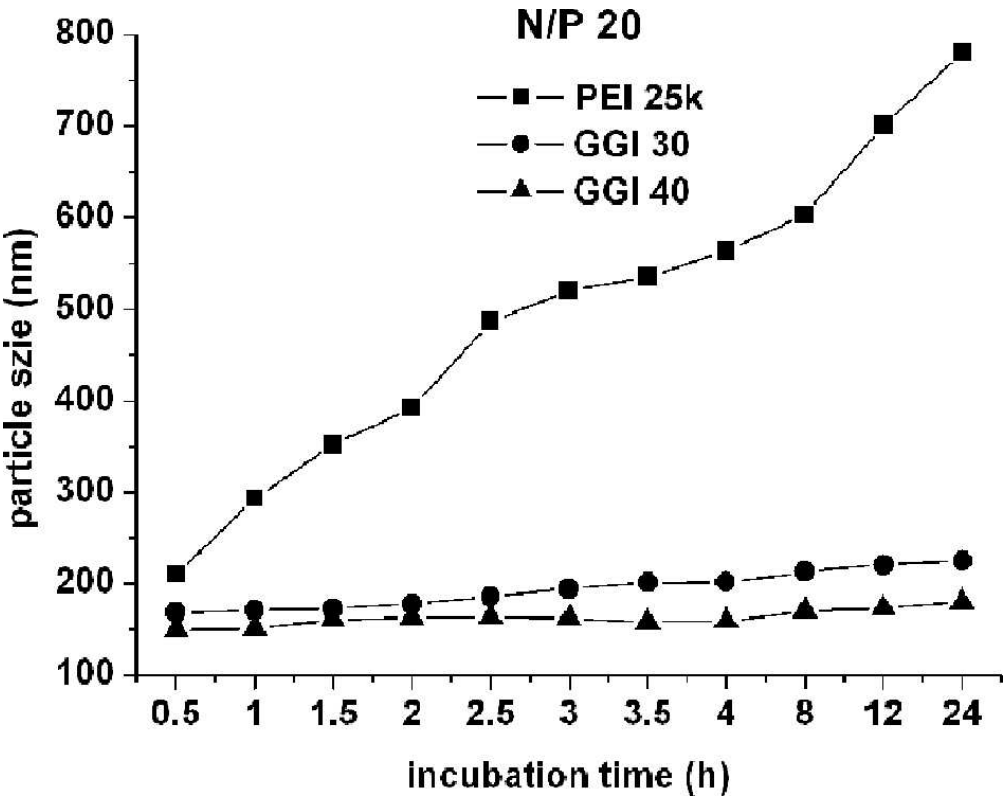

80x62mm (300 x 300 DPI)

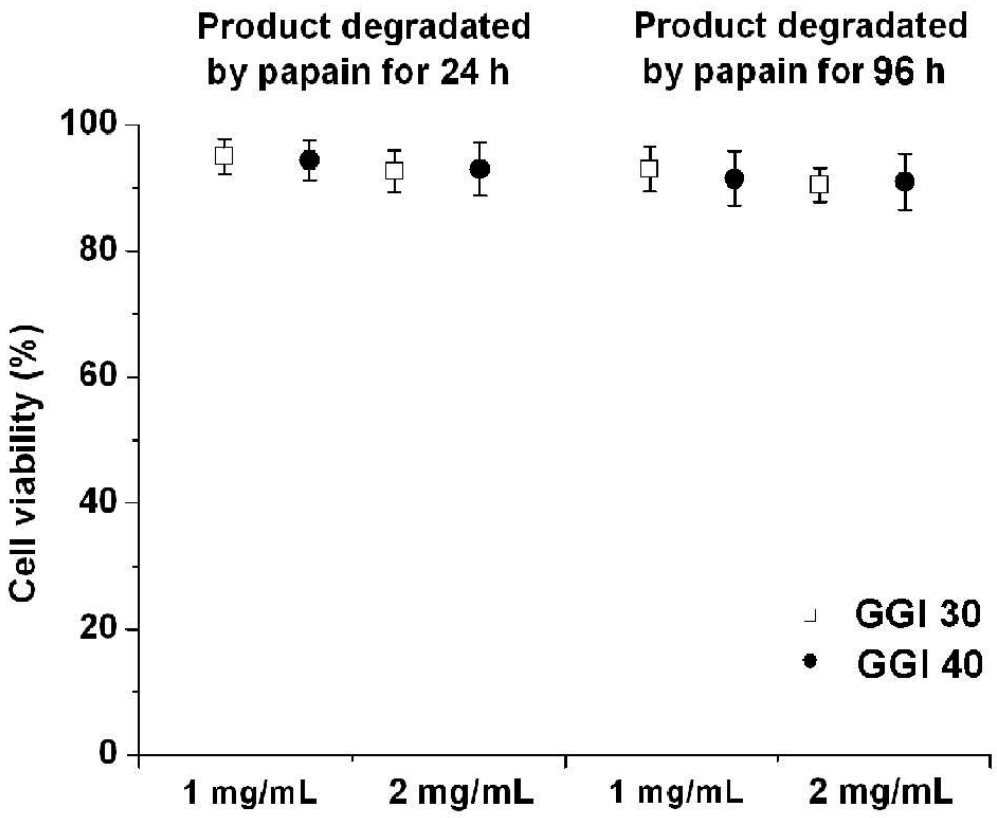

80x66mm (300 x 300 DPI)

Bioconjugate Chemistry 20th Anniversary

Subscriber access provided by SHEMYAKIN-OVCHINNIKOV INST

Article

Design and Synthesis of Biomimetic Hydrogel Scaffolds with Controlled Organization of Cyclic RGD Peptides

Junmin Zhu, Chad Tang, Kandice Kottke-Marchant, and Roger E. Marchant

Bioconjugate Chem., **2009**, 20 (2), 333-339• DOI: 10.1021/bc800441v • Publication Date (Web): 03 February 2009

Downloaded from http://pubs.acs.org on May 15, 2009

More About This Article

Additional resources and features associated with this article are available within the HTML version:

- Supporting Information
- Access to high resolution figures
- Links to articles and content related to this article
- Copyright permission to reproduce figures and/or text from this article

View the Full Text HTML

ACS Publications
High quality. High impact.

Bioconjugate Chemistry is published by the American Chemical Society. 1155 Sixteenth Street N.W., Washington, DC 20036

Design and Synthesis of Biomimetic Hydrogel Scaffolds with Controlled Organization of Cyclic RGD Peptides

Junmin Zhu,* Chad Tang, Kandice Kottke-Marchant, and Roger E. Marchant*

Department of Biomedical Engineering, Case Western Reserve University, 10900 Euclid Avenue, Cleveland, Ohio 44106, and Department of Clinical Pathology, Cleveland Clinic Foundation, 9500 Euclid Avenue, Cleveland, Ohio 44195. Received October 14, 2008; Revised Manuscript Received December 15, 2008

We report on the rational design and synthesis of a new type of bioactive poly(ethylene glycol) diacrylate (PEGDA) macromers, cyclic Arg-Gly-Asp (cRGD)-PEGDA, to mimic the cell-adhesive properties of extracellular matrix (ECM), aiming to create biomimetic scaffolds with controlled spatial organization of ligands and enhanced cell binding affinity for tissue engineering. To attach the cRGD peptide in the middle of PEGDA chain, a tailed cRGD peptide, c[RGDfE(SSSKK-NH_2)] (**1**), was synthesized with c(RGDfE) linked to a tail of SSSKK. The tail consists of a spacer with three serine residues and a linker with two lysine residues for conjugating with acryloyl-PEG-NHS (**5**) to create cRGD-PEGDA (**6**). cRGD-PEGDA possesses good photopolymerization ability to fabricate hydrogel scaffolds under UV radiation. Surface morphology and composition analysis demonstrates that cRGD-PEGDA hydrogels were well-constructed with porous three-dimensional (3D) structures and uniform distribution of cRGD ligands. Our results show that cRGD-PEGDA hydrogels facilitate endothelial cell (EC) adhesion and spreading on the hydrogel surfaces and exhibit significantly higher EC population in comparison with linear RGD-modified hydrogels at low peptide incorporation. Since ligand presentation in biomimetic scaffolds plays an important role in controlling cell behavior, cRGD-PEGDA has great advantages of controlling hydrogel properties and ligand spatial organization in the resulting scaffolds. Furthermore, cRGD-PEGDA is an attractive candidate for the future development of tissue engineering scaffolds with optimum cell adhesive strength and ligand density.

INTRODUCTION

The shortage of available organ donors has driven the growth and expansion of the field of tissue engineering as a promising alternative to organ transplantation (*1*−*6*). Scaffolds play crucial roles in tissue engineering including providing support and space for cells, encouraging cell adhesion and growth, and guiding cell function (*7*−*15*). Hydrogels are excellent scaffolding materials for repairing and regenerating a variety of tissues, such as cartilage, bone, and vasculature (*16*−*22*). They are attractive because they can provide a highly swollen three-dimensional (3D) environment similar to soft tissues and allow diffusion of nutrients and cellular waste through the elastic network. Synthetic poly(ethylene glycol) (PEG)-based hydrogels have advantages over natural hydrogels, such as the ability of photopolymerization into any shape, injectable capacity for tissue repair, and adjustable mechanical properties to fit various applications (*23*). However, most synthetic hydrogels typically exhibit minimal or no intrinsic biological activity (*16, 17*), and do not provide an ideal environment for culturing anchorage-dependent cells, such as endothelial cells (ECs) and smooth muscle cells (SMCs). To facilitate cell adhesion, small peptides derived from extracellular matrix (ECM) proteins have been important targets for the covalent coupling type of biospecific modification (*24*−*30*). For example, Arg-Gly-Asp (RGD)-modified PEG monoacrylate was copolymerized with PEG diacrylate (PEGDA) to create cell-adhesive PEG hydrogels (*31*−*33*), but the extent of incorporation of RGD-modified PEG monoacrylate into PEGDA hydrogels is limited because increasing incorporation of monoacrylated monomers affects the mechanical properties and the swelling ratio of the resultant hydrogels (*34*−*36*).

To address these limitations, we recently reported on a linear RGD-modified PEGDA macromer, RGD-PEGDA with a GRGD-SP peptide attached in the middle of PEG chain, which stimulates cell adhesion and good control over the hydrogel mechanical properties (*37*). However, a further consideration is that the RGD sequence is exposed at the tip of a loop in the cell-binding domain of fibronectin, which presents the ligand with a spatial constraint that results in increased specificity for cell binding (*38, 39*). It is a challenge to incorporate cyclic RGD (cRGD) peptides into PEGDA hydrogels with controlled spatial organization to mimic the native RGD loop structure. Previous studies have demonstrated that cRGD peptides have the advantage of increasing the specificity to integrin $\alpha_v\beta_3$ and enhance biological activity up to 240 times, in comparison with linear analogues (*40*−*43*). Research in our laboratory has shown that cyclo(Arg-Gly-Asp-D-Phe-Lys) [c(RGDfK)] and cyclo(Arg-Gly-Asp-D-Phe-Glu) [c(RGDfE)] more efficiently compete with fibronectin for specific binding to integrin $\alpha_v\beta_3$ on human pulmonary artery ECs, compared with the linear GRGDSP peptide (*44*). Therefore, we hypothesize that the incorporation of cRGD peptides into the PEGDA hydrogels will better mimic the native fibronectin cell-binding domain and benefit the cell specific adhesion.

Here, we report on the design and synthesis of a new type of bioactive PEGDA macromers, cRGD-PEGDA (**6**), to mimic the cell-adhesive properties of ECM, aiming to create biomimetic scaffolds with controlled spatial organization and enhanced cell binding affinity for tissue engineering. To attach the cRGD peptide in the middle of PEGDA chain, a tailed cRGD peptide, c[RGDfE(SSSKK-NH_2)] (**1**), was synthesized with c(RGDfE) linked to a tail of SSSKK, which consists of a spacer with three serine residues, and a linker with two lysine residues for

* Corresponding author. R. E. Marchant, Tel: 216-368-3005, Fax: 216-368-4969, E-mail: roger.marchant@case.edu. J. Zhu, Tel: 216-368-0270, Fax: 216-368-4969, E-mail: junmin.zhu@case.edu.

10.1021/bc800441v CCC: $40.75 © 2009 American Chemical Society
Published on Web 02/03/2009

conjugating with acryloyl-PEG-NHS (**5**) to create cRGD-PEGDA (**6**). Since ligand presentation in biomimetc scaffolds plays an important role in controlling cell behaviors, cRGD-PEGDA is an attractive candidate for the development of well-defined tissue engineering scaffolds with spatial control of ligand organization and optimization of adhesive strength through controlling ligand density.

EXPERIMENTAL SECTION

Materials. 9-Fluoromethoxycarbonyl (Fmoc)-protected amino acids, *O*-(benzotriazol-1-yl)-*N*,*N*,*N*′,*N*′-tetramethyluronium hexafluorophosphate (HBTU), and 1-hydroxybenzotrilazole (HOBt) were purchased from AnaSpec (San Jose, CA). Amino acids had various side chain protect groups, such as *O*-*tert*-butyl (tBu) for Asp and Ser, *O*-*tert*-butoxycarbonyl (Boc) for Lys, and 2,2,4,6,7-pentamethyldihydrobenzofurn-5-sulfonyl (Pbf) for Arg, while allyl (All) was used to protect α-COOH of Glu (Fmoc-Glu-OAll). Fmoc-aminomethyl-3,5-dimethoxyphenoxy-valeric acid (PAL) resin (with a loading of 0.6 mmol/g), tetrakis-(triphenyl phosphine) palladium (0) [$Pd(PPh_3)_4$], piperidine, *N*,*N*-dimethylformamide (DMF), and *N*,*N*-diisopropylethylamine (DIEA) were purchased from Sigma-Aldrich. 1-Hydroxy-1-azabenzotriazoleuronium (HATU) was purchased from GenScript (Piscataway, NJ). PEGDA (Mw 6000) and linear RGD-PEGDA with a sequence of GRGDSP were synthesized according to our previous method (*37*). Acryloyl-PEG-NHS (**5**, Mw 3400) was purchased from Nektar (Huntsville, AL). The cleavage cocktail of Reagent K containing 85% (v/v) TFA was prepared prior to use according to the method described previously (*45*). Irgacure 2959 (I2959, 2-hydroxy-1-[4-(hydroxyethoxy)phenyl]-2-methyl-1-propane) was used as water-soluble photoiniators, which was provided by Ciba (Tarrytown, NY).

Instrumentation. Matrix-assisted laser desorption/ionization (MALDI) mass spectrometry was performed on a Bruker Biflex III MALDI-TOF mass spectrometer by dissolving the sample and the matrix of 2,5-dihydroxybenzoic acid in 1:1 (v/v) ethanol and water, and mass spectra were typically accumulated from 200 laser shots. The surface morphology of freeze−dried hydrogels was examined by scanning electron microscopy (SEM) on a Hitachi S-4500 SEM instrument. Samples were coated with 50 Å of platinum prior to SEM imaging. Attenuated total reflectance-Fourier transform infrared (ATR-FTIR) spectra were obtained on a Bio-Rad FTS-575C FTIR spectrometer equipped with a UMA-500 microscope. A germanium crystal was used in the micro-ATR attachment to achieve a sampling depth of 0.1−0.2 μm. X-ray photoelectron spectroscopy (XPS) analysis was carried out on a PHI 5000 VersaProbe X-ray photoelectron spectrometer with the incident radiation consisting of Mg Kα X-ray and the takeoff angle fixed at 45°. Phase contrast photomicrographs of cells were obtained on a Nikon Diaphot 200 inverted phase contrast microscope with a CCD camera using *Metamorph* software package.

Synthesis of Tailed Cyclic RGD Peptide, c[RGDfE(SSSKK-NH_2)] (1). Peptides were synthesized by a three-step synthesis method in a 0.25 mmol scale with PAL resin to produce an amide C-terminus on a 433A Automatic Peptide Synthesizer (Applied Biosystems). In general, couplings were performed with a 4-fold excess of Fmoc-amino acid in the presence of HBTU/DIEA/HOBt (1:1:0.5, v/v/v) for 30 min. Fmoc groups were cleaved with 20% (v/v) piperidine in DMF for 10 min. Briefly, (1) protected linear RGD peptides on resin (**2**) with a sequence of RGDfE(SSSKK) on resin and an α-allyl protective group on Glu were synthesized using standard Fmoc strategy; (2) selectively deprotected peptides on resin (**3**) were obtained by the removal of α-allyl group on Glu manually on peptide synthesizer by 3 equiv of $Pd(PPh_3)_4$, followed by the removal of Fmoc on Arg at the N-terminus by 20% (v/v) piperidine in DMF; (3) protected cyclic RGD peptides on resin (**4**) were formed by cyclization between the amine group (NH_2) on Arg and the α-carboxylic group (COOH) on Glu using HATU. The final cyclized peptides (**1**) were cleaved from the resins using Reagent K and were further purified by reverse-phase HPLC on a Waters 2690 Alliance system (62% yield). MALDI-TOF MS: $m/z = 1121.9$ for $[M + H]^+$ (calculated mass 1122.1); $m/z = 1143.9$ for $[M + Na]^+$ (calculated mass 1144.1).

Synthesis of cRGD-PEGDA (6). c[RGDfE(SSSKK-NH_2)] **1** was dissolved in 50 mM of sodium bicarbonate buffer (pH 8.2). Acryloyl-PEG-NHS (**5**) with 2-fold molar amount as the cRGD peptide was dissolved in 50 mM of sodium bicarbonate buffer (pH 8.2) and added dropwise to the aqueous peptide solution. The mixture was stirred at room temperature for 24 h and then dialyzed against water with membranes of Mw cutoff 5000 for 48 h. The final power product was obtained by lyophilization for 48 h (65% yield). MALDI-TOF MS: a maximum peak at 7658 and a unique distribution with a repeating Mw difference of 44 (corresponding to one PEG repeating unit).

Fabrication of Hydrogels. Hydrogel solution containing 20% (w/v) of cRGD-PEGDA or PEGDA and 0.1% (w/v) of Irgacure 2959 (I2959) photoinitiator in PBS was sterilized by filtering through a 0.2 μm nylon syringe filter and was added to each well of a sterilized 6-well stainless steel mold. The plate was placed under a UV lamp (365 nm, 5−10 mW/cm^2) for 10 min irradiation. Hydrogel disks (8 mm in diameter, 1 mm in thickness) were obtained by lifting the mold plate and transferred to a 24-well culture plate. The swelling ratio (Q) of hydrogels was determined gravimetrically. The resulting hydrogel was placed in a vial containing 4 mL of PBS and incubated under gentle shaking (80 rpm) at 37° for 48 h. Excess fluid was removed to obtain the weight of the wet hydrogel (W_{wet}). The hydrogel was then freeze−dried to obtain the weight of the dried hydrogel (W_{dry}). The swelling ratio (Q) was calculated by using the equation: $Q = W_{wet}/W_{dry}$.

Cell Culturing on Hydrogels. Human pulmonary artery endothelial cells (ECs) (passage 7, Cambrex) were grown to 80−90% confluence using complete growth medium (CGM) in 25 cm^2 tissue culture flasks (Costar) at 37 °C and 5% CO_2. Confluent cells were trypsinized and resuspended in Opti-MEM I (Gibco). EC suspension (1 mL, ∼10^5 cells) was added to each well of the 24-well tissue culture plate containing hydrogel disks. Cells were allowed to attach for 2 h, and then the EC-seeded hydrogel disks were transferred to another 24-well culture plate with CGM and placed in the incubator at 37 °C and 5% CO_2. Culture media were changed every 2 days. Cells were imaged using a Nikon Diaphot 200 inverted phase contrast microscope. EC growth and viability were quantified 96 h after seeding by MTS assays, using CellTiter cell proliferation assay kit (Promega). The absorbance at 490 nm was measured. ANOVA with Tukey's comparison of means ($a = 0.05$, Minitab 15) was used to assess statistic differences.

RESULTS AND DISCUSSION

Rational Design of Well-Defined Hydrogel Scaffolds. The presentation of peptide ligands in scaffolds plays an important role in controlling cell adhesion and motility behaviors, and mechanical properties of tissue engineered constructs. Our design principle of hydrogel scaffolds is that the preconstruction of a bioactive PEGDA macromer with a cRGD peptide attachment in the middle of its chain will lead to controlled ligand spatial organization and ligand distribution in the resulting photopolymerized hydrogel scaffolds, as shown in Figure 1. Since this designed novel macromer has two C═C double bonds on both ends with a similar PEGDA backbone structure, high

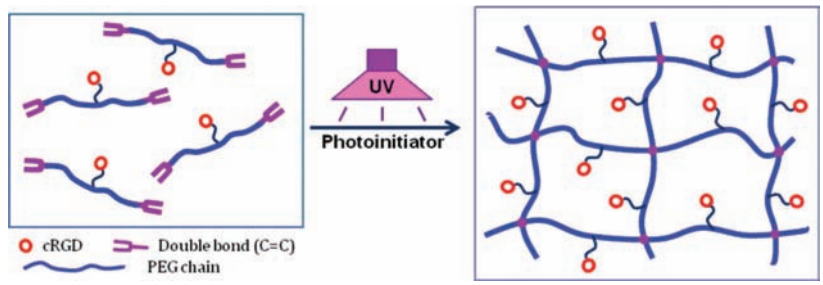

Figure 1. Rational design of cyclic RGD (cRGD)-modified PEGDA macromer for fabrication of biomimetic hydrogel scaffolds with controlled cRGD organization. A novel type of bioactive PEGDA macromers was designed with a cRGD peptide attached in the middle of PEGDA chain, which can be photopolymerized to form 3D hydrogel networks with uniform cRGD distribution.

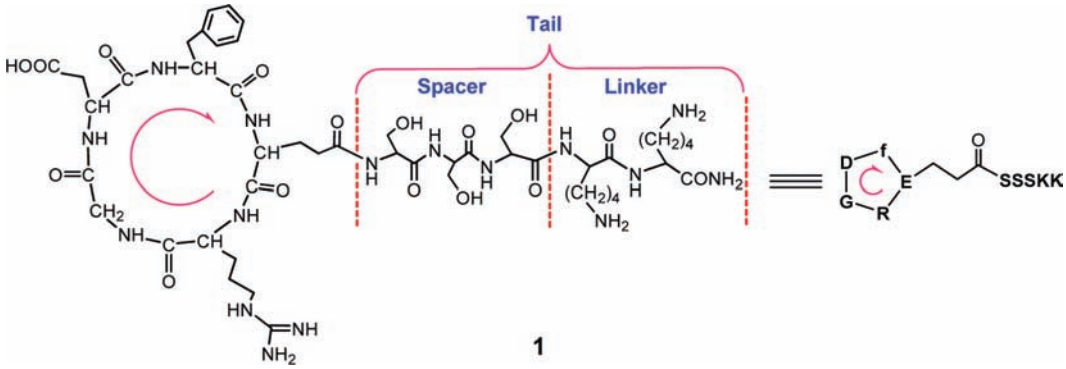

Figure 2. Chemical structure of designed cyclic RGD peptide, c[RGDfE(SSSKK-NH_2)] (**1**) with a tail of SSSKK, which consists of a spacer with three serine residues and a linker with two lysine residues for further conjugation with other molecules. The arrow shows the direction of the amino acid sequence from N-terminus to C-terminus prior to the cyclization of the linear peptide, RGDfE(SSSKK-NH_2).

cRGD peptide density can be incorporated into the hydrogels without affecting the hydrogel physical properties. Furthermore, this cRGD-modified macromer can also copolymerize with other monomers to form cell-adhesive hydrogels with less incorporation due to the higher binding ability of cRGD ligands, compared with linear RGD peptides.

Design and Synthesis of Tailed Cyclic RGD Peptide. To attach the cRGD peptide in the middle of PEGDA chain, a tailed cRGD peptide, c[RGDfE(SSSKK-NH_2)] (**1**), was designed with c(RGDfE) linked to a tail of SSSKK through the Glu (E) residue, as shown in Figure 2. The tail consists of a spacer with three serine residues and two lysine residues. The hydrophilic spacer of SSS is used to increase the mobility of the c(RGDfE) ligand, which may lead to enhanced binding ability. Another consideration is that an SSS sequence next to Glu can prevent the unexpected glutarimide formation, which took place with a GGG spacer next to Glu in our previous studies (*45*). The KK acts as a linker with two free amine groups that provide two active sites for conjugating with other molecules. Compared with c(RGDfK) (which has limited spacer length from the side chain of lysine and only one free amino group on Lys for conjugation), the design of tailed cyclic RGD peptide is more flexible (due to the spacer) and affords two or more conjugating sites through the linker, provided that two or more lysine residues are attached.

The tailed cyclic peptide **1** was synthesized by orthogonal solid-phase peptide synthesis (SPPS), as shown in Scheme 1, using Fmoc-protected glutamic acid α-allyl ester (Fmoc-Glu-OAll) on a PAL resin. The allyl group on Glu was used as the orthogonal protecting group for on-resin cyclization with Fmoc strategy. It can be selectively removed to create a free carboxylic group and enable the construction of a lactam bridge between carboxylic and N-terminal amino groups while the peptide is still attached to the resin. This synthesis includes three major steps. First, a protected linear peptide on PAL resin (**2**) was synthesized. Then, allyl and Fmoc groups were removed

Scheme 1. Orthogonal Solid Phase Synthesis of c[RGDfE(SSSKK-NH_2)] 1 by a Three-Step Method

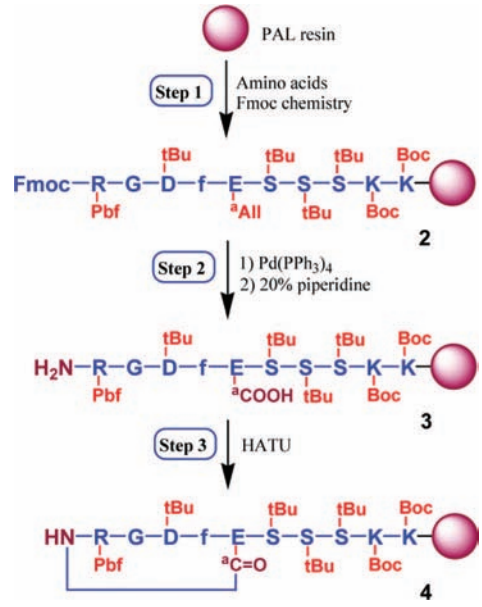

sequentially by $Pd(PPh_3)$ and piperidine to produce a selectively deprotected linear peptide on the resin (**3**). Finally, cyclization of **3** was carried out using HATU to generate the protected cyclic peptide of c[RGDfE(SSSKK-NH_2)] on the resin (**4**). The final deprotected cyclic peptide **1** was obtained by the cleavage of peptides from **4** using Reagent K containing 85% TFA, and purified by reverse-phase HPLC. Its structure was confirmed by MALDI-TOF MS analysis.

Synthesis of cRGD-PEGDA Macromer. A monoacrylated PEG macromer with a carboxylic end group activated by *N*-hydroxysuccinimide (NHS), acryloyl-PEG-NHS (**5**, Mw

Scheme 2. Synthesis of cRGD-Modified PEGDA Macromer, cRGD-PEGDA 6

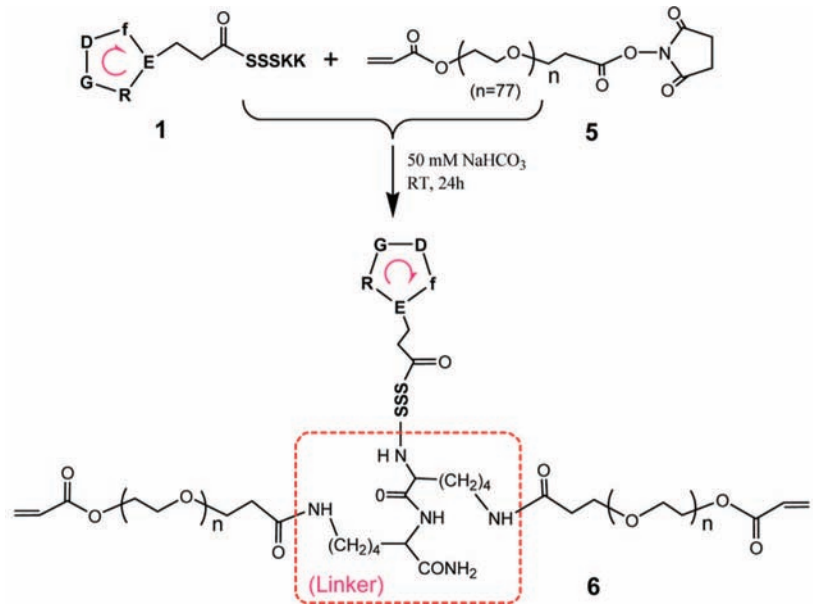

Table 1. Properties of Hydrogels from 20% (w/v) Macromers

hydrogel	Mw[a] (g/mol)	*Q*	Mc (g/mol)	ξ (Å)
PEGDA	6303	13.0	1791	64.7
cRGD-PEGDA	7658	17.6	2326	85.4

[a] Initial molecular weight of macromers determined by MALDI MS.

3400), was used to react with the two free amine groups from the linker (KK) of the tailed cyclic peptide **1** to produce cRGD-PEGDA (**6**), as shown in Scheme 2. The formation of the resulting cRGD-PEGDA macromer **6** was verified by MALDI-TOF mass analysis. The maximum peak at 7658 corresponds to the structure of **6**, which resulted from the conjugation of 2 mol **5** (Mw 3400) and 1 mol **1** (Mw 1121.1) with the elimination of 2 mol NHS (Mw 115.1). This novel bioactive PEGDA macromer **6** combines the photopolymerization ability of PEGDA and the bioactivity of cRGD peptides, and possesses the ability to form cell-adhesive hydrogels with uniform distribution of cRGD peptides in the middle of PEG chains through the whole hydrogel.

Hydrogel Fabrication and Characterization. Hydrogels with 20% (w/v) of macromers were fabricated in the form of thin disks (8 mm in diameter, 1 mm in thickness) by photopolymerization. The swelling ratio (*Q*) and mesh size (ξ) results are listed in Table 1. The number-average molecular weights between cross-links (Mc) and average mesh size were calculated according to the Peppas and Merrill model (*46*, *47*). The presence of ionic moieties in hydrogels makes the theoretical treatment of swelling much more complex (*48*). Given that the macromer of cRGD-PEGDA has only two charge groups on each long PEG chain and the resulting hydrogels are not highly charged, we still use the Peppas and Merrill model in order to simply the calculations (*49*). The hydrogel swelling properties and cross-linking density are particularly important from a tissue-engineering perspective, since they impact transport and overall cell viability and influence cell behavior. Under the same processing conditions, hydrogels made from cRGD-PEGDA exhibited a higher swelling ratio with $Q = 17.6$ than the control hydrogels from PEGDA with $Q = 13.0$, as listed in Table 1. As a result, cRGD-PEGDA hydrogels have a lower cross-linking density with a higher Mc (2326 g/mol) and greater mesh size ($\xi = 85.4$ Å) than the PEGDA hydrogels (Mc = 1791 g/mol, $\xi = 64.7$ Å). These results are consistent with the theoretical analysis that cRGD-PEGDA possesses a longer PEG chain (Mw

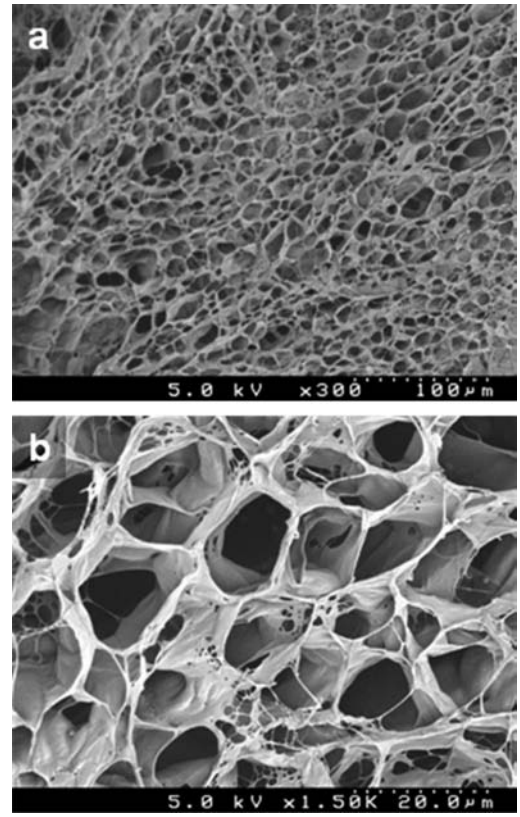

Figure 3. Surface morphology of 20% (w/v) cRGD-PEGDA hydrogel after freeze−drying. (a) SEM photograph with lower magnification (300×); (b) SEM photograph with higher magnification (1500×).

$\sim$ 6800) and much higher molecular weight (7658) after cRGD attachment, compared with PEGDA (Mw = 6303).

Hydrogel Surface Morphology. To obtain insight into the three-dimensional (3D) structure of the cRGD-PEGDA hydrogel, we used SEM to characterize the surface morphology, as shown in Figure 3. The samples were prepared by a freeze−drying method and followed by coating a thin layer of platinum (50 Å) prior to SEM imaging. There are some reports on SEM morphology of dried PEGDA hydrogels showing microporous structures (*50*, *51*), but much care must be taken when making

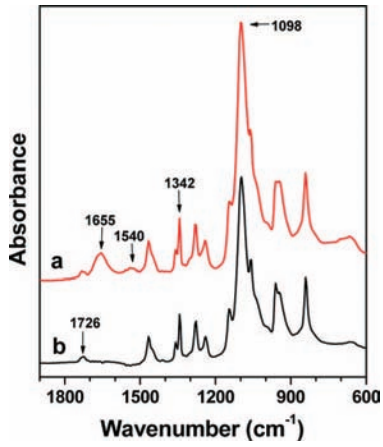

Figure 4. Surface analysis by ATR-FTIR spectroscopy. (a) ATR-FTIR spectrum of cRGD-PEGDA hydrogels after freeze−drying; (b) ATR-FTIR spectrum of PEGDA hydrogels after freeze−drying. cRGD-PEGDA hydrogels show two distinct peaks of amide I and II bands at 1655 and 1540 cm^{-1}, respectively, indicating that cRGD ligands are present on the hydrogel surface.

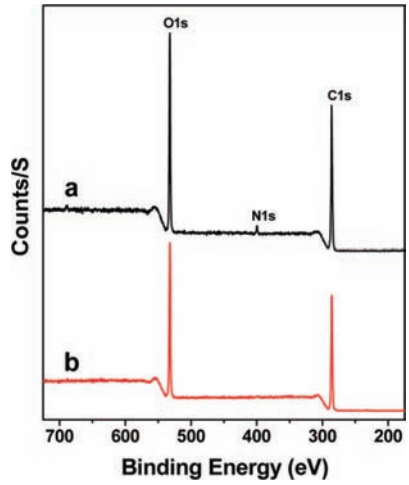

Figure 5. Surface composition analysis by XPS. (a) XPS spectrum of cRGD-PEGDA hydrogels after freeze−drying; (b) XPS spectrum of PEGDA hydrogels after freeze−drying. XPS analysis reveals that cRGD-PEGDA hydrogels have a new peak at binding energy of 398 eV, which is attributed to N_{1s} resulting from cRGD peptides. Quantitative analysis shows that there is 2.9% nitrogen present on the cRGD-PEGDA hydrogel surface.

the dried samples for SEM analysis, since the removal of water held within the porous hydrogel scaffolds may disrupt the structural stability and result in collapse and some artifacts upon drying (*52*). Our results revealed that dried cRGD-PEGDA hydrogels possess a highly porous structure (Figure 3a). The pore sizes range from 10 to 50 μm. More features were observed in the SEM image with higher amplification (Figure 3b). There are some bigger pores containing small pores and some fibrillar networks on the pore walls. In addition, most of the pores are interconnected. It demonstrates that the cRGD-PEGDA hydrogel has the microscopic porous structure with a complex 3D construction in the dried state.

Hydrogel Surface Composition analysis. The peptide ligand presentation in scaffolds plays an important role in controlling cell motility behaviors for tissue engineering (*54*, *55*). To verify the presence and distribution of cRGD peptide ligands on the cRGD-PEGDA hydrogel surface, we used ATR-FTIR (Figure 4) and XPS (Figure 5) to characterize the surface functional groups and surface composition, respectively. ATR-FTIR analysis revealed that PEGDA hydrogels (Figure 4b) show characteristic peaks at 1098, 1342, and 1726 cm^{-1}, which correspond to −C—O− symmetric stretching, −C—H_2 bending, and −C═O stretching from ester bonds, respectively. The ART-FTIR spectrum of cRGD-PEGDA hydrogel (Figure 4a) shows all three of these characteristic peaks, which demonstrates that cRGD-PEGDA hydrogel has a similar backbone structure to PEGDA. However, cRGD-PEGDA hydrogel shows two distinct peaks at 1655 and 1540 cm^{-1}, which correspond to the vibrations of amide (−CO—NH) I and II bands, respectively. These amide groups are from the cRGD peptides, indicating that cRGD ligands are present on the hydrogel surface. XPS analysis reveals that both surfaces of cRGD-PEGDA (Figure 5a) and PEGDA (Figure 5b) hydrogels have similar peaks at binding energies of 531 and 285 eV, which corresponds to O_{1s} and C_{1s}, respectively. However, cRGD-PEGDA hydrogels have a new peak at binding energy of 398 eV, which is attributed to N_{1s} resulting from cRGD peptides. Quantitative analysis shows that there is 2.9% nitrogen present on the cRGD-PEGDA hydrogel surface, which is very close to the theoretical nitrogen content of 2.8%. This indicates that the hydrogel has a well-defined structure with cRGD peptides uniformly presented on the surface and distributed through the material.

Two-Dimensional (2D) EC Seeding and Culturing on Hydrogel Surfaces. Human pulmonary artery ECs were used to test the cell responses to cRGD-PEGDA hydrogels. Cells were seeded on the material surfaces, which were made from 20% (w/v) macromers sterilized with a 0.2 μm syringe filter. Figure 6 shows phase-contrast micrographs of ECs seeded on the hydrogel surfaces at various time points. ECs seeded on the PEGDA hydrogels assumed a rounded morphology with little evidence of spreading 2 h after seeding (Figure 6a) and exhibited an apparent decrease in density 24 h postseeding (Figure 6b), suggesting that ECs have only weak, nonspecific interactions with these materials. ECs seeded on the cRGD-PEGDA hydrogels (cRGD density = 25.3 mM) showed higher initial cell attachment and cell spreading to some extent 2 h after seeding (Figure 6c), and cells were fully spreading 24 h after seeding (Figure 6d). Thus, the enhanced EC attachment and growth on cRGD-PEGDA hydrogels were attributed to the specific binding of cRGD ligands to the integrin receptors on EC surfaces.

Effect of Ligand Binding Affinity on Cell Growth. Quantitative modulation of adhesion strength can be achieved through variation of the affinity and surface density of peptide ligands. To amplify and compare the effects of ligand affinity on EC growth on hydrogels, we incorporated low ligand density into hydrogels to compare cell behaviors responding to cRGD and linear RGD ligands. Hydrogel disks from 5% (w/v) cRGD-PEGDA hydrogels (cRGD density = 6.3 mM) were fabricated by copolymerization with 15% (w/v) PEGDA. MTS cell proliferation assays were performed 96 h postseeding of ECs on the hydrogel surfaces, as shown in Figure 7. Compared with the control PEGDA hydrogel, both 5% cRGD and RGD-modified PEGDA hydrogels exhibit significantly higher ($p < 0.001$) EC population than the control PEGDA hydrogel. This is due to the specific cell adhesion with peptide ligands presented on the hydrogel surfaces. Further analysis shows that 5% cRGD-PEGDA hydrogel shows significantly higher ($p < 0.001$) EC proliferation (cell population increased 44%) than 5% RGD-PEGDA hydrogel. This is attributed to the enhanced cell adhesion resulted from the higher EC binding ability of cRGD peptides.

CONCLUSIONS

In summary, we have synthesized a new type of bioactive PEGDA macromers, cRGD-PEGDA **6**, to mimic the cell-adhesive properties of ECM, aiming to create biomimetic scaffolds with

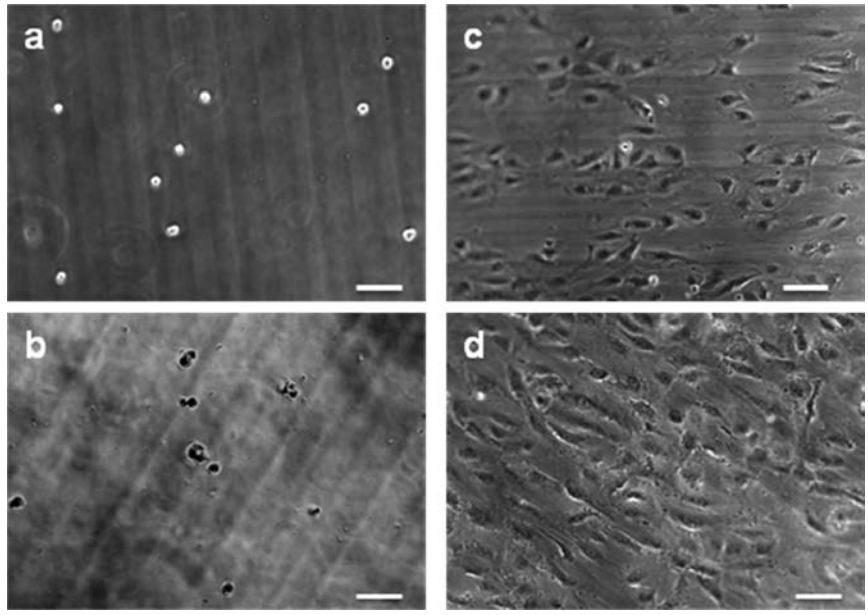

Figure 6. 2D seeding and culturing of endothelial cells (ECs) on hydrogels: (a,b) phase contrast of ECs 2 and 24 h after seeding on PEGDA hydrogel, respectively; (c,d) phase contrast of ECs 2 and 24 h after seeding on cRGD-PEGDA hydrogel, respectively. The images show that ECs seeded on cRGD-PEGDA hydrogels exhibited higher initial cell attachment, greater cell spreading, and higher cell density than on PEGDA hydrogels. (Scale bar = 100 μm).

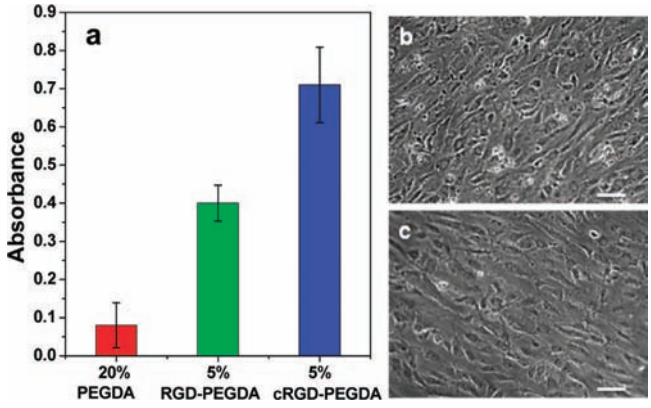

Figure 7. Comparison of EC proliferation on linear RGD-PEGDA and cRGD-PETGDA hydrogels. (a) MTS assays performed at 96 h after EC seeding; (b) phase contrast of ECs 96 h after EC seeding on 5% (w/v) cRGD-PEGDA hydrogel; (c) phase contrast of ECs 96 h after EC seeding on 5% (w/v) RGD-PEGDA hydrogel. 5% cRGD-PEGDA hydrogel shows significantly higher ($p < 0.001$) EC proliferation (cell population increased 44%) than 5% RGD-PEGDA hydrogel. (Scale bar = 100 μm.)

controlled spatial organization and enhanced cell binding affinity for tissue engineering. To attach the cRGD peptide in the middle of PEGDA chain, a tailed cRGD peptide, c[RGDfE(SSSKK-NH_2)] **1** was designed and synthesized with c(RGDfE) linked to a tail of SSSKK, which provides a hydrophilic spacer of SSS and a linker of KK for conjugation. cRGD-PEGDA possesses good photopolymerization ability to fabricate hydrogel scaffolds under UV radiation. The resulting hydrogels were well-constructed with porous 3D structures and uniform distribution of cRGD ligands. Our results show that cRGD-PEGDA hydrogels facilitate EC adhesion and spreading on the hydrogel surfaces, and exhibit significantly higher EC population in comparison with linear RGD-modified hydrogels at low peptide incorporation. Since ligand presentation in biomimetc scaffolds plays an important role in controlling cell behaviors, cRGD-PEGDA has the great advantage of controlling hydrogel properties and ligand spatial organization in the resulting scaffolds. Furthermore, cRGD-PEGDA is an attractive candidate for the future development of tissue engineering scaffolds with optimum cell adhesive strength and ligand density.

ACKNOWLEDGMENT

This work was supported by the National Institutes of Health (Grant R01EB002067). We gratefully thank Christopher Hoffman for his assistance with SEM and the facilities provided by Center for Cardiovascular Biomaterials.

LITERATURE CITED

(1) Langer, R., and Vacanti, J. P. (1993) Tissue engineering. *Science 260*, 920–926.
(2) Niklason, L. E., and Langer, R. (2001) Prospects for organ and tissue replacement. *J. Am. Med. Assoc. 285*, 573–576.
(3) Vacanti, C. A. (2006) The history of tissue engineering. *J. Cell Mol. Med. 10*, 569–576.
(4) Kaihara, S., and Vacanti, J. P. (1999) Tissue engineering: toward new solutions for transplantation and reconstructive surgery. *Arch. Surg. 134*, 1184–1188.
(5) Ogle, B., Cascalho, M., and Platt, J. L. (2004) Fusion of approaches to the treatment of organ failure. *Am. J. Transplant. 4*, S74–77.
(6) Risbud, M. (2001) Tissue engineering: implications in the treatment of organ and tissue defects. *Biogerontology 2*, 117–125.
(7) Hollister, S. J. (2005) Porous scaffold design for tissue engineering. *Nat. Mater. 4*, 518–524.
(8) Hench, L. L., and Polak, J. M. (2002) Third-generation biomedical materials. *Science 295*, 1014–1017.
(9) Griffith, L. G. (2002) Emerging design principles in biomaterials and scaffolds for tissue engineering. *Ann. N.Y. Acad. Sci. 961*, 83–95.
(10) Lee, J., Cuddihy, M. J., and Kotov, N. A. (2008) Three-dimensional cell culture matrices: state of the art. *Tissue Eng., Part B 14*, 61–86.
(11) Yang, S., Leong, K. F., Du, Z., and Chua, C. K. (2001) The design of scaffolds for use in tissue engineering. Part I. Traditional factors. *Tissue Eng. 7*, 679–689.
(12) Hutmacher, D. W. (2000) Scaffolds in tissue engineering bone and cartilage. *Biomaterials 21*, 2529–2543.
(13) Badylak, S. F. (2007) The extracellular matrix as a biologic scaffold material. *Biomaterials 28*, 3587–3593.
(14) Kasemo, B. (1998) Biological surface science. *Curr. Opin. Solid State Mater. Sci. 3*, 451–459.

(15) Stoop, R. (2008) Smart biomaterials for tissue engineering of cartilage. *Injury 39S1*, S77–87.
(16) Cushing, M. C., and Anseth, K. S. (2007) Hydrogel cell cultures. *Science 316*, 1133–1134.
(17) Lee, K. Y., and Mooney, D. J. (2001) Hydrogels for tissue engineering. *Chem. Rev. 101*, 1869–1879.
(18) Kretlow, J. D., Klouda, L., and Mikos, A. G. (2007) Injectable matrices and scaffolds for drug delivery in tissue engineering. *Adv. Drug Delivery Rev. 59*, 263–273.
(19) Chung, C., and Burdick, J. A. (2008) Engineering cartilage tissue. *Adv. Drug Delivery Rev. 60*, 243–262.
(20) Haines, L. A., Rajagopal, K., Ozbas, B., Salick, D. A., Pochan, D. J., and Schneider, J. P. (2005) Light-activated hydrogbel formation via the triggered folding and self-assembly of a designed peptide. *J. Am. Chem. Soc. 127*, 17025–17029.
(21) Elisseeff, J., Anseth, K., Sims, D., McIntosh, W., Randolph, M., and Langer, R. (1999) Transdermal photopolymerization for minimally invasive implantation. *Proc. Natl. Acad. Sci. U.S.A. 96*, 3104–3107.
(22) Buxton, A. N., Zhu, J., Marchant, R. E., West, J. L., Yoo, J. U., and Johnstone, B. (2007) Design and characterization of poly(ethylene glycol) photopolymerizable semi-interpenetrating networks for chondrogenesis of human mesenchymal stem cells. *Tissue Eng. 13*, 2549–2560.
(23) Nguyen, K. T., and West, J. L. (2002) Photopolymerizable hydrogels for tissue engineering application. *Biomaterials 23*, 4307–4314.
(24) Lutolf, M. P., and Hubbell, J. A. (2005) Synthetic biomaterials as instructive extracellular microenvironments for morphogenesis in tissue engineering. *Nat. Biotechnol. 23*, 47–55.
(25) Griffith, L. G., and Naughton, G. (2002) Tissue engineering-current challenges and expanding opportunities. *Science 295*, 1009–1014.
(26) Hirano, Y., and Mooney, D. J. (2004) Peptide and protein presenting materials for tissue engineering. *Adv. Mater. 16*, 17–25.
(27) Ito, Y. (2008) Covalently immobilized biosignal molecule materials for tissue engineering. *Soft Matter 4*, 46–56.
(28) Schaffner, P., and Dard, M. M. (2003) Structure and function of RGD peptides involved in bone biology. *Cell. Mol. Life Sci. 60*, 119–132.
(29) Hersel, U., Dahmen, C., and Kessler, H. (2003) RGD modified polymers: biomaterials for stimulated cell adhesion and beyond. *Biomaterials 24*, 4385–4415.
(30) Kantlehner, M., Finsinger, D., Meyer, J., Schaffner, P., Jonczyk, A., Diefenbach, B., Nies, B., and Kessler, H. (1999) Selective RGD-mediated adhesion of osteoblasts at surfaces of implants. *Angew. Chem., Int. Ed. 38*, 560–562.
(31) Hern, D. L., and Hubbell, J. A. (1998) Incorporation of adhesion peptides into nonadhesive hydrogels useful for tissue engineering. *J. Biomed. Mater.Res. 39*, 266–276.
(32) Burdick, J. A., and Anseth, K. S. (2002) Photoencapsulation of osteoblasts in injectable RGD-modified PEG hydrogels for bone tissue engineering. *Biomaterials 23*, 4315–4323.
(33) Yang, F., Williams, C. G., Wang, D., Lee, H., Manson, P. N., and Elisseeff, J. (2005) The effect of incorporating RGD adhesive peptide in polyethylene glycol diacrylate hydrogel on osteogenesis of bone marrow stromal cells. *Biomaterials 26*, 5991–5998.
(34) Kinoshita, T., Ishigaki, Y., Nakano, K., Yamaguchi, K., Akita, S., Nii, S., and Kawizumi, F. (2006) Application of acrylate gel having poly(ethylene glycol) side chains to recovery of gold from hydrochloric acid solutions. *Sep. Purif. Technol. 49*, 253–257.
(35) Tan, G., Wang, Y., and Guang, Y. (2008) Synthesis and properties of polyethylene glycol diacrylate/2-hydroxyethyl methacrylate hydrogels. *Key Eng. Mater. 368−372*, 1175−1177.
(36) Tan, G., Wang, Y., Li, J., and Zhang, S. (2008) Synthesis and characterization of injectable photocrosslinking poly(ethylene glycol) diacrylate based hydrogels. *Polym. Bull. 61*, 91–98.
(37) Zhu, J., Beamish, J. A., Tang, C., Kottke-Marchant, K., and Marchant, R. E. (2006) Extracellular matrix-like cell-adhesive hydrogels form RGD-containing poly(ethylene glycol) diacrylate. *Macromolecules 39*, 1305–1307.
(38) Chen, W., Chang, C., and Gilson, M. K. (2006) Concepts in receptor optimization: targeting the RGD peptide. *J. Am. Chem. Soc. 128*, 4675–4684.
(39) Leahy, D. J., Aukhil, I., and Erickson, H. P. (1996) 2.0Å crystal structure of a four-domain segment of human fibronectin encompassing the RGD loop and synergy region. *Cell 84*, 155–164.
(40) Haubner, R., Schmitt, W., Holzemann, G., Goodman, S. L., Jonczyk, A., and Kessler, H. (1996) Cyclic RGD peptides containing β-turn mimetics. *J. Am. Chem. Soc. 118*, 7881–7891.
(41) Haubner, R., Gratias, R., Diefenbach, B., Goodman, S. L., Jonczyk, A., and Kessler, H. (1996) Structural and functional aspects of RGD-containing cyclic pentapeptides as highly potent and selective integrin $\alpha_v\beta_3$ antagonists. *J. Am. Chem. Soc. 118*, 7461–7472.
(42) Locardi, E., Mullen, D. G., Mattern, R. H., and Goodman, M. (1999) Conformations and pharmacophores of cyclic RGD containing peptides which selectively bind integrin $\alpha_v\beta_3$. *J. Pept. Sci. 5*, 491–506.
(43) Lambert, J. N., Mitchell, J. P., and Roberts, K. D. (2001) The synthesis of cyclic peptides. *J. Chem. Soc., Perkin Trans. 15*, 471–484.
(44) Tang, C., Kligman, F., Larsen, C. C., Kottke-Marchant, K., and Marchant, R. E. (2008) Platelet and endothelial adhesion on flurosurfactant polymers designed for vascular graft modification *J. Biomed. Mater. Res.*. [Online early access] DOI: 10.1002/jbm.a.31888. Published Online: Feb. 19, 2008.
(45) Zhu, J., and Marchant, R. E. (2008) Solid-phase synthesis of tailed cyclic RGD peptides using glutamic acid: unexpected glutarimide formation. *J. Pept. Sci. 14*, 690–696.
(46) Canal, T., and Peppas, N. A. (1989) Correlation between mesh size and equilibrium degree of swelling of polymeric networks. *J. Biomed. Mater. Res. 23*, 1183–1193.
(47) Cruise, G. M., Scharp, D. S., and Hubbell, J. A. (1998) Characterization of permeability and network structure of interfacially photopolymerized poly(ethylene glycol) diacrylate hydrogels. *Biomaterials 19*, 1287–1294.
(48) Peppas, N. A., Bures, P., Leobandung, W., and Ichikawa, H. (2000) Hydrogels in pharmaceutical formations. *Eur. J. Pharm. Biopharm. 50*, 27–46.
(49) Raeber, G. P., Lutolf, M. P., and Hubbell, J. A. (2005) Molecularly engineered PEG hydrogels: a novel model system for proteolytically mediated cell migration. *Biophys. J. 89*, 1374–1388.
(50) Livnat, M., Beyar, R., and Seliktar, D. (2005) Endoluminal hydrogel films made of alginate and polyethylene glycol: physical characteristics and drug-eluting properties. *J. Biomed. Mater. Res. 75A*, 710–722.
(51) Kim, J. H., Kim, J. G., Kim, D., and Kim, Y. H. (2005) Preparation and properties of PEG hydrogel from PEG macromonomer with sulfonate end group. *J. Appl. Polym. Sci. 96*, 56–61.
(52) Ford, M. C., Bertram, J. P., Hynes, S. R., Michaud, M., Li, Q., Young, M., Segal, S. S., Madri, J. A., and Lavik, E. B. (2006) A macroporous hydrogel for the coculture of neural progenitor and endothelial cells to form functional vascular networks in vivo. *Proc. Natl. Acad. Sci. U.S.A. 103*, 2512–2517.
(53) Maheshwari, G., Brown, G., Lauffenburger, D. A., Wells, A., and Griffith, L. G. (2000) Cell adhesion and motility depend on nanoscale RGD clustering. *J. Cell Sci. 113*, 1677–1686.
(54) Palecek, S. P., Loftus, J. C., Ginsberg, M. H., Lauffenburger, D. A., and Horwitz, A. F. (1997) Integrin-ligand binding properties govern cell migration speed through cell-substratum adhesiveness. *Nature 385*, 537–540.
(55) Lauffenburger, D. A., and Horwitz, A. F. (1996) Cell migration: a physically integrated molecular process. *Cell 84*, 359–369.

BC800441V

Bioconjugate Chemistry 20th Anniversary

Subscriber access provided by SHEMYAKIN-OVCHINNIKOV INST

Article

Influence of Disulfide Density and Molecular Weight on Disulfide Cross-Linked Polyethylenimine as Gene Vectors

Qi Peng, Chu Hu, Juan Cheng, Zhenlin Zhong, and Renxi Zhuo

Bioconjugate Chem., **2009**, 20 (2), 340-346• DOI: 10.1021/bc800451j • Publication Date (Web): 03 February 2009

Downloaded from http://pubs.acs.org on May 15, 2009

More About This Article

Additional resources and features associated with this article are available within the HTML version:

- Supporting Information
- Access to high resolution figures
- Links to articles and content related to this article
- Copyright permission to reproduce figures and/or text from this article

View the Full Text HTML

ACS Publications
High quality. High impact.

Bioconjugate Chemistry is published by the American Chemical Society. 1155 Sixteenth Street N.W., Washington, DC 20036

Influence of Disulfide Density and Molecular Weight on Disulfide Cross-Linked Polyethylenimine as Gene Vectors

Qi Peng, Chu Hu, Juan Cheng, Zhenlin Zhong,* and Renxi Zhuo

Key Laboratory of Biomedical Polymers of Ministry of Education, Department of Chemistry, Wuhan University, Wuhan 430072, P. R. China. Received October 20, 2008; Revised Manuscript Received December 30, 2008

Disulfide cross-linked polyethylenimines (PEI_X-SS_Y, where *X* refers to the molecular weight of raw PEI, and *Y* refers to the thiolation degree) were prepared in two steps: First, thiol groups were introduced on a raw polyethylenimine (PEI) by the amine-induced ring-opening reaction of thiirane. Second, thiol groups were oxidized by DMSO to form the disulfide cross-links. The cross-linked PEI_{800}-SS_Y polymers with a moderate thiolation degree (PEI_{800}-$SS_{2.6}$, PEI_{800}-$SS_{3.5}$, and PEI_{800}-$SS_{4.5}$) could form compact polyplexes with a size of 200−300 nm at an adequate N/P ratio. In contrast, those with a too low or too high thiolation degree (*Y* below 2.6 or above 4.5) formed much looser polyplexes with a size above 600 nm. The polyplexes of PEI_X-$SS_{3.0-4.0}$ series ($X = 800$, 1800, and 25,000) formed small particles with a size below 400 nm at a wide range of N/P ratios. Efficiency of the cross-linked PEIs as gene vectors was evaluated in vitro by transfection of pGL3 to HeLa, COS7, 293T, and CHO cells. The efficiency is disulfide content and molecular weight dependent. The PEI_{800}-SS_Y series with an adequate thiolation degree between 2.6 and 4.5 have relatively lower cytotoxicity and higher gene transfection efficiency than 25 KDa PEI. The polymers with very low or very high thiolation degrees were unable to form compact polyplexes and had very poor transfection efficiency. A suitable molecular weight of raw PEI is also essential to obtain a highly efficient disulfide cross-linked PEI gene vector. Among the three raw PEIs of different molecular weights tested (800 Da, 1800 Da, and 25 KDa), the cross-linked polymer prepared from 800 Da PEI that has the lowest molecular weight gave the best results.

INTRODUCTION

Polymer-mediated gene delivery has recently appeared as a comparable alternative to viral vectors for its lower cost, large nucleic acid loading capacity, and no immunogenesis (*1*−*3*). For example, polyethylenimine (PEI) is one of the most effective nonviral gene delivery carriers. The proton sponge nature of PEI is thought to cause osmotic swelling and physical rupture of the endosome, resulting in the escape of the vector from the degradative lysosomal trafficking pathway (*4, 5*).

High molecular weight is necessary for effective gene transfection with PEI. While high molecular weight PEI possesses high gene transfection efficiency, it has a high cytotoxicity (*6, 7*). Comparatively, low molecular weight PEI showing poor gene transfection efficiency was reported to have much lower cytotoxicity (*8*). Therefore, a reasonable way for resolving the contradiction between efficiency and cytotoxicity was suggested to combine low molecular weight PEIs together with degradable links such as amides, acetals, esters, and disulfides. It was expected to produce a polymer with lower toxicity and relatively high gene transfection efficiency, as well as long-term safety. Recently, many kinds of degradable PEIs showed good transfection efficiency and low cytotoxicity (*9*−*12*).

A disulfide bond can be broken in the presence of glutathione (GSH). The intracellular glutathione concentration is 50−1000 times higher than the extracellular concentration (*13*−*15*). The presence of disulfide in gene vectors could maintain a balance of keeping pDNA polyplexes stable in the extra-cytoplasmic environment and inducing efficient release of the entrapped pDNA from the polyplexes after their movement into the reductive cytoplasmic compartment. It also would limit the toxicity of the polymers. The advantages of disulfide linkages in gene transfection polymers are exemplified in the literature (*11, 16*−*20*). Bioreducible polyamidoamines containing multiple disulfide linkages with low toxicity were able to transfect COS7 cells in vitro with transfection efficiencies significantly higher than those of 25 kDa PEI (*17*). Linear poly(ethylenimine sulfide)s were reported to be safe gene carriers with high transfection efficiencies comparable to 25 kDa PEI (*19*). Branched PEI with an M_w of 800 Da was cross-linked by the reaction with either dithiobis(succinimidylpropionate) (DSP) or dimethyl 3,3′-dithiobispropionimidate dihydrochloride (DTBP), resulting in greatly increased gene transfection efficiency. Also, cytotoxicity was decreased by avoiding long-term polymer accumulation (*21*). Recently, we demonstrated that disulfide cross-linked PEIs synthesized by oxidation of thiolated 800 Da PEI possess simultaneously higher gene transfection efficiency and lower cytotoxicity than 25 KDa PEI (*22*).

It is reasonable to assume that the properties of disulfide cross-linked PEIs as gene vectors would be determined by (i) the type and density of disulfide cross-linkages and (ii) the molecular weights of both raw and cross-linked PEIs. In this paper, the influence of disulfide density and molecular weights of raw PEIs on the molecular weights and transfection efficiency of the cross-linked PEIs is investigated.

MATERIALS AND METHODS

Materials. PEIs with M_w of 800 Da and 25 kDa were purchased from Aldrich, and PEI with a M_w of 1800 Da was from Alfa Aesar. Thiirane was synthesized by literature procedure (*23*). Plasmid pGL3 under the control of SV40 promoter and with enhancer sequences encoding luciferase was obtained from Promega, Madison, WI, USA. Plasmids were propagated in *Escherichia coli* in Luria−Bertani (LB) medium containing 60 μg/mL ampicillin respectively at 37 °C and

* To whom correspondence and reprint requests should be addressed. Phone: +86-27-6875-4061. Fax: +86-27-6875-4509. E-mail: zlzhong@yahoo.com.

10.1021/bc800451j CCC: $40.75 © 2009 American Chemical Society
Published on Web 02/03/2009

Table 1. Synthesis of PEI_X-SS_Y[a]

	starting materials			results	
PEI_X-SS_Y	raw PEI (Wt/g)	thiirane (Wt/g)	thiirane/PEI (molar ratio)	SH content in PEI_X-SH_Y (SH/PEI)	wt of PEI_X-SS_Y (g)
PEI_{800}-$SS_{0.4}$	1.436	0.051	0.47	0.4	1.040
PEI_{800}-$SS_{1.0}$	1.314	0.120	1.22	1.0	1.177
PEI_{800}-$SS_{2.6}$	0.667	0.200	4.00	2.6	0.875
PEI_{800}-$SS_{3.5}$	1.026	0.375	4.9	3.5	1.548
PEI_{800}-$SS_{4.5}$	0.990	0.458	6.17	4.5	1.664
PEI_{800}-$SS_{5.5}$	0.536	0.300	7.46	5.5	0.980
PEI_{800}-$SS_{7.0}$	0.730	0.45	8.22	7.0	1.383
PEI_{1800}-$SS_{3.5}$	1.088	0.132	3.64	3.5	1.224
PEI_{25K}-$SS_{4.0}$	3.878	0.039	4.19	4.0	5.894

[a] Reaction conditions: Step 1 (thiolation): pH 7.2 in CH_3OH, 50 °C for 24 h. Step 2 (oxidation): room temperature in DMSO for 2 days.

purified using E. Z. N. A. Fastfilter Endofree Plasmid Midi kits (Omega) according to the manufacturer's instruction. The purity of DNA was assessed spectrophotometrically by measuring absorbance at wavelengths of 260 and 280 nm (OD_{260}/OD_{280} 1.8 or greater) and confirmed using 0.7% agarose gel electrophoresis containing GelRed. The DNA concentration was determined by measuring the UV absorbance at 260 nm. DNA aliquots of pGL3 were stored at −20 °C prior to use. Dulbecco's modified eagle's medium (DMEM), penicillin−streptomycin, trypsin, Dulbecco's phosphate buffered saline, and 3-(4,5-dimethylthiazol-2-yl)-2,5-diphenyltetrazolium bromide (MTT) were purchased from Sigma. Other commercially available reagents were used as received.

Synthesis of Thiolated PEI (PEI_X-SH_Y). In a 25 mL flask, 1.00 g of PEI (800 Da, 1800 Da, or 25 kDa) was dissolved in 5 mL of deionized water. Hydrochloric acid (0.1 N) was added dropwise to the PEI solution while stirring until pH was regulated to 7.2. After removal of water by evaporation under reduced pressure, the yellow solid thus obtained was dissolved in 3 mL of CH_3OH and transferred to an ampule. After the container was purged with argon for 5 min, a calculated amount of thiirane was added. The ampule was sealed and kept in a 50 °C oil bath for 24 h with magnetic stirring. The content of the ampule was transferred to a flask, evaporated to dryness under reduced pressure, and stored under argon. The thiol group content was determined by Ellman's method (*24*, *25*) and listed in Table 1. ^{1}H NMR (300 MHz, D_2O): δ 3.15−2.55 (m, NCH_2CH_2N, NCH_2CH_2S).

Synthesis of Disulfide Cross-Linked PEI (PEI_X-SS_Y). A solution of 1.50 g of PEI_X-SH_Y in 3 mL of methanol and 1.5 mL of dimethyl sulfoxide (DMSO) was stirred for 48 h. The reaction solution was precipitated in diethyl ether three times and dried under high vacuum to give a light yellow viscous glue or solid. ^{1}H NMR (300 MHz, D_2O): δ 3.14−2.66 (m, NCH_2CH_2N, NCH_2CH_2S).

Cytotoxicity Assay of PEI_X-SS_Y. The cytotoxicity assay of PEI_X-SS_Y was performed the same way as described in the previous paper (*17*).

Molecular Weight Determination. Capillary viscosity measurements were carried out to estimate molecular weights (*26*, *27*). The polyamine polymers were neutralized with hydrochloric acid to pH 7.4 and dissolved in 150 mM NaCl at concentration from 20 mg/mL to 5 mg/mL. Viscosity measurements were carried out using a capillary viscometer at 25 °C. The molecular weights of cross-linked polymers were calculated using the Mark−Houwink equation $[\eta] = KM^{\alpha}$, where M is the molecular weight and K and α are Mark−Houwink parameters determined from PEI standards of known molecular weights.

The molecular weights of the polymers were also determined by gel permeation chromatographic (GPC) using a Waters 2690D HPLC equipped with Ultrahydrogel 120 and 250 columns. HAc/NaAc (pH 2.8) buffer solution was used as the eluent at a flow rate of 0.3 mL/min. Poly(ethylene glycol) standards with narrow distribution were used to generate a calibration curve.

Preparation of PEI_X-SS_Y /pDNA Polyplexes and Agarose Gel Retardation. A 0.1 mg/mL aqueous solution of plasmid DNA (pGL3) was diluted to designed concentration (usually 20 μg/mL) using 150 mM NaCl solution under vortexing. Designed amounts of PEI_X-SS_Y aqueous solutions were added slowly to the pDNA solutions. The amount of polymer added was calculated on the basis of chosen N/P ratios of PEI_X-SS_Y/DNA (nitrogen atoms of the polymer over phosphates of pDNA). The mixture was incubated at room temperature for 30 min for the complex formation. A 5 μL sample of the polyplex solution mixed with 1 μL of 6 × A loading buffer was loaded to agarose gel. The polyplexes were electrophoresed on a 0.7% agarose gel containing GelRed with Tris-acetate (TAE) running buffer (pH 8) at 80 V for 80 min. DNA bands were visualized by an UV (254 nm) illuminator and photographed with a Vilber Lourmat imaging system (France).

Particle Sizes and Zeta Potential Measurements. The particle size and zeta potential were measured with a Malvern Nano-ZS ZEN3600 Zeta-Sizer at room temperature. The polyplexes at various N/P ratios were prepared the same way as above. Then, the polyplexes were incubated at room temperature for 30 min. After that, the polyplexes were diluted by 150 or 10 mM NaCl solution to 1 mL volume prior to measure particle sizes or zeta potentials.

Determination of in Vitro Transfection Efficiency. The in vitro transfection efficiency of PEI_X-SS_Y/pGL3 polyplexes was evaluated in HeLa, COS7, 293T, and CHO cells by the procedure as described in the previous paper (*17*).

RESULTS AND DISCUSSION

Preparation of PEI_X-SS_Y. The strategy for preparation of PEI_X-SS_Y is shown in Scheme 1 similar to that in our previous report (*17*) except using thiirane as a thiolation regent instead of methylthiirane. First, a raw PEI is thiolated by a ring-opening reaction with a relevant quantity of thiirane to give the thiolated product PEI_X-SH_Y, where X refers to the molecular weight of the raw PEI and Y stands for the average number of thiol groups on each PEI molecule. Second, PEI_X-SH_Y is cross-linked into a higher molecular weight polymer PEI_X-SS_Y by disulfide-forming oxidation of the thiol groups with DMSO.

Three kinds of PEIs with weight-averaged molecular weights (M_w) of 800 Da, 1800 Da, and 25 kDa, respectively, were thiolated through the ring-opening reaction of thiirane with the primary and secondary amino groups of PEI at pH 7.2 in methanol, affording the thiolated products PEI_X-SH_Y. The thiolation degree Y was determined by Ellman's test (*24*, *25*) and listed in Table 1. As shown in the table, the thiolation degree was correlated to the feed ratio of thiirane/PEI and could be adjusted over a wide range.

Thiolated PEIs were cross-linked by oxidation with DMSO at room temperature, and the final products PEI_X-SS_Y were subjected to Ellman's test for the estimation of residual thiol groups. After 2 days of oxidative cross-linking reaction in DMSO, the amount of remained thiol groups was found to be less than 10% of the initial value for all samples, indicating that the disulfide-forming oxidation was near completion.

For PEI_{800}-$SS_{0.4}$, PEI_{800}-$SS_{1.0}$, PEI_{800}-$SS_{2.6}$, PEI_{800}-$SS_{3.5}$, PEI_{800}-$SS_{4.5}$, and PEI_{1800}-$SS_{3.5}$, the reaction mixtures were clear solutions during the whole oxidation process. For PEI_{800}-$SS_{5.5}$, PEI_{800}-$SS_{7.0}$, and PEI_{25K}-$SS_{4.0}$, however, gelatinous products were obtained. The gels dissolved again to become solutions gradually in one to two days at room temperature. The dissolution of the

Scheme 1. Preparation of Disulfide Cross-Linked Polyethylenimine PEI_X-SS_Y (*X* and *Y* Refer to the Molecular Weight of Raw PEI and Thiolation Degree, Respectively)

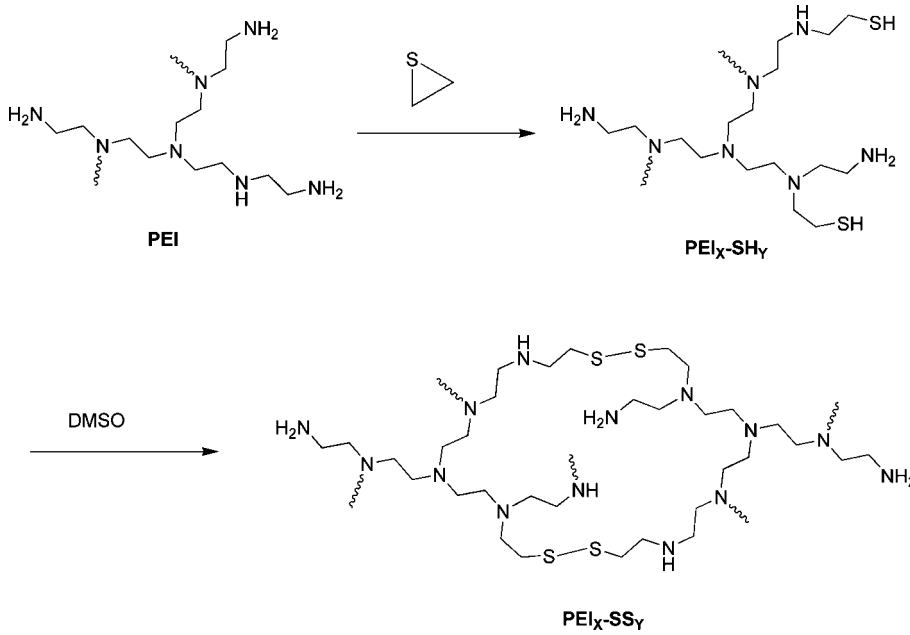

Table 2. Cytotoxicity of PEI_X-SS_Y, and the Size and Zeta Potential of PEI_X-SS_Y/pDNA Polyplexes

		particle size (nm) [b]				zeta potential (mV) [c]			
polymers	IC50 [a] (μg/mL)	N/P = 10	N/P = 20	N/P = 30	N/P = 40	N/P = 10	N/P = 20	N/P = 30	N/P = 40
PEI_{800}-$SS_{0.4}$	>1000	1069	796	696	593	13.8	14.7	14.3	15.4
PEI_{800}-$SS_{1.0}$	>500	1153	950	904	780	17.1	20.7	23.2	21.8
PEI_{800}-$SS_{2.6}$	63	460	376	290	300	13.6	15.1	22.8	25.3
PEI_{800}-$SS_{3.5}$	50	380	232	277	212	18.4	20.9	19.6	24.5
PEI_{800}-$SS_{4.5}$	41	891	281	243	238	19.1	21.1	25.8	30.3
PEI_{800}-$SS_{5.5}$	35	1626	1051	861	577	20.1	23.7	23.9	23.3
PEI_{800}-$SS_{7.0}$	34	1196	680	654	647	21.0	23.5	23.4	27.7
PEI_{1800}-$SS_{3.5}$	25	294	397	331	433	15.2	15.8	13.5	13.9
PEI_{25K}-$SS_{4.0}$	7	225	236	351	346	14.7	16.0	16.1	15.9
800 Da PEI	>1000	1190	1630	968	1038	5.8	11.6	9.8	10.7
25 KDa PEI	7	220	159	164	149	35.4	35.2	31.6	32.3

[a] IC_{50} values measured on HeLa cells at 24 h after the addition of PEI_X-SS_Y series by MTT assay. [b] Average particle sizes of PEI_X-SS_Y/pGL3 measured by DLS at different N/P ratios in 150 mM NaCl. [c] Zeta potentials of PEI_X-SS_Y/pGL3 measured at different N/P ratios in 10 mM NaCl.

gels could be explained by the transform of intermolecular disulfide bonds into intramolecular ones (*17*).

Molecular weights of the PEI_{800}-SS_Y series were estimated by viscosity measurements using a capillary viscometer. In 150 mM NaCl aqueous solution (pH 7.4, 20 °C), the molecular weights of PEI_{800}-$SS_{0.4}$, PEI_{800}-$SS_{1.0}$, PEI_{800}-$SS_{2.6}$, PEI_{800}-$SS_{3.5}$, and PEI_{800}-$SS_{4.5}$ were estimated to be 1800, 2900, 4000, 8500, and 8700, respectively. The molecular weight increases with the increase of thiolation degree *Y* when *Y* is below 3.5. The disulfide cross-linked PEIs have very similar molecular weights regardless of their thiolation degree in the range from 3.5 to 4.5. This result suggests that the majority of disulfide cross-links are intramolecular when the thiolation degree is high. Because of the phenomenon of partial gelation, we were unable to estimate the molecular weight of PEI_{800}-$SS_{5.5}$ and PEI_{800}-$SS_{7.0}$.

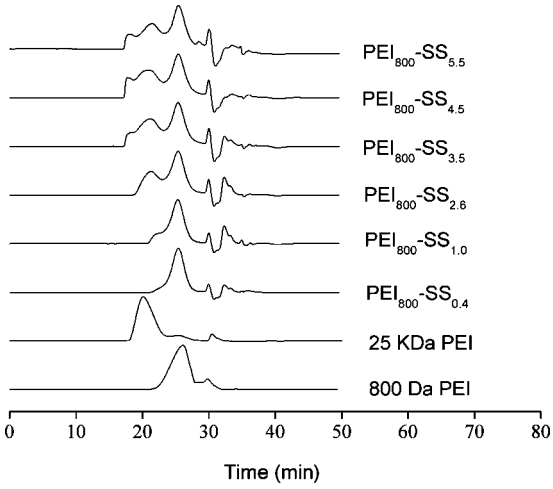

Figure 1. GPC traces of PEI_{800}-SS_Y series, 800 Da and 25 kDa PEI in HAc/NaAc (pH 2.8) buffer solution.

GPC analysis results (Figure 1) revealed that the introduction of disulfides for raw PEIs elevate the average molecular weights of the final products, and with the increase of the content of disulfide in the polymers, the molecular weights of the PEI_{800}-SS_Y ($Y = 0.4$, 1.0, 2.6, and 3.5) correspondingly increased. All PEI_{800}-SS_Ys had a similar peak nearly repeating with 800 Da PEIs. Maybe it can be explained that quite a lot of raw materials interfused the final products without reacting with thiirane. Compared to the raw material 800 Da PEI, PEI_{800}-$SS_{0.4}$ and PEI_{800}-$SS_{1.0}$ showed little improvement in their molecular weights. The peak shape of PEI_{800}-$SS_{0.4}$ seems almost the same as that of its raw materials. From PEI_{800}-$SS_{1.0}$, the cross-linked polymer was formed showing higher molecular weight from

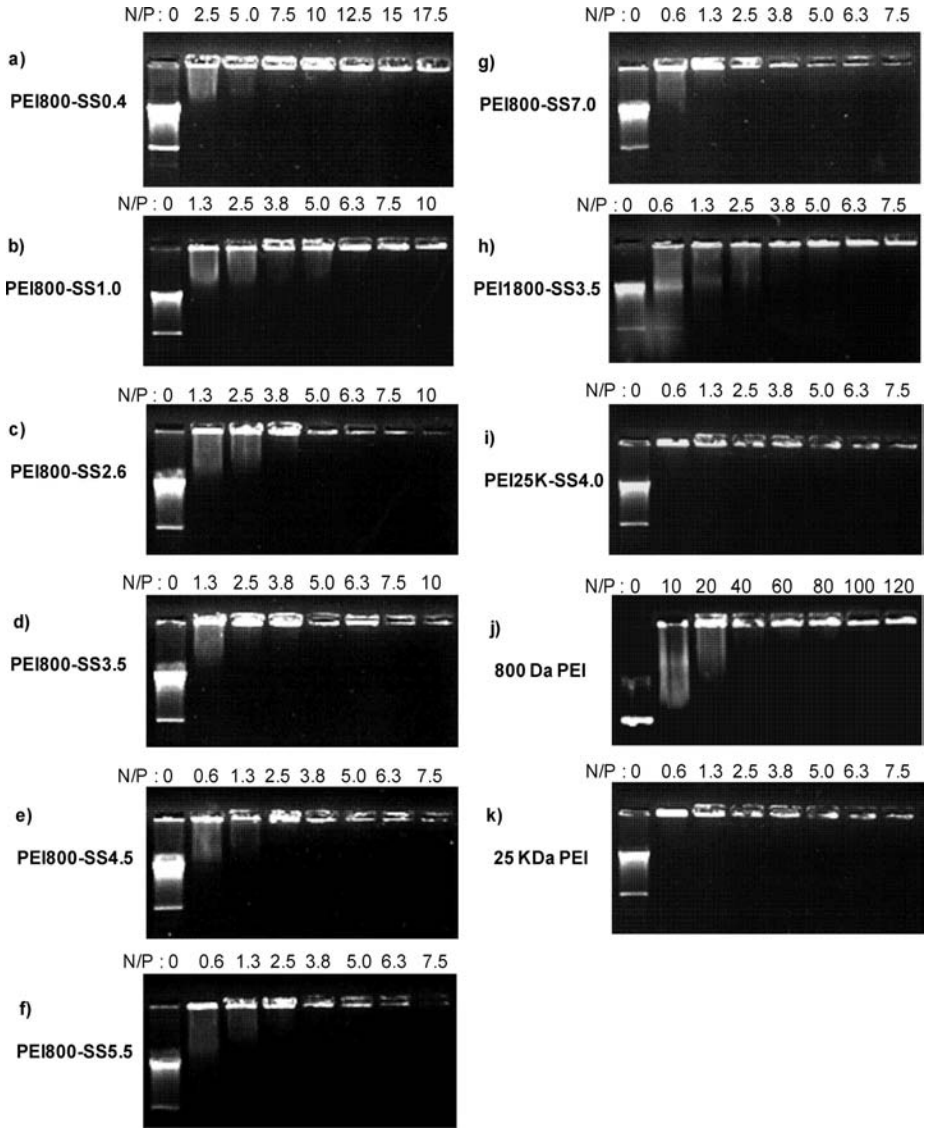

Figure 2. The effect of increasing concentration of PEI_X-SS_Y on the electrophoretic migration of pGL3 through an agarose gel. The polyplex composition (N/P ratio) was expressed as PEI nitrogen atoms per DNA phosphate. Plates a−g: PEI_{800}-$SS_{0.4}$, PEI_{800}-$SS_{1.0}$, PEI_{800}-$SS_{2.6}$, PEI_{800}-$SS_{3.5}$, PEI_{800}-$SS_{4.5}$, PEI_{800}-$SS_{5.5}$, and PEI_{800}-$SS_{7.0}$, respectively. Plates h and i: PEI_{1800}-$SS_{3.5}$ and PEI_{25K}-$SS_{4.0}$, respectively. Plate j: 800 Da PEI. Plate k: 25 KDa PEI.

the shorter outflow times of the apexes near the peak. The shapes of apexes of PEI_{800}-$SS_{3.5}$, PEI_{800}-$SS_{4.5}$, and PEI_{800}-$SS_{5.5}$ were nearly the same, and their molecular weights remained constant from the results. In HAc/NaAc buffer solution (pH 2.8, 40 °C), the molecular weights of PEI_{800}-$SS_{0.4}$, PEI_{800}-$SS_{1.0}$, PEI_{800}-$SS_{2.6}$, PEI_{800}-$SS_{3.5}$, PEI_{800}-$SS_{4.5}$ were estimated to be 1238, 1365, 1742, 2075, and 2192, respectively. The trend of the results was similar to that obtained from viscosity measurement.

Cytotoxicity of PEI_X-SS_Y. MTT assay was carried out to determine the cytotoxicity of the PEI_X-SS_Y series with the IC_{50} values listed in Table 2. The PEI_{800}-SS_Y series, regardless of the thiol group content, had a lower cytotoxicity compared to 25 kDa PEI in HeLa cells. PEI_{800}-$SS_{0.4}$ and PEI_{800}-$SS_{1.0}$ showed low cytotoxicity similar to 800 Da PEI. With the increasing content of disulfide in the polymers, their toxicity increased and reached a maximum of around 34 μg/mL (IC_{50}) at high thiolation degrees of 5.5 and 7.0. As shown in Table 2, with the similar disulfide content, PEI_X-SS_Y prepared from higher molecular weight raw PEI had higher cytotoxicity than that prepared from lower molecular weight raw PEI. PEI_{25K}-$SS_{4.0}$ showed toxicity similar to that of 25 kDa PEI.

In addition, PEI_X-SS_Y might degrade in vivo into individual low molecular weight PEI molecules with relatively low toxicity, and those low molecular weight fragments of polymers would be cleared more easily from the body.

Formation and Characterization of PEI_X-SS_Y /pDNA Polyplexes. To mediate endocytosis through cell membrane, cationic polymers need to condense DNA into compact particles via electrostatic interactions between the positively charged polymers and the negatively charged phosphates on DNA backbones (*28, 29*). The polyplex of a disulfide cross-linked PEI with a pDNA was prepared by adding PEI_X-SS_Y aqueous solution slowly to the pDNA solution. The amount of polymer added was calculated on the basis of chosen N/P ratios, nitrogen atoms of the polymer over phosphates of pDNA, in PEI_X-SS_Y/pDNA. Formation and characterization of the polyplexes was investigated by agarose gel retardation, particle size, and zeta potential.

Gel retardation assay verified that PEI_X-SS_Y series can condense plasmid DNA at low N/P ratios. As shown in Figure 2, as the concentration of the polymer increased, the capability of integrating with plasmid DNA was enhanced. 800 Da PEI formed stable complexes with DNA only at N/P ratios higher

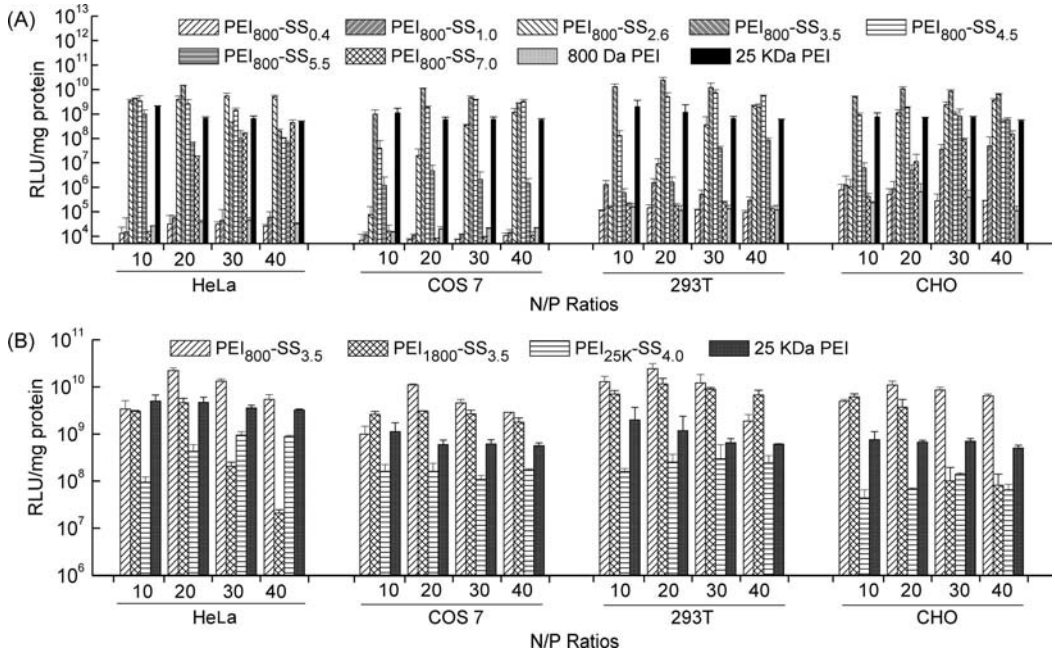

Figure 3. In vitro transfection efficiency of the polyplexes of pGL3 with PEI_{800}-SS_Y (A) and PEI_X-$SS_{3.0-4.0}$ (B) series in HeLa, COS7, 293T, and CHO cells in comparison with 800 Da and 25 kDa PEI.

than 40. In contrast, 25 kDa PEI was the most efficient that it could completely retard DNA migration at a N/P ratio of 0.6. The required N/P ratios were 7.3, 6.3, 3.8, 2.5, 2.5, 2.5, and 2.5 for PEI_{800}-$SS_{0.4}$, PEI_{800}-$SS_{1.0}$, PEI_{800}-$SS_{2.6}$, PEI_{800}-$SS_{3.5}$, PEI_{800}-$SS_{4.5}$, PEI_{800}-$SS_{5.0}$, and PEI_{800}-$SS_{7.0}$ to completely retard the pDNA, respectively. The pDNA-binding capacity of PEI_{800}-SS_Y is greatly enhanced by the disulfide cross-linking, but still significantly lower than that of 25 kDa PEI. This could be explained on the basis of GPC analysis results, which showed that there is a big portion of low molecular fraction in the cross-linked products even at high thiolation degree.

The particle sizes of the polyplexes were determined by DLS in 150 mM NaCl solution and shown in Table 2. 25 kDa PEI forms the most compact pDNA polyplexes with a size in the range 150−220 nm, and 800 Da PEI forms the loosest polyplexes with a size of about 1000 nm. The cross-linked PEI_{800}-SS_Y polymers with a moderate thiolation degree (PEI_{800}-$SS_{2.6}$, PEI_{800}-$SS_{3.5}$, and PEI_{800}-$SS_{4.5}$) could form compact polyplexes with a size of 200−300 nm at an adequate N/P ratio. In contrast, those with a too low or too high thiolation degree (Y below 2.6 or above 4.5) formed much looser polyplexes with a size above 600 nm. The polyplexes of PEI_X-$SS_{3.0-4.0}$ series (X = 800, 1800, and 25 000) form small particles with a size below 400 nm at a wide range of N/P ratios.

Zeta potentials of the polyplexes were measured in 10 mM NaCl solutions and the results are shown in Table 2. The 25 kDa PEI polyplexes have the highest zeta potential above 35 mV, and the 800 Da PEI polyplexes have the lowest zeta potential of around 10 mV. For PEI_{800}-SS_Y series, the zeta potentials are negative, showing an incomplete complexation at N/P ratios below 5 (data not shown). With increasing N/P ratio, zeta potentials of the polyplexes rapidly increase and trends to reach a plateau. For PEI_{800}-$SS_{0.4}$, PEI_{800}-$SS_{1.0}$, and PEI_{800}-$SS_{2.6}$, it reaches plateaus at N/P ratios between 30 and 40. With the increase of disulfide content in the polymers, the plateau is reached earlier at N/P ratio of about 10. For PEI_{800}-SS_Y (Y = 2.6, 3.5, and 4.5), zeta potentials plateau of the polyplexes are all around 25 mV. Surprisingly, PEI_{1800}-$SS_{3.5}$ and PEI_{25K}-$SS_{4.0}$ have lower zeta potentials of about 15 mV.

In Vitro Transfection Efficiency. The gene delivery efficiency of the PEI_X-SS_Y series was evaluated by in vitro transfection experiments of pGL3 into HeLa, COS7, 293T, and CHO cells. Branched 25 kDa PEI, which is one of the most widely used highly efficient polycation gene vectors, was used for comparison.

The transfection results of PEI_{800}-SS_Y/pGL3 polyplexes to cultured HeLa, COS7, 293T, and CHO cell lines were presented in Figure 3A. In the PEI_{800}-SS_Y series, PEI_{800}-$SS_{2.6}$, PEI_{800}-$SS_{3.5}$, and PEI_{800}-$SS_{4.5}$ showed comparable or higher transfection efficiency than 25 kDa PEI at their optimum N/P ratios. Within the range of N/P ratios tested, PEI_{800}-$SS_{3.5}$ showed maximum efficiencies at N/P ratio of 20 in all four cell lines, achieving nearly 10 times higher luciferase expression as compared with the optimal value of 25 kDa PEI. Comparison of the transfection results in Figure 3 with the size of PEI_{800}-SS_Y/pGL3 polyplexes listed in Table 2 reveals that the transfection efficiency is in good accordance with the particle size. The polymers with very low thiolation degrees of 0.4 and 1.0 unable to form compact polyplexes had very poor transfection efficiency. The polymers with moderate thiolation degrees of 2.6, 3.5, and 4.5 forming the most compact polyplexes had highest efficiency within the PEI_{800}-SS_Y series. When the thiolation degree was further increased to a very high level of 5.5 and 7.0, the polyplexes became less compact and the transfection efficiency decreased.

Figure 3B shows the transfection results of PEI_{800}-$SS_{3.5}$, PEI_{1800}-$SS_{3.5}$, and PEI_{25K}-$SS_{4.0}$, which have similar thiolation degrees but different molecular weights of raw PEIs, in HeLa, COS7, 293T, and CHO cells. Among them, PEI_{800}-$SS_{3.5}$ had the highest efficiencies in all four cell lines. PEI_{1800}-$SS_{3.5}$ had comparable efficiency to 25 kDa PEI in Hela and higher efficiency than 25 kDa PEI in COS7, 293T, and CHO cells. Surprisingly, PEI_{25K}-$SS_{4.0}$ had much poorer efficiency. Though PEI_{25K}-$SS_{4.0}$ had similar pDNA retardation capability and cell toxicity compared to 25 kDa PEI, its gene transfection efficiency was much poorer, possibly from the larger sizes and low zeta potentials of its pDNA polyplexes. These results showed that not all raw PEIs with different molecular weights are suitable for cross-linking by disulfide to form degradable polymers possessing an improved capability of gene transfection. Among

the three PEIs of different molecular weights tested (800 Da, 1800 Da, and 25 kDa), the cross-linked polymer prepared from that of the lowest molecular weight (800 Da PEI) gave the best results in all four cell lines tested.

CONCLUSIONS

Various amounts of thiol groups were readily introduced to PEIs with different molecular weights using thiirane as a thiolation agent. The thiolated PEIs were transferred to disulfide cross-linked polyethylenimines (PEI_X-SS_Y) by oxidation of the thiol groups with DMSO.

Transfection efficiency of the cross-linked polymers is dependent on the thiolation/cross-linking degree *Y*, and is in good accordance with the particle size of their pDNA polyplexes. Among the PEI_{800}-SS_Y series with different thiolation degrees prepared from identical raw PEI, the polymers with moderate thiolation degrees of 2.6, 3.5, and 4.5 forming the most compact polyplexes had highest efficiency. The polymers with very low or very high thiolation degrees were unable to form compact polyplexes and had very poor transfection efficiency.

A suitable molecular weight of raw PEI is also essential to obtain a highly efficient disulfide cross-linked PEI gene vector. Among the three raw PEIs of different molecular weights tested (800 Da, 1800 Da, and 25 kDa), the cross-linked polymer prepared from the one with the lowest molecular weight (800 Da PEI) gave the best results. Cross-linking of the high molecular weight PEI (25 kDa) led to decreased transfection efficiency.

ACKNOWLEDGMENT

This research was financially supported by National Natural Science Foundation of China (20574054), "973 Program" of the Ministry of Science and Technology of China (2005CB623903), and Program for New Century Excellent Talents in Universities (NCET) of the Ministry of Education of China.

LITERATURE CITED

(1) Remy, J. S., Sirlin, C., Vierling, P., and Behr, J. P. (1994) Gene transfer with a series of lipophilic DNA-binding molecules. *Bioconjugate Chem. 5*, 647–654.

(2) Boussif, O., Lezoualc'h, F., Zanto, M. A., Mergny, M. D., Scherman, D., Demeneix, B., and Behr, J. P. (1995) A versatile vector for gene and oligonucleotide transfer into cells in culture and in vivo: polyethylenimine. *Proc. Natl. Acad. Sci. U.S.A. 92*, 7297–7301.

(3) Felgner, P. L., Holm, T. R., Roman, R., Chan, H. W., Wenz, M., and Northrop, J. P. (1987) Lipofection—a highly efficient, lipid-mediated DNA-transfection procedure. *Proc. Natl. Acad. Sci. U.S.A. 84*, 7413–7417.

(4) Behr, J. P. (1997) The proton sponge: a trick to enter cells the viruses did not exploit. *Chimia 51*, 34–36.

(5) Akinc, A., Thomas, M., Klibanov, A. M., and Langer, R. (2005) Exploring polyethylenimine-mediated DNA transfection and the proton sponge hypothesis. *J. Gene Med. 7*, 657–663.

(6) Kircheis, R., Wightman, L., and Wagner, E. (2001) Design and gene delivery activity of modified polyethylenimines. *Adv. Drug Delivery Rev. 53*, 341–358.

(7) Uduehi, A. N., Stammberger, U., Kubisa, B., Gugger, M., Buehler, T., and Schmid, R. A. (2001) Effects of linear polyethylenimine and polyethylenimine/DNA on lung function after airway instillation to rat lungs. *Mol. Ther. 4*, 52–57.

(8) Kunath, K., Harpe, A. V., Fischer, D., Peterson, H., Bickel, U., Voigt, K., and Kissel, T. (2003) Low-molecular-weight polyethylenimine as a non-viral vector for DNA delivery: comparison of physicochemical properties, transfection efficiency and in vivo distribution with high-molecular-weight polyethylenimine. *J. Controlled Release 89*, 113–125.

(9) Ahn, C. H., Chae, S. Y., Bae, Y. H., and Kim, S. W. (2002) Biodegradable poly(ethylenimine) for plasmid DNA delivery. *J. Controlled Release 80*, 273–282.

(10) Tang, G. P., Guo, H. Y., Alexis, F., Wang, X., Zeng, S., Lim, T. M., Ding, J., Yang, Y. Y., and Wang, S. (2006) Low molecular weight polyethylenimines linked by-cyclodextrin for gene transfer into the nervous system. *J. Gene Med. 8*, 736–744.

(11) Gosselin, M. A., Guo, W., and Lee, R. J. (2001) Efficient gene transfer using reversibly crosslinked low molecular weight polyethylenimine. *Bioconjugate Chem. 12*, 989–994.

(12) Thomas, M., Ge, Q., Lu, J. J., Chen, J. Z., and Klibanov, A. M. (2005) Crosslinked small polyethylenimine: while still nontoxic, deliver DNA efficiently to mammalian cells in vitro and in vivo. *Pharm. Res. 22*, 373–380.

(13) Kakizama, Y., Harada, A., and Kataoka, K. (2001) Glutathione-sensitive stabilization of block copolymer micelles composed of antisense DNA and thiolated poly(ethylene glycol)-block-poly (L-lysine): a potential carrier for systemic delivery of antisense DNA. *Biomacromolecules 2*, 491–497.

(14) Kakizama, Y., Harada, A., and Kataoka, K. (1999) Environment-sensitive stabilization of core-shell structured polyion complex micelle by reversible cross-linking of the core through disulfide bond. *J. Am. Chem. Soc. 121*, 11247–11248.

(15) Wang, Y. X., Chen, P., and Shen, J. C. (2006) The development and characterization of a glutathione-sensitive cross-linked polyethylenimine gene vector. *Biomaterials 27*, 5292–5298.

(16) Ou, M., Wang, X. L., Xu, R. Z., Chang, C. W., Bull, D. A., and Kim, S. W. (2008) Novel biodegradable poly(disulfide amine)s for gene delivery with high efficiency and low cytotoxicity. *Bioconjugate Chem. 19*, 626–633.

(17) Lin, C., Zhong, Z. Y., Lok, M. C., Jiang, X. L., Hennink, W. E., Jan, F. J., and Engbersen, J. F. J. (2007) Novel bioreducible poly(amido amine)s for highly efficient gene delivery. *Bioconjugate Chem. 18*, 138–145.

(18) Segura, T., and Hubbell, J. A. (2007) Synthesis and in vitro characterization of an ABC triblock copolymer for siRNA delivery. *Bioconjugate Chem. 18*, 736–745.

(19) Lee, Y., Mo, H. J., Koo, H., Park, J. Y., Cho, M. Y., Jin, G. W., and Park, J. S. (2007) Visualization of the degradation of a disulfide polymer, linear poly(ethyleniminesulfide), for gene delivery. *Bioconjugate Chem. 18*, 13–18.

(20) Thierry, S., Irene, B. O., Christine, V., Gilles, P., Brigitta, L., and Andreas, B. S. (2007) Development and in vitro evaluation of a thiomer-based nanoparticulate gene delivery system. *Biomaterials 28*, 524–531.

(21) Bulmus, V., Woodward, M., Lin, L., Murthy, N., Stayton, P., and Hoffman, A. (2003) A new pH-responsive and glutathione-reactive, endosomal membrane-disruptive polymeric carrier for intracellular delivery of biomolecular drugs. *J. Controlled Release 93*, 105–120.

(22) Peng, Q., Zhong, Z. L., and Zhuo, R. X. (2008) Disulfide cross-linked polyethylenimines (PEI) prepared via thiolation of low molecular weight PEI as highly efficient gene vectors. *Bioconjugate Chem. 19*, 499–506.

(23) Scott, S, Eugene, F. L., High, R. H., and Harley, E. M. (1962) Ethylene sulfide. *Org. Synth.* 59–60.

(24) Eyer, P., Worek, F., Kiderlen, D., Sinko, G., Stuglin, A., Rudolf, V. S., and Reiner, E. (2003) Molar absorption coefficients for the reduced Ellman reagent: reassessment. *Anal. Biochem. 312*, 224–227.

(25) Riddles, P. W., Blakeley, R. L., and Zerner, B. (1979) Ellman's reagent: 5, 5′-dithiobis(2-nitrobenzoic acid)-a reexamination. *Anal. Chem. 94*, 75–81.

(26) von Harpe, A., Petersen, H., Li, Y., and Kissel, T. (2000) Characterization of commercially available and synthesized polyethylenimines for gene delivery. *J. Controlled Release 69*, 309–322.

(27) Dong, W., Jin, G. H., Li, S. F., Sun, Q. M., Ma, D. Y., and Hua, Z. C. (2006) Cross-linked polyethylenimine as potential DNA vector for gene delivery with high efficiency and low cytotoxicity. *Acta Biochim. Biophys. Sin. 38*, 780–787.

(28) Pack, D. W., Hoffman, A. S., Pun, S., and Stayton, P. S. (2005) Design and development of polymers for gene delivery. *Nat. Rev. Drug Discovery 4*, 581–593.

(29) Oupicky, D., Parker, A. L., and Seymour, L. W. (2002) Laterally stabilized complexes of DNA with linear reducible polycations: strategy for triggered intracellular activation of DNA delivery vectors. *J. Am. Chem. Soc. 124*, 8–9.

BC800451J

Bioconjugate Chemistry 20th Anniversary

Subscriber access provided by SHEMYAKIN-OVCHINNIKOV INST

Article

Hexadentate Bispidine Derivatives as Versatile Bifunctional Chelate Agents for Copper(II) Radioisotopes

Stefanie Juran, Martin Walther, Holger Stephan, Ralf Bergmann, Jo#rg Steinbach, Werner Kraus, Franziska Emmerling, and Peter Comba

Bioconjugate Chem., **2009**, 20 (2), 347-359• DOI: 10.1021/bc800461e • Publication Date (Web): 27 January 2009

Downloaded from http://pubs.acs.org on May 15, 2009

More About This Article

Additional resources and features associated with this article are available within the HTML version:

- Supporting Information
- Access to high resolution figures
- Links to articles and content related to this article
- Copyright permission to reproduce figures and/or text from this article

View the Full Text HTML

ACS Publications
High quality. High impact.

Bioconjugate Chemistry is published by the American Chemical Society. 1155 Sixteenth Street N.W., Washington, DC 20036

Hexadentate Bispidine Derivatives as Versatile Bifunctional Chelate Agents for Copper(II) Radioisotopes▽

Stefanie Juran,† Martin Walther,† Holger Stephan,*,† Ralf Bergmann,† Jörg Steinbach,† Werner Kraus,‡ Franziska Emmerling,‡ and Peter Comba*,§

Forschungszentrum Dresden-Rossendorf, Institute of Radiopharmacy, PF 510119, D-01314 Dresden, Germany, Bundesanstalt für Materialforschung and -prüfung, Richard-Willstätter-Strasse 11, D-12489, Berlin, Germany, and Universität Heidelberg, Anorganisch-Chemisches Institut, Im Neuenheimer Feld 270, D-69120 Heidelberg, Germany. Received October 24, 2008; Revised Manuscript Received December 22, 2008

The preparation and use of bispidine derivatives (3,7-diazabicyclo[3.3.1]nonane) as chelate ligands for radioactive copper isotopes for diagnosis (^{64}Cu) or therapy (^{67}Cu) are reported. Starting from the hexadentate bispidine-based bis(amine)tetrakis(pyridine) ligand **1** with a keto and two ester substituents, the corresponding mono-ol **2** and two dicarboxylic acid derivatives **3** and **5** have been synthesized. A range of techniques, including single-crystal X-ray structure analysis, UV/vis spectroscopy, cyclic voltammetry, thin-layer- (TLC), and high-performance liquid chromatography (HPLC), have been used to characterize the structure and stability of the copper(II)-bispidine complexes. A rapid formation (within 1 min) of stable copper(II)-bispidine complexes under mild conditions (ambient temperature, aqueous solution) has been observed. Challenge experiments of these complexes in the presence of a high excess of competing ligands, such as glutathione, cyclam, or superoxide dismutase (SOD), as well as in rat plasma, gave no evidence of demetalation or transchelation. The bifunctional bispidine derivative **5** can be readily functionalized with biologically active molecules at the pendant carboxylate groups. The coupling of a bombesin analogue βhomo-Glu-βAla-βAla-[Cha^{13},Nle^{14}]BBN(7−14), by condensation of a carboxylate of the bispidine backbone with the N-terminus of the peptide produced the bifunctional ligand **6**. The radiocopper(II) complex of this bombesin−bispidine conjugate has a considerable hydrophilicity (log $D_{o/w} < -2.4$), and this leads to a very fast blood clearance (blood: 0.28 ± 0.02 SUV, 1 h p.i.), low liver tissue accumulation (liver: 1.20 ± 0.27 SUV, 1 h p.i.), and rapid renal-urinary excretion (kidneys: 6.06 ± 2.96 SUV, 1 h p.i.) as shown by biodistribution studies of **^{64}Cu-6** in Wistar rats. Preliminary in vivo studies of **^{64}Cu-6** in NMRI nu/nu mice, bearing the human prostate tumor PC-3 showed an accumulation of the conjugate in the tumor (2.25 ± 0.13 SUV, 12.5 min p.i.; 0.94 ± 0.05 SUV, 55 min p.i.) and allowed a clear visualization of the gastrin-releasing peptide receptor distribution by positron emission tomography (PET).

INTRODUCTION

The extremely rigid diazaadamantane-derived bispidine ligands have first been prepared in an elegant, very versatile, and high-yielding synthesis by Mannich and recently have found extensive applications in various areas of transition metal coordination chemistry (*1*−*7*). Similar to the alkaloid sparteine, from which the bispidines are derived, various derivatives are known for their analgetic and antiarrhythmic activity (*1, 8, 9*), and the stereochemistry of the substituents is of importance for the specific receptor binding (*10*−*13*).

In the correct configuration, bispidines are highly preorganized and exceedingly rigid multidentate ligands leading to a number of very interesting properties of their transition metal coordination complexes (*14*−*18*). The distance of the ring nitrogen atoms N3−N7 of 2.9−3.1 Å allows a very stable chelation of first-row transition metals of medium size in different oxidation states, such as $V^{4+/5+}$, Mn^{2+}, $Fe^{2+/3+}$, $Co^{2+/3+}$, Ni^{2+}, Zn^{2+}, and preferably Cu^{2+}. The number, type, and position of the donor groups, which can be varied during the bispidine synthesis, provides a variety of tailor-made coordination sites for metal ions with differing preferences with respect to size, shape, and electronic properties (*1*). In particular, hexadentate ligands with pyridine units in C2, C4, N3, and N7 positions have been shown to rapidly form stable copper(II) complexes under mild conditions. The stability constants of copper(II)-bispidines are in the same range as those of macrocyclic ligand copper(II) complexes (*1, 19, 20*). As with other open-chained amine-pyridine based ligands (*21*−*23*), the relatively fast complexation kinetics of bispidine ligands in comparison with macrocyclic ligands makes the structurally reinforced bispidine derivatives with pendant pyridine donor groups attractive as chelators for copper(II) radioisotopes. Despite extensive work in this field, a number of challenges such as the specific coupling of ligands with targeting structures and detailed in vivo studies have not been accomplished to date.

^{64}Cu and ^{67}Cu have suitable nuclear decay properties with a half-life of 12.7 and 62 h, respectively, and therefore offer the possibility to be established in tumor targeting for diagnosis and therapy (*24*−*30*). Coupling of the bispidine scaffold to targeting biomolecules is therefore of particular interest. Both the C9 and the C1/5 positions are potential centers to be used for the linkage to biomolecules. The conversion of the keto group to an alcohol at C9 (*31*) and/or hydrolyzation of the C1/5 ester groups (*32*) may provide linker groups for the coupling to vector molecules.

* Corresponding authors. E-mail: h.stephan@fzd.de, Fax: +49 351 260 3232; E-mail: peter.comba@aci.uni-heidelberg.de, Fax: +49 6221 54 6617.

▽ Dedicated to Professor Dr. Fritz Vögtle on the occasion of his 70th birthday.

† Institute of Radiopharmacy.

‡ Bundesanstalt für Materialforschung and -prüfung.

§ Universität Heidelberg.

10.1021/bc800461e CCC: $40.75 © 2009 American Chemical Society
Published on Web 01/27/2009

Scheme 1. ^{64}Cu-Labeled Bispidine−Bombesin Conjugate 6 (py = pyridin-2-yl substituent)

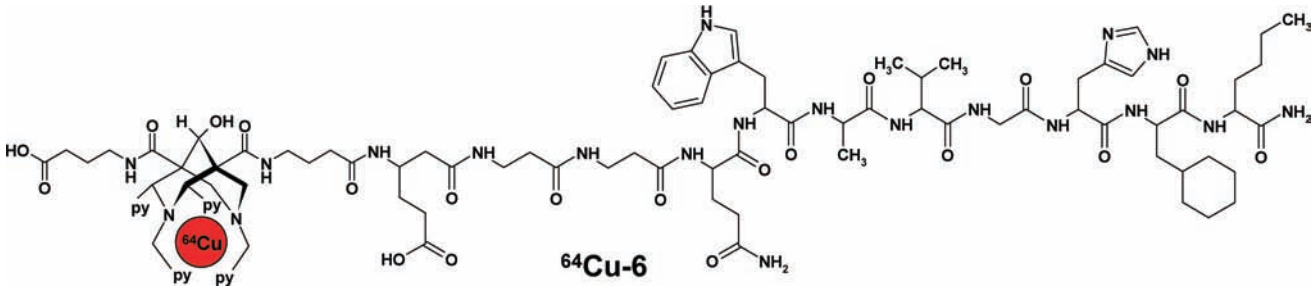

Scheme 2. Synthetic Procedure for Preparation of the Reduced Derivative 2 and Ligand 3 with Two Free Carboxylic Groups at C1 and C5 (py = pyridin-2-yl)[a]

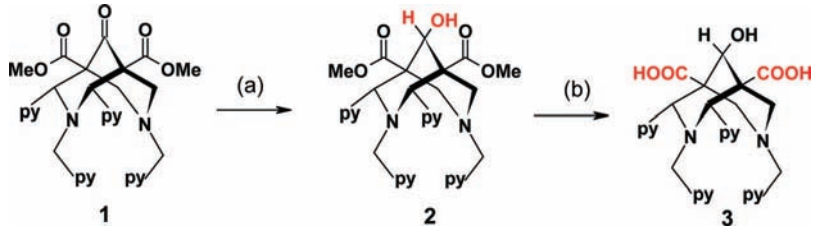

[a] (a) (i) $NaBH_4$ in dioxane/water (1/1), r.t., 24 h, (ii) H_2O, HCl, 55%; (b) CsOH, THF, r.t. 24 h, 66%.

Herein, we report the synthesis and copper coordination chemistry of the mono-ol **2** and the dicarboxylic acid derivatives **3** and **5**, starting from the hexadentate bispidine-based bis(amine)tetrakis(pyridine) ligand **1** (Scheme 2). In this first exploratory study, a stabilized bombesin (BBN) derivative βhomoGlu-βAla-βAla-[Cha^{13},Nle^{14}]BBN(7−14) (*33*) was attached as a biomolecule to the bispidine ligand **5**, yielding the bispidine−bombesin conjugate **6** (Scheme 1) as a potential imaging probe for monitoring GRP receptor expression in vivo by means of PET. The radiopharmacological characterization of the ^{64}Cu-labeled bispidine mono-ol ester **^{64}Cu-2**, the dicarboxylic acid derivative **^{64}Cu-3**, and the bispidine-bombesin conjugate **^{64}Cu-6** includes in vitro and in vivo metabolism and biodistribution studies in normal rats, and in small animal PET studies in NMRI nu/nu mice, bearing the human prostate tumor PC-3.

EXPERIMENTAL SECTION

Materials. Chemical reagents and solvents were purchased from commercial sources and used without further purification. The enzyme superoxide dismutase (from bovine liver) was purchased from Sigma. The hexadentate bispidine ligand **1** has been prepared according to a literature procedure (*34*). βhomoGlu-βAla-βAla-[Cha^{13},Nle^{14}]BBN(7−14) was obtained from Biosyntan GmbH, Berlin, Germany. The production of ^{64}Cu was performed at a PET cyclotron, similar to those recently described for the ^{64}Cu−^{61}Co-production process (*35*). For the ^{64}Ni(p,n)^{64}Cu nuclear reaction, 15 MeV protons with a beam current of 10 μA for 2 h were used. The complete separation of ^{64}Cu and ^{61}Co was confirmed by γ-ray spectroscopy. Nickel targets were prepared by electrodeposition of enriched ^{64}Ni (99.6%) on Au disks at amounts of 30−120 mg. The plated diameter was 7 mm, matching more than 80% intensity of the Cyclone 18/9 proton beam, as measured by autoradiography of a ^{nat}Ni disk irradiated with 15 MeV protons to induce the^{nat}Ni(p,x)^{57}Ni reaction. Production runs have yielded 1.5−6.0 GBq Cu-64 (130−331 MBq/μA/h) with specific activities of 30−200 GBq/μmol Cu (*35*−*37*).

Methods and Instrumentation. ^{1}H and ^{13}C NMR spectra were recorded on a 400 MHz Varian Inova spectrometer. The chemical shifts (δ, ppm) are relative to TMS or the solvent. Elemental analyses were performed on a Leco Elemental Analyzer CHNS-932. Electrospray ionization mass spectrometry (ESI-MS) was carried out using a micromass tandem quadropole mass spectrometer (Quattro LC). High-resolution mass spectra were recorded on an Agilent 6210 ESI-TOF instrument, Agilent Technologies, Santa Clara, CA, USA (ESI-TOF = electrospray ionization−time-of-flight); the solvent flow rate was adjusted to 4 μL/min; the spray voltage was set to 4 kV. The drying gas flow rate was set to 1 bar; all other parameters were adjusted to maximize $[M + H]^+$. A Cary 50 Bio UV/vis spectrometer (Varian) was used to record electronic absorption spectra. Thin layer chromatography (TLC) was performed using neutral Al_2O_3 TLC plates (Merck, F_{254}), developed in a 1:1 mixture methanol/ammonium acetate (0.1 M in water). Radioactive detection of ^{64}Cu-labeled compounds was assayed on a radioisotope thin layer analyzer (Rita Star, Raytest Isotopenmessgerät GmbH, Straubenhardt, Germany). Electrochemical measurements were carried out with a BAS100B system with a standard three-electrode cell (glassy carbon electrode, $Ag/AgNO_3$ reference electrode (0.01 M $AgNO_3$), Pt-wire auxiliary electrode) at 25 °C under argon atmosphere. All samples were measured in acetonitrile (0.1 M $(Bu)_4NPF_6$) or water (0.1 M KNO_3) with a scan rate of 100 mV/s. HPLC was performed using either of two eluents (eluent A: acetonitrile, containing 0.1% trifluoroacetic acid; eluent B: water, containing 0.1% trifluoroacetic acid), three instruments, and five methods. HPLC system 1: Knauer Smartline, including a pump 1000, a UV detector 2500, and a manager 5000. Method 1: Jupiter 4 μm C18 90 Å (Phenomenex), 250 mm × 4.6 mm, elution gradient 10% to 70% A in 20 min, 1 mL/min. Method 2: Jupiter 4 μm C18 90 Å (Phenomenex), 250 mm × 4.6 mm, elution gradient 10% to 70% A in 40 min, 1 mL/min. HPLC system 2 for the analysis of the radioactive conjugates: Perkin-Elmer, consisting of a Turbo LC System with a quarternary pump (series 200 LC pump), a programmable absorbance detector model 785A (Perkin-Elmer Instruments, Germany), and a homemade γ-ray detector (well-type, NaI(Tl) crystal). Method 3: Jupiter 4 μm C18 90 Å (Phenomenex), 250 mm × 10 mm, elution 10% to 70% A in 20 min, 2 mL/min. Method 4: Jupiter 4 μm C18 90 Å (Phenomenex), 250 mm × 10 mm, elution gradient 10% to 70% A in 40 min, 3 mL/min. HPLC system 3 for the preparative

sample purification: Knauer Wellchrom instrument, consisting of a pump K-1001, a UV detector U-2501, and a solvent organizer K-1500 for low-pressure gradient operation. Method 5: Zorbax 7 μm 300 SB-C18 Prep (Agilent), 250 mm × 21.2 mm, elution gradient 10% to 70% A in 30 min, 8 mL/min.

Dimethyl-9-hydroxy-2,4-dipyridin-2-yl-3,7-bis(pyridin-2-ylmethyl)-3,7-diazabicyclo[3.3.1]-nonane-1,5-dicarboxylate (2). 1 (500 mg, 0.844 mmol) was dissolved in 8.3 mL dioxane and mixed with 5.8 mL of water. Under ice cooling and stirring, 216 mg (5.71 mmol) sodium borohydride dissolved in 4.5 mL water was dropped into this solution. The reaction mixture was stirred 24 h at room temperature. The pH was set to 1 with dilute hydrochloric acid, the solvent was removed under reduced pressure, and the pH was set to 8 with a 1 M sodium hydroxide solution. The mixture was stirred for 1 h at room temperature and extracted five times with dichloromethane. Crystalline material suitable for X-ray analysis could be obtained from methanol. For further characterization, the crude product was purified by RP-HPLC (method 5) to yield **2** as a white solid after lyophilization. Yield: 276 mg (55%). Mp: 167 °C. Anal. Found (%): C, 64.84; H, 6.03; N, 13.36. Calcd for $C_{33}H_{34}N_6O_5 \cdot 1H_2O$ (%): C, 64.69; H, 5.92; N, 13.72. ESI-MS (*m*/*z*): 595.4 (100%) $[M + H]^+$. HPLC (method 1): $t_R = 9.4$ min.

9-Hydroxy-2,4-dipyridin-2-yl-3,7-bis(pyridin-2-ylmethyl)-3,7-diazabicyclo-[3.3.1]nonane-1,5-dicarboxylic acid (3). To 200 mg (0.336 mmol) of **2**, dissolved in 6 mL of anhydrous tetrahydrofurane, was added 565 mg (3.36 mmol) cesium hydroxide. Under ice cooling, 34 μL water was added, and after stirring 24 h at room temperature, a milky white emulsion was obtained. After setting the pH to 6 with dilute hydrochloric acid, the solvent was removed in vacuo. The crude product was dissolved in ethanol and purified by preparative RP-HPLC (method 5) to yield **3** as a white solid after lyophilization. Yield: 166 mg (87%). Mp: 174 °C. Anal. Found (%): C, 63.34; H, 5.83; N, 14.32. Calcd for $C_{31}H_{30}N_6O_5 \cdot 1H_2O$ (%): C, 63.69; H, 5.52; N, 14.37. ESI-MS (*m*/*z*): 567.3 (100%) $[M + H]^+$. HPLC (method 1): $t_R = 8.1$ min.

Diethyl 4,4′-{[9-Hydroxy-2,4-dipyridin-2-yl-3,7-bis(pyridin-2-ylmethyl)-3,7-diazabicyclo-[3.3.1]nonane 1,5-diyl]-bis(carbonylimino)}dibutanoate (4). 50 mg (0.088 mmol) of **3** and 66.9 mg (0.176 mmol) HBTU were dissolved in 500 μL dry dimethylformamide. Subsequently, 76 μL (0.412 mmol) DIPEA and 20 mg (0.154 mmol) ethyl-4-aminobutyrate, dissolved in 1 mL dry dimethylformamide, were added under ice cooling, and the reaction mixture was stirred for 3 h at room temperature. The solvent was removed under reduced pressure, and the crude product was purified by RP-HPLC (method 5) to yield **4** as a white solid after lyophilization. Yield: 14 mg (17%). Anal. Found (%): C, 53.34; H, 5.43; N, 10.62. Calcd for $C_{43}H_{52}N_8O_7 \cdot 2H_2O \cdot (TFA)_2$ (%): C, 53.41; H, 5.53; N, 10.60. ESI-MS (*m*/*z*): 793.6 (100%) $[M + H]^+$. HPLC (method 2): $t_R = 18.5$ min.

4,4′-{[9-Hydroxy-2,4-dipyridin-2-yl-3,7-bis(pyridin-2-ylmethyl)-3,7-diazabicyclo-[3.3.1]nonane-1,5-diyl]bis(carbonylimino)}dibutanic Acid (5). To 20 mg (0.019 mmol) of **4**, dissolved in 500 μL of anhydrous tetrahydrofurane, was added 32 mg (0.19 mmol) cesium hydroxide. Under ice cooling 5 μL water was added, and after stirring 24 h at room temperature, a milky white emulsion was obtained. After setting the pH to 6 with dilute hydrochloric acid, the solvent was removed in vacuo. The crude product was dissolved in ethanol and purified by preparative RP-HPLC (method 5) to yield **5** as a white solid after lyophilization. Yield: 17 mg (90%). Anal. Found (%): C, 51.64; H, 5.00; N, 11.18. Calcd for $C_{39}H_{44}N_8O_7 \cdot 2H_2O \cdot (TFA)_2$ (%): C, 51.60; H, 5.04; N, 11.20. ESI-MS (*m*/*z*): 737.4 (100%) $[M + H]^+$. HPLC (method 2): $t_R = 13.4$ min.

***N*-{6-[5-(5-Carboxypentanoyl)-9-hydroxy-2,4-dipyridin-2-yl-3,7-bis(pyridin-2-ylmethyl)-3,7-diazabicyclo-[3.3.1]non-1-yl]-6-oxohexanoyl}-*β*homo-Glu-*β*Ala-*β*Ala-[Cha^{13},Nle^{14}]BBN(7−14) (6).** Five milligrams (6.78 μmol) of **5** and 2.6 mg (6.78 μmol) HATU were dissolved in 400 μL anhydrous dimethylformamide and stirred for 10 min at room temperature. Afterward, 7 equiv of DIPEA (4.1 mg, 0.032 mmol) and 5.5 mg (4.52 μmol) βhomo-Glu-βAla-βAla-[Cha^{13},NIe^{14}]BBN(7−14) in 300 μL anhydrous dimethylformamide were added under ice cooling. The mixture was stirred for 3 h at room temperature, and the solvent was then removed in vacuo. The residue was dissolved in acetonitrile/water (1:1) and purified by RP-HPLC (method 5) to yield **6** as a white solid after lyophilization. Yield: 2.5 mg (19%). ESI-MS (*m*/*z*): 1988.94 (100%) $[M + Na]^+$. High-resolution ESI-TOF-MS (*m*/*z*): Found 983.5108 (45%); calcd 983.5103 for $[M + 2H]^{2+}$. HPLC (method 2): $t_R = 19.9$ min.

Cu-2(NO$_3$)$_2$·H$_2$O. To 100.5 mg (0.169 mmol) of **2**, dissolved in 2 mL methanol, was added a solution of 31.5 mg (0.169 mmol) $Cu(NO_3)_2$ in 1 mL methanol. The mixture was stirred for 30 min (r.t.). The color changed from pale to dark blue. Slow diffusion of diethyl ether into this solution produced crystals that were suitable for X-ray crystallography. Yield: 29.7 mg (22%). Anal. Found (%): C, 49.68; H, 4.61; N, 14.28. Calcd for $C_{33}H_{34}N_8O_{11}Cu \cdot 1H_2O$ (%): C, 49.53; H, 4.53; N, 14.00. ESI-MS (*m*/*z*): 656.4 (100%) $[M + H]^+$. HPLC (method 1): $t_R = 10.2$ min.

Cu-3(NO$_3$)$_2$·2H$_2$O. To 95.7 mg (0.169 mmol) of **3**, dissolved in 2 mL methanol, was added a solution of 31.5 mg (0.169 mmol) $Cu(NO_3)_2$ in 1 mL methanol. The mixture was stirred for 30 min (r.t.), changing the color from pale to dark blue. Slow diffusion of diethyl ether into this solution produced crystals that were suitable for X-ray crystallography. Yield: 34.7 mg (26%). Anal. Found (%): C, 47.31; H, 4.51; N, 14.08. Calcd for $C_{31}H_{30}N_8O_{11}Cu \cdot 2H_2O$ (%): C, 47.12; H, 4.34; N, 14.18. ESI-MS (*m*/*z*): 629.4 (100%) $[M - H]^-$. HPLC (method 1): $t_R = 9.7$ min.

Cu-6(TFA)$_x$. To 10 mg (0.0051 mmol) of **6** dissolved in 1 mL methanol was added a solution of 1 mg (0.0051 mmol) $Cu(NO_3)_2$ in 0.5 mL methanol. The mixture was stirred for 24 h, the solvent was then evaporated, and the resulting oily residue was purified RP-HPLC (method 3) to yield a pale blue solid after lyophilization. Yield: 6.4 mg (58%). ESI-MS (*m*/*z*): 1014.47 (100%) $[M + H]^{2+}$. High-resolution ESI-TOF-MS (*m*/*z*):Found 1013.9698 (35%); calcd 1013.9673 for $[M + Cu]^{2+}$. HPLC (method 3): $t_R = 12.9$ min.

X-ray Data Collection, Processing, and Structural Determination of Cu-1 and Cu-2. The X-ray data were collected at room temperature (293 K) on a SMART-CCD diffractometer (SIEMENS), using graphite monochromatized Mo Kα radiation ($\lambda = 0.710\ 73$ Å). The structures were solved by direct methods with SHELXS-97 (G. M. Sheldrick, Universität Göttingen, 1997). A full matrix least-squares refinement on F^2 was carried out using SHELXL-97. The hydrogen atoms were assigned with common isotropic displacement factors and included in the final refinement by the use of geometrical restrains. Further details of X-ray structure analyses are given in Table 1. Selected bond lengths and angles are listed in Table 2. CCDC 705478 (**2**), CCDC 705479 (**Cu-2**), and CCDC 705480 (**Cu-3**), contain the supplementary crystallographic data for this paper. These data can be obtained free of charge via http://www.ccdc.cam.ac.uk/data_request/cif, by e-mailing data_request@ccdc.cam.ac.uk, or by con-

Table 1. Comparison of Selected Bond Lengths [Å] and Angles [°] of Cu-1, Cu-2, and Cu-3

bond lengths [Å]	**Cu-1** (14)	**Cu-2**	**Cu-3**
Cu−N3	2.093(3)	2.063(5)	2.064(5)
Cu−N7	2.038(3)	2.028(5)	2.028(5)
$Cu-N_{(py(C2))}$	2.262(3)	2.387(6)	2.333(5)
$Cu-N_{(py(C4))}$	2.608(3)	2.538(5)	2.551(5)
$Cu-N_{(py(N3))}$	2.012(3)	1.976(5)	1.986(5)
$Cu-N_{(py(N7))}$	2.031(3)	2.001(5)	2.016(5)
$\sum_{i=1}^{6}(Cu-n_i)$	13.045(3)	12.993(5)	12.978(5)
distances [Å]			
N3−N7	2.840(3)	2.818(5)	2.803(5)
$N_{(py(C2))}$-$N_{(py(C4))}$	4.696(4)	4.719(5)	4.714(5)
angles [°]			
N3−Cu−N7	86.87(12)	87.1(2)	86.5(2)
$N3-Cu-N_{(py(C2))}$	78.54(11)	75.7(2)	77.0(2)
$N3-Cu-N_{(py(C4))}$	72.79(13)	73.6(2)	74.23(2)
$N3-Cu-N_{(py(N3))}$	84.64(11)	86.0(2)	86.6(2)
$N7-Cu-N_{(py(N7))}$	82.96(12)	83.7(2)	84.6(2)
$N3-Cu-N_{(py(N7))}$	153.31(12)	157.0(2)	156.5(2)
$N7-Cu-N_{(py(N3))}$	171.34(13)	171.5(2)	171.2(2)

Table 2. Spectroscopic and Electrochemical Data of Copper(II) Complexes with Ligands 1−3 and Cyclam

	Cu-1	**Cu-2**	**Cu-3**	**Cu-cyclam**
UV/vis (dd transition)[a]	620 (110)[b]	620 (100)	614 (110)	510 (93)[c]
$E°$ ($Cu^{II/I}$)[d] (mV)	−573[f]	−596	−690	−431
$E°$ ($Cu^{II/I}$)[e] (mV)	−502[f]	−415	−486	−

[a] λ_{max} [nm] (ε [M^{-1} cm^{-1})]. [b] From ref 14. [c] From ref 21. [d] In acetonitrile, vs $Ag/AgNO_3$; $\mu = 0.1$. [e] In water, vs $Ag/AgNO_3$; $\mu = 0.1$. [f] From ref 15.

tacting the Cambridge Crystallographic Data Centre, 12 Union Road, Cambridge CB2 1EZ, U.K.; fax: +44 1223 336033.

Preparation of Radioactive Copper Complexes ^{64}Cu-1, ^{64}Cu-2, ^{64}Cu-3, and ^{64}Cu-6[1]. To 200 μL of ligand solution (0.1 mM of **1**−**3** in acetonitrile/0.1 M NH_4OAc = 1/1), an aqueous solution of $^{64}CuCl_2$ (500 kBq, 100 μL, 0.1 M NH_4OAc) was added. The labeling efficiency was investigated as a function of time and ligand concentration. Radiochemical purity was determined by HPLC (method 3) and radio-TLC. For radiolabeling of the bioconjugate **6**, 0.5 mg ligand dissolved in 100 μL acetonitrile/water (1/1) 100 μL $^{64}CuCl_2$ (5−20 MBq, 0.1 M NH_4Oac, pH 6.5) was added. Incubation at 37 °C for 30 min yielded ≥99% radiochemical purity (HPLC, method 3).

Ligand Exchange "Challenge" Studies. UV/vis spectroscopy was used to study the stability of the copper(II) complexes with ligands **1**−**3** in the presence of glutathione. To the copper(II)-bispidine complexes (2 mM in water), 50 equiv glutathione (0.1 M) was added, and the electronic absorption spectra were recorded in the range from 400 to 800 nm as function of time (each 1 h for 24 h). To study the influence of cyclam as competing ligand, radiotracer experiments with ^{64}Cu were used. 250 μL $^{64}CuCl_2$ (500 kBq) in 0.1 M NH_4OAc was added to 500 μg **1**−**3** dissolved in 100 μL acetonitrile/water (1/1). After 15 min, full complexation of the ligand was checked by TLC. Then, 40 mg cyclam (0.2 mmol; more than 1000-fold excess (1000−10 000-fold excess, depending on varying the specific activity of different Cu-64 production runs and time of Cu-64 use after EOB) dissolved in 1 mL acetonitrile/water (1/1) was added to the complex solution, buffered to pH 6 by addition of acetic acid, and stirred for 24 h. The degree of decomposition was determined by radio-TLC and radio-HPLC (method **3**) using aliquots of the mixtures.

[1]Charges and oxidation states are all omitted in this nomenclature; all complexes investigated here are Cu^{II} complexes; ^{64}Cu-1, e.g., is a 2+ charged cation.

SOD "Challenge" Studies. 250 μL $^{64}CuCl_2$ (5 MBq) in 0.1 M NH_4OAc was added to 10 μg of the ligands **1**−**3** dissolved in 100 μL acetonitrile/water (1/1). The complete complexation of the ligand was checked by TLC after 15 min. After removal of the acetonitrile, more than a 1000-fold excess of SOD (5 mg, from bovine liver dissolved in 200 μL of 0.9 M NaCl solution) was added to the complex solution and stirred for 24 h. The degree of decomposition was determined by radio-TLC, using aliquots of the mixture.

Determination of the Partition Coefficient log $D_{o/w}$. Compounds **2**, **3**, **5**, and **6** were dissolved in 50 μL water (c_0 = 1 mM) and added to a mixture of 390 μL HEPES/NaOH buffer (0.05 M, pH = 7.2, 7.4, 7.8), 10 μL $^{64}CuCl_2$ solution in 0.1 M NH_4OAc and 50 μL 10^{-4} M $Cu(NO_3)_2$ in water. Due to the low water solubility of ligand **1**, the corresponding Cu(II) complex was used. The distribution experiments in 1-octanol/buffer systems were performed at 25 ± 1 °C in microcentrifuge tubes (2 cm^3) by means of mechanical shaking for 30 min. The phase ratio $V_{(1\text{-octanol})}$:$V_{(aq)}$ was 1:1 (0.5 cm^3 each). All samples were centrifuged, the phases separated, and the copper concentration was determined in both phases radiometrically using γ-radiation [^{64}Cu, NaI(Tl) scintillation counter automatic gamma counter 1480, Wizard 3", PerkinElmer].

In Vitro Studies. To 500 μg of the ligands (**1**−**3**, **6**), dissolved in 50 μL water/acetonitrile (1:1), 10 MBq of $^{64}CuCl_2$ was added. After complexation, 250 μL phosphate buffer (0.1 M, pH = 7.4) and 250 μL rat plasma were added, and the solution was incubated at 37 °C for 2 and 24 h, respectively. For precipitation of blood cells and proteins, cold ethanol (500 μL) was added and the supernatant was centrifuged two times. The ethanolic solution was dried under nitrogen, dissolved in 100 μL water/acetonitrile (4/1 + 0.1% TFA), the residue filtered off, and the filtrate checked by HPLC (method 3).

In Vivo Stability. The in vivo stability of **^{64}Cu-6** was analyzed using rat arterial blood samples at various time points after intravenous injection of the radiotracer. For rat arterial blood sampling, a 3.5 Fr umbilical vessel catheter, prefilled with heparinized saline, was inserted into the right carotid arteria, and 100 μL blood samples were taken at 1, 3, 5, 10, 20, 30, and 60 min after intravenous tracer application. The samples were centrifuged to precipitate the blood cells. A solution consisting of 50 μL CH_3CN, 45 μL H_2O, and 5 μL TFA was added to 200 μL of the supernatant, and the mixture was then cooled to −20 °C. After centrifugation, the supernatant was analyzed by radio-HPLC, Zorbax (Agilent) SB-C18, 300 Å, 5 μm, 250 × 9.4 mm; gradient elution using eluents C (acetonitrile containing 0.05% TFA) and D (water containing 0.04% TFA), 10% to 70% eluent C in 20 min, 3 mL/min, 28 °C. The chromatogram of **^{64}Cu-6** (plasma, 0 min) was obtained by addition of **^{64}Cu-6** to rat blood and immediately treating the mixture as described for the in vivo samples. Urine and kidney homogenate (10% in PBS) were treated analogously to the arterial blood samples.

Animals, Feeding, Husbandry, and Biodistribution Studies in Rats. The animal research committee of the Landesdirektion Dresden approved the animal facilities and the experiments according to institutional guidelines and the German animal welfare regulations. The Wistar rats (Harlan Winkelmann GmbH, Borchen, Germany) were housed under standard conditions with free access to standard food and tap water. Animals were between 7 and 9 weeks of age (body weight 227 ± 10 g). The rats were housed in an Animal Biosafety Level 1 (ABSL-1) acclimatized facility with a temperature of 22 ± 2 °C and humidity of 55 ± 5%. Animals were under a 12 h light cycle. The NMRI nu/nu mice were housed under similar conditions except temperature (27 ± 1 °C) in controlled-airflow cabinets. Animals for each time point were intravenously injected into a tail vein with approximately 8 μCi (0.3 MBq) **^{64}Cu-3** or **^{64}Cu-6** conjugate in 0.5 mL electrolyte

Scheme 3. Synthesis of 4 and 5 by Introduction of an Aminobutyric Acid Linkage into 3 to Facilitate the Attachment of Biomolecules into the Bispidine Scaffold (py = pyridin-2-yl)[a]

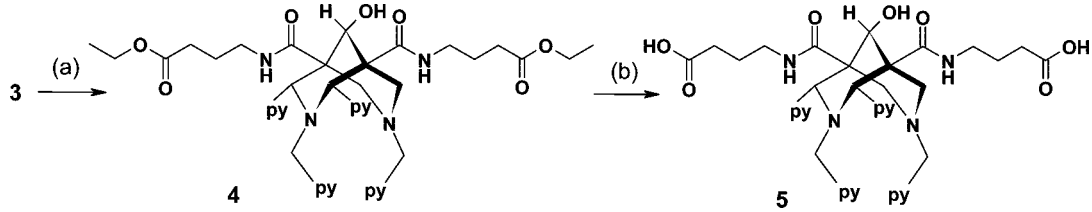

[a] (a) ethyl-4-aminobutyrate, HBTU, DIPEA, DMF, 0 °C - r.t. 3 h, 17%, (b) CsOH, THF, 0 °C - r.t., 24 h, 90% after recrystallization from ethanol.

solution E-153 (Serumwerk Bernburg, Germany) with 5% Tween 80. Animals were euthanized at 5 and 60 min postinjection. Blood and the major organs were collected, weighed, and counted in a Wallac WIZARD Automatic Gamma Counter (PerkinElmer, Germany). The radioactivity of the tissue samples was decay-corrected and calibrated by comparing the counts in tissue with the counts in aliquots of the injected tracer that had been measured in the gamma counter at the same time. The activity in the selected tissues and organs was expressed as percent injected dose per organ (% ID) or as standardized uptake value (SUV). Values are quoted as means ± standard deviation (mean ± SD) for each group of four animals.

PET Imaging. General anesthesia of rats was induced with inhalation of desflurane 9% (v/v) (Suprane, Baxter, Germany) in 40% oxygen/air (gas flow 1 L/min) and was maintained with desflurane 6% (v/v). General anesthesia of NMRI nu/nu mice was induced with inhalation of desflurane 12% (v/v) (Suprane, Baxter, Germany) in 40% oxygen/air (gas flow 1 L/min) and was maintained with desflurane 8% (v/v). In the PET experiments, approximately 0.5 mCi (18.5 MBq) of the **^{64}Cu-6** conjugate in 0.5 mL was administered intravenously over 1 min into a tail vein. PET imaging of **^{64}Cu-6** in mice was performed over 60 min with a microPET P4 scanner (Siemens CTI Molecular Imaging Inc., Knoxville). Data acquisition was performed in 3D list mode. For estimation of photon attenuation in the subjects, a transmission scan was carried out prior to the injection of **^{64}Cu-6** using a ^{57}Co point source. Emission data were collected continuously for 60 min after injection of **^{64}Cu-6**. The list mode data were sorted into sinograms using a framing scheme of 12° − 10 s, 6° − 30 s, 5° − 300 s, and 5° − 600 s frames. The data were attenuation corrected, and the frames were reconstructed by ordered subset expectation maximization applied to 3D sinograms (OSEM3D) with 14 subsets, 6 OSEM3D iterations, 2 maximum a posteriori (MAP) iterations, and 0.05 β-value for smoothing. The pixel size was 0.8 by 0.8 by 1.2 mm^3, and the resolution in the center of field of view was 1.85 mm. No correction for recovery and partial volume effects was applied. The image files were processed using the *ASIPRO* software (Siemens, CTI Molecular Imaging Inc., Knoxville) and the *ROVER* software (ABX GmbH, Radeberg, Germany). Summed frames from 30 to 90 s postinjection (p.i.) and 30 to 90 min p.i. were used to define the regions of interest (ROI). The data were normalized to the injected radioactivity by using ^{64}Cu standards from the injection solution measured in a μ-well counter (Isomed 2000, Dresden, Germany) cross-calibrated to the PET scanner and expressed in SUV.

Statistical Analysis. The data are expressed as means ± SD. One-way analysis of variance (ANOVA) was used for statistical evaluation. Means were compared using Student's *t* test. A *P* value of <0.05 was considered significant and indicated by an asterisk symbol (*).

RESULTS AND DISCUSSION

Synthetic Approach. The bispidine starting compound **1** was synthesized according to the described procedure in the *endo*−*endo* form with respect to the C2/4 positions (1, 19, 34). The chair−chair conformation of the bicycle combined with the *endo*−*endo* configuration at C2/C4 is well-organized for the complexation of metal ions like copper(II) 19. Subsequent chemical modification (reduction, saponification, peptide coupling) of the products does not alter this conformation. Full coordination of the hexadentate ligand in a distorted octahedral geometry leads to a high degree of shielding of the copper(II) ion from the environment.

The keto group in position 9 was reduced to the corresponding alcohol (ligand **2**) to stabilize the bispidine skeleton (see Scheme 2). This prevents the decarboxylation of the β-keto acid, which would be obtained through the direct ester hydrolysis of **1** *38, 39*. The reduction of the ketone was carried out in the presence of sodium borohydride in a dioxane/water mixture and led stereospecifically to the anti epimer of **2** (*31, 40*). The structure of **2** was confirmed by NMR spectroscopy and X-ray crystallography to show the chair−chair conformation as the preferred conformation in polar solvents (see Supporting Information for details) (*41*).

Experiments to alternative routes for insertion of coupling units such as imines or oximes directly at the keto group 9 fail due to the low reactivity of **1** in common carbonyl reactions (except for the reduction as described above). Therefore, the coupling is based on the ester hydrolysis to the dicarboxlic acid **3**. To increase the distance of the site of coupling to the backbone and hence the accessibility to functionalization with sterically hindered peptides, a 4-aminobutyric acid spacer was introduced (see Scheme 3). The bis ethyl ester derivative **4** was hydrolyzed with cesium hydroxide in tetrahydrofurane to yield the bispidine derivative **5** with two carboxylate functions with reduced steric demand and increased reactivity for subsequent amide coupling reactions with specific biomolecules.

The synthesis of bombesin derivative **6** was carried out in dimethylformamide with HATU, one of the most efficient auxiliary compounds for amide coupling reactions. During the attachment of the βhomo-Glu-βAla-βAla-[Cha^{13}, Nle^{14}]BBN(7−14) derivative to the bispidine **5**, the yield of **6** was limited by formation of a side product without chelate. Intramolecular cyclization of the β-homoglutamic acid residue caused by activation of the peptide leads to this undesired bombesin derivative. The product **6** was separated via HPLC and characterized by HR-MS.

Structure and Stability of Copper(II)-Bispidine Complexes. In-depth information about the complexation behavior and related structural aspects are available from single-crystal X-ray data. In the case of bispidine-type ligands, the problem of isomerism is reflected in the coordination of the copper ion, resulting in different stabilities of the complexes. The synthesis of the complexes **Cu-2** and **Cu-3** was carried out in a methanolic solution, precipitating the desired complexes with diethyl ether. Hexadentate bispidine ligands with two amine and four pyridine coordinating groups preferentially form six-coordinate copper(II) complexes with a distorted octahedral structure (*19, 20, 42, 43*). As expected, the coordination environment is only slightly

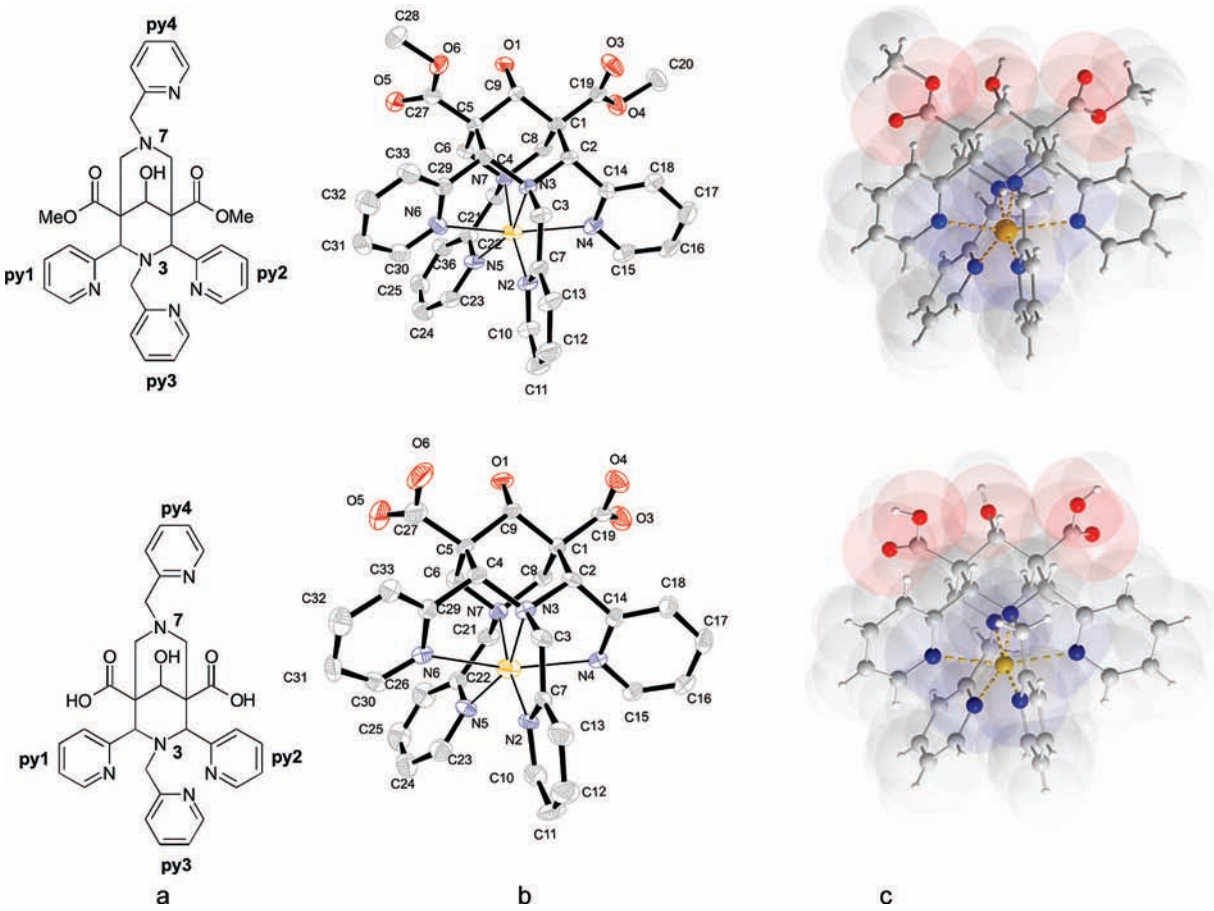

Figure 1. Coordination environment around the Cu^{II} ion in **Cu-2** (upper row) and **Cu-3** (lower row); thermal ellipsoids drawn on a 30% probability level. Gray spheres denote carbon, red spheres oxygen, blue spheres nitrogen, and yellow spheres copper atoms. Note that the crystallographic numbering scheme (b) is different from the IUPAC numbering, given in Chart a. The overlay with the space-filled model shows the efficient encapsulation of the copper ions by ligands **2** and **3** (c).

Table 3. Partition Coefficients (log $D_{o/w}$) of the ^{64}Cu Complexes of 1−3, 5, and 6 at Different pHs

pH	log $D_{o/w}$ ^{64}Cu-1	log $D_{o/w}$ ^{64}Cu-2	log $D_{o/w}$ ^{64}Cu-3	log $D_{o/w}$ ^{64}Cu-5	log $D_{o/w}$ (*64*) ^{64}Cu-6
7.2	−2.73	−2.89	−2.78	−2.14	−2.44
7.4	−2.77	−2.88	−2.76	−2.10	−2.44
7.6	−2.69	−2.85	−2.78	−2.11	−2.46

influenced by the modification of the C1...C5 ligand backbone. The crystal structures of the copper(II) complexes with the bispidol (**Cu-2**) and the corresponding dicarboxylic acid (**Cu-3**) are presented in Figure 1, and structural parameters are assembled in Table 1 (see Supporting Information for crystallographic data of **Cu-2** and **Cu-3**). The molecular structures of complexes **Cu-2** and **Cu-3** illustrate that the *endo*−*endo* geometry leads to an efficient encapsulation of the copper center. This is visualized with the space-filling models in Figure 1c, and this indicates that metal exchange in in vivo applications will be suppressed. In both complexes, the Cu^{II} ions adopts a distorted octahedral geometry which is attributed to the Jahn−Teller-type electronic effects. The Cu...N distances of the amine and pyridine donors involving py(N3) and py(N7) have comparable values in all three complexes (**Cu-1**, **Cu-2**, **Cu-3**).The Cu...N py(C2) distances are more elongated in **Cu-2** and **Cu-3** (d_{Cu-N} = 2.387(6) Å; 2.333(5) Å) than in **Cu-1** (d_{Cu-N} = 2.262 Å), whereas the equivalent distances to py(C4) are slightly shorter in **Cu-2** and **Cu-3** (d_{Cu-N} = 2.538(5) Å; 2.551(5) Å) than in **Cu-1** (d_{Cu-N} = 2.608 Å). The distances between the amine nitrogen atoms (N3...N7) in the bispidine backbone and those between the pyridine donors py(C2) and py(C4) are comparable in the three structures. As in **Cu-1**, the N3−N7-py(N3)-py(N7) plane is distorted, due to repulsion of the *ortho*-hydrogen atoms of the pyridine rings (H10A−H23A: 2.257 Å, **Cu-2**; 2.302 Å, **Cu-3**). The sum of the Cu−N bond distances of **Cu-2** and **Cu-3** is slightly shorter than that of **Cu-1**, consistent with a slightly higher stability of **Cu-2** and **Cu-3**. There are intermolecular hydrogen bonds between hydroxyl and carboxyl groups of the molecular cations and nitrates as well as water molecules in the crystal structures of **Cu-2** and **Cu-3**. In **Cu-3**, the hydrogen bonds about an inversion center lead to the formation of complex dimers (see Supporting Information).

The spectroscopic and electrochemical data of the copper(II) complexes with the bispidine ligands **1**−**3** and cyclam are summarized in Table 2. The absorption spectra of **Cu-1** to **Cu-3** exhibit broad transitions at 615−620 nm, typical for six-coordinate copper(II) complexes with distorted octahedral structure (*19*, *20*). This absorption band may be used to approximately monitor the stability of the copper(II) bispidine complexes. To an aqueous solution of the complexes (2 mM), a large excess of glutathione (100 mM) as competing ligand was added (*44*). The dd transitions remain unaffected in the presence of glutathione for at least 24 h, indicating a high stability of the copper(II) bispidine complexes.

This is further supported by the electrochemical properties of the complexes. Assuming that the copper(I) complexes have similar stability, the potential for the reduction of Cu(II) to Cu(I) can be used for the approximate determination of complex stability of the copper(II) complexes (*20*, *45*). Strongly negative reduction potentials were found as quasi-reversible reactions for the copper(II/I) couples in both acetonitrile and water. By contrast, Cu-cyclam

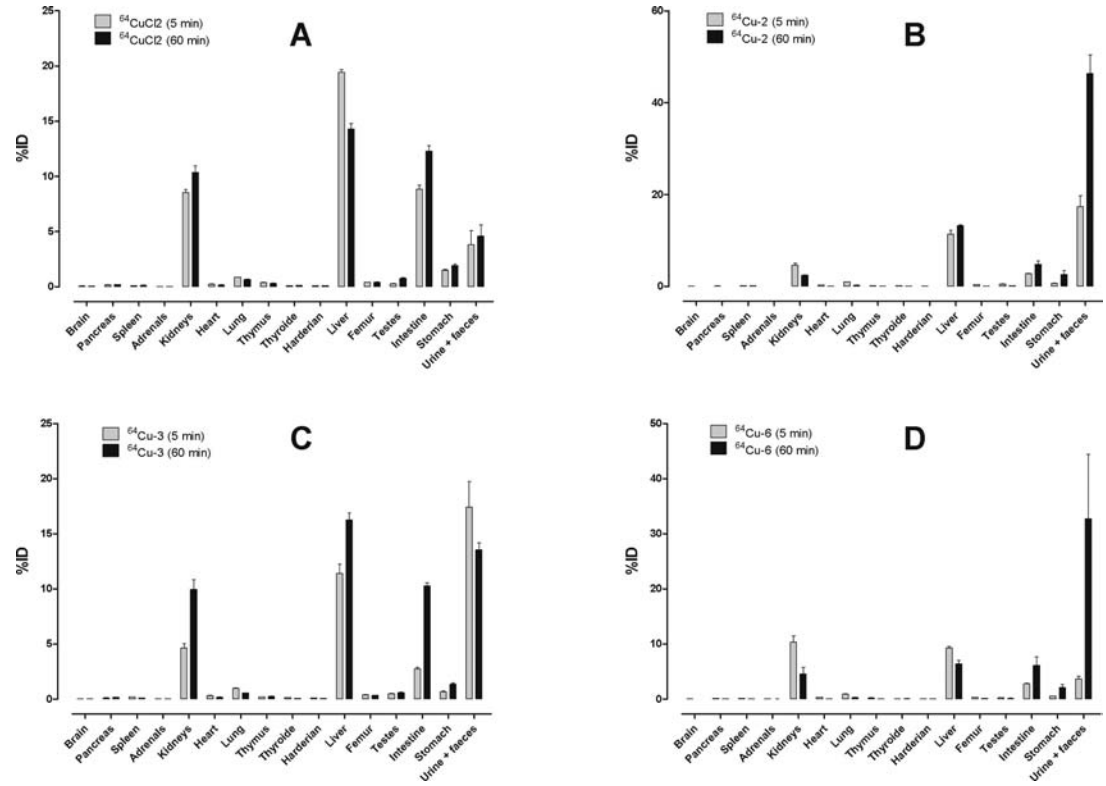

Figure 2. Biodistribution of **^{64}CuCl$_2$** (A), **^{64}Cu-2** (B), **^{64}Cu-3** (C), **^{64}Cu-6** (D) in rats at 5 and 60 min after single intravenous application. The data represent the distribution of the ^{64}Cu activity amount (%ID) in selected organs and excretions (mean ± SD of 4 animals).

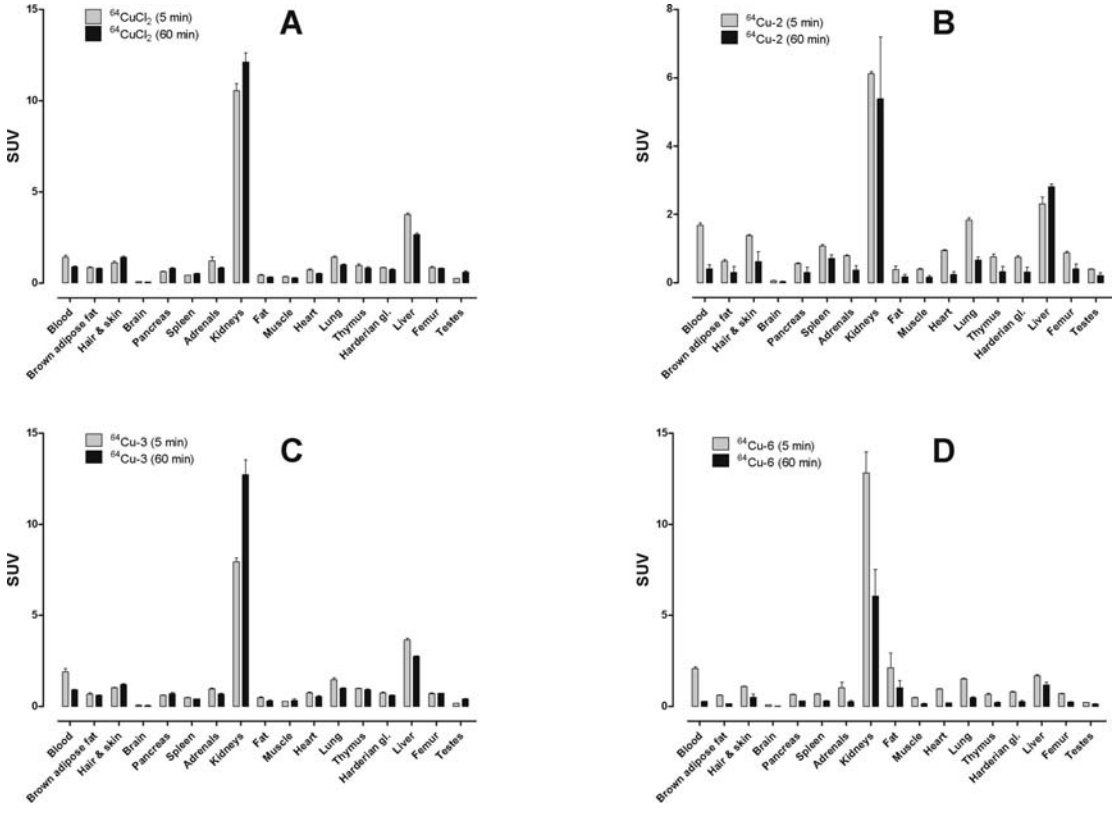

Figure 3. Biodistribution of **^{64}CuCl$_2$** (A), **^{64}Cu-2** (B), **^{64}Cu-3** (C), **^{64}Cu-6** (D) in rats at 5 and 60 min after single intravenous application. The data represent the distribution of the ^{64}Cu activity concentration (SUV) in selected organs and tissues (mean ± SD of 4 animals).

yielded an irreversible reduction in aqueous solution. The reduction potentials in acetonitrile decrease in the order **Cu-1** > **Cu-2** > **Cu-3**, indicating increasing stability from the bispidine complex (**Cu-1**) to the bispidole (**Cu-2**) and the bispidole dicarboxylic acid complex (**Cu-3**) (see above). It is worth mentioning that the reduction potentials of the copper(II) complexes with bispidine ligands are significantly lower than those of the cyclam complex, which forms one of the most stable copper complexes (log K_1 =

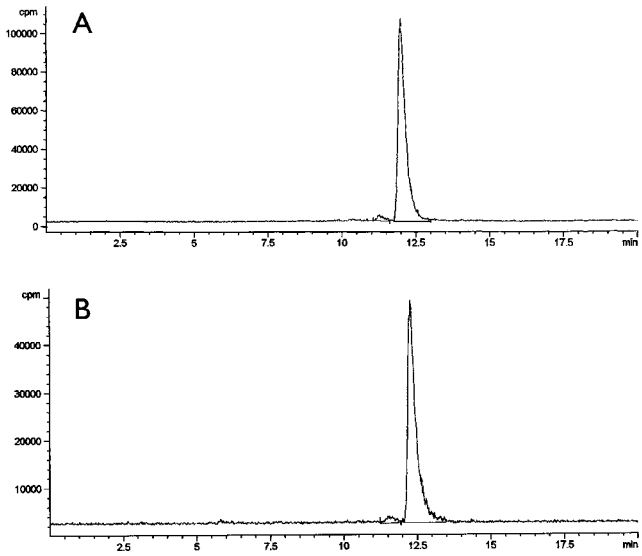

Figure 4. Examples of radio chromatograms of original **^{64}Cu-2** (A) and of rat plasma supernatant 60 min after application of **^{64}Cu-2** (B).

27.2) (*46, 47*). Note that the correlation of Cu(II/I) redox potentials with Cu(II) complex stabilities relies on the assumption of nearly constant Cu(I) stabilities, and this has been shown to be an oversimplification (*20*).

Radiochemistry. Preliminary experiments showed that the rate of copper(II) binding by bispidine ligands is very rapid at pH 6.5 and independent of the buffer system used (there is no difference among acetate, succinate, citrate, and 2-[*N*-morpholino]ethanesulfonic acid (MES) buffer, respectively). That is in contrast to the ^{64}Cu-labeling of tetraaza macrocycles, where relatively slow complexation kinetics have been observed in acetate buffer solution (*48*). ^{64}Cu-labeling of ligands **1**−**3** and **6** has been studied in detail in aqueous ammonium acetate solution. To 200 μL of 0.1 mM ligand dissolved in acetonitrile/NH_4OAc (1/1), an aqueous solution of $^{64}CuCl_2$ (500 kBq, 100 μL, 0.1 M NH_4OAc) was added. The labeling yields were monitored by thin-layer chromatography using neutral alumina plates, which were developed in 0.1 M ammonium acetate/methanol (1/1). The R_f-values of free copper and ^{64}Cu-bispidine complexes are well-separated. $^{64}CuCl_2$ remained at the origin, and the ^{64}Cu-bispidine complexes move further with R_f-values of **^{64}Cu-1**, $R_f = 0.56$; **^{64}Cu-2**, $R_f = 0.52$; **^{64}Cu-3**, $R_f = 0.46$. The bispidine ligands **1**−**3** were quantitatively labeled with ^{64}Cu within 1 min at ambient temperature under these experimental conditions. Further experiments revealed that only 1 μg of ligand is necessary to obtain complete copper complexation (5 MBq ^{64}Cu). ^{64}Cu-labeling of the bispidine bioconjugate **6** is slower than that of the unmodified ligands. Binding of copper(II) in an initial complexation step by peptide donor groups (imidazole) may lead to slower complex formation. Complexation of ^{64}Cu by **6** is complete after approximately 1 h at room temperature and 30 min at 37 °C. Altogether, a very efficient and rapid ^{64}Cu complexation of bispidine derivatives was found under mild conditions.

Challenge experiments in the presence of cyclam and the enzyme superoxide dismutase (SOD) as competing ligands have been performed to obtain further information about the stability of the radio copper bispidine complexes. HPLC (method 3) and TLC studies using neutral alumina plates (see Experimental Section) revealed that the complexes **^{64}Cu-1**, **^{64}Cu-2**, and **^{64}Cu-3** remained completely intact even in a 1000-fold excess of cyclam for at least 24 h. The stability of the radio copper complexes of these ligands was also investigated in the presence of SOD, a homodimeric enzyme which is abundant in liver, kidney, adrenal, and red blood cells. The competition assay using SOD can be used to predict the in vivo stability of radio copper complexes (*49, 50*). The challenge studies have been performed with more than 1000-fold excess of SOD compared to the ^{64}Cu bispidine complexes. The degree of decomposition was checked via TLC (neutral alumina) that allows a clear distinction of the radio copper complexes formed (**^{64}Cu-SOD**, $R_f = 0$; **^{64}Cu-1**, $R_f = 0.56$; **^{64}Cu-2**, $R_f = 0.52$; **^{64}Cu-3**, $R_f = 0.46$). Control experiments using RP-C18 plates (ethanol/MES-NaOH-buffer containing 0.001 M EDTA = 5:1) showed that free copper does not occur in the solution (**^{64}Cu-SOD**, $R_f = 0$; **^{64}Cu-EDTA**, $R_f = 0.69$). The absence of SOD-bound radioactivity indicates no transchelation of copper(II) and emphasizes a very high stability of the copper(II) bispidine complexes.

This is also confirmed by rat plasma stability studies. The plasma stability of ^{64}Cu complexes of ligands **1**−**3** and **6** was evaluated at 2 and 24 h. Radio-HPLC experiments showed that copper(II) is very tightly bound to the bispidine moiety. No demetalation of ^{64}Cu was found in rat plasma up to 24 h. In the case of the dicarboxylate **3**, the radio copper bispidine complex remains completely unchanged after rat plasma incubation. In contrast, for the radio copper complexes of the ester derivatives **1** and **2** two additional peaks appear in the chromatogram, resulting from the corresponding monoester and dicarboxylate caused by cleavage of the ester groups by esterases of the rat plasma (*51*). Furthermore, the in vitro stability studies reveal that peptidases of rat plasma attack the bombesin residue of the bioconjugate **6** (cf. in vivo stability studies).

To facilitate the interpretation of biodistribution data, the partition coefficients of the radio copper complexes have been determined in a 1-octanol/buffer system (Table 3). The copper(II) bispidine complexes are rather hydrophilic. As expected, the introduction of an aminobutyric acid spacer (**^{64}Cu-5**) leads to increased lipophilicity. The radio copper complexes of the bombesin−bispidine conjugate **^{64}Cu-6** and the bombesin−bis(2-pyridylmethyl)-triazacyclononane derivative ($\log D_{o/w} = -2.38$, pH = 7.4) possess almost the same hydrophilicity (*23*). Therefore, comparative biodistribution behavior, such as rapid blood clearance and excretion via the renal pathway, are expected for these ^{64}Cu-labeled pyridine-containing ligands.

In Vivo Studies. Due to the high affinity of the peptide bombesin to gastrin-releasing peptide receptors (GRPr), the design and synthesis of radiolabeled bombesin derivatives has recently attracted much attention (*52*−*55*). GRPs are overexpressed on a variety of human cancer cells, such as lung, breast, pancreatic, and prostate tumors. Therefore, the development of targeting vectors based on radiolabeled bombesin derivatives for imaging (PET, SPECT) and targeted radionuclide therapy is of considerable interest. Most investigations have been performed with ^{99m}Tc-labeled bombesin peptides, and to a lesser extent also with ^{18}F, ^{68}Ga, ^{125}I, ^{111}In, ^{177}Lu, ^{188}Re, ^{86}Y, and ^{90}Y (*33, 52*−*65*). Due to its favorable decay properties, the increasing availability, and the capability of producing high-quality PET images, ^{64}Cu is gaining importance in bombesin labeling (*23, 66*−*74*). In vivo studies performed so far have shown that the pharmacokinetics of the radiolabeled bombesin derivatives are influenced by the radio isotopes chosen, the chelate unit, the spacer elements, the specific modifications made to the peptide sequence and the species selected. Overall, predictions about the biodistribution of appropriate radiotracers are difficult. Therefore, we have investigated in some detail the biodistribution of various ^{64}Cu-labeled bispidine derivatives and the metabolism of the bispidine−bombesin conjugate **6**, and small-animal PET studies have also been performed.

A summary of the biodistribution and elimination data for **$^{64}CuCl_2$** (A), **^{64}Cu-2** (B), **^{64}Cu-3** (C), **^{64}Cu-6** (D) in rats is shown in Figures 2 and 3. The numeric values of %ID (% of total injected dose) and SUV (standardized uptake value) are assembled in the Supporting Information.

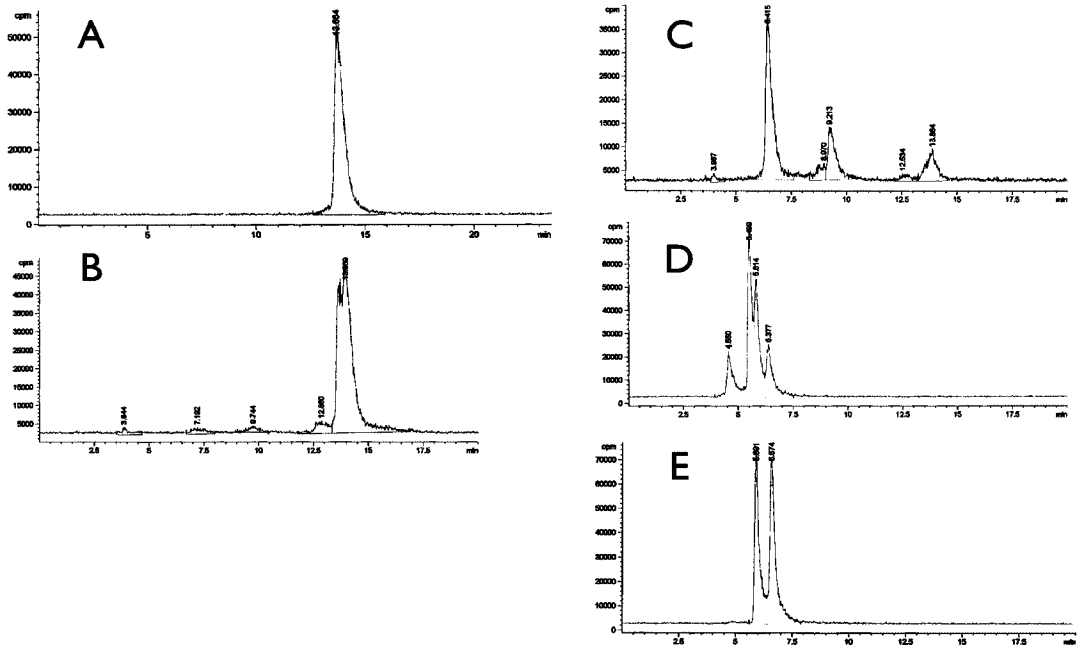

Figure 5. Radio HPLC of **^{64}Cu-6** metabolites in vitro at 1 min (A) and 60 min (B), and 60 min after application in arterial blood plasma (C), kidney homogenates (D), and urine (E).

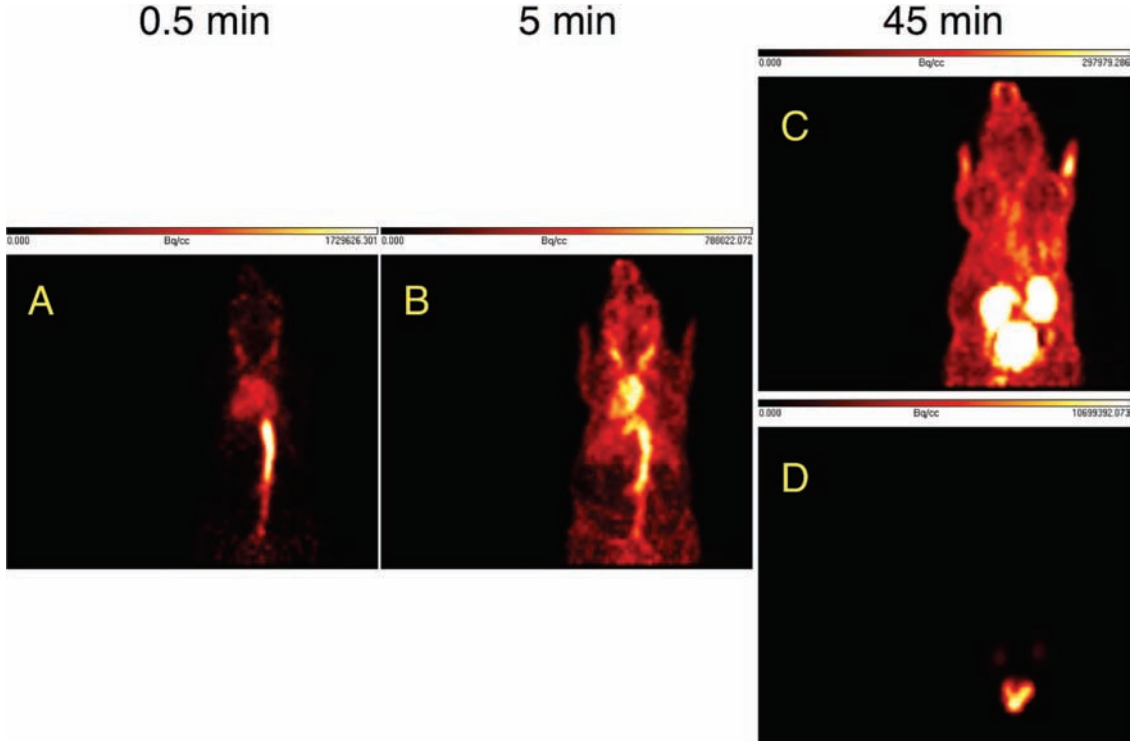

Figure 6. Coronal sections of a small animal PET study of PC-3 tumor-bearing mouse after single intravenous application of **^{64}Cu-6** at 0.5 (A), 5 (B), and 45 min (C, high intensity; D, low intensity).

The application of $^{64}CuCl_2$ resulted mostly in the accumulation of radioactive species in liver and intestine, but also in significant radioactivity retention in the kidneys. The bispidine complexes **^{64}Cu-2** and **^{64}Cu-3** were mainly eliminated into the urine as the original compounds. The metabolic analysis of **^{64}Cu-2** and **^{64}Cu-3** emphasizes the high stability of the complexes in vivo (cf., Figure 4). The initial accumulation of these compounds was similar to $^{64}CuCl_2$ in the liver, but surprisingly, the more hydrophilic acid derivative **^{64}Cu-3** was also hepatobiliary eliminated (the sum of liver and intestine activity was 26.56 ± 1.79% ID, which means more than 50% activity eliminated or on excretion pathway). The highest uptake and the resulting high activity concentration (SUV) was observed in the kidney for all compounds studied. However, the fastest elimination of radioactive species was observed for the bombesin conjugate **^{64}Cu-6**. In rats, low uptake of **^{64}Cu-6** in the pancreas, an accessible GRPr-expressing tissue, was observed. This behavior could have been caused by different effects, such as fast metabolism of the peptide residue and rapid excretion of the radiotracer. Bombesin conjugates bearing ^{99m}Tc(III) '4 + 1' complexes showed similar lack of pancreas accumulation (*64*).

The metabolic stability of **^{64}Cu-2** and **^{64}Cu-6** was determined in arterial blood samples taken at 1, 3, 5, 10, 20, 30, and 60

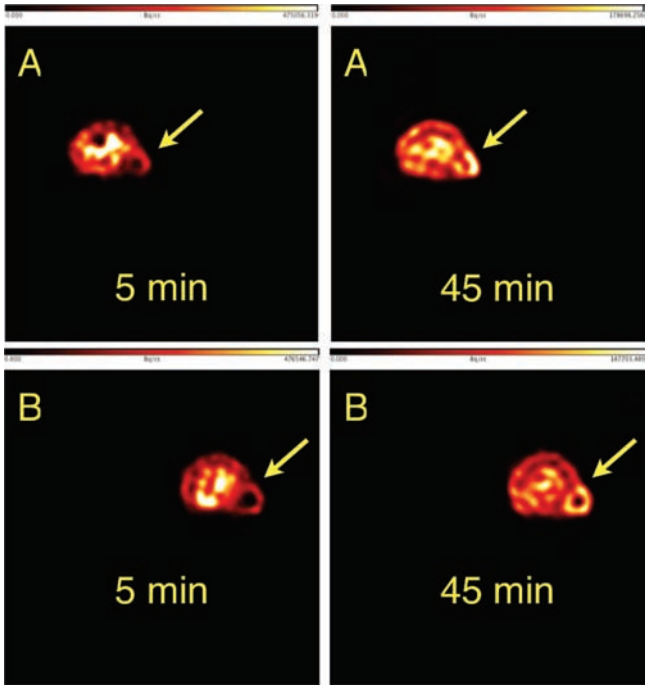

Figure 7. Coronal sections of a small animal PET study of two PC-3 tumor-bearing mice (A,B) after single intravenous application of **^{64}Cu-6** at 5 and 45 min. The arrow shows the tumor.

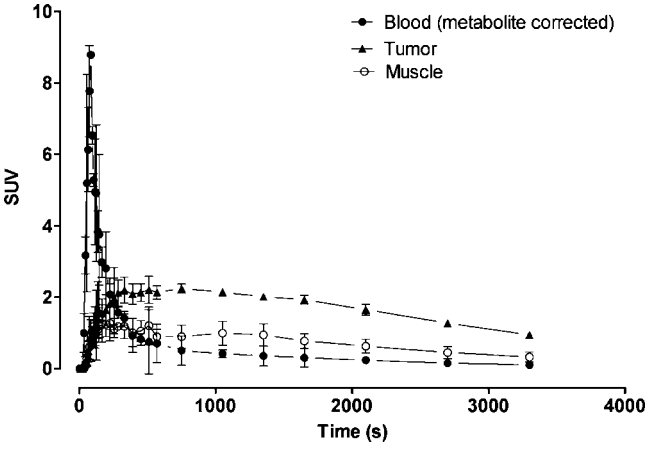

Figure 8. Biokinetics of **^{64}Cu-6** in PC-3 tumor bearing nude mice (mean ± SD of two animals). Time−activity curves were derived from ROIs over the aorta, tumor, and muscle, expressed as SUV_{mean}.

min after a single intravenous application of the radiotracer into a rat. The blood samples were centrifuged to obtain the plasma, which was treated with acetonitrile to precipitate the proteins. The supernatant is referred to as the plasma extract. After **^{64}Cu-2** was applied, the mean relative radioactivity concentration in the plasma was 90 ± 2% of the overall arterial blood activity; the plasma extract samples contained 84 ± 3% of the plasma activity. Furthermore, the plasma extract was analyzed by radio RP-HPLC for radio metabolites. Figure 5 shows the radio chromatograms of the original compound **^{64}Cu-2** and the plasma analysis after 60 min.

The main peak of in vivo samples, assigned to the original **^{64}Cu-2** complex, accounts for 98% and after 60 min for 97% of the activity (see Figure 4). The radiochromatograms of other plasma and also of urine samples are very similar. The mean relative activity of **^{64}Cu-6** in plasma was 88 ± 5% of arterial blood activity; the activity of the plasma extract samples contained 66 ± 12% of the plasma activity. The plasma extract was analyzed by RP-HPLC for radiometabolites (Figure 5).

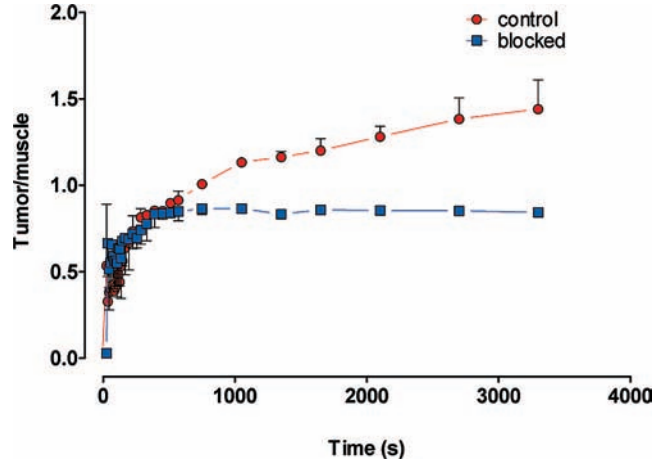

Figure 9. Time course of tumor to muscle relation of **^{64}Cu-6** in PC-3 tumor bearing nude mice (mean ± SD two animals) of control (circles) and blocked (square, 1 mg **^{nat}Cu-6**/kg body weight, simultaneously administered with **^{64}Cu-6**).

The relative amount of the original compound **^{64}Cu-6** (t_R = 13.9 min) decreased from 96% at the time of tracer application (1 min 96%, 3 min 89%, 5 min 80%, 20 min 44%, 30 min 38%) to 3% of the total plasma extract activity after 60 min. **^{64}Cu-6** was converted into three more hydrophilic radiolabeled species. The peak at 3.8 min is not due to free $^{64}Cu^{2+}$ ions, since these are eluted at 3.4 min.

The mixture of residual radioactive species in the analyzed tissues and urine was very complex. Overall, the detected radiometabolites were more hydrophilic than the native compound. The original **^{64}Cu-6** complex could not be detected in kidney extracts or urine. Extensive metabolism of **^{64}Cu-6** has occurred in both species studied (rats and tumor-mice). This is in contrast to the in vitro stability. In vitro incubation of **^{64}Cu-6** in rat blood or blood plasma yielded more than 85% of the original compound after 60 min in the nonprecipitated plasma fraction. However, the decomposition of up to 15% in vitro, which is due to partial hydrolysis, seems to be a sign of a specific effect of the bispidine complex units. A similar bombesin derivative, labeled with ^{64}Cu using 2-[4,7-bis(2-pyridylmethyl)-1,4,7-triazacyclononan-1-yl]acetic acid as bifunctional chelate, showed higher metabolic in vitro stability under analogous conditions (*23*).

Preliminary PET studies in PC-3 tumor-bearing mice have also been performed. The bombesin derivative **^{64}Cu-6** was accumulated in the GRPr-expressing tissue (see Figures 6 and 7) to allow the visualization of the tumor in the right axilla. The highest radiotracer concentration in the unblocked tumors was reached at 12.5 min (2.25 ± 0.13 SUV). However, the activity was very rapidly washed out from the tumor (Figure 8). Therefore, a high intensity is required to distinguish the tumor after 45 min, and this leads to a high background level (Figure 6C). Nonetheless, high-contrast PET images of the tumor could be produced.

The tumor to muscle ratio has been determined as function of time (Figure 9) and shows an increasing value for the unblocked (control) mice (1.78 ± 0.14 at 1 h) in contrast to the blocked animals (0.84 ± 0.01 at 1 h, 1 mg **^{nat}Cu-6**/kg body weight). This finding points to a receptor-mediated tracer uptake into tumor tissue.

CONCLUSION

Five new hexadentate pyridine-containing bispidine derivatives **2**−**6** have been synthesized. X-ray diffraction studies of the copper(II) complexes of **2** and **3** confirmed a distorted octahedral geometry with an efficiently encapsulated and shielded Cu^{2+} center. UV/vis spectra indicate that these cop-

Scheme 4. Coupling of 5 to the Bombesin Derivative Leads to Bioconjugate 6[a]

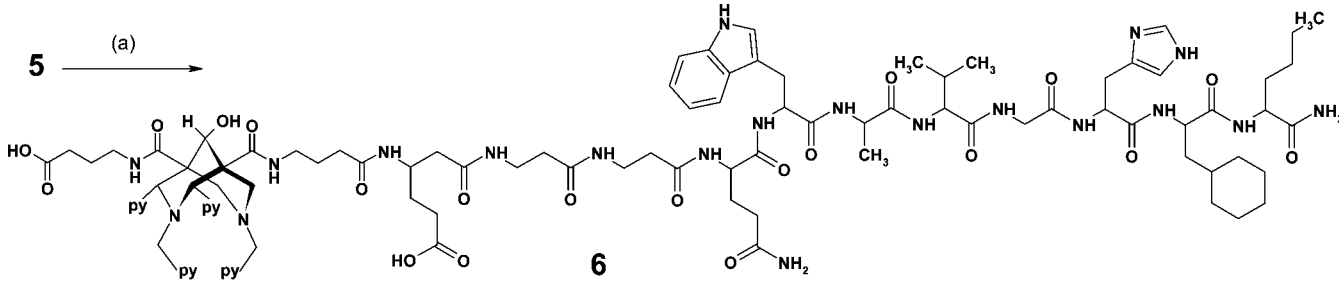

[a] (a) βhomo-Glu-βAla-βAla-[Cha[13], Nle[14]]BBN(7−14), HATU, DIPEA, DMF, 0 °C - r.t., 3 h, 19%.

Chart 1

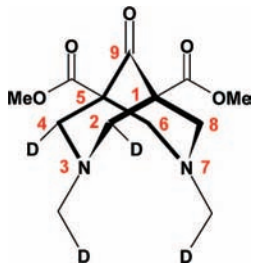

per(II)-bispidine complexes are stable in the presence of a high excess of glutathion and cyclam as competing ligands. Cyclic voltammetry with negative Cu^{II}/Cu^{I} redox potentials is in agreement with a high stability of the copper(II) complexes. The hexadentate bispidine ligands investigated here rapidly form stable radiocopper complexes under mild conditions in almost quantitative yield. Challenge experiments in the presence of superoxide dismutase and in vitro studies in rat plasma gave no evidence of transchelation or demetalation. The bispidine copper complexes **^{64}Cu-2** and **^{64}Cu-3** show in all experiments high stability in vitro and in vivo. The pendant carboxylate groups of the bispidine backbone offer good accessibility toward coupling reactions. With an aminobutyric acid spacer, the bombesin analogue as a vector molecule was conjugated to the bifunctional bispidine ligand **6**. Radiolabeling of bioconjugate **6** with ^{64}Cu was achieved at 37 °C for 30 min, yielding >99% radiochemical purity after HPLC. Comparative biodistribution and metabolic analysis of **^{64}Cu-6** indicated that there was only marginal, if any, in vivo copper demetalation. On the other side, the stabilized bombesin derivative βhomo-Glu-βAla-βAla-[Cha[13],Nle[14]]BBN(7−14) is readily metabolized. The accumulation of the radiolabeled peptide conjugate **^{64}Cu-6** in the GRPr-expressing pancreas is very low. However, PET studies on tumor-bearing PC-3 mice clearly revealed an accumulation of **^{64}Cu-6** in the GRPr-expressing tissue. The blockage study showed that **^{nat}Cu-6** was able to reduce the uptake in the receptor-rich tissue.

Bifunctional hexadentate bispidine ligands represent a versatile platform for the development of new copper radiopharmaceuticals. The two pendant carboxylate groups of the bispidines discussed here hold promising potential to tune the charge of the radiocopper complexes and consequently to influence the biodistribution and pharmacokinetic properties. Moreover, the new bispidine ligands may be readily modified with appropriate vector molecules.

ACKNOWLEDGMENT

The authors would like to thank Romy Schubert, Karin Landrock, Regina Herrlich, and Andrea Suhr for excellent technical assistance. Marion Kerscher and Madlen Matterna are acknowledged for the CV measurements, and Andreas Springer (FU Berlin) for high-resolution ESI-TOF-MS measurements.

Supporting Information Available: NMR data of compounds **2**, **3**, **4**, and **5**. Tables of crystal data, structure refinement, bond lengths and angles for compounds **2**, **Cu-2**, and **Cu-3**, and atomic coordinates and equivalent isotropic displacement parameters for **2** and **Cu-2** are presented. Figures S1 and S2 show the molecular structures of **2**, **Cu-2**, and **Cu-3**. Biodistribution data of **^{64}CuCl$_2$**, **^{64}Cu-2**, **^{64}Cu-3**, and **^{64}Cu-6** in rats are presented as %ID and SUV. This material is available free of charge via the Internet at http://pubs.acs.org.

LITERATURE CITED

(1) Mannich, C., and Mohs, P. (1963) Über Derivate eines aus zwei Piperidinringen kondensierten bicyclischen Systems. *Chem. Ber. B63*, 608–612.

(2) Comba, P., Kerscher, M., and Schiek, W. (2007) Bispidine Coordination Chemistry, in *Progress in Inorganic Chemistry* (Karlin, K. D., Ed.) pp 613−704, John Wiley and Sons, NewYork.

(3) Comba, P., Hauser, A., Kerscher, M., and Pritzkow, H. (2003) Bindungsdehnungsisomerie: lokalisierte Strukturen von sechsfach koordinierten Kupfer(II)-Bispidinkomplexen einer Jahn-Teller-aktiven Vibrationsmode. *Angew. Chem. 115*, 4675–4679. *Angew. Chem., Int. Ed. 42*, 4536−4540.

(4) Börzel, H., Comba, P., Hagen, K. S., Katsichtis, C., and Pritzkow, H. (2000) A copper(I) oxygenation precursor in the entatic state: two isomers of a copper(I) compound of a rigid tetradentate ligand. *Chem. Eur. J. 6*, 914–919.

(5) Börzel, H., Comba, P., Hagen, K. S., Kerscher, M., Pritzkow, H., Schatz, M., Schindler, S., and Walter, O. (2002) Copper-bispidine coordination chemistry: syntheses, structures, solution properties, and oxygenation reactivity. *Inorg. Chem. 41*, 5440–5452.

(6) Börzel, H., Comba, P., Katsichtis, C., Kiefer, W., Lienke, A., Nagel, V., and Pritzkow, H. (1999) Stabilization of copper dioxygen compounds: design, synthesis, and characterization. *Chem. Eur. J. 5*, 1716–1721.

(7) Comba, P., Merz, M., and Pritzkow, H. (2003) Catalytic aziridination of styrene with copper complexes of substituted 3,7-diazabicyclo[3.3.1]nonanones. *Eur. J. Inorg. Chem.* 1711–1718.

(8) Siener, T., Holzgrabe, U., Drosihn, S., and Brandt, W. (1999) Conformational and configurational behaviour of κ-agonistic 3,7-diazabicyclo[3.3.1]nonan-9-ones - synthesis, nuclear magnetic resonance studies and semiempirical PM3 calculations. *J. Chem. Soc., Perkin Trans. 2*, 1827–1834.

(9) Bailey, B. R., Berlin, K. D., Holt, E. M., Scherlag, B. J., Lazzara, R., Brachmann, J., Vanderhelm, D., Powell, D. R., Pantaleo, N. S., and Ruenitz, P. C. (1984) Synthesis, conformational-analysis, and antiarrhythmetic properties of 7-benzyl-3-thia-7-azabicyclo[3.3.1]nonan-9-one, 7-benzyl-3-thia-7-azabicyclo[3.3.1]nonane hydroperchlorate, and 7-benzyl-9-phenyl-3-thia-7-azabicyclo[3.3.1]nonan-9-ol hydroperchlorate and derivatives - single-crystal X-ray-diffraction analysis and evidence for chair-chair and chair-boat-conformers in the solid state. *J. Med. Chem. 27*, 759–767.

(10) Benyhe, S., Marki, A., Nachtsheim, C., Holzgrabe, U., and Borsodi, A. (2003) κ-Receptor selective binding of opioid ligands with a heterocyclic bicyclo[3.3.1]nonan-9-one structure. *Acta Biol. Hung. 54*, 147–155.

(11) Holzgrabe, U., and Brandt, W. (2003) Mechanism of action of the diazabicyclononanone-type κ-agonists. *J. Med. Chem. 46*, 1383–1389.

(12) Holzgrabe, U., and Erciyas, E. (1992) Synthese und Stereochemie potentiell stark analgetischer 2,4-m-diarylsubstituierter 3,7-Diazabicyclo[3.3.1]nonan-9-on-1,5-diester. *Arch. Pharm. 325*, 657–663.

(13) Kuhl, U., Engelberger, W., Haurand, M., and Holzgrabe, U. (2000) Diazabicyclo[3.3.1]nonanone-type ligands for the opioid-receptors. *Arch. Pharm. Pharm. Med. Chem. 333*, 226–230.

(14) Comba, P., Nuber, B., and Ramlow, A. (1997) The design of a new type of very rigid tetradentate ligand. *J. Chem. Soc., Dalton Trans.* 347–52.

(15) Comba, P., and Schiek, W. (2003) Fit and misfit between ligands and metal ions. *Coord. Chem. Rev. 238*, 21–29.

(16) Börzel, H., Comba, P., and Pritzkow, H. (2001) Structural studies on dicopper(II) compounds with catechol oxidase activity. *J. Chem. Soc., Chem. Commun.* 97–98.

(17) Bukowski, M. R., Comba, P., Limberg, C., Merz, M., Jr., and Wistuba, T. (2004) Bispidine ligand effects on the iron/hydrogen peroxide chemistry. *Angew. Chem. 116*, 1303–1307. *Angew. Chem., Int. Ed. 43*, 1283−1287.

(18) Bukowski, M. R., Comba, P., Lienke, A., Limberg, C., Lopez de Lorden, C., Mas-Balleste, R., and Merz, M., Jr. (2006) Catalytic oxidation of olefins in bispidine iron (II)/H_2O_2 systems. *Angew. Chem. 118*, 3524–3528. *Angew. Chem. Int. Ed. 45*, 3446−3449.

(19) Bleiholder, C., Börzel, H., Comba, P., Ferrari, R., Heydt, M., Kerscher, M., Kuwata, S., Laurenczy, G., Lawrance, G. A., Lienke, A., Martin, B., Merz, M., Nuber, B., and Pritzkow, H. (2005) Coordination chemistry of a new rigid, hexadentate bispidine-based bis(amine)tetrakis(pyridine) ligand. *Inorg. Chem. 44*, 8145–8155.

(20) Born, K., Comba, P., Ferrari, R., Lawrance, G. A., and Wadepohl, H. (2007) Stability constants: a new twist in transition metal bispidine chemistry. *Inorg. Chem. 46*, 458–464.

(21) Park, G., Dadachova, E., Przyborowska, A., Lai, S.-J., Ma, D., Broker, G., Rogers, R. D., Planalp, R. P., and Brechbiel, M. W. (2001) Synthesis of novel 1,3,5-cis,cis-triaminocyclohexane ligand based Cu(II) complexes as potential radiopharmaceuticals and correlation of structure and serum stability. *Polyhedron 20*, 3155–3163.

(22) Ma, D., Lu, F., Overstreet, T., Milenic, D. E., and Brechbiel, M. W. (2002) Novel chelating agents for potential clinical applications of copper. *Nucl. Med. Biol. 29*, 91–105.

(23) Gasser, G., Tjioe, L., Graham, B., Belousoff, M. J., Juran, S., Walther, M., Künstler, J.-U., Bergmann, R., Stephan, H., and Spiccia, L. (2008) Synthesis, copper(II) complexation, ^{64}Cu-labeling, and bioconjugation of a new bis(2-pyridylmethyl) derivative of 1,4,7-triazacyclononane. *Bioconjugate Chem. 19*, 719–730.

(24) Smith, S. V. (2004) Molecular imaging with copper-64. *J. Inorg. Biochem. 98*, 1874–1901.

(25) Adonai, N., Nguyen, K. N., Walsh, J., Iyer, M., Toyokuni, T., Phelps, M. E., McCarthy, T., McCarthy, D. W., and Gambhir, S. S. (2002) Ex vivo cell labeling with ^{64}Cu-pyruvaldehyde-bis(N-4-methylthiosemicarbazone) for imaging cell trafficking in mice with positron-emission tomography. *Proc. Natl. Acad. Sci. U.S.A. 99*, 3030–3035; *103*, 10526.

(26) Connett, J. M., Anderson, C. J., Guo, L. W., Schwarz, S. W., Zinn, K. R., Rogers, B. E., Siegel, B. A., Philpott, G. W., and Welch, M. J. (1996) Radioimmunotherapy with a ^{64}Cu-labeled monoclonal antibody: A comparison with ^{67}Cu. *Proc. Natl. Acad. Sci. U.S.A 93*, 6814–6818.

(27) Makkonen-Craig, S. (2006)^{64}Cu-Production, Ligands and biomedical Applications, Dissertation, University of Helsinki.

(28) Sun, X., and Anderson, C. J. (2004) Production and applications of copper-64 radiopharmaceuticals. *Methods Enzymol. 386*, 237–261.

(29) Sun, X., Wüst, M., Weisman, G. R., Wong, E. H., Reed, D. P., Boswell, C. A., Motekaitis, R. J., Martell, A. E., Welch, M. J., and Anderson, C. J. (2002) Radiolabeling and in vivo behaviour of copper-64-labeled cross-bridged cyclam ligands. *J. Med. Chem. 45*, 469–477.

(30) Zimmermann, K., Grünberg, J., Honer, M., Ametamey, S., Schubiger, P. A., and Novak-Hofer, I. (2003) Targeting of renal carcinoma with Cu-64/67-labeled anti-L1-CAM antibody chCE7: selection of copper ligands and PET imaging. *Nucl. Med. Biol. 30*, 417–427.

(31) Comba, P., Kanellakopulos, B., Katsichtis, C., Lienke, A., Pritzkow, H., and Rominger, F. (1998) Synthesis and characterisation of manganese(II) compounds with tetradentate ligands based on the bispidine backbone. *J. Chem. Soc., Dalton Trans.* 3997–4001.

(32) Comba, P., Kuwata, S., Linti, G., Pritzkow, H., Tarnai, M., and Wadepohl, H. (2006) Oxidative N-dealkylation in cobalt-bispidine-H_2O_2 systems. *J. Chem. Soc., Chem. Commun.* 2074–2076.

(33) García Garayoa, E., Schweinsberg, C., Maes, V., Rüegg, D., Blanc, A., Bläuenstein, P., Tourwé, D. A., Beck-Sickinger, A. G., and Schubiger, P. A. (2007) New [^{99m}Tc]bombesin analogues with improved biodistribution for targeting gastrin releasing-peptide receptor-positive tumors. *Q. J. Nucl. Med. Mol. Imaging 51*, 42–50.

(34) Börzel, H., Comba, P., Hagen, K. S., Lampeka, Y. D., Lienke, A., Linti, G., Merz, M., Pritzkow, H., and Tsymbal, L. V. (2002) Iron coordination chemistry with tetra-, penta- and hexadentate bispidine-type-ligands. *Inorg. Chim. Acta 337*, 407–419.

(35) Avila-Rodriguez, M. A., Nye, J. A., and Nickles, R. J. (2007) Simultaneous production of high specific activity ^{64}Cu and ^{61}Co with 11.4 MeV protons on enriched ^{64}Ni nuclei. *Appl. Radiat. Isot. 65*, 1115–1120.

(36) Szelecsényi, F., Blessing, G., and Qaim, S. M. (1993) Excitation functions of proton induced nuclear reactions on enriched ^{62}Ni and ^{64}Ni: Possibility of production of no-carrier-added ^{62}Cu and ^{64}Cu at a small cyclotron. *Appl. Radiat. Isot. 44*, 575–580.

(37) McCarthy, D. W., Shefer, R. E., Klinkowstein, R. E., Bass, L. A., Margeneau, W. H., Cutler, C. S., Anderson, C. J., and Welch, M. J. (1997) Efficient production of high specific activity ^{64}Cu using a biomedical cyclotron. *Nucl. Med. Biol. 24*, 35–43.

(38) Bigley, D. B., and Thurman, J. C. (1967) On the transition state for decarboxylation of β-keto acids and $\beta\gamma$-unsaturated acids. *Tetrahedron Lett. 25*, 2377–2380.

(39) Bach, R. D., and Canepa, C. (1996) Electronic factors influencing the decarboxylation of β-keto acids. A model enzyme study. *J. Org. Chem. 61*, 6346–6353.

(40) Samhammer, A., Holzgrabe, U., and Haller, R. (1989) Reduktionen an 3,7-diazabicyclo[3.3.1]nonan-9-onen und 1,3-diazaadamantan-6-onen. *Arch. Pharm. 322*, 545–550.

(41) Galvez, E., Arias, M. S., Bellanato, J., Garcia-Ramos, J. V., Florencio, F., Smith-Verdier, P., and Garcia-Blanco, S. (1985) Structural and conformational study of diazabicyclanones and diazabicyclanols. *J. Mol. Struct. 127*, 185–201.

(42) Comba, P., Kerscher, M., Merz, M., Müller, V., Pritzkow, H., Remenyi, R., Schiek, W., and Xiong, Y. (2002) Structural variation in transition metal bispidine complexes. *Chem. Eur. J. 8*, 5750–5760.

(43) Bentz, A., Comba, P., Deeth, R. J., Kerscher, M., Seibold, B., and Wadepohl, H. (2008) Modeling of the various minima on the potential energy surface of bispidine copper(II) complexes: A test for ligand field molecular mechanics structural modeling (LFMM). *Inorg. Chem. 47*, 9518–9527.

(44) Gupta, A., Seifert, S., Syhre, R., Scheunemann, M., Brust, P., and Johannsen, B. (2001) Reactivity of Tc-99m(V) "3 + 1" mixed-ligand complexes towards glutathione. *Radiochim. Acta 89*, 43–49.

(45) Rorabacher, D. B. (2004) Electron transfer by copper centers. *Chem. Rev. 104*, 651–697.
(46) Parker, D. (1990) Tumour targeting with radiolabelled macrocycle-antibody conjugates. *Chem. Soc. Rev. 19*, 271–291.
(47) Motekaitis, R. J., Rogers, B. E., Reichert, D. E., Martell, A. E., and Welch, M. J. (1996) Stability and structure of activated macrocycles. Ligands with biological applications. *Inorg. Chem. 35*, 3821–3827.
(48) Morphy, J. R., Parker, D., Kataky, R., Eaton, M. A. W., Millican, A. T., Alexander, R., Harrison, A., and Walker, C. (1990) Towards tumour targeting with copper-radiolabelled macrocycle-antibody conjugates: synthesis, antibody linkage and complexation behaviour. *J. Chem. Soc., Perkin Trans. 2*, 573–585.
(49) Bass, L. A., Wang, M., Welch, M. J., and Anderson, C. J. (2000) In vivo transchelation of copper-64 from TETA-octreotide to superoxide dismutase in rat liver. *Bioconjugate Chem. 11*, 527–532.
(50) Boswell, C. A., Sun, X., Niu, W. J., Weisman, G. R., Wong, E. H., Rheingold, A. L., and Anderson, C. J. (2004) Comparative *in vivo* stability of copper-64-labeled cross-bridged and conventional tetraazamacrocyclic complexes. *J. Med. Chem. 47*, 1465–1474.
(51) Stephan, H., Juran, S., Walther, M., Steinbach, J., Born, K., and Comba, P. (2006) Synthesis, characterization and evaluation of novel chelating agents for copper radionuclides, in *Technetium, Rhenium and other Metals in Chemistry and Nuclear Medicine* (Mazzi, U., Ed.) pp 219−222, SGE Editoriali, Padova, Italy.
(52) Smith, C. J., Volkert, W. A., and Hoffman, T. J. (2003) Gastrin releasing peptide (GRP) receptor targeted radiopharmaceuticals: A concise update. *Nucl. Med. Biol. 30*, 861–868.
(53) Smith, C. J., Volkert, W. A., and Hoffman, T. J. (2005) Radiolabeled peptide conjugates for targeting of the bombesin receptor superfamily subtypes. *Nucl. Med. Biol. 32*, 733–740.
(54) Maina, T., Nock, B., and Mather, S. (2006) Targeting prostate cancer with radiolabelled bombesins. *Cancer Imaging 6*, 153–157.
(55) Lane, S. R., Veerendra, B., Rold, T. L., Sieckman, G. L., Hoffman, T. J., Jurisson, S. S., and Smith, C. J. (2008) ^{99m}Tc(CO)$_3$-DTMA bombesin conjugates having high affinity for the GRP receptor. *Nucl. Med. Biol. 35*, 263–272.
(56) Nock, B., Nikolopoulou, A., Chiotellis, E., Loudos, G., Maintas, D., Reubi, J. C., and Maina, T. (2003) [^{99m}Tc]Demobesin 1, a novel potent bombesin analogue for GRP receptor-targeted tumour imaging. *Eur. J. Nucl. Med. 30*, 247–258.
(57) La Bella, R., Garcia-Garayoa, E., Bähler, M., Bläuenstein, P., Schibli, R., Conrath, P., Tourwé, D., and Schubiger, P. A. (2002) A ^{99m}Tc(I)-postlabeled high affinity bombesin analogue as a potential tumor imaging agent. *Bioconjugate Chem. 13*, 599–604.
(58) Nock, B. A., Nikolopoulou, A., Galanis, A., Cordopatis, P., Waser, B., Reubi, J.-C., and Maina, T. (2005) Potent bombesin-like peptides for GRP-receptor targeting of tumors with ^{99m}Tc: a preclinical study. *J. Med. Chem. 48*, 100–110.
(59) Zhang, H., Chen, J., Waldherr, C., Hinni, K., Waser, B., Reubi, J. C., and Mäcke, H. R. (2004) Synthesis and evaluation of bombesin derivatives on the basis of pan-bombesin peptides labeled with indium-111, lutetium-177, and yttrium-90 for targeting bombesin receptor-expressing tumors. *Cancer Res. 64*, 6707–6715.
(60) Maina, T., Nock, B. A., Zhang, H., Nikolopoulou, A., Waser, B., Reubi, J.-C., and Mäcke, H. R. (2005) Species differences of bombesin analog interactions with GRP-R define the choice of animal models in the development of GRP-R-targeting drugs. *J. Nucl. Med. 46*, 823–830.
(61) Dimitrakopoulou-Strauss, A., Hohenberger, P., Haberkorn, U., Mäcke, H. R., Eisenhut, M., and Strauss, L. G. (2007) ^{68}Ga-labeled bombesin studies in patients with gastrointestinal stromal tumors: comparison with ^{18}F-FDG. *J. Nucl. Med. 48*, 1245–1250.
(62) De Visser, M., Bernard, H. F., Erion, L. J., Schmidt, M. A., Srinivasan, A., Waser, B., Reubi, J., Krenning, E. P., and de Jong, M. (2007) ^{111}In-labelled bombesin analogs for molecular imaging of prostata tumors. *Eur. J. Nucl. Med. Mol. Imaging 34*, 1228–1238.
(63) García Garayoa, E., Rüegg, D., Bläuenstein, P., Zwimpfer, M., Khan, I. U., Maes, V., Blanc, A., Beck-Sickinger, A. G., Tourwé, D. A., and Schubiger, P. A. (2007) Chemical and biological characterization of new Re(CO)$_3$/[^{99m}Tc](CO)$_3$ bombesin analogues. *Nucl. Med. Biol. 34*, 17–28.
(64) Künstler, J.-U., Veerendra, B., Figueroa, Said D., Sieckmann, Gary L., Rold, Tammy L., Hoffman, T. J., Smith, C. J., and Pietzsch, H.-J. (2007) Organometallic ^{99m}Tc(III) '4 + 1' bombesin(7−14) conjugates: synthesis, radiolabeling and in vitro/in vivo studies. *Bioconjugate Chem. 18*, 1651–1661.
(65) Garrison, J. C., Rold, T. L., Sieckman, G. L., Naz, F., Sublett, S. V., Figueroa, S. D., Volkert, W. A., and Hoffman, T. J. (2008) Evaluation of the pharmacokinetic effects of various linking group using the ^{111}In-DOTA-X-BBN(7−14)NH$_2$ structural paradigm in a prostate cancer model. *Bioconjugate Chem. 19*, 1803–1812.
(66) Rogers, B. E., Bigott, H. M., McCarthy, D. W., Della Manna, D., Kim, J., Sharp, T. L., and Welch, M. J. (2003) MicroPET imaging of a gastrin-releasing peptide receptor-positive tumor in a mouse model of human prostate cancer using a ^{64}Cu-labeled bombesin analogue. *Bioconjugate Chem. 14*, 756–763.
(67) Rogers, B. E., Della Manna, D., and Safavy, A. (2004) In vitro and in vivo evaluation of a ^{64}Cu-labeled polyethylene glycol-bombesin conjugate. *Cancer Biother. Radiopharm. 19*, 25–34.
(68) Chen, X., Park, R., Hou, Y., Tohme, M., Shahinian, A. H., Bading, J. R., and Conti, P. S. (2004) microPET and autoradiographic imaging of GRP receptor expression with ^{64}Cu-DOTA-[Lys^3]bombesin in human prostate adenocarcinoma xenografts. *J. Nucl. Med. 45*, 1390–1397.
(69) Yang, Y.-S., Zhang, X., Xiong, Z., and Chen, X. (2006) Comparative *in vitro* and in vivo evaluation of two ^{64}Cu-labeled bombesin analogs in a mouse model of human prostate adenocarcinoma. *Nucl. Med. Biol. 33*, 371–380.
(70) Parry, J. J., Kelly, T. S., Andrews, R., and Rogers, B. E. (2007) In vitro and in vivo evaluation of ^{64}Cu-labeled DOTA-linker-bombesin(7−14) analogues containing different amino acids linker moieties. *Bioconjugate Chem. 18*, 1110–1117.
(71) Biddlecombe, G. B., Rogers, B. E., de Visser, M., Parry, J. J., de Jong, M., Erion, J. L., and Lewis, J. S. (2007) Molecular imaging of gastrin-releasing peptide receptor-positive tumors in mice using ^{64}Cu- and ^{86}Y-DOTA-(Pro1, Tyr4)-Bombesin(7−14). *Bioconjugate Chem. 18*, 724–730.
(72) Parry, J. J., Andrews, R., and Rogers, B. E. (2007) MicroPET imaging of breast cancer using radiolabeled bombesin analogs targeting the gastrin-releasing peptide receptor. *Breast Cancer Res. Treat. 101*, 175–183.
(73) Garrison, J. C., Rold, T. L., Sieckman, G., Figueroa, S. D., Volkert, W. A., Jurisson, S. S., and Hoffman, T. J. (2007) In vivo evaluation and small-animal PET/DT of a prostate cancer mouse model using ^{64}Cu bombesin analogs: side-by-side comparison of the CB-TE2A and DOTA chelations systems. *J. Nucl. Med. 48*, 1327–1337.
(74) Prasanphanich, A. F., Nanda, P. K., Rold, T. L., Ma, L.-J., Lewis, M. R., Garrison, J. C., Hoffman, T. J., Sieckman, G., Figueroa, S. D., and Smith, C. J. (2007) [^{64}Cu-NOTA-8-Aoc-BBN(7−14)NH$_2$] targeting vector for positron-emission tomography imaging of gastrin-releasing peptide receptor-expressing tissues. *Proc. Natl. Acad. Sci. U.S.A 104*, 12462–12467.

BC800461E

Supporting Information:

Hexadentate Bispidine Derivatives as Versatile Bifunctional Chelate Agents for Copper Radioisotopes

Stefanie Juran,[†] Martin Walther, [†] Holger Stephan,[†] Ralf Bergmann, [†] Jörg Steinbach, [†] Werner Kraus,[‡] Franziska Emmerling, [‡] and Peter Comba*[§]*

[†] Forschungszentrum Dresden-Rossendorf, Institute of Radiopharmacy, PF 510119, D-01314 Dresden, Germany; [‡] Bundesanstalt für Materialforschung und -prüfung, Richard-Willstätter-Strasse 11, D-12489, Berlin, Germany; [§] Universität Heidelberg, Anorganisch-Chemisches Institut, Im Neuenheimer Feld 270, D-69120 Heidelberg, Germany.

SUPPORTING INFORMATION

Table of contents.

NMR-data of the compounds 2, 3, 4 and 5

Table S1. Crystal data and structure refinement for compounds **2**, **Cu-2,** and **Cu-3**.

Table S2. Atomic coordinates (x 10^4) and equivalent isotropic displacement parameters (Å^2 x 10^3) for **2**. U(eq) is defined as one third of the trace of the orthogonalized Uij tensor.

Table S3. Atomic coordinates (x 10^4) and equivalent isotropic displacement parameters (Å^2 x 10^3) for **Cu-2**. U(eq) is defined as one third of the trace of the orthogonalized Uij tensor.

***Corresponding authors.** Email: h.stephan@fzd.de, Fax : +49 351 260 3232; Email: peter.comba@aci.uni-heidelberg.de, Fax : +49 6221 54 6617.

Table S4. Atomic coordinates (x 10^4) and equivalent isotropic displacement parameters ($Å^2$ x 10^3) for **Cu-3**. U(eq) is defined as one third of the trace of the orthogonalized Uij tensor.

Table S5. Bond lengths [Å] and angles [°] for **2**.

Table S6. Bond lengths [Å] and angles [°] for **Cu-2**.

Table S7. Bond lengths [Å] and angles [°] for **Cu-3**.

Figure S1. a) Molecular structure of **2,** showing the chair-chair arrangement of the bicyclic system; b) two molecules of **2** connected via hydrogen bonds.

Figure S2. Crystal structure of **Cu-2** (left, hydrogen atoms omitted for clarity) and **Cu-3** (right); gray spheres are carbon, red spheres oxygen, blue spheres nitrogen and yellow spheres copper atoms; The green lines indicate hydrogen bonds.

Table S8. Amount of **$^{64}CuCl_2$, ^{64}Cu-2**, **^{64}Cu-3,** and **^{64}Cu-6** in selected organs, tissues, and excretion in rats at 5 and 60 min after single intravenous application. Data expressed as %ID (**mean** [bold] ± SD, n=4).

Table S9. Concentration of **$^{64}CuCl_2$, ^{64}Cu-2**, **^{64}Cu-3,** and **^{64}Cu-6** in selected organs, tissues, and excretion in rats at 5 and 60 min after single intravenous application. Data expressed as SUV (**mean** [bold] ± SD, n=4).

NMR-data of the compounds 2, 3, 4 and 5

Dimethyl-9-hydroxy-2,4-dipyridin-2-yl-3,7-bis(pyridin-2-ylmethyl)-3,7-diazabicyclo[3.3.1]-nonane-1,5-dicarboxylate (2). ^{1}H-NMR (D_2O): 3.48 (d, 2H, ^{2}J = 14.8 Hz, N-CH_2), 3.51 (s, 6H, CH3), 3.67 (s, 2H, N-CH_2-py) 3.71 (d, 2H, ^{2}J = 13.2 Hz, N-CH_2), 4.48 (s, 2H, N-CH_2-py), 4.83 (s, 1H, C*H*-py), 4.92 (s, 1H, C*H*-OH), 6.90 (d, 1H ^{3}J = 8.0 Hz, C*H* pyridyl), 7.05 (m, 2H, C*H* pyridyl), 7.20 (d, 2H, ^{3}J = 7.8 Hz, C*H* pyridyl), 7.54-7.64 (m, 5H, C*H* pyridyl), 7.86-7.95 (m, 4H, C*H* pyridyl), 8.67 (d, 1H, ^{3}J = 5.6 Hz, C*H* pyridyl), 8.90 (d, 1H, ^{3}J = 4.8 Hz, C*H* pyridyl). ^{13}C-NMR (D_2O) 48.8, 53.1, 53.7, 55.9, 62.0, 70.0 (*C*H-OH), 71.2 (*C*H-py), 125.2, 125.3, 125.5, 125.8, 125.9, 127.0, 139.1, 139.3, 140.8, 146.6, 148.5, 149.8, 150.3, 153.1, 153.3, 170.2.

9-Hydroxy-2,4-dipyridin-2-yl-3,7-bis(pyridin-2-ylmethyl)-3,7-diazabicyclo-[3.3.1]nonane-1,5-dicarboxylic acid (3). ^{1}H-NMR (D_2O): 3.45 (d, 2H, ^{2}J = 13.8 Hz, N-CH_2), 3.66 (d, 2H, ^{2}J = 13.4 Hz, N-CH_2), 3.74 (s, 2H, N-CH_2-py), 4.54 (s, 2H, N-CH_2-py), 4.83 (s, 2H, C*H*-py), 4.88 (s, 1H, C*H*-OH), 6.91 (d, 1H, ^{3}J = 8.0 Hz, C*H* pyridyl), 7.12 (t, 2H, ^{3}J = 6.2 Hz, C*H* pyridyl), 7.35 (m, 2H, C*H* pyridyl), 7.66-7.71 (m, 5H, C*H* pyridyl), 7.91 (m, 2H, C*H* pyridyl), 8.02 (m, 2H, C*H* pyridyl), 8.76 (d, 1H, ^{3}J = 5.6 Hz, C*H* pyridyl), 8.96 (d, 1H, ^{3}J = 4.8 Hz, C*H* pyridyl). ^{13}C-NMR (D_2O): 49.6, 53.3, 56.2, 61.9, 70.8 (*C*H-OH), 71.7 (*C*H-py), 124.6, 124.9, 125.2, 125.6, 125.9, 126.0, 127.1, 129.2, 138.8, 139.3, 140.7, 146.5, 148.7, 149.4, 150.2, 153.9, 172.6.

Diethyl 4,4'-{[9-hydroxy-2,4-dipyridin-2-yl-3,7-bis(pyridin-2-ylmethyl)-3,7-diazabicyclo-[3.3.1]nonane 1,5-diyl]bis(carbonylimino)}dibutanoate (4). ^{1}H-NMR ($CDCl_3$): 1.21 (t, 6H, ^{3}J = 8.0 Hz, CH_3), 1.77-1.84 (m, 4H, CH_2), 2.32-2.35 (m, 4H, CH_2), 3.06-3.25 (m, 4H, CH_2), 3.59 (d, 2H, ^{2}J = 12.2 Hz, N-CH_2), 3.66 (s, 2H N-CH_2-py), 4.05-4.10 (m, 4H, OCH_2-), 4.14 (d, 2H, ^{2}J = 12.0 Hz, N-CH_2), 4.39 (s, 2H, N-CH_2-py), 5.12 (s, 2H, N-CH_2-py), 5.69 (s, 1H, *C*H-OH), 7.05-7.08 (m, 2H, C*H* pyridyl), 7.19 (m, 2H, C*H* pyridyl), 7.40 (m, 1H, C*H* pyridyl), 7.52-7.57 (m, 4H, C*H* pyridyl), 7.86-7.94 (m, 3H, C*H* pyridyl), 8.04 (m, 2H, C*H* pyridyl), 8.47 (d, 1H, ^{3}J = 5.2 Hz, C*H* pyridyl), 8.85 (broad, 2H, N*H*CO), 8.92 (d, 1H, ^{3}J = 4.4 Hz, C*H* pyridyl).^{13}C-NMR ($CDCl_3$): 14.3, 24.2, 32.2, 39.5, 50.9, 52.4, 60.4, 60.9, 69.2 (*C*H-OH), 70.9 (*C*H-py), 124.4, 125.0, 125.9, 126.2, 137.9, 138.2, 149.5, 150.5, 154.3, 168.3 (NH*C*OOCH_2-), 174.3 (*C*OOCH_2CH_3).

4,4'-{[9-Hydroxy-2,4-dipyridin-2-yl-3,7-bis(pyridin-2-ylmethyl)-3,7-diazabicyclo-[3.3.1]nonane-1,5-diyl]bis(carbonylimino)}dibutanic acid (5).

^{1}H-NMR (D_2O): 1.40-1.72 (m, 4H, CH_2), 1.85-2.02 (m, 4H, CH_2), 2.82-3.02 (m, 4H, CH_2), 3.47 (d, 2H, ^{2}J = 12.0 Hz, N-CH_2), 3.65 (s, 2H N-CH_2-py), 3.90 (d, 2H, ^{2}J = 12.0 Hz, N-CH_2), 4.53 (s, 2H, N-CH_2-py), 4.57 (s, 1H, *C*H-OH), 4.83 (s, 2H, C*H*-py), 6.94 (d, 1H, ^{3}J = 8.0 Hz, C*H* pyridyl), 7.05 (t, 2H, ^{3}J = 6.0 Hz, C*H* pyridyl), 7.20 (d, 2H, ^{3}J = 8.0 Hz, C*H* pyridyl), 7.6 (m, 3H, C*H* pyridyl), 7.85 (m, 2H, C*H* pyridyl), 7.92 (m, 2H, C*H* pyridyl), 8.60 (d, 2H, ^{3}J = 5.6, C*H* pyridyl), 8.88 (d, 1H, ^{3}J = 4.8 Hz, C*H* pyridyl). ^{13}C-NMR (D_2O): 23.3, 30.9, 39.0, 49.0, 52.2, 56.1, 60.3, 69.5 (*C*H-OH), 71.7 (*C*H-py), 124.7, 125.5, 126.4, 126.8, 128.0, 139.9, 140.6, 142.1, 146.4, 146.6, 147.7, 148.9, 152.1, 152.5, 169.0 (NH*C*OOCH$_2$-), 178.1 (*C*OOH).

Table S1. Crystal data and structure refinement for compounds **2**, **Cu-2,** and **Cu-3**.

Identification code	2	Cu-2	Cu-3
Empirical formula	$C_{33}H_{34}N_6O_5$	$Cu(C_{33}H_{36}N_6O_7)[NO_3]_2$	$Cu(C_{31}H_{34}N_6O_7)[NO_3]_2$
Formula weight	594.66	800.24	790.21
Temperature [K]	293(2)	293(3)	293(2)
Wavelength [Å]		0.71073	
Crystal system, space group	Triclinic, P-1 (No. 2)	Monoclinic, $P2_1/n$	Triclinic, P-1 (No. 2)
Unit cell dimensions [Å,°]	a = 11.814(6) b = 12.568(6) c = 13.827(7) α = 65.129(9) β = 66.488(9) γ = 65.199(9)	a = 10.498(5) b = 18.939(9) c = 17.611(8) β = 99.985(10)	a = 9.174(10) b = 13.137(15) c = 13.914(16) α = 90.488(16) β = 96.670(17) γ = 91.223(14)
Volume[$Å^3$]	1628.1(13)	3448(3)	1665(3)
Z, Calculated density [g/cm3]	2, 1.213	4, 1.541	2, 1.576
Absorption coefficient [mm^{-1}]	0.084	0.711	0.737
F(000)	628	1660	818
Theta range for data collection [°]	1.69 - 24.99.	2.11 – 24.99	1.55 - 28.75.
Limiting indices	-13 ≤h≤14, -13≤k≤14, -16≤l≤15	-11≤h≤12, -17≤k≤22, -20≤l≤20	-6≤h≤12, -17≤k≤17, -18≤l≤18
Reflections collected/unique	8543/5665 [R(int)=0.0585]	16588 / 6050 [R(int) = 0.0957]	12428 / 8499 [R(int) = 0.0955]
Refinement method		Full-matrix least squares on F^2	
Data/restraints/parameters	5665 / 0 / 385	6050 / 12 / 483	8499 / 18 / 476
Goodness-of-fitonF^2	1.137	0.907	0.968
Final R indices[I>2sigma(I)]	R1=0.1791, wR2=0.3033	R1 = 0.0660, wR2 = 0.1426	R1 = 0.0715, wR2 = 0.1463
R indices(alldata)	R1=0.2105, wR2=0.3192	R1 = 0.1765, wR2 = 0.1635	R1 = 0.2947, wR2 = 0.1822
Largest diff. peak and hole [e $Å^{-3}$]	0.455 and-0.555	0.884 and -0.374	0.806 and -0.615

Table S2. Atomic coordinates (x 10^4) and equivalent isotropic displacement parameters ($Å^2$ x 10^3) for **2**. U(eq) is defined as one third of the trace of the orthogonalized Uij tensor.

	x	y	z	U(eq)
O(1)	5535(5)	8583(5)	566(5)	44(2)
O(2)	5611(6)	7429(7)	-323(5)	56(2)
O(3)	2697(5)	10077(5)	244(4)	38(1)
O(4)	-531(6)	10654(6)	1915(6)	56(2)
O(5)	993(6)	10786(6)	2382(6)	52(2)
N(7)	1875(6)	7376(6)	1167(5)	34(2)
N(3)	2623(6)	6948(6)	3115(5)	29(1)
N(5)	608(7)	5351(7)	2166(6)	46(2)
N(6)	-474(8)	8657(8)	4435(6)	57(2)
N(4)	5896(7)	5388(7)	1987(6)	46(2)
N(2)	2658(8)	7613(8)	5168(6)	55(2)
C(43)	311(7)	6411(7)	1368(6)	34(2)
C(38)	-911(8)	6967(9)	1213(8)	47(2)
C(39)	-1860(10)	6411(11)	1879(10)	68(3)
C(40)	-1560(9)	5340(10)	2708(9)	55(3)
C(37)	-339(9)	4844(9)	2823(8)	54(3)
C(3)	310(8)	7860(8)	3888(6)	35(2)
C(7)	24(8)	6876(8)	3990(7)	40(2)
C(35)	-1136(9)	6662(10)	4691(8)	55(3)
C(26)	-1930(9)	7469(11)	5285(8)	62(3)
C(11)	3166(12)	8176(11)	5469(8)	68(3)
C(10)	-1605(10)	8472(11)	5121(9)	72(3)
C(12)	4470(12)	7957(11)	5200(9)	67(3)
C(1)	5262(11)	7144(11)	4640(9)	67(3)
C(14)	4775(8)	6584(8)	4324(6)	39(2)
C(15)	3469(8)	6848(8)	4585(6)	34(2)
C(16)	6605(9)	4279(9)	1880(9)	56(3)
C(17)	6142(9)	3430(9)	1919(7)	52(3)
C(18)	4807(10)	3746(8)	2126(7)	49(2)
C(19)	4035(9)	4884(7)	2253(7)	42(2)
C(20)	4619(7)	5685(7)	2166(6)	31(2)
C(6)	981(7)	8516(8)	1370(7)	36(2)
C(5)	1464(7)	8993(7)	1952(6)	30(2)
C(4)	1602(7)	8118(7)	3130(6)	30(2)
C(8)	3152(7)	7512(7)	501(6)	33(2)
C(1)	3688(8)	7899(7)	1092(6)	32(2)
C(2)	3846(7)	6974(7)	2248(6)	31(2)
C(9)	2818(7)	9152(7)	1281(6)	35(2)
C(28)	5036(7)	8027(7)	419(6)	30(2)
C(29)	6939(10)	7425(14)	-946(10)	90(5)
C(30)	511(8)	10232(8)	2082(7)	42(2)
C(31)	153(11)	11932(11)	2592(12)	92(5)
C(32)	2888(8)	6265(8)	4212(6)	34(2)
C(33)	1439(6)	6903(6)	611(5)	42(2)
C(34)	5767(6)	192(6)	2796(5)	102(5)
O(6)	4810(6)	760(6)	2993(5)	200(6)
C(42)	-2954(6)	9514(6)	2460(5)	99(4)

Table S3. Atomic coordinates (x 10^4) and equivalent isotropic displacement parameters ($Å^2$ x 10^3) for **Cu-2**. U(eq) is defined as one third of the trace of the orthogonalized Uij tensor.

	x	y	z	U(eq)
Cu(1)	2751(1)	9866(1)	1961(1)	51(1)
N(3)	3489(4)	9468(3)	3039(3)	42(1)
N(7)	4106(4)	10637(3)	2180(3)	39(1)
N(2)	1419(5)	9122(3)	1912(3)	49(2)
N(6)	1473(5)	10408(3)	2795(3)	53(2)
N(5)	2743(5)	10128(3)	860(3)	48(1)
N(4)	4193(5)	8835(3)	1747(3)	48(2)
O(1)	6675(4)	10878(2)	3676(2)	52(1)
O(3)	4679(5)	10897(3)	4979(3)	70(2)
O(4)	3733(4)	11698(3)	4137(2)	63(1)
O(5)	7679(4)	9575(3)	2462(3)	64(2)
O(6)	7575(4)	9274(2)	3680(3)	59(1)
C(4)	3416(5)	10021(3)	3645(3)	40(2)
C(5)	4342(6)	10641(3)	3616(3)	40(2)
C(6)	4064(5)	11074(3)	2879(3)	42(2)
C(8)	5418(5)	10309(3)	2249(3)	41(2)
C(1)	5763(5)	9864(3)	2991(3)	39(2)
C(2)	4876(5)	9233(3)	3054(3)	39(2)
C(9)	5748(5)	10344(3)	3688(3)	41(2)
C(3)	2688(6)	8833(3)	3170(4)	49(2)
C(7)	1598(6)	8675(4)	2526(4)	46(2)
C(10)	394(6)	9006(4)	1356(4)	58(2)
C(11)	-438(7)	8451(4)	1358(5)	69(2)
C(12)	-227(7)	7989(4)	1988(5)	73(2)
C(13)	800(7)	8124(4)	2580(4)	60(2)
C(29)	2024(6)	10273(3)	3529(4)	43(2)
C(30)	259(7)	10675(4)	2670(5)	60(2)
C(31)	-401(7)	10832(4)	3243(5)	66(2)
C(32)	131(7)	10697(4)	3995(5)	75(2)
C(33)	1412(6)	10400(4)	4146(4)	59(2)
C(19)	4304(6)	11084(4)	4327(4)	47(2)
C(20)	3575(7)	12169(4)	4783(4)	80(3)
C(21)	3861(6)	11123(3)	1498(3)	47(2)
C(22)	3424(6)	10717(4)	782(4)	45(2)
C(23)	2329(6)	9759(4)	221(4)	56(2)
C(24)	2542(7)	9967(4)	-511(4)	64(2)
C(25)	3192(7)	10572(4)	-577(4)	66(2)
C(26)	3662(6)	10949(4)	79(4)	57(2)
C(27)	7124(7)	9572(3)	3007(5)	51(2)
C(28)	8799(6)	8889(4)	3743(4)	78(3)
C(14)	4923(6)	8693(3)	2434(4)	44(2)
C(15)	4272(7)	8390(4)	1163(4)	56(2)
C(16)	5044(7)	7800(4)	1237(5)	68(2)
C(17)	5784(8)	7666(4)	1949(5)	76(2)
C(18)	5724(7)	8111(4)	2551(4)	65(2)
N(9)	7253(7)	11827(4)	1260(5)	90(2)
O(7)	6991(8)	11822(6)	1844(4)	215(6)
O(8)	8344(7)	11717(5)	1151(6)	208(5)
O(9)	6469(8)	11907(5)	690(4)	183(4)
N(8)	7614(8)	12048(4)	5120(4)	86(2)
O(10)	7801(10)	12417(4)	5655(4)	211(5)
O(11)	6878(9)	12204(4)	4577(5)	194(4)
O(12)	8063(7)	11459(4)	5136(4)	136(3)
O(13)	10536(9)	11392(5)	712(5)	208(4)

Table S4. Atomic coordinates (x 10^4) and equivalent isotropic displacement parameters ($Å^2$ x 10^3) for **Cu-3**. U(eq) is defined as one third of the trace of the orthogonalized Uij tensor.

	x	y	z	U(eq)
Cu(1)	6252(1)	7185(1)	7783(1)	55(1)
O(1)	3436(4)	10470(3)	7447(3)	52(1)
O(3)	6494(5)	11038(3)	9002(4)	68(2)
O(4)	6767(5)	11404(3)	7484(3)	63(1)
O(5)	1359(7)	8623(5)	6115(5)	113(2)
O(6)	2748(5)	9532(4)	5207(4)	81(2)
N(3)	6522(5)	8284(4)	6763(3)	34(1)
N(7)	4776(5)	8125(4)	8282(3)	38(1)
N(2)	7872(5)	6458(4)	7263(4)	37(1)
N(4)	8209(5)	8183(4)	8521(4)	38(1)
N(5)	5189(6)	6084(4)	8445(4)	45(1)
N(6)	4636(5)	6601(4)	6252(4)	40(1)
C(2)	7047(6)	9256(4)	7276(4)	35(2)
C(1)	5838(6)	9779(4)	7775(4)	34(2)
C(8)	5357(6)	9177(4)	8609(4)	37(2)
C(6)	3526(6)	8249(5)	7518(4)	41(2)
C(5)	3938(6)	8864(5)	6673(4)	39(2)
C(4)	5120(6)	8413(4)	6111(4)	38(2)
C(9)	4500(6)	9941(4)	7025(4)	39(2)
C(3)	7702(7)	7919(4)	6179(4)	39(2)
C(7)	8384(6)	6942(4)	6518(5)	35(2)
C(10)	8590(8)	5631(5)	7622(5)	54(2)
C(11)	9705(8)	5211(5)	7224(6)	65(2)
C(12)	10185(8)	5663(6)	6426(7)	77(3)
C(13)	9517(8)	6546(5)	6073(6)	63(2)
C(14)	8343(7)	9034(5)	8013(4)	38(2)
C(15)	9278(7)	7986(5)	9235(4)	44(2)
C(16)	10472(8)	8602(6)	9468(5)	52(2)
C(17)	10631(7)	9485(6)	8948(5)	53(2)
C(18)	9547(7)	9691(5)	8192(5)	49(2)
C(19)	6406(7)	10810(5)	8159(5)	42(2)
C(21)	4303(7)	7614(5)	9134(5)	49(2)
C(22)	4167(7)	6488(5)	8963(5)	46(2)
C(23)	5167(8)	5087(6)	8324(5)	61(2)
C(24)	4134(11)	4439(6)	8685(6)	82(3)
C(25)	3100(10)	4838(8)	9181(6)	84(3)
C(26)	3099(8)	5868(7)	9323(5)	69(2)
C(27)	2498(10)	8959(7)	5994(6)	69(2)
C(29)	4588(7)	7395(5)	5646(5)	40(2)
C(30)	3995(7)	5723(5)	5885(5)	46(2)
C(31)	3354(7)	5591(6)	4952(6)	54(2)
C(32)	3391(8)	6411(6)	4354(5)	66(2)
C(33)	4004(7)	7335(6)	4708(5)	54(2)
N(9)	9054(7)	13128(5)	8532(5)	65(2)
N(8)	2669(11)	12795(7)	6469(7)	176(2)
O(7)	7759(6)	13203(3)	8183(4)	80(2)
O(8)	9601(6)	13746(4)	9147(4)	83(2)
O(9)	9777(6)	12419(5)	8260(5)	104(2)
O(13)	12860(7)	11887(5)	9097(4)	96(2)
O(14)	330(11)	8853(13)	3908(7)	281(7)
O(12)	2365(9)	11927(5)	6231(6)	176(2)
O(11)	2085(9)	13515(6)	6160(6)	176(2)
O(10)	3859(9)	12943(6)	7018(6)	176(2)

Table S5. Bond lengths [Å] and angles [°] for **2**.

Atoms	Bondlength[Å]	Atoms	Bondlength[Å]
O(1)-C(28)	1.199(9)	C(39)-C(40)	1.371(14)
O(2)-C(28)	1.321(9)	C(40)-C(37)	1.357(13)
O(2)-C(29)	1.457(10)	C(3)-C(7)	1.352(12)
O(3)-C(9)	1.432(9)	C(3)-C(4)	1.544(10)
O(4)-C(30)	1.195(10)	C(7)-C(35)	1.386(12)
O(5)-C(30)	1.321(10)	C(35)-C(26)	1.368(14)
O(5)-C(31)	1.438(11)	C(26)-C(10)	1.372(15)
N(7)-C(6)	1.442(10)	C(11)-C(12)	1.364(15)
N(7)-C(8)	1.460(9)	C(12)-C(13)	1.343(15)
N(7)-C(33)	1.472(8)	C(13)-C(14)	1.347(13)
N(3)-C(4)	1.461(10)	C(14)-C(15)	1.359(11)
N(3)-C(2)	1.466(9)	C(15)-C(32)	1.516(11)
N(3)-C(32)	1.482(9)	C(16)-C(17)	1.364(13)
N(5)-C(37)	1.335(11)	C(17)-C(18)	1.392(13)
N(5)-C(43)	1.340(11)	C(18)-C(19)	1.378(12)
N(6)-C(3)	1.318(11)	C(19)-C(20)	1.384(11)
N(6)-C(10)	1.343(13)	C(20)-C(2)	1.518(11)
N(4)-C(16)	1.328(11)	C(6)-C(5)	1.546(10)
N(4)-C(20)	1.336(9)	C(5)-C(30)	1.526(12)
N(2)-C(15)	1.325(11)	C(5)-C(9)	1.546(10)
N(2)-C(11)	1.356(13)	C(5)-C(4)	1.563(10)
C(43)-C(38)	1.376(11)	C(8)-C(1)	1.519(10)
C(43)-C(33)	1.512(9)	C(1)-C(28)	1.528(10)
C(38)-C(39)	1.374(13)	C(1)-C(9)	1.542(11)
		C(1)-C(2)	1.560(10)

Atoms	Angle[°]	Atoms	Angle[°]
C(28)-O(2)-C(29)	116.4(7)	C(19)-C(18)-C(17	119.5(9)
C(30)-O(5)-C(31)	116.6(8)	C(18)-C(19)-C(20	118.6(8)
C(6)-N(7)-C(8)	111.0(6)	N(4)-C(20)-C(19)	122.7(8)
C(6)-N(7)-C(33)	113.2(6)	N(4)-C(20)-C(2)	115.4(7)
C(8)-N(7)-C(33)	108.6(6)	C(19)-C(20)-C(2)	121.9(7)
C(4)-N(3)-C(2)	117.7(6)	N(7)-C(6)-C(5)	112.2(6)
C(4)-N(3)-C(32)	111.0(6)	C(30)-C(5)-C(6)	109.3(6)
C(2)-N(3)-C(32)	109.7(6)	C(30)-C(5)-C(9)	108.9(6)
C(37)-N(5)-C(43)	117.3(8)	C(6)-C(5)-C(9)	111.4(6)
C(3)-N(6)-C(10)	117.7(9)	C(30)-C(5)-C(4)	107.4(6)
C(16)-N(4)-C(20)	116.9(8)	C(6)-C(5)-C(4)	114.0(6)
C(15)-N(2)-C(11)	117.9(9)	C(9)-C(5)-C(4)	105.6(6)
N(5)-C(43)-C(38)	122.3(8)	N(3)-C(4)-C(3)	109.1(6)
N(5)-C(43)-C(33)	114.8(7)	N(3)-C(4)-C(5)	113.4(6)
C(38)-C(43)-C(33	122.7(7)	C(3)-C(4)-C(5)	111.0(6)
C(39)-C(38)-C(43	119.4(9)	N(7)-C(8)-C(1)	110.3(6)
C(40)-C(39)-C(38	118.1(9)	C(8)-C(1)-C(28)	111.3(6)
C(37)-C(40)-C(39	119.5(9)	C(8)-C(1)-C(9)	111.6(7)
N(5)-C(37)-C(40)	123.3(9)	C(28)-C(1)-C(9)	107.1(6)
N(6)-C(3)-C(7)	123.0(8)	C(8)-C(1)-C(2)	114.4(6)
N(6)-C(3)-C(4)	114.9(8)	C(28)-C(1)-C(2)	105.3(6)
C(7)-C(3)-C(4)	122.1(7)	C(9)-C(1)-C(2)	106.5(6)
C(3)-C(7)-C(35)	120.6(9)	N(3)-C(2)-C(20)	109.6(6)
C(26)-C(35)-C(7)	116.3(10)	N(3)-C(2)-C(1)	114.4(6)
C(35)-C(26)-C(10	120.4(9)	C(20)-C(2)-C(1)	110.8(6)
N(2)-C(11)-C(12)	121.6(10)	O(3)-C(9)-C(1)	110.1(6)
N(6)-C(10)-C(26)	121.9(10)	O(3)-C(9)-C(5)	107.5(6)
C(13)-C(12)-C(11	118.6(10)	C(1)-C(9)-C(5)	105.7(6)
C(12)-C(13)-C(14	120.6(10)	O(1)-C(28)-O(2)	123.4(7)
C(13)-C(14)-C(15	119.1(9)	O(1)-C(28)-C(1)	123.8(7)
N(2)-C(15)-C(14)	122.1(8)	O(2)-C(28)-C(1)	112.7(7)
N(2)-C(15)-C(32)	117.5(7)	O(4)-C(30)-O(5)	124.4(9)
C(14)-C(15)-C(32	120.5(8)	O(4)-C(30)-C(5)	124.0(8)
N(4)-C(16)-C(17)	125.5(9)	O(5)-C(30)-C(5)	111.6(7)
C(16)-C(17)-C(18)	116.7(9)	N(3)-C(32)-C(15)	115.9(6)
		N(7)-C(33)-C(43)	112.4(5)

Table S6. Bond lengths [Å] and angles [°] for **Cu-2**.

Atoms	Bond length [Å]	Atoms	Bond length [Å]
Cu(1)-N(2)	1.976(5)	C(5)-C(9)	1.563(8)
Cu(1)-N(5)	2.000(5)	C(8)-C(1)	1.544(8)
Cu(1)-N(7)	2.028(5)	C(1)-C(9)	1.529(8)
Cu(1)-N(3)	2.063(5)	C(1)-C(27)	1.528(8)
Cu(1)-N(6)	2.387(6)	C(1)-C(2)	1.531(8)
Cu(1)-N(4)	2.538(5)		
N(3)-C(4)	1.507(7)	C(2)-C(14)	1.502(8)
N(3)-C(3)	1.509(7)	C(3)-C(7)	1.495(8)
N(3)-C(2)	1.519(7)	C(7)-C(13)	1.352(8)
N(7)-C(6)	1.489(7)	C(10)-C(11)	1.367(9)
N(7)-C(8)	1.497(7)	C(11)-C(12)	1.401(10)
N(7)-C(21)	1.501(7)	C(12)-C(13)	1.387(8)
N(2)-C(10)	1.341(7)	C(29)-C(33)	1.376(8)
N(2)-C(7)	1.360(8)	C(30)-C(31)	1.352(9)
N(6)-C(29)	1.345(7)	C(31)-C(32)	1.370(9)
N(6)-C(30)	1.353(8)	C(32)-C(33)	1.439(9)
N(5)-C(23)	1.331(8)	C(21)-C(22)	1.481(8)
N(5)-C(22)	1.345(7)	C(22)-C(26)	1.377(8)
N(4)-C(14)	1.344(7)	C(23)-C(24)	1.402(9)
N(4)-C(15)	1.343(8)	C(24)-C(25)	1.349(9)
O(1)-C(9)	1.406(7)	C(25)-C(26)	1.375(9)
O(3)-C(19)	1.199(7)	C(14)-C(18)	1.379(8)
O(4)-C(19)	1.325(7)	C(15)-C(16)	1.373(9)
O(4)-C(20)	1.478(7)	C(16)-C(17)	1.379(9)
O(5)-C(27)	1.205(8)	C(17)-C(18)	1.366(9)
O(6)-C(27)	1.325(7)	N(9)-O(9)	1.193(6)
O(6)-C(28)	1.465(7)	N(9)-O(7)	1.110(8)
C(4)-C(29)	1.517(8)	N(9)-O(8)	1.212(7)
C(4)-C(5)	1.531(8)	N(8)-O(11)	1.19(6)
C(5)-C(19)	1.514(9)	N(8)-O(10)	1.1635(7)
C(5)-C(6)	1.521(8)	N(8)-O(12)	1.208(7)

Atoms	Angle [°]	Atoms	Angle [°]
N(2)-Cu(1)-N(7)	171.5(2)	C(2)-C(1)-C(8)	115.5(5)
N(5)-Cu(1)-N(7)	83.7(2)	C(14)-C(2)-N(3)	109.9(5)
N(2)-Cu(1)-N(3)	86.0(2)	C(14)-C(2)-C(1)	112.5(5)
N(5)-Cu(1)-N(3)	156.9(2)	N(3)-C(2)-C(1)	111.3(5)
N(7)-Cu(1)-N(3)	87.07(2)	O(1)-C(9)-C(1)	108.2(5)
N(2)-Cu(1)-N(6)	82.2(2)	O(1)-C(9)-C(5)	112.8(5)
N(5)-Cu(1)-N(6)	125.6(2)	C(1)-C(9)-C(5)	106.9(5)
N(7)-Cu(1)-N(6)	91.37(2)	C(7)-C(3)-N(3)	114.6(5)
N(3)-Cu(1)-N(6)	75.65(2)	C(13)-C(7)-N(2)	122.3(6)
C(4)-N(3)-C(3)	110.3(5)	C(13)-C(7)-C(3)	120.2(7)
C(4)-N(3)-C(2)	111.0(4)	N(2)-C(7)-C(3)	117.5(6)
C(3)-N(3)-C(2)	108.8(5)	N(2)-C(10)-C(11)	123.8(7)
C(4)-N(3)-Cu(1)	110.0(4)	C(10)-C(11)-C(12)	118.0(7)
C(3)-N(3)-Cu(1)	107.6(3)	C(13)-C(12)-C(11)	118.4(7)
C(2)-N(3)-Cu(1)	109.2(4)	C(7)-C(13)-C(12)	120.0(7)
C(6)-N(7)-C(8)	108.8(4)	N(6)-C(29)-C(33)	122.9(6)
C(6)-N(7)-C(21)	107.2(5)	N(6)-C(29)-C(4)	115.7(6)
C(8)-N(7)-C(21)	110.3(5)	C(33)-C(29)-C(4)	121.3(6)
C(6)-N(7)-Cu(1)	115.9(4)	N(6)-C(30)-C(31)	123.4(7)
C(8)-N(7)-Cu(1)	108.8(4)	C(30)-C(31)-C(32)	120.3(7)
C(21)-N(7)-Cu(1)	105.8(3)	C(31)-C(32)-C(33)	117.5(7)
C(10)-N(2)-C(7)	117.4(6)	C(29)-C(33)-C(32)	118.2(7)
C(10)-N(2)-Cu(1)	128.4(5)	O(3)-C(19)-O(4)	124.0(7)
C(7)-N(2)-Cu(1)	114.2(4)	O(3)-C(19)-C(5)	125.2(6)
C(29)-N(6)-C(30)	117.6(6)	O(4)-C(19)-C(5)	110.7(6)
C(29)-N(6)-Cu(1)	108.4(4)	C(22)-C(21)-N(7)	110.4(5)
C(30)-N(6)-Cu(1)	132.4(5)	N(5)-C(22)-C(26)	122.7(6)
C(23)-N(5)-C(22)	116.7(6)	N(5)-C(22)-C(21)	115.8(6)
C(23)-N(5)-Cu(1)	129.5(5)	C(26)-C(22)-C(21)	121.4(7)
C(22)-N(5)-Cu(1)	113.1(4)	N(5)-C(23)-C(24)	123.3(7)
C(14)-N(4)-C(15)	117.6(6)	C(25)-C(24)-C(23)	118.8(7)
C(19)-O(4)-C(20)	116.2(5)	C(24)-C(25)-C(26)	118.8(7)
C(27)-O(6)-C(28)	116.9(6)	C(25)-C(26)-C(22)	119.6(7)
N(3)-C(4)-C(29)	106.8(4)	O(5)-C(27)-O(6)	124.6(7)
N(3)-C(4)-C(5)	113.5(5)	O(5)-C(27)-C(1)	124.3(6)
C(29)-C(4)-C(5)	111.0(5)	O(6)-C(27)-C(1)	110.9(6)
C(19)-C(5)-C(6)	112.3(5)	N(4)-C(14)-C(18)	122.2(6)
C(19)-C(5)-C(4)	106.8(5)	N(4)-C(14)-C(2)	115.6(6)
C(6)-C(5)-C(4)	114.4(5)	C(18)-C(14)-C(2)	122.1(6)
C(19)-C(5)-C(9)	107.0(5)	N(4)-C(15)-C(16)	123.5(7)
C(6)-C(5)-C(9)	107.5(5)	C(15)-C(16)-C(17)	117.8(7)

C(4)-C(5)-C(9)	108.6(5)	C(18)-C(17)-C(16)	119.8(7)
N(7)-C(6)-C(5)	112.1(5)	C(17)-C(18)-C(14)	119.1(7)
N(7)-C(8)-C(1)	111.8(5)	O(9)-N(9)-O(7)	122.3(8)
C(9)-C(1)-C(27)	109.9(5)	O(9)-N(9)-O(8)	114.9(7)
C(9)-C(1)-C(2)	108.4(5)	O(7)-N(9)-O(8)	122.6(7)
C(27)-C(1)-C(2)	107.2(5)	O(11)-N(8)-O(10)	120.7(7)
C(9)-C(1)-C(8)	108.7(5)	O(11)-N(8)-O(12)	117.2(6)
C(27)-C(1)-C(8)	107.0(5)	O(10)-N(8)-O(12)	121.7(6)

Table S7. Bond lengths [Å] and angles [°] for **Cu-3**.

Atoms	Bond length [Å]	Atoms	Bond length [Å]
Cu(1)-N(2)	1.986(5)	C(6)-C(5)	1.511(8)
Cu(1)-N(5)	2.016(5)	C(5)-C(4)	1.536(8)
Cu(1)-N(7)	2.028(5)	C(5)-C(27)	1.541(10)
Cu(1)-N(3)	2.064(5)	C(5)-C(9)	1.552(8)
Cu(1)-N(4)	2.333(5)	C(4)-C(29)	1.526(8)
O(1)-C(9)	1.392(6)	C(3)-C(7)	1.496(8)
O(3)-C(19)	1.201(7)	C(7)-C(13)	1.379(8)
O(4)-C(19)	1.293(7)	C(10)-C(11)	1.345(8)
O(5)-C(27)	1.157(9)	C(11)-C(12)	1.375(9)
O(6)-C(27)	1.372(9)	C(12)-C(13)	1.391(9)
N(3)-C(4)	1.499(7)	C(14)-C(18)	1.385(8)
N(3)-C(2)	1.501(7)	C(15)-C(16)	1.355(8)
N(3)-C(3)	1.510(6)	C(16)-C(17)	1.387(9)
N(7)-C(21)	1.471(7)	C(17)-C(18)	1.394(9)
N(7)-C(6)	1.483(7)	C(21)-C(22)	1.497(8)
N(7)-C(8)	1.518(7)	C(22)-C(26)	1.400(9)
N(2)-C(7)	1.345(7)	C(23)-C(24)	1.400(10)
N(2)-C(10)	1.352(8)	C(24)-C(25)	1.348(11)
N(4)-C(14)	1.339(7)	C(25)-C(26)	1.365(11)
N(4)-C(15)	1.344(7)	C(29)-C(33)	1.353(8)
N(5)-C(23)	1.319(8)	C(30)-C(31)	1.370(9)
N(5)-C(22)	1.360(8)	C(31)-C(32)	1.367(9)
N(6)-C(29	1.344(7)	C(32)-C(33)	1.389(9)
N(6)-C(30)	1.353(7)	N(9)-O(8)	1.231(6)
C(2)-C(14)	1.512(8)	N(9)-O(9)	1.236(6)
C(2)-C(1)	1.544(8)	N(9)-O(7)	1.237(6)
C(1)-C(19)	1.511(8)	N(8)-O(11)	1.158(8)
C(1)-C(8)	1.512(8)	N(8)-O(12)	1.203(8)
C(1)-C(9)	1.535(8)	N(8)-O(10)	1.269(8)

Atoms	Angle [°]	Atoms	Angle [°]
N(2)-Cu(1)-N(5)	103.7(2)	C(27)-C(5)-C(9)	109.2(5)
N(2)-Cu(1)-N(7)	171.2(2)	N(3)-C(4)-C(29)	110.4(5)
N(5)-Cu(1)-N(7)	84.6(2)	N(3)-C(4)-C(5)	110.6(5)
N(2)-Cu(1)-N(3)	86.6(2)	C(29)-C(4)-C(5)	110.4(5)
N(5)-Cu(1)-N(3)	156.5(2)	O(1)-C(9)-C(1)	110.0(5)
N(7)-Cu(1)-N(3)	86.5(2)	O(1)-C(9)-C(5)	111.7(5)
N(2)-Cu(1)-N(4)	81.81(19)	C(1)-C(9)-C(5)	106.2(5)
N(5)-Cu(1)-N(4)	124.9(2)	C(7)-C(3)-N(3)	114.5(5)
N(7)-Cu(1)-N(4)	91.3(2)	N(2)-C(7)-C(13)	120.8(6)
N(3)-Cu(1)-N(4)	77.0(2)	N(2)-C(7)-C(3)	118.9(5)
C(4)-N(3)-C(2)	112.3(4)	C(13)-C(7)-C(3)	120.4(6)
C(4)-N(3)-C(3)	109.7(4)	C(11)-C(10)-N(2)	123.6(7)
C(2)-N(3)-C(3)	108.8(4)	C(10)-C(11)-C(12)	118.7(7)
C(4)-N(3)-Cu(1)	110.4(4)	C(11)-C(12)-C(13)	118.8(7)
C(2)-N(3)-Cu(1)	108.7(3)	C(7)-C(13)-C(12)	119.6(7)
C(3)-N(3)-Cu(1)	106.9(3)	N(4)-C(14)-C(18)	122.2(6)
C(21)-N(7)-C(6)	111.3(5)	N(4)-C(14)-C(2)	115.1(6)
C(21)-N(7)-C(8)	107.3(4)	C(18)-C(14)-C(2)	122.6(6)
C(6)-N(7)-C(8)	108.0(5)	N(4)-C(15)-C(16)	123.6(6)
C(21)-N(7)-Cu(1)	105.3(4)	C(15)-C(16)-C(17)	119.4(7)
C(6)-N(7)-Cu(1)	109.1(3)	C(16)-C(17)-C(18)	117.8(7)
C(8)-N(7)-Cu(1)	115.8(3)	C(14)-C(18)-C(17)	119.3(7)
C(7)-N(2)-C(10)	118.1(5)	O(3)-C(19)-O(4)	124.7(6)
C(7)-N(2)-Cu(1)	113.0(4)	O(3)-C(19)-C(1)	122.6(6)
C(10)-N(2)-Cu(1)	128.4(5)	O(4)-C(19)-C(1)	112.6(6)
C(14)-N(4)-C(15)	117.8(6)	N(7)-C(21)-C(22)	110.4(5)
C(14)-N(4)-Cu(1)	109.6(4)	N(5)-C(22)-C(26)	121.0(6)
C(15)-N(4)-Cu(1)	131.8(4)	N(5)-C(22)-C(21)	115.4(6)
C(23)-N(5)-C(22)	117.6(6)	C(26)-C(22)-C(21)	123.6(7)
C(23)-N(5)-Cu(1)	130.4(5)	N(5)-C(23)-C(24)	123.1(7)
C(22)-N(5)-Cu(1)	110.9(4)	C(25)-C(24)-C(23)	119.4(8)
C(29)-N(6)-C(30)	116.1(6)	C(24)-C(25)-C(26)	118.8(8)
N(3)-C(2)-C(14)	109.0(5)	C(25)-C(26)-C(22)	120.0(7)

N(3)-C(2)-C(1)	112.9(5)	O(5)-C(27)-O(6)	123.7(8)
C(14)-C(2)-C(1)	110.0(5)	O(5)-C(27)-C(5)	126.7(9)
C(19)-C(1)-C(8)	108.1(5)	O(6)-C(27)-C(5)	109.6(8)
C(19)-C(1)-C(9)	108.2(5)	N(6)-C(29)-C(33)	123.6(6)
C(8)-C(1)-C(9)	108.9(5)	N(6)-C(29)-C(4)	115.2(6)
C(19)-C(1)-C(2)	109.1(5)	C(33)-C(29)-C(4)	121.0(6)
C(8)-C(1)-C(2)	113.3(5)	N(6)-C(30)-C(31)	124.7(7)
C(9)-C(1)-C(2)	109.1(5)	C(32)-C(31)-C(30)	116.9(7)
C(1)-C(8)-N(7)	111.4(4)	C(31)-C(32)-C(33)	120.3(7)
N(7)-C(6)-C(5)	112.8(5)	C(29)-C(33)-C(32)	118.4(7)
C(6)-C(5)-C(4)	116.1(5)	O(8)-N(9)-O(9)	121.0(6)
C(6)-C(5)-C(27)	105.0(6)	O(8)-N(9)-O(7)	120.1(6)
C(4)-C(5)-C(27)	109.5(5)	O(9)-N(9)-O(7)	119.0(6)
C(6)-C(5)-C(9)	110.0(5)	O(11)-N(8)-O(12)	126.6(9)
C(4)-C(5)-C(9)	106.9(5)	O(11)-N(8)-O(10)	116.4(8)
C(27)-C(5)-C(9)	109.2(5)	O(12)-N(8)-O(10)	116.3(8)

Figure S1. a) Molecular structure of **2,** showing the chair-chair arrangement of the bicyclic system; b) two molecules of **2** connected via hydrogen bonds.

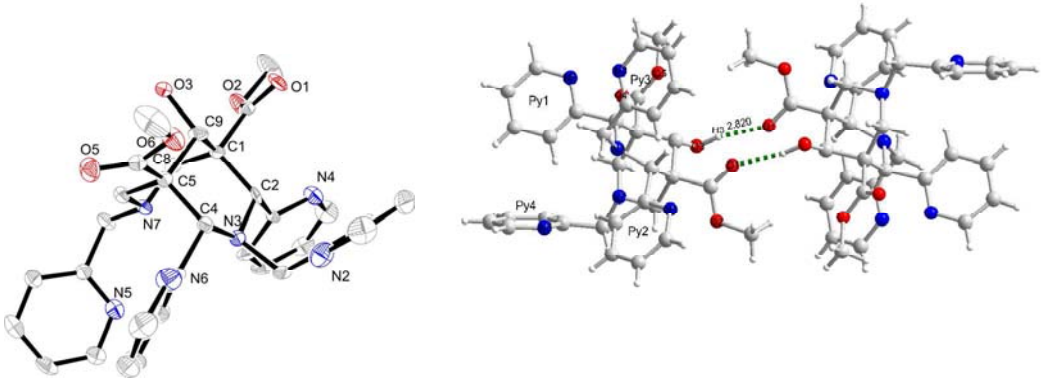

a **b**

Figure S2. Crystal structure of **Cu-2** (left, hydrogen atoms omitted for clarity) and **Cu-3** (right); gray spheres are carbon, red spheres oxygen, blue spheres nitrogen and yellow spheres copper atoms; The green lines indicate hydrogen bonds.

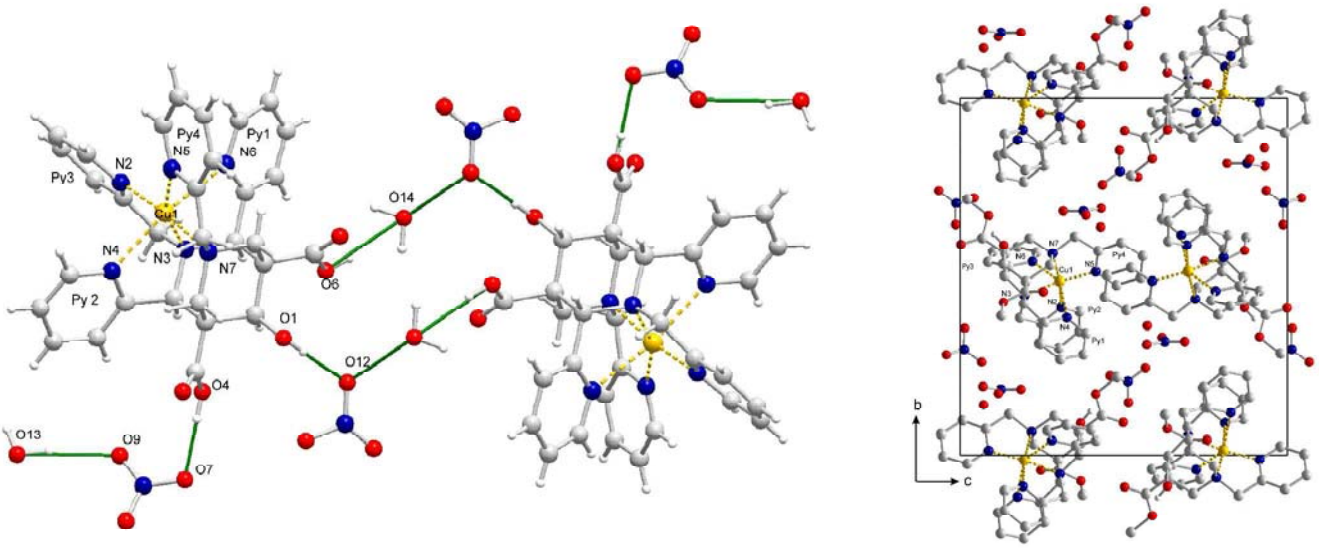

a **b**

***Corresponding authors.** Email: h.stephan@fzd.de, Fax : +49 351 260 3232; Email: peter.comba@aci.uni-heidelberg.de, Fax : +49 6221 54 6617.

Table S8. Amount of $^{64}CuCl_2$, ^{64}Cu-2, ^{64}Cu-3, and ^{64}Cu-6 in selected organs, tissues, and excretion in rats at 5 and 60 min after single intravenous application. Data expressed as %ID (**mean** [bold] ± SD, n=4).

Compound	Body weight (g)	Time p.i. (min)	Brain	Pancreas	Spleen	Adrenals	Kidneys	Heart	Lung	Thymus	Thyroide	Harderian gl.	Liver	Femur	Testes	Intestine	Stomach	Carcass	Recovery	Urine & faeces
$^{64}CuCl_2$	**170**		**0.08**	**0.17**	**0.10**	**0.02**	**8.54**	**0.25**	**0.85**	**0.38**	**0.10**	**0.10**	**19.44**	**0.39**	**0.29**	**8.85**	**1.50**	**53.55**	**96.19**	**3.81**
	15		0.01	0.03	0.01	0.01	0.54	0.04	0.03	0.02	0.01	0.02	0.51	0.03	0.05	0.69	0.17	3.27	2.54	2.54
^{64}Cu-2	**248**		**0.04**	**0.12**	**0.20**	**0.02**	**4.65**	**0.32**	**0.97**	**0.19**	**0.14**	**0.09**	**11.40**	**0.39**	**0.50**	**2.77**	**0.67**	**58.14**	**82.59**	**17.41**
	56		0.01	0.04	0.02	0.01	0.78	0.07	0.09	0.05	0.03	0.02	1.65	0.03	0.09	0.23	0.13	7.14	4.67	4.67
		5																		
^{64}Cu-3	**182**		**0.05**	**0.11**	**0.10**	**0.02**	**6.37**	**0.26**	**0.77**	**0.19**	**0.09**	**0.09**	**4.59**	**0.39**	**0.42**	**2.41**	**0.56**	**65.95**	**84.09**	**15.91**
	14		0.00	0.02	0.01	0.00	1.30	0.03	0.02	0.02	0.00	0.02	0.42	0.04	0.05	0.13	0.04	6.28	7.26	7.26
^{64}Cu-6	**226**		**0.06**	**0.14**	**0.17**	**0.03**	**10.35**	**0.36**	**0.91**	**0.22**	**0.07**	**0.09**	**9.31**	**0.33**	**0.26**	**2.80**	**0.56**	**68.29**	**96.30**	**3.70**
	13		0.01	0.02	0.01	0.02	2.30	0.03	0.20	0.07	0.02	0.01	0.62	0.03	0.01	0.12	0.05	2.36	0.95	0.95
$^{64}CuCl_2$	**181**		**0.06**	**0.20**	**0.14**	**0.02**	**10.37**	**0.18**	**0.65**	**0.30**	**0.12**	**0.09**	**14.27**	**0.41**	**0.75**	**12.30**	**1.91**	**51.93**	**95.40**	**4.60**
	8		0.01	0.03	0.02	0.00	1.18	0.02	0.08	0.07	0.01	0.01	1.00	0.03	0.18	0.94	0.29	3.22	2.01	2.01
^{64}Cu-2	**259**		**0.01**	**0.02**	**0.18**	**0.01**	**2.47**	**0.05**	**0.29**	**0.05**	**0.06**	**0.02**	**13.21**	**0.12**	**0.14**	**4.81**	**2.62**	**29.14**	**53.61**	**46.39**
	32		0.00	0.00	0.02	0.00	0.16	0.00	0.01	0.01	0.01	0.00	0.44	0.01	0.02	1.42	1.77	6.18	8.16	8.16
		60																		
^{64}Cu-3	**194**		**0.05**	**0.16**	**0.10**	**0.02**	**9.96**	**0.18**	**0.55**	**0.25**	**0.06**	**0.08**	**16.28**	**0.34**	**0.59**	**10.28**	**1.37**	**44,50**	**84,76**	**15,24**
	13		0.01	0.04	0.01	0.00	1.72	0.03	0.04	0.06	0.04	0.01	1.23	0.02	0.08	0.56	0.21	2.12	1.19	1.19
^{64}Cu-6	**196**		**0.01**	**0.06**	**0.07**	**0.02**	**4.59**	**0.06**	**0.28**	**0.06**	**0.07**	**0.03**	**6.45**	**0.13**	**0.18**	**6.16**	**2.09**	**45.80**	**67.28**	**32.72**
	21		0.00	0.01	0.02	0.02	2.35	0.01	0.06	0.02	0.09	0.02	1.24	0.02	0.03	3.01	1.15	19.61	23.42	23.42

Table S9. Concentration of **$^{64}CuCl_2$, ^{64}Cu-2**, **^{64}Cu-3,** and **^{64}Cu-6** in selected organs, tissues, and excretion in rats at 5 and 60 min after single intravenous application. Data expressed as SUV (**mean** [bold] ± SD, n=4).

Compound	Body weight (g)	Time p.i. (min)	Blood	Brown adipose fat	Hair & skin	Brain	Pancreas	Spleen	Adrenals	Kidneys	Fat	Muscle	Heart	Lung	Thymus	Harderian gl.	Liver	Femur	Testes
$^{64}CuCl_2$	**169.62**	**5**	**1.42**	**0.84**	**1.11**	**0.08**	**0.62**	**0.43**	**1.21**	**10.53**	**0.44**	**0.34**	**0.72**	**1.42**	**0.97**	**0.85**	**3.75**	**0.85**	**0.25**
	14.80		0.21	0.12	0.15	0.01	0.07	0.02	0.44	0.82	0.07	0.03	0.10	0.12	0.17	0.02	0.18	0.11	0.02
^{64}Cu-2	**248.13**		**1.68**	**0.63**	**1.38**	**0.06**	**0.56**	**1.07**	**0.79**	**6.12**	**0.38**	**0.40**	**0.94**	**1.83**	**0.76**	**0.75**	**2.31**	**0.87**	**0.40**
	55.84		0.13	0.10	0.05	0.01	0.04	0.10	0.05	0.13	0.23	0.03	0.06	0.15	0.16	0.08	0.39	0.09	0.02
^{64}Cu-3	**211.45**		**1.92**	**0.70**	**1.04**	**0.08**	**0.63**	**0.50**	**0.97**	**7.94**	**0.49**	**0.28**	**0.75**	**1.48**	**0.99**	**0.75**	**3.66**	**0.71**	**0.18**
	18.04		0.34	0.12	0.04	0.01	0.05	0.05	0.11	0.47	0.08	0.02	0.10	0.20	0.08	0.10	0.17	0.07	0.01
^{64}Cu-6	**226.23**		**2.09**	**0.63**	**1.10**	**0.09**	**0.68**	**0.70**	**1.04**	**12.80**	**2.14**	**0.49**	**0.98**	**1.51**	**0.67**	**0.79**	**1.70**	**0.71**	**0.22**
	12.82		0.18	0.02	0.05	0.01	0.04	0.02	0.60	2.35	1.59	0.05	0.03	0.12	0.13	0.10	0.13	0.03	0.01
$^{64}CuCl_2$	**180.95**	**60**	**0.88**	**0.81**	**1.41**	**0.07**	**0.81**	**0.51**	**0.83**	**12.12**	**0.32**	**0.29**	**0.52**	**1.00**	**0.83**	**0.74**	**2.65**	**0.81**	**0.61**
	7.56		0.09	0.05	0.13	0.00	0.07	0.06	0.07	0.99	0.04	0.04	0.04	0.07	0.12	0.08	0.16	0.03	0.11
^{64}Cu-2	**238.58**		**0.41**	**0.31**	**0.62**	**0.04**	**0.30**	**0.71**	**0.37**	**5.38**	**0.18**	**0.16**	**0.25**	**0.67**	**0.33**	**0.32**	**2.81**	**0.41**	**0.21**
	48.63		0.24	0.35	0.58	0.02	0.30	0.21	0.27	3.63	0.13	0.10	0.16	0.18	0.31	0.28	0.16	0.27	0.17
^{64}Cu-3	**193.60**		**0.92**	**0.63**	**1.22**	**0.06**	**0.71**	**0.43**	**0.69**	**12.72**	**0.32**	**0.34**	**0.56**	**1.02**	**0.92**	**0.62**	**2.75**	**0.73**	**0.43**
	12.55		0.07	0.02	0.10	0.01	0.14	0.02	0.07	1.62	0.09	0.19	0.07	0.03	0.11	0.07	0.09	0.01	0.05
^{64}Cu-6	**195.81**		**0.28**	**0.15**	**0.51**	**0.02**	**0.31**	**0.32**	**0.27**	**6.06**	**1.05**	**0.15**	**0.19**	**0.50**	**0.22**	**0.27**	**1.20**	**0.25**	**0.14**
	20.56		0.02	0.02	0.37	0.00	0.02	0.03	0.16	2.96	0.79	0.05	0.02	0.07	0.05	0.12	0.27	0.03	0.02

A Dual-Mode Fluorescence Strategy for Screening HAT Modulators

Nan Xie, Emilia N. Elangwe, Sabrina Asher, and Yujun George Zheng*

Department of Chemistry, Georgia State University, PO Box 4098, Atlanta, Georgia 30302. Received October 27, 2008

Histone acetyltransferases (HATs) are an important class of epigenetic enzymes involved in chromatin restructuring and transcriptional regulation. We describe in this paper a novel approach for the identification and characterization of HAT inhibitors using both fluorescence resonance energy transfer (FRET) and fluorescence polarization. Expressed protein ligation (EPL) was used to label HATs PCAF and p300 with Dabcyl (Dab) as FRET acceptors. Methoxycoumarin (Mca) is conjugated to HAT substrate analogues to function as fluorescent donors, namely, H3CoA20Mca for interacting with PCAF and LysCoAMca for p300. When a ligand−protein interaction occurs, the fluorescent intensity of the donor fluorophore decreases due to FRET quenching by the Dab acceptor. Meanwhile, the formation of ligand−protein complexes causes reduction of the molecular mobility of the donor fluorophore, resulting in increased fluorescence anisotropy. Thus, dual modes of fluorescence measurement, FRET and anisotropy, are integrated in the same assay system. In particular, we demonstrated that both FRET and anisotropy measurements can be used to effectively detect and characterize HAT inhibitors. The developed strategy should be useful in the search of new anticancer drugs that target the substrate interfaces of the HAT targets, as well as find values in mechanistic study of HATs.

INTRODUCTION

The genomes of eukaryotic organisms are tightly packed into chromatin complexes in the nucleus, which not only serve as structural scaffolds of the DNA duplexes, but also function as a dynamic regulator of various DNA-involved nuclear processes such as DNA transcription, replication, recombination, and damage repair (*1*, *2*). The core histones in chromatin are subject to a diverse post-translational modification including acetylation, methylation, and phosphorylation, which has been determined to be an important molecular process that regulates the chromatin structure and gene expression (*3*, *4*). As one of the key types of histone modifications, lysine acetylation is catalyzed by histone acetyltransferases (HATs), which elicit chromatin structural relaxation and gene transcriptional activation either by altering DNA−histone interactions or by attracting downstream effectors (*5*, *6*). HATs are grouped into several distinct families based on sequence and structural homology (*7*−*11*), which include Gcn5/PCAF, p300/CBP, and the MYST family (named after its founding members, MOZ, YBF2/SAS3, SAS2, and Tip60) (*12*). These HAT proteins not only are essential to regulate gene expression in normal cellular processes (e.g., growth, differentiation, apoptosis), but expression and/or activity deregulation of many HATs have also been observed in a range of disease states, especially cancer (*8*, *13*−*17*). It has increasingly become apparent that dysfunctional regulation of histone acetylation constitutes a significant mechanism for malignant diseases (*8*, *14*, *15*). For example, in prostate carcinoma, several HATs including PCAF, p300/CBP, and Tip60 are up-regulated and participate in the acetylation and activation of the androgen receptor and contribute to the pathway of hormone resistance (*18*, *19*). Prostate cancer cells expressing acetylation mimic AR mutants were more resistant to androgen-antagonist flutamide (*20*). Thus, inhibition of deregulated HATs represents a promising approach to new cancer therapy.

Although HDAC inhibitors have been extensively studied and several are in clinical trials (*21*−*23*), progress in developing low-molecular-weight inhibitors of HATs has been relatively slow, partly because of the lack of effective experimental tools for inhibitor screening. Most of the reported small molecule HAT inhibitors to date, such as anacardic acid, garcinol, isothiazolone, curcumin, and cinnamoyl compounds, exhibit nonspecific inhibition and have limited usage in pharmacological settings (*24*). Therefore, new endeavors are needed to develop small molecule inhibitors of HATs.

Currently, only limited approaches exist for HAT inhibitory study in a high-throughput format (*25*−*29*). The classical radioisotope-labeled assay is useful for enzymatic characterization of HATs but is difficult to be implemented to automation and high-throughput screening (HTS) (*30*). Spectrophotometric methods that rely on quantification of the product coenzyme A (CoA) have been reported (*31*−*33*). These coupled reactions contain additional components and are much more complex than a pure HAT assay, which greatly compromises their application. Immunoblotting protocols (e.g., TRF-Cellisas) that rely on antibodies recognizing acetyl-lysines are widely used to study histone acetylation and deacetylation and have also been proposed for inhibitor screening use (*28*, *29*, *34*, *35*). Although the applicability of this type of assay to natural product screening with medium throughput has been demonstrated (*36*, *37*), it suffers from several aspects of shortcomings: antibodies are expensive, the procedure involves extensive washing and is time-consuming, and achieving quantification results is technically problematic. Also, a robust deconvolution scheme is additionally required to validate the action of hits identified in a cell-based screen. Therefore, certain reservation exists concerning their practical utility in a real HTS context (*38*).

We recently developed a simple, single-step assay for direct readout of acetylation products via fluorescent intensity changes (*39*). To gain fluorescence signals adequate for use in inhibitor screening contexts, herein we present a new fluorescence strategy for the study of HAT-ligand interactions. Uniquely, we integrated two principles of photophysical measurement, namely, fluorescence resonance energy transfer (FRET) and fluorescence polarization/anisotropy, within one single system. In this approach, the HAT protein is expressed and chemoselectively labeled with an acceptor chromophore (quencher). On the other hand, a HAT-binding ligand (e.g., a modified substrate analogue)

* yzheng@gsu.edu.

10.1021/bc800467a CCC: $40.75 © 2009 American Chemical Society
Published on Web 01/15/2009

Scheme 1. Schematic Diagram of the Fluorescent Reporter System

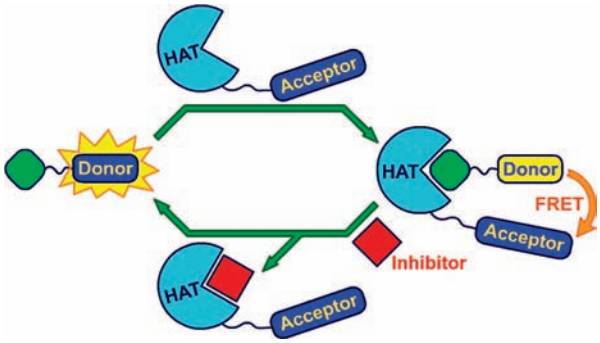

is chemically synthesized and labeled with a donor fluorophore. When the donor-labeled ligand is mixed with the acceptor-labeled HAT protein to form a complex, a FRET interaction occurs between the donor and the acceptor (e.g., coumarin and dabcyl), and thus, the fluorescence of the donor is quenched (Scheme 1). Along this process, the molecular mobility of the small-molecular-weight donor increases greatly due to complexation with the protein target. This allows for simultaneous fluorescence polarization and anisotropy readout. HAT inhibitors, on the other hand, have the potential to competitively displace the donor molecule from the enzyme, thus inversing the FRET and fluorescence anisotropy responses.

EXPERIMENTAL PROCEDURES

Materials. Fmoc-protected amino acids, Boc-protected amino acids, Rink amide resin, and preloaded Wang resin were purchased from NovaBiochem. All the other chemical reagents were purchased from Sigma-Aldrich or Fisher and used without further purification. *E. coli* strains XL1-Blue, BL-21(DE3), and BL-21(DE3) Codonplus RIPL competent cells were obtained from Stratagene. Chitin beads were purchased from New England Biolab.

Synthesis of Compounds. Solid-phase peptide synthesis (SPPS) was performed on a PS3 peptide synthesizer (Protein Technologies) using the Fmoc (*N*-(9-fluorenyl) methoxycarbonyl) strategy (*40*). All the reactions were performed at room temperature unless indicated otherwise. Removal of Fmoc was performed with 20% v/v piperidine/DMF. For the coupling of each amino acid (AA), 4 equiv of AA/HBTU/HOBt (*N*-hydroxybenzotriazole) were used. *N*-Methylmorpholine (NMM) was used as a base catalyst. The N-terminal amino group was acetylated with acetic anhydride unless indicated otherwise. After solid-phase synthesis, the resins were subsequently washed with DMF and dichloromethane and then dried in vacuum for at least 2 h before cleavage.

Peptides were cleaved from resin by treatment with 95% trifluoroacetic acid (TFA), 2.5% H_2O, and 2.5% triisopropylsilane, or with 94% TFA, 2.5% H_2O, 2.5% ethanedithiol, and 1% triisopropylsilane if the sequences of peptides contain Cysteine(Trt), or with Reagent K (82.5% trifluoroacetic acid, 5% phenol, 5% H_2O, 5% thioanisole, 2.5% ethanedithiol) if the sequences of peptides contain Arginine(Mtr) (handling of TFA must be performed in a secure hood) for 4 h. Cold diethyl ether was used to precipitate the products. Crude products were collected by centrifugation and were washed twice with cold diethyl ether. After lyophilization, the compounds were redissolved in water and purified with reverse-phase (RP) HPLC (C18, Varian) on a Varian Prostar HPLC system using linear gradients of H_2O/0.05% TFA (solvent A) vs acetonitrile/0.05% TFA (solvent B). Analytical HPLC and MALDI-MS were used for characterization.

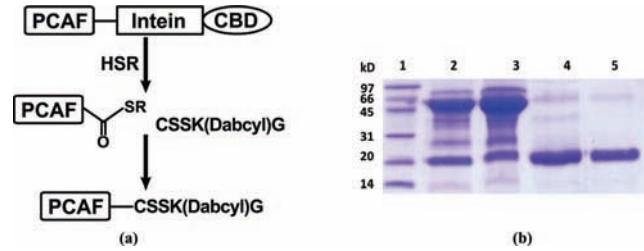

Figure 1. Preparation of PCAF-Dab acceptor with expressed protein ligation strategy. (a) Scheme of ligation. (b) 15% SDS-PAGE of PCAF expression and ligation with peptide CSSK(Dabcyl)G. Lane 1, MW marker; 2, chitin beads before ligation; 3, chitin beads after ligation; 4−5, eluting fractions of the ligated product.

Cys-Ser-Ser-Lys(Dabcyl)-Gly (1). Fmoc-Lys(Dde)-OH, Fmoc-Ser-OH, Boc-Cys(Trt)-OH, and Fmoc-Gly-Wang resin were used in SPPS. The Dde (dimethyldioxocyclohexylidene) group was removed with a solution of 2% hydrazine in DMF for 2 h (*41*). For fluorescent labeling with the Dabcyl group, the resin was treated with 4 equiv of Dabcyl-OSu and 10 equiv of *N*-methylmorpholine in DMF for 4 h. The final compound was purified with preparative RP-HPLC (gradient 5−50% B over 60 min; flow 10 mL/min; absorption detection at 460 nm), and the structure was confirmed using mass spectrometry. MALDI-MS: calcd. for $C_{32}H_{44}N_9O_9S$ [M + 1] 731.3, found 732.3.

H3(Br)20Mca (2) [Ac−K(Mca)RTKQTARKSTGGK(Br)-APRKQL]. The protected sequence Ac−K(Mca)RTKQTA-RKSTGGK(Dde)APRKQL was synthesized on preloaded Fmoc-Leu-Wang resin using SPPS protocol. After Dde removal, the resin was treated with 10 equiv of bromoacetic acid and 10 equiv diisopropylcarbodiimide (DIC) in a minimal volume of DMF for 4 h. The resins were subsequently washed with DMF and dichloromethane and then dried in vacuum for 2 h before cleavage. The compound was purified with preparative RP-HPLC (gradient 5−35% B over 60 min; flow 10 mL/min; UV detection at 214 nm), and the structure was confirmed using mass spectrometry. MALDI-MS: calcd. for $C_{110}H_{185}BrN_{36}O_{33}$ [M + 1] 2620.3, found 2620.5.

H3CoA20Mca (3). A mixture of 5.4 mg of H3(Br)20Mca and 4.7 mg of CoASH was dissolved in 100 μL of sodium phosphate buffer (100 mM, pH 8). The mixture was allowed to stand in the dark for 16 h and then purified with RP-HPLC (gradient 15−20% B over 60 min; flow 10 mL/min; UV detection at 214 nm), and the structure was confirmed using mass spectrometry. MALDI-MS: calcd. for $C_{131}H_{217}N_{43}O_{49}P_3S$ [M + Li^+] 3309.5, found 3309.2.

H3(Br)20 (4)[Ac-ARTKQTARKSTGGK(Br)APRKQL]. It was synthesized following the same procedure as for H3(Br)20Mca, but Fmoc-ALa-OH was employed in the place of Fmoc-Lys(Mca)-OH. The compound was purified with preparative RP-HPLC (gradient 5−30% B over 60 min; flow 10 mL/min; UV detection at 214 nm), and the structure was confirmed using mass spectrometry. MALDI-MS: calcd. for $C_{95}H_{170}BrN_{35}O_{29}$ [M + 1] 2347.2, found 2347.1.

H3CoA20 (5). 6.8 mg of H3(Br)20 and 6.4 mg of CoASH were dissolved in 100 μL of sodium phosphate buffer (100 mM, pH 8). The mixture was allowed to stand in the dark for 16 h and then purified with RP-HPLC (gradient 10−25% B over 60 min; flow 10 mL/min; UV detection at 214 nm), and the structure was confirmed using mass spectrometry. MALDI-MS: calcd. for $C_{116}H_{202}N_{42}O_{45}P_3S$ [M + Li^+] 3036.4, found 3034.4.

CMLVELHTQSQDRFK(Dabcyl)-NH_2 (6). The sequence was synthesized on Rink amide resin using the general SPPS protocol. Following Dde removal, then, the resin was treated with 4 equiv of Dabcyl-OSu and 10 equiv of *N*-methylmorpholine in DMF for 4 h. It should be noted that the N-terminal cysteine needs to be protected with Boc prior to the Dde removal

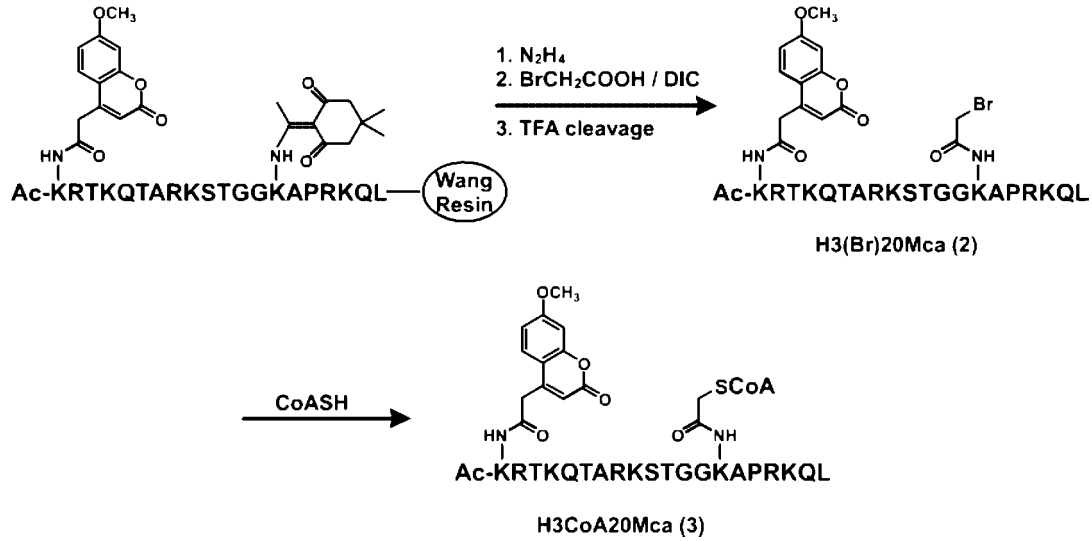

Figure 2. Chemical synthesis of the H3CoAMca donor.

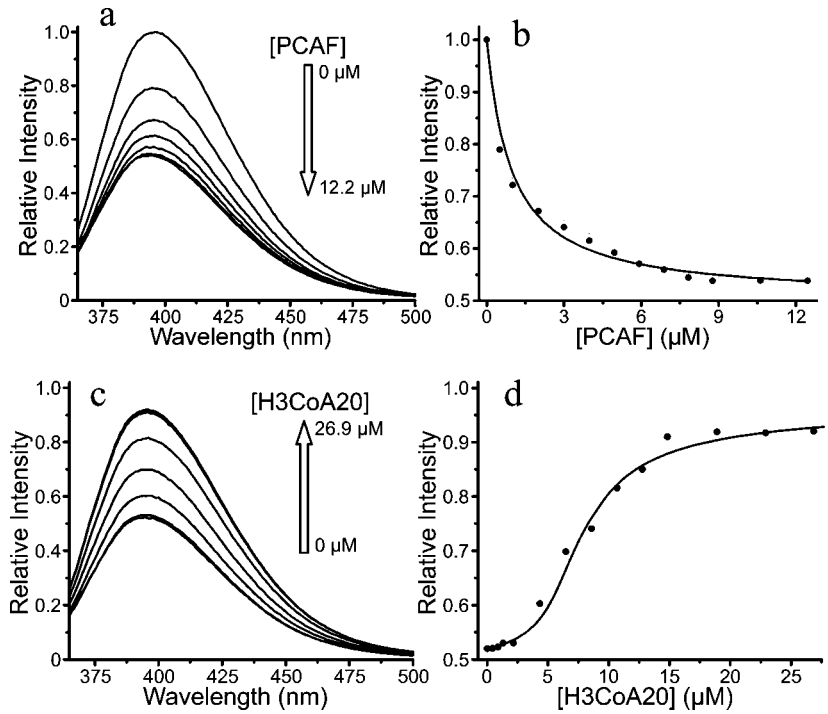

Figure 3. FRET changes of H3CoAMca. (a) The emission spectral changes of H3CoAMca (0.2 μM) at different concentrations of PCAFDab (λ_{ex} = 326 nm). (b) The titration curve of H3CoAMca emission at 396 nm (0.2 μM) vs the concentrations of PCAFDab. (c) The spectral changes of H3CoAMca (0.2 μM) at increasing concentrations of the PCAF inhibitor H3CoA20 while fixing the concentration of PCAFDab at 12 μM (λ_{ex} = 326 nm). (d) The fluorescent intensity changes of H3CoAMca (0.2 μM) at 396 nm vs the concentrations of H3CoA20 (the concentration of PCAFDab is 12 μM).

with 2% hydrazine. The compound was purified with preparative RP-HPLC (gradient 10−60% B over 70 min; flow 10 mL/min; UV−vis detection at 460 nm), and the structure was confirmed using mass spectrometry. MALDI-MS: calcd. for $C_{93}H_{141}N_{27}O_{24}S_2$ [M + 1] 2085.0, found 2085.1.

Ac-Lys(Br)-Ahx-Lys(Mca)-NH_2 (7). Fmoc-Lys(Mca)-OH, Fmoc-Ahx-OH, Fmoc-Lys(Dde)-OH, and acetic anhydride were sequentially coupled to Rink amide resin using the SPPS protocol. Then, the Dde group was removed, followed by bromoacetylation of the ε-amino group of the lysine. The resins were subsequently washed and then subjected to TFA cleavage. The compound was purified with preparative RP-HPLC (gradient 5−30% B over 60 min; flow 10 mL/min; UV detection at 214 nm), and the structure was confirmed using MALDI-MS: calcd. for $C_{34}H_{49}BrN_6O_9$ [M + Na^+] 789.26, found 789.3.

Ac-Lys-CoA-Ahx-Lys(Mca)-NH_2 (LysCoAMca) (8). A mixture of 2 mg of Ac-Lys(Br)-Ahx-Lys(Mca)-NH_2 and 4.1 mg of CoASH was dissolved in 200 μL of sodium phosphate buffer (100 mM, pH 8) and 200 μL of acetonitrile. The mixture was allowed to stand in the dark for 16 h and then purified with RP-HPLC (gradient 15−35% B over 60 min; flow 10 mL/min; UV detection at 214 nm), and the structure was confirmed by MALDI-MS: calcd. for $C_{55}H_{81}N_{13}O_{25}P_3S$ [M + Li^+] 1455.5, found 1458.3.

Ac-Lys(Br)-NH_2 (9). Fmoc-Lys(Dde)-OH and acetic anhydride were sequentially coupled to Rink amide resin using SPPS protocol. Following Dde removal with 2% hydrazine in DMF, bromoacetylation of the ε-amino group of the lysine was achieved by treating the resin with 10 equiv of bromoacetic acid and 10 equiv diisopropylcarbodiimide (DIC) in a minimal

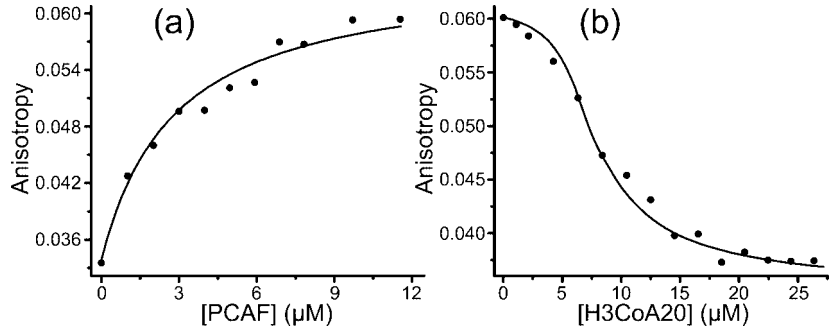

Figure 4. Use of fluorescence anisotropy for measurement of PCAF−ligand interaction. (a) Fluorescence anisotropy of H3CoAMca (0.2 μM) at 396 nm at different concentrations of PCAF-Dab. (b) Fluorescence anisotropy of the binary mixture (0.2 μM of H3CoAMca and 12 μM of PCAFDab) at 396 nm at different concentrations of the HAT inhibitor H3CoA20.

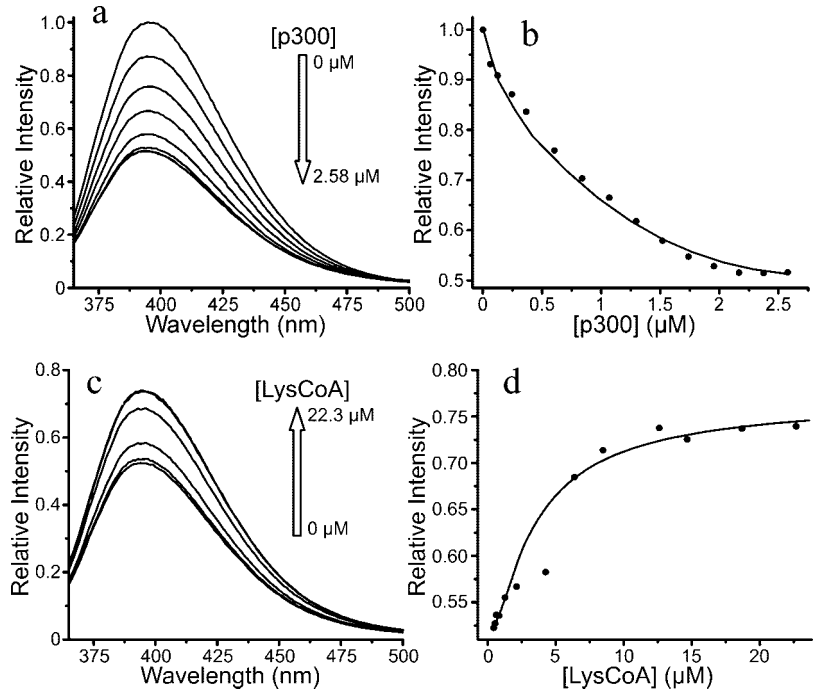

Figure 5. FRET changes of LysCoAMca. (a) The emission spectral changes of LysCoAMca (0.2 μM) at different concentrations of p300-Dabcyl (λ_{ex} = 326 nm). (b) The titration curve of LysCoAMca (0.2 μM) emission at 396 nm vs the concentrations of p300-Dabcyl. K_d is calculated to be 0.40 ± 0.06 μM. (c) The spectral changes of LysCoAMca (0.2 μM) at increasing concentrations of the p300 inhibitor LysCoA while fixing the concentration of p300Dab at 2.2 μM (λ_{ex} = 326 nm). (d) The fluorescent intensity changes of LysCoAMca (0.2 μM) at 396 nm vs the concentrations of LysCoA (the concentration of p300Dab is 2.2 μM). K_i of LysCoA is calculated to be 0.57 ± 0.07 μM.

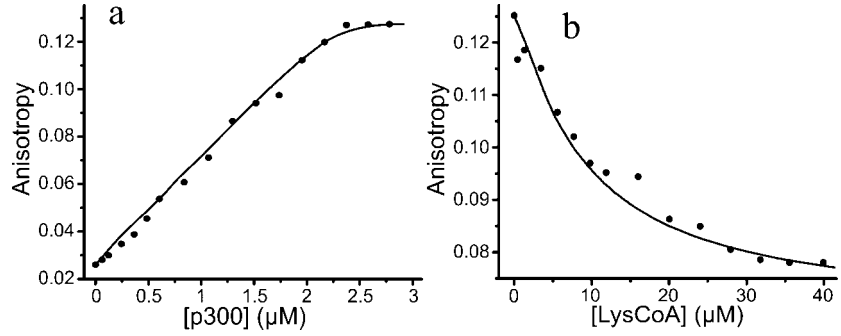

Figure 6. Fluorescence anisotropy changes of LysCoAMca. (a) Titration of LysCoAMca (0.2 μM) with p300-Dab by fluorescence anisotropy (λ_{ex} = 326 nm, λ_{em} = 396 nm). K_d is calculated to be 0.73 ± 0.15 μM. (b) Titration of the binary mixture (0.2 μM of LysCoAMca and 2.2 μM of p300Dab) with HAT inhibitor LysCoA by fluorescence anisotropy (λ_{ex} = 326 nm, λ_{em} = 396 nm). K_i of LysCoA is calculated to be 1.92 ± 0.29 μM.

volume of DMF for 4 h. The resins were subsequently washed with DMF and dichloromethane and then dried in vacuum for 2 h before cleavage. The compound was purified with preparative RP-HPLC (gradient 5−15% B over 60 min; flow 10 mL/min; UV detection at 214 nm). MALDI-MS: calcd. for $C_{10}H_{18}BrN_3O_3$ [M + Na^+] 332.04, found 332.0.

Ac-Lys-CoA-NH_2 (LysCoA) (10). A mixture of 2 mg of Ac-Lys(Br)-NH_2 and 4.1 mg of CoASH was dissolved in 50 μL of

sodium phosphate buffer (100 mM, pH 8) and 50 μL of methanol. The mixture was allowed to stand in the dark for 16 h and then purified with RP-HPLC (gradient 4−5% B over 60 min; flow 10 mL/min; UV detection at 214 nm), and the structure was confirmed using mass spectrometry. MALDI-MS: calcd. for $C_{31}H_{50}N_{10}O_{19}P_3S$ [M + Li^+] 998.2, found 995.3.

Expression of Dabcyl-Labeled PCAF Protein. The DNA construct encoding for the PCAF HAT domain (aa 493−658) in the PTYB2 vector was used for protein expression. In a typical procedure, to 50 μL of BL-21(DE3) competent cells was added 1 μL of the PCAF-pTYB2 plasmid and incubated on ice for 30 min. The tube was then heat shocked at 42 °C for 30 s and put on ice for 2 min. 0.5 mL of NZY solution was added to the cells and allowed to incubate while rotating at 37 °C, 225 rpm, for 1 h. The cells were spread to agar plates and distributed with glass-ball beads. The plates were then incubated overnight at 37 °C. One colony was selected for inoculation of 8 mL of LB media containing ampicillin. The solution was then allowed to incubate at 37 °C overnight with shaking at 225 rpm. The 8 mL cell culture was added to 1 L of LB media and cultured until the OD595 reached 0.6−0.8. Then, the temperature of the incubator was decreased to 16 °C at which point protein expression was induced with 0.3 mM of IPTG. The culture was kept in the incubator for 16−20 h. The cells were harvested by centrifugation at 5000 rpm, 4 °C, for 10 min. The cells were then resuspended in 25 mL of lysis buffer (Hepes 25 mM, pH 8.0, NaCl 500 mM, glycerol 10%, MgSO4 1 mM, PMSF 1 mM). The cells were lysed with a French Press twice, and the lysates immediately were centrifuged at 4 °C, 14,000 rpm for 30 min. The supernatant was collected and loaded to 3.0 mL of chitin beads. The beads were washed with 1× chitin column buffer (25 mM HEPES pH 8.0, 500 mM NaCl, 1 mM EDTA, 0.1% Triton X-100, glycerol 10%, and 1 mM PMSF). After washing, 2 mM of the ligation peptide (CSSK(Dabcyl)G, 1) in 3 mL of ligation buffer (25 mM HEPES pH 8.0, 500 mM NaCl, 1 mM EDTA, glycerol 10%, 1 mM PMSF, and 200 mM MESNA) was added to the beads. The ligation reaction proceeded at room temperature for 40 h. After that, the ligated product was eluted, combined, and dialyzed against a storage buffer (25 mM HEPES pH 7.0, 250 mM NaCl, 1 mM EDTA, glycerol 10%, and 5 mM DTT) and then concentrated in a Millipore centrifuge filter tube. The protein concentration was determined by Bradford assay. The final labeled protein (PCAF-Dab) was aliquoted, flash-frozen with liquid N_2, and stored at −80 °C until use.

Expression of Dabcyl-Labeled p300 Protein. Labeling of p300 protein with Dacyl was achieved using the EPL protocol essentially the same as in the literature (*33*). First, the DNA sequence encoding for the p300 HAT domain (aa 1287−1652) was subcloned into PTYB2 vector (a gift from Prof. Phil Cole). BL-21(DE3) Codonplus RIL competent cells were used for protein expression. The expressed p300-intein-CBP fusion protein was loaded to chitin beads. After extensive washing, 6 mg of the ligation peptide (**2**. CMLVELHTQSQDRFK(Dabcyl)-NH_2) in 3 mL of ligation buffer (25 mM HEPES pH8.0, 250 mM NaCl, 1 mM EDTA, and 200 mM MESNA solution) was added to the beads. The ligation reaction was kept at room temperature for 48 h. The protein product was confirmed with 12% SDS-PAGE. The combined eluents were dialyzed against the storage buffer and then concentrated in a centrifuge filter tube. The concentration of labeled p300 protein (p300Dab) was determined by Bradford assay.

Fluorescence Measurement. The fluorescence experiments were performed on a Fluoromax-4 instrument (Horiba Jobin Yvon, Edison, NJ) at 25 °C using a 0.5 mL cuvette in a buffer solution containing 50 mM Hepes (pH 8.0), 0.1 mM EDTA, 150 mM NaCl, and 1 mM DTT. The dissociation constants (K_d) were determined by measuring the fluorescence signals of Mca-labeled ligands (at fixed concentration) with increasing Dab-labeled protein concentrations.

$$\text{fraction bound} = (F - F_o)/(F_f - F_o) = \{(F_f - F_o)/2[\text{Pr}]_{tot}\}\{b(b^2 - 4[\text{L}]_{tot}[\text{Pr}]_{tot})^{1/2}\} + F_o \quad (1)$$

$$b = K_d + [\text{L}]_{tot} + [\text{PCAF}]_{tot}$$

Where F_0 and F_f are the initial and final fluorescence intensities, respectively, $[\text{Pr}]_{tot}$ is the total protein concentration, and $[\text{L}]_{tot}$ is the total concentration of Mca-labeled ligand.

The inhibition constants (K_i) were determined by measuring the fluorescence signals of the binary mixture containing Mca-labeled ligand and Dab-labeled protein (at fixed concentrations) with increasing concentrations of respective inhibitors. Equation 2 was used for K_i calculation (*42*).

$$K_i = [\text{I}]_{50}/([\text{L}]_{50}/K_d + [\text{Pr}]_o/K_d + 1) \quad (2)$$

where $[\text{I}]_{50}$ denotes the concentration of the free inhibitor at 50% inhibition, $[\text{L}]_{50}$ is the concentration of the free Mca-labeled ligand at 50% inhibition, $[\text{Pr}]_0$ is the concentration of the free protein at 0% inhibition, and K_d is the dissociation constant of the protein−ligand complex.

RESULTS AND DISCUSSION

PCAF Protein Expression and Ligation. To design the donor−acceptor reporter for HATs, it would be ideal if the HAT enzyme can be regioselectively labeled so that its active site will not be affected by the chemical labeling reaction. Mixing a protein sample with common labeling reagents (e.g., fluorescein succinimidyl ester) has a high chance of leading to random placement of introduced tags. To achieve the regioselectivity, we took advantage of expressed protein ligation (EPL), a technique widely used for site-specific protein engineering (*43*, *44*). As a proof of principle, we first conducted fluorescent labeling of the HAT PCAF (Figure 1). The gene sequence encoding for the human PCAF (493−658) was subcloned into a PTYB2 expression vector. From this system, the recombinant protein was expressed in *E. coli* in the fusion form of PCAF-intein-CBD (chitin binding domain). The CBD motif allows for purifying the fusion protein on chitin beads. After washing out impurities, the beads were treated with a ligation buffer containing peptide Cys-Ser-Ser-Lys(Dabcyl)-Gly, abbreviated as CSSK(Dab)G, and 200 mM of 2-mercaptoethanesulfonic acid (MESNA). The thiol treatment produced the PCAF protein with a thioester motif at its carboxyl terminus. In the course, PCAF-thioester reacted with CSSK(Dabcyl)G via native chemical ligation (*45*) and formed the labeled PCAF-CSSK(Dabcyl)G product (PCAFDab).

Design and Synthesis of the Fluorescent Donor Ligand H3CoAMca. PCAF was reported to acetylate the N-terminal tail of histone H3 (*46*). The bisubstrate analogue H3CoA20 in which a CoA motif is linked to the H3 N-terminal sequence at the acetylation lysine site (K14) has been shown as a potent inhibitor of PCAF/GCN5 (*47*). We modified the bisubstrate analogue H3CoA20 with a fluorophore, methoxycoumarin (Mca), to produce a fluorescent donor ligand (Figure 2). The Mca group is attached at the N-terminal end via a lysine residue, distant from the CoA-attaching site to avoid potential interference with the binding ability of the ligand to PCAF.

FRET Response of the PCAF Reporter H3CoAMca. The Mca-labeled H3CoA20 conjugate (H3CoAMca) was characterized for its fluorescence properties. The compound was excited at 326 nm (extinction coefficient ε = 11 820 M^{-1} cm^{-1}) and exhibited a maximum emission at 396 nm (Figure 3). On the other hand, PCAFDab showed a broad absorption across

360−500 nm (not shown). Therefore, excited-state energy of Mca can be effectively transferred to the Dab acceptor when the two chromophores are within the Förster distance. We tested fluorescence emission of H3CoAMca in the presence of PCAFDab. As expected, the fluorescent intensity of H3CoAMca (0.2 μM) gradually decreased as a function of PCAFDab concentration (Figure 3a,b). The maximum quenching was achieved when the concentration of PCAFDab reached 12 μM or higher. From the titration data, the apparent K_d was calculated to be 0.57 ± 0.06 μM.

Next, we evaluated the performance of the donor−acceptor reporter for use in the detection of HAT inhibitors by monitoring FRET-mediated fluorescence intensity changes. A solution of a binary mixture was prepared containing 0.2 μM of H3CoAMca and 12 μM of PCAFDab. Then, an increasing amount of the nonfluorescent HAT inhibitor, H3CoA20, was added to the solution. As shown in Figure 3c,d, the fluorescent intensity increased in response to increasing amounts of H3CoA20. This matches well with our concept that the presence of a HAT inhibitor expels the H3CoAMca donor out of the binding pocket in PCAFDab, which will release the FRET interaction between the donor and the acceptor, thus causing fluorescence enhancement of the H3CoAMca donor. The K_i of H3CoA20 can be conveniently calculated from the competitive binding curve as 0.33 ± 0.03 μM, which is in close range to the value determined from the radioactive assay (0.14 μM) (*48*).

Anisotropy Response of the PCAF Reporter. Compared to its free form, the H3CoAMca ligand in the PCAF complex possesses a larger molecular mass and more restricted molecular mobility, which will correspond to a larger fluorescence polarization and anisotropy. Therefore, the HAT binding assay can also be possibly realized using the mode of fluorescence polarization or anisotropy measurement. As shown in Figure 4a, the fluorescence anisotropy of H3CoAMca gradually increased when increasing amounts of PCAFDab were added to the solution. K_d was calculated to be 1.58 ± 0.22 μM from the titration curve. The value is slightly higher than the value obtained from the FRET measurement, which most likely reflects that not all proteins are labeled by Dab chromophore: FRET measurement is dependent on the Dab labeling, while anisotropy is not. We also tested the use of fluorescence anisotropy in the measurement of inhibitor binding (Figure 4b). A solution of binary mixture containing 0.2 μM of H3CoAMca and 12 μM of PCAF-Dab was prepared. When an increasing amount of the PCAF inhibitor H3CoA20 was added, the fluorescence anisotropy of H3CoAMca at 396 nm decreased concurrently. From the anisotropy assay, K_i of H3CoA20 was determined to be 0.83 ± 0.10 μM. These experiments substantiate that, when H3CoAMca is competitively displaced from binding to the large HAT protein by an inhibitor, its fluorescence anisotropy will decrease due to reduction in molecular mass and rigidity.

Fluorescent Reporter of p300. To demonstrate whether the dual-mode strategy can be applied as a general approach to the study of other HAT proteins, we constructed a similar donor−acceptor assay and evaluated its performance for p300, another important HAT enzyme. Like the site-specific labeling of PCAF, p300 HAT domain (1287−1652) was expressed using a pTYB2 vector and then ligated to a C-terminal peptide CMLVELHTQSQDRFK(Dabcyl) (**6**), thus generating a protein fluorescent acceptor, p300Dab. To make a corresponding fluorescent donor ligand, an Mca-labeled compound, LysCoAMa, was designed on the basis of the reported p300 inhibitor, LysCoA (*47*). As anticipated, upon addition of p300Dab, the fluorescent intensity of LysCoAMca declined in a dose-dependent manner owing to FRET quenching interaction between Dab and Mca (Figure 5a,b). Again, the fluorescence intensity was recovered when the nonfluorescent ligand LysCoA was added to the solution, competitively displacing LysCoAMca out of the binding pocket in p300 (Figure 5c,d). We also performed fluorescence anisotropy measurements of LysCoAMca (Figure 6). In this regard, the performance of LysCoAMca was analogous to that of H3CoA20Mca; the anisotropy value increased upon binding to p300Dab protein, and the change was reversed by increasing concentrations of the competitive inhibitor LysCoA. Therefore, both FRET and anisotropy signals were effective to probe and characterize the p300−inhibitor interactions.

Taken together, we demonstrated a displacement strategy for the study of HAT−inhibitor interactions. The assay is built on the binding between an acceptor-labeled HAT protein and a fluorescent donor-labeled ligand. The HAT protein (PCAF or p300) was chemoselectively labeled using the technique of EPL. FRET and fluorescence anisotropy were utilized as readout to identify and quantify ligand binding. This approach is fast, homogeneous, non-radioactive, and friendly to automation, thus holding promise as a platform for the discovery and characterization of HAT modulators. It should be noted that current screening equipments often harness capabilities to collect data in multiple modes, such as absorption, fluorescence intensity, polarization, FRET, and chemiluminescence, and so forth. Since FRET and polarization measurements are based on two totally different photophysical principles (the measurement of Mca polarization is dispensable to the Dab), availability of dual signals in a primary assay will allow for the generation of two independent data sets from one screening experiment, thus having a high efficacy in substantiating genuine hits and eliminating false positives. Apart from inhibitor discovery, this fluorescence strategy can also be used as a valuable tool to investigate binding kinetics of HAT substrate analogues as well as the enzymatic mechanisms of HAT catalysis.

ACKNOWLEDGMENT

This work is supported by Georgia Cancer Coalition Distinguished Cancer Scholar Award and a Georgia State University Research Initiation Grant.

LITERATURE CITED

(1) Holbert, M. A., and Marmorstein, R. (2005) Structure and activity of enzymes that remove histone modifications. *Curr. Opin. Struct. Biol. 15*, 673–80.
(2) Wolffe, A. (1998) *Chromatin: structure and function*, 3rd ed., Academic Press, San Diego.
(3) Strahl, B. D., and Allis, C. D. (2000) The language of covalent histone modifications. *Nature 403*, 41–5.
(4) Peterson, C. L., and Laniel, M. A. (2004) Histones and histone modifications. *Curr. Biol. 14*, R546–51.
(5) Yang, X. J. (2004) Lysine acetylation and the bromodomain: a new partnership for signaling. *Bioessays 26*, 1076–87.
(6) Taverna, S. D., Li, H., Ruthenburg, A. J., Allis, C. D., and Patel, D. J. (2007) How chromatin-binding modules interpret histone modifications: lessons from professional pocket pickers. *Nat. Struct. Mol. Biol. 14*, 1025–40.
(7) Vetting, M. W., LP, S. d. C., Yu, M., Hegde, S. S., Magnet, S., Roderick, S. L., and Blanchard, J. S. (2005) Structure and functions of the GNAT superfamily of acetyltransferases. *Arch. Biochem. Biophys. 433*, 212–26.
(8) Yang, X. J. (2004) The diverse superfamily of lysine acetyltransferases and their roles in leukemia and other diseases. *Nucleic Acids Res. 32*, 959–76.
(9) Sterner, D. E., and Berger, S. L. (2000) Acetylation of histones and transcription-related factors. *Microbiol. Mol. Biol. Rev. 64*, 435–59.
(10) Lee, K. K., and Workman, J. L. (2007) Histone acetyltransferase complexes: one size doesn't fit all. *Nat. Rev. Mol. Cell Biol. 8*, 284–95.
(11) Roth, S. Y., Denu, J. M., and Allis, C. D. (2001) Histone acetyltransferases. *Annu. Rev. Biochem. 70*, 81–120.

(12) Utley, R. T., and Cote, J. (2003) The MYST family of histone acetyltransferases. *Curr. Top. Microbiol. Immunol. 274*, 203–36.
(13) Giordano, A., and Avantaggiati, M. L. (1999) p300 and CBP: partners for life and death. *J. Cell Physiol. 181*, 218–30.
(14) Heery, D. M., and Fischer, P. M. (2007) Pharmacological targeting of lysine acetyltransferases in human disease: a progress report. *Drug Discovery Today 12*, 88–99.
(15) Avvakumov, N., and Cote, J. (2007) The MYST family of histone acetyltransferases and their intimate links to cancer. *Oncogene 26*, 5395–407.
(16) Cairns, B. R. (2001) Emerging roles for chromatin remodeling in cancer biology. *Trends Cell Biol. 11*, S15–21.
(17) Avvakumov, N., and Cote, J. (2007) Functions of myst family histone acetyltransferases and their link to disease. *Subcell Biochem. 41*, 295–317.
(18) Debes, J. D., Schmidt, L. J., Huang, H., and Tindall, D. J. (2002) p300 mediates androgen-independent transactivation of the androgen receptor by interleukin 6. *Cancer Res. 62*, 5632–6.
(19) Halkidou, K., Gnanapragasam, V. J., Mehta, P. B., Logan, I. R., Brady, M. E., Cook, S., Leung, H. Y., Neal, D. E., and Robson, C. N. (2003) Expression of Tip60, an androgen receptor coactivator, and its role in prostate cancer development. *Oncogene 22*, 2466–77.
(20) Fu, M., Wang, C., Wang, J., Zhang, X., Sakamaki, T., Yeung, Y. G., Chang, C., Hopp, T., Fuqua, S. A., Jaffray, E., Hay, R. T., Palvimo, J. J., Janne, O. A., and Pestell, R. G. (2002) Androgen receptor acetylation governs trans activation and MEKK1-induced apoptosis without affecting in vitro sumoylation and trans-repression function. *Mol. Cell. Biol. 22*, 3373–88.
(21) Yoo, C. B., and Jones, P. A. (2006) Epigenetic therapy of cancer: past, present and future. *Nat. Rev. Drug Discovery 5*, 37–50.
(22) Mai, A., Massa, S., Rotili, D., Cerbara, I., Valente, S., Pezzi, R., Simeoni, S., and Ragno, R. (2005) Histone deacetylation in epigenetics: an attractive target for anticancer therapy. *Med. Res. Rev. 25*, 261–309.
(23) Grozinger, C. M., and Schreiber, S. L. (2002) Deacetylase enzymes: biological functions and the use of small-molecule inhibitors. *Chem. Biol. 9*, 3–16.
(24) Zheng, Y. G., Wu, J., Chen, Z., and Goodman, M. (2008) Chemical regulation of epigenetic modifications: Opportunities for new cancer therapy. *Med. Res. Rev. 28*, 645–687.
(25) Wynne Aherne, G., Rowlands, M. G., Stimson, L., and Workman, P. (2002) Assays for the identification and evaluation of histone acetyltransferase inhibitors. *Methods 26*, 245–53.
(26) Berndsen, C. E., and Denu, J. M. (2005) Assays for mechanistic investigations of protein/histone acetyltransferases. *Methods 36*, 321–31.
(27) Marmorstein, R. (2004) Biochemical and structural characterization of recombinant histone acetyltransferase proteins. *Methods Enzymol. 376*, 106–19.
(28) Hardcastle, A., Boxall, K., Richards, J., Tomlin, P., Sharp, S., Clarke, P., Workman, P., and Aherne, W. (2005) Solid-phase immunoassays in mechanism-based drug discovery: their application in the development of inhibitors of the molecular chaperone heat-shock protein 90. *Assay Drug Dev. Technol. 3*, 273–85.
(29) Martinez, E. D., Dull, A. B., Beutler, J. A., and Hager, G. L. (2006) High-content fluorescence-based screening for epigenetic modulators. *Methods Enzymol. 414*, 21–36.
(30) Turlais, F., Hardcastle, A., Rowlands, M., Newbatt, Y., Bannister, A., Kouzarides, T., Workman, P., and Aherne, G. W. (2001) High-throughput screening for identification of small molecule inhibitors of histone acetyltransferases using scintillating microplates (FlashPlate). *Anal. Biochem. 298*, 62–8.
(31) Kim, Y., Tanner, K. G., and Denu, J. M. (2000) A continuous, nonradioactive assay for histone acetyltransferases. *Anal. Biochem. 280*, 308–14.
(32) Trievel, R. C., Li, F. Y., and Marmorstein, R. (2000) Application of a fluorescent histone acetyltransferase assay to probe the substrate specificity of the human p300/CBP-associated factor. *Anal. Biochem. 287*, 319–28.
(33) Thompson, P. R., Wang, D., Wang, L., Fulco, M., Pediconi, N., Zhang, D., An, W., Ge, Q., Roeder, R. G., Wong, J., Levrero, M., Sartorelli, V., Cotter, R. J., and Cole, P. A. (2004) Regulation of the p300 HAT domain via a novel activation loop. *Nat. Struct. Mol. Biol. 11*, 308–15.
(34) Zhang, Y., LeRoy, G., Seelig, H. P., Lane, W. S., and Reinberg, D. (1998) The dermatomyositis-specific autoantigen Mi2 is a component of a complex containing histone deacetylase and nucleosome remodeling activities. *Cell 95*, 279–89.
(35) Stockwell, B. R., Haggarty, S. J., and Schreiber, S. L. (1999) High-throughput screening of small molecules in miniaturized mammalian cell-based assays involving post-translational modifications. *Chem. Biol. 6*, 71–83.
(36) Haggarty, S. J., Koeller, K. M., Wong, J. C., Butcher, R. A., and Schreiber, S. L. (2003) Multidimensional chemical genetic analysis of diversity-oriented synthesis-derived deacetylase inhibitors using cell-based assays. *Chem. Biol. 10*, 383–96.
(37) Koeller, K. M., Haggarty, S. J., Perkins, B. D., Leykin, I., Wong, J. C., Kao, M. C., and Schreiber, S. L. (2003) Chemical genetic modifier screens: small molecule trichostatin suppressors as probes of intracellular histone and tubulin acetylation. *Chem. Biol. 10*, 397–410.
(38) Wegener, D., Hildmann, C., and Schwienhorst, A. (2003) Recent progress in the development of assays suited for histone deacetylase inhibitor screening. *Mol. Genet. Metab. 80*, 138–47.
(39) Wu, J., and Zheng, Y. G. (2008) Fluorescent reporters of the histone acetyltransferase. *Anal. Biochem. 380*, 106–110.
(40) Chan, W. C., and White, P. D. (2000) *Fmoc solid phase peptide synthesis: a practical approach*, Oxford University Press, Oxford.
(41) Bycroft, B. W., Chan, W. C., Chhabra, S. R., Teesdalespittle, P. H., and Hardy, P. M. (1993) A novel amino protection deprotection procedure and its application in solid-phase peptide-synthesis. *J. Chem. Soc., Chem. Commun.* 776–777.
(42) Nikolovska-Coleska, Z., Wang, R., Fang, X., Pan, H., Tomita, Y., Li, P., Roller, P. P., Krajewski, K., Saito, N. G., Stuckey, J. A., and Wang, S. (2004) Development and optimization of a binding assay for the XIAP BIR3 domain using fluorescence polarization. *Anal. Biochem. 332*, 261–73.
(43) Muir, T. W., Sondhi, D., and Cole, P. A. (1998) Expressed protein ligation: a general method for protein engineering. *Proc. Natl. Acad. Sci. U.S.A. 95*, 6705–10.
(44) Evans, T. C., Jr., Benner, J., and Xu, M. Q. (1998) Semisynthesis of cytotoxic proteins using a modified protein splicing element. *Protein Sci. 7*, 2256–64.
(45) Dawson, P. E., and Kent, S. B. (2000) Synthesis of native proteins by chemical ligation. *Annu. Rev. Biochem. 69*, 923–60.
(46) Schiltz, R. L., Mizzen, C. A., Vassilev, A., Cook, R. G., Allis, C. D., and Nakatani, Y. (1999) Overlapping but distinct patterns of histone acetylation by the human coactivators p300 and PCAF within nucleosomal substrates. *J. Biol. Chem. 274*, 1189–92.
(47) Lau, O. D., Kundu, T. K., Soccio, R. E., Ait-Si-Ali, S., Khalil, E. M., Vassilev, A., Wolffe, A. P., Nakatani, Y., Roeder, R. G., and Cole, P. A. (2000) HATs off: selective synthetic inhibitors of the histone acetyltransferases p300 and PCAF. *Mol. Cell 5*, 589–95.
(48) Zheng, Y., Mamdani, F., Toptygin, D., Brand, L., Stivers, J. T., and Cole, P. A. (2005) Fluorescence analysis of a dynamic loop in the PCAF/GCN5 histone acetyltransferase. *Biochemistry 44*, 10501–9.

BC800467A

Covalent Modification of Matrix Metalloproteinases by a Photoaffinity Probe: Influence of Nucleophilicity and Flexibility of the Residue in Position 241

Anne-Sophie Dabert-Gay,[†] B. Czarny,[†] E. Lajeunesse,[†] R. Thai,[†] H. Nagase,[‡] and V. Dive*[,†]

CEA, iBiTecS, Service d'Ingénierie Moléculaire des Protéines (SIMOPRO), CE-Saclay Gif/Yvette, F-91191, France, and Matrix Biology Department, Kennedy Institute of Rheumatology Division, Faculty of Medicine, Imperial College London, London, United Kingdom. Received November 4, 2008; Revised Manuscript Received December 12, 2008

A photoaffinity probe, developed for the specific labeling of matrix metalloproteinase (MMP) active sites, was recently shown to covalently modify a single residue in human MMP-12, namely, Lys^{241}, by reacting selectively with the side chain ε-amino group of that residue. The residue in position 241 of MMPs is not conserved; thus, variability in this position may be responsible for the dispersion in cross-linking yield observed between MMPs when labeled by this photoaffinity probe. By studying the pH dependence of the labeling properties of this probe toward different MMPs (MMP-12, MMP-3, MMP-9, and various mutants of human MMP-12) and identifying the site of covalent modification of MMP-3 by this probe, our new data demonstrated that the nucleophilicity of the residue in position 241 plays a key role in determining the cross-linking yield of MMP modification by the probe. However, these studies also reveal that subtle additional structural parameters, including local conformation and flexibility, of the residue in position 241 should also be taken into consideration, a property adding a further degree of complexity in our understanding of the photolabeling probe reactivity and in designing optimal photoaffinity probes for performing functional proteomic studies of zinc proteinases like MMPs.

INTRODUCTION

The development of photoaffinity probes able to covalently label specifically the active site of zinc proteinases (activity-base probe, ABP) may lead to important applications in functional proteomics and diagnosis (*1*−*4*). For serine and cysteine proteinases, successful development of activity-based probes (ABPs) has been achieved by exploiting the presence of highly conserved nucleophiles in the active sites of these enzymes and selecting appropriate reactive groups to perform covalent modification of the targeted enzymes (*5*, *6*). For zinc metalloproteinases, like matrix metalloproteinases (MMPs), the lack of corresponding active site nucleophiles has required the use of a photochemical group that must be incorporated into the structure of synthetic specific MMP inhibitors (*1*, *2*). Following this strategy, we recently developed a selective MMP photoaffinity probe that consists of phosphinic peptide core, able to block potently and selectively a large set of MMPs, to which has been grafted an azido group on the P_1' side chain of the inhibitor (probe **1**, Scheme 1) (*4*). While probe **1** was shown to selectively covalently modify only the active site of MMPs, high variation in the cross-linking yield was observed between different MMPs. In fact, whereas $a \approx 45\%$ of cross-linking yield was determined for the covalent modification of human MMP-12 by probe **1**, for human MMP-8, this yield decreased to few percent (*4*). As the molecular determinants controlling the cross-linking yield of photoaffinity probes to their targets remain poorly understood, we initiated a research project in order to identify in MMPs the site of their covalent modifications by probe **1**. We recently reported results of a first study of human MMP-12 (hMMP-12), showing that probe **1** covalently modifies only a single residue in this MMP, by reacting with the ε NH_3^+ group of Lys^{241} (*7*). This result was unexpected, as Lys^{241} is located on a loop segment of hMMP-12, which, based on both X-ray and NMR studies, displays high flexibility with the lysine side chain exhibiting high mobility (*8*−*10*). Another remarkable feature of this study is the fact that, at pH 7, the conditions of hMMP-12 covalent modification, photoactivated azides are expected to react with good nucleophiles, but less so with the protonated positively charged ε amino group of Lys^{241} (*11*). This remark has led us in the present study to compare the labeling of hMMP-12 by probe **1** at pH 7 and 12. On the basis of the results obtained, human MMP-3 (hMMP-3) was studied in detail, as this MMP possesses in position 241 a histidine residue, whose nucleophilicity is also pH-dependent. Two other MMPs containing an arginine residue in position 241, mouse MMP-12 (mMMP-12) and hMMP-9, were also examined. Finally, to better understand the variability in cross-linking yield observed between MMPs with probe **1**, several mutants of hMMP-12 have been produced and studied. In these mutants, position 241 has been replaced by residues observed in different MMPs in this position.

EXPERIMENTAL METHODS

Commercial reagents were used without additional purification. Buffers and salts were from Sigma. Synthesis and tritium radiolabeling of probe **1** were carried out as previously reported (*4*). Mca-Pro-Leu-Gly-Leu-Dpa-Ala-Arg-NH_2 (Mca-Mat) was from Novabiochem, and TIMP-1 inhibitor was from R&D systems.

Proteins. Synthetic genes encoding the catalytic domain of MMP-12 (Met^{98}-Lys^{266}) and murine MMP-12 (Gln^{109}-Gly^{267}) were from Geneart (Geneart-AG, Germany). Genes were inserted into the pET24a vector, between the NdeI and *Bam*HI sites, for expression under the PT7 promoter. Lys^{241} was substituted by His (primer 5'-ccgtaatgttccccac-ctacCaCtatgttgacatcaacaca-3') or Arg (primer 5'-ccgtaatgttccccacctacCGatatgttgacatcaacaca-3') or Gln (primer 5'-ccgtaatgttccccacctacCaG-

* Corresponding author. Dr. V. Dive: vincent.dive@cea.fr.
[†] Service d'Ingénierie Moléculaire des Protéines (SIMOPRO).
[‡] Imperial College London.

10.1021/bc800478b CCC: $40.75 © 2009 American Chemical Society
Published on Web 01/12/2009

Scheme 1

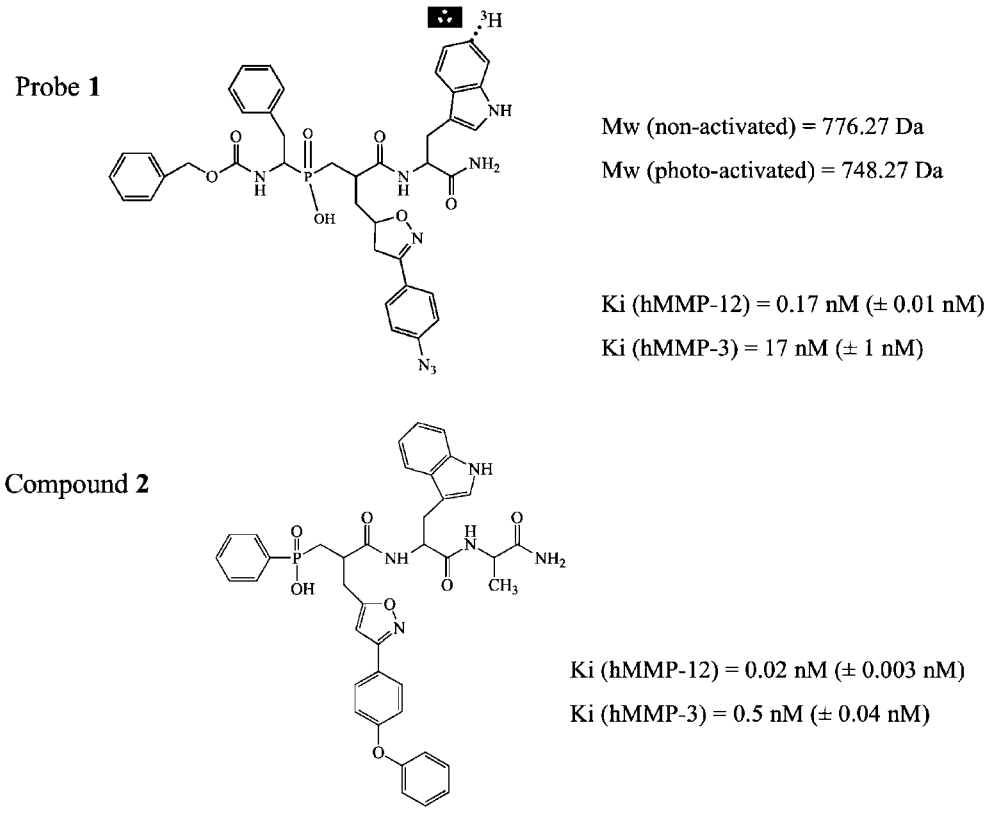

tatgttgacatcaacaca-3′) or Thr (primer 5′-ccgtaatgttccccacctaca-CGtat-gttga catcaacaca-3′). The corresponding hMMP-12 mutants were produced using the Site-Directed Mutagenesis Kit (Stratagene, Heidelberg, Germany). All plasmids were propagated in the *Escherichia coli* strain XL1-Blue at 37 °C, and all constructions were verified by DNA sequencing using the ABI PRISM 310 Genetic analyzer (Applied Biosystems). Recombinant proteins were expressed in *E. coli* BL21 (DE3 star) cells carrying the MMP-12 catalytic domain-encoding plasmids. Production and purification of MMP-12 mutants were as described in ref *7*. Protein molecular weights were determined by ESI-MS, and the presence of mutations was verified by Malti-TOF, after tryptic digestion. Human catalytic domain of MMP-3 was obtained as previously described (*12*).

Enzyme Assays. Enzyme assays and inhibition and titration experiments were carried out in 50 mM Tris/HCl buffer, pH 7, 10 mM $CaCl_2$, at 25 °C, using the Mca-Pro-Leu-Gly-Leu-Dpa-Ala-Arg-NH_2 (Mca-Mat) substrate, as described in ref *7*. Titration experiments using a calibrated TIMP-1 solution were performed to determine the exact enzyme concentration for each hMMP-12 mutant and wild-type hMMP-12. Values for k_{cat}/K_m were determined from first-order full-time course reaction curves obtained at $[S] \ll K_m$ ($[S] = 0.5$ μM), at 5 nM final enzyme concentration. The K_i of probe **1** was determined using the method proposed by Horovitz and Leviski (*13*).

Mass Spectrometry. nanoESI-MS experiments were performed in an ion trap mass spectrometer (Bruker, Esquire-HCT). Ion trap parameters were set as follows: nanoelectrospray potential, 1000 V; skimmer voltage, 40 V; capillary exit, 226 V; and a source temperature of 150 °C. The MS survey scan was *m*/*z* 400−3000 Da with a target mass fixed at *m*/*z* 1800 Da and a 5 spectrum scan average.

MS/MS Sequencing of Covalently Modified Peptides. Radioactive fractions containing covalent adduct peptides were concentrated using a C_{18} ZipTip. Off-line nanoESI-MS/MS experiments were performed in an ion trap mass spectrometer. Ion trap parameters for MS were set as above. The scan number was increased to 20 spectra over an *m*/*z* of 250−2000 Da, the isolation width was set to 1 Da, and the collision energy was tested using a range of 0.2−0.9 V in the MS/MS mode. MS/MS spectra were recorded for double-charged molecular peptide ions.

***μ*-RP-HPLC.** Peptide separation was carried out in an Agilent 1100 series apparatus using an X-Bridge (Waters) C_{18} 5 μm, 300 Å column (2.1 × 150 mm, 5 μm) at a flow rate of 200 μL/min and with detection at 214 nm. Solvent systems were as follows: (A) 100% water, 0.1% FA, and (B) 100% acetonitrile, 0.09% FA; with the following gradient, $t = 0$ min, 10% B; $t =$ 5 min, 10% B; and $t = 45$ min, 100% B.

Photoaffinity Labeling. MMPs (1 μM) were incubated with 2 μM ^{3}H-probe **1** in 50 mM Tris-HCl, pH 7, 10 mM $CaCl_2$, 0.01% Brij35, for 10 min in the dark at room temperature, as described in ref *7*. For pH dependence studies, prior probe addition, the pH was adjusted by adding ammoniac or chloride acid in order to keep the same buffer composition. After photoactivation, the reaction was quenched by the addition of Laemmli loading buffer followed by boiling (5 min, 95 °C). These samples were immediately processed for subsequent SDS gel analysis.

Electrophoresis. Radiolabeled proteins were diluted in Laemmli loading buffer (final concentration: 0.1% (w/v) bromophenol blue, 2% (w/v) SDS, 10% (v/v) glycerol, 50 mM Tris-HCL pH 6.8, and 100 mM DTT) and were resolved by SDS-PAGE electrophoresis in a 12% 1-mm-thick SDS gel, using a mini-protean III apparatus (BioRad). Silver staining was performed as previously described (*7*).

Blotting. Transfer of proteins onto PVDF (polyvinylidene fluoride) membrane was achieved using a semidry transfer blot apparatus (BioRad). Gels were rinsed in a 50 mM Tris−HCl, pH 8.5, 20% methanol, 40 mM glycine, 0.0375% SDS in distilled water (transfer buffer). The PVDF membrane was activated in a bath of methanol and was then equilibrated in

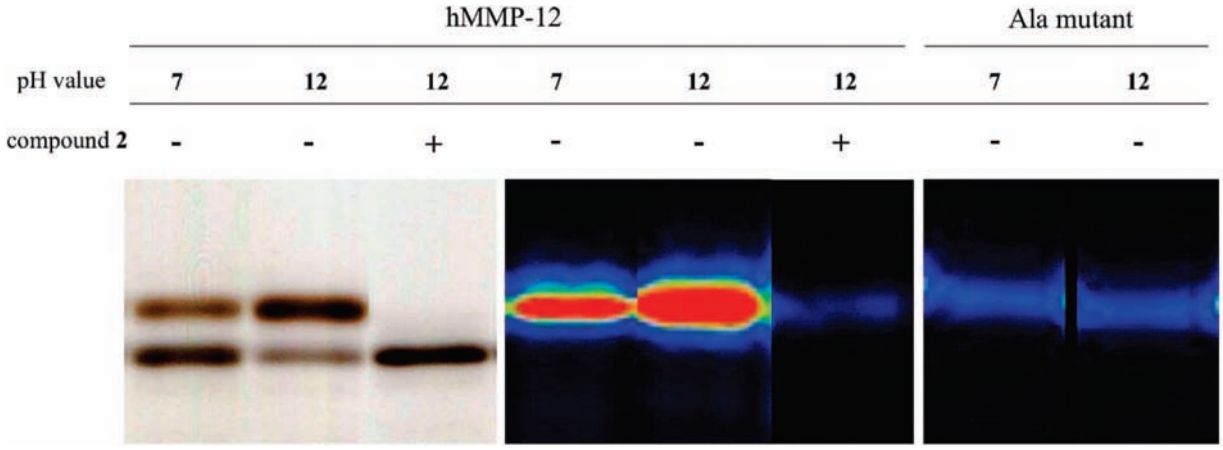

Figure 1. pH dependence for the covalent modification of wild-type h-MMP-12 and Ala-hMMP-12 mutant by probe **1**. hMMP12 or Ala mutant (1 μM) was incubated with probe **1** (2 μM) for 10 min, before UV irradiation (2 min). The corresponding complexes (5 pmol) were resolved by 1D-SDS PAGE electrophoresis and visualized on the gel by silver staining, or the proteins were transferred onto a PVDF membrane that was analyzed with a radioimager.

transfer buffer. We formed a membrane sandwich for protein transfer between the cathode and the anode: this included, from anode to cathode, a sheet of extra-thick blotting paper (BioRad), soaked in transfer buffer, the activated PVDF membrane, gels, and finally 2 sheets of extra-thick blotting paper soaked in transfer buffer. After transfer, membranes were dried before radioactivity analysis or were stained using Coomassie Blue (0.1% R_{250}, 50/49/1 water/ethanol/acetic acid).

Radioimaging. We carried out radioactivity imaging and counting on the PVDF membranes, using the beta-Imager 2000 from Biospace (Paris, France). This apparatus allows absolute counting of the tritium beta particles, with a detection threshold of 0.007 cpm/mm^2 for tritium.

PVDF-Tryptic Digestion. Pieces of PVDF membranes containing labeled or unlabeled h-MMP-12 were excised and destained using a 50/50 water/ethanol solution to remove excess R_{250}. PVDF pieces were incubated in a solution of 50 mM NH_4HCO_3 pH 8/ acetonitrile (50/50) with trypsin (12.5 ng/μL) for 18−20 h at 50 °C. PVDF pieces were then rinsed with a solution of 50% acetonitrile with 0.1% TFA.

Edman Sequencing. N-Terminal amino acid sequence analysis was performed by automated Edman degradation using an ABI model 477A/120A Protein-Peptide Sequencing/ Analysis System and Analysis Software System, model 920A (Applied Biosystems Inc., Foster City, CA). Radioactive fractions eluted from the μ-HPLC column were pooled and loaded onto a TFA-treated cartridge filter, previously conditioned with BioBrene Plus. Prior to each sequence analysis, the filters were calibrated using PTH-amino acids standard solution.

Molecular Modeling. Models of probe **1** interacting with hMMP-12 and hMMP-3 were obtained as previously described. The NMR structures in Figure 8 were selected from an ensemble of 20 NMR structures of the hMMP-12 and hMMP-3 catalytic domain deposited in RCSB PDB under access code 2POJ (*10*) and 2JNP (*14*), respectively.

RESULTS

pH Dependence of hMMP-12 Photolabeling. As shown previously, silver staining of a gel loaded with UV-irradiated hMMP-12 in complex with probe **1** in buffer pH 7 revealed two bands of approximately equal intensity (Figure 1, left panel) (*4*). The lower band was shown to represent the unlabeled form of hMMP-12, while the higher one corresponds to the covalent hMMP-12/probe **1** complex. Relative intensity of these two bands suggested that ∼45% of hMMP-12 has been cross-linked by probe **1**. As expected, a radioactive signal was only observed for the higher band (Figure 1, middle panel; probe **1** incorporates a radioactive tag which allows covalent h-MMP12/probe **1** complexes to be detected by radioimaging; Scheme 1). Under the same experimental conditions, but with photoactivation performed in a buffer pH 12, either silver staining or radioactivity counting indicated a higher cross-linking yield of hMMP-12 by probe **1** (Figure 1, from 45% to 85% based on silver staining). In contrast, when the Ala-MMP-12 mutant (Lys^{241} has been replaced by Ala) is submitted to similar probe **1** labeling, the cross-linking yield remains extremely low, a result similar to that observed at pH 7 (Figure 1, right panel). Thus, this latter observation demonstrated that the pH dependence of the cross-linking reported for the wild-type hMMP-12 relies exclusively on the presence of Lys^{241} in this MMP. When hMMP-12 was first incubated with a potent active site MMP inhibitor (compound **2**; Scheme 1), followed by probe **1** addition and UV irradiation, results reported in Figure 1 (middle panel) indicated that at pH 12 only the active site of hMMP-12 is modified by the probe, as observed previously when these experiments were performed at pH 7 (*4*). In combination with our previous study showing that probe **1** covalently modifies the ε amino group of Lys^{241} (*7*), observations reported in Figure 1 reveal that the Lys^{241} nucleophilicity determines the cross-linking yield of probe **1** toward hMMP-12.

pH Dependence and Site of Covalent Modification of hMMP-3 by Probe 1. hMMP-3 contains in position 241 a histidine residue; thus, the pH dependence of its covalent modification by probe **1** was examined. Incubation of hMMP3 with probe **1** in buffer pH 7, followed by UV irradiation and protein resolution by electrophoresis, led to the observation of two bands in a gel loaded with hMMP-3/probe **1** complex and stained with silver (Figure 2a, left panel, first lane). Radioimaging analysis indicated that only the higher band incorporated radioactivity (Figure 2a, right panel, first lane). Under the same experimental conditions, lowering the pH of the sample from 7 to 5 resulted in a strong decrease of the cross-linking yield (from 65% to less than 1%), as visualized either by silver staining or radioactivity counting (Figure 2a, second and third lanes in left and right panels). It should be mentioned that an optimum pH of 5.5 has been reported for hMMP-3 in cleaving synthetic substrates (*15*), a property explaining the low labeling of hMMP-3 by probe **1** observed previously at pH 5.5 (*4*). When hMMP-3 was first incubated at pH 7 with an excess of compound **2** (Scheme 1), and this was followed by probe **1** addition and UV irradiation, only a single band was observed by silver staining and no radioactivity was detected (Figure 2b,

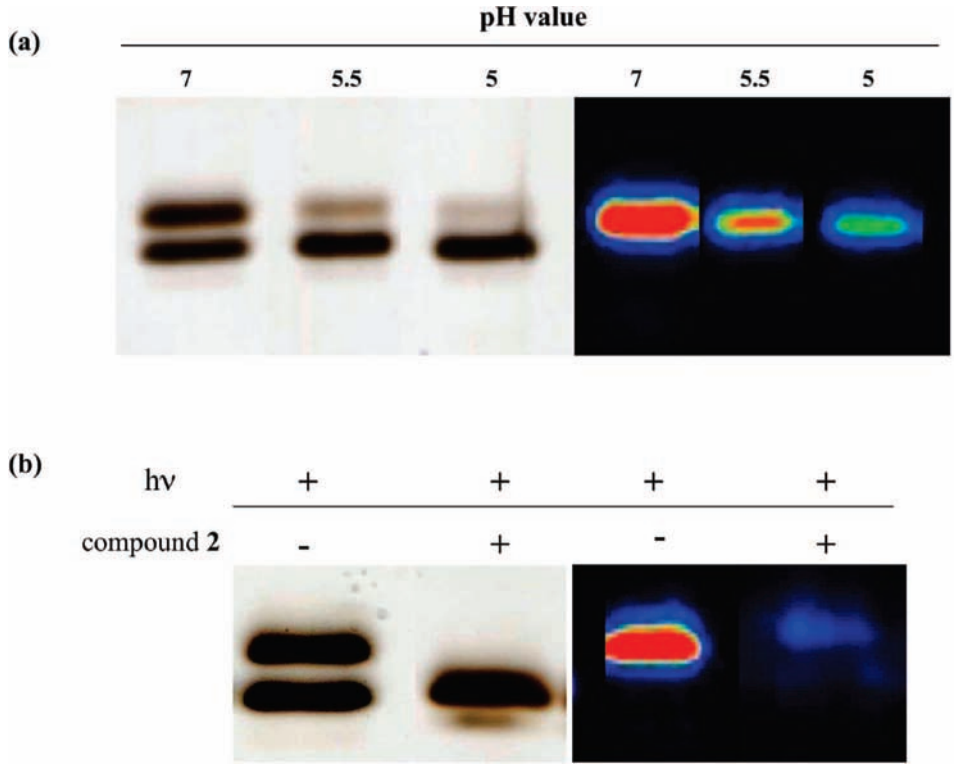

Figure 2. (a) pH dependence for the covalent modification of h-MMP-3 by probe **1**. hMMP-3 (1 μM) was incubated with probe **1** (2 μM) for 10 min, before UV irradiation (2 min). (b) Same experiments, but performed in the presence of compound **2** (10 μM) before the irradiation. The corresponding complexes (5 pmol) were resolved by 1D-SDS PAGE electrophoresis and visualized on the gel by silver staining or the proteins were transferred onto a PVDF membrane that was analyzed with a radioimager.

left and right panels). This result demonstrates that the covalent labeling of hMMP-3 involved exclusively residues of its active site. The marked pH dependence of hMMP-3 labeling by probe **1**, in a range of 5−7 that encompasses the His pK_a value (~6), and the higher labeling observed at pH 7 suggested that probe **1** probably modifies His^{241} in hMMP-3, as His is a better nucleophile at pH 7 than at pH 5.

To confirm the site of hMMP-3 modification, microsequencing and mass spectrometry experiments were carried out. Briefly, the protocol used relied on isolation of covalent hMMP-3/probe **1** complex by 1D-SDS gel, transfer of the corresponding protein species on PVDF membrane, and digestion first by trypsin and then by V-8 proteinase. Unmodified form of hMMP-3 was treated similarly for comparison. The μ-HPLC profiles of the peptide mixtures resulting from the double digestion of unlabeled and labeled hMMP-3 are reported in Figure 3. Comparison of these μ-HPLC profiles indicated that two peaks observed for unmodified hMMP-3 (labeled 1 and 2 in Figure 3, top panel) cannot be detected in the HPLC profile of modified hMMP-3 sample (Figure 3, lower panel). Mass analysis indicated that these two peaks correspond to two S_1' loop fragments of hMMP-3: the first one comprises residues from Ala^{234} to Arg^{248} and the second residues Ala^{234} to Asp^{245}. Lack of these two peaks in the μ-HPLC profile corresponding to modified hMMP-3 suggests that probe **1** probably modifies residues of the S_1' loop, an event affecting their HPLC retention time. Indeed, in the modified sample, radioactivity analysis of the μ-HPLC flowthrough indicated the presence of a radioactive signal in fractions eluting at 25−26 min (Figure 3, lower panel). These radioactive fractions were collected and analyzed by Edman sequencing. N-terminal sequencing started at Ala^{234} and went to Tyr^{240}; next, no amino acid could be assigned (His^{241} position, Figure 4). Afterward, the next sequencing step indicated a Ser^{242}; then, the sequencing identified the expected S_1' loop sequence up to Arg^{248}. Nano-ESI offline mass spectrometry analysis of the above purified radioactive fractions allowed the detection of three peaks (Figure 5), two double-charged ions, $[M_1 + 2H]^{2+} = 1094.6$ and $[M_2 + 2H]^{2+} = 1279.6$ Da, respectively, and one triple-charged ion, $[M_1 + 3H]^{3+} = 853.4$ Da. These ions represent peptide fragments of respective mass: M_w (M_1) = 2187.2 and M_w (M_2) = 2557.2 Da. The mass at 2187.2 Da corresponds to the expected mass of the S_1' loop of hMMP-3 (residues Ala^{234} to Asp^{245}, $M_w(1) = 1422.9$ Da), after trypsin and V8 protease digestion, covalently modified by probe **1** ($M_w = 776.27$ Da, minus 28 Da due to loss of N_2 after irradiation of the azide group). The difference of 16 Da between the expected theoretical mass of the S_1' loop of hMMP-3 covalently modified by probe **1** and the observed mass is explained by Met^{236} oxidation, a residue present in the S_1' loop sequence of hMMP-3. A similar methionine oxidation was also observed in related covalently modified S_1' loop fragments of hMMP-12 (*7*). The second mass at 2557.2 Da is explained by similar arguments, except that the S_1' loop fragment possesses three additional residues (Leu^{246}-Thr^{247}-Arg^{248}. This fragment, which was produced by trypsin cleavage, was not cleaved by the V8 protease. MS/MS experiments were performed on either double-charged or triple-charged ions described above in order to confirm by mass the site of covalent modification in hMMP-3. However, despite several attempts using different values of collision energy for the peptide fragmentation, only peaks of extremely low intensities were observed in the corresponding MS/MS spectra, preventing the sequencing of the covalently modified peptide fragments.

Covalent Labeling of MMP-12 Mutants. Probe **1** was previously shown to modify specifically the lysine residue located in position 241 of hMMP-12 (*7*), a position exhibiting high variability in MMPs ($Ala_{(MMP8)}$, $Gln_{(MMP14)}$, $Thr_{(MMP2,13,11)}$, $Arg_{(MMP9)}$, $His_{(MMP3)}$ (*16*). In order to see how the chemical structure of the side chain in position 241 influences the yield of covalent labeling by probe **1** in hMMP-12, independent of

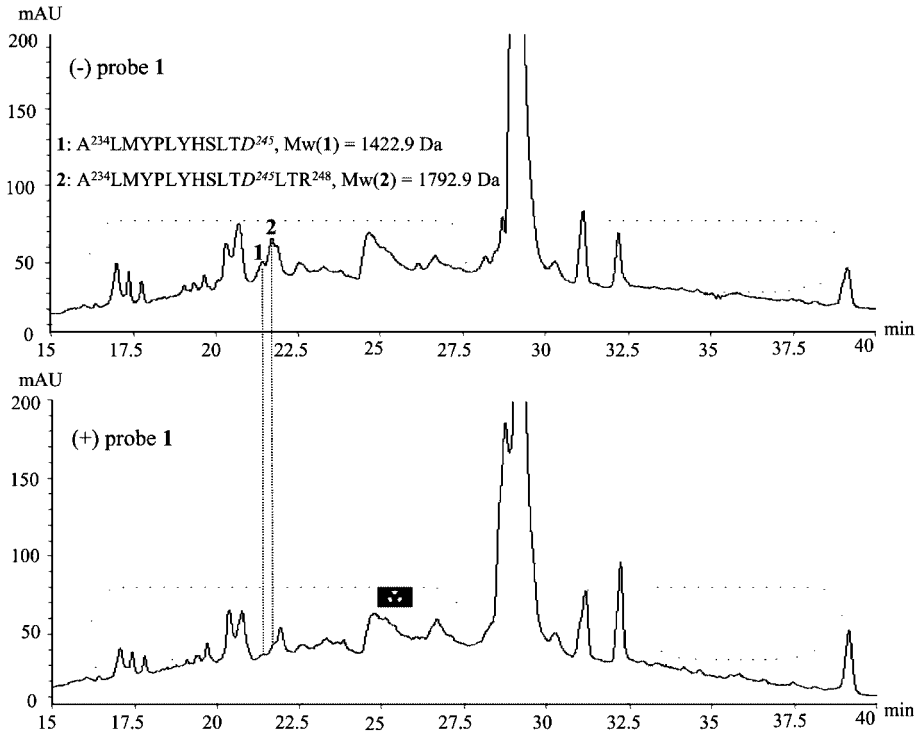

Figure 3. μ-HPLC profile of a peptide mixture obtained by trypsin and V8-protease digestion of unmodified or covalently hMMP-3 by probe **1**. UV trace (214 nm) of a PVDF digest (100 pmol) of unmodified (top panel) and modified h-MMP-3 (lower panel) by probe **1**. Peaks labeled 1 and 2 in top panel correspond to fragments reported in this figure generated by trypsin and V8 protease cleavage of the S_1' loop (2 was not cleaved by the V8 protease). In the lower panel, radioactive fractions corresponding to fragments covalently modified by probe **1** are identified by a radioactive symbol.

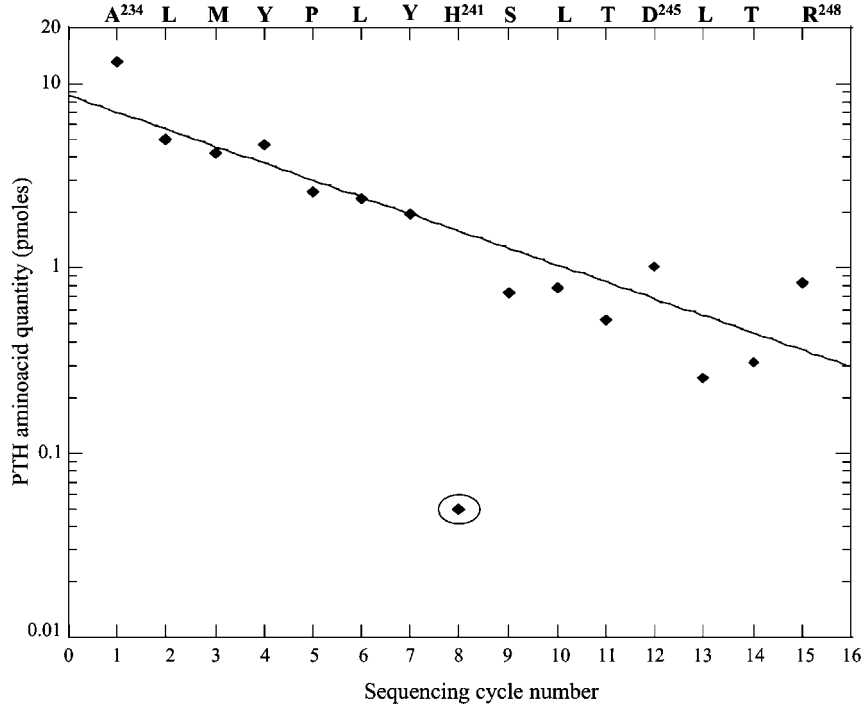

Figure 4. Edman degradation of the purified fragment peptide of h-MMP-3 (25 pmol) covalently modified by probe **1**.

the S_1' loop size which varies between MMPs, a series of mutants of hMMP-12 were produced by substituting position 241 in hMMP-12 with residues present in MMPs. Comparison of the catalytic efficiency of these mutants in cleaving a fluorogenic synthetic substrate specific for MMPs, as well as K_i values of probe **1** toward mutants, as compared with wild-type hMMP-12, indicated similar catalytic and recognition properties between mutants and wild-type enzyme (Table 1). Photolabeling of these mutants by probe **1**, analyzed either by silver staining or radioactivity counting, revealed a much lower cross-linking yield of the mutants (~3−6% based on radioactivity), as compared with a cross-linking yield value of ~45% observed in wild-type hMMP-12 (Figure 6). As previously reported, the presence of an alanine in position 241 results in lower cross-linking yield (1%) (*7*).

Covalent Labeling of mMMP-12 and hMMP-9. mMMP-12 and hMMP-9 both contain an arginine residue in position 241. Thus, the labeling of these two MMPs by probe **1** was

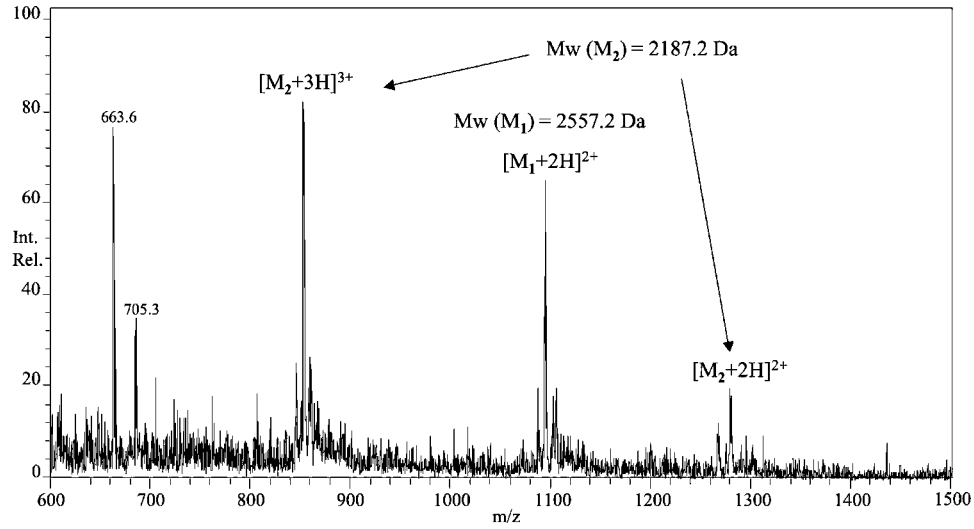

Figure 5. Nano-ESI offline mass spectra of the radioactive fractions collected after μ-HPLC purification (shown in Figure 3). Molecular weights corresponding to the double- and triple-charged ion species observed in the mass spectrum are indicated.

Table 1. Characterization of hMMP-12 Mutants (Ala, Arg, Gln, Thr, His)[a]

	hMMP-12	Ala mutant	Arg mutant	Gln mutant	Thr mutant	His mutant
k_{cat}/K_m ($M^{-1}.s^{-1}$)	$1.53 \times 10^4 \pm 0.03 \times 10^4$	$1.32 \times 10^4 \pm 0.05 \times 10^4$	$2.17 \times 10^4 \pm 0.04 \times 10^4$	$1.94 \times 10^4 \pm 0.01 \times 10^4$	$1.44 \times 10^4 \pm 0.02 \times 10^4$	$1.17 \times 10^4 \pm 0.03 \times 10^4$
K_i (nM)	0.17 ± 0.01	0.35 ± 0.04	0.15 ± 0.01	0.27 ± 0.02	0.16 ± 0.01	0.30 ± 0.02

[a] k_{cat}/K_m and K_i were determined in Tris/Hcl buffer 50 mM, pH 6.8, $CaCl_2$ 10 mM.

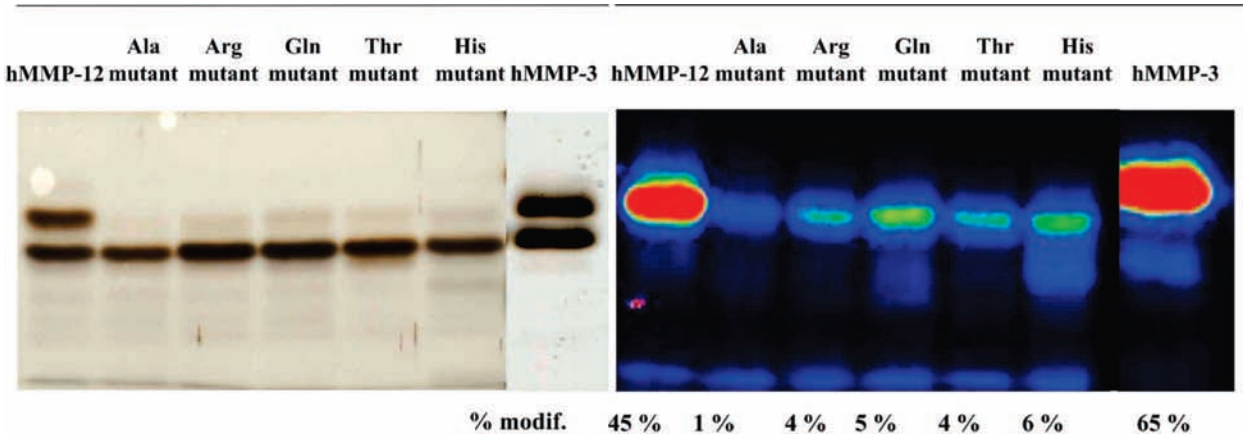

Figure 6. Labeling of hMMP-12 mutants by probe **1**, visualized by silver staining (left panel) or radioimaging (right panel), as compared with hMMP-12 and hMMP-3. Conditions as described in Figure 1.

examined at pH 7 and 13. The pH dependence of probe **1** labeling was also determined toward the Arg-hMMP-12 mutant, for comparison. As shown in Figure 7, for the three proteins stronger labeling was observed by increasing the pH from 7 to 13. Differences in cross-linking yield were observed among the three proteins, at pH 13 (11% for Arg-MMP-12, 16% for mMMP-12, and 19% for hMMP-9). As compared with hMMP-12, the cross-linking yield observed for these MMPs are smaller than that observed for hMMP-12 at pH 12 (85%).

DISCUSSION

Previous studies of the identification of the site of hMMP-12 covalent modification by photoactivated probe **1** have shown that this probe specifically modifies the ε amino group of Lys^{241} in this MMP (*7*). Taking into account the well-known efficiency of the nitrene intermediate in reacting with nucleophiles (*11*, *17*), this result led us to determine the reactivity of probe **1** at pH 12, a pH at which the ε amino group of Lys^{241} should be in its nonprotonated form (NH_2 instead NH_3^+) and thus represents a better nucleophile. The 2-fold increase in cross-linking yield observed for the labeling of hMMP-12 by probe **1** between pH 7 and 12 supports the proposal that the nucleophilicity of Lys^{241} is in fact a key parameter that determines the cross-linking yield of probe **1**. This observation suggests that other MMPs, possessing in position 241 a good nucleophile, like a lysine or any other amino acid bearing on its side chain a nucleophilic moiety, should also be modified by probe **1** with a high cross-linking yield. This led us to examine hMMP-3, the only MMP possessing in position 241 a good nucleophile too, a histidine residue. Indeed, a very high yield of cross-linking (65%) was observed for the covalent modification of this MMP by probe **1** at pH 7. In contrast, at pH 5, a pH at which the nitrogen atoms of the histidine side chain are weaker nucleophiles, a strong decrease of hMMP-3 labeling by probe **1** was observed. Microsequencing and mass spectrometry analyses identified the His^{241} as the unique site of modification of hMMP-3 by probe

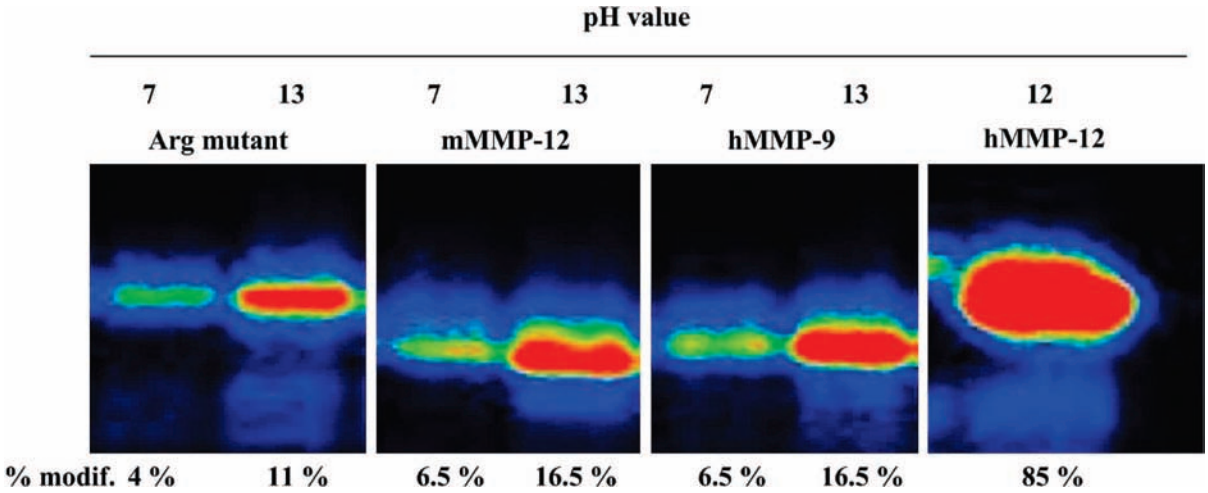

Figure 7. pH dependence for the covalent modification of, from the left to the right, Arg^{241}-hMMP-12 mutant, mMMP-12, and hMMP-9, as analyzed by radioimaging. Conditions as described in Figure 1.

1, a result explaining the observed pH cross-linking dependence. Altogether, these results again highlight the key role played by the nucleophilicity of the residue in position 241 of hMMP-3 and hMMP-12 for high labeling by probe **1**. As mentioned in the results sections, the MS/MS experiments performed to identify the site of covalent modification of hMMP-3 by probe **1** have all failed. These negative results are in contrast with those reported for hMMP-12 (*7*). In this case, it was possible to sequence by MS/MS experiments the whole S_1' loop fragment covalently modified by probe **1** and identify formally the occurrence of the probe modification on the lysine residue. Thus, even with peptides of similar size and sequence, sophisticated techniques like mass spectroscopy may not provide the expected analytical results, rendering classical Edman sequencing a still powerful technique.

According to X-ray and NMR studies, His^{241} in hMMP-3 and Lys^{241} in hMMP-12 are located on a loop segment (*8*−*10*) (*10, 14*), the S_1' loop, which exhibits high flexibility with these two residues displaying high mobility. Thus, the high yield of cross-linking observed for the modification of these two MMPs by probe **1** would be hard to predict taking into consideration this structural and dynamic information. The high cross-linking efficiency reported in this study implies the occurrence in enzyme/probe **1** complexes of conformations in which both Lys^{241} and His^{241} residues point toward the activated form of the probe **1** azide group, as shown in Figure 8. Accordingly, probe **1** can be viewed as a conformational probe providing clues about the structure and dynamics of MMPs (*9*). One important objective indicated by this study would be to determine whether the binding of probe **1**, in its nonactivated or activated form, stabilizes a particular conformation of the hMMP-3 and hMMP-12 S_1' loops; as such, a conformation selection process may have important implications for the design of highly selective inhibitors of MMPs, a challenge only partially achieved today (*18*−*20*).

The pH dependence observed for the efficient labeling of hMMP-3 and hMMP-12 led us to examine the importance of this parameter for the covalent modification of mMMP-12 and hMMP-9, two MMPs harboring an arginine in position 241. Increasing the pH form 7 to 13 resulted in a significant increase of the cross-linking yield (from 6% to 16−19% yield), a result suggesting that, in these two MMPs, like in hMMP-3 and hMMP-12, the amino acid side chain in position 241 is the target of probe **1** covalent modification. It should be noted that Arg^{241} is the only residue in the mMMP-12 and hMMP-9 active sites that can be affected by a pH variation from 7 to 13. The much

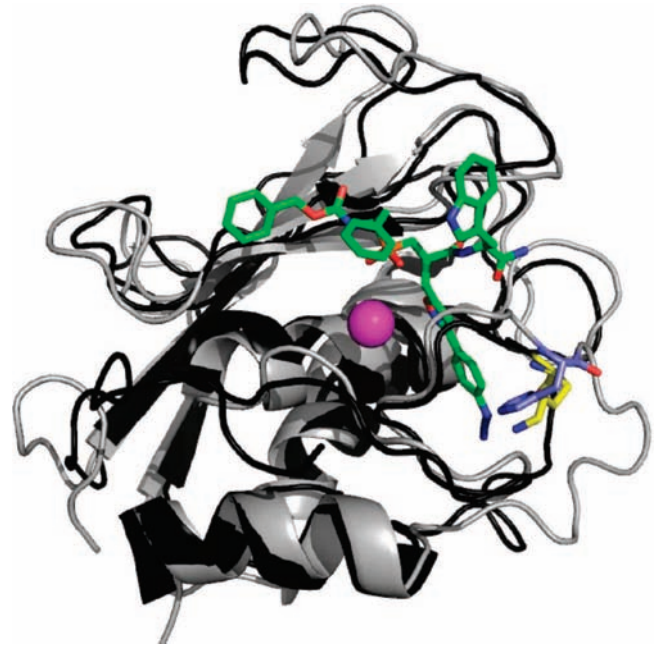

Figure 8. Superimposed model of probe **1** in complex with hMMP-12 and hMMP-3 showing the proximity between the azide group of probe **1** and the Lys^{241} and His^{241}. Ribbon plot representation of the catalytic domain of hMMP-12 (black) and hMMP-3 (gray). Lys^{241} from hMMP-12 is colored in yellow, His^{241} from hMMP-3 is blue, probe **1** in green, and catalytic zinc ion in purple.

lower yield of cross-linking observed for mMMP-12 and hMMP-9 highlights again the importance of the nucleophilicity of the residue in position 241, as the nitrogen atoms borne by the guanidinium moiety of arginine are weaker nucleophiles, as compared with the nitrogen present in the histidine and lysine residues. We previously reported that probe **1** covalently modifies MMPs, but with a very high variation in the cross-linking yield (*4*). The strict identification of the residue targeted by probe **1** in hMMP-3 and hMMP-12, plus the indirect proofs about this residue from the pH dependence observed for m-MMP-12 and hMMP-9, led us to suggest that this cross-linking yield dispersion reflects the variability of position 241 in MMPs (MMP-$8_{(Ala^{241})}$, MMP-2, 11,$13_{(Thr^{241})}$, MMP-$10_{(Asn^{241})}$, MMP-$14_{(Gln^{241})}$). The presence in these MMPs at position 241 of residues harboring weaker nucleophile atoms on their side chain, as compared with hMMP-12 and hMMP-3, explains the

lower cross-linking yield observed for these MMPs. Thus, one possibility to derive a probe displaying similar cross-linking yields toward all MMP members will be to design a new photoaffinity probe able to target conserved residues of the MMP S_1' cavity.

Analysis of hMMP-12 mutants exemplifies that the presence of a nucleophile in the side chain of residue in position 241 is mandatory, as the presence of an alanine instead a of lysine results in less than 1% cross-linking. The site of covalent modification in these mutants has not been determined directly, but the pH dependence observed for the labeling of the Arg mutant is in agreement with the proposal that probe **1** targets the Arg^{241} in this protein. Mutants with a side chain in position 241 containing weaker nucleophiles (Arg, Gln, Thr), as compared with lysine, are labeled with a lower cross-linking yield. In contrast, the observation reported for the His mutant is quiet unexpected. This result illustrates that parameters other than the soil nucleophilicity of the residue in position 241 can determine the cross-linking yield. As discussed above, the conformational properties of the residue in position 241 also play a critical role. The same arguments probably explain the differences in cross-linking yield observed among Arg241-hMMP-12, mMMP-12, and hMMP-9 at pH 13, despite the presence of the same arginine residue in these MMPs. Altogether, these results illustrate the difficulties that must be overcome in developing optimized activity-based probes incorporating photolabile groups, a strict requirement for the covalent labeling of zinc proteinases.

Probe **1** should be useful for the detection of hMMP-12 and hMMP-3 in biological fluids. At neutral pH and in buffer, the detection limit of hMMP-12 and hMMP-3 with this radioactive probe is around 2.5 fmol, a limit that can be improved by a factor two for hMMP-12 by fixing the pH at 12 before the photoactivation step. Operating at basic pH seems to be a requirement for detecting mMMP-12 and hMMP-9. At basic pH, the detection limit with probe **1** should be around 150 fmol for these MMPs, a rather good sensitivity. However, even though the results of gelatin zymography should be interpreted with great caution before drawing conclusions about the presence of active forms of MMP-9 in biological fluids (*21*), it should be kept in mind that this technique is able to detect MMP-9 with a threshold of detection of 100 amol (*22*). Actual failure in detecting active forms of MMPs by using activity-based probes has been explained by arguing that these proteases are mostly expressed as inactive zymogen forms and that most of the activated MMP fractions are blocked by endogenous inhibitors (i.e., the TIMPs) (*3*). Thus, active forms of MMPs may exist at levels that are well below the current limit of activity-based probe detection, even when using the exceptional resolution and sensitivity of multidimensional liquid chromatography coupled with mass spectroscopy. To replace gelatin zymography or to be used in proteomic profiling by mass spectroscopy, activity-based probes for detection of the MMP active form need further improvement. Our results give pointers to the development of a new generation of those probes that should be more efficient for the equivalent detection of all MMPs.

ACKNOWLEDGMENT

This work was supported by funds from the Commissariat à l'Energie Atomique and from the European Commission (FP6RT, Cancer Degradome project, LSHC-CT-2003-503297).

LITERATURE CITED

(1) Saghatelian, A., Jessani, N., Joseph, A., Humphrey, M., and Cravatt, B. F. (2004) Activity-based probes for the proteomic profiling of metalloproteases. *Proc. Natl. Acad. Sci. U.S.A. 101*, 10000–5.

(2) Chan, E. W., Chattopadhaya, S., Panicker, R. C., Huang, X., and Yao, S. Q. (2004) Developing photoactive affinity probes for proteomic profiling: hydroxamate-based probes for metalloproteases. *J. Am. Chem. Soc. 126*, 14435–46.

(3) Sieber, S. A., Niessen, S., Hoover, H. S., and Cravatt, B. F. (2006) Proteomic profiling of metalloprotease activities with cocktails of active-site probes. *Nat. Chem. Biol. 2*, 274–81.

(4) David, A., Steer, D., Bregant, S., Devel, L., Makaritis, A., Beau, F., Yiotakis, A., and Dive, V. (2007) Cross-linking yield variation of a potent matrix metalloproteinase photoaffinity probe and consequences for functional proteomics. *Angew. Chem., Int. Ed. Engl. 46*, 3275–7.

(5) Cravatt, B. F., Wright, A. T., and Kozarich, J. W. (2008) Activity-based protein profiling: from enzyme chemistry to proteomic chemistry. *Annu. Rev. Biochem. 77*, 383–414.

(6) Kato, D., Boatright, K. M., Berger, A. B., Nazif, T., Blum, G., Ryan, C., Chehade, K. A., Salvesen, G. S., and Bogyo, M. (2005) Activity-based probes that target diverse cysteine protease families. *Nat. Chem. Biol. 1*, 33–8.

(7) Dabert-Gay, A. S., Czarny, B., Devel, L., Beau, F., Lajeunesse, E., Bregant, S., Thai, R., Yiotakis, A., and Dive, V. (2008) Molecular determinants of matrix metalloproteinase-12 covalent modification by a photoaffinity probe: Insights into activity-based probe development and conformational variability of matrix metalloproteinases. *J. Biol. Chem. 283*, 31058–67.

(8) Nar, H., Werle, K., Bauer, M. M., Dollinger, H., and Jung, B. (2001) Crystal structure of human macrophage elastase (MMP-12) in complex with a hydroxamic acid inhibitor. *J. Mol. Biol. 312*, 743–51.

(9) Bertini, I., Calderone, V., Cosenza, M., Fragai, M., Lee, Y. M., Luchinat, C., Mangani, S., Terni, B., and Turano, P. (2005) Conformational variability of matrix metalloproteinases: beyond a single 3D structure. *Proc. Natl. Acad. Sci. U.S.A. 102*, 5334–9.

(10) Bhaskaran, R., Palmier, M. O., Bagegni, N. A., Liang, X., and Van Doren, S. R. (2007) Solution structure of inhibitor-free human metalloelastase (MMP-12) indicates an internal conformational adjustment. *J. Mol. Biol. 374*, 1333–44.

(11) Kotzyba-Hibert, F., and Goeldner, M. (1995) Recents trends in photoaffinity labeling. *Angew. Chem., Int. Ed. Engl. 34*, 1296–1312.

(12) Suzuki, K., Kan, C. C., Hung, W., Gehring, M. R., Brew, K., and Nagase, H. (1998) Expression of human pro-matrix metalloproteinase 3 that lacks the N-terminal 34 residues in Escherichia coli: autoactivation and interaction with tissue inhibitor of metalloproteinase 1 (TIMP-1). *Biol. Chem. 379*, 185–91.

(13) Horovitz, A., and Levitzki, A. (1987) An accurate method for determination of receptor-ligand and enzyme-inhibitor dissociation constants from displacement curves. *Proc. Natl. Acad. Sci. U.S.A. 84*, 6654–8.

(14) Alcaraz, L. A., Banci, L., Bertini, I., Cantini, F., Donaire, A., and Gonnelli, L. (2007) Matrix metalloproteinase-inhibitor interaction: the solution structure of the catalytic domain of human matrix metalloproteinase-3 with different inhibitors. *J. Biol. Inorg. Chem. 12*, 1197–206.

(15) Harrison, R. K., Chang, B., Niedzwiecki, L., and Stein, R. L. (1992) Mechanistic studies on the human matrix metalloproteinase stromelysin. *Biochemistry 31*, 10757–62.

(16) Cuniasse, P., Devel, L., Makaritis, A., Beau, F., Georgiadis, D., Matziari, M., Yiotakis, A., and Dive, V. (2005) Future challenges facing the development of specific active-site-directed synthetic inhibitors of MMPs. *Biochimie 87*, 393–402.

(17) Fleming, S. A. (1995) Chemical reagents in phtoaffinity labeling. *Tetrahedron 51*, 12479–12520.

(18) Overall, C. M., and Kleifeld, O. (2006) Validating matrix metalloproteinases as drug targets and anti-targets for cancer therapy. *Nat. Rev. Cancer 6*, 227–239.

(19) Fingleton, B. (2007) Matrix metalloproteinases as valid clinical targets. *Curr. Pharm. Des. 13*, 333–46.

(20) Yiotakis, A., and Dive, V. (2008) Synthetic active site-directed inhibitors of metzincins achievement and perspectives. *Mol. Aspects Med. 29*, 329–38.

(21) Hesek, D., Toth, M., Meroueh, S. O., Brown, S., Zhao, H., Sakr, W., Fridman, R., and Mobashery, S. (2006) Design and characterization of a metalloproteinase inhibitor-tethered resin for the detection of active MMPs in biological samples. *Chem. Biol. 13*, 379–86.

(22) Masure, S., Proost, P., Van Damme, J., and Opdenakker, G. (1991) Purification and identification of 91-kDa neutrophil gelatinase. Release by the activating peptide interleukin-8. *Eur. J. Biochem. 198*, 391–8. .

BC800478B

TECHNICAL NOTES

Microplate-Based Analysis of Protein−Membrane Binding Interactions via Immobilization of Whole Liposomes Containing a Biotinylated Anchor

Erin A. Losey, Matthew D. Smith, Meng Meng, and Michael D. Best*

Department of Chemistry, the University of Tennessee, Knoxville, Tennessee 37996. Received September 29, 2008; Revised Manuscript Received November 20, 2008

Cellular membranes play key roles in the regulation of a range of important biological processes. However, the characterization of membrane involvement in these events is difficult to achieve due to the complexity of the membrane bilayer and the challenges associated with handling and analyzing these systems. As such, rapid and reliable approaches for characterizing membrane-based processes are necessary. To address this issue, we have first developed an azide-tagged modular lipid anchor scaffold (**2**) that can be conveniently derivatized via click chemistry to functionalize the membrane surface. This was used to access biotin− and fluorescein−lipid conjugates **1a** and **1b**, respectively. These compounds were then employed to perform and characterize the immobilization of liposomes containing biotin-anchor **1a** onto streptavidin-coated microplates. Results from these studies indicated clean, biotin-dependent surface deposition. This strategy for liposome attachment was then applied to a microplate-based platform to detect the binding of receptor proteins to immobilized liposomes, specifically for the membrane binding of protein kinase Cα (PKCα). The resulting data indicated direct detection of binding to the membrane-functionalized surface. The reported approaches provide efficient methods for the derivatization of the membrane surface, which is applicable to the study of membrane-based processes. Finally, the described microplate-based liposome binding assay allows for high-throughput analysis of important protein-membrane binding events.

INTRODUCTION

Cellular membranes play vital and diverse roles in numerous intra- and extracellular molecular recognition events that correlate to important biological processes. The membrane context provides an environment in which binding interactions occurring between combinations of membrane-associated and solubilized proteins, peptides, lipids, carbohydrates, and other species control a wide range of physiological and pathophysiological events. Membrane-based binding interactions can directly modulate biomolecule function or exert indirect control, such as through the convergence of binding partners on the membrane surface resulting in subsequent pathway activation. In addition, the presentation of ligands on the membrane surface controls receptor binding affinity, as with the affect of ligand density on multivalent binding interactions (*1, 2*). Due to the prominence of membrane recognition in biological processes, it is necessary to characterize the details of these associations at the molecular level in order to fully understand roles in cellular signaling pathways. However, investigation of these interactions is complicated by several issues, including the inherent complexity of membranes due to their heterogeneous nature as well as the diverse mechanisms by which proteins interact with membrane surfaces.

In certain cases, lipids embedded in the bilayer act as site-specific ligands that recruit solubilized receptors to the membrane surface via association. This is the case with signaling lipids including diacylglycerol (DAG) (*3, 4*), phosphatidic acid (PA) (*5, 6*), and the phosphatidylinositol phosphates (PIP_ns) (*7*−*11*), which are present in low percentages in cell membranes and are tightly regulated both spacially and temporally. These ligands become up-regulated during distinct processes, which results in protein recognition that often involves the trafficking of receptors to distinct subcellular locations (*3, 4, 12, 13*). In such cases, receptors often contain a conserved binding module that interacts with the target lipid.

A particularly well studied receptor family is the protein kinase Cs (PKCs), consisting of at least eleven isozymes. PKCs represent multivalent receptors in which the binding domains (one C2 and two C1 modules) exhibit different lipid specificities among the isozymes. PKC isozymes are categorized by lipid-binding properties into conventional (calcium, DAG, and phospholipid dependent), novel (calcium independent, but DAG and phospholipid dependent) and atypical (calcium and DAG independent) subgroups (*3, 4, 14*−*16*). However, complex variations in lipid specificities and affinities are known to exist, even within the same subgroup, and are believed to control subcellular localization. PKCs have been directly implicated in tumorigenesis (*17*−*19*), and compounds that compete for PKC binding, such as the bryostatins (*20*), show promise as cancer therapeutics. However, the exact links between PKC activity and carcinogenesis have not been discerned, which is primarily a result of the difficulty in elucidating the specific activities and localizations of the different isozymes (*18*).

In addition to the actions of lipids as site-specific ligands, numerous other mechanisms exist by which proteins interact with cellular membranes. In many cases, the membrane provides the scaffold for the presentation of cell surface ligands including carbohydrates and peptides, such as with the interaction of GM1 with pentavalent toxins (*21*). Another motif involves the

* Corresponding Author. E-mail: best@ion.chem.utk.edu.

10.1021/bc800414k CCC: $40.75 © 2009 American Chemical Society
Published on Web 01/14/2009

membrane association of proteins through the insertion of hydrophobic moieties. For example, certain proteins contain post-translationally appended lipid tails that regulate membrane anchoring and subcellular localization. A prominent example involves the Ras GTPases, critical proto-oncogenes for which the cycling between the Golgi apparatus and plasma membrane is directly controlled by the extent of lipidation (*22*−*24*). This acts as a switch that controls Ras trafficking and its critical signaling activities. Receptors also interact with the membrane through the insertion of hydrophobic peptide sequences. For instance, following initial binding of the influenza virus to sialic acid on the cell surface via hemagglutinin (HA), HA then inserts a hydrophobic sequence that results in membrane fusion and viral entry (*25*). Finally, antibacterial peptides such as gramicidin act by inserting into the bacterial cell wall and increasing permeability (*26, 27*).

The challenges associated with the study of protein−membrane binding events have provided a significant barrier to understanding interactions at the molecular level. While assays based on isothermal titration calorimetry (ITC), dye leakage, membrane penetration, and surface plasmon resonance (SPR) have proven effective (*28*), these studies would benefit from an accessible high-throughput method that would allow for efficient analysis on a grand scale. Recently, a solution-phase turbidity assay was reported for detecting associations of lipid-binding domains with liposomes (*29*). While this approach is effective for high-throughput analysis, potential drawbacks include that the receptor being analyzed must be tagged, the assay relies on absorbance measurements, which generally limits sensitivity, and the fact that the receptor is dimerized for detection purposes, which may not accurately mimic the recognition event in the physiological process. For these reasons, we sought to develop a novel assay for high-throughput detection of protein−liposome binding interactions.

Microarray surface analysis offers a beneficial strategy for characterizing receptor−ligand binding interactions that has been exploited for the study of DNA (*30, 31*), protein and peptide (*32*−*34*), carbohydrate (*35*−*43*), and, to a lesser extent, lipid (*44, 45*) binding interactions. Membrane-based microarray analysis has been performed by depositing membrane bilayers onto surfaces, which has primarily been employed to study integral membrane proteins (*46, 47*). Advantages of the microarray approach include that high-throughput analysis can be performed, that miniaturization allows for the use of minute quantities of recognition components and that optical detection yields facile and accessible analysis. Herein, we report the microplate-based detection of protein−membrane binding interactions through whole liposome immobilization toward the development of a high-throughput liposome-based microarray platform.

EXPERIMENTAL PROCEDURES

General. All reagents were purchased from Acros or Aldrich and used as received. Dry solvents were obtained from a Pure Solv solvent delivery system purchased from Innovative Technology, Inc. Column chromatography was performed using 230−400 mesh silica gel purchased from Sorbent Technologies. NMR spectra were obtained using a Bruker AC250 spectrometer updated with a TecMag data collection system, a Varian Mercury 300 spectrometer, or a Bruker Avance 400 spectrometer. Mass spectra were obtained with JEOL DART-AccuTOF and ABI Voyager DE Pro MALDI spectrometers. Optical rotation values were obtained using a Perkin-Elmer 241 polarimeter. HPLC data was obtained using an HP series 1100 HPLC with an Alltech Lichrosphere SI 60 5U column with HPLC-grade solvents purchased from Fisher. L-α-Phosphatidylcholine (PC) and L-α-phosphatidylserine (PS) were purchased from Avanti Polar Lipids, Inc. (Alabaster, AL). Liposome extruder and polycarbonate membranes were obtained from Avestin (Ottawa, Canada). Microplate-based fluorescence measurements were performed using a BioTek Synergy 2 multidetection microplate reader. Clear, white and black reacti-bind streptavidin high binding capacity (HBC) coated 96-well microplates were purchased from Pierce Biotechnology (Rockford, IL). PKCα and rabbit anti-PKCα antibody were purchased from Calbiochem (San Diego, CA). Goat antirabbit igG HRP-conjugate was purchased from Chemicon International (Temecula, CA). Supersignal ELISA femto maximum sensitivity substrate was purchased from Pierce Biotechnology (Rockford, IL). All plots represent the average of at least 3 experiments with error bars included ± the standard error for each set of measurements.

(*R*)-(2,2-Dimethyl-1,3-dioxolan-4-yl)methyl 4-methylbenzenesulfonate (4). (*S*)-(2,2-Dimethyl-1,3-dioxolan-4-yl)methanol (**3**, 1 mL, 8.1 mmol), 4-(*N*,*N*-dimethylamino)pyridine (DMAP, 989 mg, 8.1 mmol), *p*-toluenesulfonyl chloride (2.28 g, 16.2 mmol), and triethylamine (2.25 mL, 16.2 mmol) were suspended in 90 mL of DMF in a round-bottomed flask. The reaction was allowed to stir at room temperature overnight, followed by solvent removal via rotary evaporation. Next, the crude was extracted with methylene chloride (3 × 50 mL) from 50 mL of 1 M HCl. The combined extracts were then dried with magnesium sulfate, filtered, and the solvent was removed under reduced pressure. The product was then purified by column chromatography over silica gel with gradient elution from 10−30% ethyl acetate/hexanes to yield **4** as a yellow oil (2.20 g, 95%). Characterizations matched previous reports (*48*).

(*S*)-4-(Azidomethyl)-2,2-dimethyl-1,3-dioxolane (5). (*R*)-(2,2-Dimethyl-1,3-dioxolan-4-yl)methyl-4-methylbenzenesulfonate (**4**, 2.03 g, 7.1 mmol) and sodium azide (1.27 g, 19.5 mmol) were suspended in a solution of DMF. The reaction was immersed in an oil bath and heated to 80 °C overnight. Next, the reaction was brought to 0 °C with an ice bath and was quenched with saturated sodium bicarbonate solution (50 mL). The mixture was extracted with diethyl ether (2 × 50 mL), and the combined extracts were then washed twice with water (50 mL). Next, the organic layer was dried with magnesium sulfate and filtered. The solvent was then removed by rotovary evaporation without heat to avoid evaporation of the volatile product, which was obtained as a yellow oil (800 mg, 72%). Characterizations matched previous reports (*49*) Note: Care must be taken when working with sodium azide and low molecular weight organic azides such as **5** due to their explosive properties (*50*).

(*S*)-3-Azidopropane-1,2-diol (6). (*S*)-4-(Azidomethyl)-2,2-dimethyl-1,3-dioxolane (**5**, 1.26 g, 8.02 mmol) and *p*-toluenesulfonic acid (76 mg, 4 mmol) were suspended in 90 mL of methanol. The reaction was allowed to stir at room temperature overnight and was then quenched by adding solid sodium bicarbonate, followed by stirring for an additional 20 min. The solvent was removed by rotary evaporation and column chromatography with a solvent gradient of 50−100% ethyl acetate/hexanes, was used to further purify the compound, which was obtained as a yellow oil (744 mg, 79%). Characterizations matched previous reports (*49*).

(*S*)-3-Azidopropane-1,2-diyl distearate (2). (*S*)-3-Azidopropane-1,2-diol (**6**, 340 mg, 2.95 mmol), *N*,*N*′-dicyclohexylcarbodiimide (DCC, 2.15 g, 10.4 mmol), 4-dimethylaminopyridine (1.27 g, 10.4 mmol), and stearic acid (2.97 g, 10.4 mmol) were suspended in 30 mL of methylene chloride in a round-bottomed flask. The reaction was allowed to stir at room temperature overnight and was then filtered through a pad of celite. The product was purified by column chromatography with a solvent gradient of 100% hexanes − 20% ethyl acetate/hexanes to yield **2** as a white solid (1.9 g, 100%).

$[\alpha]_D$ ^{296K} 0.667 (c = 1.5, $CHCl_3$). ^{1}H NMR (300 MHz, $CDCl_3$): δ 5.29 (m, 1H), 4.30 (dd, J_1 = 12 Hz, J_2 = 4.5 Hz, 1H), 4.14 (dd, J_1 = 12 Hz, J_2 = 5.4 Hz, 1H), 3.45 (m, 2H), 2.33 (m, 4H), 1.62 (m, 4H), 1.26 (m, 56H), 0.88 (t, J = 6.6 Hz, 6H). ^{13}C NMR (62.9 MHz, $CDCl_3$): δ 173.08, 172.73, 69.97, 62.33, 50.92, 34.20, 34.05, 32.03, 29.82, 29.78, 29.72, 29.66, 29.58, 29.48, 29,37, 29.20, 29.15, 24.93, 24.88, 22.78, 14.16. HRMS $[M + Na]^+$ calcd 672.5650, found 672.5667.

(2*S*)-3-(4-(3,18-Dioxo-22-(2-oxohexahydro-1*H*-thieno[3,4-*d*]imidazol-4-yl)-5,8,11,14-tetraoxa-2,17-diazadocosyl)-1*H*-1,2,3-triazol-1-yl)propane-1,2-diyl distearate (1a). (*S*)-3-Azidopropane-1,2-diyl distearate (**2**, 25 mg, 38.9 μmol) and biotin-TEG-alkyne (**7a**, 20 mg, 38.9 μmol) were suspended in 1 mL of THF. Copper iodide (7.4 mg, 38.9 μmol) and *N*,*N*-diisopropylethylamine (13 μL, 77.8 μmol) were added, and the resulting solution was allowed to stir at room temperature for 18 h. Next, the solvent was removed, and the product was purified by a short column using 12 g silica gel with a solvent gradient of 2−15% methanol/dichloromethane to obtain **1a** as a white solid (20 mg, 44%).

$[\alpha]_D^{296K}$ 12.53 (c = 1.5, $CHCl_3$). ^{1}H NMR (300 MHz, $CD_3OD/CDCl_3$): δ 7.63 (s, 1H), 5.43 (m, 1H), 4.66 (m, 1H), 4.54 (m, 1H), 4.39 (m, 6H), 4.05 (m, 2H), 3.68 (m, 12H), 3.56 (m, 2H), 3.40 (m, 3H), 2.94 (d, J = 4.8 Hz, 1H), 2.78 (m, 1H), 2.29 (m, 6H), 1.64 (m, 8H), 1.27 (m, 58H), 0.88 (m, 6H). MALDI-HRMS $[M + Na]^+$ calcd 1186.8111, found 1186.8082.

(*S*)-5(6)-((1-(2,3-Bis(stearoyloxy)propyl)-1*H*-1,2,3-triazol-4-yl)methylcarbamoyl)-2-(6-hydroxy-3-oxo-3*H*-xanthen-9-yl)benzoic acid (1b). (*S*)-3-Azidopropane-1,2-diyl distearate (**2**, 58.6 mg, 0.0901 mmol) and 2-oxo-*N*-(prop-2-ynyl)-5(6)-carboxyfluoresceinamide (**7b**, 37.2 mg, 0.0901 mmol) (*51*) were dissolved in 1:1 tetrahydrofuran/water (2 mL). Copper sulfate pentahydrate (28.8 mg, 0.115 mmol) and sodium ascorbate (35.7 mg, 0.180 mmol) were added. The reaction was stirred at room temperature in the dark overnight, at which point the solvent was removed under reduced pressure. Column chromatography with a gradient solvent system of 10−20% methanol/dichloromethane afforded **1b** as a yellow solid (65.3 mg, 68%). Note: since both fluorescein isomers (5 and 6-carboxy) were present in the ^{1}H NMR spectrum for compound **1b**, and the ratio of each isomer is unknown in the commercially available acid, integration values are not reported. ^{13}C NMR data for compound **1b** are not reported due to poor solubility of the compounds and the complex nature of the spectra due to the isomeric mixture.

$[\alpha]_D^{296K}$ 0.8 (c = 1.5, $CHCl_3$). ^{1}H NMR (300 MHz, $CD_3OD/CDCl_3$): δ 8.82 (bs), 8.41−8.29 (m), 7.99−7.87 (m), 7.42−7.26 (m), 7.12 (bs), 6.88−6.55 (m), 5.43 (bs), 4.74−4.58 (m), 4.38−4.30 (m), 4.11−4.08 (m), 3.72−3.67 (m), 2.40−2.27 (m), 1.64−1.59 (m), 1.26 (bs), 0.88 (t, J = 6.5 Hz). MALDI-HRMS $[M + H]^+$ calcd 1063.6730, found 1063.6699.

General Procedure for Liposome Preparation. Solid lipids were dissolved in chloroform to a particular concentration, and a specific amount of each lipid in solution was added to a small glass container. The chloroform was removed under a constant stream of nitrogen, and the resulting lipid film was dried under vacuum overnight. The appropriate volume of buffer (20 mM HEPES, pH 7.4, for studies not involving PKC or 100 mM NaCl, 20 mM HEPES, 1 mM $CaCl_2$, pH 7.4, for studies involving PKC) was added to the dried lipids in order to produce a specific concentration of liposomes after hydration and size reduction. The suspension of lipid and buffer was agitated at 40 °C for 40 min and then subjected to 10 freeze−thaw cycles. Vesicles were prepared by extrusion (19 times) through a 200 nm polycarbonate membrane to control liposome size.

Microplate Liposome Immobilization Experiments. Analysis of liposome microplate immobilization was performed using either clear or black streptavidin-coated microplates. A solution of 20 mM HEPES buffer pH 7.4 was employed as the wash buffer. First, the wells that were to be used for analysis were incubated with 200 μL of wash buffer for 30 min. This was removed, followed by introduction of 100 μL of the various liposome compositions at different concentrations. For the initial fluorescence immobilization study (Figure 1), liposomes containing 98% PC, 1% **1a**, and 1% **1b** were analyzed alongside a control with 99% PC, 0% **1a**, and 1% **1b**. To determine the optimal percentage of biotin for liposome surface attachment (Figure 3), studies utilized different liposome samples containing **1b** fixed at 1%, varying percentages of **1a** (0−2%), and the rest of the liposome was made up of PC (98−100%). After a

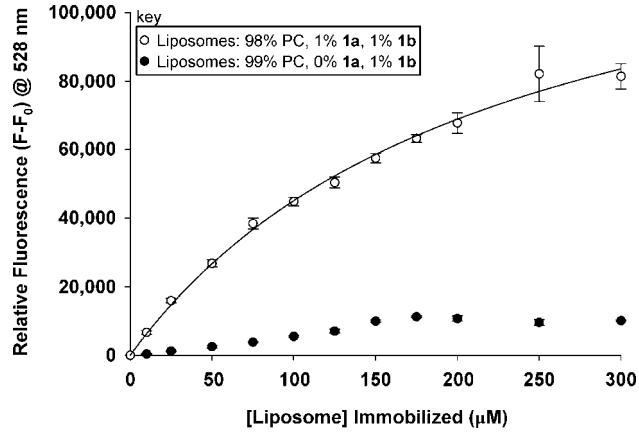

Figure 1. Microplate immobilization studies using functionalized liposomes. Liposomes containing both biotin anchor **1a** and fluorescein anchor **1b** were compared to control liposomes lacking biotin anchor **1a**.

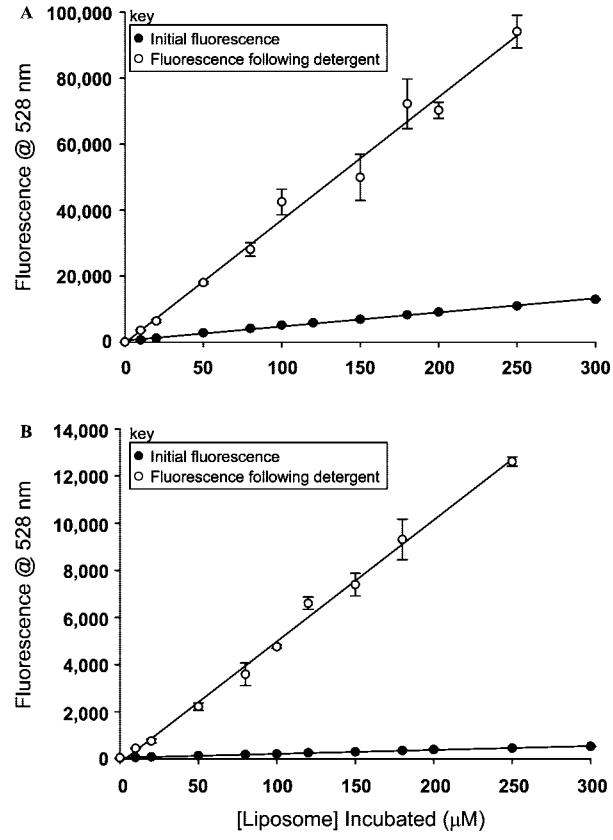

Figure 2. Dye leakage assays performed to rule out vesicle disruption on the microplate surface. Fluorescence before and after treatment of immobilized liposomes with detergent was measured both without (A) and with (B) a prior wash to remove unbound species.

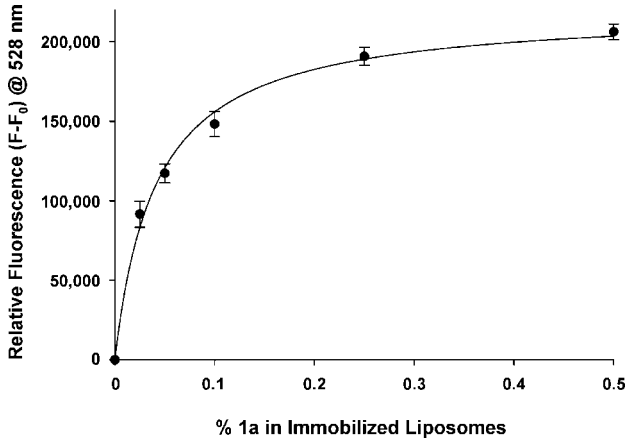

Figure 3. Immobilization of liposomes containing varying percentages of biotin anchor **1a** indicates that a low percentage (~0.25−0.5%) is effective for optimal microplate derivatization with liposomes.

1 h incubation, these solutions were removed and the wells were washed with 3 × 250 μL wash buffer. The microplate was then analyzed for fluorescence using a microplate reader with excitation using a 460 nm (±40 nm) filter and emission detected with a 528 nm (±20 nm) filter.

Procedure for Immobilized Vesicle Leakage Assay. Liposomes encapsulated with 5(6)-carboxyfluorescein (CBF) were prepared following a procedure similar to those previously reported (*52*). A solution of PC (99%) and biotin anchor **1a** (1%) in chloroform was dried under vacuum 4 h. The lipids were rehydrated with CBF buffer (50 mM CBF, 20 mM HEPES, 150 mM NaCl, pH = 7.4) according to the general procedure cited above to give a final concentration of 5 mM liposomes. Vesicles were prepared by extrusion (19 times) through a 200 nm polycarbonate membrane. Unencapsulated dye was removed using a Sephadex G-50 column equilibrated with buffer (20 mM HEPES, 150 mM NaCl, pH = 7.4). Fractions containing liposomes were determined by measuring the fluorescence (excitation λ = 490 nm) followed by the addition of 20 μL of 20% Triton X-100 to release the encapsulated CBF. Analysis of liposome microplate immobilization was performed using black streptavidin-coated microplates. Wells that were to be used for analysis were incubated with 200 μL of wash buffer (20 mM HEPES, 150 mM NaCl, pH = 7.4) for 30 min. This was removed, followed by introduction of 100 μL of liposomes at various concentrations prepared from the combined fractions after SEC chromatography. Incubation was carried out for 1 h. Following incubation, subsequent analysis was performed both with (Figure 2B) and without (Figure 2A) microplate washing (3 × 250 μL buffer) to remove unbound liposomes. In both cases, the microplate was initially analyzed for fluorescence using a microplate reader with excitation using a 460 nm (±40 nm) filter and emission detected with a 528 nm (±20 nm) filter. At this point, 30 μL of a 20% Triton X-100 solution was added to lyse the vesicles, which was followed by a repeat of the previous fluorescence measurement. Subsequent addition of detergent did not lead to a further increase in fluorescence, indicating that all liposomes had been lysed.

Microplate Analysis of Whole Liposome-PKCα Binding. Microplate protein-binding experiments were performed using white streptavidin-coated 96-well microplates. The wash buffer that was used was 20 mM HEPES buffer pH 7.4 with 100 mM sodium chloride and 1 mM calcium chloride for PKC activation. First, the wells that were to be used for analysis were washed with 200 μL of wash buffer for 30 min. This was removed, followed by introduction of different concentrations of liposomes (100 μL of solutions ranging from 0 to 200 μM in wash buffer)

Scheme 1. Synthetic Route to Modular Anchor Scaffold 2

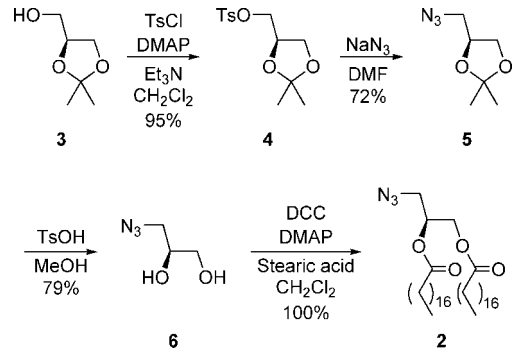

and then incubation for 1 h. Next, these solutions were removed, and the wells were washed with 3 × 250 μL wash buffer. Following this, 200 μL of a 100 ng/mL solution of PKCα in wash buffer was added to each well, followed by a 1 h incubation. At this point, the protein solution was removed, and the wells were washed with 3 × 250 μL wash buffer. Next, 200 μL of a 100 ng/mL solution of rabbit anti-PKCα antibody was added to each well and allowed to incubate for 1 h. This solution was then removed, and the wells were washed with 3 × 250 μL wash buffer. Finally, wells were incubated with goat antirabbit IgG HRP−conjugate for 1 h and then washed with 3 × 250 μL wash buffer and 1 × 100 μL water. Chemiluminescence detection of bound antibody was next performed using supersignal ELISA femto maximum sensitivity substrate. Here, a 1:1 mixture of the substrate and peroxide solutions were mixed, and 100 μL of the resulting solution was added to each well. The microplate was then immediately placed in the microplate reader, and the luminescence at 425 nm was repeatedly measured for ~5 min. Assays were run numerous times, both simultaneously and on separate occasions using newly formed solutions. The chemiluminescence data was then plotted vs the original incubation concentrations using *SigmaPlot* to curve fit the data (nonlinear regression using the Langmuir binding isotherm).

RESULTS AND DISCUSSION

The development of a microplate-based method for detecting protein−membrane binding initially requires successful immobilization of whole liposomes. For this pursuit, one must take into account issues associated with studying unilamelar liposomes, as they are known to degrade within a few days after formation and to fuse and unravel when they come in contact with certain surfaces (*53*). The former problem renders a high-throughput method for analysis particularly beneficial, as this would allow for a large number of binding studies to be performed in a short period of time prior to liposome degradation. The latter situation requires that one take care to ensure that the bilayers are not modified during the course of study. In this regard, literature precedent has shown that the immobilization of whole liposomes onto streptavidin-coated surfaces via the avidin−biotin interaction is particularly effective for avoiding decomposition of the liposomes (*53*−*57*).

The immobilization of whole liposomes has generally been achieved through the inclusion of a biotin-presenting anchor within the membrane bilayer. Previously, with a few exceptions (*58*,*59*), functionalized membrane anchors have generally been accessed through modification of the amino group of phosphatidylethanolamine (PE). However, this is not an economical or facile approach, as it employs a phospholipid as a synthetic precursor. Thus, we initially set out to develop a more cost-effective alternative that would allow for convenient and modular functionalization of a lipid anchor. Toward this end, we designed versatile azido−lipid anchor scaffold **2** (Schemes 1 and 2),

Scheme 2. Convenient Derivatization of Scaffold 2 to Obtain Membrane Anchors of Use for Functionalizing Liposomal Surfaces

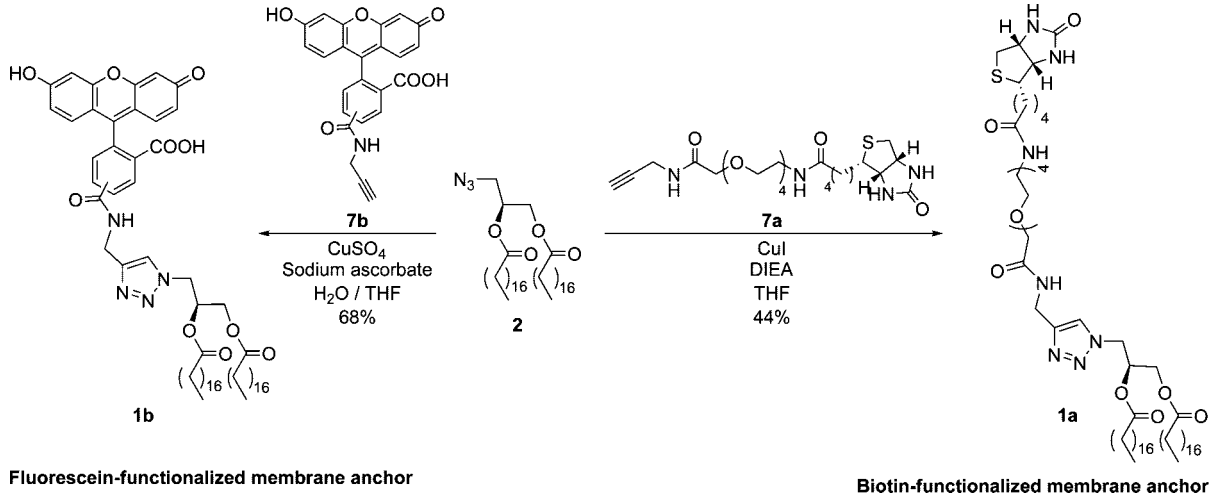

Scheme 3. Microplate-Based Assay for Rapid Characterization of Protein−Membrane Binding Interactions

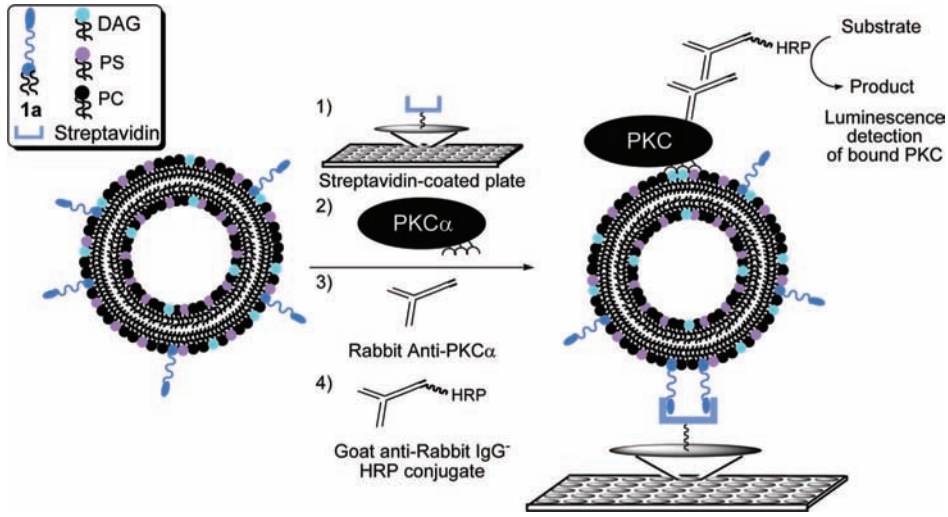

which can be easily functionalized via the azide−alkyne cycloaddition reaction (click chemistry) (*60*−*62*) to produce a range of derivatized membrane anchors in a single synthetic step.

The synthetic route to azide-tagged lipid anchor **2**, illustrated in Scheme 1, commences with commercial (S)-(+)-2,2-dimethyl-dioxolane-4-methanol (**3**). This enantiomerically pure precursor, containing stereochemistry that corresponds to that of a natural phospholipid, was used in case the stereochemistry of the anchor affected presentation in the membrane setting. Precursor **3** was converted to compound **5** via a procedure modified from that described by Martin and co-workers (*49*). First, a toluenesulfonyl (tosyl) leaving group was introduced onto the hydroxyl group of **3** to **4**, followed by substitution with azide to **5**. Care must be taken with the handling of compound **5** due to both its volatile nature as well as the fact that it is a low-molecular-weight azide, and these are known to have explosive properties (*50*). Next, the acetonide group of **5** was removed to provide diol **6**, to which stearyl chains were then appended to access azido-anchor **2**. Modular azido-anchor **2** was then conveniently derivatized to allow for subsequent presentation of desired reporters and tags on the membrane surface (Scheme 2). The first target, biotin-conjugate **1a**, was pursued in order to achieve whole liposome immobilization. Here, a tetraethylene glycol (TEG)-based tether was implemented between the biotin and lipid components to provide effective spacing of the liposomes from the microplate surface following immobilization. Fluorophore-tagged anchor **1b** (fluorescein) was also synthesized to allow for the detection of functionalized liposomes during studies.

Following the development of these compounds for efficient membrane functionalization, we moved on to study the efficacy of whole liposome immobilization using anchor **1a**. Here, unilamellar liposomes were formed using standard conditions, including the control of liposome size (200 nm), which was achieved using extrusion. The resulting samples were analyzed by dynamic light scattering (DLS) to ensure narrow polydispersity. Initial liposomes contained 98% phosphatidylcholine (PC) as the bulk lipid as well as 1% each of biotin-anchor **1a** and fluorescein−lipid conjugate **1b** (sample A). Control solutions with 99% PC and 1% **1b**, but lacking **1a** (sample B), were also implemented. Both sets of liposomes were incubated with streptavidin-coated 96-well microplates, washed thoroughly, and the fluorescence resulting from the presence of the fluorescein tag was detected using a microplate reader. As shown in Figure 1, sample A yielded an increase in fluorescence with liposome concentration. For control sample B, a small amount of nonspecific background was observed for the nonbiotinylated liposomes. Taken together, these studies indicate that biotin-dependent immobilization of whole liposomes was achieved using convenient anchor **1a**.

To provide further evidence that immobilized liposomes remain intact on the microplate surface using this approach, a traditional dye-leakage vesicle cleavage experiment was per-

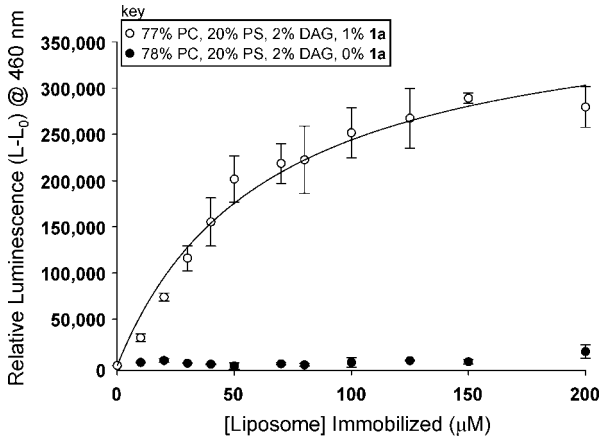

Figure 4. Results from microplate-based analysis of the binding of PKCα to immobilized whole liposomes.

formed (*52*). Here, while fluorescein emission is quenched when the dye is encapsulated within a liposomal interior, fluorescence is activated when the liposome is cleaved and the dye is released into solution. In the current study, PC liposomes containing 1% of biotin anchor **1a** were loaded with fluorescein and incubated at different concentrations for 1 h to immobilize. Initially, the microplate was not washed to remove unbound species. Following an initial fluorescence measurement (Figure 2A), the surface was treated with detergent, which led to a large increase in fluorescein emission, indicating detergent-based cleavage of intact immobilized liposomes. In a complementary experiment, the microplate surface was thoroughly washed after liposome immobilization, emission was detected, and then detergent addition was followed by another fluorescence measurement. In this case, the initial measurement yielded very low background fluorescence (Figure 2B), and the signal was once again greatly enhanced upon treatment with detergent. These studies indicate successful microplate-immobilization of intact liposomes, which were only cleaved upon traditional detergent treatment.

In a subsequent study, we sought to determine the percentage of biotin-anchor **1a** in the liposomes that is required to maximize loading onto the plate. Here, PC-based liposomes containing a variable percentage of **1a** (from 0% to 2%) and a fixed amount of fluorescein-conjugate **1b** (1%) were incubated with the plate, which was then washed and detected. The resulting emission signal was found to increase up to ~0.25−0.5% of anchor **1b**, at which point the signal reached a plateau (Figure 3). These results indicate that relatively small percentages of **1b** are effective for saturating the microplate surface with liposomes.

Following successful characterization of liposome immobilization, we moved on to the detection of protein−membrane binding interactions utilizing the microplate surface. As a proof-of-concept, we pursued the detection of the membrane-binding of PKCα. This PKC isozyme contains two C1 domains that target DAG and a calcium-dependent C1-domain that binds PS. Liposomes similar to those previously reported to be optimal for PKC-binding (*63*−*65*), which included 1% **1a**, 2% DAG, 20% PS, and 77% PC, were employed for studies. The resulting liposome formulations were analyzed via a microplate-based secondary antibody assay as depicted in Scheme 3. Here, liposome solutions of varying concentration were introduced into different wells of 96-well streptavidin-coated microplates for immobilization. This was followed by incubation with PKCα, rabbit anti-PKCα primary antibody, and finally goat antirabbit IgG horseradish peroxidase (HRP)-conjugate as a secondary antibody. Thorough buffer washes were performed after each step to remove unbound species. Finally, the secondary antibody was detected via a chemiluminescence assay catalyzed by the pendant HRP to indicate the amount of bound PKCα in each well. Results, exemplified in Figure 4, showed a typical binding isotherm for the interaction of PKCα with the immobilized liposomes. Figure 4 also indicates results from analysis using control liposomes lacking biotin anchor **1a**, which indicate the low background associated with the assay.

These results indicate the viability of whole liposome immobilization for the direct characterization of protein-membrane binding events. This assay exhibits a number of advantages over previous strategies, including that the target protein does not need to be labeled or modified, effectively mimicking the physiological system, and that chemiluminescence-based signal transduction allows for highly sensitive detection. We are currently working to advance this platform to extend the ability to detect and characterize membrane-based recognition. For instance, the large-scale immobilization of liposomes containing different lipid compositions is being pursued toward the development of a high-throughput microarray assay. In addition, a range of other membrane processes such as membrane fusion (*66*) and disruption (*27*) could also benefit from techniques involving liposome-functionalized surfaces. This approach is also not limited to the study of protein−lipid binding, but could be extended to directly characterize the binding of other ligands, such as peptides and carbohydrates. These ligands could be conveniently lipidated using azido-anchor **2** and incorporated into membrane bilayers, allowing for binding analysis in a fluid multivalent environment that mimics ligand presentation in cellular membranes. In these ways, the described liposomal microplate assay provides an excellent tool for elucidating membrane-based biological processes.

ACKNOWLEDGMENT

We acknowledge the University of Tennessee for funding of this research.

Supporting Information Available: Further procedures and characterization are included. This material is available free of charge via the Internet at http://pubs.acs.org.

LITERATURE CITED

(1) Mammen, M., Choi, S. K., and Whitesides, G. M. (1998) Polyvalent interactions in biological systems: Implications for design and use of multivalent ligands and inhibitors. *Angew. Chem., Int. Ed. 37*, 2755–2794.
(2) Kiessling, L. L., Gestwicki, J. E., and Strong, L. E. (2006) Synthetic multivalent ligands as probes of signal transduction. *Angew. Chem., Int. Ed. 45*, 2348–2368.
(3) Cho, W. H., and Stahelin, R. V. (2005) Membrane-protein interactions in cell signaling and membrane trafficking. *Annu. Rev. Biophys. Biomol. Struct. 34*, 119–151.
(4) Colon-Gonzalez, F., and Kazanietz, M. G. (2006) C1 domains exposed: From diacylglycerol binding to protein-protein interactions. *Biochim. Biophys. Acta 1761*, 827–837.
(5) Testerink, C., and Munnik, T. (2005) Phosphatidic acid: a multifunctional stress signaling lipid in plants. *Trends Plant Sci. 10*, 368–375.
(6) Stace, C. L., and Ktistakis, N. T. (2006) Phosphatidic acid- and phosphatidylserine-binding proteins. *Biochim. Biophys. Acta 1761*, 913–926.
(7) Lemmon, M. A. (2008) Membrane recognition by phospholipid-binding domains. *Nat. Rev. Mol. Cell Biol. 9*, 99–111.
(8) Lemmon, M. A. (2003) Phosphoinositide recognition domains. *Traffic 4*, 201–213.
(9) McLaughlin, S., Wang, J. Y., Gambhir, A., and Murray, D. (2002) PIP2 and proteins: Interactions, organization, and information flow. *Annu. Rev. Biophys. Biomol. Struct. 31*, 151–175.
(10) Prestwich, G. D. (2004) Phosphoinositide signaling: From

affinity probes to pharmaceutical targets. *Chem. Biol. 11*, 619–637.
(11) Di Paolo, G., and De Camilli, P. (2006) Phosphoinositides in cell regulation and membrane dynamics. *Nature 443*, 651–657.
(12) Hurley, J. H. (2006) Membrane binding domains. *Biochim. Biophys. Acta 1761*, 805–811.
(13) Schultz, A., Ling, M., and Larsson, C. (2004) Identification of an amino acid residue in the protein kinase CC1b domain crucial for its localization to the Golgi network. *J. Biol. Chem. 279*, 31750–31760.
(14) Carrasco, S., and Merida, I. (2007) Diacylglycerol, when simplicity becomes complex. *Trends Biochem. Sci. 32*, 27–36.
(15) Gomez-Fernandez, J. C., and Corbalan-Garcia, S. (2007) Diacylglycerols, multivalent membrane modulators. *Chem. Phys. Lipids 148*, 1–25.
(16) Spitaler, M., and Cantrell, D. A. (2004) Protein kinase C and beyond. *Nat. Immunol. 5*, 785–790.
(17) Gutcher, I., Webb, P. R., and Anderson, N. G. (2003) The isoform-specific regulation of apoptosis by protein kinase C. *Cell. Mol. Life Sci. 60*, 1061–1070.
(18) Griner, E. M., and Kazanietz, M. G. (2007) Protein kinase C and other diacylglycerol effectors in cancer. *Nat. Rev. Cancer 7*, 281–294.
(19) Mackay, H. J., and Twelves, C. J. (2007) Targeting the protein kinase C family: are we there yet? *Nat. Rev. Cancer 7*, 554–562.
(20) Wender, P. A., DeBrabander, J., Harran, P. G., Jimenez, J. M., Koehler, M. F. T., Lippa, B., Park, C. M., Siedenbiedel, C., and Pettit, G. R. (1998) The design, computer modeling, solution structure, and biological evaluation of synthetic analogs of bryostatin 1. *Proc. Natl. Acad. Sci. U.S.A. 95*, 6624–6629.
(21) Kitov, P. I., Sadowska, J. M., Mulvey, G., Armstrong, G. D., Ling, H., Pannu, N. S., Read, R. J., and Bundle, D. R. (2000) Shiga-like toxins are neutralized by tailored multivalent carbohydrate ligands. *Nature 403*, 669–672.
(22) Wittinghofer, A., and Waldmann, H. (2000) Ras - A molecular switch involved in tumor formation. *Angew. Chem., Int. Ed. 39*, 4193–4214.
(23) Silvius, J. R. (2002) Mechanisms of Ras protein targeting in mammalian cells. *J. Membr. Biol. 190*, 83–92.
(24) Volkert, M., Wagner, M., Peters, C., and Waldmann, H. (2001) The chemical biology of Ras lipidation. *Biol. Chem. 382*, 1133–1145.
(25) Tamm, L. K. (2008) Hypothesis: spring-loaded boomerang mechanism of influenza hemagglutinin-mediated membrane fusion. *Biochim. Biophys. Acta 1614*, 14–23.
(26) Zasloff, M. (2002) Antimicrobial peptides of multicellular organisms. *Nature 415*, 389–395.
(27) Brogden, K. A. (2005) Antimicrobial peptides: Pore formers or metabolic inhibitors in bacteria? *Nat. Rev. Microbiol. 3*, 238–250.
(28) Cho, W. W., Bittova, L., and Stahelin, R. V. (2001) Membrane binding assays for peripheral proteins. *Anal. Biochem. 296*, 153–161.
(29) Connell, E., Scott, P., and Davletov, B. (2008) Real-time assay for monitoring membrane association of lipid-binding domains. *Anal. Biochem. 377*, 83–88.
(30) Stoughton, R. B. (2005) Applications of DNA microarrays in biology. *Annu. Rev. Biochem. 74*, 53–82.
(31) Bulyk, M. L. (2006) DNA microarray technologies for measuring protein-DNA interactions. *Curr. Opin. Biotechnol. 17*, 422–430.
(32) Min, D. H., and Mrksich, M. (2004) Peptide arrays: towards routine implementation. *Curr. Opin. Chem. Biol. 8*, 554–558.
(33) Wilson, D. S., and Nock, S. (2003) Recent developments in protein microarray technology. *Angew. Chem., Int. Ed. 42*, 494–500.
(34) Kung, L. A., and Snyder, M. (2006) Proteome chips for whole-organism assays. *Nat. Rev. Mol. Cell Biol. 7*, 617–622.
(35) Feizi, T., Fazio, F., Chai, W., and Wong, C.-H. (2003) Carbohydrate microarrays - a new set of technologies at the frontiers of glycomics. *Curr. Opin. Struct. Biol. 13*, 637–645.
(36) Bryan, M. C., Fazio, F., Lee, H. K., Huang, C. Y., Chang, A., Best, M. D., Calarese, D. A., Blixt, C., Paulson, J. C., Burton, D., Wilson, I. A., and Wong, C. H. (2004) Covalent display of oligosaccharide arrays in microtiter plates. *J. Am. Chem. Soc. 126*, 8640–8641.
(37) Ratner, D. M., Adams, E. W., Disney, M. D., and Seeberger, P. H. (2004) Tools for glycomics: Mapping interactions of carbohydrates in biological systems. *ChemBioChem 5*, 1375–1383.
(38) Werz, D. B., and Seeberger, P. H. (2005) Carbohydrates as the next frontier in pharmaceutical research. *Chem. Eur. J. 11*, 3194–3206.
(39) Calarese, D. A., Lee, H. K., Huang, C. Y., Best, M. D., Astronomo, R. D., Stanfield, R. L., Katinger, H., Burton, D. R., Wong, C. H., and Wilson, I. A. (2005) Dissection of the carbohydrate specificity of the broadly neutralizing-anti-HIV-1 antibody 2G12. *Proc. Natl. Acad. Sci. U.S.A. 102*, 13372–13377.
(40) Huang, C. Y., Thayer, D. A., Chang, A. Y., Best, M. D., Hoffmann, J., Head, S., and Wong, C. H. (2006) Carbohydrate microarray for profiling the antibodies interacting with Globo H tumor antigen. *Proc. Natl. Acad. Sci. U.S.A. 103*, 15–20.
(41) Liang, P. H., Wang, S. K., and Wong, C. H. (2007) Quantitative analysis of carbohydrate-protein interactions using glycan microarrays: Determination of surface and solution dissociation constants. *J. Am. Chem. Soc. 129*, 11177–11184.
(42) Pilobello, K. T., and Mahal, L. K. (2007) Deciphering the glycocode: the complexity and analytical challenge of glycomics. *Curr. Opin. Chem. Biol. 11*, 300–305.
(43) Pohl, N. L. (2008) Fluorous tags catching on microarrays. *Angew. Chem., Int. Ed. 47*, 3868–3870.
(44) Kanter, J. L., Narayana, S., Ho, P. P., Catz, I., Warren, K. G., Sobel, R. A., Steinman, L., and Robinson, W. H. (2006) Lipid microarrays identify key mediators of autoimmune brain inflammation. *Nature Med. 12*, 138–143.
(45) Liang, P. H., Imamura, M., Li, X., Wu, D., Fujio, M., Guy, R. T., Wu, B.-C., Tsuji, M., and Wong, C. H. (2008) Quantitative microarray analysis of intact glycolipid-CD1d interaction and correlation with cell-based cytokine production. *J. Am. Chem. Soc. 130*, 12348–12354.
(46) Deng, Y., Wang, Y., Holtz, B., Li, J., Traaseth, N., Veglia, G., Stottrup, B. J., Elde, R., Pei, D., Guo, A., and Zhu, X.-Y. (2008) Fluidic air-stable supported lipid bilayer and cell-mimicking microarrays. J. Am. Chem. Soc. *130*.
(47) Fang, Y., Frutos, A. G., and Lahiri, J. (2002) Membrane protein microarrays. *J. Am. Chem. Soc. 124*, 2394–2395.
(48) Nelson, W. L., Wennerstrom, J. E., and Sankar, S. R. (1977) Absolute-configuration of glycerol derivatives 0.3. Synthesis and cupra a circular-dichroism spectra of some chiral 3-aryloxy-1,2-propanediols and 3-aryloxy-1-amino-2-propanols. *J. Org. Chem. 42*, 1006–1012.
(49) Martin, S. F., Wong, Y. L., and Wagman, A. S. (1994) Design, synthesis, and evaluation of phospholipid analogs as inhibitors of the bacterial phospholipase-C from *Bacillus cereus*. *J. Org. Chem. 59*, 4821–4831.
(50) Conrow, R. E., and Dean, W. D. Diazidomethane explosion. Org. Proc. Res. Dev., In Press.
(51) Smith, M. D., Gong, D., Sudhahar, C. G., Reno, J. C., Stahelin, R. V., and Best, M. D. (2008) Synthesis and convenient functionalization of azide-labeled diacylglycerol analogues for modular access to biologically active lipid probes. *Bioconjugate Chem. 19*, 1855–1863.
(52) Forbes, C. C., DiVittorio, K. M., and Smith, B. D. (2006) Bolaamphiphiles promote phospholipid translocation across vesicle membranes. *J. Am. Chem. Soc. 128*, 9211–9218.
(53) Kalyankar, N. D., Sharma, M. K., Vaidya, S. V., Calhoun, D., Maldarelli, C., Couzis, A., and Gilchrist, L. (2006) Arraying of intact liposomes into chemically functionalized microwells. *Langmuir 22*, 5403–5411.

(54) Liu, X. Y., Yang, Q., Nakamura, C., and Miyake, J. (2001) Avidin-biotin-immobilized liposome column for chromatographic fluorescence on-line analysis of solute-membrane interactions. *J. Chromatogr., Sect. B 750*, 51–60.

(55) Vermette, P., Meagher, L., Gagnon, E., Griesser, H. J., and Doillon, C. J. (2002) Immobilized liposome layers for drug delivery applications: inhibition of angiogenesis. *J. Controlled Release 80*, 179–195.

(56) Vermette, P., Griesser, H. J., Kambouris, P., and Meagher, L. (2004) Characterization of surface-immobilized layers of intact liposomes. *Biomacromolecules 5*, 1496–1502.

(57) Davidson, W. S., Ghering, A. B., Beish, L., Tubb, M. R., Hui, D. Y., and Pearson, K. (2006) The biotin-capture lipid affinity assay: a rapid method for determining binding parameters for apiloproteins. *J. Lipid Res. 47*, 440–449.

(58) Elliott, J. T., and Prestwich, G. D. (2000) Maleimide-functionalized lipids that anchor polypeptides to lipid bilayers and membranes. *Bioconjugate Chem. 11*, 832–841.

(59) Hassane, F. S., Frisch, B., and Schuber, F. (2006) Targeted liposomes: Convenient coupling of ligands to preformed vesicles using "click" chemistry. *Bioconjugate Chem. 17*, 849–854.

(60) Lewis, W. G., Green, L. G., Grynszpan, F., Radic, Z., Carlier, P. R., Taylor, P., Finn, M. G., and Sharpless, K. B. (2002) Click chemistry in situ: Acetylcholinesterase as a reaction vessel for the selective assembly of a femtomolar inhibitor from an array of building blocks. *Angew. Chem., Int. Ed. 41*, 1053–1057.

(61) Kolb, H. C., Finn, M. G., and Sharpless, K. B. (2001) Click chemistry: Diverse chemical function from a few good reactions. *Angew. Chem., Int. Ed. 40*, 2004–2021.

(62) Rostovtsev, V. V., Green, L. G., Fokin, V. V., and Sharpless, K. B. (2002) A stepwise Huisgen cycloaddition process: Copper(I)-catalyzed regioselective "ligation" of azides and terminal alkynes. *Angew. Chem., Int. Ed. 41*, 2596–2599.

(63) Bittova, L., Stahelin, R. V., and Cho, W. (2001) Roles of ionic residues of the C1 domain in protein kinase C-alpha activation and the origin of phosphatidylserine specificity. *J. Biol. Chem. 276*, 4218–4226.

(64) Bolen, E. J., and Sando, J. J. (1992) Effect of phospholipid unsaturation on protein-kinase-C activation. *Biochemistry 31*, 5945–5951.

(65) Stahelin, R. V., Digman, M. A., Medkova, M., Ananthanarayanan, B., Rafter, J. D., Melowic, H. R., and Cho, W. H. (2004) Mechanism of diacylglycerol-induced membrane targeting and activation of protein kinase C delta. *J. Biol. Chem. 279*, 29501–29512.

(66) Tamm, L. K., Crane, J., and Kiessling, V. (2003) Membrane fusion: a structural perspective on the interplay of lipids and proteins. *Curr. Opin. Struct. Biol. 13*, 453–466.

BC800414K

Supporting Information

Synthesis of biotin-TEG-alkyne linker 7a. Biotinylated TEG linker **7a** was synthesized from tetraethyleneglycol (**8**) as shown in Supporting Information Figure 1. First, *N*-Boc and ethyl ester-protected glycol derivative **11** was accessed in four steps using a procedure similar to that described by Lehn and co-workers*(1)*. This compound has also been synthesized with reversed order of addition of the ethyl ester and amino-functionalities*(2)*. Here, an ethylacetyl group is first appended onto **8** to **9**, followed by conversion to azide **10** via mesylation and azide substitution. Next, reduction of the azide group was performed with trapping of the resulting amine with a Boc group to **11**. The ethyl ester of **11** was then deprotected to **12**, followed coupling of the resulting carboxyl group with propargylamine to **13**. Finally, Boc deprotection was followed by direct coupling of the resulting amine with biotin-pentafluorophenyl ester (**14**) to produce biotin-TEG-alkyne conjugate **7a**.

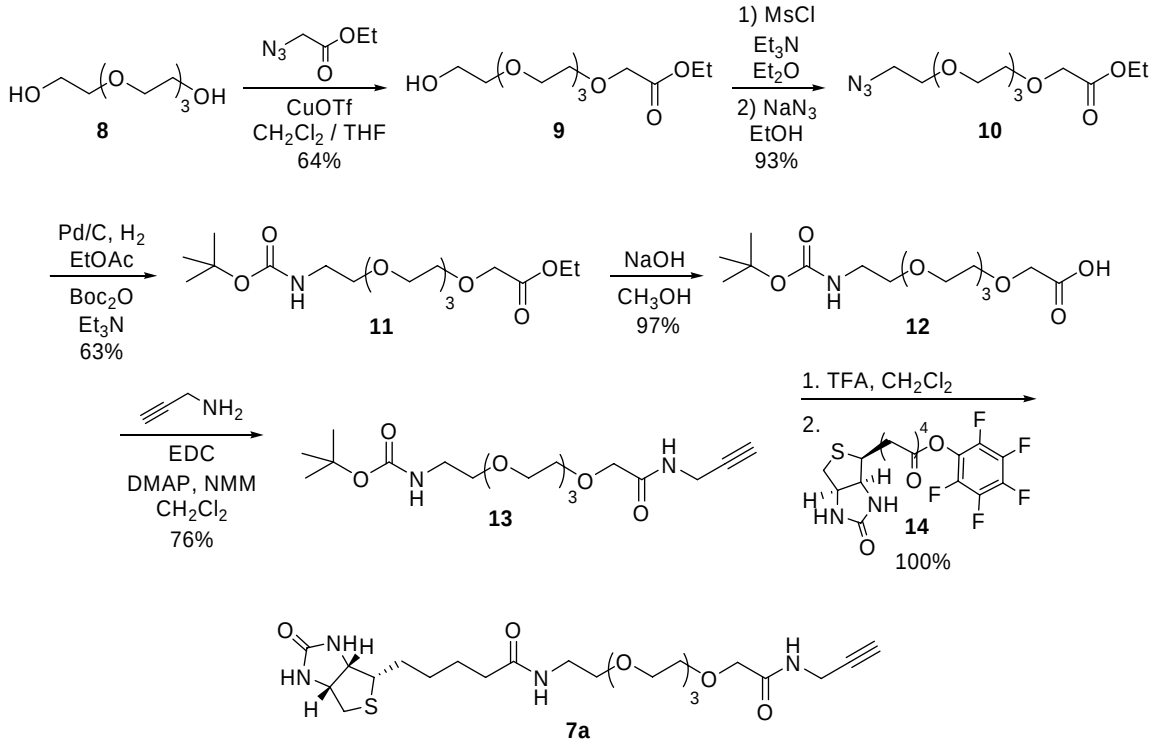

Supporting Information Figure 1. Synthesis of biotin-TEG-alkyne linker **7a**.

Ethyl 14-hydroxy-3,6,9,12-tetraoxatetradecanoate (9). In a 3-neck round bottom flask equipped with a bubbler, tetraethylene glycol (**8**, 43.2 mL, 250 mmol) was dissolved in anhydrous dichloromethane. Copper triflate (904.2 mg, 2.5 mmol) was added along with anhydrous tetrahydrofuran (7 mL). The solution was cooled to 0 °C and placed under a constant stream of nitrogen. Ethyl diazoacetate (5.3 mL, 50 mmol) was dissolved in anhydrous dichloromethane (34 mL) and added dropwise to the stirring solution. The solution was allowed to gradually warm to room temperature and stirring was continued overnight. The reaction was extracted with saturated NaCl and then washed with dichloromethane (100 mL). The combined organic layers were combined and dried with magnesium sulfate and filtered, and the solvent was removed under reduced pressure. Column chromatography with silica gel and a gradient solvent system of 0 - 10 % methanol/ethyl acetate afforded **9** as a yellow oil (8.9 g, 64%).

^{1}H NMR (300 MHz, $CDCl_3$) δ 4.20 (q, *J* = 7.2 Hz, 2H), 4.15 (s, 2H), 3.73-3.54 (m, 16H), 1.27 (t, *J* = 7.2 Hz, 3H); ^{13}C NMR (75 MHz, $CDCl_3$) δ 170.4, 72.6, 70.7, 70.54, 70.52, 70.44, 70.43, 70.2, 68.5, 61.4, 60.6, 14.2; HRMS $[M + H]^+$ cacld: 281.16003, found: 281.15895

Ethyl 14-azido-3,6,9,12-tetraoxatetradecanoate (10). Ethyl 14-hydroxy-3,6,9,12-tetraoxatetradecanoate (**9**, 1.02 g, 3.64 mmol) and triethylamine (1.5 mL, 10.92 mmol) were dissolved in anhydrous diethyl ether (7 mL) at 0 °C under a nitrogen atmosphere. Methanesulfonyl chloride (285 µL, 3.68 mmol) was added dropwise with stirring. Once the addition was complete the solution was allowed to gradually return to room temperature. Stirring was continued for a total of 1 h. At this point solvent was removed under reduced pressure. The residue was dissolved in anhydrous ethanol (10 mL) and sodium azide (239 mg, 3.68 mmol) was added. The reaction was stirred at reflux overnight. The reaction was extracted with dichloromethane (2 x 100 mL) and the organic layer was dried with magnesium sulfate, filtered and the solvent was removed under reduced pressure to yield pure **10** as a yellow oil (1.04 g, 93%).

^{1}H NMR (300 MHz, $CDCl_3$) δ 4.22 (q, *J* = 7.2 Hz, 2H), 4.15 (s, 2H), 3.73-3.67 (m, 14H), 3.40 (t, *J* = 4.8 Hz, 2H), 1.28 (t, *J* = 7.2 Hz, 3H); ^{13}C NMR (75 MHz, $CDCl_3$) δ 170.4, 70.8, 70.65, 70.62, 70.57, 70.0, 68.7, 60.8, 50.6, 14.2; HRMS $[M - N_2 + H]^+$ cacld: 278.16036, found: 278.16152

Ethyl 14-*tert*-butoxycarbonylamino-3,6,9,12-tetraoxatetradecanoate (11). Ethyl 14-azido-3,6,9,12-tetraoxatetradecanoate (**10**, 1.08 g, 3.55mmol) was dissolved in ethyl acetate. Di-tert-butyl dicarbonate (1.55 g, 7.1 mmol), triethyl amine (990 µL, 7.1 mmol) and Palladium on carbon (110 mg) were added with stirring. The flask was evacuated and refilled with hydrogen three times and stirred at room temperature overnight. The reaction mixture was filtered through a pad of celite and the solvent was removed under reduced pressure. Column chromatography with silica gel and and a gradient solvent of 5 : 1 - 2 : 1 chloroform/acetone with 0.1% triethylamine afforded **10** as a yellow oil (853 mg, 63%).

^{1}H NMR (300 MHz, $CDCl_3$) δ 5.10 (bs, 1H), 4.22 (q, *J* = 7.2 Hz, 2H), 4.16 (s, 2H), 3.73-3.53 (m, 14H), 3.34-3.31 (m, 2H), 1.44 (s, 9H), 1.29 (t, *J* = 7.2 Hz, 3H); ^{13}C NMR (75 MHz, $CDCl_3$) δ 170.5, 156.0, 79.1, 70.8, 70.62, 70.57, 70.55, 70.51, 70.21, 68.7, 60.8, 40.3, 28.4, 14.2; HRMS $[M + H]^+$ calcd: 380.22844, found: 380.22788

.

14-*tert*-butoxycarbonylamino-3,6,9,12-tetraoxatetradecanoic acid (12). Ethyl 14-*tert*-butoxycarbonylamino-3,6,9,12-tetraoxatetradecanoate (**11**, 379.4 mg, 1 mmol) was dissolved in methanol (2 mL) and 2M NaOH (2 mL) was added with stirring. The reaction was stirred 30 min. At this point Dowex® 50WX8-200 H^+ ion exchange resin was added until the pH was 4-5. The reaction was filtered and the solvent was removed under reduced pressure to afford **12** as a brown solid (340 mg, 97%).

^{1}H NMR (300 MHz, $CDCl_3$) δ 5.40 (bs, 1H), 4.08 (s, 1H), 3.66-3.54 (m, 14H), 3.34-3.24 (m, 2H) 1.44 (s, 9H); ^{13}C NMR (75 MHz, $CDCl_3$) δ 174.3, 156.3, 79.0, 70.4, 70.1, 70.0, 69.9, 69.4, 69.1, 40.1, 28.4; HRMS $[M + H]^+$ cacld: 352.19714, found: 352.19869.

***N*-(prop-2-ynyl)-14-*tert*-butoxycarbonylamino-3,6,9,12-tetraoxatetradecane carboxamide (13).** 14-*tert*-butoxycarbonylamino-3,6,9,12-tetraoxatetradecanoic acid

(**12**, 340 mg, 0.968 mmol), propargylamine (73 µL, 1.06 mmol), 4-dimethylaminopyridine (DMAP, 118 mg, 0.968 mmol), and *N*-Methylmorpholine (213 µL, 1.94 mmol) were dissolved in anhydrous *N,N*-Dimethylformamide (9mL). The solution was cooled to 0 °C and stirred for 5 min. 1-Ethyl-(3-dimethylaminopropyl)carbodiimide hydrochloride (EDC-HCl, 222 mg, 1.16 mmol) was added and the reaction was stirred at room temperature overnight. Next, the solvent was removed under reduced pressure and column chromatography with a gradient solvent system of 5 : 1 - 2 : 1 chloroform/acetone afforded **13** as a yellow oil (285 mg, 76%).

^{1}H NMR (300 MHz, $CDCl_3$) δ 7.44 (bs, 1H), 5.08 (bs, 1H), 4.11-4.09 (m, 2H), 4.03 (s, 2H), 3.70-3.53 (m, 14H), 3.33-3.31 (m, 2H), 2.24 (t, *J* = 2.3 Hz, 1H), 1.45 (s, 9H); ^{13}C NMR (75 MHz, $CDCl_3$) δ 169.9, 156.0, 79.7, 79.2, 77.3, 71.2, 71.1, 70.6, 70.5, 70.3, 70.24, 70.16, 40.3, 28.4, 28.3; HRMS $[M + H]^+$ cacld: 389.22878, found: 389.22797.

13-oxo-3,6,9,12-tetraoxa-14-azaheptadec-16-1-biotinamide(7a). Compound **13** (145 mg, 360 µmol) was dissolved in 20 mL of dry DMF. Triethylamine was added to the solution, which was then stirred for 5 minutes. Biotin-pentafluorophenyl ester (**14**, 148 mg, 360 µmol) was added and the solution was stirred at room temperature overnight. The solvent was then removed by rotary evaporation and the product was purified by column chromatography with a solvent elution of 100% acetone - 40% methanol/dichloromethane. This yielded **7a** as a colorless oil (188 mg, 100%).

$[\alpha]_D^{296K}$ 22.19 (c = 5.25, MeOH/$CHCl_3$); ^{1}H NMR (300 MHz, $CD_3OD/CDCl_3$): δ 4.54 (m, 1H), 4.34 (m, 1H), 4.08 (s, 2H), 4.04 (d, *J* = 2.4Hz, 2H), 3.72 (m, 8H), 3.68 (m, 4H), 3.60 (t, *J* = 4.9Hz, 2H), 3.43 (m, 3H), 3.20 (m, 1H), 2.94 (dd, J_1 = 12.9Hz, J_2 = 4.8Hz, 1H), 2.76 (d, *J* = 12.9Hz, 1H), 2.24 (t, *J* = 7.2Hz, 1H), 1.65 (m, 4H), 1.46 (q, J_1 = 14.4Hz, J_2 = 7.2Hz, 2H); ^{13}C NMR (100.6 MHz, $CD_3OD/CDCl_3$): δ 174.9, 171.0, 164.5, 70.3, 70.2, 70.1, 70.0, 62.2, 60.5, 55.8, 40.3, 39.4, 39.2, 35.8, 28.6, 28.4, 25.7; MALDI-HRMS $[M + H]^+$ calcd: 515.2539, found: 515.2537.

(1) Jullien, L., and Lehn, J. M. (1988) The Chundle Approach to Molecular Channels Synthesis of a Macrocycle Based Molecular Bundle. *Tetrahedron Lett. 29,* 3803-3806.

(2) Shirude, P. S., Kumar, V. A., and Ganesh, K. N. (2005) BisPNA targeting to DNA: Effect of neutral loop on DNA duplex strand invasion by aepPNA-N7G/aepPNA-C substituted peptide nucleic acids. *Eur. J. Org. Chem.,* 5207-5215.

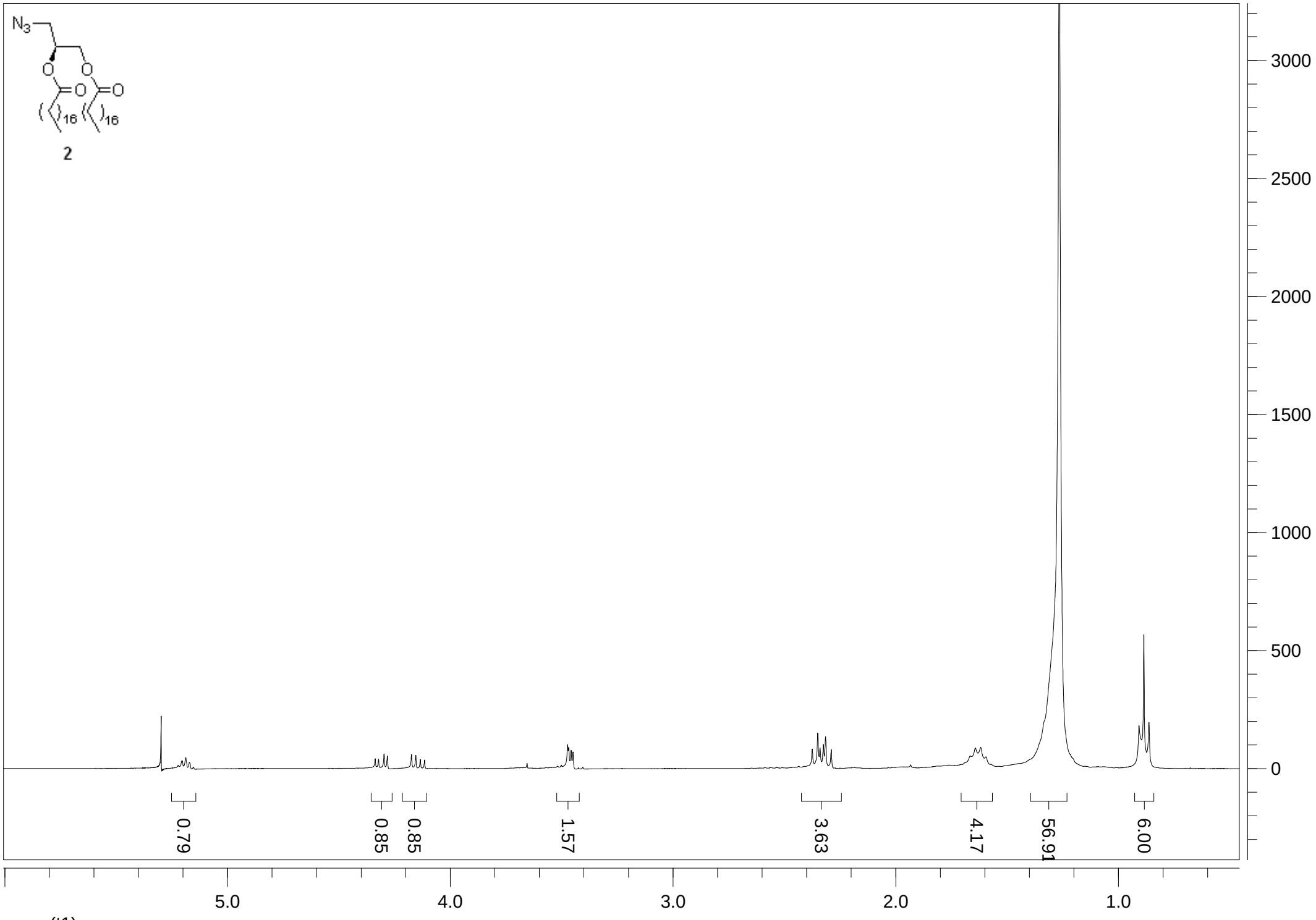
N3
O
O
O
O
O
16
16
2
3000
2500
2000
1500
1000
500
0
0.79
0.85
0.85
1.57
3.63
4.17
56.91
6.00
5.0
4.0
3.0
2.0
1.0
ppm (t1)

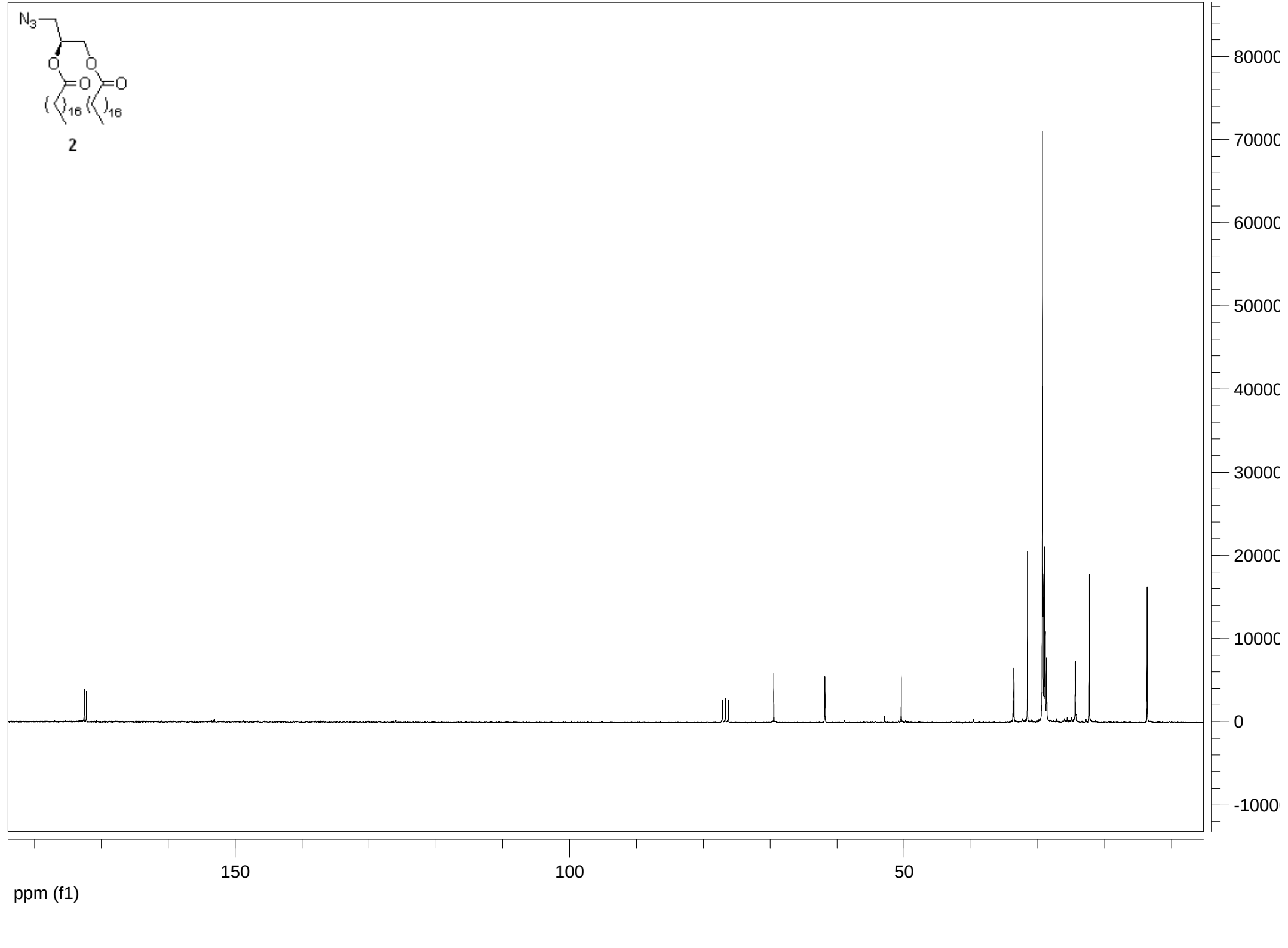
N3
O
O
O
O
16
16
2
80000
70000
60000
50000
40000
30000
20000
10000
0
-1000
150
100
50
ppm (f1)

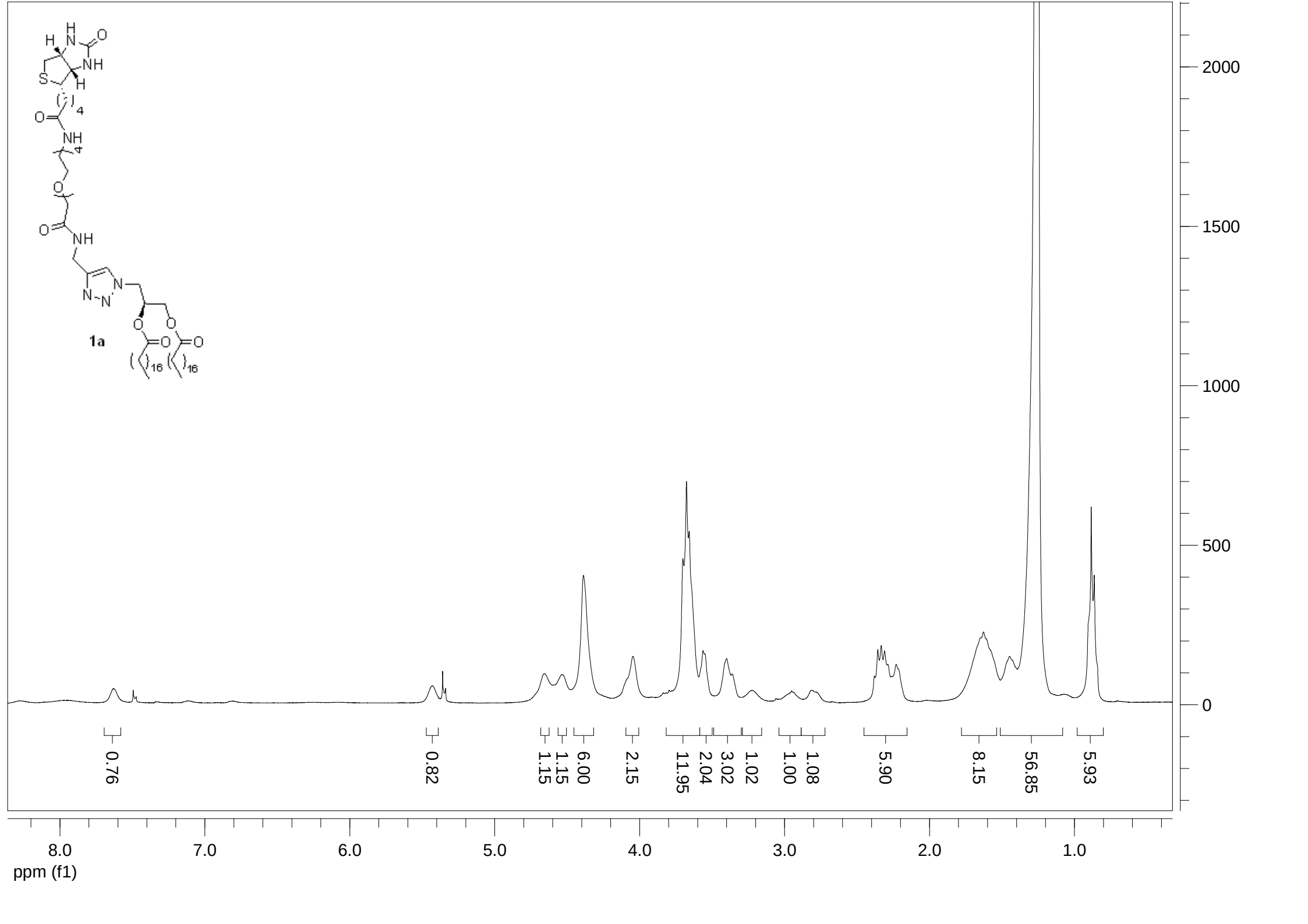
1a
0.76
0.82
1.15
1.15
6.00
2.15
11.95
2.04
3.02
1.02
1.00
1.08
5.90
8.15
56.85
5.93
2000
1500
1000
500
0
8.0
7.0
6.0
5.0
4.0
3.0
2.0
1.0
ppm (f1)

Dynamic light scattering characterization of 200 nm functional liposomes.

Sample ID	EAL_62608_1all
Operator ID	Thomas
Elapsed Time	00:01:07
Mean Diam.	245.6 (nm)
Rel. Var.	0.018
Skew	1.832
RmsError	1.8036e-03

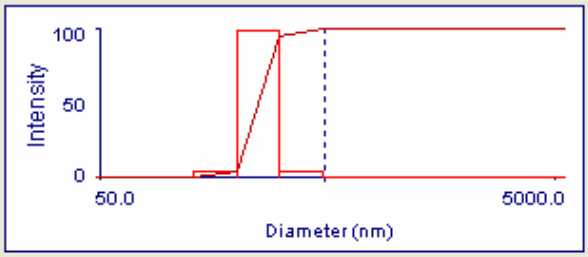

d	G(d)	C(d)	d	G(d)	C(d)	d	G(d)	C(d)
5.00	0	0	577.39	0	100			
7.70	0	0	889.14	0	100			
11.86	0	0	1369.21	0	100			
18.26	0	0	2108.48	0	100			
28.12	0	0	3246.91	0	100			
43.30	0	0	5000.00	0	100			
66.68	0	0						
102.68	0	0						
158.11	5	5						
243.48	100	95						
374.95	5	100						

Print Window

Copy For Spreadsheet

Copy to Clipboard

Close

Transglutaminase-Mediated PEGylation of Proteins: Direct Identification of the Sites of Protein Modification by Mass Spectrometry using a Novel Monodisperse PEG

Anna Mero,[†,§] Barbara Spolaore,[†,‡] Francesco M. Veronese,*[,§] and Angelo Fontana*[,‡]

CRIBI Biotechnology Centre, University of Padua, Viale G. Colombo 3, 35121 Padua, Italy, and Department of Pharmaceutical Sciences, University of Padua, Via F. Marzolo 5, 35131 Padua, Italy. Received October 6, 2008; Revised Manuscript Received December 30, 2008

Poly(ethylene glycol) (PEG) has been widely used to prolong the residence time of proteins in blood and to decrease their immunogenicity and antigenicity. A drawback of this polymer lies in its polydispersity that makes difficult the identification of the sites of protein modification. This is a mandatory requirement if a PEGylated protein should be approved as a drug. Here, a fast and reliable method is proposed to characterize proteins conjugated at the level of glutamine (Gln) residues using microbial transglutaminase (TGase). The novelty resides in the use of a monodisperse Boc-PEG-NH_2 for the derivatization that allows the direct identification of the sites of PEGylation by electrospray ionization mass spectrometry (ESI-MS). The procedure has been tested on three model proteins, namely, human granulocyte colony-stimulating factor, human growth hormone, and horse heart apomyoglobin. The Gln residues linked to the polymer chain were easily identified by ESI-MS and tandem MS analyses, demonstrating the advantage of using a monodisperse polymer in combination with mass spectrometry for an easy characterization of conjugated proteins. Interestingly, the PEGylation reaction led to the production only of mono- and bis-derivative products, indicating that the TGase-mediated PEGylation can be extremely selective and thus very useful for the derivatization of protein drugs.

INTRODUCTION

Recombinant proteins are nowadays assuming a relevant role for human therapy in a variety of diseases. However, protein drugs suffer from several limitations, including susceptibility to degradation by proteases, rapid kidney clearance, and propensity to generate immunogenic reactions. To date, the covalent attachment of poly(ethylene glycol) (PEG[1]) on the surface of proteins represents the most promising approach to improve their therapeutic efficacy, thus making them more stable to proteolytic digestion, non-immunogenic, non-aggregating, and with a longer half-life than native proteins (*1*−*3*). The most widely used chemical methods of PEGylation of proteins involve the covalent conjugation of PEG at the level of the ε-amino group of lysine residues by using acylating PEG derivatives. A drawback of these procedures resides in multiple sites of conjugation and thus in the substantial heterogeneity of the PEGylated proteins. In order to obtain site-specific PEGylation, other chemical approaches were developed, such as the selective PEGylation at the level of the thiol group of cysteine residues or at the N-terminal amino group of a polypeptide chain (*2, 4*). More recently, a very promising enzymatic method has been proposed that makes use of transglutaminase (TGase) for the covalent attachment of PEG moieties at the γ-carboxamide group of Gln residues of proteins (*5, 6*). For this purpose, a PEG derivative bearing an amino group is being used (PEG-NH_2).

The development of PEGylated biotech drugs involves the stringent need of a very detailed chemical characterization of the PEGylated proteins, as well as of the raw PEG material used for peptide and protein conjugation. Proper characterization of PEG requires determination of the end group structure, the mass of the repeating unit, and the average molecular weight (MW), as well as the MW distribution. These analyses are made rather difficult because of the polydispersity of the PEG polymer samples. Mass spectrometry (MS) has played an important role in the characterization of polymers and of polypeptide polymer conjugates. In particular, matrix-assisted laser-desorption ionization (MALDI) MS has been often employed, since this MS technique produces ions carrying few charges and thus generates mass spectra of lower complexity (*7*−*9*). Nevertheless, the MALDI technique suffers from poor ionization efficiency when applied to large synthetic polymers or PEGylated proteins. Consequently, accurate average MW can be obtained only for relatively small polymers (*10*). On the other hand, electrospray ionization mass spectrometry (ESI-MS) has a strong tendency to form multiply charged ions of PEGylated proteins, thus hampering the analysis of polymers with molecular masses above a few kilodaltons (*11, 12*).

It should be emphasized that the complete chemical characterization of PEGylated protein drugs also requires the identification of the sites of conjugation. Several analytical methods based on classical protein chemistry methodologies have so far been developed, but they are generally quite time- and protein sample-consuming. Among these methods, the peptide mapping procedure is based on the identification of peptide(s) missing in the digest of the PEGylated protein with respect to that of

* Address correspondence to angelo.fontana@unipd.it and francesco.veronese@unipd.it.

† These authors contributed equally to this work.

§ Department of Pharmaceutical Sciences.

‡ CRIBI Biotechnology Centre.

[1]Abbreviations: GCSF, human granulocyte colony stimulating factor; hGH, human growth hormone; apoMb, apomyoglobin; TGase, transglutaminase; PEG, poly(ethylene glycol); E/S, enzyme to substrate ratio; ESI-MS, electrospray-ionization mass spectrometry; MS/MS, tandem mass spectrometry; HPLC, high-performance liquid chromatography; RP, reverse-phase; TFA, trifluoroacetic acid; Tris, tris(hydroxymethyl)aminomethane; Boc, *tert*-butyloxycarbonyl; MALDI, matrix-assisted laser-desorption ionization.

10.1021/bc800427n CCC: $40.75 © 2009 American Chemical Society
Published on Web 02/02/2009

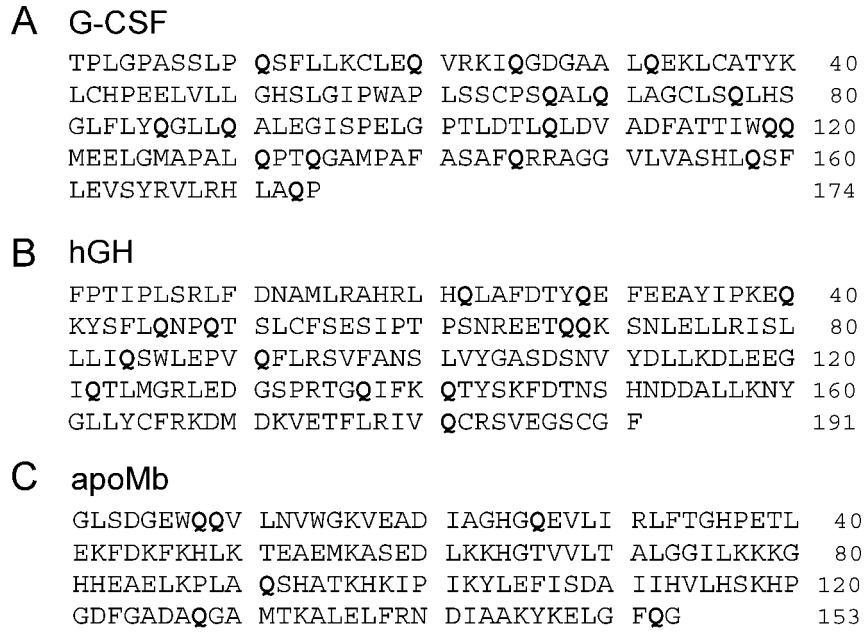

Figure 1. Amino acid sequence of human granulocyte colony stimulating factor (GCSF) (A), human growth hormone (hGH) (B), and apomyoglobin (apoMb) (C). The Gln residues potential sites of TGase PEGylation are shown in bold.

the nonmodified protein. Missing peptides are supposed to be those carrying the site of polymer conjugation. Therefore, this method is based on negative information, but it should be noted that a missing peptide may arise also from partial enzymatic hydrolysis of the protein. Moreover, confident identification of the derivatized amino acid residue(s) can be obtained only by the Edman N-terminal sequencing analysis of the purified modified peptide, which is not easy to obtain (*13*). As an alternative, mass spectrometry (MS) appears to be the most suitable technique for the identification of the sites of modification in PEGylated proteins, but until now its use has been limited by the polymer polydispersity (see above). To overcome this problem, our group has previously proposed the derivatization of proteins with a BrCN-cleavable PEG derivative. In this case, the PEGylated protein is reacted with BrCN in order to remove the polymer, while a reporter group of low molecular mass remains linked to the protein chain, thus allowing the identification of the modified amino acid residue(s) by ESI-MS (*14*).

In this paper, a method is described that exploits the sensitivity of MS analyses for the identification of the modified Gln residues in PEGylated proteins prepared using TGase. The novelty resides in the conjugation of proteins with a monodisperse Boc-PEG-NH_2, whose mass can be determined with good accuracy by ESI-MS. With respect to other procedures, in the same MS analysis and with the use of a small amount of digested protein, it is possible to identify the modified peptide and to determine the derivatized amino acid residue by MS/MS analysis. This method has been validated on three model proteins, granulocyte colony stimulating factor (GCSF) and human growth hormone (hGH) (Figure 1A,B), which represent two important pharmaceutical proteins, and apomyoglobin (apoMb), which is a most used model for studies of protein structure, folding, and stability (Figure 1C). The results of this study highlight the advantages of analyzing by MS proteins that are modified with monodisperse polymers. Moreover, it is shown that the use of TGase for the PEGylation of GCSF, hGH, and apoMb yielded only mono- and bis-derivatized products, thus emphasizing the usefulness of the TGase-mediated conjugation for the production of homogeneously modified proteins.

EXPERIMENTAL PROCEDURES

Materials. TGase from *Streptomyces mobaraensis* was purchased from Ajinomoto Co. (Tokyo, Japan), whereas V8-protease from *Staphylococcus aureus* and trypsin were from Sigma Aldrich (St. Louis, MO). GCSF and hGH were supplied by Bioker SpA (Cagliari, Italy). Boc-PEG-NH_2 (556.36 Da) was purchased from LCC Engineering GmbH (Egerkingen, Switzerland) and PEG-NH_2 (5 kDa and 20 kDa) from Shearwater Polymers Inc. (Huntsville, AL). All other chemicals where purchased from Sigma. Apomyoglobin (apoMb) was obtained from horse heart holomyoglobin by removal of heme using the acetone extraction procedure (*15*).

TGase-Mediated PEGylation of Proteins. Boc-PEG-NH_2, previously dissolved in a small amount of acetonitrile, was added at a 10-fold molar excess to solutions containing GCSF or hGH (1.5 mg/mL) in 10 mM phosphate buffer, pH 7.0. TGase was then added at an enzyme to substrate ratio (E/S) of 1:75 (by weight). The reaction mixtures were incubated at room temperature for 4 h and the product(s) purified by RP-HPLC using a Zorbax C18 column (4.6 × 250 mm; Agilent Technologies, Palo Alto, CA) with a linear gradient of 50−70% acetonitrile containing 0.05% TFA over a 25 min period, followed by an isocratic wash at 80% acetonitrile containing 0.05% TFA. The effluent from the column was monitored by measuring the absorbance at 226 nm. The PEGylated proteins of the chromatographic peaks were collected, lyophilized, and used for a peptide fingerprinting analysis by mass spectrometry.

In the case of apoMb, under the experimental conditions given above, a high yield of cross-linked dimer was obtained. Better results were obtained using a protein concentration of 0.7 mg/mL, a large excess of Boc-PEG-NH_2 (100 equiv), and TGase at an E/S ratio of 1:50 (by weight). The reaction was allowed to proceed at room temperature for 3 h and then analyzed by RP-HPLC on a Jupiter C18 column (4.6 × 150 mm; Phenomenex, Torrance, CA), eluted with a gradient of acetonitrile/0.085% TFA versus water/0.1% TFA from 5% to 40% in 5 min and from 40% to 50% in 25 min. The effluent from the column was analyzed as above.

Proteolytic Digestion of PEGylated Proteins. Native and PEGylated proteins (200 μg) were dissolved in 6 M Gdn-HCl, 50 mM Tris-HCl, pH 9.0, to reach a protein concentration of about 1 mg/mL. In order to reduce disulfide bridges, tris(2-carboxyethyl)phosphine was added to the protein solution at a final concentration of 5 mM and the reaction mixture kept for 1 h at 37 °C. The reduced protein was then reacted with 25 mM iodoacetamide, and the S-alkylation was allowed to proceed for 30 min at 37 °C in the dark. Protein samples were purified by RP-HPLC on a Zorbax C18 column as reported above.

The reduced and S-carboxamidomethylated samples of GCSF and PEG-GCSF were dissolved in 8 M urea and diluted in 50 mM phosphate buffer, pH 7.9, to reach a final protein concentration of 0.8 mg/mL and a urea concentration of 0.8 M. An aliquot from a stock solution of V8-protease in 50 mM acetic acid was then added at an E/S ratio of 1:50 (by weight), and the proteolysis was allowed to proceed at 37 °C overnight. The digestion mixtures, desalted by PepClean C-18 spin columns (Pierce, Rockford, IL), were directly analyzed by mass spectrometry. For hGH and its PEGylated samples, the same procedures were employed, but trypsin was used for protein digestion.

In the case of apoMb, the protein and its PEGylated derivative were purified by RP-HPLC, lyophilized, and digested with trypsin overnight at 37 °C in 0.1 M ammonium carbonate buffer, pH 7.8, using an E/S of 1:100 (by weight). Since apoMb does not contain cysteine residues, the steps of reduction and S-alkylation were omitted.

Mass Spectrometry Analyses. MALDI mass spectrometry measurements were performed on a REFLEX time-of-flight instrument (Bruker-Franzen Analytik, Bremen, Germany) equipped with a SCOUT ion source operating in positive linear mode. Ions generated by a pulsed UV laser beam (nitrogen laser, λ 337 nm) were accelerated to 25 kV. A saturated solution of sinapinic acid in acetonitrile/water (1:1, v/v) was used as matrix and mixed with the samples dissolved in 0.1% TFA aqueous solution at a v/v ratio of 1:1.

Electrospray mass spectrometry (ESI-MS) and tandem MS (MS/MS) measurements were performed on a Q-TOF Micro mass spectrometer (Waters, Milford, MA) equipped with a Z-spray nanoflow electrospray ionization interface. Mass spectra of the peptide digests of proteins and PEG derivatives were acquired using the nanoelectrospray source operating at capillary, cone, and extractor voltages of 2000, 30, and 1 V, respectively (positive ion mode). PEGylated derivatives purified by RP-HPLC were lyophilized, redissolved in acetonitrile/water (1:1, v/v) containing 0.1% formic acid, and then analyzed by ESI-MS. MS/MS analyses were performed only for the peptide 124−162 of GCSF and its PEG derivative utilizing the same parameters of the MS instrument as above, using argon as the collision gas and a collision energy setting of 40 V. External calibration was performed using a solution of 0.1% (v/v) phosphoric acid in 50% aqueous acetonitrile. Nanoelectrospray ionization capillaries were prepared in-house. Instrument control, data acquisition, and processing were achieved with the *Masslynx* software (Waters).

RESULTS AND DISCUSSION

TGase-Mediated PEGylation of Proteins. Figure 2 shows the mass spectra of a polydisperse 5 kDa PEG and a monodisperse PEG as Boc-PEG-NH_2. While the polydispersity of the usually employed PEG prevents analysis by ESI mass spectrometry, the recently available monodisperse one (556.36 Da) offers characteristics that make it suitable for analyzing PEGylated proteins by ESI-MS and MS/MS. This possibility was verified using two proteins of pharmaceutical interest, namely, GCSF and hGH, and a model protein as apoMb. As given by their amino acid sequences (see Figure 1), these proteins contain several Gln residues as potential sites of TGase-catalyzed conjugation.

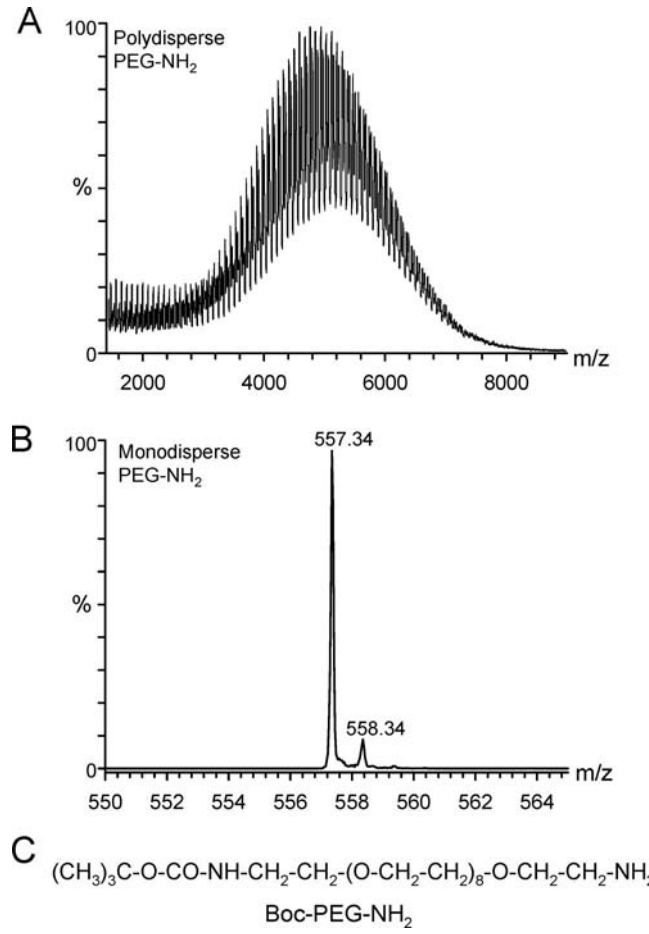

Figure 2. Analysis by mass spectrometry of polydisperse (5 kDa) and monodisperse (556.36 Da) PEG. (A) The MALDI mass spectrum of polydisperse PEG. (B) ESI-TOF mass spectrum of monodisperse PEG. (C) Chemical structure of monodisperse PEG used in this study. The derivative contains the *tert*-butoxycarbonyl (Boc) moiety as N-protecting group.

RP-HPLC analysis of the reaction mixture of GCSF with monodisperse PEG (Figure 3A) shows the complete PEGylation of the protein. The reaction product separated by RP-HPLC was analyzed by ESI-TOF mass spectrometry and a mass of 19207.2 Da was measured, which corresponds to GCSF conjugated to only one chain of PEG (Table 1). On the other hand, the RP-HPLC analysis of the TGase-mediated PEGylation of hGH showed four chromatographic peaks (Figure 3B). When analyzed by ESI-TOF mass spectrometry, these products gave masses corresponding to hGH conjugated to one or two chains of PEG (peaks 1 and 2, respectively), while the protein material of peak 3 corresponded to a mixture of hGH dimer and of hGH covalently bound to mono-PEGylated hGH; the protein material of peak 4 was a dimer of mono-PEGylated hGH (see Table 1 and Figure 3B).

PEGylated apoMb gave a mass of 17491.28 Da corresponding to a mono-PEGylated apoMb (Figure 3C). Of interest, we have observed that, by conducting the TGase-mediated reaction under identical experimental conditions and using a high molecular weight PEG (20 kDa), the same degree of protein modification was achieved with GCSF, hGH, and apoMb (data not shown).

Identification of the Sites of PEGylation by ESI-MS. In order to determine the sites of conjugation by TGase, the cysteine residues of PEG-GCSF and of native GCSF were

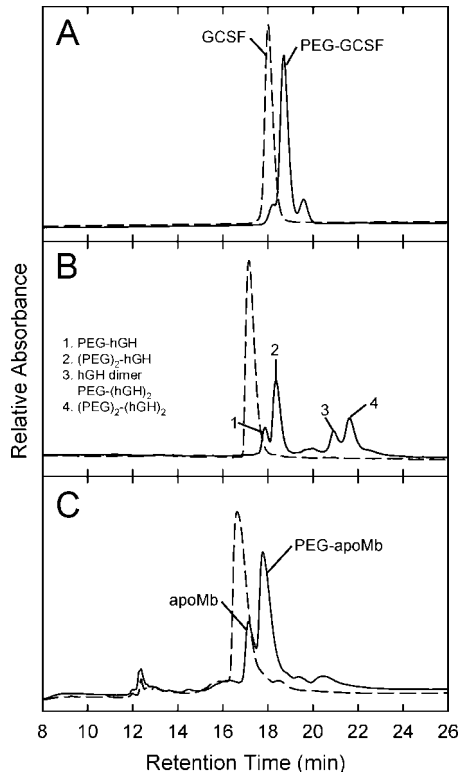

Figure 3. RP-HPLC analyses of GCSF (A), hGH (B), apoMb (C), and of the reaction mixtures of the PEGylated derivatives. A dashed line and a straight line indicate the chromatograms of native and conjugated proteins, respectively.

Table 1. Molecular Masses of Native Proteins, PEG-NH_2, and PEGylated Proteins

	molecular mass (Da)	
	calculated[a]	found[b]
Boc-PEG-NH_2	556.36	556.4
GCSF	18667.68	18666.3
PEG-GCSF	19207.34	19207.2
hGH	22125.07	22124.7
PEG-hGH	22664.73	22665.9
$(PEG)_2$-hGH	23204.39	23203.5
hGH dimer	44216.08	44216.0
PEG-$(hGH)_2$	44755.74	44756.0
$(PEG)_2$-$(hGH)_2$	45295.40	45294.0
apoMb	16951.50	16951.51
PEG-apoMb	17491.16	17491.28

[a] Calculated molecular masses. [b] Experimental molecular masses determined by ESI-MS.

reduced and S-carboxamidomethylated, and the two proteins were then digested with V8-protease. This enzyme was used instead of trypsin, since it allowed us to obtain peptide fragments with a lower molecular mass. Indeed, proteolysis with trypsin of GCSF leads to a fragment of 11.3 kDa (residues 41−146), which is not suitable for MS/MS analysis for the identification of the site of modification. Analysis by ESI-MS of the digests of PEG-GCSF and of native GCSF obtained with V8-protease led to a sequence coverage for the protein of 95%, with 10 peptide fragments identified over the 12 expected. The only fragment that was not detected by MS and that contains one Gln residue corresponds to residues 28−33 (sequence GAALQE) (Figure 1). Interestingly, all identified fragments had the same molecular mass in the digests of both PEG-GCSF and native GCSF, except peptide 124−162. Indeed, this peptide fragment deriving from the digest of conjugated GCSF showed an increase in mass corresponding to the addition of one molecule of PEG, thus indicating that PEGylation occurred at the level of this region of the protein chain (Table 2). The derivatization of the peptide 124−162 appears to be quantitative, since in the MS spectrum of the digest of PEG-GCSF, the *m*/*z* signals corresponding to a nonconjugated fragment were not observed. This is evident from an analysis of the region of the spectrum between 1000 and 1200 *m*/*z*, which contains signals of the ion $[M + 4H]^{4+}$ of this peptide (Figure 4A). In the MS spectrum of GCSF, fragment 124−162 shows a signal at 1007.18 *m*/*z* (data not shown). This signal is absent in the spectrum of the digest of PEG-GCSF, where only the signal at 1142.00 *m*/*z* is observed, which corresponds to the ion with four charges of the modified fragment.

Table 2. Molecular Masses of the Fragments Obtained upon Digestion with V8-Protease of GCSF and PEG-GCSF and with Trypsin of hGH and PEG-hGH and of apoMb and PEG-apoMb[a]

	molecular mass (Da)	
fragment[b]	calculated[c]	found[d]
124−162 (GCSF)	4025.08	4024.69
124−162 (PEG-GCSF)	4564.41	4563.96
39−41 (hGH)	403.21	[e]
39−41 (PEG-hGH)	942.54	942.67
141−145 (hGH)	625.31	[e]
141−145 (PEG-hGH)	1164.64	1164.80
80−96 (apoMb)	1852.95	1853.01
80−96 (PEG-apoMb)	2392.28	2392.39
79−96 (apoMb)	1981.05	1981.10
79−96 (PEG-apoMb)	2520.38	2520.50

[a] Only the molecular masses of the fragments which contain the Gln residues derivatized with PEG are reported. [b] Peptides obtained by proteolysis of GCSF and PEG-GCSF with V8-protease and of hGH and PEG-hGH and apoMb and PEG-apoMb with trypsin. [c] Monoisotopic molecular masses calculated from the amino acid sequence of GCSF, hGH, and apoMb. [d] Experimental molecular masses determined by ESI-MS. [e] These very short and rather hydrophilic peptides were not detected, since likely they were lost in the desalting step of the sample digest (see Experimental Procedures).

Since the GCSF fragment 124−162 contains four Gln residues (see Figure 1), the ion $[M + 4H]^{4+}$ of the derivatized peptide was subjected to MS/MS analysis in order to determine which Gln residue was modified (Figure 4B). For comparison, the nonmodified peptide was also analyzed by MS/MS (data not shown). In the case of both derivatized and non-derivatized peptides, the analysis of the MS/MS spectra indicates that the most intense product ions of the series *b* and *y* are generated from the fourteen N-terminal residues of the fragment, a region that contains two of the four Gln residues. Nevertheless, it was possible to determine the site of specific modification. In the MS/MS spectrum of the PEGylated peptide, fragment ions that contain Gln145 and Gln158 (*y*25−28) and Gln131 (*b*8) have *m*/*z* values expected for the nonmodified peptide, indicating that these Gln residues are not conjugated. On the other hand, all product ions containing Gln134 (*y*35−29) show an increase in mass of 439.28 Da, corresponding to the addition of a Boc-PEG-NH_2 with the N-protecting group (Boc) removed. Indeed, this group is conjugated to PEG via an urethane moiety, which is easily cleaved off under the conditions of the MS/MS analysis. Overall, sequence analysis by MS/MS of the modified GCSF peptide 124−162 clearly demonstrated that the TGase-mediated PEGylation occurs at Gln134.

In the case of hGH, the reduced and S-carboxamidomethylated hGH and mono- and bis-PEGylated hGH conjugates were digested with trypsin. The digested samples were analyzed by ESI-MS, and most of the tryptic fragments were identified, resulting in a sequence coverage of 88%. The only peptide fragments that were not detected in the digests were fragments 17−19, 128−134, and 179−191, with the last fragment having one Gln residue. By comparing the mass spectra of the digests of hGH and of conjugated hGH, it was observed that only the

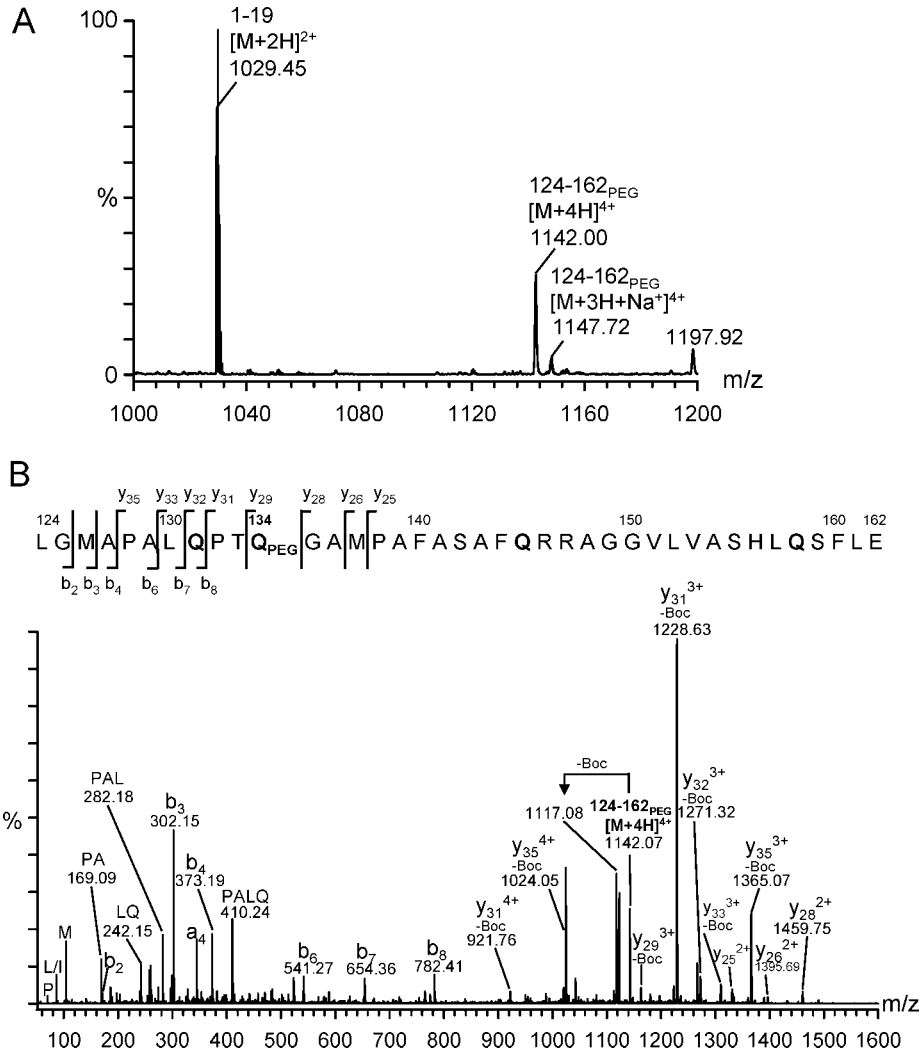

Figure 4. Electrospray mass spectrum of the digest of PEG-GCSF with V8-protease and MS/MS analysis of peptide 124−162. (A) The region of the mass spectrum between 1000 and 1200 *m*/*z* is reported in order to show the derivatization with PEG of peptide 124−162 of GCSF. The signals at 1142.00 *m*/*z* and at 1147.72 *m*/*z* of ions with four charges are indicated. (B) Electrospray MS/MS mass spectrum of the ion at 1142.00 *m*/*z* of peptide 124−162 of GCSF-PEG. (Top) Fragments of the series *b* and *y* that were identified in the MS/MS spectrum are indicated on the sequence of the peptide. Gln residues are shown in bold, and Gln134 is indicated in bold as Q_{PEG}. (Bottom) In the MS/MS spectrum, ions assigned to fragments of the series *y* and *b* are indicated. Some internal fragments and immonium ions are also labeled with their sequence in one-letter amino acid code. Fragments containing Gln134 show a mass increment corresponding to the conjugation with PEG-NH_2 without the Boc moiety, since the N-protecting group dissociates in the MS/MS analysis (-Boc).

spectrum of PEG-hGH displayed a signal at 472.34 *m*/*z*, corresponding to the triply charged ion of fragment 39−41 linked to one chain of PEG, and a signal at 583.41 *m*/*z*, corresponding to the ion with three charges of the mono-PEGylated fragment 141−145 (Figure 5A,B). Of interest, signals of the conjugated peptides without Boc were also detected in the mass spectrum, since the urethane bond, as reported above, is easily fragmented under the conditions of the ESI ionization. The detection by ESI-MS of Boc removal can be used as a further probe of the PEGylation of the peptide. Since fragments 39−41 and 141−145 contain only one Gln residue, it can be concluded that the TGase-mediated PEGylation of hGH took place at Gln40 and Gln141 in the bis-PEGylated form of the hormone, while the mono-PEGylated species was a mixture of the conjugates at Gln40 and Gln141.

In the case of apoMb, samples of native and PEGylated protein were subjected to trypsin digestion. All tryptic fragments were identified for both native apoMb and PEG-apoMb species with a sequence coverage of 98%. However, in the digest of PEG-apoMb, the tryptic fragments 80−96 and 79−96 gave only MS signals corresponding to their PEGylated species. Indeed, in the spectral region between 760−810 *m*/*z*, a signal can be observed at 794.48 *m*/*z*, which corresponds to the ion with three charges of fragment 80−96 modified with a single chain of PEG (Figure 5C). Since fragments 80−96 and 79−96 contain the single Gln91 residue, these data indicate that TGase catalyzes the conjugation of PEG at the level of Gln91 of apoMb.

CONCLUSION

The results here reported demonstrate that the use of a low molecular weight monodisperse PEG (Boc-PEG-NH_2) allows for an accurate identification of the sites of TGase-mediated PEGylation by ESI-MS and MS/MS analyses. The technique requires a small amount of protein and a limited number of analytical steps, at variance from the more laborious analyses so far employed in the characterization of proteins conjugated to high molecular weight polydisperse PEGs. A striking observation of this study is that the use of TGase in the enzymatic PEGylation yields to the specific modification of only few Gln residues, giving rise to mono- or bis-PEG derivatives. Even if GCSF, hGH, and apoMb contain 17, 11, and 6 Gln residues, respectively, just one Gln in GCSF and apoMb and two in hGH were selectively PEGylated. The reason for this selectivity resides in the fact that a flexible polypeptide substrate

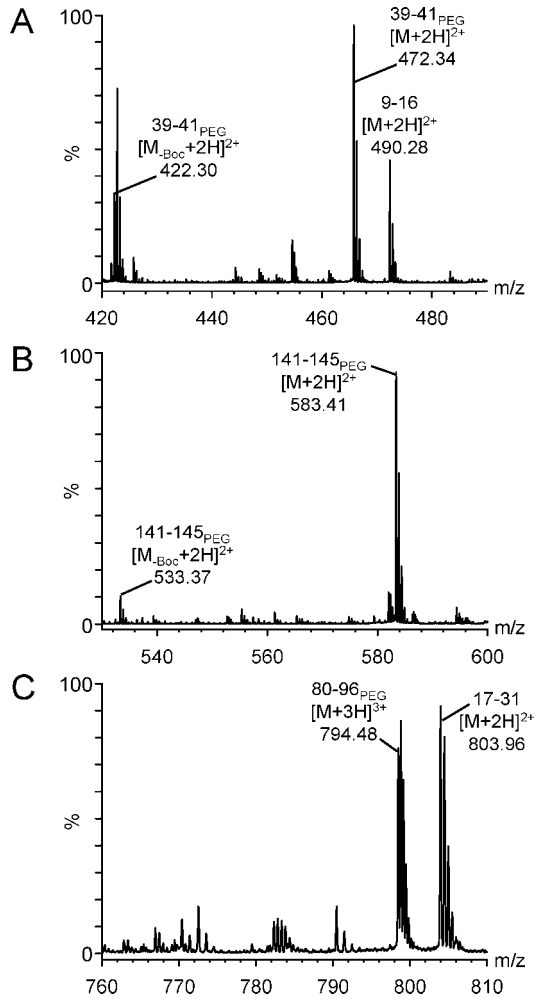

Figure 5. Electrospray mass spectra of the digests of PEG-hGH and PEG-apoMb with trypsin. (A,B) The regions between 420−500 *m*/*z* and 520−600 *m*/*z*, respectively, of the mass spectrum of the digest of PEG-hGH are shown. The signals of the modified peptides 39−41 and 141−145 are indicated. (C) The signals of PEGylated peptide 80−96 and of peptide 17−31 are indicated in the region 760−810 *m*/*z* of the mass spectrum of the digest of PEG-apoMb.

is required for a productive binding and adaptation at the active site of TGase. Indeed, the modified Gln residues of the three proteins herewith investigated are all located in disordered regions of the proteins (*16*). The method described here considers that the modification of proteins mediated by TGase with the low molecular weight PEG occurs at the same Gln residues as those derivatized with the high molecular weight polydisperse polymer. This assumption appears to be valid, since the TGase-modified Gln residues are dictated by the structure and dynamics of the protein substrate and not by features of the primary amines used as acyl acceptors (*16*). Indeed, the results of this study, based on monodisperse PEG, are in agreement with those of recent reports showing that GCSF is selectively PEGylated at the level of Gln134 (*17*) and hGH at Gln40 and Gln141 (*18*) by TGase and high molecular weight PEGs (20 kDa). Therefore, overall our results indicate that Boc-PEG-NH_2 can find a general application for the identification by ESI/MS and MS/MS of the site(s) of protein PEGylation mediated by TGase. Finally, the selectivity of the TGase-mediated reactions suggests a wider application of this enzyme for protein modification, besides PEGylation. While the TGase-mediated products can be homogeneous, a complex mixture of isomers is instead usually obtained by other chemical processes.

ACKNOWLEDGMENT

This research was supported in part by the Italian Ministry of University and Research (PRIN-2006 No. 03035 and FIRB-2003 No. RBNEOPX83). The authors are grateful to BioKer Srl (Pula, Italy) for a generous supply of protein samples of GCSF and hGH. The excellent technical assistance of Marcello Zambonin is also gratefully acknowledged.

LITERATURE CITED

(1) Delgado, C., Francis, G. E., and Fisher, D. (1992) The uses and properties of PEG-linked proteins. *Crit. Rev. Ther. Drug Carr. Sys. 9*, 249–304.

(2) Zalipsky, S. (1995) Chemistry of polyethylene glycol conjugates with biologically active molecules. *Adv. Drug Delivery. Rev. 16*, 157–182.

(3) Veronese, F. M., and Harris, J. M. (2002) Peptide and protein PEGylation I. *Adv. Drug Delivery. Rev. 54*, 453–606.

(4) Kinstler, O., Molineux, G., Treuheit, M., Ladd, D., and Gegg, C. (2002) Mono-N-terminal poly(ethylene glycol)-protein conjugates. *Adv. Drug. Delivery Rev. 54*, 477–485.

(5) Folk, J. E. (1983) Mechanism and basis for specificity of transglutaminase-catalysed ε-(γ-glutamyl)lysine bond formation. *Adv. Enzymol. Relat. Areas Mol. Biol. 54*, 1–56.

(6) Sato, H. (2002) Enzymatic procedure for site-specific PEGylation. *Adv. Drug Delivery. Rev. 54*, 487–504.

(7) Hanton, S. D. (2001) Mass spectrometry of polymers and polymer surfaces. *Chem. Rev. 101*, 527–570.

(8) Vestling, M. M., Murphy, C. M., Fenselau, C., Dedinas, J., Doleman, M. S., Harrsch, P. B., Kutny, R., Ladd, D. L., and Olsen, M. A. (1992) *Techniques in Protein Chemistry III*, pp 477−485, Academic Press, New York.

(9) Vestling, M. M., Murphy, C. M., Keller, D. A., Fenselau, C., Dedinas, J., Ladd, D. L., and Olsen, M. A. (1993) A strategy for characterization of polyethylene glycol-derivatized proteins: a mass spectrometric analysis of the attachment sites in polyethylene glycol-derivatized superoxide dismutase. *Drug Metab. Dispos. 21*, 911–917.

(10) Marie, A., Fournier, F., and Tabet, J. C. (2000) Characterization of synthetic polymers by MALDI-TOF/MS: investigation into new methods of sample target preparation and consequence on mass spectrum finger print. *Anal. Chem. 72*, 5106–5114.

(11) Fenn, J. B., Mann, M., Meng, C. K, Wong, S. F., and Whitehouse, C. M. (1989) Electrospray ionization for mass spectrometry of large biomolecules. *Science 246*, 64–71.

(12) Nohmi, T., and Fenn, J. B. (1992) Electrospray mass spectrometry of poly(ethy1ene glycols) with molecular weights up to five million. *J. Am. Chem. Soc. 114*, 3241–3246.

(13) Konigsberg, W. (1972) Subtractive Edman degradation. *Methods Enzymol. 25*, 326–332.

(14) Veronese, F. M., Saccà, B., Polverino de Laureto, P., Sergi, M., Caliceti, P., Schiavon, O., and Orsolini, P. (2001) New PEGs for peptide and protein modification, suitable for identification of the PEGylation site. *Bioconjugate Chem. 12*, 62–70.

(15) Ascoli, F., Fanelli, M. R., and Antonini, E. (1981) Preparation and properties of apohemoglobin and reconstituted hemoglobins. *Methods Enzymol. 76*, 72–87.

(16) Fontana, A., Spolaore, B., Mero, A., and Veronese, F. M. (2008) Site-specific modification and PEGylation of pharmaceutical proteins mediated by transglutaminase. *Adv. Drug Delivery Rev. 60*, 13–28.

(17) Tonon, G., and Orsini, G. (2001) G-CSF site-specific monoconjugates, Patent WO/2008/7017603.

(18) Dorwald, F., Johansen, N., and Iversen L. (2006) Transglutaminase-mediated conjugation of growth hormone, Patent WO/2006/134148, Int. Application No. PCT/EP2006/063246.

BC800427N

Development of Protein-Binding Bifunctional Linkers for a New Generation of Dual-Acting Prodrugs

Khalid Abu Ajaj,[†] Martin L. Biniossek,[‡] and Felix Kratz*,[†]

Tumor Biology Center, Breisacher Strasse 117, 79106 Freiburg, and Institute of Molecular Medicine and Cell Research, Zentrum für Biochemie and Molekulare Zellforschung, Stefan-Meier-Strasse 17, 79104 Freiburg, Germany. Received October 13, 2008; Revised Manuscript Received December 2, 2008

The aim of this work was to develop a new bifunctional maleimide linker for the development of dual-acting prodrugs that incorporate two pharmaceutically different anticancer agents independently bound by enzymatically cleavable substrates. The linker consists of a carboxyl group in one arm and an activated 1,6-self-immolative *para*-aminobenzyloxycarbonyl spacer together with a cathepsin B cleavable dipeptide Phe-Lys in the other. Aided with this linker, we have prepared a thiol-binding prodrug that contains the anticancer drugs doxorubicin and paclitaxel. Bound to the cysteine-34 position of albumin, it was cleaved efficiently by cathepsin B releasing the free drugs.

INTRODUCTION

Macromolecular prodrugs are being intensively studied, preclinically as well as clinically, in order to reduce the toxicity and improve the efficacy of anticancer agents. Modern drug antibody conjugates primarily use highly potent drugs, whereas drug conjugates with synthetic polymers or serum proteins use clinically established agents (*1, 2*). Both forms of drug conjugates couple one type of drug to the carrier (*3*).

For the development of novel prodrugs, it would be desirable to bind two different drugs to the carrier that ideally act additively or synergistically. Thus, we set out to develop such prodrugs, which we nicknamed "dual-acting prodrug" of the general formula shown in Figure 1. The dual-acting prodrug comprises two different pharmaceutically active compounds independently bound by cleavable linkers and a maleimide group as a thiol-binding moiety which is capable of binding to a carrier molecule with HS groups.

In this work, we present the first example of a dual-acting prodrug that incorporates the anticancer agents paclitaxel (*4*) and doxorubicin (*5*) that are useful drugs for treating a broad range of solid tumors. The combination of paclitaxel and doxorubicin is being intensively studied, preclinically as well as clinically. In vitro studies have shown additive (*6*) and synergistic (*7*) effects in human cancer cell lines. Recent clinical studies demonstrated that combination therapy with paclitaxel and doxorubicin was significantly better than single therapy for the treatment of patients with androgen-independent prostate cancer (*8*), advanced breast cancer (*9*−*11*), and endometrial cancer (*12*). Also, their chemical structures allow the design of prodrugs with enzymatically cleavable bonds through the amino group of doxorubicin (*5*) or the 2′-hydroxy group of paclitaxel (*13*). The target molecule with these two drugs is shown in Figure 1.

The prodrug incorporates a 1,6-self-immolative *para*-aminobenzyloxycarbonyl (PABC) spacer (*14*) between the drug and the lysosomally cleavable dipeptide Phe-Lys. This peptide is a substrate for cathepsin B, a cysteine protease that is overexpressed in solid tumors (*15*). The incorporation of a self-immolative spacer between the dipeptide and the drug ensures access to the site of cleavage by lysosomal enzymes such as cathepsin B (*16*). The self-immolative spacer hydrolytically decomposes upon deacylation, spontaneously releasing the free drug. This system has been used by Dubowchik et al. for the synthesis of monoclonal antibody conjugates with doxorubicin (*3, 16*). An additional advantage of the Phe-Lys-PABC spacer is the presence of the basic amino acid lysine that could render water solubility to the dual-acting prodrug.

Following the synthesis of such prodrugs, we wanted to ascertain whether cathepsin B can cleave the dual-acting prodrug once bound to a suitable synthetic polymer or protein carrier.

In our previous work, we have investigated a passive targeting approach in which maleimide-bearing prodrugs bind selectively to the cysteine-34 position of circulating albumin after intravenous administration. This macromolecular prodrug concept is based on two features: (i) rapid and selective binding of a maleimide functionalized prodrug to the cysteine-34 position of endogenous albumin after intravenous administration and (ii) release of the albumin-bound drugs predominantly at the tumor site due to the incorporation of an acid-sensitive or enzymatically cleavable bond between the drug and the carrier (*17*−*19*).

Albumin demonstrates preferential tumor uptake in various tumor animal models (*20*) due to the enhanced permeability and retention of macromolecules for solid tumors (*21*). In situ binding of maleimide-based prodrugs to the cysteine-34 position of circulating albumin is meanwhile a preclinically and clinically validated technology to increase the therapeutic index of anticancer agents. Besides the acid-sensitive prodrug of doxorubicin, the (6-maleimidocaproyl)hydrazone derivative of doxorubicin [INNO-206, previously DOXO-EMCH (EMC = 6-maleimidocaproic acid)] that has been studied clinically (*22*), a series of albumin-binding prodrugs with enzymatically cleavable substrates have been developed in the past five years (*15, 19, 23*−*27*).

In this work, we describe the synthesis of the maleimide bearing prodrug that incorporates both doxorubicin and pacli-

* To whom correspondence should be addressed: Dr. Felix Kratz, Head of Macromolecular Prodrugs, Tumor Biology Center, Breisacher Strasse 117, D-79106 Freiburg, Germany. Tel.: +49-761-2062930, Fax: +49-761-2062905, e-mail: felix@tumorbio.uni-freiburg.de.

[†] Tumor Biology Center.

[‡] Institute of Molecular Medicine and Cell Research.

10.1021/bc800429q CCC: $40.75 © 2009 American Chemical Society
Published on Web 01/20/2009

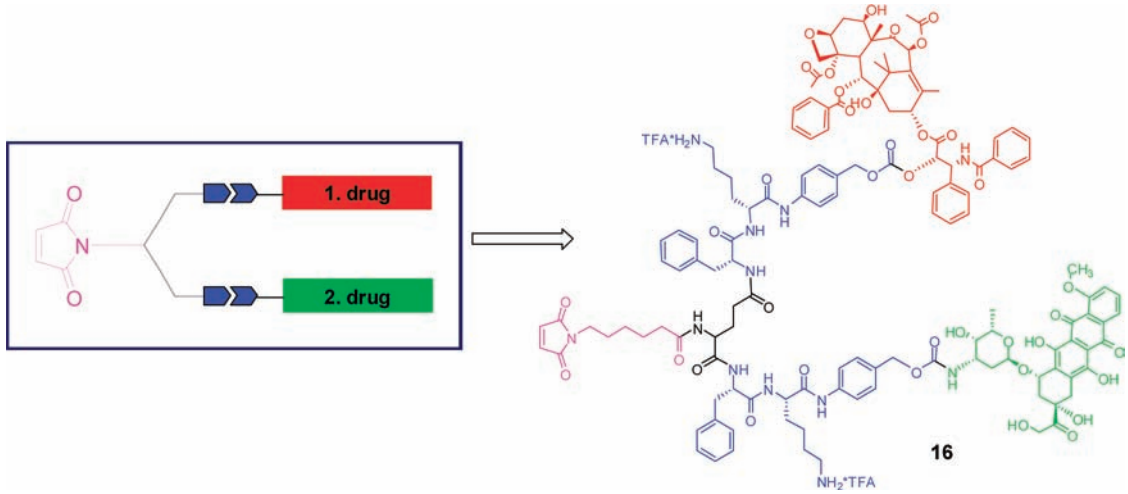

Figure 1. General structure of a dual-acting prodrug and the structure of the target compound **16**.

taxel and demonstrates cathepsin B mediated cleavage and release of doxorubicin and paclitaxel in its albumin-bound form.

EXPERIMENTAL PROCEDURES

General. Protected amino acids were purchased from Bachem and Novabiochem. Doxorubicin hydrochloride and paclitaxel were purchased from Yick-Vic Chemicals & Pharmaceuticals (HK) China. Dry solvents were Fluka Sure Seal grade. All other chemicals and solvents were purchased from Sigma-Aldrich, Fluka, Merck, and Roth and were used without further purification. Sodium sulfate was used as the drying agent for extractive workup. Human serum albumin (5% solution) was purchased from Octapharma GmbH (Langenfeld, FRG). The protein contained approximately 60% free thiol groups as assessed with the Ellmann's test. Enzymatically active cathepsin B was purchased from Calbiochem (Bad Soden, FRG). The buffers used were vacuum-filtered through a 0.2 μm membrane (Sartorius, Göttingen, FRG) and thoroughly degassed with ultrasound prior to use. Lyophilization was performed with a lyophilizer Alpha 2−4 (Christ, FRG). Centrifugation was carried out with a Tomy Capsule microcentrifuge model HF-120 (Peninsula Laboratories, Belmont, CA). The solvents were removed under reduced pressure at 30 °C.

Chromatography. Unless otherwise indicated, preparative flash chromatography (FC) was carried out using Merck grade 9385, 230−400 mesh silica gel. Analytical TLC was performed on Merck precoated plates using TLC silica gel 60F_{254} (normal phase), RP-18 F_{254S} (reversed phase), and diol F_{254S} (diol). Visualization of TLC plates was accomplished by one or several suitable detection methods; spots were identified by UV light absorption at λ = 254 and 366 nm, and/or by dipping into a solution of *p*-anisaldehyde (1 mL) and concentrated H_2SO_4 (4 mL) in ethanol (95 mL), and subsequent heating at 140 °C, and/or in a ninhydrin reagent and subsequent heating at 140 °C to color the TLC plates.

Unless otherwise indicated, analytical reversed-phase HPLC of synthetic compounds was carried out on a Kontron System using a solvent delivery system (HPLC Pump 422), a variable wavelength UV−vis detector (HPLC Detector 430) and a 25 cm nucleosil C-18 column (100−5, 250 × 4 mm, Macherey-Nagel). For peak integration, *Geminyx* software (v 1.91 by Goebel Instrumentelle Analytik, FRG) was used. HPLC conditions were as follows: flow rate, 1 mL/min; injection volume, 50 μL; gradient, 0−5 min 100% mobile phase A; 5−30 min increase to 100% mobile phase B; 30−45 min 100% mobile phase B; 45−55 min decrease to 100% mobile phase A; 55−60 min 100% mobile phase A.

System-1. mobile phase A: 80% H_2O, 20% acetonitrile, 0.05% TFA. mobile phase B: 20% H_2O, 80% acetonitrile, 0.05% TFA.

System-2. mobile phase A: 10 mM aqueous Na_2HPO_4 (pH 7)/acetonitrile 80:20. mobile phase B: 10 mM aqueous Na_2HPO_4 (pH 7)/acetonitrile 20:80.

System-3. mobile phase A: 10 mM aqueous Na_2HPO_4 (pH 7)/acetonitrile 80:20. mobile phase B: 10 mM aqueous Na_2HPO_4 (pH 7)/acetonitrile 40:60.

System-4. mobile phase A: 85% H_2O, 15% acetonitrile, 0.1% TFA containing heptane-1-sulfonic acid 2 g/L. mobile phase B: 20% H_2O, 80% acetonitrile, 0.1% TFA containing heptane-1-sulfonic acid 2 g/L.

Preparative reversed-phase HPLC for the separation of the prodrug **16** was performed with a BioLogic Duo-Flow System from Biorad (München, FRG), which was connected with a Lambda 1010 visible monitor from Bischoff (at λ = 495 nm); UV-detection at λ = 254 nm from Biorad; column, 25 cm Nucleosil C-18 column (100−7, 250 × 21 mm) with a precolumn (100−7, 50 × 21 mm) from Macherey-Nagel. Chromatographic conditions: flow rate, 10 mL/minute; injection volume, 5 mL; mobile phase A: 70% H_2O, 30% acetonitrile, 0.1% TFA; mobile phase B: 20% H_2O, 80% acetonitrile, 0.1% TFA.

Analytical reversed-phase HPLC for the synthesis of albumin conjugate **HSA-16** and its cleavage with cathepsin B was carried out on the previously described Kontron System with the following HPLC conditions: column, symmetry 300 (250 × 4.6 mm) from Waters; flow rate, 1 mL/min, λ = 495 and 220 nm; injection volume, 50 μL; gradient, 0−15 min 100% mobile phase A; 15−40 min increase to 100% mobile phase B; 40−45 min 100% mobile phase B; 45−50 min decrease to 100% mobile phase A; 50−60 min 100% mobile phase A; mobile phase A: 70% H_2O, 30% acetonitrile, 0.1% TFA; mobile phase B: 20% H_2O, 80% acetonitrile, 0.1% TFA.

Spectral Analyses. Electron spray ionization mass spectra (ESI-MS) were obtained on a Thermo Electron LCQ Advantage with associated MAT SS 200 data. Mass spectra of compounds **15** and **16** were acquired on a LTQ-FT spectrometer (ThermoFisher Scientific, Bremen, FRG) in the FT mode using electrospray ionization (ESI). Monoisotopic peaks were used for data analysis.

UV/vis-spectrophotometry was carried out with a double-beam spectrophotometer U-2000 from Hitachi. ^{1}H NMR and ^{13}C NMR spectra were run on a Varian Gemini 300 spectrometer at 300 and 75 MHz, respectively. Internal referencing was used, and chemical shifts are reported in parts per million (ppm).

Synthesis of the Bifunctional Maleimide Linker 2.

EMC-Glu(tBu)-OSu 2. A stirred solution of EMC (1 equiv, 121 mmol, 25.56 g) and HOSu (1.05 equiv, 127 mmol, 13.92 g) in dry DMF/THF, 1:6 (400 mL) at 0 °C, was treated with DCC (1.05 equiv, 127 mmol, 26.18 g). After 30 min, the mixture was allowed to warm to room temperature (RT) and was stirred for 20 h (TLC, diol, THF/hexane, 1:1). The solid byproduct was filtered off, washed with dry THF (100 mL), and the filtrate was added at room temperature to a suspension of H-Glu(OtBu)-OH (121 mmol, 24.5 g) and Et_3N (1 equiv, 121 mmol, 17.3 mL) in dry DMF (45 mL). The reaction solution was stirred for 22 h (TLC, $CHCl_3$/MeOH/AcOH, 10:1:0.2). The solvent was removed under reduced pressure, and the residue was purified by FC eluting with $CHCl_3$/MeOH/AcOH, 30:1:0.15. The solvent was removed, and the residue was subjected to another FC (diol, eluting with THF/hexane, 1:1) to remove acetic acid. **1** was obtained as a light yellow oil (29.6 g, 63%). $C_{19}H_{28}N_2O_7$, ESI-MS: calcd $[M + H]^+$ 397.19, found 396.80. HPLC analysis: (system-1; $\lambda = 254$ nm) > 95% of peak area. ^1H NMR ($CDCl_3$): $\delta = 1.30$ (multiplet, 2H), 1.40 (singlet, 9H, 3 × $(CH_3)_3C$), 1.60−1.70 (multiplet, 4H), 1.80−2.40 (multiplet, 6H), 3.50 (triplet, 2H, NCH_2,), 4.55 (triplet, 1H), 6.70 (singlet, 2H, COCHCHCO), 8.0 (singlet, 1H, NH), 9.90 (singlet, 1H, OH). ^{13}C NMR ($CDCl_3$): $\delta = 25.0$, 26.0, 27.0, 29.0, 32.0, 36.0, 39.0 (CH_2), 28.0 (3 × ($\underline{C}H_3)_3C$)), 52.0 ($\underline{C}H_2COOH$), 81.0 $(CH_3)_3\underline{C}$), 134.0 ($\underline{C}H\underline{C}H$), 171.0, 173.0, 174.0, 175.0 (CO). A stirred solution of **1** (12.6 mmol, 5.0 g) and HOSu (1.05 equiv, 13.23 mmol, 1.52 g) in dry THF (60 mL) at 0 °C was treated with DCC (1.05 equiv, 13.23 mmol, 2.73 g). After 20 min, the mixture was allowed to warm to room temperature and was stirred for 16 h (TLC, diol, THF/hexane, 1:1). The solid byproduct was filtered off, washed with dry THF, and the filtrate of **2** was used in the next step. An analytical sample was obtained by purification on FC (diol, eluting with THF/hexane, 1:1). ^1H NMR ($CDCl_3$): $\delta = 1.30$ (multiplet, 2H), 1.40 (singlet, 9H, 3 × $(CH_3)_3C$), 1.60−1.80 (multiplet, 4H), 2.10−2.30 (multiplet, 6H), 2.80 (singlet, 4H, $COCH_2CH_2CO$), 3.50 (triplet, 2H, NCH_2,), 4.90 (triplet, 1H), 6.70 (singlet, 2H, COCHCHCO), 8.0 (singlet, 1H, NH). ^{13}C NMR ($CDCl_3$): $\delta = 24.0$, 25.0, 26.0, 27.0, 29.0, 32.0, 35.0, 37.0 (CH_2), 28.0 (3 × ($\underline{C}H_3)_3C$), 50.0 ($\underline{C}H_2COOH$), 82.0 $(CH_3)_3\underline{C}$), 133.0 ($\underline{C}H\underline{C}H$), 167.0, 168.0, 171.0, 173.0, 174.0 (CO).

Synthesis of the Peptide Substrates.

Fmoc-Phe-Lys(Mtt) 4. A stirred solution of Fmoc-Phe-OH (95.0 mmol, 36.7 g) and HOSu (1.05 equiv, 99.6 mmol, 11.5 g) in dry THF (500 mL) was treated at 0 °C with DCC (1.05 equiv, 99.6 mmol, 20.5 g). After 15 min, the mixture was allowed to warm to room temperature and was stirred for 22 h (TLC-diol, $CHCl_3$/MeOH, 15:1). The solid byproduct was filtered off, washed with dry THF, and the filtrate of **3** was used in the next step without further purification. Fmoc-Lys(Mtt)-OH (80 mmol, 50 g) was dissolved in piperidine in DMF (20%, 100 mL) and stirred for 30 min (TLC, $CHCl_3$/MeOH, 10:1). The solution was added to diethyl ether (2.5 L) to precipitate H-Lys(Mtt)-OH as a white solid that was collected by suction filtration, washed well with ether, and dried in vacuo (31 g, 96%). A stirred suspension of H-Lys(Mtt)-OH (76.76 mmol, 30.9 g) and $NaHCO_3$ (1 equiv, 76.76 mmol, 6.44 g) in water (500 mL) and THF (200 mL) was treated with **3** (76.76 mmol in 500 mL dry THF). The mixture was stirred at room temperature for 22 h (TLC: $CHCl_3$/MeOH, 15:1), and then as much THF as possible was removed in vacuo at 30 °C. The resulting gummy suspension was partitioned between ethyl acetate and pH 5 buffer. The organic phase was washed with water and brine, dried, and concentrated in vacuo at 30 °C to approximately 200 mL, which was added to hexane (1 L). The white precipitate **4** was collected by suction filtration, washed well with ether, and dried in vacuo (55 g, 93%). $C_{50}H_{49}N_3O_5$, ESI-MS: calcd $[M + H]^+$ 772.37, found 772.70. HPLC analysis: (system-2; $\lambda = 254$ nm) > 88% of peak area.

Fmoc-Phe-Lys(Mtt)-PABOH 5. A solution of **4** (23.31 mmol, 18 g) and PABOH (1.2 equiv, 27.96 mmol, 3.45 g) in dry DCM (300 mL) was treated at room temperature with 2-ethoxy-1-ethoxycarbonyl-1,2-dihydroquinoline (EEDQ) (1.5 equiv, 34.95 mmol, 8.64 g) and was stirred for 20 h (TLC: $CHCl_3$/MeOH, 10:1). The solvent was then removed in vacuo at 30 °C. The solid residue was triturated with diethyl ether (600 mL), and the resulting suspension was sonicated for 20 min and left to stand at room temperature for 1 h. The resulting white solid **5** was collected by filtration, washed well with ether, and dried in vacuo (17.28 g, 85%). $C_{57}H_{56}N_4O_5$, ESI-MS: calcd $[M + Na]^+$ 899.43, found 899.40. HPLC analysis: (system-2; $\lambda = 254$ nm): > 91% of peak area.

H-Phe-Lys(Mtt)-PABOH 6. A solution of **5** (15.9 mmol, 14 g) in DCM (150 mL) at room temperature was treated with diethylamine (250 mL). The mixture was sonicated briefly and stirred at room temperature for 4 h, after which time no starting material was observed by TLC (DCM /MeOH, 10:1). The solvents were evaporated, and the residue was coevaporated twice with DCM and purified by FC eluting with DCM/MeOH 10:1 to give **6** as a white solid (8 g, 80%). $C_{42}H_{46}N_4O_3$, ESI-MS: calcd $[M + Na]^+$ 677.36, found 677.40. HPLC analysis: (system-2; $\lambda = 254$ nm) > 92%.

Fmoc-Phe-Lys(Mtt)-PABC-PNP 12. *N*,*N*-Diisopropylethylamine (DIPEA) (3 equiv, 3.42 mmol, 580 μL) was added to a solution of **5** (1 equiv, 1.14 mmol, 1.0 g) and bis-PNP carbonate (5 equiv, 5.7 mmol, 1.74 g) in dry DCM (60 mL). The reaction mixture was stirred at room temperature for 3 d (TLC: $CHCl_3$/MeOH, 10:1). The solvent was evaporated at 30 °C, and the residue was dissolved in ethyl acetate (100 mL) and extracted with pH 5 acetate buffer (2 × 20 mL). The organic phase was washed with water, brine, dried, and the solvent was evaporated at 30 °C. The oily residue was purified by FC eluting with $CHCl_3$/MeOH 15:1 to give **12** as a white solid (1.03 g, 87%). $C_{64}H_{59}N_5O_9$, ESI-MS: calcd $[M + H]^+$ 1042.43, found 1042.20; and calcd $[M + Na]^+$ 1064.43, found 1064.50. HPLC analysis: (system-1; $\lambda = 254$ nm) > 97% of peak area.

Synthesis of the Self-Immolative PABC Linker 10.

EMC-Glu-Phe-Lys(Mtt)-PABC-PNP 10. Et_3N (1.1 equiv, 11 mmol, 1.63 mL) was added at room temperature to a solution of **6** (1 equiv, 10 mmol, 7.0 g) and **2** (1 equiv, 10 mmol) in dry THF (60 mL), and the solution was stirred for 18 h (TLC, $CHCl_3$/MeOH, 10:1). The solution was added slowly to water (1 L). The white precipitate was collected by suction filtration, dissolved in DCM (50 mL), and precipitated with ether (300 mL) and dried to give **7** (8.5 g, 77%). $C_{61}H_{72}N_6O_9$, ESI-MS: calcd $[M + H]^+$ 1033.54, found 1033.20. HPLC analysis: (system-2; $\lambda = 254$ nm) > 88% of peak area. Compound **7** (8.2 mmol, 8.4 g) was then dissolved in a mixture of DCM and TFA (1:1; 20 mL) and stirred at room temperature for 2 h (TLC: DCM/MeOH/H_2O/TFA, 85:15: 1:0.2). A yellow solid precipitated upon adding the solution to diethyl ether (2 L). **8** was collected as a TFA-salt by suction filtration, washed with ether, and dried to give 6.6 g (100%). $C_{37}H_{48}N_6O_9$, ESI-MS: calcd $[M + H]^+$ 721.35, found 721.40. A stirred suspension of **8** (4.3 mmol, 3.5 g) in dry DCM (120 mL) under nitrogen at room temperature was treated with trimethylsilyl chloride (3.1 equiv, 13.3 mmol, 1.73 mL) and DIPEA (1.05 equiv, 4.5 mmol, 805 μL). The mixture was heated at reflux for 1 h, during which time it became homogeneous and then cooled to 0 °C. DIPEA (3.1 equiv, 13.3 mmol, 2.4 mL) was added, followed by 4-methyltrityl chloride (1.05 equiv, 4.3 mmol, 1.40 g). The reaction was stirred at room temperature for 16 h (TLC, DCM/MeOH/H_2O/TFA, 85:15:1:0.2). It was stirred with methanol (10

mL) for 5 min. The solvent was evaporated at 30 °C, and the residue was partitioned between DCM and pH 5 acetate buffer. The organic phase was dried, and the solvent was concentrated under vacuo to 50 mL. Precipitation with hexane yielded **9** as a light yellow solid (4 g, 96%). $C_{57}H_{64}N_6O_9$, ESI-MS: calcd $[M + H]^+$ 977.47, found 977.20. A solution of **9** (3.3 mmol 3.8 g) and bis-PNP carbonate (1.2 equiv, 3.9 mmol, 1.18 g) in dry DCM (100 mL) was treated at room temperature with DIPEA (3 equiv, 9.9 mmol, 1.99 mL) and was stirred for 16 h (TLC, DCM/MeOH/H_2O/TFA, 85:15:1: 0.2). The solvent was then removed in vacuo at 30 °C. The solid residue was triturated with diethyl ether (200 mL), and the precipitate was purified by FC eluting with $CHCl_3$/MeOH 10:1 to give **10** as a white solid (2.0 g, 45%). $C_{64}H_{67}N_7O_{13}$, ESI-MS: calcd $[M + H]^+$ 1142.48, found 1141.80. HPLC analysis: (system-3; $\lambda = 254$ nm) > 94% of peak area.

Synthesis of the Building Unit 14.

H-Phe-Lys(Mtt)-PABC-Paclitaxel 14. DMAP (1 equiv, 0.29 mmol, 36.0 mg) was added to a solution of **12** (0.29 mmol, 300 mg) and paclitaxel (1 equiv, 0.29 mmol, 246 mg) in dry DCM (12 mL), and the solution was stirred at room temperature for 18 h (TLC: $CHCl_3$/MeOH 10:1). The solvent was removed under reduced pressure at 30 °C, and the residue was purified by FC eluting with $CHCl_3$/MeOH 20:1 to give **13** as a white solid (388 mg, 77%). $C_{105}H_{105}N_5O_{20}$, ESI-MS: calcd $[M + H]^+$ 1756.74, found 1756.70. DMAP (40 equiv, 6.83 mmol, 834 mg) was added to a solution of **13** (1 equiv, 0.17 mmol, 300 mg) in dry DCM (40 mL), and the solution was stirred at room temperature for 3 days (TLC: $CHCl_3$/MeOH 10:1). The solvent was removed under reduced pressure at 30 °C, and the residue was purified by FC eluting with $CHCl_3$/MeOH 20:1 to give **14** as a white solid (189 mg, 72%). $C_{90}H_{95}N_5O_{18}$, ESI-MS: calcd $[M + H]^+$ 1534.67, found 1534.50. HPLC analysis: (system-2; $\lambda = 254$ nm) > 75% of peak area.

Synthesis of the Prodrug 16. Triethylamine (1 equiv, 1.31 mmol, 182 μL) was added to a solution of **10** (1 equiv, 1.31 mmol, 1.50 g) and doxorubicin hydrochloride (1 equiv, 1.31 mmol, 0.761 g) in dry DMF (20 mL), and the solution was stirred at room temperature for 18 h (TLC: $CHCl_3$/MeOH 7:1). The product was precipitated with ether (1 L) and was purified by FC eluting with $CHCl_3$/MeOH 15:1 to give **11** as a red solid (1.52 g, 75%). $C_{85}H_{91}N_7O_{21}$, ESI-MS: calcd $[M + H]^+$ 1546.63, found 1546.00 $[M + H]^+$. HPLC analysis: (system-3; $\lambda = 220$ nm) > 90% of peak area. A solution of **11** (0.036 mmol, 55 mg), HATU (1.1 equiv, 0.039 mmol, 14.8 mg), HOBt (1 equiv, 0.036 mmol, 4.78 mg), DIPEA (2 equiv, 0.072 mmol, 11 μL), and **14** (1 equiv, 0.036 mmol, 70 mg) in dry DMF (800 μL) was stirred at room temperature for 4 h (TLC, $CHCl_3$/MeOH, 10:1). The product was precipitated with ether (100 mL) and was then purified by FC ($CHCl_3$/MeOH, 15:1) to give after solvent removal in vacuo at 30 °C **15** as a red solid (100 mg, 93%). $C_{175}H_{184}N_{12}O_{38}$, ESI-MS: calcd $[M + 2H]^{2+}$ 1531.65, found 1531.65. HPLC analysis: (system-4; $\lambda = 495$ nm, retention time 42.62 min) > 94% of peak area. A solution of **15** (82 mg) in DCM (5 mL) was treated with a solution of 1% TFA in DCM (5 mL) and was stirred at room temperature for 24 h (HPLC; system-4). The product was precipitated with ether (80 mL), centrifuged, and further washed with ether (40 mL) and centrifuged. The residue was dissolved in MeOH/mobile phase A (1:2, 5 mL) and purified by preparative C_{18}-RP-HPLC. After lyophilization, 30 mg (44%) of **16** was obtained as a red solid. $C_{135}H_{152}N_{12}O_{38}$, ESI-MS: calcd $[M + 2H]^{2+}$ 1275.52, found 1275.52. HPLC analysis: column, symmetry 300 from Waters; ($\lambda = 495$ nm; retention time 29.38 min) > 97% of peak area; ($\lambda = 254$ nm; retention time 29.99 min) > 90% of peak area. Mass spectrum is included as Supporting Information.

Synthesis of the Albumin Conjugate of 16 (HSA-16). A solution of **16** in DMF (500 μL, 6.32 mg/791 μL, 3 mM) was diluted in EtOH (2 mL) and incubated with human serum albumin [(HSA) 5% octalbin] (4.5 mL) under stirring at 37 °C for 1 h, after which no free **16** was detectable by HPLC.

The albumin conjugate was obtained after subsequent size-exclusion chromatography (Sephacryl S-100, 50 mM sodium acetate buffer - pH 5.0). The content of anthracycline in the sample was determined using the ε-value for doxorubicin [ε_{495} (pH 7.4) = 10 650 M^{-1} cm^{-1}]. The concentration of doxorubicin in the conjugate **HSA-16** was adjusted to 290 μM by concentrating the sample with CENTRIPREP-10-concentrators (Amicon, FRG) (4 °C and 4500 rpm) to 800 μL (HPLC analysis: $\lambda = 495$ nm; retention time: 25.16 min >99% of peak area). Samples were kept frozen at −80 °C and thawed prior to use.

Cleavage Studies with Cathepsin B. 300 μL of the **HSA-16** stock solution (100 μM with respect to doxorubicin) was mixed with 10 μL cathepsin B (0.4 μg/mL, 23.8 U/mg) and 30 μL of buffer (50 mM sodium acetate buffer, pH 5.0) containing L-cysteine (8 mM). The mixture was incubated at 37 °C, and aliquots were removed at various time points and analyzed by HPLC.

RESULTS AND DISCUSSION

Chemistry. The initial step in the development of our dual-acting prodrugs was the synthesis of a bifunctional maleimide linker **2** that allows the attachment of two enzymatically cleavable substrates for both active compounds. Its synthesis (Scheme 1) is based on the bifunctional compound **1** that incorporates a protein-binding maleimide group and a free as well as a protected carboxylic acid moiety. **1** was obtained from the reaction of *tert*-butyl ester glutamic acid with 6-maleimidocaproic acid in the presence of *N*-hydroxysuccinimide (HOSu) and *N,N′*-dicyclohexylcarbodiimide (DCC). Upon its reaction with HOSu and DCC in THF, **1** was converted into the HOSu-activated ester **2** for subsequent reaction with the free amino groups of a first peptide derivative.

In our route, we wanted to introduce a self-immolative Phe-Lys-PABC-spacer (PABC = *para*-aminobenzyloxycarbonyl) in the two arms of the maleimide derivative **1**. The synthesis of the cathepsin B sensitive peptides **6** was performed according to a modified procedure of the work of Dubowchik et al. (*16*) replacing the methoxytrityl (Mmt) group in the original work with methyltrityl (Mtt) group as the protecting group of the side chain amino group of lysine. Mtt can be removed at the required step in very mild acidic media, such as with 1−2% trifluoroacetic acid (TFA) in dichloromethane (DCM) (*28*) where doxorubicin should be stable.

A triethylamine (Et_3N) catalyzed coupling of the dipeptide moiety **6** to the bifunctional maleimide linker **2** yielded the branched bifunctional peptide **7** that contains a protein-binding maleimide group, a protected carboxylic group, as well as the *para*-aminobenzyl alcohol (PABOH) moiety for conjugating with the first drug (see Scheme 1).

Prior to this, for subsequent binding of the second drug moiety, the *tert*-butyl carboxylic group of **7** needs to be deprotected and the ε-amino group of lysine has to be protected again with the acid-labile Mtt group. Thus, treatment of **7** with 50% TFA in DCM yielded **8** quantitatively. Mtt was further introduced in a one-pot tritylation procedure through activation with trimethylsilyl (TMS) (*29*) of **8** in which both the amino and carboxyl groups are silylated first with TMS-Cl, followed by a base-catalyzed reaction with 4-methyltrityl chloride (Mtt-Cl) to give **9** in high yields. The self-immolative spacer of **9** was subsequently reacted with bis(*para*-nitrophenyl) carbonate (bis-PNP carbonate) to give the activated carbonate **10**.

Scheme 1. Synthesis of Prodrug 16

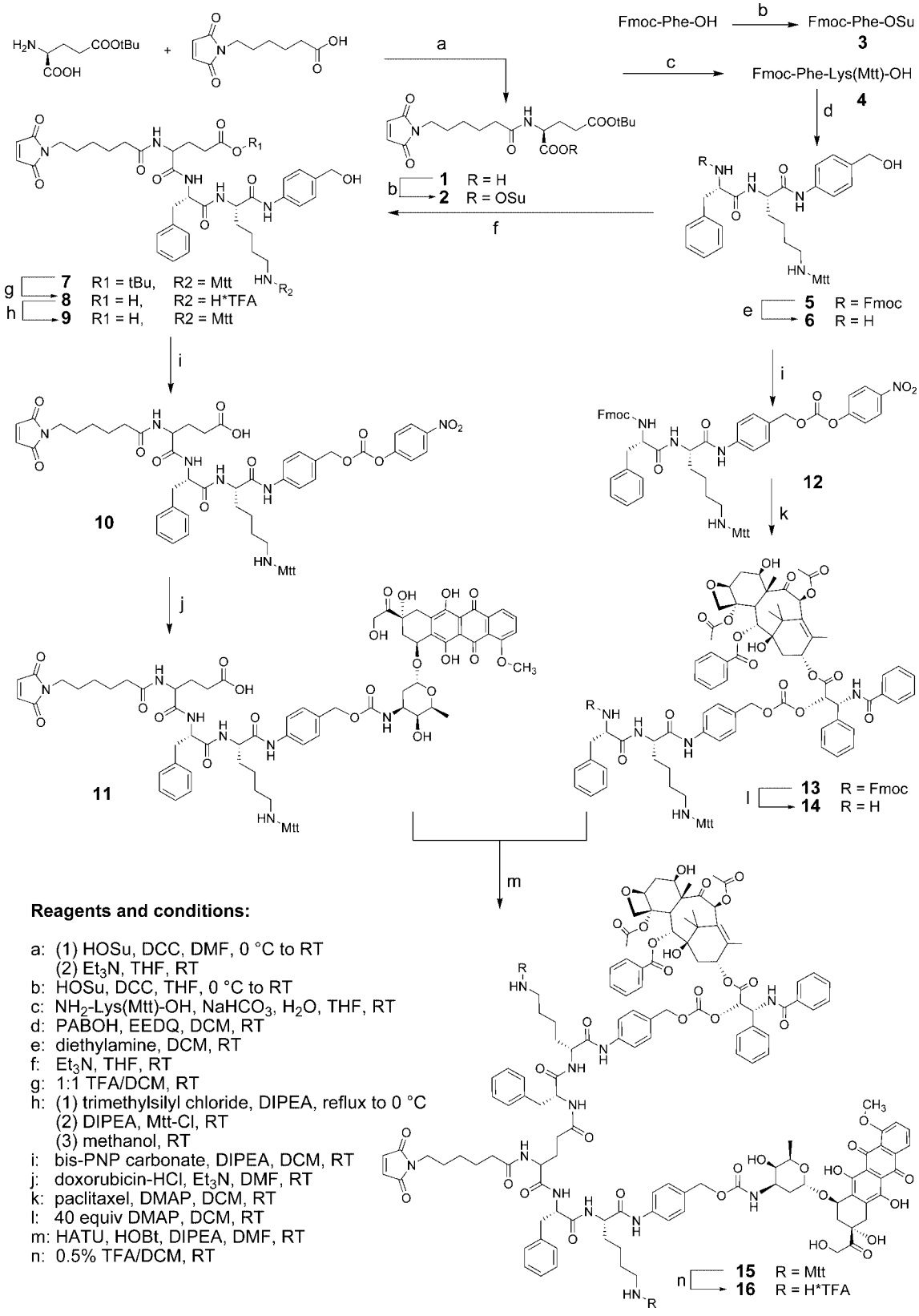

The bifunctional maleimide linker **10** represents a key building block that can be derivatized with a wide spectrum of anticancer drugs for the development of enzymatically cleavable dual-acting prodrugs. In addition to a protein-binding maleimide group, it incorporates two orthogonal functionalities for the introduction of the drugs: (i) the carbonate group for introducing the first active compound either as a carbonate or as a carbamate through its reaction with the hydroxyl or amino groups of the drug; (ii) a free carboxylic acidic group for binding the second active compound after step (i).

For preparing a doxorubicin−paclitaxel prodrug, we introduced doxorubicin in a first step by reacting the bifunctional linker **10** with doxorubicin in the presence of triethylamine, yielding **11**. To introduce paclitaxel in the prodrug, we

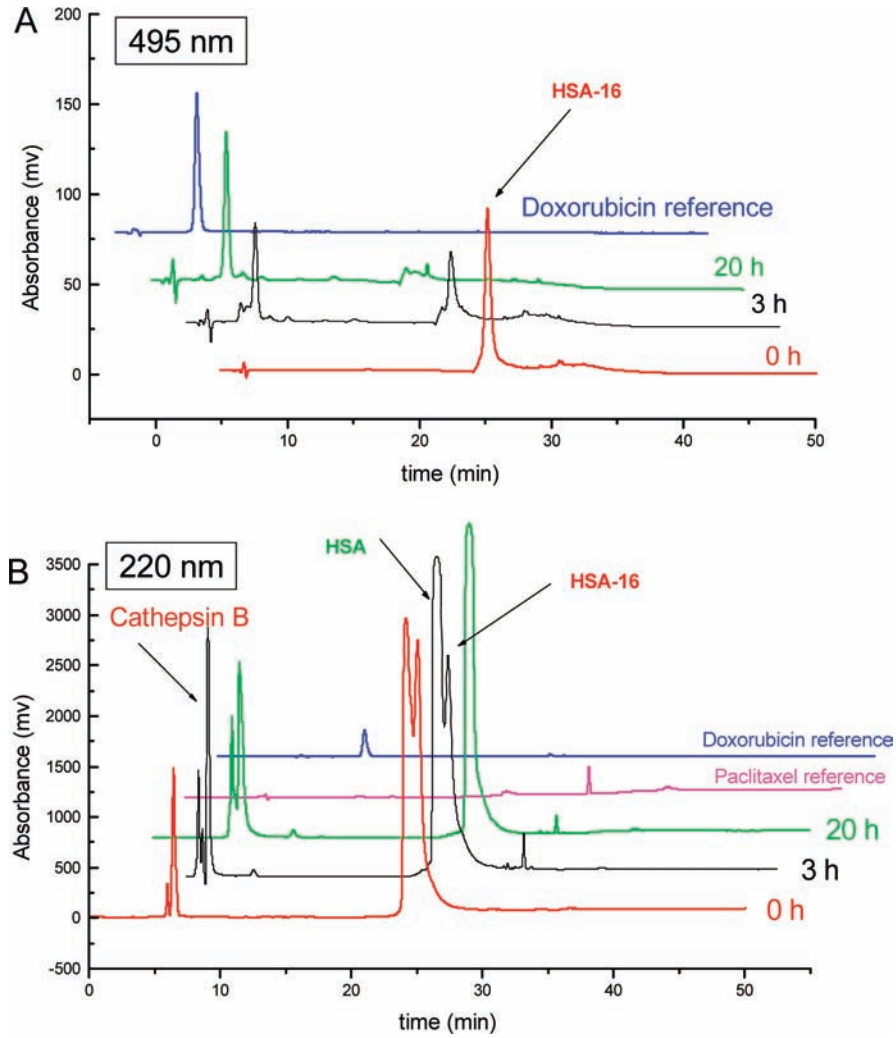

Figure 2. Chromatograms of incubation studies of **HSA-16** (100 μM) with activated cathepsin B (10 μL; 0.095 U) at 37 °C and detected at 495 nm (A) and 220 nm (B). Chromatograms of doxorubicin and paclitaxel (100 μM) are included as references.

synthesized the building block **14** in a 4-(dimethylamino)pyridine (DMAP) catalyzed reaction of paclitaxel and the activated carbonate **12** with subsequent cleavage of the Fmoc group. The desired prodrug in its protected form **15** was obtained from the reaction of **11** with **14** in the presence of *O*-(azabenzotriazol-1-yl)-*N*,*N*,*N*′,*N*′-tetramethyluronium hexafluorophosphate (HATU) and 1-hydroxybenzotriazole (HOBt).

In a final step, we attempted to remove the Mtt groups using the standard cleavage conditions (1% TFA in DCM) of the Mtt-protecting groups in **15**. However, under these conditions, doxorubicin was not stable, producing large amounts of aglycone. To overcome these problems, we optimized the cleavage conditions by dissolving **15** in DCM before it was treated with DCM containing 1% TFA. Cleavage of both groups was successfully performed with a final concentration of 0.5% TFA in DCM. The desired doxorubicin−paclitaxel prodrug **16** was then purified by preparative C_{18}-RP-HPLC chromatography and lyophilized to obtain a red product. The prodrug **16** was characterized by analytical HPLC and ESI-MS (see Supporting Information).

Cleavage Studies with the Albumin-Bound form of 16. Our second aim after the synthesis of the dual-acting prodrug **16** was to ascertain whether cathepsin B can cleave the dual-acting prodrug once bound to a protein carrier. Thus, prodrug **16** was bound through its maleimide moiety to the cysteine-34 group of human serum albumin (HSA) to give the albumin-bound prodrug **HSA-16**. The incubation of **HSA-16** with activated cathepsin B is monitored at two different wavelengths. Doxorubicin and **HSA-16** can be detected at 495 and 220 nm, whereas paclitaxel and cathepsin B can only be observed at 220 nm. The chromatographic profile at 220 nm showed two peaks: the first at 24.2 min corresponding to nonmercaptalbumin, and the second at 25.0 min that we assigned to **HSA-16**, considering that for the synthesis the employed octalbin (5%) contained ~60% free thiol groups (see Figure 2).

The cleavage properties of compound **HSA-16** were evaluated using enzymatically active cathepsin B at pH 5.0. Reverse phase HPLC showed that incubation with cathepsin B resulted in an efficient and almost complete cleavage over a period of 20 h (Figure 2). At 220 nm, the peak at 25.0 min that corresponds to **HSA-16** disappears after incubation with cathepsin B for 20 h. The main cleavage products were identified by HPLC to be the free anticancer agents doxorubicin (eluting at 10.8 min) and paclitaxel (eluting at 30.8 min).

In conclusion, for the development of dual-acting prodrugs we have synthesized for the first time a bifunctional maleimide linker which consists of a maleimide group, a carboxylic acid group, and an activated Phe-Lys(Mtt)-PABC linker **10**. Aided with this linker, we have prepared an albumin-binding prodrug containing the anticancer drugs doxorubicin and paclitaxel **16**. **16** binds rapidly and selectively to the cysteine-34 position of endogenous serum albumin and is cleaved specifically by cathepsin B releasing the free drugs.

We anticipate that such bifunctional linkers will pave the way for the development of a next generation of albumin-binding

prodrugs that contain two anticancer agents. The bifunctional linker **10** has proven to be fruitful in the synthesis of other prodrugs under development in our group (*30*).

Supporting Information Available: ESI-Mass spectrum of prodrug **16**. This material is available free of charge via the Internet at http://pubs.acs.org.

LITERATURE CITED

(1) Kratz, F., Abu Ajaj, K., and Warnecke, A. (2007) Anticancer carrier-linked prodrugs in clinical trials. *Expert Opin. Invest. Drugs 16*, 1037–1058.

(2) Kratz, F., Muller, I. A., Ryppa, C., and Warnecke, A. (2008) Prodrug strategies in anticancer chemotherapy. *ChemMedChem 3*, 20–53.

(3) King, H. D., Dubowchik, G. M., Mastalerz, H., Willner, D., Hofstead, S. J., Firestone, R. A., Lasch, S. J., and Trail, P. A. (2002) Monoclonal antibody conjugates of doxorubicin prepared with branched peptide linkers: inhibition of aggregation by methoxytriethyleneglycol chains. *J. Med. Chem. 45*, 4336–4343.

(4) Sugahara, S., Kajiki, M., Kuriyama, H., and Kobayashi, T. R. (2002) Paclitaxel delivery systems: the use of amino acid linkers in the conjugation of paclitaxel with carboxymethyldextran to create prodrugs. *Biol. Pharm. Bull. 25*, 632–641.

(5) Kratz, F., Warnecke, A., Schmid, B., Chung, D. E., and Gitzel, M. (2006) Prodrugs of anthracyclines in cancer chemotherapy. *Curr. Med. Chem. 13*, 763–771.

(6) Akutsu, M., Kano, Y., Tsunoda, S., Suzuki, K., Yazawa, Y., and Miura, Y. (1995) Schedule-dependent interaction between paclitaxel and doxorubicin in human cancer cell lines in vitro. *Eur. J. Cancer 31A*, 2341–2346.

(7) Koechli, O. R., Sevin, B. U., Perras, J. P., Chou, T. C., Angioli, R., Steren, A., Untch, M., and Averette, H. E. (1993) Characteristics of the combination paclitaxel plus doxorubicin in breast cancer cell lines analyzed with the ATP-cell viability assay. *Breast Cancer Res. Treat. 28*, 21–27.

(8) Amato, R. J., and Sarao, H. (2006) A phase I study of paclitaxel/ doxorubicin/ thalidomide in patients with androgen- independent prostate cancer. *Clin. Genitourin Cancer 4*, 281–286.

(9) Zielinski, C. C. (2003) Gemcitabine, anthracycline, and taxane combinations for advanced breast cancer. *Oncology (Williston Park) 17*, 36–40.

(10) Piccart-Gebhart, M. J., Burzykowski, T., Buyse, M., Sledge, G., Carmichael, J., Luck, H. J., Mackey, J. R., Nabholtz, J. M., Paridaens, R., Biganzoli, L., Jassem, J., Bontenbal, M., Bonneterre, J., Chan, S., Basaran, G. A., and Therasse, P. (2008) Taxanes alone or in combination with anthracyclines as first-line therapy of patients with metastatic breast cancer. *J. Clin. Oncol. 26*, 1980–1986.

(11) Passardi, A., Massa, I., Zoli, W., Gianni, L., Milandri, C., Zumaglini, F., Nanni, O., Maltoni, R., Frassineti, G. L., and Amadori, D. (2006) Phase II study of gemcitabine, doxorubicin and paclitaxel (GAT) as first-line chemotherapy for metastatic breast cancer: a translational research experience. *BMC Cancer 6*, 76.

(12) Shimada, M., Kigawa, J., Terakawa, N., Yoshizaki, A., Shoji, T., Suzuki, M., Hatae, M., Tsuda, H., Ohwada, M., and Sugiyama, T. (2007) Phase I trial of paclitaxel, doxorubicin, and carboplatin (TAC) for the treatment of endometrial cancer. *Int. J. Gynecol. Cancer 17*, 210–214.

(13) Rodrigues, P. C. A., Scheuermann, K., Stockmar, C., Maier, G., Fiebig, H. H., Unger, C., Mülhaupt, R., and Kratz, F. (2003) Synthesis and *in vitro* efficacy of acid-sensitive poly(ethylene glycol) paclitaxel conjugates. *Bioorg. Med. Chem. Lett. 13*, 355–360.

(14) Carl, P. L., Chakravarty, P. K., and Katzenellenbogen, J. A. (1981) A novel connector linkage applicable in prodrug design. *J. Med. Chem. 24*, 479–480.

(15) Schmid, B., Chung, D. E., Warnecke, A., Fichtner, I., and Kratz, F. (2007) Albumin-binding prodrugs of camptothecin and doxorubicin with an Ala-Leu-Ala-Leu-linker that are cleaved by cathepsin B: synthesis and antitumor efficacy. *Bioconjugate Chem. 18*, 702–716.

(16) Dubowchik, G. M., Firestone, R. A., Padilla, L., Willner, D., Hofstead, S. J., Mosure, K., Knipe, J. O., Lasch, S. J., and Trail, P. A. (2002) Cathepsin B-labile dipeptide linkers for lysosomal release of doxorubicin from internalizing immunoconjugates: model studies of enzymatic drug release and antigen-specific in vitro anticancer activity. *Bioconjugate Chem. 13*, 855–869.

(17) Kratz, F., Mueller-Driver, R., Hofmann, I., Drevs, J., and Unger, C. (2000) A novel macromolecular prodrug concept exploiting endogenous serum albumin as a drug carrier for cancer chemotherapy. *J. Med. Chem. 43*, 1253–1256.

(18) Kratz, F., Warnecke, A., Scheuermann, K., Stockmar, C., Schwab, J., Lazar, P., Drückes, P., Esser, N., Drevs, J., Rognan, D., Bissantz, C., Hinderling, C., Folkers, G., Fichtner, I., and Unger, C. (2002) Probing the cysteine-34 position of endogenous serum albumin with thiol-binding doxorubicin derivatives: improved efficacy of an acid-sensitive doxorubicin derivative with specific albumin-binding properties compared to that of the parent compound. *J. Med. Chem. 45*, 5523–5533.

(19) Mansour, A. M., Drevs, J., Esser, N., Hamada, F. M., Badary, O. A., Unger, C., Fichtner, I., and Kratz, F. (2003) A new approach for the treatment of malignant melanoma: enhanced antitumor efficacy of an albumin-binding doxorubicin prodrug that is cleaved by matrix metalloproteinase 2. *Cancer Res. 63*, 4062–4066.

(20) Kratz, F., and Beyer, U. (1998) Serum proteins as drug carriers of anticancer agents: a review. *Drug Delivery 5*, 281–299.

(21) Maeda, H., Wu, J., Sawa, T., Matsumura, Y., and Hori, K. (2000) Tumor vascular permeability and the EPR effect in macromolecular therapeutics: a review. *J. Controlled Release 65*, 271–284.

(22) Kratz, F. (2007) DOXO-EMCH (INNO-206): the first albumin-binding prodrug of doxorubicin to enter clinical trials. *Expert Opin. Investig. Drugs 16*, 855–66.

(23) Kratz, F., Mansour, A., Soltau, J., Warnecke, A., Fichtner, I., Unger, C., and Drevs, J. (2005) Development of albumin-binding doxorubicin prodrugs that are cleaved by prostate-specific antigen. *Arch. Pharm. (Weinheim) 338*, 462–472.

(24) Chung, D. E., and Kratz, F. (2006) Development of a novel albumin-binding prodrug that is cleaved by urokinase-type-plasminogen activator (uPA). *Bioorg. Med. Chem. Lett. 16*, 5157–5163.

(25) Graeser, R., Chung, D. E., Esser, N., Moor, S., Schachtele, C., Unger, C., and Kratz, F. (2008) Synthesis and biological evaluation of an albumin-binding prodrug of doxorubicin that is cleaved by prostate-specific antigen (PSA) in a PSA-positive orthotopic prostate carcinoma model (LNCaP). *Int. J. Cancer 122*, 1145–1154.

(26) Fiehn, C., Kratz, F., Sass, G., Muller-Ladner, U., and Neumann, E. (2008) Targeted drug delivery by in vivo coupling to endogenous albumin: an albumin-binding prodrug of methotrexate (MTX) is better than MTX in the treatment of murine collagen-induced arthritis. *Ann. Rheum. Dis. 67*, 1188–1191.

(27) Warnecke, A., Fichtner, I., Sass, G., and Kratz, F. (2007) Synthesis, cleavage profile, and antitumor efficacy of an albumin-binding prodrug of methotrexate that is cleaved by plasmin and cathepsin B. *Arch. Pharm. (Weinheim) 340*, 389–395.

(28) Kadereit, D., Deck, P., Heinemann, I., and Waldmann, H. (2001) Acid-labile protecting groups for the synthesis of lipidated peptides. *Chem. Eur. J. 7*, 1184–1193.

(29) Dubowchik, G. M., and Radia, S. (1997) Monomethoxytrityl (MMT) as a versatile amino protecting group for complex prodrugs of anticancer compounds sensitive to strong acids, bases and nucleophiles. *Tetrahedron Lett. 38*, 5257–5260.

(30) Abu Ajaj, K., and Kratz, F. (2009) Development of dual-acting prodrugs for circumventing multidrug resistance in breast cancer. Bioorg. Med. Chem. Lett., online, DOI: 10.1016/j.bmcl.2008.11.063.

BC800429Q

SUPPORTING INFORMATION

Development of protein-binding bifunctional linkers for a new generation of dual-acting prodrugs

Khalid Abu Ajaj[1], Martin L. Biniossek[2], Felix Kratz[1*]

[1]Tumor Biology Center, Breisacher Straße 117, 79106 Freiburg, Federal Republic of Germany

[2]Institut für Molekulare Medizin und Zellforschung, Zentrum für Biochemie und Molekulare Zellforschung, Stefan-Meier-Straße 17, 79104 Freiburg, Federal Republic of Germany

[*] To whom correspondence should be addressed: Dr. Felix Kratz, Tumor Biology Center, Department of Medical Oncology, Clinical Research, Breisacher Straße 117, D-79106 Freiburg, Federal Republic of Germany; Tel.: 0049-761-2062930; Fax.: 0049-761-2062905; e-mail: felix@tumorbio.uni-freiburg.de

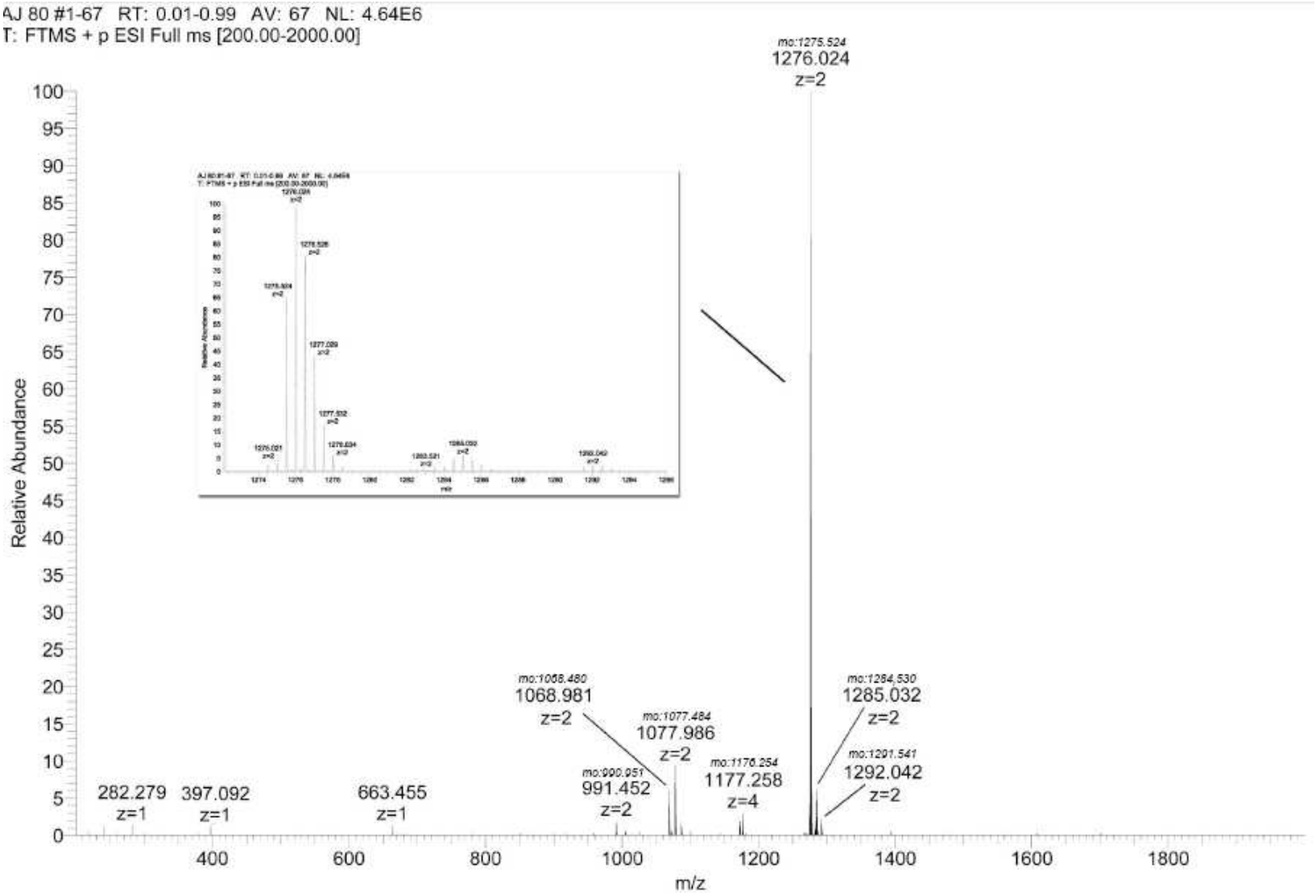

Figure S1. ESI-MS mass spectrum of thedual-acting prodruprodrug **16**. Labels correspond to the *m/z* value of the most intense peak of the isotopic distribution as well as the monoisotopic peaks (mo).

^{18}F Labeled Nanoparticles for *in Vivo* PET-CT Imaging

Neal K. Devaraj,† Edmund J. Keliher,† Greg M. Thurber, Matthias Nahrendorf, and Ralph Weissleder*

Center for Systems Biology, Massachusetts General Hospital and Harvard Medical School, Simches Research Building, 185 Cambridge Street, Boston, Massachusetts 02114, and Center for Molecular Imaging Research, Massachusetts General Hospital and Harvard Medical School, Building 149, 13th Street, Charlestown, Massachusetts 02129. Received October 27, 2008; Revised Manuscript Received December 5, 2008

We report the synthesis and in vivo characterization of an ^{18}F modified trimodal nanoparticle (^{18}F-CLIO). This particle consists of cross-linked dextran held together in core−shell formation by a superparamagnetic iron oxide core and functionalized with the radionuclide ^{18}F in high yield via "click" chemistry. The particle can be detected with positron emission tomography, fluorescence molecular tomography, and magnetic resonance imaging. The presence of ^{18}F dramatically lowers the detection threshold of the nanoparticles, while the facile conjugation chemistry provides a simple platform for rapid and efficient nanoparticle labeling.

INTRODUCTION

Polymer-coated metal core nanoparticles have emerged as important platforms for a variety of biological applications such as bioseparation, sensing, molecular imaging, and drug delivery. Examples of such materials include carbohydrate-coated iron oxide nanoparticles (*1*−*3*) for magnetic applications, synthetic polymer coated cores for molecular imaging (*4*, *5*), gold nanoshells for therapy, or biocompatible quantum dots (*6*, *7*). Magnetic nanoparticles, in particular, have received much attention, as they were shown to be biocompatible (*8*) and have low clinical toxicity (*9*), and subsequently were among the first nanomaterials tested in clinical trials (*10*). While native carbohydrate-coated preparations primarily target macrophages, monocytes, and other phagocytic cells in vivo, conjugation of affinity ligands has been used to image other molecular targets in vivo (*11*, *12*). We have recently shown that small molecule modifications (*13*) can yield uniquely targeted nanoparticles with low toxicities (*14*). Despite these advances, the in vivo detection threshold of nanoparticles via magnetic resonance is generally in the micromolar range requiring an estimated ∼200−700 mg (Fe) for a 70 Kg patient.

One avenue to substantially decrease the detection threshold and therefore the clinical dose is to label nanoparticles with positron emitters and detect them by position emission tomography (PET) imaging. Recently, we reported the use of a ^{64}Cu labeled trireporting nanoparticle that could be used at ∼100 times lower doses for PET imaging as compared to MRI and was employed to image macrophages in inflammatory atherosclerotic plaques (*15*). This material was based on aminated cross-linked dextran iron oxide (CLIO) decorated with diethylene triamine pentaacetic acid (DTPA) to transchelate ^{64}Cu. While we showed proof of principle, ^{64}Cu is not widely available, complicating clinical day-to-day on-demand syntheses. On the contrary, ^{18}F is a widely available PET isotope that is produced daily in cyclotrons of most major hospitals and distribution centers. ^{18}F has additional advantages over ^{64}Cu such as higher sensitivity, shorter half-life, and the ability of irreversible covalent bonding. Despite these advantages, the addition of ^{18}F to functionally complex materials is chemically challenging and is a major reason for the absence of reports of ^{18}F iron nanoparticles. Here, we report a facile and straightforward synthesis method for an ^{18}F trimodal nanoparticle (^{18}F-CLIO, Figure 1) and demonstrate its use for in vivo PET imaging. In this work, we have used "click" chemistry (*16*, *17*), the copper-catalyzed azide−alkyne cycloaddition, to introduce ^{18}F onto an azide-modified nanoparticle.

The introduction of ^{18}F to functionally complex molecules has been an outstanding problem in nuclear chemistry. Though there are many reported conjugation methods, most suffer from the requirement of harsh coupling conditions, long reactions times, multistep protocols, or poor overall yields. A number of ^{18}F labeling methods have been described and are conceivable for nanoparticle labeling. One such method, nucleophilic aromatic substitution, used to prepare *N*-succinimidyl 4-[^{18}F]fluorobenzoate and 4-[^{18}F]fluorobenzaldehyde, either requires multiple steps post-labeling to obtain an amine-reactive species for the former or produces a volatile compound difficult to concentrate for subsequent bimolecular reactions in the case of the latter (*18*, *19*). In contrast, "click" chemistry, specifically copper-catalyzed azide−alkyne cycloaddition, has proven to be an extremely robust, mild, conceptually simple, and chemoselective method to conjugate function to complex macromolecules and biomolecules. Recently, there have been a variety of reports demonstrating that the "click" reaction can be used efficiently and mildly to conjugate an ^{18}F label to a variety of peptides and small molecules (*20*, *21*). These reports motivated us to explore the application of "click" chemistry to modify nanoparticles with ^{18}F.

MATERIALS AND METHODS

Materials. All reagents were purchased from from Sigma-Aldrich and used without further purification unless otherwise noted. 1-Amino-11-azido-3,6,9-trioxaundecane was purchased from Toronto Research Chemicals and used as received. Sodium [^{18}F]-fluoride (Na[^{18}F]F) in ^{18}O -enriched water was purchased from PETNET (Woburn, MA). The well-characterized nanoparticle MION (MGH-CMIR, Charlestown, MA) served as starting material (*2*). The dextran coating of the nanoparticle was cross-linked with epichlorin hydrin, aminated, and labeled with near-infrared fluorochrome Vivotag-680 (VT680, VisEn Medical, Woburn, MA) (*22*). The ratio of VT680 per nanopar-

* Corresponding author. Ralph Weissleder, MD, PhD, MGH-CSB, 185 Cambridge St., Boston, MA 02114, Tel: 617-726-8226, Fax: 617-726-5708, rweissleder@mgh.harvard.edu.

† These authors contributed equally to this work.

10.1021/bc8004649 CCC: $40.75 © 2009 American Chemical Society
Published on Web 01/12/2009

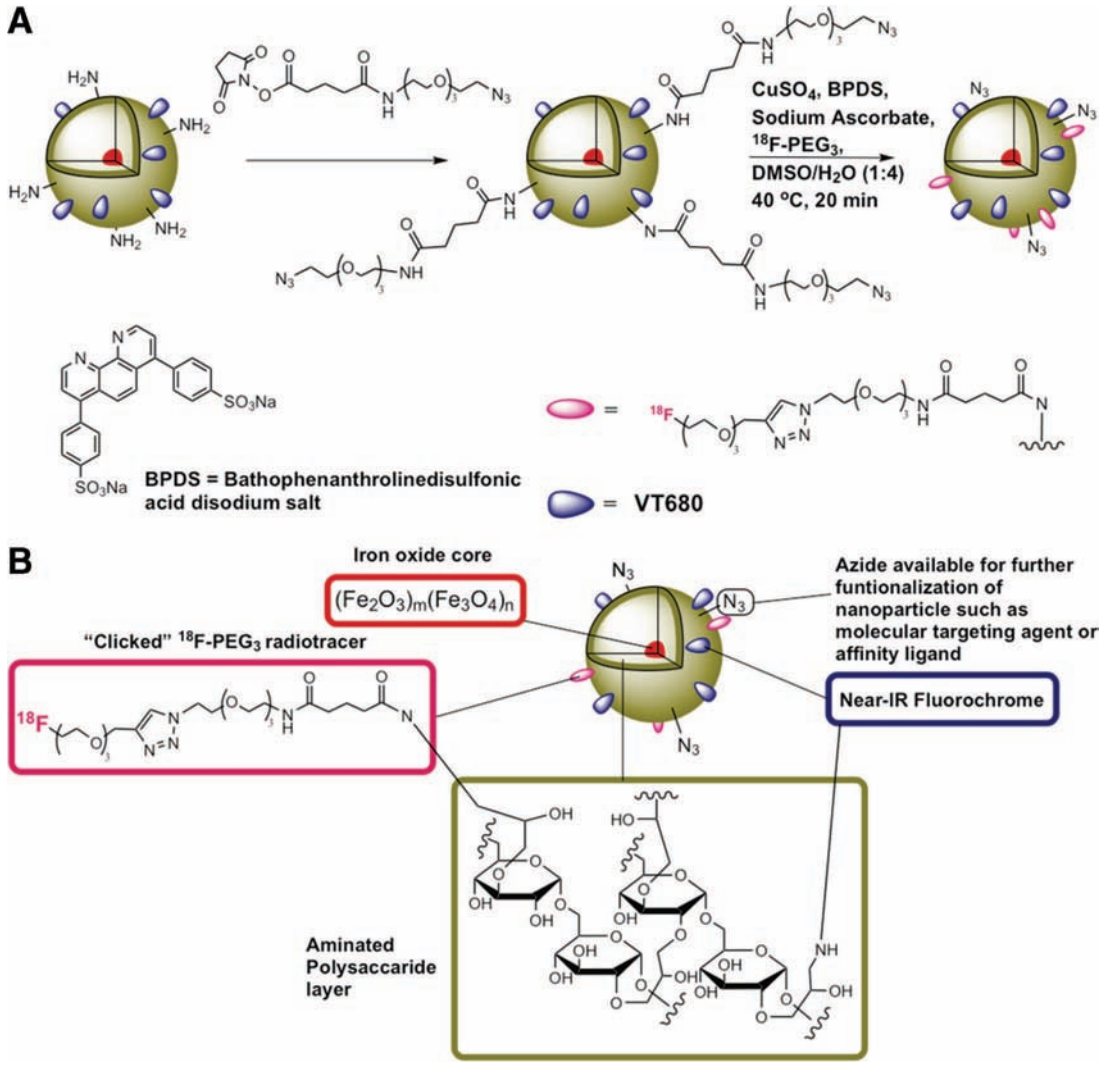

Figure 1. Preparation of ^{18}F-CLIO. (A) Derivatization of primary amines on CLIO-VT680 with the NHS ester of 1-azido-13-oxo-3,6,9-trioxa-12-azaheptadecan-17-oic acid followed by chemoselective "click" of ^{18}F-PEG$_3$ radiotracer. (B) Schematic of ^{18}F-CLIO.

ticle was approximately 5 dye moieties/particle. Preparative-scale high-performance liquid chromatography (HPLC) purification was achieved using a Machery-Nagel Nucleodur C18 Pyramid 250 × 10 mm Vario-Prep column (60:40 0.1% trifluoroacetic acid (v/v) in water−acetonitrile (AcCN) at 5.5 mL.min^{-1}) with a 254 nm UV detector and radiodetector connected in series. Analytical HPLC was performed employing a Grace VYDAC (218TP510) C18 reversed-phase column (eluents 0.1% TFA (v/v) in water and AcCN; gradient: 0−17 min, 5−60% B; 17−21 min, 60−95% B; 21−24 min, 95% B; 24−25 min, 95−5% B; 25−30 min, 5% B; 2 mL.min^{-1}) with a dual-wavelength UV−vis detector and a flow-through gamma detector connected in series. HyperSep C18 cartridges were purchased from Thermo Electron (Bellefonte, PA) and Sep-pak VAC Alumina-N cartridges from Waters (Milford, MA).

Synthesis of ^{18}F-PEG$_3$. The preparation of the 2-(2-(2-(prop-2-ynyloxy)ethoxy)ethoxy)ethyl tosylate (*20*) precursor started from the monopotassium salt of triethylene glycol, which was alkylated with propargyl bromide. This propargyl PEG$_3$ was treated with tosyl chloride in the presence of triethyl amine. 3-(2-(2-(2-[^{18}F]-Fluoroethoxy)-ethoxy)ethoxy)prop-1-yne (^{18}F-PEG$_3$) was prepared using Synthra RN Plus automated synthesizer (Synthra GmbH, Hamburg, Germany) operated by *Explora View* software in an average time of 40 min. The target well was charged with Na[^{18}F]F, n.c.a., (∼1850 MBq, 50 mCi) in $H_2{}^{18}O$ (150 μL), 150 μL of a 74 mM K_2CO_3 solution in water, and 250 μL of 49 mM Kryptofix 2.2.2 in AcCN. The synthesizer reagent vials were filled as follows: A2 with AcCN (350 μL), A3 with tosylate **2** (1.0 mg, 19.2 μmol) in DMSO (400 μL), A5 with DMSO (50 μL), and B2 with H_2O (900 μL). The Na[^{18}F]F/K_2CO_3/K2.2.2 solution was transferred to Reaction Vessel #1 and dried by azeotropic distillation of the acetonitrile/water solution by heating to 60 °C under reduced pressure and a flow of argon to achieve ∼310 mbar for 2 min followed by 98 °C and 270 mbar for 3 min. Reaction Vessel #1 was cooled to 50 °C, tosylate **2** in DMSO (400 μL) added, and the reaction vessel pressurized to 2000 mbar and heated to 110 °C for 15 min. After cooling to 30 °C, the mixture was filtered through an Alumina-N cartridge (100 mg, 1 mL, Waters) into Reaction Vessel #2. The Alumina-N cartridge was washed with DMSO (50 μL), and the combined filtrates were diluted with water (900 μL). This solution was subjected to preparative HPLC purification. ^{18}F-PEG$_3$ was collected (t_R = 4.9 min) in 3−4 mL of solvent and isolated by C18 solid-phase extraction. Elution of the collected material with CH_2Cl_2 (600 μL) to give ^{18}F-PEG$_3$ in 57% average decay-corrected radiochemical yield (RCY). Analytical HPLC demonstrated >99% radiochemical purity of ^{18}F-PEG$_3$, Figure 2.

Preparation of Azido-PEG Modified CLIO. 1-Amino-11-azido-3,6,9-trioxaundecane (218 mg, 1 mmol) and glutaric anhydride (114 mg, 1 mmol) were dissolved in 1 mL methylene chloride and refluxed for 1 h. Evaporation of solvent yielded

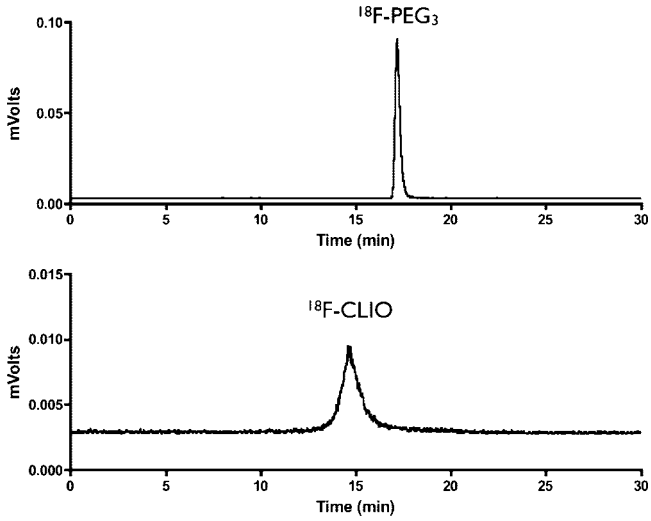

Figure 2. HPLC analysis of purified ^{18}F-PEG$_3$ and ^{18}F-CLIO demonstrating >98% purity.

1-azido-13-oxo-3,6,9-trioxa-12-azaheptadecan-17-oic acid quantitatively, verified by LRMS-ESI $[M + H]^+$ *m*/*z* calc. $[C_{13}H_{25}N_4O_6]^+$ 333.17, found 333.3. The azido−acid (33 mg, 0.1 mmol) was stirred for 3 h in 0.3 mL AcCN with 8 μL of pyridine and 26 mg of disuccinimidylcarbonate. The AcCN was evaporated, and the resulting crude *N*-hydroxysuccinimide ester was used directly with amine-terminated iron oxide nanoparticles. The aminated cross-linked dextran iron oxide (CLIO) nanoparticle was prepared as previously described (*23*). Nanoparticles were approximately 30 nm in diameter and contained on average 40 primary amines. Aminated CLIO was functionalized first with NHS modified VT680 (VisEn Medical, Woburn, MA) such that there were approximately 5 molecules of VT680 per particle. The remaining amines were capped with the NHS ester of 1-azido-13-oxo-3,6,9-trioxa-12-azaheptadecan-17-oic acid to give the CLIO-azide. In a typical coupling procedure, 0.4 mg of amine-terminated CLIO was dissolved in 0.5 mL of 0.1 M sodium bicarbonate buffered to a pH of 8.5. To this solution was added 40 μL of DMSO containing 1 mg of the azido *N*-hydroxysuccinimide ester. The solution was stirred at room temperature for 2 h, purified by centrifuge filtration, and stored in PBS buffered to pH 7.4.

Conjugation. ^{18}F-PEG$_3$ in 50−100 μL water added to the azido-CLIO (50 μL of a 400 μg/100 μL 1×PBS (phosphate buffered solution)) was subjected to water-soluble copper-catalyzed 1,3-dipolar cycloaddition reaction conditions: 40 μL 10 mM $Cu^{(II)}SO_4$/bathophenanthrolinedisulfonic acid disodium salt (BPDS) in distilled water/DMSO (3:1) and 40 uL 100 mM Na-ascorbate in distilled water (*24*). The reaction mixture was incubated for 40 min at 40 °C and filtered to remove the ^{18}F-CLIO from unreacted ^{18}F-PEG$_3$. ^{18}F-CLIO was washed with 1×PBS until no activity was collected in the filtrate (>1 μCi). HPLC analysis demonstrated >99% radiochemical purity of ^{18}F-CLIO (Figure 2). The ^{18}F-labeled nanoparticle was suspended in DPBS (Dulbecco's phosphate buffered solution with Ca^{2+} and Mg^{2+}).

Phantom Experiment. To compare the sensitivity of nanoparticle detection with MRI and PET, ^{18}F-CLIO was diluted in 2% low melting agarose to concentrations ranging from 0.005 to 10 μg Fe /mL and added to wells in a precast gel. PET-CT imaging of 2 gels was followed by MRI using a 7 T Pharmascan magnet (Bruker, Billerica, MA) and employing a T2* weighted gradient echo sequence (TE 140 ms, matrix 128 × 128, FOV 60 × 40 mm^2, slice thickness 0.8 mm).

Mice. Inbred male BALB/c (B/c, H-2d) mice (8−12 weeks old) were obtained from Jackson Laboratory (Bar Harbor, ME). The mice were maintained at the animal facilities of Massachusetts General Hospital, accredited by the American Association of Laboratory Animal Care. All experiments conformed to animal care protocols approved by the institutional review board.

PET Imaging. Mice were imaged with PET-CT one hour after injection of 998 ± 74 μCi of ^{18}F -CLIO (n = 6). This concentration was about 1 order of magnitude lower than previously used for MRI (10−20 mg Fe/kg). PET-CT was performed on an Inveon system (Siemens Preclinical Solutions). PET scans were terminated after 600 million events were recorded, with a typical acquisition time of 45 min. Spatial resolution of PET imaging approximated 1 mm isotropic. Acquisition coincidence data were rebinned using Fourier rebinning in 3D, and the resulting sinogram was reconstructed using an ordered subsets expectation maximization (OSEM) algorithm. For quantification of standard uptake values (SUV), images were reconstructed using 2D filtered back projection (FBP). The CT X-ray source was used with a power of 80 kVp and 500 μA and an exposure time of 370−400 ms. The effective 3D resolution was 90 μm isotropic. Typically, 360 projections were acquired. The reconstruction protocol was set to interpolate bilinearly, used a Shepp-Logan filter, and signal intensity was scaled to Hounsfield units. To achieve appropriate intravascular contrast, iopamidol 61% (Bracco Diagnostics, Princeton, NJ) was continuously infused via tail vein at a rate of 65 μL/min for the time of CT acquisition, which was approximately 7 min. Fused images were converted into DICOM format and analyzed using OsiriX shareware (Geneva, Switzerland, www.osirix-viewer.com) by placing volumes of interest in the various organs for calculation of target-to-background ratios. Standard uptake values (SUV) were calculated as (tissue activity/volume of tissue)/(body activity/body weight).

Pharmacokinetic Analysis. Blood half-life data obtained from the heart (blood pool organ) were fit to a biexponential model, and the half-life is reported as the weighted average of the distribution and clearance phases. For fitting permeability surface area product (PS/V) values, the average concentration of activity (decay corrected) in a region of interest determined by CT was measured for the time series. The interstitial concentration was obtained by subtracting the blood contribution using the plasma fraction for each organ. Assuming an interstitial void fraction of 0.05 for these particles, PS/V was fit using the plasma clearance and specific organ data. Due to the early imaging sequence with ^{18}F, clearance was assumed to be negligible for all organs (uptake only) except the lung. The lung had similar low levels of activity as the kidney but demonstrated decreasing signal at later time points. Here, a value for lymphatic clearance was assumed to obtain a reasonable fit.

RESULTS

3-(2-(2-(2-[^{18}F]-Fluoroethoxy)ethoxy)ethoxy)prop-1-yne (^{18}F-PEG$_3$) was prepared in 57% average decay-corrected radiochemical yield from an alkynyl tosylate (see Supporting Information for full experimental details). ^{18}F-PEG$_3$ is prepared in one step and when compared with 4-[^{18}F]fluorobenzaldehyde is relatively nonvolatile. This quality allows concentration of ^{18}F-PEG$_3$ to almost dryness, thus increasing the yield of the bimolecular second step. "Click" reaction with an azide-terminated CLIO yielded ^{18}F-CLIO with a decay-corrected yield of 58%. Both ^{18}F-PEG$_3$ and ^{18}F-CLIO were analyzed by HPLC to determine radiochemical purity. Following preparative HPLC purification of ^{18}F-PEG$_3$ and microcentrifuge filtration of ^{18}F-CLIO, both were observed to be >98% pure (Figure 2). Average total ^{18}F-CLIO synthesis time was 120 min from the start of radiolabeling of ^{18}F-PEG$_3$. ^{18}F-CLIO had an average specific activity of 1.1 mCi/0.1 mg of nanoparticles. Control experiments

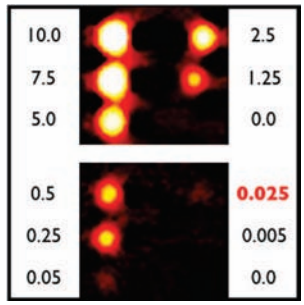

Figure 3. PET imaging of 2 agar phantoms with decreasing concentrations of ^{18}F-CLIO (μg Fe/mL).

using nanoparticles without azides or the absence of the copper catalyst failed in demonstrating the chemoselectivity of the conjugation.

The detection threshold of ^{18}F-CLIO suspended in the agar phantom was 0.025 μg Fe/mL for PET-CT imaging, approximately 200 times lower than by T2*-weighted MR imaging (Figure 3). This is an improvement from ^{64}Cu-labeled nanoparticles of comparable specific activity. The increased sensitivity was expected due to the increased branching ratio for the decay of ^{18}F over ^{64}Cu (*25*). As previously determined, the lowest observed concentration of the nanoparticles by MRI was 5 μg Fe/mL (*15*), demonstrating a PET detection threshold 200 times more sensitive than MRI at current specific activities. It is expected that optimization of reaction yields will further decrease the PET detection threshold.

Purified ^{18}F-CLIO was injected into the tail vein of 3 mice, and dynamic PET imaging was performed to determine organ biodistribution and blood clearance over time. Figure 4 summarizes one imaging series in which data were collected over the course of 16 h after intravenous injection of ^{18}F-CLIO and shows images acquired at 2, 7, and 16 h. Initially, high sustained activity was detected in the blood pool, demonstrated by high PET signal in the cardiac chambers. Over time, this signal declined, while an increase of activity was observed in the liver and spleen. Using compartmental analysis, the uptake rate in the liver was much higher than uptake by the kidney (~4-fold, Table 1), and some of the renal activity may have indeed been due to the close proximity of the region of interest to the liver. The low renal and bladder uptake emphasizes that ^{18}F-CLIO is stable in vivo, and the tracer is not excreted via the kidneys. Taken together, these PET data follow the typical pharmacokinetics of CLIO, showing redistribution of the blood pool signal to the liver and lymphatic organs over the course of several hours (Figure 4D−F).

In vivo dynamic PET imaging showed very high signal-to-noise ratios for injected ^{18}F-CLIO. As summarized in Figures 4 and 5, the nanoparticle has a vascular half-life of 5.8 h in mice and is subsequently internalized into macrophages of liver, spleen, and phagocytic cells of other lymphatic organs. The nanoparticle is biodegradable and had previously been shown to be broken down into elemental components in weeks−months time frames (*8*). There was negligible urine and/or bowel excretion (<2%) over 24 h. The iron is metabolized and is reused in heme synthesis (*8*). The 10 kDa dextran coating is slowly excreted as determined by ^{14}C labeling studies. While long-term toxicity experiments have not been conducted for this agent, an adverse reaction is not expected due to the substantially lower iron doses administered than those of previous studies that demonstrated no adverse acute, subacute, or chronic effects (*8, 15*).

DISCUSSION

A major future application of the above approach is to use nanoparticle platforms for targeted molecular imaging. Nanoparticles allow multivalent attachment of small affinity ligands, vastly increasing avidity. This together with optimized pharmacokinetics of parent materials would allow a modular approach to rapidly building and testing such materials. Our

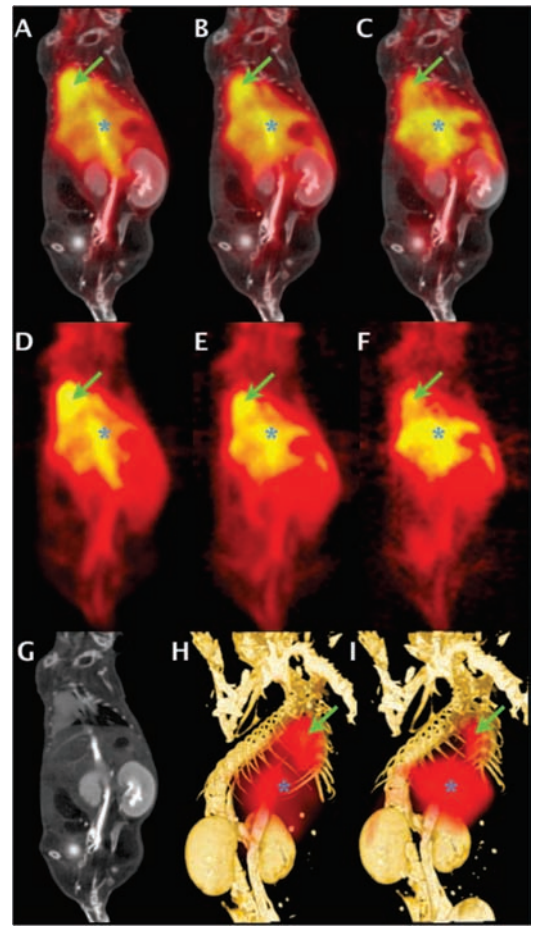

Figure 4. Dynamic PET/CT imaging of BALB/C mouse injected with ^{18}F-CLIO**.** Fused PET/CT coronal images at 2 h (A), 7 h (B), and 16 h (C) postinjection of ^{18}F-CLIO. PET only coronal images at 2 h (D), 7 h (E), and 16 h (F) postinjection of ^{18}F-CLIO. CT only coronal image (G). Three-dimensional rendering of fused PET-CT images at 2 h (H) and 16 h (I) postinjection. Arrow (green) indicates blood pool region of interest (ROI) and asterisk indicates liver ROI.

Table 1. Permeability Surface Area Product (PS/V) for Major Organs[a]

organ	PS/V (10^{-5}/s)	clearance
liver	32.9	-
spleen	20.4	-
kidney	8.64	-
lung	33.2	0.000089/s

[a] Values were fit to ROI data from serial PET imaging.

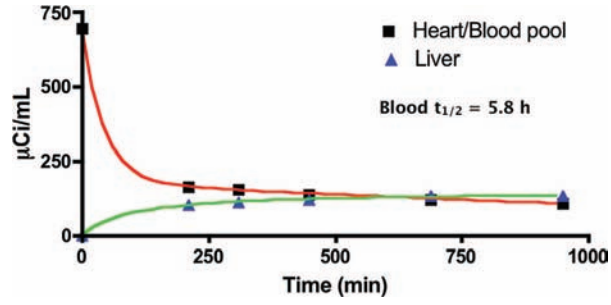

Figure 5. Activity density vs time curves for blood pool of the heart and liver. Blood half-life ($t_{1/2}$) was calculated to be 5.8 h.

approach for ^{18}F labeling of such materials is yet another step to rapidly test their efficacy in vivo. The ability to use targeted nanomaterials at 2−4 orders of magnitude lower doses than those required for MR imaging will likely make PET imaging an important platform for clinical molecular imaging.

ACKNOWLEDGMENT

The Center of Cancer Nanotechnology Excellence (U54-CA119349), the Translational Program of Excellence in Nanotechnology (UO1-HL080731), and NIH training grant T32-CA79443 supported this work. The authors would like to thank Jose-Luiz Figureiredo for helpful discussions, Brett Marinelli for conducting the PET-CT imaging, and Nikolay Sergeyev for preparing the CLIO nanoparticles.

Supporting Information Available: Methods and Materials. This material is available free of charge via the Internet at http://pubs.acs.org.

LITERATURE CITED

(1) Nahrendorf, M., Sosnovik, D. E., Waterman, P., Swirski, F. K., Pande, A. N., Aikawa, E., Figueiredo, J. L., Pittet, M. J., and Weissleder, R. (2007) Dual channel optical tomographic imaging of leukocyte recruitment and protease activity in the healing myocardial infarct. *Circ. Res. 100*, 1218–1225.

(2) Shen, T., Weissleder, R., Papisov, M., Bogdanov, A. J. R., and Brady, T. J. (1993) Monocrystalline iron oxide nanocompounds(MION): physicochemical properties. *Mag. Reson. Med. 29*, 599–604.

(3) Yu, M. K., Jeong, Y. Y., Park, J., Park, S., Kim, J. W., Min, J. J., Kim, K., and Jon, S. (2008) Drug-loaded superparamagnetic iron oxide nanoparticles for combined cancer imaging and therapy in vivo. *Angew. Chem., Int. Ed. Engl. 47*, 5362–5365.

(4) Aikawa, E., Nahrendorf, M., Sosnovik, D., Lok, V. M., Jaffer, F. A., Aikawa, M., and Weissleder, R. (2007) Multimodality molecular imaging identifies proteolytic and osteogenic activities in early aortic valve disease. *Circulation 115*, 377–386.

(5) Swirski, F. K., Berger, C. R., Figueiredo, J. L., Mempel, T. R., von Andrian, U. H., Pittet, M. J., and Weissleder, R. (2007) A near-infrared cell tracker reagent for multiscopic in vivo imaging and quantification of leukocyte immune responses. *PLoS ONE 2*, e1075.

(6) Liu, W., Howarth, M., Greytak, A. B., Zheng, Y., Nocera, D. G., Ting, A. Y., and Bawendi, M. G. (2008) Compact biocompatible quantum dots functionalized for cellular imaging. *J. Am. Chem. Soc. 130*, 1274–1284.

(7) Shi, X., Wang, S., Meshinchi, S., Van Antwerp, M. E., Bi, X., Lee, I., and Baker, J. R. (2007) Dendrimer-entrapped gold nanoparticles as a platform for cancer-cell targeting and imaging. *Small 3*, 1245–1252.

(8) Weissleder, R., Stark, D. D., Engelstad, B. L., Bacon, B. R., Compton, C. C., White, D. L., Jacobs, P., and Lewis, J. (1989) Superparamagnetic iron oxide: pharmacokinetics and toxicity. *Am. J. Roentgen. 152*, 167–173.

(9) Harisinghani, M. G., Barentsz, J., Hahn, P. F., Deserno, W. M., Tabatabaei, S., van de Kaa, C. H., de la Rosette, J., and Weissleder, R. (2003) Noninvasive detection of clinically occult lymph-node metastases in prostate cancer. *New Eng. J. Med. 348* (25), 2491–2499.

(10) Weissleder, R., Hahn, P. F., and Stark, D. D. (1988) Superparamagnetic iron oxide: enhanced detection of focal splenic tumors with mr imaging'. *Radiology 169*, 399–403.

(11) Kelly, K. A., Bardeesy, N., Anbazhagan, R., Gurumurthy, S., Berger, J., Alencar, H., Depinho, R. A., Mahmood, U., and Weissleder, R. (2008) Targeted nanoparticles for imaging incipient pancreatic ductal adenocarcinoma. *PLoS Med. 5*, e85.

(12) Weissleder, R., Lee, A. S., Khaw, B. A., Shen, T., and Brady, T. J. (1992) Antimyosin-labeled monocrystalline iron oxide allows detection of myocardial infarct: MR antibody imaging. *Radiology 182*, 381–385.

(13) Weissleder, R., Kelly, K., Sun, E. Y., Shtatland, T., and Josephson, L. (2005) Cell-specific targeting of nanoparticles by multivalent attachment of small molecules. *Nat. Biotechnol. 23*, 1418–1423.

(14) Shaw, S. Y., Westly, E. C., Pittet, M. J., Subramanian, A., Schreiber, S. L., and Weissleder, R. (2008) Perturbational profiling of nanomaterial biologic activity. *Proc. Nat. Acad. Sci. 105*, 7387–7392.

(15) Nahrendorf, M., Zhang, H., Hembrador, S., Panizzi, P., Sosnovik, D. E., Aikawa, E., Libby, P., Swirski, F. K., and Weissleder, R. (2008) Nanoparticle PET-CT imaging of macrophages in inflammatory atherosclerosis. *Circulation 117*, 379–387.

(16) Rostovtsev, V. V., Green, L. G., Fokin, V. V., and Sharpless, K. B. (2002) A stepwise huisgen cycloaddition process: Copper (I)-catalyzed regioselective"ligation" of azides and terminal alkynes. *Angew. Chem., Int. Ed. Engl. 41*, 2596–2599.

(17) Wang, Q., Chan, T. R., Hilgraf, R., Fokin, V. V., Sharpless, K. B., and Finn, M. G. (2003) Bioconjugation by copper (I)-catalyzed azide-alkyne [3,2] cycloaddition. *J. Am. Chem. Soc. 125*, 3192–3193.

(18) Poethko, T., Schottelius, M., Thumshirn, G., Hersel, U., Herz, M., Henriksen, G., Kessler, H., Schwaiger, M., and Wester, H. J. (2004) Two-step methodology for high-yield routine radiohalogenation of peptides: (18) F-labeled RGD and octreotide analogs. *J. Nucl. Med. 45*, 892–902.

(19) Vaidyanathan, G., and Zalutsky, R. (2006) Synthesis of N-succinimidyl 4-[18F]fluorobenzoate, an agent for labeling proteins and peptides with 18F. *Nat. Prot. 1*, 1655–1661.

(20) Li, Z. B., Wu, Z., Chen, K., Chin, F. T., and Chen, X. (2007) Click chemistry for ^{18}F-labeling of RGD peptides and microPET imaging of tumor integrin $\alpha v\beta 3$ expression. *Bioconjugate Chem.* 1987–1994.

(21) Marik, J., and Sutcliffe, J. L. (2006) Click for PET: rapid preparation of [18F] fluoropeptides using CuI catalyzed 1,3-dipolar cycloaddition. *Tetrahedron Lett. 47*, 6681–6684.

(22) Kelly, K. A., Waterman, P., and Weissleder, R. (2006) In vivo imaging of molecularly targeted phage. *Neoplasia 8*, 1011–1018.

(23) Josephson, L., Kircher, M. F., Mahmood, U., Tang, Y., and Weissleder, R. (2002) Near-infrared fluorescent nanoparticles as combined MR/optical imaging probes. *Bioconjugate Chem. 13*, 554–560.

(24) Lewis, W. G., Magallon, F. G., Fokin, V. V., and Finn, M. G. (2004) Discovery and characterization of catalysts for azide-alkyne cycloaddition by fluorescence quenching. *J. Am. Chem. Soc. 126*, 9152–9153.

(25) Cherry, S. R., Sorenson, J. A., Phelps, M. E. (2003) *Physics in Nuclear Medicine*, Saunders, Philadelphia.

BC8004649

Supporting Information

^{18}F labeled Nanoparticles for in vivo PET-CT Imaging

Neal Devaraj*, Edmund J. Keliher*, Greg Thurber, Matthias Nahrendorf, Ralph Weissleder
(*equal contributions)

All authors: Center for Systems Biology, Massachusetts General Hospital and Harvard Medical School, Simches Research Building, 185 Cambridge St., Boston, MA 02114; Center for Molecular Imaging Research, Massachusetts General Hospital and Harvard Medical School, Building 149, 13th St., Charlestown, MA 02129.

Corresponding author: Ralph Weissleder, MD, PhD
MGH-CSB
185 Cambridge St
Boston, MA 02114
Tel: 617-726-8226
Fax: 617-726-5708
rweissleder@mgh.harvard.edu

MATERIALS AND METHODS

Materials

All reagents were purchased from from Sigma-Aldrich and used without further purification unless otherwise noted. 1-Amino-11-azido-3,6,9-trioxaundecane was purchased from Toronto Research Chemicals and used as received. Sodium [^{18}F]-fluoride (Na[^{18}F]F) in ^{18}O-enriched water was purchased from PETNET (Woburn, MA). The well characterized nanoparticle MION (MGH-CMIR, Charlestown, MA) served as starting material. (1) The dextran coating of the nanoparticle was crosslinked with epichlorin hydrin, aminated and labeled with near infrared fluorochrome Vivotag-680 (VT680, VisEn Medical, Woburn, MA). (2) The ratio of VT680 per nanoparticle was approximately 5 dye moieties/particle. Preparative scale high-performance liquid chromatography (HPLC) purification was achieved using a Machery-Nagel Nucleodur

C18 Pyramid 250 x 10 mm Vario-Prep column (60:40 0.1 % trifluoroacetic acid (v/v) in water-acetonitrile (AcCN) at 5.5 $ml \cdot min^{-1}$) with a 254 nm UV detector and radiodetector connected in series. Analytical HPLC was performed employing a Grace VYDAC (218TP510) C18 reversed-phase column (eluents 0.1% TFA (v/v) in water and AcCN; gradient: 0-17 min, 5-60% B; 17-21 min, 60-95% B; 21-24 min, 95% B; 24-25 min, 95-5% B; 25-30 min, 5% B; 2 $mL \cdot min^{-1}$) with a dual-wavelength UV-Vis detector and a flow-through gamma detector connected in series. HyperSep C18 cartridges were purchased from Thermo Electron (Bellefonte, PA) and Sep-pak VAC Alumina-N cartridges from Waters (Milford, MA).

Synthesis of ^{18}F-PEG$_3$. The preparation of the 2-(2-(2-(prop-2-ynyloxy)ethoxy)ethoxy)ethyl tosylate(3) precursor started from the mono-potassium salt of triethylene glycol which was alkylated with propargyl bromide. This propargyl PEG_3 was treated with tosyl chloride in the presence of triethyl amine. 3-(2-(2-(2-[^{18}F]-Fluoroethoxy)-ethoxy)ethoxy)prop-1-yne (^{18}F-PEG_3) was prepared using Synthra RN Plus automated synthesizer (Synthra GmbH, Hamburg, Germany) operated by Explora View software in an average time of 40 min. The target well was charged with Na[^{18}F]F, n.c.a., (~1850 MBq, 50 mCi) in $H_2{}^{18}O$ (150 μ L), 150 μ L of a 74 mM K_2CO_3 solution in water, and 250 μ L of 49 mM Kryptofix 2.2.2 in AcCN. The synthesizer reagent vials were filled as follows: A2 with AcCN (350 μ L), A3 with tosylate **2** (1.0 mg, 19.2 μ mol) in DMSO (400 μ L), A5 with DMSO (50 μ L), and B2 with H_2O (900 μ L). The Na[^{18}F]F/K_2CO_3/K2.2.2 solution was transferred to Reaction Vessel #1 and dried by azeotropic distillation of the acetonitrile/water solution by

heating to 60 ^{o}C under reduced pressure and a flow of argon to achieve ~310 mbar for 2 min followed by 98 ^{o}C and 270 mbar for 3 min. Reaction Vessel #1 was cooled to 50 ^{o}C, tosylate **2** in DMSO (400 μ L) added, the reaction vessel pressurized to 2000 mbar, and heated to 110 ^{o}C for 15 min. Cooled to 30 ^{o}C, the mixture was filtered through an Alumina-N cartridge (100 mg, 1 mL, Waters) into Reaction Vessel #2. The Alumina-N cartridge was washed with DMSO (50 μ L) and the combined filtrates were diluted with water (900 μ L). This solution was subjected to preparative HPLC purification. ^{18}F-PEG$_3$ was collected (t_R = 4.9 min) in 3-4 mL of solvent and isolated by C18 solid phase extraction. Elution of the collected material with CH_2Cl_2 (600 μ L) to give ^{18}F-PEG$_3$ in 57% average decay-corrected radiochemical yield (RCY). Analytical HPLC demonstrated >99% radiochemical purity of ^{18}F-PEG$_3$, Figure 2.

Preparation of Azido-PEG modified CLIO. 1-Amino-11-azido-3,6,9-trioxaundecane (218 mg, 1 mmol) and glutaric anhydride (114 mg, 1 mmol) were dissolved in 1 mL methylene chloride and refluxed for 1 h. Evaporation of solvent yielded 1-azido-13-oxo-3,6,9-trioxa-12-azaheptadecan-17-oic acid quantitatively, verified by LRMS-ESI $[M+H]^+$ m/z calc. $[C_{13}H_{25}N_4O_6]^+$ 333.17 found 333.3. The azido-acid (33 mg, 0.1 mmol) was stirred for 3 h in 0.3 mL AcCN with 8 μL of pyridine and 26 mg of disuccinimidylcarbonate. The AcCN was evaporated and the resulting crude N-hydroxysuccinimide ester was used directly with amine-terminated iron oxide nanoparticles. The aminated cross-linked dextran iron oxide (CLIO) nanoparticle was prepared as previously described. (4) Nanoparticles were approximately 30 nm in diameter and contained on average 40 primary amines. Aminated CLIO was

functionalized first with NHS modified VT680 (VisEn Medical, Woburn, MA) such that there were approximately 5 molecules of VT680 per particle. The remaining amines were capped with the NHS ester of 1-azido-13-oxo-3,6,9-trioxa-12-azaheptadecan-17-oic acid to give the CLIO-azide. In a typical coupling procedure, 0.4 mg of amine terminated CLIO was dissolved in 0.5 mL of 0.1 M sodium bicarbonate buffered to a pH of 8.5. To this solution was added 40 μL of DMSO containing 1 mg of the azido N-hydroxysuccinimide ester. The solution was stirred at room temperature for 2 h, purified by centrifuge filtration, and stored in PBS buffered to pH 7.4.

Conjugation. **^{18}F-PEG$_3$** in 50-100 μ L water added to the azido-CLIO (50 μ L of a 400 μ g/100 μ L 1xPBS (phosphate buffered solution)) was subjected to water soluble copper catalyzed 1,3-dipolar cycloaddition reaction conditions: 40 μ L 10 mM $Cu^{(II)}SO_4$/bathophenanthrolinedisulfonic acid disodium salt (BPDS) in distilled water/DMSO (3:1) and 40 uL 100 mM Na-ascorbate in distilled water. (5) The reaction mixture was incubated for 40 min at 40 ^{o}C and filtered to remove the ^{18}F-CLIO from unreacted ^{18}F-PEG$_3$. ^{18}F-CLIO was washed with 1xPBS until no activity was collected in the filtrate (>1 μ Ci). HPLC analysis demonstrated >99% radiochemical purity of ^{18}F-CLIO (Figure 2). The ^{18}F-labeled nanoparticle was suspended in DPBS (Dulbecco's phosphate buffered solution with Ca^{+2} and Mg^{+2}).

Phantom experiment

To compare the sensitivity of nanoparticle detection with MRI and PET, ^{18}F-CLIO was diluted in 2 % low melting agarose to concentrations ranging from .005 to 10 μ g Fe /mL

and added to wells in a precast gel. PET-CT imaging of 2 gels was followed by MRI using a 7 Tesla Pharmascan magnet (Bruker, Billerica, MA) and employing a T2* weighted gradient echo sequence (TE 140 ms, matrix 128x128, FOV 60x40 mm, slice thickness 0.8 mm).

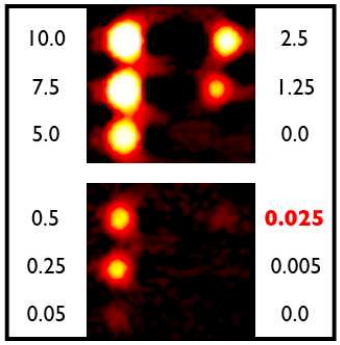

Figure S1. PET imaging of 2 agar phantoms with decreasing concentrations of 18F-CLIO (μg Fe/mL)

Mice

8-12 weeks old inbred male BALB/c (B/c, H-2d) mice were obtained from Jackson Laboratory (Bar Harbor, ME). The mice were maintained at the animal facilities of Massachusetts General Hospital, accredited by the American Association of Laboratory Animal Care. All experiments conformed to animal care protocols approved by the institutional review board.

PET Imaging

Mice were imaged with PET-CT one hour after injection of 998 ± 74 μ Ci of ^{18}F-CLIO

(n=6). This concentration was about one order of magnitude lower than previously used for MRI (10-20 mg Fe/kg). PET-CT was performed on an Inveon system (Siemens Preclinical Solutions). PET scans were terminated after 600 million events were recorded, with a typical acquisition time of 45 minutes. Spatial resolution of PET imaging approximated 1mm isotropic. Acquisition coincidence data were rebinned using Fourier rebinning in 3D, and the resulting sinogram was reconstructed using an Ordered Subsets Expectation Maximization (OSEM) algorithm. For quantification of standard uptake values (SUV), images were reconstructed using 2D Filtered Back Projection (FBP). The CT x-ray source was used with a power of 80 kVp and 500 µA and an exposure time of 370–400 ms. The effective 3D resolution was 90 µm isotropic. Typically, 360 projections were acquired. The reconstruction protocol was set to interpolate bilinearly, used a Shepp-Logan filter, and signal intensity was scaled to Hounsfield units. To achieve appropriate intravascular contrast, iopamidol 61% (Bracco Diagnostics, Princeton, NJ) was continuously infused via tail vein at a rate of 65 μ L/min for the time of CT acquisition, which was approximately 7 minutes. Fused images were converted into DICOM format and analyzed using OsiriX shareware (Geneva, Switzerland, www.osirix-viewer.com) by placing volumes of interest in the various organs for calculation of target to background ratios. Standard uptake values (SUV) were calculated as (tissue activity/volume of tissue)/(body activity/body weight).

PHARMACOKINETIC ANALYSIS

Blood half life data obtained from the heart (blood pool organ) was fit to a biexponential model, and the half life is reported as the weighted average of the distribution and

clearance phases. For fitting permeability surface area product (PS/V) values, the average concentration of activity (decay corrected) in a region of interest determined by CT was measured for the time series. The interstitial concentration was obtained by subtracting the blood contribution using the plasma fraction for each organ. Assuming an interstitial void fraction of 0.05 for these particles, PS/V was fit using the plasma clearance and specific organ data. Due to the early imaging sequence with ^{18}F, clearance was assumed to be negligible for all organs (uptake only) except the lung. The lung had similar low levels of activity as the kidney but demonstrated decreasing signal at later time points. Here a value for lymphatic clearance was assumed to obtain a reasonable fit.

(1) Shen, T., Weissleder, R., Papisov, M., Bogdanov, A. J. R., Brady, T. J. (1993) Monocrystalline iron oxide nanocompounds(MION): physicochemical properties. *Mag. Reson. Med. 29*, 599-604.

(2) Kelly, K. A., Waterman, P., Weissleder, R. (2006) In vivo imaging of molecularly targeted phage. *Neoplasia 8*, 1011-1018.

(3) Li, Z. B., Wu, Z., Chen, K., Chin, F. T., Chen, X. (2007) Click Chemistry for 18 F-Labeling of RGD Peptides and microPET Imaging of Tumor Integrin α vß3 Expression. *Bioconjug. Chem.* 1987-1994.

(4) Josephson, L., Kircher, M. F., Mahmood, U., Tang, Y., Weissleder, R. (2002) Near-infrared fluorescent nanoparticles as combined MR/optical imaging probes. *Bioconjug. Chem. 13*, 554-560.

(5) Lewis, W. G., Magallon, F. G., Fokin, V. V., Finn, M. G. (2004) Discovery and Characterization of Catalysts for Azide-Alkyne Cycloaddition by Fluorescence Quenching. *J. Am. Chem. Soc. 126*, 9152-9153.

CORRECTIONS

Volume 19, Number 12, 2008.

Furong Ye, Eun-Kee Jeong, Zhanjun Jia, Tianxin Yang, Dennis Parker, and Zheng-Rong Lu*

A Peptide Targeted Contrast Agent Specific to Fibrin−Fibronectin Complexes for Cancer Molecular Imaging with MRI

The name of author Xueming Wu was inadvertently omitted and not included in the author byline. He should be listed as the second author. Please view the corrected author byline and affiliations here:

Furong Ye,[†] Xueming Wu,[†] Eun-Kee Jeong,[‡] Zhanjun Jia,[§] Tianxin Yang,[§] Dennis Parker,[‡] and Zheng-Rong Lu[†,*]

[†]Department of Pharmaceutics and Pharmaceutical Chemistry, Department of Radiology, and [§]Department of Internal Medicine, University of Utah, Salt Lake City, and [§]Veterans Affairs Medical Center, Salt Lake City, Utah.

BC8005682

10.1021/bc8005682
Published on Web 01/13/2009

MARCH 2009
Volume 20, Number 3

© *Copyright 2009 by the American Chemical Society*

Bioconjugate Chemistry

Editorial: "Conjugates of Oligonucleotides and Modified Oligonucleotides": A Memorable Review by John Goodchild

DNA and RNA oligonucleotides and oligonucleotide conjugates play a critical role in modern day biochemistry and molecular biology research. For example, these agents are used as hybridization probes to detect and characterize DNA; as primers to amplify DNA through polymerase chain reactions (PCR); as primers for DNA sequencing; as substrates for site-directed mutagenesis; as agents for controlling gene expression at both the DNA and RNA level; and as substrates for a variety of biochemical and biophysical studies. In addition, there have been intensive efforts to develop oligonucleotide-based diagnostic and therapeutic agents.

The extensive use of oligonucleotides in these applications has been made possible by the development of automated synthetic procedures. Equally important has been the development of methods to synthesize oligonucleotide conjugates containing various linkers, functional groups, fluorescent tags, and other modifications that impart specific properties, such as nuclease resistance, to the oligonucleotides. The syntheses and properties of oligonucleotide conjugates were extensively reviewed in an article by John Goodchild that appeared in the May/June issue of *Bioconjugate Chemistry* in 1990 *(1)*. This article, which has been cited at least 370 times since its appearance, described methods, both chemical and enzymatic, for preparing backbone modified oligonucleotides and oligonucleotide conjugates, and summarized the general biophysical and biological properties of these molecules. The preparation of modified oligonucleotides and their conjugates continues to be an active and productive area of research as evidenced by the many articles in this area that continue to appear in this journal. Many of the methods described in Goodchild's review are still used today, and reagents for preparing an ever-widening variety of conjugates are commercially available. Because of their central role in molecular biology and their emerging importance as diagnostic/therapeutic tools, it is safe to say that we can look forward to even more novel types and applications of oligonucleotide conjugates in the years to come.

Paul S. Miller

Bloomberg School of Public Health, Biochemistry and Molecular Biology, Johns Hopkins University, 615 North Wolfe Street, Baltimore, Maryland, United States, 21205

LITERATURE CITED

(1) Goodchild, J. (1990) Conjugates of oligonucleotides and modified oligonucleotides: a review of their synthesis and properties. *Bioconjugate Chem. 1*, 165–187.

BC9000855

* pmiller@jhsph.edu.

10.1021/bc9000855 CCC: $40.75 © 2009 American Chemical Society
Published on Web 03/18/2009

REVIEWS

Bioconjugation with Stable Luminescent Lanthanide(III) Chelates Comprising Pyridine Subunits

Jari Hovinen*,† and Pamela M. Guy‡

PerkinElmer Life and Analytical Sciences, Turku Site, POB 10, FI-20101 Turku, Finland, and PerkinElmer Incorporated, Winter Street, Waltham, Massachusetts 02451. Received August 30, 2008; Revised Manuscript Received October 30, 2008

The use of long-lifetime emitting lanthanide(III) chelate labels or probes together with time-resolved fluorometry in detection provides a method to generate sensitive bioaffinity assays. However, the use of stable chelates demands very complicated optimization of the chelate structure. A great number of chelates have been synthesized, but usually, only the most prominent structures were then converted to corresponding biomolecule labeling reactants. This review covers the syntheses of luminescent lanthanide chelates comprising a pyridine subunit that allow solution and solid-phase bioconjugation.

INTRODUCTION

The idea of using lanthanide chelates as labels in time-resolved fluoroimmunoassays was described almost three decades ago (*1, 2*). The use of long-lifetime emitting lanthanide(III) chelate labels or probes together with time-resolved fluorometry in detection has proven its value in the development of highly sensitive bioaffinity assays (*3*). The heterogeneous DELFIA time-resolved fluorometry assay method uses non-luminescent lanthanide(III) chelates as the labels (*4*−*6*). After immunoreaction, lanthanide(III) ions are dissociated from the non-luminescent chelates by lowering pH, and luminescence is enhanced with a mixture of β-diketone, detergent, and trioctylphosphine oxide (TOPO). The resultant chelates have a very high luminescence, giving excellent detection sensitivity. However, the DELFIA time-resolved fluorometry technology is not useful for applications requiring site-specificity. Furthermore, the use of the additional chelator TOPO is essential for high luminescence. In contrast, the FIAgen time-resolved fluorometry system uses a fluorescent 4,7-bis(chlorosulfophenyl)-1,10-phenanthonine-2,9-dicarboxylate europium(III) as the label, and thus in contrast to the DELFIA system, the signal enhancement step is avoided (*7*−*10*). Due to limited chelate stability, FIAgen assays are performed in the presence of an excess of lanthanide ion. Another assay system, sold under trademark TRACE, was the first real homogeneous time-resolved fluorometry system and is based on an energy transfer between a europium(III) chelate of tris(bipyridine)cryptate and an organic fluorophore (*11*). However, detection sensitivity of the FIAgen and TRACE technologies is considerably lower than in assays based on DELFIA technology. To overcome these limitations, better luminescent lanthanide(III) chelates have to be developed.

For time-resolved fluorometry assay systems, a luminescent lanthanide(III) chelate should fulfill several requirements: (a) the molecule has to be photochemically stable, in both the ground and excited states; (b) the molecule has to be kinetically stable; (c) the molecule has to be chemically stable; (d) the excitation wavelength has to be as high as possible, preferably over 330 nm; (e) the molecule must have a high excitation coefficient in the excitation wavelength; (f) the energy transfer from the ligand to the central ion has to be efficient; (g) the luminescence decay time has to be long; (h) the chelate should be readily soluble in water; and (i) the bioactive molecules have to retain their affinities after the coupling to the lanthanide chelate.

Although organic chelators and their substituents have a significant effect on the photophysical properties of lanthanide(III) chelates, no general rules for the estimation of these effects are available. Thus, finding a highly fluorescent chelate structure to fulfill all the requirements for a label with respect to signal, conjugation, stability, and biocompatibility remains as a challenge. Hundreds of stable fluorescent chelates have been developed at numerous laboratories. A great number of chelates synthesized are basic structures that do not allow biomolecule derivatization; usually, only the most prominent structures have been converted to the corresponding biomolecule labeling reactants. Although there are several excellent review articles on the photophysical properties and bioanalytical applications of lanthanide(III) chelates (*12*−*23*), syntheses of luminescent lanthanide(III) chelates has not been reviewed.

Stable luminescent lanthanide(III) chelates consist of a ligand with a reactive group for covalent conjugation to bioactive molecules, an aromatic structure, which absorbs the excitation energy and transfers it to the lanthanide ion, and additional chelating groups such as carboxylic acid moieties and amines. Unlike organic chromophores, these molecules do not suffer from Raman and Rayleigh scattering or concentration quenching. This allows multilabeling and development of chelates bearing several light-absorbing moieties.

The pyridine moiety is by far the most common chromophoric subunit in luminescent lanthanide chelates. When appropriately

* Corresponding author. Dr. Jari Hovinen. Tel + 358 2 2678 513; fax + 358 2 2678 380; jari.hovinen@perkinelmer.com.
† PerkinElmer Life and Analytical Sciences.
‡ PerkinElmer Incorporated.

10.1021/bc800370s CCC: $40.75 © 2009 American Chemical Society
Published on Web 12/15/2008

Scheme 1. Derivatization of Pyridine[a]

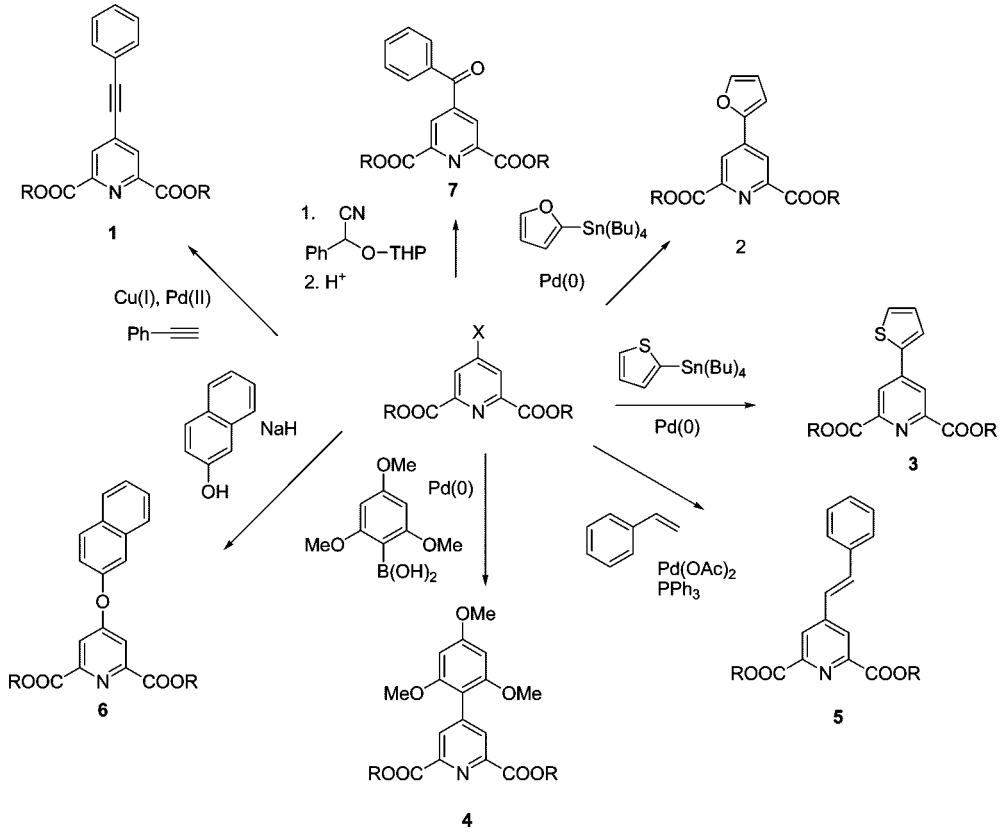

[a] X = Br, I, or Cl; R = an alkyl group.

derivatized, pyridine can serve as the chromophoric moiety alone. Alternatively, it can be present in multimeric forms in open-chain structures and macrocyclic cage-type complexes such as cryptates and cyclic Schiff bases. This review mainly describes synthesis of luminescent lanthanide chelates comprising pyridine subunits that can undergo bioconjugation. Accordingly, luminescent stable chelates with no pyridine subunits, such as those comprising DTPA and DOTA tethered to light-harvesting groups, and chelates based on β-diketones and phenolic compounds, are not discussed here.

THE CHROMOPHORE

A single unsubstituted pyridine moiety is not efficient enough to serve as a light-absorbing and triplet-sensitizing aromatic group in stable luminescent chelates. Thus, pyridine has often been substituted with various energy-absorbing groups. Pyridine analogues conjugated to five-membered heteroaromatic rings have also been prepared. The chromophores of stable chelates are often composed from one to three conjugated pyridine rings, or the pyridine moieties are connected to each other via N, O, or S-containing hydrocarbon chains. While bipyridine and terpyridine moieties are commercially available, preparation of chromophores based on 4-substituted pyridines and pyridines conjugated to five-membered hetereocyclic rings require numerous synthetic manipulations.

Derivatization of C4 of Pyridine. There are numerous methods for attaching additional light absorbing groups to 4-halopyridines (Scheme 1). Phenylethynyl substitution (**1**) has been performed using the Sonogashira reaction (*24*−*26*). Furyl (**2**) and thienyl (**3**) substituted pyridines have been synthesized using the palladium(0)-catalyzed Stille reaction with the corresponding stannyl derivatives of the additional light-absorbing groups (*28*−*31*). Suzuki coupling of the halopyridine with alkoxyphenylboronates gives rise to the alkoxyphenylpyridine chromophore **4** (*32*). The *trans*-4-styrylpyridine derivative (**5**) has been synthesized by Heck coupling with 4-chloropyridine-2,6-dicarboxylate using the mixture of palladium(II) acetate and triphenyl phosphine (*29*). Aromatic nucleophilic substitution has been exploited in the preparation the 4-(2-napthoxy)pyridine derivative (**6**). The 4-benzoylpyridine-2,6-dicarboxylate **7** was obtained under similar conditions using *O*-(tetrahydropyran-2-yl)mandelonitrile followed by acid-catalyzed cleavage of the THP group (*29*).

Derivatization of Terpyridine. This has most commonly been performed using Claisen-Schmidt condensation of various aromatic aldehydes (*33*−*42*) with 2-acetylpyridine to give the (*E*)-propen-2-enones **8** (Scheme 2). Their reaction with *N*-[2-(pyrid-2-yl)-2-oxoethyl]pyridinium iodide and sodium acetate in methanol yielded the terpyridine derivatives **9a**−**d**. Stille reaction between terpyridine 4-triflate **10** and tributylstannyl furan has been utilized in the preparation of 4-furyl terpyridine **11** (*28*).

Pyridine Conjugated to Five-Membered Heteroaromatic Rings. A wide range of lanthanide chelates comprising a pyridine subunit conjugated to one or two heteroaromatic rings have been synthesized and claimed (*29*, *43*−*50*). The conjugated chromophore often exhibits a high excitation coefficient, long excitation wavelength, and good energy transfer from the ligand to the lanthanide ion, giving rise to improvements in detection sensitivity. However, only few of these chelates have been converted to the corresponding biomolecule labeling reactants. The key steps of the syntheses of their chromophores are shown in Scheme 3. The preparation of 2,2′-(1*H*-pyrazole-1,3-diyl)-bispyridine chromophore **15** involves treatment of 6-methyl-2-acetylpyridine **12** with *N*,*N*-dimethylformamide dimethyl acetal to give rise to (*E*)-3-(dimethylamino)-1-(6-methylpyridin-2-yl)prop-2-en-1-one **13**, which is cyclized to 2-methyl-6-(1*H*-pyrazol-3-yl)pyridine **14** with hydrazine hydrate followed by

Scheme 2. Derivatization of Terpyridine

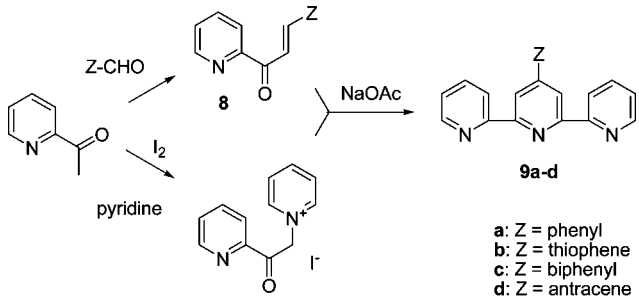

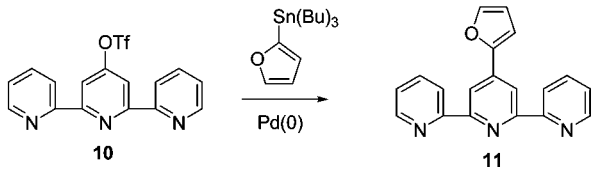

Scheme 3. Preparation of Chromophores Comprising Pyridine Conjugated to Five-Membered Heteroaromatic Ring

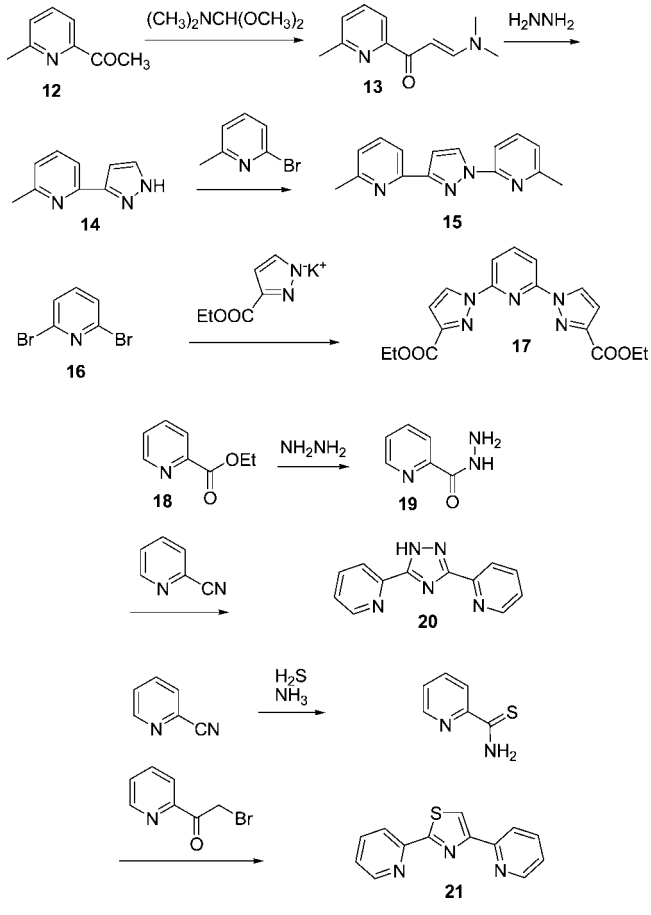

reaction with 2-bromo-6-methylpyridine (*29*). The key reaction of the most recent synthesis of 2,6-bis(3-methyl-1-pyrazolyl)pyridine **17** starts from nucleophilic substitution of the bromine atoms of 2,6-dibromopyridine **16** with potassium 3-ethoxycarbonylpyrazole in diglyme (*50*). The triazole derivative **20** has been prepared using 2-pyridinecarboxylate **18** as the starting material that was initially treated with hydrazine hydrate to give 2-pyridylhydrazide **19**, the reaction of which with picolinonitrile at 160 °C gave the desired heterocycle (*43*). Synthesis of the thiazole derivative **21** includes treatment of picolinonitrile with

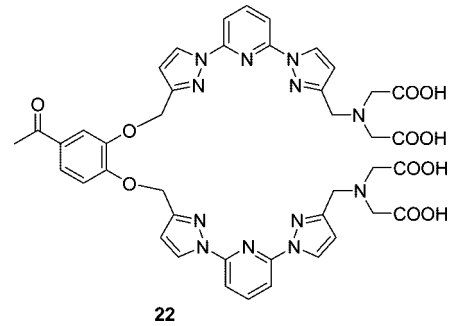

Figure 1. A ligand with two 2,6-bis(*N*-pyrazol-11-yl)pyridine subunits.

hydrogen sulfide in ammonia followed by cyclization with 2-bromoacetylpyridine (*43*).

Lanthanide(III) chelates based on 2,6-bis(*N*-pyrazolyl)pyridine **17** and 6,6′-(1*H*-pyrazole-1,3-diyl)bis(pyridine) **15** are among the best and most widely used luminescent terbium(III) chelates synthesized: they have excellent photophysical properties including high luminescent quantum yield and relatively high energy of their lowest triplet state. The chromophore of the lanthanide chelate comprising 1,2,4-triazol-3,5-ylene subunit **20** is negatively charged, a property that stabilizes the chelate. Its suitability in immunoassays has been demonstrated (*43*). No applications for the chelate comprising the chromophore **21** have been published. Also, chelates derived from 2,6-bis(*N*-pyrazol-11-yl)pyridine motif attached to aceto/benzophenone and iminodiatetic subunits **22** (Figure 1) have been synthesized (*51*); however, their quantum yields were significantly lower than those of simpler complexes.

THE CHELATING PART

The lanthanide chelate has to be stable in the presence of external chelators such as EDTA and relatively low pH conditions sometimes used in biochemical assays. Tolerance to high temperatures is required in nucleic acid based assays employing thermal cycling. Because the chromophoric moiety binds weakly to the lanthanide ion, the chelate requires additional metal coordination sites. Enhancement in stability has been obtained by adding chelating groups such as carboxylic acid and phosphonate moieties to the chromophore. Alternatively, incorporating several fluorogenic ligands into one structure (*52*) or encapsulating the metal ion to the chromophoric structure forming polycyclic cage-type compounds such as cryptates and macrocyclic Schiff's bases have been used to enhance stability.

Carboxylic Acid Derivatives. Methods for attaching chelating carboxylic and phosphonic acid moieties to chromophores are shown in Scheme 4. A pyridine ring **23** has been converted to the *N*-oxide **24** using an oxidizer such as *m*-chloroperbenzoic acid or magnesium perphthalate (*29*, *35*, *40*, *53*). There are enormous differences in the reactivities of the pyridine rings: while the terminal pyridine rings of terpyridine are readily oxidized with *m*-chloroperbenzoic acid in dichloromethane in a few hours at ambient temperature, a prolonged reaction time (perphthalate in acetic acid; 8 days at 80 °C) was required for the preparation of the di-*N*-oxide of **15** (*29*). The *N*-oxides have been converted to the corresponding carbonitriles **25** by a modified Reissert-Henze reaction, the reduction of which with borane yields the amines **26** that have been carboxymethylated with alkyl bromoacetate followed by hydrolysis to give the iminoacetic acid derivatives **27**. The nitrile **25** has also been hydrolyzed to carboxylic acid **28**, which was esterified followed by reduction to the alcohol **29** (*29, 53*−*57*). The cyanide **25** has also been obtained by nucleophilic substitution of 2-bro-

Scheme 4[a]

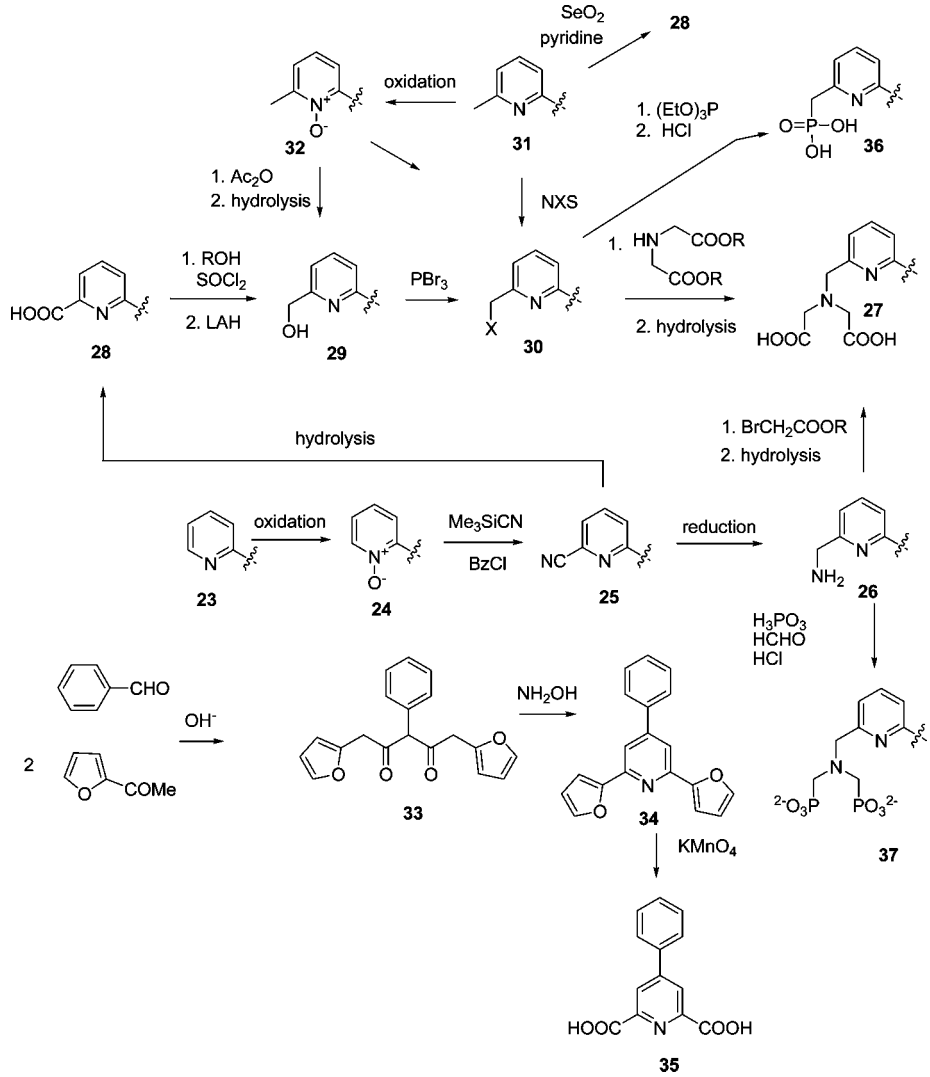

[a] X = Br or Cl; some substituents are omitted for clarity.

mopyridine derivative with cyanide ion (*54*). Treatment of **29** with phosphorus tribromide in DMF or chloroform gives the bromide **30** that has been allowed to react with iminoacetic acid ester followed by hydrolysis to give **27**.

Several alternative approaches have been used when 2-methylpyridine or its derivatives **31** have been used as the key intermediates. One route involves free radical halogenation (*24*, *48*, *53*, *55*) to **30** followed by substitution with iminoacetic acid ester and ester hydrolysis. However, the yield of the free radical reaction may be low due to the formation of unsymmetrical byproduct and the products of different halogenation steps. The yield is highly related to the structure of the alkylpyridine derivative (*57*). Another route comprises oxidation of **31** to the corresponding *N*-oxide **32**. Treatment of this with acetic anhydride followed by base-catalyzed hydrolysis gives the methanol **29** that was converted to the bromide **30** (*29*). The picolinate **31** has also been oxidized to carboxylic acid **28** using selenium(IV) oxide in refluxing pyridine (*53*).

When 2-alkyl picolinates are used as key intermediates, the ester is either hydrolyzed to acid (*23*) or it is reduced to alcohol with $NaBH_4$, followed by bromination with PBr_3, substitution with iminoacetic acid ester, and hydrolysis (*23*).

A method disclosed by Hale and Solas (*52*) includes base-catalyzed condensation of 2-acetylfuran and benzaldehyde to give the pentanedione **33**, which was further converted to the furylpyridine **34** by treatment with hydroxylamine that was finally oxidized to the desired acid **35**.

Phosphonate ligands (**36**, **37**) have been synthesized by an Arbuzov reaction between the bromide **30** and triethyl phosphate followed by ester hydrolysis and by treatment of the amine **26** with H_3PO_3 and formaldehyde in the presence of HCl (*53*). Because there are fewer water molecules coordinated to the lanthanide ion than in the corresponding carboxylate chelate, the phosphonate group has a positive effect on the luminescence. The phosphonate chelates have a high negative charge, and therefore, their coupling to bioactive molecules could change the physical properties of the conjugate. No biomolecule labeling reactants containing phosphonates as chelating units have been synthesized.

Azamacrocycles. Macrocyclic lanthanide chelates comprising an intracyclic chromophoric unit (pyridine, bipyridine, terpyridine, bis(pyrazol-1-yl)pyridine) and pendant carboxylate groups have been shown to exhibit high chelate stability and promising photophysical properties (*23*, *40*, *58*−*63*). Also, macrocycles in which the chromphore comprises two nonconjugated pyridine subunits tethered to each other via a nitrogen-containing hydrocarbon chain has been described and claimed in patents (*28*,*32*). The crucial step in the ligand synthesis is the macrocyclization reaction. Azamacrocyles have been traditionally synthesized via the method of Richman and Atkins (*64*) by condensing disodium

Scheme 5. Preparation of Azamacrocycles[a]

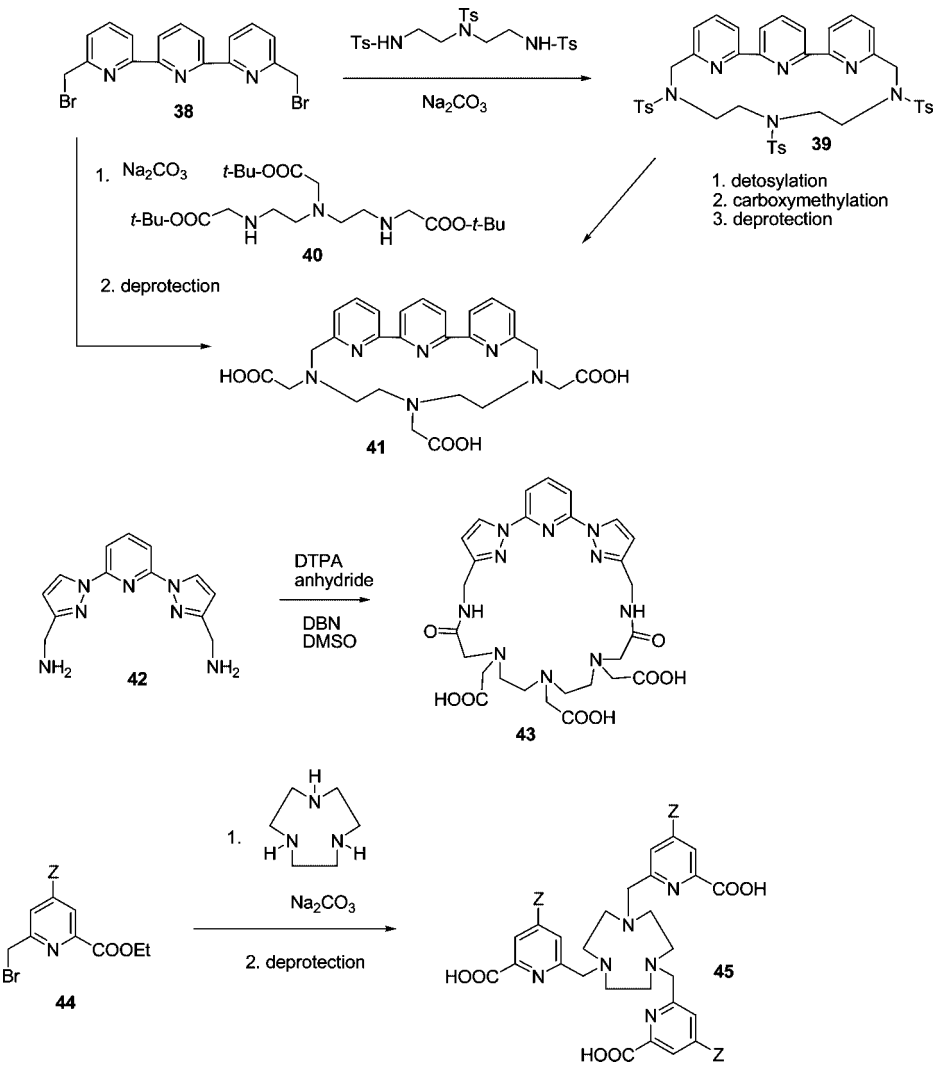

[a] Z = an aromatic group.

salts of pertosylated amines with dihalogeno fragments of the chromophore (Scheme 5). According to the latest modification of this reaction, the synthesis involves a reaction between a bifunctional electrophile (e.g., a dibromide or ditosylate) and a pernosylated amine in dry DMF at an elevated temperature in the presence of cesium or sodium carbonate (*65*−*67*). Finally, the tosyl or nosyl groups are removed with acid or thiol in the presence of base, respectively, giving the desired azamacrocycle. Carboxyalkylation of the secondary amines gives the desired ligands. Also, a cyclization reaction utilizing the Mitsunobu reaction between a dihydroxy fragment of the chromophore and a pernosylated amine has been used (*68*). Galaup et al. have reported an elegant direct method to 18-membered hexaazamacrocyles comprising a functionalized 2,2′:6′,2″-terpyridine moiety **41**, exploiting a metal template ion effect on the macrocylization step (*60*). The acetate pedant arm **40** was synthesized in five steps starting from diethylenetriamine.

Brunet et al. allowed a diamino fragment of the chromophore to react with DTPA anhydride in the presence of base (*63*) to give **43**. The reaction was performed in high dilution, and the yield of the desired ligand was relatively low.

Lanthanide chelates based on 1,4,7-triazacyclononane **45** and 1,4,7-triazacyclodecane also exhibit high kinetic and thermodynamic stabilities (*28*, *32*). Their synthesis is straightforward and involves alkylation of the azacycloalkane with the bromomethyl derivatives of the desired chromophore **44**.

Cryptates. Macropolycyclic inclusion complexes, cryptates, have been designed to provide lanthanide chelates of high kinetic and thermodynamic stability. Practically, all lanthanide chelate cryptates containing bivalent heterocyclic unsaturated five-membered rings and/or one or more pyridine derivatives as a chromophore have been claimed in patents (*42*, *43*, *62*, *69*, *70*). However, only few of these compounds have been synthesized and converted to the corresponding biomolecule labeling reactants. Preparation of cryptates comprising the 4,13-diaza-18-crown 6 ether moiety involves alkylation of the secondary amines with a chromophore having two bromoalkyl groups (Scheme 6). The cryptand formation is assisted by using a metal ion as a directing template. When the metal ion used is a lanthanide (*42*, *71*), the desired lanthanide chelate is formed; otherwise, an additional prolonged metal exchange reaction is needed. The usefulness of cryptates containing a 4,13-diaza-18-crown 6 ether subunit for biomolecule derivatization has not been demonstrated.

The only commercialized lanthanide cryptant is the europium chelate based on three bipyridine moieties **46**. It has been synthesized by treatment of 2,6′-aminomethylbipyridine and 2 equiv of the corresponding dibromide in the presence of base.

Cryptates are kinetically inert and have good stability, because the lanthanide ion is tightly closed inside the molecular cavity. However, the positive net charge may have an adverse effect on antibodies, which are widely used bioactive components in

Scheme 6. Synthesis of Cryptands and Schiff'S Bases[a]

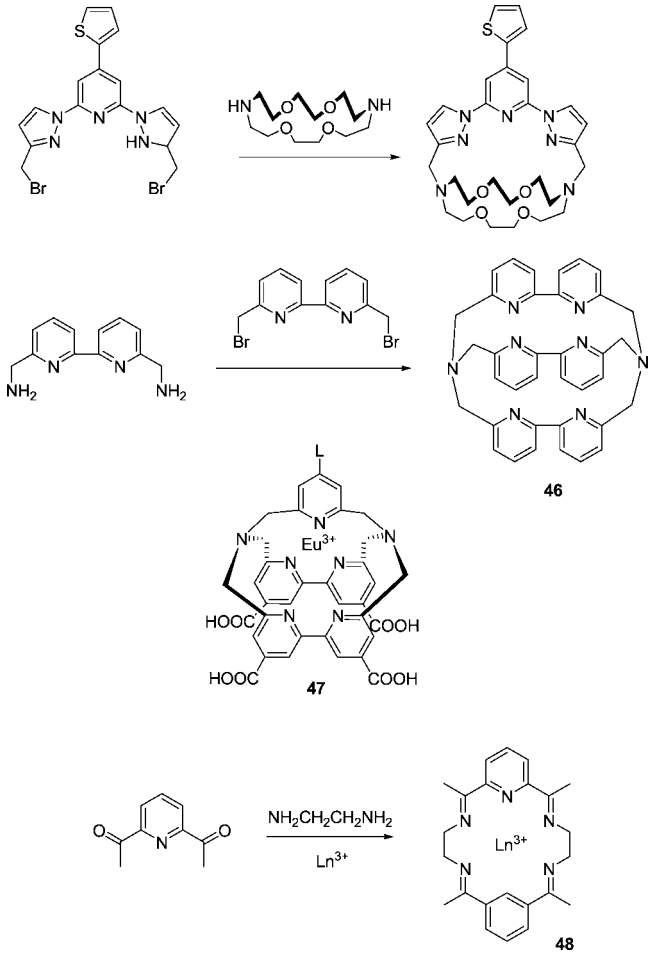

[a] L = a linker.

common assay formats. In addition, water and negatively charged quenchers present in samples must be removed by treatment with fluoride ion. These disadvantages are not present in **47**, since the molecule has a net charge of −1. Also, its quantum yield is relatively high (*70*).

Macrocyclic Schiff Bases. Lanthanide chelates having a macrocyclic Schiff base **48** as a ligand can be prepared from 2,6-diacetylpyridine and diaminoalkane by using a lanthanide ion as a template (Scheme 6). Although Schiff bases are normally labile, the lanthanide ion stabilizes the macrocyclic moiety if the structure formed is an 18-membered macrocycle (*72*). Due to limited chelate stability, assays have been performed in the presence of excess lanthanide ion. Detection sensitivity has been enhanced by using the chelate in association with dissociative enhancement (*73*) or as a mixed ligand chelate with thenoyltrifluoroacetone (*74*).

Figure 2 shows different ligands containing the pyridinyl-4-phenylethynyl chromophore. The corresponding chelates differ from each other with regard to lanthanide/ligand ratio and stability constants of the formed complex. The tridentate pyridine dicarboxylic acid **49** forms 1/1, 1/2, and 1/3 complexes with lanthanide(III) ions, but only the 1/3 complex is highly luminescent. Thus, this ligand is unsuitable for biomolecule derivatization. Ligands with seven or more chelating groups **50**−**56** form luminescent 1/1 chelates with lanthanide(III) ions and thus are suitable for bioconjugation. The stability of the chelate is usually increased as the number of ligating atoms of the chelate are increased. Simultaneously, the number of coordinating water molecules in the first coordinating sphere of the lanthanide ion and the quenching effect of O−H vibrations are decreased, giving rise to enhanced luminescence. Chelate stability has been enhanced by linking several chelates together to give rise to multidentate structures. However, the chelate has to be saturated using an excess of lanthanide ion if the single subunit is tridentate (*75*).

Since lanthanide chelates do not suffer from concentration quenching, development of chelates bearing several light-absorbing moieties is possible. In particular, chelates comprising a triazacyclononane **56** backbone have been shown to be highly luminescent (*28, 30, 32*). The corresponding triazacyclododecane **57** is practically nonluminescent (*30*).

THE LINKER

Although in many applications a reactive group for biomolecule conjugation can be attached directly to the chromophoric group or to the chelating part, it is often desirable, for steric reasons, to have a linker between the reactive group and the chromophoric group or chelating part, respectively. The linker is especially important in case the chelate should be used in solid-phase syntheses of oligopeptides and oligonucleotides, but it is often desirable also when labeling biomolecules in solution.

In one strategy for attaching a linker, an aromatic bromide or iodide was allowed to react with a linker tethered to a terminal alkynyl group using Sonogashira reaction (*28*). Elongation of an amine function was performed using reactions of peptide bond formation. Aromatic amino groups of low reactivity require the use of reactive activators such as HATU (*76*) and 1-(2-mesitylenesulfonyl)-3-nitro-1,2,4-triazole (*24*).

For the preparation of terpyridyl ethers with an ω-substituent, three methods have been reported. The method of Newkome and He (*77*) involves nucleophilic substitution of 4′-chloro-2,2′:6′,2″-terpyridine with various ω-substituted alcohols or thiols in the presence of an excess of KOH in DMSO at elevated temperature (Scheme 7, route A). Although the reactions have to be performed in rather drastic reaction conditions, a wide variety of linkers have been introduced in high yield (*78, 79*). Another tethering strategy, developed by Constable and co-workers (*80*) involves an S_N2 reaction between the nucleophilic 2,6-di(pyridin-2-yl)pyridin-4(1*H*)-one and a tether molecule bearing a good leaving group in its structure (Scheme 7, route B). The third method is based a reaction 2,6-di(pyridin-2-yl)pyridin-4(1*H*)-one and an alcohol under Mitsunobu reaction (Scheme 7, route C). Since the reaction conditions are mild, a wide range of linkers tethered to various substituents can be synthesized (*81*). The reaction has shown to be applicable to pyridine derivatization also.

The addition of a binding arm to energetically isolated positions, such as to the chelating imidoacetate group, allows development of structures without changing the energetic profile of the aromatic part on conjugation. However, synthesis of these structures is more challenging unless the presence of two linker arms for biomolecule derivatization is accepted. Attachment of a single linker arm to the chelating imidoacetate group involves two S_N2 reactions with different amines of similar reactivities reducing the yield of the desired product (*82*). The method also calls for preparation of a modified iminoacetic acid ester (Scheme 8).

When the chromophores are linked to each other via a nitrogen-containing hydrocarbon chain, the linker has been attached to this unit (Scheme 9). Several nine dentate derivatives have been synthesized by a S_N2 reaction of a primary amine in the presence of an excess of a bromide (*28, 32, 83*). The corresponding azamacrocycles have been synthesized using a carbon-substituted cyclic amine (*28, 32, 84*) (Scheme 10). Site-specific derivatization of azacycloalkane bearing a single tether

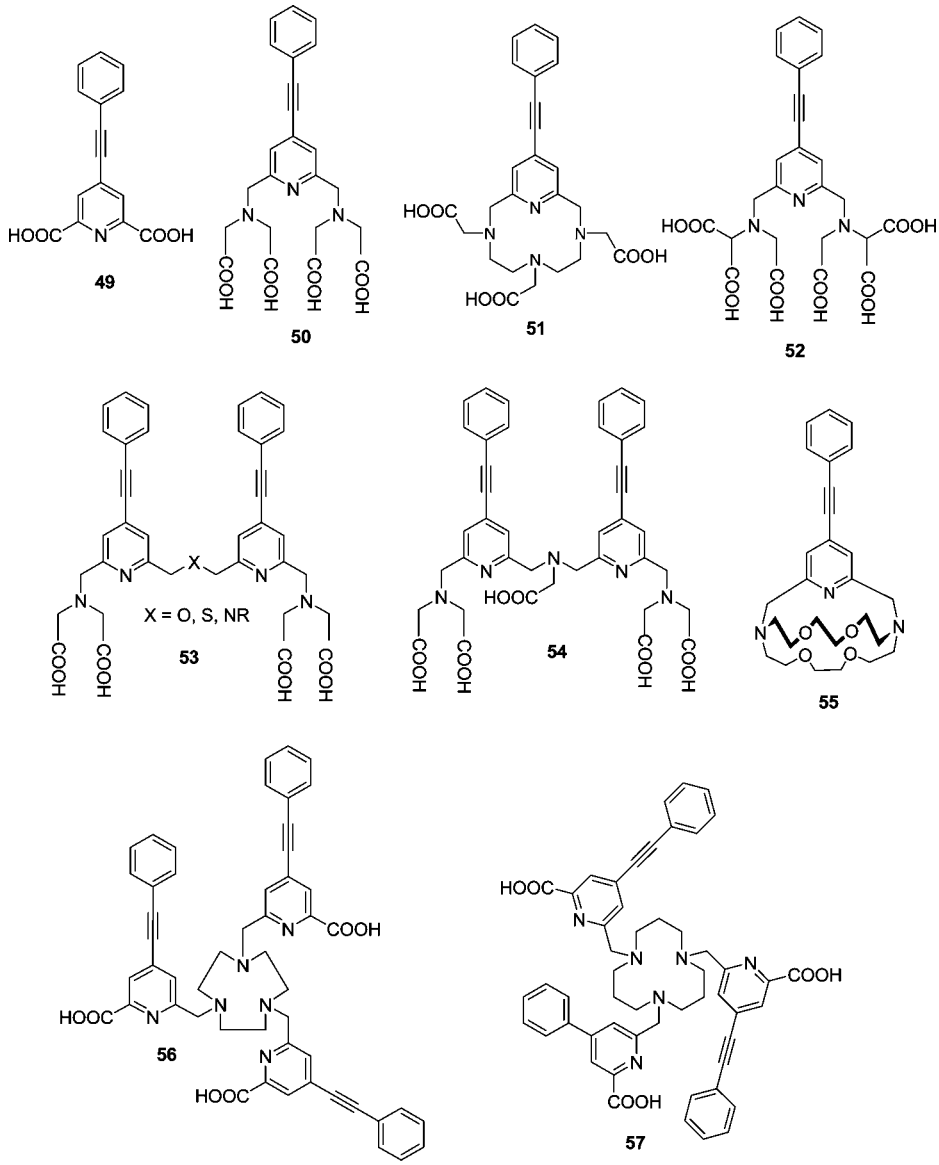

Figure 2. Ligands containing 4-(phenylethynyl)pyridine chromophore.

Scheme 7

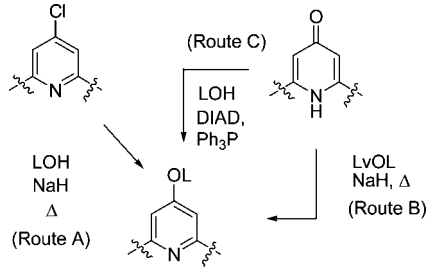

L = a Linker; Lv = a leaving group.

arm at one of the chromophores was performed using a bis-protected triazacyclononane (*28, 32*).

THE REACTIVE GROUP

In several applications, covalent conjugation of the chelate to bioactive molecules is required. Most commonly, this is performed in solution by allowing a chelate with a reactive group to react with a functional group of a bioactive molecule (*85*). Although derivatization of synthetic biomolecules can be conveniently performed on solid phase using standard oligopeptide and oligonucleotide synthesizers, solution-phase labeling of large biomolecules, such as proteins, is also important. In these cases, the labeling reaction must be as selective and effective as possible. Preparation of the most common activations is depicted in Scheme 11.

Labeling in Solution. Synthesis of the activated chelate often involves reaction of an amino chelate with the desired activator. Treatment of an amine with thiourea gives rise to the corresponding isothiocyanate (*86*). An aromatic isothiocyanate reacts smoothly with primary amino groups forming thiourea bonds (optimal pH of the reaction is 9.0−9.5). Aromatic isothiocyanate is commonly employed for the coupling of lanthanide chelates to proteins, oligopeptides, and oligonucleotides tethered to primary amino groups. Since the aliphatic isothiocyanate is considerably less reactive, this group does not have preparative value.

Amino groups of biomolecules can be selectively labeled also with arenesulfonyl activated chelates (*10*). Due to quite drastic reaction conditions, the activation has to be performed before chelate formation. Although the activated chelate contains two reactive arenesulfonyl groups in its structure, no formation of protein polymers during labeling (protein−protein cross-links)

Scheme 8. Introduction of the Linker Arm to an Energetically Isolated Position of Terpyridine[a]

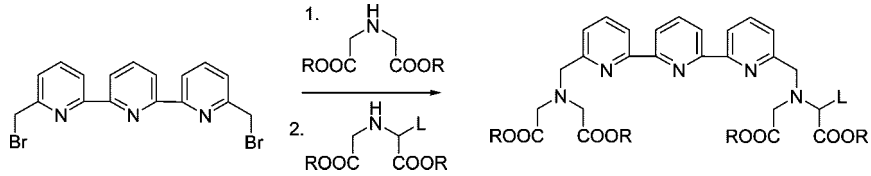

[a] L = a linker; R = an alkyl group.

Scheme 9. Introduction of the Linker between the Chromophores[a]

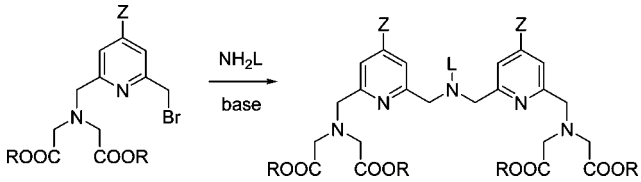

[a] L = a linker; R = an alkyl group; Z = an aromatic group.

have been observed. The same has been later observed for an europium chelate tethered to two aromatic isothiocyanate groups (*87*).

When high reactivity is required, the 4,6-dichloro-1,3,5-triazin-3-yl group (DTA) is the activation of choice. The activated chelate has been prepared by treating the amino chelate with cyanuric acid. DTA allows labeling of all functional groups of proteins (*87, 88*). This function has been used even in the labeling of hydroxy groups of sugars. Due to the high reactivity, the selectivity is lost. A study has been conducted to evaluate various less reactive DTA derivatives and their effects on chelate luminescence and antibody functionality by replacing one of the chlorine atoms in the triazine ring with a deactivating substituent (*89*). Histidine and tyrosine residues can be selectively labeled using diazonium coupling. Although no luminescent lanthanide chelates tethered to diazo groups have been synthesized (*90*), they have been claimed in several patents.

Thiols are know to react with haloacetamides, maleimides, disulfides and their analogues, mercurials, vinyl sulfones, aryl halides, aziridines, and oxiranes (*91*). For coupling purposes, the reactions of haloacetamides, maleimides, and disulfides are most commonly employed. From them, the haloacetyl derivatives display a wide range of other reactivities, while disulfides are practically completely specific to thiols. The reactivity of maleimides is intermediate between them. The problem with using disulfides is lability of the bioconjugate in the presence of reducing agents, which are often present in the conjugation reaction. The haloacetamide chelates have been synthesized by allowing the amino chelates or ligands to react with the haloacetic anhydride or halide (*87*). Because of the high reactivity of haloacetamides, the pH of the conjugation reaction has to be carefully controlled. At too low pH, the reaction is slow, while at too high pH, amino functions, often abundantly present in the bioactive molecule to be labeled, compete with the target mercapto function for the label. Accordingly, the haloacetamides are most specific toward thiols at neutral pH. Maleimides have been synthesized by allowing amino chelates or ligands to react with carboxylic acid derivatives bearing an ω-maleimide substituent in the presence of appropriate activating agents (*76*). Disulfides have been prepared by allowing amino chelates to react with the NHS ester of 3-(2-(pyridin-2-yl)-disulfanyl)propanoic acid (*92*). Ge and Selvin allowed a modified DTPA anhydride to react with primary maleimidopropionic acid hydrazide and aminoethylmethanethiosulfonate to give the corresponding mercapto selective labeling reactants (*93*).

Although *N*-hydroxysuccinimidyl (NHS) ester is one of the most common functional groups used in bioanalytical chemistry for covalent coupling of labels to primary amino groups of biomolecules, this activation has not been widely applied to lanthanide chelate conjugation. The coupling reaction with NHS esters is performed under mild alkaline conditions under which the ester reacts specifically with primary amino groups. NHS coupling is not harmful to biologically active compounds, and high reaction yields can be achieved, minimizing protein denaturation. Wieder et al. allowed a chelate comprising an aromatic amino group to react with bis NHS ester of dicarboxylic acid to give rise to the chelate tethered to NHS group (*92*). NHS ester **58** was prepared by allowing the corresponding carboxylic acid to react with *N*-hydroxysuccinimide in the presence of DCC (*46*) (Scheme 12). In this case, the reactive group is attached to the energetically isolated position, but the net charge of the chelate is changed. The NHS ester was not isolated but used in situ for bioconjugation. Weibel et al. (*94*) prepared a europium chelate based on a glutamic acid skeleton bis-functionalized on its nitrogen atoms by 6-methylene-6′-carboxy-2,2′-bipyridine chromophoric units **59**. Since the propionate function on the glutamic residue remained uncoordinated to the central ion, its esterification into an activated *N*-hydroxysuccinimidyl ester could be performed.

Amino groups can be conjugated directly to carboxylic acid groups in the presence of water soluble carbodiimides such as EDAC. This reaction has been utilized especially for antibody and steroid conjugation (*92, 95, 96*).

O-Alkyl hydroxylamines are known to react chemoselectively with ketones and aldehydes under mild conditions, giving stabile oximes in excellent yield. Although aminooxy chelates have been claimed in numerous patents and patent applications, only one stable luminescent europium chelate tethered to a aminooxy group **60** (Figure 3) has been prepared and used for carbonyl group conjugation (*97*). The same chelate structure tethered to a mercapto group **61** has been synthesized and exploited in the detection of phosphopeptides by phosphate elimination and subsequent Michael addition (*98*). Poupart et al. synthesized the aldehyde **62** and used it in oligonucleotide conjugation (*99*). The Schiff base formed was further stabilized by reduction with borohydride to the corresponding amine.

The thioester-mediated ligation of unprotected peptide segments, called natural chemical ligation, has been demonstrated to be extremely effective for the rapid and efficient chemical synthesis of proteins and long oligopeptides (*100*). The method is based on the reaction of a peptide containing a thioester at the α-carboxy group with the *N*-terminal Cys residue of another peptide. The initial thioester ligation product then undergoes rapid intramolecular reaction giving rise to a native peptide bond at the ligation site. In addition to the synthesis of proteins and long oligopeptides, natural chemical ligation has been successfully used in the introduction of affinity groups and organic fluorophores to proteins. A lanthanide chelate tethered to thioester bond **63** has been prepared by allowing a chelate bearing a primary amine to react with pentafluorophenyl *S*-benzyl thiosuccinate (*99*).

Scheme 10. Derivatization of Ligands Comprising Azacycloalkane Backbone[a]

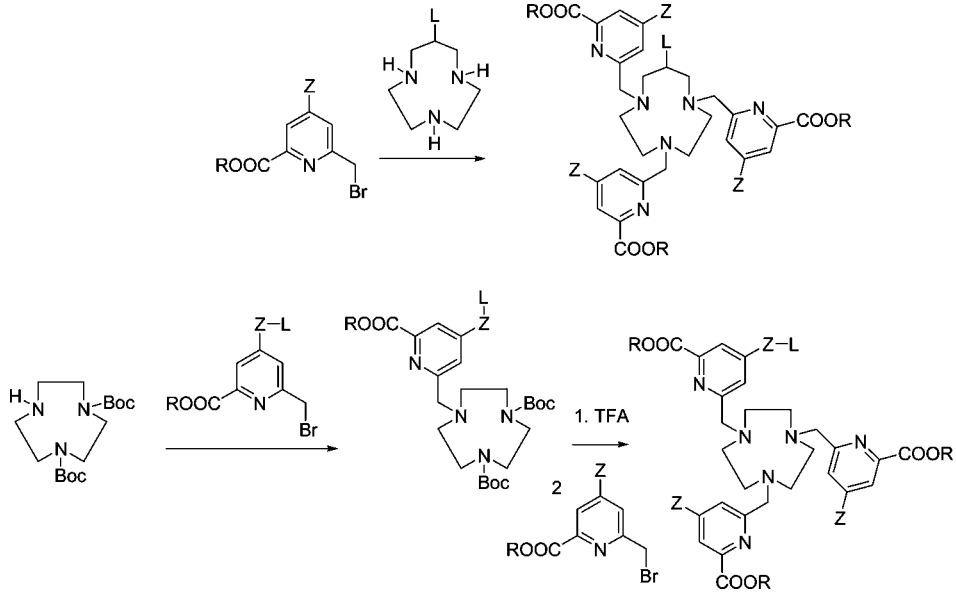

[a] L = a linker; R = an alkyl group; Z = an aromatic group.

Scheme 11. Activation of an Aromatic Amino Group[a]

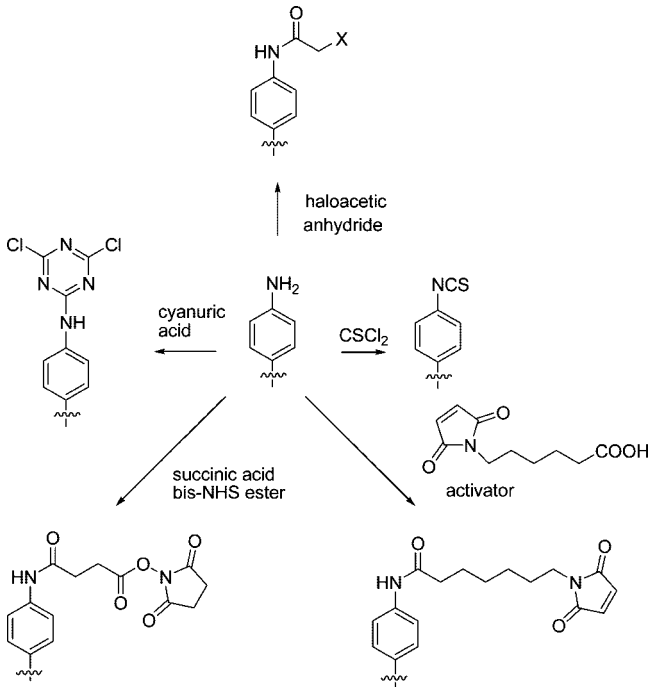

[a] X = Br or I.

The copper(I) catalyzed Huisgen's dipolar [2 + 3] cycloaddition of azide and alkynes, called "click chemistry", is a powerful direct method to prepare 1,4-disubstituted 1,2,3-triazoles (*101*). This reaction has been utilized increasingly also in the conjugation of various label molecules to nanomaterials and biomolecules. Recently, this reaction has been utilized with lanthanide chelates (*99*). For example, a protected ligand tethered to an azido group **64** has been reacted with a steroid tethered to an ethynyl group in the presence of copper(I). Removal of the protecting groups followed by treatment with europium ion gave the desired steroid conjugate.

Statistical labeling of oligonucleotides, DNA, RNA and proteins was done using labels tethered to derivatives of *cis*-platinum (*102*). In nucleic acids, the platinum predominantly coordinates to N7 of guanine residues. Although no luminescent lanthanide chelates tethered to platinum have been synthesized, the patent (*102*) has claims directed to platinum tethered to any detectable group. Statistical phosphate labeling using lanthanide titanocene conjugates, such as **65** has also been proposed (*103*).

It has been shown that detection sensitivity can be dramatically enhanced by incorporating lanthanide(III) chelates into particles. Beads containing lanthanide(III) chelates as dye molecules have most commonly been prepared simply by swelling chelates into the bead polymer (*104*). Few of this type of labeled beads are currently commercially available (*23*). If the lanthanide(III) chelates are not covalently bound to the polymer particles, the signal obtained from the particles may decrease as a function of the time because of leaking. This problem has been avoided by linking the chelate covalently to a matrix (*31, 105*−*107*). In case the chelate should be attached to a microparticle or nanoparticle during the manufacturing process of the particles, a lanthanide chelate tethered to a polymerizable group is required. For this purpose, europium(III) chelates based on thienylpyridine subunits tethered to an acrylamide function **66** have been synthesized (*31*).

Labeling on Solid Phase. In almost all biomolecule labelings, the reaction is performed with an excess of an activated label, and accordingly, laborious purification procedures cannot be avoided. In particular, when attachment of several label molecules, or site-specific labeling in the presence of several functional groups of similar reactivity, is desired the isolation and characterization of the resultant biomolecule conjugate is extremely difficult, and often practically impossible. The biomolecule conjugates used in many applications, such as homogeneous quenching assays, must be extremely pure, because even small amounts of fluorescent impurities considerably increase luminescence background and thereby reduce detection sensitivity. Thus, it is highly desirable to perform conjugation of biomolecules on a solid phase, allowing removal of most impurities by washing while the biomolecule is anchored to the solid support. Once the complex is released into the solution, only a single chromatographic or electrophoretic purification is required.

Solid-phase labeling of oligopeptides calls for preparation of the corresponding oligopeptide building blocks (*108*−*110*). Most commonly, the block has an activatable carboxylic acid function and an α-amino group bearing a transient protecting group. The chelating part has to be masked with permanent protecting

Scheme 12. NHS Activation at the Energetically Isolated Position

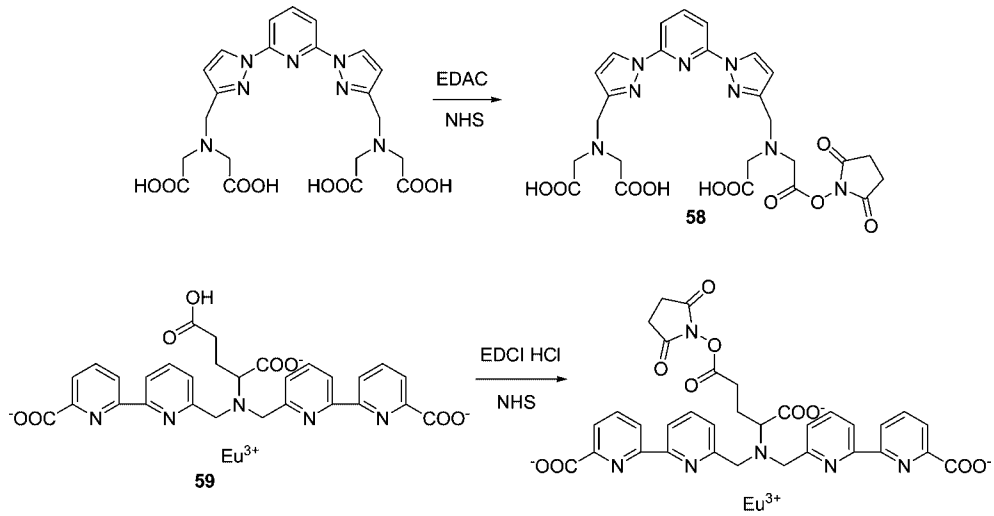

groups. Building blocks that allow solid-phase introduction of luminescent europium and terbium chelates to olipeptides using standard Fmoc chemistry are shown in Figure 4. The blocks have been coupled either to the amino or carboxyl terminus or to the internal position of the coding sequence using prolonged coupling time but otherwise standard conditions (Scheme 13). The coupling efficiencies of these blocks are comparable to natural amino acid analogues. After completion of the oligopeptide synthesis, the oligopeptides were deprotected and released from the resin using standard procedures. Treatment of the

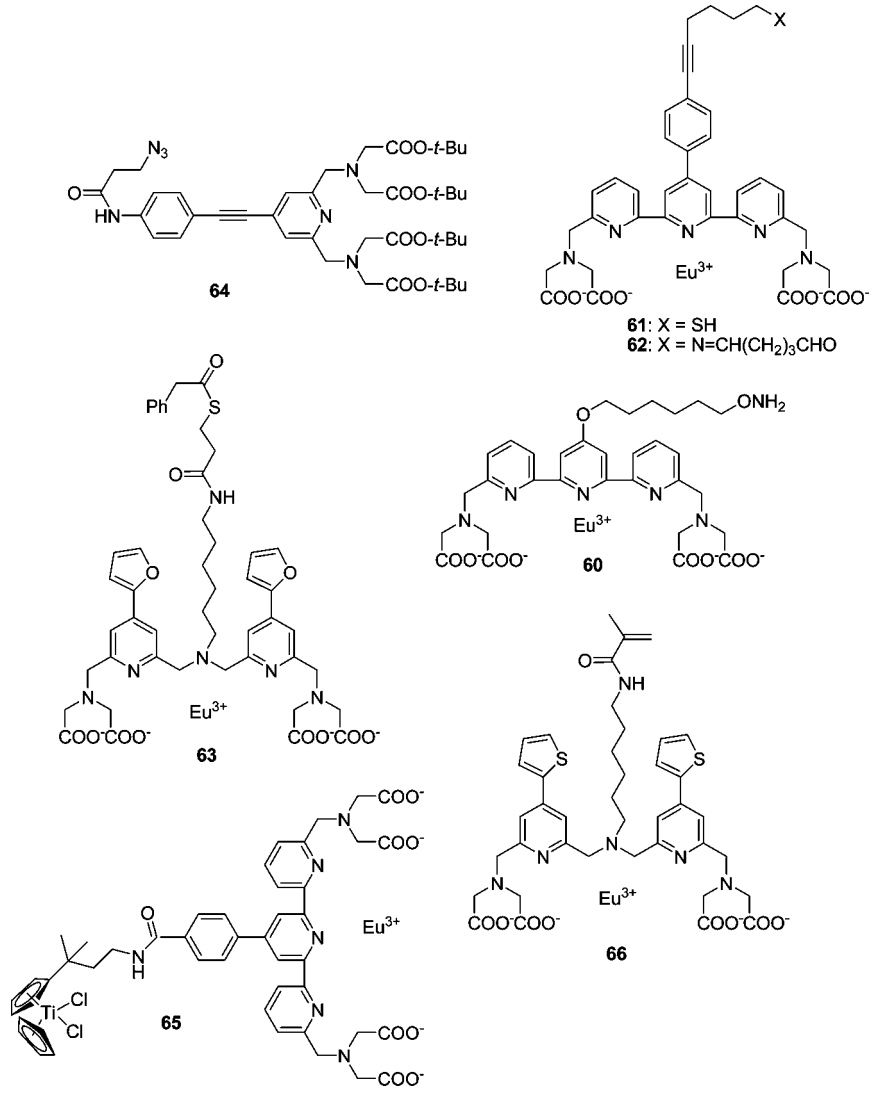

Figure 3. Europium(III) chelates tethered to reactive groups.

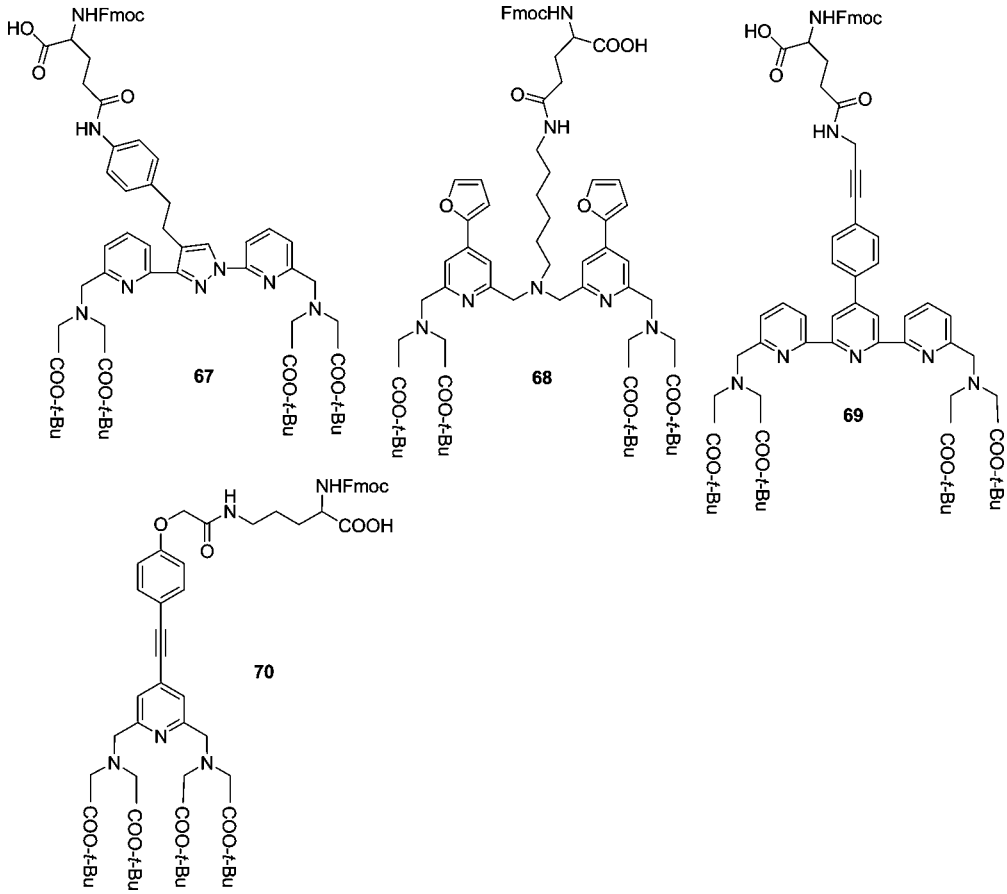

Figure 4. Oligopeptide labeling reactants.

Scheme 13. Labeling of Oligopeptides on Solid Phase

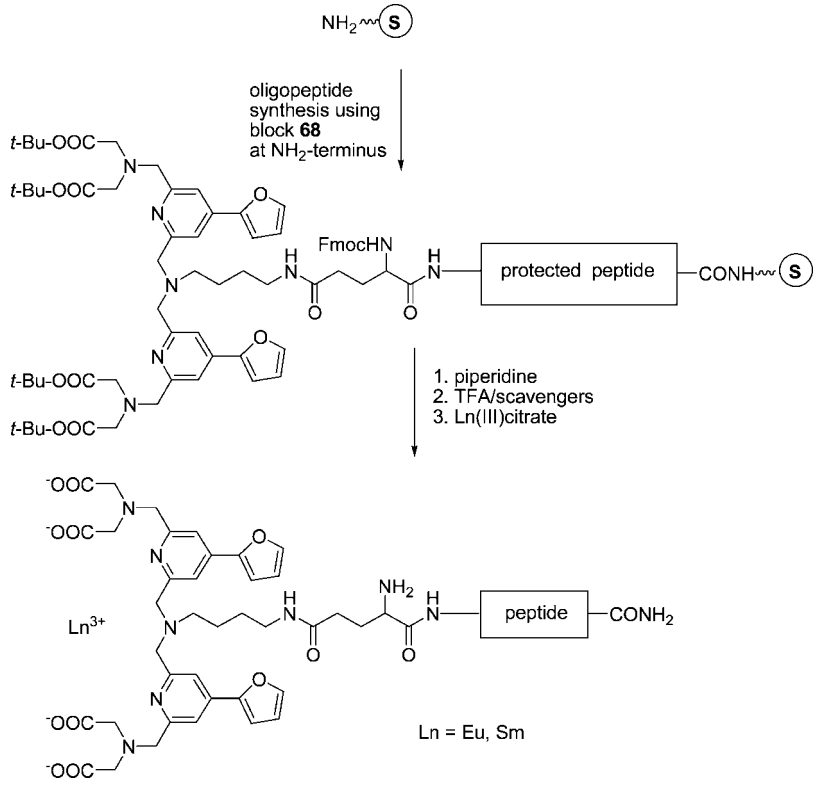

deblocked oligomers with lanthanide(III) salt converts the oligopeptide conjugate to the corresponding lanthanide chelate. These blocks have been shown to be suitable for solid-phase steroid derivatization also (*108*).

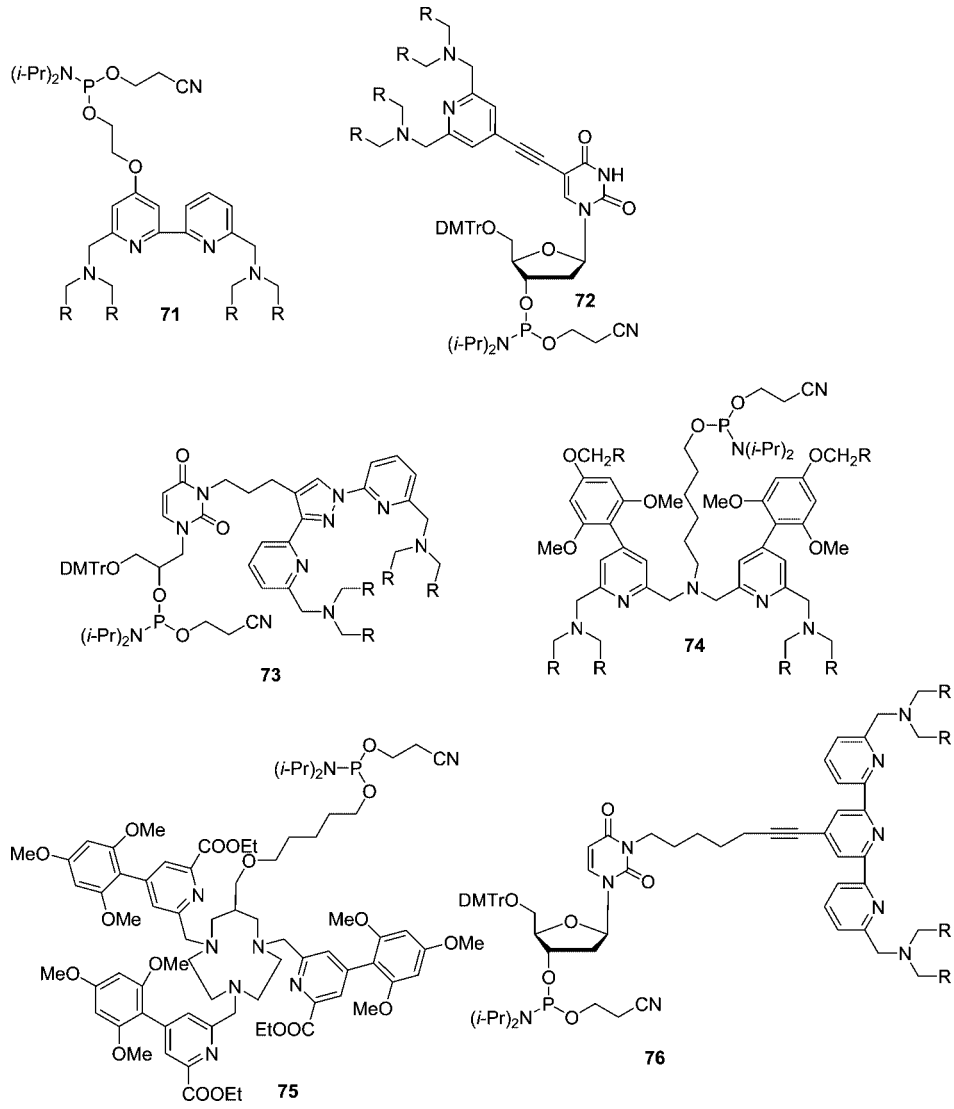

Figure 5. Oligonucleotide labeling reactants. R = COOMe.

Several nucleosidic and non-nucleosidic building blocks useful for solid-phase oligonucleotide derivatization with lanthanide chelates have been prepared. Illustrative examples are shown in Figure 5. The key step in this labeling reaction is the phosphitylation of the corresponding protected ligand tethered to a hydroxy group. Synthesis of the hydroxy group comprising the precursor has been performed as described above. The chelating carboxylic acid functions were protected with base labile groups compatible with standard oligonucleotide synthesis. Originally, Kwiatkowski et al. synthesized a non-nucleosidic bipyridine derivative **71** that can be coupled to oligonucleotide by phosphoramidite chemistry (*111*). Later, various non-nucleosidic terbium, dysprosium, samarium, and europium blocks in which the linker was attached at the chromophore have been prepared (*28, 112*). The non-nucleosidic blocks are suitable for introduction of a single label molecule to the 5′-terminus of an oligonucleotide. The first nucleosidic blocks including **72** were published by Kwiatkowski et al. (*113*). These blocks comprise a chromophore conjugated to uracil and cytosine base via ethynyl moieties. Accordingly, the nucleobase is a part of the chelate chromophore. They can be introduced also within the coding sequence, since the chelates do not restrict the formation of Watson−Crick base pairs. Later, a more versatile method for the preparation of nucleosidic and acyclo-nucleosidic oligonucleotide building blocks was developed in which the linker is attached at the N3 of uracil and thymine base using a Mitsunobu reaction (*112*−*116*). This approach was applied to multilabeling of oligonucleotides and in the preparation of solid supports that allow 3′-derivatization. Since the labels are attached at sites involved in base pairing, incorporation of these blocks within coding sequences has not been recommended.

The oligonucleotide building blocks described in the literature have been introduced into oligonucleotide structures with high efficiency using a modified deprotection protocol (Scheme 14). Hydrolysis of the protecting groups of the chelating moieties was performed by treatment with aqueous sodium hydroxide prior to ammonialysis to avoid carboxamide formation. The lanthanide ion was introduced as a lanthanide citrate in which the lanthanide is chelated and in solution even under basic conditions.

It is known that trivalent lanthanide ions promote hydrolysis of phosphoesters very effectively (*117*). The catalytic efficiency can be attributed to the formation of a metal hydroxide gel, and the catalysis was suggested to be a complicated heterogenic process (*118*). The lanthanide clusters are formed already in slightly alkaline solutions. Accordingly, it is extremely important that the excess lanthanide ion is not precipitated under the basic conditions needed. It is also known that certain europium chelates based on Schiff bases hydrolyze RNA (*119*). The catalytic activity is considerably reduced with negatively charged

Scheme 14. Labeling of Oligonucleotides on Solid Phase

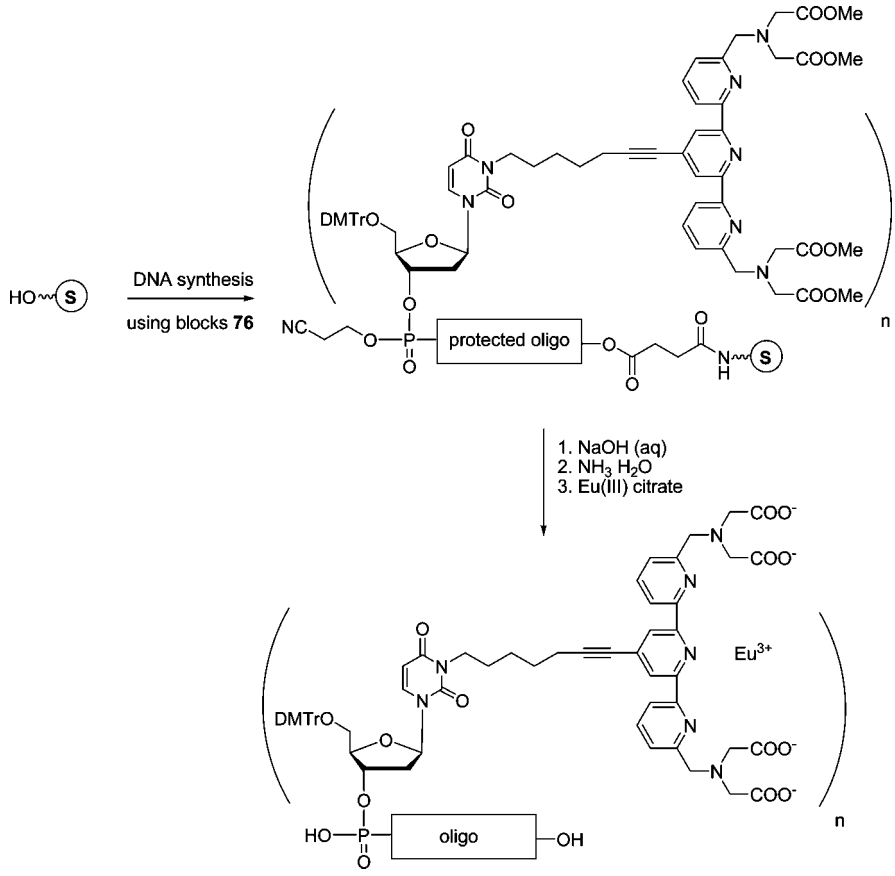

ligands (*120*). Accordingly, the choice of ligand structure is highly important.

Noncovalent Binding. There exist assay formats in which no covalent binding between biomolecule and label is necessary. The example of preparation of nanobeads by swelling chelates into particles was discussed above. As another example, a cytotoxicity assay in which target cells are labeled with the acetoxymethyl ester of 2,2′:6′,2″-terpyridine-6,6′-dicarboxylic acid has been developed (*121*). The hydrophobic ligand **76** penetrates easily through cellular membranes of viable cells. Upon the action of intracellular esterases, the acetoxymethyl esters are hydrolyzed, generating impermeable hydrophilic ligands within cells. The ligand leakage upon cell disintegration is monitored by enhancing the supernatant with an excess of Eu^{3+}. Another example of an assay application in which no reactive group is needed is the separation of eosinophilic and basophilic cells (*122*). In this application, positively and negatively charged chelates bind with negatively and positively charged cell surfaces, respectively. Reaction of the almost nonluminescent chelate **9d** (Figure 6) with singlet oxygen converts it to the luminescent endoperoxide **77**. This has been utilized in the quantitation of $^1O_2$ generated in various biological systems (*38*).

SOLUBILITY

In general, lanthanide chelates exhibit good water solubility. However, large aromatic chromophores may cause hydrophophic aggregation. The problem has been solved by introduction of hydrophilic substituents to the chelate structure. For example, the aqueous solubility of compound **50** has been enhanced by the addition of COOH (*83*) or carbohydrate (*123*) groups to the chromophore (Figure 7). Also, the nonspecific binding of labeled biomolecules is reduced, whereas the affinity properties of the used biomolecules are almost unchanged. The same strategy has been used also for terbium chelates (*124, 125*).

Very recently, Romieu et al. reported an elegant method for improvement of water solubility of organic dyes (*126*). The method involves the addition of 3-amino-2-sulfopropanoic acid to dyes tethered to active esters of carboxylic acids. The new labeling reactant formed contains a carboxylic acid group for biomolecule conjugation. Although the applicability of 3-amino-2-sulfopropanoic acid to derivatization of lanthanide chelates has not been published, the molecule is worth trying if enhanced water solubility is needed.

Since lanthanide chelates are often extremely hydrophilic, their solubilities in organic solvents are low. This is a serious problem when developing luminescent chelates to be polymerized to produce nanobeads. However, certain europium(III) chelates having thienylpyridine subunits have moderate solubil-

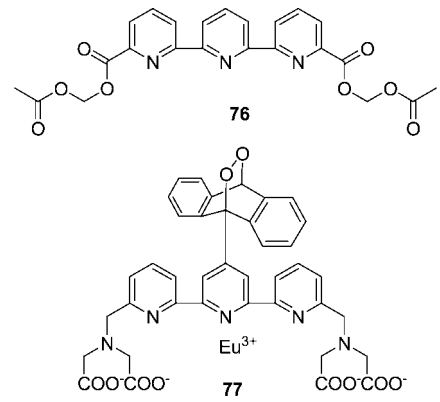

Figure 6. Labels for applications where no covalent binding between biomolecule and label is needed.

ity in organic solvents such as THF that allow the preparation of the beads (*31*).

THE LANTHANIDE(III) ION

Lanthanide(III) chelates are most commonly prepared by the treatment of the free ligand with a slight excess of lanthanide chloride at pH 6−7. When the chelation is completed, the excess of lanthanide is conveniently removed by increasing the pH of the reaction mixture to ca. 11 where the uncomplexed lanthanide ion precipitates as lanthanide hydroxide (*86*). Alternatively, the chelate formation is achieved by passing the ligand through a column of strong cation exchange resin loaded with the appropriate lanthanide ion (*76*).

Eu^{3+}, Tb^{3+}, Sm^{3+}, and Dy^{3+} are the four lanthanide ions that can be used as central ions of luminescent lanthanide chelates. Since there are larger differences in the vibrational levels of the lowest excited state and the highest ground state of Eu^{3+} and Tb^{3+} than of Sm^{3+} and Dy^{3+}, europium and terbium chelates are more efficient light emitters, and thus they are applied more often. The decay times of Sm^{3+} and especially Dy^{3+} chelates are short (*39, 127, 128*). Due to the similarities in the energy levels of Eu^{3+} and Sm^{3+}, ligands highly luminescent with europium are useful with samarium (*129*). This is the case with the terbium and dysprosium pair also. For example, electron releasing substituents in the aromatic moiety of phenyl and naphthyl substituted 2,6-[*N*,*N*-di(carboxyalkyl)aminoalkyl]pyridines have advantageous effects on the photophysical properties on their chelates with terbium and dysprosium, while the corresponding europium and samarium chelates are practically nonluminescent (*131*). However, ligands based on 2,6-bis(*N*-pyrazolyl)pyridine and 6,6′-(1*H*-pyrazole-1,3-diyl)bis(pyridine) have been shown to form luminescent chelates with Eu^{3+}, Sm^{3+}, Tb^{3+}, and Dy^{3+} ions. Accordingly, these ligands are highly useful for multiparametric homogeneous assays simplifying considerably the preparation of chelates needed in these applications. Also, dual-label assays based on luminescent Eu^{3+} and Tb^{3+} chelates of terpyridine have been proposed (*82*).

It has been observed repeatedly that even small modifications in the structure of labeling reagents may cause significant changes in the luminescence properties of the chelate. In this respect, europium is the most robust metal: it is possible to develop assays in which the labeling reagents coupled to a bioactive molecule have luminescence properties almost identical to their parent compounds (*40*). The use of terbium chelates is more complex due to their greater sensitivity to the environment. Li and Selvin have shown that the emission intensity of certain luminescent Tb^{3+} but not the corresponding Eu^{3+} chelates decreases upon conjugation to single-stranded oligonucleotides, and that the signal increases upon hybridization (*132*). The emission intensity is at its highest for unconjugated chelate. This unique property of Tb^{3+} chelates has been exploited in the development of homogeneous DNA hybridization assays (*133*−*137*).

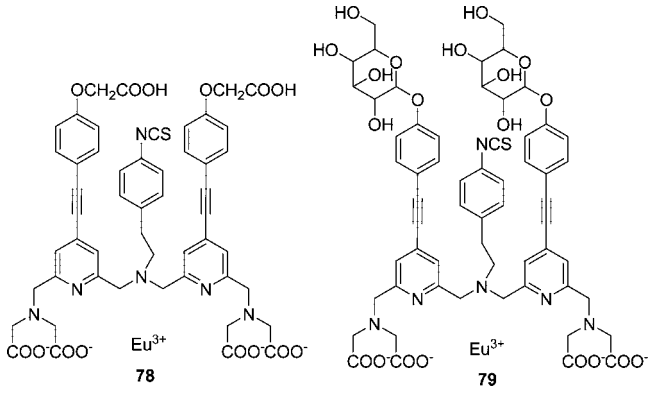

Figure 7. Europium(III) chelates with enhanced water solubility.

Traditionally, the lanthanide-based assay chemistries have allowed only limited multiplexing since the number of usable chelates is limited to four (chelates of Eu^{3+}, Tb^{3+}, Sm^{3+}, and Dy^{3+}) (*138*). However, when luminescent lanthanide chelates are combined with different homogeneous FRET techniques, more multiplexed detections can be performed, since the same donor chelate can be exploited for different analytes in the reaction. With appropriate selection of acceptor labels, one can use either the emission of donor itself (TR-FQA) (*139*) or wavelengths in the Red/NIR region (TR-FRET) (*140*), or wavelengths shorter than the donor emission spectrum (anti Stokes' shift TR-FRET) (*141*) to detect the analyte. In addition, extra signal resolution can be obtained by adjusting the decay time of the acceptor signal (*142*). Accordingly, by using multiple assay chemistries, a single lanthanide chelate can be utilized for measuring at least five analytes simultaneously.

FREEDOM TO OPERATE

Patent literature provides a rich source of information about luminescent lanthanide chelates. Although there are numerous excellent scientific publications, only a small fraction of luminescent lanthanide chelates described in the patent literature have also been described in the non-patent literature. Moreover, many chelates published in the non-patent literature were first described in the patent literature. Thus, a search of chemical literature concerning luminescent lanthanide chelates, as well as many other classes of structures, would be incomplete without a review of published patent applications and patents.

Fortunately, there are many public resources available for patent literature searching, and the patent laws of most countries require publication of a patent application as a condition of granting a patent. Typically, patent applications are published about 18 months from the date of filing in a patent office, for the public benefit of describing the invention in a manner sufficient for others to practice it after the term of protection granted with the patent has expired. Useful patent information is available free of charge, for example, from www.espacenet.com. This worldwide database was designed especially for nonprofessionals and offers efficient contextual help and help files. In addition to providing millions of uploadable patents and patent application publications, this resource provides information about the legal status of specific patents, as well as the countries in which patent applications are pending and patents are granted. More detailed information on patents and pending patent application is available at many governmental patent offices, such as WIPO (www.wipo.int), EPO (www.epoline.org). and USPTO (www.uspto.gov), academic Internet sites, professional societies' sites, and fee-based Internet sources, such as Delphion (www.delphion.com), Micropatent (www.micopat.com), and Nerac, Inc. (www.nerac.com).

Briefly turning to the value of patents to their owners, a patent is a form of intellectual property that grants to the owner the right to exclude others from making, using, importing, and selling the claimed invention. Notably, a patent does not give the owner the right to practice the invention. Patent rights are based on laws of the granting country and most often provide 20 years of protection from the first filing date of the application. In most countries, a patent can protect any subject matter that falls into one of the following categories: a process, machine, article of manufacture, or composition of matter, or any new and useful improvement thereof. From a chemistry perspective, in most countries a patent can protect a new and useful compound, a composition containing the compound, an article

containing or made from the compound, a process for synthesizing the compound, and a method that involves using the compound. Certain subject matter is not patentable in various countries due to specific prohibitions in patent laws or as a result of court decisions ruling on these laws. In particular, laws of nature, physical phenomena, scientific principles, abstract ideas, purely mental processes, and mathematical algorithms are typically nonpatentable subject matter. Given the inherent complexities of patents, from selecting a type of patent application, meeting patentability requirements, and complying with rules in patent offices throughout the world to more commercial aspects such as exercising provisional rights, licensing, and enforcing patent rights, this review article mentions a minute fraction of patent-related issues of interest to chemists. Readers are encouraged to pursue additional information, which fortunately is increasingly available as professional societies and publishers of chemical research literature more frequently provide educational information about patents.

CONCLUSION

Stable luminescent lanthanide chelates have made homogeneous bioaffinity assays possible. However, the use of stable chelates demands very complicated optimization of the chelate structure. The optimal luminescent lanthanide chelate is stable in the presence of additional chelators even at low pH and high temperature. The ideal chelate has an optimal emission profile, high hydrophilicity, small size, good biocompactibility, little effect on biomolecules, and good energy transfer properties. In addition, the chelate should be compatible with different energy acceptors. The synthesis of the molecule should be simple, affordable, and scalable. Naturally, it is advantageous from a commercial perspective that new luminescent lanthanide chelates are protected by patents in relevant international markets.

ACKNOWLEDGMENT

J.H. wish to thank Dr. Ilkka Hemmilä (PerkinElmer Life and Analytical Sciences, Turku Site) for valuable discussions.

LITERATURE CITED

(1) Wieder, I. (1978) Background rejection in fluorescence immunoassay. In *Immunofluorescence and related staining techniques* (Knapp, W., Holubar, K., and Wick, G., Eds.) pp 67−80, Elsevier, New York.
(2) Soini, E., and Hemmilä, I. (1979) Fluoroimmunoassays: present status and key problems. *Clin. Chem. 25*, 353−361.
(3) Hemmilä, I., Dakubu, S., Mukkala, V.-M., Siitari, H., and Lövgren, T. (1984) Europium as a label in time-resolved immunofluorometric assays. *Anal. Biochem. 137*, 335–343.
(4) Hemmilä, I., and Dabuku, S. (1986) Method for fluorescence spectroscopic determination of a biologically active substance, U.S. Patent 4,565,790.
(5) Mukkala, V.-M., Mikola, H., and Hemmilä, I. (1989) Determination method utilizing reagents covalently labelled with essentially non-fluorescent lanthanide chelates in combination with time-resolved fluorescence spectroscopy and the reagents to be used in the method, U.S. Patent 4,808,541.
(6) Hemmilä, I., Blomberg, K., Mukkala, V.-M., and Hakala, H. (2007) Dissociative fluorescence enhancement assay, U.S. Patent 7,211,440.
(7) Diamanthis, E. P., and Lowden, J. A. (1992) Immunoassay methods and reagents and methods for producing the latter, CA Patent 1300007.
(8) Diamanthis, E. P., and Lowden, J. A. (1988) Immunoassay methods and reagents and methods for producing the latter, Eur. Patent 0290269.
(9) Diamandis, E. P. (1988) Immunoassays with time-resolved fluorescence spectroscopy: principle and applications. *Clin. Biochem. 21*, 139–150.
(10) Evangelista, R., Pollak, A., Allore, B., Templeton, E. F., Morton, R. C., and Diamandis, E. O. (1988) A new europium chelate for protein labelling an time-resolved fluorometric applications. *Clin. Biochem. 21*, 173–178.
(11) Mathis, G. (1995) Probing molecular interactions with homogeneous techniques based on rare earth cryptates and fluorescence energy transfer. *Clin. Chem. 41*, 1391–1397.
(12) Sabbatini, N., Guardigli, M., and Lehn, J.-M. (1993) Luminescent lanthanide complexes as phorochemical supramolecular devices. *Coord. Chem. Rev. 123*, 201–228.
(13) Hemmilä, I., and Mukkala, V.-M. (2001) Time-resolution in fluorometry technologies, labels, and applications in bioanalytical assays. *Crit. Rev. Clin. Lab. Sci. 38*, 441–519.
(14) Hemmilä, I., Stahlberg, T., and Mottram, P. (1994) *Bioanalytical Applications of Labeling Technologies*, Wallac Oy.
(15) Hemmilä, I. (1991) Applications of fluorescence in immunoassays, In *Chemical Analysis: A Series of Monographs on Analytical Chemistry and Its Applications* (Winefordner, J. D., Ed.) Vol. 117, John Wiley & Sons, Inc., New York.
(16) Pope, A. J. (1999) LANCE vs HTRF technologies (or vice versa). *J. Biomol. Screen. 6*, 301–302.
(17) Hemmilä, I. (1999) LANCE: homogeneous assay platform for HTS. *J. Biomol. Screen. 6*, 303–307.
(18) Mathis, G. (1999) HTRF technology. *J. Biomol. Screen. 6*, 309–313.
(19) Mathis, G. (1993) Rare earth cryptates and homogeneous fluoroimmunoassays with human sera. *Clin. Chem. 39*, 1953–1969.
(20) Dickson, E. F. G., Pollak, A., and Diamandis, E. F. (1995) Ultrasensitive bioanalytical assays using time-resolved fluorescence detection. *Pharmac. Ther. 66*, 207–235.
(21) Selvin, P. R. (2002) Principles and biophysical applications of lanthanide-based probes. *Annu. Rev. Biomol. Struct. 31*, 275–320.
(22) Hemmilä, I., and Laitala, V. (2005) Progress in lanthanides as luminescent probes. *J. Fluoresc. 15*, 529–542.
(23) Yan, J., and Wang, G. (2006) Lanthanide-based luminescence probes and time-resolved luminescence bioassays. *Trends Anal. Chem. 25*, 490–500.
(24) Kankare, J., Takalo, H., and Pasanen, P. (1990) Fluorescent lanthanide chelates, U.S. Patent 4,920,195.
(25) Takalo, H., and Kankare, J. (1987) Synthesis of dimethyl and diethyl 4-(phenylethynyl)-2,6- pyridinedicarboxylate. *Acta Chem. Scand. B42*, 373–375.
(26) Takalo, H., Pasanen, P., and Kankare, J. (1988) Synthesis of 4-(phenylethynyl)-2,6-bis[*N*,*N*- bis(carboxymethyl)aminomethyl]pyridine. *Acta Chem. Scand. Ser. B 42*, 373.
(27) Takalo, H., Hänninen, E., and Kankare, J. (1993) Luminescence of europium(III) chelates of substituted 4-phenylethynylpyridines as ligands. *Helv. Chim. Acta 76*, 877–883.
(28) Hovinen, J., Mukkala, V.-M., Hakala, H., and Peuralahti, J. (2005) Novel chelating agents and chelates and their use, U.S. Patent Application 2005/084451.
(29) Jaakkola, L., Peuralahti, J., Hakala, H., Kunttu, J., Tallqvist, P., Mukkala, V.-M., Ylikoski, A., and Hovinen, J. (2005) Solid-phase synthesis of oligonucleotides labeled with luminescent lanthanide(III) chelates. *Bioconjugate Chem. 16*, 700–709.
(30) Latva, M., Takalo, H., Mukkala, V.-M., Matachescu, C., Rodryguez-Ubis, J. C., and Kankare, J. (1997) Correlation between the lowest triplet state energy level of the ligand and lanthanide(III) luminescence quantum yield. *J. Lumin. 75*, 149–169.
(31) Hakala, H., Mukkala, V.-M., Sutela, T., and Hovinen, J. (2006) Synthesis and properties of nanospheres copolymerised with luminescent europium(III) chelates. *Org. Biomol. Chem. 4*, 1383–1386.
(32) Hovinen, J., Mukkala, V.-M., Hakala, H., and Peuralahti, J. (2005) Novel chelating agents and highly luminescent and stable chelates and their use, U.S. Patent Application 2005/181393.

(33) Hinshaw, J. C., Toner, J. L., and Reynolds, G. A. (1987) Fluorescent labels for immunoassay, U.S. Patent 4,637,988.

(34) Toner, J. L. (1989) Polypyridine fluorescent labels for immunoassay, U.S. Patent 4,837,169.

(35) Kankare, J., Takalo, H., Hänninen, E., Helenius, M., and Mukkala, V.-M. (1994) Chelating terpyridine derivatives and their use, U.S. Patent 5,324,825.

(36) Wang, Z., Yan, J., and Matsumoto, K. (2005) Synthesis and fluorescence properties of the europium(III) chelate of a polyacid derivative of terpyridine. *Luminescence 20*, 347–351.

(37) Yan, J., Tan, M., and Wang, G. (2004) Synthesis and luminescence properties of lanthanide(III) chelates with polyacid derivatives of thienylsubstituted terpyridine analogues, *J. Luminesc. 106*, 91−101.

(38) Song, B., Wang, G., Tan, M., and Yan, J. (2005) Synthesis and time-resolved fluorimetric application of a europium chelate-based phosphorescene probe specific for singlet oxygen. *New J. Chem. 29*, 1431–1338.

(39) Coates, J., Sammes, P. G., and West, R. M. (1996) Enhancement of luminescence of europium(III) ions in water by use of synergistic chelation. Part 1. 1:1 and 2:1 complexes. *J. Chem. Soc., Perkin Trans. 2*, 1275–1282.

(40) Mukkala, V.-M., Helenius, M., Hemmilä, I., Kankare, J., and Takalo, H. (1993) Development of luminescent europium(III) and terbium(III) chelates of 2,2′:6′,2″-terpyridine derivatives for protein labelling. *Helv. Chim. Acta 76*, 1361–1378.

(41) Cooper, M. E., and Sammes, P. G. (2000) Synthesis and spectral properties of a new luminescent europium(III) terpyridyl chelate. *J. Chem. Soc., Perkin Trans. 2*, 1695–1700.

(42) Matsumoto, K., Yan, J., Wang, G. and Tan, M. (2004) Novel fluorescent label compounds, Eur. Patent Application 1489418.

(43) Takalo, H. and Mukkala, V.-M. (1996) Luminescent lanthanide chelates, U.S. Patent 5,571,897.

(44) Rodrigues-Ubis, J.-C., Takalo, H., and Mukkala, V.-M. (1999) Biospecific binding reactants labelled with luminescent lanthanide chelates and their use, U.S. Patent 5,859,215.

(45) Ketola, J., Katajisto, J., Hakala, H., and Hovinen, J. (2007) Synthesis of lanthanide(III) chelates by using ′click′ chemistry. *Helv. Chim. Acta 90*, 607–615.

(46) Yan, J., Wang, G., Majima, K., and Matsumoto, K. (2001) Synthesis of a terbium fluorescent chelate and its application to time-resolved fluoroimmunoassay. *Anal. Chem. 73*, 1869–1876.

(47) Remuinan, M. J., Roman, H., Alonso, M. T., and Rodrigues-Ubis, J.-C. (1993) Synthesis and luminescence properties of europium(III) and terbium(III) complexes with polyacid chelates derived from 2,6-bis(*N*-pyrazolyl)pyridine. *J. Chem. Soc., Perkin Trans. 2*, 1099–1102.

(48) Rodrígues-Ubis, J.-C., Sedano, R., Barroso, G., Juanes, O., and Brunet, E. (1997) Lanthanide complexes of polyacid ligands derived from 2,6-bis(pyrazol-1-yl)pyridine, pyrazine, and 6,6′-bis(pyrazol-1-yl) 2,2′-bipyridine: synthesis and luminescence properties. *Helv. Chim. Acta 80*, 86–96.

(49) Takalo, H., Mukkala, V.-M., Meriö, L., Rodrígues-Ubis, J.-C., Sedano, R., Juanes, O., and Brunet, E. (1997) Development of luminescent terbium(III) chelates for protein labelling: effect of triplet-state energy level. *Helv. Chim. Acta 80*, 372–387.

(50) Brunet, E., Juanes, O., Sedano, R., and Rodrígues-Ubis, J.-C. (2002) Lanthanide complexes of polycarboxylate- bearing dipyrazolylpyridine ligands with near-unity luminescence quantum yields: the effect of pyridine substitution. *Photochem. Photobiol. Sci. 1*, 613–618.

(51) Brunet, E., Juanes, O., Sedano, J. C., and Rodriques-Ubis, J.-C. (2005) Lanthanide complexes of new polyaminocarboxylate complexes with two chromophores derived from bispyrazolylpyridine and aceto or benzophenone: synthesis, characterization and photophysicaal properties. *Tetrahedron 61*, 6757–6763.

(52) Hale, R. N., and Solas, D. W. (1991) Fluorescent poly(arylpyridine) rare earth chelates, U.S. Patent 5,055,578.

(53) Mukkala, V.-M., Kwiatkowski, M., Kankare, J., and Takalo, H. (1993) Influence of chelating groups on the luminescence properties of europium(III) and terbium(III) chelates in the 2,2′-bipyridine series. *Helv. Chim. Acta 76*, 893–899.

(54) Dürr, H., Zengerle, K., and Trierweiler, H.-P. (1988) Podanden, Coronaden und Kryptanden als neue Komplex-Liganden für Photoelektronentransfer-Reaktionen Synthese und erste photophysikalische Studien. *Z. Naturforsch. B43*, 361–367.

(55) Mameri, S., Charbonniere, L. J., and Ziessel, R. F. (2003) Synthesis of amino-bridged 6,6′- disubstituted-2,2′-bipyridine ligands for lanthanide coordination chemistry. *Synthesis* 2713–2719.

(56) Newkome, G. R., Kiefer, G. E., Xia, Y.-A., and Gupta, V. K. (1994) α-Methyl functionalization of electron-poor heterocycles: free radical chlorination. *Synthesis* 676–679.

(57) Mukkala, V.-M., and Kankare, J. J. (1992) New 2,2′-bipyridine derivatives and their luminescence properties with europium(III) and terbium(III). *Helv. Chim. Acta 75*, 1578–1592.

(58) Kim, W. D., Kiefer, G. E., Maton, F., McMillan, K., Muller, R. N., and Sherry, A. D. (1995) Relaxometry, luminescence measurements, electrophoresis, and animal biodistribution of lanthanide(III) complexes of some polyaza macrocyclic acetates containing pyridine. *Inorg. Chem. 34*, 2233–2243.

(59) Galaup, C., Carrie, M.-C., Tisnes, P., and Picard, C. (2001) Time-resolved luminescence in aqueous solution−new europium labels derived from macro(bi)cyclic ligands with aminocarboxylic units. *Eur. J. Org. Chem.* 2165–2175.

(60) Galaup, C., Couchet, J.-M., Bedel, S., Tisnes, P., and Picard, C. (2005) Direct access to terpyridine-containing polyazamacrocycles as photosensitizing ligands for Eu(III) luminescence in aqueous media. *J. Org. Chem. 70*, 2274–2284.

(61) Nasso, I., Galaup, C., Havas, F., Tisnès, P., Picard, C., Laurent, S., Vander Elst, L., and Muller, R. N. (2005) Bimodal system (luminophore and paramagnetic contrastophore) derived from Ln(III) complexes based on a bipyridine-containing macrocyclic ligand. *Inorg. Chem. 44*, 8293–8305.

(62) Kazumi, S., Daikichi, H., Masahiro, N., and Hiroshi, M. (1992) Fluorescent compound, complex, reagent, and specific binding assay employing said reagent, Eur. Patent 0493745.

(63) Brunet, E., Juanes, O., Sedano, R., and Rodriques-.Ubis, J.-C. (2002) Synthesis of novel macrocyclic lanthanide chelates derived from bis-pyrazolylpyridine. *Org. Lett. 4*, 213–216.

(64) Richman, J. E., and Atkins, T. J. (1974) Nitrogen analogs of crown ethers. *J. Am. Chem. Soc. 96*, 2268–2270.

(65) Burguete, M. I. U., Escuder, B., Caraca-Espana, E., Luis, S. V., and Miravet, J. V. (2002) Polyaza[*n*](1,4)naphthalenophanes and polyaza[*n*](9,10)anthracenophanes. *Tetrahedron 58*, 2839–2846.

(66) An, H., and Cook, P. D. (1996) Solution phase combinatorial chemistry I. Synthesis of polyazacyclophane scaffolds and tertiary amine libraries. *Tetrahedron Lett. 37*, 7233–7236.

(67) Siaugue, J. M., Segat-Dioury, F., Sylvestre, I., FavreReguillon, A., Foos, J., Madic, C., and Guy, A. (2001) Regioselective synthesis of *N*-functionalized 12-membered azapyridinomacrocycles bearing trialkylcarboxylic acid side chains. *Tetrahedron 57*, 4713–4718.

(68) Hovinen, J., and Sillanpää, R. (2005) Synthesis of azamacrocycles via a Mitsunobu reaction. *Tetrahedron Lett. 46*, 4387–4389.

(69) Mathis, G., and Lehn, J.-M. (1990) Macropolycyclic rare earth compexes and applications and fluorescent tracers, U.S. Patent 4,927,923.

(70) Autiero, H., Bazin, H., and Mathis, G. (2006) Rare earth metal cryptates with are not very sensitive to the fluorescence quenching, U.S. Patent 7,087,384.

(71) Takalo, H., and Kankare, J. (1988) Synthesis of pyridocryptate using europium(III) acetate as a template. *Finn. Chem. Lett. 15*, 95–99.

(72) De Cola, L., Smailes, D. L., and Vallarino, L. M. (1986) Hexaaza macrocyclic complexes of the lanthanides. *Inorg. Chem. 25*, 1729–1732.

(73) Saito, K., Lee, R. T., and Lee, Y. C. (1998) Quantification of Eu^{3+} in quantum-dye-labeled materials by ashing and dissociation enhancement. *Anal. Biochem. 258*, 311–314.
(74) Leif, L. C., and Vallarino, L. M. (1991) Rare-earth chelates as fluorescent markers in cell separation and analysis, In *Cell Separation Science and Technology* (Kompala, D. S., and Todd, P., Eds.) ACS Symposium Series 46, pp 42−58, Oxford University Press, Cary, NC.
(75) Bush, C. E., Di Michele, L. J., Peterson, W. R., Sherman, D. G., and Godsey, J. H. (1992) Solid-phase time-resolved fluorescence detection of human immunodeficiency virus polymerase chain reaction amplification products. *Anal. Biochem. 202*, 146–151.
(76) Hovinen, J. (2007) Maleimido-derivatized luminescent lanthanide(III) chelates for mercapto-group conjugation. *Bioconjugate Chem. 18*, 587–600.
(77) Newkome, G. R., and He, E. (1997) Nanometric dendritic macromolecules: stepwise assembly by double(2,2′:6′,2”-terpyridine)ruthenium(I) connectivity. *J. Mater. Chem. 7*, 1237–1244.
(78) Schubert, U. S., Eschbaumer, C., Hien, O., and Anders, P. R. (2001) 4′-Functionalized 2,2′:6′,2″- terpyridines as building blocks for supramolecular chemistry and nanoscience. *Tetrahedron Lett. 42*, 4705–4707.
(79) Sampath, U. S., Putnam, W. C., Osiek, T. A., Touami, S., Xie, J., Cohen, D., Cagnolini, A., Droege, P., Klug, D., Barnes, C. L., Modak, A., Bashkin, J. K., and Jurisson, S. S. (1999) Terpyridyl derivatives as bifunctional chelates: synthesis and crystal structures of 4′-[2-(1,3- dioxolan-2-yl)ethylsulfanyl]-2,2′**:** 6′,2″-terpyridine and chloro(4′-methylsulfanyl-2,2′**:**6′,2″-terpyridine)gold(III) bis(trifluoromethanesulfonate). *J. Chem. Soc., Dalton Trans.* 2049–2058.
(80) Armspach, D., Constable, E. C., Housecroft, C. E., Neuburger, M., and Zehneder, M. (1998) Carbaborane-functionalised 2,2′:6′,2″-terpyridine ligands for metallosupramolecular chemistry: syntheses, complex formation, and the crystal and molecular structures of 4′-(ortho-carboranyl)- 2,2′:6′,2″-terpyridine and 4′-(ortho-carboranylpropoxy)-2,2′:6′,2″-terpyridine. *J. Organomet. Chem. 550*, 193–206.
(81) Hovinen, J. (2004) Synthesis of 4′-functionalized 2,2′:6′,2″-terpyridines via a Mitsunobu reaction. *Tetrahedron Lett. 45*, 5707–5708.
(82) Mukkala, V.-M., Takalo, H., Liitti, P., and Hemmilä, I. (1995) Synthesis and luminescence properties of some Eu(III) and Tb(III) chelate labels having 2,2′:6′,2″-terpyridine as an energy absorbing part. *J. Alloys Compd. 225*, 507–510.
(83) Takalo, H., Hemmilä, I., Sutela, T., and Latva, M. (1996) Synthesis and luminescence of novel Eu(III) complexing agents and labels with 4-(phenylethyny1)pyridine subunits. *Helv. Chim. Acta 79*, 789–802.
(84) Hovinen, J. (2007) Biomolecule labeling reactants based on azacycloalkanes and conjugates derived thereof, International Patent Application WO2007/104834.
(85) Brinkley, M. (1992) A brief survey of methods for preparing protein conjugates with dyes, haptens, and cross-linking reagents. *Bioconjugate Chem. 3*, 2–13.
(86) Takalo, H., Mukkala, V.-M., Mikola, H., Liitti, P., and Hemmilä, I. (1994) Synthesis of europium(III) chelates suitable for labeling of bioactive molecules. *Bioconjugate Chem. 5*, 278–282.
(87) Takalo, H., and Rosenberg, J. (2006) Biospecific binding reactants labeled with new luminescent lanthanide chelates and their use, U.S. Patent 7,018,851.
(88) Nishioka, T., Yan, J., Yamamoto, Y., Sumitomo, K., Wang, Z., Hashino, K., Hosoya, C., Ikawa, K., Wang, G., and Matsumoto, K. (2006) New luminescent europium(III) chelates for DNA labeling. *Inorg. Chem. 45*, 4088–4096.
(89) Karsüilayan, H., Hemmilä, I., Takalo, H., Toivonen, A., Pettersson, K., Lövgren, T., and Mukkala, V.-M. (1997) Influence of coupling method on the luminescence properties, coupling efficiency, and binding affinity of antibodies labeled with europium(III) chelates. *Bioconjugate Chem. 8*, 71–75.
(90) For the preparation of diazo derivative of EDTA, see Sundberg, M. W., Meares, C., Goodwin, D. A., and Diamanti, C. I. Selective binding of metal ions to macromolecules using bifunctional analogs of EDTA, *J. Med. Chem.* 1974, *17*, 1304−1307.
(91) Aslam, M., and Dent, A. *Bioconjugation. Protein Coupling Techniques for the Biomedical Sciences*, Macmillan Reference Ltd, London, 1998.
(92) Wieder, I., and Hale, R. L. (1998) Homogenous fluoroassay methods employing fluorescent background rejection and water soluble rare earth metal chelates, U.S. Patent 5,830,769.
(93) Ge, P., and Selvin, P. R. (2003) Thiol-reactive luminescent lanthanide chelates. Part 2. *Bioconjugate Chem. 14*, 870–876.
(94) Weibel, N., Charbonniere, L. J., Guardigli, M., Roda, A., and Ziessel, R. (2004) Engineering of highly luminescent lanthanide tags suitable for protein labeling and time-resolved luminescence imaging. *J. Am. Chem. Soc. 126*, 4888–4896.
(95) Hovinen, J. (1999) An alternative method for the preparation of 11-derivatized progesterone. *Acta Chem. Scand. 53*, 530.
(96) Meltola, N., Jauria, P., Saviranta, P., and Mikola, H. (1999) Synthesis of novel europium-labeled estradiol derivatives for time-resolved fluoroimmunoassays. *Bioconjugate Chem. 10*, 325–331.
(97) Hovinen, J. (2006) Synthesis of aminooxy chelates and their use in carbonyl group conjugation. *Chem. Biodivers. 3*, 296–303.
(98) Ketola, J., Jaakkola, L., and Hovinen, J. (2008) Lanthanide(III) chelates for selective solution phase labeling of bioactive molecules. *Lett. Org. Chem. 5*, 444–448.
(99) Poupart, S., Boudon, C., Peixoto, P., Massonneau, M., Renard, P.-Y., and Romieu, A. (2006) Aminopropargyl derivative of terpyridine bis(methyl-enamine) tetraacetic acid chelate of europium (Eu(TMT)-AP3): a new reagent for fluorescent labelling of proteins and peptides. *Org. Biomol. Chem. 4*, 4165–4177.
(100) Dawson, P. E., Muir, T. W., Clark-Lewis, I. C., and Kent, S. H. B. (1994) Synthesis of proteins by native ligation. *Science 266*, 776–779.
(101) Kolb., H. C., Finn, M. G., and Sharpless, K. B. (2001) Click chemistry: diverse chemical function from a few good reactions. *Angew. Chem., Int. Ed. Engl. 40*, 2004–2021.
(102) Houthoff, H. J., Reedijk, J., Tinka, J. VanesRemco, M. VandenBerg, F. M., Lempers, E. L. M., and Bloemink, M. J. (1999) Platinum-containing compounds, methods for their preparation and applications thereof, U.S. 5,985,566.
(103) Hovinen, J. Titanocens for labeling biospecific binding reactants, International Patent Application WO 2007/12291.
(104) Huhtinen, P., Kivelä, M., Kuronen, O., Hagren, V., Takalo, H., Tenhu, H., Lövgren, T., and Härmä, H. (2005) Synthesis, characterization, and application of Eu(III), Tb(III), Sm(III), and Dy(III) lanthanide chelate nanoparticle labels. *Anal. Chem. 77*, 2643.
(105) Ye, Z., Tan, M., Wang, G., and Yuan, J. (2005) Preparation, characterization and application of fluorescent terbium complex-doped zirconia nanoparticles. *J. Fluoresc. 15*, 499–505.
(106) Hai, X., Tan, M., Wang, G., Ye, Z., Yuan, J., and Matsumoto, K. (2004) Preparation and a time- resolved fluoroimmunoassay application of new europium fluorescent nanoparticles. *Anal. Sci. 20*, 245–246.
(107) Tan, M., Ye, Z., Wang, G., and Yuan, J. (2004) Preparation and time-resolved fluorometric application of luminescent europium nanoparticles. *Chem. Mater. 16*, 2494–2498.
(108) Takalo, H., Hovinen, J., Mukkala, V.-M., Mikola, H., and Liitti, P. (2000) Labeling reactants and their use, U.S. Patent 6,080,839.
(109) Peuralahti, J., Hakala, H., Mukkala, V.-M., Hurskainen, P., Mulari, O., and Hovinen, J. (2002) Introduction of lanthanide(III) chelates to oligopeptides on solid phase. *Bioconjugate Chem. 13*, 870–875.
(110) Peuralahti, J., Jaakkola, L., Hakala, H., Mukkala, V.-M., Hurskainen, P., and Hovinen, J. (2006) Labeling of oligopeptides and proteins with luminescent lanthanide(III) chelates. *J. Peptide*

Sci. 12, 199–205.
(111) Mukkala, V.-M., Sund, C., and Kwiatkowski, M. (1993) Spectrofluorometric method and compounds that are of value for the method, U.S. Patent 5,216,134.
(112) Hovinen, J., and Hakala, H. (2001) Versatile strategy for oligonucleotide derivatization. Introduction of lanthanide(III) chelates to oligonucleotides. *Org. Lett. 3*, 2473–2476.
(113) Kwiatkowski, M., Samiotaki, M., Lamminmäki, U., Mukkala, V.-M., and Landegren, U. (1994) Solid-phase synthesis of chelate-labelled oligonucleotides: application in triple-color ligase mediated gene analysis. *Nucleic Acids Res. 22*, 2604–2611.
(114) Hovinen, J., and Takalo, H. (2005) Oligonucleotide labeling reactants and their use, U.S. Patent 6,949,639.
(115) Hovinen, J. (2007) Oligonucleotide labeling reactants based on acyclonucleosides and conjugates derived thereof, U.S. Patent 7,282,581.
(116) Hakala, H., Ollikka, P., Degerholm, J., and Hovinen, J. (2002) Oligonucletide conjugates based on acyclonucleotides and their use in DNA hybridization assays. *Tetrahedron 58*, 8771–8777.
(117) Komiyama, M., Takeda, N., and Shigekawa, H. (1999) Hydrolysis of DNA and RNA by lanthanide ions: mechanistic studies leading to new applications. *Chem. Comm.* 1443–1451.
(118) Franklin, S. J. (2001) Lanthanide-mediated DNA hydrolysis. *Curr. Opin. Chem. Biol. 5*, 201–208.
(119) Butcher, W. W., and Westheimer, F. H. (1955) The lanthanum hydroxide gel promoted hydrolysis of phosphate esters. *J. Am. Chem. Soc. 77*, 2420–2424.
(120) Mukkala, V.-M., Takalo, H., Liitti, P., Kankare, J., Kuusela, S., and Lönnberg, H. (1994) Lanthanide chelates as a tool in nucleic acid chemistry. *Metal-Based Drugs 1*, 201–211.
(121) Blomberg, K., Hautala, R., Lövgren, J., Mukkala, V.-M., Lindqvist, C., and Åkerman, K. (1996) Time-resolved fluorometric assay for natural killer activity using target cells labeled with a fluorescence enhancing ligand. *J. Immunol. Methods 193*, 199–206.
(122) Kuusisto, A., and Seveus, L. Method for analysing a sample, International Patent Application WO2006/072668.
(123) von Lode, P., Rosenberg, J., Pettersson, K., and Takalo, H. (2003) A europium chelate for quantitative point-of-care immunoassays using direct surface measurement. *Anal. Chem. 75*, 3193–3201.
(124) Hovinen, J., Mukkala, V.-M., Hakala, H., and Peuralahti, J. Novel chelating agents and highly luminescent and stable chelates and their use, U.S. Patent Application 2008/01677443.
(125) Takalo, H., Kankare, J., and Tienari, R. Luminescent lanthanide labeling reagents and their use, International Patent Application WO2008/020113.
(126) Romieu, A., Brossard, B., Hamon, M., Outaabout, H., Portal, C., and Renard, P. Y. (2008) Postsynthetic derivatization of fluorophores with α-sulfo-β-alanine dipeptide linker. Application to the preparation of water soluble cyanine and rhodamine dyes. *Bioconjugate Chem. 18*, 279–289.
(127) Hakala, H., Liitti, P., Puukka, K., Peuralahti, J., Karvinen, J., Ollikka, P., Ylikoski, A., Mukkala, V.-M., and Hovinen, J. (2002) Novel luminescent samarium(III) chelates. *Inorg. Chem. Commun. 5*, 1059–1063.
(128) Hakala, H., Liitti, P., Peuralahti, J., Karvinen, J., Mukkala, V.-M., and Hovinen, J. (2005) Development of luminescent samarium(III) chelates containing hexadentate to nonadentate ligands: synthesis, photophysical propertiens and coupling to biomolecules. *J. Lumin. 113*, 17–26.
(129) Soini, E., and Lövgren, T. (1987) Time-resolved fluorescence of lanthanide probes and applications in biotechnology. *Crit. Rev. Anal. Chem. 18*, 105–154.
(130) Hale, R. L., and Solas, D. W. (1988) Substituted pyridine derivatives, U.S. Patent 4,761,481.
(131) Hemmilä, I., Mukkala, V.-M., Latva, M., and Kiilholma, P. (1993) Di- and tetracarboxylate derivatives of pyridines, bipyridines and terpyridines as luminogenic reagents for time-resolved fluorometric determination of terbium and dysprosium. *J. Biochem. Biophys. Methods 26*, 283–290.
(132) Li, M., and Selvin, P. R. (1997) Amine-reactive forms of a luminescent diethylenetriaminepentaacetic acid of terbium and europium: attachment to DNA and energy transfer measurements. *Bioconjugate Chem. 8*, 127–132.
(133) Nurmi, J., Ylikoski, A., Soukka, T., Karp, M., and Lövgren, T. (2000) A new label technology for the detection of specific polymerase chain reaction products in a closed tube. *Nucleic Acids Res. 28*, E28.
(134) Nurmi, J. (2008) Homogenous method for the detection of a polynucleotide, with e.g. cleavable lanthanide chelate label, U.S. Patent 7,371,544.
(135) Nurmi, J., Lilja, H., and Ylikoski, A. (2000) Time-resolved fluorometry in end-point and real-time PCR quantification of nucleic acids. *Luminescence 15*, 381–388.
(136) Nurmi, J., Kiviniemi, M., Kujanpää, M., Sjöroos, M., Ilonen, J., and Lövgren, T. (2001) High- throughput genetic analysis using time-resolved fluorometry and closed-tube detection. *Anal. Biochem. 299*, 211–217.
(137) Nurmi, J., Wikman, T., Karp, M., and Lövgren, T. (2002) High-performance real-time quantitative RT-PCR using lanthanide probes and a dual-temperature hybridization assay. *Anal. Chem. 74*, 3525–3532.
(138) Karvinen, J., Elomaa, A., Mäkinen, M.-L., Hakala, H., Mukkala, V.-M., Peuralahti, J., Hurskainen, P., Hovinen, J., and Hemmilä, I. (2004) Caspase multiplexing: simultaneous homogeneous time-resolved quenching assay (TruPoint) for caspases 1, 3, and 6. *Anal. Biochem. 325*, 317–325.
(139) Ollikka, P., and Ylikoski, A. Integrated nucleic acid analysis, U.S. Patent Application 2006/014185.
(140) Laitala, V. Improved homogenous time-resolved energy transfer assay, International Patent Application WO2005/033709.
(141) Laitala, V. Highly sensitive homogenous assay based on anti-Stokes'shift FRET measurement, U.S. Patent Application 2006/115842.
(142) Laitala, V., and Ylikoski, A. Novel probe and its use in bioaffinity assays, U.S. Patent Application 2006/147954.

BC800370S

Bioconjugate Chemistry 20th Anniversary

Subscriber access provided by SHEMYAKIN-OVCHINNIKOV INST

Communication

Knocking (Anti)-Sense into Cells: The Microsphere Approach to Gene Silencing

Lois M. Alexander, Rosario M. Sa#nchez-Marti#n, and Mark Bradley

Bioconjugate Chem., **2009**, 20 (3), 422-426• DOI: 10.1021/bc800529r • Publication Date (Web): 26 February 2009

Downloaded from http://pubs.acs.org on April 8, 2009

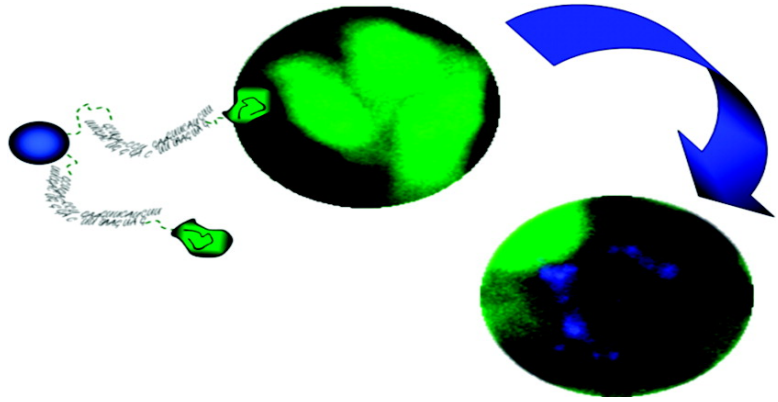

More About This Article

Additional resources and features associated with this article are available within the HTML version:

- Supporting Information
- Access to high resolution figures
- Links to articles and content related to this article
- Copyright permission to reproduce figures and/or text from this article

View the Full Text HTML

ACS Publications
High quality. High impact.

Bioconjugate Chemistry is published by the American Chemical Society. 1155 Sixteenth Street N.W., Washington, DC 20036

COMMUNICATIONS

Knocking (Anti)-Sense into Cells: The Microsphere Approach to Gene Silencing

Lois M. Alexander, Rosario M. Sánchez-Martín, and Mark Bradley*

School of Chemistry, University of Edinburgh, West Mains Road, Edinburgh, EH9 3JJ United Kingdom. Received December 9, 2008; Revised Manuscript Received February 2, 2009

200 and 500 nm polymeric microspheres have been conjugated to siRNA targeted against EGFP expressed in human cervical cancer (HeLa) cells and shown to efficiently silence protein expression over 72 h, without detrimental cytotoxicity. Furthermore, with use of an independent Cy5 tracking label on the siRNA-laden microsphere, silencing of EGFP could be assessed by selecting only those cells that contained the delivery vehicle (and thus the siRNA) generating a more accurate picture of microsphere-induced gene silencing.

Since it was first described in the 1990s (*1, 2*), interest in the area of RNA interference or the so-called RNAi pathway has grown dramatically. This interest has been heightened by the increased understanding of the role of short interfering RNA (siRNA) (*3*) and the possible therapeutic applications it may have (*4, 5*). However, naked, synthetic siRNA is cell-impermeable and requires a delivery system, which includes, for example, viral methods (*6, 7*) which generate siRNA in vivo, microinjection (*8*), lipofection (*9*), and carbon nanotubes (*10*). Microspheres have been shown to be efficient delivery agents of a range of biological cargos, including sensors, proteins, and reporters (*11*−*14*). As well as having high uptake efficiencies in a wide range of cells, they have additionally been shown to be nontoxic (*14*) and may be readily and easily functionalized. Here, we report the attachment of double-stranded siRNA to 200 and 500 nm polystyrene microspheres via cleavable (disulfide) and noncleavable (amide) linkages and demonstrate the efficient silencing of enhanced green fluorescent protein (EGFP) stably expressed in human cervical cancer (HeLa) cells.

Polystyrene microspheres (200 and 500 nm) with divinylbenzene cross-linking were prepared by dispersion or emulsion polymerization and PEGylated as previously reported (*14*). Initially, in order to quantify the uptake of these microspheres in HeLa cells, fluoresceinamine was coupled to PEGylated microspheres via a noncleavable (amide) linker (Scheme 1, **2a**−**b**) using standard solid-phase techniques (*14*). Analysis of cellular uptake was made by flow cytometry following incubation with the microspheres for 6−72 h and was observed to be over 70% after 24 h and over 80% after 72 h (see Supporting Information, Graph S-1). All flow cytometric analysis was performed in 0.2% trypan blue, which quenches any extracellular fluorescence associated with microspheres on the outside of the cell, ensuring that only fluorescence originating from microspheres inside the cell is measured (*15, 16*). Uptake was additionally confirmed by confocal microscopy, showing fluorescein microspheres localized within the cytoplasmic regions of the cell (see Supporting Information, Figure S-3).

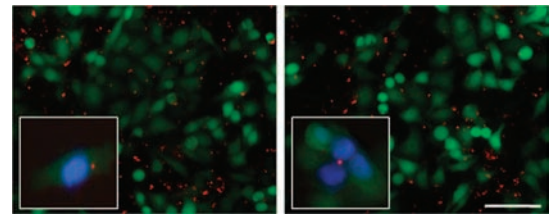

Figure 1. Pseudoconfocal microscopy of HeLa-EGFP cells (green) incubated with (a) 200 nm TAMRA siRNA microspheres (red); (b) 500 nm TAMRA siRNA microspheres (red). Images taken after 24 h (scale bar is 200 μm). Inset images are a 4 × magnification, where nuclei are stained with Hoechst 33342.

In order to achieve an intracellularly cleavable functionality, PEGylated microspheres (**1a**−**b**) were functionalized with a disulfide linker, yielding **3a**−**b**. To evaluate the cleavability of the disulfide linkage, fluoresceinamine was coupled, yielding disulfide-FAM microspheres (Scheme 1, **4a**−**b**) and the constructs were treated with glutathione (10 mM) to facilitate release of thiolated fluoresceinamine, which was assessed by flow cytometry. Reduction of the disulfide linkage was evident after just 1 h and maximal after 24 h (Supporting Information, Graph S-2). **4a** and **4b** were subsequently incubated with HeLa cells and release of the fluorophore into the intracellular environment examined and was found to be prevalent after 12 h when microspheres as fluorescently localized points within cells were no longer extensively visible (see Supporting Information, Figure S-2a,b). In contrast, microspheres exhibiting fluoresceinamine via a noncleavable (amide) linkage retained their fluorescent label regardless of glutathione treatment or the length of incubation time within HeLa cells (see Supporting Information, Graph S-2 and Figure S-3).

Subsequently, the efficiency of siRNA loading onto microspheres was studied using siRNA with a 5′-amino functionality on the sense strand for coupling to the microspheres (Scheme 1) and a 5′ fluorescent label (TAMRA) on the antisense strand allowing quantification of coupling and hybridization by spec-

* Corresponding author. Professor Mark Bradley, School of Chemistry, University of Edinburgh, West Mains Road, Edinburgh, EH9 3JJ (United Kingdom), E-mail: mark.bradley@ed.ac.uk, Tel: +44 (0) 131 651 3307, Fax: +44 (0) 131 650 6453.

10.1021/bc800529r CCC: $40.75 © 2009 American Chemical Society
Published on Web 02/26/2009

Scheme 1. Preparation of siRNA and Fluoresceinamine Loaded 200 and 500 nm Microspheres with Noncleavable (Amide) and Cleavable (Disulfide) Linkages[a]

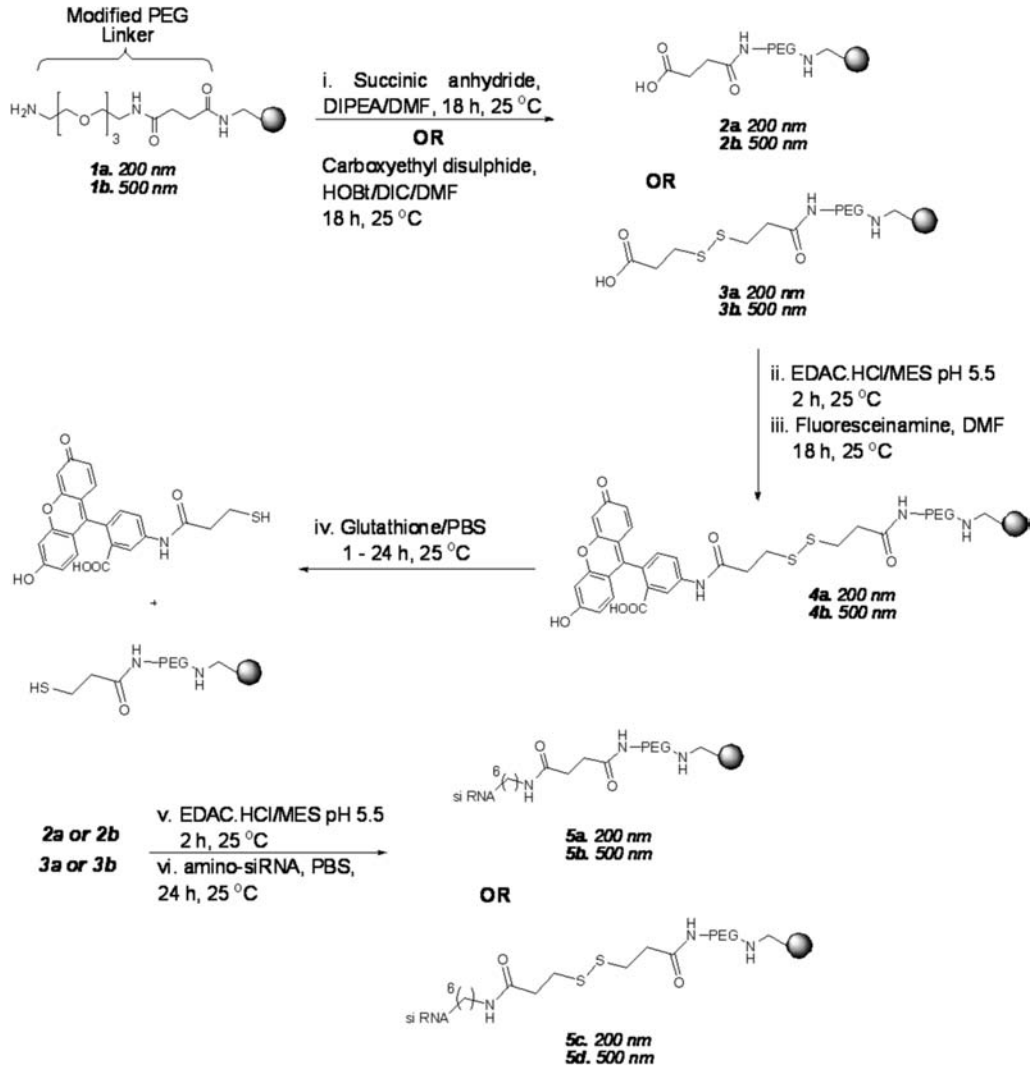

[a] For siRNA sequences, see Supporting Information.

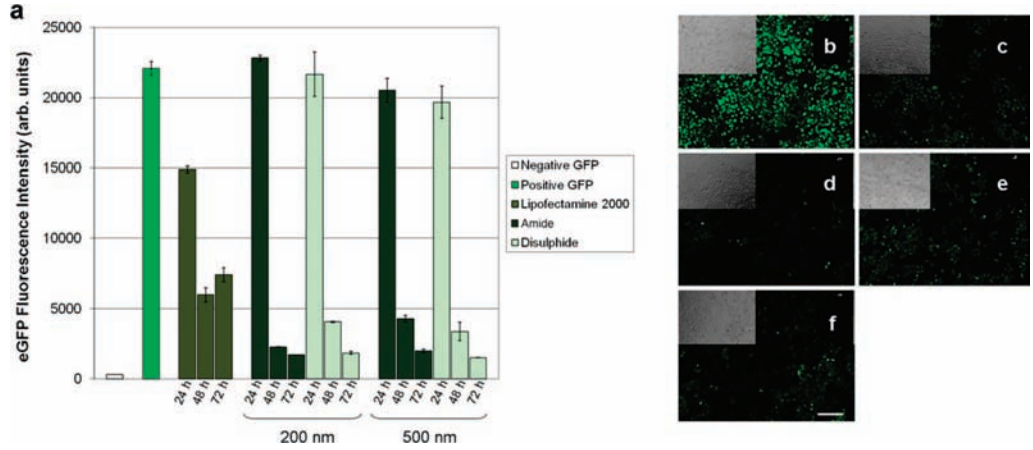

Figure 2. EGFP fluorescence expression in HeLa cells (a) by flow cytometry after 24, 48 and 72 h incubations with siRNA microspheres (200 and 500 nm, amide and disulphide, **5a–d**) and siRNA transfected via Lipofectamine 2000. siRNA concentration = 28 nM in all incubations. Negative GFP = HeLa cells untreated and not transfected with EGFP; Positive GFP = HeLa cells untreated and stably transfected with EGFP. *Right:* by microscopy after 72 h (b) Untreated cells; (c) with 200 nm amide-siRNA microspheres (**5a**); (d) with 200 nm disulphide-siRNA microspheres (**5c**); (e) with 500 nm amide-siRNA microspheres (**5b**); (f) with 500 nm disulphide-siRNA microspheres (**5d**). Scale bar is 350 μm. Inset are phase contrast images, showing approximately 70−80% cell confluency.

trofluorimetric analysis (see Supporting Information). The quantity of siRNA present on the microspheres was found to be ca. 13 000 molecules (2.2×10^{-20} mol) of siRNA per 500 nm microsphere and ca. 780 chains (1.3×10^{-21} mol) of siRNA

Scheme 2. Preparation of Dual-Labeled 500 nm Cy5-*co*-siRNA Microspheres with Disulfide and Amide Linkages (Fmoc-PEG-OH is Fmoc-NH-CH_2-(CH_2-O-CH_2)$_3$-CH_2-NH-C(O)-CH_2-CH_2-COOH)

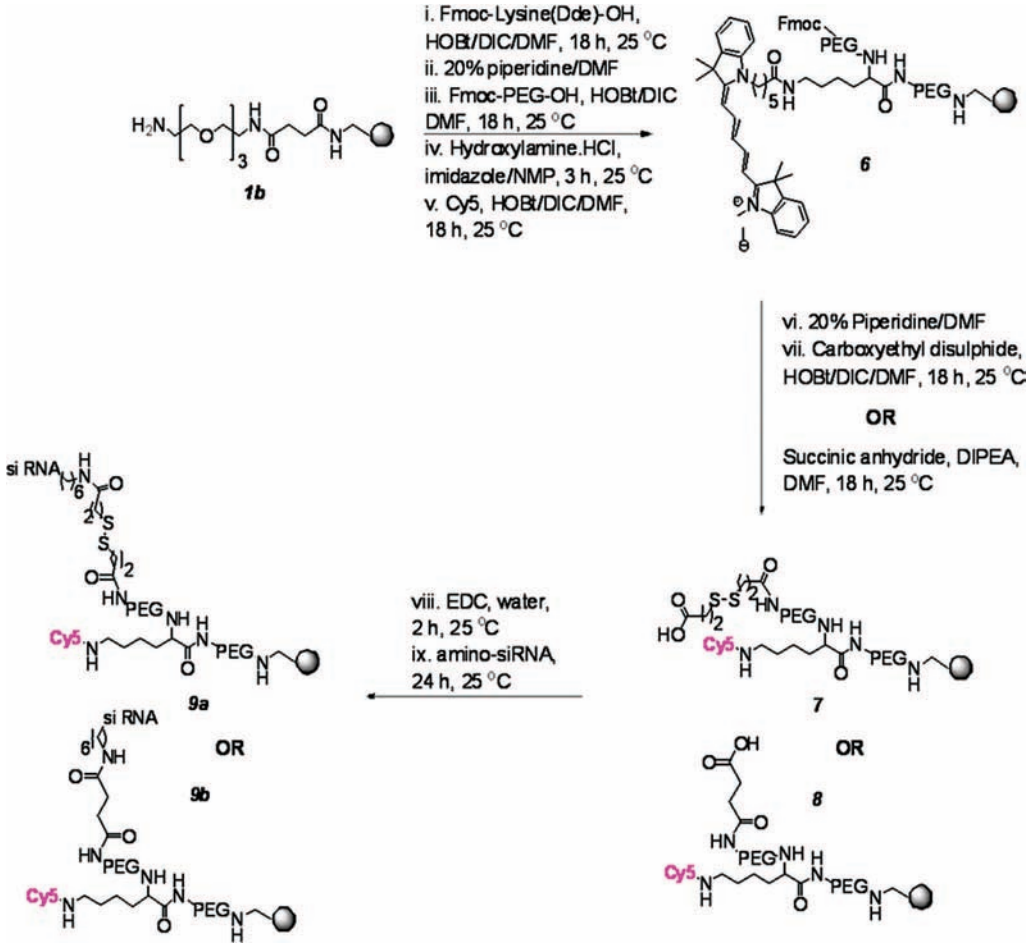

per 200 nm microsphere. As such, with a microsphere concentration of 86 μg mL^{-1} (which has been demonstrated to afford excellent and uniform cellular uptake), this equates to a siRNA concentration of 28 nM in cell cultures (assuming all siRNA on the microspheres is cleaved in solution; see Supporting Information, Graphs S4−6). Examining this on a single bead

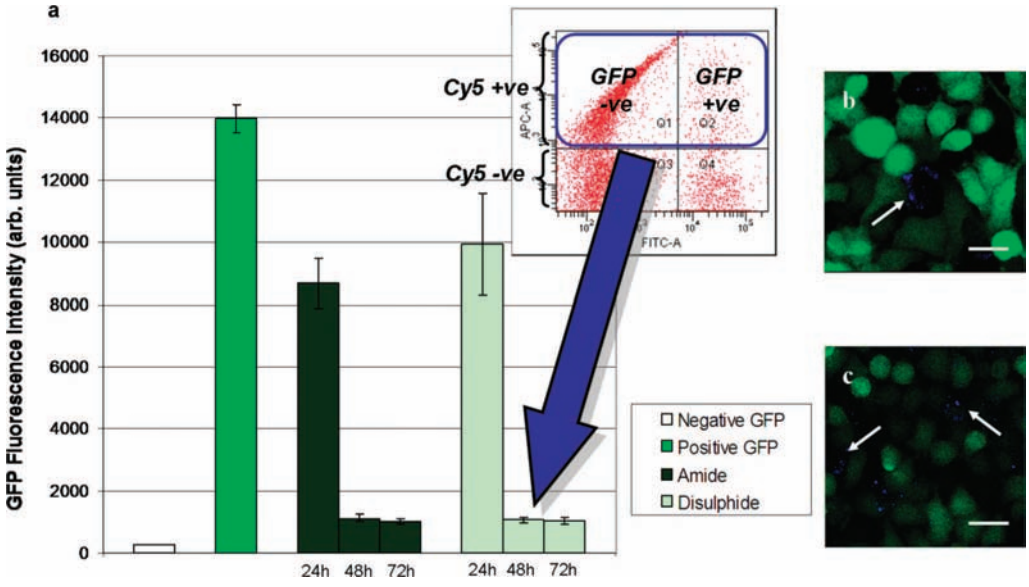

Figure 3. (a) EGFP Intensity in HeLa-EGFP cells after 24, 48, and 72 h incubation with Cy5-*co*-siRNA microspheres (**9a**−**b**). Negative GFP = HeLa cells untreated with beads and not transfected with EGFP; positive GFP = HeLa cells untreated with beads and stably transfected with EGFP. Inset: Dot plot of EGFP (FITC-A) vs Cy5 (APC-A) showing beadfected cells (Q1 and Q2) have a substantial reduction in EGFP intensity. *Right:* Confocal microscopy of HeLa-EGFP cells (green) treated with (b) amide-siRNA 500 nm Cy5 microspheres (**9b**) (scale bar is 70 μm); (c) Disulfide-siRNA 500 nm Cy5 microspheres (**9a**) (scale bar is 100 μm). Microspheres (blue) are indicated with white arrows. Images were collected using a Leica DM IRE2 inverted confocal microscope.

per cell basis, we equate this to an intracellular siRNA concentration of 0.3 nM (200 nm microspheres) to 4 nM (500 nm microspheres), assuming that all siRNA is disengaged from the delivery device and cell volume average of 5000 μ^3 (*17*). However, it must be noted that, in general, cells take up more 200 nm microspheres than 500 nm microspheres. Accordingly, in order to qualify siRNA-laden microsphere uptake, HeLa-EGFP cells were incubated with microspheres loaded with TAMRA labeled siRNA (**5a**−**b**) and assessed for uptake via pseudoconfocal microscopy (Figure 1) (a control was established using TAMRA-siRNA not conjugated to microspheres to measure background staining). Uptake was evident after 24 h, and the siRNA label could be seen localized on the polymer microspheres within cells. Previous studies have indicated that these microspheres enter cells by a mechanism that does not result in their endosomal capture (*11*, *13*), avoiding the need to apply endosomal disrupting agents to achieve cytoplasmic localization.

While siRNA functionalized with a fluorophore can achieve efficient gene knockdown (*18*), labeling of the antisense strand can result in poor silencing (see Supporting Information, Graph S-7) (*19*). As a consequence, **2a**−**b** and **3a**−**b** were conjugated to *unlabeled* siRNA, and HeLa-EGFP cells were subsequently treated with these microspheres (86 μg mL^{-1}, 28 nM siRNA) for 24, 48, and 72 h, before analysis of EGFP expression by microscopy and flow cytometry. After 48 h, excellent reductions in EGFP intensities were observed in cells incubated with all siRNA bead types, which was even more prominent after 72 h (Figure 2), with up to a 90% reduction in EGFP intensity. Positive controls were established using a commercially available transfection agent, Lipofectamine 2000, which achieved a 70% reduction in EGFP after 72 h using the same concentration of siRNA as the microspheres (28 nM, Figure 2). Negative controls included lipofection and beadfection of scrambled siRNA, siRNA without a carrier system, and microspheres without siRNA (Supporting Information, Graph S-8). In addition, the concentration of siRNA-microspheres incubated with HeLa-EGFP cells was varied and the knockdown efficiency was found to be dose- as well as time-dependent (see Supporting Information, Graph S-9). Furthermore, siRNA microspheres were shown to be nontoxic by MTT assay, even after 72 h, at all concentrations analyzed (see Supporting Information, Graph S-3).

Although EGFP silencing was clear, it was considered that a more accurate assessment of the knockdown would be to obtain a system whereby the beadfected cells could be assessed independently from non-beadfected cells. To this affect, a dual-functionalized system was developed. Thus, orthogonally protected lysine (*20*) was employed to allow functionalization of the microspheres with both a fluorophore (Cy5) and siRNA (Scheme 2). As such, HeLa-EGFP cells were incubated with Cy5-*co*-siRNA 500 nm microspheres (**9a**−**b**, 86 μg mL^{-1}, 28 nM siRNA), and EGFP silencing was analyzed after 24, 48, and 72 h by flow cytometry selecting only those cells that were positive for Cy5 (beadfected cells, thus containing siRNA) (Figure 3a). Silencing of EGFP was evident after 24 h and extensive at 48 and 72 h using both cleavable (disulfide) and noncleavable (amide) linkages to the microspheres. Reduction in EGFP expression was confirmed by confocal microscopy (Figure 3b,c), whereby cells containing microspheres (indicated by white arrows) were negative for EGFP expression. Using this method, the gene silencing capabilities of microspheres could be more accurately depicted, since only those cells known to contain the delivery device were considered in analysis of the EGFP expression.

In conclusion, enhanced green fluorescent protein stably expressed in human cervical cancer (HeLa) cells was successfully silenced (by approximately 90%) using siRNA linked to 500 and 200 nm microspheres via cleavable (disulfide) and noncleavable (amide) linkers, exceeding the silencing capabilities of commercially available lipofection products. In addition, a system employing dual-functionalized (Cy5-*co*-siRNA) microspheres allowed independent evaluation of only those cells that had been beadfected with siRNA, yielding gene silencing data based only on those cellular populations that had received the delivery vehicle, generating a more accurate analysis of the gene silencing capabilities of microspheres. This approach additionally allowed HeLa-EGFP cells beadfected with siRNA to be tracked over time, both visually by microscopy and by fluorescence-based flow cytometric methods.

Importantly, the nontoxic nature of the microspheres along with their facile functionalization and controllability over cellular loading makes these constructs particularly suitable to this application in a day and age when efficient, nontoxic, and versatile delivery devices are strongly desired.

ACKNOWLEDGMENT

The authors would like to thank the EPSRC and the BBSRC for funding. R.M. Sánchez-Martín would like to thank the Royal Society for a Dorothy Hogdkin Fellowship. The authors are grateful to M. Lopalco for the Cy5 dye.

Supporting Information Available: Microsphere preparation, functionalization, and cellular uptake (including siRNA sequences); disulfide cleavage; MTT toxicity assays; controls in gene silencing; and dose−response of siRNA microspheres. This material is available free of charge via the Internet at http://pubs.acs.org.

LITERATURE CITED

(1) Fire, A., Xu, S., Montgomery, M. K., Kostas, S. A., Driver, S. E., and Mello, C. C. (1998) Potent and specific genetic interference by double-stranded RNA in *Caenorhabditis elegans*. *Nature 391*, 806–810.

(2) Hamilton, A. J., and Baulcombe, D. C. (1999) A species of small antisense RNA in post-transcriptional gene silencing in plants. *Science 286*, 950–952.

(3) Elbashir, S. M., Harborth, J., Lendeckel, W., Yalcin, A., Weber, K., and Tuschl, T. (2001) Duplexes of 21-nucleotide RNAs mediate RNA interference in cultured mammalian cells. *Nature 411*, 494–497.

(4) Dykxhoorn, D. M., Novina, C. D., and Sharp, P. A. (2003) Killing the messenger: Short RNAs that silence gene expression. *Nat. Rev. Mol. Cell Biol. 4*, 457–467.

(5) Song, E. W., Zhu, P. C., Lee, S. K., Chowdhury, D., Kussman, S., Dykxhoorn, D. M., Feng, Y., Palliser, D., Weiner, D. B., Shankar, P., Marasco, W. A., and Lieberman, J. (2005) Antibody mediated *in vivo* delivery of small interfering RNAs via cell-surface receptors. *Nat. Biotechnol. 23*, 709–717.

(6) Brummelkamp, T. R., Bernards, R., and Agami, R. (2002) Stable suppression of tumorigenicity by virus mediated RNA interference. *Cancer Cell 2*, 243–248.

(7) Xia, H., Mao, Q., Paulson, H. L., and Davidson, B. L. (2002) siRNA-mediated gene silencing in vitro and in vivo. *Nat. Biotechnol. 20*, 1006–1010.

(8) Kennerdell, J. R., and Carthew, R. W. (1998) Use of dsRNA-mediated genetic interference to demonstrate that *frizzled* and *frizzled 2* act in the wingless pathway. *Cell 95*, 1017–1026.

(9) Arnold, A. S., Tang, Y. L., Qian, K., Shen, L., Valencia, V., Phillips, M. I., and Zhang, Y. C. (2007) Specific β1-adrenergic receptor silencing with small interfering RNA lowers high blood pressure and improves cardiac function in myocardial ischemia.

J. Hypertens. 25, 197–205.
(10) Liu, Z., Winters, M., Holodniy, M., and Dai, H. (2007) siRNA Delivery into Human T cells and primary cells with carbon-nanotube transporters. *Angew. Chem., Int. Ed. 46*, 2023–2027.
(11) Sánchez-Martín, R. M., Cuttle, M., Mittoo, S., and Bradley, M. (2006) Microsphere-based real-time calcium sensing. *Angew. Chem., Int. Ed. 45*, 5472–5474.
(12) Bradley, M., Alexander, L., and Sánchez-Martín, R. M. (2008) Cellular uptake of fluorescent labelled biotin−streptavidin microspheres. *J. Fluoresc. 18*, 733–739.
(13) Bradley, M., Alexander, L., Duncan, K., Chennaoui, M., Jones, A. C., and Sánchez-Martín, R. M. (2008) pH sensing in living cells using fluorescent microspheres. *Bioorg. Med. Chem. Lett. 18*, 313–317.
(14) Sánchez-Martín, R. M., Muzerelle, M., Chitkul, N., How, S. E., Mittoo, S., and Bradley, M. (2005) Bead-based cellular analysis, sorting and multiplexing. *ChemBioChem 6*, 1341–1345.
(15) Mosiman, V. L., Patterson, B. K., Canterero, L., and Goolsby, C. L. (1997) Reducing cellular autofluorescence in flow cytometry: An in situ method. *Cytometry Part B: Clinical Cytometry 30*, 151–156.
(16) Rejman, J., Oberle, V., Zuhorn, I. S., and Hoesktra, D. (2004) Size-dependent internalization of particles via the pathways of clathrin- and caveolae-mediated endocytosis. *Biochem. J. 377*, 159–170.
(17) Korchev, Y. E., Gorelik, J., Lab, M. J., Sviderskaya, E. V., Johnston, C. L., Coombes, C. R., Vodyanoy, I., and Edwards, C. R. W. (2000) Cell volume measurement using scanning ion conductance microscopy. *Biophys. J. 78*, 451–457.
(18) Berezhna, S. Y., Supekova, L., Supek, F., Schultz, P. G., and Deniz, A. A. (2006) siRNA in human cells selectively localizes to target RNA sites. *Proc. Natl. Acad. Sci. U.S.A. 103*, 7682–7687.
(19) Järve, A., Müller, J., Kim, I., Rohr, K., MacLean, C., Fricker, G., Massing, U., Eberle, F., Dalpke, A., Fischer, R., Trendelenburg, M. F., and Helm, M. (2007) Surveillance of siRNA integrity by FRET imaging. *Nucleic Acids Res.* , e124.
(20) Díaz-Mochón, J. J., Bialy, L., and Bradley, M. (2004) Full orthogonality between Dde and Fmoc: The direct synthesis of PNA-peptide conjugates. *Org. Lett. 6*, 1127–1129.

BC800529R

Supporting Information for
Knocking (Anti)-Sense into Cells – The Microsphere Approach to Gene Silencing

Lois Alexander, Rosario Sanchez-Martin and Mark Bradley

School of Chemistry, Joseph Black Building, King's Buildings, West Mains Road, Edinburgh, EH9 3JJ; Tel: +44(0)1316513307; Fax: : +44(0)1316506453;
E-mail: mark.bradley@ed.ac.uk

Preparation of siRNA Microspheres

200 and 500 nm amino microspheres were firstly functionalised with a modified PEG linker as follows: Microspheres were washed and suspended in DMF (3% solid content, 0.5 mL). Separately, Fmoc-amino carboxy poly(ethylene glycol) (10 equiv.) was dissolved in DMF (0.5 mL) with HOBt and DIC (10 equiv.) and mixed for 10 minutes. After this time, the solution was added to microspheres and mixed for 18 hours at 25 ºC. Subsequently, the microspheres were washed by centrifugation (13,000 rpm, 3 – 10 minutes) with DMF, methanol and water. Fmoc deprotection was subsequently achieved via treatment with 20% piperidine/DMF (3 × 20 minutes) and microspheres (**1a-b**) were sequentially washed as previously.

200 and 500 nm succinic microspheres (**2a-b**) were prepared by the addition of succinic anhydride (10 equiv.) and DIPEA (10 equiv.) in DMF and mixed at 25 ºC for 18 hours. Microspheres were then sequentially washed as described.

200 and 500 nm disulphide microspheres (**3a-b**) were prepared by the addition of carboxyethyl disulphide (10 equiv.), HOBt and DIC (10 equiv.) in DMF and mixed at 25 ºC for 18 hours. Microspheres were then sequentially washed as described.

Microspheres (**2a-b, 3a-b,** 100 µL, 3% solid content) were sterilized by U.V. radiation and with RNase Zap solution (Invitrogen) before pre-activation in MES buffer (pH 5.5) with EDAC.HCl (10 equiv.) for 2 hours at 25 ºC. The microspheres were isolated by centrifugation (as previous) and amino-siRNA (1 nmol) was then added in sterile RNase-Free water (100 µL) and mixed for 24 hours at 25 ºC.

Microspheres were subsequently isolated by centrifugation and stored in sterile RNase-Free water at 4 ºC.

siRNA Sequences: For EGFP silencing: Sense 5'-amino-C6-GCU GAC CCU GAA GUU CAU CUU-3'; Anti-sense 5'-GAU GAA CUU CAG GGU CAG CUU-3' (21).

Scrambled siRNA: Sense 5'-amino-C6-GUG AAA ACC AGG ACA AAA GUU-3'; Anti-sense 5'-CUU UUG UCC UGG UUU UCA CUU-3'.

Preparation of Fluorescein Microspheres

Microspheres (**2a-b, 3a-b**) were pre-activated in MES buffer (pH 5.5) with EDAC.HCl (10 equiv.) for 2 hours at 25 ºC before the addition of fluoresceinamine (10 equiv.) and mixing at 25 ºC for 18 hours. Microspheres were washed sequentially as previous and stored in water at 4 ºC.

Preparation of Dual-Functionalized Microspheres

PEGylated microspheres (**1a-b**), were treated with orthogonally protected Fmoc-Lysine(Dde)-OH (10 equiv.), HOBt and DIC (10 equiv.) in DMF for 18 hours at 25 ºC. Microspheres were subsequently washed as previous and Fmoc deprotected with 20% piperidine/DMF, yielding free amino residues, which were PEGylated as described above. Subsequently, Dde deprotection was afforded by treatment of microspheres with hydroxylamine.HCl (0.4 mmol) and imidazole (0.3 mmol) in NMP (1 mL) for 30 minutes – 1 hour. Microspheres were subsequently labelled with Cy5 by addition of Cy5 (5 equiv.) in the presence of HOBt (5 equiv.) and DIC (5 equiv.) in DMF and mixed for 18 hours at 25 ºC yielding **6**. After washing, microspheres were Fmoc deprotected and then coupled with carboxyethyl disulphide (yielding **7**) or succinic anhydride (yielding **8**) as described above.

Microspheres were activated and conjugated to siRNA as described above.

Cell Cultures

HeLa and HeLa-EGFP cells were grown in Roswell Park Memorial Institute Medium supplemented with 10% fetal bovine serum, 100 units/mL penicillin/streptomycin and 4 mM L-glutamine to 70 - 80% confluency. The cells were harvested via trypsin/EDTA and collected in growth media. They were seeded at a density of 2×10^4 cell per well in a 24-well plate and incubated at 37 ºC/5% CO_2.

HeLa Cell Uptake of Succinic-Fluorescein Microspheres

HeLa cells were cultured as described above. After 24 hours, 500 nm and 200 nm amide-fluorescein microspheres were added to the cells in fresh growth media at a concentration of 86 μg/mL. After 6, 12, 24, 48 and 72 hours the cells were detached by trypsination, collected in media and pelleted by centrifugation (1200 rpm, 4 minutes). The cell pellet was then resuspended in 0.2% trypan blue in Hank's Balanced Saline Solution (HBSS) for analysis by flow cytometry on a FACS Aria system (BD Biosciences). Excitation was made at 488 nm and emission collected with a 530/30 band pass filter. FACS Diva software was used for analysis. The % uptake is summarized in Graph S-1.

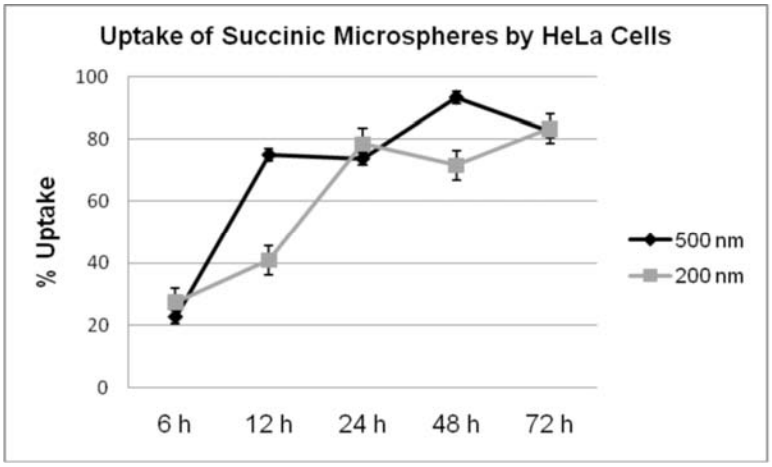

Graph S-1. Uptake of 200 and 500 nm amide-fluorescein microspheres by HeLa cells over 72 hours. % Uptake is calculated as the total % of the cell population that contains a fluorescent microsphere, where 0% uptake is untreated cells.

Disulphide Cleavage with Glutathione

200 and 500 nm disulphide-fluorescein beads (Figure S-1) were treated with 10 mM glutathione in phosphate buffered saline (PBS, pH 7.4) for 1, 6 and 24 hours. Cleavage was assessed on the reduction in fluorescence intensity of the microspheres compared to untreated control beads (Graph S-2).

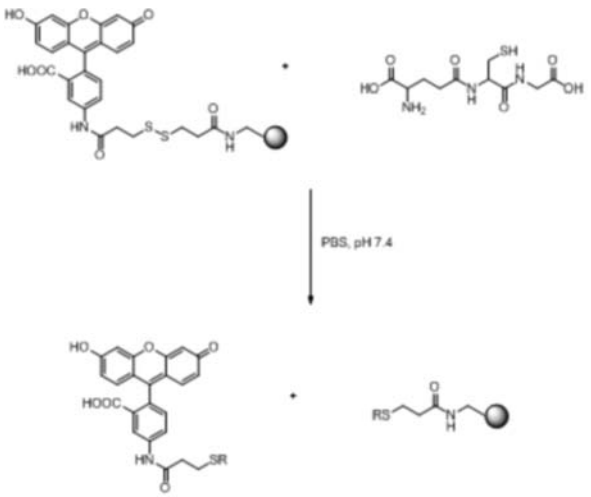

Figure S-1. Cleavage of disulphide-fluorescein beads by treatment with glutathione

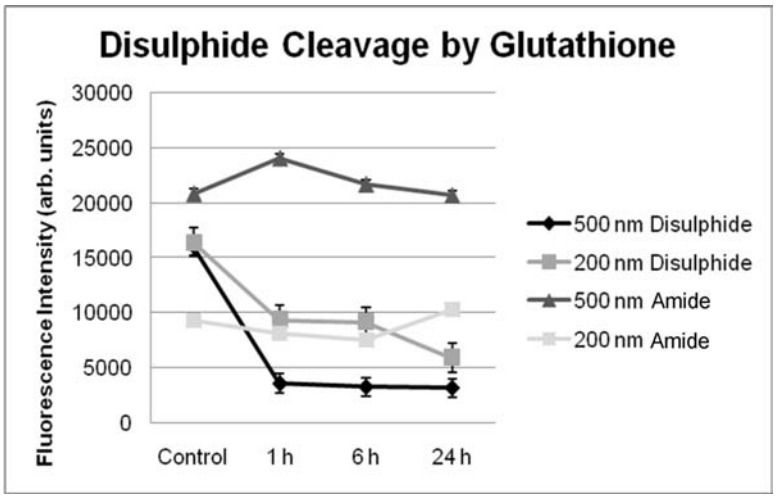

Graph S-2. Cleavage of disulphide-fluorescein beads by treatment with glutathione over 24 hours.

For *in vitro* analysis, HeLa cells (not expressing EGFP) were cultured as described and disulphide-fluorescein microspheres (200 and 500 nm, 86 µg/mL) were added. Microscopy was performed after 6, 12 and 24 hours.

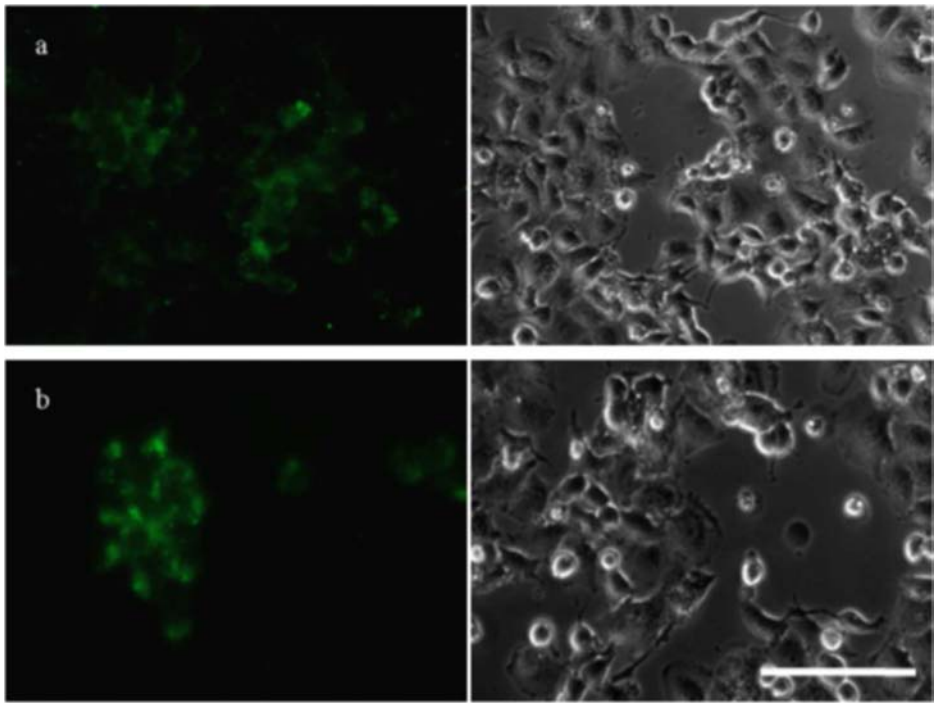

Figure S-2. Microscopy of HeLa cells incubated with **a.** 500 nm disulphide-fluorescein microspheres (**4b**); **b.** 200 nm disulphide-fluorescein microspheres (**4a**). Images taken after 12 hours (scale bar is 100 μm).

MTT Assays of HeLa-EGFP cells with siRNA Microspheres

HeLa-EGFP cells were cultured as described above. They were seeded into a 96-well plate in growth media. 200 and 500 nm amide and disulphide siRNA microspheres were added to fresh phenol-red free growth media at day 1, day 2 and day 3. After 72 hours after the first microsphere addition, 3-(4,5-Dimethylthiazol-2-yl)-2,5-diphenyltetrazolium bromide in phenol red-free media (5 mg/mL, 10 μL per well) was added and the cells incubated for a further 5 hours. After this time, MTT solubilization solution was added (10% Triton-X, 0.1 N HCl in isopropanol, 100 μL) and the well plate was gently shaken overnight. Analysis was made at 570 nm. See Graph S-3.

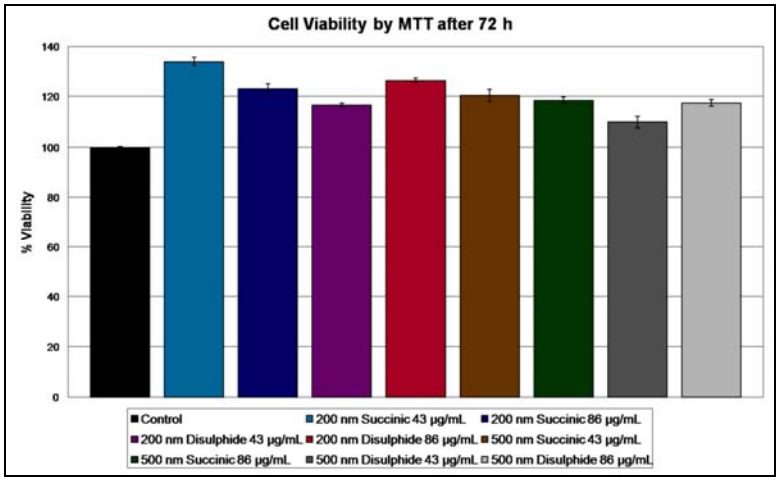

Graph S-3. Toxicity by MTT assay after 72 hours with siRNA microspheres in HeLa-GFP cells

Cell Staining

Staining with Hoechst 33342: Hoechst 33342 (1 µg/mL) was added in PBS (pH 7.4) to cell cultures previously washed with PBS and incubated at 25 ºC for 10 minutes. Cell cultures were washed sequentially with PBS.

Staining with Alexa Fluor® 568-Phalloidin: Cells stained with Hoechst 33342 were fixed in 3% *p*-formaldehyde solution in PBS for 20 minutes. Cultures were then washed with PBS and Alexa Fluor® 568-Phalloidin (1 unit) added in PBS (200 µL) supplemented with 1% Bovine Serum Albumin. Cells were incubated at 25 ºC for 20 minutes before washing with PBS and finally stored in PBS at 4 ºC.

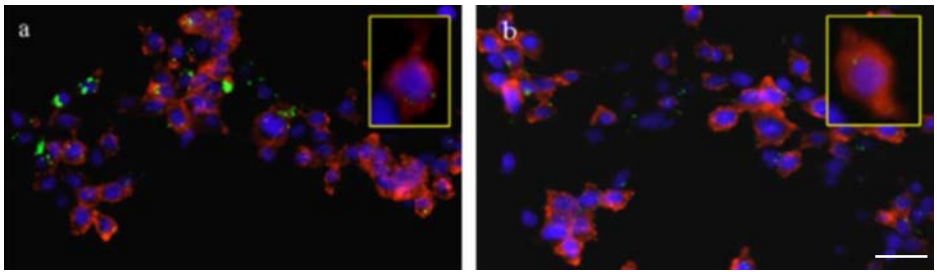

Figure S-3. Uptake of fluorescein labelled succinic **a.** 500 and **b.** 200 nm microspheres by HeLa cells. Actin filaments stained with Alexa Fluor® 568-Phalloidin and nuclei stained with Hoechst 33342. Inset is 2× magnification. Scale bar is 100 µm.

Analysis of siRNA Loading by Spectrofluorometry

The supernatant was collected from the siRNA-bead coupling by centrifugation (13,000 rpm, 2 minutes). Calibration solutions were prepared at concentrations of 0.25, 0.15, 0.1 and 0.05 µM TAMRA labelled siRNA in sterile RNase-free water and analysed on a FluoroMax spectrofluorometer and compared with the supernatant from the coupling reactions exciting at 542 nm and collecting emission from 500 – 750 nm. The emission maximum was found at 578 nm (Graph S-4 and S-5).

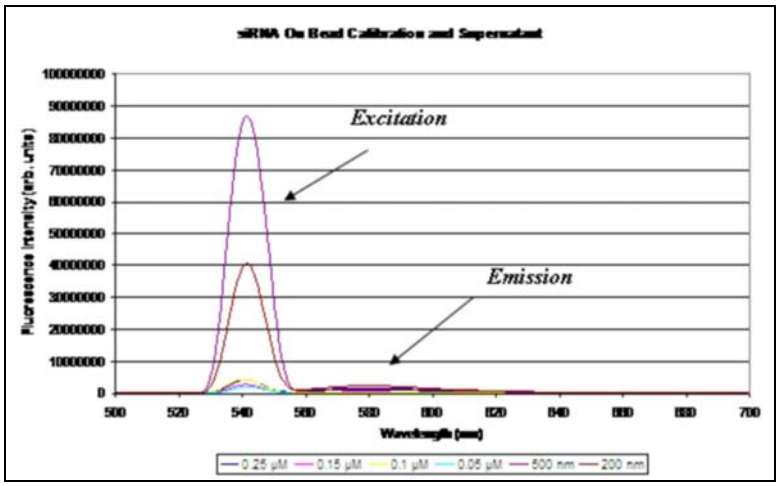

Graph S-4. Fluorescence excitation and emission collected by spectrofluorometry of calibration solutions and coupling supernatant, exciting at 542 nm and collecting emissions over 500 – 750 nm.

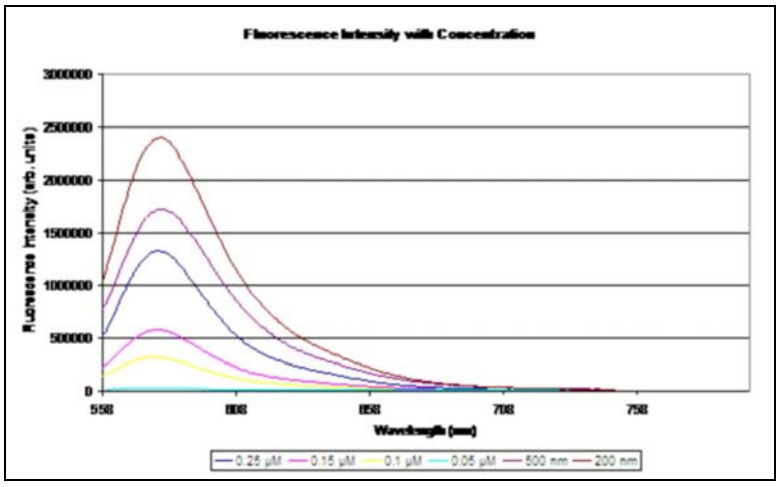

Graph S-5. Fluorescence emission only collected by spectrofluorometry of calibration solutions and coupling supernatant, exciting at 542 nm. Emission maximum was at 578 nm.

The calibration solutions were used to correlate TAMRA siRNA concentration to the intensity of fluorescence emission, which was found to be a linear relationship (Graph S-6).

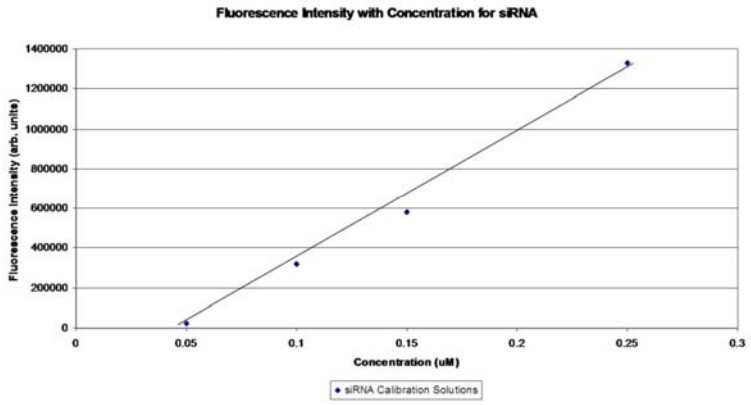

Graph S-6. Fluorescence emission collected by spectrofluorometry of calibration solutions plotted as a function of concentration.

Using the equation of the graph (Equation S-1), the fluorescence emission recorded for the supernatant of the 200 and 500 nm bead-siRNA couplings were used to calculate the concentration of siRNA present in the samples and found to be 0.4 µM for 200 nm bead-siRNA supernatant and 0.3 µM for 500 nm bead-siRNA supernatant.

$$y = 7 \times 10^6 x - 332854 \qquad \textbf{Equation S-1}$$

Therefore: $x = (y + 332854)/7 \times 10^6$

Where x is the concentration (µM) and y is the fluorescence intensity (arb. units).

The 200 nm bead-siRNA supernatant contained 4×10^{-11} moles of siRNA and the 500 nm bead-siRNA supernatant 3×10^{-11} mol of siRNA. A total of 1×10^{-9} moles siRNA was added to the beads originally thus the 200 nm beads must have retained 9.6×10^{-10} moles siRNA (96% of siRNA coupled to microspheres) and the 500 nm beads must have retained 9.7×10^{-10} moles siRNA (97% of siRNA coupled to microspheres).

The number of beads per gram of solid can be calculated by Equation S-2.

$$Number\ of\ beads/g = 6 \times 10^{12}/(\pi \times \rho \times d^3) \qquad \textbf{Equation S-2}$$

Where ρ is the density of the microspheres (1.0 g/mL for polystyrene microspheres) and d is the diameter of the microspheres. Equation from Bangs Laboratories, Technical Note.

Thus, in the case of 200 nm microspheres, there are 2.4×10^{14} beads/g and in a 100 µL aliquot at a solid content of 3% (as used in the siRNA couplings) there is 3 mg of solid beads. This equates to 7.2×10^{11} beads, therefore each bead holds, on average, 1.3×10^{-21} moles of siRNA, which equates to 783 molecules of siRNA per bead.
In a typical culture where 86 µg/mL microspheres (or 2.1×10^{10} beads/mL) are added to cells, 1.3×10^{-21} moles of siRNA per bead equates to 9.4×10^{-12} siRNA per culture. Given the cell culture volume is 350 µL, this gives a concentration of 2.7×10^{-8} moldm^{-3}.

In the case of 500 nm microspheres, there are 1.5×10^{13} beads/g and in a 100 µL aliquot at a solid content of 3% (as used in the siRNA couplings) there is 3 mg of solid beads. This equates to 4.5×10^{10} beads, therefore each bead holds, on average, 2.2×10^{-20} moles of siRNA, which equates to 13,244 chains of siRNA per bead.
In a typical culture where 86 µg/mL (or 1.3×10^{9} beads/mL) microspheres are added to cells, 2.2×10^{-20} moles of siRNA per bead equates to 1.0×10^{-11} siRNA per culture. Given then cell culture volume is 350 µL, this gives a concentration of 2.8×10^{-8} moldm^{-3}.

Gene Silencing by Beadfection with Fluorescently Labelled and Unlabelled siRNA
HeLa-EGFP cells were cultured in the normal manner (described above) prior to the addition of siRNA conjugated 200 and 500 nm microspheres (86 µg/mL beads or 28 nM siRNA per culture) in serum free media. After 24 hours, the serum-free media was exchanged from complete media and EGFP expression was evaluated by flow cytometry after 24, 48 and 72 hours (results shown after 72 hours) in 2% FBS/PBS. A positive control was established with Lipofectamine 2000 used as according to the manufacturer's instructions using 28 nM siRNA.

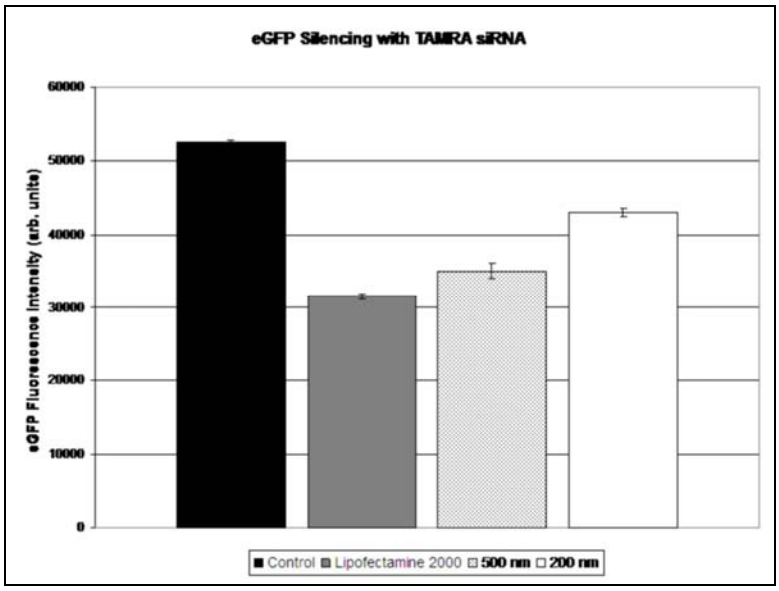

Graph S-7. EGFP silencing in HeLa-EGFP cells after 72 hours by 500 and 200 nm microspheres carrying TAMRA labelled siRNA via an amide linkage (concentration of beads: 86 µg/mL; concentration of siRNA: 28 nM).

Controls for Gene Silencing

HeLa-EGFP cells were incubated with a range of controls and analysed by flow cytometry (2% FBS/PBS) after 24, 48 and 72 hours.

The concentration of siRNA used was 28 nM to reflect that concentration used in beadfections. Lipofectamine 2000 was used as according to the manufacturer's instructions.

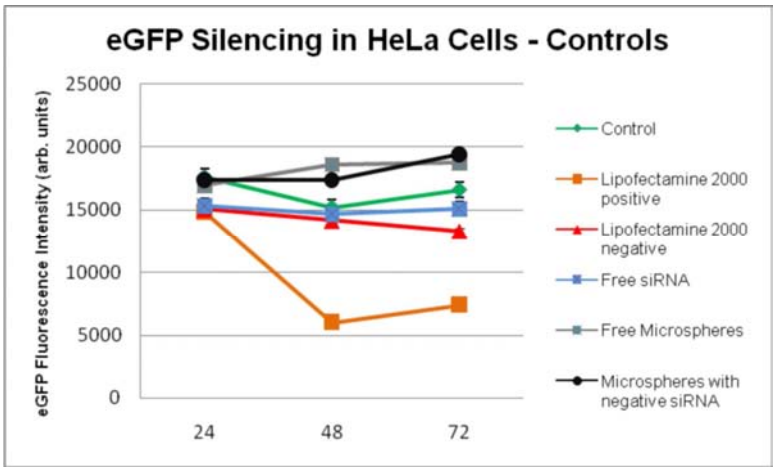

Graph S-8. Controls for gene silencing of EGFP in HeLa cells. (*Control*: untreated cells; Lipofectamine 2000 positive = siRNA transfected with Lipofectamine 2000; *Lipofectamine 2000 negative* = scrambled siRNA transfected with Lipofectamine

2000; *Free siRNA* = siRNA targeted against GFP, without a carrier device; *Free Microspheres* = 500 nm microspheres without siRNA; *Microspheres with negative siRNA* = 500 nm microspheres bound to scrambled siRNA (via an amide linkage).

Dose Response Analysis of Gene Silencing

HeLa-EGFP cells were cultured as stated above and siRNA microspheres (500 and 200 nm, amide linkages) were added to the cultures (86 µg/mL = 28 nM and 43 µg/mL = 14 nM) in serum-free media. After 24 hours, the old media was exchanged from complete media and flow cytometric analysis was carried out as described after 24, 48 and 72 hours (data not shown for 24 and 48 hours) in 2% FBS/PBS.

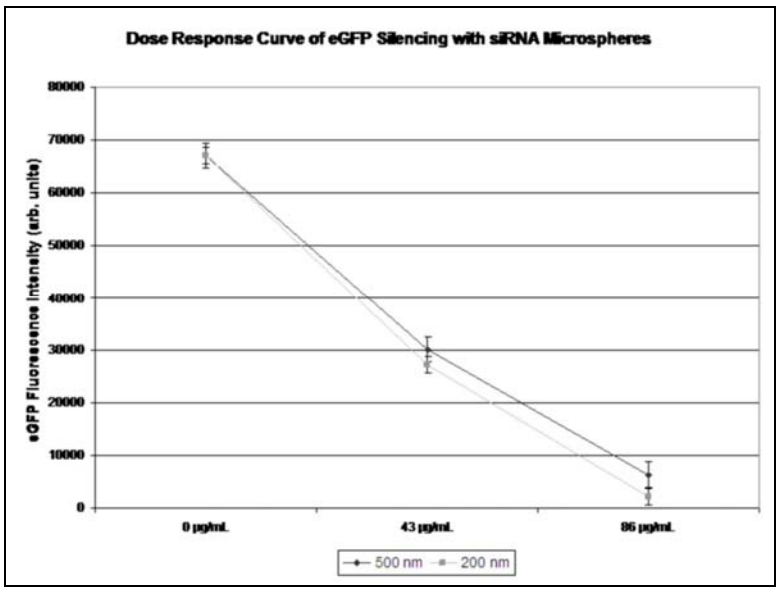

Graph S-9. Dose response curve following the addition of 500 and 200 nm siRNA microspheres (amide linkage, 86 and 43 µg/mL *or* 28 nM and 14 nM siRNA respectively) to HeLa-EGFP cells. Results shown are after 72 hours.

Subscriber access provided by SHEMYAKIN-OVCHINNIKOV INST

Communication

Conjugation of Antisense Oligonucleotides to PEGylated Carbon Nanotubes Enables Efficient Knockdown of PTPN22 in T Lymphocytes

Lucia G. Delogu, Andrea Magrini, Antonio Bergamaschi, Nicola Rosato, Marcia I. Dawson, Nunzio Bottini, and Massimo Bottini

Bioconjugate Chem., **2009**, 20 (3), 427-431• DOI: 10.1021/bc800540j • Publication Date (Web): 25 February 2009

Downloaded from http://pubs.acs.org on April 8, 2009

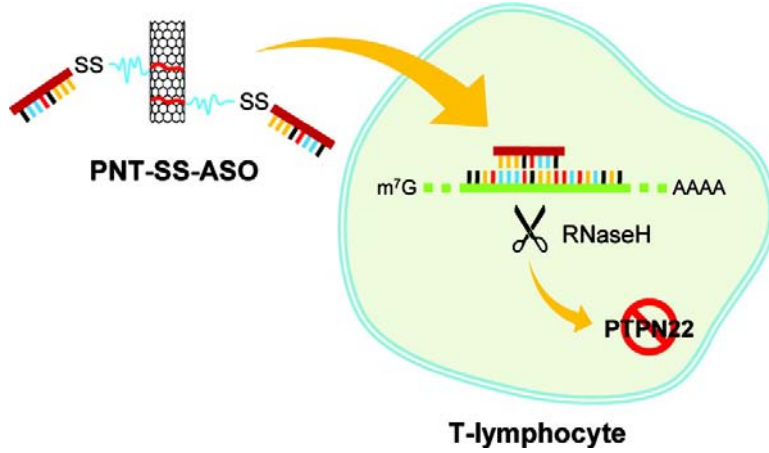

More About This Article

Additional resources and features associated with this article are available within the HTML version:

- Supporting Information
- Access to high resolution figures
- Links to articles and content related to this article
- Copyright permission to reproduce figures and/or text from this article

View the Full Text HTML

ACS Publications
High quality. High impact.

Bioconjugate Chemistry is published by the American Chemical Society. 1155 Sixteenth Street N.W., Washington, DC 20036

Conjugation of Antisense Oligonucleotides to PEGylated Carbon Nanotubes Enables Efficient Knockdown of PTPN22 in T Lymphocytes

Lucia G. Delogu,[†] Andrea Magrini,[‡,§] Antonio Bergamaschi,[||] Nicola Rosato,[‡,⊥] Marcia I. Dawson,[#] Nunzio Bottini,*[,†] and Massimo Bottini*[,‡,⊥,#]

Department of Biochemistry and Molecular Biology and Institute for Genetic Medicine, Keck School of Medicine of the University of Southern California, Los Angeles, California 90033, NAST Centre for Nanoscience & Nanotechnology & Innovative Instrumentation, Department of Environmental, Occupational, and Social Medicine, and Department of Experimental Medicine and Biochemical Sciences, University of Rome Tor Vergata, Via Montpellier 1, 00133 Rome, Italy, Institute of Occupational Medicine, Università Cattolica del Sacro Cuore, Largo Agostino Gemelli 8, 00168 Rome, Italy, and Burnham Institute for Medical Research, 10901 North Torrey Pines Road, La Jolla, California 92037. Received December 12, 2008; Revised Manuscript Received February 4, 2009

PEGylated-carbon nanotubes (PNTs) were evaluated as nanocarriers of antisense oligonucleotides into T-cells using protein tyrosine phosphatase N22 (PTPN22) as a model target gene. PTPN22 is an important predisposing gene and drug target in type 1 diabetes and several other human autoimmune diseases. Here, we generated the first anti-PTPN22 20-mer antisense oligonucleotides (ASOs) and tethered them to PNTs through a cleavable disulfide bond. Spectroscopic and atomic force microscopy analyses were used to determine the loading of ASO onto PNTs, whereas the cleavable nature of the disulfide bond connecting the oligonucleotide to the nanocarrier was confirmed by incubation with dithiothreitol followed by agarose gel electrophoresis. PNT-conjugated ASOs achieved efficient (>50%) knockdown of PTPN22 expression in T-lymphocytes in culture at the mRNA and protein level, as measured by quantitative real-time PCR and Western blotting, respectively. Considering the high biocompatibility and low in vivo toxicity of PNTs, we expect that our approach will be easily translated to achieve in vivo knockdown of PTPN22 and other T lymphocyte targets, thus enabling novel ASO-mediated immunotherapies for type 1 diabetes and other autoimmune diseases.

Gene silencing can be achieved using antisense oligomers, ribozymes, DNAzymes, and RNA interference (*1*). Antisense technology permits knockdown in expression of a specific gene for both research and medicinal applications. Typically, a 20-mer antisense oligonucleotide (ASO) is designed to complement the mRNA of a particular target for cleavage by RNaseH endonuclease or by inhibiting translation (*2*). ASOs have been chemically modified to improve their affinity for target mRNA, potency, nuclease resistance, and biostability and to elicit RNaseH-mediated cleavage of target mRNA (*3, 4*). The so-called first generation of ASOs is based on phosphorothioate deoxynucleotides. These sequences have a net negative charge, elicit RNase H-mediated message degradation, and are stable to nuclease degradation (*5*). Systemic injection of ASOs enables the therapeutic knockdown of disease-related genes in important tissues, including liver and bone (*6*). However, their use for immunotherapy has been hampered by inefficient transport across the plasma membranes of immune cells. For example, the negatively charged phosphorothioates have very low bioavailability in B- and T-lymphocytes (*7*).

Chemically engineered nanotechnology-derived carriers (nanocarriers) have recently improved drug delivery into difficult cell targets (*8*). These nanocarriers have been shown to be able to deliver cargo (nucleic acids, peptides, small molecules, etc.) into such specific cell types as B- and T-lymphocytes after injection in mice without causing significant toxicity. Carbon nanotubes (NTs), due to their extremely high aspect ratio (length/diameter), represent a potential scaffold for constructing multivalent delivery systems capable of binding many membrane receptors (*9, 10*). In particular, NTs functionalized with poly(ethylene glycol) (PEG) chains (PEGylated NTs or PNTs) have been reported to deliver small-interfering RNA into cultured cells (including T-lymphocytes) (*11*) and target integrin-positive tumors in mice (*12*). Moreover, PNTs exhibit long circulation times in the blood, low uptake by the reticuloendothelial system (RES) (*13*), and lack of toxicity in vivo (*14*). Both in vitro and in vivo, PNTs were taken into the cytoplasm of T-lymphocytes (*15*). These reports led us to investigate whether PNTs could be used as nanocarriers to deliver ASOs into immune cells.

Here, we used PNT-conjugated ASOs to achieve knockdown of protein tyrosine phosphatase N22 (PTPN22) in T cells. PTPN22 is an important drug target for autoimmune diseases (*16*−*18*). A mutation in its gene is a well-recognized predisposing factor for type 1 diabetes (*19*−*22*), rheumatoid arthritis (*23, 24*), and several other autoimmune diseases (*25*). PTPN22 is found in white blood cells and has a particularly critical function in T-lymphocytes, in which it negatively regulates growth and activation (*26*−*29*). The autoimmune-predisposing C1858T mutation (R620W) (*29, 30*) in the *PTPN22* gene produces a

* Address correspondence to Nunzio Bottini, M.D., Ph.D., nunzio@usc.edu, Institute for Genetic Medicine, Keck School of Medicine of the University of Southern California, Los Angeles, CA 90033, USA, Phone (323) 442-2634; or Massimo Bottini, Ph.D., mbottini@burnham.org, Burnham Institute for Medical Research, 10901 North Torrey Pines Road, La Jolla, CA 92037, USA, Phone (858) 646-3100 x3063.

[†] Keck School of Medicine of the University of Southern California.

[‡] NAST Centre for Nanoscience & Nanotechnology & Innovative Instrumentation, University of Rome Tor Vergata.

[§] Department of Environmental, Occupational, and Social Medicine, University of Rome Tor Vergata.

[||] Università Cattolica del Sacro Cuore.

[⊥] Department of Experimental Medicine and Biochemical Sciences, University of Rome Tor Vergata.

[#] Burnham Institute for Medical Research.

10.1021/bc800540j CCC: $40.75 © 2009 American Chemical Society
Published on Web 02/25/2009

Scheme 1. Fabrication of Antisense Oligonucleotide- And Carboxyfluorescein-Functionalized PEGylated Carbon Nanotubes[a]

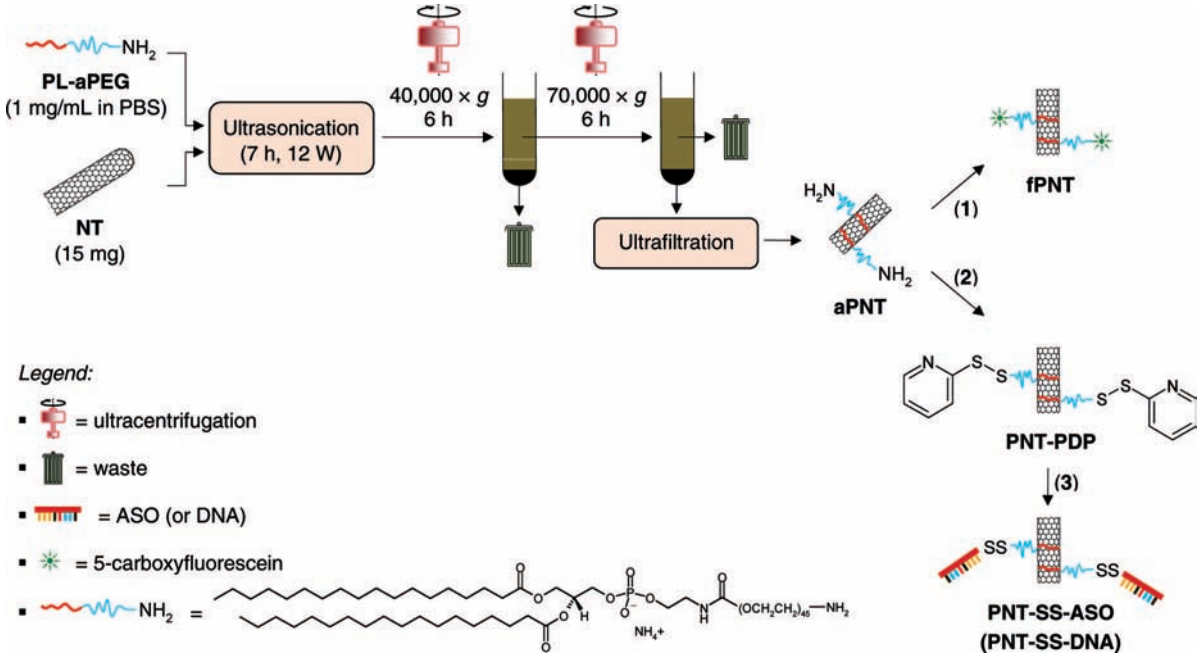

[a] Pristine carbon nanotubes (NTs) were sonicated in the presence of 1,2-distearoyl-*sn*-glycero-3-phosphoethanolamine-*N*-[amino(poly(ethylene glycol))$_{2000}$] (PL-aPEG), fractionated by stepwise centrifugation, and purified away from small molecules by ultrafiltration. The amino-functionalized PEGylated NTs (aPNTs) obtained were capped with 5-carboxyfluorescein by reaction with 5-carboxyfluorescein *N*-hydroxysuccinimide ester to give fluorescent PEGylated NTs (fPNTs, **(1)**). Alternatively, aPNTs were capped with ASO8 phosphorothioate by stepwise activation with sulfosuccinimidyl 6-(3′-[2-pyridyldithio]propionamido)hexanoate (sulfo-LC-SPDP) (to give pyridyldithio-functionalized PEGylated NTs, PNT-PDP **(2)**) followed by displacement with 5′-mercapto-terminated ASO8 to give the PTPN22 antisense oligonucleotide tethered to PEGylated NTs through a disulfide bond (PNT-SS-ASO, (**3**)). This procedure was repeated to produce DNA tethered to PNTs through a disulfide bond as a model conjugate (PNT-SS-DNA).

gain-of-function-W620 variant that is a more potent inhibitor of T-lymphocyte activation. Reduced T-lymphocyte growth and activation are important predisposing factors for autoimmune disease (*31*, *32*). Thus, systemic inhibition of *PTPN22* expression is considered to be beneficial for prevention or early treatment of autoimmunity (*18*). Our goal is to develop nucleotide-based *PTPN22* inhibitors and optimize their delivery into T-lymphocytes for treatment of type 1 diabetes and other autoimmune diseases.

PNTs were obtained by hydrophobic adsorption of phospholipids terminated with amino-functionalized PEG chains onto NT sidewalls by using a procedure previously reported by us (*15*) and others (*11*). Pristine (nonfunctionalized) NTs were ultrasonicated with phospholipids terminated with approximately 12-nm-long amino-functionalized PEG chains {1,2-distearoyl-*sn*-glycero-3-phosphoethanolamine-*N*-[amino(polyethylene glycol)$_{2000}$]} (PL-aPEG, Scheme 1), fractionated by stepwise ultracentrifugation to isolate short hydrophilic amino-terminated PEGylated NTs and purified by ultrafiltration to remove free phospholipids (aPNTs). The collected nanocarriers were found to disperse under physiologic conditions and did not display any visible flocculation upon standing for several months at room temperature in PBS pH 7.4. Atomic force microscopy (AFM) images of aPNTs showed the presence of individual particles and small bundles (Figure 1A) having a length of 164 ± 46 nm. We calculated that aPNTs had an approximate molecular weight of 450 kDa and were decorated with 85 ± 14 PEG chains per nanoparticle (see Supporting Information).

The exposed amino groups of the aPNTs were acylated with 5-carboxyfluorescein *N*-hydroxysuccinimide ester to introduce a fluorescent label (Scheme 1). The fluorescent PNTs (fPNTs) were visible by conventional light optical and confocal microscopy (data not shown). The Jurkat human acute lymphoblastoma leukemia T-cell line expressing the SV40 T antigen (TAg) (*33*) was kept at logarithmic growth in RPMI 1640 medium supplemented with 10% FCS, 2 mM L-glutamine, 1 mM sodium pyruvate, 10 mM HEPES pH 7.3, 2.5 mg/mL D-glucose, 100 units/mL of penicillin, and 100 μg/mL streptomycin. The internalization of fPNTs by Jurkat TAg cells was investigated by flow cytometry using a Beckman FC500 instrument. In the presence of fPNTs, 100% cells showed internalization of the nanocarriers already at 30 min and the internal fluorescence of the cells kept increasing during the first 18 h (Figure 1B, cell fluorescence was read in the presence of Trypan blue in order to quench fluorescence of noninternalized fluorescein). Next, we loaded the aPNTs with oligonucleotides using a tether with a cleavable disulfide bond that enables the release of the oligonucleotide cargo once the nanocarrier is transported into intracellular compartments. We acylated the aPNT primary amino groups with sulfosuccinimidyl 6-[3′-(2-pyridyldithio)-propionamido]hexanoate (sulfo-LC-SPDP) to give pyridyldithio-functionalized PNTs (PNT-PDP) and, subsequently, used a SH-terminated 21-mer single-stranded oligonucleotide to displace the pyridyl group and produce the oligonucleotide-tethered PNTs (PNT-SS-DNA) as a model conjugate (Scheme 1). The PNT-SS-DNA were purified by filtration, and the cleavable nature of the disulfide bond connecting the oligonucleotide to the nanocarrier was confirmed by incubation with dithiothreitol (DTT) followed by agarose gel electrophoresis (Figure 1C). The electrophoretic mobility of PNT-SS-DNA (lane 2), which was greater than that of PNT-PDP (lane 1), was decreased after incubation with DTT (lane 3), which cleaved the oligonucleotide off the PNTs by reducing the disulfide bond.

Next, we generated and characterized anti-PTPN22 ASOs. PTPN22 ASO sequences have not been reported. We used the Sfold software (http://sfold.wadsworth.org, Supporting Information) to design a set of 20-mer ASOs against human PTPN22 (Accession: NM_017774; GI: 48928053). After passing a

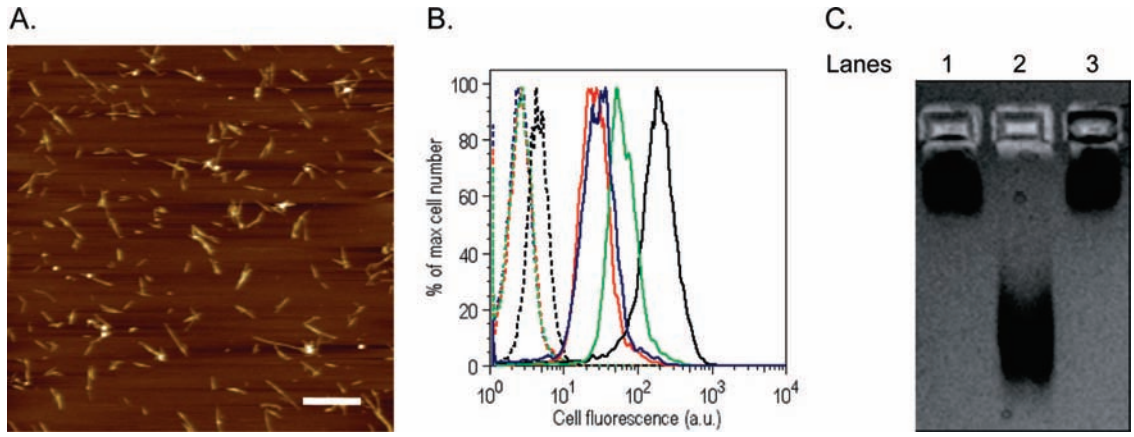

Figure 1. Characterization of PNT-based nanoassemblies. (A) Atomic force microscope (AFM) image of aPNTs (bar length 500 nm). (B) Flow cytometry plot of Jurkat TAg cell fluorescence after incubation with 6 nM fPNT for 30 min (blue line), 1 h (red line), 6 h (green line), or 18 h (black line) compared to nontreated control cells after the same times (dotted lines). Cell fluorescence was measured in the presence of 0.4% (w/v) trypan blue in order to quench fluorescence from noninternalized fluorescein. The histogram shows ungated data from approximately 5000 events; cell fluorescence is reported in arbitrary units (a.u.). (C) Reversible conjugation of a 21-mer single-stranded SH-terminated DNA oligomer to activated aPNTs through a disulfide bond. PNT-PDP (lane 1), PNT-SS-DNA (lane 2), and PNT-SS-DNA incubated with 0.1 M DTT for 30 min (lane 3) were analyzed by 1% agarose gel electrophoresis and visualized under visible light.

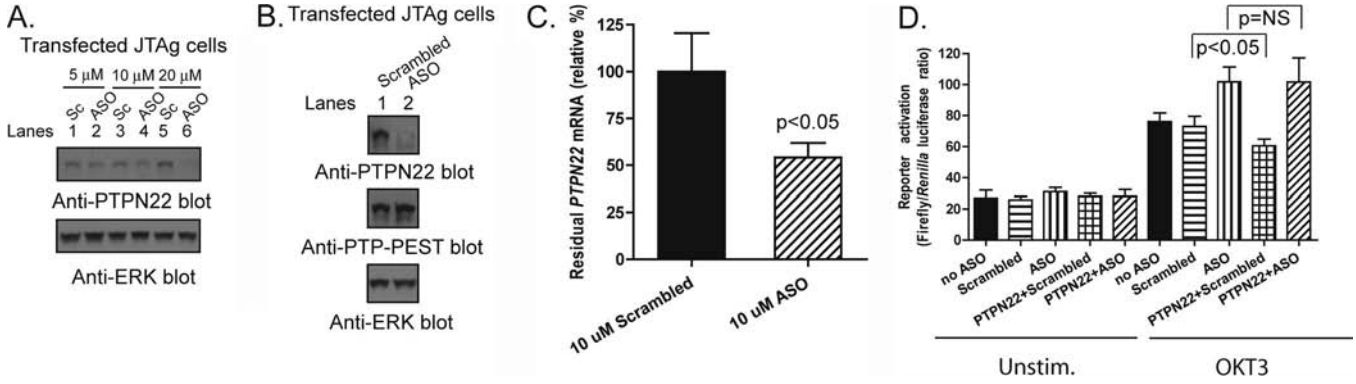

Figure 2. Characterization of a new anti-PTPN22 ASO. (A) Dose-dependent knockdown of PTPN22 using ASO. JTAg cells were electroporated with 5 μM (lanes 1, 2), 10 μM (lanes 3, 4), or 20 μM (lanes 5, 6) scrambled ASO (lanes 1, 3, 5) or ASO8 (lanes 2, 4, 6). Cells were lysed 24 h after transfection. Upper panel shows anti-PTPN22 blot, and lower panel shows control anti-ERK2 blot of total lysates. (B) PTPN22-specific knockdown by ASO8. Jurkat TAg cells were electroporated with a plasmid encoding PTP-PEST and with 10 μM scrambled ASO (lane 1) or ASO8 (lane 2) and lysed 24 h later. Cell lysates were subjected to Western blotting using antibodies to PTPN22, PTP-PEST, and Erk2. (C) ASO8 possesses endonuclease-inducing activity. Jurkat TAg cells were electroporated with 10 μM scrambled ASO or ASO8 and lysed 24 h later for isolation of total RNA. PTPN22 mRNA levels were measured in triplicate by quantitative real-time PCR. The histogram shows residual PTPN22 mRNA (%) in cells treated with ASO8 relative to those treated with scrambled ASO (100%). The statistical significance of differences between the two samples was calculated on the raw data by two-tailed Student's *t* test. (D) ASO8 induces increased T cell receptor (TCR) signaling and rescues the inhibitory effects of PTPN22 overexpression on a TCR reporter activation. Jurkat TAg cells were electroporated with a NFAT/AP1-firefly luciferase reporter plasmid and a pGL3 *Renilla* control plasmid alone (columns 1, 2, 3, 6, 7, 8) or combined with 10 μM scrambled ASO (columns 2, 4, 7, 9) or ASO8 (columns 3, 5, 8, 10) and with a plasmid for hemagglutinin (HA)-tagged PTPN22 (columns 4, 5, 9, 10). Samples represented in columns 1 and 6 represent negative controls and contained no ASO. At 24 h after transfection, half of the samples were stimulated using 1.5 mg/mL of OKT3 for 6 h (columns 6−10) to induce reporter activation, while the remainder (columns 1−5) were not stimulated. The histogram shows reporter activation (firefly/renilla luciferase ratios) as measured by the dual-luciferase assay (see Supporting Information for details). Statistical significance of differences was calculated by one-way ANOVA with Tukey post-test.

counter-screen to disallow nonspecific cross-hybridizers, the three top-scoring antisense sequences (ASO7, ASO8, and ASO9) were synthesized as phosphorothioates. A 20-mer scrambled ASO (*34*) was used as a control in the experiments. Jurkat TAg were transfected with the ASO by electroporation at 240 V with a single 25-ms pulse (*29*), and the expression of PTPN22 protein was assessed by Western blotting (WB) using an anti-PTPN22 antibody (R&D Systems, Minneapolis, MN) compared to that of ERK2, which was detected using anti-ERK2 Ab (Santa Cruz Biotechnology, Santa Cruz, CA) and used as a loading control. Comparison of PTPN22 protein levels in the ASO7, ASO8, ASO9, and scrambled ASO-electroporated Jurkat TAg cells after 24 and 48 h revealed that ASO8 had most effectively knocked down expression by 50% or more (as assessed by densitometric scanning of Western blotting) when compared with the scrambled ASO (Figure S1 in Supporting Information) and showed the highest potency at 24 h. In ASO8-electroporated T-cells PTPN22, knockdown was dose-dependent and became evident at 5 μM concentration (Figure 2A). The specificity of knockdown by ASO8 was next evaluated by controlling for knockdown of the closely related PTP proline, glutamate, serine, and threonine-rich sequence (PTP-PEST) (*35*). Jurkat TAg cells were electroporated with 10 μM of ASO8 or scrambled ASO and with a plasmid encoding PTP-PEST. Western blots of T-cell lysates using an anti-PTPN22 antibody compared to anti-PTP-PEST and anti-ERK2 antibodies showed that ASO8 only caused knockdown of PTPN22 expression without affecting the levels of PTP-PEST (Figure 2B). RT-PCR analysis of T-cells electroporated with 10 μM ASO8 or scrambled ASO showed that PTPN22 mRNA levels were reduced in cells treated with ASO8 compared to cells treated with scrambled ASO, suggesting that ASO8 possesses RNase-activating effects (Figure 2C). We

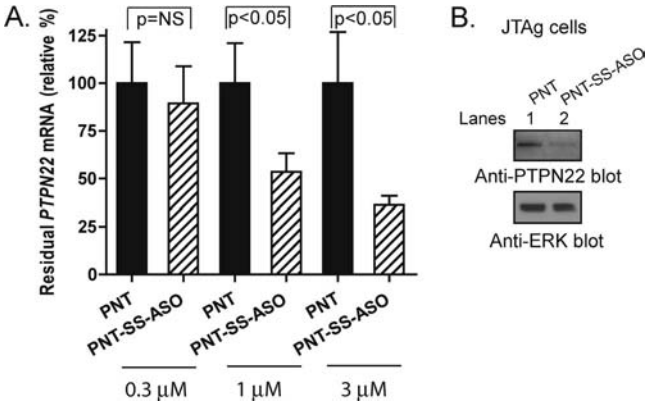

Figure 3. PNT-SS-ASO mediated knock-down of PTPN22 expression in Jurkat TAg cells. (A) Dose-dependent knockdown of PTPN22 mRNA using ASO8-conjugated PEGylated nanotubes (PNT-SS-ASO). Jurkat TAg cells were incubated with approximately 3.5 nM (column 1), 12 nM (column 3), or 35 nM (column 5) aPNT (black column) or approximately 3.5 nM (approximately 0.3 μM ASO8, column 2); 12 nM (approximately 1 μM ASO8, column 4), or 35 nM (approximately 3 μM ASO8, column 6) PNT-SS-ASO (lined columns). Total mRNA was extracted after 24 h. PTPN22 mRNA levels were measured in triplicate by quantitative real time PCR. *Y*-axis shows residual PTPN22 mRNA (%) in cells after treatment with PNT-SS-ASO relative to cells treated with aPNTs (100%). Statistical significance of differences was calculated on the raw data by two-tailed Student's *t* test. (B) Knockdown of PTPN22 protein expression using PNT-SS-ASO. Jurkat TAg cells were incubated with 12 nM aPNT alone (lane 1) or 12 nM PNT-SS-ASO (approximately 1 μM ASO8 or 85 ASO8/PNT, lane 2) and then lysed 24 h later. Anti-PTPN22 antibody staining of total cell lysates is shown in upper panel compared to anti-ERK2 antibody staining in lower panel.

completed the characterization of ASO8 with a functional evaluation of its effect on T cell receptor (TCR) signaling using an NFAT/AP1-luciferase reporter assay in Jurkat TAg cells. This assay monitors the TCR-induced activation of the distal IL-2 promoter following its recruitment of activated NFAT and AP1 transcription factors (see Supporting Information). As shown in Figure 2D, ASO8-mediated knockdown of PTPN22 expression led to increased TCR signaling. ASO8 was also able to rescue the TCR-inhibiting effect of PTPN22 overexpression in Jurkat TAg, as indicated by reduced inhibition of TCR-induced reporter activation in cells overexpressing PTPN22 and treated with ASO8 compared to cells treated with scrambled ASO.

Finally, we conjugated anti-PTPN22 ASO to PNTs and assessed the ability of the PNT-ASO conjugate to enable knockdown of PTPN22 expression in Jurkat TAg cells. Activated PNT-PDP was treated with 5′-SH-terminated-ASO8 (purchased as 5′-C6-S-S(disulfide)-modified ASO from IDT, modification cat. no. 5ThioMC6-D) to produce PNTs conjugated with ASO8 through a cleavable disulfide bond (PNT-SS-ASO). The cleavable nature of the disulfide bond was confirmed by incubation with DTT followed by agarose gel electrophoresis (data not shown). Knockdown of PTPN22 message and protein expression in Jurkat TAg cells incubated for 24 h with PNT-SS-ASO or the same amount of aPNTs was assessed using RT-PCR and Western blotting, respectively. Incubation of cells with PNT-SS-ASO enabled a dose-dependent knockdown of PTPN22 mRNA (Figure 3A) and a significant reduction of PTPN22 protein levels (Figure 3B). Interestingly, a significant reduction of PTPN22 expression was also achieved in these experiments by treating cells with approximately 1 μM PNT-conjugated ASO, which is below the threshold ASO concentration needed to achieve detectable knockdown when ASO8 was introduced by electroporation. The increased potency of the PNT-SS-ASO could be due to the SH termination of the ASO, or it might indicate that silencing of PTPN22 expression through PNT delivery is more efficient than that achieved by the electroporation method.

In conclusion, we generated and characterized the first anti-PTPN22 antisense oligomer and achieved its PNT-mediated delivery into T-cells. Incubation of T cells with PNT-SS-ASO enabled knockdown of PTPN22 expression at the mRNA and protein levels. Considering the high biocompatibility and low in vivo toxicity of PNTs (*14*), we expect that, after appropriate functionalization for targeting of selected immune cell subpopulations, PNT−ASO conjugates could enable ASO-mediated in vivo immunotherapy. Previously, we achieved selective delivery of PNTs to T-cells in vivo by functionalization with anti-CD3 and anti-CD28 antibodies (*15*). Future objectives are to prepare antibody-conjugated PNT−ASOs to achieve specific T-cell specific knockdown of PTPN22 and later translate this approach to in vivo knockdown of PTPN22 for therapy of type 1 diabetes and other autoimmune diseases.

ACKNOWLEDGMENT

This work was supported by a Baxter Foundation Grant (N.B.), PRIN Grant No. 2006069554 from the Italian Ministry of University and Scientific Research (A.M.) and a Master & Back Fellowship from the Sardinian government (L.G.D.). The authors are grateful to Sanjay K. Pandey for the gift of the scrambled ASO and for critically revising the manuscript.

Supporting Information Available: Materials and methods, characterization of PEGylated carbon nanotubes and knockdown of PTPN22 by ASOs. This material is available free of charge via the Internet at http://pubs.acs.org.

LITERATURE CITED

(1) Scherer, L. J., and Rossi, J. J. (2003) Approach for the sequence-specific knockdown of mRNA. *Nat. Biotechnol. 21*, 1457–65.
(2) Crooke, S. T. (2004) Progress in antisense technology. *Annu. Rev. Med. 55*, 61–95.
(3) Kurreck, J. (2003) Antisense technologies. Improvement through novel chemical modification. *Eur. J. Biochem. 270*, 1628–44.
(4) Chan, J. H., Lim, S., and Wong, W. S. (2006) Antisense oligonucleotides: from design to therapeutic application. *Clin. Exp. Pharmacol. Physiol. 33*, 533–40.
(5) Eckstein, F. (2000) Phosphorothioate oligonucleotides: What is their origin and what is unique about them? *Antisense Nucleic Acids Drug Dev. 10*, 117–21.
(6) Lysik, M. A., and Wu-Pong, S. (2003) Innovations in oligonucleotide drug delivery. *J. Pharm. Sci. 92*, 1559–73.
(7) Marshall, N. B., Oda, S. K., London, C. A., Moulton, H. M., Iversen, P. L., Kerkvliet, N. I., and Mourich, D. V. (2007) Arginine-rich cell-penetrating peptides facilitate delivery of antisense oligomers into murine leukocytes and alter pre-mRNA splicing. *J. Immunol. Methods 325*, 114–26.
(8) Moghimi, S. M., Hunter, A. C., and Murray, J. C. (2005) Nanomedicine: current status and future. *FASEB J. 19*, 311–30.
(9) Bianco, A., Kostarelos, K., Partidos, C. D., and Prato, M. (2005) Biomedical applications of functionalized carbon nanotubes. *Chem. Commun.* 571–7.
(10) Bottini, M., Cerignoli, F., Dawson, M. I., Magrini, A., Rosato, N., and Mustelin, T. (2006) Full-length single-walled carbon nanotubes decorated with streptavidin-conjugated quantum dots as multivalent intracellular fluorescent nanoprobes. *Biomacromolecules 7*, 2259–63.
(11) Kam, N. W. S., Liu, Z., and Dai, H. (2005) Functionalization of carbon nanotubes via cleavable disulfide bond for efficient intracellular delivery of siRNA and potent gene silencing. *J. Am. Chem. Soc. 127*, 12492–3.
(12) Liu, Z., Cai, W., He, L., Nakayama, N., Chen, K., Sun, X., Chen, X., and Dai, H. (2007) In vivo biodistribution and highly

efficient tumor targeting of carbon nanotubes in mice. *Nat. Nanotechnol. 2*, 47–52.
(13) Liu, Z., Davis, C., Cai, W., He, L., Chen, X., and Dai, H. (2008) Circulation and long-term fate of functionalized, biocompatible single-walled carbon nanotubes in mice probed by Raman spectroscopy. *Proc. Natl. Sci. U.S.A. 105*, 1410–5.
(14) Schipper, M. L., Nakayama-Ratchford, N., Davis, C. R., Kam, N. W., Chu, P., Liu, Z., Sun, X., Dai, H., and Gambhir, S. S. (2008) A pilot toxicology study of single-walled carbon nanotubes in a small sample of mice. *Nat. Nanotechnol. 3*, 216–21.
(15) Cato, M. H., D'Annibale, F., Mills, D. M., Cerignoli, F., Dawson, M. I., Bergamaschi, E., Bottini, N., Magrini, A., Bergamaschi, A., Rosato, N., Rickert, R. C., Mustelin, T., and Bottini, M. (2008) Cell-type specific and cytoplasmic targeting of PEGylated carbon nanotube-based nanoassemblies. *J. Nanosci. Nanotechnol. 8*, 2259–69.
(16) Bottini, N., Vang, T., Cucca, F., and Mustelin, T. (2006) Role of PTPN22 in type 1 diabetes and other autoimmune diseases. *Semin. Immunol. 18*, 207–13.
(17) Gregersen, P. K., Lee, H. S., Batliwalla, F., and Begovich, A. B. (2006) PTPN22: setting thresholds for autoimmunity. *Semin. Immunol. 18*, 214–23.
(18) Yu, X., Sun, J. P., He, Y., Guo, X., Liu, S., Zhou, B., Hudmon, A., and Zhang, Z. Y. (2007) Structure, inhibitor, and regulatory mechanism of Lyp, a lymphoid-specific tyrosine phosphatase implicated in autoimmune diseases. *Proc. Natl. Acad. Sci. U.S.A. 104*, 19767–72.
(19) Bottini, N., Musumeci, L., Alonso, A., Rahmouni, S., Nika, K., Rostamkhani, M., MacMurray, J., Meloni, G. F., Lucarelli, P., Pellecchia, M., Eisenbarth, G. S., Comings, D., and Mustelin, T. (2004) A functional variant of lymphoid tyrosine phosphatase is associated with type I diabetes. *Nat. Genet. 36*, 337–8.
(20) Smyth, D., Cooper, J. D., Collins, J. E., Heward, J. M., Franklyn, J. A., Howson, J. M., Vella, A., Nutland, S., Rance, H. E., Maier, L., Barratt, B. J., Guja, C., Ionescu-Tirgoviste, C., Savage, D. A., Dunger, D. B., Widmer, B., Strachan, D. P., Ring, S. M., Walker, N., Clayton, D. G., Twells, R. C., Gough, S. C., and Todd, J. A. (2004) Replication of an association between the lymphoid tyrosine phosphatase locus (LYP/PTPN22) with type 1 diabetes, and evidence for its role as a general autoimmunity locus. *Diabetes 53*, 3020–3.
(21) Onengut-Gumuscu, S., Ewens, K. G., Spielman, R. S., and Concannon, P. (2004) A functional polymorphism (1858C/T) in the PTPN22 gene is linked and associated with type I diabetes in multiplex families. *Genes Immun. 5*, 678–80.
(22) Todd, J. A., Walker, N. M., Cooper, J. D., Smyth, D. J., Downes, K., Plagnol, V., Bailey, R., Nejentsev, S., Field, S. F., Payne, F., Lowe, C. E., Szeszko, J. S., Hafler, J. P., Zeitels, L., Yang, J. H., Vella, A., Nutland, S., Stevens, H. E., Schuilenburg, H., Coleman, G., Maisuria, M., Meadows, W., Smink, L. J., Healy, B., Burren, O. S., Lam, A. A., Ovington, N. R., Allen, J., Adlem, E., Leung, H. T., Wallace, C., Howson, J. M., Guja, C., Ionescu-Tirgoviste, C., Simmonds, M. J., Heward, J. M., Gough, S. C., Dunger, D. B., Wicker, L. S., and Clayton, D. G. (2007) Robust associations of four new chromosome regions from genome-wide analyses of type 1 diabetes. *Nat. Genet. 39*, 857–64.
(23) Begovich, A. B., Carlton, V. E., Honigberg, L. A., Schrodi, S. J., Chokkalingam, A. P., Alexander, H. C., Ardlie, K. G., Huang, Q., Smith, A. M., Spoerke, J. M., Conn, M. T., Chang, M., Chang, S. Y., Saiki, R. K., Catanese, J. J., Leong, D. U., Garcia, V. E., McAllister, L. B., Jeffery, D. A., Lee, A. T., Batliwalla, F., Remmers, E., Criswell, L. A., Seldin, M. F., Kastner, D. L., Amos, C. I., Sninsky, J. J., and Gregersen, P. K. (2004) A missense single-nucleotide polymorphism in a gene encoding a protein tyrosine phosphatase (PTPN22) is associated with rheumatoid arthritis. *Am. J. Hum. Genet. 75*, 330–7.
(24) Orozco, G., Sanchez, E., Gonzalez-Gay, M. A., Lopez-Nevot, M. A., Torres, B., Caliz, R., Ortego-Centeno, N., Jimenez-Alonso, J., Pascual-Salcedo, D., Balsa, A., de Pablo, R., Nunez-Roldan, A., Gonzalez-Escribano, M. F., and Martin, J. (2005) Association of a functional single-nucleotide polymorphism of PTPN22, encoding lymphoid protein phosphatase, with rheumatoid arthritis and systemic lupus erythematosus. *Arthritis Rheum. 52*, 219–24.
(25) Gregersen, P. K. (2005) Gaining insight into PTPN22 and autoimmunity. *Nat. Genet. 37*, 1300–2.
(26) Cloutier, J. F., and Veillette, A. (1999) Cooperative inhibition of T-cell antigen receptor signaling by a complex between a kinase and a phosphatase. *J. Exp. Med. 189*, 111–21.
(27) Gjorloff-Wingren, A., Saxena, M., Williams, S., Hammi, D., and Mustelin, T. (1999) Characterization of TCR-induced receptor-proximal signaling events negatively regulated by the protein tyrosine phosphatase PEP. *Eur. J. Immunol. 29*, 3845–54.
(28) Hill, R. J., Zozulya, S., Lu, Y. L., Ward, K., Gishizky, M., and Jallal, B. (2002) The lymphoid protein tyrosine phosphatase Lyp interacts with the adaptor molecule Grb2 and functions as a negative regulator of T-cell activation. *Exp. Hematol. 30*, 237–44.
(29) Vang, T., Congia, M., Macis, M. D., Musumeci, L., Orrú, V., Zavattari, P., Nika, K., Tautz, L., Taskén, K., Cucca, F., Mustelin, T., and Bottini, N. (2005) Autoimmune-associated lymphoid tyrosine phosphatase is a gain-of-function variant. *Nat. Genet. 37*, 1317–9.
(30) Rieck, M., Arechiga, A., Onengut-Gumuscu, S., Greenbaum, C., Concannon, P., and Buckner, J. H. (2007) Genetic variation in PTPN22 corresponds to altered function of T and B lymphocytes. *J. Immunol. 179*, 4704–10.
(31) Sakaguchi, N., Takahashi, T., Hata, H., Nomura, T., Tagami, T., Yamazaki, S., Sakihama, T., Matsutani, T., Negishi, I., Nakatsuru, S., and Sakaguchi, S. (2003) Altered thymic T-cell selection due to a mutation of the ZAP-70 gene causes autoimmune arthritis in mice. *Nature 426*, 454–60.
(32) Siggs, O. M., Miosge, L. A., Yates, A. L., Kucharska, E. M., Sheahan, D., Brdicka, T., Weiss, A., Liston, A., and Goodnow, C. C. (2007) Opposing functions of the T cell receptor kinase ZAP-70 in immunity and tolerance differentially titrate in response to nucleotide substitutions. *Immunity 27*, 912–26.
(33) Northrop, J. P., Ullman, K. S., and Crabtree, G. R. (1993) Characterization of the nuclear and cytoplasmic components of the lymphoid-specific nuclear factor of activated T cells (NF-AT) complex. *J. Biol. Chem. 268*, 2917–23.
(34) Pandey, S. K., Yu, X. X., Watts, L. M., Michael, M. D., Sloop, K. W., Rivard, A. R., Leedom, T. A., Manchem, V. P., Samadzadeh, L., McKay, R. A., Monia, B. P., and Bhanot, S. (2007) Reduction of low molecular weight protein-tyrosine phosphatase expression improves hyperglycemia and insulin sensitivity in obese mice. *J. Biol. Chem. 282*, 14291–9.
(35) Alonso, A., Sasin, J., Bottini, N., Friedberg, I., Friedberg, I., Osterman, A., Godzik, A., Hunter, T., Dixon, J., and Mustelin, T. (2004) Protein tyrosine phosphatases in the human genome. *Cell 117*, 699–711.

BC800540J

Conjugation of antisense oligonucleotides to PEGylated carbon nanotubes enables efficient knock-down of PTPN22 in T cells

Supporting Information

Lucia G. Delogu[†,‡], Andrea Magrini[§⌈], Antonio Bergamaschi[¶], Nicola Rosato[§ǁ], Marcia I. Dawson[#], Nunzio Bottini[†,‡,*] & Massimo Bottini[#,§,ǁ,*]

[†] Department of Biochemistry and Molecular Biology, Keck School of Medicine of the University of Southern California, Los Angeles, CA 90033, USA

[‡] Institute for Genetic Medicine, Keck School of Medicine of the University of Southern California, Los Angeles, CA 90033, USA

[§] NAST Centre for Nanoscience & Nanotechnology & Innovative Instrumentation, University of Rome Tor Vergata, Via Montpellier 1, 00133 Rome, Italy

[⌈] Department of Environmental, Occupational, and Social Medicine, University of Rome Tor Vergata, Via Montpellier 1, 00133 Rome, Italy

[¶] Institute of Occupational Medicine, Università Cattolica del Sacro Cuore, Largo Agostino Gemelli 8, 00168 Rome, Italy

[ǁ] Department of Experimental Medicine and Biochemical Sciences, University of Rome Tor Vergata, Via Montpellier 1, 00133 Rome, Italy

[#] Burnham Institute for Medical Research, 10901 North Torrey Pines Road, La Jolla, CA 92037, USA

Address correspondence to: Nunzio Bottini, MD, PhD, nunzio@usc.edu, Institute for Genetic Medicine, Keck School of Medicine of the University of Southern California, Los Angeles, CA 90033, USA, Phone: (323) 442-2634 or Massimo Bottini, PhD, mbottini@burnham.org, Burnham Institute for Medical Research, 10901 North Torrey Pines Road, La Jolla, CA 92037, USA, Phone: (858) 646-3100 x3063.

MATERIALS AND METHODS

Antibodies and other reagents. The monoclonal anti-hemagglutinin (HA) antibody (Ab) clone 16B12 was purchased from Covance (Berkeley, CA). The anti-ERK2 (C14) antibody was from Santa Cruz Biotech (Santa Cruz, CA), the anti-PTP-PEST antibody was from Cell Signaling Technology (Danvers, MA), and the anti-PTPN22 goat antibody (raised against the human protein) was from R&D (Minneapolis, MN). OKT3 (*1*) was purified from hybridoma supernatants by ultrafiltration on Falcon Amicon ultra-15 (Millipore cat. n. ufc910024). $F(ab)_2$ antibody and anti-mouse IgG used for cross-linking were purchased from Jackson Immunoresearch (West Grove, PA) and Upstate/Millipore (Billerica, MA), respectively. SDS sample buffer, pre-cast gels, dNTPs, and Taq polymerase were from Invitrogen (Carlsbad, CA). Hybond-ECL nitrocellulose was from GE Healthcare (Piscataway, NJ). Trypan blue was purchased from Sigma (cat.n.T8154). The protein molecular weight standard for polyacrylamide gel electrophoresis was purchased from Fermentas (Glen Burnie, MD). DNA oligonucleotides and all phosphorothioate ASOs against PTPN22 were purchased from IDT (San Diego, CA). The sequence of the anti-PTPN22 ASOs was as follows: ASO7: 5'-CCATTTTTGTCCTTTGTTGG-3', ASO8: 5'-GTTGTGTCAGCATTTTTGTC-3', ASO9: 5'-GCTGTCCACCTCCTTGGTTT-3'. Scrambled ASO was a gift from Dr. Sanjay K. Pandey of Isis Pharmaceuticals (Carlsbad, CA). Unless otherwise specified, other chemicals were from Sigma (St. Louis, MO).

Plasmids, cell culture, transfections, and Western blotting. Full-length human PTPN22 and PTP-PEST were cloned in the *Bam*HI site of the plasmid pEF5 (*2*), which allows the expression of constructs in fusion with an N-terminal HA tag, and under control of the EFalpha promoter. Jurkat cells expressing the SV-40 large T Antigen (Jurkat TAg) (*3*) were were kept at

logarithmic growth in RPMI 1640 medium supplemented with 10% fetal calf serum (FCS, purchased from the USC Norris Cancer Center Cell Culture Core), 2mM L-glutamine, 1 mM sodium pyruvate, 10 mM HEPES pH 7.3, 2.5 mg/mL D-glucose, 100 units/mL of penicillin and 100 μg/mL streptomycin.

Jurkat TAg cell transfections were performed by electroporation at 240 V with a single 25-ms pulse. Cells were lysed in 20 mM Tris/HCl, pH 7.4, containing 150 mM NaCl, 1 mM EDTA, 1% NP40 (TNE buffer), 1 mM PMSF, 10 mg/ml of aprotinin/leupeptin and 10 mg/ml of soybean trypsin inhibitor. Lysates were pre-cleared by centrifugation at 16,000 g for 30 min. For western blotting, proteins were run on denaturing SDS-polyacrylamide gels (Invitrogen, Carlsbad, CA), transferred to nitrocellulose membranes, and identified using appropriate dilutions of unconjugated primary antibodies, followed by HRP-conjugated secondary antibodies (GE Healthcare). Filters were then subjected to a chemiluminescent detection protocol using ECL Plus (GE Healthcare) followed by autoradiography using light or blue film (Kodak, Rochester, NY)**.** Expression of endogenous/transfected PTPN22 and of transfected PTP-PEST proteins (expression levels of endogenous PTP-PEST in Jurkat are extremely low (*4*)) was assessed by Western blotting using an anti-PTPN22 antibody (R&D) or anti-PTP-PEST antibody (Cell Signaling Technology) compared to anti-Erk2 antibody (Santa Cruz Biotech) as a control.

Reporter assays. Luciferase reporter assays were performed as described (*5*). The NFAT/AP-1 reporter plasmid (kindly provided by Dr. Gerald Crabtree, Stanford University, Stanford, CA, USA) carries three tandem copies of the distal NFAT/AP-1 composite element of the human *IL2* promoter (*3*), which are cloned upstream of the minimal *IL2* promoter (from -89 to +51) and the

luciferase reporter gene. The NFAT/AP-1 reporter plasmid and the control pGL3 plasmid, driving constitutive expression of *Renilla* luciferase for use as a transfection control, were cotransfected in Jurkat TAg cells together with and without 10 μM ASO. Cells were subjected to T cell receptor (TCR) stimulation with 1.5 μg/ml of OKT3 (*1*) for 6 h, before luciferase assays were performed in triplicate on cell lysates using the dual luciferase kit from Promega (Madison, WI) according to manufacturer's instructions Luminescence was read on a 1420 Multilabel Counter Victor^3 V plate reader (Perkin-Elmer, Turku, Finland). The difference in the ratio between firefly and *Renilla* luciferase activities in stimulated versus nonstimulated cells was assessed.

Flow cytometry. Flow cytometry was carried out on a Cytomics FC500 cytometer (Beckman Coulter, Fullerton, CA) at the USC Immune Monitoring Core. Cell fluorescence was measured after the cells were washed with a 0.4% (w/v) Trypan Blue solution in order to quench fluorescence from non-internalized fluorescein(*6, 7*). Flow cytometry data analysis and graph preparation were carried out using FlowJo (Tree Star, Inc., Ashland, OR).

mRNA quantification by real-time PCR. Total RNA was extracted from transfected cells using Tryzol (Sigma) to quantify for PTPN22 mRNA expression levels. cDNA was generated by reverse transcription using RETROscript (Ambion, Austin, TX). RT-PCR was performed using Cyber-green (Invitrogen, Carlsbad, CA) and primers 5'- CCAAGAGGATGACAGTGTTCCC -3' (nt 2291-2310 of *PTPN22* coding sequence - NCBI accession#NM_015967, GI#48928053) and 5'- GTGCTTGATTTAGCAGGGTGC -3' (nt 2396-2377 of *PTPN22* coding sequence -

NCBI accession#NM_015967, GI#48928053) on a MJ Research DNA Engine Opticon 2 (Waltham, MA).

Preparation of amino-functionalized PEGylated NTs (aPNTs). Single walled NTs (15 mg) (Carbon Solutions, Riverside, CA) were added to a 1.0 mg/mL solution of 1,2-distearoyl-*sn*-glycero-3-phosphoethanolamine-*N*-[amino(polyethylene glycol)$_{2000}$] (PL-aPEG) (Avanti Polar Lipids, Alabaster, AL) in PBS (25 mL) (2.7 mM KCl, 1.5 mM KH_2PO_4, 137 mM NaCl and 8.1 mM Na_2HPO_4, pH 7.4 from Mediatech, Inc., Herndon, VA). The mixture was ultrasonicated (Misonix, Inc., Farmingdale, NY) in an ice-bath for 7 h at a constant power of 15 W and centrifuged (Beckman Optima™ XL-80K Ultracentrifuge, Palo Alto, CA) at 40,000 × *g* for 6 h. Approximately 80% of the supernatant was carefully collected by aspiration and centrifuged at 70,000 × *g* for 6 h. The pellet was dispersed in PBS by brief sonication and filtered six times through a 100-kDa molecular weight cutoff centrifugal filter device (Ultrafree, Millipore Corp., Temecula, CA) to remove free phospholipids from aPNTs.

Preparation of carboxyfluorescein-conjugated PEGylated NTs (fPNTs). aPNTs (50 µg in 1.0 mL of PBS) were incubated with 5-carboxyfluorescein *N*-hydroxysuccinimide ester (25 µg in 25 µL of anhydrous DMF) for 2 h at room temperature in the dark. fPNTs were purified from unlinked 5-carboxyfluorescein molecules by filtration through 10-kDa molecular weight cutoff centrifugal filter devices (Ultrafree).

Preparation of ASO-conjugated PEGylated NTs (PNT-SS-ASO). aPNTs (50 µg in 1.0 mL of PBS) were incubated with sulfosuccinimidyl 6-(3'-[2-pyridyldithio]-propionamido)hexanoate

(sulfo-LC-SPDP, 30 ug in 25 μL of anhydrous DMF) (PNT-PDP) for 2 h at room temperature in the dark and then filtered through a NAP-5 gravity column (GE Healthcare UK Ltd), previously equilibrated with PBS supplemented with 10 mM EDTA. SH-ASO (5'-GTTGTGTCAGCATTTTTGTC-3') or SH-DNA (5'-ATTGATGTAGCTGGAATCCTC-3') in PBS was treated with 100 mM dithiothreitol (DTT) for 30 min and then filtered though a Microspin G-25 column (GE Healthcare UK Ltd) previously equilibrated with PBS supplemented with 10 mM EDTA. PNT-PDP and reduced SH-ASO (or SH-DNA) were mixed in an approximate molar ratio of 1:250 in PBS supplemented with 10 mM EDTA and allowed to react overnight at room temperature. PNT-SS-ASO (or PNT-SS-DNA) were purified from unlinked ASO by several cycles of dilution in PBS followed by ultrafiltration through 100-kDa molecular weight cutoff centrifugal filter devices (Ultrafree).

AFM of PEGylated NTs. A solution of aPNTs in PBS (10 μL) was dropped onto a freshly cleaved mica substrate (Ted Pella, Redding, CA). The droplet was allowed to stand for approximately 10 min at room temperature, and then the mica surface was rinsed with water and dried under a nitrogen stream. Atomic force microscope (5500 AFM, Agilent Technologies, Santa Clara, CA) images were taken using the acoustic alternate current mode (AAC).

Graphs and Statistics. Histograms were prepared using the Prism software package (Graphpad, San Diego, CA). Statistics (ANOVA or Student t-test) were calculated using the Prism or Excel (Microsoft, Redmond, WA) softwares. Standard deviations of differences and ratios were calculated according to error propagation rules described by Taylor (*8*).

Characterization of PEGylated carbon nanotubes. The spectroscopic contribution of 5-carboxyfluorescein grafted onto fPNTs in PBS was calculated by subtracting from the absorbance spectrum of fPNTs that of aPNTs with matching absorption at 830 nm (the spectroscopic contribution of 5-carboxyfluorescein was absent at 830 nm). The calculated absorbance spectrum of 5-carboxyfluorescein grafted onto fPNTs exhibited a 496-nm peak that, under the assumption that all PEG chains were capped with 5-carboxyfluorescein, was used to calculate the concentration (K, [μM]) of PEG chains onto PNTs (aPNTs and fPNTs) having an absorbance value at 830 nm equal to one (A_{830} =1) in PBS.

Next, the concentration (c_{NT}, [mg/L]) of underneath (non-PEGylated)-NTs having A_{830} = 1 in PBS was determined. aPNTs in PBS were dialyzed against water, vacuum dried, carefully weighed, redispersed in PBS by brief sonication and the absorbance at 830 nm recorded. The concentration (c_{aPNT}, [mg/L]) of aPNTs having A_{830} = 1 in PBS was then calculated. Finally, c_{NT} was obtained by subtracting the contribution of PL-aPEGa from c_{aPNT}:

$$c_{NT} = c_{aPNT} - c_{PL\text{-}aPEG} = c_{aPNT} - K \times w_{PL\text{-}aPEG} \quad \textbf{(eq. 1)},$$

where $w_{PL\text{-}aPEG}$ = 2800 Daltons is the molecular weight of PL-aPEG.

AFM images of aPNTs showed individual and small bundles of PNTs having a length of 164 ± 46 nm. We calculated the molecular weight (w_{NT}) of underneath (non-PEGylated) NTs and the concentration (C_{NT}, [μM]) of underneath (non-PEGylated)-NTs having A_{830} = 1 in PBS:

$$w_{NT} = (d_{NT} - 0.34) \times \pi \times \sigma_{graphene} \times L_{NT} \quad \textbf{(eq. 2)},$$

$$C_{NT} = c_{NT} / w_{NT} \quad \textbf{(eq. 3)},$$

where L_{NT} and d_{NT} = 1.4 nm are the length and average outer diameter (the latter from the supplier), respectively, 0.34 nm is the van der Waals diameter of carbon and $\sigma_{graphene}$ = 458.3

[Daltons × nm^{-2}] is the sheet density of graphene. Finally, we calculated the number of PEG chains per aPNT (X) and the molecular weight of aPNT (w_{aPNT}):

$X = K / C_{NT}$ (**eq. 4**),

$w_{aPNT} = w_{NT} + (X \times w_{PL\text{-}aPEG})$ (**eq. 5**).

SUPPLEMENTARY FIGURES

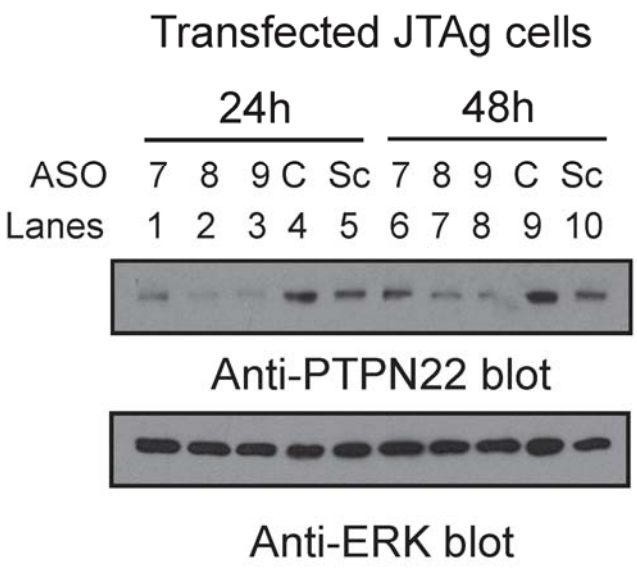

Figure S1. Knock-down of PTPN22 by ASOs. Jurkat TAg cells were electroporated with 20 µM ASO7 (lanes 1 and 6), ASO8 (lanes 2 and 7), ASO9 (lanes 3 and 8) or scrambled ASO (lanes 5 and 10). Cells were lysed 24 h (lanes 1-5) or 48h (lanes 6-10) after electroporation and protein analyzed by Western blotting. Upper panel shows anti-PTPN22 Ab blot, and lower panel shows control anti-ERK2 Ab blot of total lysates. Lanes 4 and 9 show control lysates of non-electroporated cells.

References

(1) Kung, P., Goldstein, G., Reinherz, E. L., and Schlossman, S. F. (1979) Monoclonal antibodies defining distinctive human T cell surface antigens. *Science 206*, 347-9.

(2) Saito, K., Williams, S., Bulankina, A., Honing, S., and Mustelin, T. (2007) Association of protein-tyrosine phosphatase MEG2 via its Sec14p homology domain with vesicle-trafficking proteins. *J Biol Chem 282*, 15170-8.

(3) Shaw, J. P., Utz, P. J., Durand, D. B., Toole, J. J., Emmel, E. A., and Crabtree, G. R. (1988) Identification of a putative regulator of early T cell activation genes. *Science 241*, 202-5.

(4) Arimura, Y., Vang, T., Tautz, L., Williams, S., and Mustelin, T. (2008) TCR-induced downregulation of protein tyrosine phosphatase PEST augments secondary T cell responses. *Mol Immunol 45*, 3074-84.

(5) Vang, T., Congia, M., Macis, M. D., Musumeci, L., Orru, V., Zavattari, P., Nika, K., Tautz, L., Tasken, K., Cucca, F., Mustelin, T., and Bottini, N. (2005) Autoimmune-associated lymphoid tyrosine phosphatase is a gain-of-function variant. *Nat Genet 37*, 1317-9.

(6) Rejman, J., Oberle, V., Zuhorn, I. S., and Hoekstra, D. (2004) Size-dependent internalization of particles via the pathways of clathrin- and caveolae-mediated endocytosis. *Biochem J 377*, 159-69.

(7) Wang, R., Kovalchin, J. T., Muhlenkamp, P., and Chandawarkar, R. Y. (2006) Exogenous heat shock protein 70 binds macrophage lipid raft microdomain and stimulates phagocytosis, processing, and MHC-II presentation of antigens. *Blood 107*, 1636-42.

(8) Taylor, J. R. (1997) An introduction to error analysis, Second Edition. *University Science Books*.

Subscriber access provided by SHEMYAKIN-OVCHINNIKOV INST

Communication

A Novel Method for Direct Site-Specific Radiolabeling of Peptides Using [F]FDG

Mohammad Namavari, Zhen Cheng, Rong Zhang, Abhijit De, Jelena Levi, Joshua K. Hoerner, Shahriar S. Yaghoubi, Faisal A. Syud, and Sanjiv S. Gambhir

Bioconjugate Chem., **2009**, 20 (3), 432-436• DOI: 10.1021/bc800422b • Publication Date (Web): 18 February 2009

Downloaded from http://pubs.acs.org on April 8, 2009

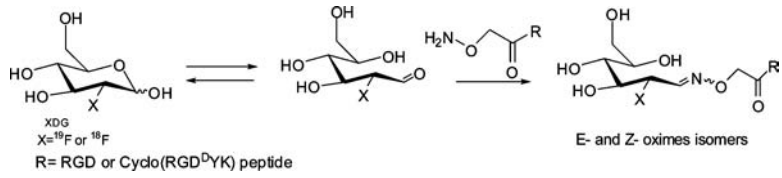

More About This Article

Additional resources and features associated with this article are available within the HTML version:

- Supporting Information
- Access to high resolution figures
- Links to articles and content related to this article
- Copyright permission to reproduce figures and/or text from this article

View the Full Text HTML

ACS Publications
High quality. High impact.

Bioconjugate Chemistry is published by the American Chemical Society. 1155 Sixteenth Street N.W., Washington, DC 20036

A Novel Method for Direct Site-Specific Radiolabeling of Peptides Using [^{18}F]FDG

Mohammad Namavari,[†] Zhen Cheng,[†] Rong Zhang,[‡] Abhijit De,[†] Jelena Levi,[†] Joshua K. Hoerner,[‡] Shahriar S. Yaghoubi,[†] Faisal A. Syud,[‡] and Sanjiv S. Gambhir*[,†]

Molecular Imaging Program at Stanford (MIPS), Departments of Radiology and Bioengineering, Bio-X Program, Stanford University, and Global Research, General Electric. Received October 2, 2008; Revised Manuscript Received February 3, 2009

We have used the well-accepted and easily available 2-[^{18}F]fluoro-2-deoxyglucose ([^{18}F]FDG) positron emission tomography (PET) tracer as a prosthetic group for synthesis of ^{18}F-labeled peptides. We herein report the synthesis of [^{18}F]FDG-RGD (^{18}F labeled linear RGD) and [^{18}F]FDG-cyclo(RGD^{D}YK) (^{18}F labeled cyclic RGD) as examples of the use of [^{18}F]FDG. We have successfully prepared [^{18}F]FDG-RGD and [^{18}F]FDG-cyclo(RGD^{D}YK) in 27.5% and 41% radiochemical yields (decay corrected) respectively. The receptor binding affinity study of FDG-cyclo(RGD^{D}YK) for integrin $\alpha_v\beta_3$, using $\alpha_v\beta_3$ positive U87MG cells confirmed a competitive displacement with ^{125}I-echistatin as a radioligand. The IC_{50} value for FDG-cyclo(RGD^{D}YK) was determined to be 0.67 ± 0.19 μM. High-contrast small animal PET images with relatively moderate tumor uptake were observed for [^{18}F]FDG-RGD and [^{18}F]FDG-cyclo(RGD^{D}YK) as PET probes in xenograft models expressing $\alpha_v\beta_3$ integrin. In conclusion, we have successfully used [^{18}F]FDG as a prosthetic group to prepare ^{18}F]FDG-RGD and [^{18}F]FDG-cyclic[RGD^{D}YK] based on a simple one-step radiosynthesis. The one-step radiosynthesis methodology consists of chemoselective oxime formation between an aminooxy-functionalized peptide and [^{18}F]FDG. The results have implications for radiolabeling of other macromolecules and would lead to a very simple strategy for routine preclinical and clinical use.

Currently, time-sensitive methods used for ^{18}F-labeling of peptides for positron emission tomography (PET) imaging involve the development of unique ^{18}F-containing prosthetic groups for attachment to the peptides that will likely require significant effort to pervasively implement for routine preclinical and clinical application. Therefore, the ability to utilize reagents currently well-accepted and easily available in the PET community at the final formulation step will likely be highly beneficial. The use of 2-[^{18}F]fluoro-2-deoxyglucose ([^{18}F]FDG) is well-established in clinical PET centers (*1*), and we show here the potential use of this tracer, without further chemical modifications, to label peptides that can be used to report on one or more biomarkers in vivo.

We herein report the synthesis of a ^{18}F-labeled linear trimeric-peptide, [^{18}F]FDG-RGD, and ^{18}F-labeled cyclic trimeric-peptide, [^{18}F]FDG-cyclo(RGD^{D}YK), by using [^{18}F]FDG without further modification. We chose $\alpha_v\beta_3$ integrin and its peptide ligand because the trimeric peptide sequence argenine-glycine-aspartic acid (RGD) recognizes the $\alpha_v\beta_3$ integrin found on new blood vessels and tumor cells. RGD peptide binds to $\alpha_v\beta_3$ integrin and inhibits angiogenesis (*2*). The $\alpha_v\beta_3$ integrin is highly expressed in activated endothelial and solid tumor cells (*3, 4*). The synthesis of the radiolabeled peptides utilizes the reaction between the aldehyde functionality in the linear, open form of [^{18}F]FDG with an aminooxy functionality in the peptide to form an oxime bond. The resulting ^{18}F-labeled RGD molecules were evaluated in vitro for their binding affinity and ultimately as PET probes in xenograft models expressing $\alpha_v\beta_3$ integrin to demonstrate the integrity of the binders post-labeling.

Chemoselective oxime formation between an aminooxy group and a carbonyl functionality has recently been successfully utilized for [^{18}F]-labeling of peptides (*5, 6*), and we hypothesized that it can be used to directly attach [^{18}F]FDG to biomarker-targeted peptides. The highly specific oxime formation between an aminooxy-functionalized peptide and an 4-[^{18}F]fluorobenzaldehdey ([^{18}F]FBA) has previously offered high-yield, two-step synthesis for ^{18}F-labeled peptides (*6*−*9*). [^{18}F]FBA can be obtained in a nonoptimized radiochemical yield of 50% in 30 min, with reported radiochemical yields of 60−80% for the final ^{18}F-peptides. The hypothesis is further supported by a recent report by Wuest et al., which reported the oxime formation between [^{18}F]FDG and *N*-[6-(aminooxy)hexyl]maleimide to create a thiol-reactive prosthetic group [^{18}F]FDG-maleimide-hexyloxime ([^{18}F]FDG-MHO) in moderately high yield (45−69%) at 100 °C over 15 min (*10*). The basis of this chemistry lies in the fact that, at 100 °C, FDG exists in a dynamic equilibrium between its cyclic form and a linear form, where the latter contains an aldehyde functionality at position 1 that can potentially react with the aminooxy functionality under appropriate conditions. We wanted to understand the feasibility of whether such conditions could be translated directly to a targeting peptide while maintaining the peptide's biological efficacy in cell culture and small living subjects.

[^{18}F]FDG-Peptide Conjugation. The synthesis of FDG-RGD and [^{18}F]FDG-RGD were carried out as outlined in Scheme 1. The linear aminooxy-RGD (RGD-ONH_2, 2 mg) was incubated with 3.7 equiv cold FDG in 16% ethanol in saline (120 μL) in the presence of 0.4% TFA at 100 °C for 40 min to afford FDG-RGD (E- and Z-oximes) in 39.5% yield. The formation of E- and Z-oximes was expected. It has been reported that, in a similar case, the reaction of glucose with *O*-(4-nitrobenzyl)-hydroxylamine afforded E- and Z-oxime isomers (*11*). The mass

* Author to whom correspondence should be addressed: Sanjiv Sam Gambhir M.D., Ph.D., Molecular Imaging Program at Stanford, Departments of Radiology and Bioengineering, Bio-X Program, 318 Campus Dr., Clark Center, E-150, Stanford University, Stanford, CA 94305, 650-725-2309 (V), 650-724-4948 (Fax), E-mail: sgambhir@stanford.edu.

[†] MIPS.

[‡] General Electric.

10.1021/bc800422b CCC: $40.75 © 2009 American Chemical Society
Published on Web 02/18/2009

Scheme 1. Schematic Synthesis of FDG-RGD and FDG-cyclo(RGD^{D}YK) (X = ^{19}F) from FDG or [^{18}F]FDG-RGD and [^{18}F]FDG-cyclo(RGD^{D}YK) (X = ^{18}F) from [^{18}F]FGD

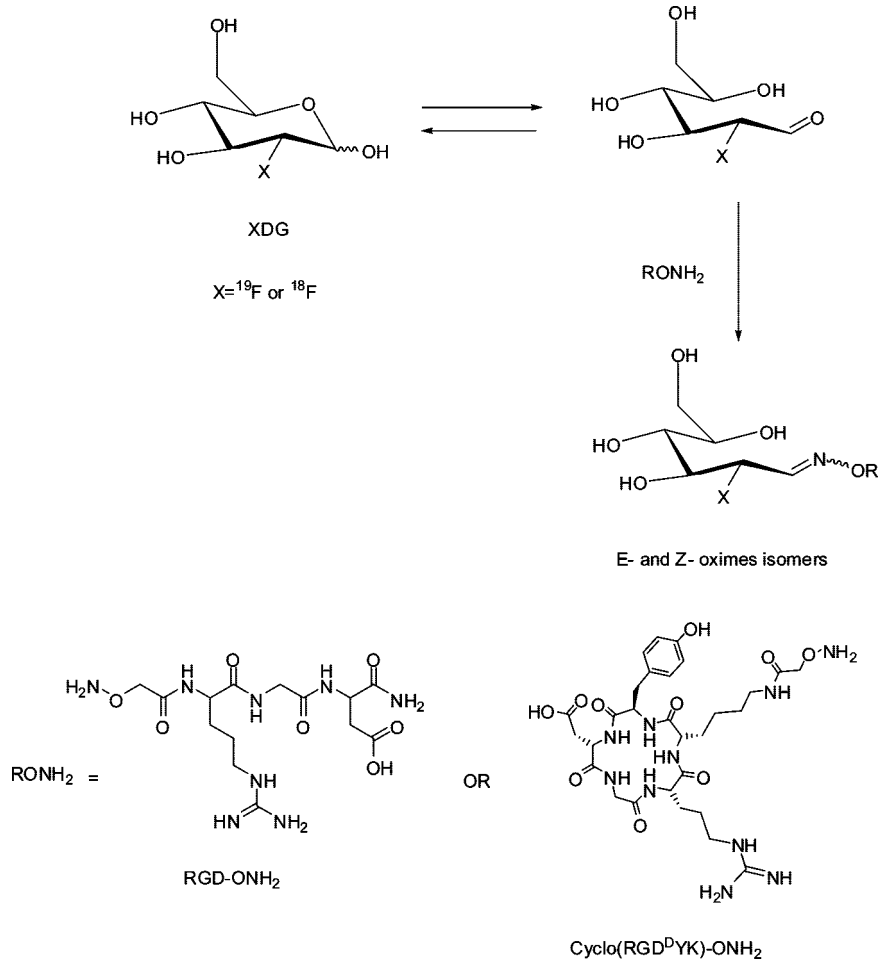

spectrometry (ESI-MS) analysis of the isolated product showed two identical mass peaks of 584.2 ([M+H]$^{+}$), which correspond to FDG-RGD (E- and Z-oximes) (calcd [M+H] for RGD-FDG is 584.5). Similarly, aminooxy-RGD (2 mg) was reacted with 4−6 mCi of [^{18}F]FDG in the same condition as above but in 30 min to afford [^{18}F]FDG-RGD (E- and Z-oximes) in 27.5% radiochemical yields based on [^{18}F]FDG (decay-corrected). [^{18}F]RGD-FDG oximes were purified by HPLC and used for biological studies. Similar stereochemistry has been observed in the synthesis of ^{18}F-lableled peptide Gluc-s-Dpr ([^{18}F]BOAT)-TOACF by using an ^{18}F-benzaldehyde (*6*).

Likewise, conjugation of FDG and [^{18}F]FDG to cyclo(RGD-^{D}YK)-ONH$_2$ were achieved according to Scheme 1. Cyclo-(RGD^{D}YK)-ONH$_2$ (2 mg) was incubated with 5.7 equiv of FDG in 16% ethanol in saline (120 μL) and 0.4% TFA at 100 °C for 60 min to give FDG-cyclo(RGD^{D}YK) (E- and Z-oximes) in 41.4% yield. The purified FDG-cyclo(RGD^{D}YK) showed two identical mass peaks of 857.35 ([M+H]$^{+}$) in ESI-MS, which correspond to FDG-cyclo(RGD^{D}YK) (E- and Z-oximes) (calcd M+H for FDG-cyclo(RGD^{D}YK) is 857.47). Conjugation of

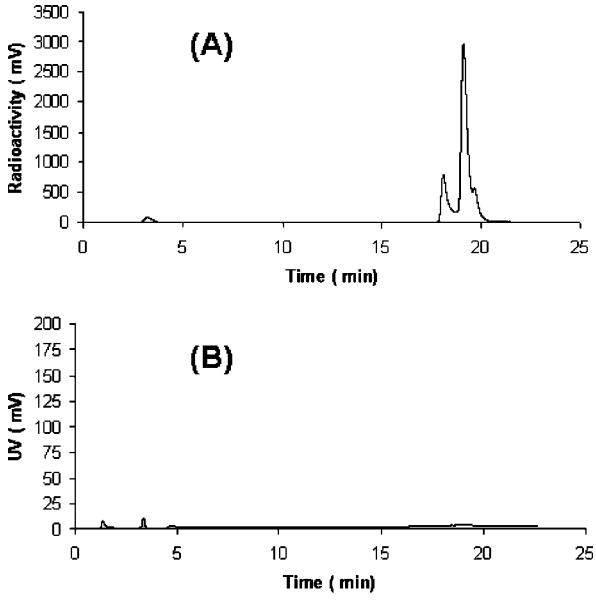

Figure 1. Analytical HPLC profiles of [^{18}F]FDG-cyclo(RGD^{D}YK) (E- and Z-oximes) after semiprep HPLC. A is radioactive trace and B is UV trace.

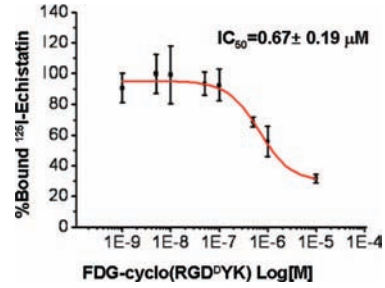

Figure 2. Inhibition of ^{125}I-echistatin (integrin $\alpha_v\beta_3$-specific) binding to $\alpha_v\beta_3$ intgrin on U87MG cells by FDG-cyclo(RGD^{D}YK).

Table 1. Biodistribution of [^{18}F]FDG-RGD in Mice Bearing U87MG Xenografts[a]

Organ (%ID/g)	0.5 h	2 h
U87MG	0.94 ± 0.25	0.27 ± 0.06
blood	0.43 ± 0.05	0.02 ± 0.00
heart	3.56 ± 1.11	3.67 ± 0.26
liver	0.44 ± 0.03	0.22 ± 0.04
lungs	0.78 ± 0.05	0.47 ± 0.37
muscle	0.27 ± 0.07	0.09 ± 0.03
kidney	1.95 ± 0.17	0.55 ± 0.51
spleen	0.49 ± 0.10	0.64 ± 0.68
brain	0.58 ± 0.04	0.16 ± 0.02
intestine	0.32 ± 0.03	0.19 ± 0.09
stomach	0.61 ± 0.50	0.30 ± 0.32
bone	0.29 ± 0.03	0.23 ± 0.20
ratios		
T/Blood	2.19 ± 0.55	13.27 ± 1.05
T/Muscle	3.71 ± 1.49	3.50 ± 1.90
T/Liver	2.17 ± 0.76	1.25 ± 0.08
T/Kidney	0.49 ± 0.14	0.74 ± 0.43

[a] Data are expressed as of percentage of injected radioactivity per gram of organ or tissue (% ID/g) after intravenous injection of [^{18}F]FDG-RGD (10−30 μCi) at different times postinjection (n = 3 for each group).

Table 2. Biodistribution of [^{18}F]FDG-cyclo(RGD^{D}YK) in Mice Bearing U87MG Xenografts[a]

Organ (%ID/g)	0.5 h	1 h	2 h
kidney	4.75 ± 5.60	3.75 ± 1.42	16.1 ± 13.0
liver	1.32 ± 1.3		0.43 ± 0.40
brain	0.80 ± 1.09		0.13 ± 0.07
heart	1.11 ± 0.22		2.57 ± 2.53
lung	0.54 ± 45		0.60 ± 0.66
muscle	0.30 ± 0.10		0.13 ± 0.06
stomach	0.17 ± 0.03		0.46 ± 0.52
intestine	0.50 ± 0.02		0.28 ± 0.19
bone	0.71 ± 0.65		0.13 ± 0.21
blood	2.04 ± 2.28	0.84 ± 0.19	0.54 ± 0.31
U87MG	0.63 ± 0.13	0.95 ± 0.40	1.53 ± 1.59
spleen	0.19 ± 0.16		0.17 ± 0.20
ratios			
T/Blood	0.32 ± 0.17	1.19 ± 0.63	2.75 ± 1.62
T/Muscle	3.72 ± 2.16		12.9 ± 9.41
T/Liver	0.49 ± 0.30		6.02 ± 6.08
T/Kidney	0.15 ± 0.08	0.28 ± 0.17	0.17 ± 0.08

[a] Data are expressed as of percentage of injected radioactivity per gram of organ or tissue (% ID/g) after intravenous injection of [^{18}F]FDG-cyclo(RGD^{D}YK) (10−30 μCi) at different times postinjection (n = 3 for each group).

^{18}FDG to cyclo(RGD^{D}YK)-ONH$_2$ (2 mg) afforded [^{18}F]FDG-cyclo(RGD^{D}YK) (E- and Z-oximes) in 41% radiochemical yield based on [^{18}F]FDG (decay-corrected). [^{18}F]FDG-cyclo(RGD-^{D}YK) (E- and Z-) oximes were purified but not separated by HPLC, and the two ^{18}F-labeled products (E- or Z-oximes) were isolated as a mixture and analyzed by analytical HPLC (Figure 1). The exact stereochemistry (E- and Z-) of these two products has not been determined yet. We found that under our experimental conditions maximum radiochemical yields were obtained at pH values of 1.5−2.5. When the reaction was performed at pH 4 in ammonium acetate buffer, no significant products were produced. In our previous report (*9*), we addressed the selectivity of aldehyde toward the aminooxy groups over the amine groups in conjugation of RGD peptides with a simple aldehyde such as 4-flurobenzaldehyde. We found that, when, for example, two RGD aminooxy-functionalized peptides NH$_2$-OCH$_2$CO-Arg-Gly-Asp-NH$_2$ and NH$_2$OCH$_2$CO-Lys-Arg-Gly-Asp-NH$_2$ were reacted at the same condition (8.5−150 equiv, 45−60 min, 70 °C, pH 4) with 4-fluorobenzaldehyde, in each case only one oxime product was formed. It strongly suggests that in conjugation of RGD-ONH$_2$ or cyclo(RGD^{D}YK)-ONH$_2$ with FDG oximes are the major products. Similar selectivity was observed by Poethko et al. (*6*) where they tested the selectivity of 4-[^{18}F]fluorobenzaldehyde for aminooxy groups vs amine groups in amino acids argentine serine, histidine, and lysine in both the presence and the absence of 2-aminooxyacetic acid. The major limitations of our ^{18}F-labeling methodology are the high-temperature (100 °C) and acidic pH conditions. High-temperature and acidic pH are tolerated for the small unprotected peptides but might not be suitable for the large peptides.

Cell Culture Binding Studies. To determine whether FDG-cyclo(RGD^{D}YK) has similar receptor binding affinity for integrin $\alpha_v\beta_3$ as cyclo(RGD^{D}YK), we studied the receptor binding affinity of FDG-cyclo(RGD^{D}YK) for integrin $\alpha_v\beta_3$, using $\alpha_v\beta_3$ positive U87MG cells. The receptor binding affinity study of FDG-cyclo(RGD^{D}YK) for integrin $\alpha_v\beta_3$, using $\alpha_v\beta_3$ positive U87MG cells, confirmed a competitive displacement with ^{125}I-echistatin as a radioligand (Figure 2). The IC$_{50}$ value

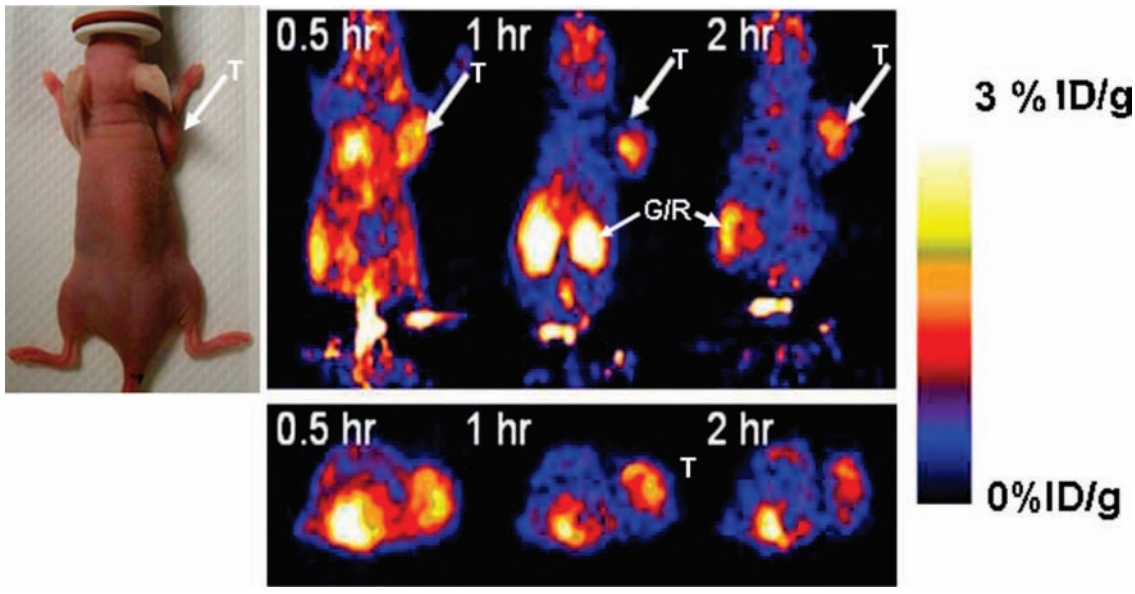

Figure 3. Decay-corrected microPET images (coronal top and trnsaxial bottom) of a nude mouse (photograph shown on left) bearing U87MG xenograft at 0.5, 1, and 2 h after tail injection of 100 μCi of [^{18}F]FDG-RGD. T is for tumor, G/R is gastrointestinal/renal activities, and color bar represents % ID/g.

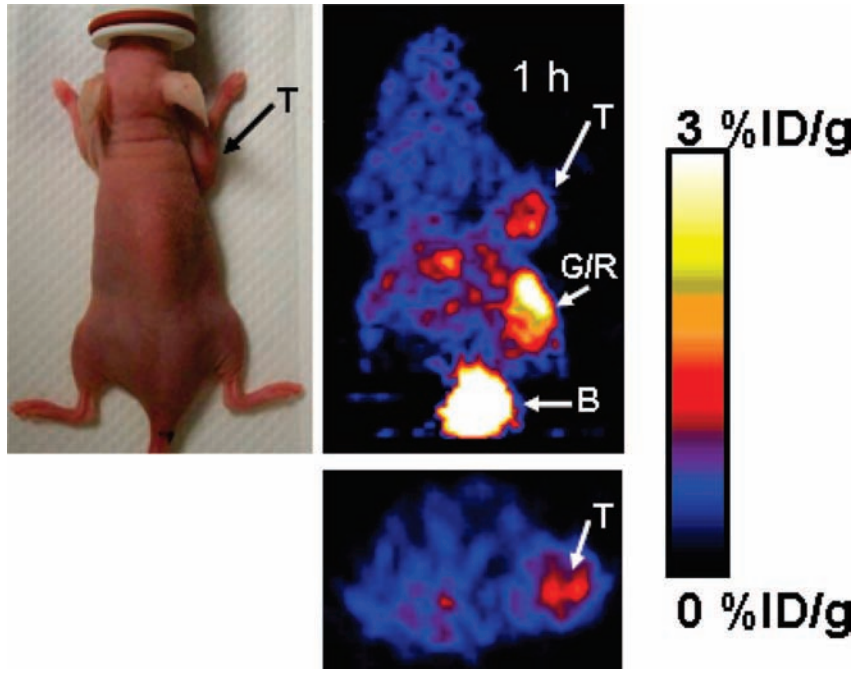

Figure 4. Decay-corrected microPET images (coronal top and trnsaxial bottom) of a nude mouse bearing a U87MG xenograft at 1 h after tail injection of 72 μCi of [^{18}F]FDG-cyclo(RGD^{D}YK). T, tumor; B, bladder; G/R, gastrointestinal/renal activities; and color bar represents % ID/g.

for FDG-cyclo(RGD^{D}YK) was determined to be 0.67 ± 0.19 μM. The corresponding IC_{50} value of cyclo(RGD^{D}YK) is 0.23 μM (*12*).This result suggests that fluorine labeling and the conditions (100 °C and acidic pH) did not have a dramatic affect on its binding affinity.

Biodistribution and Imaging. In order to determine the in vivo imaging performance of [^{18}F]-labeled FDG-RGD over alternatively ^{18}F-labeled RGD analogues, we evaluated [^{18}F]FDG-RGD in U87MG tumor-bearing nude mice that express $\alpha_v\beta_3$ integrin on both tumor vasculature and tumor cells. In vivo biodistribution of [^{18}F]FDG-RGD in U87MG tumor-bearing nude mice ($n = 6$) expressing $\alpha_v\beta_3$ integrin is shown in Table 1. The ratios of tumor to blood, tumor to liver, and tumor to kidney at 2 h postinjection of the probe are comparable to [^{18}F]Galacto-RGD analogue that has been used for biodistribution of [^{18}F]Galacto-RGD in osteosarcoma tumor-bearing nude mice that express $\alpha_v\beta_3$ integrin (*13*). MicroPET images of U87MG tumor-bearing nude mice ($n = 6$) 0.5, 1, and 2 h after tail vein injection of ^{18}F-labeled [^{18}F]FDG-RGD probe were obtained. Figure 3 shows the microPET image of one representative mouse. The subcutaneous U87MG mice tumors could be clearly visualized from surrounding background tissue.

To evaluate in vivo imaging performance of [^{18}F]FDG-cyclo(RGD^{D}YK) in small living subjects, we investigated biodistribution and microPET imaging of U87MG tumor-bearing nude mice expressing $\alpha_v\beta_3$ integrin by using [^{18}F]FDG-cyclo(RGD^{D}YK) as a probe. Biodistribution of [^{18}F]FDG-cyclo(RGD^{D}YK) in U87MG tumor-bearing nude mice ($n = 9$) expressing $\alpha_v\beta_3$ integrin is shown in Table 2. The ratios of tumor to blood, tumor to muscle, and tumor to liver at 2 h postinjection of the probe were 3, 13, and 6, respectively. MicroPET images of U87MG tumor-bearing nude mice ($n = 3$) 60 min after tail vein injection of [^{18}F]FDG]-cyclo(RGD^{D}YK) were also obtained. Figure 4 shows the microPET image of one representative mouse. The subcutaneous U87MG mouse tumor could be clearly visualized from surrounding background tissue. Tracer activity within the tumor was determined to be 1.06 ± 0.20% ID/g, by region of interest (ROI) analysis of the three mice, which matches with the value of 0.95 ± 0.4% ID/g determined by the biodistribution studies (Table 2), and muscle uptake was 0.20 ± 0.12% ID/g. Although the reasons for the relatively fast clearance and moderate tumor uptake after 60 min of injection of [^{18}F]FDG-cyclo(RGD^{D}YK) are not clear, the use of ^{18}F-labeled dimeric or tetrameric ^{18}FDG-labeled RGD should be explored. Recent reports (*14*−*16*) on the radiolabeled DOTA conjugated-cyclic-RGD, monomer, dimer, and tetramer with ^{64}Cu showed that tetrameric cyclic-RGD peptide tracer had about twice as much tumor uptake as the corresponding dimer. Also, the dimer had significantly higher uptake than the monomer counterpart. Likewise, it has been shown that ^{18}F-labeled dimeric RGD peptide, [^{18}F]FB-E[c(RGDYK)]$_2$, has superior imaging characteristics to the corresponding monomer (*17*).

CONCLUSION

We have successfully prepared [^{18}F]FDG-RGD and [^{18}F]FDG-cyclo(RGD^{D}YK) based on a simple one-step radiosynthesis by using [^{18}F]FDG as a prosthetic group. The one-step radiosynthesis methodology consists of chemoselective oxime formation between an easily synthesized aminooxy-functionalized peptide and [^{18}F]FDG. The [^{18}F]FDG labeled RGD peptides can be used to image tumors expressing in living subjects. Imaging of integrin ´$\alpha_v\beta_3$ expression in living subjects would offer a potentially useful approach to diagnose tumors and their metastasis, to help us better understand tumor angiogenesis, and to monitor target-specific antiangiogenesis treatment efficacy. The preliminary mice data support further investigation of the tracers and more comparisons to alternately labeled RGD peptides. The major limitations for generalization of our ^{18}F-labeling methodology are the relatively high temperature (100 °C) and acidic pH conditions required. High temperature and acidic pH are tolerated for the small unprotected peptides but might not be suitable for larger peptides. This approach may also be useful for labeling other biomolecules and would lead to a very simple strategy for routine preclinical and clinical use. The methodology additionally provides benefits such as the use of unprotected aminooxy precursor and the ability to form oximes in aqueous media, providing easy formulation for in vivo use. Indeed, the chemistry has been proven through many biological applications in the synthesis of glycopeptides (*18, 19*), oligonucleotide−peptide conjugates (*20, 21*), complex proteins

(from peptide fragments) (*22*), and conjugation of oligoribonucleotides and proteins with metal chelates (*23*).

ACKNOWLEDGMENT

This work was supported, in part, by Medical Diagnostics, GE Healthcare, National Cancer Institute (NCI) Small Animal Imaging Resource Program (SAIRP) grant R24 CA93862, and NCI In Vivo Cellular Molecular Imaging Center (ICMIC) grant P50 CA114747 (SSG). We also thank Dr. David Dick for [^{18}F] production, Dr. Frederick T. Chin for modification of a GE TRACERlab FX-FN synthetic module for radiosynthesis, Dr. Alan Cuthbertson and Dr. Alex Gibson of GE Healthcare for their review of the manuscript.

Supporting Information Available: Detailed experimental procedures. This material is available free of charge via the Internet at http://pubs.acs.org.

LITERATURE CITED

(1) Gambhir, S. S. (2002) Molecular imaging of cancer with positron emission tomography. *Nat. Rev. Cancer 2*, 683–693.
(2) Brooks, P. C., and Clark, R. (1994) Requirement of vascular integrine $\alpha_v\beta_3$ for angiogenesis. *Science 264*, 569–571.
(3) Cairns, R. A., Khokha, R., and Hill, R. P. (2003) Molecular mechanisms of tumor invasion and metastasis: an integrated view. *Curr. Mol. Med. 3*, 659–671.
(4) Felding-Habermann, B. (2003) Integrin adhesion receptors in tumor metastasis. *Clin. Exp. Metastasis 20*, 203–213.
(5) Toyokuni, T., Walsh, J. C., Dominguez, A., Phelps, M. E., Barrio, J. R., Gambhir, S. S., and Satyamurthy, N. (2003) Synthesis of a new heterobifunctional linker, N-[4-(aminooxy) butyl]maleimide, for facile access to a thiol-reactive ^{18}F-labeling agent. *Bioconjugate Chem. 14*, 1253–1259.
(6) Poethko, T., Schottelius, M., Thumshirn, G., Hersel, U., Herz, M., Henriksen, G., Kessler, H., Schwaiger, M., and Wester, H.-J. (2004) Two-step methodology for high yield routine radiohalogenation of peptides, ^{18}F-labeled RGD and octreotide analogs. *J. Nucl. Med. 45*, 892–902.
(7) Berndt, M., Pietzsch, J., and Wuest, F. (2007) Labeling of low-density lipoproteins: ^{18}F-labeled thio-reactive reagent N-[6-[^{18}F]fluorobenzylidine)aminooxyhexyl]maeimide. *Nucl. Med. Biol. 34*, 5–25.
(8) Cheng, Z., De Jesus, O. P., Namavari, M., De, A., Levi, J., Webster, J. M., Zhang, R., Lee, B., Syud, F. A., and Gambhir, S. S. (2008) Small-animal PET imaging of human epidermal growth factor receptor type 2 expression with site-specific ^{18}F-labeled protein scaffold. *J. Nucl. Med. 49*, 804–813.
(9) Namavari, M., De Jesus, O. P., Cheng, Z., De, A., Kovacs, E., Levi, J., Zhang, R., Joshua, K., Hoerner, J. K., Grade, H., Syud, F. A., and Gambhir, S. S. (2008) Direct site-specific radiolabeling of an affibody protein with 4-[^{18}F]fluorobenzaldehyde via oxime chemistry. *Mol. Imaging Biol. 10*, 177–181.
(10) Berndt, M., Pietzsch, J., Bergmann, R., and Wuest, F. (2006) A novel role for [^{18}F]FDG: Synthesis and application of a [^{18}F]FDG-based prosthetic group for peptides and protein labeling. *J. Nucl. Med. 47* (Supplement 1), 29p.
(11) Ramsy, S. L., Freeman, C., Grace, P. B., Remond, J. W., and MacLeod, J. K. (2001) Mild tagging procedures for the structural analysis of glycans. *Carbohydr. Res. 333*, 59–71.
(12) Cai, W., Chen, K., Li, Z.-B., Gambhir, S. S., and Chen, X. (2007) Dual-function probe for PET and near-infrared fluorescence imaging of tumor vasculature. *J. Nucl. Med. 48*, 1862–1870.
(13) Haubner, R., Wester, H. J., Weber, W. A., Mang, C., Ziegler, S. I., Goodman, S. L., Senekowitsch-Schmidtke, R., Kessler, H., and Schwaiger, M. (2001) Noninvasive imaging of alpha(v)beta3 integrin expression using ^{18}F-labeled RGD-containing glycopeptides and positron emission tomography. *Cancer Res. 61*, 1781–1785.
(14) Chen, X., Park, R., Tohme, M., Shahinian, A. H., Bading, J. R., and Conti, P. S. (2004) MicroPET and autoradiographic imaging of breast cancer α_v-integrin expression using ^{18}F- and ^{64}Cu-labeled RGD peptide. *Bioconjugate Chem. 15*, 41–49.
(15) Chen, X., Liu, S., Hou, Y., Tohme, M., Park, R., Bading, J. R., and Conti, P. S. (2004) MicroPET imaging of breast cancer α_v-integrin expression with ^{64}Cu-labeled dimeric RGD peptides. *Mol. Imaging Biol. 6*, 350–359.
(16) Wu, Y., Zhang, X., Xiong, Z., Cheng, Z., Fisher, D. R., Liu, S., Gambhir, S. S., and Chen, X. (2005) MicroPET imaging of glioma α_v-integrin expression using ^{64}Cu labeled tetrameric RGD peptide. *J. Nucl. Med. 46*, 1707–1718.
(17) Chen, X., Tohme, M., Park, R., Hou, Y., Bading, J. R., and Conti, P. S. (2004) MicroPET imaging of $\alpha_v\beta_3$-integrin expression with ^{18}F-flabeled dimeric RGD peptide. *Mol. Imaging 3*, 96–104.
(18) Renaudet, O., and Dumy, P. (2003) Chemoselectively template-assembled glycoconjugates as mimics for multivalent presentation of carbohydrates. *Org. Lett. 5*, 243–246.
(19) Dey, S., and Sheppard, T. L. (2001) Ketone-DNA: A versatile postsynthetic DNA decoration platform. *Org. Lett. 3*, 3983–3986.
(20) Hamma, T., and Miller, P. S. (2003) 4-(2-Aminooxy)-2-(ethylureido)quinoline-oligonucleotide conjugates: synthesis binding interactions and derivatization with peptides. *Bioconjugate Chem. 14*, 320–330.
(21) Zatsepin, T. S., Stetsenko, D. A., Arzumanov, A. A., Romonova, E. A., Gait, M. J., and Oretskaya, T. S. (2002) Synthesis of peptide−oligonucleotide conjugates with single and multiple peptide attached to 2′-aldehydes through thiazolidine, oxime, and hydrazine linkages. *Bioconjugate Chem. 13*, 822–830.
(22) Bure, C., Leliever, D., and Delmas, A. (2000) Identification of by-products from an orthogonal peptide ligation by oxime bonds using spectrometry and tandem mass spectrometry. *Rapid Commun. Mass Spectrom. 14*, 2158–2164.
(23) Peuralahti, J., Puukka, K., Hakala, H., Mukkala, V.-M., Mulari, Q., Hurskainen, P., and Hovinen, J. (2002) Synthesis of nonluminescent lanthanide (III) chelates tethered to an aminooxy group and their applicability to biomolecules derivatization. *Bioconjugate Chem. 13*, 876–880.

BC800422B

A Novel Method for Direct site-specific Radiolabeling of Peptides Using [^{18}F]FDG

Mohammad Namavari[†], Zhen Cheng[†], Rong Zhang[‡], Abhijit De[†], Jelena Levi[†], Joshua K. Hoerner[‡], Shahriar S. Yaghoubi[†], Faisal A. Syud[‡] and Sanjiv S. Gambhir [†]

[†]Molecular Imaging Program at Stanford (MIPS), Departments of Radiology and Bioengineering, Bio-X Program, Stanford University, and [‡]Global Research, General Electric.

SUPPLEMENTRY INFORMATION

Experimental Procedures……S3

General……S3

Synthesis of FDG-RGD……..S5

Synthesis of [^{18}F]FDG-RGD…… S5

Synthesis of FDG-Cyclo(RGD^{D}YK)…… S6

Synthesis of [^{18}F]FDG-Cyclo(RGD^{D}YK)…… S6

U87MG Glioblastoma Xenograft Model……S7

Biodistribution……S7

Integrin Binding Characteristics *in vitro*.....S8

MicroPET Imaging…… S8

Experimental Procedures

General: Cyclic peptide *cyclo*[Arg(Pbf)-Gly-Asp(tBu)-^{D}Tyr(But)-Lys] was purchased from Peptides International (Louisville, KY). All other N-α-Fmoc (Fluorenylmethoxycarbonyl)-protected amino acids, O-benzotriazole-N,N,N',N'-tetramethyluronium hexafluorophosphate (HBTU), O-(7-azabenzotriazol-1-yl)-N,N,N',N'-trimethyluronium hexafluorophosphate (HATU), 1-hydroxy-7-Azabenzotriazole (HOAt), trifluoroacetic acid (TFA), and rink amide resin (100-200 mesh, 1% DVB, 0.5 mmol/g) were purchased from Advanced Chemtech (Louisville, KY). Dimethylformamide (DMF) and methylene chloride were obtained from Fisher Scientific (Fair Lawn, NJ). 20% piperidine in DMF was obtained from Protein Technologies Inc. (Tucson, AZ). Pyridine, acetic anhydride, acetic acid, and anhydrous ether were obtained from J.T.Baker (Phillipsburg, NJ). N-methylmorpholine (NMM), Boc-(aminooxy)acetic acid, N,N-diisopropylethylamine, 1, 2-Ethanedithiol (EDT), and triisopropylsilane (TIPS) were purchased from Aldrich Chemical Company (Milwaukee, WI). HPLC grade acetonitrile (CH_3CN) and Millipore 18 mΩ water were used for peptide purifications. ^{125}I-Echistatin labeled by the lactoperoxidase method with specific activity of 2,000 Ci/mmol was purchased from Amersham Biosciences (Piscataway, NJ). Purification and analysis of the peptides was done on a Dionex Summit HPLC system (Dionex Corporation, Sunnyvale, CA) equipped with a 340 U 4-Channel UV-Vis

absorbance detector and radioactivity detector (Carroll & Ramsey Associates, model 105S, Berkeley, CA). UV detection wavelengths were 218 nm, 254 nm and 280 nm for all the experiments and HPLC reveres phase column (Vydac, Hesperia, CA. 218TP510-C18, 5μ, 10 mm × 250 mm) was used for analysis of labeled peptides. The mobile phase was 0.1% TFA in water , and 0.1% TFA in acetonitrile. Radioactivity measurements were performed by A CRC-15R PETdose calibrator (Capintec Inc., Ramsey, NJ). Electron spray ionization (ESI) mass spectrometry was done by Vincent Coates Foundation Mass Spectrometry Laboratory, Stanford University or an electrospray ionization time of flight mass spectrometer (ESI-TOF-MS, model: JMS-T100LC) (JEOL, Tokyo, Japan) was performed by the Mass Spectrometry Lab at GE Global Research (Niskayuna, NY).

Linear RGD (Arg-Gly-Asp) peptide was synthesized using standard solid phase techniques with N-Fmoc-protected amino acids using substitution 2,4-dimethoxybenzhydrylamine resin (Rink Resin LS, Advanced Chemtech) on a 100 μmol scale. The synthesis was performed in a Rainin/Protein Technology, Inc. Symphony solid phase peptide synthesizer. N-terminal functionalized with aminooxy acetyl group was achieved by using Boc-(aminooxy)acetic acid. Cleavage from the solid support and removal of the acid-labile protecting groups was performed by 95% TFA: 2.5% TIPS (triisopropylsilae): 2.5% water (v/v/v) and purified to afford aminooxy-RGD (RGD-ONH_2) in 72 % yield. Analysis of the peptide by HPLC followed by ESI-MS showed *m/z* = 419.22 for $[M+H]^+$ ($C_{14}H_{27}N_8O_7$, Calculated $[M+H]^+$ = 419.19). For preparation of aminooxyacetyl Cyclo(RGD^{D}YK) [Cyclo(RGD^{D}YK)-ONH_2], initially the protected cyclo[Arg (pbf)-Gly-Asp(tBU)-^{D}Tyr(But)-Lys]-ONH-Boc was prepared by the reaction

of Boc-(aminooxy)acetic acid, O-(7-azabenzotriazol-1-yl)-N,N,N',N'-trimethyluronium hexafluorophosphate (HATU) and Hunig's base with commercially available cyclo[Arg (pbf)-Gly-Asp(tBU)-^{D}Tyr(But)-Lys] in DMF. The protected Cyclo[Arg(pbf)-Gly-Asp(tBU)-^{D}Tyr(But)-Lys]-ONH-Boc was purified by HPLC (white powder,78 % yield). Analysis of peptide by ESI-MS showed *m/z* = 1157.48 for $[M+H]^+$ ($C_{55}H_{85}N_{10}O_{15}S$, calculated $[M+H]^+$ = 1157.58). Removal of the acid-labile protecting groups of cyclo[Arg(pbf)-Gly-Asp(tBU)-^{D}Tyr(But)-Lys]-ONH-Boc was performed as above and purified by HPLC to afford Cyclo(RGD^{D}YK)-ONH_2 in 92 % yield. Analysis of the peptide by ESI-MS showed *m/z* = 693.26 for $[M+H]^+$ ($C_{29}H_{45}N_{10}O_{10}$, calculated $[M+H]^+$ =693.32).

Synthesis of FDG-RGD: The linear aminooxy-RGD (RGD-ONH_2, 2 mg) was incubated with 3.7 equivalents cold FDG in 16 % ethanol in saline (120 μl) in the presence of 0.4 % TFA at 100 °C for 40 min. After cooling to room temperature, the reaction mixture was diluted to 300 μL with water. The resulting solution was injected into a HPLC column (Vydac 218TP54, C18, 5 u, 4.6 X 250 mm, 1mL/min flow rate). The eluent changed from 95% solvent A (0.1 % TFA in H_2O) and 5 % solvent B (0.1% TFA in acetonitrile) (0-3 min) to 35 % solvent A and 65 % solvent B at 33 min. The E and Z oximes were collected (retention time 6.0-7.0 min) and solvents were removed under reduced pressure to yield FDG-RGD (1.1 mg, 39.5 %). The mass spectrometry (ESI-MS) analysis of the isolated product showed two identical mass peaks of 584.2 ($[M+H]^+$) which correspond to FDG-RGD (E- and Z-oximes) (cal. [M+H] for FDG-RGD is 584.5.).

Synthesis of [^{18}F]FDG-RGD: Aminooxy-RGD (RGD-ONH_2, 2 mg) was reacted with 4-6 mCi of [^{18}F]FDG in 100 μl saline in the same condition as above but in 30 minutes.

The poducts (E and Z oximes) were isolated by the above HPLC conditions but with a different gradients. The eluent changed from 97% solvent A (0.1 % TFA in H_2O) and 3 % solvent B (0.1% TFA in acetonitrile) (0-3 min) to 85 % solvent A and 15 % solvent B at 33 min. After products collection, solvents were removed under reduced pressure to afford [^{18}F]FDG-RGD (E and Z) in 27.5 % radiochemical yields based on [^{18}F]FDG (decay corrected).

Synthesis of FDG-Cyclo(RGD^{D}YK): Cyclo(RGD^{D}FK)-ONH_2 (2 mg) was incubated with 5.7 equivalents of FDG in 16 % ethanol in saline (120 μl) and 0.4 % TFA at 100 °C for 60 min. After cooling to room temperature, the reaction mixture was diluted to 300 μL with water. The resulting solution was injected into a HPLC column (above). The eluent changed from 95% solvent A (0.1 % TFA in H_2O) and 5 % solvent B (0.1% TFA in acetonitrile) (0-3 min) to 35 % solvent A and 65 % solvent B at 33 min. The products were collected (retention times 17.5-19 min) and solvents were removed under reduced pressure to yield (E and Z) FDG-cyclo(RGDDYK) (1.03 mg, 41.4 %). The purified FDG-cyclo(RGD^{D}YK) showed two identical mass peaks of 857.35 ([M+H]$^{+}$) in ESI-MS which are corresponding to FDG-cyclo(RGD^{D}YK) (E- and Z-oximes) (cal. M+H for FDG-cyclo(RGD^{D}YK) is 857.47.).

Synthesis of [^{18}F]FDG-Cyclo(RGD^{D}YK): Cyclo(RGD^{D}FK)-ONH_2 (2 mg) was incubated with [^{18}F]FDG (4-6 mCi) in 16 % ethanol in saline (120 μl) and 0.4 % TFA at 100 °C for 45 min. After cooling to room temperature, the products (E and Z oximes) were isolated by the above HPLC conditions which used for the synthesis of FDG-cyclo(RGD^{D}YK)**.** After products collection, solvents were removed under reduced pressure to afford [^{18}F]FDG-cyclo(RGD^{D}YK) (E and Z oximes) in 41 % radiochemical

yields based on [^{18}F]FDG (decay corrected). [^{18}F]FDG-cyclo(RGD^{D}YK) (E- and Z-) oximes were purified but not separated by HPLC and the two ^{18}F-labeled products (E- or Z-oximes) were isolated as a mixture and analyzed by analytical HPLC. The exact stereochemistry (E- and Z-) of these two products has not been determined yet.

U87MG Glioblastoma Xenograft Model

U87MG human glioblastoma cell line was obtained from American Type Culture Collection (Manassas, VA) and was maintained at 37 ºC in a humidified atmosphere containing 5% CO_2 in Iscove's modified Dulbecco's medium and 5% fetal bovine serum (Life Technologies, Inc., Grand island, NY). Animal studies were carried out according to a protocol approved by the Stanford University Administrative Panels on Laboratory Animal Care (A-PLAC). Female athymic nude mice (*nu/nu*), purchased from Charles River Laboratories, Inc. (Cambridge, MA) at 4-6 weeks of age, were inoculated subcutaneously in the flanks with 5×10^6 U87MG glioblastoma cells suspended in 100 μL of phosphate buffered saline (PBS). The tumor bearing mice were subjected to *in vivo biodistribution and* imaging studies when the tumors reached 0.4-0.6 cm in diameter (14-21 d after implant).

Biodistribution

For biodistribution studies, the U87MG tumor-bearing mice (20 g each, n = 3 for each group) were injected with radiolabeled [^{18}F]FDG-RGD or [^{18}F]FDG-cyclo(RGD^{D}YK) (10-30 μCi, 0.37–1.11 MBq) via tail vein and sacrificed and dissected at 30 min to 2 h after injection. Tumor, blood and major tissues of interest were removed

and weighed, and their radioactivity was measured in a gamma-counter. The radioactivity uptake in the tumor and normal tissues was expressed as a percentage of the injected radioactive dose per gram of tissue (% ID/g).

Integrin Binding Characteristics *in vitro*

The receptor binding affinity study of conjugate FDG-cyclo(RGD^{D}YK) for integrin $\alpha_v\beta_3$ was carried out using $\alpha_v\beta_3$ positive U87MG cells. We compared the receptor binding affinity of FDG-cyclo(RGD^{D}YK) by performing competitive displacement studies with ^{125}I-echistatin as radioligand. FDG-cyclo(RGD^{D}YK) inhibited the binding of ^{125}I-echistatin to U87MG cells in a dose dependent manner. The IC_{50} value for FDG-cyclo(RGD^{D}YK) was 0.66 ± 0.22 μM.

MicroPET Imaging

PET scans were performed on a microPET R4 rodent model scanner (Concorde Microsystem Inc.). The mice bearing U87MG were injected with [^{18}F]FDG-RGD or [^{18}F]FDG-cyclo(RGD^{D}YK) via the tail vein and the mice were imaged at 30 min to 2 h after post injection (pi). At different time p.i. (0.5, 1 and 2 h), the mice were anesthetized with 2% isoflurane, and placed in the prone position and near the center of the filed of view of microPET. The 5-min static scans were obtained and the images were reconstructed by a two-dimensional ordered subsets expectation maximum (OSEM) algorithm. Regions of interest (ROIs) were then drawn over the tumor on decay-corrected whole-body coronal images.

Subscriber access provided by SHEMYAKIN-OVCHINNIKOV INST

Communication

A Modular Monolayer Coating Enables Cell Targeting by Luminescent Yttria Nanoparticles

Christopher A. Traina, T. Joseph Dennes, and Jeffrey Schwartz

Bioconjugate Chem., **2009**, 20 (3), 437-439• DOI: 10.1021/bc800551x • Publication Date (Web): 18 February 2009

Downloaded from http://pubs.acs.org on April 8, 2009

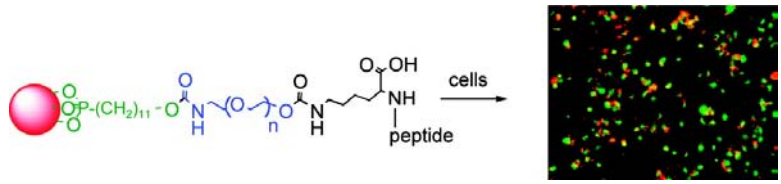

More About This Article

Additional resources and features associated with this article are available within the HTML version:

- Supporting Information
- Access to high resolution figures
- Links to articles and content related to this article
- Copyright permission to reproduce figures and/or text from this article

View the Full Text HTML

ACS Publications
High quality. High impact.

Bioconjugate Chemistry is published by the American Chemical Society. 1155 Sixteenth Street N.W., Washington, DC 20036

A Modular Monolayer Coating Enables Cell Targeting by Luminescent Yttria Nanoparticles

Christopher A. Traina, T. Joseph Dennes, and Jeffrey Schwartz*

Department of Chemistry, Princeton University, Princeton, New Jersey 08544-1009. Received December 18, 2008; Revised Manuscript Received February 7, 2009

Luminescent Eu^{3+}-doped Y_2O_3 nanoparticles are functionalized for cell targeting using a modular, multisegmented approach based on a phosphonate monolayer platform. The first segment provides hydrolytic stability for the particle−organic interface; the second enables aqueous suspendability; the third is used to bond cell attachment molecules. In vitro imaging experiments showed enhanced cell attachment of activated nanoparticles conjugated with cell attachment peptides compared to control nanoparticles. Peptide-derivatized nanoparticles are not displaced from the cells by their soluble peptide analogue, which suggests strong, polyvalent cell−particle interactions.

Effective biotargeting luminescent nanoparticles must be nontoxic, small relative to the system they are imaging, stable over the course of the experiment, and able to efficiently bond to the desired entity. Rare earth ion-doped yttria (Y_2O_3) nanoparticles are an appealing class of such targeting agents: they are benign in vitro (*1*) and in vivo (*2*) and can be made with diameters of <20 nm (*3*); they can be synthesized to have strong emission in the UV, visible, or IR (*4*) by varying lanthanide dopant ions (so narrow particle size distributions are not necessary as they are for quantum dots (*5*)); and they can be doped for down- (*6*) or up-conversion (*7*) emission. Despite these attractive features, rare earth ion-doped Y_2O_3 nanoparticles have seen only limited use heretofore for targeting biological systems (*2, 8*), which may be due to their limited suspendability in aqueous media and lack of acceptable bioconjugation schemes. We showed that we could control wettability of yttria nanoparticles by bonding monolayers of simple phosphonic acids to them (*9*); these monolayers are stable in organic or aqueous media and are about 1 nm thick. We now report that modular, multifunctional phosphonate monolayers can be synthesized on Y_2O_3 particles to enable their use as cell targeting agents. These tailored monolayers are stable to physiological conditions; they protect the particle−phosphonate interface from hydrolysis, impart particle suspendability in aqueous media, and enable polyvalent bonding of targeting biomolecules to the particles. We also show that luminescent, europium-doped Y_2O_3 nanoparticles that are surface-treated with one such modular monolayer are selective for cell attachment in an in vitro test that can serve as a model for targeting applications.

Monolayers of 11-hydroxyundecylphosphonate attached to micrometer- or nanoscale Y_2O_3 particles (**1**) (*9*) are stable to hydrolysis at pH 7.5 for >12 days; thus, **1** is used as our first module. Treating **1** with *p*-nitrophenyl chloroformate readily gives activated *p*-nitrophenyl carbonate-derivatized **2**, and the second module is introduced by reaction with tri(ethylene glycol) monoamine to give **3**; **3** has good aqueous suspendability and is also stable to hydrolysis at physiological pH. Treating **3** with *p*-nitrophenyl chloroformate gives **4**, which can then bond the desired biotargeting molecule via reaction with a primary amino group (see Scheme 1).

In a typical procedure, Y_2O_3 powder (ca. 1 g; Aldrich) was dispersed by sonication in 60 mL THF. A solution of 11-hydroxyundecylphosphonic acid (*10*) (**5**; 12 mg, 4.76×10^{-5} mol, in 25 mL THF) was added to the suspension, and the reaction mixture was stirred for 3 h at room temperature. The powder was collected by centrifugation, washed to remove excess phosphonic acid, and then dried in vacuo to give **1**, which was then resuspended in 60 mL THF. *p*-Nitrophenyl chloroformate (80 mg) and diisopropylethylamine (0.75 mL) were added, and the mixture was stirred for 15 h. The powder was then recovered by centrifugation and washed to give **2** ($\nu_{C=O} = 1768$ cm^{-1}). It was then treated with tri(ethylene glycol) monoamine (35 mg) and diisopropylethylamine (0.75 mL) in THF with stirring for 20 h. The powder was collected by centrifugation, and excess reagents were removed to give **3**, which was then treated with *p*-nitrophenyl chloroformate (80 mg) as described above. The product was then washed to give **4** ($\nu_{C=O} = 1768$; 1700 cm^{-1}). To determine the surface loading of the two modules on Y_2O_3 particles, a fluorescent dye was coupled to **4**, cleaved, and quantified in solution (*11*); in this way, the surface loading was measured to be 0.25 ± 0.01 mol/cm^2. Full synthesis and characterization details are given as Supporting Information.

As a first step to determining their biocompatibility, cell culture studies using NIH 3T3 fibroblasts were performed to probe cell adhesion on untreated and treated Y_2O_3 particles. Using a standard IR pellet press, aliquots of **4** were pressed into disks ($d = 12$ mm, $h = 1.5$ mm) that were then kept in a solution of Gly-Arg-Gly-Asp-Ser-Pro-Lys (GRGDSPK; 20 mg in 40 mL deionized water adjusted to pH 8−8.5 with aqueous NaOH) for 24 h; peptides containing the RGDS sequence are well-known models for the cell recognition site in fibronectin (*12*). The disks were then removed and rinsed with aqueous NaOH (pH 8.5), deionized water, then methanol to give peptide-terminated **6a** (see Scheme 1). Three surfaces were examined for cell adhesion: unmodified Y_2O_3, **3**, and **6a**. Samples of these particles were pressed into disks and put into cell culture (Supporting Information Figure 2). Quantification of cell adhesion for each surface was assessed by counting the number of cells in randomly generated microscope fields (Figure 1; 10× magnification, minimum of six fields for each type of sample; for cell counting data, see Supporting Information Figure 3). Unmodified Y_2O_3 supported some cell adhesion; importantly, the number of adherent cells was reduced by almost half on **3** and was doubled on **6a**. A two-way analysis of variance (ANOVA) showed a statistically significant difference between

* E-mail: jschwartz@princeton.edu.

10.1021/bc800551x CCC: $40.75 © 2009 American Chemical Society
Published on Web 02/18/2009

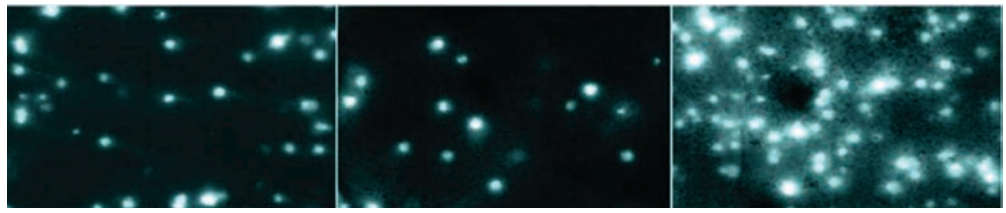

Figure 1. Cell adhesion images for pelletized Y_2O_3: untreated (left), **3** (middle), **6a** (right); cell counting data are given in Supporting Information.

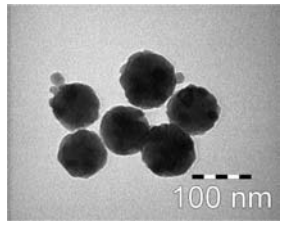

Figure 2. TEM image of Y_2O_3/Eu^{3+}nanoparticles shows diameters of ca. 100 nm.

the mean number of cells attached to RGD-coated and control pellets (for untreated Y_2O_3 vs **3** $p = 0.02$; for untreated Y_2O_3 vs **6a**, $p = 0.001$; for **3** vs **6a**, $p = 0.0001$).

To demonstrate the utility of this modular approach for bioimaging purposes, bioconjugation of luminescent nanoparticles was investigated. Eu^{3+}-doped (5%) Y_2O_3 nanoparticles were synthesized by precipitation of $Y(OH)CO_3$ particles from a refluxing, aqueous solution of Y^{3+} and Eu^{3+} salts and urea (*13*); calcining at 785 °C for 1 h gave cubic Y_2O_3:Eu^{3+} (by powder X-ray diffraction (*13*)). Particles with diameters ranging from ~40 to 180 nm (by TEM) could be obtained by adjustment of reagent concentrations; those with diameters between 80 and 120 nm (Figure 2) were used for subsequent experimentation. A strong band at 612 nm and less intense peaks at 591 and 630 nm were recorded in the particle emission spectrum and are characteristic of Eu^{3+} luminescence (*14*). Importantly, these nanoparticles can be easily visualized using a standard fluorescence microscope under UV (~365 nm) or blue (~488 nm) excitation.

The luminescent yttria nanoparticles were sonicated in THF to break up any agglomeration prior to and during monolayer deposition of **5** to give **1**, which was derivatized with tetra(ethylene glycol) monoamine and then GRGDSPK to give **6a** as described above. Similarly prepared control **6b** used cell adhesion-inactive GRADSPK (*12*) as a control. Suspensions of **6a** and **6b** were introduced into separate fibroblast cell culture dishes (10^5 cells/mL; cells were prestained with cell-tracker dye) which had a confluent cell layer on the plating substrate and the particles were allowed to attach for 3 h; the cells were then washed to remove unbound particles, fixed, and visualized by fluorescence microscopy. There was no change in the emission spectra for **6a**- or **6b**-treated vs untreated nanoparticles; only the doped nanoparticles were visible under UV (365 nm) illumination, but blue (488 nm) irradiation excited both dye-stained cells and nanoparticles. Images of cells treated with control **6b** showed only some large particle aggregates but no specific particle binding to the cells. In contrast, **6a** showed cell attachment with little aggregation (see Supporting Information Figure 8). Since **6a** and **6b** have similar wetting properties and charges, it is unlikely that they would have different aggregative properties in the absence of cell binding opportunities.

Nanoparticle−cell binding was further distinguished from simple precipitation using a nonconfluent cell layer (~50% substrate coverage) that was treated with **6a** or **6b**. Most of the

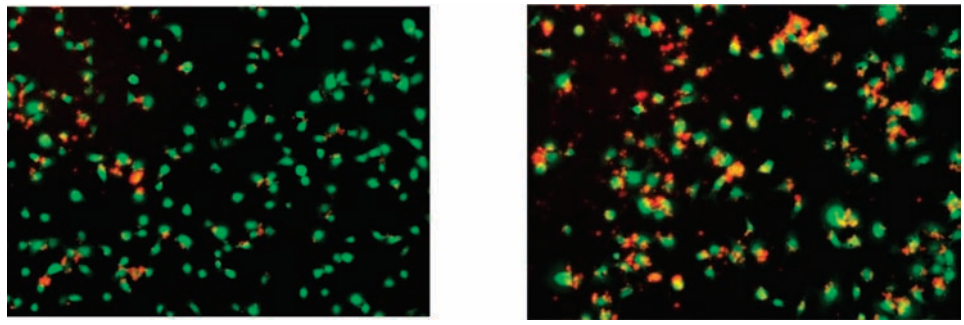

Figure 3. Nonspecific adsorption/aggregation of RAD-modified nanoparticles **6b** (left) versus adherence to cells (green) by RGD-modified nanoparticles **6a** (right) in nonconfluent cell layers. The nanoparticles luminesce red.

Scheme 1. The Modular Approach to Surface Functionalization of Undoped and Doped Yttria Particles (Red Spheres)

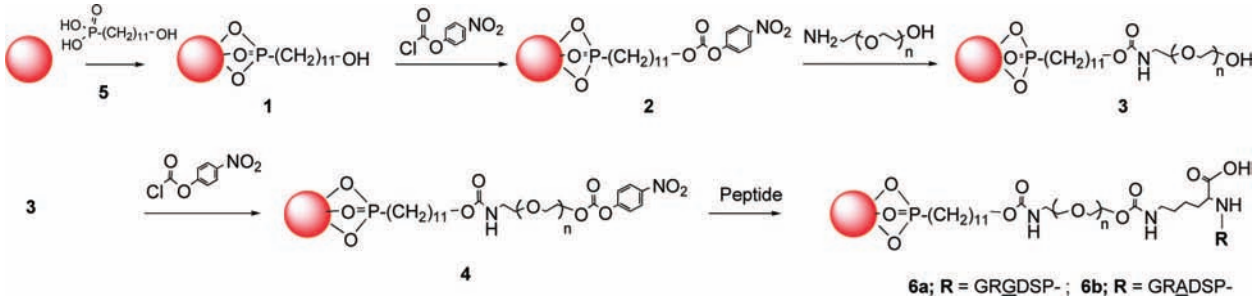

cells treated with **6a** were covered with nanoparticles but very little **6a** deposited on the substrate between the cells; few cells exposed to **6b** were bound to particles (Figure 3). Cell binding by **6a** was not inhibited by soluble GRGDSPK. RGD−integrin binding is reversible (*15*), but due to their size, particles of **6a** cannot be resuspended after cell interaction, which inhibits displacement by the soluble peptide. Importantly for cellular targeting, nanoparticles of **6a** may act as polyvalent binding species (*16*), which would greatly enhance cell binding of the bioconjugated particles vs the soluble peptide: On the basis of calculated surface loadings of the two modules on the Y_2O_3 particles, and assuming an average particle diameter of ∼100 nm, each nanoparticle can have $>10^4$ surface-attached peptide molecules on it, thus making it possible for each particle to bind simultaneously to several receptor sites on the cell surface.

We have shown that the Y_2O_3 surface can be easily and reproducibly functionalized in high yield via a modular scheme based on organophosphonate monolayers that enables control of nanoparticle surface properties. The nanoparticles can be made more cell adhesive or more cell resistant than the native ones by bonding an RGD-containing peptide or an oligo(ethylene glycol) moiety, respectively. This modular scheme was used to derivatize luminescent, Eu^{3+}-doped nanoparticles with an RGD peptide; in vitro experiments showed that increased cell surface−nanoparticle binding interactions could be visualized, and this binding was not suppressed by added soluble peptide. The modular concept may be expanded to examine peptide−receptor specificities; a small library of differently "colored" nanoparticles, each terminated with a different peptide sequence, might in principle be used to identify the presence of peptide-ligand specific cell surface receptor sites.

ACKNOWLEDGMENT

The authors thank the National Science Foundation, CHE-0612572, for support of this research. They also thank Prof. Jean E. Schwarzbauer, Department of Molecular Biology, Princeton University, for critical assistance.

Supporting Information Available: Full experimental details for synthesis of **1**, **2**, **3**, **4**, and **6**; a calibration curve for measuring surface loading of **4**; calculation of surface loading; cell adhesion cartoon and counting data; IR spectra for **1**, **2**, **3**, and **4**; images of nanoparticles of **6a** and **6b** on a confluent layer of cells. This material is available free of charge via the Internet at http://pubs.acs.org.

LITERATURE CITED

(1) Schubert, D., Dargusch, R., Raitano, J., and Chan, S.-W. (2006) Cerium and yttrium oxide nanoparticles are neuroprotective. *Biochem. Biophys. Res. Commun. 342*, 86–91.

(2) Lim, S. F., Riehn, R., Ryu, W. S., Khanarian, N., Tung, C.-k., Tank, D., and Austin, R. H. (2006) In Vivo and Scanning Electron Microscopy Imaging of Upconverting Nanophosphors in *Caenorhabditis elegans*. *Nano Lett. 6*, 169–174.

(3) Qin, X., Yokomori, T., and Ju, Y. (2007) Flame synthesis and characterization of rare-earth (Er^{3+}, Ho^{3+}, and Tm^{3+}) doped upconversion nanophosphors. *Appl. Phys. Lett. 90*, 073104−1−3.

(4) Maas, H., Currao, A., and Calzaferri, C. (2002) Encapsulated lanthanides as luminescent materials. *Angew. Chem., Int. Ed. 41*, 2495–2497.

(5) Michalet, X., Pinaud, F., Lacoste, T. D., Dahan, M., Bruchez, M. P., Alivisatos, A. P., and Weiss, S. (2001) Properties of fluorescent semiconductor nanocrystals and their application to biological labeling. *Single Mol. 2*, 261–276.

(6) He, C., Guan, Y., Yao, L., Cai, W., Li, X., and Yao, Z. (2003) Synthesis and photoluminescence of nano-Y_2O_3:Eu^{3+} phosphors. *Mater. Res. Bull. 38*, 973–979.

(7) Matsuura, D. (2002) Red, green, and blue upconversion luminescence of trivalent-rare-earth ion-doped Y_2O_3 nanocrystals. *Appl. Phys. Lett. 81*, 4526–4528.

(8) Texier, I., Heinrich, E., Berger, M., Tillement, O., Louis, C., and Peltie, P. (2007) Luminescent up-converting nano-crystals for in vivo imaging. *Proc. SPIE 6449*, 64490D-1–64490D-11.

(9) Traina, C. A., and Schwartz, J. (2007) Surface modification of Y_2O_3 nanoparticles. *Langmuir 23*, 9158–9161.

(10) Putvinski, T. M., Schilling, M. L., Katz, H. E., Chidsey, C. E. D., Mujsce, A. M., and Emerson, A. B. (1990) Self-assembly of organic multilayers with polar order using zirconium phosphate bonding between layers. *Langmuir 6*, 1567–1571.

(11) Silverman, B. M., Wieghaus, K. A., and Schwartz, J. (2005) Comparative stabilities of siloxane vs. phosphonate monolayers on a key titanium alloy. *Langmuir 21*, 225–228.

(12) Pierschbacher, M. D., and Ruoslahti, E. (1984) Variants of the cell recognition site of fibronectin that retain attachment-promoting activity. *Proc. Natl. Acad. Sci. U.S.A. 81*, 5985–5988.

(13) Kaczmarek, W. A., and Riesen, H. (2006) Structural and morphological properties of RE^{3+} doped sesquioxide Y_2O_3 spherical nanoparticles. *J. Mater. Sci. 41*, 8320–8328.

(14) Pang, Q., Shi, J., Liu, Y., Xing, D., Gong, M., and Xu, N. (2003) A novel approach for preparation of Y_2O_3:Eu^{3+} nanoparticles by microemulsion-microwave heating. *Mater. Sci. Eng., B 103*, 57–61.

(15) Ruoslahti, E., and Pierschbacher, M. D. (1987) New perspectives in cell adhesion: RGD and integrins. *Science 238*, 491–497.

(16) Mammen, M., Choi, S.-K., and Whitesides, G. M. (1998) Polyvalent interactions in biological systems: implications for design and use of multivalent ligands and inhibitors. *Angew. Chem., Int. Ed. 37*, 2754–2794.

BC800551X

A MODULAR MONOLAYER COATING ENABLES CELL TARGETING BY LUMINESCENT YTTRIA NANOPARTICLES

Christopher A. Traina, T. Joseph Dennes, and Jeffrey Schwartz*

Department of Chemistry, Princeton University, Princeton, NJ 08544

Supporting Information

Full experimental details for synthesis of **1**, **2**, **3**, **4**, and **6**; a calibration curve for measuring surface loading of **4**; calculation of surface loading; cell adhesion cartoon and counting data; IR spectra for **1**, **2**, **3**, and **4**; images of nanoparticles of **6a** and **6b** on a confluent layer of cells.

General. Tetrahydrofuran (ACS grade, EMD) was distilled from Na/benzophenone before use. Acetonitrile (HPLC grade, EMD) was distilled from CaH_2 prior to use. Methanol (EMD), tetra(ethylene glycol), trimethylsilyl bromide (TMS-Br), sodium 5-([2-aminoethyl]amino)naphthalene-1-sulfonate (EDANS), urea, europium(III) chloride hexahydrate, yttrium(III) chloride hexahydrate, *p*-nitrophenyl chloroformate, N,N-diisopropylethylamine, yttrium oxide, sodium hydroxide, tetra(ethylene glycol) monoamine and tri(ethylene glycol) monoamine (Molecular Bioscience) were used as received. Methylene chloride (EMD) was dried over 4Å molecular sieves prior to use. GRGDSPK peptide (99% purity, 80% peptide) and GRADSPK peptide (98% purity, 74% peptide, American Peptide) were used as received. IR spectra were recorded using a Smart Orbit diamond attenuated total reflectance (ATR) attachment on a Nicolet 6700 FT-IR spectrometer (solids) or neat on NaCl plates using a Nicolet 730 FT-IR spectrometer (liquids). Fluorescence measurements were acquired on a Perkin Elmer LS 50 fluorescence spectrometer. Luminescence spectra of nanoparticles were obtained by dispersing particles onto a glass slide fitted with double-sided tape. ^{1}H and ^{31}P NMR spectra were obtained on a Varian Mercury 300 MHz spectrometer. ^{13}C NMR spectra were acquired on a Varian Inova 400 or Inova 500 MHz spectrometer. TEM images were acquired on a Zeiss 910 TEM and powder X-ray diffraction patterns were recorded on a Rigaku MiniFlex X-Ray Diffractometer.

Phosphonate film depositions on Y_2O_3 powder.[1] Yttrium oxide powder (~1 g) was dispersed by sonication in 60 ml THF in a 250 ml round-bottom flask. A solution of 11-hydroxyundecylphosphonic acid (**5**, 12 mg, 4.76×10^{-5} mol, in 25 ml THF) was added to the powder suspension, and the reaction mixture was stirred for 3 hrs at room temperature. The powder was then collected by centrifugation and subsequently washed to remove excess

phosphonic acid. The washing procedure consisted of dispersing the powder in 80 ml methanol containing 0.65 ml 0.05M NaOH/methanol solution and shaking this suspension for 6 min. The particles were then collected by centrifugation and the washing procedure was performed again. The powder was then washed a third time in a similar way but with a solution of 60 ml methanol, 20 ml deionized water, and 0.3 ml 0.05 M aqueous NaOH. The powder was subsequently dried *in vacuo* to give coated particles of **1**.

Reaction of 1 with *p*-nitrophenyl chloroformate. Phosphonate-coated **1** (1 g) was put into a 100 ml round-bottom flask equipped with an argon inlet and stir bar. Dry THF (60 ml) was added, and the suspension was stirred under argon for 5 min. *p*-Nitrophenyl chloroformate (80 mg) and diisopropylethylamine (0.75 ml) were added, and the reaction was stirred for 15 hrs under argon. The powder was then recovered by centrifugation and was subsequently washed twice (sonication for 10 min in 80 ml dry acetonitrile) to give **2**.

Reaction of 2 with tri(ethylene glycol) monoamine. *p*-Nitrophenyl carbonate-derivatized **2** was added to a 100 ml round-bottom flask equipped with an argon inlet and stir bar. Dry THF (60 ml) was added and the suspension was stirred under argon for 5 min. A solution of tri(ethylene glycol) monoamine (35 mg) in dry THF (5 ml) was added along with diisopropylethylamine (0.75 ml), and the reaction was stirred under argon for 20 hrs. The powder was then collected by centrifugation. Excess reagents were removed by dispersing the powder in 80 ml methanol containing 0.65 ml of a 0.05 M NaOH/methanol solution and manually shaking this suspension for 6 min. The powder was recovered by centrifugation. This washing procedure was performed twice to give **3**.

Reaction of 3 with *p*-nitrophenyl chloroformate. The reaction of **3** with *p*-nitrophenyl chloroformate was done as for the preparation of **2**. The product was then washed to give **4**.

Reaction of 4 with GRGDSPK peptide. Powder of **4** was pressed into disks (d = 12 mm, h = 1.5 mm) using a standard IR pellet press. The disks were placed in a solution of GRGDSPK (20 mg in 40 ml deionized water, adjusted to pH 8 – 8.5 with aqueous NaOH) and allowed to react for 24 hrs. The disks were then removed and rinsed by immersion for 12 min in aqueous NaOH (pH 8.5) followed by immersion in deionized water, then methanol, each for 20 sec. Each disk was washed five times using this procedure to give peptide terminated **6a**.

Reaction of 4 with sodium 5-([2-aminoethyl]amino)naphthalene-1-sulfonate (EDANS). To quantify surface bonding to the functionalized nanoparticles, green fluorescent dye sodium 5-([2-aminoethyl]amino)naphthalene-1-sulfonate (EDANS) was attached to **4**, which gives **7a** (Supporting Information Scheme 1); by cleaving the dye from the nanoparticles, surface bonding can be quantified from the amount of dye cleaved from the surface (obtained from fluorescence measurements of the cleaved dye solution), particle mass and surface area[2] (see Supporting Information Figure 1 and Calculation). A solution of EDANS (35 mg in 45 ml deionized water and 3 ml acetonitrile) was adjusted to pH 8.5, and **4** (350 mg) was added. The reaction mixture was stirred at room temperature for 24 hrs and was subsequently centrifuged to collect the powder. The product was washed until no significant fluorescence was visible in the supernatant under UV illumination. The washing procedure consisted of suspending the powder in a solution of 0.15 ml 0.05M NaOH/methanol in 20 ml methanol and manually shaking for 6 min. The powder was recovered by centrifugation to give **7a** (Supporting Information Scheme 1). A

control sample was prepared in a similar way by substituting powder **3** for **4** to give **7b** (not shown).

Surface loading of EDANS dye. Product **7a** or control **7b** (20 mg) was put into a 50 ml centrifuge tube. Aqueous NaOH (10.0 ml, pH 7.5) was added, and the samples were placed on a shaker for 24 hrs after which time the samples were centrifuged and fluorescence readings of the supernatant were measured. The supernatant was removed, and fresh pH 7.5 solution was added. Fluorescence measurements and supernatant replacement were repeated every 24 hrs until no significant fluorescence was detected. The supernatant was then removed, and aqueous NaOH (10.0 ml, 0.1 M) was added to cleave the remaining covalently-bound dye from the particles. The samples were shaken for 24 hrs after which time they were centrifuged and the fluorescence intensity of the supernatant was measured. The supernatant was removed, fresh aqueous NaOH (10.0 ml, 0.1 M) was added, and the samples were shaken for an additional 24 hrs. The samples were then centrifuged and fluorescence intensity measurements of the supernatant were taken. To obtain the EDANS concentration in the supernatant, a linear plot of fluorescence intensity versus concentration was constructed from a set of EDANS calibration standards (130 nM – 7 mM in 0.1 M NaOH) (see Supporting Information Figure 1) and the concentration of cleaved EDANS dye was calculated using this linear fit (See Supporting Information Calculation). The concentration of cleaved EDANS along with the volume of supernatant, the amount of powder used for each experiment, and the measured specific surface area of the powder were used to calculate the amount of EDANS dye covalently bound to the yttrium oxide. In this way, the surface loading of dye on **7a** was calculated to be 0.25 ± 0.01 nmol/cm^2, which is similar to

peptide loadings on PUL monolayers on TiO_2/Ti;[2, 3] this loading is assumed to be comparable for attachment of biomolecules of similar "footprint" to that of EDANS.

Supporting Information Scheme 1. Fluorescence-based procedure for determination of surface loading.

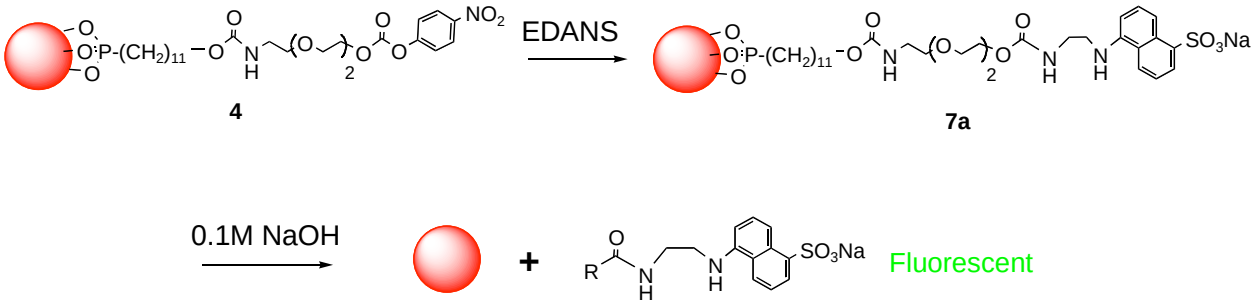

Supporting Information Figure 1. EDANS calibration curve used for surface loading calculation of **7a**.

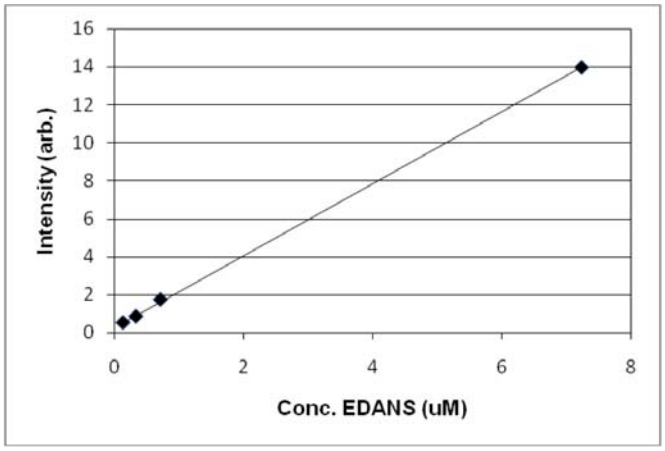

Surface loading calculation

Surface loading = $(nmol_{EDANS,\ total})/(\ SA\ (cm^2)\ )$ (Eq. 1)

$nmol_{EDANS,\ total}$

$intensity_{supernatant} = (m * concentration_{EDANS}) + b$ (Eq. 2)

(from linear fit to calibration curve)

$conc._{sample} = (int_{sample} – b)/m$ (Eq. 3)

$conc._{sample}$ (mM) * $vol._{supernatant}$ (L) = $mmol_{EDANS}$ (Eq. 4)

$mmol_{EDANS,\ day\ 1} + mmol_{EDANS,\ day\ 2} = mmol_{EDANS,\ total}$ (Eq. 5)

(day 1 – first 24 hrs cleavage, day 2 – second 24 hrs cleavage)

$mmol_{EDANS,\ total} * 10^3 = nmol_{EDANS,\ total}$ (Eq. 6)

Surface Area of powder (cm^2)

Surface Area, SA (m^2) = $mass_{sample}$ (g) * 1.2 m^2/g (Eq. 7)

(Surface area per gram measured from Y_2O_3 powder)

SA (cm^2) = SA (m^2) * 10^4 (Eq. 8)

***In vitro* adhesion study (pellet substrate).** NIH 3T3 cells were maintained in Dulbecco's Modified Eagle's Medium (DMEM) with 10% calf serum (Hyclone) and were prepared for cell adhesion experiments as previously described.[4] Cells (10^4 cells/ml in Tris buffer), pre-stained with Cell Tracker Green (30 min at 37 ^oC), were added to tissue culture wells containing peptide-modified pellets pressed from particles of **6a**, tri(ethylene glycol)-modified pellets pressed from particles of **3**, or unmodified Y_2O_3 pellets (See Supporting Information Figure 2). Cells were allowed to attach for 90 min after which time non-adherent cells were removed by several washings with Tris buffer. The cells were then fixed (15 min, 3.7% formaldehyde in PBS) and visualized using a Nikon Optiphot-2 microscope. Images were obtained using a Photometrics

Coolsnap camera, and image analysis was performed using IPLab software. Cell counting data are summarized in Supporting Information Figure 3.

Supporting Information Figure 2. Cartoon illustrating the in vitro pellet experiment.

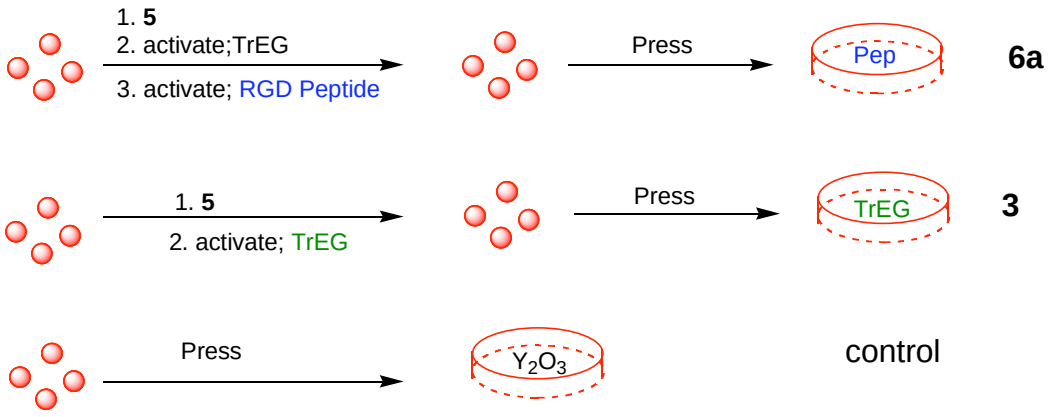

Supporting Information Figure 3. Cell adhesion count data for Y_2O_3 (left), **3** (middle), **6a** (right).

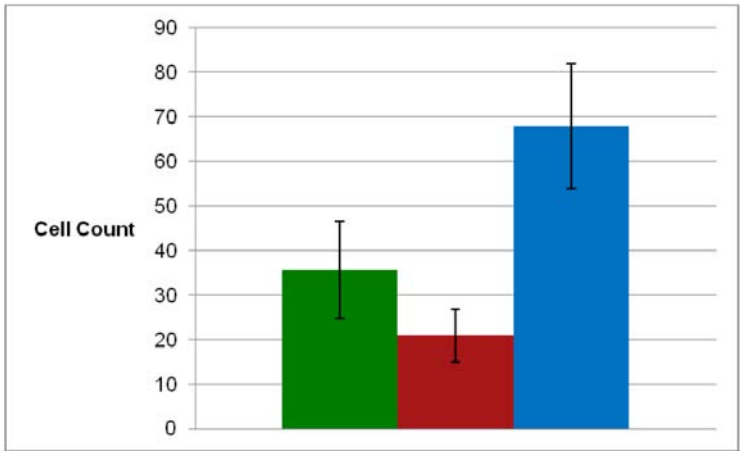

Synthesis of 5% Europium-Doped Y_2O_3 Nanoparticles (Y_2O_3:Eu^{3+}). A modification of a literature procedure was used.[5] Lanthanide salts $YCl_3 \cdot 6H_2O$ (0.364g, 1.2 mmol) and $EuCl_3 \cdot 6H_2O$ (0.023g, 0.063 mmol) were dissolved in 100 ml deionized (DI) water in a 250 ml round-bottom flask, and urea (1.44g, 24 mmol) was added. The pH was adjusted to between 5.5 and 6, and the solution was heated to 90-100 ^oC. A slight turbidity was visible, and the reaction was allowed to proceed for 90 min. The white suspension that formed was then cooled by immersing the flask in a water bath; ice was added until the flask reached room temperature. The $Y(OH)CO_3$ nanoparticles were then collected by centrifugation (~5000 x g, 40 min) and washed four times with 80 ml DI water followed by centrifugation. The particles were air-dried overnight and then dried for 3 hrs at 110 ^oC under vacuum (~0.5 torr). Annealing at 785 ^oC for 1 hr in air (~2-3 hrs to reach 785 ^oC and <1 hr cool down) converted the nanoparticles from the yttrium hydroxycarbonate precursor to yttrium oxide. X-ray powder diffraction patterns conformed to published data as did low resolution luminescence spectra that were taken to confirm dopant presence;[5] TEM images indicated particle sizes between 80 and 120 nm (Supporting Information Figure 4).[18]

Supporting Information Figure 4. TEM image of Y_2O_3:Eu^{3+}nanoparticle show diameters of ca. 100 nm.

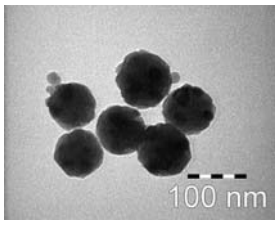

Supporting Information Figure 5. Excitation (left, excitation wavelengths scanned with emission monitored at 612 nm) and emission spectra (right, emission wavelengths scanned with sample excitation at 460 nm) for Y_2O_3:Eu3+ nanoparticles.

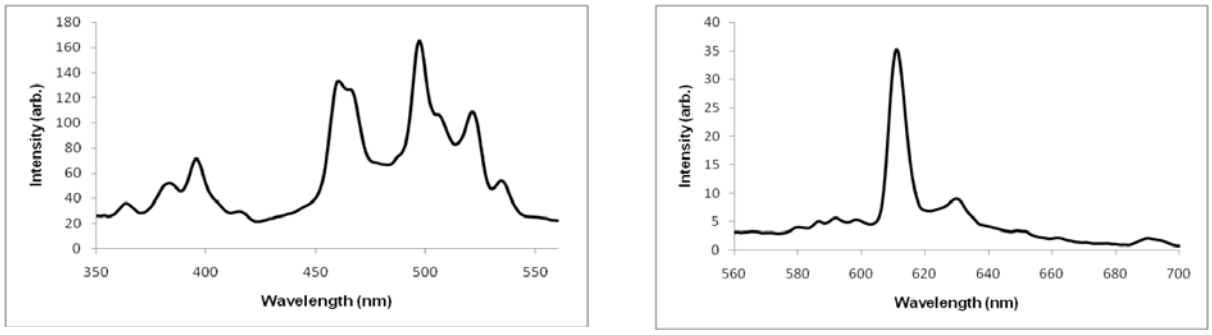

Supporting Information Figure 6. IR spectra of **1** (top) and **2** (bottom), showing *p*-nitrophenyl carbonate $\nu_{C=O}$ = 1768 cm^{-1}.

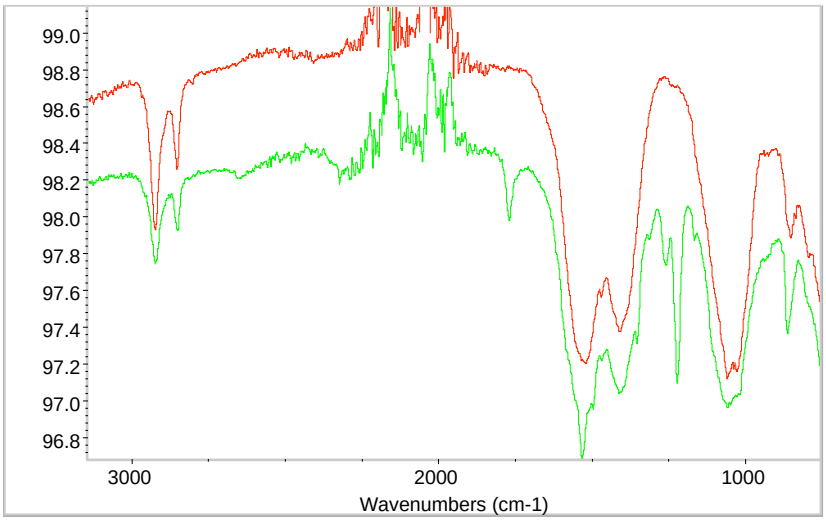

Supporting Information Figure 7. IR spectra of **3** (top) with carbamate $\nu_{C=O}$ = 1700 cm^{-1} and **4** (bottom) with both carbamate and carbonate bands ($\nu_{C=O}$ = 1768 cm^{-1} and 1700 cm^{-1}).

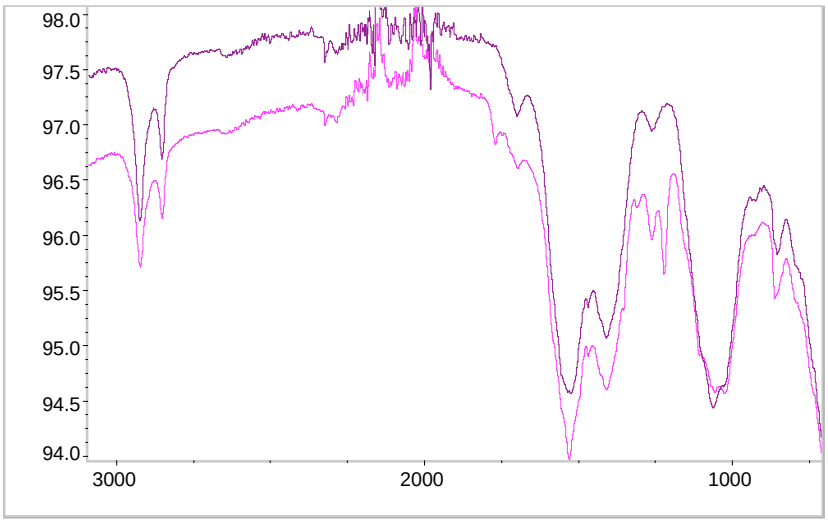

Supporting Information Figure 8. Nanoparticles of **6a** and **6b** on a confluent layer of cells. In vitro labeling experiment with (A) RGD-terminated **6a** and (B) control RAD-conjugated **6b**. Cells are stained green and nanoparticles emit red luminescence.

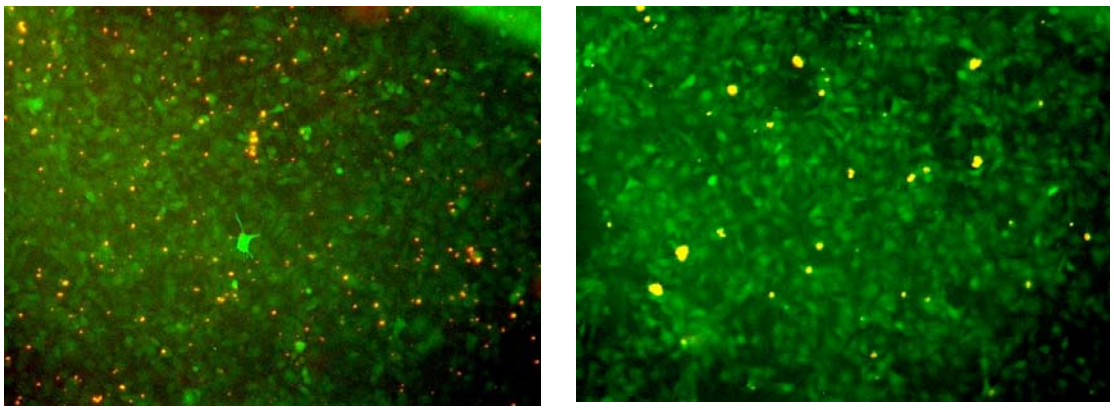

References for Supporting Materials

1. Traina, C. A.; Schwartz, J., Surface Modification of Y_2O_3 Nanoparticles. *Langmuir* **2007,** *23*, 9158-9161.
2. Silverman, B. M.; Wieghaus, K. A.; Schwartz, J., Comparative Stabilities of Siloxane vs. Phosphonate Monolayers on a Key Titanium Alloy. *Langmuir* **2005,** *21*, 225-228.
3. Gawalt, E. S.; Avaltroni, M. J.; Danahy, M. P.; Silverman, B. M.; Hanson, E. L.; Midwood, K. S.; Schwarzbauer, J. E.; Schwartz, J., Bonding Organics to Ti Alloys: Facilitating Human Osteoblast Attachment and Spreading on Surgical Implant Materials. *Langmuir* **2003,** *19*, 200-204 (correction, *Langmuir* **2003**, *19*, 7147).
4. Midwood, K.; Schwarzbauer, J., Tenascin-C moldulates matrix contraction via focal adhesion kinase- and Rho-mediated signaling pathways. *Mol. Biol. Cell* **2002,** *13*, 3601-3613.
5. Kaczmarek, W. A.; Riesen, H., Structural and Morphological Properties of RE^{3+} Doped Sesquioxide Y_2O_3 Spherical Nanoparticles. *J. Mater. Sci.* **2006,** *41*, 8320-8328.

Bioconjugate Chemistry 20th Anniversary

Subscriber access provided by SHEMYAKIN-OVCHINNIKOV INST

Article

Polyaspartamide-Based Oligo-ethylenimine Brushes with High Buffer Capacity and Low Cytotoxicity for Highly Efficient Gene Delivery

Min Zhang, Min Liu, Ya-Nan Xue, Shi-Wen Huang, and Ren-Xi Zhuo

Bioconjugate Chem., **2009**, 20 (3), 440-446• DOI: 10.1021/bc800214u • Publication Date (Web): 10 February 2009

Downloaded from http://pubs.acs.org on April 8, 2009

More About This Article

Additional resources and features associated with this article are available within the HTML version:

- Supporting Information
- Access to high resolution figures
- Links to articles and content related to this article
- Copyright permission to reproduce figures and/or text from this article

View the Full Text HTML

ACS Publications
High quality. High impact.

Bioconjugate Chemistry is published by the American Chemical Society. 1155 Sixteenth Street N.W., Washington, DC 20036

ARTICLES

Polyaspartamide-Based Oligo-ethylenimine Brushes with High Buffer Capacity and Low Cytotoxicity for Highly Efficient Gene Delivery

Min Zhang, Min Liu, Ya-Nan Xue, Shi-Wen Huang,* and Ren-Xi Zhuo*

Key Laboratory of Biomedical Polymers, Ministry of Education, Department of Chemistry, Wuhan University, Wuhan 430072, P. R. China. Received May 23, 2008; Revised Manuscript Received December 11, 2008

Polyaspartamide-based oligo-ethylenimine brushes (PASP-EDA, PASP-TEPA, PASP-PEHA, and PASP-PEI 423) were synthesized from polysuccinimide (PSI) via a ring-opening reaction with N-Boc protected ethylenediamine, tetraethylenepentamine, pentaethylenehexamine, and linear polyethylenimine (Mn 423), respectively. PASP-TEPA, PASP-PEHA, and PASP-PEI 423 possess high buffer capacity between pH 5 and pH 7, which is comparable to that of branched PEI 25000. The cytotoxicity assay indicated that they all are less toxic than PEI 25000. At an *N*/*P* ratio of above 2, all of the four synthetic polycation brushes can condense plasmid DNA to form small sized (160−400nm) polyelectrolyte complexes with positive surface charge. The transfection of HEK 293 cells with oligo-ethylenimine brush/pRE Luc polyplexes indicated that the transfection efficiencies increased with increasing the length of oligo-ethylenimine side chains. The luciferase expression with PASP-PEHA and PASP-PEI 423 were as high as or even a little higher than that of PEI 25000. The results demonstrate that polyaspartamide-based oligo-ethylenimine brushes are a very promising class of novel polycations for highly efficient and less toxic gene delivery.

INTRODUCTION

In the past decade, cationic polymers, as nonviral gene delivery vectors, have received more and more attention and have been widely used to deliver foreign DNA into cells and achieve efficient gene expression in cells (*1*−*3*). A variety of natural and synthetic polycations, such as poly(L-lysine) (PLL) (*4, 5*), poly(ethylenimine) (PEI) (*6*−*8*), polyamidoamine dendrimer (*9*−*13*), cationic polyester (*14*−*18*), cationic polyphosphoester and polyphosphoramidate (*19*−*23*), chitosan (*24*−*26*), etc., have been used as gene carriers. Among the current polymeric gene delivery vectors, PEI is undoubtedly the most successful one and has become the gold standard for designing new polymeric gene carriers. PEI/DNA complexes often show high efficiencies for transfecting a large number of cell lines. It is widely accepted that the good transfection property of PEI is due to its high buffer capacity over a broad pH range, which is called proton sponge theory (*27, 28*). Further protonation of PEI in PEI/DNA complexes localized in the endosomal compartments leads to transfer protons and chloride counterions into the endosomes, which result in destabilization of endosomes and release of PEI/DNA complexes into the cytoplasm. Similarly, the proton sponge mechanism is also applicable for other polycations with a pK_a at or below physiological pH, such as polyamidoamine (*29*,*30*), imidazole-containing polylysine (*31*−*33*), etc.

Both branched PEI and linear PEI have been tested for in vitro and in vivo gene delivery. The transfection efficiencies of branched PEI as gene carriers are dependent on the polymer structures, such as molecular weight and degree of branching (*34*). It was found that high molecular weight branched PEI up to 800 K shows superior ability to form compact and stable PEI/DNA complexes and higher transfection efficiency, compared to lower molecular weight PEI. However, high molecular weight branched PEI is more toxic than lower molecular weight branched PEI. Linear PEI-based gene carriers have also been investigated in recent years. In comparison to branched PEI, linear PEI shows different characteristics, such as DNA compaction, nuclear uptake, transfection efficiency, and toxicity. Linear PEI is often more effective and less toxic than branched PEI. It is more attractive that lower molecular weight linear PEI is almost nontoxic to cells. It is possible to combine the low cytotoxicity of low molecular weight linear PEI and high transfection by grafting low molecular weight linear PEI into a suitable polymer. In the previous work, Zhong et al. reported ABA triblock copolymers PEI-PEG-PEI composed of PEG 3400 and relatively low molecular weight linear PEI (2100 and 4000) as gene carriers (*35*). The optimized transfection efficiency of PEI-PEG-PEI (PEI 4000) is higher than linear PEI 25K. Low molecular weight linear PEI-grafted cyclodextrin, polyaspartamide, chitosan, and dextrane have also been used as highly efficient and less toxic gene carriers (*36*−*43*). However, although many polyaspartamide-derived polycations have been applied to in vitro gene delivery, the transfection efficiencies are often relatively low (*44*−*47*). We here report oligo-ethylenimine brushes, a new kind of polycation, as polymer gene delivery vectors. Oligo-ethylenimine brushes were synthesized from polysuccinimide (PSI) reacting with excess of oligo(ethylenimine). The goal of this work is to develop new types of highly efficient polycation brush gene delivery vectors by the introduction of low toxicity of lower molecular weight PEI side chains into polyaspartamide. The effects of the length of oligo-

* To whom correspondence should be addressed. Fax: 86-27-68754509. E-mail: swhuang@public.wh.hb.cn (S.-W.H.); pibmp@public.wh.hb.cn (R.-X.Z.).

10.1021/bc800214u CCC: $40.75 © 2009 American Chemical Society
Published on Web 02/10/2009

ethylenimine side chains on the transfection efficiencies have also been investigated.

EXPERIMENTAL PROCEDURES

Materials and Methods. Tetraethylenepentamine (TEPA), pentaethylenehexamine (PEHA), linear polyethylenimine (Mn 423) (PEI 423), and branched PEI 25000 (M_w = 25000) were purchased from Aldrich-Sigma Chemical Co. MTT (3-{4,5-dimethylthiazol-2-yl}-2,5-diphenyltetrazolium bromide) was purchased from BDH Laboratory Supplies. Dulbecco's modified Eagle's medium (DMEM) and L-glutamine were purchased from Gibco BRL. Giga plasmid purification kit was purchased from Qiagen in China. Fetal bovine serum (FBS) was the product of HyClone. Other reagents and solvents were of analytical grade, obtained from domestic suppliers and used directly. Poly-L-succinimide (PSI) (M_w = 3.41 × 10^4, M_w/M_n = 1.32) was synthesized by thermal polycondensation of L-aspartic acid according to the previously reported method (*48*). *N*-*t*-Butoxycarbonyl-ethylenediamine (N-Boc-EDA) was synthesized according to the literature method (*49*). The luciferase encoding plasmid pRE Luc is an 11.9 kb pcDNA driven by a Rous sarcoma virus promoter inserted into an Invitrogen (Sandiego, CA) pREP7 vector. The plasmid was amplified in *Escherichia coli* and isolated and purified using Qiagen endotoxin free plasmid Gigaprep kits according to the supplier's protocol. The quantity and quality of plasmid DNA was analyzed by spectrophotometric analysis at 260 and 280 nm and by electrophoresis in 0.8% agarose gel. Purified plasmid DNA was diluted in TE buffer and stored at −20 °C.

FTIR spectra were measured on a Perkin-Elmer Spectrum one spectrometer. ^{1}HNMR spectra were recorded on a Mercury VX-300 MHz instrument. Gel permeation chromatography (GPC) measurements were carried out by using a Waters-2690D HPLC equipped with an Ultrahydrogel 120, 250, and 2000 column. Samples were detected with a Wyatt multiangle light-scattering detector and a Waters 2100 differential refractive index detector. PBS (0.1 mol L^{-1}, pH 7.4) was used as the mobile phase at a flow rate of 0.8 mL min^{-1}. The column temperature was 25 °C.

Synthesis of PASP-EDA, PASP-TEPA, PASP-PEHA, and PASP-PEI 423. *PASP-EDA.* A solution of 0.485 g of poly-L-succinimide (PSI) in 10 mL of DMF was added dropwise to a solution of 1.6 g of N-Boc-ethylenediamine (N-Boc-EDA) in 5 mL of DMF at 0 °C. The reaction mixture was stirred for 2 h at 0 °C and stirred for a further 24 h at room temperature, and then poured into 150 mL of ether. The formed precipitate was filtered, dried, and added into 60 mL of 2 mol L^{-1} hydrochloride to remove the protective N-Boc group of polyaspartamide derivative. The suspension mixture was stirred for 4 h at room temperature until the solid gradually dissolved in dilute hydrochloride, and then alkalized with 2 mol L^{-1} sodium hydroxide to pH 12. Next, the solution was dialyzed against distilled water for two days and lyophilized to yield 0.43 g of slightly yellow solid. FT-IR (KBr, cm^{-1}): 3431, 3068, 2923, 2819, 1660, 1533, 1384, 1171 cm^{-1}. ^{1}H NMR (D_2O, ppm) δ: 2.5−2.7 (2H, m, CH_2); 3.0 (2H, m, CH_2); 3.3 (2H, m, CH_2); 4.7 (1H, m, CH). M_w = 1.78 × 10^4. M_w/M_n = 1.40.

PASP-TEPA, PASP-PEHA, and PASP-PEI 423 were synthesized according to the general procedure described below. A solution of 0.097 g of poly-L-succinimide (PSI) in 4 mL of DMF was separately added dropwise to a solution of 10-fold molar excess oligoethylenimine (for TEPA, 1.89 g; PEHA, 2.32 g; and PEI423, 4.23 g) in 5 mL of DMF at 0 °C. The reaction mixture was stirred for 2 h at 0 °C and stirred for a further 24 h at room temperature, then dialyzed against distilled water for two days, and lyophilized to yield PASP-TEPA, PASP-PEHA, and PASP-PEI 423.

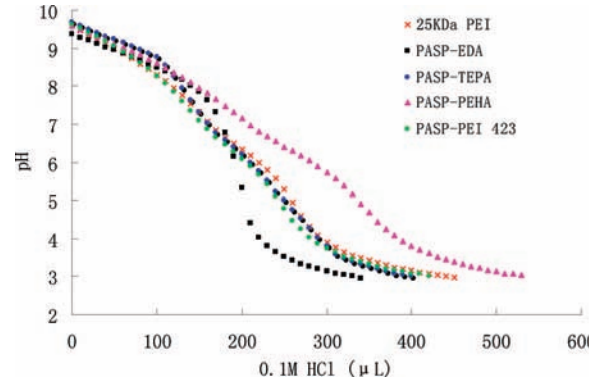

Figure 1. Titration curve of polyaspartamide-based oligo-ethylenimine brushes. A solution of polymer (5 mM total amine) in 0.15 mol L^{-1} NaCl was titrated with 0.1 mol L^{-1} HCl. Branched PEI (M_w 25000) was used as a control.

PASP-TEPA. 68.7 mg. FT-IR (KBr, cm^{-1}): 3436, 2926, 2853, 1643, 1547, 1398, 1128. ^{1}H NMR (D_2O, ppm) δ: 2.4−2.8 (CH_2NH); 2.9 (CH_2CO); 3.2 (CH_2); 4.7 (CH). M_w = 0.98 × 10^4, M_w/M_n = 1.47.

PASP-PEHA. 68.5 mg. FT-IR (KBr, cm^{-1}): 3401, 3081, 2947, 2844, 1649, 1551, 1385, 1123 cm^{-1}. ^{1}H NMR (D_2O, ppm) δ: 2.3−2.8 (CH_2); 2.9 (CH_2); 3.2 (CH_2); 4.7 (CH). M_w = 1.09 × 10^4, M_w/M_n = 1.43.

PASP-PEI 423. 125.9 mg. FT-IR (KBr, cm^{-1}): 3434, 2956, 2851, 1650, 1554, 1384, 1122 cm^{-1}. ^{1}H NMR (D_2O, ppm) δ: 2.3−2.8 (CH_2); 2.9 (CH_2); 3.2 (CH_2); 4.7 (CH). M_w = 1.45 × 10^4, M_w/M_n = 1.22.

Acid−Base Titration. The buffer capacity of synthetic polymers and branched PEI 25000 was determined by acid−base titration. Each polymer was dissolved in 10 mL of 0.15 mol L^{-1} sodium chloride aqueous solution to give a final concentration of total amino groups in the polymer of 5 mmol L^{-1}. Each polymer solution was separately titrated with 0.1 mol L^{-1} HCl at 25 °C. The pH values were recorded with a Microprocessor pH Meter.

In Vitro Cytotoxicity. PASP-EDA, PASP-TEPA, PASP-PEHA, PASP-PEI 423, and branched PEI 25000 were separately dissolved in Dulbecco's modified Eagle's medium (DMEM) supplemented with 4 mmol L^{-1} glutamine, 10% FBS, penicillin, and streptomycin (100U/mL), and sterile-filtered. The solution was diluted with complete DMEM to different concentrations ranging from 3.7 μg mL^{-1} to 4000 μg mL^{-1}. HEK293 cells were seeded into a 96-well plate at a density of 5000 cells/well in 50 μL of complete DMEM. After the cells were cultured at 37 °C for 24 h in an atmosphere containing 5% CO_2, 50 μL of polymer solutions at different concentrations were separately added into the wells. Cells treated with polymers were cultured for a further 24 h at 37 °C, and then MTT solution (5 mg mL^{-1}, 20 μL) in PBS (0.1 mol L^{-1}, pH 7.4) was added into each well except that PBS (20 μL) was added into the background wells, and then incubated at 37 °C for 4 h. After the removal of the medium in each well, 150 μL of DMSO was added to each well to dissolve the formed formazan blue crystal inside the cells. After shaking for 10 min, the absorbance of the solution was measured using a microplate reader (Bio-Rad 550) at 570 nm. The percent relative viability in reference to control wells containing complete DMEM without the added polymer was calculated by the following equation (A = absorbance at 570 nm; A_0 is the absorbance of the solution containing cells and complete DMEM without MTT and polymer): relative cell viability (%) = 100 × $(A_{test} - A_0)/(A_{control} - A_0)$.

Preparation of Polycation/Plasmid DNA Complexes. Polycation/ pRE Luc complexes at various *N*/*P* ratios were separately prepared by rapidly adding 50 μL of polycation solution in 150

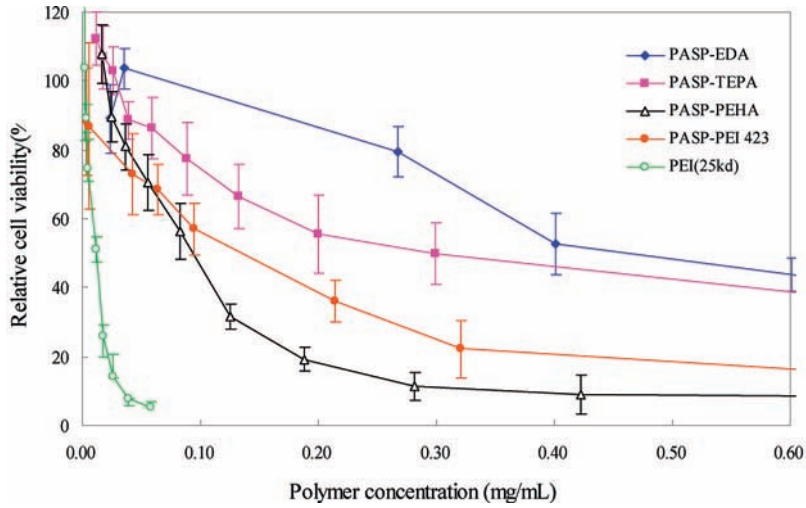

Figure 2. In vitro cytotoxicity of polyaspartamide-based oligo-ethylenimine brushes in HEK 293 cells ($n = 4$).

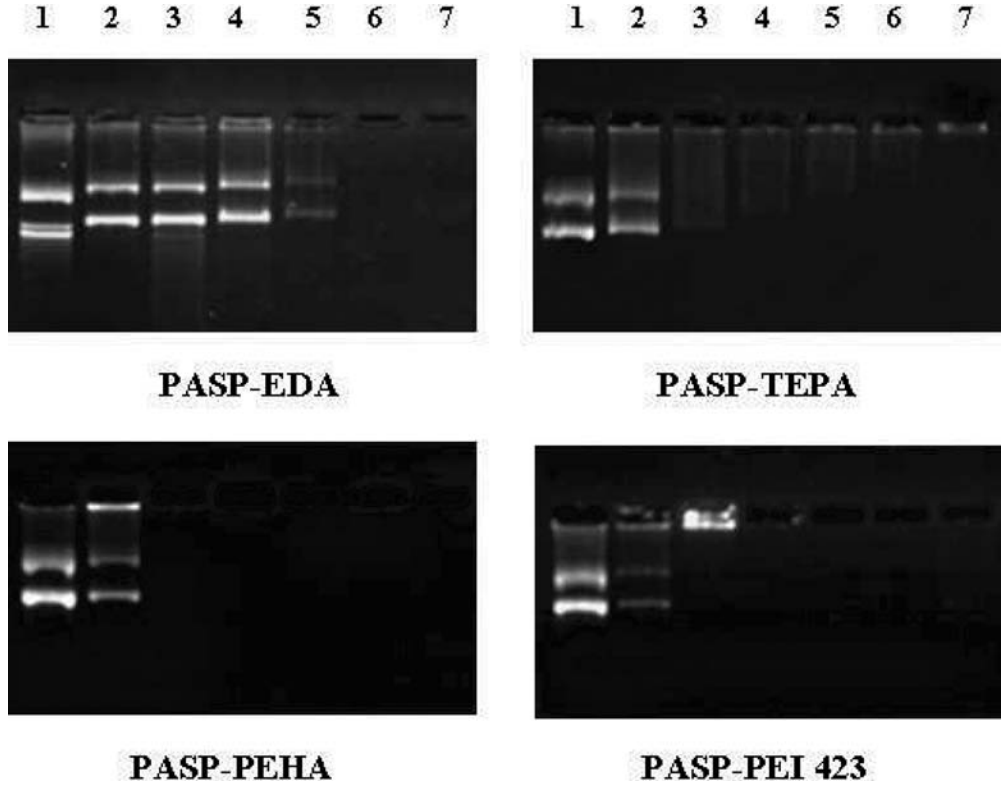

Figure 3. Agarose gel electrophoresis images of complexes formed from polyaspartamide-based oligo-ethylenimine brushes and plasmid DNA. Lane 1, naked DNA; lane 2−7, *N*/*P* ratios of 0.5/1, 1/1, 2/1, 5/1, 10/1, and 20/1, respectively.

mmol L^{-1} sodium chloride at calculated concentration to an equal volume of 150 mmol L^{-1} sodium chloride containing 1 μg of pRE Luc with gentle vortexing and allowed to incubate at room temperature for half an hour.

Agarose Gel Electrophoresis. Polycation/pRE Luc complexes at various *N*/*P* ratios, ranging from 0.5:1 up to 20:1 were separately electrophoresed on 0.8% (W/V) agarose gel containing of 0.1% gel red (V/V) for 80 min at 80 V. Then the gel was illuminated on a UV illuminator to show the mobility of the DNA. Naked DNA was used as reference.

Particle Size and Zeta Potential Measurement. The particle size and zeta potential of the freshly prepared polycation/pRE Luc complexes were measured using a Zetasizer (Nano ZS, Malvern Instruments Ltd., U.K.). The complexes were prepared as described above and directly used without further filtration before measurement.

In Vitro Transfection and Luciferase Assay. HEK 293 cells were seeded into a 24-well plate at a density of 5×10^4 cells/well and incubated in 1 mL of complete DMEM for 24 h prior to transfection. The medium was removed and washed gently with PBS (pH 7.4) when the cells were cultured to 40−50% confluency in the 24-well plate. Serum-free DMEM (1 mL) and 100 μL of 1 μg of DNA-containing polycation/pRE Luc complexes in saline were added into each well. After 4 h of incubation at 37 °C, the serum-free DMEM was replaced by 1 mL of complete DMEM. After 48 h of incubation at 37 °C, the medium was removed and washed with PBS7.4. Then, the cells were treated with 200 μL of reporter lysis buffer (Promega). The lysate was subjected to two cycles of freezing and thawing, and then centrifuged at 10000 rpm for 3 min. Ten microliters of supernatant was mixed with 100 μL of luciferase assay substrate (Promega). The light emission was measured using a

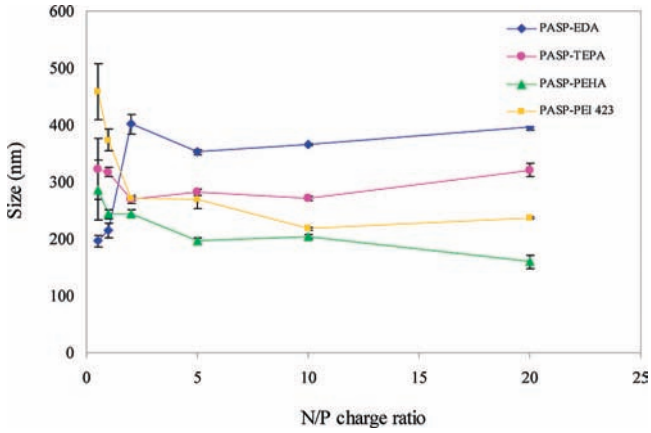

Figure 4. Average sizes of polyaspartamide-based oligo-ethylenimine brushes/DNA complexes prepared at *N*/*P* ratios ranging from 0.5 to 20 in 0.15 M NaCl.

Lumat 9507 luminometer (Berthold, Germany) for 10 s. The relative light units (RLU/mg protein) were normalized against the total protein concentration in the cell extracts, which was determined using a BCA assay kit (Pierce). All of the transfection tests were carried out in duplicate.

RESULTS AND DISCUSSION

Synthesis and Characterization of Cationic Polymer Brushes. Typically, cationic polyaspartamide derivatives (PASP-TEPA, PASP-PEHA, and PASP-PEI 423) were synthesized from poly-L-succinimide (PSI) by direct ring-opening reaction with oligo-ethlyenimine. However, only a small amount of low-molecular-weight PASP-EDA was obtained by direct ring-opening of PSI with ethlyenediamine. We used a two-step strategy to successfully synthesize PASP-EDA. First, PSI reacted with *N*-*t*-butyloxycarbonyl-ethlyenediamine, and then N-Boc was deprotected in diluted hydrochloride solution. The synthesis of cationic polyaspartamide derivatives is shown in Scheme 1. These cationic polyaspartamide derivatives, we named them oligo-PEI brushes, have polyaspartamide main chains and pendant aminoethyl or oligo-ethylenimine.

The reaction temperature should be strictly controlled at 0 °C for the first 4 h to avoid cross-linking of polyaspartamide. Because there are several amino groups in tetraethylenepentamine, pentaethylenehexamine, and linear PEI 423, the reaction would be very complicated. Either primary amines or secondary amines in polyamine could attract the ring of PSI. The lower temperature was helpful for yielding the polyamide with well-defined structures. The four polyaspartamide deravatives were purified by dialysis against distilled water (molecular weight cut off 3500) and lyophilization. The substituted degrees of PASP-EDA, PASP-TEPA, PASP-PEHA, and PASP-PEI 423, calculated by ^{1}HNMR integral, were 100%, 62%, 56%, and 35%, respectively. The results indicated that the substituted degrees of pendant groups decreased with increasing lengths of oligo-ethylenimine. The partial grafting of polyaspartamide may have resulted from steric hindrance and/or electrostatic repulsion. The four polyaspartamide-based oligo-PEI brushes were characterized with FT-IR and ^{1}HNMR. Polymers were analyzed by size exclusion chromatography combined with multiangle laser light scattering, using PBS (0.1 mol L^{-1}, pH 7.4) as eluent. The weight average molecular weights (M_w) of PASP-EDA, PASP-TEPA, PASP-PEHA, and PASP-PEI 423 were 1.78×10^4, 0.98×10^4, 1.09×10^4, and 1.45×10^4, respectively. We can find that the polymerization degrees of PASP-EDA, PASP-TEPA, PASP-PEHA, and PASP-PEI 423 are lower than that of PSI, which means that the cleavage of the main chain of PSI occurred in the process of ring-opening of PSI with amine. The four polymers are all soluble in water and various buffers at pH 3−10 because of the introduction of hydrophilic amino groups into the polymer side chains.

Buffer Capacity of Cationic Polymers. It has been widely accepted that high buffer capacity of PEI facilitates osmotic swelling and rupture of endosomes by proton sponge effect, which results in the release of polycation/DNA complexes into the cytoplasm and improves the transfection efficiency. We

Scheme 1. Synthesis of Polyaspartamide-Based Oligo-ethylenimine Brushes

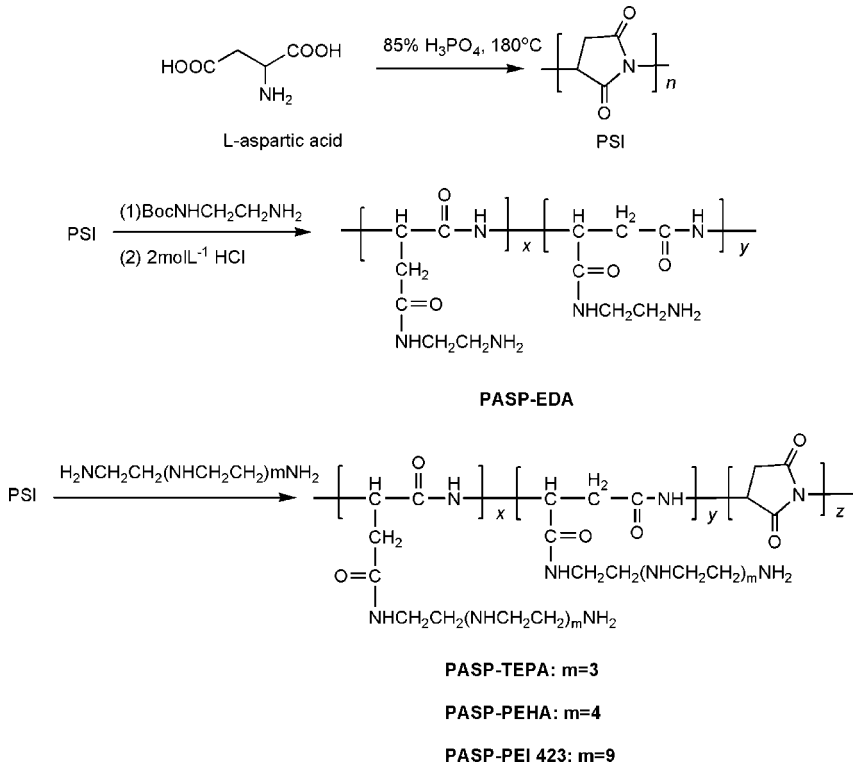

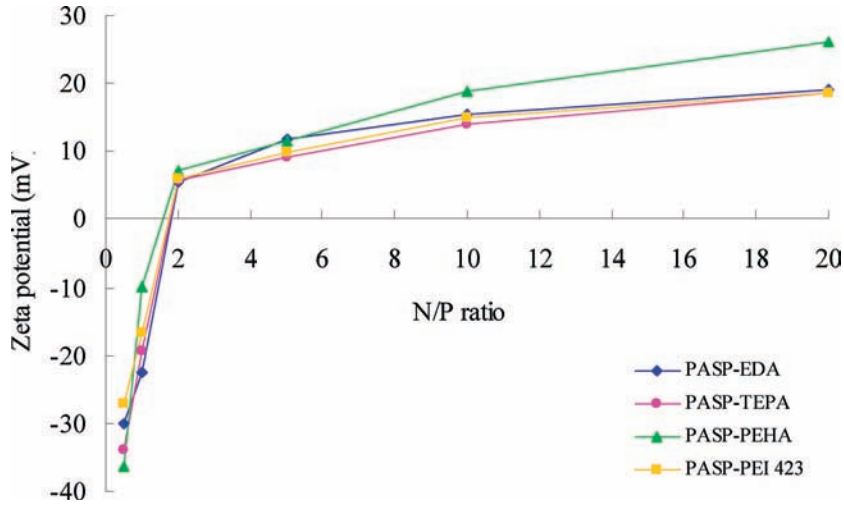

Figure 5. Zeta potential of polyaspartamide-based oligo-ethylenimine brushes/DNA complexes prepared at *N*/*P* ratios ranging from 0.5 to 20 in 0.15 M NaCl.

investigated the buffer capacity of the polycations by acid−base titration of the polymer solution (total amines of 5 mmol L^{-1}) in 0.15 M aqueous sodium chloride with 0.1 mol L^{-1} hydrochloride. Branched PEI (M_w = 25KDa) was also titrated under the same conditions as a control. As shown in Figure 1, the data indicated that there were no significant differences in the acid−base titration curves of the tested 5 polymers at pH ranging from 10 to 7, which means that they all have the same buffer capacity at these pH values. However, we found that the acid−base titration curves of PASP-TEPA and PASP-PEI 423 were still almost the same as that of PEI 25000 at pH from 7 to 5, which implied that the buffer capacities of PASP-TEPA and PASP-PEI 423 were equal to that of PEI 25000 at pH ranging from 7 to5. Meanwhile, PASP-PEHA exhibited relatively higher buffer capacity at pH ranging from 7 to 5 than that of PEI 25000. In contrast, PASP-EDA has very low buffer capacity at pH ranging from 7 to 5 in comparison to that of PASP-TEPA, PASP-PEHA, PASP-PEI 423, and PEI 25000.

Cytotoxicity of Cationic Polymers. The biocompatibility is an important factor for evaluating the application of polycations in nonviral gene delivery. The significant disadvantage of high-molecular-weight PEI as a gene carrier is that PEI shows high cytotoxicity to many types of cells. We used the MTT assay to measure the cytotoxicity of synthesized polycations to HEK 293 cells. Branched PEI (M_w = 25000) was used as a reference. The results, shown in Figure 2, indicated that PEI 25000 had high cytotoxicity to HEK 293 cells (LC50 ~10 μg mL^{-1}), which was in agreement with the results we observed previously (*12, 50*). Although the cell viability also decreased with increasing concentrations of the synthesized polycations in this work, the LC50 of PASP-EDA, PASP-TEPA, PASP-PEHA, and PASP-PEI 423, in the range of 92−452 mg mL^{-1}, are generally 1 order of magnitude higher than that of PEI 25000. The results indicated that PASP-EDA, PASP-TEPA, PASP-PEHA, and PASP-PEI 423 were less toxic than PEI 25000, which confirmed our hypothesis that the graft of oligo-PEI to polyaspartamide partially maintains the low toxicity characteristic of oligo-PEI.

Agarose Gel Electrophoresis. The condensation of DNA into nanosized polyelectrolyte complexes is a prerequisite for polycations as nonviral gene carriers. The binding ability of the polycations to plasmid DNA was investigated by agarose gel electrophoresis. The complexes of polycation and pRE Luc at various amino groups of polycation/phosphate of DNA (*N*/*P* ratio), ranging from 0.5/1, 1/1, 2/1, 5/1, 10/1, and 20/1, were separately electrophoresed in agarose gel. Naked DNA was used as a reference. The migration of naked DNA and polycation/DNA complexes in agarose gel is shown in Figure 3. In the cases of PASP-TEPA, PASP-PEHA, and PASP-PEI 423, a fraction of plasmid DNA was free to migrate in the gel at an *N*/*P* ratio of 0.5:1; however, no migration bands of plasmid DNA were observed at *N*/*P* ratios of 1:1 or above. PASP-EDA could fully retard the migration of DNA in agarose gel at an *N*/*P* ratio higher than 5:1. The results indicated that the DNA binding ability of PASP-TEPA, PASP-PEHA, and PASP-PEI 423 is stronger than that of PASP-EDA.

Particle Size and Zeta Potential of Polycation/DNA Complexes. Small size and positive surface charge of polycation/DNA polyelectrolyte complexes are important for cell uptake and efficient transfection. Dynamic light scattering (DLS) measurement results in Figure 4 showed that small sized polycation/DNA complexes with diameters less than 400 nm were obtained by mixing the polymer solution and DNA solution in 150 mmol L^{-1} of sodium chloride at *N*/*P* ratios above 5:1. The diameters of polycations/DNA complexes are dependent on the structures of polycations. At *N*/*P* ratios of above 5:1, the diameters of PASP-EDA/pRE Luc, PASP-TEPA/pRE Luc, and PASP-PEI 423/pRE Luc were around 400, 300, and 250 nm, respectively. Different from these three polycations, PASP-PEHA condensed pRE Luc to from complexes with diameters less than 200 nm. The diameters of PASP-PEHA/pRE Luc decreased with increasing *N*/*P* ratios from 5:1 to 20:1.

The zeta potential data of polycation/DNA complexes in Figure 5 showed a trend that the zeta potentials of complexes increased with increasing *N*/*P* ratios of polycation amino groups to DNA phosphates. In the case of PASP-EDA, PASP-TEPA, and PASP-PEI 423, the zeta potentials of complexes reached 20 mV when *N*/*P* ratios were 20:1. The zeta potential of PASP-PEHA /pRE Luc was 26 mV when the *N*/*P* ratio was 20:1, which was also different from that of the above three polycations.

In Vitro Transfection of HEK 293 Cells. To evaluate the potential of the synthetic polycations as gene carriers, the tranfection experiments were conducted using polycation/pRE Luc, expressing luciferase, at *N*/*P* ratios of 5:1, 10:1, and 20:1 on the HEK 293 cell line. Naked DNA was used as a negative control and branched PEI 25000 at an optimized *N*/*P* ratio of 10:1 was used as a positive control. The results were shown in Figure 6. We can find that the transfection efficiencies of polycation/DNA complexes in HEK 293 cells are greatly dependent on the structures of polymer side chains. Very low luciferase expression in HEK 293 cells transfected with PASP-EDA/pRE Luc and PASP-TEPA/pRE Luc complexes was observed at various *N*/*P* ratios. The transfection efficiencies of

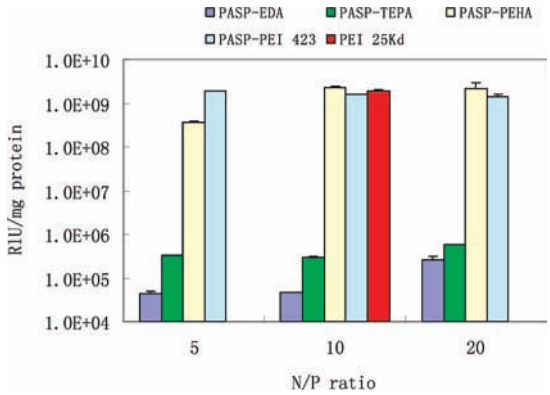

Figure 6. Transfection efficiencies of polyaspartamide-based oligo-ethylenimine brushes/pRE Luc complexes in HEK293 cells. Branched PEI (M_w 25000) was used as a control. Data represent the mean standard deviation ($n = 2$).

PASP-EDA/pRE Luc and PASP-TEPA/pRE Luc complexes in the HEK 293 cell line were almost as low as that of naked DNA. In the case of PASP-PEHA and PASP-PEI 423, the transfection results were interesting and significantly different from that of PASP-EDA and PASP-TEPA. The luciferase expression in HEK 293 cells with PASP-PEHA/pRE Luc and PASP-PEI 423/pRE Luc complexes at various *N*/*P* ratios was as high as that of branched PEI 25000 under optimized conditions (*N*/*P* ratio of 10:1), even a little higher than that of PEI. The high transfection efficiencies of PASP-PEHA/pRE Luc and PASP-PEI 423/pRE Luc in HEK 293 cells ascribe to the combination of high buffer capacity of PASP-PEHA and PASP-PEI 423 and relatively small particle size of PASP-PEHA/pRE Luc and PASP-PEI 423/pRE Luc. The results suggested that the length of oligo-ethylenimine side chains is an important factor for the high transfection efficiencies of polyaspartamide-based oligo-ethylenimine brushes, which provides useful experimental evidence for the design of novel cationic polymer gene carriers.

CONCLUSIONS

We have synthesized polyaspartamide-based oligo-ethylenimine brushes as novel promising nonviral gene delivery vectors. Their in vitro cytotoxicity was significantly lower than that of branched PEI 25000. The four synthetic polycations showed excellent DNA binding ability and condensed DNA to form small sized polyelectrolyte complexes with positive surface charge at higher *N*/*P* ratios. The transfection efficiencies increased with increasing the length of oligo-ethylenimine of polymer side chains. These results will provide some useful evidence for the design of novel highly efficient and less toxic cationic polymer gene delivery vectors.

ACKNOWLEDGMENT

This work was financially supported by National Natural Science Foundation of China (20474045, 20674058) and National Key Basic Research Program of China (2005CB623903, 2009CB930300).

LITERATURE CITED

(1) Luo, D., and Saltzman, W. M. (2000) Synthetic DNA delivery systems. *Nat. Biotechnol. 18*, 33–37.
(2) Huang, S. W., and Zhuo, R. X. (2003) Recent progress in polymer-based gene delivery vectors. *Chin. Sci. Bull. 48*, 1304–1309.
(3) Wong, S. Y., Pelet, J. M., and Putnam, D. (2007) Polymer systems for gene delivery-past, present, and future. *Prog. Polym. Sci. 32*, 799–837.
(4) Kwoh, D. Y., Coffin, C. C., Lollo, C. P., Jovenal, J., Banaszczyk, M. G., Mullen, P., Phillips, A., Amini, A., Fabrycki, J., Bartholomew, R. M., Brostoff, S. W., and Carlo, D. J. (1999) Stabilization of poly-L-lysine/DNA polyplexes for in vivo gene delivery to the liver. *Biochim. Biophys. Acta 1444*, 171–190.
(5) Mannisto, M., Vanderkerken, S., Toncheva, V., Elomaa, M., Ruponen, M., Schacht, E., and Urtti, A. (2002) Structure-activity relationships of poly(L-lysines): effects of pegylation and molecular shape on physicochemical and biological properties in gene delivery. *J. Controlled Release 83*, 169–182.
(6) Boussif, O., Lezoualc'h, F., Zanta, M. A., Mergny, M. D., Scherman, D., Demeneix, B., and Behr, J. P. (1995) A versatile vector for gene and oligonucleotide transfer into cells in culture and in vivo: polyethylenimine. *Proc. Natl. Acad. Sci. U.S.A. 92*, 7297–7301.
(7) Godbey, W. T., Wu, K. K., and Mikos, A. G. (1999) Poly(ethylenimine) and its role in gene delivery. *J. Controlled Release 60*, 149–160.
(8) Neu, M., Fischer, D., and Kissel, T. (2005) Recent advances in rational gene transfer vector design based on poly(ethylene imine) and its derivatives. *J. Gene Med. 7*, 992–1009.
(9) Haensler, J., and Szoka, F. C. (1993) Polyamidoamine cascade polymers mediate efficient transfection of cells in culture. *Bioconjugate Chem. 4*, 372–379.
(10) Kukowska-Latallo, J. F., Bielinska, A. U., Johnson, J., Spindler, R., Tomalia, D. A., and Baker, Jr, J. R. (1996) Efficient transfer of genetic material into mammalian cells using starburst polyamidoamine dendrimers. *Proc. Natl. Acad. Sci. U.S.A. 93*, 4897–4902.
(11) Huang, S. W., Fu, L. Z., Zhang, X. Q., Liu, H., Li, W. X., and Zhuo, R. X. (2003) Syntheses of polyamidoamine dendrimers starting from a hexadimensional core and application in gene transfer. *Sci. China Ser. B 46*, 271–279.
(12) Zhang, X. Q., Wang, X. L., Huang, S. W., Zhuo, R. X., Liu, Z. L., Mao, H. Q., and Leong, K. W. (2005) In vitro gene delivery using polyamidoamine dendrimers with a trimesyl core. *Biomacromolecules 6*, 341–350.
(13) Dufes, C., Uchegbu, I. F., and Schatzleinm, A. G. (2005) Dendrimers in gene delivery. *Adv. Drug Delivery Rev. 57*, 2177–2202.
(14) Lim, Y. B., Kim, C. H., Kim, K., Kim, S. W., and Park, J. S. (2000) Development of a safe gene delivery system using biodegradable polymer, poly[alpha-(4-aminobutyl)-L-glycolic acid]. *J. Am. Chem. Soc. 122*, 6524–6525.
(15) Lim, Y. B., Han, S. O., Kong, H. U., Lee, Y., Park, J. S., Jeong, B., and Kim, S. W. (2000) Biodegradable polyester, poly[alpha-(4 aminobutyl)-L-glycolic acid], as a non-toxic gene carrier. *Pharm. Res. 17*, 811–816.
(16) Putnam, D., and Langer, R. (1999) Poly(4-hydroxy-L-proline ester): Low-temperature polycondensation and plasmid DNA complexation. *Macromolecules 32*, 3658–3662.
(17) Lynn, D. M., and Langer, R. (2000) Degradable poly(beta-amino esters): Synthesis, characterization, and self-assembly with plasmid DNA. *J. Am. Chem. Soc. 122*, 10761–10768.
(18) Akinc, A., Lynn, D. M., Anderson, D. G., and Langer, R. (2003) Parallel synthesis and biophysical characterization of a degradable polymer library for gene delivery. *J. Am. Chem. Soc. 125*, 5316–5323.
(19) Wang, J., Mao, H. Q., and Leong, K. W. (2001) A novel biodegradable gene carrier based on polyphosphoester. *J. Am. Chem. Soc. 123*, 9480–9481.
(20) Wang, J., Huang, S. W., Zhang, P. C., Mao, H. Q., and Leong, K. W. (2003) Effect of side-chain structures on gene transfer efficiency of biodegradable cationic polyphosphoesters. *Int. J. Pharm. 265*, 75–84.
(21) Lu, Z. Z., Wu, J., Sun, T. M., Ji, J., Yan, L. F., and Wang, J. (2008) Biodegradable polycation and plasmid DNA multilayer film for prolonged gene delivery to mouse osteoblasts. *Biomaterials 29*, 733–741.
(22) Wang, J., Zhang, P. C., Lu, H. F., Ma, N., Wang, S., Mao, H. Q., and Leong, K. W. (2002) New polyphosphoramidate with

a spermidine side chain as a gene carrier. *J. Controlled Release 83*, 157–168.
(23) Wang, J., Gao, S. J., Zhang, P. C., Wang, S., Mao, M. Q., and Leong, K. W. (2004) Polyphosphoramidate gene carriers: effect of charge group on gene transfer efficiency. *Gene Ther. 11*, 1001–1010.
(24) Mao, H. Q., Roy, K., Troung-Le, V. L., Janes, K. A., Lin, K. Y., Wang, Y., August, J. T., and Leong, K. W. (2001) Chitosan-DNA nanoparticles as gene carriers: synthesis, characterization and transfection efficiency. *J. Controlled Release 70*, 399–421.
(25) Jiang, X., Dai, H., Leong, K. W., Goh, S. H., Mao, H. Q., and Yang, Y. Y. (2006) Chitosan-g-PEG/DNA complexes deliver gene to the rat liver via intrabiliary and intraportal infusions. *J. Gene Med. 8*, 477–487.
(26) Mao, Z. W., Ma, L., Jiang, Y., Yan, M., Gao, C. Y., and Shen, J. C. (2007) N, N, N-Trimethylchitosan chloride as a gene vector: Synthesis and application. *Macromol. Biosci. 7*, 855–863.
(27) Behr, J. P. (1997) The proton sponge: a trick to enter cells the viruses did not exploit. *Chimia 51*, 34–36.
(28) Akinc, A., Thomas, M., Klibanov, A. M., and Langer, R. (2005) Exploring polyethylenimine-mediated DNA transfection and the proton sponge hypothesis. *J. Gene Med. 7*, 657–663.
(29) Liu, Y. M., and Reineke, T. M. (2006) Poly(glycoamidoamine)s for gene delivery: Stability of polyplexes and efficacy with cardiomyoblast cells. *Bioconjugate Chem. 17*, 101–108.
(30) Liu, Y. M., and Reineke, T. M. (2007) Poly(glycoamidoamine)s for gene delivery. Structural effects on cellular internalization, buffering capacity, and gene expression. *Bioconjugate Chem 18*, 19–30.
(31) Midoux, P., and Monsigny, M. (1999) Efficient gene transfer by histidylated polylysine/pDNA complexes. *Bioconjugate Chem. 10*, 406–411.
(32) Putnam, D., Gentry, C. A., Pack, D. W., and Langer, R. (2001) Polymer-based gene delivery with low cytotoxicity by a unique balance of side-chain termini. *Proc. Natl. Acad. Sci. U.S.A. 98*, 1200–1205.
(33) Pack, D. W., Putnam, D., and Langer, R. (2000) Design of imidazole-containing endosomolytic biopolymers for gene delivery. *Biotechnol. Bioeng. 67*, 217–223.
(34) Godbey, W. T., Wu, K. K., and Mikos, A. G. (1999) Size matters: Molecular weight affects the efficiency of poly(ethylenimine) as a gene delivery vehicle. *J. Biomed. Mater. Res. 45*, 268–275.
(35) Zhong, Z. Y., Feijen, J., Lok, M. C., Hennink, W. E., Christensen, L. V., Yockman, J. W., Kim, Y. H., and Kim, S. W. (2005) Low molecular weight linear polyethylenimine-b-poly(ethylene glycol)-b-polyethylenimine triblock copolymers: Synthesis, characterization, and in vitro gene transfer properties. *Biomacromolecules 6*, 3440–3448.
(36) Huang, H. L., Tang, G. P., Wang, Q. Q., Li, D., Shen, F. P., Zhou, J., and Yu, H. (2006) Two novel non-viral gene delivery vectors: low molecular weight polyethylenimine cross-linked by (2-hydroxypropyl)-beta-cyclodextrin or (2-hydroxypropyl)-gamma-cyclodextrin. *Chem. Commun.* 2382–2384.
(37) Yang, C. A., Li, H. Z., Goh, S. H., and Li, J. (2007) Cationic star polymers consisting of alpha-cyclodextrin core and oligoethylenimine arms as nonviral gene delivery vectors. *Biomaterials 28*, 3245–3254.
(38) Li, J., Yang, C., Li, H. Z., Wang, X., Goh, S. H., Ding, J. L., Wang, D. Y., and Leong, K. W. (2006) Cationic supramolecules composed of multiple oligoethylenimine-grafted β-cyclodextrins threaded on a polymer chain for efficient gene delivery. *Adv. Mater. 18*, 2969–2974.
(39) Yang, C., Wang, X., Li, H. Z., Goh, S. H., and Li, J. (2007) Synthesis and characterization of polyrotaxanes consisting of cationic α-cyclodextrins threaded on poly[(ethylene oxide)-*ran*-(propylene oxide)] as gene carriers. *Biomacromolecules 8*, 3365–3374.
(40) Li, J., and Loh, X. J. (2008) Cyclodextrin-based supramolecular architectures: Syntheses, structures, and applications for drug and gene delivery. *Adv. Drug Delivery Rev. 60*, 1000–1017.
(41) Xiong, M. P., Forrest, M. L., Ton, G., Zhao, A., Davies, N. M., and Kwon, G. S. (2007) Poly(aspartate-g-PEI800), a polyethylenimine analogue of low toxicity and high transfection efficiency for gene delivery. *Biomaterials 28*, 4889–4900.
(42) Wong, K., Sun, G. B., Zhang, X. Q., Dai, H., Liu, Y., He, C. B., and Leong, K. W. (2006) PEI-g-chitosan, a novel gene delivery system with transfection efficiency comparable to polyethylenimine in vitro and after liver administration in vivo. *Bioconjugate Chem. 17*, 152–158.
(43) Sun, Y. X., Zhang, X. Z., Cheng, H., Cheng, S. X., and Zhuo, R. X. (2008) Low-toxic and efficient gene vector: Carboxymethyl dextran-*graft*-polyethylenimine. *J. Biomed. Mater. Res. 84*, 1102–1110.
(44) Xue, W. H., Diao, H. J., Chen, X., Wang, C. M., Chen, J. N., and Zhang, J. F. (2007) An efficient vector for gene delivery: alpha,beta-poly(3-dimethylaminopropyl-D, L-aspartamide). *Eur. J. Pharm. Biopharm. 66*, 327–333.
(45) Pedone, E., Cavallaro, G., Richardson, S. C. W., Duncan, R., and Giammona, G. (2001) Alpha,beta-poly(asparthylhydrazide)-glycidyltrimethylammonium chloride copolymers (PAHy-GTA): novel polymers with potential for DNA delivery. *J. Controlled Release 77*, 139–153.
(46) Licciardi, M., Campisi, M., Cavallaro, G., Carlisi, B., and Giammona, G. (2006) Novel cationic polyaspartamide with covalently linked carboxypropyl-trimethyl ammonium chloride as a candidate vector for gene delivery. *Eur. Polym. J. 42*, 823–834.
(47) Ogris, M., Kotha, A. K., Tietze, N., Wagner, E., Palumbo, F. S., Giammona, G., and Cavallaro, G. (2007) Novel biocompatible cationic copolymers based on polyaspartylhydrazide being potent as gene vector on tumor cells. *Pharm. Res. 24*, 2213–2222.
(48) Neri, P., Antoni, G., Benvenuti, F., Cocola, F., and Gazzei, G. (1973) Synthesis of α,β-poly[(2-hydroxyethyl)-D, L-aspartamide], a New Plasma Expander. *J. Med. Chem. 16*, 893–897.
(49) Hobson, L. J., and Feast, W. J. (1999) Poly(amidoamine) hyperbranched systems: synthesis, structure and characterization. *Polymer 40*, 1279–1297.
(50) Huang, S. W., Wang, J., Zhang, P. C., Mao, H. Q., Zhuo, R. X., and Leong, K. W. (2004) Water-soluble and nonionic polyphosphoester: synthesis, degradation, biocompatibility and enhancement of gene expression in mouse muscle. *Biomacromolecules 5*, 306–311.

BC800214U

Subscriber access provided by SHEMYAKIN-OVCHINNIKOV INST

Article

Ruthenium(II) Complexes of Bipyridine#Glycoluril and their Interactions with DNA

Megha S. Deshpande, Anupa A. Kumbhar, Avinash S. Kumbhar, Manoj Kumbhakar, Haridas Pal, Uddhavesh B. Sonawane, and Rajendra R. Joshi

Bioconjugate Chem., **2009**, 20 (3), 447-459• DOI: 10.1021/bc800298t • Publication Date (Web): 23 February 2009

Downloaded from http://pubs.acs.org on April 8, 2009

More About This Article

Additional resources and features associated with this article are available within the HTML version:

- Supporting Information
- Access to high resolution figures
- Links to articles and content related to this article
- Copyright permission to reproduce figures and/or text from this article

View the Full Text HTML

ACS Publications
High quality. High impact.

Bioconjugate Chemistry is published by the American Chemical Society. 1155 Sixteenth Street N.W., Washington, DC 20036

Ruthenium(II) Complexes of Bipyridine−Glycoluril and their Interactions with DNA

Megha S. Deshpande,[†] Anupa A. Kumbhar,[†] Avinash S. Kumbhar,*[,†] Manoj Kumbhakar,[‡] Haridas Pal,[‡] Uddhavesh B. Sonawane,[§] and Rajendra R. Joshi[§]

Department of Chemistry, University of Pune, Pune - 411 007, Radiation and Photochemistry Division, BARC, Mumbai - 400 085, and Bioinformatics Team, Scientific and Engineering Computing Group, Centre for Development of Advanced Computing (C-DAC), Pune University Campus, Pune - 411 007, India. Received July 15, 2008; Revised Manuscript Received January 12, 2009

Nine complexes of the type $[Ru(N-N)_2(BPG)]Cl_2$ **1**−**4**, $[Ru(N-N)(BPG)_2]Cl_2$ **5**−**8**, and $[Ru(BPG)_3]Cl_2$ **9** where N−N is 2,2′-bipyridine (bpy), 1,10-phenanthroline (phen), dipyrido[3,2-*d*:2′,3′-*f*]quinoxaline (dpq), dipyrido[3,2-*a*:2′,3′-*c*]phenazine (dppz), which incorporates bipyridine−glycoluril (BPG-4*b*,5,7,7*a*-tetrahydro-4*b*,7*a*-epiminomethanoimino-6*H*-imidazo[4,5-*f*][1,10]phenanthroline-6,13-dione) as the ancillary ligand, have been synthesized and characterized. These complexes with the peripheral polypyridyl ligands have the ability to form conjugates with DNA. The DNA binding (absorption spectroscopy, steady-state and time-resolved emission measurements, steady-state emission quenching measurements) and cleavage (under dark and irradiated conditions) by these complexes has been studied to investigate the influence of the ancillary ligand. The binding ability of these complexes to DNA is dependent on the planarity of the intercalative polypyridyl ligand, which is further affected by the ancillary bipyridine−glycoluril ligand. The complexes **3**, **4**, **7**, and **8** bind to CT-DNA with binding constants on the order of 10^4 M^{-1}. Time-resolved emission measurements on the DNA-bound complexes **1**, **3**, **5**−**7**, and **9** show monoexponential decay of the excited states, whereas complexes **2**, **4**, and **8** show biexponential decay with short- and long-lived components. Interaction of complexes **2**−**9** with plasmid *pBR322* DNA studied by gel electrophoresis experiments reveals that all complexes cleave DNA efficiently at micromolar concentrations under dark and anaerobic conditions probably by a hydrolytic mechanism. Complexes **3**, **4**, **7**, **8**, and $[Ru(bpy)_2(dppz)]^{2+}$ show extensive DNA cleavage in the presence of light with a shift in mobility of form I of DNA probably due to the high molecular weight of DNA−complex conjugates. However, the extent of the cleavage is augmented on irradiation in the case of complexes **3**, **4**, **7**, and **8**, which include the planar dpq and dppz ligands, suggesting a combination of hydrolytic and oxidative mechanism for the DNA scission. Molecular mechanics calculations of these systems corroborate the DNA binding and cleavage mechanisms.

INTRODUCTION

The interaction of transition metal complexes with DNA is a vibrant area of research (*1*−*4*). An advantage of using these complexes in such studies is that their ligands and metals can be conveniently varied to suit individual applications. Ruthenium(II) complexes with intercalating polypyridyl ligands have been extensively studied in this context, as their luminescence and photochemical reactivity are significantly altered on interaction with DNA (*1*−*11*). Ruthenium polypyridyl complexes are useful probes of DNA structure and DNA oxidation chemistry and in addition are used as sensors (*12*−*49*). Among them, $[Ru(bpy)_2(dppz)]^{2+}$ and $[Ru(phen)_2(dppz)]^{2+}$ are found to be high-affinity intercalators with interesting light switch behavior with potential applications in sensing and signaling, as well as in data storage and communication (*14*, *15*). The versatility of these complexes is modulated by the ligand set, which controls whether a complex is an intercalator, hemi-intercalator, or electrostatic binder (*12*−*49*). In general, ruthenium polypyridyl intercalators like $[Ru(bpy)_2(dppz)]^{2+}$ and $[Ru(phen)_2(dppz)]^{2+}$ have $K = 10^6-10^7$ M^{-1}, whereas electrostatic binders like $[Ru(bpy)_3]^{2+}$ have binding affinities on the order of 10^3 M^{-1}. The affinity of dppz intercalators for DNA can be further enhanced by increasing the surface area of the ancillary ligand (*45*).

Adding groups to the edges of the ruthenium polypyridyl complexes further expands the functionality of these complexes. For example, insertion of two polyamine tridentate arm-like segments in a macrochelating ligand in the complex $[Ru(DIP)_2(macro)]^{n+}$ enables binding of certain divalent metal cations so as to deliver its coordinated nucleophile to the phosphate backbone for hydrolysis of the anionic diester (*50*). In a previous study, we have explored the possibility of modifying reactivity by using the urea-fused bipyridine ligand (BPG) that contains hydrogen bond donor (N−H) and acceptor (C═O) groups. This ligand is capable of forming extensive H-bonding networks resulting in diverse frameworks encapsulating water/solvent molecules depending upon the number of bipyridine−glycoluril ligands (*51*−*53*). We have also demonstrated that the urea groups of the BPG ligand are involved in DNA binding and facilitate hydrolytic cleavage of DNA by the complex $[Ru(bpy)_2(BPG)]^{2+}$ **1** (*54*). Thus, the molecules that can hydrolyze the DNA phosphodiester at specific positions are valuable tools in biotechnology, thus facilitating DNA manipulation in a variety of applications.

To test whether the hydrolytic DNA cleavage mechanism is unique to a ruthenium polypyridyl complex containing a single BPG ligand, we synthesized the series of compounds containing one, two, or three BPG ligands. In complexes with one or two BPG ligands, the remaining ligands were varied to include

* E-mail: askum@chem.unipune.ernet.in. Tel: (+91)-020-25601225 (534); Fax:(+91)-020-25691728.
[†] University of Pune.
[‡] Radiation and Photochemistry Division, BARC.
[§] Centre for Development of Advanced Computing (C-DAC).

10.1021/bc800298t CCC: $40.75 © 2009 American Chemical Society
Published on Web 02/23/2009

ligands that favor a particular binding mode (i.e., intercalation, electrostatic binding, etc.) to assess the influence of the BPG ligands on the binding mode and reactivity. If the reactivity and binding mode of these complexes is dominated by the BPG−DNA interactions, these complexes should cleave DNA via a hydrolytic mechanism, consistent with our previous work on $[Ru(bpy)_2(BPG)]^{2+}$ **1**. Here, we present data on the DNA binding and cleavage ability of these complexes probed by spectroscopic methods, gel electrophoresis, and molecular mechanics calculations.

EXPERIMENTAL SECTION

A. Materials. *1. General Details.* All reagents and solvents were purchased commercially and were used as received. $RuCl_3 \cdot xH_2O$ and $K_4[Fe(CN)_6]$ were obtained from S. D. Fine Chemicals Limited (India). Calf thymus DNA and plasmid *pBR322* DNA were purchased from SRL (India). The enzyme superoxide dismutase (SOD EC1.15.1.1) was purchased from Sigma Chemical Co. USA. Deionized water was used for the preparation of the buffers. Supercoiled *pBR322* DNA (CsCl) purified was obtained from Bangalore Genei (Bangalore, India) and used as received. The concentration of DNA in nucleotide phosphate (NP) was determined by UV absorbance at 260 nm using the molar absorption coefficient as 6600 M^{-1} cm^{-1}. Solutions of calf thymus DNA in phosphate buffer gave a ratio of UV absorbance at 260 and 280 nm, A_{260}/A_{280}, of 1.8−1.9:1, indicating that the DNA was sufficiently free of protein (*55*).

2. Syntheses. The ligands 1,10-phenenthroline-5,6-dione (phendione) (*56*), dipyrido[3,2-*d*:2′,3′-*f*]quinoxaline (dpq) (*57*), and dipyrido[3,2-*a*: 2′,3′-*c*]phenazine (dppz) (*58*) were synthesized according to the literature protocols. BPG [4*b*,5,7,7*a*-tetrahydro-4*b*,7*a*-epiminomethanoimino-6*H*-imidazo[4,5-*f*] [1,10] phenanthroline-6,13-dione] was prepared by modifying the literature method (*59, 60, 51*−*54*). The precursor complexes of the type *cis*-$[Ru(N-N)_2Cl_2]$ (*61, 62*), $[Ru(N-N)Cl_4]$ (*63*) were prepared by using the literature methods, and the synthesis of the complex $[Ru(bpy)_2(BPG)]Cl_2$ **1** (*51, 54*) was reported previously by us.

*3. Series I - Ru/BPG Ratio (1:1). [Ru(phen)$_2$(BPG)]Cl$_2$·4H$_2$O (**2**).* This complex was prepared by the method described for complex **1** (*51, 54*) using *cis*- $[Ru(phen)_2Cl_2] \cdot 2H_2O$ in place of *cis*-$[Ru(bpy)_2Cl_2] \cdot 2H_2O$. The precursor complex *cis*-$[Ru(phen)_2Cl_2] \cdot 2H_2O$ (0.125 g, 0.21 mmol) and BPG (0.0608 g, 0.21 mmol) in a 1:1 molar ratio were dissolved in 50% methanol/50% water (50 mL), and the mixture was heated to reflux for 8 h, whereupon the color of the solution changed from dark purple to red. The red solution was filtered hot and was cooled to room temperature. After evaporation of the solvent, the red solid was collected and washed with small amounts of methanol and diethyl ether and then dried under vacuum. The product was purified by column chromatography on active alumina using acetone and methanol as eluent. The red fraction was collected and concentrated in vacuum, a small amount of diethyl ether was added to the concentrated solution, and a red solid was obtained.

Yield: (67%). Elemental analysis calcd for $RuC_{38}H_{34}N_{10}O_6Cl_2$ (898.35): C 50.76, H 3.81, N 15.59%. Found: C 49.80, H 3.71, N 14.90%. ^{1}H NMR (300 MHz, DMSO-d_6, 25 °C): δ = 8.92 (2H), 8.80 (2H), 8.51 (2H), 8.45 (4H), 8.41 (2H), 8.24 (2H), 8.03 (4H), 7.74 (4H), 7.57 (2H) ppm. IR (KBr): $\nu^{\sim}$ = 1708 cm^{-1} (C═O), 3215 cm^{-1} (N−H), 3421 cm^{-1} (O−H), 1647 cm^{-1} (C═N), 1427 cm^{-1} (C═C). UV−visible (H_2O), λ_{max}, nm (log ε): 441 (4.01), 263 (4.77), 223 (4.70). $E_{1/2}$ (V vs Ag/AgCl in DMF 25 °C, 0.1 M [([Bu^t]$_4$ NPF$_6$)]): +1.18.

Complexes $[Ru(dpq)_2(BPG)]Cl_2 \cdot 4H_2O$ (**3**) and $[Ru(dppz)_2(BPG)]Cl_2 \cdot 4H_2O$ (**4**) were prepared similarly to the method described for complex **1**, with *cis*-$[Ru(dpq)_2Cl_2] \cdot 2H_2O$ and *cis*-$[Ru(dppz)_2Cl_2] \cdot 2H_2O$ in place of *cis*-$[Ru(bpy)_2Cl_2] \cdot 2H_2O$. However, in the case of **4** the precursor complex *cis*-$[Ru(dppz)_2Cl_2] \cdot 2H_2O$ and BPG in a 1:1 molar ratio was refluxed in ethylene glycol (20 mL) for 12 h whereupon the color of the solution changed to red. The purification was also carried out by column chromatography on an active alumina column.

*[Ru(dpq)$_2$(BPG)]Cl$_2$·4H$_2$O (**3**).* Yield: (60%). Elemental analysis calcd for $RuC_{42}H_{34}N_{14}O_6Cl_2$ (1002.38): C 50.29, H 3.41, N 19.56%. Found: C 50.78, H 3.60, N 19.10%. ^{1}H NMR (300 MHz, DMSO-d_6, 25 °C): δ = 9.57 (d, 2H), 9.47 (d, 2H), 9.33 (s, 4H), 8.69 (s, 2H), 8.47 (s, 2H), 8.40 (d, 2H), 8.15 (m, 6H), 7.83 (dd, 2H), 7.75 (d, 2H), 7.49 (dd, 2H) ppm. IR (KBr): $\nu^{\sim}$ = 1703 cm^{-1} (C═O), 3217 cm^{-1} (N−H), 3413 cm^{-1} (O−H), 1645 cm^{-1} (C═N), 1448 cm^{-1} (C═C). UV−visible (H_2O), λ_{max}, nm (log ε): 452 (4.13), 296 (4.60), 256 (4.85), 205 (4.77). $E_{1/2}$ (V vs Ag/AgCl in DMF 25 °C, 0.1 M [([Bu^t]$_4$ NPF$_6$)]): +1.16.

*[Ru(dppz)$_2$(BPG)]Cl$_2$·4H$_2$O (**4**).* Yield: (25%). Elemental analysis calcd for $RuC_{50}H_{38}N_{14}O_6Cl_2$ (1102.42): C 56.06, H 3.57, N 18.32%. Found: C 55.99, H 3.87, N 17.98%. ^{1}H NMR (300 MHz, DMSO-d_6, 25 °C): δ = 8.85 (m, 8H), 8.45 (s, 4H), 8.12 (m, 5H), 8.02 (d, 4H), 7.82 (m, 9H) ppm. IR (KBr): $\nu^{\sim}$ = 1705 cm^{-1} (C═O), 2923 cm^{-1} (N−H), 3336 cm^{-1} (O−H), 1602 cm^{-1} (C═N), 1407 cm^{-1} (C═C). UV−visible (H_2O), λ_{max}, nm (log ε): 443 (4.05), 371 (4.03), 263 (4.83), 224 (4.68). $E_{1/2}$ (V vs Ag/AgCl in DMF 25 °C, 0.1 M [([Bu^t]$_4$ NPF$_6$)]): +1.24.

*4. Series II - Ru/BPG Ratio (1:2). [Ru(bpy)(BPG)$_2$]Cl$_2$·4H$_2$O (**5**).* The precursor complex $[Ru(bpy)Cl_4]$ (0.100 g, 0.190 mmol) and BPG (0.112 g, 0.381 mmol) in a 1:2 molar ratio were refluxed in 50% methanol/50% water (50 mL) for 8 h, whereupon the color of the solution changed from dark green to red. The red solution was filtered hot and was cooled to room temperature. After evaporation of the solvent, the brownish red solid was collected and washed with small amounts of methanol and diethyl ether and then dried under vacuum. The product was purified by column chromatography on active alumina using acetone and methanol as eluent. The red fraction was collected and concentrated in vacuum, a small amount of diethyl ether was added to the concentrated solution and red solid was obtained.

Yield: (65%). Elemental analysis calcd for $RuC_{38}H_{36}N_{14}O_8Cl_2$ (988.38): C 46.13, H 3.67, N 19.84%. Found: C 46.70, H 3.70, N 19.20%. ^{1}H NMR (300 MHz, DMSO-d_6, 25 °C): δ = 8.82 (1H), 8.63 (2H), 8.51(3H), 8.38 (2H), 7.79 (12H), 7.60 (8H). IR (KBr, cm^{-1}): $\nu^{\sim}$ = C═O (1709), N−H (3207, 3411), C═N (1616), C═C (1454). UV−visible (H_2O), λ_{max}, nm (log ε): 460 (4.07), 301.5 (4.48), 287.5 (4.53), 255 (4.29), 232.5 (4.47), 204.5 (4.74). $E_{1/2}$ (V vs Ag/AgCl in DMF 25 °C, 0.1 M [([Bu^t]$_4$ NPF$_6$)]): + 1.18. Complexes $[Ru(phen)(BPG)_2]Cl_2 \cdot 4.4H_2O$ (**6**), $[Ru(dpq)(BPG)_2]Cl_2 \cdot 3H_2O$ (**7**), and $[Ru(dppz)(BPG)_2]Cl_2 \cdot 2CH_3OH$ (**8**) were prepared similarly to the method described for **5**, with the precursor complexes $[Ru(phen)Cl_4]$, $[Ru(dpq)Cl_4]$, and $[Ru(dppz)Cl_4]$ in place of $[Ru(bpy)Cl_4]$. The purification was also carried out by column chromatography on an active alumina column. Single crystals were grown by slow evaporation of the methanol−water solution.

*[Ru(phen)(BPG)$_2$]Cl$_2$·4.4H$_2$O (**6**).* Yield: (70%). Calcd for $RuC_{40}H_{36.8}N_{14}O_{8.4}Cl_2$ (1019.59): C 47.08, H 3.64, N 19.23%. Found: C 47.63, H 3.83, N 19.63%. ^{1}H NMR (300 MHz, DMSO-d_6, 25 °C): δ = 8.57(m, 6H), 8.33(s, 8H), 8.17(s, 2H), 8.05 (d, 2H), 7.97 (d, 3H), 7.70 (m, 3H), 7.54 (d, 2H), 7.27 (d, 2H). IR (KBr, cm^{-1}): $\nu^{\sim}$ = C═O (1703), N−H (3207, 3408), C═N (1616), C═C (1452). UV−visible (H_2O), λ_{max}, nm (log ε): 457 (4.11), 375.5 (3.87), 301 (4.43), 262.5 (4.72), 224 (4.70), 205 (4.84). $E_{1/2}$ (V vs Ag/AgCl in DMF 25 °C, 0.1 M [([Bu^t]$_4$ NPF$_6$)]): +1.17.

*[Ru(dpq)(BPG)$_2$]Cl$_2$·3H$_2$O (**7**).* Yield: (63%). Calcd for $RuC_{42}H_{36}N_{16}O_8Cl_2$ (1046.39): C 48.16, H 3.27, N 21.41%. Found: C 47.86, H 3.90, N 21.70%. ^{1}H NMR (300 MHz,

DMSO-d_6, 25 °C): δ = 9.43 (dd, 2H), 9.14 (dd, 2H), 8.85 (s, 6H), 8.34 (m, 3H), 8.22 (m, 6H), 8.19 (dd, 2H), 7.91 (dd, 2H), 7.88 (m, 4H), 7.41 (dd, 1H). IR(KBr, cm^{-1}) $\nu^{\sim}$ = C═O (1699), N−H (3091, 3178), C═N (1614), C═C (1450). UV−visible (H_2O), λ_{max}, nm (log ε): 454 (4.20), 297.5 (4.67), 256.5 (4.84), 206.5 (4.85). $E_{1/2}$ (V vs Ag/AgCl in DMF 25 °C, 0.1 M [([Bu^t]$_4$ NPF_6)]): +1.17.

*[Ru(dppz)(BPG)$_2$]Cl$_2$·2CH$_3$OH (**8**).* Yield: (67%). Calcd for $RuC_{48}N_{16}O_6H_{38}Cl_2$: C 52.01, H 3.48, N 20.23%. Found: C 52.06, H 3.43, N 19.46%. ^{1}H NMR (300 MHz, DMSO-d_6, 25 °C): δ = 9.60 (dd, 2H), 9.18 (d, 1H), 8.78 (d, 4H), 8.46 (s, 8H), 8.39 (d, 4H), 8.25 (m, 5H), 8.09 (m, 3H), 7.75 (m, 3H). IR (KBr, cm^{-1}): $\nu^{\sim}$ = C═O (1699), N−H (3095, 3186), C═N (1616), C═C (1454). UV−visible (H_2O), λ_{max}, nm (log ε): 457 (3.90), 359.5 (4.10), 277.5 (4.64), 205.5 (4.73). $E_{1/2}$ (V vs Ag/AgCl in DMF 25 °C, 0.1 M [([Bu^t]$_4$ NPF_6)]): +1.18.

*5. Series III - Ru/BPG Ratio (1:3). [Ru(BPG)$_3$]Cl$_2$·4H$_2$O (**9**).* This complex was prepared by the reaction of $RuCl_3 \cdot xH_2O$ (0.100 g, 0.444 mmol) and BPG (0.392 g, 1.331 mmol) in a 1:3 molar ratio in 1:1 methanol/water at reflux for 12 h whereupon the color of the solution changed to red. The resulting red solution was cooled to room temperature and filtered. After evaporation of the solvent, the complex was collected and washed with water and diethyl ether. The product was purified by column chromatography on active alumina using methanol and water as eluent. The red fraction was collected.

Yield: (75%). Elemental analysis calcd. for $RuC_{42}H_{38}N_{18}O_{10}Cl_2$ (1126.43): C 44.71, H 3.39, N 22.36%. Found: C 43.80, H 3.09, N 22.63%. ^{1}H NMR (300 MHz, DMSO-d_6, 25 °C): δ = 8.79 (s, 6H), 8.50 (s, 6H), 8.28 (d, 6H), 7.79 (d, 6H), 7.75 (d, 6H) ppm. ^{1}H NMR (300 MHz, D_2O, 25 °C): δ = 8.15 (d, 6H), 7.90 (d, 6H), 7.57 (d, 6H) ppm. IR (KBr) $\nu^{\sim}$ = 1703 cm^{-1} (C═O), 3213 cm^{-1} (N−H), 3417 cm^{-1} (O−H), 1643 cm^{-1} (C═N), 1454 cm^{-1} (C═C). UV−visible (H_2O), λ_{max}, nm (log ε): 456 (4.10), 304 (4.48), 262 (4.29), 231 (4.52). $E_{1/2}$ (V vs Ag/AgCl in DMF 25 °C, 0.1 M [([Bu^t]$_4$ NPF_6)]): +1.14.

B. Methods. *1. Spectroscopy.* The microanalyses (C, H, and N) were carried out with a Perkin-Elmer 240 Q elemental analyzer at NCL, Pune. UV−vis spectra were recorded on a Shimadzu UV-1601 spectrophotometer. ^{1}H NMR spectra were measured on a Varian-Mercury 300 MHz spectrometer with (d_6) DMSO as a solvent at room temperature, and all chemical shifts are given relative to TMS. The infrared spectra of solid samples dispersed in KBr were recorded on a Shimadzu FTIR-8400 spectrophotometer. Electrochemical experiments with Ru(II) polypyridyl complexes in DMF solution were performed on a CH-660A (USA) electrochemical instrument in a conventional three-electrode cell assembly with a saturated Ag/AgCl reference electrode, platinum as working electrode for all measurements. Electrochemical measurements were performed using dimethylformamide as solvent and 0.1 M tetrabutylammonium hexafluorophosphate ([Bu^t]$_4$$NPF_6$) as supporting electrolyte. Steady-state emission titrations were carried out on a Shimadzu RF-5301 spectrofluorometer at room temperature. The emission lifetimes were measured with a time-correlated-single-photon-counting spectrometer from IBH, UK, using 455 nm nanosecond light-emitting diode (NanoLed-01) for the excitation of the samples.

2. DNA Binding and Cleavage Studies. a. Absorption Spectral Studies. For electronic absorption titration, a stock 10 μM solution of the complex was made up in a phosphate buffer (pH 7.2); 3000 μL of the solution was loaded into an optical glass cuvette with a path length of 1 cm, and 200 μL was removed with a micropipette and replaced with 200 μL of the complex solution. This cuvette was then loaded into the spectrometer sample block, controlled at 25 °C; 3000 μL of the buffer was loaded to an identical cuvette and placed in the reference cell. Both the cuvettes were mixed 30 times with a micropipette, and all bubbles were removed. After the cuvettes had been allowed to reach equilibrium over the course of 20 min, a spectrum was recorded between 700 and 200 nm. One to 55 mL of CT-DNA was added to both cuvettes and mixed 30 times. The spectrum was recorded after checking for bubbles and showed a drop in absorptivity showing interaction between the DNA and the metal complex. The intrinsic binding constant of the complex with CT-DNA was determined from eq 1 (*64, 65*) where [DNA] is the concentration of DNA in base pairs.

$$[DNA]/[\varepsilon_a - \varepsilon_f] = [DNA]/[\varepsilon_b - \varepsilon_f] + 1/K_b[\varepsilon_b - \varepsilon_f] \quad (1)$$

The apparent absorption coefficients ε_a, ε_f, and ε_b correspond to A_{obsd}/[Ru], the extinction coefficient for the free complex and the extinction coefficient for the complex in the fully bound form, respectively. The slope and the intercept of the linear fit of [DNA]/[ε_a − ε_f] versus [DNA] plot give 1/[ε_a − ε_f] and 1/K_b[ε_b − ε_f], respectively. The intrinsic binding constant K_b can be obtained from the ratio of the slope to the intercept (*64*).

b. Viscosity Measurements. Viscosity experiments were carried out using a semimicro viscometer maintained at 28 °C in a thermostatic water bath. Flow time of solutions in phosphate buffer (pH 7.2) was recorded in triplicate for each sample, and an average flow time was calculated. Data were presented as $(\eta/\eta^0)^{1/3}$ versus binding ratio, where η is the viscosity of DNA in the presence of complex and η^0 is the viscosity of DNA alone (*65*).

c. Thermal Denaturation Study. DNA melting studies were carried out with a JASCO V-630 spectrophotometer equipped with a Peltier temperature-controlling programmer ETC-717 (±0.1 °C) in phosphate buffer. The DNA melting studies were done by controlling the temperature of the sample cell with a water-circulating bath. UV melting profiles were obtained by scanning A_{260} absorbance was monitored at a heating rate of 1 °C/min for solutions of CT-DNA (100 μM) in the absence and presence of ruthenium(II) complexes (20 μM) from 30 to 90 °C. The data were analyzed with the use of separate thermal melting program; the temperature of the cell containing the cuvette was ramped from 50 to 90 °C. The melting temperature T_m which is defined as the temperature where half of the total base pairs are unbound was determined from the midpoint of the melting curves.

d. Steady-State and Time-Resolved Luminescence Spectral Studies. For calculating emission quantum yields, the optical densities of the samples were adjusted to about 0.3 at the excitation wavelength. Emission quantum yields (ϕ) were calculated by integrating the area under the fluorescence curves and by using the formula (*66*)

$$\varphi_{Sample} = \{OD_{Standard}/OD_{Sample}\} \times \{A_{Sample}/A_{Standard}\} \times \varphi_{Standard} \quad (2)$$

where OD is optical density of the compound at the excitation wavelength (450 nm) and A is the area under the emission spectral curve. The standard used for the fluorescence quantum yield measurements was [Ru(bpy)$_3$]Cl$_2$ (*67*). The rate constant, k_0, includes both radiative k_r and nonradiative k_{nr} contributions to the rate of the ^{3}MLCT excited-state decay. Radiative (k_r) and nonradiative (k_{nr}) decay rate constants were determined using the values of τ and ϕ_r (radiative quantum yield) estimated at room temperature (*66*).

The excitation and emission slit widths employed were 5 nm each. Emission titration experiments were performed by using a fixed metal complex concentration to which increments of the stock DNA solutions were added. Typical concentration of metal complex used was 0.025 mM and [DNA]/[Ru] ratio is in the range 0−30. After the addition of DNA to metal complex,

the resulting solution was allowed to equilibrate for 20−30 min at room temperature before being excited in their intense metal to ligand charge-transfer band between 400 and 500 nm.

Steady-state quenching experiments were conducted by adding 75−750 μL aliquots of a 4 mM ferrocyanide stock solution to 3 mL sample solutions containing 0.8 mM nucleic acid concentration and 0.02 mM Ru(II) complex concentration in phosphate buffer. All solutions were allowed to equilibrate thermally for ∼15 min before measurements were made. The Stern-Volmer quenching constant is calculated according to the classical Stern-Volmer equation (*66, 68*)

$$I_0/I = 1 + K_{SV}[Q] \quad (3)$$

where I_0 and I are the fluorescence intensities of the complex in the absence and presence of $[Fe(CN)_6]^{4-}$, and K_{sv} is the Stern-Volmer quenching constant, which is a measure of the efficiency of fluorescence quenching by $[Fe(CN)_6]^{4-}$.

For time-resolved single photon counting measurements, the samples were excited in their intense metal to ligand charge-transfer band between 400 and 500 nm. Emission was detected in the wavelength range 590−630 nm depending on the sample, using a photomultiplier tube based detection module (model TBX-04 from IBH). The instrument response function for the present setup is ∼1.2 ns (fwhm). The decay curves were analyzed by reconvolution procedure (*69*), using DAS-6 software, obtained from IBH, considering a suitable functional form (mono- or biexponential) of the decays. The quality of the fits were judged by the reduced chi-square (χ^2) values and the distribution of the weighted residuals among the data channels (*69*). For good fits, the χ^2 values were close to unity and the weighted residuals were distributed randomly among the data channels (*69*).

e. DNA Cleavage. The DNA cleavage was carried out by agarose gel electrophoresis as described previously (*54, 70, 71*). A 10 μL total sample volume in 0.5 mL transparent Eppendorf microtubes containing *pBR322* DNA (90 μM in base pairs). For the gel electrophoresis experiments, plasmid *pBR322* DNA was treated with the metal complex (20 μM) and the mixture was incubated in the dark for 2 and 18 h at 37 °C for the dark experiments. The samples were analyzed by 1% agarose gel electrophoresis (Tris-Boric acid-EDTA (TBE) buffer, (pH 8.2) for 2 h at 60 mV. The gel was stained with a 0.5 μg/mL ethidium bromide and visualized by UV light and photographed for analysis. The extent of cleavage of the plasmid *pBR322* DNA was determined by measuring the intensities of the bands using the Alpha Innotech Gel documentation system (AlphaImager 2200). Irradiation experiments were carried out under illuminated conditions using a UV lamp of 365 nm. In irradiation experiments, *pBR322* DNA (90 μM in base pairs) was treated with 20 μM samples of the metal complexes, and the mixtures were incubated for 30 min in the dark followed by 20 min irradiation at 365 nm. For mechanistic investigations, experiments were carried out under irradiated conditions in the presence of radical scavenging agents DMSO, mannitol, DABCO, NaN_3, L-histidine, and SOD, which were added to the plasmid *pBR322* DNA prior to the addition of the complexes.

f. Dialysis Experiments. A typical dialysis experiment was carried out as follows. Three milliliters solution of the ruthenium(II) complexes **1**−**9** ([Ru] = 20 μM) in the presence of CT-DNA ([DNA] = 200 μM) under dark conditions in phosphate buffer (pH 7.2) solution was transferred to the dialysis tubing (molecular weight cutoff 12 000, 14 000) and dialysed with gentle stirring against buffer solution in the dark, with three changes of buffer over a 24 h period. Changes in the absorption spectrum of complexes **1**−**9** in the presence of calf thymus DNA with dialysis (24 h) compared with the dialyzed samples and undialyzed samples were monitored by UV−vis spectroscopy.

Scheme 1. Structure of BPG and Various Polypyridyl Ligands Used in the Present Study

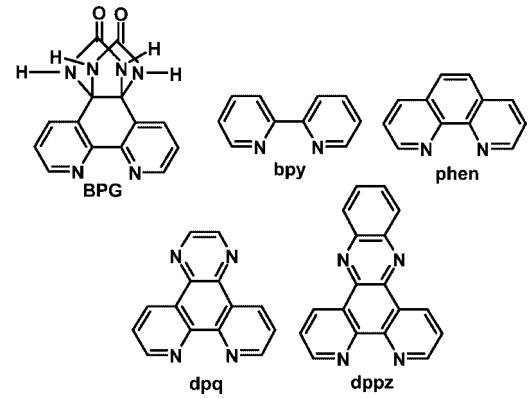

g. Molecular Modeling. Molecular modeling studies were performed on a Silicon Graphics Octane workstation using the software Insight II 2000 (*72*) with the Discover 3 module. Initial models of right-handed B-DNA of sequence $d(C:G)_{12}$ were constructed using the Biopolymer module of Insight II. The coordinates for the metal complex $[Ru(bpy)_2(BPG)]^{2+}$ and derivatives were taken from its crystal structure as a CIF file and were converted to the PDB format using Mercury software (*73*). The all atom extensible systematic force field (ESFF) was used for the entire modeling study. The $[Ru(bpy)_2(BPG)]^{2+}$ and derivative-bound DNA was then soaked in a water box of dimensions 35.0 × 50.0 × 35.0, and periodic boundary conditions were applied. A dielectric constant of 1.0 for electrostatic energy and a cutoff of 9.5 A were used for both the Coulomb as well as van der Waals energies. The nonbonded electrostatic terms were calculated using the Ewald summation method (*74*). The accuracy of convergence for the Ewald Coulomb energy summation was kept to 0.0001 kcal/mol. The system was minimized using the steepest descent gradient algorithm for 1000 steps, followed by the conjugate gradient algorithm for 1000 steps or until the maximum derivative was below 0.1 kcal/mol/A. The Ewald summation method that expands the simple sum of the Coulomb's law terms into several sums including a direct, reciprocal term was used to calculate the long-range electrostatics. As the Ewald sum method is valid for a neutral system, B−DNA−Ru(II) polypyridyl complex, the Ewald summation method calculates charges by homogeneous charge density distribution. The initial 1000 steps of steepest descent minimization were performed to relax the initial strain on the molecule.

RESULTS AND DISCUSSION

A. Syntheses and Properties. The urea fused bipyridine ligand bipyridine−glycoluril (BPG) (Scheme 1) and a series of nine new ruthenium(II) polypyridyl complexes of the type $[Ru(N-N)_2(BPG)]Cl_2$ **1**−**4**, $[Ru(N-N)(BPG)_2]Cl_2$ **5**−**8**, and $[Ru(BPG)_3]Cl_2$ **9** were synthesized and obtained in a racemic form by the reactions of precursor complexes *cis*-$[Ru(N-N)_2Cl_2]$, $[Ru(N-N)Cl_4]$, and $RuCl_3 \cdot xH_2O$ by varying the number of BPG (Scheme 2). Crystal structures of BPG ligand and its complexes **1**, **6**, and **9** have been reported elsewhere (*51, 52*).

The electronic absorption spectra of complexes **1**−**9** are dominated by two sets of transitions (i) low-energy metal-to-ligand charge transfer (MLCT) transitions in the range 440−460 nm and (ii) high-energy ligand-centered $\pi-\pi^*$ transitions (IL) in the range 200−380 nm for all complexes which are similar to the parent $[Ru(bpy)_3]^{2+}$ and other Ru(II) polypyridyl complexes (*75, 76*). The peaks at 371 and 360 nm in compounds **4** and **8** are characteristic of the $\pi-\pi^*$ transition of the dppz

Scheme 2. Synthetic Route for Complexes 1−9

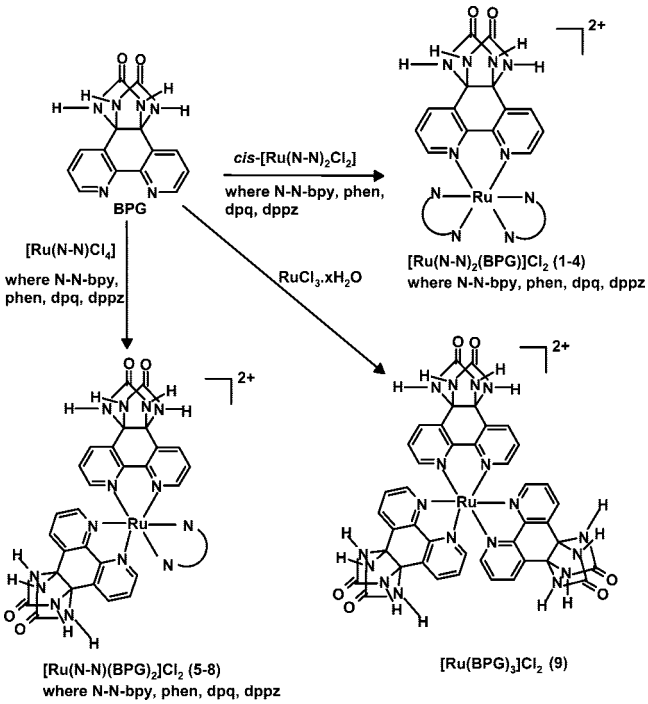

Table 1. Photophysical Data for Ruthenium(II) Polypyridyl Complexes 1−7 and 9

	emission (buffer)					
complex	λ_{em} (nm)	τ (ns)	ϕ_{em}	K_r (s^{-1})	K_{nr} (s^{-1})	K_0 (s^{-1})
1	624	253	0.0096	3.8×10^4	3.9×10^6	3.9×10^6
2	622	369	0.0149	4.0×10^4	2.7×10^6	2.7×10^6
3	605	147	0.049	3.4×10^4	6.5×10^6	6.8×10^6
4	601	348	0.0119	3.4×10^4	2.8×10^6	2.8×10^6
5	612	346	0.027	7.7×10^4	2.8×10^6	2.9×10^6
6	609	384	0.032	8.4×10^4	2.5×10^6	2.6×10^6
7	598	332	0.033	1.0×10^5	2.9×10^6	3.0×10^6
9	596	342	0.0178	5.2×10^4	2.9×10^6	2.9×10^6

ligand. The synthesized ruthenium(II) complexes **1**−**7** and **9** emit in phosphate buffer at room temperature with maximum between 590 and 640 nm. The emission quantum yields for **1**−**7** and **9** are calculated by using eq 2 and summarized in Table 1. The radiative rate constants for complexes **1**−**7** and **9** are on the order of 10^4-10^5 and nonradiative rate constants are on the order of 10^6 (Table 1) that are in the range expected for Ru(II) polypyridyl emitters (*75, 76*). No detectable luminescence is observed for complex **8** in buffer solution. Single exponential decays are observed for **1**−**7** and **9** in buffer solutions, and the results are tabulated in Table 1.

DNA Binding Studies. *Absorption Spectroscopy Studies.* Absorption spectral titrations are the most common method to investigate the interactions of metal complexes with DNA. Binding of the complexes to DNA through intercalation results in hypochromism and red shift of the bands due to noncovalent stacking of the planar aromatic chromophore between the base pairs of DNA (*77*−*82*). Changes in the electronic absorption spectra of complexes **1**−**9** were measured as a function of DNA concentration, and the titration curves for **3**, **4**, **7**, and **8** are shown in Figure 1. There was insignificant change in the absorption profile of complexes **1**, **5**, **6**, and **9** on sequential addition of DNA, indicating an electrostatic binding similar to that of $[Ru(bpy)_3]^{2+}$ (*3, 78*−*82*), as the nonplanar bpy and urea moiety of BPG precludes intercalation. The binding constants estimated using eq 1 for complexes **2**, **3**, **4**, **7**, and **8** are $(3.86 \pm 0.2) \times 10^3$, $(3.14 \pm 0.1) \times 10^4$, $(6.19 \pm 0.1) \times 10^4$, $(2.87 \pm 0.2) \times 10^4$, and $(9.14 \pm 0.2) \times 10^4$, respectively (Table 2). The absorption spectra of **3** on addition of DNA shows 5.1% hypochromism in the MLCT band at the [DNA]/[Ru] ratio of 8, whereas complex **4** shows 9.6% and 19.5% hypochromicity in both MLCT and IL bands, respectively, at the same [DNA]/[Ru] ratio. The extent of hypochromism and red shift is more in **4** than **3**, indicating strong binding of this complex to CT-DNA. A comparison of the binding constants of **3** and **4** with strong intercalators such as $[Ru(phen)_2dppz]^{2+}$ reveals a weak binding due to hindrance to the intercalation by the second planar dppz and the nonplanar BPG ancillary ligand. For the complex **7**, the hypochromism in the MLCT and IL bands are 3.0% and 5.1% at the same [DNA]/[Ru] ratio. However, for complex **8**, the absorption spectra on addition of DNA shows pronounced hypochromism in both MLCT and IL bands of about 12.3% and 31.0%, respectively, at the ratio of [DNA]/[Ru] of 8. The extent of hypochromism and red shift is particularly pronounced in the interligand absorption band (∼360 nm) for **8** and is typical for stacking interaction of the dppz ligand with the DNA base pairs. These spectral characteristics suggest that complexes **7** and **8** interact with DNA through a mode that involves a stacking interaction of the planar aromatic chromophore and the base pairs of DNA, but with a moderate binding constant as compared to classical intercalators ($[Ru(phen)_2(dppz)]^{2+}$, $K_b = 5.1 \times 10^6$ M^{-1}) probably due to the influence of ancillary BPG ligand. Similar results have been observed for the $[Ru(NH_3)_4(dppz)]^{2+}$, $K_b = 1.8 \times 10^5$ M^{-1} (see Table 2 for comparative data on dppz complexes) for which the NH_3 ligand which has the potential for hydrogen bonding is found to be detrimental for DNA binding (*46*). In the present series, the ancillary ligand bipyridine−glycoluril has the potential for hydrogen bonding interactions with the phosphates or bases of DNA, resulting in lowering the binding constant value as compared to classical intercalators.

Viscosity and Thermal Denaturation Studies. Viscosity measurements, which are sensitive to length change, are regarded as most critical tests for binding mode and were studied in order to assess the binding mode of these complexes with DNA. Changes in relative viscosity provide a reliable method for distinguishing between intercalators and electrostatic binders of DNA. Intercalation of a ligand into DNA is known to cause a significant increase in the viscosity of a DNA solution due to an increase in the separation of the base pairs at the intercalation site and, hence, an increase in the overall DNA molecular length. In contrast, a ligand that binds in the DNA grooves causes a less pronounced change (positive or negative) or no change in the viscosity of a DNA solution. The changes in the relative viscosity of solutions containing DNA upon addition of increasing concentrations of **1**−**9** are shown in Supporting Information Figures S1 and S2. The maximum increase in viscosity of DNA on increasing the [Ru]/[DNA] ratio for complexes **3**, **4**, **7**, and **8** suggest an intercalative binding mode, while a minute/negligible increase in viscosity for the complexes **1** and **2** indicate an electrostatic binding. The incorporation of non-intercalating BPG ligands with bulky peripheral urea groups are expected to influence the efficacy of the intercalative ligand. A similar effect was observed in the case of $[Ru(bpyMe_2)_2(dpq)]^{2+}$ where the orientation of the peripheral $bpyMe_2$ ligands results in partial intercalation of the classical intercalator dpq (*12*). Addition of complexes **5**, **6**, and **9** has no effect on the DNA viscosity, suggesting an electrostatic binding similarly observed previously for $[Ru(bpy)_3]^{2+}$ (*78, 87*). The viscosity data taken together with the hypochromism observed in the absorption data upon addition of DNA are in accord with the fact that the peripheral urea groups influence the ability of the intercalative ligand.

The thermal behavior of the DNA in the presence of complexes would offer some information about the interaction

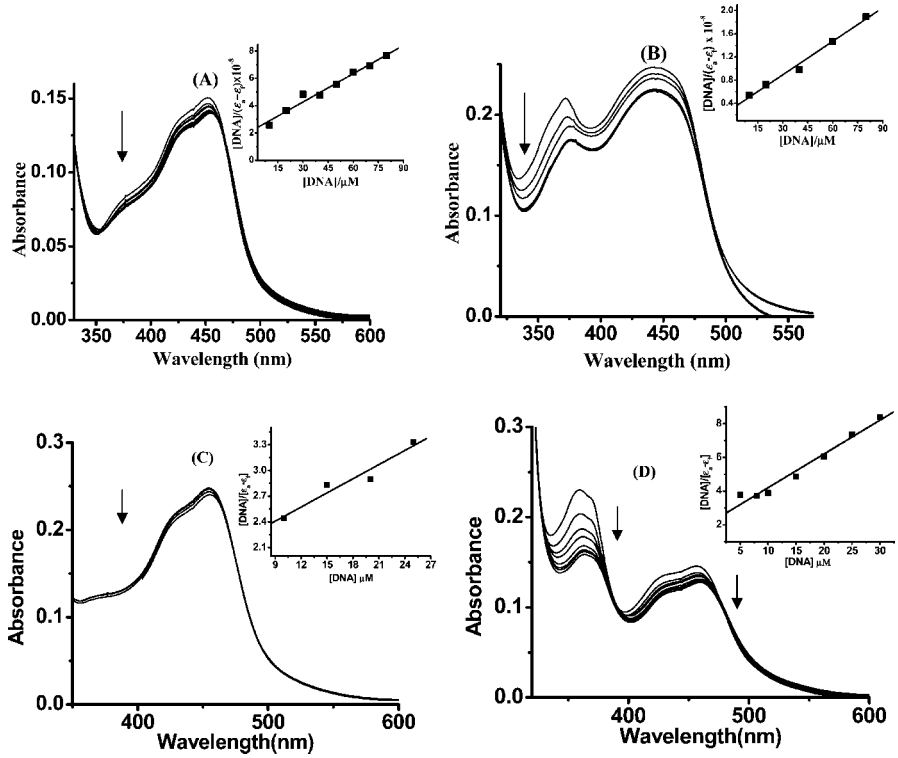

Figure 1. Changes in the electronic absorption spectra of (A) **3** (10 μM), (B) **4** (10 μM), (C)**7** (10 μM), and (D) **8** (10 μM) with increasing the concentrations (0−100 μM) of CT-DNA (phosphate buffer pH 7.2); the inset graph shows a fit of the absorbance data used to obtain the binding constant.

Table 2. Spectroscopic Properties of the Complexes 3, 4, 7, and 8 in the presence of CT-DNA

complexes	K_b (M^{-1})	hypochromism[b] H (%) MLCT	LMCT	ref
3	$(3.14 \pm 0.1) \times 10^4$	3.0	5.1	[a] this work
4	$(6.19 \pm 0.1) \times 10^4$	9.6	19.5	[a] this work
7	$(2.87 \pm 0.2) \times 10^4$	3.0	5.1	[a] this work
8	$(9.14 \pm 0.2) \times 10^4$	12.3	31.0	[a] this work
$[Ru(bpy)_2(dppz)]^{2+}$	5.0×10^6	14.5	40.1	*37, 20*
$[Ru(phen)_2(dppz)]^{2+}$	5.1×10^6	-	35.0	*78−82*
$[Ru(dmp)_2(dppz)]^{2+}$	2.3×10^6	11.2	31.1	*37, 43*
$[Ru(dmb)_2(dppz)]^{2+}$	4.5×10^6	15.6	38.5	*37*
$[Ru(NH_3)_4(dppz)]^{2+}$	1.8×10^5	13.6	-	*46*
$[Ru(tpm)(py)(dppz)]^{2+}$	4.7×10^6	-	-	*41*
$[Ru(terpy)(dppz)(OH_2)]^{2+}$	7.0×10^5	9.6	-	*47*
$[Ru(IP)_2(dppz)]^{2+}$	2.1×10^7	40.4	46.3	*37, 42*

[a] [DNA]/[Ru] = 8:1 [b] $H\ \% = 100(A_{free} - A_{bound})/A_{free}$.

Table 3. Luminescence and Thermal Properties of Complexes 1−9 in the Absence and Presence of CT-DNA

complexes	ΔT_m/°C	I/I_0[a]	Stern-Volmer quenching constant[b] (M^{-1}) without DNA	with DNA
1	2	1.13	2.12×10^3	1.96×10^3
2	2	1.23	1.02×10^3	1.00×10^3
3	2	1.69	2.59×10^3	2.69×10^2
4	3	3.70	2.35×10^3	1.49×10^2
5	2	1.09	3.32×10^3	2.68×10^3
6	2	1.13	3.09×10^3	2.31×10^3
7	3	1.65	2.64×10^3	4.11×10^2
8	4	23.31	-	2.83×10^2
9	1	1.05	2.45×10^3	2.40×10^3

[a] Relative emission intensity enhancement in the presence of CT-DNA at $R = 30$. [b] Stern-Volmer constants for the quenching of the complexes by $K_4[Fe(CN)_6]$ in the absence and presence of DNA.

affinities of these complexes with DNA and characterizes the transition from double-stranded to single-stranded DNA. The extinction coefficient of DNA bases at 260 nm in the double helical form is much less than in the single-stranded form; hence, melting of the helix leads to an increase in the absorption at this wavelength. Thus, the melting temperature (T_m) of DNA, which can characterize the transition from double-stranded to single-stranded form of DNA, is usually determined (*43*, *49*). Thermal denaturation Figures S3 and S4 in the Supporting Information and the data for DNA in the presence and absence of ruthenium(II) complexes **1**−**9** investigated in this study are summarized in Table 3. Thermal denaturation experiments carried out on CT-DNA in the absence of added complex revealed that the T_m value for the duplex is 63° ± 1°. It is clear from the data given in the Table 3 that the complexes containing the non-intercalative/partial intercalative ligands shift the T_m values only by up to 2° compared to that of the pure DNA sample. However, the complexes containing the intercalative ligands dpq/dppz shift the T_m values by up to 4° compared to that of the pure DNA sample. This increase in the helix melting temperature indicates the increased stability of the double helix when these compounds **3**, **4**, **7**, and **8** bind to DNA. However, the increase in the melting temperature is relatively lower than the classical intercalators, suggesting that the dpq/dppz complexes bind with DNA through a mode that involves a stacking interaction of the planar aromatic chromophore and the base pairs of DNA, but with a moderate binding, probably due to the influence of ancillary BPG ligand, thus lowering the T_m values for these complexes.

Steady-State Emission Studies. The changes in the emission spectra of Ru(II) polypyridyl complexes in the presence of DNA are a diagnostic means to determine DNA binding (*19, 76*). The emission spectra of complexes **1**−**9** have been measured in the absence and in the presence of CT-DNA (Supporting Information Figures S5 and S6). The dependence of relative emission intensities as a function of DNA concentration in buffered solution at pH 7.2 is shown in Figure 2 (in terms of [DNA]/[Ru]). The spectra profiles and emission maxima for the complexes **1**−**3**, **5**−**7**, and **9** exhibit weak luminescence

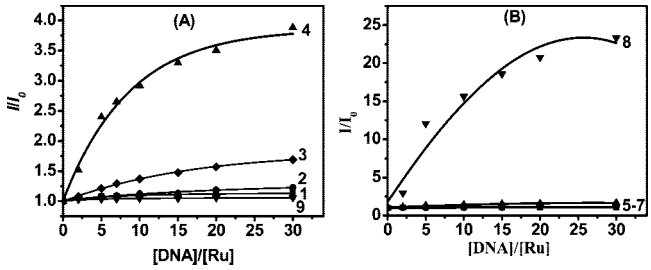

Figure 2. Plots of relative integrated emission intensity versus [DNA]/[Ru] for the complexes: (A) Complexes (■) **1**, (●) **2**, (◆) **3**, (▲) **4**, and (▼) **9** (24 μM). (B) Complexes (●) **5**, (■) **6**, (▲) **7**, (▼) **8** (24 μM) in phosphate buffer, pH 7.2 at 298 K with increasing [DNA]/[Ru] ratio from 0−30.

enhancements in the range 1−1.7 after adding CT-DNA at a ratio of [DNA]/[Ru] = 30 indicating a weak binding of these complexes with CT-DNA by partial intercalation or electrostatic association (Table 3). However, complex **4** exhibits luminescence enhancement of 3.7 indicating strong binding by intercalation of this complex with CT-DNA. On the other hand, complex **8** is nonluminescent in aqueous solution but emits intensely in the presence of CT-DNA. In this case, observed emission enhancement was ascribed to the protection of the phenazine nitrogen atoms of DNA-intercalated excited-state complex from accessibility by water molecules. The fluorescence intensity is observed to vary with the [DNA]/[Ru] ratio. The remarkable sensitivity is observed for complex **8** in the presence of CT-DNA ($R = 0-30$) with the relative emission intensity enhancement of a factor 23.31, much higher than that for the other complexes (Figure S6 in the Supporting Information) that supports the stacking interaction of the planar aromatic dppz ligand into the DNA base pairs, which is consistent with other spectroscopic studies.

Steady-State Emission Quenching Experiment Using $K_4[Fe(CN)_6]$. The fluorescence intensities of the ruthenium polypyridyl complexes, upon visible excitation, are enhanced on binding to DNA (*83*−*85*). Quenching of this luminescent excited state with the use of an anionic quencher such as $[Fe(CN)_6]^{4-}$ has been shown to be able to distinguish bound ruthenium(II) species (*86*). A highly negatively charged quencher is expected to be repelled by the negatively charged phosphate backbone, and therefore, a DNA-bound cationic molecule should be protected from quenching while free complexes should be readily quenched. The results of steady-state emission quenching experiments using $[Fe(CN)_6]^{4-}$ as the quencher are shown in Figures S7 and S8 in the Supporting Information. The results are interpreted in terms of two binding modes: electrostatic, which is easily quenched by ferrocyanide; and intercalative, which is protected from ferrocyanide quenching. Stern-Volmer quenching constants for complexes **1**−**7** and **9** in the absence and presence of DNA are shown in Table 3. In the absence of DNA, complexes **1**−**7** and **9** are efficiently quenched by $[Fe(CN)_6]^{4-}$ with the Stern-Volmer quenching constants on the order of $1.02-3.32 \times 10^3$. The nonlinear nature of the graph for complex **2** indicates that two differential binding modes, viz., partial intercalation and surface binding, may be possible. Barton et al. interpreted the curved Stern-Volmer plots obtained with the anionic quencher $[Fe(CN)_6]^{4-}$ as having two binding modes, one intercalative and one groove-bound, with Δ preferring the former and Λ the latter mode in the case of $[Ru(phen)_3]^{2+}$ (*87*, *88*). However, in the presence of DNA, the maximum decrease in the Stern-Volmer quenching constant is obtained for the complexes **3**, **4**, **7**, and **8**. For these complexes, the Stern-Volmer plot is a straight line, implying that the luminescent complex is homogeneous. The linear nature with negligible difference in the Stern-Volmer quenching constants for complexes **1**, **5**−**6**, and **9** indicates a single component donor−quencher system with electrostatic binding similar to that for $[Ru(bpy)_3]^{2+}$.

Time-Resolved Emission Measurements in the Presence of DNA. The above-mentioned trends in DNA binding are further corroborated by time-correlated single photon counting fluorescence measurements. In the absence of DNA, all the complexes strictly exhibit monoexponential emission decay. Table S1 in the Supporting Information summarizes the luminescence lifetime of the complexes **1**−**9** in the presence of CT-DNA for a ratio [DNA]/[Ru] of 2−30. Complexes **1**, **5**, and **9** show monoexponential decay with negligible change in τ_o value, indicating an electrostatic interaction of these complexes with DNA. Complex **3**, **6**, and **7** also exhibits monoexponential decay; however, the lifetime increases from 330 to 432 ns for **3**, 386 to 404 ns for **6**, and 357 to 426 ns for **7** exhibits monoexponential decay, indicating intercalative/partial intercalative binding mode with DNA. The luminescent characteristics of the complexes **2** and **4** bound to DNA shows biexponential decay in emission indicating the presence of two distinguishable DNA binding modes for the complexes. Two binding modes were proposed for the complex **2**; one may be partial intercalation, while the other is groove-bound interaction or electrostatic interaction in which the excited-state lifetime is comparable to that of the free form. When the binding ratio [DNA]/[Ru] is varied from 2:1 to 30:1 for the complex **4**, the excited-state lifetimes increased from 207 ns to 290 ns for short-lifetime component and from 677 to 1679 ns for long-lifetime component and for the complex **2** from 183 to 334 ns for short-lifetime component and from 329 to 761 ns for long-lifetime component. The steady-state quenching experiments and time-resolved emission measurements on complex **4** suggest that both lifetime components could be assigned to partial intercalative binding depending on the orientations of the two dppz ligands in the complex. The results also are consistent with intercalation and electrostatic binding being the two binding modes. This complex contains the sterically demanding bipyridine glycoluril ancillary ligand, and the other planar dppz ligand, which increases hydrophobicity (*17*). The presence of multiple binding modes for osmium and ruthenium polypyridyl complexes has been suggested recently on the basis of DNA film voltammetry (*21*). The luminescent characteristics of the complex **8** bound to DNA show biexponential decay in emission indicating the presence of two distinguishable DNA binding modes. When the binding ratio [DNA]/[Ru] varied from 2:1 to 30:1 for the complex **8**, the excited-state lifetimes increased up to 125 ns for short-lifetime component and from 346 to 611 ns for long-lifetime component. The lifetimes obtained for long-lived species of complex **8** are higher than the others, confirming its stronger intercalative DNA binding, and does not differ from the excited-state lifetimes in the presence of DNA for $[Ru(phen)_2dppz]^{2+}$ (*10*, *11*, *17*−*21*) indicating that the intercalated dppz ligand is well-protected from solvent.

Preliminary DNA Cleavage Studies under Dark and Light Conditions. Majority of ruthenium−polypyridyl complexes noncovalently bind to DNA by different modes, viz., electrostatic, surface binding, or intercalation, and initiate DNA cleavage reactions on photoirradiation either by electron transfer to base forming covalent photoadducts or by energy transfer to molecular oxygen generating $^1O_2$ or rarely by a hydrolytic mechanism (*50*, *54*, *89*−*95*). We have recently reported the hydrolytic cleavage of plasmid *pBR322* DNA by $[Ru(bpy)_2(BPG)]^{2+}$ **1** in an enzyme-like manner and detailed the kinetic aspects of DNA cleavage by **1** under pseudo and true Michaelis−Menten conditions (*54*). Therefore, in the present study the potential of complexes **2**−**9** to cleave DNA under

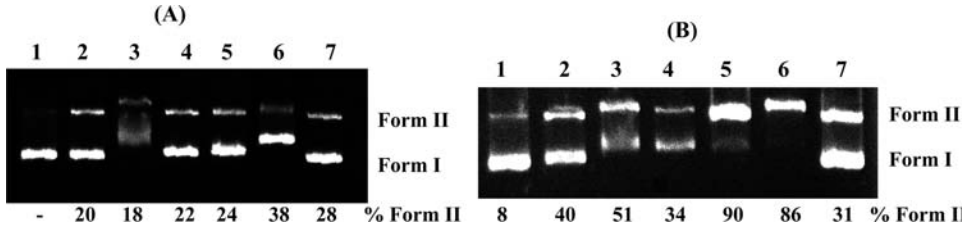

Figure 3. Ethidium bromide-stained agarose gel (1%) of plasmid *pBR322* DNA (90 μM in base pairs) in the presence of 20 μM Ru(II) complexes **2**−**4** and **9**. (A) Dark experiments for **2**−**4** and **9** (incubation for 2 h in air atmosphere): Form I - supercoiled plasmid DNA, Form II - nicked circular plasmid DNA; Lane 1 - DNA control, Lane 2 - DNA + $[Ru(bpy)_3]^{2+}$, Lane 3 - DNA + $[Ru(bpy)_2(dppz)]^{2+}$, Lane 4 - DNA + **2**, Lane 5 - DNA + **3**, Lane 6 - DNA + **4**, Lane 7 - DNA + **9**. (B) Light experiments for **2**−**4** and **9** in air (incubation 30 min, irradiation 20 min; $\lambda_{irr} = 365$ nm): Lane 1 - DNA control, Lane 2 - DNA + $[Ru(bpy)_3]^{2+}$, Lane 3 - DNA + $[Ru(bpy)_2(dppz)]^{2+}$, Lane 4 - DNA + **2**, Lane 5 - DNA + **3**, Lane 6 - DNA + **4**, Lane 5 - DNA + **9**.

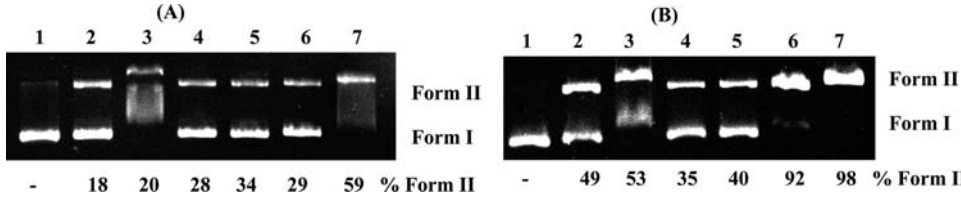

Figure 4. Ethidium bromide-stained agarose gel (1%) of plasmid *pBR322* DNA (90 μM in base pairs) in the presence of 20 μM Ru(II) complexes **5**−**8**. (A) Dark experiments for **5**−**8** (incubation for 2 h in air atmosphere): Form I - supercoiled plasmid DNA, Form II - nicked circular plasmid DNA; Lane 1 - DNA control, Lane 2 - DNA + $[Ru(bpy)_3]^{2+}$, Lane 3 - DNA + $[Ru(bpy)_2(dppz)]^{2+}$, Lane 4 - DNA + **5**, Lane 5 - DNA + **6**, Lane 6 - DNA + **7**, Lane 7 - DNA + **8**. (B) Light experiments for **5**−**8** in air (incubation 30 min, irradiation 20 min; $\lambda_{irr} = 365$ nm): Lane 1 - DNA control, Lane 2 - DNA + $[Ru(bpy)_3]^{2+}$, Lane 3 - DNA + $[Ru(bpy)_2(dppz)]^{2+}$, Lane 4 - DNA + **5**, Lane 5 - DNA + **6**, Lane 6 - DNA + **7**, Lane 5 - DNA + **8**.

dark and light conditions was studied by gel electrophoresis using plasmid *pBR322* DNA.

When incubated for 2 h at 37 °C under dark conditions, it is observed that micromolar concentration of complexes **2**−**4** and **9** shows 22−40% (Figure 3A) and **5**−**8** shows 28−60% (Figure 4A) DNA cleavage as evidenced by the disappearance of form I (supercoiled form) of the plasmid and the appearance of the form II (nicked circular form). A band migration of the supercoiled form of DNA relative to the control lane is observed for complexes **2**−**4** (Figure 3A; lanes 4−6) and for complexes **7** and **8** (Figure 4A; lanes 6 and 7). An increase in DNA cleavage is observed for **2**−**9** after incubation for 2 h in argon atmosphere (Figures S9 and S10A in the Supporting Information) implying an oxygen-independent cleavage mechanism under dark conditions. Extensive DNA cleavage is observed for complexes **2**−**9** in dark conditions when incubated for 18 h at 37 °C (Figures S9B and S10B in the Supporting Information) indicating a hydrolytic mechanism, which suggests that these complexes are oriented in such a way so as to facilitate intramolecular H-bonding with the phosphate group or with the nucleobases. Under similar conditions $[Ru(bpy)_3]^{2+}$ and $[Ru(bpy)_2(dppz)]^{2+}$, which binds to DNA by electrostatic binding and intercalation, respectively, and are not capable of H-bonding, cleave DNA to a lesser extent after 2 h incubation as compared to complexes **2**−**9**. Here, we have observed DNA cleavage under dark conditions by ruthenium polypyridyl complexes containing one, two, and three BPG ligands without any bound water molecule, but with the pheripheral urea moiety of the ancillary bipyridyl glycoluril ligand hydrolyzes the phosphodiester bond efficiently.

The rate of RNA hydrolysis is enhanced 3300-fold by monometallic Zn(II) complexes of terpyridine-based ligands with ammonium and guanidinium groups capable of H-bonding to the phosphodiester group compared to the parent complex without the functional H-bonding groups (*96*). A similar effect of enhancing the phosphodiester cleavage was observed by a Zn(II) complex with three aminopyridyl hydrogen bond donors, which orient the complex and the substrate for efficient proximity interactions (*97*−*99*). A series of organometallic ruthenium and *cis*-platin like ethylenediamine based complexes also exploit these H-bonding interactions to direct DNA binding by the NH_2 groups of the metal-bound ethylenediamine ligand favoring H-bonding interactions with nucleobases resulting in site-selectivity (*100*−*102*).

Rhodium(III) intercalators attached to peptide moieties $[Rh(phi)_2(bpy'\text{-peptide})]$ (phi = intercalative ligands), macrocyclic complexes of lanthanides, polyamine derivatives such as cyclen, trpn, and tamen complexes of cobalt(III) can act as catalysts for the hydrolysis of the phosphate esters of DNA and ammonium-functionalized copper(II) complexes and copper(II) complexes of macrocycles, *cis*,*cis*-1,3,5-triaminocyclohexane and neamine have been reported (*103*−*105*). Of those, however, the most highly efficient hydrolytic cleavage agents are mononuclear copper(II) complexes in which a copper-bound hydroxyl group is the active species in the hydrolysis of the nucleic acid phosphate backbone. As far as we are aware, the only other hydrolytic cleavage of DNA by the ruthenium−polypyridyl complex was reported by Barton et al. for the $[Ru(DIP)_2(macro)]^{2+}$, where $Ru(DIP)_2$ binds to DNA via intercalation and macro is a chelating ligand with two polyamine tridentate arm-like segments which bind certain divalent metal cations so as to deliver its coordinated nucleophile to the phosphate backbone for the hydrolysis of the anionic diester (*50*).

Photocleavage of DNA by ruthenium(II) polypyridyl complexes on irradiation is well-documented in the literature (*89*−*95*). Therefore, the photocleavage of plasmid *pBR322* DNA in the presence of complexes **2**−**9** on irradiation at 365 nm was carried out, and the results are shown in Figure 3B and Figure 4B. The complexes **2** and **9** show only 3−12% increase in conversion of form I (SC) of DNA to form II (NC) of DNA, and the complexes **5** and **6** show only 6−7% increase in conversion of form I (SC) of DNA to form II (NC) of DNA as compared to DNA cleavage under dark conditions. The fact that the observed photocleavage for complexes **2**, **5**, **6**, and **9** in air is significantly lower than what is observed for $[Ru(bpy)_3]^{2+}$ possibly indicates lower levels of $^1O_2$ generation. The complexes **3**, **4**, **7**, and **8** and $[Ru(bpy)_2(dppz)]^{2+}$ shows extensive DNA cleavage in the

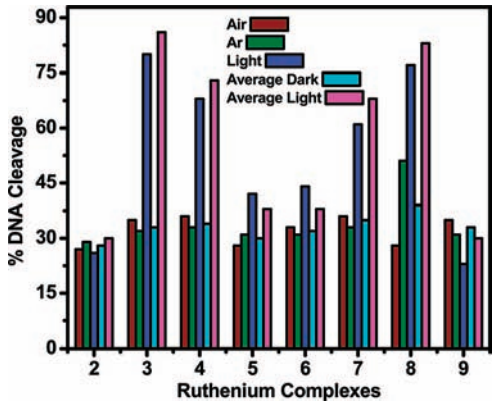

Figure 5. DNA cleavage efficiency of ruthenium(II) complexes containing one, two, and three BPG ligands **2**−**9** in the dark and light conditions.

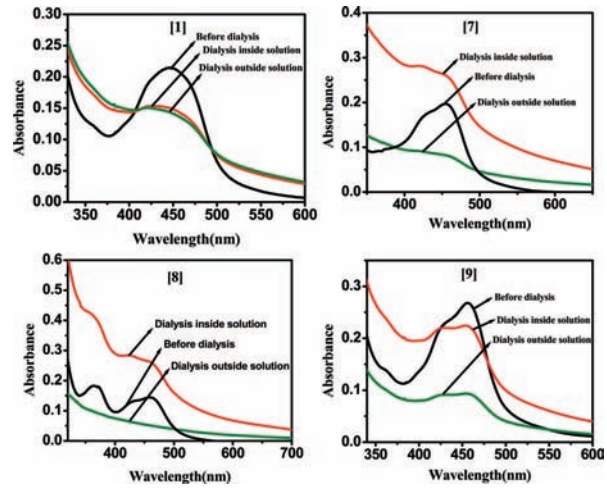

Figure 6. Changes in the absorption spectras of complexes **1** and **7**−**9** in the presence of calf thymus DNA under dark conditions with dialysis (24 h) compared with the dialyzed samples and undialyzed samples in phosphate buffer pH 7.2 solutions. ([Ru] = 20 μM, [DNA] = 200 μM).

presence of light with a shift in mobility of form I of DNA probably due to the high molecular weight of DNA−complex conjugates.

In order to investigate the role of radicals in the DNA damage by these complexes **2**−**9**, reactions were performed under aerobic conditions by incubating the complexes for half an hour and irradiation for 20 min with DNA in the presence of hydroxyl radical scavengers (DMSO and mannitol), singlet oxygen scavengers (NaN_3, histidine, and DABCO) and superoxide scavenger (superoxide dismutase, SOD) (Figures S11−S18, Tables S2−S9 in the Supporting Information). It is observed that the photocleavage by complexes **2** and **9** was not inhibited by reactive oxygen species scavengers indicating hydrolytic pathway for these complexes. However, complexes **5** and **6** show small amounts of inhibition in the presence of reactive oxygen species indicating hydrolytic mechanism. Complexes **3**, **4**, **7**, and **8** containing dpq and dppz intercalating ligands show extensive DNA cleavage in the presence of light, and the photocleavage experiments in the presence of different radical scavengers show inhibition indicating that hydroxyl radicals and singlet oxygen are responsible for DNA cleavage by these complexes upon irradiation. From the above results, it appears that the mechanism of DNA cleavage photoinduced by complexes **3**, **4**, **7**, and **8** involve either singlet oxygen or hydroxyl radicals. However, the photocleavage by these complexes is higher than $[Ru(bpy)_2(dppz)]^{2+}$ complex implying that complexes **3**, **4**, **7**, and **8** with an inherent intercalating ability cleave DNA by a combination of oxidative and hydrolytic cleavage. The cleavage data for all complexes **2**−**9** under dark conditions in the presence and absence of air and under light conditions are tabulated in Table S10 in the Supporting Information and depicted as a histogram in Figure 5.

DNA−Complex Conjugate Investigation by UV−vis Spectroscopy: In order to further investigate the formation of the DNA−complex conjugates, dialysis experiments followed by UV−vis spectroscopy were performed on the ruthenium(II) bipyridine−glycoluril complexes in the presence of CT-DNA under dark conditions in phosphate buffer (pH 7.2). If the complex is covalently bound to the DNA, then this can be verified by dialysis of the samples where the parent metal complex, but not the DNA, would pass through the dialysis membrane (*106, 107*). The formation of the product is monitored by UV−vis spectroscopy, and the results are given in Figure 6 and Figure S19 in the Supporting Information. Figure 6 shows the spectrum of the complexes **1**, **7**, **8**, and **9** kept in the dark for 24 h in the presence of CT-DNA, both before and after dialysis. With complexes **1** and **9**, the large decrease in absorption is observed showing that most of the product is diffused through the dialysis membrane as would be expected for the complexes which are not bound strongly to the CT-DNA. However, the absorption spectrum of the dialyzed samples **2**−**8** in the presence of DNA reveals that the complex remains bound to DNA inside the membrane (Figure 6 and Figure S19 in the Supporting Information). The complexes **2**−**8** after dialysis in the presence of CT-DNA show large increases in absorption in the 345−500 nm region suggesting that these complexes are strongly bound to the CT-DNA and the conjugate formed is retained after dialysis. The UV−vis spectroscopic observations together with the electrophoresis results presented earlier suggests that the DNA−complex conjugates are formed with CT-DNA. A hyperchromic effect and mobility shift in electrophoresis experiments were reported previously for the complexes of the type $[Ru(bpy)_{3-n}(TAP/HAT)_n]^{2+}$ (n = 2, 3), which result in the formation of adducts on irradiation (*106, 107*).

Molecular Modeling. Molecular mechanics calculations have been carried out for complexes **1**−**9** with the models of right-handed B-DNA of sequence $d(C:G)_{12}$. Different modes of binding with different orientations of ruthenium complexes, including groove binding through major/minor groove, and intercalation through major and minor groove, were attempted with the model of right-handed B-DNA of sequence $d(C:G)_{12}$. It was observed that the minimized structure maintains the octahedral form of the complexes and shows the H-bonding to the bases and phosphates of DNA without disrupting the helical structure of B-DNA. The H-bonding distances for **1**−**9** after minimizations are summarized in Table S11 in the Supporting Information. All complexes are stabilized by H-bonding interactions between the DNA and the complexes. It is found that **1** and **2** orients in the minor and major groove, respectively, with hydrogen bonding interactions of the N−H and C−H groups preferably to O1P and O10P phosphate oxygen atoms of DNA for **1** and preferably to O2P phosphate oxygen atom in case of **2** (Figure 7 and Figure S18 in the Supporting Information), while for **9** in the major groove with the H- bonding between the N−H and C═O groups of the bipyridine−glycoluril ligand and the N7 of the guanine. (Figure S24 in the Supporting Information). Such N−H···O H-bonding interactions between one ethylenediamine NH proton and the guanine O6 oxygen have been shown by Sadler and co-workers in the case of organomatallic ruthenium(II) arene complexes of the type $[(\eta^6\text{-arene})Ru^{II}(en)Cl](PF_6)$ (en = ethylenediamine, arene = biphenyl, 5,8,9,10-tetrahydroanthracene, and 9,10-dihydroanthracene) specifically target guanine bases of DNA oligomers (*102*). It is found that

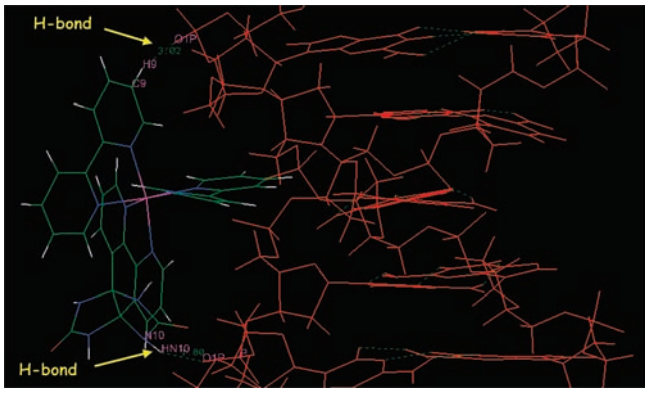

Figure 7. The core view of the bound **1** to DNA with the H-bond patterns observed showing phosphate interactions.

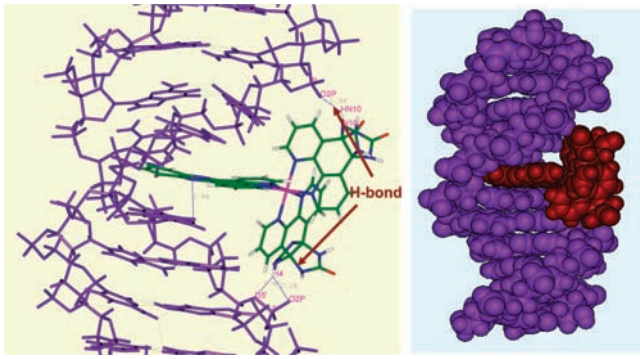

Figure 8. The core view of the bound **8** to DNA showing the intercalation of the dppz ligand between the base pairs of DNA along with the H-bonding interactions of the two BPG ligands with the phosphate groups of DNA.

the binding of **5** and **6** in the major groove with H-bonding interactions of the N−H groups preferably to O2P phosphate oxygen atoms of DNA (Figure S21 and Figure S22 in the Supporting Information). In the complexes **1**, **2**, and **9**, the urea groups exclusively bind with phosphate oxygens of the nucleic acids. Recently, Farrell et al. have reported a phosphate backbone binding mode for a polynuclear platinum(II) complex that has planar arrays of hydrogen bond donors, leading to association with the DNA backbone (*108*). For complexes **3** and **4**, the molecular modeling reveals that the planar dpq and dppz ligands interact with the bases and the other planar ligand with the phosphate oxygens. (Figure S19 and S20 in the Supporting Information). However, the complexes **7** and **8** containing planar aromatic dpq and dppz ligands and with the two ancillary bipyridine−glycoluril ligands show the intercalative binding mode in which the stacking interaction of the planar dpq (Figure S23 in the Supporting Information) and dppz ligand between the base pairs of DNA through major groove side take place along with the phosphate interactions of the N−H groups of the two ancillary bipyridine-glycoluril ligands preferably to O2P oxygen atoms (Figure 8), Such H-bonding suggests that the bipyridine−glycoluril ligand is located in a specific position of the H-bond to the neighboring oxygen atoms of the bases or a phosphate group and thus influences the binding ability of these complexes with DNA.

CONCLUDING REMARKS

In summary, in the present study we have synthesized a series of new Ru(II) polypyridyl complexes containing urea fused bipyridine−glycoluril ligand and characterized by various physical methods. By the incorporation of the simple modification on the ancillary ligand of bipyridine, different DNA binding behaviors for complexes **1**−**9** were observed. The planar aromatic ligands have the potential for intercalation, and the bipyridine−glycoluril ligand with inherent H-bond donor and acceptor groups are accessible for H-bonding with the phosphate groups or with the nucleobases of DNA. The DNA binding and photocleavage measurements revealed that the complexes that favor electrostatic binding mode cleave DNA by hydrolytic mechanism while those that contain intercalating ligands form conjugates with and then cleave DNA by a combination of oxidative and hydrolytic mechanism.

ACKNOWLEDGMENT

M.S.D. acknowledges Bhabha Atomic Research Centre (BARC) for providing research fellowship through collaborative research scheme of Pune University - BARC, Mumbai, India. A.A.K. acknowledges the financial assistance from Department of Science and Technology (DST), New Delhi, for the award of Fast Track Project for Young Scientist (SR/FTP/CSA-15/2003). A.S.K. thanks University of Pune for partial funding. The time correlated single photon-counting spectrophotometer facility in the Department was created by funding from the University Grants Commission, New Delhi, under the Centre for Advanced Studies funds (CAS). The authors thank Dr. Amitava Das CSMCRI, Bhavnagar, India, for cyclic voltammetry data.

Supporting Information Available: Changes in the relative specific viscosity of solutions **1**−**9** in the presence of CT-DNA (Figure S1 and S2); melting curves of CT-DNA in the absence and presence of complexes **1**−**9** (Figure S3 and S4); emission spectra of Ru(II) complexes **1**−**9** (25 μM) in phosphate buffer with increasing [DNA]/[Ru] ratio from 0 to 30 (Figure S5 and S6), emission spectra of Ru(II) complexes **1**−**9** using anionic quencher $K_4[Fe(CN)_6]$ in the presence and absence of DNA in phosphate buffer (Figure S7 and S8), luminescence decay lifetime of the complexes **1**−**9** in the presence of CT-DNA (Table S1), DNA cleavage experiment in the presence of 20 μM Ru(II) complexes **2**−**9**; dark experiments incubation for 2 h in argon atmosphere and dark experiments incubation for 18 h in air (Figure S9 and S10); DNA cleavage experiment in the presence of different radical scavengers for Ru(II) complexes **2**−**9** (Figure S11−S18 and Table S2−S9); DNA cleavage efficiency of ruthenium(II) complexes containing one, two, and three BPG ligands **2**−**9** in the dark and light conditions (Table S10); changes in the absorption spectras of complexes **2**−**6** in the presence of DNA before and after dialysis (Figure S19); the core view of the bound **2**−**7** and **9** (Figure S20−S26) to DNA, binding energies in kcal/mol and hydrogen bond information of Ru(II) polypyridyl complexes **1**−**9** with right-handed B-DNA of sequence $d(C:G)_{12}$ (Table S11). This material is available free of charge via the Internet at http://pubs.acs.org.

LITERATURE CITED

(1) Zeglis, B. M., Pierre, V. C., and Barton, J. K. (2007) Metallo-intercalators and metallo-insertors. *Chem. Commun.* 4565–4579.
(2) Metcalfe, C., and Thomas, J. A. (2003) Kinetically inert transition metal complexes that reversibly bind to DNA. *Chem. Soc. Rev. 32*, 215–224.
(3) Erkkila, K. E., Odom, D. T., and Barton, J. K. (1999) Recognition and reaction of metallointercalators with DNA. *Chem. Rev. 99*, 2777–2796.
(4) Sigman, D. S., Mazumder, A., and Perrin, D. M. (1993) Chemical nucleases. *Chem. Rev. 93*, 2295–2316.
(5) Eriksson, M., Leijon, M., Hiort, C., Norden, B., and Graslund, A. (1994) Binding of Δ- and Λ-$[Ru(phen)_3]^{2+}$ to [d(CGCGATCGCG)]2 Studied by NMR. *Biochemistry 33*, 5031–5040.

(6) Hudson, B. P., Dupureur, C. M., and Barton, J. K. (1995) 1H NMR structural evidence for the sequence-specific design of an intercalator: Δ-α-[Rh[(R, R)-Me2trien]phi]$^{3+}$ bound to d(GAGTGCACTC)$_2$. *J. Am. Chem. Soc. 117*, 9379–9380.

(7) Terbrueggen, R. H., and Barton, J. K. (1995) Sequence-specific DNA binding by a rhodium complex: recognition based on sequence-dependent twistability. *Biochemistry 34*, 8227–8234.

(8) Lecomte, J. P., Kirsch-De Mesmaeker, A., and Kelly, J. M. (1996) Photoreactions of metal complexes with DNA, especially those involving a primary photo-electron transfer. *Top. Curr. Chem. 177*, 25–76.

(9) Lincoln, P., and Norden, B. (1998) DNA binding geometries of ruthenium(II) complexes with 1,10-phenanthroline and 2,2′-bipyridine ligands studied with linear dichroism spectroscopy. borderline cases of intercalation. *J. Phys. Chem. B 102*, 9583–9594.

(10) Hermana, L., Ghosh, S., Defrancq, E., and Mesmaeker, A. K.-D. (2008) Ru(II) complexes and light: molecular tools for biomolecules. *J. Phys. Org. Chem. 21*, 670–681.

(11) Tuite, E., Lincoln, P., and Norden, B. (1997) Photophysical evidence that Δ- and Λ-[Ru(phen)$_2$(dppz)]$^{2+}$ intercalate DNA from the minor groove. *J. Am. Chem. Soc. 119*, 239–240.

(12) Collins, J. G., Aldrich-Wright, J. R., Greguric, I. D., and Pellegrini, P. A. (1999) Binding of the Δ and Λ-enantiomers of [Ru(dmphen)$_2$dpq]$^{2+}$ to the hexanucleotide d(GTCGAC)$_2$. *Inorg. Chem. 38*, 5502–5509.

(13) Greguric, I. D., Aldrich-Wright, J. R., and Collins, J. G. (1997) A ^{1}H NMR study of the binding of Δ-[Ru(phen)$_2$DPQ]$^{2+}$ to the hexanucleotide d(GTCGAC)$_2$. Evidence for intercalation from the minor groove. *J. Am. Chem. Soc. 119*, 3621–3622.

(14) De Silva, A. P., and McClenaghan, N. D. (2004) Molecular-scale logic gates. *Chem. Eur. J. 10*, 574–586.

(15) Jiang, Y., Fang, X., and Bai, C. (2004) Signaling aptamer/protein binding by a molecular light switch complex. *Anal. Chem. 76*, 5230–5235.

(16) O'Donoghue, K., Penedo, J. C., Kelly, J. M., and Kruger, P. E. (2005) Photophysical study of a family of [Ru(phen)$_2$(Me$_n$-dpq)]$^{2+}$ complexes in different solvents and DNA: a specific water effect promoted by methyl substitution. *Dalton Trans.* 1123–1128.

(17) Hartshorn, R. M., and Barton, J. K. (1992) Novel dipyridophenazine complexes of ruthenium(II): exploring luminescent reporters of DNA. *J. Am. Chem. Soc. 114*, 5919–5925.

(18) Jenkins, Y., and Barton, J. K. (1992) A sequence-specific molecular light switch: tethering of an oligonucleotide to a dipyridophenazine complex of ruthenium(II). *J. Am. Chem. Soc. 114*, 8736–8738.

(19) Jenkins, Y., Friedman, A. E., Turro, N. J., and Barton, J. K. (1992) Characterization of dipyridophenazine complexes of ruthenium(II): The light switch effect as a function of nucleic acid sequence and conformation. *Biochemistry 31*, 10809–10816.

(20) Friedman, A. E., Chambron, J. C., Sauvage, J. P., Turro, N. J., and Barton, J. K. (1990) A molecular light switch for DNA: Ru(bpy)$_2$(dppz)$_2^+$. *J. Am. Chem. Soc. 112*, 4960–4962.

(21) Guo, L.-H., Wei, M.-Y., and Chen, H. (2006) Multiple DNA binding modes of a metallointercalator revealed by DNA film voltammetry. *J. Phys. Chem. B 110*, 20568–20571.

(22) Hiort, C., Lincoln, P., and Norden, B. (1993) DNA binding of Δ- and Λ-[Ru(phen)$_2$DPPZ]$^{2+}$. *J. Am. Chem. Soc. 115*, 3448–3454.

(23) Arounaguiri, S., and Maiya, B. G. (1999) "Electro-photo switch" and "molecular light switch" devices based on ruthenium(II). Complexes of modified dipyridophenazine ligands: modulation of the photochemical function through ligand design. *Inorg. Chem. 38*, 842–843.

(24) Ambroise, A., and Maiya, B. G. (2000) Ruthenium(II) complexes of redox-related, modified dipyridophenazine ligands: synthesis, characterization, and DNA interaction. *Inorg. Chem. 39*, 4256–4263.

(25) Ambroise, A., and Maiya, B. G. (2000) Ruthenium(II) complexes of 6,7-dicyanodipyridoquinoxaline: synthesis, luminescence studies, and DNA interaction. *Inorg. Chem. 39*, 4264–4272.

(26) Liu, Y., Chouai, A., Degtyareva, N. N., Lutterman, D. A., Dunbar, K. R., and Turro, C. (2005) Chemical control of the DNA light switch: cycling the switch ON and OFF. *J. Am. Chem. Soc. 127*, 10796–10797.

(27) Tysoe, S. A., Kopelman, R., and Schelzig, D. (1999) Flipping the molecular light switch off: formation of DNA-bound heterobimetallic complexes using Ru(bpy)$_2$tpphz^{2+} and transition metal ions. *Inorg. Chem. 38*, 5196–5197.

(28) Lo, K. K.-W., Chung, C.-K., and Zhu, N. (2006) Nucleic acid intercalators and avidin probes derived from luminescent cyclometalated iridium(III)-dipyridoquinoxaline and -dipyridophenazine complexes. *Chem. Eur. J. 12*, 1500–1512.

(29) Albano, G., Belser, P., De Cola, L., and Gandolfi, M. T. (1999) New luminescent ruthenium complexes with extended π-systems. *Chem. Commun.* 1171–1172.

(30) Jackson, B. A., Alekseyev, V. Y., and Barton, J. K. (1999) A versatile mismatch recognition agent: specific cleavage of a plasmid DNA at a single base mispair. *Biochemistry 38*, 4655–4662.

(31) Bergman, S. D., Gut, D., Kol, M., Sabatini, C., Barbieri, A., and Barigelletti, F. (2005) Eilatin complexes of ruthenium and osmium. Synthesis, electrochemical behavior, and near-IR luminescence. *Inorg. Chem. 44*, 7943–7950.

(32) Kirk, S. R., Luedtke, N. W., and Tor, Y. (2001) 2-Aminopurine as a real-time probe of enzymatic cleavage and inhibition of hammerhead ribozymes. *Bioorg. Med. Chem. 9*, 2295–2301.

(33) Luedtke, N. W., Hwang, J. S., Nava, E., Gut, D., Kol, M., and Tor, Y. (2003) The DNA and RNA specificity of eilatin Ru(II) complexes as compared to eilatin and ethidium bromide. *Nucleic Acids Res. 31*, 5732–5740.

(34) Luedtke, N. W., and Tor, Y. (2003) Fluorescence-based methods for evaluating the RNA affinity and specificity of HIV-1 Rev-RRE inhibitors. *Biopolymers 70*, 103–119.

(35) Chouai, A., Wicke, S. E., Turro, C., Bacsa, J., Dunbar, K. R., Wang, D., and Thummel, R. P. (2005) Ruthenium(II) complexes of 1,12-diazaperylene and their interactions with DNA. *Inorg. Chem. 44*, 5996–6003.

(36) Stemp, E. D. A., Arkin, M. K., and Berton, J. K. (1995) Electron transfer between metallointercalators bound to DNA: Spectral identification of the transient intermediate. *J. Am. Chem. Soc. 117*, 2375–2376.

(37) Liu, J. G., Zhang, Q. L., Shi, X. F., and Ji, L. N. (2001) Interaction of [Ru(dmp)$_2$(dppz)]$^{2+}$ and [Ru(dmb)$_2$(dppz)]$^{2+}$ with DNA: Effects of the ancillary ligands on the DNA-binding behaviors. *Inorg. Chem. 40*, 5045–5050.

(38) Nair, R. B., Yeung, L. K., and Murphy, C. J. (1999) Synthesis and solvent-dependent properties of Ru(acac)$_2$dppz. *Inorg. Chem. 38*, 2536–2538.

(39) Ji, L. N., Zon, X. H., and Ziu, J. G. (2001) Shape- and enantioselective interaction of Ru(II)/Co(III) polypyridyl complexes with DNA. *Coord. Chem. Rev. 216−217*, 513–536.

(40) Foxon, S. P., Metcalfe, C., Adams, H., Webb, M., and Thomas, J. A. (2007) Electrochemical and photophysical properties of DNA metallo-intercalators containing the ruthenium(II) Tris(1-pyrazolyl)methane unit. *Inorg. Chem. 46*, 409–416.

(41) Metcalfe, C., Adams, H., Haq, I., and Thomas, J. A. (2003) A ruthenium dipyridophenazine complex that binds preferentially to GC sequences. *Chem. Commun.* 1152–1153.

(42) Liu, J. G., Ye, B. H., Li, H., Ji, L. N., Li, R. H., and Zhou, J. Y. (1999) Synthesis, characterization and DNA-binding properties of novel dipyridophenazine complex of ruthenium(II): [Ru(IP)$_2$(DPPZ)]$^{2+}$. *J. Inorg. Biochem. 73*, 117–122.

(43) Maheswari, P. U., Rajendiran, V., Palaniandavar, M., Parthasarathi, R., and Subramanian, V. (2006) Synthesis, characterization -and DNA-binding properties of rac-[Ru(5,6 dmp)$_2$-(dppz)]$^{2+}$- Enantiopreferential DNA binding and co-ligand promoted exciton coupling. *J. Inorg. Biochem. 100*, 3–17.

(44) Sentagne, C., Chambron, J.-C., Sauvage, J.-P., and Paillous, N. (1994) Tuning the mechanism of DNA cleavage photosensitized by ruthenium dipyridophenazine complexes by varying the structure of the two non intercalating ligands. *J. Photochem. Photobiol. B: Biology 26*, 165–174.

(45) Liu, Y., Hammitt, R., Lutterman, D. A., Thummel, R. P., and Turro, C. (2007) Marked differences in light-switch behavior of Ru(II) complexes possessing a tridentate DNA intercalating ligand. *Inorg. Chem. 46*, 6011–6021.

(46) Nair, R. B., Teng, E. S., Kirkland, S. L., and Murphy, C. J. (1998) Synthesis and DNA-binding properties of $[Ru(NH_3)_4$-dppz$]^{2+}$. *Inorg. Chem. 37*, 139–141.

(47) Neyhart, G. A., Grover, N., Smith, S. R., Kalsbeck, W. A., Fairley, T. A., Cory, M., and Thorp, H. H. (1993) Binding and kinetics studies of oxidation of DNA by oxoruthenium(IV). *J. Am. Chem. Soc. 115*, 4423–4428.

(48) Puckett, C. A., and Barton, J. K. (2007) Methods to explore cellular uptake of ruthenium complexes. *J. Am. Chem. Soc. 129*, 46–47.

(49) Kelly, J. M., Tossi, A. B., McConnell, D. J., and OhUigin, C. (1985) A study of the interactions of some polypyridylruthenium(II) complexes with DNA using fluorescence spectroscopy, topoisomerisation and thermal denaturation. *Nucleic Acids Res. 13*, 6017–6034.

(50) Basile, L. A., Raphael, A. L., and Barton, J. K. (1987) Metal-activated hydrolytic cleavage of DNA. *J. Am. Chem. Soc. 109*, 7550–7551.

(51) Deshpande, M. S., Kumbhar, A. S., Puranik, V. G., and Selvaraj, K. (2006) Supramolecular self-assembled ruthenium-polypyridyl framework encapsulating discrete water cluster. *Cryst. Growth Des. 6*, 743–748.

(52) Deshpande, M. S., Kumbhar, A. S., and Puranik, V. G. (2008) Hydrogen bonding-directed metallosupramolecular structural motifs based on a peripheral urea fused bipyridine tecton. *Cryst. Growth Des. 8*, 1952–1960.

(53) Kumbhar, A. S., Deshpande, M. S., and Butcher, R. J. (2008) Hydrogen bond directed open-framework of bis(bipyridine-glycoluril) phosphatocobalt(III) with solvent accessible void space. *CrystEngComm. 10*, 1520–1523.

(54) Deshpande, M. S., Kumbhar, A. A., and Kumbhar, A. S. (2007) Hydrolytic cleavage of DNA by a Ruthenium(II). Polypyridyl complex. *Inorg. Chem. 46*, 5450–5452.

(55) Marmur, J. (1961) Procedure for isolation of deoxyribonucleic acid from micro-organisms. *J. Mol. Biol. 3*, 208–218.

(56) Yamada, M., Tanaka, Y., Yoshimoto, Y., and Kuroda, S. (1992) Synthesis and properties of diamino-substituted dipyrido[3,2-*a*:2′,3′-*c*]phenazine. *Bull. Chem. Soc. Jpn. 65*, 1006–1011.

(57) Collins, J. G., Sleeman, A. D., Aldrich-Wright, J. R., Greguric, L., and Hambley, T. W. (1998) A ^{1}H NMR study of the DNA binding of ruthenium(II) polypyridyl complexes. *Inorg. Chem. 37*, 3133–3141.

(58) Dickerson, J. E., and Summers, L. A. (1970) Derivatives of 1,10-phenanthroline-5,6-quinone. *Aust. J. Chem. 23*, 1023–1027.

(59) Elemans, J. A. A. W., Gelder, R. D., Rowan, A. E., and Nolte, R. J. M. (1998) Bipyridine functionalized molecular clips. Self-assembly of their ruthenium complexes in water. *Chem. Commun.* 1553–1554.

(60) Kurth, D. G., Fromm, K. M., and Lehn, J. M. (2001) Hydrogen-bonding and metal-ion-mediated self-assembly of a nanoporous crystal lattice. *Eur. J. Inorg. Chem.* 1523–1526.

(61) Sullivan, B. P., Salmon, D. J., and Meyer, T. J. (1978) Mixed phosphine 2,2′-bipyridine complexes of ruthenium. *Inorg. Chem. 17*, 3334–3341.

(62) Sprintschnik, G., Sprintschnik, H. W., Kirsch, P. P., and Whitten, D. G. (1977) Photochemical reactions in organized monolayer assemblies. 6. Preparation and photochemical reactivity of surfactant ruthenium(II) complexes in monolayer assemblies and at water-solid interfaces. *J. Am. Chem. Soc. 99*, 4947–4954.

(63) Krause, R. A. (1977) Synthesis of mixed complexes of ruthenium(II) with 2,2′-dipyridyl. *Inorg. Chim. Acta 22*, 209–213.

(64) Wolfe, A., Shimer, G. H., and Meehan, T. (1987) Polycyclic aromatic hydrocarbons physically intercalate into duplex regions of denatured DNA. *Biochemistry 26*, 6392–6396.

(65) Cohen, G., and Eisenberg, H. (1969) Viscosity and sedimentation study of sonicated DNA-proflavine complexes. *Biopolymers 8*, 45–55.

(66) Lakowicz, J. R. (2006) *Principles of fluorescence spectroscopy*, 3rd ed., New York.

(67) Caspar, J. V., and Meyer, T. J. (1983) Photochemistry of tris(2,2′-bipyridine)ruthenium(2+) ion (Ru(bpy)32+). Solvent effects. *J. Am. Chem. Soc. 105*, 5583–5590.

(68) Lakowicz, J. R., and Webber, G. (1973) Quenching of fluorescence by oxygen. Probe for structural fluctuations in macromolecules. *Biochemistry 12*, 4161–4170.

(69) O'Connor, D. V. and Phillips, D. (1984) *Time Correlated Single Photon Counting*, Academic Press, New York.

(70) Tonde, S. S., Kumbhar, A. S., Padhye, S. B., and Butcher, R. J. (2006) Self-activating nuclease activity of copper (II). Complexes of hydroxyl-rich ligands. *J. Inorg. Biochem. 100*, 51–57.

(71) Ghosh, S., Barve, A. C., Kumbhar, A. A., Kumbhar, A. S., Puranik, V. G., Datar, P. A., Sonawane, U. B., and Joshi, R. R. (2006) Synthesis, characterization, X-ray structure and DNA photocleavage by *cis*-dichloro bis(diimine). Co(III) complexes. *J. Inorg. Biochem. 100*, 331–343.

(72) Insight II2000, (1997) Molecular Modeling Program Package, Accelrys Inc., San Diego.

(73) Mercury, Cambridge Crystallographic Data Centre,12 Union Road, Cambridge CB21EZ, United Kingdom. Available from http://www.ccdc.cam.ac.uk/.

(74) Darden, T., Perera, L., Li, L., and Pedersen, L. (1999) New tricks for modelers from the crystallography toolkit: the particle mesh Ewald algorithm and its use in nucleic acid simulations. *Structure 7*, R55−R60.

(75) Allen, G. H., White, R. P., Rillema, D. P., and Meyer, T. J. (1984) Synthetic control of excited-state properties. Tris-chelate complexes containing the ligands 2,2′-bipyrazine, 2,2′-bipyridine, and 2,2′-bipyrimidine. *J. Am. Chem. Soc. 106*, 2613–2620.

(76) Treadway, J. A., Loeb, B., Lopez, R., Anderson, P. A., Keene, F. R., and Meyer, T. J. (1996) Effect of delocalization and rigidity in the acceptor ligand on MLCT excited-state decay. *Inorg. Chem. 35*, 2242–2246.

(77) Barton, J. K., Danishefsky, A. T. And, and Goldberg, J. M. (1984) Tris(phenanthroline)ruthenium(II): stereoselectivity in binding to DNA. *J. Am. Chem. Soc. 106*, 2172–2176.

(78) Friedman, A. E., Kumar, C. V., Turro, N. J., and Barton, J. K. (1991) Luminescence of ruthenium(II). Polypyridyls: evidence for intercalative binding to Z-DNA. *Nucleic Acids. Res. 19*, 2595–2601.

(79) Tang, T.-C., and Huang, H.-J. (1999) Electrochemical studies of the intercalation of ethidium bromide to DNA. *Electroanalysis 11*, 1185–1190.

(80) Paoletti, C., Le Pecq, J. B., and Lehman, I. R. (1971) The use of ethidium bromide-circular DNA complexes for the fluorometric analysis of breakage and joining of DNA. *J. Mol. Biol. 55*, 75–100.

(81) Suh, D., Oh, Y.-K., and Chaires, J. B. (2001) Determining the binding mode of DNA sequence specific compounds. *Process Biochem. 37*, 521–525.

(82) Aldrich-Wright, J. R., and Pellegrini, P. P. (2003) Evidence for chiral discrimination of ruthenium(II). polypyridyl complexes by DNA. *Dalton Trans.* 176–183.

(83) Satyanarayana, S., Dabrowiak, J. C., and Chaires, J. B. (1992) Neither Δ- nor Λ-tris(phenanthroline)ruthenium(II) binds to DNA by classical intercalation. *Biochemistry 31*, 9319–9324.

(84) Juris, A., Balzani, V., Barigelleti, F., Campagna, S., Belser, P., and Zelewsky, A. V. (1988) Ru(II) polypyridine complexes: photophysics, photochemistry, eletrochemistry, and chemiluminescence. *Coord. Chem. Rev. 84*, 85–277.
(85) Hager, G. D., and Crosby, G. A. (1975) Charge-transfer exited states of ruthenium(II). Complexes. I. Quantum yield and decay measurements. *J. Am. Chem. Soc. 97*, 7031–7037.
(86) Elfring, W. H. J., and Crosby, G. A. (1981) Excited states of mixed-ligand chelates of ruthenium(II). Quantum yield and decay time measurements. *J. Am. Chem. Soc. 103*, 2683–2687.
(87) Kumar, C. V., Barton, J. K., and Turro, N. J. (1985) Photophysics of ruthenium complexes bound to double helical DNA. *J. Am. Chem. Soc. 107*, 5518–5523.
(88) Barton, J. K., Goldberg, J. M., Kumar, C. V., and Turro, N. J. (1986) Binding modes and base specificity of tris(phenanthroline)ruthenium(II) enantiomers with nucleic acids: tuning the stereoselectivity. *J. Am. Chem. Soc. 108*, 2081–2088.
(89) Tan, L.-F., Chao, H., Li, H., Liu, Y. - J., Sun, B., Wei, W., and Ji, L.-N. (2005) Synthesis, characterization, DNA-binding and photocleavage studies of $[Ru(bpy)_2(PPIP)]^{2+}$ and $[Ru(phen)_2(PPIP)]^{2+}$. *J. Inorg. Biochem. 99*, 513–520.
(90) Sastri, C. V., Eswaramoorthy, D., Giribabu, L., and Maiya, B. G. (2003) DNA interactions of new mixed-ligand complexes of cobalt(III) and nickel(II) that incorporate modified phenanthroline ligands. *J. Inorg. Biochem. 94*, 138–145.
(91) Liu, Y.-J., Chao, H., Tan, L.-F., Yuan, Y.-X., Wei, W., and Ji, L.-N. (2005) Interaction of polypyridyl ruthenium (II) complex containing asymmetric ligand with DNA. *J. Inorg. Biochem. 99*, 530–537.
(92) Shi, S., Liu, J., Li, J., Zheng, K.-C., Huang, X. M., Tan, C. P., Chen, L.-M., and Ji, L.-N. (2006) Synthesis, characterization and DNA-binding of novel chiral complexes Δ- and Λ-$[Ru(bpy)_2L]^{2+}$ (L = o-mopip and p-mopip). *J. Inorg. Biochem. 100*, 385–395.
(93) Zhang, Q.-L., Liu, J.-H., Liu, J.-Z., Zhang, P.-X., Ren, X.-Z., Liu, Y., Huang, Y., and Ji, L.-N. (2004) DNA-binding and photoactivated enantiospecific cleavage of chiral polypyridyl ruthenium(II) complexes. *J. Inorg. Biochem. 98*, 1405–1412.
(94) Mei, H. Y., and Barton, J. K. (1988) Sequence-specific binding and photocrosslinking of α and β oligodeoxynucleotides to the major groove of DNA via triple-helix formation. *Proc. Natl. Acad. Sci. U.S.A. 85*, 1339–1343.
(95) Schoch, T. K., Hubbard, J. L., Zoch, C. R., Yi, G.-B., and Soerlie, M. (1996) Synthesis and structure of the ruthenium(II) complexes $[(\eta C_5Me_5)Ru(NO)(bipy)]^{2+}$ and $[(\eta C_5Me_5)Ru(NO)(dppz)]^{2+}$. DNA cleavage by an organometallic dppz complex (bipy = 2,2′-bipyridine; dppz = Dipyrido[3,2-*a*:2′,3′-*c*]phenazine). *Inorg. Chem. 35*, 4383–4390.
(96) Ait-Haddoun, H., Sumaoka, J., Wiskur, S. L., Folmer-Andersen, J. F., and Anslyn, E. V. (2002) Remarkable cooperativity between a Zn^{II} ion and guanidinium/ammonium groups in the hydrolysis of RNA. *Angew. Chem., Int. Ed. 41*, 4013–4016.
(97) Feng, G., Mareuqe-Rivas, J. C., Torres Martin de Rosales, R., and Williams, N. H. (2005) A highly reactive mononuclear Zn(II) complex for phosphodiester cleavage. *J. Am. Chem. Soc. 127*, 13470–13471.
(98) Feng, G., Mareuqe-Rivas, J. C., and Williams, N. H. (2006) Comparing a mononuclear Zn(II) complex with hydrogen bond donors with a dinuclear Zn(II) complex for catalysing phosphate ester cleavage. *Chem. Commun.* 1845–1847.
(99) Feng, G., Natale, D., Prabaharan, R., Mareuqe-Rivas, J. C., and Williams, N. H. (2006) Efficient phosphodiester binding and cleavage by a Zn^{II} complex combining hydrogen-bonding interactions and double Lewis acid activation. *Angew. Chem., Int. Ed. 45*, 7056–7059.
(100) Reedjik, J. (2003) New clues for platinum antitumor chemistry: Kinetically controlled metal binding to DNA. *Proc. Natl. Acad. Sci. U.S.A. 100*, 3611–3616.
(101) Chen, H., Parkinson, J. A., Morris, R. E., and Sadler, P. J. (2003) Highly selective binding of organometallic ruthenium ethylenediamine complexes to nucleic acids: novel recognition mechanisms. *J. Am. Chem. Soc. 125*, 173–186.
(102) Chen, H., Parkinson, J. A., Parsons, S., Coxall, R. A., Gould, R. O., and Sadler, P. J. (2002) Organometallic ruthenium(II). Diamine anticancer complexes: arene-nucleobase stacking and stereospecific hydrogen-bonding in guanine adducts. *J. Am. Chem. Soc. 124*, 3064–3082.
(103) Boerner, L. J. K., and Zaleski, J. M. (2005) Metal complex-DNA interactions: from transcription inhibition to photoactivated cleavage. *Curr. Opin. Chem. Biol. 9*, 135–144.
(104) Liu, C., Yu, S., Li, D., Liao, Z., Sun, X., and Xu, H. (2002) DNA hydrolytic cleavage by the Diiron(III). Complex $Fe_2(DTPB)(\mu\text{-}O)(\mu\text{-}Ac)Cl(BF_4)_2$: comparison with other binuclear transition metal complexes. *Inorg. Chem. 41*, 913–922.
(105) Cowan, J. A. (2001) Chemical nucleases. *Curr. Opin. Chem. Biol. 5*, 634–642.
(106) Kelly, J. M., Feeney, M. M., Jacquet, L., Kirsch-De Mesmaeker, A., and Lecomte, J.-P. (1997) Photoinduced electron transfer between ruthenium complexes and nucleotides or DNA. *Pure Appl. Chem. 69*, 767–772.
(107) Moucheron, C., Kirsch-De Mesmaeker, A., and Kelly, J. M. (1997) Photoreactions of ruthenium(II) and osmium(II) complexes with deoxyribonucleic acid (DNA). *J. Photochem. Photobiol. B: Biology 40*, 91–106.
(108) Komeda, S., Moulaei, T., Woods, K. K., Chikuma, M., Farrell, N. P., and Williams, L. D. (2006) A third mode of DNA binding: Phosphate clamps by a polynuclear platinum complex. *J. Am. Chem. Soc. 128*, 16092–16103.

BC800298T

Supporting Information

Ruthenium(II) Complexes of Bipyridine-Glycoluril and their Interactions with DNA

Megha S. Deshpande,[†] Anupa A. Kumbhar,[†] Avinash S. Kumbhar,[*†] Manoj Kumbhakar,[‡] Haridas Pal,[‡] Uddhavesh B. Sonawane,[#] Rajendra R. Joshi [#]

[†]Department of Chemistry, University of Pune, Pune - 411 007 (India)

[‡]Radiation and Photochemistry Division, BARC, Mumbai - 400 085, (India)

[#]Bioinformatics Team, Scientific and Engineering Computing Group, Centre for Development of Advanced Computing (C-DAC), Pune University Campus, Pune - 411 007 (India)

Email: askum@chem.unipune.ernet.in

Tel: (+91) - 020 - 25601225 (534); Fax: (+91) - 020 - 25691728

List of Contents:

Figure S1 and S2: Changes in the relative specific viscosity of solutions **1-9** in the presence of CT-DNA.

Figure S3 and S4: Melting curves of CT-DNA in the absence and presence of complexes **1-9.**

Figure S5 and S6: Emission spectra of Ru(II) complexes **1-9** (25 μM) in phosphate buffer with increasing [DNA]/[Ru] ratio from 0-30.

Figure S7 and S8: Emission spectra of Ru(II) complexes **1-9** using anionic quencher $K_4[Fe(CN)_6]$ in the presence and absence of DNA in phosphate buffer.

Table S1: Luminescence decay lifetime of the complexes **1-9** in the presence of CT-DNA.

Figure S9 and S10: DNA cleavage experiment in the presence of 20 μM Ru(II) complexes **2-9**; dark experiments incubation for 2 h in argon atmosphere and dark experiments incubation for 18 h in air.

Figure S11-S18 and Table S2-S9: DNA cleavage experiment in the presence of different radical scavengers for Ru(II) complexes **2-9.**

Table S10: DNA cleavage efficiency of ruthenium(II) complexes containing one, two and three BPG ligands **2-9** in the dark and light conditions.

Figure S19: Changes in the absorption spectra of complexes **2-6** in the presence of DNA before and after dialysis.

Figure S20-S26: The core view of the bound **2-7 and 9** to DNA.

Table S11: Binding energies in Kcal/mol and hydrogen bond information of Ru(II) polypyridyl complexes **1-9** with right handed B-DNA of sequence $d(C:G)_{12}$.

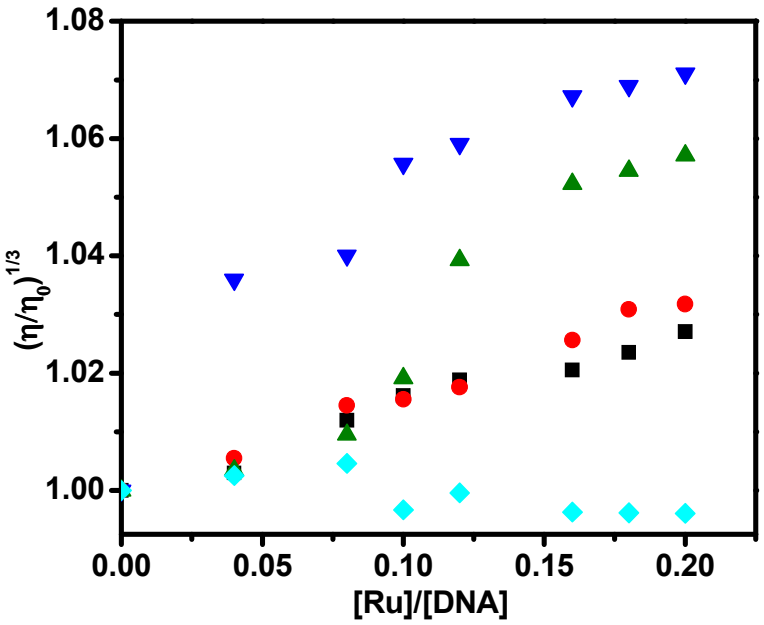

Figure S1. Changes in the relative viscosity of solutions containing 200 μM CT-DNA (Phosphate buffer, pH 7.2) as a function of concentration of (■) **1**, (●) **2**, (▲) **3**, (▼) **4**, (♦) **9;** ([Ru]/[DNA] = 0.02-0.20).

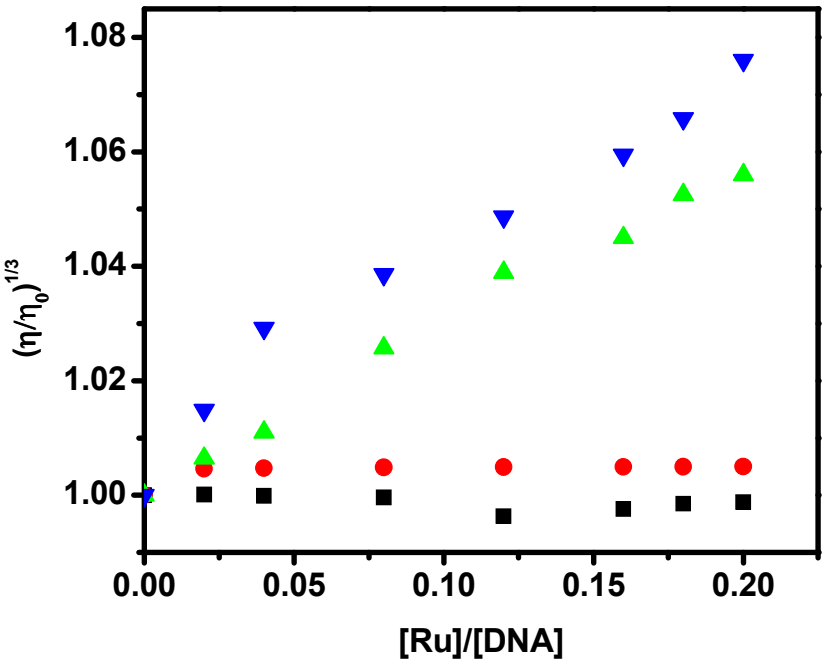

Figure S2. Changes in the relative viscosity of solutions containing 200 μM CT-DNA (Phosphate buffer, pH 7.2) as a function of concentration of (■) **5**, (●) **6**, (▲) **7**, (▼) **8;** ([Ru]/[DNA] = 0.02-0.20).

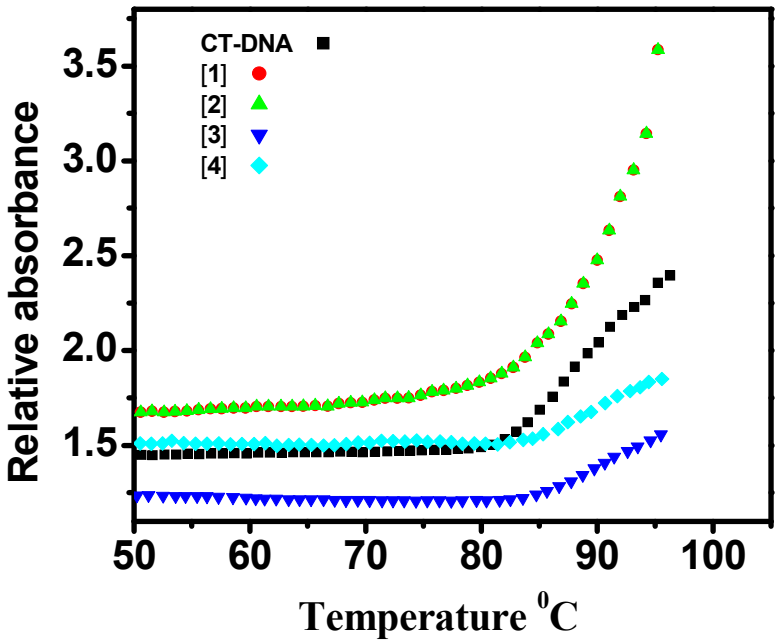

Figure S3. Melting curves of CT-DNA (200 μM) alone (■), DNA + [**1**] (•), DNA + [**2**] (▲), DNA + [**3**] (▼), DNA + [**4**] (♦). ([Ru] = 20 μM, [DNA] = 200 μM).

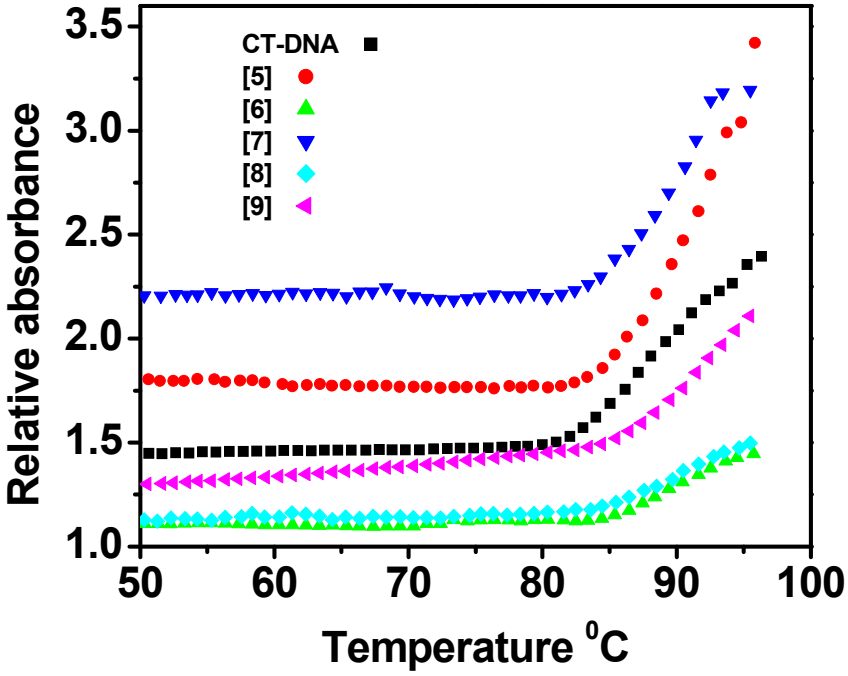

Figure S4. Melting curves of CT-DNA (200 μM) alone (■), DNA + [**5**] (•), DNA + [**6**] (▲), DNA + [**7**] (▼), DNA + [**8**] (♦), DNA + [**9**] (◄). ([Ru] = 20 μM, [DNA] = 200 μM).

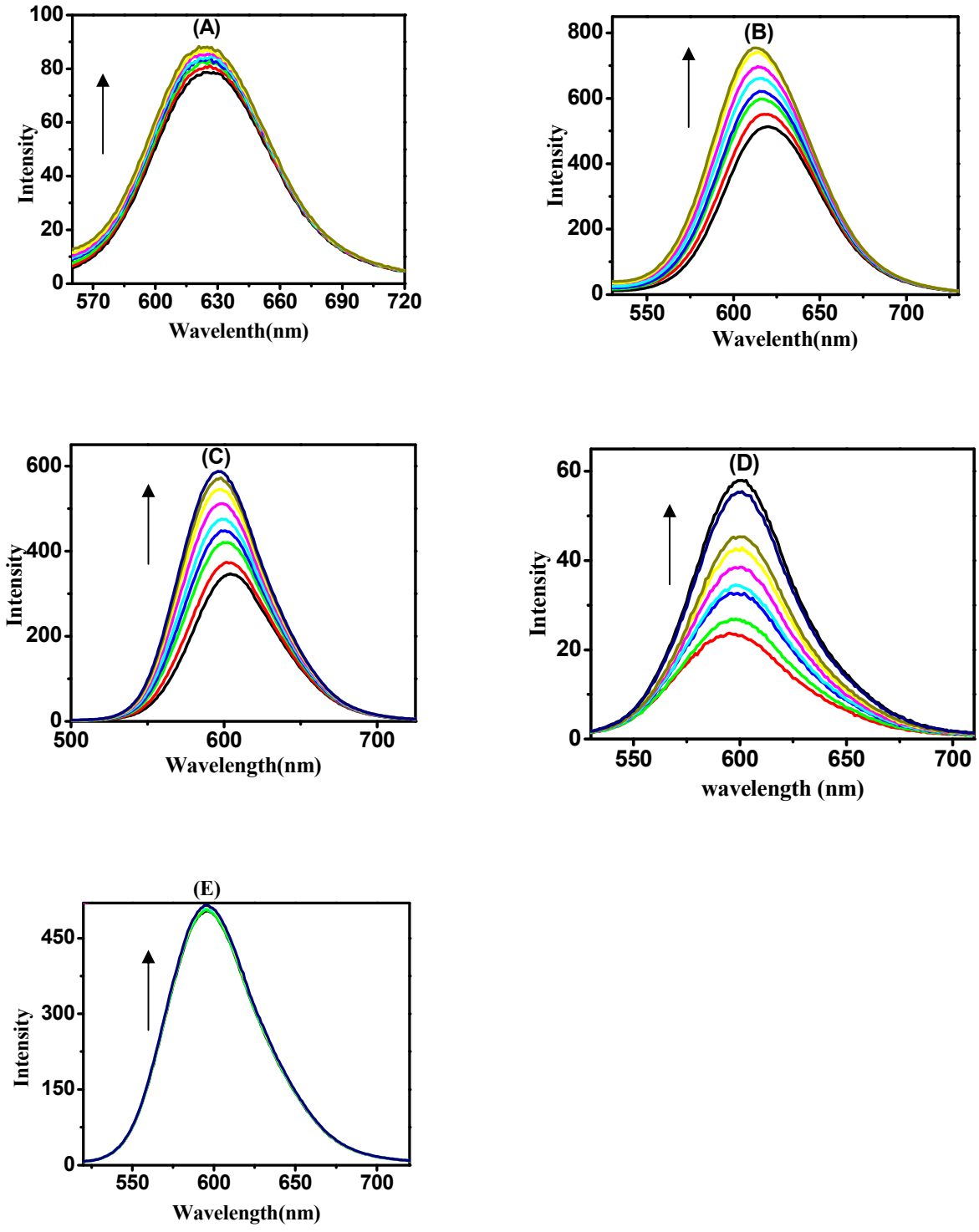

Figure S5. Emission spectra of Ru(II) complexes (A) **1** , (B) **2**, (C) **3**, (D) **4** and (E) **9** (25 μM) in phosphate buffer (pH 7.2) at 298 K with increasing [DNA]/[Ru] ratio from 0-30. Arrow shows the intensity changes upon increasing DNA concentrations.

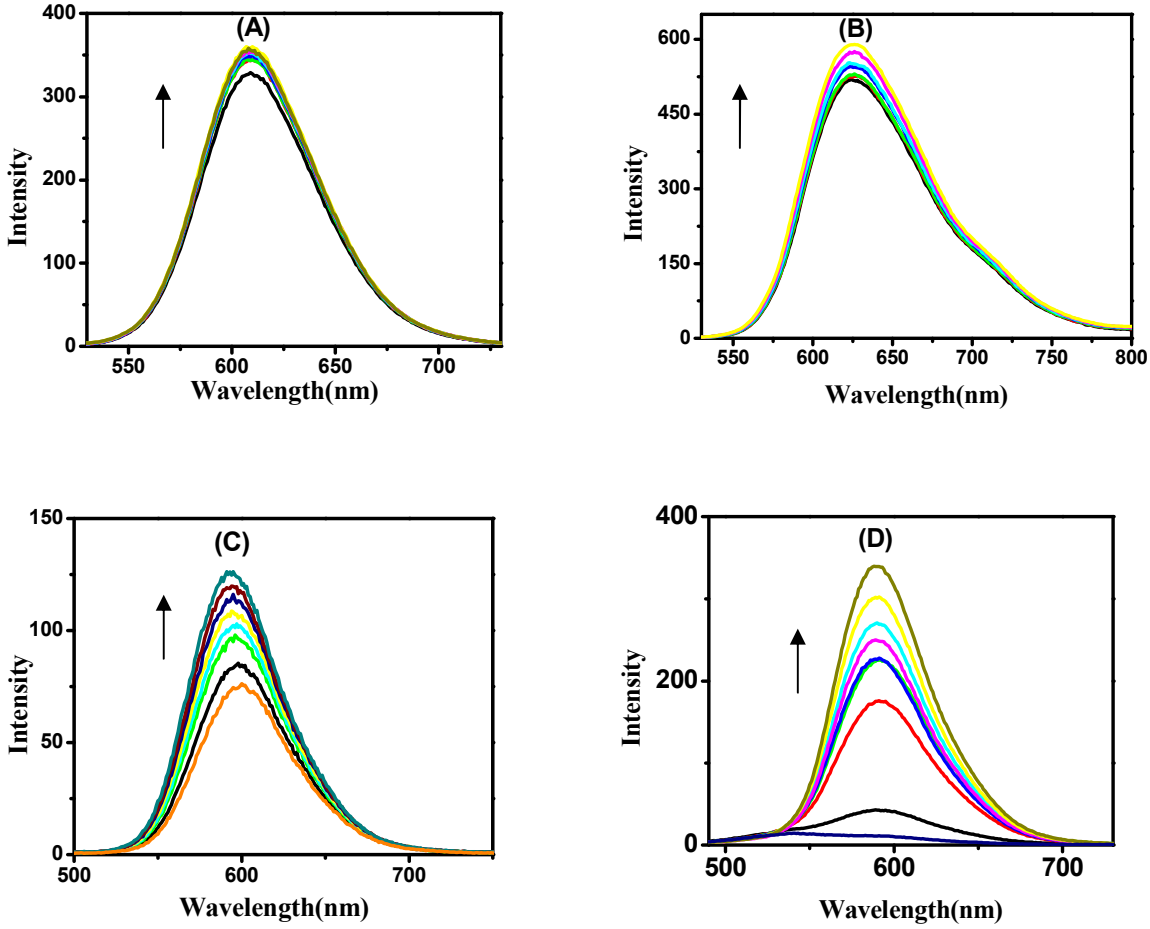

Figure S6. Emission spectra of complexes (A) **5**, (B) **6**, (C) **7, (D) 8** (25 μM) in phosphate buffer (pH 7.2) at 298 K with increasing [DNA]/[Ru] ratio from 0-30. Arrow shows the intensity changes upon increasing DNA concentrations.

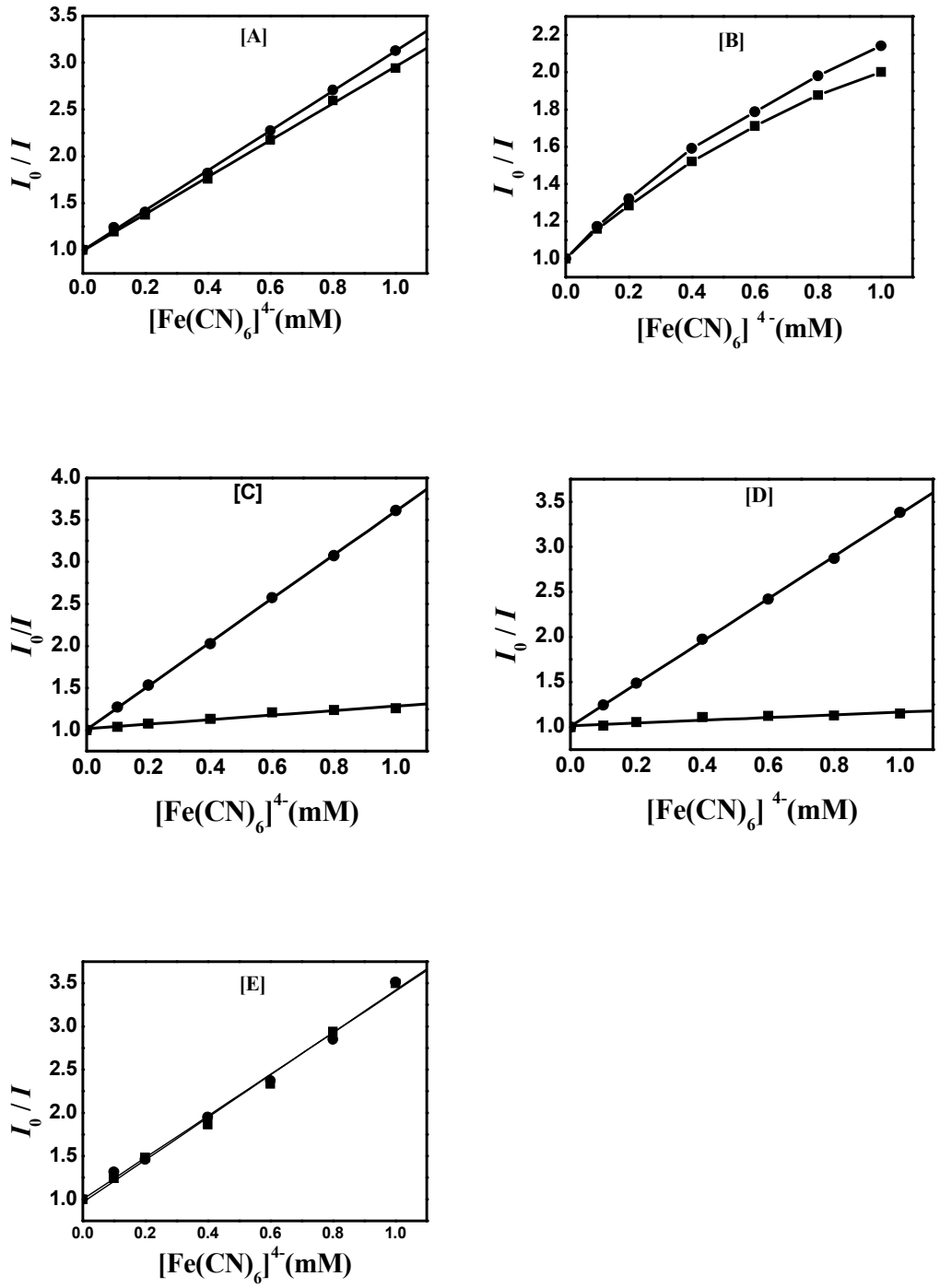

Figure S7. Emission quenching of the ruthenium(II) complexes with increasing concentration of quencher $[Fe(CN)_6]^{4-}$ in the absence (●) and presence (■) of CT-DNA (phosphate buffer pH 7.2); ([Ru] = 20 μM, [DNA]/[Ru] = 40:1), (A) **1**, (B) **2**, (C) **3**, (D) **4**, (E) **9**.

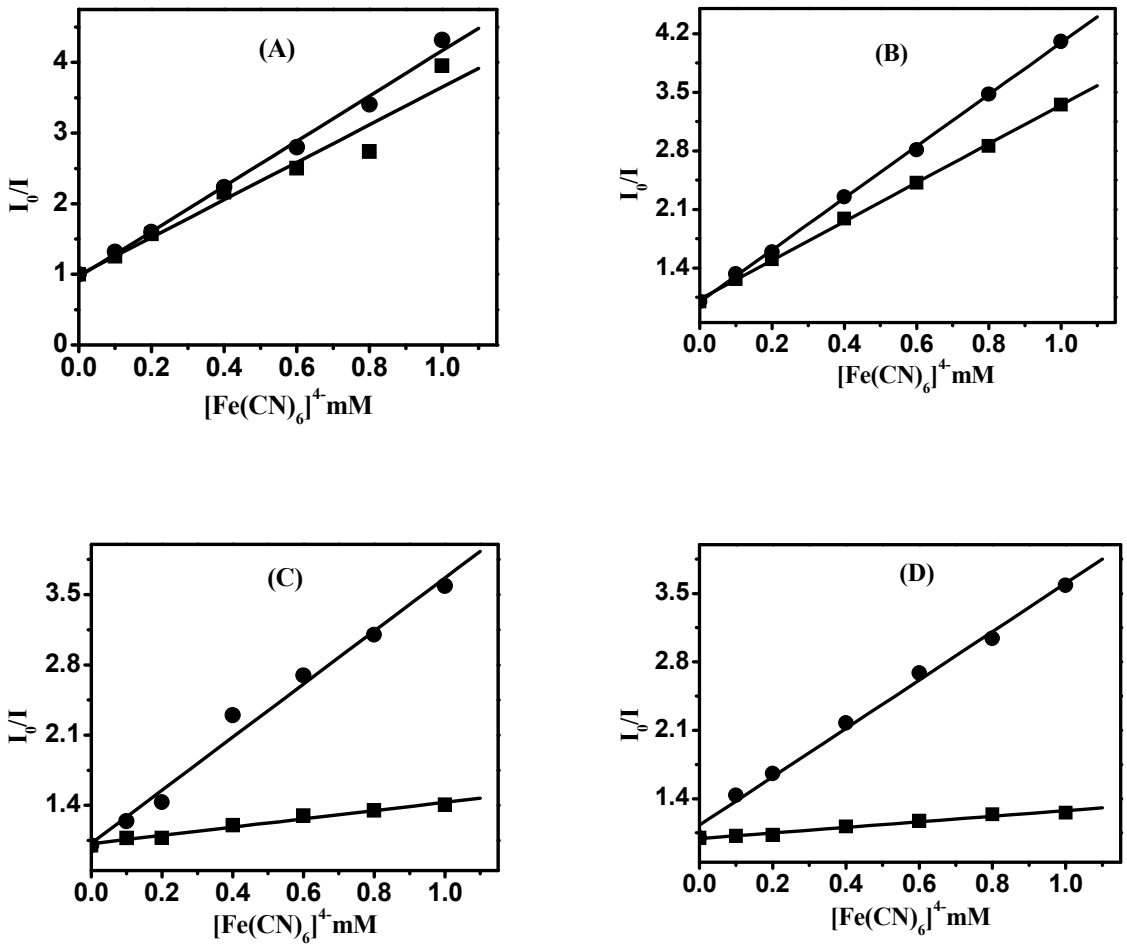

Figure S8. Emission quenching of the Ru(II) complexes with increasing concentration of quencher $[Fe(CN)_6]^{4-}$ in the absence (●) and presence (■) of DNA (phosphate buffer pH 7.2); ([Ru] = 20 μM, [DNA]/[Ru] = 40:1), (A) **5**, (B) **6**, (C) **7**, (D) **8**.

Table S1. Luminescence decay lifetime of the complexes **1-9** in the presence of CT-DNA.

[DNA]/[Ru]	**1**	**2**		**3**	**4**		**5**	**6**	**7**	**8**		**9**
	τ(ns)	τ_S(ns)	τ_l(ns)	τ(ns)	τ_S(ns)	τ_l(ns)	τ(ns)	τ(ns)	τ(ns)	τ_S(ns)	τl(ns)	τ(ns)
2	248	183	329	330	207	677	343	392	369	112	510	339
5	246	303	515	346	251	1348	341	393	381	119	576	337
10	248	320	919	382	256	1513	348	396	398	129	597	334
15	247	294	523	407	247	1476	346	393	407	134	608	335
20	248	284	502	420	275	1587	345	397	416	126	606	334
30	248	334	761	432	290	1679	347	404	426	125	611	334

Measurements performed at 25°C in air equilibrated aqueous solutions (25 μM complex, [DNA]/[Ru] = 2-30, (phosphate buffer pH 7.2). The subscripts s and l stand for short and long components of the biexponential decays.

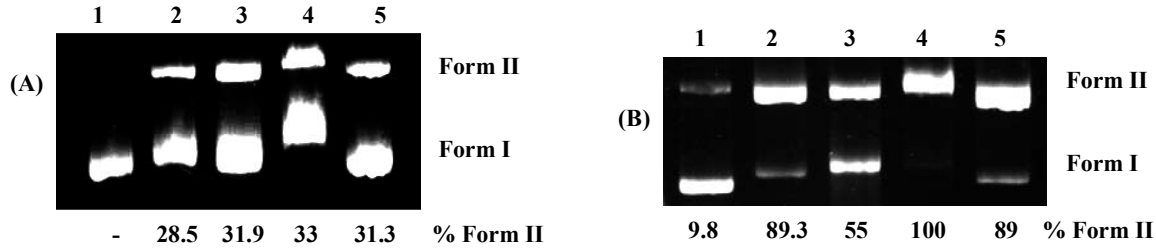

Figure S9. Ethidium bromide-stained agarose gel (1 %) of plasmid *pBR322* DNA (90 μM in base pairs) in the presence of 20 μM Ru(II) complexes **2-4** and **9**; (A) Dark experiments (incubation for 2 h in argon atmosphere); Lane 1 – DNA control; Lane 2 - DNA + **2**, Lane 3 - DNA + **3**, Lane 4 - DNA + **4**, Lane 5 - DNA + **9**; (B) Dark Experiments (incubation for 18 h in air atmosphere): Lane 1 – DNA control; Lane 2 - DNA + **2**, Lane 3 - DNA + **3**, Lane 4 - DNA + **4**, Lane 5 - DNA + **9.**

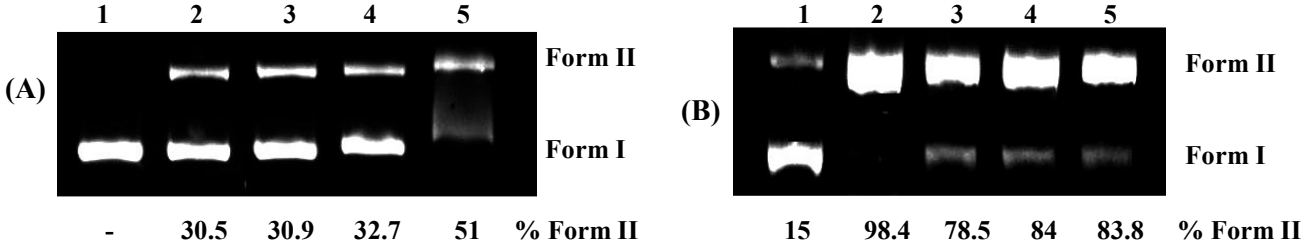

Figure S10. Ethidium bromide-stained agarose gel (1 %) of plasmid *pBR322* DNA (90 μM in base pairs) in the presence of 20 μM ruthenium(II) complexes **5-8**; Form I - supercoiled plasmid DNA; Form II - nicked circular plasmid DNA; (A) Dark Experiments (incubation for 2 h in argon atmosphere): Lane 1 – DNA control; Lane 2 - DNA + **5**, Lane 3 - DNA + **6**, Lane 4 - DNA + **7**, Lane 5 - DNA + **8**; (B) Dark Experiments (incubation for 18 h in air atmosphere): Lane 1 – DNA control; Lane 2 - DNA + **5**, Lane 3 - DNA +**6**, Lane 4 - DNA + **7**, Lane 5 - DNA + **8.**

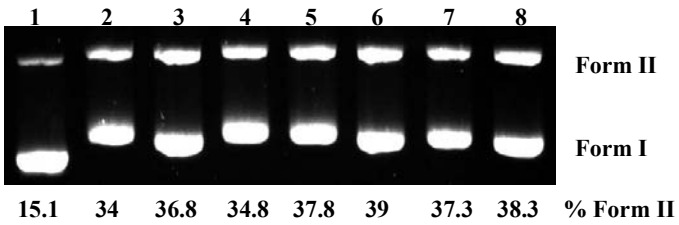

Figure S11. Effect of inhibitors on the photocleavage activity of (20 μM) **2** (plasmid *pBR322* DNA 90 μM, in base pairs); 30 min incubation and 20 min irradiation in air; (λ_{irr} = 365 nm); Form I - supercoiled plasmid DNA; Form II - nicked circular plasmid DNA; Lane 1- untreated *pBR322* DNA upon irradiation for 20 min, Lane 2 - DNA + **2**, Lane 3 - DNA + **2** + DMSO (1 mM), Lane 4 - DNA + **2** + mannitol (50 mM), Lane 5 - DNA + **2** + DABCO (10 mM), Lane 6 - DNA + **2** + NaN_3 (20 mM), Lane 7 - DNA + **2** + L-Histidine (20 mM), Lane 8 - DNA + **2** + SOD (15 units).

Table S2. Comparison of the *pBR322* DNA cleavage efficiency of complex **2** in presence of inhibitors when irradiated for 20 min, after 30 min incubation at 37 ºC.

Serial No.	Reaction Condition	Form (%)	
		Form I	Form II
1.	*pBR322* DNA control	84.9	15.1
2.	DNA + **2**	66	34
3.	DNA + DMSO + **2**	63.2	36.8
4.	DNA + mannitol + **2**	65.2	34.8
5.	DNA + DABCO + **2**	62.2	37.8
6.	DNA + NaN_3 + **2**	61	39
7.	DNA + L-Histidine + **2**	62.7	37.3
8.	DNA + SOD + **2**	61.7	38.3

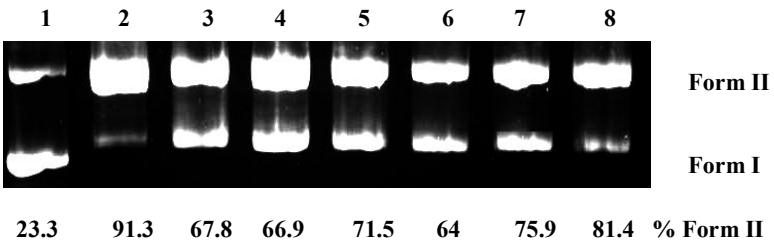

Figure S12. Photocleavage of plasmid *pBR322* DNA (90 μM, in base pairs) in the presence of 20 μM **3** and different inhibitors after 30 min incubation and 20 min irradiation in air. (λ_{irr} = 365 nm); Form I - supercoiled plasmid DNA; Form II - nicked circular plasmid DNA; Lane 1 – untreated *pBR322* DNA upon irradiation for 20 min, Lane 2 - DNA + **3**, Lane 3 - DNA + **3** + DMSO (1 mM), Lane 4 - DNA + **3** + mannitol (100 mM), Lane 5 - DNA + **3** + DABCO (20 mM), Lane 6 – DNA + **3** + NaN_3 (40 mM), Lane 7 - DNA + **3** + L-Histidine (40 mM), Lane 8 - DNA + **3** + SOD (15 units).

Table S3. Comparison of the *pBR322* DNA cleavage efficiency of complex **3** in presence of inhibitors when irradiated for 20 min, after 30 min incubation at 37 ºC.

Serial No.	Reaction Condition	Form I	Form II
1.	*pBR322* DNA control	76.7	23.3
2.	DNA + **3**	8.7	91.3
3.	DNA + DMSO + **3**	32.2	67.8
4.	DNA + mannitol + **3**	33.1	66.9
5.	DNA + DABCO + **3**	28.5	71.5
6.	DNA + NaN_3 + 3	36	64
7.	DNA + L-Histidine + **3**	24.1	75.9
8.	DNA + SOD + **3**	18.6	81.4

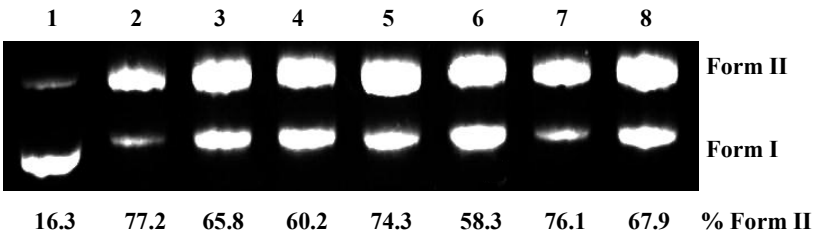

Figure S13. Photocleavage of plasmid *pBR322* DNA (90 μM, in base pairs) in the presence of 20 μM **4** and different inhibitors after 30 min incubation and 20 min irradiation in air (λ_{irr} = 365 nm); Form I - supercoiled plasmid DNA; Form II - nicked circular plasmid DNA; Lane 1 – untreated *pBR322* DNA upon irradiation for 20 min, Lane 2 - DNA + **4**, Lane 3 - DNA + **4** + DMSO (1 mM), Lane 4 - DNA + **4** + mannitol (100 mM), Lane 5 - DNA + **4** + DABCO (20 mM), Lane 6 - DNA + **4** + NaN_3 (40 mM), Lane 7 - DNA + **4** + L-Histidine (40 mM), Lane 8 - DNA + **4** + SOD (15 units).

Table S4. Comparison of the *pBR322* DNA cleavage efficiency of complex **4** in presence of inhibitors when irradiated for 20 min, after 30 min incubation at 37 ºC.

Serial No.	Reaction Condition	Form I	Form II
1.	*pBR322* DNA control	83.7	16.3
2.	DNA + **4**	22.8	77.2
3.	DNA + DMSO + **4**	34.2	65.8
4.	DNA + mannitol + **4**	39.8	60.2
5.	DNA + DABCO + **4**	25.7	74.3
6.	DNA + NaN_3 + **4**	41.7	58.3
7.	DNA + L-Histidine + **4**	23.9	76.1
8.	DNA + SOD + **4**	32.1	67.9

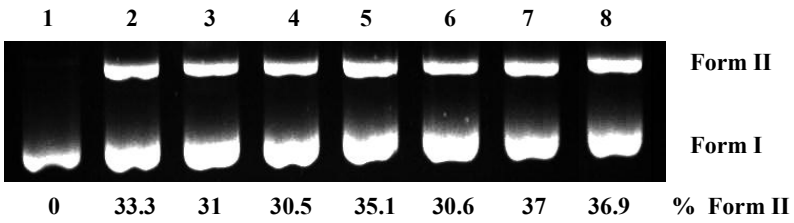

Figure S14. Effect of inhibitors on the photocleavage activity of **5** (20 μM) (plasmid *pBR322* DNA 90 μM, in base pairs); 30 min incubation and 20 min irradiation in air; (λ_{irr} = 365 nm); Form I - supercoiled plasmid DNA; Form II - nicked circular plasmid DNA; Lanes 1- DNA control, Lane 2 - DNA + **5**, Lane 3 - DNA + **5** + DMSO (1 mM), Lane 4 - DNA + **5** + mannitol (50 mM), Lane 5 - DNA + **5** + DABCO (10 mM), Lane 6 - DNA + **5** + NaN_3 (20 mM), Lane 7 - DNA + **5** + L-Histidine (20 mM), Lane 8 - DNA + **5** + SOD (15 units).

Table S5. Comparison of the *pBR322* DNA cleavage efficiency of complex **5** in presence of inhibitors when irradiated for 20 min, after 30 min incubation at 37 ºC.

Serial No.	Reaction Condition	Form (%)	
		Form I	Form II
1.	DNA control	100	-
2.	DNA + **5**	66.7	33.3
3.	DNA + DMSO + **5**	69	31
4.	DNA + mannitol + **5**	69.5	30.5
5.	DNA + DABCO + **5**	64.9	35.1
6.	DNA + NaN_3 + **5**	69.4	30.6
7.	DNA + L-Histidine + **5**	63	37
8.	DNA + SOD + **5**	63.1	36.9

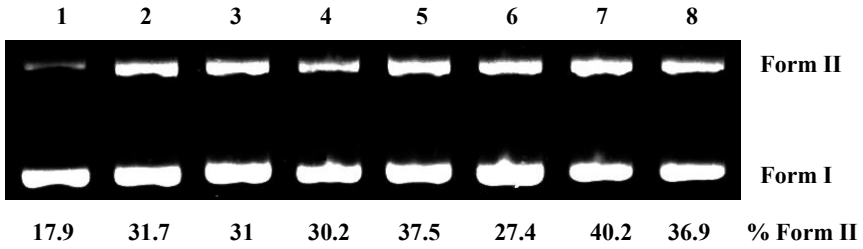

Figure S15. Effect of inhibitors on the photocleavage activity of **6** (20 μM) (plasmid *pBR322* DNA 90 μM, in base pairs); 30 min incubation and 20 min irradiation in air; (λ_{irr} = 365 nm); Form I - supercoiled plasmid DNA; Form II - nicked circular plasmid DNA; Lanes 1- DNA control, Lane 2 - DNA + **6**, Lane 3 - DNA + **6** + DMSO (1 mM), Lane 4 - DNA + **6** + mannitol (50 mM), Lane 5 - DNA + **6** + DABCO (10 mM), Lane 6 - DNA + **6** + NaN_3 (20 mM), Lane 7 - DNA + **6** + L-Histidine (20 mM), Lane 8 - DNA + **6** + SOD (15 units).

Table S6. Comparison of the *pBR322* DNA cleavage efficiency of complex **6** in presence of inhibitors when irradiated for 20 min, after 30 min incubation at 37 ºC.

Serial No.	Reaction Condition	Form (%)	
		Form I	Form II
1.	DNA control	82.1	17.9
2.	DNA + **6**	68.3	31.7
3.	DNA + DMSO + **6**	69	31
4.	DNA + mannitol + **6**	69.8	30.2
5.	DNA + DABCO + **6**	62.5	37.5
6.	DNA + NaN_3 + **6**	72.6	27.4
7.	DNA + L-Histidine + **6**	59.8	40.2
8.	DNA + SOD + **6**	63.1	36.9

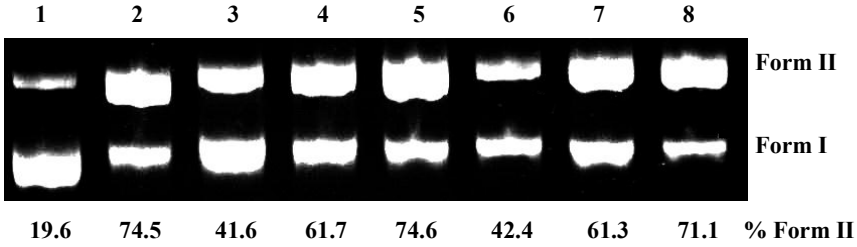

Figure S16. Effect of inhibitors on the photocleavage activity of **7** (20 μM) (plasmid *pBR322* DNA 90 μM, in base pairs); 30 min incubation and 20 min irradiation in air; (λ_{irr} = 365 nm); Form I - supercoiled plasmid DNA; Form II - nicked circular plasmid DNA; Lanes 1- DNA control, Lane 2 - DNA + **7**, Lane 3 - DNA + **7** + DMSO (1 mM), Lane 4 - DNA + **7** + mannitol (50 mM), Lane 5 - DNA + **7** + DABCO (10 mM), Lane 6 - DNA + **7** + NaN_3 (20 mM), Lane 7 - DNA + **7** + L-Histidine (20 mM), Lane 8 - DNA + **7** + SOD (15 units).

Table S7. Comparison of the *pBR322* DNA cleavage efficiency of complex **7** in presence of inhibitors when irradiated for 20 min, after 30 min incubation at 37 ºC.

Serial No.	Reaction Condition	Form (%)	
		Form I	Form II
1.	DNA control	80.4	19.6
2.	DNA + **7**	25.5	74.5
3.	DNA + DMSO + **7**	58.4	41.6
4.	DNA + mannitol + **7**	38.3	61.7
5.	DNA + DABCO + **7**	25.4	74.6
6.	DNA + NaN_3 + **7**	57.6	42.4
7.	DNA + L-Histidine + **7**	38.7	61.3
8.	DNA + SOD + **7**	28.9	71.1

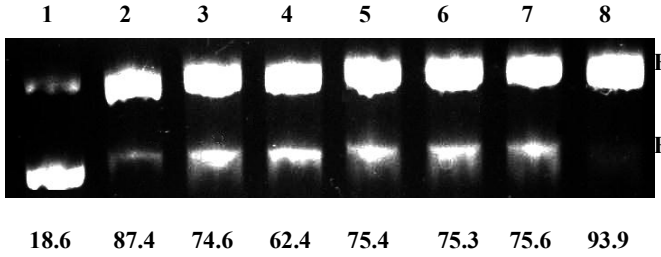

Figure S17. Effect of inhibitors on the photocleavage activity of **8** (20 μM) (plasmid *pBR322* DNA 90 μM, in base pairs); 30 min incubation and 20 min irradiation in air; (λ_{irr} = 365 nm); Form I - supercoiled plasmid DNA; Form II - nicked circular plasmid DNA; Lanes 1- DNA control, Lane 2 - DNA + **8**, Lane 3 - DNA + **8** + DMSO (1 mM), Lane 4 - DNA + **8** + mannitol (50 mM), Lane 5 - DNA + **8** + DABCO (10 mM), Lane 6 - DNA + **8** + NaN_3 (20 mM), Lane 7 - DNA + **8** + L-Histidine (20 mM), Lane 8 - DNA + **8** + SOD (15 units).

Table S8. Comparison of the *pBR322* DNA cleavage efficiency of complex **8** in presence of inhibitors when irradiated for 20 min, after 30 min incubation at 37 ºC.

Serial No.	Reaction Condition	Form (%)	
		Form I	Form II
1.	DNA control	81.4	18.6
2.	DNA + **8**	12.6	87.4
3.	DNA + DMSO + **8**	25.4	74.6
4.	DNA + mannitol + **8**	31.6	62.4
5.	DNA + DABCO + **8**	24.6	75.4
6.	DNA + NaN_3 + **8**	24.7	75.3
7.	DNA + L-Histidine + **8**	24.4	75.6
8.	DNA + SOD + **8**	6.1	93.9

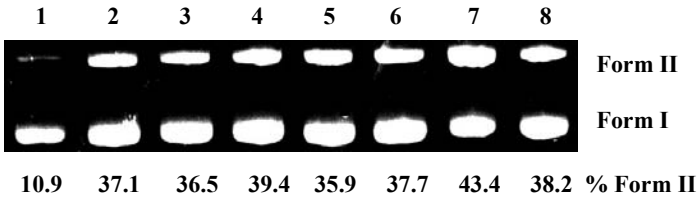

Figure S18. Effect of inhibitors on the photocleavage activity of (20 μM) **9** (plasmid *pBR322* DNA 90 μM, in base pairs); 30 min incubation and 20 min irradiation in air; (λ_{irr} = 365 nm); Form I - supercoiled plasmid DNA; Form II - nicked circular plasmid DNA; Lane 1- untreated *pBR322* upon irradiation for 20 min, Lane 2 - DNA + **9**, Lane 3 - DNA + **9** + DMSO (1 mM), Lane 4 - DNA + **9** + mannitol (50 mM), Lane 5 - DNA + **9** + DABCO (10 mM), Lane 6 - DNA + **9** + NaN_3 (20 mM), Lane 7 - DNA + **9** + L-Histidine (20 mM), Lane 8 - DNA + **9** + SOD (15 units).

Table S9. Comparison of the *pBR322* DNA cleavage efficiency of complex **9** in presence of inhibitors when irradiated for 20 min, after 30 min incubation at 37 ºC.

Serial No.	Reaction Condition	Form I	Form II
1.	*pBR322* DNA control	82.5	10.9
2.	DNA + **9**	62.9	37.1
3.	DNA + DMSO + **9**	63.5	36.5
4.	DNA + mannitol + **9**	60.6	39.4
5.	DNA + DABCO + **9**	54.7	35.9
6.	DNA + NaN_3 + **9**	62.3	37.7
7.	DNA + L-Histidine + **9**	56.6	43.4
8.	DNA + SOD + **9**	61.8	38.2

Table S10. DNA cleavage efficiency of Ruthenium(II) complexes containing one, two and three BPG ligands **2-9** in the Dark and Light conditions.

Complex	L(n)	Air	Argon	Average without Light	Air+Light	Air+ Light (From SI figures)	Average with Light
2	$phen_2$	22	29	25.5	34	34	34
3	dpq_2	24	32	28	90	91	90.5
4	$dppz_2$	38	33	35.5	86	77	81.5
5	bpy	28	31	29.5	35	33	34
6	phen	34	31	32.5	40	32	38
7	dpq	29	33	31	92	75	83.5
8	dppz	59	51	55	98	87	92.5
9	BPG_3	28	31	29.5	31	37	34

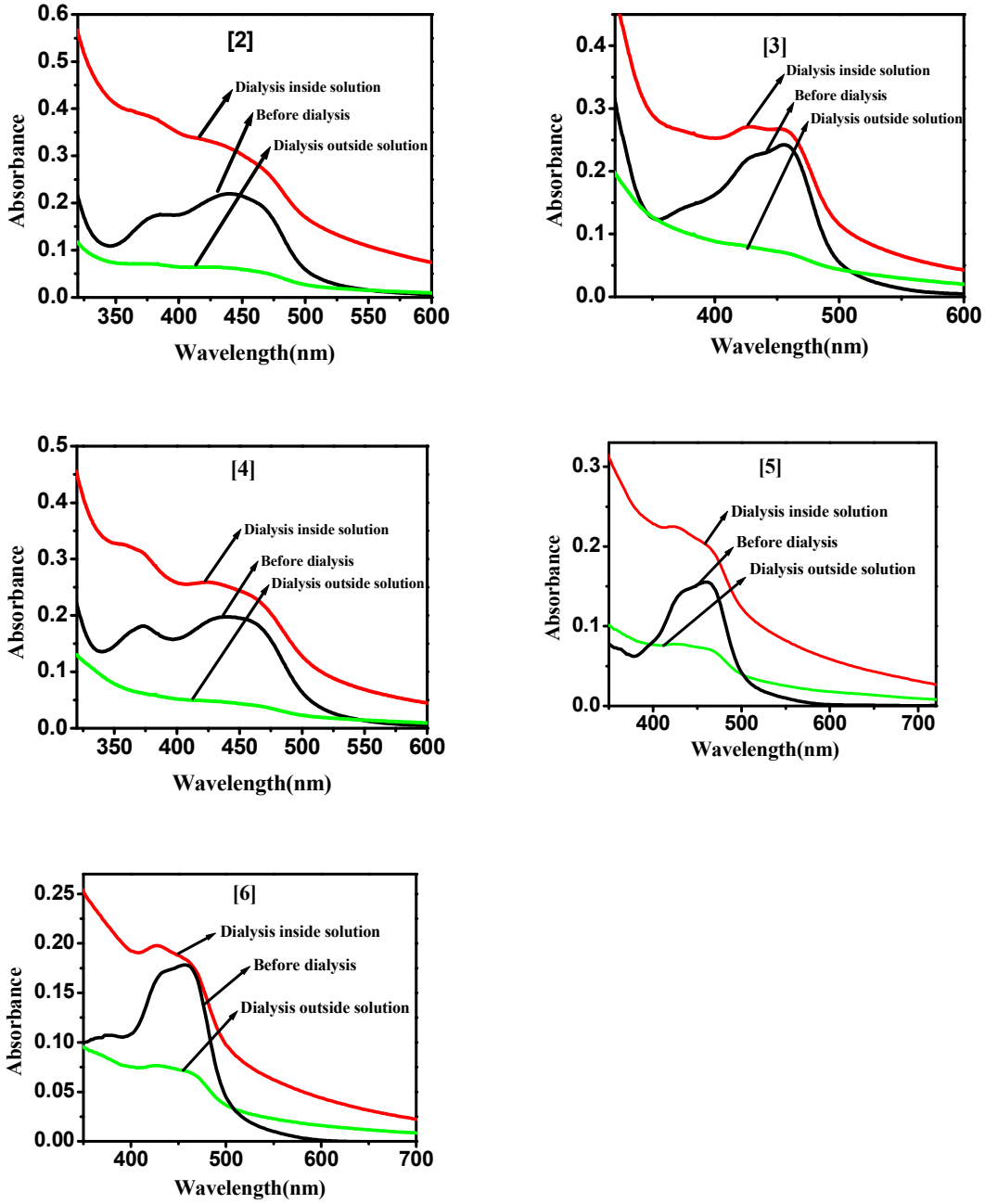

Figure S19. Changes in the absorption spectras of complexes **2-6** in the presence of calf-thymus DNA under dark conditions with dialysis (24 h) compared with the dialysed samples and undialysed samples in phosphate buffer pH 7.2 solutions. ([Ru] = 20 μM, [DNA] = 200 μM).

Molecular modeling of ruthenium(II) complexes with right handed B-DNA of sequence d(C:G)$_{12}$.

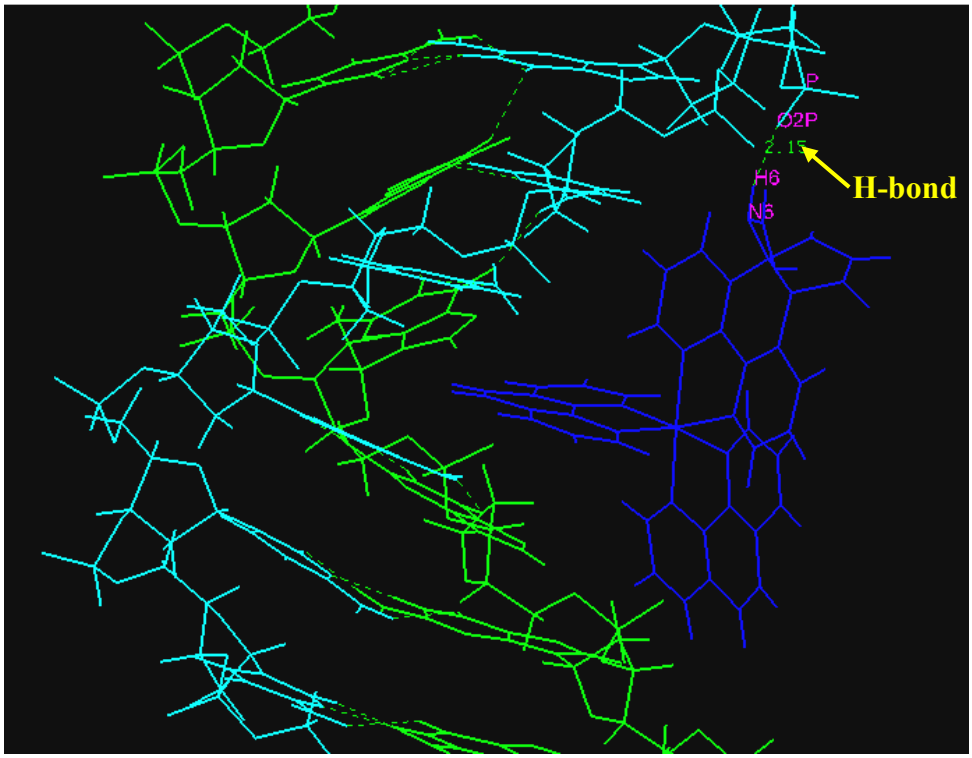

Figure S20. The core view of the bound **2** to DNA with the H-bond patterns observed showing the phosphate interactions.

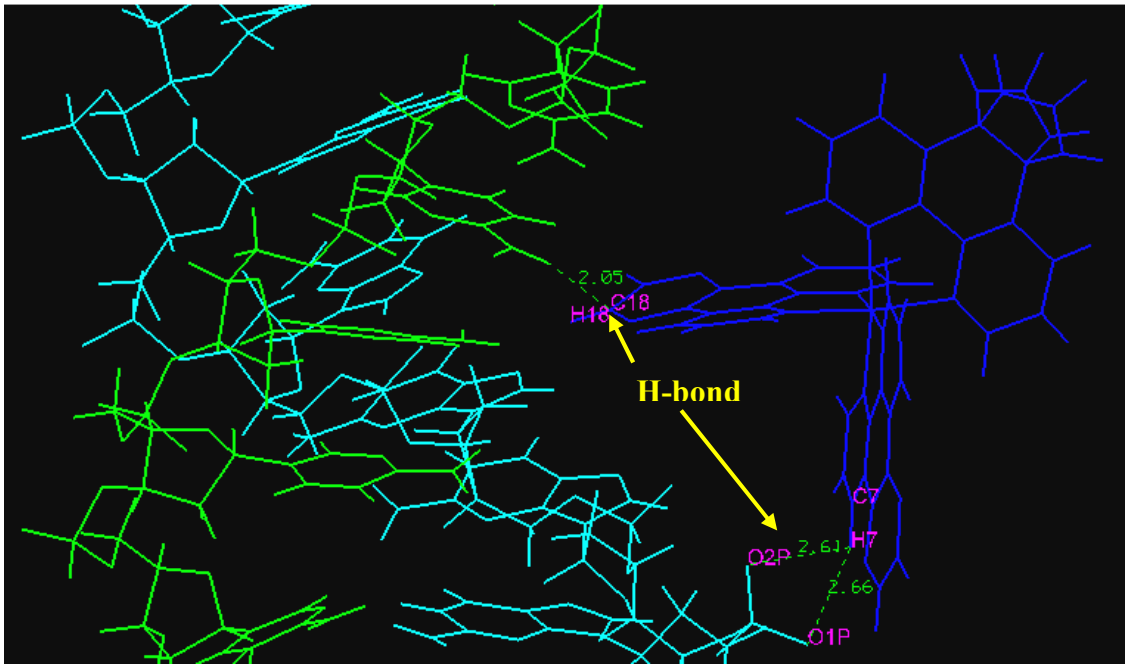

Figure S21. The core view of the bound **3** to DNA with the H-bond patterns observed showing the base and phosphate interactions.

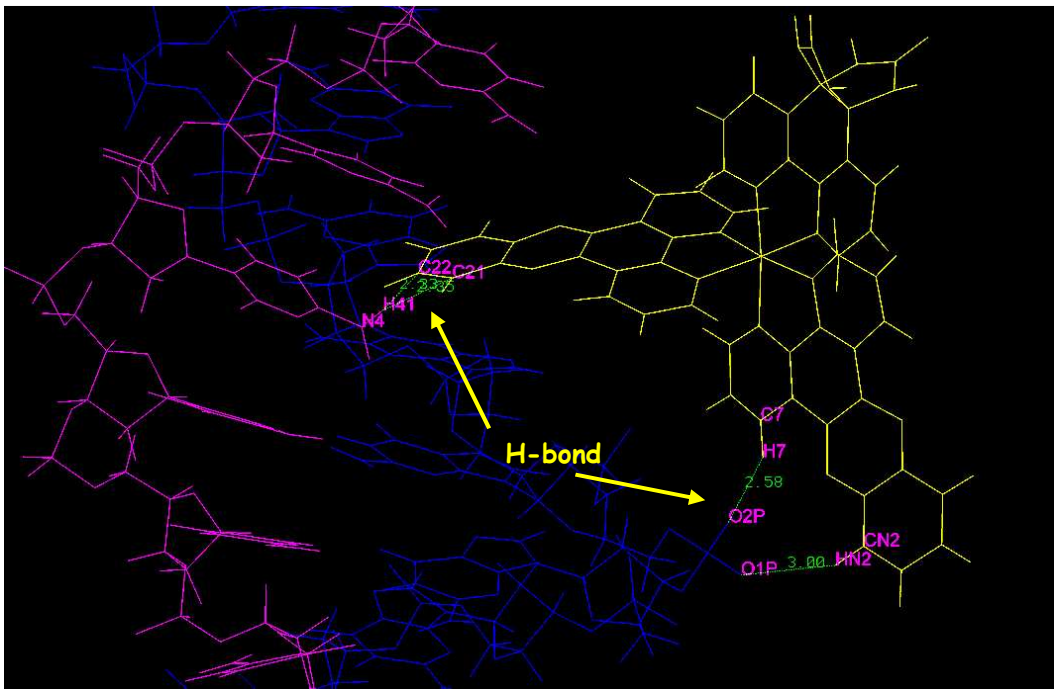

Figure S22. The core view of the bound **4** to DNA with the H-bond patterns observed showing base and phosphate interactions.

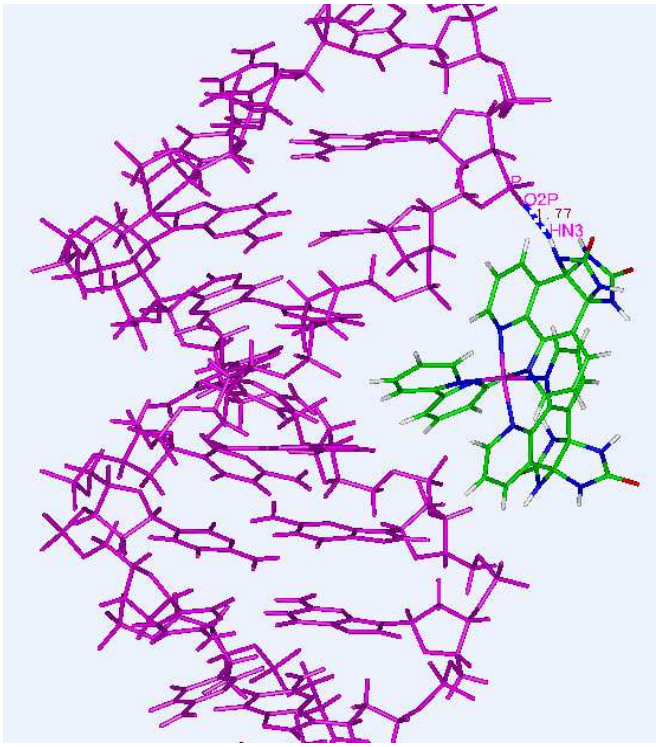

Figure S23. The core view of the bound **5** to DNA showing the hydrogen bonding interactions of the BPG ligand with the phosphate groups of DNA.

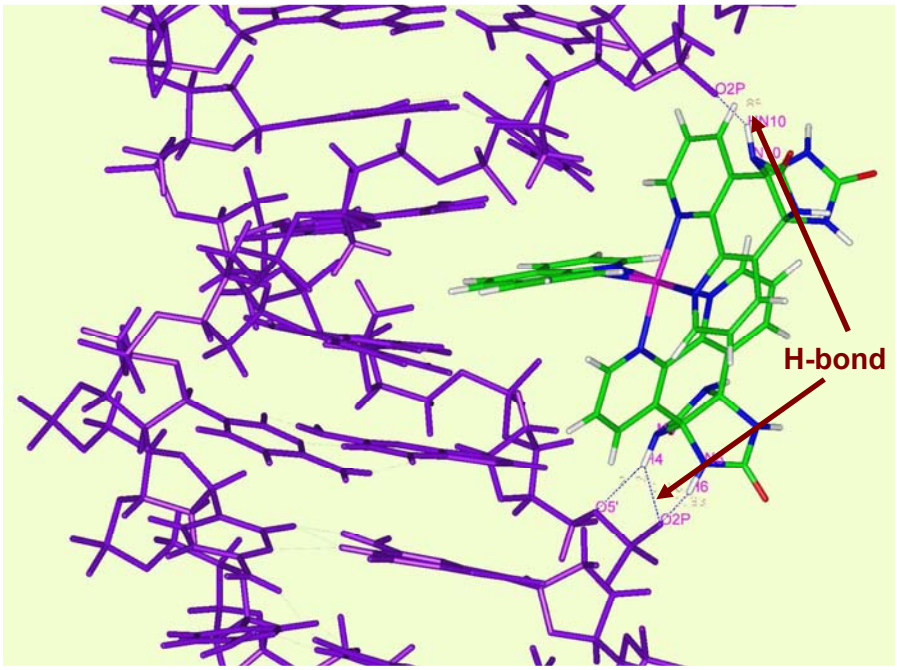

Figure S24. The core view of the bound **6** to DNA showing the partial intercalation of the phen ligand between the base pairs of DNA along with the hydrogen bonding interactions of the two BPG ligands with the phosphate groups of DNA.

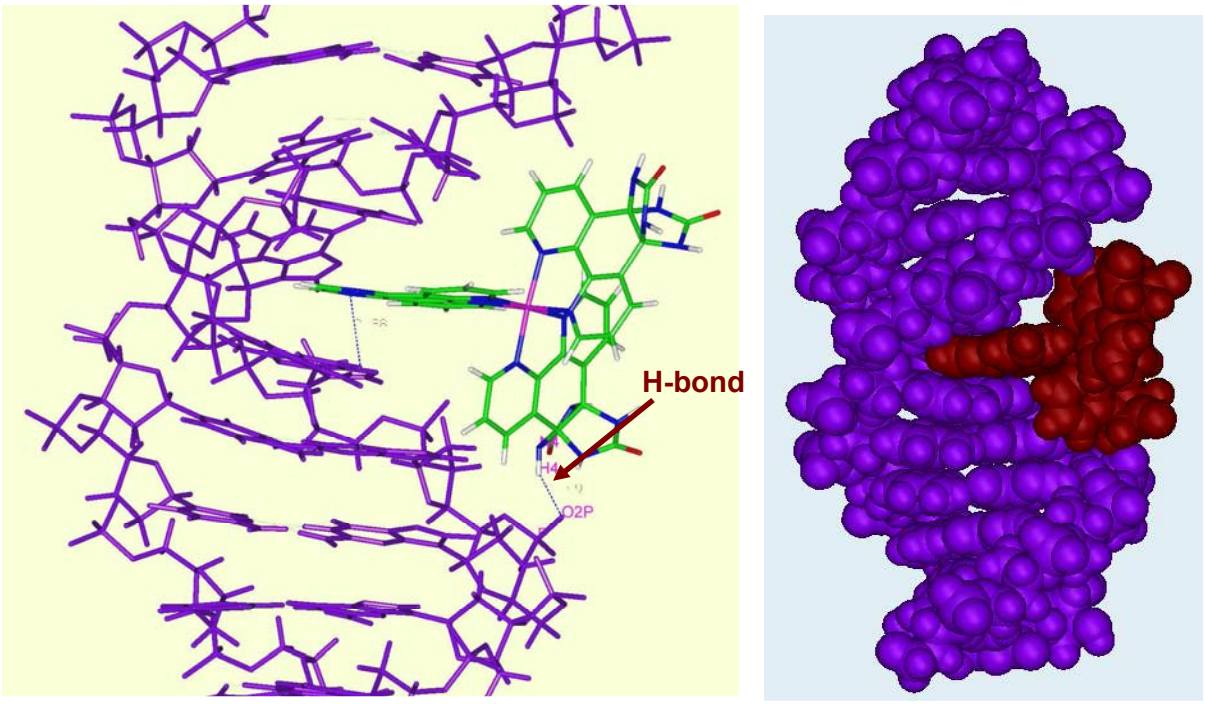

Figure S25. The core view of the bound **7** to DNA showing the intercalation of the dpq ligand between the base pairs of DNA along with the hydrogen bonding interactions of the BPG ligand with the phosphate group of DNA.

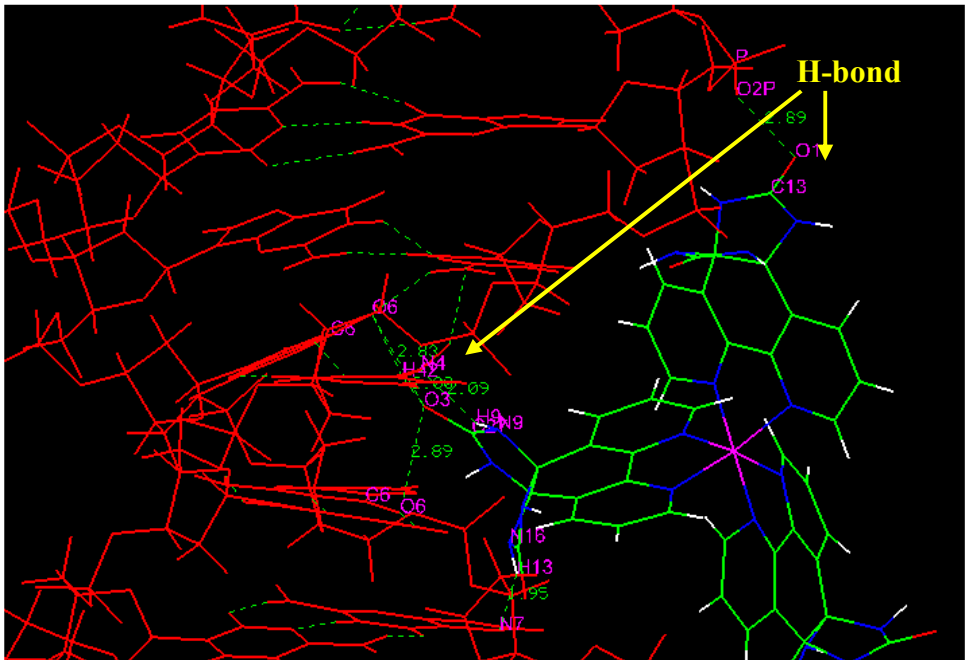

Figure S26. The core view of the bound **9** to DNA with the H-bond patterns observed showing the base and phosphate interactions.

Table S11. Binding energies in Kcal/mol and Hydrogen bond distances of Ru(II) polypyridyl complexes **1-9** with right handed B-DNA of sequence $d(C:G)_{12}$.

Complexes	Energy kcal/mol	H-bond	Distance (A˚)
$[Ru(bpy)_2(BPG)]Cl_2$ (**1**)	-20912.523	N10-HN10···O10P C9-H9···O1P	1.80 3.02
$[Ru(phen)_2(BPG)]Cl_2$ (**2**)	-21627.585	N6-H6···O2P	2.15
$[Ru(dpq)_2(BPG)]Cl_2$ (**3**)	-29789.396	C7-H7···O1P N4-H41···C18	2.66 2.05
$[Ru(dppz)_2(BPG)]Cl_2$ (**4**)	-29657.974	C7-H7···O2P CN2-HN2···O1P N4-H41···C22 N4-H41···C21	2.58 3.00 2.33 2.35
$[Ru(bpy)(BPG)_2]Cl_2$ (**5**)	-24058.515	N3- HN3···O2P-P	1.77
$[Ru(phen)(BPG)_2]Cl_2$ (**6**)	-25238.197	N10-HN10···O2P-P N4-H4···O2P-P N6-H6···O2P-P N4-H4···O5'-P	1.89 1.96 1.83 2.29
$[Ru(dpq)(BPG)_2]Cl_2$ (**7**)	-21341.273	N4-H4···O2P-P	1.99
$[Ru(dppz)(BPG)_2]Cl_2$ (**8**)	-21174.937	N10-HN10···O2P-P N4-H4···O2P-P N4-H4···O5'-P	1.94 2.28 2.46
$[Ru(BPG)_3]Cl_2$ (**9**)	-29440.145	N9-H9···N4 O3···H42-N4 N16-H13···N7	2.09 2.00 1.95

Bioconjugate Chemistry 20th Anniversary

Subscriber access provided by SHEMYAKIN-OVCHINNIKOV INST

Article

Immobilization of His-Tagged Proteins on Nickel-Chelating Nanolipoprotein Particles

Nicholas O. Fischer, Craig D. Blanchette, Brett A. Chromy, Edward A. Kuhn, Brent W. Segelke, Michele Corzett, Graham Bench, Peter W. Mason, and Paul D. Hoeprich

Bioconjugate Chem., **2009**, 20 (3), 460-465• DOI: 10.1021/bc8003155 • Publication Date (Web): 24 February 2009

Downloaded from http://pubs.acs.org on April 8, 2009

More About This Article

Additional resources and features associated with this article are available within the HTML version:

- Supporting Information
- Access to high resolution figures
- Links to articles and content related to this article
- Copyright permission to reproduce figures and/or text from this article

View the Full Text HTML

ACS Publications
High quality. High impact.

Bioconjugate Chemistry is published by the American Chemical Society. 1155 Sixteenth Street N.W., Washington, DC 20036

Immobilization of His-Tagged Proteins on Nickel-Chelating Nanolipoprotein Particles

Nicholas O. Fischer,[†] Craig D. Blanchette,[†] Brett A. Chromy,[†] Edward A. Kuhn,[†] Brent W. Segelke,[†] Michele Corzett,[†] Graham Bench,[†] Peter W. Mason,[‡] and Paul D. Hoeprich*[,†]

Chemistry, Materials, Earth, and Life Sciences, Lawrence Livermore National Laboratory, Livermore, California 94551 and Department of Pathology and Microbiology & Immunology, University of Texas Medical Branch, Galveston, Texas 77555.
Received July 23, 2008; Revised Manuscript Received January 12, 2009

Nanolipoprotein particles (NLPs) are nanometer-sized, discoidal particles that self-assemble from purified apolipoprotein and phospholipid. Their size and facile functionalization suggest potential application of NLPs as platforms for the presentation and delivery of recombinant proteins. To this end, we investigated incorporation of nickel-chelating lipids into NLPs (NiNLPs) and subsequent sequestration of polyhistidine (His)-tagged proteins. From initial lipid screens for NLP formation, the two phospholipids DMPC and DOPC were identified as suitable bulk lipids for incorporation of the nickel-chelating lipid DOGS-NTA-Ni into NLPs, and NiNLPs were successfully formed with varying amounts of DOGS-NTA-Ni. NiNLPs consisting of 10% DOGS-NTA-Ni with 90% bulk lipid (either DMPC or DOPC) were thoroughly characterized by size exclusion chromatography (SEC), nondenaturing gradient gel electrophoresis (NDGGE), and atomic force microscopy (AFM). Three different His-tagged proteins were sequestered on NiNLPs in a nickel-dependent manner, and the amount of immobilized protein was contingent on the size and composition of the NiNLP.

INTRODUCTION

Nanolipoprotein particles (NLPs) are self-assembled, nanometer-sized discoidal particles comprising lipoproteins and phospholipids (*1, 2*). Recently, NLPs have been used as model membrane mimetics for stabilizing and studying membrane proteins (*3*). While NLP formation requires only purified apolipoprotein and lipid reagents, the diversity in both the protein (*4*−*6*) and the lipid (*4, 7, 8*) components successfully used in NLP assemblies demonstrates the robust nature of the assembly process and hints at facile NLP functionalization by incorporating modified starting materials. Hence, the ability to vary the size and composition of NLPs suggests that they will be versatile platforms for immobilization of biomolecules. Functional NLPs can be used to capture recombinant proteins for a range of applications, such as facilitating the study of receptor−antigen interactions (*9*), providing a versatile platform for in vivo protein delivery (*10, 11*), or functioning as adjuvant-free particulate vaccine carriers for the delivery and presentation of immunogens (*12*−*14*).

With the goal of functionalizing NLPs with recombinant proteins, we have developed nickel-chelating nanolipoprotein particles (NiNLPs) for the targeted immobilization of any polyhistidine-tagged protein (Figure 1). Recombinant engineering of His-tagged proteins is a common intermediary in molecular biology and proteomics and is readily achievable in a variety of expression systems. As such, a substantial library of recombinant His-tagged proteins is available for NiNLP immobilization. Nickel-chelating lipids (*15*−*19*) represent a facile means of imparting NLPs with the ability to bind His-tagged proteins and have been developed for myriad applications, including two-dimensional protein crystallization (*16, 20*), functionalization of supported lipid bilayers or liposomes (*21, 22*), and liposomal or microemulsion antigen delivery (*17, 23*−*25*).

* hoeprich2@llnl.gov.
[†] Lawrence Livermore National Laboratory.
[‡] University of Texas Medical Branch.

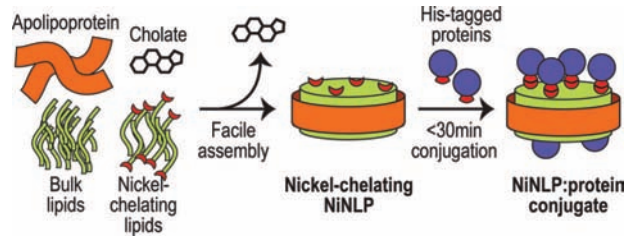

Figure 1. Schematic of NiNLP formation and conjugation of His-tagged proteins. The apolipoprotein E422K is incubated with cholate-solubilized bulk and Ni-chelating lipids. Upon removal of cholate by dialysis, discrete discoidal nanolipoprotein particles form that present nickel-chelating headgroups at the lipid bilayer periphery. The chelated nickel enables binding of polyhistidine-tagged proteins.

Herein, we describe the successful incorporation of nickel-chelating lipids into NLPs. Specifically, varying ratios of a nickel-chelating lipid (1,2-dioleoyl-*sn*-glycero-3-{[*N*-(5-amino-1-carboxypentyl) iminodiacetic acid] succinyl}(nickel salt) (DOGS-NTA-Ni)) were doped into NLP assembly reactions, which consisted of bulk lipids (either 1,2-dimyristoyl-*sn*-glycero-3-phosphocholine (DMPC) or 1,2-dioleoyl-*sn*-glycero-3-phosphocholine (DOPC)), the 22 kDa N-terminal truncation of human apolipoprotein E4 (denoted as apoE422K or E422K in the absence or presence of lipid, respectively) (*26*) and sodium cholate. The NLPs assembled with DOGS-NTA-Ni and bulk lipids (subsequently referred to as NiNLPs) were competent in binding various His-tagged recombinant proteins, including the bacteriocin pesticin (Pst) from *Yersinia pestis*, the *Y. pestis* quorum sensing protein lsrG, and the light chain of botulinum neurotoxin A.

EXPERIMENTAL SECTION

Materials. 1,2-Dimyristoyl-*sn*-glycero-3-phosphocholine (DMPC), 1,2-dioleoyl-*sn*-glycero-3-phosphocholine (DOPC), 1-palmitoyl-2-oleoyl-*sn*-glycero-3-phosphocholine (POPC), 1,2-

10.1021/bc8003155 CCC: $40.75 © 2009 American Chemical Society
Published on Web 02/24/2009

dioleoyl-*sn*-glycero-3-phosphoserine (DOPS), 1,2-dioleoyl-*sn*-glycero-3-phosphoethanolamine (DOPE), 1,2-dioleoyl-*sn*-glycero-3-ethylphosphocholine (DOEPC), 1,2-dioleoyl-3-trimethylammonium-propane (DOTAP), and the nickel salt of 1,2-dioleoyl-*sn*-glycero-3-{[*N*-(5-amino-1-carboxypentyl)iminodiacetic acid] succinyl} (DOGS-NTA-Ni) were purchased from Avanti Polar Lipids (Alabaster, AL). All other reagents were ordered from Sigma-Aldrich (St. Louis, MO).

Protein Expression and Purification. The expression clone for the 22 kDa N-terminal fragment of apolipoprotein E4 (apoE422K, kindly provided by Dr. Karl Weisgraber) featuring a cleavable His-tag (*26*) was expressed and purified as previously described (*4*). To generate the two *Y. pestis* proteins used in this study, lsrG and Pst, expression clones for each protein were generated by amplification from genomic DNA (*Y. pestis* KIM D27), and the full-length ORFs were directly cloned into a modified pETBlue expression plasmid encoding a C-terminal hexa-His tag. Plasmids were subsequently transformed into BL21(DE3)pLacI competent cells (Novagen, Madison, WI). Cells were grown in LB media with 50 μg/mL ampicillin, pelleted, and lysed using a high-pressure homogenizer (Emulsiflex-C5, Avestin, Ottawa, Canada). Insoluble material was pelleted, and soluble His-tagged protein was purified with Ni-NTA agarose (Qiagen, Valencia, CA). Immobilized protein was eluted with imidazole and further purified by SEC using a HiLoad 26/60 Superdex 75 prep-grade column (GE Healthcare, Piscataway, NJ). His-tagged botulinum neurotoxin type A light chain was expressed and purified according to the published protocol (*27*). Protein concentrations were determined using the Advanced Protein Assay Reagent (Cytoskeleton Inc., Denver, CO).

NLP Assemblies. NLPs were assembled according to a previously reported procedure (*4*) with slight modifications. Briefly, lipids were either prepared or obtained in chloroform and aliquoted into glass vials. Chloroform was then removed using a stream of N_2 under agitation to form a thin lipid film, which was further dried in vacuo for at least 4 h. Lipids were then solubilized in TBS buffer (10 mM Tris, 150 mM NaCl, 0.05% NaN_3, pH 7.4) using sodium cholate. A typical assembly contained 20 mM cholate, although during the initial lipid screen, up to 45 mM cholate was added to ensure lipid solubilization. After addition of E422K apolipoprotein, samples were either incubated at 4 °C for at least 18 h (for those lipids with transition temperatures below 4 °C) or transitioned between 30 and 20 °C three times, followed by an incubation at 23.8 °C for at least 18 h (specifically for DMPC). Assemblies were then dialyzed overnight against TBS to remove cholate and subsequently analyzed and purified by SEC (Superdex 200, 10/300 GL column, GE Healthcare, Piscataway, NJ) in TBS buffer (0.5 mL/min flow rate). NLP fractions were concentrated using a 50 kDa molecular weight cutoff (MWCO) spin concentrators (Agilent Technologies, Santa Clara, CA) and analyzed by NDGGE and/or AFM. Prior to SEC analysis, all samples were filtered using a 0.22 μm spin filter to remove any particulates (Agilent Technologies). A gel filtration calibration kit (GE Healthcare) was used to calibrate the column. The exclusion limit of the column was determined with Blue Dextran 2000. All assemblies were prepared at a 100:1 molar ratio of lipid to E422K, except assemblies with DMPC, which were prepared at a 132:1 molar ratio. Lipid concentrations during assembly typically ranged between 2 and 8 mM (see Supporting Information for details). For nondenaturing gradient gel electrophoresis (NDGGE), 4−20% Tris-glycine polyacrylamide gels were used (Invitrogen, Carlsbad, CA), and subsequently stained with SyproRuby (BioRad, Hercules, CA) and imaged using the Typhoon 9410 Variable Mode Imager (GE Healthcare). Assemblies with various ratios of bulk lipid and DOGS-NTA-Ni were essentially prepared as described above. Higher final concentrations of cholate were required for assemblies incorporating higher fractions of DOGS-NTA-Ni, with up to 35 mM cholate used for 100% DOGS-NTA-Ni assemblies.

NiNLP Component Analysis. To determine the component ratios of assembled NiNLPs, phospholipid, lipoprotein, and nickel content were quantified. Phospholipid content was determined using an enzymatic method to detect choline (Phospholipids C Assay kit, Wako Diagnostics, Richmond, VA). Protein content was assessed using the Advanced Protein Assay Reagent (Cytoskeleton Inc., Denver, CO). Nickel content was quantified by inductively coupled plasma atomic emission spectroscopy (ICP-AES) using a Thermo Elemental inductively coupled plasma - atomic emission spectrometer (Waltham, MA). Briefly, triplicate samples were aspirated using a glass nebulizer into a conical spray chamber. The instrument was calibrated using a five-point calibration curve prepared from NIST traceable certified reference materials. Calibration checks were performed before, during, and after analysis, and were within 5% of the true value of the calibrant (typically <1%). Matrix spikes ensured that the sample matrix did not interfere with the analysis. Samples were acidified (to 2% ultrapure nitric acid) in the dilution process, which was based on mass. Analyses were conducted using three wavelengths: one analytical wavelength (221.647 nm) and two confirmatory wavelengths (231.604 and 341.476 nm). All the wavelengths were in agreement within 1%. The Ni concentration was extrapolated by the instrument from a calibration curve. The correlation coefficients for the calibration curves were 0.99998 (221.647 nm), 0.99999 (231.604 nm), and 0.99952 (341.476 nm).

AFM Analysis of NLPs. Atomic force microscopy was conducted as previously described (*28*). Briefly, samples were incubated for 2 min on an atomically flat muscovite mica surface in imaging buffer (10 mM $MgCl_2$, 10 mM Tris-HCl, 100 mM NaCl, pH 8.0), then lightly rinsed. Height, amplitude, and phase images were collected using a MFP-3D-CFM AFM (Asylum Research, Santa Barbara, CA). NLP diameters were determined by full width half-maximum (fwhm) analysis of particles in the slow scan direction using IgorPro software (WaveMetrics Inc., Portland, OR). To limit instrument broadening during lateral particle sizing, only tips revealing sharp imaging were used for diameter analysis. We have previously determined, based on NLP size and molecular dynamics simulations, that the average tip broadening effect was ∼2−3 nm (*28*). Due to tip architecture, it is assumed that the tip directly contacts the NLP bilayer, rather than the peripheral lipoproteins. Hence, the ∼2−3 nm tip convolution is essentially abrogated as the proteins are estimated to extend ∼2−3 nm from the bilayer (i.e., ∼1.0−1.5 nm on each side of the NLP). To determine the reproducibility of the procedure used for measuring NLP diameters, randomly selected particles were repeatedly imaged to verify consistent diameter measurements. Heights of particles were elucidated from histogram analysis.

Protein−NLP Conjugation. To immobilize His-tagged proteins on NiNLPs, NiNLPs (0.1 μg/μL) were incubated in TBS buffer with various concentrations of His-tagged proteins at room temperature for 45 min in a volume of 100 μL. A portion from each sample (60 μL) was subsequently filtered through a 100 kDa MWCO Microcon spin concentrator (Millipore, Burlington, MA) and washed three times with 200 μL of buffer. For control experiments, NiNLPs were preincubated in TBS buffer supplemented with 4 mM ethylenediaminetetraacetic acid (EDTA) for 45 min at room temperature prior to His-tagged protein addition. For these samples, the wash buffer also contained 4 mM EDTA. Samples were then analyzed by denaturing gel electrophoresis on 16% Tris-tricine polyacrylamide gels (Invitrogen). Gels were stained and imaged as

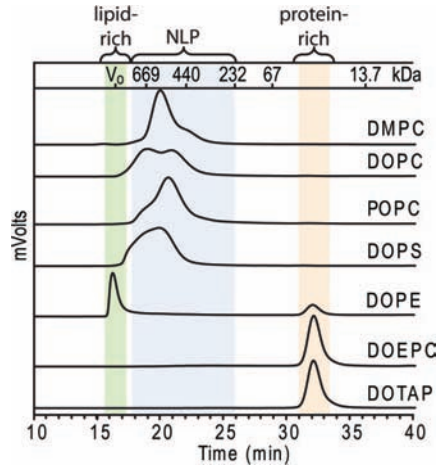

Figure 2. NLP formation with apolipoprotein E422K in the presence of seven bulk lipids (DMPC, DOPC, POPC, DOPS, DOPE, DOEPC, and DOTAP) was screened by SEC. Three important regions of the SEC traces are indicated, corresponding to lipid-rich (~15−17 min), NLP (17−26 min), and protein-rich fractions (31−34 min). Molecular weights of protein standards are indicated, as well as the exclusion limit of the column (V_o).

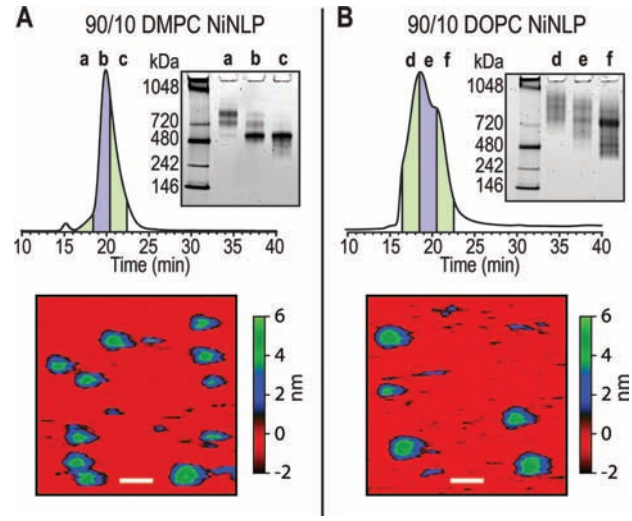

Figure 3. Formation of NiNLPs incorporating nickel-chelating lipids. Characterization of (A) DMPC- and (B) DOPC-based NiNLPs incorporating 10% DOGS-NiNTA using SEC (top), NDGGE of indicated SEC fractions (inset), and AFM (bottom). Scale bar is 50 nm.

indicated above. ImageQuant (GE Healthcare) was used for densitometry measurements. The NiNLPs used for these studies were both composed of pooled SEC fractions. Previously published experimental and modeling data (*28*) were used to extrapolate NiNLP concentration assuming DMPC- and DOPC-based NiNLPs contain five and six E422K lipoproteins per NiNLP, respectively. For AFM analysis of protein binding, samples were prepared as indicated above. In lieu of ultrafiltration, samples were diluted in imaging buffer and pipetted onto the AFM mica surface.

RESULTS

Survey of Lipid Compatibility with NLP Formation. The formation of nickel-presenting lipid bilayers has been extensively demonstrated for a variety of applications and is typically accomplished by mixing low concentrations of a nickel-chelating lipid with a bulk lipid. The first step in developing NiNLPs was to determine the effects of several bulk lipids on NLP assembly. To this end, seven different lipids were tested for NLP formation: DMPC, DOPC, DOPS, POPC, DOPE, DOTAP, and DOEPC. SEC was then used to determine proper assembly of NLPs. As demonstrated in Figure 2, assemblies with DMPC, DOPC, DOPS, and POPC all formed particles with the expected NLP retention times of 18 to 26 min (*4*), indicating NLPs ranging in apparent molecular weight (MW) between 350 and 900 kDa. NDGGE of these samples also indicated particle formation, while AFM confirmed the presence of discoidal particles (data not shown). No NLP formation was observed with DOPE, as the SEC trace depicts two discrete, non-NLP peaks. The first peak at ~17 min is attributed to large lipid-rich aggregates (corresponding to the ~1.5 MDa exclusion limit of the column), while the second peak at ~32 min is characterized as a protein-rich species. The retention time of the protein-rich peak was identical to pure apolipoprotein (data not shown). Assemblies with DOTAP and DOEPC were cloudy after dialysis, and seemingly all precipitated lipids were removed in the prefiltration (0.22 μm) step prior to SEC analysis. No NLP species were observed in the SEC traces, though a peak in the protein-rich region was observed in both samples. These data demonstrate that, by using the assembly conditions and stoichiometry described above, NLPs were successfully formed with DMPC, DOPC, DOPS, and POPC.

NLP Formation with DOGS-NTA-Ni. On the basis of the survey of NLP formation with the bulk lipids, DMPC and DOPC were chosen to evaluate DOGS-NTA-Ni incorporation into NLPs. Initially, NLP assemblies with 1%, 3%, 10%, 30%, and 100% (molar) DOGS-NTA-Ni were tested. All lipid ratios formed NiNLPs (data not shown), so formulations incorporating 10% DOGS-NTA-Ni were deemed acceptable for further study, as 10% ensures the presence of chelated nickel at the NiNLP surface without requiring excessive amounts of costly DOGS-NTA-Ni lipid. These NiNLPs were further analyzed by SEC, NDGGE, and AFM (Figure 3). The NiNLPs consisting of 90% DMPC and 10% DOGS-NTA-Ni (henceforth referred to as 90/10 DMPC NiNLPs) were characterized by a relatively narrow SEC peak with a retention time of ~20 min, indicating an apparent MW of 680 kDa (Figure 3A). NDGGE analysis of the indicated fractions suggested a mixed population of NiNLPs with apparent MW of ca. 800, 710, and 570 kDa (based on a calibration curve using the protein marker standards). The larger NLPs eluted primarily in the first SEC fraction (fraction a), while the main SEC peak (fractions b and c) was dominated by 570 kDa NiNLPs. In contrast, 90/10 DOPC NiNLPs had a larger size distribution (Figure 3B). By SEC, at least two peaks are apparent, corresponding to 950 and 615 kDa (at 18.5 and 20.3 min, respectively). SEC fractions d and e were composed of large particles, whereby three equally intense bands at approximately 950, 890, and 730 kDa could be discerned by NDGGE. The SEC fraction f, on the other hand, was dominated by the 730 kDa NiNLP species.

The NiNLPs prepared with either DMPC or DOPC were further characterized by AFM to elucidate both particle size and morphology. AFM analysis of 90/10 DMPC NiNLP fraction c demonstrated that the majority of NLP species were either 14.5 or 19.0 nm in diameter, with an average of 17.5 ± 3.5 nm. The heights of these particles were measured at 5.24 ± 0.25 nm, illustrating the discoidal morphology of these NiNLPs. AFM indicated that 90/10 DOPC NiNLPs were overall larger in diameter than the 90/10 DMPC NiNLPs, with an average diameter of 21.0 ± 4.2 nm. The heights of these NiNLPs were 5.16 ± 0.18 nm, again demonstrating that these particles are discoidal.

To understand the compositional stoichiometry of the NiNLPs, the protein, phospholipid, and DOGS-NTA-Ni constituents were quantified (see Experimental Section for details). Elemental nickel analysis indicated that both 90/10 DMPC and 90/10 DOPC NiNLPs incorporated similar molar ratios of DOGS-NTA-Ni (11.1 ± 0.1% and 9.3 ± 0.3%, respectively), consistent

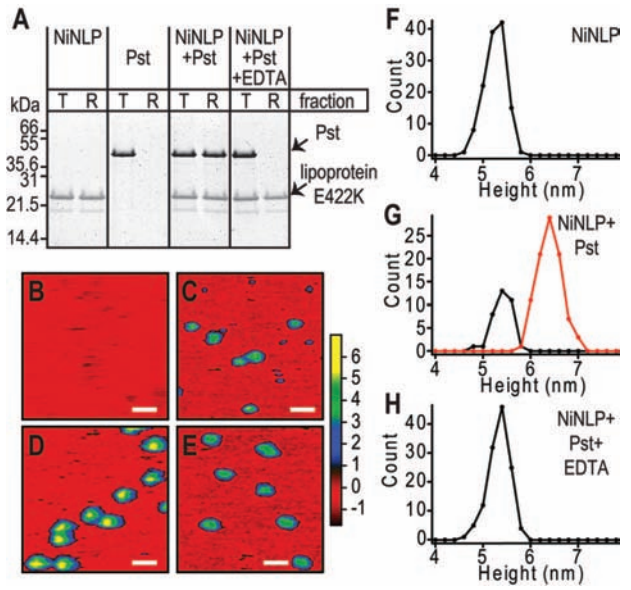

Figure 4. NiNLPs can bind His-tagged proteins. (A) NiNLPs incubated with His-tagged pesticin (Pst) at room temperature for 30 min were analyzed by denaturing SDS-PAGE. Total sample (*T*) was compared to retentate fraction (*R*) after size-exclusion partitioning using a 100 kDa MWCO membrane (see Experimental Section), enabling NiNLPs (>400 kDa) to be separated from unconjugated Pst (40 kDa). Addition of EDTA abrogates any interaction between the protein and the NiNLP. (B−E) Atomic force micrographs of Pst alone (B), NiNLPs alone (C), NiNLPs+Pst (D), and NiNLPs+Pst in the presence of EDTA (E). Scale bar is 50 nm. (F−H) Summary height analyses of NiNLPs (F), NiNLPs with Pst (G), and NiNLPs with Pst in the presence of EDTA (H).

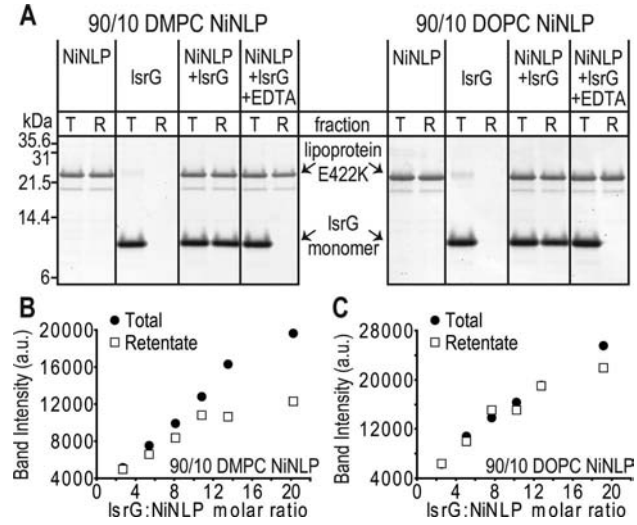

Figure 5. Protein loading of NiNLPs can be controlled by coupling stoichiometry. (A) NiNLPs incubated with His-tagged lsrG at room temperature for 30 min were analyzed by denaturing SDS-PAGE. Total sample (*T*) was compared to retentate fraction (*R*) after size-exclusion partitioning using a 100 kDa MWCO membrane to separate NiNLPs (>400 kDa) from unconjugated lsrG (11.4 kDa). The 90/10 DMPC and 90/10 DOPC NiNLPs are equally competent in protein binding. The faint bands at 24 kDa in the lsrG (*T*) lanes correspond to nondenatured lsrG dimers. (B,C) Incubation of lsrG with NiNLPs at various molar ratios demonstrates conjugation stoichiometry with 90/10 DMPC NiNLPs (B) and the larger 90/10 DOPC NiNLPs (C).

with an initial feed ratio of 10%. When prepared at a 130:1 lipid/E422K molar ratio, the 90/10 DMPC NiNLPs contained a final lipid/E422K ratio of 103.3 ± 6.1. The 100:1 molar ratio used for the DOPC-based NiNLPs resulted in a final lipid/E422K ratio of 86.2 ± 15.0.

Conjugation of His-Tagged Proteins to NiNLPs. To demonstrate functionalization of NiNLPs, the ability to conjugate several His-tagged proteins to NiNLPs was tested. To assess conjugation, samples were partitioned using 100 kDa MWCO spin filters, which retained NiNLPs (and proteins conjugated to the NiNLPs), whereas the unbound His-tagged proteins were passed to the filtrate. Thus, by performing denaturing gel electrophoresis on NiNLP/His-tagged protein mixtures and the 100 kDa MWCO filter retentate, conjugation could be readily assessed. A His-tagged 40 kDa soluble protein from *Y. pestis*, pesticin (Pst), was successfully immobilized on 90/10 DMPC NiNLPs (Figure 4A, lane NiNLP+Pst (R)). To demonstrate that Ni was required for this interaction, NiNLPs were preincubated with EDTA to chelate the Ni from the NiNLP bilayer surface and then mixed with Pst. Under these conditions, no retention of Pst was observed, indicating that specific conjugation to the Ni-chelating lipids had been abrogated. To verify these results, nonpartitioned samples were analyzed by AFM (Figure 4B−H). Upon incubation with Pst, the height profile of the majority of NiNLPs shifted from ∼5.4 nm to ∼6.4 nm. This height shift was absent in the presence of EDTA, demonstrating that the chelated Ni was required for the observed interaction between the His-tagged protein and the NiNLP. Similarly, a partially purified preparation of recombinant His-tagged botulinum neurotoxin A light chain (BoNT/A LC) was successfully immobilized on 90/10 DMPC NiNLPs (see Supporting Information).

To further demonstrate the universal applicability of this approach, conjugation of another His-tagged *Y. pestis* protein, lsrG, was shown with both DMPC and DOPC-based NiNLPs containing 10% DOGS-NTA-Ni (Figure 5A). Various molar ratios of NiNLP to lsrG were tested in the hopes of elucidating conjugation stoichiometry. To simplify analysis, previous modeling data were used to extrapolate the average number of lipoprotein molecules per NiNLP from the NiNLP diameters (*28*). On the basis of these models, the DMPC- and DOPC-based NiNLPs were estimated to have incorporated an average of 5 and 6 lipoprotein molecules, respectively, enabling an approximation of NiNLP molar concentration from measured lipoprotein concentrations. Samples were partitioned and run on denaturing gels, demonstrating that both NiNLPs efficiently bound lsrG (Figure 5B,C). Densitometry of the bands detected in these gels was used to quantify the relative retention of lsrG, and post-partitioned samples were normalized to pre-partitioned samples based on E422K band intensity. This normalization was required to account for the slight loss of material due to filter membrane retention observed at higher concentrations of lsrG, presumably due to an alteration of the NiNLP surface charge and/or polar characteristics by lsrG. On the basis of these data, 90/10 DOPC NiNLPs can accommodate significantly more lsrG molecules prior to saturation than the smaller 90/10 DMPC NiNLPs.

DISCUSSION

We have demonstrated the successful incorporation of nickel-chelating lipids into NLPs that enables direct conjugation of His-tagged proteins to the resultant NiNLP surface. The nickel-chelating lipid DOGS-NTA-Ni has been extensively used for myriad applications (*19, 21, 24, 25*) and always in conjunction with a bulk (non-Ni-chelating) lipid. The use of bulk lipids in these reports permitted control of the number of Ni-chelate groups on the bilayer surface, reduced cost by using an inexpensive bulk lipid, and took advantage of the overall bilayer-formation properties of the bulk lipid. Hence, we screened a variety of bulk lipids that have previously been used in conjunction with DOGS-NTA-Ni for NLP formation using a previously established NLP assembly protocol (*4*). NLP forma-

tion was successful with four of the tested phospholipids: DMPC, DOPC, POPC, and DOPS (Figure 2). NLPs incorporating DMPC have been extensively studied (*4, 5, 28, 29*), in contrast to DOPC-based NLPs. Subsequently, these two lipids were tested for incorporation of DOGS-NTA-Ni. Discoidal NLPs were readily formed with the nickel-chelating lipid and either DMPC or DOPC (Figure 3). At a 10% DOGS-NTA-Ni feed ratio, the DMPC-based NiNLPs had an average diameter of 17.5 ± 2.2 nm as measured by AFM. DOPC-based NiNLPs were more heterogeneous in size, exhibiting a major species ca. 21.0 ± 4.2 nm in size. These results reaffirm published studies indicating that the identity of the bulk lipid as well as the stoichiometry of lipid to apolipoprotein influence the average size of the resultant NiNLPs (*4*). Stoichiometry also plays a role in the heterogeneity of NLPs. Although heterogeneity in this case does not necessarily affect potential applications, certain uses may require particles that are highly monodisperse in size. In these cases, greater homogeneity can be achieved through both optimization of lipid/protein ratios and subsequent SEC fractionation.

It is important to note that the NLP diameters obtained by AFM are not in complete agreement with SEC and NDGGE (which are in greater agreement with each other). Direct comparison of discoidal NLPs to globular protein standards (used for both SEC and NDGGE calibration) proved difficult. To address these discrepancies, we have previously demonstrated a high degree of NLP diameter correlation from three independent single-molecule techniques: AFM, transmission electron microscopy, and ion mobility spectroscopy (*4, 28*). As SEC- and NDGGE-based size determinations are derived from averages of particle ensembles, we have utilized SEC and NDGGE as screening techniques to understand general trends in NLP size, while using AFM for more direct quantification.

Here, we have shown that NiNLPs are functionally active, as they can be readily conjugated with His-tagged proteins. The conjugation of His-tagged proteins to nickel-chelating moieties is an integral process in protein purification and proteomics applications (*30*−*32*). This interaction has also been adapted for functionalization of myriad lipid-based particles and surfaces for biotechnology applications (*15*−*25*). The ease and speed of the conjugation process, coupled with the simplicity of generation of His-tagged proteins, make this a very powerful approach for surface functionalization. We have demonstrated that this process works very well for NiNLPs by demonstrating that all three His-tagged proteins tested were readily immobilized on the NiNLPs. The conjugation was monitored by two independent techniques: denaturing gel electrophoresis of partitioned NiNLPs and AFM. Gel electrophoresis demonstrated that His-tagged proteins were successfully immobilized on NLPs, as partitioning was used to isolate the large NiNLPs from unbound material using a 100 kDa MWCO membrane. The presence of any His-tagged protein in the high molecular weight retentate was possible only through conjugation of the protein to the NiNLP. When the NiNLP was treated with EDTA to remove nickel, no protein was found in the retentate, demonstrating the importance of chelated nickel in the immobilization process. Also, a significant height increase was observed with AFM upon the addition of the His-tagged protein to NiNLPs (Figure 4). Again, this was abrogated if NiNLPs were preincubated with EDTA.

Both size and lipid composition are anticipated to be important determinants in the degree of His-tagged protein loading on the NiNLP. This was demonstrated when overall protein immobilization was compared between the DMPC- and DOPC-based NiNLPs (Figure 5). The larger diameter 90/10 DOPC NiNLPs were able to accommodate more lsrG protein than the smaller 90/10 DMPC NiNLPs. While these data suggest that the diameter of the NiNLPs dictates the amount of immobilized protein, the composition of the lipid can also play a role in bilayer packing and DOGS-NTA-Ni distribution. Performing immobilization assays with a panel of discretely sized NiNLP of uniform composition may provide a means to identify the contribution of both particle size and bilayer composition to protein loading.

In conclusion, we have demonstrated the preparation of NLPs incorporating chelated nickel and that these NiNLPs bind His-tagged proteins. NiNLP technology may be applied to the study of receptor−target interactions at a bilayer surface or to the in vivo delivery or targeting of biological macromolecules. These latter applications suggest that NiNLPs may represent a rapid and versatile means to immobilize a protein or multiple proteins for potential use as vaccines, including multivalent vaccines. The development of a universal particulate platform for the delivery and controlled presentation of recombinant proteins for vaccine applications (*12, 33, 34*) would provide an important step toward greater applicability of recombinant immunogens.

ACKNOWLEDGMENT

The authors thank Dr. Karl Weisgraber for providing reagents and Dr. Roger Martinelli for ICP-AES nickel quantification. This work performed under the auspices of the U.S. Department of Energy by Lawrence Livermore National Laboratory (LLNL-JRNL-405192) under Contract DE-AC52-07NA27344 with support from Lawrence Livermore National Laboratory (LDRD, 06-SI-003).

Supporting Information Available: Experimental details of NLP assemblies and results of BoNT/A LC conjugation to NiNLPs. This material is available free of charge via the Internet at http://pubs.acs.org.

LITERATURE CITED

(1) Jonas, A. (1986) Reconstitution of high-density-lipoproteins. *Methods Enzymol. 128*, 553–582.

(2) Brouillette, C. G., Jones, J. L., Ng, T. C., Kercret, H., Chung, B. H., and Segrest, J. P. (1984) Structural studies of apolipoprotein-A-I phosphatidylcholine recombinants by high-field proton NMR, nondenaturing gradient gel-electrophoresis, and electron-microscopy. *Biochemistry 23*, 359–367.

(3) Nath, A., Atkins, W. M., and Sligar, S. G. (2007) Applications of phospholipid bilayer nanodiscs in the study of membranes and membrane proteins. *Biochemistry 46*, 2059–2069.

(4) Chromy, B. A., Arroyo, E., Blanchette, C. D., Bench, G., Benner, H., Cappuccio, J. A., Coleman, M. A., Henderson, P. T., Hinz, A. K., Kuhn, E. A., Pesavento, J. B., Segelke, B. W., Sulchek, T. A., Tarasow, T., Walsworth, V. L., and Hoeprich, P. D. (2007) Different apolipoproteins impact nanolipoprotein particle formation. *J. Am. Chem. Soc. 129*, 14348–14354.

(5) Fang, Y. L., Gursky, O., and Atkinson, D. (2003) Lipid-binding studies of human apolipoprotein A-I and its terminally truncated mutants. *Biochemistry 42*, 13260–13268.

(6) Weers, P. M. M., and Ryan, R. O. (2006) Apolipophorin III: Role model apolipoprotein. *Insect Biochem. 36*, 231–240.

(7) Bhat, S., Sorci-Thomas, M. G., Tuladhar, R., Samuel, M. P., and Thomas, M. J. (2007) Conformational adaptation of apolipoprotein A-I to discretely sized phospholipid complexes. *Biochemistry 46*, 7811–7821.

(8) Denisov, I. G., McLean, M. A., Shaw, A. W., Grinkova, Y. V., and Sligar, S. G. (2005) Thermotropic phase transition in soluble nanoscale lipid bilayers. *J. Phys. Chem. B 109*, 15580–15588.

(9) Tuthill, T. J., Bubeck, D., Rowlands, D. J., and Hogle, J. M. (2006) Characterization of early steps in the poliovirus infection process: Receptor-decorated liposomes induce conversion of the virus to membrane-anchored entry-intermediate particles. *J. Virol. 80*, 172–180.

(10) Devalapally, H., Chakilam, A., and Amiji, M. M. (2007) Role of nanotechnology in pharmaceutical product development. *J. Pharm. Sci. 96*, 2547–2565.

(11) Rawat, M., Singh, D., Saraf, S., and Saraf, S. (2006) Nanocarriers: Promising vehicle for bioactive drugs. *Biol. Pharm. Bull. 29*, 1790–1798.

(12) Bramwell, V. W., Eyles, J. E., and Alpar, H. O. (2005) Particulate delivery systems for biodefense subunit vaccines. *Adv. Drug Delivery Rev. 57*, 1247–1265.

(13) Friede, M., and Aguado, M. T. (2005) Need for new vaccine formulations and potential of particulate antigen and DNA delivery systems. *Adv. Drug Delivery Rev. 57*, 325–331.

(14) Jennings, G. T., and Bachmann, M. F. (2007) Designing recombinant vaccines with viral properties: a rational approach to more effective vaccines. *Curr. Mol. Med. 7*, 143.

(15) Venien-Bryan, C., Balavoine, F., Toussaint, B., Mioskowski, C., Hewat, E. A., Helme, B., and Vignais, P. M. (1997) Structural study of the response regulator HupR from Rhodobacter capsulatus. Electron microscopy of two-dimensional crystals on a nickel-chelating lipid. *J. Mol. Biol. 274*, 687–692.

(16) Kubalek, E. W., Legrice, S. F. J., and Brown, P. O. (1994) 2-Dimensional crystallization of histidine-tagged, HIV-1 reverse-transcriptase promoted by a novel nickel-chelating lipid. *J. Struct. Biol. 113*, 117–123.

(17) van Broekhoven, C. L., and Altin, J. G. (2005) The novel chelator lipid 3(nitrilotriacetic acid)-ditetradecylamine (NTA(3)-DTDA) promotes stable binding of His-tagged proteins to liposomal membranes: Potent anti-tumor responses induced by simultaneously targeting antigen, cytokine and costimulatory signals to T cells. *Biochim. Biophys. Acta 1716*, 104–116.

(18) Schmitt, L., Dietrich, C., and Tampe, R. (1994) Synthesis and characterization of chelator-lipids for reversible immobilization of engineered proteins at self-assembled lipid interfaces. *J. Am. Chem. Soc. 116*, 8485–8491.

(19) Wilson-Kubalek, E. M., Brown, R. E., Celia, H., and Milligan, R. A. (1998) Lipid nanotubes as substrates for helical crystallization of macromolecules. *Proc. Natl. Acad. Sci. U.S.A. 95*, 8040–8045.

(20) Bischler, N., Balavoine, F., Milkereit, P., Tschochner, H., Mioskowski, C., and Schultz, P. (1998) Specific interaction and two-dimensional crystallization of histidine tagged yeast RNA polymerase I on nickel-chelating lipids. *Biophys. J. 74*, 1522–1532.

(21) Nye, J. A., and Groves, J. T. (2008) Kinetic control of histidine-tagged protein surface density on supported lipid bilayers. *Langmuir 24*, 4145–4149.

(22) Sun, J. J., Vernier, G., Wigelsworth, D. J., and Collier, R. J. (2007) Insertion of anthrax protective antigen into liposomal membranes - Effects of a receptor. *J. Biol. Chem. 282*, 1059–1065.

(23) Ruger, R., Muller, D., Fahr, A., and Kontermann, R. E. (2005) Generation of immunoliposomes using recombinant single-chain Fv fragments bound to Ni-NTA-liposomes. *J. Drug Targeting 13*, 399–406.

(24) Ruger, R., Muller, D., Fahr, A., and Kontermann, R. E. (2006) In vitro characterization of binding and stability of single-chain Fv Ni-NTA-liposomes. *J. Drug Targeting 14*, 576–582.

(25) Patel, J. D., O'Carra, R., Jones, J., Woodward, J. G., and Mumper, R. J. (2007) Preparation and characterization of nickel nanoparticles for binding to his-tag proteins and antigens. *Pharm. Res. 24*, 343–352.

(26) Morrow, J. A., Arnold, K. S., and Weisgraber, K. H. (1999) Functional characterization of apolipoprotein E isoforms overexpressed in Escherichia coli. *Protein Expr. Purif. 16*, 224–230.

(27) Kadkhodayan, S., Knapp, M. S., Schmidt, J. J., Fabes, S. E., Rupp, B., and Balhorn, R. (2000) Cloning, expression, and one-step purification of the minimal essential domain of the light chain of botulinum neurotoxin type A. *Protein Expr. Purif. 19*, 125–130.

(28) Blanchette, C. D., Law, R., H., B. W., Pesavento, J. B., Cappuccio, J. A., Walsworth, V., Kuhn, E. A., Corzett, M., Chromy, B. A., Segelke, B. W., Coleman, M. A., Bench, G., Hoeprich, P. D., and Sulchek, T. A. (2008) Quantifying size distributions of nanolipoprotein particles with single-particle analysis and molecular dynamic simulations. *J. Lipid Res. 49*, 1420–1430.

(29) Denisov, I. G., Grinkova, Y. V., Lazarides, A. A., and Sligar, S. G. (2004) Directed self-assembly of monodisperse phospholipid bilayer nanodiscs with controlled size. *J. Am. Chem. Soc. 126*, 3477–3487.

(30) Porath, J., Carlsson, J., Olsson, I., and Belfrage, G. (1975) Metal chelate affinity chromatography, a new approach to protein fractionation. *Nature 258*, 598–599.

(31) Hochuli, E., Bannwarth, W., Dobeli, H., Gentz, R., and Stuber, D. (1988) Genetic approach to facilitate purification of recombinant proteins with a novel metal chelate adsorbent. *Bio-Technology 6*, 1321–1325.

(32) Terpe, K. (2003) Overview of tag protein fusions: from molecular and biochemical fundamentals to commercial systems. *Appl. Microbiol. Biotechnol. 60*, 523–533.

(33) Liljeqvist, S., and Stahl, S. (1999) Production of recombinant subunit vaccines: protein immunogens, live delivery systems and nucleic acid vaccines. *J. Biotechnol. 73*, 1–33.

(34) Pashine, A., Valiante, N. M., and Ulmer, J. B. (2005) Targeting the innate immune response with improved vaccine adjuvants. *Nat. Med. 11*, S63−S68.

BC8003155

Immobilization of His-tagged proteins on nickel-chelating nanolipoprotein particles

Nicholas O. Fischer[1], Craig D. Blanchette[1], Brett A. Chromy[1], Edward A. Kuhn[1], Brent W. Segelke[1], Michele Corzett[1], Graham Bench[1], Peter W. Mason[2], and Paul D. Hoeprich[,1]*

[1]Chemistry, Materials, Earth, and Life Sciences, Lawrence Livermore National Laboratory, Livermore, California 94551

[2]Department of Pathology and Microbiology & Immunology, University of Texas Medical Branch, Galveston, Texas 77555

Supporting Information

Table S1. NLP assembly parameters

NLP identity[a]	[E422K], mM	[Lipid], mM	[Cholate], mM	Incubation time, hr	Transition[b]	Incubation temperature
DMPC	0.05	6.5	20.0	22	yes	23.8°C
DOPC	0.05	5.0	20.0	22	no	4°C
DOPE	0.05	5.0	45.0	22	no	4°C
DOPS	0.05	5.0	21.5	22	no	4°C
DOEPC	0.05	5.0	20.0	22	no	4°C
DOTAP	0.05	5.0	20.0	22	no	4°C
POPC	0.07	6.5	25.0	22	no	4°C
90/10 DMPC/DOGS-NTA-Ni	0.05	6.5	20.0	18	yes	23.8°C
90/10 DOPC/DOGS-NTA-Ni	0.05	5.0	20.0	18	no	4°C

[a] NLP identity based on lipid constituents

[b] Temperature transitions consisted of 10 minute incubations at 30°C and 20°C, repeated 3 times

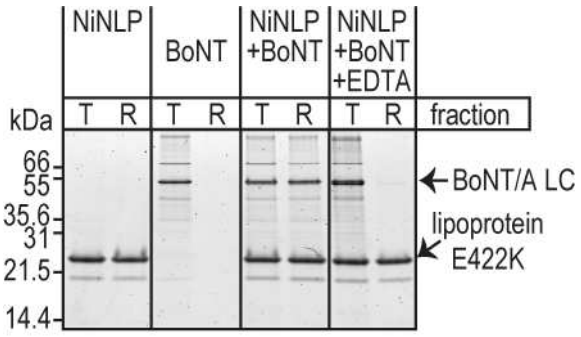

Figure S1. NiNLPs incubated with a partially purified preparation of the His-tagged light chain of botulinum neurotoxin A (BoNT/A LC) at room temperature for 30 minutes were analyzed by denaturing SDS-PAGE. Total sample (T) was compared to retentate fraction (R) after size-exclusion partitioning using a 100 kDa MWCO membrane. Addition of EDTA abrogates any interaction between the protein and the NiNLP.

Subscriber access provided by SHEMYAKIN-OVCHINNIKOV INST

Article

Receptor Arrays for the Selective and Efficient Capturing of Viral Particles

Philipp D. Pollheimer, Markus Kastner, Andreas Ebner, Dieter Blaas, Peter Hinterdorfer, Hermann J. Gruber, and Stefan Howorka

Bioconjugate Chem., **2009**, 20 (3), 466-475• DOI: 10.1021/bc800357j • Publication Date (Web): 05 February 2009

Downloaded from http://pubs.acs.org on April 8, 2009

More About This Article

Additional resources and features associated with this article are available within the HTML version:

- Supporting Information
- Access to high resolution figures
- Links to articles and content related to this article
- Copyright permission to reproduce figures and/or text from this article

View the Full Text HTML

ACS Publications
High quality. High impact.

Bioconjugate Chemistry is published by the American Chemical Society. 1155 Sixteenth Street N.W., Washington, DC 20036

Receptor Arrays for the Selective and Efficient Capturing of Viral Particles

Philipp D. Pollheimer,[†,‡] Markus Kastner,[†] Andreas Ebner,[†] Dieter Blaas,[§] Peter Hinterdorfer,[†] Hermann J. Gruber,[†] and Stefan Howorka*[,‡,||]

Institute of Biophysics, Johannes Kepler University, 4040 Linz, Austria, Center for Biomedical Nanotechnology, Upper Austrian Research GmbH, 4020 Linz, Austria, Max F. Perutz Laboratories, Medical University of Vienna, 1030 Vienna, Austria, and Department of Chemistry, Institute of Structural Molecular Biology, University College London, London WC1H 0AJ, United Kingdom. Received August 20, 2008; Revised Manuscript Received December 22, 2008

We describe microarrays of receptors on gold/glass substrates for the selective capturing of viral particles at high density. Microscale gold squares were surface-modified with alkanethiol derivatives which enabled the immobilization of the His_6-tagged virus-binding domain from the very-low density lipoprotein (VLDL) receptor. The free glass areas surrounding the gold squares were passivated with a dense film of poly(ethylene glycol) (PEG). As assessed by atomic force microscopy, human rhinovirus particles were captured onto the VLDL-receptor patches with a high surface coverage but were effectively repelled by the PEG layer, resulting in a 330 000-fold higher density of the particles on the gold as compared to the glass surfaces. The metal chelate-based coupling strategy was found to be superior to two alternative routes, which used the covalent coupling of viral particles or viral receptors to the substrate surface. The high-density receptor arrays were employed for sensing and characterizing viral particles with so far unprecedented selectivity.

INTRODUCTION

Capturing viral particles from solution onto micropatterned substrates is of relevance for applications in biotechnology, diagnostics, and biomedical research. Similar to the specific binding of DNAs and proteins onto microarrays, selective detection and biophysical characterization of viruses via surface-immobilized receptors is becoming increasingly important (*1*−*5*). Particularly useful in this respect is the combination with high-resolution read-out technologies such as atomic force microscopy (AFM) (*6*−*10*). This technique introduces an additional dimension because the virions are analyzed by AFM with regard to their characteristic morphology and size (*1, 2*).

Microarray patterns of receptor molecules have been generated by microspotting (*11*−*13*), microcontact printing (*14*−*16*), microfluidic networks (*17*), chemical photolithography (*18, 19*), and photochemical patterning (*20, 21*). However, several of these methodologies are either chemically incompatible with the attachment of virus receptors (*18, 19*) or cannot be easily scaled down for the production of small micrometer or submicrometer-sized receptor spots as required in high throughput AFM read-out (*11, 12, 14*−*17*). Recently, an AFM cantilever has been successfully used as a stylus to scratch soft protein layers and thereby generate nanoscale patterns of receptor spots (*1, 22*). However, the procedure is serial and does not benefit from the scalability and ease of parallel processing. Furthermore, virus nanoarrays have been obtained by the AFM-based dip-pen nanolithography approach (*23, 24*) leading to the immobilization of single virions (*2, 6, 7*). The particles were either bound onto chemically activated surfaces (*6, 7*) or captured onto antibody spots (*2*).

By using a human rhinovirus (HRV2) and a recombinant very-low-density lipoprotein receptor (VLDLR) as the model system, we report a new parallel approach toward the specific and high-density immobilization of virions onto solid substrates. HRVs are the main causative agent of the common cold (*25*) and belong to the family of *Picornaviridae*, which comprise small, nonenveloped icosahedral viruses with a single-stranded positive sense RNA genome (*26*). Twelve HRV types (among them HRV2) use very-low density lipoprotein receptor and other members of the low-density lipoprotein receptor family for cell attachment (*27*). These receptors are mosaic proteins with a ligand-binding domain composed of various numbers of similar modules that bind to symmetry-related sites around the icosahedral 5-fold axes of the virion (*28*).

Here, we describe a new strategy that achieves (i) the selective immobilization of VLDL receptors on gold surfaces of microstructured glass substrates and (ii) the high-density capturing of HRV2 particles onto the receptor areas. Using orthogonal chemistries, glass areas were coated with a dense layer of trimethoxy-silane-terminated poly(ethylene glycol) (PEG) to avoid the nonspecific adsorption of protein, while gold surfaces were specifically modified with self-assembled monolayers (SAMs) of alkanethiol derivatives. Two different SAMs were tested for coupling VLDLR and HRV2 to the gold surfaces. The first SAM surface carried terminal bis-nitrilo-triacetic acid (bis-NTA) groups (Figure 1A) to bind His_6-tagged VLDLR via metal−chelate complexes. The second SAM surface featured a layer of carboxyl groups, which were activated with *N*-hydroxysuccinimide (NHS) (Figure 1B) to covalently couple VLDLR or HRV2 via amide bonds. SAM and PEG surfaces were characterized by using water contact angle goniometry and atomic force microscopy (AFM), respectively. The ability of the SAMs to couple protein was assessed using fluorescence microscopy and AFM. Our data show that gold and glass surfaces of the microstructured substrates could be specifically addressed to achieve 330,000-fold higher binding of viral particles to the former as related to the latter surface. By comparing coupling via covalent bonds, metal−chelate bonds, or noncovalent molecular recognition, our article provides

* Corresponding author. Phone: 0044 20 7679 4702. Fax: 0044 20 7679 7463. E-mail: s.howorka@ucl.ac.uk.
[†] Johannes Kepler University.
[‡] Upper Austrian Research GmbH.
[§] Medical University of Vienna.
[||] University College London.

10.1021/bc800357j CCC: $40.75 © 2009 American Chemical Society
Published on Web 02/05/2009

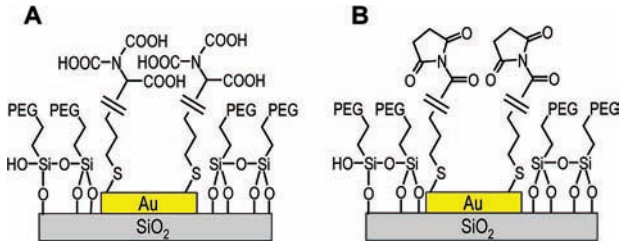

Figure 1. Schematic drawing of microstructured substrates featuring a PEG-layer on the glass areas and gold surfaces derivatized with a self-assembled monolayer of alkanethiols terminated with (A) bis-NTA groups and (B) NHS-activated carboxyl groups. For reason of visual clarity, the simplified structures of the SAM components are displayed. See Scheme 1 for the detailed structures.

important insight into which factors govern the immobilization and capturing of protein assemblies.

EXPERIMENTAL SECTION

Reagents. All chemicals were of the highest purity available unless stated otherwise. Glass slides ($50 \times 24 \times 0.15$ mm^3), 30% ammonia, 30% hydrogen peroxide, and 37% hydrochloric acid were purchased from Carl Roth GmbH (Karlsruhe, Germany). Glass slides coated with a layer of 10 nm Cr and 100 nm Au were obtained from Epluse (Engerwitzdorf, Austria). Octylmercaptan (1-octanethiol), 16-mercaptohexadecanoid acid, 1-ethyl-3-(3-dimethylaminopropyl)carbodiimide (EDC), and *N*-hydroxysuccinimide (NHS) were from Aldrich (Milwaukee, WI). 12-Mercaptododecanoic acid was synthesized as described (*29*). 2-[Methoxy(polyethyleneoxy)propyl] trimethoxysilane (PEG-silane) was purchased from ABCR GmbH (Karlsruhe, Germany). 16-Mercapto-hexadecanoic acid 2-[2-(2-hydroxy-ethoxy)-ethoxy]-ethyl ester (triethylene glycol matrix thiol) and 16-mercapto-hexadecanoic acid 2-[2-(2-{1,3-bis-[5-(biscarboxymethyl-amino)-5-carboxypentylcarbamoyl]-propylcarbamoyloxy}-ethoxy)-ethoxy]-ethyl ester (bis-NTA thiol) were kindly provided by Robert Tampé (Institute of Biochemistry, Biocenter, Johann Wolfgang Goethe University, Frankfurt, Germany).

MBP-VLDLR-His_6, a recombinant derivative of VLDLR that binds minor group HRVs, such as HRV2, with high affinity, was produced in bacteria as described (*30*). It carries a C-terminal hexahistidine tag and maltose binding protein fused to its N-terminus (*1*). HRV2 was isolated from infected HeLa-H1 suspension cultures and purified by sucrose density gradient centrifugation as described (*1*).

Microfabrication of Substrates. Glass substrates with microscale gold features were fabricated using a photolithographic process. Slides were first spin-coated with a layer of positive photoresist (thickness 500 nm, Photoresist Microposit S1805, Rohm & Haas, PA). An array of squares (50×50 μm, 150 μm center-to-center spacing) was then patterned on the photoresist by placing a mask over the substrate and exposing it to UV light. After developing the resist (Microposit MF319, Rohm & Haas, PA) to remove the exposed photoresist areas, a 5 nm Cr layer and a 50 nm gold film were sequentially deposited onto the substrates by sputtering and thermal evaporation, respectively. The photoresist areas, which had not been exposed to UV light, were then dissolved in acetone, leading to an array of gold-squares.

Targeted Functionalization of Microstructured Substrates using a Multi-Step Procedure. Microstructured substrates were subjected to a selective surface modification procedure in order to coat the glass areas with a dense film of PEG, and to derivatize gold features with a self-assembled monolayer of carboxyl- or bis-NTA-terminated alkanethiol SAMs. The multistep procedure (Scheme 1) followed an adapted version of a published protocol (*31*, *32*) and involved (i) the selective coating of the gold features with a SAM composed of octylmercaptan, (ii) the formation of a PEG layer on the nonblocked glass areas, (iii) the removal of the octylmercaptan SAM by heating the slides to 120 °C, and (iv & vi) the coating of the blank gold surface with a new SAM composed of alkanethiols with terminal carboxyl or bis-NTA groups. The carboxyl SAM was also further derivatized to display NHS-activated esters (v).

Surface Cleaning. Prior to surface functionalization, slides were cleaned in 10:90, 50:50, and 90:10 mixtures of methanol/$CHCl_3$ for 15 min each in an ultrasonic bath, followed by washing in deionized (DI) water, and drying in a stream of nitrogen. The substrates were then incubated twice for 20 min in a mixture of DI water/ammonia/hydrogen peroxide 30% (v/v/v 100/25/20) at 90 °C, rinsed thoroughly with DI water and dried in a stream of nitrogen gas.

Formation of a SAM Composed of Octylmercaptan. An octylmercaptan SAM was formed on the gold regions of the microstructured substrates by immersing the slides in ethanol for 5 min, followed by incubation in a 1 mM ethanolic solution of octylmercaptan for 16−24 h. Subsequently, the modified substrates were sonicated in ethanol for 3 min, rinsed with DI water, and dried with nitrogen gas.

Generation of a PEG Film via Silanization. A PEG-silane layer was formed on the glass areas between the octylmercaptan-coated microstructured gold areas. The slides were immersed in a solution of PEG-silane in anhydrous toluene (10 mg/mL) supplemented with 0.08% HCl. After incubation for 20−24 h, the slides were sonicated in toluene and ethanol for three min each, rinsed with DI water, and dried in a nitrogen stream.

Removal of the Octylmercaptan SAM. After the formation of the PEG layer, the passivating octylmercaptan SAM was removed by baking the substrates in an oven at 120 °C for 1 h, thereby regenerating bare gold surfaces suitable for the functionalization with mercaptoalkane derivatives carrying carboxyl or bis-NTA groups.

Formation of a Carboxyl-Terminated SAM. Bare gold regions were coated with a SAM of carboxyl-terminated alkanethiols by incubating the slides in an ethanolic solution of 1 mM 12-mercaptododecanoic acid and 0.1 mM 16-mercaptohexadecanoic acid following a published procedure (*33*). After 16−24 h of incubation, the slides were sonicated for 5 min in ethanol, rinsed with DI water, and blown dry with nitrogen. The resulting substrates were either used without further modification or surface-treated to activate the COOH groups. NHS-activated carboxyl groups were formed by immersing the slides in an aqueous solution of 200 mM EDC and 50 mM NHS for 15 min, followed by briefly rinsing in deionized water. To avoid hydrolysis, which would decrease the reactivity of the activated ester, NHS-derivatized slides were used for further experiments immediately after their modification with NHS.

Generation of a SAM with Terminal Bis-NTA Groups. Alkanethiols with terminal bis-NTA groups were chemisorbed on bare gold squares by immersing the microstructured substrates in acetonitrile containing 19 μM triethylene glycol-terminated matrix thiol (16-mercapto-hexadecanoic acid 2-[2-(2-hydroxy-ethoxy)-ethoxy]-ethyl ester) and 1 μM bis-NTA thiol (16-mercapto-hexadecanoic acid 2-[2-(2-{1,3-bis-[5-(biscarboxymethyl-amino)-5-carboxypentylcarbamoyl]-propylcarbamoyloxy}-ethoxy)-ethoxy]-ethyl ester) for 24−36 h. The substrates were then sonicated for 5 min in ethanol, rinsed with DI water, and blown dry with nitrogen.

Surface Modification of Gold Substrates for Contact Angle Measurements. Slides with a homogeneous 10 nm Cr and 100 nm Au layer were coated with SAMs for contact angle measurements. Prior to the formation of SAMs, all slides were cleaned as described in Surface Cleaning.

Scheme 1. Multi-Step Functionalization of Gold-on-Glass Substrates to Obtain NHS-Carboxyl and Bis-NTA SAMs on Gold, and a PEG Film on Glass

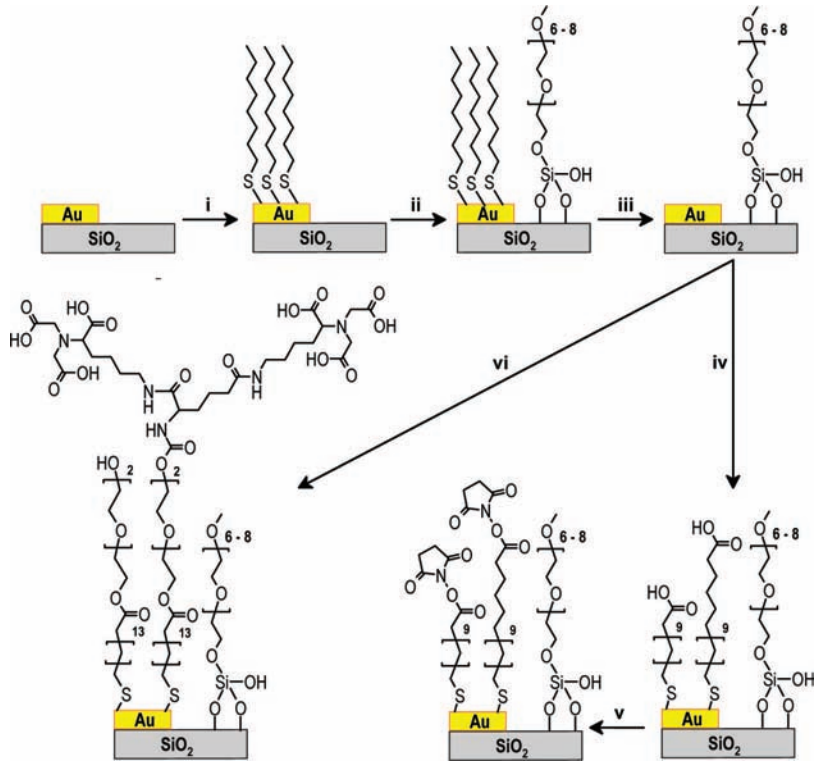

The octylmercaptan SAM was obtained as detailed in Formation of a SAM Composed of Octylmercaptan and evaporated as described in Removal of the Octylmercaptan SAM without the intermediate PEGylation step. Carboxyl or bis-NTA SAMs were generated by coating gold surfaces (whose octylmercaptan had been removed) with mercaptoalkane derivatives as specified in Formation of a Carboxyl-Terminated SAM and Generation of a SAM with Terminal bis-NTA Groups, respectively. Alternatively, mixed SAMs exhibiting carboxyl or bis-NTA functions were chemisorbed directly onto freshly cleaned gold surfaces without the intermediate steps of formation and removal of an octylmercaptan SAM.

Contact Angle Measurements. Contact angles were determined using a Dataphysics OCA 20 goniometer in combination with the SCA-20 software package (Dataphysics, Filderstadt, Germany). All measurements were performed with DI water under ambient laboratory conditions. Advancing and receding contact angles were measured with a starting volume of 5 μL, an oscillating volume of 8 μL, and a velocity of 0.2 μL/s.

Immobilization of Immunoglobulin-Cy3 and Streptavidin-Cy3 on Microstructured Substrates. The experiments were conducted using structured substrates with gold areas coated with SAMs of NHS-activated alkanethiols, and with glass areas displaying a PEG film. The slides were exposed to 0.1 μM Cy3-labeled immunoglobulin or 0.2 μM Cy3-streptavidin in HEPES buffer (10 mM HEPES, 140 mM NaCl, 5 mM KCl, 1 mM MgCl, pH 7.4) for 1 h. The surfaces were then rinsed in HEPES buffer and DI water, and analyzed using fluorescence microscopy.

Fluorescence Microscopy. Images of patterned surfaces were acquired using a fluorescence scanning device (*34*) based on an inverted epifluorescence microscope (Axiovert 200, Zeiss, Oberkochen, Germany). For all measurements, a 100× objective (Zeiss, α Plan-FLUAR 100×/1.45) was used. After mounting on a scanning stage (Märzhäuser, Wetzlar-Steindorf, Germany), the slides were illuminated with a diode-pumped solid-state laser with an emission line of 532 nm (Millennia Iis, Spectra Physics, Irvine, CA). Images were taken with a Photometrics CoolSnap HQ digital camera (Roper Scientific, Trenton, NJ) (1392 × 1040-element CCD; pixel pitch, 6.45 μm × 6.45 μm; 12-bit; QE, 0.6) using a time delayed integration mode (*34*). Bright fluorescent spots exceeding the maximum detection limit of the CCD camera were visualized by using a filter of optical density 1. V++ (Roper Scientific) was employed for image processing and analysis.

Immobilization of Virus Particles and VLDL-Receptors. To achieve covalent coupling of virus particles, slides with NHS-activated carboxyl SAMs were incubated with 10 μg/mL HRV2 in HEPES buffer followed by rinsing the slides with HEPES buffer. Covalent coupling of the MBP-VLDLR-His_6 was achieved by incubating slides with NHS-activated carboxyl SAMs in 20 μg/mL MBP-VLDLR-His_6 in HEPES buffer. Afterward, the slides were washed and incubated with 10 μg/mL HRV2 in HEPES buffer. Alternatively, MBP-VLDLR-His_6 was bound via metal−chelate complexes to bis-NTA-functionalized gold patterns by covering the slides with a protein solution of 20 μg/mL in Tris-Ni buffer (50 mM Tris, 1 mM $NiCl_2$, pH 7.4) for 2 h followed by rinsing in HEPES buffer. HRV2 was subsequently captured onto the VLDL-receptor surfaces by incubating the slides with the virus at 10 μg/mL (approximately 7.5×10^{11} particles/mL) for 2 h followed by rinsing in Tris-Ni buffer.

Atomic Force Microscopy. *Contact Mode AFM.* For contact-mode imaging, an Agilent 5500 AFM (Agilent Technologies Inc., Chandler, AZ) was used in combination with oxide-sharpened standard silicon nitride cantilevers (Veeco Instruments Inc., NY) with a nominal tip radius of 10 nm and spring constants *k* between 0.3 and 0.01 N/m. The contact mode images were acquired at a scan rate of 1.5 lines/s.

MAC Mode AFM. For acquiring images in MAC Mode, a magnetically driven dynamic force microscope (Agilent Technologies, Chandler, AZ) and magnetically coated MacLevers with a nominal spring constant of 0.1 N/m (Agilent Technologies) were used. During imaging, the vertical position of the cantilever was adjusted by using an electronic feedback loop

Table 1. Water Contact Angles of Carboxyl and Bis-NTA SAMs on Gold

surface	(θ_a) (deg)[a,b]	(θ_r) (deg)[a,b]	hysteresis[a]
cleaned gold	87 ± 3	65 ± 2	22 ± 2
gold/octylmercaptan	102 ± 1	84 ± 1	18 ± 1
gold/octylmercaptan/thermal treatment	94 ± 2	74 ± 3	20 ± 3
gold/octylmercaptan/thermal treatment/12-mercaptododecanoic acid and 16-mercaptohexadecanoic acid	51 ± 2	44 ± 3	7 ± 2
gold/12-mercaptododecanoic acid and 16-mercaptohexadecanoic acid	51 ± 1	43 ± 1	8 ± 1
gold/octylmercaptan/thermal treatment/triethylene glycol matrix thiol and bis-NTA thiol	33 ± 1	28 ± 1	5 ± 1
gold/triethylene glycol matrix thiol and bis-NTA thiol	33 ± 1	27 ± 2	5 ± 2

[a] The values represent the arithmetic mean ± SD of six different places on two independently prepared samples. [b] Advancing (θ_a) and receding (θ_r) contact angles of water.

in order to keep the amplitude of the oscillating tip constant. A scanning frequency of 1.5 lines/s was employed for all images. The peak-to-peak oscillation amplitude was set to 5 nm at 7.5 kHz oscillation frequency. Images were acquired in HEPES buffer (for the covalent coupling strategy) or Tris-Ni buffer (for the metal−chelate complex strategy) using a commercial AFM fluid cell.

RESULTS AND DISCUSSION

Targeted Surface Modification of Gold and Glass Areas on Microstructured Substrates. Solid supports composed of glass with 50 × 50 μm gold features were modified by chemically addressing the two different surface types (*32, 35, 36*). Self-assembled monolayers (SAMs) of carboxyl or bis-NTA alkanethiols were formed on gold squares (Figure 1A and B) to facilitate the binding of the viral receptors, while a dense layer of PEG was grafted onto the surrounding glass areas (Figure 1A and B) to render the surface nonadsorptive for the virus. The targeted modification of glass and gold was achieved by using a multistep procedure (Scheme 1). The first step involved the selective coating of the gold squares with a SAM composed of octylmercaptan (Scheme 1, step i), which rendered the surface nonreactive against further chemical modification. In the next step, a PEG layer was formed on the nonblocked glass areas (Scheme 1, step ii) by reacting trimethoxysilane-terminated PEG with the silanol groups of glass. The octylmercaptan SAM was then removed by heating the slides, leaving behind blank gold surfaces (Scheme 1, step iii) (*31*). The gold squares were subsequently coated with a SAM composed of alkanethiols carrying terminal carboxyl groups (Scheme 1, step iv), which were activated with *N*-hydroxysuccinimide (Scheme 1, step v). Alternatively, the bare gold features were functionalized with alkanethiols carrying terminal bis-NTA groups (Scheme 1, step vi).

Analysis of SAMs Using Contact Angle Measurements. The multistep formation of SAMs (Scheme 1, steps i, iii, iv, and vi) was monitored using water contact angle goniometry. Goniometry detects changes in the composition of surfaces with high sensitivity (*37−42*). Our measurements were conducted with slides carrying homogeneous gold films rather than microstructured substrates because the 50 × 50 μm features were much smaller than the water drops. The advancing (θ_a) and receding (θ_r) contact angles of water were measured (Table 1). Treating freshly cleaned gold surfaces (θ_a and θ_r values of 87 ± 3° and 65 ± 2°, respectively) with octylmercaptan increased the contact angles by 15 and 19°, respectively (Table 1), in line with the formation of a hydrophobic SAM. Removal of the octylmercaptan layer by heating lowered the contact angles close to the initial values of cleaned gold (Table 1). The subsequent formation of a carboxyl SAM composed of 12-mercaptododecanoic acid and 16-mercaptohexadecanoic acid was accompanied by a substantial reduction of θ_a and θ_r to 51 ± 2 and 44 ± 3°, respectively (Table 1), in agreement with literature values of related carboxyl SAMs (*43*). Importantly, the hysteresis of the COOH surface with a value of 7 ± 2° was much lower than the hysteresis of the octylmercaptan surface (18 ± 1°) or of thermally treated gold (20 ± 1°) (Table 1). A reduction in hysteresis is typical for hydrophilic surface coatings of high homogeneity (*39*) and therefore indicates the quality of the carboxyl surface. Furthermore, contact angles and hysteresis of the carboxyl SAM are identical, within experimental error, to the corresponding values of surfaces that were obtained by direct modification from bare gold surfaces which had not been subjected to coating and removal of the octylmercaptan SAM (Table 1). The data strongly suggest that the stepwise surface modification procedure was able to reversibly coat gold surface with octylmercaptan as well as to form a SAM carrying terminal carboxyl groups.

By comparison, generating SAMs with bis-NTA groups on thermally treated slides led to advancing and receding contact angles of 33 ± 1 and 28 ± 1°, respectively (Table 1), which is lower than the values of the carboxyl surface (Table 1). The bis-NTA SAM is more hydrophilic than the carboxyl SAM because it contains a 20-fold excess of oligo(ethylene glycol), which is known to result in low contact angles (*44, 45*). Similar to the carboxyl surface, bis-NTA SAMs had a low hysteresis value of 5 ± 1° (Table 1) indicative of a homogeneous surface layer (*44−46*). As a further indication of a dense film, direct bis-NTA modification using bare gold surfaces led to contact angle and hysteresis values, which were identical to those obtained using the octylmercaptan route (Table 1).

AFM Analysis of the PEG Film on Glass. The PEG layer on glass surfaces obtained in step (ii) of Scheme 1 was characterized by AFM in order to determine the film's homogeneity and thickness. AFM is a sensitive tool to probe the quality of PEG films (*38, 46*). Typical topographic images of a bare glass surface before and after PEG coating are shown in Figure 2A and B, respectively. The root-mean-square (rms) noise of the surface roughness for bare glass (Figure 2A) was 1.46 ± 0.23 nm (n = 14), in line with the visible topographic structures, which are partially caused by the cleaning procedure. The rms roughness dropped to 0.22 ± 0.01 nm (n = 14) for PEG-coated glass (Figure 2B), indicative of a compressible polymeric film. In further support of a homogeneous layer, AFM images of the PEGylated glass did not reveal any visible surface defects (Figure 2B). The thickness of the PEG layer was determined by using the AFM cantilever as a stylus to scratch a hole into the film and then measuring the step of the height profile. The observed step size of 2 nm (Figure 2C) compares well with the thickness of PEG films in other studies (*47−49*). On the basis of the known polymer density of PEG and its MW of 500 Da, we calculated (*50*) a high surface density (400 pmol/cm^2) and a corresponding average molecular cross-sectional area of 41 Å^2 per polymer chain. This value indicates a very compact PEG layer because the molecular cross-section of PEG in a crystal of idealized helical form is 21.3 Å^2 (*51*).

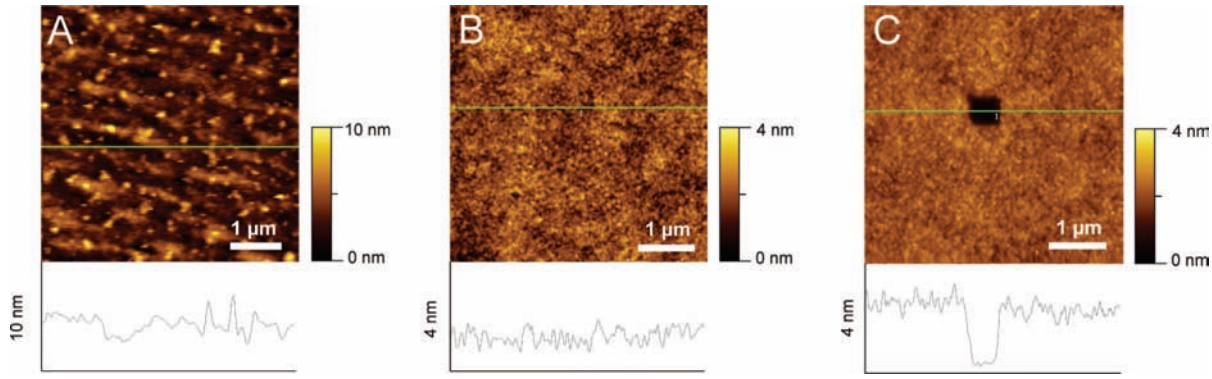

Figure 2. AFM analysis of PEG films on glass areas. (A) Topographic image of a cleaned bare glass surface. (B) Image of a PEG film on a glass surface. (C) A 500 × 500 nm square was scratched into the PEG film. The step size in the height profile is ~2 nm. The scan range is 5 × 5 μm for all images.

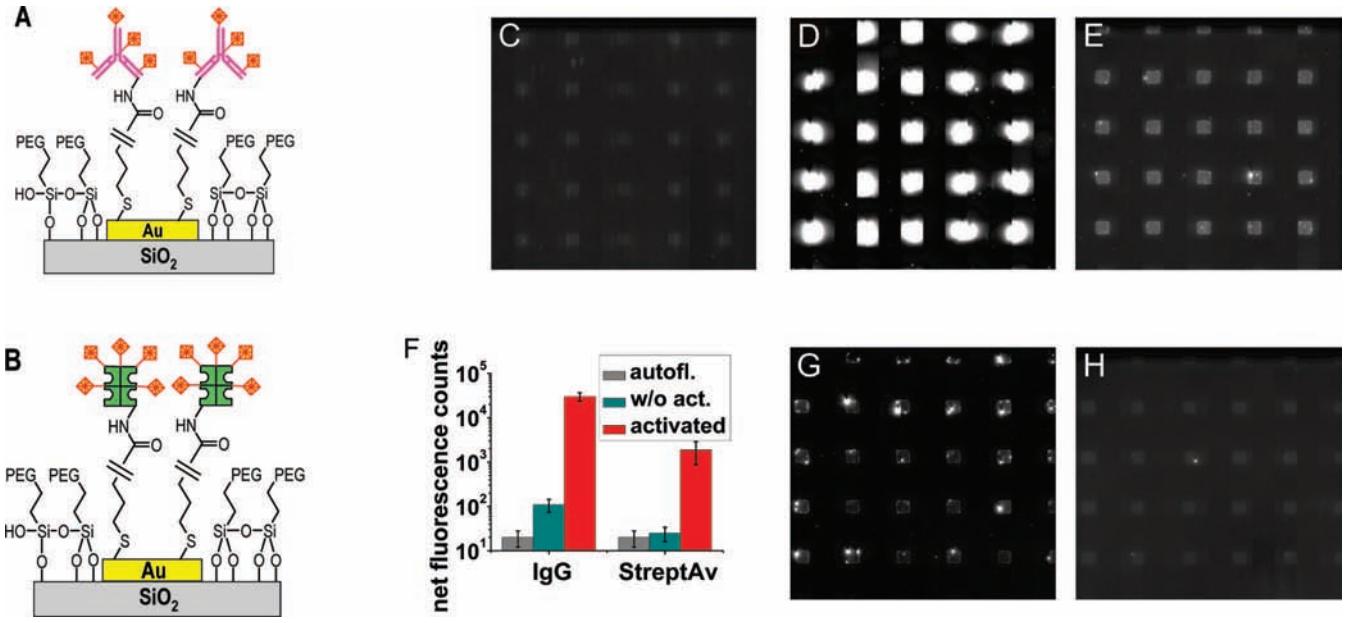

Figure 3. Fluorophore-labeled IgG and streptavidin covalently couple onto NHS-activated carboxyl SAMs on gold squares. (A,B) Schematic illustration of IgG-Cy3 and streptavidin-Cy3 covalently coupled onto NHS-carboxyl SAMs. (C,D) Fluorescence images of bare NHS-carboxyl slides prior to (C) and after (D) exposure to 0.1 μM IgG-Cy3. (E) Image of a nonactivated carboxyl SAM after exposure to IgG-Cy3. (F) Average fluorescence counts on gold squares before and after exposure to fluorescence-labeled protein. The values represent the arithmetic mean ± SD of ten different places on two independently prepared samples. (G,H) Fluorescence images of NHS (G) and carboxyl-coated gold (H) after incubation with 0.2 μM streptavidin-Cy3. Images D and G were obtained using a filter of optical density 1; all other images were acquired without attenuation. The stripes in D are an artifact of the fluorescence scanning procedure but do not interfere with the quantitative analysis of the fluorescence counts. The bright features deviate from the expected square structure as their brightness was within saturation of the fluorescence scanner. The micrographs show an area of 750 × 750 μm^2.

Covalent Coupling of Fluorescence-Labeled Proteins onto NHS-Activated Carboxyl SAMs. Selective covalent attachment of labelled proteins to the NHS-carboxyl gold surfaces was assessed using a fluorescence-based assay. The same assay also probed the absence of nonspecific adsorption of the protein to the PEGylated glass areas. Slides carrying either NHS-activated carboxyl or –for control purposes- non-activated carboxyl groups were incubated with solutions of Cy3 fluorescence-labeled IgG (Figure 3A) and streptavidin (Figure 3B). After removing loosely adsorbed protein in a washing step, the amount of surface-bound protein was quantified by using epifluorescence microscopy. Figure 3C depicts the fluorescence image of an NHS-carboxyl surface, prior to incubation with protein. The regular pattern of gold squares with 150 ± 8 fluorescence counts is discernible from the glass substrate (130 ± 4 cts) because the incident light is weakly reflected from the gold surface. Incubation with 0.1 μM IgG-Cy3 in HEPES buffer (pH 7.2) led to a drastic increase in the fluorescence on the gold squares (Figure 3D, 30130 ± 6390 cts) indicating coupling of the immunoglobulin to the NHS-carboxyl surface. The immobilization was certainly due to the formation of amide bonds between lysine residues of IgG and the carboxyl groups of the SAM because nonactivated carboxyl SAMs without NHS ester functions bound much less protein (Figure 3E, 239 ± 35 cts). The fluorescence counts are also summarized in Figure 3F. A quantitative comparison of these values using the factor ($counts_{NHS,IgG} - counts_{carboxyl,IgG}$)/$counts_{Gold}$ reveals that the NHS-decorated surface leads to a 200-fold higher binding of IgG compared to carboxyl-terminated gold substrates.

The ability of NHS ester surfaces to couple protein was also tested with streptavidin-Cy3. The tetrameric streptavidin possesses a total of 12 surface-exposed lysine residues. This is less than the approximately 30 surface-exposed lysine residues in IgG (PDB ID, 1IGT) (*52*). Given that the covalent coupling to NHS surfaces is mediated by primary amines, it was expected that streptavidin with fewer lysines would be more challenging to immobilize. Moreover, the number of available lysines on the streptavidin-Cy3 surface is further reduced because on

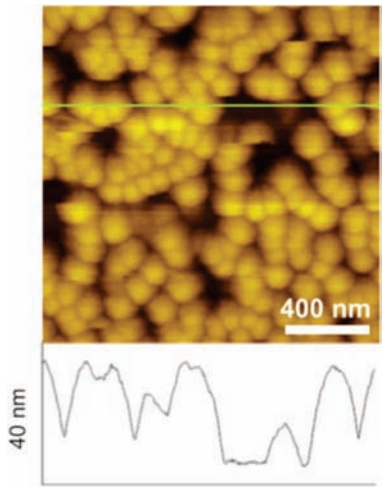

Figure 4. Topographic AFM image of human rhinovirus type 2 adsorbed in Tris-Ni buffer onto mica.

average, six residues are coupled to the Cy3 fluorophores. By comparison, the molar labeling ratio for IgG-Cy3 is four. Images of NHS and carboxyl surfaces incubated with 0.2 μM streptavidin-Cy3 are shown in Figure 3G (2000 $\pm$ 1000 cts) and 3H (155 $\pm$ 9 cts), respectively. The gold areas are less bright than the corresponding surfaces covered with IgG-Cy3 (Figure 3D and 3E). This is in line with the expected lower extent of immobilization for streptavidin. A lower degree of covalent coupling was also apparent from the analysis of fluorescence counts. NHS activation only led to a 12-fold increase in coupled streptavidin when compared to that of carboxyl-terminated gold surfaces (Figure 3F).

All samples displayed low fluorescence counts on the PEG-coated areas, implying that the polymeric layer effectively repelled the labeled protein. For example, the fluorescence counts of PEG areas from NHS-activated slides before incubation with IgG-Cy3 was 132 $\pm$ 3 cts, while incubation with IgG-Cy3 resulted in a very similar fluorescence count of 128 $\pm$ 3. The passivation of the glass surface by a dense layer of PEG is in line with other reports (*33, 35, 38, 53, 54*).

The analysis of fluorescence counts provides insight into the ability of the NHS and PEG surfaces to couple and repel, respectively, proteins. A quantitative comparison between gold and glass surfaces is, however, not possible because of the partial fluorescence quenching by gold (*55, 56*).

Targeted Binding of Viral Receptors and Viral Particles to NHS-Carboxyl and Bis-NTA Surfaces. We compared the ability of NHS-carboxyl and bis-NTA surfaces to bind receptors and viral particles. For the binding assays, MBP-VLDLR-His_6 and HRV2 were used. The appended MPB and His_6 tags in the receptor do not affect its ability to recognize and bind human rhinoviruses (*1*).

HRVs have a diameter of 30 nm as determined by X-ray crystallography (*57*). The same size was also obtained via AFM from the step height in the topographic profile (Figure 4). The AFM image was acquired in the MAC Mode, which uses an external oscillating magnetic field to deflect the cantilever. As the imaging forces are smaller than those in contact mode, the MAC Mode is better suited to image soft biological materials (*58, 59*).

Three different coupling strategies were compared to determine the best one for high-density surface capture of viral particles. In approach A, virions were covalently coupled onto NHS-carboxyl SAMs (Figure 5A). In strategy B, MBP-VLDLR-His_6 was covalently immobilized onto the NHS-carboxyl surface, and viral particles were then captured onto the receptor spots via molecular recognition (Figure 5B). Route C also used the receptor-mediated capture of viral particles, but MBP-VLDLR-His_6 was bound via Ni−chelate bridges to the bis-NTA SAM (Figure 5C). In all three cases, the gold squares were surrounded by PEG-coated glass areas. A secondary aim of the experiments was therefore to probe the ability of the polymer film to prevent the nonspecific adsorption of viral particles onto the glass surfaces.

Binding assay A was conducted by incubating microstructured slides featuring NHS-carboxyl-coated gold squares with a 10 μg/mL suspension of HRV2 in 10 mM HEPES buffer for 2 h. In strategy B, the NHS-carboxyl slides were first treated with a 20 μg/mL solution of MBP-VLDLR-His_6, followed by a washing step and incubation with 10 μg/mL HRV2 in HEPES buffer for 2 h. For strategy C, MBP-VLDLR-His_6 was used in 50 mM Tris buffer supplemented with 1 mM $NiCl_2$ to facilitate metal−chelate-mediated binding onto the bis-NTA-coated gold. HRV2 was captured onto the receptor spots in the same Ni(II)-containing buffer. After each incubation step, the slides were rinsed to remove loosely bound protein or virus particles and imaged using contact mode or MAC Mode AFM, as specified below.

Samples from the direct covalent coupling strategy A (Figure 5A) yielded a typical topographic contact mode image as shown in Figure 6A. The 50 $\times$ 50 μm gold square in the center of the image is clearly visible. The brighter areas on top and at the bottom of the gold square are glass surfaces but their apparent height is skewed by a flattening artifact (*60*). A magnified image of the gold surface (Figure 6B) revealed elevated features with a height of approximately 30 nm, which represent individual or clusters of viral particles. Their surface density had a value of 756 $\pm$ 158 particles per 100 μm^2 (four independent

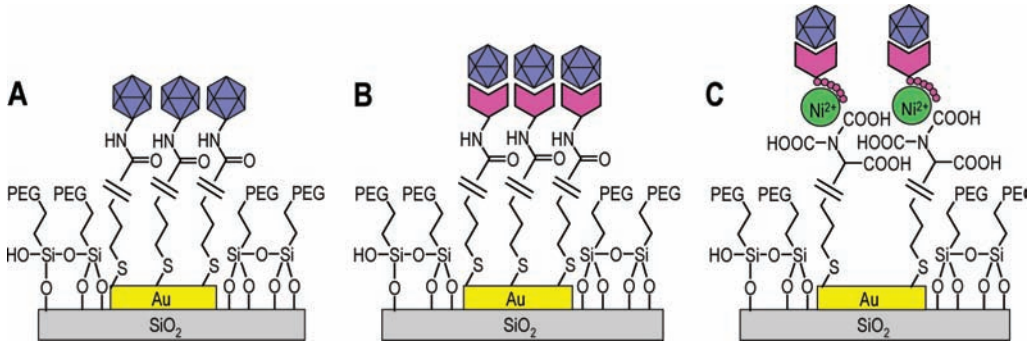

Figure 5. Schematic representation of three coupling strategies used for the immobilization of viral particles onto gold surfaces. (A) Covalent coupling of viral particles onto NHS-carboxyl surfaces. (B) Coupling of viral MBP-VLDLR-His_6 receptors onto NHS SAMs, and the binding of viral receptors via molecular recognition. (C) Immobilization of the His_6-tagged VLDL receptors onto bis-NTA SAMs via Ni(II) chelate complexes, and the molecular recognition of viral particles. For reason of visual clarity, the simplified structures of the SAM components are displayed. See Scheme 1 for the detailed structures.

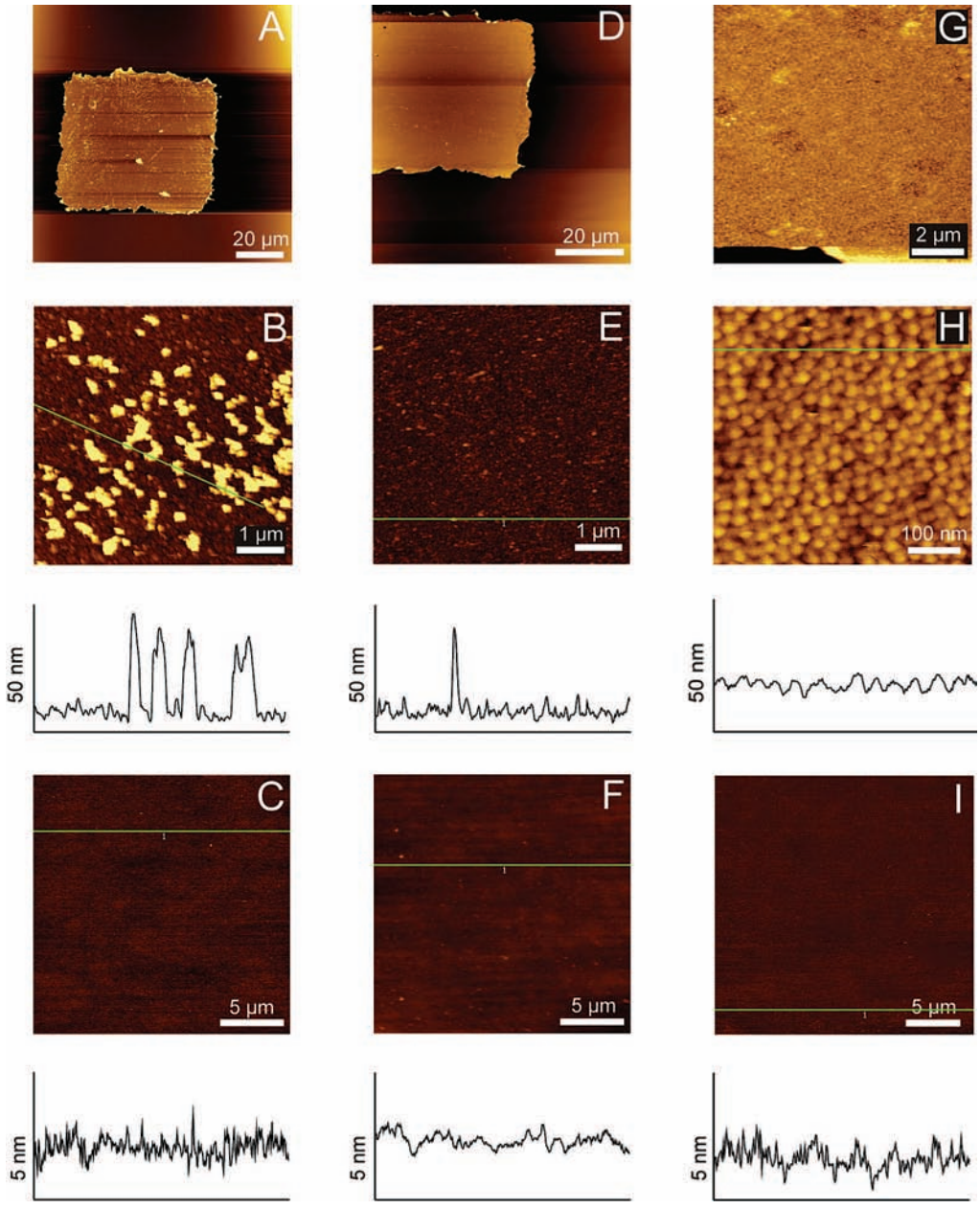

Figure 6. Capturing of viral particles onto receptor-coated gold surfaces via coupling strategies A, B, and C as shown in Figure 5. Topographic AFM images of slides were obtained via strategies A (A−C), B (D−F), and C (G−I). The images display an overview of functionalized gold squares and surrounding glass areas (A, D, and G), a magnified view of the gold surfaces (B, E, and H), and a zoom-in of the PEG-coated glass surfaces (C, F, and I). All images were acquired using the AFM contact mode except for images G, H, and I, which were obtained in MAC Mode. The experiments were repeated twice and gave the same results.

measurements), as determined using an algorithm. The algorithm was based on the detection of topographic peaks above a threshold value of 20 nm, which compares to a diameter of 30 nm for the viral particle. The AFM analysis of the PEG surface showed much fewer peaks (Figure 6C, 1.0 ± 0.8 particles per 100 μm^2), thereby demonstrating that the polymeric layer had effectively prevented the nonspecific adsorption of viral particles, in agreement with the known surface passivating properties of PEG against proteins, cells, or DNA (*33*, *35*, *38*, *53*, *54*).

Strategy B, that is, covalent coupling of MBP-VLDLR-His_6 and the molecular capturing of HRV2 particles (Figure 5B), yielded a contact mode image as shown in Figure 6D. The gold square appeared smoother than the surface from the previous coupling strategy A (Figure 6A). Indeed, a magnified image of the gold area displayed almost no viral particles (Figure 6E). The low density of particles (2.5 ± 1.3 per 100 μm^2) may reflect that very little or no MBP-VLDLR-His_6 had covalently coupled onto the NHS surface. Alternatively, it is also possible that the viral receptor was coupled but lost its binding activity due to steric hindrance or denaturation. Nevertheless, it can be ruled out that MBP-VLDLR-His_6 generally loses its binding activity upon immobilization because the surface-tethered receptor has been used successfully in previous virus-binding studies (*1*).

In contrast, strategy C takes advantage of metal−chelate binding of MBP-VLDLR-His_6 (Figure 5C), and yielded gold surfaces that were densely packed with viral particles (Figure 6G, MAC Mode). A section of the gold square (Figure 6G, top) featured a corrugated surface, while the PEG surface was smooth (Figure 6G, bottom stripe at left). The gold surface was covered with densely spaced clusters of viral particles as displayed in a magnified view (Figure 6H) corresponding to a surface density of 99200 ± 3100 particles per 100 μm^2. In comparison, the very few particles that nonspecifically adsorbed onto PEG areas (Figure 6I) resulted in a low surface density of 0.3 ± 0.2

particles per 100 μm^2. Using the measured surface densities on bis-NTA-derivatized gold and PEG-coated glass, we calculated the very high selectivity factor of over 330 000 for the preferential binding of viral particles onto MBP-VLDLR-His_6 patches.

In this study, we have explored strategies to selectively immobilize viral particles and their cognate receptors onto gold surfaces. Two types of alkanethiol-coated gold surfaces were examined. SAMs were either modified with terminal *N*-hydroxysuccinimide-activated carboxyl or bis-nitrilo-triacetic acid groups. The ability of activated esters to bind protein via covalent amide bonds was confirmed using fluorescence-based assays. The experiments with fluorophore-labeled IgG and streptavidin also highlighted that a higher number of surface-exposed lysine residues increases the extent of immobilization to NHS groups.

The effectiveness of bis-NTA and NHS surfaces was assayed by measuring the density of the captured particles with AFM. Among the three strategies, A, covalent binding of virions, B, covalent binding of viral receptor, and C, binding of the receptor via metal chelate bonds followed by non-covalent binding of virus, route B produced the lowest density of captured particles. It is unlikely that no MBP-VLDLR-His_6 was coupled to the NHS-derivatized SAM because the receptor construct contains 30 surface-exposed lysine residues, which are all located in the N-terminally fused maltose-binding protein. It is therefore most likely that the inability to capture viral particles is accounted for by an unfavorable orientation of the surface-bound receptor, which sterically blocks interaction with the virions. It is possible that the lysine-rich maltose binding protein covalently tethers the N terminus of MBP-VLDLR-His_6 to the surface, while the C-terminal hexahistidine tag electrostatically interacts with the negatively charged, hydrolyzed NHS groups.

Immobilization strategy A, direct covalent binding of virions, yielded higher surface densities. The better performance of approach A as compared to that of route B is somewhat surprising because the molar concentration of virions of 1.3 nM is much lower than the concentration of the VLDL-receptor (280 nM). In addition, the lower diffusion coefficient of the bigger viral particles should slow down the reaction with the NHS surface. Apparently, these factors were outweighed by the high number of surface-exposed lysines (>200) on the viral surface and the concomitant increased extent of reaction with the activated esters.

Approach C resulted in the highest surface densities of viral particles. The excellent performance can be singularly attributed to the use of the bis-NTA surface and the coupling of MBP-VLDLR-His_6 via metal−chelate complexes, because, in comparison to strategy B, all other parameters such as the concentration of viral receptors and particles were the same. It is most probable that bis-NTA is superior to NHS because the chelate-forming group maintains its capacity to bind receptors, while the activated ester suffers hydrolysis and inactivation (*61*). In addition, bis-NTA tethers MBP-VLDLR-His_6 via its C-terminal His_6 tag, which orients the virus-binding moiety of the receptor away from the surface, rendering it highly accessible, while the coupling of protein to the NHS surface can occur for all exposed lysine residues leading to a more randomized orientation of the receptor molecules on the substrate. The advantage of oriented immobilization for protein function has been demonstrated in the context of other studies (*62*−*65*). Here, we have shown a particular realization of this principle, which can be employed in the orthogonal biofunctionalization of micropatterned surfaces.

CONCLUSIONS

In conclusion, this study describes methods with thus far unprecedented selectivity for capturing viral particles on gold-over-glass surfaces. The high-density immobilization of viral receptors is the result of a combination of several advantages such as the conservation of the bis-NTA reactivity and its ability to bind His_6-tagged proteins in an oriented fashion. By comparing the coupling of proteins via covalent bond formation, metal chelation, molecular recognition, or a combination of them, our study provides insight into factors that influence the immobilization of proteins. By providing an experimental strategy for maintaining the biological activity of immobilized receptors (*35*, *65*−*67*) while averting nonspecific binding of ligands using passivating PEG layers, this work is relevant to the wide field of micropatterned biofunctionalization because efficiently addressing glass and gold surfaces for the high-density immobilization of receptors may also be used to selectively capture other protein assemblies, proteins, or cells. We expect that our surface modification approach can be applied to further miniaturize viral arrays to nanoscale dimensions.

ACKNOWLEDGMENT

This work was supported by the Austrian Science Foundation (project N00104-NAN), the European Fund for Regional Development (EFRE), and the government of Upper Austria.

LITERATURE CITED

(1) Artelsmair, H., Kienberger, F., Tinazli, A., Schlapak, R., Zhu, R., Preiner, J., Wruss, J., Kastner, M., Saucedo-Zeni, N., Hoelzl, M., Rankl, C., Baumgartner, W., Howorka, S., Blaas, D., Gruber, H., Tampe, R., and Hinterdorfer, P. (2008) Atomic force microscopy-derived nanoscale chip for the detection of human pathogenic viruses. *Small 4*, 847–854.

(2) Lee, K. B., Kim, E. Y., Mirkin, C. A., and Wolinsky, S. M. (2004) The use of nanoarrays for highly sensitive and selective detection of human immunodeficiency virus type 1 in plasma. *Nano Lett. 4*, 1869–1872.

(3) Cooper, M. A., Dultsev, F. N., Minson, T., Ostanin, V. P., Abell, C., and Klenerman, D. (2001) Direct and sensitive detection of a human virus by rupture event scanning. *Nat. Biotechnol. 19*, 833–837.

(4) Patolsky, F., Zheng, G. F., Hayden, O., Lakadamyali, M., Zhuang, X. W., and Lieber, C. M. (2004) Electrical detection of single viruses. *Proc. Natl. Acad. Sci. U.S.A. 101*, 14017–14022.

(5) Eun, A. J. C., Huang, L. Q., Chew, F. T., Li, S. F. Y., and Wong, S. M. (2002) Detection of two orchid viruses using quartz crystal microbalance (QCM) immunosensors. *J. Virol. Methods 99*, 71–79.

(6) Smith, J. C., Lee, K., Wang, Q., Finn, M. G., Johnson, J. E., Mrksich, M., and Mirkin, C. A. (2003) Nanopatterning the chemospecific immobilization of cowpea mosaic virus capsid. *Nano Lett. 3*, 883–886.

(7) Vega, R. A., Maspoch, D., Salaita, K., and Mirkin, C. A. (2005) Nanoarrays of single virus particles. *Angew. Chem., Int. Ed. 44*, 6013–6015.

(8) Kuznetsov, Y. G., Victoria, J. G., Robinson, W. E., and McPherson, A. (2003) Atomic force microscopy investigation of human immunodeficiency virus (HIV) and HIV-Infected lymphocytes. *J. Virol. 77*, 11896–11909.

(9) Drygin, Y. F., Bordunova, O. A., Gallyamov, M. O., and Yaminsky, I. V. (1998) Atomic force microscopy examination of tobacco mosaic virus and virion RNA. *FEBS Lett. 425*, 217–221.

(10) Falvo, M. R., Washburn, S., Superfine, R., Finch, M., Brooks, F. P., Chi, V., and Taylor, R. M. (1997) Manipulation of individual viruses: Friction and mechanical properties. *Biophys. J. 72*, 1396–1403.

(11) MacBeath, G., and Schreiber, S. L. (2000) Printing proteins as microarrays for high-throughput function determination. *Science 289*, 1760–1763.

(12) Schena, M., Shalon, D., Davis, R. W., and Brown, P. O. (1995) Quantitative monitoring of gene expression patterns with a complementary DNA microarray. *Science 270*, 467–470.
(13) Houseman, B. T., and Mrksich, M. (2002) Carbohydrate arrays for the evaluation of protein binding and enzymatic modification. *Chem. Biol. 9*, 443–454.
(14) Bernard, A., Fitzli, D., Sonderegger, P., Delamarche, E., Michel, B., Bosshard, H. R., and Biebuyck, H. (2001) Affinity capture of proteins from solution and their dissociation by contact printing. *Nat. Biotechnol. 19*, 866–869.
(15) Bernard, A., Delamarche, E., Schmid, H., Michel, B., Bosshard, H. R., and Biebuyck, H. (1998) Printing patterns of proteins. *Langmuir 14*, 2225–2229.
(16) Pammer, P., Schlapak, R., Sonnleitner, M., Ebner, A., Zhu, R., Hinterdorfer, P., Höglinger, O., Schindler, H. G., and Howorka, S. (2005) Nanopatterning of biomolecules with microscale beads. *ChemPhysChem 6*, 900–903.
(17) Delamarche, E., Bernard, A., Schmid, H., Michel, B., and Biebuyck, H. (1997) Patterned delivery of immunoglobulins to surfaces using microfluidic networks. *Science 276*, 779–781.
(18) Fodor, S. P., Rava, R. P., Huang, X. C., Pease, A. C., Holmes, C. P., and Adams, C. L. (1993) Multiplexed biochemical assays with biological chips. *Nature 364*, 555–556.
(19) Pellois, J. P., Zhou, X., Srivannavit, O., Zhou, T., Gulari, E., and Gao, X. (2002) Individually addressable parallel peptide synthesis on microchips. *Nat. Biotechnol. 20*, 922–926.
(20) Dillmore, W. S., Yousaf, M. N., and Mrksich, M. (2004) A photochemical method for patterning the immobilization of ligands and cells to self-assembled monolayers. *Langmuir 20*, 7223–7231.
(21) Ryan, D., Parviz, B. A., Linder, V., Semetey, V., Sia, S. K., Su, J., Mrksich, M., and Whitesides, G. M. (2004) Patterning multiple aligned self-assembled monolayers using light. *Langmuir 20*, 9080–9088.
(22) Tinazli, A., Piehler, J., Beuttler, M., Guckenberger, R., and Tampe, R. (2007) Native protein nanolithography that can write, read and erase. *Nat. Nanotechnol. 2*, 220–225.
(23) Piner, R. D., Zhu, J., Xu, F., Hong, S., and Mirkin, C. A. (1999) "Dip-Pen" nanolithography. *Science 283*, 661–663.
(24) Rosi, N. L., and Mirkin, C. A. (2005) Nanostructures in biodiagnostics. *Chem. Rev. 105*, 1547–1562.
(25) Heikkinen, T., and Jarvinen, A. (2003) The common cold. *Lancet 361*, 51–59.
(26) Semler, B. L., and Wimmer, E. (2002) *Molecular Biology of Picornaviruses*, pp 20036−2904, ASM Press, Washington, DC.
(27) Hofer, F., Gruenberger, M., Kowalski, H., Machat, H., Huettinger, M., Kuechler, E., and Blaas, D. (1994) Members of the low-density-lipoprotein receptor family mediate cell dntry of a minor-group common cold virus. *Proc. Natl. Acad. Sci. U.S.A. 91*, 1839–1842.
(28) Verdaguer, N., Fita, I., Reithmayer, M., Moser, R., and Blaas, D. (2004) X-ray structure of a minor group human rhinovirus bound to a fragment of its cellular receptor protein. *Nat. Struct. Mol. Biol. 11*, 429–434.
(29) Kienberger, F., Kada, G., Gruber, H. J., Pastushenko, V. P., Riener, C., Trieb, M., Knaus, H.-G., Schindler, H., and Hinterdorfer, P. (2000) Recognition force spectroscopy studies of the NTA-His6 bond. *Single Mol. 1*, 59–65.
(30) Ronacher, B., Marlovits, T. C., Moser, R., and Blaas, D. (2000) Expression and folding of human very-low-density lipoprotein receptor fragments: Neutralization capacity toward human rhinovirus HRV2. *Virology 278*, 541–550.
(31) Boozer, C., Yu, Q., Chen, S., Lee, C.-Y., Homola, J., Yee, S. S., and Jiang, S. (2003) Surface functionalization for self-referencing surface plasmon resonance (SPR) biosensors by multi-step self-assembly. *Sens. Actuators, B 90*, 22–30.
(32) Veiseh, M., and Zhang, M. (2006) Effect of silicon oxidation on long-term cell selectivity of cell-patterned Au/SiO2 platforms. *J. Am. Chem. Soc. 128*, 1197–1203.
(33) Lan, S., Veiseh, M., and Zhang, M. (2005) Surface modification of silicon and gold-patterned silicon surfaces for improved biocompatibility and cell patterning selectivity. *Biosens. Bioelectron. 20*, 1697–1708.
(34) Hesse, J., Sonnleitner, M., Sonnleitner, A., Freudenthaler, G., Jacak, J., Höglinger, O., Schindler, H., and Schutz, G. J. (2004) Single molecule reader for high-throughput bioanalysis. *Anal. Chem. 76*, 5960–5964.
(35) Veiseh, M., Zareie, M. H., and Zhang, M. Q. (2002) Highly selective protein patterning on gold-silicon substrates for biosensor applications. *Langmuir 18*, 6671–6678.
(36) Rozkiewicz, D. I., Ravoo, B. J., and Reinhoudt, D. N. (2005) Reversible covalent patterning of self-assembled monolayers on gold and silicon oxide surfaces. *Langmuir 21*, 6337–6343.
(37) Whitesides, G. M., and Laibinis, P. E. (1990) Wet chemical approaches to the characterization of organic-surfaces: self-assembled monolayers, wetting, and the physical organic-chemistry of the solid liquid interface. *Langmuir 6*, 87–96.
(38) Schlapak, R., Pammer, P., Armitage, D., Zhu, R., Hinterdorfer, P., Vaupel, M., Fruhwirth, T., and Howorka, S. (2006) Glass surfaces grafted with high-density poly(ethylene glycol) as substrates for DNA oligonucleotide microarrays. *Langmuir 22*, 277–285.
(39) Piehler, J., Brecht, A., Valiokas, R., Liedberg, B., and Gauglitz, G. (2000) A high-density poly(ethylene glycol) polymer brush for immobilization on glass-type surfaces. *Biosens. Bioelectron. 15*, 473–481.
(40) Folkers, J. P., Gorman, C. B., Laibinis, P. E., Buchholz, S., Whitesides, G. M., and Nuzzo, R. G. (1995) Self-assembled monolayers of long-chain hydroxamic acids on the native oxides of metals. *Langmuir 11*, 813–824.
(41) Robbins, M. O., and Joanny, J. F. (1987) Contact-angle hysteresis on random surfaces. *Europhys. Lett. 3*, 729–735.
(42) Good, R. J. (1952) A thermodynamic derivation of Wenzel's modification of Young's equation for contact angles; together with a theory of hysteresis. *J. Am. Chem. Soc. 74*, 5041–5042.
(43) Kim, Y.-K., Koo, J.-P., and Ha, J. S. (2005) Replacement of adsorbed alkanethiolate on Au with carboxyl-terminated thiol in solution: effect of alkyl chain length. *Appl. Surf. Sci. 249*, 7–11.
(44) Herrwerth, S., Eck, W., Reinhardt, S., and Grunze, M. (2003) Factors that determine the protein resistance of oligoether self-assembled monolayers - Internal hydrophilicity, terminal hydrophilicity, and lateral packing density. *J. Am. Chem. Soc. 125*, 9359–9366.
(45) Andruzzi, L., Senaratne, W., Hexemer, A., Sheets, E. D., Ilic, B., Kramer, E. J., Baird, B., and Ober, C. K. (2005) Oligo(ethylene glycol) containing polymer brushes as bioselective surfaces. *Langmuir 21*, 2495–2504.
(46) Schlapak, R., Armitage, D., Saucedo-Zeni, N., Hohage, M., and Howorka, S. (2007) Dense passivating poly(ethylene glycol) films on indium tin oxide substrates. *Langmuir 23*, 10244–10253.
(47) Doi, M. (1996) *Introduction to Polymer Physics*, Clarendon Press, Oxford.
(48) Kenworthy, A. K., Hristova, K., Needham, D., and McIntosh, T. J. (1995) Range and magnitude of the steric pressure between bilayers containing phospholipids with covalently attached poly(ethylene glycol). *Biophys. J. 68*, 1921–1936.
(49) Rex, S., Zuckermann, M. J., Lafleur, M., and Silvius, J. R. (1998) Experimental and Monte Carlo simulation studies of the thermodynamics of polyethyleneglycol chains grafted to lipid bilayers. *Biophys. J. 75*, 2900–2914.
(50) Zhu, X. Y., Jun, Y., Staarup, D. R., Major, R. C., Danielson, S., Boiadjiev, V., Gladfelter, W. L., Bunker, B. C., and Guo, A. (2001) Grafting of high-density poly(ethylene glycol) monolayers on Si(111). *Langmuir 17*, 7798–7803.
(51) Harder, P., Grunze, M., Dahint, R., Whitesides, G. M., and Laibinis, P. E. (1998) Molecular conformation in oligo(ethylene glycol)-terminated self-assembled monolayers on gold and silver surfaces determines their ability to resist protein adsorption. *J. Phys. Chem. B 102*, 426–436.

(52) Liu, G. Y., and Amro, N. A. (2002) Positioning protein molecules on surfaces: a nanoengineering approach to supramolecular chemistry. *Proc. Natl. Acad. Sci. U.S.A. 99*, 5165–5170.

(53) Ostuni, E., Chapman, R. G., Holmlin, R. E., Takayama, S., and Whitesides, G. M. (2001) A survey of structure-property relationships of surfaces that resist the adsorption of protein. *Langmuir 17*, 5605–5620.

(54) Huang, N. P., Michel, R., Voros, J., Textor, M., Hofer, R., Rossi, A., Elbert, D. L., Hubbell, J. A., and Spencer, N. D. (2001) Poly(L-lysine)-g-poly(ethylene glycol) layers on metal oxide surfaces: Surface-analytical characterization and resistance to serum and fibrinogen adsorption. *Langmuir 17*, 489–498.

(55) Ishida, A., and Majima, T. (2000) Surface plasmon enhanced fluorescence measurement on flat and constructed gold surfaces. *Analyst 125*, 535–540.

(56) Lee, C. Y., Gong, P., Harbers, G. M., Grainger, D. W., Castner, D. G., and Gamble, L. J. (2006) Surface coverage and structure of mixed DNA/alkylthiol monolayers on gold: characterization by XPS, NEXAFS, and fluorescence intensity measurements. *Anal. Chem. 78*, 3316–3325.

(57) Verdaguer, N., Blaas, D., and Fita, I. (2000) Structure of human rhinovirus serotype 2 (HRV2). *J. Mol. Biol. 300*, 1179–1194.

(58) Han, W., Lindsay, S. M., and Jing, T. A. (1996) A magnetically driven oscillating probe microscope for operation in liquid. *Appl. Phys. Lett. 69*, 1–3.

(59) Leuba, S. H., Yang, G., Robert, C., Samori, B., Van Holde, K., Zlatanova, J., and Bustamante, C. (1994) Three-dimensional structure of extended chromatin fibers as revealed by tapping-mode scanning force microscopy. *Proc. Natl. Acad. Sci. U.S.A. 91*, 11621–11625.

(60) Kienberger, F., Pastushenko, V. P., Kada, G., Puntheeranurak, T., Chtcheglova, L., Riethmueller, C., Rankl, C., Ebner, A., and Hinterdorfer, P. (2006) Improving the contrast of topographical AFM images by a simple averaging filter. *Ultramicroscopy 106*, 822–828.

(61) Hermanson, G. T. (2008) *Bioconjugate Techniques*, 2nd ed., Academic Press,, London.

(62) Dabrowski, M. J., Chen, J. P., Shi, H., Chin, W. C., and Atkins, W. M. (1998) Strategies for protein-based nanofabrication: Ni2+-NTA as a chemical mask to control biologically imposed symmetry. *Chem. Biol. 5*, 689–97.

(63) Huang, N. P., Voros, J., De Paul, S. M., Textor, M., and Spencer, N. D. (2002) Biotin-derivatized poly(L-lysine)-g-poly(ethylene glycol): A novel polymeric interface for bioaffinity sensing. *Langmuir 18*, 220–230.

(64) Breitwieser, A., Kupcu, S., Howorka, S., Weigert, S., Langer, C., Hoffmann-Sommergruber, K., Scheiner, O., Sleytr, U. B., and Sára, M. (1996) 2-D protein crystals as an immobilization matrix for producing reaction zones in dipstick-style immunoassays. *Biotechniques 21*, 918–25.

(65) Chen, X. X., Ferrigno, R., Yang, J., and Whitesides, G. A. (2002) Redox properties of cytochrome c adsorbed on self-assembled monolayers: A probe for protein conformation and orientation. *Langmuir 18*, 7009–7015.

(66) Gaubert, H. E., and Frey, W. (2007) Highly parallel fabrication of nanopatterned surfaces with nanoscale orthogonal biofunctionalization imprint lithography. *Nanotechnology 18*, 135101–135108.

(67) Zoller, F. A., Padeste, C., Ekinci, Y., Solak, H. H., and Engel, A. (2008) Nanostructured substrates for high density protein arrays. *Microelectron. Eng. 85*, 1370–1374.

BC800357J

Optical Properties and Application of a Reactive and Bioreducible Thiol-Containing Tetramethylrhodamine Dimer

R. James Christie, Constantino J. Tadiello, Lisa M. Chamberlain, and David W. Grainger*

Department of Chemistry, Colorado State University, Fort Collins, Colorado 80523-1872. Received August 28, 2008; Revised Manuscript Received January 20, 2009

Thiolated dimeric tetramethylrhodamine (TAMRA) was synthesized in a straightforward procedure utilizing commercially available 5(6)-succinimidyl TAMRA and cystamine hydrochloride. The thiol-containing TAMRA dimer displayed distinct spectral properties in reduced and oxidized forms; covalent dimer formation produced greater effects on the spectral properties than previously reported for noncovalent TAMRA dimers or dimers formed with shorter carbon spacers. The resulting TAMRA disulfide dimer exhibited a hypsochromic shift of 34 nm relative to the reduced monomer species and an isosbestic point at 532 nm between reduced monomeric and oxidized dimeric forms. Molar extinction coefficients of the monomer and dimer relative to moles of TAMRA were similar (6.61×10^4 M^{-1} cm^{-1} and 6.42×10^{-4} M^{-1} cm^{-1}, respectively). However, fluorescence emission was altered with >93% of dye fluorescence quenched in phosphate buffered saline upon dimer formation. A 520:554 nm absorbance intensity ratio of 2.64 was observed for the oxidized ssTAMRA dimer, almost twice as high as values reported for noncovalent TAMRA dimers. The resulting disulfide dye was easily reduced using both soluble and agarose gel immobilized tris(2-carboxyethyl) phosphine and fresh cell lysate from cultured RAW 264.7 macrophage cells. Absorbance intensity ratios at 554 and 520 nm were used to determine the oxidation half-life of a 1.2×10^{-5} M solution of reduced TAMRA stored in ambient atmosphere to be ~50 h at 22 °C. The free thiol dye was further reacted with maleimide-derivatized poly(hydroxypropyl methacrylamide) to yield the dye-labeled polymer conjugate. This dye derivative should prove useful as a dithiol reduction-sensitive fluorescent probe in cellular tracking systems, as well as a thiol-based dye-labeling reagent due to its easy preparation from readily available materials, environmental sensitivity, and simple activation to produce distinct spectral states. The enhanced spectral properties of the covalent TAMRA dimer described here could be useful to prepare more advanced reporter molecules and bioconjugates.

INTRODUCTION

Reactive fluorescent dyes have many biological and biomedical applications as assay reporters and tracking molecules both in vitro and in vivo (*1*−*4*). A number of reactive fluorescent dyes are commercially available containing functional groups such as *N*-hydroxy succinimide (NHS) esters, isothiocyanates, maleimides, or iodoacetamides to couple with naturally occurring reactive amine and thiol functional groups on peptides, nucleic acids, saccharides, proteins, and other biomolecules (*5*). Currently, several thiolated fluorescent dyes are commercially available, produced by modification of fluoresceine (Invitrogen and Toronto Research Chemicals Inc.), tetramethylrhodamine (TAMRA), sulforhodamine, dansyl, and Texas Red (Toronto Research Chemicals Inc.). These dyes are available with protective groups (acetyl, methanethiosulfonate) attached to the desired reactive thiol or sold as the free mercaptan form (although a mixture of disulfide and mercaptan dyes is likely). Of the above-mentioned reactive dyes, care must be taken when using fluorescein-based derivatives, as they are known to be pH-sensitive, with quantum yield decreasing by ~70−80% upon acidification and formation of the neutral molecule (*6, 7*). Observing such fluorescein-labeled molecules that are trafficked to lysosomes within cells is difficult due to decreased dye fluorescence signal within these acidic subcellular compartments.

Corresponding author. Currently at the Department of Pharmaceutics and Pharmaceutical Chemistry, College of Pharmacy, University of Utah, Salt Lake City, UT 84112 USA; Email: david.grainger@pharm.utah.edu. Phone: +1 801.581.4532; Fax: +1 801.581.3674.

The current popularity of reducible disulfide-containing polymeric cellular delivery systems for therapeutic transgenes, tumor drugs, and imaging agents merits development of new disulfide exchange reagents capable of providing intracellular reporting information on cell-based polymer degradation (*8*−*10*). Investigation of a nonexotic dimeric thiol-containing, pH-insensitive, reactive fluorescent dye reagent was the focus of this work. Tetramethylrhodamine (TAMRA) was chosen for this study because of its excellent photostability, and its quantum yield is unaffected at acidic pH (*11*). In fact, several intracellular pH estimates have been described on basis of the ratio of fluorescence signal from simultaneous observations of fluorescein and TAMRA (*12*−*14*).

In this short work, we reevaluate the optical properties of dimeric TAMRA with the dimer covalently linked via a disulfide bond. This dimer was reversibly converted to monomer by addition of disulfide reducing agent or biological milieu. The observed effect of covalent dimer formation on fluorescence and absorption spectra was significantly higher than previously observed in noncovalent dimer systems.

EXPERIMENTAL PROCEDURES

General. All solvents and reagents were purchased from commercial sources and used as received. NMR spectra were recorded on a Magnex Scientific Inova 400 MHz instrument in DMSO-d_6 containing 5% w/v tetramethylsilane as an internal standard. Absorbance measurements were obtained on a Varian Cary 500 Scan and BioTek Synergy 2 plate reader instruments. All samples were weighed to the nearest 0.01 mg using a Mettler Toledo Pro Balance 220/81 GX 0.1/0.01MG analytical balance.

10.1021/bc800367e CCC: $40.75 © 2009 American Chemical Society
Published on Web 02/27/2009

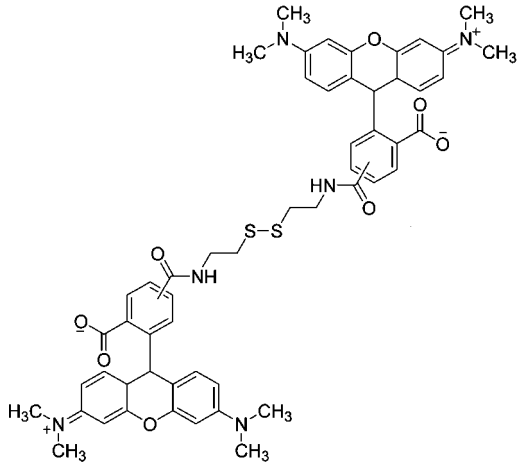

Figure 1. Structure of ssTAMRA dimer.

Size exclusion chromatography was performed using a HP1050 HPLC system equipped with a HP1040A refractive index detector and Biosil 125 column. Sodium phosphate buffer (0.05 M, pH 7.4) mobile phase, 100 μL sample injection, and 0.5 mL/min flow rate was used for each analysis. RAW 264.7 murine monocyte-macrophage cells were obtained from the American Type Culture Collection (Manassas, VA) and cultured in RPMI 1640 (Mediatech) supplemented with 10% fetal bovine serum (FBS, HyClone, Inc.) and 1% penicillin−streptomycin (Life Technologies). Cultures were maintained in T-175 TCPS flasks (Nunc) under standard conditions: incubation at 37 °C, 98% humidity, and 5% CO_2, and dissociated from culture flasks by incubation with Ca^{2+}- and Mg^{2+}-free cell culture grade Hank's balanced salt solution (HBSS, Life Technologies).

Synthesis of Disulfide TAMRA Dimer. TAMRA disulfide dimer (ssTAMRA) was prepared by reacting 5-(6)-carboxytetramethylrhodamine, succinimidyl ester (5(6) TAMRA-NHS, AnaSpec) with cystamine hydrochloride activated using diisopropylethylamine (DIPEA). In a typical experiment, 9.6 mg cystamine hydrochloride (0.085 mmol, 0.9 equiv amines) was activated in 2.5 mL dimethylformamide (DMF) containing 30 μL DIPEA (0.17 mmol, 1.8 equiv). This solution was then added to a solution of 50.0 mg TAMRA-NHS (0.095 mmol, 1.0 equiv) in 1.5 mL DMF and stirred at room temperature for 30 min. Then, 15 μL (0.086 mmol, 1.0 equiv) of DIPEA was added and the reaction was stirred for an additional hour. Product was precipitated by addition of 50 mL cold diethyl ether, washed several times with diethyl ether, and dried under vacuum overnight. Solids were further purified by repeated precipitation from methanol into cold ether. Product yield: 75%. Formation of the desired dimer was confirmed by mass spectrometry, MS-FAB M[H^+] calculated = 977.336, found = 977.334. ^{1}H NMR analysis confirmed formation of the new amide bonds, with four relevant peaks observed in an unambiguous region of the spectrum, corresponding to combinations of 5 and 6 TAMRA isomers (8.58, 8.91, 9.00, 9.07 ppm, triplets, total integration = 2H). The structure of ssTAMRA is shown in Figure 1.

Determination of Molar Extinction Coefficients. ssTAMRA was dried under vacuum overnight, then weighed to the nearest 0.01 mg inside a 200 mL (±0.1 mL) volumetric flask and subsequently dissolved in 200 mL buffer (0.01 M sodium phosphate, 0.15 M NaCl, 10 mM EDTA, pH = 7.2). This solution was then serially diluted using 25 mL (±0.03 mL) volumetric flasks. The absorbance at 520 nM was measured to the nearest 1×10^{-6} absorbance units using a Varian Cary 500 Scan spectrometer. The molar extinction was determined as the slope of the best-fit line of a plot of absorbance vs concentration ($y = 128\,358x$, $R^2 = 0.9999$), and further normalized to moles TAMRA by dividing this value by 2. The molar extinction of reduced sTAMRA was determined in a similar fashion, except that ssTAMRA was dissolved in phosphate buffer supplemented with 10 mM TCEP·HCl and then incubated for 30 min at room temperature before preparing diluted samples. The resulting best-fit line from a plot of absorbance vs concentration was found to be $y = 66\,131x$, $R^2 = 0.9999$. The sample purity was assumed to be 100%, as no starting material was observed in mass spectrometry or NMR measurements.

Oxidation of sTAMRA. Disulfide oxidation was determined following complete reduction of ssTAMRA with agarose gel-immobilized TCEP (Pierce) in buffer (0.01 M sodium phosphate, 0.15 M NaCl, 10 mM EDTA, pH 7.2). Upon removal of reducing agent by filtration, the resulting sTAMRA solution (1.2×10^{-5} M) was capped under ambient atmosphere and maintained in the dark at room temperature (22 °C), and absorbance spectra were recorded at various times. The rate of disulfide formation was determined by plotting the 554/520 nm absorbance ratios.

Reduction of ssTAMRA with Cell Lysate. Reduction of ssTAMRA was monitored in RAW 264.7 murine monocyte−macrophage cell lysate over time. In this experiment, 1 mL of M-PER cell lysate solution (Pierce, Rockford, IL) was added per 1 g of cell pellet, and the resulting solution was processed per manufacturer recommendations and stored at −20 °C prior to use. Cell lysate solution was diluted 1:1 with ssTAMRA solution to yield a final TAMRA concentration of 1.15×10^{-5} M and then incubated at room temperature in a microwell plate. TAMRA absorbance at both 554 and 520 nm was measured at various times using a BioTek Synergy 2 plate reader.

Conjugation of sTAMRA to Poly[*N*-(2-hydroxypropyl)methacrylamide]. Poly *N*-(2-hydroxypropyl)methacrylamide] (HPMA) copolymer containing reactive esters, further converted to hydrazide groups, was prepared as previously described (*15*). Prior to hydrazide modification, a portion of reactive esters were used to conjugate Oregon Green 488 fluorescent dye to the polymer backbone (~0.7 dyes/polymer) by reaction with amine-containing Oregon Green 488 cadaverine in the presence of DIPEA in DMF. Finally, hydrazides were converted to maleimide groups by reaction with the heterobifunctional cross-linker *N*-4-(acetylphenyl) maleimide (APM). Preparation of the reactive HPMA copolymer is outlined in the Supporting Information.

Dimeric ssTAMRA (7.0 mg, 1.6 μmol) was reduced using TCEP reducing gel (2.5 mL slurry/μmol ssTAMRA dimer) for 45 min, followed by removal of the reducing agent by filtration through a 0.2 μm filter. Reduced sTAMRA was then reacted with maleimide-derivatized poly(HPMA) (40.45 mg, 1.60×10^{-6} mol maleimide groups) for 1.5 h in 0.01 M sodium phosphate, 0.15 M NaCl, 10 mM EDTA, pH 7.2; then, remaining maleimide groups were quenched by addition of 2 μL β-mercaptoethanol. The dual dye-labeled poly(HPMA) product was separated from free sTAMRA dye and desalted using size exclusion chromatography (SEC) (Sephadex G-25, 15 × 1 cm, H_2O mobile phase), then isolated using a speed-vac. TAMRA content was determined by absorbance measurements at 554 nm using $\varepsilon = 6.4 \times 10^4$ M^{-1} cm^{-1}. The polymer−TAMRA conjugate was analyzed by SEC; BioSilect 125 column, 0.5 mL/min 0.01 M sodium phosphate buffer containing 0.15 M NaCl and 10 mM EDTA, pH 7.2.

RESULTS AND DISCUSSION

Synthesis of the disulfide-containing ssTAMRA probe was readily achieved by nucleophilic displacement of NHS esters contained on TAMRA by cysteamine's two terminal amines. Cysteamine was selected as the starting material, because it contains an internal disulfide bond; thus, only amide formation between cysteamine and TAMRA facilitates formation of the

Table 1. Spectral Properties of Oxidized and Reduced Thiolated TAMRA.

	λ_{max} absorbance (nm)	ε (M^{-1} cm^{-1})[a]	554/520 ratio	520/554 ratio	λ_{max} emission (nm)	relative fluorescence[b]
reduced sTAMRA	554	$6.61 \times 10^4 \pm 0.18 \times 10^4$	2.37	0.42	578	1.00
oxidized ssTAMRA	520	$6.42 \times 10^4 \pm 0.17 \times 10^4$	0.38	2.64	578	0.061

[a] Expressed relative to moles TAMRA, determined at λ_{max}. [b] Excitation at isosbestic point, 532 nm.

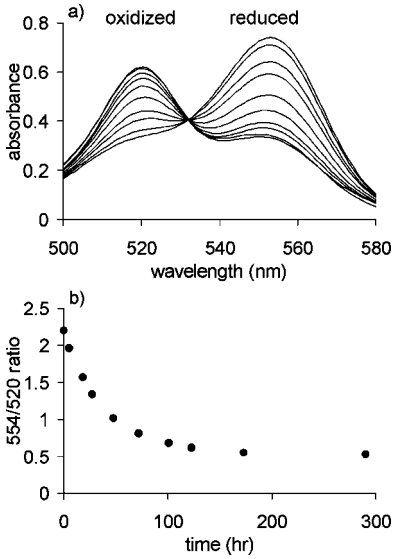

Figure 2. Oxidation of sTAMRA monomer in 0.1 M sodium phosphate, 0.15 M NaCl, 10 mM EDTA, pH 7.2. (a) absorbance spectra of 1.2×10^{-5} M sTAMRA at various times. (b) Ratio of 554/520 nm absorbance spectra showing disulfide formation rate.

disulfide-containing dimer. Preparation of dimeric fluorescent reporter molecules has received much attention due to the different spectral properties of these molecules in monomeric and dimeric forms (*16*−*18*). Spectral properties of the reduced monomeric TAMRA (sTAMRA) and oxidized dimeric thiolated TAMRA (ssTAMRA) are summarized in Table 1. Reduction of the disulfide was readily achieved after incubation in 10 mM tris(2-carboxyethyl) phosphine hydrochloride (TCEP·HCl), with no increase in 554 nm sTAMRA monomer absorbance observed after 30 min, indicating complete reduction. Oxidized ssTAMRA exhibited a hypsochromic shift of 34 nm relative to the reduced sTAMRA absorption maximum, which was close to native TAMRA (Figure 2a, Table 1). This phenomenon has been observed for concentrated aqueous solutions of rhodamine B with the formation of noncovalent dimers (dissociation constant of 6.8×10^{-4} M) observed at mM concentrations (*19, 20*). This hypsochromic shift has also been used to study conformation and subunit exchange of *E. coli* ribosomal protein L7/L12, and conformation of the muscle protein, titin, with cysteine thiol groups labeled with tetramethylrhodamine iodoacetamide (*21, 22*). These studies utilized the ratio of noncovalent dimer absorbance at 518 nm to monomer absorbance at 555 nm to determine proximity of TAMRA labels on the protein, with a 518/554 absorbance ratio of 1−1.3 reported for noncovalent dimeric TAMRA (*21*). Additionally, a 519/550 ratio for an analogous covalent TAMRA dimer linked by thiourea bonds and an ethylene spacer has been reported to be 1.5 (*23*). Results for ssTAMRA in this study show a 520/554 ratio of 2.64 for the covalent disulfide dimer, exceeding all spectral ratios previously described and indicating significantly that the longer disulfide 4-carbon spacer used in this study allows for increased dye interaction and enhanced spectral properties. This ratio might also be further increased by using pure starting material, instead of mixed 5 and 6 TAMRA-NHS isomers as reported here.

Dimer formation had no affect on optical absorption of attached TAMRA, as molar extinction coefficients for reduced and oxidized species were nearly identical. However, fluorescence emission was nearly extinguished upon dimer formation, with fluorescence intensity reduced by >93% in ssTAMRA when excited at the isosbestic point (532 nm). This is likely due to self-quenching from stacked xanthene rings as previously described for analogous rhodamine B, rhodamine 6G, and TAMRA dimers in aqueous solution (*20*, *24*, *25*). Stacking proximity of a folded covalent TAMRA dimer containing an ethylenediamine spacer has been estimated as 0.9 nm (*23*). Fluorescence quenching of rhodamine dimers appears to be solvent-dependent, with no quenching observed in mixed water/organic solvent systems but observed in aqueous buffered systems as also described here (*22*−*25*).

The reversibility of disulfide reduction/oxidation was determined following complete reduction of ssTAMRA and removal of reducing agent. Reduced dye is susceptible to oxidation by divalent metals such as Zn^{2+}, Cu^{2+}, and Mg^{2+}, or oxygen in aqueous media resulting in formation of the dye disulfide dimer. However, in the conditions used in this experiment the major cause of sTAMRA oxidation is likely dissolved oxygen, as deionized water and EDTA were used to reduce ion effects and the solution was not degassed or stored under inert atmosphere. Absorbance spectra at various times are shown in Figure 2a with an isosbestic point apparent at 532 nm. The rate of ssTAMRA disulfide formation was determined by plotting the 554/520 nm absorbance ratios as shown in Figure 2b. The absorbance spectra shown in Figure 2a confirm sTAMRA oxidation and reformation of disulfide bonds by the increasing 520 nm absorbance value over time. In this experiment, the absorbance value for oxidized ssTAMRA never reached the same value as the initial absorbance value shown for reduced sTAMRA, despite very similar extinction coefficients reported in Table 1. This is likely due to the fact that reformation of the ssTAMRA dimer does not proceed to 100% conversion in this time. The reduced dye thiol is relatively stable at μM concentrations in this buffer system for several hours ($t_{1/2} \sim 50$ h), but stability could likely be enhanced by degassing the storage solution and storing it under inert atmosphere. This type of experiment could be useful for preparation of bioconjugates when confirmation of disulfide reduction or sulfhydryl stability information for specific reaction or storage conditions is required.

The utility of ssTAMRA as a disulfide reduction reporter molecule in vitro was demonstrated using fresh lysate from cultured harvested RAW 264.7 macrophage cells. These cells were selected since they are common models for phagocytosis and processing of drugs, toxins, polymers, and particles in the endosomal/lysosomal cell trafficking pathway (*26*). The ssTAMRA dye was effectively reduced in lysed RAW 264.7 cells over time, with ~80% reduction observed after 4 h (Figure 3). Recently, a disulfide-reducible FRET reporter molecule containing folate was used to evaluate disulfide reduction during endocytosis (*27*). In this approach, the FRET pair is prepared by attachment of dyes to the reporter molecule in different synthetic steps; however, reporter systems based on self-quenching of TAMRA molecules covalently bound in close proximity by disulfide groups may reduce synthetic steps and cost by reaction of the reporter molecule with an excess of relatively inexpensive TAMRA derivative.

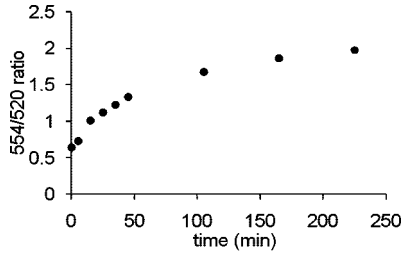

Figure 3. Reduction of ssTAMRA (1.15×10^{-5} M TAMRA) in fresh cell lystae from cultured RAW 264.7 cells at room temperature. Cell lysate background absorbance has been subtracted at both wavelengths for ratios calculated for each data point.

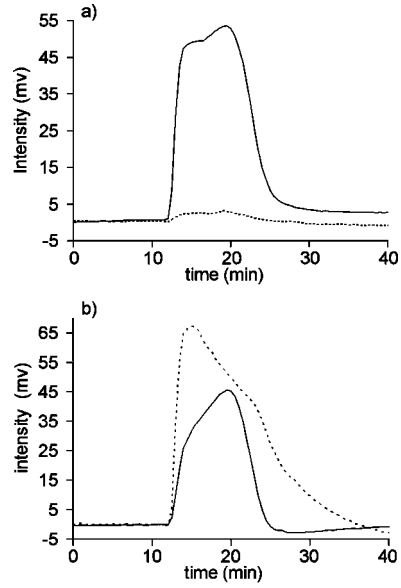

Figure 4. Size exclusion chromatography trace of dual-labeled poly(HPMA) in 0.01 M sodium phosphate buffer containing 0.15 M NaCl and 10 mM EDTA, pH 7.2, before (a) and after (b) sTAMRA conjugation. Detection at 496 nm (solid) corresponds to polymer backbone (Oregon Green), and 554 nm detection (dashed) corresponds to sTAMRA.

Further application of sTAMRA as a traditional reactive probe was realized by covalent reaction with Oregon Green-labeled, maleimide-derivatized, poly[*N*-(2-hydroxypropyl)methacrylamide] (polyHPMA), a polymer often selected as a model for polymer-mediated uptake and processing of drugs and other agents to cells both in vitro and in vivo, and much is known about its endosomal and lysosomal trafficking within cells (*28, 29*). This particular fluorescent-labeled HPMA copolymer was designed for reversible attachment of thiol-containing peptides via hydrazone and maleimide chemistries, and the thiolated ssTAMRA described here served as a model reporter molecule to confirm thiol coupling to the polymer backbone. This dual-labeled water-soluble polymer allowed simultaneous observation of the Oregon Green backbone and reacted sTAMRA using diode array detection at absorption wavelengths for Oregon Green 488 (496 nm) and sTAMRA (554 nm) during SEC analysis. It should be noted that, once conjugated to the polymer backbone in this fashion, the dye loses its environmental sensitivity, so this experiment was performed to confirm the utility of ssTAMRA as a reactive dye probe analogous to other thiolated dyes. Conjugation of reduced sTAMRA to the polymer backbone was confirmed, as TAMRA eluted in the polymer fraction at 12−22 min as shown in Figure 4 (free dye elutes from this column after 30 min under these conditions). The small amount of free dye observed after the polymer peak in Figure 4b is a characteristic of the degradable cross-linker used to incorporate maleimide groups into poly(HPMA), designed for intracellular delivery and release of peptides. The amount of dye conjugated to the polymer backbone was 25.9 μmol/g, corresponding to ~10% conjugation under the conditions described here. This coupling efficiency could likely be increased by longer reaction time and reaction with more stable precursors, as polymer degradation is evidenced as the tailing peak in Figure 4b.

CONCLUSION

In summary, a reactive thiolated dimeric TAMRA-based fluorescent reporter is described that is inexpensive and convenient to produce. The covalent ssTAMRA disulfide dimer exhibits unique spectral properties useful in the study of disulfide exchange or other disulfide redox processes by either absorbance shifts or increases in fluorescence emission after generation of monomeric sTAMRA. Reduction of ssTAMRA dimers is readily achieved using TCEP, with reduced sTAMRA being reactive to maleimide functionality. Conjugation of this reduced sTAMRA to nucleic acids, enzymes, peptides, polymers, proteins, saccharides, or other relevant targets useful for cell trafficking studies is shown to be feasible for application as a reactive fluorescent probe. The sensitivity of ssTAMRA to reduction by biological milieu (i.e., cell lysate) shows its potential as a reporter molecule in cell or organism-based studies where local oxidizing or reducing environmental changes would produce probe spectral shifts in situ.

The enhanced spectral properties of the covalent TAMRA dimer described here could be useful to prepare more advanced reporter molecules and bioconjugates. It would be rather simple to build specialty probes containing dimeric TAMRA that are attached to moieties that affect and track activity in biological systems. For example, many heterobifunctional PEGs and multifunctional cross-linkers are available that could be used to build probes for specific applications. The utility of dimeric TAMRA is not limited to disulfide dimers; TAMRA dimers formed using an acetal as the anchor point would result in a pH-sensitive probe. With TAMRA dimers, environmentally specific information can be obtained using a single fluorophore rather than two as needed in FRET experiments. This would simplify preparation of probes, eliminating the need for extensive purification and complex reaction schemes. Covalent TAMRA dimers could serve as powerful yet simple tools to investigate biological systems.

ACKNOWLEDGMENT

Dr. George Barisas and Dr. James Herron are recognized for fluorescence assay technical assistance. This work was supported by NIH grant EB000894.

Supporting Information Available: Experimental details regarding poly(HPMA) synthesis and subsequent polymer modifications are described. This material is available free of charge via the Internet at http://pubs.acs.org.

LITERATURE CITED

(1) Slavík, J. (1994) *Fluorescent probes in cellular and molecular biology*, CRC Press, Boca Raton.
(2) Andersson-Engels, S., Klinteberg, C., Svanberg, K., and Svanberg, S. (1997) In vivo fluorescence imaging for tissue diagnostics. *Phys. Med. Biol. 42*, 815–24.
(3) Hassan, M., and Klaunberg, B. A. (2004) Biomedical applications of fluorescence imaging in vivo. *Comp. Med. 54*, 635–44.
(4) Rudin, M., and Weissleder, R. (2003) Molecular imaging in drug discovery and development. *Nat. Rev. Drug Discovery 2*, 123–31.

(5) Haugland, R. P. (2002) *Handbook of fluorescent probes and research products*, 9th ed., Molecular Probes, Inc., Eugene, OR.
(6) Martin, M. M., and Lindqvist, L. (1975) Ph-dependence of fluorescein fluorescence. *J. Lumin. 10*, 381–390.
(7) Yguerabide, J., Talavera, E., Alvarez, J. M., and Quintero, B. (1994) Steady-state fluorescence method for evaluating excited state proton reactions: application to fluorescein. *Photochem. Photobiol. 60*, 435–441.
(8) Ou, M., Wang, X. L., Xu, R. Z., Chang, C. W., Bull, D. A., and Kim, S. W. (2008) Novel biodegradable poly(disulfide amine)s for gene delivery with high efficiency and low cytotoxicity. *Bioconjugate Chem. 19*, 626–633.
(9) Lu, Z. R., Ye, F. R., and Vaidya, A. (2007) Polymer platforms for drug delivery and biomedical imaging. *J. Controlled Release 122*, 269–277.
(10) Oupicky, D., Carlisle, R. C., and Seymour, L. W. (2001) Triggered intracellular activation of disulfide crosslinked polyelectrolyte gene delivery complexes with extended systemic circulation in vivo. *Gene Ther. 8*, 713–724.
(11) Geisow, M. J. (1984) Fluorescein conjugates as indicators of subcellular Ph - a critical-evaluation. *Exp. Cell Res. 150*, 29–35.
(12) Ichimura, T., Hatae, T., and Ishida, T. (1997) Direct measurement of endosomal pH in living cells of the rat yolk sac epithelium by laser confocal microscopy. *Eur. J. Cell Biol. 74*, 41–8.
(13) McNamara, K. P., Nguyen, T., Dumitrascu, G., Ji, J., Rosenzweig, N., and Rosenzweig, Z. (2001) Synthesis, characterization, and application of fluorescence sensing lipobeads for intracellular pH measurements. *Anal. Chem. 73*, 3240–3246.
(14) Chen, Y., and Arriaga, E. A. (2006) Individual acidic organelle pH measurements by capillary electrophoresis. *Anal. Chem. 78*, 820–826.
(15) Etrych, T., Jelinkova, M., Rihova, B., and Ulbrich, K. (2001) New HPMA copolymers containing doxorubicin bound via pH-sensitive linkage: synthesis and preliminary in vitro and in vivo biological properties. *J. Controlled Release 73*, 89–102.
(16) Wang, C., Leffler, S., Thompson, D. H., and Hrycyna, C. A. (2005) A general fluorescence-based coupled assay for S-adenosylmethionine-dependent methyltransferases. *Biochem. Biophys. Res. Commun. 331*, 351–6.
(17) Johansson, M. K., Fidder, H., Dick, D., and Cook, R. M. (2002) Intramolecular dimers: a new strategy to fluorescence quenching in dual-labeled oligonucleotide probes. *J. Am. Chem. Soc. 124*, 6950–6.
(18) Galande, A. K., Weissleder, R., and Tung, C. H. (2006) Fluorescence probe with a pH-sensitive trigger. *Bioconjugate Chem. 17*, 255–7.
(19) Selwyn, J. E., and Steinfeld, J. I. (1972) Aggregation equilibria of xanthene dyes. *J. Phys. Chem. 76*, 762–774.
(20) Lopez Arbeloa, I., and Ruiz Ojeda, P. (1982) Dimeric states of rhodamine B. *Chem. Phys. Lett. 87*, 556–560.
(21) Hamman, B. D., Oleinikov, A. V., Jokhadze, G. G., Bochkariov, D. E., Traut, R. R., and Jameson, D. M. (1996) Tetramethylrhodamine dimer formation as a spectroscopic probe of the conformation of *Escherichia coli* ribosomal protein L7/L12 dimers. *J. Biol. Chem. 271*, 7568–73.
(22) Grama, L., Somogyi, B., and Kellermayer, M. S. Z. (2001) Global configuration of single titin molecules observed through chain-associated rhodamine dimers. *Proc. Natl. Acad. Sci. U.S.A. 98*, 14362–14367.
(23) Hernando, J., van der Schaaf, M., van Dijk, E. M. H. P., Sauer, M., Garcia-Parajo, M. F., and van Hulst, N. F. (2003) Excitonic behavior of rhodamine dimers: A single-molecule study. *J. Phys. Chem. A 107*, 43–52.
(24) Ilich, P., Mishra, P. K., Macura, S., and Burghardt, T. P. (1996) Direct observation of rhodamine dimer structures in water. *Spectrochim. Acta, Part A 52*, 1323–1330.
(25) Burghardt, T. P., Lyke, J. E., and Ajtai, K. (1996) Fluorescence emission and anisotropy from rhodamine dimers. *Biophys. Chem. 59*, 119–131.
(26) Groves, E., Dart, A. E., Covarelli, V., and Caron, E. (2008) Molecular mechanisms of phagocytic uptake in mammalian cells. *Cell. Mol. Life Sci. 65*, 1957–76.
(27) Yang, J., Chen, H., Vlahov, I. R., Cheng, J. X., and Low, P. S. (2006) Evaluation of disulfide reduction during receptor-mediated endocytosis by using FRET imaging. *Proc. Natl. Acad. Sci. U.S.A. 103*, 13872–13877.
(28) Jensen, K. D., Nori, A., Tijerina, M., Kopeckova, P., and Kopecek, J. (2003) Cytoplasmic delivery and nuclear targeting of synthetic macromolecules. *J. Controlled Release 87*, 89–105.
(29) Kopecek, J., Kopeckova, P., Minko, T., and Lu, Z. R. (2000) HPMA copolymer-anticancer drug conjugates: design, activity, and mechanism of action. *Eur. J. Pharm. Biopharm. 50*, 61–81.

BC800367E

SUPPORTING INFORMATION

1. Poly(HPMA) monomer synthesis

1.1 N-2-hydroxypropyl methacrylamide

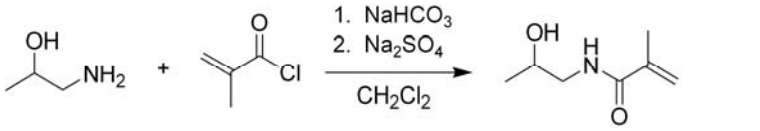

N-2-hydroxypropyl methacrylamide
"HPMA"

Scheme S1. Synthesis of N-2-hydroxypropyl methacrylamide monomer.

N-(2-hydroxypropyl)methacrylamide (HPMA) was synthesized by reaction of DL-1-amino-2-propanol with methacryloyl chloride as shown in Scheme S1. 1-amino-2-propanol (24.3 mL, 0.311 mol, 1 eq) and sodium bicarbonate (33.6 g, 0.40 mol, 1.3 eq) was added to CH_2Cl_2 (85 mL) and the suspension was purged with N_2, capped, and placed in an ice bath. A second solution containing methacryloyl chloride (29.5 mL, 0.304 mol, 0.98 eq) in CH_2Cl_2 (40 mL) was prepared and cooled to –20 ^oC. Next, the methacryloyl chloride solution was slowly added to the 1-amino-2-propanol solution under N_2 with vigorous stirring. After complete addition the reaction was stirred for 15 min at 25 ^oC, and anhydrous Na_2SO_4 (10 g) was added. The solution was manually stirred for an additional 10 minutes and the solution was filtered through paper. Solids were washed twice with 20 mL CH_2Cl_2 and the filtrates were combined. The combined filtrates were concentrated under vacuum to ~ 50% of the original volume then placed in a –20 ^oC freezer overnight. HPMA crystals were collected by filtration and washed with cold acetone. Product was purified by repeated crystallization from acetone. Typical yield: ~15.0 g, 30%, semi-transparent white crystals. ^1H NMR, δ ppm: 1.008 (d, 3H), 1.848 (s, 3H), 3.041 (t, 2H), 3.678 (m, 1H), 4.693 (s, 1H), 5.483 (d, 2H), 7.820 (s, 1H). Mp = 72 ^oC (sharp).

Reference: Ulbrich K, Subr V, Strohalm J, Plocova D, Jelinkova M, Rihova B. (2000) Polymeric drugs based on conjugates of synthetic and natural macromolecules I. Synthesis and physico-chemical characterisation. J. Controlled Release *64(1-3)*, 63-79.

1.2 Methacryloyl glycylglycine

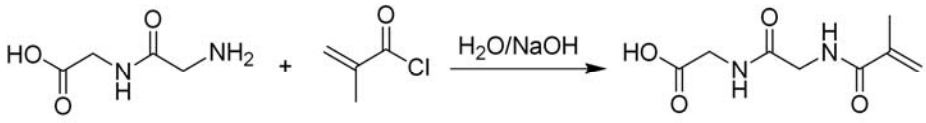

methacryloyl glycylglycine
"MAGG"

Scheme S2. Synthesis of methacryloyl glycylglycine.

N-methacryloyl glycylglycine 4-nitrophenyl ester (MAGGONP) synthesis began with preparation of methacryloyl glycylglycine (MAGG) using the Schotten-Baumann procedure in aqueous alkaline medium as shown in Scheme S2. Glycylglycine (10 g, 76 mmol, 1 eq) was dissolved in 0.5 M NaOH (15.1 mL, 76 mmol, 1 eq) over 30 minutes then cooled to 0 ^oC. Methacryloyl chloride (7.5 mL, 77 mmol, 1eq) and 5.0 M NaOH (15.1 mL, 76 mmol, 1 eq) were added dropwise and simultaneously to the glycylglycine solution while stirring at 0 ^oC. After complete addition, the reaction was stirred for an

additional hour at room temperature, then concentrated HCl was added until a dense white precipitate formed. Solids were collected by filtration and washed with cold water until the filtrate was neutral. Crude solid product was dried under vacuum and further purified by repeat crystallization from 50/50 (v/v) ethanol/water. Typical yield: ~5.0 g, 30%, small white crystals. ^{1}H NMR: (400 MHz, DMSO-d_6) δ ppm: 1.876 (s, 3H), 3.766 (d, 4H), 5.561 (d, 2H), 8.132 (t, 1H), 8.190 (t, 1H), 12.594 (s, 1H). Mp = 175-205 ^{o}C.

Reference: Kopecek J. (1977) Reactive Copolymers of N-(2-Hydroxypropyl)Methacrylamide with N-Methacryloylated Derivatives of L-Leucine and L-Phenylalanine .1. Preparation, Characterization, and Reactions with Diamines. Makromol. Chem. Macromol. Chem. Phys. *178(8)*, 2169-83.

1.3 Methacryloyl glycylglycine 4-nitrophenyl ester

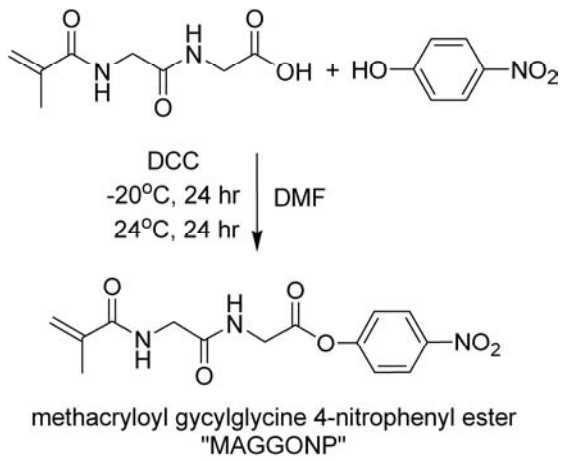

Scheme S3. Synthesis of methacryloyl glycylglycine 4-nitrophenyl ester

Methacryloyl glycylglycine (MAGG) was esterified with 4-nitrophenol using carbodiimide chemistry to yield methacryloyl glycylglycine 4-nitrophenyl ester as shown in Scheme S3. MAGG (5.23 g, 26.1 mmol, 1 eq) was dissolved in dry dimethyl formamide (DMF, 50 mL) and cooled to –15 ^{o}C. 4-nitrophenol (4.0 g, 28.71 mmol, 1.1 eq) and dicyclohexylcarbodiimide (DCC) (5.39 g, 26.1 mmol, 1.0 eq) were each dissolved in DMF (26 mL) in separate flasks and cooled to –15 ^{o}C. After all solutions were cooled, the 4-nitrophenol and DCC solutions were added dropwise to the MAGG solution sequentially while stirring. The reaction was stirred for 4 hr at –15 ^{o}C followed by 24 hr at –20 ^{o}C. Upon complete reaction, dicyclohexyl urea (DCU) byproduct was removed by filtration. The filtrate was collected and allowed to sit at room temperature for 24 hrs under N_2 and then cooled to –20 ^{o}C. The solution was again filtered to remove DCU crystals. The filtrate was retained and 100 mL cold water was added. This mixture was placed on ice for 1 hr. The pale-yellow solids were collected by filtration and dried under vacuum. Hot 50/50 water/ethanol was added to the dried solids until ~ 80% dissolved. The solution was boiled for an additional 10 minutes then filtered. Small, pale-yellow, fish-scale crystals formed slowly in the filtrate over a 3 hr period at room temperature. Solids were collected by filtration and dried under vacuum. Typical yield ~ 2.0 g, 22%, yellow crystals. ^{1}H NMR, δ ppm: 1.884 (s, 3H), 3.809 (d, 2H), 4.176 (d, 2H), 5.577 (d, 2H), 7.435 (m,2H), 8.267 (t, 1H), 8.326 (m, 2H), 8.479 (t, 1H). Mp = 143-160 ^{o}C.

Reference: Kopecek J. (1977) Reactive Copolymers of N-(2-Hydroxypropyl)Methacrylamide with N-Methacryloylated Derivatives of L-Leucine and L-Phenylalanine .1. Preparation, Characterization, and Reactions with Diamines. Makromol. Chem. Macromol. Chem. Phys. *178(8)*, 2169-83.

2. HPMA copolymer synthesis

2.1 Free radical initiated polymerization

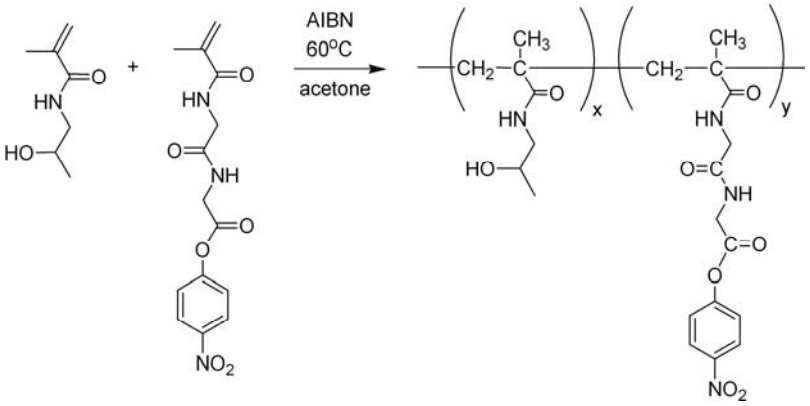

Scheme S4. Free radical initiated copolymerization of N-2-hydroxypropyl methacrylamide and methacryloyl glycylglycine nitrophenyl ester.

HPMA copolymer was prepared by free radical initiated polymerization as previously described using 12.5% (w/v) monomer and 0.6% initiator (AIBN) in freshly distilled acetone. Reactive side chain content in the polymer product was controlled by feed ratio of MAGGONP. The following is a typical procedure to produce an HPMA copolymer with 95 mole % HPMA units and 5 mole % MAGGONP units. HPMA monomer (3.35 g, 23.4 mmol, 1 eq), MAGGONP (0.40 g, 1.2 mmol, 0.05 eq), and AIBN (0.18 g, 1.1 mmol, 0.05 eq) were added to acetone (26 mL) in a Chemglass 50 mL pressure flask containing a magnetic stirbar. The solution was degassed by sonication under N_2 flow for 5 minutes and then capped. This solution was stirred until all solids dissolved (~ 30 minutes) and placed in a hot water bath and stirred at 60 ^oC for 24 hrs. After complete reaction, solids were collected by filtration, washed with cold acetone, and dried under vacuum. Solids were further purified by repeat precipitation from 90/10 CH_2Cl_2/MeOH (v/v) into a 10-fold excess of cold acetone. Typical yield: ~ 2.2 g, 56%, cream colored powder.

Reference: Kopecek J. (1977) Reactive Copolymers of N-(2-Hydroxypropyl)Methacrylamide with N-Methacryloylated Derivatives of L-Leucine and L-Phenylalanine .1. Preparation, Characterization, and Reactions with Diamines. Makromol. Chem. Macromol. Chem. Phys. *178(8)*, 2169-83.

2.2 Detemination of Active Ester Content in HPMA Copolymers.

HPMA copolymer product was dissolved in 0.05 M NaOH at concentrations of 0.08-0.1 mg/mL then stirred at 37 ^oC for 3 hrs. The absorbance of the resulting bright-yellow solutions was measured at 400 nm and ester content was estimated using the molar extinction coefficient ($\varepsilon = 1.74 \times 10^4\ M^{-1}cm^{-1}$) of the released p-nitrophenolate anion and the original mass of the polymer sample. The molar extinction coefficient was determined by serial dilution of a p-nitrophenol solution in 0.05 M NaOH. No increase

in absorbance after incubation for 3 hr at 37 ^{o}C was observed, showing complete cleavage p-nitrophenol esters. The reactive ester content was determined to be 4.9% +/- 1.5%.

2.3 Molecular Weight Estimation of HPMA Copolymers

Molecular weight of synthesized poly(HPMA) copolymer was estimated following displacement of reactive ester groups with 1-amino-2-propanol by size exclusion chromatography using an HP1050 HPLC system equipped with an HP1040A refractive index detector and Biosil 125 column. The instrument was calibrated with poly(HPMA) samples of known molecular weight. For each characterization, sodium phosphate buffer (0.05 M, pH 7.4) was used as the mobile phase with a 100 μL sample injection and a 0.5 mL/min flow rate.

2.4 Hydrazide modification

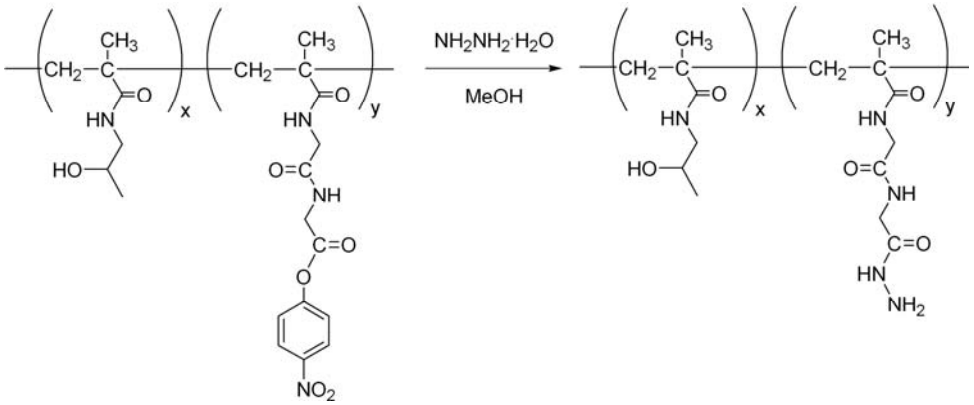

Scheme S5. Conversion of reactive esters to hydrazide groups

Hydrazide groups were generated on HPMA copolymers by reaction of hydrazine with active esters present on MAGGONP side chains as previously described (Scheme S5). A representative procedure follows: HPMA/MAGGONP copolymer (5 mole % MAGGONP, 2.0 g, 0.51 mmol active esters, 1 eq) was dissolved in methanol (25 mL). Hydrazine monohydrate (267 uL, 5.1 mmol, 10 eq) was added to 25 mL methanol in a separate flask. The HPMA copolymer solution was added to the hydrazine monohydrate solution dropwise while stirring over ~ 30 minutes then purged with N_2, capped, and stirred for 3 hr at room temperature. After complete reaction, the mixture was slowly added to 75 mL cold water while stirring, then transferred to dialysis tubing (SpectraPore 7, 6-8 kDa MWCO) and dialyzed against water for 3 days with frequent changing of the dialysis water. Polymer product was isolated by lyophilization. Typical yield: ~ 1.2 g, 60%, white powder.

Reference: Etrych, T., Chytil, P., Jelinkova, M., Rihova, B., Ulbrich, K. (2002) Synthesis of HPMA copolymers containing doxorubicin bound via a hydrazone linkage. Effect of spacer on drug release and in vitro cytotoxicity. *Macromol. Biosci. 2*, 43-52.

2.5 Analysis of HPMA Copolymer Hydrazide Content

Hydrazide content in HPMA copolymers was estimated using a modified trinitrobenzene sulfonic acid (TNBSA) assay. TNBSA assay compared ethyl carbazate and methacryloyl glycylglycine hydrazide (MAGGH) as standards. MAGGH was synthesized by reaction of MAGGONP with hydrazine monohydrate. MAGGONP (750 mg, 2.33 mmol, 1 eq) was dissolved in methanol (90 mL) and then slowly added to a solution of hydrazine monohydrate (567 µL, 11.7 mmol, 5 eq) in 10 mL methanol. The reaction was stirred for 5 hr at room temperature under N_2. After complete reaction, solvent was removed under vacuum to yield crude solids. The resulting solids were dissolved in 90/10 CH_2Cl_2/methanol (40 mL), filtered and loaded onto a silica gel column (2.5 x 17.5 cm) equilibrated with 90/10 CH_2Cl_2/MeOH. After the sample was loaded onto the column, the elution solvent was changed to MeOH. MAGGH eluted after the visible yellow 4-nitrophenol band. Yield: 0.156 g, 31%, white powder. ^{1}H NMR, δ ppm: 1.836 (s, 1H), 3.619 (d, 2H), 3.712 (d, 2H), 4.165 (d, 2H), 5.341 (d, 1H), 5.698 (d, 1H), 8.048 (t, 1H), 8.131 (t, 1H), 8.907 (s, 1H). ^{13}C NMR, δ ppm: 18.479, 40.779, 42.402, 119.752, 139.356, 167.597, 168.011, 169.204. MS-FAB m/z = 215.1147 $[M+H]^+$(calculated m/z = 215.1144 $[M+H]^+$)

For each poly(HPMA) hydrazide content analysis, stock solutions of 0.1% w/v TNBSA, ~ 2 x 10^{-4} M MAGGH, and ~ 2 x10^{-4} M ethyl carbazate were prepared in 0.1 M $NaHCO_3$, pH 8.5. MAGGH and ethyl carbazate solutions were further diluted with 0.1 M $NaHCO_3$ to generate standards in the range of ~0.3 - 2 x 10^{-4} M. Next, hydrazide-derivatized HPMA copolymers were dissolved in 0.1 M $NaHCO_3$ at a concentration of 0.2-0.4 mg/mL. Sample or standard solutions (1.0 mL) were combined with 0.5 mL TNBSA stock solution and stirred for 1.5 – 48 hr at 37 °C. After incubation, sample absorbance was measured at 505 nm and hydrazide content was estimated from the equation of the line fit to MAGGH or ethyl carbazate standards plotted as concentration vs. absorbance.

3. Preparation of HPMA-APM conjugate

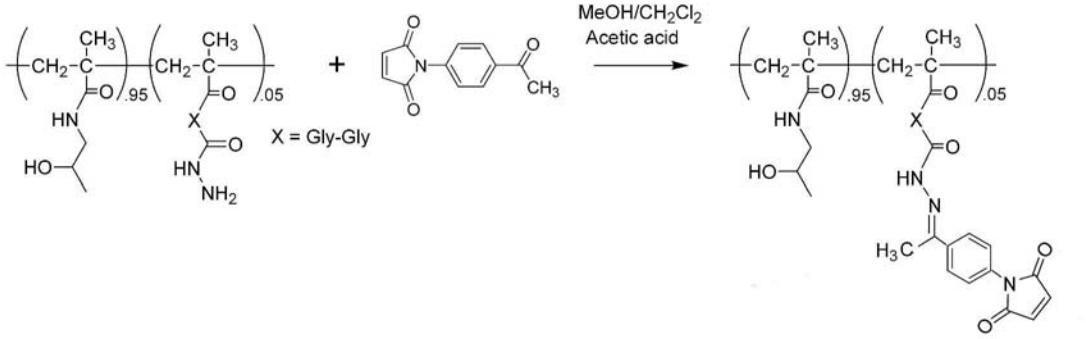

Scheme S6. Conjugation of *N*-4-(acetylphenyl) maleimide to HPMA copolymer

Hydrazide derivatized poly(HPMA), (0.20 g, 1.0 equiv, 52 µmol hydrazide) was dissolved in 50/50 methylene chloride/methanol (2 mL), and 100 mg Na_2SO_4 was added. *N*-4-(acetylphenyl) maleimide solution (34.0 mg, 3.1 equiv, 160 µmol) was prepared in 50/50 methylene chloride/methanol (2 mL) and then added to the poly(HPMA) solution dropwise. After complete addition, acetic acid (5 µL of 34% v/v solution in methylene chloride, 0.6 equiv, 30 µmol) was added and the reaction was stirred under nitrogen at room temperature for 24 hr. The reaction was terminated by precipitation of poly(HPMA) product into ether. Product was further purified by size exclusion chromatography (Sephadex LH-20, 1 x 15 cm, methanol mobile phase). Typical yield: 126 mg, 63%, white powder. Hydrazide content post-

conjugation was determined using a TNBSA assay, as described above. Crosslinker content was determined by an absorbance measurement at λ_{max} and using the molar extinction coefficients of corresponding ethyl carbazate-crosslinker hydrazone derivative at 288 nm, $\varepsilon = 1.9 \times 10^4\ M^{-1}\ cm^{-1}$. Polymer-crosslinker conjugates were analyzed by ^1H NMR and maleimide functionality was confirmed in the polymer backbone as a sharp singlet at 7.2 ppm.

Bioconjugate Chemistry 20th Anniversary

Subscriber access provided by SHEMYAKIN-OVCHINNIKOV INST

Article

Targeted Gene Delivery Mediated by Folate-polyethylenimine-block-poly(ethylene glycol) with Receptor Selectivity

Han Cheng, Jing-Ling Zhu, Xuan Zeng, Yue Jing, Xian-Zheng Zhang, and Ren-Xi Zhuo

Bioconjugate Chem., **2009**, 20 (3), 481-487• DOI: 10.1021/bc8004057 • Publication Date (Web): 03 February 2009

Downloaded from http://pubs.acs.org on May 8, 2009

More About This Article

Additional resources and features associated with this article are available within the HTML version:

- Supporting Information
- Access to high resolution figures
- Links to articles and content related to this article
- Copyright permission to reproduce figures and/or text from this article

View the Full Text HTML

ACS Publications
High quality. High impact.

Bioconjugate Chemistry is published by the American Chemical Society. 1155 Sixteenth Street N.W., Washington, DC 20036

Targeted Gene Delivery Mediated by Folate-polyethylenimine-block-poly(ethylene glycol) with Receptor Selectivity

Han Cheng, Jing-Ling Zhu, Xuan Zeng, Yue Jing, Xian-Zheng Zhang,* and Ren-Xi Zhuo

Key Laboratory of Biomedical Polymers of the Ministry of Education, Department of Chemistry, Wuhan University, Wuhan 430072, P. R. China. Received September 22, 2008; Revised Manuscript Received December 30, 2008

The folate receptor (FR) is a tumor marker overexpressed in large numbers of cancer cells. Folic acid has high affinity to the FR and retains its binding affinity upon derivatization via its γ-carboxyl. Therefore, in this article, folate-polyethylenimine-block-poly(ethylene glycol) (FOL-PEI-b-PEG) was designed for specific receptor targeted gene delivery. Physicochemical characterizations of resulting FOL-PEI-b-PEG/DNA complexes in terms of agarose gel electrophoresis, particle size, and zeta potential measurements were investigated. The results indicated that FOL-PEI-b-PEG was able to condense plasmid DNA tightly with a suitable particle size. The cytotoxicity study indicated that the copolymer exhibited less toxicity in comparison with that of 25 kDa PEI. Luciferase assay and green fluorescent protein (GFP) detections were also used to confirm that FOL-PEI-b-PEG could be an effective gene vector. Importantly, transfection efficiency of FOL-PEI-b-PEG with free folic acid was much lower than that of the copolymer without free folic acid on FR-positive HeLa cells, suggesting that FOL-PEI-b-PEG has great potential as a targeting gene vector.

INTRODUCTION

In recent years, gene therapy has attracted much attention for its pharmaceutical application in treating chronic diseases and genetic disorders (*1, 2*). There are two categories of gene delivery vectors: viral and nonviral vectors (*3*−*6*). Nonviral gene vectors are considered to have several advantages over viral gene vectors, such as flexibility in formulation design, ability to be modified with ligands and delivered selectively to a specific tissue/cell, no limitation of carrying capacity in DNA size, and so on (*7*−*10*). Cationic lipids and cationic polymers are the most widely used nonviral vectors that have been extensively studied (*11, 12*). Compared with cationic lipids, cationic polymers are stable, easy to be manipulated, and more economical. Polyethylenimine (PEI), one of the most successful and efficient nonviral vectors, is a cationic polymer and has been broadly utilized for gene delivery both in vitro and in vivo (*13*−*16*). PEI has been shown to form compact interpolyelectrolyte complexes with DNA, and the PEI/DNA polyplexes have been found to be able to mediate efficient transfection of cells in culture.

As we know, transfection efficiency and toxicity of PEI depend on its molecular weight, and it is recognized that high molecular weight PEI shows high transfection activity and cytotoxicity. For example, the well-known commercial branched 25 kDa PEI, as an effective transfection reagent in vitro and in vivo, has high transfection efficiency but has high cytotoxicity too. In order to enhance transfection efficiency and decrease cytotoxicity, synthetic cationic copolymers based on PEI and poly(ethylene glycol) (PEG) were investigated as nonviral gene vectors (*17*−*20*). In recent years, PEG has been widely applied in gene delivery systems. The presence of PEG on the surface of gene vectors can enhance biocompatibility, reduce cytotoxicity, and protect DNA from degradation.

Polycationic gene vector modified with folic acid (FA) was expected to identify specific tissue/cell surface receptors and transfect cells by receptor-mediated endocytosis (*21*−*23*). In this study, folate-polyethylenimine-block-poly(ethylene glycol) (FOL-PEI-b-PEG) was prepared as an effective gene vector. Folic acid was conjugated to PEI to increase the transfection efficiency for targeting purposes, while PEG was used as the biocompatible outer hydrophilic shell to protect the genes and reduce the cytotoxicity of PEI. The in vitro cytotoxicity of the resulting copolymers was examined, while the physiochemical characteristics of the copolymer/DNA complexes were analyzed by agarose gel electrophoresis, particle size, and zeta potential measurements. In addition, the in vitro transfection efficiency of FOL-PEI-b-PEG/DNA complexes in terms of the luciferase assay and green fluorescent protein (GFP) detections were also examined with three cell lines using the branched 25KDa PEI as the control.

EXPERIMENTAL PROCEDURES

Materials. Methoxy polyethylene glycol with a molecular weight of 5000 (PEG 5 kDa) was purchased from Acros and dried by azeotropic distillation with toluene. Polyethylenimine (PEI, 25 kDa, branched) and sodium cyanoborohydride ($NaBH_3CN$) were purchased from Sigma and used as received. Folic acid (FA) and acetic anhydride (Ac_2O) were purchased from Sinopharm Chem. Reagent Co. Ltd., China. The Micro BCA protein assay kit and GelRed were purchased from Pierce and Biotium (CA, USA), respectively. Dulbecco's modified Eagle's medium (DMEM) with a folate concentration of 4 mg/L, fetal bovine serum (FBS), penicillin-streptomycin, trypsin, Dubelcco's phosphate buffered saline (PBS), and 3-(4,5-dimethylthiazol-2-yl)-2,5-diphenyltetrazolium bromide (MTT) were obtained from Invitrogen Corp. All other reagents and solvents were used as received without further purification.

Two different types of plasmid DNAs, pGL-3 and pEGFP-C1 plasmids, were used in the study. Plasmid pGL3-control with SV40 promoter and enhancer sequences encoding luciferase was obtained from Promega, Madison, WI, USA. Plasmid pEGFP-C1 encoding a red-shifted variant of wild-type green fluorescent protein (GFP) was purchased from Clontech, Mountain View, CA, USA. The former was transformed in *E. coli* JM109, and the latter was transformed in *E. coli* DH5α. Both plasmids were

* Corresponding author. Tel./Fax: 86-27-6875 4509. E-mail: xz-zhang@whu.edu.cn.

10.1021/bc8004057 CCC: $40.75 © 2009 American Chemical Society
Published on Web 02/03/2009

amplified in LB medium at 37 °C overnight at 250 rpm. Then the plasmids were purified as described by means of EndoFree plasmid purification. The purified plasmid was diluted by TE buffer solution and stored at −20 °C. The integrity of the plasmid was confirmed by agarose gel electrophoresis. The purity and concentration of the plasmid were determined by ultraviolet (UV) absorbance at 260 and 280 nm.

Cell Culture. Human embryonic kidney 293T cells (HEK293T), human cervix carcinoma cells (HeLa), and human hepatocellular carcinoma cells (HepG2) were incubated in DMEM containing 10% FBS and 1% antibiotics (penicillin-streptomycin, 10000 U/mL) at 37 °C in a humidified atmosphere containing 5% CO_2, respectively.

Synthesis of Aldehyde-PEG (PEG-CHO). PEG-CHO was prepared as follows: dried PEG (3 g) was dissolved in 10 mL of dried DMSO and 1 mL of $CHCl_3$, and then Ac_2O (2 mL) was added to the reaction mixture. The reaction was performed at room temperature for 12 h. Then the product was precipitated into diethyl ether. The precipitated product was isolated by filtration and dried under vacuum.

Synthesis of PEI-b-PEG. PEI (2 g) was dissolved in 20 mL of CH_3OH. Then PEG-CHO (2 g) in 20 mL of CH_3OH was added dropwise to the reaction mixture. After 24 h at room temperature under N_2 atmosphere, 0.16 g of $NaBH_3CN$ was added, and the reaction was performed at room temperature for another 48 h. Then the product was dialyzed against distilled water using a dialysis membrane (MWCO 8000-12000) for purification. The aqueous solution in the dialysis bag was freeze-dried to obtain PEI-b-PEG.

Synthesis of FOL-PEI-b-PEG. PEI-b-PEG (480 mg) and FA (15 mg) were dissolved in 10 mL of DMSO, and then DCC (8.5 mg) and DMAP (5 mg) were added to the reaction mixture. The reaction mixture was magnetically stirred for 24 h at 35 °C under N_2 atmosphere to produce FOL-PEI-b-PEG. Thereafter, the mixture was dialyzed against distilled water using a dialysis membrane (MWCO 8000-12000) for further purification. The aqueous solution in the dialysis bag was freeze-dried to obtain the product.

Folic Acid Content of FOL-PEI-b-PEG. The content of folic acid conjugated in FOL-PEI-b-PEG was obtained on the basis of the standard curve by using the UV−vis spectrophotometer. FOL-PEI-b-PEG and folic acid were dissolved in distilled water. FOL-PEI-b-PEG aqueous solution of 290 mg/L, and folic acid aqueous solutions of 13.9−111 mg/L were prepared. Optical absorbance of folic acid aqueous solution at room temperatures was measured from 250 to 400 nm by UV−vis spectrometer and the absorbance at a wavelength of 280 nm was determined. The absorbance values of the peak intensities at 280 nm of the absorbance spectra were analyzed as a function of folic acid concentration. Also, the absorbance value of the peak intensity at 280 nm of FOL-PEI-b-PEG was obtained. The concentration of folic acid in FOL-PEI-b-PEG aqueous solution was calculated according to the calibration curve made from free folic acid, while the content of folic acid was calculated by the concentration ratio of the folic acid and FOL-PEI-b-PEG.

^{1}H NMR Measurements. ^{1}H NMR spectra were recorded on a Varian Unity 300 MHz spectrometer using D_2O as the solvent.

Formation of the Copolymer/DNA Complexes. PEI-b-PEG or FOL-PEI-b-PEG was dissolved in NaCl solution (150 mM pH 7.4) to form a solution of 1 mg/mL. A plasmid DNA stock solution (120 ng/μL) was prepared in Tris-HCl buffer solution (pH 7.4). The volume of the polycation solution and the DNA stock solution was adjusted to 50 μL with 150 mM NaCl solution. Then the polycation solution and DNA stock solution were mixed together to form complexes with different weight ratios of copolymer/DNA. The complexes were incubated at 37 °C for 30 min.

Agarose Gel Retardation Assay. The complexes at different weight ratios were prepared by adding an appropriate volume of PEI-b-PEG or FOL-PEI-b-PEG (in 150 mM NaCl solution) to 96 ng of pEGFP-C1 plasmid DNA (120 ng/μL in 40 mM Tris-HCl buffer solution), the complexes were diluted by 150 mM NaCl solution to 6 μL, and then the complexes were incubated at 37 °C for 30 min. After that the complexes were electrophoresed in the 0.7% (w/v) agarose gel containing GelRed with Tris-acetate (TAE) running buffer at 80 V for 80 min. DNA was visualized with a UV lamp using a Vilber Lourmat imaging system (France).

Particle Size Measurement. The particle size was measured by Nano-ZS ZEN3600 (MALVERN Instr.). PEI-b-PEG/DNA or FOL-PEI-b-PEG/DNA complexes at various weight ratios were prepared by adding an appropriate volume of PEI-b-PEG or FOL-PEI-b-PEG (in 150 mM NaCl solution) to 1 μg of plasmid DNA (in Tris-HCl buffer solution, pH 7.4). The complexes were diluted by 150 mM NaCl solution to 1 mL and incubated at 37 °C for 30 min before the measurement.

Zeta Potential Measurement. The zeta potentials of coplolymer/DNA complexes were measured using Nano-ZS ZEN3600 based on the principle of phase analysis light scattering. The zeta potentials quoted were averages obtained from at least six measurements over duplicate samples.

In Vitro Cytotoxicity Test. For each well in a 96-well plate, 200 μL of cells (HEK293T, HepG2 or HeLa) in DMEM, with a concentration of 2.5×10^4 cells/mL was added. The number of cells in each well was 5000. After incubation for 24 h in an incubator (37 °C, 5% CO_2), the culture medium was changed to 200 μL of DMEM containing polymers with particular concentrations, and the mixture was further incubated for 48 h. Then, DMEM with polymers was replaced by fresh DMEM, and 20 μL of MTT solution (5 mg/mL) was added to the cells. After incubation for 4 h, 150 μL of DMSO was added and shaken at room temperature. The optical density (OD) was measured at 570 nm with a Microplate Reader Model550 (BIO-RAD, USA). The relative cell viability was calculated by the following equation:

$$\text{relative cell viability (\%)} = (\text{OD}_{\text{treated}}/\text{OD}_{\text{control}}) \times 100 \quad (1)$$

where $\text{OD}_{\text{control}}$ was obtained in the absence of copolymers, and $\text{OD}_{\text{treated}}$ was obtained in the presence of copolymers.

Gene Transfection. For the in vitro transfection study, the HEK293T, HepG2, and HeLa cells were split one day prior to transfection and plated in 24-well plates at a density of 5×10^4 cells/well. Before transfection, the cell culture medium was replaced with serum-free DMEM. The cells were transfected with gene delivery complexes containing 1 μg of plasmid DNA at 37 °C for 4 h. Then the complexes were removed and incubated in fresh DMEM with 10% FBS at 37 °C for another 48 h.

Luciferase Assay. The cells were washed by PBS and lysed with the reporter lysis buffer (Promega, USA). The luciferase activity in cell extracts was measured using a luciferase assay kit (Promega, USA). Each measurement was carried out for 10 s in a single-well luminometer (Berthold Lumat LB 9507, Germany). The relative light units (RLU) were normalized by the total protein concentration of the cell extracts, and the total protein was measured with a BCA protein assay kit (PERBIO, USA). Luciferase activity was expressed as RLU/mg Protein. The statistical significance between two sets of data was calculated using Student's *t*-test. $P < 0.05$ was considered statistically significant.

GFP Detection. The cells expressing green fluorescent proteins were directly observed by an inverted microscope (IX 70, Olympus, Japan).

Scheme 1. Synthesis Route of FOL-PEI-b-PEG

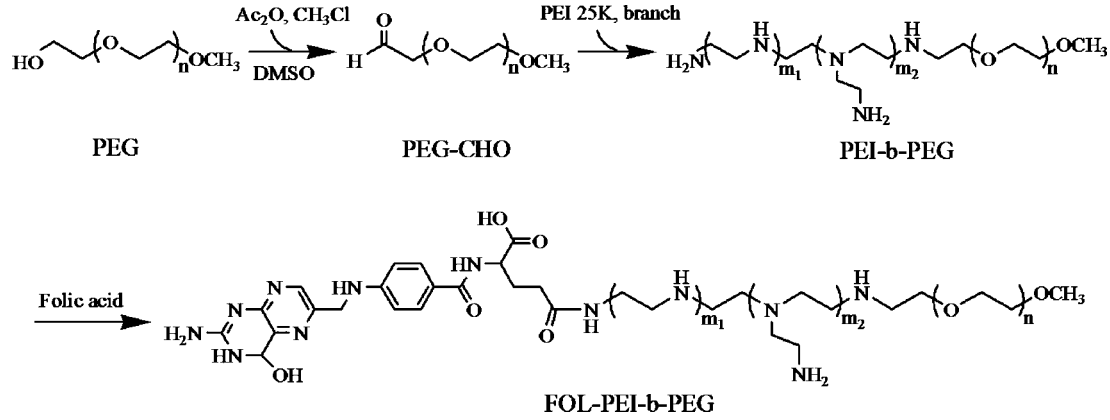

Folic Acid Competition Study. HepG2 cells and HeLa cells were cultured in the same conditions as that of the transfection tests. Cells were seeded into 24-well plates at 5×10^4 cell density per well and incubated for 24 h. The first series of stock solutions containing FOL-PEI-b-PEG/DNA complexes with predetermined weight ratios were prepared. The second series of stock solutions containing the same predetermined weight ratios of FOL-PEI-b-PEG/DNA complexes with free folic acid were prepared by fixing the weight ratio of FOL-PEI-b-PEG/free FA to 32/1 (molar ratio of FOL-PEI-b-PEG/free FA: 43.4/100). The third series of stock solutions containing free folic acid at varied weight ratios of FOL-PEI-b-PEG/free FA ranging from 10/0 to 10/40 were prepared with a fixed FOL-PEI-b-PEG/DNA weight ratio of 10. All of the stock solutions contained 1 μg of plasmid DNA with predetermined weight ratios of FOL-PEI-b-PEG/DNA (the amount of DNA used in each well is 1 μg). Cells were subsequently incubated at 37 °C with one of these solutions for 4 h in the presence of 5% CO_2, respectively. After that, cells were washed once with PBS solution and further incubated with fresh DMEM medium and maintained at 37 °C in 5% CO_2 for another 48 h. The transfection efficiency was then assessed using the same way described in the luciferase assay section.

RESULTS AND DISCUSSION

Synthesis of FOL-PEI-b-PEG. The FOL-PEI-b-PEG copolymer was synthesized through three steps as illustrated in Scheme 1. The first step was to prepare PEG-CHO by the oxidation of the hydroxyl end group of PEG. Then, PEI (25 kDa, branch) was combined with PEG-CHO to form PEI-b-PEG. FOL-PEI-b-PEG was finally synthesized by activating the γ-carboxyl group in folic acid with DCC/DMAP for the conjugating to primary amine groups of PEI-b-PEG.

The ^{1}H NMR analysis was used to determine the molecular weight and composition of the resulting polymers. Figure 1 shows the ^{1}H NMR spectrum of PEI-b-PEG in D_2O. The signal at δ 3.6 ppm related to the PEG, which was marked b. The signals of the NCH_2CH_2N protons of PEI backbone were found in the range of 2.4−3.4 ppm (a). The ratio of integral *a* and integral *b* was 4.63, and the molecular weights (M_n) of the polymers can be calculated from the ratio of these two integrals. The M_n of PEI-b-PEG was calculated to be 3.05×10^4 since that of PEI was 2.5×10^4. The results indicate that about one PEG molecular chain was conjugated to one PEI molecular chain.

As shown in Figure 2, the content of folic acid conjugated in FOL-PEI-b-PEG was 2.48 wt %, i.e., the molar ratio of folate/PEI in the FOL-PEI-b-PEG was around 1.8/1, obtained on the basis of the standard curve by using the UV absorbance at 280 nm as the reference. According to the reference, α- and γ-carboxyl groups on the folic acid have been reported to undergo coupling reactions, but only the γ-conjugate can bind to the folate receptor (FR) (*24*). The DCC-mediated polycondensation reaction involves about 80% γ-linked and 20% α-linked conjugates.

Physicochemical Characterization of Copolymers. The DNA-binding capability of the copolymers is very important for gene vectors (*25*). The condensed form of the copolymer/DNA complexes can protect the plasmid DNA from cell barriers during gene delivery. In order to study complexation and condensation capabilities of copolymers with DNA, agarose gel retardation assays were performed. In this study, the weight ratio instead of the *N*/*P* ratio (*N*/*P* refers to the ratio of moles of the amine groups of copolymer to moles of phosphates of DNA) was used to represent the properties of the copolymer. When the weight ratio of PEI-b-PEG/DNA or FOL-PEI-b-PEG/DNA is 1, the *N*/*P* ratio of corresponding complexes is 6.15 or 5.99, respectively. The agarose gel electrophoresis of copolymer/DNA complexes were examined at varied weight ratios. As shown in Figure 3, the copolymers could efficiently bind DNA at a weight ratio of 3. The complete retardation of DNA was achieved at a copolymer/DNA weight ratio of 5. These results proved that the copolymers might be used to bind DNA as an efficient gene vector.

The particle size of the copolymer/DNA complexes at different weight ratios was shown in Figure 4. All of the sizes of complexes were measured at weight ratios ranging from 2.3 to 11.7. At the lowest weight ratio, the particle size was 325 nm. With the increasing weight ratios of the copolymer/DNA complexes, the particle size increased from 325 to 647 nm. In

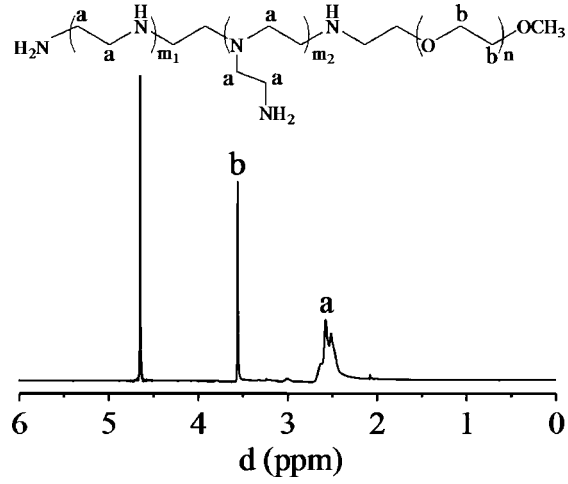

Figure 1. ^{1}H NMR of PEI-b-PEG in D_2O.

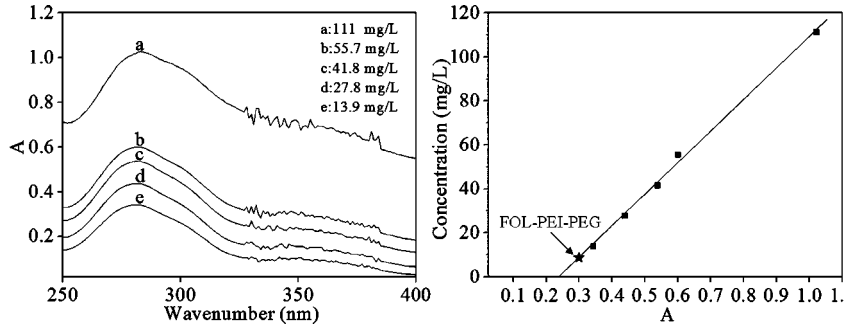

Figure 2. UV absorbance of folic acid solutions. (Light transmittance of FOL-PEI-b-PEG aqueous solution at room temperatures was measured from 250 to 400 nm by UV−vis spectrometer.)

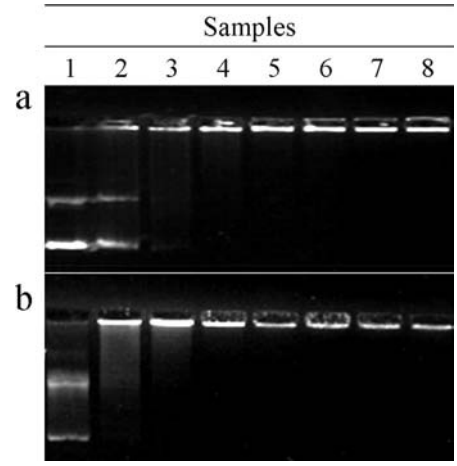

Figure 3. Agarose gel electrophoresis retardation assay of FOL-PEI-b-PEG/DNA (a) and PEI-b-PEG/DNA (b) complexes. Lane 1, naked DNA (plasmid only); lanes 2−8, weight ratios 1 to 13 with increments of 2.

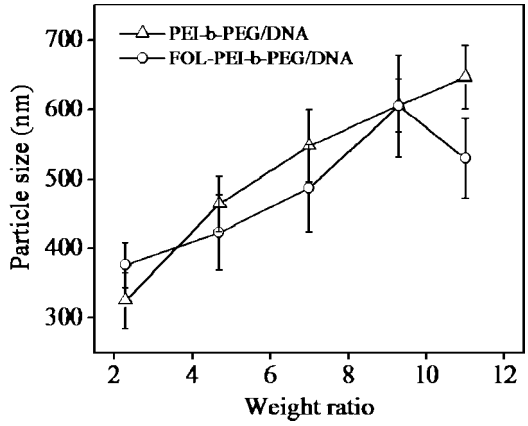

Figure 4. Particle size of FOL-PEI-b-PEG/DNA (a) and PEI-b-PEG/DNA (b) complexes at weight ratios ranging from 2.3 to 11.7.

addition, the two copolymer/DNA complexes, i.e., PEI-b-PEG/DNA and FOL-PEI-b-PEG/DNA had similar particle size at the same weight ratio. Obviously, the complex size of the copolymer/DNA depends on weight ratios.

As shown in Table 1, the zeta potential of the FOL-PEI-b-PEG/DNA complex increased from −6.4 mV to 7.99 mV with increasing weight ratio while that of the PEI-b-PEG/DNA complex increased from 2.11 mV to 13.2 mV correspondingly. At a higher weight ratio, the copolymer/DNA complex possessed a higher zeta potential due to the increasing amount of cationic copolymer. The positive zeta potential of copolymers is necessary to ensure the uptake of complexes by cells due to electrostatic interactions between negatively charged cellular membranes and positively charged complexes (*26, 27*).

Biological Characterization of the Copolymers. The gene vector should not induce cytotoxic effects (*28, 29*). In order to evaluate the cytotoxicity of resulting copolymers, the viability of three different cell lines was tested in the presence of PEI-b-PEG and FOL-PEI-b-PEG at various concentrations. Here, PEI 25 kDa was used as the control. Figure 5 shows that both PEI-b-PEG and FOL-PEI-b-PEG exhibited much lower cytotoxicity compared with that of 25 kDa PEI regardless of cell lines, and the difference of cytotoxicity between FOL-PEI-b-PEG and PEI-b-PEG is not significant. The cytotoxicity of PEI-b-PEG and FOL-PEI-b-PEG increased gradually with increasing concentration. Concurrently, it was found that the cytotoxicity of PEI-b-PEG and FOL-PEI-b-PEG was a little lower in HepG2 cells than that in HEK293T and HeLa cells.

FR is normally elevated in cancer cells. For targeting purposes, the folic acid molecule was conjugated to the PEI-b-PEG copolymer. To investigate the transfection efficiency mediated by PEI-b-PEG and FOL-PEI-b-PEG copolymers, we performed in vitro transfection activity assays using FR-positive (HEK293T and HeLa) and FR-negative (HepG2) cells. The transfection efficiency of copolymer/DNA complexes was visualized by a fluorescence microscope. The images in Figure 6 show that HEK293T, HeLa, and HepG2 cells were transfected with FOL-PEI-b-PEG/pEGFP-C1 or PEI-b-PEG/pEGFP-C1 complexes, respectively. As shown in Figure 6AI and BI, for HEK293T cells no obvious difference of fluorescent density was found because HEK293T cells have been proved to be the kind of cells with high transfection efficiency, and the difference of the transfection efficiency between PEI-b-PEG and FOL-PEI-b-PEG was not significant (*30*). In contrast to HEK293T cells, the fluorescent density showed obvious differences when HeLa cells were transfected with two copolymer/pEGFP-C1 complexes. The fluorescent density of HeLa cells was decreased when we used PEI-b-PEG/pEGFP-C1 complexes instead of FOL-PEI-b-PEG/pEGFP-C1 complexes, while there was not much difference in HepG2 cells. It was also noted that HepG2 cells showed the lowest transfection efficiency among the three cell lines and that the fluorescent spots were markedly reduced. These results indicate that the transfection efficiency, mediated by PEI-b-PEG or FOL-PEI-b-PEG, depended on cell types.

Table 1. Zeta Potential of Copolymer/DNA Complexes with Varied Weight Ratios

weight ratio	2.3	4.7	7	9.3	11.7
FOL-PEI-b-PEG/DNA	−6.4 ± 0.37 mV	5.08 ± 0.36 mV	4.54 ± 0.27 mV	7.57 ± 0.35 mV	7.99 ± 0.65 mV
PEI-b-PEG/DNA	2.11 ± 0.39 mV	6.37 ± 0.26 mV	5.65 ± 0.33 mV	7.19 ± 0.29 mV	13.2 ± 0.41 mV

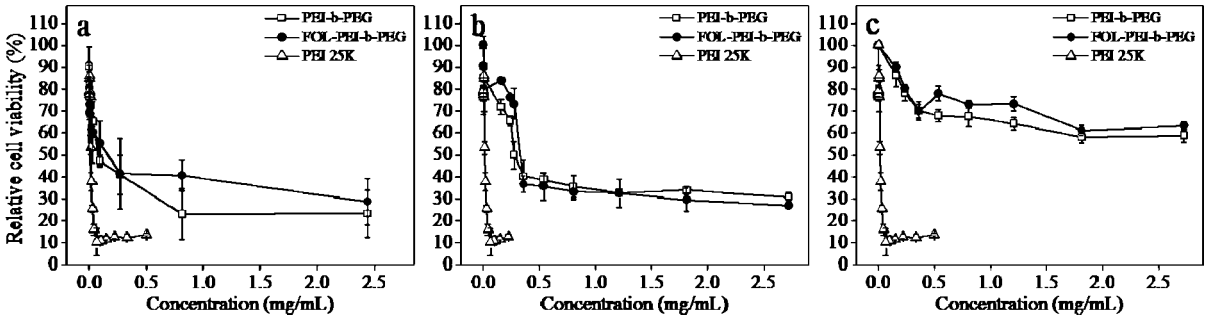

Figure 5. Cytotoxicity of FOL-PEI-b-PEG and PEI-b-PEG copolymers in comparison with 25 kDa PEI in HEK293T cells (a), HeLa cells (b), and HepG2 cells (c).

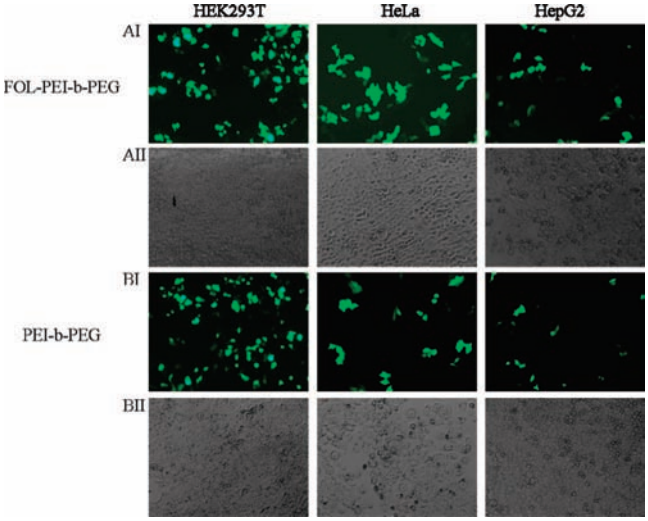

Figure 6. GFP detection of the transfected HEK293T cells, HeLa cells, and HepG2 cells observed by an inverted microscope. Images (AI, BI) are the fluorescent images, and images (AII, BII) are the bright-field images. Images (AI, AII) were observed in HEK293T cells with an FOL-PEI-b-PEG/DNA weight ratio of 14, in HeLa cells with an FOL-PEI-b-PEG/DNA weight ratio of 11, and in HepG2 cells with an FOL-PEI-b-PEG/DNA weight ratio of 14; images (BI, BII) were observed in HEK293T cells with a PEI-b-PEG/DNA weight ratio of 14, in HeLa cells with a PEI-b-PEG/DNA weight ratio of 11, and in HepG2 cells with a PEI-b-PEG/DNA weight ratio of 14. The images were obtained at magnification of 100×.

FOL-PEI-b-PEG/DNA complexes exhibited higher transfection efficiency than that of PEI-b-PEG/DNA complexes in FR-positive HeLa cells, whereas no difference in FR-negative HepG2 cells was found.

To quantify the transfection efficiency, the plasmid pGL-3 was used as the luciferase reporter gene, and the luciferase expression assay induced by the copolymers/pGL-3 complexes was carried out. The luciferase activities of the copolymer/DNA complexes were similar to the results of GFP detection. As shown in Figure 7a, the luciferase activity of PEI/pGL-3 complexes was 3.72×10^8 RLU/mg at an N/P ratio of 10. PEI-b-PEG/pGL-3 complex showed comparable or higher luciferase activities ($1.09 \times 10^8 - 7.82 \times 10^8$ RLU/mg) at certain weight ratios when compared with that of PEI/pGL-3 complexes in HEK293T cell lines, indicating that the conjugation of PEG could reduce the cytotoxicity of copolymers and increase the gene expression to some extent. Compared with the one of FOL-PEI-b-PEG/pGL-3 complexes, the luciferase activity was obviously higher when HEK293T cells were transfected with PEI-b-PEG/pGL-3 complexes at a weight ratio of 4.6, whereas no significant difference (nonsignificant: $P = 0.475$) between PEI-b-PEG/pGL-3 complexes and FOL-PEI-b-PEG/pGL-3 complexes was observed when the weight ratio increased. On the basis of the results, we also found that the PEI-b-PEG/pGL-3 complexes possessed the highest transfection efficiency in HEK293T cells at the weight ratio of 14 (7.82×10^8 RLU/mg).

In HeLa and HepG2 cells, the results became different from those described above. As shown in Figure 7b, the luciferase activities of FOL-PEI-b-PEG/pGL-3 complexes were $0.84 \times 10^8 - 1.97 \times 10^8$ RLU/mg, and the luciferase activities of PEI-b-PEG/pGL-3 complexes were $3.82 \times 10^6 - 5.81 \times 10^7$ RLU/mg at varied weight ratios. These results indicate that luciferase expression was significantly higher ($P < 0.05$) when HeLa cells were transfected with FOL-PEI-b-PEG. By contrast, there was no significant difference (nonsignificant: $P > 0.05$) when HepG2 were transfected with copolymers/DNA complexes of FOL-PEI-b-PEG or PEI-b-PEG. The gene transfection efficiency of the copolymers was initially increased and then decreased with an increasing weight ratio of copolymer/DNA (Figure 7c). Besides, both copolymer/DNA complexes at a weight ratio 14 got the highest transfection efficiency. Obviously, the transfection efficiency of complexes depends on weight ratios, and it seems that there exists a weight ratio equilibrium between the

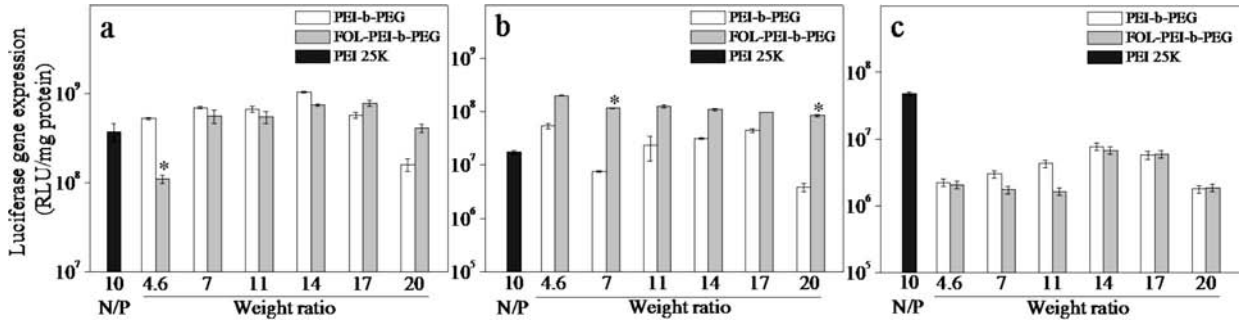

Figure 7. Luciferase expression efficiency in HEK293T cells (a), HeLa cells (b), and HepG2 cells (c). Transfection efficiency of FOL-PEI-b-PEG/DNA and PEI-b-PEG/DNA complexes were evaluated at weight ratios ranging from 4.6/1 to 20/1 with 25 kDa PEI/DNA complexes at the optimal ratio ($N/P = 10$) as the control. Data are shown as the mean ± SD ($n = 3$) (*$P < 0.05$ as compared with the data of PEI-b-PEG).

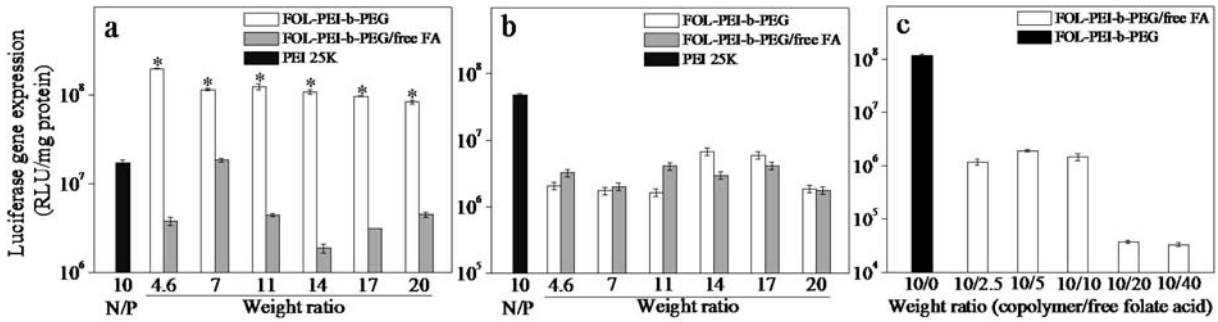

Figure 8. Folic acid competition study. Transfection efficiency of FOL-PEI-b-PEG/DNA complexes, free folic acid with FOL-PEI-b-PEG/DNA complexes, and 25 kDa PEI/DNA complexes in the FR-positive HeLa cells (a) and FR-negative HepG2 cells (b). FOL-PEI-b-PEG/DNA complexes were evaluated at weight ratios ranging from 4.6/1 to 20/1, with fixed FOL-PEI-b-PEG/free FA weight ratio of 32/1, and 25 kDa PEI at the optimal ratio ($N/P = 10$) was taken as control. Transfection efficiency of FOL-PEI-b-PEG/DNA at the fixed weight ratio of FOL-PEI-b-PEG/DNA of 10 with varied weight ratios of FOL-PEI-b-PEG/free FA ranging from 10/0 to 10/40 were evaluated in the FR-positive HeLa cells (c). Data are shown as the mean ± SD ($n = 3$) (*$P < 0.05$ as compared with the data of FOL-PEI-b-PEG/free FA).

copolymer and DNA. Weight ratios of copolymer and DNA that are too high or too low are not favorable to form an effective gene delivery system. These results indicate that gene transfection efficiency could be adjusted by controlling the weight ratio of copolymer/DNA.

The FR-positive HeLa cells and FR-negative HepG2 cells were chosen to further evaluate the targeting effect with free folic acid in the transfection process. First, HeLa cells and HepG2 cells were incubated with the complexes in medium containing varied amounts of free folic acid with a fixed weight ratio of FOL-PEI-b-PEG/free FA. As seen in Figure 8a, luciferase expression was significantly higher ($P < 0.05$) when plasmids were complexed to FOL-PEI-b-PEG to transfection than when the complexes were prepared with FOL-PEI-b-PEG/free FA. The transfection efficiency of HeLa cells was much decreased due to the existence of free FA in culture medium, whereas no significant difference (nonsignificant: $P > 0.05$) was found when HepG2 were transfected in the presence of free folic acid in medium (Figure 8b). Additionally, to further investigate the relationship between the amount of free FA and the transfection efficiency, a series of stock solutions containing free FA at varied weight ratios of FOL-PEI-b-PEG/free FA were added to HeLa cells with a fixed FOL-PEI-b-PEG/DNA weight ratio of 10. As shown in Figure 8c, the transfection efficiency of HeLa cells decreased with increasing amounts of free FA, and when the weight ratio of free FA/FOL-PEI-b-PEG was above 20/10, the transfection efficiency decreased greatly. These findings suggest that free folic acid molecules would prevent the cellular uptake of the complexes by competitive binding to the folate receptors on the cell surface. From another point of view, the conjugation of folic acid indeed improved the transfection efficiency of FOL-PEI-b-PEG for FR-positive cell gene delivery in normal conditions without excess free folic acid.

CONCLUSIONS

In this study, PEG and PEI 25 kDa were combined to prepare PEI-b-PEG; thereafter, FA was further conjugated to prepared FOL-PEI-b-PEG as a cell targeting gene vector. Both PEI-b-PEG and FOL-PEI-b-PEG showed good capability to form complexes with plasmid DNA and exhibited much lower cytotoxicity compared with PEI 25 kDa. PEI-b-PEG/DNA and FOL-PEI-b-PEG/DNA complexes displayed comparable or higher transfection efficiency at certain weight ratios in comparison to that of PEI 25 kDa. Importantly, FOL-PEI-b-PEG/DNA complexes exhibited higher transfection efficiency than that of PEI-b-PEG in FR-positive HeLa cells, whereas no difference in FR-negative HepG2 cells was found. FOL-PEI-b-PEG might be a potential safe and efficient gene vector, particularly for FR-positive cell gene delivery.

ACKNOWLEDGMENT

This work was supported by National Natural Science Foundation of China (Grant No.: 20504024) and National Key Basic Research Program of China (Grant No.: 2005CB623903).

LITERATURE CITED

(1) El-Aneed, A. (2004) An overview of current delivery systems in cancer gene therapy. *J. Controlled Release 94*, 1–14.
(2) Olefsky, J. M. (2000) Diabetes Gene therapy for rats and mice. *Nature 408*, 420–421.
(3) Zhang, X. J., and Godbey, W. T. (2006) Viral vectors for gene delivery in tissue engineering. *Adv. Drug Delivery Rev. 58*, 515–534.
(4) Song, S., Goudy, K., Campbell-Thompson, M., Wasserfall, C., Scott-Jorgensen, M., Wang, J., Tang, Q., Crawford, J. M., Ellis, T. M., Atkinson, M. A., and Flotte, T. R. (2004) Recombinant adeno-associated virusmediated alpha-1 antitrypsin gene therapy prevents type I diabetes in NOD mice. *Gene Ther. 11*, 181–186.
(5) Laporte, L. D., Rea, J. C., and Shea, L. D. (2006) Design of modular non-viral gene therapy vectors. *Biomaterials 27*, 947–954.
(6) Merdan, T., Kopecek, J., and Kissel, T. (2002) Prospects for cationic polymers in gene and oligonucleotide therapy against cancer. *Adv. Drug Delivery Rev. 54*, 715–758.
(7) Lehrman, S. (1999) Virus treatment questioned after gene therapy death. *Nature 401*, 517–518.
(8) Gore, M. E. (2003) Adverse effects of gene therapy, gene therapy can cause leukaemia, no shock, mild horror but a probe. *Gene Ther. 10*, 4.
(9) Sun, J. Y., Anand-Jawa, V., Chatterjee, S., and Wong, K. K. (2003) Immune responses to adeno-associated virus and its recombinant vectors. *Gene Ther. 10*, 964–976.
(10) Liu, Q., and Muruve, D. A. (2003) Molecular basis of the inflammatory response to adenovirus vectors. *Gene Ther. 10*, 935–940.
(11) Kunath, K., von Harpe, A., Fischer, D., Peterson, H., Bickel, U., Voigt, K., and Kissel, T. (2003) Low-molecular-weight polyethylenimine as a non-viral vector for DNA delivery, comparison of physicochemical properties, transfection efficiency and in vivo distribution withhigh-molecular-weight polyethylenimine. *J. Controlled Release 89*, 113–125.
(12) Itaka, K., Yamauchi, K., Harada, A., Nakamura, K., Kawaguchi, H., and Kataoka, K. (2003) Polyion complex micelles from plasmid DNA and poly(ethyleneglycol)-poly(l-lysine) block copolymer as serum-tolerable polyplexsystem, physicochemical properties of micelles relevant to genetransfection efficiency. *Biomaterials 24*, 4495–4506.

(13) Fischer, D., Bieber, T., Li, Y. X., Elsässer, H. P., and Kissel, T. (1999) A novel non-viral vector for DNA delivery based on low molecular weight, branched polyethylenimine: effect of molecular weight on transfection efficiency and cytotoxicity. *Pharm. Res. 16*, 1273–1279.

(14) Tang, M. X., and Szoka, F. C. (1997) The influence of polymer structure on the interactions of cationic polymers with DNA and morphology of the resulting complexes. *Gene Ther. 4*, 823–832.

(15) Clamme, J. P., Azoulay, J., and Mely, Y. 2003) Monitoring of the formation and dissociation of polyethylenimine/DNA complexes by two photon fluorescence correlation spectroscopy*Biophys. J. 84*, 1960–1968.

(16) Kichler, A., Leborgne, C., Coeytaux, E., and Danos, O. (2001) Polyethylenimine-mediated gene delivery: a mechanistic study. *J. Gene. Med. 3*, 135–144.

(17) Petersen, H., Fechner, P. M., Martin, A. L., Kunath, K., Snjezana, S., Roberts, C. J., Martin, A. L., and Kunath, K. (2002) Polyethylenimine-*graft*-poly(ethylene glycol) copolymers: influence of copolymer block structure on DNA complexation and biological activities as gene delivery system. *Bioconjugate Chem. 13*, 845–854.

(18) Harada-Shiba, M., Yamauchi, K., Harada, A., Takamisawa, I., Shimokado, K., and Kataoka, K. (2002) Polyion complex micelles as vectors in gene therapy-pharmacokinetics and *in vivo* gene transfer. *Gene Ther. 9*, 407–414.

(19) Petersen, H., Fechner, P. M., Fischer, D., and Kissel, T. (2002) Synthesis, characterization, and biocompatibility of polyethylenimine-*graft*-poly(ethylene glycol) block copolymers. *Macromolecules 35*, 6867–6874.

(20) Brus, C., Petersen, H., Aigner, A., Czubayko, F., and Kissel, T. (2004) Physicochemical and biological characterization of polyethylenimine-graft-poly(ethylene glycol) block copolymers as a delivery system for oligonucleotides and ribozymes. *Bioconjugate Chem. 15*, 677–684.

(21) Guo, W. J., and Lee, R. J. (1999) Receptor-targeted gene delivery via folate-conjugated polyethylenimine. *AAPS PharmSci. 1*, E19.

(22) Liang, B., He, M. L., Xiao, Z. P., Li, Y., Chan, C., Kung, H. F., Shuai, X. T., and Peng, Y. (2008) Synthesis and characterization of folate-PEG-grafted- hyperbranched-PEI for tumor-targeted gene delivery. *Biochem. Biophys. Res. Commun. 367*, 874–880.

(23) Liu, S. Q., Wiradharma, N., Gao, S. J., Tong, Y. W., and Yang, Y. Y. (2007) Bio-functional micelles self-assembled from a folate-conjugated block copolymer for targeted intracellular delivery of anticancer drugs. *Biomaterials 28*, 1423–1433.

(24) Gabizon, A., Horowitz, A. T., Goren, D., Tzemach, D., Mandelbaum-Shavit, F., Qazen, M. M., and Zalipsky, S. (1999) Targeting folate receptor with folate linked to extremities of poly(ethylene glycol)-grafted liposomes: in vitro studies. *Bioconjugate Chem. 10*, 289–298.

(25) Bozkir, A., and Saka, O. M. (2004) Chitosan-DNA nanoparticles: effect on DNA integrity, bacterial transformation and transfection efficiency. *J. Drug Target 12*, 281–288.

(26) Avgoustakis, K. (2004) Pegylated poly(lactide) and poly(lactide-co-glycolide) nanoparticles: preparation, properties and possible applications in drug delivery. *Curr. Drug Delivery 1*, 321–333.

(27) Mansouri, S., Cuie, Y., Winnik, F., Shi, Q., Lavigne, P., Benderdour, M., Beaumont, E., and Fernandes, J. C. (2006) Characterization of folate-chitosan-DNA nanoparticles for gene therapy. *Biomaterials 27*, 2060–2065.

(28) Clements, B. A., Bai, J., Kucharski, C., Farrell, L. L., Lavasanifar, A., Ritchie, B., Ghahary, A., and Uludag, H. (2006) RGD conjugation to polyethyleneimine does not improve DNA delivery to bone marrow stromal cells. *Biomacromolecules 7*, 1481–1488.

(29) Conwell, C. C., and Huang, L. (2005) Recent advances in non-viral gene delivery. *Adv. Genet. 53*, 1–18.

(30) Deery, E. C., Vithana, E. N., Newbold, R. J., Gallon, V. A., Bhattacharya, S. S., Warren, M. J., Hunt, D. M., and Wilkie, S. E. (2002) Disease mechanism for retinitis pigmentosa (RP11) caused by mutations in the splicing factor gene PRPF31. *Hum. Mol. Genet. 11*, 3209–3219.

BC8004057

Bioconjugate Chemistry 20th Anniversary

Subscriber access provided by SHEMYAKIN-OVCHINNIKOV INST

Article

Acid-Responsive Linear Polyethylenimine for Efficient, Specific, and Biocompatible siRNA Delivery

Min Suk Shim, and Young Jik Kwon

Bioconjugate Chem., **2009**, 20 (3), 488-499• DOI: 10.1021/bc800436v • Publication Date (Web): 06 February 2009

Downloaded from http://pubs.acs.org on May 8, 2009

More About This Article

Additional resources and features associated with this article are available within the HTML version:

- Supporting Information
- Access to high resolution figures
- Links to articles and content related to this article
- Copyright permission to reproduce figures and/or text from this article

View the Full Text HTML

ACS Publications
High quality. High impact.

Bioconjugate Chemistry is published by the American Chemical Society. 1155 Sixteenth Street N.W., Washington, DC 20036

Acid-Responsive Linear Polyethylenimine for Efficient, Specific, and Biocompatible siRNA Delivery

Min Suk Shim[†,‡] and Young Jik Kwon*[,‡,§,||]

Department of Macromolecular Science and Engineering, Case Western Reserve University, 10900 Euclid Avenue, Cleveland, Ohio 44106, and Department of Chemical Engineering and Materials Science, Department of Pharmaceutical Sciences, and Department of Biomedical Engineering, University of California, Irvine, California 92697. Received October 13, 2008; Revised Manuscript Received December 23, 2008

Efficient intracellular processes including cytosolic release and unpackaging of siRNA from the carrier in the cytoplasm are efficiency-determining steps in achieving successful gene silencing. In this study, acid-degradable ketalized linear polyethylenimine (KL-PEI) was synthesized for efficient, intracellular target-specific, and biocompatible siRNA delivery. The siRNA/KL-PEI polyplexes resulted in much higher RNA interference efficiency than unmodified L-PEI via selective cytoplasmic localization of the polyplexes and efficient disassembly of siRNA from the polyplexes, which were promoted upon acid-hydrolysis of amino ketal linkages. Confocal laser scanning microscopy demonstrated that siRNA was efficiently disassembled from the siRNA/KL-PEI polyplexes that were selectively localized in the cytoplasm. On the contrary, siRNA and unmodified linear PEI were colocalized in both the cytoplasm and the nucleus, and limited unpackaging of siRNA from the polyplexes was observed. In addition, ketalization further reduced the cytotoxicity of linear PEI but did not alter its serum-independent gene delivery efficiency. Therefore, KL-PEI is a promising nonviral vector for efficient and biocompatible siRNA delivery.

INTRODUCTION

Silencing gene expression in a sequence-specific manner by double stranded small interfering RNA (siRNA) has attracted great attention as a potential therapeutic approach for treating diseases arising from genetic defects (*1*−*3*). However, the use of siRNA is restricted by its inherent low stability against degradation and poor cellular uptake into cells in vitro or in vivo (*4, 5*). Therefore, the development of effective carrier systems, which can protect and deliver siRNA to the cytoplasm, where siRNA encounters target mRNA, is a major key to exploit the successful therapeutic and research use of siRNA in mammalian cells (*6, 7*). Among the gene carriers that have been investigated, nonviral vectors have recently attracted more and more attention in comparison to viral vectors, due to their advantages, including the ease of synthesis, delivery of large quantities of genes, and low immune response (*8*). Recently, cationic polymer-based nonviral systems for siRNA delivery have been popularly developed since the cationic polymers form stable polyplexes via electrostatic interaction and protect siRNA from enzymatic digestion (*9*−*13*). Common challenges in using the cationic polymer for siRNA delivery often involve high toxicity and limited siRNA delivery efficiency (*14*).

One of the major bottleneck steps in nonviral gene transfer is the escape of nucleic acid-containing carriers from the endosomal compartment, where acidic pH and nucleases efficiently digest nucleic acids, and the release of nucleic acids in their desired intracellular targets (e.g., cytoplasm for siRNA) (*15*−*18*). Therefore, the facilitated release of siRNA-containing polyplexes from the digestive endosome and efficient polyplex unpackaging in the cytoplasm are indispensible design goals of developing efficient carriers for gene silencing. In recent years, polyethylenimine (PEI)-based carriers have been highlighted as efficient nonviral nucleic acid delivery carriers (*4, 15, 19*−*22*). Among a variety of selections in terms of molecular weights (0.8−800 kDa) and topological isomers (branched or linear structures), linear high molecular weight PEI (L-HMW PEI) (e.g, 22 kDa) and branched high molecular weight PEI (B-HMW PEI) (e.g., 25 kDa) have demonstrated sufficient efficiency. Although both polymers have shown high gene delivery efficiency in vitro (*15, 23*), L-HMW PEI has shown much higher in vivo gene expression with less cytotoxicity in comparison to branched PEI (B-PEI) (*22*−*26*). However, linear PEI shows limited efficiency in siRNA delivery, although the reason for such a discrepancy between DNA and siRNA delivery efficiencies is unclear (*20, 27*). For this reason, finding a strategy to improve siRNA delivery efficiency using linear PEI is of great interest.

In this study, 25 kDa linear PEI was modified to accomplish enhanced siRNA delivery with low cytotoxicity. It was hypothesized that the incorporation of acid-degradable amino ketal branches to secondary amines of linear PEI would facilitate endosomal escape, by broadened buffering capacity of primary, secondary, and tertiary amines, and the subsequent release of siRNA to the cytoplasm, thus resulting in efficient RNA interference. Under the acidic conditions in the endosome, hydrolyzed ketal side branches were expected to induce endosomal destabilization by increased osmotic forces and swollen polyplexes. It was shown that ketalized linear PEI resulted in high RNA interference (RNAi) efficiency, even in the presence of serum, through exclusive cytoplasmic localization of the siRNA-containing polyplexes and efficient unpackaging of

* Corresponding author. 916 Engineering Tower, Irvine, CA 92697-2575. Tel: +949 824 8714. Fax: +949 824 2545. E-mail: kwonyj@uci.edu.

† Case Western Reserve University.

‡ Department of Chemical Engineering and Materials Science, University of California, Irvine.

§ Department of Pharmaceutical Sciences, University of California, Irvine.

|| Department of Biomedical Engineering, University of California, Irvine.

10.1021/bc800436v CCC: $40.75 © 2009 American Chemical Society
Published on Web 02/06/2009

siRNA from the hydrolyzed polyplexes. This study implies that ketalized linear PEI is a promising siRNA delivery carrier offering substantially improved RNAi efficiency and biocompatibility.

MATERIALS AND METHODS

Materials. Linear polyethylenimine (25 kDa, 2.5 kDa) was purchased from Polyscience, Inc. (Warrington, PA). Branched polyethylenimine (25 kDa) and 3-(4,5-dimethyl-2-thiazolyl)-2,5-diphenyltetrazoliumbromide (MTT) were purchased from Sigma Aldrich (Milwaukee, WI). 2-Aminoethanol, pyridinium *p*-toluenesulfonate, ethyl trifluoroacetate, 2-methoxypropene, molecular sieves, and 1,4-diaminobutane dihydrochloride were supplied from Acros (Morris Plains, NJ). Acryloyl chloride was supplied from Alfa Aesar (Ward Hill, MA). Ethidium bromide was purchased from Fisher Scientific (Pittsburgh, PA). Enhanced green fluorescent protein (eGFP)-encoding plasmid DNA was a generous gift from Dr. Pamela Davis (Department of Physiology and Biophysics, Case Western Reserve University, Cleveland, OH). Alexa Fluor 488 carboxylic acid succinimidyl ester dye was purchased from Molecular Probes (Eugene, OR), and DRAQ5 nuclear dye was purchased from BioStatus (Leicestershire, UK). Silencer GFP siRNA and Silencer Cy3-labeled negative control siRNA were purchased from Ambion (Austin, TX). NIH 3T3 cells (ATCC, Rockville, MD) were cultured in Dulbecco's modified Eagle's medium (DMEM) (MediaTech, Herndon, VA) with 10% fetal bovine serum (FBS) (Hyclone, Logan, UT), unless otherwise noted.

Polymer Characterization. Electrospray mass spectra of various monomers were obtained on a Micromass LCT mass spectrometer (Micromass Ltd., Manchester, UK). ^{1}H NMR spectrum of various ketalized linear PEI was obtained by a Bruker Avance 500 MHz NMR spectrometer (Bruker Biospin Corporation, Billerica, MA). Chemical shifts for ^{1}H NMR spectra were reported relative to (2,2-dimethyl-2-silapentane-5-sulfonate sodium salt) (DSS, $\delta = 0.015$ ppm) when D_2O was used as solvent. The molecular weights and molecular weight distributions of various ketalized linear PEI were determined by a gel permeation chromatography (GPC) system equipped with Agilent 1100 series (Agilent Technologies, Santa Clara, CA). The eluent was water, and a flow rate of 1.0 mL/min was used. The sample was diluted to 0.5 mg/mL in DI water and filtered through 0.45 μm PVDF syringe filters, and 100 μL of sample was injected into the GPC system for analysis. The molecular weights were calibrated against poly(ethylene oxide) standards.

Synthesis of Ketalized Linear Polyethylenimine (KL-PEI). Acid-degradable ketalized linear polyethylenimine in which acid-degradable ketal linkages were grafted was synthesized via Michael addition conjugation of acrylated ketal monomers (Scheme 1).

Synthesis of Compound 2 [*N*-(2-(2-(2-Aminoethoxy)propan-2-yloxy)ethyl)-2,2,2-trifluoroacetamide]. [1,1′-(2,2′-(Propane-2,2-diylbis(oxy))bis(ethane-2,1-diyl))diurea] (compound **1**) was prepared as previously reported (*28*). Compound **1** (2.2 g, 13.58 mmol, 1 equiv) was dissolved in 10 mL of methanol with 2.06 g of triethylamine (20.37 mmol, 1.5 equiv). Ethyl trifluoroacetate (1.93 g, 13.58 mmol, 1 equiv) was dissolved in 10 mL of methanol, and the resulting mixture was slowly added dropwise to the solution of compound **1** on ice. The reaction mixture was stirred for 6 h on ice, and then the mixture was extracted with 3 × 30 mL of dichloromethane. The organic layers were combined and evaporated. The product was purified by silica gel chromatography using a gradient from hexane to 60/40 hexane/tetrahydrofuran to obtain the product as a white solid (1.57 g, 6.11 mmol, 45% yield). ESI-MS $[M + H]^+$ calcd 259.1; found, 259.2. ^{1}H NMR (500 MHz, $CDCl_3$): δ 1.37 (s, 6H, $CF_3CONHCH_2CH_2OC(C\underline{H_3})_2OCH_2CH_2NH_2$); δ 1.51 (br, 2H, $CF_3CONHCH_2CH_2OC(CH_3)_2OCH_2CH_2N\underline{H_2}$); δ 2.88 (t, 2H, $CF_3CONHCH_2CH_2OC(CH_3)_2OCH_2C\underline{H_2}NH_2$); δ 3.52 − 3.56 (m, 4H, $CF_3CONHC\underline{H_2}C\underline{H_2}OC(CH_3)_2OCH_2CH_2NH_2$); δ 3.70 (t, 2H, $CF_3CONHCH_2CH_2OC(CH_3)_2OC\underline{H_2}CH_2NH_2$); δ 9.50 (br, 1H, $CF_3CON\underline{H}CH_2CH_2OC(CH_3)_2OCH_2CH_2NH_2$).

Scheme 1. Synthesis of Ketalized Linear PEI

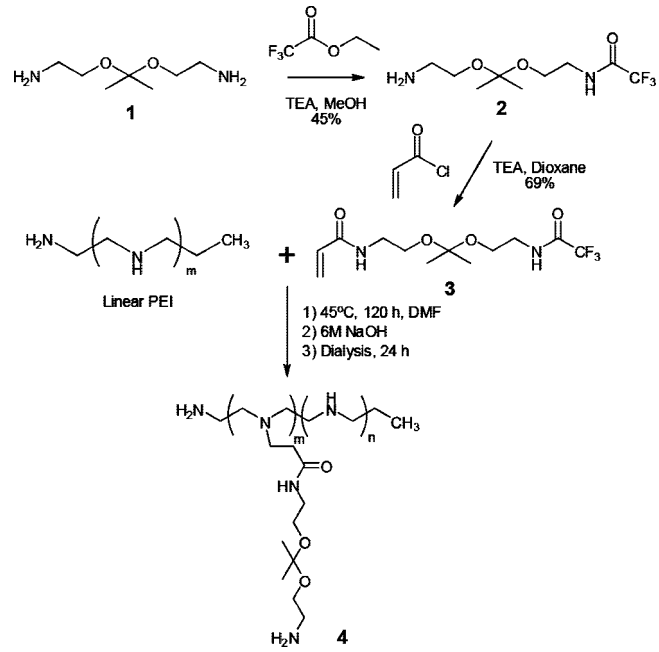

Synthesis of Compound 3 [*N*-(2-(2-(2-(2,2,2-Trifluoroacetamido)ethoxy)propan-2-yloxy)ethyl)acrylamide. Compound **2** (1.40 g, 5.42 mmol, 1 equiv) was dissolved in 10 mL of dioxane with 2.19 g of triethylamine (21.68 mmol, 4 equiv), and the mixture solution was kept in an ice bath. Acryloyl chloride solution (0.98 g, 10.84 mmol, 2 equiv) was prepared in 10 mL of dioxane and slowly added to the solution of compound **2**. The reaction mixture was stirred for 10 min, and the product was extracted using 3 × 100 mL of ethyl acetate and then purified by silica gel chromatography using a gradient from hexane to 1/1 hexane/ethyl acetate to obtain the product as a yellow oil (1.17 g, 3.75 mmol, 69% yield). ESI-MS $[M + H]^+$ calcd 313.1; found, 313.2. ^{1}H NMR (500 MHz, $CDCl_3$): δ 1.36 (s, 6H, $CF_3CONHCH_2CH_2OC(C\underline{H_3})_2OCH_2CH_2NHCOCHCH_2$); δ 3.48 − 3.53 (m, 8H, $CF_3CONHC\underline{H_2}C\underline{H_2}OC(CH_3)_2OC\underline{H_2}C\underline{H_2}NHCOCHCH_2$); δ 5.67 (dd, 1H, $CF_3CONHCH_2CH_2OC(CH_3)_2OCH_2CH_2NHCOCHCH'\underline{H''}$); δ 6.01 (br, 1H, $CF_3CON\underline{H}CH_2CH_2OC(CH_3)_2OCH_2CH_2NHCOCHCH_2$); δ 6.14 (dd, 1H, $CF_3CONHCH_2CH_2OC(CH_3)_2OCH_2CH_2NHCOC\underline{H}CH_2$); δ 6.33 (dd, 1H, $CF_3CONHCH_2CH_2OC(CH_3)_2OCH_2CH_2NHCOCHC\underline{H'}H''$); δ 7.05 (br, 1H, $CF_3CONHCH_2CH_2OC(CH_3)_2OCH_2CH_2N\underline{H}COCHCH_2$).

Synthesis of Compound 4. Linear low molecular weight PEI (L-LMW PEI, 2.5 kDa) and linear high molecular weight PEI (L-HMW PEI, 25 kDa) (0.1 g, 2.33 mmol of secondary amine groups, 1 equiv) were dissolved in 2 mL of methanol followed by evaporating the methanol under high vacuum for 30 min. The resulting solution was dissolved in 10 mL of dimethylformamide (DMF) with 0.73 g of compound **3** (2.33 mmol, 1 equiv), and 0.23 g of triethylamine (2.33 mmol, 1 equiv), which served as a deprotonating agent as well as a preventer of hydrolysis of ketals, was added. The resulting mixture was stirred for 120 h at 45 °C, and the polymer was precipitated into anhydrous diethyl ether and dried under vacuum. The precipitated polymer was dissolved in 10 mL of 1:9 MeOH/6 M NaOH solution and stirred for 12 h to deprotect trifluoro-

acetate groups. After deprotection, the polymer was dissolved in DI water and purified by dialysis against DI water at 4 °C (Mw cutoff of dialysis membrane = 500 for L-LMW PEI and Mw Cutoff = 6000 for L-HMW PEI). After 24 h of dialysis, each polymer was lyophilized overnight to obtain the product as a powder with a hint of yellow color [60 mg of ketalized linear low molecular weight PEI (KL-LMW PEI) (26% yield) and 72 mg of ketalized linear high molecular weight PEI (KL-HMW PEI) (36% yield)]. ^{1}H NMR (500 MHz, D_2O): δ 1.41 (s, -$NCH_2CH_2CONHCH_2CH_2OC(C\underline{H}_3)_2OCH_2CH_2NH_2$); δ 2.7 − 3.0 (m, -C$\underline{H}_2$-C$\underline{H}_2$-NH-, -NC$\underline{H}_2C\underline{H}_2$$CONHCH_2CH_2OC(CH_3)_2$-$OCH_2CH_2NH_2$, and - $NCH_2CH_2CONHCH_2CH_2OC(CH_3)_2OCH_2$-C$\underline{H}_2NH_2$); δ 3.3 − 3.7 (m, -$NCH_2CH_2CONHC\underline{H}_2CH_2OC(CH_3)_2$-$OCH_2CH_2NH_2$, -$NCH_2CH_2CONHCH_2C\underline{H}_2OC(CH_3)_2OCH_2CH_2$-$NH_2$, and - $NCH_2CH_2CONHCH_2CH_2OC(CH_3)_2OC\underline{H}_2CH_2NH_2$).

Hydrolysis Kinetics of KL-PEI. The hydrolysis rates of KL-PEI at different molecular weights and pH values were investigated by incubating KL-PEI in (10 mg) pH 5.0 acetate, 6.0 acetate, and pH 7.4 Tris-HCl buffers in D_2O at 37 °C (0.6 mL) for various periods of time. Disappearance of the ketal linkage peak (1.41 ppm) was quantified by using ^{1}H NMR spectroscopy in comparison with the constant buffer salt peak. Half-lives of the various PEI at different pH values were obtained by using the Arrhenius equation.

Preparation and Characterization of siRNA/PEI Polyplexes. Two micrograms of siRNA with various amounts of polymers were mixed in 100 μL of DI water at various N/P ratios, followed by incubation for 30 min at room temperature. Then the resulting polyplex solution was diluted with additional 800 μL of DI water. Mean particle diameter (Z-average) and zeta potential of various siRNA/PEI polyplexes were measured at 25 °C by using ZEN3600 Zetasizer (Malvern Instruments, Worcestershire, UK)y. The viscosity (0.887 mPa/s) and the refractive index (1.333) of water at 25 °C were used to analyze the data. The mean values of each sample were yielded from the data obtained from at least 10 measurements. Each sample was analyzed in triplicate.

Ethidium Bromide Exclusion Assay. The ability of KL-PEI to condense siRNA was evaluated by a standard ethidium bromide exclusion assay. After one microgram of ethidium bromide and 1 μg of siRNA in 40 μL of DI water were incubated for 15 min at room temperature, desired amounts of the polymer solution in 60 μL of DI water were added in order to achieve various N/P ratios. After 30 min of incubation, fluorescence intensity was measured using a fluorescence microplate reader (Molecular Devices, Sunnyvale, CA) with an excitation wavelength (λ_{ex}) of 320 nm and an emission wavelength (λ_{em}) of 600 nm. Normalized fluorescence was determined as $(F - F_0)/(F_{siRNA} - F_0)$, where F, F_0, and F_{siRNA} represent the fluorescence of the solution containing ethidium bromide and the polyplexes, the solution of ethidium bromide without siRNA and polymers, and siRNA/ethidium bromide solution, respectively. Reduced fluorescence intensity was used as a quantitative indicator of siRNA condensation in polyplexes.

Agarose Gel Electrophoresis Assay. The binding of siRNA with PEI was determined by 1.2% agarose gel electrophoresis. Desired amounts of ketalized and unketalized L-PEI dissolved in phosphate buffered saline (PBS) were mixed with 1 μg of siRNA in DI water (17 μL in total) to yield various N/P ratios, followed by incubation for 15 min. Three μL of a gel loading dye was added to each polyplex solution, and 20 μL of the resulting polyplex solution was loaded on a gel containing 1 μg/mL of ethidium bromide. To verify the dissociation of the siRNA from the polymers upon hydrolysis, 2 μg of siRNA and desired amounts of polymer were mixed in 8 μL of DI water to obtain various N/P ratios. Then the mixture was incubated for 20 min at R.T. followed by the addition of 26 μL of pH 5.0 acetate buffer. The polyplexes were further incubated for 4 h at 37 °C. A 17 μL aliquot of the sample containing 1 μg of siRNA was mixed with 3 μL of gel loading dye, and 20 μL of the mixture solution was loaded on the agarose gel. The samples were electrophoresed in Tris-acetate-EDTA (TAE) buffer at 60 V for 15 min. The siRNA bands were then visualized under a UV transilluminator at a wavelength of 365 nm.

Transmission Electron Microscopy. Size and morphological changes of various polyplexes upon hydrolysis were analyzed by transmission electron microscopy (TEM). Briefly, siRNA/KL-PEI polyplexes were prepared by mixing 1 μg of siRNA with various PEI in 20 μL of DI water to obtain the N/P ratio of 100. A 2 μL aliquot of the sample solution was dropped on a carbon-coated copper TEM grid (Electron Microscopy Sciences, Hatfield, PA) and air-dried for 10 min at R.T. Grids were then stained with uranyl acetate and dried. To prepare hydrolyzed particles, 20 μL of siRNA/KL-PEI polyplex solution was mixed with 40 μL of pH 5.0 acetate buffer and further incubated for 4 h at 37 °C. Then a 6 μL aliquot of the resulting polyplex solution was deposited on a grid and dried. TEM images were acquired using Philips CM20 (Philips Electronic Instruments, Mahwah, NJ) operated at 200 kV.

Fluorescence Labeling of Polyplexes and Quantification. Desired amounts of various polymers were mixed with 4 μg of siRNA in DI water (400 μL total) to obtain various N/P ratios. The polyplexes were incubated for 30 min at room temperature and then fluorescently labeled with Alexa Fluor 488 dye (Molecular Probes, Inc., Eugene, OR) by following the manufacturer's instructions. Labeled siRNA/L-PEI polyplexes were purified from unreacted dyes by a PD-10 size exclusion column (GE Healthcare, Piscataway, NJ) using DMEM as eluent. To quantify Alexa Fluor 488 conjugation to siRNA/KL-PEI polyplexes, the fluorescence intensity of the Alexa Fluor 488-conjugated polyplexes was compared with the one of Alexa Fluor 488 added for conjugation. Briefly, siRNA/KL-PEI polyplexes were prepared by mixing 71.3 μg of KL-LMW PEI with 4 μg of siRNA in DI water (500 μL total) to achieve the N/P ratio of 100. After 30 min of incubation, KL-LMW PEI (0.11 mmol of primary amines linked to ketal branches, 1 equiv) complexing siRNA reacted with Alexa Fluor 488 carboxylic acid succinimidyl ester dye (1 equiv), and the resulting mixture was incubated for 2 h at R.T. Then unreacted Alexa Fluor 488 dyes were removed using a PD-10 size exclusion column. Fluorescence of the Alexa Fluor 488 labeled-polyplexes was measured using a microplate reader with an excitation wavelength (λ_{ex}) of 488 nm and an emission wavelength (λ_{em}) of 520 nm. In addition, a fluorescence standard curve was constructed using various concentrations of Alexa Fluor 488 dye stock solution in the range of 0.01 mM to 10 mM. In order to quantitatively estimate the amount of free Alexa Fluor 488 released from the ketalized linear PEI upon hydrolysis, Alexa Fluor 488-labeled polyplexes were incubated in pH 5.0 acetate buffer for 4 h at 37 °C. Released free Alexa Fluor 488 dye was removed by eluting the polyplexes through a PD-10 size exclusion column, and the reduced fluorescence intensity of the eluted solution was compared with the one of the unhydrolyzed ploxyplexes-containing solution.

Confocal Laser Scanning Microscopy. Confocal laser scanning microscopy was performed to observe the intracellular localization of various siRNA/PEI polyplexes. NIH 3T3 cells were inoculated at a density of 2.0×10^4 cells/well in a Falcon 8-well cultureslide (BD Biosciences, Franklin Lakes, NJ), 15 h prior to the incubation with the polyplexes. Five hundred twenty microliters of polyplex solution containing 0.6 μg of siRNA in DMEM, prepared as described above, was added to each well. After 6 h of incubation, the cells were washed with PBS four times and fixed with 2% *p*-formaldehyde solution for 30 min

at 4 °C. Then, the nuclei of the cells were counter-stained by treating 1 μM nuclear dye DRAQ5 solution in PBS (BioStatus, Leicestershire) for 20 min, and the cells were washed with PBS. Fluorescence images were acquired using an Olympus IX2 inverted microscope equipped with a Fluoview 1000 confocal scanning microscopy setup (FV10-ASW, Olympus America, Melville, NY) and a 40X/1.3 NA oil immersion planapochromat objective lens. Alexa Fluor 488 was excited with a 488 nm multiple argon laser light, and emission was collected using a SDM 560 dichroic mirror and a 505−605 nm band-pass filter. Images of DRAQ5-stained nuclei were acquired using a 635 nm helium−neon laser excitation light, a 635 nm dichroic mirror, and a 655−755nm band-pass barrier filter. Digital image recording and analysis were carried out using FV10-ASW 1.6 viewer (Olympus America). The cells were scanned in three dimensions as a z-stack of two-dimensional images (1024 × 1024 pixels). An image cutting horizontally through approximately the middle of the cellular height was selected out of a z-stack of images to differentiate the fluorescence from the polyplexes located in the perinuclear and intranuclear areas. To observe siRNA and polymer in NIH 3T3 cells, polyplexes were prepared with Cy3-labeled siRNA, as described earlier. Then linear PEI complexing Cy3-labeled siRNA were labeled with Alexa Fluor 488 dye. Unreacted dyes were removed using PD-10 size exclusion columns. Desired amounts of polyplex solutions containing 0.6 μg of siRNA in DMEM were added to each well containing NIH 3T3 cells inoculated at a density of 2.0×10^4 cells. After 4 h of incubation, the cells were washed several times with PBS and fixed with 2% *p*-formaldehyde solution for 30 min at 4 °C. Then, the fixed cells were counter-stained by DRAQ5 and washed with PBS. Fluorescence images of Alexa Fluor 488 were acquired using a 488 nm excitation light from a multiple argon laser, a SDM560 dichroic mirror, and a 505−540 nm band-pass barrier filter. A 559 nm helium−neon laser, a SMD640 dichroic mirror, and a 575−620 nm band-pass barrier filter were used to obtain the images of Cy3-labeled siRNA. Images of DRAQ5-stained nuclei were acquired using a 635 nm helium−neon laser, a 635 nm dichroic mirror, and a 655−755 nm band-pass barrier filter. Each excitation light was scanned separately for the individual excitation of the dyes to eliminate cross-talk.

RNA Interference. eGFP-expressing NIH 3T3 cells were obtained by retroviral transduction and subsequent G418 selection (*29*). Cells were seeded in a 24-well plate at a density of 2×10^4 cells/well. siRNA-containing polyplexes were prepared by mixing various amounts of polymer stock solutions in PBS with anti-eGFP siRNA or nonspecific control siRNA solutions (75 pmol) in DI water to obtain various N/P ratios in the final volume of 75 μL, followed by 30 min of incubation at R.T. After 24 h, the culture medium in each well was replaced with 300 μL of FBS-free DMEM or 10% FBS-containing DMEM. Then 75 μL of polyplex solutions was added to the cells to obtain a final siRNA concentration of 200 nM. After 4 h of incubation, the medium in the well was replaced with 0.5 mL of fresh DMEM containing 10% FBS, and the cells were further cultured for 72 h. After the cells were harvested by trypsinization and washed with PBS, their eGFP fluorescence was analyzed by using a Guava EasyCyte Plus flow cytometer (Guava Technologies, Hayward, CA). The silencing of eGFP gene expression was quantified by mean fluorescence intensities of the cells incubated with various siRNA-containing polyplexes in comparison with the cells incubated without polyplexes.

Cytotoxicity Assay. eGFP-expressing NIH 3T3 were inoculated at a density of 4×10^3 cells/well in a 96-well plate and incubated for 24 h. The culture medium was replaced with the mixtures of 60 μL of FBS-free DMEM and 15 μL of anti-eGFP siRNA or nonspecific control siRNA (15 pmol) polyplex solutions in a final siRNA concentration of 200 nM in a well. After 4 h of incubation, the medium was replaced with 100 μL of fresh DMEM supplemented 10% FBS. After the cells were further incubated for 24 h at 37 °C, the medium was replaced with the mixture of 10 μL of 3-(4,5-dimethyl-2-thiazolyl)-2,5-diphenyltetrazolium bromide (MTT) in PBS (10 mg/mL) and 90 μL of growth medium. After 3 h of incubation, the MTT solution was discarded from each well, and the mixtures of 200 μL of DMSO and 20 μL of glycine buffer (0.1 M glycine, 0.1 M NaCl) were added to dissolve the blue formazan crystals formed by live cells. The relative viability of the cells treated with various polyplexes was determined by UV absorbance of formazan products at 561 nm.

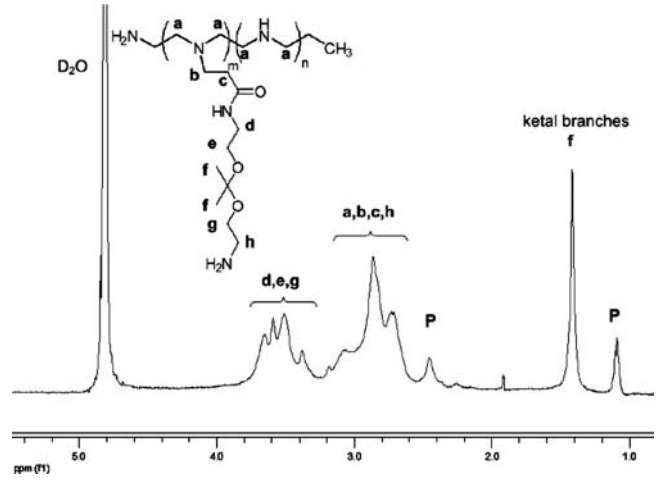

Figure 1. ^{1}H NMR spectrum of ketalized linear low molecular weight PEI (KL-LMW PEI). The peaks appearing at 1.1 ppm and at 2.4 ppm (denoted by P) indicate the -CH_3 and -CH_2- protons of the residual propionyl moiety in commercial linear PEI, respectively.

Statistics. Triplicate data were analyzed using one-way analysis of variance (ANOVA) on the significance level of $p < 0.01$ and presented as mean ± standard deviation.

RESULTS AND DISCUSSION

Design and Synthesis of Ketalized Linear PEI. As intracellular targets for DNA transfection and RNA interference are different (*30, 31*), the design of nonviral carrier for siRNA delivery should be distinguished from the one for DNA delivery in order to obtain desired therapeutic effects. It is hypothesized that efficient cytoplasmic release of free siRNA is required to maximize the therapeutic efficacy and avoid undesirable effects. Therefore, in this study, acid-degradable ketalized linear PEI (KL-PEI) was specifically designed and synthesized to achieve efficient cytoplasmic localization of polyplexes and unpackaging of the polyplexes through hydrolysis of ketal branches grafted to the polymer backbone. Acrylamide groups at the end of amino ketal monomers were conjugated to secondary amines of linear PEI via a Michael addition reaction. A sharp singlet peak at 1.41 ppm (i.e., methyl protons of ketal linkage) in the ^{1}H NMR spectrum of ketalized linear low molecular weight (KL-LMW) PEI indicates successful conjugation of acid-degradable branches (Figure 1). It was found that ketal hydrolyzed at pH 7.4 at 4 °C with a half-life of approximately 200 h. The hydrolysis test using ^{1}H NMR showed that approximately 8.0% of ketal linkages hydrolyzed during the dialysis for the purification of ketalized linear PEI. To quantify the degree of hydrolysis during the dialysis, integral ratios of methyl protons (1.41 pm) of ketal linkage peak to methyl protons (1.1 ppm) of the residual propionyl moiety of linear PEI in ^{1}H NMR spectra were measured before and after dialysis, respectively. Ketalization ratios relative to available secondary amines were calculated

Table 1. Characterization and Hydrolysis Kinetics of Various Ketalized Linear PEI

polymer	degree of ketalization (mol %)	Mn (kDa)	Mw (kDa)	PDI	half-lives (h) pH 5.0	pH 6.0	pH 7.4
L-HMW PEI	0	23.8	45.5	1.91	N/A	N/A	N/A
L-LMW PEI	0	2.2	3.4	1.55	N/A	N/A	N/A
KL-HMW PEI	24	47.2	85.8	1.82	2.3	6.0	21.6
KL-LMW PEI	22	5.0	8.2	1.65	1.9	4.7	20.3

to be approximately 22% for ketalized linear low molecular weight PEI (KL-LMW PEI) and 24% for ketalized linear high molecular weight PEI (KL-HMW PEI), by integral ratios of the peak at 1.41 ppm to the peak at 2.7−3.0 ppm. The polydispersity of the ketalized PEI was not increased during the synthesis (Table 1). It was also found that the buffering capacity of linear PEI was not significantly changed by ketalization (Supporting Information, Figure S1).

Acid-Degradability of KL-PEI. Hydrolysis rates of KL-PEI at endosomal and physiological pH values were investigated by incubating the polymer in acetate and Tris-HCl buffers in D_2O at 37 °C for various periods of time. The disappearance of the ketal linkage peak at 1.41 ppm relative to the constant buffer salt peak at different incubation time points was quantified by ^1H NMR spectroscopy. As shown in Table 1, the half-lives of KL-LMW PEI at pH 5.0, 6.0, and 7.4 were calculated to be 1.9, 4.7, and 20.3 h, respectively, while the half-lives of KL-HMW PEI at each different pH were 2.3, 6.0, and 21.6 h, respectively (Table 1). The results show that the KL-PEI hydrolyzed about 10 times faster at an endosomal pH of 5.0 than at a physiological pH of 7.4, regardless of molecular weights. It is desirable for nucleic acids to be released from the carrier by an intracellular stimulus (e.g., low pH) (*32*), and KL-PEI was found to be capable of intracellular release of siRNA via effective hydrolysis in the acidic endosome, which facilitates endosomal membrane destabilization and unpackaging of siRNA/KL-PEI polyplexes.

Acid hydrolysis of ketal linkages in a test tube depends on the concentration of amines, which can scavenge protons and change pH, but roles of the polymer concentration dependency of ketal hydrolysis in a cell have not been confirmed. In this study, ketal hydrolysis was tested at the concentration of 16.7 mg/mL in a test tube, which was substantially higher than the highest polymer concentration of incubation (i.e., 66 μg/mL at the N/P ratio of 140), although it is very difficult to assess what exactly would be the concentration of the polymer (or amines) in the endosome/lysosome. In addition, the proton concentration in the endosome/lysosome changes by active influx via proton pumps.

Complexation of siRNA with KL-PEI. Condensation of nucleic acids by a gene carrier plays a key role in determining extracellular stability, endocytosis of polyplexes, and eventual gene expression (*33, 34*). The effects of ketalization on siRNA condensation in various PEI polyplexes were confirmed by size reduction. As shown in Figure 2A, the size of siRNA/B-PEI (25 kDa) polyplexes at the N/P ratio of 5 and above was relatively constant in the range of 110 to 160 nm. Unmodified L-LMW and L-HMW PEI formed siRNA-containing polyplexes in similar sizes of 130 to 220 nm in diameter at the N/P ratio of 10 to 120. It was shown that KL-PEI effectively condensed siRNA into nanosized particles at high N/P ratios, allowing them to enter the cell through nonreceptor-mediated endocytosis. The size of siRNA/KL-LMW PEI polyplexes was in the range of 120 to 190 nm at the N/P ratio of 10 to 120, which was close to the size of siRNA/L-LMW PEI and siRNA/L-HMW PEI polyplexes. However, KL-HMW PEI formed polyplexes with diameters of 170 to 400 nm at the observed N/P ratios, indicating lower complexation efficiency of siRNA by KL-HMW PEI than by the other types of PEI.

Ethidium bromide exclusion analysis was also conducted to quantitatively evaluate the abilities of polymers to condense siRNA in the polyplexes. As shown in Figure 2B, siRNA/B-PEI, siRNA/L-LMW PEI, and siRNA/L-HMW PEI showed

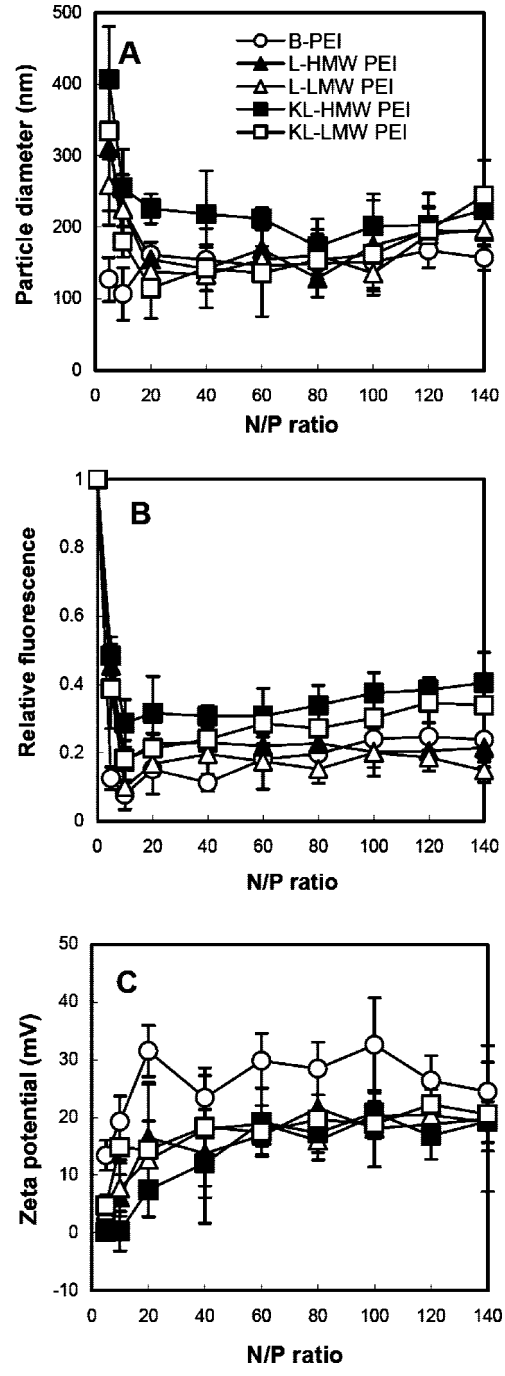

Figure 2. (A) Particle size of various siRNA/PEI polyplexes at various N/P ratios, determined by DLS analysis. (B) siRNA condensation efficiency of various siRNA/KL-PEI polyplexes at various N/P ratios, measured by ethidium bromide exclusion assay. (C) Surface charge density of various siRNA/PEI polyplexes at various N/P ratios.

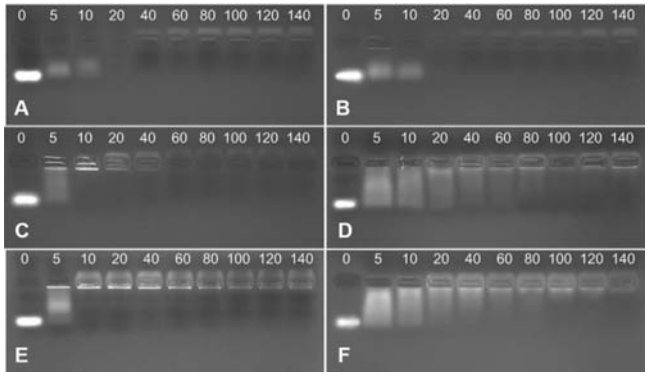

Figure 3. Agarose gel electrophoresis of various siRNA/linear PEI polyplexes at different N/P ratios. (A) siRNA/L-LMW PEI polyplexes, (B) siRNA/L-HMW PEI polyplexes, (C) siRNA/KL-LMW PEI polyplexes before hydrolysis, (D) siRNA/KL-LMW PEI polyplexes after hydrolysis, (E) siRNA/KL-HMW PEI polyplexes before hydrolysis, and (F) siRNA/KL-HMW PEI polyplexes after hydrolysis. Numbers indicate N/P ratios. (0 N/P ratio: naked siRNA only.)

efficient fluorescence quenching, indicating their abilities to efficiently condense siRNA. In contrast, both KL-LMW PEI and KL-HMW PEI showed less efficient siRNA condensation ability compared to unmodified L-PEI. Particularly, siRNA/KL-HMW PEI polyplexes exhibited relatively low condensation efficiency, even at high N/P ratios. The reason for the low condensation efficiency of siRNA by both KL-LMW PEI and KL-HMW PEI can be explained by their spatially hampered interactions with siRNA resulting from bulky ketal arms, especially when they were conjugated to high molecular weight linear PEI (*28*). Generally, it was observed that the siRNA condensation efficiency of various polyplexes determined by the ethidium bromide exclusion assay corresponded to size reduction of the polyplexes (Figure 2A and B).

The measured zeta potentials of various siRNA/PEI polyplexes were shown in Figure 2C. All of the polyplexes had positive surface charges at the observed range of N/P ratios, suggesting that negatively charged siRNA was successfully condensed into the polymers. All KL-PEI and unmodified L-PEI polyplexes prepared at the N/P ratio of 60 and above exhibited relatively constant positive zeta potentials of +16 to +22 mV. The polyplexes formed by both KL-LMW PEI and KL-HMW PEI did not show a noticeable difference in surface charges compared to those of the polyplexes formed by unmodified L-LMW PEI and L-HMW PEI ($p > 0.3$). Polyplexes prepared by siRNA and B-PEI showed the highest cationic surface charge among the various polyplexes, obviously due to the highest cationic density of the B-PEI (*35*).

Efficient Dissociation of siRNA from Hydrolyzed KL-PEI Polyplexes. The formation of various siRNA/PEI polyplexes and the dissociation of the siRNA from the polyplexes upon hydrolysis were demonstrated by agarose gel electrophoresis assay. As shown in Figure 3A and B, siRNA was partially retained by unmodified L-PEI at the N/P ratio up to 20 and completely retarded at the N/P ratios of 40 and above. However, for siRNA/KL-PEI polyplexes, the siRNA was completely retarded even at the N/P ratio of 10, indicating that KL-PEI could efficiently interact with negatively charged siRNA at lower N/P ratios than unmodified L-PEI (Figure 3C and E). This result is expected because of improved interactions of siRNA with amine-bearing branches, which can more closely access to siRNA than the linear cationic backbone of PEI. By the incorporation of ketal branches to linear PEI, secondary amines of linear PEI were altered to tertiary amines, and additional primary amines were generated from the ketal branches. Therefore, the newly added primary amines will make

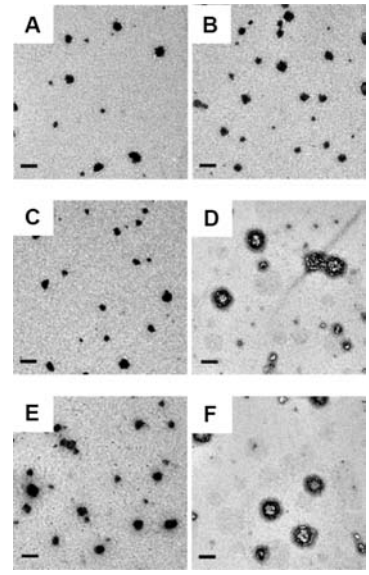

Figure 4. TEM micrographs of (A) siRNA/L-LMW PEI polyplexes (N/P = 40), (B) siRNA/L-HMW PEI PEI polyplexes (N/P = 40), (C) siRNA/KL-LMW PEI polyplexes (N/P = 100) before hydrolysis, (D) siRNA/KL-LMW PEI polyplexes (N/P = 100) after hydrolysis, (E) siRNA/KL-HMW PEI polyplexes (N/P = 100) before hydrolysis, and (F) siRNA/KL-HMW PEI polyplexes (N/P = 100) after hydrolysis. Scale bar = 100 nm.

linear PEI more protonatable and can interact more closely with siRNA than unmodified linear PEI. Various siRNA/KL-PEI polyplexes were treated with pH 5.0 acidic buffer and electrophoresed to demonstrate the disassembly of siRNA from polyplexes upon hydrolysis of ketal branches, which simulates the release of siRNA in the acidic endosome. It was clearly confirmed that the hydrolysis of ketal branches in KL-PEI at mild acidic pH 5.0 facilitated siRNA release from the polyplexes even at high N/P ratios (e.g., 100 and 120) as shown in Figure 3D and F. No detectable degradation of naked siRNA incubated at pH 5.0 for 4 h at 37 °C was observed (data not shown). The results obtained from the gel electrophoresis assay indicate that ketalization of L-PEI did not alter siRNA condensation but facilitated siRNA release from the polyplexes upon hydrolysis in mild acidic environments.

Morphological Changes of siRNA/KL-PEI Polyplexes upon Hydrolysis. Transmission electron microscopy images were acquired to observe the changes of sizes and the morphologies of various siRNA/PEI polyplexes before and after hydrolysis (Figure 4). All of the unmodified L-PEI and KL-PEI formed spherical and compact siRNA-containing polyplexes with a diameter of 40−100 nm (Figure 4A, B, C, and E). In addition, no significant size difference among the polyplexes formed by L-LMW PEI, L-HMW PEI, and KL-LMW PEI was observed ($p > 0.8$). However, the size of siRNA/KL-HMW PEI polyplexes formed at the N/P ratio of 100 was slightly larger that of siRNA/unmodified L-PEI polyplexes (Figure 4E). The larger size of siRNA/KL-HMW PEI polyplexes compared to those of other polyplexes was consistent with the results obtained from DLS analysis (Figure 2A). Again, taken together with the results from ethidium bromide exclusion assay, these results imply that the siRNA complexation ability of KL-HMW PEI was lower than the ones of unmodified L-PEI and KL-LMW PEI, possibly because of steric hindrance from ketal branches. Importantly, the TEM images showed swollen and disrupted siRNA/KL-PEI polyplexes after hydrolysis (Figure 4D and F), indicating that hydrolysis of ketal branches of KL-PEI at the endosomal pH of 5.0 may be able to destabilize the polyplexes and therefore facilitate the disassembly of siRNA from the destabilized polyplexes.

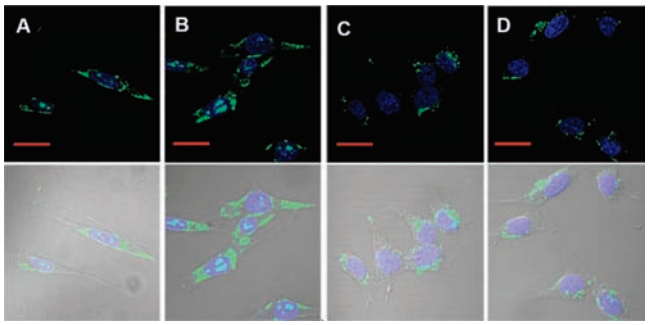

Figure 5. Laser scanning confocal micrographs illustrating the intracellular localization of various siRNA/L-PEI polyplexes in NIH 3T3 cells. (A) siRNA/L-LMW PEI polyplexes (N/P = 30), (B) siRNA/L-HMW PEI polyplexes (N/P = 30), (C) siRNA/KL-LMW PEI polyplexes (N/P = 100), and (D) siRNA/KL-HMW PEI polyplexes (N/P = 100). The upper panel depicts merged images of Alexa Fluor 488-stained polyplexes (green) and DRAQ5-counter-stained nuclei of the cells (blue). The lower panel depicts overlaid images of the upper panel and differential interference contrast (DIC) images of the cells. Images cutting horizontally through approximately the middle of the cell were selected out of a z-stack of images to differentiate the polyplexes in the perinuclear area from ones in the nucleus. Scale bar = 25 μm.

Intracellular Localization of Polyplexes. The intracellular localization of siRNA is an important factor for successful RNA interference. To investigate the intracellular localization of various siRNA/PEI polyplexes after cellular uptake, NIH 3T3 cells were incubated with various siRNA/PEI polyplexes and observed by confocal laser scanning microscopy. Various ketalized and unmodified L-PEI were used to complex unlabeled siRNA or Cy3-labeled siRNA, and the resulting polyplexes were further labeled with Alexa Fluor 488 dye. It was quantified that 42% of primary amines of KL-PEI were conjugated with Alexa Fluor 488. Since 1 equivalent Alexa Fluor 488 was used to react with the 1 equivalent primary amines of the entire KL-PEI complexing siRNA, and Alexa Fluor 488 was conjugated after siRNA complexation, it is presumed that most primary amines on the surface of the polyplexes were conjugated with Alexa Fluor 488 (i.e., actual conjugation ratio of Alex Fluor 488 to primary amines on the surface of the polyplexes was significantly higher than 1). Since Alexa Fluor 488 conjugation to ketalized linear PEI with abundant primary amines and unmodified linear PEI with mainly secondary amines in the backbone is not identical, internalizations of fluorescently labeled and unlabeled polyplexes cannot be directly compared. Therefore, relative numbers of the polyplexes in the cytoplasm to the ones in the nucleus were considered to explore intracellular localizations.

Localization of the various polyplexes was observed in the middle focal plane, which traverses both the cytoplasm and the nucleus of a cell (Figure 5). As shown in Figure 5A and B, a large number of the polyplexes prepared by using unmodified L-PEI were found inside cells regardless of their molecular weights, and these polyplexes were localized not only in the cytoplasm but also in the nucleus. This observation was in agreement with a previous study reporting that L-PEI delivers nucleic acids to the nucleus (*36, 37*). On the contrary, siRNA/KL-LMW PEI and siRNA/KL-HMW PEI polyplexes (and possibly free Alexa Fluor dye released by acid hydrolysis) were exclusively localized in the cytoplasm where siRNA mediates its function (Figure 5C and D), demonstrating that ketalization of L-PEI greatly redirects the intracellular distributions of the polyplexes to the cytoplasm. Hydrolysis of siRNA/KL-PEI polyplexes is hypothesized to make the polyplexes become larger and destabilized as the hydrolyzed KL-PEI has neutrally charged hydroxyl side chains, which hinder tight complexation with the siRNA. Therefore, cytoplasmic localization of the

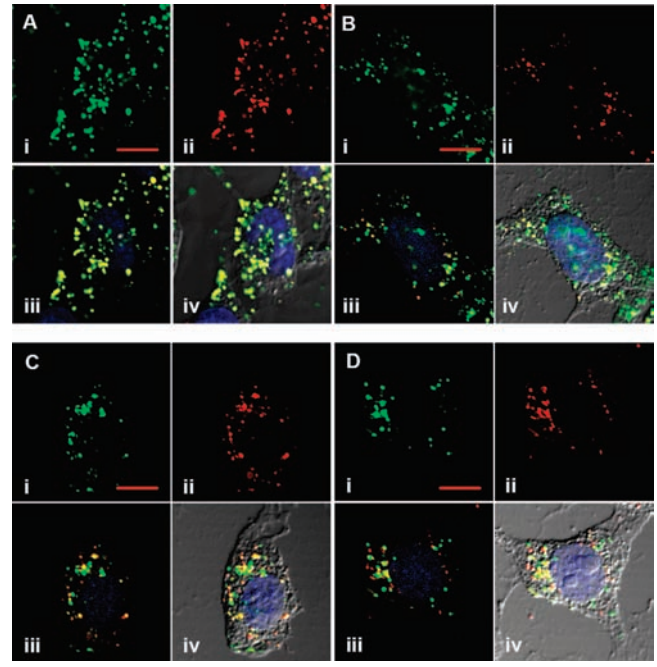

Figure 6. Laser scanning confocal micrographs illustrating the intracellular colocalization of Cy3 labeled-siRNA (red) and Alexa fluor 488 (green)-labeled linear PEI in NIH 3T3 cells. (A) siRNA/L-LMW PEI polyplexes (N/P = 30), (B) siRNA/L-HMW PEI polyplexes (N/P = 30), (C) siRNA/KL-LMW PEI polyplexes (N/P = 100), and (D) siRNA/KL-HMW PEI polyplexes (N/P = 100). The left upper panel depicts images of Alexa Fluor 488-labeled linear PEI (i), and the right upper panel depicts images of Cy3-labeled siRNA (ii). The left lower panel depicts merged images of Alexa Fluor 488-stained polyplexes and Cy3-labeled siRNA with nucleus staining (blue) (iii). The right lower panel depicts overlaid images of image (iii) and DIC image of the cells. Scale bar = 10 μm.

siRNA/KL-PEI polyplexes might be ascribed to their increased size and loose siRNA complexation in the cytoplasm, which prevent transport through nuclear pores.

Localization of Alexa fluor 488-labeled linear PEI (green, i) and Cy3-labeled siRNA (red, ii) was investigated, and the colocalized polymer and siRNA were represented as yellow dots (iii) in Figure 6. When the siRNA/unmodified linear PEI polyplexes were incubated with cells, siRNA and unmodified linear PEI were clearly colocalized both in the cytoplasm and the nucleus as shown in Figure 6A and B. On the contrary, when siRNA/KL-PEI polyplexes were incubated with the cells, both siRNA and the KL-PEI were mainly colocalized in the cytoplasm instead of entering the nucleus as shown in Figure 6C and D. More importantly, there were significantly more red spots, which represent stably labeled siRNA alone, in the cell incubated with siRNA/KL-PEI polyplexes than the ones incubated with siRNA/unmodified L-PEI polyplexes [Figure 6C (iii) and D (iii)] after 4 h of incubation in the cells. In comparison, siRNA/unmodified linear PEI polyplexes resulted in exclusive colocalization of siRNA and unmodified PEI [(Figure 6A (iii) and B (iii)]. Quantitative estimation of the amount of free Alexa Fluor 488 dye released from the ketalized linear PEI upon hydrolysis showed that 70% of the conjugated Alexa Fluor 488 dye was released during hydrolysis. This indicates that some yellow spots in the cells incubated with siRNA/KL-PEI polyplexes probably represent colocalized siRNA and free Alexa Fluor 488. Again, attention should be given to the fact that there were more red spots (i.e., free siRNA alone) in the cells incubated with KL-PEI polyplexes than the ones incubated with unketalized L-PEI polyplexes. This finding clearly demonstrates efficient intracellular disassembly of siRNA from ketalized linear

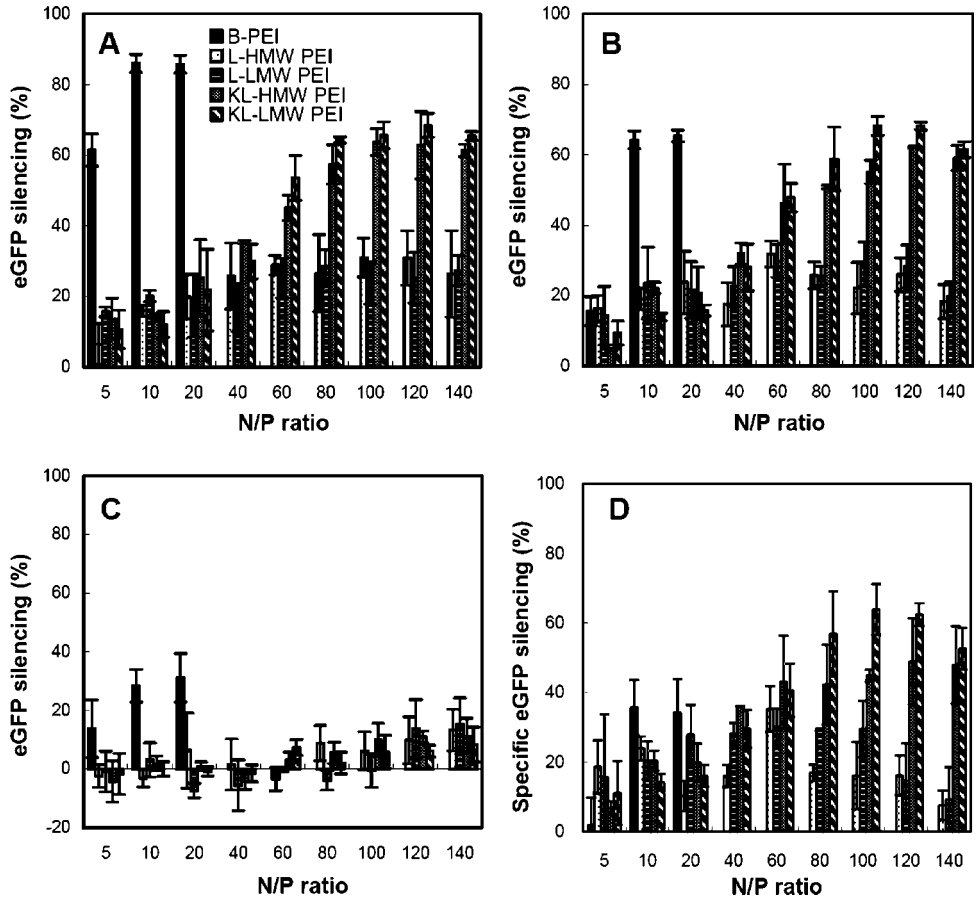

Figure 7. eGFP gene silencing efficiency of various siRNA/PEI polyplexes at various N/P ratios. eGFP knockdown in NIH 3T3 cells by various (A) siRNA/PEI polyplexes in the absence of serum, (B) siRNA/PEI polyplexes in the presence of serum, and (C) siRNA/PEI polyplexes synthesized with control (nonspecific) siRNA in the presence of serum. Specific eGFP silencing efficiency (D) was determined by subtracting nonspecific gene silencing efficiency of siRNA/PEI polyplexes synthesized with control siRNA from the gene silencing efficiency of siRNA/PEI polyplexes synthesized with anti-eGFP siRNA in the presence of serum. Notice that there was an insufficient number of live cells to analyze for gene silencing after being incubated with siRNA/B-PEI at N/P ratio of 40 and above due to severe cytotoxicity.

PEI polyplexes in the cytoplasm and efficient subsequent processes toward RNA interference.

Efficient Gene Silencing with Low Cytotoxicity by siRNA/KL-PEI Polyplexes. RNAi efficiency of various siRNA/PEI polyplexes at various N/P ratios was evaluated by quantifying the reduced expression of eGFP in NIH 3T3 cells. As shown in Figure 7A, to some extent, KL-PEI-mediated RNAi efficiency tended to increase with N/P ratios. This might be due to increased endosomal escape caused by higher numbers of amines (*17*). siRNA/B-PEI polyplexes showed the highest gene silencing efficiency among the various polyplexes in the absence of serum as shown in Figure 7A. Both unmodified L-HMW PEI and L-LMW PEI showed minimal RNAi efficiency at the entire N/P ratios in contrast to their superior DNA transfection efficiency as previously reported (*22*−*26*). In contrast, ketalization of L-PEI remarkably enhanced the RNAi efficiency ($p \ll 0.001$), and the highest gene silencing efficiencies of KL-HMW PEI and KL-LMW PEI were observed at N/P ratios of 100 and 120, respectively. A confocal laser scanning microscopy study showed that siRNA and unmodified L-PEI were exclusively colocalized in both the cytoplasm and the nucleus, although a large number of siRNA/unmodified L-PEI polyplexes were localized in the cytoplasm (Figure 6A and B). This finding indicates limited dissociation of siRNA from the polyplexes in the cytoplasm possibly due to highly stable siRNA complexation by L-PEI, resulting in limited RNAi activity (Figures 2B and 7A). However, acid-degradable KL-PEI was able to facilitate efficient polyplex unpackaging in the cytoplasm and subsequent siRNA release (Figure 6C and D), suggesting that the improvement of RNAi efficiency mediated by KL-PEI compared to that of unmodified L-PEI might be ascribed to more efficient endosomal escape and unpackaging of siRNA/KL-PEI polyplexes in the cytoplasm as well as its targeted cytosolic delivery of siRNA. As shown in Figure 7A, both KL-LMW PEI and KL-HMW PEI resulted in still slightly lower gene silencing efficiencies than B-PEI in the absence of serum. However, the gene silencing efficiency of siRNA/B-PEI polyplexes dramatically decreased in the presence of serum ($p < 0.005$), which might be attributed to an undesirable interaction of the polyplexes with negatively charged serum proteins (*38*). For example, the gene silencing by siRNA/B-PEI polyplexes reduced from 85.7% in the absence of serum to 65.3% in the presence of 10% serum at the N/P ratio of 20. Regardless of molecular weights, unmodified linear PEI did not show significant decrease in RNAi efficiency in the presence of serum ($p > 0.3$), as previously reported (*39*). Similarly, high gene silencing efficiencies of siRNA/KL-HMW PEI and siRNA/KL-LMW PEI polyplexes prepared at the N/P ratio of 80 to 140 remained without significant changes (Figure 7A and B). This result was also clearly presented by confocal laser scanning micrographs (Figure 8) as well as a flow cytometry histogram (Supporting Information, Figure S2). The effects of various serum concentrations on gene silencing efficiency by ketalized PEI were also investigated (Supporting Information, Figure S3). Results showed that KL-PEI, regardless of molecular weights, was able to silence eGFP expression more efficiently than unketalized branched and linear PEI in the presence of up to 50% serum as shown in Figure S3B (Supporting Information)

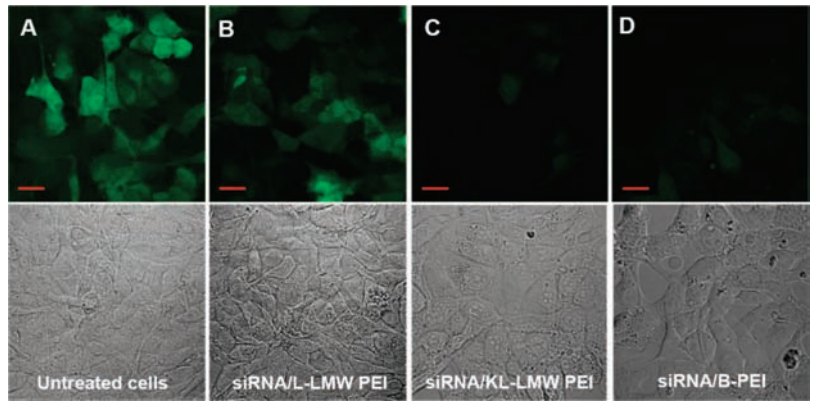

Figure 8. Confocal micrographs of eGFP-expressing NIH 3T3 cells (A) untreated used as a control and incubated with (B) siRNA/L-LMW PEI polyplexes (N/P = 60), (C) siRNA/KL-LMW PEI polyplexes (N/P = 120), and (D) siRNA/B-PEI polyplexes (N/P = 10), in the presence of 10% serum. The upper panel depicts fluorescent images of eGFP-expressing NIH 3T3 cells. The lower panel depicts differential interference contrast (DIC) images of the cells. Scale bar = 20 μm.

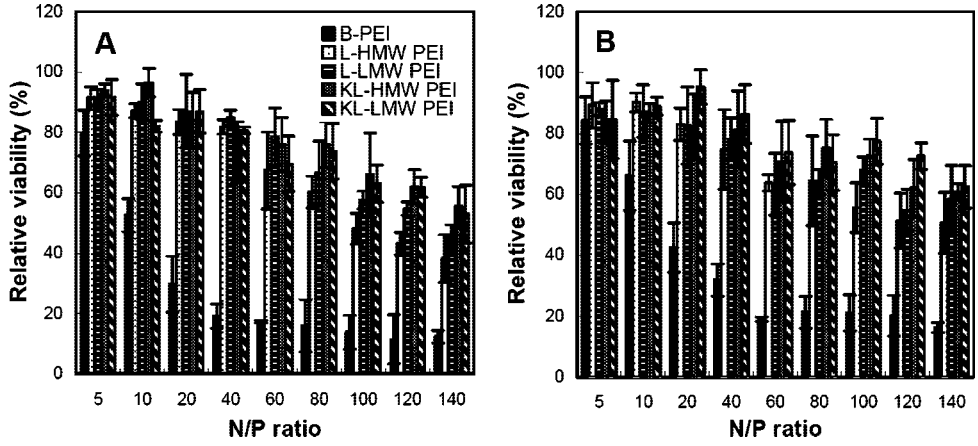

Figure 9. Viability of NIH 3T3 cells incubated with siRNA/PEI polyplexes at different N/P ratios (A) in the absence of serum and (B) in the presence of serum (10%). NIH 3T3 cells were incubated with polyplexes in serum-free or serum-containing medium for 4 h followed by 24 h of incubation with fresh medium supplemented with 10% FBS.

($p < 0.003$), although KL-PEI showed slightly less efficient siRNA condensation capability than unketalized branched and linear PEI (Figure 2B).

In order to exclude nonspecifically reduced gene expression by the polyplexes in gene silencing quantification, the eGFP expressing NIH 3T3 cells were also incubated with the polyplexes prepared by nonsequence-specific (control) siRNA and PEI. For the polyplexes prepared by using unmodified and ketalized linear PEI, nonspecific eGFP knockdown was found to be very minimal (e.g., less than 8% of gene silencing) at low N/P ratios (e.g., N/P $\leq$ 60), although nonspecific effects slightly increased with N/P ratios (Figure 7C). However, siRNA/B-PEI polyplexes showed significant nonspecific gene silencing in a N/P ratio-dependent way ($p \ll 0.001$) (Figure 7C). In other words, specific gene silencing by siRNA/PEI polyplexes must be considered after subtracting nonspecific effects (Figure 7D). Specific eGFP silencing by siRNA/KL-LMW PEI and siRNA/KL-HMW PEI polyplexes in the presence of serum was much higher than that of siRNA/B-PEI polyplexes. The maximum specific eGFP silencing by siRNA/KL-LMW PEI polyplexes at the N/P ratio of 100 was around 63%, which was about 2-fold higher than specific eGFP silencing efficiency by siRNA/B-PEI polyplexes at the N/P ratio of 10.

Cytotoxicity of siRNA/KL-PEI polyplexes was slightly lower than that of siRNA/unketalized L-PEI polyplexes ($p > 0.02$) but significantly lower than that of siRNA/B-PEI polyplexes as shown in Figure 9 ($p \ll 0.001$). Cells incubated with the siRNA/KL-PEI polyplexes remained more than 70% viable at the N/P ratios up to 80 whether they were incubated with serum or not. On the contrary, siRNA/B-PEI polyplexes showed significant cytotoxicity even at the N/P ratio of 20, regardless of the presence of serum ($p \ll 0.001$). This high cytotoxicity seems to contribute to nonspecific gene silencing by siRNA/B-PEI polyplexes (Figure 7C). Unmodified linear PEI showed relatively low cytotoxicity compared to B-PEI as previously reported (*27, 36*). It is well-known that high cytotoxicity of B-PEI is correlated with its high charge density (*40*). Since zeta potentials of siRNA/L-PEI and siRNA/KL-PEI polyplexes were a lot lower than that of B-PEI ($p \ll 0.001$), this low cationic charge density of the polyplexes probably contributed to high cell viability even at high N/P ratios. It seems that low cytotoxicity of KL-PEI is not only a consequence of the inherently low cytotoxicity of L-PEI but also the reduced interactions of hydrolyzed KL-PEI, which has neutral hydroxyl overhangs, with endogenous genes as previously discussed (*28, 41*). The reason for similar characteristics of KL-PEI to ones of unmodified L-PEI with regard to serum-independent gene transfer and low cytotoxicity might be due to a low degree of ketalization (i.e., 22 and 24%). Although linear PEI was transformed to a branched form to a certain extent by ketalization, its advantageous properties (e.g., low cytotoxicity and serum-independence) seem to be preserved. One of the practical challenges for in vivo gene delivery mediated by cationic nonviral vectors is inhibition of gene delivery efficiency by serum and high cytotoxicity (*42*). Although branched PEI, one of the efficient cationic nonviral gene delivery carriers, has been

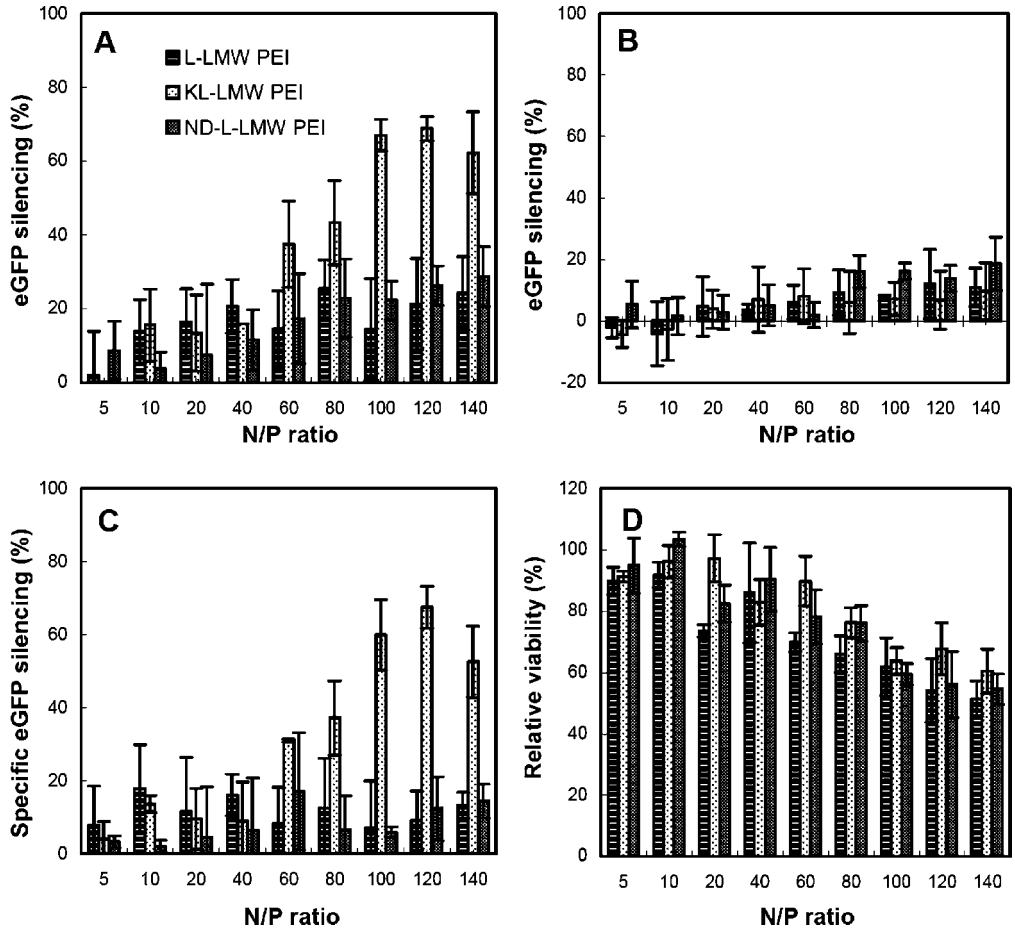

Figure 10. Effects of ketalization of L-PEI on eGFP gene silencing efficiency and cytotoxicity. eGFP knockdown in NIH 3T3 cells mediated by various (A) siRNA/PEI polyplexes in the presence of serum and (B) siRNA/PEI polyplexes synthesized with control (nonspecific) siRNA in the presence of serum, and (C) specific eGFP silencing efficiency of various siRNA/PEI polyplexes in the presence of serum. (D) Cytotoxicity of acid-degradable KL-LMW PEI and nondegradable modified L-LMW PEI (ND-L-LMW PEI) at various N/P ratios. eGFP expressing NIH 3T3 cells were incubated with various siRNA-containing polyplexes in the 10% FBS supplemented medium. After 4 h of incubation, the medium was replaced with fresh DMEM containing 10% FBS, and the cells were further cultured for 72 h.

popularly used for years due to its high transfection efficiency in vitro (*15*), its in vivo application has been limited because of its serum-dependent gene transfection efficiency and high cytotoxicity (*25, 36, 38, 43*). In contrast to branched PEI, KL-PEI showed serum-independent high RNAi efficiency and low cytotoxicity. Moreover, KL-PEI showed higher specific eGFP silencing efficiency than B-PEI (Figure 7D). Our previous study showed that the transfection efficiency of ketalized low molecular weight branched PEI was also influenced by the presence of serum to some extent such as unmodified 25 kDa branched PEI, although ketalized low molecular weight PEI showed enhanced transfection efficiency and significantly reduced cytotoxicity (*28*). Therefore, serum-independent and nontoxic siRNA delivery by KL-PEI in this study implies that the critical drawbacks of PEI-mediated gene delivery for clinical trials can be ameliorated.

Enhanced Gene Silencing by Acid-Degradable Ketal Branches. Contribution of the acid-degradability of KL-PEI to the improved RNA interference was evaluated by comparing RNAi efficiency of modified L-LMW PEI with nondegradable amine-bearing branches. This nondegradable counterpart was prepared by conjugating L-LMW PEI with nondegradable *N*-(4-(2,2,2-trifluoroacetamido)butyl)acrylamide followed by deprotecting the trifluoroacetate group. The synthetic scheme, detailed synthesis procedures, and characterization are described in Supporting Information (Figure S4). As shown in Figure 10A, the eGFP knockdown by siRNA/KL-LMW PEI polyplexes in NIH 3T3 cells was much higher than the one by nondegradable L-LMW PEI (ND-L-LMW PEI) at all observed N/P ratios ($p < 0.004$). Interestingly, siRNA/ND-L-LMW PEI polyplexes showed a similar level of RNAi efficiency in comparison to that of siRNA/unmodified L-LMW PEI polyplexes. This result clearly demonstrates that the acid degradability of KL-LMW PEI remarkably contributed to the efficient RNAi by siRNA/KL-LMW PEI polyplexes. Moreover, siRNA/ND-L-LMW PEI polyplexes showed some nonspecific gene silencing at high N/P ratios (e.g., 80−140) (nonspecific gene silencing degree: ≥ 10%), although it was not significantly different from the one by siRNA/KL-LMW PEI polyplexes (e.g., less than 10% of nonspecific gene silencing) ($p > 0.08$) (Figure 10B). The cytotoxicity result shown in Figure 10D indicates no significant difference in cell viability between degradable and nondegradable polyplexes ($p > 0.34$). These results imply that ketalization of L-PEI indeed increased gene silencing, while keeping the minimal nonspecific RNA interference and cytotoxicity of L-PEI.

CONCLUSIONS

In this study, pH-sensitive ketalized linear PEI was synthesized for siRNA delivery. The conjugation of acid-degradable amino ketal branches resulted in enhanced cytoplasmic release of free siRNA, which could be a crucial part of the reason for the achieved efficient RNA interference. The ketalization preserved the advantages of linear PEI including low cytotoxicity, serum-independent gene delivery, and sequence-specific

gene silencing. It appeared that KL-PEI could be a promising candidate for a nonviral siRNA delivery carrier in vivo.

ACKNOWLEDGMENT

We thank the staff at the Optical Biology Core (OBC) facility in UC Irvine for assistance with the confocal laser scanning microscopy and Ms. Shirley Wong (UC Irvine) for proofreading the manuscript. The authors are also grateful to Dr. Jian-Guo Zheng for his assistance of TEM imaging and analysis at the Materials Characterization Center in UC Irvine.

Supporting Information Available: Buffering capacity of KL-PEI, flow cytometry histogram of eGFP-exprssing cells incubated with various polyplexes, effects of various serum concentrations on RNA interference, and synthesis of nondegradable modified linear polyethylenimine (ND-L-PEI). This material is available free of charge via the Internet at http://pubs.acs.org.

LITERATURE CITED

(1) McManus, M. T., and Sharp, P. A. (2002) Gene silencing in mammals by small interfering RNAs. *Nat. Rev. Genet. 3*, 737–747.

(2) Caplen, N. J., Parrish, S., Imani, F., Fire, A., and Morgan, R. A. (2001) Specific inhibition of gene expression by small double-stranded RNAs in invertebrate and vertebrate systems. *Proc. Natl. Acad. Sci. U.S.A. 98*, 9742–9747.

(3) Elbashir, S. M., Harborth, J., Lendeckel, W., Yalcin, A., Weber, K., and Tuschl, T. (2001) Duplexes of 21-nucleotide RNAs mediate RNA interference in cultured mammalian cells. *Nature 411*, 494–498.

(4) Urban-Klein, B., Werth, S., Abuharbeid, S., Czubayko, F., and Aigner, A. (2005) RNAi-mediated gene-targeting through systemic application of polyethylenimine (PEI)-complexed siRNA in vivo. *Gene Ther. 12*, 461–466.

(5) Lu, P. Y., Xie, F., and Woodle, M. C. (2005) In vivo application of RNA interference: from functional genomics to therapeutics. *Adv. Genet. 54*, 117–142.

(6) de Fougerolles, A. R. (2008) Delivery vehicles for small interfering RNA in vivo. *Hum. Gene Ther. 19*, 125–132.

(7) Gary, D. J., Puri, N., and Won, Y. Y. (2007) Polymer-based siRNA delivery: perspectives on the fundamental and phenomenological distinctions from polymer-based DNA delivery. *J. Controlled Release 121*, 64–73.

(8) Read, M. L., Singh, S., Ahmed, Z., Stevenson, M., Briggs, S. S., Oupicky, D., Barrett, L. B., Spice, R., Kendall, M., Berry, M., Preece, J. A., Logan, A., and Seymour, L. W. (2005) A versatile reducible polycation-based system for efficient delivery of a broad range of nucleic acids. *Nucleic Acids Res. 33*, e86.

(9) Werth, S., Urban-Klein, B., Dai, L., Höbel, S., Grzelinski, M., Bakowsky, U., Czubayko, F., and Aigner, A. (2006) A low molecular weight fraction of polyethylenimine (PEI) displays increased transfection efficiency of DNA and siRNA in fresh or lyophilized complexes. *J. Controlled Release 112*, 257–270.

(10) Oishi, M., Nagasaki, Y., Itaka, K., Nishiyama, N., and Kataoka, K. (2005) Lactosylated poly(ethylene glycol)-siRNA conjugate through acid-labile beta-thiopropionate linkage to construct pH-sensitive polyion complex micelles achieving enhanced gene silencing in hepatoma cells. *J. Am. Chem. Soc. 127*, 1624–1625.

(11) Kim, S. H., Jeong, J. H., Cho, K. C., Kim, S. W., and Park, T. G. (2005) Target-specific gene silencing by siRNA plasmid DNA complexed with folate-modified poly(ethylenimine). *J. Controlled Release 104*, 223–232.

(12) Chien, P. Y., Wang, J., Carbonaro, D., Lei, S., Miller, B., Sheikh, S., Ali, S. M., Ahmad, M. U., and Ahmad, I. (2005) Novel cationic cardiolipin analogue-based liposome for efficient DNA and small interfering RNA delivery in vitro and in vivo. *Cancer Gene Ther. 12*, 321–328.

(13) Segura, T., and Hubbell, J. A. (2007) Synthesis and in vitro characterization of an ABC triblock copolymer for siRNA delivery. *Bioconjugate Chem. 18*, 736–745.

(14) Richards Grayson, A. C., Ma, J., and Putnam, D. (2006) Kinetic and efficacy analysis of RNA interference in stably and transiently expressing cell lines. *Mol. Pharmaceutics 3*, 601–613.

(15) Boussif, O., Lezoualc'h, F., Zanta, M. A., Mergny, M. D., Scherman, D., Demeneix, B., and Behr, J.-P. (1995) A versatile vector for gene and oligonucleotide transfer into cells in culture and in vivo: polyethyleneimine. *Proc. Natl. Acad. Sci. U.S.A. 92*, 7297–7301.

(16) Godbey, W. T., Wu, K. K., and Mikos, G. A. (1999) Poly(ethylenimine) and its role in gene delivery. *J. Controlled Release 60*, 149–160.

(17) Akinc, A., Thomas, M., Klibanov, A. M., and Langer, R. (2005) Exploring polyethylenimine-mediated DNA transfection and the proton sponge hypothesis. *J. Gene Med. 7*, 657–663.

(18) Plank, C., Oberhauser, B., Mechtler, K., Koch, C., and Wagner, E. (1994) The influence of endosome-disruptive peptides on gene transfer using synthetic virus-like gene transfer systems. *J. Biol. Chem. 269*, 12918–12924.

(19) Suh, J., Paik, H. J., and Hwang, B. K. (1994) Ionization of poly(ethyleneimine) and poly(allylamine) at various pH's. *Bioorg. Chem. 22*, 318–327.

(20) Hassani, Z., Lemkine, G. F., Erbacher, P., Palmier, K., Alfama, G., Giovannangeli, C., Behr, J.-P., and Demeneix, B. A. (2005) Lipid-mediated siRNA delivery down-regulates exogenous gene expression in the mouse brain at picomolar levels. *J. Gene Med. 7*, 198–207.

(21) Goula, D., Becker, N., Lemkine, G. F., Normandie, P., Rodrigues, J., Mantero, S., Levi, G., and Demeneix, B. A. (2000) Rapid crossing of the pulmonary endothelial barrier by polyethylenimine/DNA complexes. *Gene Ther. 7*, 499–504.

(22) Zou, S. M., Erbacher, P., Remy, J. S., and Behr, J.-P. (2000) Systemic linear polyethylenimine (L-PEI)-mediated gene delivery in the mouse. *J. Gene Med. 2*, 128–134.

(23) Brissault, B., Leborgne, C., Guis, C., Danos, O., Cheradame, H., and Kichler, A. (2006) Linear topology confers in vivo gene transfer activity to polyethylenimines. *Bioconjugate Chem. 17*, 759–765.

(24) Bragonzi, A., Boletta, A., Biffi, A., Muggia, A., Sersale, G., Cheng, S. H., Bordignon, C., Assael, B. M., and Conese, M. (1999) Comparison between cationic polymers and lipids in mediating systemic gene delivery to the lungs. *Gene Ther. 6*, 1995–2004.

(25) Goula, D., Benoist, C., Mantero, S., Merlo, G., Levi, G., and Demeneix, B. A. (1998) Polyethylenimine-based intravenous delivery of transgenes to mouse lung. *Gene Ther. 5*, 1291–1295.

(26) Goula, D., Remy, J. S., Erbacher, P., Wasowicz, M., Levi, G., Abdallah, B., and Demeneix, B. A. (1998) Size, diffusibility and transfection performance of linear PEI/DNA complexes in the mouse central nervous system. *Gene Ther. 5*, 712–717.

(27) Richards Grayson, A. C., Doody, A. M., and Putnam, D. (2006) Biophysical and structural characterization of polyethylenimine-mediated siRNA delivery in vitro. *Pharm. Res. 23*, 1868–1876.

(28) Shim, M. S., and Kwon, Y. J. (2008) Controlled delivery of plasmid DNA and siRNA to intracellular targets using ketalized polyethylenimine. *Biomacromolecules 9*, 444–455.

(29) Kwon, Y. J., Yu, H., and Peng, C.-A. (2001) Enhanced retroviral transduction of 293 cells cultured on liquid-liquid interfaces. *Biotechnol. Bioeng. 72*, 331–338.

(30) Martinez, J., Patkaniowska, A., Urlaub, H., Lührmann, R., and Tuschl, T. (2002) Single-stranded antisense siRNAs guide target RNA cleavage in RNAi. *Cell 110*, 563–574.

(31) Zeng, Y., and Cullen, B. R. (2002) RNA is restricted to the cytoplasm. *RNA 8*, 855–860.

(32) Schaffer, D. V., Fidelman, N. A., Dan, N., and Lauffenburger, D. A. (2000) Vector unpacking as a potential barrier for receptor mediated polyplex gene delivery. *Biotechnol. Bioeng. 67*, 598–606.

(33) Ogris, M., Steinlein, P., Kursa, M., Mechtler, K., Kircheis, R., and Wagner, E. (1998) The size of DNA/transferrin-PEI complexes is an important factor for gene expression in cultured cells. *Gene Ther. 5*, 1425–1433.

(34) Dunlap, D. D., Maggi, A., Soria, M. R., and Monaco, L. (1997) Nanoscopic structure of DNA condensed for gene delivery. *Nucleic Acids Res. 25*, 3095–3101.

(35) Furgeson, D. Y., Chan, W. S., Yockman, J. W., and Kim, S. W. (2003) Modified linear polyethylenimine-cholesterol conjugates for DNA complexation. *Bioconjugate Chem. 14*, 840–847.

(36) Wightman, L., Kircheis, R., Rössler, V., Carotta, S., Ruzicka, R., Kursa, M., and Wagner, E. (2001) Different behavior of branched and linear polyethylenimine for gene delivery in vitro and in vivo. *J. Gene Med. 3*, 362–372.

(37) Brunner, S., Furtbauer, E., Sauer, T., Kursa, M., and Wagner, E. (2002) Overcoming the nuclear barrier: cell cycle independent nonviral gene transfer with linear polyethylenimine or electroporation. *Mol. Ther. 5*, 80–86.

(38) Guo, W., and Lee, R. J. (2001) Efficient gene delivery via non-covalent complexes of folic acid and polyethylenimine. *J. Controlled Release 77*, 131–138.

(39) Boussif, O., Zanta, M. A., and Behr, J.-P. (1996) Optimized galenics improve in vitro gene transfer with cationic molecules up to 1000-fold. *Gene Ther. 3*, 1074–1080.

(40) Fischer, D., Li, Y., Ahlemeyer, B., Krieglstein, J., and Kissel, T. (2003) In vitro cytotoxicity testing of polycations: influence of polymer structure on cell viability and hemolysis. *Biomaterials 24*, 1121–1131.

(41) Dindo, D., Dahm, F., Szulc, Z., Bielawska, A., Obeid, L. M., Hannun, Y. A., Graf, R., and Clavien, P.-A. (2006) Cationic long-chain ceramide LCL-30 induces cell death by mitochondrial targeting in SW403 cells. *Mol. Cancer Ther. 5*, 1520–1529.

(42) Goldman, C. K., Soroceanu, L., Smith, N., Gillespie, G. Y., Shaw, W., Burgess, S., Bilbao, G., and Curiel, D. T. (1997) In vitro and in vivo gene delivery mediated by a synthetic polycationic amino polymer. *Nat. Biotechnol. 15*, 462–466.

(43) Kircheis, R., Wightman, L., and Wagner, E. (2001) Design and gene delivery activity of modified polyethylenimines. *Adv. Drug Delivery Rev. 53*, 341–358.

BC800436V

Supporting Information

Acid-responsive Linear Polyethylenimine for Efficient, Specific, and Biocompatible siRNA Delivery

Min Suk Shim[†,‡] and Young Jik Kwon[‡,§,‖*]

[†]Department of Macromolecular Science and Engineering, Case Western Reserve University, 10900 Euclid Avenue, Cleveland, Ohio 44106

[‡]Department of Chemical Engineering and Materials Science, University of California, Irvine, CA 92697

[§]Department of Pharmaceutical Sciences, University of California, Irvine, CA 92697

[‖]Department of Biomedical Engineering, University of California, Irvine, CA 92697

Buffering capacity of KL-PEI. 10 mg of KL-LMW and L-LMW PEI were dissolved in 1.5 mL of DI water and adjusted to pH at approximately 12.5 with 2M NaOH in DI water. The pHs of the polymer solutions at R.T. were measured as aliquots of 1M HCl solution was subsequently added.

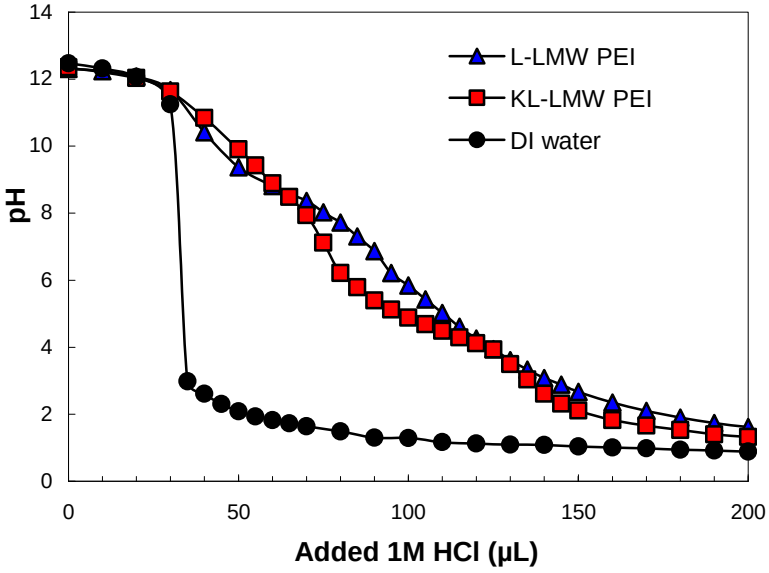

Figure S1. Titration curve of polymer solutions in DI water.

Flow cytometry histogram of eGFP silencing by various polyplexes. eGFP-expressing NIH 3T3 cells were incubated with various siRNA/PEI polyplexes in the presence of 10% FBS. Each polyplex solution was prepared at the optimized N/P ratios for maximum eGFP silencing (e.g., N/P ratio of 60 for siRNA/L-LMW PEI and siRNA/L-HMW PEI, N/P ratio of 120 for siRNA/KL-LMW PEI and siRNA/KL-HMW PEI, and N/P ratio of 10 for siRNA/B-PEI). eGFP silencing was analyzed after 76 h

of incubation. The results demonstrated that both KL-LMW PEI and KL-HMW PEI showed higher gene silencing efficiency than unmodified L-LMW PEI and L-HMW PEI.

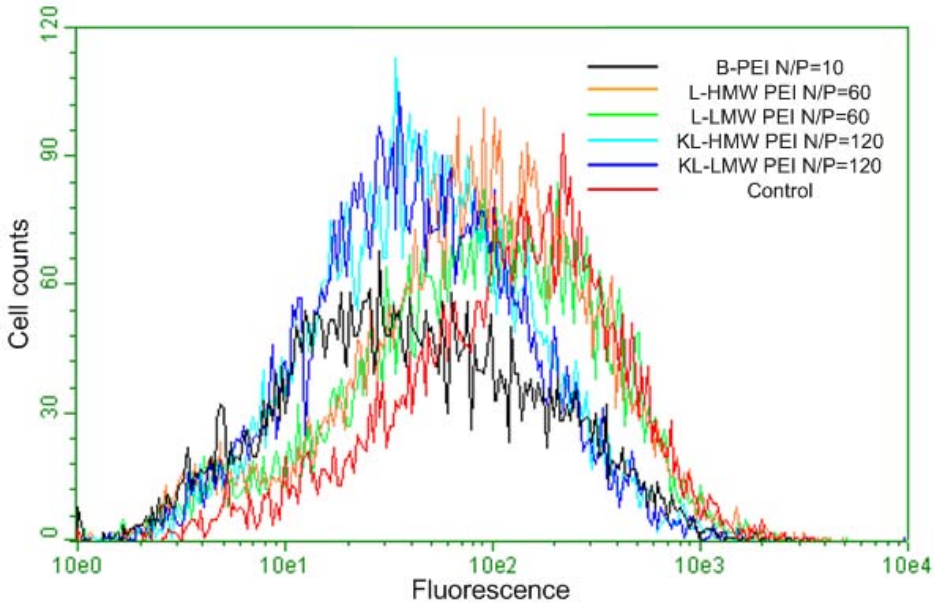

***Figure S2*.** Flow cytometry histogram of eGFP-expressing NIH 3T3 cells incubated with various polyplexes in the presence of 10% serum.

Effects of various serum concentrations on RNA interference. eGFP-expressing NIH 3T3 cells were inoculated in a 24-well plate at a density of 2×10^4 cells/well, 24 h prior to siRNA treatment. siRNA-containing polyplexes were prepared by mixing various amounts of polymer stock solutions in PBS with anti-eGFP siRNA or non-specific control siRNA solutions (75 pmol) in DI water (total in 75 μL). Each polyplex solution was prepared at the optimized N/P ratios for maximum eGFP silencing (e.g., N/P ratio of 60 for siRNA/unmodified linear PEI, N/P ratio of 120 for siRNA/ketalized linear PEI, and N/P ratio of 10 for siRNA/branched PEI). The culture medium in each well was replaced with 300 μL of DMEM containing different concentrations of FBS (e.g., FBS-free, 10% FBS, 20% FBS, 50% FBS, and 100% FBS). After 4 h of incubation, the medium in the well was replaced with 0.5 mL of fresh DMEM containing 10% FBS, and the cells were further cultured for 72 h. After the cells were harvested by trypsinization and washed with PBS, silenced eGFP expression was analyzed by flow cytometry. Specific eGFP silencing efficiency was determined by subtracting non-specific gene silencing by non-specific control siRNA/PEI polyplexes from the gene silencing by anti-eGFP siRNA/PEI polyplexes. RNAi efficiencies of both ketalized linear PEI and unketalized linear PEI decreased as serum concentrations increased. However, ketalized linear PEI, regardless of molecular weights of PEI, was able to induce specific eGFP silencing above the level of 25% at high serum concentrations that were up to 50%, while branched PEI showed almost no specific gene silencing at high serum concentrations (e.g., 50% and 100% FBS). siRNA/unketalized linear PEI polyplexes showed minimal specific eGFP knockdown regardless serum concentrations (e.g., less than 30% of specific gene silencing).

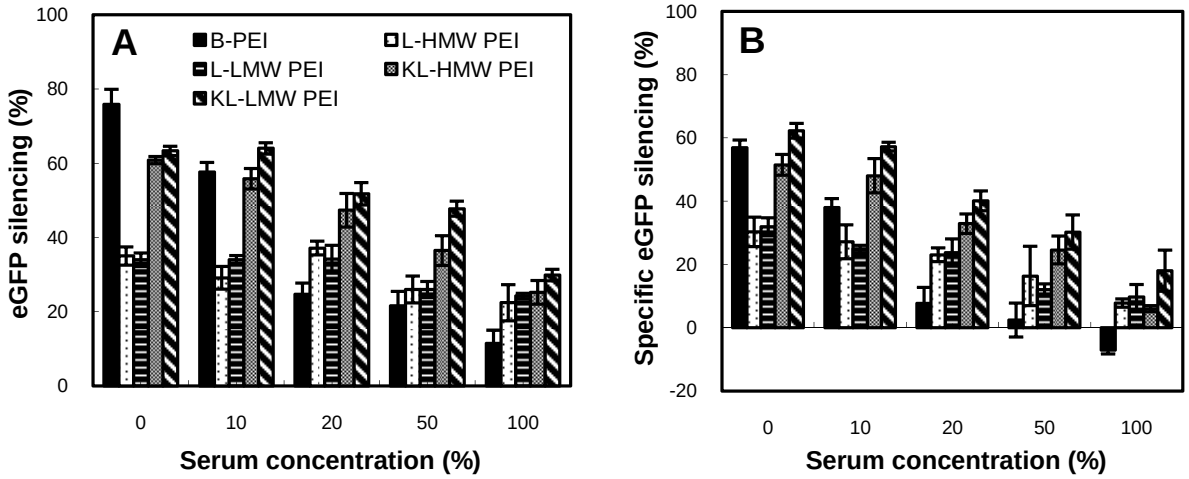

Figure S3. Effects of serum concentrations on eGFP gene silencing by various polyplexes. (A) Overall eGFP silencing by various siRNA/PEI polyplexes in the presence of different serum concentrations. (B) Specific eGFP silencing by various siRNA/PEI polyplexes at different serum concentrations.

Synthesis of non-degradable modified linear polyethylenimine (ND-L-PEI). Non-degradable branch-grafted linear polyethylenimine was synthesized via Michael addition conjugation of (N-(4-(2,2,2-trifluoroacetamido)butyl)acrylamide) as shown in Figure S4.

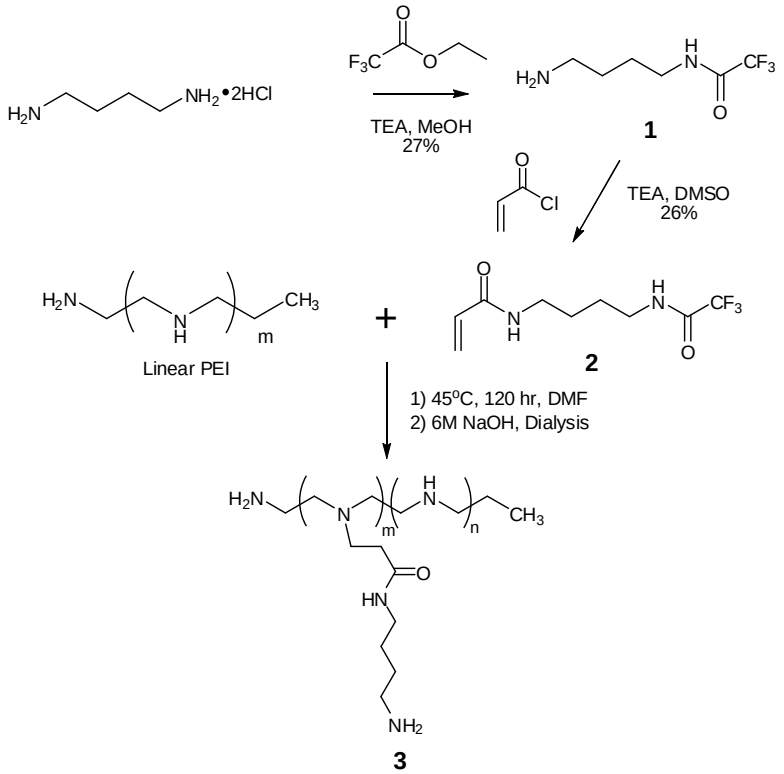

Figure S4. Synthesis of non-degradable modified linear polyethylenimine (ND-L-PEI).

Synthesis of Compound 1 [*N*-(4-aminobutyl)-2,2,2-trifluoroacetamide]. 1,4-diaminobutane dihydrochloride (2.0 g, 12.42 mmol, 1 equiv) was dissolved in 10 mL of methanol with 2.50 g of triethylamine (24.84 mmol, 2 equiv). The solution of ethyl trifluoroacetate (1.76 g, 12.42 mmol, 1 equiv) in 10 mL of methanol was slowly added dropwise to the solution of 1,4-diaminobutane dihydrochloride on ice, and the resulting mixture was stirred for 4 h on ice. After evaporating the solvent, the mixture was extracted with 3 × 50 mL of dichloromethane. The organic layers were collected and evaporated. The product was purified by silica gel chromatography using a gradient from tetrahydrofuran to 80/20 tetrahydrofuran/methanol to obtain the product as a white solid (0.62 g, 3.36 mmol, 27% yield). ^{1}H-NMR (500MHz, DMSO-d6): δ 1.57 (m, 4H, $CF_3CONHCH_2C\underline{H_2}C\underline{H_2}CH_2NH_2$); δ 2.78 (t, 2H, $CF_3CONHCH_2CH_2CH_2C\underline{H_2}NH_2$); δ 3.21 (t, 2H, $CF_3CONHC\underline{H_2}CH_2CH_2CH_2NH_2$); δ 8.08 (br, 2H, $CF_3CONHCH_2CH_2CH_2CH_2N\underline{H_2}$); δ 9.58 (br, 1H, $CF_3CON\underline{H}CH_2CH_2CH_2CH_2NH_2$). ESI-MS $[M + H]^+$ calcd 185.1, found 185.1.

Synthesis of Compound 2 [*N*-(4-(2,2,2-trifluoroacetamido)butyl)acrylamide]. Compound 1 (0.60 g, 3.25 mmol, 1 equiv) was dissolved in 10 mL of DMSO, followed by adding 1.32 g of triethylamine (13.0 mmol, 4 equiv). Acryloyl chloride solution (0.59 g, 6.50 mmol, 2 equiv) prepared in 10 mL of DMSO was slowly added dropwise to the solution of compound 1 on ice. The reaction mixture was stirred for 10 min, and the product was extracted using 3 × 100 mL of ethyl acetate. The product was purified by silica gel chromatography using a gradient from hexane to ethyl acetate to obtain the product as a powder with a hint of yellow color (0.20 g, 0.84 mmol, 26% yield). ^{1}H-NMR (500MHz, $CDCl_3$): δ 1.63 (m, 4H, $CF_3CONHCH_2C\underline{H_2}C\underline{H_2}CH_2NHCOCHCH_2$); δ 3.34 - 3.41 (m, 4H, $CF_3CONHC\underline{H_2}CH_2CH_2C\underline{H_2}NHCOCHCH_2$); δ 5.64 (dd, 1H, $CF_3CONHCH_2CH_2CH_2CH_2NHCOCHCH'\underline{H''}$); δ 6.12 (dd, 1H, $CF_3CONHCH_2CH_2CH_2CH_2NHCOC\underline{H}CH_2$); δ 6.16 (br, 1H, $CF_3CON\underline{H}CH_2CH_2CH_2CH_2NHCOCHCH_2$); δ 6.29 (dd, 1H, $CF_3CONHCH_2CH_2CH_2CH_2NHCOCHC\underline{H'}H''$); δ 7.51 (br, 1H, $CF_3CONHCH_2CH_2CH_2CH_2N\underline{H}COCHCH_2$). ESI-MS $[M + Na]^+$ calcd 261.1, found 261.1.

Synthesis of Compound 3. Linear low molecular weight PEI (L-LMW PEI, 2.5 kDa) (0.03 g, 0.70 mmol of secondary amine groups, 1 equiv) was dissolved in 2 mL of methanol, and the solvent was removed by evaporation under high vacuum for 30 min. The resulting solution was dissolved in 10 mL of dimethylformamide (DMF) containing 0.17 g of compound 2 (0.70 mmol, 1 equiv) and mixed with 0.07 g of triethylamine (0.70 mmol, 1 equiv). The resulting mixture was stirred for 120 h at 45 °C, and the polymer was precipitated into anhydrous diethyl ether and dried under vacuum. The obtained product was dissolved in 5 mL of 1:9 MeOH:6 M NaOH solution and stirred for 12 h to deprotect trifluoroacetate groups. Then the polymer was purified by dialysis against DI water at 4 °C (Mw Cutoff of dialysis membrane = 500) for 24 h, and the resulting polymer was freeze-dried overnight to obtain a white powder (21 mg, 40% yield). The grafting ratio of nondegradable branches relative to available secondary amines was calculated to be approximately 18% by integral ratio of methylene protons (1.59 - 1.67 ppm) of branches to methylene protons (2.7 - 3.1 ppm) of PEI backbone. The molecular weights of the product were determined by GPC using water as eluent, and they were calculated to be M_n = 3810

and M_w = 7164 with polydispersity index (PDI) of 1.88 by using poly(ethylene oxide) standards. ^{1}H-NMR (500MHz, D_2O): δ 1.59 - 1.67 (m, -$NCH_2CH_2CONHCH_2C\underline{H_2}C\underline{H_2}CH_2NH_2$); δ 2.47 (br, -$NCH_2CH_2CONHCH_2CH_2CH_2C\underline{H_2}NH_2$); δ 2.7 - 3.1 (m, -$C\underline{H_2}$-$C\underline{H_2}$-NH- and -$NC\underline{H_2}C\underline{H_2}CONHCH_2CH_2CH_2CH_2NH_2$); δ 3.5 - 3.6 (m, - $NCH_2CH_2CONHC\underline{H_2}CH_2CH_2CH_2NH_2$).

Bioconjugate Chemistry 20th Anniversary

Subscriber access provided by SHEMYAKIN-OVCHINNIKOV INST

Article

A Novel Antitumor Prodrug Platform Designed to Be Cleaved by the Endoprotease Legumain

Liron Stern, Rotem Perry, Paula Ofek, Ariel Many, Doron Shabat, and Ronit Satchi-Fainaro

Bioconjugate Chem., **2009**, 20 (3), 500-510• DOI: 10.1021/bc800448u • Publication Date (Web): 05 February 2009

Downloaded from http://pubs.acs.org on May 8, 2009

More About This Article

Additional resources and features associated with this article are available within the HTML version:

- Supporting Information
- Access to high resolution figures
- Links to articles and content related to this article
- Copyright permission to reproduce figures and/or text from this article

View the Full Text HTML

ACS Publications
High quality. High impact.

Bioconjugate Chemistry is published by the American Chemical Society. 1155 Sixteenth Street N.W., Washington, DC 20036

A Novel Antitumor Prodrug Platform Designed to Be Cleaved by the Endoprotease Legumain

Liron Stern,[†,||] Rotem Perry,[‡,||] Paula Ofek,[†] Ariel Many,[§] Doron Shabat,[‡] and Ronit Satchi-Fainaro*[,†]

Department of Physiology and Pharmacology, Sackler School of Medicine, Tel Aviv University, Ramat Aviv, Tel Aviv 69978, Israel, Department of Organic Chemistry, School of Chemistry, Raymond and Beverly Sackler Faculty of Exact Sciences, Tel Aviv University, Tel Aviv 69978, Israel, and Lis Maternity Hospital, Sourasky Medical Center, Tel Aviv, Israel. Received October 20, 2008; Revised Manuscript Received December 30, 2008

Chemotherapeutic treatment of neoplastic diseases is often restricted by adverse systemic toxicity, which limits the dose of drug that can be administered, or by the appearance of drug resistance. Therefore, novel targeted therapeutic approaches are being developed to improve current conventional therapy in order to increase specificity and biocompatibility, and decrease toxicity. Legumain represents a recently identified lysosomal protease that has been reported to be overexpressed in the majority of human solid tumors, to promote cell migration and is associated with enhanced tissue invasion and metastases. Therefore, it serves as a promising candidate for prodrug therapy. We synthesized a novel legumain-cleavable prodrug, carbobenzyloxy-alanine-alanine-asparagine-ethylenediamine-etoposide, which releases the chemotherapeutic agent, etoposide, as the active drug. The prodrug was characterized and analyzed by ^{1}H NMR and HPLC. 293 Human embryonic kidney (293 HEK) cells were stably transfected with human legumain, to achieve overexpression in vitro (293 HEK-Leg). 293 HEK-Leg cells expressed both active and inactive legumain and secreted it to the medium. Legumain expression was found to be elevated because of serum starvation in both 293 HEK cells and PC3 human prostate carcinoma cells. The commercial substrate of legumain, carbobenzyloxy-alanine-alanine-asparagine-amino-4-methyl coumarin (CBZ-Ala-Ala-Asn-AMC) and the synthesized prodrug were both cleaved by recombinant human legumain (rhlegumain) and legumain expressed in the 293 HEK-Leg cell lysate. Upon cleavage by rhlegumain, the prodrug showed an inhibitory effect on the proliferation of 293 HEK and 293 HEK-Leg cells. This study suggests a novel platform for prodrug therapy activated by legumain as a promising approach for cancer therapy.

INTRODUCTION

Current conventional chemotherapy, though widely used in cancer treatments, is still far from reaching its optimal potential. Clinically used chemotherapeutic drugs exhibit a short half-life in the bloodstream and a high overall clearance rate. Most chemotherapeutic drugs are considered to be low-molecular-weight compounds, and as such, they diffuse rapidly and are distributed evenly within the body, into tumor tissues as well as healthy ones (*1*). Thus, small amounts of the drug reach the target cancerous site, whereas healthy tissues suffer from many side effects that limit the maximum tolerated dose (MTD[1]) that can be administered (*1*).

The development of cancer prodrug therapies is implemented to solve the limitations of conventional chemotherapy. Prodrugs have been designed for optimal structure, size, and surface characteristics to increase their circulation time in the bloodstream. They are able to carry their loaded active agents to cancer cells by selectively using the unique pathophysiology of tumors, such as the acidic, neoplastic supporting microenvironment. As such, the microenvironment surrounding the tumor has been found to overexpress specific proteases that are active in these acidic conditions (*2*−*4*). It can be utilized for prodrug-targeting by linking a spacer cleavable by hydrolysis at low pH or by lysosomal or tumor-associated overexpressed enzymes resulting in the release of the active drug.

Legumain is a member of the C13 family of peptidases that specifically cleaves asparaginyl bonds. It was first discovered in plants (*5*−*7*) and later in parasites (*8*, *9*) and mammals (*10*, *11*). All legumains are synthesized as a 50−60 kDa pro-enzyme that undergoes activation upon autocleavage at acidic conditions (pH 3.0−6.0). Mature, active mammalian legumain varies in size from 30 kDa to 40 kDa, due to different degrees of glycosylation. Chen et al. detected 3 bands of human legumain in an immunoblot from a cell lysate consisting of a 56 kDa inactive pro-enzyme, a 46 kDa active form, and a 36 kDa mature active

* To whom correspondence should be addressed. Tel: +972-3-640 7427. Fax: +972-3-640 9113. E-mail: ronitsf@post.tau.ac.il.
† Department of Physiology and Pharmacology.
‡ Department of Organic Chemistry.
§ Sourasky Medical Center.
|| These authors contributed equally to this work.

[1]Abbreviations: 293 HEK, 293 human embryonic kidney; 293 HEK-Leg, 293 HEK cells stably transfected to overexpress legumain; ACN, acetonitrile; AMC, amino-4-methyl coumarin; AUC, area under the curve; BCA, bicinchoninic acid; CBZ, carbobenzyloxy; CT26, murine colon carcinoma cells; cDNA, complementary DNA; DMEM, Dulbecco's modified Eagle's medium; DMF, dimethyl formamide; DNA, deoxyribonucleic acid; ECGS, endothelial cell growth supplement; EDTA, ethylene diamine tetraacetic acid; EtOAc, ethylacetate; FBS, fetal bovine serum; FDA, food and drug administration; G418, neomycin; HUVEC, human umbilical vein endothelial cells; HPLC, high pressure liquid chromatography; HRP, horseradish peroxidase; IC_{50}, inhibitory concentration of 50% of the cells; IgG, immunoglobulin G; kDa, kilo Dalton; MeOH, methanol; MES, 2-(*N*-morpholino)ethanesulfonic acid sodium salt; MTD, maximum tolerated dose; PAGE, polyacrylamide gel electrophoresis; PBS, phosphate buffered saline; PNP, *p*-nitrophenyl; rhlegumain, recombinant human legumain; RP, reverse phase; t_R, retention time; s.c., subcutaneously; TFA, trifluoroacetic acid; THF, tetrahydrofuran; TLC, thin layer chromatography; TRAMP C2, transgenic adenocarcinoma of the mouse prostate C2; XTT assay, cell proliferation kit based on the tetrazolium salt XTT.

10.1021/bc800448u CCC: $40.75 © 2009 American Chemical Society
Published on Web 02/05/2009

enzyme. Pro-legumain is autocleaved at asparaginyl residues as well as aspartic ones, upon activation at pH 4.5 to produce the 46 kDa active form. Further autocleavage at acidic conditions results in the mature form of the 36 kDa, active human legumain. Once the enzyme is in its active form, raising the pH level up to 7.0 results in enzyme denaturation and therefore inactivation (*12*). The precise physiological role of mammalian legumain in human biology is still poorly understood. It has been found to be involved in the processing of the microbial tetanus toxin (*13*) and to play a role in osteoclast inhibition (*14*). Furthermore, it has been suggested that legumain is responsible for the processing of cathepsins B, H, and L (*15*) and activating progelatinase A to produce mature active gelatinase A (MMP-2) in cultured cells (*16*). A recently published study has also found legumain to regulate the degradation of fibronectin in renal proximal tubular cells. This implicates legumain in the control of extracellular matrix remodeling and turnover, a well-known process in various pathological conditions such as tumor growth, development of metastases and progression of atherosclerosis (*17*). In recent years, legumain has been reported to be overexpressed in tumors (*18*). High levels of legumain were found in tumor cells, as well as in tumor-associated endothelial cells, tumor-associated macrophages, and other stromal cells. Though never explored or examined empirically, legumain has been indicated to be up-regulated in vitro as a result of stress such as serum starvation or in vivo growth (*19*). Legumain is almost undetectable in vitro, suggesting that its expression is highly dependent on the unique microenvironment of the tumor (*19*). Therefore, we generated a cell line stably overexpressing legumain, in order to characterize its activity in vitro. Legumain is not only highly expressed in the lysosomal cell fraction (*10*), but it is also associated with the cell surface and colocalized with integrin β1. In addition, in vitro assays showed that tumor cells overexpressing legumain exhibit increased migration and invasion through the extracellular matrix. Furthermore, legumain was suggested to play a role in promoting tumor progression and correlated with a more aggressive behavior and a poorer prognosis (*20*). Legumain's unique specificity to cleavage of asparaginyl bonds and its connection to cancer progression led to the interesting notion regarding legumain as a target for various prodrug designs in targeted chemotherapeutics (*19*, *21*, *22*).

In this study, we designed and synthesized a legumain-activated prodrug of etoposide. Etoposide, 4′-demethyl-epipodophyllotoxin-9-[4,6-*O*-(*R*)-ethylidene-β-D-glucopyranoside], is a semisynthetic derivative of podophillotoxin, classified as a cell cycle-specific, plant alkaloid antineoplastic chemotherapeutic drug. It was the first topoisomerase II inhibitor to be discovered (*23*). Etoposide does not block the activity of this essential enzyme, but rather increases the steady-state concentration of the covalent DNA cleavage complexes, converting them into physiological toxins. High level of DNA breaks arise in the genome, becoming targets for recombination, sister chromatids exchange, insertions, deletions, chromosomal aberrations, and translocations. These alterations trigger a series of events, resulting in cell death and apoptosis, thus killing the tumor cells (*24*). Etoposide is one of the most highly prescribed anticancer drugs in the world, even though it possesses the same characteristics as most chemotherapeutic drugs do. Being a hydrophobic low-molecular-weight compound (588 g/mol), etoposide diffuses through the bloodstream to healthy tissues and causes many side effects. The primary dose-limiting toxicity of etoposide in clinical use is severe myelosuppression (*25*). Etoposide undergoes hydrolysis and epimerization to generate metabolites that are 100-fold and 500-fold less cytotoxic, or not active at all (*26*). Its low water-solubility forces it to either be solubilized in toxic solvents, such as tween-80 or ethanol, or to be diluted to low concentrations and administered in high volumes of an isotonic solution, causing discomfort either way (*27*). Accumulation of DNA breaks, caused by etoposide, generate potential mutations and chromosomal translocations that may also lead to myeloid/lymphoid or mixed lineage leukemia (*28*). Furthermore, it undergoes nonspecific hydrolysis, and it induces drug resistance in repeated treatment. New drug delivery systems are currently being developed in the hope of evading etoposide's limitations and toxicities while preserving and even elevating its antitumor activity, thus increasing its therapeutic index.

A well-established etoposide−prodrug system will prevail etoposide limitations and improve its efficacy and specificity in various cancer treatments. Here, we show a prodrug of etoposide linked to a tripeptide cleavable by legumain. We hypothesize that this prodrug will be activated by the overexpressed legumain in tumor epithelial and endothelial cells in vivo or by the ectopically or stress-induced overexpressed legumain in model systems in vitro.

EXPERIMENTAL PROCEDURES

Materials. DMEM (Dulbecco's modified Eagle's medium), FBS (fetal bovine serum), androstan, nonessential amino acids, sodium pyruvate, insulin, and penicillin−streptomycin−nystatin were obtained from Biological Industries, Israel; EGM-2 MV medium was obtained from Cambrex; Neomycin (G418) was obtained from Chemicon International; XTT reagent was obtained from biological industries; rhlegumain was obtained from R&D systems, USA; ketamine was obtained from Ketaset, Canada; xylazin was obtained from Medical Market; etoposide, polybrene, *n*-octyl β-D-glucopyranoside, protease inhibitor cocktail (P2714−1BTL), and CHAPS were obtained from Sigma Aldrich, Israel. CBZ-Ala-Ala-Asn-AMC (compound **1**) was obtained from Bachem. CBZ-Ala-Ala-Asn(Trt)-OH (compound **2**) was obtained from Chinese Peptide Company. Bicinchoninic acid (BCA) kit and enhanced chemiluminescence kit (SuperSignal) were obtained from Pierce, USA. Nitrocellulose membrane was obtained from Whatman, Germany. Endothelial mitogen was obtained from Biomedical Technologies, Stoughton, USA. Heparin was obtained from Laboratoire Choay, Paris, France. Monoclonal mouse antiactin was obtained from Sigma (A 1978); goat antimouse immunoglobulin G (IgG) horseradish peroxidase (HRP) was obtained from Jackson Immunoresearch (115-035-166); goat polyclonal antilegumain was obtained from R&D Systems (AF2199); goat polyclonal antilegumain was obtained from Santa Cruz (sc-47105); rabbit antigoat HRP was obtained from Chemicon International (AP106P); rabbit anti-p38 was obtained from Sigma; and goat antirabbit IgG HRP was obtained from Jackson Immunoresearch (11-035-144). The pcDNA3/legumain plasmid was kindly provided by David Roodman and Chang-Sook Hong (University of Texas Health Science Center, San-Antonio, Texas, USA).

Cell Culture. 293 HEK cells were kindly provided by Professor Sara Lavi (Tel Aviv University, Tel Aviv, Israel); U87-human glioblastoma and PC3-human prostate adenocarcinoma cells were obtained from the American Type Culture Collection (ATCC), Manassas, VA; TRAMP C2 cells were kindly provided by Professor Norman Greenberg (Fred Hutchinson Cancer Research Center, Seattle, Washington, USA.); CT26 murine colon carcinoma cells were kindly provided by Professor Eliezer Flescher (Tel Aviv University, Tel Aviv, Israel); human umbilical vein endothelial cells (HUVEC) were isolated in our laboratory as previously described (*29*). Umbilical cords were collected at Lis Maternity Hospital, Sourasky Medical Center, Tel Aviv, Israel. This was approved by the Institutional Review Board (IRB). CT26 colon carcinoma, 293 HEK, PC3-human prostate adenocarcinoma cells were cultured

in DMEM supplemented with 10% FBS, 100 μg/mL penicillin, 100 U/mL streptomycin, 12.5 U/mL nystatin, and 2 mM L-glutamine. TRAMP-C2: cells were cultured in DMEM supplemented with 10% FBS, 100 μg/mL penicillin, 100 U/mL streptomycin, 12.5 U/mL nystatin, 15 un/mL insulin, nonessential amino acids X 1, 10 μM androstan, 1 mM sodium pyruvate, and 2 mM L-glutamine. 293 HEK-Leg and U87 human glioblastoma cells were cultured in DMEM supplemented with 10% FBS, 100 μg/mL penicillin, 100 U/mL streptomycin, 12.5 U/mL nystatin, and 2 mM L-glutamine. For selection purposes, 200 μg/mL of G418 was added. HUVEC: Cells were cultured in M-199 supplemented with with 20% FBS, 100 μg/mL penicillin, 100 U/mL streptomycin, 12.5 U/mL nystatin and 2 mM L-glutamine, 50 μg/mL endothelial mitogen, and 5 U/mL heparin. All cells were grown at 37 °C; 5% CO_2.

Prodrug Synthesis. *Compound* **3.** Compound **2** was dissolved in dry THF (1 g, 1.53 mmol), and the mixture was cooled to −15 °C. *N*-Methyl morpholine (170 μL, 1.53 mmol) was added, and then isobutylchloroformate (239 μL, 1.843 mmol) was added dropwise. The reaction was stirred for 15 min, then, the commercially available *N*-Boc,*N*-methyl ethylenediamine (401.4 mg, 2.30 mmol) was added. The reaction was allowed to warm to room temperature, was stirred for 1 h, and was monitored by TLC (EtOAc/hexane, 85:15). Upon completion of the reaction, the solvent was removed under reduced pressure, and the crude product was purified by using column chromatography on silica gel (EtOAc/hexane, 85:15) to give compound **3** (808 mg, 65%) as a white solid.

^{1}H NMR (400 MHz, MeOD): $\delta = 7.33-7.14$ (20H, m); 5.09 (2H, bs); 4.67 (1H, m); 4.14−4.09 (2H, m); 3.45−3.25 (4H, bs); 3.08 (1H, dd); 2.84 (3H, s); 2.58 (1H, dd); 1.43 (9H, s); 1.34 (6H, s). ^{13}C NMR (100 MHz, MeOD): $\delta = 174.96$, 174.34, 173.74, 172.66, 158.41, 158.11, 146.16, 138.20, 130.43, 81.57, 68.85, 68.85, 52.50, 50.20, 40.39, 39.56, 37.21, 20.20, 19.33, 18.99.

Compound **4.** Compound **3** (100 mg, 0.123 mmol) was dissolved in 1 mL of TFA and stirred for 10 min. The excess of acid was removed under reduced pressure, and the crude amine salt was dissolved in 1 mL of DMF. The activated carbonate of etoposide (*30*) (111 mg, 0.147 mmol) was added, followed by the addition of triethylamine (163 μL, 1.17 mmol). The reaction was stirred for 30 min and was monitored by TLC (EtOAc/MeOH 90:10). Upon completion of the reaction, the solvent was removed under reduced pressure, and the crude product was purified by using column chromatography on silica gel (EtOAc/MeOH 90:10) to give compound **4** (98 mg, 75%) as a white powder.

^{1}H NMR (400 MHz, MeOD): $\delta = 7.33$ (5H, bs); 6.97 (1H, s); 6.49 (1H, s); 6.30 (2H, s); 5.92 (2H, s); 5.06 (2H, m); 4.95 (1H, m); 4.80 (1H, m); 4.66 (2H, m); 4.30 (2H, m); 3.63 (6H, s); 3.50 (7H, m); 2.94 (4H, m); 2.67 (3H, m); 1.32−1.2 (9H, m). ^{13}C NMR (100 MHz, MeOD): $\delta = 177.97$, 176.93, 173.88, 159.09,156.59, 155.58,153.83, 150.53, 148.98, 140.29, 134.28, 130.93,130.01, 129.81, 129.41, 111.72, 111.42, 109.41, 109.28, 103.79, 103.44, 101.25, 82.22, 76.35, 74.98, 74.49, 70.22, 69.61, 68.36, 68.05, 57.10, 52.92, 49.84, 48.88, 48.54, 45.77, 42.69, 39.75, 37.83, 21.12, 18.43, 17.66. HRMS (MALDI-TOF) calculated for $C_{51}H_{62}N_6O_{20}$ 1101.3911 [M + Na^+], found 1101.3899.

Evaluation of the Activity of Rhlegumain and Endogenous Legumain on Its Commercial Substrate CBZ-Ala-Ala-Asn-AMC. Prior to all activity assays, rhlegumain (R&D, Lot MVY01651) was activated by incubation at a concentration of 100 μg/mL in 50 mM NaOAc and 0.1 M NaCl, pH 4.0, for 2 h at 37 °C.

The specific activity of rhlegumain was measured using 100 μM of rhlegumain's commercial substrate CBZ-Ala-Ala-Asn-AMC and 50 ng of active enzyme in 100 μL of 50 mM MES and 0.25 M NaCl at pH 5.0. Cleavage of CBZ-Ala-Ala-Asn-AMC was measured at excitation $\lambda = 380$ nm and emission $\lambda = 460$ nm, in a fluorescence plate reader.

In order to measure the activity of the endogenous cellular legumain, confluent cells were first harvested in PBS and centrifuged at 3,000 rpm for 3 min at 4 °C. The pellet was resuspended in lysis buffer (40 mM citric acid, 121 mM $NaHPO_4$, 1 mM EDTA, and 1% w/v *n*-octyl-β-D-glucopyranoside, pH 5.8) and incubated on ice for 10 min with occasional vortexing. Three cycles of freezing and thawing were performed. Cells were centrifuged at 14,000 rpm for 20 min at 4 °C. The supernatant was collected and tested for its protein concentration using the BCA kit. Then, the enzymatic activity of endogenous legumain was measured using 5−10 μL of cell lysate (depending on total protein concentration), which were placed in a 96-well microtiter plate. The reaction was initiated by the addition of 190 μL of CBZ-Ala-Ala-Asn-AMC solution in assay buffer (40 mM citric acid and 121 mM $NaHPO_4$, pH 5.8, containing 1 mM dithiothreitol, 1 mM EDTA, and 0.1% CHAPS) to give a final concentration of 10 μM substrate. The plates were incubated at 25 °C, and the level of legumain activity was calculated from the obtained cleaved substrate. Fluorescence levels of the released AMC were measured at excitation $\lambda = 360$ nm and emission $\lambda = 460$ nm, in a fluorescence plate reader.

HPLC Analysis. To test etoposide prodrug cleavage by rhlegumain, 100 μL (50 mM MES and 0.25 M NaCl, pH 5.0) of 500 μM prodrug was incubated with 250 ng of activated rhlegumain overnight at 37 °C. A control tube with 100 μL of 500 μM prodrug without rhlegumain was incubated under the same conditions. HPLC analysis was performed using a C-18 RP (reverse phase) analytical column; $\lambda = 290$ nm; flow, 1 mL min^{-1}; eluent, ACN/H_2O; gradient program, $t = 0$ (10% ACN/90% H_2O)−$t = 30$ (100% ACN/0% H_2O).

To test etoposide prodrug cleavage by cell lysates, 293 HEK-Leg, 293 HEK, and CT26 cells were lysed according to cell lysis (endogenous legumain activity assay) described in this section. The etoposide prodrug (250 μM) was incubated with 75 μL of cell lysate (giving total volume of 200 μL) at 37 °C. HPLC analysis was performed using a C-18 RP analytical column; $\lambda = 290$ nm; flow, 1 mL min^{-1}; eluent, ACN/H_2O; gradient program, $t = 0$ (10% ACN/90% H_2O)−$t = 30$ (100% ACN/0% H_2O).

Stable Transfection of Legumain into 293 HEK Cells. 293 HEK cells were plated a day before tranfection to reach 80% confluency during transfection. Cells were stably transfected with pcDNA3/legumain by calcium phosphate/DNA precipitation (*31*). Transfected cells were cultured in medium containing 1.2 mg/mL of G418. Every 3 days, the selection media containing G418 was changed. Following 2 weeks of culture in selection media, cell lysates and conditioned medium were tested for legumain expression by Western blot.

Cell Starvation. CT26 murine colon carcinoma, 293 HEK, TRAMP C2, PC3 human prostate adenocarcinoma, and U87 human glioblastoma cells were plated to reach 90% confluence at starvation. The medium of each cell line was replaced with serum-free medium. An additional plate of each cell line was left with cultured medium as the control. All plates were further incubated at 37 °C and 5% CO_2 for 6 h. Cells were harvested and kept in −80 °C.

Western Blot Analysis. Prior to Western blot analysis, the medium was concentrated and lyophilized O.N. (Benchtop-K, VirTis). The powder was resuspended in 1 mL of DDW.

For cell lysate analysis by Western blot, confluent cells were harvested with PBS and centrifuged at 3,000 rpm for 3 min at 4 °C. The pellet was resuspended in lysis buffer (50 mM Tris-HCl, pH 7.5, 150 mM NaCl, 5 mM EDTA, and 1% triton,

supplemented with 1% protease inhibitor cocktail) and incubated on ice for 20 min with occasional vortex. Cells were centrifuged at 14,000 rpm for 20 min at 4 °C. The supernatant was collected and tested for its protein concentration by the BCA kit.

For tumor and organ analysis by Western blot, murine tumors and organs were weighed. Lysis buffer (50 mM sodium citrate, pH 5.8, 0.1 M NaCl, 1 mM EDTA, and 2 mM β-mercaptoethanol) was added in 8 parts (v/w). Tissues were homogenized using a homogenizer (Politron, Kinematika, Switzerland), and three cycles of freezing and thawing were performed. The homogenates were centrifuged at 14,000 rpm at 4 °C for 20 min. The supernatant was collected and tested for its protein concentration using the BCA kit.

All cell lysates, tissue lysates, and cell medium were boiled in sample buffer × 2 and loaded onto a 12% PAGE gel. Following electrophoresis, the proteins were transferred to nitrocellulose membranes, which were blocked with nonfat milk. For legumain detection, goat antilegumain was incubated with the membrane O.N. (1:1,000 dilution with R&D or 1:200 with Santa Cruz, depending on the samples). The membrane was washed three times with TBST and then incubated with HRP-labeled antigoat IgG (1:5,000) for 1 h. For p38 detection, rabbit anti-p38 was incubated with the membrane for 2 h (1:10,000 dilution). The membrane was washed three times with TBST and incubated with HRP labeled antirabbit IgG (1:10,000) for 1 h. Following incubation with the antibodies, membranes were washed three times with TBST, incubated with Supersignal kit, exposed to film, and developed.

Cell Proliferation Assay. 293 HEK or 293 HEK-Leg cells were plated at 4000 cells/well in a 96-well plate (37 °C; 5% CO_2). For serum-starved cell lines, medium was replaced with serum-free DMEM for 6 h. Cells were then challenged with etoposide, etoposide prodrug, or etoposide prodrug preincubated O.N. with rhlegumain, at serial concentrations. Control cells were grown with DMEM with growth factors and serum. Following 72 h, cell growth was evaluated by an XTT assay (*32*).

For HUVEC proliferation assay, cells were plated at 15,000 cells/well (37 °C; 5% CO_2). Following 24 h, cells were challenged with etoposide, etoposide prodrug, etoposide prodrug preincubated O.N. with rhlegumain, at serial concentrations, Control cells were grown with EGM2-MV. Following 72 h, HUVEC were counted with a Z1-Coulter particle counter (Beckman Coulter).

Animal Studies. All animal procedures were performed in compliance with Tel Aviv University, Sackler School of Medicine guidelines and protocols approved by the Institutional Animal Care and Use Committee. Animal were treated as follows: (a) 7 week old male Balb/c mice were inoculated s.c. with 1×10^6 CT26 cells. Upon exceeding 1000 mm^3 in volume, mice were euthanized by cervical dislocation, and immediately, all tumors and organs were removed and kept at −80 °C. Tumor volume was measured with a caliper and calculated according to the formula width × length^2 × 0.52. (b) 7 weeks old male C57/BL6 mice were inoculated orthotopically into the prostate with 1×10^6 TRAMP C2 cells. Following 2 weeks, mice were euthanized by cervical dislocation, and immediately, all tumors and organs were resected and kept at −80 °C.

Semiquantitative RT-PCR. Total RNA extraction was performed using the EZ-RNA kit (Biological Industries) according to the manufacturer's instructions. The reverse transcriptase reaction was performed with the EZ-first Strand cDNA Synthesis kit (Biological Industries) using oligo(dT) primers. The PCR reactions were carried out using PCR-ReadyTM High Specificity (Syntezza) in an ATC 401 thermocycler (Apollo, CLP). To get semiquantitative results, the number of cycles for each reaction was kept at a minimum.

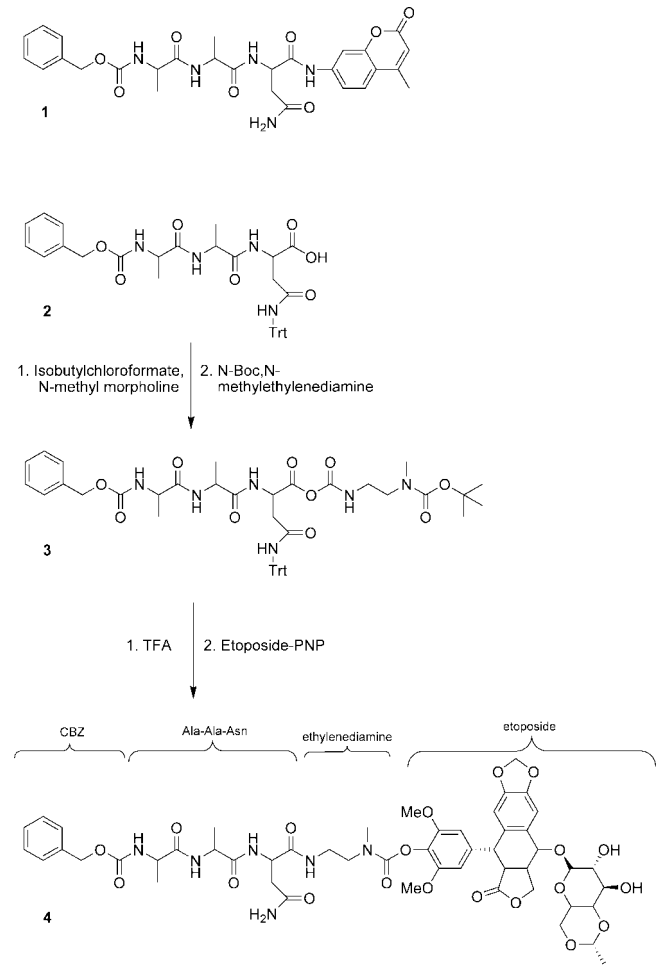

Figure 1. Synthesis of etoposide prodrug (compound **4**). Etoposide was conjugated to the tripeptide (legumain substrate) through an amine spacer (*N*-Boc,*N*-methyl ethylenediamine) to give the final prodrug-compound **4.**

PCR primers: Legumain, 5′-AAGCACTGGGTGGTGATTG-3′ and 5′-TGAGGTCAAGGT GTGTGA-3′; GAPDH, 5′-CCATCACCATCTTCCAGGAGC-3′ and 5′-GGCATGGACT-GTGGTCATGAG-3′.

RESULTS

Etoposide Prodrug Synthesis. On the basis of the standard substrate of legumain, we synthesized a tripeptide substrate, linked to an amine spacer (which is used for etoposide conjugation). The synthesis of the etoposide prodrug is presented in Figure 1. Compound **2**, CBZ-Ala-Ala-Asn(Trt)-OH, was coupled with the commercially available, *N*-Boc,*N*-methylethylenediamine, yielding compound **3**. Compound **3** was dissolved in TFA for deprotection of both the Trityl and the Boc protecting groups. Then, the carbonate derivative of etoposide was reacted with the deprotected substrate, generating the final prodrug **4** (Figure 1).

rhLegumain Cleaved Its Substrate CBZ-Ala-Ala-Asn-AMC More Potently at pH 6.5 than at pH 5.0. Enzymatic activity of legumain was first evaluated by incubating rhlegumain with the commercially available substrate CBZ-Ala-Ala-Asn-AMC. Unexpectedly, the enzymatic activity was greater at a pH value of 6.5 rather than at 5.0. No enzymatic activity was noted at pH 7.0 due to the fact that legumain undergoes denaturation at these basic conditions. The substrate alone showed no spontaneous release of AMC, when incubated without rhlegumain (Figure 2a).

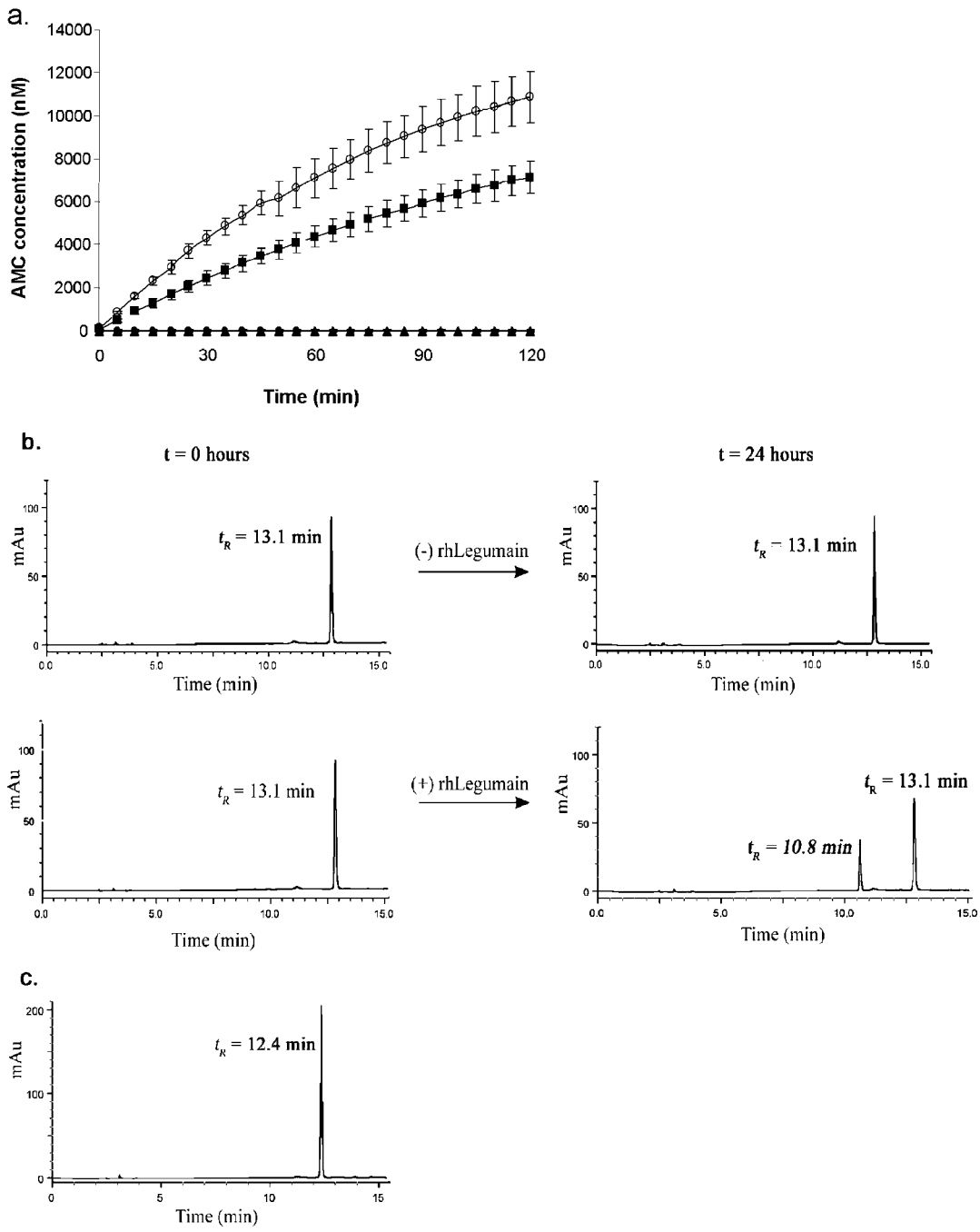

Figure 2. Active rhlegumain potently cleaves its substrate CBZ-Ala-Ala-Asn-AMC and the etoposide prodrug. (a) AMC release at pH 5.0 (■), pH 6.5 (○), pH 7.0 (♦), or in the absence of rhlegumain (▲). Data represent the mean ± SD (b) HPLC analysis of etoposide prodrug in the absence or presence of rhlegumain at $t = 0$ and $t = 24$ h. (c) HPLC analysis of free etoposide.

Characterization of the Etoposide Prodrug. In order to establish its capability to be cleaved by legumain, the etoposide prodrug was incubated with rhlegumain and evaluated using HPLC. The etoposide prodrug eluted as a single peak with an average retention time of $t_R = 13.1$ min and exhibited no self-degradation for 24 h. Incubation of the prodrug with rhlegumain for 24 h resulted in 33% of an inactive etoposide−ethylenediamine (Figure 2b). Further basic conditions were supplied in order for the linker to be released and free active etoposide to be generated, as previously described (*33*). Under the tested conditions, the ethylenediamine failed to undergo cyclization and release free etoposide. Free etoposide eluted as a single peak with $t_R = 12.4$ min (Figure 2c).

293 HEK-Leg Express Legumain. It has been previously reported that legumain expression in vitro is scarce (*19*). Therefore, 293 HEK cells were stably transfected to constitutively overexpress legumain. Legumain expression was evaluated by Western blot analysis. Commercial active (46 kDa) and inactive (56 kDa) rhlegumain were used as size reference controls (Figure 3a). Active legumain was detected in 293 HEK-Leg cells as 46 and 36 kDa bands (mature and nonmature protein) and inactive legumain as a 56 kDa band. 293 HEK-Leg cells also secreted legumain to the conditioned medium. No signal was found in the nontransfected 293 HEK cell lysate and medium. p38 was used as the loading control (Figure 3b).

Expression of Legumain Was Elevated due to Serum Starvation. As previously described, the tumor microenvironment is characterized by a defective supply of blood and nutrients, which exposes the tumor cells to hypoxia and starvation.

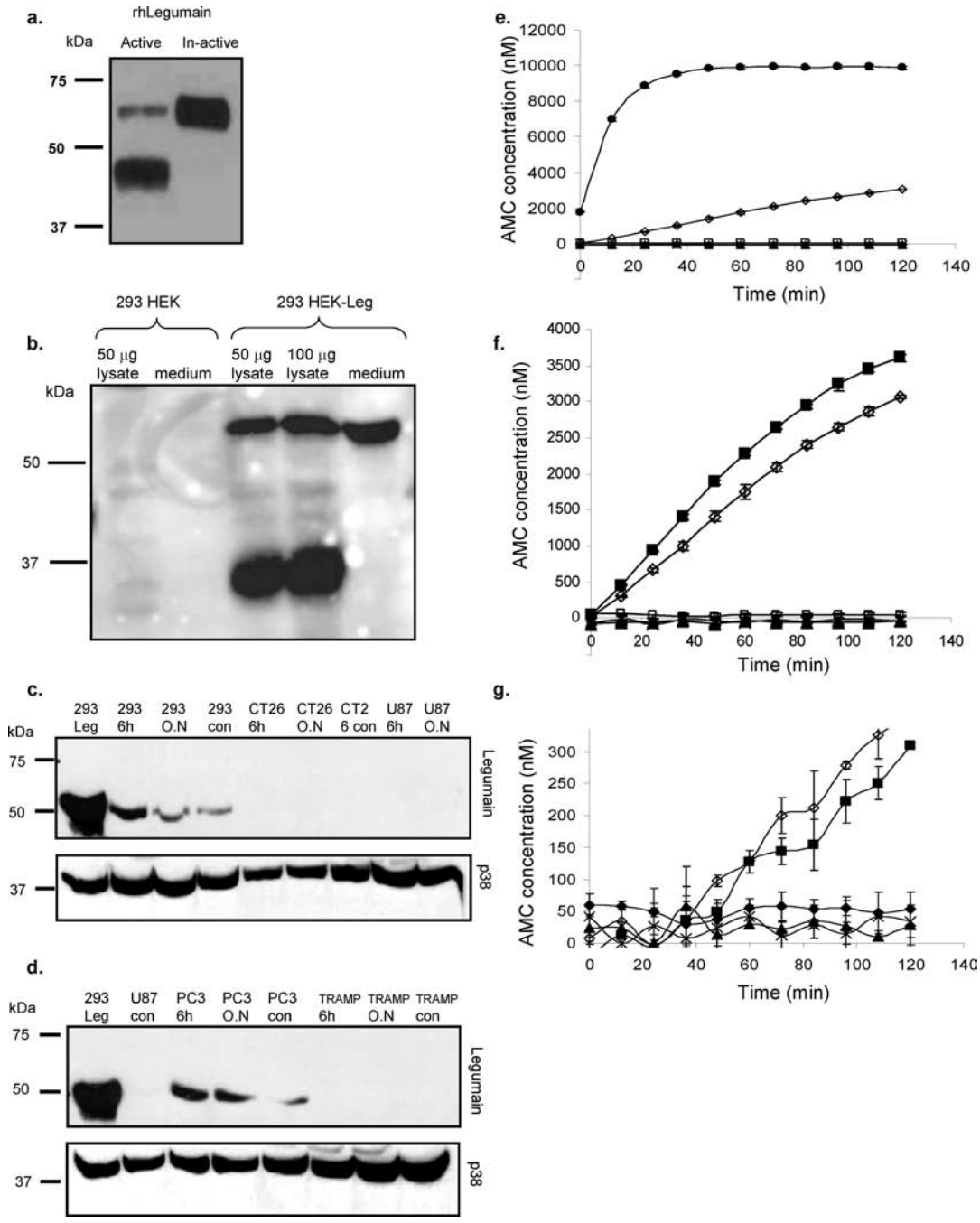

Figure 3. Legumain expression pattern and activity. (a) Western blot analysis of active (46 kDa) and inactive (56 kDa) rhlegumain. (b) Western blot analysis of cell lysate and conditioned medium of 293 HEK and 293 HEK-Leg cells. Active legumain is detected at 46 and 36 kDa (nonmature and mature forms, respectively), and inactive legumain is detected as a band of 56 kDa. p38 antibody was used as loading control. (c,d) 293 HEK, CT26 colon carcinoma, U87-human glioblastoma, PC3-human prostate adenocarcinoma, and TRAMP C2 murine prostate adenocarcinoma cells were serum starved for 6 h, O.N., or not starved at all, respectively. Cells were then harvested, lysed, and analyzed by Western blot. (e) Legumain commercial substrate was incubated with 293 HEK-Leg (●) or 293 HEK cell lysate (◊). Substrate alone (□), 293 HEK cell lysate (▲), and 293 HEKLeg cell lysate (×) were controls. A legumain activity assay was performed as described in Experimental Procedures. (f) Control (◊) or serum-starved (■) 293 HEK cell lysates were incubated with substrate. Substrate alone (□) and 293 HEK cell lysate alone, either serum starved (×) or nonstarved (▲) were controls. A legumain activity assay was performed. Data represent the mean ± SD. (g) Control (◊) or serum-starved (▲) PC3 cell lysate were incubated with the substrate. Substrate alone (♦) and PC3 cell lysate alone, either starved (×) or nonstraved (■) were controls. A legumain activity assay was performed. Data represent the mean ± SD.

Therefore, we wanted to determine whether endogenous legumain elevates as a result of serum starvation. Different cell lines were serum-starved and examined for their legumain expression. Only 293 HEK and PC3 prostate adenocarcinoma cell lines expressed legumain in vitro, and the levels of its inactive form increased following serum starvation. p38 antibody was used as the loading control (Figure 3c,d).

Overexpressed Legumain in 293 HEK-Leg Cells Potently Cleaved CBZ-Ala-Ala-Asn-AMC. 293 HEK-Leg cells were found to overexpress the active form of legumain (Figure 3b). Therefore, we evaluated the enzymatic activity of endogenous and overexpressed legumain. 293 HEK-Leg cell lysates were incubated with legumain's commercial substrate CBZ-Ala-Ala-Asn-AMC and released high levels of AMC. 293

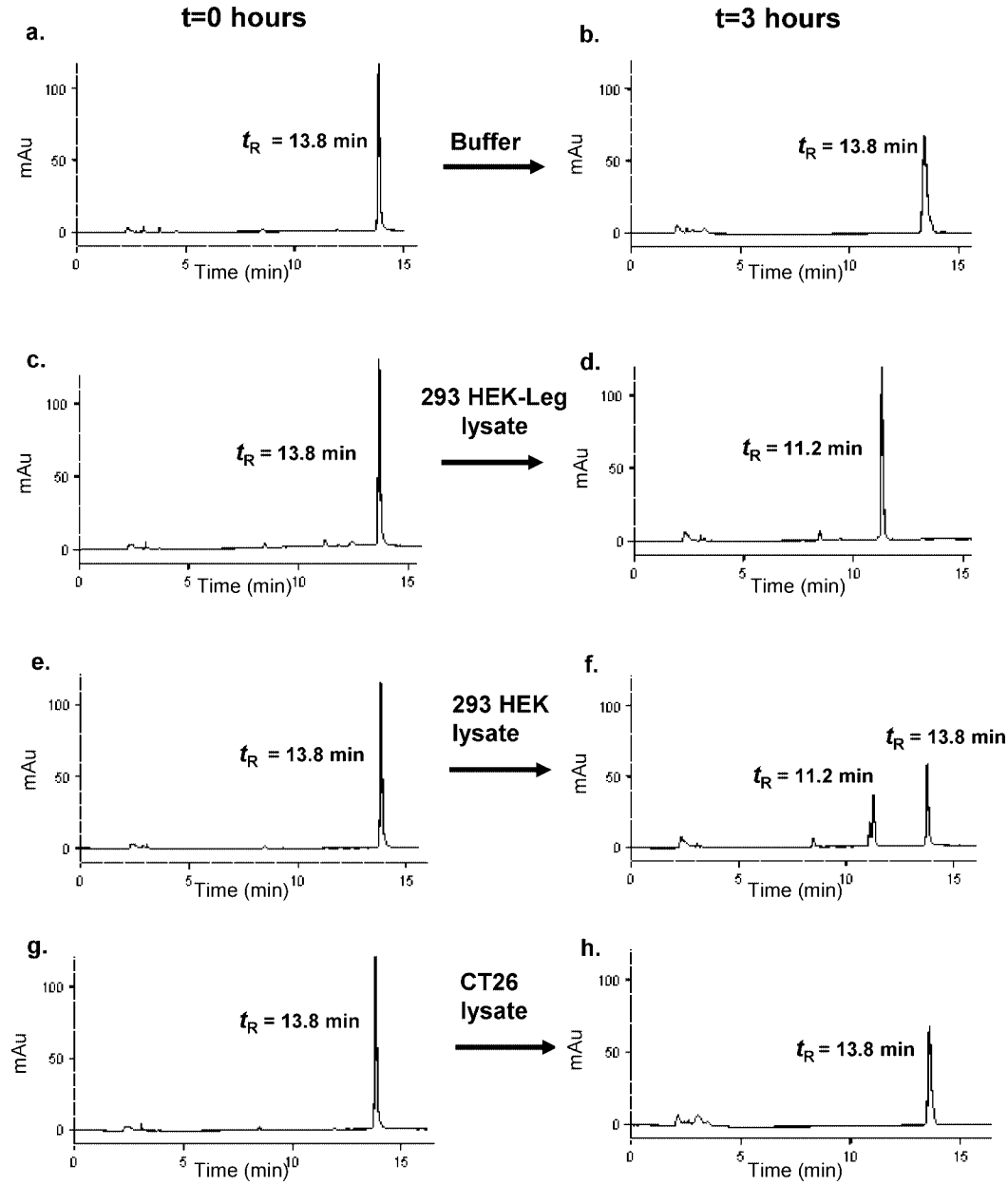

Figure 4. Both endogenous and exogenous legumain effectively and selectively cleave the etoposide prodrug as evaluated by HPLC analysis. (a,b) Etoposide prodrug in buffer at $t = 0$ and 3 h following incubation in buffer. (c,d) Etoposide prodrug with 293 HEK-Leg cell lysate at $t = 0-3$ h. (e,f) Etoposide prodrug with 293 HEK cell lysate at $t = 0-3$ h. (g,h) Etoposide prodrug with CT26 cell lysate at $t = 0-3$ h.

HEK cell lysates showed only a minor enzymatic activity releasing very low levels of AMC (Figure 3e). We further explored whether the elevation in expression of legumain due to serum starvation correlates with an increase in its enzymatic activity. 293 HEK serum-starved cells showed a slight 1.2-fold increase in enzymatic activity toward CBZ-Ala-Ala-Asn-AMC compared to that of nonstarved 293 HEK cells (Figure 3f), while PC3 serum-starved or nonstarved cells showed no significant difference in enzymatic activity (Figure 3g). Substrate alone and cell lysates of starved and nonstarved cells were used as controls.

Overexpressed Legumain Potently and Selectively Cleaved the Etoposide Prodrug. In order to examine whether ectopically expressed legumain specifically cleaves the etoposide prodrug, the prodrug was incubated separately with 293 HEK-Leg, 293 HEK, and CT26 cell lysates. Cleavage was evaluated using HPLC analysis. While the etoposide prodrug alone did not undergo self-hydrolysis within 3 h and elute as a single pick with $t_R = 13.8$ min (Figure 4a,b), incubation of 3 h with 293 HEK-Leg cell lysates resulted in 100% cleavage, generating etoposide−ethylenediamime (etoposide-linker) with $t_R = 11.2$ min (Figure 4c,d). 293 HEK cell lysates, which were previously found to scarcely express legumain, resulted in only 33% cleavage (Figure 4e,f), and CT26 cell lysates left the etoposide prodrug 100% intact following 3 h of incubation (Figure 4g,h).

Etoposide and Etoposide Prodrug Inhibited the Proliferation of 293 HEK and 293 HEK-Leg Cells. To determine the in vitro activity of etoposide and the etoposide prodrug, their inhibitory effect was tested on 293 HEK and 293 HEK-Leg cells. Free etoposide inhibited the proliferation of both cell lines with an IC_{50} of 700 nM. Treatment with the etoposide prodrug alone on both 293 HEK-Leg and 293 HEK cells did not reach the IC_{50} at the concentrations tested ($IC_{50} > 100$ μM). However, when cleaved externally with rhlegumain prior to the proliferation assay, the etoposide prodrug inhibited 293 HEK and 293 HEK-Leg cells with an IC_{50} of 4 μM (Figure 5a).

Serum-Starvation-Induced Inhibition of the Proliferation of 293 HEK Cells by the Legumain-Activated Pro-

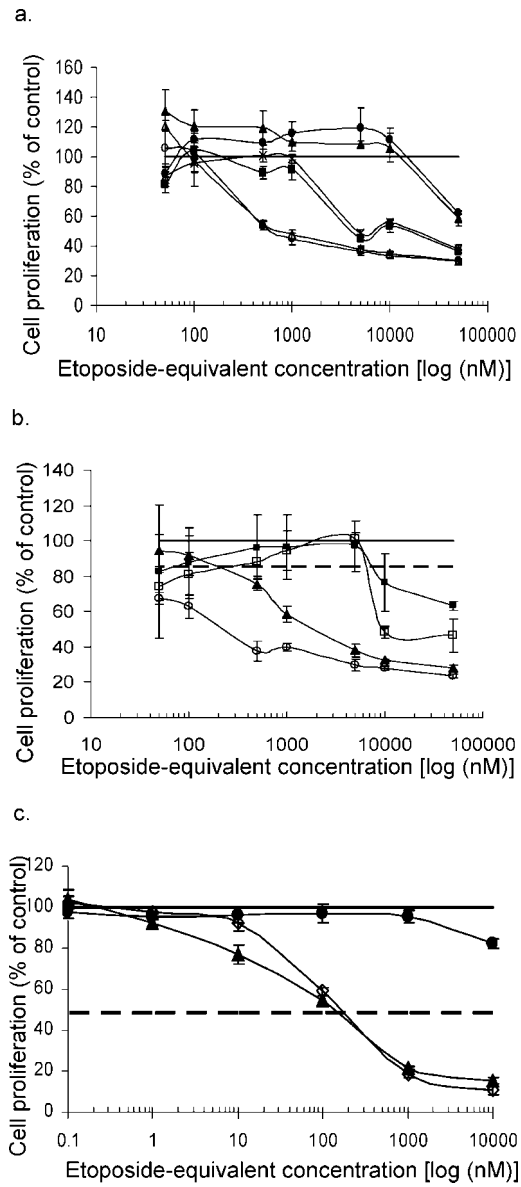

Figure 5. Etoposide and the etoposide prodrug inhibit cell proliferation in vitro. (a) Proliferation assay of 293 HEK-Leg (△,▲) and 293 HEK cells (○,●), following treatment with free etoposide and etoposide prodrug, respectively. 293 HEK cells were also assayed for proliferation following treatment with the externally cleaved etoposide prodrug (■). (b) Proliferation assay of control (black triangles and squares) and serum-starved (white circles and squares) 293 HEK cells, following treatment with free etoposide and etoposide prodrug, respectively. (c) HUVEC proliferation assay following incubation with free etoposide (◊), the etoposide prodrug (●), and the legumain-activated etoposide prodrug (▲). Data represent the mean ± SD.

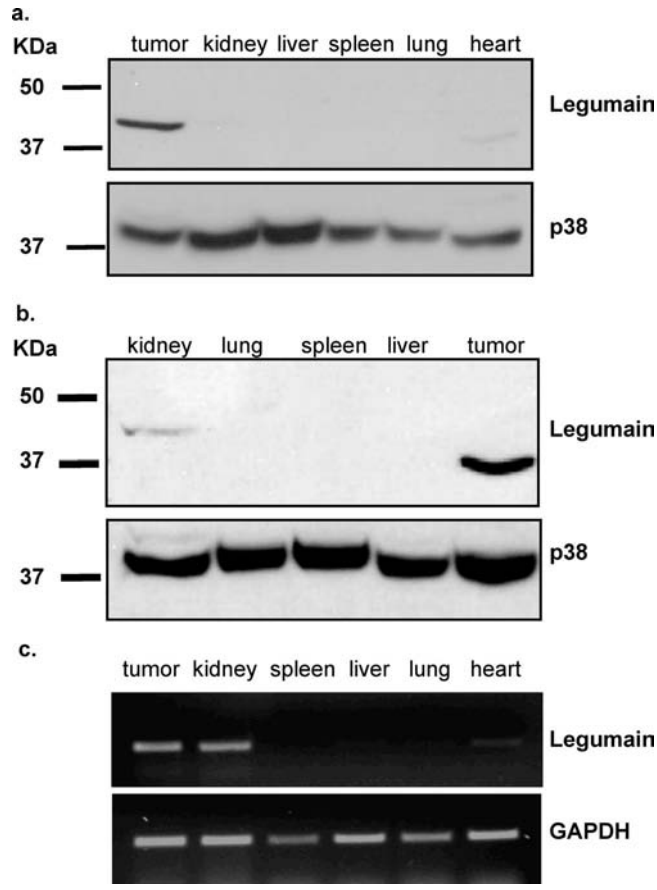

Figure 6. Legumain is overexpressed in murine tumors inoculated in mice compared to normal organs. (a) CT26 tumors inoculated s.c. in Balb/c mice and their normal organs were dissected, homogenized, lysed, and analyzed for legumain expression by Western blot. p38 antibody was used as the loading control. (b) Orthotopic TRAMP-C2 prostate tumors inoculated in C57/BL6 and their normal organs were dissected, homogenized, lysed, and analyzed for legumain expression by Western blot. p38 antibody was used as the loading control. (c) Orthotopic TRAMP-C2 prostate tumors inoculated in C57/BL6 and their normal organs were dissected and homogenized, and RNA was isolated. Legumain mRNA levels were monitored and calibrated to GAPDH mRNA levels (semiquantitive RT-PCR).

drug at High Concentrations. To determine whether the potency of the etoposide prodrug elevates because of the increase in legumain expression, the inhibitory effect of etoposide and the etoposide prodrug was tested on 293 HEK serum-starved or nonstarved cells. Serum starvation of 293 HEK cells was performed in order to elevate legumain expression. Free etoposide inhibited proliferation of both starved and nonstarved cells with IC_{50} values of 200 nM and 2 μM, respectively. The prodrug also had a more toxic effect on serum-starved cells, but only at concentrations higher than 5 μM. At lower concentrations, the prodrug had the same effect on cells grown in the presence or absence of serum (Figure 5b).

Etoposide and the Etoposide Prodrug Inhibited HUVEC Proliferation. It has been recently shown that legumain is also overexpressed in tumor endothelial cells in vivo (*18*). Hence, having shown the inhibitory effect of etoposide on 293 HEK cells, its ability to inhibit HUVEC proliferation was evaluated. Free etoposide and the legumain-activated etoposide prodrug (cleaved externally with rhlegumain prior to the proliferation assay) inhibited HUVEC proliferation with an IC_{50} of 150 nM (Figure 5c). The prodrug alone did not have any inhibitory effect on HUVEC proliferation.

Legumain Is Overexpressed in Murine Tumors Inoculated in Mice Compared to Healthy Organs. In order to demonstrate the potential of an etoposide prodrug activated by legumain in vivo, we examined the expression of legumain in murine tumors inoculated in mice and their healthy organs. CT26 derived tumors and organs of Balb/c mice (Figure 6a) and TRAMP-C2 murine prostate adenocarcinoma and organs of C57/BL6 mice (Figure 6b,c) were lysed and evaluated for legumain expression by Western blot and semiquantitive RT-PCR. Legumain is highly expressed in tumor tissues as opposed to other healthy organs. CT26 cells, subcutaneously inoculated in a Balb/c mouse, showed high expression of murine legumain, while only low levels of legumain were detected in the heart, and no legumain at all in the kidney, liver, spleen, or lung lysates (Figure 6a). TRAMP-C2 prostate tumors, orthotopically inoculated in C57/BL6 mice, expressed high levels of legumain, while

the kidney tissue lysate expressed low levels, and in other organs tested no legumain was detected (Figure 6b). Accordingly, legumain mRNA levels were also higher in the tumor and the kidney in comparison to that in other tissues tested (Figure 6c).

DISCUSSION

The pursuit for effective strategies of targeted chemotherapy treatments for various neoplastic pathologies is still ongoing, as many novel compounds are already in clinical trials. A common method for targeting chemotherapeutic agents specifically to the tumor is the design of a prodrug platform that covalently links the drug to a peptide cleavable by a certain overexpressed protease in the tumor and its microenvironment. Such is legumain, which represents a novel candidate target for chemotherapeutic and antiangiogenic prodrug therapy.

To date, there are only two ongoing prodrug preclinical studies based on legumain, one of which covalently links a peptide cleavable by legumain to doxorubicin. Wu et al. showed that *N*-Suc-Ala-Ala-Asn-Leu-doxorubicin, named LEG-3, was cleavable by legumain and released Leu-doxorubicin at the tumor site (*19*). The second prodrug therapy is a legumain-based DNA vaccine, which leads to suppression of tumor growth and metastasis (*21, 22*).

In this study, we described the synthesis of a prodrug that covalently links the chemotherapeutic agent etoposide to legumain's substrate, CBZ-Ala-Ala-Asn-ethylenediamine-etoposide. The prodrug is designed to be cleaved at acidic conditions by legumain, at the asparagine residue bound to ethylenediamine through a carbamate bond, creating an ethylenediamine−etoposide moiety. According to the chemical synthesis technique established by Perry et al. (*33*), the ethylenediamine linker undergoes cyclization at physiological pH, releasing free etoposide. Thus, the prodrug is designed to be cleaved by legumain in the cell lysosome at acidic pH values and undergo cyclization and etoposide release in the cell cytoplasm.

Enzymatic activity of rhlegumain is known to be optimal at pH 5.0. We evaluated its activity at a pH value of 6.5, an acidic level that better reflects the neoplastic environment, in comparison to the supposedly optimal pH 5 and 7 (Figure 2a). Legumain's enzymatic activity was the highest at pH 6.5, further establishing the concept of it being a suitable target for anticancer prodrug therapy. Evaluation of the enzymatic activity of the commercial legumain led to testing its ability to cleave the prodrug using HPLC analysis (Figure 2b). Our results revealed that the prodrug is in fact cleavable by legumain and generates the ethylenediamine−etoposide moiety at acidic conditions.

We have transfected cells to overexpress legumain in vitro (293 HEK-Leg), which was shown to be highly active against CBZ-Ala-Ala-Asn-AMC (Figure 3b,e). We were also interested in exploring whether stress such as serum starvation would elevate legumain expression in vitro in various cell lines. Our interest was based on the notion that legumain is a stress-responsive gene, as previously suggested by Lui et al. (*18*). This idea was not investigated or tested empirically. Thus, we serum starved various cell lines and examined their endogenous legumain expression (Figure 3d,e). Our findings revealed that legumain expression, though in its inactive form of 56 kDa, is elevated in both 293 HEK and PC3 cell lines following 6 h of serum starvation. Overnight serum starvation did not further elevate legumain expression, probably due to a decrease in cell metabolism, caused by the prolonged stress. The present study is the first to show an increase in legumain expression due to serum starvation in vitro, in any kind of cell line. Although the level of legumain expression was raised, only a slight increase in the enzymatic activity was detected in the serum-starved versus the control 293 HEK cells. There was no difference between the level of legumain enzymatic activity in the control or serum-starved PC3 cells, when tested on the commercial substrate of legumain. This is probably due to the fact that upon serum starvation, only the inactive form of legumain expression level was augmented (Figure 3c,d).

293 HEK-Leg cells cleaved 100% of the prodrug, whereas 293 HEK cells, which express low levels of legumain, cleaved only 33% of it. CT26 cell lysate, in which no legumain expression was found, similarly to our working buffer alone, did not cleave the prodrug at all (Figure 4). This result indicates not only that our transfected 293 HEK-Leg cells successfully cleaved the prodrug but also that the prodrug is specifically and exclusively cleaved by legumain and not by other proteases, as demonstrated by the CT26 cell line, which does not express legumain. Furthermore, the prodrug remains stable and does not undergo nonspecific self-hydrolysis within 72 h.

Establishment of the specificity of the prodrug to be cleaved by legumain enabled us to test its cytotoxic potential. We evaluated the inhibitory effect of the prodrug on the proliferation of 293 HEK and 293 HEK-Leg cells (Figure 5a). As expected, the prodrug did not inhibit the proliferation of 293 HEK cells, and free etoposide inhibited the proliferation of both 293 HEK and 293 HEK-Leg in the same manner, achieving similar IC_{50} values. In contrast to our expectation, the prodrug failed to inhibit the proliferation of 293 HEK-Leg cells. This disappointing result might be due to the fact that upon cleavage by legumain at acidic conditions, the ethylenediamine−etoposide either failed to exit the lysosome and reach the cytoplasm or that cyclization did not occur. Another possibility that can explain the failure of the prodrug to inhibit the proliferation of 293 HEK-Leg cells concerned its uptake by the cells. Even though the prodrug is relatively small in its molecular size and is compact in structure, it is possible that the prodrug failed to enter the cells and therefore did not inhibit cell proliferation. Furthermore, it is plausible that the prodrug did internalize into the cell but did not succeed in entering the lysosome in order to be cleaved. A suitable uptake assay on an adequate prodrug pathway examination is necessary and would reveal whether the prodrug internalizes the cell through passive endocytosis, as expected, or whether it is adsorbed around the cell membrane. A future confocal microscopy analysis of a fluorescently labeled prodrug would disclose its subcellular trafficking and localization. Since etoposide is not fluorescent by itself (unlike doxorubicin), it will be necessary to link a suitable fluorescent molecule for detection purposes that does not interfere with the prodrug's cleavage site.

We have demonstrated that expression levels of endogenous legumain elevate in 293 HEK cells following stress. We hypothesized that cells expressing high levels of endogenous legumain may better cleave and activate the prodrug than 293 HEK-Leg cells, which overexpress ectopic legumain. The inhibitory effect of the prodrug on the proliferation of serum-starved 293 HEK cells revealed that serum starvation turned the cells more susceptible to etoposide (Figure 5b). However, serum starvation in itself had no significant inhibitory effect on the proliferation of 293 HEK cells treated with low concentrations of the etoposide prodrug. The influence of serum starvation was noted at concentrations higher than 5 μM etoposide prodrug. The IC_{50} of the etoposide prodrug on serum-starved 293 HEK cells was lower than the IC_{50} of the etoposide prodrug on nonstarved 293 HEK cells. Thus, at relatively high concentrations of the etoposide prodrug, serum starvation increased the prodrug's potency on the inhibition of proliferation of 293 HEK cells by increasing legumain's expression and augmenting the sensitivity of the cells to the treatment.

Legumain has also been reported to be overexpressed in tumor endothelial cells. Therefore, we evaluated the effect of the etoposide prodrug on tumor angiogenesis by examining the

inhibitory potential of etoposide on proliferating endothelial cells (Figure 5c). Our results indicate that etoposide inhibits HUVEC proliferation at concentrations 1 log-lower than tumor cells; hence, tumor endothelial cells would be sensitive to lower doses of etoposide released from the prodrug.

We inoculated two different cell lines in two different strains of mice (CT26 in Balb/c mice and TRAMP C2 in C57BL/6 mice) in order to show that overexpression of legumain is not cell line-dependent or strain-dependent. Western blot and RT-PCR analysis revealed that legumain is in fact overexpressed in tumor tissues rather than in normal tissues, in both cell lines in both strains (Figure 6). Interestingly, although there was no substantial difference between the mRNA levels of legumain in the tumor and kidney tissues from C57/BL6 mice, the legumain protein levels were substantially higher in tumor tissues. This finding suggests that the expression level of legumain is not governed by enhanced transcription and points to the involvement of post-translational events. Further studies should clarify this issue.

In summary, this study describes the synthesis and characterization of an etoposide prodrug designed to be cleaved by the endoprotease legumain. The prodrug was found to be potently and selectively cleaved by all three forms of legumain: the commercial, overexpressed, and endogenous legumain. Therefore, the prodrug should specifically be cleaved at the tumor site, which will warrant this approach as a novel anticancer targeted therapy.

ACKNOWLEDGMENT

This research was partly supported by the Israel Science Foundation (grant no. 1300/06) and a grant from the Igal Alon Foundation (to R.S.-F.). We thank Daniella Ben-Meir for her very skillful assistance.

LITERATURE CITED

(1) Haag, R., and Kratz, F. (2006) Polymer therapeutics: concepts and applications. *Angew. Chem., Int. Ed. 45*, 1198–1215.

(2) Foekens, J. A., Kos, J., Peters, H. A., Krasovec, M., Look, M. P., Cimerman, N., Meijer-van Gelder, M. E., Henzen-Logmans, S. C., van Putten, W. L., and Klijn, J. G. (1998) Prognostic significance of cathepsins B and L in primary human breast cancer. *J. Clin. Oncol. 16*, 1013–1021.

(3) Vartak, D. G., and Gemeinhart, R. A. (2007) Matrix metalloproteases: underutilized targets for drug delivery. *J. Drug Target 15*, 1–20.

(4) Lah, T. T., Kalman, E., Najjar, D., Gorodetsky, E., Brennan, P., Somers, R., and Daskal, I. (2000) Cells producing cathepsins D, B, and L in human breast carcinoma and their association with prognosis. *Hum. Pathol. 31*, 149–160.

(5) Hara-Nishimura, I., Inoue, K., and Nishimura, M. (1991) A unique vacuolar processing enzyme responsible for conversion of several proprotein precursors into the mature forms. *FEBS Lett. 294*, 89–93.

(6) Kembhavi, A. A., Buttle, D. J., Knight, C. G., and Barrett, A. J. (1993) The two cysteine endopeptidases of legume seeds: purification and characterization by use of specific fluorometric assays. *Arch. Biochem. Biophys. 303*, 208–213.

(7) Csoma, C., and Polgar, L. (1984) Proteinase from germinating bean cotyledons. Evidence for involvement of a thiol group in catalysis. *Biochem. J. 222*, 769–776.

(8) El-Sayed, L. H., Ghoneim, H., Demian, S. R., El-Sayed, M. H., Tawfik, N. M., Sakr, I., Abou-Basha, L. M., Renganathan, E., Klinkert, M. Q., and Abou-Rawash, N. (1998) Diagnostic significance of *Schistosoma mansoni* proteins Sm31 and Sm32 in human schistosomiasis in an endemic area in Egypt. *Trop. Med. Int. Health 3*, 721–727.

(9) el Meanawy, M. A., Aji, T., Phillips, N. F., Davis, R. E., Salata, R. A., Malhotra, I., McClain, D., Aikawa, M., and Davis, A. H. (1990) Definition of the complete *Schistosoma mansoni* hemoglobinase mRNA sequence and gene expression in developing parasites. *Am. J. Trop. Med. Hyg. 43*, 67–78.

(10) Chen, J. M., Dando, P. M., Stevens, R. A., Fortunato, M., and Barrett, A. J. (1998) Cloning and expression of mouse legumain, a lysosomal endopeptidase. *Biochem. J. 335* (Pt. 1), 111–117.

(11) Chen, J. M., Dando, P. M., Rawlings, N. D., Brown, M. A., Young, N. E., Stevens, R. A., Hewitt, E., Watts, C., and Barrett, A. J. (1997) Cloning, isolation, and characterization of mammalian legumain, an asparaginyl endopeptidase. *J. Biol. Chem. 272*, 8090–8098.

(12) Chen, J. M., Fortunato, M., and Barrett, A. J. (2000) Activation of human prolegumain by cleavage at a C-terminal asparagine residue. *Biochem. J. 352* (Pt. 2), 327–334.

(13) Manoury, B., Hewitt, E. W., Morrice, N., Dando, P. M., Barrett, A. J., and Watts, C. (1998) An asparaginyl endopeptidase processes a microbial antigen for class II MHC presentation. *Nature 396*, 695–699.

(14) Choi, S. J., Reddy, S. V., Devlin, R. D., Menaa, C., Chung, H., Boyce, B. F., and Roodman, G. D. (1999) Identification of human asparaginyl endopeptidase (legumain) as an inhibitor of osteoclast formation and bone resorption. *J. Biol. Chem. 274*, 27747–27753.

(15) Shirahama-Noda, K., Yamamoto, A., Sugihara, K., Hashimoto, N., Asano, M., Nishimura, M., and Hara-Nishimura, I. (2003) Biosynthetic processing of cathepsins and lysosomal degradation are abolished in asparaginyl endopeptidase-deficient mice. *J. Biol. Chem. 278*, 33194–33199.

(16) Chen, J. M., Fortunato, M., Stevens, R. A., and Barrett, A. J. (2001) Activation of progelatinase A by mammalian legumain, a recently discovered cysteine proteinase. *Biol Chem 382*, 777–783.

(17) Morita, Y., Araki, H., Sugimoto, T., Takeuchi, K., Yamane, T., Maeda, T., Yamamoto, Y., Nishi, K., Asano, M., Shirahama-Noda, K., Nishimura, M., Uzu, T., Hara-Nishimura, I., Koya, D., Kashiwagi, A., and Ohkubo, I. (2007) Legumain/asparaginyl endopeptidase controls extracellular matrix remodeling through the degradation of fibronectin in mouse renal proximal tubular cells. *FEBS Lett. 581*, 1417–1424.

(18) Liu, C., Sun, C., Huang, H., Janda, K., and Edgington, T. (2003) Overexpression of legumain in tumors is significant for invasion/metastasis and a candidate enzymatic target for prodrug therapy. *Cancer Res. 63*, 2957–2964.

(19) Wu, W., Luo, Y., Sun, C., Liu, Y., Kuo, P., Varga, J., Xiang, R., Reisfeld, R., Janda, K. D., Edgington, T. S., and Liu, C. (2006) Targeting cell-impermeable prodrug activation to tumor microenvironment eradicates multiple drug-resistant neoplasms. *Cancer Res. 66*, 970–980.

(20) Murthy, R. V., Arbman, G., Gao, J., Roodman, G. D., and Sun, X. F. (2005) Legumain expression in relation to clinicopathologic and biological variables in colorectal cancer. *Clin. Cancer Res. 11*, 2293–2299.

(21) Luo, Y., Zhou, H., Krueger, J., Kaplan, C., Lee, S. H., Dolman, C., Markowitz, D., Wu, W., Liu, C., Reisfeld, R. A., and Xiang, R. (2006) Targeting tumor-associated macrophages as a novel strategy against breast cancer. *J. Clin. Invest. 116*, 2132–2141.

(22) Lewen, S., Zhou, H., Hu, H. D., Cheng, T., Markowitz, D., Reisfeld, R. A., Xiang, R., and Luo, Y. (2008) A Legumain-based minigene vaccine targets the tumor stroma and suppresses breast cancer growth and angiogenesis. *Cancer Immunol. Immunother. 57*, 507–515.

(23) Stahelin, H. F., and von Wartburg, A. (1991) The chemical and biological route from podophyllotoxin glucoside to etoposide: ninth Cain memorial Award lecture. *Cancer Res. 51*, 5–15.

(24) Hande, K. R. (1998) Etoposide: four decades of development of a topoisomerase II inhibitor. *Eur. J. Cancer 34*, 1514–1521.

(25) Kobayashi, K., and Ratain, M. J. (1994) Pharmacodynamics and long-term toxicity of etoposide. *Cancer Chemother. Pharmacol. 34*, S64−S68.

(26) Clark, P. I., and Slevin, M. L. (1987) The clinical pharmacology of etoposide and teniposide. *Clin. Pharmacokinet. 12*, 223–252.

(27) Meresse, P., Dechaux, E., Monneret, C., and Bertounesque, E. (2004) Etoposide: discovery and medicinal chemistry. *Curr. Med. Chem. 11*, 2443–2466.

(28) Baldwin, E. L., and Osheroff, N. (2005) Etoposide, topoisomerase II and cancer. *Curr. Med. Chem. Anticancer Agents 5*, 363–372.

(29) Larrivee, B., and Karsan, A. (2005) Isolation and culture of primary endothelial cells. *Methods Mol. Biol. 290*, 315–329.

(30) Shabat, D., Lode, H. N., Pertl, U., Reisfeld, R. A., Rader, C., Lerner, R. A., and Barbas, C. F. (2001) In vivo activity in a catalytic antibody-prodrug system: Antibody catalyzed etoposide prodrug activation for selective chemotherapy. *Proc. Natl. Acad. Sci. U.S.A. 98*, 7528–7533.

(31) Sambrook, J., and Russell, D. W. (2001) *Molecular Cloning: A Laboratory Manual*, 3rd ed., Cold Spring Harbor Laboratory Press, Cold Spring Harbor, NY.

(32) Scudiero, D. A., Shoemaker, R. H., Paull, K. D., Monks, A., Tierney, S., Nofziger, T. H., Currens, M. J., Seniff, D., and Boyd, M. R. (1988) Evaluation of a soluble tetrazolium/formazan assay for cell growth and drug sensitivity in culture using human and other tumor cell lines. *Cancer Res. 48*, 4827–4833.

(33) Perry, R., Amir, R., and Shabat, D. (2007) Substituent-dependent disassembly of self-immolative dendrimers. *New J. Chem. 31*, 1307–1312.

BC800448U

Subscriber access provided by SHEMYAKIN-OVCHINNIKOV INST

Article

Ring-Opening Metathesis Polymerization-Based Synthesis of ICG-Containing Amphiphilic Triblock Copolymers for in Vivo Tumor Imaging

Koji Miki, Yoshiaki Kuramochi, Kazuaki Oride, Satoru Inoue, Hiroshi Harada, Masahiro Hiraoka, and Kouichi Ohe

Bioconjugate Chem., **2009**, 20 (3), 511-517• DOI: 10.1021/bc800449s • Publication Date (Web): 04 February 2009

Downloaded from http://pubs.acs.org on May 8, 2009

More About This Article

Additional resources and features associated with this article are available within the HTML version:

- Supporting Information
- Access to high resolution figures
- Links to articles and content related to this article
- Copyright permission to reproduce figures and/or text from this article

View the Full Text HTML

ACS Publications
High quality. High impact.

Bioconjugate Chemistry is published by the American Chemical Society. 1155 Sixteenth Street N.W., Washington, DC 20036

Ring-Opening Metathesis Polymerization-Based Synthesis of ICG-Containing Amphiphilic Triblock Copolymers for in Vivo Tumor Imaging

Koji Miki,[†] Yoshiaki Kuramochi,[†] Kazuaki Oride,[†] Satoru Inoue,[†] Hiroshi Harada,[‡,§] Masahiro Hiraoka,[‡,§] and Kouichi Ohe*[,†]

Department of Energy and Hydrocarbon Chemistry, Graduate School of Engineering, Kyoto University, Nishikyo-ku, Kyoto 615-8510, Japan, Department of Radiation Oncology and Image-Applied Therapy, Graduate School of Medicine, Kyoto University, 54 Shogoin Kawahara-cho, Sakyo-ku, Kyoto 606-8507, Japan, and Nano-Medicine Merger Education Unit, Kyoto University, Nishikyo-ku, Kyoto 615-8530, Japan. Received October 20, 2008; Revised Manuscript Received January 6, 2009

Water-soluble triblock copolymers consisting of hydrophobic−hydrophilic−dye segments were synthesized by ring-opening metathesis polymerization (ROMP) of norbornadiene monomers, copper-catalyzed click reaction, osmium-catalyzed dihydroxylation, and the following transformations. These polymers in aqueous conditions could form spherical assemblies, whose diameters were 50−60 nm by TEM measurement. From in vivo optical imaging experiments, the spherical assemblies of these copolymers could be efficiently accumulated in tumor cells. In addition, the spherical assemblies of water-soluble polymers accumulated in a tumor cell over two weeks.

INTRODUCTION

Molecular imaging is an important topic that has gained significant attention in the fields of chemical biology and noninvasive diagnosis of diseases (*1*, *2*). Optical imaging strategies using dyes (*3*−*8*) and quantum dots (QDs) (*9*−*13*) emitting near-infrared fluorescence (NIRF) have been widely investigated in the past decades. The NIRF imaging technique has many benefits such as the high permeability of biological tissue to the fluorescence and resultant noninvasive imaging for patients. In order to carry probes and drugs efficiently to the targets, spherical amphiphilic molecular assemblies, such as liposomes and related self-assemblies (*7*, *14*−*16*) and micelles or vesicles of polymer conjugates (*17*−*29*), have been developed. Recently, to improve the specificity of probe and drug delivery and to prolong their retention time in the target tumor tissues, much attention has been paid to cross-conjugation between polymer conjugate units using further functionalization and polymerization (*30*, *31*). Although triblock copolymers consisting of hydrophobic, hydrophilic, and dye segments have been widely accepted as appropriate components of spherical self-assemblies for optical tumor imaging utilizing the enhanced permeability and retention effect (*32*, *33*), there still exists a problem with selective accumulation of the imaging probe in the target tissue.

Ring-opening metathesis polymerization (ROMP) of strained alkenes, such as bicyclo[2.2.1]hept-2-ene (norbornene) and bicyclo[2.2.1]hept-2,5-diene (norbornadiene), gives multiblock copolymers in high yields with a small polydispersity index (PDI) (*34*, *35*). Since a wide range of functional groups can be introduced in a monomer skeleton, metathesis-based syntheses of amphiphilic block copolymers to construct micellar or vesicular nanoparticles have been well investigated (*36*, *37*). Although amphiphilic polymers synthesized by the ROMP method are known to form stable nanoparticles having low critical micelle concentration (cmc) values in water (0.5−1.0 g/L) (*38*, *39*), the further modification of polymer conjugates is still necessary to use them as imaging probes in vivo. More recently, Grubbs and a co-worker demonstrated the powerful ROMP method followed by cross-linking for the size-tunable synthesis of micellar nanoparticles aimed at a PET imaging probe (*30*). However, Kane and co-workers reported the synthesis of block copolymers from two types of norbornenes using ROMP followed by dihydroxylation of olefin moieties in the polymer to gain solubility in water (*40*). The high water-solubility of polymer conjugates, in the latter case, would be caused by the formation of stable micellar nanoparticles assembled with flexible polymer conjugates having many hydroxyl groups. This successful synthesis of highly water-soluble polymer conjugates prompted us to investigate the ROMP of norbornadienes instead of norbornenes followed by dihydroxylation, which can lead to further enhancement of water-solubility and stability of nanoparticles. Here, we wish to report the synthesis of water-soluble polymer conjugates using ROMP of three types of norbornadiene monomers and osmium-catalyzed dihydroxylation, and their application as an efficient optical tumor imaging probe.

EXPERIMENTAL PROCEDURES

Materials. Grubbs' third catalyst was prepared from Grubbs' second catalyst according to the reported procedure (*35*). Grubbs' second catalyst and potassium osmate dihydrate were purchased from Sigma-Aldrich (St. Louis, MO). Ethyl vinyl ether, sodium azide, L(+)-ascorbic acid sodium salt, copper (II) sulfate pentahydrate, thiophenol, potassium carbonate, chloroform ($CHCl_3$), *N*,*N*-dimethylformamide (DMF), methanol (MeOH), acetone, and dichloromethane (CH_2Cl_2) were purchased from Nacalai Tesque (Japan). 4-Methylmorpholine *N*-oxide and tetrahydrofuran (THF) were purchased from Wako Pure Chemicals Inc. (Japan). Spectra/Por 6 (MW:1000) was purchased from Spectrum Laboratories Inc. (Rancho Dominguez, CA). All monomers containing the norbornadiene (bicyclo-

* Corresponding author. Phone: +81-75-383-2495. Fax: +81-75-383-2499. E-mail: ohe@scl.kyoto-u.ac.jp.
[†] Department of Energy and Hydrocarbon Chemistry.
[‡] Department of Radiation Oncology and Image-Applied Therapy.
[§] Nano-Medicine Merger Education Unit.

10.1021/bc800449s CCC: $40.75 © 2009 American Chemical Society
Published on Web 02/04/2009

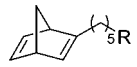

1a : R = OC_5H_{11} **1b** : R = Br **1c** : R = NHNs

Figure 1. Norbornadiene monomers. Ns = 2-nitrobenzenesulfonyl.

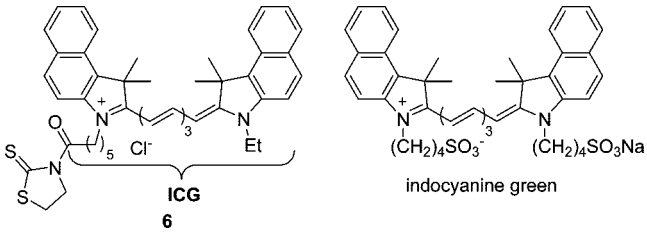

Figure 2. Indocyanine green derivative **6**.

Scheme 1. Synthesis of ICG-Containing Block Copolymers 4[a]

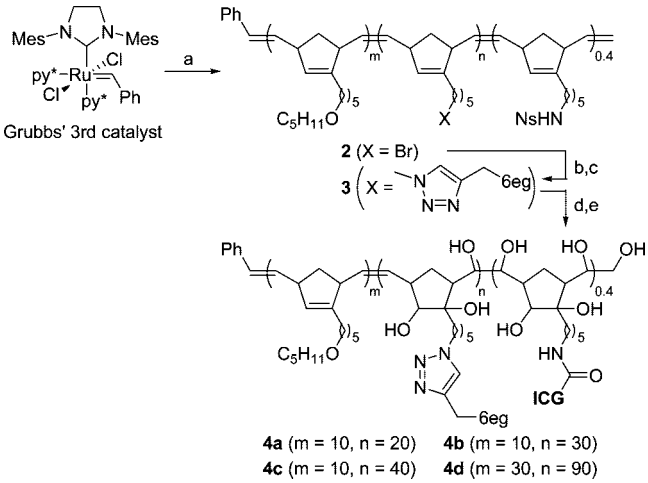

[a] Reaction conditions: (a) **1a** (m equiv), **1b** (n equiv), **1c** (0.4 equiv), CH_2Cl_2, rt, then ethyl vinyl ether; (b) NaN_3, DMF, 50 °C, 15 h; (c) HC≡CCH_2-6eg (**5**), $CuSO_4 \cdot 5H_2O$, sodium ascorbate, THF/H_2O, rt, 48 h; (d) K_2OsO_4, 4-methylmorpholine-*N*-oxide, acetone/MeOH/H_2O, rt, 12 h, then dialysis; (e) PhSH, K_2CO_3, DMF, rt, overnight, then (**6**), rt, 24 h, then dialysis. Mes = 2,4,6-trimethylphenyl, py* = 3-bromopyridine, and 6eg = -$(OCH_2CH_2)_6OCH_3$.

[2.2.1]hepta-2,5-diene) moieties used are shown in Figure 1, and the preparation of monomers from norbornadiene is summarized in Supporting Information. All monomers were purified by gel permeation chromatography (GPC, recycling preparative HPLC LC-908, Japan Analytical Industry Co., Ltd., Japan) with $CHCl_3$ as an eluent and stocked as a dried and degassed CH_2Cl_2 solution in the dark.

Synthesis of Triblock Copolymers 4. We synthesized triblock copolymer **4** by using norbornadiene monomers, 2-(5-pentyloxypentyl)bicyclo[2.2.1]hepta-2,5-diene (**1a**), 2-(5-bromopentyl)bicyclo[2.2.1]hepta-2,5-diene (**1b**), and *N*-(5-bicyclo-[2.2.1]hepta-2,5-dien-2-yl)pentyl-2-nitrobenzensulfonamide (**1c**) (Scheme 1). When the ROMP of **1a**−**c** with a catalytic amount of Grubbs' third catalyst was consequently carried out at room temperature, triblock copolymer **2** was obtained in a nearly quantitative yield. After the nucleophilic substitution of bromide with azide, the Cu-catalyzed [2 + 3] dipolar cyclization reaction (click reaction) (*41*−*44*) of the resulting alkyl azide with propargyl ether **5** gave triblock copolymer **3**. The double bonds in polymer **3** surrounded by hexaethylene glycol moieties were selectively oxidized to vicinal diols using standard Os-catalyzed dihydroxylation under aqueous conditions (*45, 46*). The transamidation with ICG derivative **6** (*47*) gave the ICG-containing water-soluble triblock copolymer **4** after careful dialysis to remove unreacted **6** and lyophilization.

Synthesis of Triblock Copolymer 2. A catalytic amount of Grubbs' third catalyst (4.4 mg, 0.005 mmol) was placed in a flame-dried Schlenk flask and dissolved in CH_2Cl_2 (0.5 mL) under N_2. A 0.10 M solution of **1a** in dried and degassed CH_2Cl_2 (0.50 mL, 0.050 mmol, 10 equiv) was added to the flask at room temperature. After stirring for 20 min at room temperature, to the brown solution was added a 0.075 M solution of **1b** in dried and degassed CH_2Cl_2 (2.0 mL, 0.15 mmol, 30 equiv) at room temperature. After stirring for 20 min, to the brown solution was added a 0.10 M solution of **1c** in dried and degassed CH_2Cl_2 (20 μL, 0.0020 mmol, 0.40 equiv) at room temperature. The resulting pale brown reaction mixture was stirred for 20 min at room temperature and then quenched by ethyl vinyl ether (0.1 mL). After stirring for an additional 30 min, the organic solvent and excess amounts of ethyl vinyl ether were removed under reduced pressure. The crude triblock copolymer **2** (49 mg, >99%, theoretical molecular weight (MW) = 1.00×10^4) was obtained quantitatively and used for the next oxidation reaction without further purification. Triblock copolymer **2** was purified and collected by precipitation in CH_2Cl_2/hexane for spectral measurements (47 mg, 96%).

2: ^{1}H NMR (300 MHz, $CDCl_3$): δ = 0.87−0.91 (m, 26H), 1.21−1.65 (m, 291H), 1.71−2.14 (m, 142H), 2.30−2.36 (m, 34H), 3.01−3.30 (m, 32H), 3.30−3.70 (m, 147H), 5.00−5.45 (m, 120H), 7.72−7.75 (m, 1.0H), 7.80−7.85 (m, 0.6H), 8.10−8.15 (m, 0.5H).

Synthesis of Triblock Copolymer 3. To a crude triblock copolymer **2** (49 mg) in DMF (3.0 mL) was added sodium azide (53 mg, 0.82 mmol) at room temperature. The reaction mixture was stirred at room temperature for 24 h. The organic solvent was reduced to ca. 0.5 mL under reduced pressure. To the solution was added H_2O (3.0 mL), and the precipitate was collected by filteration and dried under reduced pressure to afford a brown solid (44 mg, >99%, MW = 0.88×10^4).

To a solution of the obtained solid in THF (1.0 mL) were sequentially added a solution of propargyl ether **5** (0.25 g, 0.73 mmol) in THF (1.0 mL), a solution of $CuSO_4 \cdot 5H_2O$ (8.8 mg, 0.035 mmol) in H_2O (1.0 mL), and a solution of sodium ascorbate (13.9 mg, 0.070 mmol) in H_2O (1.0 mL) at room temperature. After stirring the reaction mixture overnight at room temperature, the organic solvent was removed under reduced pressure, and the residue was dialyzed by using Spectra/Por 6 (MW:1000) against H_2O for 1 day. Triblock copolymer **3** (95 mg, >99%, MW = 1.89×10^4) was obtained after lyophilization.

3: ^{1}H NMR (300 MHz, $CDCl_3$): δ = 0.87−0.91 (m, 34H), 1.19−1.65 (m, 321H), 1.78−2.20 (m, 263H), 2.42−2.47 (m, 25H), 3.38 (br s, 151H), 3.53−3.88 (m, 1014H), 4.34 (br s, 61H), 4.67 (br s, 61H), 4.98−5.50 (m, 120H). The peaks of aromatic protons could not be detected because of high intensity of protons on ethylene glycol moieties. The peaks of unreacted propargyl ether **5** were included at δ 3.38 and δ 3.53−3.88.

Synthesis of Triblock Copolymer 4. To a solution of crude copolymer **3** suspended in acetone (1.0 mL) and MeOH (1.0 mL) was added an aqueous solution of 4-methylmorpholine *N*-oxide (NMO, 71 mg, 0.61 mmol) and K_2OsO_4 (1.0 mg) in H_2O (2.0 mL) at room temperature. The reaction mixture was stirred for 12 h at room temperature, and the organic solvents were removed under reduced pressure. The residue was dialyzed to remove excess amounts of NMO and osmium compound by using Spectra/Por 6 (MWCO:1000) against H_2O.

To a solution of the resulting amphiphilic copolymer in DMF (2.0 mL) were added potassium carbonate (7.5 mg, 0.050 mmol) and thiophenol (10 μL, 0.10 mmol) at room temperature. After stirring overnight at room temperature, a solution of ICG derivative **6** (8.0 mg, 0.01 mmol) in DMF (1.0 mL) was added at room temperature. After stirring overnight at room temper-

Table 1. Properties of Polymers 4 and Their Self-Assemblies

	2			self-assemblies of **4**		
polymer	MW[a]	M_n[b]	PDI[b]	D_{TEM} (nm)[c]	D_{DLS} (nm)[d]	cmc (g/L)[e]
4a	7.6×10^2	5.2×10^2	1.27	52.2 ± 19.3	*f*	$2.2 \times 10^{-4} - 3.6 \times 10^{-4}$
4b	1.0×10^3	6.4×10^2	1.48	52.4 ± 18.3	90.6 ± 27.2	$7.6 \times 10^{-4} - 1.8 \times 10^{-3}$
4c	1.2×10^3	6.8×10^2	1.17	49.3 ± 14.3	*f*	$5.0 \times 10^{-3} - 7.6 \times 10^{-3}$
4d	2.9×10^3	2.4×10^3	1.36	60.0 ± 16.2	115.9 ± 30.8	$2.2 \times 10^{-3} - 4.3 \times 10^{-3}$

[a] Theoretical molecular weight by assuming quantitative conversion. [b] Number-average molecular weight (M_n) and polydispersity index (PDI) determined by GPC ($CHCl_3$, polystyrene standards). [c] Distribution of diameters of nanoparticles determined by transmission electron microscopy (TEM). [d] Hydrodynamic diameters of nanoparticles in H_2O measured by dynamic light scattering (DLS). [e] Measured by static light scattering (SLS). [f] Not determined after several attempts because of large error values (residual > 0.01).

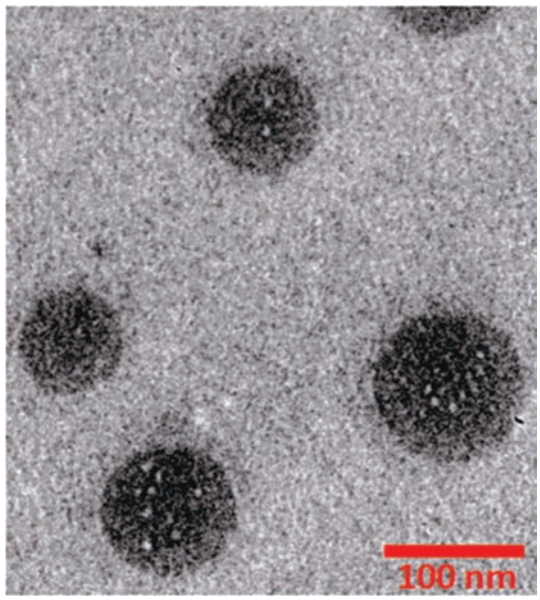

Figure 3. TEM images of the spherical assemblies of the amphiphilic copolymers **4b**.

ature, the solvent was removed under reduced pressure. The resulting mixture was diluted with H_2O (2.0 mL), and this aqueous solution was washed at least 10 times with Et_2O until the green color of the etheral solution disappeared. (ICG derivative **6** does not show water-solubility. On the basis of this, we believe that the ICG moiety is attached covalently with the polymer side chain. However, we do not exclude the fact that a small amount of **6** is contained inside the polymer assemblies.) The volume of solvent was reduced by using lyophilization, and the resulting aqueous solution was dialyzed by using Spectra/Por 6 (MWCO:1000) against H_2O. ICG-containing amphiphilic triblock copolymer **4** (84% from **3b** ($m = 10$, $n = 30$); MW $= 2.16 \times 10^4$; 68−80% of double bonds were oxidized) was obtained after lyophilization for 48 h. In this case, MW (theoretical molecular weight) means the polymer molecular weight by assuming quantitative conversion of double bonds to vicinal diols and quantitative transformation of all free NH_2 groups from the Ns-protected amino groups with **6**. **4b**: ^{1}H NMR (300 MHz, $CDCl_3$): $\delta = 0.70-0.96$ (m, 17H), 0.96−1.50 (m, 171H), 1.50−1.70 (m, 67H), 1.70−2.15 (m, 147H), 2.20−2.42 (m, 35H), 3.20−3.45 (m, 158H), 3.45−4.05 (m, 910H), 4.10−4.52 (m, 71H), 4.52−4.84 (m, 60H), 4.95−5.80 (m, 27H), 7.50−8.00 (m, 43H).

4a (97% from **3a** ($m = 10$, $n = 20$); MW $=1.57 \times 10^4$; 65−75% of double bonds were oxidized): ^{1}H NMR (300 MHz, $CDCl_3$): $\delta = 0.70-0.96$ (m, 10H), 0.96−1.50 (m, 71H), 1.50−1.70 (m, 35H), 1.70−2.15 (m, 35H), 2.20−2.42 (m, 65H), 3.20−3.45 (m, 113H), 3.45−4.05 (m, 967H), 4.10−4.52 (m, 69H), 4.52−4.84 (m, 40H), 4.95−5.80 (m, 22H), 7.50−8.00 (m, 18H).

4c (92% from **3c** ($m = 10$, $n = 40$); MW $=2.77 \times 10^4$; 70−87% of double bonds were oxidized): ^{1}H NMR (300 MHz, $CDCl_3$): $\delta = 0.70-0.96$ (m, 12H), 0.96−1.50 (m, 136H), 1.50−1.70 (m, 69H), 1.70−2.15 (m, 163H), 2.20−2.42 (m, 65H), 3.20−3.45 (m, 195H), 3.45−4.05 (m, 991H), 4.10−4.52 (m, 144H), 4.52−4.84 (m, 80H), 4.95−5.80 (m, 20H), 7.50−8.00 (m, 39H).

4d (59% from **3d** ($m = 30$, $n = 90$); MW $=6.43 \times 10^4$; 65−75% of double bonds were oxidized): ^{1}H NMR (300 MHz, $CDCl_3$): $\delta = 0.70-0.96$ (m, 101H), 0.96−1.50 (m, 569H), 1.50−1.70 (m, 230H), 1.70−2.15 (m, 402H), 2.20−2.42 (m, 100H), 3.20−3.45 (m, 474H), 3.45−4.05 (m, 2328H), 4.10−4.52 (m, 216H), 4.52−4.84 (m, 180H), 4.95−5.80 (m, 98H), 7.50−8.00 (m, 89H).

Transmission Electron Microscopy (TEM) Image Analysis. Transmission electron microscopy (TEM, Model H-9000NAR, Power Supply 200 V, 60 Hz, 15 kVA, Single phase, Hitachi, Ltd., Tokyo, Japan) was used to visualize the morphology of nanoparticles. Samples were dropped onto a TEM copper grid covered with a carbon film (200 mesh, Nisshin EM, Japan) and air-dried for 3 h.

Size Distribution Using Dynamic Light Scattering (DLS) Measurement. The hydrodynamic diameters of spherical assemblies were determined by dynamic light scattering (DLS, FPAR-1000, Otsuka Electronics Co, Ltd., Japan) at 20 °C. The sample solutions were diluted in H_2O and filtered prior to analysis (syringe filter, 0.45 μm pore size, PVDF filter membrane, Whatman, Florham Park, NJ). The light source was a semiconductor laser ($\lambda_0 = 658$ nm), and the correlation function for each solution was obtained at 90°. The measurements of all samples were conducted at least three times. Apparent hydrodynamic diameters of polymer assemblies were obtained using the method of Marquadt. The copolymer concentrations of the analyzed sample solutions were 0.05 mg/mL, in which concentration polymer assemblies were formed according to the results of cmc measurements.

Measurement of Critical Micelle Concentration (cmc). The cmc values of the dye-containing triblock copolymers were determined using static light scattering (SLS, SLS-6000, Otsuka Electronics Co Ltd., Japan) measurements. Several concentrations of the copolymer solution were filtered prior to analysis (syringe filter, 0.45 μm pore size, PVDF filter membrane, Whatman, Florham Park, NJ). The measurements were done with He−Ne laser ($\lambda_0 = 633$ nm) in the angular range of 90−95°. The measurement of samples in each concentration was conducted at least two times, and the intensity of the scattering light (I_s) is an average of all measured values in each concentration. The intensities of the scattering light over the incident light (I_s/I_0) was plotted against log *C* (C = concentration (g/L)), and the ranges of cmc values were determined at the area where I_s/I_0 changed from a constant (near zero) to a larger value (see Supporting Information).

Imaging Experiments. *Cell Culture and Tumor-Bearing Mice.* The human cervical epithelial adenocarcinoma cell line (HeLa) was purchased from American type Culture Collection.

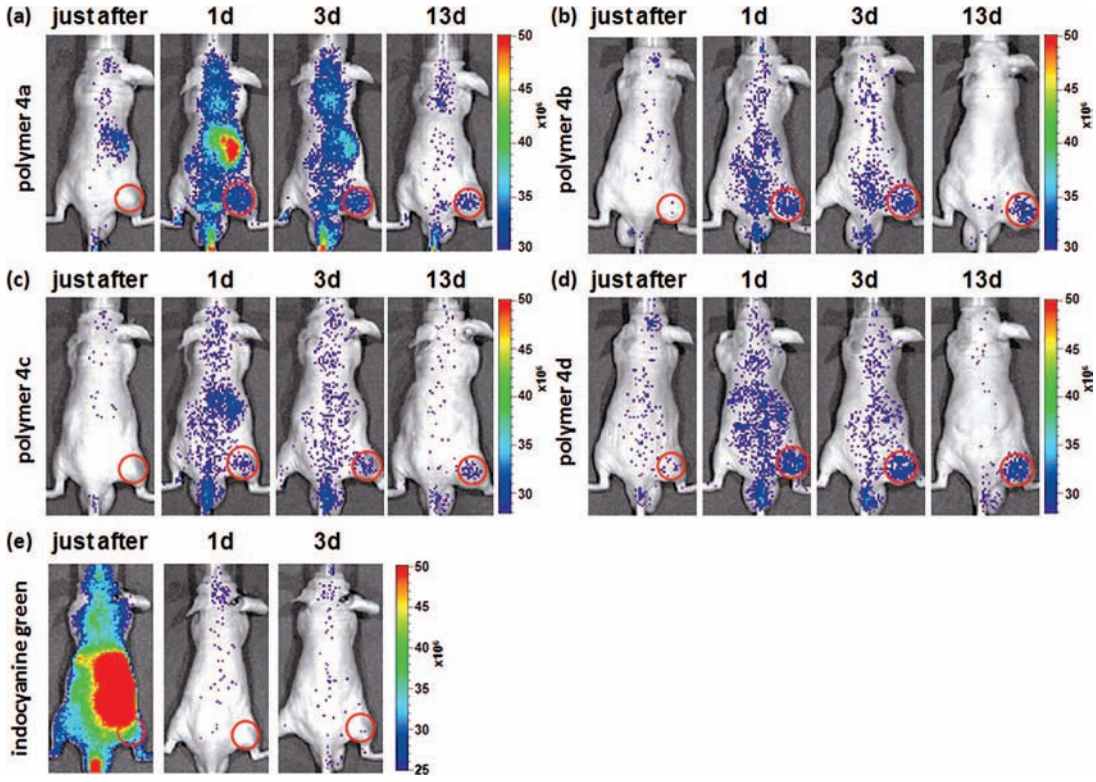

Figure 4. NIRF tomographic images of tumor-bearing mice after injection (just after, 1 day, 3 days, and 13 days) of 100 μL of ICG-containing imaging probes (a) **4a**, (b) **4b**, (c) **4c**, (d) **4d**, and (e) indocyanine green (1.0 mg/mL). Purple, low intensity; red, high intensity; and red circle, tumor site. In order to clarify the data, the fluorescence intensities lower than 3.0×10^7 (polymers **4a** and **4b**), 2.8×10^7 (polymers **4c** and **4d**), or 2.5×10^7 (indocyanine green), and higher than 5.0×10^7 were omitted.

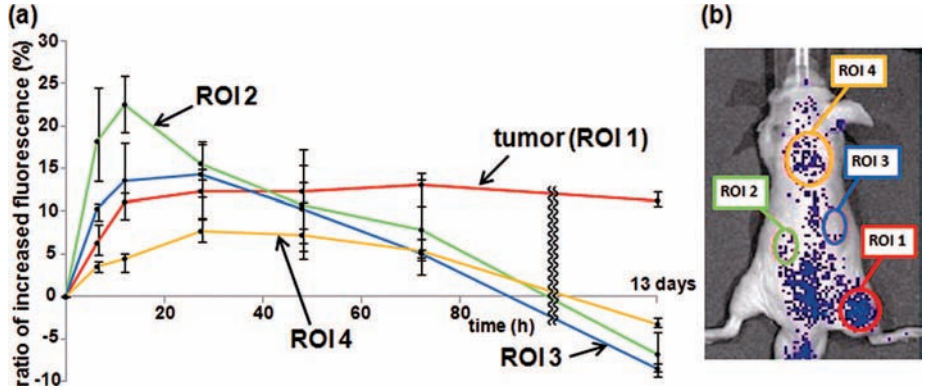

Figure 5. (a) Ratio of increased fluorescence intensity (%) of **4b**. (b) ROI (region of interest). The ratios of increased fluorescence intensity were calculated from the equation: $\{(I_t/I_0) - 1\} \times 100$ (I_t = average fluorescence intensity in each ROI at each time; I_0 = average fluorescence intensity in each ROI just after injection). ROI 1 was located at a tumor, and ROIs 2−4 were located around a lung and a kidney. The photon in each ROI was counted at least three times, and the ranges of these values are shown as error bars.

Cells were maintained in 10% FBS-Dulbecco's modified Eagle's medium and cultured in a well-humidified incubator with 5% CO_2 and 95% air at 37 °C. The suspension of HeLa cells (2×10^6) was subcutaneously inoculated into the right hind leg or left shoulder of 6-week-old nude mice (BALB/c nu/nu mice, SHIMIZU Laboratory Supplies Co. Ltd., Kyoto, Japan).

Fluorescent Imaging in Vivo. Polymers **4a**−**d** in pure water (1 mg/mL) as fluorescence probes were prepared and kept in the dark at room temperature for at least 24 h before injection. One hundred microliters of fluorescence probes were intravenously injected for each experiment. Optical imaging experiments to detect the distribution of the fluorescent probes in tumor-bearing mice were carried out with an IVIS-200 in vivo imaging device (Xenogen, Alameda, CA). During imaging, mice were anesthetized with 2.5% isoflurane gas in the oxygen flow (1.5 L/min). Images were analyzed using Living Image 2.50-Igor Pro 4.09 software (Xenogen), according to the manufacturer's instructions. In all imaging experiments, the fluorescence probe in the same batch was injected to at least two mice, and one set of experiments was repeated at least twice to confirm reproducibility, and representative images are shown. Fluorescence imaging in vitro was carried out with the same device described above.

Ethics of Animal Experiments. All of our animal experiments were approved by the Animal Research Committee of Kyoto University and carried out in accordance with its guidelines.

RESULTS AND DISCUSSION

Synthesis of ICG-Containing Amphiphilic Triblock Copolymers. Water-soluble triblock copolymer **4** was synthesized from norbornadiene monomers **1a**−**c**. At first, triblock copoly-

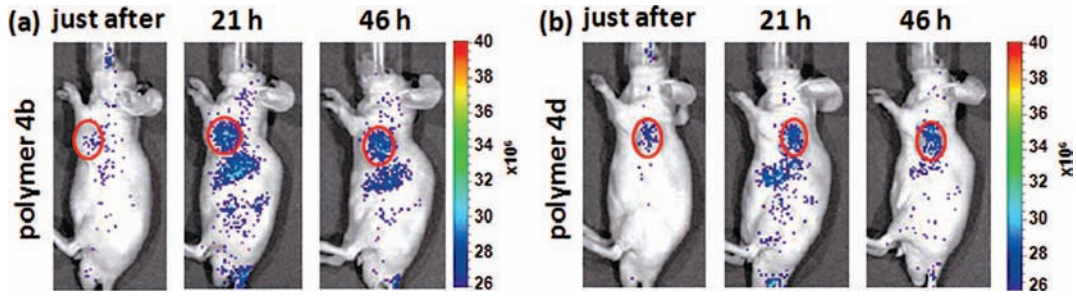

Figure 6. NIRF tomographic images of tumor-bearing mice after injection (just after, 21 h, and 46 h) of 100 μL of ICG-containing imaging probes (a) **4b** and (b) **4d** (1.0 mg/mL). Red circle at a left shoulder indicates the tumor site. In order to clarify the data, the fluorescence intensities lower than 2.6×10^7 and higher than 4.0×10^7 were omitted.

mers **2a**−**d** with different molar ratios of monomers **1a**−**c** to a Grubbs' third catalyst were synthesized by using ROMP in nearly quantitative yields. The number-average molecular weight (M_n) and polydispersity index (PDI) are summarized in Table 1. Although all M_ns were estimated as a little lower value by GPC compared with the theoretical molecular weight (MW) by assuming quantitative conversion of monomers, PDIs indicated that the polymer had a precisely controlled length. The complete consumption of norbornadiene monomers was checked by ^{1}H NMR spectra; three vinyl protons of all mono alkyl-substituted norbornadiene skeletons observed at δ 6.1 (1H) and 6.7 (2H) disappeared, and both a vinyl proton of cyclopentene and two vinyl protons of 1,2-disubstituted ethene newly appeared around δ 5.2. Azide formation followed by Cu-catalyzed [2 + 3] cyclization with propargyl ether HC≡CCH$_2$-6eg (**5**) gave triblock copolymer **3** with >95% introduction efficiency of hexaethylene glycol moiety. The efficiency of the click reaction was estimated by ^{1}H NMR measurement; the integration values of newly appeared methylene protons at α-position of a triazole ring observed around δ 4.3 and 4.7 were compared with that of vinyl protons observed at δ 5.2 before and after the click reaction (see Supporting Information). The obtained copolymer **3** was unfortunately difficult to dissolve in water. To improve the water-solubility of polymer **3**, the double bonds in the polymer backbone surrounded by hexaethylene glycol moieties were selectively oxidized to vicinal diols by using Os-catalyzed dihydroxylation with 4-methylmorpholine *N*-oxide in aqueous conditions. The proportions of vicinal diols were estimated to be 65−75% by ^{1}H NMR spectra; the integration value of vinyl protons observed around δ 5.2 was compared with that of methylene protons next to a triazole ring observed at δ 4.7 before and after the Os-catalyzed dihydroxylation (see Supporting Information). The transamidation of 1,3-thiazolidine-2-thione **6** gave the ICG-containing water-soluble triblock copolymers **4**, which were purified by dialysis and lyophilization.

Size Distribution and cmc. Average diameters of nanometer-size spherical self-assemblies formed by the ICG-containing triblock copolymers **4** in H_2O were measured by TEM and DLS (Table 1). The diameters of nanoparticles were estimated at 50−60 nm by TEM (Figure 3). When the images were measured without osmium tetroxide exposure, 10% of nanoparticles were observed as a black spot. This indicates that a part of the spherical assemblies would contain transition metal species in their supermolecular structure. The self-assembly of the longest polymer **4d** was slightly larger than **4a**−**c**, whose sizes were almost same. The reason why the sizes of nanoparticles were not significantly affected by polymer length might come from large PDI values. The theoretical molecular length of **4a**−**c** as the extended form is estimated to be 25−35 nm, and the diameters of nanoparticles measured by TEM are reasonable as polymer self-assemblies. Although the diameter of **4d** is estimated at ca. 60 nm in the extended form, the nanoparticle size of **4d** was a little smaller than the expected one. However, the diameters of nanoparticles in water measured by DLS were much larger than even twice the extended length of polymers. This might indicate that the polymer assemblies formed larger assemblies such as vesicles in water media. The diameters of self-assemblies of **2a** and **2c** were not determined with certainty by DLS because of large residual values ($>1.0 \times 10^{-2}$).

The cmc values of **4** were determined by static light scattering (SLS) (see Supporting Information). These values are much lower than those of the other polymers synthesized by ROMP without dihydroxylation (*39*, *40*). Low cmc values of self-assemblies of **4** indicate that these polymers form stable assemblies in aqueous media and are good candidates for tumor imaging in vivo.

In Vivo Tumor Imaging. To examine the characteristics of the polymer conjugates as tumor-specific fluorescent probes in vivo, we performed a series of optical imaging experiments. We intravenously injected the polymer conjugates **4a**−**d** and indocyanine green into tumor-bearing nude mice and monitored their distribution using an optical in vivo imaging device (Figure 4). To emphasize the areas where imaging probes specifically accumulated, lower and higher fluorescence intensities were omitted. In the case of imaging data just after, the probes were diffused in a whole body, and the fluorescence intensities could not reach to the lower limit. All nanoparticles could accumulate in the tumor xenograft on the right leg as well as in other organs such as the liver and kidney within one day. Despite the low selectivity, all nanoparticles could stay for at least two weeks in the tumor. The self-assembly of **4a** showed slightly higher fluorescence intensity than those of **4b** and **4c** because **4a** contained larger amounts of the fluorescence probe (Figures 4a-c). In Figure 5, the ratios of increased fluorescence intensities in each region of interest (ROI) for polymer **4b** were calculated and summarized. Interestingly, the accumulation of nanoparticles in all ROIs reached a peak 12−24 h after the injection and decreased gradually in all regions thereafter except ROI 1. When the sizes of ROIs were changed, the fluorescence intensities were also changed, but the tendencies of the increase or decrease in ratios were quite similar to the graphs shown in Figure 5 (see Supporting Information). This phenomenon was also observed using polymers **4c** and **4d**, while the intensities were decreased gradually in all regions in the case of polymer **4a**. The long time retention in the tumor xenograft might be caused by the stability of polymer assemblies predicted from cmc values. A tumor transplanted to another part, such as a left shoulder, could also be visualized (Figure 6).

In conclusion, we have synthesized amphiphilic block copolymers containing the indocyanine green moiety, of the form hydrophobic−hydrophilic−dye segments, using a combination of ROMP, Cu-catalyzed [2 + 3]-dipolar click reaction, and Os-catalyzed dihydroxylation. The amphiphilic polymers modified by dihydroxylation on a polymer backbone exhibit much lower cmc values and form 50−60 nm size nanoparticles in water. Although further modification such as PEGylation (*48*, *49*)

using click chemistry to conjugate a much longer polyethylene glycol chain for a hydrophilic segment is necessary to restrain accumulation in other normal organs, it appears that the prolonged retention of nanoparticles of **4** in solid tumors will be useful for medical treatment using sterically rigid hydrophobic antitumor drugs, such as Taxol, and for cancer diagnosis using conjugating quantum dots (QDs), positron emission tomography, or magnetic resonance imaging probes.

ACKNOWLEDGMENT

This research was supported in part by the Global COE Program "International Center for Integrated Research and Advanced Education in Materials Science" (No. B-09) of the Ministry of Education, Culture, Sports, Science and Technology of Japan. We acknowledge Professor Yoshiki Chujo and Dr. Yasuhiro Morisaki, Kyoto University for DLS measurement, Professor Hideki Matsuoka and Dr. Rati Ranjan Nayak, Kyoto University for SLS measurement, and Ms. Akiyo Morinibu and Ms. Kazumi Shinomiya, Kyoto University for technical assistance in in vivo imaging experiments. We appreciate Nano-Medicine Merger Education Unit, Kyoto University for giving us this opportunity to collaborate.

Supporting Information Available: Preparation of monomers, efficiencies of transformation of polymer side chain, SLS measurements, and the graphs of ratio of increased fluorescence intensity in in vivo tumor imaging. This material is available free of charge via the Internet at http://pubs.acs.org.

LITERATURE CITED

(1) Weissleder, R., and Mahmood, U. (2001) Molecular imaging. *Radiology 219*, 316–333.
(2) Herschman, H. R. (2003) Molecular imaging: looking at problems, seeing solutions. *Science 302*, 605–608.
(3) Lee, H., Yu, M. K., Park, S., Moon, S., Min, J. J., Jeong, Y. Y., Kang, H.-W., and Jon, S. (2007) Thermally cross-linked superparamagnetic iron oxide nanoparticles: synthesis and application as a dual imaging probe for cancer in vivo. *J. Am. Chem. Soc. 129*, 12739–12745.
(4) Hama, Y., Urano, Y., Koyama, Y., Bernardo, M., Choyke, P. L., and Kobayashi, H. (2006) A comparison of the emission efficiency of four common green fluorescence dyes after internalization into cancer cells. *Bioconjugate Chem. 17*, 1426–1431.
(5) Yao, H., So, M.-K., and Rao, J. (2007) A bioluminogenic substrate for in vivo imaging of β-lactamase. *Angew. Chem., Int. Ed. 46*, 7031–7034.
(6) Chen, J., Corbin, I. R., Li, H., Cao, W., Glickson, J. D., and Zheng, G. (2007) Ligand conjugated low-density lipoprotein nanoparticles for enhanced optical cancer imaging in vivo. *J. Am. Chem. Soc. 129*, 5798–5799.
(7) Tanisaka, H., Kizaka-Kondoh, S., Makino, A., Tanaka, S., Hiraoka, M., and Kimura, S. (2008) Near-infrared fluorescent labeled peptosome for application to cancer imaging. *Bioconjugate Chem. 19*, 109–117.
(8) Yang, Z., Zheng, S., Harrison, W. J., Harder, J., Wen, X., Gelovani, J. G., Qiao, A., and Li, C. (2007) Long-circulating near-infrared fluorescence core-cross-linked polymeric micelles: synthesis, characterization, and dual nuclear/optical imaging. *Biomacromolecules 8*, 3422–3428.
(9) Tada, H., Higuchi, H., Watanabe, T. M., and Ohuchi, N. (2007) In vivo real-time tracking of single quantum dots conjugated with monoclonal anti-HER2 antibody in tumors of mice. *Cancer Res. 67*, 1138–1144.
(10) Gao, X., Cui, Y., Levenson, R. M., Chung, L. W. K., and Nie, S. (2004) In vivo cancer targeting and imaging with semiconductor quantum dots. *Nat. Biotechnol. 22*, 969–976.
(11) Cai, W., Shin, D.-W., Chen, K., Gheysens, O., Cao, Q., Wang, S. X., Gambhir, S. S., and Chen, X. (2006) Peptide-labeled nearinfrared quantum dots for imaging tumor vasculature in living subjects. *Nano Lett. 6*, 669–676.
(12) Al-Jamal, W. T., Al-Jamal, K. T., Tian, B., Lacerda, L., Bomans, P. H., Frederik, P. M., and Kostarelos, K. (2008) Lipid-quantum dot bilayer vesicles enhance tumor cell uptake and retention in vitro and in vivo. *ACS Nano 2*, 408–418.
(13) Smith, B. R., Cheng, Z., De, A., Koh, A. L., Sinclair, R., and Gambhir, S. S. (2008) Real-time intravital imaging of RGD-quantum dot binding to luminal endothelium in mouse tumor neovasculature. *Nano Lett. 8*, 2599–2606.
(14) Lyass, O., Uziely, B., Ben-Yosef, R., Tzemach, D., Heshing, N. I., Lotem, M., Brufman, G., and Gabizon, A. (2000) Correlation of toxicity with pharmacokinetics of pegylated liposomal doxorubicin (Doxil) in metastatic breast carcinoma. *Cancer 89*, 1037–1047.
(15) Muggia, F. M., Hainsworth, J. D., Jeffers, S., Miller, P., Groshen, S., Tan, M., Roman, L., Uziely, B., Muderspach, L., Garcia, A., Burnett, A., Greco, F. A., Morrow, C. P., Paradiso, L. J., and Liang, L. J. (1997) Phase II study of liposomal doxorubicin in refractory ovarian cancer: antitumor activity and toxicity modification by liposomal encapsulation. *J. Clin. Oncol. 15*, 987–993.
(16) Koide, A., Kishimura, A., Osada, K., Jang, W.-D., Yamasaki, Y., and Kataoka, K. (2006) Semipermeable polymer vesicle (PICsome) self-assembled in aqueous medium from a pair of oppositely charged block. *J. Am. Chem. Soc. 128*, 5988–5989.
(17) Discher, D. E., and Eisenberg, A. (2002) Polymer vesicles. *Science 297*, 967–973.
(18) Choucair, A., Lavigueur, C., and Eisenberg, A. (2004) Polystyrene-*b*-poly(acrylic acid) vesicle size control using solution properties and hydrophilic block length. *Langmuir 20*, 3894–3900.
(19) Hoste, K., Winne, K. D., and Schacht, E. (2004) Polymeric prodrugs. *Int. J. Pharm. 277*, 119–131.
(20) Hamaguchi, T., Matsumura, Y., Suzuki, M., Shimizu, K., Goda, R., Nakamura, I., Nakatomi, I., Yokoyama, M., Kataoka, K., and Kakizoe, T. (2005) NK105, a paclitaxel-incorporating micellar nanoparticle formation, can extend in vivo antitumor activity and reduce the neurotoxicity of paclitaxel. *Br. J. Cancer 92*, 1240–1246.
(21) Uchino, H., Matsumura, Y., Negishi, T., Koizumi, F., Hayashi, T., Honda, T., Nishiyama, N., Kataoka, K., Naito, S., and Kakizoe, T. (2005) Cisplatin-incorporating polymeric micelles (NC-6004) can reduce nephrotoxicity and neurotoxicity of cisplatin in rats. *Br. J. Cancer 93*, 678–687.
(22) Bae, Y., Nishiyama, N., Fukushima, S., Koyama, H., Matsumura, Y., and Kataoka, K. (2005) Preparation and Biological characterization of polymeric micelle drug carriers with intracellular pH-triggered drug release property: tumor permeability, controlled subcellular drug distribution, and enhanced in vivo antitumor efficacy. *Bioconjugate Chem. 16*, 122–130.
(23) Greish, K., Nagamitsu, A., Fang, J., and Maeda, H. (2005) Copoly(styrene-maleic acid)-pirarubicin micelles: high tumor-targeting efficiency with little toxicity. *Bioconjugate Chem. 15*, 230–236.
(24) Okuda, T., Kawakami, S., Akimoto, N., Niidome, T., Yamashita, F., and Hashida, M. (2006) PEGlylated lysine dendrimers for tumor-selective targeting after intravenous injection in tumor-bearing mice. *J. Controlled Release 116*, 330–336.
(25) Osada, K., and Kataoka, K. (2006) Drug and gene delivery based on supramolecular assembly of PEG-polypeptide hybrid block copolymers. *Adv. Polym. Sci. 202*, 113–153.
(26) Heyes, J., Hall, K., Tailor, V., Lenz, R., and Maclachlan, I. (2006) Synthesis and characterization of novel poly(ethylene glycol)-lipid conjugates suitable for use in drug delivery. *J. Controlled Release 112*, 280–290.
(27) Vincent, M. J., and Duncan, R. (2006) Polymer conjugates: nanosized medicines for treating cancer. *Trends Biotechnol. 24*, 39–47.

(28) Torchilin, V. P. (2007) Micellar Nanoparticles: Pharmaceutical Perspectives. *Pharm. Res. 24*, 1–16.
(29) Kim, J.-H., Kim, Y.-S., Park, K., Lee, S., Nam, H. Y., Min, K. H., Jo, H. G., Park, J. H., Choi, K., Jeong, S. Y., Park, R.-W., Kim, I.-S., Kim, K., and Kwon, I. C. (2008) Antitumor efficacy of cisplatin-loaded glyocol chitosan nanoparticles in tumor-bearing mice. *J. Controlled Release 127*, 41–49.
(30) Matson, J. B., and Grubbs, R. H. (2008) Synthesis of fluorine-18 functionalized nanoparticles for use as in vivo molecular imaging agents. *J. Am. Chem. Soc. 130*, 6731–6733.
(31) Rodríguez-Hernández, J., Chécot, F., Gnanou, Y., and Lecommandoux, S. (2005) Toward 'smart' nano-objects by self-assembly of block copolymers in solution. *Prog. Polym. Sci. 30*, 691–724.
(32) Matsumura, Y., and Maeda, H. (1986) A new concept for macromolecular therapeutics in cancer chemotherapy: mechanism of tumoritropic accumulation of proteins and the antitumor agent smancs. *Cancer Res. 46*, 6387–6392.
(33) Iyer, A. K., Khaled, G., Fang, J., and Maeda, H. (2006) Exploiting the enhanced permeability and retention effect for tumor imaging. *Drug Discovery Today 11*, 812–818.
(34) Trnka, T. M., and Grubbs, R. H. (2001) The development of $L_2X_2Ru{=}CHR$ olefin metathesis catalysts: an organometallic success story. *Acc. Chem. Res. 34*, 18–29.
(35) Choi, T.-L., and Grubbs, R. H. (2003) Controlled living ring-opening-metathesis polymerization by a fast-initiating ruthenium catalyst. *Angew. Chem., Int. Ed. 42*, 1743–1746.
(36) Stubenrauch, K., Moitzi, C., Fritz, G., Glatter, O., Trimmel, G., and Stelzer, F. (2006) Precise tuning of micelle, core, and chell size by the composition of amphiphilic block copolymers derived from ROMP investigated by DLS and SAXS. *Macromolecules 39*, 5865–5874.
(37) Bertin, P. A., Watson, K. J., and Nguyen, S. T. (2004) Indomethacin-containing nanoparticles derived from amphiphilic polynorbornene: a model ROMP-based drug encapsulation system. *Macromolecules 37*, 8364–8372.
(38) Liaw, D.-J., Chen, T.-P., and Huang, C.-C. (2005) Self-assembly aggregation of highly stable copolynorbornenes with amphiphilic architecture via ring-opening metathesis polymerization. *Macromolecules 38*, 3533–3538.
(39) Sutthasupa, S., Sanda, F., and Masuda, T. (2008) Copolymerization of amino acid functionalized norbornene monomers. Synthesis of amphiphilic block copolymers forming reverse micelles. *Macromolecules 41*, 305–311.
(40) Carrillo, A., Yanjarappa, M. J., Gujraty, K. V., and Kane, R. S. (2006) Biofunctionalized block copolymer nanoparticles based on ring-opening metathesis polymerization. *J. Polym. Sci., Part A: Polym. Chem. 44*, 928–939.
(41) Kolb, H. C., Finn, M. G., and Sharpless, K. B. (2001) Click chemistry: diverse chemical function from a few good reactions. *Angew. Chem. Int. Ed. 40*, 2004–2021.
(42) Kluger, C., and Binder, W. H. (2007) Functionalized poly-(oxanorbornene)-block-copolymers: preparation via romp/click-methodology. *J. Polym. Sci., Part A: Polym. Chem. 45*, 485–499.
(43) Binder, W. H., and Kluger, C. (2004) Combining ring-opening metathesis polymerization (ROMP) with Sharpless-type "click" reactions: an easy method for the preparation of side chain functionalized poly(oxanorbornenes). *Macromolecules 37*, 9321–9330.
(44) Opsteen, J. A., Brinkhuis, R. P., Teeuwen, R. L. M., Löwik, D. W. P. M., and van Hest, J. C. M. (2007) "Clickable" polymersomes. *Chem. Commun.* 3136–3138.
(45) Kolb, H. C., VanNieuwenhze, M. S., and Sharpless, K. B. (1994) Catalytic asymmetric dihydroxylation. *Chem. Rev. 94*, 2483–2547.
(46) Dupau, P., Epple, R., Thomas, A. A., Fokin, V. V., and Sharpless, K. B. (2002) Osmium-catalyzed dihydroxylation of olefins in acidic media: old process, new tricks. *Adv. Synth. Catal. 344*, 421–433.
(47) Hirata, T., Kogiso, H., Morimoto, K., Miyamoto, S., Taue, H., Sano, S., Muguruma, N., Ito, S., and Nagao, Y. (1998) Synthesis and reactivities of 3-indocyanine-green-acyl-1,3-thiazoline-2-thione (ICG-ATT) as a new near-infrared fluorescent-labeling reagent. *Bioorg. Med. Chem. 6*, 2179–2184.
(48) Gao, J.-G., Eto, Y., Yoshioka, Y., Sekiguchi, F., Kurachi, S., Morishige, T., Yao, X., Watanabe, H., Asavatanabodee, R., Sakurai, F., Mizuguchi, H., Okada, Y., Mukai, Y., Tsutsumi, Y., Mayumi, T., Okada, N., and Nakagawa, S. (2007) Effective tumor targeted gene transfer using PEGylated adenovirus vector via systemic administration. *J. Controlled Release 122*, 102–110.
(49) Suzuki, R., Takizawa, T., Kuwata, Y., Mutoh, M., Ishiguro, N., Utoguchi, N., Shinohara, A., Eriguchi, M., Yanagie, H., and Maruyama, K. (2008) Effective anti-tumor activity of oxaliplatin encapsulated in transferring-PEG-liposome. *Int. J. Pharm. 346*, 143–150.

BC800449S

--Supporting Information--

Ring-Opening Metathesis Polymerization-Based Synthesis of ICG-Containing Amphiphilic Triblock Copolymers for in Vivo Tumor Imaging

Koji Miki,[†] Yoshiaki Kuramochi,[†] Kazuaki Oride,[†]Satoru Inoue,[†] Hiroshi Harada,[‡,§] Masahiro Hiraoka,[‡,§] and Kouichi Ohe[*,†]

[†]*Department of Energy and Hydrocarbon Chemistry, Graduate School of Engineering, Kyoto University, Nishikyo-ku, Kyoto, 615-8510, Japan*

[‡]*Department of Radiation Oncology and Image-Applied Therapy, Graduate School of Medicine, Kyoto University, 54 Shogoin Kawahara-cho, Sakyo-ku, Kyoto 606-8507, Japan*

[§]*Nano-Medicine Merger Education Unit, Kyoto University, Nishikyo-ku, Kyoto, 615-8530, Japan*

* Corresponding author. Kouichi Ohe. E-mail: ohe@scl.kyoto-u.ac.jp, Department of Energy and Hydrocarbon Chemistry, Graduate School of Engineering, Kyoto University, Nishikyo-ku, Kyoto 615-8510, Japan. Phone +81-75-383-2495. Fax +81-75-383-2499.

<Index>

1. Experimental Section S2-S6
1.1. Preparation of Monomers S2
1.2. Efficiencies of Transformation of Polymer Side Chain (Estimated from ^{1}H NMR Spectra) S4
1.3. SLS Measurements S6
1.4. Ratio of increased fluorescence intensity S7-9

2. References S9

1. Experimental Section

Materials. Bicycle[2.2.1]hepta-2,5-diene (norbornadiene), triethylene glycol monomethyl ether, were purchased from Sigma-Aldrich (St. Louis, MO). 1-Pentanol, potassium carbonate, (DMF), chloroform and dichloromethane were purchased from nacalai tesque (Japan). 2-Nitrobenzenesulfonamide was purchased from Tokyo Chemical Industry Co., Ltd. (Japan). Sodium hydride (60 wt% in oil), propargyl bromide, and tetrahydrofuran (THF) were purchased from Wako Pure Chemicals Inc. (Japan). Silica gel (230-400 mesh) for column chromatography was purchased from Silicycle (Canada). All monomers containing norbornadiene (bicycle[2.2.1]hepta-2,5-diene) moieties used are shown in Figure S1 and the preparation of monomers from norbornadiene is summarized in Supporting Information. All monomers were purified by gel permeation chromatography (GPC, recycling preparative HPLC LC-908, Japan Analytical Industry Co., Ltd., Japan) with $CHCl_3$ as an eluent and stocked as a dried and degassed CH_2Cl_2 solution.

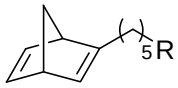

1A: R = OC_5H_{11} **1B**: R = NHNs **1C**: R = Br

Figure S1. Norbornadiene monomers. Ns = 2-nitrobenzenedulfonyl.

1.1. Preparation of Monomers. The synthetic scheme for norbornadiene monomers from bicycle[2.2.1]hepta-2,5-diene (norbornadiene) is shown in Scheme S1. HC≡C-CH_2-6eg (**5**, 6eg = –$(OCH_2CH_2)_6OCH_3$) was prepared from hexaethylene glycol monomethyl ether (Scheme S2).

SCHEME S1.

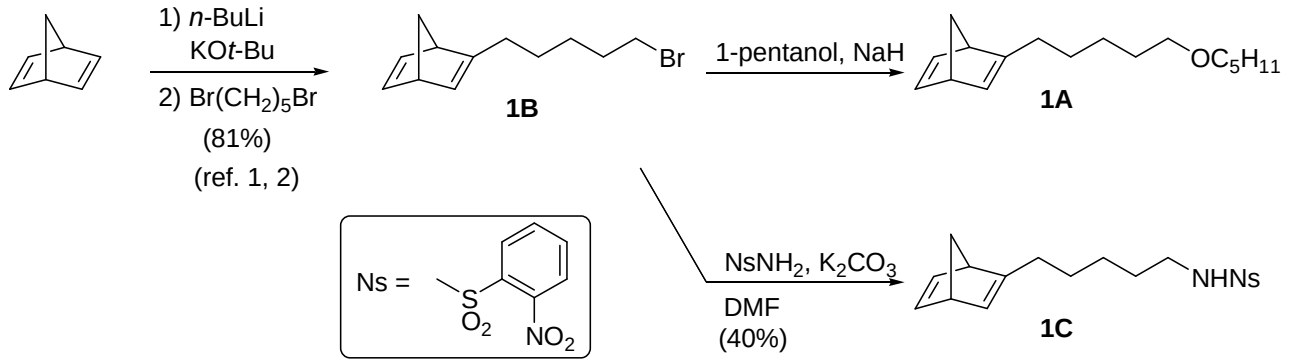

SCHEME S2.

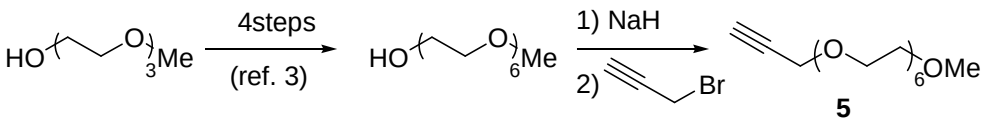

*Synthesis of 2-(5-pentyloxypentyl)bicyclo[2.2.1]hepta-2,5-diene (**1a**).* To a solution of 1-pentanol (2.1 g, 24 mmol) in THF (20 mL) was slowly added sodium hydride (60 wt% in oil, 1.2 g, 30 mmol) at 0 °C. After stirring for 1 h at room temperature, to this solution was added a solution of **1b** (*1*,*2*) (3.9 g, 16 mmol) in THF (20 mL) at 0 °C. The reaction mixture was stirred overnight at 60 °C. The reaction mixture was cooled down to room temperature and washed with brine (15 mL x 3). The aqueous layer was extracted with AcOEt (20 mL x 3) and the combined organic solution was dried over $MgSO_4$. The solvents were removed under reduced pressure and the

crude product was subjected to column chromatography on SiO_2 with hexane as an eluent to afford **1a** (1.5 g, 6.1 mmol, 38%) as a colorless oil. IR (neat) 694, 879, 1116, 1302, 1376, 1464, 2859, 2932, 3056cm^{-1}; ^{1}H NMR (400 MHz, $CDCl_3$): δ 0.90 (t, J = 6.0 Hz, 3H), 1.24-1.47 (m, 8H), 1.53-1.60 (m, 4H), 1.95 (dd, J = 5.4, 15.0 Hz, 2H), 2.12-2.25 (m, 2H), 3.27 (s, 1H), 3.38 (t, J = 6.6 Hz, 2H), 3.48 (s, 1H), 6.12 (d, J = 8.8 Hz, 1H), 6.75 (m, 2H); ^{13}C NMR (100 MHz, $CDCl_3$): δ 14.1, 22.6, 26.0, 27.1, 28.4, 29.5, 29.7, 31.5, 50.0, 53.5, 70.8, 70.9, 73.4, 133.1, 142.3, 143.7, 158.7. HRMS calcd for $C_{17}H_{29}O$ ($M+H^+$) 249.2218, found 249.2212. Anal calcd for $C_{17}H_{28}O$: C, 82.20; H, 11.36. Found: C, 81.99; H, 11.40.

*Synthesis of Amino Moiety-Containing Norbornadiene Monomer **1c***. To a solution of **1b** (*1*,*2*) (2.2 g, 9.0 mmol) in DMF (8.5 mL) was added 2-nitrobenzenesulfonamide (0.97 g, 4.8 mmol) and K_2CO_3 (1.3 g, 9.6 mmol) at 0 °C. The reaction mixture was stirred overnight at 60 °C. The reaction mixture was poured into ice water (50 mL) and the aqueous layer was extracted with AcOEt (20 mL x 3). The organic layer was washed with brine (20 mL) and dried over $MgSO_4$. The solvents were removed under reduced pressure and the crude product was subjected to column chromatography on SiO_2 with ethyl acetate/hexane (v/v = 1/7) as an eluent to afford **1c** (0.70 g, 1.9 mmol, 40%) as a colorless oil. IR (neat) 592, 732, 912, 1170, 1362, 1415, 1541, 2932, 3350 cm^{-1}; ^{1}H NMR (400 MHz, $CDCl_3$): δ 1.25-1.58 (m, 6H), 1.92 (dd, J = 5.6, 11.6 Hz, 2H), 2.03-2.21 (m, 2H), 3.08 (dd, J = 6.8, 13.2 Hz, 2H), 3.22 (s, 1H), 3.46 (s, 1H), 5.35 (t, J = 6.3 Hz, 1H), 6.07 (s, 1H), 6.71-6.72 (m, 2H), 7.74-7.76 (m, 2H), 7.83-7.85 (m, 1H), 8.10-8.12 (m, 1H); ^{13}C NMR (100 MHz, $CDCl_3$) δ 25.9, 26.3, 29.1, 31.0, 43.6, 49.8, 53.2, 73.2, 125.0, 130.6, 132.5, 133.2, 133.4, 133.4, 141.9, 143.4, 147.6, 157.9. HRMS calcd for $C_{18}H_{22}N_2O_4S$ ($M+H^+$): 363.1379. Found: 363.1381. Anal calcd for $C_{18}H_{22}N_2O_4S$: C, 59.65; H, 6.12. Found: C, 59.43; H, 5.96.

*Synthesis of Propargyl Ether **5***. Propargyl ether **5** was synthesized according to the similar reported procedure (*4*). Ether **5** was purified by GPC with $CHCl_3$ as an eluent before use. IR (neat) 733, 849, 921, 1034, 1104, 1200, 1249, 1300, 1351, 1456, 1645, 1739, 2113, 2871, 3245, 3543 cm^{-1}; ^{1}H NMR (400 MHz, $CDCl_3$): δ 2.44 (t, J = 2.0 Hz, 1H), 3.38 (s, 3H), 3.53-3.80 (m, 24H), 4.20 (d, J = 2.0 Hz, 2H); ^{13}C NMR (100 MHz, $CDCl_3$) δ 58.3, 59.0, 69.1, 70.4, 70.5, 70.5, 70.6, 71.9, 74.5, 79.6. Anal calcd for $C_{16}H_{30}O_7$: C, 57.47; H, 9.04. Found: C, 57.24; H, 8.74.

1.2. Efficiencies of Transformation of Polymer Side Chain (Estimated from ^{1}H NMR Spectra)

The click reaction of azide, and the Os-catalyzed dihydroxylation were estimated from ^{1}H NMR spectra. The NMR charts of the nucleophilic substitution of bromide with azide were also summarized below.

1.2.1. Nucleophilic Substitution of Bromide with Azide.

^{1}H NMR spectra before and after the nucleophilic substitution of **2b** were shown below (Figures S2). The conversion were difficult to be estimated, however these might be estimated indirectly around >95% because the efficiency of the click reaction after azide formation was estimated at >95% (see the next page). A vibration peak of -N=N=N: was newly appeared at 2096 cm^{-1} in IR spectra.

(a) Before the substitution reaction of 2b

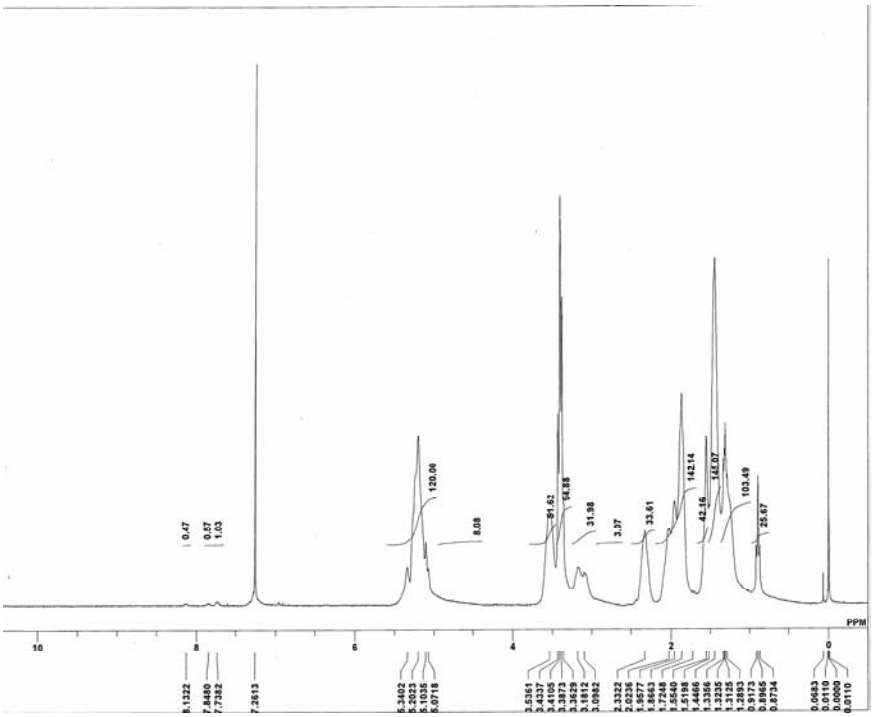

(b) After the substitution reaction of 2b

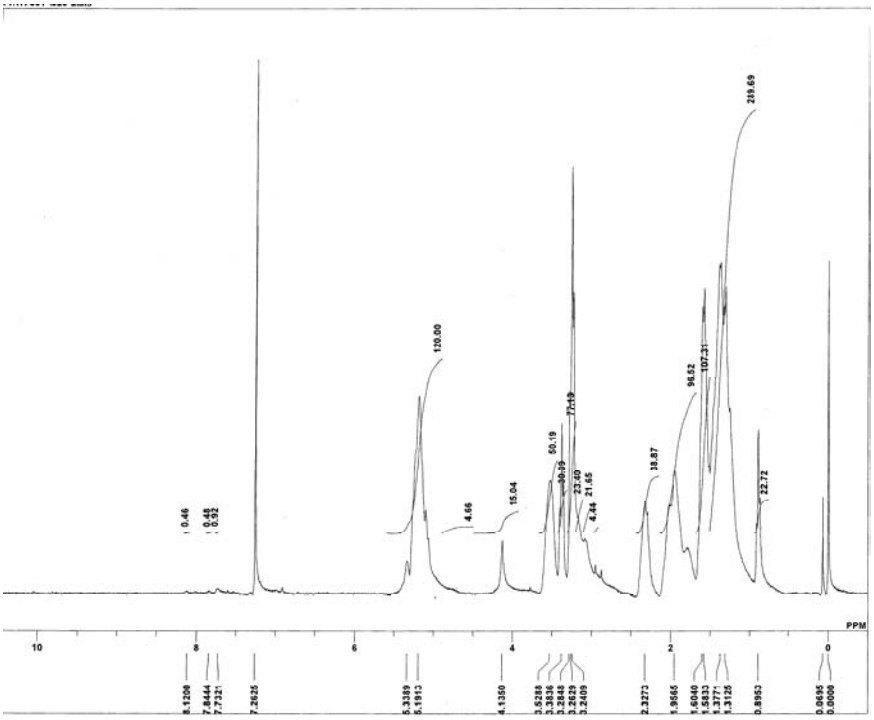

Figure S2. ^{1}H NMR spectra (300 MHz) before (a) and after (b) the substitution of **2b** with azide.

1.2.2. Click Reaction of Azide and Os-Catalyzed Reaction of the Resulting 3b.

The efficiencies of the click reactions were estimated at >95% (Figure S3). Two proton pairs at α-position of triazole ring were assigned at δ 4.3 and 4.7 (The peak at δ 4.2 was assigned as HC≡CCH_2–6eg (**5**)). The integrated values of these peaks were theoretically 60 compared with vinyl protons at δ 5.2 (121.2H), respectively. Based on these values, the efficiencies of conversion on the click reactions were estimated over 95% from the results of several runs. A vibration peak of an azide at 2096 cm^{-1} on IR spectra was disappeared and the broad peak around 1102-1105 cm^{-1} was newly appeared. This might be assigned as a vibration peak of C-O-C bonds in ethylene glycol moieties. Since the integration values at δ 4.7 and 5.2 were theoretically 60 and 121.2, the efficiency of conversion of double bonds was estimated at 68-80% from the results of several runs (Figure S3).

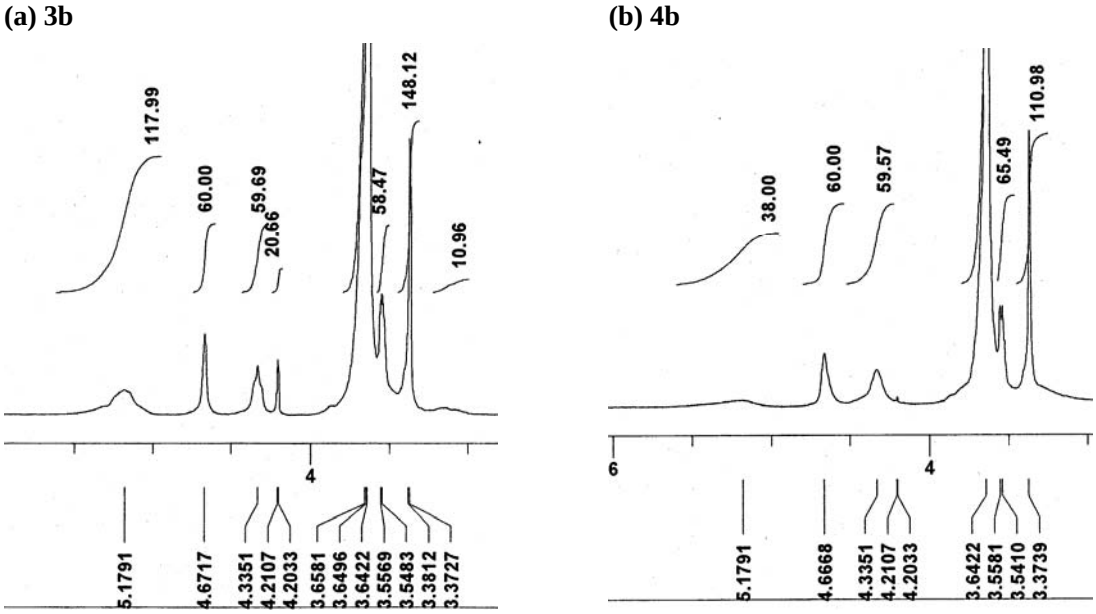

Figure S3. ^{1}H NMR spectra (300 MHz) of **3b** (a) and **4b** (b).

1.3. SLS Measurements

The obtained values of I_s/I_0 from SLS measurement were plotted against log C (see below). I_s : the intensity of the scattering light, I_0 : the intensity of the incident light, C: polymer concentration (g/L).

Since the scattering light could not find in lower concentration and the values (I_s/I_0) converged within 0.2-0.3 in all cases, the ranges of cmc value were determined between two intersections of "y (I_s/I_0) = k (k: the lowest value of I_s/I_0 or average of two or three low I_s/I_0 values)" and two tangent lines of an approximate curve contacted at "y = 1.1 x constant" and "y = 1.0". Each approximate curve was determined by fitting with exponential or polynomial approximation.

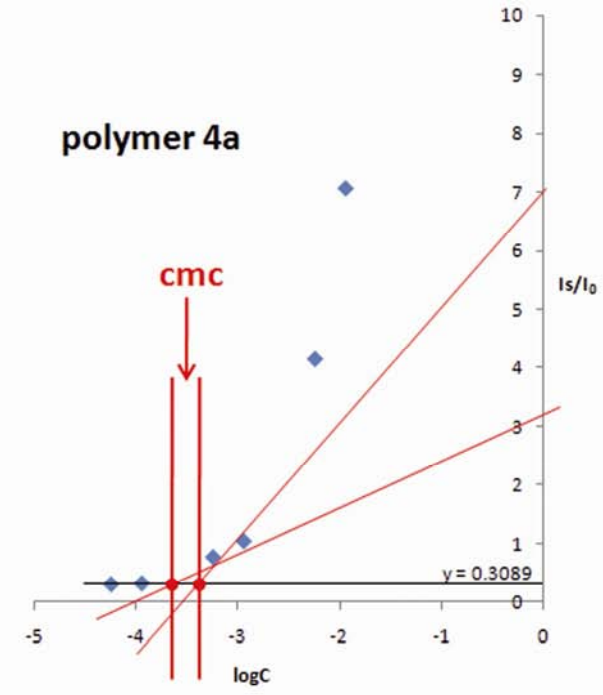

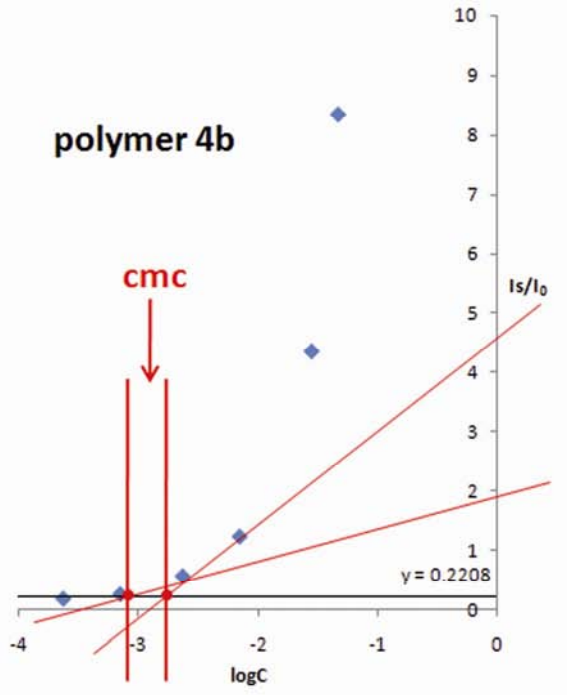

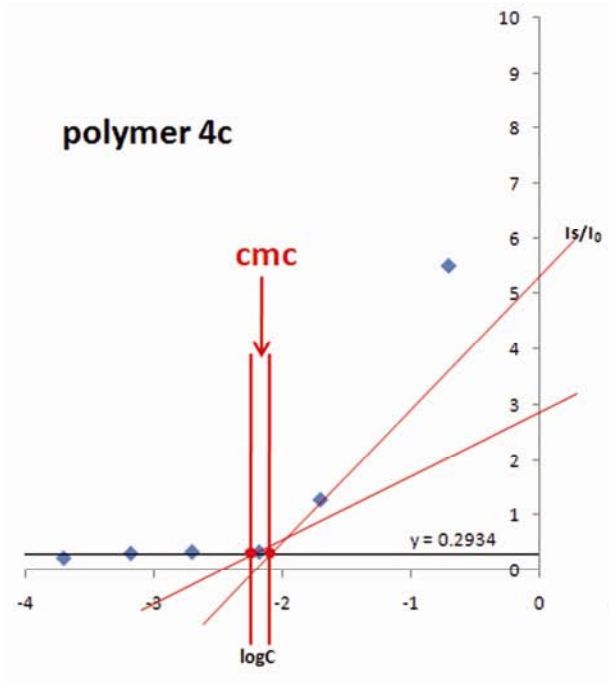

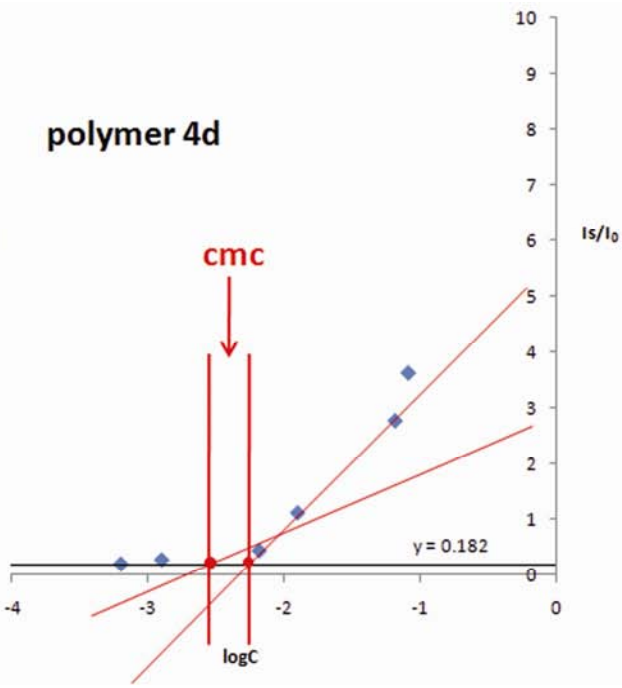

1.4. Ratio of increased fluorescence intensity.

The ratio of increased fluorescence intensity in in vivo tumor imaging by using polymer conjugates **4a-d** are summarized in Figure S4 . The sums of fluorescence intensities in all ROI, which was obtained as an average of fluorescence intensity in a ROI measured at least four times, were summarized in Table S1-S4. The accumulation of nanoparticles in all ROIs reached a peak 12–24 hours after the injection and decreased gradually in all regions thereafter except ROI 1, in all cases.

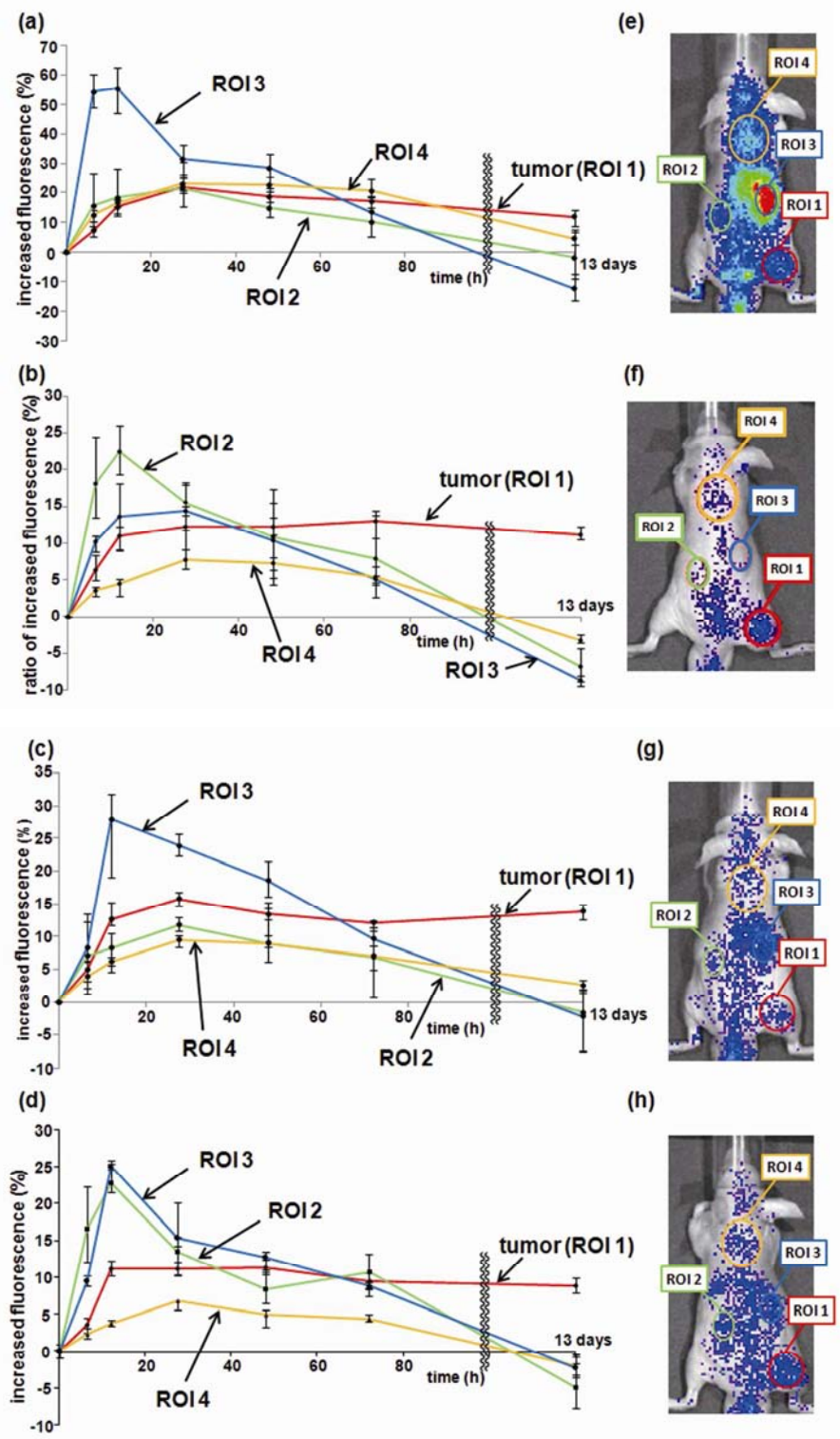

Figure S4. (a) Ratio of increased fluorescence intensity (%) of **4a**, (b) **4b**, (c) **4c** and (d) **4d**. (e) Region of interest (ROI) of **4a**, (f) **4b**, (g) **4c**, and (h) **4d**. The ratios of increased fluorescence intensity were calculated from the equation: $\{(I_t/I_0)-1\}x100$ (I_t: average fluorescence intensity in each ROI at each time, I_0: average fluorescence intensity in each ROI just after injection). ROI 1 was located at a tumor, and ROIs 2-4 were located around a lung and a kidney. The photon in each ROI was counted at least three times and the ranges of these values are shown as error bars.

Table S1. The Sum of Fluorescence Intensities and Ratio of Increased Fluorescence Intensities in All ROI Using Polymer **4a**.

time	sums of fluorescence intensity in ROI				ratio of increased fluorescence intensity (%)			
	ROI 1	ROI 2	ROI 3	ROI 4	ROI 1	ROI 2	ROI 3	ROI 4
just after	2.726E+08	1.160E+08	1.332E+08	4.291E+08	0.0	0.0	0.0	0.0
6.5 h	2.923E+08	1.340E+08	2.056E+08	4.825E+08	7.2	15.5	54.4	12.4
12 h	3.141E+08	1.372E+08	2.071E+08	5.001E+08	15.2	18.3	55.5	16.5
27.5 h	3.320E+08	1.409E+08	1.750E+08	5.274E+08	21.8	21.5	31.4	22.9
48 h	3.233E+08	1.332E+08	1.711E+08	5.257E+08	18.6	14.8	28.5	22.5
72 h	3.194E+08	1.278E+08	1.511E+08	5.177E+08	17.2	10.2	13.4	20.6
13 days	3.053E+08	1.139E+08	1.166E+08	4.488E+08	12.0	-1.8	-12.5	4.6

Table S2. The Sum of Fluorescence Intensities and Ratio of Increased Fluorescence Intensities in All ROI Using Polymer **4b**.

time	sums of fluorescence intensity in ROI				ratio of increased fluorescence intensity (%)			
	ROI 1	ROI 2	ROI 3	ROI 4	ROI 1	ROI 2	ROI 3	ROI 4
just after	2.773E+08	1.114E+08	1.145E+08	4.210E+08	0.0	0.0	0.0	0.0
6.5 h	2.949E+08	1.317E+08	1.263E+08	4.360E+08	6.3	18.2	10.3	3.6
12 h	3.080E+08	1.365E+08	1.302E+08	4.403E+08	11.1	22.5	13.7	4.6
27.5 h	3.113E+08	1.288E+08	1.310E+08	4.538E+08	12.3	15.6	14.4	7.8
48 h	3.097E+08	1.235E+08	1.264E+08	4.517E+08	11.7	10.9	10.4	7.3
72 h	3.136E+08	1.202E+08	1.204E+08	4.443E+08	13.1	7.9	5.2	5.5
13 days	3.084E+08	1.038E+08	1.047E+08	4.074E+08	11.2	-6.8	-8.6	-3.2

Table S3. The Sum of Fluorescence Intensities and Ratio of Increased Fluorescence Intensities in All ROI Using Polymer **4c**.

time	sums of fluorescence intensity in ROI				ratio of increased fluorescence intensity (%)			
	ROI 1	ROI 2	ROI 3	ROI 4	ROI 1	ROI 2	ROI 3	ROI 4
just after	2.479E+08	1.059E+08	1.062E+08	3.902E+08	0.0	0.0	0.0	0.0
6.5 h	2.602E+08	1.134E+08	1.150E+08	4.055E+08	5.0	7.1	8.3	3.9
12 h	2.793E+08	1.147E+08	1.358E+08	4.145E+08	12.7	8.3	27.9	6.2
27.5 h	2.869E+08	1.184E+08	1.316E+08	4.272E+08	15.7	11.8	23.9	9.5
48 h	2.811E+08	1.155E+08	1.259E+08	4.253E+08	13.4	9.1	18.5	9.0
72 h	2.777E+08	1.132E+08	1.165E+08	4.178E+08	12.0	6.9	9.7	7.1
13 days	2.822E+08	1.043E+08	1.039E+08	4.006E+08	13.8	-1.5	-2.2	2.7

Table S4. The Sum of Fluorescence Intensities and Ratio of Increased Fluorescence Intensities in All ROI Using Polymer **4d**.

time	fluorescence intensity in ROI				ratio of increased fluorescence intensity (%)			
	ROI 1	ROI 2	ROI 3	ROI 4	ROI 1	ROI 2	ROI 3	ROI 4
just after	2.70E+08	1.06E+08	1.09E+08	4.00E+08	0.0	0.0	0.0	0.0
6.5 h	2.80E+08	1.23E+08	1.19E+08	4.10E+08	3.5	16.6	9.5	2.3
12 h	3.01E+08	1.30E+08	1.36E+08	4.15E+08	11.2	22.8	25.0	3.8
27.5 h	3.01E+08	1.20E+08	1.25E+08	4.27E+08	11.1	13.5	15.4	6.8
48 h	3.01E+08	1.15E+08	1.22E+08	4.20E+08	11.4	8.4	12.7	4.9
72 h	2.96E+08	1.17E+08	1.18E+08	4.18E+08	9.5	10.7	8.7	4.3
13 days	2.94E+08	1.00E+08	1.06E+08	3.92E+08	8.8	-5.0	-2.3	-1.9

2. References

(1) Tranmer, G. K., and Tam, W. (2001) Intramolecular 1,3-dipolar cycloadditions of norbornadiene-tethered nitrones. *J. Org. Chem*. *66*, 5113-5123.

(2) Yip, C., Handerson, S., Tranmer, G. K., and Tam, W. (2001) Intramolecular 1,3-dipolar cycloadditions of norbornadiene-tethered nitrile oxides. *J. Org. Chem*. *66*, 276-286.

(3) Yam, C. M., Deluge, M., Tang, D., Kumar, A., and Cai, C. (2006) Preparation, characterization, resistance to protein adsorption, and specific avidin-biotin binding of poly(amidoamine) dendrimers functionalized with oligo(ethylene glycol) on gold. *J. Colloid Interface Sci*. *296*, 118-130.

(4) Maeda, H., Maeda, T., Mizuno, K., Fujimoto, K., Shimizu, H., and Inouye, M. (2006) Alkynylpyrenes as improved pyrene-based biomolecular probes with the advantages of high fluorescence quantum yields and long absorption/emission wavelengths. *Chem. Eur. J*. *12*, 824-831.

Bioconjugate Chemistry 20th Anniversary

Subscriber access provided by SHEMYAKIN-OVCHINNIKOV INST

Article

Stabilized Integrin-Targeting Ternary LPD (Lipopolyplex) Vectors for Gene Delivery Designed To Disassemble Within the Target Cell

M. Firouz Mohd Mustapa, Stephanie M. Grosse, Laila Kudsiova, Martin Elbs, Eun-Ang Raiber, John B. Wong, Anthony P. R. Brain, Hannah E. J. Armer, Alice Warley, Melanie Keppler, Tony Ng, M. Jayne Lawrence, Stephen L. Hart, Helen C. Hailes, and Alethea B. Tabor

Bioconjugate Chem., **2009**, 20 (3), 518-532• DOI: 10.1021/bc800450r • Publication Date (Web): 20 February 2009

Downloaded from http://pubs.acs.org on May 8, 2009

More About This Article

Additional resources and features associated with this article are available within the HTML version:

- Supporting Information
- Access to high resolution figures
- Links to articles and content related to this article
- Copyright permission to reproduce figures and/or text from this article

View the Full Text HTML

ACS Publications
High quality. High impact.

Bioconjugate Chemistry is published by the American Chemical Society. 1155 Sixteenth Street N.W., Washington, DC 20036

Stabilized Integrin-Targeting Ternary LPD (Lipopolyplex) Vectors for Gene Delivery Designed To Disassemble Within the Target Cell

M. Firouz Mohd Mustapa,[†] Stephanie M. Grosse,[‡] Laila Kudsiova,[§] Martin Elbs,[†,¶] Eun-Ang Raiber,[†] John B. Wong,[†] Anthony P. R. Brain,[||] Hannah E. J. Armer,[||,□] Alice Warley,[||] Melanie Keppler,[⊥] Tony Ng,[⊥] M. Jayne Lawrence,[§] Stephen L. Hart,[‡] Helen C. Hailes,[†] and Alethea B. Tabor*[,†]

Department of Chemistry, University College London, Christopher Ingold Laboratories, 20 Gordon Street, London WC1H 0AJ, Wolfson Centre for Gene Therapy of Childhood Disease, Institute of Child Health, University College London, 30 Guilford Street, London WC1N 1EH, School of Biomedical and Health Sciences, Pharmaceutical Science Research Division, King's College London, Franklin-Wilkins Building, Stamford Street, London SE1 9NH, Centre for Ultrastructure Imaging, King's College London, New Hunt's House, Guy's Campus, London SE1 1UL, and School of Biomedical and Health Sciences, Randall Division of Cell and Molecular Biophysics, King's College London, Henriette Raphael Building, Guy's Campus, London SE1 1UL, United Kingdom. Received October 20, 2008

Recent research in the field of nonviral gene delivery vectors has focused on preparing nanoparticles that are stabilized by the incorporation of a PEG coating and where one of the vector components is also cleavable. Here,we describe the synthesis, formulation, transfection properties, and biophysical studies of a PEG-stabilized ternary lipopolyplex vector in which, for the first time, both the lipid and peptide components are designed to be cleaved once the vector has been internalized. A series of cationic lipids, bearing short tri- or hexaethylene glycol groups, attached to the headgroup via an ester linkage, has been prepared. Trifunctional peptides have also been prepared, consisting of a Lys_{16} sequence at the N-terminus (to bind and condense plasmid DNA); a spacer group (containing a sequence recognized and cleaved by endosomal enzymes) and an optional PEG4 amino acid; and an integrin-targeting cyclic peptide sequence (allowing the resulting nanoparticle to be internalized via receptor-mediated endocytosis). Differing combinations of these lipids and peptides have been formulated with DOPE and with plasmid DNA, and complex stability, transfection, and cleavage studies carried out. It was shown that optimal transfection activities in a range of cell types and complex stabilities were achieved with lipids bearing short cleavable triethylene glycol moieties, whereas the incorporation of PEG4 amino acids into the cleavable peptides had little effect. We have synthesized appropriate fluorescently labeled components and have studied the uptake of the vector, endosomal escape, peptide cleavage, and plasmid transport to the nucleus in breast cancer cells using confocal microscopy. We have also studied the morphology of these compact, stabilized vectors using cryo-EM.

INTRODUCTION

Nonviral vectors are now regarded as a clinically important approach for the therapeutic delivery of DNA into cells. They have several advantages over viral vectors; their unlimited packaging capacity, ease of structural modification, and potential for large-scale production are all important for the manufacturing of gene delivery agents. Most importantly, their low immunogenicity means that they have few of the toxicity and safety issues associated with viral gene delivery vectors (*1*, *2*). In early studies, packaging was achieved by the condensation of DNA with polycationic polymers such as polyethylenimine (PEI), peptides, and dendrimers, giving polyplexes (*3*), or with cationic lipids, giving lipoplexes (*4*−*6*). However, these gene delivery complexes initially lacked any mechanisms to overcome the multiple barriers to successful gene transfer (*7*), and frequently, only low transfection efficiencies and poor in vivo stabilities were achieved. As a consequence, very few nonviral vectors have so far reached clinical trials (*8*).

A recent important advance in the design of high-efficiency nonviral gene delivery vectors was the recognition that incorporating targeting moieties on the surface of the complex would lead to vector internalization by receptor-mediated endocytosis, and hence higher transfection efficiencies (*9*). Multicomponent nonviral vectors, incorporating more than one type of carrier molecule, and more closely imitating viruses in their assembly and cell targeting properties, have recently been investigated and have been shown to have enhanced transfection properties (*10*−*12*). Several groups have reported the use of ternary lipid−peptide−DNA lipopolyplex vectors, combining the advantages of polyplexes and lipoplexes and incorporating receptor-targeting moieties (*13*, *14*). Hart et al. (*13*) described the use of the LPD vector, which consists of a self-assembling combination of lipids (L), polycationic peptide (P), and plasmid DNA (D). The dual functional peptide (**1**) comprises both a K_{16} DNA-binding and compaction domain and a cyclic peptide (CRRETAWAC) domain targeted to the $\alpha_5\beta_1$ integrin; the lipids DOTMA (**2**) and DOPE (**3**) are used as a 1:1 mixture (Lipofectin) (Figure 1). The LPD system

* To whom all correspondence should be addressed. Department of Chemistry, University College London, Christopher Ingold Laboratories, 20 Gordon Street, London WC1H 0AJ, United Kingdom. Phone: +44 20 7679 4695. Fax: +44 20 7679 7463. Email: a.b.tabor@ucl.ac.uk.

[†] Department of Chemistry, UCL.

[‡] Institute of Child Health, UCL.

[§] School of Biomedical and Health Sciences, Pharmaceutical Science Division, KCL.

[||] CUI, KCL.

[⊥] School of Biomedical and Health Sciences, Randall Division of Cell and Molecular Biophysics, KCL.

[¶] Present address: Ciba AG, Postfach 4002 Basel, Switzerland.

[□] Present address: Electron Microscopy Unit, London Research Institute, Cancer Research UK, 44 Lincoln's Inn Fields, London, WC2A 3PX, UK.

10.1021/bc800450r CCC: $40.75 © 2009 American Chemical Society
Published on Web 02/20/2009

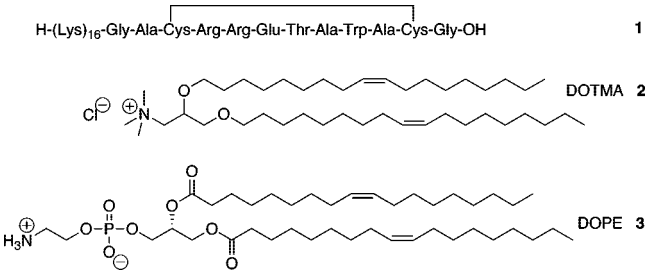

Figure 1. Components of first-generation LPD vector.

was shown to display high transfection efficiencies and, in particular, to efficiently transfect nondividing cells. Moreover, these complexes exhibited low toxicity in vitro and in vivo, with low immunogenicity in vivo (*13, 15*−*17*). We have recently established the stoichiometry of these particles using fluorescence correlation spectroscopy (FCS) and, using freeze-fracture electron microscopy and fluorescence quenching, have demonstrated that the LPD vectors have a tightly compacted DNA−peptide inner core surrounded by a disordered lipid layer, from which the integrin-targeting peptide partially protrudes (*18*). We have also established that this system can be used with a wide variety of targeting peptides, enabling delivery to specific cell types (*19*−*22*).

An additional problem with many nonviral vectors is that cationic polyplexes, lipoplexes, and lipopolyplexes are bound by plasma proteins and are quickly cleared by the reticuloendothelial system (RES). In addition, these formulations are unstable in buffers and plasma and tend to aggregate (*23, 24*). In order for nonviral vectors to be therapeutically useful, these problems must be overcome. It has been shown that coating the surface of these complexes with polymeric poly(ethylene glycol) (PEG) units prevents aggregation, lowers residual toxicity, and prolongs the circulation time (*25*−*29*). However, although the stabilities of such sterically shielded complexes are greatly enhanced, in many cases greatly reduced cell transfection activities are also observed. This has been attributed to a number of factors including particle charge masking (*30*), steric hindrance of targeting ligands (*31*), interference with the ability of the liposome to undergo membrane fusion and destabilization once internalized in the endosome (*32*−*34*), and blocking of intracellular trafficking of the plasmid DNA (*35*). Even when the surface of the stabilized particles was coated with receptor-targeting ligands, in many cases the transfection efficiencies did not improve (*36*). Recent advances in the synthesis of chemically dynamic gene delivery complexes containing components that can be triggered to disassemble or degrade within the liposome (*37, 38*) have been applied to the preparation of PEG-stabilized gene delivery vectors, and more effective transfections have been reported (*39*−*42*). However, all of these studies have been carried out with large polymeric PEG moieties attached, and until very recently, there have been no reports of stabilized gene delivery vectors formulated with components containing shorter ethylene glycol oligomer units of defined length (*43, 44*).

The aim of this work was to design and synthesize gene delivery vectors that would be stable in the circulation and would not be cleared rapidly by the RES, but would retain their capacity to target specific cells and to transfect them efficiently. We report herein the synthesis of lipids and peptides containing short ethylene glycol oligomer units of defined lengths, and our studies of the stability, transfection, structural, and biophysical properties of LPD complexes formulated using these components. These lipids and peptides have, additionally, been designed to incorporate features that can be cleaved by enzymes found in endosomes, ensuring that these components can degrade within the endosome and thus trigger endocytotic release and partial complex disassembly. We have also carried out a detailed study of the uptake and disassembly of these complexes using confocal microscopy.

EXPERIMENTAL PROCEDURES

General Synthetic Methods and Materials for Cell Biology are given in the Supporting Information.

Peptide Synthesis. Protected amino acids, coupling reagents, and solid supports were purchased from Novobiochem (U.K.) or AGTC Bioproducts (U.K.).

Lipids. DOTMA was purchased from Invitrogen Life Technologies, U.K., and TCI Europe N. V. Belgium, respectively. 2-(4,4-Difluoro-5-methyl-4-bora-3*a*,4*a*-diaza-*s*-indacene-3-dodecanoyl)-1-hexadecanoyl-*sn*-glycero-3-phosphocholine (*β*-BODIPY 500/510 C_{12}−HPC) (**21**) was purchased from Invitrogen Molecular Probes, U.K. DOPE (dioleoylphosphatidylethanolamine) was supplied from Avanti Polar Lipids, USA. 2,3-Di-((9*Z*)-octadecenyloxy)propyl-*N*,*N*-dimethylamine **13** was prepared as previously described (*45*).

Cell Lines. The human bronchial epithelial (16HBE14o-) cell line was kindly given by D. C. Gruenert (University of Vermont, Burlington, VT, USA) (*46*). Mouse neuroblastoma (Neuro 2A) and endothelial (bEND.3) cell lines were obtained from ATCC (Manassas, VA, USA). Primary porcine vascular smooth muscle cells (PVSMCs) were prepared using the explant method described previously (*47*). AJ3.1 is a mouse embryonic fibroblast line derived from A/J embryos. MDA-MB-231 breast cancer cells were a gift from the Randall Division of Cell and Molecular Biophysics, King's College London.

Lipid Synthesis. *5-Bromopentanoic Acid 8-Hydroxy-3,6-dioxooctyl Ester (***15***).* To a stirred solution of triethylene glycol (7.50 mL, 50 mmol, 10 equiv) in dry dichloromethane (20 mL) was added, dropwise, 5-bromopentanoyl chloride (0.670 mL, 5.0 mmol), and the reaction was stirred for 18 h. The mixture was then concentrated in vacuo and the crude oil purified by flash column chromatography (0−4% methanol in dichloromethane), yielding the desired product **15** as a golden yellow oil (1.47 g, 95%). ^{1}H NMR (300 MHz, $CDCl_3$): δ 1.68 (2H, m), 1.80 (2H, m), 2.28 (2H, t, $J = 7.2$ Hz), 3.31 (2H, t, $J = 6.5$ Hz), 3.47−3.62 (10H, m), 4.14 (2H, t, $J = 4.7$ Hz). ^{13}C NMR (75 MHz, $CDCl_3$): δ 23.4, 31.9, 33.0, 33.1, 61.5, 63.3, 69.0, 70.2, 70.4, 72.5, 173.1. HRMS *m*/*z* (ES+) calcd 335.04707, found 335.04651 ($[M + Na]^+$).

*5-Bromopentanoic Acid 3,6,9-Trioxodecyl Ester (***16***).* A solution of triethylene glycol monomethylether (0.880 g, 5.5 mmol, 1.1 equiv) in dry dichloromethane (10 mL) was stirred for 10 min at room temperature. 5-Bromopentanoyl chloride (0.670 mL, 5.0 mmol) was then added dropwise, and the reaction was stirred for a further 18 h. The mixture was concentrated in vacuo, and the crude material was purified by flash column chromatography (2−7% methanol in dichloromethane) to yield the title compound as a yellow oil (0.805 g, 51%). ^{1}H NMR (300 MHz, $CDCl_3$): δ 1.70 (2H, m), 1.81 (2H, m), 2.30 (2H, t, $J = 7.2$ Hz), 3.30 (3H, s), 3.33 (2H, t, $J = 6.5$ Hz), 3.45−3.64 (10H, m), 4.15 (2H, m). ^{13}C NMR (75 MHz, $CDCl_3$): δ 23.4, 31.9, 33.0, 33.1, 59.0, 63.5, 69.1, 70.49 (signals overlap), 70.54, 71.9, 173.0. HRMS *m*/*z* (ES+) calcd 349.06272, found 349.06202 ($[M + Na]^+$).

*5-Bromopentanoic Acid 17-Hydroxy-3,6,9,12,15-pentaoxoheptadecyl Ester (***17***).* A solution of hexaethylene glycol (3.75 mL, 15 mmol, 3 equiv) was stirred in dry dichloromethane (10 mL) for 10 min at room temperature. 5-Bromopentanoyl chloride (0.670 mL, 5.0 mmol) was then added dropwise, and the reaction was stirred for a further 18 h. The mixture was concentrated in vacuo, and the crude material was purified by flash column chromatography (5−10% methanol in dichloromethane) to yield

the title product as a yellow oil (1.43 g, 64%). ^{1}H NMR (300 MHz, $CDCl_3$): δ 1.64 (2H, m), 1.75 (2H, m), 2.24 (2H, t, J = 7.2 Hz), 3.31 (2H, t, J = 6.5 Hz), 3.42−3.58 (22H, m), 4.08 (2H, t, J = 4.8 Hz). ^{13}C NMR (75 MHz, $CDCl_3$): δ 23.2, 31.6, 32.8, 33.0, 61.1, 63.2, 68.8, 70.0−70.3 (signal overlap), 72.4, 172.6. HRMS *m/z* (ES+) calcd 467.12571, found 467.12615 ($[M + Na]^+$).

(2,3-Bis-octadec-9-enyloxypropyl)-(8-hydroxy-3,6-dioxooctyloxycarbonylbutyl)dimethylammonium Bromide (4). A mixture of **13** (0.515 g, 0.83 mmol) and **15** (0.312 g, 1.0 mmol, 1.2 equiv) was stirred in a sealed tube at 100 °C for 96 h. Upon cooling, the crude mixture was purified by flash column chromatography (0−20% ethanol in dichloromethane) to give the title compound as a pale yellow oil (0.427 g, 60%). ^{1}H NMR (300 MHz, $CDCl_3$): δ 0.89 (6H, t, J = 6.7 Hz), 1.25 (44H, m), 1.53 (4H, m), 1.72 (2H, m), 1.85 (2H, m), 1.99 (8H, m), 2.45 (2H, t, J = 6.8 Hz), 3.36−3.43 (10H, m), 3.54−3.72 (16H, m), 3.88 (1H, d, J = 13.2), 4.06 (1H, m), 4.23 (2H, t, J = 4.6 Hz), 5.32 (4H, m). ^{13}C NMR (75 MHz, $CDCl_3$): δ 14.1 (signal overlap), 21.5, 22.1, 22.7, 26.0, 26.2, 27.2, 29.1−30.2 (signal overlap), 32.6, 33.2, 52.3 (signal overlap), 61.4, 63.4, 65.1, 65.7, 68.4, 69.0, 69.3, 70.2, 70.5, 72.0, 72.5, 73.3, 129.7 (signal overlap), 130.0 (signal overlap), 172.7. HRMS *m/z* (ES+) calcd 852.76558, found 852.76483 (M^+).

(2,3-Bis-octadec-9-enyloxypropyl)-(3,6,9-trioxodecyloxycarbonylbutyl)dimethylammonium Bromide (5). A mixture of **13** (0.430 g, 0.69 mmol) and **16** (0.252 g, 0.80 mmol) in acetone (5 mL) was stirred in a sealed tube at room temperature for 24 h, followed by another 24 h at 80 °C. Upon cooling, the solvent was evaporated in vacuo, and the crude material was purified by flash column chromatography (10% methanol in dichloromethane) to give the title compound as an orange oil (0.264 g, 44%). ^{1}H NMR (300 MHz, $CDCl_3$): δ 0.85 (6H, t, J = 6.7 Hz), 1.24 (44H, m), 1.53 (4H, m), 1.69 (2H, m), 1.84 (2H, m), 1.99 (8H, m), 2.44 (2H, t, J = 6.8 Hz), 3.34−3.45 (14H, m), 3.54−3.72 (16H, m), 3.88 (1H, m), 4.05 (1H, m), 4.21 (2H, t, J = 4.7 Hz), 5.32 (4H, m). ^{13}C NMR (75 MHz, $CDCl_3$): δ 14.1 (signal overlap), 21.5, 22.1, 22.6, 26.0, 26.2, 27.2, 29.1−30.0 (signal overlap), 31.8, 32.6, 33.1, 52.2, 52.3, 59.0, 63.6, 65.0, 65.6, 68.4, 69.0, 69.2, 70.5 (signal overlap), 70.5, 71.86, 71.92, 73.3, 129.7 (signal overlap), 129.9 (signal overlap), 172.6. HRMS *m/z* (ES+) calcd 866.78123, found 866.78074 (M^+).

(2,3-Bis-octadec-9-enyloxypropyl)-(17-hydroxy-3,6,9,12,15-pentaoxoheptadecyloxycarbonylbutyl)dimethylammonium bromide (6). A mixture of **13** (0.395 g, 0.64 mmol) and **17** (0.330 g, 0.74 mmol) in acetone (5 mL) was stirred in a sealed tube at room temperature for 24 h followed by another 24 h at 80 °C. Upon cooling, the solvent was removed in vacuo and the crude material was purified by flash column chromatography (5−10% methanol in dichloromethane) to yield the title compound as an orange oil (0.300 g, 47%). ^{1}H NMR (300 MHz, $CDCl_3$): δ 0.85 (6H, t, J = 6.7 Hz), 1.24 (44H, m), 1.52 (4H, m), 1.69 (2H, m), 1.84 (2H, m), 1.98 (8H, m), 2.44 (2H, t, J = 6.9 Hz), 3.37−3.43 (14H, m), 3.54−3.70 (28H, m), 3.92 (1H, m), 4.06 (1H, m), 4.22 (2H, t, J = 4.7 Hz), 5.31 (4H, m). ^{13}C NMR (75 MHz, $CDCl_3$): δ 14.1 (signal overlap), 21.5, 22.1, 22.6, 26.0, 26.2, 27.1, 29.1−29.7 (signal overlap), 30.0, 31.8, 32.5, 33.2, 52.2 (signal overlap), 61.1, 63.5, 65.0, 65.6, 68.5, 69.1, 69.2, 69.9, 70.2−70.3 (signal overlap), 71.9, 72.3, 73.3, 129.7 (signal overlap), 129.9 (signal overlap), 172.8. HRMS *m/z* (ES+) calcd 984.84421, found 984.84335 (M^+).

Peptide Synthesis. All peptides were synthesized on a MultiSynTech Syro peptide synthesizer. Preloaded solid support (Fmoc-Gly-NovaSyn TGT (0.20 mmol/g loading, 0.180 g, 36 μmol)) was used and was preswelled in DMF for at least 30 min before the start of synthesis. All reagents were dissolved in HPLC-grade DMF, with the exception of DIPEA where it was dissolved in NMP. Automated protocols were employed as follows:

Fmoc Deprotection. To a sintered reaction vessel containing the solid support was added the piperidine solution (40% v/v, 0.90 mL, excess), and the resulting mixture was agitated by vortex for 20 s with a 1 min break for a total of 3 min. The excess reagents were removed by filtering under vacuum. A second deprotection step was carried out with a 20% piperidine/DMF (v/v) solution by adding the piperidine solution (40% v/v, 0.45 mL, excess) followed by DMF (0.45 mL), and the resulting mixture was agitated by vortex for 20 s with a 1 min break for a total of 10 min. The excess reagents were removed by filtering under vacuum, and the resin was washed with DMF (6 × 1 mL).

Amino Acid Coupling. To a sintered reaction vessel containing the solid support was added the Fmoc-protected amino acid solution (0.360 mL, 0.40 M, 4 equiv), followed by HBTU (0.360 mL, 0.40 M, 4 equiv) and DIPEA (0.180 mL, 1.6 M, 8 equiv). The resulting mixture was agitated by vortex for 20 s with a 2 min break for a total of 40 min. The excess reagents were removed by filtering under vacuum, and the resin was washed with DMF (4 × 1 mL).

Disulfide Bond Formation. To a sintered reaction vessel containing the solid support with the completed peptide sequence was manually added a solution of iodine (0.100 g) in DMF (1 mL), and the resulting mixture was agitated by vortex for 20 s with a 4 min break for a total of 4 h.

Peptide Cleavage from Resin. Upon completion of the synthesis, the peptidyl resin was washed thoroughly with DCM to remove traces of DMF, and to the sintered vessel was added a cocktail solution of either TFA/TIS/water (95:2.5:2.5, 2 mL, for peptides with disulfide bonds already formed) or TFA/EDT/waterTIS (94:2.5:2.5:1, 2 mL, for peptides containing Cys), and the reaction was left to stand for at least 3 h. The resulting solution was removed from the vessel and the resin was washed with neat TFA (2 × 1 mL). The combined TFA solution was concentrated in vacuo followed by addition of ice−cold ether to precipitate the peptide. This was left in the freezer for a further 2 h, and the mixture was centrifuged. The liquid was decanted, and fresh ether was added. The centrifugation/decanting procedure was repeated twice more. The isolated pellet was dissolved in water or ^{t}BuOH/water and freeze−dried.

Labeled Peptides. Assembly of the linear sequences were carried out as described above (with the use of Fmoc-Lys(ivDde)-OH (0.360 mL, 0.40 M, 4 equiv) on the labeling site and Boc-Lys(Boc)-OH (0.360 mL, 0.40 M, 4 equiv) on the *N*-terminus). This was followed by removal of the ivDde group by treatment with a hydrazine monohydrate solution in DMF (2% v/v, 5 × 1 mL, agitated by vortex for 20 s with a 1 min break for a total of 3 min each) and on resin coupling with either tetramethylrhodamine (0.150 mL, 0.20 M, 2 equiv with HBTU (0.150 mL, 0.40 M, 2 equiv) and DIPEA (0.038 mL, 1.60 M, 4 equiv)) (peptide **19**) or Pacific Blue (succinimidyl ester, 0.150 mL, 0.20 M, 2 equiv, with DIPEA (0.038 mL, 1.60 M, 4 equiv)) (peptide **20**), all with agitation by vortex for 20 s with a 4 min break for a total of 18 h. The peptidyl resin was then washed with DMF (6 × 1 mL), followed by DCM (6 × 1 mL) for cleavage preparation. Labeled peptides were first cleaved from the solid support and worked up as described previously, and the lyophilized solid was dissolved in doubly distilled water (≤0.25 mg/mL) and stirred for 10 days.

Peptide Purification by HPLC. Each peptide was purified by preparative reverse-phase HPLC with aqueous TFA (0.1% v/v) and acetonitrile (with 0.1% TFA, v/v) using a Supelco column (25 cm × 21.2 mm). Each purified peptide was then analyzed by analytical reverse-phase chromatography using a Supelco

column (25 cm × 4.6 mm) with either a 10−100% MeCN or a 10−50% MeCN gradient run over 25 min (Gradient P and Gradient Q, respectively).

Peptide **9.** Purification was carried out as described above (10% to 20% MeCN over 30 min), Gradient Q R_T 7.7 min, *m*/*z* (ES+) 1157.0 ($[M + 3H]^{3+}$), 867.9 ($[M + 4H]^{4+}$), 694.6 ($[M + 5H]^{5+}$), 579.1 ($[M + 6H]^{6+}$), 496.7 ($[M + 7H]^{7+}$).

Peptide **10.** Purification was carried out as described above (10% to 25% MeCN over 30 min), Gradient P R_T 5.2 min, *m*/*z* (ES+) 1829.6 ($[M + 2H]^{2+}$), 1220.4 ($[M + 3H]^{3+}$), 915.6 ($[M + 4H]^{4+}$), 732.7 ($[M + 5H]^{5+}$), 610.5 ($[M + 6H]^{6+}$).

Peptide **11.** Purification was carried out as described above (10% to 25% MeCN over 30 min), Gradient P R_T 5.4 min, *m*/*z* (ES+) 1829.8 ($[M + 2H]^{2+}$), 1220.34 ($[M + 3H]^{3+}$), 915.4 ($[M + 4H]^{4+}$), 733.0 ($[M + 5H]^{5+}$), 610.4 ($[M + 6H]^{6+}$).

Peptide **12.** Purification was carried out as described above (10% to 20% MeCN over 30 min), Gradient P R_T 4.8 min, *m*/*z* (ES+) 1129.3 ($[M + 3H]^{3+}$), 847.1 ($[M + 4H]^{4+}$), 678.1 ($[M + 5H]^{5+}$), 565.3 ($[M + 6H]^{6+}$).

Peptide **19.** Purification was carried out as described above (10% to 25% MeCN over 30 min), Gradient Q R_T 10.5 and 11.4 min (corresponding to the two isomers of tetramethylrhodamine). *m*/*z* (ES+) 1003.2 ($[M + 4H]^{4+}$), 802.8 ($[M + 5H]^{5+}$), 669.3 ($[M + 6H]^{6+}$), 573.7 ($[M + 7H]^{7+}$).

Peptide **20.** Purification was carried out as described above (10% to 25% MeCN over 30 min), Gradient Q R_T 10.8 min, *m*/*z* (ES+) 970.3 ($[M + 4H]^{4+}$), 776.4 ($[M + 5H]^{5+}$), 647.3 ($[M + 6H]^{6+}$), 554.9 ($[M + 7H]^{7+}$).

Plasmid DNA. The plasmid pCI-Luc (5.7 kb) consists of pCI (Promega, Southampton, U.K.) containing the luciferase gene driven by the cytomegalovirus (CMV) immediate/early promoter−enhancer. It was grown in *Escherichia coli* DH5α and purified, after bacterial alkaline lysis, on resin columns (Qiagen Ltd., Crawley, UK). Isopropanol-precipitated DNA pellets were washed with 70% ethanol, then dissolved in water at 1 mg/mL.

Preparation of Lipoplexes and Lipopolyplexes. Small unilamellar vesicles were prepared using the cationic lipid mixed with DOPE (**3**) at 1:1 weight ratio. One milligram of DOPE and 1 mg of cationic lipid were weighed out into a 25 mL round-bottom flask and dissolved in chloroform. The solvent was rotary-evaporated to produce a thin film of lipid, and then evaporated under high vacuum for 24 h. The film was then rehydrated with an appropriate volume of water at 4 °C for 24 h and then sonicated on ice for 2 min using a Lucas Dawes probe sonicator to produce vesicles.

LPD lipopolyplexes were prepared essentially as described previously (*13*). Briefly, the LPD components were mixed in the following order: 50 μL of lipid (L) at 400 μg/mL in PBS, prepared as described above, 70 μL of peptide (P) at 550 μg/mL in PBS, and 50 μL of plasmid pCI-Luc (D) at 200 μg/mL in PBS (10 μg of pCI-Luc plasmid), and diluted in PBS to a final volume of 1 mL. The weight ratio used was 2:4:1 for L:P:D, respectively, which was shown to be the best ratio for gene transfer, corresponding to a charge ratio of +7 (ratio of positive equivalents of the cationic groups to negative charge equivalents of the nucleic acid).

Complex Stability/Particle Size. Complex size was determined in three independent experiments by dynamic light scattering using a Zetasizer 3000 (Malvern Instruments, Worcestershire, U.K.) with the following specifications: automatic sampling time, 10 measurements per sample, refractive index medium of 1.33, and temperature of 25 °C.

Cell Culture. Human bronchial epithelial (16HBE14o-) cell line was maintained in Eagle's minimum essential medium (MEM) HEPES modification supplemented with 10% fetal bovine serum (FBS), 2 mM L-glutamine, 100 U/mL penicillin, and 100 μg/mL streptomycin. Mouse neuroblastoma (Neuro 2A) and endothelial (bEND.3) cell lines were maintained in Dulbecco's modified Eagle's medium (DMEM) with Glutamax-1 supplemented with 10% FBS, 1% NEAA solution, 1% sodium pyruvate, 100 U/mL penicillin, and 100 μg/mL streptomycin. AJ3.1 is a mouse embryonic fibroblast line derived from A/J embryos 13.5 days postcoitum as follows: the crania and red organs were removed and the remaining tissue minced using scalpels, digested with trypsin, then passed through a cell strainer. The resulting suspension was plated in DMEM with Glutamax-1 containing 10% FCS and 100 U/mL penicillin and 100 μg/mL streptomycin, with each embryo maintained as a separate culture. Cells were passaged every few days to maintain sparse colonies until the cultures reached senescence, and after 7−10 days, growing colonies of cells were observed. One culture was selected for all further work and is hereafter referred to as AJ3.1. PVSMCs were maintained in DMEM with Glutamax-1 supplemented with 20% FBS and 100 U/mL penicillin and 100 μg/mL streptomycin and used in transfections between passages 3−8. All cells were adherent and grew in Falcon 75 cm^2 plastic tissue culture flasks and were maintained in a humidified atmosphere of 95% air and 5% CO_2 at 37 °C.

MDA-MB-231 cells were cultured in tissue flasks in DMEM cell culture media supplemented with 10% FBS, 1% NEAA solution, 1% L-glutamine, and 1% penicillin−streptomycin solution, at 37 °C, 5% CO_2, and 90% relative humidity. The cells were fed every other day and passaged every three to four days at around 70−80% confluency, using 0.25% trypsin−EDTA solution.

In Vitro Transfections. Cells were seeded into 96 well plates at 2.5 × 10^3 cells per well for bEND.3 cells and at 2 × 10^4 cells per well for all the other cells, then incubated overnight at 37 °C in complete growth medium. The following day, lipopolyplex (LPD) formulations were prepared by mixing the components in the following order: 50 μL of lipid (L) at 80 μg/mL in OptiMEM, 70 μL of peptide (P) at 110 μg/mL in OptiMEM, and 50 μL of plasmid pCI-Luc (D) at 40 μg/mL in OptiMEM corresponding to a weight ratio of 2:4:1, respectively. All the complexes were mixed by pipetting briefly, kept for 1 h at room temperature, and then diluted in OptiMEM to a final volume of 1.57 mL. Two hundred microliters of complexes corresponding at 0.25 μg of plasmid DNA were added to each culture well after removal of the complete growth medium. All the transfections were carried out in 6 wells each. A centrifugation (1500 rpm, during 5 min) was performed to promote the complexe sedimentation and cell contact. The cells were incubated with the complexes for 4 h at 37 °C before replacing with fresh media for 24 h, after which reporter gene expression was analyzed by luciferase assay. For bEND.3 cells, 5 mM sodium butyrate was added to the transfection medium and to the fresh media to achieve optimal expression levels.

MDA-MB-231 cells were seeded on 24 well plates at 1.2 × 10^5 cells per well and incubated at 37 °C for 24 h. On the day of the experiment, the growth media was removed, and the cells were washed twice with PBS buffer and replaced with 200 μL of serum free DMEM. 200 μL of the complexes at 1:4:1 weight ratio were then added to each well, as above, at a final concentration of 1 μg of plasmid per well. The plates were incubated at 37 °C for 4 h after which the cells were washed once with PBS buffer and replaced with FBS containing culture medium. The cells were incubated for a further 48 h, to allow for luciferase expression, which was then measured as below.

Luciferase and Protein Assays. Cells were washed once with PBS before the addition of 20 μL (or 100 μL into a 24 well plate) of 1× Reporter Lysis Buffer to the cells for 20 min at 4 °C before freezing at −80 °C for at least 30 min, followed by thawing at room temperature. Then, the luciferase activity was measured during 10 s using the Luciferase Assay System and

a FLUOstar Optima (BMG Labtech, U.K.). The amount of protein present in each transfection lysate was determined with the Bio-Rad (Hercules, CA, USA) protein assay reagent by the manufacturer's instructions, adding 20 μL from the luciferase test to 180 μL of the reagent diluted 1 in 5 and incubating at room temperature for 10 min before comparing the OD590 to a range of BSA standards. Luciferase activity was expressed as relative light units (RLU) per milligram of protein (RLU/mg).

Cell Viability Assays. Cell viability of MDA-MB-231 cells was tested in the presence of free **4** without DNA or in the presence of **4**/calf thymus DNA complexes using the MTT assay. The cells were seeded at 1.5×10^5 cells per well in 24 well plates and left incubated at 37 °C for 48 h prior to use. On the day of the experiment, the cells were washed once with PBS and replaced with 200 μL of serum-free DMEM media before introducing 200 μL of various concentrations of lipids or lipid/DNA complexes and incubating for 4 h at 37 °C. The controls wells were treated with DMEM media with the same amount of water as the test wells but without the lipids. After incubation, the test solutions were removed and the cells washed once with PBS buffer. One milliliter of 0.8 mg/mL MTT solution in PBS was then introduced to all wells and left incubated for 3 h at 37 °C. 200 μL of neat isopropanol was then applied to solubilize the formazan crystals and the plates stored at 4 °C for 1 h. The contents of the wells were transferred to a clear 96-well plate and the absorbance measured at 550 nm using a Spectromax 190 Microplate Spectrophotometer (Molecular Devices, USA).

In Vitro Cleavage Experiments. *Esterase Cleavage of* **4.** A phosphate buffer stock solution (0.1 M, pH 7.5) was prepared by mixing an aqueous solution of potassium dihydrogen phosphate (0.1 M, 50 mL) with an aqueous solution of sodium hydroxide (0.1 M, 41 mL), all using Baxter water. A stock solution of **4** was prepared (2 mg/mL) according to the method described above, omitting the colipid DOPE. A solution of the pig liver esterase (28 mg, 672 units, capable of hydrolyzing 28 μmol of ethyl butyrate) was prepared by dissolving it in the phosphate buffer (875 μL). To the liposome (125 μL, 250 μg, 0.294 μmol) was added the buffered enzyme solution (875 μL), and the resulting mixture was incubated at 37 °C for 24 h. Aliquots (200 μL) were taken at $T = 1$, 2, 4, 6, and 24 h and immediately freeze−dried. The lyophilized material was dissolved in dichloromethane (50 μL) and analyzed by thin layer chromatography (15% methanol in dichloromethane + acetic acid) with phosphomolybdic acid staining. A sample of the hydrolyzed lipid **18** was previously run under the same conditions and the R_f value determined as a standard. R_f values: **4**, 0.35; **18**, 0.22 (15% methanol, 84% dichloromethane, 1% acetic acid).

Esterase Cleavage of ***4*** *in LPD Complex.* Stock solutions for peptide **9** and pCI-Luciferase were prepared (50 mg/mL and 5 mg/mL, respectively) using Baxter water. Formulation of the stock **4**/DOPE solution (2 mg/mL) was prepared according to the description above. Secondary solutions of the liposome (125 μL), peptide **9** (10 μL), and pCI-Luciferase (12.5 μL) in the phosphate buffer (125 μL, 250 and 250 μL, respectively) were then prepared. The resulting peptide solution was added to the buffered liposome. To the resulting mixture was added the pCI-Luciferase solution, and the mixture was left to equilibrate at RT for 1 h. A solution of the pig liver esterase (28 mg, 672 units, capable of hydrolyzing 28 μmol of ethyl butyrate) in phosphate buffer (223 μL) was then added to the LPD mixture followed by incubation at 37 °C for 24 h. Aliquots (200 μL) were taken at $T = 1$, 2, 4, 6, and 24 h and immediately freeze−dried. The lyophilized material was dissolved in dichloromethane (50 μL) and analyzed by thin layer chromatography (15% methanol in dichloromethane + acetic acid) with phosphomolybdic acid staining. Samples of the hydrolyzed lipid **18** and of DOPE were previously run under the same conditions and the R_f values determined. R_f values: **4**, 0.35; **18**, 0.22; DOPE, 0.07 (15% methanol, 84% dichloromethane, 1% acetic acid).

Furin Cleavage of **9.** A buffer solution was prepared by mixing HEPES (2.38 g, 100 mM), $CaCl_2$ (11 mg, 1 mM), mercaptoethanol (7 μL, 1 mM), Triton X100 (0.5 mL, 0.5%) in Millipore water (100 mL) and adjusted to pH 7.5 with sodium hydroxide (2 M). To the furin (2 units) was added the peptide solution (14 mM, 5 μL) and the buffer (494 μL), and the mixture was incubated at 30 °C. Aliquots (100 μL) were taken at $T =$ 0, 1, 2, and 4 h and transferred to a vial containing acetic acid (5 M, 100 μL) to inactivate the enzyme. The mixture was then freeze−dried, redissolved in water, and analyzed by analytical reverse-phase HPLC (10−50% MeCN in 25 min).

Furin Cleavage of **12.** To the furin (2 units) was added the peptide solution (2.9 mM, 25 μL) and the buffer (473 μL), and the mixture was incubated at 30 °C. Aliquots (100 μL) were taken at $T = 0$, 1, 2, and 4 h and transferred to a vial containing acetic acid (5 M, 100 μL) to inactivate the enzyme. The mixture was then freeze−dried, redissolved in water, and analyzed by analytical reverse-phase HPLC (10−50% MeCN in 25 min).

Cathepsin B Cleavage of **12.** Lyophilized cathepsin B was divided into aliquots, each containing approximately 2 units of cathepsin B, immediately after delivery and stored at −20 °C. An acetate buffer solution (Buffer A) was prepared by mixing sodium acetate (0.164 g, 20 mM) and EDTA (0.0372 g, 1 mM) in Millipore water (100 mL) and adjusted to pH 5.0 with acetic acid. A similar acetate buffer solution (Buffer B) was prepared with the addition of cysteine (0.1202 g, 5 mM). To the cathepsin B (2 units) was added Buffer A (10 μL). To this buffered enzyme solution was added the peptide solution (2.9 mM, 25 μL) and Buffer B (464 μL), and the mixture was incubated at 37 °C. Aliquots (100 μL) were taken at $T = 0$, 1, 2, 4, and 24 h and transferred to a vial containing acetic acid (5 M, 100 μL) to inactivate the enzyme. The mixture was then freeze−dried, redissolved in water, and analyzed by analytical reverse-phase HPLC (10−50% MeCN in 25 min).

Cathepsin B Cleavage of **9.** Lyophilized cathepsin B was divided into aliquots, each containing approximately 2 units of cathepsin B, immediately after delivery and stored at −20 °C. An acetate buffer solution (Buffer A) was prepared by mixing sodium acetate (0.164 g, 20 mM) and EDTA (0.0372 g, 1 mM) in Millipore water (100 mL) and adjusted to pH 5.0 with acetic acid. A similar acetate buffer solution (Buffer B) was prepared with the addition of cysteine (0.1202 g, 5 mM). To the cathepsin B (2 units) was added Buffer A (10 μL). To this buffered enzyme solution was added the peptide solution (13.5 mM, 5 μL) and Buffer B (485 μL) and the mixture was incubated at 37 °C. Aliquots (100 μL) were taken at $T = 0$, 1, 2, 3, and 4 h and transferred to a vial containing acetic acid (5 M, 20 μL) to inactivate the enzyme. The mixture was then freeze−dried, redissolved in water, and analyzed by analytical reverse-phase HPLC (10−50% MeCN in 25 min).

Cathepsin B Cleavage on Peptide **9** *in LPD Complex.* Lipid **4** was formulated with DOPE as described above (2 mg/mL). To this solution (62.5 μL) was added Buffer B (120 μL). To the peptide solution (13.5 mM, 5 μL) was added Buffer B (120 μL). The buffered lipid and peptide mixtures were then mixed together, followed by the addition of a buffered pCI-Luciferase solution (pCI-Luciferase solution at 5 mg/mL (12.5 μL) in Buffer B (160 μL). The resulting LPD complex mixture was left to equilibrate at rt for 1 h. To the cathepsin B (2 units) was added Buffer A (10 μL). To this buffered enzyme solution was added the LPD solution, and the mixture was incubated at 37 °C. Aliquots (100 μL) were taken at $T = 0$, 1, 2, 3, and 4 h and transferred to a vial containing acetic acid (5 M, 20 μL) to

inactivate the enzyme. The mixture was then freeze−dried, redissolved in water, and analyzed by analytical reverse-phase HPLC (10−50% MeCN in 25 min).

Acid Hydrolysis of Lipid **4.** Three buffered solutions were prepared: pH 5.5 (Buffer A from the cathepsin B experiments), pH 3 of citric acid solution (adjusted with sodium hydroxide (2 M)) and pH 1 of 0.1 M HCl solution. Lipid **4** was formulated as described above (2 mg/mL) and diluted 1:10 (v/v) with the buffered solutions and incubated at 37 °C. Aliquots were taken at $T = 1$ and 5 h and spotted onto a thin layer chromatography plate (10% methanol in dichloromethane) and stained with phosphomolybdic acid.

Confocal Fluorescence Microscopy. The pGL-3 plasmid luciferase reporter vector was purified from a transformed *E. coli* JM109 strain using a QIAGEN EndoFree plasmid Giga kit, according to manufacturer's instructions. The purified plasmid was then characterized and tested for yield and purity using UV spectroscopy and gel electrophoresis. The pGL-3 plasmid was then labeled with FluoroRed (rhodamine-4-dUTP) using a Nick translation kit. The manufacturer's protocol was modified in order to increase the yield of the labeled DNA. In an Eppendorf tube containing 30 μg of plasmid in 22 μL of water, 6 μL of 10 mM of each dCTP, dGTP, and dATP and 2.5 μL of 25 nmol tetramethyl-rhodamine-5-dUTP were added, together with 5 μL of polymerase/DNase mix (supplied in the kit) and 2 μL of DNA polymerase I. To all the above, 5.5 μL of NT buffer (10× strength, supplied in the kit) with 1 mM DTT was added. The mixture was gently vortexed and incubated at 15 °C for 4 h, after which the enzyme activity was stopped by the addition of 5 μL of 0.5 M EDTA (pH 8.0) while being placed on ice. The labeled DNA was then purified using a Biospin 6 column (from Bio-Rad, UK) by centrifuging the mixture twice for 5 min at 1000 × *g*. The concentration and purity of the labeled DNA was assessed using UV spectroscopy.

Confocal fluorescence images were acquired on a confocal fluorescence laser-scanning microscope (model LSM 510; Carl Zeiss Inc.) equipped with both 40×/1.3Plan-Neofluar and 63×/1.4Plan-APOCHROMAT oil immersion objectives. MDA-MB-231 cells were transfected with the complexes in 24 well plates fitted with 13 mm circular coverslips as described above using various combinations of labeled (β-BODIPY 500/510 C_{12}−HPC **21**) and unlabeled (DOPE, **3**) lipids with **4**; various combinations of labeled (**19** or **20**) and unlabeled (**9**) peptide; and either labeled or unlabeled plasmid DNA. For experiments where labeled lipid was used, labeled liposomes were initially formulated as described earlier, using a 10:9:1 weight ratio of **4**/DOPE/**21** and used in the preparation of the LPD lipopolyplexes. For experiments where labeled peptide was used, LPD complexes were formulated using 100% of either peptide **19** or peptide **20**. For experiments where the plasmid was being tracked, labeled DNA was either prepared by mixing 25% of the rhodamine-labeled plasmid with 75% of unlabeled plasmid or used at 100%.

After a 4 h incubation period, the LPD complexes were removed and the cells washed once with PBS before changing to serum-containing media. The cells were then fixed with 4% paraformaldehyde at time intervals of 0, 4, 24, and 48 h after the 4 h incubation time. The cells were permeabilized with a 0.2% Triton X-100 solution and DAPI stained by adding a 1 μg/mL solution of DAPI in PBS for 2 min. Washed coverslips were mounted with Mowiol 4−88 mounting media containing 2.5% DABCO as an antifade agent.

Electron Microscopy. Samples were negatively stained with 1% uranyl acetate in water and examined in either a Philips Tecnai T12 or an FEI Tecnai T20 transmission electron microscope. For cryo transmission electron microscopy, approximately 5 μL of the sample was placed on a holey carbon film on a 300 mesh gold grid and blotted to leave a thin film of sample across the holes. It was then rapidly frozen in "slushed" nitrogen and examined by low dose imaging at −170 °C in an FEI Tecnai T20 transmission electron microscope fitted with a Gatan 626DH cryotransfer system.

Statistical Analysis. All experiments were carried out more than three times, and the results are shown as means ± standard deviation. The statistical significance of results was assessed using the Student *t*-test, and results were taken to be significant when $p < 0.05$.

RESULTS

Design of the Lipid and Peptide Components. The lipid components were based on the structure of DOTMA, with short ethylene glycol oligomer units, appended to the headgroup, designed to detach in the endosomal environment. Various studies of vesicles with PEG attached have shown that the PEG molecular weight and loading, and whether the PEG is capped or uncapped, both have a significant influence on the vesicle aggregation process and on prolonging circulation times (*25, 48*). For the LPD system, it was necessary for the ethylene glycol oligomer layer to be relatively shallow, in order to allow the integrin-binding portion of the peptide to be exposed. Although few studies have been reported on the stabilization of lipid structures by short PEG layers, Tirrell et al. have investigated PEG-lipids with different lengths of oligoethylene glycol units, incorporated into a membrane containing a peptide−amphiphile (at a 1:1 ratio of PEG−lipid to peptide−amphiphile) and have determined that shorter PEG chains were required to ensure accessibility of the peptide ligand to cell surface receptors (*49*). Other studies have demonstrated that the use of surfactants conjugated to shorter PEG headgroups (4 to 30 units, MW approximately 180 to 1320), even at 1% PEG-modified surfactant or above, still results in significantly less aggregation compared to controls lacking the PEG units (*50*). All of these factors indicated that PEG headgroups bearing three or six units, capped and uncapped, should be investigated. Indeed, we have previously synthesized DOTMA analogues bearing PEG chains directly attached to the quaternary ammonium headgroup (*43*) and have showed that lipopolyplexes formulated with these lipids have increased serum stability and transfection efficiencies compared to lipopolyplexes formulated with DOTMA. This effect was particularly pronounced with tetraethylene glycol-bearing lipids.

The lipids were designed with an ester as a cleavable linkage between the PEG chain and the quaternary ammonium moiety of the lipid. Ester linkages have been extensively used in drug delivery applications, as they generally remain stable at pH 7 in plasma and in the early endosome, but hydrolyze when the pH changes to 5.5 in the late endosome (*51, 52*). Although aliphatic esters are not generally readily hydrolyzed in vivo (*53*), several studies have indicated that amino esters (*54*−*56*) and mercapto esters (*52, 57, 58*) can be hydrolyzed either within the circulation or within endosomes. It has been shown that in some cases the rate of hydrolysis depends upon the linker length (*58*) and that esterase hydrolysis within the endosome may represent an alternative pathway for degradation (*55*). Taking all of these factors into consideration, lipids **4**, **5**, and **6** were selected for synthesis (Figure 2) and compared with the noncleavable tetraethylene glycol lipid **7** (*43*) that we had prepared previously.

The peptides were designed to incorporate the following: a targeting element; short, ethylene glycol oligomeric chains of defined lengths; and peptide sequences that could be cleaved within the endosome. The end goals of this project are to produce gene delivery vectors that are sufficiently stable in vivo to be administered intravenously, and also to produce vectors

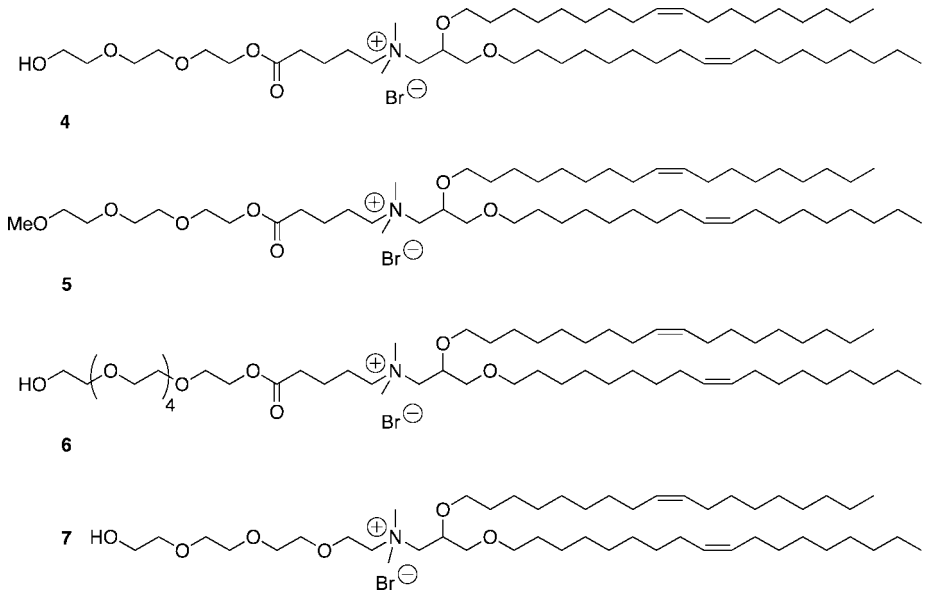

Figure 2. Structures of lipids investigated in this study.

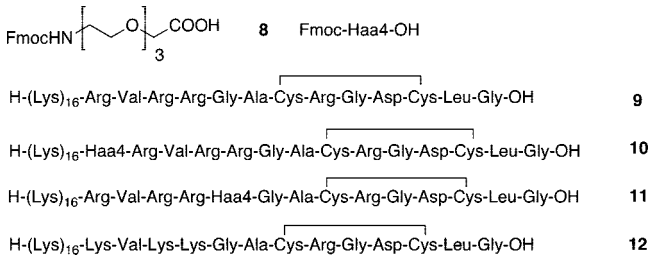

Figure 3. Sequences of peptides investigated in this study.

that will target and deliver genes to tumors that are currently hard to treat, such as neuroblastoma, or that have metastatized. Accordingly, a cyclic peptide sequence, CRDGCLG (*59*), was selected as the targeting element. This sequence is known to bind to the α_v integrin receptors expressed on neuroblastoma (*60*) endothelial (*61*) and breast cancer (*62, 63*) cell lines, as models for the tumor types that would eventually be studied in vivo. We have previously synthesized a range of Fmoc-protected PEG-amino acids and used these to incorporate ethylene glycol oligomer spacers into peptides based on the sequence of **1** using standard solid-phase methods. These peptides, with the short ethylene glycol oligomeric chains, were then used to formulate LPD particles (*64*). In this work, the optimum ethylene glycol oligomer chain length was found to vary with the cell type; however, the amino acid Fmoc-Haa4 **8** (Figure 3) had shown promising transfection properties in some cell lines, and this was therefore selected as a spacer for some peptide sequences.

There are several enzymes that are known to operate efficiently within the acidic environment of the endosome and have been implicated in the processing of endocytosed proteins: in particular, the enzyme furin (*65*) is known to be active within the endosome. Similarly, there are a range of enzymes active within the lysosome, such as cathepsin B (*66*). Peptides containing consensus sequences for cathepsin B (*67*−*69*) have previously been successfully used as cleavable linkers in drug delivery applications. The sequence RVRR was therefore chosen, as this is a consensus sequence for furin cleavage (*65*) and RR a consensus sequence for cathepsin B cleavage (*66*).

The peptides shown in Figure 3 were designed and synthesized, taking all of these factors into consideration. Peptide **9** has the integrin-targeting sequence CRDGCLG attached via the enzymatically cleavable RVRR linker sequence to the K_{16} DNA binding sequence used in our previous work. Peptides **10** and **11** also have this sequence, but with the tetraethylene glycol spacer, Haa4, on either the K_{16} (peptide **10**) or CRDGCLG (peptide **11**) side of the cleavable linker. Finally, peptide **12**, which lacks both the tetraethylene glycol spacer and a sequence which can be cleaved by processing enzymes, but which retains the overall charge of peptides **9**, **10**, and **11**, was prepared as a control.

Synthesis of Endosomally Cleavable PEG-Containing Lipids. DOTMA analogues can be conveniently prepared via 1,2-dialkyloxy-3-aminopropane or 3-dimethylamino-1,2-propandiol intermediates (*45, 70*), and this approach has been used to synthesize DOTMA analogues bearing ethylene glycol oligomer chains directly attached to the quaternary ammonium headgroup (*43*). The synthesis of 2,3-di-((9*Z*)-octadecenyloxy)propyl-*N*,*N*-dimethylamine **13** was carried out as previously described (*45*). The noncleavable tetraethylene glycol-bearing lipid **7** was also synthesized as a control, as it had previously shown promising transfection and stability properties when formulated with DOPE, peptide **1**, and plasmid DNA (*43*). The approach was then adapted to synthesize the cleavable lipids **4**, **5**, and **6** (Scheme 1). Quaternization of **13** with esters such as **14** to afford cleavable lipids bearing ethylene glycol oligomer chains, linked via a shorter β-amino acid linker, was initially investigated. However, competing elimination reactions resulted in consistently low yields and impure products. Instead, 5-bromopentanoyl chloride was reacted with commercially available triethylene glycol, triethylene glycol monomethyl ester, or hexaethylene glycol, to yield bromoalkyl-oligo(ethylene glycol) esters **15**, **16**, and **17**, respectively. These were then heated in a sealed tube with **13**, to afford the target lipids **4**, **5**, and **6**, respectively, in 47−60% yield.

Synthesis of Endosomally Cleavable PEG-Containing Peptides. For the synthesis of the endosomally cleavable peptides **10** and **11**, containing tetraethylene glycol spacers, Fmoc-Haa4-OH **8** was prepared as previously reported (*64*). Peptides **9**, **10**, **11**, and **12** were then prepared by standard Fmoc-based solid-phase peptide synthesis (SPPS) using HBTU/DIPEA coupling protocol. Prior to peptide cleavage from the solid support, the disulfide linkages were formed by treatment of the Cys(Trt) residues with a solution of iodine in DMF to simultaneously cleave the Trt group and form the disulfide linkage (*71*).

Formulation of LPD Complexes and Measurement of Complex Stability. With a range of cleavable lipids and peptides, with and without ethylene glycol oligomers, in hand,

Scheme 1. Synthesis of Cleavable PEG-Containing Lipids 4, 5, and 6[a]

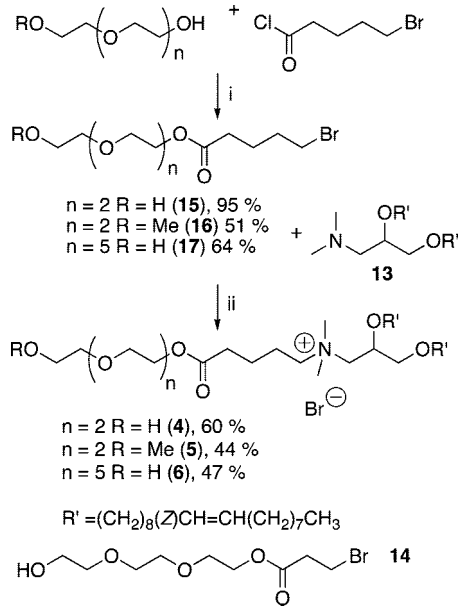

[a] Reagents: i, CH_2Cl_2; ii, sealed tube, with or without acetone, RT to 100 °C.

LPD formulations using different combinations of peptides and lipids were investigated. It was anticipated that the use of a high density (50% or 100%) of lipid and/or peptide components bearing the short ethylene glycol oligomeric units would result in complexes with a uniform hydrophilic surface that would confer stability on the lipopolyplex, and it was desirable to ascertain which features of each component were important to achieve gene delivery vectors that would be stable in the circulation but would disassemble in the endosome. Initially, the size and stability of the integrin-targeting ternary LPD lipopolyplexes was studied in saline buffer (as a model for physiological conditions), since incorporating lipids or peptides bearing ethylene glycol oligomeric units could have an effect on both the size and the stability of complexes. Four complexes were therefore formulated: one with no ethylene glycol oligomer containing components (Complex **A**); one where only the peptide component had an ethylene glycol oligomer unit (Complex **B**); one where only the lipid component had an ethylene glycol oligomer unit (Complex **C**); and one where both lipid and peptide components had ethylene glycol oligomer units (Complex **D**) (Table 1). The sizes of these complexes were measured by laser-light scattering (Figure 4). Preliminary measurements in water (Table 1) showed the four complexes to be of approximately similar sizes, with complex **A** the largest. Sizing measurements in saline solution were then carried out over a period of 1 h, to ascertain whether the complexes would aggregate in a physiologically relevant buffer. Initially, the size difference between the four complexes was again very small, although complexes **C** and **D**, with lipids containing ethylene glycol oligomers, were slightly smaller, and in the saline solution the complexes were overall larger than in water (in line with previous literature observations (*72*)). However, after 1 h, the size of complexes **A** and **B** had increased dramatically, whereas complexes **C** and **D**, containing lipid **4** with a triethylene glycol unit, had remained at a constant size, indicating the greater stability of these complexes.

In Vitro Transfections. Preliminary transfection experiments, to investigate the effect of the ethylene glycol oligomeric layer on the transfection efficiency of LPD complexes formulated from lipids **4**, **5**, **6**, and **7**, were first carried out. The cleavable hexaethylene glycol lipid **6** was compared with lipopolyplexes formulated with the cleavable triethylene glycol lipid **4** and the noncleavable tetraethylene glycol lipid **7** (and with peptide **9** and plasmid DNA). Complexes formulated with **6** had significantly poorer transfection efficiencies (Supporting Information). This was consistent with our previous studies with noncleavable hexaethylene glycol lipids (*43*) and **6** was therefore not investigated further.

Since the size of the lipopolyplexes could have an effect on transfection efficiencies, in vitro transfections of the integrin-targeting ternary LPD complexes using lipids **4**, **5**, and **7** were then studied following an additional centrifugation (1500 rpm, during 5 min), which was performed to help with sedimentation of the smaller LPD complexes with lipids containing ethylene glycol oligomers, on to the cells.

Transfection Efficiencies of Endosomally Cleavable PEG-Containing Peptides. Transfection efficiencies of endosomally cleavable peptide **9**, and endosomally cleavable peptides **10** and **11** bearing tetraethylene glycol units, complexed with Lipofectin and a plasmid encoding the luciferase gene (pCI-Luc), were studied in Neuro 2A, bEND.3, AJ3.1, 16HBE14o- cell lines and PVSMC primary cells. These complexes were compared with those formulated using the noncleavable control peptide **12** (Figure 5a). In all cells studied, peptide **9** was significantly the best endosomally cleavable peptide, and the transfection efficiencies were not improved with complexes formulated with peptides containing the Haa4 amino acid ($p < 0.05$). Peptide **9** was also significantly more efficient than the noncleavable control peptide **12** in all cells ($p < 0.05$) with the exception of Neuro 2A, where it was as efficient as **12**.

Transfection Efficiencies of Endosomally Cleavable PEG-Containing Lipids. Transfection efficiencies of endosomally cleavable, triethylene glycol-containing lipids **4** and **5** complexed with cleavable peptide **9** and pCI-Luc were then studied in Neuro 2A, bEND.3, AJ3.1, 16HBE14o- cell lines and PVSMCs primary cells. These were compared with complexes formulated using the noncleavable tetraethylene glycol lipid **7**, identified in our earlier work, as a control (Figure 5b). Preliminary studies showed that lipoplex formulations (lacking the peptide) were ineffective transfection agents, and also that the inclusion of the colipid DOPE was necessary (data not shown). Lipid **4**/DOPE was significantly more efficient compared to lipid **5**/DOPE in Neuro 2A, AJ3.1, 16HBE14o-, and PVSMCs cells ($p < 0.05$), and as efficient as in the bEND.3 cells. Therefore, the best-performing lipid was the cleavable, triethylene glycol lipid **4**/DOPE, which was shown to be as efficient as the noncleavable tetraethylene glycol control lipid (lipid **7**/DOPE) in Neuro 2A, AJ3.1, and16HBE14o- cells, and more efficient than the same control lipid in bEND.3 and PVSMCs cells ($p < 0.05$). Similar results were shown when lipids were complexed to a noncleavable peptide (data not shown).

The optimal combination of lipid and peptide for a range of cells was thus identified to be complex **C** (lipid **4**/DOPE/peptide **9**/DNA). This complex was also tested in MDA-MB-231 breast cancer cells and showed it to have greater transfection efficiency than the commercially available transfection agent Lipofectamine (Supporting Information). The viability of cells when treated with the tetraethylene glycol-bearing lipid **4**, alone or formulated as lipoplexes with DNA (Supporting Information), was then investigated. In this cell line, very little toxicity was observed (in line with the low reported toxicities (*73*) of triethylene glycol and tetraethylene glycol) except at much higher lipid/DNA ratios than those used in the present study, where significant amounts of uncomplexed lipid **4** would be expected.

In Vitro Cleavage Studies. As these LPD complexes were designed to cleave and to disassemble during the transfection process, it was necessary to demonstrate that the component

Table 1. Comparison of the Sizes and Stabilities of Different Lipopolyplex Formulations in Water and in Saline Buffer

	composition of complex	size (nm) in water	size (nm) after 5 min in buffer	size (nm) after 1 h in buffer
Complex **A** (no ethylene glycol oligomer)	lipofectin/peptide **9**/pCI-Luc	131 ± 1.0	457 ± 46	1388 ± 198
Complex **B** (tetraethylene glycol on peptide)	lipofectin/peptide **11**/pCI-Luc	n/d	456 ± 46	1417 ± 146
Complex **C** (tetraethylene glycol on lipid)	**4**/DOPE/peptide **9**/pCI-Luc	119 ± 1.3	335 ± 11	394 ± 14
Complex **D** (tetraethylene glycol on peptide and lipid)	**4**/DOPE/peptide **11**/pCI-Luc	n/d	346 ± 15	417 ± 10

peptides and lipids could be degraded under conditions likely to be encountered within the endosome. Model cleavage studies on lipid **4** and peptide **9**, both individually and within LPD complexes, were therefore carried out.

Cleavage Studies on Lipid 4, Alone and in LPD Complex. The expected cleavage product from lipid **4**, lipid **18**, was prepared by hydrolysis of **4** (Scheme 2) in order to serve as a control for the lipid cleavage studies. The conditions required for acid-catalyzed cleavage of **4** were first investigated. Formulated lipid **4** was treated with solutions of sodium acetate, citric acid, and aqueous HCl buffers at pH 5.5, 3, and 1, respectively. The reaction was monitored by taking aliquots at $T = 1$ and 5 h and analysis by thin layer chromatography. The results indicated that hydrolysis of the ester bond occurred only at very low levels (data not shown).

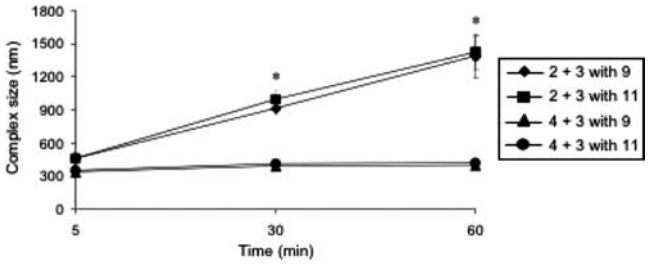

Figure 4. Effect of PEG group on particle stability, illustrated in dynamic light scattering measurements of complex particle size. Lipid/peptide/plasmid complexes containing the PEGylated lipid **4** were stable in physiological saline buffers: non-PEGylated lipids (Lipofectin) rapidly aggregated. (* $p < 0.05$ when complex size was compared between vectors).

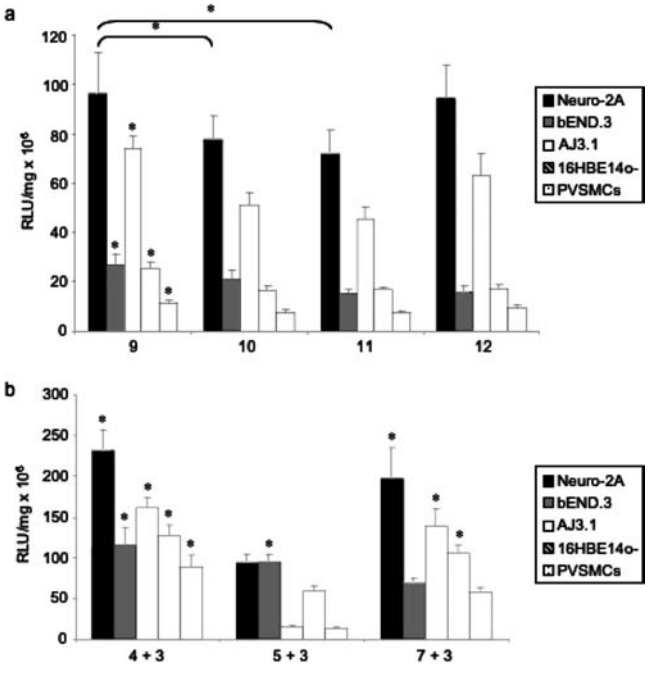

Figure 5. Transfection efficiencies of (a) endosomally cleavable PEG-containing peptides complexed with Lipofectin lipid and pCI-Luc plasmid and of (b) endosomally cleavable PEG-containing lipids complexed with peptide **9** and pCI-Luc plasmid, performed in mouse neuroblastoma (Neuro 2A) cells, mouse endothelial (bEND.3) cells, mouse embryonic fibroblast (AJ3.1) cells, human bronchial epithelial (16HBE14o-) cells, and primary porcine vascular smooth muscle (PVSMCs) cells. Complexes were prepared with a weight ratio of 2:4:1. Transfection incubation was performed for 4 h and luciferase activity was measured 24 h later. The relative light units (RLU) measured for 10 s are expressed as means ± sem per mg of protein. (*$p < 0.05$ when peptide **9** and lipid **4**/DOPE were compared with other peptides and lipids, respectively).

Scheme 2. Hydrolysis of lipid 4[a]

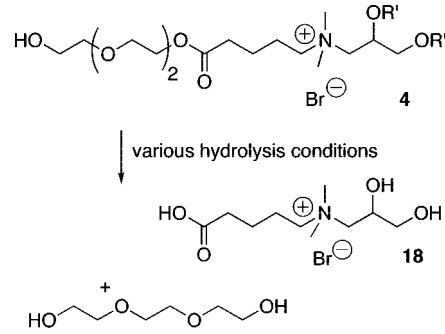

[a] Hydrolysis conditions: NaOH (1 M), H_2O, 2 h; or sodium acetate buffer (pH 5.5); or citric acid (pH 3); or HCl (pH 1); or pig liver esterase (pH 7.5).

As a model (*55*) for the effects of endosomal esterases, **4** was then treated with pig liver esterase buffered at pH 7.5, and the reaction again monitored by thin layer chromatography. Within 1 h, a spot had appeared corresponding to compound **18** (which also has a similar R_f value to that of the other half of the cleaved material, triethylene glycol). The intensity of this spot steadily increased as the reaction proceeded over 24 h. LPD complex **C**, containing **4**/DOPE, peptide **9**, and plasmid pCI-Luc, was then formulated. This was again treated with pig liver esterase buffered at pH 7.5, and a similar pattern of lipid cleavage was observed, indicating that the ester linkage of **4** is still accessible to esterase enzymes even when the lipid forms part of the LPD complex (Supporting Information).

Cleavage Studies on Peptide 9, Alone and in LPD Complex. The cleavage of peptide **9** by two enzymes known to be active within the endosome or the lysosome was then investigated. Peptide **9** was initially treated with the endosomal enzyme furin, with the reaction monitored by HPLC, and after 4 h complete cleavage of **9** was observed (Supporting Information). In contrast, when peptide **12**, which lacks the RVRR consensus cleavage sequence, was treated with furin under the same conditions, significant cleavage was only observed after 24 h. Unfortunately, the buffer required for optimum stability of the enzyme disrupted the LPD complex, and conversely, the furin was inactive in buffer solutions suitable for the LPD complex. Hence, further studies with furin could not be carried out on the complex itself. To investigate whether the peptide consensus cleavage sequence is accessible to proteolytic enzymes when the peptide is within the LPD complex, further studies were carried out with the lysosomal enzyme cathepsin B. Uncomplexed peptide **9** was first treated with cathepsin B, buffered at pH 5.5, with the reaction again monitored by HPLC. Immediate cleavage was observed, evidenced by the appearance of a new signal on the analytical HPLC chromatogram with a retention time (R_T) of 8.5 min compared to **9**, which appeared

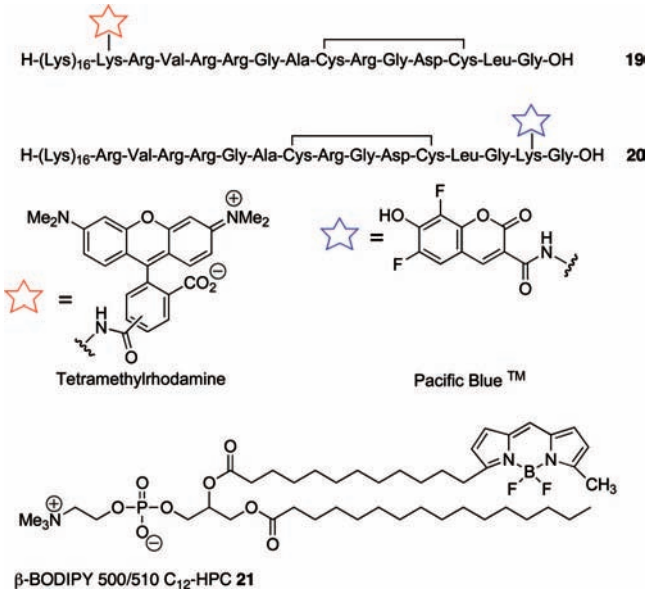

Figure 6. Fluorophore-Labeled Peptides and Lipid for Confocal Microscopy.

at R_T 7.8 min. The intensity of the peak at 8.5 min steadily increased as the reaction proceeded over 4 h, while the intensity of the peak for peptide **9** decreased. (Immediate cleavage, complete within 1 h, was also observed with the control peptide **12**; however, cathepsin B has relatively low sequence specificity, and VKK is also known to be a cleavage sequence for this enzyme (*66*).) Complex **C** was then prepared and treated with cathepsin B, and a very similar cleavage pattern was observed by HPLC (Supporting Information), indicating that the peptide is accessible to proteolytic enzymes within the complex.

Confocal Fluorescence Microscopy. In order to verify the location of the various components of the LPD vector during the transfection process, and also to further investigate the hypothesis that environmentally responsive vector components could be designed to disassemble in the endosome, the transfection process was then studied by confocal microscopy. Fluorescently labeled lipid, peptide, and plasmid DNA components were therefore needed. For the peptide component, selective labeling of residues on either the N-terminal or C-terminal side of the RVRR linker sequence would allow visualization of when the peptide was cleaved during transfection and would allow the movement of the peptide within the cell to be followed. Peptide **19**, where a tetramethylrhodamine label is appended on the N-terminal side of the RVRR sequence, and peptide **20**, where a Pacific Blue label is attached on the C-terminal side (Figure 6), were therefore required. These particular fluorophores were selected to give good contrast in the confocal experiments. In addition, in order to ensure regioselective labeling of the desired residues, it was expedient to prepare the labeled peptides by solid-phase peptide synthesis, using orthogonal protecting group chemistry to reveal only one lysine side chain for labeling, and there was precedent to suggest that both Pacific Blue and tetramethylrhodamine would be robust to treatment with TFA during the peptide cleavage and side chain deprotection steps. Fluorescently labeled peptides **19** and **20** were prepared by initially assembling the desired linear sequences, incorporating Lys(ivDde) at the point where the fluorophore was to be attached (Scheme 3). This was then followed by selective removal of the ivDde group with hydrazine hydrate, on-resin coupling with either tetramethylrhodamine or Pacific Blue, cleavage of the peptide from solid support, and aerial oxidation to form the disulfide bridge, as shown in Scheme 3 for peptide **20**.

For the lipid component, the large size of most fluorescent probes relative to the size of the lipid component meant that attempting to synthesize analogues of lipid **4** with fluorophores either side of the ester linkage was likely to peturb the system to an unacceptable extent. The commercially available fluorescent lipid β-BODIPY 500/510 C_{12}-HPC (**21**, an analogue of DOPE) was therefore used as a general probe to track the movement of lipids within the cell. Finally, rhodamine-labeled plasmid DNA was prepared by standard techniques.

With these materials in hand, transfection of MDA-MB-231 breast cancer cells with labeled LPD complexes was investigated. LPD complexes incorporating lipid **4**, the fluorescent lipid **21** (green), and the fluorescent peptide **19** (red), with unlabeled plasmid DNA, were used to transfect MDA-MB-231 breast cancer cells (Figure 7). The cell nucleus is stained with DAPI (blue). Directly after the initial 4 h incubation period (Figure 7a), both the lipid and the peptide are largely colocated in the cytoplasm of the cell (giving rise to a yellow color), and both components were able to enter the nucleus at that early stage. A similar image was obtained 4 h later, with the cross section images clearly showing the incorporation of both the lipid and the peptide within the center of the nucleus, which is highlighted in blue (Figure 7b). The peptide, unlike the lipid, was still detectable in the nucleus 24 h after incubation (Figure 7c).

In a second set of experiments (Figure 8), LPD complexes were prepared, again incorporating lipid **4** and the fluorescent lipid **21** (green), labeled pGL3 plasmid (red), and the fluorescent peptide **20** (blue). Peptide **20** was selected in order to assess whether the headgroup of the peptide was cleaved from the Lys_{16} DNA-binding moiety after endocytosis. The cell nucleus was not stained. If cleavage of the RVRR sequence takes place in the endosome, then it would be expected that the blue dye (attached to the integrin-binding headgroup) would remain in the endosome or the cytoplasm, whereas the labeled plasmid would be trafficked to the nucleus. Indeed (Figure 8a,b), it can be seen that, at 0 and 4 h after the initial 4 h incubation, there is no obvious internalization of the peptide into the nucleus, although some free DNA has been internalized at 4 h. However, at 24 h (Figure 8c), blue fluorescence is detected in the nuclear region of the cell, suggesting either that the cleaved peptide eventually enters the nucleus or that the peptide is further degraded over 24 h, releasing free dye that then enters the nucleus.

Cryo-Electron Microscopy of LPD Complexes. We had previously studied the morphology of the first generation of LPD complexes using freeze−fracture electron microscopy (*18*). To compare the first-generation LPD complexes with the complexes discussed in this paper, the more sensitive technique of cryo-electron microscopy was used. Cryo-EM images of lipoplexes formulated using Lipofectin and plasmid DNA (Figure 9a) were similar to those formulated from lipid **4**, DOPE, and plasmid DNA (Figure 9b) and showed the spherical shape and absence of internal structure previously observed for similar lipoplexes (*33*). LPD complexes formulated from Lipofectin, peptide **1**, and plasmid DNA produced particles with condensed cores and irregular outer layers, as expected from the freeze−fracture electron microscopy studies (Figure 9c). In contrast to cryo-EM studies of other LPD complexes (*74*), no lamellar structures were seen in the outer layers of the particles. The images (Figure 9d) of the new LPD complex, Complex **C**, formulated from **4**/DOPE, peptide **9**, and plasmid DNA, however, showed marked differences. First, there was a small but significant reduction in the size of the particles when lipid **4** was used, consistent with the smaller particle size observed by laser light scattering (Figure 4). Second, for many of the particles there was a change in the morphology of the internal core, with subdivisions clearly visible. Similar morphologies have been

Scheme 3. Synthesis of Fluorophore-Labeled Peptide 20[a]

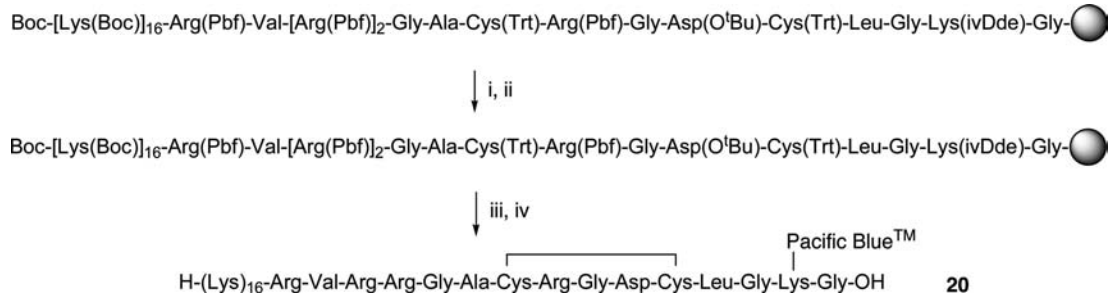

[a] Reagents: i, 2% H_2NNH_2/DMF; ii, Pacific Blue-OSu/DIPEA; iii, TFA/EDT/TIPS/H_2O; iv, aerial oxidation.

previously observed for some lipoplex systems (*75*) and attributed to a phase change in the lipid/DNA complexes, but it is currently unclear what these represent in this system.

DISCUSSION

On the basis of our previous work (*43, 64*), it was postulated that incorporating short ethylene glycol oligomeric moieties of defined length into both lipid and peptide components of the LPD vector would result in increased vector stability. However, whereas complexes formulated with ethylene glycol oligomer-bearing lipid components resulted in minimal aggregation and higher stability of the complexes, compared to complexes formulated with unmodified lipids, peptides incorporating the amino acid Haa4 did not further contribute to the size and stability of the resulting lipopolyplexes (Figure 4). Furthermore, LPD vectors formulated with the triethylene glycol lipid **4** gave particles with discernibly smaller size and altered morphology (Figure 9) compared with the first-generation LPD vectors lacking the ethylene glycol oligomers.

Previous work on sterically stabilized liposomes for drug and gene delivery applications indicated that large polymeric PEG molecules are necessary to inhibit binding to proteins and to prevent aggregation. PEG2000 to PEG5000 molecules are typically used, with larger polymers significantly inhibiting liposome uptake (*25*−*27*). However, these liposomes typically have a low surface density (5−15 mol %) of the surface-anchored PEG; at greater concentrations, the lipid bilayer becomes unstable due to the lateral pressure between the polymer chains (*25*). In these liposomes, therefore, the PEG takes up a "mushroom" configuration: the longer the PEG chain, the larger the mushroom and the more effective the shielding. With lipopolyplexes formulated with lipids such as **4**, in which 50% of the lipid content carries the short ethylene glycol oligomers, complete coverage of the surface can be achieved even with these short oligomers at a high density. Similar observations have been made by Whitesides (*76*) in which it was demonstrated that monolayers formed from monoethylene glycol-conjugated alkanethiols (100%) effectively prevented protein adhesion to the monolayers.

Attachment of ethylene glycol oligomers to the lipid component also appears to improve the transfection efficiencies of the complexes. LPD lipopolyplex (**4**/DOPE/**9**) was 2, 7, 3, 7,

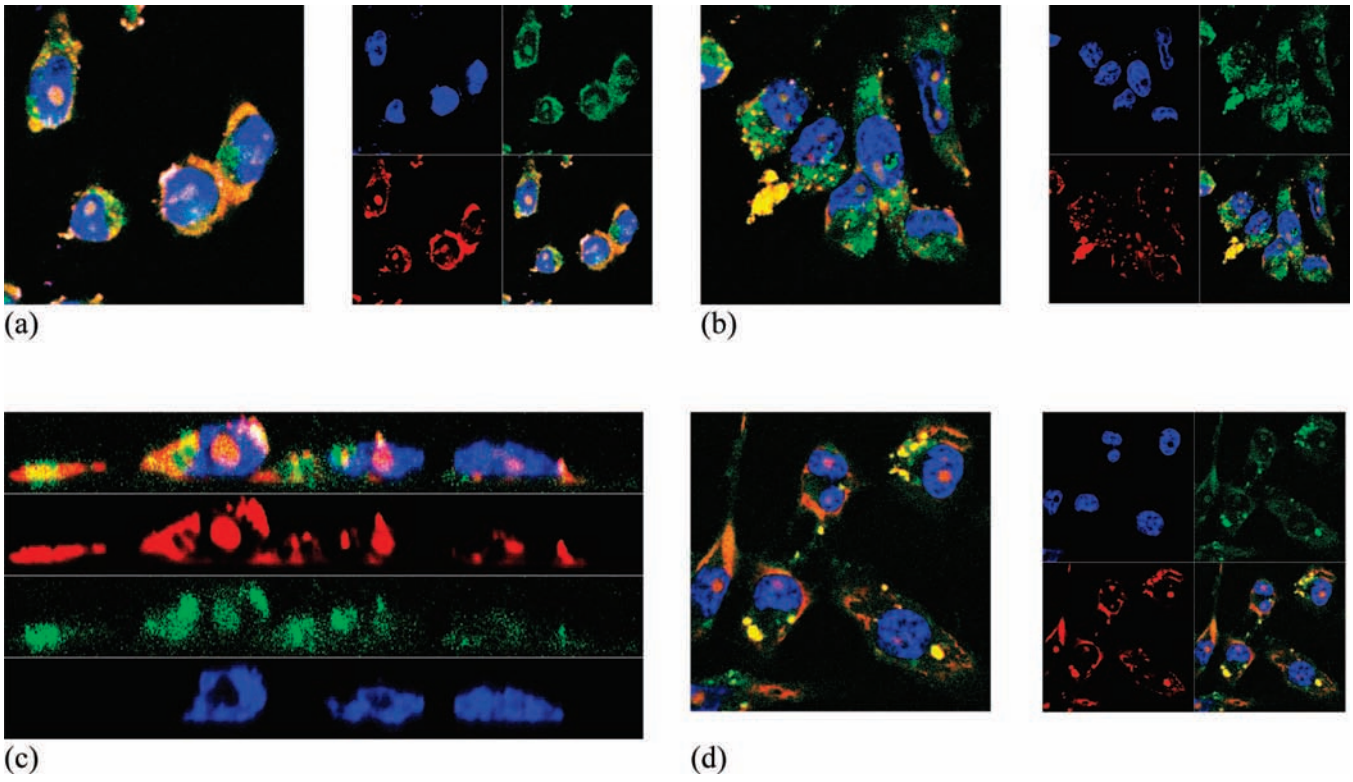

Figure 7. Confocal fluorescence microscopy studies. MDA-MB-231 breast cancer cells were transfected with LPD complexes incorporating the fluorescent lipid **21** (green) at a ratio of lipid **4**:DOPE:**21** of 10:9:1; and the fluorescent peptide **19** (red). The pGL3 plasmid is unlabelled and the cell nucleus is stained with DAPI (blue). Cells were fixed at (a) 0 h (b) 4 h and (d) 24 h after the initial 4 h incubation period. In Figure 7(c), a cross-sectional XZ plane image was taken at 4 h to show the position of the peptide and lipid in relation to the nucleus.

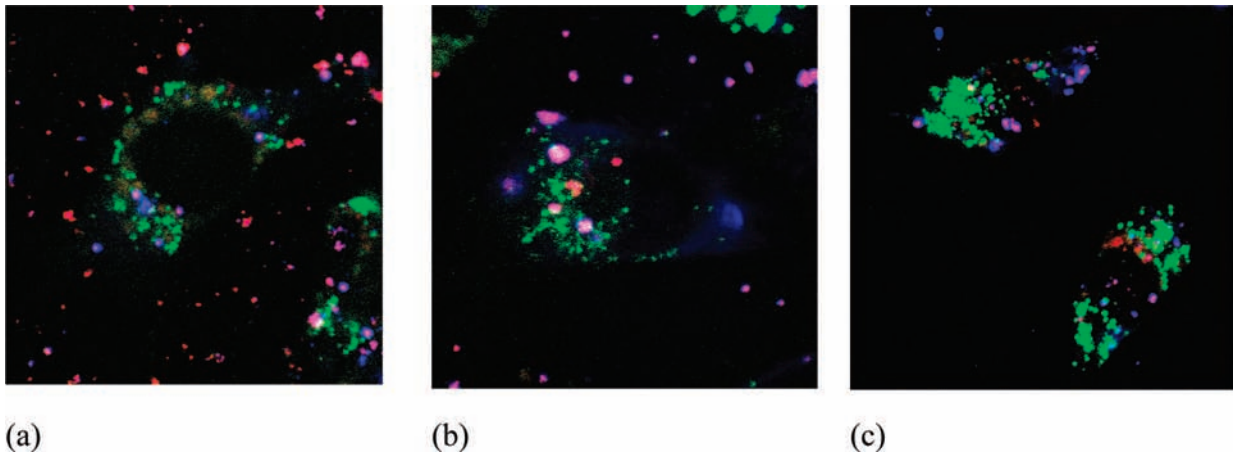

Figure 8. Confocal fluorescence microscopy studies. MDA-MB-231 breast cancer cells were transfected with LPD complexes incorporating the fluorescent lipid **21** (green) at a ratio of lipid **4**/DOPE/**21** of 10:9:1; the fluorescent peptide **20** (blue); and the labeled pGL3 plasmid (red) mixed with unlabeled pGL3 at a 1:3 ratio. The cell nucleus is not stained. Cells were fixed at (a) 0 h, (b) 4 h, and (c) 24 h after the initial 4 h incubation period.

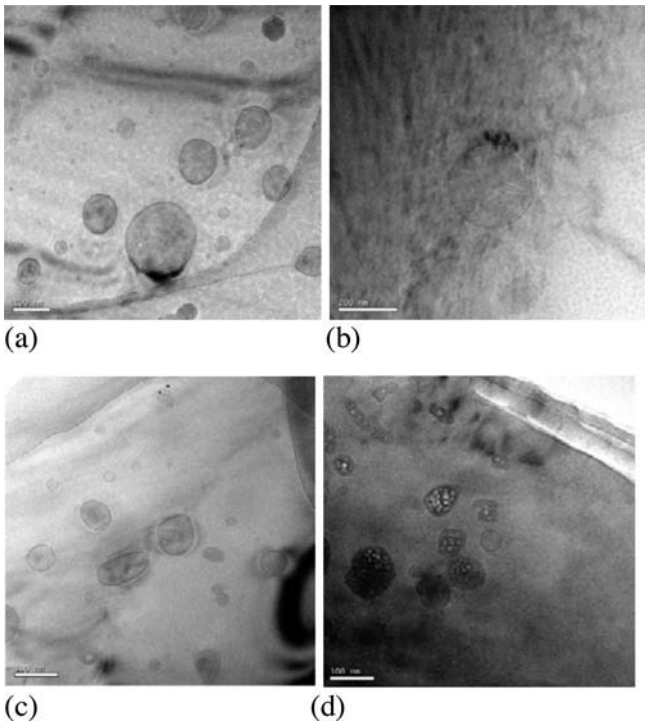

Figure 9. Cryo-EM images of lipoplexes and lipopolyplexes. (a) Lipoplex formed from plasmid DNA and Lipofectin (DOTMA/DOPE). (b) Lipoplex formed from plasmid DNA and **4**/DOPE. (c) LPD complexes formed from plasmid DNA, peptide **1**, and Lipofectin. (d) LPD complexes formed from plasmid DNA, peptide **9**, and **4**/DOPE. All complexes were formulated at 1 mg/mL.

and 9 more efficient for gene transfer than the first generation of noncleavable LPD lipopolyplexes (Lipofectin/**1**), in Neuro 2A, bEND.3, AJ3.1, 16HBE14o-, and PVSMCs cells, respectively ($p < 0.05$). The length and structure of the ethylene glycol oligomeric moieties attached to the lipid also have an important effect on the transfection properties of the resulting complexes. Lipids "capped" with an −OMe group (**5**) performed significantly less well in the majority of cell lines than the "uncapped" lipid **4** when formulated (Figure 5b). Complexes formed with the hexaethylene glycol-bearing lipid **6** had very poor transfection efficiencies, which may be attributable to a reduction in the accessibility of the peptide targeting sequence to the integrin receptors (*49*) or may simply be due to a less compact particle being formed. By contrast (Figure 5a), the inclusion of the amino acid, Haa4, in the peptide sequence had very little effect, marginally reducing the transfection efficiencies of the resulting complexes.

Incorporating lipids and peptides that have the potential to be cleaved within the endosome also results in vectors with enhanced transfection properties. Introduction of the enzyme-cleavable RVRR sequence in the peptide in between the Lys_{16} DNA-binding moiety and the integrin-binding C-terminal amino acids, giving peptide **9**, significantly increases lipopolyplex transfection efficiency (Figure 5a). Similarly, the triethylene glycol-bearing lipid **4**, with an ester linkage which can be cleaved in the endosome, gave LPD complexes with similar, or enhanced, transfection properties compared with the non-cleavable analogue **7** (Figure 5b).

The proposed mechanism for transfection by these stabilized, environmentally responsive lipopolyplexes is as follows. Initial binding of the vector to the α_v integrin receptors expressed on the surface, via the CRGDCLG sequence, which partially protrudes from the complex (*18*), is followed by receptor-mediated endocytosis. Once the particle is encapsulated within the endosome, both the lipid and the peptide undergo cleavage. Removal of the triethylene glycol unit from the cationic lipid reduces steric hindrance and allows the cationic lipids to merge effectively with the endosomal membrane, destabilizing it and allowing the gene delivery particle to escape (*77*). This results in the dispersal of the lipids within the cytoplasm, as demonstrated by confocal microscopy (Figures 7 and 8). In addition, cleavage of the peptide at the RVRR sequence will detach the CRGDCLG sequence, which may still be bound to the α_v integrin, from the DNA/K_{16} complex. The DNA/K_{16} complex will thus be released from both the receptor and the disintegrating endosome and will be able to travel to the nucleus at a very early stage (within 4 h). This is demonstrated by the confocal images of the complex containing peptide **19**, an analogue of **9** bearing the TMR fluorophore on the K_{16} side of the RVRR sequence (Figure 7): the TMR label is rapidly trafficked to the nucleus, presumably complexed to the plasmid DNA. It is additionally possible that the K_{16}-RVRR sequence, being composed of basic, charged amino acids, may function as a nuclear localization sequence (*78, 79*) although it does not correspond to any nuclear localization sequence so far reported (*80*).

We have demonstrated that both the RVRR-linked peptide **9** and the ester-linked lipid **4** can be cleaved in vitro under conditions approximating those found in the endosome. It is noteworthy that, although these LPD complexes are highly

compact, and are clearly stabilized by the incorporation of ethylene glycol oligomer-bearing lipids, both the lipid and the peptide components of the complex are accessible to cathepsin B and to PLE, suggesting that enzyme-mediated cleavage of these components, within the complex and within the endosome, is a viable proposition. Furthermore, we have demonstrated in vitro that the RVRR sequence can be cleaved by furin within 4 h, consistent with the confocal data (Figure 7), which would suggest that endosomal release, complex disassembly, and nuclear trafficking have taken place within this period. In contrast, when peptide **20** (an analogue of **9** with a Pacific Blue label between the RVRR sequence and the integrin-binding CRGDCLG sequence) was used in the LPD complex, the label initially remained in the cytoplasm (Figure 8) and is only visible in the nucleus after 24 h. This may indicate that the Pacific Blue label initially remains, after enzymatic cleavage, associated with the α_v integrin: from there it may be recycled to the outer membrane, or further degradation of the peptide may release free dye, which is later trafficked to the nucleus.

It is also notable that the triethylene glycol lipid **4** was able to enhance the transfection efficiencies of these LPD complexes. Literature precedent strongly suggests that the five-carbon linker used in **4** would be suboptimal for acid-catalyzed cleavage within the endosome (*58*), and, indeed, we saw only very low levels of ester cleavage under acidic conditions.

CONCLUSIONS

We have designed and developed a new class of ternary lipopolyplex gene delivery vectors, with lipids incorporating short ethylene glycol oligomer units of defined length and with both lipid and peptide components designed to degrade within the endosome after internalization of the vector, leading to disassembly of the complexes and release from the endosome. These gene delivery vectors are very compact and show very promising stabilities under physiologically relevant conditions, while maintaining excellent transfection activities. These desirable properties bring us one step closer to developing vectors that can be administered systemically, will be stable enough to persist in circulation and not be cleared by the RES, and yet will be able to find, target, and transfect specific cell types (in this case, specific tumor types) within living organisms. The development of targeted, environmentally responsive vector systems that are able to deliver therapeutic genes efficiently and specifically to the target cells after application into the systemic blood circulation will be vital in treating a range of cancers, particularly metastatic tumors. Detailed studies of the effects of centrifugation of these smaller LPD particles on the efficiency of in vitro transfection and of the in vivo stability and tumor-specific targeting of the complexes are ongoing, and will be published in due course.

ACKNOWLEDGMENT

The BBSRC are thanked for grants to M. F. M. M., S. M. G., and M. E. (BBS/B/03645) and E.-A. R. (BB/D005469/1). The EPSRC is thanked for a DTA studentship (to J. B. W.) and Kings College London for the award of a Maplethorpe Fellowship (to L. K.). We thank Dieter Gruenert, California Pacific Medical Centre Research Institute, San Francisco, CA, USA, for kindly providing the 16HBE14o-cell line.

Supporting Information Available: Bar chart showing the transfection efficiencies of LPD complexes formulated with peptide **9**, plasmid DNA and **4**/DOPE, **6**/DOPE, or **7**/DOPE. Transfection of MDA-MB-231 breast cancer cells by the lipid **4**/DOPE/peptide **9**/DNA complex, compared with transfection by lipofectamine. Comparison of cell viability between free lipid **4** and lipid **4**/DNA complexes of the same corresponding lipid concentrations. General Synthetic Methods. Materials for Cell Biology. Experimental procedure for the synthesis of **18**. ^{1}H NMR spectra for compounds **15**, **16**, **17**, **4**, **5**, **6**, **18**.This material is available free of charge via the Internet at http://pubs.acs.org.

LITERATURE CITED

(1) Somia, N., and Verma, I. M. (2000) Gene therapy: Trials and tribulations. *Nat. Rev. Genet. 1*, 91–99.

(2) Hacein-Bey-Abina, S., Von Kalle, C., Schmidt, M., McCcormack, M. P., Wulffraat, N., Leboulch, P., Lim, A., Osborne, C. S., Pawliuk, R., Morillon, E., Sorensen, R., Forster, A., Fraser, P., Cohen, J. I., de Saint Basile, G., Alexander, I., Wintergerst, U., Frebourg, T., Aurias, A., Stoppa-Lyonnet, D., Romana, S., Radford-Weiss, I., Gross, F., Valensi, F., Delabesse, E., Macintyre, E., Sigaux, F., Soulier, J., Leiva, L. E., Wissler, M., Prinz, C., Rabbitts, T. H., Le Deist, F., Fischer, A., and Cavazzana-Calvo, M. (2003) LMO2-associated clonal T cell proliferation in two patients after gene therapy for SCID-X1. *Science 302*, 415–419.

(3) Godbey, W. T., Wu, K. K., and Mikos, A. G. (1999) Poly(ethylenimine) and its role in gene delivery. *J. Controlled Release 60*, 149–160.

(4) Davis, M. E. (2002) Non-viral gene delivery systems. *Curr. Opin. Biotechnol. 13*, 128–131.

(5) Miller, A. D. (1998) Cationic liposomes for gene therapy. *Angew. Chem., Int. Ed. Engl. 37*, 1769–1785.

(6) Niidome, T., and Huang, L. (2002) Gene therapy progress and prospects: Nonviral vectors. *Gene Ther. 9*, 1647–1652.

(7) Wiethoff, C. M., and Middaugh, C. R. (2003) Barriers to nonviral gene delivery. *J. Pharm. Sci. 92*, 203–217.

(8) Edelstein, M. L., Abedi, M. R., and Wixon, J. (2007) Gene therapy clinical trials worldwide to 2007−an update. *J. Gene Med. 9*, 833–842.

(9) Varga, C. M., Wickham, T. J., and Lauffenburger, D. A. (2000) Receptor-mediated targeting of gene delivery vectors: Insights from molecular mechanisms for improved vehicle design. *Biotechnol. Bioeng. 70*, 593–605.

(10) Demeneix, B., Hassani, Z., and Behr, J. P. (2004) Towards multifunctional synthetic vectors. *Curr. Gene Ther. 4*, 445–455.

(11) Miller, A. D. (2003) The problem with cationic liposome/micelle-based non-viral vector systems for gene therapy. *Curr. Med. Chem. 10*, 1195–1211.

(12) Kostarelos, K., and Miller, A. D. (2005) Synthetic, self-assembly ABCD nanoparticles; a structural paradigm for viable synthetic non-viral vectors. *Chem. Soc. Rev. 34*, 970–994.

(13) Hart, S. L., Arancibia-Cárcamo, C. V., Wolfert, M. A., Mailhos, C., O'Reilly, N. J., Ali, R. R., Coutelle, C., George, A. J. T., Harbottle, R. P., Knight, A. M., Larkin, D. F. P., Levinsky, R. J., Seymour, L. W., Thrasher, A. J., and Kinnon, C. (1998) Lipid-mediated enhancement of transfection by a nonviral integrin-targeting vector. *Hum. Gene Ther. 9*, 575–585.

(14) Tagawa, T., Manvell, M., Brown, N., Keller, M., Perouzel, E., Murray, K. D., Harbottle, R. P., Tecle, M., Booy, F., Brahimi-Horn, M. C., Coutelle, C., Lemoine, N. R., Alton, E. W. F. W., and Miller, A. D. (2002) Characterisation of LMD virus-like nanoparticles self-assembled from cationic liposomes, adenovirus core peptide μ (mu) and plasmid DNA. *Gene Ther. 9*, 564–576.

(15) Hart, S. L., Collins, L., Gustafsson, K., and Fabre, J. W. (1997) Integrin-mediated transfection with peptides containing arginine-glycine-aspartic acid domains. *Gene Ther. 4*, 1225–1230.

(16) Jenkins, R. G., Herrick, S. E., Meng, Q.-H., Kinnon, C., Laurent, G. J., McAnulty, R. J., and Hart, S. L. (2000) An integrin-targeted non-viral vector for pulmonary gene therapy. *Gene Ther. 7*, 393–400.

(17) Parkes, R., Meng, Q. H., Siapati, K. E., McEwan, J. R., and Hart, S. L. (2002) (2002) High efficiency transfection of porcine vascular cells in vitro with a synthetic vector system. *J. Gene Med. 4*, 292–299.

(18) Mohd Mustapa, M. F., Bell, P. C., Hurley, C. A., Nicol, A., Guénin, A., Sarkar, S., Writer, M. J., Barker, S. E., Wong, J. B.,

Pilkington-Miksa, M. A., Papahadjopoulos-Sternberg, B., Ayazi Shamlou, P., Hailes, H. C., Hart, S. L., Zicha, D., and Tabor, A. B. (2007) Biophysical characterization of an integrin-targeted lipopolyplex gene delivery vector. *Biochemistry 46*, 12930–12944.

(19) Writer, M. J., Marshall, B., Pilkington-Miksa, M. A., Barker, S. E., Jacobsen, M., Bell, P. C., Lester, D. H., Tabor, A. B., Hailes, H. C., Klein, N., and Hart, S. L. (2004) Targeted gene delivery with synthetic vectors to human airway epithelial cells with novel targeting peptides selected by phage display. *J. Drug Targeting 12*, 185–194.

(20) Irvine, S. A., Meng, Q.-H., Afzal, F., Ho, J., Wong, J. B., Hailes, H. C., Tabor, A. B., McEwan, J. R., and Hart, S. L. (2008) Receptor-targeted nanocomplexes optimized for gene transfer to primary vascular cells and explant cultures of rabbit aorta. *Mol. Ther.* 508–515.

(21) Tagalakis, A. D., McAnulty, R. J., Devaney, J., Bottoms, S. E., Wong, J. B., Elbs, M., Writer, M. J., Hailes, H. C., Tabor, A. B., O'Callaghan, C., Jaffe, A., and Hart, S. L. (2008) A receptor-targeted nanocomplex vector system optimized for respiratory gene transfer. *Mol. Ther. 16*, 907–915.

(22) Sarkar, S., Lee, L. K., Hart, S. L., Hailes, H. C., Levy, S. M., Tabor, A. B., and Ayazi Shamlou, P. (2005) Fractal structure of polycation-DNA complexes. *Biotechnol. Appl. Biochem. 41*, 127–136.

(23) Plank, C., Mechtler, K., Szoka, F. C., and Wagner, E. (1996) Activation of the complement system by synthetic DNA complexes: A potential barrier for intravenous gene delivery. *Hum. Gene Ther. 7*, 1437–1446.

(24) Dash, P. R., Read, M. L., Barrett, L. B., Wolfert, M., and Seymour, L. W. (1999) Factors affecting blood clearance and in vivo distribution of polyelectrolyte complexes for gene delivery. *Gene Ther. 6*, 643–650.

(25) Lasic, D. D., and Needham, D. (1995) The "stealth" liposome: A prototypical biomaterial. *Chem. Rev. 95*, 2601–2628.

(26) Allen, T. M. (1994) Long-circulating (sterically stabilized) liposomes for targeted drug-delivery. *Trends Pharmacol. Sci. 15*, 215–220.

(27) Ogris, M., Brunner, S., Schuller, S., Kircheis, R., and Wagner, E. (1999) PEGylated DNA/transferrin-PEI complexes: reduced interaction with blood components, extended circulation in blood and potential for systemic gene delivery. *Gene Ther. 6*, 595–605.

(28) Wheeler, J. J., Palmer, L., Ossanlou, M., MacLachlan, I., Graham, R. W., Zhang, Y. P., Hope, M. J., Scherrer, P., and Cullis, P. R. (1999) Stabilized plasmid-lipid particles: construction and characterization. *Gene Ther. 6*, 271–281.

(29) Palmer, L. R., Chen, T., Lam, A. M. I., Fenske, D. B., Wong, K. F., MacLachlan, I., and Cullis, P. R. (2003) Transfection properties of stabilized plasmid-lipid particles containing cationic PEG lipids. *Biochim. Biophys. Acta 1611*, 204–216.

(30) Erbacher, P., Bettinger, T., Belguise-Valladier, P., Zou, S. M., Coll, J. L., Behr, J. P., and Remy, J. S. (1999) Transfection and physical properties of various saccharide, poly(ethylene glycol), and antibody-derivatized polyethylenimines (PEI). *J. Gene Med. 1*, 210–222.

(31) Ogris, M., Steinlein, P., Carotta, S., Brunner, S., and Wagner, E. (2001) DNA/polyethylenimine transfection particles: Influence of ligands, polymer size, and PEGylation on international and gene expression. *AAPS Pharm. Sci. 3*, 1–11.

(32) Holland, J. W., Hui, C., Cullis, P. R., and Madden, T. D. (1996) Poly(ethylene glycol)-lipid conjugates regulate the calcium-induced fusion of liposomes composed of phosphatidylethanolamine and phosphatidylserine. *Biochemistry 35*, 2618–2624.

(33) Shi, F., Wasungu, L., Nomden, A., Stuart, M. C. A., Polushkin, E., Engberts, J. B. F. N., and Hoekstra, D. (2002) Interference of poly(ethylene glycol)-lipid analogues with cationic-lipid-mediated delivery of oligonucleotides; role of lipid exchangeability and non-lamellar transitions. *Biochem. J. 366*, 333–341.

(34) Song, L. Y., Ahktong, Q. F., Rong, Q., Wang, Z., Ansell, S., Hope, M. J., and Mui, B. (2002) Characterization of the inhibitory effect of PEG-lipid conjugates on the intracellular delivery of plasmid and antisense DNA mediated by cationic lipid liposomes. *Biochim. Biophys. Acta 1558*, 1–13.

(35) Keller, M., Harbottle, R. P., Perouzel, E., Colin, M., Shah, L., Rahim, A., Vaysse, L., Bergau, A., Moritz, S., Brahimi-Horn, C., Coutelle, C., and Miller, A. D. (2003) Nuclear localiation sequence templated nonviral gene delivery vectors: Investigation of intracellular trafficking events, of LMD and LD vector systems. *ChemBioChem 4*, 286–298.

(36) Rudolph, C., Schillinger, U., Plank, C., Gessner, A., Nicklaus, P., Müller, R. H., and Rosenecker, J. (2002) Nonviral gene delivery to the lung with copolymer-protected and transferrin-modified polyethylenimine. *Biochim. Biophys. Acta 1573*, 75–83.

(37) Guo, X., and Szoka, F. C. (2003) Chemical approaches to triggerable lipid vesicles for drug and gene delivery. *Acc. Chem. Res. 36*, 335–341.

(38) Wolff, J. A., and Rozema, D. B. (2008) Breaking the bonds: non-viral vectors become chemically dynamic. *Mol. Ther. 16*, 8–15.

(39) Walker, G. F., Fella, C., Pelisek, J., Fahrmeir, J., Boeckle, S., Ogris, M., and Wagner, E. (2005) Toward synthetic viruses: Endosomal pH-triggered deshielding of targeted polyplexes greatly enhances gene transfer in vitro and in vivo. *Mol. Ther. 11*, 418–425.

(40) Park, M. R., Han, K. O., Han, I. K., Cho, M. H., Nah, J. W., Choi, Y. J., and Cho, C. S. (2005) Degradable polyethylenimine-alt-poly(ethylene glycol) copolymers as novel gene carriers. *J. Controlled Release 105*, 367–380.

(41) Li, W. J., Huang, Z. H., MacKay, J. A., Grube, S., and Szoka, F. C. (2005) Low-pH-sensitive poly(ethylene glycol) (PEG)-stabilized plasmid nanlipoparticles: effects of PEG chain length, lipid composition and assembly conditions on gene delivery. *J. Gene Med. 7*, 67–79.

(42) Hatakeyama, H., Akita, H., Kogure, K., Oishi, M., Nagasaki, Y., Kihira, Y., Ueno, M., Kobayashi, H., Kikuchi, H., and Harashima, H. (2007) Development of a novel systemic gene delivery system for cancer therapy with a tumor-specific cleavable PEG-lipid. *Gene Ther. 14*, 68–77.

(43) Hurley, C. A., Wong, J. B., Ho, J., Writer, M., Hart, S. L., Lawrence, M. J., Tabor, A. B., and Hailes, H. C. (2008) Di- and monocationic short PEG and methylene dioxyalkylglycerols for use in synthetic gene delivery systems. *Org. Biomol. Chem. 6*, 2554–2559.

(44) Wong, J. B., Grosse, S. M., Tabor, A. B., Hart, S. L., and Hailes, H. C. (2008) Acid cleavable PEG-lipids for applications in ternary gene delivery vectors. *Mol. Biosyst. 4*, 532–541.

(45) Hurley, C. A., Wong, J. B., Hailes, H. C., and Tabor, A. B. (2004) Asymmetric synthesis of dialkyloxy-3-alkylammonium cationic lipids. *J. Org. Chem. 69*, 980–983.

(46) Cozens, A. L., Yezzi, M. J., Kunzelmann, K., Ohrui, T., Chin, L., Eng, K., Finkbeiner, W. E., Widdicombe, J. H., and Gruenert, D. C. (1994) CFTR expression and chloride secretion in polarized immortal human bronchial epithelial cells. *Am. J. Respir. Cell Mol. Biol. 10*, 38–47.

(47) Ross, R. (1971) Smooth muscle cell. 2. Growth of smooth muscle in culture and formation of elastic fibers. *J. Cell. Biol. 50*, 172–186.

(48) Ward, C. M., Pechar, M., Oupicky, D., Ulbrich, K., and Seymour, L. W. (2002) Modification of pLL/DNA complexes with a multivalent hydrophilic polymer permits folate-mediated targeting in vitro and prolonged plasma circulation in vivo. *J. Gene Med. 4*, 536–547.

(49) Dori, Y., Bianco-Peled, H., Satija, S., Fields, G. B., McCarthy, J. B., and Tirrell, M. (2000) Ligand accessibility as means to control cell response to bioactive bilayer membranes. *J. Biomed. Mater. Res. 50*, 75–81.

(50) Guo, Y. Q., and Hui, S. W. (1997) Poly(ethylene glycol)-conjugated surfactants promote or inhibit aggregation of phospholipids. *Biochim. Biophys. Acta 1323*, 185–194.

(51) Lucas, M., Karrer, U., Lucas, A., and Klenerman, P. (2001) Viral escape mechanisms - escapology taught by viruses. *Int. J. Exp. Pathol. 82*, 269–286. .

(52) Oishi, M., Nagasaki, Y., Itaka, K., Nishiyama, N., and Kataoka, K. (2005) Lactosylated poly(ethylene glycol)-siRNA conjugate through acid-labile SS-thiopropionate linkage to construct pH-sensitive polyion complex micelles achieving enhanced gene silencing in hepatoma cells. *J. Am. Chem. Soc. 127*, 1624–1625.

(53) Ali, S., Ahmad, I., Peters, A., Masters, G., Minchey, S., Janoff, A., and Mayhew, E. (2001) Hydrolyzable hydrophobic taxanes: synthesis and anti-cancer activities. *Anti-Cancer Drugs 12*, 117–128.

(54) Mathew, A. E., Mejillano, M. R., Nath, J. P., Himes, R. H., and Stella, V. J. (1992) Synthesis and evaluation of some water-soluble prodrugs and derivatives of taxol with antitumor activity. *J. Med. Chem. 35*, 145–151.

(55) Giammona, G., Cavallaro, G., Fontana, G., De Guidi, G., and Giuffrida, S. (1996) Macromolecular prodrug of diflunisal. II. Investigations of in vitro release and of photochemical behaviour. *Eur. J. Pharm. Sci. 4*, 273–282.

(56) Kloeckner, J., Wagner, E., and Ogris, M. (2006) Degradable gene carriers based on oligomerized polyamines. *Eur. J. Pharm. Sci. 29*, 414–425.

(57) Oishi, M., Sasaki, S., Nagasaki, Y., and Kataoka, K. (2003) pH-Responsive oligodeoxynucleotide (ODN)-poly(ethylene glycol) conjugate through acid-labile beta-thiopropionate linkage: Preparation and polyion complex micelle formation. *Biomacromolecules 4*, 1426–1432.

(58) Schoenmakers, R. G., van de Wetering, P., Elbert, D. L., and Hubbell, J. A. (2004) The effect of the linker on the hydrolysis rate of drug-linked ester bonds. *J. Controlled Release 95*, 291–300.

(59) Koivunen, E., Wang, B., and Ruoslahti, E. (1995) Phage libraries displaying cyclic-peptides with different ring sizes−ligand specificities of the RGD-directed integrins. *Bio-Technology 13*, 265–270.

(60) Meitar, D., Crawford, S. E., Rademaker, A. W., and Cohn, S. L. (1996) Tumor angiogenesis correlates with metastatic disease, N-myc amplification, and poor outcome in human neuroblastoma. *J. Clin. Oncol. 14*, 405–414.

(61) Zitzmann, S., Ehemann, V., and Schwab, M. (2002) Arginine-glycine-aspartic acid (RGD)-peptide binds to both tumor and tumor-endothelial cells in vivo. *Cancer Res. 62*, 5139–5143.

(62) Gasparini, G., Brooks, P. C., Biganzoli, E., Vermeulen, P. B., Bonoldi, E., Dirix, L. Y., Ranieri, G., Miceli, R., and Cheresh, D. A. (1998) Vascular integrin $\alpha(v)\beta(3)$: A new prognostic indicator in breast cancer. *Clin. Cancer Res. 4*, 2625–2634.

(63) Sengupta, S., Chattopadhyay, N., Mitra, A., Ray, S., Dasgupta, S., and Chatterjee, A. (2001) Role of $\alpha_v\beta_3$ integrin receptors in breast tumor. *J. Exp. Clin. Cancer Res. 20*, 585–590.

(64) Pilkington-Miksa, M. A., Sarkar, S., Writer, M. J., Barker, S. E., Ayazi Shamlou, P., Hart, S. L., Hailes, H. C., and Tabor, A. B. (2008) Synthesis of bifunctional integrin-binding peptides containing PEG spacers of defined length for non-viral gene delivery. *Eur. J. Org. Chem. 17*, 2900–2914.

(65) Molloy, S. S., Anderson, E. D., Jean, F., and Thomas, G. (1999) Bi-cycling the furin pathway: from TGN localization to pathogen activation and embryogenesis. *Trends Cell Biol. 9*, 28–35.

(66) Barrett, A. J., and Kirschke, H. (1981) Cathepsin B, Cathepsin H, and Cathepsin L. *Methods Enzymol. 80*, 535–561.

(67) Soyez, H., Schacht, E., and Vanderkerken, S. (1996) The crucial role of spacer groups in macromolecular prodrug design. *Adv. Drug Delivery Rev. 21*, 81–106.

(68) Pechar, M., Ulbrich, K., Subr, V., Seymour, L. W., and Schacht, E. H. (2000) Poly(ethylene glycol) multiblock copolymer as a carrier of anti-cancer drug doxorubicin. *Bioconjugate Chem. 11*, 131–139.

(69) Schmid, B., Chung, D.-E., Warnecke, A., Fichtner, I., and Kratz, F. (2007) Albumin-binding prodrugs of camptothecin and doxorubicin with an Ala-Leu-Ala-Leu-linker that are cleaved by cathepsin B: Synthesis and antitumor efficacy. *Bioconjugate Chem. 18*, 702–716.

(70) Felgner, P. L., Gadek, T. R., Holm, M., Roman, R., Chan, H. W., Wenz, M., Northrop, J. P., Ringold, G. M., and Danielsen, M. (1987) Lipofection−a highly efficient, lipid-mediated DNA-transfection procedure. *Proc. Natl. Acad. Sci. U.S.A. 84*, 7413–7417.

(71) Kamber, B., Hartmann, A., Eisler, K., Riniker, B., Rink, H., Sieber, P., and Rittel, W. (1980) The synthesis of cystine peptides by iodine oxidation of *S*-trityl-cysteine and *S*-acetamidomethyl-cysteine peptides. *Helv. Chim. Acta 63*, 899–915.

(72) Fajac, I., Allo, J.-C., Souil, E., Merten, M., Pichon, C., Figarella, C., Monsigny, M., Briand, P., and Midoux, P. (2000) Histidylated polylysine as a synthetic vector for gene transfer into immortalised cystic fibrosis airway surface and airway gland serous cells. *J. Gene Med. 2*, 368–378.

(73) (2006) Final report on the safety assessment of Triethylene Glycol and PEG-4. *Int. J. Toxicol. 25*, 121−138.

(74) Stewart, L., Manvell, M., Hillery, E., Etheridge, C. J., Cooper, R. G., Stark, H., van Heel, M., Preuss, M., Alton, E. W. F. W., and Miller, A. D. (2001) Cationic lipids for gene therapy part 4 - Physico-chemical analysis of cationic liposome-DNA complexes (lipoplexes) with respect to in vitro and in vivo gene delivery efficiency. *J. Chem. Soc., Perkin Trans. II* 624–632.

(75) Scarzello, M., Smisterova, J., Wagenaar, A., Stuart, M. C. A., Hoeksra, D., Engberts, J. B. F. N., and Hulst, R. (2005) Sunfish cationic amphiphiles: Toward an adaptative lipoplex morphology. *J. Am. Chem. Soc. 127*, 10420–10429.

(76) Prime, K. L., and Whitesides, G. M. (1993) Adsorption of proteins onto surfaces containing end-attached oligo(ethylene oxide): a model system using self-assembled monolayers. *J. Am. Chem. Soc. 115*, 10714–10721.

(77) Felgner, J. H., Kumar, R., Sridhar, C. N., Wheeler, C. J., Tsai, Y. J., Border, R., Ramsey, P., Martin, M., and Felgner, P. L. (1994) Enhanced gene delivery and mechanism studies with a novel series of cationic lipid formulations. *J. Biol. Chem. 269*, 2550–2561.

(78) van der Aa, M. A. E. M., Mastrobattista, E., Oosting, R. S., Hennink, W. E., Koning, G. A., and Crommelin, D. J. A. (2006) The nuclear pore complex: The gateway to successful nonviral gene delivery. *Pharm. Res. 23*, 447–459.

(79) Colin, M., Moritz, S., Fontanges, P., Kornprobst, M., Delouis, C., Keller, M., Miller, A. D., Capeau, J., Coutelle, C., and Brahimi-Horn, M. C. (2001) The nuclear pore complex is involved in nuclear transfer of plasmid DNA condensed with an oligolysine-RGD peptide containing nuclear localisation properties. *Gene Ther. 8*, 1643–1653.

(80) Cokol, M., Nair, R., and Rost, B. (2000) Finding nuclear localization signals. *EMBO Rep. 1*, 411–415.

BC800450R

Supporting Information

Stabilised Integrin-Targeting Ternary LPD (Lipopolyplex) Vectors for Gene Delivery Designed To Disassemble Within the Target Cell†

M. Firouz Mohd Mustapa, Stephanie M. Grosse, Laila Kudsiova, Martin Elbs, Eun-Ang Raiber, J. B. Wong, Anthony P. R. Brain, Hannah E. J. Armer, Alice Warley, Melanie Keppler, Tony Ng, M. Jayne Lawrence, Stephen L. Hart, Helen C. Hailes, Alethea B. Tabor

Contents

S2 Supplementary Figure 1

S3 Supplementary Figure 2

S4 Supplementary Figure 3: Comparison of cell viability between free lipid **4** and lipid **4**:DNA complexes of the same corresponding lipid concentrations

S5 Supplementary Figure 4: In vitro cleavage results for lipid **4** with pig liver esterase

S6-S8 Supplementary Figure 5: In vitro cleavage results for peptides **9** and **12** with furin and cathepsin

S9 General Synthetic Methods and Methods for Cell Biology

S10 Synthesis of **18**

S11 – S17 ^{1}H NMR spectra of **15**, **16**, **17**, **4, 5**, **6**, **18**.

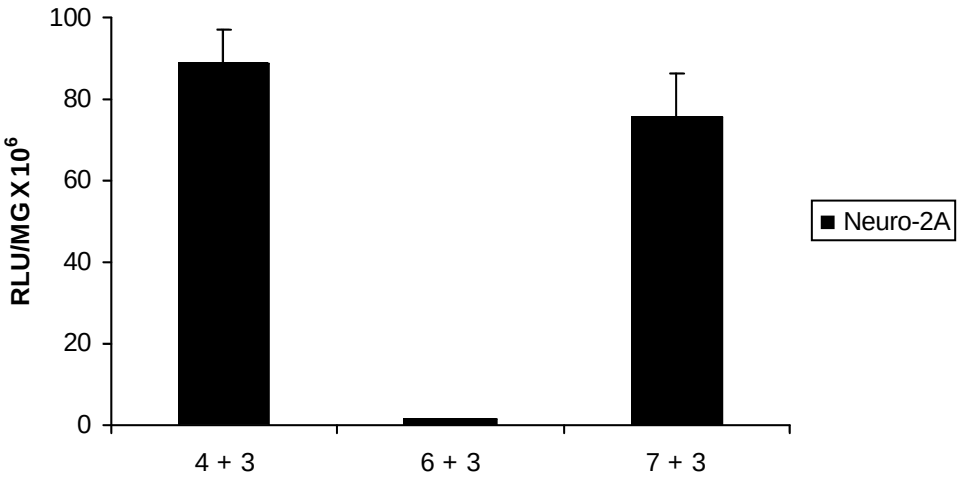

Supplementary Figure 1. Transfection efficiencies of LPD complexes formulated with peptide **9**, plasmid DNA and either **4**/DOPE, **6**/DOPE or **7**/DOPE, in Neuro-2A cells.

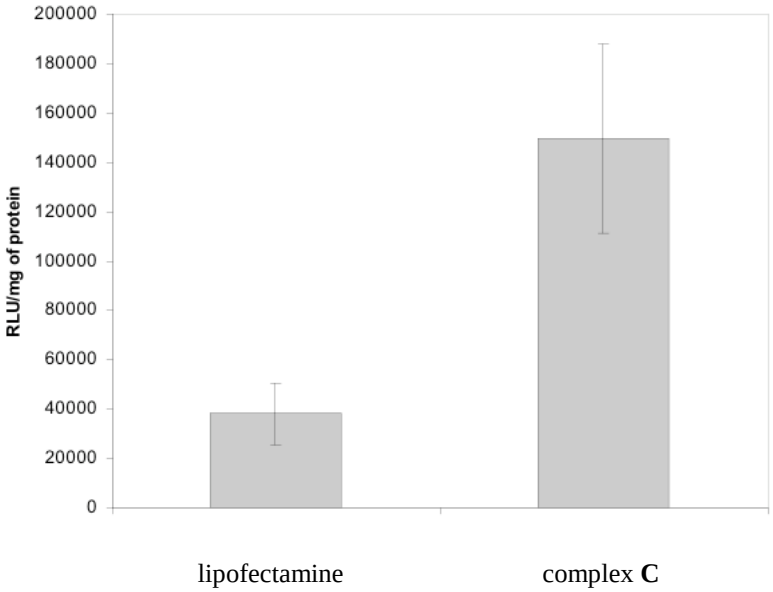

Supplementary Figure 2. Transfection of MDA-MB-231 breast cancer cells by the lipid **4**/DOPE/peptide **9**/DNA complex (complex **C**), compared with transfection by lipofectamine.

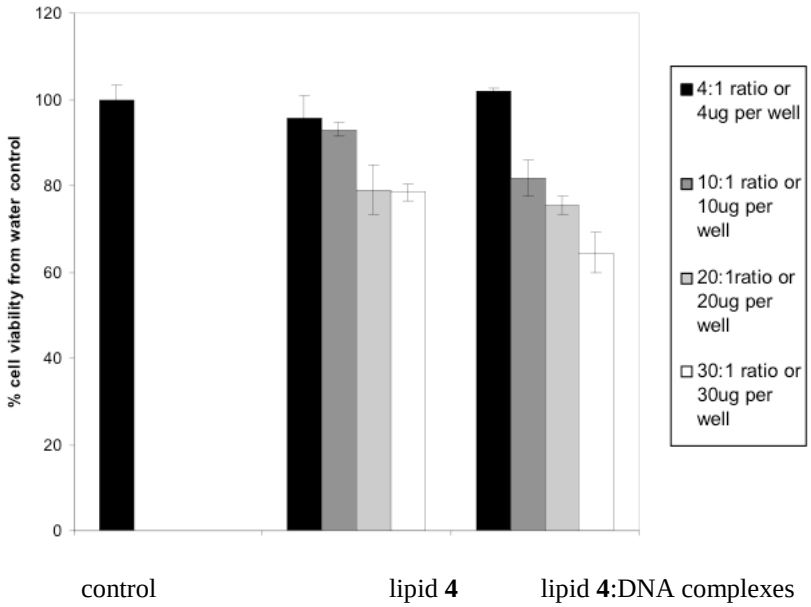

Supplementary Figure 3. Comparison of cell viability between free lipid **4** and lipid **4**:DNA complexes of the same corresponding lipid concentrations.

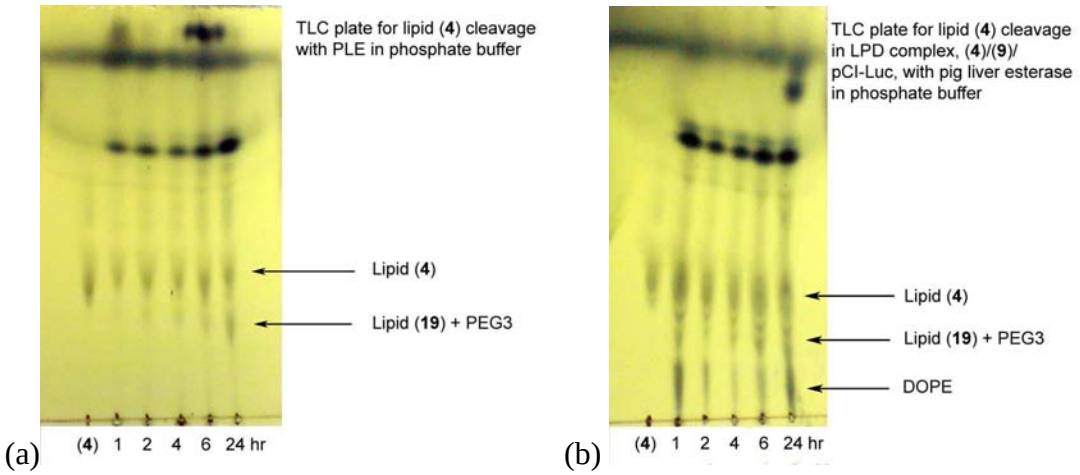

Supplementary Figure 4. In vitro cleavage results for (a) lipid **4** with pig liver esterase, (b) **4**/DOPE/**9**/pCI-Luc with pig liver esterase.

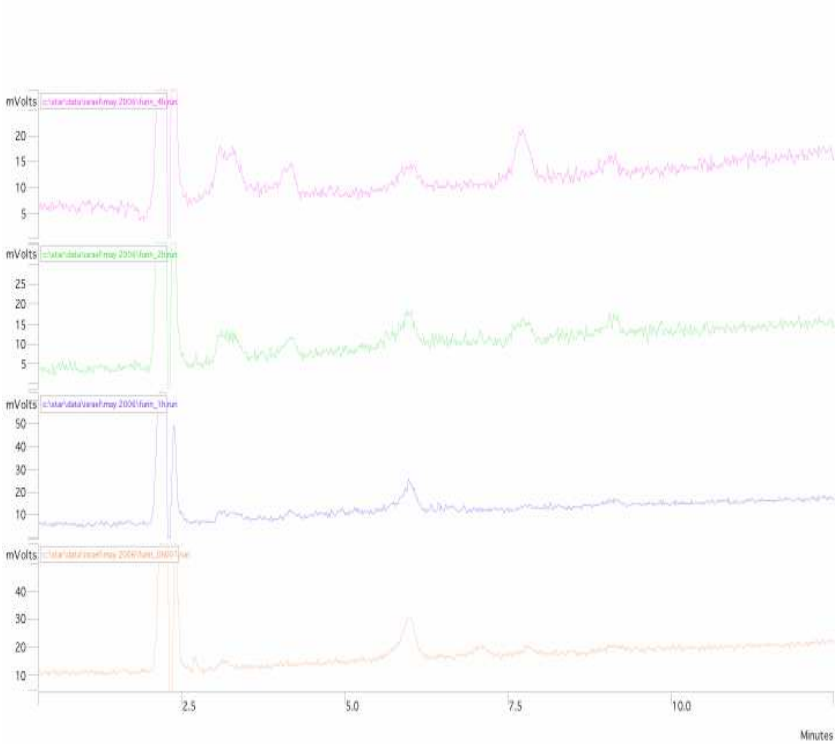
mVolts
20
15
10
5
mVolts
25
20
15
10
5
mVolts
50
40
30
20
10
mVolts
40
30
20
10
2.5
5.0
7.5
10.0
Minutes

(a)

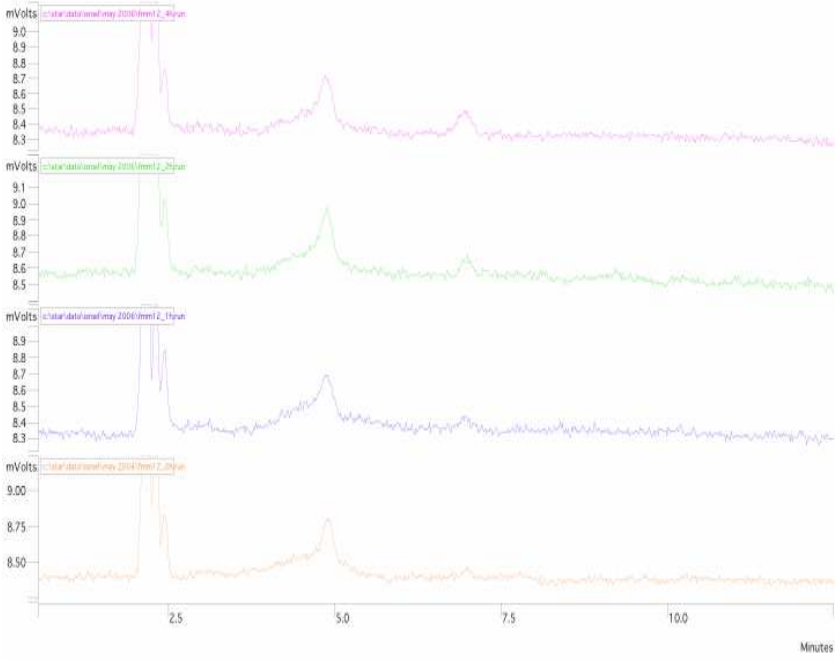
mVolts
9.0
8.9
8.8
8.7
8.6
8.5
8.4
8.3
mVolts
9.1
9.0
8.9
8.8
8.7
8.6
8.5
mVolts
8.9
8.8
8.7
8.6
8.5
8.4
8.3
mVolts
9.00
8.75
8.50
2.5
5.0
7.5
10.0
Minutes

(b)

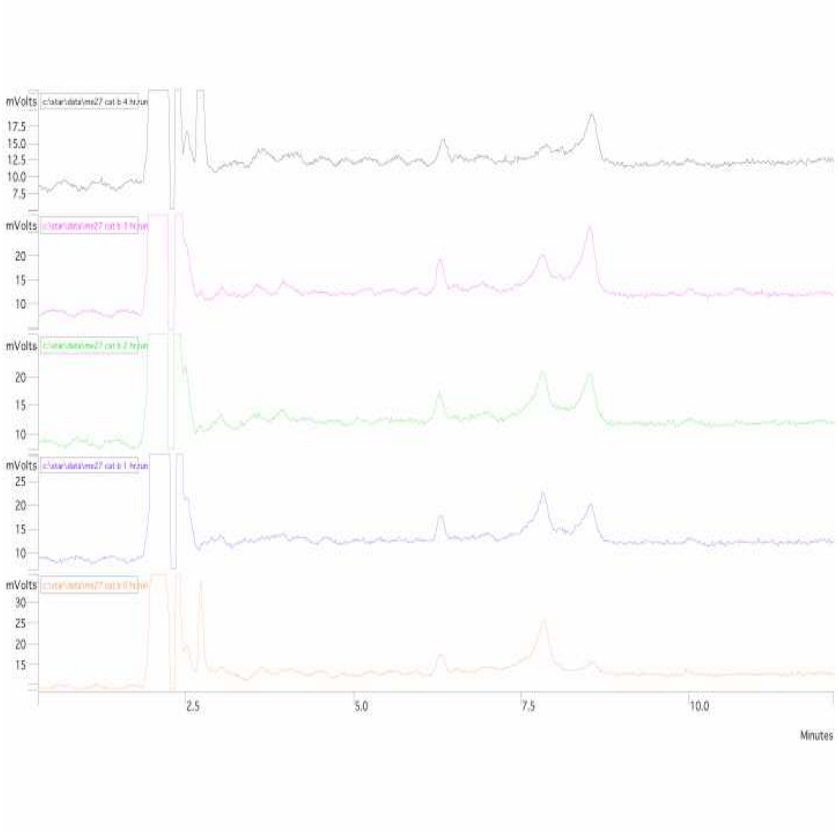
mVolts
17.5
15.0
12.5
10.0
7.5
mVolts
20
15
10
mVolts
20
15
10
mVolts
25
20
15
10
mVolts
30
25
20
15
2.5
5.0
7.5
10.0
Minutes

(c)

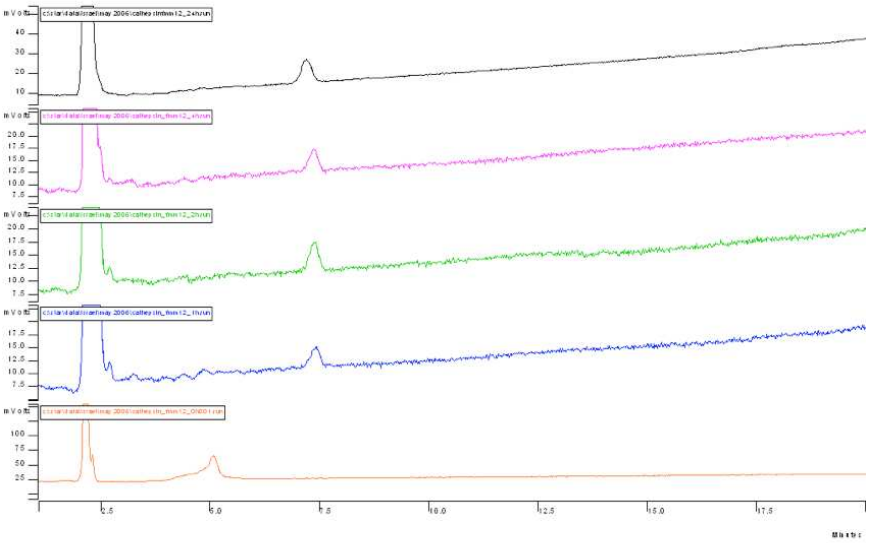

(d)

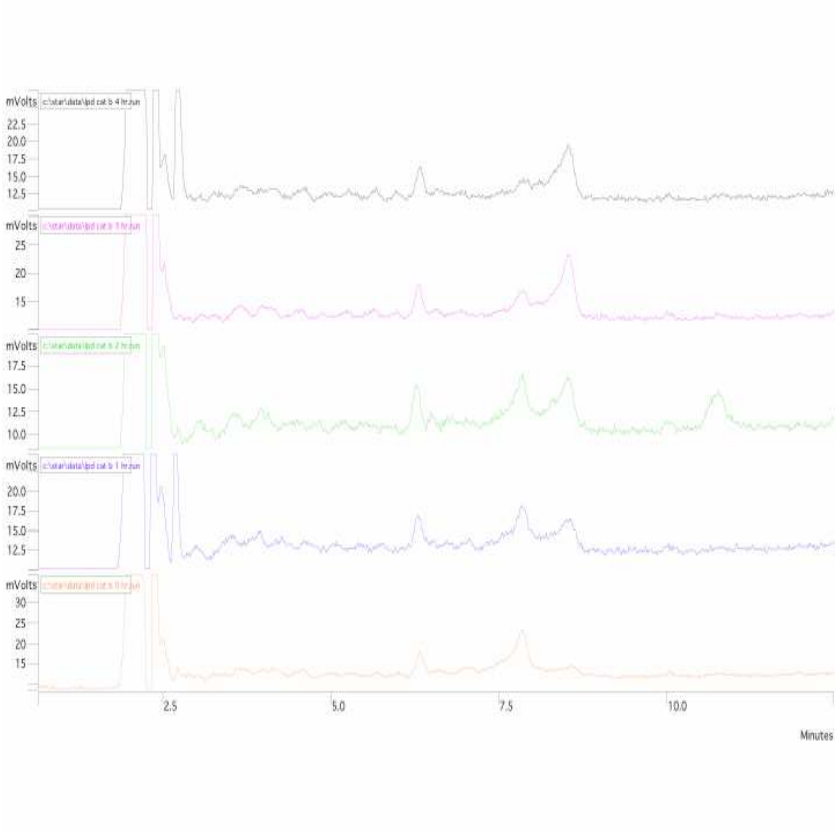

(e)

Supplementary Figure 5. In vitro cleavage results for (a) peptide **9** with furin; (b) peptide **12** (non-cleavable) with furin; (c) peptide **9** with cathepsin B; (d) peptide **12** with cathepsin B; (e) complex **C** (**4**/DOPE/**9**/pCI-Luc) with cathepsin B. The traces are shown at 0 hr (—), 1 hr (—), 2 hr (—), 4 hr (—) and 24 hr (—).

General Synthetic Methods

All reagents used for synthesis were purchased from commercial suppliers. Cathepsin B and furin were purchased from Sigma. Dichloromethane was dried over anhydrous alumina columns (*1*) moisture levels were usually <15 ppm by Karl Fischer titration. ^{1}H and ^{13}C NMR spectra were recorded on a Bruker AMX300 spectrometer; chemical shifts (δ) are reported in parts per million (ppm) using residual isotopic solvent as an internal reference. Coupling constants (*J*) are reported in Hertz (Hz). Electrospray mass spectra were recorded on Micromass Quattro LC, Thermo Finnegan MAT 900XP or VG ZAB 2SE instruments, and fast atom bombardment mass spectra on Thermo Finnegan MAT 900XP or VG ZAB 2SE instruments.

Materials for Cell Biology

Dulbecco's Modified Eagle's medium (DMEM), foetal bovine serum (FBS), penicillin/streptomycin solution, trypan blue solution 0.4 % w/v, 0.25% Trypsin-EDTA, thiazolyl blue reagent (MTT), 4',6-Diamidino-2-phenylindole dihydrochloride (DAPI) and SYBR-green 10,000x solution were all supplied from Sigma Ltd, UK. Luciferase assay system with reporter lysis buffer was obtained from Promega, UK. RC DC protein assay was purchased from Bio-Rad laboratories. Paraformaldehyde (PFA), Triton-X and sodium borohydride were supplied from Sigma-Aldrich. 100 U/mL penicillin, Glutamax-1, sodium pyruvate, PBS and streptomycin were supplied by InVitrogen (Paisley, UK). MEM-non-essential amino acids (NEAA) and L-glutamine were supplied by either InVitrogen or Sigma. 1X Reporter Lysis Buffer was supplied by Promega (Madison, WI, USA). Mowiol solution was supplied by the Randall division of cell and molecular biophysics department, King's College London.

The pGL-3 plasmid was initially purchased from Promega, UK and grown in a transformed *E. coli* JM109 strain then purified using a QIAGEN® EndoFree plasmid Giga kit (from QIAGEN, UK). A nick translation kit for plasmid fluorescence labelling together with 10mM of dCTP, dGTP and dATP were all purchased form Amersham Bioscience, UK. Tetramethyl-rhodamine-5-dUTP 25nmol/25μL was obtained from Roche, UK, DNA polymerase I and 10mg/ml bovine serum albumin (BSA) were

purchased from New England Biolabs and 0.5M EDTA, 1M Tris HCl and dithiothreitol (DTT) were from Promega, UK.

(2,3-Bis-octadec-9-enyloxypropy)-(carboxybutyl)-dimethylammonium bromide (18) Lipid (**11**) (0.177 g, 0.18 mmol) was dissolved in NaOH (1M, 2 mL) and stirred at room temperature for 2 h. Dichloromethane was then added, and the mixture was washed with saturated $NaHCO_3$ and brine. The separated organic layer was dried over $MgSO_4$ and the solvent was removed *in vacuo*. Purification by flash column chromatography (10% methanol in dichloromethane changing to pure methanol) gave the titled compound (0.017 g, 13%) as a pale yellow oil. ^{1}H (300 MHz, $CDCl_3$): δ 0.87 (6H, t, J = 6.6 Hz) 1.24 (44H, m), 1.53 (4H, m), 1.67 (2H, m), 1.86 (2H, m), 1.99 (8H, m), 2.31 (2H, m), 3.28-3.45 (10 H, m), 3.52-3.68 (7H, m), 3.98 (1H, m), 5.32 (4H, m). ^{13}C (75 MHz, $CDCl_3$): δ 14.05, 22.08, 22.58, 25.94, 26.11, 27.12, 29.10–29.67 (signals overlap), 29.94, 31.80, 32.52, 51.74, 52.30 (signals overlap), 65.26, 65.85, 68.75, 69.32, 71.89, 73.21, 129.67 (signals overlap), 129.85 (2 signals overlap) HRMS *m/z* (ES+) calcd 720.68699, found 720.68512 (M^+).

References

1. Pangborn, A. B., Giardello, M. A., Grubbs, R. H., Rosen, R. K., and Timmers, F. J. (1996) Safe and Convenient Procedure for Solvent Purification. *Organometallics 15*, 1518 - 1520.

5-Bromopentanoic acid 8-hydroxy-3,6-dioxooctyl ester (15).

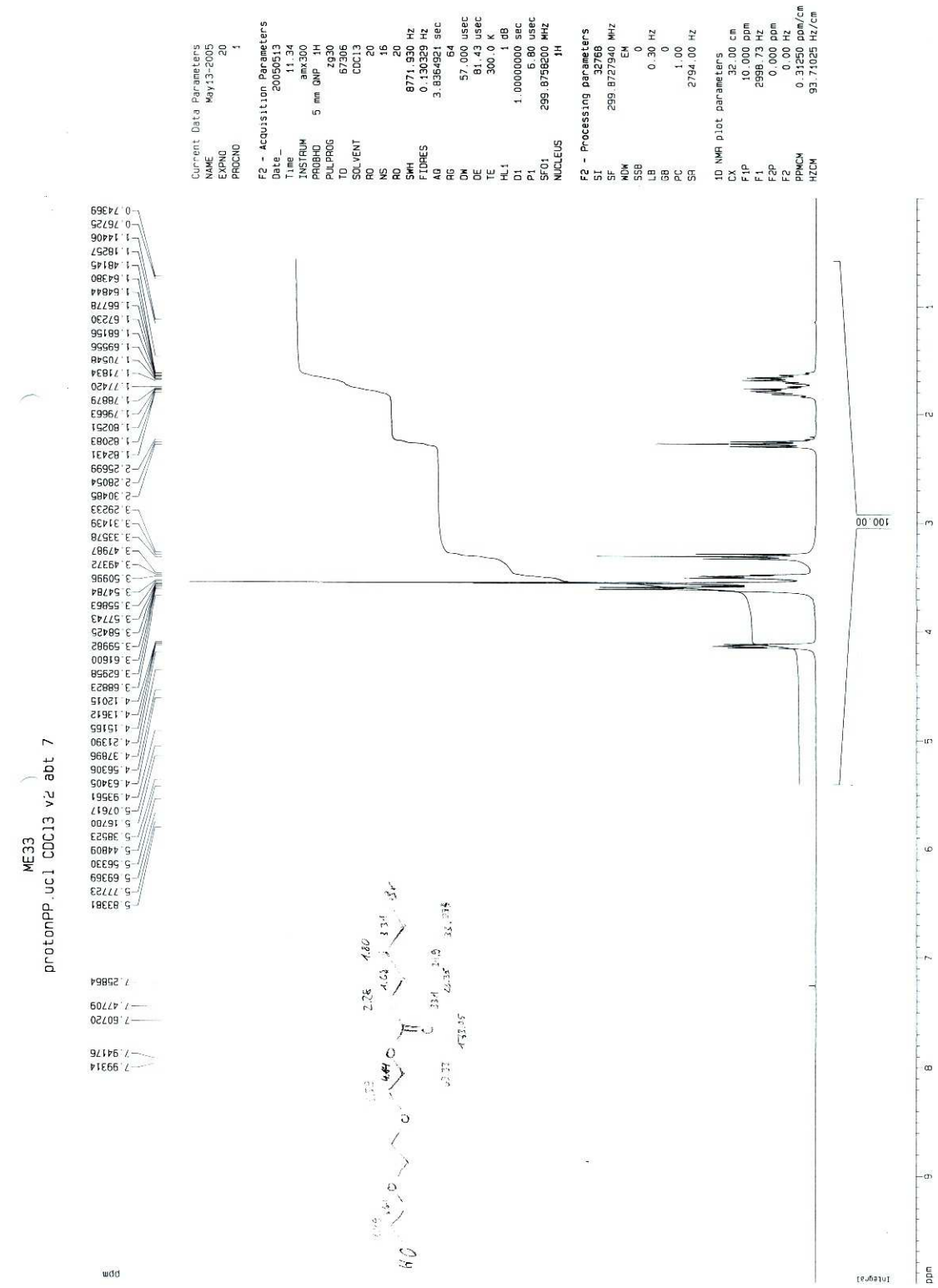

5-Bromopentanoic acid 3,6,9-trioxodecyl ester (16).

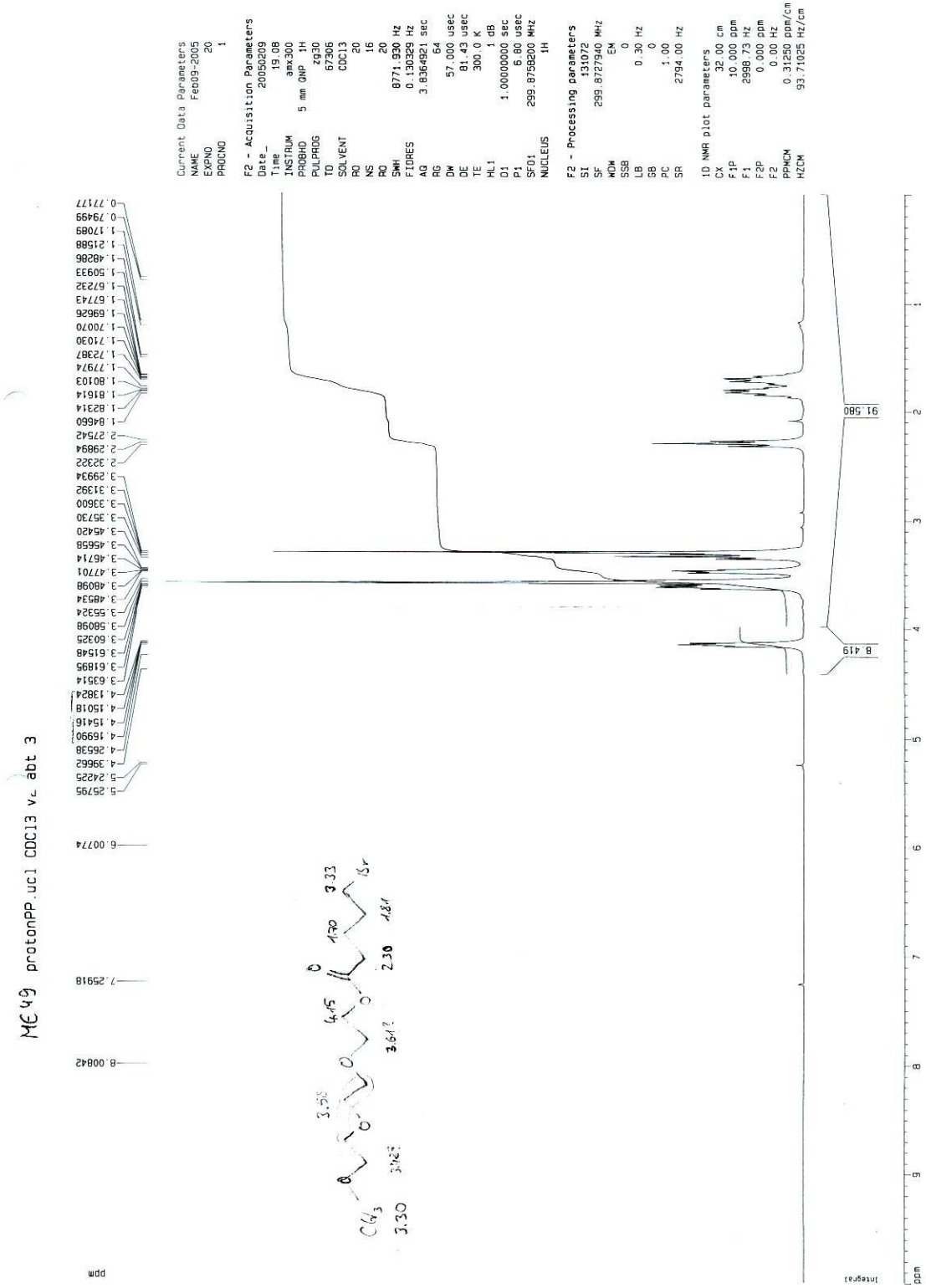

5-Bromopentanoic acid 17-hydroxy-3,6,9,12,15-pentaoxoheptadecyl ester (17).

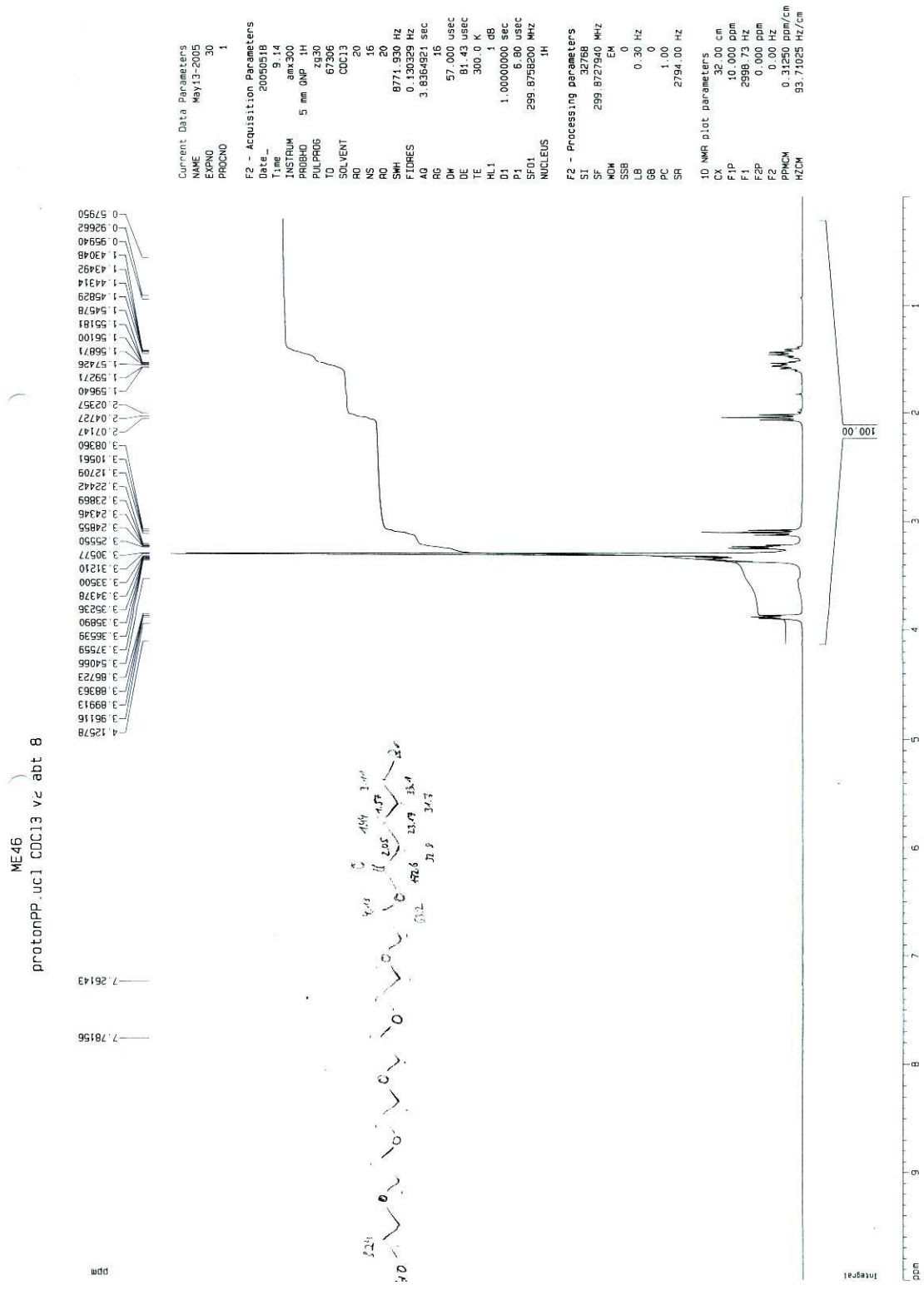

(2,3-Bis-octadec-9-enyloxypropyl)-(8-hydroxy-3,6-dioxooctyloxycarbonylbutyl)-dimethyl-ammonium bromide (4).

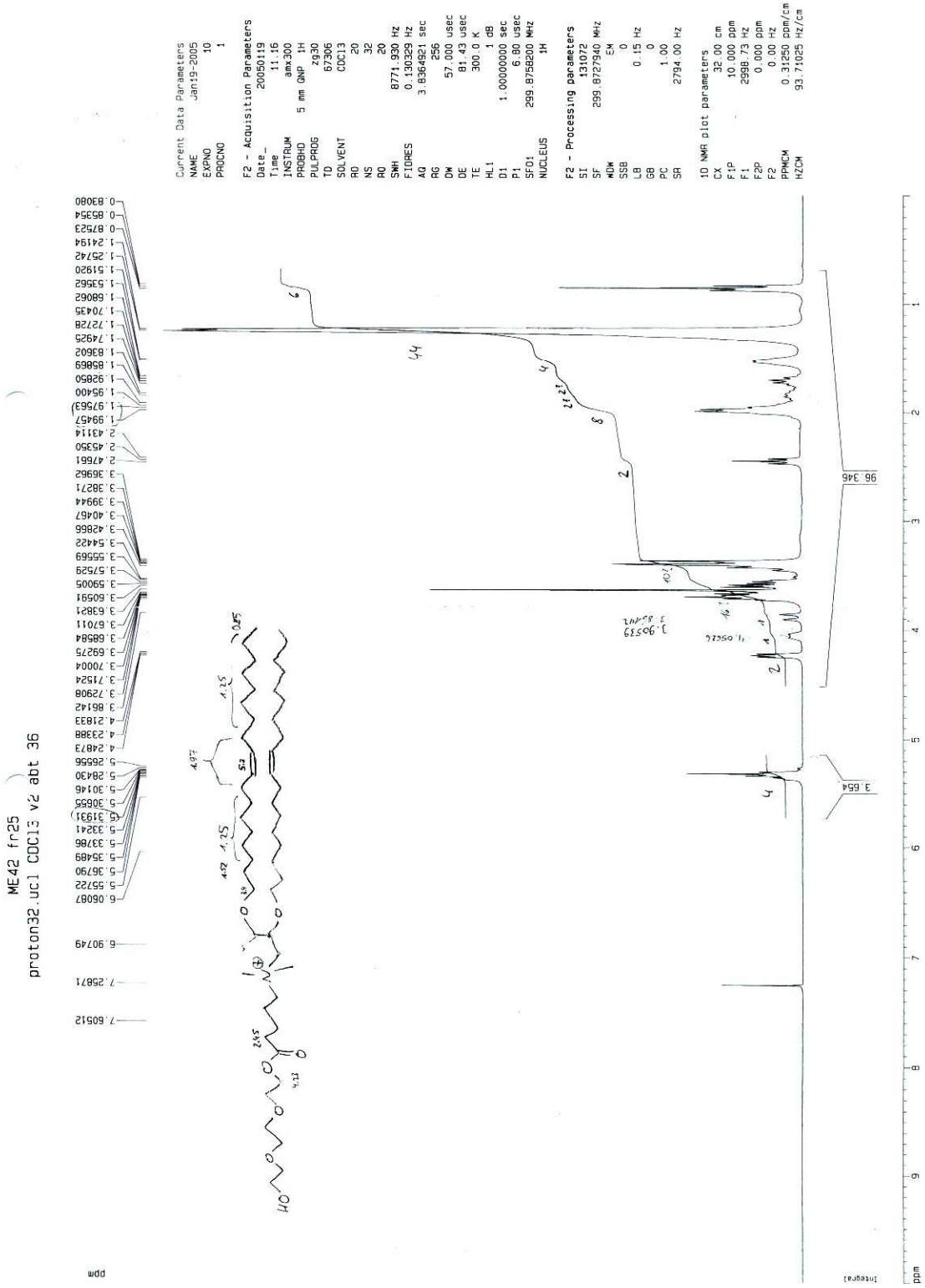

(2,3-Bis-octadec-9-enyloxypropyl)-(3,6,9-trioxodecyloxycarbonylbutyl)-dimethylammonium bromide (5).

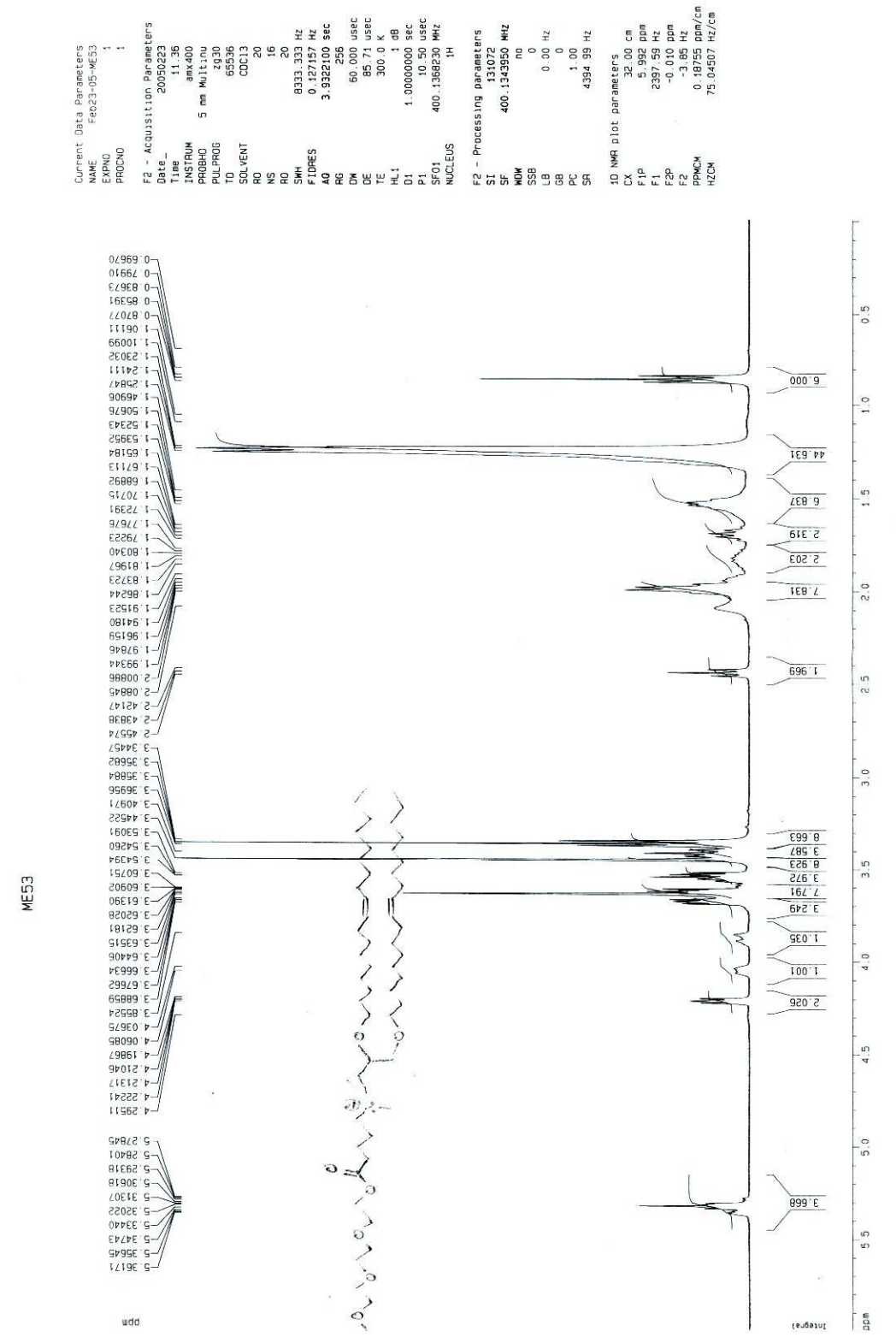

(2,3-Bis-octadec-9-enyloxypropyl)-(17-hydroxy-3,6,9,12,15-pentaoxoheptadecyloxycarbonyl-butyl)-dimethylammonium bromide (6).

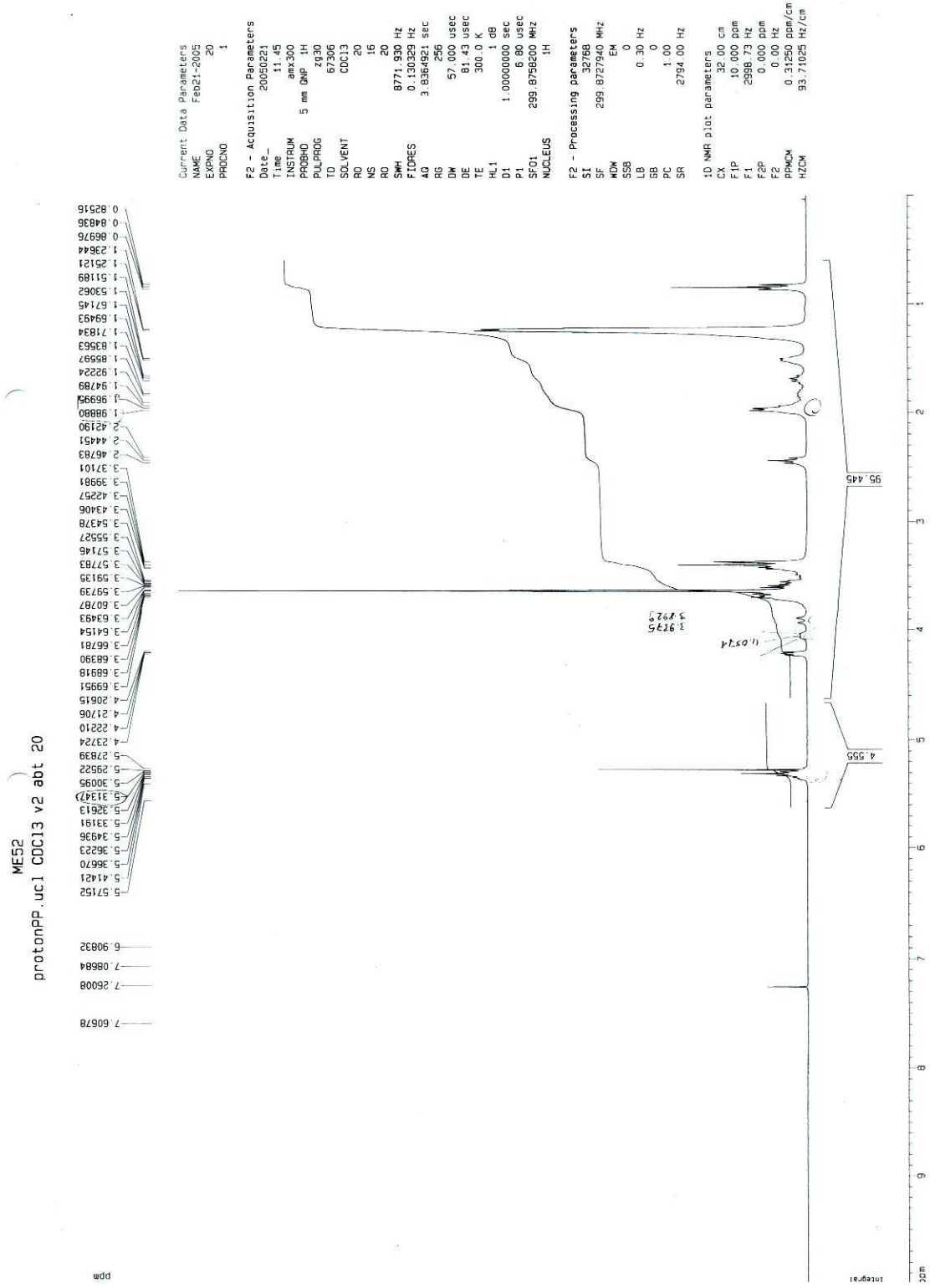

(2,3-Bis-octadec-9-enyloxypropy)-(carboxybutyl)-dimethylammonium bromide (18)

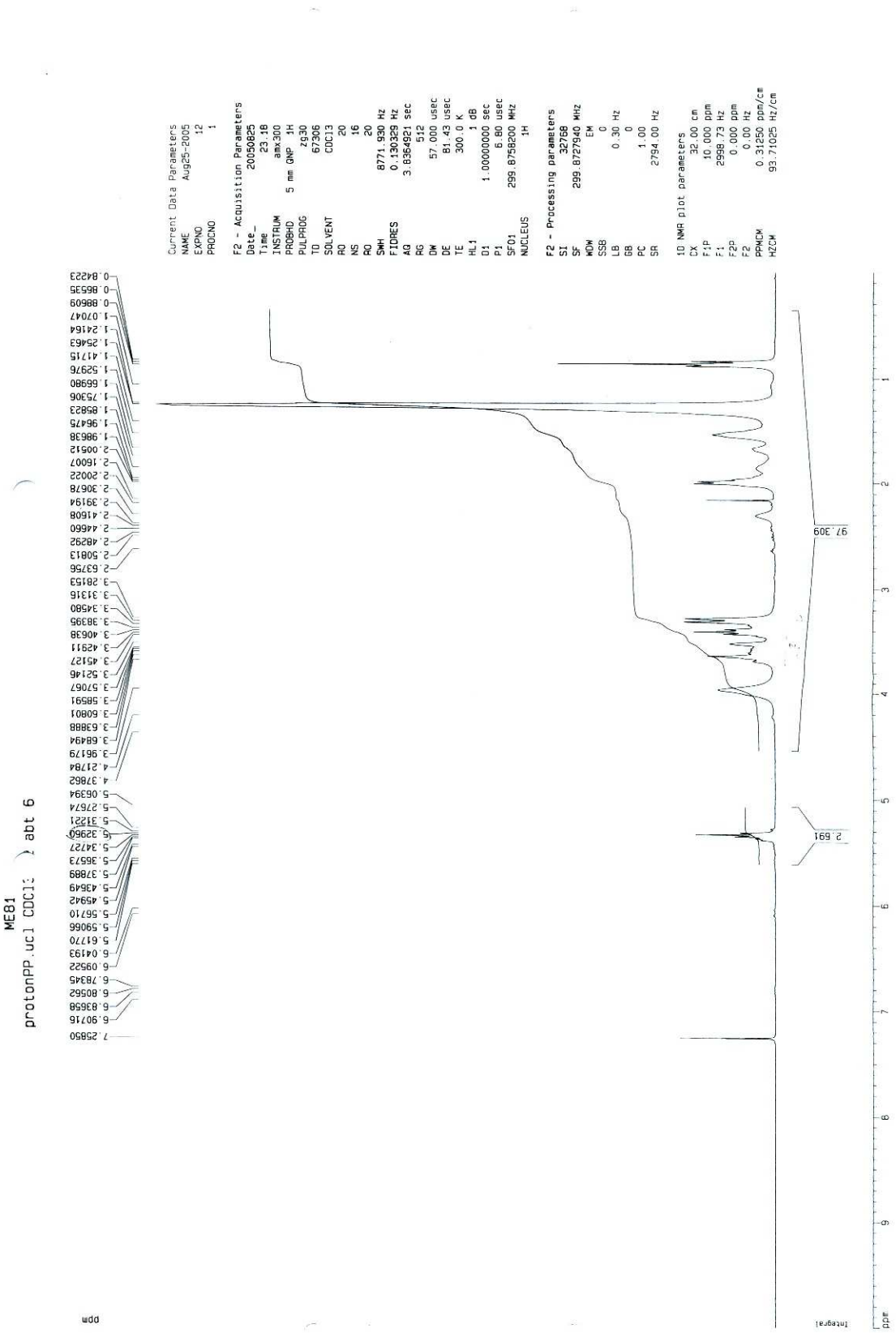

Bioconjugate Chemistry 20th Anniversary

Subscriber access provided by SHEMYAKIN-OVCHINNIKOV INST

Article

Construction of Effective Receptor for Recognition of Avian Influenza H5N1 Protein HA1 by Assembly of Monohead Glycolipids on Polydiacetylene Vesicle Surface

Jieli Deng, Zhonghan Sheng, Kai Zhou, Mingxing Duan, Chu-yi Yu, and Long Jiang

Bioconjugate Chem., **2009**, 20 (3), 533-537• DOI: 10.1021/bc800453u • Publication Date (Web): 23 February 2009

Downloaded from http://pubs.acs.org on May 8, 2009

More About This Article

Additional resources and features associated with this article are available within the HTML version:

- Supporting Information
- Access to high resolution figures
- Links to articles and content related to this article
- Copyright permission to reproduce figures and/or text from this article

View the Full Text HTML

ACS Publications
High quality. High impact.

Bioconjugate Chemistry is published by the American Chemical Society. 1155 Sixteenth Street N.W., Washington, DC 20036

Construction of Effective Receptor for Recognition of Avian Influenza H5N1 Protein HA1 by Assembly of Monohead Glycolipids on Polydiacetylene Vesicle Surface

Jieli Deng,[†] Zhonghan Sheng,[†] Kai Zhou,[‡] Mingxing Duan,*[,‡] Chu-yi Yu,*[,†] and Long Jiang*[,†]

Beijing National Laboratory for Molecular Sciences, Institute of Chemistry, Chinese Academy of Sciences, Beijing 100190, and State Key Laboratory of Biomembrane and Membrane Biotechnology, Department of Biological Sciences and Biotechnology, Tsinghua University, Beijing 100084, P.R. China. Received October 21, 2008; Revised Manuscript Received January 16, 2009

Fast and sensitive detection of epidemic virus is of the utmost importance for human being in nowadays. Various biosensors have been designed for this goal based on conjugation event between host cell glycolipids and invading virus. However, multihead glycolipids analogous to native receptors on cell surface are known to be very difficult to mimic because of the complexity of chemical synthesis. Here, we developed a new approach where two types of monohead glycolipids, active sialic acid-β-glucoside (G1) and inactive lactose-β-glucoside (G2), are embedded onto the surface of a polydiacetylene (PDA) vesicle to mimic native glycolipids on the cell surface. Vesicles prepared in this manner show good selectivity with a 10 ng/mL detection limit and 5 min response time to Hemagglutinin (HA1), which is more sensitive than any HA1 biosensors ever known. Moreover, in the formation of color-changeable vesicles, a very strong synergistic effect between G1 and G2 has been found, offering a novel strategy to construct effective biosensor receptors, as well as a new way to study the surface combination effect that is potentially important to the immunology study of epidemic disease.

INTRODUCTION

Fast and sensitive detection of epidemic viruses is of the utmost importance for human beings nowadays. A commonly used approach is to mimic biological interfaces upon which specific molecular events could occur (*1*). Such interfacial biological processes have been found to be detectable with the help of a polydiacetylene (PDA) vesicle (*2*−*4*).

Many efforts have been devoted to developing PDA-based vesicles for detection of various biologically important analytes, such as lipophilic enzymes (*5*) (*6*), antibacterial peptides (*7*), mammalian peptides (*8*), ions (*9*), antibodies (*10*−*12*), proteins (*13*), and pharmacologically active compounds (*14*). It is generally believed that the PDA vesicle is a good model system to mimic the cell surface in the study of the surface conjugation events. To the best of our knowledge, however, there are only a few studies on the detection of the key polysaccharide or carbohydrate−protein interaction (*15*−*17*), although it is one of the most widely existing and important types of conjugation in cell membranes. Furthermore, almost all the epidemic virus invading processes involve polysaccharides on cell surfaces. One major limitation to the PDA-based approach is the difficulty of synthesizing complicated probes that contain more than one saccharide group in a molecule as effective binding sites. If these obstacles could be overcome by self-assembly technology, for example, by inserting receptors and various saccharide groups into the same vesicle to make it analogous to natural complex polysaccharide receptors on the cell, a much easier approach for biosensor design and construction would be developed, which may lead to a wide range of applications.

Herein, we report an approach based on the strategy mentioned above. The recognition element assembled in the colorimetric mixed PCDA sensor consists of sialic acid-β-glucoside (G1) and lactose-β-glucoside (G2) receptors, both having a tetraethylene glycol spacer and C12 hydrocarbon. The fragment of influenza virus H5N1 protein of Hemagglutinin (HA1) on the cell surface is used to act as the target for detection.

EXPERIMENTAL PROCEDURES

Materials. 10,12-pentacosadiynoic acid (PDA) was purchased from Lancaster Co. in 98% purity, which was further purified by dissolving in chloroform and then filtered to remove polymerized monomers before use. Dimyristoylphosphatidycholine (DMPC) was purchased from Sigma, and bovine serum albumin (BSA) was purchased from Beijing Reagent Co. *E.coli DH5*α was provided by Institute of Zoology of the Chinese Academy of Sciences. Sialic acid-acid-β-glucoside (G1) and lactose-β-glucoside (G2) receptors were synthesized according to previously reported procedures (*18*−*24*). The fragments of the influenza virus protein of Hemagglutinin on the cell surface (HA1) were obtained as reported (*25*−*29*), with details of abstraction and synthesis procedures given in the Supporting Information (SI).

Preparation of PDA Mixed Vesicles. The PDA vesicles were prepared according to literature procedures (*12, 17*). The typical procedure for the mixed vesicles preparation is as follows. The mixed components (PDA, DMPC, G1, G2) with various molecular fractions were dissolved in $CHCl_3$ followed by solvent evaporation. After adding 0.01 mol/L phosphate buffer (pH 6.9), the suspension (1 mmol L^{-1} of the mixed component) was probe sonicated for 5−6 min at approximately 80 °C. After the sonication, the solution was cooled to room temperature and then stored overnight at 4 °C to induce crystallization of lipid membranes. Polymerization was carried out under irradiation at 254 nm wavelength for 10 s. All vesicles used in our experiment have the same DMPC to PDA ratio of 4:6. The ratios of G1 and G2 in the vesicles were 1:0, 9:1, 7:3,

* Tel.: +86 10 82612084; fax: +86 10 82612084; E-mail jiangl@iccas.ac.cn.

[†] Chinese Academy of Sciences.

[‡] Tsinghua University.

10.1021/bc800453u CCC: $40.75 © 2009 American Chemical Society
Published on Web 02/23/2009

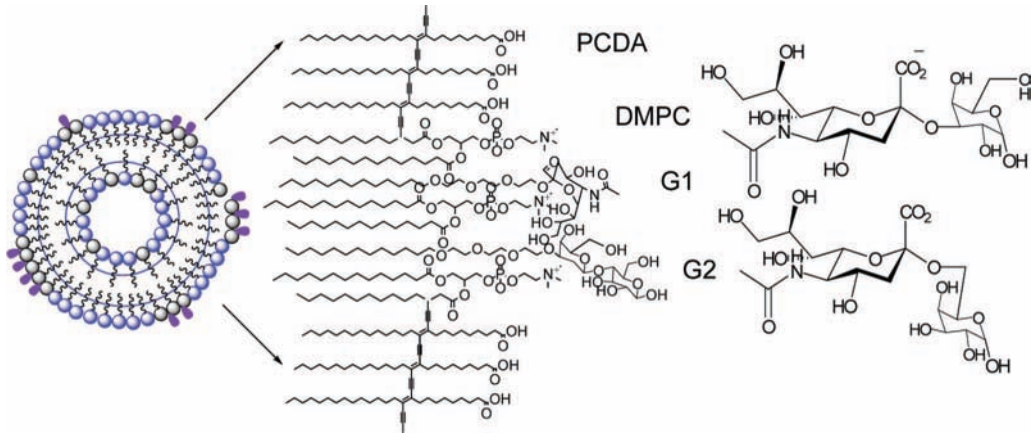

Figure 1. Schematic structure of the PDA vesicle functionalized with glicolipids: Receptors/DMPC/PDA assemblies (left) and the natural receptors found in the cell surface: α-Neu5Ac(2−3)-β-Gal,α-Neu5Ac(2−6)-β-Gal (right).

5:5, 3:7, 1:9, and 0:1, respectively, and the total molar ratio of (G1+G2) to PDA to DMPC is 0.2:6:4.

UV−vis Spectroscopy. Measurement of UV−vis spectra for the mixed lipid vesicles in water were carried out using a two-beam Hitachi U2800 UV−vis spectrometer. The pH of the vesicle solutions was maintained at 6.9 with phosphate buffer. During the measurement, a certain amount of aqueous analyte solution was injected stepwise into the vesicle solution with a syringe. All measurements were carried out at 35 °C.

Colorimetric transition from blue to red was monitored quantitatively by the colorimetric response (CR), which is defined as (*2, 11, 17*)

$$CR = [(PB_0 - PB_f)/PB_0] \times 100\% \quad (1)$$

where $PB = A_{blue}/(A_{blue} + A_{red})$, and A_{blue} and A_{red} are the absorbances of the blue component ($\lambda_{max} \approx 650$ nm) and the red component ($\lambda_{max} \approx 540$ nm) in the UV−vis spectrum; PB_0 and PB_f are the initial and final percentages of the blue component in the vesicle solution before and after adding the analyte, respectively.

RESULTS AND DISCUSSION

The design of a new system for rapid detection of interfacial biomolecular interactions in general, and receptor−ligand recognition in particular, has to fulfill two main objectives. First, the system structure should allow the interaction event to take place readily. Second, the specific interactions between the receptor and the ligand should be easily transformed into a quantified chemical or physical signal, such as transferring the conjugation event into a color change. The Vesicle-(G1+G2) we have designed, shown schematically in Figure 1, satisfies the above two requirements.

We synthesized glycolipids with sialic acid (G1) and lactose (G2), respectively, and designed the headgroups pointing outward from the PDA vesicle surface in order to assemble them to form an analogue to the complicated influenza virus H5N1 receptors where sialic acid linked to galactose by α-2,3 linkage [α-Neu5Ac(2−3)-β-Gal] and α-2,6 linkage [α-Neu5Ac(2−6)-β-Gal], the minimal recognition site for the HA1 (*25*). In our experiment, galactose is replaced by lactose, because the lactose is composed of two galactoses so that a "trap" with sialic acid to HA1 can be formed. In order to make the glycolipids extend in water, a tetraethylene glycol spacer was chosen as linker; G1 and G2 both ended with a C_{12} hydrocarbon chain for the immobilization to the vesicles.

It has been found that local dimyristoylphosphatidylcholine (DMPC) domains incorporated into PDA vesicles not only increase the detection sensitivity, but also open a new avenue for lipophilic biological molecules physically inserting the mixed vesicles. DMPC was used as a component of vesicles. The molar ratio of glycolipid/DA/DMPC equals 0.2:6:4, where the glycolipids can be G1, G1+G2, or G2. A series of vesicles were prepared to study how the combined glycolipids affect the conjugation. In these vesicles, the ratio of G1 to G2 in the vesicles changes in the following way: 1:0, 9:1, 7:3, 5:5, 3:7, 1:9, and 0:1. After photopolymerization, the PDA mixed vesicles appeared to be clear blue to the naked eye and exhibited a maximal absorption at 640 nm, which is due to their backbone alternating ene−yne conjugated structure.

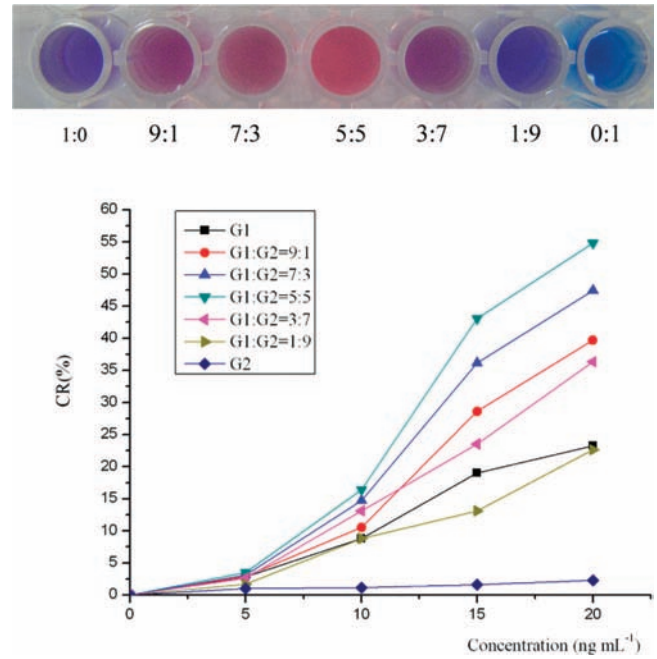

Figure 2. The color of the seven different vesicles with 20 ng mL^{-1} HA1, from left to right, with the ratio of G1 to G2 indicated (up), and the CR% of seven mixed vesicles with addition of different amount of HA1(down).

According to our experiment, the larger the concentration of DMPC in the vesicle, the more sensitive the PDA vesicle will be. However, if the amount of receptor G1+G2 or DMPC exceeds a certain threshold value, the blue-colored PDA vesicle could not be observed, which is believed to be due to the destruction of the effective conjugation length of the PDA backbone.

In Figure 2, the color of PDA vesicles functionalized with G1, G2, or G1+G2 shaded from blue into purple, amaranth,

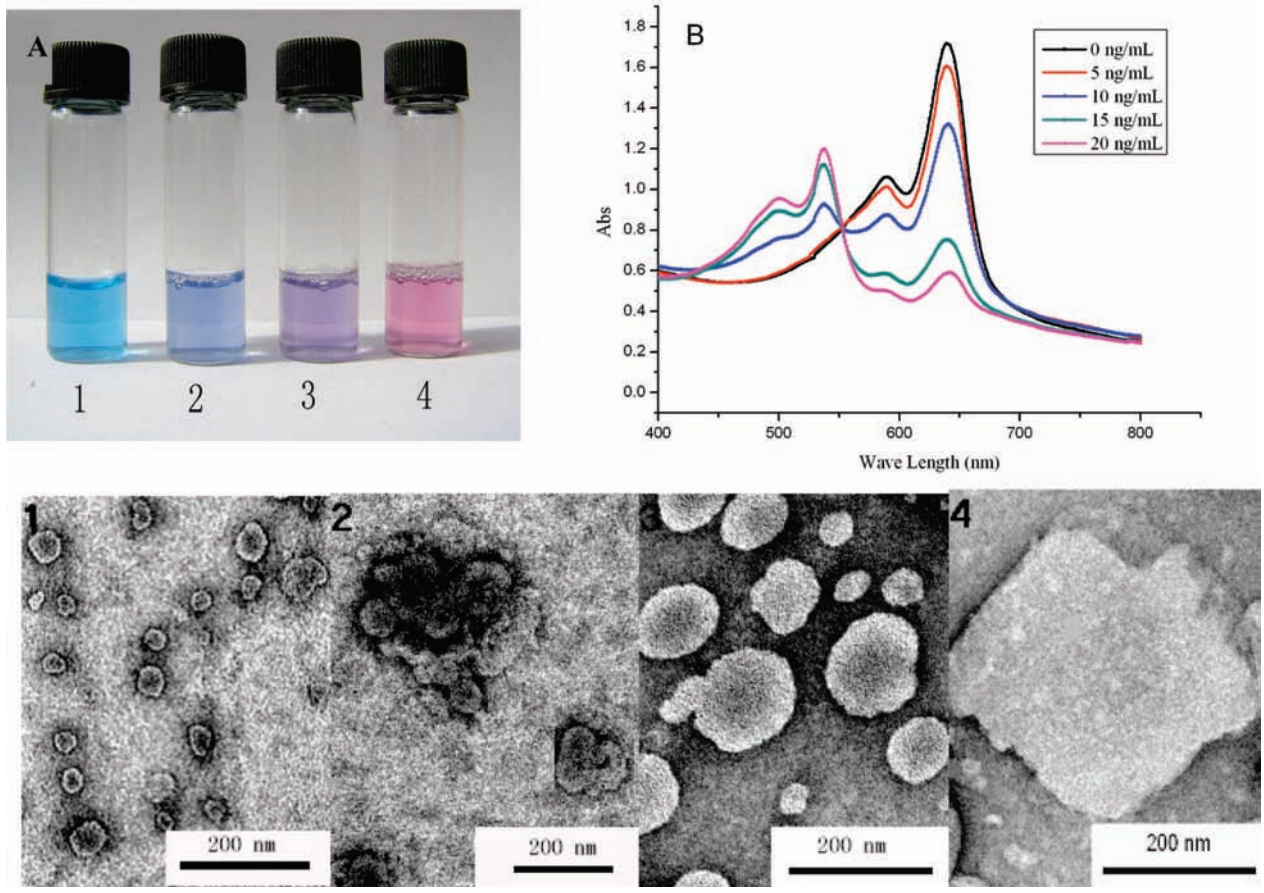

Figure 3. Interaction of vesicle-(G1+G2 = 5:5) with different amounts of HA1 in solution. (A) Photographs. (1) Control without HA1. (2) 5 ng mL^{-1}. (3) 10 ng mL^{-1}. (4) 20 ng mL^{-1}. (B) Visible adsorption spectra of vesicle-(G1+G2 = 5:5) solution mixed with HA1. (C)TEM images of vesicle-(G1+G2 = 5:5) solution tested with different concentration of HA1: (1) control. (2) 5 ng mL^{-1}. (3) 15 ng mL^{-1}. (4) 20 ng mL^{-1}.

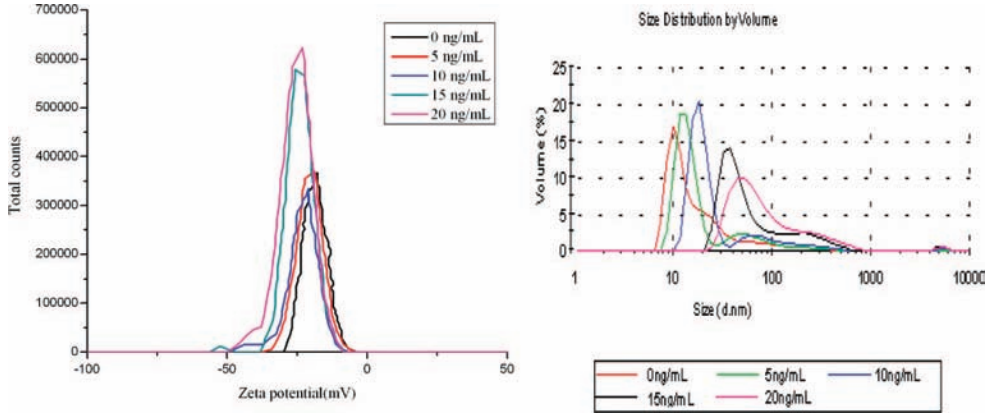

Figure 4. ζ potential and volume distribution of vesicles measured by using a Zetasizer, Nano ZS Malvern Instruments Ltd.

magenta, and red when the surface-assembled receptor was bound to different amounts of HA1. It is intriguing that the degree of the color change of the polymerized vesicles functionalized with G1 or G2 alone was much less than those functionalized with (G1+G2) when HA1 was added; vesicle-G1 underwent a color change from blue to purple as the HA1 concentration reached 20 ng mL^{-1}, whereas the color of vesicle-G2 still remained blue, meaning no conjugation occurred at all. On the other hand, vesicle-(G1+G2), especially G1/G2 = 5:5, causes a remarkabe color change even at a very low concentration of HA1 (ca. 10 ng mL^{-1}), showing a very strong synergistic effect for the recognition of virus HA1. This behavior can also be found in the change of CR% of seven mixed vesicle, as shown in Figure 3, where the value of CR is ordered as follows: vesicle-(G1/G2 = 5:5) > vesicle-(G1/G2 = 7:3) > vesicle-(G1/G2 = 3:7) > vesicle-(G1/G2 = 9:1) > vesicle-G ≈ vesicle-(G1/G2 = 1:9) > vesicle-G2 when 10 ng mL^{-1} HA1 was added. However, the value of CR of the vesicle-(G1/G2 = 9:1) is higher than that of the vesicle-(G1/G2 = 3:7) when HA1 was added from 15 ng mL^{-1} to 20 ng mL^{-1}. These results show that there is some synergistic effect between G1 and G2. It was reported previously (*2*) that lactose (receptor G2) is not a ligand for the hemagglutinin lectin, whereas sialoside (receptor G1) is the selective and sensitive one. To the best of our knowledge, this kind of synergistic effect and high sensitivity have not yet been reported previously.

Figure 3A,B shows the relationship between the color change and the visible absorption spectra of the vesicle-(G1/G2 = 5:5)

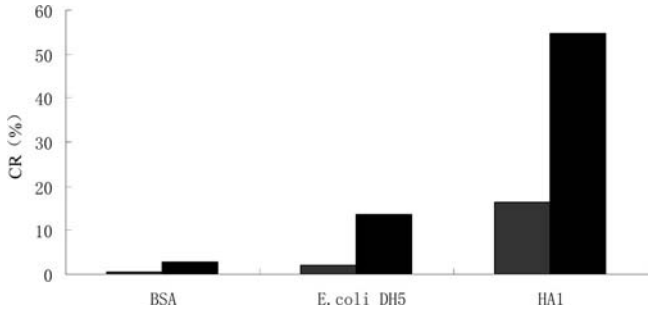

Figure 5. Absorbance difference at 640 nm of vesicle-(G1+G2) changed with different species of biomolecules: (1) BSA. Left: 10 ng mL^{-1}. Right: 25 ng mL^{-1}. (2) *E.coli DH5*. Left: 10 ng mL^{-1}. Right: 25 ng mL^{-1}. (3) HA1. Left: 10 ng mL^{-1}. Right: 20 ng mL^{-1} within 5 min.

as it encountered HA1. When the color changed, the absorption maximum at 640 nm decreased with a concurrent absorption increase in the maximum at 540 nm in visible absorption spectra. It is commonly accepted that the blue−red chromatic transitions observed in PDA can be attributed to the disturbance of the conjugation length of the polydiacetylene backbone. Our experiment showed that binding of the viral hemoglotinen to the glycolipids affects the vesicle conformation to a great extent, which was clearly demonstrated in the TEM picture (Figure 3C). TEM images demonstrated that the vesicle packing shape after recognition with HA1 is much different from that of its original form. As more HA1 adsorbed on the vesicle surface, the size of vesicles-(G1+ G2) grows bigger, accompanied by the shape change due to fusion from spherical to flat rectangular. This occurs presumably because of the interaction between the HA1 proteins on the vesicle surfaces.

Two interesting results were found in these experiments: (1) It is possible to form a highly sensitive biosensing element in the vesicle surface simply by inserting G1 and G2 into the PDA vesicle, thus providing an easy way to mimic the receptors containing multiple saccharide complex on the cell surface. (2) A very strong synergistic effect between sensitive receptor (G1) and nonsensitive receptor (G2) was observed, indicating the importance of the receptor combination effect for the ligand conjugation on the vesicle surface that was less known previously, thus providing us an open area for further investigation.

To gain a deeper insight into the property of the vesicle surface, electrophoresis experimentation for the ζ potential measurement was carried out. It was found that, after adding more HA1, the ζ potential of the vesicles-(G1+G2) gradually changed to a more negative and constant value as shown in Figure 4. In combination with the volume changing in TEM pictures showed in Figure 3, it is reasonable to assume that after conjugating with HA1, the receptor surface was gradually covered by HA1 and reached a constant ζ value mainly due to HA1 no matter how large the vesicle was. TEM and CR measurements show that the agglomeration of particles still continued by the increase of HA1 concentration caused by the interaction between proteins on the vesicle surfaces or protein fragments in the bulk, which further made the aggregate volume and morphology change, and caused CR% to increase, respectively.

In order to further assess the color response due to nonspecific adhesion of the vesicles, some large biomolecules such as *E.coli DH5*α and bovine serum albumin were tested as controls. It appears that these molecules do not cause any vesicle color change even for a long time (at least 5 min) as shown in Figure 5. This is completely different from the case of vesicle-(G1+G2), whose color change from deep blue to amaranth or red may occur within less than 5 min when treated with HA1 10 ng mL^{-1} or 20 ng mL^{-1}. Together, our results show that vesicles-(G1+G2) prepared in this manner are promising candidates for biosensors. It shows very good specificity, high sensitivity, and short respondent time, thus being of great significance in its application in influenza virus H5N1 diagnosis.

CONCLUSIONS

This study describes an approach to the preparation of an effective biosensor for HA1 recognition on a chromatic vesicle surface based on a molecular assembly technique. It overcomes the limitation of current synthesis methods, which were known to be both complicated and difficult. The colorimetric assay is robust and easy to carry out, yielding results that are much faster and more sensitive than commonly used traditional biochemical techniques. Although the exact mechanism of the synergistic effect is not clear yet, the phenomenon itself has already shown great significance in application. Further study of the mechanism of this finding and its applicability by assembling glycolipids to improve the sensitivity in bioconjugate events shall be an attractive area in the future. Our results also show that, in combination with the self-assembly technology, the chromatic vesicle protocol could be utilized as a platform for various biochemical applications, such as for new drug metabolism and for pharmacokinetics of the H5N1 virus, including the establishment of a receptor library for disease diagnostics.

ACKNOWLEDGMENT

This research is supported by the Chinese Academy of Sciences and National Natural Science Foundation of China (grant numbers 90206035, 20503036). We thank Prof. Jianping Wang for thoughtful review of the manuscript.

Supporting Information Available: Experimental procedures, synthesis of sialic acid-β-glucoside (G1) and lactose-β-glucoside (G2), expression and purification of HA1 and preparation of PDA mixed vesicles. This material is available free of charge via the Internet at http://pubs.acs.org.

LITERATURE CITED

(1) Mallouk, T., and Harrison, D. J. (1993) *Interfacial design and chemical sensing*, American Chemical Society, Washington, DC.
(2) Charych, D. H., Nagy, J. O., Spevak, W., and Bednarski, M. D. (1993) Direct colorimetric detection of a receptor-ligand interaction by a polymerized bikayer assembly. *Science 261*, 585–588.
(3) Reichert, A., Nagy, J. O, Spevak, W., and Charych, D. (1995) Polydiacetylene liposomes functionalized with sialic acid bind and colorimetrically detect influenza virus. *J. Am. Chem. Soc. 117*, 829–830.
(4) Kim, K. -W., Choi, H., Lee, G. S., Ahn, D. J., Oh, M. -K., and Kim, J. -M. (2006) Micro-patterned polydiacetylene vesicle chips for detecting protein-protein interactions. *Macromol. Res. 14*, 483–485.
(5) Jelinek, R., Okada, S., Norvez, S., and Charych, D. (1998) Interfacial catalysis by phospholipases at conjugated lipid vesicles: colorimetric detection and NMR spectroscopy. *Chem. Biol. 5*, 619–629.
(6) Okada, S., Peng, S., Spevak, W., and Charych, D. (1998) Color and chromism of polydiacetyl ene vesicles. *Acc. Chem. Res. 31*, 229–239.
(7) Kolusheva, S., Boyer, L., and Jelinek, R. (2000) Colormetric assay for rapid screening of antimicrobial peptides. *Nat. Biotechnol. 18*, 225–227.
(8) Satchell, D. P., Sheynis, T., Shirafuji, Y., Kolusheva, S., Ouellette, A. J., and Jelinek, R. J. (2003) Interactions of mouse paneth cell α-defensins and α-defensin precursors with membranes. *J. Biol. Chem. 278* (16), 13838–13846.

(9) Kolusheva, S., Shahal, T., and Jelinek, R. (2000) Cation-selective color sensors composed of ionophore- phospholipid-polydiacetylene mixed vesicles. *J. Am. Chem. Soc. 122*, 776–780.

(10) Gill, I., and Ballesteros, A. (2003) Immunoglobulin-polydiacetylene sol-gel nanocomposites as solid-state chomatic biosensors. *Angew. Chem., Int. Ed. Engl. 42*, 3264–3267.

(11) Kolusheva, S., Kafri, R., Katz, M., and Jelinek, R. (2001) Rapid colorimetric detection of antibody-epitope recognition at a biomimetic membrane interface. *J. Am. Chem. Soc. 123*, 417–422.

(12) Su, Y. L., Li, J. R., Jiang, L., and Cao, J. (2005) Biosensor signal amplification of vesicles functionalized with glycolipid for colorimetric detection of *Escherichia coli*. *Colloid Interface Sci. 284*, 114–119.

(13) Trester-Zedlitz, M., Kamada, K., Burley, S. K., Fenyo, D., Chait, B. T., and Muir, T. W. (2003) A modular cross-linking approach for exploring protein interactions. *J. Am. Chem. Soc. 125* (9), 2416–2425.

(14) Jelinek, R., and Kolusheva, S. (2001) Polymerized lipid vesicles as colorimetric biosensors for biotechnological applications. *Biotechnol. Adv. 19*, 109–118.

(15) Pan, J. J., and Charych, D. (1997) Molecular recognition and colorimetric detection of cholera toxin by poly(diacetylene) liposomes incorporating G_{m1} Ganglioside. *Langmuir 13*, 1365–1367.

(16) Jung, Y. K., Park, H. G., and Kim, J, M. (2006) Polydiacetylene (PDA)-based colorimetric detection of biotin-streptavidin interactions. *Biosens. Bioelectron. 21*, 1536–1544.

(17) Ma, Z. F., Li, J. R., Liu, M. H., Cao, J., Zou, J. Y., Zhou, J., and Jiang, L. (1998) Colorimetric detection of *Escherichia coli* by polyacetylene visicles functionalized with glycolipid. *J. Am. Chem. Soc. 120*, 12678–12679.

(18) Lu, S.-F., O'yang, Q., Guo, Z.-W., Yu, B., and Hui, Y.-Z. (1997) Total synthesis of tricolorin A. *J. Org. Chem. 62*, 8400–8405.

(19) Baughman, T. W., Sworen, J. C., and Wagener, K. B. (2004) The facile preparation of alkenyl metathesis synthons. *Tetrahedron 60*, 10943–10948.

(20) Wrigley, A. N., Stirton, A. J., and Howard, E. (1960) Higher alkyl monoethers of mono- to tetraethylene glycol2a,b. *J. Org. Chem. 25*, 439–444.

(21) Katsuraya, K., Nakashima, H., Yamamoto, N., and Uryu, T. (1999) Synthesis of sulfated oligosaccharide glycosides having high anti-HIV activity and the relationship between activity and chemical structure. *Carbohydr. Res. 315*, 234–242.

(22) Ikeda, K., Nagao, Y., and Achiwa, K. (1992) Synthesis of sialic acid-containing nucleotide sugars: CMP-sialic acid analogs. *Carbohydr. Res. 224*, 123–131.

(23) Chatterjee, S. K., and Nuhn, P. (1998) Stereoselective α-glycosidation using $FeCl_3$ as a Lewis acid catalyst. *Chem. Commun. 1998*, 1729–1730.

(24) Ogura, H., Furuhata, K., Itoh, M., and Shitori, Y. (1986) Syntheses of 2-O-glycosyl derivatives of N-acetyl--neuraminic acid. *Carbohydr. Res. 158*, 37–51.

(25) Wiley, D. C., Wilson, I. A., and Skehel, J. J. (1981) Structural identification of the antibody-binding sites of Hong Kong influenza haemagglutinin and their involvement in antigenic variation. *Nature 289*, 373–378.

(26) Johansson, B. E., Bucher, D. J., and Kilbourne, E. D. (1989) Purified influenza virus hemagglutinin and neuraminidase are equivalent in stimulation of antibody response but induce contrasting types of immunity to infection. *J. Virol. 63*, 1239–1246.

(27) Gibbs, M. J., Armstrong, J. S., and Gibbs, A. J. (2001) Recombination in the hemagglutinin gene of the "1918 spanish Flu". *Science 293*, 1842–1845.

(28) Cregg, J. M., Barringer, K. J., Hessler, A. Y., and Madden, K. R. (1985) Pichia pastoris as a host system for transformations. *Mol. Cell. Biol. 5*, 3376–3385.

(29) Rodriguez, E., Han, Y., and Lei, X. G. (1999) Cloning, sequencing, and expression of an Escherichia coli acid phosphatase/phytase gene (appA2) isolated from pig colon. *Biochem. Biophys. Res. Commun. 257*, 117–123.

(30) Wilson, J, C., and Itzstein, M. V. (2003) Recent strategies in the search for new anti-influenza therapies. *Curr. Drug Targets 4*, 389–408.

BC800453U

Supporting information for

“Construction of effective receptor for recognition of avian influenza H5N1 protein HA1 by assembly of mono-head glycolipids on polydiacetylene vesicle surface”

Jieli Deng[†], Zhonghan Sheng[†], Kai Zhou[‡], Mingxing Duan[*‡], Chu-Yi Yu[*†], Long Jiang[*†]

Synthesis of sialic acid- β -glucoside (G1) **2-5page**

Synthesis of lactose- β -glucoside(G2) **6-8page**

Express and purification of HA1 **9-10page**

[*] Tel.: +86 10 82612084; fax: +86 10 82612084
jiangl@iccas.ac.cn

Synthesis of sialic acid- β -glucoside (G1):

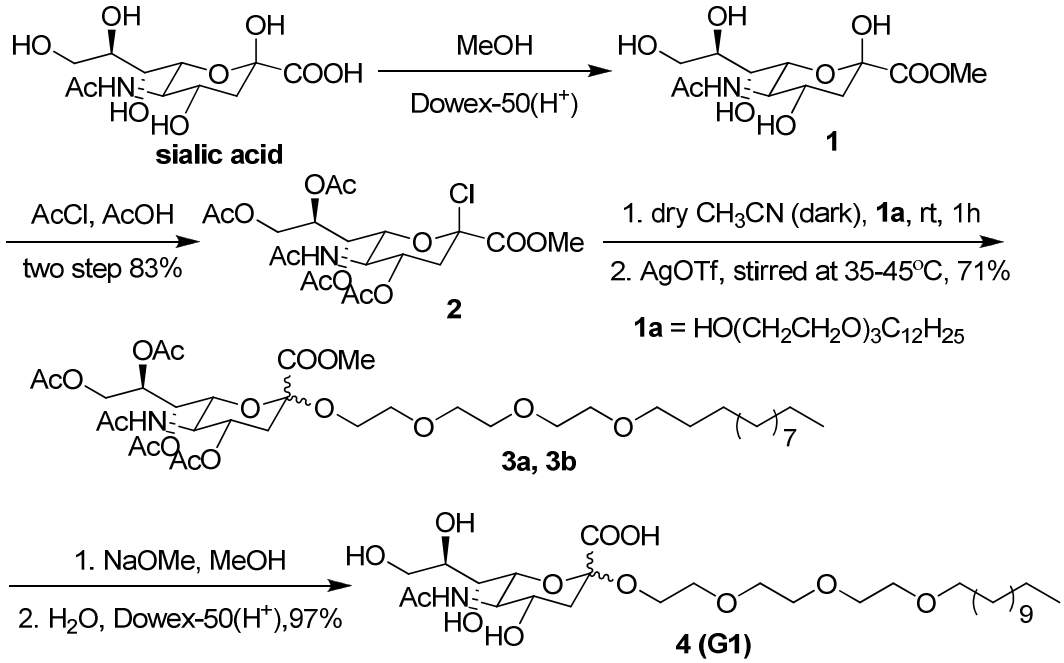

Figure S1. Schematic diagram for the synthesis of glycolipid **G1**

Preparation of Methyl 5-acetamido-3,5-dideoxy-D-glycero-D-galacto-2-nonulopyranosonate **1**:

N-acetylneuraminate (5.0g) was dissolved in MeOH (50 ml). The H^+ ion exchange resin (10.0g) was added at room temperature. After 40 h, the solution was filtrated and the resin was washed by MeOH, the organic layer was concentrated to afford the desired product **1** white solid (4.35g, 83% yield).

R_f=0.60 (EA:MeOH=1:1)

Preparation of

5-Acetamido-4,7,8,9-tetra-O-acetyl-2-chloro-2,3,5-trideoxy-D-glycero-β-

D-galacto-2-nonulosonic acid methyl ester **2**:

A mixture of acetyl chloride (70 ml) and acetic acid (35 ml) was cooled to 0 ℃. **1** (3.55 g) was added. The reaction was stirring at room temperature for 48 h. The reaction solution was concentrated to yield compound **2** as a white solid (3.70 g, 83% yield).

R_f=0.50(EA)，melting point: 65 ℃–67 ℃. ^{1}HNMR ($CDCl_3$, 300MHz) δ 5.90 (d, *J*=10.2,1H), 5.41-5.52 (m, 4H), 5.18 (br, 1H), 4.36-4.43 (m, 2H), 4.20-4.24 (m, 2H), 4.09 (m, 1H), 3.90 (s, 3H), 3.80-3.82 (m, 2H), 2.79 (dd, *J*=4.8, 13.8, 1H), 1.92-2.23 (m, 18H) ppm. ^{13}C NMR (300MHz, $CDCl_3$): δ 175.45, 171.00, 170.78, 170.68, 169.98, 169.84, 165.59, 96.62, 73.86, 70.14, 68.80, 65.95, 62.12, 48.62, 40.59, 22.99, 20.88, 20.80, 20.73, 20.68, 20.65 ppm.

Preparation of 5-Acetamido-4,7,8,9-tetra-O-acetyl-2-(diethylene glycol mono-dodecyl ethyl) -3,5-dideoxy-D-glycero-D-galacto-2-nonulosonic acid methyl ester **3a-3b**:

Compound **2** (0.50 g), 4Å molecular sieve (1.0 g) and triethylene glycol mono-dodecyl ether (0.62 g) was mixed in dry CH_3CN (20 ml), and stirred for 1h at room temperature. The TfOAg (0.50 g) was added in the dark at 35-40 ℃. After 72h, the reaction was stopped and the insoluble solids in reaction mixture were removed by filtration. The organic layer

was washed by saturated $NaHCO_3$ aq, saturated $Na_2S_2O_3$ aq and saturated brine, dried by anhydrous sodium sulfate. The resulting crude mixture of products were separated and purified by column chromatography to afford two pure isomers (**3α:**21% yield, **3β**:21% yield).

α-Isomer **3a**

R_f=0.31(PE:acetone=2:1). ^{1}HNMR ($CDCl_3$, 300MHz): δ 5.36-5.41 (m, 1H), 5.30-5.33 (m, 1H), 5.24-5.27 (m, 1H), 4.81-4.920 (m, 1H), 4.31 (dd, *J*=2.4, 12.4, 1H), 4.00-4.12 (m, 2H), 3.87-3.93 (m, 1H), 3.80 (s, 3H), 3.56-3.65 (m, 9H), 3.42-3.50 (m, 3H), 2.62 (dd, *J*=4.5, 12.9, 1H), 1.81-2.14 (m, 16H), 1.53-1.60(m, 2H), 1.26(br, 18H), 0.86-0.90 (m, 3H) ppm. ^{13}C NMR (300MHz, $CDCl_3$): δ 170.98, 170.60, 170.19, 170.12, 170.00, 168.29, 98.82, 72.48, 71.55, 70.61, 70.56, 70.54, 70.10, 70.05, 69.11, 67.35, 64.50, 62.37, 52.71, 49.45, 31.89, 29.61, 29.59, 29.48, 29.32, 26.08, 23.16, 22.66, 21.07, 20.81, 20.73, 14.08 ppm. MALDITOF-MS: *m/z* 792.4376 $[M + H]^+$ Calcd for $C_{38}H_{66}O_{16}N$: 792.4382.

β-Isomer **3b**

R_f= 0.24 (PE:acetone=2:1). ^{1}HNMR ($CDCl_3$, 300MHz): δ 6.40 (d, *J*=10.2, 1H), 5.31-5.33 (m, 1H), 5.23-5.27 (m, 1H), 5.11-5.22 (m, 1H), 4.82 (dd, *J*=2.4, 12.4, 1H), 4.55 (dd, *J*=2.1, 10.8), 4.01-4.08 (m, 2H), 3.46-3.80 (m,

15H), 3.36 (t, J=6.9, 2H), 2.37 (dd, *J*=5.1, 12.9, 1H), 2.07(s, 3H), 1.93-1.99 (m, 9H), 1.75-1.83 (m, 4H), 1.46-1.51(m, 2H), 1.19 (br, 18H), 0.76-0.83(m, 3H) ppm. ^{13}C NMR (300MHz, $CDCl_3$): δ 170.46, 170.42, 170.37, 170.08, 167.47, 97.72, 72.09, 71.33, 70.63, 70.19, 69.85, 69.77, 69.45, 68.57, 62.75, 62.65, 52.48, 37.12, 31.80, 29.54, 29.51, 29.44, 29.38, 29.23, 25.98, 22.81, 22.57, 20.86, 20.70, 13.99 ppm. MALDITOF-MS: *m/z* 815.4216 $[M + Na]^+$ Calcd for $C_{38}H_{66}O_{16}NNa$: 815.4279.

Preparation of

(2-(triethylene glycol mono-dodecyl ethyl) -3,5-dideoxy-D-glycero-β-D-galacto- 2-nonulosonic acid **4** (**G1**): 80mg of **3β** was dissolved in dry MeOH (2mL), and NaOMe (1M in MeOH, 20μL) was added. After 5 h, water (2 mL) and NaOMe (1M in MeOH, 50μL) was added. After 4h, the H^+ ion exchange resin (1.0g) was added, stirring for 10min. The reaction mixture was filtrated and the filtrate was concentrated to give the desired product **4** (**G1**) as colorless oil (50mg, 97% yield).

^{1}HNMR ($CDCl_3$, 300MHz): δ 3.34-3.84 (m, 23H), 3.20-3.22 (m, 1H), 2.60 (dd, *J*=3.9, 12.3, 1H), 1.90 (s, 3H), 1.42-1.49 (m, 2H), 1.19 (br, 18H), 0.78-0.82(m,3H) ppm. ^{13}C NMR (300MHz, $CDCl_3$): δ 175.20, 170.90, 100.22, 72.47, 72.42, 71.63, 71.58, 71.56, 71.24, 71.19, 64.76, 64.71,

53.82, 53.48, 33.11, 30.82, 30.78, 30.63, 30.50, 27.24, 23.77, 22.77, 14.52 ppm. MALDITOF-MS: *m/z* 610.3799[M + H]$^+$ Calcd for $C_{29}H_{56}O_{12}N$: 610.3803.

Preparation of lactose- β -glucoside(G2)

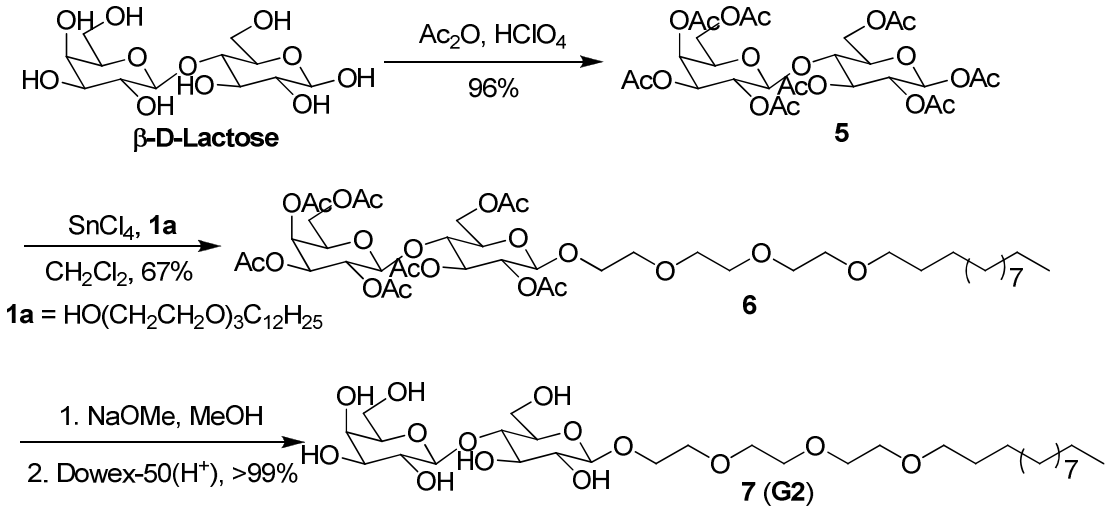

Figure S2. Schematic diagram for the synthesis of glycolipid **G2**

Preparation of β-D-Lactose octylacetate **5**:

$HClO_4$ (3 drops, 70% aq.) was added dropwise to acetic anhydride (20 ml) at 0℃, and β-D-Lactose (5.0g) was the added to the solution under stirring. After stirring at room temperature for 3h, the solution was diluted with CH_2Cl_2 (20 mL), and then poured into ice water (40 mL). The organic layer was washed by $NaHCO_3$ and brine, dried by anhydrous sodium sulfate. The resulting crude product was purified by column

chromatography (96% yield). R_f=0.33 (PE:EA=1:1)

Preparation of triethylene glycol mono-dodecyl ethyl heptacetyl β-D-Lactoside **6** :

The molecular sieve (1.0 g) was added to the solution of triethylene glycol mono-dodecyl ether (0.45 g) and **5** (0.50 g) in CH_2Cl_2 under argon. After 20min, $SnCl_4$ (0.17mL) was added at 35 ℃. After 2 days, the reaction was stopped and the reaction mixture was filtered. The filtrate was washed by saturated NH_4Cl aq, saturated $NaHCO_3$ aq and saturated brine, dried by anhydrous sodium sulfate. The crude product was purified by column chromatography (67% yield).

R_f=0.14(PE:acetone=3:1). ^{1}HNMR ($CDCl_3$, 300MHz): δ 5.34 (d, J=1.8, 1H), 5.07-5.22 (m, 2H), 4.86-4.98 (m, 2H), 5.56 (d, J=11.1, 1H), 4.46-4.50 (m, 2H), 4.07-4.13 (m, 3H), 3.56-5.93 (m, 15H), 3.42-3.46 (m, 2H), 2.17 (s, 3H), 2.15(s, 3H), 2.04-2.06 (m, 12H), 1.96 (s, 3H), 1.56-1.59 (m, 2H), 1.26 (br, 18H), 0.86-0.90 (m, 3H) ppm. ^{13}C NMR (300MHz, $CDCl_3$): δ 170.27, 170.05, 169.95, 169.66, 169.57, 168.98, 101.03, 100.62, 72.84, 71.49, 70.97, 70.68, 70.61, 70.57, 70.22, 70.02, 69.04, 60.80, 31.86, 29.60, 29.55, 29.43, 29.28, 26.05, 22.62, 20.78, 20.74, 20.62, 30.54, 20.42, 14.04 ppm. MALDITOF-MS: *m/z* 959.4458 $[M + H]^+$ Calcd for $C_{44}H_{72}O_{21}Na$: 959.4464.

Preparation of triethylene glycol mono-dodecyl ethyl β-D-Lactoside **7** (**G2**):

6 (340mg) was dissolved in MeOH (10ml), and then NaOMe (1M in MeOH, 100μL) was added to the solution. After the reaction solution had been stirred for 24 h, H^+ ion exchange resin (1.0g) was added to the solution, stirring for another 20min. The reaction mixture was then filtered and the filtrate was concentrated to yield the desired product **7** (**G2**) as white solid (99% yield).

R_f=0.5(EA:MeOH=3:1)，熔点 160 ℃ --161 ℃

^{1}HNMR($CDCl_3$, 300MHz): δ 4.37 (t, J=6.9, 2H), 3.26-4.07 (m, 26H), 3.31-3.33 (m, 3H), 1.56-1.60 (m, 2H), 1.31 (br, 18H), 0.89-0.94 (m, 3H) ppm. ^{13}C NMR (300MHz, $CDCl_3$): δ 105.14, 104.35, 80.74, 77.10, 76.52, 76.33, 74.88, 72.58, 72.42, 71.54, 71.50, 71.17, 70.33, 69.78, 62.50, 33.08, 30.75, 30.60, 30.47, 27.23, 23.74, 14.46 ppm. MALDITOF-MS: *m/z* 643.3899 $[M + H]^+$ Calcd for $C_{30}H_{59}O_{14}$: 643.3905.

Express and purification of HA1

Construction of the expression plasmid. The HA1 gene (Figure S3) was cloned from HA full-length gene with PCR method and then was inserted separately into pET21b vector with T4 DNA ligase. Proper

construction of the final vector pET21b-HA1 was verified by restriction analysis and DNA sequencing. Transformation of BL21 was achieved by $CaCl_2$ with pET21b-HA1 and pET21b (negative control). The recombinant BL21 with pET21b-HA1 was inducted with 0.1mmol L^{-1} IPTG in 37ºC for 2.5 hours. After that, the culture supernatant and cells were separated by centrifugation at 12000 rpm for 5 min and frozen in -20 ºC. Ni-ATA column was used for purification of culture supernatant and cells. The supernatant of E.coli BL21 was analyzed with 12% SDS–PAGE according to an established protocol. Then total proteins were resolved on a 12% SDS-polyacrylamide gel and transferred onto a nylon membrane and incubated with avian influenza positive antigens, followed by incubation with rabbit conjugated anti-chicken IgG secondary antibody (Sigma). The DNA sequence of HA1 is shown in Figure S3.

HA1-3→gggaagctctgc→gatctaaatggagtgaagcctctcattttgagagattgtagtgtagctggatggctcctc
ggaaaccctatgtgtgacgaattcatcaatgtgccggaatggtcttacatagtggagaaggccagtccagccaatgacctct
gttacccaggggatttcaacgactatgaagaactgaaacacctattgagcagaacaaaccattttgagaaaattcagatcatc
cccaaaagttcttggtccaatcatgatgcctcatcaggggtgagctcagcatgtccataccatgggaggtcctccttttttcaga
aatgtggtatggcttatcaaaaagaacagtgcatacccaacaataaagaggagctacaataataccaaccaagaagatcttt
tagtactgtgggggattcaccatcctaatgatgcggcagagcagacaaagctctatcaaaacccaaccacttacatttccgtt
ggaacatcaacactgaaccagagattggttccagaaatagctactagacccaaagtaaacgggcaaagtggaagaatgg
agttcttctggacaattttaaagccgaatgatgccatcaatttcgagagtaatggaaatttcattgctccagaatatgcatacaa
aattgtcaagaaaaggggactcagcaattatgaaaagtgaattggaatatggtaac←tgcaacaccaag←HA1-3

Figure S3. The DNA sequence of the HA1

Bioconjugate Chemistry 20th Anniversary

Subscriber access provided by SHEMYAKIN-OVCHINNIKOV INST

Article

Chemoenzymatic Synthesis of Sialoglycopolypeptides As Glycomimetics to Block Infection by Avian and Human Influenza Viruses

Makoto Ogata, Kazuya I. P. J. Hidari, Takeomi Murata, Shizumi Shimada, Wataru Kozaki, Enoch Y. Park, Takashi Suzuki, and Taichi Usui

Bioconjugate Chem., **2009**, 20 (3), 538-549• DOI: 10.1021/bc800460p • Publication Date (Web): 12 February 2009

Downloaded from http://pubs.acs.org on May 8, 2009

More About This Article

Additional resources and features associated with this article are available within the HTML version:

- Supporting Information
- Access to high resolution figures
- Links to articles and content related to this article
- Copyright permission to reproduce figures and/or text from this article

View the Full Text HTML

ACS Publications
High quality. High impact.

Bioconjugate Chemistry is published by the American Chemical Society. 1155 Sixteenth Street N.W., Washington, DC 20036

Chemoenzymatic Synthesis of Sialoglycopolypeptides As Glycomimetics to Block Infection by Avian and Human Influenza Viruses

Makoto Ogata,[△,†] Kazuya I. P. J. Hidari,[△,‡] Takeomi Murata,[†] Shizumi Shimada,[‡] Wataru Kozaki,[§] Enoch Y. Park,[†] Takashi Suzuki,[‡] and Taichi Usui*[,†]

Department of Bioscience, Graduate School of Science and Technology, Shizuoka University, Ohya 836, Suruga ward, Shizuoka 422-8529, Japan, Department of Biochemistry, University of Shizuoka, School of Pharmaceutical Sciences and Global COE Program, and Department of Applied Biological Chemistry, Faculty of Agriculture, Shizuoka University. Received October 23, 2008; Revised Manuscript Received December 31, 2008

We designed a series of γ-polyglutamic acid (γ-PGA)-based glycopolypeptides carrying long/short α2,3/6 sialylated glycans to act inhibitors of the influenza virus. As an alternative design, sialoglycopolypeptides carrying long-spacer linked glycans were engineered by replacement of the *N*-acetyllactosamine (LN) unit by an alkyl chain. The structure−activity relationship of the resulting sialoglycopolypeptides with different glycans in the array has been investigated by in vitro and in vivo infection experiments. The avian viruses specifically bound to glycopolypeptides carrying a short sialoglycan with higher affinity than to a long glycan. In contrast, human viruses, preferentially bound not only to long α2,3/6 sialylated glycan with LN repeats in the receptors, but also to more spacer-linked glycan in which the inner sugar has been replaced by a nonsugar structural unit such as a pentylamido group. Taken together, our results indicate that a spaced tandem/triplet pentylamido repeat is a good mimetic of a tandem/triplet LN repeat. Our strategy provides a facile way to design strong polymeric inhibitors of infection by avian and human influenza viruses.

INTRODUCTION

Influenza viruses infect host cells through the binding of viral hemagglutinins (HAs) to sialoglycoproteins or sialoglycopeptides of the receptors on the host cell surfaces (*1*−*3*). Because the molecular recognition process leads to the adhesion of host cell and virus, molecules having a high affinity for the viral HA act as potent inhibitors of infection by influenza viruses (*4*−*6*). Host cell specificity of the virus is dependent not only on linkage of sialic acids (SAs) to the penultimate galactose, but also on the number of SA residues and the precise nature of the core structure (*7*−*10*). The recognition ability of glycol signals is also known to be greatly enhanced by clustering the sialooligosaccharides on macromolecular scaffolds such as the synthetic glycopolymers (*6, 11*−*16*). The multivalent interactions have been amplified by the so-called glycoside cluster effects (*17*). Various factors are known to influence the affinity and specificity of multivalent binding events including the structure of the individual saccharide residues (*8*−*10*). In this respect, a variety of synthetic glycopolymers carrying multivalent sialooligosaccharides that target HAs have been produced for the influenza virus inhibitors using polyacrylamide (*11, 17*−*22*), poly(acrylacid) (*14, 23*), polystyrene (*12*), and dendrimers (*24*) as polymer backbone. However, synthetic glycopolymers potentially pose several problems for in vivo use, such as low solubility, significant cytotoxicity, and immunogenicity. We have already reported that sialoglycopolypeptides with α- or γ-PGA backbones can be used as a scaffold in the synthesis of multivalent inhibitors of the influenza viruses (*6, 9, 16*). Glycopolypeptides possessing either multivalent SAα2,3Gal or SAα2,6Gal have aided our understanding of human adaptation of the H5N1 influenza virus (*9*). The length of the asialo portion in glycopolypeptides also increased binding affinity to the viral HA in a glycan length-dependent manner (*8*). Recent studies using cocrystal structures with glycan microarrays also showed that human viral HAs specifically bound to long α2,6 sialylated glycans with a length beyond trisaccharide, whereas avian viral HAs bound to short α2,3 sialylated glycans (*25*). These findings indicate that glycan length of the receptors is another determinant of human viral HAs binding to the terminal α2,6 linked sialoside in the core glycan structures.

Thus far in these macromolecular approaches, the use of ligands has been limited to small carbohydrate units containing sialodi- or sialotrisaccharide. Spatial arrangement of the side chains is not usually considered during the design of the ligand. Our strategy of molecular design is to construct an amphiphilic structure, taking into account the contribution of the asialo portion of the glycan chain, by arranging multivalent short or long glycans attached to a polypeptide backbone. We therefore planned to chemoenzymatically synthesize a series of γ-PGA-based sialoglycopolymers carrying glycans or spacers of different lengths in the array, in order to identify the specific SA motifs recognized by the influenza virus. Using these glycopolymers, the structure−activity relationship was elucidated by measurement of the inhibition of infection by avian and human influenza viruses.

EXPERIMENTAL SECTION

Materials. γ-PGA-Na (MW 990 000) from *Bacillus subtilis* was a kind gift from Meiji Food Materia Co. UDP-GlcNAc, UDP-Gal, and CMP-Neu5Ac were gifts from Yamasa Corporation (Chiba, Japan). Bovine milk β1,4-galactosyltransferase (β4GalT), α2,3-(*N*)-sialyltransferase (α2,3SiaT, rat recombinant, *Spodoptera frugiperda*), and α2,6-(*N*)-sialyltransferase (α2,6SiaT, rat recombinant, *S. frugiperda*) were purchased from Calbiochem-Novabiochem (San Diego, CA). β1,3-*N*-Acetylglucosami-

* Corresponding author. Fax: +81-54-238-4873; e-mail: actusui@agr.shizuoka.ac.jp.
△ These authors contributed equally to this work.
† Shizuoka University.
‡ University of Shizuoka and Global COE Program.
§ Faculty of Agriculture, Shizuoka University.

10.1021/bc800460p CCC: $40.75 © 2009 American Chemical Society
Published on Web 02/12/2009

Table 1. Synthesis of Asialoglycopolypeptides with Different Degrees of Polymerization of Glutamic Acid Residues

products	compound	PGA[a] (mg)	BOP[b] (mg)	HOBt[c] (mg)	amino-sugar[d] (mg)	yield (mg)	DS[e] (%)
Poly[LNβ-O(CH2)5NH—/γ-PGA]	**16**	15	118	15	46	19	40
Poly[LNnTβ-O(CH2)5NH—/γ-PGA]	**17**	15	118	15	39	22	35
Poly[(LN)2β-O(CH2)5NH—/γ-PGA]	**18**	15	118	15	83	32	48
Poly[LNβ1,3LNnTβ-O(CH2)5NH—/γ-PGA]	**19**	15	118	15	58	28	31
Poly[(LN)3β-O(CH2)5NH—/γ-PGA]	**20**	15	118	15	119	39	44
Poly[LNβ-O(CH2)5NHCO(CH2)5NH—/γ-PGA]	**21**	35	276	34	79	42	47
Poly{LNβ-O[(CH2)5NHCO]2(CH2)5NH—/γ-PGA}	**22**	35	276	34	95	59	49

[a] γ-PGA: MW = 990 000. [b] Benzotriazol-1-yloxvtris-(dimethylamino)phosphonium hexafluorophosphate. [c] 1-Hydroxybenzotriazole hydrate. [d] 5-AP-β-LN for **16**, 5-AP-β-LNnT for **17**, 5-AP-β-$(LN)_2$ for **18**, 5-AP-β-LNβ1−3LNnT for **19**, 5-AP-β-$(LN)_3$ for **20**, 5-(5′-aminopentanecarboxamido)-pentyl β-LN for **21**, and 5-[5′-(5″-aminopentanecarboxamido)pentanecarboxamido]pentyl β-LN for **22**. [e] Degree of substitution of sugar derivatives based on DP of g-PGA as 100%. Calculated from ^{1}H NMR data at 25 °C.

nyltransferase (β3GnT) was prepared by our previously described methods (*26*). 5-Trifluoroacetamidopentyl β-lactoside (5-TFAP-β-Lac), 5-TFAP-β-LN, and 5-aminopentyl β-LacNAc (5-AP-β-LN) were synthesized by our previously described methods (*6*). The human and avian influenza virus strains used in this study were propagated and purified as described previously (*2, 27*). Viral hemagglutination units (HAUs) of purified viruses were determined as described previously (*28*). All other reagents were of the highest quality commercially available and were used without further purification.

Enzyme Assay. β3GnT activity was assayed as follows. UDP-GlcNAc (40 mM), LNβ-*p*NP (20 mM), and $MnCl_2$ (16 mM) were dissolved in 150 mM Tris-HCl (pH 6.8) followed by 100 μL of enzyme solution (total vol 200 μL). The reaction was started by addition of β3GnT. At each sample time, 10 μL of the reaction mixture was added to 190 μL of distilled water, followed by immediate boiling for 5 min. After filtration through a 0.45 μm nitrocellulose filter (Millipore, Bedford, MA), the filtrates were analyzed by HPLC using a TSK-gel ODS 80TsQA (4.6 × 250 mm, TOSOH Co.) column. Reaction products were eluted with 10% MeOH containing 0.1% TFA and detected at the absorbance of 300 nm. HPLC was done at 40 °C with a flow rate 1.0 mL/min. One unit of enzyme activity is defined as the amount of enzyme capable of catalyzing the transfer of 1 μmol of GlcNAc per minute.

β4GalT activity was assayed as follows. UDP-Gal (40 mM), GlcNAcβ1,3LNβ-*p*NP (20 mM), and $MnCl_2$ (16 mM) were dissolved in 150 mM Tris-HCl (pH 6.8) followed by 100 μL of enzyme solution (total vol 200 μL). The reaction was initiated by addition of β4GalT. At each sample time, 10 μL of the reaction mixture was added to 190 μL of distilled water, followed by immediate boiling for 5 min. After filtration through a 0.45 μm nitrocellulose filter (Millipore, Bedford, MA), the filtrates were analyzed by HPLC using a TSK-gel ODS 80TsQA (4.6 × 250 mm, TOSOH Co.) column. Reaction products were eluted with 10% MeOH containing 0.1% TFA and detected at the absorbance of 300 nm. HPLC was done at 40 °C with a flow rate 1.0 mL/min. One unit of enzyme activity is defined as the amount of enzyme capable of catalyzing the transfer of 1 μmol of Gal per minute.

HPLC Determination of Neutral Sugar Units in Asialoglycopolypeptides. The artificial asialoglycopolypeptides (0.02 μM, 250 μL) were hydrolyzed with 4 M trifluoroacetic acid (250 μL) at 100 °C for 4 h to release sugar units and the hydrolysates were then freeze-dried. In brief, to dry samples were added water (10 μL) and ethyl 4-aminobenzoate (ABEE) solution (40 μL). Derivatization was carried out at 80 °C for 1 h. The reaction mixture of ABEE derivatization in 10 μL portions was directly injected into a Honenpak C18 column (4.6 × 75 mm) and eluted using 10% CH_3CN containing 0.02% TFA. A JASCO LC-2000 plus HPLC system equipped with an UV-2070 plus UV detector (305 nm), operating isocratically at 1.0 mL/min at a column temperature of 45 °C, was used (Table 2) (*29*).

HPLC Determination of Sialic Acids in Sialoglycopolypeptides. The artificial sialoglycopolypeptides (0.1 μM, 5 μL) were hydrolyzed with 0.05 M HCl (45 μL) at 80 °C for 1 h to release sialic acid units. Next, the samples were added to a 1,2-diamino-4,5-methylenedioxybenzene (DMB) solution (200 μL). Derivatization was carried out at 50 °C for 2.5 h in the dark. All labeled compounds were kept at 4 °C in the dark to prevent degradation. The reaction mixture of DMB derivatization in 10 μL portions was directly injected into a Shodex ODP2 HP-4E column (4.6 × 250 mm, Shodex) and eluted with water/methanol/acetonitrile (84:7:9, v/v/v). A JASCO LC-2000 plus HPLC system equipped with an FP-2020 plus fluorescence detector (excitation, 373 nm; emission, 448 nm), operating isocratically at 0.5 mL/min at a column temperature of 40 °C, was used (Table 2) (*30*).

Analytical Methods. HPLC analysis was carried out using an Asahipak NH2-P50 4-E column (4.6 × 250 mm, Shodex) with a JASCO Intelligent system liquid chromatograph and detection at 210 nm. The bound material was eluted with 80% CH_3CN at a flow rate of 1.0 mL/min at 40 °C. FAB-mass analysis was carried out in positive ion mode using a JEOL JMS DX-303HF mass spectrometer coupled to a JEOL DA-800 mass data system. An accelerating voltage of 10 kV and a mass resolution of 1000 were employed. A sample in distilled water (1 μL) was loaded onto a probe tip and mixed with glycerol (1 μL) as a matrix. ^{1}H and ^{13}C NMR spectra were recorded on a JEOL JNM-LA 500 spectrometer at 25 °C. Chemical shifts are expressed in δ relative to sodium 3-(trimethylsilyl) propionate as an external standard. The amount of protein was determined using a Bio-Rad protein assay kit.

Synthesis of LN-Repeating Tetra- And Hexasaccharide Glycosides. 5-Trifluoroacetamidopentyl β-lacto-*N*-neotetraoside (5-TFAP-β-LNnT, **3**) was synthesized by the alternative addition of β1−3 linked GlcNAc and β1−4 linked Gal to 5-TFAP-β-Lac (**1**), using two kinds of glycosyltransferase. Compound **1** (300 mg, 0.56 mmol) and UDP-GlcNAc (725 mg, 1.11 mmol) were dissolved in 150 mM Tris-HCl buffer pH 6.8 (50.3 mL) containing $MnCl_2$ (88.2 mg) and 1% (w/v) NaN_3 (0.56 mL), followed by addition of 540 mU (4.8 mL) of partially purified β3GnT preparation from the cell culture supernatant. The mixture was incubated for 168 h at 37 °C, and the reaction was terminated by boiling for 5 min. UDP-Gal (679 mg, 1.11 mmol) was dissolved the mixture, followed by addition of 4 U (0.2 mL) of β4GalT from bovine milk. The mixture was incubated for 124 h at 37 °C, and the reaction was terminated by boiling for 5 min. The precipitate was removed by centrifugation (8000 *g*, 20 min) and the supernatant was loaded onto a ODS column (3.5 × 60 cm) equilibrated with 10% MeOH at flow rate of 2.0 mL/min. After washing the column with 1500 mL of 10% MeOH, absorbed portion was eluted with 20% MeOH and a fraction size of 25 mL/tube. The eluate was monitored by measuring the absorbance at 210 nm using a spectrometer. An aliquot from fractions 14−28 was then concentrated and lyophilized: compound **3** was obtained in a total yield of 90% (451 mg) based on the acceptor substrate **1**. $[\alpha]_D^{30}$ + 7.0° (*c*

Table 2. Glycopolypeptides Carrying LN-Repeating and Long-Spacer Linked Aminoalkyl Oligosaccharide Glycosides for Inhibition of Binding by Influenza Viruses

			DS (%)		
sugar moiety	spacer	compound	NS[a]	Sia[b]	kDa[c]
LNβ-	-O$(CH_2)_5$NH—	16	40[d] (33)[e]	—	2100
LNnTβ-	-O$(CH_2)_5$NH—	17	35 (30)	—	2700
$(LN)_2\beta$-	-O$(CH_2)_5$NH—	18	48 (45)	—	3500
LNβ1,3LNnTβ-	-O$(CH_2)_5$NH—	19	31 (28)	—	3300
$(LN)_3\beta$-	-O$(CH_2)_5$NH—	20	44 (44)	—	4300
LNβ-	-O$(CH_2)_5$NHCO$(CH_2)_5$NH—	21	47 (46)	—	2700
LNβ-	-O$[(CH_2)_5$NHCO$]_2(CH_2)_5$NH—	22	49 (40)	—	3100
SAα2,3LNβ-	-O$(CH_2)_5$NH—	23	0	40 (37)	2800
SAα2,3LNnTβ-	-O$(CH_2)_5$NH—	24	0	35 (32)	3400
SAα2,3$(LN)_2\beta$-	-O$(CH_2)_5$NH—	25	0	48 (45)	4400
SAα2,3LNβ1,3LNnTβ-	-O$(CH_2)_5$NH—	26	0	31 (33)	3900
SAα2,3(LN)3β-	-O$(CH_2)_5$NH—	27	0	44 (40)	5200
SAα2,3LNβ-	-O$(CH_2)_5$NHCO$(CH_2)_5$NH—	28	0	47 (48)	3600
SAα2,3LNβ-	-O$[(CH_2)_5$NHCO$]_2(CH_2)_5$NH—	29	0	49 (46)	4000
SAα2,6LNβ-	-O$(CH_2)_5$NH—	30	0	40 (39)	2800
SAα2,6LNnTβ-	-O$(CH_2)_5$NH—	31	0	35 (39)	3400
SAα2,6(LN)2β-	-O$(CH_2)_5$NH—	32	0	48 (48)	4400
SAα2,6LNβ1,3LNnTβ-	-O$(CH_2)_5$NH—	33	0	31 (33)	3900
SAα2,6(LN)3β-	-O$(CH_2)_5$NH—	34	0	44 (42)	5200
SAα2,6LNβ-	-O$(CH_2)_5$NHCO$(CH_2)_5$NH—	35	0	47 (44)	3600
SAα2,6LNβ-	-O$[(CH_2)_5$NHCO$]_2(CH_2)_5$NH—	36	0	49 (47)	4000

[a] Neutral sugar derivatives substituted. [b] Sialyl sugar derivatives substituted (=Sia contents). [c] Calculated kDa. [d] Degree of substitution of asialo- or sialo-sugar derivatives based on DP of γ-PGA as 100%. Calculated from ^{1}H NMR data at 25 °C. [e] Degree of substitution of asialo- or sialo-sugar derivatives based on DP of γ-PGA as 100%.Calculated from two type HPLC analyses (ABEE and DMB methods). (All data normalized to those of ^{1}H NMR.)

0.1, water). FAB-mass: *m*/*z* 889 $[M + H]^+$ (matrix: glycerol). ^{1}H NMR (D_2O, 500 MHz): δ 4.70 (d, 1H, $J_{1'',2''}$ 8.6 Hz, H-1″), 4.48 (d, 1H, $J_{1',2'}$ 8.0 Hz, H-1′), 4.47 (d, 1H, $J_{1,2}$ 8.0 Hz, H-1), 4.43 (d, 1H, $J_{1''',2'''}$ 7.6 Hz, H-1‴), 4.16 (1H, H-4′), 3.99−3.94 (2H, H-6b, H-6″b), 3.93 (1H, H-4‴), 3.91 (1H, H-αb), 3.87−3.63 (15H of sugar protons), 3.60−3.56 (4H, H-αa, H-5″, H-5, H-2′), 3.54 (dd, 1H, $J_{1'',2''}$ 8.6, $J_{2'',3''}$ 10 Hz, H-2″), 3.34 (t, 2H, H-ε), 3.29 (t, 1H, $J_{1,2}$ 8.0, $J_{2,3}$ 8.0 Hz, H-2), 2.03 (s, 3H, C<u>H</u>$_3$CONH″-), 1.66 (q, 2H, H-β), 1.61 (q, 2H, H-ω), 1.40 (q, 2H, H-γ). ^{13}C NMR (D_2O, 500 MHz): δ 177.7 (CH_3<u>C</u>ONH″-), 161.6 (CF_3<u>C</u>O), 118.8 (<u>C</u>F_3CONH—), 105.8 (C-1‴), 105.7 (C-1′), 105.6 (C-1″), 104.8 (C-1), 84.9 (C-3′), 81.2 (C-4), 81.0 (C-4″), 78.2 (C-5‴), 77.7 (C-5′), 77.6 (C-5), 77.4 (C-5″), 77.2 (C-3), 75.6 (C-2), 75.3 (C-3‴), 75.0 (C-3″), 73.8 (C-2‴), 73.1 (C-α), 72.8 (C-2′), 71.4 (C-4‴), 71.2 (C-4′), 63.8 (C-6‴, C-6′), 62.9 (C-6), 62.7 (C-6″), 58.0 (C-2″), 42.5 (C-ε), 31.1 (C-β), 30.2 (C-ω), 25.2 (C-γ), 25.0 (<u>C</u>H_3CONH″-). 5-TFAP-β-$(LN)_2$ (**4**) was synthesized by the alternative addition of GlcNAc and Gal residue to 5-TFAP-β-LN (**2**) in a similar manner. Compound **4** was obtained in a total yield of 72% (356 mg) based on the acceptor substrate **2**. $[\alpha]_D^{30}$−12.3° (*c* 0.1, water). FAB-mass: *m*/*z* 930 $[M + H]^+$ (matrix: glycerol). ^{1}H NMR (D_2O, 500 MHz): δ 4.71 (d, 1H, $J_{1'',2''}$ 8.3 Hz, H-1″), 4.52 (d, 1H, $J_{1,2}$ 7.6 Hz, H-1), 4.48 (d, 1H, $J_{1''',2'''}$ 8.0 Hz, H-1‴), 4.46 (d, 1H, $J_{1',2'}$ 7.9 Hz, H-1′), 4.16 (1H, H-4′), 4.04−3.97 (2H, H-6b, H-6″b), 3.94 (1H, H-4‴), 3.90 (1H, H-αb), 3.87−3.66 (16H of sugar protons), 3.60−3.56 (4H, H-αa, H-5″, H-5, H-2′), 3.55 (dd, 1H, $J_{1'',2''}$ 8.3, $J_{2'',3''}$ 10 Hz, H-2″), 3.33 (t, 2H, H-ε), 2.04 (s, 3H, C<u>H</u>$_3$CO), 2.03 (s, 3H, C<u>H</u>$_3$CONH″-), 1.62−1.56 (4H, H-β, H-ω), 1.35 (2H, H-γ). ^{13}C NMR (D_2O, 500 MHz): δ 177.7 (CH_3<u>C</u>ONH″-), 177.2 (CH_3<u>C</u>O), 161.6 (CF_3<u>C</u>ONH—), 118.8 (<u>C</u>F_3CO), 105.72 (C-1′), 105.68 (C-1‴), 105.6 (C-1″), 103.8 (C-1), 84.9 (C-3′), 81.3 (C-4), 80.9 (C-4″), 78.2 (C-5‴), 77.7 (C-5′), 77.6 (C-5), 77.4 (C-5″), 75.3 (C-3‴, C-3), 75.0 (C-3″), 73.8 (C-2‴), 73.1 (C-α), 72.8 (C-2′), 71.4 (C-4‴), 71.1 (C-4′), 63.8 (C-6‴, C-6′), 62.9 (C-6), 62.7 (C-6″), 58.0 (C-2″), 57.9 (C-2), 42.5 (C-ε), 31.0 (C-β), 30.2 (C-ω), 25.2 (C-γ), 25.0 (<u>C</u>H_3CONH″-), 24.9 (<u>C</u>H_3CO). 5-TFAP-β-(LNβ1,3LNnT) (**5**) was synthesized by the alternative addition of GlcNAc and Gal residue to **3** in a similar manner. Compound **5** was obtained in a total yield of 75% (153 mg) based on the acceptor substrate **3**. $[\alpha]_D^{30}$+ 7.2° (*c* 0.1, water). FAB-mass: *m*/*z* 1255 $[M + H]^+$ (matrix: glycerol). ^{1}H NMR (D_2O, 500 MHz): δ 4.70 (d, 2H, $J_{1'''',2''''}$ 8.6, $J_{1'',2''}$ 8.6 Hz, H-1‴″, H-1″), 4.48 (d, 2H, $J_{1''',2'''}$ 7.0, $J_{1',2'}$ 7.0 Hz, H-1‴, H-1′), 4.47 (d, 1H, $J_{1,2}$ 8.3 Hz, H-1), 4.44 (d, 1H, $J_{1'''',2''''}$ 7.7 Hz, H-1‴″), 4.16 (2H, H-4‴, H-4′), 3.99−3.90 (5H, H-6b, H-6′29b, H-6‴″b, H-4‴″, H-αb), 3.87−3.53 (30H of sugar protons and aglycon α-methylene protons), 3.34 (t, 2H, H-ε), 3.30 (t, 1H, $J_{1,2}$ 8.3, $J_{2,3}$ 8.3 Hz, H-2), 2.04 (s, 6H, C<u>H</u>$_3$CONH‴″-, C<u>H</u>$_3$CONH″-), 1.66 (q, 2H, H-β), 1.62 (q, 2H, H-ω), 1.41 (q, 2H, H-γ). ^{13}C NMR (D_2O, 500 MHz): δ 177.7 (CH_3<u>C</u>ONH‴″-, CH_3<u>C</u>ONH″-), 161.6 (CF_3<u>C</u>ONH—), 118.8 (<u>C</u>F_3CO), 105.8 (C-1‴″), 105.7 (C-1‴, C-1′), 105.6 (C-1‴″, C-1″), 104.8 (C-1), 84.9 (C-3‴, C-3′), 81.2 (C-4), 81.0 (C-4‴″, C-4″), 78.2 (C-5‴″), 77.7 (C-5‴, C-5′), 77.6 (C-5), 77.4 (C-5‴″, C-5″), 77.2 (C-3), 75.6 (C-2), 75.3 (C-3‴″), 75.0 (C-3‴″, C-3″), 73.8 (C-2‴″), 73.1 (C-α), 72.8 (C-2‴, C-2′), 71.4 (C-4‴″), 71.2 (C-4‴, C-4′), 63.9 (C-6‴″), 63.8 (C-6‴, C-6′), 62.9 (C-6), 62.7 (C-6‴″, C-6″), 58.0 (C-2‴″, C-2″), 42.5 (C-ε), 31.1 (C-β), 30.2 (C-ω), 25.2 (C-γ), 25.0 (<u>C</u>H_3CONH‴″-, <u>C</u>H_3CONH″-). 5-TFAP-β-$(LN)_3$ (**6**) was synthesized by the alternative addition of GlcNAc and Gal residues to **4** in a similar manner. Compound **6** was obtained in a total yield of 85% (232 mg) based on the acceptor substrate **4**. $[\alpha]_D^{30}$−10.7° (*c* 0.1, water). FAB-mass: *m*/*z* 1296 $[M + H]^+$ (matrix: glycerol). ^{1}H NMR (D_2O, 500 MHz): δ 4.71 (d, 2H, $J_{1'''',2''''}$ 8.2, $J_{1'',2''}$ 8.2 Hz, H-1‴″, H-1″), 4.52 (d, 1H, $J_{1,2}$ 7.4 Hz, H-1), 4.48 (d, 1H, $J_{1''',2'''}$ 7.3 Hz, H-1‴), 4.47 (d, 1H, $J_{1'''',2''''}$ 7.0 Hz, H-1‴″), 4.46 (d, 1H, $J_{1',2'}$ 8.0 Hz, H-1′), 4.16 (2H, H-4‴, H-4′), 4.00−3.94 (3H, H-6b, H-6″b, H-6‴″b), 3.93 (1H, H-4‴″), 3.90 (1H, H-αb), 3.87−3.66 (23H of sugar protons), 3.60−3.56 (5H, H-αa, H-5‴″, H-5″, H-5, H-2‴, H-2′), 3.55 (dd, 2H, $J_{1'''',2''''}$ 8.2, $J_{2''''3''''}$ 10, $J_{1'',2''}$ 8.3, $J_{2'',3''}$ 10 Hz, H-2‴″, H-2″), 3.33 (t, 2H, H-ε), 2.04 (s, 6H, C<u>H</u>$_3$CONH‴″-, C<u>H</u>$_3$CONH—), 2.03 (s, 3H, C<u>H</u>$_3$CONH″-), 1.62−1.57 (4H, H-β, H-ω), 1.36 (2H, H-γ). ^{13}C NMR (D_2O, 500 MHz): δ 177.7 (CH_3<u>C</u>ONH‴″-, CH_3<u>C</u>ONH″-), 177.2 (CH_3<u>C</u>ONH—), 161.6 (CF_3<u>C</u>ONH—), 118.8 (<u>C</u>F_3CONH—), 105.7 (C-1‴″, C-1‴, C-1′), 105.6 (C-1‴″, C-1″), 103.8 (C-1), 84.9 (C-3‴, C-3′), 81.3 (C-4), 81.0 (C-4‴″, C-4″), 78.2 (C-5‴″), 77.7

(C-5‴, C-5′), 77.6 (C-5), 77.4 (C-5⁗, C-5″), 75.3 (C-3⁗, C-3), 75.0 (C-3‴, C-3′), 73.8 (C-2⁗), 73.1 (C-α), 72.8 (C-2‴, C-2′), 71.4 (C-4⁗), 71.1 (C-4‴, C-4′), 63.8 (C-6⁗, C-6‴, C-6′), 62.9 (C-6), 62.7 (C-6⁗, C-6″), 58.0 (C-2⁗, C-2″), 57.9 (C-2), 42.5 (C-ε), 31.0 (C-β), 30.2 (C-ω), 25.2 (C-γ), 25.0 ($\underline{C}H_3CONH‴$-, $\underline{C}H_3CONH″$-), 24.9 ($\underline{C}H_3CONH—$).

Synthesis of More Spaced Disaccharide Glycosides. Compound **9** (180 mg, 0.39 mmol), HOBT (208 mg, 1.54 mmol) and 6-trifluoroacetamidohexanoic acid (350 mg, 1.54 mmol) were dissolved in DMF (7.0 mL). Then, DIPCD (240 μL, 1.54 mmol) was added to the solution with continuous stirring for 24 h at room temperature. After the reaction mixture was concentrated to a solid, it was dissolved in 5 mL of $CHCl_3$/CH_3OH/H_2O = 7.5/2.5/0.35 and then loaded onto a silica gel 60N column (2.0 × 30 cm). The column was developed with the same solvent at a flow rate of 10 mL/min and a fraction size of 20 mL/tube. Fractions 26−66 were pooled and concentrated: 5-[5′-(trifluoroacetamido) pentanecarboxamido]pentyl β-LN (**7**) was obtained in a total yield of 59% (154 mg). $[\alpha]_D^{30}$−2.9° (*c* 0.1, water). FAB-mass: *m/z* 678 $[M + H]^+$ (matrix: glycerol). ^{1}H NMR (D_2O, 500 MHz): δ 4.52 (d, 1H, $J_{1,2}$ 7.0 Hz, H-1), 4.47 (d, 1H, $J_{1′2′}$ 8.0 Hz, H-1′), 3.98 (dd, 1H, $J_{5,6b}$ 1.2, $J_{6a,6b}$ 12.2 Hz, H-6b), 3.93 (1H, H-4′), 3.90 (m, 1H, H-αb), 3.83 (dd, 1H, $J_{5,6a}$ 4.6, $J_{6a,6b}$ 12.2 Hz, H-6a), 3.78−3.75 (2H, H-6′a, H-6′b), 3.73−3.70 (4H, H-5′, H-4, H-3, H-2), 3.67 (dd, 1H, $J_{2′,3′}$ 10, $J_{3′,4′}$ 4.9 Hz, H-3′), 3.61 (m, 1H, H-αa), 3.60 (1H, H-5), 3.54 (dd, 1H, $J_{1′,2′}$ 8.0, $J_{2′,3′}$ 10 Hz, H-2′), 3.32 (t, 2H, H-ε′), 3.17 (t, 2H, H-ε), 2.24 (t, 2H, H-α′), 2.03 (s, 3H, $C\underline{H}_3CONH—$), 1.64−1.54 (6H, H-β′, H-β, H-ω′), 1.51 (m, 2H, H-ω), 1.32 (4H, H-γ′, H-γ). ^{13}C NMR (D_2O, 500 MHz): δ 179.5 (-$\underline{C}ONH—$), 177.2 ($CH_3\underline{C}ONH—$), 161.8 ($CF_3\underline{C}ONH—$), 117.6 ($\underline{C}F_3CONH—$), 105.7 (C-1′), 103.8 (C-1), 81.3 (C-4), 78.2 (C-5′), 77.6 (C-5), 75.32 (C-3′), 75.28 (C-3), 73.8 (C-2′), 73.1 (C-α), 71.4 (C-4′), 63.8 (C-6′), 62.9 (C-6), 57.9 (C-2), 42.4 (C-ε′), 42.0 (C-ε), 38.4 (C-α′), 31.0 (C-β), 30.7 (C-ω), 30.2 (C-ω′), 28.1 (C-γ′), 27.8 (C-β′), 25.3 (C-γ), 25.0 ($\underline{C}H_3CONH—$). 5-{5′-[5″-(Trifluoroacetamido) pentanecarboxamido]pentanecarboxamido}pentyl β-LN (**8**) was synthesized by the addition of spacer parts to **7** in a similar manner. Compound **8** was obtained in a total yield of 64% (260 mg). $[\alpha]_D^{30}$+8.3° (*c* 0.1, water). FAB-mass: *m/z* 791 $[M + H]^+$ (matrix: glycerol). ^{1}H NMR ($CDCl_3$, 500 MHz): δ 4.40 (d, 1H, $J_{1,2}$ 7.9 Hz, H-1), 4.38 (d, 1H, $J_{1′2′}$ 7.3 Hz, H-1′), 3.87 (dd, 1H, $J_{5,6b}$ 2.5, $J_{6a,6b}$ 12.5 Hz, H-6b), 3.84−3.81 (3H, H-αb, H-4′, H-6a), 3.74 (dd, 1H, $J_{5′,6′b}$ 7.7, $J_{6′a,6′b}$ 11.7 Hz, H-6′b), 3.67 (dd, 1H, $J_{5′,6′a}$ 4.3, $J_{6′a,6′b}$ 11.7 Hz, H-6′a), 3.64−3.59 (4H, H-5′, H-4, H-3, H-2), 3.54−3.48 (2H, H-3′, H-2′), 3.46 (m, 1H, H-αa), 3.41 (m, 1H, H-5), 3.26 (t, 2H, H-ε″), 3.16−3.08 (4H, H-ε′, H-ε), 2.16 (4H, H-α″, H-α′), 1.96 (s, 3H, $C\underline{H}_3CONH—$), 1.63−1.52 (8H, H-β″, H-β′, H-β, H-ω″), 1.46 (4H, H-ω′, H-ω), 1.31 (6H, H-γ″, H-γ′, H-γ). ^{13}C NMR ($CDCl_3$, 500 MHz): δ 175.7 (-$\underline{C}ONH′$-), 175.6 (-$\underline{C}ONH—$), 173.5 ($CH_3\underline{C}ONH—$), 158.8 ($CF_3\underline{C}ONH—$), 115.6 ($\underline{C}F_3CONH—$), 104.1 (C-1′), 102.0 (C-1), 79.9 (C-4), 76.3 (C-5′), 75.6 (C-5), 73.8 (C-3′), 73.3 (C-3), 71.9 (C-2′), 70.4 (C-α), 69.5 (C-4′), 61.9 (C-6′), 61.2 (C-6), 56.0 (C-2), 40.2 (C-ε″), 39.9 (C-ε), 39.8 (C-ε′), 36.63 (C-α′), 36.55 (C-α″), 29.5 (C-β), 29.4 (C-ω, C-ω′), 28.8 (C-ω″), 26.9 (C-γ″), 26.7 (C-β″), 26.1 (C-γ′), 25.9 (C-β′), 23.8 (C-γ), 23.0 ($\underline{C}H_3CONH—$).

Synthesis of Various Aminoalkyl Di-, Tetra- And Hexasaccharide Glycosides. 5-AP-β-LN **9**, 5-AP-β-LNnT **10**, 5-AP-β-$(LN)_2$ **11**, 5-AP-β-(LNβ1,3LNnT) **12**, 5-AP-β-$(LN)_3$ **13**, 5-(5′-aminopentanecarboxamido)pentyl β-LN **14**, and 5-[5′-(5″-aminopentanecarboxamido)pentanecarboxamido]pentyl β-LN **15** were synthesized from **2**−**8** by alkaline hydrolysis according to our previously reported method (*6*).

Synthesis of Asialoglycopolypeptides with γ-PGA Backbones. The amino functions of oligosaccharide glycosides (**9**−**15**) were coupled with the carboxyl group of γ-PGA by a condensation reaction. DSs of the substituted residues in glycopolypeptide were adjusted to 31−49% (Table 1). Poly[LNβ-$O(CH_2)_5NH—$/γ-PGA] **16**, poly[LNnTβ-$O(CH_2)_5NH—$/γ-PGA] **17**, poly[$(LN)_2$β-$O(CH_2)_5NH—$/γ-PGA] **18**, poly[LNβ1,3LNnTβ-$O(CH_2)_5NH—$/γ-PGA] **19**, poly[$(LN)_3$β-$O(CH_2)_5NH—$/γ-PGA] **20**, poly[LNβ-$O(CH_2)_5NHCO(CH_2)_5NH—$/γ-PGA] **21**, and poly{LNβ-$O[(CH_2)_5NHCO]_2(CH_2)_5NH—$/γ-PGA} **22** were prepared from **9**−**15**, respectively, according to our previously reported method (*6*).

Synthesis of Sialoglycopolypeptides with γ-PGA Backbones. α2,3-Sialoglycopolymers **23**−**29** were synthesized from **16**−**22**, respectively, using rat recombinant α2,3-(*N*)-sialyltransferase. In addition, α2,6-sialoglycopolymers **30**−**36** were also synthesized from **16**−**22**, respectively, using rat recombinant α2,6-(*N*)-sialyltransferase according to our previously reported method (*6*).

Focus-Forming Assay. Virus titers were determined by focus-forming assay using Madine-Darby canine kidney (MDCK) cells. MDCK cells were seeded at 1.5 × 10^4 cell/well in 96-well plates and cultured in MEM supplemented with 10% fetal bovine serum at 37 °C. After removal of medium, virus solutions were serially diluted with serum-free DMEM and inoculated onto the plates. The cells were then incubated for 30 min at 34.5 °C. After removing the virus solution, overlay medium (DMEM containing 0.5% (w/v) tragacanth gum (Wako, Osaka) and 0.2% (w/v) bovine serum albumin) was added, and the plates were incubated at 34.5 °C for 20−24 h. The cells were then fixed with methanol. Infectious foci were detected with mouse antinucleoprotein (NP) monoclonal antibody (clone H16L-10−4R55, ATCC) as the primary antibody and HRP-conjugated goat antimouse immunoglobulin as the secondary antibody. Detected foci were counted under a light microscope. Virus infectivity was determined as focus-forming units (FFU).

Inhibition of Influenza Virus Infection by Glycopolypeptides. Influenza viruses were mixed on ice with or without glycopolypeptides at the indicated concentrations. The virus-glycopolypeptide mixtures (50 μL) were then inoculated for 30 min at 34.5 °C onto MDCK cells grown in 96-well plates. After washing three times with serum-free DMEM, overlay medium was added and plates were incubated at 34.5 °C for 20−24 h. Virus infectivity was then determined by focus-forming assay as described above. The optimal titer of inoculated virus was predetermined such that more than 80−100 foci appeared per well. Each experiment was performed in triplicate wells. Significant analysis of means of focus numbers between control and treatment was performed by *t* test.

Solid-Phase Binding Assay. The assay measuring direct binding activity of influenza virus to glycopolymers was performed by our method (*9, 31*). Glycopolymers were briefly immobilized on polystyrene Universal-Bind microplates (Corning) under an ultraviolet irradiation method. After blocking with PBS containing 2% bovine serum albumin, the plates were incubated in solutions containing influenza virus in PBS (2^7 HAU of A/WSN/33) at 4 °C overnight. After five washes with ice-cold PBS, the plates were incubated in a substrate solution containing 40 μM of 2′-(4-methylumbelliferyl)-α-D-*N*-acetylneuraminic acid in PBS at 37 °C for 1 h. The reactions were terminated by the addition of a 500 mM carbonate buffer (pH 10.2). Fluorescence was measured at 355 nm (excitation) and 460 nm (emission). The direct virus-binding activity was determined by the quantity of 4-methylumbelliferon released by viral neuraminidases.

Influenza Virus Infection in Mice. Influenza A/WSN/33 virus was used in this study to evaluate antiviral effects of

Scheme 1. Enzymatic Synthesis of LN-Repeating Tetra- And Hexasaccharide Glycosides

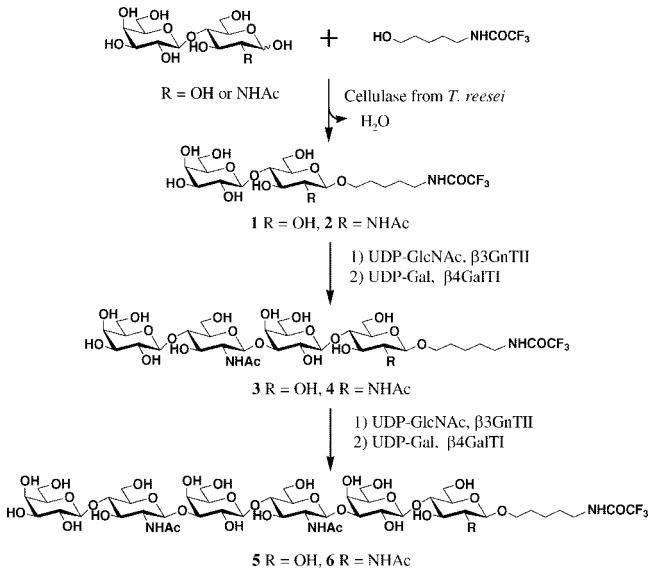

synthetic glycopolymers as described previously (*31*). Briefly, groups of six female BALB/c mice (five weeks old, 14−18 g) were inoculated intranasally with 25 μL of premixes containing viral suspension (2.0×10^4 pfu/mL) and glycopolymers at the indicated concentrations. Control was treated with 25 μL of viral suspension and asialo-glycopolymers. Mice were observed for 13 days after infection. Anti-influenza efficacy was determined by prevention of loss of body weight and protection against lethality caused by influenza virus infection. The significance of differences in the ratios of survival mice between groups treated with asialo- and α2,3-sialoglycopolymers was analyzed by Log-rank test (*32*) on Kaplan−Meier survival curves (*33*). Animal care and experiments were performed in accordance with the guidelines for the care and use of laboratory animals of the Shizuoka University.

Hemagglutination Inhibition Assay. The hemagglutination inhibition (HI) assay was carried out using 96-well microtiter plates as described previously (*22*). Phosphate-buffered saline (PBS, pH 6.5) was used as a dilution buffer. Virus suspension (2^2 HA units in 0.025 mL of PBS) was added to each well containing the synthetic glycopolypeptides (200 to 0.024 nM) in a 2-fold serial dilution in dilution buffer. After incubation for 1 h at 4 °C, 0.05 mL of 0.6% (v/v) guinea pig suspension erythrocytes was added to the plates, and allowed to settle for 2 h at 4 °C. The maximum dilution of the samples showing complete inhibition of hemagglutination was defined as the HI titer.

RESULTS

Convenient Synthetic Route to a New Type of Artificial Glycopolymer. *Synthesis of Oligosaccharide Glycosides Carrying LN Repeats.* We have recently reported that a condensation reaction between lactose (Lac) or LN and 5-trifluoroacetamido-1-pentanol can be catalyzed by cellulase from *Trichoderma reesei* to obtain 5-TFAP-β-Lac (**1**) and 5-TFAP-β-LN (**2**), respectively (**6**). O-Linked oligosaccharide glycosides carrying LN repeats were then derived from the resulting products (Scheme 1). Thus, consecutive additions of β1,3 linked GlcNAc and β1,4 linked Gal to respective **1** and **2** acceptors led to the synthesis of tetrasaccharide glycosides **3** and **4** carrying LNnT and tandem LN repeats, respectively, by using either β3GnT or β4GalTI. GlcNAc and Gal residues can then be added to the resulting glycosides **3** and **4** in a similar way to form hexasaccharide glycosides **5** and **6** carrying LN repeats. The target products **3**−**6** were obtained in high yields of 90−75%, based on the acceptors.

Scheme 2. Synthesis of More Spaced Disaccharide Glycosides

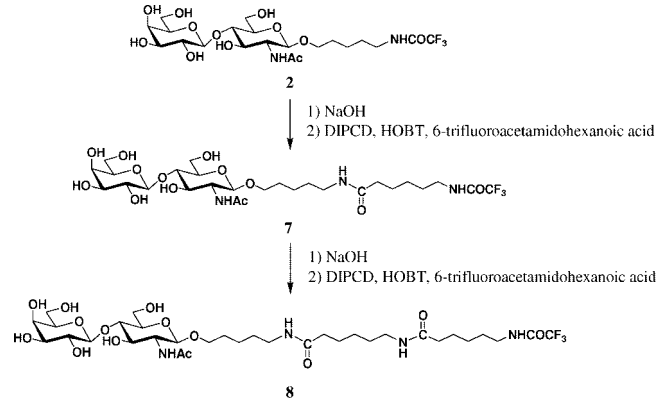

Synthesis of More Spaced Disaccharide Glycosides. The aglycon trifluoroacetamido group of **2** was deacylated to 5-aminopentyl β-LN (5-AP-β-LN) **9** by hydrolysis in an alkaline solution as shown in Scheme 2. The resulting amino function was coupled to 6-trifluoroacetamidohexanoic acid with DIPCD and HOBt in DMF to produce **7** with tandem alkylamido repeats in the aglycon moiety. The resulting glycoside **7** was then subjected to the condensation reaction to produce **8** with triplet alkylamido repeats. The longer spaced disaccharide glycosides **7** and **8** were easily purified with a silica gel column, in yields of 59% and 64% based on the corresponding glycosides, respectively.

Synthesis of Asialoglycopolypeptides. The resulting oligosaccharide glycosides with different glycans in the array were similarly deacylated to the corresponding amino group by alkali treatment as mentioned above (Scheme 3). The amino function of the resulting oligosaccharide glycosides **9**−**15** was reacted with the carboxyl groups of γ-PGA in the presence of the condensation reagents BOP and HOBt, as described earlier. In the synthesis, γ-PGA of 990 kDa was used as the polypeptide base of the glycopolymers. The reaction solution was applied to a column of Sephadex G-25 M PD-10 to separate the glycosylated γ-PGA from the low molecular weight reactants. The degree of substitution (DS) in mole fraction of the substituted residues in the asialoglycopolypeptides **16**−**22** was calculated by two methods: ^{1}H NMR and chemical analyses. The ^{1}H NMR results were based on the relative intensities of signals due to peptide methylene protons and those due to spacer-linked methylene protons in the aglycon. The chemical analysis procedure used the method of Yasuno et al. (*29*). The DS in those asialoglycopolypeptides was limited to the extent of 30−50% by controlling the coupling conditions of the aminated spacer-linked glycosides with γ-PGAs (Tables 1 and 2).

Synthesis of Sialoglycopolypeptides. A series of asialoglycopolypeptides with different glycans in the array were sialylated to **23**−**29** carrying SAα2,3Gal and **30**−**36** carrying SAα2,6Gal by α2,3- and α2,6-SiaTs, respectively (Scheme 3). After separation through a column of Sephadex G-25 M PD-10, the target glycopolypeptides were obtained. The structures of the synthesized glycopolymers were confirmed by ^{1}H and ^{13}C NMR analyses with reference to our previous report (*6*). The DS of sialyl sugar derivatives in the sialoglycopolypeptides was determined by ^{1}H NMR and chemical analyses, such as those of asialoglycopolypeptides mentioned above. The structures of sialoglycopolypeptides **27** and **34** as representative examples were analyzed from the corresponding ^{1}H NMR spectrum. In the ^{1}H NMR spectrum of **27**, characteristic signals at δ 2.76 (dd, 1H, $J_{3''''',\,3''''_{ax}}$, $_{3''''_{eq}}$ 11.6,

Scheme 3[a]

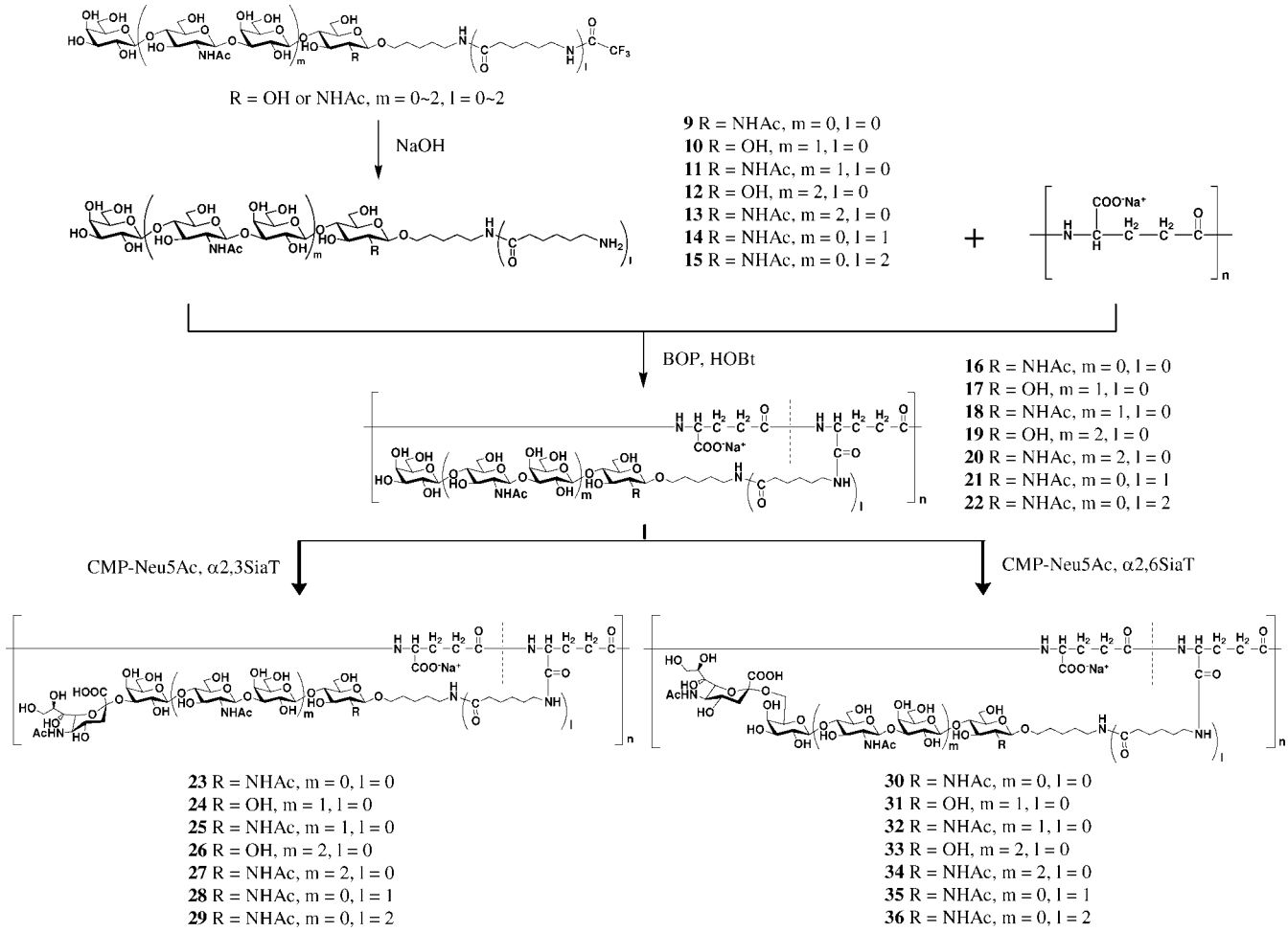

[a] (1) Chemoenzymatic synthesis of LN-repeating and long-spacer linked aminoalkyl oligosaccharide glycosides, (2) coupling of the resulting glycoside with γ-PGA, and (3) sialylation to highly water-soluble glycopolypeptides carrying clustered identical sialooligosaccharide segments.

$J_{3''''eq,\ 4''''}$ 3.7 Hz, H-3′′′′′eq) and δ 1.81 (t, 1H, $J_{3''''ax,\ 3''''eq}$ 11.6, $J_{3''''ax,\ 4''''}$ 11.6 Hz, H-3′′′′′ax) were assigned to the H-3′′′′′ proton. In **34**, δ 2.67 (dd, 1H, $J_{3''''ax,\ 3''''eq}$ 12.2, $J_{3''''eq,\ 4''''}$ 4.3 Hz, H-3′′′′′eq) and δ 1.73 (t, 1H, $J_{3''''ax,\ 3''''eq}$ 12.2, $J_{3''''ax,\ 4''''}$ 12.2 Hz, H-3′′′′′ax) were assigned to the H-3′′′′′ proton. It was possible to evaluate the extent of sialylation from the integration data of the resulting proton signals (Table 2). The properties of the synthesized glycopolypeptides are summarized in Table 2. The chemical analysis was performed using the method of Sato et al. (*30*). The degree of substitution of neutral sugar derivatives (NS) and sialyl sugar derivatives (Sia) was based on the DP of γ-PGA, which was arbitrarily given a value of 100% (Table 2). In the ^{13}C NMR spectra of **27** and **34**, the respective C-3′′′′ and C-6′′′′ signals were distinguished by a downfield position with chemical shifts at δ 78.0 and δ 66.2. These data indicate that the terminal Gal residues of the sugar chains are regiospecifically sialylated in the α2−3 and α2−6 linkages.

Interaction of Synthetic Glycopolypeptides with Influenza Viruses. *Inhibition of Influenza Virus Infection by Glycopolypeptides.* To investigate the inhibitory effects of glycopolypeptides carrying different length glycans in the array on infection of MDCK cells by influenza virus, virus and test agents were inoculated concurrently. The inhibitory activity was determined by focus-forming assay. This experiment was performed to determine whether glycopolymers act directly on viruses in the early stages of viral infection, particularly adsorption. The results are summarized in Table 3. Infection of the avian strains, A/Duck/HongKong/313/4/78 (H5N3), A/Duck/HongKong/47/5/76 (H3N2), and A/Duck/HongKong/47/5/76 (H7N2) were inhibited by sialoglycopolymers carrying the α2,3 sialylated glycan, but not by those carrying the α2,6 sialylated glycan. Inhibition by **23**, **25**, and **27** decreased in a glycan length-dependent manner. Compound **23**, carrying a short glycan of trisaccharide, was shown to be the most effective inhibitor among the glycopolymers tested. The polymer showed 4−10-fold higher inhibitory activity than **27** carrying triplet LN repeats. The virus appears to recognize a short α2,3 sialylated glycan in preference to the long glycan.

In contrast, the human virus, A/WSN/33 (H1N1) was inhibited by glycopolymers carrying long α2,3/6 sialylated glycan with LN repeats. The inhibition clearly occurred in a glycan length-dependent manner. Viral infection was strongly inhibited by **27** and **34** carrying long glycans at a very low concentration (IC_{50} 0.06 pM). Inhibition by **27** displayed 13×10^6-fold higher activity compared to that of **23**, which carries a short glycan. In this case, the sugar elongation of the inner glycan for **27** resulted in a remarkable increase of inhibition activity to enhance the virus binding. IC_{50} of **27** and **34** in the present study is 7.5×10^5-fold stronger than α-PGA-based glycopolypeptide carrying the same LN repeat (*31*). The human virus, A/Aichi/2/68 (H3N2), which has high susceptibility to compounds **32** and **34** (IC_{50} 0.1−0.2 pM), also showed a similar pattern of inhibitory effect. Taken together, our results indicate that the length of the sialylated glycan critically influences binding to the human virus, which is favored by long glycan

Table 3. IC_{50} of Sialoglycopolypeptides Carrying LN-Repeating Glycoside in Focus-Forming Assays of Human and Avian Influenza Viruses

		IC_{50}[a] (Sia nM)					
		α2,3-sialopolypeptides			α2,6-sialopolypeptides		
virus	subtype	**23**[b] (single[c])	**25** (tandem)	**27** (triplet)	**30** (single)	**32** (tandem)	**34** (triplet)
			Avian				
A/Duck/HongKong/313/4/78	H5N3	10	40	100	N.E.[d]	N.E.	N.E.
A/Duck/HongKong/24/76	H3N2	20	60	100	N.E.	N.E.	N.E.
A/Duck/HongKong/47/5/76	H7N2	80	200	300	N.E.	N.E.	N.E.
			Human				
A/WSN/33	H1N1	800	0.1 (pM)	0.06 (pM)	0.02	1 (pM)	0.06 (pM)
A/Aichi/2/68	H3N2	2	0.4	0.04	3 (pM)	0.1 (pM)	0.2 (pM)

[a] Concentration of Sia units. [b] Compound no. [c] Single, tandem, and triplet means respective LN repeats. [d] No effect means that inhibitory effect was not observed up to 300 μg/mL of glycopolymers.

units such as LN repeats. As controls, asialoglycopolymers did not affect the virus binding.

Direct Binding Activity of Influenza Virus to Glycopolypeptides. For further investigation, we directly determined the binding activity of glycopolymers to human virus by a solid-phase virus binding assay. We have recently established a direct binding assay with artificial glycopolymers for human and avian influenza viruses (*9*, *31*). In this study, we applied the assay for determination of direct binding dynamics of artificial glycopolymers carrying long glycan units such as LN repeats to human virus, A/WSN/33.

The binding signals were detected when α2,3/6-sialoglycopolymers, but not asialoglycopolymers (data not shown), were used as ligands. As the concentration of sialoglycopolymers with LN repeats increased, the signals from human virus bound to glycopolymers increase in a dose-dependent manner regardless of the core carbohydrate structure. The inhibition by α2,3-sialopolymers **23**, **25**, and **27** carrying single, tandem, and triplet LN repeats increased in a glycan length-dependent manner (Figure 1A). Also, the α2,6-sialopolymers **30**, **32**, and **34** with different LN repeats showed a similar pattern of inhibitory effect as those of the α2,3-sialopolymers (Figure 1B). These results were comparable with those obtained by in vitro infection experiments. Taken together, the human viruses bind exclusively to sialoglycopolymers carrying elongated core carbohydrates with higher affinity.

Protection of Mice by Intranasal Administration of Glycopolypeptides from Death Induced by A/WSN/33 Infection. We examined the protective effects of sialoglycopolymers (**23** and **27**) with single and triplet LN repeats in a murine model of respiratory tract viral infection with A/WSN/33 strain. Asialoglycopolymer (**20**) was used as control to examine influenza infection. Groups of mice were administered glycopolymers at five weeks old. Compound **27** with triplet LN repeats, administered at a dose of 3 nmol/kg corresponding to approximately 15.6 mg/kg, reduced mortality below 0% on day 13 postinfection (Figure 2A). In contrast, compound **23** with a single LN, administered at 3 nmol/kg did not significantly affect lethality in mice induced by infection with A/WSN/33 as compared to administration of asialoglycopolymer **20** (Figure 2A). In mice treated with compound **27** with triplet LN repeat, but neither compound **23** with a single LN or asialoglycopolymer **20** at a dose of 3 nmol/kg, we also observed improvement in the weight gain of mice surviving to day 13 postinfection (Figure 2B). Thus, sialoglycopolymers with an elongated LN chain as core structure showed a significant protective effect in this murine model of influenza virus infection. The protective effect of this glycopolymer is comparable to that observed in vitro (Table 3). Glycopolymer-related toxicity was not observed in any of the groups examined.

Hemagglutinin Inhibition Assay of the Glycopolypeptides Carrying Spacer-Linked Alkylamido Repeats as Sugar Mimetics. Various substances carrying sialooligosaccharide glycosides are known to inhibit hemagglutination by binding to viral HA (*6*). We tested the inhibitory effect of the glycopolypeptides with different glycans and spacers in the array on hemagglutination using human and avian influenza viruses. The hemagglutination inhibition activity toward glycopolypeptides showed a distinct difference between the avian and human strains as in Table 4. The avian viruses reacted with **23**, **25**, and **27** carrying α2,3 sialylated glycans (Table 4A and Figure 3A). Inhibition by the sialopolymers tended to decrease in a glycan length-dependent manner. Furthermore, we prepared different length spacer linked polymers **28**, **29**, **35**, and **36** carrying a trisaccharide α2,3/6 motif (SAα2,3/6LN) in order to elucidate whether the inner sugar should be replaced by a nonsugar structural unit, such as an alkylamido group. The avian virus A/Duck/HongKong/313/4/78 was not greatly affected to inhibition by replacement of alkylamido group (**28** and **29**) by sugar unit (the corresponding **25** and **27**). Thus, the α2,3-sialoglycopolypeptides carrying tandem and triplet alkylamido repeats showed a similar pattern of inhibitory effect to those of the α2,3-

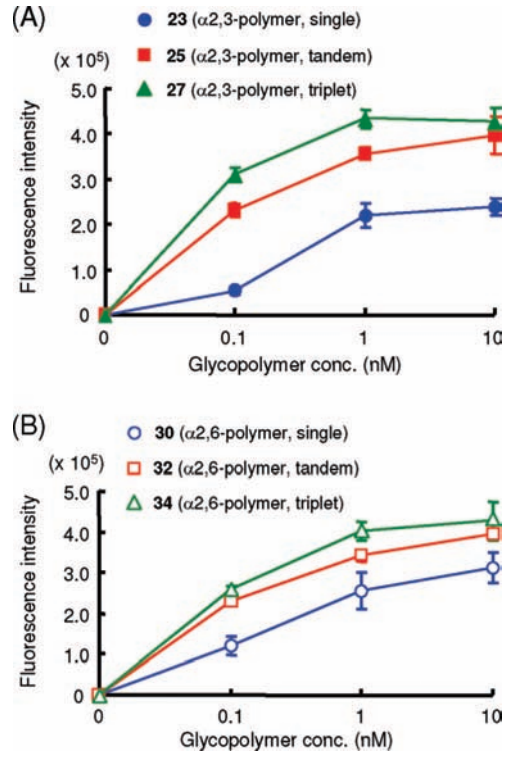

Figure 1. The direct binding activity of human influenza virus, A/WSN/33 (H1N1), to glycopolypeptides carrying a single, tandem, or triplet LN-repeating glycoside was determined by our method (*9*, *31*). (A) SAα2,3-glycopolymers, (B) SAα2,6-glycopolymers.

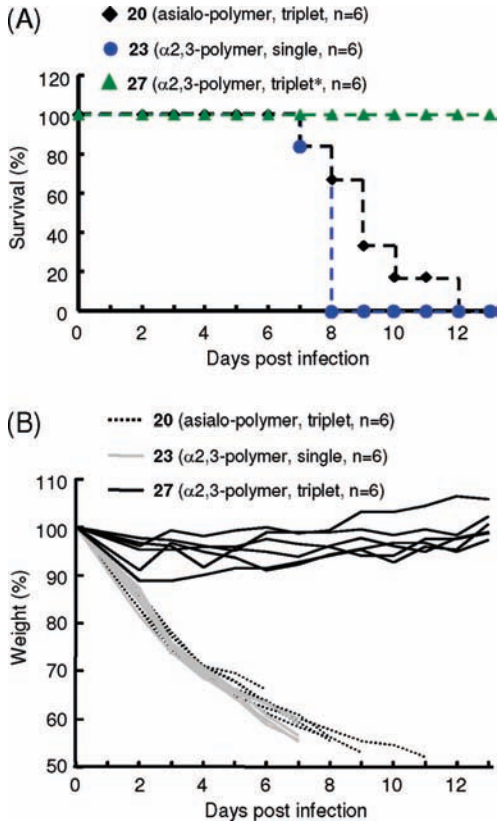

Figure 2. Effect of glycopolymer influenza virus (AWSN/33) infection in mice was performed as described in the Experimental Section. Graph (A) indicates Kaplan−Meier survival curves (*P < 0.01, Log-rank test). Mice were intranasally inoculated with viral suspension and asialo- (**20**, triplet) or SAα2,3- (**23**, single; and **27**, triplet) glycopolymers at a dose of 3 nmol/kg. Graph (B) shows body weight dynamics of mice.

sialoglycopolypeptides carrying tandem and triplet LN repeats (Table 4B and Figure 3A).

In contrast, the human viruses preferentially bound not only to long α2,3/6 sialylated glycan **27** (**26**) and **34** (**33**) with LN repeats in the receptors, but also to more spacer-linked glycan (Table 4A). For the human virus, A/Aichi/2/68, inhibition by α2,6-sialopolymers **30**, **31**, and **33** carrying a single LN, LNnT, and LN-LNnT unit increased in a glycan length-dependent manner (Figure 3B). This result was consistent with in vitro and in vivo infection experiments, suggesting that enhancement of the binding affinity of glycopolymers with viral HA is accompanied with the extension of LN repeats as the core structure. Furthermore, inhibition by the human virus, A/Aichi/2/68, was also strongly inhibited by α2,6-sialopolymers **35** (IC_{50} 0.73 μM) and **36** (IC_{50} 1.5 μM) carrying tandem and triplet alkylamido repeats with 4−8-fold higher affinity compared to **30** carrying a single alkylamido spacer (Table 4B). The inhibitory activity of **35** and **36** gave somewhat similar values to that of **31** and **33** carrying tandem and triplet LN repeats (Figure 3B). It indicates that a spaced tandem/triplet alkylamido repeat is a good mimetic of a tandem/triplet LN repeat. Indeed, **35** and **36** displayed 21−43-fold higher affinities for the viral hemagglutinins relative to the control fetuin (IC_{50} 31.5 μM), which binds both avian and human types of influenza virus due to the presence of two different SA linkages, α2,3 and α2,6. As controls, asialoglycopolymers did not affect influenza virus-mediated hemagglutination (data not shown).

DISCUSSION

The binding specificity of influenza viral HA involves both recognition of the SA linkages as well as the core glycan sequence (*8, 9, 25, 34, 35*). We therefore designed a series of sialoglycopolypeptides to act as potential polymeric inhibitors of infection by avian and human influenza viruses in order to analyze the structure−activity relationship on the viral HA. Each of these compounds comprised three parts: glycan, spaced-linker, and polypeptide backbone. Here, we propose a convenient synthesis of asialo-type polymers with LN repeats starting LN or Lac. Schemes 1−3 represent the pathway via the following three steps: (1) enzymatic and chemical glycosylations of the respective spaced-disaccharide (LN/Lac) glycosides; (2) enzymatic sugar elongation of the LN unit to the resulting disaccharide glycosides by consecutive use of β3GnT and β4GalT to produce tetra- and hexasaccharide glycosides with tandem and triplet LN repeats; (3) coupling of the resulting glycoside to γ-PGA. High molecular-weight γ-PGA was used as a backbone for each glycopolymer. As an alternative design, the resulting disaccharide glycosides were converted to long spacer-linked disaccharide glycosides with tandem and triplet alkylamido repeats by consecutive coupling reactions. These units were then coupled to γ-PGA. The DS (%) of asialoglycan in the resulting glycopolypeptides was adjusted to a proportion of around 40% by controlling the coupling reaction (Table 1). Finally, a series of asialoglycopolypeptides were sialylated to obtain glycopolypeptides carrying α2,3/6 sialylated glycans in the array by the use of α2,3- and α2,6-SiaTs. We have already reported that γ-PGA-based glycopolypeptide carrying a single LN unit can be used as an acceptor of a CMP-Neu5Ac donor by utilizing rat recombinant α2,3/6-SiaTs (*6*). This method was applicable to the sialylation of the present asialoglycopolypeptides. The rat recombinant α2,3/6-SiaTs regiospecifically catalyzed sialylation to the terminal Gal residue in the short asialoglycan as well as the Gal in the long asialoglycan, such as LN repeats (*36*). As a result, sialylation of the asialo-portion of the glycopolymers was almost quantitative at around 40%, whose proportion is based on the optimum result on inhibition of viral infection (Table 2).

To date, infections by influenza viruses have been successively inhibited by sialoglycopolymers carrying short glycans, such as sialyllactose and sialyl LN, no matter how short the glycan chain (*12*). However, recent studies have demonstrated that the length of the glycan beyond a trisaccharide critically influences viral HA binding contacts (*9, 25, 34*). In the present study, the contribution of the asialo portion in the sugar chains was examined by in vitro or in vivo infection experiments, solid-phase binding assay, and hemagglutination inhibition assay using glycopolypeptides carrying different lengths of glycan or spacer-linked glycan in the array. Five strains of avian and human influenza viruses were used as models for studies aimed at identifying the HA glycan binding specificity. First, the in vitro infection experiments (focus-forming assay) examined that artificial glycopolypeptide effectively inhibited cellular infection by avian and human strains (Table 3). The avian viruses specifically recognized a short α2,3 sialylated glycan to an LN/Lac motif in a trisaccharide. In addition, the virus did not bind to the terminal SA-linked α2,6 of the LN/Lac motif. In contrast to this result, human viruses preferentially bound to a long α2,3/6 sialylated glycan with LN repeats that are at least pentasaccharide in length. These results were further supported by solid-phase binding assays that elongation of core carbohydrate portion markedly enhances binding affinity of α2,3/6-sialopolymers with the human viral HA (Figure 1). A possible explanation could lie with the difference in the conformation of the terminal trisaccharides resulting from sialic acid linkage in the cocrystal structures (*25, 34*). Chandrasekaran et al. have proposed that the cone-like and umbrella-like topologies are governed by conformation of

Table 4

A. Inhibition of Human and Avian Influenza Virus Hemagglutination by Sialoglycopolypeptides Carrying LN-Repeating Glycoside

		IC_{50}[a] (Sia μM)					
		α2,3-sialopolypeptides			α2,6-sialopolypeptides		
virus	subtype	**23** (single[c])	**25** (tandem)	**27** (triplet)	**30** (single)	**32** (tandem)	**34** (triplet)
			Avian				
A/Duck/HongKong/313/4/78	H5N3	99	145	317	ND[b]	ND	ND
A/Duck/HongKong/24/76	H3N2	8.8	5.7	14	ND	ND	ND
A/Duck/HongKong/47/5/76	H7N2	35	46	54	ND	ND	ND
			Human				
A/WSN/33	H1N1	0.22	0.71 (nM)	0.34 (nM)	4.3 (nM)	1.4 (nM)	0.34 (nM)
A/Aichi/2/68	H3N2	231	188[d]	94[e]	6	2.7[f]	1.2[g]

B. Inhibition of Human and Avian Influenza Virus Hemagglutination by Sialoglycopolypeptides Carrying Long-spacer Linked Disaccharide Glycoside

		IC_{50}[a] (Sia μM)					
		α2,3-sialopolypeptides			α2,6-sialopolypeptides		
virus	subtype	**23** (single[c])	**28** (tandem)	**29** (triplet)	**30** (single)	**35** (tandem)	**36** (triplet)
			Avian				
A/Duck/HongKong/313/4/78	H5N3	99	120	240	ND[b]	ND	ND
			Human				
A/Aichi/2/68	H3N2	231	47	94	6	0.73	1.5

[a] Minimum concentrations required for complete inhibition of hemagglutination. [b] ND: not detected (No activity). [c] Single, tandem, and triplet means respective LN repeats. Single, tandem, and triplet means respective alkylamido repeats. [d] Compound **24** was used. [e] Compound **26** was used. [f] Compound **31** was used. [g] Compound **33** was used.

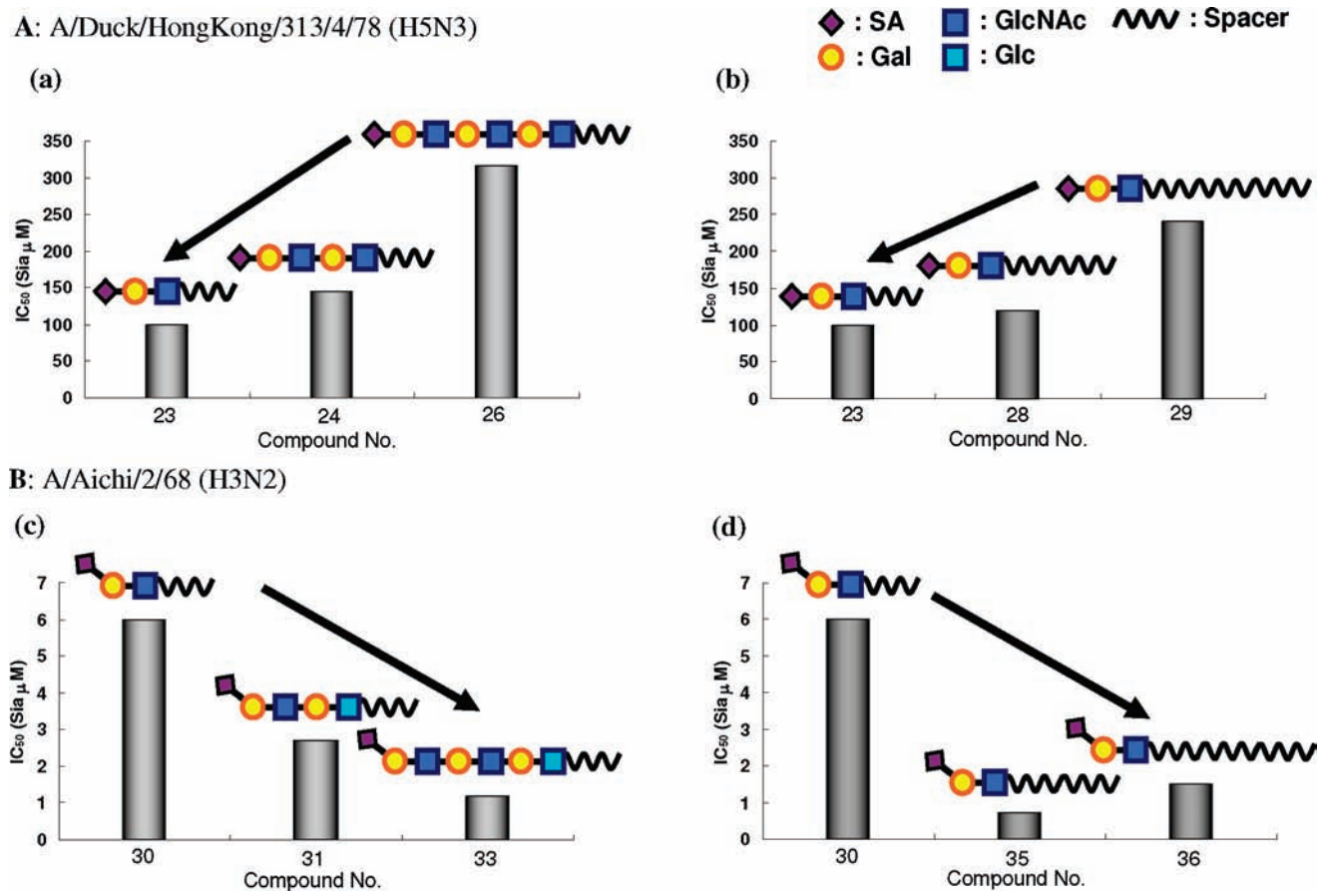

Figure 3. Inhibitory effects of glycopolypeptides with different glycans (**a** and **c**) and spacers (**b** and **d**) on hemagglutination using two strains of influenza viruses: (**A**) Avian strain A/Duck/HongKong/313/4/78 (H5N3) and (**B**) human strain A/Aichi/2/68 (H3N2). (**A**) **a** and **b**: SAα2,3-polymer **23** carrying a short glycan and spacer, was shown to be the most effective inhibitor. (**B**) **c**: Inhibition by SAα2,6-polymers **30**, **31**, and **33** carrying single LN, LNnT, and LN-LNnT units increased in a glycan length-dependent manner. **d**: Inhibition by SAα2,6-polymers **30**, **35**, and **36** carrying single, tandem, and triplet alkylamido repeats increased in a spacer length-dependent manner.

the α2,3 and α2,6 sialylated trisaccharides, respectively (*25*). In the umbrella-like topology, longer α2,6 oligosaccharides (at least pentasaccharide residues) favor this conformation (*25*). Thus, in the umbrella-like topology, which is unique

to α2,6, the specificity for a kink motif of a least five sugar residues long could indicate that a kinked sugar chain of comparable residues is able to reach into the binding locus on the HA surface. This concept was also the case for the present viral HA binding. Therefore, whereas the avian viral HA interactions with the glycans is characteristic of short α2,3 glycans, such as single LN/Lac, human viral HA interactions involve α2,6 and is typically adopted by long glycans with multiple repeating LN units.

To examine the inhibitory activity of sialoglycopolymers carrying multiple LN repeats, we administered glycopolymers to mice as an infection model. After inoculation with A/WSN/33, virus invades and propagates in various tissues, particularly in the lung and brain. As a result, mice develop mortality and typical morbidity, such as loss of movement and food consumption, resulting in loss of weight. Compound **27** carrying sialylated triplet LN repeats, but not with compound **23** carrying sialylated single LN, effectively protected mice from lethal challenge of A/WSN/33. At 13 days postinfection, only mice administered 3 nmol/kg of compound **27** all survived. No toxic effect was observed in mice inoculated with the same concentration of glycopolymer alone. This observation was consistent with the results of in vitro infection experiments. In vitro and in vivo infection experiments clearly showed that the extended structure of the glycan enhanced the inhibitory activity.

Furthermore, we tested the inhibitory effect of glycopolypeptides designed by replacement of nonsugar glycomimetics in the asialo portion of the molecule in order to identify the specific SA motifs recognized by influenza virus. The mimetics under discussion here, such as the spaced sugars, were anticipated to act as functional sugar mimetics, which typically display the activity of a carbohydrate. However, the relationship between the viral binding activity and the core determinant of the glycan is still unclear. Acyclic spacers were used to replace sugar units in a rather flexible way. Long spacer-linked polymers carrying alkylamido repeats linked to a terminal trisaccharide motif (SAα2,3/6LN) were prepared, based on the assumption that the seven-atom spacer of pentylamido group would be a mimetic for two glycosyl units. Interestingly, the mimetics turned out to be strong viral inhibitors against the human strain A/Aichi/2/68 by hemagglutinin inhibition assay. Thus, in the human virus, **35**/**36** carrying a tandem/triplet alkylamido repeat showed 2−4-fold higher inhibitory potency over **31**/**33** carrying a α2,6 sialylated long glycans. The length of the alkylamido chain linked to the terminal SAα2,3/6LN appeared to be critical for recognition by the human viral HA. A tandem alkylamido repeat constituted the minimum length of the bound spacer-linked glycan. Whitesides and colleagues reported that the crucial factors for influenza virus inhibition by conventional SA-conjugated glycopolymers are the cluster of SA units, the molecular weight, electrostatic considerations, presence of bulky/hydrophobic groups, and steric stabilization of the glycopolymer (*17*). Numerous types of synthetic multivalent glycoconjugates have been synthesized with regard to the multivalency principle occurring in the viral HA interactions with glycans. However, contribution of the asialo portion of the glycopolymer on inhibitory activity has not been extensively examined, because the length of glycan was limited to mono-, di-, and trisaccharides. Our study indicates that replacement of a part of the glycan by a nonsugar structural unit, such as pentylamido group, results in good inhibitory activity. This type of structure is suited to build up glycopolypeptides carrying more spacer-linked glycans by replacement of a long glycan. Conventional procedures for obtaining extended glycans, such as LN repeats, are cumbersome and involve several steps. However, nonsugar glycomimetics in the asialo portion of the molecule simplifies the large-scale preparation of the glycopolypeptides. Furthermore, γ-PGA is an obvious starting point to prepare polymeric inhibitors, because it is a readily available and inexpensive polymer. Indeed, the γ-PGA backbone from *B. subtilis* is commercially available in large quantities. The physiological merits of α- and γ-PGAs as the backbone to a glycopolymer in terms of cytotoxicity and immunogenicity have already been investigated. We have demonstrated that sialoglycopolymers with a α-PGA backbone have relatively low immunogenicity (*16*). Generally, conventional glycopolymers with a backbone such as PA can be toxic (*17*, *20*). In our previous study, acrylamide monomer, which is known to be a potent neurotoxin, and PAA-Na were found to be cytotoxic to MDCK cells under the conditions used for the tests (*16*). It has also been shown that sugar-bovine serum albumin (BSA) and PA conjugates act as antigens or immunogens (*16*).

CONCLUSION

Artificial sialoglycopolymers with a γ-PGA backbone that possess a single type of SA linkage (either α2,3 or α2,6) were chemoenzymatically synthesized. These compounds were then used as a tool to study the molecular interactions between receptors and viruses. Replacement by nonsugar glycomimetics in the asialo portion of the molecule made it possible to generate strongly active glycopolypeptides carrying more spacer-linked short glycans that were suitable for large-scale synthesis. It should be emphasized that our PGA-based polymers have an extremely high solubility in water (>10% w/v), as compared with PA-based polymers (1<%), and that they are remarkably heat-stable with no aggregation, even in boiling water. Therefore, PGA-based glycopolymers have ideal characteristics as potential in vivo polymeric inhibitors. Furthermore, precise analysis of the asialo moiety in the array of glycopolypeptides provides a facile way to explore the role of the glycan sequence in the binding of glycopolymers to the viruses, as well as increasing our understanding of the molecular basis to infection by influenza virus.

ACKNOWLEDGMENT

We are grateful to the Yamasa Corporation for the generous gift of the CMP-Neu5Ac, UDP-GlcNAc, and UDP-Gal. This work was supported by a grant-in-aid for Scientific Research (Nos. 19310141, 16380077) and Scientific Research on Priority Areas (18570135 to K.I.H.) from the Ministry of Education, Science, Sports, and Culture of Japan, and a research grant from Cooperation of Innovative Technology and Advanced Research in Evolutional Area (CITY AREA) in the Central Shizuoka Area-, Ministry of Education, Culture, Sports, Science and Technology (MEXT) of Japan.

LITERATURE CITED

(1) Paulson, J. C., Sadler, J., and Hill, R. L. (1979) Restoration of specific myxovirus receptors to asialoerythrocytes by incorporation of sialic acid with pure sialyltransferases. *J. Biol. Chem. 254*, 2120–2124.

(2) Suzuki, Y., Nagano, Y., Kato, H., Matsumoto, M., Nerome, K., Nakajima, K., and Nobusawa, E. (1986) Human influenza A virus hemagglutinin distinguishes sialyloligosaccharides in membrane-associated gangliosides as its receptor which mediates the adsorption and fusion processes of virus infection. *J. Biol. Chem. 261*, 17057–17061.

(3) Rogers, G. N., and D'Souza, B. L. (1989) Receptor binding properties of human and animal H1 influenza virus isolates. *Virology 173*, 317–322.

(4) Gambaryan, A. S., Tuzikov, A. B., Piskarev, V. E., Yamnikova, S. S., Lvov, D. K., Robertson, J. S., Bovin, N. V., and Matrosovich, M. N. (1997) Specification of receptor-binding phenotypes of influenza virus isolates from different hosts using synthetic sialylglycopolymers: non-egg-adapted human H1 and H3 influenza A and B viruses share a common high binding affinity for 6′-sialyl(*N*-acetyllactosamine). *Virology 232*, 345–350.

(5) Schengrund, C.-L. (2003) "Multivalent" saccharides: development of new approaches for inhibiting the effects of glycosphingolipid-binding pathogens. *Biochem. Pharmacol. 65*, 699–707.

(6) Ogata, M., Murata, T., Murakami, K., Suzuki, T., Hidari, K. I.-P.J., Suzuki, Y., and Usui, T. (2007) Chemoenzymatic synthesis of artificial glycopolypeptides containing multivalent sialyloligosaccharides with a γ-polyglutamic acid backbone and their effect on inhibition of infection by influenza viruses. *Bioorg. Med. Chem. 15*, 1383–1393.

(7) Suzuki, Y. (1994) Gangliosides as influenza virus receptors. Variation of influenza viruses and their recognition of the receptor sialo-sugar chains. *Prog. Lipid Res. 33*, 429–457.

(8) Hidari, K. I.-P.J., Shimada, S., Suzuki, Y., and Suzuki, T. (2007) Binding kinetics of influenza viruses to sialic acid-containing carbohydrates. *Glycoconj. J. 24*, 583–590.

(9) Yamada, S., Suzuki, Y., Suzuki, T., Li, M. Q., Nidom, C. A., Sakai-Tagawa, Y., Muramoto, Y., Ito, M., Kiso, M., Hiromoto, T., Shinya, K., Sawada, T., Kiso, M., Usui, T., Murata, T., Lin, Y., Hay, A., Haire, L. F., Stevens, D. J., Russell, R. J., Gamblin, S. J., Skehel, J. J., and Kawaoka, Y. (2006) Hemagglutinin mutations responsible for the binding of H5N1 influenza A viruses to human-type receptors. *Nature 444*, 378–382.

(10) Gambaryan, A. S., Tuzikov, A. B., Pazynina, G. V., Webster, R. G., Matrosovich, M. N., and Bovin, N. V. (2004) H5N1 chicken influenza viruses display a high binding affinity for Neu5Acα2−3Galβ1−4(6-HSO_3)GlcNAc-containing receptors. *Virology 326*, 310–316.

(11) Wu, W.-Y., Jin, B., Krippner, G. Y., and Watson, K. G. (2000) Synthesis of a polymeric 4-*N*-linked sialoside which inhibits influenza virus hemagglutinin. *Bioorg. Med. Chem. Lett. 10*, 341–343.

(12) Tsuchida, A., Kobayashi, K., Matsubara, N., Muramatsu, T., Suzuki, T., and Suzuki, Y. (1998) Simple synthesis of sialyllactose-carrying polystyrene and its binding with influenza virus. *Glycoconj. J. 15*, 1047–1054.

(13) Ohta, T., Miura, N., Fujitani, N., Nakajima, F., Niikura, K., Sadamoto, R., Guo, C.-T., Suzuki, T., Suzuki, Y., Monde, K., and Nishimura, S.-I. (2003) Glycotentacles: synthesis of cyclic glycopeptides, toward a tailored blocker of influenza virus hemagglutinin. *Angew. Chem., Int. Ed. 42*, 5186–5189.

(14) Choi, S.-K., Mammen, M., and Whitesides, G. M. (1997) Generation and in situ evaluation of libraries of poly(acrylic acid) presenting sialosides as side chains as polyvalent inhibitors of influenza-mediated hemagglutination. *J. Am. Chem. Soc. 119*, 4103–4111.

(15) Umemura, M., Itoh, M., Makimura, Y., Yamazaki, K., Umekawa, M., Masui, A., Matahira, Y., Shibata, M., Ashida, H., and Yamamoto, K. (2008) Design of a sialylglycopolymer with a chitosan backbone having efficient inhibitory activity against influenza virus infection. *J. Med. Chem. 51*, 4496–4503.

(16) Totani, K., Kubota, T., Kuroda, T., Murata, T., Hidari, K. I.-P.J., Suzuki, T., Suzuki, Y., Kobayashi, K., Ashida, H., Yamamoto, K., and Usui, T. (2003) Chemoenzymatic synthesis and application of glycopolymers containing multivalent sialyloligosaccharides with a poly(L-glutamic acid) backbone for inhibition of infection by influenza viruses. *Glycobiology 13*, 315–326.

(17) Sigal, G. B., Mammen, M., Dahmann, G., and Whitesides, G. M. (1996) Polyacrylamides bearing pendant α-sialoside groups strongly inhibit agglutination of erythrocytes by influenza virus: The strong inhibition reflects enhanced binding through cooperative polyvalent interactions. *J. Am. Chem. Soc. 118*, 3789–3800.

(18) Gamian, A., Chomik, M., Laferriere, C. A., and Roy, R. (1991) Inhibition on influenza A virus hemagglutinin and induction by synthetic sialylated glycoconjugates. *Can. J. Microbiol. 37*, 233–237.

(19) Spaltenstein, A., and Whitesides, G. M. (1991) Polyacrylamides bearing pendant α-sialoside groups strongly inhibit agglutination of erythrocytes by influenza virus. *J. Am. Chem. Soc. 113*, 686–687.

(20) Lees, W. J., Spaltenstein, A., Kingery-Wood, J. E., and Whitesides, G. M. (1997) Polyacrylamides bearing pendant alpha-sialoside groups strongly inhibit agglutination of erythrocytes by influenza A virus: multivalency and steric stabilization of particulate biological systems. *J. Med. Chem. 37*, 3419–3433.

(21) Itoh, M., Hetterich, P., Isecke, R., Brossmer, R., and Klenk, H. (1995) Suppression of influenza virus infection by an *N*-thioacetylneuraminic acid acrylamide copolymer resistant to neuraminidase. *Virology 212*, 340–347.

(22) Furuike, T., Aiba, S., Suzuki, T., Takahashi, T., Suzuki, Y., and Yamada, K. (2000) Synthesis and anti-influenza virus activity of novel glycopolymers having triantennary oligosaccharide branches. *J. Chem. Soc., Perkin Trans. 1*, 3000–3005.

(23) Mammen, M., Dahmann, G., and Whitesides, G. M. (1995) Effective inhibitors of hemagglutination by influenza virus synthesized from polymers having active ester groups. Insight into mechanism of inhibition. *J. Med. Chem. 38*, 4179–4190.

(24) Reuter, J. D., Myc, A., Hayes, M. M., Gan, Z., Roy, R., Qin, D., Yin, R., Piehler, L. T., Esfand, R., Tomalia, D. A., and Baker, J, Jr. (1999) Inhibition of viral adhesion and infection by sialic-conjugated dendritic polymers. *Bioconjugate Chem. 10*, 271–278.

(25) Chandrasekaran, A., Srinivasan, A., Raman, R., Viswanathan, K., Raguram, S., Tumpey, T. M., Sasisekharan, V., and Sasisekharan, R. (2008) Glycan topology determines human adaptation of avian H5N1 virus hemagglutinin. *Nat. Biotechnol. 26*, 107–113.

(26) Kato, T., Murata, T., Usui, T., and Park, E. Y. (2003) Improvement of GFPuv-β3GnT2 fusion protein production by suppressing protease in baculovirus expression system. *Biosci. Biotechnol. Biochem. 67*, 2388–2395.

(27) Suzuki, Y., and Matsumoto, M. (1985) N-Acetylneuraminyllactosylceramide, GM3-NeuAc, a new influenza A virus receptor which mediates the adsorption fusion process of viral infection. Binding specificity of influenza virus A/Aichi/2/68 (H3N2) to membrane-associated GM3 with different molecular species of sialic acid. *J. Biol. Chem. 260*, 1362–1365.

(28) Suzuki, Y., Suzuki, T., and Matsumoto, M. (1983) Isolation and characterization of receptor sialoglycoprotein for hemagglutinating virus of Japan (Sendai virus) from bovine erythrocyte membrane. *J. Biochem. (Tokyo) 93*, 1621–1633.

(29) Yasuno, S., Murata, T., Kokubo, K., Yamaguchi, T., and Kamei, M. (1997) Two-mode analysis by high-performance liquid chromatography of p-aminobenzoic ethyl ester-derivatized monosaccharides. *Biosci. Biotechnol. Biochem. 61*, 1944–1946.

(30) Sato, C., Inoue, S., Matsuda, T., and Kitajima, K. (1998) Development of a highly sensitive chemical method for detecting α2,8-linked oligo/polysialic acid residues in glycoproteins blotted on the membrane. *Anal. Biochem. 261*, 191–197.

(31) Hidari, K. I.-P.J., Murata, T., Yoshida, K., Minamijima, Y., Adachi, S., Ogata, M., Usui, T., Suzuki, Y., and Suzuki, T. (2008) Chemoenzymatic synthesis, characterization, and application of glycopolymers carrying lactosamine repeats as entry inhibitors against influenza virus infection. *Glycobiology 18*, 779–788.

(32) Peto, R., Pike, M. C., Armitage, P., Breslow, N. E., Cox, D. R., Howard, S. V., Mantel, N., McPherson, K., Peto, J., and Smith,

P. G. (1997) Design and analysis of randomized clinical trials requiring prolonged observation of each patient. II. Analysis and examples. *Br. J. Cancer 35*, 1–39.

(33) Kaplan, E. L., and Meier, P. (1958) Nonparametric estimation from incomplete observations. *J. Am. Statist. Assoc. 53*, 457–481.

(34) Srinivasan, A., Viswanathan, K., Raman, R., Chandrasekaran, A., Raguram, S., Tumpey, T. M., Sasisekharan, V., and Sasisekharan, R. (2008) Quantitative biochemical rationale for differences in transmissibility of 1918 pandemic influenza A viruses. *Proc. Natl. Acad. Sci. U.S.A. 105*, 2800–2805.

(35) Stevens, J., Blixt, O., Glaser, L., Taubenberger, J. K., Palese, P., Paulson, J. C., and Wilson, I. A. (2006) Glycan microarray analysis of the hemagglutinins from modern and pandemic influenza viruses reveals different receptor specificities. *J. Mol. Biol. 355*, 1143–1155.

(36) Blixt, O., Allin, K., Bohorov, O., Liu, X., Andersson-Sand, H., Hoffmann, J., and Razi, N. (2008) Glycan microarrays for screening sialyltransferase specificities. *Glycoconj. J. 25*, 59–68.

BC800460P

Subscriber access provided by SHEMYAKIN-OVCHINNIKOV INST

Article

In Situ Ligation between Peptides and Silica Nanoparticles for Making Peptide Microarrays on Polycarbonate

Vianney Souplet, Re#mi Desmet, and Oleg Melnyk

Bioconjugate Chem., **2009**, 20 (3), 550-557• DOI: 10.1021/bc800474g • Publication Date (Web): 17 February 2009

Downloaded from http://pubs.acs.org on May 8, 2009

More About This Article

Additional resources and features associated with this article are available within the HTML version:

- Supporting Information
- Access to high resolution figures
- Links to articles and content related to this article
- Copyright permission to reproduce figures and/or text from this article

View the Full Text HTML

ACS Publications
High quality. High impact.

Bioconjugate Chemistry is published by the American Chemical Society. 1155 Sixteenth Street N.W., Washington, DC 20036

In Situ Ligation between Peptides and Silica Nanoparticles for Making Peptide Microarrays on Polycarbonate

Vianney Souplet, Rémi Desmet, and Oleg Melnyk*

Institut de Biologie de Lille, UMR CNRS 8161, Universités de Lille 1 et 2, Institut Pasteur de Lille, IFR 142, 1 rue du Professeur Calmette, 59021 Lille Cedex, France. Received October 31, 2008; Revised Manuscript Received January 14, 2009

Bisphenol A polycarbonate (PC) is emerging as an interesting alternative to silicon oxide substrates for making microarrays. We show that the printing of peptide/nanoparticle mixtures allows the creation of complex peptide microarrays. Semicarbazone ligation was used for linking the peptides to the nanoparticles. The reaction occurred probably after printing due to solvent evaporation and to the in situ concentration of the reagents. Peptide microarrays were used successfully for the specific capture of purified antibodies or of antibodies from serum.

INTRODUCTION

The detection of antibodies in biological samples using polypeptide probes has a wide range of potential applications. Enzyme-linked immunosorbent assays (ELISA) are often used in this field. However, the need for studying large collections of antigens and biological samples has stimulated the development of high-throughput systems. In particular, peptide or protein microarrays (*1*−*3*) are now increasingly used for the study of autoimmune (*4*) or infectious diseases (*5*−*8*) to cite only few applications. Besides the parallelization of the assay, the great advantage of miniaturization is that microspot assay sensitivities can be higher than those obtainable by conventional methods (*9*−*11*). Various methods are used to detect the antibodies captured by the immobilized antigens. Among them, fluorescence is probably the most frequently used detection technique (*12, 13*).

The physicochemical properties of the substrate and the bond formed between the peptide probes and the surface play a crucial role in the performance of the microarray (*14*). A microscope glass slide is a standard substrate for making microarrays. This substrate is cheap, has a low intrinsic fluorescence, and can be easily functionalized with silanes. The attachment of polypeptides to silicon oxide substrates was achieved using different methods (*15*). Chemoselective methods include native (*15*−*17*), oxime (*18*), semicarbazone (*6, 19, 20*), or Staudinger (*21*) ligations as well as various thiol chemistries (*18*). Other methods include random attachment of the polypeptide chain to the surface using amide chemistry (*22*), Ni(II) coordination chemistry (*23*), or the biotin/avidin interaction (*17, 24, 25*). Immobilization of polypeptides can also be achieved by physisorption (*5*−*7*).

The widespread use of microarrays for diagnostic applications requires the development of safe systems. Because glass can break and cut, the analysis of potentially contaminating samples with glass-based devices must be avoided. Bisphenol A polycarbonate is emerging as an interesting material in this field: it is shock-resistant, and it can be easily molded and eliminated by incineration. This polymer is also used for compact disc manufacturing, and the use of this substrate as a platform for high-throughput binding assays has attracted much attention recently (*26*−*29*). Unfortunately, only few chemical methods are available for linking molecules to PC. In the work of La Clair et al., terminal OH residues of PC were first converted to surface-bound chlorophosphate groups, which were subsequently reacted with alcohol-functionalized probes to yield a phosphodiester bond (*30*). In the work of Soper et al., UV-ozone treatment of PC led to the formation of surface-exposed carboxylic acid residues which, upon activation, permitted the immobilization of amine-modified oligonucleotides through an amide bond (*31*). Bańuls et al. derivatized PC compact discs by spin-coating the support with a hydroxy-modified PMMA polymer, followed by treatment with (3-isocyanatopropyl)triethoxysilane (*32*). The same group described recently the preparation of amine- or thiol-derivatized PC discs (*33*). The surfaces were used for immobilizing aminated oligonucleotides (*32*). Bora et al. described the photochemical activation of PC (96-well plates) using 1-fluoro-2-nitro-4-azidobenzene and UV irradiation. Proteins were immobilized randomly by nucleophilic aromatic substitution of fluorine atoms by amine groups. Finally, we have recently shown that silica nanoparticles can be adsorbed on PC to form micropatterns (*34*). These micropatterns were subsequently reacted chemoselectively using semicarbazone ligation with peptides by covering the whole PC substrate with the peptide solution. Consequently, the same peptide was attached to all the micropatterns. Clearly, the methods described cannot be used for the chemoselective attachment of peptides to PC or for the creation of complex peptide microarrays.

We have examined here the possibility of creating different peptide micropatterns on PC by printing mixtures of peptides and nanoparticles and by allowing the ligation to proceed in situ. The influence of different parameters such as the buffer used for printing and the peptide concentration on peptide micropattern formation was examined. The microarrays were used for detecting antibodies using fluorescence detection. The method was first optimized using HA and FLAG tag peptides and their corresponding murine antibodies. Subsequently, a collection of overlapping peptides derived from amyloid beta Aβ 1−42 peptide was synthesized and used to probe an anti-Aβ monoclonal antibody using either the microarray or the ELISA methods. Finally, the specific detection of antibodies in serum was examined to test the usefulness of the microarray method in real detection experiments.

MATERIALS AND METHODS

Peptide Synthesis. *COCHO*−*HA, COCHO*−*FLAG.* The synthesis of COCHO−HA (CHOCO-GYPYDVPDYAGYPYD-VPDYAGYPYDVPDYAS-NH_2) (*35*) and CHOCO-FLAG (CO-

* Corresponding author. Phone: 333 20 87 12 14. Fax: 333 20 87 12 35. E-mail oleg.melnyk@ibl.fr.

10.1021/bc800474g CCC: $40.75 © 2009 American Chemical Society
Published on Web 02/17/2009

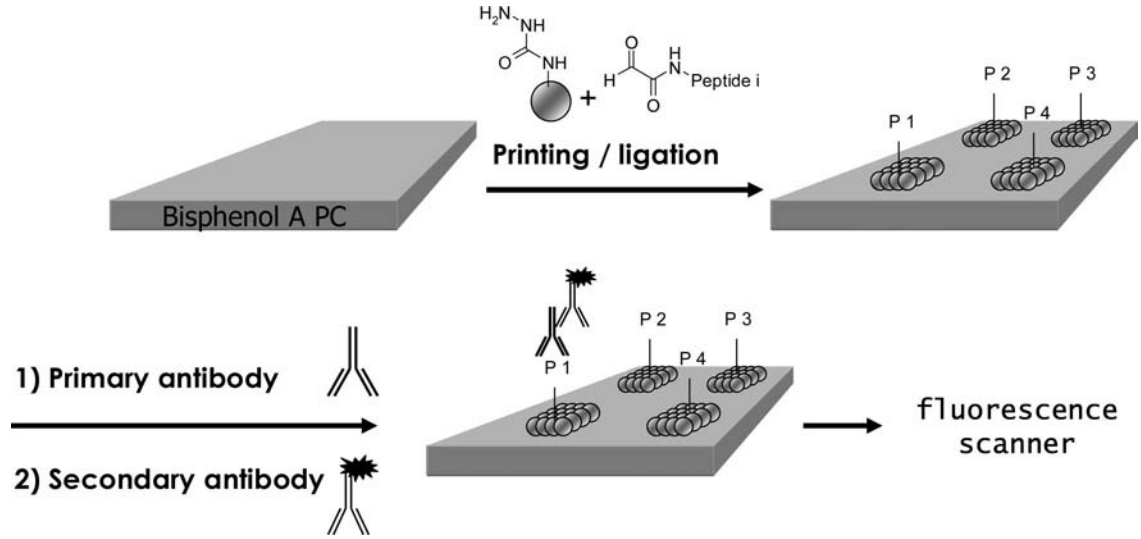

Figure 1. Preparation of peptide microarrays on PC slides by printing mixtures of SSN and COCHO−peptides as microspots. Microarrays were used to detect antibodies using a tetramethylrhodamine-labeled secondary antibody and fluorescence detection at 532 nm.

CHO−DYKDHDGDYKDHDIDYKDDDDKGGS-NH_2) (*36*) peptides was performed by treating the Ser-HA or Ser-FLAG precursors with sodium periodate (*37*). The detailed procedures and characterization data are presented elsewhere (*34*).

APP-COCHO **1**−**12.** APP-COCHO peptides were synthesized on the solid phase using standard Fmoc/*tert*-butyl chemistry and Pioneer synthesizer (Applied Biosystems, CA, USA) (*38*). The peptides were assembled on a tartaramide-NovaSyn TG resin (0.1 mmol, Novabiochem, France) using 1,3-diaminopropane as linker (*39*−*41*). For peptides APP-COCHO **1**−**7** and **9**−**12**, the N-terminal Fmoc group was removed using DMF/piperidine: 4/1 by vol on the synthesizer. The resin was washed with DMF and MeOH and dried. For peptide APP-COCHO 8, the N-terminal Fmoc group was left on the resin to avoid oxidation of N-terminal Ser residue. All the peptidyl resins were deprotected using TFA/water/triisopropylsilane: 95/2.5/2.5 by vol (10 mL) at rt during 1 h 30, washed, and dried.

The resins were resuspended in 20% aqueous AcOH (5 mL). Oxidative cleavage was then performed by adding $NaIO_4$ (0.60 mmol, 128 mg dissolved in 2 mL of 10% aqueous AcOH) in one portion to the peptidyl resins. The resins were agitated 2 min 30 s. Ethanolamine (2.4 mmol, 144 μL) was added to stop the reaction. The resins were filtered and washed with water (2 × 5 mL). The combined filtrates were immediately purified by RP-HPLC on a 120 Å 5 μm C18 Nucleosil column using a linear water/acetonitrile gradient containing 0.05%TFA by vol (6 mL/min, detection 225 nm). The fractions were collected and lyophilized to give APP-COCHO **1**−**7**, **9**−**12** (56−72 mg), and Fmoc-APP-COCHO **8** (70 mg).

Fmoc-APP-COCHO **8** (9.6 μmol, 19.0 mg) was dissolved in DMF (500 μL). DBU (95.7 μmol, 14.3 μL) was added in one portion. After 10 min at rt, the reaction was stopped by adding 10% aqueous TFA (191 μmol, 145.4 μL). The crude peptide was precipitated in Et_2O (30 mL), centrifugated, and purified by RP-HPLC as above to give 9.8 mg of APP-COCHO **8**.

Analytical RP-HPLCs and MALDI-TOF for all peptides are presented in Supporting Information.

Rho-KR-NH(CH_2)$_3$NH-COCHO and Rho-KR-NH_2 Peptides. Peptide Rho-KR-NH(CH_2)$_3$NH-COCHO was prepared on the solid phase using the tartaramide linker as described for APP-COCHO peptides. Rho-KR-NH_2 was prepared on the solid phase using standard Fmoc/*tert*-butyl chemistry. Detailed protocols are available elsewhere (*19, 42*).

Typical Printing Procedure. Commercially available polycarbonate sheets 300 × 300 × 1 mm (Goodfellow, Huntingdon, UK) were cut by high-pressure water jet at the size of microscope glass slides 75 × 25 × 1 mm^3 (Economos, Dunkerque, France). Polycarbonate slides were washed twice with deionized water and absolute ethanol (ACROS Organics, Geel, Belgium), respectively, before use.

The preparation of semicarbazide silica nanoparticles (SSN) was described in detail elsewhere (*34*). These particles are typically prepared as a 10 mg/mL suspension in DMF. This suspension is stable for months when stored at 4 °C. Before printing, the suspension is centrifuged at 21 000 × *g* for 30 min at 10 °C and resuspended under sonication in DMF to obtain a 20 mg/mL suspension.

The peptide/SSN mixtures were prepared in V-bottomed 96-well microtiter plates (ABgene, Surrey, UK, AB-1058, 40 μL/per well) by mixing SSN suspension with peptides dissolved at 20 μM in 5 mM sodium acetate buffer (pH 5.5). The final peptide concentration is 10 μM.

Each peptide/SSN mixture was printed in triplicate on each microarray. The mixtures (3 drops, 300 pL each, 3 replicates per peptide) were printed on PC slides using either a BCA1 Microarrayer (Perkin-Elmer, MA, USA used with long piezoarray tips ref 7601831) or a Qarray2 contact microarrayer (1 hit per dot, Genetix, New Milton, UK, used with tungsten pins ref PTS200, European Biotech Nnetwork, Belgium). The piezoarray tips were washed under sonication with DMF/water: 1/1 by vol buffered at pH 5.5 with 5 mM sodium acetate and water after each sample. The tips used with the Qarray2 microarrayer were washed three times with water and then with ethanol.

Up to 24 patterns can be printed per PC slide. The position of these patterns must be carefully controlled to allow the correct positioning of the patterns in the 96 well microplate microarray hardware used for the subsequent incubations and washing steps (TeleChem International, Inc. CA, USA, ref MMH4 × 24, ref GMMH4 × 24). The printed slides were incubated overnight in an oven at 37 °C and 60% relative humidity to favor ligation of the peptides to the nanoparticles. The slides were stored under nitrogen atmosphere at rt until use.

Typical Incubation Procedure for Microarrays. *PBS-A: 2% w/v BSA in PBS. PBS-B: 0.05% v/v Tween20 in PBS.* Each experiment was performed in triplicate (3 wells or microarrays per incubation). Incubations were performed in an incubator (Biosan, MI, USA, ref PST-60HL-4). The plate was warmed at 37 °C during 15 min and then saturated with PBS-A for 5 min at 37 °C (150 μL per well). The wells were washed twice with PBS-B and then incubated with the primary antibody diluted

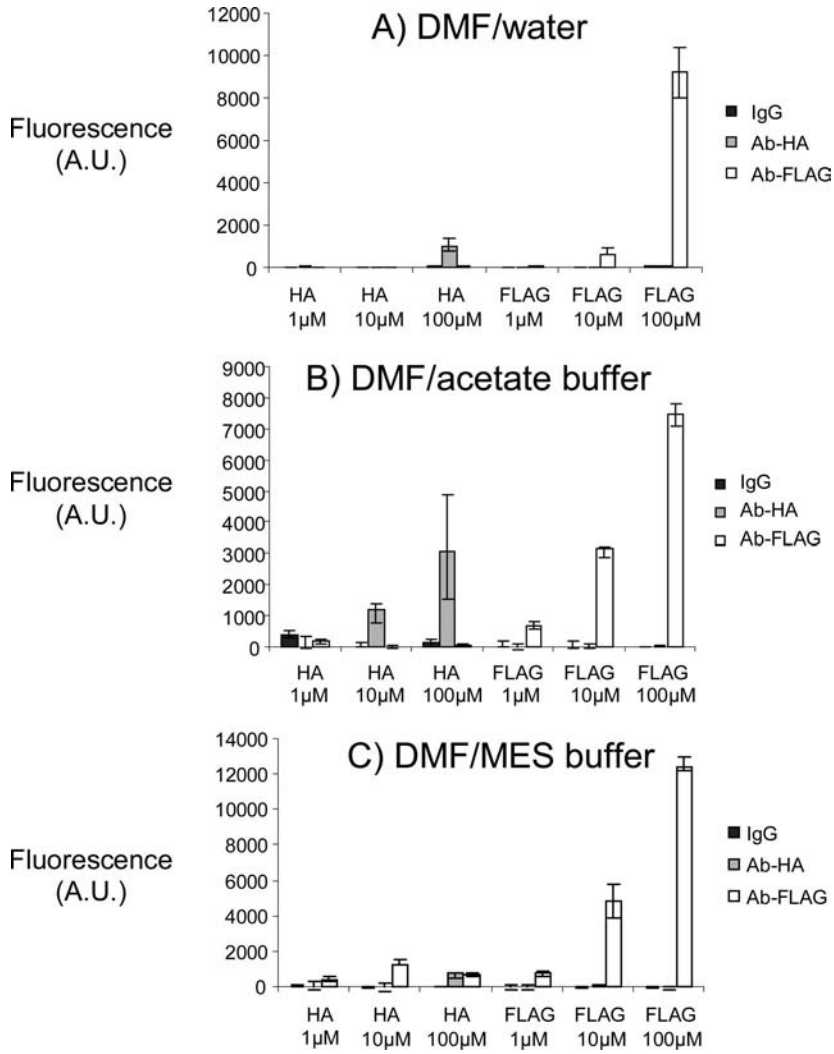

Figure 2. Effect of the buffer on the in situ ligation of COCHO−peptides to semicarbazide nanoparticles. Peptides were printed at 1, 10, or 100 μM in DMF/buffer: 1/1 v/v mixture (final nanoparticle concentration 1% w/v, BCA1 piezoelectric arrayer, 3 drops/spot, 1 nL overall, 5 replicates). (A) DMF/water, (B) DMF/pH 5.5 5 mM sodium acetate, (C) DMF/pH 5.5 5 mM MES. The microarrays were incubated in triplicate with Ab-HA, AbFLAG, or murine IgGs (10 μg/mL) 1 h at 37 °C and then with tetramethylrhodamine-labeled antimurine antibodies. Detection was performed at 532 nm using a standard fluorescence microarray scanner. The data represent the median and interquartile range for 3 microarrays.

in PBS-A for 1 h at 37 °C (120 μL per well). The wells were washed 3 times with PBS-B and incubated immediately with secondary antibody (120 μL per well, 1 h at 37 °C, typically at 10 μg/mL in PBS-A). The wells were washed 3 times with PBS-B and water. The slides were then removed from the microplate hardware, washed with EtOH, dried under N_2, and analyzed at 532 nm with a standard microarray scanner (Innoscan 700, Innopsys, France). 16-bit images were analyzed using Mapix software (Innopsys, France). Fluorescence intensities are expressed in arbitrary units (A.U.). The data presented correspond to the median of the pixel intensities for the analyzed spots.

ELISA. *PBS-C: 3% w/v BSA in PBS.* Peptides were solubilized in pH 9.6 sodium carbonate/sodium bicarbonate buffer at 0.57 μM. The wells (Nunc Immuno Maxisorp 96-well plates, VWR) were coated overnight at 4 °C with the peptide solutions diluted 1/100 (100 μL per well, 2 wells per peptide), washed 3 times with PBS, and saturated 1 h at 37 °C with PBS-C (200 μL per well). The wells were washed 3 times with PBS-B and then incubated 2 h at rt with 6E10 antibody diluted 1/10 000 in PBS-C (100 μL per well, Eurogentec, Belgium). The wells were washed 3 times with PBS-B and then incubated 1 h at 37 °C with horseradish peroxidase (HRP)-labeled goat antimurine antibodies diluted 1/10 000 in PBS-C (100 μL per well, SouthernBiotech, AL, USA). The wells were washed 6 times with PBS-B. TMB solution (100 μL per well, Interchim, France) was added to the wells at rt. After 30 min in the dark, the reaction was stopped with 2 N H_2SO_4 (50 μL per well) and the absorbance at 450 nm was measured immediately.

RESULTS AND DISCUSSION

The derivatization of PC by chemical groups allowing the site-specific immobilization of peptides is difficult to achieve. In this context, the use of silica nanoparticles for functionalizing PC is an attractive strategy because the introduction of various functional group on silica nanoparticles can be performed easily by silanization. In this work, peptides were immobilized within silica micropatterns formed on PC. Besides the use of small amounts of reagents, the advantage of creating micropatterns is that the PC substrate between the microspots and thus its interesting physicochemical properties remain unchanged.

We have recently described a method for micropatterning PC using semicarbazide silica nanoparticles. A suspension of SSN in DMF/water was printed on PC using a piezoelectric non-contact microarrayer. The evaporation of the solvent resulted in an SSN layer on PC. The micropatterns were subsequently reacted chemoselectively with a COCHO−peptide by covering

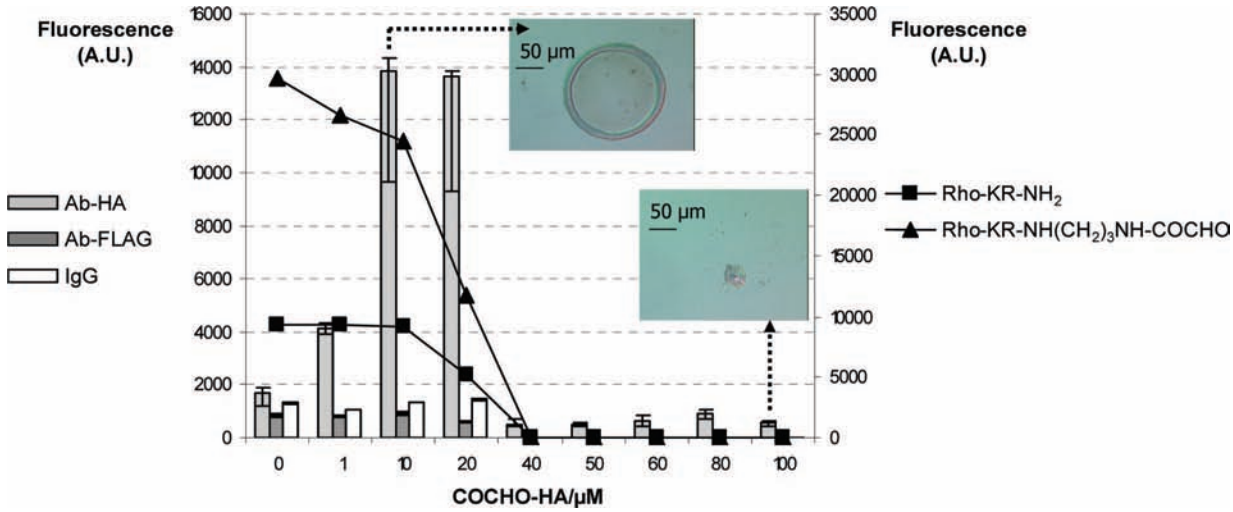

Figure 3. Effect of COCHO−peptide concentration. Peptides were printed at 0−100 μM in DMF/pH 5.5 5 mM sodium acetate buffer: 1/1 v/v mixture containing 1% w/v of SSN (BCA1 piezoelectric arrayer, 3 drops/spot, 1 nL overall, 5 replicates). The microarrays were incubated in triplicate with Ab-HA, Ab-FLAG, or murine IgG (10 μg/mL) 1 h at 37 °C and then with tetramethylrhodamine-labeled antimurine antibodies (left scale) or with peptide Rho-KR-NH$(CH_2)_3$NH-COCHO or Rho-KR-NH_2 (10^{-4} M, 0.1 M pH 5.5 sodium acetate buffer). Detection was performed at 532 nm using a standard fluorescence microarray scanner. The data represent the median and interquartile range. Images correspond to COCHO−HA/SSN microspots at 10 or 100 μM imaged using a microscope operating in the DIC mode.

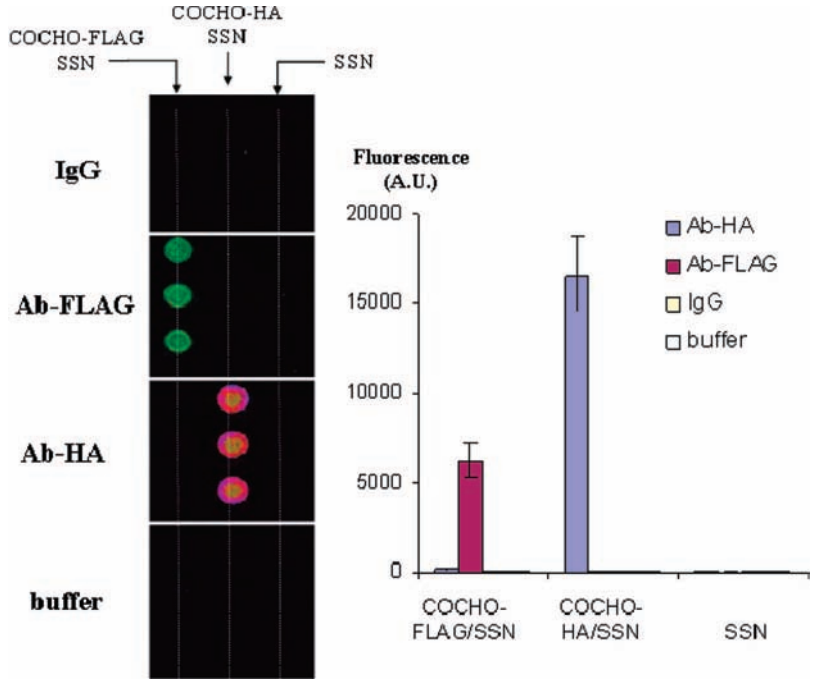

Figure 4. Peptides were printed at 10 μM in DMF/pH 5.5 5 mM sodium acetate buffer: 1/1 v/v mixture (final nanoparticle concentration 1% w/v, Qarray2 microarrayer (Genetix), 3 replicates) on PC slides (75 × 25 × 1 mm^3). The PC slides were inserted in a 96 well microplate microarray hardware (Telechem, Inc., CA, USA) equipped with a silicone gasket. The microarrays were incubated in triplicate with Ab-HA, Ab-FLAG, or murine IgG (10 μg/mL) or the buffer during 1 h at 37 °C and then with tetramethylrhodamine-labeled antimurine antibodies. Incubations and washings were performed using standard 96 well plates incubation and washing stations. Detection was performed at 532 nm using a standard fluorescence microarray scanner. The data represent the median and the interquartile range.

the whole substrate with the aqueous peptide solution. The method is of great interest for immobilizing peptides or proteins which require an aqueous environment to be soluble or to retain their active conformation. However, the method limits the number of probes which can be immobilized within PC-based miniaturized devices.

The preparation of complex peptide microarrays on PC required addressing a collection of peptides on different silica micropatterns in a simple way. SSN are stable for months in DMF/water but aggregate immediately in water. Hopefully, most peptides are soluble in DMF/water mixtures, thus opening the possibility to mix SSN and COCHO−peptides prior to the printing step for addressing a collection of peptides on PC (Figure 1). Ligation between the COCHO−peptide and SSN was expected to occur in solution and/or after printing due the concentration of the reagents on the microspot.

Optimization of the Printing Buffer. The buffer used for printing the mixtures of SSN and COCHO−peptides was expected to play a crucial role, since Schiff base formation between hydrazine derivatives and aldehydes is known to be pH-dependent. The best kinetics for hydrazone or semicarbazone bond formation are generally observed around pH 5.

This parameter was examined using COCHO−HA and COCHO−FLAG peptides derived from well-known tag se-

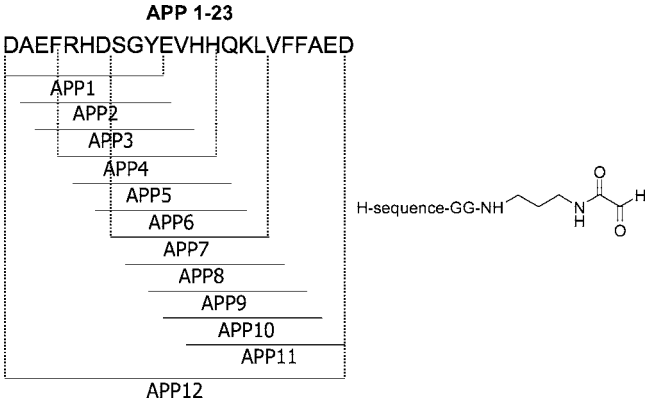

Figure 5. β-amyloid peptides APP **1**−**12** synthesized in this study. The peptides are derived from the N-terminal sequence **1**−**23** of amyloid precursor protein (APP). The peptides were modified by a COCHO group at the C-terminus, separated from the backbone by a 1,3-diaminopropyl spacer and two glycines.

quences. The peptides were printed from 1 to 100 μM in DMF/water, DMF/pH 5.5 acetate buffer, or DMF/pH 5.5 MES buffer. The final SSN concentration was 1% w/v. The substrates were incubated with anti-HA, anti-FLAG, or murine IgG antibodies used as negative control and then tetramethylrhodamine-labeled secondary antibodies (Figure 1). Fluorescence was detected at 532 nm.

The data are presented in Figure 2. At low peptide concentration (1 or 10 μM), the use of buffered mixtures (B and C) gave better results in terms of signal strength than DMF/water mixture (Figure 2A). Examination of the data obtained for COCHO−HA peptide shows that, between the two buffers tested, sodium acetate was by far superior to MES buffer in terms of both signal strength and specificity. Thus, the DMF/sodium acetate buffer was used in the rest of the study.

Effect of COCHO−Peptide Concentration. In the preceding experiment, the highest COCHO−peptide concentration used was 100 μM. Subsequently, the quality of the microarrays prepared using these experimental conditions appeared to be highly variable. Thus, the influence of COCHO−peptide concentration on the formation of the micropatterns was studied in detail using COCHO−HA peptide. After printing, a series of microarrays were incubated with Ab-HA to probe the presence of HA peptide on the micropattern (Figure 3, left-hand-side scale). Another series was incubated with peptide Rho-KR-NH$(CH_2)_3$-COCHO, as a probe for the presence of unreacted semicarbazide groups on the micropattern. Peptide Rho-KR-NH_2 was used as a control to estimate the level of physisorption (Figure 3, right-hand-side scale).

The signal strength of COCHO−HA/SSN microspots after incubating with HA-Ab increased significantly for concentrations up to 20 μM, whereas the signal strength after incubating with peptide Rho-KR-NH$(CH_2)_3$-COCHO decreased significantly in the same concentration range. The same trend was observed with COCHO−FLAG/SSN microspots (data not shown). The concomitant increase of COCHO−HA peptides and decrease of semicarbazide groups on silica nanoparticles is expected if immobilization occurs through site-specific semicarbazone ligation. However, concentrations above 40 μM led to very low signal strengths for both experiments, suggesting that aggregation of the COCHO−HA/SSN mixture occurred before printing. Observation of the PC substrates with an optical microscope operating in the differential interference contrast (DIC) mode showed the presence of a SSN layer at 10 μM but not at 100 μM, thus confirming the probable aggregation of the COCHO−HA/SSN mixture above 40 μM.

Aggregation of COCHO−peptide/SSN mixtures occurred frequently above 40 μM COCHO−peptide concentration. The aggregation kinetics also probably depends on how the COCHO−peptides and the SSN are mixed together, a parameter which cannot be easily controlled due to the small volumes manipulated. Interestingly, COCHO−peptide/SSN mixtures were always found to be stable at 10 μM. Consequently, these experimental conditions were used in the rest of this study.

The reaction between a semicarbazide and an aldehyde group is chemoselective, and the equilibrium usually favors the formation of the semicarbazone in aqueous solution. However, the equilibration kinetics can be slow, especially if concentrations lower than millimolar are used. Because ligation of the COCHO−peptide to the surface of the SSN is not favored at 10 μM, the surface of the SSN is probably unchanged in the COCHO−peptide/SSN mixture, thus explaining the stability of the suspension. We hypothesize that ligation between SSN and COCHO−peptides occurs predominantly on the microspot after printing due to the evaporation of the solvents (in a few seconds) which leads to a concentration of the ligation partners on the PC substrate.

COCHO−peptide/SSN mixtures can be printed using a piezoelectric noncontact microarrayer as above or using a standard contact microarrayer (Figure 4). In this experiment, COCHO−HA or COCHO−FLAG/SSN mixtures were printed on PC slides using tungsten pins. The slides were then inserted in a 96 well device for the incubations and washings using standard ELISA incubation or washing stations. The data illustrate the good specificity of the interaction taking place on the COCHO−peptide/SSN microspots and the absence of carryover between the different COCHO−peptide/SSN mixtures.

Preparation of APP Microarray. The principal aim of the following experiment was to show the interest of the method for preparing microarrays of higher complexity. We have also compared PC microarray data with those obtained using a standard ELISA assay. For this purpose, a series of COCHO-peptides derived from APP protein and monoclonal antibody 6E10 raised against amino acids 4−9 of APP (FRHDSG) were selected (Figure 5) (*43*). APP-COCHO **1**−**11** are overlapped by nine amino acids, whereas APP-COCHO **12** span the whole **1**−**23** sequence of APP. Alzheimer disease (AD) is the major cause of senile dementia. Degradation of APP by several enzymes leads to the formation of β-amyloid (Aβ) peptides which aggregate extracellularly into senile plaques (*44*). Neurodegeneration in AD is due in part to the accumulation of these senile plaques. A huge effort is currently dedicated to the design of vaccines against amyloid deposits since the discovery of Schenk et al. that immunization of APP transgenic mice with Aβ reduces senile plaques and prevents new deposits of β-amyloid (*45*−*47*). The fine control of the specificity of the antibodies produced by immunization is of prime importance to avoid side effects. Thus, besides this model experiment, a peptide microarray presenting different Aβ peptides should be useful for determining the specificity of anti-Aβ antibodies and the relationships between specificity and vaccine efficacy.

APP-COCHO peptides were synthesized on the solid phase using Fmoc/*tert*-butyl chemistry (*38*). For peptides APP-COCHO **1**−**7** and **9**−**12**, the COCHO group was introduced at the C-terminus of the peptides using a tartaramide linker and a solid-phase oxidative cleavage of the tartaramide with sodium periodate (Scheme 1) (*39*−*41*). APP-COCHO **8** features a N-terminal Ser residue and could not be synthesized using the procedure used for the other APP-COCHO peptides, because in this position, Ser residue is also oxidatively cleaved by periodate (*37*). Thus, the N-terminal Fmoc protecting group was left on the peptidyl resin to protect the β-amino alcohol moiety of Ser. Deprotection of the side chains in TFA and periodate cleavage of the tartaramide moiety provided Fmoc-APP-

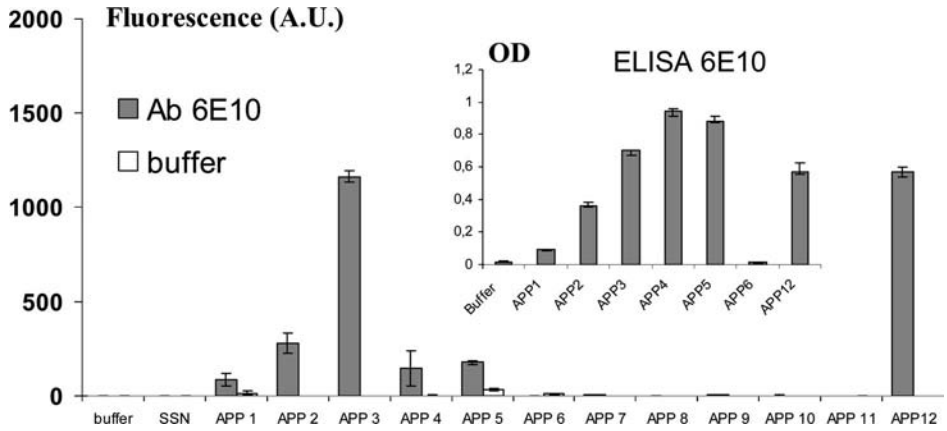

Figure 6. The binding of APP-COCHO **1**−**12** peptides to 6E10 antibody was examined using microarrays prepared on PC slides or the ELISA technique on standard polystyrene 96 well plates. The microarrays were incubated with 6E10 antibody diluted 1/10 000 in PBS and secondary antimurine antibodies labeled with tetramethylrhodamine detected at 532 nm. ELISA assay was performed using an antimurine antibody-HRP conjugate diluted 1/10 000. The absorbance was measured at 450 nm.

Scheme 1. Synthesis of APP-COCHO Peptides

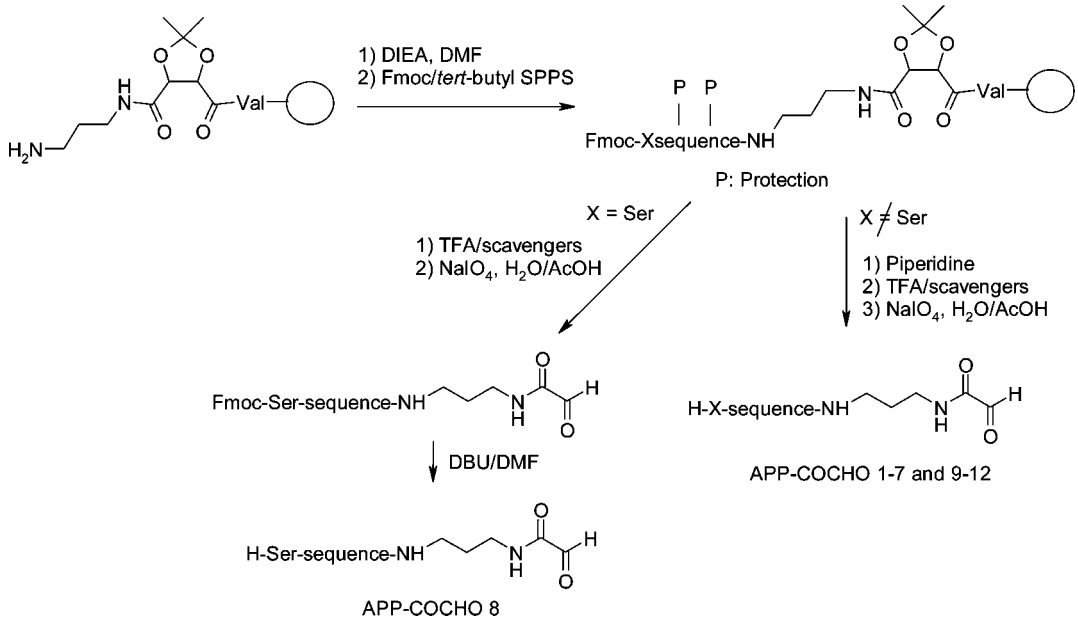

COCHO **8**, which was subsequently deprotected in the presence of DBU to give APP-COCHO **8**.

The APP-COCHO/SSN mixtures were printed using the contact microarrayer and tungsten pins as above. The concentration of each APP-COCHO peptide solution was verified by RP-HPLC as described elsewhere (*48*). No aggregation was observed before or during printing. The microarrays were incubated with murine 6E10 antibody and tetramethylrhodamine-labeled antimurine antibodies for fluorescence detection at 532 nm. APP-COCHO peptides were also coated on standard polystyrene 96 well plates for ELISA. The data are presented in Figure 6.

Examination of Figure 6 reveals that both assays displayed similar results: (i) peptides APP-COCHO **1**−**5** and **12** bind to 6E10 monoclonal antibody, (ii) APP-COCHO **6** did not react with the antibody, highlighting the critical role of R5 for binding to the 6E10 antibody. APP-COCHO **3** gave the best signal using the microarray method, whereas the highest signal was observed for APP-COCHO **4** using the ELISA. The use of microarrays prepared by printing the APP-COCHO **1**−**12** peptides on semicarbazide-functionalized glass slides led to results very similar to polycarbonate microarrays: APP-COCHO **3** was the best binder, and the signal displayed by APP-COCHO **6** was not significantly different from the background (data not shown). These results suggest that the differences observed between the two detection techniques are probably due to the difference in the mode of binding of the peptides to the substrates rather than to other parameters such as substrate chemical composition or roughness. In the microarray experiment, the peptides were attached site-specifically to the substrate through their C-terminus, whereas in the ELISA assay, the peptides were randomly physisorbed on the polystyrene substrate.

Detection of Antibodies in Biological Samples. The utility of the in situ ligation technique for detecting antibodies in serum was documented using peptide COCHO−HA and Ab-HA antibodies diluted in murine serum. SSN or COCHO−FLAG/SSN microspots were used as controls. The data presented in Figure 7 show the good specificity of the detection since the SSN or COCHO−FLAG microspots were nearly indistinguishable from the background in the entire Ab-HA concentration range. Figure 5B details the data obtained for the lowest Ab-HA concentrations. Ab-HA could be still detected at 10 ng/mL. In this experiment, the same scanning parameters were used for the entire Ab-HA concentration range. The sensitivity of the detection can probably be improved by adjusting the scanning parameters in the low Ab concentration range. Overall,

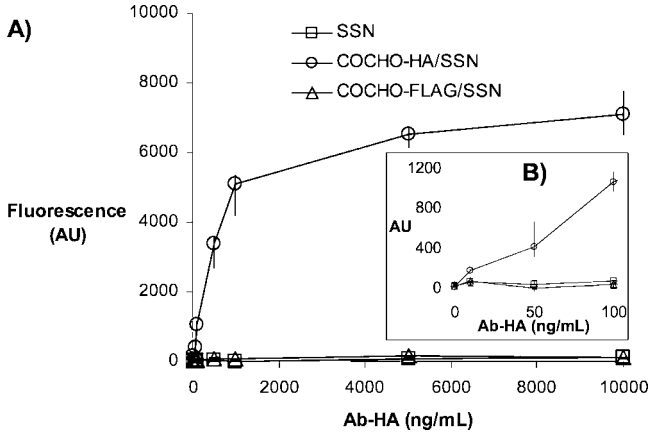

Figure 7. Peptides were printed at 10 μM in DMF/pH 5.5 5 mM sodium acetate buffer: 1/1 v/v mixture (final nanoparticle concentration 1% w/v, Qarray2 microarrayer (Genetix), 3 replicates) on PC slides (75 × 25 × 1 mm^3). The PC slides were inserted in a 96 well microplate microarray hardware (Telechem, Inc., CA, USA) equipped with a silicone gasket. The microarrays were incubated in triplicate during 1 h at 37 °C with Ab-HA diluted from 0 to 10 μg/mL in murine serum (final dilution of serum: 1/50) and then with tetramethylrhodamine-labeled antimurine antibodies. Incubations and washings were performed using standard 96 well plates incubation and washing stations. Detection was performed at 532 nm using a standard fluorescence microarray scanner. The data represent the median and interquartile range for SSN (open squares), COCHO−HA (open circles), or COCHO−FLAG/SSN (open triangles) microspots. Insert (B) shows the data for the lowest concentrations of Ab-HA (0, 10, 50 ng/mL).

these results show the utility of the in situ ligation of COCHO−peptides on SSN for detecting antibodies in complex samples such as serum.

CONCLUSION

We have shown that in situ site-specific ligation of COCHO−peptides on semicarbazide silica nanoparticles allows the preparation of peptide microarrays on polycarbonate. The concentration of the peptide solution used for printing must be in the 10 μM range to avoid the aggregation of the silica nanoparticles. These experimental conditions permitted the preparation of an APP peptide microarray, which was incubated with monoclonal 6E10 antibody. Microarray data were in accordance with ELISA data. Moreover, the microarrays were used successfully for the detection of antibodies in serum.

ACKNOWLEDGMENT

We thank the financial support from the French Ministry of Research, grants from the EEC, from the Région Nord Pas-de-Calais and from Cancéropôle Nord-Ouest. The work was performed in Chemistry Systems Biology platform facility of the Institute of Biology (Lille, France, http://csb.ibl.fr).

Supporting Information Available: RP-HPLC and MALDI-TOF analyses for APP-COCHO peptides. This material is available free of charge via the Internet at http://pubs.acs.org.

LITERATURE CITED

(1) Templin, M. F., Stoll, D., Schrenk, M., Traub, P. C., Vohringer, C. F., and Joos, T. O. (2002) Protein microarray technology. *Drug Discovery Today 7*, 815–22.

(2) Talapatra, A., Rouse, R., and Hardiman, G. (2002) Protein microarrays: challenges and promises. *Pharmacogenomics 3*, 527–36.

(3) Ryan, T. E., and Patterson, S. D. (2002) Proteomics: drug target discovery on an industrial scale. *Trends Biotechnol. 20*, S45–51.

(4) Robinson, W. H., DiGennaro, C., Hueber, W., Haab, B. B., Kamachi, M., Dean, E. J., Fournel, S., Fong, D., Genovese, M. C., de Vegvar, H. E., Skriner, K., Hirschberg, D. L., Morris, R. I., Muller, S., Pruijn, G. J., van Venrooij, W. J., Smolen, J. S., Brown, P. O., Steinman, L., and Utz, P. J. (2002) Autoantigen microarrays for multiplex characterization of autoantibody responses. *Nat. Med. 8*, 295–301.

(5) Duburcq, X., Olivier, C., Malingue, F., Desmet, R., Bouzidi, A., Zhou, F., Auriault, C., Gras-Masse, H., and Melnyk, O. (2004) Peptide-protein microarrays for the simultaneous detection of pathogen infections. *Bioconjugate Chem. 15*, 307–16.

(6) Duburcq, X., Olivier, C., Desmet, R., Halasa, M., Carion, O., Grandidier, B., Heim, T., Stievenard, D., Auriault, C., and Melnyk, O. (2004) Polypeptide semicarbazide glass slide microarrays: characterization and comparison with amine slides in serodetection studies. *Bioconjugate Chem. 15*, 317–25.

(7) Mezzasoma, L., Bacarese-Hamilton, T., Di Cristina, M., Rossi, R., Bistoni, F., and Crisanti, A. (2002) Antigen microarrays for serodiagnosis of infectious diseases. *Clin. Chem. 48*, 121–30.

(8) Petrik, J. (2001) Microarray technology: the future of blood testing? *Vox Sang. 80*, 1–11.

(9) Ekins, R., Chu, F., and Biggart, E. (1990) Multispot, multianalyte, immunoassay. *Ann. Biol. Clin. (Paris) 48*, 655–66.

(10) Ekins, R. P., and Chu, F. W. (1991) Multianalyte microspot immunoassay--microanalytical "compact disk" of the future. *Clin. Chem. 37*, 1955–67.

(11) Ekins, R. P. (1998) Ligand assays: from electrophoresis to miniaturized microarrays. *Clin. Chem. 44*, 2015–30.

(12) Schaferling, M., and Nagl, S. (2006) Optical technologies for the read out and quality control of DNA and protein microarrays. *Anal. Bioanal. Chem. 385*, 500–17.

(13) Ekins, R., Chu, F., and Micallef, J. (1989) High specific activity chemiluminescent and fluorescent markers: their potential application to high sensitivity and 'multi-analyte' immunoassays. *J. Biolumin. Chemilumin. 4*, 59–78.

(14) Angenendt, P., Glokler, J., Sobek, J., Lehrach, H., and Cahill, D. J. (2003) Next generation of protein microarray support materials: evaluation for protein and antibody microarray applications. *J. Chromatogr., Sect. A 1009*, 97–104.

(15) Yeo, D. S., Panicker, R. C., Tan, L. P., and Yao, S. Q. (2004) Strategies for immobilization of biomolecules in a microarray. *Comb. Chem. High Throughput Screen 7*, 213–21.

(16) Yeo, D. S., Srinivasan, R., Chen, G. Y., and Yao, S. Q. (2004) Expanded utility of the native chemical ligation reaction. *Chemistry 10*, 4664–72.

(17) Uttamchandani, M., Chen, G. Y., Lesaicherre, M. L., and Yao, S. Q. (2004) Site-specific peptide immobilization strategies for the rapid detection of kinase activity on microarrays. *Methods Mol. Biol. 264*, 191–204.

(18) Falsey, J. R., Renil, M., Park, S., Li, S., and Lam, K. S. (2001) Peptide and small molecule microarray for high throughput cell adhesion and functional assays. *Bioconjugate Chem. 12*, 346–53.

(19) Olivier, C., Hot, D., Huot, L., Ollivier, N., El-Mahdi, O., Gouyette, C., Huynh-Dinh, T., Gras-Masse, H., Lemoine, Y., and Melnyk, O. (2003) Alpha-oxo semicarbazone peptide or oligodeoxynucleotide microarrays. *Bioconjugate Chem. 14*, 430–9.

(20) Melnyk, O., Duburcq, X., Olivier, C., Urbes, F., Auriault, C., and Gras-Masse, H. (2002) Peptide arrays for highly sensitive and specific antibody-binding fluorescence assays. *Bioconjugate Chem. 13*, 713–20.

(21) Soellner, M. B., Dickson, K. A., Nilsson, B. L., and Raines, R. T. (2003) Site-specific protein immobilization by Staudinger ligation. *J. Am. Chem. Soc. 125*, 11790–1.

(22) MacBeath, G., and Schreiber, S. L. (2000) Printing proteins as microarrays for high-throughput function determination. *Science 289*, 1760–3.

(23) Zhu, H., Bilgin, M., Bangham, R., Hall, D., Casamayor, A., Bertone, P., Lan, N., Jansen, R., Bidlingmaier, S., Houfek, T., Mitchell, T., Miller, P., Dean, R. A., Gerstein, M., and Snyder, M. (2001) Global analysis of protein activities using proteome chips. *Science 293*, 2101–5.

(24) Pritchard, D. J., Morgan, H., and Cooper, J. M. (1995) Patterning and regeneration of surfaces with antibodies. *Anal. Chem. 67*, 3605–7.
(25) Delehanty, J. B., and Ligler, F. S. (2002) A microarray immunoassay for simultaneous detection of proteins and bacteria. *Anal. Chem. 74*, 5681–7.
(26) Alexandre, I., Houbion, Y., Collet, J., Hamels, S., Demarteau, J., Gala, J. L., and Remacle, J. (2002) Compact disc with both numeric and genomic information as DNA microarray platform. *Biotechniques 33* (435−6), 438–9.
(27) La Clair, J. J., and Burkart, M. D. (2006) Geometry in digital molecular arrays. *Org. Biomol. Chem. 4*, 3052–5.
(28) Morais, S., Carrascosa, J., Mira, D., Puchades, R., and Maquieira, A. (2007) Microimmunoanalysis on standard compact discs to determine low abundant compounds, *Anal. Chem.*
(29) Ko, K. S., Najmabadi, P., La Clair, J. J., and Burkart, M. D. (2008) Affinity analyses on moldable optical polycarbonate. *ChemBioChem 9*, 201–5.
(30) La Clair, J. J., and Burkart, M. D. (2003) Molecular screening on a compact disc. *Org. Biomol. Chem. 1*, 3244–9.
(31) Soper, S. A., Hashimoto, M., Situma, C., Murphy, M. C., McCarley, R. L., Cheng, Y. W., and Barany, F. (2005) Fabrication of DNA microarrays onto polymer substrates using UV modification protocols with integration into microfluidic platforms for the sensing of low-abundant DNA point mutations. *Methods 37*, 103–13.
(32) Banuls, M. J., Gonzalez-Pedro, V., Puchades, R., and Maquieira, A. (2007) PMMA isocyanate-modified digital discs as a support for oligonucleotide-based assays. *Bioconjugate Chem. 18*, 1408–14.
(33) Banuls, M. J., Garcia-Pinon, F., Puchades, R., and Maquieira, A. (2008) Chemical derivatization of compact disc polycarbonate surfaces for SNPs detection. *Bioconjugate Chem. 19*, 665–72.
(34) Carion, O., Souplet, V., Olivier, C., Maillet, C., Medard, N., El-Mahdi, O., Durand, J. O., and Melnyk, O. (2007) Chemical micropatterning of polycarbonate for site-specific peptide immobilization and biomolecular interactions. *ChemBioChem 8*, 315–322.
(35) Field, J., Nikawa, J., Broek, D., MacDonald, B., Rodgers, L., Wilson, I. A., Lerner, R. A., and Wigler, M. (1988) Purification of a RAS-responsive adenylyl cyclase complex from *Saccharomyces cerevisiae* by use of an epitope addition method. *Mol. Cell. Biol. 8*, 2159–65.
(36) Brizzard, B. L., Chubet, R. G., and Vizard, D. L. (1994) Immunoaffinity purification of FLAG epitope-tagged bacterial alkaline phosphatase using a novel monoclonal antibody and peptide elution. *Biotechniques 16*, 730–5.
(37) Geoghegan, K. F., and Stroh, J. G. (1992) Site-directed conjugation of nonpeptide groups to peptides and proteins via periodate oxidation of a 2-amino alcohol. Application to modification at N-terminal serine. *Bioconjugate Chem. 3*, 138–46.
(38) Fields, G. B., and Noble, R. L. (1990) Solid phase peptide synthesis utilizing 9-fluorenylmethoxycarbonyl amino acids. *Int. J. Pept. Protein Res. 35*, 161–214.
(39) Melnyk, O., Fruchart, J. S., Grandjean, C., and Gras-Masse, H. (2001) Tartric acid-based linker for the solid-phase synthesis of C-terminal peptide alpha-oxo aldehydes. *J. Org. Chem. 66*, 4153–60.
(40) Melnyk, O., Fehrentz, J. A., Martinez, J., and Gras-Masse, H. (2000) Functionalization of peptides and proteins by aldehyde or keto groups. *Biopolymers 55*, 165–86.
(41) Fruchart, J.-S., Gras-Masse, H., and Melnyk, O. (1999) A new linker for the synthesis of C-terminal peptide [alpha]-oxo-aldehydes. *Tetrahedron Lett. 40*, 6225–6228.
(42) Melnyk, O., Olivier, C., Ollivier, N., Lemoine, Y., Hot, D., Huot, L., and Gouyette, C. (2005) Preparation of alpha-Oxo semicarbazone oligonucleotide microarrays, In *Current Protocol Nucleic Acid Chemistry*, Chapter 12, Unit 12 6.
(43) Ida, N., Hartmann, T., Pantel, J., Schroder, J., Zerfass, R., Forstl, H., Sandbrink, R., Masters, C. L., and Beyreuther, K. (1996) Analysis of heterogeneous A4 peptides in human cerebrospinal fluid and blood by a newly developed sensitive Western blot assay. *J. Biol. Chem. 271*, 22908–14.
(44) Wilquet, V., and De Strooper, B. (2004) Amyloid-beta precursor protein processing in neurodegeneration. *Curr. Opin. Neurobiol. 14*, 582–8.
(45) Schenk, D., Barbour, R., Dunn, W., Gordon, G., Grajeda, H., Guido, T., Hu, K., Huang, J., Johnson-Wood, K., Khan, K., Kholodenko, D., Lee, M., Liao, Z., Lieberburg, I., Motter, R., Mutter, L., Soriano, F., Shopp, G., Vasquez, N., Vandevert, C., Walker, S., Wogulis, M., Yednock, T., Games, D., and Seubert, P. (1999) Immunization with amyloid-beta attenuates Alzheimer-disease-like pathology in the PDAPP mouse. *Nature 400*, 173–7.
(46) Tabira, T. (2007) Vaccination therapy for Alzheimer's disease. *Brain Nerve 59*, 375–82.
(47) Woodhouse, A., Dickson, T. C., and Vickers, J. C. (2007) Vaccination strategies for Alzheimer's disease: A new hope? *Drugs Aging 24*, 107–19.
(48) Garcia, J. M., Far, S., Diesis, E., and Melnyk, O. (2006) Determination of glyoxylyl-peptide concentration using oxime chemistry and RP-HPLC analysis. *J. Pept. Sci. 12*, 734–8.

BC800474G

In situ ligation between peptides and silica nanoparticles for making peptide microarrays on plastic

Vianney Souplet, Rémi Desmet, Oleg Melnyk*

Institut de Biologie de Lille, UMR CNRS 8161, Universités de Lille 1 et 2, Institut Pasteur de Lille, IFR 142, 1 rue du Professeur Calmette, 59021 Lille Cedex, France

Supporting Information
Table of Contents

RP-HPLC COCHO-APP1	S2
MALDI-TOF analysis COCHO-APP1	S3
RP-HPLC COCHO-APP2	S4
MALDI-TOF analysis COCHO-APP2	S5
RP-HPLC COCHO-APP3	S6
MALDI-TOF analysis COCHO-APP3	S7
RP-HPLC COCHO-APP4	S8
MALDI-TOF analysis COCHO-APP4	S9
RP-HPLC COCHO-APP5	S10
MALDI-TOF analysis COCHO-APP5	S11
RP-HPLC COCHO-APP6	S12
MALDI-TOF analysis COCHO-APP6	S13
RP-HPLC COCHO-APP7	S14
MALDI-TOF analysis COCHO-APP7	S15
RP-HPLC Fmoc-COCHO-APP8	S16
MALDI-TOF analysis fmoc-COCHO-APP8	S17
RP-HPLC COCHO-APP8	S18
MALDI-TOF analysis COCHO-APP8	S19
RP-HPLC OCHO-APP9	S20
MALDI-TOF analysis COCHO-APP9	S21
RP-HPLC OCHO-APP10	S22
MALDI-TOF analysis COCHO-APP10	S23
RP-HPLC OCHO-APP11	S24
MALDI-TOF analysis COCHO-APP11	S25
RP-HPLC OCHO-APP12	S26
MALDI-TOF analysis COCHO-APP12	S27

COCHO-APP1

RP-HPLC

Eluent A is 0.05% TFA in water, eluent B is 0.05% TFA in CH_3CN/water: 4/1 by vol. RP-HPLC on a 120 Å 5 µm C18 Nucleosil column (4.6 × 250 mm) using a linear water/acetonitrile gradient 0-100%B in 30 min (1 mL/min, detection 215 nm).

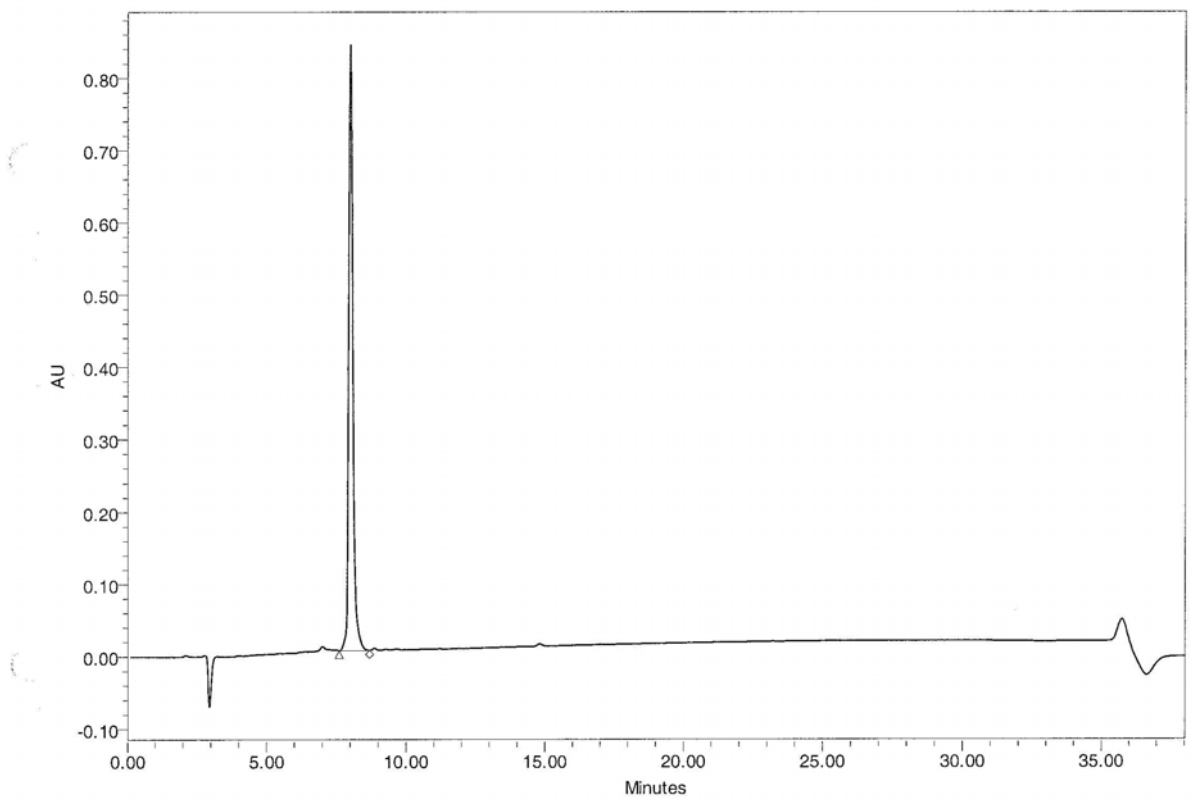

	RT	Height	Area	% Area
1	8.016	836308	8564430	100.00

MALDI-TOF spectrum COCHO-APP1

MALDI-TOF matrix : α-cyano-4-hydroxycinnamic acid

Calcd. For C60H83N19O22 [M+H]+ 1422.60, found 1422.6

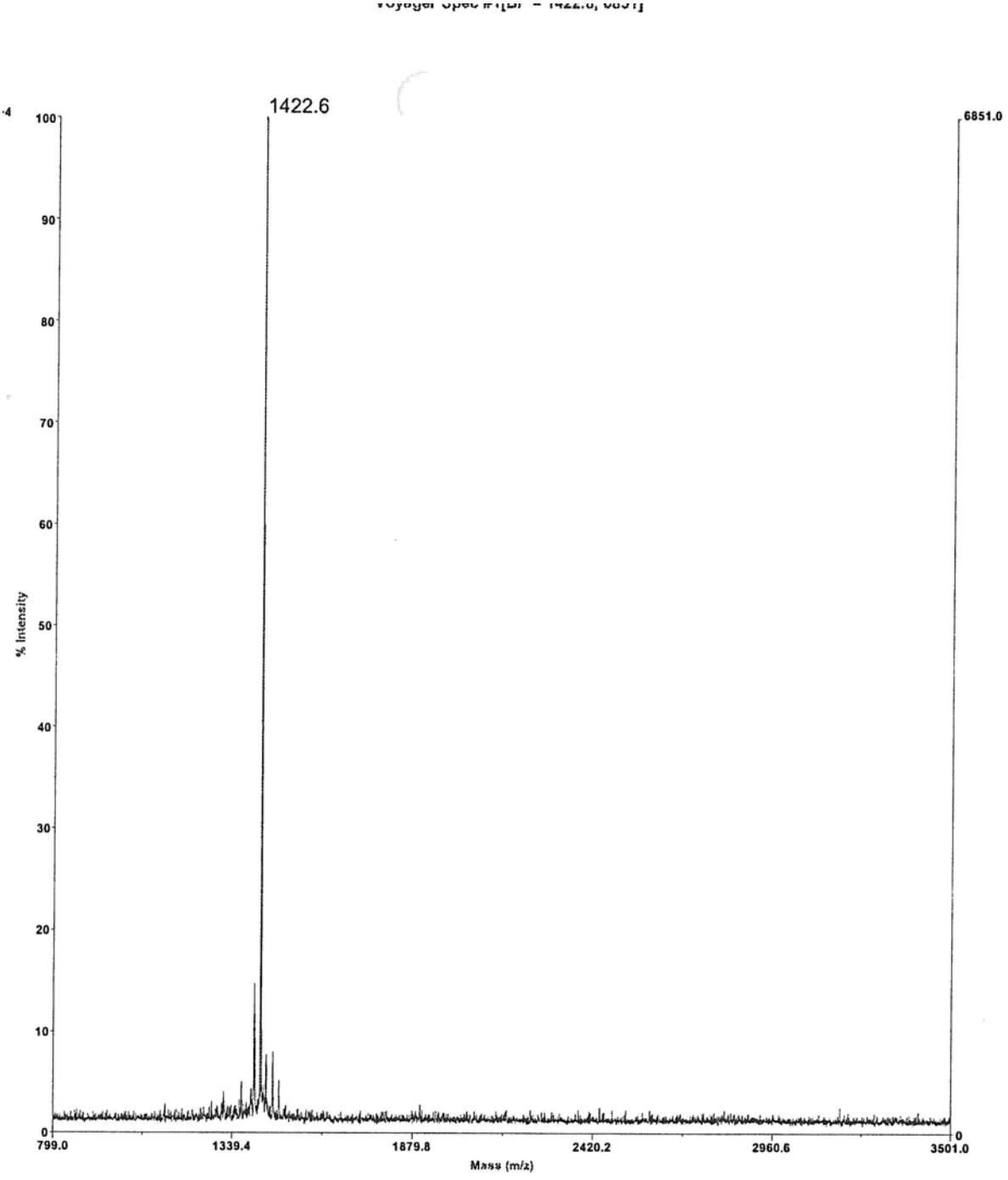

COCHO-APP2

RP-HPLC

Eluent A is 0.05% TFA in water, eluent B is 0.05% TFA in CH_3CN/water: 4/1 by vol. RP-HPLC on a 120 Å 5 µm C18 Nucleosil column (4.6 × 250 mm) using a linear water/acetonitrile gradient 0-100%B in 30 min (1 mL/min, detection 215 nm).

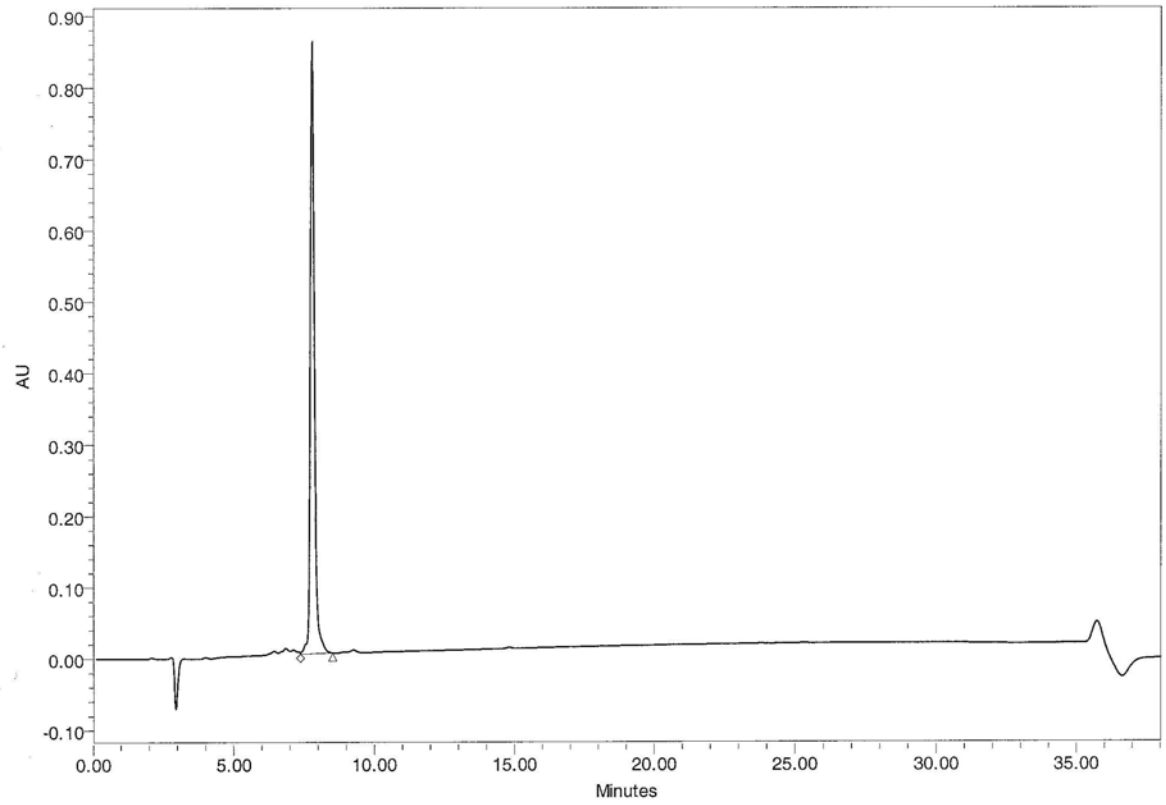

	RT	Height	Area	% Area
1	7.797	857483	8737376	100.00

MALDI-TOF spectrum COCHO-APP2

MALDI-TOF matrix : α-cyano-4-hydroxycinnamic acid

Calcd. For C61H85N19O22 [M+H]+ 1436,62, found 1422.8

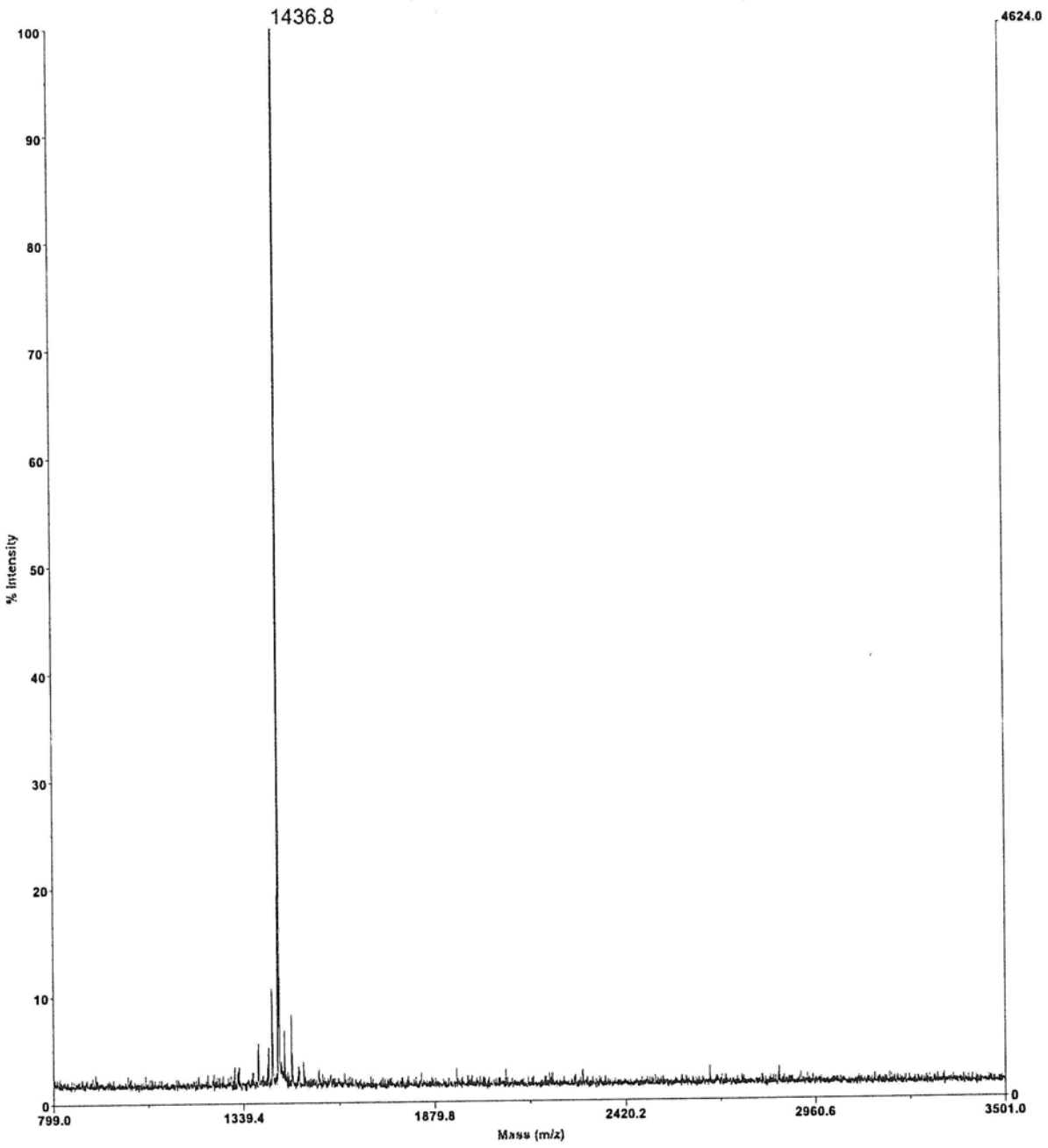

COCHO-APP3

RP-HPLC

Eluent A is 0.05% TFA in water, eluent B is 0.05% TFA in CH_3CN/water: 4/1 by vol. RP-HPLC on a 120 Å 5 µm C18 Nucleosil column (4.6 × 250 mm) using a linear water/acetonitrile gradient 0-100%B in 30 min (1 mL/min, detection 215 nm).

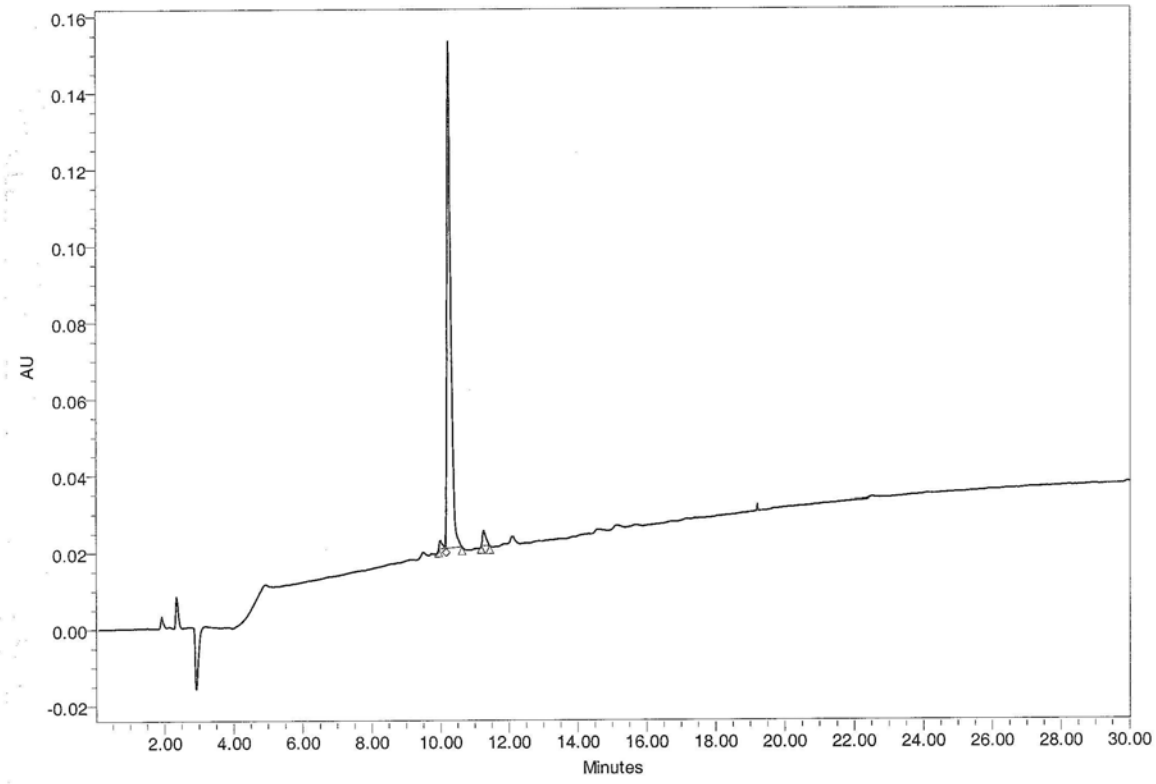

	RT	Height	Area	% Area
1	10.167	8942	19644	1.91
2	10.240	132408	980293	95.40
3	11.272	3905	27570	2.68

MALDI-TOF spectrum COCHO-APP3

MALDI-TOF matrix : α-cyano-4-hydroxycinnamic acid

Calcd. For C63H89N19O22 [M+H]+ 1464.65, found 1465.0

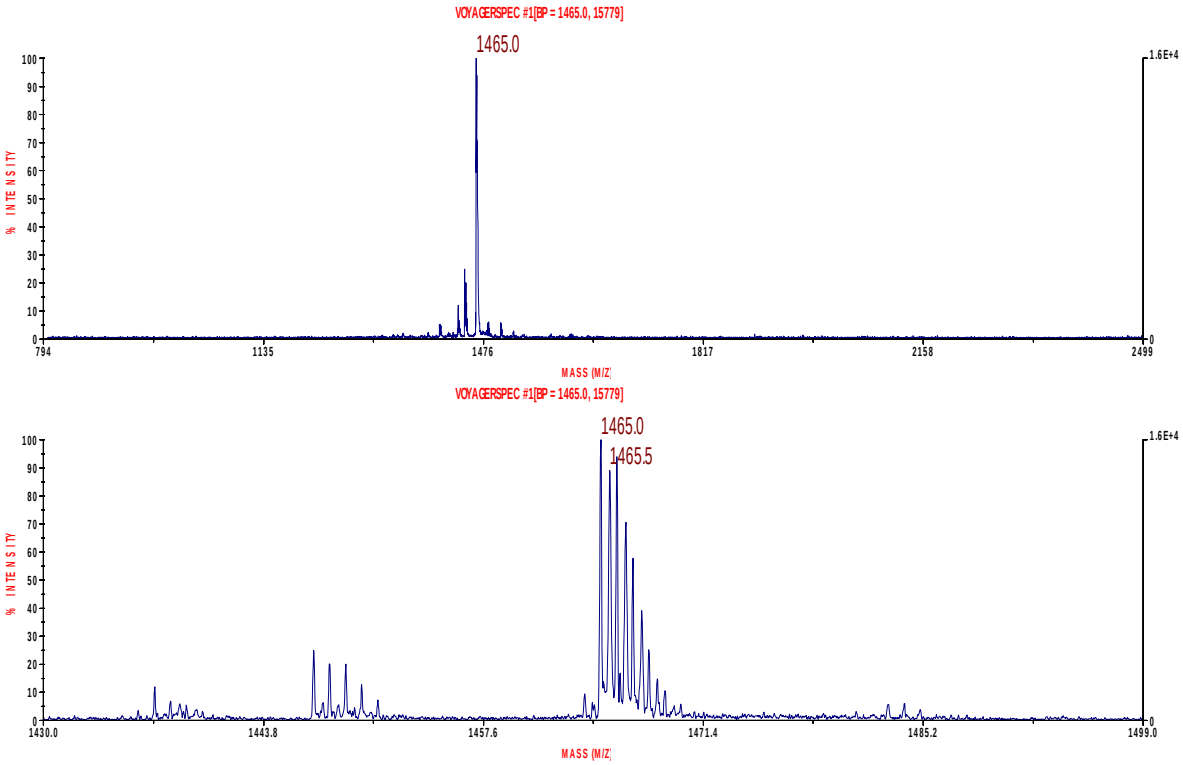

COCHO-APP4

RP-HPLC

Eluent A is 0.05% TFA in water, eluent B is 0.05% TFA in CH_3CN/water: 4/1 by vol. RP-HPLC on a 120 Å 5 µm C18 Nucleosil column (4.6 × 250 mm) using a linear water/acetonitrile gradient 0-100%B in 30 min (1 mL/min, detection 215 nm).

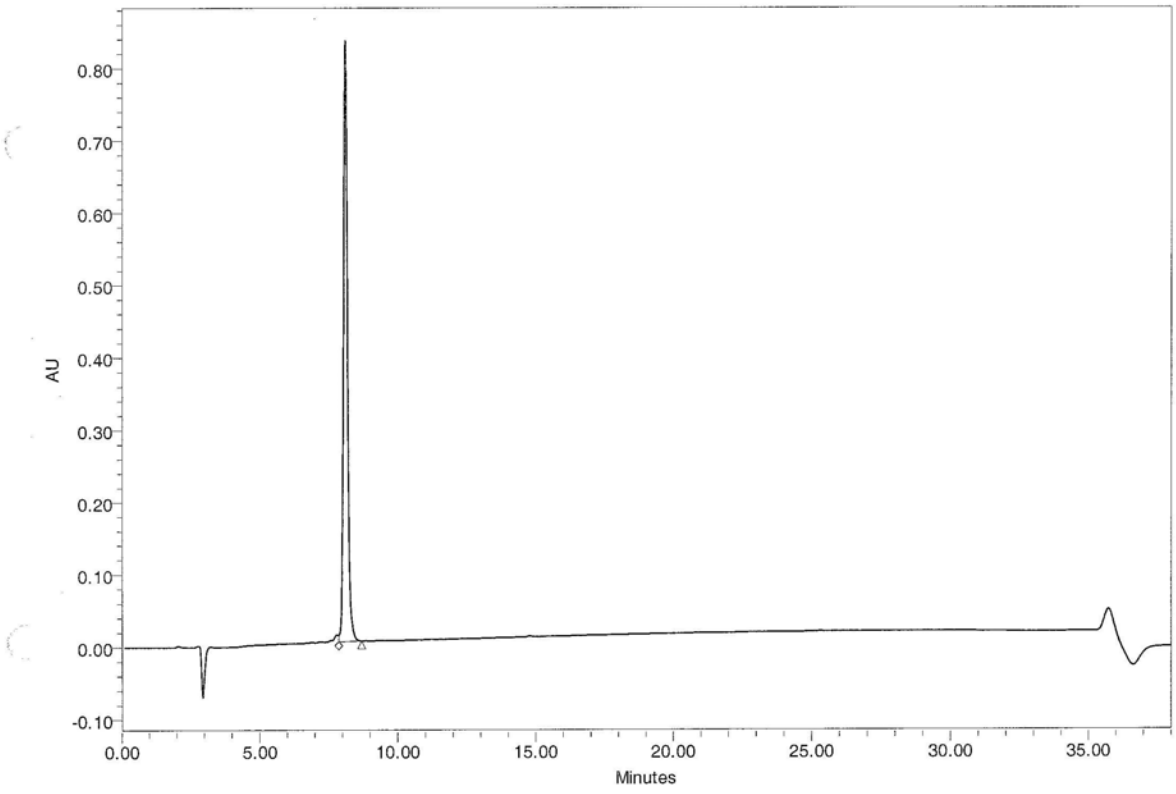

	RT	Height	Area	% Area
1	8.097	830232	8279542	100.00

MALDI-TOF spectrum COCHO-APP4

MALDI-TOF matrix : α-cyano-4-hydroxycinnamic acid

Calcd. For C64H89N21O20 [M+H]+ 1472.67, found 1472.8

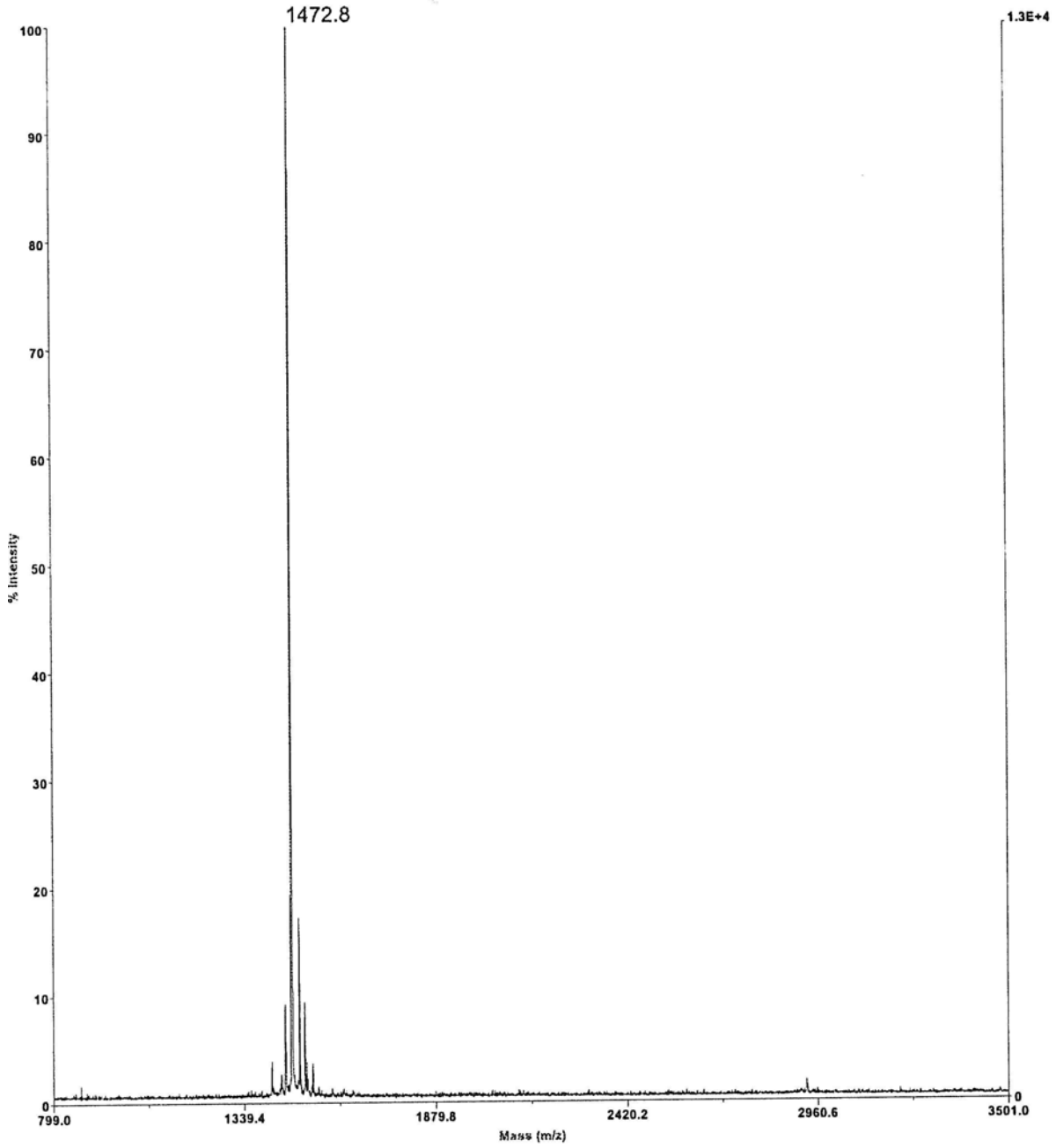

COCHO-APP5

RP-HPLC

Eluent A is 0.05% TFA in water, eluent B is 0.05% TFA in CH_3CN/water: 4/1 by vol. RP-HPLC on a 120 Å 5 µm C18 Nucleosil column (4.6 × 250 mm) using a linear water/acetonitrile gradient 0-100%B in 30 min (1 mL/min, detection 215 nm).

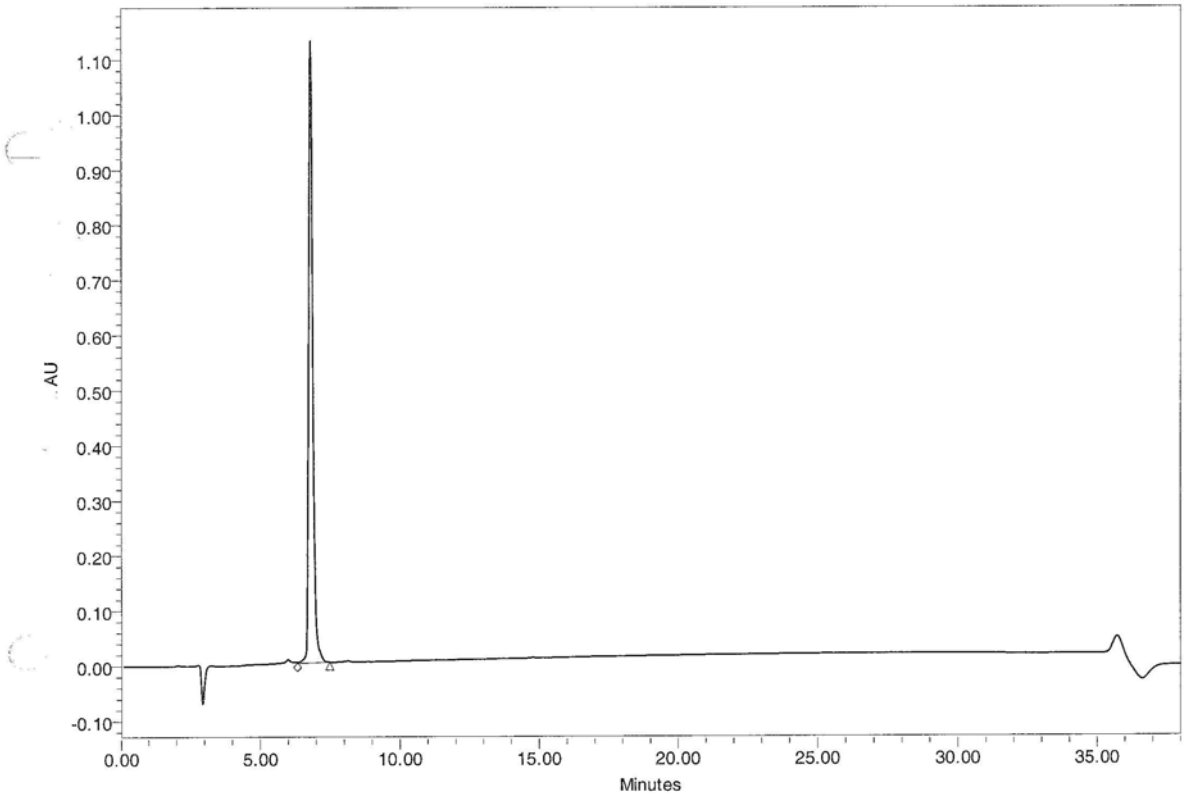

	RT	Height	Area	% Area
1	6.803	1128057	11550744	100.00

MALDI-TOF spectrum COCHO-APP5

MALDI-TOF matrix : α-cyano-4-hydroxycinnamic acid

Calcd. For C61H87N23O20 [M+H]+ 1462.66, found 1462.9

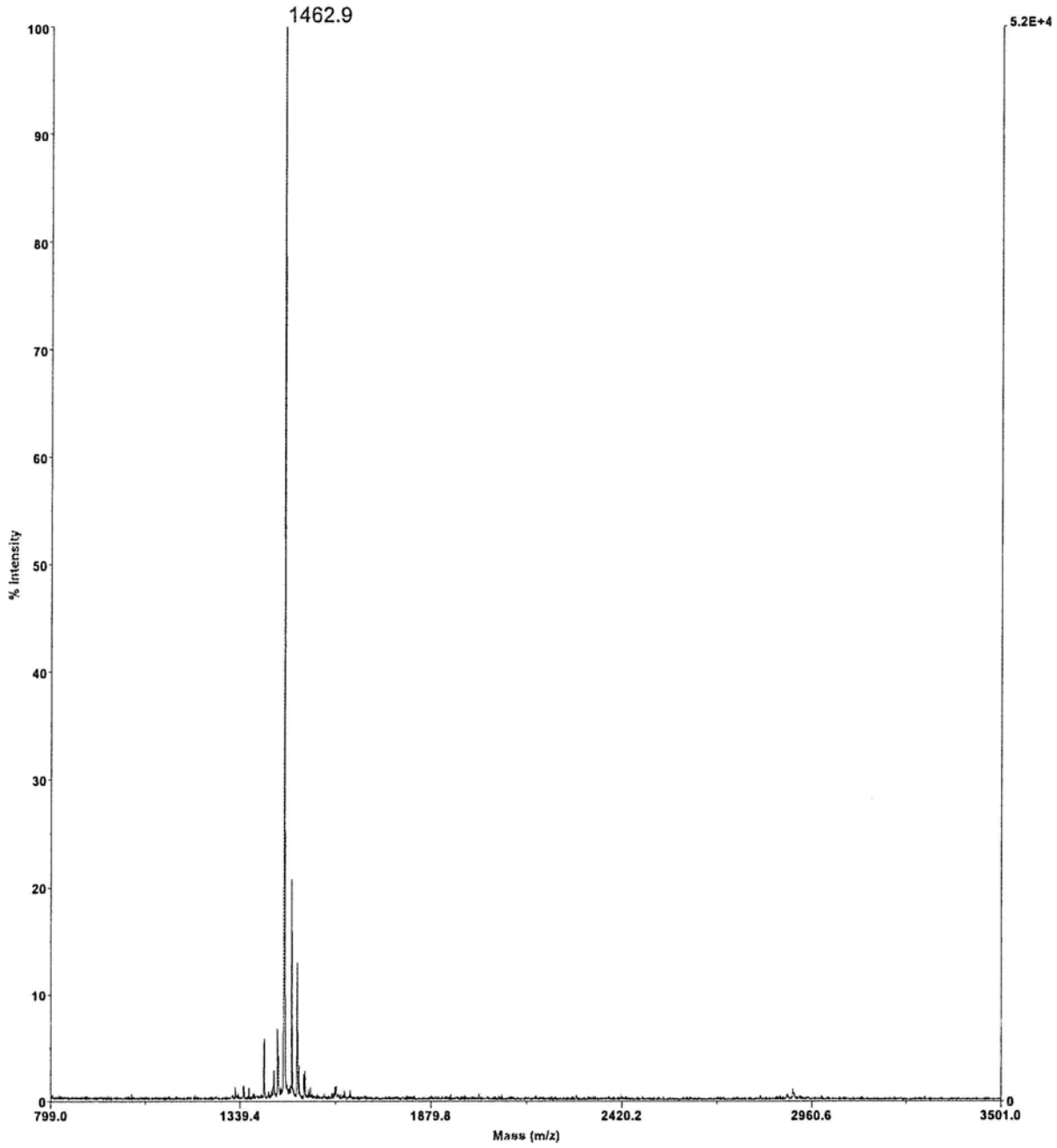

COCHO-APP6

RP-HPLC

Eluent A is 0.05% TFA in water, eluent B is 0.05% TFA in CH_3CN/water: 4/1 by vol. RP-HPLC on a 120 Å 5 µm C18 Nucleosil column (4.6 × 250 mm) using a linear water/acetonitrile gradient 0-100%B in 30 min (1 mL/min, detection 215 nm).

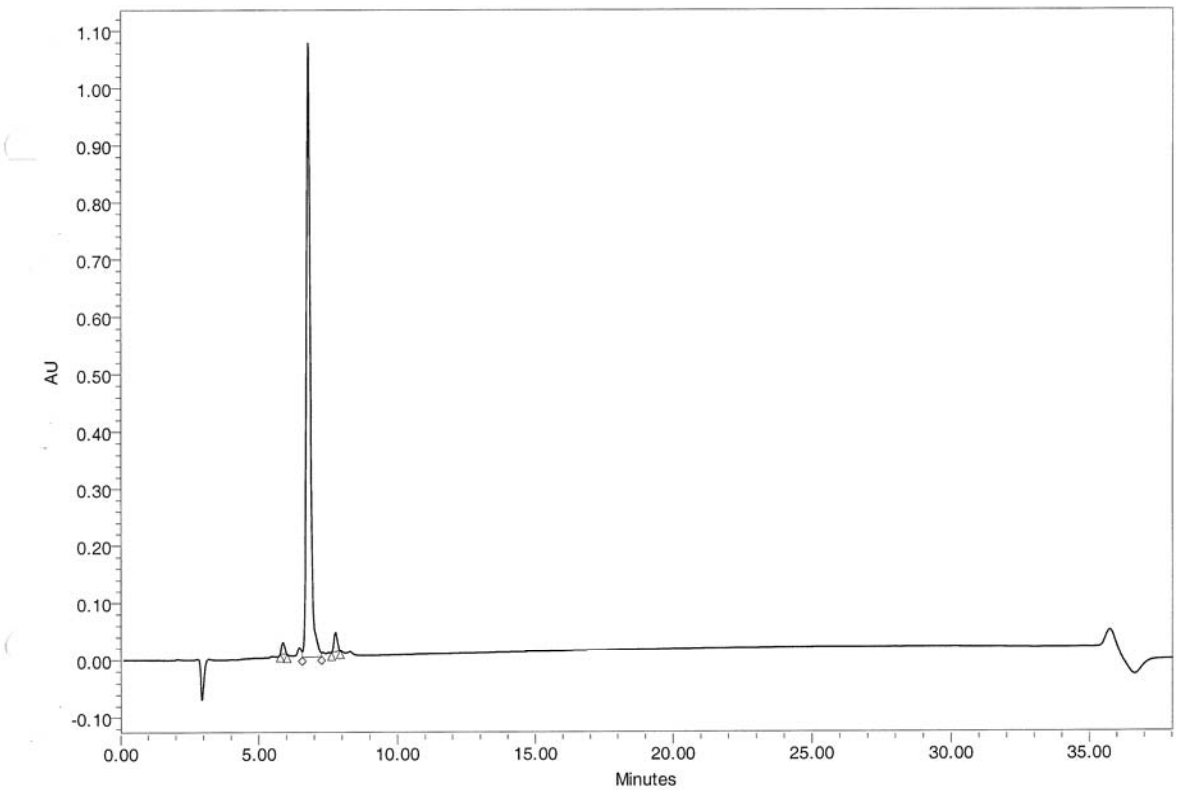

	RT	Height	Area	% Area
1	5.883	20463	156638	1.41
2	6.789	1077103	10639134	95.99
3	7.777	33678	287694	2.60

MALDI-TOF spectrum COCHO-APP6

MALDI-TOF matrix : α-cyano-4-hydroxycinnamic acid

Calcd. For C60H83N21O21 [M+H]+ 1434.62, found 1434.8

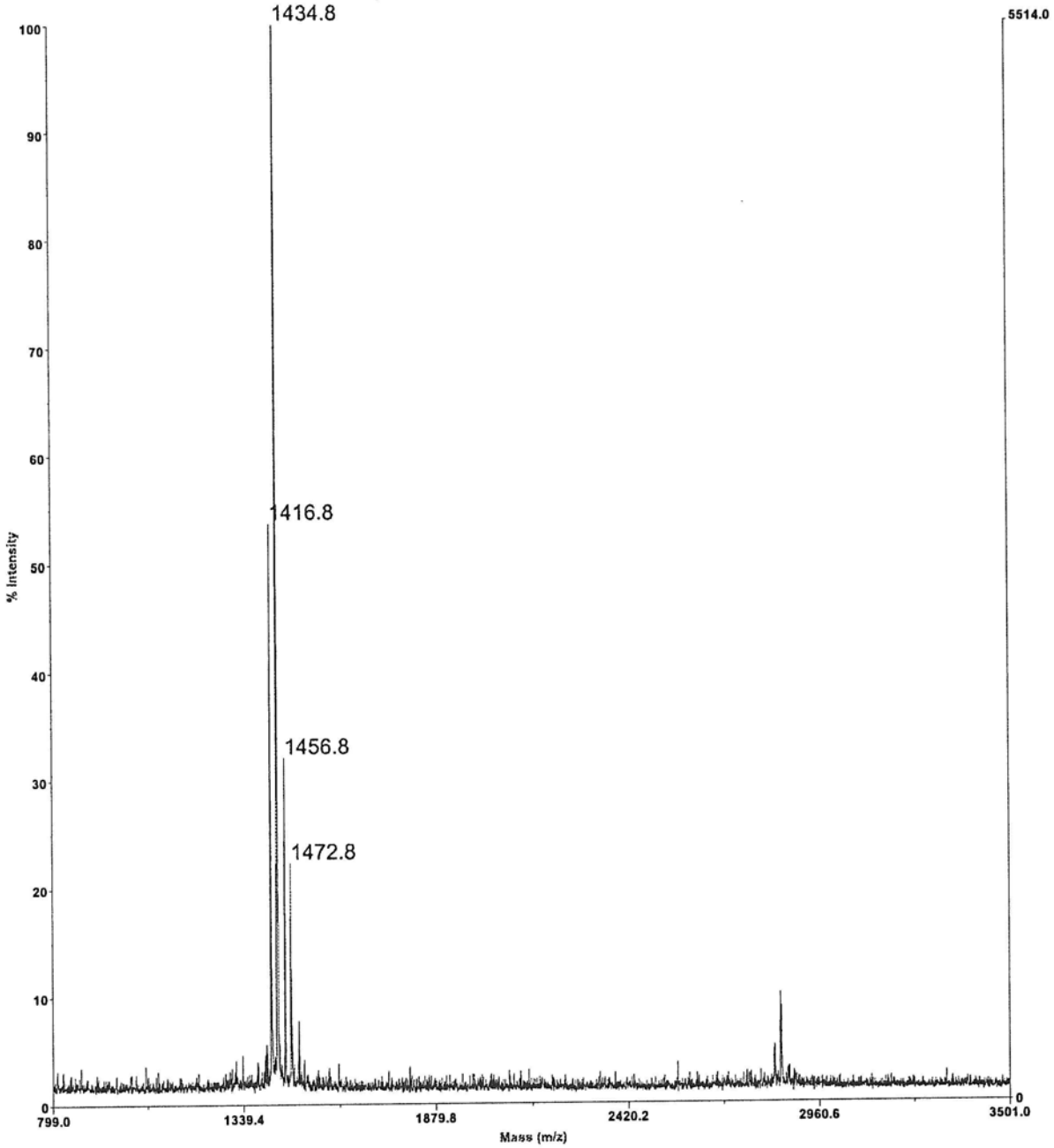

COCHO-APP7

RP-HPLC

Eluent A is 0.05% TFA in water, eluent B is 0.05% TFA in CH_3CN/water: 4/1 by vol. RP-HPLC on a 120 Å 5 µm C18 Nucleosil column (4.6 × 250 mm) using a linear water/acetonitrile gradient 0-100%B in 30 min (1 mL/min, detection 215 nm).

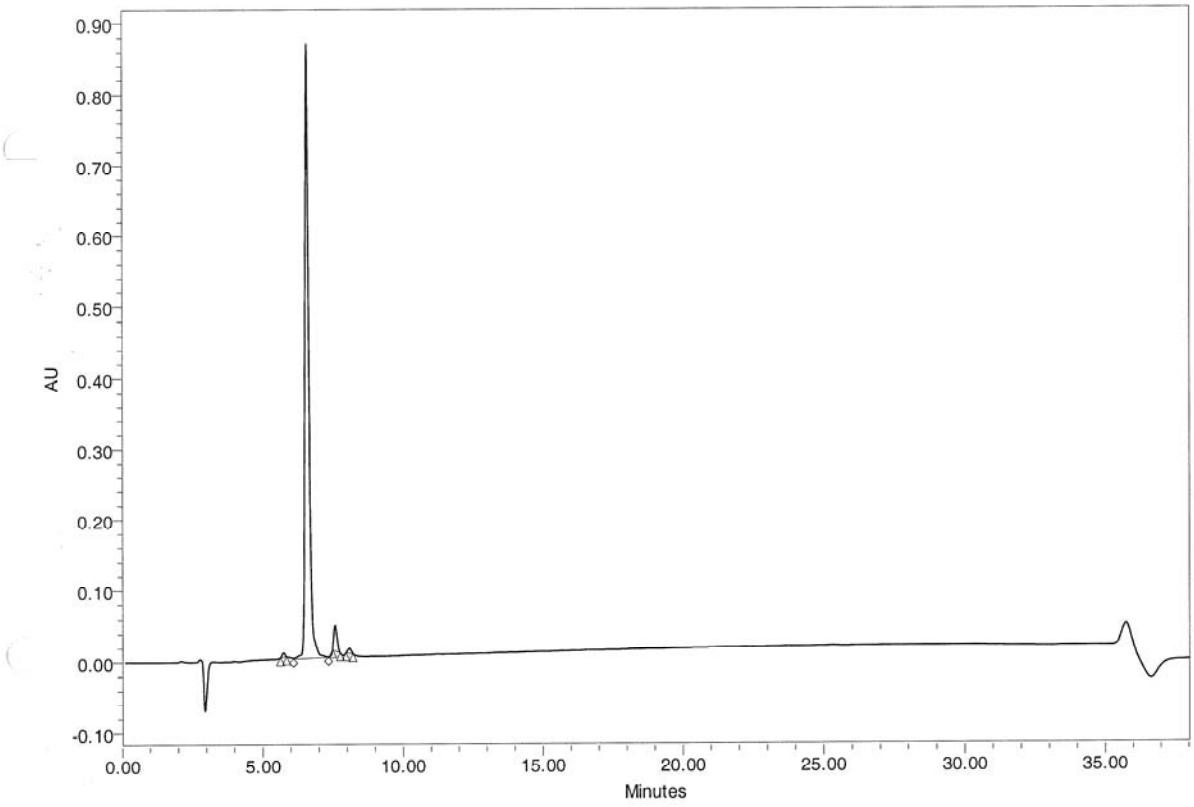

	RT	Height	Area	% Area
1	5.740	6351	43945	0.50
2	6.587	866365	8379860	95.49
3	7.585	35734	290306	3.31
4	8.091	7013	61341	0.70

MALDI-TOF spectrum COCHO-APP7

MALDI-TOF matrix : α-cyano-4-hydroxycinnamic acid

Calcd. For C60H88N20O21 [M+H]+ 1425.65, found 1425.9

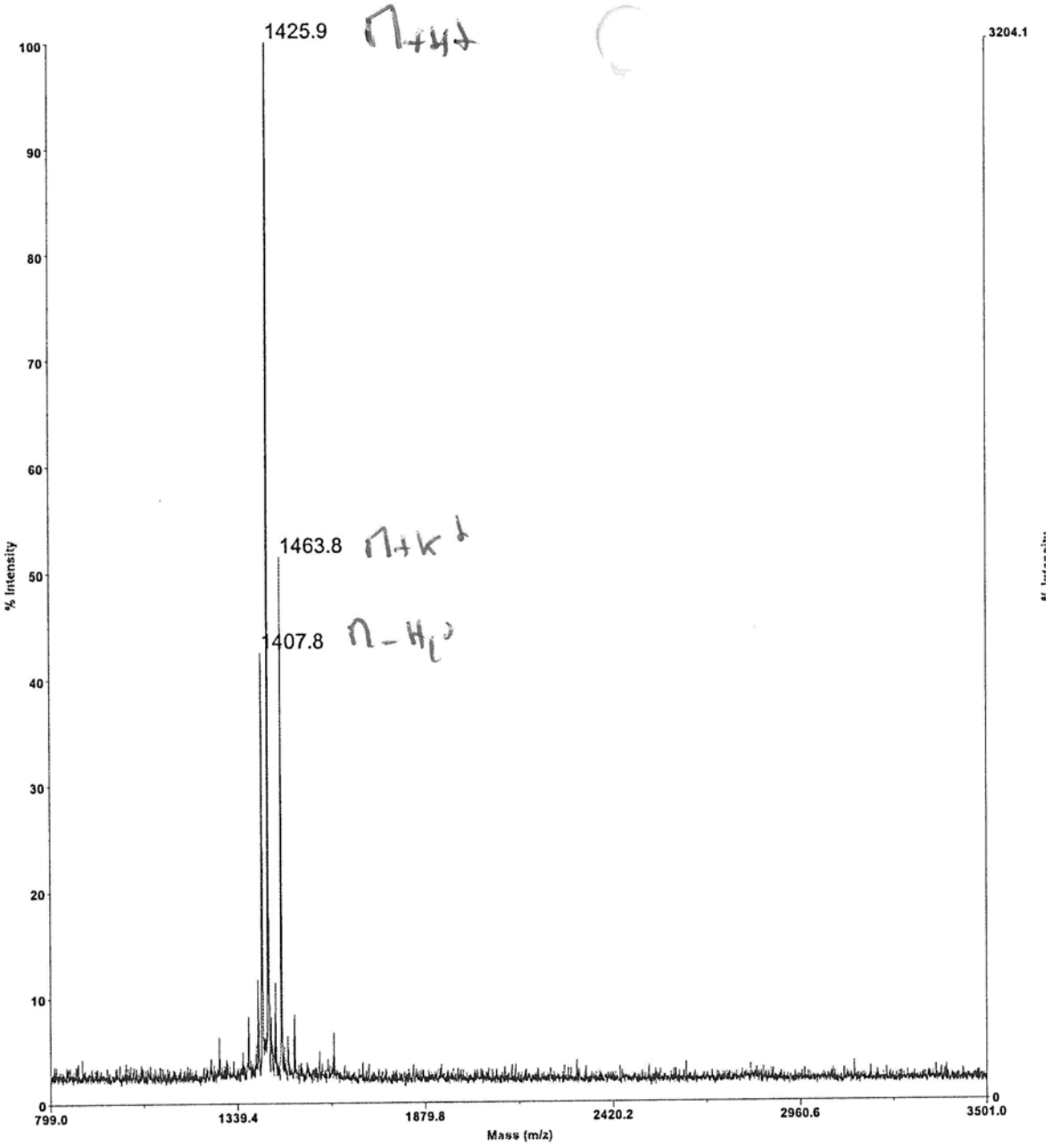

Fmoc-COCHO-APP8

RP-HPLC

Eluent A is 0.05% TFA in water, eluent B is 0.05% TFA in CH_3CN/water: 4/1 by vol. RP-HPLC on a 120 Å 5 µm C18 Nucleosil column (4.6 × 250 mm) using a linear water/acetonitrile gradient 0-100%B in 60 min (1 mL/min, detection 215 nm).

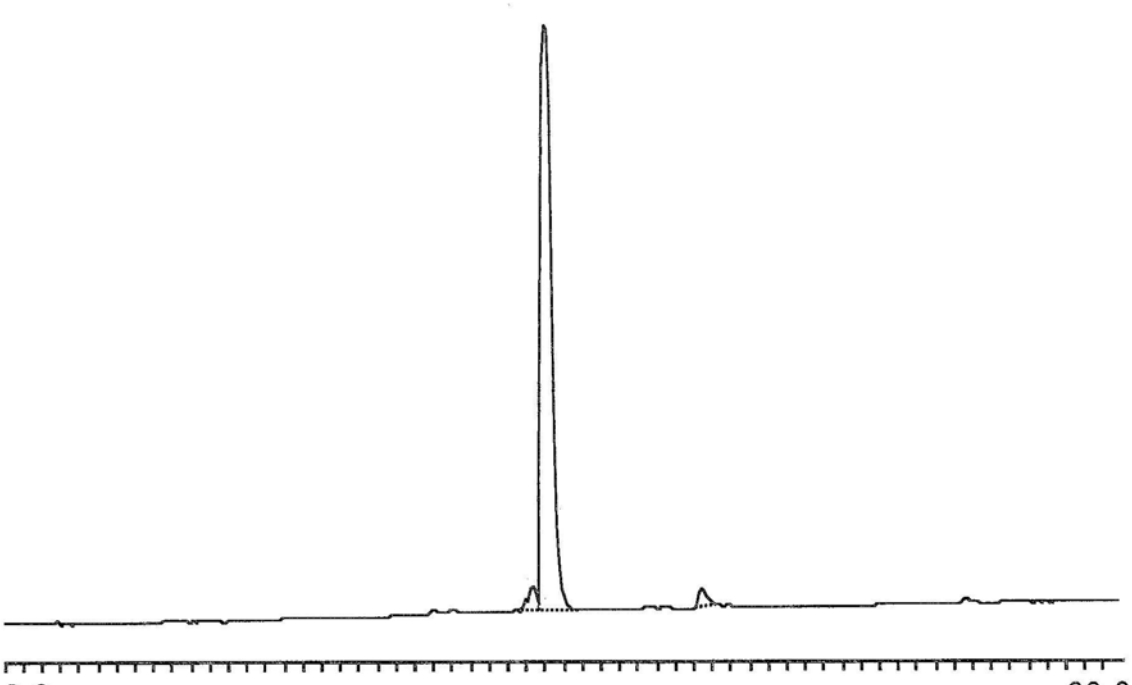

Analysis: Channel A

Peak No.	Time	Type	Height(µV)	Area(µV-sec)	Area%
1	28.345	*N1	9617	251465	2.807
2	28.953	*N2	241736	8527479	95.214
3	37.393	N	7225	177119	1.977
Total Area				8956063	99.998

MALDI-TOF spectrum Fmoc-COCHO-APP8

MALDI-TOF matrix : α-cyano-4-hydroxycinnamic acid

Calcd. For C77H104N20O21/C62H94N20O19 [M+H]+ 1645,78, found 1645.9

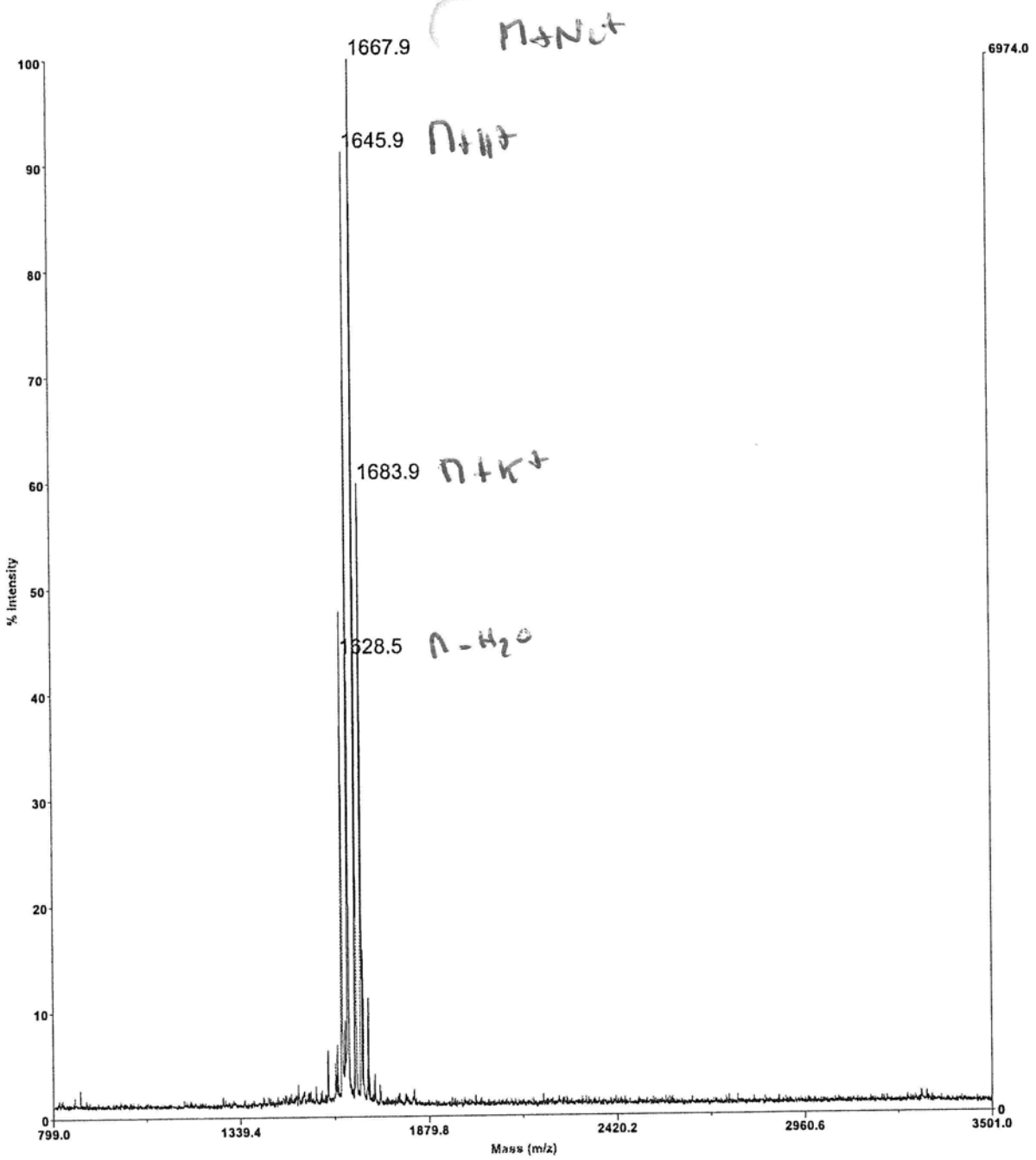

COCHO-APP8

RP-HPLC

Eluent A is 0.05% TFA in water, eluent B is 0.05% TFA in CH_3CN/water: 4/1 by vol. RP-HPLC on a 120 Å 5 µm C18 Nucleosil column (4.6 × 250 mm) using a linear water/acetonitrile gradient 0-100%B in 60 min (1 mL/min, detection 215 nm).

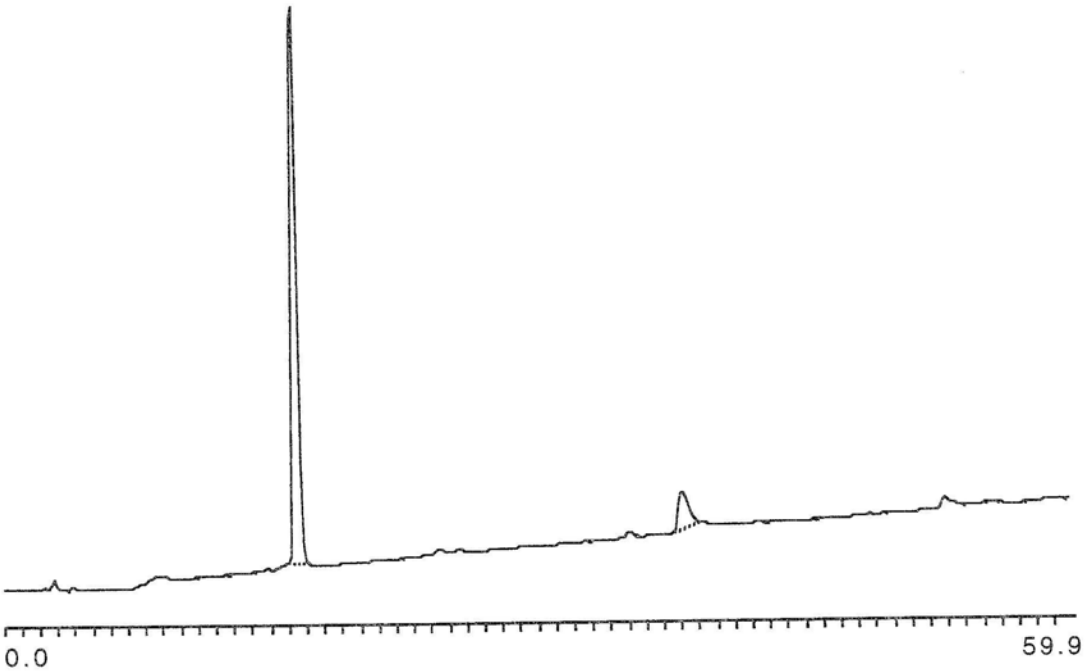

Analysis: Channel A

Peak No.	Time	Type	Height(µV)	Area(µV-sec)	Area%
1	16.381	*N	92319	1333554	87.470
2	37.975	*N	6244	191022	12.529
Total Area				1524576	99.999

The peak at 37.9 min is due to the column.

MALDI-TOF spectrum COCHO-APP8

MALDI-TOF matrix : α-cyano-4-hydroxycinnamic acid

Calcd. For C62H94N20O19 [M+Na]+ 1445,69, found 1445.7

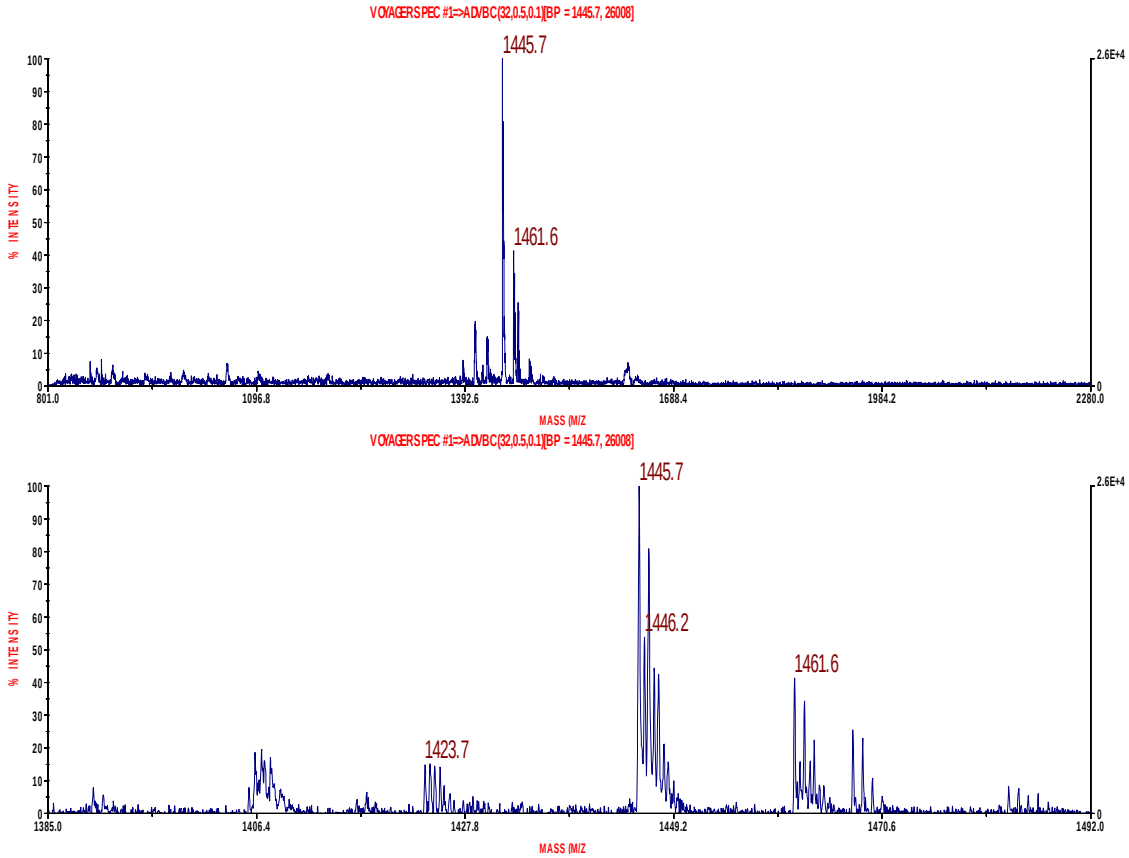

COCHO-APP9

RP-HPLC

Eluent A is 0.05% TFA in water, eluent B is 0.05% TFA in CH_3CN/water: 4/1 by vol. RP-HPLC on a 120 Å 5 µm C18 Nucleosil column (4.6 × 250 mm) using a linear water/acetonitrile gradient 0-50%B in 30 min (1 mL/min, detection 215 nm).

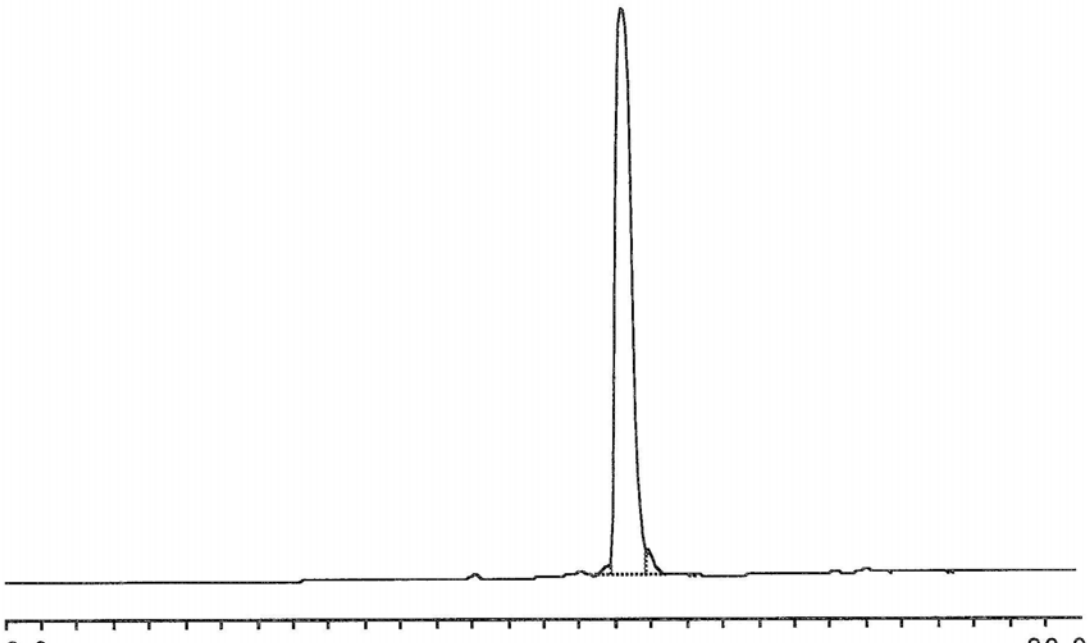

Analysis: Channel A

Peak No.	Time	Type	Height(µV)	Area(µV-sec)	Area%
1	16.781	N1	3137	36348	0.571
2	17.166	N2	229049	6197340	97.408
3	17.878	N3	9751	128537	2.020
Total Area				6362225	99.999

MALDI-TOF spectrum COCHO-APP9

MALDI-TOF matrix : α-cyano-4-hydroxycinnamic acid

Calcd. For C64H98N20O18 [M+H]+ 1435.74, found 1435.7

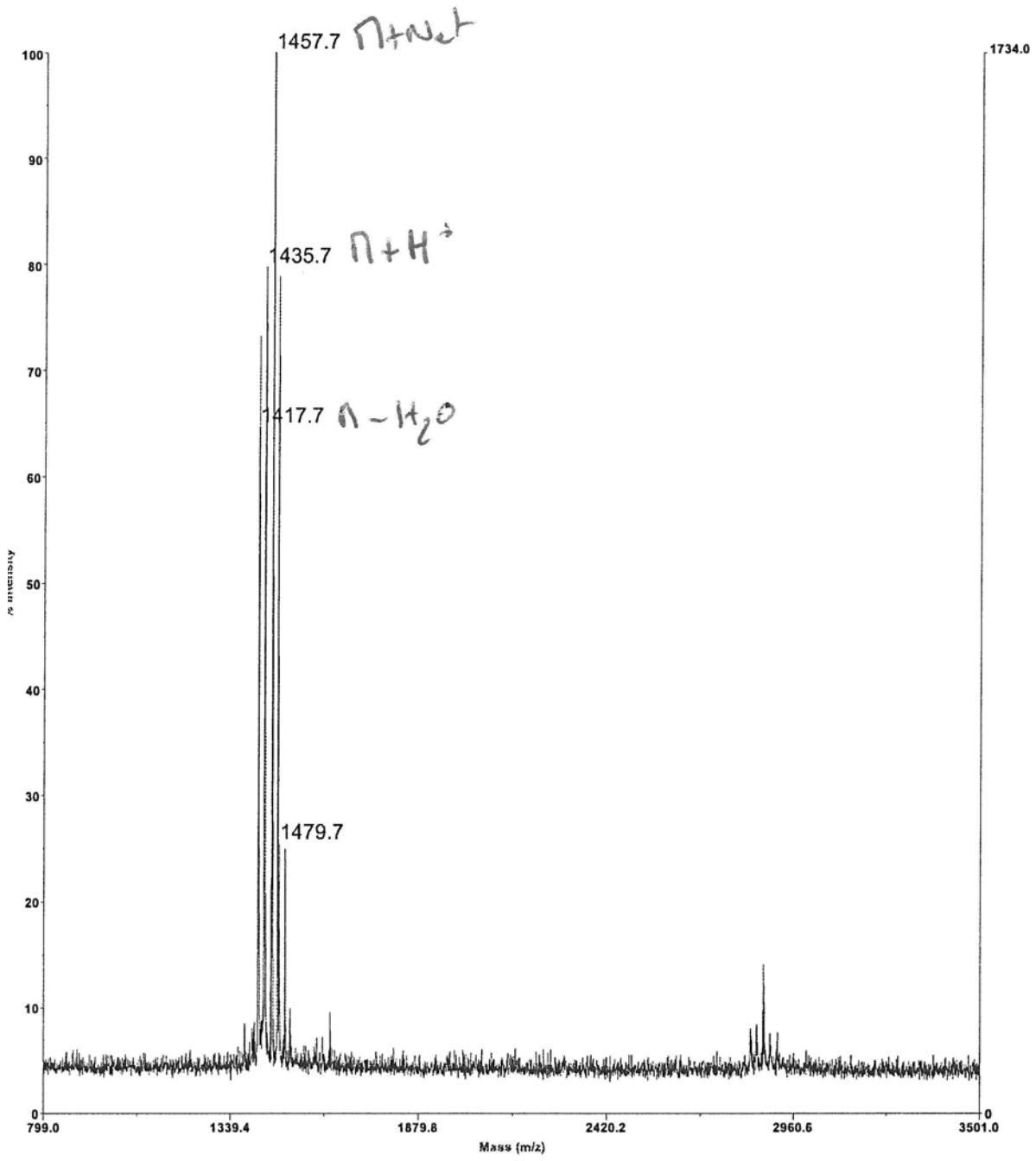

COCHO-APP10

RP-HPLC

Eluent A is 0.05% TFA in water, eluent B is 0.05% TFA in CH_3CN/water: 4/1 by vol. RP-HPLC on a 120 Å 5 µm C18 Nucleosil column (4.6 × 250 mm) using a linear water/acetonitrile gradient 0-100%B in 60 min (1 mL/min, detection 215 nm).

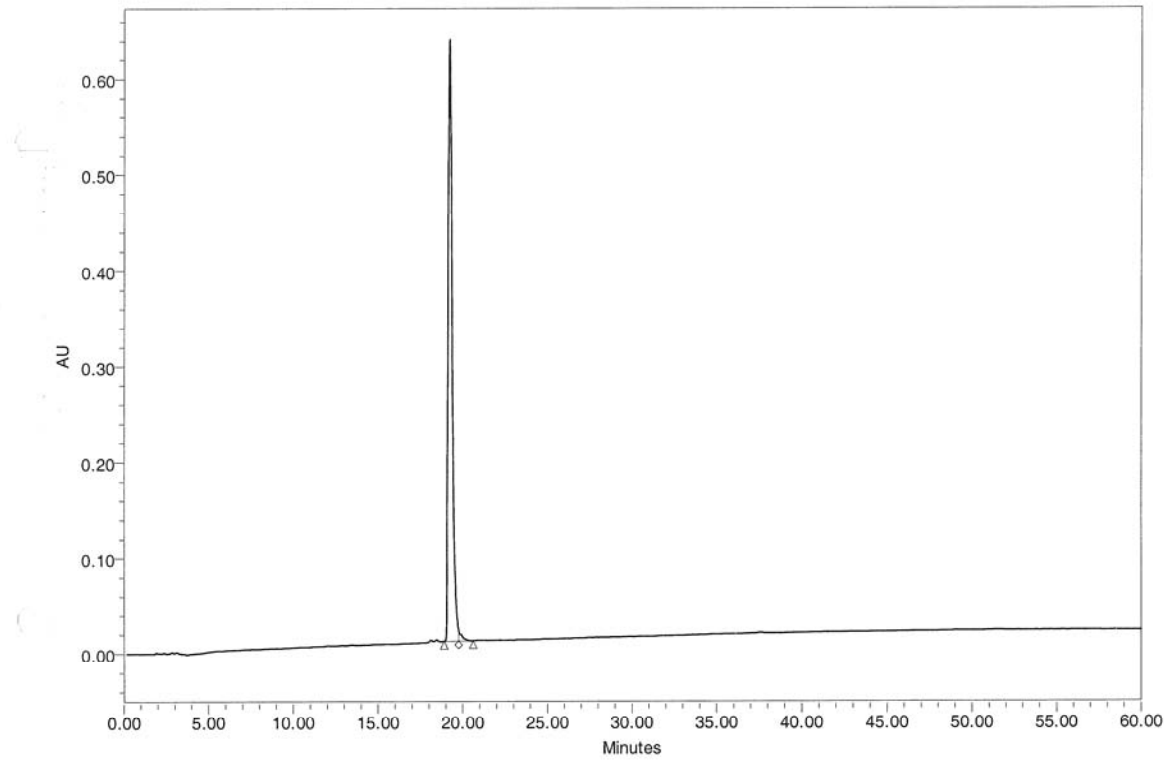

RT	Height	Area	% Area
19.218	628451	10614407	98.69
19.767	11414	140587	1.31

MALDI-TOF spectrum COCHO-APP10

MALDI-TOF matrix : α-cyano-4-hydroxycinnamic acid

Calcd. For C71H104N20O18 [M+H]+ 1525.79, found 1526.0

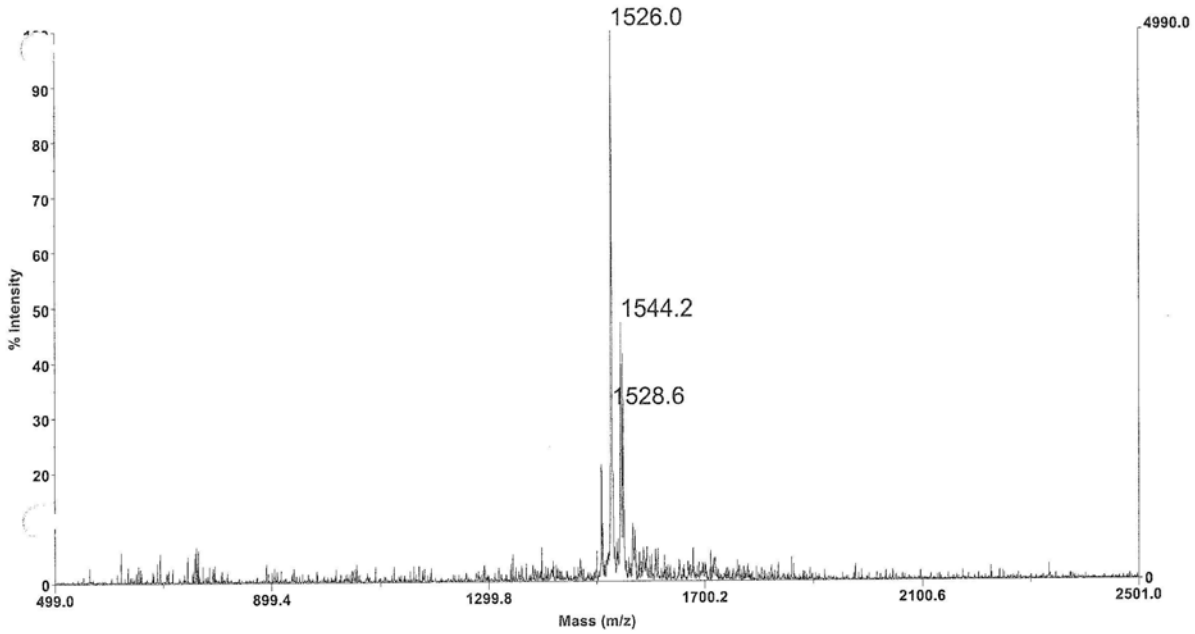

COCHO-APP11

RP-HPLC

Eluent A is 0.05% TFA in water, eluent B is 0.05% TFA in CH_3CN/water: 4/1 by vol. RP-HPLC on a 120 Å 5 µm C18 Nucleosil column (4.6 × 250 mm) using a linear water/acetonitrile gradient 0-100%B in 60 min (1 mL/min, detection 215 nm).

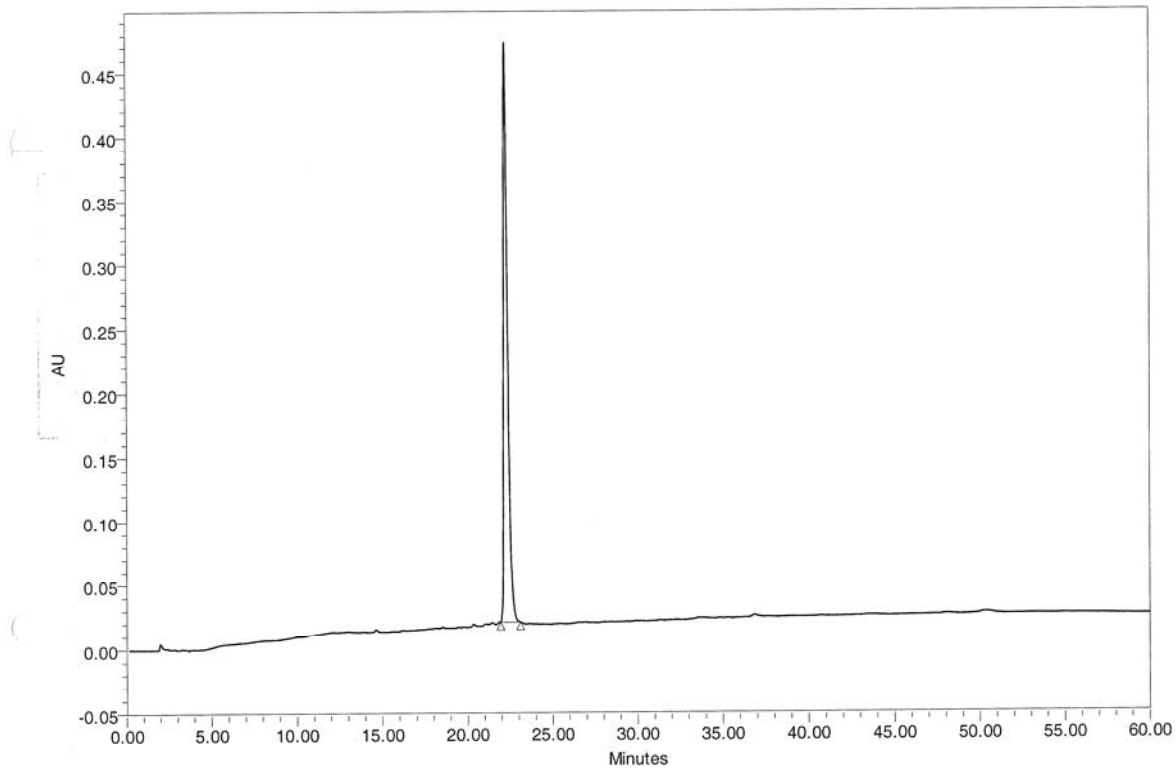

RT	Height	Area	% Area
22.231	453620	7420104	100.00

MALDI-TOF spectrum COCHO-APP11

MALDI-TOF matrix : α-cyano-4-hydroxycinnamic acid

Calcd. For C71H104N20O17 [M+H]+ 1509.80, found 1509.7

Reflector mode

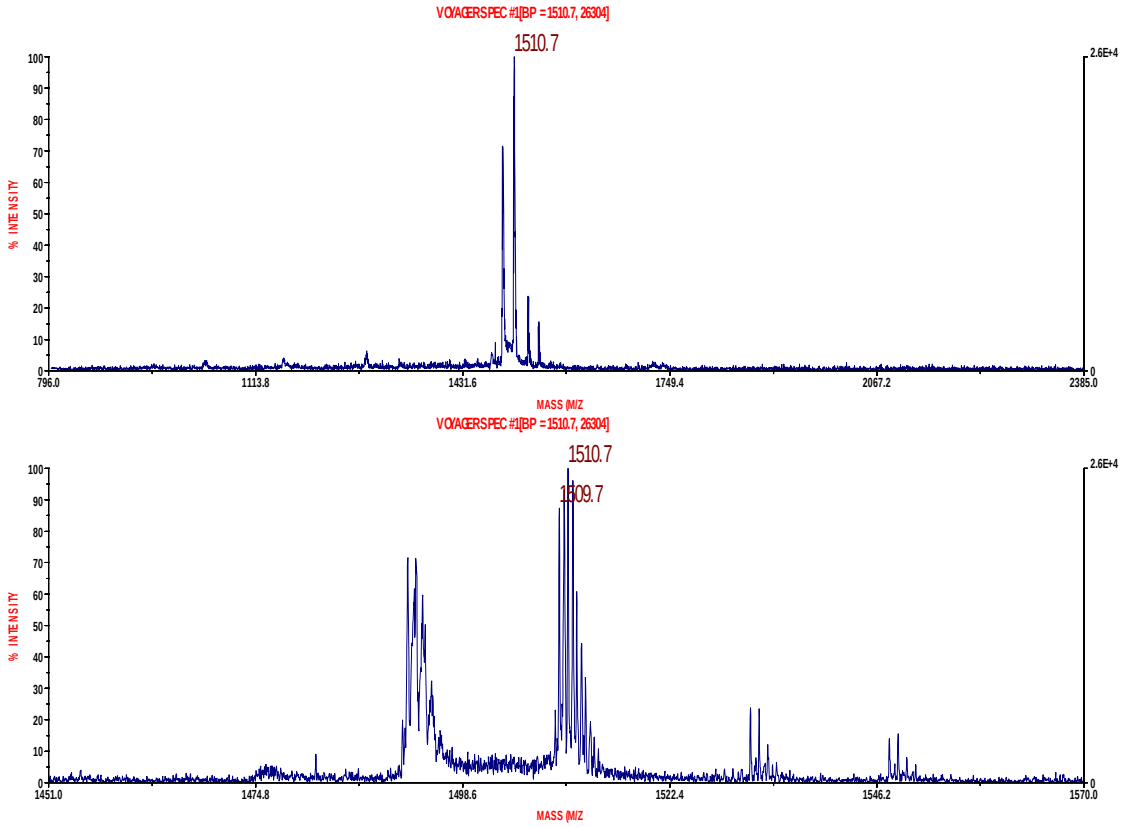

Linear mode

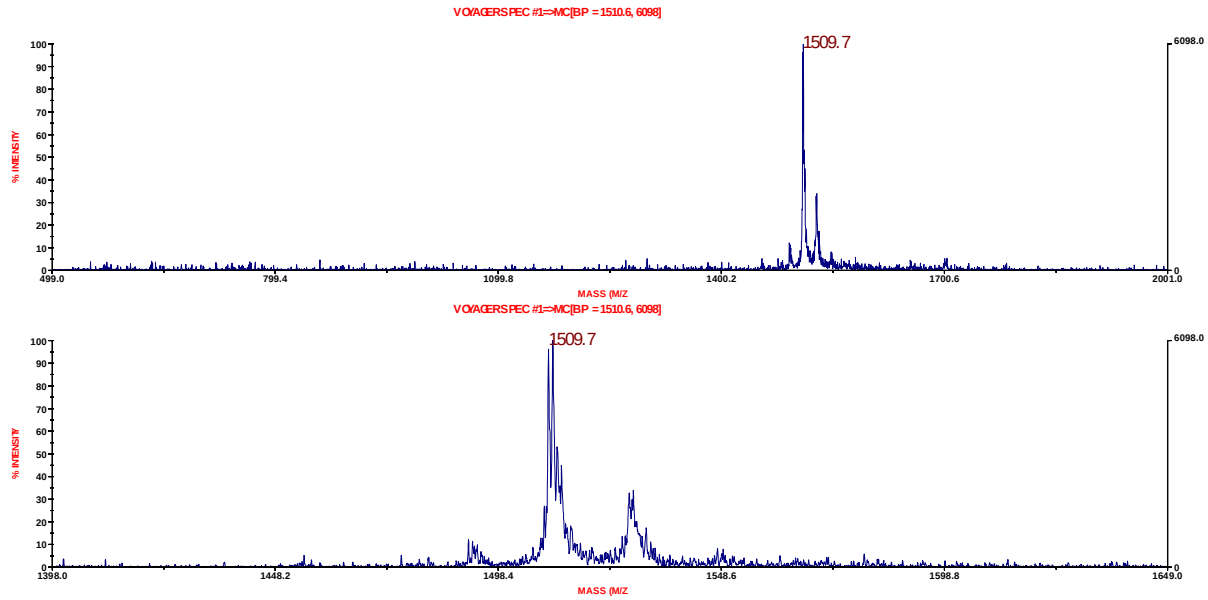

COCHO-APP12

RP-HPLC

Eluent A is 0.05% TFA in water, eluent B is 0.05% TFA in CH_3CN/water: 4/1 by vol. RP-HPLC on a 120 Å 5 µm C18 Nucleosil column (4.6 × 250 mm) using a linear water/acetonitrile gradient 0-100%B in 30 min (1 mL/min, detection 215 nm).

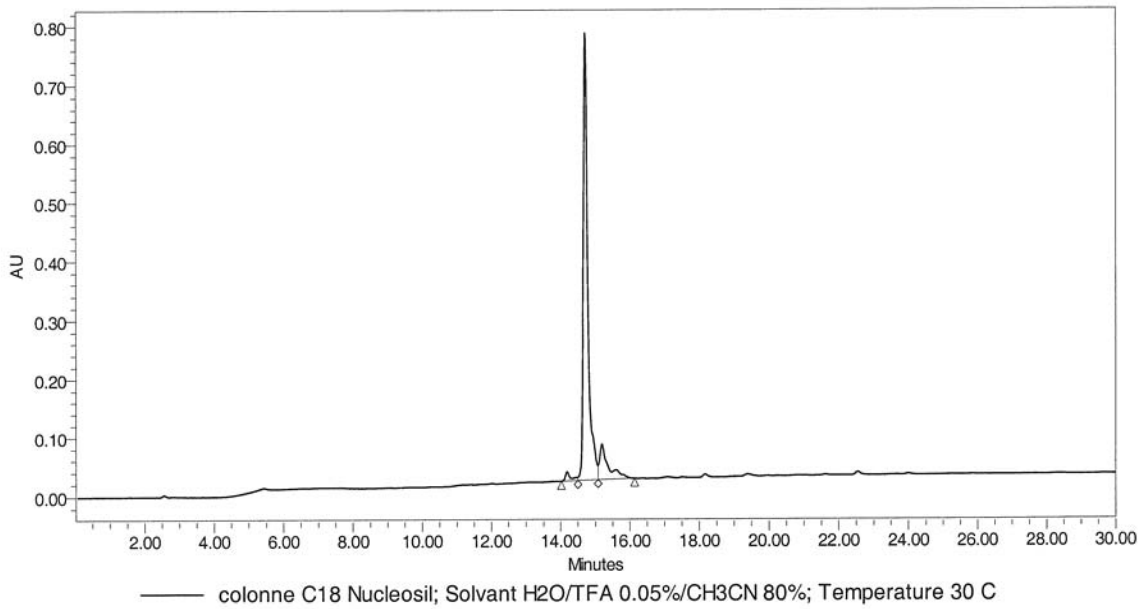

	RT	Area	% Area	Height
1	14.186	167351	2.05	15580
2	14.708	6962456	85.10	766925
3	15.193	1051442	12.85	60900

MALDI-TOF spectrum COCHO-APP12

MALDI-TOF matrix : α-cyano-4-hydroxycinnamic acid

Calcd. For C122H171N35O35 [M+H]+ 2687.28, found 2687.5

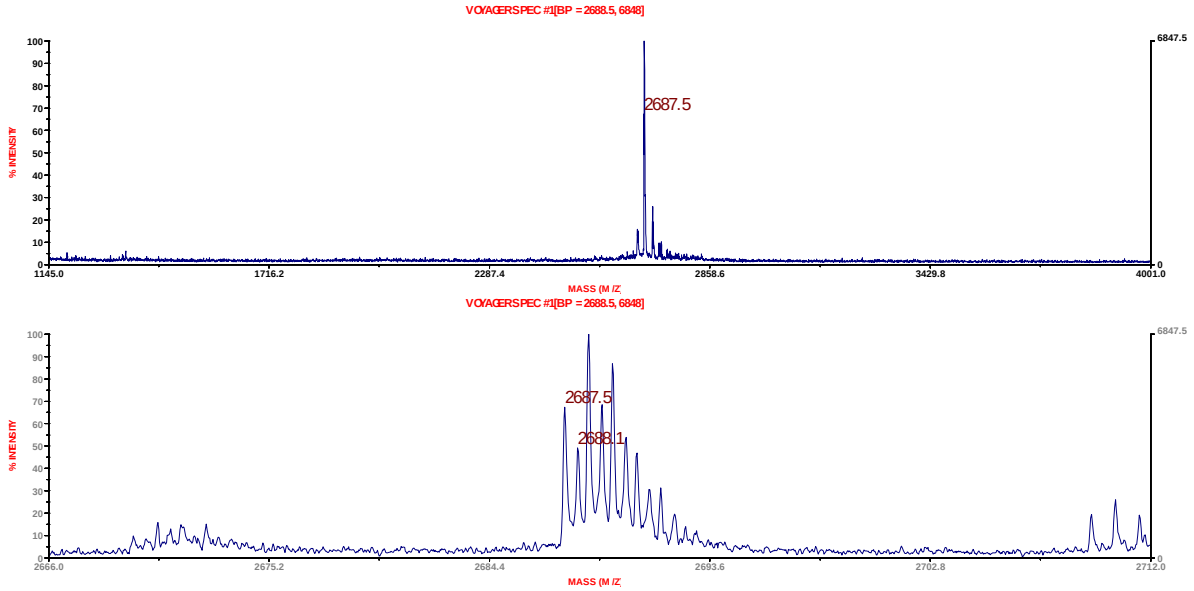

Comparison of a Nucleosidic vs Non-Nucleosidic Postsynthetic "Click" Modification of DNA with Base-Labile Fluorescent Probes

Sina Berndl,[†] Nadine Herzig,[†] Péter Kele,[‡] Daniel Lachmann,[†] Xiaohua Li,[‡] Otto S. Wolfbeis,[‡] and Hans-Achim Wagenknecht*,[†]

Institute of Organic Chemistry, University of Regensburg, D-93040 Regensburg, Germany and Institute of Analytical Chemistry, Chemo- and Biosensors, University of Regensburg, D-93040 Regensburg, Germany. Received November 7, 2008; Revised Manuscript Received January 8, 2009

The azides **1** and **2** bearing a phenoxazinium and a coumarin fluorophore, respectively, were applied in postsynthetic "click"-type bioconjugation and coupled to oligonucleotides modified with alkyne groups using two alternative approaches: (i) as a nucleotide modification at the 2′-position of uridine and (ii) as a nucleotide substitution using (*S*)-(−)-3-amino-1,2-propanediol as an acyclic linker between the phosphodiester bridges. The corresponding alkynylated phosporamidites **3** and **6** were used as DNA building blocks for the preparation of alkyne-bearing DNA duplexes. The base pairs adjacent to the site of modification and the base opposite to it were varied in the DNA sequences. The modified duplexes were investigated by UV/vis absorption spectroscopy (including melting temperatures) and fluorescence spectroscopy in order to study the different optical properties of the two chromophores and to evaluate their potential for bioanalytical applications. The sequence-selective fluorescence quenching of phenoxazinium **1** differs only slightly and does not depend on the type of modification, meaning whether it has been attached to the 2′-position of uridine or as DNA base surrogate using the acyclic glycol linker. The 2′-chromophore-modified uridine still recognizes adenine as the counterbase, and the duplexes exhibit a sufficient thermal stability that is comparable to that of unmodified duplexes. Thus, the application of the 2′-modification site of uridine is preferred in comparison to glycol-assisted DNA base surrogates. Accordingly, the coumarin dye azide **2** was attached only to the 2′-position of uridine. The significant Stokes shift of ∼100 nm and the good quantum yields make the coumarin chromophore a powerful fluorescent label for nucleic acids.

INTRODUCTION

Bioanalytical methods based on nucleic acids often require the use of bright DNA labels for fluorescence readout (*1*−*12*). The standard phosphoramidite DNA building block strategy enables a large variety of organic fluorophores to be routinely incorporated at specific positions within the oligonucleotide. Alternatively, postsynthetic labeling with fluorophores can be performed via amide bond formation to internal, 3′- and 5′-terminal modifiers that are commercially or synthetically available as phosphoramidites (*13*). In recent years, the "click" ligation strategy has become an important alternative. Huisgen originally described the [2 + 3]-cycloaddition between alkynes and azides yielding 1,2,3-triazoles (*14*). The utility of this reaction as a bioligation method has grown incredibly after Sharpless had reported that the addition of Cu(I) led to a significant increase in the reaction rate and in regioselectivity (*15*). This type of "click" chemistry has been widely used as a bioconjugation method (*16*−*27*) due to the mild reaction conditions and the bioorthogonal functional groups meaning that both alkynes and azides typically are not present in biopolymers (*28*−*31*). Using the "click" chemistry, up to six modifications have been incoporated simultaneously (*32*) and up to three modifications consecutively into oligonucleotides (*33*). Highly modified DNA can be prepared by a combination of PCR with triphosphates bearing alkynes (*34*).

It became clear that "click" chemistry is predestined for the application as a postsynthetic ligation for nucleic acids in order to avoid the time-consuming synthesis of phosphoramidites as DNA building blocks (*20, 21*). This is especially important for a number of remarkable and brightly emitting fluorophores that are not compatible with the acidic, oxidative, or basic conditions of automated DNA phosphoramidite chemistry and DNA workup. For instance, phenoxazinium and coumarin dyes represent brightly emitting organic fluorophores that are not stable under the typically strong basic conditions during DNA cleavage and deprotection. Hence, these labels cannot be incorporated into oligonucleotides using the conventional phosphoramidite chemistry.

Herein, we present the application of "click" chemistry for postsynthetic attachment of the fluorescent azides *N*-(5-(3-azidopropylamino)-9*H*-benzo[*a*]phenoxazin-9-ylidene)-*N*-methylmethanaminium (**1**) (*35*) and (*E*)-1-(3-azidopropyl)-4-(2-(7-(diethylamino)-2-oxo-2*H*-chromen-3-yl)vinyl)pyridinium (**2**) (*35,36*) (Scheme 1) as representatives of a phenoxazinium and a coumarin dye, respectively. They were coupled to oligonucleotides that are modified with alkyne groups using two alternative structural approaches: (i) as a nucleotide modification at the 2′-position of uridine and (ii) as a nucleotide substitution using (*S*)-(−)-3-amino-1,2-propanediol as an acyclic linker between the phosphodiester bridges. The resulting duplexes were investigated by optical spectroscopy in order to study the different stacking situations of the chromophores and to evaluate their potential in oligonucleotide-based assays.

EXPERIMENTAL PROCEDURES

Materials and Methods. Chemicals were purchased from Aldrich, Alfa Aesar, and Merck. Unmodified oligonucleotides

* Corresponding author. E-mail: achim.wagenknecht@chemie.uni-regensburg.de, Fax: 49 941 9434802.

[†] Institute of Organic Chemistry, University of Regensburg, D-93040 Regensburg, Germany.

[‡] Institute of Analytical Chemistry, Chemo- and Biosensors, University of Regensburg, D-93040 Regensburg, Germany.

10.1021/bc8004864 CCC: $40.75 © 2009 American Chemical Society
Published on Web 02/16/2009

Scheme 1. Building Blocks for the Postsynthetic "Click" Chemistry with Oligonucleotides[a]

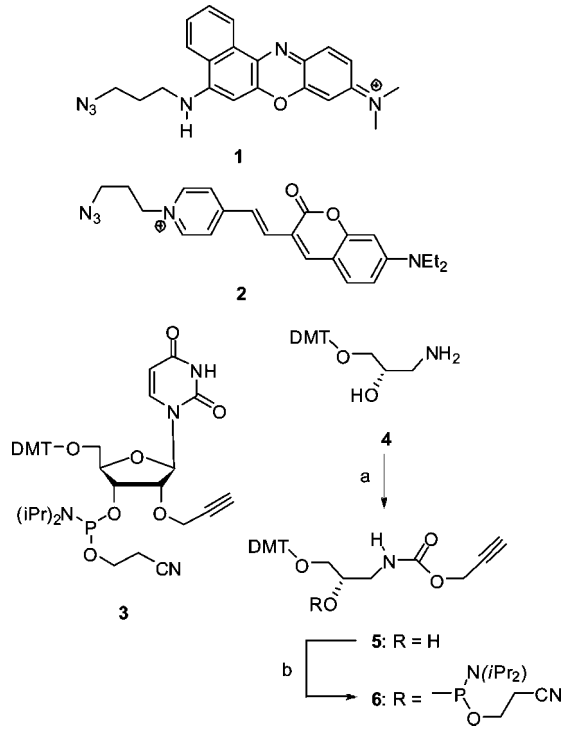

[a] Azides **1**, **2** and alkyne phosphoramidites **3**, **4**: (a) 2-propyn-1-ol, 1,1′-carbonyldiimidazole, DMF, r.t., 27 h; 76%; (b) 2-cyanoethyl-*N*,*N*-diisopropylchlorophosphoramidite, $EtN(iPr)_2$, CH_2Cl_2, r.t., 3 h.

were purchased from Metabion. TLC was performed on Fluka silica gel 60 F_{254} coated aluminum foil. Flash chromatography was carried out with silica gel 60 from Aldrich (60−43 μm). Spectroscopic measurements were recorded in sodium phosphate buffer solution (10 mM) using quartz glass cuvettes (10 mm). ESI mass spectra were acquired in the central analytical facility of the faculty on a ThermoQuest Finnigan TSQ 7000 in negative and positive ionization mode. NMR spectra were recorded on a Bruker Avance 300 spectrometer in deuterated solvents that had been dried over basic alumina. Chemical shifts are given in ppm relative to TMS. Absorption spectra and the melting temperatures (2.5 μM DNA, 250 mM NaCl, 10−90 °C, 0.7 °C/min, step width 0.5 °C) were recorded on a Varian Cary 100 spectrometer equipped with a 6 × 6 cell changer unit. Fluorescence spectra were acquired on a Jobin-Yvon Fluoromax 3 fluorimeter in spectral steps of 1 nm and an integration time of 0.2 s. All spectra were recorded with an excitation and emission bandpass of 2 nm and are corrected for Raman emission from the buffer solution.

Synthesis of 5. 2-Propyn-1-ol (40 μL, 700 μmol) was dissolved in DMF (5 mL). 1,1′-carbonyldiimidazole (114 mg, 700 μmol) was added and the solution was stirred at room temperature for 3 h. (3-(4,4′-Dimethoxytrityl)-2-hydroxy-propylamine (**4**) (268 mg, 700 μmol) was added and the solution was stirred for another 24 h at room temperature and then evaporated to dryness. The crude product was purified by flash chromatography (CH_2Cl_2, 0.1% NEt_3) yielding a yellow solid (76%). TLC (CH_2Cl_2/MeOH 100:2) R_f = 0.3. ^{1}H NMR (300 MHz, [d_6]-acetone): δ = 7.51−7.48 ppm (m, 2H, arom. DMT), 7.37−7.28 (m, 7H, arom. DMT), 6.89−6.86 (m, 4H, arom. DMT), 6.26 (m, 1H, NH), 4.64 (d, J = 2.47, 2H, C$\underline{H_2}$CCH), 4.17 (d, J = 5.21, 1H, OH), 3.92−3.86 (m, 1H, CH_2CHCH_2), 3.79 (s, 6H, OMe), 3.45−3.37 (m, 1H, CH_2CHCH_2), 3.22−3.15 (m, 1H, CH_2CHCH_2), 3.13−3.05 (m, 2H, CH_2CHCH_2), 2.98 (t, J = 2.47, 1H, CCH). MS (FAB): m/z (%) 303.1 (100) [DMT]$^+$, 475.5 [MH$^+$]. HRMS (FAB): M$^+$ calcd for $C_{28}H_{30}NO_6$ [MH$^+$]: 476.2073. Found: 476.2085.

Synthesis of 6. Compound **5** (350 mg, 0.74 mmol) was dissolved under nitrogen in dry CH_2Cl_2 (5 mL). Dry ethyldiisopropylamine (380 μL, 2.21 mmol) and 2-cyanoethyl-*N*,*N*-diisopropylchlorophosphoramidite (181 μL, 0.81 mmol) were added, and the solution was stirred for 3 h at r.t. The mixture was washed with freshly prepared sat. aqueous $NaHCO_3$, dried over Na_2SO_4, and evaporated to dryness. The crude product was purified by flash chromatography (CH_2Cl_2/MeOH 100:2, 0.1% $(^iPr)_2NEt$). The resulting yellow foam (80%) was dissolved in dry MeCN (6.1 mL) and applied directly for automated DNA synthesis. TLC (CH_2Cl_2/MeOH 100:2): R_f = 0.6. ^{1}H NMR (300 MHz, [d_6]-C_3D_6O): δ = 1.06−1.19 (m, 12H, 4 × Me (^{i}Prop)), 2.58 (t, J_z = 6.04, 1H, ≡H), 2.76 (m, 2H), 2.95 (m, 1H), 3.07 (m, 1H), 3.22 (m, 1H), 3.36 (m, 1H), 3.54 (m, 1H), 3.61 (m, 2H), 3.85 (m, 1H), 3.75 (s, 6H, 2 × OMe), 4.10 (m, 1H), 4.60 (dd, J_z = 2.47, CH_2≡), 6.20 (m, 1H, NH), 6.83−6.88 (m, 4H, arom.), 7.25−7.35 (m, 7H, arom.), 7.46−7.49 (m, 2H, arom.). ^{31}P NMR (121 MHz, [d_6]-acetone): = 150.6.

Preparation of Modified Oligonucleotides. Oligonucleotides were prepared on an Expedite 8909 Synthesizer from Applied Biosystems (ABI) using standard phosphoramidite chemistry. Reagents and controlled pore glass (CPG) (1 μmol) were purchased from ABI and Glen Research. The synthesis of DNA oligonucleotides modified with the acyclic linked acetylene was performed using a modified protocol. Activator solution (0.45 M tetrazole in acetonitrile) was pumped together with the building block (0.15 M in acetonitrile) through the CPG vial. The coupling time was extended to 61 min with an intervening step after 30.8 min for washing and refreshing the activator/phosphoramidite solution in the CPG vial. The CPG vial was flushed with dry acetonitrile after coupling. Acetylene-modified uridine was introduced into DNA by using standard coupling conditions. The concentration of the building block was increased to 0.1 M. After preparation, the trityl-off oligonucleotides were cleaved from the resin and deprotected by treatment with conc. NH_4OH at room temperature for 24 h.

"Click" Ligation. The azides **1** (blue) and **2** (red) were synthesized according to the literature (*35*, *36*). The azide **1** or **2** (114 μL, 10 mM), Cu(I) (17 μL, 100 mM), TBTA (34 μL, 100 mM), each in DMSO/^{t}BuOH = 3:1, and sodium ascorbate (25 μL, 400 mM) in H_2O was added to the oligonucleotide (1 μmol). The reaction mixture was vortexed, shaken overnight at room temperature, and then evaporated to dryness using a speedvac. Sodium acetate (100 μL, 0.15 mmol) was added and the mixture stored for 1 h at room temperature. Ethanol (1 mL) was added and the mixture vortexed and frozen (−20 °C) overnight. The suspension was centrifuged (13 000 rpm, 15 min) and the supernatant removed. The pellet was washed twice with ethanol (500 μL) and then dissolved in water (500 μL). Prior to purification by HPLC, the DNA was desalted by NAP-5 column (GE Healthcare).

DNA Purification. The modified oligonucleotides were purified by HPLC on a semipreparative RP-C18 column (300 Å, Supelco) using the following conditions: A = NH_4OAc buffer (50 mM), pH = 6.5; B = acetonitrile; gradient 0−30% B over 50 min, flow rate 2.5 mL/min, UV/vis detection at 260 and 641 nm. The oligonucleotides were lyophilized and quantified by their absorbance in 10 mM sodium phosphate buffer at 260 nm on a Varian Cary 100 spectrometer. Duplexes were formed by heating to 90 °C (15 min) followed by slow cooling. MS (ESI): **DNA1** calc. 5453, found m/z = 1092.1 [M/5]$^{5+}$, 1364.8 [M/4]$^{4+}$, 1819.5 [M/3]$^{3+}$; ε (260 nm) = 159 090 [mol L^{-1} cm^{-1}]. **DNA2** calc. 5562, found m/z = 1390.0 [M/4]$^{4-}$, 1853.8 [M/3]$^{3-}$; ε (260 nm) = 181 650 [mol L^{-1} cm^{-1}]; **DNA3** calc. 5594, found m/z = 1397.9 [M/4]$^{4-}$, 1864.4 [M/3]$^{3-}$; ε (260 nm) = 166 270 [mol

L^{-1} cm^{-1}]; **DNA5** calc. 5503, found m/z = 1833.9 [M/3] $^{3-}$; ε (260 nm) = 164 290 [mol L^{-1} cm^{-1}]; **DNA6** calc. 5612, found m/z = 1402.3 [M/4] $^{4-}$, 1869.9 [M/3] $^{3-}$; ε (260 nm) = 186 850 [mol L^{-1} cm^{-1}]; **DNA7** calc. 5644, found m/z = 1410.3 [M/4]$^{4-}$, 1881.3 [M/3]$^{3-}$; ε (260 nm) = 171 470 [mol L^{-1} cm^{-1}].

RESULTS

"Click" Bioconjugations. The fluorophore azides **1** (blue) and **2** (red) were incorporated oligonucleotides bearing the alkyne group either as a nucleotide modification at the 2′-position of uridine or as a nucleotide substitution using (*S*)-(−)-3-amino-1,2-propanediol as an acyclic linker between the phosphodiester bridges. The first DNA building block, 5′-*O*-dimethoxytrityl-N^3-pivaloyloxymethyl-2′-*O*-propargyluridine-3′-*O*-(2-cyanoethyl-*N*,*N*-diisopropylphosphoramidite (**3**), can be synthesized according to the literature procedure (*37*). In the second DNA building block, ethynyl (2*S*)-3-(bis(4-methoxyphenyl)(phenyl)methoxy)-2-((2-cyanoethoxy)(diisopropylamino)phosphinooxy)propylcarbamate (**6**), the 2′-deoxyribofuranoside moiety was replaced by an acyclic linker. Similar glycol linkers have been used by others in order to prepare glycol nucleic acid (GNA) (*38*, *39*), twisted intercalating nucleic acids (TINA) (*25*, *40*), and alkyne-modified oligonucleotides for the "click" cycloaddition as a postsynthetic modification (*33*). We had previously used this structural approach for the incorporation of ethidium (*41*, *42*), indole (*43*), perylene bismimide (*44*, *45*), phenothiazine (*46*), and thiazole orange (*47*) into oligonucleotides via the corresponding phosphoramidites as DNA building blocks. In contrast to the latter examples, we have connected the glycol linker not directly to the propargyl group but via a carbamate function. This facilitates the synthesis of the corresponding DNA building block **6**, since the protection of the N−H group of the linker part is not necessary. The DMT-protected (*S*)-3-amino-1,2-propanediol **4** as the precursor was synthesized according to the literature (*41*). The hydroxy function of commercially available 2-propyn-1-ol was converted into an activated ester by 1,1′-carbonyldiimidazole, and the subsequent nucleophilic acyl substitution with **4** gave the conjugate **5** in 76% yield. The synthesis of the phosphoramidite **6** was accomplished by standard procedures.

The detritylated oligonucleotides were automatically synthesized at the 1 μmol scale using the synthetic phosphoramidites **3** or **6** and coupled to the azides **1** or **2**, respectively, in the presence of an excess of Cu(I), TBTA, and sodium ascorbate in a DMSO/^{t}BuOH (3:1) solvent mixture at room temperature overnight. After lyophilization and ethanol precipitation, the modified single strands **DNA1**-**DNA3** and **DNA5**-**DNA7** were purified by semipreparative HPLC and finally desalted. All modified oligonucleotides were studied by UV/vis absorption and fluorescence spectroscopy (including quantum yields); the corresponding duplexes **DNA1Y**-**DNA3Y** and **DNA5Y**-**DNA7Y** additionally by measurement of the melting temperature (T_m). The unmodified duplexes **DNA4Y** and **DNA8Y** were used as references (Scheme 2).

Phenoxazinium-Modified DNA. The sequences of **DNA1Y**, **DNA2Y**, **DNA5Y**, and **DNA6Y** bear the blue phenoxazinium chromophore in three different structural variations (Scheme 2): (I) The chromophore was either connected to the 2′-position of uridine (**DNA2Y** and **DNA6Y**) or as a non-nucleosidic DNA base replacement (**DNA1Y** and **DNA5Y**). (II) The base pairs directly adjacent to the phenoxazinium modification site were varied (A-T in **DNA1Y**/**DNA2Y** or G-C in **DNA5Y**/**DNA6Y**). (III) The base opposite to the modification site was varied (Y = A, T, C, or G).

First, we measured the melting temperatures (T_m) of the phenoxazinium-modified duplexes at 260 nm (Tables 1 and 2) in order to study the influence of the phenoxazinium moiety on the duplex stability. The following major effects have been observed: (i) The phenoxazinium chromophore as a non-nucleosidic base surrogate in **DNA1Y** and **DNA5Y** does not exhibit any preferential base pairing with the counterstrand. (ii) In contrast, the phenoxazinium-modified uridine in **DNA2Y** and **DNA6Y** clearly prefers the adenine opposite to the modification site. (iii) Regardless of the type of modification and the sequential context, the "mismatched" modified duplexes **DNA1Y**, **DNA2Y**, **DNA5Y**, and **DNA6Y** (Y = T, C, G) are

Scheme 2. Sequences and Numbering of the Modified Duplexes DNA1Y-DNA8Y[a]

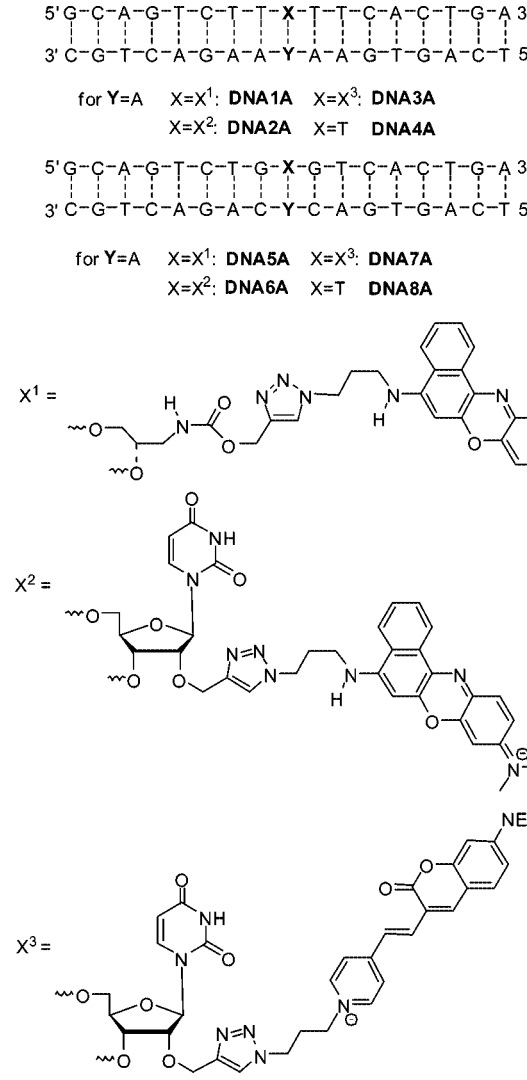

[a] Representatively shown for **Y** = A. For **Y** = T, C, G, structures are numbered accordingly (see Table 1 and Table 2).

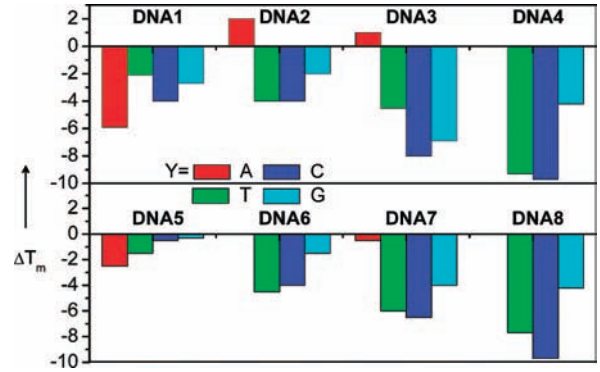

Figure 1. Melting temperature differences of duplexes **DNA1**-**DNA4** in comparison to **DNA4A** as the reference and **DNA5**-**DNA8** in comparison to **DNA8A** as the reference.

Table 1. Quantum Yields (Θ_F) and Melting Temperatures (T_m) of DNA1Y-DNA4Y

		X = X^1/R^1	X = X^2/R^1	X = X^2/R^1	X = T
		DNA1 (ss)	**DNA2** (ss)	**DNA3** (ss)	**DNA4** (ss)
	Θ_F	0.159	0.176	0.283	–
Y = A		**DNA1A**	**DNA2A**	**DNA3A**	**DNA4A**
	Θ_F	0.151	0.122	0.317	–
	T_m (°C)	56.6	64.5	63.5	62.5
Y = T		**DNA1T**	**DNA2T**	**DNA3T**	**DNA4T**
	Θ_F	0.188	0.147	0.346	–
	T_m (°C)	60.4	58.5	58.0	53.2
Y = C		**DNA1C**	**DNA2C**	**DNA3C**	**DNA4C**
	Θ_F	0.221	0.163	0.305	–
	T_m (°C)	58.5	58.5	54.5	52.8
Y = G		**DNA1G**	**DNA2G**	**DNA3G**	**DNA4G**
	Θ_F	0.055	0.030	0.299	–
	T_m (°C)	59.8	60.5	55.6	55.0

Table 2. Quantum Yields (Θ_F) and Melting Temperatures (T_m) of DNA5Y-DNA8Y

		X = X^1/R^1	X = X^2/R^1	X = X^2/R^1	X = T
		DNA5 (ss)	**DNA6** (ss)	**DNA7** (ss)	**DNA8** (ss)
	Θ_F	0.051	0.041	0.312	–
Y = A		**DNA5A**	**DNA6A**	**DNA7A**	**DNA8A**
	Θ_F	0.015	0.025	0.202	–
	T_m (°C)	65.5	68.0	67.5	68.0
Y = T		**DNA5T**	**DNA6T**	**DNA7T**	**DNA8T**
	Θ_F	0.016	0.029	0.199	–
	T_m (°C)	66.5	63.5	62.0	60.3
Y = C		**DNA5C**	**DNA6C**	**DNA7C**	**DNA8C**
	Θ_F	0.011	0.014	0.266	–
	T_m (°C)	67.5	64.0	61.5	58.3
Y = G		**DNA5G**	**DNA6G**	**DNA7G**	**DNA8G**
	Θ_F	0.009	0.018	0.255	–
	T_m (°C)	67.7	66.5	62.0	63.8

more stable compared to the corresponding unmodified mismatched duplexes **DNA4Y** and **DNA8Y**, respectively. This result indicates a stabilization of base mismatches by the stacking interactions with the phenoxazinium chromophore. The following additional effects can be drawn if the unmodified and matched **DNA4A** and **DNA8A** are regarded as the references (Figure 1): (iv) The replacement of the 2′-deoxyribofuranoside by the acyclic glycol linker results in a decrease of thermal stability by 5.9 °C in **DNA1A** and 4.0 °C in **DNA5A**. (v) In contrast, the incorporation of the phenoxazinium chromophore as a nucleosidic 2′-modification yields duplexes of equal (**DNA2A**) or even by 2 °C higher thermal stability (**DNA6A**).

The UV/vis spectra of all modified single strands and all duplexes show the typical absorption of the blue chromophore with maxima in the small range between 652 and 661 nm (Supporting Information Figures S1, S2, S4, S5). The absorption properties do not reflect a systematic change of properties as a result of any of the three different structural variations **I**−**III**. In contrast, the fluorescence of the duplexes show the influence of the sequential neighborhood (Figure 2). The quantum yield of the fluorescence of the phenoxazinium duplexes ranges from 12% to 22% provided guanines are not placed in the vicinity of the phenoxazinium dye (Figure 3). The fluorescence is quenched significantly if a guanine is present as the counterbase or as part of the adjacent base pairs, or both. It is important to point out that this profile of emission properties is observed regardless of whether the chromophore has been attached to the 2′-position of uridine or as a non-nucleosidic DNA base surrogate using the acyclic glycol linker. In fact, the quantum yields of the corresponding duplex pairs are similar, e.g., **DNA1A** vs **DNA2A**.

Coumarin-Modified DNA. Due to this similarity that has been observed between the nucleosidic and non-nucleosidic approaches for phenoxazinium-modified DNA duplexes, we decided to incorporate the red coumarin label (azide **2**) only to the 2′-position of uridine. Those modified duplexes would show

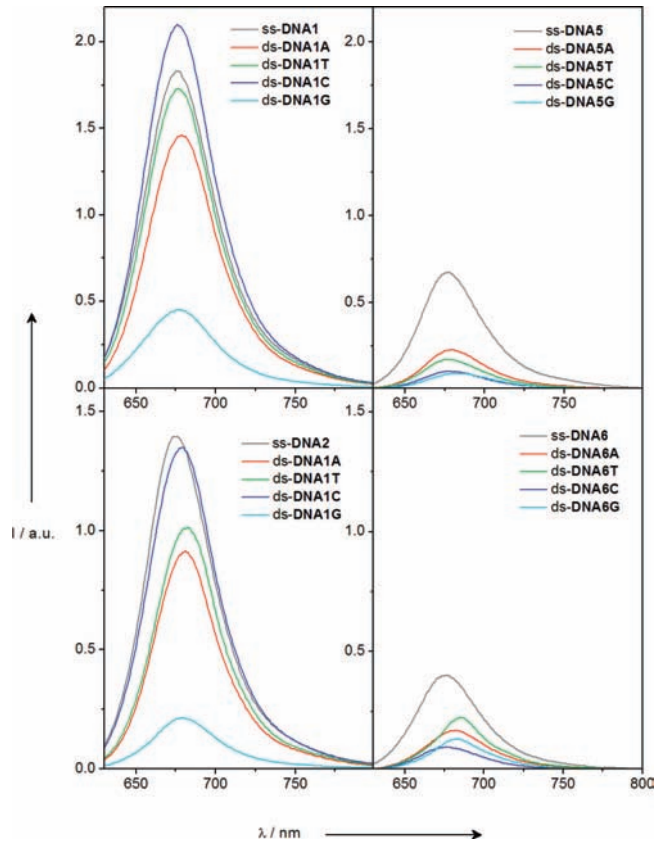

Figure 2. Fluorescence spectra of single-stranded **DNA1**, **DNA2**, **DNA5**, and **DNA6** and the corresponding duplexes (2.5 μM) in sodium phosphate buffer (10 mM) of pH 7.0, NaCl (250 mM), λ_{exc} = 610 nm.

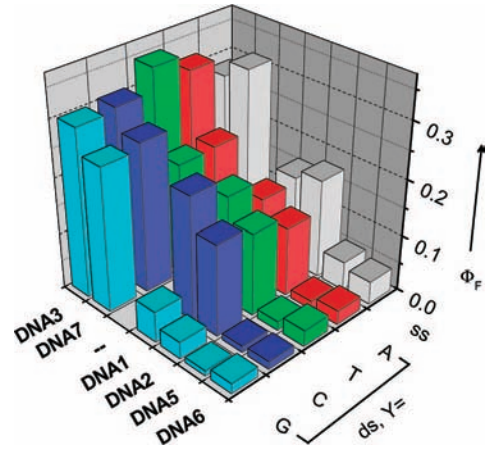

Figure 3. Graphical display of the quantum yields (Θ_F) of the coumarin-modified **DNA3** and **DNA7** and the phenoxazinium-modified **DNA1**, **DNA2**, **DNA5**, and **DNA6**.

defined Watson−Crick base pairing and exhibit a similar thermal stability to that of the unmodified matched duplexes (**DNA4A** and **DNA8A**). Accordingly, we have prepared **DNA3Y** and **DNA7Y** that bear variations of the adjacent base pairs and the counterbase. The melting temperatures show two major trends that are similar to the phenoxazinium-modified **DNA2Y** and **DNA6Y**. (i) As expected, the coumarin-modified uridine clearly prefers the adenine opposite to the modification site. (ii) Compared to the corresponding matched and unmodified duplexes **DNA4A** and **DNA8A**, respectively, the thermal stabilities of the matched but modified duplexes are only slightly lower (−0.5 °C for **DNA7A**) or even higher (+1.0 °C for

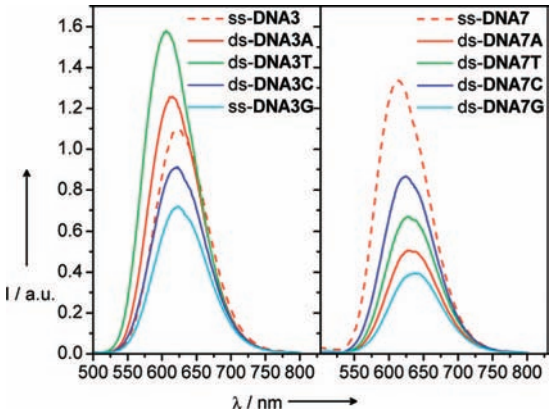

Figure 4. Fluorescence spectra of single-stranded **DNA3** and **DNA7** and the corresponding duplexes (2.5 μM) in sodium phosphate buffer (10 mM) of pH 7.0, NaCl (250 mM), $\lambda_{exc} = 500$ nm.

DNA3A). (iii) The coumarin dye stabilizes mismatches in **DNA3Y** and **DNA7Y** (Y = T, C, G), but not to such an extent as that observed in the case of the corresponding phenoxazinium-modified duplexes.

The UV/vis spectra of the modified single strands and duplexes show an absorption maximum in the range between 515 and 534 nm (Supporting Information Figures S3, S6). It is interesting to note that the duplexes bearing guanine as the counterbase (**DNA3G**) or as the base adjacent to the coumarin modification site (**DNA7Y**) show the most red-shifted absorption, particularly significant in **DNA7G** (534 nm). The steady-state fluorescence spectra of the coumarin-modified duplexes display maxima in the range 606−637 nm (Figure 4). It is important to point out that all modified duplexes exhibit a significant Stokes' shift of approximately 100 nm. The duplexes **DNA3Y** show quantum yields in the range between 30% and 35%. Compared to other coumarins, this is a very large Stokes' shift that is of particular interest with respect to potential fluorescence resonance energy transfer (FRET) studies. In fact, labels **1** and **2** form a well-matched FRET pair excitable with the argon ion laser. The quantum yields of the duplexes with adjacent G-C base pairs (**DNA7Y**) are lower (20−27%); however, a nearly complete fluorescence quenching as in the case of the corresponding phenoxazinium-modified duplexes is not observed.

DISCUSSION

Both the blue phenoxazinium fluorophore of **1** and the red coumarin of **2** are unstable under the basic conditions typically applied for DNA workup. Using the appropriate phosphoramidites as DNA building blocks is therefore a difficult task for the incorporation of these dyes into oligonucleotides. Postsynthetic "click" chemistry, however, allowed the modification of presynthesized alkynylated oligonucleotides with the fluorescent azides **1** and **2** to prepare the corresponding modified duplexes **DNA1Y-DNA3Y** and **DNA5Y-DNA7Y**.

The most critical issue with respect to fluorescent labeling of nucleic acids is fluorescence quenching caused by charge transfer and oxidation of guanines (*48*). Accordingly, there is a major difference between the two fluorophores of **1** and **2** based on photophysical and electrochemical data in the literature. The oxidation potential of guanine is ∼1.3−1.4 V vs normal hydrogen electrode (NHE) (*49*). According to the Rehm−Weller equation, the energy of the singlet−singlet transition E_{00} has to be added to the reduction potential E_{red} in order to calculate the excited-state potential and the driving force of a potential charge transfer reaction. In the case of fluorophore **1**, the excited-state potential is estimated to be $E^*_{red} = 2.2$ eV (vs NHE) using $E_{red} = -0.26$ V (vs decamethylferrocen), $E_{00} = 1.88$ eV, and a correction value of +0.54 V (from decamethylferrocen to NHE reference) (*50*). The excited-state potential of fluorophore **2** is significantly lower and estimated to be $E^*_{red} = 1.5$ eV using $E_{red} = -1.27$ V (vs Ferrocen), $E_{00} = 2.16$ eV and a correction value of +0.63 V (from ferrocen to NHE reference) (*50*). Conclusively, these values indicate that the phenoxazinium label **1** is capable of oxidizing guanines in the sequential neighborhood, whereas the coumarin label **2** represents a borderline case. Hence, we expected sequence-dependent fluorescence quenching of the phenoxazinium dye of azide **1**, and it is important to point out that we decided to use this property as a sensitive tool to compare the electronic interactions of the phenoxazinium chromophore with the DNA base stack in order to evaluate the role of the modification type (nucleosidic vs non-nucleosidic).

Accordingly, azide **1** was incorporated into oligonucleotides either as a nucleotide modification at the 2′-position of uridine (**DNA2Y** and **DNA6Y**) or as a non-nucleosidic base substitution (**DNA1Y** and **DNA5Y**). As expected based on the photophysical data given above, the emission is quenched significantly if a guanine is present as the counterbase, as part of the adjacent base pair, or both. In fact, the fluorescence of the phenoxazinium-modified single strands and duplexes has a quantum yield of >6% only if guanines are not located in direct vicinity of the chromophore. Most importantly, the quantum yield profiles (Figure 3) of the two duplex sets with the nucleoside modification (**DNA2Y** and **DNA6Y**) are very similar in comparison to the duplexes with the non-nucleosidic modification (**DNA1Y** and **DNA5Y**). This is a remarkable result that shows that the optical properties of fluorescent DNA do not depend on whether the dye has been incorporated as a DNA base substitution or as a 2′-nucleoside modification. In both cases, the interactions of the phenoxazinium dye with the counterbase and the adjacent DNA base pairs seem to be electronically similar.

In contrast to the similarity of the fluorescence properties, the phenoxazinium-modified duplexes show different thermal stabilities with respect to the type of modification. Compared to the unmodified and matched duplexes **DNA4A** and **DNA8A**, the replacement of the 2′-deoxyribofuranoside by the non-nucleosidic glycol linker (**DNA1A** and **DNA5A**) result not only in the loss of a preferred base pairing but also in a decrease of thermal stability. Both effects have been expected on basis of the design of the two types of modification (nucleosidic vs non-nucleosidic). However, the second effect is not very pronounced and thus surprising. Typical for single glycol linker substitutions in DNA is a thermal destabilization of more than 10 °C (*43*, *46*, *51*). For the phenoxazinium-modified **DNA1Y** and **DNA5Y**, the values are significantly lower. Obviously, some of the lost thermal stability can be regained by the hydrophobic stacking interactions of the phenoxazinium chromophore, presumably intercalated. The stabilizing effects are highest especially in the presence of adjacent G-C base pairs (**DNA5Y**).

This interpretation is supported by the observation that the mismatched modified duplexes are more stable against thermal dehybridization compared to the corresponding mismatched but unmodified duplexes. This represents another remarkable result, since it indicates that the phenoxazinium dye, presumably intercalated, stabilizes single-base mismatches by its hydrophobic interactions. It is important to point out that, for this effect, similar to the fluorescence quenching, it does not matter whether the phenoxazinium dye has been incorporated as a non-nucleosidic DNA base substitute or as a 2′-nucleoside modification.

Taking together with the results of the phenoxazinium-modified duplexes, it becomes clear that the application of the 2′-modification site of uridine is preferred in comparison to the non-nucleosidic, glycol-assisted DNA base substitution. Hence,

the red coumarin label **2** was attached only to the 2′-position of uridine. The steady-state fluorescence spectra of all coumarin-modified duplexes show a significant Stokes' shift of approximately 100 nm and quantum yields in the ranges 30−35% (**DNA3Y**) and 20−27% (**DNA7Y**). In contrast to the phenoxazinium-modified duplexes, nearly quantitative fluorescence quenching by charge transfer to guanines is not observed here. The lower quantum yields in **DNA7Y** are accompanied by a red-shifted absorption of the coumarin label. Obviously, guanine strongly interacts with the coumarin in the ground state, which also affects the exciplex-type fluorescence originating from the excited state, most significantly observed in the case of **DNA7G**. Nevertheless, the coumarin represents a powerful label for fluorescent nucleic acids based on the Stokes' shift and the quantum yields.

CONCLUSIONS

The blue phenoxazinium azide **1** and the red coumarin azide **2** represent examples of two structurally different but novel types of fluorophores (*35*). A common feature of both dyes is the instability under strongly basic conditions that are typically used for DNA workup. Hence, both chromophores cannot be easily incorporated into DNA using the standard phosphoramidite building block chemistry. However, "click" chemistry allows the postsynthetic modification of oligonucleotides that were presynthesized and modified with an alkyne group. A range of DNA duplexes was modified with the blue phenoxazinium azide **1**; one set of duplexes carried the chromophore attached at the 2′-position of uridine, and a second set contained the chromophore as a non-nucleosidic DNA base surrogate that has been inserted using an acyclic glycol linker. These phenoxazinium-modified duplexes were characterized by optical spectroscopy. A sequence-dependent fluorescence quenching of the phenoxazinium **1** was applied as a sensitive tool to compare the stacking interactions with respect to the structural variations (nucleosidic vs non-nucleosidic). Remarkably, the fluorescence properties do not depend on the modification site. It does not matter whether the chromophore has been attached to the 2′-position of uridine or as DNA base surrogate using the acyclic glycol linker. Thus, the application of the 2′-modification site of uridine is preferred in comparison to glycol-assisted DNA base surrogates. The 2′-chromophore-modified uridine still recognizes adenine as the counterbase and the duplexes do not exhibit a reduced thermal stability in comparison to the unmodified duplexes. Accordingly, the coumarin dye azide **2** was attached only using the nucleosidic approach that means by modification of the 2′-position of uridine. The significant Stokes' shift of ∼100 nm and the good quantum yields make the coumarin chromophore a powerful fluorescent label for nucleic acids in assays or cell biology. The postsynthetic "click" chemistry makes this dye now accessible to fluorescent labeling of nucleic acids.

ACKNOWLEDGMENT

This work was supported by the Deutsche Forschungsgemeinschaft, the Fonds der Chemischen Industrie, and the University of Regensburg. P.K. thanks the Alexander von Humboldt Foundation for a Humboldt fellowship (3.3-UNG/1126507).

Supporting Information Available: Absorption spectra of all modified DNA single strands and duplexes (Figure S1−S6); images of MS, ^{1}H NMR, and ^{13}C NMR for **5**, ^{1}H NMR and ^{31}P NMR for **6**, HPLC analysis and MS of **DNA1**−**3** and **DNA5**−**7**. This material is available free of charge via the Internet at http://pubs.acs.org.

LITERATURE CITED

(1) Epstein, J. R., Biran, I., and Walt, D. R. (2002) Fluorescence-based nucleic acid detection and microarrays. *Anal. Chim. Acta 469*, 3–36.
(2) Johansson, M. K., and Cook, R. M. (2003) Intramolecular dimers: a new design strategy for fluorescence-quenched probes. *Chem. Eur. J. 9*, 3466–3471.
(3) Tan, W., Wang, K., and Drake, T. J. (2004) Molecular beacons. *Curr. Opin. Chem. Biol. 8*, 547–553.
(4) Ranasinghe, R. T., and Brown, T. (2005) Fluorescence bases strategies for genetic analysis. *Chem. Commun.* 5487–5502.
(5) Waggoner, A. (2006) Fluorescent labels for proteomics and genomics. *Curr. Opin. Chem. Biol. 10*, 62–66.
(6) Niemeyer, C. M., and Blohm, D. (1999) DNA microarrays. *Angew. Chem., Int. Ed. Engl. 38*, 2865–2869.
(7) Pirrung, M. C. (2002) How to make a DNA chip. *Angew. Chem., Int. Ed. Engl. 41*, 1276–1289.
(8) Tyagi, S., and Kramer, F. R. (1996) Molecular beacons: probes that fluoresce upon hybridization. *Nat. Biotechnol. 14*, 303–308.
(9) Heyduk, T., and Heyduk, E. (2002) Molecular beacons for detecting DNA binding proteins. *Nat. Biotechnol. 20*, 171–176.
(10) Strerath, M., and Marx, A. (2005) Genotyping-from genomic DNA to genotype in a single tube. *Angew. Chem., Int. Ed. Engl. 44*, 7842–7849.
(11) Socher, E., Jarikote, D. V., Knoll, A., Röglin, L., Burmeister, J., and Seitz, O. (2008) FIT probes: peptide nucleic acid probes with a fluorescent base surrogate enable real-time DNA quantification and single nucleotide polymorphism discovery. *Anal. Biochem. 375*, 318–330.
(12) Wagenknecht, H.-A. (2008) Fluorescent DNA base modifications and substitutes: multiple fluorophore labeling and the DETEQ concept. *Ann. N.Y. Acad. Sci. 1130*, 122–130.
(13) Wojczewski, C., Stolze, K., and Engels, J. W. (1999) Fluorescent oligonucleotides - versatile tools as probes and primers for DNA and RNA analysis. *Synlett* 1667–1678.
(14) Huisgen, R. (1962) 1,3-dipolar cycloaddition. Past and future. *Angew. Chem., Int. Ed. 2*, 565–598.
(15) Lewis, W. G., Green, L. G., Grynszpan, F., Radic, Z., Carlier, P. R., Taylor, P., Finn, M. G., and Sharpless, K. B. (2002) Click chemistry in situ: acetylcholinesterase as a reaction vessel for the selective assembly of a femtomolar inhibitor from an array of building blocks. *Angew. Chem., Int. Ed. Engl. 41*, 1053–1057.
(16) Beckmann, H. S. G., and Wittmann, V. (2007) One-pot procedure for diazo transfer and azide-alkyne cycloaddition: triazole linkages from amines. *Org. Lett. 9*, 1–4.
(17) Lutz, J.-F. (2007) 1,3-Dipolar cycloadditions of azides and alkynes: a universal ligation tool in polymer and materials science. *Angew. Chem., Int. Ed. 46*, 1018–1025.
(18) Agard, N. J., Baskin, J. M., Prescher, J. A., Lo, A., and Bertozzi, C. R. (2006) A comparative study of bioorthogonal reactions with azides. *ACS Chem. Biol. 1*, 644–648.
(19) Wolfbeis, O. S. (2007) The click reaction in the luminescent probing of metal ions, and its implications on biolabeling techniques. *Angew. Chem., Int. Ed. 46*, 2980–2982.
(20) Weisbrod, S. H., and Marx, A. Novel strategies for the site-specific labelling of nucleic acids. *Chem. Commun.*, DOI: 10.1039/b809528k.
(21) Gramlich, P. M. E., Wirges, C. T., Manetto, A., and Carell, T. Postsynthetic DNA modification through the copper-catalyzed azide-alkyne cycloaddition reaction. *Angew. Chem. Int.*, Ed. DOI: 10.1002/anie.200802077.
(22) Seela, F., Sirivolu, V., and Chittepu, P. (2008) Modification of DNA with octadiynyl side chains: synthesis, base pairing, and formation of fluorescent coumarin dye conjugates of four nucleobases by the alkyne-azide "click" reaction. *Bioconjugate Chem. 19*, 211–224.
(23) Kocalka, P., Andersen, N. K., Jensen, F., and Nielsen, P. (2007) Synthesis of 5-(1,2,3-triazol-4-yl)-2′-deoxyuridines by a click chemistry approach: stacking of triazoles in the major

groove gives increases nucleic acid stability. *ChemBioChem 8*, 2106–2116.
(24) Kocalka, P., El-Sagheer, A. H., and Brown, T. (2008) Rapid and efficient DNA Strand cross-linking by click chemistry. *ChemBioChem 9*, 1280–1285.
(25) Geci, I., Filichev, V. V., and Pedersen, E. B. (2007) Stabilization of parallel triplexes by twisted intercalating nucleic acids (TINAs) incorporating 1,2,3-triazole units and prepared by microwave-accelerated click chemistry. *Chem. Eur. J. 13*, 6379–6386.
(26) Salic, A., and Mitchison, T. J. (2008) A chemical method for fast and sensitive detection of DNA synthesis *in vivo*. *Proc. Natl. Acad. Sci. U.S.A. 105*, 2415–2420.
(27) Jawalekar, A. M., Meeuwenoord, N., Cremers, J. S. G. O., Rutjes, F. P. J. T., and Delft, F. L. v. (2008) Conjugation of nucleosides and oligonucleotids by [3 + 2] cycloaddition. *J. Org. Chem. 73*, 287–290.
(28) Link, A. J., Vink, M. K. S., and Tirrell, D. A. (2004) Presentation and detection of azide functionality in bacterial cell surface proteins. *J. Am. Chem. Soc. 126*, 10598–10602.
(29) Iida, S., Asakura, N., Tabata, K., Okura, I., and Kamachi, T. (2006) Incorporation of unnatural amino acids into cytochrome c_3 and specific viologen binding to the unnatural amino acid. *ChemBioChem 7*, 1853–1855.
(30) Humenik, M., Huang, Y., Wang, Y., and Sprinzl, M. (2007) C-Terminal incorporation of bio-orthogonal azide groups into a protein-oligodeoxynucleotide conjugates by Cu^{I}-catalyzed cycloaddition. *ChemBioChem 8*, 1103–1106.
(31) Weisbrod, S. H., and Marx, A. (2007) A nucleoside triphosphate for site-specific labelling of DNA by the Staudinger l;igation. *Chem. Commun.* 1828–1830.
(32) Gierlich, J., Burley, G. A., Gramlich, P. M. E., Hammond, D. M., and Carell, T. (2006) Click chemistry as a reliable method for the high-density postsynthetic functionalization of alkyne-modified DNA. *Org. Lett. 8*, 3639–3642.
(33) Gramlich, P. M. E., Warncke, S., Gierlich, J., and Carell, T. (2008) Click-click-click: single to triple modification of DNA. *Angew. Chem., Int. Ed. 47*, 3442–3444.
(34) Gierlich, J., Gutsmiedl, K., Gramlich, P. M. E., Schmidt, A., Burley, G. A., and Carell, T. (2007) Synthesis of highly modified DNA by a combination of PCR with alkyne-bearing triphophates and click chemistry. *Chem. Eur. J. 13*, 9486–9494.
(35) Mader, H., Li, X., Saleh, S., Link, M., Kele, P., and Wolfbeis, O. S. (2008) Fluorescent silica nanoparticles. *Ann. N.Y. Acad. Sci. 1130*, 218–223.
(36) Kele, P., Mezo, G., Achatz, D., and Wolfbeis, O. S. (2008) Dual labeling of biomolecules by click chemistry: a sequential approach. *Angew. Chem., Int. Ed.* in press.
(37) Grotli, M., Douglas, M., Eritja, R., and Sproat, B. S. (1998) 2′-*O*-Propargyl oligoribonucleotides: synthesis and hybridisation. *Tetrahedron 54*, 5899–5914.
(38) Zhang, L., Peritz, A. E., Carroll, P. J., and Meggers, E. (2006) Synthesis of glycol nucleic acids. *Synthesis* 645–653.
(39) Schlegel, M. L., Essen, L.-O., and Meggers, E. (2008) Duplex structure of a minimal nucleic acid. *J. Am. Chem. Soc. 130*, 8158–8159.
(40) Filichev, V. V., Christensen, U. B., Pedersen, E. B., Babu, B. R., and Wengel, J. (2004) Locked nucleic acids and intercalating nucleic acids in the design of easily denaturing nucleic acids: thermal stability studies. *ChemBioChem 5*, 1673–1679.
(41) Huber, R., Amann, N., and Wagenknecht, H.-A. (2004) Synthesis of DNA with phenanthridinium as an artificial DNA base. *J. Org. Chem. 69*, 744–751.
(42) Amann, N., Huber, R., and Wagenknecht, H.-A. (2004) Phenanthridinium as an artificial base and charge donor in DNA. *Angew. Chem., Int. Ed. Engl. 43*, 1845–1847.
(43) Wanninger, C., and Wagenknecht, H.-A. (2006) Indole as an artificial DNA base incorporated via an acyclic DNA base surrogate. *Synlett* 2051–1054.
(44) Wagner, C., and Wagenknecht, H.-A. (2006) Perylene-3,4: 9,10-tetracarboxylic acid bisimide dye as an artificial DNA base surrogate. *Org. Lett. 8*, 4191–4194.
(45) Baumstark, D., and Wagenknecht, H.-A. (2008) Perylene bisimide dimers as fluorescent glue for DNA and for base mismatch detection. *Angew. Chem., Int. Ed. 47*, 2652–2654.
(46) Wagner, C., and Wagenknecht, H.-A. (2008) Phenothiazine as a redox-active DNA base substitute: comparison with phenothiazine-modified uridine. *Org. Biomol. Chem. 6*, 48–50.
(47) Menacher, F., Rubner, M., Berndl, S., and Wagenknecht, H.-A. (2008) Thiazole orange and Cy3: improvement of fluorescent DNA probes using short range electron transfer. *J. Org. Chem. 73*, 4263–4266.
(48) Kurata, S., Kanagawa, T., Yamada, K., Torimura, M., Yokomaku, T., Kamagata, Y., and Kurane, R. (2001) Fluorescent quenching-based quantitative detection of specific DNA/RNA using a BODIPY FL-labeled probe or primer. *Nucleic Acids Res. 29*, e34.
(49) Steenken, S., Jovanovic, S. V., Candeias, L. P., and Reynisson, J. (2001) Is "Frank" DNA-strand breakage via the guanine radical thermodynamically and sterically possible. *Chem. Eur. J. 7*, 2829–2833.
(50) Pavlishchuk, V. V., and Addison, A. W. (2000) Conversion constants for redox potentials measured versus different reference electrodes in acetonitrile solutions at 25 °C. *Inorg. Chim. Acta 298*, 97–102.
(51) Schlegel, M. K., Peritz, A. E., Kittigowittana, K., Zhang, L., and Meggers, E. (2007) Duplex formation of the simplified nucleic acid GNA. *ChemBioChem 8*, 927–932.

BC8004864

Comparison of a nucleosidic vs. non-nucleosidic postsynthetic "Click" modification of DNA with base-labile fluorescent probes

Sina Berndl,[†] Nadine Herzig,[†] Péter Kele,[‡] Daniel Lachmann,[†] Xiaohua Li, [‡] Otto S. Wolfbeis,[‡] Hans-Achim Wagenknecht[†]*

Supporting Information

[†]Institute for Organic Chemistry
University of Regensburg
Universitätsstr. 31
D-93053 Regensburg, Germany

[‡]Institute for Analytical Chemistry, Chemo- and Biosensors
University of Regensburg
Universitätsstr. 31
D-93053 Regensburg, Germany

*Corresponding author
Email: achim.wagenknecht@chemie.uni-regensburg.de
Fax : 49 941 9434802

Table of Content **Page**

UV/Vis absorption spectra
Figure S1: Duplex set **DNA1** 2
Figure S2: Duplex set **DNA2** 2
Figure S3: Duplex set **DNA3** 3
Figure S4: Duplex set **DNA5** 3
Figure S5: Duplex set **DNA6** 4
Figure S6: Duplex set **DNA7** 4

Spectra and analyses
Compound **5**
Image of ^{1}H NMR spectrum 5
Image of ^{13}C NMR spectrum 5
Image of ESI-MS 6
Image of HR-MS analysis 6
Compound **6**
Image of ^{1}H NMR spectrum 7
Image of ^{31}P NMR spectrum 7
DNA1
Image of HPLC analysis 8
Image of ESI-MS 8
DNA2
Image of HPLC analysis 9
Image of ESI-MS 9
DNA3
Image of LC-ESI-MS 10
DNA5
Image of LC-ESI-MS 11
DNA6
Image of HPLC analysis 12
Image of ESI-MS 12
DNA7
Image of LC-ESI-MS 13

Figure S1
UV/Vis absorption spectra of the single strand **DNA1** and the corresponding duplex set (2.5 μM) in sodium phosphate buffer (10 mM) of pH 7.0, NaCl (250 mM).

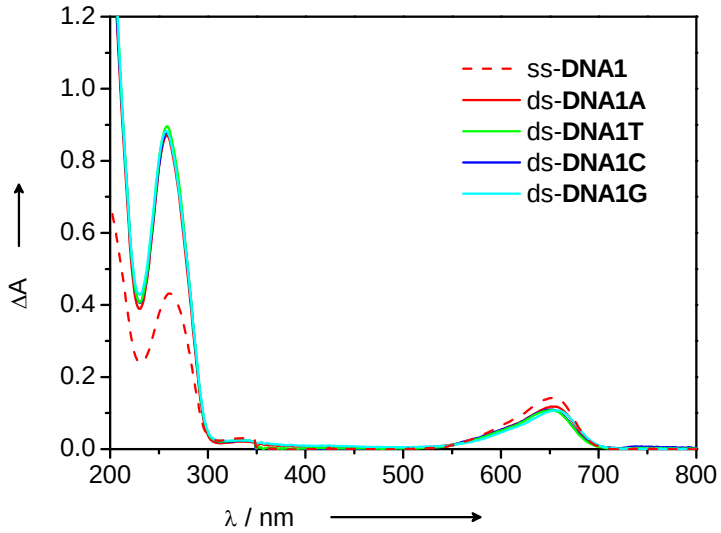

Figure S2
UV/Vis absorption spectra of single strand **DNA2** and the corresponding duplex set (2.5 μM) in sodium phosphate buffer (10 mM) of pH 7.0, NaCl (250 mM).

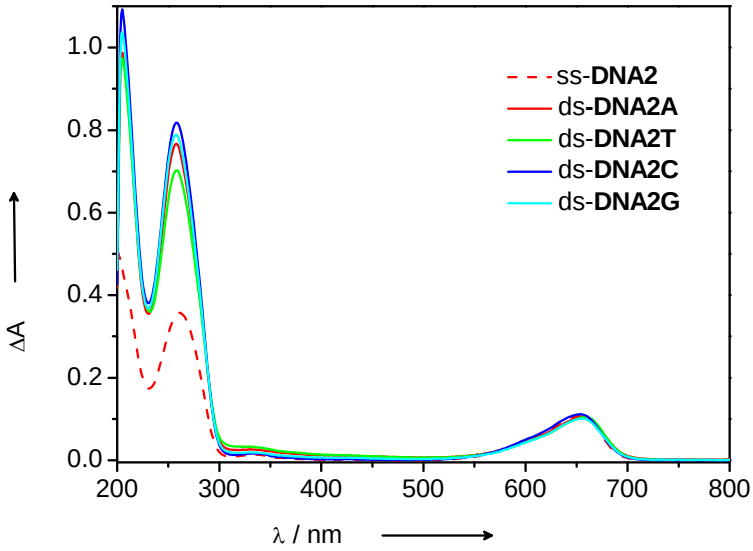

Figure S3
UV/Vis absorption spectra of single strand **DNA3** and the corresponding duplex set (2.5 μM) in sodium phosphate buffer (10 mM) of pH 7.0, NaCl (250 mM).

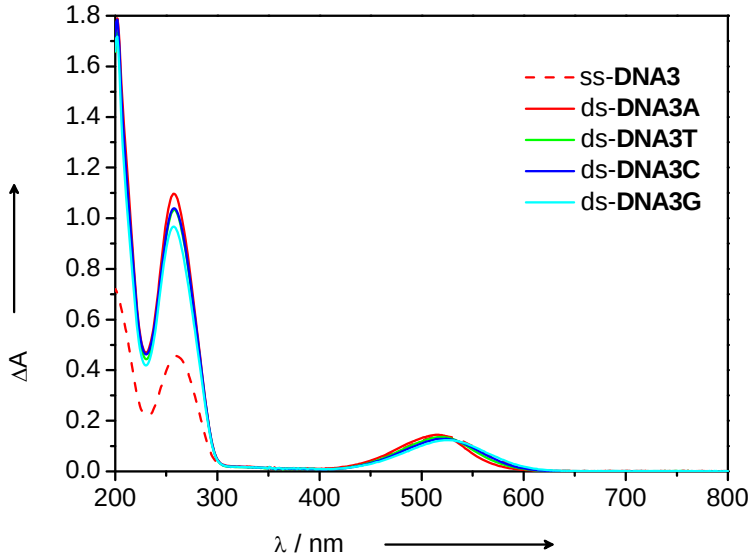

Figure S4
UV/Vis absorption spectra of single strand **DNA5** (2.5 μM) and the corresponding duplex set in sodium phosphate buffer (10 mM) of pH 7.0, NaCl (250 mM).

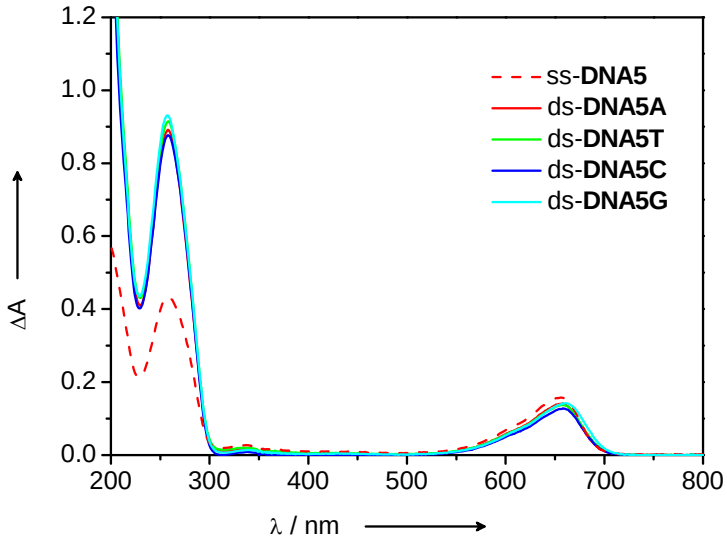

Figure S5
UV/Vis absorption spectra of single strand **DNA6** and the corresponding duplex set (2.5 μM) in sodium phosphate buffer (10 mM) of pH 7.0, NaCl (250 mM).

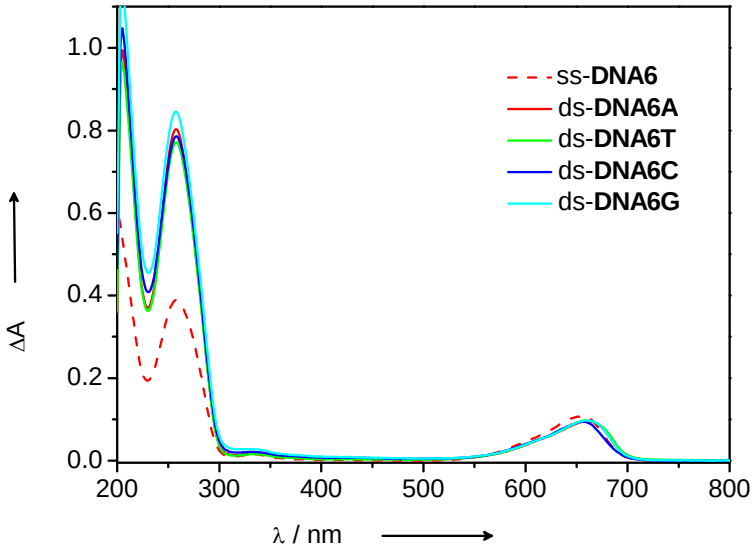

Figure S6
UV/Vis absorption spectra of single strand **DNA7** and the corresponding duplex set (2.5 μM) in sodium phosphate buffer (10 mM) of pH 7.0, NaCl (250 mM).

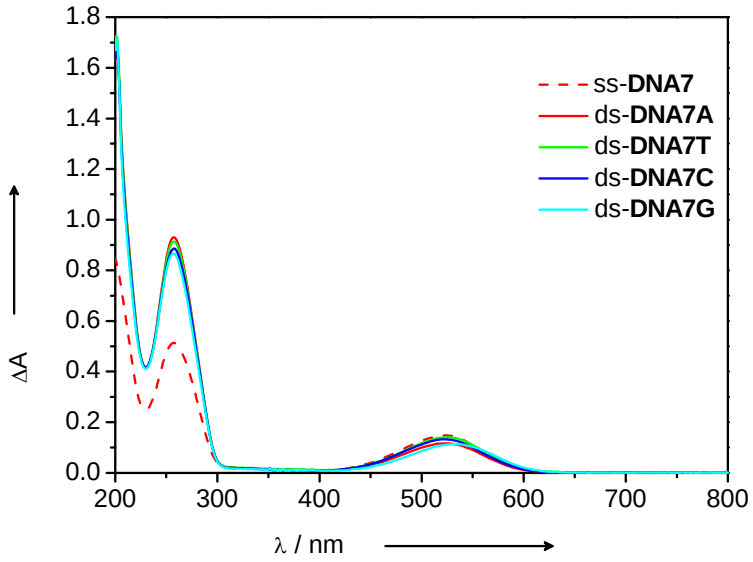

Compound **5**

^{1}H-NMR

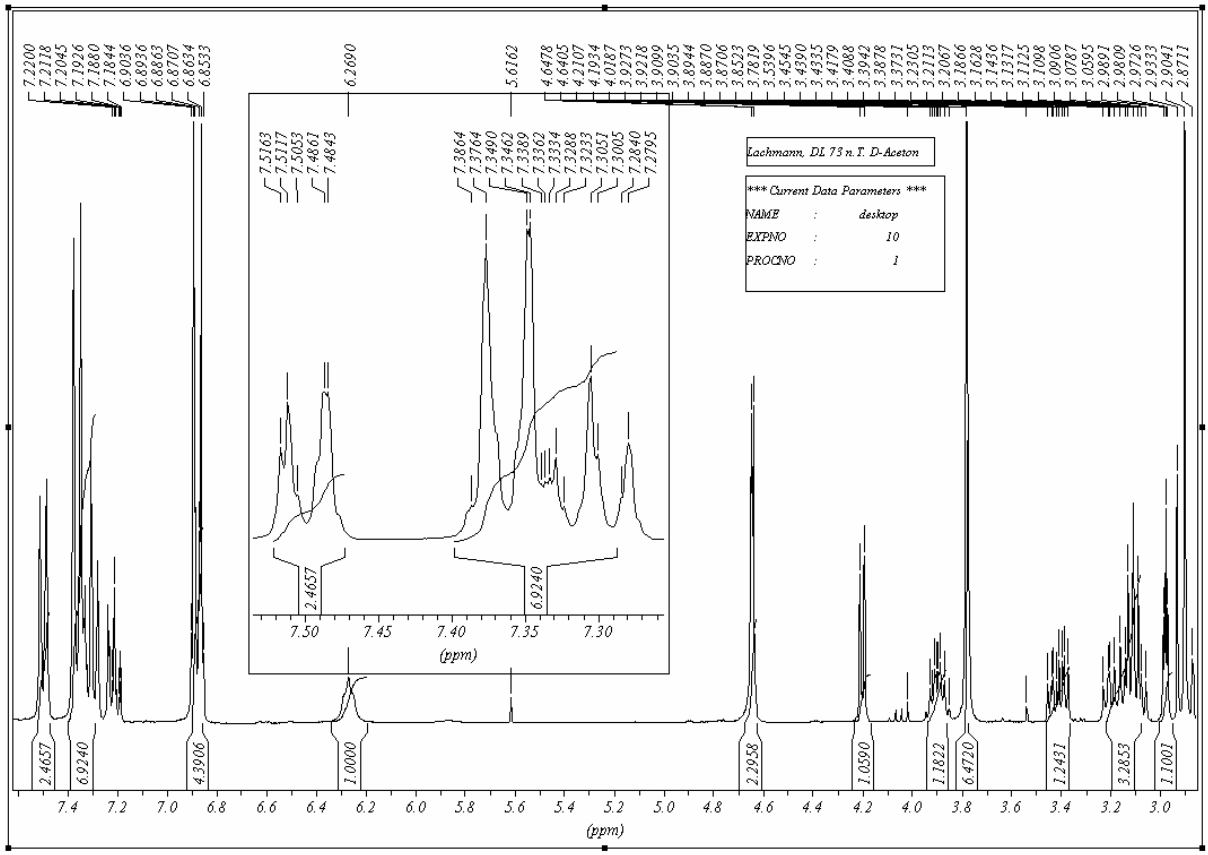

^{13}C-NMR

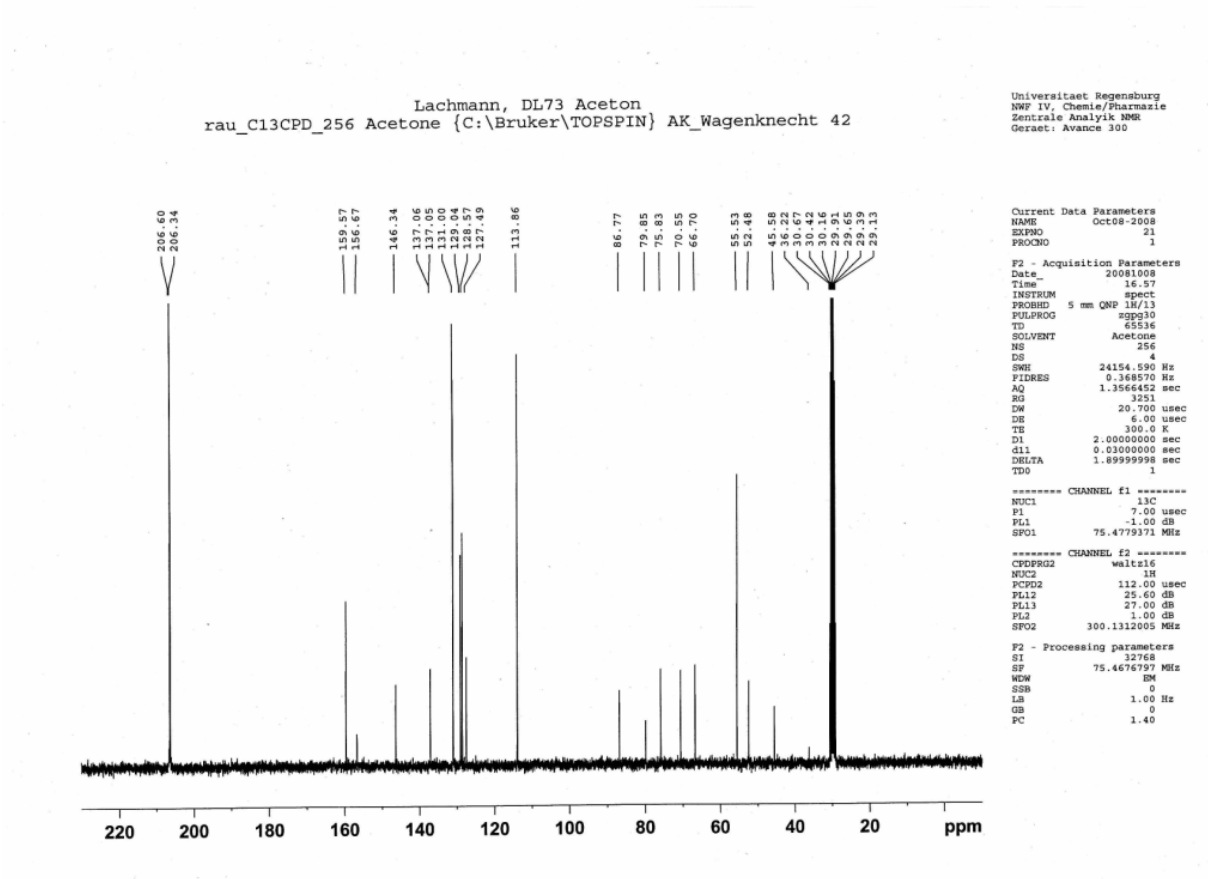

ESI-MS

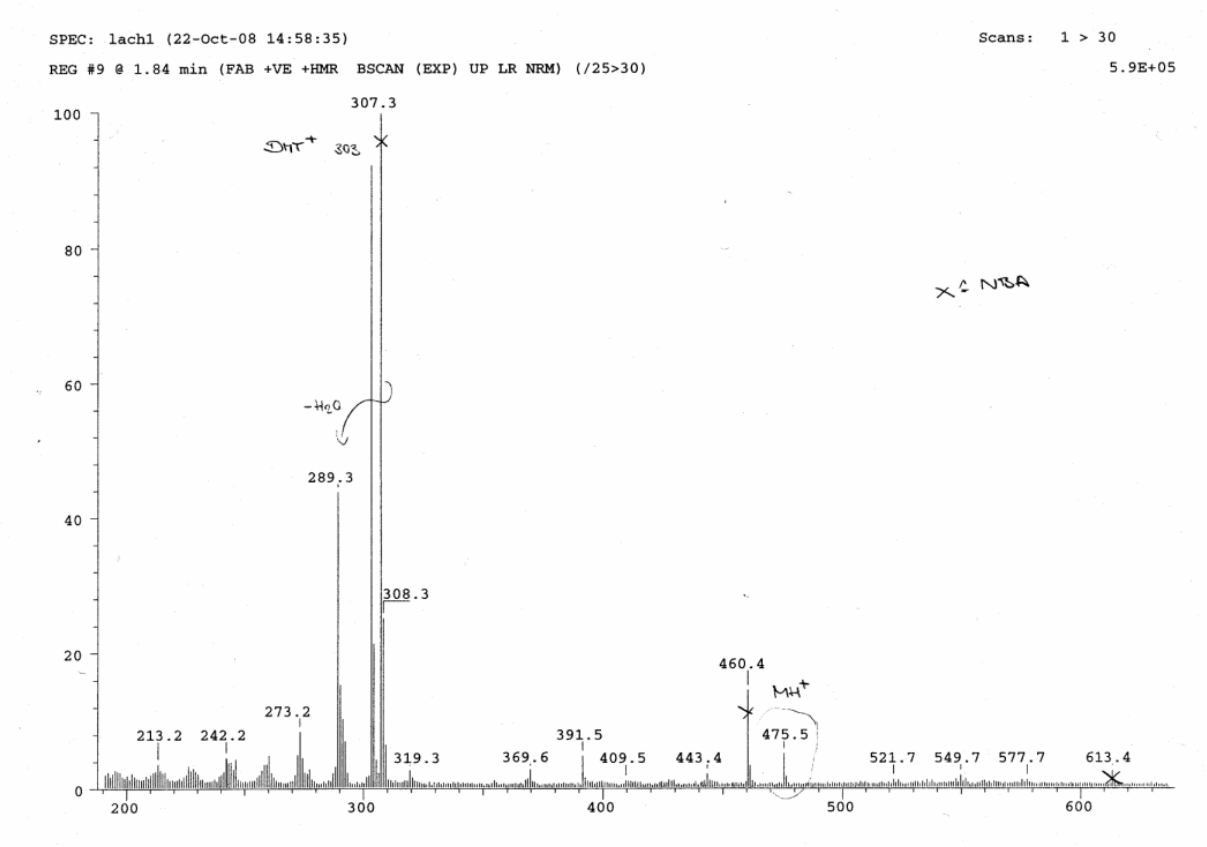

HR-MS analysis:

```
Limt: (     0 )     .     .     .
    : ( 160 )  C100.H100.N10.O10
Peak:   400.00   mmu      R+D:   -0.5 > 50.0

Mass of (  476.2085 ) = 476.208500000  (found) PI-LSIMS
Abs Abun.    .7153375745

Delta (ppm)    R+    Formula
.314946       19.5   C29.H26.N5.O2
1.38099        7.0   C15.H28.N10.O8
-2.4937       14.5   C28.H30.N.O6  (calcd. for C28H30NO6 [MH+]: 476,2073)
-2.5045       20.0   C27.H24.N8.O
3.13443       19.0   C31.H28.N2.O3
4.20047        6.5   C17.H30.N7.O9
-5.3131       15.0   C26.H28.N4.O5
7.01995        6.0   C19.H32.N4.O10
-8.1217       10.0   C25.H32.O9
-8.1326       15.5   C24.H26.N7.O4
8.76251       23.5   C34.H26.N3
 9.8286       11.0   C20.H28.N8.O6
```

Coumpound **6**

^{1}H-NMR

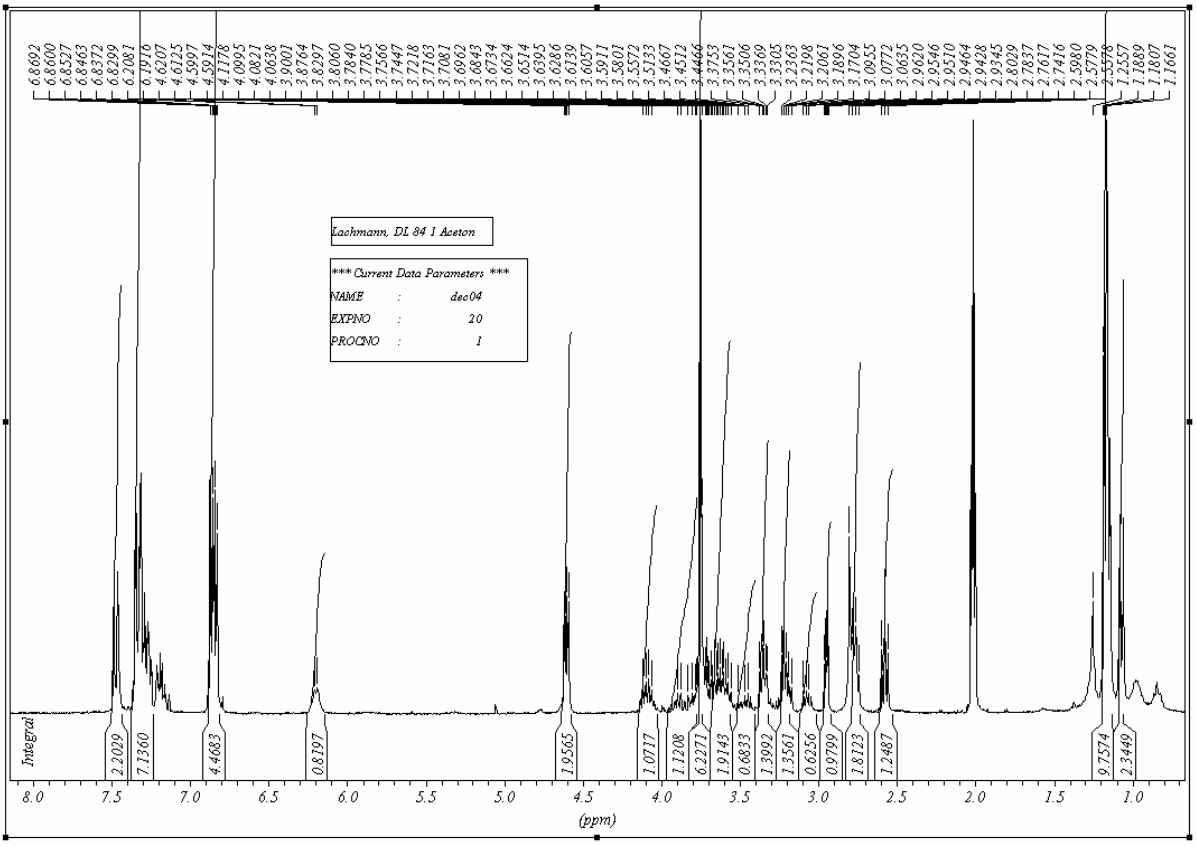

^{31}P-NMR:

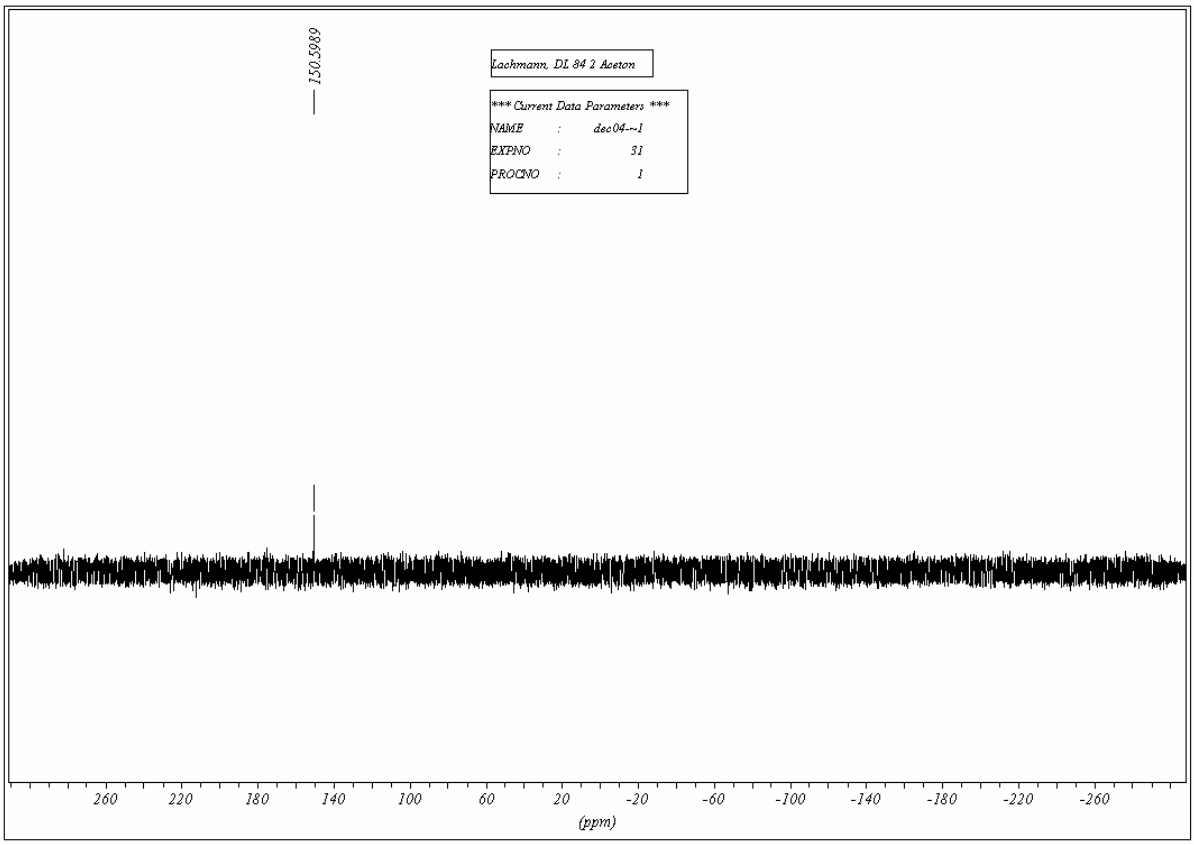

DNA1
HPLC

Sample Information

Universität Regensburg
AK Prof. Wagenknecht

Sample Name:	**DL-DNA3.1T2-0.3**
Injection Volume:	**25 µL**
Date Acquired:	**24/06/2008 21:05:01**
File Name:	**D:\Janez\Müll\DL-DNA3.0T2-0.3**
Method Name:	**D:\Methoden\Analytik\0-30A641A507.met**

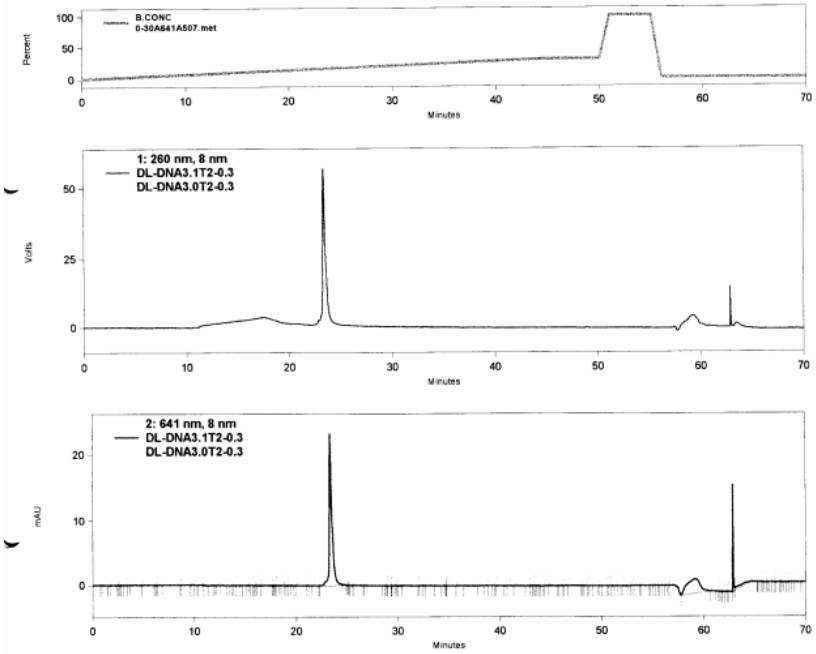

ESI-MS

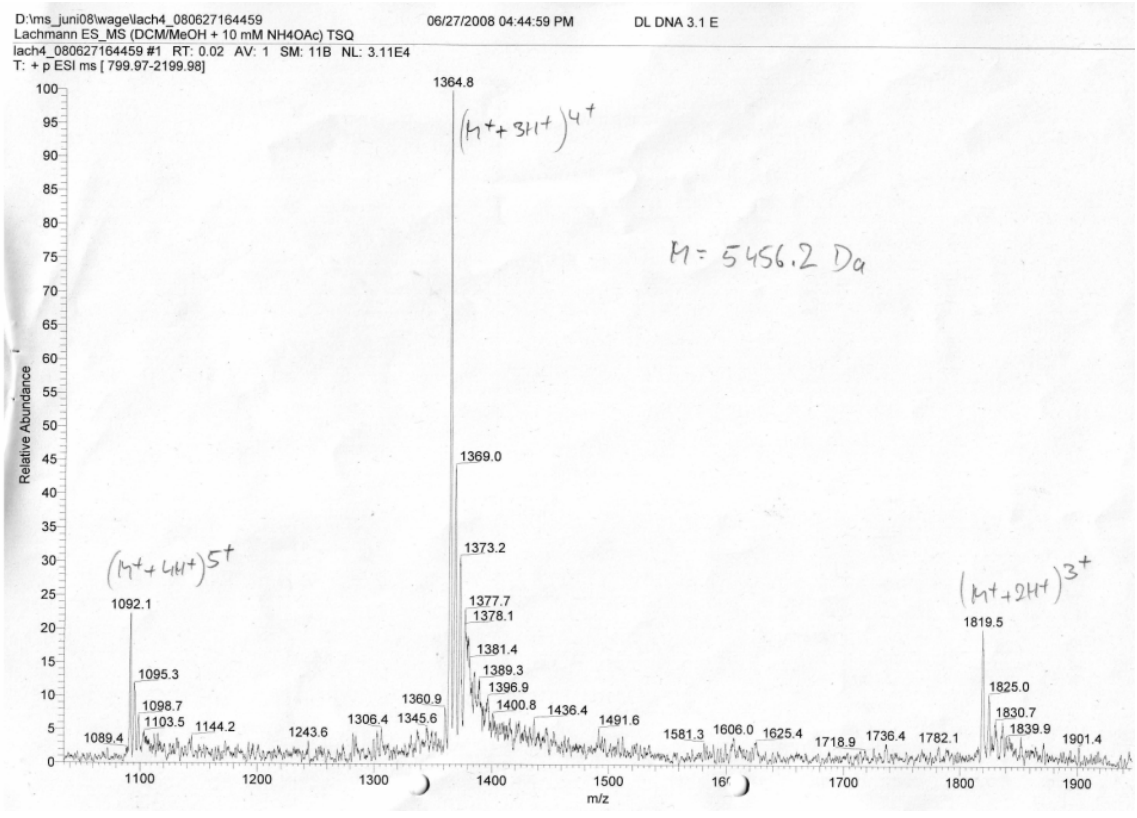

DNA2
HPLC

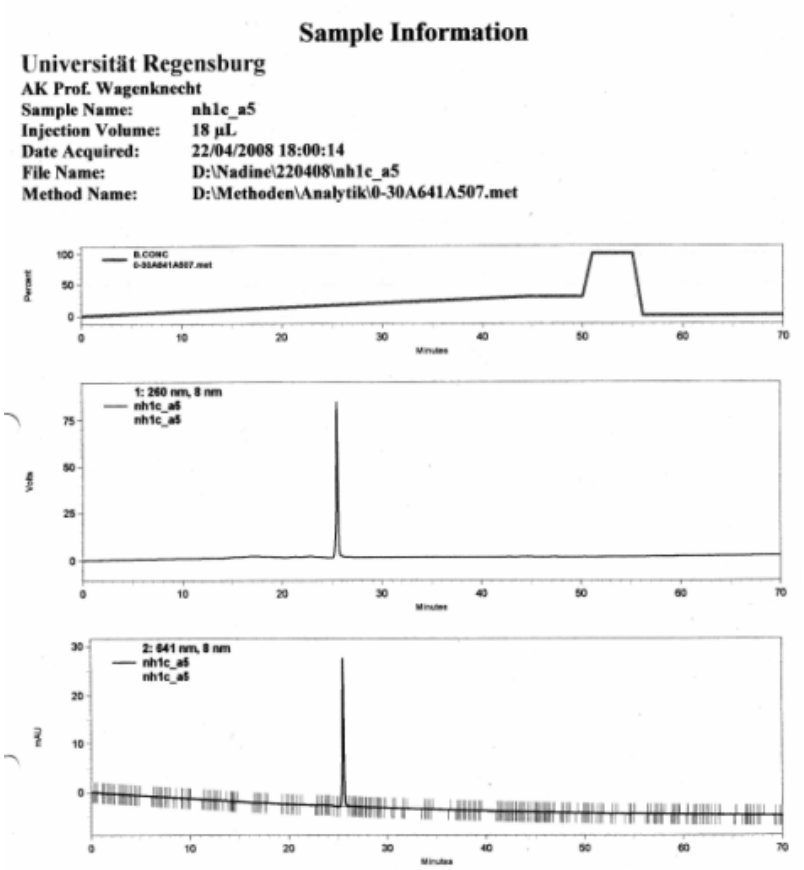
Sample Information
Universität Regensburg
AK Prof. Wagenknecht
Sample Name: nh1c_a5
Injection Volume: 18 µL
Date Acquired: 22/04/2008 18:00:14
File Name: D:\Nadine\220408\nh1c_a5
Method Name: D:\Methoden\Analytik\0-30A641A507.met
B.CONC
0-30A641A507.met
Percent
Minutes
1: 260 nm, 8 nm
nh1c_a5
nh1c_a5
Volts
Minutes
2: 641 nm, 8 nm
nh1c_a5
nh1c_a5
mAU
Minutes

MS

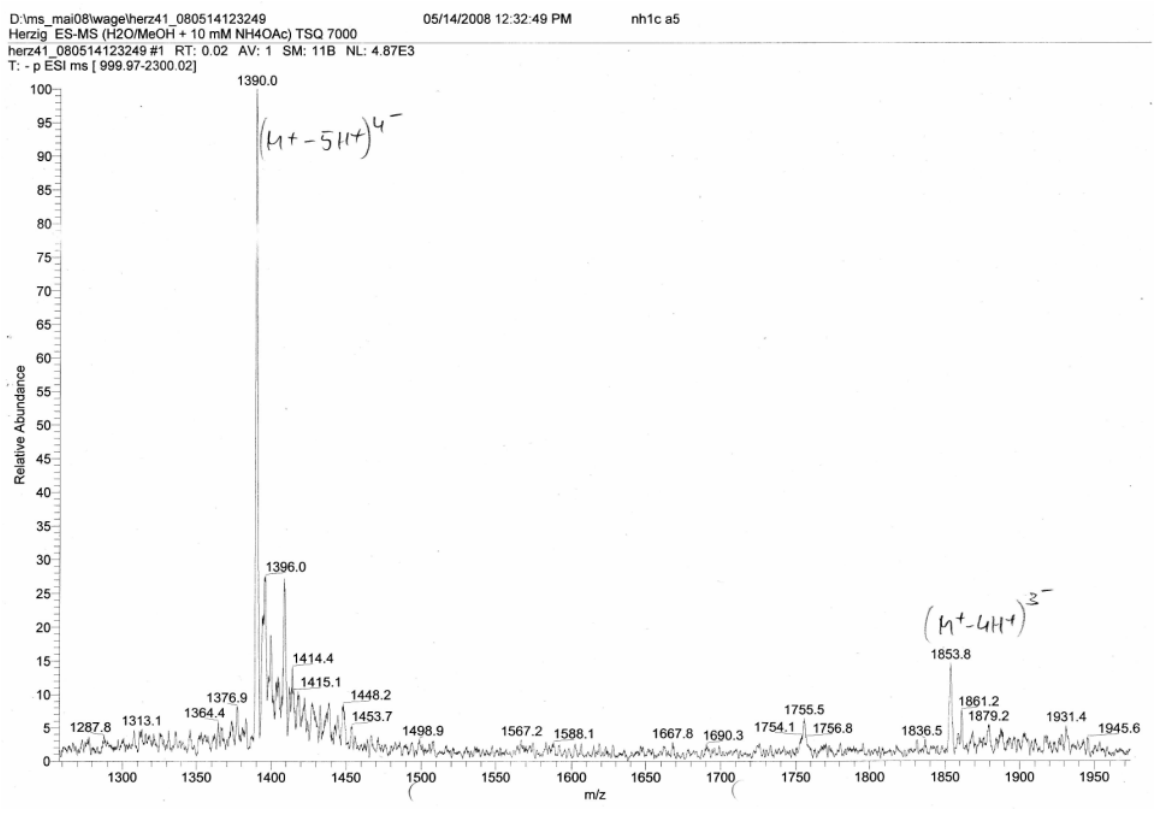
D:\ms_mai08\wage\herz41_080514123249 05/14/2008 12:32:49 PM nh1c a5
Herzig ES-MS (H2O/MeOH + 10 mM NH4OAc) TSQ 7000
herz41_080514123249 #1 RT: 0.02 AV: 1 SM: 11B NL: 4.87E3
T: - p ESI ms [999.97-2300.02]
Relative Abundance
m/z
1390.0
(M+-5H+)4-
1396.0
1414.4
1415.1
1448.2
1453.7
1376.9
1364.4
1313.1
1287.8
1498.9
1567.2
1588.1
1667.8
1690.3
1755.5
1754.1
1756.8
1836.5
1853.8
1861.2
1879.2
1931.4
1945.6
(M+-4H+)4-

DNA3
LC-ESI-MS

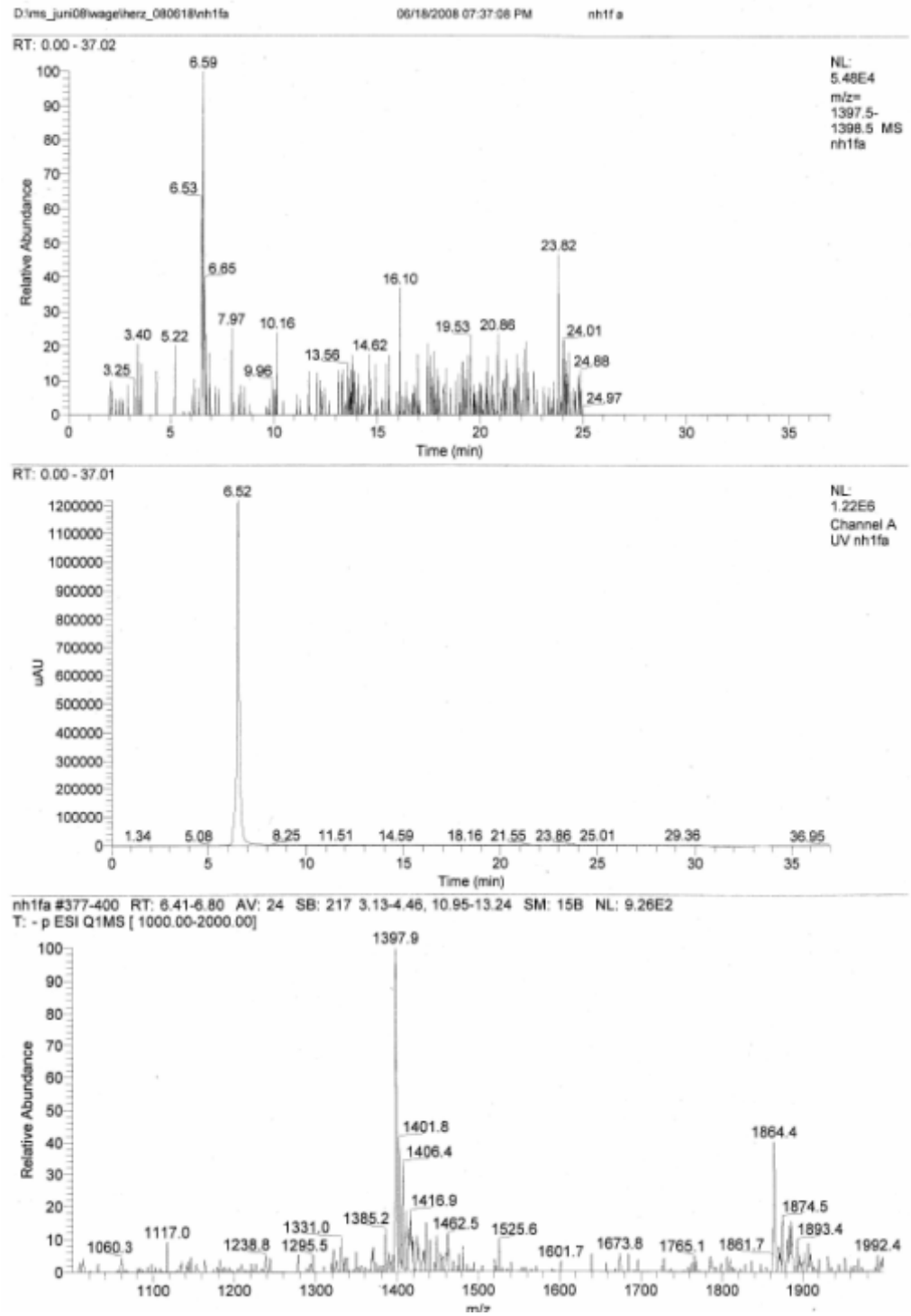

DNA5
LC-ESI-MS

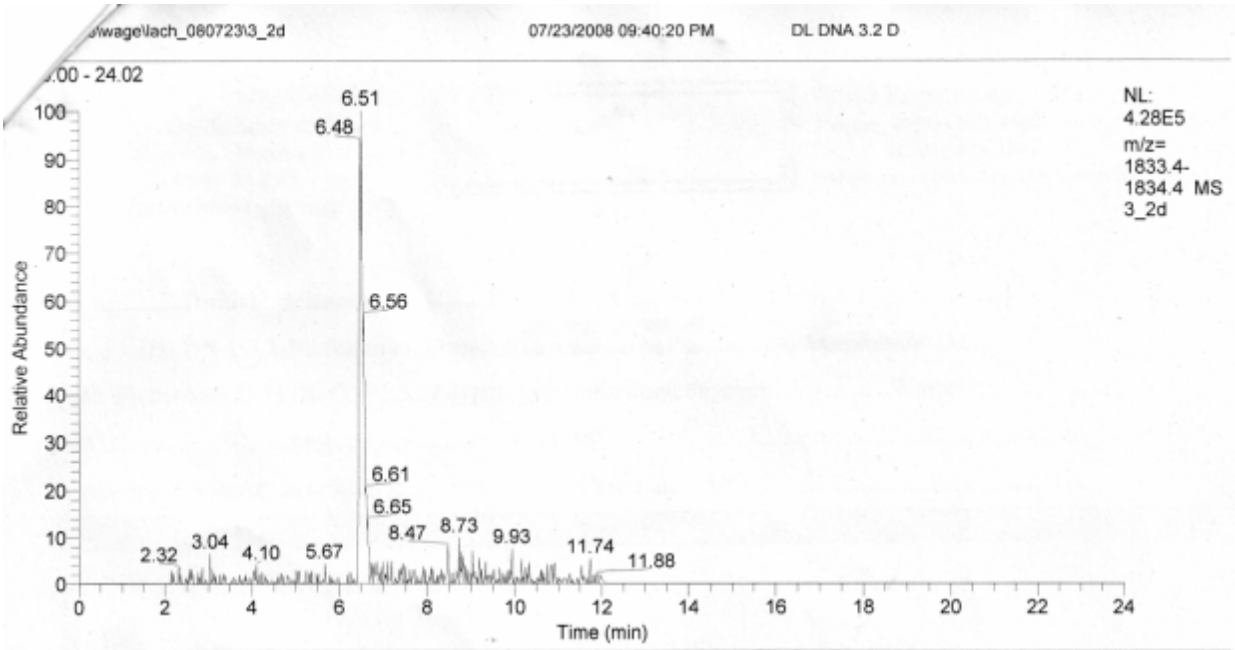

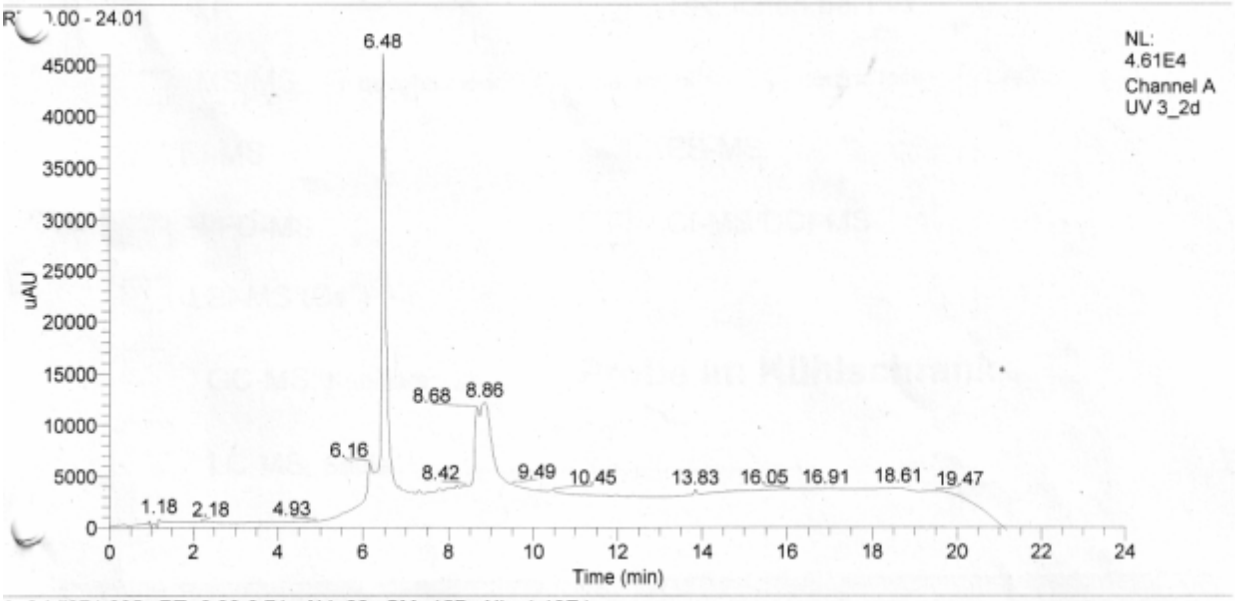

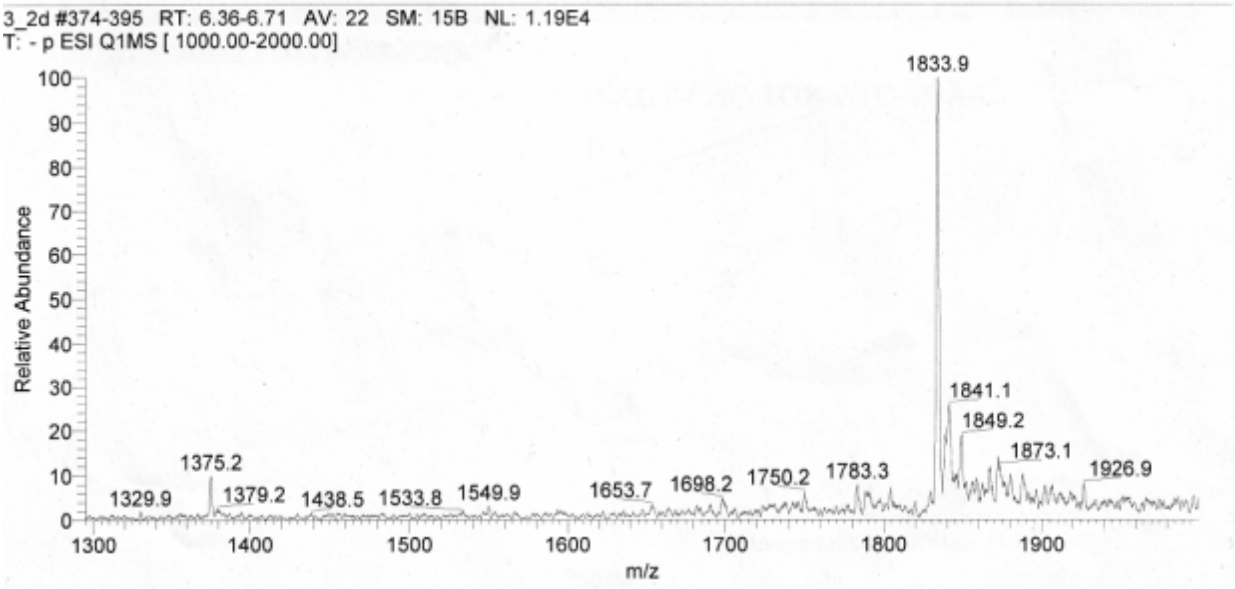

DNA6
HPLC

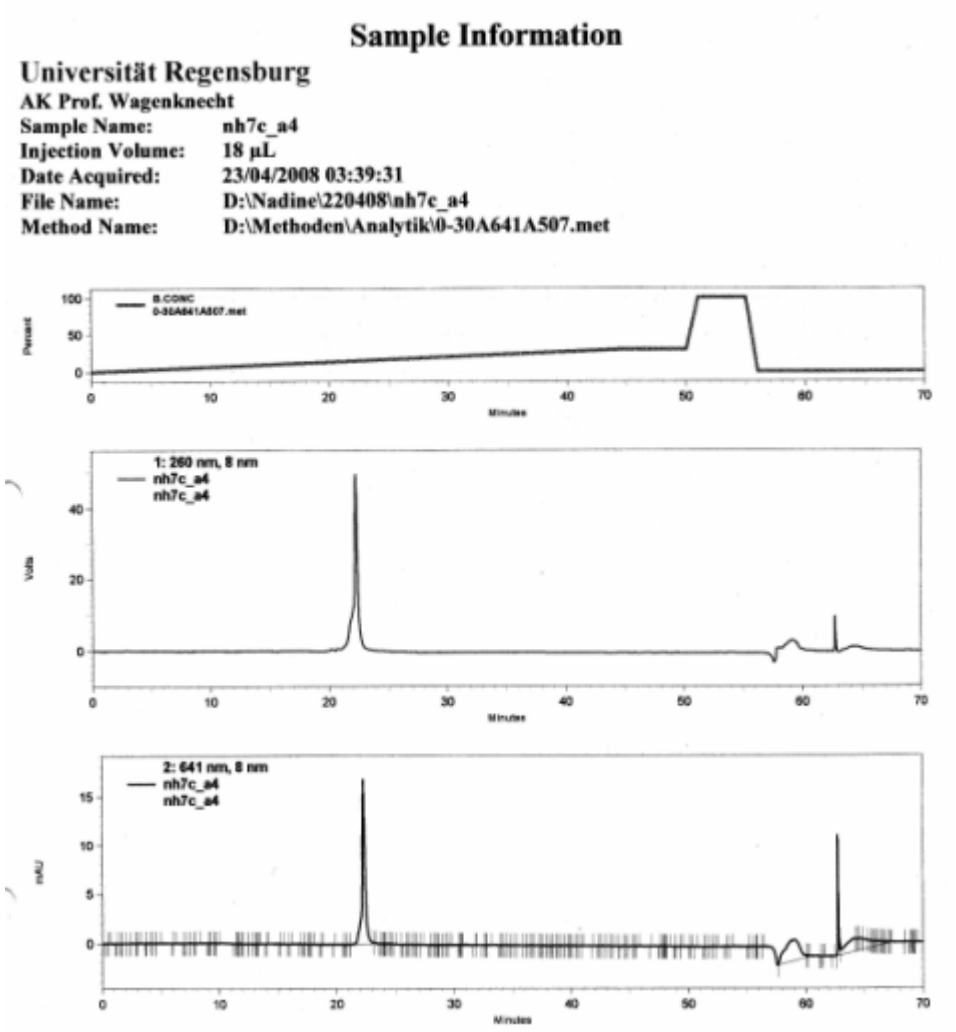
Sample Information
Universität Regensburg
AK Prof. Wagenknecht
Sample Name: nh7c_a4
Injection Volume: 18 µL
Date Acquired: 23/04/2008 03:39:31
File Name: D:\Nadine\220408\nh7c_a4
Method Name: D:\Methoden\Analytik\0-30A641A507.met
B,CONC
0-30A641A507.met
Percent
Minutes
1: 260 nm, 8 nm
nh7c_a4
nh7c_a4
Volts
Minutes
2: 641 nm, 8 nm
nh7c_a4
nh7c_a4
mAU
Minutes

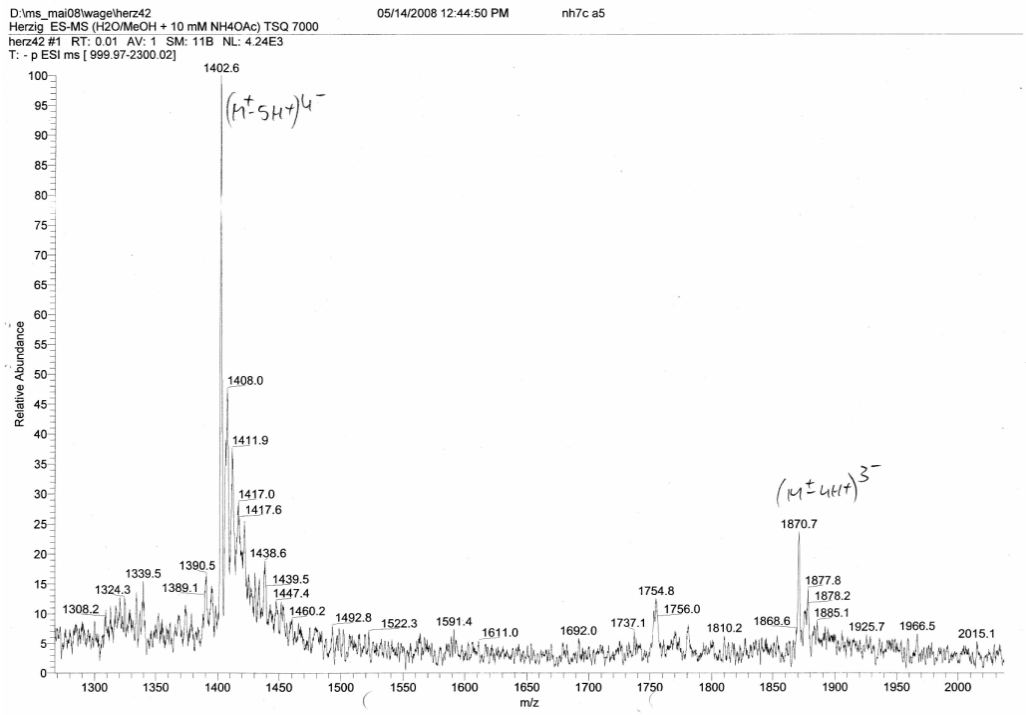
D:\ms_mai08\wage\herz42
05/14/2008 12:44:50 PM
nh7c a5
Herzig ES-MS (H2O/MeOH + 10 mM NH4OAc) TSQ 7000
herz42 #1 RT: 0.01 AV: 1 SM: 11B NL: 4.24E3
T: - p ESI ms [999.97-2300.02]
Relative Abundance
m/z
1402.6
(M+5H+)4-
1408.0
1411.9
1417.0
1417.6
1438.6
1439.5
1447.4
1460.2
1492.8
1522.3
1591.4
1611.0
1692.0
1737.1
1754.8
1756.0
1810.2
1868.6
1870.7
1877.8
1878.2
1885.1
1925.7
1966.5
2015.1
(M+4H+)3-
1390.5
1389.1
1339.5
1324.3
1308.2

DNA7
LC-MS

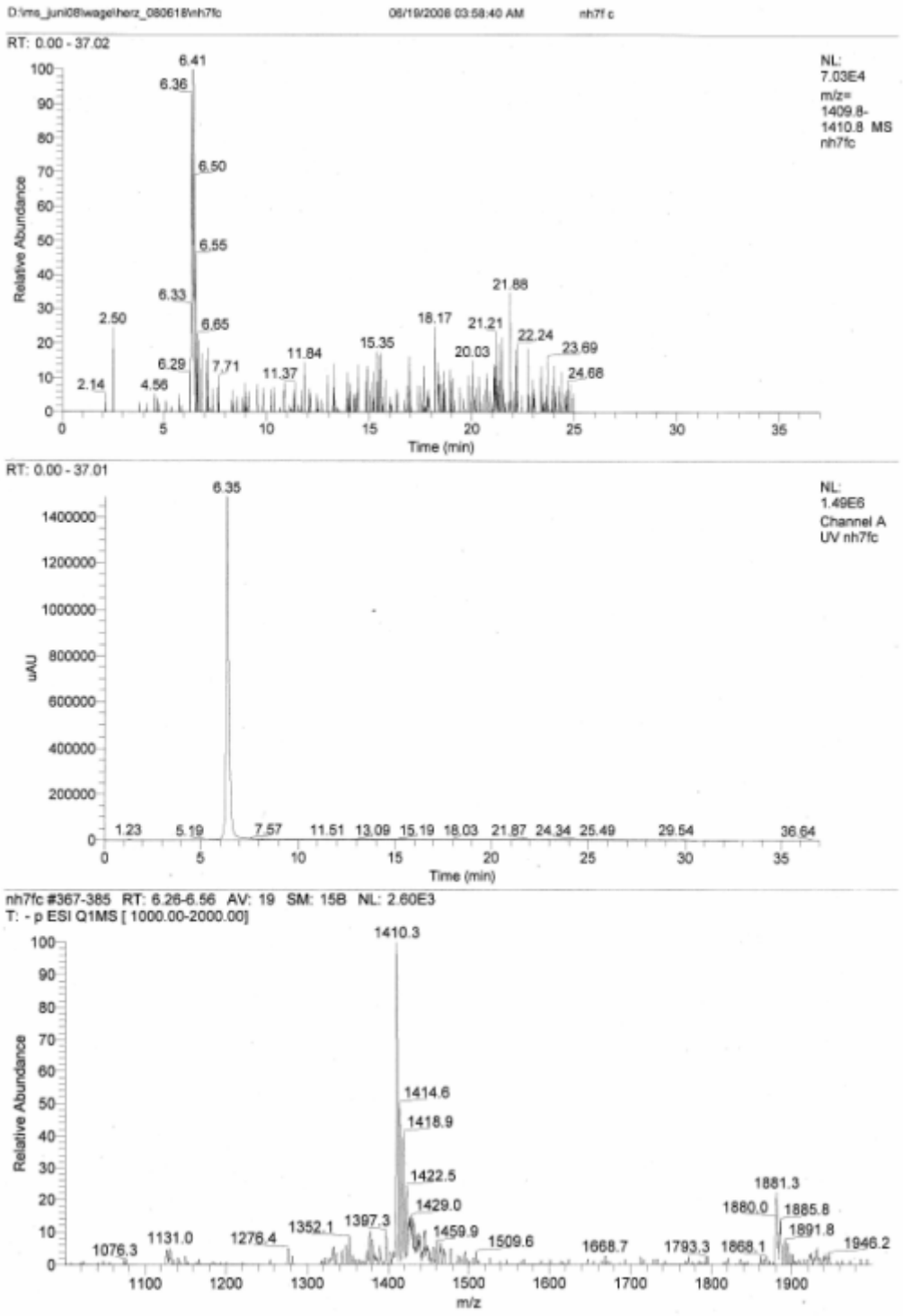
D:\ms_juni08\wagelherz_080618\nh7fc
06/19/2008 03:58:40 AM
nh7f c
RT: 0.00 - 37.02
NL:
7.03E4
m/z=
1409.8-
1410.8 MS
nh7fc
Relative Abundance
Time (min)
RT: 0.00 - 37.01
NL:
1.49E6
Channel A
UV nh7fc
uAU
Time (min)
nh7fc #367-385 RT: 6.26-6.56 AV: 19 SM: 15B NL: 2.60E3
T: - p ESI Q1MS [1000.00-2000.00]
Relative Abundance
m/z

Bioconjugate Chemistry 20th Anniversary

Subscriber access provided by SHEMYAKIN-OVCHINNIKOV INST

Article

(*S*)-5-(*p*-Nitrobenzyl)-PCTA, a Promising Bifunctional Ligand with Advantageous Metal Ion Complexation Kinetics

Gyula Tircso#, Eniko# Tircso#ne# Benyo#, Eul Hyun Suh, Paul Jurek, Garry E. Kiefer, A. Dean Sherry, and Zolta#n Kova#cs

Bioconjugate Chem., **2009**, 20 (3), 565-575• DOI: 10.1021/bc8004914 • Publication Date (Web): 16 February 2009

Downloaded from http://pubs.acs.org on May 8, 2009

More About This Article

Additional resources and features associated with this article are available within the HTML version:

- Supporting Information
- Access to high resolution figures
- Links to articles and content related to this article
- Copyright permission to reproduce figures and/or text from this article

View the Full Text HTML

ACS Publications
High quality. High impact.

Bioconjugate Chemistry is published by the American Chemical Society. 1155 Sixteenth Street N.W., Washington, DC 20036

(*S*)-5-(*p*-Nitrobenzyl)-PCTA, a Promising Bifunctional Ligand with Advantageous Metal Ion Complexation Kinetics

Gyula Tircsó,[†,||] Enikő Tircsóné Benyó,[†,||] Eul Hyun Suh,[‡] Paul Jurek,[§] Garry E. Kiefer,[†,§] A. Dean Sherry,[†,‡] and Zoltán Kovács*[,‡]

Department of Chemistry, University of Texas at Dallas, P.O. Box 830660, Richardson, Texas 75080, Advanced Imaging Research Center, University of Texas Southwestern Medical Center, 5323 Harry Hines Boulevard, Dallas, Texas 75390, and Macrocyclics, 2110 Research Row, Suite 425, Dallas, Texas 75235. Received November 12, 2008; Revised Manuscript Received December 24, 2008

A bifunctional version of PCTA (3,6,9,15-tetraazabicyclo[9.3.1]pentadeca-1(15),11,13-triene-3,6,9,-triacetic acid) that exhibits fast complexation kinetics with the trivalent lanthanide(III) ions was synthesized in reasonable yields starting from *N*,*N*′,*N*″-tristosyl-(*S*)-2-(*p*-nitrobenzyl)-diethylenetriamine. pH-potentiometric studies showed that the basicities of *p*-nitrobenzyl-PCTA and the parent ligand PCTA were similar. The stability of M(NO_2-Bn-PCTA) (M = Mg^{2+}, Ca^{2+}, Cu^{2+}, Zn^{2+}) complexes was similar to that of the corresponding PCTA complexes, while the stability of Ln^{3+} complexes of the bifunctional ligand is somewhat lower than that of PCTA chelates. The rate of complex formation of Ln(NO_2-Bn-PCTA) complexes was found to be quite similar to that of PCTA, a ligand known to exhibit the fastest formation rates among all lanthanide macrocyclic ligand complexes studied to date. The acid-catalyzed decomplexation kinetic studies of the selected Ln(NO_2-Bn-PCTA) complexes showed that the kinetic inertness of the complexes was comparable to that of Ln(DOTA) chelates making the bifunctional ligand NO_2-Bn-PCTA suitable for labeling biological vectors with radioisotopes for nuclear medicine applications.

INTRODUCTION

The choice of chelating system for biomedical imaging and therapeutic applications is largely determined by the nature of the metal ion required for the given application. Several rare earth metal ions (lanthanides and yttrium) and main group III elements are frequently selected for diagnostic (^{111}In, ^{67}Ga, ^{68}Ga, ^{86}Y, ^{177}Lu) and/or therapeutic (^{90}Y, ^{177}Lu, ^{166}Ho,^{149}Pm, ^{153}Sm) nuclear medicine applications (*1, 2*). A common characteristic feature of these metals is their tendency to exist as trivalent cations that form stable complexes in aqueous media with polyamino polycarboxylate type ligands such as the acyclic H_5DTPA (diethylenetriamine-*N*,*N*,*N*′,*N*′*N*″-pentaacetic acid) and the macrocyclic H_4DOTA (1,4,7,10-tetraazacyclododecane-1,4,7,10-teraacetic acid) systems (Figure 1). Bifunctional derivatives of DOTA are increasingly used to radiolabel peptides, proteins, and other biomolecules (*3*). The success of DOTA-bifunctionals is largely due to their ability to form complexes with these metal ions with high thermodynamic stability and extraordinary kinetic inertness. However, slow complex formation kinetics with DOTA under mild conditions can be a disadvantage, especially when sensitive biological vectors are labeled or when short half-lived isotopes are used (*4, 5*). Therefore, macrocyclic ligands that are complex radioisotopes faster than DOTA and still retain reasonably high kinetic inertness are very desirable. The acyclic octadentate DTPA and its bifunctional versions form complexes much faster than DOTA derivatives, but these complexes have significantly lower kinetic inertness than the corresponding DOTA derivatives despite recent improvements achieved by substituting one of the flexible ethane-1,2-diamine units of DTPA by the more rigid propane-1,2-diamine (MX-DTPA) or cyclohexane-1,2-diamine bridge (CHX-DTPA) (Figure 1) (*6*).

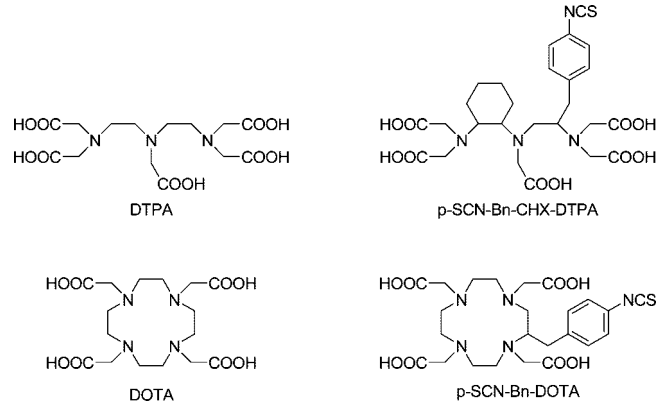

Figure 1. DTPA, DOTA, and two bifunctional derivatives commonly used in nuclear medicine.

Recently, a few attempts have been reported to overcome the problem of slow complex formation involving DOTA-based ligands (Figure 2). Brechbiel and co-workers have synthesized a new class of ligands that integrate a macrocyclic triazacyclononane-diacetic acid and acyclic iminodiacetic acid moiety (bimodal or hybrid ligands). When the two units are linked together through an ethylene bridge, the resulting ligand (NETA) was shown to have improved complexation kinetics (fast complexation with Y^{3+}, excellent serum stability, and rapid clearance of the radiolanthanide chelates) (*7*). A bifunctional version of NETA has also been reported recently (*4, 8*).

Aime and colleagues synthesized an interesting cyclic heptadentate ligand, AAZTA (*9*). Although detailed formation

* To whom correspondence should be addressed. Phone: (+1) 214-645-2750. E-mail: zoltan.kovacs@utsouthwestern.edu.
† University of Texas at Dallas.
‡ University of Texas Southwestern Medical Center.
§ Macrocyclics.
|| Present address: University of Debrecen, Department of Inorganic and Analytical Chemistry, P.O. Box 21, Egyetem tér 1, Debrecen H-4010, Hungary.

10.1021/bc8004914 CCC: $40.75 © 2009 American Chemical Society
Published on Web 02/16/2009

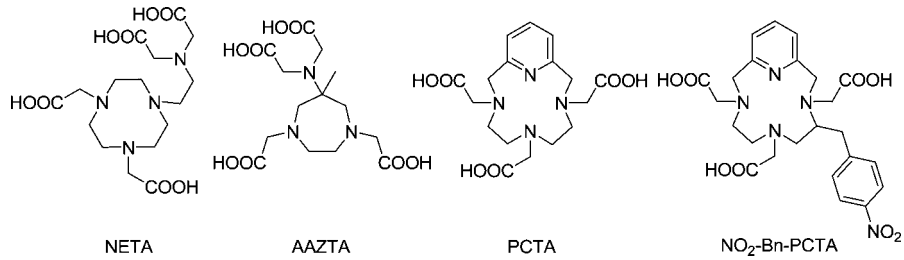

Figure 2. Structure of NETA, AAZTA, PCTA, and NO_2-Bn-PCTA.

kinetic data have not been reported for this system, the reaction of AAZTA with lanthanide ions appears to be almost instantaneous (*9*).

Our approach to a bifunctional macrocyclic chelator with improved metal ion complexation kinetics is based on the ligand H_3PCTA (3,6,9,15-tetraazabicyclo[9.3.1]pentadeca-1(15),11,13-triene-3,6,9-triacetic acid, Figure 2). We recently reported that PCTA forms complexes with lanthanide ions about an order of magnitude faster than DOTA (*10*). Furthermore, the acid-catalyzed dissociation rates of the Ln(PCTA) complexes were found to be satisfactorily slow despite their somewhat low thermodynamic stabilities (*10*). Here, we report the synthesis of a bifunctional version of PCTA, (NO_2-Bn-PCTA), the protonation constants of the ligand, the stability constants of the ligand with various metal ions, and the formation and dissociation rates of some Ln(NO_2-Bn-PCTA) complexes.

EXPERIMENTAL SECTION

Synthesis. The detailed synthetic procedures for the bifunctional ligand (*S*)-5-(*p*-nitrobenzyl)-PCTA (NO_2-Bn-PCTA) is reported in the Supporting Information. Analytically pure samples of the ligand used in the equilibrium and kinetics studies were obtained by preparative HPLC purification on a Phenomenex Luna 5u C18(2) column [elution with H_2O (0.038% HCl)/MeCN (gradient elution from 0% MeCN to 50% MeCN in 30 min)].

Equilibrium Studies. pH-potentiometric titrations were carried out with a Thermo Orion EA940 expandable ion analyzer using a Thermo Orion semimicro combination electrode 8103BN in a thermostatted (at 25.0 °C) vessel. A Metrohm DOSIMATE 665 autoburette (5 mL capacity) was used for base additions, and 1.0 M KCl was used to maintain the ionic strength. All equilibrium measurements (direct titrations) were carried out in 10.00 mL sample volumes with magnetic stirring. During the titrations, argon gas was passed over the sample surface to maintain a CO_2-free environment. Standard buffers (borax, 0.01 M, pH 9.180; and KH-phthalate 0.05 M, pH 4.005) were used to calibrate the electrode. The titrant, a carbonate-free KOH solution, was standardized against 0.05 M KH-phthalate solution by pH-potentiometry. The H^+ ion concentrations corresponding to the measured pH values were calculated by the method proposed by Irving et al. (*11*) The ion-product of water was established in a separate acid−base titration experiment ($pK_w = 13.747$) and used in our calculations.

Stock solutions of $MgCl_2$, $CaCl_2$, $ZnCl_2$, $CuCl_2$, YCl_3, $InCl_3$, and $LnCl_3$ were prepared from analytical grade salts (Aldrich and Sigma, 99.9%). The concentration of the stock solutions were determined by complexometric titration using standardized Na_2H_2EDTA solution in the presence of an appropriate end-point indicator (eriochromeblack-T for $MgCl_2$, and $ZnCl_2$, calconcarboxylic acid for $CaCl_2$, murexide for $CuCl_2$, and xylenol orange for YCl_3, $InCl_3$, and $LnCl_3$ stock solutions) (*12*). The concentration of the ligand stock solution was determined by pH-potentiometry from the titration data obtained in the absence and in the presence of about 50-fold excess $CaCl_2$.

The protonation constants of the ligand were calculated from the data obtained by titrating 2.5 mM and 4.4 mM ligand solutions (total 506 data pairs) with standardized KOH solution (0.1713 M) in the pH range of 1.8−11.9. The protonation constants of the ligand (log K_i^H) are defined as follows:

$$K_i^H = \frac{[H_iL]}{[H_{i-1}L][H^+]} \quad (1)$$

where $i = 1, 2,..., 5$ and $[H_{i-1}L]$ and $[H^+]$ are the equilibrium concentrations of the ligand ($i = 1$) and protonated forms of the ligand ($i = 2,.. 5$) and hydrogen ions, respectively.

In the systems containing Mg^{2+}, Ca^{2+}, Zn^{2+}, or Cu^{2+}, equilibrium in acidic media was reached rapidly enough to use a direct titration data for stability constant determinations. The titrations were carried out at 1:1 and 2:1 metal to ligand concentration ratio ($C_{Lig} = 2.5$ mM). The data obtained at different concentration ratios were combined and fitted simultaneously. Even though the rate of complex formation of the Ln(NO_2-Bn-PCTA) complexes is faster than that of the Ln-(DOTA) complexes, they are not fast enough to determine the stability of the complexes by direct titration. Because of the slow formation reactions of Y(NO_2-Bn-PCTA) In(NO_2-Bn-PCTA) and the Ln(NO_2-Bn-PCTA) complexes, the out-of-cell technique was applied for the stability constant determinations. The same method was used earlier to determine the stability constants of some Ln(PCTA) complexes, and further details may be found elsewhere (*10*, *13*).

The program PSEQUAD was used to process the titration data (calculation of the protonation and stability constants) (*14*). The reliability of the protonation and stability constants are characterized by the calculated standard deviation values shown in parenthesis and the fitting parameter values (ΔV is the difference between the experimental and the calculated titration curves expressed in mL of the titrant) given in the footnotes of the tables.

Formation Kinetics. The rates of complex formation of Ce(NO_2-Bn-PCTA), Eu(NO_2-Bn-PCTA), and Yb(NO_2-Bn-PCTA) were studied at 25 °C and 1.0 M KCl ionic strength using an Applied Photophysics RX.2000 rapid mixing accessory attached to a Cary 300 Bio UV−vis spectrophotometer. The formation reactions at low pH were sufficiently slow and were followed by conventional UV−vis spectroscopy. The formation rate of Yb(PCTA) was also reexamined in the current study. A typical concentration of PCTA was 0.2 mM, while the concentration of NO_2-Bn-PCTA was approximately 0.075 mM. The concentration of the metal ions was varied in the range 4−40 mM (20 × to 200 × metal excess) when the saturation curves were studied while it was set to 200-fold metal excess for the pH dependent measurements. Yb(PCTA) complex formation was studied in the pH range 3.59−5.16, while in the studies involving the NO_2-Bn-PCTA ligand, the following pH ranges were used: pH 3.93−5.69 for Ce^{3+} and Eu^{3+}, and pH 3.93−5.45 for Yb^{3+}.

Both PCTA and NO_2-Bn-PCTA contain a convenient built-in chromophore (pyridine unit), and both the formation and

Scheme 1. Synthesis of the Bifunctional Ligand, NO_2-Bn-PCTA

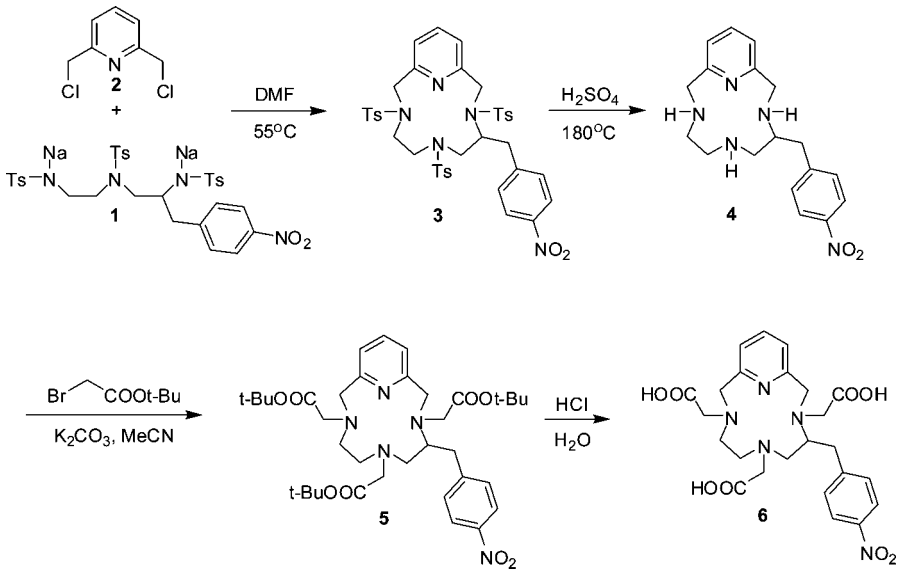

dissociation kinetics studies were performed by following the changes in the $\pi \rightarrow \pi^*$ transition at 278 nm. At this wavelength, the absorbance of the metal ions is either weak (Ce^{3+} and Eu^{3+}) or zero (Y^{3+} and Yb^{3+}). During the formation kinetic studies, the noncoordinating buffers *N*-methylpiperazine (NMP, log $K_2^H = 4.83$) and dimethylpiperazine (DMP, log $K_2^H = 4.18$) were used to maintain the pH constant at a concentration of 0.05 M (*14*).

Equation 2 was used to calculate the first order rate constants (k_{obs} for formation and k_p for dissociation), where A_0, A_e, and A_t are the absorbance values measured at the start of the reaction ($t = 0$), at equilibrium, and at time t, respectively. The data were fitted to eq 2 with the Scientist (Micromath) software using a standard least-squares procedure.

$$A_t = A_e + (A_0 - A_e) \cdot e^{(-k_{obs} \cdot t)} \quad (2)$$

The relative error for fitting of the absorbance versus time data was less than 1%, while the calculated first order rate constants, k_{obs} and k_p, were reproduced to within ±3% as determined in 12−15 identical experiments (each point on the curves reflects an average of 12−15 identical kinetic runs) for formation and 3 experiments for the dissociation reactions.

Kinetics of Dissociation. The acid-catalyzed dissociation kinetics of Ce(NO_2-Bn-PCTA), Eu(NO_2-Bn-PCTA), and Yb(NO_2-Bn-PCTA) complexes were measured under pseudofirst-order conditions by mixing the appropriate complexes with a large excess hydrochloric acid (0.25−2.0 M) while keeping the ionic strength constant at 3.0 M with added KCl [$(H^+ + K^+)Cl^-$]. A total of eight reactions was followed by direct spectrophotometry at 25 °C until the conversion reached 80−100% in 0.075 mM complex solutions. Under these conditions, changes of ∼0.2 abs. units were detected throughout the dissociation reaction. In addition, the absorbance data, recorded as a function of time at 278 nm, showed no evidence of significant amplitude loss during the mixing of the components (usually 6−8 s) and were fitted to eq 2 as a single-exponential decay with excellent confidence.

RESULTS AND DISCUSSION

Ligand Design and Synthesis. The aromatic isothiocyanato group is one of the most commonly used reactive functionalities for bioconjugation. It readily reacts with primary amino groups of peptides or proteins to form a stable thiourea linkage under mild conditions. The isothiocyanato functionality can easily be synthesized by reducing the corresponding nitro derivative and reacting the resulting aniline with thiophosgene. Both the aromatic isothiocyanato and amino compounds are sensitive to hydrolysis and oxidation, respectively, and have limited shelf-lives; therefore, they are not suitable for extended equilibrium and kinetic measurements lasting several days (such as the out-of-cell technique). The nitro derivative, however, is stable at room temperature in aqueous solutions and can conveniently be used in these studies. Considering the parent ligand PCTA, the aromatic isothiocyanato function can be attached to three chemically distinct positions: one of the pyridine carbons, one of the acetate sidearms, or one of the carbon atoms of the ethylene bridges in the pyclen backbone. Each of these options has advantages and disadvantages. For example, functionalization of the pyridine moiety would be expected to have the least effect on the chelation properties of the ligand (the *p*-NO_2-benzyl substituent does not have a strong inductive or mesomeric effect, and therefore, it is not expected to significantly alter the electron density on the pyridine N-atom), while sidearm functionalization may have an adverse effect on the metal binding ability of the acetate pendant arms. We have chosen the ethylene bridge for functionalization because our assumption was that this would eliminate any unwanted interference with metal binding, and the rigidifying effect of macrocyclic backbone substitution may actually add to the kinetic inertness of the resulting complexes. In addition, the backbone functionalized PCTA would structurally be analogous to the nitro precursor of the most frequently used bifunctional ligand, *p*-isothiocyanatobenzyl-DOTA, and therefore, comparison of the equilibrium and kinetic properties of these two ligands could provide further insight into the design of new bifunctional chelators. The synthesis of the new bifunctional ligand, (*S*)-5-(*p*-nitrobenzyl)-PCTA (NO_2-Bn-PCTA, **6**) is outlined in Scheme 1. *N*,*N*′,*N*″-tritosyl (*S*)-2-(*p*-nitrobenzyl)-diethylenetriamine was prepared starting from L-nitrophenyl alanine following published procedures (*16*). The key step of the synthesis is the Richman−Atkins-type cyclization of the disodium salt of *N*,*N*′,*N*″-tritosyl-(*S*)-2-(*p*-nitrobenzyl)-diethylenetriamine (tosyl = *p*-toluenesulfonyl) **1** with 2,6-bis(chloromethyl)pyridine **2** in DMF giving about 55% yield of the tritosyl-nitrobenzyl-pyclen (*17*). It is worth noting that the analogous cyclization reaction between the disodium salt of ditosyl-nitrobenzyl ethylenediamine and the tetratosyl derivative of *N*,*N*′-bis(2-hydroxyethyl)-ethylenediamine failed to give the expected tetratosyl nitrobenzyl-cyclen due to side reactions

Table 1. Protonation Constants of DO3A, PCTA, NO_2-Bn-PCTA, DOTA, and NO_2-Bn-DOTA Ligands (25 °C)

ligand	DO3A	PCTA	**NO_2-Bn-PCTA**	DOTA	NO_2-Bn-DOTA
I	0.1 M Me_4NCl[a,b]	1.0 M KCl[c], 0.1 M Me_4NNO_3[d]	**1.0 M KCl**[e]	0.1 M KNO_3[f], 0.1 M Me_4NCl[g]	1.0 M Me_4NCl[h]
log K_1^H	11.59[a], 12.46[b]	11.36[c], 10.90[d]	**11.29 (0.01)**	12.09[f], 12.60[g]	10.93
log K_2^H	9.24[a], 9.49[b]	7.35[c], 7.11[d]	**6.70 (0.02)**	9.76[f], 9.70[g]	9.14
log K_3^H	4.43[a], 4.26[b]	3.83[c], 3.88[d]	**3.96 (0.03)**	4.56[f], 4.50[g]	4.44
log K_4^H	3.48[a], 3.51[b]	2.12[c], 2.27[d]	**2.08 (0.04)**	4.09[f], 4.14[g]	4.14
log K_5^H	–[a], 1.97[b]	1.29[c], –[d]	**1.82 (0.03)**	–[f], 2.32[g]	2.33
Σ log K_i^H	28.74[a], 29.36[b]	25.96[c], 24.16[d]	**25.84**	30.45[f], 33.26[g]	32.43

[a] Ref *19*. [b] Ref *20*. [c] Ref *10*. [d] Refs *21, 22*. [e] $\Delta V = 9.74 \cdot 10^{-3}$ cm^3 for 506 data pairs. [f] Ref *23*. [g] Ref *24*. [h] The log K_6^H for this ligand is 1.40; ref *13*.

Table 2. Stability Constants of the Complexes Formed with Mg^{2+}, Ca^{2+}, Cu^{2+}, and Zn^{2+} Ions (I = 1.0 M KCl; 25 °C)

M^{2+}	equilibrium	PCTA	**NO_2-Bn-PCTA**	DO3A[c]	DOTA[g]
Mg^{2+}	[ML]/[M][L]	11.82[a], 12.35[b]	**12.39 (0.01)**	11.3[d]	11.92
	[MHL]/[ML][H]	3.70[a], 3.82[b]	**3.52 (0.07)**		4.09
Ca^{2+}	[ML]/[M][L]	12.38[a], 12.72[b]	**12.72 (0.01)**	13.39, 11.74[e]	17.23, 17.22[e]
	[MHL]/[ML][H]	3.66[a], 3.79[b]	**3.66 (0.03)**		3.54
Cu^{2+}	[ML]/[M][L]	17.79[a], 18.79[b]	**19.11 (0.08)**	21.65, 22.87[e]	22.25, 22.44[e]
	[MHL]/[ML][H]	4.03[a], 3.58[b]	**3.67 (0.05)**	3.86, 3.2[e,f]	3.78, 4.31[e]
	[ML]/[ML(OH)][H]	10.3[a], 11.28[b]			
Zn^{2+}	[ML]/[M][L]	18.22[a], 20.48[b]	**21.36 (0.11)**	21.87, 19.26[e]	21.10[h] 20.52[e]
	[MHL]/[ML][H]	3.64[a], 3.10[b]	**3.02 (0.03)**	3.27[f], 3.77[e]	4.18[h] 4.35[e]
	[ML]/[ML(OH)][H]	9.4[a], 12.31[b]		11.44[e]	

[a] Ref *26*. [b] Ref *10*. [c] Ref *20*. [d] Ref *27*. [e] Ref *28*. [f] The second protonation constant of Cu(DO3A) is log K = 2.8, for Zn(DO3A) log K = 2.81, for Zn(DOTA) log K = 3.49, and for Cu(DOTA) log K = 3.52 (MHL + H = MH_2L). [g] Ref *29*. [h] Ref *23*.

involving the nitro group (*18*). Interestingly, in this case, the aromatic nitro group did not affect the cyclization reaction, probably because the benzyl-halide type bis(chloromethyl)pyridine is a more reactive alkylating agent than the O-tosyl derivative of *N*,*N*′-bis(2-hydroxyethyl)-ethylenediamine or diethanolamine. The tosyl groups of **3** were removed in concentrated sulfuric acid at 180 °C to afford (*S*)-5-(*p*-nitrobenzyl)-pyclen **4** in good yield. The ^{1}H NMR spectrum of this cyclic tetramine is quite complicated as all the protons are magnetically nonequivalent, and correct assignement could only be achieved with the help of ^{1}H−^{1}H COSY, ^{13}C APT, and ^{13}C−^{1}H HMQC NMR experiments (Supporting Information, Figures S1−S3). Nitrobenzyl pyclen **4** was alkylated with *tert*-butyl bromoacetate in the presence of anhydrous potassium carbonate in acetonitrile to yield the *tert*-butyl ester **5**. The *tert*-butyl ester groups were subsequently cleaved in aqueous hydrochloric acid to afford ligand **6** as the HCl salt in about 35% overall yield.

Protonation and Stability Constant Determinations. The bifunctional ligand (*S*)-5-(*p*-nitrobenzyl)-PCTA has seven protonation sites, and five protonation steps of these were detected in the pH range 1.8−11.8 when the ligand was titrated with strong base (KOH). The protonation constants obtained by pH-potentiometric measurements are presented in Table 1 along with the previously reported values for PCTA, DOTA, and the bifunctional NO_2-Bn-DOTA.

The first and the second protonation constants can be assigned to nitrogen atoms of the macrocyclic ring, while the next 3 protonation steps occur most likely at the acetate pendant arms. The first protonation constant of PCTA and NO_2-Bn-PCTA are nearly identical, but there is a noticeable difference in the second protonation constant (about 0.5 log K units). This was not unexpected as a similar trend has been observed for the protonation constants of DOTA and *p*-NO_2-Bn-DOTA. The somewhat smaller log K_2 values found for the bifunctional versions are likely due to the conformational changes in the ethylene bridge of the macrocyclic ring induced by the *p*-nitrobenzyl substituent (*13*). Interestingly, in the case of NO_2-Bn-DOTA, both the first and the second protonation constants were affected, while for NO_2-Bn-PCTA, only the second protonation constant is affected. This may be explained by the considerably lower conformational flexibility of PCTA derivatives as compared to the DOTA-based ligands due to the rigidifying effect of the pyridine ring. Consequently, the extra strain introduced by the *p*-nitrobenzyl substituent will have a smaller effect on the pyclen macrocycle. Differences in the protonation sequence of NO_2-Bn-PCTA and NO_2-Bn-DOTA may also play a role. According to ^{1}H NMR studies, the most basic site in PCTA is the nitrogen atom opposite the pyridine ring (*25*). Addition of a second proton results in a rearrangement of the protonation sites to the two tertiary nitrogen atoms positioned *trans* to each other and *cis* to the pyridine nitrogen (*25*). In NO_2-Bn-PCTA, the *p*-nitrobenzyl substituent is attached next to a tertiary nitrogen atom positioned *cis* to the pyridine nitrogen, and the extra strain induced at this nitrogen atom reduces its basicity. The total basicity (Σ log K_i^H) of PCTA and NO_2-Bn-PCTA is similar, around 25.8−25.9. Although this value is reasonably favorable, it is about 3 log K units lower than that of the DO3A and 6 to 7 log K units lower than that of DOTA and NO_2-Bn-DOTA. As a consequence, the thermodynamic stability constants for the complexes of PCTA-based ligands are expected to be somewhat lower than the corresponding DOTA complexes.

The stability constants of the complexes of Mg^{2+}, Ca^{2+}, Zn^{2+}, and Cu^{2+} ions with NO_2-Bn-PCTA were determined by pH-potentiometry in the presence of 1.0 M KCl as the ionic background. The stability constants of these complexes along with the constants characterizing the stability of the M(DO3A), M(PCTA) and M(DOTA) complexes are listed in Table 2 (the stability constants of Mg^{2+}, Ca^{2+}, Zn^{2+}, and Cu^{2+} complexes of NO_2-Bn-DOTA have not been reported yet). The pH-potentiomeric titration data for both the 1:1 and 1:2 metal to ligand concentration ratios could be fitted well by assuming the formation of ML and MHL species only. The stability and protonation constants characterizing the formation of the Mg^{2+} and Ca(NO_2-Bn-PCTA) complexes are in excellent agreement with data obtained for the Mg^{2+} and Ca(PCTA) complexes. Unlike the Cu^{2+} and Zn(PCTA) systems, no evidence of formation of ternary hydroxo complexes, MLH_{-1}, was found in titrations with these same metal ions and NO_2-Bn-PCTA, likely due to the higher stability of the latter complexes.

The data in Table 2 show that, unlike DOTA-based ligands, both PCTA and NO_2-Bn-PCTA form more stable complexes with Zn^{2+} than with Cu^{2+}. This observation is in accordance with the results reported earlier by Delgado et al. on the

Table 3. Stability Constants of ML Type Complexes Formed with Y^{3+}, In^{3+}, and some Ln^{3+} Ions (I = 1.0 M KCl; 25 °C)

M^{3+}	DO3A[a]	PCTA[d]	**NO_2-Bn-PCTA**	DOTA[h]	*p*-NO_2-Bn-DOTA[k]
Ce^{3+}	19.7	18.15	**17.89(0.12)**	23.39	
Nd^{3+}		20.15	**18.74(0.04)**	22.99	
Eu^{3+}	20.6[b]	20.26, 20.9−21.1[e]	**19.02(0.09)**	23.45	
Gd^{3+}	21.0	20.39, 21.0[f]	**19.42(0.07)**	24.0[i], 24.67, 25.3[j]	24.2
Ho^{3+}		20.24	**19.66(0.06)**	24.54	
Yb^{3+}		20.63		25.00	
Lu^{3+}	23.0		**19.85(0.09)**	25.41	24.9
Y^{3+}	21.1[c]	20.28	**18.78(0.09)**	24.9[j]	24.5
In^{3+}		21.42[g] **24.7 (0.1)**	**23.91(0.09)**	23.9[i]	

[a] Refs *31* and *32*. [b] Determined by luminescence refs *33* and *34*. [c] Ref *19*. [d] Ref *10*. [e] Refs *21, 22*. [f] Ref *25*. [g] I = 0.1 mol/dm^3 Me_4NNO_3 from ref *26*. [h] Ref *35*. [i] I = 0.1 M KCl from ref *36*. [j] Ref *19*. [k] Ref *13*. The fitting parameters for trivalent metal ions ranged from 1.1810^{-3} cm^3 (Nd^{3+}) to 7.7410^{-3} cm^3 (Ce^{3+})

selectivity of some pyridine-containing macrocyclic ligands for Zn^{2+} over Cu^{2+} (*26*). Interestingly, the selectivity was observed exclusively for the 12-membered PCTA ligand (*26*). This unexpected selectivity is likely due to the rigid nature of the pyclen backbone and the slightly different type of interaction required (angle) between the pyridine nitrogen atom and Zn^{2+} and Cu^{2+} ions. This explanation is supported by the crystal structure of the [Cu(pyclen)Br]ClO_4, which shows that the pyridine nitrogen−Cu^{2+} bond length is shorter than the secondary amine−Cu^{2+} bonds, while in the ([Zn(pyclen)Cl])$_2ZnCl_4$ complex, the length of the pyridine−N−Zn^{2+} bond is comparable to that of the secondary amine−Zn^{2+} bonds (*26, 30*).

The stability constants (log K_{ML}) of the complexes formed with some Ln^{3+}, Y^{3+}, and In^{3+} ions with NO_2-Bn-PCTA were determined by the out-of-cell potentiometric titration technique because of their slow formation rates. There was evidence for the formation of MHL species only for the larger metal ions (Ce^{3+} and Nd^{3+}, log $K_{CeL}{}^{H}$ = 2.17 and log $K_{NdL}{}^{H}$ = 1.93, respectively), while ternary hydroxo complex formation was not considered. The stability constants of NO_2-Bn-PCTA complexes with these trivalent ions are listed in Table 3 along with previously reported values for structurally related ligands.

As expected, the stability of the Ln(NO_2-Bn-PCTA) complexes increases substantially from Ce^{3+} to Eu^{3+}, then increases only gradually with decreasing ion size, maximizing at Lu^{3+}. This trend is similar to that seen previously for complexes of macrocyclic ligands with a similar size and number of donor atoms (Ln(PCTA), Ln(DO3A), and Ln(DOTA)) (*10, 31, 32, 35, 36*). Despite the similar basicities of PCTA and NO_2-Bn-PCTA, the stability of the Ln(III) complexes formed with the bifunctional ligand are about 0.5−1 log K units lower than those of the parent ligand, PCTA. Since the basicities of these ligands are similar, this difference is likely due to the steric effect of the *p*-nitrobenzyl substituent. Although the thermodynamic stabilities of lanthanide complexes of NO_2-Bn-PCTA are somewhat lower than the stability of the corresponding DOTA complexes, they remain reasonably favorable for potential in vivo applications (*37*).

It is of interest to note that In^{3+} forms quite stable complexes with both PCTA and NO_2-Bn-PCTA (the log K_{ML} value is comparable to the value published for In(DOTA)). However, for a more meaningful comparison, the available literature data on In^{3+}-ligand stability constants should be analyzed carefully because these are often measured in the presence of Cl^- containing electrolytes (e.g., KCl, NaCl, and Me_4NCl) used to maintain the constant ionic strength during titrations. However, Cl^- ions can form relatively stable complexes with the In^{3+} ion with log β_1, log β_2, and log β_3 values of 2.58, 3.84, and 4.20, respectively (25 °C, I = 3.0 M $NaClO_4$) (*38*). If the formation of $InCl_x^{(3-x)+}$ species is not taken into account, then the resulting stability constants only represent the lower limits of stability, and the actual stability constants are somewhat higher (with about 4 log K units). This appears to be the case for In(DOTA), as its stability was measured in the presence of 0.1 M KCl, and the formation of $InCl_x^{(3-x)+}$ species was ignored by Clarke et al. (*36*), whereas it was accounted for in the calculated stabilities of In(PCTA) and In(NO_2-Bn-PCTA) here. In the pH range 1.5−2.5, the conditional stabilities of the In(PCTA) and In(NO_2-Bn-PCTA) complexes are relatively low, and the Cl^- ions can compete well with these ligands. Under the conditions employed in our study (I = 1.0 M KCl), only the complexes $InCl_2^-$, $InCl_3$, and In(PCTA) are present in equilibrium (there is no free In^{3+}), and the stability of the In complexes listed in Table 3 were calculated with the use of the known log β_X values. It is worth noting that the stability of In(PCTA) published by Delgado et al. is 3.3 log K units lower than that measured here (Table 3) (*26*). The competitive Cl^- complex formation cannot explain the discrepancy in this case since Delgado et al. used MeN_4NO_3 to set the ionic strength of the samples (*26*). It is more likely that these differences originate from differences in the protonation constants of the ligand due to the different methods used to evaluate these constants.

Kinetics of Complex Formation. The formation kinetics of the complexes involving macrocyclic ligands are usually considerably slower than the corresponding complexes formed with multidentate, open-chain ligands (*39*). Unlike the polycarboxylate ligands derived from linear polyamines, the corresponding polycarboxylate macrocyclic ligands tend to form relatively stable protonated out-of-cage complexes as intermediates, which then rearrange slowly to the thermodynamically stable complex in a general base-catalyzed step (*40*−*42*). Mono-, di-, and occasionally triprotonated intermediates have been demonstrated by different spectroscopic techniques (UV−vis, luminescence, NMR, EXAFS, etc.) (*43*−*53*). The formation kinetics of Ln(III) complexes are most easily studied by UV−vis spectroscopy (Ce^{3+} and Eu^{3+}) or relaxivity measurements (Gd^{3+}) (*43, 46*−*49*). Complexation of the smaller ionic radii Ln(III) ions that have no absorption in the UV−vis (Yb^{3+} or Lu^{3+}) can be followed indirectly by UV−vis spectroscopy using an appropriate acid−base indicator to register slight pH changes during the course of the reaction (*43, 46, 54*). Fortunately, PCTA and NO_2-Bn-PCTA have a convenient built-in chromophore arising from the $\pi \rightarrow \pi^*$ transition of the pyridine moiety (ε_{max} = 1.25 × 10^4 dm^3 mol^{-1} cm^{-1}, λ_{max} = 269 nm, and pH 3.97, for NO_2-Bn-PCTA) that undergoes a bathochromic shift upon metal ion encapsulation (λ_{max} = 278 nm) (Figure 3). As the bathochromic shift and the molar extinction coefficient are almost independent of which metal ion is encapsulated, this transition can be used to monitor complex formation for a large variety of metal ions. Here, formation kinetics were examined for three lanthanide ions, one of larger ionic radius (Ce^{3+} 103 pm), one of medium ionic radius (Eu^{3+} 95 pm) and one of smaller ionic radius (Yb^{3+} 86 pm) to compare the effect of metal ion size on the rates of complex formation.

The formation kinetics of Ln(NO_2-Bn-PCTA) (Ln = Ce^{3+}, Eu^{3+}, and Yb^{3+}) were studied at different pH and metal ion concentrations (20 to 200-fold metal excess) under pseudofirst-order conditions. In the presence of excess Ln^{3+}, the rate of complex formation may be described as follows:

$$\frac{d[LnL]_t}{dt} = k_{obs}[L]_t \quad (3)$$

where $[L]_t$ is the total concentration of the NO_2-Bn-PCTA (complexed and uncomplexed forms), and k_{obs} is a pseudofirst-order rate constant. Plots of k_{obs} versus Ln^{3+} ion concentraton showed saturation kinetics at high Ln^{3+} concentration. The shape of these plots is characteristic of the rapid formation of an intermediate that rearranges slowly to the final product in a slow, rate-determining step. A similar mechanism has been reported for other Ln(III) complexes formed with macrocyclic polyaminopolycarboxylic acid ligands including Ln(NOTA), Ln(DOTA)$^-$, Ln(TRITA)$^-$, and Ln(PCTA) (*10, 43, 46, 49*). The intermediate formed along the pathway to stable Ln(DOTA) and Ln(PCTA) complexes has been shown to be a diprotonated species, while the intermediate formed in the Ln(NOTA) and Ln(DETA) complexes is monoprotonated (*46, 55*). In each case, the number of protons in the intermediate reflects the basicity of the macrocyclic nitrogen donor atoms in these systems. Tetraazamacrocycles generally have two very basic nitrogen atoms, while triaza macrocycles typically have one basic and one moderately basic nitrogen (*56*); the difference between the first and second protonation constants ($\log K_1^H - \log K_2^H$) is generally larger for triaza macrocycles (4.74 − 6.31 for NOTA) than for tetraaza-macrocyclic ligands ($\log K_1^H - \log K_2^H = 2.33 - 2.90$ for DOTA (the range of the protonation constant differences reflect the literature data reported for the given ligand). The difference between the first and second protonation constants of NO_2-Bn-PCTA (4.59) is somewhat greater than the same difference in PCTA (3.99) and lies between the corresponding differences for DOTA, NO_2-Bn-DOTA, and NOTA. This comparison suggests that the Ln(NO_2-Bn-PCTA) intermediates will likely also be diprotonated. This was verified experimentally for the Yb^{3+} complex in weakly buffered solutions by a UV−vis spectroscopic method described earlier (*43, 46, 54*). Changes in the absorbance of a sample containing an acid−base indicator (methyl orange) in weakly buffered solutions (0.01 M DMP) were calibrated by the addition of a known amount of strong acid stock solution. Using this calibration curve, the concentration (number of moles) of protons released immediately after the mixing of the two components (ligand and metal-ion solution) and at the end of the complexation reaction was determined and compared. The components (ligand and metal ion solutions) were mixed at pH 3.95; a slight pH change was registered upon mixing followed by a more pronounced change in pH during the approach to equilibrium (∼6 h). From the volume of acid needed to return the pH to its original value, it was estimated that about 4 times more protons were released in the slow process than in the fast one. Since the ligand exists as $H_{2.5}L$ at pH ∼4, the release of 0.5 equiv of H^+ upon mixing followed by the liberation of 2 equiv of H^+ after reaching equilibrium is consistent with the formation of a diprotonated intermediate.

Since no major differences in the mechanism of complex formation of Ln(NO_2-Bn-PCTA) and Ln(PCTA) complexes could be detected, the raw data measured for the formation of Ln(NO_2-Bn-PCTA) complexes were treated the same way as the Ln(PCTA) complexes, the details of which will not be repeated here (*10*). Briefly, the pseudofirst-order rate constants obtained at various pH and metal concentrations were fitted to eq 4 (additional information can be found in Supporting Information), and the k_r rate constants and the stability constants of the intermediates $K_{Ln(H_2L)^*}$ were calculated as described for the Ln(PCTA) complexes.

$$k_{obs} = \frac{k_r \frac{K_{Ln(H_2L)^*}}{\alpha_{H_2L}}[Ln^{3+}]}{1 + \frac{K_{Ln(H_2L)^*}}{\alpha_{H_2L}}[Ln^{3+}]} \quad (4)$$

The stability constants of the Ce^{3+} and Eu(H_2NO_2-Bn-PCTA) intermediates determined from the kinetics data were 2.83 ± 0.16 and 2.90 ± 0.11, respectively. The stability of the Yb(H_2PCTA) was also redetermined in the present study and found to be in excellent agreement with our previously published value (2.70 ± 0.08). The stability constants of the intermediates calculated from the kinetic data are lower than those obtained from pH-potentiometric titration for the Ce^{3+}, Eu^{3+}, and Yb(H_2DOTA)$^+$ complexes ($\log K = 4.5$, 4.3, and 4.2, respectively), consistent with differences in the acid-base properties of the ligands as well as differences in the structures expected for these intermediates. The nature of this intermediate has been thoroughly investigated for DOTA. Recent pH-potentiometry, luminescence, and extended X-ray absorption fine structure (EXASF) spectroscopy studies have indicated that the formation of Ln(DOTA) chelates actually involves two diprotonated intermediates (*51, 52*), the first of which is formed instantaneously where the central Ln^{3+} ion is coordinated to oxygens of each of the four carboxylate groups and five water molecules ($q = 5$). This intermediate rapidly converts into the more stable diprotonated species in which the metal ion is coordinated to four oxygens of the acetate side arms, two N-atoms of the macrocyclic ring, and three water molecules ($q = 3$). The stability of the more stable ($q = 3$) intermediate has been determined by both pH-potentiometry and spectrophotometry ($\log K = 4.5$, 4.3, and 4.2 for Ce^{3+}, Eu^{3+}, and Yb^{3+}, respectively, by pH-potentiometry) (*43*). For ligands with three acetate side arms (PCTA, DO3A), the stability of the intermediate is expected to be lower (*57*). There are no stability data available for the intermediates in Ln(DO3A) systems, but q was found to be 4.6 for the Eu(DO3A) complex (*52*). Data published for [10-[2,3-dihydroxy-1-(hydroxymethyl)propyl]-DO3A (DO3A-butriol) ($\log K = 2.4$, 2.5, and 2.43 for the Ce^{3+}, Eu^{3+}, and Yb^{3+} intermediates, respectively) suggest that only the acetate oxygens coordinate (*57*). Considering the Eu^{3+} aqua ion as nine-coordinate, one can assume that the PCTA and NO_2-Bn-PCTA ligands also coordinate to the metal by the three acetate oxygen donor atoms. This assumption is supported by the fact that the stability of the intermediates are higher than the stability of the monoacetate complexes and are very similar to the stability of Ln-dicarboxylic acid complexes (*15*).

It is now generally accepted that the mechanism of complex formation for DOTA and DOTA-like ligands involves the rearrangement of the diprotonated intermediates through rapid deprotonation of the intermediate to a monoprotonated species in a fast equilibrium step. This is followed by the release of the second proton in a slow, rate-determining step and the rapid structural rearrangement of the fully nonprotonated complex to the final product. In accordance with this mechanism, the validity of general base catalysis has been confirmed in some cases (*10, 24, 57*).

Equation 4 can further be simplified if the experimental conditions are chosen so that the conditional stability constant of the intermediate will be high ($K^C_{Ln(H_2L)^*} = K_{Ln(H_2L)^*}/\alpha_{H_2L}$), and the reaction will be pseudofirst-order ($C_{Ln} \geq 10C_L$). Under these conditions, $K^C_{Ln(H_2L)^*} \times [Ln]_{tot} \gg 1$, and thus 1 can be neglected in the denominator of eq 4. This simplifies eq 4 to $k_{obs} \approx k_r$, (k_r is the saturation value of the rate constant k_{obs} when the formation of the intermediate is complete). In other words, the k_r values can be approximated with k_{obs} if a large excess of

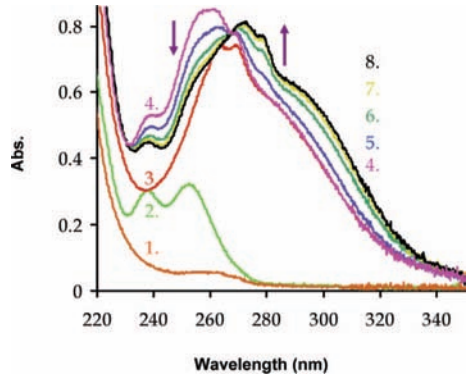

Figure 3. Absorbance changes in the UV region during the formation of Ce(NO_2-Bn-PCTA) after mixing Ce^{3+} and the ligand at 10:1 metal to ligand concentration ratio at pH 4.20 (in 0.04 M DMP, $I = 1.0$ M KCl, and $C_{Lig} = 6 \times 10^{-5}$ M). The curves represent the UV-spectrum of (1) 40 mM buffer, (2) 6×10^{-4} M $CeCl_3$ in DMP buffer, (3) 6×10^{-5} M ligand in DMP buffer, (4) immediately after mixing the Ce^{3+} with the ligand (0 min), (5) after 2 min, (6) after 7 min, (7) after 12 min, and (8) after 70 min (equilibrium).

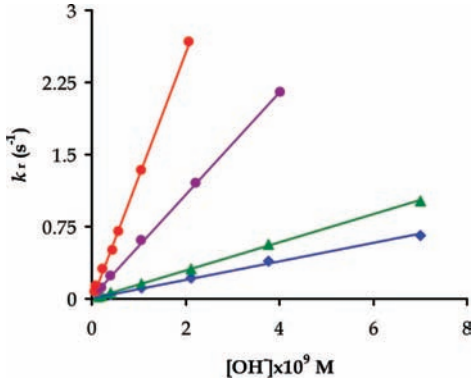

Figure 4. Formation rates of Ce(NO_2-Bn-PCTA) (blue diamonds), Eu(NO_2-Bn-PCTA) (green triangles), Yb(NO_2-Bn-PCTA) (purple circles), and Yb(PCTA) (red circles) vs OH^- ion concentration ($I =$ 1.0 M KCl; 25 °C).

Ln^{3+} is used over the ligand. The necessary excess of the Ln^{3+} to reach the $k_{obs} \approx k_r$ condition can be determined from the expression of the stability constant of the accumulated intermediate (eq 5):

$$K_{Ln(H_2L)^*}[Ln^{3+}] = \frac{[Ln(H_2L)^*]}{[H_2L]} \quad (5)$$

To ensure quantitative formation of the intermediate, the ratio $[Ln(H_2L)^*]/[H_2L]$ ([bound]/[unbound]) in eq 5 should be $\gg 1$. The ratio [bound]/[unbound] will be equal to 1 when the ratio $[Ln^{3+}]/[H_2L] = 19$ (as calculated from the stability constant of the intermediate); therefore, for a more detailed pH dependence study, the ratio $[Ln^{3+}]/[H_2L]$ was set to 200.

The rate constants k_r obtained under these conditions were found to be inversely proportional to the H^+ ion concentration (eq 6) for all of the metal ions and ligands studied in the present work (Figure 4). The k_{OH} values were obtained from the fitting of k_r values gained at different pH values to eq 6 (Table 4).

$$k_r = \frac{k_H}{[H^+]} = k_{OH}[OH^-] \quad (6)$$

The rate of complex formation (rearrangement of the intermediates) increases with decreasing lanthanide-ion size. This decreasing tendency of the k_{OH} values along the lanthanide series is not surprising since it has been reported for numerous cyclen derivatives with acetate pendant arms

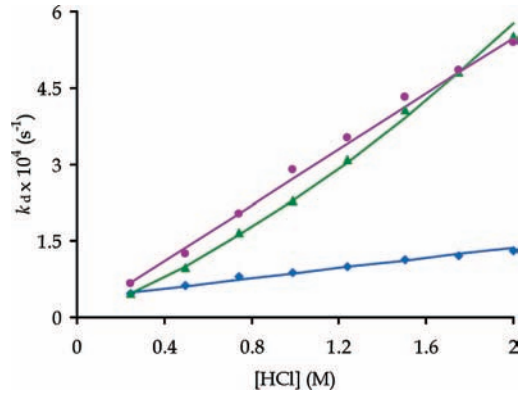

Figure 5. Dependence of the dissociation rate constants (k_d) on the H^+ ion concentration in the dissociation of Ce(NO_2-Bn-PCTA) (blue diamonds), Eu(NO_2-Bn-PCTA) (green triangles), and Yb(NO_2-Bn-PCTA) (purple circles) complexes at 25 °C.

and can be explained by the higher charge density of the heavier lanthanides (the OH^- ion catalyzed deprotonation is faster for the metal ions with greater positive charge density) (*42*). The Ln(NOTA) complexes do not follow this trend, and for some DOTA-tetra(amides), the opposite order of formation constants was recently reported (*46*, *61*, *62*). For the latter complexes, the extremely slow water exchange that is typical of DOTA-tetraamide systems seems to be responsible for this unusual behavior across the lanthanide series (*61*, *62*).

Kinetics of Dissociation. The kinetic inertness of a complex will largely determine its fate in vivo (*63*). Even if the thermodynamic stability of the complex is not very high, it is possible that it can safely be used for biomedical applications if the complex does not dissociate in vivo. The usefulness of acid-catalyzed dissociation rates in predicting the fate of a complex in vivo was first noted by Wedeking when it was found that the extent of long-term Gd-deposition in the whole body, liver, and femur of mice correlated well with the ex vivo acid-catalyzed dissociation rates of various open chain and macrocyclic ^{153}Gd-labeled complexes (*64*). The deposition of Gd was the lowest for Gd(DOTA), and this is in good agreement with its extremely slow proton assisted dissociation rate (*64*). Generally, the dissociation of Ln(III) complexes of DOTA-like ligands are very slow under physiological conditions (*63*), probably because of their tightly packed and highly rigid structure (*45*). Later it was realized that the in vivo dissociation mechanism of acyclic and macrocyclic lanthanide complexes is quite different. The dominant pathway for in vivo dissociation of Ln-chelates of DOTA-like ligands involves the acid-catalyzed dissociation and the acid-independent spontaneous dissociation. However, Ln-complexes of open chain ligands (EDTA and DTPA) dissociate in vivo through a metal ion [Zn(II) and Cu(II)] catalyzed pathway, which is acid-independent above pH 4.5 (*63*). Therefore, the in vitro dissociation kinetic studies of macrocyclic chelates are focused on the acid-catalyzed dissociation, and from the kinetic data, the k_1 and k_2 rate constants corresponding to acid-assisted dissociation of the mono and diprotonated complexes as well as the k_0 rate constant that describes the acid-independent spontaneous dissociation can be estimated (*43*, *45*). Since at pH >2, Ln(NO_2-Bn-PCTA) complexes dissociate too slowly to collect kinetic data over a reasonable period of time, the acid-catalyzed dissociation of Ln(NO_2-Bn-PCTA) complexes was examined at pH $\ll$2, where the complexes are thermodynamically unstable. Under these experimental conditions, proton-assisted dissociation follows first-order kinetics with respect to the complex ($[H^+] \gg$ [Ln(NO_2-Bn-PCTA)]), and

Table 4. Rate Constants, k_{OH}, Characterizing the Rearrangement of the Intermediates in Ce(NO_2-Bn-PCTA), Eu(NO_2-Bn-PCTA), and Yb(NO_2-Bn-PCTA) (I = 1.0 M KCl; 25 °C)

	k_{OH} (M^{-1} s^{-1})			
	Ce^{3+}	Eu^{3+}	Y^{3+}	Yb^{3+}
DO3A[a]		2.1×10^7 [b]		
PCTA[c]	9.7×10^7	1.74×10^8	1.13×10^8	1.11×10^9 **$(1.28 \pm 0.03) \times 10^9$** [d]
NO_2-Bn-PCTA	**$(1.01 \pm 0.01) \times 10^8$**	**$(1.45 \pm 0.03) \times 10^8$**		**$(5.59 \pm 0.10) \times 10^8$**
DOTA[e]	3.5×10^6, 1.16×10^6 [f], 2.7×10^6 [g]	1.1×10^7, 7.2×10^6 [h]	5.9×10^6 [b,i] 6.4×10^5 [h]	4.1×10^7, 9.3×10^7 [g]

[a] Ref *58*. [b] Data corresponds to the Gd(III) complex. [c] Ref *10*. [d] remeasured with stopped-flow method in the current study. [e] Ref *43*. [f] Ref *59*. [g] Ref *24*. [h] Ref *44*. [i] From Ref *45*. [j] Ref *60*.

Table 5. Comparison of Acid-Assisted Dissociation Rate Constants (k_1, M^{-1} s^{-1}) for Ce^{3+}, Eu^{3+}, and Yb(NO_2-Bn-PCTA) Complexes (I = 1.0 M KCl; 25 °C)[a]

	Ce^{3+}	Gd^{3+}	Yb^{3+}
DO3A[b]	1.12×10^{-1}	2.7×10^{-2}, 1.17×10^{-2} [c] 5.2×10^{-2} [d]	2.8×10^{-2}
PCTA[e]	9.6×10^{-4} [g]	5.1×10^{-4} [f], 1.1×10^{-3} [d,g]	3.9×10^{-4}, 2.8×10^{-4} [g]
NO_2-Bn-PCTA	**$(4.77 \pm 0.22) \times 10^{-5}$**	**$(1.75 \pm 0.06) \times 10^{-4}$** [h]	**$(2.78 \pm 0.03) \times 10^{-4}$**
DOTA[i]	8×10^{-4} [j]	2.0×10^{-5} [k], 8.4×10^{-6} [l], 1.4×10^{-5} [m]	

[a] Data for some other complexes formed with macrocyclic ligands are also listed for comparison. [b] Calculated from saturation kinetics from ref *32*. [c] Ref *66*. [d] Data corresponds to the YL complex. [e] Ref *10*. [f] Data corresponds to the EuL complex. [g] Calculated from saturation kinetics obtained in a wide concentration range. [h] Second-order dependence on H^+ ion concentration with third-order rate constant $(5.7 \pm 0.4) \times 10^{-5}$ M^{-2} s^{-1} was also observed. [i] Ref *47*. [j] Second-order dependence on H^+ ion concentration with third-order rate constant 2.0×10^{-3} M^{-2} s^{-1} was also observed (*47*). [k] t = 37 °C; ref *43*. [l] Ref *45*. [m] Data corresponds to EuL (*43*).

the rate of the dissociation is directly proportional to the total concentration of the complex:

$$-\frac{d[LnL]_t}{dt} = k_d[LnL]_t \quad (7)$$

where k_d is a pseudofirst-order rate constant. Under the conditions employed in the current work (0.25 M HCl < C < 2.00 M HCl), complex dissociation proceeds via some combination of acid-assisted and spontaneous dissociation, and consequently, the total concentration of the complex will be a sum of equilibrium concentrations of the complex ([LnL]) and its different protonated forms ([LnH_xL] where x = 1, 2,...).

The dependence of the pseudofirst-order dissociation rate constants (k_d) on the H^+ ion-concentration was measured for Ce^{3+}, Eu^{3+}, and Yb(NO_2-Bn-PCTA) (Figure 5, each point on this figure is an average of two identical kinetic runs). These data demonstrate that the rate of dissociation of the complexes is either proportional to the acid concentration (Ce and Yb) or shows a second-order dependence and can be described by eqs 8 and 9, respectively

$$k_d = k_0 + k_1[H^+] \quad (8)$$

$$k_d = k_0 + k_1[H^+] + k_2[H^+]^2 \quad (9)$$

where k_0 is a constant that describes the acid-independent dissociation (spontaneous dissociation), while k_1 and k_2 correspond to acid-assisted dissociation of the protonated complexes. Ln^{3+} complexes of the parent PCTA behaved slightly differently since Eu(PCTA) and Yb(PCTA) exhibited linear dependence at low acid concentrations, while saturation type dependence was observed for Ce(PCTA), Y(PCTA), and Yb(PCTA) at higher acid concentration. This is likely a consequence of the lower thermodynamic stability of Ln(NO_2-Bn-PCTA) complexes. As a result, the mono and diprotonated intermediates are also expected to have lower stability, and the dissociation curves reach saturation at higher acidity beyond the range of acid concentration used in the study.

The acid-catalyzed dissociation of NO_2-Bn-PCTA complexes very likely follows the same mechanism that accounts for the dissociation of DOTA complexes, with protonation of a carboxylate oxygen as the initial step. The protonated species then undergoes rearrangement, while the proton is transferred from the acetate arm to a ring nitrogen atom. Electrostatic repulsion between the protonated nitrogen and the central metal ion in the macrocyclic cavity of the ligand causes the formation of an out-of-basket complex, which may then dissociate directly or can simultaneously follow a pathway that involves an attack by a second proton. Proton transfer and rearrangement of the complex occurs concurrently, and either of these processes can be the rate-limiting step. The rigidity of the macrocyclic ligand is responsible for the high kinetic inertness of these complexes.

In the physiologically relevant pH range, the contribution of the spontaneous dissociation of the complex, characterized by the k_0 rate constant, may be significant. The value of k_0 can be estimated from the kinetic data (eq 8), but normally its value is zero within the experimental error because under the experimental conditions (pH ≪2), the contribution of the spontaneous dissociation to the dissociation process is very small. In our studies, fitting of dissociation kinetics data for the Eu^{3+} and Yb^{3+} complexes returned a small and negative value for k_0. Similar conclusions were reached by other researchers who determined the rate constant characterizing the spontaneous dissociation of Gd(DOTA) from the kinetic data, and the contribution of the acid-independent dissociation was neglected (*43, 45*). We have found a positive $k_0 = (4.0 \pm 0.3) \times 10^{-5}$ s^{-1} with acceptable uncertainty for Ce(NO_2-Bn-PCTA). However, this value appears to be too high for the spontaneous dissociation of this type of complexes. As reported earlier (*10*), the rate of spontaneous dissociation can be predicted from acid-catalyzed dissociation rate data. By comparing data obtained for complexes of macrocyclic ligands of similar ring size, number, and quality of donor atoms, it was found that the rate of spontaneous dissociation is usually 4−6 orders of magnitude lower than the acid-catalyzed dissociation rate constant, k_1 (*10*). This approximation gives about 10^{-8} to 10^{-9} s^{-1} as the lower limit of the rate constant characterizing spontaneous dissociation of the Ln(NO_2-Bn-PCTA) complexes. In order to determine the k_0 value more precisely, the measurements must be performed at a pH range closer to 7. Preliminary data collected for Gd(PCTA) and Gd(NO_2-Bn-PCTA) in the pH range of 3.0−6.0 and in the presence of Zn^{2+} as scavenger metal ion indicate that an estimate for k_0 is about 10^{-8} to 10^{-9} s^{-1}. Moreover, a recent study on the transmetalation of Gd(PCTA) and its rigidified derivative, Gd(CHX-PCTA) as well as other cyclen based macrocyclic Gd(III) complexes in the presence of Zn^{2+} ions and at physiological pH showed no measureable dissociation of the complexes over the time period of 9000 min (*37, 65*).

The acid-catalyzed dissociation rate constants for some Ln(NO_2-Bn-PCTA) complexes are listed and compared to those of other macrocyclic complexes in Table 5. Interestingly, when compared to the parent ligand, PCTA, the introduction of the *p*-nitrobenzyl substituent did not adversely affect the kinetic inertness of the Ln(NO_2-Bn-PCTA) complexes. Even though the thermodynamic stability of Ln(NO_2-Bn-PCTA) is slightly lower than the corresponding PCTA complexes, their kinetic inertness toward acid-catalyzed dissociation is somewhat higher. This is likely due to the rigidifying effect of the *p*-nitrobenzyl subtituent attached to the pyclen backbone. A similar trend was observed for open-chain and macrocylic ligands when their structures were rigidified. For example, the half-life of Gd(cyclohexyl DOTA) in 1 M HCl is 50 h compared to 23 h of Gd(DOTA) (*67*). The improvement in kinetic inertness is the most pronounced for the Ce^{3+} complex where the rate constant k_1 was found to be at least an order of magnitude lower than it is for the Ce(PCTA). Furthermore, Ce(NO_2-Bn-PCTA) was found to be even more inert toward acid-assisted dissociation than Ce(DOTA).

CONCLUSIONS

The novel bifunctional ligand *p*-nitrobenzyl-PCTA was synthesized in reasonable yields. The total basicity of *p*-nitrobenzyl-PCTA was very similar to that of PCTA and about 6 orders of magnitude less than the basicity of DOTA. As expected, the stability of the complexes of M(NO_2-Bn-PCTA) (M = Mg^{2+}, Ca^{2+}, Cu^{2+}, and Zn^{2+}) is very similar to that of the corresponding PCTA complexes. The stability of the Ln complexes of this new bifunctional ligand is slightly lower ($\Delta\log K = 0.5 - 1.0$) than that of the parent ligand, but the trend of the stability constants across the Ln^{3+} series remains unaffected. The stabilities of In(PCTA) and In(NO_2-Bn-PCTA) were found to be quite high ($\log K \sim 24$), about 3.3 $\log K$ units higher than that previously reported for In(PCTA). This difference is a consequence of competitive complex formation between the Cl^- and In^{3+}. As expected, the formation of Ln(NO_2-Bn-PCTA) complexes proceeds through a diprotonated intermediate, and the rate constant characterizing the OH^- ion catalyzed deprotonation and rearrangement of the intermediate was found to be comparable to that of PCTA complexes. The kinetic inertness of selected Ln(NO_2-Bn-PCTA) (Ln = Ce, Eu, and Yb) complexes was studied by measuring the rate constant characterizing the acid-catalyzed dissociation and was found to be higher than the corresponding PCTA chelates probably due to the rigidifying effect of the *p*-nitrobenzyl substituent. In summary, structural modification of the pyclen backbone with a *p*-nitrobenzyl substiuent does not have an unfavorable influence on either the thermodynamic or kinetic properties of PCTA. The bifunctional ligand forms complexes about an order of magnitude faster than DOTA, while the kinetic inertness of the Ln(NO_2-Bn-PCTA) complexes are comparable to that of DOTA chelates. The rapid complex formation kinetics combined with satisfactory thermodynamic stability and excellent kinetic inertness of the complexes renders this bifunctional ligand particularly suitable for nuclear medicine applications when rapid complex formation is required under mild conditions. In addition, the pyridine moiety is a good sensitizer for luminescent lanthanides such as Eu(III) and Tb(III), and using time gating imaging techniques, the lanthanide emission can be easily separated from the background tissue fluorescence because of the much longer luminescent lifetime (ms) of these ions (*68*). Thus, *p*-nitrobenzyl-PCTA could also be used in the design and construction of in vivo bimodal (nuclear/optical or MRI/optical) imaging probes (*69, 70*).

ACKNOWLEDGMENT

This article is dedicated to Dr Róbert Király (University of Debrecen, Hungary) on the occasion of his retirement. We are grateful to Professor Lynn A. Melton (University of Texas at Dallas) for the access to the RX.2000 Rapid Mixing Accessory. This work was supported in part by grants from the National Institutes of Health (CA-115531, RR-02584 & EB-004582), the Robert A. Welch Foundation (AT-584), the EMIL Project funded by the EC FP6 Framework Program (LSCH-2004-503569), and the Hungarian Science Foundation (OTKA K-69098).

Supporting Information Available: Detailed synthesis of the ligand, $^1H-^1H$ COSY, ^{13}C APT and $^{13}C-^1H$ HMQC NMR spectra of nitrobenzyl pyclen, evaluation of kinetic data, the rate constants characterizing the rearrangement of the intermediates to the final products in formation reactions of Ce(NO_2-Bn-PCTA), Eu(NO_2-Bn-PCTA) and Yb(NO_2-Bn-PCTA) complexes, the k_p values for dissociation of Ce(NO_2-Bn-PCTA), Eu(NO_2-Bn-PCTA), and Yb(NO_2-Bn-PCTA) complexes. This material is available free of charge via the Internet at http://pubs.acs.org.

LITERATURE CITED

(1) Boswell, C. A., and Brechbiel, M. W. (2007) Development of radioimmunotherapeutic and diagnostic antibodies: an inside-out view. *Nucl. Med. Biol. 34*, 757–778.

(2) Kassis, A. I. (2008) Therapeutic radionuclides: biophysical and radiobiologic principles. *Semin. Nucl. Med. 38*, 358–366.

(3) De Leon-Rodriguez, L. M., and Kovacs, Z. (2008) The synthesis and chelation chemistry of DOTA-peptide conjugates. *Bioconjugate Chem. 19*, 391–402.

(4) Chong, H. S., Ma, X., Le, T., Kwamena, B., Milenic, D. E., Brady, E. D., Song, H. A., and Brechbiel, M. W. (2008) Rational design and generation of a bimodal bifunctional ligand for antibody-targeted radiation cancer therapy. *J. Med. Chem. 51*, 118–125.

(5) Breeman, W. A. P., de Blois, E., Bakker, W. H., and Krenning, E. P. (2006) Radionuclide Peptide Cancer Therapy, in *Radionuclide Peptide Cancer Therapy* (Chinol, M., and Paganelli, G., Eds.) pp 119−125, Taylor & Francis, New York.

(6) Camera, L., Kinuya, S., Garmestani, K., Wu, C., Brechbiel, M. W., Pai, L. H., McMurry, T J., Gansow, O. A., Pastan, I., and Paik, C. H. (1994) Evaluation of the serum stability and in vivo biodistribution of CHX-DTPA and other ligands for yttrium labeling of monoclonal antibodies. *J. Nucl. Med. 35*, 882–889.

(7) Chong, H. S., Garmestani, K., Ma, D. S., Milenic, D. E., Overstreet, T., and Brechbiel, M. W. (2002) Synthesis and biological evaluation of novel macrocyclic ligands with pendent donor groups as potential yttrium chelators for radioimmunotherapy with improved complex formation kinetics. *J. Med. Chem. 45*, 3458–3464.

(8) Chong, H. S., Song, H. A., Ma, X., Milenic, D. E., Brady, E. D., Lim, S., Lee, H., Baidoo, K., Cheng, D., and Brechbiel, M. W. (2008) Novel bimodal bifunctional ligands for radioimmunotherapy and targeted MRI. *Bioconjugate Chem. 19*, 1439–1447.

(9) Baranyai, Z., Uggeri, F., Giovenzana, G. B., Bényei, A., Brücher, E., and Aime, S. (2009) Equilibrium and kinetic properties of the lanthanoids(III) and various divalent metal complexes of the heptadentate ligand AAZTA. *Chem. -Eur. J. 15*, 1696–1705.

(10) Tircso, G., Kovacs, Z., and Sherry, A. D. (2006) Equilibrium and formation/dissociation kinetics of some Ln(III)PCTA complexes. *Inorg. Chem. 45*, 9269–9280.

(11) Irving, H. M., Miles, M. G., and Pettit, L. D. (1967) A study of some problems in determining stoicheiometric proton dissociation constants of complexes by potentiometric titrations using a glass electrode. *Anal. Chim. Acta 38*, 475–488.

(12) Schwarzenbach, G., and Flaschka, H. (1969) *Complexometric Titrations*, 2nd Ed., Methuen, London.
(13) Woods, M., Kovacs, Z., Kiraly, R., Brucher, E., Zhang, S. R., and Sherry, A. D. (2004) Solution dynamics and stability of lanthanide(III) (*S*)-2-(*p*-nitrobenzyl)DOTA complexes. *Inorg. Chem. 43*, 2845–2851.
(14) Zekany, L., and Nagypal, I. (1985) Computational Methods for the Determination of Formation Constants, in *Computational Methods for the Determination of Formation Constants* (Leggett, D. J., Ed.) p 291, Plenum Press, New York.
(15) Martell, A. E., Smith, R. M., and Motekaitis, R. J. (2004) *Critically Selected Stability Constants of Metal Complexes, Database Version 8.0.* National Institute of Standards and Technology, Standard Reference Data Program, Gaithersburg.
(16) Ansari, M. H., Ahmad, M., and Dicke, K. A. (1993) Synthesis of 2-(*p*-aminobenzyl) derivatives of 1,4,7-triazacyclononane-*N*,*N*′,*N*″-triacetic acid (NOTA) and 1,4,7,10-tetraazacyclododecane-N, *N*′,*N*″,*N*‴-tetraacetic acid (DOTA): macrocyclic bifunctional chelating-agents useful for antibodies labeling. *Bioorg. Med. Chem. Lett. 3*, 1067–1070.
(17) Richman, J. E., and Atkins, T. J. (1974) Nitrogen analogs of crown ethers. *J. Am. Chem. Soc. 96*, 2268–70.
(18) McMurry, T. J., Brechbiel, M., Kumar, K., and Gansow, O. A. (1992) Convenient synthesis of bifunctional tetraaza macrocycles. *Bioconjugate Chem. 3*, 108–117.
(19) Kumar, K., Chang, C. A., Francesconi, L. C., Dischino, D. D., Malley, M. F., Gougoutas, J. Z., and Tweedle, M. F. (1994) Synthesis, stability, and structure of gadolinium(III) and yttrium(III) macrocyclic poly(amino carboxylates). *Inorg. Chem. 33*, 3567–3575.
(20) Bianchi, A., Calabi, L., Giorgi, C., Losi, P., Mariani, P., Paoli, P., Rossi, P., Valtancoli, B., and Virtuani, M. (2000) Thermodynamic and structural properties of Gd^{3+} complexes with functionalized macrocyclic ligands based upon 1,4,7,10-tetraazacyclododecane. *J. Chem. Soc., Dalton Trans.* 697–705.
(21) Siaugue, J. M., Favre-Reguillon, A., Dioury, F., Plancque, G., Foos, J., Madic, C., Moulin, C., and Guy, A. (2003) Effect of mixed pendant groups on the solution properties of 12-membered azapyridinomacrocycles: evaluation of the protonation constants and the stability constants of the europium(III) complexes. *Eur. J. Inorg. Chem.* 2834–2838.
(22) Siaugue, J. M., Segat-Dioury, F., Favre-Reguillon, A., Wintgens, V., Madic, C., Foos, J., and Guy, A. (2003) Europium(III) complex formed with pyridine containing azamacrocyclic triacetate ligand: characterization by sensitized Eu(III) luminescence. *J. Photochem. Photobiol. A 156*, 23–29.
(23) Chaves, S., Delgado, R., and Dasilva, J. J. R. F. (1992) The stability of the metal-complexes of cyclic tetra-aza tetraacetic acids. *Talanta 39*, 249–254.
(24) Burai, L., Fabian, I., Kiraly, R., Szilagyi, E., and Brucher, E. (1998) Equilibrium and kinetic studies on the formation of the lanthanide(III) complexes, [Ce(dota)](-) and [Yb(dota)](-) (H(4)dota=1,4,7,10-tetraazacyclododecane-1,4,7,10-tetraacetic acid). *J. Chem. Soc., Dalton Trans.* 243–248.
(25) Aime, S., Botta, M., Crich, S. G., Giovenzana, G. B., Jommi, G., Pagliarin, R., and Sisti, M. (1997) Synthesis and NMR studies of three pyridine-containing triaza macrocyclic triacetate ligands and their complexes with lanthanide ions. *Inorg. Chem. 36*, 2992–3000.
(26) Delgado, R., Quintino, S., Teixeira, M., and Zhang, A. (1997) Metal complexes of a 12-membered tetraaza macrocycle containing pyridine and N-carboxymethyl groups. *J. Chem. Soc., Dalton Trans.* 55–63.
(27) Chang, C. A. (1996) Selectivity of macrocyclic aminocarboxylates for alkaline-earth metal ions and stability of their complexes. *J. Chem. Soc., Dalton Trans.* 2347–2350.
(28) Kumar, K., Tweedle, M. F., Malley, M. F., and Gougoutas, J. Z. (1995) Synthesis, stability, and crystal structure studies of some Ca^{2+}, Cu^{2+} and Zn^{2+} complexes of macrocyclic polyamino carboxylates. *Inorg. Chem. 34*, 6472–6480.
(29) Delgado, R., and Dasilva, J. J. R. F. (1982) metal-complexes of cyclic tetra-azatetra-acetic acids. *Talanta 29*, 815–822.
(30) Alcock, N. W., Busch, D. H., and Liu, C. Y. (2006) Bis(chloro-(3,6,9,15-tetra-azabicyclo(9.3.1)pentadeca-1(15),11,13-triene)-zinc) tetrachlorozincate, CCDC 628572 Identifier: LESSEI.
(31) Kumar, K., and Tweedle, M. F. (1993) Macrocyclic polyaminocarboxylate complexes of lanthanides as magnetic-resonance-imaging contrast agents. *Pure Appl. Chem. 65*, 515–520.
(32) Kumar, K., Chang, C. A., and Tweedle, M. F. (1993) Equilibrium and kinetic-studies of lanthanide complexes of macrocyclic polyamino carboxylates. *Inorg. Chem. 32*, 587–593.
(33) Wu, S. L., and Horrocks, W. D. (1996) General method for the determination of stability constants of lanthanide ion chelates by ligand ligand competition: laser-excited Eu^{3+} luminescence excitation spectroscopy. *Anal. Chem. 68*, 394–401.
(34) Wu, S. L., and Horrocks, W. D. (1997) Direct determination of stability constants of lanthanide ion chelates by laser-excited europium(III) luminescence spectroscopy: application to cyclic and acyclic aminocarboxylate complexes. *J. Chem. Soc., Dalton Trans.* 1497–1502.
(35) Cacheris, W. P., Nickle, S. K., and Sherry, A. D. (1987) Thermodynamic study of lanthanide complexes of 1,4,7-triazacyclononane-*N*,*N*′,*N*″-triacetic acid and 1,4,7,10-tetraazacyclododecane-*N*,*N*′,*N*″,*N*‴-tetraacetic acid. *Inorg. Chem. 26*, 958–960.
(36) Clarke, E. T., and Martell, A. E. (1991) Stabilities of trivalent metal-ion complexes of the tetraacetate derivatives of 12-membered, 13-membered and 14-membered tetraazamacrocycles. *Inorg. Chim. Acta 190*, 37–46.
(37) Laurent, S., Elst, L. V., and Muller, R. N. (2006) Comparative study of the physicochemical properties of six clinical low molecular weight gadolinium contrast agents. *Contrast Media Mol. Imaging 1*, 128–137.
(38) Ferri, D. (1972) On the complex formation equilibria between indium(III) and chloride ions. *Acta Chem. Scand. 26*, 733–746.
(39) Brucher, E. (2002) Kinetic stabilities of gadolinium(III) chelates used as MRI contrast agents. *Top. Curr. Chem. Contrast Agents I 221*, 103–122.
(40) Cossy, C., and Merbach, A. E. (1988) Recent developments in solvation and dynamics of the lanthanide(III) Ions. *Pure Appl. Chem. 60*, 1785–1796.
(41) Lincoln, S. F., and Merbach, A. E. (1995) Substitution reactions of solvated metal ions. *Adv. Inorg. Chem. 42*, 1–88.
(42) Lincoln, S. F. (1986) Solvation, solvent exchange, and ligand substitution reactions of the trivalent lanthanide ions. *Adv. Inorg. Bioinorg. Mech. 4*, 217–87.
(43) Toth, E., Brucher, E., Lazar, I., and Toth, I. (1994) Kinetics of formation and dissociation of lanthanide(III)-dota complexes. *Inorg. Chem. 33*, 4070–4076.
(44) Wu, S. L., and Horrocks, W. D. (1995) Kinetics of complex-formation by macrocyclic polyaza polycarboxylate ligands - detection and characterization of an intermediate in the Eu^{3+}-dota system by laser-excited luminescence. *Inorg. Chem. 34*, 3724–3732.
(45) Wang, X. Y., Jin, T. Z., Comblin, V., Lopezmut, A., Merciny, E., and Desreux, J. F. (1992) A kinetic investigation of the lanthanide dota chelates: stability and rates of formation and of dissociation of a macrocyclic gadolinium(III) polyaza polycarboxylic MRI contrast agent. *Inorg. Chem. 31*, 1095–1099.
(46) Brucher, E., and Sherry, A. D. (1990) Kinetics of formation and dissociation of the 1,4,7-triazacyclononane-*N*,*N*′,*N*″-triacetate complexes of cerium(III), gadolinium(III), and erbium(III) ions. *Inorg. Chem. 29*, 1555–1559.
(47) Brucher, E., Laurenczy, G., and Makra, Z. (1987) Studies on the kinetics of formation and dissociation of the cerium(III)-dota complex. *Inorg. Chim. Acta 139*, 141–142.
(48) Balogh, E., Tripier, R., Fouskova, P., Reviriego, F., Handel, H., and Toth, E. (2007) Monopropionate analogues of DOTA(4-) and DTPA(5-): kinetics of formation and dissociation of their lanthanide(III) complexes. *Dalton Trans.* 3572–3581.

(49) Balogh, E., Tripier, R., Ruloff, R., and Toth, E. (2005) Kinetics of formation and dissociation of lanthanide(III) complexes with the 13-membered macrocyclic ligand TRITA(4-). *Dalton Trans.* 1058–1065.

(50) Moreau, J., Pierrard, J. C., Rimbault, J., Guillon, E., Port, M., and Aplincourt, M. (2007) Thermodynamic and structural properties of Eu^{3+} complexes of a new 12-membered tetraaza macrocycle containing pyridine and N-glutaryl groups as pendant arms: characterization of three complexing successive phases. *Dalton Trans.* 1611–1620.

(51) Moreau, J., Guillon, E., Pierrard, J. C., Rimbault, J., Port, M., and Aplincourt, M. (2004) Complexing mechanism of the lanthanide cations Eu^{3+}, Gd^{3+}, and Tb^{3+} with 1,4,7,10-tetrakis-(carboxymethyl)-1,4,7,10-tetraazacyclododecane (dota): characterization of three successive complexing phases: study of the thermodynamic and structural properties of the complexes by potentiometry, luminescence spectroscopy, and EXAFS. *Chem.—Eur. J. 10*, 5218–5232.

(52) Taborsky, P., Svobodova, I., Lubal, P., Hnatejko, Z., Lis, S., and Hermann, P. (2007) Formation and dissociation kinetics of Eu(III) complexes with H(5)do3ap and similar dota-like ligands. *Polyhedron 26*, 4119–4130.

(53) Taborsky, P., Svobodova, I., Hnatejko, Z., Lubal, P., Lis, S., Forsterova, M., Hermann, P., Lukes, I., and Havel, J. (2005) Spectroscopic characterization of Eu(III) complexes with new monophosphorus acid derivatives of H(4)dota. *J. Fluoresc. 15*, 507–512.

(54) Kasprzyk, S. P., and Wilkins, R. G. (1982) Kinetics of interaction of metal-ions with 2 tetraaza tetraacetate macrocycles. *Inorg. Chem. 21*, 3349–3352.

(55) Brucher, E., Cortes, S., Chavez, F., and Sherry, A. D. (1991) Synthesis, equilibrium, and kinetic properties of the gadolinium(III) complexes of 3 triazacyclodecanetriacetate ligands. *Inorg. Chem. 30*, 2092–2097.

(56) Kovacs, Z., and Sherry, A. D. (1997) pH-controlled selective protection of polyaza macrocycles. *Synthesis* 759–763.

(57) Szilagyi, E., Toth, E., Kovacs, Z., Platzek, J., Raduchel, B., and Brucher, E. (2000) Equilibria and formation kinetics of some cyclen derivative complexes of lanthanides. *Inorg. Chim. Acta 298*, 226–234.

(58) Kumar, K., Jin, T., Wang, X., Desreux, J. F., and Tweedle, M. F. (1994) Effect of ligand basicity on the formation and dissociation equilibria and kinetics of Gd^{3+} complexes of macrocyclic polyamino carboxylates. *Inorg. Chem. 33*, 3823–3829.

(59) Chang, C. A., Liu, Y. L., Chen, C. Y., and Chou, X. M. (2001) Ligand preorganization in metal ion complexation: molecular mechanics/dynamics, kinetics, and laser-excited luminescence studies of trivalent lanthanide complex formation with macrocyclic ligands TETA and DOTA. *Inorg. Chem. 40*, 3448–3455.

(60) Forsterova, M., Svobodova, I., Lubal, P., Taborsky, P., Kotek, J., Hermann, P., and Lukes, I. (2007) Thermodynamic study of lanthanide(III) complexes with bifunctional monophosphinic acid analogues of H(4)dota and comparative kinetic study of yttrium(III) complexes. *Dalton Trans.* 535–549.

(61) Pasha, A., Tircso, G., Benyo, E. T., Brucher, E., and Sherry, A. D. (2007) Synthesis and characterization of DOTA-(amide)4 derivatives: equilibrium and kinetic behavior of their lanthanide(III) complexes. *Eur. J. Inorg. Chem.* 4340–4349.

(62) Baranyai, Z., Banyai, I., Brucher, E., Kiraly, R., and Terreno, E. (2007) Kinetics of the formation of [Ln(DOTAM)](3+) complexes. *Eur. J. Inorg. Chem.* 3639–3645.

(63) Brucher, E., and Sherry, A. D. (2001) Stability and Toxicity of Contrast Agents, in *The Chemistry of Contrast Agents in Medical Magnetic Resonance Imaging* (Merbach, A. E., and Toth, E, Eds.) pp 243−279, Chapter 6, John Wiley and Sons Ltd., Chichester, U.K.

(64) Wedeking, P., Kumar, K., and Tweedle, M. F. (1992) Dissociation of gadolinium chelates in mice: relationship to chemical characteristics. *Magn. Reson. Imaging 10*, 641–8.

(65) Port, M., Raynal, I., Elst, L. V., Muller, R. N., Dioury, F., Ferroud, C., and Guy, A. (2006) Impact of rigidification on relaxometric properties of a tricyclic tetraazatriacetic gadolinium chelate. *Contrast Media Mol. Imaging 1*, 121–127.

(66) Cai, H. Z., and Kaden, T. A. (1994) Metal-complexes with macrocyclic ligands. 36. Thermodynamic and kinetic studies of bivalent and trivalent metal-ions with 1,4,7,10-tetraazacyclododecane-1,4,7-triacetic acid. *Helv. Chim. Acta 77*, 383–398.

(67) Comblin, V., Gilsoul, D., Hermann, M., Humblet, V., Jacques, V., Mesbahi, M., Sauvage, C., and Desreux, J. F. (1999) Designing new MRI contrast agents: a coordination chemistry challenge. *Coord. Chem. Rev. 186*, 451–470.

(68) Faulkner, S., Pope, S. J. A., and Burton-Pye, B. P. (2005) Lanthanide complexes for luminescence imaging applications. *Appl. Spectrosc. Rev. 40*, 1–31.

(69) Bornhop, D. J., Griffin, J. M. M., Goebel, T. S., Sudduth, M. R., Bell, B., and Motamedi, M. (2003) Luminescent lanthanide chelate contrast agents and detection of lesions in the hamster oral cancer model. *Appl. Spectrosc. 57*, 1216–22.

(70) Manning, H. C., Goebel, T., Thompson, R. C., Price, R. R., Lee, H., and Bornhop, D. J. (2004) Targeted molecular imaging agents for cellular-scale bimodal imaging. *Bioconjugate Chem. 15*, 1488–1495.

BC8004914

Electronic Supporting Information

(*S*)-5-(*p*-nitrobenzyl)-PCTA, a Promising Bifunctional Ligand with Advantageous Metal Ion Complexation Kinetics

*Gyula Tircsó[#&], Enikő Tircsóné Benyó[#&], Eul Hyun Suh[§], Paul Jurek[@], Garry E. Kiefer[@#], A. Dean Sherry[#§] and Zoltán Kovács[§]**

[#] Department of Chemistry, University of Texas at Dallas, P.O. Box 830660, Richardson, Texas 75080, USA

[§] Advanced Imaging Research Center, University of Texas Southwestern Medical Center, 5323 Harry Hines Boulevard, Dallas, Texas 75390, USA

[@] Macrocyclics, 2110 Research Row, Suite 425, Dallas, Texas 75235, USA

[&] Present address: University of Debrecen, Department of Inorganic and Analytical Chemistry, P. O. Box 21, Egyetem tér 1, Debrecen 4010, Hungary

Table of Contents

Synthesis S1

^{1}H-^{1}H COSY, ^{13}C APT and ^{13}C-^{1}H HMQC NMR experiments with nitrobenzyl cyclen S6

Equations used for the formation kinetics data fitting S10

Formation rate constants S12

Observed k_p values S13

Synthesis

General. Reagents were purchased from Sigma-Aldrich (St. Louis, MO) and solvents were obtained from Fisher Scientrific, (Houston, TX) unless otherwise stated. ^{1}H and ^{13}C NMR data were recorded o a Varian Inova 400MHz or a JEOL Eclipse 200MHz FT NMR spectrometer. Chemical shifts are reported as δ in ppm relative to TMS. MALDI-TOF MS spectra were recorded on a Voyager-DE^{TM} PRO (Applied Biosystems) for MALDI-TOF using an α-cyano-4-hydroxycinnamic acid matrix. Electrospray (ESI) mass spectra were obtained from HT Laboratories, San Diego, CA. Elemental analyses were performed by Galbraith Laboratories, Knoxville, TN.

N, N,' N''-Tritosyl-(S)-2-(p-nitrobenzyl)-diethylenetriamine was prepared from L-nitrophenyl alanine following literature procedures.*(1, 3, 4*).

N, N', N"–Tritosyl-2-(p-nitrobenzyl)-diethylenetriamine disodium salt (1). The disodium salt of N, N,' N''-tristosyl-(S)-2-(p-nitrobenzyl)-diethylenetriamine was prepared by the adaptation of the literature procedure for the disodium salt of N,N',N"-tritosyldiethylenetriamine (*2, 5*) N, N', N"–tritosyl-2-(p-nitrobenzyl)-diethylenetriamine (23.00 g) was suspended in absolute ethanol (250 mL) and the mixture was heated to reflux. Sodium ethoxide (freshly prepared by dissolving 1.85 g of sodium metal in 50 mL of absolute ethanol) was added to the hot, stirred reaction mixture in one portion resulting in a clear yellow solution. The mixture was heated at reflux for an additional 5 min. while a fine precipitate formed. The mixture was allowed to cool to room temperature and then it was placed into the refrigerator overnight.

The product was filtered on a fritted glass filter and was washed with ethanol (2x50 mL) and ether (2x50 mL) and dried in high vacuum to give 23.18 g of a pale yellow solid. This product was used without further purification and characterization.

N, N', N"–Tritosyl-5-(p-nitrobenzyl)-pyclen (3). N, N', N"–Tritosyl-2-(p-nitrobenzyl)-diethylenetriamine disodium salt (**1**) (16.00 g) was suspended in DMF (500 mL) and bis(chloromethyl) pyridine (**2**) (4.00 g) was added. The mixture was stirred at 55 °C for 3 days. The solvent was removed by rotary evaporation and the residue was taken up in water (200 mL). The yellow solid was filtered on a Buchner funnel, washed with water (4x200 mL) and dried with air suction. The yield for the crude product was 16.08 g. The crude product was dissolved in hot ethyl acetate (40 mL) and hot absolute ethanol (80 mL) was added. The mixture was boiled until all of the solid dissolved. Upon cooling to room temperature, a large amount solid started to crystallize. It was placed into the refrigerator overnight. The product was filtered on a fritted glass filter, washed with ethanol (2x10 mL) and with ether (2x10 mL) and dried by air suction to give 9.71 g of a yellow solid (56.16%). An analytical sample was obtained by another recrystallization from MeCN. ^{1}H NMR (400MHz, CDCl3) δ: 8.05 (2H, s br, Ar) 7.68 (5H, s br, Ar), 7.34-7.26 (12H, m, Ar), 4.87-3.08 (12H, m br, O$\underline{CH_2}$Ar, N$\underline{CH_2}$ ring) 2.44 (3H, s, CH_3Ar), 2.40 (3H, s, CH_3Ar), 2.36 (3H, CH_3Ar). ^{13}C NMR (100MHz, CDCl3) δ: 153.87, 144.79, 142.00, 141.87, 136.79, 133.80, 128.07, 127.84, 125.41, 125.19, 121.67, 59.90, 53.38, 46.36, 35.18, 19.69, 19.66, 19.55. MS (MALDI-TOF): *m/z* calcd. for $[M + H]^+$: 804.22; found: 804.59. Anal. Calcd for $C_{39}H_{41}N_5O_8S_3$: C, 58.26, H, 5.14, N.8.71. Found: C, 58.15, H, 5.09, N, 9.05.

5-(p-Nitrobenzyl)-pyclen (4). N, N', N"–Tritosyl-5-(p-nitrobenzyl)-pyclen (**3**) (9.00 g) was dissolved in sulfuric acid (40 mL) and the solution was heated at 180 °C for 10 min. The mixture was allowed to cool to room temperature and then placed into an ice bath and ether (500mL) was carefully added in small portions. *Caution! Addition of ether to sulfuric acid generates heat!* A large amount of grey precipitate formed. The ether was decanted and the grey residue was washed and decanted with ether (2x500 mL). The residue was dissolved in water (50 mL) and NaOH solution (15g NaOH in 20 mL of water) was added. A dark oil separated, which was extracted into chloroform (3x150 mL) and the combined chloroform extracts were dried over sodium sulfate, clarified with activated carbon, filtered and evaporated by rotary evaporation to give a yellow oil that crystallized in high vacuum. Yield :3.00 g (78.53%). ^{1}H NMR (400MHz, $CDCl_3$) δ: 8.05 (2H, dd, Ar, *J* = 8.8Hz), 7.45 (1H, t, Ar), 7.25 (2H, dd, Ar, *J* = 8.8Hz), 6.93 (1H, d, Ar, *J* = 7.6Hz), 6.86 (1H, d, Ar, *J* = 7.6Hz), 4.12 (1H, d, N$\underline{CH_2}$ ring, *J* = 16.0Hz), 4.03 (1H, d, N$\underline{CH_2}$ ring, *J* = 16.0Hz), 3.64 (1H, d, N$\underline{CH_2}$ ring, *J* = 16.0Hz), 3.57 (1H, d, N$\underline{CH_2}$ ring *J* = 16.0Hz), 2.89-2.75 (2H, m, NCH$\underline{CH_2}$Ar, N$\underline{CH_2}$ ring), 2.65-2.60 (2H, m, NCH$\underline{CH_2}$Ar, N$\underline{CH}CH_2$Ar), 2.51-2.46 (1H, m, N$\underline{CH_2}$ ring), 2.32 (1H, dd, N$\underline{CH_2}$ ring, *J* = 12.0Hz), 2.25-2.21 (1H, m, N$\underline{CH_2}$ ring), 2.03 (1H, dd, N$\underline{CH_2}$ ring, *J* = 12.0Hz), 1.76-1.70 (1H, m, N$\underline{CH_2}$ ring). ^{13}C NMR (100MHz, $CDCl_3$) δ: 160.43, 159.40, 148.22, 146.65, 136.67, 130.22, 123.66, 120.42, 119.97, 57.00, 54.55, 53.85, 51.84, 50.33, 49.54, 40.36. MS (MALDI-TOF): *m/z* calcd. for $[M + H]^+$: 342.20; found: 342.44 (overlaps with peaks from the matrix). MS (ESI) *m/z* calcd. for $[M + H]^+$: 342.20; found: 342. Anal. Calcd for $C_{18}H_{23}N_5O_2$: C, 63.32, H, 6.79, N, 20.51. Found: C, 62.86, H, 6.82, N, 20.41.

5-(p-Nitrobenzyl)-PCTA (6). 5-(p-Nitrobenzyl)-pyclen (**4**) (2.85 g) was dissolved in acetonitrile (200 mL) and potassium carbonate (9.0 g, anhydrous, -325 mesh) was added. Tert-butyl bromoacetate (5.33 g) was dissolved in acetonitrile (10 mL) and the solution was added to the reaction mixture in small portions over a period of 30 min. The mixture was stirred at 50 °C for five days. The inorganic salts were filtered off and the filtrate was evaporated by rotary evaporation. The residue was dissolved in ether (100 mL) and the solution was washed with water (3x50 mL), dried over sodium sulfate, filtered and evaporated by rotary evaporation to give 5-(p-nitrobenzyl)-PCTA tris(tert-butyl ester) (**5**) as a yellow oil. ^{13}C NMR, 50MHz, $CDCl_3$) δ: 170.99, 170.92, 170.42, 157.30, 156.38, 149.71, 145.90, 136,74, 130.13, 122.71, 122.30, 122.06, 80.93, 80.78, 80.57, 60.26, 59.59, 59.09, 58.47, 58.32, 54.21, 50.14, 49.93, 47.61, 37.58, 28.00, 27.98. MS (ESI) *m/z* calcd. for $[M + H]^+$: 684.39; found: 685. This product was used in the next step without further purification. 5-(p-Nitrobenzyl)-PCTA tris(tert-butyl ester) (**5**) (5.83 g) was dissolved in hydrochloric acid (20%, 100 mL) and the solution was stirred at room temperature for two days. The mixture was treated with activated carbon (0.5 g), filtered and evaporated by rotary evaporation. The residue was redissolved in water and freeze dried to give 4.35 g of a yellow solid (83% from 6). The crude product was purified on a Waters DeltaPrep preparative chromatography system and a Phenomenex Luna C18(2) (250x50 mm, 10 μm) column. Mobile phase was 15/85 CH_3CN/H_2O 0.01 M HCl total. Four injections of 0.5 g in 10 mL of mobile phase were performed. Using a flow rate of 100 mL/min and monitoring the output at 210 nm, a single fraction was collected each run with a retention time of ~9.8 – 13.0 min. All four fractions were placed on the freeze-dryer to remove the solvent. Final solid samples were homogenized by shaking.

The yield was 1.30 g (65%). The chromatographic purity of the final product was 99.1%. ^{1}H NMR (400MHz, D_2O, ND_4OD) δ: 7.87 (2H, s br, Ar) 7.52 (1H, dd, Ar, *J* = 8.0Hz), 7.22 (2H, s, br, Ar), 6.96 (2H, d Ar, *J* = 8.0Hz), 3.83-2.86 (18H, d, m,O$\underline{CH_2}$Ar, N$\underline{CH_2}$ ring, N$\underline{CH_2}$COOH). ^{13}C NMR (100MHz, D_2O, ND_4OD) δ: 178.97, 178.44, 171.29, 159.26, 147.14, 146.35, 138.70, 130.32, 124.08, 121.08, 61.38, 60.49, 58.10, 54.28, 52.43, 51.85, 50.57, 48.22, 33.34. MS (MALDI-TOF): *m/z* calcd. for $[M + H]^+$: 516.21; found: 516.49. Anal. Calcd for $C_{24}H_{29}N_5O_8 \cdot 3HCl \cdot 2H_2O$: C, 43.61, H, 5.49, N.10.60. Found: C, 43.34, H, 5.77, N, 10.59.

Literature references

(1) Ansari, M. H., Ahmad, M., and Dicke, K. A. (1993) Synthesis of 2-(p-aminobenzyl) derivatives of 1,4,7-triazacyclononane-N,N',N''-triacetic acid (NOTA) and 1,4,7,10-tetraazacyclododecane-N,N',N'',N'''-tetraacetic acid (DOTA) - macrocyclic bifunctional chelating-agents useful for antibodies labeling. *Bioorg. Med. Chem. Lett. 3*, 1067-1070.

(2) Richman, J. E., and Atkins, T. J. (1974) Nitrogen analogs of crown ethers. *J. Am. Chem. Soc. 96*, 2268-70.

(3) Garrity, M. L., Brown, G. M., Elbert, J. E., and Sachleben, R. A. (1993) A new synthetic route to 2-(p-nitrobenzyl)-1,4,7,10-tetraazacyclododecane. *Tetrahedron Lett. 34*, 5531-5534.

(4) Corson, D. T., and Meares, C. F. (2000) Efficient multigram synthesis of the bifunctional chelating agent (S)-1-p-isothiocyanatobenzyl-diethylenetetraminepentaacetic acid. *Bioconjugate Chem. 11*, 292-299.

(5) Atkins, T. J., Richman, J. E., and Oettle, W. F. (1978) Macrocyclic polyamines: 1,4,7,10,13,16-hexaazacyclooctadecane. *Org. Synth. 58*, 86-98.

^{1}H-^{1}H COSY, APT ^{13}C and ^{13}C-^{1}H HMQC NMR experiments with nitrobenzyl cyclen

Due to the presence of the nitrobenzyl group, all the protons of nitrobenzyl pyclen are magnetically nonequivalent. The correct assignment of the ^{1}H and ^{13}C NMR spectra were accomplished with the help of APT (attached proton test), ^{1}H-^{1}H COSY (correlated spectroscopy) and HMQC (heteronuclear multiple quantum coherence) experiments. The ^{1}H-^{1}H-COSY spectrum (Figure S1) confirmed the connection of C-5 to C-6 and C-16, C-8 to C-9, C-14 to C-13 and C-15, C-18 to C-19, and C21 to C-22.

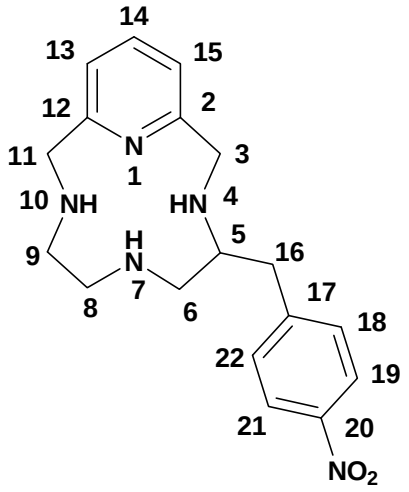

The numbering of the nitrobenzyl pyclen skeleton as used here to identify the protons and carbons in the NMR spectra

The APT experiment detected the multiplicity (number of protons attached) of the carbons (Figure S2) while the HMQC experiment established the correlations between the protons and the ^{13}C nuclei by showing the directly coupled C-H peaks (Figure S3). The COSY, APT and HMQC experiments were performed on a Varian Inova 400MHz NMR spectrometer.

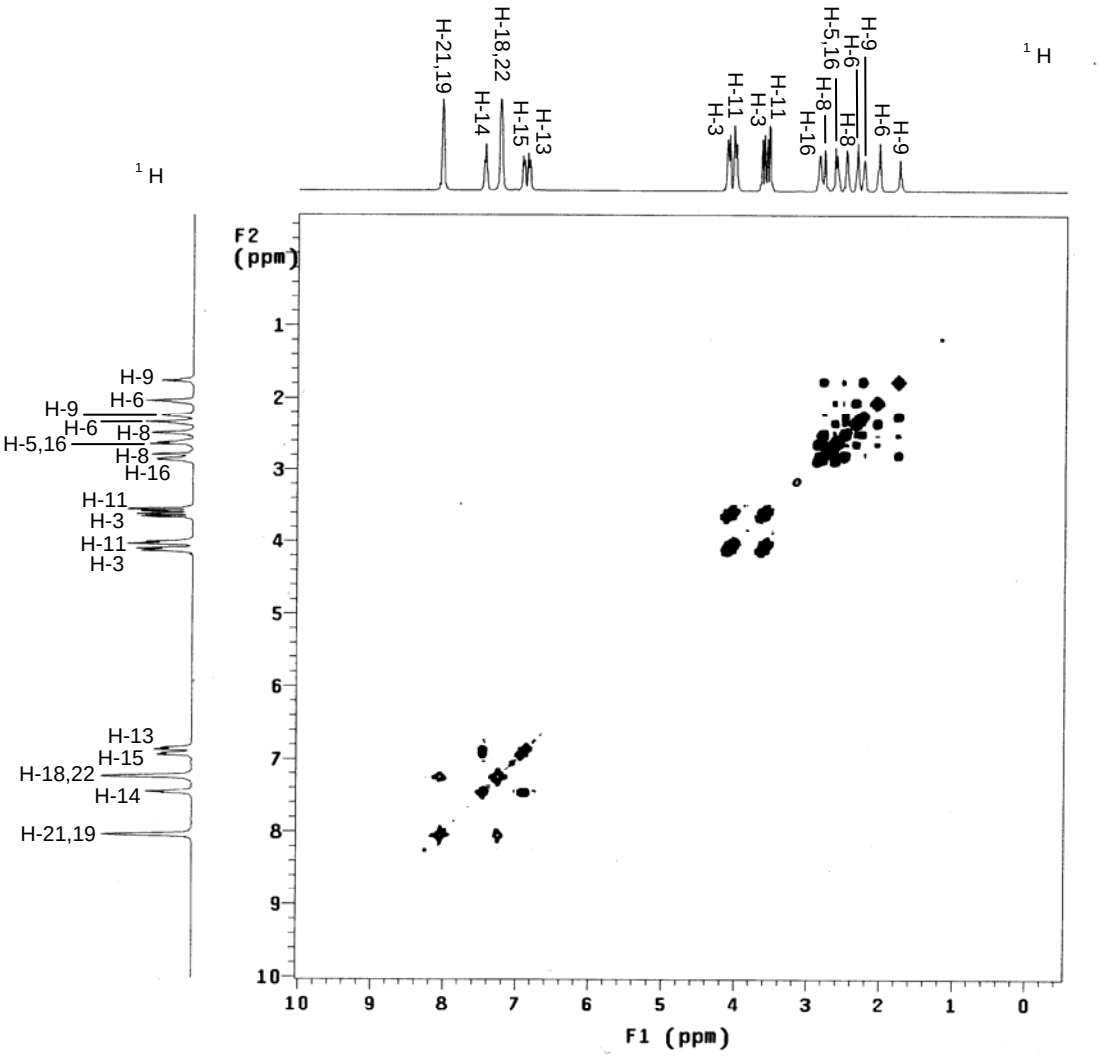

Figure S1. ^{1}H-^{1}H COSY experiment

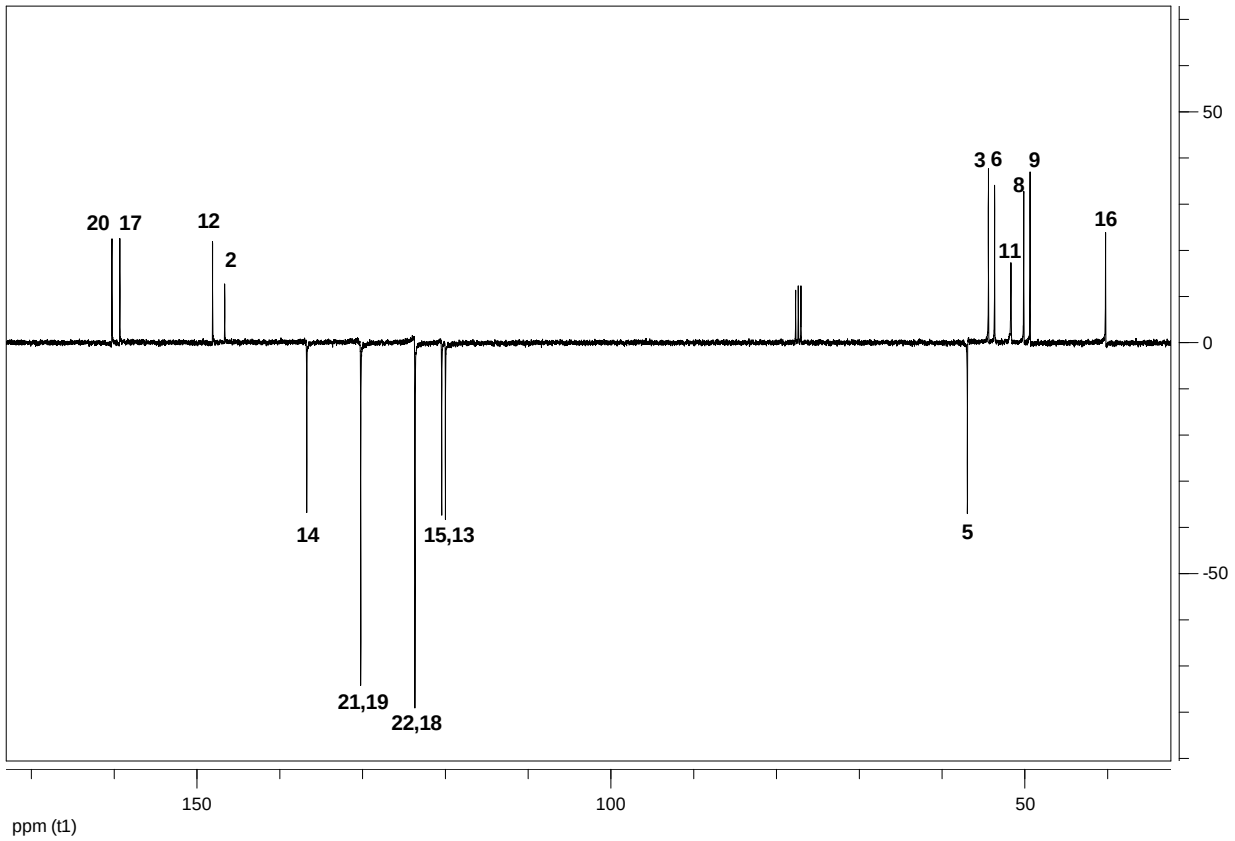

Figure S2. ^{13}C APT NMR spectrum of nitrobenzyl pyclen.

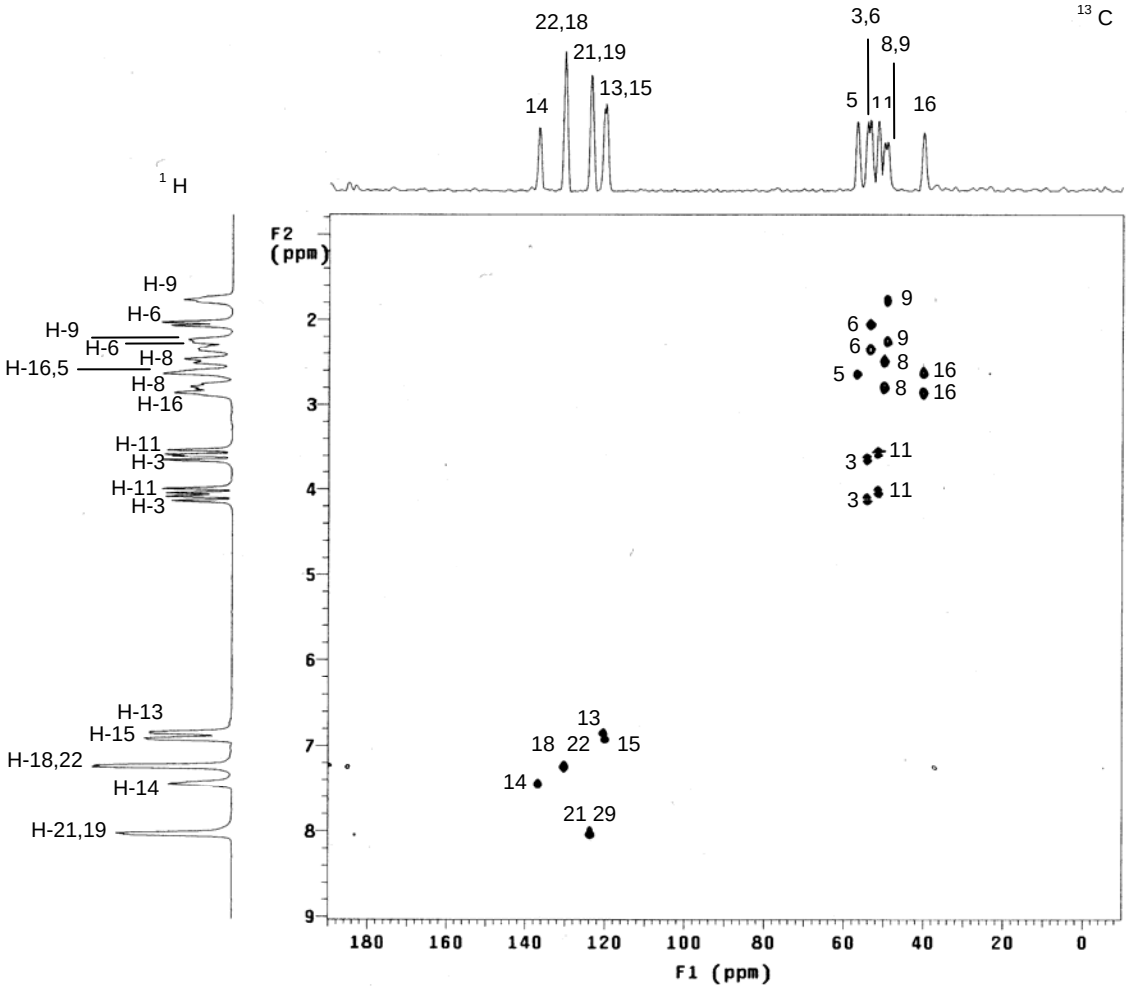

Figure S3. ^{13}C-^{1}H HMQC spectrum of nitrobenzyl pyclen.

Equations used for the formation kinetics data fitting.

The relation of conditional equilibrium constant ($K_{cond}^{Ln(H_2L)}$) and $K_{therm}^{Ln(H_2L)}$ can be obtained from the following equations (where H_2L is the diprotonated form of the ligand NO_2-Bn-PCTA):

$$K_{therm}^{Ln(H_2L)} = \frac{[Ln(H_2L)^{2+}]}{[Ln^{3+}][H_2L^-]} \qquad \text{(S1)}$$

Since we assumed that the rate determining step is the deprotonation and rearrangement of the diprotonated intermediate, the rate of this first-order process can be expressed as in eqn. (S2):

$$\frac{d[LnL]_t}{dt} = k_{obs}[L]_0 = k_r[Ln(H_2L)^-] \qquad \text{(S2)}$$

The total concentration of the ligand can be obtained by summarizing the concentration of the complexed and uncomplexed forms of ligand:

$$[L]_0 = [Ln(H_2L)^-] + [L^{3-}]_{free} \qquad \text{(S3)}$$

The concentration of uncomplexed ligand can be derived by summarizing the concentrations of all ligand species:

$$[L^{3-}]_{free} = [H_5L^{2+}] + [H_4L^-] + [H_3L] + [H_2L^-] + [HL^{2-}] + [L^{3-}] \qquad \text{(S4)}$$

Eqn. S4 can be rewritten using the protonation constants of the ligand:

$$[L^{3-}]_{free} = [H_2L^-](K_1^H K_2^H [H^+]^2 + K_2^H [H^+] + 1 + \frac{1}{K_3^H [H^+]} + \frac{1}{K_3^H K_4^H [H^+]^2} + \frac{1}{K_3^H K_4^H K_5^H [H^+]^3}) \quad \text{(S5)}$$

The term in parenthesis is the α_{H_2L} according to eqn. S6:

$$\alpha_{H_2L} = \frac{K_1^H K_2^H [H^+]^2}{1 + K_1^H [H^+] + K_1^H K_2^H [H^+]^2 + K_1^H K_2^H K_3^H [H^+]^3 + K_1^H K_2^H K_3^H K_4^H [H^+]^4 + K_1^H K_2^H K_3^H K_4^H K_5^H [H^+]^5} \quad \text{(S6)}$$

Thus, $[L^{3-}]_{free}$ can be expressed with α_{H2L} as:

$$[L^{3-}]_{free} = [H_2L^-]\alpha_{H_2L} \quad \text{(S7)}$$

The conditional stability constant ($K_{cond}^{Ln(H_2L)^{2+}}$) of the intermediates are related to the thermodynamics stability constant ($K_{therm}^{Ln(H_2L)^{2+}}$) of the intermediate by the following equation:

$$K_{therm}^{Ln(H_2L)^{2+}} = K_{cond}^{Ln(H_2L)^{2+}} \alpha_{H_2L} \quad \text{(S8)}$$

Finally, from equations S1, S2, S7 and. S8, the final equation used for fittings (eqn. 4) can be derived.

Formation rate constants

Table S1. The rate constant characterizing the rearrangement of the intermediates to the final products in formation reactions of Ce(NO_2-Bn-PCTA), Eu(NO_2-Bn-PCTA) and Yb(NO_2-Bn-PCTA) complexes (I=1.0 M KCl, t=25 ^{o}C).

$[OH]^- \times 10^9$ (M)	$Ce(H_2L)^-$	$Eu(H_2L)^-$	$Yb(H_2L)^-$	$[OH]^- \times 10^9$ (M)	$Yb(H_2PCTA)$
0.1216	-	0.01666	0.07112	0.05559	0.05559
0.2113	0.02119	0.02951	0.1142	0.08222	0.08222
0.4121	0.04126	0.06016	0.2403	0.2265	0.2265
1.059	0.1163	0.1591	0.6106	0.4416	0.4416
2.113	0.2112	0.3069	1.202	0.5689	0.5689
3.758	0.3880	0.5702	2.150	1.059	1.059
6.998	0.6621	1.018	-	2.065	2.065

Observed k_p values

Table S2. Observed k_p values for dissociation of Ce(NO_2-Bn-PCTA), Eu(NO_2-Bn-PCTA) and Yb(NO_2-Bn-PCTA) complexes (I=1.0 M KCl, t=25 ^{o}C).

$[H]^+$ (M)	Ce(PCTA) $\times 10^4$ (s^{-1})	Eu(PCTA) $\times 10^4$ (s^{-1})	Yb(PCTA) $\times 10^4$ (s^{-1})
0.247	0.4611	0.4634	0.6647
0.495	0.6181	0.9854	1.243
0.743	0.8038	1.654	2.038
0.990	0.8889	2.277	2.884
1.238	0.9888	3.093	3.511
1.503	1.127	4.066	4.311
1.750	1.215	4.816	4.853
1.998	1.318	5.519	5.403

Bioconjugate Chemistry 20th Anniversary

Subscriber access provided by SHEMYAKIN-OVCHINNIKOV INST

Article

Influence of Streptavidin on the Absorption and Fluorescence Properties of Cyanine Dyes

Franziska Luschtinetz, Carsten Dosche, and Michael U. Kumke

Bioconjugate Chem., **2009**, 20 (3), 576-582• DOI: 10.1021/bc800497v • Publication Date (Web): 18 February 2009

Downloaded from http://pubs.acs.org on May 8, 2009

More About This Article

Additional resources and features associated with this article are available within the HTML version:

- Supporting Information
- Access to high resolution figures
- Links to articles and content related to this article
- Copyright permission to reproduce figures and/or text from this article

View the Full Text HTML

ACS Publications
High quality. High impact.

Bioconjugate Chemistry is published by the American Chemical Society. 1155 Sixteenth Street N.W., Washington, DC 20036

Influence of Streptavidin on the Absorption and Fluorescence Properties of Cyanine Dyes

Franziska Luschtinetz, Carsten Dosche,* and Michael U. Kumke

Institute of Chemistry, University of Potsdam, Karl-Liebknecht-Str. 24−25, 14476 Potsdam-Golm, Germany. Received November 17, 2008; Revised Manuscript Received January 22, 2009

Cyanine dyes have become widely used fluorescence labels in clinical and biological chemistry. In particular, cyanine dyes with excitation wavelengths $\lambda_{ex} > 600$ nm are often used in biological applications. However, aggregation behavior and matrix effects on cyanine fluorescence are not fully understood yet and interfere with the data interpretation. In this study, we analyzed the spectroscopic characteristics of a model system consisting of the biotinylated cyanine dyes DY-635 and DY-647 and their streptavidin conjugates. On the basis of the spectroscopic data, the interaction processes between cyanine dye molecules and proteins are discussed. Binding to streptavidin had a significant influence on both fluorescence and anisotropy decays of the cyanine dyes investigated. In particular, the fluorescence anisotropy was significantly altered, making it a promising detection parameter for bioanalytical applications in connection with the cyanine dyes used in the present study. In order to evaluate the time-resolved anisotropy, the introduction of a sophisticated kinetic model was required to describe the contributions from different fluorescing species properly. The rotational motion of streptavidin-bound dyes was analyzed using the associated anisotropy model, which allowed discrimination between contributions from different microenvironments. The anisotropy decay times increased by a factor of up to 20 due to protein binding.

INTRODUCTION

In life sciences, medicine, and clinical diagnostics, fluorescence-based analytical techniques, such as fluorescence immuno analysis (FIA) or fluorescence lifetime imaging microscopy (FLIM), have proven to be most versatile for qualitative and quantitative analysis as well as for basic research. For using fluorescent labels in biological samples, several drawbacks have to be overcome, e.g., (i) the autofluorescence of the sample, (ii) cell damage due to irradiation (by laser light), (iii) the often limited penetration depth of excitation light, and (iv) problems arising from the fluorescence probes such as quenching phenomena or low solubility. Additional important properties needed especially for single molecule detection applications are very high photostability and high fluorescence quantum yield.

By using red- and NIR-absorbing dyes, the autofluorescence of the sample and problems arising from scattered light can be greatly reduced. Because of excitation wavelength $\lambda_{ex} > 600$ nm, the risk of cell damage is reduced and indicates such dyes to be especially suited as fluorescence probes in biological systems. Due to the high fluorescence efficiency, the good photostability, and the high potential to design tailor-made fluorescence probes covering a wide spectral range in absorption and fluorescence, cyanine dyes are highly attractive as fluorescence probes for bioanalytical applications such as cytometry or heterogeneous and homogeneous FIA. However, problem arising from low solubility, self-quenching, and self-aggregation have to be overcome.

Generally, cyanine dyes are based on two heteroarenes coupled by a polymethine chain which determines the spectral properties of the particular cyanine dye. Problems due to low solubility, self-quenching, and self-aggregation can be reduced by the introduction of functional groups like sulfonic acid groups or by applying only very low concentrations (*1*−*4*). Also, the addition of detergents such as Tween20 has been reported to increase the solubility of the cyanine dyes in aqueous solution (*5*). However, the effect of detergents on the fluorescence properties of probes such as cyanine dyes has to be evaluated from case to case.

By implementing reactive groups, the cyanine dyes can be covalently labeled, e.g., to biotin. Particularly, biotinylation of fluorescence probes is an often used approach for detecting and analyzing interaction processes of biomolecules. The biotin−streptavidin binding is widely used for biological sensors since the biotin−streptavidin system is a well-characterized model system for biological binding. Streptavidin is a 52.8 kDa tetrameric protein and binds four biotins per molecule with high affinity ($K_D = 10^{-13}$ M). The neutral isoelectric point of the non-glycosylated streptavidin leads to a high specificity of this binding (*6*). However, binding of biotinylated fluorescence markers to proteins like streptavidin might alter the fluorescence properties of the probe. The frequently used fluorescence probe ATTO 655 was reported to be quenched by the aromatic amino acids tryptophan and tyrosine (*7*). Furthermore, the interaction with neighboring binding sites of proteins can block them from binding another biotinylated probe molecule (*4*). In addition, dye−dye interactions can occur after binding to biological samples. In DNA-bound cyanine dyes, the formation of dimers and H-aggregates was described (*8*). It is also known that the presence of liposomes can lead to dimerization of fluorophores such as cyanine dyes (*9*). Depending on the layout of the bioanalytical application, such alterations in the fluorescence properties of the probe represent a large benefit or drawback (e.g., in a homogeneous FIA, the binding is monitored due to the change of the fluorescence; on the other side in a heterogeneous FIA such change might render the fluorescence probe useless for the application). Therefore, for using fluorescence probes such as cyanine dyes in tailor-made biological applications and for further improved fluorescence probe design, a sound understanding of fundamental molecular interactions among probe molecules, possible matrix components, and proteins (e.g., aggregation effects) is essential.

* dosche@chem.uni-potsdam.de.

10.1021/bc800497v CCC: $40.75 © 2009 American Chemical Society
Published on Web 02/18/2009

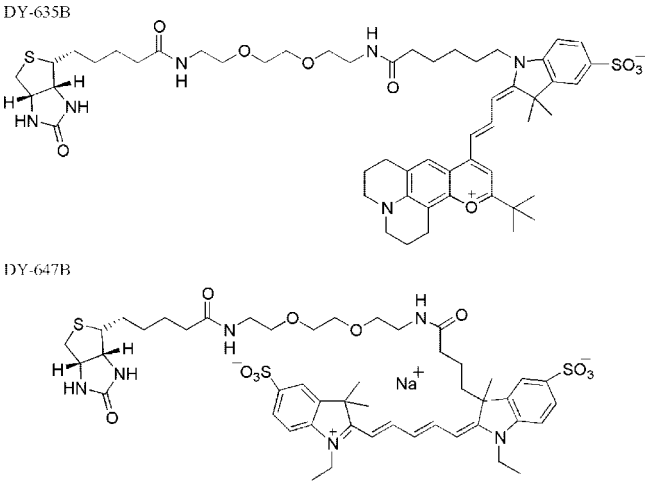

Figure 1. Molecular structures of biotinylated cyanine dyes (DY-635B, DY-647B) used in this study.

In the present study, two fluorescence probes of the cyanine dye class were investigated. DY-635 and DY-647, their biotinylated analogues (DY-635B, DY-647B) (see Figure 1), and complexes with streptavidin were characterized in steady-state and time-resolved fluorescence experiments. In particular, the binding of the biotinylated compounds (DY-635B, DY-647B) to streptavidin was analyzed in detail using steady-state and time-resolved anisotropy. To describe the rotational dynamics of the biotinylated dyes and their corresponding complexes with streptavidin, a global analysis of the time-dependent anisotropy was performed and the rotational correlation times ϕ_i were determined.

EXPERIMENTAL PROCEDURES

Materials. The dyes DY-635, DY-647 (as carboxylic acid), and the corresponding biotin conjugates (DY-635B, DY-647B) (Figure 1) were obtained from Dyomics (Jena, Germany) (CAS Registry Numbers: 375396-02-4 (DY-635), 709668-85-9 (DY-647)). For biotin−streptavidin studies, purified streptavidin was purchased from Promega (Madison, WI).

Stationary Fluorescence and Extinction Measurements. Absorption and fluorescence studies were carried out in a 0.1 M PBS buffer solution (pH 7.4 and $T = 298$ K). To avoid inner filter effects, the maximum absorbance was kept below 0.1 for fluorescence measurements. For low-temperature measurements, a nitrogen-cooled cryostat equipped with an external temperature control (Optistat DN1704, ITC4; both Oxford Instruments, Wiesbaden, Germany) was used. Absorption spectra were recorded in the range 400 nm $< \lambda_{abs} <$ 800 nm using a Cary 500 UV−vis−NIR spectrometer (Varian, Darmstadt, Germany). The extinction coefficients for the unconjugated dyes (DY-635, DY-647) were provided by the product data sheet of the manufacturer.

A Fluoromax-3 spectrofluorometer (Horiba Jobin Yvon, Munich) was used to measure the steady-state fluorescence and anisotropy spectra. For steady-state fluorescence measurements, a spectral bandwidth of $\Delta\lambda = 1.5$ nm in the excitation and emission channel was set, and for fluorescence anisotropy measurements, $\Delta\lambda = 4$ nm was applied. All emission spectra were background-corrected. In the anisotropy measurements, the sample was excited with vertically (I_v) and horizontally (I_h) polarized light. The steady-state anisotropy r was determined according to

$$r = \frac{I_{vv} - I_{vh}G}{I_{vv} + 2I_{vh}G} \tag{1}$$

G is the instrumental correction factor

$$G = \frac{I_{hv}}{I_{hh}} \tag{2}$$

The subscripts v and h refer to the vertical and horizontal orientations of the polarizers in the excitation and emission beam.

Fluorescence Quantum Efficiency. The fluorescence quantum efficiencies were determined using an integrating sphere setup (PL Quantum Yield Measurement System C9920−02, Hamamatsu). Samples with concentrations of 5×10^{-7} M were excited at $\lambda_{ex} = 610$ nm.

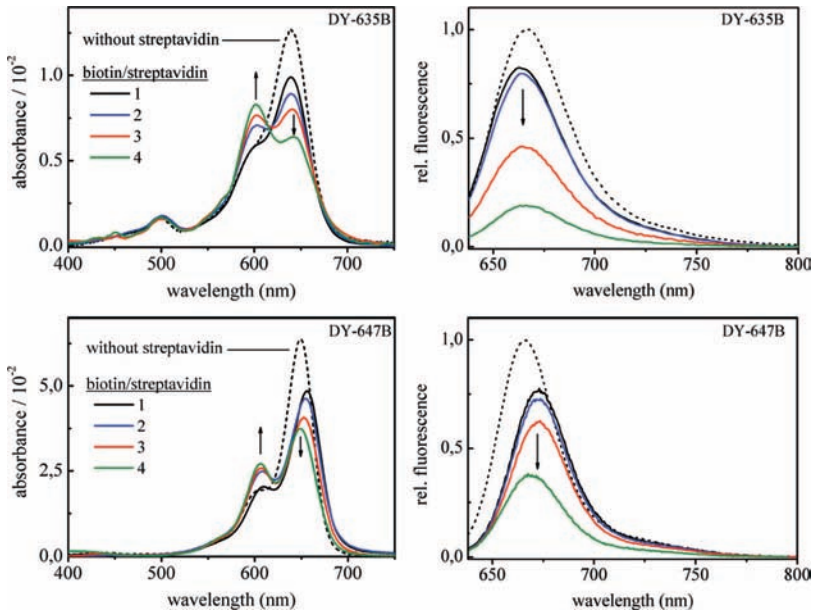

Figure 2. Normalized absorption and fluorescence spectra ($\lambda_{ex} = 620$ nm) of DY-635B ($c = 9 \times 10^{-8}$ M, top) and DY-647B ($c = 2.9 \times 10^{-7}$ M, bottom). Free dyes in absence of streptavidin (dashed lines) and streptavidin-bound biotinylated dyes (solid lines) at different biotin/streptavidin ratios (black, 1:1; blue, 2:1; red, 3:1; green, 4:1) in PBS buffer (pH 7.4).

Fluorescence Decay Measurements. For the measurements of the fluorescence decays, a FL920 fluorescence lifetime spectrophotometer (Edinburgh Instruments, Edinburgh, UK) operated in the time-correlated single photon counting (TCSPC) mode was used. To avoid polarization effects, fluorescence decays were recorded under magic angle conditions (54.8°). With respect to the fluorescence anisotropy decay measurements, the instrument was set up in an L-geometry configuration (*10*). A pulsed laser diode (Picoquant, Berlin, Germany) ($\lambda_{ex} = 635$ nm, rep. rate 2.5 MHz, pulse width (FWHM) 90 ps) was attached as the excitation source. In all time-resolved emission measurements, the excitation beam was vertically polarized. A multichannel plate (Europhoton GmbH, Berlin, Germany) with a Glenn-Thomson polarizer in front of the emission monochromator was used for signal collection.

The experimental data were analyzed using least-squares deconvolution, and the goodness of the fit was judged on the reduced χ_R^2-values. The fluorescence decays were fitted according to a single- or double-exponential decay model

$$I(t) = \sum_{i=1}^{n} \alpha_i \exp\left(-\frac{t}{\tau_i}\right) + B \quad \text{with } i = 1...2 \tag{3}$$

The α_i is the amplitude of the component i with the corresponding fluorescence decay times τ_i. The parameter B accounts for the background. The fractional amounts A_i of the fluorescence decay times are calculated according to

$$A_i = \frac{\alpha_i \tau_i}{\sum_{j=1}^{2} \alpha_j \tau_j} \quad \text{with } i, j = 1...2 \tag{4}$$

Anisotropy Decay Measurements r(t). To obtain anisotropy decays, the values $r(t)$ were determined by measuring the fluorescence decay with the emission polarizer set in a vertical ($I_{vv}(t)$) and horizontal ($I_{vh}(t)$) position, respectively. From the experimental data, $r(t)$ was calculated according to eq 1. The G-factor was obtained by fitting the synthesized fluorescence decay curve $I_{vv}(t) + 2GI_{vh}(t)$ and is described in detail elsewhere (*11*).

The fit for the anisotropy $r(t)$ was weighted according eq 5

$$w_i = \frac{3[I_{vv}(t_i) + 2I_{vh}(t_i)]}{2 + r(t_i) + 5[r(t_i)]^2 - 2[r(t_i)]^3} \quad \text{with } i = 1...2 \tag{5}$$

The rotational diffusion of molecules in a homogeneous environment can be described by the model of general ellipsoids (*8*). In that case, an exponential decay of the anisotropy $r(t)$ can be assumed. As the fundamental anisotropy r_0 at the time $t = 0$ is known from low-temperature steady-state fluorescence anisotropy measurements, the anisotropy decay $r(t)$ can be analyzed using eq 6

$$r(t) = r_0 \sum_j \exp\left(-\frac{t}{\varphi_j}\right) \quad \text{with } j \leq 5 \tag{6}$$

ϕ_j are the rotational correlation times for rotations around the different rotational axes of the molecule. In this simple case, the fluorescence decay time τ_i does not influence the anisotropy decay.

In contrast to a homogeneous distribution of fluorophores, often the anisotropy decay of a heterogeneous environment cannot be described by a simple exponential approach (*12*).

Due to the binding of the fluorescent probes to a protein like streptavidin, a second microenvironment for the fluorophore can subsequently lead to a change in the fluorescence decay time τ_i as well as in the rotational correlation time ϕ_j. For a mixture of free and streptavidin-bound fluorescent probes, a more complex model to account for the observed anisotropy decay has to be used. In particular, the fluorescent decay time τ_i has to be properly considered in the data analysis. The concept of an "associated" anisotropy can be applied in order to account for the correlation of anisotropy and fluorescence decay (*12*−*16*). Assuming that each fluorescence decay time τ_i is directly associated with one rotational correlation time ϕ_j, the observed anisotropy decay $r(t)$ in the case of two microenvironments results in a complex decay and can be described by eq 7

$$r(t) = \frac{\sum_{i=1}^{2} \alpha_i \beta_i \left[-t\left\{\frac{1}{\tau_i} + \frac{1}{\varphi_i}\right\}\right]}{\sum_{i=1}^{2} \alpha_i \exp\left(-\frac{t}{\tau_i}\right)} \quad \text{with } i = 1...2 \tag{7}$$

Here, β_i are the pre-exponential factors of the anisotropy decay. It has to be stressed that in this model the anisotropy decay $r(t)$ is influenced by the fluorescence decay time τ_i of the fluorophores in each environment. In case τ_i is altered due to conjugation and it is correlated to one rotational correlation time, the anisotropy decay curve is found to be nonexponential. Only the special case of an identical fluorescent decay time in both microenvironments results in a biexponential decay of the anisotropy, and $r(t)$ would be independent of the fluorescence decay time τ_i.

The fluorescence and anisotropy decay data were evaluated in a global fitting approach with at least nine different biotin/streptavidin ratios. The values β_i were set as global parameters and kept constant, because no alteration in the fundamental anisotropy r_0 of the dyes due to the binding to streptavidin is expected.

In order to get a rough first approximation for the rotational correlation times, a spherical protein geometry was assumed and the Stokes−Einstein relation was used to estimate the rotation correlation time ϕ_i by means of the molar mass M and the hydration properties (ν, h) of the protein (*10*, *17*):

$$\varphi_i = \frac{\eta M}{RT}(\nu + h) \tag{8}$$

In eq 8, η represents the dynamic viscosity of the solvent and T the absolute temperature. For streptavidin assuming a molar mass of $M = 52.800$ g/mol (provided by the manufacturer), the expected rotational correlation time is around 18 ns (viscosity of water at 298 K: $\eta = 0.89$ cp, hydrodynamic properties (specific protein volume: $\nu = 0.23$ mL/g, hydration $h = 0.73$ mL/g) were taken from the literature (*10*)).

From the rotational correlation time of the free diffusing fluorophores, the theoretical stationary anisotropy r_{calc} was determined according to the Perrin relation (*10*, *18*):

$$r_{calc} = r_0\left(\frac{1}{1 + \tau/\varphi}\right) \tag{9}$$

RESULTS AND DISCUSSION

Steady-State Absorbance and Fluorescence Measurements. The comparison of the parent and biotinylated cyanine dyes showed that the photophysical properties of the dyes were not altered due to biotinylation. However, binding to streptavidin resulted in significant changes in the steady-state photophysical characteristics of DY-635B and DY-647B (see Figure 2). The biotin/streptavidin ratio has a strong effect on the absorption and fluorescence intensity as well as the spectral position of the corresponding maxima. Compared to the absorbance of the free biotinylated dyes, the complex formation of 1:1 complexes

Table 1. Spectroscopic Characteristics[a] of Free Biotinylated Dyes and in the Presence of a 5-Fold Excess of Streptavidin in 0.1 M PBS buffer pH 7.4[b]

	Spectroscopic Data in Absence/Presence of Streptavidin (1:1 Complexes)						
dye	λ_{abs} (nm)	λ_{em} (nm)	τ_1/ns	A_1	τ_2/ns	A_2	Φ_F
DY-635B	640/640	668/663	0.9/0.9	1.00/0.11	-/2.2	-/0.89	0.09/-
DY-647B	649/655	666/672	1.1/1.1	1.00/0.24	-/1.7	-/0.76	0.25/-

[a] (Longest wavelength absorption maxima λ_{abs}, emission maxima λ_{em}, fluorescence decay times τ_i (excitation at $\lambda_{Ex} = 635$ nm), fractional amounts A_i of the fluorescence decay time, quantum yield Φ_F). [b] Quantum yields Φ_F of biotinylated dyes in PBS buffer are given for free biotinylated dyes.

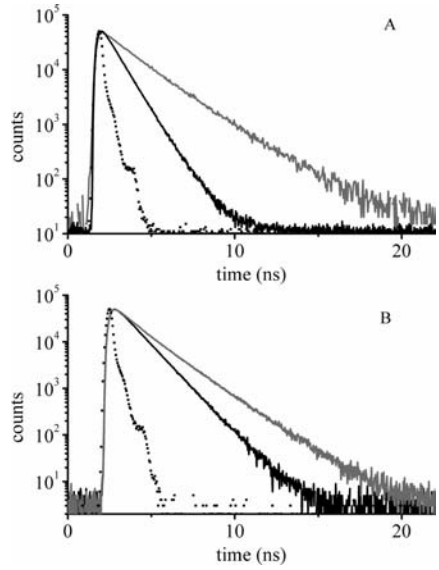

Figure 3. Fluorescence decay curves of DY-635B (A) and DY-647B (B) in PBS buffer in the absence (black line) and presence (gray line) of streptavidin (biotin/streptavidin ratio 1:1). The emission was detected at $\lambda_{em} = 670$ nm with excitation at $\lambda_{ex} = 635$ nm. Instrument response functions are shown as a dotted line.

results in a decrease of 20%. The absorption and fluorescence maxima of DY-647B are red-shifted by 6 nm upon binding to streptavidin (Figure 2 - bottom, Table 1). For DY-635B, the fluorescence maximum was blue-shifted (5 nm), while no influence of streptavidin on the absorption maximum was observed in 1:1 complexes (see Figure 2 - top, Table 1).

At higher ratios, these trends became more pronounced (see Figure 2). Moreover, at higher biotin/streptavidin ratios an enhancement of the absorption band at $\lambda \sim 600$ nm was found, which was accompanied by a decrease of the main absorption band of the dyes (see Figure 2). Such spectral change was observed for other cyanine dyes conjugated to biomolecules before and has been attributed to dye−dye interactions (e.g., dimerization) (*15, 19*−*24*).

In order to minimize dye−dye interactions, such as association in following time-resolved experiments, an excess of streptavidin to the solution of the biotinylated dyes was added. Under such conditions, it can be assumed that predominantly 1:1 biotin−streptavidin complexes are formed (*5, 19*). Consequently, it is tempting to attribute the observed enhancement of the absorption band at $\lambda \sim 600$ nm in 1:1 complexes to an (electronic) interaction of the dyes and streptavidin.

Fluorescence Decay Times. In the absence of streptavidin, DY-635B and DY-647B exhibit monoexponential fluorescence decays (in PBS buffer, pH 7.4). The fluorescence of both dyes decays more slowly after binding to streptavidin (Figure 3, Table 1), and for the analysis, a second decay component has to be

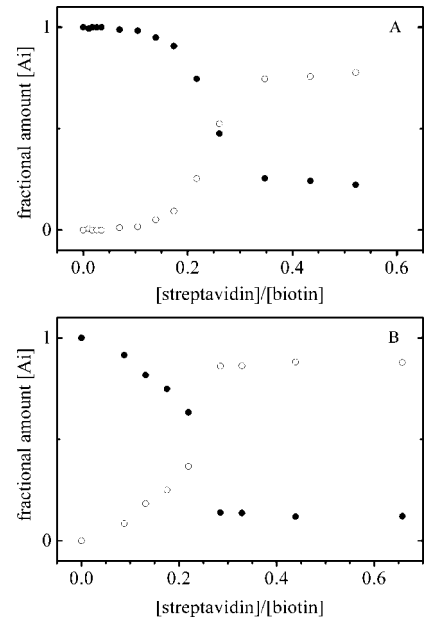

Figure 4. Fractional amounts [A_i] of the fluorescence decay times at different streptavidin/biotin ratios in PBS buffer pH 7.4. (A) DY-647B: $\tau_1 = 1.1$ ns (•) and $\tau_2 = 1.7$ ns (○) (c(DY-647B) = 2.3×10^{-7} M) and (B) DY-635B: $\tau_1 = 0.9$ ns (•) and $\tau_2 = 2.2$ ns (○) (c(DY-635B)= $1.3 \cdot \times 10^{-7}$ M).

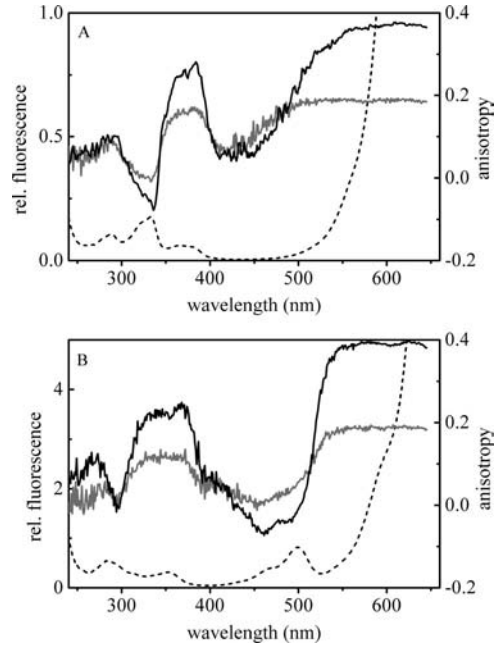

Figure 5. Anisotropy measurements of (A) DY-635B and (B) DY-647B: Stationary fluorescence excitation (dashed line) and anisotropy spectra in PBS buffer pH 7.4 at 298 K (gray line). Anisotropy spectra in glycerol at 223 K (black line).

introduced in order to properly fit the experimental data. The appearance of a second fluorescence decay time for DY-647B and DY-635B in the presence of streptavidin is attributed to the localization of these dyes in two different microenvironments. The longer fluorescence decay time τ_2 points to a more rigid conformation of the dyes due to binding to streptavidin, e.g., the formation of hydrogen bonds between the dyes and streptavidin (see also the changes in the absorption spectrum of the dyes); e.g., due to the reduced flexibility of the dye, the internal conversion rate is decreased (*21*).

The allocation between the two microenvironments is displayed by the fractional amount A_i of the corresponding

Table 2. Fundamental Anisotropy r_0 (at 223 K in glycerol), Measured Steady-State Anisotropy r, and Estimated Value r_{calc} of Free DY-635B and DY-647B at Room Temperature in PBS Buffer (pH 7.4)[a]

dye	r_0	r	r_{calc}	τ_1/ns	τ_2/ns	ϕ_1/ns	ϕ_2/ns
DY-635	0.39	0.19	0.18	0.9	2.2	0.8	17.8
DY-647	0.37	0.18	0.16	1.1	1.7	0.8	17.4

[a] Fluorescence decay times τ_i (with excitation at $\lambda_{ex} = 635$ nm) and rotational correlation times ϕ_i of the biotinylated dyes (τ_1, ϕ_1) and their biotin−streptavidin complexes (τ_2, ϕ_2).

fluorescence decay times τ_i (Figure 4). For both DY-635B and DY-647B, at low concentrations of streptavidin the fractional amount A_2 remains low due to the large amount of unbound dye molecules in solution. Starting at a ratio of about 0.1, a steady increase of the fraction A_2 was found. At a streptavidin/biotin ratio of 0.25, an inflection point can be seen. Above this ratio, all biotinylated dyes are bound to streptavidin resulting in constant values of A_2 of 89% for DY-635B and of 76% for DY-647B, respectively. The remaining amount 11% (24%) of the fluorescence decay time τ_1 can be attributed to a small amount of non-biotinylated dyes in solution or to the presence of different (micro)environments of the biotinylated dyes when bound to streptavidin: (i) closely bound (e.g., via H-bonds, etc.) to the streptavidin, which would also be supported by the changes in the absorption spectra and (ii) a relatively uninfluenced situation, e.g., in which the dye is free to rotate around its linker in solution. From literature (*23*), it is known that the structural similar cyanine dye Cy5 shows two different fluorescent decay times after binding to streptavidin. The referred fluorescent states are converted by light.

Stationary and Time-Resolved Fluorescence Anisotropy Measurements. In order to further characterize the binding of the biotinylated dyes by streptavidin, the rotational correlation times ϕ_i in the absence and presence of streptavidin were determined. Excitation anisotropy measurements of DY-635B and DY-647B in glycerol at 223 K were used to determine the fundamental anisotropy r_0, since the rotation of the dyes is prevented at this temperature (*10*). From the anisotropy spectra (Figure 5), it becomes obvious that only one electronic transition is observed in the spectral range 520 nm $< \lambda_{ex} <$ 650 nm, which can be attributed to the S_0-S_1 transition. In the spectral region of the S_0-S_1 transition, the anisotropy value was determined close to the theoretical limit of 0.4 indicating that the absorption and emission dipole moments are nearly parallel (see also Table 2). In the shorter wavelength region, high electronic transitions (S_0-S_n transitions) are observed as well. In buffer solution at room temperature, anisotropy values of 0.18 (0.19) were found for DY-647B (DY-635B) in the spectral range of the S_0-S_1 transition. The anisotropy data of DY-647B and DY-635B are consistent with data reported for other cyanine dyes (*25*−*28*)

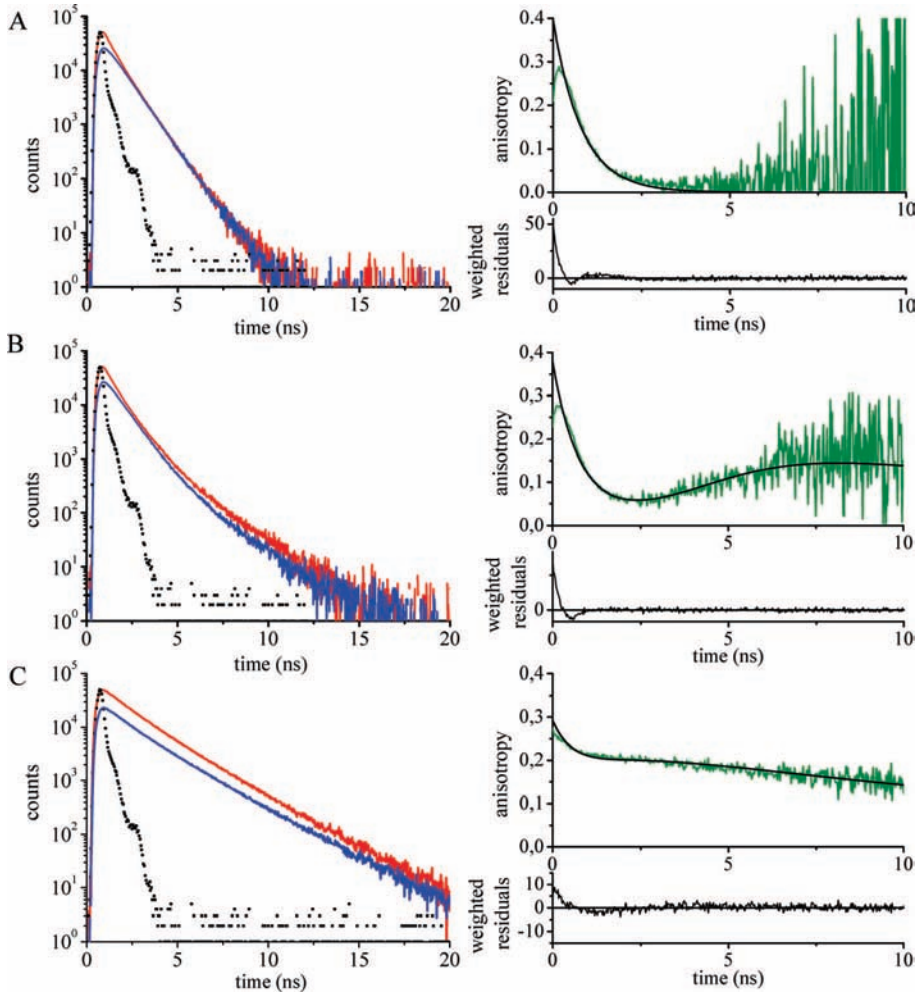

Figure 6. Time-resolved anisotropy measurements for DY-635B at different streptavidin/biotin ratios in PBS buffer pH 7.4 (c(DY-635) = 1.3 × 10^{-7} M). (A) DY-635B in the absence of streptavidin. (B) Streptavidin/biotin: 0.1. (C) Streptavidin/biotin: 1. Left side: polarized fluorescence decay curves (*G*-factor corrected): $I_{vv}(t)$ (red line) and ($I_{vh}(t)$ (blue line). Emission at $\lambda_{em} = 670$ nm, excitation at $\lambda_{ex} = 635$ nm. Instrument response functions are shown (dotted line). Right side: anisotropy decay data (green lines) and the corresponding global fit curve (black line).

For DY-635B the polarized fluorescence decay curves $I_{vv}(t)$ and $I_{vh}(t)$ and the corresponding anisotropy decay data $r(t)$ at different streptavidin/biotin ratios are shown in Figure 6.

In the absence of streptavidin (Figure 6A), the anisotropy of DY-635B decays monoexponentially with a rotational correlation time ϕ of 0.8 ns. By means of the fluorescence decay time τ (0.9 ns) and the fundamental anisotropy r_0, a theoretical value of the steady-state anisotropy r_{calc} at 298 K of 0.18 was obtained with the Perrin equation (eq 9). That value is in good agreement with the stationary fluorescence anisotropy value of 0.19. Similar results were obtained for DY-647B (Table 2).

After addition of a small amount of streptavidin to a solution of DY-635B (10 times excess of biotinylated dye), the anisotropy decay curves show a significant change (Figure 6B, right side). At low streptavidin concentrations (streptavidin/biotin <0.4; see also Figure 4A,B), not all biotinylated dyes are tightly bound to streptavidin (e.g., via H-bonds), and subsequently, the fluorophores are located in two different environments, each with a characteristic fluorescence decay time and rotational correlation time.

At short times, the anisotropy $r(t)$ initially decays with rotational correlation time ϕ_1 very similar to that of biotinylated dyes in streptavidin-free solutions. This could be either due to the presence of nonbound biotinylated dye molecules or to the fact that a fraction of the dye molecules are free to rotate around the linker chain, which would make them appear as "free" molecules. However, at times above 2 ns (after the excitation pulse, see Figure 6B) an increase in anisotropy is found. This rise of the anisotropy at longer times can be associated to streptavidin-bound dyes, which are expected to show a much longer rotational correlation time ϕ_2 due to the increased overall rotational volume (e.g., see also eq 8). To analyze the nonexponential anisotropy decay, the use of an associated model was applied (*11*). Using a global fitting approach, the anisotropy as well as the fluorescence decay curves were fitted simultaneously with the fluorescence decay times τ_1 and τ_2, as well as the rotation correlation times ϕ_1 and ϕ_2 set as global parameters for all streptavidin/biotin ratios. The corresponding global fit curves for the anisotropy decay at streptavidin/biotin ratios of 0, 0.1, and 1 are displayed in Figure 6 (right side). Figure 6C presents the polarized fluorescence and anisotropy decay curves for a streptavidin/biotin ratio of 1. In that case, it is expected that all biotinylated dyes are bound to streptavidin, and consequently, the anisotropy decays monoexponentially with a long rotational correlation time ϕ_2 of about 17 ns. In the anisotropy curve shown in Figure 6C, the remaining fast decay at short times can be attributed to remaining unbound dyes in solution.

CONCLUSION

In our study, two biotinylated fluorophores of the cyanine family and their binding to streptavidin were characterized by time-resolved emission spectroscopy.

Due the sulfonation of the indolene rings of indocarbocyanine dyes, the hydrophilicity of the dyes was increased, and subsequently, it was expected that dimerization in aqueous solution should be greatly reduced. It could be shown that in the case of the biotinylated dyes upon binding to streptavidin spectral changes are induced, which are attributed to dye−protein interactions. Depending on the molecular topography of the dye molecules, the interactions can be strong, which is found as a significant change in the absorptivity of the samples and in an overall alteration of the absorption and/or emission bands. Moreover, for the investigated polymethine dyes both the fluorescence decay times and the anisotropy decays are strongly affected by the complexation to streptavidin. On the basis of the molecular structures (Figure 1), it can be hypothesized that dye DY-635B (compared to DY-647B) is more rigid and hydrophobically judged. Therefore, a strong interaction, e.g., via H-bonding, with the protein can be assumed. This is reflected in the longer fluorescence decay time τ_2 and the corresponding amplitude A_2. However, for dye DY-647B a significant change of the absorption band intensities was observed, which points to a stronger electronic coupling to the protein.

Both the stationary and time-resolved measurements show that four molecules of biotinylated dyes are bound to one streptavidin tetramer. For both biotinylated dyes, the binding to streptavidin greatly changed the rotational motion of the dye molecules. Using an associated anisotropy decay model and global fitting in combination with the fluorescence decay time parameters, it is possible to attribute the upward curvature of time-dependent anisotropy curves in solutions to different microenvironments of the dye molecules. Upon binding, the rotational correlation times increased by a factor of about 20. Consequently, for the investigated dyes anisotropy-based detection schemes can be envisaged for future analytical applications, such as in homogeneous FIA or in fundamental research on the interaction processes between antigens and antibodies in single molecule detection studies. For the latter, but also for the design of improved tailor-made fluorescence probes, in particular, time-resolved fluorescence measurements in combination with anisotropy are valuable tools for an in-depth understanding of the underlying fundamental processes in dye−protein as well as protein−protein interactions.

ACKNOWLEDGMENT

This work was supported by the German Federal Department for Science and Education BMBF (IP 03/517). The authors wish to Dr. Frank Lehmann (Dyomics, Germany) for providing the dyes.

LITERATURE CITED

(1) Mujumdar, S. R., Mujumdar, R. B., Grant, C. M., and Waggoner, A. S. (1996) Cyanine-labeling reagents: sulfobenzindocyanine succinimidyl esters. *Bioconjugate Chem. 7*, 356–362.

(2) Briggs, M. S., Burns, D. D., Cooper, M. E., and Gregory, S. J. (2000) A pH sensitive fluorescent cyanine dye for biological applications. *Chem. Commun. 23*, 2323–2324.

(3) Mishra, A., Behera, R. K., Behera, K., Mishra, B. K., and Behera, G. B. (2000) Cyanines during the 1990s: A review. *Chem. Rev. 100*, 1973–2011.

(4) Panchuk-Voloshina, N., Haugland, R. P., Bishop-Stewart, J., Mahesh, K., Bhalgat, P. J. M., Mao, F., Leung, W., and Haughland, R. P. (1999) Alexa dyes, a series of new fluorescent dyes that yield exceptionally bright, photostable conjugates. *J. Histochem. Cytochem. 47*, 1179–1188.

(5) Buschmann, V., Weston, K. D., and Sauer, M. (2003) Spectroscopic study and evaluation of red-absorbing fluorescent dyes. *Bioconjugate Chem. 14*, 195–204.

(6) Green, N. M. (1966) Thermodynamics of the binding of biotin and some analogues by avidin. *Biochem. J. 101*, 774–780.

(7) Marmé, N., Knemeyer, J., Sauer, M., and Wolfrum, J. (2003) Inter- and intramolecular fluorescence quenching of organic dyes by tryptophan. *Bioconjugate Chem. 14*, 1133–1139.

(8) Randolph, J. B., and Waggoner, A. S. (1997) Stability, specificity and fluorescence brightness of multiply-labeled fluorescent DNA probes. *Nucleic Acids Res. 25*, 2923–2929.

(9) Chen, R. F., and Knutson, J. R. (1988) Mechanism of fluorescence concentration quenching of carboxyfluorescein in liposomes: energy transfer to nonfluorescent dimers. *Anal. Biochem. 172*, 61–77.

(10) Lakowicz, J. R. (2006) Fluorescence Anisotropy, In *Principles of fluorescence spectroscopy*, 3rd ed., pp 353−382, Kluwer Academic, Plenum Publishers, New York.

(11) O'Connor, D. V., and Phillips, D. (1984) Time Dependence of Fluorescence Anisotropy, In *Time-correlated single photon counting*, pp 252−283, Academic Press Harcourt Brace Jovanovich Publishers, London.

(12) Bialik, C. N., Wolf, B., Rachofsky, E. L., Ross, J. B. A., and Laws, W. R. (1998) Dynamics of biomolecules: assignment of local motions by fluorescence anisotropy decay. *Biophys. J. 75*, 2564–2573.

(13) Wahl, P. (1979) Analysis of anisotropy decays by a least square technique. *Biophys. Chem. 10*, 91–104.

(14) Brand, L., Knutson, J., Davenport, L., Beechem, J., Dale, R., Walbridge, D., and Kowalczyk, A. (1985) Time-resolved fluorescence spectroscopy: some applications of associative behaviour to studies of proteins and membranes, In *Spectroscopy and the dynamics of molecular biological systems*, pp 259−305, Academic Press, London.

(15) Guest, C. R., Hochstrasser, R. A., Dupuy, C. G., Allen, D. J., Benkovic, S. J., and Millar, D. P. (1991) Interaction of DNA with the Klenow fragment of DNA polymerase I studied by time-resolved fluorescence spectroscopy. *Biochemistry 30*, 8759–8770.

(16) Peng, K., Visser, A. J., van Hoek, A., Wolfs, C. J., Sanders, J. C., and Hemminga, M. A. (1990) Analysis of time-resolved fluorescence anisotropy in lipid-protein systems. I. Application to the lipid probe octadecyl rhodamine B in interaction with bacteriophage M13 coat protein incorporated in phospholipid bilayers. *Eur. Biophys. J. 18*, 277–283.

(17) van den Berg, P. A., van Hoek, A., and Visser, A. J. (2004) Evidence for a novel mechanism of time-resolved flavin fluorescence depolarization in glutathione reductase. *Biophys. J. 87*, 2577–2586.

(18) Feinstein, E., Deikus, G., Rusinova, E., Rachofsky, E. L., Ross, J. B. A., and Laws, W. R. (2003) Constrained analysis of fluorescence anisotropy decay: application to experimental protein dynamics. *Biophys. J. 84*, 599–611.

(19) Gruber, H. J., Hahn, C. D., Kada, G., Riener, C. K., Harms, G. S., Ahrer, W., Dax, T. G., and Knaus, H. (2000) Anomalous fluorescence enhancement of Cy3 and Cy3.5 versus anomalous fluorescence loss of Cy5 and Cy7 upon covalent linking to IgG and noncovalent binding to avidin. *Bioconjugate Chem. 11*, 696–704.

(20) Schobel, U., Egelhaaf, H. J., Brecht, A., Oelkrug, D., and Gauglitz, G. (1999) New donor-acceptor pair for fluorescent immunoassays by energy transfer. *Bioconjugate Chem. 10*, 1107–1114.

(21) Cooper, M., Ebner, A., Briggs, M., Burrows, M., Gardner, N., Richardson, R., and West, R. (2004) Cy3B: improving the performance of cyanine dyes. *J. Fluoresc. 14*, 145–150.

(22) Patonay, G., Kim, J. S., Kodagahally, R., and Strekowski, L. (2005) Spectroscopic study of a novel bis(heptamethine cyanine) dye and its interaction with human serum albumin. *Appl. Spectrosc. 59*, 682–690.

(23) Gregor, I., and Enderlein, J. (2007) Time-resolved methods in biophysics. 3. Fluorescence lifetime correlation spectroscopy. *Photochem. Photobiol. Sci. 6*, 13–18.

(24) Berlier, J. E., Rothe, A., Buller, G., Bradford, J., Gray, D. R., Filanoski, B. J., Telford, W. G., Yue, S., Liu, J., Cheung, C., Chang, W., Hirsch, J. D., Beechem, J. M., Haugland, R. P., and Haugland, R. P. (2003) Quantitative comparison of long-wavelength Alexa Fluor dyes to Cy dyes: fluorescence of the dyes and their bioconjugates. *J. Histochem. Cytochem. 51*, 1699–1712.

(25) Lepkowicz, R. S., Cirloganu, C. M., Przhonska, O. V., Hagan, D. J., Van Stryland, E. W., Bondar, M. V., Slominsky, Y. L., Kachkovski, A. D., and Mayboroda, E. I. (2004) Absorption anisotropy studies of polymethine dyes. *Chem. Phys. 306*, 171–183.

(26) Levitus, M., Negri, R. M., and Aramendia, P. F. (1995) Rotational relaxation of carbocyanines. comparative study with the isomerization dynamics. *J. Phys. Chem. 99*, 14231–14239.

(27) Aramendía, P. F., Negri, R. M., and San Román, E. (1994) Temperature dependence of fluorescence and photoisomerization in symmetric carbocyanines. influence on medium viscosity and molecular structure. *J. Phys. Chem. 98*, 3165–3173.

(28) Sanborn, M. E., Connolly, B. K., Gurunathan, K., and Levitus, M. (2007) Fluorescence properties and photophysics of the sulfoindocyanine Cy3 linked covalently to DNA. *J. Phys. Chem. B 111*, 11064–11074.

BC800497V

Subscriber access provided by SHEMYAKIN-OVCHINNIKOV INST

Article

Design, Synthesis, and Preliminary in Vitro and in Vivo Evaluation of *N*-(2-diethylaminoethyl)-4-[F]fluorobenzamide ([F]-DAFBA): A Novel Potential PET Probe to Image Melanoma Tumors

Sudha Garg, Kanchan Kothari, Shankar R. Thopate, Aniruddha K. Doke, and Pradeep K. Garg

Bioconjugate Chem., **2009**, 20 (3), 583-590• DOI: 10.1021/bc8005094 • Publication Date (Web): 17 February 2009

Downloaded from http://pubs.acs.org on May 8, 2009

More About This Article

Additional resources and features associated with this article are available within the HTML version:

- Supporting Information
- Access to high resolution figures
- Links to articles and content related to this article
- Copyright permission to reproduce figures and/or text from this article

View the Full Text HTML

ACS Publications
High quality. High impact.

Bioconjugate Chemistry is published by the American Chemical Society. 1155 Sixteenth Street N.W., Washington, DC 20036

Design, Synthesis, and Preliminary in Vitro and in Vivo Evaluation of *N*-(2-diethylaminoethyl)-4-[^{18}F]fluorobenzamide ([^{18}F]-DAFBA): A Novel Potential PET Probe to Image Melanoma Tumors

Sudha Garg, Kanchan Kothari, Shankar R. Thopate, Aniruddha K. Doke, and Pradeep K. Garg*

PET Center, Department of Radiological Sciences, Wake Forest University Medical Center, Winston Salem, North Carolina 27157. Received November 26, 2008; Revised Manuscript Received January 9, 2009

In order to develop a PET radiopharmaceutical to image malignant melanoma, we synthesized *N*-(2-diethylaminoethyl)-4-[^{18}F]fluorobenzamide ([^{18}F]-DAFBA). In vitro studies show a high uptake of [^{18}F]-DAFBA by the B16F1 melanoma cells. No significant binding was seen for DAFBA to the sigma-1 and sigma-2 receptors in vitro. The in vivo biodistribution studies performed in normal ICR mice showed a low uptake in the normal tissues followed by further elimination of radioactivity from these tissues with time. The biodistribution studies performed in C57 mice bearing the melanoma tumor xenograft showed a rapid uptake of radioactivity in the tumor that reached a plateau within 30 min postinjection. The F-18 uptake in the tumor was 7.00 ± 2.76, 6.57 ± 1.66, and 5.80 ± 0.98%ID/g at 60, 120, and 180 min, respectively. A steady uptake of radioactivity in the tumor and low uptake in normal tissues resulted in high tumor to normal tissue ratios. For example, at 180 min postinjection, the tumor to tissue ratios were 14.90 ± 6.47, 21.90 ± 4.68, 32.91 ± 6.11, 39.73 ± 11.78, and 6.33 ± 1.9, for the spleen, lungs, muscle, blood, and liver, respectively. The radioactivity rapidly cleared from the blood pool, and it decreased from 0.68 ± 0.21%ID/g at 60 min to 0.13 ± 0.03%ID/g at 180 min. The F-18 uptake in the bones at 60, 120, and 180 min was 0.91 ± 0.27, 0.57 ± 0.32, and 0.17 ± 0.05%ID/g, respectively. This low uptake in the bones reflects its in vivo resistance toward defluorination. A low residual activity in normal tissues and a high tumor uptake signifies the superior imaging potential of this compound. Because of these positive traits, [^{18}F]-DAFBA could help delineate the tumor and its metastases when used for imaging applications. Further in vivo studies are underway to assess the potential of [^{18}F]-DAFBA as a promising PET imaging probe.

INTRODUCTION

Skin cancer is one of the most common cancers in the USA, and one in five people will develop it over the course of their lives. While melanoma accounts for only 3% of all skin cancer cases, 75% of deaths in this group are associated with melanoma. Unfortunately, the incidence of melanoma is increasing more rapidly than any other cancer. The prognosis and the patient's survival heavily depend on the clinical stage of the disease at the time of diagnosis. For example, a 10 year survival rate for stage 1 melanoma patients is 90−97% and only 3% for stage IV melanoma patients. Therefore, an early diagnosis of this disease and accurate assessment of its metastases remain the keys for improved outcome and disease free survival. Several scintigraphic probes such as monoclonal antibodies to melanoma associated antigens (*1, 2*), peptides (*3, 4*), iodoquinolines (*5, 6*), iodoamphetamine (*7, 8*), and guanidines (*9*) have been developed over the years to detect melanoma and localize metastatic lesions. While some of these compounds showed their potential in preliminary evaluations, none of these agents could achieve clinical significance. Therefore, the goal of many research groups including ours has been to develop diagnostic imaging agents with higher specificity and sensitivity to melanoma. More recently, a series of iodinated benzamides were synthesized as potential melanoma imaging agents. Because of the high affinity of iodobenzamides toward melanocytes and favorable tissue distribution characteristics, some of these radioiodinated benzamides were further pursued in humans to image melanoma tumors. This concerted effort yielded several clinically useful scintigraphic probes with good imaging characteristics (*10*−*13*). For an effective treatment outcome, it is important to accurately localize the tumor and its micrometastatic lesions. While positron emission tomography (PET) has recently emerged as an effective and noninvasive three-dimensional (3-D) tomographic imaging modality to provide absolute quantitative data on tracer uptake in the tissues, efforts to develop a PET probe to image melanoma have been rather sparse. The advantages of PET imaging include its ability to provide absolute quantitative data, ease in background subtraction, and tomographic imaging. At present, F-18 FDG PET imaging remains the only available imaging probe to localize melanoma cancer, despite its inherent drawbacks. For example, it is difficult to detect smaller tumor volumes using FDG (*14*). In addition, the sensitivity of these scans depends largely on the stage of the disease. FDG PET sensitivity to detect stage 1 melanoma is 0% but improves to 81% for stage III (*15*), thus ruling out its utility in the early detection of melanoma. In previous studies, FDG failed to detect metastatic disease in all patients with positive sentinel node biopsy (*16*). The presence of infection, inflammation, or recent surgery further increases the rate of false positive results, thus diminishing its efficacy as a reliable diagnostic tool (*17*). F-18 FDG lacking specificity toward melanoma underscores the need to search for more effective probes for early detection of melanoma cancer.

Since *N*-diethylaminoethyl-4-[*I]iodobenzamide (4-[*I]BZA) and *N*-diethylaminoethyl-2-[*I]iodobenzamide (2-[*I]IBZA) show clinical potential and are currently used in the clinics to image melanoma (*10, 18*−*21*), it was imperative that we focus

* To whom correspondence should be addressed. PET Center, Department of Radiological Sciences, Wake Forest University Health Sciences, Winston Salem, NC 27157. Phone: 336-716-5624. Fax: 336-716-5639 (FAX). E-mail: pgarg@wfubmc.edu.

10.1021/bc8005094 CCC: $40.75 © 2009 American Chemical Society
Published on Web 02/17/2009

our initial efforts to develop a PET analogue using the same structural motif. Toward that goal, we replaced the 4-iodo group of 4-[*I]IBZA with a 4-fluoro group while keeping the remainder of the molecule unchanged. If successfully synthesized and promising biological characteristics are observed, this new PET probe could be a useful technique for the early detection of melanoma, especially when lesions are small in size and difficult to detect. In order to develop this PET probe, we initially synthesized the nonradioactive compound *N*-(2-diethylaminoethyl)-4-fluorobenzamide (DAFBA, **1**). This compound was synthesized using a one step synthesis procedure. The radiochemistry to incorporated F-18, a PET radioisotope to prepare *N*-(2-diethylaminoethyl) 4-[^{18}F]fluorobenzamide ([^{18}F]-DAFBA) was accomplished using a three step synthesis. Herein, we describe the synthesis of [^{18}F]-DAFBA, the in vitro uptake to melanoma cells, and its in vivo distribution characteristics in normal mice and in mice with a melanoma tumor xenograft.

EXPERIMENTAL PROCEDURES

All reactions were carried out under an inert argon atmosphere using dry solvents under anhydrous conditions, unless otherwise stated. Reagents and solvents were purchased from commercial suppliers and were used without further purification. The C-18 plus Sep-Pack and the QMA cartridges were obtained from Waters Corporation, USA. Melting points were determined on an Electrothermal MEL-TEMP melting point apparatus and are uncorrected. Flash column chromatography was carried out over silica gel (60 Å, Mallinckrodt, Baker). ^{1}H NMR data was acquired on a Bruker Advance 300 DPX spectrometer. All chemical shift values are reported in ppm (δ).

High performance liquid chromatography (HPLC) was performed in isocratic mode using a Varian 9010 LC pump, a variable wavelength 9050UV VIS detector (Varian Corp, Palo Alto, CA, USA) set at 254 λ, and a radioisotope detector (Bioscan Inc., Washington, DC. USA) attached to Varian's chromatography software package. The radiochemical yields reported are decay corrected and are calculated to the end of bombardment (EOB) time. The HPLC system used for the purification of [^{18}F]-DAFBA was a C-18 reverse-phase, 7.5 × 250 mm 5 μm column (Phenomenex, Torrence, CA) eluted with MeOH/0.1 M ammonium formate (30:70) using a flow rate of 3 mL/min. Quality control of the purified product was carried out on C-18 QC column (4.6 mm × 250 mm, 5 μm) eluted with the methanol/0.1 M ammonium acetate (50:50) containing 40 μL of triethyl amine/100 mL of solvent with a flow rate of 1 mL/min. The kryptofix solution was prepared by dissolving 120 mg of K222 and 72 mg of K_2CO_3 in 720 μL water followed by the addition of 12 mL of acetonitrile. The C-18 Sep-Pak cartridge was activated by passing 5 mL of ethanol followed by 5 mL of sterile water. The QMA cartridge was activated by washing with 5 mL of 1 N sodium bicarbonate solution followed by flushing with 10 mL of water, and then drying the cartridge by passing air for ~30 s.

The melanoma cells (B16F1) were purchased from American Type Culture Collection (ATCC, Rockville, MD) and were grown in Dulbecco's modified Eagle's medium (DMEM) supplemented with 10% fetal bovine serum at 37 °C in an incubator maintaining a 5% CO_2 environment. The ICR and the C57 mice (6−8 weeks old) were purchased from Charles River Laboratories. Animal studies were performed under the guidelines established by the Wake Forest University Institutional Animal Care and Use Committee. The radioactivity levels in tissues were assessed with a Packard Cobra γ-counter.

Chemistry. *Preparation of N-(2-Diethylaminoethyl)-4-fluorobenzamide (DAFBA,* **1***).* This compound was synthesized as shown in Scheme 1. A solution of 4-fluorobenzoic acid (1.42 g, 10.3 mmol) in 50 mL of dichloromethane was cooled to 0 °C using an ice bath. To this ice cooled solution, triethylamine (1.3 g, 12.9 mmol) and ethyl chloroformate (1.2 g, 11.1 mmol) were added, and the reaction mixture was stirred for 1 h at 0 °C. A solution of *N*,*N*-diethylethylenediamine (1.0 g, 8.6 mmol) in dichloromethane (10 mL) was added slowly to this reaction mixture. After the addition was completed, the flask was removed from the ice bath, and the reaction mixture was stirred for 2 h at room temperature. Subsequently, the reaction mixture was cooled in the ice bath, and the reaction was quenched with 10 mL of 3 N NaOH. The product was extracted from the crude reaction mixture using dichloromethane (2 × 30 mL). The combined organic layer was dried over sodium sulfate. After evaporating the solvent, a light-yellow colored oil was obtained that was further purified using flash column chromatography (acetone). The desired product **1** was collected as a colorless viscous oil (1.96 g, 96% yield). ^{1}H NMR ($CDCl_3$, δ): 1.04 (t, 6H, J = 7.2 Hz, 2× -CH_2−C**H**$_3$), 2.56 (q, 4H, J = 7.2 Hz, 2× -C**H**$_2$−CH_3), 2.64 (t, 2H, J = 6.3 Hz, -C**H**$_2$−N-(CH_2−CH_3)$_2$), 3.44 − 3.49 (m, 2H, -CONH-C**H**$_2$-), 6.87 (br S, 1H, -N**H**), 7.07 − 7.14 (m, 2H, Ar−H @ C3 and C5), 7.75 − 7.81 (m, 2H, Ar−H @ C2 and C6).

Scheme 1. Reaction Scheme for the Synthesis of *N*-(2-Diethylamino ethyl) 4-fluorobenzamide (DAFBA; 1)

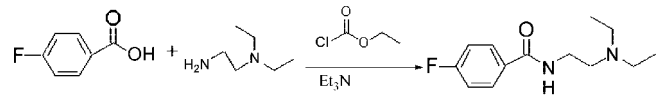

1

Ethyl-4-(N,N,N-trimethylammonium trifluoromethanesulfonyl)-benzoate. This compound was prepared as a precursor for the radiofluorination reaction by using a method analogous to that reported earlier with minor modifications (*22*−*24*). Briefly, ethyl 4-(dimethylamino) benzoate (0.5 g) was dissolved in dichloromethane (20 mL), and the solution was cooled in an ice bath. To this ice cold solution, methyl trifluoromethanesulfonate (0.5 mL) was slowly added while stirring. After the addition was completed, the reaction mixture was stirred for an additional 30 min and filtered, and a colorless to whitish crystalline product was collected as the target compound (0.84 g) mp 110−112 °C (Lit mp 112−114 °C (*24*)). ^{1}H NMR ($CDCl_3$, δ): 1.37 (t, 3H, J = 7.2 Hz, -OCH_2C**H**$_3$), 3.66 (s, 9H, -N(C**H**$_3$)$_3$, 4.40 (q, 2H, J = 7.2 Hz, -OC**H**$_2$$CH_3$), 7.94 (d, 2H, J = 9.3 Hz, Ar−H close to N(Me_3)$_3$), 8.21 (d, 2H, J = 9.3 Hz, Ar−H close to -COOEt).

Radiochemical Synthesis of N-[2-(diethylamino)ethyl]-4-[^{18}F]fluorobenzamide ([^{18}F]-DAFBA). The radiochemical synthesis of [^{18}F]-DAFBA was accomplished by first synthesizing 4-[^{18}F]fluorobenzoic acid followed by its coupling to *N*,*N*-diethylethylenediamine, using 1-(3-dimethylaminopropyl)-3-ethylcarbodiimide hydrochloride (EDC) as the coupling agent. The radiochemical synthesis of this compound is shown in Scheme 2.

Synthesis of 4-[^{18}F]Fluorobenzoic Acid (4). Aqueous [^{18}F]fluoride was produced by using an ^{18}O(p, n)^{18}F reaction on 95% enriched [^{18}O]-H_2O in a high volume, high pressure [^{18}F]fluoride target irradiated with a 45 μA beam current. After the irradiation, the ^{18}O−H_2O bolus containing 450−800 mCi of [^{18}F]-fluoride was transferred from the cyclotron onto an AG1 × 8 (Bio-Rad) anion exchange resin cartridge in the hot-cell, and the [^{18}O]-H_2O was recovered. The trapped [^{18}F]fluoride was eluted from the cartridge with aqueous Cs_2CO_3 (0.3 mL, 1 mM) into a reaction vessel. The remainder of water from this mixture was removed azeotropically using acetonitrile. The dried [^{18}F]fluoride was resolubilized in 10 μL of aqueous Cs_2CO_3 solution (1 mM) and reacted with 4-formyl *N*,*N*,*N*-trimethylbenzeneaminium trifluoromethane sulfonate dissolved in 120 μL of DMSO, following the procedure described earlier (*24*). The 4-[^{18}F]fluo-

Scheme 2. Reaction for the Preparation of Radiolabeled Compound *N*-(2-Diethylaminoethyl) 4-[^{18}F]fluorobenzamide ([^{18}F]-DAFBA) Using 4-[^{18}F]Fluorobenzoic acid (4) as the Intermediate[a]

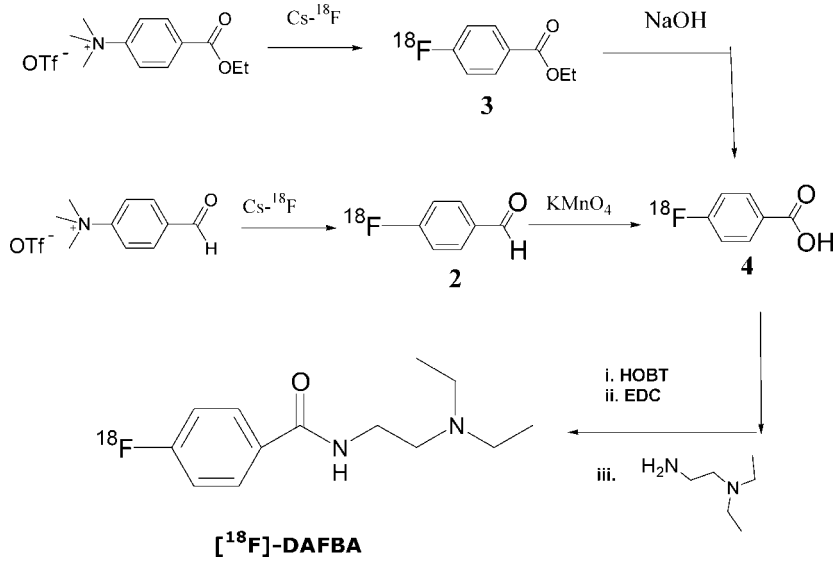

[a] Compound **4** was prepared utilizing either 4-[^{18}F]fluorobenzaldehyde (**2**) or ethyl 4-[^{18}F]fluorobenzoate (**3**). Subsequent coupling of **4** with *N*-*N*-diethylethylenediamine in the presence of 1-hydroxybenzotriazole hydrate (HOBT) and 1-(3-dimethylaminopropyl)-3-ethylcarbodiimide hydrochloride (EDC) provided the desired compound.

robenzaldehyde (**2**) thus obtained was oxidized by reacting with a 5% solution of $KMnO_4$ in 1 N NaOH (300 μL) at 120 °C for 10 min. Subsequently, sodium bisulphate solution (150 μg in 300 μL water) and 5 N HCl (0.5 mL) were added. The contents were diluted with 6 mL of water, passed through a C-18 Sep-Pak cartridge, and rinsed with 10 mL of water, and the 4-[^{18}F] fluorobenzoic acid (**4**) was eluted from the cartridge in 72 ± 11% (n = 12) radiochemical yield with 3 mL of acetonitrile.

Alternate Synthesis of 4-[^{18}F]Fluorobenzoic Acid via Ethyl-4-[^{18}F]fluorobenzoate as an Intermediate. After the irradiation, the $^{18}O-H_2O$ bolus containing 450−800 mCi of [^{18}F]-fluoride was transferred from the cyclotron onto a preactivated QMA cartridge in the hot-cell, and [^{18}O]-H_2O was recovered. The trapped [^{18}F]fluoride was eluted from the cartridge with 1.5 mL of K2.2.2. solution prepared as described above. The remainder of water from this mixture was removed azeotropically using acetonitrile. The dried [^{18}F]fluoride was reacted with a freshly prepared solution of 5 mg of ethyl-4-(trimethylammonium triflate)benzoate in 120 μL of anhydrous DMSO at 106 °C for 10 min as described earlier (*25*). Subsequently, the reaction vessel was cooled to room temperature, 500 μL of 1 N NaOH was added, and the reaction mixture was heated for 5 min at 100 °C to hydrolyze the ester group without isolating intermediate **3**. After cooling the reaction mixture to room temperature, the contents were acidified using 1 N HCl (∼600 μL) and loaded onto a C-18 Sep-Pak cartridge for purification. The Sep-Pak was washed with 10 mL of water, and 4-[^{18}F]fluorobenzoic acid (**4**) was eluted from the cartridge using 3.5 mL of acetonitrile.

Coupling of 4-[^{18}F]Fluorobenzoic acid with *N*-*N*-diethylethylenediamine to Prepare [^{18}F]-DAFBA. The solvent from the 4-[^{18}F]fluorobenzoic acid solution (**4**) obtained using either of the above two methods was reduced to ∼300 μL. (Note: evaporating to lesser volume resulted in the loss of radioactivity). A solution of 1-hydroxybenzotriazole hydrate (HOBT, 3 mg) in 100 μL of DMF, 1-(3-dimethylaminopropyl)-3-ethylcarbodiimide hydrochloride (EDC, 3.5 mg), and *N*-*N*-diethylethylenediamine (1 mg) in DMF (100 μL) were added sequentially to the reaction vessel containing 4-[^{18}F]fluorobenzoic acid, and the reaction mixture was stirred for 30 min at room temperature. The solvent was evaporated to ∼150 μL using a gentle stream of nitrogen, diluted with 1 mL of HPLC mobile phase, and the contents were loaded onto the HPLC column. The desired product was collected from HPLC and the solvent evaporated using a rotary evaporator. The residue was redissolved in 0.5 mL ethanol, and 9.5 mL of water was added. The product solution was then filtered through a 0.22 μm filtering cartridge and collected in a 20 mL sterile product vial.

Stability Measurement. A solution of [^{18}F]-DAFBA (5 mCi) in 2 mL of saline was assayed for its room temperature shelf life stability assay using the HPLC method. An aliquot (100 μL) of the above solution was injected into HPLC at 10, 60, 180, 240, and 360 min postsynthesis and analyzed for change in radiochemical purity over time by using the QC HPLC procedure.

Lipophilicity Measurement. Lipophilicity of [^{18}F]-DAFBA was determined via the shake flask method using a 1-octanol and phosphate-buffered saline (pH 7.4) system as described by Wilson et al. (*26*). Briefly, ∼500 Kcpm of [^{18}F]-DAFBA was added to test tubes containing a 1-octanol (1 mL) and PBS (1 mL) mixture (in triplicate), and the test-tubes were vortexed for 3 min. Subsequently, the two layers were allowed to separate, aliquots (100 μL) of the organic and the aqueous layers were withdrawn from each tube, measured for radioactivity, and the log *P* value calculated (*26, 27*).

In Vitro Uptake Assay. The cells were grown to 80−90% confluence in flasks before trypsinizing and then were resuspended in PBS at pH 7.4. After assessing the cell counts, 1×10^5, 5×10^5, 8×10^5, and 1×10^6 cells were aliquoted in triplicate in Eppendorf tubes. To each tube, ∼200 Kcpm of [^{18}F]-DAFBA was added, and the tubes were incubated at 22 °C (ambient temperature) for 1 h. After incubation, the tubes were centrifuged, the media was removed, the pellet was washed with PBS, and the combined wash and the pellets were counted for radioactivity using a gamma counter. The percent uptake (% uptake) was calculated as the percent of the total added radioactivity found in the pellet.

Sigma Receptor Binding Assay. The IC_{50} values for the binding of DAFBA to sigma receptors were performed by using a competitive binding assay. For sigma-1 receptor binding, the assay was performed using the guinea pig brain membrane and the ligand ^{3}H-PENT as described earlier (*28*). For sigma-2 receptor binding, the assay was performed using rat liver

membrane prepared from Sprague−Dawley rats and the ligand ^{3}H-DTG in the presence of 1 μM dextrallorphane to mask sigma-1 receptors, as described earlier (*29*). The competition binding assays for both of the receptors was performed using 7 concentrations of DAFBA ranging from 10^{-6} to 10^{-9} M. The IC_{50} and K_i values were calculated using Prism Software (GraphPad Software Inc., La Jolla, CA).

Tissue Distribution Studies in Normal ICR Mice. The biodistribution studies were performed using ICR mice. The mice were injected with ~15 μCi of [^{18}F]-DAFBA in 100 μL of saline via the tail vein. At 30, 60, 120, and 180 min postinjection, the animals were euthanized, tissues of interest removed, washed with PBS, weighed, and counted for radioactivity using a gamma-counter. The accumulation of radioactivity in various tissues is expressed as percent-injected dose per gram of tissue (%ID/g) by counting the injected dose standard of appropriate count rate along with the tissues. The statistical significance of differences was determined by an unpaired Student's *t*-test using the Microsoft Excel program. Differences were considered significant when $P < 0.05$ was obtained.

Tissue Distribution Studies Using C57 Mice Bearing the B16F1 Tumor Xenograft. Mouse melanoma cells B16F1 were grown in DMEM media as described above. When the flasks were 80−90% confluent, the cells were trypsinized, removed from flask, centrifuged, and resuspended in a 50:50 mixture of Matrigel (Becton Dickinson, San Jose, CA) and PBS (pH 7.4) for inoculation in the animals. The mice were inoculated with 0.1 mL of cell suspension in PBS-containing ~5×10^6 cells in the right flank with a 23-gauge needle. Tumor growth was monitored periodically. The biodistribution studies were performed when the tumor volume reached >200 mm^3. The tumor bearing mice were injected with of ~15 μCi of [^{18}F]-DAFBA in 100 μL of saline via the tail vein. F-18 uptake in the tumor and other tissues was assessed at 30, 60, 120, and 180 min postinjection. At preset time points, the animals were euthanized, tissues of interest removed, washed with PBS, weighed and counted for radioactivity using a gamma-counter.

RESULTS AND DISCUSSION

Synthesis of DAFBA, the nonradioactive compound, is shown in Scheme 1. The desired product was obtained in 84% yield and in 98% chemical purity after flash column chromatography. DAFBA was eluted at 22 ± 1 min using a semipreparatory HPLC column. On the QC column, this product was eluted at 11.1 ± 0.4 min. This nonradiolabeled DAFBA was prepared as an HPLC reference standard for the production of radioactive compound [^{18}F]-DAFBA. The radiochemical synthesis of [^{18}F]-DAFBA was accomplished using two separate routes and is shown in Scheme 2. For the first method, initially 4-[^{18}F]fluorobenzaldehyde was prepared followed by oxidation of the aldehyde group to the carboxylic acid group. Using this route, 4-[^{18}F]Fluorobenzoic acid was synthesized in 72 ± 11% (n = 12) radiochemical yield. Alternatively, 4-[^{18}F]fluorobenzoic acid **4** was prepared in 82 ± 8% (n = 11) radiochemical yield in two steps, first by preparing ethyl [^{18}F]fluorobenzoate followed by hydrolyzing the ester group to yield 4-[^{18}F]fluorobenzoic acid **4** without isolating the intermediate ethyl ester. The coupling of *N*-*N*-diethylethylenediamine to 4-[^{18}F]fluorobenzoic acid **4** was accomplished using EDC as the coupling agent. After the reaction, the mixture was loaded on a semiprep HPLC column, and the desired product was eluted from the column (retention time 22.2 min) in 54 ± 18% radiochemical yield (n = 17) and 97 ± 2% radiochemical purity. The purity and the specific activity of this product were determined using the QC HPLC system. The retention time of [^{18}F]-DAFBA on the QC-HPLC column was 11.3 min, and the specific activity remained >1000 mCi/μmol for all preparations. The overall synthesis time for

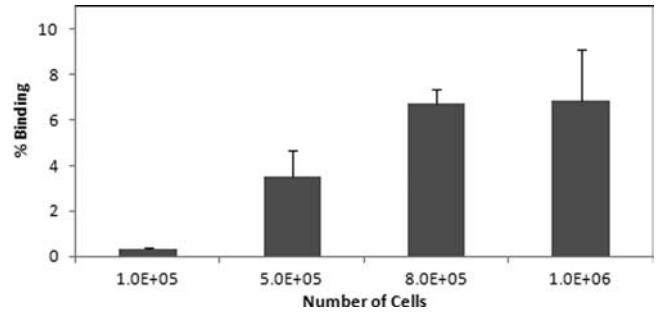

Figure 1. In vitro binding of [^{18}F]-DAFBA to B16F1 melanoma cells. Various concentrations of cells were incubated with [^{18}F]-DAFBA for 60 min at room temperature. The results are presented as a percent of total added radioactivity that was taken up by the cells (mean ± standard deviation; n = 3 tubes for each concentration).

[^{18}F]-DAFBA including the HPLC purification and the final formulation was 175 ± 15 min (n = 17). To assess the stability of [^{18}F]-DAFBA over an extended period of time, an aliquot of the product was injected on a QC-HPLC column at various time points for up to 6 h postpreparation of the product. The shelf life stability studies showed that the radiochemical purity of [^{18}F]-DAFBA remained >95% at all time points, demonstrating the stability of the radiotracer over the 6 h storage period. While these studies were performed to assess the expiration time for this radioactive compound, this data does not reflect in vivo stability of the molecule. While the assessment of biostability and metabolic fate of this compound in vivo remains outside the scope of this study, these important parameters are part of an extensive characterization of [^{18}F]-DAFBA as an imaging probe.

Cell uptake studies were performed using the B16F1 mouse melanoma cells.Triplicate sets of Eppendorf tubes containing various concentrations of cells were incubated with [^{18}F]-DAFBA at room temperature for 60 min. The cells were separated, washed, and counted for radioactivity to determine the percentage of added radioactivity taken up by the cells. The cell uptake data is shown in Figure 1. As see in Figure 1, the uptake of [^{18}F]-DAFBA increased with increasing number of cells with an uptake of 5.60 ± 2.67% when 1×10^6 cells/tube were incubated with [^{18}F]-DAFBA.

Role of Sigma Receptors. The role of sigma receptors on tumor cells has been implicated in the uptake of radioiodinated benzamides in certain tumors. Although it is not known whether B16F1 cells used in our study express sigma receptors, various other tumor cell lines such as PC12, A375 amelanotic melanoma, T47D breast ductal carcimona, SK-N-SH neuroblastoma, and C6 glioma cells highly express sigma receptors. Since these tumor cell lines also show high binding to iodobenzamides, several investigators hypothesized that the binding ability of iodobenzamides to sigma receptors could be exploited to image melanoma and other tumors (*30*−*33*). For that reason, John et al. synthesized a series of iodobenzamides that showed high sigma receptor binding and displayed varying efficacy to image various tumors (*34*, *35*). Therefore, we evaluated sigma receptor binding of DAFBA in vitro. Surprisingly, the in vitro binding assay showed lack of any appreciable binding of DAFBA to sigma-1 and sigma-2 receptors, and the IC_{50} for DAFBA was >1000 nM for both of these receptors. Despite the lack of affinity toward sigma receptors, we observed encouraging [^{18}F]-DAFBA uptake results using the B16F1 melanoma cells. A more expanded in vivo structure−activity-relationship study performed by Eisenhut et al. revealed that the binding of iodinated benzamide to the melanoma tumor does not correlate with sigma receptor binding and concluded that sigma receptors are not important for the uptake of iodobenzamides by the melanoma

Table 1. Biodistribution of *N*-(2-Diethylaminoethyl) 4-[^{18}F]fluorobenzamide ([^{18}F]-DAFBA) in Normal Balb/c ICR Mice at Various Time Points after Injection (Mean ± SEM; $n = 5$)

	percent injected dose per gram tissue (%ID/g)			
organ	30 min	60 min	120 min	180 min
liver	3.12 ± 0.62	3.61 ± 0.48	1.14 ± 0.41	1.12 ± 0.20
spleen	2.35 ± 0.07	1.87 ± 0.46	0.43 ± 0.25	0.53 ± 0.08
lung	1.75 ± 0.43	1.84 ± 0.41	0.42 ± 0.14	0.49 ± 0.07
heart	1.10 ± 0.14	0.92 ± 0.10	0.28 ± 0.05	0.23 ± 0.03
kidneys	4.13 ± 0.68	4.20 ± 0.41	1.58 ± 0.51	1.34 ± 0.36
intestine	0.91 ± 0.32	1.39 ± 0.54	0.26 ± 0.26	0.40 ± 0.11
muscle	0.88 ± 0.13	0.65 ± 0.11	0.18 ± 0.10	0.16 ± 0.03
bone	0.81 ± 0.19	0.69 ± 0.08	0.20 ± 0.06	0.24 ± 0.10
blood	0.78 ± 0.07	0.67 ± 0.05	0.20 ± 0.04	0.21 ± 0.03
brain	2.16 ± 0.32	1.54 ± 0.24	0.52 ± 0.07	0.46 ± 0.07

tumors and cells (*36*). Interestingly, an attempt to block sigma receptors in vivo by injecting DuP 734 prior to iodobenzamide administration resulted in a 2-fold increased uptake in the tumor, while it significantly reduced its uptake in the brain and the lungs. These findings further demonstrate that uptake in melanoma tumors is independent of sigma receptors (*33*). The low in vitro binding affinity toward sigma-1 and sigma-2 receptors along with a modest in vitro cell uptake to B16F1 cells seen in our study using [^{18}F]-DAFBA further support those findings.

To explore in vivo tissue distribution characteristics of [^{18}F]-DAFBA, the biodistribution studies were performed using ICR normal mice. The F-18 uptake in various tissues from that study is summarized in Table 1. In general, a low F-18 uptake was observed in most normal tissues. As expected, at earlier time points (30 min), the uptake in the liver and kidneys was somewhat higher than that in other normal tissues (liver 3.12 ± 0.62%ID/g; kidneys 4.13 ± 0.68%ID/g). Nonetheless, the radioactivity from the liver rapidly washed out with time, approaching the levels seen in other normal tissues (liver 1.12 ± 0.20 at 180 min). Similarly, the radioactivity in blood was quite low at all time point studies with radioactivity levels of 0.20 ± 0.04%ID/g at 120 min postinjection.

Since only a few studies have reported the biodistribution characteristics of iodinated benzamides in normal mice, we could only compare our results to biodistribution results reported for the [*I]*N*-(2-diethylaminoethyl)-3-iodo 4-methoxybenzamide ([*I]IMBA), a closely matched structural analogue, that used the C57 normal mice (*37*). The radioiodine uptake levels in most tissues reported for [*I]IMBA were similar to F-18 uptake observed in the current study. For example, in the current study at 60 min postinjection, the F-18 in the liver, lungs, and blood was 3.12 ± 0.62, 1.75 ± 0.43, and 0.78 ± 0.07%ID/g, respectively, as compared to 3.09 ± 0.45, 1.06 ± 0.23, and 0.84 ± 0.08%ID/g, respectively, reported for the [*I]IMBA (*37*). The uptake differences in various tissues between the two studies were small and statistically insignificant ($p > 0.01$). Although the thyroid uptake data was not reported for the [*I]IMBA, a high uptake in the stomach (9.72 ± 1.51%ID/g) and in intestine (7.70 ± 4.70%ID/g) indicated extensive in vivo dehalogenation. In contrast, the [^{18}F]-DAFBA was found to be quite stable in vivo as evident from its low F-18 uptake in the bones (60 min: 0.69 ± 0.08%ID/g) that continued to decrease further with time. Despite disparate specific activities of the tracers used in these two studies (IMBA 0.1−1.0 mCi/μmol; [^{18}F]DAFBA >1000 mCi/μmol) and varied lipophilicities, the tissue distribution results for the two molecules were fairly similar.

To further characterize [^{18}F]-DAFBA for its tumor uptake properties, the biodistribution studies were performed using C57 mice bearing B16F1 melanoma tumor xenografts. The F-18 uptake in various tissues is shown in Table 2. The F-18 accumulation for the tumor bearing mice was quite similar to

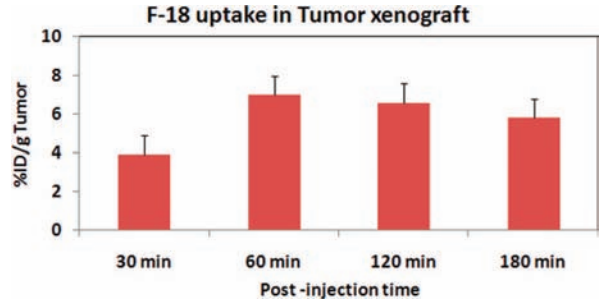

Figure 2. F-18 uptake in the tumor at 30, 60, 120, and 180 min postinjection of [^{18}F]-DAFBA using C57 mice bearing the B16F1 melanoma tumor. The data is expressed as percent injected dose per gram of tumor (%ID/g average ± standard deviation; $n = 5$).

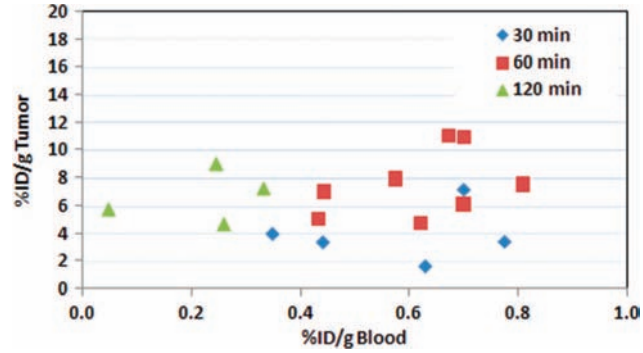

Figure 3. Correlation plot for [^{18}F]-DAFBA uptake in the melanoma tumor versus the radioactivity present in the blood at 30, 60, and 120 min. Each data point represents data from a single mouse. The plot shows that the radioactivity levels in the blood pool is independent of radioactivity in the tumor and that the two variables exhibit a poor Pearson correlation ($r = 0.398$).

that observed using the ICR normal mice. Most normal tissues from tumor bearing mice showed a low accumulation at all time points studied. The radioactivity continued to clear out from normal tissues with time. For example, F-18 uptake in the muscles was 1.1 ± 0.14%ID/g at 30 min, which was further reduced to 0.17 ± 0.03%ID/g at 180 min postinjection, exhibiting a 6-fold reduction. Similarly, the F-18 level in the blood was 0.58 ± 0.18%ID/g and 0.13 ± 0.03%ID/g at 30 and 180 min, respectively. A rapid in vivo clearance of radioactivity and low levels of circulating radioactivity in the blood pool reflected a low affinity of this compound toward erythrocytes and serum proteins. One of the advantages of this low circulating radioactivity in blood would be clear visualization of tumor and metastases in vivo using this probe. The metabolic tissues such as the liver and spleen also showed low uptake of radioactivity that continued to clear out further with time. The bone uptake in normal mice and tumor bearing mice remained significantly low, thereby underscoring the stability of [^{18}F]-DAFBA toward in vivo dehalogenation.

In this study, [^{18}F]-DAFBA displayed a rapid and high uptake in the tumor. The [^{18}F]-DAFBA uptake in the B16F1melanoma tumor xenograft is shown in Figure 2. The tumor uptake reached 7.00 ± 2.76%ID/g by 60 min. While the tumor accumulation decreased slightly by 180 min (5.80 ± 0.98%ID/g), the tumor uptake differences between 60 and 180 min time points were small and statistically insignificant ($p > 0.2$).

Earlier, Pham et al. suggested that iodobenzamides with higher lipophilicity would show better tumor uptake properties. They further hypothesized that a log $P_{7.4}$ of greater than 1.4 is necessary for the enhanced tumor uptake characteristics (*38*). Using the Chem-Draw Ultra software (Cambridge Sof.Com, Cambridge, MA), the calculated log *P* values for the [*I]IBZA

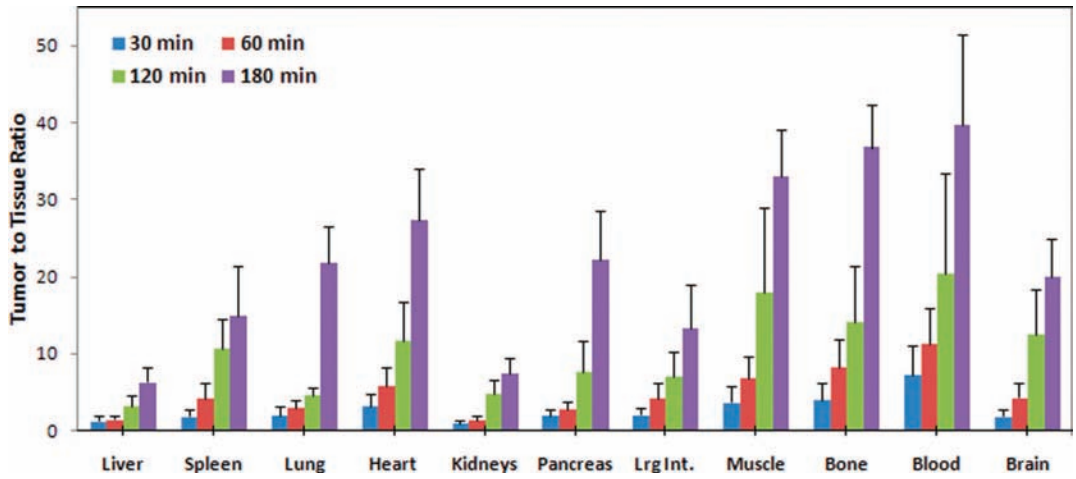

Figure 4. Tumor to normal tissue ratios of [^{18}F]-DAFBA using C57 mice bearing the B16F1 melanoma tumor at 30, 60, 120, and 180 min postinjection. While modest tumor to normal tissue ratios were observed at 30 min, these ratios continued to improve significantly with time.

Table 2. Biodistribution of *N*-(2-Diethylaminoethyl) 4-[^{18}F]fluorobenzamide ([^{18}F]-DAFBA) in C57 Mice Bearing the B16F1 Melanoma Tumor Xenograft at Various Time Points after Injection (Mean ± SEM; $n = 5$)

	percent injected dose per gram tissue (%ID/g)			
organ	30 min	60 min	120 min	180 min
liver	3.27 ± 0.90	5.01 ± 2.06	2.35 ± 1.20	0.80 ± 0.35
spleen	2.14 ± 0.41	1.83 ± 0.54	0.71 ± 0.37	0.44 ± 0.25
lung	2.46 ± 1.27	2.48 ± 1.27	1.47 ± 0.47	0.27 ± 0.07
heart	1.25 ± 0.28	1.27 ± 0.50	0.61 ± 0.20	0.21 ± 0.04
kidneys	4.50 ± 1.33	5.38 ± 1.86	1.41 ± 0.11	0.83 ± 0.23
intestine	1.94 ± 0.51	1.98 ± 0.88	1.02 ± 0.33	0.46 ± 0.22
muscle	1.09 ± 0.18	1.10 ± 0.38	0.57 ± 0.54	0.17 ± 0.03
bone	1.00 ± 0.14	0.90 ± 0.27	0.57 ± 0.32	0.17 ± 0.05
blood	0.58 ± 0.18	0.68 ± 0.21	0.43 ± 0.47	0.13 ± 0.03
brain	2.02 ± 0.35	1.68 ± 0.43	0.64 ± 0.40	0.29 ± 0.05

and [^{18}F]-DAFBA were 3.21 and 2.01, respectively. Both of these compounds showed higher than the minimal suggested log *P* value of 1.4, indicating that they should be useful melanoma imaging agents (*38*). Since Pham et al. suggested the lipophilicity of benzamides as one of the important determinants for their biological efficacy, we experimentally measured the partition coefficient of [^{18}F]-DAFBA using the 1-octanol/PBS method described earlier (*26*). The measured partition coefficient for [^{18}F]-DAFBA was 1.7, a value similar to its calculated log *P* value as stated above. It is possible that iodine for fluoride substitution may have resulted in significantly decreased lipophilicity of [^{18}F]-DAFBA. While the lipophilicity remains an important feature for improved tissue membrane penetration, multiple factors play a critical role to achieve favorable tracer uptake and kinetics (*27, 39*). A higher lipophilicity (higher log *P*) may enhance tissue penetration to improve tumor uptake; it simultaneously would increase the nontarget tissue uptake and lead to higher nonspecific uptake in target and in nontarget tissues. Therefore, it is important to carefully balance physicochemical parameters when designing new probes. In essence, several investigations explicate that the lipophilicity measure of melanoma-specific compounds remains a less reliable predictor of their in vivo behavior (*27, 40*). Physiological parameters such as specific activity of radioactive probe, metabolism, clearance, and excretion are some of the other factors that play vital role in defining the merits of a potentially useful imaging probe.

In order to assess the correlation between the radioactivity levels in blood and its uptake in the tumor, the blood uptake values (%ID/g) from individual mice were plotted against the respective tumor uptake values (%ID/g). The data presented in Figure 3 suggest that the tumor uptake is not dependent on the amount of radioactivity present in the blood pool. While the radioactivity levels in the blood decreased significantly by 120 min, the radioactivity levels in the tumor remained unchanged. No correlation was noted between blood and tumor uptake values. The Pearson coefficient of correlation for these two variables was 0.32.

A high F-18 uptake in the tumor and low accumulation of radioactivity in normal tissues resulted in a favorable tumor to tissue ratio for [^{18}F]-DAFBA. The tumor to normal tissue ratios for various tissues is presented in Figure 4. The tumor to blood ratio increased from 8.3 ± 3 at 60 min to 39 ± 12 by 180 min, a 5-fold increase. Similarly, tumor to lung and tumor to muscle ratios for [^{18}F]-DAFBA were >20 at 180 min. Except for the kidneys, the tumor to tissue ratio for most tissues remained high at 180 min. These results were quite similar to that reported by Moins et al. using the [*I]IBZA (*27*). A rapid and high tumor uptake along with a high tumor to normal tissue ratios seen herein are exceedingly significant because it underscores the potential of this compound for aiding in clear visualization of tumors and its metastases noninvasively and within a time frame compatible with the PET isotope half-life.

The brain is one of the common sites that develop melanoma metastases. Therefore, we were interested in exploring whether [^{18}F]-DAFBA crosses the blood−brain barrier to enter the brain. The tissue distribution studies performed in normal and tumor-bearing mice showed that [^{18}F]-DAFBA enters in the brain within 30 min. At early time points, the radioactivity levels were 2-fold higher in the brain than that in other normal organs. After initial high uptake, the radioactivity cleared from the brain with time. For example, the F-18 uptake in the brain was 2.02 ± 0.35%ID/g at 30 min and reduced to one-seventh of this value by 180 min. While initial accumulation in the brain showed its ability to enter the brain, a rapid washout displayed a low affinity of [^{18}F]-DAFBA toward nontumoral tissues, a positive attribute for a potentially useful imaging agent. [^{18}F]-DAFBA also showed encouraging uptake characteristics in the lungs and the liver, two other tissues known to anchor melanoma metastases. As evident from data presented in Table 2, the uptake and clearance of [^{18}F]-DAFBA in the lungs is similar to that seen for the brain. At 30 min, the F-18 uptake in the lungs was slightly higher than that in the brain, and it decreased exponentially with time and reached radioactivity levels similar to that in the blood by 180 min. The initial modest uptake following a rapid elimination of radioactivity from the organs of metastatic potential would constitute a positive trait of this

probe. If developed further, this probe may have significant potential in delineating brain and lung metastases from normal tissues.

Two of the major traits for a successful imaging agent are high uptake of radioactivity in the tumor and low retention of radioactivity in normal tissues. In the current study, [^{18}F]-DAFBA exhibits both of these properties. A high uptake and retention of radioactivity in tumor along with low retention of radioactivity in normal tissues suggests that if developed further, [^{18}F]-DAFBA could be a potentially useful PET imaging probe to image melanoma.

In summary, we successfully synthesized a melanoma-seeking PET imaging agent [^{18}F]-DAFBA. The radiochemical synthesis was achieved in high radiochemical yields and in a synthesis time compatible with F-18 half-life. The in vitro studies showed that [^{18}F]-DAFBA binds to the melanoma cells. Biodistribution studies in mice showed a rapid and high uptake in the tumor and a low accumulation of F-18 in normal tissues pointing to its potential to provide a high signal-to-noise ratio and to its ability to clearly visualize tumors with low background signals. Besides, a low bone uptake signifies the stability of this ligand toward in vivo dehalogenation. On the basis of these promising in vitro and in vivo results, it is tempting to envision the potential of [^{18}F]-DAFBA as a useful melanoma imaging agent using PET. Additional studies are necessary to fully explore the potential of [^{18}F]-DAFBA as a melanoma imaging agent using PET.

ACKNOWLEDGMENT

We thank Kimberly Black, Holly Smith, and Li Wu for their excellent technical help with the cell uptake assay and tissue distribution studies. We also thank the cyclotron staff for their help with radioisotope production. The partial financial support for this study from the NIH (CA 105383 to PKG) is greatly appreciated.

LITERATURE CITED

(1) Chen, J., Giblin, M. F., Wang, N., Jurisson, S. S., and Quinn, T. P. (1999) In vivo evaluation of 99mTc/188Re-labeled linear alpha-melanocyte stimulating hormone analogs for specific melanoma targeting. *Nucl. Med. Biol. 26*, 687–693.

(2) Buraggi, G. L., Callegaro, L., Mariani, G., Turrin, A., Cascinelli, N., Attili, A., Bombardieri, E., Terno, G., Plassio, G., Dovis, M., et al. (1985) Imaging with 131I-labeled monoclonal antibodies to a high-molecular-weight melanoma-associated antigen in patients with melanoma: efficacy of whole immunoglobulin and its F(ab′)2 fragments. *Cancer Res. 45*, 3378–3387.

(3) Garg, P. K., Alston, K. L., Welsh, P. C., and Zalutsky, M. R. (1996) Enhanced binding and inertness to dehalogenation of alpha-melanotropic peptides labeled using N-succinimidyl 3-iodobenzoate. *Bioconjugate Chem. 7*, 233–239.

(4) Miao, Y., Benwell, K., and Quinn, T. P. (2007) ^{99m}Tc- and ^{111}Inlabeled α-melanocyte-stimulating hormone peptides as imaging probes for primary and pulmonary metastatic melanoma detection. *J. Nucl. Med 48*, 73–80.

(5) Boyd, C. M., Lieberman, L. M., Beierwaltes, W. H., and Varma, V. M. (1970) Diagnostic efficacy of a radioiodinated chloroquine analog in patients with malignant melanoma. *J. Nucl. Med. 11*, 479–486.

(6) Lambrecht, R. M., Packer, S., Wolf, A. P., Lloyd, D., and Atkins, H. L. (1984) Detection of ocular melanoma with 4-(3-dimethylaminopropylamino)-7-[123I]-iodoquinoline. *J. Nucl. Med. 25*, 800–804.

(7) Ono, S., Fukunaga, M., Otsuka, N., Nagai, K., Morita, K., Furukawa, T., Muranaka, A., Yanagimoto, S., Tomomitsu, T., Tabuchi, A., et al. (1988) Visualization of ocular melanoma with N-isopropyl-p-[123I]-iodoamphetamine. *J. Nucl. Med. 29*, 1448–1450.

(8) Cohen, M. B., Saxton, R. E., Lake, R. R., Cagle, L., Graham, L. S., Nizze, A., Yamada, L. S., Gan, M., Bronca, G., Greenwell, K., et al. (1988) Detection of malignant melanoma with iodine-123 iodoamphetamine. *J. Nucl. Med. 29*, 1200–1206.

(9) Osei-Bonsu, A., Kokoschka, E. M., Ulrich, W., and Sinzinger, H. (1989) 131I-metaiodobenzylguanidine (mIBG) for bronchial oat cell cancer and melanoma detection? *Eur. J. Nucl. Med. 15*, 629–631.

(10) Michelot, J. M., Moreau, M. F., Veyre, A. J., Bonafous, J. F., Bacin, F. J., Madelmont, J. C., Bussiere, F., Souteyrand, P. A., Mauclaire, L. P., Chossat, F. M., et al. (1993) Phase II scintigraphic clinical trial of malignant melanoma and metastases with iodine-123-N-(2-diethylaminoethyl 4-iodobenzamide). *J. Nucl. Med. 34*, 1260–1266.

(11) Moins, N., D'Incan, M., Bonafous, J., Bacin, F., Labarre, P., Moreau, M. F., Mestas, D., Noirault, E., Chossat, F., Berthommier, E., Papon, J., Bayle, M., Souteyrand, P., Madelmont, J. C., and Veyre, A. (2002) 123I-N-(2-diethylaminoethyl)-2-iodobenzamide: a potential imaging agent for cutaneous melanoma staging. *Eur. J. Nucl. Med. Mol. Imaging 29*, 1478–1484.

(12) Brenner, W., Klomp, H. J., Bohuslavizki, K. H., Szonn, B., Kampen, W. U., and Henze, E. (1999) Limited sensitivity of iodine-123−2-hydroxy-3-iodo-6-methoxy-N-[(1-ethyl-2-pyrrolidinyl)methyl] benzamide whole-body scintigraphy in patients with malignant melanoma: a comparison with thallium-201 imaging. *Eur. J. Nucl. Med. 26*, 1567–1571.

(13) Maffioli, L., Mascheroni, L., Mongioj, V., Gasparini, M., Baldini, M. T., Seregni, E., Castellani, M. R., Cascinelli, N., and Buraggi, G. L. (1994) Scintigraphic detection of melanoma metastases with a radiolabeled benzamide ([iodine-123]-(S)-IBZM). *J. Nucl. Med. 35*, 1741–1747.

(14) Wagner, J. D., Schauwecker, D., Davidson, D., Logan, T., Coleman, J. J., 3rd, Hutchins, G., Love, C., Wenck, S., and Daggy, J. (2005) Inefficacy of F-18 fluorodeoxy-D-glucose-positron emission tomography scans for initial evaluation in early-stage cutaneous melanoma. *Cancer 104*, 570–579.

(15) Wagner, J. D. (2004) A role for FDG-PET in the surgical management of stage IV melanoma. *Ann. Surg. Oncol. 11*, 721–722.

(16) Acland, K. M., Healy, C., Calonje, E., O'Doherty, M., Nunan, T., Page, C., Higgins, E., and Russell-Jones, R. (2001) Comparison of positron emission tomography scanning and sentinel node biopsy in the detection of micrometastases of primary cutaneous malignant melanoma. *J. Clin. Oncol. 19*, 2674–2678.

(17) Hafner, J., Schmid, M. H., Kempf, W., Burg, G., Kunzi, W., Meuli-Simmen, C., Neff, P., Meyer, V., Mihic, D., Garzoli, E., Jungius, K. P., Seifert, B., Dummer, R., and Steinert, H. (2004) Baseline staging in cutaneous malignant melanoma. *Br. J. Dermatol. 150*, 677–686.

(18) Michelot, J. M., Moreau, M. F., Labarre, P. G., Madelmont, J. C., Veyre, A. J., Papon, J. M., Parry, D. F., Bonafous, J. F., Boire, J. Y., Desplanches, G. G., et al. (1991) Synthesis and evaluation of new iodine-125 radiopharmaceuticals as potential tracers for malignant melanoma. *J. Nucl. Med. 32*, 1573–1580.

(19) Brandau, W., Kirchner, B., Bartenstein, P., Sciuk, J., Kamanabrou, D., and Schober, O. (1993) N-(2-diethylaminoethyl)-4-[123I]iodobenzamide as a tracer for the detection of malignant melanoma: simple synthesis, improved labelling technique and first clinical results. *Eur. J. Nucl. Med. 20*, 238–243.

(20) Mansard, S., Papon, J., Moreau, M. F., Miot-Noirault, E., Labarre, P., Bayle, M., Veyre, A., Madelmont, J. C., and Moins, N. (2005) Uptake in melanoma cells of N-(2-diethylaminoethyl)-2-iodobenzamide (BZA2), an imaging agent for melanoma staging: relation to pigmentation. *Nucl. Med. Biol. 32*, 451–458.

(21) Sillaire-Houtmann, I., Bonafous, J., Veyre, A., Mestas, D., D'Incan, M., Moins, N., Kemeny, J. L., Chossat, F., and Bacin, F. (2004) [Phase 2 clinical study of 123I-N-(2-diethylaminoethyl)-2-iodobenzamide in the diagnostic of primary and metastatic ocular melanoma]. *J. Fr. Ophtalmol. 27*, 34–39.

(22) Wilson, A. A., Dannals, R. F., Ravert, H. T., and Wagner, H. N. (1990) Reductive Amination of [18F]fluorobenzaldehydes: Radiosynthesis of 2-[18F] and 4-[18F]fluorodexetimides. *J. Label. Compound Radiopharm. XXXVIII*, 1189–1199.

(23) Garg, P. K., Garg, S., and Zalutsky, M. R. (1994) Synthesis and preliminary evaluation of *para*- and *meta*-[^{18}F]fluorobenzylguanidine. *Nucl. Med. Biol. 21*, 97–103.

(24) Haka, M. S., Kilbourn, M. R., Watkins, G. L., and Torongian, S. (1989) Arylmethylammonium trifluoromethanesulfonates as precursors to aryl [F-18]fluorides: Improved synthesis of [F-18]GBR-13119. *J. Label. Compound Radiopharm. 27*, 823–833.

(25) Marik, J., and Sutcliffe, J. L. (2007) Fully automated preparation of n.c.a. 4-[18F]fluorobenzoic acid and N-succinimidyl 4-[18F]fluorobenzoate using a Siemens/CTI chemistry process control unit (CPCU). *Appl. Radiat. Isot. 65*, 199–203.

(26) Wilson, A. A., Jin, L., Garcia, A., DaSilva, J. N., and Houle, S. (2001) An admonition when measuring the lipophilicity of radiotracers using counting techniques. *Appl. Radiat. Isot. 54*, 203–208.

(27) Moins, N., Papon, J., Seguin, H., Gardette, D., Moreau, M. F., Labarre, P., Bayle, M., Michelot, J., Gramain, J. C., Madelmont, J. C., and Veyre, A. (2001) Synthesis, characterization and comparative biodistribution study of a new series of p-iodine-125 benzamides as potential melanoma imaging agents. *Nucl. Med. Biol. 28*, 799–808.

(28) Bowen, W. D., de Costa, B. R., Hellewell, S. B., J, M., W., and Rice, K. C. (1993) [^{3}H]-(+)-Pentazocine: a potent and highly selective benzomorphane based probe for sigma-1 receptors. *Mol. Neuropharmacol. 3*, 117–126.

(29) Hellewell, S. B., Bruce, A., Feinstein, G., Orringer, J., Williams, W., and Bowen, W. D. (1994) Rat liver and kidney contain high densities of sigma 1 and sigma 2 receptors: characterization by ligand binding and photoaffinity labeling. *Eur. J. Pharmacol. 268*, 9–18.

(30) John, C. S., Vilner, B. J., Gulden, M. E., Efange, S. M., Langason, R. B., Moody, T. W., and Bowen, W. D. (1995) Synthesis and pharmacological characterization of 4-[125I]-N-(N-benzylpiperidin-4-yl)-4-iodobenzamide: a high affinity sigma receptor ligand for potential imaging of breast cancer. *Cancer Res. 55*, 3022–3027.

(31) Staelens, L., Oltenfreiter, R., Dumont, F., Waterhouse, R. N., Vandenbulcke, K., Blanckaert, P., Dierckx, R. A., and Slegers, G. (2005) In vivo evaluation of [123I]-4-iodo-N-(4-(4-(2-methoxyphenyl)-piperazin-1-yl)butyl)-benzamide: a potential sigma receptor ligand for SPECT studies. *Nucl. Med. Biol. 32*, 193–200.

(32) Vilner, B. J., John, C. S., and Bowen, W. D. (1995) Sigma-1 and sigma-2 receptors are expressed in a wide variety of human and rodent tumor cell lines. *Cancer Res. 55*, 408–413.

(33) Waterhouse, R. N., Chapman, J., Izard, B., Donald, A., Belbin, K., Obrien, J. C., and Collier, T. L. (1997) Examination of four 123I labeled piperidine-based sigma receptor ligands as potential melanoma imaging agents— initial studies in mouse tumor models. *Nucl. Med. Biol. 24*, 587–593.

(34) John, C. S., Bowen, W. D., Saga, T., Kinuya, S., Vilner, B. J., Baumgold, J., Paik, C. H., Reba, R. C., Neumann, R. D., Varma, V. M., et al. (1993) A malignant melanoma imaging agent: synthesis, characterization, in vitro binding and biodistribution of iodine-125-(2-piperidinylaminoethyl)4-iodobenzamide. *J. Nucl. Med. 34*, 2169–2175.

(35) John, C. S., Vilner, B. J., and Bowen, W. D. (1994) Synthesis and characterization of [^{125}I]-*N*-(*N*-benzylpiperidin-4-yl)-4-iodobenzamide, a new sigma receptor radiopharmaceutical: high affinity binding to MCF-7 breast tumor cells. *J. Med. Chem. 37*, 1737–1739.

(36) Eisenhut, M., Hull, W. E., Mohammed, A., Mier, W., Lay, D., Just, W., Gorgas, K., Lehmann, W. D., and Haberkorn, U. (2000) Radioiodinated N-(2-diethylaminoethyl)benzamide derivatives with high melanoma uptake: structure-affinity relationships, metabolic fate, and intracellular localization. *J. Med. Chem. 43*, 3913–3922.

(37) Edreira, M. M., and Pozzi, O. R. (2006) Iodide benzamides for the in-vivo detection of melanoma and metastases. *Melanoma Res. 16*, 37–43.

(38) Pham, T. Q., Greguric, I., Liu, X., Berghofer, P., Ballantyne, P., Chapman, J., Mattner, F., Dikic, B., Jackson, T., Loc'h, C., and Katsifis, A. (2007) Synthesis and evaluation of novel radioiodinated benzamides for malignant melanoma. *J. Med. Chem. 50*, 3561–3572.

(39) Brandau, W., Niehoff, T., Pulawski, P., Jonas, M., Dutschka, K., Sciuk, J., Coenen, H. H., and Schober, O. (1996) Structure distribution relationship of iodine-123-iodobenzamides as tracers for the detection of melanotic melanoma. *J. Nucl. Med. 37*, 1865–1871.

(40) Nicholl, C., Mohammed, A., Hull, W. E., Bubeck, B., and Eisenhut, M. (1997) Pharmacokinetics of iodine-123-IMBA for melanoma imaging. *J. Nucl. Med. 38*, 127–133.

BC8005094

Subscriber access provided by SHEMYAKIN-OVCHINNIKOV INST

Article

Reagents for Astatination of Biomolecules. 3. Comparison of *closo*-Decaborate(2-) and *closo*-Dodecaborate(2-) Moieties as Reactive Groups for Labeling with Astatine-211

D. Scott Wilbur, Ming-Kuan Chyan, Donald K. Hamlin, and Matthew A. Perry

Bioconjugate Chem., **2009**, 20 (3), 591-602• DOI: 10.1021/bc800515d • Publication Date (Web): 23 February 2009

Downloaded from http://pubs.acs.org on May 15, 2009

More About This Article

Additional resources and features associated with this article are available within the HTML version:

- Supporting Information
- Access to high resolution figures
- Links to articles and content related to this article
- Copyright permission to reproduce figures and/or text from this article

View the Full Text HTML

ACS Publications
High quality. High impact.

Bioconjugate Chemistry is published by the American Chemical Society. 1155 Sixteenth Street N.W., Washington, DC 20036

Reagents for Astatination of Biomolecules. 3. Comparison of *closo*-Decaborate(2-) and *closo*-Dodecaborate(2-) Moieties as Reactive Groups for Labeling with Astatine-211

D. Scott Wilbur,* Ming-Kuan Chyan, Donald K. Hamlin, and Matthew A. Perry

Department of Radiation Oncology, University of Washington, Seattle, Washington 98195. Received December 3, 2008; Revised Manuscript Received January 22, 2009

In vivo deastatination has been a major problem in the development of reagents for therapeutic applications of the α-particle emitting radionuclide ^{211}At. Our prior studies demonstrated that the use of a *closo*-decaborate(2-) ([*closo*-$B_{10}H_9R]^{2-}$) moiety for ^{211}At labeling of biomolecules provides conjugates that are stable to *in vivo* deastatination. In this investigation, the *closo*-decaborate(2-) moiety was compared with the structurally similar *closo*-dodecaborate(2-) ([*closo*-$B_{12}H_{11}R]^{2-}$) to determine if one has more favorable properties than the other for use in pendant groups as ^{211}At labeling molecules. To determine the differences, two sets of structurally identical molecules, with the exception that they contained either a *closo*-decaborate(2-) or a *closo*-dodecaborate(2-) moiety, were compared with regard to their synthesis, radiohalogenation, stability to in vivo deastatination and tissue distribution. Quite different rates of reaction were noted in the synthetic steps for the two *closo*-borate(2-) moieties, but ultimately the yields were similar, making these differences of little importance. Differences in radiohalogenation rates were also noted between the two *closo*-borate(2-) moieties, with the more electrophilic *closo*-decaborate(2-) reacting more rapidly. This resulted in somewhat higher yields of astatinated *closo*-decaborate(2-) derivatives (84% vs 53%), but both cage moieties gave good radioiodination yields (e.g., 79−96%). Importantly, both *closo*-borate(2-) cage moieties were shown to have high stability to in vivo deastatination. The largest differences between pairs of compounds containing the structurally similar boron cage moieties were in their in vivo tissue distributions. For example, $[Et_3NH]_2B_{12}H_{10}I$−CONHpropyl, [^{125}I]**2b** had high concentrations in kidney (1 h, 19.8%ID/g; 4 h, 26.5%ID/g), whereas $[Et_3NH]_2B_{10}H_8I$−CONHpropyl, [^{125}I]**1e** had much lower concentrations in kidney (1 h, 6.6%ID/g; 4 h, 0.27%ID/g). Interestingly, when another salt of the *closo*-decaborate(2-), $[nBu_4N]_2B_{10}H_8I$−CONHpropyl, [^{125}I]**1b**, was evaluated, the route of excretion appeared to be hepatobiliary rather than renal. Identical biotin derivatives containing the two *closo*-borate(2-) cage moieties had similar tissue distributions, except the *closo*-decaborate(2-) derivative had lower concentrations in kidney (1 h, 19.9%ID/g; 4 h, 24.4%ID/g vs 1 h, 38.9%ID/g; 4 h, 40.6%ID/g). In summary, the higher reactivity, faster tissue clearance, and lower kidney concentrations make the *closo*-decaborate(2-) more favorable for further studies using them in reactive groups for ^{211}At labeling of biomolecules.

INTRODUCTION

The radionuclide, ^{211}At ($t_{1/2}$ = 7.21 h) is one of only a few α-emitting radionuclides considered useful for targeted radionuclide therapy of cancer (*1*−*4*). Although ^{211}At has a relatively short half-life ($t_{1/2}$ = 7.21 h), 100% of its decays (in a branched chain) emit an α-particle and the decay process does not result in production of α-particle emitting daughters (*5*). The short pathlengths of α-particle emissions (e.g., 50−80 μm) and the high linear energy deposition (>100 keV/μm) of those emissions make α-particles very effective in cell killing. Most importantly, the cell-killing properties of α-emissions make them potentially useful for killing micrometastatic disease, which is a major impediment to successful therapy of cancer (*6*).

Coupling ^{211}At with biomolecules that target cancer cells is very important for its application to therapy of cancer. Unfortunately, in vivo deastatination of biomolecules labeled with ^{211}At has been problematic in the development of therapeutic radiopharmaceuticals (*7*). In fact, the deastatination of labeled compounds has severely limited the in vivo application of ^{211}At. To circumvent this shortcoming, several research groups have evaluated the use of aryl pendant groups to stabilize the ^{211}At-labeled biomolecules in vivo (*8*−*11*). However, in many examples astatinated aryl groups are not stable to deastatination when the carrier biomolecule is rapidly metabolized. More recently, our research group has focused on using anionic boron cage pendant groups for labeling with ^{211}At. While the in vivo stability was found to be low for ^{211}At-bonded *nido*-carborane[1] pendant groups (*12*), we have found that the pendant groups containing *closo*-decaborate(2-) moieties, $[B_{10}H_9R]^{2-}$, can be used to provide high ^{211}At labeling yields and result in high stability in vivo (*13*).

Other investigators have reported the use of a similar boron cage moiety, *closo*-dodecaborate(2-), [*closo*-$B_{12}H_{11}R]^{2-}$ for radioiodine (*14, 15*) and ^{211}At labeling (*16*). Our interest in using *closo*-borate(2-) cage derivatives as pendant groups in ^{211}At

* Corresponding author. D. Scott Wilbur, Department of Radiation Oncology, University of Washington, Box 355016, 616 N.E. Northlake Place, Seattle, WA 98105. Phone: 206-616-9246, 206-616-8798. dswilbur@u.washington.edu.

[1]Nomenclature of compounds: (a) The designations "*nido*-" refers to a polyhedral structure that is open or "nest-like", and "*closo*-" refers to a polyhedral "cage" (from Greek "*clovo*" (*45*)) structure that is closed such as an icosahedran; (b) the naming of *closo*-borate(2-) compounds is simplified herein for brevity. For example, tetrabutylammonium 2-(*n*-propylamido)-nonahydro-*closo*-decaborate(2-), **1a**, is designated as $[nBu_4N]_2$[*closo*-$B_{10}H_9$-CONHpropyl], and triethylammonium 2-(*n*-propylamido)-undecahydro-*closo*-dodecaborate(2-), **2a**, is designated as $[Et_3NH]_2$[*closo*-$B_{12}H_{11}$-CONHpropyl].

10.1021/bc800515d CCC: $40.75 © 2009 American Chemical Society
Published on Web 02/23/2009

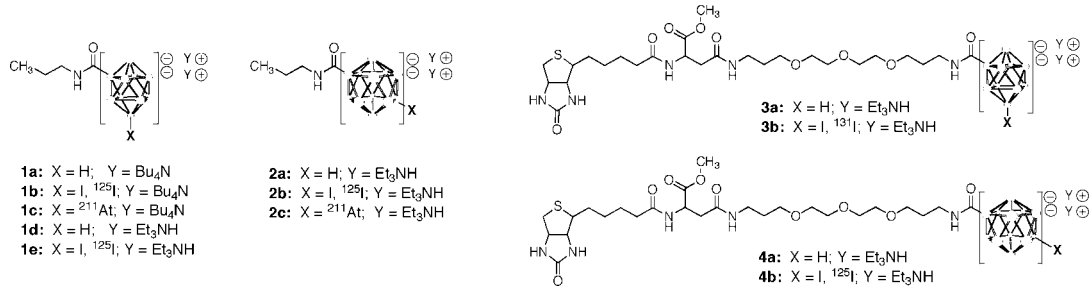

Figure 1. *closo*-Decaborate(2-) derivatives (**1a**−**1e**, **3a**, **3b**) and *closo*-dodecaborate(2-) derivatives (**2a**−**2c**, **4a**, **4b**) were prepared and evaluated. For simplicity in the *closo*-borate(2-) cage depictions, the open circles represent B (where substituted) or BH atoms.

labeling led to an investigation to determine which of the two *closo*-borate(2-) cage moieties has the most favorable properties for in vivo applications. In the investigation, we compared the chemical syntheses, radiolabeling efficiency, and in vivo stability of two pairs of identical compounds containing *closo*-decaborate(2-) and *closo*-dodecaborate(2-) moieties as depicted in Figure 1 (i.e., **1** vs **2** and **3** vs **4**). Use of pairs of compounds having the same structure except for the *closo*-borate(2-) cage permits evaluation of the effect of those moieties on chemical and in vivo properties of the compounds studied. Although the test compounds were identical except for the *closo*-borate(2-) moiety, it was anticipated that differences would be observed, as it is known that the chemistry and properties of *closo*-decaborate (2-) and *closo*-dodecaborate(2-) derivatives can be quite different (*17*−*19*).

In the first part of the investigation, carbonyl derivatives of the two boron cage moieties were modified by *n*-propylamine to provide simple *closo*-borate(2-) derivatives, **1a** and **2a**, which have a (small) lipophilic propylamide moiety attached. In an initial study, the nBu$_4$N salt of *closo*-decaborate(2-), **1a**, was prepared to facilitate its isolation and characterization. The Et$_3$NH salt was used with the *closo*-dodecaborate(2-), **2a**. The propionamide derivatives **1a** and **2a** were radioiodinated and astatinated, and then each radiolabeled *closo*-borate(2-) pair (i.e., [^{125}I]**1b**/[^{211}At]**1c** and [^{125}I]**2b**/[^{211}At]**2c**) was mixed and coinjected into mice to determine their biodistributions and the relative in vivo stability of the ^{211}At attachment. Due to unexpected in vivo distributions of the [^{125}I]**1b**/[^{211}At]**1c** pair of radiolabeled compounds, another biodistribution study was carried out with [^{125}I]**1e**, in which the counterions were changed from nBu$_4$N to Et$_3$NH. As another part of the investigation, biotin derivatives **3a** and **4a** were prepared, again incorporating the two *closo*-borate(2-) cage moieties into otherwise identical chemical structures. To evaluate the differences in their in vivo distributions, the biotin derivatives were radioiodinated to yield [^{131}I]**3b** and [^{125}I]**4b**, and that pair of radiolabeled compounds was coinjected into mice. The results of our investigation to compare chemistry and properties of structurally similar compounds containing the *closo*-decaborate(2-) and *closo*-dodecaborate(2-) moieties are reported herein.

MATERIALS AND METHODS

Materials. All chemicals obtained from commercial sources were analytical grade or better and were used without further purification. 4,7,10-Trioxa-1,13-tridecanediamine, solvents, and most other chemicals were obtained from Aldrich (Sigma-Aldrich, Milwaukee, WI). L-Aspartate-α-methyl ester (H-Asp-OMe) was obtained from Bachem (Bachem California, Inc., Torrance, CA). Biotin *N*-hydroxysuccinimide ester, **9**, was obtained from Quanta BioDesign, Ltd. (Powell, OH). Trifluoroacetyl tetrafluorophenol (TFA-O-TFP) was prepared as previously described (*20*). Silica gel chromatography was conducted with 70−230 mesh 60 Å silica gel (Aldrich). Decaborane was obtained from Alfa (Alfa Aesar, Ward Hill, MA).

Radioactivity. All radioactive materials were handled according to approved protocols at the University of Washington. Na[^{125}I]I and Na[^{131}I]I were purchased from Perkin-Elmer Life and Analytical Sciences, Inc. (Waltham, MA) as a high concentration solution in 0.1 N NaOH. ^{211}At was produced by irradiation of a thin layer of bismuth metal (99.999%, Aldrich) with a 28 MeV α-particle beam on a Scandatronix MC-50 cyclotron (University of Washington). Isolation of Na[^{211}At]At was conducted in a charcoal-filtered glovebox (Innovative Technologies, Inc., radioisotope glovebox) by distillation from the irradiated target using the conditions previously described (*13*, *21*). Radiohalogenations were conducted within a charcoal-filtered Plexiglas enclosure (Biodex Medical Systems Inc., Shirley, NY) housed in a radiochemical fume hood. Radiohalogenation reactions were carried out in vials capped with Teflon-coated septa vented through a 10 mL charcoal-filled syringe.

Measurement of ^{125}I, ^{131}I, and ^{211}At was accomplished on the Capintec CRC-15R Radioisotope Calibrator using the manufacturer's settings for those radionuclides. In the experiment evaluating an admixture of ^{131}I with ^{125}I, the ^{125}I counts were compensated for spillover from the ^{131}I window (32%). Tissue samples were counted in a Wallac 1480 gamma counter with the following window settings: channels 35−102 and 165−185 for ^{125}I and ^{131}I were counted together, and channels 20−2000 (open window) when ^{211}At and ^{125}I were counted together. In experiments containing an admixture of ^{211}At/^{125}I counting was conducted twice, soon after animal sacrifice to obtain total counts and again after samples had decayed for 3−5 days to obtain the ^{125}I counts. ^{211}At counts were obtained by subtracting ^{125}I counts from the total counts. All ^{211}At counts were corrected for decay during the counting process.

Spectral Analyses. ^{1}H/^{11}B NMR and mass spectral analyses were obtained on new compounds. The data obtained are provided with the experimental procedures. Spectral data for compounds previously reported are not listed, but were consistent with the reported data. ^{1}H and ^{11}B NMR spectra were obtained on a Bruker AV-300 (300 MHz for ^{1}H; 96.3 MHz for ^{11}B); or a Bruker AV-500 (500 MHz ^{1}H and 160.4 MHz for ^{11}B). ^{1}H NMR data are referenced to tetramethylsilane as an internal standard (δ = 0.0 ppm), and ^{11}B NMR data are referenced to $BF_3 \cdot OEt_2$ as an external standard. Infrared spectra were obtained on a Bruker Vector 33 Fourier transform infrared spectrophotometer. Mass spectral data (both low and high resolution) were obtained on a VG Analytical (Manchester, England) VG-70 SEQ mass spectrometer with associated 11250J Data System. Although several attempts were made, we were unsuccessful in obtaining mass spectral data for two of the *closo*-dodecaborate(2-) derivatives, **2b** and **4b**.

Analytical Chromatography. HPLC separations of the nonradioactive compounds were obtained using a system that contained a Hewlett-Packard quaternary 1050 gradient pump, a variable wavelength UV detector (254 nm), and an ELSD 2000 evaporative light-scattering detector (Alltech, Deerfield, IL). Analysis of the HPLC data was conducted on Hewlett-

Packard HPLC ChemStation software. Reversed-phase HPLC chromatography was carried out on an Alltech Altima C-18 column (5 μm, 250 × 4.5 mm) using a gradient solvent system at a flow rate of 1 mL/min. The gradient mixture was composed of MeOH (eluant A) and 0.05 M, pH 5.5, aqueous triethylammonium acetate (eluant B). The gradient started with 20% MeOH and 80% eluant B for 2 min; then, the % MeOH was increased linearly to 100% over a 13 min period; following this, the elution continued with 100% MeOH for an additional 5 min. The retention time (t_R) of each iodinated compound is provided with the experimental procedure.

Preparative Chromatography. Products were purified from crude reaction mixtures using a Biotage SP Flash Purification System (Charlottesville, VA) on a reversed-phase C18 FLASH 25+M column. The purification used a gradient mixture composed of MeOH and 0.05 M Et_3NHOAc (TEAA). The gradient started with 80% 0.05 M TEAA, and MeOH was increased linearly to 100% over the next 20 min. Fractions were collected on the basis of UV detection at 215 or 254 nm. Fractions containing pure products were determined by analytical HPLC and were combined, solvent evaporated, and isolated to provide the yields listed.

Radio-HPLC. The product mixtures from radioiodination and astatination reactions were analyzed by HPLC using a C-18 column (Altima C-18, 5 μm, 250 × 4.5 mm; Alltech, Deerfield, IL) eluting at a flow rate of 1 mL/min with a gradient beginning with 20% MeOH/80% of an aqueous Et_3NHOAc solution. The HPLC equipment used in the analyses consisted of a Hewlett-Packard quaternary 1050 gradient pump, Waters 601 UV detector, and a Beckman model 170 radioisotope detector. Analysis of the HPLC data was conducted on Hewlett-Packard HPLC ChemStation software. Isolation of radiolabeled compounds was accomplished by collection of part of (when broad) or the entire radioactive peak. The retention times (t_R) of the radioiodinated and astatinated compounds are provided with the analytical data for individual compounds.

$[Et_3NH]_2$[*closo*-$B_{10}H_{10}$], 5a. This compound was prepared by a modification of the procedure described by Hawthorne and Pilling (*22*). A 25 g quantity (0.21 mol) of decaborane ($B_{10}H_{14}$) was dissolved in 400 mL xylene in a three-necked flask. The flask was flushed with Ar, and then 75 mL (0.54 mol) of Et_3N was added dropwise over 30 min. Following the addition, the reaction mixture was heated to 105 °C for 3 h, then refluxed (140 °C) for another 5 h. The reaction mixture was allowed to cool to room temperature, transferred to a round-bottom flask, and the xylene was removed with heating on a rotary evaporator. Addition of 250 mL of MeOH to the residue gave a colorless precipitate. The precipitate was filtered and set aside. The remaining solution was triturated with EtOAc (750 mL), filtered, and washed with EtOAc (1 L). The combined precipitate was placed under high vacuum to yield 62.3 g (94%) of **5a**. Spectral properties of this compound were as previously reported (*22*).

$[n-Bu_4N]_2$[*closo*-$B_{10}H_{10}$], 5b. A 2.0 g (6.20 mmol) quantity of $[Et_3NH]_2[B_{10}H_{10}]$ was dissolved in water (100 mL), then a solution containing *n*-Bu_4NBr (6.0 g, 18.61 mmol) in water (20 mL) was added slowly with stirring at room temperature. The precipitate was filtered, washed with water (1 L), dried under vacuum for overnight to afford the product as a colorless solid. 3.2 g (86%).

Na_2[*closo*-$B_{10}H_{10}$], 5c. A 25 × 1.5 cm column was filled with Amberlite IR120 resin (Sigma-Aldrich, St. Louis, MO) in deionized H_2O. Then, a 200 mL quantity of 3 M HCl was run across the column, followed by 750 mL of deionized H_2O. After acid conditioning, 250 mL of a NaCl solution (1 M) was passed over the column, followed by 750 mL of deionized H_2O. After conversion to the Na form, 100 mg sample of **5a** (0.31 mmol) was dissolved in 2 mL of a 1:1 mixture of CH_3CN/H_2O and was loaded on the column. The column was eluted with deionized H_2O (100 mL). The eluted aqueous solution was evaporated to a solid residue on a rotoevaporator, then placed under high vacuum overnight to give 51 mg (0.31 mmol, 100%) of **5c**.

$[Et_3NH]_2$[*closo*-$B_{12}H_{12}$], 6. This compound was prepared by a modification of a procedure described by Miller and Muetterties (*23*). A 240 mL quantity of undecane was placed in a 1 L three-necked flask equipped with a thermometer on one neck and a condenser with an addition funnel on top on the middle neck and a septum on the third neck. The addition funnel was capped with a septum for Ar introduction (with bubbler) and hydrogen release. The system was placed under argon and heated to 190−197 °C. In a separate flask, 32.0 g decaborane (262 mmol) was placed in a flask under argon and 84 mL of borane−triethylamine complex (65.3 g, 567 mmol) was added. When the decaborane was dissolved, it was filtered through glass wool into the addition funnel. The mixture was then slowly dripped into the hot undecane, keeping the temperature above 190 °C. Large amounts of hydrogen evolved. After addition of the decaborane solution, the mixture was heated for an additional 30 min. The mixture became thick with white/yellow solid and was difficult to stir. After cooling, the precipitate was filtered by gravity and the solid was washed with 200 mL ether to remove residual undecane. The solid was air-dried, then was dissolved in 1.5 L boiling water and heated for 30 min. A thick gummy material collected, floating on top of the solution. This was then filtered hot, and the resultant solution was allowed to cooled to room temperature, then placed in a refrigerator at 4 °C. After 3 h at 4 °C, the colorless solid was collected by vacuum filtration and dried under high vacuum to yield 34.6 g. The filtrate was concentrated to 200 mL, yielding another 15.9 g. A total yield 50.5 g (53.7%) of **6** was obtained. Spectral properties of isolated **6** were as previously reported (*23*).

$[n-Bu_4N]$[*closo*-$B_{10}H_9$-CO], 7a. This compound was prepared using a procedure similar from that previously reported (*24*). A 0.5 mL quantity (5.26 mmol) of oxalyl chloride was added slowly over 5 min to a solution of $[n-Bu_4N]_2[B_{10}H_{10}]$ (1 g, 1.66 mmol) in anhydrous CH_2Cl_2 (15 mL) at 0 °C. The mixture was stirred at 0 °C for 30 min, then allowed to warm to room temperature while stirring for additional 30 min. The reaction solution was evaporated to dryness on a rotary evaporator under vacuum. The residue was recrystallized from CH_2Cl_2/Et_2O to yield 0.74 g (71%) of brown tacky solid. IR (cm^{-1}, KBr disk): 2389 (s), 2340 (s), 2308 (s). ^{11}B NMR (DMSO-d_6, 160.43 MHz): δ 5.71 (1B), −4.52 (4B), −15.70 (2B), −21.64 (2B), −25.80 (1B).

$[Et_3NH]$[*closo*-$B_{10}H_9$-CO], 7b ((*24*)). A 1.08 mL (12.4 mmol) quantity of oxalyl chloride was added slowly over 5 min to a solution of $[Et_3NH]_2[B_{10}H_{10}]$ (2 g, 6.2 mmol) in anhydrous CH_3CN (30 mL) at 0 °C. The mixture was stirred at 0 °C for 30 min, then allowed to warm to room temperature while stirring for an additional 30 min. The reaction solution was evaporated to dryness on a rotary evaporator under vacuum. The residue was recrystallized from CH_3CN/Et_2O to yield 1.8 g (83%) of a brown tacky solid.

$[Et_3NH]$[*closo*-$B_{12}H_{11}$-CO], 8. A 1 mL (11.46 mmol) quantity of oxalyl chloride was added to a solution of $[Et_3NH]_2[B_{12}H_{12}]$ (1 g, 2.89 mmol) in anhydrous CH_3CN (20 mL) at room temperature, and then the mixture was stirred and heated to reflux for 3 h. The solution was allowed to cool to room temperature, then was evaporated to dryness on a rotary evaporator under vacuum. The residue was recrystallized from CH_3CN/Et_2O to yield 0.84 g (78%) of a brown tacky solid. IR (cm^{-1}, KBr disk): 2392 (s), 2336 (s), 2284 (s). ^{11}B NMR (DMSO-d_6, 160.43 MHz): δ −10.96 (1B), −11.98 (1B), −13.11 (1B), −14.20 (2B), −15.16 (3B), −15.82 (4B).

[*n*Bu$_4$N]$_2$[*closo*-B$_{10}$H$_9$-CONHpropyl], 1a. A solution of [*n*Bu$_4$N][*closo*-B$_{10}$H$_9$-CO], **7a** (400 mg, 1.032 mmol), *n*-propylamine (0.75 mL, 9.12 mmol), Et$_3$N (0.72 mL, 5.16 mmol) in anhydrous CH$_3$CN (10 mL) was stirred at room temperature for 16 h. EtOAc (15 mL) was added and the resultant solution was stirred at room temperature for 20 min. The solvents were decanted, and the crude residue was redissolved in 4 mL of MeOH/CH$_3$CN (1/1) and purified via preparative reversed-phase chromatography. Purification yielded 410 mg (83%) of **1a**. ^{1}H NMR (CD$_3$OD, 500 MHz): δ −0.25−0.75 (m, 9H), 0.86(t, J = 7.4 Hz, 3H), 1.02 (t, J = 7.2 Hz, 24 H), 1.36−1.48 (m, 16 H), 1.65−1.75 (m, 18 H), 2.98 (t, J = 6.8 Hz, 2 H), 3.26−3.29 (m, 16H). ^{11}B NMR (CD$_3$OD, 160.43 MHz): δ −0.62 (1B), −1.39 (1B), −23.90 (1B), −28.26 (7B). LRMS (ES$^-$) calcd for C$_4$H$_{17}$B$_{10}$NO (M)$^-$: 205.2. Found: 205.1. HPLC: t_R = 11.6 min.

[Et$_3$NH]$_2$B$_{10}$H$_8$I-CONH-propyl, 1b. A 746 μL aliquot of a 10 mg/mL solution of chloramine-T (32.7 μmol) in H$_2$O was added to a solution containing 20 mg (65.5 μmol) [Et$_3$NH]$_2$B$_{10}$H$_9$-CONH-Pr, **1a**, and 4.9 mg NaI (49 μL of 100 mg/mL in H$_2$O, 32.7 μmol) in 1 mL MeOH/H$_2$O with 5% HOAc (1:1). The reaction mixture was stirred at room temperature for 30 s, and then Na$_2$S$_2$O$_5$ (622 μL, 32.7 μmol, 10 mg/mL in H$_2$O) was added. The product was identified as a new, more lipophilic, species by reversed-phase HPLC (**1b** had approximately the same peak area as **1a** by ELSD detection). LRMS (ES$^-$) calcd for C$_4$H$_{16}$B$_{10}$INO (M)$^-$: 331.1. Found: 331.1. HPLC: t_R = 4.0 min.

[*n*Bu$_4$N]$_2$B$_{10}$H$_8$I-CONHpropyl, [^{125}I]1b. To 100 μL of 1 mg/mL **1a** in 50/50 water/MeOH with 5% HOAc was added 3 μL of Na[^{125}I]I (980 μCi in 0.1 N NaOH) followed by 10 μL of 1 mg/mL chloramine-T in H$_2$O. After 2 min at room temperature, 10 μL of 1 mg/mL Na$_2$S$_2$O$_5$ was added to quench the reaction. Analytical radioHPLC indicated that an 86% labeling efficiency was obtained. The remainder of the radiolabeled material was injected on the HPLC in two fractions and collected in a peak at 4.2 min to give 250 μCi of isolated product (26% isolated from leading portion of product peak). This was concentrated on a rotary evaporator, diluted with PBS, and neutralized with NaOH for the animal study.

[*n*Bu$_4$N]$_2$B$_{10}$H$_8$At-CONHpropyl, [^{211}At]1c. To 100 μL of 1 mg/mL **1a** in 50/50 water/MeOH with 5% HOAc was added 100 μL of Na[^{211}At]At (500 μCi in 0.05 N NaOH) followed by 10 μL of 1 mg/mL chloramine-T in H$_2$O. After 5 min at room temperature, 10 μL of 1 mg/mL Na$_2$S$_2$O$_5$ in H$_2$O was added to quench the reaction. Analytical radioHPLC indicated that an 84% labeling efficiency was obtained. The remainder of the radiolabeled material was injected on the HPLC, and the leading portion of the peak at 4.8 min to give 180 μCi was isolated (36%). This was concentrated on a rotary evaporator, diluted with PBS, and neutralized with NaOH for an animal study.

[Et$_3$NH]$_2$[*closo*-B$_{10}$H$_9$-CONHpropyl], 1d. This compound was prepared in 79% yield using the same reaction conditions as used to prepare **1a**. HPLC: t_R = 3.8 min.

[Et$_3$NH]$_2$B$_{10}$H$_8$I-CONHpropyl, [^{125}I]1e. To 100 μL of 1 mg/mL **1d** in 50/50 MeOH/5% HOAc was added 4 μL of Na[^{125}I]I (1.4 mCi) in 0.1 N NaOH followed by 20 μL of 1 mg/mL chloramine-T in water. After 1 min at rt, the reaction was quenched with 20 μL of 1 mg/mL Na$_2$S$_2$O$_5$ in H$_2$O. The reaction mixture was injected on the HPLC, and the peak at 12 min was collected for an isolated yield of 81% (HPLC indicated 82% reaction efficiency).

[Et$_3$NH]$_2$[*closo*-B$_{12}$H$_{11}$-CONHpropyl], 2a. A 500 mg (1.84 mmol) quantity of [Et$_3$NH][B$_{12}$H$_{11}$-CO], **8** was dissolved in 10 mL *n*-propylamine and was stirred at room temperature for 16 h. Excess *n*-propylamine was removed under vacuum. The crude residue was dissolved in 6 mL of MeOH/DMF/H$_2$O (1/1/1) and was purified via preparative reversed-phase chromatography. Isolation of the product yielded 510 mg (84%) of **8**. ^{1}H NMR (DMSO-d_6, 500 MHz): δ 0.39−1.30 (m, 11H), 0.87 (t, J = 7.4 Hz, 3H), 1.16 (t, J = 7.2 Hz, 18H), 1.50−1.58 (m, 2H), 2.73 (t, J = 7.4 Hz, 2H), 3.01 (q, J = 7.3 Hz, 12H), 3.15 (s, 1H). ^{11}B NMR (CD$_3$OD, 160.43 MHz): δ −0.43 (1B), −14.92 (5B), −15.54 (6B). LRMS (ES$^-$) calcd for C$_4$H$_{19}$B$_{12}$NO (M)$^-$: 229.2. Found: 229.1. HPLC: t_R = 3.7 min.

[Et$_3$NH]$_2$B$_{12}$H$_{10}$I-CONH-propyl, 2b. A 692 μL (30.4 μmol) aliquot of a 10 mg/mL solution of chloramine-T in H$_2$O was added to a solution containing 20 mg (60.8 μmol) [Et$_3$NH]$_2$-B$_{12}$H$_{11}$−CONH-Pr, **2a**, and 4.56 mg NaI (30.4 μmol; 45.6 μL of a 100 mg/mL solution in H$_2$O) in 1 mL of MeOH/H$_2$O with 5% HOAc (1:1). The solution was stirred at room temperature for 30 s, and then Na$_2$S$_2$O$_5$ (578 μL, 30.4 μmol, 10 mg/mL in H$_2$O) was added. The product was identified as a new, more lipophilic species by reversed-phase HPLC (**2b** had approximately the same peak area as **2a** by ELSD detection). HPLC: t_R = 4.0 min.

[Et$_3$NH]$_2$B$_{12}$H$_{10}$I-CONHpropyl, [^{125}I]2b. To 120 μL of 1 mg/mL **1a** in 50/50 water/MeOH with 1% HOAc was added 1 μL of Na[^{125}I]I (566 μCi in 0.1 N NaOH) followed by 20 μL of 1 mg/mL chloramine-T in H$_2$O. After 2 min at room temperature, 20 μL of 1 mg/mL Na$_2$S$_2$O$_5$ in H$_2$O was added to quench the reaction. Analytical radioHPLC indicated that a 79% labeling efficiency was obtained. The remainder of the radiolabeled material was injected on the HPLC in two fractions and collected in a broad peak at 10 min to give 306 μCi (68%) of isolated product. This was concentrated on a rotary evaporator, diluted with PBS, and neutralized with NaOH for use in the animal study.

[Et$_3$NH]$_2$B$_{12}$H$_{10}$At-CONHpropyl, [^{211}At]2c. To 120 μL of 1 mg/mL **1a** in 50/50 water/MeOH with 1% HOAc was added 100 μL of Na[^{211}At]At (633 μCi in 0.05 N NaOH) followed by 20 μL of 1 mg/mL chloramine-T in H$_2$O. After 10 min at room temperature, 20 μL of 1 mg/mL Na$_2$S$_2$O$_5$ in H$_2$O was added to quench the reaction. Analytical radioHPLC indicated that a 53% labeling efficiency was obtained. A portion of the reaction mixture (250 μCi) was injected on the HPLC and a broad peak at 9 min was collected to give 126 μCi of isolated product (45%). This was concentrated on a rotary evaporator, diluted with PBS, and neutralized with NaOH for the animal study.

Biotin-Asp-α-OMe, 11. H-Asp-OMe, **10** (516 mg, 3.51 mmol), was dissolved in a solution of H$_2$O (15 mL) and NaHCO$_3$ (738 mg, 8.78 mmol), and then biotin *N*-hydroxysuccinimide ester, **9** (1.0 g, 2.93 mmol), and acetone (15 mL) were added, respectively. The resulting solution was stirred at room temperature for 16 h, and then the solution was evaporated to dryness on a rotary evaporator under vacuum. The residue was dissolved in water (50 mL), and the aqueous solution was acidified to pH 2.0 by 1 N HCl. After storage at 5 °C overnight, the white precipitate was filtered, washed with water (500 mL), and dried under vacuum to yield 791 mg (73%) of **11** as a colorless solid. ^{1}H NMR (DMSO-d_6, 500 MHz): δ 1.24−1.36 (m, 3H), 1.41−1.53 (m, 4H), 1.57−1.64 (m, 1H), 2.08−2.12 (m, 2H), 2.56−2.61 (m, 2H), 2.70 (dd, J = 5.9, 16.2 Hz, 1H), 2.82 (dd, J = 5.3, 12.3 Hz, 1H), 3.07−3.11 (m, 1H), 3.61 (s, 3H), 4.11−4.14 (m, 1H), 4.30 (dd, J = 5.4, 7.6 Hz, 1H), 4.57 (dd, J = 7.5, 13.4 Hz, 1H), 6.37 (s, 1H), 6.41 (s, 1H), 8.28 (d, J = 7.5 Hz, 1H), 12.44 (br s, 1H). HRMS (ES$^+$) calcd for C$_{15}$H$_{23}$N$_3$NaO$_6$S (M + Na)$^+$: 396.1205. Found: 396.1202. HPLC: t_R = 4.9 min.

Biotin-Asp-α-OMe Tetrafluorophenyl Ester, 12. TFA-O-TFP (182 mg, 0.70 mmol) was added slowly to a solution of biotin-Asp-OMe, **11** (200 mg, 0.54 mmol), Et$_3$N (0.112 mL, 0.80 mmol), and anhydrous DMF (8 mL) at 0 °C. After stirring at 0 °C for 30 min, the solution was evaporated on a rotary

evaporator under vacuum. The crude product was then purified by silica gel column (1.5 cm × 25 cm) eluting with a gradient solution from 50% EtOAc/hexanes to 100% EtOAc. Purification yielded 235 mg (84%) of **12** as a colorless solid. mp 127−128 °C. ^{1}H NMR (DMSO-d_6, 500 MHz): δ 1.25−1.38 (m, 3H), 1.42−1.55 (m, 4H), 1.58−1.65 (m, 1H), 2.09−2.15 (m, 2H), 2.57 (d, J = 12.6 Hz, 1H), 2.81 (dd, J = 5.9, 16.4 Hz, 1H), 3.06−3.10 (m, 1H), 3.16 (dd, J = 7.1, 16.5 Hz, 1H), 3.29 (dd, J = 6.2, 16.8 Hz, 1H), 3.66 (s, 3H), 4.11−4.14 (m, 1H), 4.30 (dd, J = 5.0, 7.8 Hz, 1H), 4.76 (dd, J = 7.3, 14.5 Hz, 1H), 6.36 (s, 1H), 6.42 (s, 1H), 7.92−7.99 (m, 1H), 8.52 (d, J = 7.7 Hz, 1H). HRMS (ES$^+$) calcd for $C_{21}H_{23}F_4N_3NaO_6S$ (M + Na)$^+$: 544.1141. Found: 544.1126. HPLC: t_R = 11.6 min.

[Et$_3$NH]B$_{10}$H$_9$-CONH-trioxatridecane-NH$_2$, 13. This compound was prepared in 68% yield by reaction of **7b** with 4,7,10-trioxa-1,13-tridecanediamine at room temperature for 3 days as previously reported (*13*).

[Et$_3$NH]B$_{12}$H$_{11}$-CONH-trioxatridecane-NH$_2$, 14. A solution of [Et$_3$NH][B$_{12}$H$_{11}$-CO], **8** (0.30 g, 1.11 mmol), and 4,7,10-trioxa-1,13-tridecanediamine (6.0 mL) was stirred at room temperature for 16 h. EtOAc (10 mL) was added, and the resulting solution was stirred at room temperature for 20 min. The solution was decanted, and the residue was washed with EtOAc (3 × 15 mL). The crude product was dissolved in 4 mL of MeOH/DMF/water (1/1/1) and purified via preparative reversed-phase chromatography. Purification yielded 407 mg (75%) of **14**. ^{1}H NMR (DMSO-d_6, 500 MHz): δ 0.21−1.50 (m, 11H), 1.12 (t, J = 7.2 Hz, 9H), 1.66−1.76 (m, 4H), 1.78 (s, 1H), 2.68−2.75 (m, 4H), 2.94−2.97 (m, 8H), 3.38−3.52 (m, 12H). ^{11}B NMR (DMSO-d_6, 160.43 MHz): δ −6.20 (1B), −15.54 (5B), −16.15 (6B). LRMS (ES-) calc for $C_{11}H_{33}B_{12}N_2O_4LiNa$ (M + Li + Na) 419.4, found 419.4. HPLC: t_R = 3.8 min.

[Et$_3$NH]$_2$B$_{10}$H$_9$-CONH-trioxatridecane-NHCO-Asp-α-OMe-Biotin, 3a. [Et$_3$NH]B$_{10}$H$_9$-trioxatridecane-NH$_2$, **13** (116 mg, 0.249 mmol), was added to a solution of biotin-Asp-OMe TFP ester, **12** (100 mg, 0.192 mmol), Et$_3$N (0.08 mL, 0.575 mmol), and anhydrous DMF (10 mL). The resulting solution was stirred at room temperature for 1 h, and then the volatile materials were removed on a rotary evaporator under vacuum. The residue was dissolved in 5 mL of MeOH/CH$_3$CN (1/1) and purified via preparative reversed-phase chromatography. Purification yielded 108 mg (69%) of **3a**. ^{1}H NMR (CD$_3$OD, 500 MHz): δ −0.18−0.79 (m, 9H), 1.22 (t, J = 7.3 Hz, 18H), 1.38−1.44 (m, 2H), 1.52−1.73 (m, 6H), 2.19−2.27 (m, 2H), 2.66−2.69 (m, 3H), 2.91 (dd, J = 5.0, 12.8 Hz, 1H), 3.06 (q, J = 7.2 Hz, 12H), 3.17−3.23 (m, 4H), 3.48 (t, J = 6.4 Hz, 3H), 3.53−3.56 (m, 2H), 3.58−3.61 (m, 3H), 3.62−3.67 (m, 16H), 3.69 (s, 3H), 4.29 (dd, J = 4.4, 7.8 Hz, 1H), 4.46 (dd, J = 5.0, 8.0 Hz, 1H), 4.69 (t, J = 6.0 Hz, 1H). ^{11}B NMR (CD$_3$OD, 160.43 MHz): δ −0.91 (2B), −23.79 (2B), −27.99 (6B). LRMS (ES$^-$) calcd for $C_{26}H_{53}B_{10}N_5O_9S$ (M)$^-$: 721.5, Found: 721.5. HPLC: t_R = 12.1 min.

[Et$_3$NH]$_2$B$_{10}$H$_8$I-CONH-trioxatridecane-NHCO-Asp-α-OMe-Biotin, 3b. A 246 μL aliquot of chloramine-T solution (11 μmol, 10 mg/mL in H$_2$O) was added to a solution of **3a** (20 mg, 22 μmol), NaI (16 μL, 11 μmol, 100 mg/mL in water), and 5% HOAc of MeOH/water (50/50, 1 mL). The solution was allowed to stir at room temperature for 1 min, then 205 μL of Na$_2$S$_2$O$_5$ (11 μmol, 10 mg/mL in H$_2$O) was added. The product was identified as a new, more lipophilic species by reversed-phase HPLC (**3b** had approximately the same peak area as **3a** by ELSD detection). LRMS (ES$^-$) calcd for $C_{26}H_{53}B_{10}IN_5O_9S$ (M + H + Na): 871.3, Found: 871.3. HPLC: t_R = 4.3 min.

[Et$_3$NH]$_2$B$_{10}$H$_8$[^{131}I]I-CONH-trioxatridecane-NHCO-Asp-OMe-Biotin, [^{131}I]3b. A 20 μL aliquot of a 1 mg/mL solution of chloramine-T was added to a solution containing **3a** (100 μg, 0.11 μmol), Na[^{131}I]I (3 μL, 780 μCi, 0.1 N NaOH solution), and 100 μL of 5% HOAc in 1:1 H$_2$O/MeOH. The reaction was quenched with Na$_2$S$_2$O$_5$ (20 μL of 1 mg/mL solution in H$_2$O) after 1 min at room temperature. Analytical radioHPLC indicated that a 96% labeling efficiency was obtained. A portion of the eluted [^{131}I]**3b** was isolated for the animal study (44%).

[Et$_3$NH]B$_{12}$H$_{11}$-CONH-trioxatridecane-NHCO-Asp-OMe-Biotin, 4a. [Et$_3$NH]B$_{12}$H$_{11}$-CONH-trioxatridecane-NH$_2$, **14** (122 mg, 0.249 mmol) was added to a solution of biotin-Asp-OMe TFP ester, **12** (100 mg, 0.192 mmol), Et$_3$N (0.08 mL, 0.575 mmol), and anhydrous DMF (10 mL). The resulting solution was stirred at room temperature for 1 h, and then the volatile materials were removed on a rotary evaporator under vacuum. The residue was dissolved in 5 mL of MeOH/CH$_3$CN (1/1) and purified via preparative reversed-phase chromatography. Purification yielded 86 mg (53%) of **4a**. ^{1}H NMR (DMSO-d_6, 500 MHz): δ 0.22−1.44 (m, 13H), 1.22 (t, J = 7.3 Hz, 9H), 1.52−1.73 (m, 6H), 2.19−2.27 (m, 2H), 2.66−2.69 (m, 3H), 2.91 (dd, J = 5.0, 12.8 Hz, 1H), 3.06 (q, J = 7.2 Hz, 6H), 3.17−3.23 (m, 4H), 3.48 (t, J = 6.4 Hz, 3H), 3.53−3.56 (m, 2H), 3.58−3.61 (m, 3H), 3.62−3.67 (m, 16H), 3.59 (s, 3H), 4.13 (dd, J = 4.7, 7.8 Hz, 1H), 4.31 (dd, J = 4.8, 7.7 Hz, 1H), 4.55 (dd, J = 6.9, 13.8 Hz, 1H), 6.35 (s, 1H), 6.40 (s, 1H), 7.89 (t, J = 5.3 Hz, 1H), 8.16 (d, J = 7.9 Hz, 1H). ^{11}B NMR (DMSO-d_6, 160.43 MHz) δ −4.55 (1B), −15.88 (5B), −16.55 (6B). LRMS (ES$^-$) calcd for $C_{26}H_{55}B_{12}N_5O_9SNa$ (M + Na): 768.5, Found: 768.5. HPLC: t_R = 3.7 min.

[Et$_3$NH]$_2$B$_{12}$H$_{10}$I-CONH-trioxatridecane-NHCO-Asp-α-OMe-Biotin, 4b. A 240 μL aliquot of a chloramine-T solution (11 mmol, 10 mg/mL in water) was added to a solution of [Et$_3$NH]B$_{12}$H$_{11}$-trioxa-Asp-OMe-biotin (20 mg, 21 μmol), NaI (16 μL, 11 mmol, 100 mg/mL in water), and 5% HOAc of MeOH/water (50/50, 1 mL). After the solution was stirred at room temperature for 1 min, 200 μL of Na$_2$S$_2$O$_5$ (11 mmol, 10 mg/mL in water) was added. The product was identified as a new, more lipophilic species by reversed-phase HPLC (**4b** had approximately the same peak area as **4a** by ELSD detection). HPLC: t_R = 4.5 min.

[Et$_3$NH]$_2$B$_{12}$H$_{11}$[^{125}I]I-CONH-trioxatridecane-NHCO-Asp-OMe-Biotin, [^{125}I]4b. A 20 μL aliquot of a 1 mg/mL solution of chloramine-T was added to a solution containing **4a** (100 μg, 0.11 μmol), Na[^{125}I]I (2 μL, 1 mCi, 0.1 N NaOH solution), and 100 μL of 5% HOAc in 1:1 H$_2$O/MeOH. The reaction was quenched with Na$_2$S$_2$O$_5$ (20 μL of 1 mg/mL solution in H$_2$O) after 10 min at room temperature. Analytical radioHPLC indicated that a 86% labeling efficiency was obtained. A portion of the eluted [^{125}I]**4b** was isolated for the animal study (33%).

Biodistribution Studies. The biodistribution studies were conducted under a protocol approved by the Institutional Animal Care and Use Committee (IACUC) at the University of Washington. Procedures were conducted in compliance with U.S. laws relating to the conduct of animal experimentation. Male athymic mice (*nu*/*nu*), obtained from Simonson Laboratories (Gilroy, CA), were housed for 1 week in the isolator facility prior to beginning the study. In each experiment, the peaks corresponding to the desired products were isolated from the HPLC and were mixed in appropriate quantities to prepare an admixture containing predetermined quantities of each astatinated and/or radioiodinated compound. The admixture was diluted with phosphate buffered saline (PBS) to prepare injection quantities of ∼100 μL. This quantity was injected into each of 10 athymic mice via the lateral tail vein. The actual amount of injectate each animal received was determined by weighing the administering syringe before and after injection. Groups of 5

Scheme 1. Synthesis and Radiohalogenation of *n*-Propylamide Derivatives of *closo*-Decaborate(2-) and *closo*-Dodecaborate(2-)†

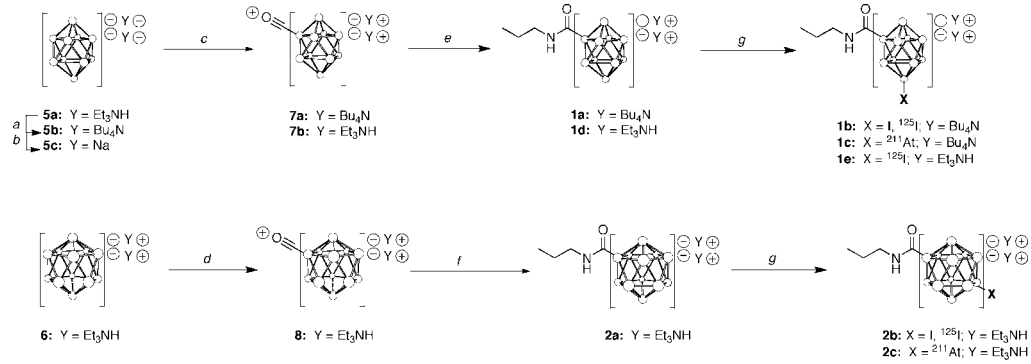

† Circles in cage structures represent B (when substituted) or BH atoms. (*a*) $(n\text{Bu})_4\text{NBr}$, H_2O, 86%. (*b*) 120 IR ion exchange (Na), 100%. (*c*) oxalyl chloride, anhyd. CH_2Cl_2, 0 °C-rt, 30 min: **7a**, 71%, **7b**, 83%. (*d*) oxalyl chloride, anhyd. CH_2Cl_2, reflux, 3 h, 8, 78%. (*e*) *n*-propylNH_2, Et_3N, anhyd. CH_3CN, rt, 16 h, **1a**, 83%, **1d**, 79%. (*f*) *n*-propylNH_2, rt, 16 h, **2a**, 84%; ^{f}Na[*X], ChT, MeOH/H_2O, rt: [^{125}I]**1b**, 2 min, 86%, [^{211}At]**1c**, 5 min, 84%, [^{125}I]**1e**, 1 min, 82%; [^{125}I]**2b**, 2 min, 68%; [^{211}At]**2c**, 10 min, 53%.

mice were sacrificed by cervical dislocation at 1 and 4 h post-injection. The tissues were excised, blotted free of blood, weighed, and counted. Blood weight was estimated to be 6% of the total body weight (*25*). Calculation of the percent injected dose per gram (%ID/g) in the tissues was accomplished using internal standards for the ^{211}At and ^{125}I or ^{131}I counts. The quantities injected and data obtained in the biodistribution studies are provided in Tables S1−S4 (Supporting Information).

RESULTS

Preparation of *closo*-Borate(2-) Derivatives. The *closo*-borate(2-) derivatives, **1a**−**1e** and **2a**−**2c**, were prepared by the reaction sequences shown in Scheme 1. $[Et_3NH]_2$[*closo*-$B_{10}H_{10}$], **5a**, was prepared in 94% yield by reaction of decaborane ($B_{10}H_{14}$) with Et_3N in xylene at 105−140 °C (*22*). $[n\text{Bu}_4\text{N}]_2$[*closo*-$B_{10}H_{10}$], **5b**. was prepared in 86% yield from **5a** by counterion exchange in H_2O after mixing with $n\text{Bu}_4\text{NBr}$. The Na salt Na_2[*closo*-$B_{10}H_{10}$], **5c**, was prepared from **5a** by elution over an Amberlite IR120 ion-exchange resin (Na form). $[Et_3NH]_2$[*closo*-$B_{12}H_{12}$], **6**, was prepared in 54% yield by reaction of decaborane with a triethylamine borane complex ($Et_3N\cdot BH_3$) at 190 °C in undecane (*23*). $[n\text{Bu}_4\text{N}]_2$[*closo*-$B_{10}H_{10}$], **5b**, was substituted with carbon monoxide by reaction of oxalyl chloride in anhydrous acetonitrile, initially in an ice bath for 30 min, then at room temperature for 30 min, to provide [$n\text{Bu}_4$N][*closo*-$B_{10}H_9$-CO], **7a**, in 71% yield. [Et_3NH][*closo*-$B_{10}H_9$-CO], **7b**, was prepared in 83% yield using the same reaction conditions. Similarly, $[Et_3NH]_2[B_{12}H_{12}]$, **6**, was substituted with carbon monoxide using the same reaction at reflux for 3 h to provide [Et_3NH][$B_{12}H_{11}$-CO], **10**, in 78% yield. Reaction of **7a** with *n*-propylamine and triethylamine in anhydrous acetonitrile at room temperature for 16 h provided the adduct $[n\text{Bu}_4\text{N}]_2[B_{10}H_9]$-CONHpropyl, **1a**, in 83% yield. Reaction of **8** with *n*-propylamine was slower, requiring it to be used as a solvent. However, the reaction was complete when run at room temperature for 16 h, yielding the adduct, $[Et_3NH]_2[B_{12}H_{11}]$-CONHpropyl, **2a**, in 84%.

The biotin derivatives **3a** and **4a** were prepared in multistep syntheses as depicted in Scheme 2. The reaction sequence began with preparation of a biotinidase-stabilized biotin derivative, the aspartate methyl ester adduct of biotin, **11** (*26*). Reaction of biotin *N*-hydroxylsuccinimide ester **9** with the α-methyl ester of aspartic acid, **10**, in aqueous sodium bicarbonate provided **11** in 73% yield. Activation of the free carboxylate of **11** was accomplished by reaction with trifluoroacetyl tetrafluorophenol (TFA-O-TFP) with Et_3N in DMF at 0 °C for 30 min to give an 84% yield of the tetrafluorophenyl ester, **12**. Reaction of **7b** with 4,7,10-trioxa-1,13-tridecanediamine for 3 days at room temperature gave a 68% yield of the adduct, **13**. Similarly, reaction of **8** with 4,7,10-trioxa-1,13-tridecanediamine for 16 h at room temperature gave a 75% yield of **14**. Reaction of biotin derivative **12** with **13** for 1 h at room temperature in anhydrous DMF containing Et_3N gave the targeted biotin derivative **3a** in 69% yield. Reaction of **12** with **14** under the same reaction conditions gave **4a** in 53% yield.

Iodination reactions were performed on **1a**, **2a**, **3a**, and **4a** to provide HPLC reference standards (**1b**, **2b**, **3b**, and **4b**) for use in the radiohalogenation studies. In the iodination reactions, 0.5 equiv of both NaI and chloramine-T were reacted with each *closo*-borate(2-) derivative in H_2O. This stoichiometry was used to ensure that the reaction did not substitute chlorine or multiple iodine atoms on the *closo*-borate(2-) moiety, and to distinguish the product from starting material (which had 50% remaining) by HPLC. Both of the *closo*-borate(2-) moieties are known to add multiple halogen atoms to the same molecule (*27*) and are reactive with all of the electrophilic halogen species (*28, 29*). Yields of the iodinated products were measured by HPLC (ELSD detection), and in each case were approximately 50% due to limited quantities of iodination reagent used. (Reactions containing 1 equiv each of NaI and chloramine-T have provided isolated iodinated products in >80% after separation of the other halogenated products by Biotage Flash Chromatograpy. In these studies, adequate quantities of products for MS analyses and HPLC standards was obtained by using only 0.5 equiv of reagents.) Iodinated products were isolated from HPLC to obtain a pure sample for use as a HPLC standard. Although attempts were made to obtain mass spectra data for identification of the iodinated standards, this was unsuccessful for some derivatives even though several attempts were made using negative ion electrospray mass spectrometry.

HPLC of *closo*-Decaborate(2-) Salts. The Na, Et_3N, and $n\text{Bu}_4\text{N}$ salts of *closo*-decaborate(2-) (**5c**, **5a**, **5b**, respectively) were prepared and analyzed by reversed-phase HPLC using two different solvent mixtures under the same gradient conditions. One solvent mixture was composed of [solvent A] MeOH and [solvent B] H_2O containing 0.1% HOAc (v/v). The second solvent mixture also employed MeOH as solvent A, but solvent B was 50 mM aqueous Et_3NHOAc. The Et_3NHOAc modifier was used to determine if the Et_3NH ion would displace the counterions on the isolated *closo*-decaborate(2-) under the elution conditions. Detection of the eluted non-chromophoric ions and salts was accomplished by an evaporative light scattering detector (ELSD). Using the ELSD, Na ions are detected, but organic ammonium salts were not (due to volatility). Therefore, the peaks observed are those of nonvolatile Na ions and/or the *closo*-decaborate(2-) derivative salts. Chromatograms showing the peak

Scheme 2. Synthesis and Radioiodination of Biotin Derivatives Containing Decaborate(2-) and Dodecaborate(2-) Moieties‡

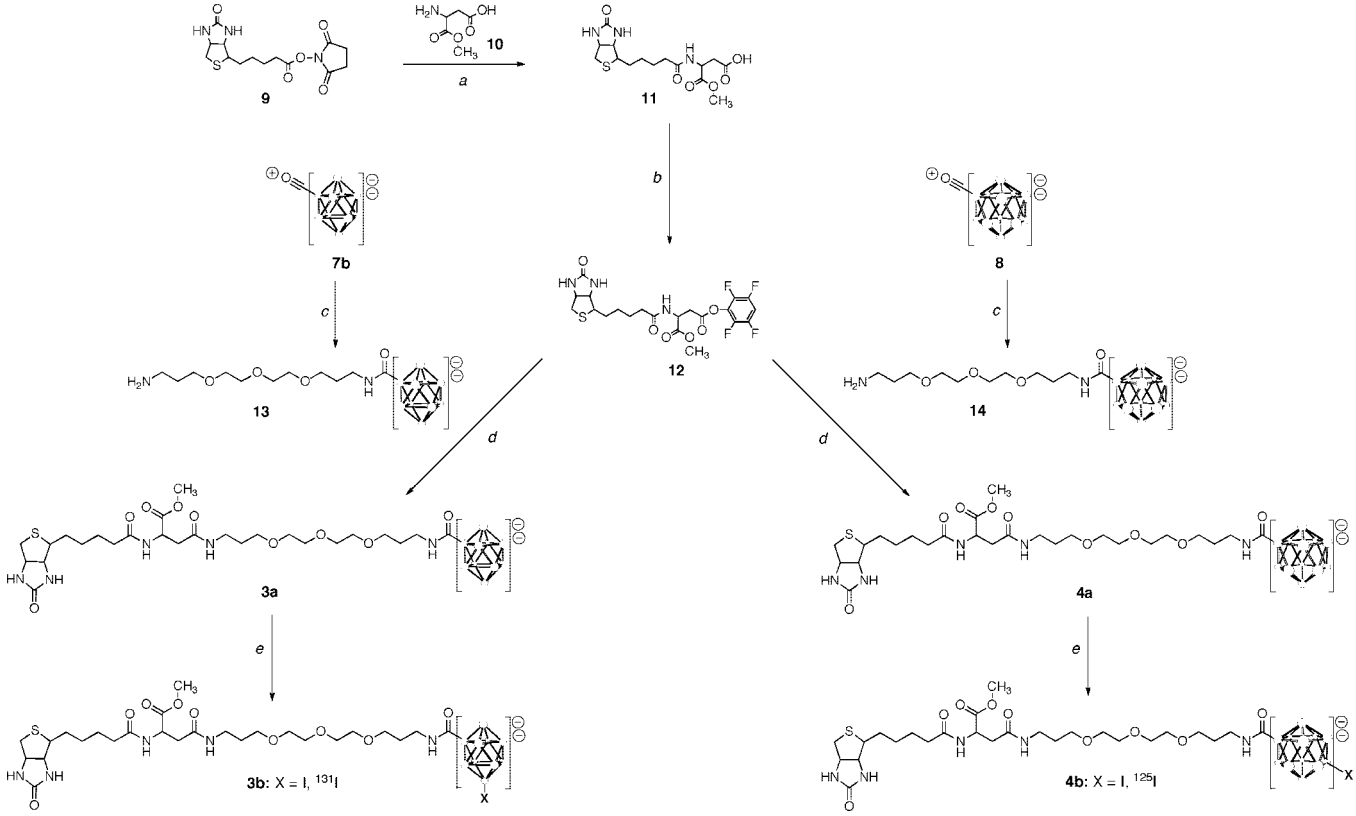

‡ Circles in cage structures represent B or BH atoms. The Et_3NH counterions for *closo*-borate(2-) derivatives are not shown for simplicity. (*a*) H_2O, $NaHCO_3$, acetone, rt, 16 h, 73%. (*b*) **10**, TFA-O-TFP, Et_3 N, anhyd. DMF, 0 °C, 30 min, 84%. (*c*) trioxtridecanediamine, rt: **13**, 3 d, 68%; **14**, 16 h, 75%. (*d*) Et_3N, anhyd. DMF, rt, 1 h: **3a**, 69%, **4a**, 53%. (*e*) ChT, H_2O/MeOH/HOAc, rt: **3b**, 1 min, 96%; **4b**, 10 min, 86%.

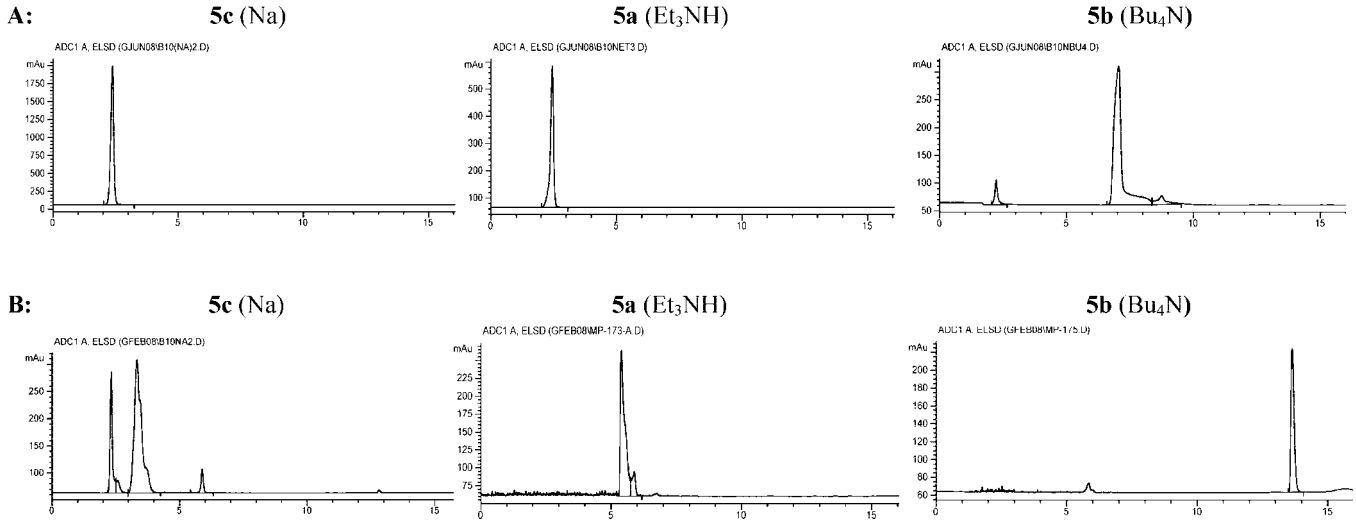

Figure 2. HPLC chromatograms of *closo*-decaborate(2-) having Na (**5c**), Et_3NH (**5a**), or Bu_4N (**5b**) counterions. Identities of the compound and its counterion (in parentheses) are shown above each chromatogram. Panel A chromatograms (3 across) were obtained using MeOH/0.1% aqueous HOAc (v/v) as eluant. Panel B chromatograms (3 across) were obtained using MeOH/50 mM aqueous Et_3NHOAc as the eluant. An evaporative light scattering detector (ELSD) was used for detection. (Note that the small peak at t_R = ~6 min in chromatograms in panel B is likely to be an impurity.)

retention times (t_R) after injecting the same quantity of each salt are shown in Figure 2, panels A and B. The left and middle chromatograms in panel A (3 chromatograms across) show that the Na and Et_3NH salts of *closo*-decaborate(2-) are highly ionic, eluting with the solvent front. In contrast, it appears from the right chromatogram in panel A that at least one of the nBu_4N ions remains with the *closo*-decaborate(2-) under the same conditions, as it elutes with a t_R of ~7 min. Chromatograms in panel B are also informative. As expected, the left chromatogram shows that the Na ions in **5c** are readily displaced by at least one Et_3NH ion. In the case where the isolated compound has two Et_3NH counterions (i.e., **5a**), as in the middle chromatogram of panel B, both Et_3NH counterions appear to elute with the *closo*-decaborate(2-) ion. Interestingly, it appears from the right chromatogram in panel B that both of the nBu_4N ions also elute with the *closo*-decaborate(2-) derivative **5b** when Et_3NHOAc is in the eluting solvent.

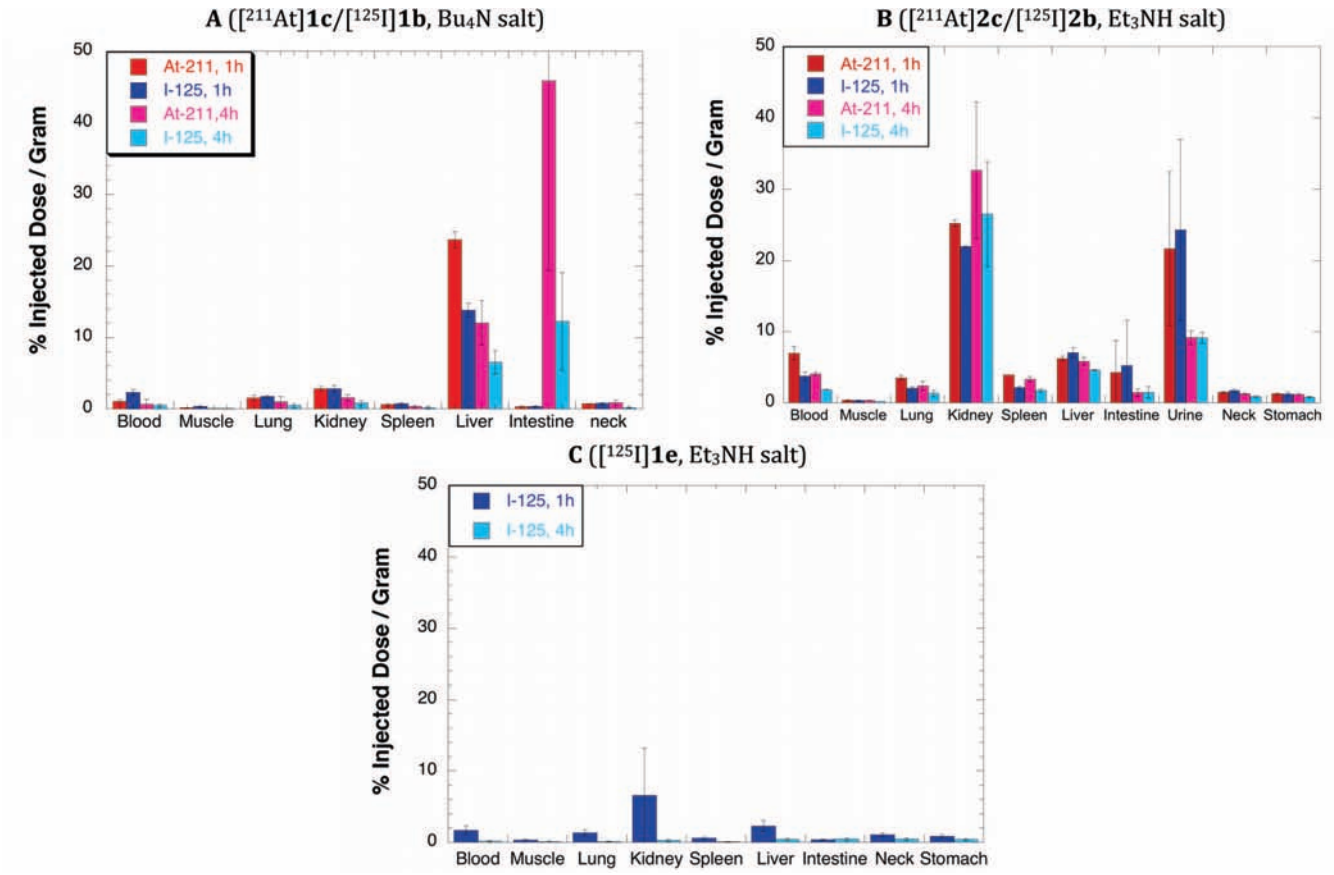

Figure 3. Graphed data from tissue biodistributions in mice at 1 and 4 h after injection of (panel A) *n*Bu4 *closo*-decaborate(2-) labeled with ^{211}At ([^{211}At]**1c**)/^{125}I ([^{125}I]**1b**); (panel B) Et_3NH salt of 2 propylamido closo dodecaborate labeled with ^{211}At ([^{211}At]**2c**]/^{131}I ([^{125}I]**2b**); and (panel C) Et_3NH salt of 2 propylamido-*closo*-decaborate(2-) labeled with ^{125}I ([^{125}I]**1e**). Red bars represent concentration of ^{211}At at 1 h post injection (pi), pink bars represent concentration of ^{211}At at 4 h pi, dark blue bars represent ^{125}I at 1 h pi, and light blue bars represent ^{125}I at 4 h pi. Data have been plotted on the same scale for all three graphs for comparison purposes.

Radiohalogenation Reactions. Radioiodinations (*nca*) were conducted using Na*I/chloramine T in a mixture of 5% HOAc/MeOH/H_2O at room temperature for 1−10 min. Radioiodinations of both *closo*-decaborate(2-) and *closo*-dodecaborate(2-) derivatives were facile, giving labeled compounds in 68−96% yields by HPLC analyses, but the *closo*-dodecaborate(2-) derivatives were slower, requiring up to 10 min to complete. Astatination yields were also high for the *closo*-decaborate(2-) derivative **1c**, providing 84% radiochemical yield after a 5 min reaction time. However, the slower reaction of the *closo*-dodecaborate derivative **2c** gave only 53% yield after 10 min reaction time. No studies were conducted to optimize the reaction conditions, including reaction times. However, radiohalogenations of the *closo*-decaborate(2-) derivatives appeared to be complete within 1 min. and no improvements in labeling yields were observed after 10 min reaction time for the *closo*-dodecaborate. Previous studies by Orlova et al. (*15*) indicated that the astatinataion reaction of *closo*-dodecaborate(2-) was "essentially complete" within 5 min under the conditions they studied. In some examples, isolated radiochemical yields were considerably lower than what the HPLC indicated, as only portions of the prepared radiolabeled compounds were collected from the HPLC effluent. The quantities of radioactivity collected were not optimized, as only small quantities of activity were required for the animal studies.

Biodistribution Studies. Four biodistribution studies were conducted with radiolabeled *closo*-borate(2-) derivatives in this investigation. In the first biodistribution study, radiolabeled *closo*-decaborates [^{211}At]**1c** and [^{125}I]**1b** were mixed and coinjected into athymic mice. At 1 and 4 h post-injection (pi), concentrations of radionuclides were evaluated in blood, urine, and selected tissues. Tissue concentrations (%ID/g) for selected tissues are plotted in Figure 3, panel A, and all data obtained are provided in Table S1 (Supporting Information). Surprisingly, the highest concentrations of both ^{211}At and ^{125}I were found in the liver and intestines. While most tissues had concentrations of ^{211}At and ^{125}I that are not significantly different (paired Student's *t*-test; $P < 0.05$), the concentrations of the two radionuclides in blood, urine, liver, and stomach were significantly different. Interestingly, the concentration of ^{125}I in urine at 1 h pi (174.43 ± 90.33%ID/g) was much higher than that of the ^{211}At (33.11 ± 14.06%ID/g), suggesting that there is a difference in the route of excretion of the otherwise identical radiolabeled *closo*-decaborate(2-) derivatives. In fact, the higher concentration of ^{211}At than ^{125}I observed in liver also supports having different excretion routes. Although ^{211}At concentrations were found to be higher than ^{125}I concentrations in stomach, the fact that there are no significant differences in the concentrations of radionuclides in lung and spleen suggests that only very small amounts, if any, of the free [^{211}At]astatide were present (*7*).

In the second biodistribution study, coadministered radiolabeled *closo*-dodecaborates, [^{211}At]**2c** and [^{125}I]**2b**, were evaluated at the 1 and 4 h pi time points. Selected tissue concentrations (%ID/g) are plotted in Figure 3, panel B, and all data obtained are provided in Table S2 (Supporting Information). The highest tissue concentrations of ^{211}At and ^{125}I were found in kidney, indicating that the kidney was likely to be the route of excretion for this pair of radiolabeled *closo*-dodecaborate(2-) compounds. Unlike the radiolabeled *closo*-decaborate(2-) derivatives [^{211}At]**1c** and [^{125}I]**1b**, there was no significant difference in the concentration of ^{211}At and ^{125}I in urine (at sacrifice). There were

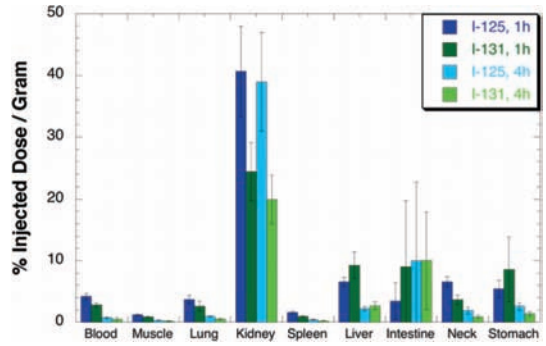

Figure 4. Biodistribution of radioiodinated biotin derivatives in mice at 1 and 4 h postinjection. Dark blue bars show concentrations of biotin derivative containing the *closo*-decaborate(2-) moiety ([^{131}I]**3b**) at 1 h pi and light blue bars show concentrations of that compound at 4 h pi. Dark green bars show concentrations of biotin derivative containing *closo*-dodecaborate ([^{125}I]**4b**) at 1 h pi and light green bars show concentrations of that compound at 4 h pi.

signficant differences (paired Student's *t*-test; $P < 0.05$) between the concentrations of ^{211}At and ^{125}I in lung, spleen, neck, and stomach suggesting that some free ^{211}At was present. However, the %ID/g concentrations of ^{211}At in those tissues indicates that the amount of deastatination was small.

The surprising differences in routes of excretion for the radiolabeled *closo*-decaborate(2-) and *closo*-dodecaborate(2-) led to a third biodistribution study where the tissue distribution of the Et_3NH salt of *closo*-decaborate(2-), [^{125}I]**1e**, was evaluated at 1 and 4 h pi. Selected tissue concentrations (%ID/g) are plotted in Figure 3, panel C, and all data obtained are provided in Table S3 (Supporting Information). The tissue concentration data from the Et_3NH salt, [^{125}I]**1e**, are strikingly different from that obtained with the nBu$_4$N salt, [^{125}I]**1b**, of the same compound. The highest concentration of ^{125}I is in kidney after injection of [^{125}I]**1e**, suggesting that renal clearance is the primary route of excretion. The high concentration in urine at 1 h (320 ± 135%ID/g) also supports renal clearance. Importantly, all tissue concentrations for the Et_3NH salt of [^{125}I]**1e**-labeled *closo*-decaborate(2-) (panel B, blue bars) were much lower than those observed for the nBu$_4$N salt.

In the fourth biodistribution, the biotin derivatives containing the *closo*-decaborate(2-) moiety, [^{131}I]**3b**, and the *closo*-dodecaborate(2-) moiety, [^{125}I]**4b**, were coinjected into athymic mice and evaluated at 1 and 4 h pi. Concentrations (%ID/g) of radionuclides in selected tissues are plotted in Figure 4, and all data obtained are provided in Table S4 (Supporting Information). The highest concentrations were found in the kidney for both radiolabeled compounds, but the biotin derivative containing the *closo*-dodecaborate(2-) moiety, [^{125}I]**4b**, had considerably higher concentrations than the *closo*-decaborate(2-) derivative, [^{131}I]**3b**. The high kidney concentrations may be due, at least in part, to the higher lipophilicity of the methyl esters, as other similar biotin derivatives did not show as high kidney concentrations. For example, the biotin derivative having the same structure as [*I]**3b** without the methyl ester had kidney concentrations of 12.27 ± 1.30 at 1 h pi and 16.24 ± 2.71 at 4 h pi (unpublished data), and in a series of biotin derivatives containing *nido*-carborane moieties, the highest kidney concentrations were <8% ID/g at 1 h pi and <4%ID/g at 4 h pi (*30*).

Significant differences (paired Student's *t*-test; $P < 0.05$) were seen between the two radiolabeled biotin derivatives in blood, lung, kidney, spleen, liver, and neck at 1 h pi, and in lung, kidney, spleen, neck, and stomach at 4 h pi. However, the differences, while significant, were small in most tissues, making the kidney localization/retention the most important factor in deciding between the two *closo*-borate(2-) moieties.

DISCUSSION

Our previous studies demonstrated that biomolecule-conjugated pendant groups having ^{211}At bonded to an aryl carbon can be quite unstable in vivo, releasing [^{211}At]astatide to localize to lung, spleen, stomach, and thyroid (*7, 31*). Since there are no stable nuclides of At found in nature, it is unlikely that there are specific enzymes to cleave the C−At bond. One possible explanation for the in vivo deastatination is that the low bond energy of the C−At bond (*32, 33*) makes it possible for nonspecific processes to release ^{211}At from metabolized biomolecules. We reasoned that the in vivo stability of ^{211}At-labeled compounds might be increased if the At was coupled to the carrier molecule through a stronger bond. This led us to consider boron−halogen bonds, which are considerably stronger than the corresponding carbon−halogen bonds (*34*). We further reasoned that ^{211}At bonded to a boron atom on an aromatic boron cage moiety would likely provide the highest bond energy, as is the case with aromatic C−At bonding (*33*). Thus, we became interested in boron cage moieties as components of pendant (conjugation) groups for ^{211}At labeling.

Our boron-^{211}At labeling studies began with the *nido*-carborane moiety (*12*). While that moiety was relatively easy to modify and incorporate into biomolecules, its conjugation appeared to increase the half-life of the biomolecule in blood compared with the same biomolecule astatinated with an astatobenzoate pendant group (*12, 30*). Importantly, when ^{211}At-labeled molecules containing conjugated *nido*-carborane groups were metabolized, the ^{211}At was released. Following those studies, we evaluated the reactivity of monocarbon carboranes and found that the cage system has a low reactivity for radioiodinations, so astatinations were not conducted (*35*). Subsequently, we evaluated bis-*nido*-carboranes (also called venus flytrap cluster (*36*)) and found that they provided high astatine stability in vivo, but dramatically affected the nature of the biomolecule to which they were attached (*13*). In the later studies, we also found that another boron cage moiety, *closo*-decaborate(2-), **5**, provided high in vivo stability with minimal effect on the biomolecules investigated (*13*).

Orlova et al. reported that a similar boron cage moiety, the *closo*-dodecaborate(2-) cage, could be astatinated in high yield (*16*). The same research group described several modified *closo*-dodecaborate(2-) derivatives that can be used for conjugation to biomolecules (*14, 37*−*39*). The reported *closo*-dodecaborate(2-) derivatives all had hetero atoms (N, O, S) attached to the *closo*-borate(2-) cage. We prepared two of the reported derivatives and found that the rate of halogenation was very slow under the conditions studied (unreported results). It was postulated that the heteroatom attached to the boron cage moiety was protonated under the reaction conditions, resulting in an adjacent positive charge that deactivated the cage to halogenation. To circumvent that situation, we sought derivatives of dianionic *closo*-borate(2-) cage moieties that would not have a protonated heteroatom adjacent to the boron cage. We found that derivatives of *closo*-borate(2-) moieties, which were conjugated to another moiety through an amide bond, retained their high reactivity with halogens. Therefore, our recent studies have focused on derivatives containing amido-bonded *closo*-borate(2-) moieties for ^{211}At labeling.

This investigation was conducted to assess the differences in chemistry and in vivo properties associated with using *closo*-decaborate(2-) or *closo*-dodecaborate(2-) moieties as the labeling components of pendant groups for astatination of biomolecules. To illustrate the differences, 2-*n*-propylamido derivatives of two *closo*-borate(2-) moieties were prepared and evaluated in vivo.

As expected based on prior literature reports, the synthetic chemistry and radiolabeling chemistry differed significantly between the two cage systems. First, while the yields of amine reactions with the two *closo*-borate(2-) carbon monoxide adducts, [*closo*-$B_{10}H_9$−CO]$^{1-}$, **7**, and [*closo*-$B_{12}H_{11}$−CO]$^{1-}$, **8**, were similar (i.e., 78% and 83%), the reaction times for coupling amines with **7** were considerably longer than with **8** (3 days vs 16 h). The low reactivity of **7** with amines most likely reflects the higher electron density of the *closo*-decaborate(2-) cage, which makes the carbon on the carbon monoxide moiety less electrophilic. Importantly, the higher electron density of the *closo*-decaborate(2-) cage makes it more reactive in the no-carrier-added radiohalogenations. Although the radioiodination yields were similar (**1b**, **1f**, **3b** 82−96% vs **2b**, **4b** 79−86%) the astatination yields (**1c**, 84% vs **2c**, 53%) yields favor the use of the *closo*-decaborate(2-) moiety.

An important finding of the investigation was that biodistributions of radiolabeled molecules differing only in the type of *closo*-borate(2-) cage incorporated were significantly different. Indeed, tissue distributions of the radiolabeled *n*-propylamido derivatives of *closo*-decaborate(2-), **1b**/**1c** (Figure 3A), and *closo*-dodecaborate(2-), **2b**/**2c** (Figure 3B), were surprisingly different. Biodistribution data from the Et_3NH salt of radiolabeled *closo*-dodecaborate(2-) derivatives **2b**/**2c** indicated that it was excreted primarily by the kidney. This was not surprising, as renal clearance is the route of excretion that was anticipated for both *closo*-borate(2-) derivatives. However, the biodistribution data from the *n*Bu_4N salt of *closo*-decaborate(2-) indicated that it is primarily excreted by the hepatobiliary system. This surprising result made us consider the other difference in the molecules, the nature of the ammonium counterion used. In our initial study of the in vivo distributions of the *n*Bu_4N salt of *closo*-decaborate(2-) derivatives, [^{211}At]**1c** and [^{125}I]**1b** were investigated. The Bu_4NH salt was employed with the *closo*-decaborate(2-) derivatives to aid purification of the radiolabeled compounds by HPLC. Under the elution conditions employed, the Et_3NH salt eluted at the solvent front whereas the *n*Bu_4N salt eluted at a later time allowing collection of the purified material from the HPLC eluant. The *n*Bu_4N salt was also used in the preparation of *closo*-decaborate(2-) derivatives to assist in isolation and purification of products, as the salts have very low solubility in H_2O. The Et_3NH salts of *closo*-decaborate(2-) derivatives are fairly water soluble (*17*). The *n*Bu_4N salts were not used with the *closo*-dodecaborate(2-) derivatives, as their Et_3NH salts are fairly insoluble in water, making isolation and purification readily achieved.

We surmised that the observed differences in tissue concentrations between the radiolabeled 2-propylamido derivatives of *closo*-decaborate(2-) [^{125}I]**1b** and *closo*-dodecaborate(2-) [^{125}I]**2b** could be due the differences in counterion used. We reasoned that, if the *n*Bu_4N counterion was not readily exchanged by other counterions in the blood, the radiolabeled *closo*-decaborate(2-) derivative would remain highly lipophilic, causing it to bind with proteins in blood, ultimately leading to excretion by the hepatobiliary system. As a cursory assessment of the extent of counterion association with the *closo*-decaborate(2-) derivatives, a simple reversed-phase HPLC comparison was carried out. For the HPLC comparison, the Na, Et_3N, and nBu_4N salts of unsubstituted *closo*-decaborate(2-) (i.e., **5a**, **5b**, **5c**) were prepared and analyzed by reversed-phase HPLC. To create different challenges to the *closo*-decaborate(2-) counterions, two solvent mixtures were used for elution. In one solvent mixture, the counterions were challenged by hydronium ion (H_3O^+), and in the other solvent mixture, the counterions were challenged with ammonium ions (Et_3NH^+). The chromatograms obtained are shown in Figure 2, panels A and B. It appears from the HPLC analyses that the *n*Bu_4N counterions of the *closo*-decaborate(2-) are not readily displaced, even under conditions that would seem to favor their displacement (i.e., high concentrations of H_3O^+ or Et_3NH^+). In contrast, both the Na and Et_3NH salts appear to be highly ionic as they elute at the solvent front when there are no ammonium ions in the eluant. As expected, the Na and Et_3NH ions appear to exchange rapidly with Et_3NH when it is present in the eluant.

The HPLC elution data did not prove that the *n*Bu_4N counterions remain with the radiolabeled *closo*-decaborate(2-) derivative in vivo. Thus, the ultimate test was to evaluate the Et_3NH salt in vivo and compare the biodistributions of the two identical compounds that only differ in the nature of their counterions. The tissue distributions for the *n*Bu_4N salt, [^{125}I]**1b**, and the Et_3NH salt, [^{125}I]**1e**, at 1 and 4 h pi are very different (Figure 3, panels A and C). While the *n*Bu_4N salt had high concentrations in the liver, the Et_3NH salt had its highest tissue concentration in the kidney. This finding suggests that the highly lipophilic *n*Bu_4N counterion remains associated with the *closo*-decaborate(2-) derivative in vivo. Importantly, all of the tissue concentrations were substantially lower when the Et_3NH salt was used, making this counterion preferred for use when the compounds have in vivo applications. Although the Na salts of *closo*-decaborate(2-) can be prepared and used in vivo, it does not seem to be a requirement. This is fortunate, as we now routinely use Et_3NHOAc as a modifier in the HPLC eluant to move the radiolabeled *closo*-decaborate(2-) derivative away from the solvent front, resulting in isolation of the Et_3NH salt.

The fourth biodistribution evaluated the differences in tissue distributions between the *closo*-decaborate(2-) and *closo*-dodecaborate(2-) moieties (both as Et_3NH salts) in a more complex biomolecule, a biotinidase-stabilized biotin derivative. For in vivo evaluation, stabilization of the biotinamide bond to cleavage from the serum enzyme biotinidase (*40*−*42*) is required so that the radiolabel remains with the biotin moiety. Our previous studies have demonstrated that a number of functional groups can be built into the carbon α to the biotinamide bond to block enzymatic cleavage of that bond (*26*, *43*, *44*). In this study, a carboxylate methyl ester was used in the biotin derivatives. The carboxylate methyl ester is not generally used for biotinidase blocking due to its high lipophilicity. However, for this comparison, optimization of the biotin derivative was not required, so the methyl ester was used in the study because it can be readily prepared. The radioiodinated derivatives [^{131}I]**3b** and [^{125}I]**4b** were evaluated in mice at 1 and 4 h pi. The biodistribution data (Figure 4) show that the only substantive difference between the two radioiodinated biotin derivatives is in the kidney concentrations. As might be expected based on the prior studies with simple *n*-propylamide-substituted *closo*-borate(2-) moieties, the *closo*-dodecaborate(2-) derivative, [^{125}I]**4b**, had significantly higher kidney concentrations than the corresponding *closo*-decaborate(2-) derivative, [^{131}I]**3b**.

SUMMARY

The goal of this investigation was to compare the synthetic chemistry, radioiodine and ^{211}At labeling efficiencies, and in vivo tissue distributions between compounds that were identical except that they contained either a *closo*-decaborate(2-) or a *closo*-dodecaborate(2-) moiety. Synthesis of *closo*-borate(2-) derivatives **1a**, **2a**, **3a**, and **4a** pointed out differences in reaction rates between the two *closo*-borate(2-) moieties. However, the differences are not considered important in choosing one *closo*-borate(2-) moiety over the other, as both could be substituted with carbon monoxide and subsequently coupled with amine-containing molecules. While only one comparison was done, it appears that ^{211}At-labeling efficiency is higher in compounds containing the more electron-rich *closo*-decaborate(2-). The tissue distribution data indicated that the ^{211}At-labeled derivatives

with both *closo*-borate(2-) moieties have high stability toward in vivo deastatination, making this parameter unimportant in the decision between the use of two *closo*-borate(2-) moieties. However, the tissue distribution indicated that the *closo*-dodecaborate(2-) is highly sequestered and retained in the kidney, whereas the *closo*-decaborate(2-) is not. An interesting finding was the fact that the counterion can have a large influence on the tissue distribution, with the highly lipophilic nBu$_4$N salt causing the compound to be excreted by the hepatobiliary system, whereas the Et$_3$NH salt appears to have much less influence on the distribution. In the final analysis, the low kidney sequestration and rapid tissue clearance of the *closo*-decaborate(2-) make it the better candidate for use as a pendant group in ^{211}At-labeling (or radioiodination) of biomolecules for in vivo therapy applications.

ACKNOWLEDGMENT

We thank Holly Nguyen and Dr. Robert Vessella for assistance with the animal studies conducted in this investigation. Funding for this research was provided by NCI, NIH (CA11343).

Supporting Information Available: Additional data as described in the text. This material is available free of charge via the Internet at http://pubs.acs.org.

LITERATURE CITED

(1) Couturier, O., Supiot, S., Degraef-Mougin, M., Faivre-Chauvet, A., Carlier, T., Chatal, J. F., Davodeau, F., and Cherel, M. (2005) Cancer radioimmunotherapy with alpha-emitting nuclides. *Eur. J. Nucl. Med. Mol. Imaging 32*, 601–14.

(2) Mulford, D. A., Scheinberg, D. A., and Jurcic, J. G. (2005) The promise of targeted α-particle therapy. *J. Nucl. Med. 46*, 199S–204S.

(3) Zalutsky, M. R. (2006) Targeted alpha-particle therapy of microscopic disease: Providing a further rationale for clinical investigation. *J. Nucl. Med. 47*, 1238–40.

(4) Cherel, M., Davodeau, F., Kraeber-Bodere, F., and Chatal, J. F. (2006) Current status and perspectives in alpha radioimmunotherapy. *Q. J. Nucl. Med. Mol. Imaging 50*, 322–9.

(5) Zalutsky, M. R., Reardon, D. A., Pozzi, O. R., Vaidyanathan, G., and Bigner, D. D. (2007) Targeted alpha-particle radiotherapy with ^{211}At-labeled monoclonal antibodies. *Nucl. Med. Biol. 34*, 779–85.

(6) American Cancer Society. (2008) Cancer Facts and Figures.

(7) Wilbur, D. S. (2008) [^{211}At]Astatine-labeled compound stability: issues with released [^{211}At]astatide and development of labeling reagents to increase stability. *Curr. Radiopharm. 1*, 144–176.

(8) Zalutsky, M. R., and Narula, A. S. (1988) Astatination of proteins using an N-succinimidyl tri-*n*-butylstannyl benzoate intermediate. *Appl. Radiat. Isot. 39*, 227–232.

(9) Wilbur, D. S. (1992) Radiohalogenation of proteins: an overview of radionuclides, labeling methods, and reagents for conjugate labeling. *Bioconjugate Chem. 3*, 433–70.

(10) Vaidyanathan, G., Affleck, D. J., Bigner, D. D., and Zalutsky, M. R. (2003) N-succinimidyl 3-[^{211}At]astato-4-guanidinomethylbenzoate: an acylation agent for labeling internalizing antibodies with α-particle emitting ^{211}At. *Nucl. Med. Biol. 30*, 351–359.

(11) Talanov, V. S., Yordanov, A. T., Garmestani, K., Milenic, D. E., Arora, H. C., Plascjak, P. S., Eckelman, W. C., Waldmann, T. A., and Brechbiel, M. W. (2004) Preparation and in vivo evaluation of novel linkers for ^{211}At labeling of proteins. *Nucl. Med. Biol. 31*, 1061–1071.

(12) Wilbur, D. S., Chyan, M. K., Hamlin, D. K., Kegley, B. B., Risler, R., Pathare, P. M., Quinn, J., Vessella, R. L., Foulon, C., Zalutsky, M., Wedge, T. J., and Hawthorne, M. F. (2004) Reagents for astatination of biomolecules: comparison of the in vivo distribution and stability of some radioiodinated/astatinated benzamidyl and *nido*-carboranyl compounds. *Bioconjugate Chem. 15*, 203–23.

(13) Wilbur, D. S., Chyan, M. K., Hamlin, D. K., Vessella, R. L., Wedge, T. J., and Hawthorne, M. F. (2007) Reagents for astatination of biomolecules. 2. Conjugation of anionic boron cage pendant groups to a protein provides a method for direct labeling that is stable to in vivo deastatination. *Bioconjugate Chem. 18*, 1226–40.

(14) Tolmachev, V., Koziorowski, J., Sivaev, I., Lundqvist, H., Carlsson, J., Orlova, A., Gedda, L., Olsson, P., Sjoberg, S., and Sundin, A. (1999) *Closo*-Dodecaborate(2-) as a linker for iodination of macromolecules. Aspects on conjugation chemistry and biodistribution. *Bioconjugate Chem. 10*, 338–45.

(15) Orlova, A., Lebeda, O., Tolmachev, V., Sjoberg, S., Carlsson, J., and Lundqvist, H. (2000) *Closo*-dodecaborate (2-) anion as a potential prosthetic group for attachment of astatine to proteins. Aspects of the labelling chemistry with Chloramine-T. *J. Labelled Compds. Radiopharm. 43*, 251–260.

(16) Orlova, A., Lebeda, O., Tolmachev, V., Sjoberg, S., Carlsson, J., and Lundqvist, H. (1999) Astatination of *closo*-dodecaborate(2-) anion. *J. Labelled Compd. Radiopharm. 42*, S735−S737.

(17) Muetterties, E. L., Balthis, J. H., Chia, Y. T., Knoth, W. H., and Miller, H. C. (1964) Chemistry of boranes. VIII. Salts and acids of $B_{10}H_{10}^{-2}$ and $B_{12}H_{12}^{-2}$. *Inorg. Chem. 3*, 444–451.

(18) Knoth, W. H., Sauer, J. C., Balthis, J. H., Miller, H. C., and Muetterties, E. L. (1967) Chemistry of boranes. XXX. Carbonyl derivatives of $B_{10}H_{10}^{2-}$ and $B_{12}H_{12}^{2-}$. *J. Am. Chem. Soc. 89*, 4842–4850.

(19) Hertler, W. R., Knoth, W. H., and Muetterties, E. L. (1965) Chemistry of boranes. XXIV. Carbonylation of derivatives of $B_{10}H_{10}^{2-}$ and $B_{12}H_{12}^{2-}$ with oxalyl chloride. *Inorg. Chem. 4*, 288–293.

(20) Gamper, H. B., Reed, M. W., Cox, T., Virosco, J. S., Adams, A. D., Gall, A. A., Scholler, J. K., and Meyer, R. B., Jr. (1993) Facile preparation of nuclease resistant 3′ modified oligodeoxynucleotides. *Nucleic Acids Res. 21*, 145–50.

(21) Wilbur, D. S., Vessella, R. L., Stray, J. E., Goffe, D. K., Blouke, K. A., and Atcher, R. W. (1993) Preparation and evaluation of *para*-[^{211}At]astatobenzoyl labeled anti-renal cell carcinoma antibody A6H F(ab′)$_2$. In vivo distribution comparison with para-[^{125}I]iodobenzoyl labeled A6H F(ab′)$_2$. *Nucl. Med. Biol. 20*, 917–27.

(22) Hawthorne, M. F., and Pilling, R. L. (1967) 5. Bis(triethylammonium) decahydrodecaborate (2-). *Inorg. Synth. 9*, 16–19.

(23) Miller, H. C., and Muetterties, E. L. (1967) 16. Borane anions. *Inorg. Synth. 10*, 81–91.

(24) Shelly, K., Knobler, C. B., and Hawthorne, M. F. (1992) Synthesis of monosubstituted derivatives of *closo*-decahydrodecaborate(2-). X-ray crystal structures of [*closo*-2-$B_{10}H_9CO]^-$ and [*closo*-2-$B_{10}H_9NCO]^{2-}$. *Inorg. Chem. 31*, 2889–2892.

(25) Kaplan, H. M., Brewer, N. R., and Blair, W. H. (1983) Physiology, In *The Mouse in Biomedical Research* (Foster, H. L., Small, J. D., and Fox, J. G., Eds.) pp 248−292, Academic Press, New York.

(26) Wilbur, D. S., Hamlin, D. K., Chyan, M. K., Kegley, B. B., and Pathare, P. M. (2001) Biotin reagents for antibody pretargeting. 5. Additional studies of biotin conjugate design to provide biotinidase stability. *Bioconjugate Chem. 12*, 616–23.

(27) Bührens, K.-G., and Preetz, W. (1977) Isolation of halohydroborates of type $[B_{10}H_{10-n}X_n]^{2-}$. *Angew. Chem., Int. Ed. 16*, 173–174.

(28) Knoth, W. H., Miller, H. C., Sauer, J. C., Balthis, J. H., Chia, Y. T., and Muetterties, E. L. (1964) Chemistry of boranes. IX. Halogenation of $B_{10}H_{10}^{-2}$ and $B_{12}H_{12}^{-2}$. *Inorg. Chem. 3*, 159–167.

(29) Ivanov, S. V., Ivanova, S. M., Miller, S. M., Anderson, O. P., Solntsev, K. A., and Strauss, S. H. (1996) Fluorination of $B_{10}H_{10}^{2-}$ with an N-fluoro reagent. A new way to transform B-H bonds into B-F bonds. *Inorg. Chem. 35*, 6914–6915.

(30) Wilbur, D. S., Hamlin, D. K., Chyan, M. K., Kegley, B. B., Quinn, J., and Vessella, R. L. (2004) Biotin reagents in antibody pretargeting. 6. Synthesis and in vivo evaluation of astatinated and radioiodinated aryl- and *nido*-carboranyl-biotin derivatives. *Bioconjugate Chem. 15*, 601–16.

(31) Hamilton, J. G., Durbin, P. W., and Parrott, M. (1954) The accumulation and destructive action of astatine^{211} (EKA- Iodine) in the thyroid gland of rats and monkeys. *J. Clin. Endocrinol. Metab. 14*, 1161–1178.

(32) Eberle, S. H. (1985) Chemical behavior and compounds of astatine, In *Gmelin Handbook of Chemistry, Astatine* (Kugler, H. K., and Keller, C., Eds.) pp 183−259, Springer-Verlag, Berlin.

(33) Coenen, H. H., Moerlein, S. M., and Stöcklin, G. (1983) No-carrier-added radiohalogenation methods with heavy halogens. *Radiochim. Acta 34*, 47–68.

(34) Kerr, J. A. (1993) Strengths of chemical bonds, In *CRC Handbook of Chemistry and Physics* (Lide, D. R., Ed.) pp 9−123−9−145, CRC Press, Boca Raton.

(35) Wilbur, D. S., Hamlin, D. K., Srivastava, R. R., and Chyan, M. K. (2004) Synthesis, radioiodination, and biodistribution of some *nido*- and *closo*-monocarbon carborane derivatives. *Nucl. Med. Biol. 31*, 523–30.

(36) Paxton, R. J., Beatty, B. G., Hawthorne, M. F., Varadarajan, A., Williams, L. E., Curtis, F. L., Knobler, C. B., and Shively, J. E. (1991) A transition metal complex (Venus flytrap cluster) for radioimmunodetection and radioimmunotherapy. *Proc. Nat. Acad. Sci. U.S.A. 88*, 3387–3391.

(37) Sivaev, I. B., Sjuberg, S., Bregadze, V. I., and Gabel, D. (1999) Synthesis of alkoxy derivatives of dodecahdro-*closo*-dodecaborate anion $[B_{12}H_{12}]^{2-}$. *Tetrahedron Lett. 40*, 3451–4.

(38) Sivaev, I. B., Bruskin, A. B., Nesterov, V. V., Antipin, M. Y., Bregadze, V. I., and Sjoberg, S. (1999) Synthesis of Schiff bases derived from the ammoniaundecahydro-*closo*-dodecaborate(1-) anion, $[B_{12}H_{11}NH{=}CHR]^-$, and their reduction into monosubstituted amines $[B_{12}H_{11}NH_2CH_2R]^-$: A new route to water soluble agents for BNCT. *Inorg. Chem. 38*, 5887–5893.

(39) Nestor, M., Persson, M., Cheng, J., Tolmachev, V., Van Dongen, G., Anniko, M., and Kairemo, K. (2003) Biodistribution of the chimeric monoclonal antibody U36 radioiodinated with a *closo*-dodecaborate-containing linker. Comparison with other radioiodination methods. *Bioconjugate Chem. 14*, 805–810.

(40) Pispa, J. (1965) Animal biotinidase. *Ann. Med. Exptl. Bio. Fenniae 43*, 3–40.

(41) Chauhan, J., Ebrahim, H., Bhullar, R. P., and Dakshinamurti, K. (1985) Human serum biotinidase. *Ann. N.Y. Acad. Sci. 447*, 386–388.

(42) Hymes, J., Fleischhauer, K., and Wolf, B. (1997) Biotinidase in serum and tissues. *Methods Enzymol. 279*, 422–434.

(43) Wilbur, D. S., Hamlin, D. K., Pathare, P. M., and Weerawarna, S. A. (1997) Biotin reagents for antibody pretargeting. Synthesis, radioiodination and in vitro evaluation of water soluble, biotinidase resistant biotin derivatives. *Bioconjugate Chem. 8*, 572–584.

(44) Wilbur, D. S., Hamlin, D. K., and Chyan, M. K. (2006) Biotin reagents for antibody pretargeting. 7. Investigation of chemically inert biotinidase blocking functionalities for synthetic utility. *Bioconjugate Chem. 17*, 1514–22.

(45) Adams, R. (1963) Cage borane nomenclature. *Inorg. Chem. 2*, 1087–1088.

BC800515D

Supporting Information For:

Reagents for Astatination of Biomolecules. 3. Comparison of *closo*-Decaborate(2-) and *closo*-Dodecaborate(2-) Moieties as Reactive Groups for Labeling with Astatine-211.

D. Scott Wilbur*, Ming-Kuan Chyan, Donald K. Hamlin and Matthew A. Perry

Department of Radiation Oncology, Univ. of Washington, Seattle, WA 98195

Table S1: **Distribution of Radioactivity for Co-injected [^{125}I]- and [^{211}At]-Labeled *closo*-Decaborate, [^{125}I]1b and [^{211}At]1c, in BALB/c mice.**

Table S2: **Distribution of Radioactivity for Co-injected [^{125}I]- and [^{211}At]-Labeled *closo*-Dodecaborate, [^{125}I]2b and [^{211}At]2c, in BALB/c mice.**

Table S3: **Distribution of Radioactivity for [^{125}I]B_{10}CONHpropyl, [^{125}I]1e (Et_3NH salt) in BALB/c mice.**

Table S4: **Distribution of Radioactivity for Co-injected [^{131}I]B_{10}-Biotin, [^{131}I]3b and [^{125}I]B_{12}-Biotin, [^{125}I]4b in BALB/c mice.**

Table S1: Distribution of Radioactivity for Co-injected [^{125}I]- and [^{211}At]-Labeled *closo*-Decaborate, [^{125}I]1b and [^{211}At]1c, in BALB/c mice.[a]

Tissues	1 h[b,c]		4 h	
	I-125	At-211	I-125	At-211
blood	2.30 ± 0.41*	1.07 ± 0.26*	0.47 ± 0.23	0.67 ± 0.67
muscle	0.33 ± 0.11*	0.17 ± 0.04*	0.05 ± 0.01	0.04 ± 0.01
lung	1.72 ± 0.16	1.52 ± 0.34	0.48 ± 0.28	0.96 ± 0.76
kidney	2.84 ± 0.48	2.83 ± 0.32	0.82 ± 0.30*	1.59 ± 0.41*
spleen	0.77 ± 0.16	0.60 ± 0.15	0.20 ± 0.14	0.35 ± 0.17
liver	13.80 ± 0.96*	23.66 ± 1.13*	6.52 ± 1.67*	12.04 ± 3.11*
intestine	0.38 ± 0.80	0.29 ± 0.12	12.23 ± 6.84*	45.89 ± 26.55*
neck	0.79 ± 0.07	0.74 ± 0.02	0.21 ± 0.07*	0.90 ± 0.30*
stomach	2.30 ± 1.00*	6.92 ± 4.10*	0.45 ± 0.12*	1.45 ± 0.44*
urine[d]	174.43 ± 90.33*	33.11 ± 14.06*	34.39 ± 13.26	23.04 ± 8.50

[a]Values shown are % injected dose / gram ± standard deviation. [b]Time of sacrifice from injection of radiolabeled *closo*-decaborate(2-) derivatives, [^{125}I]**1b** and [^{211}At]**1c**. [c]Data were obtained for n = 5 mice at each time point; average animal weight, 29.28 ± 2.68 g; Radiolabeled compounds were isolated (purified) from the HPLC and diluted with saline for injection; Injectate for each animal had 3 μCi of [^{125}I]**1b** and 3 μCi of [^{211}At]**1c** in approximately 100 μL of 0.9% sterile saline. [d]Urine was collected by syringe bladder tap after sacrifice. *Significant difference found in values by paired Student's t test, $P<0.05$.

Table S2: Distribution of Radioactivity for Co-injected [^{125}I]- and [^{211}At]-Labeled *closo*-Dodecaborate, [^{125}I]2b and [^{211}At]2c, in BALB/c mice.[a]

Tissues	1 h[b,c]		4 h	
	I-125	At-211	I-125	At-211
blood	3.20 ± 1.05	5.99 ± 1.83	1.84 ± 0.20*	4.04 ± 0.26*
muscle	0.27 ± 0.08	0.29 ± 0.10	0.20 ± 0.00*	0.32 ± 0.02*
lung	1.94 ± 0.21	3.55 ± 0.24	1.33 ± 0.43*	2.40 ± 0.59*
kidney	19.84 ± 3.62	22.70 ± 4.28	26.50 ± 7.38	32.62 ± 9.58
spleen	1.98 ± 0.33*	3.69 ± 0.40*	1.73 ± 0.24*	3.33 ± 0.39*
liver	6.80 ± 0.63	5.88 ± 0.64	4.58 ± 0.10*	5.84 ± 0.49*
intestine	5.22 ± 4.50	4.20 ± 3.20	1.46 ± 0.80	1.46 ± 0.50
neck	1.66 ± 0.14	1.46 ± 0.11	0.88 ± 0.14*	1.29 ± 0.13*
stomach	1.17 ± 0.21	1.13 ± 0.27	0.88 ± 0.14*	1.29 ± 0.13*
urine[d]	26.38 ± 9.71	22.26 ± 7.72	9.13 ± 0.76	9.15 ± 0.96

[a]Values shown are % injected dose / gram ± standard deviation. [b]Time of sacrifice from injection of radiolabeled *closo*-dodecaborate(2-) derivatives, [^{125}I]**2b** and [^{211}At]**2c**. [c]Data were obtained for n = 3 mice at the 1h timepoint and n = 5 mice at the 4h time point; average animal weight, 27.87 ± 1.58 g; Radiolabeled compounds were isolated (purified) from the HPLC and diluted with saline for injection; Injectate for each animal had 5 μCi of [^{125}I]**2b** and 5 μCi of [^{211}At]**2c** in approximately 100 μL of 0.9% sterile saline. [d]Urine was collected by syringe bladder tap after sacrifice. *Significant difference found in values by paired Student's t test, $P<0.05$.

Table S3: Distribution of Radioactivity for [^{125}I]B_{10}CONHpropyl, [^{125}I]1e (Et_3NH salt) in BALB/c mice.[a]

Tissues	1 h[b,c]	4 h
	I-125	I-125
blood	1.67 ± 0.61	0.13 ± 0.09
muscle	0.32 ± 0.11	0.08 ± 0.05
lung	1.31 ± 0.38	0.10 ± 0.06
kidney	6.56 ± 6.65	0.27 ± 0.17
spleen	0.56 ± 0.12	0.07 ± 0.04
liver	2.27 ± 0.73	0.40 ± 0.18
intestine	0.35 ± 0.07	0.44 ± 0.19
neck	1.03 ± 0.23	0.44 ± 0.19
stomach	0.84 ± 0.20	0.39 ± 0.11
urine[d]	320 ± 135	32.9 ± 25.3

[a]Values shown are % injected dose / gram ± standard deviation. [b]Time of sacrifice from injection of radiolabeled rSAv derivatives, [^{125}I]**1e**. [c]Data were obtained for *n* = 5 mice at 1h and 4h timepoints; average animal weight, 29.48 ± 1.95 g; Radiolabeled compounds were isolated (purified) from the HPLC and diluted with saline for injection; Injectate for each animal had 5 μCi of [^{125}I]**1e** in approximately 100 μL of 0.9% sterile saline. [d]Urine was collected by syringe bladder tap after sacrifice.

Table S4: Distribution of Radioactivity for Co-injected [^{131}I]B_{10}-Biotin, [^{131}I]3b and [^{125}I]B_{12}-Biotin, [^{125}I]4b in BALB/c mice.[a]

Tissues	1 h[b,c]		4 h	
	I-125	I-131	I-125	I-131
blood	4.22 ± 0.50*	2.84 ± 0.35*	0.74 ± 0.12	0.49 ± 0.30
muscle	1.20 ± 0.12*	0.88 ± 0.08*	0.30 ± 0.07*	0.18 ± 0.05*
lung	3.72 ± 0.68*	2.61 ± 0.77*	0.98 ± 0.08*	0.53 ± 0.08*
kidney	40.64 ± 7.33*	24.38 ± 4.68*	38.92 ± 8.01*	19.94 ± 3.90*
spleen	1.62 ± 0.22*	0.96 ± 0.10*	0.42 ± 0.07*	0.21 ± 0.05*
liver	6.54 ± 0.77*	9.27 ± 2.16*	2.20 ± 0.31	2.68 ± 0.61
intestine	3.45 ± 2.98	9.02 ± 10.67	4.17 ± 2.69	10.02 ± 7.93
neck	6.57 ± 0.83*	3.63 ± 0.79*	1.92 ± 0.58*	0.87 ± 0.26*
stomach	5.43 ± 1.44	8.55 ± 5.27	2.62 ± 0.62*	1.37 ± 0.31*
urine[d]	112.33 ± 62.72	103.85 ± 56.46	28.13 ± 15.28	16.04 ± 9.12

[a]Values shown are % injected dose / gram ± standard deviation. [b]Time of sacrifice from injection of radiolabeled biotin derivatives, [^{125}I]**4b** and [^{131}I]**3b**. [c]Data were obtained for n = 5 mice at each time point; average animal weight, 23.71 ± 1.04 g; Radiolabeled compounds were isolated (purified) from the HPLC and diluted with saline for injection; Injectate for each animal had 8 μCi of [^{125}I]**4b** and 8 μCi of [^{125}I]**3b** in approximately 100 μL of 0.9% sterile saline. [d]Urine was collected by syringe bladder tap after sacrifice. *Significant difference found in values by paired Student's t test, $P<0.05$.

Bioconjugate Chemistry 20th Anniversary

Subscriber access provided by SHEMYAKIN-OVCHINNIKOV INST

Article

Osmium Complexation of Mismatched DNA: Effect of the Bases Adjacent to Mismatched 5-Methylcytosine

Akiko Nomura, Kazuki Tainaka, and Akimitsu Okamoto

Bioconjugate Chem., **2009**, 20 (3), 603-607• DOI: 10.1021/bc800531z • Publication Date (Web): 13 February 2009

Downloaded from http://pubs.acs.org on May 15, 2009

More About This Article

Additional resources and features associated with this article are available within the HTML version:

- Supporting Information
- Access to high resolution figures
- Links to articles and content related to this article
- Copyright permission to reproduce figures and/or text from this article

View the Full Text HTML

ACS Publications
High quality. High impact.

Bioconjugate Chemistry is published by the American Chemical Society. 1155 Sixteenth Street N.W., Washington, DC 20036

Osmium Complexation of Mismatched DNA: Effect of the Bases Adjacent to Mismatched 5-Methylcytosine

Akiko Nomura, Kazuki Tainaka, and Akimitsu Okamoto*

Advanced Science Institute, RIKEN (The Institute of Physical and Chemical Research), Wako, Saitama 351-1098, Japan.
Received December 10, 2008; Revised Manuscript Received January 12, 2009

The efficiency of osmium complex formation at 5-methylcytosine in mismatched DNA duplexes is a key point for the design of sequence-specific detection of DNA methylation. Osmium complexation was not observed in fully matched duplexes, whereas the complexation site and efficiency in mismatched duplexes changed depending on the type of 5′-neighboring base of the 5-methylcytosine forming a mismatched base pair. In particular, when the base adjacent to the 5′ side of the mismatched base pair was thymine, a unique "side reaction" was observed. However, the nature of the mismatched base pairs in the reaction site did not influence the selectivity of osmium complex formation with methylated DNA.

INTRODUCTION

A number of reactions for pyrimidine bases have been reported, such as photodimerization (*1, 2*), Michael addition (*3*−*5*), and oxidation (*6*−*9*). Osmium oxidation is one of the known pyrimidine-targeting sequencing methods, and in this case, the C5−C6 double bonds of thymine and 5-methylcytosine are oxidized (*10*−*15*). A highly stable pyrimidine glycol−osmate−bipyridine triad is formed on reaction with osmium tetroxide (*10, 11*) or potassium osmate activated by potassium hexacyanoferrate(III) in the presence of bipyridine as a ligand (Figure 1a) (*12*−*15*). On the other hand, the oxidation of cytosine is much slower than that of 5-methylcytosine (*10, 12*).

Cytosine methylation, in which the C5 position of the cytosine base is methylated enzymatically, is an epigenetic modification that can play an important role in the control of gene expression in mammalian cells, and about 70% to 80% of cytosines are methylated in the CpG sequence. The sequence-selective distinction between methylated and unmethylated cytosines is very important for studies of gene deactivation (*16, 17*). In addition, erroneous DNA methylation may contribute to the etiopathogenesis of tumorigenesis (*18*−*20*). Cytosine methylation is one of the most important epigenetic events in cells, and its detection is very significant. The oxidation of pyrimidine bases may be useful for the detection of the presence/absence of a methyl group at cytosine C5.

A 5-methylcytosine-adenine mismatched base pair made possible the sequence-selective formation of an osmium complex at 5-methylcytosine (*21*). This is different from the negligible reactivity of the fully matched duplex, because the formation of a cytosine-adenine mismatched pair causes partial disruption of π-stacking of the DNA duplex and facilitates oxidation at the C5−C6 double bond of the cytosine forced out of the DNA major groove. This system was applied to a new DNA probe for methylation detection, the so-called ICON probe (Figure 1b). The formation of a mismatched base pair by hybridization with the ICON probe and the location of bipyridine attached to the probe DNA results in complexation at a specific 5-methylcytosine. Toward development of more effective, sequence-selective 5-methylcytosine detection based on the formation of mismatched base pairs, a more detailed investigation of the osmium complexation efficiency and selectivity depending on the nature of the mismatched base pairs and neighboring sequences is required. This knowledge facilitates prior estimation of the reaction abilities of probes and helps in the design of highly methylation sensitive probes.

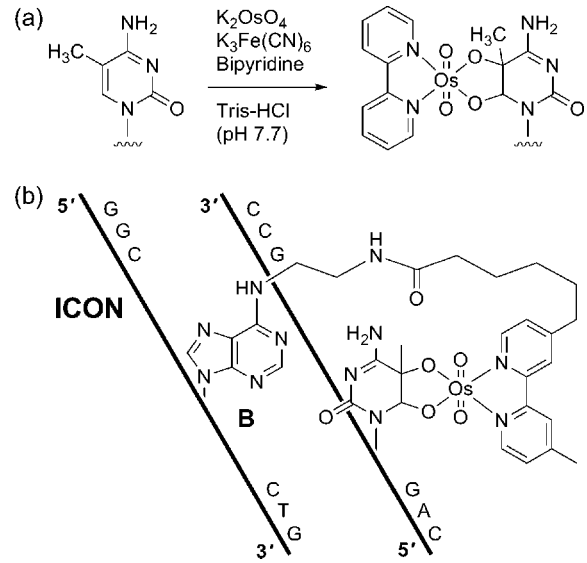

Figure 1. Osmium complex formation at 5-methylcytosine. (a) Formation of a ternary complex with 5-methylcytosine, osmate, and bipyridine. (b) Interstrand cross-link by osmium complexation with the ICON probe.

In this paper, we describe the osmium oxidation efficiency at methylated CpG (MpG) in a series of duplexes with a single base mismatch. The oxidation efficiency was investigated through alkaline strand cleavage for a variety of duplexes with different complementary bases of 5-methylcytosine and different 5′-flanking base pairs of MpG. Sequence-selective osmium complexation at the target 5-methylcytosine was detected for mismatched duplexes, and the unique reactivity of 5′-neighboring thymine was also observed.

EXPERIMENTAL PROCEDURES

General. The reagents for 5-methylcytosine oxidation were purchased from Wako, and the reagents for the DNA synthe-

* To whom correspondence may be addressed. Phone: (+81) 48-467-9238. Fax: (+81) 48-467-9205. E-mail: aki-okamoto@riken.jp.

10.1021/bc800531z CCC: $40.75 © 2009 American Chemical Society
Published on Web 02/13/2009

sizer, such as A, G, C, T, and M-β-cyanoethyl phosphoramidite, were purchased from Glen Research. Oligodeoxynucleotides (ODNs) were purchased from Gene Design. HPLC was performed on a Cosmosil 5C-18AR or Chemcobond 5-ODS-H column (10 × 150 mm) with a Gilson Chromatography model 305 using a UV detector model 118 at 254 nm. Micro Bio-Spin chromatography columns used for desalting were purchased from Bio-Rad. ICON probes were prepared as in our previous report (*21*).

Preparation of ^{32}P-5′-End-Labeled DNA. The ODNs (400 pmol-strand) were 5′-end-labeled by phosphorylation with 4 μL of [γ-^{32}P]ATP (GE Healthcare) and T4 polynucleotide kinase using a standard procedure. The 5′-end-labeled ODN was recovered by ethanol precipitation and further purified by 15% denaturing polyacrylamide gel electrophoresis (PAGE).

Osmium Oxidation of ^{32}P-5′-End-Labeled DNA. The 5′-end-labeled ODN (10 pmol-strand) to be examined was incubated in a solution of 1 μM mismatch-forming ODN or ICON probe, 5 mM potassium osmate, 100 mM potassium hexacyanoferrate(III), 100 mM bipyridine, and 1 mM EDTA in 100 mM Tris-HCl buffer (pH 7.7) and 10% acetonitrile at 0 °C for 5 min. The reaction mixture was ethanol precipitated with the addition of 15 μL of 3 M sodium acetate (pH 5.0), 10 μL of salmon sperm DNA (1 mg/mL), and 1 mL of cold ethanol. The precipitate was washed with 150 μL of 80% cold ethanol and dried in vacuo. The residue was redissolved in 50 μL of 10% piperidine (v/v), heated at 90 °C for 20 min, and then evaporated to dryness by vacuum rotary evaporation. The dried reaction sample was resuspended in 5−20 μL of 80% formamide loading buffer (a solution of 80% formamide (v/v), 1 mM EDTA, 0.1% xylenecyanol, and 0.1% bromophenol blue). The samples (1 μL, 3−10 kcpm) were loaded onto 15% denaturing 19:1 acrylamide−bisacrylamide gel containing 7 M urea, electrophoresed at 1900 V for approximately 1 h, transferred to a cassette, and stored at −80 °C with X-ray film.

Melting Temperature (T_m) Measurement. All T_m values of the ODN duplexes (2.5 μM, duplex concentration) were taken in a buffer containing 1 mM EDTA, 100 mM Tris-HCl buffer, and 100 mM sodium chloride, pH 7.7. Absorbance vs temperature profiles were measured at 260 nm using a Shimadzu UV-2550 UV/vis spectrometer connected to a Shimadzu TMSPC-8 temperature controller. The absorbance of the samples was monitored at 260 nm from 5 to 90 °C at a heating rate of 1 °C/min. From these profiles, first derivatives were calculated to determine T_m values.

RESULTS AND DISCUSSION

Osmium Oxidation at Mismatched 5-Methylcytosine. We prepared ^{32}P-labeled DNA containing an MpG or CpG dinucleotide with different 5′-flanking bases, or ODN(XNG), 5′-^{32}P-d(AAAAGAXNGAGAAAA)-3′ (N = M or C; X = C, G, A, or T), which were hybridized with ODN′(CN′X′) 5′-d(TTTTCTCN′X′TCTTTT)-3′ (N′ = G, A, C, or T; X′ = G, C, T, or A), to examine the reactivity on osmium oxidation (Figure 2a and Supporting Information Figure S1). The duplex was incubated in a solution of 5 mM potassium osmate, 100 mM potassium hexacyanoferrate(III), 100 mM bipyridine, 1 mM EDTA in 100 mM Tris-HCl (pH = 7.7) and 10% acetonitrile at 0 °C for 5 min. The oxidized strand was cleaved at the damaged pyrimidine base with hot piperidine (90 °C, 20 min), and the products were analyzed as bands representing the shortened strands using PAGE. Typical results of PAGE are shown in Figure 2b. No cleavage band was observed for the fully Watson−Crick base-paired duplex (N′ = G). The strong suppression of oxidation of bases was due to the protection of the C5−C6 double bond by the stacking of the flanking base pairs. On the other hand, the osmium oxidation specifically

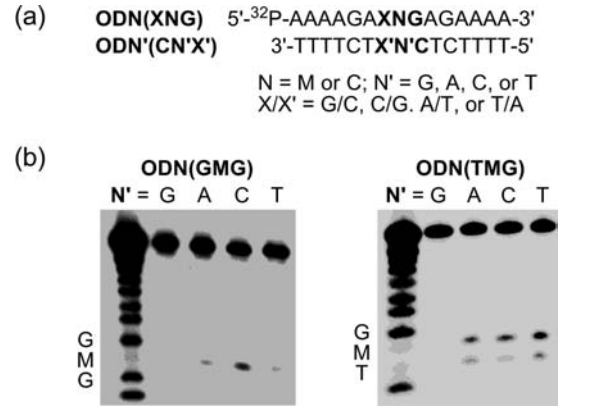

Figure 2. Osmium oxidation of mismatched duplexes. (a) The sequence of the duplex ^{32}P-ODN(XNG)/ODN′(CN′X′). (b) Two typical examples of gel images after PAGE of the oxidation products. The duplexes were incubated in a solution of 5 mM potassium osmate, 100 mM potassium hexacyanoferrate(III), 1 mM EDTA, and 100 mM bipyridine in 100 mM Tris-HCl (pH = 7.7), and 10% acetonitrile at 0 °C for 5 min. Recovered DNA was treated with piperidine (10% v/v, 90 °C, 20 min) to cleave the oxidized strand. (Left) Oxidation of ^{32}P-ODN(GMG)/ODN′(CN′C). (Right) Oxidation of ^{32}P-ODN(TMG)/ODN′(CN′A).

proceeded at the mismatched 5-methylcytosine of ODN(GMG), ODN(AMG), and ODN(CMG), although some difference in strand cleavage efficiency between the types of bases opposite 5-methylcytosine appeared (Figure 3). The small difference in the reactivity can be explained by duplex stability or T_m values. Higher duplex stability resulted in the appearance of the weaker strand cleavage band at 5-methylcytosine (Figure 4). For example, the T_m value of ODN(CMG)/ODN′(CAG) was slightly higher (34 °C) among those of the mismatched duplexes. This mismatched duplex showed relatively low strand cleavage intensity (the relative band intensity was 9%). It is more difficult for oxidants to access the 5-methylcytosine of stable mismatched duplexes compared with 5-methylcytosines in less stable mismatched duplexes, as well as strong suppression of oxidation because of low accessibility in the fully matched duplex. Cleavage of unmethylated ODNs, namely, ODN(GCG), ODN(ACG), and ODN(CCG), was negligible regardless of the nature of the base opposite cytosine.

Unique Reaction Site Selectivity in TMG Sequence. The site selectivity of the strand cleavage observed for ODN(TMG) was quite different from that of the sequences described above (Figures 2 and 3). The ODN(TMG) strand was oxidized at 5-methylcytosine regardless of the nature of the base opposite 5-methylcytosine. In addition, the 5′-neighboring thymine also reacted in spite of the formation of a Watson−Crick base pair with the complementary adenine base. This may be because the accessibility of oxidants to the C5−C6 double bond of the thymine base adjacent to the mismatched base pair is higher compared with a thymine base in a fully matched duplex. ODN(TCG) also showed oxidation of the mismatch-neighboring thymine base, but the efficiency was lower. Oxidation at cytosine was negligible, as well as of other unmethylated cytosine sequences. To learn more about the reactivity of mismatch-neighboring thymine, we prepared an artificial methylation sequence GMT, where a thymine base was located at the 3′ side of 5-methylcytosine, and the oxidation site was examined (Supporting Information Figure S2). In the GMT sequence, 5-methylcytosine was predominantly oxidized. Oxidation at the 3′-neighboring thymine was much lower. The site selectivity of oxidation for the GMT sequence is quite different from oxidation at the 5′-neighboring thymine, but this is an expected result because the thymine forms a stable base pair with the complementary adenine. Compared with the oxidation of the

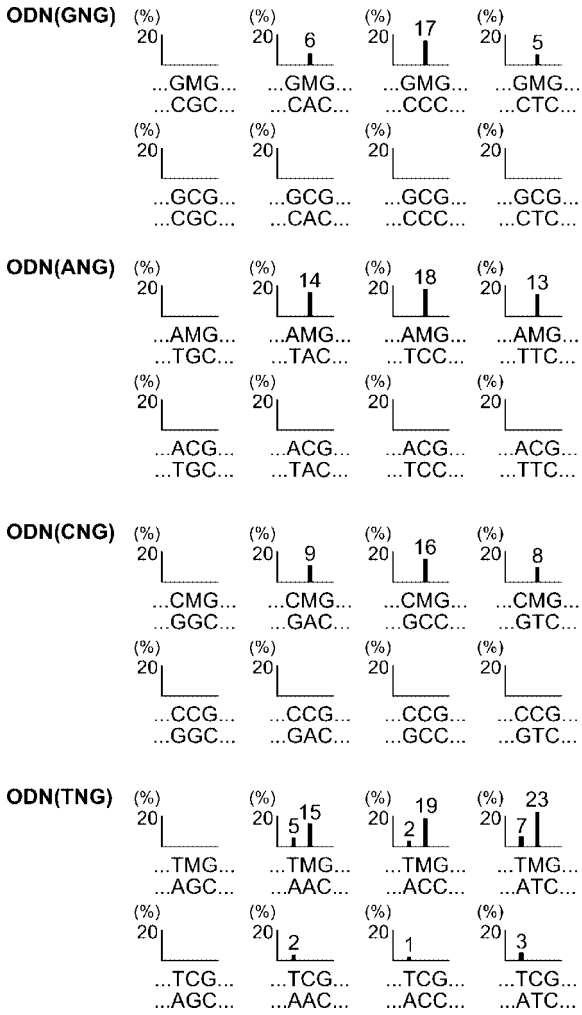

Figure 3. The reactivity at each base of the duplex ^{32}P-ODN(XNG)/ODN′(CN′X′). The heights of bars were determined from the ratio of the band intensity at the corresponding base among the total band intensity of each lane.

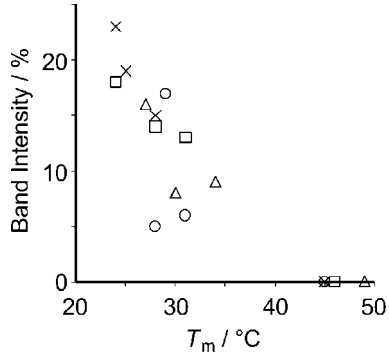

Figure 4. Relationship between the value of T_m and osmium complexation at 5-methylcytosine. Circles, ODN(GMG) hybridized with ODN′(CN′C); squares, ODN(AMG) hybridized with ODN′(CN′T); triangles, ODN(CMG) hybridized with ODN′(CN′G); crosses, ODN(TMG) hybridized with ODN′(CN′A).

thymine located at the 3′ side of the mismatched 5-methylcytosine, the reactivity of the 5′-neighboring thymine is higher and unique.

We have reported that osmium complexation proceeds rapidly at thymines and 5-methylcytosines in a single-stranded DNA, and also that methylated and unmethylated cytosines are clearly distinguished by the oxidation rate (*12*). In addition, we have shown that enhancement of osmium oxidation is observed for

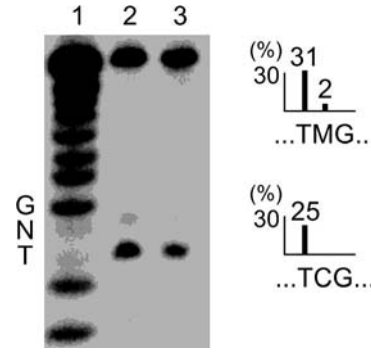

Figure 5. Osmium complexation of single-stranded ODN(TNG). Reaction time was 15 s. Lane 1, G + A sequencing lane; lane 2, N = M; lane 3, N = C.

5′ thymine of TT and TM sequences, whereas it is low at the thymine of the TC sequence (*22*). In brief, the reactivity at thymine greatly depended on the pyrimidine bases located at the 3′ side. This phenomenon seems to indicate that a methyl group at C5 of the 3′-neighboring pyrimidine base enhanced the reactivity of thymine. The result of osmium oxidation of single-stranded ODN(TNG) is shown in Figure 5. This figure exhibits not only the high reactivity of thymine bases, but also the enhancement of reaction at thymine by a methylated cytosine located at the 3′ side of thymine. The unique reactivity of mismatched ODN(TNG) described above can be explained by these phenomena. Mismatched ODN(TMG) reacted at 5-methylcytosine, but the 5′-neighboring thymine base was also oxidized in spite of the Watson−Crick base pair formation of thymine. The high accessibility of oxidants to thymine is supported by the predominant formation of a (5*R*,6*S*)-thymine glycol complex (*23*) showing that the oxidant approached the target thymine from the 3′ mismatched base pair side. In addition, the fact that a methyl group of 5-methylcytosine enhanced the reactivity of 5′-neighboring thymine would also support the reaction at thymine of mismatched ODN(TMG). On the other hand, the reaction efficiency of ODN(TCG) was lower at thymine and negligible at cytosine. The thymine can be oxidized because of high accessibility from the 3′ mismatched base pair side, but the oxidation efficiency decreased because of lack of enhancement of oxidation ability by the "methyl group effect". The reason the modification of cytosine with a methyl group enhanced the reactivity of 5′-neighboring thymine is unclear, but the methyl group of a 3′-neighboring 5-methylcytosine base may play an important role in electronic or hydrophobic promotion of oxidant approach or might have worked as a bridgehead for the approach of oxidants to 5′-neighboring thymine (*22*). The low reactivity of thymine of the GMT sequence can also be explained by the difficulty of approach of oxidants from the 3′ side and loss of the "methyl group effect" by the 3′-neighboring base.

ICON Probe. The ICON probe is a conceptually new DNA for sequence-specific short-term methylation analysis supported by a chemical basis (*21*). The formation of a methylated/unmethylated cytosine-adenine mismatched base pair in hybridization of the probe and the target DNA is applied for sequence-selective methylation detection because this mismatched base pair is well-known to adopt a wobble-type structure with the cytosine displaced laterally into the major groove and the adenine into the minor groove by hydrogen bonding between the 6-amino group of adenine and the N3 of cytosine (*24, 25*). Osmium complexation using the probe may also result in oxidation of the thymine base in the TNG sequence. We examined the oxidation site of TNG sequences using ICON probes under the same reaction conditions as described above except for the absence of bipyridine, which

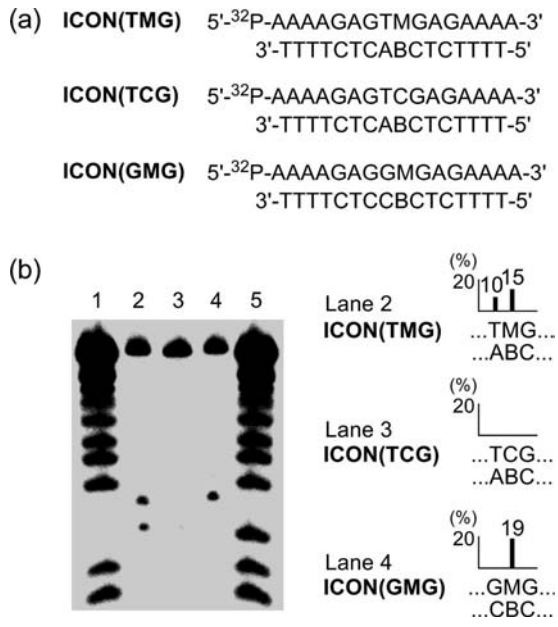

Figure 6. Osmium oxidation using the ICON probe. (a) The sequence of the duplexes formed by hybridization of ^{32}P-labeled target DNA and ICON probes. (b) The reactivity at each base. Lane 1, G + A sequencing lane for ICON(TMG) and ICON(TCG); lane 2, ICON-(TMG); lane 3, ICON(TCG); lane 4, ICON(GMG); lane 5, G + A sequencing lane for ICON(GMG).

was replaced by the ICON probe (Figure 6). For a TMG sequence, oxidation was observed at both thymine and 5-methylcytosine. In contrast, for a TCG sequence, oxidation was negligible at both thymine and cytosine. Because the bipyridine ligand of the ICON probe is fixed near the target 5-methylcytosine base because of the linker length, the reaction efficiency at the thymine neighboring the target is significantly decreased. The reaction at thymine was suppressed in the TCG sequence. However, even though the bipyridine was fixed, oxidation of thymine was still observed for the TMG sequence. Oxidation suppression at the neighboring thymine is due to the combination of three effects: Watson−Crick base pair formation at thymine, small enhancement of thymine reactivity by 3′-neighboring cytosine, and limitation of the reaction site by the bipyridine-connecting linker. As a result, the function of the ICON probes, which discriminate methylated cytosine from unmethylated cytosine using osmium complexation efficiency, is completely maintained, although complexation at the thymine of TMG occurs. There is no problem in quantification of 5-methylcytosine through interstrand cross-linking between the target methylated DNA and the ICON probe.

In conclusion, the efficiency of osmium complex formation at 5-methylcytosine in mismatched DNA duplexes is a key point for the design of sequence-specific detection of DNA methylation. We have described the osmium oxidation efficiency at 5-methylcytosines in a series of duplexes with a single base mismatch. The complexation site and efficiency in mismatched duplexes changed depending on the type of 5′-neighboring base of the 5-methylcytosine forming a mismatched base pair. In particular, when the base neighboring the 5′ side of the mismatched base pair was thymine, oxidation at thymine was also observed. The nature of the mismatched base pairs and their neighboring bases influences the reaction site and efficiency. However, the variation of the reaction site does not degrade the characteristic function of ICON probes, in that it captures only methylated DNA although 5′-neighboring thymine may react. The osmium complexation efficiency and selectivity depending on the nature of mismatched base pairs and neighboring sequences is demonstrated. This knowledge facilitates prior estimation of the reaction abilities of probes and helps in the design of highly methylation sensitive probes.

Supporting Information Available: PAGE analysis of osmium oxidation. This material is available free of charge via the Internet at http://pubs.acs.org.

LITERATURE CITED

(1) Wacker, A., Dellweg, H., Träger, L., Kornhauser, A., Lodemann, E., Türck, G., Selzer, R., Chandra, P., and Ishimoto, M. (1964) Organic photochemistry of nucleic acids. *Photochem. Photobiol. 3*, 369–394.

(2) Weinblum, D., and Johns, H. (1966) Isolation and properties of isomeric thymine dimers. *Biochim. Biophys. Acta 114*, 450–459.

(3) Hayatsu, H. (1976) Bisulfite modification of nucleic acids and their constituents. *Prog. Nucleic Acids Res. Mol. Biol. 16*, 75–124.

(4) Shapiro, R. (1981) Damage to DNA caused by hydrolysis. *Chromosome Damage and Repair* (Seeberg, E., and Kleppe, K., Eds.) pp 3−12, Plenum Publishing Corp., New York.

(5) Chen, H., and Shaw, B. R. (1993) Kinetics of bisulfate-induced cytosine deamination in single-stranded DNA. *Biochemistry 32*, 3535–3539.

(6) Beer, M., Stern, S., Carmalt, D., and Mohlhenrich, K. H. (1966) Determination of base sequence in nucleic acids with the electron microscope. V. The thymine-specific reactions of osmium tetroxide with deoxyribonucleic acid and its components. *Biochemistry 5*, 2283–2288.

(7) Frenkel, K., Goldstein, M. S., Duker, N. J., and Teebor, G. W. (1981) Identification of the cis-thymine glycol moiety in oxidized deoxyribonucleic acid. *Biochemistry 20*, 750–754.

(8) Demple, B., and Linn, S. (1982) 5,6-Saturated thymine lesions in DNA-Production by ultraviolet light or hydrogen peroxide. *Nucleic Acids Res. 10*, 3781–3789.

(9) Jovanovic, S. V., and Simic, M. G. (1986) Mechanism of OH radical reactions with thymine and uracil derivatives. *J. Am. Chem. Soc. 108*, 5968–5972.

(10) Subbaraman, L. R., Subbaraman, J., and Behrman, E. J. (1971) The reaction of osmium tetroxide-pyridine complexes with nucleic acid components. *Bioinorg. Chem. 1*, 35–55.

(11) Chang, C.-H., Ford, H., and Behrman, E. J. (1981) Reactions of cytosine and 5-methylcytosine with osmium(VIII) reagents: Synthesis and deamination to uracil and thymine derivatives. *Inorg. Chim. Acta 55*, 77–80.

(12) Okamoto, A., Tainaka, K., and Kamei, T. (2006) Sequence-selective osmium oxidation of DNA: Efficient distinction between 5-methylcytosine and cytosine. *Org. Biomol. Chem. 4*, 1638–1640.

(13) Tanaka, K., Tainaka, K., and Okamoto, A. (2007) Methylation-selective fluorescence quenching by osmium complexation. *Bioorg. Med. Chem. 15*, 1615–1621.

(14) Tanaka, K., Tainaka, K., Kamei, T., and Okamoto, A. (2007) Direct labeling of 5-methylcytosine and its applications. *J. Am. Chem. Soc. 129*, 5612–5620.

(15) Okamoto, A. (2009) Chemical approach toward efficient DNA methylation analysis. *Org. Biomol. Chem. 7*, 21–26.

(16) Pfeifer, G. P., Steigerwald, S. D., Mueller, P. R., Wold, B., and Riggs, A. D. (1989) Genomic sequencing and methylation analysis by ligation mediated PCR. *Science 246*, 810–813.

(17) Riggs, A. D., and Pfeifer, G. P. (1992) X-chromosome inactivation and cell memory. *Trends Genet. 8*, 169–174.

(18) Herman, J. G., Latif, F., Weng, Y., Lerman, M. I., Zbar, B., Liu, S., Samid, D., Duan, D. S., Gnarra, J. R., Linehan, W. M., and Baylin, S. B. (1994) Silencing of the *VHL* tumor-suppressor gene by DNA methylation in renal carcinoma. *Proc. Natl. Acad. Sci. U.S.A. 91*, 9700–9704.

(19) Merlo, A., Herman, J. G., Mao, L., Lee, D. J., Gabrielson, E., Burger, P. C., Baylin, S. B., and Sidransky, D. (1995) 5′

CpG island methylation is associated with transcriptional silencing of the tumor suppressor p16/CDKN2/MTS1 in human cancers. *Nat. Med. 1*, 686–692.
(20) Herman, J. G., Jen, J., Merlo, A., and Baylin, S. B. (1996) Hypermethylation-associated inactivation indicates a tumor suppressor role for p15(INK4B1). *Cancer Res. 56*, 722–727.
(21) Tanaka, K., Tainaka, K., Umemoto, T., Nomura, A., and Okamoto, A. (2007) An osmium-DNA interstrand complex: Application to facile DNA methylation analysis. *J. Am. Chem. Soc. 129*, 14511–14517.
(22) Nomura, A., and Okamoto, A. (2008) Heterogeneity of osmium oxidation efficiency at consecutive thymines. *Org. Biomol. Chem. 6*, 3905–3907.
(23) Umemoto, T., and Okamoto, A. (2008) Synthesis and characterization of the 5-methyl-2′-deoxycytidine glycol-dioxoosmium-bipyridine ternary complex in DNA. *Org. Biomol. Chem. 6*, 269–271.
(24) Kalnik, M. W., Kouchakdjian, M., Li, B. F. L., Swann, P. F., and Patel, D. J. (1988) Base pair mismatches and carcinogen-modified bases in DNA: an NMR study of A-C and A-O4meT pairing in dodecanucleotide duplexes. *Biochemistry 27*, 100–108.
(25) Okamoto, A., Tanaka, K., and Saito, I. (2004) DNA logic gates. *J. Am. Chem. Soc. 126*, 9458–9463.

BC800531Z

Supporting Information

Osmium Complexation of Mismatched DNA: Effect of the Bases Adjacent to Mismatched 5-Methylcytosine

Akiko Nomura, Kazuki Tainaka, Akimitsu Okamoto*

Advanced Science Institute, RIKEN (The Institute of Physical and Chemical Research), Wako, Saitama 351-1098, Japan.

Fax: +81 48 467 9205; Tel: +81 48 467 9238; E-mail: aki-okamoto@riken.jp

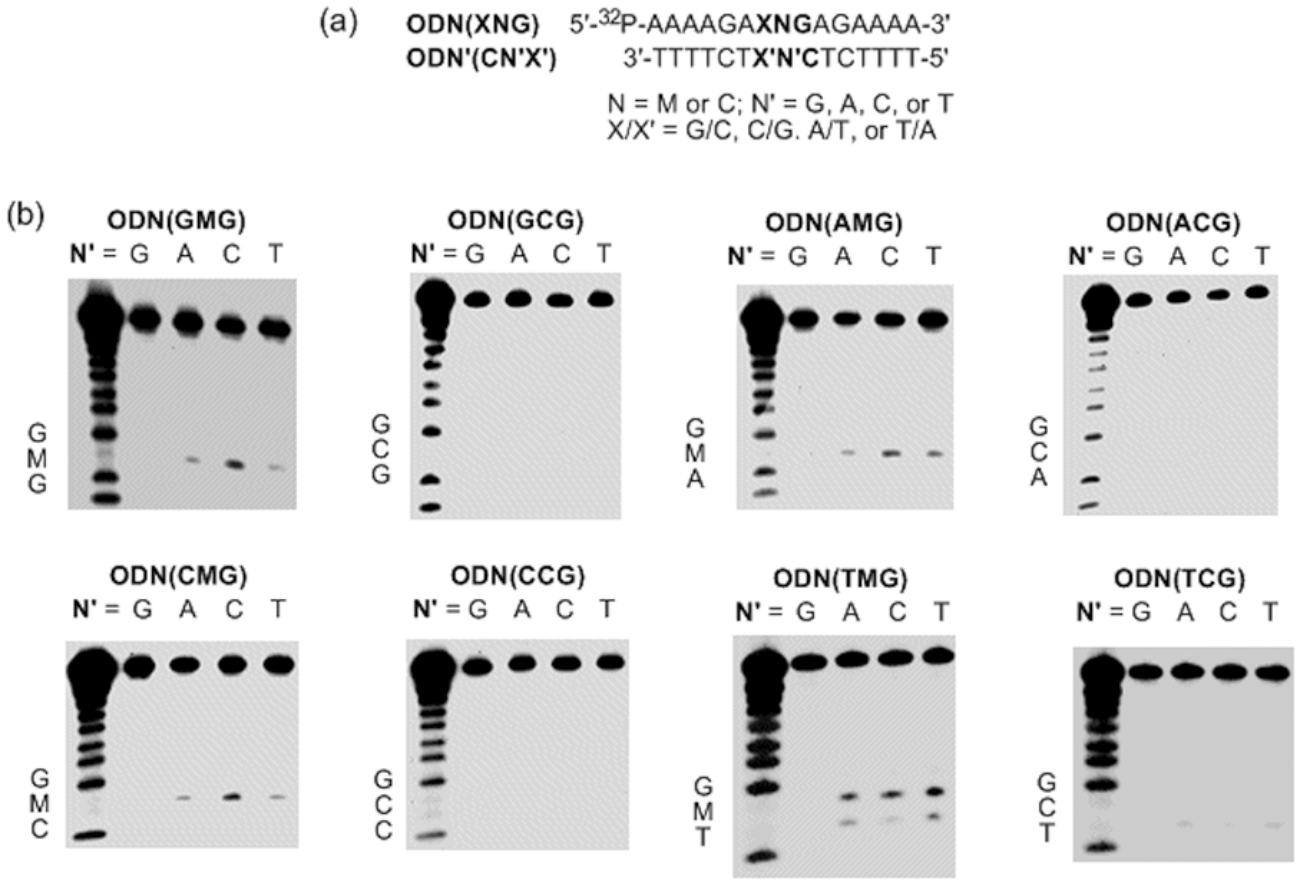

Figure S1. Osmium oxidation of mismatched duplexes. (a) The sequence of the duplex ^{32}P-ODN(XNG)/ODN′(CN′X′). (b) Gel images after PAGE of the oxidation products.

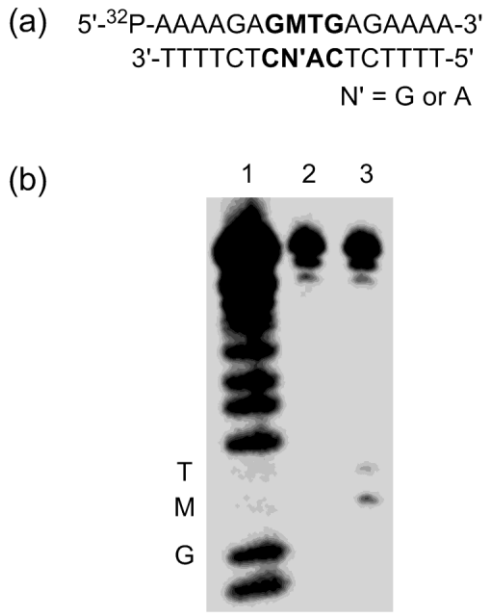

Figure S2. Osmium complexation of a GMT sequence. (a) The sequence of the duplex. (b) Gel image. Lane 1, G + A sequencing lane; lane 2, N' = G (matched); lane 3, N' = A (mismatched).

Subscriber access provided by SHEMYAKIN-OVCHINNIKOV INST

Article

Bioconjugation and Detection of Lactosamine Moiety using #1,3-Galactosyltransferase Mutants That Transfer C2-Modified Galactose with a Chemical Handle

Marta Pasek, Boopathy Ramakrishnan, Elizabeth Boeggeman, Maria Manzoni, Timothy J. Waybright, and Pradman K. Qasba

Bioconjugate Chem., **2009**, 20 (3), 608-618• DOI: 10.1021/bc800534r • Publication Date (Web): 26 February 2009

Downloaded from http://pubs.acs.org on May 15, 2009

More About This Article

Additional resources and features associated with this article are available within the HTML version:

- Supporting Information
- Access to high resolution figures
- Links to articles and content related to this article
- Copyright permission to reproduce figures and/or text from this article

View the Full Text HTML

ACS Publications
High quality. High impact.

Bioconjugate Chemistry is published by the American Chemical Society. 1155 Sixteenth Street N.W., Washington, DC 20036

Bioconjugation and Detection of Lactosamine Moiety using α1,3-Galactosyltransferase Mutants That Transfer C2-Modified Galactose with a Chemical Handle

Marta Pasek,[†] Boopathy Ramakrishnan,[†,‡] Elizabeth Boeggeman,[†,‡] Maria Manzoni,[†] Timothy J. Waybright,[§] and Pradman K. Qasba*[,†]

Structural Glycobiology Section, Nanobiology Program, NCI-Frederick, Basic Research Program, and Laboratory of Proteomics and Analytical Technologies, SAIC-Frederick, Inc., Center for Cancer Research, NCI-Frederick, Frederick, Maryland 21702.
Received December 11, 2008; Revised Manuscript Received January 27, 2009

Studies on wild-type and mutant glycosyltransferases have shown that they can transfer modified sugars with a versatile chemical handle, such as keto or azido group, that can be used for conjugation chemistry and detection of glycan residues on glycoconjugates. To detect the most prevalent glycan epitope, *N*-acetyllactosamine (LacNAc (Galβ1−4GalNAcβ)), we have mutated a bovine α1,3-galactosyltransferse (α3Gal-T) enzyme which normally transfers Gal from UDP-Gal to the LacNAc acceptor, to transfer GalNAc or C2-modified galactose from their UDP derivatives. The α3Gal-T enzyme belongs to the α3Gal/GalNAc-T family that includes human blood group A and B glycosyltransferases, which transfer GalNAc and Gal, respectively, to the Gal moiety of the trisaccharide Fucα1−2Galβ1−4GlcNAc. On the basis of the sequence and structure comparison of these enzymes, we have carried out rational mutation studies on the sugar donor-binding residues in bovine α3Gal-T at positions 280 to 282. A mutation of His280 to Leu/Thr/Ser/Ala or Gly and Ala281 and Ala282 to Gly resulted in the GalNAc transferase activity by the mutant α3Gal-T enzymes to 5−19% of their original Gal-T activity. We show that the mutants ^{280}SGG^{282} and ^{280}AGG^{282} with the highest GalNAc-T activity can also transfer modified sugars such as 2-keto-galactose or GalNAz from their respective UDP-sugar derivatives to LacNAc moiety present at the nonreducing end of glycans of asialofetuin, thus enabling the detection of LacNAc moiety of glycoproteins and glycolipids by a chemiluminescence method.

INTRODUCTION

Glycan moieties of glycoproteins and glycolipids, by mediating protein−carbohydrate (*1*−*4*) and carbohydrate−carbohydrate interactions (*5*−*7*), play an important role in several cellular processes and are implicated in human diseases and cancer. The terminal sugar residues of the glycans are often important for their specific protein−carbohydrate interactions; for example, only the sialyated glycans have high affinity for CD22, a regulatory molecule that prevents the overactivation of the immune system and the development to autoimmune diseases (*4*). Similarly, desialyated glycans with terminal galactose bind mostly to galectin molecules. The pathophysiological role of glycans, as seen in the presence of the unusually short glycans, such as Tn carbohydrate in Core 1 glycan or elongated glycans, such as the polylactosamine moiety in N-glycans, have been associated with cancer (*8*−*10*). Therefore, the ability to detect different terminal sugar moieties is vital for determining the association of these moieties with different cellular states. The detection of these sugar moieties have been achieved mostly through lectin- or antibody-binding studies. These methods, however, lack high specificity and sensitivity. In limited situations, modified sugars with a unique chemical handle have been used for in vivo incorporation in the metabolic pathway to enable the detection of sugar residues on the glycoconjugates of a cell (*11*−*14*). Consequently, a highly specific and sensitive chemoenzymatic method to detect β-GlcNAc[1] residue at the nonreducing end of glycans using the mutant enzyme of β1,4-galactosyltransferase, Y289L β4Gal-T1, has been recently developed (*15*−*18*).

A mutation of the residueTyr289 to Leu289 in bovine β4Gal-T1 broadens the sugar donor specificity of the enzyme in such a way that the mutant enzyme, Y289L β4Gal-T1, transfers GalNAc from UDP-GalNAc to a sugar acceptor with the same efficiency as Gal from UDP-Gal (*15*). The mutant enzyme also transfers galactose analogues that have a chemical handle at the C2 position of the galactose and are similar in size and shape to the N-acetyl group, such as 2-keto-galactose (*16*) or GalNAz (Gal-2-NH-CO-CH_2-N_3) from their respective UDP-sugar substrates (*17*). The transfer of these galactose analogues with a unique chemical handle at the C2 position, such as a keto or azido group, by the mutant enzyme enables one to detect GlcNAc residue using a sensitive chemiluminescence method or to conjugate a variety of molecules in a site-specific manner via GlcNAc residue (*17*, *18*). Similarly, the polypeptide-α-

* Corresponding author. Structural Glycobiology Section, Nanobiology Program, CCR, NCI-Frederick, Building 469, Room 221, Frederick, Maryland 21702. E-mail: qasba@helix.nih.gov. Phone: (301) 846-1934. Fax: (301) 846-7149.

† Structural Glycobiology Section, Nanobiology Program.

‡ Basic Research Program, Center for Cancer Research.

§ Laboratory of Proteomics and Analytical Technologies, Center for Cancer Research.

[1]Abbreviations: α3Gal-T, α1,3-galactosyltransferase; β4Gal-T1, β1,4-galactosyltransferase; GlcNAc, *N*-acetylglucosamine; GalNAc, *N*-acetylgalactosamine; *N*-acetyl-azido-galactosamine (Gal-2-NH-CO-CH_2-N_3), GalNAz; UDP-Gal, uridine 5′-diphosphogalactose; UDP-2-keto-Gal, uridine 5′-diphospho-2-acetonyl-2-deoxy-galactose; UDP-GalNAc, uridine 5′-diphospho-*N*-acetylgalactosamine; UDP-GalNAz, uridine 5′-diphospho-*N*-acetyl-azido-galactosamine; MALDI, matrix-assisted laser desorption ionization; DHB, 2,5-dihydroxybenzoic acid; DMA, *N*,*N*-dimethylalinine; MS, mass spectra; AOB, *N*-aminooxymethylcarbonylhydrazino-D-biotin; HRP, horseradish peroxidase; lac, lactose; LacNAc, *N*-acetyllactosamine.

10.1021/bc800534r CCC: $40.75 © 2009 American Chemical Society
Published on Web 02/26/2009

GalNAc-T2, which transfers GalNAc from UDP-GalNAc to the side chain hydroxyl group of a Thr/Ser residue of a specific peptide sequence, has been shown to transfer the modified galactose with a chemical handle, either 2-keto-galactose or GalNAz, from its respective UDP-sugar (*19*).

It has been shown that only a few residues in the sugar donor-binding pocket of glycosyltransferases determine the sugar donor specificity of these enzymes and that mutation of these residues can alter their sugar donor specificity (*15, 20*−*22*). Consequently, novel glycosyltransferases with broader donor specificities can be designed to transfer a sugar residue with a chemically reactive functional group to specific terminal moieties of glycoconjugates. To detect the terminal *N*-acetyllactosamine (LacNAc (Galβ1−4GlcNAc)) moiety that is the most prevalent sugar moiety found on cells, we engineered the bovine α3Gal-T enzyme, which has high acceptor specificity toward LacNAc, to transfer GalNAc or C2-modified galactose which can be used to detect LacNAc. Because of its high acceptor specificity, α3Gal-T enzyme has been previously used to transfer Gal from UDP-Gal to asialo-glycoprotein with the free LacNAc moiety at its N-linked glycans (*23*).

The α3Gal-T enzyme transfers only galactose from UDP-Gal to the terminal galactose sugar of the LacNAc or lactose moiety forming the product with Galα1−3-linkage. It belongs to a family of α3Gal/GalNAc glycosyltransferases to which human blood group transferases A and B also belong. The blood group transferases A (α1,3-GalNAc-T-A) and B (α1,3-Gal-T-B) transfer GalNAc and Gal, respectively, to galactose moiety of the fucosylated LacNAc acceptor, Fucα1−2Galβ1−4GlcNAc. The amino acid sequences of transferase A and transferase B are identical (*24, 25*) except for four amino acids. Two of the four residues at positions 266 and 268, Leu266 and Gly268 in blood group A transferase, and Met266 and Ala268 in blood group B transferase, determine their respective sugar donor specificities. In fact, in blood group A and B enzymes a mutation of the residue at position 266 is sufficient to alter the donor specificity of these enzymes (*20, 21*). Since α3Gal-T exhibits high sequence similarity and nearly identical crystal structure with the blood group A and B enzymes, a mutation of the corresponding sugar donor-binding residue in α3Gal-T, specifically, His280, is expected to alter the sugar donor specificity of the α3Gal-T enzyme (*26*). Indeed, recently the mutations of the residues in the sugar donor-binding site of bovine α3Gal-T have been shown to enhance the GalNAc transfer from UDP-GalNAc (*27, 28*). In the present study, we have rationally mutated not only His280 residue, but also its neighboring residues to alter its sugar donor specificity from Gal to GalNAc. We show that the mutants also selectively transfer the modified sugar 2-keto-Gal from its UDP derivative to LacNAc. This handle is used in biotinylation and subsequent detection of terminal LacNAc moiety in glycoproteins by chemiluminescence.

MATERIALS AND METHODS

The pET23a vector, His-Bind resin, His-Bind kit buffers, and BL21 (DE3) LysS cells were purchased from Novagen. XL2 blue ultracompetent cells were purchased from Stratagene. The Taq DNA polymerase, PCR nucleotide mix, and rapid DNA ligation kit were purchased from Roche Pharmaceuticals. DNA miniprep spin, PCR purification, and low-melting agarose extraction kits were from Qiagen. Restriction enzymes and PNGase F were purchased from New England Biolabs Inc. DNA primers were synthesized by Integrated Technologies Inc. Ampicillin, UDP-Gal, UDP-GalNAc, lactose, and asialofetuin was obtained from Sigma-Aldrich. UDP-[6-^{3}H] galactose was purchased from Amersham Biosciences, and UDP-[6-^{3}H]-N-acetylgalactosamine was from American Radiolabeled Chemicals. AG 1-X8 chloride resin, form 200−400 mesh, was from Bio-Rad. The micro spin column with active charcoal was from Harvard Apparatus. UDP-GalNAz was purchased from Invitrogen Inc., and UDP-2-keto-Gal was synthesized using the method described (*16*). The *N*-aminooxymethylcarbonylhydrazino-D-biotin (AOB), an aldehyde reacting probe (ARP), was purchased from Dojindo Laboratories.

Site-Directed Mutagenesis and Protein Expression. Site-directed mutagenesis was performed using PCR. Construction of the mutants was carried out using the plasmid pET23a-αGal-T-d79, described previously (*29*), that contains a *Bam*HI/*EcoRI* DNA fragment that codes for residues 80−368 of bovine α3Gal-T. The mutation primers corresponding to the upper and lower DNA strands, respectively, for each mutant were

^{280}SGG^{282}: 5′-GGGGATTTTTATTAC***TCCGGA*****GGC**ATTTTTGGGGGAACACCC-3′ and 5′-TCCCCCAAAAATGCC***TCCGGA*****GTA**ATAAAAATCCCCTTCGCC-3′,

^{280}AGG^{282}: 5′-GATTTTTATTAC***GCCGGC*****GGC**ATTTTTGGGGGAACACCCACT-3′and 5′-TCCCCCAAAAATGCC***GCCGGC*****GTA**ATAAAAATCCCCTTCGCC-3′,

^{280}AAA^{282}: 5′-GATTTTTATTAC**G*CGGCCG*C**C**ATTTTTGGGGGAACACCCACT-3′ and 5′- TCCCCCAAAAAT**G*GCGGCCG*C**GTAATAAAAATCCCCTTCGCC-3′,

^{280}GAG^{282}: 5′-TTTTATTAC**GGG*GCCGGC***ATTTTTGGGGGAACACCCACTCAGGTC-3′ and 5′-TCCCCCAAAAAT***GCCGGC*****CCC**GTAATAAAAATCCCCTTCGCCGAA-3′,

^{280}VGG^{282}: 5′-TATTAC**GTAGGAGGA***ATATT*TGGGGGAACACCCACTCAGGTCCTT-3′ and 5′-TGTTCCCCCA*AATAT***TCCTCCTAC**GTAATAAAAATCCCCTTCGCC-3′, and

^{280}TGG^{282}: 5′-TTTTATTAC***ACCGGTGGC***ATTTTTGGGGGAACACCCACTCAGGTCCTT-3′and 5′-AAAAAT**GCCAC***CGGT*GTAATAAAAATCCCCTTCGCCGAAGGGAATGA-3′.

Mutation codons are shown in bold letters The restriction sites, which are part of the mutation codons, are shown in italics and are underlined. Typically, the entire α3Gal-T cDNA was PCR amplified as two fragments. For the amplification of fragment 1, the primers used were the lower-strand mutation primer and the terminal cloning primer, 5′-CGC*GGATCC*CACCACCACCACCACGAAAGCAAG*C*TTAAGCTA-3′, that introduced *BamH I* restriction site. For the amplification of fragment 2, the primers used were the upper-strand mutation primer and the terminal cloning primer, 5′-CCG*GAATTC*TCAGACATTATTTCTAACCACATTATACTCTTT-3′, that introduced the *EcoRI* restriction site. The fragments were then cut with the restriction enzymes *BspE I, NgoM IV, Eag I, NgoM IV, SspI*, and *Age I* for mutants ^{280}SGG^{282}, ^{280}AGG^{282}, ^{280}AAA^{282}, ^{280}GAG^{282}, ^{280}VGG^{282}, and ^{280}TGG^{282}, respectively, and ligated. The full α3Gal-T cDNA with the mutation was PCR amplified using the terminal cloning primers and then inserted at the *BamHI*/*EcoRI* restriction site into the pET23a vector and transfected in ultracompetent XL2-blue cells. Clones were selected for the unique restriction site introduced with the mutagenesis primer. Each mutation was confirmed by sequence analysis of the insert in the plasmid DNA. Clones that were positive for the desired mutation were transformed into BL21(DE3)LysS cells. The proteins were expressed and purified according to the published method (*29*). The protein concentrations were measured using the Bio-Rad Protein Assay kit, based on the Bradford method, and further confirmed by SDS-the PAGE electrophoresis using ovalbumin as the standard protein marker.

Enzymatic Assay for Wild-Type and Mutant α1,3Gal-T. For specific activity measurements, reactions were carried out at 37 °C for 15 min in a 100 μL volume containing 5 mmol $MnCl_2$, 25 mmol Tris/HCl (pH 7.0), 500 μmol UDP-Gal, or UDP-GalNAc, 0.5 μCi of ^{3}H-labeled sugar nucleotide and 20

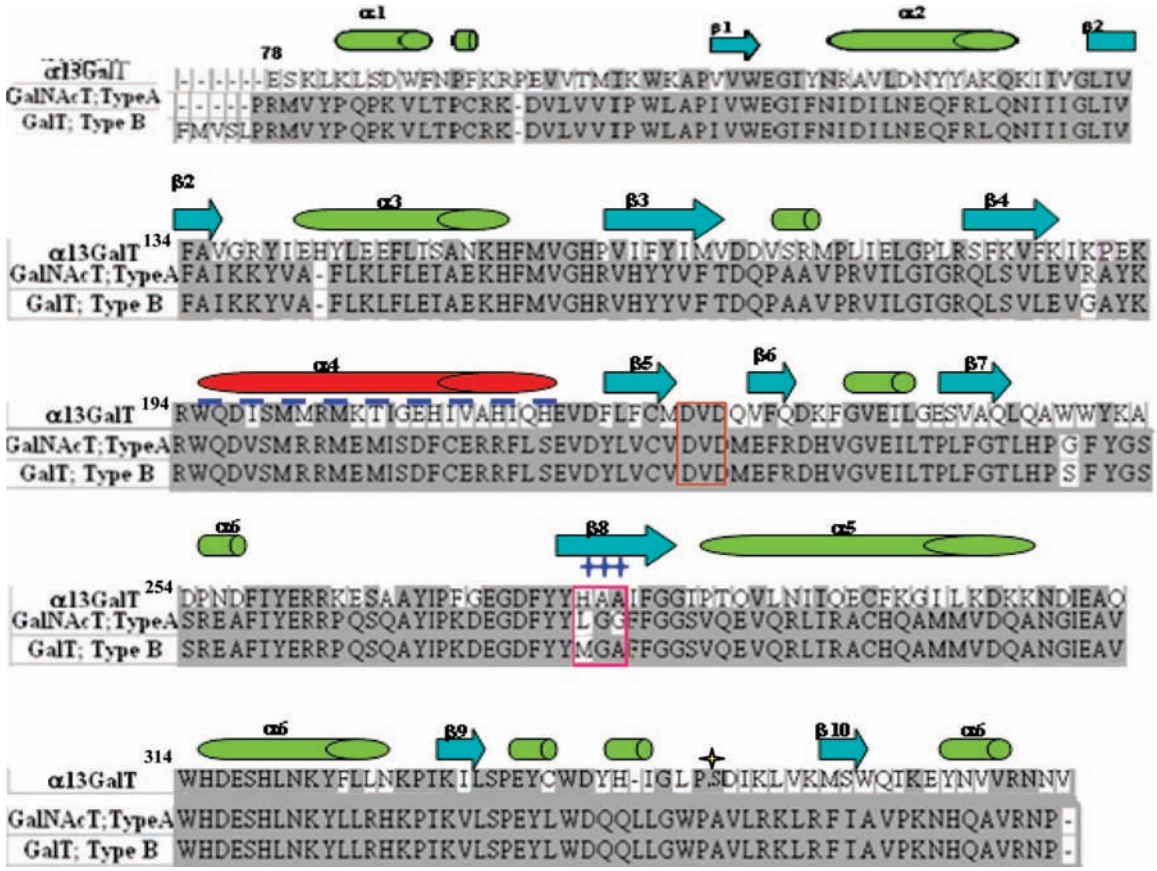

Figure 1. Sequence comparison of the catalytic domain of α3Gal-T with the blood group A and B transferases. The DVD motif (red box) and the sugar donor binding site residues (pink box) are labeled. Secondary structural motifs of these proteins are shown above the sequence; green and red tubes indicate α helix; blue arrows indicate *β* strands; dashed navy line indicates missed internal loop in blood group A and B transferase structure. Sites of mutation of α3Gal-T are indicated by navy stars at positions 280−282.

mmol lactose for wild-type and 200 mmol lactose for mutants with 1 μg of enzyme. The reactions were terminated by the addition of 200 μL ice-cold water to the incubation mixture and analyzed as described (*29*).

Kinetic Analysis for Wild-Type and Mutant α1,3GalT. Different concentrations of the sugar donor, UDP-Gal in the range 10−500 μmol, and UDP-GalNAc in the range 100−1000 μmol, and six different concentrations of the lactose were used in a range that allowed for an accurate Michaelis−Menten plot to be derived. Data were analyzed for a two-substrate system using the following equation:

$$v = \frac{v[\mathrm{A}][\mathrm{B}]}{K_{ia}K_{\mathrm{B}} + K_{\mathrm{B}}[\mathrm{A}] + K_{\mathrm{A}}[\mathrm{B}] + [\mathrm{A}][\mathrm{B}]}$$

The EnzFitter Program, a nonlinear curve-fitting program for Windows from Biosoft, was used to obtain the kinetic parameters K_a, K_b, K_{ia}, and V_{max} from the fitted curves using the rate equation above.

MALDI Mass Spectroscopic Analysis of Oligosaccharides. MALDI mass spectrometry was performed using a 4700 Proteomics Analyzer (Applied Biosystems, Framingham, MA). Two microliters of sample was mixed with 2 μL of DHB/DMA matrix on a stainless steel plate and air-dried or dried under a light vacuum at room temperature as described (*30*). MS spectra were obtained using a laser intensity between 4500 and 6000 kW, with 2000 shots per sample.

Transfer of Modified Sugars from Their UDP Derivatives to the LacNAc Residue on Galactosylated Chitotetrose and on a Glycoprotein, Asialofetuin. Reactions were carried out at 37 °C overnight in a 25 μL volume containing 5 mmol $MnCl_2$, 25 mmol Tris/ HCl (pH 7.0), 500 μmol UDP-Gal-2-keto or UDP-GalNAz, and 0.1 mmol sugar acceptor galactosylated chitotetrose (Galβ1−4GlNAc(β1−4GlcNAc)$_3$) and 2 μg of mutant enzymes SGG, AGG, or TGG. The samples were analyzed by MALDI-MS as described above. The *N*-acetyllactosaminyl-chitoriose (galacto-chitotetrose) used as an acceptor

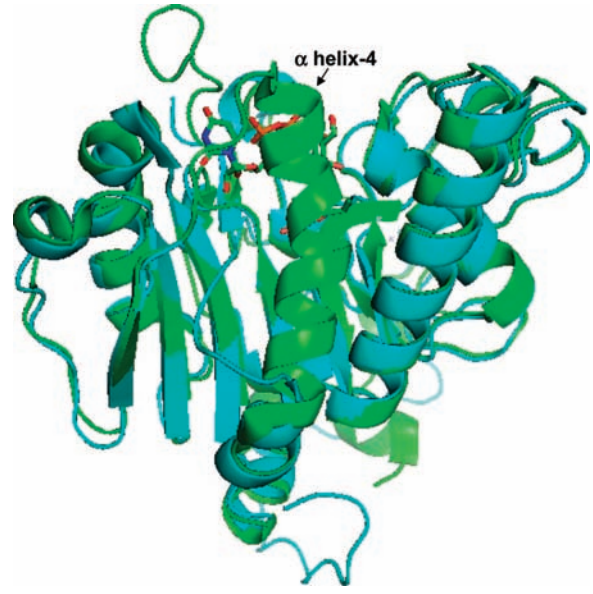

Figure 2. Superposition of the structure of α3Gal-T with UDP-Gal complex (green) with blood group A transferase (cyan). The structural similarity of the two enzymes is very high. The α helix-4 is visible in α3Gal-T and is disordered in the blood group A and B transferase structures.

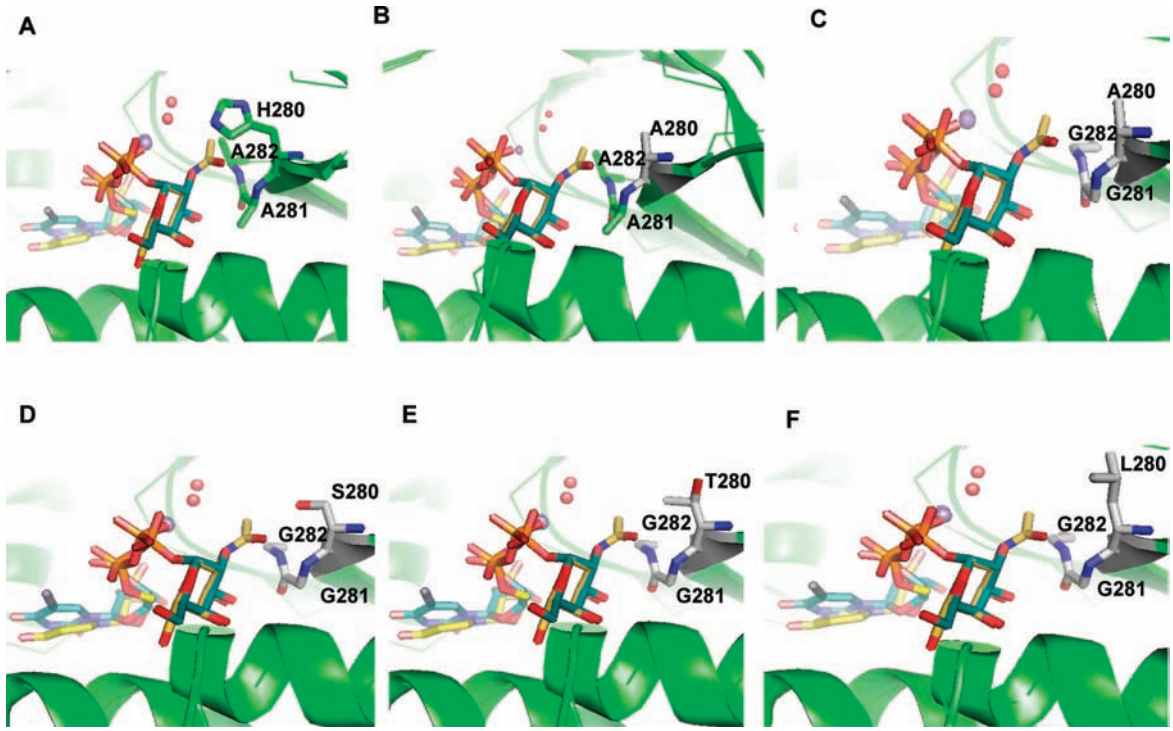

Figure 3. Comparison of sugar donor binding site residues of wild-type α3Gal-T with the bound UDP-Gal (green) (A) (PDB 1fg5) with the modeled structures of the mutants AAA (B), LGG (C), TGG (D), AGG (E), and SGG (F). The UDP-GalNAc structure (yellow) (from PDB 1oqm) is superimposed in these structures. H280 residue causes steric hindrance with the *N*-acetyl moiety of GalNAc. A mutation of H280 to S280 or A280 and a mutation of residues A281 and A282 to G281 and G282, respectively, accommodate the N-acetyl group from UDP-GalNAc in the sugar donor binding site.

Table 1. Catalytic Activity of the Wild-Type α3Gal-T with Ser347, and Mutants of α3Gal-T Enzymes at Different Lactose Concentrations with Each Sugar Nucleotides, UDP-Gal and UDP-GalNAc[a]

	donor substrates			
	UDP-Gal		UDP-GalNAc	
enzyme	20 mmol lac (%)	200 mmol lac (%)	20 mmol lac (%)	200 mmol lac (%)
α1,3 GalT ^{280}HAA^{282} (WT)	100	100	N/A	N/A
α1,3 GalT ^{280}AAA^{282}	14	41	4	6
α1,3 GalT ^{280}GAG^{282}	5	27	0.3	2
α1,3 GalT ^{280}AGG^{282}	0.4	1	3	19
α1,3 GalT ^{280}SGG^{282}	5	5	2	11
α1,3 GalT ^{280}TGG^{282}	3	15	1	6
α1,3 GalT ^{280}LGG^{282}	2	1	3	2
α1,3 GalT ^{280}VGG^{282}	4	16	0.5	3

[a] The 100% specific activity of the wild type (WT) is 1.100 ± 0.20 pmol/ng/min.

substrate in the transfer reactions was synthesized by galactosylation of chitotetrose (GlcNAcβ1−4-GlcNAcβ1−4 GlcNAcβ1−4GlcNAcβ) with wild-type β-1,4-galactosyltransferase. Full conversion of chitotetrose to galacto-chitotetrose (Galβ1−4GlcNAcβ1−4-(GlcNAcβ1−4)$_3$) was achieved by incubating 100 μL of the mixture containing 1 mmol chitotetrose, 3 μg of recombinant bovine C342T-Gal-T1 (15), 500 μM UDP-Gal, 5 mmol $MnCl_2$, and 25 mmol Tris-HCl (pH 8.0), overnight at 37 °C.

Asialofetuin (200 μg) was incubated with 1 mmol UDP-2-keto-Gal and 4 μg of the α3Gal-T1 SGG and AGG mutants in a 10 μL final incubation mixture containing 5 mmol $MnCl_2$ and 25 mmol Tris-HCl (pH 7.0). Reactions were incubated overnight at 37 °C. The samples were placed on a Microcon YM-10 filter, washed with 1 mL of water, and samples were eluted into 20 μL of water. A portion of the sample was analyzed by conjugation with AOB and detected by the chemiluminescence method as described previously (*17*) (see below). Meanwhile, a portion of the sample that contained 10 μg of 2-keto-galctosylated asialofetuin was digested with 2500 units of PNGase F in 20 μL of 50 mmol sodium phosphate buffer for18 h at 37 °C. The oligosaccharides released from the PNGase F-treated samples were purified on a micro SpinColumn with active charcoal prior to MALDI-MS analysis.

Biotinylation and Western Blotting of 2-Keto-Galactosylated Asialofetuin. The 2-keto-galactosylated asialofetuin samples (100 μg) were diluted to 30 μL in a mixture containing 50 mmol NaOAc (pH 3.9) and 3 mmol AOB. The AOB reaction mixtures were incubated with gentle shaking for 12 h at 25 °C, and the reaction was stopped by boiling in Tris-glycine-SDS sample buffer containing β-mercaptoethanol. The biotinylated protein, 25 and 50 ng, was analyzed by Western blotting and detected by chemiluminescence using streptavidin conjugated with HRP as described previously (*16*, *17*).

RESULTS AND DISCUSSION

Comparison of Sequence and Structure of α3Gal-T with the Human Blood Group A and B Glycosyltransferases. The protein sequence of the catalytic domain of bovine α3Gal-T used in our present and past studies (*29*) is identical to the sequence reported by Zhang et al. (*26*) except at position 347, where there is Ser instead of Ala (Figure 1). Comparison of the α3Gal-T sequences from different species in the sequence database show that mouse, rat, and capuchin also have Ser at the corresponding position. We have mutated the Ser347 in our clone of bovine α3Gal-T to Ala347 and found that the two enzymes have comparable enzymatic and kinetic parameters (see Supporting Information). All our mutational studies reported here have been carried out with Ser at position 347 and are considered, in this paper, as the wild-type α3Gal-T.

A comparison of the protein sequences of the catalytic domain of bovine α3Gal-T with the human blood group A (α3GalNAc-

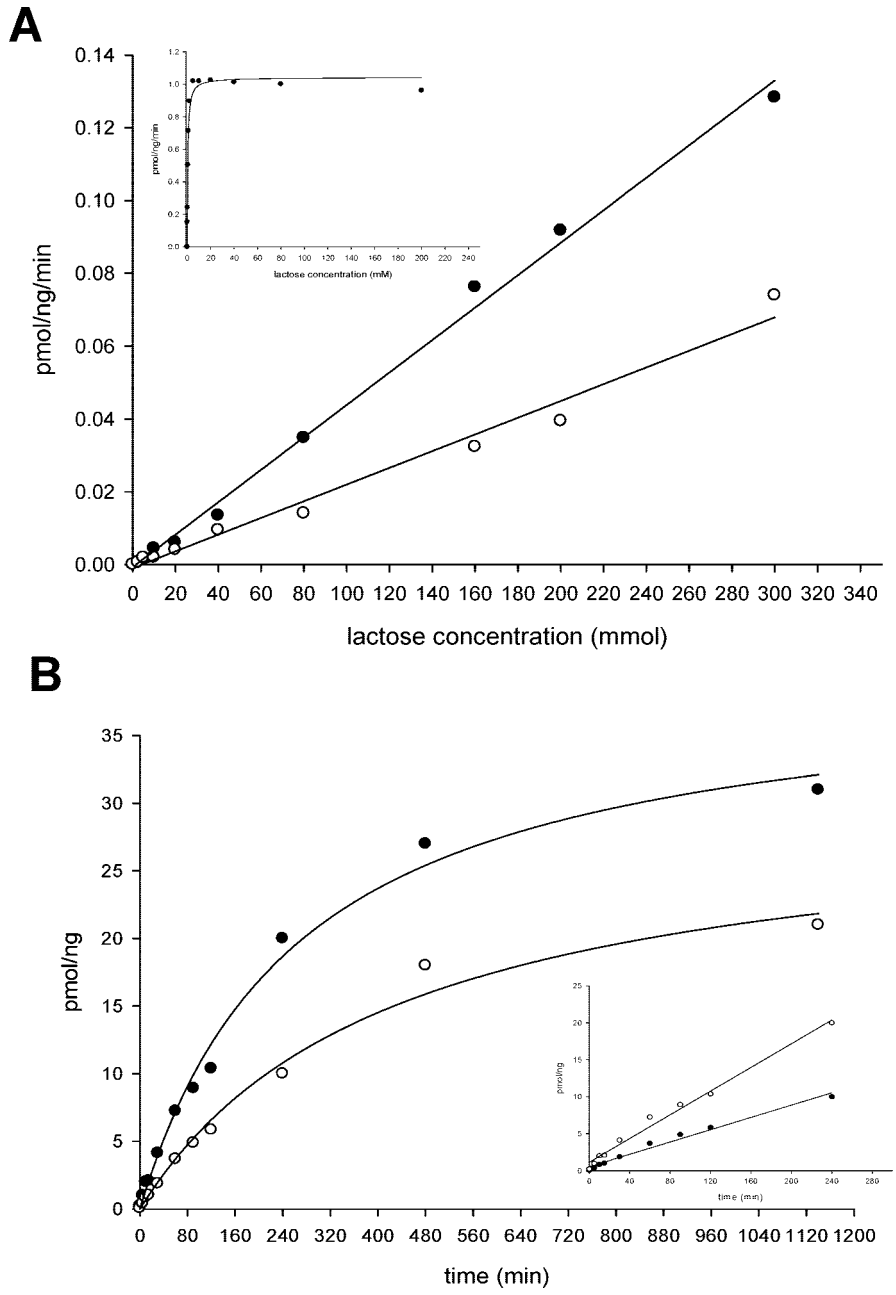

Figure 4. (A) The catalytic activities of the α3Gal-T mutants ^{280}SGG^{282} (*o*) and ^{280}AGG^{282} (•) with UDP-GalNAc as the donor substrate at different concentrations of lactose. The insert shows the catalytic activity of the wild-type α3Gal-T with UDP-Gal as the sugar donor at different concentrations of lactose. Each assay was carried out for 15 min with 1 μg of enzyme, as described in Materials and Methods. (B) Time course of GalNAc transfer with 1 μg of mutant enzymes ^{280}SGG^{282} (*o*) and ^{280}AGG^{282} (•) at 200 mmol lactose and 500 μmol UDP-GalNAc.

Table 2. Kinetic Parameters for Donor Substrates UDP-Gal and UDP-GalNAc and the Acceptor Substrate Lactose with Wild-Type (WT with Ser347) and Mutant Enzymes

UDP-Gal							
enzyme	K_a (mmol)	K_b (mmol)	K_{ia} (mmol)	K_{ib} (mmol)	k_{cat} (s^{-1})	k_{cat}/K_a (s^{-1} mmol)	k_{cat}/K_b (s^{-1} mmol)
α1,3 GalT^{280}HAA^{282} (WT)	0.790 ± 0.001	4.50 ± 0.01	0.13 ± 0.01	0.74 ± 0.02	3.40	4.30	7.5×10^{-1}
α1,3 GalT^{280}AGG^{282}	0.042 ± 0.012	270 ± 21	0.004 ± 0.0007	25.70 ± 3	0.02	0.50	7.4×10^{-5}
α1,3 GalT^{280}SGG^{282}	0.070 ± 0.001	180 ± 24	0.014 ± 0.001	36 ± 5	0.10	1.40	5.5×10^{-4}
UDP-GalNAc							
enzyme	K_a (mmol)	K_b (mmol)	K_{ia} (mmol)	K_{ib} (mmol)	k_{cat} (s^{-1})	k_{cat}/K_a (s^{-1} mmol)	k_{cat}/K_b (s^{-1} mmol)
α1,3 GalT^{280}HAA^{282} (WT)	N/A	N/A	N/A	N/A	N/A	N/A	N/A
α1,3 GalT^{280}AGG^{282}	0.500 ± 0.04	258 ± 25	0.068 ± 0.002	36.1 ± 2	0.30	0.60	1.1×10^{-3}
α1,3 GalT^{280}SGG^{282}	0.740 ± 0.001	330 ± 30	0.101 ± 0.004	45.8 ± 8	0.40	0.50	7.0×10^{-4}

T-A) and B (α3Gal-T-B) shows a 46% similarity (Figure 1). On the contrary, the blood group A and B transferases differ by only four amino acids: Gly176, Ser235, Leu266, and Ala268 for transferase A; and Arg176, Gly235, Met266, and Gly268 for transferase B. Among these four amino acids, the residue at position 266, Met (for B) and Leu (for A), largely determines the sugar

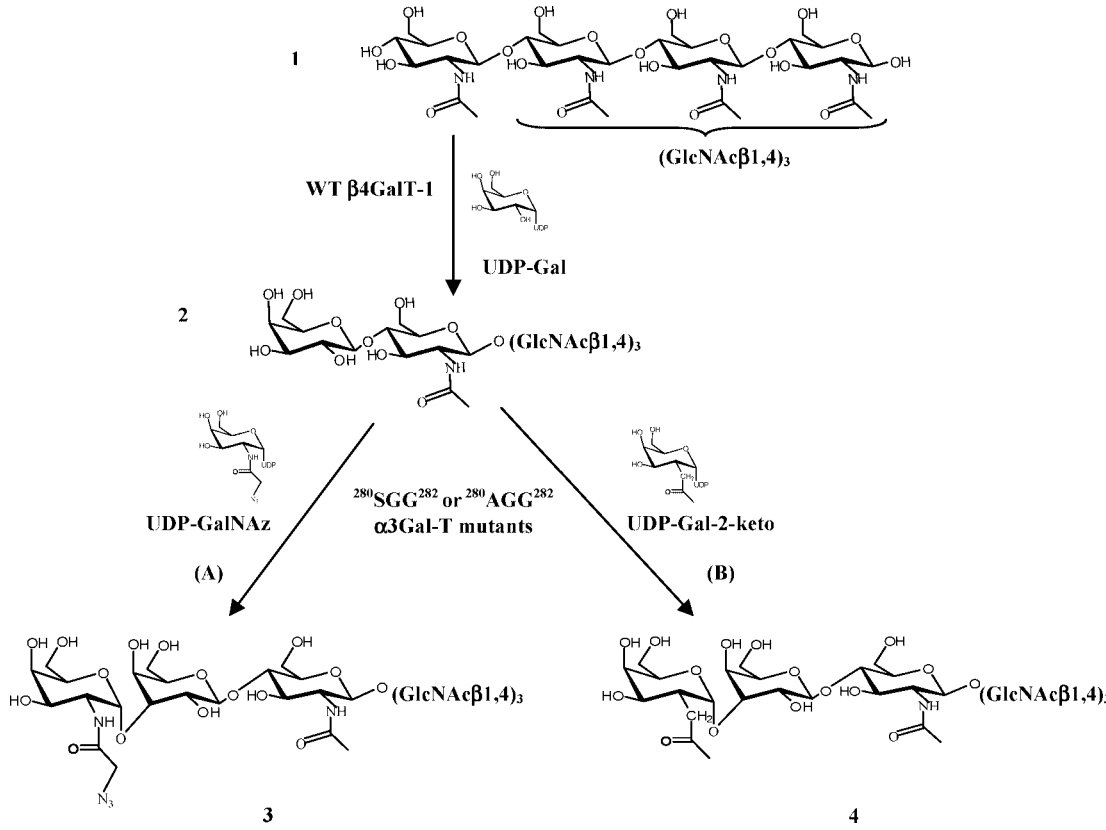

Figure 5. Scheme of the chemoenzymatic synthesis of galacto-chitotetrose, Galβ1,4-GlcNAcβ1,4-(GlcNAcβ1,4)$_3$) (**2**) and the transfer of modified sugars by the α3Gal-T mutants, SGG or AGG. Galactose was transferred to chitotetrose (**1**) by the wild-type (WT) β1,4Gal-T1 to give galacto-chitotetrose (**2**) that has a terminal LacNAc disaccharide moiety. Modified sugars, GalNAz (A) or 2-keto-Gal (B), were transferred from their UDP derivatives to galacto-chitotetrose, synthesizing the products **3** or **4**, respectively, by the mutants SGG or AGG.

donor specificity for Gal or GalNAc, respectively (*24, 25*). At the corresponding position in α3Gal-T is the residue His280. Several other differences are found between α3Gal-T and the blood group A and B transferases, such as residues in the sugar acceptor-binding site.

A number of crystal structures of both bovine α3Gal-T (*26, 31*−*33*) and human blood group A and B enzymes (*34*−*36*), with and without substrates, are available, and they show that the crystal structure of the bovine α3Gal-T is quite similar to that of the human blood group A and B enzyme, with an rms deviation of Cα atoms of only 0.8 Å (Figure 2). These crystal structure studies have shown that, in these enzymes, two similar, flexible regions undergo conformational changes upon Mn^{2+} and UDP-Gal/GalNAc binding. In α3Gal-T, the first flexible region is found between residues 190 and 199, and the second region is its C-terminal 11 amino acids (*26, 31*−*33*); in the blood group A and B transferases, the first flexible region is between residues 177 and 195, and the second is its C-terminal 10 amino acids (*34, 35*). Although these two flexible regions belong to the same part of their three-dimensional structure, the nature of the conformational change in the first region between the two proteins is quite different, while the conformational change in the C-terminal region is the same. During the conformational changes in α3Gal-T, the first flexible region positions the side chain of Trp195 residue (corresponding residue Trp181 in blood group A and B) to form hydrophobic interactions with the bound donor sugar substrate. The second flexible region, the C-terminal end, in addition to burying the bound donor substrate, positions the side chain of Arg359 residue (Arg352 in blood group A and B) in such a way that it forms a stacking interaction with the side chain of Trp195 residue from the first flexible loop (*32*).

Although the crystal structures of the donor substrate, UDP-Gal, bound to α3Gal-T and blood group B enzymes are available, the crystal structure of UDP-GalNAc bound to blood group A enzyme is not yet known. While the conformation of the bound UDP-Gal is the same in these crystal structures, its molecular interactions with the protein molecules show few differences. In the UDP-Gal-bound α3Gal-T crystal structure (*32*), the side chain NH atom of His280 forms a strong hydrogen bond with the O2 hydroxyl group of the galactose sugar; in the blood group B structure, however, the corresponding residue, Met266, forms only hydrophobic interactions with the O2 hydroxyl group (*36*).

A simple modeling of an N-acetyl moiety at the C2 of galactose that converts the donor residue to GalNAc in the crystal structure of UDP-Gal-bound bovine α3Gal-T indicates that the side chains of His280 and Ala282 residues cause steric hindrance with the N-acetyl moiety of GalNAc (Figure 3A). Interestingly, the corresponding residues in the blood group A and B transferases are the ones that determine the sugar donor specificity of these enzymes, indicating that His280 and Ala282 may determine the sugar donor specificity of α3Gal-T toward galactose. In addition, the sequence comparison reveals that the Ala281 residue, the backbone of which forms a hydrogen bond with O3′ of galactose in α3Gal-T (*32*), is also naturally present as a Gly residue in both human blood group A and B transferases. Thus, to accommodate a substitution at the C-2 position of galactose in the sugar donor-binding site of bovine α3Gal-T enzyme, the three contiguous residues, His280-Ala281-Ala282, were considered potential target residues for mutagenesis. A previous study on bovine α3Gal-T (which has Ala at position 347) has shown that, when the His280 residue was mutated to the Ala residue, the mutant enzyme exhibited weak

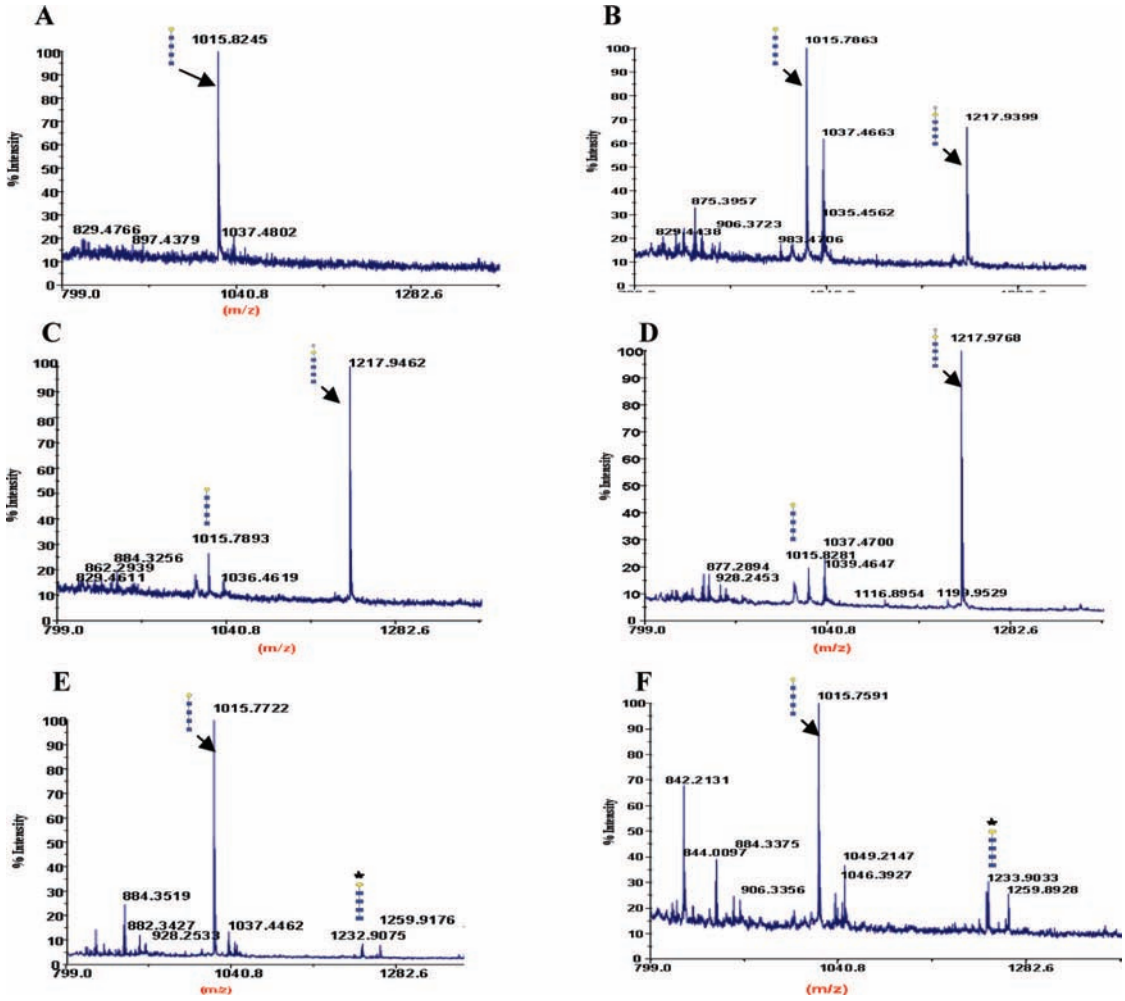

Figure 6. MALDI mass spectra of the acceptor galacto-chitotetrose, Galβ1,4-GlcNAcβ1,4-(GlcNAcβ1,4)$_3$) (A) and after the transfer of 2-keto-Gal (B,C,D) and GalNAz (E,F) to the sugar acceptor. Major peaks are annotated with the carbohydrate structure shown in the symbols for monosaccharides, according to the nomenclature adopted by the consortium for functional glycomics, http://www.functionalglycomics.org/static/consortium/. (GlcNAc [blue square], Gal [yellow circle], 2-keto-Gal [yellow stars], and GalNAz [blue stars]). The symbols were drawn using the *GlycoWorkbench* program found in the eurocarb database http://www.eurocarbdb.org/. The transferred 2-keto-Gal moiety by the mutants TGG (B), SGG (C), and AGG (D), and the transferred GalNAz by the mutants SGG (E) and AGG (F) are shown. (A) Peak at 1015 *m*/*z* corresponds to the linear glycan structure, galacto-chitotetrose. (B−D) Shift in the molecular mass after addition of 2-keto-Gal moiety to galacto-chitotetrose, from the starting ion at 1015 *m*/*z* to a peak of 1218 *m*/*z* (Material and Methods section). (E,F) Shift in the molecular mass after addition of a GalNAz moiety to galacto-chitotetrose, from the starting ion at 1015 *m*/*z* to a peak of 1232 *m*/*z*.

GalNAc-T activity at 20 mmol lactose concentration and was very unstable (*26*). To convert α3Gal-T (which has Ser at position 347) into an efficient α3GalNAc-T, based on the structural details of the two enzymes, we have considered (1) substituting the His280 residue to Ala, Gly, Ser, Thr, Leu, and Val, and (2) substituting the next two residues, Ala281 and Ala282, to Gly281 and Gly282, which are the residues at the corresponding positions in the blood group A and B transferases. A mutation of His280 to Gly (GAA) did not produce stable protein and thus could not be analyzed. Thus, in this study we have characterized the following α3Gal-T mutants: Ala280-Ala281-Ala282 (AAA); Gly280-Ala281-Gly282 (GAG); Ala280-Gly281-Gly282 (AGG); Ser280-Gly281-Gly282 (SGG); Thr280-Gly281-Gly-282 (TGG); Leu280-Gly281-Gly282 (LGG); and Val280-Gly281-Gly282 (VGG) (Table 1). The final yield of the purified mutant proteins ranged from 2 to 6 mg per liter of bacterial culture, and they were stable at a concentration of 2 to 4 mg/mL.

Mutation of His280 Residue Affects the Acceptor Affinity of the Enzyme. In the Gal-T activity, the K_m value of the acceptor substrate lactose is only 4.5 mmol, which is 4-fold lower than the value (20 mmol) found by Zhang et al. (*26*). At the saturation concentration of UDP-Gal, the wild-type enzyme reached its maximum catalytic activity at less than 20 mmol lactose concentration and only very little inhibition even at 200 mmol lactose concentration (Figure 4A and insert; Table 1). A mutation of His280 residue to Ala, mutant AAA, reduces Gal-T activity to 14% at 20 mmol lactose, while at 200 mmol lactose, the reduction is 41%, indicating that the mutant has also lost the affinity for the acceptor substrate (Table 1). The AAA mutant, and including other mutants, shows linear catalytic activity from 20 to 200 mmol lactose concentration for nearly 4 h (Figure 4B and insert). In the crystal structure of bovine α3Gal-T, the side chain of the acceptor substrate-binding residue Gln247 stacks on the side chain imidazole ring of the His280 residue. Therefore, a mutation of His residue to a smaller side chain residue is expected to affect the side chain conformation of Gln247, which may cause a loss of acceptor substrate affinity. This hypothesis is confirmed by the K_m values found for the acceptor substrate in the enzyme kinetic data of both the Gal-T and GalNAc-T mutants (Table 2).

Mutation of His280 to Gly280, the mutant GAA, produces unstable protein that precipitated during purification and thus could not be analyzed further. In contrast, mutation of His280 to Ala280, the mutant AAA, produced stable and active protein. This mutant was analyzed for GalNAc-T activity. In contrast

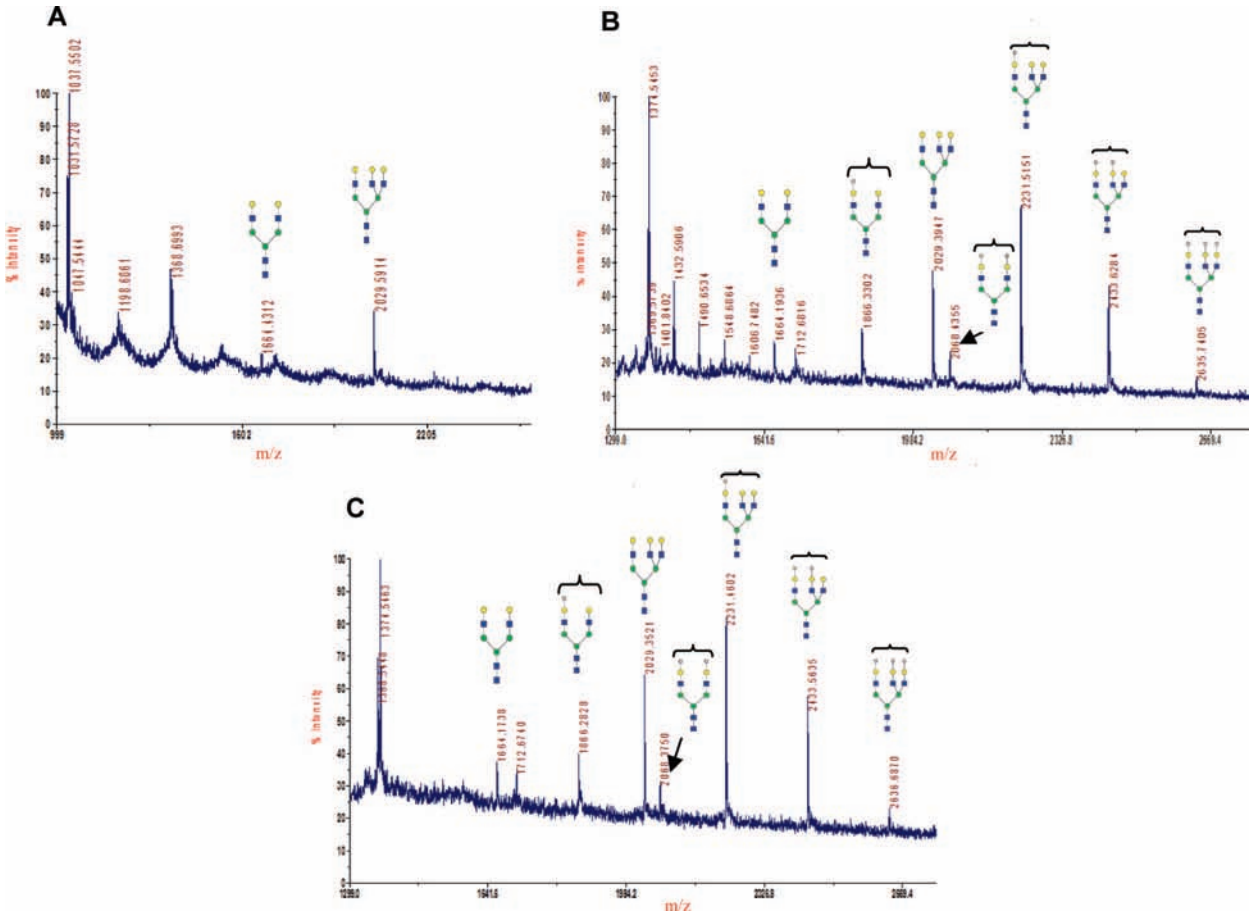

Figure 7. MALDI mass spectra of the glycans released from asialofetuin. After PNGase F treatment of asialofetuin, the released oligosaccharides were passed through SpinColumn with active charcoal and analyzed by MALDI mass spectrometry. Only the peaks of interest are annotated, showing their molecular mass and possible structures. All carbohydrate structures are shown in symbol form, as described in the Figure 6 legend, and Man is drawn as a green circle. Glycans released from the commercial sample (Sigma) of asialofetuin before 2-keto-Gal transfer (A). Ions at 1664 *m*/*z* (biantennary galactosylated N-glycans) and 2029 *m*/*z* (triantennary galactosylated N-glycans) are assigned to N-glycan structures reported for asialofetuin (*37*). Glycan structures released from asialofetuin after the transfer of 2-ket-Gal from UDP-2-keto-Gal with the mutant enzymes α3Gal-T1-SGG (B) and AGG (C). Ions at 1866 and 2068 *m*/*z* indicate mass of biantennary N-glycans with transferred 2-keto-Gal on one and two arms, respectively. Ions at 2231, 2433, and 2635 *m*/*z* indicate mass of triantennary N-glycans with one, two, and three transferred 2-keto-Gal residues to the three arms, respectively.

to wild-type enzyme HAA, the mutant enzyme AAA has 4% and 6% GalNAc-T activity at 20 and 200 mmol lactose concentration, respectively. Thus, the substitution of His280 by Ala280 seems to have reduced the steric hindrance and created a space to accommodate the N-acetyl group of the sugar donor GalNAc (Figure 3B). A mutation of His280 to Gly280, together with the mutation of Ala282 to Gly282 (GAG mutant), shows reduced activity at 200 mmol lactose with both UDP-Gal (27%) and UDP-GalNAc (2%) as donor substrates, compared with the AAA mutant (Table 1).

With sugar donor substrate UDP-Gal, the mutants AGG, SGG, TGG, VGG, and LGG with a Gly residue at both positions 281 and 282 (which is similar to the blood group A and B transferases) exhibit only 0.4%, 5%, 3%, 4%, and 2% Gal-T activity, respectively, at 20 mmol lactose concentrations, and 1%, 5%, 15%, 16%, and 1% Gal-T activity, respectively, at 200 mmol lactose. When UDP-GalNAc was used as the donor substrate, the wild-type α3Gal-T enzyme exhibited no GalNAc-T activity; however, the mutant enzymes at 20 mmol lactose concentration exhibited GalNAc-T activity that corresponds to 3%, 2%, 1%, 0.5%, and 3%, respectively, of the Gal-T activity of the wild-type α3Gal-T at 20 mM lactose (Table 1). Nevertheless, at 200 mmol lactose, the mutants showed higher GalNAc-T activity, with the AGG and SGG mutants showing 19% and 11% activity, respectively (Table 1). Recently, Tumbale et al. (*28*) have generated bovine α3Gal-T mutants with altered donor specificity from the wild-type α3Gal-T that has Ala at position 347 (α3Gal-T-Ala347). The donor substrate mutants of α3Gal-T-Ala347 where ^{280}HisAlaAla^{282} is mutated to ^{280}AlaGlyGly^{282} require mutation of Ile283 to Leu283 to make the mutant proteins stable (*28*). As stated above the mutations in the donor substrate site affects the acceptor binding (Table 1), increasing the lactose concentration from 20 to 200 mM increases the specific activity toward UDP-GalNAc (Figure 4), the observation also made by Tumbale et al. (*28*). However, in their studies this observation was not exploited for screening the mutants from the library at higher acceptor concentrations of lactose.

In the present studies, the mutants AGG and SGG with highest activity toward UDP-GalNAc were selected for kinetic studies.

Kinetic Parameters of SGG and AGG Mutants. The results of the kinetic analysis with UDP-Gal and UDP-GalNAc for the wild-type α3Gal-T (HAA) and the mutants AGG and SGG are presented in Table 2. The k_{cat} values for the UDP-Gal of the mutants AGG and SGG were 170- and 34-fold lower, respectively, than that of the wild-type. The K_m values for the UDP-Gal (K_a) and K_{ia} decreased by about 20- and 10-fold for AGG and SGG, respectively, while the K_m for the acceptor lactose (K_b) of the two mutants increased 60- and 40-fold, respectively. Thus, a mutation of HAA to either AGG or SGG results in increased binding and decreased dissociation of UDP-Gal and

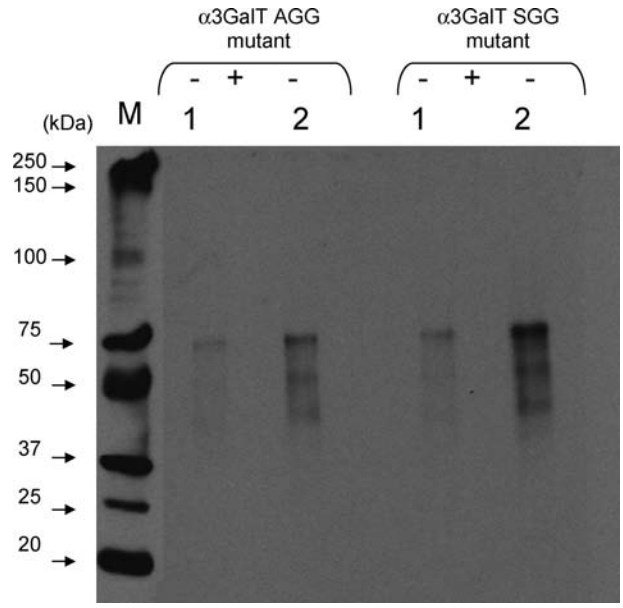

Figure 8. Chemoenzymatic detection of the transferred 2-keto-Gal on asialofetuin. The transfer of 2-keto-galctose to LacNAc residues on the N-glycans chains of asialofetuin by the α3Gal-T mutant enzyme SGG and AGG was monitored by linking with the AOB, followed by Western blotting and chemiluminescence detection. The chemiluminescence was detected only in the samples that contained UDP-2-keto-Gal and mutant enzyme and 25 ng (1) and 50 ng (2) of asialofetuin. After the transfer of 2-keto-Gal, asialofetuin samples were treated with PNGase F (see Materials and Methods section), which removes the N-glycan chains from the protein (+). In contrast to the untreated samples (−), the PNGase F-treated samples (+) exhibited no chemiluminescence indicating that the transfer of 2-keto-Gal is selective for the glycan portion of asialofetuin.

lower affinity for the acceptor lactose. However, in contrast to the wild-type enzyme, the mutants have GalNAc-T activity and the k_{cat} for UDP-GalNAc about 0.3−0.4 s^{-1}, which is one-tenth the wild-type k_{cat} for UDP-Gal. In these mutants, the K_m and K_{ia} for the UDP-GalNAc are similar to the K_m and K_{ia} for the UDP-Gal of the wild-type enzyme, while the K_m for the acceptor lactose (K_b) is nearly 60-fold higher.

In the modeled structures, the "HAA residue" in the sugar nucleotide-binding pocket of the wild-type enzyme was mutated to AAA, AGG, SGG, TGG, or LGG. Moreover, the UDP-GalNAc structure was superimposed on the bound UDP-Gal structure in these models (Figure 3B−F). The N-acetyl group of GalNAc moiety in the AGG mutant has no steric hindrance and is well-accommodated in the substrate-binding pocket (Figure 3C). In contrast, in the SGG mutant, the side chain of the Ser residue seems to have some steric hindrance to the N-acetyl group (Figure 3D). For this mutant, the K_m for UDP-GalNAc is also one-and-a-half-times higher than that for the AGG mutant. The mutants TGG (Figure 3E), LGG (Figure 3F), and VGG (not shown), which have a residue with a more extended side chain than that of Ser, exhibit much lower GalNAc-T activity (Table 1).

Transfer of Modified Sugars UDP-Gal-2-keto and UDP-GalNAz by α3Gal-T SGG and AGG Mutants to LacNAc Acceptor. In our previous studies with the Y289L-β1,4-galactosyltransferase mutant (*15*−*18*) and the polypeptide *N*-acetylgalactosaminyltransferase (*19*), we have shown that the enzymes that accommodate the N-acetyl group of the sugar donor GalNAc in the binding pocket also accommodate C2-modified galactose, which has a chemical handle, such as a 2-keto- or N-2-azido group. In this study, we show that the α3Gal-T mutants SGG and AGG, which transfer GalNAc from UDP-GalNAc, also transfer the modified sugars 2-keto-galactose or GalNAz from their respective UDP derivatives to the LacNAc residues linked to chitotriose (galacto-chitotetrose, *N*-acetyl-lactosaminyl-chitotrios) (Figures 5 and 6) or the LacNAc on the glycoprotein, asialofetuin (Figure 7).

Transfer of 2-Keto-Galactose or 2-Azido-Galactose to LacNAc Moiety in *N*-Acetyl-Lactosaminyl-Chitotriose (Galacto-Chitotetrose). The transfer of C2 modified galactose, 2-keto-galactose, and GalNAz by the mutant enzymes was followed by MALDI mass profiling, and the results are shown in Figure 6E, F. The galacto-chitotetrose (Galβ1−4-GlcNAcβ1−4-(GlcNAcβ1−4-)$_3$) used as an acceptor substrate in the transfer reactions was prepared by galactosylation of chitotetrose (GlcNAcβ1−4-(GlcNAcβ1−4-)$_3$) with β-1,4-galactosyltransferase (Figure 5(2)). The MS analysis of the starting material used as an acceptor substrate for the transfer of 2-keto-galactose or GalNAz from their UDP derivatives by the α3Gal-T mutants showed one peak at 1015 *m*/*z* corresponding to the mass of galacto-chitotetrose (Figure 6A). The mutant enzymes SGG (Figure 6C) and AGG (Figure 6D), in contrast to TGG (Figure 6B), transferred 2-keto-galactose efficiently, converting the acceptor substrate galacto-chitotetrose (1015 *m*/*z* in Figure 6A) completely into 2-keto-galactosylated galacto-chitotetrose, which has a mass of 1218 *m*/*z* (Figure 6C,D). The mutant enzymes SGG and AGG transferred the GalNAz very poorly in contrast to the transfer of 2-keto-galactose (Figure 6E, F).

Transfer of 2-Keto-Galactose to LacNAc Moiety on Asialofetuin. The transfer of 2-keto-Gal to the LacNAc moiety of glycoprotein asialofetuin, known to have N-linked glycans with terminal LacNAc residues, by the mutant enzymes SGG and AGG, is shown in Figure 7B,C. The MALDI analysis of the N-glycans released after the PNGase F treatment of asialofetuin show biantennary (1664 *m*/*z*) and triantennary (2029 *m*/*z*) structures (Figure 7A) as reported (*37*). Both mutants, SGG (Figure 7B) and AGG (Figure 7C), transfer 2-ket-Gal to one (1886 *m*/*z*) or both (2086 *m*/*z*) arms of the biantennary glycan, and to one (2231 *m*/*z*), two (2433 *m*/*z*), or all three (2636 *m*/*z*) arms of the triantennary structure. The MS analyses indicate that the preferred transfer of 2-keto-Gal is to one arm of the biantennary and triantennary structures.

After the 2-keto-galactose was transferred to LacNAc residues on the N-glycans of asialofetuin by SGG and AGG mutants, the ketone moiety at the C-2 position of galactose was coupled with AOB (Figure 8). The biotinylated product was analyzed on Western blots and detected by chemiluminescence with streptavidin conjugated to HRP (Figure 8, (−) samples). Chemiluminescence was detected only when samples were not treated with PNGase F before Western blot analysis (Figure 8, (−) samples), in contrast to samples treated with PNGase F (Figure 8, (+) samples), indicating that the transfer of 2-keto-galactose occurred only to the N-linked carbohydrate moiety. These results show that the transfer of 2-keto-galactose to the LacNAc moieties of glycoproteins can be used for detection of LacNAc moieties of glycoproteins with very high sensitivity and to conjugate glycoproteins via glycan chains. The transfer of modified galactose with a chemical handle at the C-2 position to the LacNAc residues of a glycoprotein using the AGG and SGG mutants makes it possible to (1) detect a LacNAc disaccharide unit in a glycoprotein with high sensitivity and (2) site-specifically conjugate a glycoprotein via its glycan chain.

CONCLUSION

Lactosamine (LacNAc) moiety on glycoconjugates is the most prevalent sugar found on cells. α3Gal-T transfers Gal moiety to LacNAc (Galβ1−4GlcNAc), forming a Galα1−3Galβ-linkage. On the basis of the structural information of wild-type α3Gal-T and human blood group A and B glycosyltransferases, we have engineered bovine α3Gal-T enzyme in such a way that

it can transfer a galactose residue with a chemical handle at the C2 position, such as a keto group to lactosamine that can be used for conjugation chemistry and detection of LacNAc residues on glycoconjugates. In the blood group A glycosyltransferase sugar donor binding site, three residues (Leu266, Gly267, and Gly268) allow transfer of 2-N-acetylated galactose (GalNAc) to fucosylated LacNAc. At the corresponding positions in the α3Gal-T, three residues (His280, Ala281, and Ala282) determine the sugar−donor specificity toward Gal. We have mutated these three residues to Ala280, Gly281, and Gly282 (AGG mutant) and to Ser280, Gly281, and Gly282 (SGG mutant). These mutants lost Gal-T activity by 95% but gained the GalNAc transferase activity, which is 10−20% of the Gal-T activity at 200 mmol lactose concentration. The mutation results show that creation of a cavity in the sugar-donor binding site allows the transfer of galactose with a C2 substitution of a bulky group. The transfer of modified sugar that has a chemical handle at the C2 position of galactose, e.g., 2-keto-Gal to the LacNAc moiety of a pentasaccharide, galactochitotetrose, and of a glycoprotein, asialofetuin, was demonstrated by MS analysis of the product and by bioconjugation of the transferred 2-keto-Gal to the aminooxy-biotinylated derivative, which was detected by the chemiluminescence method.

ACKNOWLEDGMENT

We thank Dr. Linda Hsieh-Wilson, CalTech, for helping Dr. Maria Manzoni during the synthesis of UDP-2-keto galactose and Dr. Natalia Mercer for the critical reading of the manuscript. This project has been funded in whole or in part with federal funds from the National Cancer Institute, National Institutes of Health, under contract N01-CO-12400. The content of this publication does not necessarily reflect the views or policies of the Department of Health and Human Services, nor does mention of trade names, commercial products or organizations imply endorsement by the U.S. Government. This Research was supported in part by the Intramural Research Program of the NIH, National Cancer Institute, Center for Cancer Research.

Supporting Information Available: Additional information as described in the text. This material is available free of charge via the Internet at http://pubs.acs.org.

LITERATURE CITED

(1) Sacchettini, J. C., Baum, L. G., and Brewer, C. F. (2001) Multivalent protein-carbohydrate interactions: a new paradigm for supermolecular assembly and signal transduction. *Biochemistry 40*, 3009–3015.

(2) Sharon, N., and Lis, H. (2002) How proteins bind carbohydrates: lessons from legume lectins. *J. Agric. Food Chem. 50*, 6586–6591.

(3) Wormald, M. R., and Sharon, N. (2004) Carbohydrates and glycoconjugates: progress in non-mammalian glycosylation, glycosyltransferases, invertebrate lectins and carbohydrate-carbohydrate interactions. *Curr. Opin. Struct. Biol. 14*, 591–592.

(4) Varki, A. (2007) Glycan-based interactions involving vertebrate sialic-acid-recognizing proteins. *Nature 446*, 1023–1029.

(5) Hakomori, S. (2004) Carbohydrate-to-carbohydrate interaction, through glycosynapse, as a basis of cell recognition and membrane organization. *Glycoconj. J. 21*, 125–137.

(6) Hakomori, S. (2004) Carbohydrate-to-carbohydrate interaction in basic cell biology: a brief overview. *Arch. Biochem. Biophys. 426*, 173–181.

(7) Bucior, I., and Burger, M. M. (2004) Carbohydrate-carbohydrate interaction as a major force initiating cell-cell recognition. *Glycoconj. J. 21*, 111–123.

(8) Dennis, J. W., Granovsky, M., and Warren, C. E. (1999) Glycoprotein glycosylation and cancer progression. *Biochim. Biophys. Acta 1473*, 21–34.

(9) Glinsky, V. V., Glinsky, G. V., Rittenhouse-Olson, K., Huflejt, M. E., Glinskii, O. V., Deutscher, S. L., and Quinn, T. P. (2001) The role of Thomsen-Friedenreich antigen in adhesion of human breast and prostate cancer cells to the endothelium. *Cancer Res. 61*, 4851–4857.

(10) Desai, P. R. (2000) Immunoreactive T and Tn antigens in malignancy: role in carcinoma diagnosis, prognosis, and immunotherapy. *Transfus. Med. Rev. 14*, 312–325.

(11) Laughlin, S. T., and Bertozzi, C. R. (2007) Metabolic labeling of glycans with azido sugars and subsequent glycan-profiling and visualization via Staudinger ligation. *Nat. Protoc. 2*, 2930–2944.

(12) Saxon, E., and Bertozzi, C. R. (2000) Cell surface engineering by a modified Staudinger reaction. *Science 287*, 2007–2010.

(13) Hang, H. C., Yu, C., Kato, D. L., and Bertozzi, C. R. (2003) A metabolic labeling approach toward proteomic analysis of mucin-type O-linked glycosylation. *Proc. Natl. Acad. Sci. U.S.A 100*, 14846–14851.

(14) Sawa, M., Hsu, T. L., Sugiyama, M., Hanson, S. R., Vogt, P. K., and Wong, C. H. (2006) Glycoproteomic probes for fluorescent imaging of fucosylated glycans in vivo. *Proc. Nat. Acad. Sci. U.S.A. 103*, 12371–12376.

(15) Ramakrishnan, B., and Qasba, P. K. (2002) Structure-based design of beta 1,4-galactosyltransferase I (beta 4Gal-T1) with equally efficient N-acetylgalactosaminyltransferase activity: point mutation broadens beta 4Gal-T1 donor specificity. *J. Biol. Chem. 277*, 20833–20839.

(16) Khidekel, N., Arndt, S., Lamarre-Vincent, N., Lippert, A., Poulin-Kerstien, K. G., Ramakrishnan, B., Qasba, P. K., and Hsieh-Wilson, L. C. (2003) A chemoenzymatic approach toward the rapid and sensitive detection of O-GlcNAc posttranslational modification. *J. Am. Chem. Soc. 31*, 16162–16163.

(17) Boeggeman, E., Ramakrishnan, B., Kilgore, C., Khidekel, N., Hsieh-Wilson, L. C., Simpson, J. T., and Qasba, P. K. (2007) Direct identification of nonreducing GlcNAc residues on N-glycans of glycoproteins using a novel chemoenzymatic method. *Bioconjugate Chem. 18*, 806–814.

(18) Qasba, P. K., Boeggeman, E., and Ramakrishnan, B. (2008) Site-specific linking of biomolecules via glycan residues using glycosyltransferases. *Biotechnol. Prog. 24*, 520–526.

(19) Ramakrishnan, B., Boeggeman, E., and Qasba, P. K. (2007) Novel method for in vitro O-glycosylation of proteins: application for bioconjugation. *Bioconjugate Chem. 18*, 1912–1918.

(20) Seto, N. O., Palcic, M. M., Compston, C. A., Li, H., Bundle, D. R., and Narang, S. A. (1997) Sequential interchange of four amino acids from blood group B to blood group A glycosyltransferase boosts catalytic activity and progressively modifies substrate recognition in human recombinant enzymes. *J. Biol. Chem. 272*, 14133–14138.

(21) Seto, N. O., Compston, C. A., Evans, S. V., Bundle, D. R., Narang, S. A., and Palcic, M. M. (1999) Donor substrate specificity of recombinant human blood group A, B and hybrid A AND B glycosyltransferases expressed in *Escherichia coli*. *Eur. J. Biochem. 259*, 770–775.

(22) Qasba, P. K., Ramakrishnan, B., and Boeggeman, E. (2005) Substrate-induced conformational changes in glycosyltransferases. *Trends Biochem. Sci. 30*, 53–62.

(23) Joziasse, D. H., Lee, R. T., Lee, Y. C., Biessen, E. A., Schiphorst, W. E., Koeleman, C. A., and van den Eijnden, D. H. (2000) Alpha3-galactosylated glycoproteins can bind to the hepatic asialoglycoprotein receptor. *Eur. J. Biochem. 267*, 6501–6508.

(24) Yamamoto, F., Clausen, H., White, T., Marken, J., and Hakomori, S. (1990) Molecular genetic basis of the histo-blood group ABO system. *Nature 345*, 229–233.

(25) Yamamoto, F., and Hakomori, S. (1990) Sugar-nucleotide donor specificity of histo-blood group A and B transferases is

based on amino acid substitutions. *J. Biol. Chem. 265*, 19257–19262.
(26) Zhang, Y., Swaminathan, G. J., Deshpande, A., Boix, E., Natesh, R., Xie, Z., Acharya, K. R., and Brew, K. (2003) Roles of individual enzyme-substrate interactions by alpha-1,3-galactosyltransferase in catalysis and specificity. *Biochemistry. 42*, 13512–13521.
(27) Qasba, P. K., Ramakrishnan, B., Boeggeman, E., and Pasek, M. (2007) Structure-based design of alpha-1,3 N-Acetylgalactosaminyltransferase (α3GalNAc-T) from alpha-1,3galactosyltransferase (a3Gal-T) that can transfer 2′-modified galactose from the corresponding UDP-derivatives. PCT Patent Application No. PCT/US2007/018678 filed 22 Aug 2007.
(28) Tumbale, P., Jamaluddin, H., Thiyagarajan, N., Acharya, K. R., and Brew, K. (2008) Screening a limited structure-based library identifies UDP-GalNAc-specific mutants of {alpha}−1,3 galactosyltransferase. *Glycobiology 18*, 1036–1043.
(29) Shah, P. S., Bizik, F., Dukor, R. K., and Qasba, P. K. (2001) Active site studies of bovine alpha3-galactosyltransferase and its secondary structure prediction. *Biochim. Biophys. Acta 1480*, 222–234.
(30) Snovida, S. I., and Perreault, H. (2007) A 2,5-dihydroxybenzoic acid/N,N-dimethylaniline matrix for the analysis of oligosaccharides by matrix-assisted laser desorption/ionization mass Spectrometry. *Rapid Commun. Mass Spectrom. 21*, 3711–3715.
(31) Boix, E., Swaminathan, G. J., Zhang, Y., Natesh, R., Brew, K., and Acharya, K. R. (2001) Structure of UDP complex of UDP-galactose:beta-galactoside-alpha-1,3-galactosyltransferase at 1.53-A resolution reveals a conformational change in the catalytically important C terminus. *J. Biol. Chem. 276*, 48608–48614.
(32) Tumbale, P., Jamaluddin, H., Thiyagarajan, N., Brew, K., and Acharya, K. R. (2008) Structural basis of UDP-galactose binding by alpha-1,3-galactosyltransferase (alpha3GT): role of negative charge on aspartic acid 316 in structure and activity. *Biochemistry 47*, 8711–8718.
(33) Jamaluddin, H., Tumbale, P., Withers, S. G., Acharya, K. R., and Brew, K. (2007) Conformational changes induced by binding UDP-2F-galactose to alpha-1,3 galactosyltransferase- implications for catalysis. *J. Mol. Biol. 369*, 1270–1281.
(34) Patenaude, S. I., Seto, N. O. L., Borisova, S. N., Szpacenko, A., Marcus, S. L., Palcic, M. M., and Evans, S. V. (2002) The structural basis for specificity in human ABO(H) blood group biosynthesis. *Nat. Struct. Biol. 9*, 685–690.
(35) Letts, J. A., Rose, N. L., Fang, Y. R., Barry, C. H., Borisova, S. N., Seto, N. O., Palcic, M. M., and Evans, S. V. (2006) Differential recognition of the type I and II H antigen acceptors by the human ABO(H) blood group A and B glycosyltransferases. *J. Biol. Chem. 281*, 3625–3632.
(36) Alfaro, J. A., Zheng, R. B., Persson, M., Letts, J. A., Polakowski, R., Bai, Y., Borisova, S. N., Seto, N. O., Lowary, T. L., Palcic, M. M., and Evans, S. V. (2008) ABO (H) blood group A and B glycosyltransferases recognize substrate via specific conformational changes. *J. Bio.Chem 283*, 10097–10108.
(37) Palm, A. K., and Novotny, M. V. (2005) A monolithic PNGase F enzyme microreactor enabling glycan mass mapping of glycoproteins by mass spectrometry. *Rapid Commun. Mass Spectrom. 19*, 1730–1738.

BC800534R

SM-Table 1 Comparison of the kinetic parameters of α3 Gal-T S347 (wt) (a) used in the current studies, with the α3 Gal-T A347 constructed in the lab (b) and that used in the references (26 (c)) and (28 (d)).

Enzyme	K_a (mM)	K_b (mM)	K_{ia} (mM)	K_{ib} (mM)	k_{cat} (s -1)	k_{cat}/K_{ia} (s -1 mM)	k_{cat}/K_{ib} (s -1 mM)
α3 Gal-T 280HAA282..S347[a]	0.790±0.001	4.50±0.01	0.13±0.01	0.90±0.02	3.4	4.3	7.5x10-1
α3 Gal-T 280HAA282..A347[b]	0.400 ±0.001	1.80±0.02	0.20±0.01	0.20±0.01	2.3	5.7	1.3
α3 Gal-T 280HAA282..A347[c]	0.430±0.070	19.9±3.40	0.14±0.03	N/A	6.4	2.3	N/A
α3 Gal-T 280HAA282..A347[d]	0.16	30	N/D	N/D	4.8	N/D	N/D

a α3Gal-T wild type with Ser at 347 used in this paper
b α3Gal-T wild type mutated at position 347 to Ala
c α3Gal-T wild type published (26)
d α3Gal-T wild type published (28)

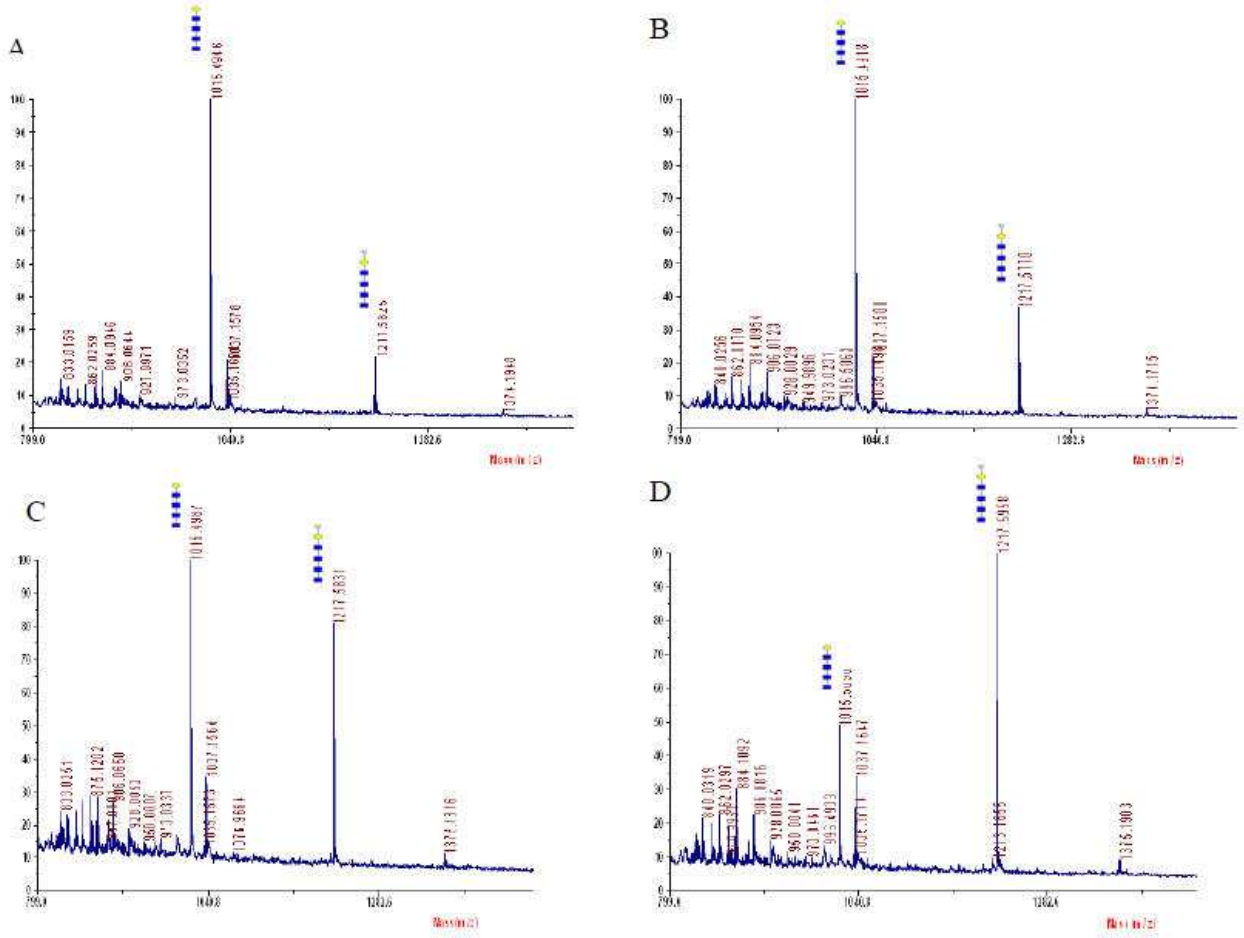

SM-Figure 1. MALDI mass spectra of glycans after the transfer of 2-keto-Gal by the mutant enzyme SGG to a sugar acceptor galacto-chitotetrose Galβ1,4-GlcNAcβ1,4-(GlcNAcβ1,4-)$_3$. Incubation mixtures of 25 µl, containing 0.5 µg of the enzyme, 0.1 mM acceptor, 500 µM UDP-2-keto-Gal, 5 mM $MnCl_2$ and 25 mM Tris/HCl (pH 7.0), were incubated at 37^0 C for 1 h, 2 h, 6 h and overnight and analyzed by MS (A–D). The major peaks are annotated with the carbohydrate structure shown in the symbols for monosaccharides, according to the nomenclature adopted by the consortium for functional glycomics, http://www.functionalglycomics.org/static/consortium/. GlcNAc (blue squares), and 2-keto-Gal (yellow stars). MS analysis shows a shift in the molecular mass from the starting ion at 1015 *m/z* to a peak of 1217 *m/z* after the addition of 2-keto-Gal moiety (see Material and Methods section), for 1 h (A), 2 h (B), 6 h (C) and overnight incubation (D). A peak after the transfer of 2-keto-Gal moiety (1217 *m/z*) increases with time compared to the starting ion 1015 *m/z,* showing that the enzyme is stable and transfers modified sugar donor during the entire incubation time.

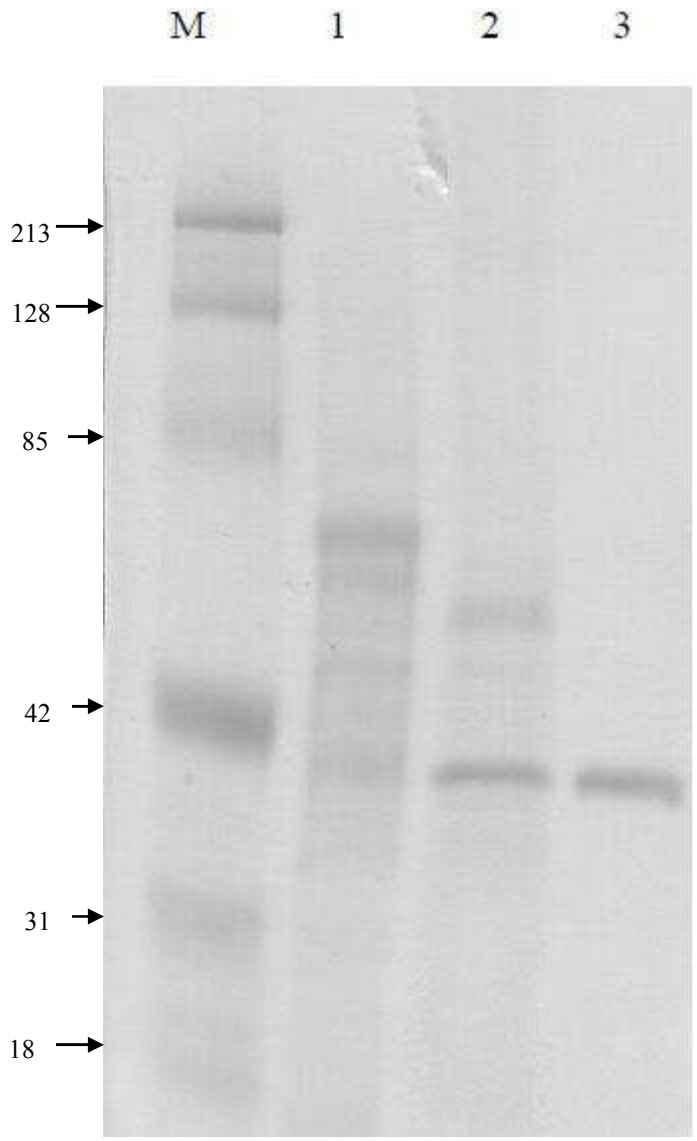

SM-Figure 2 SDS-PAGE analysis of asialofetuin under reduced conditions showing the protein stained bands. (M) Marker, (1) asialofetuin under reduced conditions, (2) asialofetuin under reduced condition after removal of N-glycans by PNGase F treatment, and (3) the PNGase F protein alone under reduced conditions. The chemiluminescence bands in the Figure 7 of the manuscript, with a main band of about 55 kD, correspond to the stained protein bands in the lane 1.

Subscriber access provided by SHEMYAKIN-OVCHINNIKOV INST

Technical Note

A Multidentate Peptide for Stabilization and Facile Bioconjugation of Gold Nanoparticles

Z#eljka Krpetic#, Paola Nativo, Francesca Porta, and Mathias Brust

Bioconjugate Chem., **2009**, 20 (3), 619-624• DOI: 10.1021/bc8003028 • Publication Date (Web): 16 February 2009

Downloaded from http://pubs.acs.org on May 15, 2009

More About This Article

Additional resources and features associated with this article are available within the HTML version:

- Supporting Information
- Access to high resolution figures
- Links to articles and content related to this article
- Copyright permission to reproduce figures and/or text from this article

View the Full Text HTML

ACS Publications
High quality. High impact.

Bioconjugate Chemistry is published by the American Chemical Society. 1155 Sixteenth Street N.W., Washington, DC 20036

TECHNICAL NOTES

A Multidentate Peptide for Stabilization and Facile Bioconjugation of Gold Nanoparticles

Željka Krpetić,[†] Paola Nativo,[‡] Francesca Porta,[†] and Mathias Brust*,[‡]

Dipartimento di Chimica Inorganica Metallorganica Analitica "Lamberto Malatesta", University of Milan, Via Venezian 21, Milan 20133, Italy, and Centre for Nanoscale Science, Department of Chemistry, University of Liverpool, Liverpool L697ZD, United Kingdom. Received July 16, 2008; Revised Manuscript Received January 22, 2009

Gold nanoparticles of two different sizes stabilized by a 15-*mer* peptide ligand specifically designed for this purpose have been prepared in aqueous solution and characterized by UV−vis spectroscopy and TEM. The presence of the ligand and its binding mode to the particles via its four cystein thiols is evidenced by FTIR and NMR spectroscopy. Biotinylation of the particles via binding to a freely accessible lysine residue is demonstrated.

INTRODUCTION

There is increasing interest in the preparation of nanoparticles that are stable in aqueous media and can be readily functionalized with biomolecules by established bioconjugation procedures. Such materials have many applications including biolabeling for a range of optical and electron microscopic techniques, biosensing, and as potential carriers for drug and gene delivery (*1*−*4*). Gold nanoparticles have been investigated extensively in this context owing to their unique optical properties, excellent stability, and relative ease of preparation (*5, 6*). Several efficient stabilization methods based on capping the particles with protective thiol-based ligands have been reported, including the use of mercaptodextranes (*7*), thiolated PEG derivatives (*8*−*14*), and peptides (*15*−*25*). A number of different approaches to conjugating such particles to biomolecules have also been reported. These include click chemistry (*26*), biotin−avidin coupling (*27*−*29*), ligand exchange (*30, 31*), and a range of standard bioconjugation procedures (*32, 33*). Recently, peptides containing several regularly spaced amine (lysine) or thiol (cysteine) functions have been introduced as very strongly binding "multidentate" ligands to stabilize gold nanoparticles (*34*). A special feature of these peptides is that unlike most compounds that contain more than one thiol group they do not generally lead to particle aggregation by cross-linking. This frequently observed adverse side effect is avoided if a sufficient amount of peptide is used and the pH of the solution is controlled so that the acid group of the peptide is present in anionic form. Under such conditions, the peptide molecule readily replaces citrate and binds to the gold particle with all its thiol moieties comparable to the behavior of the well-established hand-in-glove effect observed when multiply thiolated dextranes are used as ligands (*7*). Here, we report the use of a new peptide of this family, specifically designed for the stabilization and subsequent bioconjugation of gold nanoparticles. This ligand can bind to the nanoparticle via the thiol groups of four cysteine moieties and contains a central lysine that provides an amine function to which biomolecular functionality can be readily attached. This protection method is very robust and can be used either for the one-step synthesis of relatively small (2−4 nm) particles or for the stabilization of preprepared, larger (10−20 nm) colloids. The materials have been characterized by TEM, UV−vis, ATR-FTIR, and ^{1}H NMR spectroscopy. As an example of facile bioconjugation, a biotin moiety has been introduced via a standard coupling procedure, and binding of the biotinylated particles to streptavidin-modified surfaces has been demonstrated.

EXPERIMENTAL PROCEDURES

Chemicals. All the chemicals were of the highest grade available and purchased from Aldrich. As a biotin labeling agent *N*-hydroxy sulfosuccinimidobiotin (Sulfo-NHS-Biotin) was used. Water-soluble 15-*mer* peptide with amino acidic sequence H_2N-G**C**GG**C**GG**K**GG**C**GG**C**G-COOH (Figure 1), named GCK15, was purchased from Aldrich (purity >95%). GCK15 aqueous stock solution and Au@Citrate colloidal solution were filtered through 0.45 m Millipore syringe filters prior to use.

Spectroscopy and Microscopy. UV−vis spectra were recorded on a Thermo Spectronic spectrometer, Genesys 20-S. Transmission electron microscopy (TEM) micrographs of the colloidal dispersions were obtained using a FEI Tecnai Spirit instrument operated at an accelerating voltage of 120 kV. Carbon-supported copper grids were used to support the colloidal dispersions. Specimens for imaging by TEM were prepared by evaporating a droplet of gold nanoparticle solutions onto carbon-coated copper grids. A histogram of the particle size distribution and the average particle diameter were obtained by measuring about 200 particles.

ATR FTIR analysis was performed on a JASCO FT/IR-4100 spectrometer. For the ATR FTIR analysis, the samples of gold colloids were freeze−dried, and the analysis of the free peptide and GCK15 stabilized gold particles was performed in the solid state.

^{1}H and COSY ^{1}H NMR spectra were recorded on a Bruker AVANCE 400 MHz spectrometer. For analysis, purified samples

* Crown Street, Liverpool, L697ZD, United Kingdom, E-mail: M.Brust@liv.ac.uk; tel. +44 151 7943554, fax +44 151 7943588.
[†] University of Milan.
[‡] University of Liverpool.

10.1021/bc8003028 CCC: $40.75 © 2009 American Chemical Society
Published on Web 02/16/2009

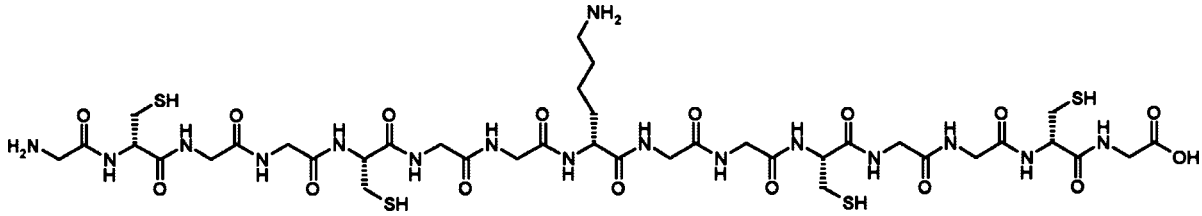

Figure 1. Structure of GCK15 peptide.

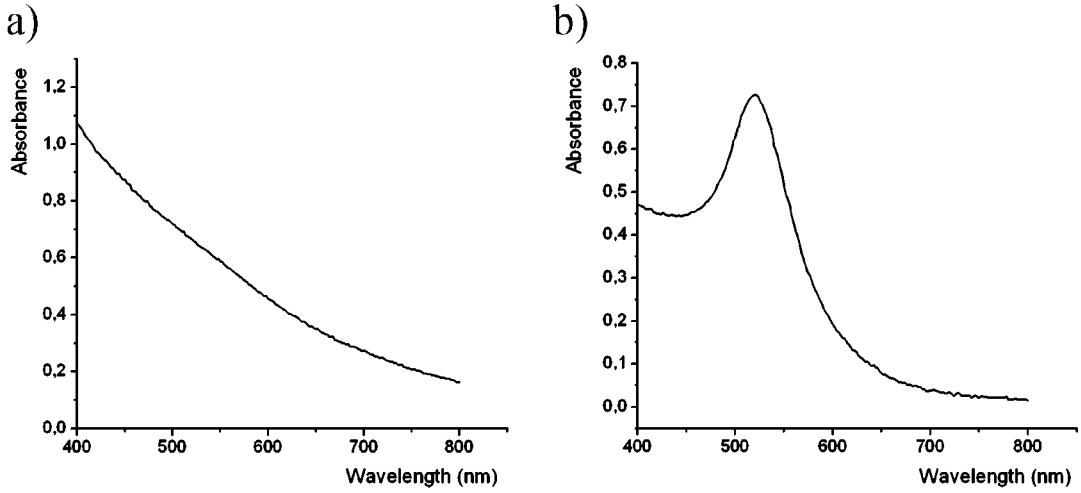

Figure 2. UV−visible spectra of (a) 2.5 nm Au@GCK15 nanoparticles and (b) 15 nm Au@GCK15 nanoparticles.

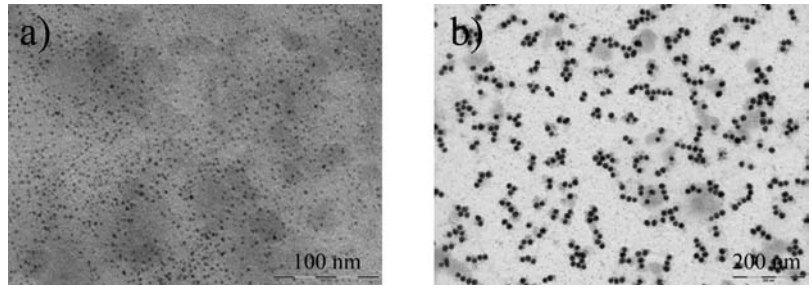

Figure 3. TEM images of GCK15 stabilized gold nanoparticles (a) 2.5 nm Au@GCK15, (b) 15 nm Au@GCK15.

were redispersed in a H_2O/D_2O (9:1) mixture. Chemical shifts (δ ppm) were referenced to 3-(trimethylsilyl) propionic-2,2,3,3-d_4 acid sodium salt (δ Me = 0).

HR-MAS (high-resolution magic angle spinning) ^{1}H NMR spectra were recorded on a Bruker AVANCE 500 MHz spectrometer, spinning at 3 KHz and operating at T = 302 K. For analysis, the sample was prepared by centrifugation of gold nanoparticles (13000 rpm, 15 min), subsequent redispersion in 50 μL of D_2O, and placing of the sample into a 12 mm high precision ceramic rotor (sample tube).

Preparation of Au-GCK15 (2.4 nm). To a 13 mL of mQ water, an aqueous solution of $NaAuCl_4$ (0.162 mL; 6.16×10^{-2} M) was added. Under vigorous stirring, an aqueous solution of GCK15 peptide (1.51 mL, 1.98×10^{-2} M) was added, in order to set up the molar ratio between Au and the peptide 1:0.3. After 5 min, an aqueous solution of $NaBH_4$ was added (0.3 mL, 0.1 M) and a brown sol was immediately formed. It was left under stirring for further 60 min. The particles were purified by dialysis for 48 h (Sigma-Aldrich dry dialysis tubing).

Preparation of Au-GCK15 (15 nm). 15 nm citrate-capped gold nanoparticles were prepared by the Turkevich/Frens method, showing a typical UV−vis plasmon peak at 520 nm. To 20 mL of citrate-capped gold nanoparticles ($C_{NPs} = 1.9 \times 10^{-9}$ M), 9.5 μL of GCK15 aqueous solution (1.98×10^{-3} M) was added, and the mixture was left overnight to allow the complete ligand exchange between citrate ligand and the peptide molecule. The amount of peptide was calculated in order to have 500 molecules of the GCK15 15-*mer* peptide on the surface of each gold particle. Prior to peptide addition, the pH of the gold sol was adjusted to 8 by adding dilute NaOH. The particles

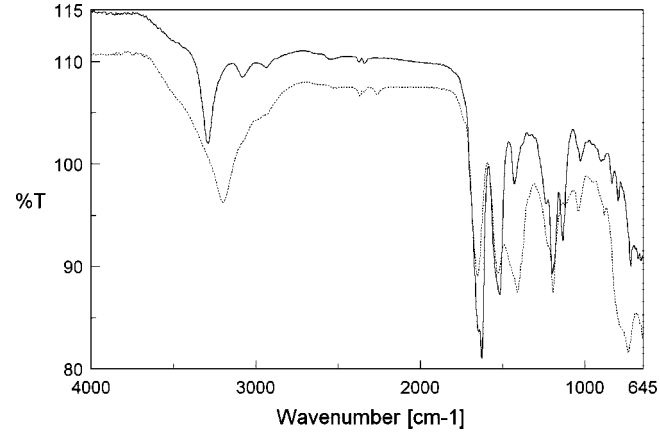

Figure 4. ATR FTIR spectra of GCK15 (solid line) and Au@GCK15 (dotted line) in 4000−650 cm^{-1}region.

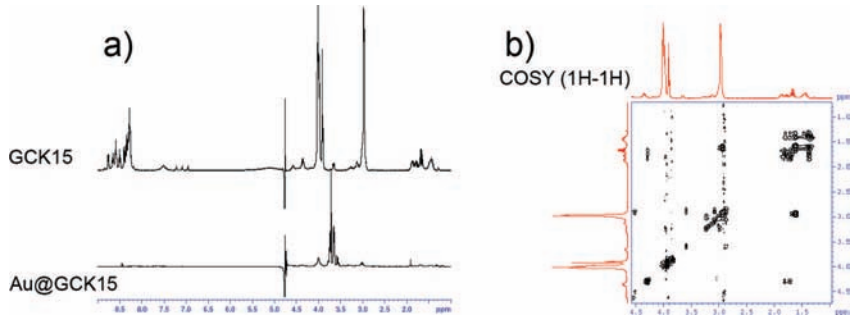

Figure 5. (a) ^{1}H NMR spectra of GCK15 and Au@GCK15 in H_2O/D_2O (9:1), (b) COSY (^{1}H−^{1}H) of Au@GCK15 nanoparticles.

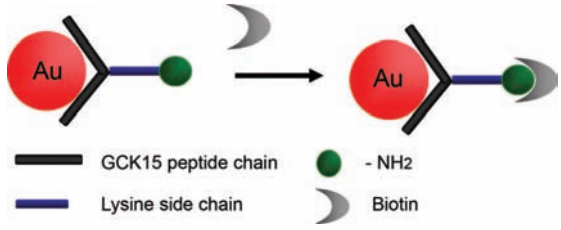

Figure 6. Scheme of biotinylation of peptide-stabilized gold nanoparticles using the standard sulfo-NHS-biotin labeling agent.

were centrifuged (13 000 rpm, 15 min) and purified by 3 cycles of repetitive centrifugation and redispersion in fresh mQ water.

Characterization of Au-GCK15 (2.4 nm). GCK15 coated gold nanoparticles were characterized using UV−vis (Figure 2a), ATR-FTIR (Figure 4), and NMR spectroscopy (Figure 5), while the morphology and size distribution of these particles were investigated by TEM (Figure 3a).

Characterization of Au-GCK15 (15 nm). GCK15 coated gold nanoparticles obtained by ligand exchange reaction were characterized using UV−vis (Figure 2b) and HR-MAS ^{1}H NMR spectroscopy (Figure 8), while the morphology and size distribution of these particles were investigated by TEM (Figure 3b). UV−visible spectra of Au-Citrate-GCK15 particles before and after biotinylation redispersed in PBS showed no significant changes in the plasmon peak absorption (520 nm) and particle size distribution (Figure A, Supporting Information).

Biotinylation Procedure for 15 nm Au-GCK15 Nanoparticles. *N*-Hydroxy sulfosuccinimidobiotin (Sulfo-NHS-Biotin) was used as the biotin-labeling agent. By mixing 300 μL of GCK15 coated gold nanoparticles redispersed in PBS (pH 7.4) and 20 μL of Sulfo-NHS-Biotin (50 mM) in dimethylsulfoxide. The excess of the biotin label was set up to be at least 1000 times more than lysine molecules present in the peptide. The excess of biotin ligand was removed by centrifugation and subsequent redispersion in PBS.

Biotin Detection Methods. *Streptavidin Beads Assay.* Biotin labeled nanoparticles were added to the suspension of streptavidin beads (commercially available suspension in 0.01 M sodium phosphate, pH 7.2, 0.15 M NaCl, 0.02% NaN_3) and stirred for 10 min. After centrifugation (2 min, 2000 rpm), the color change of the beads was observed passing from colorless to red, as a demonstration of biotin molecule specifically bounded to the GCK15 peptide.

Dot Blot Specific Biodetection of Biotin. Samples of capped gold nanoparticles were deposited onto a PVDF membrane (previously prepared by soaking in 70% EtOH/H_2O for 5 min and then two times for 2 min in H_2O). The membrane was blocked 40 min with phosphate buffer containing 5 mg/mL bovine serum albumin (BSA) and then incubated with streptavidin-horseradish peroxidase (HRP). After the rinsing with H_2O, a luminol reagent (ECL reagents) was pippeted for 5 min continually. The membrane was then placed between a cling film and the X-ray image was recorded. In the case of a positive outcome, for biotinylated Au NPs, the dark spot appeared on the place where biotinylated Au NPs were placed.

RESULTS AND DISCUSSION

Gold nanoparticles of 2.4 nm diameter were prepared in a one-step reaction by borohydride reduction of tetrachloroaurate in the presence of the stabilizing peptide H_2N-G**C**GG**C**GG**K**G-G**C**GG**C**G-COOH (Figure 1). The four cysteine (C) residues binding to the particle surface and the lysine (K) available for subsequent bioconjugation are represented in bold. The particles were purified by dialysis. A clear brown solution was obtained indicating the formation of gold particles in the size range below 3 nm. This conclusion was confirmed by the absence of a plasmon absorption band in the UV−vis spectrum (Figure 2a) and by the observation of very small (2 to 5 nm) particles by TEM (Figure 3a). These results are typical for preparations of monolayer protected clusters (MPCs), although usually much simpler thiol ligands are employed, which generally do not lend themselves to facile bioconjugation (*35*). Structural investigations of the ligand shell of MPCs always represent a formidable challenge, even in the case of alkane thiol ligands (*36*−*38*). Only recently, the complete molecular structure of an MPC, $Au_{102}MBA_{44}$ (MBA: *p*-mercaptobenzoic acid), has been determined by X-ray crystallography (*39*). Usually, IR and NMR signatures of the MPCs are compared to those of the free ligands in solution, and the formation of the ligand shell is inferred from the similarity of the spectra. In some cases, it is possible to assign conformational features that are specific to the molecules in the ligand shell, based on subtle spectroscopic differences between bound and free ligands (*40, 41*). Usually, the ligand shell contributes to the broadening and blurring of spectral features, particularly in NMR experiments (*42*−*45*). We have used both FTIR and NMR spectroscopy to demonstrate that our peptide indeed constitutes the ligand shell of the particles. A comparison between the FTIR spectrum of the free peptide and that of the peptide-protected particles is shown in Figure 4. As found previously for peptide ligands of this family, it can be inferred from the spectra that the amide functions participate in the bonding of the ligand to the surface (*34*). This is concluded from the shift of the amide A band from 3291 cm^{-1} in the free peptide to 3197 cm^{-1} in the particles suggestive of unusually strong hydrogen bonding. Otherwise, both spectra are very similar and thus indicate that the intact peptide indeed acts as a surface bound stabilizing agent. Hydrogen bonding is supported also by NMR results, as shown in Figure 5a, where peaks in the NH region (6.8−8.8 ppm) had significantly changed their position and shape upon binding to gold particles, suggesting possible interaction between vicinal peptides on the gold surface, besides coordination to gold.

Unfortunately, the S−H vibration of the cysteine thiols is not visible in the IR spectrum of the free peptide, and hence, its absence in the spectrum of the particles is not diagnostic for

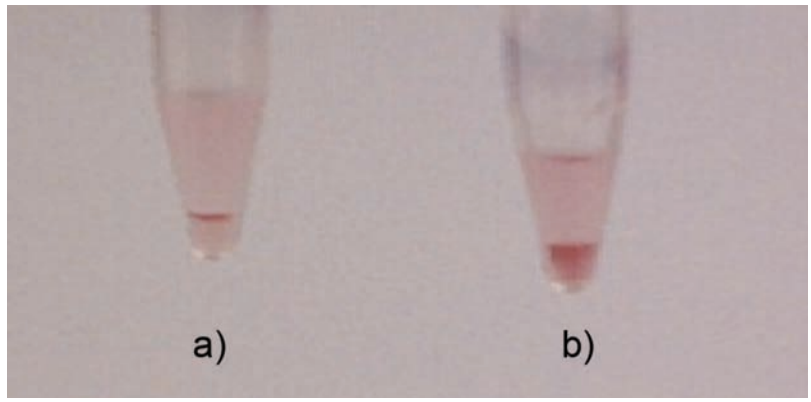

Figure 7. Specific binding of the biotinylated particles to streptavidin-modified agarose beads. (a) 15 nm Au@GCK15 nanoparticles and (b) biotinylated 15 nm Au@GCK15 nanoparticles attached onto streptavidin-modified agarose beads.

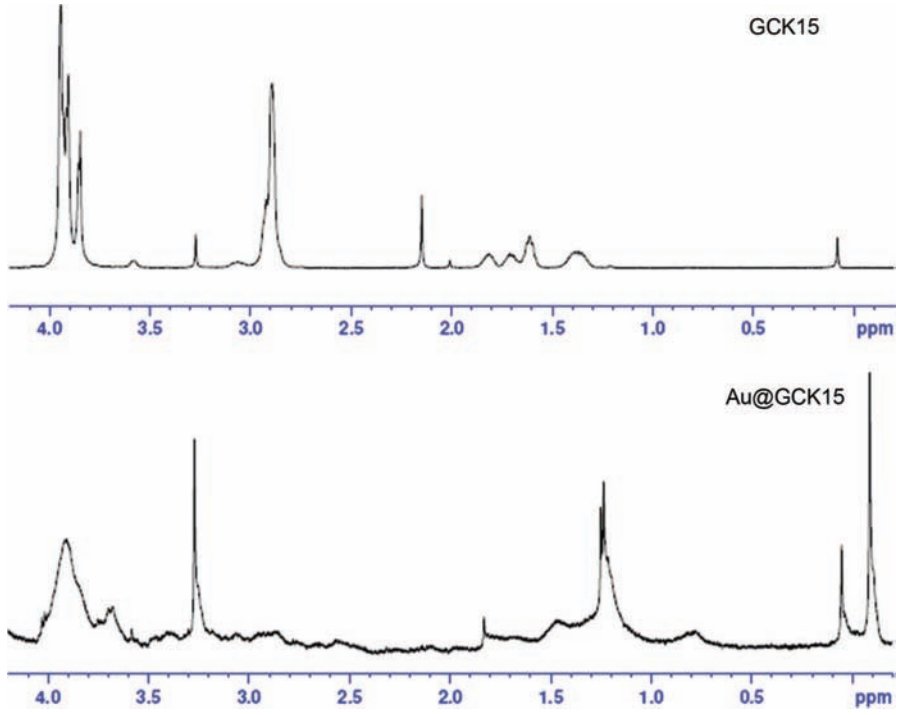

Figure 8. HR-MAS ^{1}H NMR of GCK15 peptide and 15 nm Au@GCK15 nanoparticles.

binding to the gold surface via the thiols. This, however, can be demonstrated by ^{1}H NMR spectroscopy. The NMR spectra of the free peptide and of the particles in 9:1 H_2O/D_2O mixtures are shown in Figure 5. In the spectrum of the free peptide, the 8 cysteine β-methylene groups vicinal to the thiol groups appear, as expected, as a sharp doublet centered at 2.90 ppm. Upon binding to the particles, this feature disappears. This is commonly observed for signals that are due to hydrogen atoms very close to the gold surface (*46*, *47*). What remains is a weak triplet centered at 3.01 ppm that we attribute to the ε-methylene group of the central lysine side chain, which is occulted in the spectrum of the free peptide by the strong β-methylene doublet (Figure 5b). From these observations, we conclude that the ligand binds to the surface of the particles via all its thiol functions leaving the lysine amine group freely accessible, as intended.

Gold nanoparticles of 15 nm diameter were obtained via the classic Turkevich/Frens method (*48*, *49*), subsequently protected by addition of our peptide and purified by repeated centrifugation and redispersion. The particles are extremely stable and can be centrifuged and redispersed in pure water many times without detectable loss of material, whereas the as-prepared citrate-stabilized particles cannot be redispersed in pure water after the first centrifugation. The UV−vis spectrum in Figure 2b shows a plasmon absorption band at 520 nm typical for gold particles of this size range. The TEM image of the peptide-coated gold particles in Figure 2b indicates a narrow size distribution centered at 14 nm. The type of aggregation of particles on the sample grid observed here is fairly common for charged particles derived from hydrosols and does not suggest that particles are aggregated in solution. In addition, the UV−vis spectrum and the ruby red color of the hydrosol rule out the presence of a significant number of aggregates.

There are many reports in the literature on the passivation of gold nanoparticles with polythiolated ligands. While such ligands often cause irreversible aggregation of particles by cross-linking (*50*−*56*), there are also several reports in which their use results in the formation of stable colloids (*7*, *57*). In our case, we have in fact also observed aggregation but only when the peptide ligand was added at a pH value of 6 or below. On the other hand, at pH 8 no aggregation occurs, presumably because the acid group of the peptide is deprotonated, which facilitates the rapid and efficient replacement of citrate.

The analysis of the ligand shell in the case of these larger particles is more difficult due to the very small proportion

of peptide present in the total amount of material, which is predominantly gold. However, using high-resolution magic angle spinning (HR-MAS) well-resolved ^{1}H NMR spectra of 15 nm Au@GCK15 nanoparticles were obtained (Figure 8). The absence of citrate peaks (quartet centered at 2.5−2.7 ppm) suggests complete ligand exchange by exposure to the peptide. The sharp doublet centered at 2.90 ppm in the spectrum of the free peptide ligand is due to the 8 cysteine β-methylene groups vicinal to the thiol groups and disappears completely upon binding to the particles. This indicates that all cysteine thiol groups are involved in the surface binding process.

Biotinylation of peptide-stabilized gold nanoparticles was achieved using the standard sulfo-NHS-biotin labeling agent. This is illustrated in Figure 6. Binding of the particles to streptavidin-modified substrates was demonstrated as evidence for successful biotinylation. Specific binding of the biotinylated particles to streptavidin-modified agarose beads leading to an intense coloration of the beads is shown in Figure 7. Particles that have not been biotinylated do not attach to the beads. Dot blot experiments (not shown) also clearly indicate efficient biotinylation of the particles.

CONCLUSIONS

A simple and versatile new route to stable biofunctional gold nanoparticles in aqueous media has been described. Stabilization is robust owing to the presence of four thiol groups per ligand molecule, which are all capable of binding to the surface of the particles. This binding configuration has been confirmed by NMR spectroscopy. Subsequent attachment of biomolecular functionality of choice, e.g., biotin, is possible by standard procedures due to the presence of a central lysine residue that is not involved in the binding of the ligand to the surface of the particles. The same capping ligand can be used to cover a range of particle size from ca. 1 to 20 nm. Preliminary results indicate that larger particles (up to 50 nm) can also be stabilized by this ligand. Custom-made variations of the ligand are readily available from commercial peptide suppliers. To date, it has been difficult to determine the exact number of ligands per particle, which will strongly depend on particle size. Once this figure is known, the stabilizing approach shown here will allow controlling the precise number of biomolecules attached to each particle, by ligand design.

ACKNOWLEDGMENT

Financial support from the European Union (NACARDIO, PATTERNS) is gratefully acknowledged. We also acknowledge Fondazione CARIPLO (Progetti Internazionali Finalizzati al Reclutamento di Giovani Ricercatori) for financial support.

Supporting Information Available: UV−visible spectra of 15 nm Au@GCK15 before (blue line) and after biotinylation (green line). This material is available free of charge via the Internet at http://pubs.acs.org.

LITERATURE CITED

(1) Brisson, A., and Mornet, S. (2007) Functionalization of gold nanoparticles with oriented proteins. Application to the high-density labelling of cell membranes. *PCT Int. Appl.* 89.

(2) Han, G., Ghosh, P., De, M., and Rotello, V. M. (2007) Drug and gene delivery using gold nanoparticles. *Nanobiotechnology 3*, 40–45.

(3) Sharma, P., Brown, S., Walter, G., Santra, S., and Moudgil, B. (2006) Nanoparticles for bioimaging. *Adv. Colloid Interface Sci. 123−126*, 471–485.

(4) Glomm, W. R. (2005) Functionalized gold nanoparticles for applications in bionanotechnology. *J. Dispersion Sci. Technol. 26*, 389–414.

(5) Daniel, M. C., and Astruc, D. (2004) Gold nanoparticles: Assembly, supramolecular chemistry, quantum-size-related properties, and applications toward biology, catalysis, and nanotechnology. *Chem. Rev. 104*, 293–346.

(6) Maye, M. M., Lim, I-I. S., Luo, J., Rab, Z., Rabinovich, D., Liu, T., and Zhong, C.-J. (2005) Mediator-template assembly of nanoparticles. *J. Am. Chem. Soc. 127*, 1519–1529.

(7) Wilson, R., Chen, Y., and Aveyard, J. (2004) One molecule per particle method for functionalising nanoparticles. *Chem. Commun.* 1156–1157.

(8) Bartz, M., Kuther, J., Nelles, G., Weber, N., Seshadri, R., and Tremel, W. (1999) Monothiols derived from glycols as agents for stabilizing gold colloids in water: synthesis, self-assembly and use as crystallization templates. *J. Mater. Chem. 9*, 1121–1125.

(9) Kanaras, A. G., Kamounah, F. S., Schaumburg, K., Kiley, C., and Brust, M. (2002) Thioalkylated tetraethylene glycol: a new ligand for water soluble monolayer protected gold clusters. *Chem. Commun. 20*, 2294–2295.

(10) Tshikhudo, T. R., Wang, Z., and Brust, M. (2004) Biocompatible gold nanoparticles. *Mater. Sci. Technol. 20*, 980–984.

(11) Gao, X., Tao, W., Lu, W., Zhang, Q., Zhang, Y., Jiang, X., and Fu, S. (2006) Lectin-conjugated PEG -PLA nanoparticles: preparation and brain delivery after intranasal administration. *Biomaterials 27*, 3482–3490.

(12) Kommareddy, S., and Amiji, M. (2007) Poly(ethylene glycol)-modified thiolated gelatin nanoparticles for glutathione-responsive intracellular DNA delivery. *Nanomedicine 3*, 32–42.

(13) Tracy, J. B., Kalyuzhny, G., Crowe, M. C., Balasubramanian, R., Choi, J.-P., and Murray, R. W. (2007) Poly(ethylene glycol) ligands for high-resolution nanoparticle mass spectrometry. *J. Am. Chem. Soc. 129*, 6706–6707.

(14) Becker, C. F. W., Marsac, Y., Hazarika, P., Moser, J., Goody, R. S., and Niemeyer, C. M. (2007) Functional immobilization of the small GTPase Rab6A on DNA-gold nanoparticles by using a site-specifically attached poly(ethylene glycol) linker and thiol-place exchange reaction. *ChemBioChem 8*, 32–36.

(15) Kim, Y.-P., Oh, E., Oh, Y.-H., Moon, D. W., Lee, T. G., and Kim, H.-S. (2007) Protein kinase assay on peptide-conjugated gold nanoparticles by using secondary-ion mass sectrometric imaging. *Angew. Chem., Int. Ed. 46*, 6816–6819.

(16) Slocik, J. M., Tam, F., Halas, N. J., and Naik, N. N. (2007) Peptide-assembled optically responsive nanoparticle complexes. *Nano Lett. 7*, 1054–1058.

(17) Si, S., and Mandal, T. K. (2007) pH-controlled reversible assembly of peptide-functionalized gold nanoparticles. *Langmuir 23*, 190–195.

(18) Higuchi, M., Ushiba, K., and Kawaguchi, M. (2007) Structural control of peptide-coated gold nanoparticle assemblies by the conformational transition of surface peptides. *J. Colloid Interface Sci. 308*, 356–363.

(19) Tkachenko, A. G., Xie, H., Liu, Y., Coleman, D., Ryan, J., Glomm, W. R., Shipton, M. K., Franzen, S., and Feldheim, D. L. (2004) Cellular trajectories of peptide-modified gold particle complexes: comparison of nuclear localization signals and peptide transduction domains. *Bioconjugate Chem. 15*, 482–490.

(20) Oyelere, A. K., Chen, P. C., Huang, X., El-Sayed, I. H., and El-Sayed, A. M. (2007) Peptide-conjugated gold nanorods for nuclear targeting. *Bioconjugate Chem. 18*, 1490–1497.

(21) Pengo, P., Baltzer, L., Pasquato, L., and Scrimin, P. (2007) Substrate modulation of the activity of an artificial nanoesterase made of peptide-functionalized gold nanoparticles. *Angew. Chem., Int. Ed. 46*, 400–404.

(22) Fillon, Y., Verma, A., Ghosh, P., Ernenwein, D., Rotello, V. M., and Chmielewski, J. (2007) Peptide ligation catalyzed by functionalized gold nanoparticles. *J. Am. Chem. Soc. 129*, 6676–6677.

(23) Satyabrata, S., Manoj, R., Tapas, K. P., and Tarun, K. M. (2008) Reversible self-ssembly of carboxylated peptide-functionalized gold nanoparticles driven by metal-ion coordination. *ChemPhysChem 9*, 1578–1584.
(24) Levy, R., Thanh, N. T. K., Doty, R. C., Hussain, I., Nichols, R. J., Schiffrin, D. J., Brust, M., and Fernig, D. G. (2004) Rational and combinatorial design of peptide capping ligands for gold nanoparticles. *J. Am. Chem. Soc. 126*, 10076–10084.
(25) Levy, R. (2006) Peptide-capped gold nanoparticles: towards artificial proteins. *ChemBioChem 7*, 1141–1145.
(26) Brennan, J. L., Hatzakis, N. S., Tshikhudo, T. R., Dirvianskyte, N., Razumas, V., Patkar, S., Vind, J., Svendsen, A., Nolte, R. J. M., Rowan, A. E., and Brust, M. (2006) Bionanoconjugation via click chemistry: the creation of functional hybrids of lipases and gold nanoparticles. *Bioconjugate Chem. 17*, 1373–1375.
(27) Park, J.-A., Lee, J.-J., Kim, I.-S., Park, B.-H., Lee, G.-H., Kim, T.-J., Ri, H.-C., Kim, H.-J., and Chang, Y. (2008) Magnetic and MR relaxation properties of avidin-biotin conjugated superparamagnetic nanoparticles. *Colloids Surf., A 31*, 288–291.
(28) Prosperi, D., Morasso, C., Tortora, P., Monti, D., and Bellini, T. (2007) Avidin decorated core-shell nanoparticles for biorecognition studies by elastic light scattering. *ChemBioChem 8*, 1021–1028.
(29) Weiss, B., Schneider, M., Muys, L., Taetz, S., Neumann, D., Schaefer, U. F., and Lehr, C.-M. (2007) Coupling of biotin-(poly(ethylene glycol))amine to poly(D,L-lactide-*co*-glycolide) nanoparticles for versatile surface modification. *Bioconjugate Chem. 18*, 1087–1094.
(30) Ackerson, C. J., Jadzinsky, P. D., Jensen, G.-J., and Kornberg, R. D. (2006) Rigid, specific, and discrete gold nanoparticle/antibody conjugates. *J. Am. Chem. Soc. 128*, 2635–2640.
(31) You, C.-C., Verma, A., and Rotello, V. M. (2006) Engineering the nanoparticle-biomacromolecule interface. *Soft Mater. 2*, 190–204.
(32) Shang, L., Wang, Y., Jiang, J., and Dong, S. (2007) pH-Dependent protein conformational changes in albumin: gold nanoparticle bioconjugates: a spectroscopic study. *Langmuir 23*, 2714–2721.
(33) Schroedter, A., and Weller, H. (2002) Ligand design and bioconjugation of colloidal gold nanoparticles. *Angew. Chem., Int. Ed. 41*, 3218–3221.
(34) Porta, F., Speranza, G., Krpetic, Z., Dal Santo, V., Francescato, P., and Scari, G. (2007) Gold nanoparticles capped by peptides. *Mater. Sci. Eng., B. 140*, 187–194.
(35) Zheng, M., and Huang, X. (2004) Nanoparticles comprising a mixed monolayer for specific bindings with biomolecules. *J. Am. Chem. Soc. 126*, 12047–12054.
(36) Cervellino, A., Giannini, C., and Guagliardi, A. (2003) Determination of nanoparticle structure type, size and strain distribution from X-ray data for monatomic f.c.c.-derived non-crystallographic nanoclusters. *J. Appl. Crystallogr. 36*, 1148–1158.
(37) Yang, Y.-C., Wang, C.-H., Hwu, Y.-K., and Je, J.-H. (2006) Synchrotron X-ray synthesis of colloidal gold particles for drug delivery. *Mater. Chem. Phys. 100*, 72–76.
(38) Fabris, L., Antonello, S., Armelao, L., Donkers, R. L., Polo, F., Toniolo, C., and Maran, F. (2006) TGold nanoclusters protected by conformationally constrained peptides. *J. Am. Chem. Soc. 128*, 326–336.
(39) TJadzinsky, P. D., Calero, G., Ackerson, C. J., Bushnell, D. A., and Kornberg, R. D. (2007) TStructure of a thiol monolayer-protected gold nanoparticle at 1.1 Å resolution. *Science 318*, 430–433.
(40) Shang, L., Wang, Y., Jiang, J., and Dong, S. (2007) pH-dependent protein conformational changes in albumin: gold nanoparticle bioconjugates: a spectroscopic study. *Surf. Colloid. 23*, 2714–2721.
(41) Chah, S., Hammond, M. R., and Zare, R. N. (2005) Gold nanoparticles as a colorimetric sensor for protein conformational changes. *Chem. Biol. 12*, 323–328.
(42) Hostetler, M. J., Wingate, J. E., Zhong, C.-J., Harris, J. E., Vachet, R. W., Clark, M. R., Londono, J. D., Green, S. J., Stokes, J. J., Wignall, G. D., Glish, G. L., Porter, M. D., Evans, N. D., and Murray, R. W. (1998) TTAlkanethiolate gold cluster molecules with core diameters from 1.5 to 5.2 nm: core and monolayer properties as a function of core size. *Langmuir 14*, 17–30.
(43) Kohlmann, O., Steinmetz, W. E., Mao, X.-A., Wuelfing, P., Templeton, A. C., Murray, R. W., and Johnson, C. S. (2001) TTNMR diffusion, relaxation, and spectroscopic studies of water soluble, monolayer-protected gold nanoclusters. *J. Phys. Chem. B 105*, 8801–8809.
(44) Cooke, G., Garety, J. F., Hewage, S. G., Rabani, G., Rotello, V. M., and Woisel, P. (2006) The tuneable complexation of gold nanoparticles. *Chem. Commun.* 4119–4121.
(45) Zubarev, E. R., Xu, J., Sayyad, A., and Gibson, J. D. (2006) Amphiphilic gold nanoparticles with V-shaped arms. *J. Am. Chem. Soc. 128*, 4958–4959.
(46) Shaffer, A. W., Worden, J. G., and Huo, Q. (2004) Comparison study of the solution phase versus solid phase place exchange reactions in the controlled functionalization of gold nanoparticles. *Langmuir 20*, 8343–8351.
(47) Kumar, A., Mandal, S., Selvakannan, P. R., Pasricha, R., Mandale, A. B., and Sastry, M. (2003) Investigation into the interaction between surface-bound alkylamines and gold nanoparticles. *Langmuir 19*, 6277–6282.
(48) Turkevich, J., Stevenson, P. C., and Hillier, J. (1951) A study of the nucleation and growth process in the synthesis of colloidal gold. *J. Discuss. Faraday Soc. 11*, 55–75.
(49) Frens, G. (1973) Controlled nucleation for the regulation of the particle size in monodisperse gold suspensions. *Nat: Phys. Sci. 241*, 20–22.
(50) Bethell, D., Brust, M., Schiffrin, D. J., and Kiely, C. (1996) From monolayers to nanostructured materials: an organic chemist's view of self-assembly. *J. Electroanal. Chem. 409*, 137–143.
(51) Mayya, K. S., Patil, V., and Sastry, M. (2000) An optical absorption investigation of cross-linking of gold colloidal particles with a small dithiol molecule. *Bull. Chem. Soc. Jpn. 73*, 1757–1761.
(52) Maye, M. M., Chun, S. C., Han, L., Rabinovich, D., and Zhong, C.-J. (2002) Novel spherical assembly of gold nanoparticles mediated by a tetradentate thioether. *J. Am. Chem. Soc. 124*, 4958–4959.
(53) Guarise, C., Pasquato, L., and Scrimin, P. (2005) Reversible aggregation/deaggregation of gold nanoparticles induced by a cleavable dithiol linker. *Langmuir 21*, 5537–5541.
(54) Guarise, C., Pasquato, L., De Filippis, V., and Scrimin, P. (2006) Gold nanoparticles-based protease assay. *Proc. Natl. Acad. Sci. U.S.A. 103*, 3978–3982.
(55) Srisombat, L., Park, J.-S., Zhang, S., and Lee, R. (2008) Preparation, characterization, and chemical stability of gold nanoparticles coated with mono-, bis-, and tris-chelating alkanethiols. *Langmuir 24*, 7750–7754.
(56) Wei, A. (2006) Calixarene-encapsulated nanoparticles: self-assembly intro functional nanomaterials. *Chem. Commun.* 1581–1591.
(57) Tshikhudo, T. R., Demuru, D., Wang, Z., Brust, M., Secchi, A., Arduini, A., and Pochini, A. (2005) Molecular recognition by calix[4] arene-modified gold nanoparticles in aqueous solution. *Angew. Chem., Int. Ed. 44*, 2913–2916.

BC8003028

Supporting Information for

"A multidentate peptide for stabilisation and facile bioconjugation of gold nanoparticles"

Željka Krpetić, Paola Nativo, Francesca Porta and Mathias Brust*

Figure A. UV-visible spectra of 15 nm Au@GCK15 before (blue line) and after biotinylation (green line)

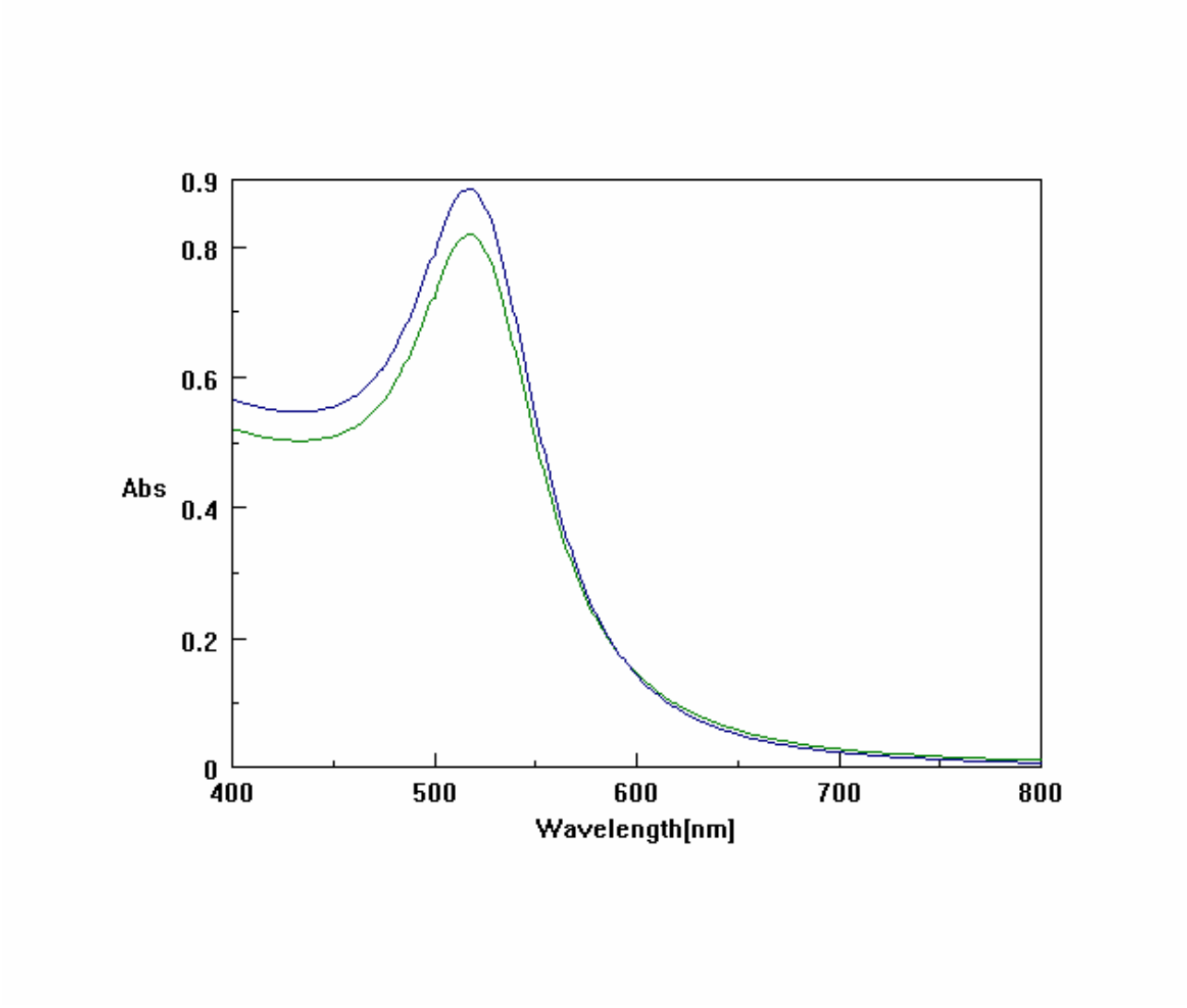

Bioconjugate Chemistry 20th Anniversary

Subscriber access provided by SHEMYAKIN-OVCHINNIKOV INST

Technical Note

Derivatization of 11-#-Hydroxyprogesterone using Phosphoramidite Chemistry

Janne Ketola, Pertti Hurskainen, and Jari Hovinen

Bioconjugate Chem., **2009**, 20 (3), 625-628• DOI: 10.1021/bc800513h • Publication Date (Web): 16 February 2009

Downloaded from http://pubs.acs.org on May 15, 2009

More About This Article

Additional resources and features associated with this article are available within the HTML version:

- Supporting Information
- Access to high resolution figures
- Links to articles and content related to this article
- Copyright permission to reproduce figures and/or text from this article

View the Full Text HTML

ACS Publications
High quality. High impact.

Bioconjugate Chemistry is published by the American Chemical Society. 1155 Sixteenth Street N.W., Washington, DC 20036

Derivatization of 11-α-Hydroxyprogesterone using Phosphoramidite Chemistry

Janne Ketola, Pertti Hurskainen, and Jari Hovinen*

PerkinElmer, Genetic Screening, P.O. Box 10, FI-20101 Turku, Finland. Received December 3, 2008; Revised Manuscript Received January 22, 2009

The well-known phosphoramidite chemistry routinely used in solid-phase oligonucleotide synthesis is exploited here in the preparation of steroid conjugates in solution. The applicability of the method is tested by conjugating one nucleosidic and one non-nucleosidic phosphoramidite building block to 11-α-hydroxyprogesterone. The suitability of one of the conjugates synthesized (**5**) for a competitive binding assay is also demonstrated.

INTRODUCTION

Steroids with additional functional and label groups are often needed for biochemical, diagnostic, microbiological, and medicinal applications. For example, in immunoassays haptens are coupled covalently to carrier protein prior to immunization. In competitive immunoassays, in turn, haptens coupled to label molecule are used as tracers. Most commonly, a spacer arm with a reactive ω-substituent is introduced into the steroid structure before the coupling reaction. Since the coupling site and the length and chemical structure of the spacer play a very important role in antibody recognition, a wide range of methods for steroid tethering have been developed (*1*−*3*).

Since the glucuronide bridge is a weakly antigenic subunit (*4*), steroid glucuronides have been widely used as tracers in competitive immunoassays. Although several efficient glucuronization reactions have been developed (*5*−*9*), derivatization of certain steroids is still challenging. One of the most difficult steroids to glucuronize is progesterone at position C11. The only reported synthesis of progesterone 11-α-glucuronide (**1**, Figure 1) is based on the classical Koenigs-Knorr method starting from glucuronolactone, which is initially converted to methyl 1-bromo-1-deoxy-2,3,4,-tri-*O*-acetyl-α-D-glucopyranoate followed by reaction with 11-α-hydroxyprogesterone (*4*). Accordingly, the synthesis is laborious, and the overall yield of the desired isomer is low. In addition, attachment of a label molecule to the carboxylic acid function of **1** is also needed.

Here is presented a simple method for the preparation of labeled progesterone derivatives using phosphoramidite chemistry. Also, the suitability of one of the steroid conjugates prepared for a competitive binding assay was tested.

EXPERIMENTAL PROCEDURES

General Methods. Adsorption column chromatography was performed on columns packed with silica gel 60 (Merck). 6-[*N*-4′-Carboxy-4-(dimethylamino)azobenzene]aminohexyl-1-*O*-(2-cyanoethyl)-(*N*,*N*-diisopropyl)phosphoramidite (dabcyl), **6**, and 11-α-hydroxyprogesterone were purchased from Glen Research and Sigma, respectively. 2′-Deoxy-5′-*O*-(4,4′-dimethoxytrityl)-3-{[4-(5-hexyn-1-yl)phenyl]-2,2′:6′,2″-terpyridine-6,6″-diyl]-methylenenitrilotetrakis(acetato)}uridine 3′-*O*-(2-cyanoethyl *N*,*N*-diisopropyl) phosphoramidite, **3**, was synthesized as disclosed in the literature (*10*). The DELFIA progesterone kit and DELFIA Inducer were from PerkinElmer (Turku, Finland). The oxidizer used was 0.1 M I_2 in pyridine/water from Sigma-Proligo. All solvents were from Merck, and they were used as received. HPLC was performed using a Shimadzu LC 10 AT instrument equipped with a diode array detector, a fraction collector, and a reversed-phase column (LiChrocart 125−3 Purospher RP-18e, particle size 5 μm). Mobile phase: (Buffer A) 0.02 M triethylammonium acetate (pH 7.0); (Buffer B) A in 50% (v/v) acetonitrile. Gradient: from 0 to 1 min 95% A, from 1 to 21 min from 95% A to 100% B. Flow rate was 0.6 mL min^{-1}. NMR spectra were recorded on a Jeol LA 400 spectrometer operating at 161.9 MHz for ^{31}P. The signal H_3PO_4 was used as an external reference. ESI-TOF mass spectra were recorded on an Applied Biosystems Mariner instrument.

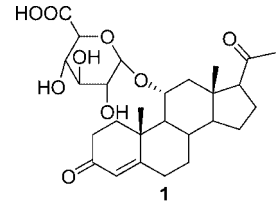

1

Figure 1. Progesterone 11-α-glucuronide.

Reaction of 11-α-Hydroxyprogesterone with Phosphoramidites. General Procedure. The phosphoramidite (compound **3** (16.1 mg) or **6** (6.6 mg); 11 μmol) and 11-α-hydroxyprogesterone (**2**, 32 mg, 22 μmol; 2.0 equiv) were dissolved in a mixture of dichloromethane and acetonitrile (150 μL, 1:1, v/v). 1*H*-tetrazole in acetonitrile (250 μL, 0.45 M) was added, and the mixture was stirred for 1 h at RT after which the oxidizer (220 μL; 2.0 equiv) was added, and the mixture was stirred for an additional 5 min. All volatiles were removed in vacuo. The residue was dissolved in dichloromethane, washed with aq $Na_2S_2O_3$, dried over Na_2SO_4, and concentrated. Purification on silica gel (eluent 10% (v/v) methanol in dichloromethane) yielded the desired progesterone conjugates. Compound **4** (14.3 mg, 76%). ESI-TOF MS: found, 1709.25; calcd for $C_{95}H_{106}N_8O_{20}P^+$ 1709.87. Compound **7** (9.25 mg, 99%). ESI-TOF MS: found, 850.48; calcd for $C_{44}H_{61}N_5O_8PS^+$ 850.40.

11-α-Hydroxyprogesterone Labeled with a Nucleosidic Europium(III) Chelate. Compound **4** (12 mg, 7 μmol) was dissolved in dichloromethane (1 mL). TFA (40 μL) was added, and the mixture was stirred for 15 min at RT before methanol (1 mL) was added, and the stirring was continued for an additional 15 min. Water (1 mL) was added, and volatiles

* Dr. Jari Hovinen, Tel + 358 2 2678 513; fax + 358 2 2678 380, jari.hovinen@perkinelmer.com.

10.1021/bc800513h CCC: $40.75 © 2009 American Chemical Society
Published on Web 02/16/2009

Scheme 1. Synthesis of Europium(III) Chelate Labeled 11-α-Hydroxyprogesterone

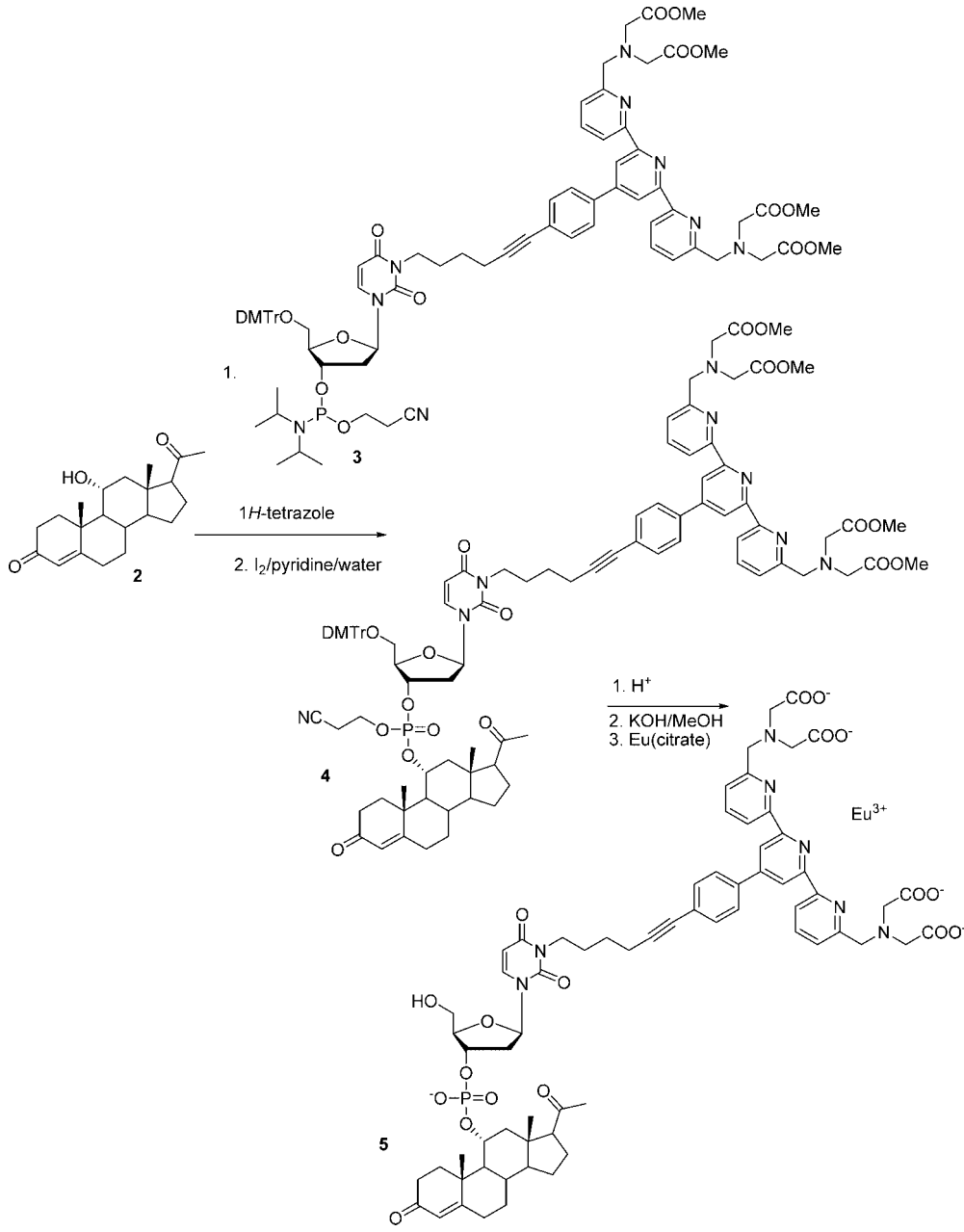

were removed in vacuo. Aqueous NaOH (0.1 M; 200 μL) was added, and the mixture was stirred for 3 h at RT, after which the pH was adjusted to 8.5 with 0.2 M HCl. Europium citrate (40 μL, 0.2 M) was added, and the mixture was stirred for 4 h. Compound **5** was precipitated from the reaction mixture by adding cold acetone (50 mL). Final purification was performed on HPLC. ESI-TOF MS: found, 1447.56; calcd for $C_{67}H_{73}EuN_7O_{18}P^+$ 1447.27. The product was stored at −18 °C.

11-α-Hydroxyprogesterone Labeled with Dabcyl. Compound **7** (54 mg, 0.066 mmol) was dissolved in THF (50 μL). Aq ammonia (25% v/v; 100 μL) was added, and the mixture was stirred for 10 min at RT before being concentrated in vacuo to give compound **8**. ^{31}P NMR ($CDCl_3$): δ −4.94. ESI-TOF MS: found, 795.33; calcd for $C_{41}H_{56}N_4O_8PS^-$ 795.36. The product was stored at −18 °C.

The Displacement Assay. Compound **5** was tested in a displacement assay using components of the DELFIA Progesterone kit. The assay was performed essentially as instructed in the kit manual. Accordingly, progesterone standards (25 μL) were added in triplicate to antirabbit IgG coated microtitration plate wells. The progesterone conjugate **5**, diluted with DELFIA progesterone assay buffer to 11.3 nM, was added to the wells (100 μL/well; final concentration 5 nM) followed by rabbit antiprogesterone antiserum diluted 1:10 in assay buffer (100 μL/well). The wells were shaken on DELFIA Plateshake (setting: slow) for 2 h at RT. After washing the wells four times in DELFIA Platewash using DELFIA wash solution, DELFIA inducer was added to the wells (200 μL/well). The wells were shaken on DELFIA Plateshake for 15 min (setting: slow) and then measured using a Victor 2V multiplate reader using the factory-set DELFIA Eu protocol. The results were analyzed using *GraphPad Prism* software (GraphPad Software, Inc.).

RESULTS AND DISCUSSION

Solid-phase oligonucleotide synthesis is routinely performed using phosphoramidite chemistry. The key step of this method is the highly efficient coupling reaction between the 5′-hydroxyl

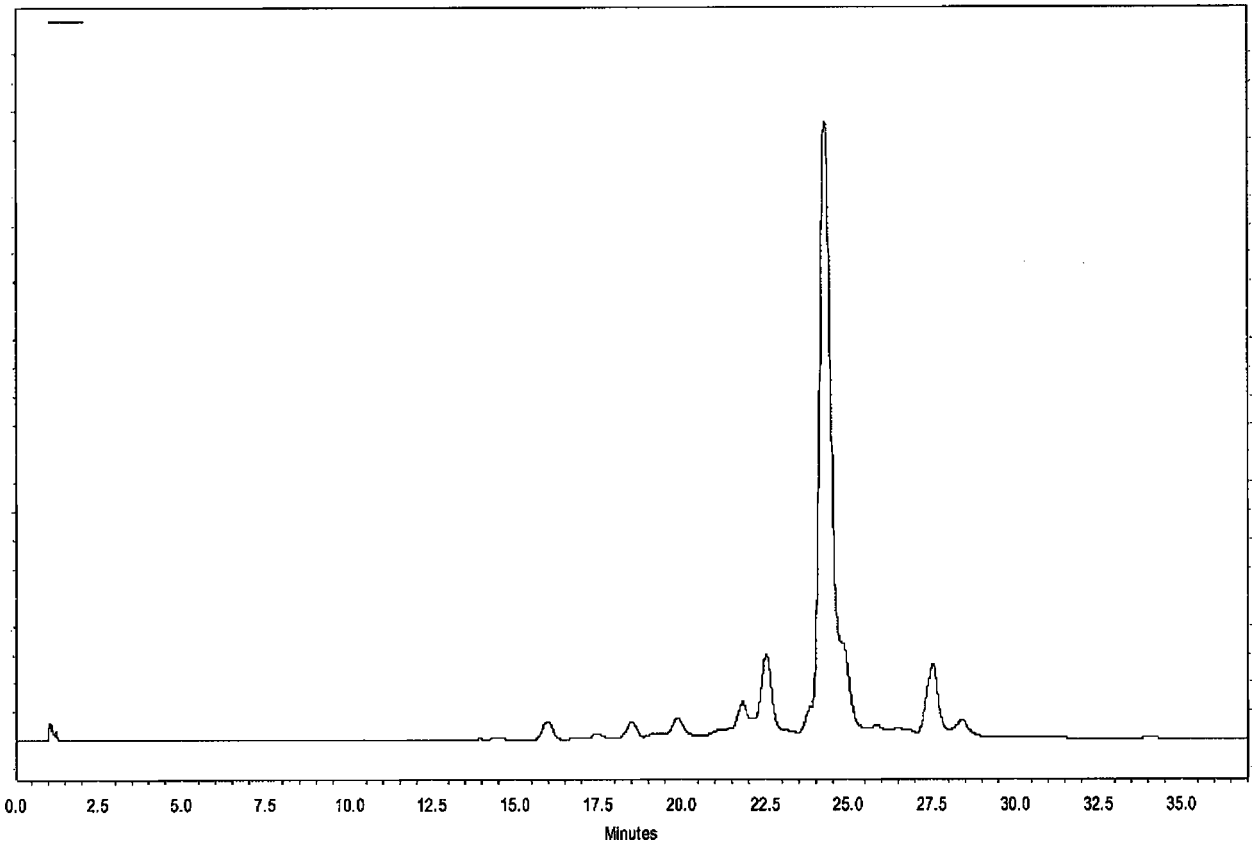

Figure 2. Reversed-phase HPLC trace of the progesterone derivative **5**, synthesized with the aid of the phosphoramidite **3** (crude reaction mixture) detected at 270 nm. The major peak (ca. 90% based on the integral areas) is the desired conjugate as judged on ESI-TOF MS. For chromatographic conditions, see Experimental Procedures.

Scheme 2. Synthesis of 11-α-Hydroxyprogesterone Labeled with an Organic Dye

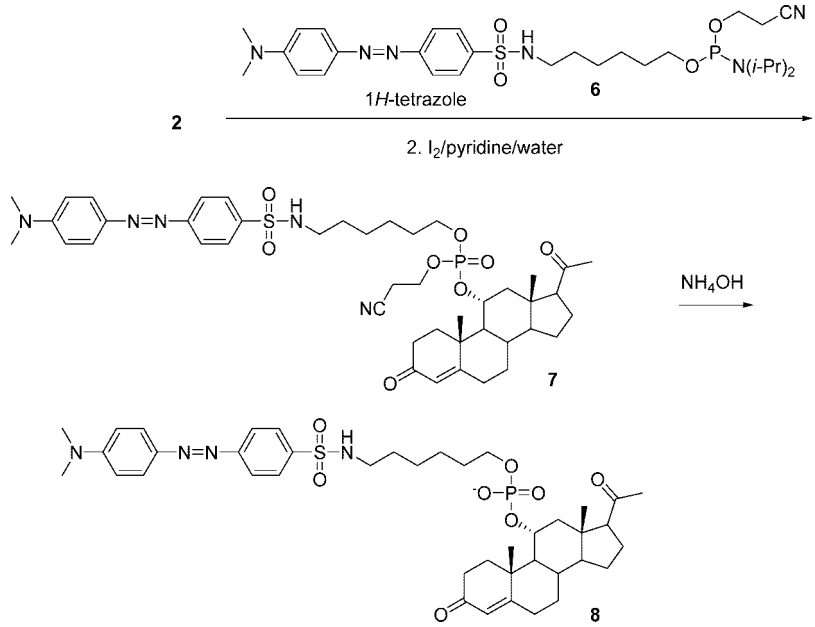

group of a nucleoside bound to a resin and a nucleoside 3′-phosphoramidite catalyzed by 1*H*-tetrazole. Oxidation of the phosphite triester formed by iodine gives rise to stable phosphotriesters. Removal of the protecting groups completes the synthesis. The method has been widely applied also to the preparation of oligonucleotide conjugates (*11*). Although few solution-phase phosphoramidite methods have been reported, they describe large-scale synthesis of unmodified oligodeoxyribonucleotides (*12, 13*).

In order to study the applicability of phosphoramidite chemistry for the preparation of steroid conjugates, 11-α-hydroxyprogesterone (**2**) was allowed to react with a nucleosidic terpyridine phosphoramidite (**3**) in the presence of 1*H*-tetrazole followed by iodine oxidation (Scheme 1). The desired product, **4**, was isolated by silica gel column chromatography in good yield. Removal of the DMTr and cyanoethyl protecting groups of **4** with TFA and sodium hydroxide, respectively, followed by treatment with europium citrate (*7*) yielded the progesterone

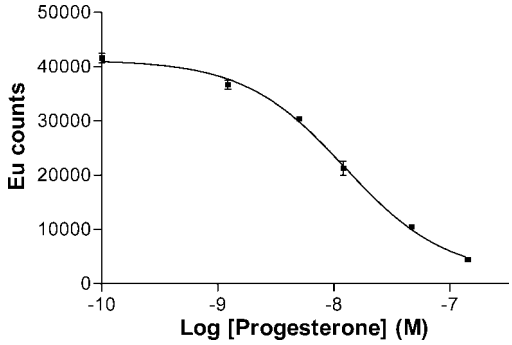

Figure 3. A competitive binding assay of 11-α-hydroxyprogesterone labeled with the nucleosidic terpyridine chelate. The experiments were performed with a 5 nM solution of compound **5** using a commercial progesterone kit and recommended protocols.

conjugate **5**. The product was easily isolated by precipitation from acetone. A reversed-phase HPLC trace (crude reaction mixture) of compound **5** is shown in Figure 2. The major peak is the desired steroid conjugate. The final purification was performed on HPLC.

The more general applicability of the method was also tested by allowing **2** to react with a commercially available dabcyl phosphoramidite **6** (Scheme 2). The reaction was practically quantitative giving compound **7** in 99% yield after purification on silica gel column chromatography. The final product, **8**, was obtained by standard ammonolysis.

Competition Assay. Figure 3 shows the competitive binding assay of progesterone. The experiment was performed with 5 nM of compound **5** using a commercial progesterone kit and the recommended protocols. It was found that antiprogesterone antiserum binds to compound **5**, and that progesterone displaces compound **5** from the antiserum. The assay using compound **5** was as sensitive as the commercial progesterone kit wherein progesterone 11-α-glucuronide (**1**) labeled with a europium(III) chelate is used. Accordingly, the glucuronide moiety can be replaced by a conjugate group including a deoxyribose subunit, the latter being considerably easier to synthesize.

As shown here, the phosphoramidite approach works well in the solution phase, too. Accordingly, steroid tethering using phosphoramidite chemistry may be the method of choice when conjugation of steroids at positions of low reactivity is needed. Since a wide range of phosphoramidites tethered to label groups is commercially available, the rather laborious post-labeling can also be avoided. Although the applicability of phosphoramidite chemistry is demonstrated here only for progesterone conjugation, the method is, in all likelihood, applicable to other steroids and other type of tracers as well, as long as the target molecule has a hydroxy group in its structure, and all other functional groups are protected. Since the reaction intermediates are fully protected lipophilic phosphotriesters, they can be easily purified by silica gel chromatography, with the final step thus comprising deprotection of the purified material. If desired, the method also allows the preparation of phosphorothioates simply by changing the oxidant (*14*). This might be needed if resistance toward nucleases is required.

LITERATURE CITED

(1) Franek, M. (1987) Structural aspects of steroid-antibody specificity. *J. Steroid Biochem. 27*, 95–108.
(2) Niswender, G. D. (1973) Influence of the site of conjugation on the specificity of antibodies to progesterone. *Steroids 22*, 413–424.
(3) Wu, Y., Mitchell, J., Cook, C., and Main, L. (2002) Evaluation of progesterone-ovalbumin conjugates with different length linkers in enzyme-linked immunosorbant assay and surface plasmon resonance-based immunoassay. *Steroids 67*, 565–572.
(4) Corrie, J. E. T., Hunter, W. M., and Macpherson, J. S. (1981) A strategy for radioimmunoassay of plasma progesterone with use of a homologous-site ^{125}I labeled radioligand. *Clin. Chem. 27*, 594–599.
(5) Fischer, B., Nudelman, A., Ruse, M., Herzig, J., and Gottlieb, H. E. (1984) A novel method for stereoselective glucuronidation. *J. Org. Chem. 49*, 4984–4988.
(6) Dayal, B., Salen, G., Padia, J., Sheref, S., Tint, G. S., Sasso, G., and Williams, T. H. (1993) Bile alcohol glucuronides: regioselective O-glucuronidation of 5β-cholestane-3α,7α,12α,25-tetrol and 24-nor-5β-cholestane-3α,7α,12α,25-tetrol. *Carbohydr. Res. 240*, 133–142.
(7) Kim, N.-C., Kinghorn, A. D., and Kim, D. S. H. L. (1999) Semisynthesis of abrusoside A methyl ester. *Org. Lett. 1*, 223–224.
(8) Jäntti, S. E., Kiriazis, A., Reinilä, R. R., Kostiainen, R. K., and Ketola, R. A. (2007) Enzyme-assisted synthesis and characterization of glucuronide conjugates of neuroactive steroids. *Steroids 72*, 287–296.
(9) Hintikka, L., Kuuranne, T., Aitio, O., Thevis, M., Schänzer, W., and Kostiainen, R. (2008) Enzyme-assisted synthesis and structure characterization of glucuronide conjugates of eleven anabolic steroid metabolites. *Steroids 73*, 257–265.
(10) Hovinen, J., and Hakala, H. (2001) Versatile strategy for oligonucleotide derivatization. Introduction of lanthanide(III) chelates to oligonucleotides. *Org. Lett. 3*, 2473–2476.
(11) Beaucage, S. L., and Ivyer, R. P. (1993) The synthesis of modified oligonucleotides by the phosphoramidite approach and their applications. *Tetrahedron 49*, 6123–6194.
(12) Bonora, G. M., Biancotto, G., Maffini, M., and Scremin, C. L. (1993) Large scale, liquid phase synthesis of oligonucleotides by the phosphoramidite approach. *Nucleic Acids Res. 21*, 1213–1217.
(13) De Koning, M. C., Ghisaidoobe, A. B. T., Duynstee, H. I., Ten Kortenaar, P. B. W., Filippov, D. V., and van der Marel, G., A. (2006) Simple and efficient solution-phase synthesis of oligonucleotides using extractive work-up. *Org. Process Res. Dev. 10*, 1238–1245.
(14) Beaucage, S. L., and Caruthers, M. H. (1996) The chemical synthesis of DNA/RNA. In *Bioorganic Chemistry Nucleic Acids* (Hecht, S. M., Ed.) Oxford University Press, Oxford, UK.

BC800513H

Subscriber access provided by SHEMYAKIN-OVCHINNIKOV INST

Correction

The Role of Polyamine Architecture on the Pharmacological Activity of Open Lactone Camptothecin#Polyamine Conjugates

Cristian Samori#, Andrea Guerrini, Greta Varchi, Giovanni Luca Beretta, Gabriele Fontana, Ezio Bombardelli, Nives Carenini, Franco Zunino, Carlo Bertucci, Jessica Fiori, and Arturo Battaglia

Bioconjugate Chem., **2009**, 20 (3), 629-629• DOI: 10.1021/bc800535j • Publication Date (Web): 02 March 2009

Downloaded from http://pubs.acs.org on May 15, 2009

More About This Article

Additional resources and features associated with this article are available within the HTML version:

- Supporting Information
- Access to high resolution figures
- Links to articles and content related to this article
- Copyright permission to reproduce figures and/or text from this article

View the Full Text HTML

ACS Publications
High quality. High impact.

Bioconjugate Chemistry is published by the American Chemical Society. 1155 Sixteenth Street N.W., Washington, DC 20036

CORRECTIONS

Volume 19, Number 11, 2008.

Cristian Samorì,* Andrea Guerrini, Greta Varchi, Giovanni Luca Beretta, Gabriele Fontana, Ezio Bombardelli, Nives Carenini, Franco Zunino, Carlo Bertucci, Jessica Fiori, and Arturo Battaglia

The Role of Polyamine Architecture on the Pharmacological Activity of Open Lactone Camptothecin−Polyamine Conjugates

Page 2270. A misspelled author name was found on the last name of the first author in the version published on the Web October 8, 2008 (ASAP), and published in the November 19 issue. Dr. Samor's name should be spelled Cristian Samorì.

BC800535J

10.1021/bc800535j
Published on Web 03/02/2009

Subscriber access provided by SHEMYAKIN-OVCHINNIKOV INST

Review

Molecular Imaging with Bioconjugates in Mouse Models of Cancer

Stephen Mather

Bioconjugate Chem., **2009**, 20 (4), 631-643• DOI: 10.1021/bc800401x • Publication Date (Web): 16 December 2008

Downloaded from http://pubs.acs.org on May 8, 2009

More About This Article

Additional resources and features associated with this article are available within the HTML version:

- Supporting Information
- Access to high resolution figures
- Links to articles and content related to this article
- Copyright permission to reproduce figures and/or text from this article

View the Full Text HTML

ACS Publications
High quality. High impact.

Bioconjugate Chemistry is published by the American Chemical Society. 1155 Sixteenth Street N.W., Washington, DC 20036

Bioconjugate Chemistry

APRIL 2009
Volume 20, Number 4

© *Copyright 2009 by the American Chemical Society*

REVIEWS

Molecular Imaging with Bioconjugates in Mouse Models of Cancer

Stephen Mather*

Barts and The London Queen Mary's School of Medicine and Dentistry, Centre for Cancer Imaging Institute of Cancer and the CR-UK Clinical Centre, St. Bartholomew's Hos, London, EC1A 7BE, United Kingdon. Received September 18, 2008; Revised Manuscript Received November 12, 2008

The definition of molecular imaging provided by the Society of Nuclear Medicine is "the visualization, characterization and measurement of biological processes at the molecular and cellular levels in humans and other living systems". This review gives an overview of the technologies available for and the potential benefits from molecular imaging at the preclinical stage. It focuses on the use of imaging probes based on bioconjugates and for reasons of brevity confines itself to discussion of applications in the field of oncology, although molecular imaging can be equally useful in many fields including cardiovascular medicine, neurosciences, infection, and others.

WHY PRECLINICAL MOLECULAR IMAGING

Researchers may wish to use molecular imaging for a number of reasons. Basic researchers in the in vivo sciences may wish to measure physiological parameters such as receptor or enzyme concentrations, organ function such as cardiac output or renal excretion, or metabolic processes such as bone turnover or glucose metabolism. All of these parameters are accessible by imaging. More common will be a desire to measure how these parameters change during disease. Since a major reason for the study of disease in small animals is to try and model human diseases in such species, it is important to compare the effects of a particular disease in mouse and man. If such a disease results in a change in a biological function, then there will normally be a desire to correct this change by the use of drugs or other interventions, and it will therefore be valuable to screen drugs to compare their effects on this function using imaging in an animal model before proceeding to clinical trials. If this is successful, then the subsequent application of the imaging technology in human subjects may prove useful as a biomarker for the assessment of the performance of a drug in such trials. The disposition of drugs in the body may be monitored by imaging in some case directly or alternatively after tagging with an imaging probe, and last (but not least), imaging studies in small animals can be very useful (essential in fact) for the development of clinically useful imaging agents and, to a lesser extent, for the validation of clinically applicable imaging protocols.

ANIMAL MODELS OF CANCER

Normal Animals. As the genetic mutations responsible for malignancy are identified, there is a desire to duplicate these changes in animal models in order to determine their phenotypic consequences, and many highly sophisticated systems have now been developed as described below. However, useful information can also often be gained by the use of much simpler animal models including normal rodents. The physiology of such animals bears many similarities to and some differences from that of man. Thus, the basic layout and function of most organs is preserved, and many of the functional molecules expressed

* E-mail: stephen.mather@cancer.org.uk.

10.1021/bc800401x CCC: $40.75 © 2009 American Chemical Society
Published on Web 12/16/2008

in healthy tissues are also conserved. In the early stages of the development of a new biomolecular contrast agent, there is a need to assess its pattern of biodistribution, its stability in vivo, and its ability to interact with a molecular target in a biological environment. Such studies can often be performed in normal animals. Neuropeptide receptors, for example, are targets of current interest in radiopharmaceutical development (*1*), and such receptors are widely expressed in mice and often interact as efficiently as human receptors with radiolabeled complementary peptides. For example, the development of radiolabeled somatostatin analogues has been significantly informed by such studies (*2*). However, this is not always the case. For example, Maina et al. found significant differences between bombesin analogues in their ability to interact with gastrin-releasing peptide receptors originating from mouse and man (*3*). While such receptors may be highly conserved throughout mammals, their pattern of distribution may not be; for example, many neuropeptide receptors are highly expressed in the mouse pancreas but may not be expressed in the human organ (*4*). While the functional binding sites of receptors may be highly conserved across mammalian species, this is not necessarily true of the their nonfunctional framework regions, and this can cause problems in the study of monoclonal antibodies and their related constructs, which represent a very important class of biomolecular conjugates (*5*). Such molecules only rarely bind to the same sites as the native ligands, and many antibody-based agents that bind well to human-derived targets will not bind to their rodent equivalents. For such targets, it is therefore necessary to express the human homologue in a mouse background. Other differences between rodent and human physiology are quantitative rather than qualitative. It is well-recognized, for example, that the mouse heart beats much faster than the human and that mice breathe much faster. Because of the much smaller size, tissue perfusion times are much shorter, and compounds will show more rapid pharmacokinetics in mouse than man. Gastrointestinal transit times in man are roughly twice those in mice, and there are also differences in relative organ perfusion so that, for example, renal blood flow in the mouse is 75% of the blood volume per minute, while in man, it is only 15% (*6*).

Tumor-Bearing Animals. If the purpose of the preclinical imaging study is to predict the likely behavior of a drug or contrast agent in a patient with cancer, then it is likely that, at some stage, tumor-bearing animals will be utilized. These fall into several types depending on the source of the tumor, the immunocompetence of the host, and the degree of genetic manipulation employed.

Syngeneic Models. Perhaps the simplest model is the use of normal mice or rats bearing tumors derived from their own species. Tumors may arise spontaneously (although this is rare in normal laboratory strains); they may be induced by administration of carcinogens or transplanted by a variety of administration routes. Spontaneous and carcinogen-induced tumors have the advantage that they develop in a "natural" tumor environment. Thus, the blood supply and stromal and cellular interactions can be considered to closely mimic those occurring in human tumors apart from the fact that they involve murine rather than human homologues. Specific genetic mutations can be induced by the selection of appropriate carcinogens (*7*). The exogenous administration of tumor cells by typically subcutaneous, intravenous, or intraperitoneal routes, on the other hand, often results in the tumors developing in an unnatural location—pancreatic tumors in the lungs, for example—and this results in changes in the intratumoral signaling that might normally occur. Such approaches are, however, widely used, because it is quicker to produce the large numbers of animals often required for such studies. It is possible to use orthotopic routes of administration, i.e., to transplant the tumor to the same site as its origin, but although useful in superficial tissues such as the mammary gland (*8*), this is technically much more difficult to perform in less accessible organs, and most commonly, the precise anatomical microlocation of origin cannot be reproduced.

Xenogeneic Models. Perhaps the main limitation of syngeneic models is that the target molecules expressed within the tumor are of animal rather than human origin. If this represents a problem for the target of interest, then the next level of complexity is to implant cells of human origin in the mouse tissues. These can again be administered by various routes, although subcutaneous administration is by far the most common, since it is technically simple to perform and it is easy to monitor tumor growth, which is clearly visible. Since the administered cells are derived from a different species from the host, the animal's immune system would normally recognize them as foreign and mount an effective immune response against them, resulting in very low "take" rates—perhaps as low as 1 in 100. To overcome this problem, animals with disabled immune systems are normally used. In the past, this was often done by irradiation or treatment with cytotoxic drugs, but most commonly today, genetically immunodeficient animals are used, the most common being various strains of "nude" mice (or rats), which lack a thymus (*9*) and therefore cannot generate mature T-cells, or severe combined immunodeficient (SCID) mice (*10*), which have a mutation that prevents V(D)J recombination of DNA resulting in a complete loss of both humoral and cellular immune systems. "Take"-rates of close to 100% can be achieved following injection of human-derived tumor cells into such strains, making it easy to generate large numbers of relatively homogeneous tumor-bearing mice for imaging studies. Immunodeficient mice are more expensive (typically 5−10 times more) than their normal counterparts and, since they are very prone to infection, must also be housed in cages with a filtered air supply to prevent ingress of microorganisms. However, the nude/SCID mouse−human xenograft probably represents the most widely used animal model for preclinical imaging studies. A large number of well-characterized tumor types are available, which enables the expression of a great number of potential molecular targets in a living environment. Since these targets are of human origin, such models can successfully be used for contrast agents, which do not bind to mouse homologues such as antibody-based agents (*5*). However, such models still have their limitations: While the tumor cells may be of human origin, the stromal cells and blood vessels around them are derived from the murine host, and in particular, the immune environment in the tumor is very abnormal. In man, target molecule expression is rarely restricted to tumor cells but is also present at lower levels in normal tissues; however, this is not the case in such models where the patterns of expression on the host tissues are quite different from those on the implanted cells. Such problems can, to some extent, be addressed by the use of genetically modified animal models (*11*).

Genetically Modified Models. At the simplest level, genetic modifications can be employed to simply alter the nature of target molecule expression on the transplanted tumor cells. Although many different cell lines derived from spontaneously occurring tumors expressing many different combinations of target molecules exist, the use of transfected cell lines provides the potential for greater control over the nature, pattern, and levels of expression of these molecules. For example, it is possible to restrict expression to a particular receptor subtype, to vary the levels of expression from high to low, and to generate control cell lines which differ only in one specific detail from others. A good example of such an approach is the recent study by Ginj et al. which studied the uptake of somatostatin receptor

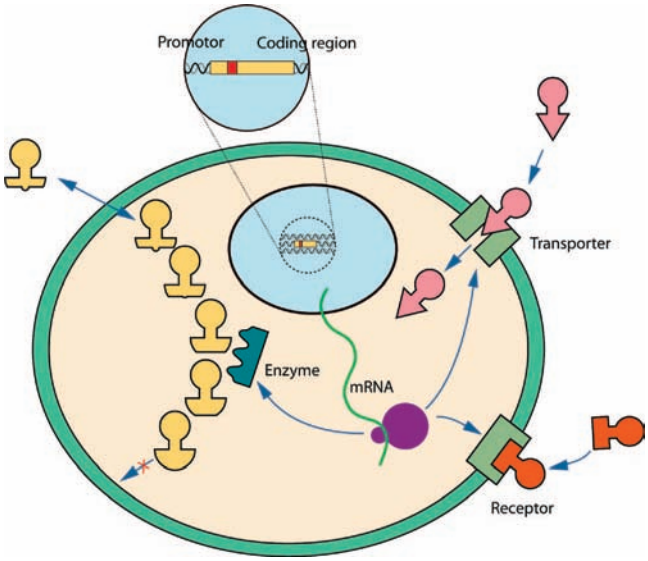

Figure 1. Reporter gene imaging. A gene coding for the expression of a desired reporter construct is introduced into cells. This construct is typically an enzyme such as HSV-TK, a transporter such as the sodium/iodide symporter, or a receptor such as the dopamine subtype 2 receptor. To image cells in which the transduced gene is present, a contrast agent consisting of a suitably tagged substrate that interacts with the construct is administered. If the reporter gene is present in the cell, it will result in increased uptake of the contrast agent. If the gene is not present, then there will no specific uptake of the agent.

subtype-specific antagonists in nude mice bearing transfected human embryonic kidney (HEK293) cell lines (*12*).

An increasingly popular application of genetically modified transplanted tumor cells is for "reporter-gene imaging" (*13*). The aim of such approaches is to put the expression of the target molecule under the control of a particular gene so that the effect of subsequent changes on the activity of this gene can be directly imaged by the binding of a contrast agent with the target molecule. As illustrated in Figure 1, the reporter gene will typically consist of a coding region—transcription and translation of which results in the cellular expression of the target molecule—and a promotor region, which determines the extent and level of transcription of the coding region. The reporting target molecule is typically an enzyme, a receptor, or a transporter, which interacts with a contrast agent in such a way as to increase its uptake by cells in which the reporter gene is active. An example of reporter gene imaging using the sodium/iodide symporter (NIS) reporter gene system is shown in Figure 2. Control of the level and site of transcription is provided by the promotor region of the reporter gene. Promotors may be strong or weak and result in constitutive expression in all tissues in which the gene is present or provide expression that is restricted to certain tissues (such as the prostate, for example) through the use of tissue-specific promoters. A list of some popular reporter gene systems is shown in Table 1. Promotors can also be rendered inducible by the incorporation of response elements that are either turned on or off by administration of drugs that interact directly or with transcription factors that bind to these elements (*11*). The advantages of such systems is that they allow transient expression of a protein that may be directly toxic and therefore compromise the design of the study, or even result in embryonic lethality, so that the function of a particular gene in a mature animal could not otherwise be determined. They also allow the results of different combinations of gene transcription to be studied in the same animal. Some examples of inducible promotor systems are shown in Figure 3.

Such genetic modifications are most simply applied by stable transduction of cells in culture with the gene of interest, followed

Figure 2. SPECT-CT scan showing uptake of ^{99m}Tc-pertechnetate mediated by the sodium/iodide symporter. Uptake is seen in the thyroid gland, the stomach, and around the rim of a tumor following viral transduction of the symporter gene (30).

Table 1. List of the Most Popular Report Gene Imaging Systems (Adapted from Ref 13)

imaging modality	reporter	ref(s)
optical reporter genes	fluorescent proteins	14,15
	luciferase	16,17
nuclear medicine reporter genes	herpes simplex virus-thymidine kinase-1	18,19
	dopamine-2 receptor	20,21
	sodium/iodide symporter	22,23
	norepinephrine transporter	24,25
	somatostatin receptor	26
MRI reporter genes	transferrin receptor	27
	ferritin	28,29

by administration of the cells to a (typically immunodeficient) animal. However, such models still suffer from many of the disadvantages described above. A model that more closely matches the phenotype of the ultimate human recipient can be provided by the generation of transgenic mice (*11*). In such animals, typically an additional human gene will be incorporated into the mouse genome so that on translation it is widely expressed in many mouse tissues and not only by cells that are exogenously administered. So-called "knock-in" mice were originally developed by microinjection of the transduct into the fertilized eggs of mice, followed by implantation and maturation in pseudopregnant foster mothers (*31*). However, this results in random, transient, and rather inefficient insertion into the genome and has more recently largely been replaced by the "gene targeting" approach shown in Figure 4 which resulted in 2007 in the award of the Nobel Prize to Capecchi, Evans, and Smithies (*32*). This involves the biosynthesis of a vector that contains human DNA homologous to the target mouse gene together with an antibiotic resistance sequence that enables successfully transduced cells to be selected. This vector is introduced into cultured embryonic stems cells obtained from harvested mouse blastocysts whereupon the vector is incorporated into a precise location in the genome of one or more cells

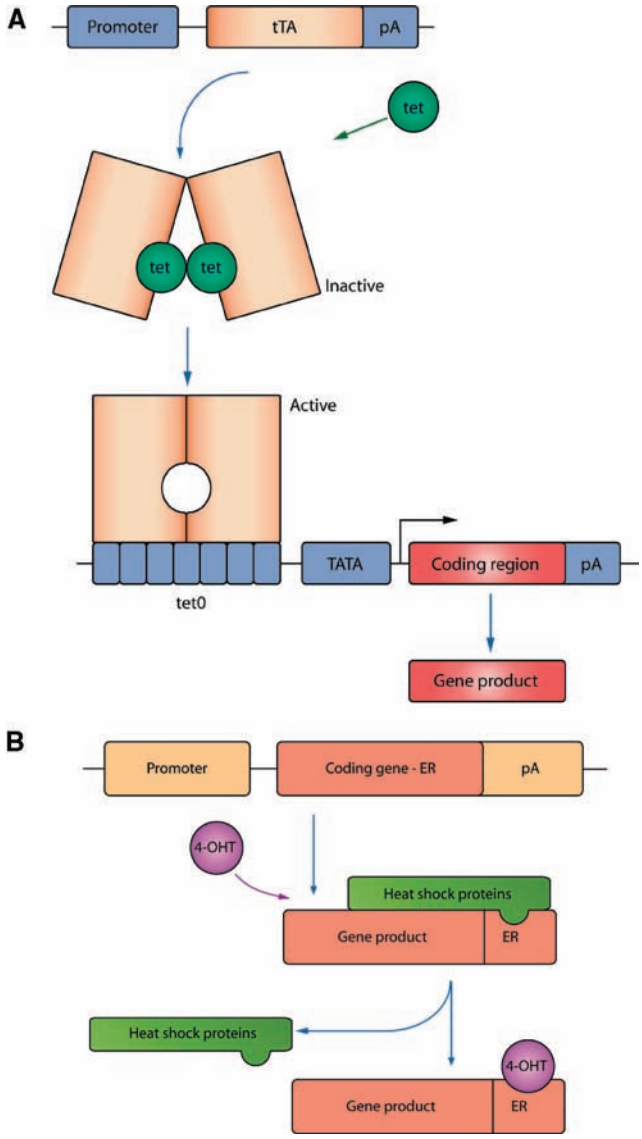

Figure 3. Inducible promotor systems (adapted from ref 11). (A) A tetracycline regulated transcriptional transactivator system. Cells are co-transfected with genes coding for a tetracycline-dependent transactivator, the desired gene expression of which is controlled by a promotor containing a concatamer of seven TetO sequences. In the presence of tetracycline, binding of the transactivator to the promotor is inhibited resulting in low or no levels of protein expression. In the absence of tetracycline, the transactivator binds and promotes transcription of the desired gene. (B) Tamoxifen-induced expression system. The desired gene is linked with that encoding for the transciption of a mutated ligand binding site from the estrogen receptor, and this results in the production of a fusion protein containing both sequences. In the absence of tamoxifen (4-OHT), heat shock proteins bind to the ER-domain of the protein and prevent its function. Addition of tamoxifen displaces the heat shock protein, allowing the protein to function correctly.

by a process known as homologous recombination. These cells can be selected by antibiotic treatment and implanted into foster mothers, which give birth to chimeric mice bearing cells derived from both the original and transduced cells. Further mating of the offspring with normal mice results in the birth of mice that carry only either the knock-in human gene or the original mouse gene. The human gene will be present in all the cells in the transgenic mice and, depending on its nature, will result in a pattern of molecular expression similar to that seen in man (*33*). Recent examples of the use of such models for imaging include a study of proliferation in gliomas using PET imaging (*34*) and the use of MRI for studying spontaneous lesions following insertion of a gene inducing tuberous sclerosis (*35*).

The last refinement of genetically modified animal model to be described here is the "knockout" mouse. Instead of resulting in the added expression of a human gene to a mouse background, this results in the disruption of function of a selected gene. The gene-targeting approach described above can also be used here, except that an inactivated mouse gene would be substituted for the human gene (*36*). However, another route to knockout mice is by site-specific recombination approaches such as the Cre-lox system (Figure 5). In such an approach, two transgenic mice must first be generated. One is a mouse that expresses the enzyme Cre recombinase, and the other is a mouse in which the gene of interest is flanked by two recognition sites—called "LoxP" sites. When these two strains are mated, some mice inherit both genes, and in these, the recombinase enzyme binds to the two LoxP sites, thereby tying together the ends of the target gene, preventing its transcription, and resulting in a mouse in which the function of this gene is lacking. Such models are very useful for determining the function of a particular gene or for studying the interaction of its gene product with contrast agents, an example of which is the study by de Jong et al. who elucidated the role of megalin in the tubular reabsorption of labeled peptides by the use of megalin-knockout mice (*37*). Potential disadvantages of the use of genetically engineered animals is that they are complex to produce and not generally available. These drawbacks are, to some extent, ameliorated by initiatives such as the NIH Transgenic Mouse consortium (http://www.nih.gov/science/models/mouse/index.html), which aims to improve the availability of transgenic models as well as provide a useful source of information.

Molecular Imaging Modalities. Each of the different imaging technologies that can be employed for molecular imaging has its own inherent strengths and weaknesses. These are summarized in Table 2 and will be discussed, together with the basic principles of each modality, below.

Radionuclide Imaging. As the name implies, radionuclide imaging maps the in vivo biodistribution of radiotracers. It comes in two distinct flavors, single photon emission tomography (SPECT) and positron emission tomography (PET). (For a useful overview on the instrumentation used for PET and SPECT imaging, see ref 38).

SPECT or gamma camera imaging is based on the detection of gamma photons or X-rays emitted by radionuclides decaying by electron capture or isomeric transition. After the administration of a contrast agent labeled with an appropriate radioisotope, the emitted radiation is picked up by a suitable detector (normally a sodium iodide crystal) and the distribution of γ rays converted into an electrical pulse and subsequently into an image. In order to remove scattered radiation and to ensure that the detected events can be traced back to their point of origin in the tissue, a collimator consisting of a sheet of lead containing many small parallel holes is placed between the subject and the detector system as shown in Figure 6. Radionuclides decaying in this fashion emit γ radiation with a range of energies, and for successful imaging, this energy must be high enough to penetrate the tissues of the body and interact with the detector but not so high that it passes completely through the crystal. For clinical imaging, the preferred energies lie in the range 80−250 keV, but for preclinical imaging, lower energies can be used owing to the lower attenuation provided by the smaller body mass. One of the advantages of single photon imaging is that the signals arising from photons of different energies can be discriminated, and so the images arising from two or three different radionuclides can be acquired simultaneously. Although radionuclide imaging is, in principle, one of the most sensitive imaging modalities, the sensitivity of SPECT imaging is degraded by the presence of the lead collimator, which absorbs the great majority of events issuing

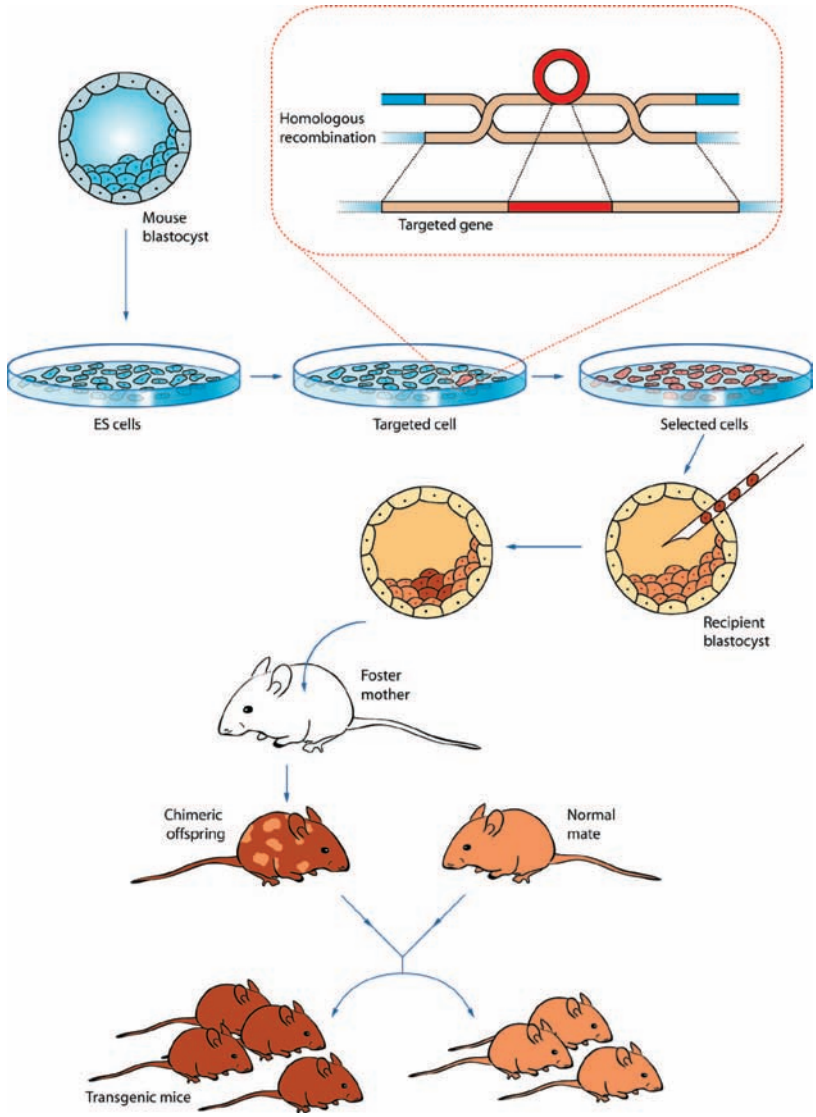

Figure 4. Gene targeting. Adapted from ref (*32*). Embryonic stem cells from mouse blastocyst are transfected with the gene of interest, which inserts by homologous recombination into the genome of the recipient cell. After selection, the cells are transferred to a recipient blastocsyt and implanted into the uterus of a foster mother. This results in the birth of mice who are chimeric for both the targeted cells and those of the parent blastocyst. Mating of these chimeric mice with normal mice results in the production of mice transgenic for the targeted gene by a process of normal Mendelian inheritance.

from the subject. The consequence is that only about 0.1% of the emitted γ rays are normally measured, and this results in a requirement for relatively high administered doses of radioactivity and long imaging times—typically on the order of tens of minutes.

PET imaging, in contrast, operates on a somewhat different principle. When a positron (a positively charged electron) is emitted by the nucleus of the radioactive atom, it almost immediately interacts with an electron in the immediate vicinity, and this interaction results in the production of two 511 keV γ rays emitted simultaneously in (almost) opposite directions. These photons are detected by a ring of detectors around the subject as shown in Figure 7, and when two such events are recorded simultaneously ("in coincidence"), they can be traced back to the point at which the annihilation occurs, thus creating a map of the distribution of the radioactivity in the animal. Because no collimation is required for PET imaging, it is much (about 100 times) more sensitive than SPECT imaging, and consequently, lower levels of radioactivity can be administered, larger numbers of radioactive events detected, and shorter imaging times used. The list of suitable positron emitting radionuclides for PET is not as extensive as those available for SPECT imaging, and because all PET isotopes result in the production of 511 keV photons, it is not possible to perform simultaneous multi-isotope acquisitions. Either radionuclide imaging approach is able to produce images with an intermediate resolution, typically around 1 mm for SPECT and 2 mm for PET in practice. For a detailed description of PET imaging technology, especially in combination with other imaging modalities, please see the reviews by Pichler et al. (*39*, *40*).

Both radionuclide imaging techniques are to a large degree quantitative—thus, the measured signal is directly proportional to the concentration of radioactivity in the tissue, which in turn *may* be proportional to the levels of the target molecule to which it binds. Consideration needs to be given to attenuation of the signal by overlying tissues, but this is less of a problem in small animals than in human-sized subjects, and provided that the system is appropriately calibrated, it is possible to draw quantitative conclusions from the images obtained (*41*). Because of the large numbers of events detected in PET imaging, it is possible, by the use of compartmental modeling, to calculate the molar concentration of radiotracer in a tissue of interest, provided that a measure of the arterial concentration of radioactivity (input function) can be obtained (*42*).

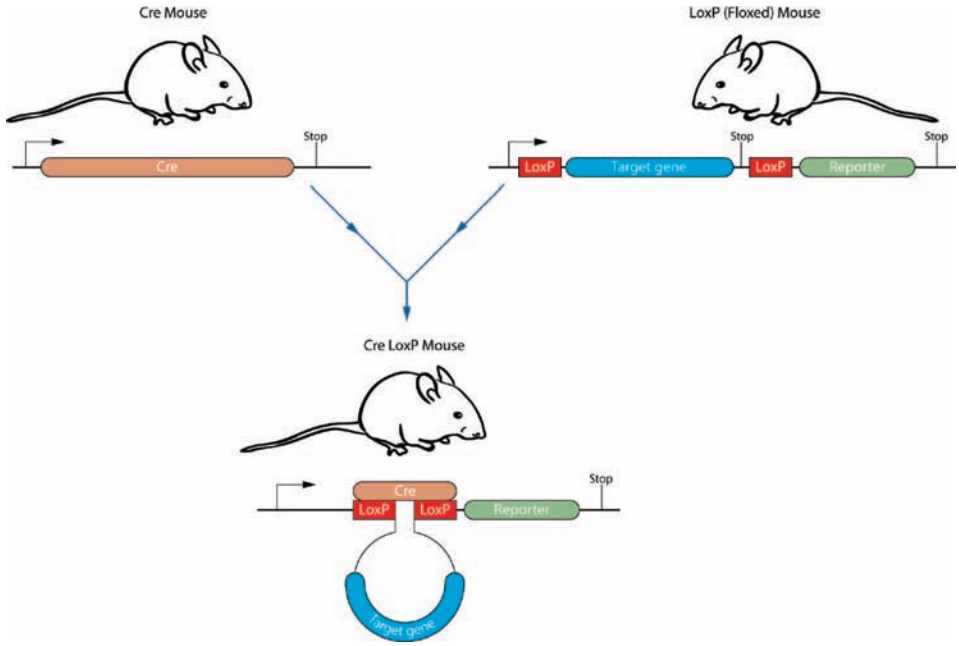

Figure 5. Adapted from ref 11. Generation of transgenic mice by Cre-Lox site-specific recombination. Introduction of Cre-recombinase and a "floxed" gene into a cell results in the floxed gene being inactivated and a reporter gene transcribed instead.

Table 2. Comparison of Small-Animal Imaging Modalities

modality	resolution	sensitivity	quantitation	time	cost
US	50 μm	v. low	-	minutes	low-medium
CT	50 μm	v. low	-	minutes	medium
MRI	25 μm	low	+	secs-tens of mins	v. high
PET	2 mm	high	+++	mins-tens of mins	high
SPECT	1 mm	high	++	tens of mins	high
BLI	5 mm	v. high	++	secs-mins	low
NIR	5 mm	high	+	secs-mins	low-medium

Optical Imaging. Optical imaging also comes in two distinct flavors—bioluminescence and fluorescence imaging. For a useful overview of the fundamentals of optical imaging, see ref 43. Bioluminescence imaging is a form of reporter-gene imaging and relies upon the emission of light generated in vivo by the action of luciferase enzymes produced by transduced cells. Although a very useful, sensitive, inexpensive, simple, and rapid imaging technique, it does not depend on the use of contrast agents and will therefore not be further discussed in this article.

Fluorescence imaging depends on the detection of fluorescent light induced by excitement of fluorophores in the animal tissues as illustrated in Figure 8. Fluorophores may be endogenously produced by transduction of tissues to express, for example, green or red fluorescent proteins, or may be exogenously administered in the form of fluorescent contrast agents. Fluorescence imaging is also a relatively inexpensive, sensitive, and rapid imaging technique, but the main disadvantage of both optical imaging modalities is the high degree of scatter and absorption of light by overlying tissues. This severely degrades the resolution of the system and also means that, apart from its use in very superficial tissues, it cannot be considered quantitative. A further disadvantage of fluorescent imaging over bioluminescence is the fluorescence that arises from normal tissues, in particular, from blood (hemoglobin) and foods in the stomach and intestines. This latter problem can be reduced by feeding animals on a special diet of non-chlorophyll-containing foods and the former by the use of fluorophores that emit light in the near-infrared (NIR) window of 650−900 nm. A number of new optical imaging techniques are seeking to overcome the problems of light scatter, such as time-domain (fluorescence lifetime) imaging (*44*), frequency domain imaging (*45*), and optical coherence tomography (*46*); however, such techniques to a large extent lose the advantages of simplicity and high sensitivity associated with planar imaging.

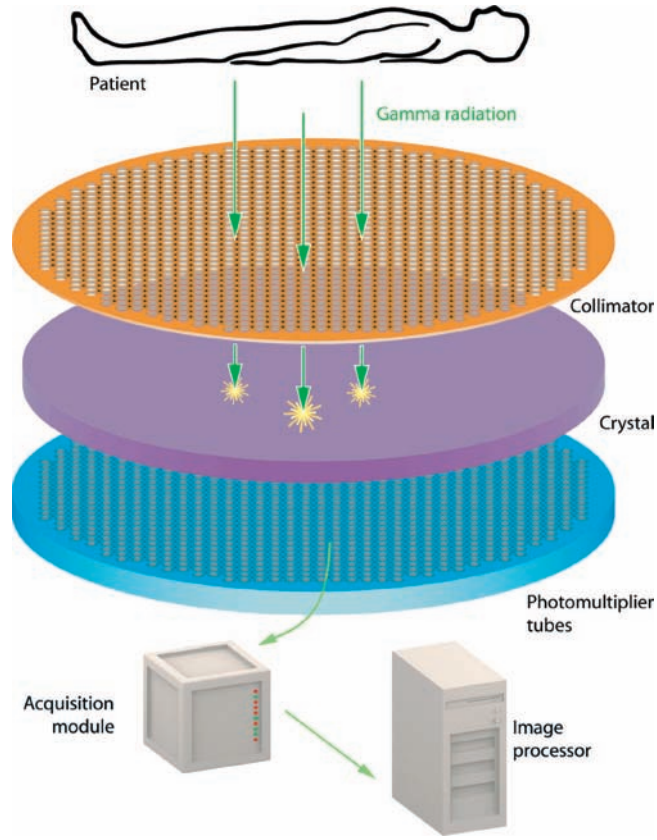

Figure 6. Principle of the gamma camera for SPECT imaging. Photons emitted from the patient after injection of a radiotracer pass through a lead collimator and impinge in a crystal producing a flash of light, which is detected by an array of photomultiplier tubes and converted into an image such as that shown in Figure 2.

Ultrasound Imaging. Ultrasound imaging depends on the reflection of high-frequency sound waves by anatomical struc-

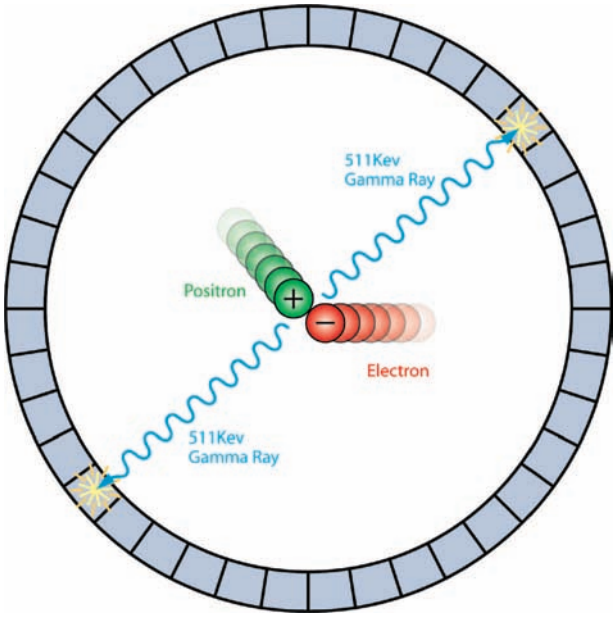

Figure 7. Principle of PET imaging. An emitted positron annihilates with a circulating electron resulting in the emission of two photons in opposite directions. Simultaneous interaction of these photons with crystals in a ring around the subject results in the detection of an event that can be traced back to the point of annihilation. Many millions of these events are built up into a PET image such as the example shown in Figure 11.

tures in the body, especially the boundaries between different tissue types (*47*) and, through the use of Doppler techniques, is particularly useful for measuring blood flow. An example is shown in Figure 9. It is a relatively inexpensive technique, which is simple and rapid to perform but is considered to be somewhat operator-dependent in its use. Since it is essentially an anatomical imaging tool, until recently ultrasound imaging would not have been considered part of the panel of molecular imaging techniques, but recent developments have resulted in a very significant increase in its use for small animal imaging. These developments hinge upon a combination of (i) the use of very high frequency probes, which emit sound waves with frequencies up to 100 MHz and result in a very high imaging resolution of the order of 25 μm, and (ii) ultrasound contrast agents based on the use of gas-filled microbubbles, although since such agents are too large to leave the vascular space, their application is limited to intravascular structures such as endothelial target molecules. A tradeoff against the excellent resolution of high-frequency ultrasound is its poor tissue penetration, and the sensitivity of detection of contrast agents is low (*48*). Modern semiautomated small animal ultrasound systems overcome to some extent the intraoperator variability of this modality, but it should still be considered a generally qualitative rather than quantitative tool.

Magnetic Resonance Imaging (MRI). MRI depends upon the measurement of the concentration and rates of relaxation of hydrogen atoms in a high magnetic field. The spinning single proton in a hydrogen atom creates a magnetic field, and each hydrogen atom therefore acts like a tiny magnet. In the absence of an external magnetic field, hydrogen nuclei magnetic moments are randomly oriented, but in the presence of an external magnetic field, a small proportion of the hydrogen protons align themselves in one of two directions, parallel or antiparallel to the net magnetic field producing a net magnetic field. The hydrogen atoms are not still but "precess" like a spinning top in the direction of the external magnetic field at a particular frequency known as the Larmor (or precessional) frequency. If a magnetic field pulse at the Larmor frequency is then applied perpendicular to the main magnetic field by a radiofrequency coil, the protons will absorb some energy and alter their alignment away from the direction of the main magnetic field. As well as changing direction, the protons also begin to precess "in phase" resulting in a net magnetic moment transverse to the external field, which induces a current and is detected in the transceiver coil. When the RF pulse is switched off, the protons give up the energy they have absorbed and start to return to their previous direction and to precess out of frequency. This results in a gradual increase in the longitudinal magnetization—called T1 or spin−lattice relaxation—and a gradual decrease in the transverse magnetization—called T2 or spin−spin relaxation. The rate at which these processes occur vary from tissue to tissue. These parameters can be converted into images that can be "weighted" toward T1 or T2 in order to increase the contrast between the tissues of interest. For a useful overview of the physics of MRI, see ref 49. Contrast agents in MRI work by influencing the T1 and T2 relaxation times. Most contrast agents are based on paramagnetic metals such as gadolinium, which have unpaired electrons in their outer shells. These interact with the water molecules in the vicinity resulting in a reduction in T1 relaxation times and a corresponding increase in signal intensity on T1-weighted images. Superparamagnetic iron oxide (SPIO) based agents on the other hand cause a significant reduction in T2 relaxation with a resultant decrease in image intensity on T2-weighted images.

Although MRI is a very powerful high-resolution anatomical imaging tool, its sensitivity for detection of changes at the molecular level is very low—typically 10^6 times lower than that of PET imaging, although this can be increased somewhat by the use of superparamagnetic contrast agents (*50*). It is probably the most expensive of the molecular imaging modalities, and long image acquisition times are often required, especially for high-resolution images and if low-strength magnetic fields are employed.

X-ray Computed Tomography (CT). CT imaging is not a molecular imaging tool per se since it provides only anatomical information as a result of the differential absorption of X-rays by different tissues. However, functional molecular imaging especially PET/SPECT is often combined with CT, either by using dual-modality instrumentation or by software image fusion, in order to provide enhanced anatomical localization of the functional information or, in the case of PET imaging, for attenuation correction.

BIOCONJUGATE CONTRAST AGENTS

All of the imaging modalities described above depend to some extent on the use of contrast agents to either provide or enhance the signals required for image generation. Irrespective of the modality employed, all molecular imaging contrast agents consist of (at least) two main components: (i) a targeting component that interacts with the target molecule of interest in vivo and (ii) a signaling component, sometimes called a "molecular beacon", which is detected by the instrument and provides information on the location and concentration of the signal, and consequently the target molecule. These two components are normally conjugated together to form a contrast agent using a range of chemistries, a rich variety of which are described every month in this journal. The targeting requirements for the contrast agent are essentially shared by each of the modalities—it should bind with high affinity and selectivity to the molecular target and show low-nonspecific binding to other tissues, should be stable in vivo, and be nontoxic. Stability is of particular importance in avoiding metabolites that might contribute to a signal but have lost their capacity for molecular targeting. The signaling component of the contrast agent, however, will be specific to the imaging method being used:

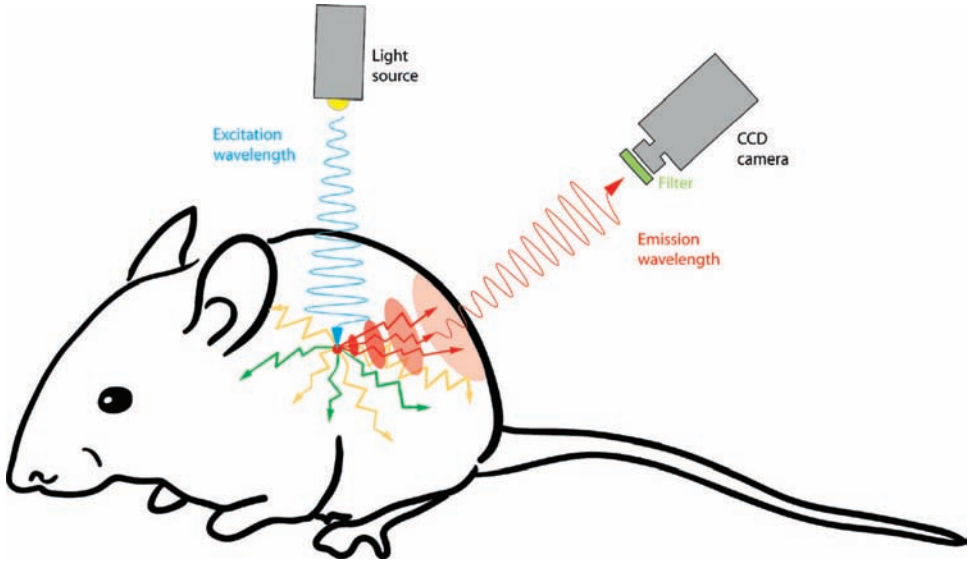

Figure 8. Fluorescence imaging. The presence of an endogenous or exogenously introduced fluorophore can be imaged following excitation with a laser. Scattering of the emitted light by tissue overlying the event results in absorption and degradation of the imaging resolution.

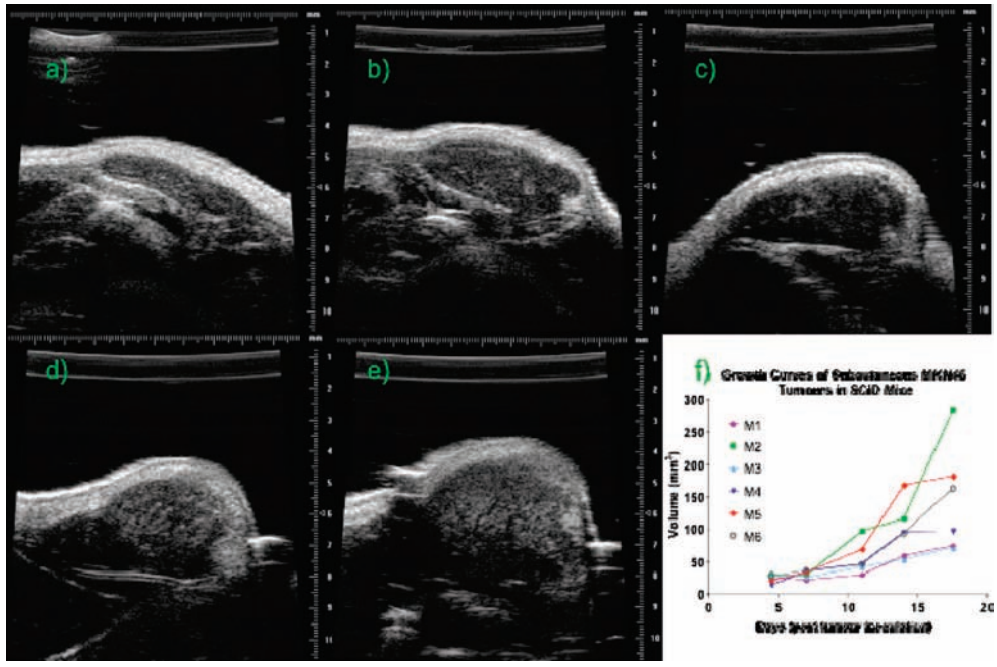

Figure 9. Example of ultrasound imaging. A subcutaneous MKN45 tumor on the right flank of a female SCID mouse (M1). (a−e) Sonograms showing the tumor 4, 7, 11, 14, and 17 days after inoculation, respectively. (f) Growth of MKN45 tumors measured by 3D ultrasound volume quantification.

radionuclides for PET/SPECT, fluorochrome for fluorescence imaging, microbubble for ultrasound, and paramagnetic chelate for MRI. The methodology used for attachment should ensure that the conjugation does not impact on the desired properties of the contrast agent (binding affinity, stability, etc.) but will depend on the chemical properties of the particular agent to be used, and when short-lived radionuclides are employed, clearance rates need to be commensurate with isotope lifetimes. The reader is again referred to elsewhere in this journal for many examples.

APPLICATIONS

Molecular Targets and Design Considerations. The performance of any molecular imaging approach is determined by the characteristics of the modality of choice, the contrast agent developed, and the molecular target of interest. Ultimately, the most important performance criterion for any imaging approach is the signal-to-noise ratio (SNR) that is achieved where "signal" represents the signal arising from the contrast agent that is bound to the target and "noise" represents the signal arising from background, which comprises nontargeted contrast agent plus that arising from extraneous "noise" intrinsic to the detection system. The higher the SNR, the better, in general terms, is the imaging approach, and therefore, the higher the signal and the lower the noise, the better.

There are many thousands of biochemical pathways that could usefully be explored with molecular imaging, and it is outside the scope of this review to discuss more than a few of these, but some general considerations apply in selecting targets worthy of pursuit (*52*, *53*). In the context of optimizing the SNR, the

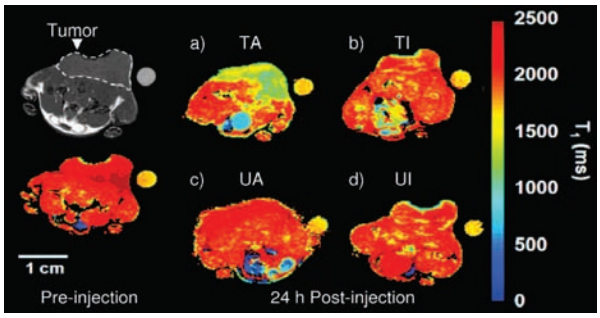

Figure 10. Example of a contrast enhanced MRI study. Reproduced with permission from ref 51. Transverse T1 maps of drug-treated and untreated tumors in animals injected with PS-active (GST-C2A-Gd) and PS-inactive (GST-C2A-Gd) contrast agents. Color scale indicates T1 values for image voxels. Images were acquired immediately before injection of contrast agent (a T1 map acquired from a tumor before injection is shown on the left-hand side) and at 24 h after injection. A reference capillary was placed adjacent to the tumors, the position of which is indicated on the grayscale image. (A) Drug-treated tumor in animal injected with PS-active GST-C2A-Gd (TA). (B) Drug-treated tumor in animal injected with PS-inactive GST-C2A-Gd (TI). (C) Untreated tumor in animal injected with PS-active GST-C2A-Gd (UA). (D) Untreated tumor in animal injected with PS-inactive GST-C2A-Gd (UI). Drug-treated tumor in animal injected with PS-active contrast agent shows greater accumulation 24 h after injection (A).

Figure 11. Example of PET-CT image of a mouse bearing a AR42J pancreatic tumor imaged with ^{18}FDG. Uptake is seen in the tumor (in the left thigh), muscle, brown fatty tissue, bladder, and intestines.

two most important considerations are accessibility and abundance. Since an interaction between the contrast agent and its target is the basis of the imaging approach, the tracer must be able to reach its destination. Targets located within the vascular lumen of the blood supply represent the most accessible site and those buried deep within the cell the least, while those expressed on the cell surface of tissues represent the middle ground. Consideration must be given to the way in which the ligand will reach its target. Extravascular delivery demands that the agent is able to leave the bloodstream, and in cancer, this is facilitated by the highly fenestrated capillaries present in many tumors. Intracellular delivery requires that the contrast agent pass through the cell membrane and into the appropriate intracellular compartment, and this places severe restrictions on its design.

While great emphasis is naturally placed on optimizing the interaction between the target and the contrast agent, in practice a greater impact on SNR can be made by reducing the background signal. Typically, only 1−2% of the administered dose will accumulate at the target at best. This leaves 98−99% of the dose free to contribute to the background. Consideration should therefore be given to reducing this contribution by accelerating blood clearance times, lowering nonspecific protein binding, and reducing accumulation in organs of excretion such as the liver, kidneys, and gastrointestinal tract. A significant impact on such parameters can be achieved by reducing the size and enhancing the hydrophilicity of the contrast agent by judicious choice of conjugation chemistry or by the introduction of pharmacokinetic modifiers such as poly(ethylene glycol) (*54*). If desired, metabolically labile chemical bonds can also be introduced to accelerate clearance from nontarget tisssues (*55*).

Drug Development. As indicated above, one of the main areas of application of preclinical imaging is in the field of pharmaceutical development. It is hoped that preclinical imaging has the potential to reduce the high attrition rates in the development of new drugs and the long time scales and great expense involved in this process. Applications can be found at all stages of the drug development process from evaluation of target expression through screening of candidate compounds, assessment of activity in animal models of disease to measurement of pharmacokinetics, comparisons of different formulations, and determination of appropriate doses for clinical trials. (For detailed reviews of the role of molecular imaging in drug development, please see *refs* 56, 57).

Biomarkers. In the field of oncology, there is particular interest in the development of imaging biomarkers as a result of the development of molecularly targeted therapies that aim to interact with a defined molecular target rather than induce relatively nonspecific toxicity and the desire the reduce unnecessary drug-related expenditure in the face of the increasing costs of novel drug treatments. Biomarkers provide a means of measuring a particular pathological process that is associated with the progression of a disease or the effectiveness of a drug used for its treatment. Most useful among the range of biomarkers is a "surrogate end point", which can be considered to provide a direct measure of the severity of a disease such as, for example, the measurement of blood glucose levels in diabetes. However, in the absence of such a direct correlative measure, any biomarker that provides an early indication of drug effectiveness or safety can be useful. Biomarkers can originate from many different types of measurement ranging in complexity (and cost) from the simple measurement of a chemical or cell type in a blood sample, e.g., CD-4 counts in HIV infection, through immunohistochemical analysis of biopsy samples, e.g., the Herceptest used to measure HER-2 expression in breast cancer, through to the use of imaging biomarkers.

The most widely used imaging biomarker in oncology is the anatomical imaging techniques to measure the size of tumor masses before and after treatment. To be most valuable, a biomarker should be universally applicable and generalizable to a range of situations and localities, and in order to standardize the use of MRI and CT in this regard, a set of criteria known as the RECIST criteria have been internationally agreed upon (*58*). However, although a reduction in the size of a tumor can be considered a useful indicator of cytotoxic treatments for cancer, which result directly in cell death, it may not be an appropriate measure of success of a

molecularly targeted treatment that may result only initially in tumoristasis. In such a situation, molecular imaging biomarkers may prove to be useful in a number of ways: the first requirement is to identify those patients who are most likely to benefit from a particular molecularly targeted treatment. An example is the use of antiangiogenic drugs targeted against the $\alpha_v\beta_3$ integrin. $\alpha_v\beta_3$ is one of the most widely explored targets for molecular imaging with preclinical imaging applications developed for all of the modalities described above including both gadolinium (*59*−*61*) and SPIO-based (*62*, *63*) agents for MRI, targeted microbubbles for ultrasound (*64*), and NIR probes (*65*) or quantum dots (*66*) for optical imaging. However, radionuclide imaging applications for both SPECT and PET have been most widely explored (*67*). Importantly, developments initially explored in the preclinical imaging arena have since been translated into clinical practice. For example, Beer at al. have shown that PET imaging with [(^{18})F]Galacto-RGD is able to measure the levels of $\alpha_v\beta_3$ integrin in patients with cancer (*68*) and explored its applicability in the context of breast (*69*) and head and neck (*70*) cancers.

Having identified those patients most likely to benefit from a particular treatment, the next aim is to identify a pharmacodynamic response (or lack of it) as soon as possible. This would be valuable for several reasons. Prediction of treatment failure early in the course of therapy would indicate that the treatment should be withdrawn to avoid unnecessary toxicity and expense and would provide an early indication that an individual should change to an alternative therapy before drug resistance mechanisms have been induced. Early detection of tumor sensitivity, on the other hand, indicates that treatment should be continued and also raises the possibility of treatment intensification, since any resulting side effects or increased costs could be justified by the likelihood of improved response.

By far, the most widely used imaging biomarker of treatment response is [(^{18})F] fluorodeoxyglucose (FDG) (see Figure 11). Glucose metabolism is intricately linked to many of the metabolic processes involved in the development of malignancy (for reviews, see refs 71, 72), and as a consequence, glucose transport and utilization are elevated in most types of cancer. Importantly, in the context of assessment of therapy response FDG uptake is often reduced following treatment with anticancer drugs, and its use is beginning to be clinically accepted as a standard biomarker of response (*73*). However, a number of questions arise relating to the use of FDG imaging in this regard. One issue is the actual cause of reduction in signal. In some cases, this reduction does appear to be due to a reduction in the number of metabolically active cells as a direct consequence of cell death and in such instances could therefore be considered a marker of treatment response; however, in other cases the reduction appears to be due to a translocation of the glucose transporter from the cell membrane to the cytosol (*74*). In other examples, the reduction in glucose metabolism seems to be a direct consequence of signaling downstream from the molecular target of the drug. Thus, treatment with rapamycin and its analogues results in a direct inhibition of glucose metabolism via the Akt and Hif-1α pathways (*75*), while in endocrine-sensitive breast cancer, transient stimulation of tumors with estradiol results in a consequent increase in FDG uptake, thereby predicting a likely response to endocrine therapies, because it indicates that the estrogen receptor system is functional (*76*). It could be argued therefore that although FDG imaging does provide a readout of drug activity, it cannot be considered to provide a surrogate end point in this regard. The other significant drawback of FDG imaging is that it is taken up not only by cancer cells but also by some metabolically active normal cells such as macrophages, as well as by microrganisms present in sites of infection. As a result of this perceived lack of specificity, efforts are being made to develop more specific imaging biomarkers of response.

One such approach is to try and measure the rate of cell proliferation. Perhaps the most widely explored imaging approach is the use of [(^{18})F] 3′-deoxy-3′-fluorothymidine (FLT) for PET (*77*). Retention of FLT by cells is primarily mediated by the action of the enzyme thymidine kinase-1 (TK1), which phosphorylates the tracer resulting in intracellular trapping. If cancer treatment results in a reduction in the rate of cell division within the tumor, then it would result in a down-regulation in the concentration of TK1 and a consequent reduction in FLT uptake. However, a reduction in TK1 can also be caused by drugs such as actinomycin D or cisplatin that have a direct effect on thymidine and DNA metabolism (*78*). On the other hand, the use of some drugs such as Fluorouracil that deplete the thymidine triphosphate pool can actually cause a transient increase in FLT uptake (*79*). Interpretation of the use of such agents therefore requires an understanding of the mechanism of action of the drug in use and its effects on DNA and thymidine metabolism.

An alternative means of assessing treatment response is to try and image cell death directly. One of the earliest events in the induction of this process in cancer therapy is apoptosis—also known as programmed cell death (*80*). The molecular events that occur in apoptosis are now well-understood, and a number of attempts have been made to develop imaging biomarkers that interact with these events (*81*). The most widely exploited of these is the translocation of phosphatidylserine (PS) from the inner to the outer surface of the cell membrane. Molecules such as Annexin V (*82*) or synaptotagmin (*51*, *83*) that bind to PS can be tagged with Molecular Beacons and potentially used to measure the induction of apoptosis after drug treatment (see Figure 10, for example). Because of the relatively large size of these targeting agents and their extracellular location, a variety of imaging modalities have been studied. PET and SPECT imaging probes again are the most widely explored (*81*), but contrast agents for optical imaging (*84*), gadolinium (*85*), and SPIO (*86*)-based MRI agents, as well as multimodality contrast agents (*87*), have been described.

CONCLUSIONS

A number of different imaging modalities in combination with a wide range of contrast agents can be employed to provide different types of information from small animal models of cancer and other diseases. Each technology has its own strengths and weaknesses, and each is able to provide unique insights into the status of biological pathways and processes of interest. Great care should be exercised, however, in directly extrapolating the information obtained in animal model systems to the human situation, but particularly in view of the increasing regulatory difficulties in performing experimental studies in human subjects, preclinical imaging can be very helpful in optimizing contrast agents and developing imaging protocols in order to reduce the number and complexity of studies in humans required to answer a particular medical or scientific question.

ACKNOWLEDGMENT

Thanks go to Kevin Brindle, Julie Foster, and Andrew Merron for examples of small animal images and to Tim Bacon for the illustrations.

LITERATURE CITED

(1) Breeman, W. A., Kwekkeboom, D. J., de Blois, E., de Jong, M., Visser, T. J., and Krenning, E. P. (2007) Radiolabelled

regulatory peptides for imaging and therapy. *Anticancer Agents Med. Chem. 7*, 345–57.
(2) Decristoforo, C., and Mather, S. J. (1999) 99m-Technetium-labelled peptide-HYNIC conjugates: effects of lipophilicity and stability on biodistribution. *Nucl. Med. Biol. 26*, 389–96.
(3) Maina, T., Nock, B. A., Zhang, H., Nikolopoulou, A., Waser, B., Reubi, J. C., and Maecke, H. R. (2005) Species differences of bombesin analog interactions with GRP-R define the choice of animal models in the development of GRP-R-targeting drugs. *J. Nucl. Med. 46*, 823–30.
(4) Harmar, A. J., Sheward, W. J., Morrison, C. F., Waser, B., Gugger, M., and Reubi, J. C. (2004) Distribution of the VPAC2 receptor in peripheral tissues of the mouse. *Endocrinology 145*, 1203–10.
(5) Pegram, M., and Ngo, D. (2006) Application and potential limitations of animal models utilized in the development of trastuzumab (Herceptin): a case study. *Adv. Drug Delivery Rev. 58*, 723–34.
(6) Davies, B., and Morris, T. (1993) Physiological parameters in laboratory animals and humans. *Pharm. Res. 10*, 1093–5.
(7) Beissert, S., and Loser, K. (2008) Molecular and cellular mechanisms of photocarcinogenesis. *Photochem. Photobiol. 84*, 29–34.
(8) Ottewell, P. D., Coleman, R. E., and Holen, I. (2006) From genetic abnormality to metastases: murine models of breast cancer and their use in the development of anticancer therapies. *Breast Cancer Res. Treat. 96*, 101–13.
(9) Pelleitier, M., and Montplaisir, S. (1975) The nude mouse: a model of deficient T-cell function. *Methods Achiev. Exp. Pathol. 7*, 149–66.
(10) Mueller, B. M., and Reisfeld, R. A. (1991) Potential of the scid mouse as a host for human tumors. *Cancer Metastasis Rev. 10*, 193–200.
(11) Jonkers, J., and Berns, A. (2002) Conditional mouse models of sporadic cancer. *Nat. Rev. Cancer 2*, 251–65.
(12) Ginj, M., Zhang, H., Waser, B., Cescato, R., Wild, D., Wang, X., Erchegyi, J., Rivier, J., Macke, H. R., and Reubi, J. C. (2006) Radiolabeled somatostatin receptor antagonists are preferable to agonists for in vivo peptide receptor targeting of tumors. *Proc. Natl. Acad. Sci. U.S.A. 103*, 16436–41.
(13) Kang, J. H., and Chung, J. K. (2008) Molecular-genetic imaging based on reporter gene expression. *J. Nucl. Med. 49 Suppl. 2* 164S–79S.
(14) Chudakov, D. M., Lukyanov, S., and Lukyanov, K. A. (2005) Fluorescent proteins as a toolkit for in vivo imaging. *Trends Biotechnol. 23*, 605–13.
(15) Muller-Taubenberger, A. (2006) Application of fluorescent protein tags as reporters in live-cell imaging studies. *Methods Mol. Biol. 346*, 229–46.
(16) Troy, T., Jekic-McMullen, D., Sambucetti, L., and Rice, B. (2004) Quantitative comparison of the sensitivity of detection of fluorescent and bioluminescent reporters in animal models. *Mol. Imaging 3*, 9–23.
(17) Contag, C. H., Spilman, S. D., Contag, P. R., Oshiro, M., Eames, B., Dennery, P., Stevenson, D. K., and Benaron, D. A. (1997) Visualizing gene expression in living mammals using a bioluminescent reporter. *Photochem. Photobiol. 66*, 523–31.
(18) Gambhir, S. S., Barrio, J. R., Phelps, M. E., Iyer, M., Namavari, M., Satyamurthy, N., Wu, L., Green, L. A., Bauer, E., MacLaren, D. C., Nguyen, K., Berk, A. J., Cherry, S. R., and Herschman, H. R. (1999) Imaging adenoviral-directed reporter gene expression in living animals with positron emission tomography. *Proc. Natl. Acad. Sci. U.S.A. 96*, 2333–8.
(19) Tjuvajev, J. G., Stockhammer, G., Desai, R., Uehara, H., Watanabe, K., Gansbacher, B., and Blasberg, R. G. (1995) Imaging the expression of transfected genes in vivo. *Cancer Res. 55*, 6126–32.
(20) Auricchio, A., Acton, P. D., Hildinger, M., Louboutin, J. P., Plossl, K., O'Connor, E., Kung, H. F., and Wilson, J. M. (2003) In vivo quantitative noninvasive imaging of gene transfer by single-photon emission computerized tomography. *Hum. Gene Ther. 14*, 255–61.
(21) MacLaren, D. C., Gambhir, S. S., Satyamurthy, N., Barrio, J. R., Sharfstein, S., Toyokuni, T., Wu, L., Berk, A. J., Cherry, S. R., Phelps, M. E., and Herschman, H. R. (1999) Repetitive, non-invasive imaging of the dopamine D2 receptor as a reporter gene in living animals. *Gene Ther. 6*, 785–91.
(22) Groot-Wassink, T., Aboagye, E. O., Glaser, M., Lemoine, N. R., and Vassaux, G. (2002) Adenovirus biodistribution and noninvasive imaging of gene expression in vivo by positron emission tomography using human sodium/iodide symporter as reporter gene. *Hum. Gene Ther. 13*, 1723–35.
(23) Haberkorn, U. (2001) Gene therapy with sodium/iodide symporter in hepatocarcinoma. *Exp. Clin. Endocrinol. Diabetes 109*, 60–2.
(24) Boyd, M., Cunningham, S. H., Brown, M. M., Mairs, R. J., and Wheldon, T. E. (1999) Noradrenaline transporter gene transfer for radiation cell kill by ^{131}I meta-iodobenzylguanidine. *Gene Ther. 6*, 1147–52.
(25) Moroz, M. A., Serganova, I., Zanzonico, P., Ageyeva, L., Beresten, T., Dyomina, E., Burnazi, E., Finn, R. D., Doubrovin, M., and Blasberg, R. G. (2007) Imaging hNET reporter gene expression with ^{124}I-MIBG. *J. Nucl. Med. 48*, 827–36.
(26) Rogers, B. E., Parry, J. J., Andrews, R., Cordopatis, P., Nock, B. A., and Maina, T. (2005) MicroPET imaging of gene transfer with a somatostatin receptor-based reporter gene and (94m)Tc-Demotate 1. *J. Nucl. Med. 46*, 1889–97.
(27) Gilad, A. A., Winnard, P. T., Jr., van Zijl, P. C., and Bulte, J. W. (2007) Developing MR reporter genes: promises and pitfalls. *NMR Biomed. 20*, 275–90.
(28) Cohen, B., Dafni, H., Meir, G., Harmelin, A., and Neeman, M. (2005) Ferritin as an endogenous MRI reporter for noninvasive imaging of gene expression in C6 glioma tumors. *Neoplasia 7*, 109–17.
(29) Genove, G., DeMarco, U., Xu, H., Goins, W. F., and Ahrens, E. T. (2005) A new transgene reporter for in vivo magnetic resonance imaging. *Nat. Med. 11*, 450–4.
(30) Merron, A., Peerlinck, I., Martin-Duque, P., Burnet, J., Quintanilla, M., Mather, S., Hingorani, M., Harrington, K., Iggo, R., and Vassaux, G. (2007) SPECT/CT imaging of oncolytic adenovirus propagation in tumours in vivo using the Na/I symporter as a reporter gene. *Gene Ther. 14*, 1731–8.
(31) Gordon, K., and Ruddle, F. H. (1986) Gene transfer into mouse embryos. *Dev. Biol. (N Y 1985) 4*, 1–36.
(32) The Nobel Prize in Physiology or Medicine 2007, http://nobelprize.org/nobel_prizes/medicine/laureates/2007/press.html, Date Accessed 30/10/2008.
(33) Mak, T. W., Penninger, J. M., and Ohashi, P. S. (2001) Knockout mice: a paradigm shift in modern immunology. *Nat. Rev. Immunol. 1*, 11–9.
(34) Bradbury, M. S., Hambardzumyan, D., Zanzonico, P. B., Schwartz, J., Cai, S., Burnazi, E. M., Longo, V., Larson, S. M., and Holland, E. C. (2008) Dynamic small-animal PET imaging of tumor proliferation with 3′-deoxy-3′-^{18}F-fluorothymidine in a genetically engineered mouse model of high-grade gliomas. *J. Nucl. Med. 49*, 422–9.
(35) Brown, A. B., Mahmood, U., Cortes, M. L., Tang, Y., Dai, G., Stemmer-Rachamimov, A., Prabhakar, S., Leishear, K., Onda, H., Kwiatkowski, D., Weissleder, R., and Breakefield, X. (2005) Magnetic resonance imaging and characterization of spontaneous lesions in a transgenic mouse model of tuberous sclerosis as a model for endothelial cell-based transgene delivery. *Hum. Gene Ther. 16*, 1367–76.
(36) Koller, B. H., and Smithies, O. (1989) Inactivating the beta 2-microglobulin locus in mouse embryonic stem cells by homologous recombination. *Proc. Natl. Acad. Sci. U.S.A. 86*, 8932–5.
(37) de Jong, M., Barone, R., Krenning, E., Bernard, B., Melis, M., Visser, T., Gekle, M., Willnow, T. E., Walrand, S., Jamar, F., and Pauwels, S. (2005) Megalin is essential for renal proximal

tubule reabsorption of (111)In-DTPA-octreotide. *J. Nucl. Med. 46*, 1696–700.
(38) Spanoudaki, V. C., and Ziegler, S. I. (2008) PET & SPECT Instrumentation. *Handb. Exp. Pharmacol.* 53–74.
(39) Pichler, B. J., Judenhofer, M. S., and Pfannenberg, C. (2008) Multimodal imaging approaches: PET/CT and PET/MRI. *Handb. Exp. Pharmacol.* 109–32.
(40) Pichler, B. J., Wehrl, H. F., and Judenhofer, M. S. (2008) Latest advances in molecular imaging instrumentation. *J. Nucl. Med. 49*, 5S–23S.
(41) Forrer, F., Valkema, R., Bernard, B., Schramm, N. U., Hoppin, J. W., Rolleman, E., Krenning, E. P., and de Jong, M. (2006) In vivo radionuclide uptake quantification using a multi-pinhole SPECT system to predict renal function in small animals. *Eur. J. Nucl. Med. Mol. Imaging 33*, 1214–7.
(42) Wu, H. M., Sui, G., Lee, C. C., Prins, M. L., Ladno, W., Lin, H. D., Yu, A. S., Phelps, M. E., and Huang, S. C. (2007) In vivo quantitation of glucose metabolism in mice using small-animal PET and a microfluidic device. *J. Nucl. Med. 48*, 837–45.
(43) Schulz, R. B., and Semmler, W. (2008) Fundamentals of optical imaging. *Handb. Exp. Pharmacol.* 3–22.
(44) Kumar, A. T., Raymond, S. B., Dunn, A. K., Bacskai, B. J., and Boas, D. A. (2008) A time domain fluorescence tomography system for small animal imaging. *IEEE Trans. Med. Imaging 27*, 1152–63.
(45) van Munster, E. B., and Gadella, T. W. (2005) Fluorescence lifetime imaging microscopy (FLIM). *Adv. Biochem. Eng. Biotechnol. 95*, 143–75.
(46) Cobb, M. J., Chen, Y., Bailey, S. L., Kemp, C. J., and Li, X. (2006) Non-invasive imaging of carcinogen-induced early neoplasia using ultrahigh-resolution optical coherence tomography. *Cancer Biomark. 2*, 163–73.
(47) Hauff, P., Reinhardt, M., and Foster, S. (2008) Ultrasound basics. *Handb. Exp. Pharmacol.* 91–107.
(48) Hauff, P., Reinhardt, M., and Foster, S. (2008) Ultrasound contrast agents for molecular imaging. *Handb. Exp. Pharmacol.* 223–45.
(49) Schaeffter, T., and Dahnke, H. (2008) Magnetic resonance imaging and spectroscopy. *Handb. Exp. Pharmacol.* 75–90.
(50) Sosnovik, D. E., Nahrendorf, M., and Weissleder, R. (2008) Magnetic nanoparticles for MR imaging: agents, techniques and cardiovascular applications. *Basic Res. Cardiol. 103*, 122–30.
(51) Krishnan, A. S., Neves, A. A., de Backer, M. M., Hu, D. E., Davletov, B., Kettunen, M. I., and Brindle, K. M. (2008) Detection of cell death in tumors by using MR imaging and a gadolinium-based targeted contrast agent. *Radiology 246*, 854–62.
(52) Mather, S. J. (2007) Design of radiolabelled ligands for the imaging and treatment of cancer. *Mol. Biosyst. 3*, 30–5.
(53) Mather, S. J. (2006) Functional targets in cancer for radiopharmaceutical development, In *Technetium, Rhenium and Other Metals in Chemistry and Nuclear Medicine* (Mazzi, U., Ed.) SGE Editoriali, Padova.
(54) Ryan, S. M., Mantovani, G., Wang, X., Haddleton, D. M., and Brayden, D. J. (2008) Advances in PEGylation of important biotech molecules: delivery aspects. *Expert Opin. Drug Delivery 5*, 371–83.
(55) Akizawa, H., Uehara, T., and Arano, Y. (2008) Renal uptake and metabolism of radiopharmaceuticals derived from peptides and proteins. *Adv. Drug Delivery Rev. 60*, 1319–28.
(56) Willmann, J. K., van Bruggen, N., Dinkelborg, L. M., and Gambhir, S. S. (2008) Molecular imaging in drug development. *Nat. Rev. Drug Discovery 7*, 591–607.
(57) Gross, S., and Piwnica-Worms, D. (2006) Molecular imaging strategies for drug discovery and development. *Curr. Opin. Chem. Biol. 10*, 334–42.
(58) Therasse, P., Eisenhauer, E. A., and Verweij, J. (2006) RECIST revisited: a review of validation studies on tumour assessment. *Eur. J. Cancer 42*, 1031–9.
(59) Schmieder, A. H., Winter, P. M., Caruthers, S. D., Harris, T. D., Williams, T. A., Allen, J. S., Lacy, E. K., Zhang, H., Scott, M. J., Hu, G., Robertson, J. D., Wickline, S. A., and Lanza, G. M. (2005) Molecular MR imaging of melanoma angiogenesis with alphanubeta3-targeted paramagnetic nanoparticles. *Magn. Reson. Med. 53*, 621–7.
(60) Sipkins, D. A., Cheresh, D. A., Kazemi, M. R., Nevin, L. M., Bednarski, M. D., and Li, K. C. (1998) Detection of tumor angiogenesis in vivo by $\alpha_V\beta_3$-targeted magnetic resonance imaging. *Nat. Med. 4*, 623–6.
(61) Winter, P. M., Caruthers, S. D., Kassner, A., Harris, T. D., Chinen, L. K., Allen, J. S., Lacy, E. K., Zhang, H., Robertson, J. D., Wickline, S. A., and Lanza, G. M. (2003) Molecular imaging of angiogenesis in nascent Vx-2 rabbit tumors using a novel α(nu)β3-targeted nanoparticle and 1.5 T magnetic resonance imaging. *Cancer Res. 63*, 5838–43.
(62) Thorek, D. L., Chen, A. K., Czupryna, J., and Tsourkas, A. (2006) Superparamagnetic iron oxide nanoparticle probes for molecular imaging. *Ann. Biomed. Eng. 34*, 23–38.
(63) Zhang, C., Jugold, M., Woenne, E. C., Lammers, T., Morgenstern, B., Mueller, M. M., Zentgraf, H., Bock, M., Eisenhut, M., Semmler, W., and Kiessling, F. (2007) Specific targeting of tumor angiogenesis by RGD-conjugated ultrasmall superparamagnetic iron oxide particles using a clinical 1.5-T magnetic resonance scanner. *Cancer Res. 67*, 1555–62.
(64) Ellegala, D. B., Leong-Poi, H., Carpenter, J. E., Klibanov, A. L., Kaul, S., Shaffrey, M. E., Sklenar, J., and Lindner, J. R. (2003) Imaging tumor angiogenesis with contrast ultrasound and microbubbles targeted to α(v)β3. *Circulation 108*, 336–41.
(65) von Wallbrunn, A., Holtke, C., Zuhlsdorf, M., Heindel, W., Schafers, M., and Bremer, C. (2007) In vivo imaging of integrin $\alpha_v\beta_3$ expression using fluorescence-mediated tomography. *Eur. J. Nucl. Med. Mol. Imaging 34*, 745–54.
(66) Cai, W., Shin, D. W., Chen, K., Gheysens, O., Cao, Q., Wang, S. X., Gambhir, S. S., and Chen, X. (2006) Peptide-labeled near-infrared quantum dots for imaging tumor vasculature in living subjects. *Nano Lett. 6*, 669–76.
(67) Beer, A. J., and Schwaiger, M. (2008) Imaging of integrin $\alpha_v\beta_3$ expression, *Cancer Metastasis Rev.*
(68) Beer, A. J., Haubner, R., Sarbia, M., Goebel, M., Luderschmidt, S., Grosu, A. L., Schnell, O., Niemeyer, M., Kessler, H., Wester, H. J., Weber, W. A., and Schwaiger, M. (2006) Positron emission tomography using [^{18}F]Galacto-RGD identifies the level of integrin α(v)β3 expression in man. *Clin. Cancer Res. 12*, 3942–9.
(69) Beer, A. J., Niemeyer, M., Carlsen, J., Sarbia, M., Nahrig, J., Watzlowik, P., Wester, H. J., Harbeck, N., and Schwaiger, M. (2008) Patterns of $\alpha_v\beta_3$ expression in primary and metastatic human breast cancer as shown by ^{18}F-Galacto-RGD PET. *J. Nucl. Med. 49*, 255–9.
(70) Beer, A. J., Grosu, A. L., Carlsen, J., Kolk, A., Sarbia, M., Stangier, I., Watzlowik, P., Wester, H. J., Haubner, R., and Schwaiger, M. (2007) [^{18}F]galacto-RGD positron emission tomography for imaging of $\alpha_v\beta_3$ expression on the neovasculature in patients with squamous cell carcinoma of the head and neck. *Clin. Cancer Res. 13*, 6610–6.
(71) Gillies, R. J., Robey, I., and Gatenby, R. A. (2008) Causes and consequences of increased glucose metabolism of cancers. *J. Nucl. Med. 49*, 24S–42S.
(72) Plathow, C., and Weber, W. A. (2008) Tumor cell metabolism imaging. *J. Nucl. Med. 49*, 43S–63S.
(73) Cheson, B. D., Pfistner, B., Juweid, M. E., Gascoyne, R. D., Specht, L., Horning, S. J., Coiffier, B., Fisher, R. I., Hagenbeek, A., Zucca, E., Rosen, S. T., Stroobants, S., Lister, T. A., Hoppe, R. T., Dreyling, M., Tobinai, K., Vose, J. M., Connors, J. M., Federico, M., and Diehl, V. (2007) Revised response criteria for malignant lymphoma. *J. Clin. Oncol. 25*, 579–86.

(74) Cullinane, C., Dorow, D. S., Kansara, M., Conus, N., Binns, D., Hicks, R. J., Ashman, L. K., McArthur, G. A., and Thomas, D. M. (2005) An in vivo tumor model exploiting metabolic response as a biomarker for targeted drug development. *Cancer Res. 65*, 9633–6.

(75) Wei, L. H., Su, H., Hildebrandt, I. J., Phelps, M. E., Czernin, J., and Weber, W. A. (2008) Changes in tumor metabolism as readout for mammalian target of rapamycin kinase inhibition by rapamycin in glioblastoma. *Clin. Cancer Res. 14*, 3416–26.

(76) Dehdashti, F., Mortimer, J. E., Trinkaus, K., Naughton, M. J., Ellis, M., Katzenellenbogen, J. A., Welch, M. J., and Siegel, B. A. (2008) PET-based estradiol challenge as a predictive biomarker of response to endocrine therapy in women with estrogen-receptor-positive breast cancer. *Breast Cancer Res. Treat*.

(77) Shields, A. F., Grierson, J. R., Dohmen, B. M., Machulla, H. J., Stayanoff, J. C., Lawhorn-Crews, J. M., Obradovich, J. E., Muzik, O., and Mangner, T. J. (1998) Imaging proliferation in vivo with [F-18]FLT and positron emission tomography. *Nat. Med. 4*, 1334–6.

(78) Bading, J. R., and Shields, A. F. (2008) Imaging of cell proliferation: status and prospects. *J. Nucl. Med. 49*, 64S–80S.

(79) Dittmann, H., Dohmen, B. M., Kehlbach, R., Bartusek, G., Pritzkow, M., Sarbia, M., and Bares, R. (2002) Early changes in [^{18}F]FLT uptake after chemotherapy: an experimental study. *Eur. J. Nucl. Med. Mol. Imaging 29*, 1462–9.

(80) Kerr, J. F., Wyllie, A. H., and Currie, A. R. (1972) Apoptosis: a basic biological phenomenon with wide-ranging implications in tissue kinetics. *Br. J. Cancer 26*, 239–57.

(81) Blankenberg, F. G. (2008) In vivo detection of apoptosis. *J. Nucl. Med. 49*, 81S–95S.

(82) Belhocine, T., Steinmetz, N., Hustinx, R., Bartsch, P., Jerusalem, G., Seidel, L., Rigo, P., and Green, A. (2002) Increased uptake of the apoptosis-imaging agent (99m)Tc recombinant human Annexin V in human tumors after one course of chemotherapy as a predictor of tumor response and patient prognosis. *Clin. Cancer Res. 8*, 2766–74.

(83) Zhao, M., Zhu, X., Ji, S., Zhou, J., Ozker, K. S., Fang, W., Molthen, R. C., and Hellman, R. S. (2006) ^{99m}Tc-labeled C2A domain of synaptotagmin I as a target-specific molecular probe for noninvasive imaging of acute myocardial infarction. *J. Nucl. Med. 47*, 1367–74.

(84) Prinzen, L., Miserus, R. J., Dirksen, A., Hackeng, T. M., Deckers, N., Bitsch, N. J., Megens, R. T., Douma, K., Heemskerk, J. W., Kooi, M. E., Frederik, P. M., Slaaf, D. W., van Zandvoort, M. A., and Reutelingsperger, C. P. (2007) Optical and magnetic resonance imaging of cell death and platelet activation using annexin a5-functionalized quantum dots. *Nano Lett. 7*, 93–100.

(85) Hiller, K. H., Waller, C., Nahrendorf, M., Bauer, W. R., and Jakob, P. M. (2006) Assessment of cardiovascular apoptosis in the isolated rat heart by magnetic resonance molecular imaging. *Mol. Imaging 5*, 115–21.

(86) Smith, B. R., Heverhagen, J., Knopp, M., Schmalbrock, P., Shapiro, J., Shiomi, M., Moldovan, N. I., Ferrari, M., and Lee, S. C. (2007) Localization to atherosclerotic plaque and biodistribution of biochemically derivatized superparamagnetic iron oxide nanoparticles (SPIONs) contrast particles for magnetic resonance imaging (MRI). *Biomed. Microdevices 9*, 719–27.

(87) Schellenberger, E. A., Sosnovik, D., Weissleder, R., and Josephson, L. (2004) Magneto/optical annexin V, a multimodal protein. *Bioconjugate Chem. 15*, 1062–7.

BC800401X

Subscriber access provided by SHEMYAKIN-OVCHINNIKOV INST

Communication

Synthesis and Characterization of Circular Structures of i-Motif Tagged with Fluoresceins

Tianyan Zhou, Xinming Li, Magdeline Tao Tao Ng, Yifan Wang, Ngee Mien Quek, Ji Luo, Weixing Yuan, Choon-Hong Tan, Huaqiang Zeng, and Tianhu Li

Bioconjugate Chem., **2009**, 20 (4), 644-647• DOI: 10.1021/bc8004599 • Publication Date (Web): 30 March 2009

Downloaded from http://pubs.acs.org on May 8, 2009

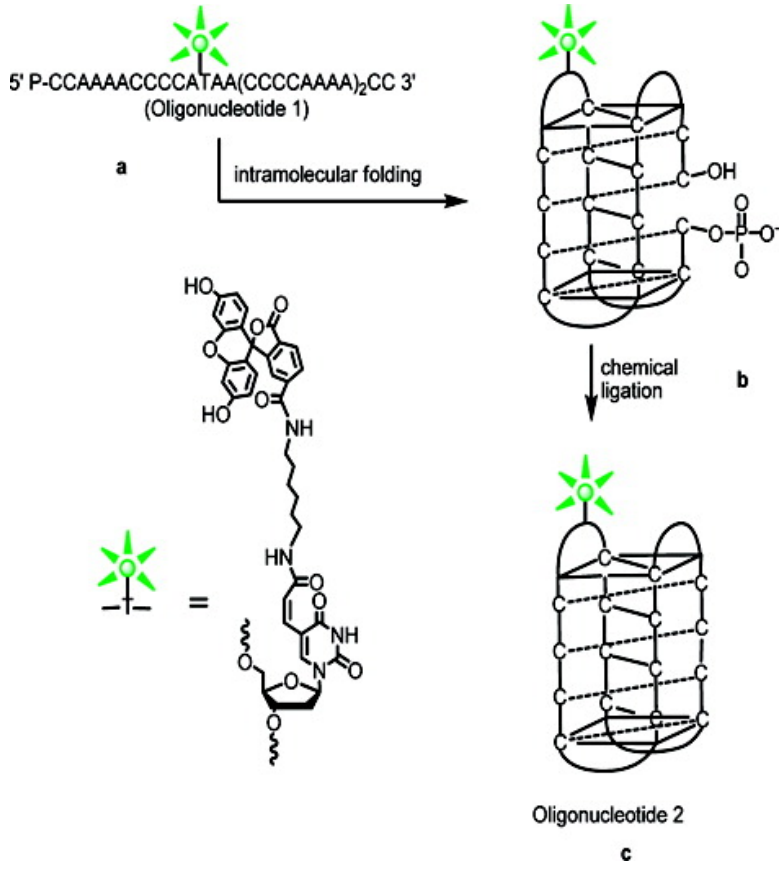

More About This Article

Additional resources and features associated with this article are available within the HTML version:

ACS Publications
High quality. High impact.

Bioconjugate Chemistry is published by the American Chemical Society. 1155 Sixteenth Street N.W., Washington, DC 20036

Subscriber access provided by SHEMYAKIN-OVCHINNIKOV INST

- Supporting Information
- Access to high resolution figures
- Links to articles and content related to this article
- Copyright permission to reproduce figures and/or text from this article

View the Full Text HTML

ACS Publications
High quality. High impact.

Bioconjugate Chemistry is published by the American Chemical Society. 1155 Sixteenth Street N.W., Washington, DC 20036

COMMUNICATIONS

Synthesis and Characterization of Circular Structures of i-Motif Tagged with Fluoresceins

Tianyan Zhou,[†] Xinming Li,*[,‡] Magdeline Tao Tao Ng,[§] Yifan Wang,[§] Ngee Mien Quek,[‡] Ji Luo,[‡] Weixing Yuan,[‡] Choon-Hong Tan,[§] Huaqiang Zeng,[§] and Tianhu Li*[,‡]

State Key Laboratory of Natural and Biomimetic Drugs, (Peking University), 38 Xueyuan Road, Haidian District, Beijing 100191, The People's Republic of China, Division of Chemistry and Biological Chemistry, School of Physical & Mathematical Sciences, Nanyang Technological University, 21 Nanyang Link, Singapore 637371, and Department of Chemistry, National University of Singapore, 3 Science Drive 3, Singapore 117543. Received October 23, 2008; Revised Manuscript Received January 27, 2009

Synthesis of a fluorescein-tagged circular structure of i-motif was accomplished during our investigations. The backbone circularity of this molecular probe and the presence of the fluorescent moiety within its structure were also confirmed through exonuclease hydrolysis and fluorescence spectroscopy.

Held together by hemiprotonated $C-C^+$ base pairing, i-motif is a four-stranded structural entity composed of two parallel-stranded duplexes zipped together in an antiparallel orientation (*1*−*15*). In vitro studies in the past demonstrated that such a tetraplex structural assembly could form by human telomere repeats $[d(C_3TAA)_n]$ and many other biologically significant cytosine-rich sequences (*8*−*15*) under some physiological-like conditions. Further investigations illustrated that some proteins isolated from *Drosophila* could selectively interact with cytosine-rich repeats of the centromere (*16*). In addition, the cytosine-rich strands of the human telomere were reportedly capable of being bound by some human nuclear proteins such as hnRNP K and ASF/SF2 (*17*). Consequently, it has been assumed that i-motif structures could play some significant roles in certain biological processes (*18*). With the aim of developing molecular probes that could be used to identify new types of i-motif-binding proteins, fluorescein-tagged circular i-motif was constructed in our laboratory recently. We present herein the design and synthesis of these new types of fluorescein-containing circular oligonucleotides as well as characterizations of these circular molecular probes by using exonuclease VII and fluorescence spectroscopy. It is our expectation that such newly designed probes could be useful for identifying a new i-motif-binding protein as well as determining the location and distribution of i-motif-binding proteins in acidic cancer cells upon the introduction of these probes through microinjection.

Our approaches for synthesizing a circular i-motif structure tagged with a fluorescein moiety (oligonucleotide **2**) are illustrated in Figure 1. A linear 32-mer oligonucleotide containing a fluorescein moiety covalently linked to carbon-5 of a thymine (oligonucleotide **1** in Figure 1a) was accordingly designed in our studies. The 5′-phosphate and 3′-hydroxyl ends of oligonucleotide **1** would be proximal to each other once this

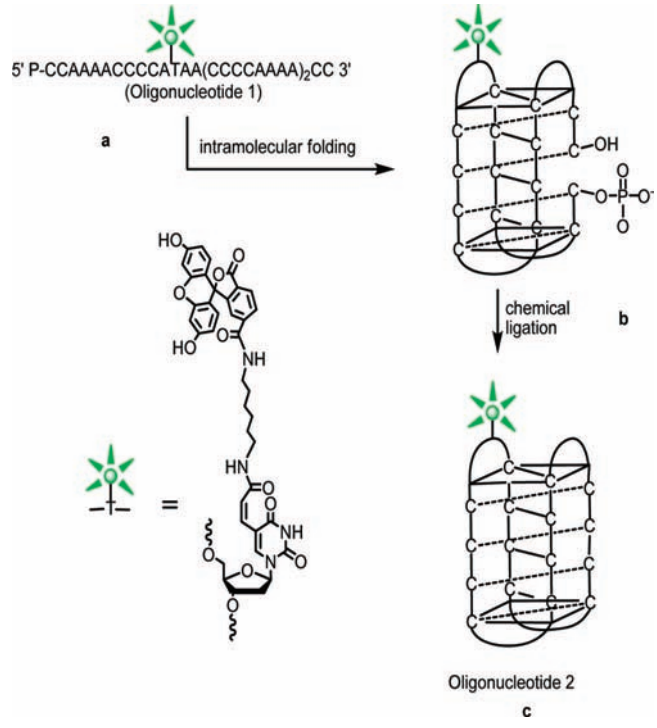

Figure 1. Schematic representation of the synthesis of a fluorescein-tagged circular structure of i-motif.

oligonucleotide self-assembles into intramolecular i-motif conformation (Figure 1b) under slightly acidic conditions (*1*, *2*). A new phosphodiester bond was expected to form between 5′-phosphate and 3′-hydroxyl ends upon the subsequent chemical activation. A mixture was accordingly prepared during our investigation that contained 1 μM sequence A, 100 mM MES (pH 5.0), and 50 mM KCl. This solution was heated next to 90 °C and kept at the same temperature for 3 min followed by cooling the mixture to 25 °C over 2 h to allow the formation of the i-motif structure (Figure 1b). The chemical ligation reactions

* xmli@ntu.edu.sg; thli@ntu.edu.sg.
[†] Peking University.
[‡] Nanyang Technological University.
[§] National University of Singapore.

10.1021/bc8004599 CCC: $40.75 © 2009 American Chemical Society
Published on Web 03/30/2009

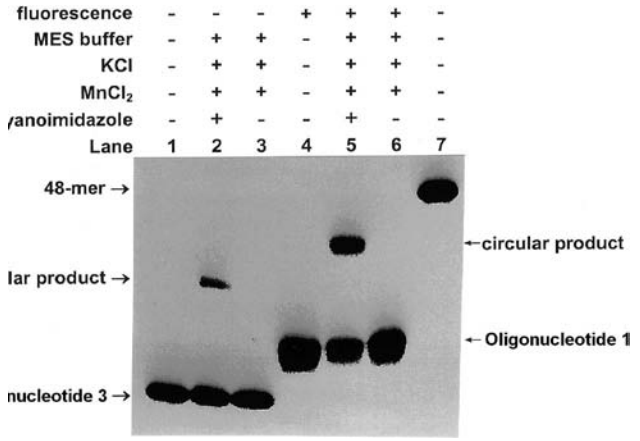

Figure 2. Electrophoretic analysis of the fluorescein-tagged circular structure of i-motif constructed through chemical ligation reactions. A linear precursor (oligonucleotide **1** or oligonucleotide **3**) with free 5′-hydroxyl terminus was labeled with [γ-^{32}P] ATP (GE Healthcare) at its 5′-end catalyzed by T4 polynucleotide kinase (New England Biolabs). A mixture containing 100 mM MES (pH 5.0) and 50 mM KCl and 1 μM linear precursor (oligonucleotide **1** or oligonucleotide **3**) was then kept at 90 °C for 3 min and further allowed to cool down to 25 °C over 120 min. The chemical ligation reactions were next initiated by addition of *N*-cyanoimidazole in the presence of $MnCl_2$, and the resultant solution contains 500 nM annealed linear precursor (oligonucleotide **1** or oligonucleotide **3**), 100 mM MES (pH 5.0), 50 mM KCl, 10 mM $MnCl_2$, and 10 mM *N*-cyanoimidazole. After being further incubated at 4 °C for 24 h, the reaction mixtures were analyzed by polyacrylamide gel electrophoresis (20%) followed by visualization using a PhosphorImager (Typhoon Trio, GE Healthcare). Lane 1: linear prescusor oligonucleotide (oligonucleotide **3**) alone. Lane 2: mixture of ligation reaction containing non-fluorescein-tagged linear oligonucleotide (oligonucleotide **3**). Lane 3: same reaction as in lane 2 except for the absence of **N**-cyanoimidazole. Lane 4: linear precursor oligonucleotide (oligonucleotide **1**) alone. Lane 5: mixture of ligation reaction containing fluorescein-tagged linear oligonucleotide (oligonucleotide **1**). Lane 6: same reaction as the one loaded in lane 5 except for the absence of **N**-cyanoimidazole. Lane 7: 48-mer oligonucleotide as a molecular weight marker.

were then initiated by addition of *N*-cyanoimidazole in the presence of $MnCl_2$ (*19*−*21*). After being further incubated at 4 °C for 24 h, the reaction was terminated by adding loading buffer. The resultant ligation products were analyzed by polyacrylamide gel electrophoresis.

As illustrated in Figure 2, a slow-moving band was observed (upper band of lane 5) when the ligation reaction of oligonucleotide **1** (Figure 1b) was activated by addition of *N*-cyanoimidazole, which corresponds to the desired fluorescein-labeled circular i-motif (*22, 23*) (Figure 1c). For comparison, a linear oligonucleotide (5′-pCCAAAACCCCATAACCCCAAAACCCCAAAACC-3′, oligonucleotide **3**) that contains no fluorescent tag was also designed and circularized (lane 2) during our investigations. As shown in Figure 2, a new band was generated as well in the circularization processes of oligonucleotide **3**. It is worth noting that the circularization product obtained from oligonucleotide **1** (fluorescein-tagged oligonucleotide) (lane 5) has a slower rate of mobility than that of oligonucleotide **3** (non-fluorescein-tagged oligonucleotide) (lane 2). The possession of an extra fluorescein moiety within oligonucleotide **1** could be the cause of the mobility shift difference between these two circular products (Figure 1c).

With the aim of confirming the absence of open ends in oligonucleotide **2**, the newly formed ligation product (upper band in lane 5 of Figure 2) was purified and further hydrolyzed with exonuclease VII (an exodeoxyribonuclease that degradates linear DNA from both 3′ and 5′ termini). As seen in Figure 3, there was an absence of degradation product observed when the purified ligation product was incubated with exonuclease VII

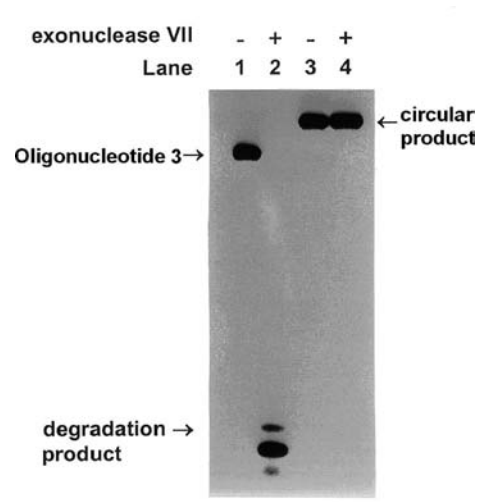

Figure 3. Hydrolysis of purified fluorescein-tagged circular i-motif (oligonucleotide **2**) by exonuclease VII. The ^{32}P-labeled reaction products in the upper band in lane 5 in Figure 2 were cut out and further purified. Solutions containing 100 mM Tris-acetate, 100 mM potassium phosphate, 16.6 mM ethylenediamine tetraacetic acid, and 20 mM 2-sulfanylethanol, pH 7.9, 10 units of exonuclease VII, and the newly purified ^{32}P-labeled oligonucleotides were then incubated at 37 °C for 2 h. The hydrolysis products were further analyzed using polyacrylamide gel electrophoresis (20%). Lane 1: 32-mer linear precursor oligonucleotide (oligonucleotide **3**) alone. Lane 2: the reaction mixture of 32-mer linear precursor oligonucleotide (oligonucleotide **3**) and exonuclease VII. Lane 3: fluorescein-tagged circular products (oligonucleotide **2**) alone. Lane 4: the reaction mixture of purified fluorescein-tagged circular products (oligonucleotide **2**) and exonuclease VII.

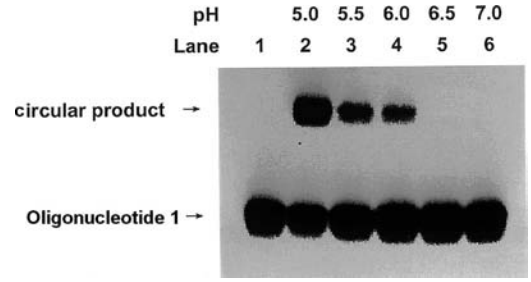

Figure 4. pH dependency of the circularization reaction of fluorescein-tagged linear oligonucleotide (oligonucleotide **1**). Ligation reactions were carried out in the same way as the one loaded in lane 5 in Figure 2 except that pH values of the buffer solutions were 5.0 (lane 2), 5.5 (lane 3), 6.0 (lane 4), 6.5 (lane 5), and 7.0 (lane 6), respectively. Lane 1: linear precursor oligonucleotide (oligonucleotide **1**) alone.

(lane 4 in Figure 3). For comparison, oligonucleotide **3** (a linear precursor) was also degraded by exonuclease VII under the same reaction conditions, which led to the complete disappearance of this linear precursor and generation of fast-moving degradation products (lane 2 in Figure 3). The complete resistance of the purified ligation product (oligonucleotide **2**) to the hydrolysis by this exonuclease is the indication that there is absence of open terminus within its backbone (*24*).

In addition, the variation of pH value on our circularization reactions was examined during our investigations. As shown in Figure 4, the efficiency of these ligation reactions decreased with the increase of pH values of the corresponding buffer solutions. The circularization reaction of oligonucleotide **1** proceeded in 45%, 11%, and 6% yields at pH 5 (lane 2), pH 5.5 (lane 3), and pH 6.0 (lane 4), respectively, while there were no circularization products from the reaction observable at pH 6.5 (lane 5) and pH 7.0 (lane 6). The above observations suggest

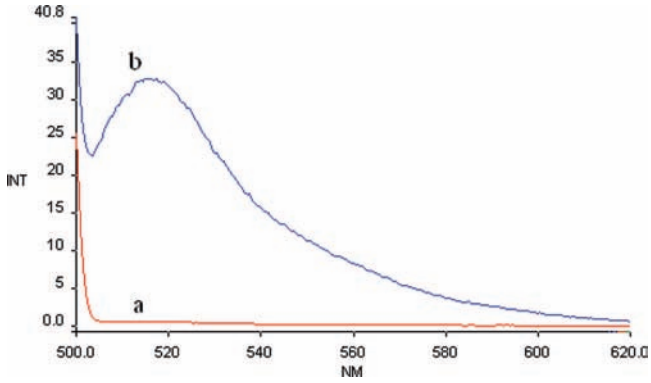

Figure 5. Fluorescence emission spectra of fluorescein-labeled circular i-motif (oligonucleotide **2**) (a) and non-fluorescein-labeled circular oligonucleotide (b). Samples containing 1 μM oligonucleotides and 10 mM Tris buffer (pH 7.0) were examined at 20 °C with excitation set at 495 nm using a fluorescence spectrometer (Perkin-Elmer LS 55).

that the formation of the i-motif structure is a prerequisite for the i-motif-based ligation reactions (*1*−*15*).

With the aim of confirming that the molecular moiety of fluorescein was indeed present in oligonucleotide **2**, fluorescence spectroscopic examinations were carried out in our studies. As seen in Figure 5, oligonucleotide **2** displayed an emission maximum at 520 nm when excited at 495 nm wavelength. For comparison, the circular product of oligonucleotide **3** (a non-fluorescence-tagged oligonucleotide) was also examined during our studies, which lacks emission from 500 to 620 nm. In addition, MALTI-TOF mass spectroscopic examination on oligonucleotide **2** and oligonucleotide **1** was carried out during our investigations. It turned out that the obtained molecular weights of the ligation product (oligonucleotide **2** in Figure 1) and its linear precursor (oligonucleotide **1** in Figure 1) were 10 145.35 Da (calculated molecular weight: 10 141.8 Da) and 10 163.09 Da (calculated molecular weight: 10 159.8 Da), respectively. The observed molecular weight difference between oligonucleotide **2**and oligonucleotide **1** was ∼18, which is consistent with the suggestion that a condensation reaction took place between the two termini of oligonucleotide **1**.

In conclusion, circular i-motif structure tagged with fluorescein was synthesized in our laboratory through chemical ligation reactions. Our subsequent studies confirmed that this newly obtained oligonucleotide resists the hydrolysis by exonucleases and the fluorescent moiety is indeed present in the ligation product. Since many cancer cells are acidic (*25*−*27*), it is our expectation that these newly designed fluorescein-labeled circular i-motifs could serve as useful probes for identifying new types of i-motif-interacting enzymes and other functional proteins in these fast-dividing cells.

ACKNOWLEDGMENT

The authors would like to express their gratitude to Ministry of Education of Singapore and Nanyang Technological University for financial support (ARC and SUG to T.L.).

Supporting Information Available: Additional experimental details about oligonucleotide **1**. This material is available free of charge via the Internet at http://pubs.acs.org.

LITERATURE CITED

(1) Gehring, K., Leroy, J.-L., and Gueron, M. (1993) A tetrameric DNA structure with protonated cytosine-cytosine base pairs. *Nature 363*, 561–564.

(2) Kang, C., Berger, I., Lockshin, C., Ratliff, R., Moyzis, R., and Rich, A. (1995) Stable loop in the crystal structure of the intercalated four-stranded cytosine-rich metazoan telomere. *Proc. Natl. Acad. Sci. U.S.A. 92*, 3874–3878.

(3) Ahmed, S., Kintanar, A., and Henderson, E. (1994) Human telomeric C-strand tetraplexes. *Nat. Struct. Mol. Biol. 1*, 83–88.

(4) Mergny, J.-L. (1999) Fluorescence energy transfer as a probe for tetraplex formation: the i-motif. *Biochemistry 38*, 1573–1581.

(5) Kanaori, K., Maeda, A., Kanehara, H., Tajima, K., and Makino, K. (1998) 1H nuclear magnetic resonance study on equilibrium between two four-stranded solution conformations of short d(C_nT). *Biochemistry 37*, 12979–12986.

(6) Feigon, J. (1993) A new DNA quadruplex. *Curr. Biol. 3*, 611–613.

(7) Mergny, J.-L., Lacroix, L., Han, X., Leroy, J.-L., and Helene, C. (1995) Intramolecular folding of pyrimidine oligodeoxynucleotides into an i-DNA motif. *J. Am. Chem. Soc. 117*, 8887–8898.

(8) Guo, K., Pourpak, A., Beetz-Rogers, K., Gokhale, V., Sun, D., and Hurley, L. H. (2007) Formation of pseudosymmetrical G-quadruplex and i-motif structures in the proximal promoter region of the *RET* oncogene. *J. Am. Chem. Soc. 129*, 10220–10228.

(9) Mathur, V., Verma, A., Maiti, S., and Chowdhury, S. (2004) Thermodynamics of *i*-tetraplex formation in the nuclease hypersensitive element of human *c-myc* promoter. *Biochem. Biophys. Res. Commun. 320*, 1220–1227.

(10) Jolad, V. V., Murad, F., Arnold, K. J. R. P., and Fisher, J. (2005) Solution conformation of d($C_4ACAC_4TGT)_2$; an intramolecularly folded i-motif from the insulin minisatellite. *Org. Biomol. Chem. 3*, 2234–2236.

(11) Kanaori, K., Shibayama, N., Gohda, K., Tajima, K., and Makino, K. (2001) Multiple four-stranded conformations of human telomere sequence d(CCCTAA) in solution. *Nucleic Acids Res. 29*, 831–840.

(12) Phan, A. T., Gueron, M., and Leroy, J.-L. (2000) The solution structure and internal motions of a fragment of the cytidine-rich strand of the human telomere. *J. Mol. Biol. 299*, 123–144.

(13) Catasti, P., Chen, X., Deaven, L. L., Moyzis, R. K., Bradbury, E. M., and Gupta, G. (1997) Cystosine-rich strands of the insulin minisatellite adopt hairpins with intercalated Cytosine$^+$·Cytosine pairs. *J. Mol. Biol. 272*, 369–382.

(14) Xu, Y., and Sugiyama, H. (2006) Formation of the G-quadruplex and i-motif structures in retinoblastoma susceptibility genes (Rb). *Nucleic Acids Res. 34*, 949–954.

(15) Khan, N., Avino, A., Tauler, R., Gonzalez, C., Eritja, R., and Gargallo, R. (2007) Solution equilibria of the i-motif-forming region upstream of the B-cell lymphoma-2 P1 promoter. *Biochimie 89*, 1562–1572.

(16) Cortes, A., Huertas, D., Fanti, L., Pimpinelli, S., Marsellach, F. X., Pina, B., and Azorin, F. (1999) DDP1, a single-stranded nucleic acid-binding protein of *Drosophila*, associates with pericentric heterochromatin and is functionally homologous to the yeast Scp160p, which is involved in the control of cell ploidy. *EMBO J. 18*, 3820–3833.

(17) Lacroix, L., Liénard, H., Labourier, E., Djavaheri-Mergny, M., Lacoste, J., Leffers, H., Tazi, J., Helene, C., and Mergny, J.-L. (2000) Identification of two human nuclear proteins that recognise the cytosine-rich strand of human telomeres *in vitro*. *Nucleic Acids Res. 28*, 1564–1575.

(18) Nonin, S., Phan, A. T., and Leroy, J.-L. (1997) Solution structure and base pair opening kinetics of the i-motif dimer of d(5mCCTTTACC): a noncanonical structure with possible roles in chromosome stability. *Structure 5*, 1231–1246.

(19) Luebke, K. J., and Dervan, P. B. (1989) Nonenzymatic ligation of oligodeoxyribonucleotides on a duplex DNA template by triple-helix formation. *J. Am. Chem. Soc. 111*, 8733–8735.

(20) Luebke, K. J., and Dervan, P. B. (1992) Nonenzymatic ligation of double-helical DNA by alternatestrand triple helix formation. *Nucleic Acids Res. 20*, 3005–3009.

(21) Liu, D., Chen, J., Lee, A. L. F., Chow, L. M. C., Chan, A. S. C., and Li, T. (2003) Small circular oligodeoxynucleotides

achieved from self-assembling entities. *Angew. Chem., Int. Ed. 42*, 797–799.
(22) Wang, S., and Kool, E. T. (1994) Circular RNA oligonucleotides. Synthesis, nucleic acid binding properties, and a comparison with circular DNAs. *Nucleic Acids Res. 22*, 2326–2333.
(23) Li, T., Liu, D., Chen, J., Lee, A. L. F., Qi, J., and Chan, A. S. C. (2001) Construction of circular oligodeoxyribonucleotides on the new structural basis of i-motif. *J. Am. Chem. Soc. 123*, 12901–12902.
(24) Kool, E. T. (1991) Molecular recognition by circular oligonucleotides: increasing the selectivity of DNA binding. *J. Am. Chem. Soc. 113*, 6265–6266.
(25) Schornack, P. A., and Gillies, R. J. (2003) Contributions of cell metabolism and H^+ diffusion to the acidic pH of tumors. *Neoplasia 5*, 135–145.
(26) Wike-Hooley, J. L., Haveman, J., and Reinhold, H. S. (1984) The relevance of tumour pH to the treatment of malignant disease. *Radiother. Oncol. 2*, 343–366.
(27) Glunde, K., Gugginoy, S. E., Solaiyappan, M., Pathak, A. P., Ichikawaz, Y., and Bhujwalla, Z. M. (2003) Extracellular acidification alters lysosomal trafficking in human breast cancer cells. *Neoplasia 5*, 533–545.

BC8004599

SUPPORTING INFORMATION

Synthesis and characterization of circular structures of i-motif tagged with fluoresceins

Tianyan Zhou[†], Xinming Li[‡*], Magdeline Tao Tao Ng[§], Yifan Wang[§], Weixing Yuan[‡], Choonhong Tan[§], Huaqiang Zeng[§] and Tianhu Li[‡*]

[†]State Key Laboratory of Natural and Biomimetic Drugs
Peking University
38 Xueyuan Road, Haidian District
Beijing 100191
The People's Republic of China

[‡]Division of Chemistry and Biological Chemistry
School of Physical & Mathematical Sciences
Nanyang Technological University
21 Nanyang Link
Singapore 637371

[§]Department of Chemistry
National University of Singapore
3 Science Drive 3
Singapore 117543

Experimental Section

General Methods. All of our linear 32-mer oligonucleotide containing a fluorescein moiety covalently linked to carbon-5 of a thymine (Oligonucleotide 1 in Fig. 1) were purchased from Integrated DNA Technologies, Inc. (USA). A mixture containing 100 mM MES (pH 5.0) and 50 mM KCl and 1 μM linear precursor (Oligonucleotide 1) was kept at 90 °C for 3 min and was then allowed to cool down to 25 °C over 120 min. The chemical ligation reactions were next initiated by addition of N-cyanoimidazole in the presence of $MnCl_2$, and the resultant solution contains 500 nM annealed linear precursor (Oligonucleotide 1), 100 mM MES (pH 5.0), 50 mM KCl, 10 mM $MnCl_2$ and 10 mM *N*-cyanoimidazole. The reaction mixture was further incubated at 4 ˚C for 24 h and analyzed next using denaturing polyacrylamide gel electrophoresis. The ligating reagent used in the studies, N-cyanoimidazole, was prepared according to literature-reported procedures (20) starting with cyanogen bromide.

Bioconjugate Chemistry 20th Anniversary

Subscriber access provided by SHEMYAKIN-OVCHINNIKOV INST

Article

Folate Receptor Targeted Bimodal Liposomes for Tumor Magnetic Resonance Imaging

Nazila Kamaly, Tammy Kalber, Maya Thanou, Jimmy D. Bell, and Andrew D. Miller

Bioconjugate Chem., **2009**, 20 (4), 648-655• DOI: 10.1021/bc8002259 • Publication Date (Web): 10 March 2009

Downloaded from http://pubs.acs.org on May 8, 2009

More About This Article

Additional resources and features associated with this article are available within the HTML version:

- Supporting Information
- Access to high resolution figures
- Links to articles and content related to this article
- Copyright permission to reproduce figures and/or text from this article

View the Full Text HTML

ACS Publications
High quality. High impact.

Bioconjugate Chemistry is published by the American Chemical Society. 1155 Sixteenth Street N.W., Washington, DC 20036

ARTICLES

Folate Receptor Targeted Bimodal Liposomes for Tumor Magnetic Resonance Imaging

Nazila Kamaly,[†,‡] Tammy Kalber,[‡] Maya Thanou,[†] Jimmy D. Bell,[‡] and Andrew D. Miller*[,†,§]

Imperial College Genetic Therapies Centre, Department of Chemistry, Flowers Building, Armstrong Road, Imperial College London, London, SW7 2AZ, Metabolic and Molecular Imaging Group, Imaging Sciences Department, MRC Clinical Sciences Centre, Imperial College London, Hammersmith Hospital, London, W12 0HS, and ImuThes Ltd, Flowers Building, Armstrong Road, London SW7 2AZ, United Kingdom. Received June 1, 2008; Revised Manuscript Received February 8, 2009

Folate-targeted bimodal paramagnetic and fluorescent liposomes were developed and showed enhanced accumulation in a folate receptor expressing tumor model. These bimodal liposomes were composed of both a paramagnetic and a fluorescent lipid, and utilized a PEG-lipid amphiphile for prolonged in vivo circulation. The particles were formulated to ensure a size distribution of approximately 100 nm with a low polydispersity index. IGROV-1 cells were used to induce tumors in nude Balb/c mice, and the folate-targeted liposomes were injected intravenously. Rapid accumulation of the folate-targeted liposomes within the tumor tissue compared to nontargeted liposomes was observed. Furthermore, folate-labeled liposomes showed a 4-fold increase in tumor T_1 signal intensity at just 2 h postinjection with similar results being obtained for the nontargeted liposomes only 24 h postinjection. In addition, the folate-targeted liposomes were injected at half the nontargeted liposome dose, further demonstrating their effectiveness. Histological analysis of sectioned tumor slices revealed distinct fluorescence patterns between the targeted and nontargeted systems, with a more localized and hyperintense fluorescence signal observed from tumor sections post-folate-targeted liposome injections. These results demonstrate the effectiveness of folate targeting for dynamic real-time solid tumor MRI and provide insight into kinetics of targeted and nontargeted nanoparticles to solid tumors.

INTRODUCTION

Folate based targeting systems present an effective means of selectively delivering therapeutic or imaging agents to tumors (*1*−*11*). It has been shown that aggressive or undifferentiated tumors at an advanced stage have an increased folate receptor (FR) density, indicating that cancer therapy could benefit from the broad approach that FR mediated drug delivery offers (*12, 13*). The FR is overexpressed in several cancer types, such as brain, kidney, lung, and breast cancers, and, in particular, in epithelial carcinomas such as ovarian cancers (*14*). The FR ligand, folate (or folic acid), is a vitamin that is used for the biosynthesis of nucleotides and is utilized in high levels to meet the needs of proliferating cancer cells (*15*).

In addition to numerous drug delivery efforts, folate-targeted technology has been successfully applied to radio-imaging of therapeutic agents (*16*), fluorescence imaging of cancer cells (*17*), MRI contrast agents (*18*), and gadolinium liposomes (*19*). Choi et al. have demonstrated the use of folate-targeted iron oxide nanoparticles for the imaging of induced KB tumors and showed these particles to have a 38% signal intensity increase compared to controls (*20*). Successful tumor MRI with a nontargeted bimodal liposomal contrast agent was shown recently, whereby bimodal paramagnetic and fluorescent liposomes of ∼100 nm in size were seen to accumulate in a mouse xenograft model of ovarian cancer (*21*). Liposomes are able to accumulate within tumor tissue due to the widely reported enhanced permeation and retention effect (EPR) which relies on the passive accumulation of colloidal macromolecules of ∼40 kDa and above in tumors (*22*). The EPR effect arises due to aberrant tumor endothelium, which as a result of its "leakiness" allows the penetration of nanoparticles into tumor tissue. Liposome accumulation in tumor tissue could be improved through the use of receptor targeting moieties that are either postconjugated to the surface of liposomes or attached to lipids that become incorporated within the liposomal bilayer. Since FR binding affinity ($K_d = 1 \times 1^{-10}$ M) does not appear to be affected when its ligand, folate, is conjugated to an imaging agent or therapeutic moiety via its γ-carboxyl (*10, 23*), a folate ligand tethered onto the distal end of a lipidic PEG amphiphile allows for the development of a FR targeted liposomal system.

The human nasopharyngeal KB carcinoma cell line is considered to have the highest level of FR expression, yet the number of cases for this cancer are low in comparison to ovarian cancer, which has the highest frequency (>90% of cases) (*6*). In particular, the α-FR isoform which is a glycosyl phosphatidylinositol (GPI)-anchored membrane protein is highly expressed in ovarian carcinoma (*24*). Additionally, the α-FR isoform has also been shown to have a specific biomarker value, aiding in the identification of metastatic tumor site origin (*25*). Therefore, we were interested in using this receptor in order to test the efficacy of folate-targeted bimodal liposomes for the imaging of ovarian tumors using MRI. Folate-based liposomal drug delivery has been studied extensively (*7, 24, 26*); however,

* Author e-mail address: Nazila.Kamaly@imperial.ac.uk.
† Imperial College Genetic Therapies Centre.
‡ MRC Clinical Sciences Centre.
§ ImuThes Ltd.

10.1021/bc8002259 CCC: $40.75 © 2009 American Chemical Society
Published on Web 03/10/2009

the rate-enhancing effect of liposome accumulation in tumors due to folate targeting has not been studied dynamically in real time to a great extent. Effective tumor signal enhancement was anticipated, since the FR is expressed in significantly lower amounts in normal tissue, limited mainly to kidney tubuli, lung epithelium, and placenta tissue (*27*).

To asses the value of the addition of a targeting ligand on the rate and extent of accumulation of liposomes in solid tumors, FR targeted bimodal fluorescent and paramagnetic liposomes were formulated and compared to nontargeted liposomes by both MRI and fluorescence microscopy.

EXPERIMENTAL RESULTS

Materials. Phosphatidylethaolamine-lissamine rhodamine B (DOPE-Rhodamine), 1,2-dioleoyl-*sn*-glycero-3-phosphocholine (DOPC), 1,2-distearoyl-*sn*-glycero-3-phosphoethanolamine-*N*-methoxy(poly(ethylene glycol))-2000 (DSPE-PEG2000), and 1,2-distearoyl-*sn*-glycero-3-phosphoethanolamine-*N*-[folate(poly-(ethylene glycol))-2000] (DSPE-PEG(2000)folate, ammonium salt) were purchased from Avanti Polar Lipids Inc. (Alabaster, AL, USA). All other chemicals were of analytical grade or the best grade available and purchased from Sigma-Aldrich (UK). Gadolinium (III) 2-{4,7-bis-carboxymethyl-10-[(*N*,*N*-distearylamidomethyl-*N*′-amido-methyl]-1,4,7,10-tetra azacyclododec-1-yl}-acetic acid (Gd.DOTA.DSA) was synthesized in-house as shown previously (*21*).

General Procedures. Liposome zeta potentials were recorded on a Nanoseries Nano-ZS zetasizer (Malvern instruments). Microscopy experiments were conducted on a Nikon Eclipse E600 microscope. FACS analysis was conducted on a Becton Dickinson FACSCalibur machine. ICP-AES experiments were run on a Varian VISTA PRO instrument. All MRI experiments were conducted on a 4.7 T Magnex magnet (Oxford, UK) with a Varian Unity Inova console (Palo Alto, CA, USA). All procedures on animals were carried out in accordance with UK Home Office regulations and the Guidance for the Operation of Animals (Scientific Procedures) Act (1986).

Liposome Preparations. All lipids were stored as stock solutions in anhydrous organic solvents ($CHCl_3$, MeOH, or a mixture of both), at −20 °C under argon. Liposomes were made with defined molar ratios of individual lipids to give a predetermined total lipid concentration of 15 (folate-targeted) or 30 (nontargeted) mg mL^{-1} in HEPES (20 mM, NaCl 135 mM, pH 6.5) for in vivo experiments. Targeted liposomes consisted of Gd.DOTA.DSA/DOPC/Cholesterol/DSPE-PEG2000/DSPE-PEG(2000)Folate/DOPE-Rhodamine 30/32/30/4/3/1 mol %, and nontargeted liposomes were made up of Gd.DOTA.DSA/DOPC/Cholesterol/DSPE-PEG2000/DOPE-Rhodamine 30/32/30/7/1 mol %. Appropriate volumes of each lipid stock were placed in a round-bottom flask (typically 5 mL) containing distilled $CHCl_3$ (500 μL) and stirred to ensure thorough mixing of the lipids. The solvent was slowly removed in vacuo to ensure production of an even lipid film. The film was rehydrated with buffer at a defined volume. The resulting solution was sonicated for 30 min (at 30 °C) for in vivo formulations in order to form gadolinium liposomes of appropriate size. For each preparation, the size of liposomes was measured by photon correlation spectroscopy (PCS) to ensure a size distribution of, on average, below 100 nm. Folate-targeted liposomes were prepared containing a total of ∼4.94 μmol of Gd and control nontargeted liposomes contained ∼9.87 μmol of Gd.

Zeta Potential Measurements of Folate-Targeted and Nontargeted Liposomes. Targeted or nontargeted liposomes were added to plastic electrode cuvettes (1 mL, total liposome concentration: 1.2 mg mL^{-1}) and their electrophoretic mobility measured. Measurements were carried out at 25 °C, on a Zetasizer Nanoseries, Nano-ZS.

Relaxivity Measurement of Folate-Targeted and Nontargeted Liposomes. Liposomes were prepared in HEPES (20 mM, NaCl, 135 mM, pH 6.5) buffer. These liposomes were prepared and diluted in order to obtain five different Gd atom concentrations ranging from 1.973 to 0.246 mM. The liposome solutions were placed in small Eppendorf tubes (200 μL), imaged at 4.7 T in the coronal plane, T_1 values obtained, and the molar relaxivity r_1 (mM^{-1} s^{-1}) determined. T_1 values were acquired using saturation recovery experiments performed with a standard spin−echo sequence and a 2 mm single slice acquisition (TR = 50, 100, 200, 300, 500, 700, 1200, 3000, 5000, 7000 ms, TE = 15 ms), number of signal averages; 2, FOV; 70 × 70 mm^2, collected into a matrix of 256 × 128.

Immunohistochemical Analysis of Folate Receptor Expression. At 48 h prior to FACS experiment, adherent IGROV-1, OVCAR-3, HeLa, and SKBR-3 cells were grown in RPMI media (folic acid free) with 10% FCS and 1% penicillin−streptomycin (Sigma-Aldrich). Cells were grown in 25 cm^3 culture flasks (5 × 10^5 cells per well, 5 mL of growth medium) and in a wet (37 °C) 10% CO_2/90% air atmosphere. The cells were grown until 80% confluence. The media was then removed and the cells washed with PBS. The cells were then treated with trypsin−EDTA (500 μL trypsin, 1 mM EDTA) for 2 min at 37 °C, then transferred to 25 mL Falcon tubes and centrifuged (1500 rpm for 5 min). The PBS was removed, and the cells were washed further with PBS and centrifuged (1500 rpm for 5 min). The cells were then incubated in 10% FCS, 1% NaN_3 solution (1 mL) for 1 h at 4 °C, then spun down (1500 rpm for 5 min), washed with PBS (1 mL), and then this washing step was repeated twice more. The primary antibody (mAb Mov18/ZEL, Axxora, UK) selective for the α-FR was then added to each Falcon (5 μg/mL in 3% BSA/PBS (total volume 1 mL)) and the cells incubated at 4 °C for 1 h (for each cell line, one tube contained no antibody). The cells were centrifuged (1500 rpm for 5 min) and washed with PBS (3 × 1 mL, followed by centrifugation), and the secondary antibody (goat antibody IgG, FITC conjugated, Santa Cruz Biotechnology, Inc., USA) was then added to the cells (1:1000 dilution, in 3% BSA/PBS (total volume 1 mL)) and the cells were incubated at 4 °C for a further hour. The cells were then washed with PBS (3 × 1 mL) and centrifuged (400 rpm for 5 min), diluted in 10% FCS/PBS 1% NaN_3 (1 mL), and analyzed for their FITC fluorescence on a flow cytometer.

Inductively Coupled Plasma−Atomic Emission Spectrometry (ICP-AES) Analysis of Cell Lysates Postincubation with Liposomes. At 48 h prior to gadolinium liposome uptake experiments, adherent IGROV-1 cells were grown in RPMI media (folic acid free) with 10% FCS and 1% penicillin−streptomycin (Sigma-Aldrich) in 48 welled plates. The cells were grown until 80% confluence. The media was then removed and replaced with fresh media (same volume as previous). Folate-targeted and nontargeted liposomes were added in a dose of 12 μg to each well, swirled to ensure even dispersion, and then incubated in a wet (37 °C) 10% CO_2/90% air atmosphere for 6 h. After liposome uptake, the cells were washed with PBS (2 × 200 μL) and then treated with lysis buffer (200 μL per well). Samples containing the cell lysate (200 μL) were submitted for ICP-AES measurements of ^{157}Gd content. Briefly, 150 μL of each sample was pipetted and diluted to 3.75 mL with 2% nitric acid to give a total dilution of 1 in 25 and then analyzed on a Varian VIST PRO instrument. All data were corrected for these dilutions, and a blank 2% nitric acid sample was also analyzed.

Mouse Tumor Model. IGROV-1 cells (5 × 10^6/1 mL PBS) were implanted into the flanks of 6−8 week old Balb/c nude mice for generation of subcutaneous tumors. After ∼2 weeks (estimated tumor weights 40−50 mg), the mice were anaesthetized with an isoflurane/O_2 mix and placed into a quadrature

^{1}H volume coil and positioned into the magnet. Baseline scans were obtained, and then the mice were injected intravenously via lateral tail vein with a 200 μL liposome solution (HEPES (20 mM, NaCl 135 mM, pH 6.5)) and imaged at 4.7 T (spin−echo sequence: TR = 400−2800 ms; TE = 10 ms; FOV = 45 × 45 cm^2; averages, 1; matrix size, 256 × 128; thickness, 2.0 mm; and 20 slices). The mice were imaged prior to injection to obtain baseline images and subsequently placed in the scanner at 2, 16, and 24 h postinjection intervals and scanned further.

Histology Experiments. Following MRI, the animals were sacrificed; and the tumors, livers, and kidneys were excised, frozen on liquid nitrogen, embedded in OCT (VWR) embedding fluid, and 10 μm thick sections cut, mounted on slides, and studied by fluorescence microscopy.

RESULTS

Folate Receptor Expression. In order to establish whether the IGROV-1 cell line, a human ovarian carcinoma cell line, expresses a sufficient level of the folate receptor, FACS analysis of four different cell lines was carried out. For this purposes, the α-folate receptor (α-FR) isoform, which is a folate transporter with restricted expression levels in normal tissues, was chosen. To measure the α-FR expression levels of the human ovarian cell lines IGROV-1, OVCAR-3, and HeLa (cervical cancer) cells, flow cytometry experiments were carried out. In addition to these cell lines, a breast cancer cell line (SKBR-3) was also analyzed as a negative control cell line with no α-FR expression. Cells were grown in folic acid free media and incubated with serum to block any nonspecific interactions. Immunostaining was carried out with a monoclonal antibody (mAb Mov18/ZEL) specific for the α-FR, and post incubation with this antibody, a secondary FITC labeled antibody (Goat antibody IgG, FITC conjugated), was allowed with the cells. Poststaining, the cells were fixed and analyzed by fluorescence microscopy.

From the FACS α-FR expression analysis (Figure 1), where all cell lines were cultured under the same standardized conditions using folate free cell culture medium, it was shown that the IGROV-1 cell line exhibited a distinctly higher level of α-FR expression. From these typical FACS data, the α-FR expression was measured to be in the order IGROV-1 ≫ OVCAR-3 > HeLa > SKBR-3 (three days postseeding).

Folate-Targeted Gadolinium Liposomes for Tumor Imaging. Having established the overexpression of the α-FR on the IGROV-1 cell line, folate-targeted gadolinium liposomes were prepared for specific cell receptor binding and uptake into IGROV-1 tumor cancer cells. These folate-targeted bimodal liposomes consisted of Gd.DOTA.DSA/DOPC/Cholesterol/DSPE-PEG2000/DSPE-PEG(2000)Folate/DOPE-Rhodamine 30/32/30/4/3/1 mol % (see Figure 2). The synthesis of Gd.DOTA.DSA, a lipidic T_1 MRI contrast agent, has been shown elsewhere (*21*). Briefly, Gd.DOTA.DSA is made from the metal-free ligand 2-{4,7-bis-carboxymethyl-10-[(*N*,*N*-distearylamidomethyl-*N*′-amidomethyl]-1,4,7,10-tetra-azacyclododec-1-yl}-acetic acid (DOTA.DSA) by the addition of a gadolinium source such as gadolinium chloride. DOTA.DSA is formed by amide coupling of *N*,*N*-distearylamidomethylamine with 2-(4,7,10-tris(2-*tert*-butyloxycarbonylmethyl)-1,4,7,10-tetra-azacyclododecan-1yl)acetic acid and the subsequent removal of the *tert*-butyl groups in acidic conditions (*21*).

Nontargeted bimodal control liposomes contained no targeting moiety and consisted of Gd.DOTA.DSA/DOPC/Cholesterol/DSPE-PEG2000/DOPE-Rhodamine 30/32/30/7/1 mol %. The serum aggregation of these liposomes was also assessed, and no significant change in liposome size was observed over a 24 h incubation period of folate-targeted and nontargeted liposomes in a 1:1 FCS/HEPES mixture at 37 °C (data not shown).

Relaxivity of Folate-Targeted Liposomes. The relaxivities of both the folate-targeted and nontargeted liposomes were measured by formulating liposomes with varying concentrations of the Gd.DOTA.DSA lipid to obtain five formulations with atomic Gd concentrations within the range 1.972 to 0.2466 mM. The r_1 and r_2 relaxivities measured for the folate-targeted liposomes were 1.30 mM^{-1} s^{-1} and 5.38 mM^{-1} s^{-1}, respectively. For the nontargeted liposomes, r_1 and r_2 were measured as 0.926 mM^{-1} s^{-1} and 5.096 mM^{-1} s^{-1}, respectively, and were comparable to the targeted liposomes relaxivities.

Zeta Potential Measurements. The zeta potentials of both the folate-targeted and nontargeted PEGylated liposomes were also obtained, and these values were found to be close to zero, indicating an overall neutral charge for these liposomes (zeta potential for folate-targeted liposomes was measured to be 3.21 ± 0.284 mV and that for the control nontargeted liposomes was 5.76 ± 0.0673 mV). These liposomes were also formulated using the thin-film technique and sonicated to obtain particles of approximately 100 nm in size with a polydispersity index of <0.5.

In Vitro IGROV-1 Cell Uptake Experiments. Having established that the IGROV-1 cell line overexpresses the FR receptor, to additionally ascertain the targeting efficacy of our folate ligand bearing liposomes to the IGROV-1 cell line, IGROV-1 cells were incubated with folate-targeted and nontargeted liposomes. After 5 h of incubation, the cells were washed and lysed, and the cell lysate destroyed with nitric acid and subjected to ICP-AES measurements of ^{157}Gd content. Figure 3 shows the amount of Gd in ppm that was measured from the cell lysate of IGROV-1 cells incubated with nontargeted liposomes (white bar), folate-targeted liposomes with 0.03 mol % folate lipid incorporated (black bar), and folate-targeted liposomes containing 3 mol % of the folate lipid (gray bar). It is evident that the higher folate ratio bearing targeted liposomes are taken up to a much greater degree by the IGROV-1 cells compared to the nontargeted liposomes and folate-targeted liposomes containing 100 times less folate-lipid.

In Vivo Tumor MRI. Folate-targeted Gd liposomes (total liposome concentration; 15 mg mL^{-1}) and nontargeted control liposomes (total liposome concentration; 30 mg mL^{-1}) were prepared in HEPES buffer (20 mM, NaCl, 135 mM, pH 6.5) and injected through the tail vein of tumor bearing mice, a method that ensures rapid entry of the liposomes into the blood circulation. Prior to injection, baseline MRI scans were obtained on a 4.7 T magnet in order to identify the tumor and measure T_1 baseline values. The mice were then imaged at 2, 16, and 24 h intervals postinjection. T_1-weighted images for each time point were obtained, and the percent signal enhancement as a result of the accumulation of the PEGylated gadolinium liposomes within the tumor tissue was calculated from T_1 values generated from the tumors. It was proposed that, due to the presence of the folate targeting moiety, an increase in tumor signal will be apparent postinjection by MRI, in comparison to the control liposomes (nontargeted). Indeed, this increase was apparent at just 2 h postinjection of the folate-targeted liposomes (see Figure 4).

The measured tumor T_1 values show that within just 2 h post i.v. injection the active and specific targeting effect of the folate liposomes is apparent and a substantial 65% T_1 reduction is achieved within 16 h postinjection compared to ∼15% for the nontargeted liposomes. This substantial enhancement is observed despite injection of folate-targeted liposomes at half the concentration of the nontargeted liposomes.

Figure 5 shows images of IGROV-1 tumors from mice injected with folate-targeted liposomes and control liposomes. The tumor signal enhancement of the targeted liposomes is visible at just 2 h postinjection, and this effect is persistent up to the 24 h imaging end point.

Histology of IGROV-1 Tumors. Following MRI, the mice were then sacrificed and the tumors excised, frozen, fixed, and

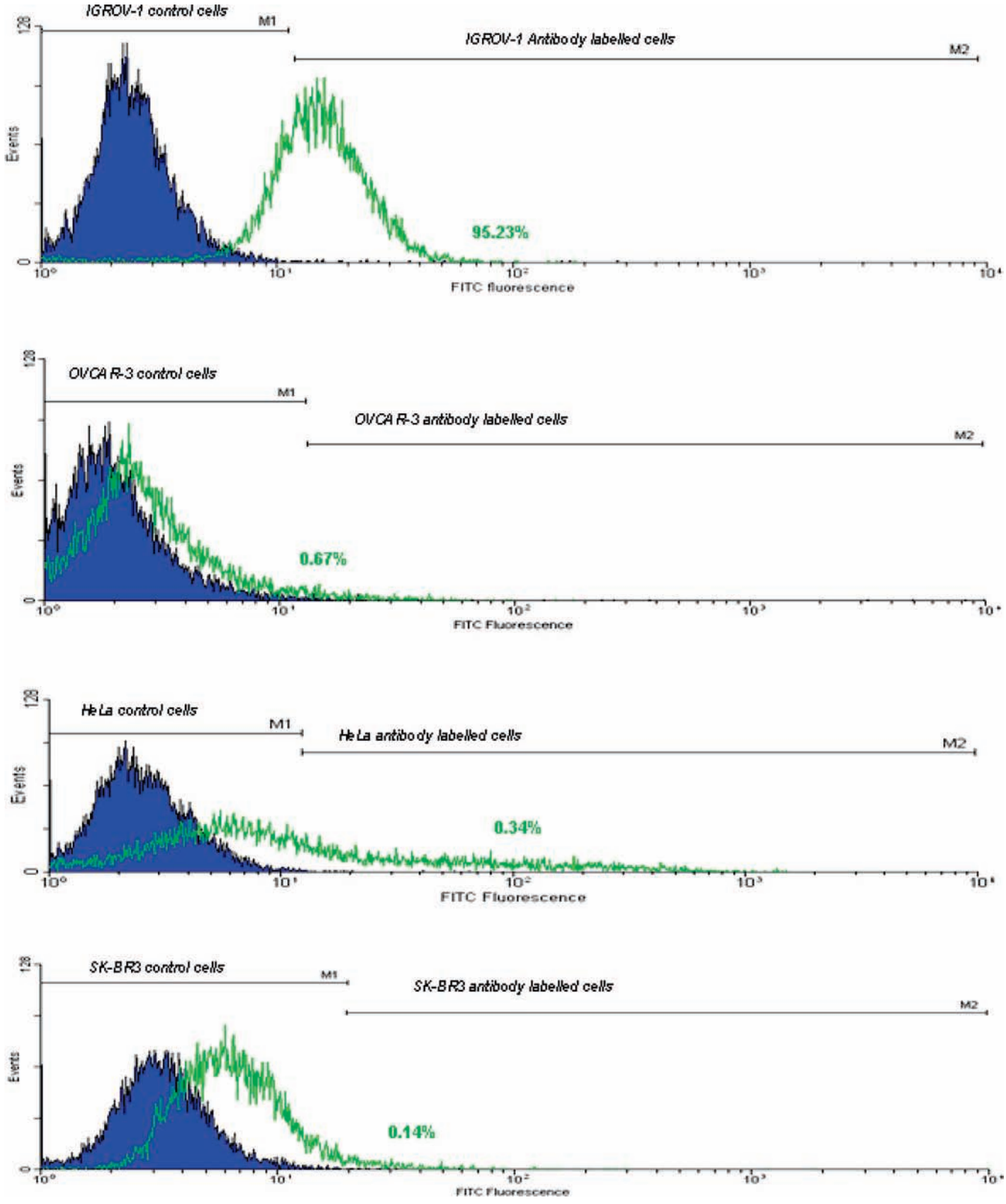

Figure 1. FACS analysis of four cell lines for α-FR expression levels.

sectioned for histological analysis. The inclusion of the fluorescent DOPE-Rhodamine lipid in the liposome formulation allows for postmortem analysis by fluorescence microscopy, which is a sensitive indication for the presence of liposomes within the tumor tissue. Figure 6 presents fluorescence microscopy images of sectioned tumors 24 h post folate-liposome injection. The presence of intense red fluorescence from these sectioned tumor slices is indicative of the accumulation of the targeted liposomes in the tumor tissue. The T_1 tumor signals measured (Figure 4) indicate a rapid accumulation of the targeted liposomes, and histological results show that the folate-targeted gadolinium liposomes may be accumulating at areas of hyperpermeability within the viable tumor tissue. In addition to the sectioned tumors, the liver and kidney tissue of the folate-

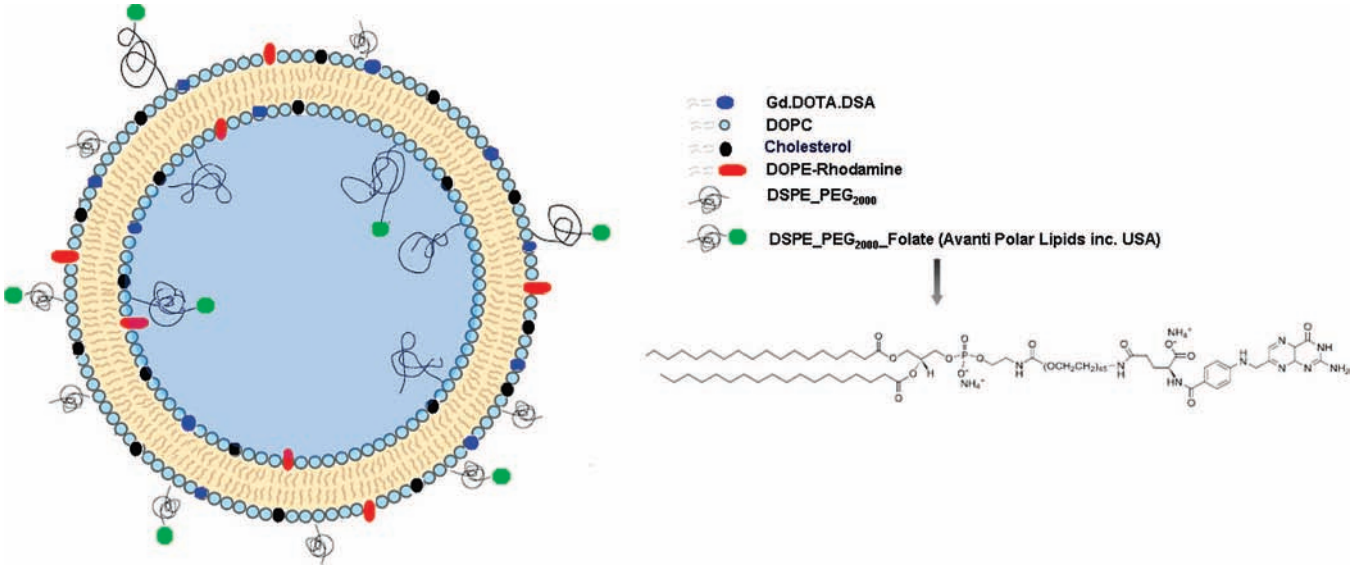

Figure 2. Folate-targeted gadolinium liposomes for IGROV-1 tumor imaging.

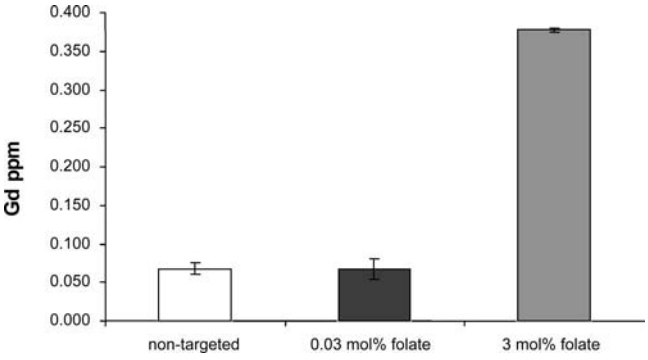

Figure 3. ICP-AES measurements of cellular ^{157}Gd content 6 h post-uptake of low ratio folate-targeted liposomes (black bar), high folate ratio targeted liposomes (gray bar), and nontargeted liposomes (white bar).

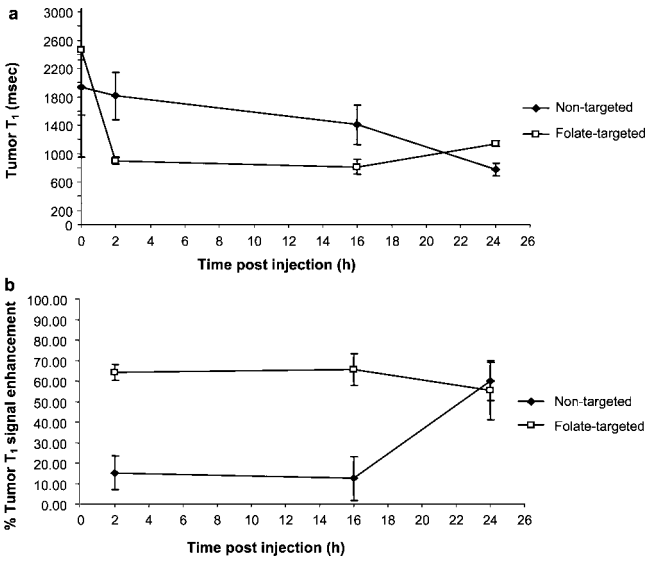

Figure 4. Mouse tumor signal enhancement with folate-targeted and nontargeted gadolinium liposomes: (a) tumor T_1 measurements at 4.7 T, (b) signal enhancement (%) calculated from mean tumor T_1 values pre- and post-liposome injection.

targeted liposome injected mice were also removed and analyzed for their fluorescence (see Figure 7). The results revealed that

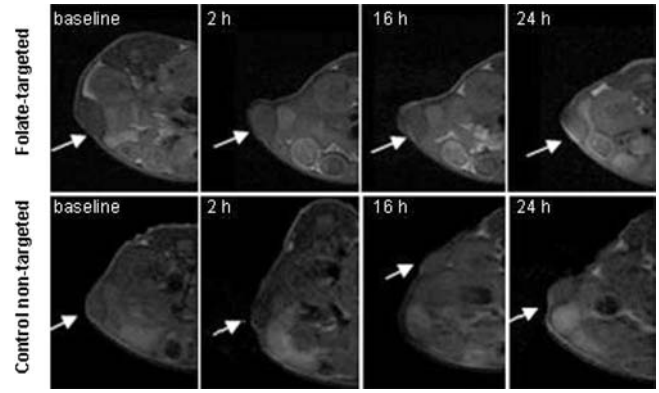

Figure 5. MRI of IGROV-1 tumor bearing Balb/C nude mice: top images are of mice injected with folate-targeted liposomes; bottom images are from control mice injected with nontargeted liposomes (white arrow shows location of tumor).

there is very little accumulation of the folate-targeted liposomes within the liver or kidney tissues 24 h post-administration and suggests their clearance from the liver and their major accumulation in tumor tissue as observed at this time point.

DISCUSSION

Liposomes not only are versatile carriers used successfully for drug delivery, but also present great potential when used in molecular imaging, as thousands of contrast agent molecules can be incorporated within a single particle, increasing contrast agent concentration. In this study, bimodal ligand-targeted paramagnetic and fluorescent liposomes were prepared and used to image xenograft tumors in mice. At just 2 h postinjection the folate-targeted liposomes had achieved a similar signal enhancement attained by the nontargeted liposomes at 24 h postinjection. In the case of the targeted liposomes, the folate ligand binds to the FR receptor in the IGROV-1 tumor, and as a result, the folate-targeted liposomes are effectively "halted" in place through receptor binding and are therefore unavailable for recirculation. We believe that this receptor-binding effect explains the rapid tumor signal enhancement at just 2 h postinjection of the folate-targeted liposomes (Figure 4). The nontargeted liposomes, on the other hand, may be able to recirculate in the blood and undergo several passages before becoming trapped and accumulating in the tumor. Since a 60%

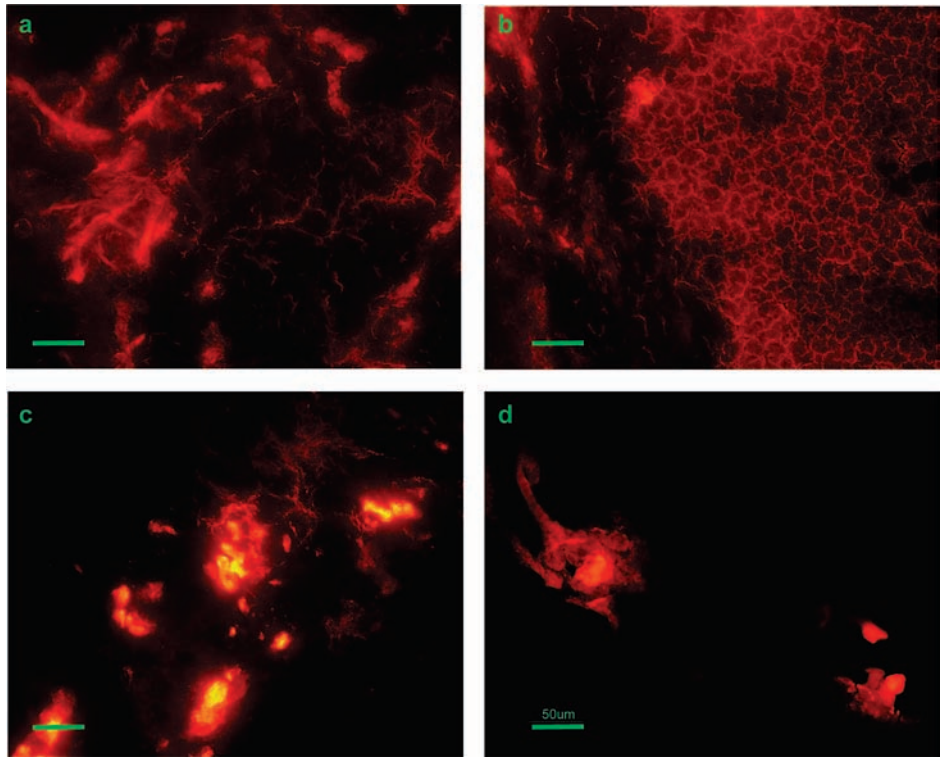

Figure 6. Fluorescence microscopy images of sectioned IGROV-1 tumors 24 h post liposome injection. (a) surface tumor slices, nontargeted liposomes, (b) midtumor slices, nontargeted liposomes, (c) surface tumor slices, folate-targeted liposomes, and (d) midtumor slices, folate-targeted liposomes (green bar represents 50 μm).

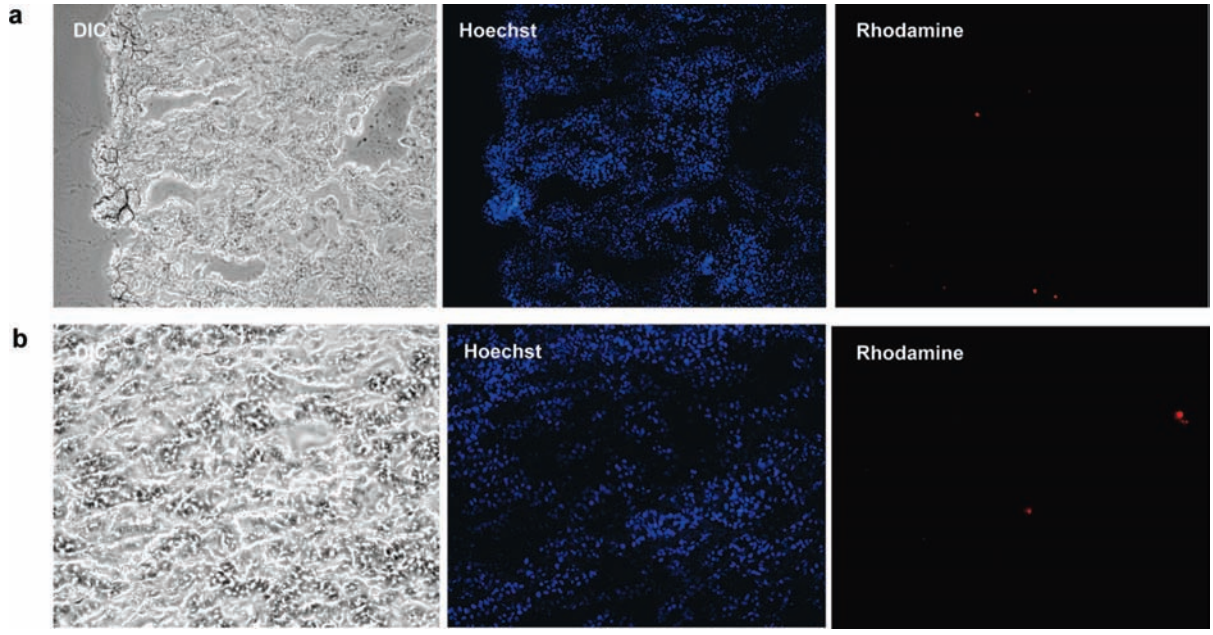

Figure 7. (a) Microscopy images of sectioned liver from tumor-bearing mice injected with folate-targeted liposome; the results show that there is no significant accumulation of the liposomes in the liver. (b) Microscopy images of sections from excised kidneys, where the presence of the fluorescent lipid DOPE-Rhodamine and therefore folate-targeted liposomes is minimal 24 h postadministration ($\times$20 magnification).

signal enhancement is achieved for the nontargeted liposomes only after 24 h postinjection, suggesting continuous circulation and gradual accumulation of these passively targeted liposomes. This is in line with current EPR theories, suggesting that the rate-limiting step for nontargeted liposomes is indeed extravasation (*28, 29*). These trends in active and passive targeting to tumors are also observed by others investigating the effect of targeting on the EPR mechanism (*30*).

The drop in tumor signal intensity at the 24 h postinjection time point for the folate-targeted liposomes is perhaps indicative of cellular internalization and endosomal or cytoplasmic retention of the liposomes and therefore the Gd signaling lipid.

The fluorescence pattern observed for the folate-targeted liposomes appears to be more localized, and the type of diffused and dispersed fluorescence observed for the passively accumulated liposomes is not reflected from these images (Figure 6). It has been suggested that, in particular with immunoliposomes targeted to tumors, there may exist a "binding site barrier" that affects targeted liposome binding in tumors. Weinstein et al. have suggested that immunoliposomes will not penetrate

deeply into the tumor but will bind to the first target cells encountered (*31*). The "binding site barrier" hypothesis suggests that antibodies or ligand-targeted nanoparticles bind to the first target cells they encounter, which retards their diffusion through the tumors (*32*). Additionally, the observed difference in tumor fluorescence localization may be due to macrophage activity within the tumor. A limitation to note is the complicating factor that tumor infiltrating macrophages are also likely to be FR positive. In fact, Turk et al. showed that FR targeted liposomes preferentially target macrophages even in the presence of FR+ tumor cells (*33*). This raises the possibility that FR+ tumor infiltrating macrophages may constitute the actual target cell population in solid tumors and thus will also be investigated in our future studies. A further elucidation for the distinction in fluorescence patterns observed in the case of the folate-targeted particles may be that these particles can distinguish between necrotic and viable tumor areas, leading to more intense fluorescence observed in the viable proliferating tumor areas where more folate-targeted liposomes are able to bind to the growing cells. On the other hand, the nontargeted liposomes cannot make this distinction and will be more uniformly distributed throughout the tumor due to a purely EPR dominating effect.

As such, it appears that the nontargeted gadolinium liposomes may show better penetration into solid tumors; however, the folate-targeted liposomes show a more rapid accumulation within the IGROV-1 tumors. Further work to clarify the localization of the folate-targeted liposomes within the tumor could involve the direct antibody staining of the sectioned tumor slices for α-FR expression.

The lack of fluorescence signal from the sectioned kidneys and liver of mice injected with both the folate-targeted and nontargeted liposomes (see Figure 7) is attributed to the heavily PEGylated nature of these particles and provides further evidence for their prolonged circulation and tumor accumulation through EPR.

In this study, we used a 3 mol % folate-PEG-lipid to ensure multivalency, and liposomes with this folate ratio were taken up in greater amounts by IGROV-1 cells compared to low folate ratio bearing liposomes (Figure 3). However, it has been shown that effective in vivo tumor folate targeting may only require less than 0.3 mol % of the ligand (*34*). It has been suggested that the folate receptor function is regulated by cellular folate requirements, and therefore, a small amount of folic acid is sufficient to trigger the down-regulation of the folate receptor cycle (*5*). However, the observed maximum 68% signal enhancement in our case for the folate-targeted liposomes may suggest that perhaps only a slight decrease in ligand ratio may be necessary to achieve even higher tumor signal enhancement rates. Further studies will focus on optimizing the folate molar ratio of liposomes for in vivo imaging.

Furthermore, it has been shown that the folate ligand indeed remains intact on the liposome surface during circulation. If the ligand is lost in vivo during circulation, the liposome particles would have lost the ability to bind to the tumor cells. Gabizon et al. tested the ligand−liposome association of folate-targeted liposomes in vivo using an ascetic tumor that did not express folate receptors (*12*). In this study, the injected folate liposomes were collected from the ascetic fluid 48 h after i.v injection and were tested ex vivo for their FR binding on relevant FR expressing cell lines. They successfully showed that the folate-targeted liposomes retain their FR receptor binding post in vivo injection and extravasation to the ascetic fluid. These findings in addition to our study suggest that folate targeting for the in vivo imaging of tumors presents a robust and broad platform for both tumor imaging and the delivery of therapeutic agents over a prolonged period of time to tumor tissue.

CONCLUSION

We have demonstrated the utility of folate-targeted liposomes for the imaging of solid tumors and compared these liposomes to nontargeted bimodal liposomes. The folate bearing liposomes showed over 4-fold increase in their accumulation rate at just 2 h postinjection as observed by a drop in tumor T_1 signal due to their effective targeting to the α-FR of the IGROV-1 tumor cells. Here, active targeting versus passive targeting to solid tumors was shown. The rapid and persistent tumor signal enhancement of the folate-targeted liposomes beyond the 24 h experimental end-point will be further investigated. Targeting solid tumors in vivo is challenging due to the rate-limiting step of extravasation and the limited potential for liposomes to diffuse within a solid tumor based on their size. In the quest for ever more optimal nanoparticles for the effective imaging of solid tumors, considerations of particle size, charge, and targeting elements are key requirements for successful particle development for tumor imaging.

ACKNOWLEDGMENT

We thank Dr. Ian McNeish (CRUK) for the kind gift of IGROV-1 cells and Ms. Lorraine Lawrence (Imperial College London) for assistance with histology experiments. Funding for Nazila Kamaly was provided by the GTC and MRC.

LITERATURE CITED

(1) Ke, C. Y., Mathias, C. J., and Green, M. A. (2004) Folate-receptor-targeted radionuclide imaging agents. *Adv. Drug Delivery Rev. 56*, 1143–1160.

(2) Reddy, J. A., Allagadda, V. M., and Leamon, C. P. (2005) Targeting therapeutic and imaging agents to folate receptor positive tumors. *Curr. Pharm. Biotechnol. 6*, 131–150.

(3) Wang, Z. J., Boddington, S., Wendland, M., Meier, R., Corot, C., and Daldrup-Link, H. (2008) MR imaging of ovarian tumors using folate-receptor-targeted contrast agents. *Pediatric Radiol. 38*, 529–537.

(4) Saul, J. M., Annapragada, A. V., and Bellamkonda, R. V. (2006) A dual-ligand approach for enhancing targeting selectivity of therapeutic nanocarriers. *J. Controlled Release 114*, 277–287.

(5) Ghaghada, K. B., Saul, J., Natarajan, J. V., Bellamkonda, R. V., and Annapragada, A. V. (2005) Folate targeting of drug carriers: A mathematical model. *J. Controlled Release 104*, 113–128.

(6) Müller, C., Schubiger, P. A., and Schibli, R. (2006) In vitro and in vivo targeting of different folate receptor-positive cancer cell lines with a novel 99mTc-radiofolate tracer. *Eur. J. Nucl. Med. Mol. Imaging 33*, 1162–1170.

(7) Hilgenbrink, A. R., and Low, P. S. (2005) Folate receptor-mediated drug targeting: from therapeutics to diagnostics. *J. Pharm. Sci. 94*, 2135–2146.

(8) Henriksen, G., Bruland, O. S., and Larsen, R. H. (2005) Preparation and preclinical assessment of folate-conjugated, radiolabelled antibodies. *Anticancer Res. 25*, 9–16.

(9) Wang, S., Luo, J., Lantrip, D. A., Waters, D. J., Mathias, C. J., Green, M. A., Fuchs, P. L., and Low, P. S. (1997) Design and synthesis of [^{111}In]DTPA-folate for use as a tumor-targeted radiopharmaceutical. *Bioconjugate Chem. 8*, 673–679.

(10) Sudimack, J., and Lee, R. J. (2000) Targeted drug delivery via the folate receptor. *Adv. Drug Delivery Rev. 41*, 147–162.

(11) Hofland, H. E., Masson, C., Iginla, S., Osetinsky, I., Reddy, J. A., Leamon, C. P., Scherman, D., Bessodes, M., and Wils, P. (2002) Folate-targeted gene transfer in vivo. *Mol. Ther. 5*, 739–744.

(12) Gabizon, A., Horowitz, A. T., Goren, D., Tzemach, D., Shmeeda, H., and Zalipsky, S. (2003) In vivo fate of folate-targeted polyethylene-glycol liposomes in tumor-bearing mice. *Clin. Cancer Res. 9*, 6551–6559.

(13) Salazar, M. D., and Ratnam, M. (2007) The folate receptor: What does it promise in tissue-targeted therapeutics? *Cancer Metastasis Rev. 26*, 141–152.
(14) Low, P. S., Henne, W. A., and Doorneweerd, D. D. (2008) Discovery and development of folic-acid-based receptor targeting for imaging and therapy of cancer and inflammatory diseases. *Acc. Chem. Res. 41*, 120–129.
(15) Gupta, Y., Jain, A., Jain, P., and Jain, S. (2007) Design and development of folate appended liposomes for enhanced delivery of 5-FU to tumor cells. *J. Drug Targeting 15*, 231–240.
(16) Sega, E. I., and Low, P. S. (2008) Tumor detection using folate receptor-targeted imaging agents. *Cancer Metastasis Rev. 27*, 655–664.
(17) Kim, I. B., Shin, H., Garcia, A. J., and Bunz, U. H. F. (2007) Use of a folate-PPE conjugate to image cancer cells in vitro. *Bioconjugate Chem. 18*, 815–820.
(18) Konda, S. D., Aref, M., Wang, S., Brechbiel, M., and Wiener, E. C. (2001) Specific targeting of folate-dendrimer MRI contrast agents to the high affinity folate receptor expressed in ovarian tumor xenografts. *Magma 12*, 104–113.
(19) Oyewumi, M. O., Yokel, R. A., Jay, M., Coakley, T., and Mumper, R. J. (2004) Comparison of cell uptake, biodistribution and tumor retention of folate-coated and PEG-coated gadolinium nanoparticles in tumor-bearing mice. *J. Controlled Release 95*, 613–626.
(20) Choi, H., Choi, S. R., Zhou, R., Kung, H. F., and Chen, I. W. (2004) Iron oxide nanoparticles as magnetic resonance contrast agent for tumor imaging via folate receptor-targeted delivery. *Acad. Radiol. 11*, 996–1004.
(21) Kamaly, N., Kalber, T., Ahmad, A., Oliver, M. H., So, P. W., Herlihy, A. H., Bell, J. D., Jorgensen, M. R., and Miller, A. D. (2008) Bimodal paramagnetic and fluorescent liposomes for cellular and tumor magnetic resonance imaging. *Bioconjugate Chem. 19*, 118–129.
(22) Torchilin, V. P. (2007) Targeted pharmaceutical nanocarriers for cancer therapy and imaging. *AAPS J. 9*, E128–E147.
(23) Sun, C., Sze, R., and Zhang, M. (2006) Folic acid-PEG conjugated superparamagnetic nanoparticles for targeted cellular uptake and detection by MRI. *J. Biomed. Mater. Res. Part A 78*, 550–557.
(24) Wu, J., Liu, Q., and Lee, R. J. (2006) A folate receptor-targeted liposomal formulation for paclitaxel. *Int. J. Pharm. 316*, 148–153.
(25) Wu, M., Gunning, W., and Ratnam, M. (1999) Expression of folate receptor type α in relation to cell type, malignancy, and differentiation in ovary, uterus, and cervix. *Cancer Epidemiology Biomarkers and Prevention 8*, 775–782.
(26) Stevens, P. J., Sekido, M., and Lee, R. J. A. (2004) Folate receptor-targeted lipid nanoparticle formulation for a lipophilic paclitaxel prodrug. *Pharm. Res. 21*, 2153–2157.
(27) Gabizon, A. A., Shmeeda, H., and Zalipsky, S. (2005) Liposome advances: progress in drug and vaccine delivery, In *Pros and cons of the liposome platform in cancer drug targeting. international liposome society (ILS 2005)* pp 175−184, Taylor & Francis, London.
(28) Maeda, H., Greish, K., and Fang, J. (2006) The EPR effect and polymeric drugs: a paradigm shift for cancer chemotherapy in the 21st century. *Adv. Polym. Sci. 193*, 103–122.
(29) Iyer, A. K., Khaled, G., Fang, J., and Maeda, H. (2006) Exploiting the enhanced permeability and retention effect for tumor targeting. *Drug Discovery Today 11*, 812–818.
(30) Pirollo, K. F., and Chang, E. H. (2008) Does a targeting ligand influence nanoparticle tumor localization or uptake? *Trends Biotechnol. 26*, 552–558.
(31) Mastrobattista, E., Koning, G. A., and Storm, G. (1999) Immunoliposomes for the targeted delivery of antitumor drugs. *Adv. Drug Delivery Rev. 40*, 103–127.
(32) Weinstein, J. N., and van Osdol, W. (1992) Early intervention in cancer using monoclonal antibodies and other biological ligands: micropharmacology and the ”binding site barrier”. *Cancer Res. 52*, 2747s–2751s.
(33) Turk, M. J., Waters, D. J., and Low, P. S. (2004) Folate-conjugated liposomes preferentially target macrophages associated with ovarian carcinoma. *Cancer Lett. 213*, 165–172.
(34) Reddy, J. A., Abburi, C., Hofland, H., Howard, S. J., Vlahov, I., Wils, P., and Leamon, C. P. (2002) Folate-targeted, cationic liposome-mediated gene transfer into disseminated peritoneal tumors. *Gene Ther. 9*, 1542–1550.

BC8002259

Bioconjugate Chemistry 20th Anniversary

Subscriber access provided by SHEMYAKIN-OVCHINNIKOV INST

Article

Development of an Oxime Bond Containing Daunorubicin-Gonadotropin-Releasing Hormone-III Conjugate as a Potential Anticancer Drug

Ildiko# Szabo#, Marilena Manea, Erika Orba#n, Antal Csa#mpai, Szilvia Bo#sze, Rita Szabo#, Miguel Tejeda, Dezso# Gaa#l, Bence Kapuva#ri, Michael Przybylski, Ferenc Hudecz, and Ga#bor Mezo#

Bioconjugate Chem., **2009**, 20 (4), 656-665• DOI: 10.1021/bc800542u • Publication Date (Web): 18 March 2009

Downloaded from http://pubs.acs.org on May 8, 2009

More About This Article

Additional resources and features associated with this article are available within the HTML version:

- Supporting Information
- Access to high resolution figures
- Links to articles and content related to this article
- Copyright permission to reproduce figures and/or text from this article

View the Full Text HTML

ACS Publications
High quality. High impact.

Bioconjugate Chemistry is published by the American Chemical Society. 1155 Sixteenth Street N.W., Washington, DC 20036

Development of an Oxime Bond Containing Daunorubicin-Gonadotropin-Releasing Hormone-III Conjugate as a Potential Anticancer Drug

Ildikó Szabó,[#,†] Marilena Manea,[#,§,||] Erika Orbán,[†] Antal Csámpai,[‡] Szilvia Bősze,[†] Rita Szabó,[†] Miguel Tejeda,[⊥] Dezső Gaál,[⊥] Bence Kapuvári,[⊥] Michael Przybylski,[§] Ferenc Hudecz,[†,‡] and Gábor Mező*[,†]

Research Group of Peptide Chemistry, Hungarian Academy of Sciences, and Institute of Chemistry, Eötvös Loránd University, 1117 Budapest, Hungary, Laboratory of Analytical Chemistry and Biopolymer Structure Analysis, Department of Chemistry and Zukunftskolleg, University of Konstanz, 78457 Konstanz, Germany, and National Institute of Oncology, 1122 Budapest, Hungary. Received December 14, 2008; Revised Manuscript Received February 9, 2009

Here, we report on the synthesis and biological properties of a conjugate in which daunorubicin (Dau) as chemotherapeutic agent was attached through an oxime bond to gonadotropin-releasing hormone-III (GnRH-III) as targeting moiety. In vitro toxicity and the cytostatic effect of the conjugate on MCF-7 human breast and C26 murine colon cancer cell lines were determined, and the results were compared with those obtained for the free daunorubicin, as well as with the doxorubicin containing derivative. In vivo antitumor effect of daunorubicin−GnRH-III was studied on Balb/c female mice transplanted with C26 tumor. Our data indicate that the daunorubicin−GnRH-III conjugate had a lower toxic effect than the free daunorubicin and it was essentially nontoxic up to 15 mg (Dau content)/kg body weight. The treatment of the C26 tumor bearing mice with the conjugate led to tumor growth inhibition and longer survival time in comparison with the controls and with the administration of the free drug. When mice were treated twice with the conjugate (on days 4 and 7 after tumor transplantation), 46% tumor growth inhibition was obtained. In this case, the increase of the median survival time was 38% compared to the controls.

INTRODUCTION

Chemotherapy is still one of the primary modalities for the treatment of cancer. However, the application of free anticancer drugs has several drawbacks. Frequently applied high doses are required for the efficacy because of the fast elimination of the drugs from the circulation. Furthermore, the lack of selectivity generally results in toxic side effects. Also, the aquired or intrinsic multidrug resistance (MDR) of cancer cells may restrict the use of chemotherapy. Targeted chemotherapy has been developed to overcome these disadvantages (*1*, *2*) and it has been suggested as an alternative for differentiating healthy and afflicted cells (*3*). Tumor targeting is usually achieved by conjugation of the chemotherapeutic agent to a targeting moiety consisting of sugars (*4*), lectins (*5*−*7*), receptor ligands (*1*, *3*, *8*, *9*), or antibodies (*10*−*12*), which is specifically directed to certain types of binding sites on cancer cells.

One of the various targeted chemotherapeutic approaches is based on the finding that receptors of several peptide hormones (e.g., gonadotropin-releasing hormone (GnRH[1]), bombesin, somatostatin) are overexpressed on cancer cells compared to normal cells and organs. GnRH receptor (GnRH-R) expression was identified on different tumors (breast, ovarian, endometrial, prostate, renal, brain, pancreatic, melanomas, and non-Hodgkin's lymphomas) with high percentages in specimens (*1*, *13*, *14*).

The primary biological function of the hormonal decapeptide GnRH (also called LH-RH) is the regulation of gonadal functions by releasing gonadotropic hormones, luteinizing hormone (LH), and follicle stimulating hormone (FSH), and therefore it plays a pivotal role in vertebrate reproduction (*15*). However, it was demonstrated that high doses of human GnRH (hGnRH) and its superagonist analogues inhibit the growth of hormone-dependent mammary and prostate cancers through chemical castration (*16*). Some of the GnRH agonists and antagonists not only have an indirect effect on tumors, but also can affect the cancer cells directly by the interaction with GnRH receptors that activate a G-protein-dependent transducing mechanism (*17*−*19*).

GnRH derivatives not only might be anticancer agents, but also could serve as targeting moieties to deliver chemotherapeutic agents to tumor cells. Chemotherapeutic antineoplastic radicals including alkylating nitrogen mustard derivatives (e.g., D-melphalan), antimetabolites (e.g., methotrexate), and anthracycline derivatives (e.g., doxorubicin and 2-pyrrolinodoxorubicin), were conjugated to [D-Lys[6]]-GnRH through amide or ester bonds (*1*, *20*−*22*). However, in the case of the application of this superactive GnRH agonist as the targeting moiety, temporary damage to the pituitary was observed, which was recovered in about two weeks (*23*).

* Correspondence to Gábor Mező, Research Group of Peptide Chemistry, Hungarian Academy of Sciences, Eötvös L. University, 1117 Budapest, Pázmány P. stny. 1/A, Hungary. Tel.: (+36)-1-209-0555/1433; Fax: (+36)-1-372-2620; e-mail: gmezo@elte.hu.

[#] Ildikó Szabó and Marilena Manea contributed equally to this work.

[†] Hungarian Academy of Sciences, Eötvös Loránd University.

[‡] Institute of Chemistry, Eötvös Loránd University.

[§] Department of Chemistry, University of Konstanz.

[||] Zukunftskolleg, University of Konstanz.

[⊥] National Institute of Oncology.

[1] Abbreviations: Aoa, aminooxyacetic acid; Dau, daunorubicin; Dox, doxorubicin; GnRH, gonadotropin-releasing hormone; LH-RH, luteinizing hormone releasing hormone; MTT, 3-(4,5-dimethylthiazol-2-yl)-2,5-diphenyltetrazolium bromide; C26 tumor, solid murine colon carcinoma; MCF-7 tumor, solid human estrogen receptor positive breast carcinoma.

10.1021/bc800542u CCC: $40.75 © 2009 American Chemical Society
Published on Web 03/18/2009

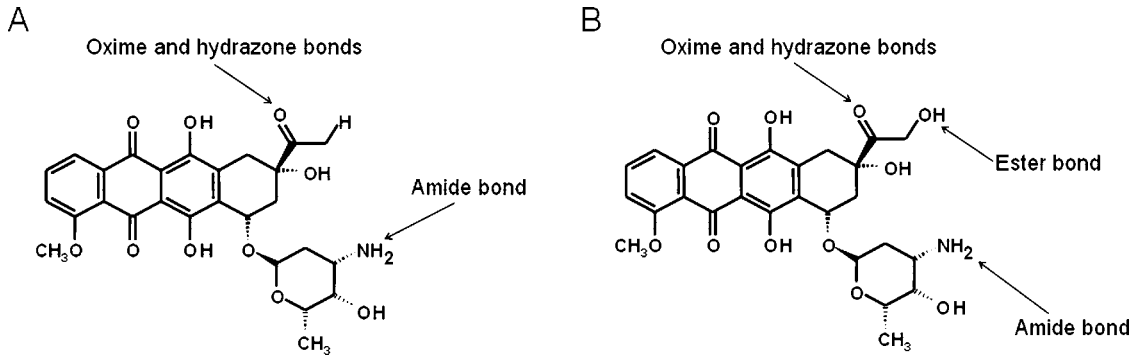

Figure 1. Conjugation sites of daunorubicin (A) and doxorubicin (B).

The antitumor effect of the conjugate Dox-[Lys^6]-GnRH (AN-152), which is currently in the phase III clinical trial, was studied on many types of tumors. The highest antitumor effect was determined on human epithelial ovarian cancers. The clinical trials are performed in female patients with LH-RH-receptor expressing gynecological tumors (advanced or recurrent ovarian and endometrial tumors).

The selectivity of the antitumor effect in targeted chemotherapy can be increased by using GnRH analogues that have lower binding to gonadotropic cells. One of the weak agonistic analogues of GnRH is the variant (Glp-His-Trp-Ser-His-Asp-Trp-Lys-Pro-Gly-NH_2; GnRH-III) isolated from sea lamprey (*Petromyzon marinus*) (*24*) that specifically binds to receptors on cancer cells and recognizes not only the high- but also the low-affinity binding sites of GnRH receptors (*25*). GnRH-III has 500−1000 times less potency in LH and FSH secretion both in vitro and in vivo indicating its selective antitumor activity (*26, 27*). It was also demonstrated that the modification of ^{8}Lys by conjugation (*28*), cyclization (*29*), Ala-scan (*30*), or dimerization (*31*) did not result in the loss of the antiproliferative activity of GnRH-III. However, the absence of the free ε-amino group of lysine decreased the endocrine effect of the compounds (*27, 31, 32*)

The aim of our study was to prepare bioconjugates in which daunorubicin (also called daunomycin, Dau) as the chemotherapeutic agent was covalently attached to GnRH-III as a targeting moiety with its own antiproliferative effect. Daunorubicin is an anthracycline derivative which differs from doxorubicin (Dox) in the substitution at the C-14 position (H instead of OH). It has been shown that daunorubicin has less cardiotoxic side effect than doxorubicin (*33, 34*). However, the lack of the aliphatic OH-group in daunorubicin prevents the possibility of synthesizing conjugates containing ester bonds (Figure 1). Also, the conjugation through the amino group of the aminosugar moiety (daunosamine) might lead to a significant loss of bioavailability of the compound (*32, 35*). Therefore, daunorubicin is not a common part of the conjugates tested in experiments for targeted chemotherapy. Here, we report on the conjugation of daunorubicin to GnRH-III(GFLG) via an oxime bond. In vitro and in vivo toxicity of the conjugate was studied. The cytostatic effect of the compound on MCF-7 human breast and C26 murine colon tumor cell lines was determined. The results were compared with those obtained for the free daunorubicin, as well as with the doxorubicin containing derivative. The in vivo antitumor effect of the GnRH-III(Dau=Aoa-GFLG) conjugate (throughout the manuscript, the conjugate will be abbreviated as Dau-GnRH-III) was studied on mice transplanted with C26 murine colon tumor xenograft.

The oxime bond containing Dau-GnRH-III conjugate had in vitro and in vivo antitumor effects and enhanced the survival of treated mice bearing C26 tumor compared to the untreated

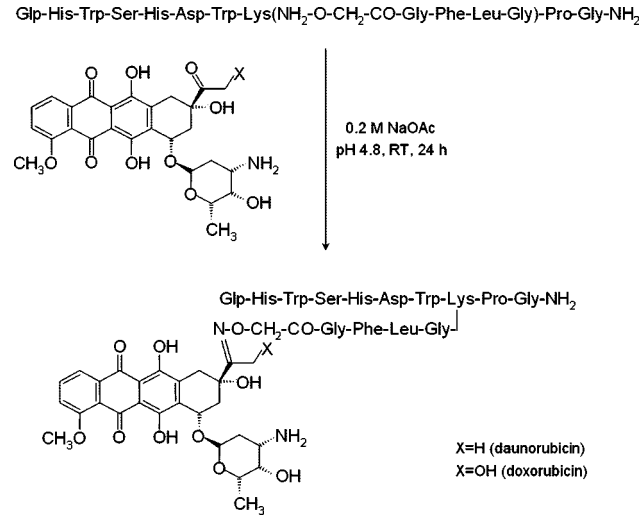

Figure 2. Conjugation of anthracyclines to GnRH-III derivative.

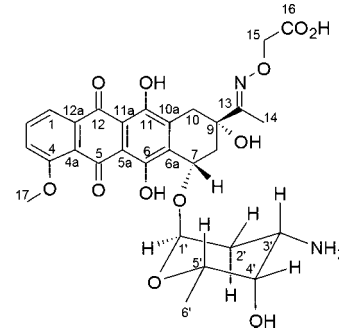

Figure 3. Numbering of atoms used for NMR assignments (arbitrary).

control group. The conjugate also prevented the toxic side effects of the free drug.

EXPERIMENTAL SECTION

Materials. All amino acid derivatives and MBHA resin were purchased from NovaBiochem (Läufelfingen, Switzerland) or Reanal (Budapest, Hungary). Scavengers, coupling agents, and cleavage reagents (*p*-cresol, dithiothreitol (DTT), *N*,*N*′-dicyclohexylcarbodiimide (DCC), *N*,*N*′-diisopropylcarbodiimide (DIPCI), 1,2-ethanedithiol (EDT), (benzotriazol-1-yloxy)-tris-(dimethylamino)phosphonium hexafluorophosphate (BOP), *N*-diisopropyl-ethylamine (DIEA), 1-hydroxybenzotriazole (HOBt), 1,8-diazabicyclo-[5.4.0]undec-7-ene (DBU), piperidine, trifluoroacetic acid (TFA), and hydrogen fluoride (HF)), as well as daunorubicin (Dau), doxorubicin (Dox), aminooxyacetic acid (Aoa), and Boc-aminooxyacetic acid (Boc-Aoa-OH), were Fluka

Table 1. Characteristics of Conjugates, Dau-Aminooxyacetic Acid Derivative and GnRH-III(GFLG)[a]

	RP-HPLC[b]	ESI-MS[c]	
compound	R_t (min)	$[M + H]^+_{calc.}$	$[M + H]^+_{exp.}$
Dau-GnRH-III	32.3	2217.3	2216.8
Dox-GnRH-III	31.9	2233.3	2232.9
Dau-Aoa-OH	31.6	601.2	601.2
GnRH-III(GFLG)	26.3	1634.8	1634.6

[a] HPLC chromatograms and mass spectra are shown in the Supporting Information (S3−S5). [b] Column: Phenomenex Jupiter C_{18} (250 mm × 4.6 mm) with 5 μm silica (300 Å pore size); gradient: 0 min 0% B; 5 min 0% B; 50 min 90% B; eluents 0.1% TFA in water (A) and 0.1% TFA in acetonitrile−water (80:20, v/v) (B); flow rate: 1 mL/min; detection: λ = 220 nm. [c] Bruker Daltonics Esquire 3000+ ion trap mass spectrometer.

products (Buchs, Switzerland). Solvents for synthesis (dichloromethane (DCM) and *N*,*N*′-dimethylformamide (DMF)) were purchased from Reanal (Budapest, Hungary). HPLC-grade acetonitrile (MeCN) and 3-(4,5-dimethylthiazol-2-yl)-2,5-diphenyltetrazolium bromide (MTT) were from Sigma-Aldrich Kft (Budapest, Hungary).

Synthesis of Conjugates. Branched GnRH-III derivative (<EHWSHDWK(Aoa-GFLG)PG-NH_2; where <E is pyroglutamic acid) was built up on 4-methylbenzhydrylamine (MBHA) resin (1.04 mmol/g coupling capacity) using mixed Boc/Bzl and Fmoc/^{t}Bu chemistries as previously reported (*31, 36*). The first two amino acids (Gly and Pro) were attached as Boc-protected derivatives followed by the coupling of Fmoc-Lys(Boc)-OH to the peptidyl resin. After removal of the Boc protecting group from the $^\epsilon NH_2$ function of Lys, the GFLG tetrapeptide branch was prepared by Boc strategy. The remaining part of the GnRH-III sequence was built up by Fmoc strategy, except pyroglutamic acid, which was attached without any protection. The removal of the side-chain protecting groups, as well as the Boc-group from the *N*-terminus of the branch, was carried out with a mixture of TFA-water-EDT (95:2.5:2.5, v/v/v) at RT for 1 h. A part of the resin was used for the preparation of GnRH-III(GFLG) hormone derivative. On the other part of the resin, Boc-aminooxyacetic acid was attached to the *N*-terminus of the branch after preactivation with BOP reagent in the presence of DIEA (2 equiv each to the resin capacity). The Boc group was cleaved with a mixture of TFA-water-EDT (95:2.5:2.5, v/v/v) at RT for 15 min. After washing and neutralization, the peptide−resin was dried in a desiccator. After that, the peptides were cleaved from the resin with anhydrous HF in the presence of *p*-cresol and DTT (HF-*p*-cresol-DTT = 10 mL:1 g:0.1 g). The crude products were purified by semipreparative RP-HPLC and the purified compounds were characterized by analytical HPLC and mass spectrometry (Table 1). The yields were 54% (Aoa containing peptide) and 66% (GnRH-III(GFLG)) to the resin capacity.

The conjugation via oxime bond formation was carried out in 0.2 M sodium acetate buffer, pH 4.8. Daunorubicin or doxorubicin was used in 20% excess compared to the GnRH-III derivative. The reaction mixture was stirred at RT for 24 h; then, the conjugate was separated from the excess of anthracycline derivative by RP-HPLC. The yield was 72% in the case of daunorubicin and 70% in the case of doxorubicin. The purity of the conjugates was determined by analytical RP-HPLC, and the identity of the compounds was confirmed by ESI-ion trap mass spectrometry (Table 1; Supporting Information S3−S5). Conjugation of Dau to aminooxyacetic acid (compound prepared for NMR analysis) was carried out in the same way as described above (83% yield).

High-Performance Liquid Chromatography (HPLC). Analytical RP-HPLC was performed on a Knauer (H. Knauer, Bad Homburg, Germany) system using a Phenomenex Jupiter C_{18} column (250 mm × 4.6 mm) with 5 μm silica (300 Å pore size) (Torrance, CA) as a stationary phase. Linear gradient elution (0 min 0% B; 5 min 0% B; 50 min 90% B) with eluent A (0.1% TFA in water) and eluent B (0.1% TFA in acetonitrile−water (80:20, v/v)) was used at a flow rate of 1 mL/min. Peaks were detected at λ = 220 nm. The crude products were purified on a semipreparative Phenomenex Jupiter C_{18} column (250 mm × 10 mm) with 10 μm silica (300 Å pore size). The flow rate was 4 mL/min. The same eluents with a linear gradient of 20−60% B in 40 min were applied.

Mass Spectrometry (MS). Mass spectrometric analyses were carried out on a Bruker Daltonics Esquire 3000+ ion trap mass spectrometer (Bremen, Germany). Spectra were acquired in the 50−2000 *m*/*z* range. Samples were dissolved in acetonitrile−water = 1:1 (v/v) solvent mixture containing 0.1% acetic acid.

Liquid chromatography in combination with mass spectrometry (LC/MS) was carried out on a Bruker Esquire 3000+ ion trap mass spectrometer (Bruker Daltonics, Bremen, Germany) equipped with an Agilent 1100 HPLC system (Agilent, Waldbronn, Germany). Peptides were separated on a Vydac MS C_{18} column (150 × 1 mm; 300 Å, 3 μm) using a linear gradient from 90% solvent A (0.1% formic acid in water (v/v)) and 10% solvent B (0.1% formic acid in acetonitrile (v/v)) to 70% solvent B over 65 min and a flow rate of 50 μL/min. Spectra were recorded in positive ion mode in the 100−2000 *m*/*z* range.

^{1}H and ^{13}C NMR Study. The ^{1}H and ^{13}C NMR spectra were recorded in DMSO-d_6 solution in a 5 mm tube at RT, on a Bruker DRX-500 spectrometer at 500.13 (^{1}H) and 125.76 (^{13}C) MHz, with the deuterium signal of the solvent as the lock and TMS as the internal standard. The standard Bruker microprogram NOEMULT to generate NOE and to get DIFFNOE spectra was used with a selective pre-irradiation time (50 ms). DEPT spectrum was run in a standard manner, using only a $\Theta = 135°$ pulse to separate the CH/CH_3 and CH_2 lines phased "up" and "down", respectively. The 2D-COSY, 2D-HMQC, and 2D-HMBC spectra were obtained by using the standard Bruker pulse programs.

^{1}H NMR (δ_{TMS} = 0 ppm): 14.0 (br, ∼1H, CO_2H); 13.2 (very br, ∼2H, 6- and 11-OH); 7.8 (br ∼1H, OH or NH); 5.5 (br, ∼2H, OH or NH); 5.2 (br ∼1H, OH or NH); 7.88 (br m, 2H, 1- and 2-H); 7.63 (br m, 1H, 3-H); 5.28 (br s, 1H, 1′-H); 4.91 (t, J = 4.9 Hz, 1H, 7-H); 4.46 (s, 2H, 15-H); 4.14 (qa, J = 6.6 Hz, 1H, 5′-H); 3.97 (s, 3H, 17-H); 3.56 (br s, 1H, 4′-H); 3.37 (br d, J = 12.4 Hz, 3′-H); 2.98 and 2.89 (AB spin system, J_{AB} = 18.1 Hz, 2 × 1H, 10-H_{ax} and 10-H_{eq}); 2.23 (br s, 2H, 8-H_{ax} and 8 H_{eq}); 1.89 (td, J = 12.4 and 3.0 Hz, 1H, 2′-H_{ax}); 1.69 (dd, J = 12.4 and 3.0 Hz, 1H, 2′-H_{eq}); 1.91 (s, 3H, 14-H); 1.16 (d, J = 6.6 Hz, 6′-H).

^{13}C NMR (δ_{TMS} = 0 ppm): 187.2 and 187.3 (C-5 and C-12); 171.8 (C-16); 161.4 (C-13); 161.7 (C-4); 157.3 (C-11); 155.3 (C-6); 137.6 (C-2); 137.0, 136.64, 164.63, 135.99, 135,96, 135.6 (C-4a, C-5a, C-6a, C-10a, C-11a, C-12a); 120.6 (C-3); 119.9 (C-1); 100.1 (C-1′); 72.2 (C-7); 71.7 (C-9); 71.0 (C-15); 67.1 (C-5′); 67.0 (C-4′); 57.4 (C-17); 47.5 (C-3′); 39.0 (C-8); 33.8 (C-10); 29.0 (C-2′); 17.6 (C-6′); 10.8 (C-14).

Enzymatic Digestion of Dau-GnRH-III Conjugate by Cathepsin B. Dau-GnRH-III was dissolved at a concentration of 0.1 μg/μL in 0.1 M NaOAc, 0.01 M DTT, pH 5, and then human liver Cathepsin B (Calbiochem, Germany; c = 0.4 μg/μL in 20 mM NaOAc containing 1 mM EDTA, pH 5) was added at an enzyme to substrate ratio of 1:50, w/w. The reaction mixture was incubated at 37 °C, and aliquots of 20 μL were taken after 5 min, 2 h, 4 h, 8 h, and 24 h (the reaction was quenched by adding 2 μL of acetic acid, followed by freezing the sample with liquid nitrogen). The digestion mixtures were analyzed by LC/MS.

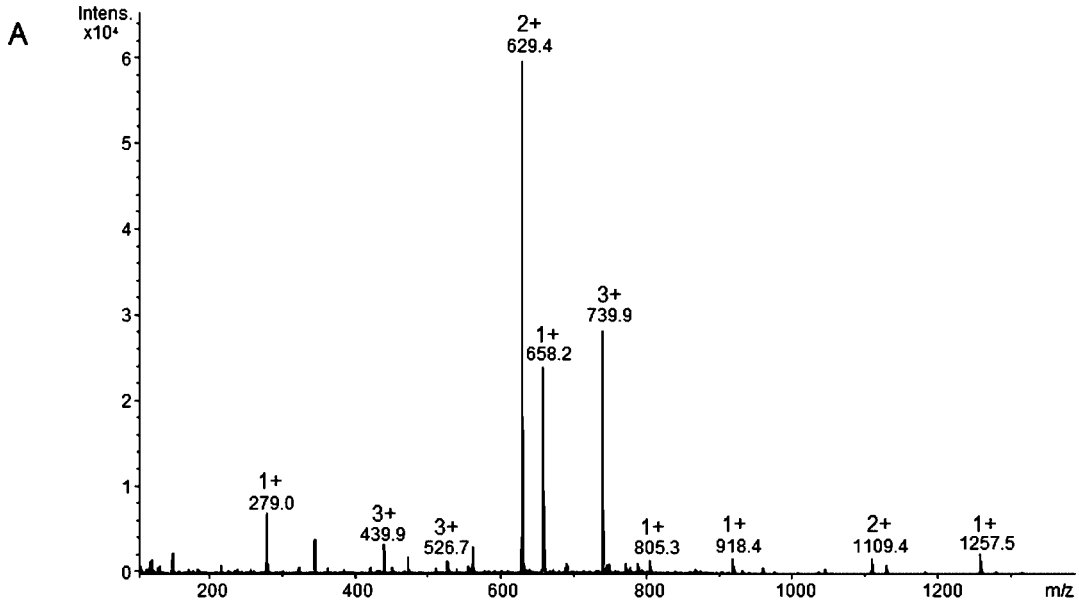

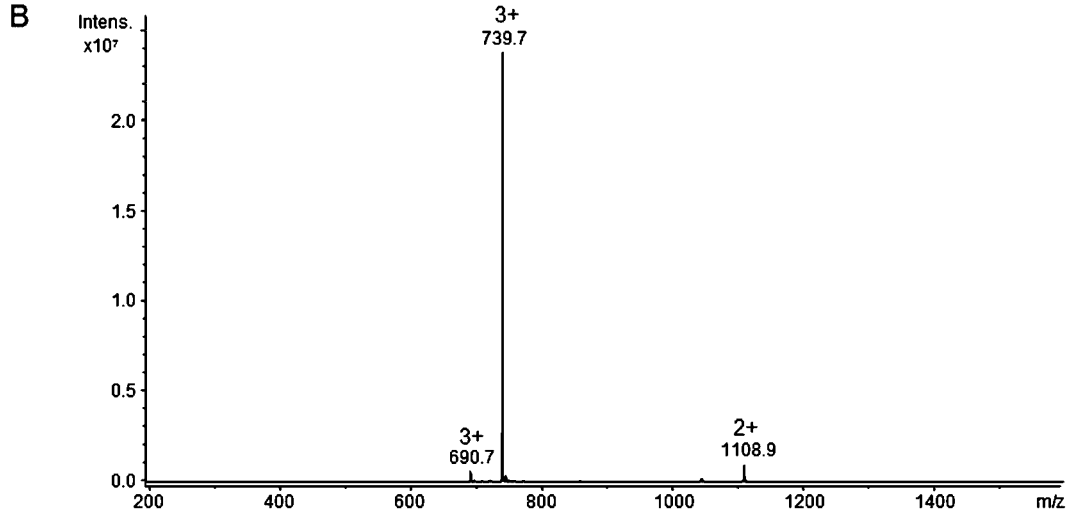

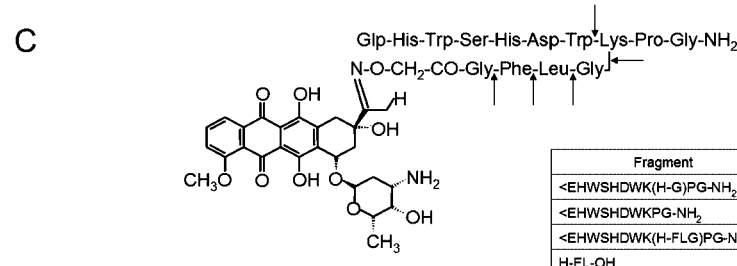

Fragment	MW_{calc}/MW_{exp}
<EHWSHDWK(H-G)PG-NH_2	1316.43/1316.65
<EHWSHDWKPG-NH_2	1259.35/1259.65
<EHWSHDWK(H-FLG)PG-NH_2	1576.75/1577.35
H-FL-OH	278.16/278.00
H-K(Dau=Aoa-GFLG)PG-NH_2	1256.31/1256.60
Dau=Aoa-G-OH	657.55/657.20
Dau=Aoa-GF-OH	804.58/804.30
Dau=Aoa-GLF-OH	917.66/917.40

Figure 4. ESI-ion trap mass spectra of Dau-GnRH-III conjugate after Cathepsin B digestion for 24 h (A) and in the absence of Cathepsin B (B). (C) Cathepsin B cleavage sites and fragments produced by proteolysis of Dau-GnRH-III.

A control experiment in which a solution of 0.1 μg/μL Dau-GnRH-III in 0.1 M NaOAc, 0.01 M DTT, pH 5, was incubated at 37 °C for 24 h was also performed.

Cells. MCF-7 cells (human breast adenocarcinoma cell line) were maintained in DMEM (Sigma Ltd., St. Louis, MO) containing 10% FCS (fetal calf serum, Sigma Ltd.), L-glutamine (2 mM), gentamicine (160 μg/mL) at 37 °C in a humidified 5% CO_2 atmosphere. C26 cells (mouse colon adenocarcinoma cell line) were cultured in DMEM F12 (Sigma Ltd.) containing 10% FCS (fetal calf serum), L-glutamine (2 mM), and pyruvate (1 mM) at 37 °C in a humidified 5% CO_2 atmosphere.

Cytotoxicity and Cytostatic Studies by MTT Assay. For the study of in vitro cytotoxicity, MCF-7 human breast or C26 murine colon cancer cells were plated into 96-well tissue culture plate in 100 μL culture medium with the initial cell number of 5×10^3 cells/well. The compounds used in the (5×10^{-4}) to

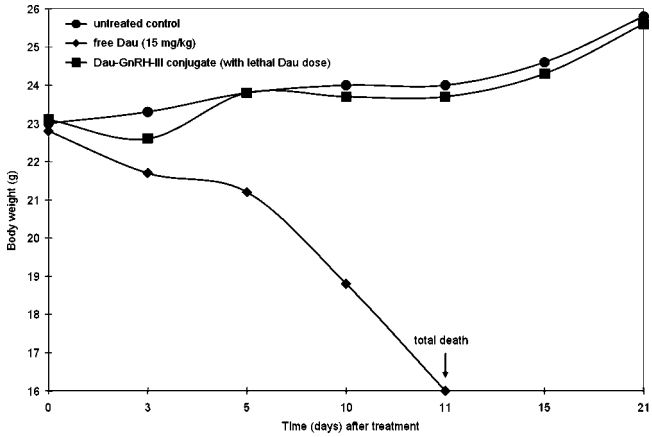

Figure 5. Effect of free daunorubicin (Dau) and Dau-GnRH-III conjugate on changes of the body weight and survival of healthy BDF-1 female mice (7 animals/group, values report the average).

Table 2. In Vitro Cytotoxicity and Cytostatic Effect on MCF-7 and C26 Cancer Cell Lines

compound	cytotoxicity (MCF-7) ($LC_{50}/\mu M$)	cytostasis (MCF-7) ($IC_{50}/\mu M$)	cytostasis (C26) ($IC_{50}/\mu M$)
Dau·HCl	0.67 ± 0.01	0.23 ± 0.03	1.95 ± 0.01
Dox·HCl	0.68 ± 0.01	0.07 ± 0.02	4.51 ± 0.16
Dau-GnRH-III	40.11 ± 25.31	3.94 ± 1.18	22.46 ± 1.74
Dox-GnRH-III	85.18 ± 3.81	5.38 ± 1.86	46.10 ± 6.06
GnRH-III(GFLG)	>200	>100	>100

(2×10^2) μM concentration range were dissolved in fresh culture medium and added to the cells. After 6 h incubation at 37 °C, the amount of living cells was determined by MTT assay using 0.367 mg/mL final concentration of MTT in each well. After 3.5 h incubation with MTT, cells were centrifuged at 2000 rpm for 5 min, supernatant was removed, and crystals were dissolved in DMSO. The absorbance was measured using an ELISA-reader (Labsystems MS Reader, Finland) at $\lambda = 540$ nm and at $\lambda = 620$ nm as reference wavelengths. Statistical analysis of data was performed by Student's *t*-test of Origin7.5 at the 95% confidence level.

In the case of the measurement of cytostatic effect, cells were plated into 96-well tissue culture plates in 100 μL culture medium with an initial cell number of 5×10^3 cells/well, 24 h prior to the treatment. The compounds or serum free medium as a control were added to the wells in 100 μL in serum free medium at a 200 μL final volume. After 6 h incubation, cells were washed twice with serum free medium, and then fresh culture medium was added to each well. Cells were maintained at 37 °C for a further 72 h, and then the quantity of living cells was determined by MTT-assay as described above.

Four parallel measurements were performed in all cases, and they were repeated twice.

Acute Toxicity Measurement. First-generation hybrid BDF_1 (C57BL/6 female and DBA/2 male) adult female mice, weighing 22−23 g, specified pathogen free (SPF) from Department of Exprimental Pharmacology, National Institute of Oncology, Budapest, Hungary, were used. Colonies were used for these experiments. The animals were kept in macrolon cages at 22−24 °C (40−50% humidity), with a lighting regimen of 12/12 h light/dark. The animals had free access to tap water and were fed a sterilized standard diet (Charles River VRF1, autoclavable, Germany) ad libitum. The animals used in these studies were cared for according to the "Guiding Principles for the Care and Use of Animals" based upon the Helsinki declaration, and they were approved by the local ethical committe. Our permission for breeding and performing experiments with laboratory animals is valid up to 10/06/2010.

Daunorubicin and Dau-GnRH-III conjugate were dissolved in distilled water at a concentration that allowed the dose to be given at a volume of 0.1 mL/10 g body weight. In this experiment, 7−7 mice/group were used. The mice were treated by i.p. administration. Toxicity in mice was characterized on the basis of lifespan and body weight. Survival time was followed over 21 days.

In Vivo Antitumor Effect of Daunorubicin and Dau-GnRH-III Conjugate on Colon-26 Carcinoma. Balb/c female mice, weighing 22−24 g, kept under the same conditions described above were used in this experiment. Tumor tissue fragments (Colon-26 mouse carcinoma, SRI, Birmingham, AL) were transplanted (3−4 mm, ∼25 mg weight) subcutaneously (s.c.) into the intrascapulare region of the mice using a tweezers. In the first trial, the treatments started on day 7 after tumor transplantation by i.p. administration of the compounds dissolved in d.i. water. In this experiment, 5−5 mice/group were used. Except for the control group, the mice were treated with either free daunorubicin (once 5 mg (8.86 μmol)/kg body weight or 2 mg (3.55 μmol)/kg 5 times on every second day) or Dau-GnRH-III conjugate (once 62.5 mg/kg (26.6 μmol; 15 mg Dau content) or 20.8 mg/kg (8.86 μmol; 5 mg Dau content) 5 times on every second day. In the second experiment, tumor bearing mice (7 mice in each group) were treated twice with the conjugate using 62.5 mg (26.6 μmol)/kg. Treatments were carried out either on days 4 and 7 or days 7 and 10. In this case, the antitumor activity of the free GnRH-III(GFLG) was also studied. The hormone derivative was injected i.p. on days 4 and 7 using 45 mg (26.6 μmol)/kg body weight. The tumor growth inhibitory effect of various treatments was controlled 7 times within three weeks following the tumor transplantation using a digital caliper. Tumor volume was calculated using the following formula: $V = a^2 \times b \times \pi/6$ (where "*a*" and "*b*" mean the shortest and the longest diameter, respectively of a given tumor) (*37*). Changes of tumor volume and body weight were controlled and evaluated. Mean values and standard deviations were calculated. The evaluation of antitumor activity on the basis of survival time was evaluated as well. The survival probability was presented according to the Kaplan−Meier curve calculated/drawn by the MedCalc9 program.

RESULTS AND DISCUSSION

Due to the limited conjugation sites of daunorubicin (Figure 1), the drug was attached to GnRH-III derivative as homing device via oxime bond formation. The in vitro antitumor effect of the conjugate was determined on MCF-7 and C26 tumor cell lines. Similar experiments were performed with a conjugate containing doxorubicin instead of daunorubicin, as well as with the free drugs. In spite of the higher in vitro activity of the conjugate on MCF-7 tumor cells, the C26 tumor bearing mice was a suitable animal model for in vivo experiments, because C26 colon tumor is a fast-growing and aggressive tumor type. It is worth noting that colon carcinomas are rarely used for the study of in vivo antitumor activity.

However, the first results of the treatment of colon cancer bearing mice with Dox and Dox-[Lys^6]-GnRH (AN-152) were recently reported (*38*). The treatment of nude mice bearing HT-29 tumor started 14 days after tumor transplantation and continued for 55 days. The conjugate was administered intraperitoneally (i.p.) on days 1 and 28, whereas Dox (20.7 μmol/kg; 13.6 mg/kg) was injected only once on day 1. AN-152 (20.7 μmol/kg) inhibited the tumor growth by 41% (735 ± 158 mm^3 tumor volume), while Dox only by 28% (885 ± 201 mm^3) compared to the controls (1219 ± 372 mm^3). All animals were alive at the end of the experiment in the group treated with AN-152, but 6/9 mice Dox treated and 2/9 from the controls died. Some other colon tumors, such as HCT-116, HCT-15,

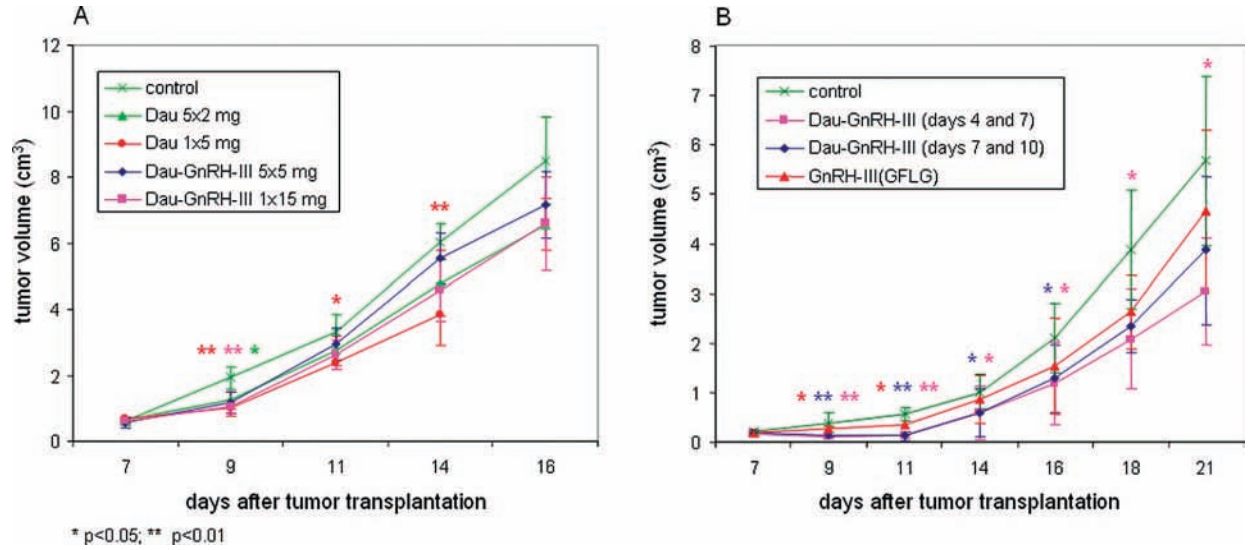

Figure 6. In vivo antitumor effect of daunorubicin and Dau-GnRH-III conjugate on mice bearing C26 colon tumor.

Table 3. Antitumor Effect of Daunorubicin and Dau-GnRH-III Conjugate on Mice Bearing C26 Tumor (Experiment 1)

		tumor volume (cm^3) ± SD								
days after tumor transplant	number of mice	control	Dau 2 mg/kg 5 × q2d	*T/C* (%)[a]	Dau 5 mg/kg 1 ×	*T/C* (%)	Dau-GnRH-III conjugate 5 mg/kg Dau 5 × q2d	*T/C* (%)	Dau-GnRH-III conjugate 15 mg/kg Dau 1 ×	*T/C* (%)
7	5	0.60 ± 0.10	0.64 ± 0.10		0.67 ± 0.11		0.58 ± 0.16		0.59 ± 0,05	
9	5	1.91 ± 0.35	1.24 ± 0.26	64.9	1.00 ± 0.23	52.4[c]	1.18 ± 0.32	61.3[d]	1.04 ± 0.21	54.4[c]
11	5	3.33 ± 0.51	2.75 ± 0.44	82.6	2.40 ± 0.23	72.1[d]	2.95 ± 0.47	88.6	2.63 ± 0.45	79.0
14	5	6.04 ± 0.53	4.78 ± 0.98	79.1	3.84 ± 0.93	63.6[c]	5.54 ± 0.78	91.7	4.58 ± 0.96	75.8
16	5	8.47 ± 1.33	6.56 ± 0.80	77.4	nt[b]	---	7.14 ± 1.01	84.3	6.59 ± 1.41	77.7

[a] Treated/control in percentage. [b] Not tested because of the death of mice. [c] $p < 0.01$. [d] $p < 0.05$.

LoVo, and Colo320DM, were examined. A lower amount of compounds (6.9 μmol/kg) but more frequent treatments (days 1, 7, 11, 15, 22, 28, 49) were applied. The tumor growth inhibition of AN-152 was 20%, 75%, 67%, and 74%, respectively. These are the only reported data on the treatment of colon cancer bearing mice to which our results can be compared.

Conjugates. Daunorubicin, an antineoplastic agent widely used in tumor therapy, was attached to GnRH-III as a targeting moiety, which has itself an antiproliferative effect on cancer cells. The oxo group at the C-13 position was used as a conjugation site, because the acylation of the amino group of daunosamine by GnRH peptide led to the loss of biological activity (Figure 1). An oxime bond was formed between the keto group of daunorubicin and the aminooxyacetyl group of the GnRH-III derivative (Figure 2). As the oxime bond is relatively stable between pH 3 and 8 (*39*), as well as under in vitro and in vivo biological experimental conditions (*40*), an enzyme-labile GFLG tetrapeptide spacer was incorporated between the decapeptide and daunorubicin. This spacer sequence can be cleaved by lysosomal enzymes (e.g., Cathepsin B) (*41, 42*), and it was successfully applied in methotrexate and doxorubicin containing conjugates (*42, 43*). For comparative studies, the doxorubicin containing conjugate (Dox-GnRH-III) was also prepared under the same conditions. The purified conjugates were characterized by RP-HPLC and ESI-MS (Table 1; Supporting Information S3−S5).

^{1}H and ^{13}C NMR Analyses of the Carboxymethyloxime Derivative of Daunorubicin (Dau-Aoa-OH). A simple model compound was prepared in order to analyze the oxime bond structure of Dau conjugate. The structure of O-carboxymethyloxime is unambiguously evidenced by the ^{1}H and ^{13}C NMR data assigned on the basis of DEPT, 2D-COSY, 2D-HMQC, 2D-HMBC, and DNOE measurements (Figure 3). The relative configuration of the daunoseamine motif is clearly reflected from the split of the signals originated from the skeletal hydrogens and the mutual NOEs (3.7−4.2%) measured between the axial 3′-H and 5′-H protons. The broad singlets of 1′-H and 4′-H associated with weak vicinal couplings refer to their equatorial position, and consequently to the axial position of 1′-cycloalkoxy- and 4′-OH groups, respectively. The relatively small split (4.9 Hz) of the triplet from the 7-H cyclohexene proton points to its pseudoequatorial orientation. In the ^{1}H−^{13}C-HMBC spectrum, 7-H exhibits a cross peak with the C-13 signal originated from their 4*J* coupling along a special "W"-arrangement of the bonds transmitting the interaction. Accordingly, the cyclohexene ring condensed to antraquinone carries the pseudoequatorial oxime moiety in the trans position relative to the pseudoaxial daunosamine unit.

The weak NOEs (1.6−1.8%) detected between the 14-H methyl- and 15-H O-carboxymethyl protons in the oxime moiety with "*E*" configuration can be ascribed to the increased lifetime of the rotamer stabilized by a quasi six-membered chelate ring involving the imino nitrogen and the carboxyl proton [δ·(CO_2H) ∼ 14.0 ppm]. This downfield-shifted signal is considerably broadened due to exchange. The "*E*"-oxime configuration is also supported by the upfield-shifted carbon line of C-14 (10.8 ppm), of the which signal would be expected at around 16−17 ppm in a "*Z*"-oxime isomer.

Enzymatic Digestion of Dau-GnRH-III Conjugate by Cathepsin B. Cathepsin B, known to be overexpressed in cancer cells (*44*), is one of the lysosomal enzymes involved in the intracellular digestion of extracellular proteins taken up by endocytosis. The cleavage specificity of Cathepsin B can be used as a basis for controlled intracellular drug release. In the present work, oxime bond linked Dau-GnRH-III conjugate containing a GFLG tetrapeptide spacer between the anticancer drug and the GnRH-III decapeptide was subjected to Cathepsin B catalyzed hydrolysis. Liquid chromatography in combination with mass

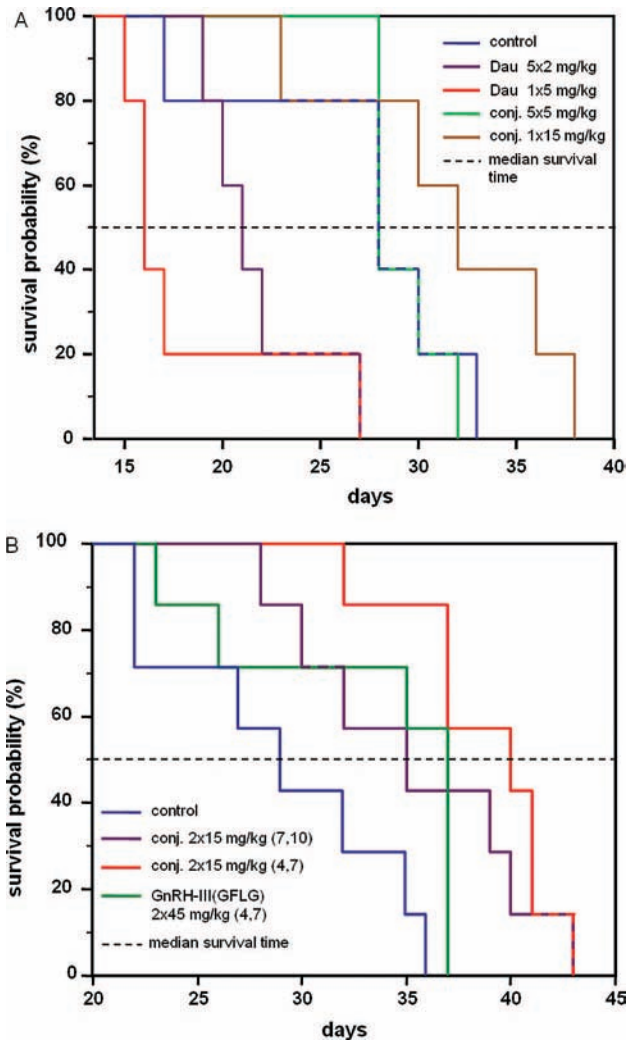

Figure 7. (A) Survival according to the Kaplan−Meier analysis. Control group compared to the groups treated with different doses of Dau or Dau-GnRH-III conjugate (B) Survival according to the Kaplan−Meier analysis. Control group compared to the groups treated twice with Dau-GnRH-III conjugate on different days or with GnRH-III(GFLG).

spectrometric analysis of the reaction mixture indicated several Cathepsin B cleavage sites, namely, the peptide bonds -Gly-Phe-, -Phe-Leu-, -Leu-Gly- inside the spacer sequence and the isopeptide bond -Lys(Gly)-. In addition, the cleavage of the peptide bond -^{7}Trp-^{8}Lys- in the GnRH-III sequence was determined (Figure 4A,C). Total ion chromatogram and mass spectra of each fragment produced by Cathepsin B digestion are presented in the Supporting Information S6 and S7. LC/MS analysis of a solution of Dau-GnRH-III which was incubated at 37 °C for 24 h revealed no degradation of the conjugate in the absence of Cathepsin B (Figure 4B).

In Vitro Cytotoxicity and Cytostatic Effect. In vitro cytotoxicity of free drugs and their GnRH-III conjugates was measured on MCF-7 tumor cell lines by MTT assay. The cells were incubated with the compounds in the (5.1×10^{-4}) to (2×10^{2}) μM concentration range for 6 h at 37 °C. Daunorubicin and doxorubicin elicited similar cytotoxicity with LC_{50} values of 0.67 and 0.68 μM, respectively (Table 2, Supporting Information S8). The conjugates were toxic at a higher concentration, with Dau-GnRH-III having significant higher toxicity than Dox-GnRH-III (LC_{50} values are 40.11 ± 25.31 μM and 85.18 ± 3.85 μM, respectively). Long-term tumor cell growth inhibition was also studied on MCF-7 and C26 tumor cell lines that express GnRH receptors (Supporting Information S1). In this case, cells were incubated with Dau-GnRH-III or Dox-GnRH-III conjugates for 6 h; then, the treated cells were maintained in fresh culture medium at 37 °C for a further 72 h. The Dau or Dox conjugates showed a higher cytostatic effect on MCF-7 tumor cells than on C26. The difference between the IC_{50} values of Dau-GnRH-III (3.94 ± 1.18 μM) and Dox-GnRH-III (5.38 ± 1.86 μM) was not significant on MCF-7 cells (Table 2, Supporting Information S8). On C26 tumor cells, the conjugates were less potent, and the Dau-GnRH-III conjugate had a lower IC_{50} value (22.46 ± 1.74 μM) than Dox-GnRH-III (46.10 ± 6.06 μM). The GnRH-III(GFLG) hormone derivative had no cytostatic effect in the 10^{-4}−10^{2} μM concentration range (IC_{50} > 100 μM).

In Vivo Toxicity. In vivo toxicity of the free daunorubicin and Dau-GnRH-III conjugate was studied on healthy BDF-1 female mice (7 mice in each group) in our preliminary toxicological experiments. The BDF-1 inbred mouse strain is internationally accepted for maintenance of the most transplantable tumors. Mice were treated i.p. once with 15 mg (26.6 μmol)/kg body weight free daunorubicin or equivalent daunorubicin containing conjugate (62.5 mg/kg, 24% Dau content). The experiment lasted for 21 days. All mice treated with the free drug died between days 10 and 12 (11.3 ± 0.76 days). However, all mice treated with the Dau-GnRH-III conjugate survived until the end of the experiment (day 21). The body weight of the Dau-GnRH-III treated mice slightly decreased during the first three days, and then it increased up to the body weight values observed in the case of the control group (Figure 5).

In Vivo Antitumor Effect. For the study of the in vivo antitumor effect, Balb/c mice were transplanted with C26 tumor (5 mice in each group), because the maintenance of colon-26 solid carcinoma tumor is realizable exclusively in Balb/c inbred mouse strain. Both free daunorubicin and Dau-GnRH-III conjugate showed a moderate in vivo antitumor activity on C26 colon tumor bearing mice. The first treatment in all cases was performed on day 7 after tumor trasplantation. The compounds were administered once or 5 times on every second day. Measurement of the tumor volume was continued until day 16 after tumor transplantation, because one mouse from the nontreated control group died on day 17. The application of the free drug at 5 mg (8.86 μmol)/kg body weight (only one injection) resulted in the most effective inhibition of the tumor growth (36.4% on average to the control) in one week after treatment (Figure 6A, Table 3). However, 4 of 5 mice died between days 15 and 17 (median survival day is 16; $p = 0.0009$, log-rank test) because of the toxicity of daunorubicin (Figure 7A). Using a lower dose of free daunorubicin, 5 × 2 mg (3.55 μmol)/kg, resulted in average 22.6% inhibition of tumor growth as compared to the control group before terminating the experiment (Figure 6A, Table 3). The toxic side effect of daunorubicin was also observed in this case, because the median survival time calculated from the Kaplan−Meier survival curve (*45*) was 21 days ($p = 0.0342$, log-rank test) compared with 28 days for control population (Figure 7A). A similar level of inhibition (22.3% on average) was determined in the case of Dau-GnRH-III conjugate treatment when 62.5 mg (26.6 μmol)/kg body weight dose was used (Figure 6A, Table 3). However, a lower dose (20.8 mg (8.86 μmol/kg) of conjugate was less effective even in the case of 5× repeated treatments of tumor bearing mice (15.7% on average) (Figure 6A, Table 3). Using the conjugate (62.5 mg/kg), the data of median survival time showed a moderate increase to the control (32 days (14.3%), $p = 0.1650$ log-rank test), while the increase was significant in comparison to the group of mice treated with free drug (>52%) (Figure 7A).

In the second experiment, the treatments with Dau-GnRH conjugate (62.5 mg (26.6 μmol)/kg) were carried out either on

Table 4. Antitumor Effect of Dau-GnRH-III Conjugate and GnRH-III(GFLG) on Mice Bearing C26 Tumor (Experiment 2)

		tumor volume (cm^3) ± SD						
days after tumor transplant.	number of mice	control	Dau-GnRH-III conjugate treatment on days 4, 7	*T/C* (%)[a]	Dau-GnRH-III conjugate treatment on days 7, 10	*T/C* (%)	GnRH-III(GFLG) treatment on days 4, 7	*T/C* (%)
7	7	0.203 ± 0.03	0.172 ± 0.06		0.182 ± 0.06		0.193 ± 0.06	
9	7	0.387 ± 0.20	0.118 ± 0.03	30.5[b]	0.144 ± 0.04	37.2[b]	0.273 ± 0.05	70.5[c]
11	7	0.569 ± 0.14	0.125 ± 0.04	22.0[b]	0.127 ± 0.09	22.3[b]	0.344 ± 0.20	60.5[c]
14	7	1.010 ± 0.36	0.586 ± 0.54	58.0[c]	0.597 ± 0.48	59.1[c]	0.861 ± 0.48	85.4
16	7	2.094 ± 0.70	1.191 ± 0.85	56.9[c]	1.281 ± 0.68	61.2[c]	1.544 ± 0.97	73.7
18	7	3.888 ± 1.20	2.078 ± 1.01	53.3[c]	2.344 ± 0.53	60.3	2.630 ± 0.74	67.6
21	7	5.677 ± 1.71	3.044 ± 1.07	53.6[c]	3.866 ± 1.50	68.1	4.665 ± 1.63	82.2

[a] Treated/control in percentage. [b] $p < 0.01$. [c] $p < 0.05$.

days 4 and 7 or on days 7 and 10 after the transplantation of tumor xenograft. Significantly higher tumor growth inhibition was observed in both cases at the end of the experiment (46% and 32% inhibition, respectively, measured on day 21) (Figure 6B, Table 4). Even if the tumor growth was slower in this experiment, we could conclude that until day 11 the tumor volume decreased due to the treatments, with 70−80% tumor growth inhibition being detected during this time. The antitumor effect of the free GnRH-III(GFLG) hormone derivative was also studied. The data indicated slight but not significant inhibition (18%) of tumor growth compared to the control group at the end of the experiment. However, during the treatment period (until day 11) 30−40% tumor growth inhibition induced by the hormone peptide alone was observed using the same amount (26.6 μmol; 45 mg/kg) of peptide as was in conjugate (Figure 6B, Table 4). These data indicate that GnRH-III(GFLG) hormone derivative had its own in vivo antitumor effect on C26 colon cancer, which was only 40−50% of the inhibition determined in the case of treatment with the conjugate.

In this experiment, the median survival probability of the control and treated animals (on days 7 and 10 or 4 and 7) was 29, 35, and 40 days, respectively. The increase of the survival time of treated animals was 21% and 38% compared to the control group. The group of mice treated only with the GnRH-III derivative also showed increased survival time, but the last 4 of 7 mice died on day 37 after tumor transplantation; in this way, the median survival time cannot be used properly for comparison. However, the average survival time of the control group (29 days) and the group treated with GnRH-III derivative (33 days) shows 14% increase. According to the Kaplan−Meier curves, the longest survival (40 days) was found in the case of the group treated with Dau-GnRH-III conjugate on days 4 and 7 (compared to the control group, $p = 0.0009$, log-rank test).

The results show that the animals survived the lethal dose of daunorubicin if it was conjugated to GnRH-III derivative as a targeting moiety even in the case of repeated treatments. A single treatment with Dau-GnRH-III conjugate using 15 mg Dau content/kg body weight provided tumor growth inhibition similar to the treatment with daunorubicin 5 × 2 mg, but the lifetime was lengthened by using the conjugate instead of the free drug. Furthermore, the elevation of the number as well as the earlier start of treatments increased the efficiency of the conjugate. Significant tumor growth inhibition and survival of mice were observed in the case of treatment on days 4 and 7 using 62.5 mg (26.6 μmol)/kg body weight. Further optimization of the treatment schedule and doses (determination of MTD; maximal tolerated dose) is in progress.

CONCLUSIONS

In the present study, we report on the conjugation of daunorubicin to GnRH-III through the oxime bond. Considering the chemical and biological stability of the oxime bond, a tetrapeptide spacer cleavable by Cathepsin B was incorporated between the drug and the hormone. Dau-GnRH-III and Dox-GnRH-III conjugates had less but significant in vitro antitumor effects on MCF-7 human breast and C26 murine colon carcinoma cells compared to the free drugs. It is worth mentioning that daunorubicin conjugates previously prepared in our laboratory using branched-chain polypeptides with polylysine backbone (EAK and SAK) as carriers and *cis*-aconitic acid (cA) pH labile spacer had significantly less antiproliferative effect in vitro on C26 tumor cells (IC_{50} = 117.4 μM (cAD-SAK) and 629.9 μM (cAD-EAK)) and MDA-MB 435 P human breast cancer cells (IC_{50} = 195.2 μM for both) (*46*).

The in vivo antitumor effect of the new Dau-GnRH conjugate was determined on mice transplanted with a fast-growing, aggressive tumor type (C26 colon tumor). We found that higher daunorubicin content than the lethal dose was well-tolerated in the case of Dau-GnRH-III conjugate administration. Dau-GnRH-III could decrease the tumor growth similarly to daunorubicin (∼23%) in the case of a single treatment. The animals treated with Dau-GnRH-III had longer survival times compared to the untreated control group, while mice treated with the free drug died early. The repeated treatment with the conjugate (15 mg daunorubicin content/kg body weight) increased significantly the tumor growth inhibition (∼32%). We also found that the earlier start of the treatment had a positive effect on the efficiency (∼46% inhibition). In conclusion, the Dau-GnRH-III conjugate in which the components are connected by an oxime bond exhibited antitumor effect both in vitro and in vivo. To our knowledge, this is the first Dau-peptide conjugate containing an oxime bond that has in vivo antitumor activity. The conjugate was well-tolerated and did not show significant toxic side effects even in high doses. In spite of the significant tumor inhibition of Dau, the effect on survival was considerably decreased by the late toxic effect. In contrast to Dau, in addition to the tumor inhibitory effect, the prolongation of the lifetime was observed in the case of conjugate-treated tumor bearing mice. The pharmacological optimization of the treatment using the Dau-GnRH-III conjugate as well as the detailed study of the mechanism of action of the conjugate are in progress. Furthermore, in vitro and in vivo antitumor activity of Dau-GnRH-III conjugate will be tested on other types of tumors.

ACKNOWLEDGMENT

This work was supported by grants from the Hungarian National Science Fund (OTKA T 049814 and K-68285), the Ministy of Education ("Medichem 2" 1/A/005/2004), the Ministry of Health (ETT 202/2006), GVOP-3.2.1.-2004-04-0005/3.0, GVOP-3.2.1-2004-04-0352/3.0, and the Zukunftskolleg, University of Konstanz. The authors thank Anikó Horváth for her excellent technical support.

Supporting Information Available: (i) Western blot analysis of solubilized membrane proteins from C26 (mouse colon), HT-29 (human colon), and MCF-7 (human breast) cells; (ii) HPLC chromatograms and mass spectra of the compounds; (iii) enzymatic digestion of Dau-GnRH-III conjugate by Cathepsin

B: LC/MS analysis of the reaction mixture (24 h reaction time). (iv) Cytostatic effect of the compounds on MCF-7 human breast cancer cells. This material is available free of charge via the Internet at http://pubs.acs.org.

LITERATURE CITED

(1) Nagy, A., and Schally, A. V. (2005) Targeting of cytotoxic luteinizing hormone-releasing hormone analogs to breast, ovarian, endometrial, and prostate cancers. *Biol. Reprod. 73*, 851–859.

(2) Dharap, S. S., Wang, Y., Chandna, P., Khandare, J. J., Qui, B., Gunaseelan, S., Sinko, P. J., Stein, S., Farmanfarmaian, A., and Minko, T. (2005) Tumor-specific targeting of an anticancer drug delivery system by LHRH peptide. *Proc. Natl. Acad. Sci. U.S.A. 102*, 12962–12967.

(3) Rahimipour, S., Ben-Aroya, N., Ziv, K., Chen, A., Fridkin, M., and Koch, Y. (2003) Receptor-mediated targeting of a photosensitizer by its conjugation to gonadotropin-releasing hormone analogues. *J. Med. Chem. 46*, 3965–3974.

(4) David, A., Kopeckova, P., Minko, T., Rubinstein, A., and Kopecek, J. (2004) Design of a multivalent galactoside ligand for selective targeting of HPMA copolymer-doxorubicin conjugates to human colon cancer cells. *Eur. J. Cancer 40*, 148–157.

(5) Yamazaki, N., Kojima, S., Bovin, N. V., Andre, S., Gabius, S., and Gabius, H. J. (2000) Endogenous lectins as targets for drug delivery. *Adv. Drug Delivery Rev. 43*, 225–244.

(6) Wirth, M., Gerhardt, K., Wurm, C., and Gabor, F. (2002) Lectin-mediated drug delivery: influence of mucin on cytoadhesion of plant lectins in vitro. *J. Controlled Release 79*, 183–191.

(7) Wroblewski, S., Rihova, B., Rossmann, P., Hudcovicz, T., Rehakova, Z., Kopeckova, P., and Kopecek, J. (2001) The influence of a colonic microbiota on HPMA copolymer lectin conjugates binding in rodent intestine. *J. Drug Targeting 9*, 85–94.

(8) Minko, T., Dharap, S. S., Pakunlu, R. I., and Wang, Y. (2004) Molecular targeting of drug delivery systems to cancer. *Curr. Drug Targets 5*, 389–406.

(9) Low, P. S., and Antony, A. C. (2004) Folate receptor-targeted drugs for cancer and inflammatory diseases. *Adv. Drug Delivery Rev. 56*, 1055–1058.

(10) Cho, N., Chueh, P. J., Kim, C., Caldwell, S., Morre, D. M., and Morre, D. J. (2002) Monoclonal antibody to a cancer-specific and drug-responsive hydroquinone (NADH) oxidase from the sera of cancer patients. *Cancer Immunol., Immunother. 51*, 121–129.

(11) Trail, P. A., King, H. D., and Dubowchik, G. W. (2003) Monoclonal antibody drug immunoconjugates for targeted treatment of cancer. *Cancer Immunol., Immunother. 52*, 328–337.

(12) Mao, W., Luis, E., Ross, S., Silva, J., Tan, C., Crowley, C., Chui, C., Franz, G., Senter, P., Koeppen, H., and Polakis, P. (2004) EphB2 as a therapeutic antibody drug target for the treatment of colorectal cancer. *Cancer Res. 64*, 781–788.

(13) Keller, G., Schally, A. V., Gaiser, T., Nagy, A., Baker, B., Westphal, G., Halmos, G., and Engel, J. B. (2005) Human malignant melanomas express receptors for luteinizing hormone releasing hormone allowing targeted therapy with cytotoxic luteinizing hormone releasing hormone analogue. *Cancer Res. 65*, 5857–5863.

(14) Keller, G., Schally, A. V., Gaiser, T., Nagy, A., Baker, B., Halmos, G., and Engel, J. B. (2005) Receptors for luteinizing hormone releasing hormone (LHRH) expressed in human non-Hodgkin's lymphomas can be targeted for therapy with cytotoxic LHRH analogue AN-207. *Eur. J. Cancer 41*, 2196–2202.

(15) Schally, A. V., Arimura, A., Kastin, A. J., Matsuo, H., Baba, Y., Redding, T. W., Nair, R. M. G., Debeljuk, L., and White, W. F. (1971) Gonadotropin-releasing hormone: one polypeptide regulates secretion of luteinizing and follicle-stimulating hormones. *Science 173*, 1036–1038.

(16) Chengalvala, M. V., Pelletier, J. C., and Kopf, G. S. (2003) GnRH agonists and antagonists in cancer therapy. *Curr. Med. Chem. 3*, 399–410.

(17) Sharoni, Y., Bosin, E., Münster, A., Levy, L., and Schally, A. V. (1989) Inhibition of growth of human mammary tumor cells by potent antagonists of luteinizing hormone-releasing hormone. *Proc. Natl. Acad. Sci. U.S.A. 86*, 1648–1651.

(18) Segal-Abramson, T., Kitroser, H., Levy, J., Schally, A. V., and Sharoni, Y. (1992) Direct effects of luteinizing hormone-releasing hormone agonists and antagonists on MCF-7 mammary cancer cells. *Proc. Natl. Acad. Sci. U.S.A. 89*, 2336–2339.

(19) Gründker, C., Völker, P., and Emons, G. (2001) Antiproliferative signaling of luteinizing hormone-releasing hormone in human endometrial and ovarian cancer cells through G protein alpha(I)-mediated activation of phosphotyrosine phosphatase. *Endocrinology 142*, 2369–2380.

(20) Janáky, T., Juhász, A., Bajusz, S., Csernus, V. J., Skralovic, G., Bokser, L., Milovanovics, S., Redding, T. W., Rékasi, Z., Nagy, A., and Schally, A. V. (1991) Analogues of luteinizing hormone-releasing hormone containing cytotoxic groups. *Proc. Natl. Acad. Sci. U.S.A. 89*, 972–976.

(21) Nagy, A., Szöke, B., and Schally, A. V. (1993) Selective coupling of methotrexate to peptide hormone carrier through a γ-carboxamide linkage of its glutamic acid moiety: Benzotriazol-1-yloxytris(dimethylamino)phosphonium hexafluorophosphate activation in salt coupling. *Proc. Natl. Acad. Sci. U.S.A. 90*, 6373–6376.

(22) Nagy, A., Schally, A. V., Armatis, P., Szepesházi, K., Halmos, G., Kovács, M., Zarándi, M., Groot, K., Miyazaka, M., Jungwirth, A., and Horváth, J. (1996) Cytotoxic analogs of luteinizing hormone-releasing hormone containing doxorubicin or 2-pyrrolinodoxorubicin, a derivative 500−1000 times more potent. *Proc. Natl. Acad. Sci. U.S.A. 93*, 7269–7273.

(23) Kovács, M., Schally, A. V., Nagy, A., Koppán, M., and Groot, K. (1997) Recovery of pituitary function after treatment with a targeted cytotoxic analog of luteinizing hormone-releasing hormone. *Proc. Natl. Acad. Sci. U.S.A. 94*, 1420–1425.

(24) Sower, S. A., Chiang, Y.-C., Lovas, S., and Conlon, J. M. (1993) Primary structure and biological activity of a third gonadotropin-releasing hormone from lamprey brain. *Endocrinology 132*, 1125–1131.

(25) Lovas, S., Pályi, I., Vincze, B., Horváth, J., Kovács, M., Mezö, I., Tóth, G., Teplán, I., and Murphy, R. F. (1998) Direct anticancer activity of gonadotropin-releasing hormone-III. *J. Pept. Res. 52*, 384–389.

(26) Kovács, M., Seprödi, J., Koppán, M., Horváth, J. E., Vincze, B., Teplán, I., and Flerkó, B. (2002) Lamprey gonadotropin hormone-releasing hormone-III has no selective follicle-stimulating hormone-releasing effect in rats. *J. Neuroendocrinol. 14*, 1–14.

(27) Kovács, M., Vincze, B., Horváth, J. E., and Seprödi, J. (2007) Structure-activity study on the LH- and FSH-releasing and anticancer effects of gonadotropin-releasing hormone (GnRH)-III analogs. *Peptides 28*, 821–829.

(28) Pályi, I., Vincze, B., Lovas, S., Mezö, I., Pató, J., Kálnai, A., Túri, G., Gaál, D., Mihalik, R., Péter, I., Teplán, I., and Murphy, R. F. (1999) Gonadotropin-releasing hormone analogue conjugates with strong selective antitumor activity. *Proc. Natl. Acad. Sci. U.S.A. 96*, 2361–2366.

(29) Mezö, I., Lovas, S., Pályi, I., Vincze, B., Kálnay, A., Turi, G., Vadász, Zs., Seprödi, J., Idei, M., Tóth, G., Gulyás, É., Ötvös, F., Mák, M., Horváth, J. E., Teplán, I., and Murphy, R. F. (1997) Synthesis of gonadotropin-releasing hormone III analogs. Structure-antitumor activity relationship. *J. Med. Chem. 40*, 3353–3358.

(30) Herédi-Szabó, K., Lubke, J., Tóth, G., Murphy, R. F., and Lovas, S. (2005) Importance of the central region of lamprey gonadotropin-releasing hormone III in the inhibition of breast cancer cell growth. *Peptides 26*, 419–422.

(31) Mezö, G., Czajlik, A., Manea, M., Jakab, A., Farkas, V., Majer, Z., Vass, E., Bodor, A., Kapuvári, B., Boldizsár, M.,

Vincze, B., Csuka, O., Perczel, A., Przybylski, M., and Hudecz, F. (2007) Structure, enzymatic stability and antitumor activity of sea lamprey GnRH-III and its dimer derivatives. *Peptides 28*, 806–820.

(32) Mezö, G., Manea, M., Szabó, I., Vincze, B., and Kovács, M. (2008) New derivatives of GnRH as potential anticancer therapeutic agents. *Curr. Med. Chem. 15*, 2366–2379.

(33) Gilladoga, A. C., Manuel, C., Tan, C. T., Wollner, N., Sternberg, S. S., and Murphy, M. L. (1976) The cardiotoxicity of adriamycin and daunorubicin in children. *Cancer 37*, 1070–1078.

(34) Minotti, G., Cavaliere, A. F., Mordente, A., Rossi, M., Schiavello, R., Zamparelli, M., and Possati, G.-F. (1995) Secondary alcohol metabolites mediate iron delocalization in cytosolic fractions of myocardial biopsies exposed to anticancer anthracyclines. Novel linkage between anthracycline metabolism and iron-induced cardiotoxicity. *J. Clin. Invest. 95*, 1595–1605.

(35) Gao, Y.-G., Liaw, Y.-C., Li, Y.-K., van der Marel, G. A., van Boom, J. H., and Wang, A. H.-J. (1991) Facile formation of crosslinked adduct between DNA and daunorubicin derivative MAR70 mediated by formaldehyde: Molecular structure of the MAR70-dCGT^{n}ACG) covalent adduct. *Proc. Natl. Acad. Sci. U.S.A. 88*, 4845–4849.

(36) Mezö, G., Manea, M., Jakab, A., Kapuvári, B., Bösze, S., Schlosser, G., Przybylski, M., and Hudecz, F. (2004) Synthesis and structural characterization of bioactive peptide conjugates using thioether linkage approaches. *J. Pept. Sci. 10*, 701–713.

(37) Tomayko, M. M., and Reynolds, C. P. (1989) Determination of subcutaneous tumor size in athymic (nude) mice. *Cancer Chemother. Pharmocol. 24*, 148–154.

(38) Szepesházi, K., Schally, A. V., and Halmos, G. (2007) LH-RH receptors in human colorectal cancers: Unexpected molecular targets for experimental therapy. *Int. J. Oncol. 30*, 1485–1492.

(39) Shao, J., and Tam, J. P. (1995) Unprotected peptides as building blocks for the synthesis of peptide dendrimers with oxime, hydrazone and thiazolidine linkages. *J. Am. Chem. Soc. 117*, 3893–3899.

(40) Braslawsky, G. R., Kadow, K., Knipe, J., McGoff, K., Edson, M., Kaneko, T., and Greenfields, R. S. (1991) Adriamycin(hydrazone)-antibody conjugates require internalization and intracellular acid hydrolysis for antitumor activity. *Cancer Immunol. Immunother. 33*, 367–374.

(41) Omelyanenko, V., Gentry, C., Kopeckova, C., and Kopecek, J. (1998) HPMA copolymer-anticancer drug-OV-TL16 antibody conjugates. II. Processing in epithelial ovarian carcinoma cells in vitro. *Int. J. Cancer 75*, 600–608.

(42) Bai, K. B., Láng, O., Orbán, E., Szabó, R., Köhidai, L., Hudecz, F., and Mezö, G. (2008) Design, synthesis, and in vitro activity of novel drug delivery systems containing tuftsin derivatives and methotrexate. *Bioconjugate Chem. 19*, 2260–2269.

(43) Veronese, F. M., Schiavon, O., Pasut, G., Mendichi, R., Andersson, L., Tsirk, A., Ford, J., Wu, G., Kneller, S., Davis, J., and Duncan, R. (2005) PEG-doxorubicin conjugates: influence of polymer structure on drug release, in vitro cytotoxicity, biodistribution, and antitumor activity. *Bioconjugate Chem. 16*, 775–784.

(44) Sibrian-Vazquez, M., Jensen, T. J., and Vicente, M. G. H. (2008) Synthesis, characterization, and metabolic stability of porphyrin-peptide conjugates bearing bifunctional signaling sequences. *J. Med. Chem. 51*, 2915–2923.

(45) Kaplan, E. L., and Meier, P. (1958) Nonparametric estimation from incomplete observations. *J. Am. Stat. Assoc. 53*, 457–481.

(46) Reményi, J., Csík, G., Kovács, P., Reig, F., and Hudecz, F. (2006) The effect of the structure of branched polypeptide carrier on intracellular delivery of daunorubicin. *Biochim. Biophys. Acta 1758*, 280–289.

BC800542U

Supporting Information

Development of an Oxime Bond Containing Daunorubicin-Gonadotropin-Releasing Hormone-III Conjugate as a Potential Anticancer Drug

Ildikó Szabó, Marilena Manea, Erika Orbán, Antal Csámpai, Szilvia Bősze, Rita Szabó, Miguel Tejeda, Dezső Gaál, Bence Kapuvári, Michael Przybylski, Ferenc Hudecz, Gábor Mező*

*Correspondence to: Prof. Dr. Gábor Mező, Research Group of Peptide Chemistry, Hungarian Academy of Sciences, Eötvös L. University, 1117 Budapest, Pázmány P. stny. 1/A, Hungary; Tel.: (+36)-1-209-0555/1433; Fax: (+36)-1-372-2620; e-mail: gmezo@elte.hu

Table of Contents:

Western blot analysis of solubilized membrane proteins from C26 (mouse colon), HT-29 (human colon) and MCF-7 (human breast) cells…….....S2
HPLC chromatogram and mass spectrum of Dau-GnRH-III conjugate…….....S3
HPLC chromatogram and mass spectrum of Dox-GnRH-III conjugate …….....S4
HPLC chromatogram and mass spectrum of Dau-Aoa-OH.....……S5
Enzymatic digestion of Dau-GnRH-III conjugate by Cathepsin B: LC/MS analysis of the reaction mixture (24 hrs reaction time)…….……..S6-S7
Cytostatic effect of Dau, Dau-GnRH-III, Dox-GnRH-III and GnRH-III(GFLG) on MCF-7 human breast cancer cell lines (results of one experiment)……..S8

Figure 1: Western blot analysis of solubilized membrane proteins from C26 (mouse colon), HT-29 (human colon) and MCF-7 (human breast) cells

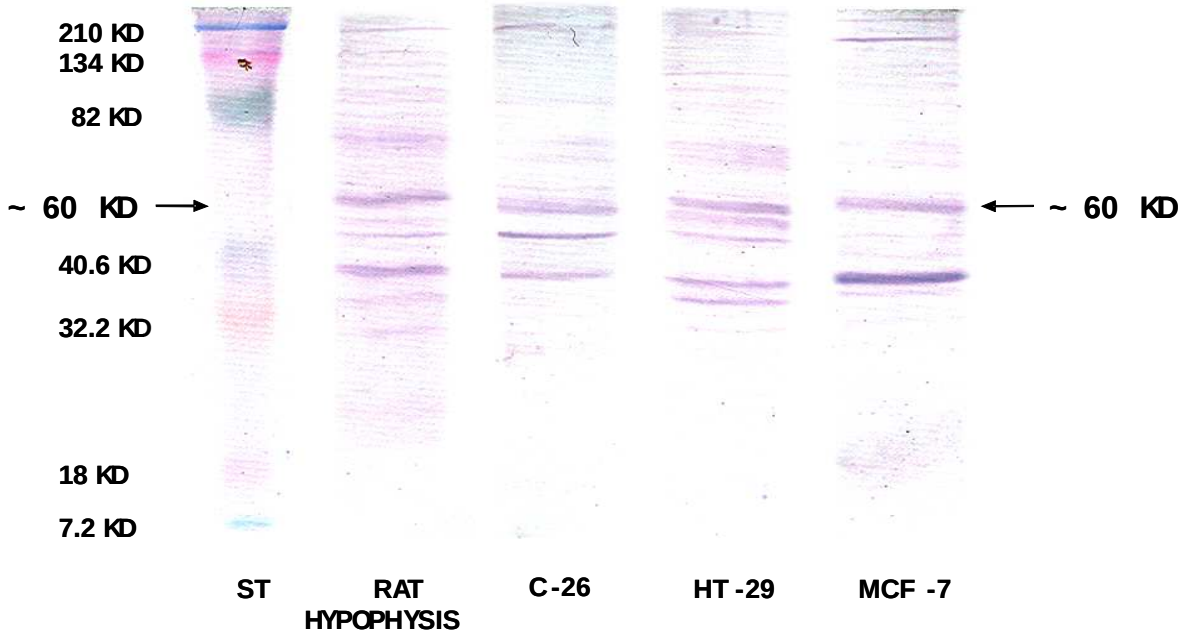

Figure 2: HPLC chromatogram and mass spectrum of Dau-GnRH-III conjugate

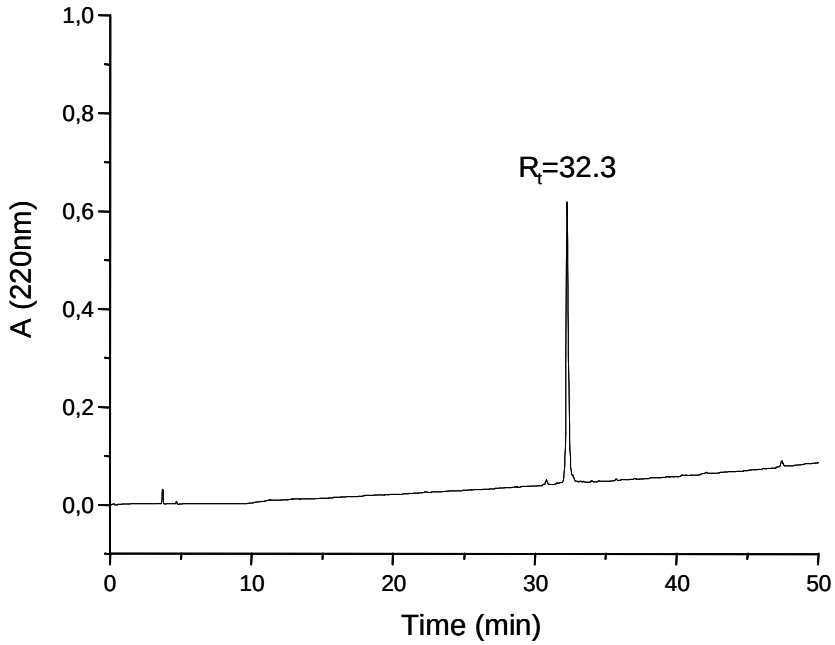

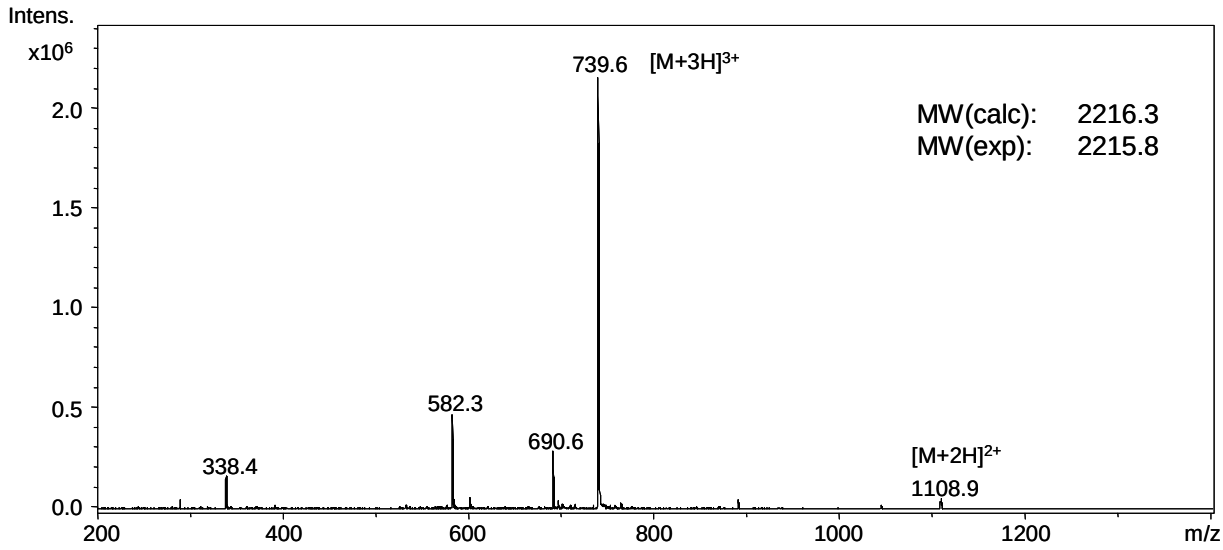

Figure 3: HPLC chromatogram and mass spectrum of Dox-GnRH-III conjugate

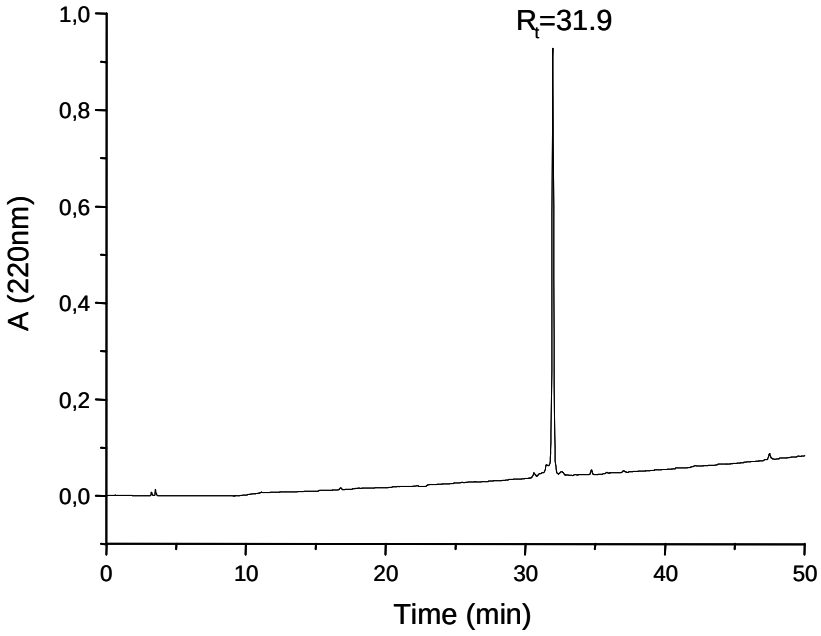

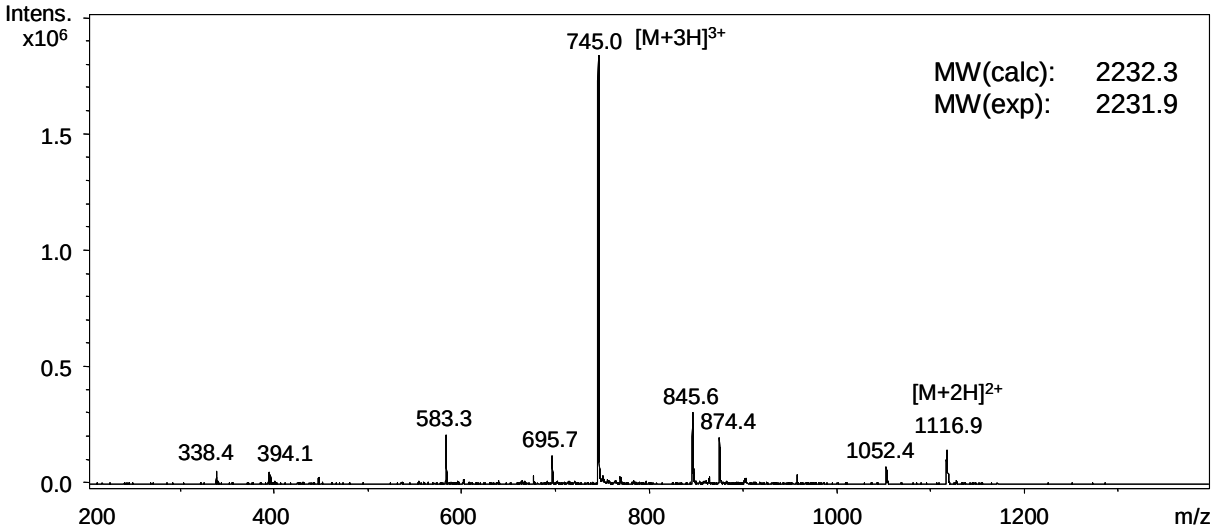

Figure 4: HPLC chromatogram and mass spectrum of Dau-Aoa-OH

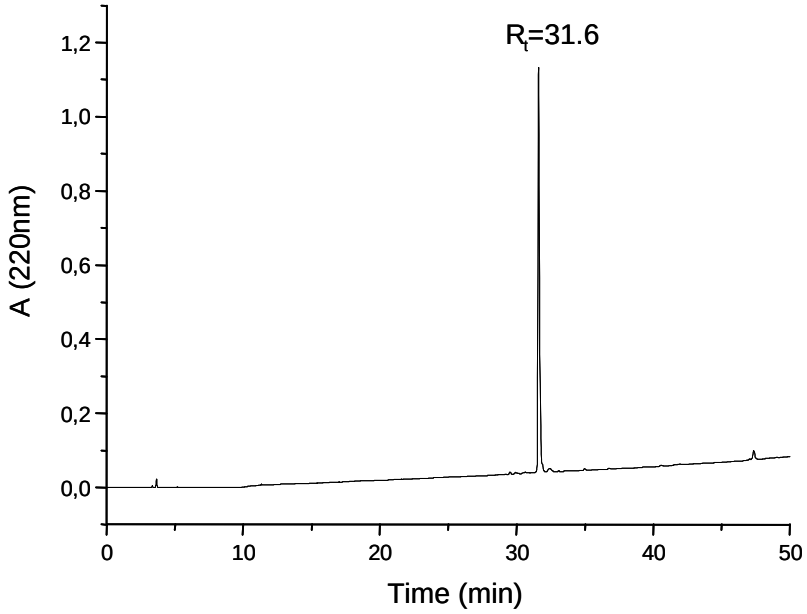

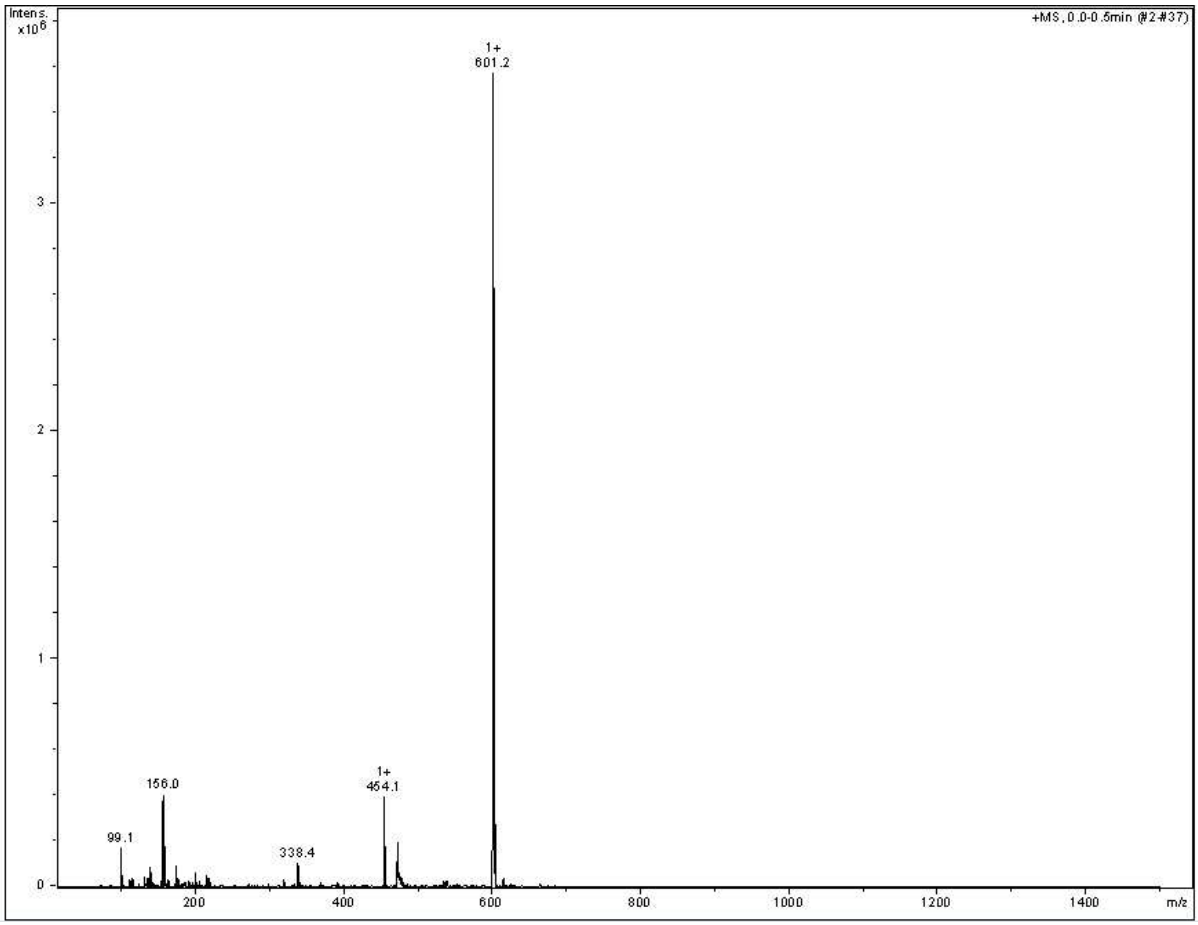

Figure 5: Enzymatic digestion of Dau-GnRH-III conjugate by Cathepsin B: LC/MS analysis of the reaction mixture (24 hrs reaction time)

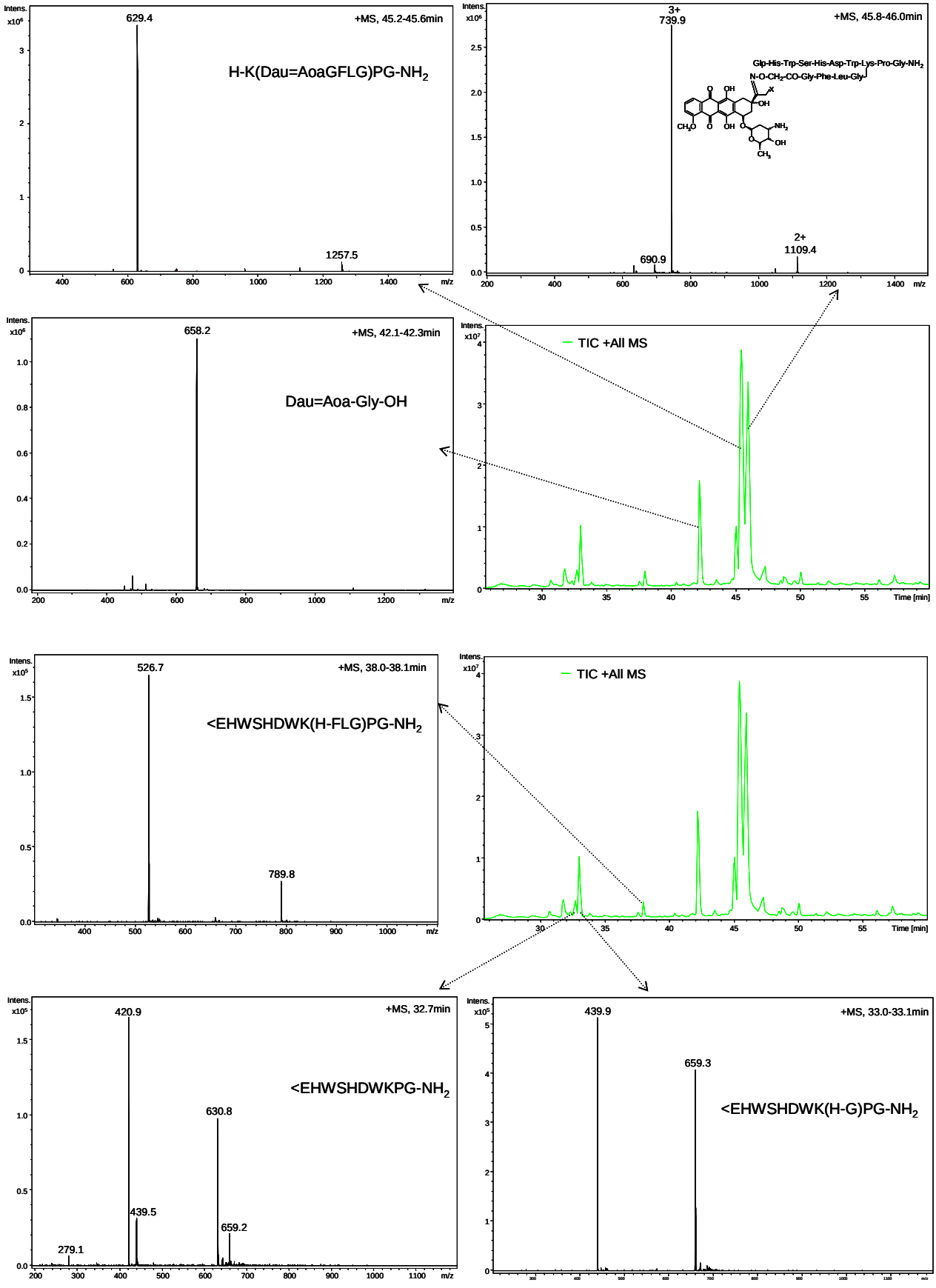

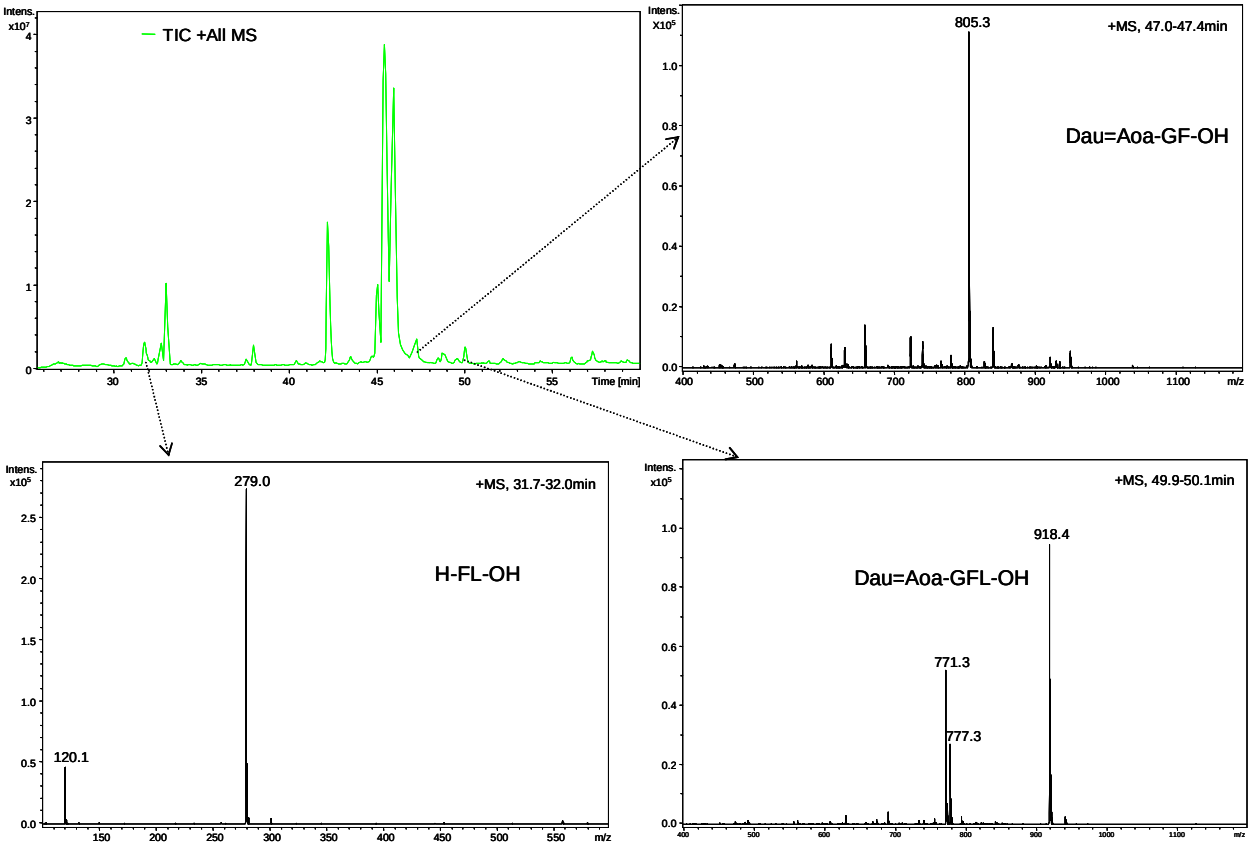
TIC +All MS
Intens.
x10^7
Time [min]
805.3
+MS, 47.0-47.4min
Dau=Aoa-GF-OH
Intens.
X10^5
m/z
279.0
+MS, 31.7-32.0min
H-FL-OH
120.1
Intens.
x10^5
m/z
+MS, 49.9-50.1min
Dau=Aoa-GFL-OH
918.4
771.3
777.3
Intens.
x10^5
m/z

Figure 6. Cytostatic effect of Dau-GnRH-III, Dox-GnRH-III and GnRH-III(GFLG) on MCF-7 human breast cancer cell lines (results of one experiment)

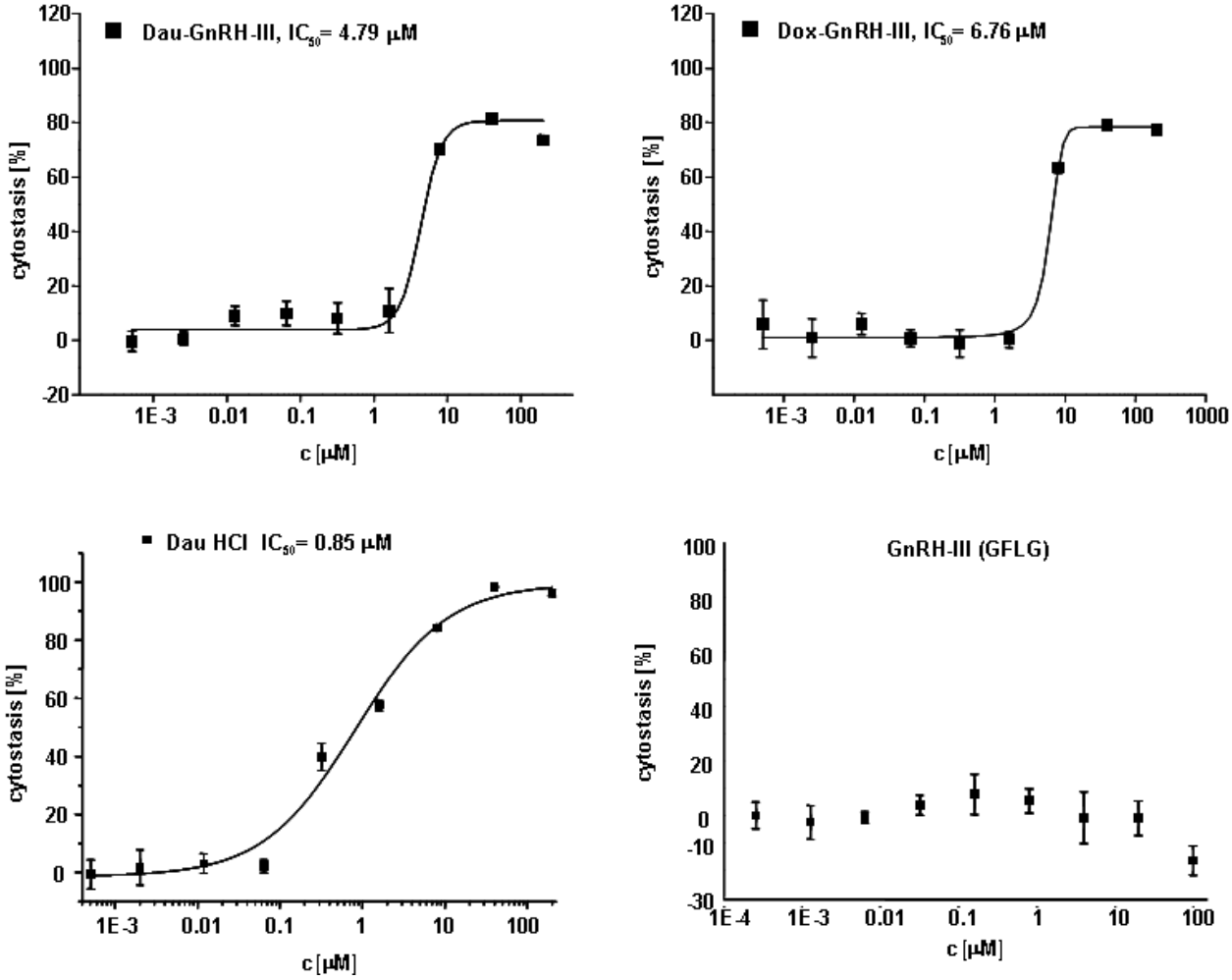

Bioconjugate Chemistry 20th Anniversary

Subscriber access provided by SHEMYAKIN-OVCHINNIKOV INST

Article

Optimized Synthesis and Enhanced Efficacy of Novel Triplex-Forming Camptothecin Derivatives Based on Gimatecan

Pierre Vekhoff, Ludovic Halby, Kahina Oussedik, Sabrina Dallavalle, Lucio Merlini, Christine Mahieu, Ame#lie Lansiaux, Christian Bailly, Alexandre Boutorine, Claudio Pisano, Giuseppe Giannini, Domenico Alloatti, and Paola B. Arimondo

Bioconjugate Chem., **2009**, 20 (4), 666-672• DOI: 10.1021/bc800494y • Publication Date (Web): 23 March 2009

Downloaded from http://pubs.acs.org on May 8, 2009

More About This Article

Additional resources and features associated with this article are available within the HTML version:

- Supporting Information
- Access to high resolution figures
- Links to articles and content related to this article
- Copyright permission to reproduce figures and/or text from this article

View the Full Text HTML

ACS Publications
High quality. High impact.

Bioconjugate Chemistry is published by the American Chemical Society. 1155 Sixteenth Street N.W., Washington, DC 20036

Optimized Synthesis and Enhanced Efficacy of Novel Triplex-Forming Camptothecin Derivatives Based on Gimatecan

Pierre Vekhoff,[†,‡,§] Ludovic Halby,[†,‡] Kahina Oussedik,[†,‡,§] Sabrina Dallavalle,[||] Lucio Merlini,[||] Christine Mahieu,[⊥] Amélie Lansiaux,[⊥] Christian Bailly,[⊥] Alexandre Boutorine,[†,‡] Claudio Pisano,[#] Giuseppe Giannini,[#] Domenico Alloatti,[#] and Paola B. Arimondo*[,†,‡]

CNRS UMR5153, Muséum National d'Histoire Naturelle USM0503, and INSERM U565, 43 rue Cuvier, 75231 Paris cedex 05, France, UPMC, Paris 75005, France, DISMA, Università di Milano, via Celoria 2, 20133 Milano, Italy, INSERM U-837, COL, IRCL, Place Verdun, 59045 Lille, France, and Sigma-tau Industrie Farmaceutiche Riunite SpA, Pomezia, Italy. Received November 13, 2008; Revised Manuscript Received January 18, 2009

Sequence-specific camptothecins are useful tools to inhibit specifically gene expression. The camptothecins are attached to the 3′ end of triplex-forming oligonucleotides (TFO), sequence-specific DNA ligands that position the camptothecin moiety exclusively in proximity to their binding site. We studied here different gimatecan derivatives or analogues, a potent lipophilic camptothecin compound in clinical trials. We optimized the synthesis procedure in order to increase the yields and the purity and obtain the conjugates on a large scale. The greatly improved synthesis is now based on the conjugation of a bromoalkyl analogue of gimatecan to the 3′ phosphorothioate of the TFO. We showed that the most efficient conjugate, both in vitro and in HeLa cells, bears the TFO on position 7 of the gimatecan analogue, and it is more efficient than the previous camptothecin conjugates. In addition, the gimatecan-like moiety at the 3′ end of the TFO protects from nuclease degradation.

INTRODUCTION

Topoisomerase I (topo I) is a ubiquitous DNA-cleaving enzyme and an important therapeutic target in cancer chemotherapy (*1*). It controls tightly DNA topology by cleaving transiently DNA on one strand (formation of a cleavage complex), changing its topology by control rotation of the cleaved strand around the intact strand, and religating it to give an intact DNA (*2*). Camptothecins (CPTs, Figure 1), potent topo I poisons, reversibly trap the topo I in the covalent complex with DNA, inducing an accumulation of DNA damage that conducts to cell death (*3*). Two derivatives, topotecan and irinotecan, are used in clinics as anticancer agents. However, a major drawback to their use is the fact that CPTs and other topo I poisons exhibit limited sequence preference. The strategy that we have developed consists of targeting topo I poisons to a specific DNA site upon covalent linkage of the poison, such as CPT, to a sequence-specific DNA ligand and binding of the ligand to DNA. As DNA ligands, we have used triplex-forming oligonucleotides (TFO) and hairpin polyamides (MGB for minor groove binders) (*4*, *5*). We have shown that these sequence-specific CPTs are able to induce a topo I-mediated DNA cleavage specifically at the ligand binding site and represent a valid and efficient tool to inhibit the expression of a reporter gene in cells (*6*). In order to extend their use in vivo, it is necessary to optimize the synthesis of the TFO−CPT conjugates, their activity, and cellular stability. For the synthetic procedure, we aimed to increase the yield and scale-up the process; while to increase the chemical stability and the activity of the conjugates, we studied various derivatives or analogues of gimatecan (ST), a potent CPT derivative actually in clinical trials (*7*) (Figure 1). We tested the roles of (1) the attachment site of the TFO on CPT, (2) the linker arm between the two entities, and (3) the steric hindrance of the oxime substitution.

* To whom correspondence should be addressed. CNRS UMR5153, MNHN USM503, INSERM U565, 43 rue Cuvier 75005 Paris, France. Phone: 33-1-40793859, fax: 33-1-40793705; e-mail: arimondo@mnhn.fr.

[†] CNRS UMR5153.

[‡] INSERM U565.

[§] UPMC.

[||] DISMA.

[⊥] INSERM U-837.

[#] Sigma-tau Industrie Farmaceutiche Riunite SpA.

EXPERIMENTAL PROCEDURES

Mass determination was accomplished by electrospray ionization on a Q-STAR pulsar I (Appleura), and HPLC purifications were performed upon Agilent 1100 using a Xterra reverse-phase C_{18} column (4.6 × 50 mm, 2.5 μm). ^{1}H NMR spectra were recorded in Me_2SO-d_6 on a Varian spectrometer (300 MHz). Oligonucleotides (TFO, sequence reported in Figure 1B) were purchased from Eurogentec and purified using quick spin columns and Sephadex G-25 fine (Biorad). Concentrations were determined spectrophotometrically at 25 °C using molar extinction coefficients at 260 nm calculated from a nearest-neighbor model (*8*). All the drugs were dissolved in dimethyl sulfoxide. 10-HydroxyCPT and other chemicals were purchased from Sigma Aldrich. Radioactive gels were analyzed with a Typhoon 9410 (GE Healthcare) and quantified by ImageQuant. Cell media Dulbecco's modified Eagle's medium (DMEM) and Roswell Park Memorial Institute medium 1640 (RPMI) and other related products were from Invitrogen.

Chemistry. *Attachment of an Aminolinker Arm to 10-Hydroxy-CPT (10OH-CPT), NCPT, or 10-Hydroxy-Gimatecan (10OH-G), N10G.* 10OH-G was synthesized as previously described in ref 7. The synthesis of NCPT was described previously (*9*) and N10G was synthesized according to the same procedure. 6-BOC-aminohexylbromide (8.6 mg, 31 μmol) was reacted with 10OH-G (27 μmol) in anhydrous acetone (10 mL) 12 h at reflux in presence of K_2CO_3 (4.5 mg, 32 μmol). The reaction mixture was filtered and the solvent was removed. The residue was purified by column chromatography using a ethyl acetate/cyclohexane 6:4 as an eluent to give a yellow powder (13.1 mg, 19.7 μmmol (73%)). The protected compound was dissolved

10.1021/bc800494y CCC: $40.75 © 2009 American Chemical Society
Published on Web 03/23/2009

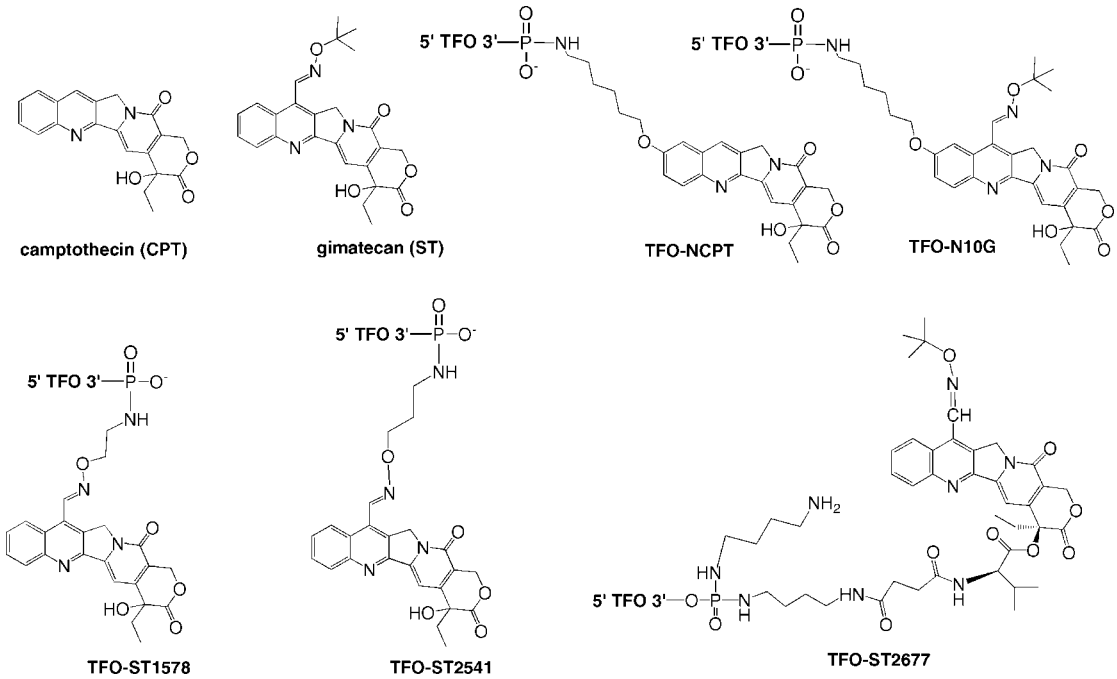

Figure 1. (A) Chemical structures of camptothecin (CPT), gimatecan (ST), and the TFO conjugates. (B) Target DNA and TFO sequence: the triplex site on the target is underlined and the CPT cleavage sites are indicated by arrows. M = 5-methyl-deoxycytidine and P = 5-propynyl-deoxyuridine.

in CH_2Cl_2 /TFA 1:1 and kept at room temperature for 10 min. Solvents were removed under reduced pressure to give a yellow powder (11.1 mg, 19.7 μmmol). ES-MS $[M+H]^+$: found 563.28, calculated 563.28 ($C_{31}H_{38}N_4O_6$). ^{1}H NMR (Me_2SO-d_6): δ (ppm) = 0.88 (t, 3H, J = 7.4 Hz), 1.35−1.65 (m, 15H), 1.79−2.26 (m, 4H), 2.71−2.83 (m, 2H), 4.15 (t, 2H, J = 6.3 Hz), 5.27 (s, 2H), 5.43 (s, 2H), 6.40 (s, 1H), 7.28 (s, 1H), 7.48−7.54 (m, 1H), 7.61 (m, 2H), 8.05 (d, 1H, J = 9.3 Hz), 9.32 (s, 1H).

Synthesis of 7-(2-Aminoethoxy)iminomethylcamptothecin, ST1578. This derivative was synthesized as previously described in ref 7.

Synthesis of 20-O-[N-succinyl-valine]-Gimatecan ST2677. A suspension of gimatecan (1 mmol), $Dy(OTf)_3$ (0.6 mmol), BOC-Valine (3 mmol), DMAP (3 mmol) in 15 mL of dry CH_2Cl_2 was cooled down to −10 °C and after 30 min DCC (3.1 mmol) was added. The reaction mixture was kept 30 min at −10 °C and then 2 h at room temperature. Upon completion, the reaction mixture was diluted with CH_2Cl_2 (20 mL), washed with 1 N aq HCl, the organic fraction was neutralized with sat $NaHCO_3$ and dried over anhydrous Na_2SO_4. Purification by chromatography on silica gel with CH_2Cl_2/MeOH 97:3 gave the desired product as a yellow solid in 92% yield. Rf = 0.72 in CH_2Cl_2/MeOH 96:4. MS (IS): $[M+H]^+$ = 647.1, mp 207 °C (dec).

After BOC-deprotection with CH_2Cl_2/TFA 75:25 at 0 °C and removal of the solvent and excess TFA under reduced pressure, the residue was dissolved in dry pyridine (10 mL), and succinic anhydride (2.5 mmol) was added at 0 °C. The reaction mixture was kept under stirring at room temperature for 1 h until completion. The solvent was removed under vacuum and then the residue dissolved in CH_2Cl_2 and washed with 0.5 N aq HCl. Chromatography on silica gel with CH_2Cl_2/MeOH 95:5 gave the final product with a 90% yield. Rf = 0.41 in CH_2Cl_2/MeOH 92:8. $[M+H]^+$ = 647.5. $[M-H]^-$ = 645.1. ^{1}H NMR (200 MHz, $CDCl_3$): δ = 9.06 (s, 1H, CH), 8.39 (d, J = 8.3 Hz, 1H, CH), 8.29 (d, J = 8.3 Hz, 1H, CH), 7.89 (t, J = 7.7 Hz, 1H, CH), 7.79 (t, J = 7.7 Hz, 1H, CH), 7.69 (s, 1H, CH), 6.39 (d, J = 8.6 Hz, 1H, NH), 5.69 (d, J = 17.7 Hz, 1H, CH), 5.50 (d, J = 17.7 Hz, 1H, CH), 5.46 (s, 2H, CH_2), 4.57 (dd, J = 10.0 Hz, J = 5.3 Hz, 1H, CH), 2.6 (m, 7H, $3CH_2$+CH), 1.53 (s, 9H, tBu), 1.07 (d, J = 6.4 Hz, 6H, $2CH_3$), 0.92 (t, J = 7.1 Hz, 3H, CH_3).

Synthesis of 7-(3-Aminopropoxy)iminomethylcamptothecin ST2541. To a suspension of CPT-7-aldehyde (235 mg, 0.625 mmol), synthesized as in ref 7, in 20 mL of absolute ethanol, *O*-(3-aminopropyl)-hydroxylamine hydrochloride (203 mg, 1.25 mmol) and anhydrous pyridine (0.7 mL) were added. The solution was refluxed for 1 h. After cooling at room temperature, the precipitate was filtered and washed with cold ethanol and diethyl ether to give the title compound as a a yellow solid (138 mg, 49%), mp 187 °C (dec.). R_f = 0.11 CH_3OH/H_2O 9:1 (RP). ^{1}H NMR (300 MHz, DMSO-d_6): δ = 0.86 (t, H_3-18, J = 7.44 Hz), 1.86 (m, H_2-19), 2.07 (m, $-OCH_2CH_2CH_2NH_2$), 2.96 (m, $-OCH_2CH_2CH_2NH_2$), 4.43 (t, $H_2-OCH_2CH_2CH_2NH_2$, J = 5.95 Hz), 5.34 (s, H_2-5), 5.41 (s, H_2-17), 6.52 (bs, -OH), 7.35 (s, H-14), 7.70−8.04 (bs, $-NH_2$), 7.76 (dd, H-10, J = 7.44, 8.19), 7.90 (dd, H-11, J = 7.44, 7.82), 8.22 (d, H-9, J = 8.19 Hz), 8.60 (d, H-12, J = 7.82), 9.34 (s, CH=N).

The synthesis of SCR-CPT and TFO-Ph2 was previously described in ref 6. TFO-ST1578, TFO-NCPT, TFO-ST2541, TFO-L4-ST2677, and TFO-N10G were synthesized as described in refs 9, 10. In the case of ST2677, the CPT derivative was attached through a tetramethylene linker arm. As an example, the synthesis of TFO-N10G is reported.

Synthesis of Conjugate TFO-N10G. A sample of 500 μg (97 nmol) of 3′-phosphorylated oligonucleotide was precipitated as the hexadecyltrimethylammonium salt and dissolved in 50 μL of dry dimethylsulfoxide. Solutions of 4-dimethylaminopyridine (5 mg in 25 μL of DMSO, 41 μmol), dipyridyl disulfide (6.6 mg in 25 μL of DMSO, 30 μmol) and triphenylphosphine (7.9 mg in 50 μL of DMSO, 30 μmol) were added. After 15 min of incubation at room temperature, the activated oligonucleotide was precipitated from the mixture by the addition of 2% $LiClO_4$ in acetone. A solution of 10-aminohexyloxygimatecan (N10G) (0.5 mg, 1 μmol) in 50 μL of DMSO/water 8:2 was added to the activated oligonucleotide. The mixture was kept at room temperature for 2 h. The oligonucleotide conjugate was precipitated by the addition of 2% $LiClO_4$ in acetone, rinsed with acetone, and resuspended from the mixture with double-distilled water to be purified by reversed-phase HPLC using a linear acetonitrile gradient (0→80% CH_3CN in 0.2 M $(NH_4)OAc$)) to obtain 310 μg (54 nmol), yield 56%.

All conjugates were analyzed by UV spectrophotometry and mass spectrometry. TFO-NCPT: ES-MS $[M-H]^-$ = found 5589.5, calculated 5589. TFO-ST1578: ES-MS $[M-H]^-$ = found 5559.7, calculated 5560. TFO-N10G: ES-MS $[M-H]^-$ = found 5688.6, calculated 5688. TFO-ST2677: ES-MS $[M-H]^-$ = found 5596.1, calculated 5578. TFO-ST2541: ES-MS $[M-H]^-$ = found 5573.6, calculated 5574.

Synthesis of Bromoacetamido-ST1578. 3 mg (6 μmol) of ST1578 and 0.8 mg (7 μmol) of DMAP were dissolved in 200 μL of DMSO and 10 μL of TEA. 1 μL (11 μmol) of bromoacetylbromide was added, and the reaction mixture was stirred at room temperature for 2 h under N_2. 500 μL of CH_2Cl_2/acetone 9:1 was added, and the organic phase was extracted 3 times with 500 μL of water and then concentrated. The resulting residue was purified by reverse-phase HPLC using linear acetonitrile gradient (0−90% CH_3CN in 0.1% of TFA) to give a yellow powder (1.3 mg, yield 34%). ES-MS (*m*/*z*): found 554.08 and 556.09. $C_{25}H_{23}BrN_4O_6$ calculated 554.08 and 556.08.

Synthesis of Conjugate TFOPS-ST1578. The salt of a TFO-PS (300 μg, 60 nmol) (NH_4^+ as counterions) was dissolved in 14 μL of water, 7 μL of 18-crown-6, 1.4 μL of DTT 0.5 M, 0.5 mg (0.9 μmol) of bromoacetamide-ST1578 in 70 μL of DMF, and a catalytic quantity of KI were added. The reaction mixture was kept for 16 h at 45 °C. The crude mixture was diluted with 150 μL of water and extracted with a 15/85 v/v mixture of MeOH/CH_2Cl_2. The aqueous phase was concentrated and the oligonucleotide conjugate was purified by reverse phase HPLC using linear acetonitrile gradient (0−80% CH_3CN in 0.02 M (NH_4)OAc), to give 150 μg, yield 47%. MS (*m*/*z*): found 5632.6, calculated 5633.

Biology. *Sequence-Specific DNA Cleavage by the Conjugates.* Sequence-specific Topo I-mediated DNA cleavage was assessed as in ref 5 at 37 °C and pH 7.2. In the presence of the conjugates, the number of cleavage sites is reduced to one, located right downstream of the 3′-end of the triple helix site, as expected from the experimental design (Figure 1B).

Cell Cultures. Human HeLa cells were grown in DMEM supplemented with 10% heat-inactivated fetal bovine serum (FBS), 2 mM L-glutamine and 1% penicillin−streptomycin, at 37 °C and 5% CO_2.

Conjugates Stability in Cells or Cellular Media. Conjugates were 5′-OH labeled with [γ-^{32}P]ATP (GE Healthcare) by T4 polynucleotides kinase (New England Biolabs).

Stability Assay in RPMI 1640 or DMEM Medium Alone. 15 nM of each radiolabeled conjugate and TFOP (3′ phosphorylated TFO) were incubated at 37 °C in 300 μL of RPMI 1640 or DMEM medium (containing 10% FBS, 1% penicillin−streptomycin, and 2 mM L-glutamine). After 24 h and 72 h, 150 μL of this medium was precipitated in ethanol. Samples were then resuspended in 95% formamide and heated at 90 °C for 3 min before being loaded onto a denaturating 15% polyacrylamide gel (19:1 acrylamide/bisacrylamide) containing 7 M urea in 1 × TBE.

Stability Assay in HeLa Cells. This experiment was performed in a 96-well plate containing 125 μL of HeLa cells at a concentration of 122 000 cells/mL and 61 000 cells/mL, for 24 h and 72 h, respectively, in DMEM cell medium containing 10% FBS, 2 mM L-glutamine, and 1% penicillin−streptomycin at 5% CO_2 and 37 °C. 15 nM of each radiolabeled conjugate or TFOP were added. After 24 h or 72 h, the supernatant was precipitated in ethanol.

In parallel, after supernatant removal, the cells in the wells were lysed with 200 μL 10 mM Tris HCl pH 8, 10 mM EDTA, 0.5% Triton X-100, and incubated 15 min on ice, followed by centrifugation 15 min at 1500 *g* and 4 °C. The soluble supernatant was retired and treated with RNase A (50 μg/mL 20 min at 37 °C) and proteinase K (50 μg/mL 35 min at 50 °C) and precipitated in ethanol.

After ethanol precipitation, all samples were resuspended in 95% formamide and heated at 90 °C for 3 min before being loaded onto a denaturating 15% polyacrylamide gel (19:1 acrylamide/bisacrylamide) containing 7 M urea in 1 × TBE buffer.

Transient Expression Experiments. Transfections were performed by using Superfect (Qiagen) as described in ref 6. Both luciferase activities (*Pyralis* and *Renilla*) were measured in cell lyses by using the dual-Luciferase Reporter Assay System (Promega). A luminometer (Victor, Wallac) was used to measure light signal output. The experiments were run as triplicates. The results are reported as mean *Pyralis*/*Renilla* ratio and are further normalized to the ratio of the cells not treated by the conjugates. The total protein amount was measured with the Bio-Rad Protein assay, according to the manufacture instructions. Experiments were repeated from 3 times.

ICE (in vivo Complex of Enzyme) Bioassay. HeLa cell nuclei were prepared as described previously (*6*) and the in vivo Topo I link kit of TopoGEN, Inc. (Columbus, OH) was used to determine the ability of the conjugates to induce Topo I-mediated DNA breaks in treated HeLa cell nuclei. The recommended protocol was followed with a few modifications as described in ref 6. Fractions 1−4 contain free Topo I. DNA-Topo I covalent complexes can be detected in fractions 8−11 of the drug-treated samples. To quantify the amount of cleavage complexes formed in the presence of free or conjugated CPT, the percentage of signal in the fractions 8−11 was normalized to the total amount of Topo I signal in all fractions for each sample.

RESULTS AND DISCUSSION

Optimization of the Conjugate. We have already clearly shown that the efficacy of the conjugates depends on the potency of the inhibitor, the linker arm and the attachment site (*5, 11, 12*). Here, we chose to covalently link gimatecan (Figure 1), a very potent camptothecin derivative actually in clinical trials (*1, 7, 13*). Gimatecan has an oxime group that confers high antitumoral activity due to the lipophilic character of the compound, the improved pharmacokinetics, the more stable cleavage complexes, and the slower lactone ring opening (*7, 14*).

We tested different attachment points on gimatecan and its analogues (Figure 1A): positions 10 (N10G), 7 (ST1578), and 20 (ST2677). The first two attachment points gave very active conjugates in the case of CPT (*5*), while it has been shown that 20 ester derivatives of CPT (attachment of poly(L-glutamic acid), maleimide, or sugars) improve the intratumoral delivery and increase water solubility, giving enhanced antitumoral activity (*15*−*17*). In all experiments, we used, for comparison, CPT attached through position 10 (10-hydroxyCPT). 10-hydroxyCPT (10OH-CPT) and 10-hydroxygimatecan (10OH-G) were attached through an hexamethyleneamino linker to the 3′ phosphorylated TFO following the described procedure (*10*). ST2677 was attached through a tetramethylene linker following the same procedure, while ST1578 was reacted directly without the addition of a linker arm.

As TFO model system, we used the one previously described in our studies, consisting of a 16-mer triplex site and a pyrimidine-motif TFO containing 5-methyl-deoxycytidines instead of deoxycytidines and 5-propynyl-deoxyuridine instead of thymidines (Figure 1B) (*12*).

Figure 2A,B shows the ability of these newly synthesized conjugates (TFO-N10G, TFO-ST1578, TFO-ST2677) to induce topo I-mediated DNA cleavage at the target site. All conjugates strictly restricted DNA cleavage by topo I to the 3′-side of the duplex/triplex junction at site *b*. Cleavage at sites *a*, *c*, and *d* of

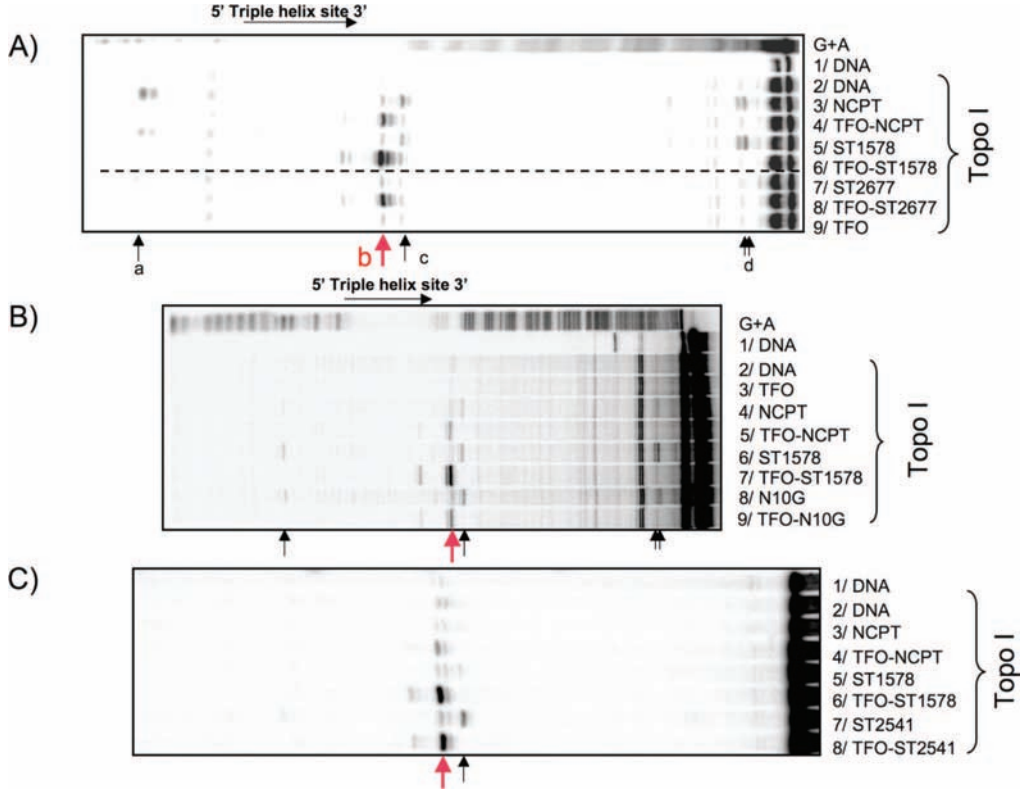

Figure 2. Cleavage products mediated by topo I were resolved on a 8% polyacrylamide gel containing 7 M urea. Adenine/guanine-specific Maxam−Gilbert chemical cleavage reaction were used as markers (lane G+A). (A) Target duplex alone (lane 1), incubated with 10 units of topo I (lane 2) and in the presence of 10 μM NCPT (lane 3); 1 μM TFO-NCPT (lane 4); 10 μM ST1578 (lane 5); 1 μM TFO-ST1578 (lane 6); 10 μM ST2677 (lane 7); 1 μM TFO-ST2677 (lane 8); and 1 μM TFO (lane 9). The three latter samples were investigated at pH 6.2, because the TFO does not contain the 5-propynyl-deoxyuridine modification that stabilizes the triplex at pH 7.2. (B) Target duplex alone (lane 1), incubated with 10 units of topo I (lane 2) and in the presence of 1 μM TFO (lane 3); 10 μM NCPT (lane 4); 1 μM TFO-NCPT (lane 5); 10 μM ST1578 (lane 6); 1 μM TFO-ST1578 (lane 7); 10 μM N10G (lane 8); and 1 μM TFO-N10G (lane 9). (C) Target duplex alone (lane 1), incubated with 10 units of topo I (lane 2) and in the presence of 10 μM NCPT (lane 3); 1 μM TFO-NCPT (lane 4); 10 μM ST1578 (lane 5); 1 μM TFO-ST1578 (lane 6), 10 μM ST2541 (lane 7); 1 μM TFO-ST2541 (lane 8).

the free camptothecins completely disappeared. This is a strong indication that the enzyme has been targeted to a specific region. The efficacy of cleavage by TFO-ST1578 is six times stronger than the efficacy of cleavage by TFO-NCPT and three times stronger than the efficacy of cleavage by TFO-N10G. TFO-ST2677 is equivalent to TFO-NCPT. Therefore, the most efficient conjugate is the TFO-ST1578, where the TFO is attached to the oxime substituent in position 7.

To further optimize the TFO-ST1578 conjugate, we increased the length of the side chain on the oxime group of ST1578 by a methylene group, obtaining conjugate TFO-ST2541 (Figure 1A). As shown in Figure 2C, the two conjugates, TFO-ST1578 and TFO-ST2541, are equivalent in efficacy.

Optimization of the Synthesis. Biological tests need large amounts of conjugates; therefore, it is necessary to develop a large-scale synthesis. The question that we addressed was whether it is possible to do semipreparative synthesis in the liquid phase. We used two classical pathways (Scheme 1): (A) the reaction of a primary amino group of the drug on the terminal phosphate (P) of the TFO upon activation by triphenylphosphine and dipyridylsulfide, routinely used to synthesize TFO-CPT conjugates (*10*), and (B) the reaction of an halide linker arm on the drug to a terminal thiophosphate group (PS) on the TFO, used to couple daunomycin to TFOs (*18*). A major advantage of the latter is that the drug is attached to the TFO through a chemical bond resistant to acidic treatment.

Conjugate TFOPS-ST1578. An haloacetamido linker has been attached to the amino side chain of the ST1578 derivative and then reacted with the TFO bearing a thiophosphate group (PS) at the 3′ end (Figure 3A). While we were not able to obtain the iodoacetamido derivative of ST1578, the bromoacetamido one gave high yields of the wanted conjugate. The ability of the conjugate TFOPS-ST1578 to induce sequence-specific topo I-mediated DNA cleavage was compared to that of TFO-ST1578, obtained by procedure A (Figure 3B). The two conjugates give comparable results: they both induce a selective cleavage on the DNA at the site where the drug is positioned specifically by the formation of the triple helix with a comparable efficacy of cleavage.

Scheme 1. Two Chemical Pathways Were Used for the Formation of the Conjugates

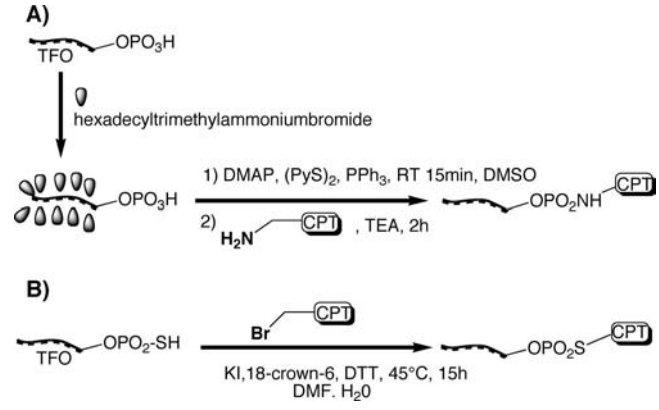

Comparison of the Two Synthetic Pathways. The two methods were compared in parallel. Increasing quantities of TFO were engaged in the two pathways. At the end of the synthesis, a

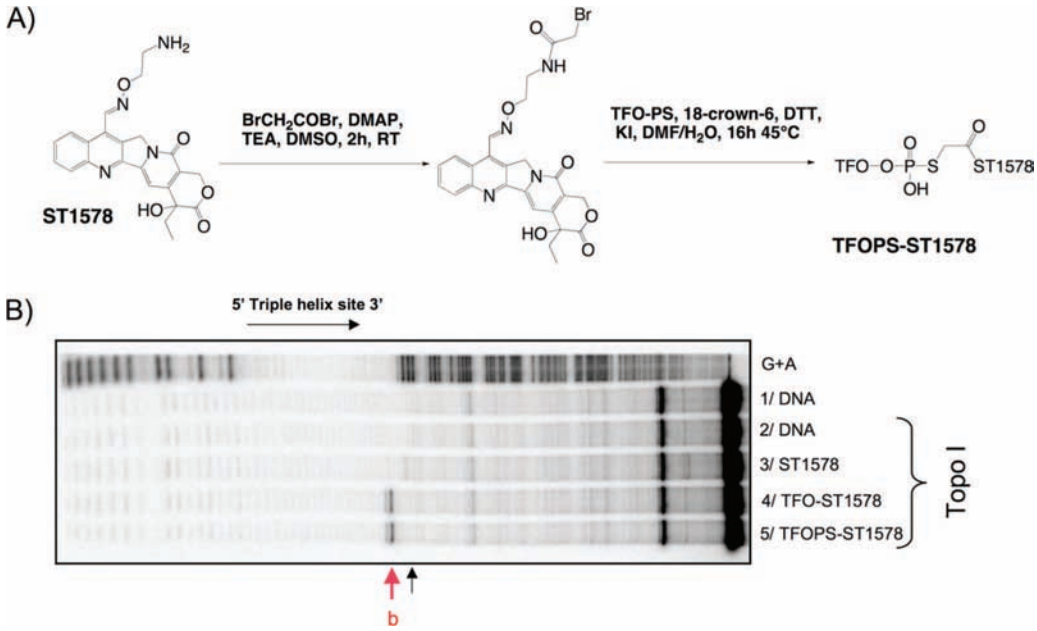

Figure 3. (A) Synthesis of TFOPS-ST1578. (B) Cleavage products mediated by topo I were resolved on a 8% polyacrylamide gel containing 7 M urea. Adenine/guanine-specific Maxam−Gilbert chemical cleavage reaction were used as markers (lane G+A). Target duplex alone (lane 1), incubated with 10 units of topo I (lane 2) and in the presence of 10 μM ST1578 (lane 3); 1 μM TFO-ST1578 (lane 4); and 1 μM TFOPS-ST1578 (lane 5).

Table 1. Yields of Pathway 1 where TFOP Was Reacted with ST1578 and of Pathway 2 where TFOPS Was Reacted with Bromoacetamido-ST1578 (Scheme 1 and Figure 3A)

TFO (mg)		1	2	5	10
total yield (%)	TFOP	61	51	26	21
	TFOPS	71	68	65	64

sample of the reaction mixture was analyzed by gel electrophoresis to determine the relative quantities of free oligonucleotide and of conjugate, in order to deduce the apparent yield of synthesis. In addition, after HPLC purification and characterization by UV−vis spectrometry and mass spectrometry, the final yield of the reaction was determined by standard quantification of the conjugate by UV absorbance. The yields obtained in the two pathways are compared in Table 1.

We observed an important decrease in yield upon increase of the quantities of TFOP engaged when pathway A was used. We think that this is due to the presence of CTAB in the reaction mixture during the precipitation with acetone/$LiClO_4$. Pathway B did not present this problem; the yields are constant, and furthermore, it works at higher quantities of TFOPS (up to 50 mg). In conclusion, pathway B presents several advantages: it is easier to carry out, is more reproducible, no side products are formed, large-scale synthesis is possible, the covalent linkage between the drug and the TFO is more stable, and the conjugate is equally efficient. Therefore, this is the pathway of choice for the liquid-phase synthesis of the conjugates.

Cellular Stability of the Conjugates. It is commonly known that unprotected oligonucleotides are rapidly degraded in cells by the action of nucleases and, in particular, 3′ exonucleases (*19*). Therefore, we tested whether the presence of the ST derivative at the 3′ end of the TFO would protect it from degradation. Unconjugated TFOP, phosphorylated at the 3′ end, was used as control. The 5′-radiolabeled TFOP or conjugates were added to RPMI 1640 or DMEM cell medium or to HeLa cells.

TFOP is strongly degraded both in the cellular media (RPMI 1640 and DMEM) and in cells. Noteworthy, the degradation of TFOP is higher in RPMI 1640 than in DMEM. This is related to the different composition of the two media (http://www.invitrogen.com/site/us/en/home/support/Product-Technical-Resources/media_formulation.116.html and http://www.invitrogen.com/site/us/en/home/support/Product-Technical-Resources/media_formulation.220.html). The presence of a camptothecin derivative, attached through position 7 or 10, protects the conjugates from nuclease degradation (Table 2). This is most evident after 72 h incubation. Samples were also analyzed by HPLC and MS: no free CPT or ST derivatives were found.

Table 2. Cellular Stability of the Conjugates[a]

	DMEM	RPMI	cells
TFOP	29	20	40
TFO-ST1578	80	74	100
TFO-ST2541	95	90	100
TFOPS-ST1578	95	97	100
TFO-NCPT	86	97	n.d.
TFO-N10G	100	95	98

[a] Percentage of the remaining amount of conjugate after 24 h incubation in DMEM or RPMI media or in HeLa cells. S.E. 5%. n.d. = not determined.

We also tested their stability in cells. Cells were lysed after 24 or 72 h, and the radiolabeled oligonucleotides were recovered and analyzed on a denaturing gel (Table 2, Supporting Information Figure 1). In general, degradation is less important than in just the cell media. However, we still observe a strong degradation of TFOP, while the conjugates are stable in these conditions, protected by the presence of the drug at their 3′ end. Once we had confirmed the chemical stability of the conjugates in cells, we tested their ability to modulate gene expression in cells.

Cellular Activity. The experimental design was described previously (*6*). Briefly, the duplex containing the triplex site and CPT cleavage sites a, b, and c was cloned in the pGL3 Promoter vector in the transcribed region upward of the *Pyralis* luciferase gene. This expression vector is cotransfected by Superfect together with the expression vector for *Renilla* luciferase (pRL-TK) in the absence or in the presence of different conjugates at the indicated concentration. 24 h after transfection, the cells are lysed and tested for luciferase activity. Figure 4A shows the mean value of the ratio between the

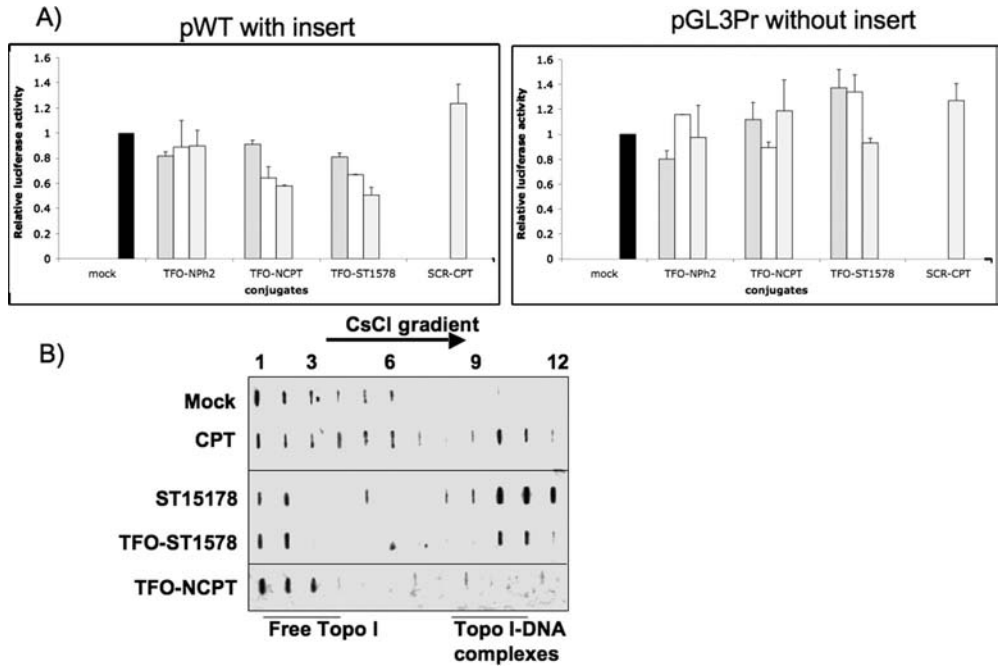

Figure 4. (A) HeLa cell lysates were assayed for firefly and *Renilla* luciferase activities after transfection by Superfect. The firefly luciferase construct was introduced with the control expressing vector RL-TK in the absence (black bars) or presence of the various oligonucleotides, TFO-NPh2, TFO-NCPT, TFO-ST1578, or SCR-CPT at 0.05 μM (hatched bars), 0.1 μM (white bars), or 0.5 μM (dotted bars). The results are presented as mean firefly/*Renilla* luminescence intensity ratios of triplicates (relative luciferase activity) and normalized to the value obtained in the absence of the oligonucleotides (none). Left panel, pWT construct at 24 h after transfection. Right panel, pGL3Pr control vector at 24 h after transfection. (B) Immunoblot analysis of topo I-DNA covalent complexes stabilized by topo I inhibitor in HeLa cell nuclei. 5×10^6 HeLa cell nuclei were incubated for 3 h at 37 °C in the presence or absence of compounds (5 μM). The lysates obtained were applied to a CsCl gradient and centrifuged overnight. Twelve fractions were collected and analyzed by the slot blot. Fractions 1−4 contained free topo I. Topo I/DNA covalent complexes were detected in fractions 8−11. Results are representative of three independent experiments.

luminescence signal of *Pyralis* and *Renilla* normalized to untreated cells.

We compared the activity of conjugate TFO-ST1578 to conjugate TFO-NCPT, the former being the most efficient conjugate in vitro of the gimatecan family. As control, we used the TFO linked at its 3′ end to NH_2-$(CH_2)_4$-NH_2 and then to a diphenylacetic acid (TFO-NPh2) to protect it from 3′-exonuclease degradation, and SCR-CPT, where CPT is attached through a NH_2-$(CH_2)_6$-NH_2 linker to an oligonucleotide, containing the same modified bases, that cannot bind to the target sequence. Clearly, while the controls have no effect even at 0.5 μM, the highest concentration tested, TFO-ST1578 efficiently inhibits luciferase expression up to 50% at 0.5 μM, slightly better than TFO-NCPT. TFO-ST2541 gave comparable results to TFO-ST1578, and both conjugates are active up to 72 h (Supporting Information Figure 2). The conjugates have no effect on the parent reporter gene plasmid pGL3Pr that has no insert (and thus no triplex can be formed).

In order to evaluate if TFO-ST1578 induced the stabilization of the topo I/DNA cleavage complex in cells, we performed ICE bioassays, which detect the formation of the covalent topo I/DNA complexes in cells (*20*). HeLa cell nuclei were incubated for 3 h at 37 °C with CPT or ST1578 alone or the conjugates or the control oligonucleotide TFO-NPh2. The samples were lysed with an ionic detergent, and proteins that were covalently attached to genomic DNA were separated from free proteins by sedimentation through a CsCl gradient by ultracentrifugation. As shown in Figure 4B, 12 fractions were recovered and analyzed by Western slot blot to detect the fractions containing topo I. In the control samples with no drug, topo I was found exclusively at the top of the CsCl gradient as free protein (fractions 1−3). In contrast, with drug-treated cells, Topo I was found in the top fractions as well as in the lower fractions 8−11 near the bottom of the gradient where the nucleic acids were localized (as judged from absorbance measurements at 260 nm), corresponding to TopoI/DNA complexes. In fact, in these complexes the enzyme is covalently linked to the DNA; therefore, the Topo I is found also in the fractions containing DNA (the lower fractions). Such complexes (bands in fractions 8−11) were visualized in the presence of CPT and ST1578, as expected, but also with conjugates and in particular with TFO-ST1578. These data indicate that TFO-ST1578 and TFO-NCPT are able to stabilize topo I/DNA complexes. Table 3 shows that the ratio of Topo I bound to DNA/TFO-ST1578 is very efficient in trapping the enzyme on the DNA.

Table 3. Ratio of the Topo I Bound/Topo I Free from ICE Experiments[a]

	Topo bound/Topo free
mock	0
CPT 5 μM	0.56
CPT 1 μM	0.40
ST1578 5 μM	3
ST1578 1 μM	1
TFO-NPh2	0.02
TFO-NCPT	0.32
TFO-ST1578	0.95

[a] S.E. 20%.

CONCLUSIONS

We have shown that the novel sequence-specific camptothecins based on gimatecan analogues are able to induce a targeted DNA cleavage mediated by topoisomerase I with a highly increased efficacy. Therefore, these triplex-forming gimatecan analogues are very promising for applications in cells. The synthesis of the camptothecin conjugates has been greatly improved upon use of halido derivatives and optimized for scale-up development. Finally, these new conjugates show an

increased resistance to nuclease degradation. In conclusion, a new step forward has been made in the development of a new family of compounds aimed at a targeted therapy.

ACKNOWLEDGMENT

This work was supported by grants from Ligue Nationale Contre le Cancer and Sigma Tau collaboration grant; from Assocation pour la Recherche sur les Tumeurs de la Prostate; and from Association pour la Recherche sur le Cancer to KO.

Supporting Information Available: Additional information as described in the text. This material is available free of charge via the Internet at http://pubs.acs.org.

LITERATURE CITED

(1) Pommier, Y. (2006) Topoisomerase I inhibitors: camptothecins and beyond. *Nat. Rev. Cancer 6*, 789–802.

(2) Wang, J. C. (2002) Cellular roles of DNA topoisomerases: a molecular perspective. *Nat. Rev. Mol. Cell Biol. 3*, 430–40.

(3) Thomas, C. J., Rahier, N. J., and Hecht, S. M. (2004) Camptothecin: current perspectives. *Bioorg. Med. Chem. 12*, 1585–604.

(4) Arimondo, P. B., Bailly, C., Boutorine, A., Ryabinin, V., Syniakov, A., Sun, J. S., Garestier, T., and Helene, C. (2001) Directing topoisomerase I-mediated DNA cleavage to specific sites by camptothecin tethered to minor and major groove ligands. *Angew. Chem. Int. Ed. 40*, 3045–3048.

(5) Arimondo, P. B., Boutorine, A., Baldeyrou, B., Bailly, C., Kuwahara, M., Hecht, S. M., Sun, J. S., Garestier, T., and Helene, C. (2002) Design and optimization of camptothecin conjugates of triple helix- forming oligonucleotides for sequence-specific DNA cleavage by topoisomerase I. *J. Biol. Chem. 277*, 3132–40.

(6) Arimondo, P. B., Thomas, C. J., Oussedik, K., Baldeyrou, B., Mahieu, C., Halby, L., Guianvarc'h, D., Lansiaux, A., Hecht, S. M., Bailly, C., and Giovannangeli, C. (2006) Exploring the cellular activity of camptothecin-triple-helix-forming oligonucleotide conjugates. *Mol. Cell. Biol. 26*, 324–33.

(7) Dallavalle, S., Ferrari, A., Biasotti, B., Merlini, L., Penco, S., Gallo, G., Marzi, M., Tinti, M. O., Martinelli, R., Pisano, C., Carminati, P., Carenini, N., Beretta, G., Perego, P., De Cesare, M., Pratesi, G., and Zunino, F. (2001) Novel 7-oxyiminomethyl derivatives of camptothecin with potent in vitro and in vivo antitumor activity. *J. Med. Chem. 44*, 3264–74.

(8) Cantor, C. R., Warshaw, M. M., and Shapiro, H. (1970) Oligonucleotides interactions. III. Circular dichroism studies of the conformation of deoxyoligonucleotides. *Biopolymers 9*, 1059–1077.

(9) Koster, D. A., Czerwinski, F., Halby, L., Crut, A., Vekhoff, P., Palle, K., Arimondo, P. B., and Dekker, N. H. (2008) Single-molecule observations of topotecan-mediated TopIB activity at a unique DNA sequence. *Nucleic Acids Res. 36*, 2301–10.

(10) Arimondo, P. B., Laco, G. S., Thomas, C. J., Halby, L., Pez, D., Schmitt, P., Boutorine, A., Garestier, T., Pommier, Y., Hecht, S. M., Sun, J. S., and Bailly, C. (2005) Activation of camptothecin derivatives by conjugation to triple helix-forming oligonucleotides. *Biochemistry 44*, 4171–80.

(11) Arimondo, P. B., Bailly, C., Boutorine, A., Prudhomme, M., Sun, J.-S., Garestier, T., and Hélène, C. (2000) Recognition and cleavage of DNA by rebeccamycin- or benzopyridoquinoxaline-triplex-forming oligonucleotide conjugates. *Bioorg. Med. Chem. 8*, 777–784.

(12) Arimondo, P. B., Bailly, C., Boutorine, A., Sun, J. S., Garestier, T., and Hélène, C. (1999) Targeting topoisomerase I cleavage to specific sequences of DNA by triple helix-forming oligonucleotide conjugates. A comparison between a rebeccamycin derivative and camptothecin. *C. R. Acad. Sci. III/Life Sciences 322*, 785–90.

(13) Dallavalle, S., Delsoldato, T., Ferrari, A., Merlini, L., Penco, S., Carenini, N., Perego, P., De Cesare, M., Pratesi, G., and Zunino, F. (2000) Novel 7-substituted camptothecins with potent antitumor activity. *J. Med. Chem. 43*, 3963–9.

(14) De Cesare, M., Pratesi, G., Perego, P., Carenini, N., Tinelli, S., Merlini, L., Penco, S., Pisano, C., Bucci, F., Vesci, L., Pace, S., Capocasa, F., Carminati, P., and Zunino, F. (2001) Potent antitumor activity and improved pharmacological profile of ST1481, a novel 7-substituted camptothecin. *Cancer Res. 61*, 7189–95.

(15) Bhatt, R., de Vries, P., Tulinsky, J., Bellamy, G., Baker, B., Singer, J. W., and Klein, P. (2003) Synthesis and in vivo antitumor activity of poly(L-glutamic acid) conjugates of 20S-camptothecin. *J. Med. Chem. 46*, 190–3.

(16) Lerchen, H. G., Baumgarten, J., von dem Bruch, K., Lehmann, T. E., Sperzel, M., Kempka, G., and Fiebig, H. H. (2001) Design and optimization of 20-O-linked camptothecin glycoconjugates as anticancer agents. *J. Med. Chem. 44*, 4186–95.

(17) Warnecke, A., and Kratz, F. (2003) Maleimide-oligo(ethylene glycol) derivatives of camptothecin as albumin-binding prodrugs: synthesis and antitumor efficacy. *Bioconjugate Chem. 14*, 377–87.

(18) Capobianco, M. L., De Champdore, M., Arcamone, F., Garbesi, A., Guianvarc'h, D., and P, B. A. (2005) Improved synthesis of daunomycin conjugates with triplex-forming oligonucleotides. The polypurine tract of HIV-1 as a target. *Bioorg. Med. Chem. 13*, 3209–18.

(19) Agrawal, S., Temsamani, J., and Tang, J. Y. (1991) Pharmacokinetics, biodistribution, and stability of oligodeoxynucleotide phosphorothioates in mice. *Proc. Natl. Acad. Sci. U.S.A. 88*, 7595–9.

(20) Subramanian, D., Kraut, E., Staubus, A., Young, D. C., and Muller, M. T. (1995) Analysis of topoisomerase I/DNA complexes in patients administered topotecan. *Cancer Res. 55*, 2097–103.

BC800494Y

Supplementary Information

Optimized synthesis and enhanced efficacy of novel triplex-forming camptothecin derivatives based on gimatecan

Pierre Vekhoff [†‡§]; Ludovic Halby [†‡]; Kahina Oussedik [†‡§]; Sabrina Dallavalle [¥]; Lucio Merlini [¥]; Christine Mahieu [∫]; Amélie Lansiaux [∫]; Christian Bailly [∫]; Alexandre Boutorine [†‡]; Claudio Pisano [£]; Giuseppe Giannini [£]; Domenico Alloatti [£]; Paola B. Arimondo [†‡*]

† *CNRS UMR5153; Muséum National d'Histoire Naturelle USM0503; 43, rue Cuvier, 75231 Paris cedex 05 France*

‡ *INSERM U565; 43, rue Cuvier, 75231 Paris cedex 05 France*

§ *UPMC Paris 75005 France*

¥ *DISMA, Università di Milano, via Celoria 2, 20133 Milano, Italy*

∫ *INSERM U-837, COL, IRCL, Place Verdun, 59045 Lille, France*

£ *Sigma-tau Industrie Farmaceutiche Riunite SpA, Pomezia, Italy*

The chemical stability of the conjugates was evaluated in HeLa cells and in DMEM and RPMI1640 cellular media. The 5'-end radiolabeled oligonucleotides were incubated in cell culture medium containing 10% fetal bovine serum at 37°C or in 96-wells plate containing HeLa cells at 37°C and 5% CO_2. Aliquots were removed after 5 min., 24h or 72h and analyzed on a 20% denaturing gel. Figure S1 shows a typical result: conjugate TFO-ST2541 is protected from degradation by the ST derivative in 3' while the parent TFOP is degradated. Degradation is more important in the cell media (Fig.S1B) than in the cells directly (Fig.S1A).

Figure S1

A) Stability in HeLa cells at 24 and 72h for TFOP and TFO-ST2541. B) Stability in DMEM and RMPI1640 media: TFOP was collected after 5 min. incubation at 37°C, TFO-ST2541 was analyzed after 5 min., 24h and 72h. Control represents the radiolabled TFOP or TFO-ST2541 without further treatment.

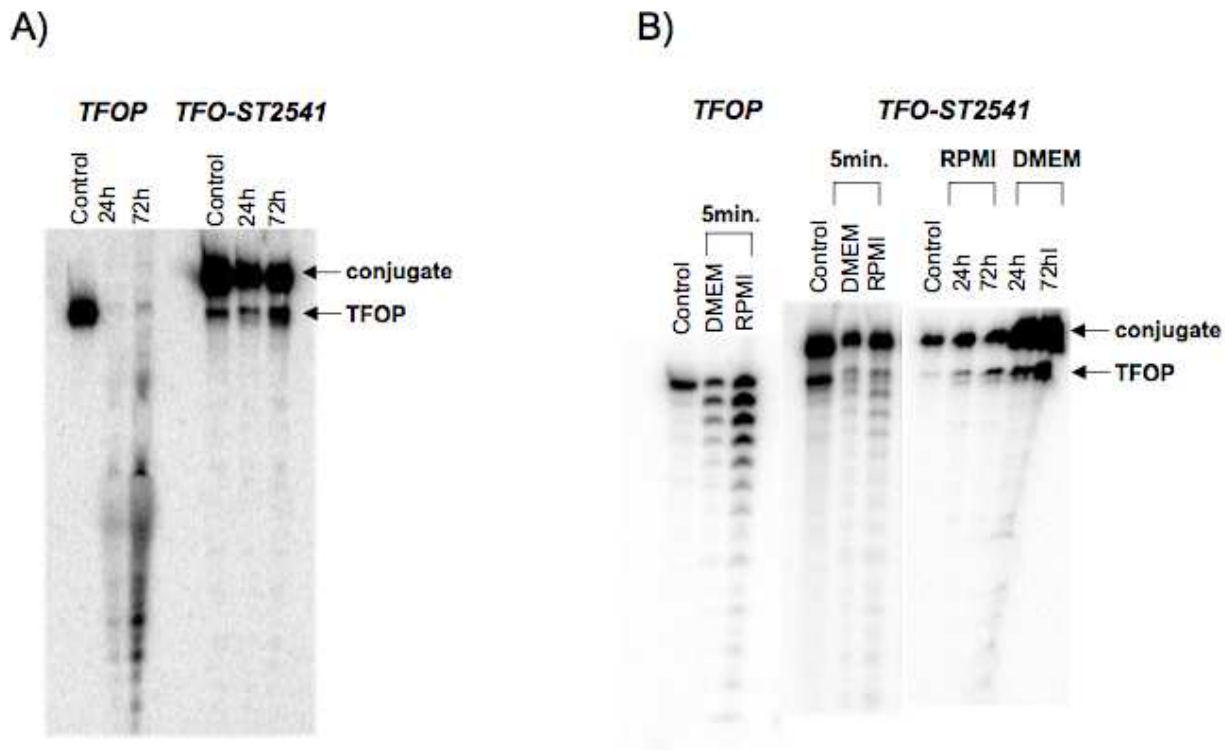

Conjugates TFO-ST1578 and TFO-ST2541were able to inhibit the expression of *Pyralis* reporter gene in HeLa cells up to 72h after transfection with Superfect™. Conjugate TFO-NCPT was used as positive control and TFO-NPh2 and SCR-CPT as negative controls.

Figure S2

HeLa cell lysats were assayed for *firefly* and *Renilla* luciferase activities after transfection by Superfect™. The *firefly luciferase* construct was introduced with the control expressing vector RL-TK in the absence (black bars) or presence of the various oligonucleotides, TFO-NPh2, TFO-NCPT, TFO-ST1578 or HIV-CPT at 0.05 μM (hatched bars), 0.1 μM (white bars) or 0.5 μM (dotted bars). The results are presented as mean *firefly/Renilla* luminescence intensity ratios of triplicates (relative luciferase activity) and normalized to the value obtained in the absence of the oligonucleotides (none). Left panel, pWT construct at 72h after transfection. Right panel, pGL3Pr control vector at 72h after transfection.

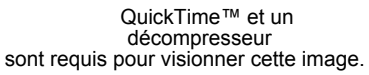
QuickTime™ et un
décompresseur
sont requis pour visionner cette image.

Bioconjugate Chemistry 20th Anniversary

Subscriber access provided by SHEMYAKIN-OVCHINNIKOV INST

Article

Glycan Tagging to Produce Bioactive Ligands for a Surface Plasmon Resonance (SPR) Study via Immobilization on Different Surfaces

F. Javier Mun#oz, Jose# Pe#rez, A#ngel Rumbero, J. Ignacio Santos, F. Javier Can#ada, Sabine Andre#, Hans-Joachim Gabius, Jesu#s Jime#nez-Barbero, Jose# V. Sinisterra, and Mari#a J. Herna#iz

Bioconjugate Chem., **2009**, 20 (4), 673-682• DOI: 10.1021/bc800350q • Publication Date (Web): 06 March 2009

Downloaded from http://pubs.acs.org on May 8, 2009

More About This Article

Additional resources and features associated with this article are available within the HTML version:

- Supporting Information
- Access to high resolution figures
- Links to articles and content related to this article
- Copyright permission to reproduce figures and/or text from this article

View the Full Text HTML

ACS Publications
High quality. High impact.

Bioconjugate Chemistry is published by the American Chemical Society. 1155 Sixteenth Street N.W., Washington, DC 20036

Glycan Tagging to Produce Bioactive Ligands for a Surface Plasmon Resonance (SPR) Study via Immobilization on Different Surfaces

F. Javier Muñoz,[†,⊥] José Pérez,[†,⊥] Ángel Rumbero,[‡] J. Ignacio Santos,[§] F. Javier Cañada,[§] Sabine André, Hans-Joachim Gabius,[||] Jesús Jiménez-Barbero,[§] José V. Sinisterra,[†,⊥] and María J. Hernáiz*[,†,⊥,#]

Departamento de Química Orgánica y Farmacéutica, Universidad Complutense de Madrid, Pz/ Ramón y Cajal s/n. 28040 Madrid, Spain, Departamento de Química Orgánica, Universidad Autónoma de Madrid, Campus de Cantoblanco, 28049 Madrid, Spain, Departamento de Ciencia de Proteínas, CIB-CSIC, c/Ramiro de Maeztu 9, 28040 Madrid, Spain, Institut für Physiologische Chemie, Tierärztliche Fakultät, Ludwig-Maximilians-Universität, München, Veterinärstr 13, 80539 München, Germany, Servicio de Biotransformaciones Industriales, Parque Científico de Madrid C/Santiago Grisolía, 28760 Tres Cantos, Spain, and Servicio de Interacciones Biomoleculares, Parque Científico de Madrid, Pz/Ramón y Cajal s/n. 28040 Madrid, Spain.
Received August 15, 2008; Revised Manuscript Received December 23, 2008

Suitable glycan derivatives will find immediate application in the study of their interactions. Here, we present an efficient synthetic strategy to introduce a fluorescent tag functionalized with an amino group into a model disaccharide structure (lactose). This strategy led to the maintenance of bioactivity, checked by the study of the interaction of this bioconjugate with a plant lectin (mistletoe lectin 1) by NMR spectroscopy, computational docking, and surface plasmon resonance (SPR). To demonstrate the versatility of this approach, we immobilized the new glycan derivatives on different surfaces, and a comparative analysis is presented and can be successfully used for biomimetic carbohydrate−protein interaction studies on the SPR biochip.

INTRODUCTION

The emerging concept of the sugar code defines glycans as biochemically ideal for high-density coding and ascribes the table to translate these sugar-encoded messages into cellular responses to receptor proteins such as lectins. Because of the wide range of glycan functionality, it is obvious that the development of analytical procedures to probe carbohydrate−protein and carbohydrate−carbohydrate interactions and of suitably tailored glycans is a challenge with medical implications. In terms of synthetic aspects, there is a need for approaches that enable proper functionalization of the glycans. One of the strategies for glycan derivatization goes through the generation of amine reactive compounds by conversion of free glycans into glycosylamines (*1*−*3*). However, these glycosylamines derivatives are generally unstable so that they are recovered in poor yields, are readily hydrolyzed, and often afford undesirable side products.

Furthermore, it is well established that glycans with free reducing ends readily react by reductive amidation with primary aryl amine reagents, such as fluorescent compounds 2-aminopyridine (*4, 5*) or 2,6-diaminopyridine (*6*−*8*). However, for the first molecule, monoaminated derivatives preclude further derivatization of the obtained molecule, for instance, by biotinylation or by covalent attachment to protein carriers or solid supports. Also, in both methods the structural integrity of the glycan is modified, which may influence its biological function, e.g., its binding properties to lectins in biological information transfer.

At the same time, surface plasmon resonance (SPR) has proven particularly suitable for the study of lectin−carbohydrate interactions (*9*−*11*). A major issue in all surface-based techniques is the immobilization of the desired ligand onto a solid surface. Covalent attachment is preferred over other specific immobilization methods, such as biotin/streptavidin-mediated attachment or hydrophobic interactions, as it allows an easy control of the immobilization level. One of the more important requirements for a covalent carbohydrate immobilization on a surface is the spacer between the glycan and the surface. This linker chain should provide optimal presentation of glycans and prevent nonspecific binding (*12*). A number of investigators have tackled the challenges of carbohydrate immobilization. Mainly, one linker system has been devised for the attachment of carbohydrate to a surface. This approach relies on the formation of alkane thiolate monolayers on a gold surface (*13, 14*).

Here, we present an efficient synthesis of a new fluorescent-glycan that can readily be immobilized on different surfaces. This methodology involves the derivatization of a model disaccharide (lactose) with 1,5-diaminonaphtalene (DN). The new glycan derivative is detectable by UV−visible or fluorescence spectroscopy and, in addition, the free amino group enables its coupling to different surfaces functionalized with carboxylic groups in order to carry out SPR studies lowering the nonspecific interactions.

EXPERIMENTAL PROCEDURES

General Procedures. All commercial products were used without any further purification steps. TLC was used to monitor the course of the reactions on Kieselgel plates 60 F_{254} (SDS), a UV-lamp light as well as 10% H_2SO_4 in MeOH, and heating for compound visualization. Column chromatography was carried out, if necessary, on silicagel 60, AC, 40−63 μm (purchased from SDS). Elemental analysis and mass spectrometry were carried out by the Support Services (CAI) of the UCM.

* Corresponding author. Departamento de Química Orgánica y Farmacéutica, Facultad de Farmacia, Universidad Complutense de Madrid, Pz/Ramón y Cajal s/n. 28040 Madrid, Spain. Phone: (+34) 913947208. Fax: (+34) 913941822. E-mail: mjhernai@farm.ucm.es.
† Universidad Complutense de Madrid.
‡ Universidad Autónoma de Madrid.
§ CIB-CSIC.
|| Ludwig-Maximilians-Universität.
⊥ Servicio de Biotransformaciones Industriales.
Servicio de Interacciones Biomoleculares.

10.1021/bc800350q CCC: $40.75 © 2009 American Chemical Society
Published on Web 03/06/2009

NMR spectra were recorded on Bruker 250, 300, and 500 MHz equipment. Samples were dissolved in the appropriate deuterated solvent ($CDCl_3$ and D_2O), and chemical shifts (δ) are expressed in parts per million (ppm). If necessary for correct assignment, COSY and $^1H-^{13}C$ heteronuclear experiments were performed. Determination of protein concentration was carried out by the method of Bradford (*15*). SPR experiments were performed in a BIACORE-3000 SPR sensor chips, and solutions used for the SPR assays were purchased from BIAcore. The sensorgrams and fittings were processed by the software BIAEvaluation (version 4.1, 2003). Synthesis of compounds **1** to **3** followed published procedures (*16*).

Synthesis of 2-Oxoethyl-(2,3,4,6-tetraacetyl-β-D-galactopyranosyl)-(1→4)-2,3,6-triacetyl-β-D-glucopyranoside (4). Allyllactoside **3** (1 g, 1.48 mmol) was dissolved in anhydrous CH_2Cl_2 (50 mL) at −78 °C, and ozone was introduced in constant flow. After 40 min, remaining ozone was removed with a constant flow of argon for 5 min and an excess of $(CH_3)_2S$ (2 mmol). When the mixture lost its blue color, the cooling bath was removed, and the organic solvent was then evaporated (*R*f: 0.2, hexane/EtOAc 1:2). Purification of the final product was carried out by column chromatography (hexane/EtOAc 1:2), yielding **4** in 75% yield.

^1H NMR (250 MHz, $CDCl_3$): 9.65 (dd, $J = 1.43$, $J = 0.77$, 1H; H-1), 5.35 (dd, $J = 3.3$, $J = 2.5$ Hz, 1H, H-4″), 5.22 (t, $J = 9.3$ Hz, 1H; H-3′), 5.11 (dd, $J = 10.4$, $J = 7.8$ Hz, 1H; H-2″), 5.00 (dd, $J = 9.4$, $J = 7.8$ Hz, 1H; H-2′), 4.96 (dd, $J = 10.3$, $J = 6.8$ Hz, 1H; H-3″), 4.55 (d, $J = 7.9$ Hz, 1H; H-1′), 4.49 (d, $J = 7.8$ Hz, 1H; H-1″), 4.47 (dd, $J = 12.0$, $J = 2.2$ Hz, 1H; H-6′a), 4.26 (dd, $J = 16.0$, $J = 0.8$, 1H; H-1a), 4.17 (d, $J = 15.0$, $J = 0.8$, 1H; H-1b), 4.12 (dd, $J = 11.9$, $J = 2.4$ Hz, 1H; H-6″a), 4.08 (dd, $J = 12.1$, $J = 5.6$ Hz, 1H; H-6′b), 4.06 (dd, $J = 11.9$, $J = 5.7$ Hz, 1H; H-6″b), 3.87 (t, $J = 6.8$ Hz, 1H; H-5″), 3.81 (t, $J = 9.4$, 1H; H-4′), 3.62 (m, 1H; H-5′), 2.16−1.97 (21H; CH_3CO). ^{13}C NMR (63 MHz, $CDCl_3$): 200.04 (C-1), 170.33−169.03 (7-COO-), 101.00 (C-1″), 100.70 C-1′), 76.10 (C-4′), 74.21 (C-1), 72.80 (C-5′), 72.36 (C-3′), 71.10 (C-2′), 70.83 (C-3″), 70.60 (C-5″), 68.94 (C-2″), 66.48 (C-4″), 61.58 (C-6′), 60.70 (C-6″), 20.72−20.46 (7 -CH_3CO). Analysis calculated for $C_{28}H_{38}O_{19}$: C, 49.56%; H, 5.64%. Found: C, 49.57%; H, 5.63%.ESI-MS: [M + Na] Calcd: 701.2. Found: 701.0.

Synthesis of 2-Bromoethyl-(2,3,4,6-tetraacetyl-β-D-galactopyranosyl)-(1→4)-2,3,6-triacetyl-β-D-glucopyranoside (5). To a solution of octaacetyl-lactose (500 mg, 0.74 mmol) in anhydrous CH_2Cl_2 (2 mL) at 0 °C (ice−water bath), 2-bromoethanol (63 μL, 0.89 mmol) was added, and the reaction mixture was stirred under argon atmosphere. After 30 min, $BF_3{\cdot}(EtO)_2$ (600 μL, 3.70 mmol) was dropped over the mixture at 0 °C for 1 h; afterward, the cooling bath was removed and stirred overnight at room temperature. The reaction mixture was finally added over a stirring ice−water bath. The aqueous fraction was extracted with CH_2Cl_2. The organic phase was washed with water, neutralized with $NaHCO_3$, and then again with water. Afterward, the organic phase was dried with Na_2SO_4, and the solvent was removed. Compound **5** was purified by a chromatography column (hexane/EtOAc 1:1). Yield: 40%.

^1H NMR (250 MHz, $CDCl_3$): 5.35 (dd, $J = 3.3$, $J = 2.8$ Hz, 1H; H-4″), 5.14 (t, $J = 9.8$ Hz, 1H; H-3′), 5.03 (dd, $J = 9.8$, $J = 7.8$ Hz, 1H; H-2″), 4.95 (dd, $J = 9.8$, $J = 3.3$ Hz, 1H; H-3″), 4.85 (dd, $J = 9.8$, $J = 7.8$ Hz, 1H; H-2′), 4.43 (d, $J = 7.8$ Hz, 1H; H-1′), 4.41 (d, $J = 7.8$ Hz, 1H; H-1″), 4.42 (dd, $J = 11.9$, $J = 2.4$ Hz, 1H; H-6′a), 4.13 (dd, $J = 11.9$, $J = 2.4$ Hz, 1H; H-6″a), 4.06 (dd, $J = 11.9$, $J = 5.6$ Hz, 1H; H-6″b), 4.02 (dd, $J = 11.9$, $J = 5.6$ Hz, 1H; H-6′b), 3.85 (m, 1H; H-5″), 3.74 (t, $J = 9.8$, 1H; H-4′), 3.73 (t, $J = 6.8$ Hz, 2H; H-1), 3.55 (m, 1H, H-5′), 3.37 (t, $J = 6.8$ Hz, 2H; H-2), 2.1−1.9 (21H; CH_3CO). ^{13}C NMR (63 MHz, $CDCl_3$): 170.76−169.49 (7-COO-), 101.45 (C-1″), 101.45 (C-1′), 76.55 (C-4′), 73.08 (C-5′), 72.92 (C-3′), 71.73 (C-2′), 71.33 (C-3″), 71.02 (C-5″), 70.19 (C-1), 69.42 (C-2″), 66.96 (C-4″), 62.22 (C-6′), 61.18 (C-6″), 30.33 (C-2), 21.29−20.94 (7 -CH_3CO). Analysis calculated for $C_{28}H_{39}BrO_{18}$: C, 45.23%; H, 5.29%. Found: C, 45.26%; H, 5.28%. FAB-MS: [M + Na] Calcd: 765.1300. Found: 765.1297.

Synthesis of 2-Iodoethyl-(2,3,4,6-tetraacetyl-β-D-galactopyranosyl)-(1→4)-2,3,6-triacetyl-β-D-glucopyranoside (6). To a solution of compound **5** (250 mg, 0.34 mmol) in acetone (25 mL), NaI (1.4 g, 9.36 mmol) was added. The mixture was stirred for 3 h at reflux temperature. When reaction was completed, solvent was removed, and the solid substance was redissolved in EtOAc and washed gently with water. Organic phase was then collected, dried with Na_2SO_4, filtered, and the solvent removed. Compound **6** was obtained in quantitative yield.

^1H NMR (250 MHz, $CDCl_3$): 5.37 (dd, $J = 3.3$ $J = 2.8$ Hz, 1H; H-4″), 5.22 (t, $J = 9.8$ Hz, 1H; H-3′), 5.13 (dd, $J = 9.8$, $J = 7.8$ Hz, 1H; H-2″), 4.97 (dd, $J = 9.8$, $J = 3.3$ Hz, 1H; H-3″), 4.92 (dd, $J = 9.8$, $J = 7.8$, Hz, 1H; H-2′), 4.54 (d, $J = 7.8$ Hz, 1H; H-1′), 4.49 (d, $J = 7.8$ Hz, 1H; H-1″), 4.45 (dd, $J = 11.9$, $J = 2.4$ Hz, 1H; H-6′a), 4.15 (dd, $J = 11.9$, $J = 2.4$ Hz, 1H; H-6″a), 4.08 (dd, $J = 11.9$, $J = 5.6$ Hz, 1H; H-6″b), 4.05 (dd, $J = 11.9$, $J = 5.6$ Hz, 1H; H-6′b), 3.80 (m, 1H; H-5″), 3.75 (t, $J = 7.2$ Hz, 1H; H-1), 3.71 (t, $J = 9.8$, 1H; H-4′), 3.63 (ddd, $J = 9.8$, $J = 5.0$, $J = 2.0$, 1H; H-5′), 3.24 (t, $J = 7.2$ Hz, 2H; H-2), 2.1−1.9 (21H; CH_3CO). ^{13}C NMR (63 MHz, $CDCl_3$): 170.80−169.51 (7-COO-), 101.48 (C-1″), 100.93 (C-1′), 76.58 (C-4′), 73.09 (C-5′), 72.98 (C-3′), 71.75 (C-2′), 71.34 (C-3″), 71.04 (C-5″), 70.91 (C-1), 69.43 (C-2″), 66.95 (C-4″), 62.22 (C-6′), 61.18 (C-6″), 2.63 (C-2), 21.33−20.95 (7 -CH_3CO). Analysis calculated for $C_{28}H_{39}IO_{18}$: C, 45.54%; H, 4.97%. Found: C, 45.52%; H, 4.96%. FAB-MS: [M + Na] Calcd: 813.1200. Found: 813.1780.

Synthesis of 2-[1′-(5′-aminonaphthyl)amino]ethyl-*O*-(2,3,4,6-tetraacetyl-β-D-galactopyranosyl)-(1→4)-2,3,6-triacetyl-β-D-glucopyranoside (7). *Method 1.* To a solution of aldehyde lactoside **4** (100 mg, 0.15 mmol) in anhydrous MeOH (5 mL), 1,5-diaminonaphthalene (DN) (117 mg, 0.74 mmol) and AcOH (20 μL) were added, and the reaction mixture was stirred at room temperature under argon atmosphere. After 1 h, compound **4** had reacted completely as determined by TLC (CH_2Cl_2/acetone 12:1), then $NaBH_3CN$ (19 mg, 0.30 mmol) was added, and the mixture was further stirred for 20 h at room temperature. The solvent was then evaporated, and EtOAc was added to the residue and quenched with brine and water. The organic phase was dried (Na_2SO_4), filtered, and the solvent removed with a vacuum pump. Compound **7** was purified by column chromatography (CH_2Cl_2/acetone 12:1) with 50% yield.

Method 2. To a solution of compound 6 (50 mg, 0.07 mmol) in the toluene anhydrous (5 mL) an excess of DN (5 eq) was added, the reaction mixture was stirred under argon atmosphere, at the reflux temperature of toluene. Reaction was monitored by TLC (CH_2Cl_2/MeOH 20:1). Product 7 was purified, by column chromatography (CH_2Cl_2/MeOH 20:1) and isolated in 70% yield.

^1H NMR (300 MHz, $CDCl_3$): 7.28 (t, $J = 7.4$ Hz, 1H; H-3), 7.20 (d, $J = 7.4$ Hz, 1H; H-4), 7.16 (d, $J = 7.4$ Hz, 1H; H-8), 7.12 (t, $J = 7.4$ Hz, 1H; H-7), 6.70 (d, $J = 7.4$ Hz, 1H; H-6), 6.52 (d, $J = 7.4$ Hz, 1H; H-2), 5.27 (dd, $J = 3.3$, $J = 2.8$ Hz, 1H; H-4″), 5.13 (t, $J = 9.2$ Hz, 1H; H-3′), 5.04 (dd, $J = 9.2$, $J = 7.8$ Hz, 1H; H-2″), 4.89 (dd, $J = 9.2$, $J = 3.3$ Hz, 1H; H-3″), 4.86 (dd, $J = 9.2$, $J = 7.8$ Hz, 1H; H-2′), 4.49 (d, $J = 7.8$ Hz, 1H; H-1′), 4.40 (dd, $J = 11.9$, $J = 2.4$ Hz, 1H; 6′a), 4.38 (d, $J = 7.8$, 1H; H-1″), 4.07 (dd, $J = 11.9$, $J = 2.4$ Hz, 1H; H-6″a), 4.03 (dd, $J = 11.9$, $J = 5.6$ Hz, 1H; H-6″b), 4.01 (dd, $J = 11.9$, $J = 5.6$ Hz, 1H; H-6′b), 3.86 (m, 1H; H-5″), 3.80 (t, $J =$

6.8 Hz, 1H; H-10), 3.72 (t, J = 9.2, 1H; H-4′), 3.57 (m, 1H; H-5′), 3.38 (t, J = 6.8 Hz, 1H; H-9), 1.8−2.01 (21H; CH_3CO). ^{13}C NMR (63 MHz, $CDCl_3$): 170.87−169.56 (7-COO-), 143.91 (C-1), 143.07 (C-5), 125.90 (C-3), 125.67 (C-8), 124.90 (C-4a), 124.64 (C-8a), 111.06 (C-4), 110.84 (C-7), 110.46 (C-6), 105.33 (C-2), 101.53 (C-1″), 100.89 (C-1′), 76.71 (C-4′), 73.18 (C-5′), 73.08 (C-3′), 72.03 (C-2′), 71.38 (C-3″), 71.04 (C-5″), 69.43 (C-2″), 68.77 (C-10), 66.97 (C-4″), 62.49 (C-6′), 61.18 (C-6″), 44.02 (C-9), 21.26−20.96 (7-CH_3CO). Analysis calculated for $C_{38}H_{48}N_2O_{18}$: C, 55.61%; H, 5.89%; N, 3.41%. Found: C, 55.62%; H, 5.88%; N, 3.41%. FAB-MS: [M + H] Calcd: 821.2975. Found: 821.2954.

Synthesis of 2-[1′-(5′-Aminonaphthyl)aminoethylene]-*O*-*β*-D-galactopyranosyl-(1→4)-*β*-D-glucopyranoside (8). To a solution of compound **7** in MeOH, catalytic amounts of MeONa were added. The reaction mixture was stirred at room temperature until complete conversion of the acetylated compound was observed by TLC (2-propanol/nitromethane/water, 10:9:2). The reaction mixture was then neutralized with Amberlite-IR 120 [H^+] and filtered. The filtrate was collected, and the solvent was removed. Compound **8** was obtained in quantitative yield.

^1H NMR (500 MHz, D_2O): The assignment is shown in Table 1 of the Supporting Information. ^{13}C NMR (125 MHz, D_2O): 143.42 (C-1), 141.28 (C-5), 126.38 (C-3), 126.08 (C-8), 125.05 (C-4a,C-8a), 113.20 (C-4), 112.64 (C-7), 112.33 (C-6), 107.48 (C-2), 103.20 (C-1″), 102.60 (C-1′), 78.52 (C-4′), 75.61 (C-5′), 75.17 (C-3′), 75.00 (C-2′), 74.56 (C-3″), 73.08 (C-5″), 72.77 (C-2″), 71.20 (C-10), 68.80 (C-4″), 61.31 (C-6′), 60.29 (C-6″), 44.00 (C-9). Analysis calculated for $C_{19}H_{31}N_3O_{11}$: C, 54.75%; H, 6.51%; N, 5.32%. Found: C, 54.78%; H, 6.53%; N, 5.32%. ESI-MS: [M + Na] Calcd: 526.2. Found: 548.9.

Synthesis of 20-Bromo-3,6,9,12-tetraoxatrieicosan-1-ol (9). To a solution of tetraethylen glycol (1 g, 5 mmol) in THF anhydrous, NaH (160 mg, 6.5 mmol) was added, and the reaction mixture was stirred under argon atmosphere at 0 °C. After 3 h, the reaction mixture was dropped over a solution of 1,8-dibromooctane (1.4 g, 5 mmol) under argon atmosphere at 0 °. After 4 h, NaBr formed, and the solvent was removed. Purification of the final product was carried out by column chromatography (CH_2Cl_2/MeOH 20:1), yielding **9** in 40%.

^1H NMR (300 MHz, $CDCl_3$): 3.62 (m, 16H, H-1 to H-8), 3.43 (t, 2H, J = 6.56 Hz, H-9), 3.38 (t, 2H, J = 7.03 Hz, H-19), 1.83 (q, 2H, J = 7.2 Hz, H-18), 1.55 (q, 2H, J = 6.90 Hz, H-10), 1.38 (m, 2H, H-11), 1.25 (m, 12H, H-12 to H-17).^{13}C NMR (125 MHz, $CDCl_3$): 72.63 (C-9), 71.52 (C-7), 70.61 (C-3,C-4,C-5,C-6), 70.28 (C-8), 70.05 (C-2), 61.50 (C-1), 34.00 (C-19), 32.89 (C-18), 29.56 (C-10,C-12,C-13,C-14, C-15), 28.72 (C-11), 28.18 (C-16), 26.13 (C-17). Analysis calculated for $C_{16}H_{33}BrO_5$: C, 49.87%; H, 8.63%; Found: C, 49.88%; H, 8.65%. ESI-MS: [M + Na] Calcd: 407.2. Found: 407.3.

Synthesis of 20-Bromo-3,6,9,12-tetraoxatrieicosan-1-oic Acid (10). Over a solution of **9** (650 mg, 1.7 mmol) in acetone (50 mL), 1 mL of Jones reagent (2.4 mmol of CrO_3) was dropped, and the reaction was stirred for 30 min followed by the addition of a few drops of 2-propanol. Afterward, saturated NaCl solution (20 mL) was added to the mixture and stirred for an additional 30 min followed by the removal of the acetone. The aqueous mixture was extracted with CH_2Cl_2 (3 × 30 mL), and the solvent was then removed. Compound **10** was finally purified by column chromatography (CH_2Cl_2/MeOH 10:1) in 70% yield.

^1H NMR (300 MHz, $CDCl_3$): 6.71 (s, 1H, COOH), 4.13 (s, 2H, H-2), 3.56 (m, 12H, H-3 to H-8), 3.39 (t, 2H, J = 6.90 Hz, H-9), 3.34 (t, 2H, J = 6.85 Hz, H-14), 1.81 (q, 2H, J = 7.16 Hz, H-15), 1.52 (m, 2H, H-10), 1.34 (m, 2H, H-11), 1.28 (m, 6H, H-12,H-13 and H-14). ^{13}C NMR (125 MHz, $CDCl_3$): 173.03 (C-1), 72.07 (C-9), 71.97 (C-8), 70.84 (C-7), 70.74 (C-6), 70.65 (C-5), 70.45 (C-4), 70.34 (C-3), 69.11 (C-2), 34.44 (C-16), 33.10 (C-15), 29.70 (C-10), 29.55 (C-12), 29.00 (C-11), 28.41 (C-13), 26.24 (C-14). Analysis calculated for $C_{16}H_{31}BrO_6$: C, 48.12%; H, 7.82%. Found: C, 48.20%; H, 7.81%. ESI-MS: [M + Na] Calcd: 421.1. Found: 421.0.

Scheme 1. Synthesis of Fluorescent Glycans via Reductive Amination[a]

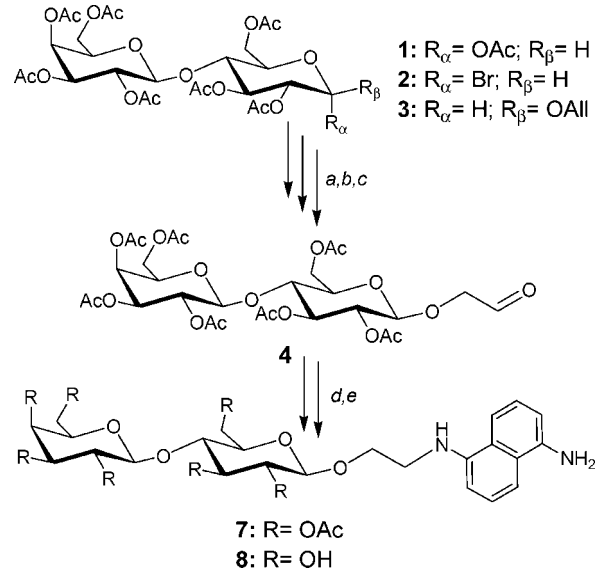

[a] (a) HBr, CH_2Cl_2 (90% yield). (b) Allyl alcohol, $HgBr_2$, HgO, CH_2Cl_2 (50% yield). (c) O_3, −78°C, CH_2Cl_2. (75% yield). (d) 1. DN, $AcOH_{cat}$, MeOH. 2. $NaCNBH_3$ (50% yield). (e) MeONa, MeOH (quantitative yield).

Scheme 2. Synthesis of Iodoethyl Derivative and Binding to the DN[a]

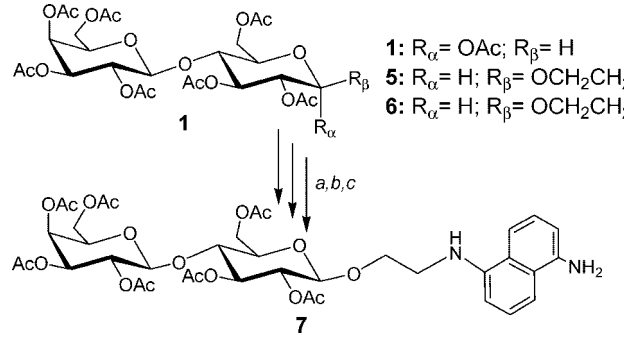

[a] (a) $BF_3 \cdot Et_2O$, Br-ethanol, CH_2Cl_2 (40% yield). (b) NaI, acetone, reflux (100% yield). (c) DN, toluene, reflux (70% yield).

Synthesis of 20-Mercapto-3,6,9,12-tetraoxatrieicosan-1-oic Acid (11). A solution of **10** (230 mg, 0.5 mmol) and thiourea (120 mg, 1.5 mmol) in 30 mL of water was heated to reflux temperature. After 6 h, NaOH (600 mg, 15 mmol) was added and the mixture stirred for an additional period of 6 h. The mixture was finally cooled to room temperature, and the pH was adjusted to 1 with concentrated HCl. The resulting solution was extracted with CH_2Cl_2 (3 × 20 mL). The combined extracts were dried (MgSO4), evaporated to dryness, and the resulting oil was purified by column chromatography (CH_2Cl_2/MeOH 5:2.) affording compound **11** with a 60% yield.

^1H NMR (300 MHz, $CDCl_3$): 8.23 (s, 1H, COOH), 4.00 (s, 2H, H-2), 3.56 (m, 12H, H-3 to H-8), 3.38 (t, 2H, J = 6.93 Hz, H-9), 2.58 (t, 2H, J = 7.35 Hz, H-19), 1.58 (m, 4H, H-10 and H-18), 1.20 (m, 14H, H-11 to H-17). ^{13}C NMR (125 MHz, $CDCl_3$): 173.03 (C-1), 72.07 (C-9), 71.97 (C-8), 70.84 (C-7), 70.74 (C-6), 70.65 (C-5), 70.45 (C-4), 70.34 (C-3), 69.11(C-2), 34.44 (C-16), 33.10 (C-15), 29.70 (C-10), 29.55 (C-12), 29.00 (C-11), 28.41 (C-13), 26.24 (C-14). Analysis calculated

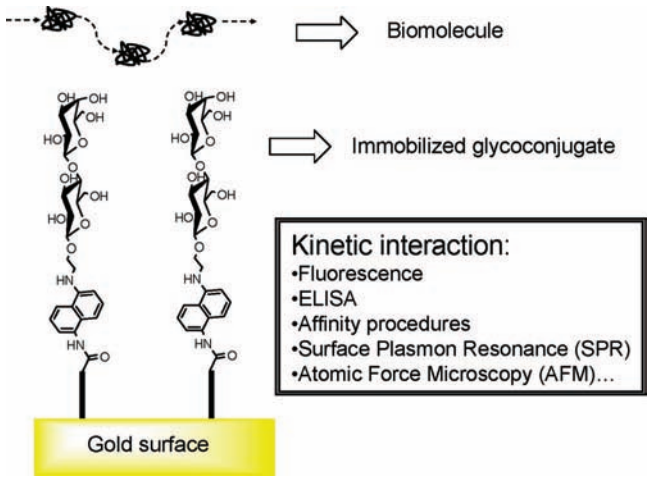

Figure 1. New fluorescent glycan is immobilized on different carboxylated surfaces. This is a versatile way to functionalize carbohydrates for their application in different techniques for biological studies.

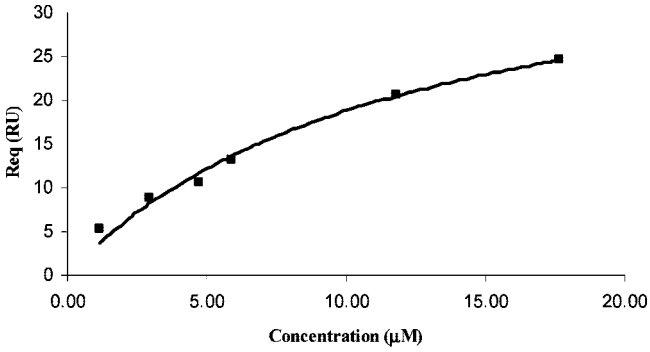

Figure 2. Steady state affinity study of the interaction between VAA and LacDAN immobilized on a C1 chip.

for $C_{16}H_{32}O_6S$: C, 54.52%; H, 9.15%; S, 9.10%. Found: C, 54.53%; H, 9.17%; S: 9.09%. ESI-MS: [M + Na] Calcd: 375.2. Found: 375.0.

Lectin Purification and Quality Controls. The galactoside-specific lectin from mistletoe (*Viscum album* agglutinin; VAA) was purified from aqueous extracts of dried leaves by affinity chromatography as a crucial step, using divinyl sulfone activation of Sepharose 4B and lactose as ligand for optimal yields (*17*, *18*). The purity of the product was ascertained by gel electrophosesis and gel filtration and the activity by solid-phase and cell-binding assays, and the activity of both binding sites in the 1α and 2γ subdomains (Trp/Tyr sites) was determined by spectroscopic methods (*19*−*22*).

Conformational Analysis and Molecular Recognition Studies. To record the nuclear Overhauser enhancements (NOE) of the compounds in the free state, a double pulse field-gradient spin−echo (DPFGSE) module was used (*23*). NOE intensities were normalized with respect to the diagonal peak at zero mixing time. Selective T_1 measurements were performed on anomeric and several other protons. Experimental NOEs were fitted to a double exponential function, as described (*23*) $f(t) = p0(e^{-p1t})(1 - e^{-p2t})$, where $p0$, $p1$, and $p2$ are adjustable parameters. The initial slope was determined from the first derivative at time $t = 0$, $f(0) = p0p2$. From the initial slopes, interproton distances were obtained by employing the isolated spin-pair approximation (ISPA).

STD experiments (*24*) were performed without saturation of the residual HDO signal for molar ratios between 20:1 and 50:1 of compound/lectin. A series of Gaussian-shaped pulses of 50 ms was run, with a total saturation time of the protein of 2 s and a maximum B1 field strength of 50 Hz. An off-resonance frequency of $\delta = 40$ ppm and on-resonance frequencies between $\delta = -1.0$ ppm (protein aliphatic signals region) were applied. In all cases, line-broadening of ligand protons was monitored. The STD experiments were repeated twice. Basically, similar results were obtained in both sets. In each case, the intensities were normalized with respect to the highest response, which always corresponded to the Gal H4 proton.

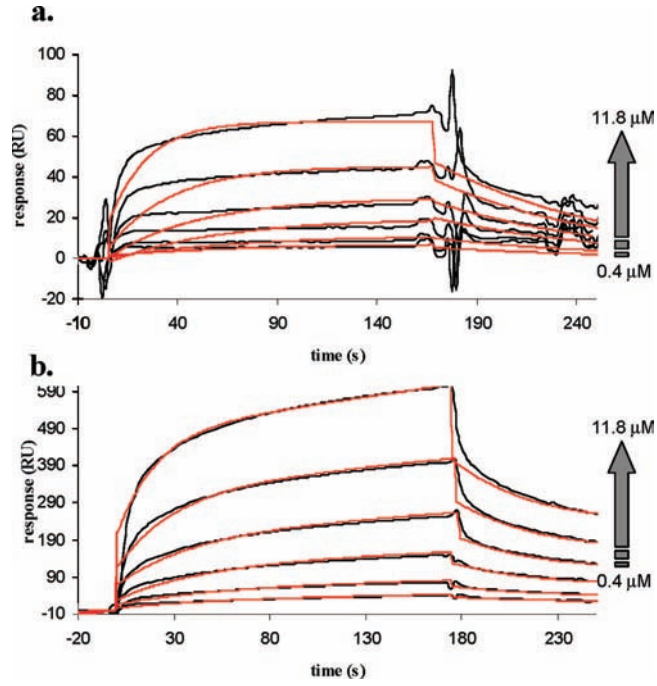

Figure 3. Kinetic study of the interaction between LacDN immobilized on a CM5 sensor chip and VAA. (a) Low density (96 RU). (b) High density (660 RU).

Table 1. Kinetic Parameters Determined by SPR of the Interaction between VAA and LacDN Immobilized on Different Surfaces (1:1 Langmuir Binding Model)

	kinetic study				steady state study
surface	k_{on} ($M^{-1}s^{-1}$)	k_{off} (s^{-1})	K_D (μM)	χ^2	K_D (μM)
C1 (111 RU)					11.9
CM5 (96 RU)	3.45×10^3	1.2×10^{-2}	3.3	3.7	15.3 ± 2.2
CM5 (660 RU)	2.79×10^3	1.7×10^{-2}	6.2	1.6	11.8 ± 1.0
SAM (530 RU)	3.0×10^3	9.2×10^{-3}	3.2	107	7.8 ± 0.1

For the bound ligands, trNOE experiments were performed as described previously (*25*, *26*). The cvff and cff91 force-fields were applied in computational conformational analysis, and also AMBER-based molecular mechanics and dynamics calculations for methyl β-lactoside were performed. Measurements were done with a freshly prepared ligand/lectin mixture, with mixing times of 100, 150, and 200 ms, at an approximately 30:1 molar ratio of ligand/protein. A concentration between 2−3 mM of the ligand was employed in all cases. No purging spin-lock period was employed to remove the NMR signals of the macromolecule background. First, line-broadening of the ligand protons was monitored after the addition of the lectin. Strong negative NOE cross-peaks were observed, in contrast to the free state, indicating binding of the sugars to the lectin preparation (*27*).

Additional experiments were performed with concanavalin A (ConA) as a receptor for negative control. ConA binds glucose or mannose moieties and displays no binding activity for galactose derivatives. No STD or trNOE signals were observed, thus indicating the specificity of the synthetic probe for galactose-binding proteins.

Table 2. Kinetic Parameters Determined by SPR of the Interaction between VAA and LacDN Immobilized on Different Surfaces (Bivalent Analyte Model)

surface	k_{on1} ($M^{-1}s^{-1}$)	k_{off1} (s^{-1})	k_{on2} ($M^{-1}s^{-1}$)	k_{off2} (s^{-1})	K_{D1} (μM)	K_{D2} (M)	χ^2
CM5 (96 RU)	1.64×10^3	4.4×10^{-2}	6.7×10^{-5}	3.1×10^{-4}	26.8	4.6	12
CM5 (660 RU)	8.09×10^2	6×10^{-2}	6.2×10^{-6}	1.2×10^{-3}	74.2	193	19
SAM (530 RU)	6.0×10^2	2.8×10^{-3}	2.4×10^{-5}	4.4×10^{-3}	4.66	183	114

Molecular Mechanics and Dynamics Calculations. All molecular mechanics and dynamics calculations for the free molecules were performed using the MAESTRO package and the MM3* force field (*28*). Charges were taken from the force field (all-atom charge option), and water solvation was simulated using the generalized Born GB/SA continuum solvent model (*29*). The torsion angles Φ are defined as H1Gal-C1Gal−O-C4Glc and Ψ as H4Glc-C4Glc−O-C1Gal. For the pendant chain, Φ chain is H1Glc-C1Glc-O-CH_2, and Ψ chain is C1Glc-O-CH_2−CH_2. The torsion angle around the C5−C6 linkage (ω) is defined as O5−C5−C6-O6. Two different conformers were considered gt ($\omega = +60°$) and gg ($\omega = -60°$) for the Gal and Glc moieties, respectively. The Φ/Ψ maps computed (*30*) from the 3 ns MD simulations (1.5 fs integration sep, 300 K) were built and analyzed as described (*31*). A temperature of simulation of 300 K was employed with a time step of 1.5 fs and an equilibration time of 100 ps. The total simulation time was 3 ns. The GB/SA solvation model was employed. The numbering is given in the corresponding scheme in the Supporting Information.

Docking Calculations. The prevalent conformer of **8** (as observed by NMR) was manually docked into the two carbohydrate-binding sites of VAA in the 1α and 2γ subdomains of the B-subunit of VAA by superimposing the terminal Gal residue (pdb code 1PUM). Then, different possibilities of arranging the side chain of the glycan were used as input geometries for AutoDock 3.0 simulations (*32*) with the multiple Lamarckian genetic algorithm. Only local searches were performed centered in the two experimental galactoside-specific VAA X-ray sites. Grids of probe atom interaction energies and electrostatic potential were generated by the AutoGrid program present in AutoDock 3.0. Grid spacings of 0.6 and 0.375 Å were used for the global and local searches, respectively. For each calculation, 100 docking runs were performed using a population of 200 individuals and an energy evaluation number of 3×10^6.

Immobilization of Compound 8 on a Carboxylated Surface (C1, Biacore). For the immobilization of the fluorescent lactoside **8**, a standard C1 chip (BIAcore) was activated by the injection of the amino coupling kit (BIAcore): EDC/NHS (35 μL) at a flow rate of 5 μL min^{-1}, at 28 °C, and 10 mM Hepes, 150 mM NaCl, pH 7.4 (HBS-P) as running buffer. At the same conditions of flow and temperature, a solution of **8** (1 mM, 150 μL) in 10 mM sodium acetate buffer, pH 4.5, was injected 3 consecutive times to get the maximum immobilization, followed by the injection of ethanolamine (1 M, 35 μL) to block the possible remaining active sites on the dextran matrix. The final response reached was 111 RU (flow cell-1). On a second flow cell, the activation and blocking standard procedures were carried out as described above, and it was left as the negative control of the interaction.

For the interaction assays, different concentrations (1.2, 2.9, 4.7, 5.9, 11.8, and 17.7 μM) of a solution of VAA in the running buffer were injected (15 μL), at a flow rate of 5 μL min^{-1}, at 28 °C. After the injection of the sample, the same buffer (without added protein) was injected to the sensor chip surface to allow dissociation. After a suitable dissociation phase, the sensor surface was regenerated for the next protein sample by injecting of 50 mM (5 μL) NaCl. The data were double reference subtracted, and the apparent K_D value was calculated by nonlinear fitting of the plot of R_{eq} versus the VAA concentration using the average model with steady-state affinity as given in the BIAEvaluation software from BIAcore.

Immobilization of Compound 8 on a Carboxylated Dextran Surface (CM5, Biacore). For the immobilization of the fluorescent lactoside **8** (flow cell-1), a standard CM-5 chip (BIAcore) was activated by injection of the amino coupling kit (BIAcore): EDC/NHS (35 μL) at a flow rate of 5 μL min^{-1}, at 28 °C, and 10 mM Hepes, 150 mM NaCl, pH 7.4 (HBS-P) as running buffer. At the same conditions of flow and temperature, a solution of **8** (1 mM, 180 μL) in 10 mM sodium acetate buffer, pH 4.5, was injected 3 consecutive times to get the maximum immobilization, followed by the injection of ethanolamine (1 M, 35 μL) to block the possible remaining active sites on the dextran matrix. The final response reached was 660 RU (flow cell-1). The same procedure was repeated to obtain less density of the immobilization on the SPR chip. In this case, LacDN **8** (96 RU) was immobilized on the surface (flow cell-2). On a third flow cell, the activation and blocking standard procedures were carried out as described above, and it was left as the negative control of the interaction.

For the interaction assays, different concentrations (0.4, 0.7, 1.7, 2.9, 5.9, and 11.8 μM) of a solution of VAA in the running buffer were injected (15 μL), at a flow rate of 5 μL min^{-1}, at 28 °C. After injection of the sample, the same buffer (without added protein) was flowed through the sensor chip surface to allow dissociation. After a suitable dissociation phase, the sensor surface was regenerated for the next protein sample by injecting of 50 mM (5 μL) NaCl. In each experiment the response unit (RU) was monitored as a function of time (sensorgram). The data were fitted to a single biomolecular reaction model using the BIAEvaluation software from BIAcore.

Immobilization of Compound 8 on a Self-Assembled Monolayer (SAM) Prepared with a Gold Chip (Au). Compound **11** was immobilized on a gold surface from an Au chip (Biacore) to create a SAM. For that purpose, a solution of **11** in water-P_{20} (10 μL) was injected on an Au chip, at a flow rate of 2 μL min^{-1}, at 25 °C. After each injection, the surface of the flow cell was washed with 50% MeOH (5 μL) and 75% MeOH (5 μL) at a flow rate of 5 μL min^{-1}, at 25 °C. The same procedure was repeated in another flow cell so that both cells reached a similar response in RU (720 and 1000 RU).

For the immobilization of the fluorescent lactoside **8**, the previous chip was activated by the injection of the amino coupling kit (BIAcore): EDC/NHS (35 μL) at a flow rate of 5 μL min^{-1}, at 25 °C, and 10 mM Hepes, 150 mM NaCl, pH 7.4 (HBS-P), as running buffer. At the same conditions of flow and temperature, a solution of **8** (1 mM, 150 μL) in sodium acetate 10 mM buffer, pH 4.5, was injected to get the maximum immobilization, followed by the injection of ethanolamine (1 M, 35 μL) to block the possible remaining active carboxylate groups of the SAM. The final response reached was 530 RU (flow cell-1). On a second flow cell, the activation and blocking standard procedures were carried out as described above, and it was left as negative control of the interaction.

For the interaction assays, different concentrations (1.1, 2.2, 4.4, 8.8, 17.7, and 35.3 μM) of a solution of VAA in the running buffer were injected (15 μL), at a flow rate of 5 μL min^{-1}, at 25 °C. After injection of the sample, the same buffer (without added protein) was injected to the sensor chip surface to allow dissociation. After a suitable dissociation phase, the sensor

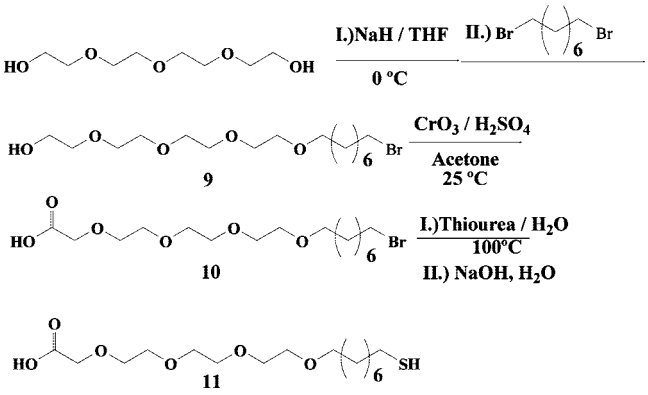

Figure 4. Synthesis of compound **11**.

surface was regenerated for the next protein sample by injecting 50 mM (5 μL) NaCl. The data collected were fitted to a single biomolecular reaction model using the BIAEvaluation software from BIAcore.

RESULTS AND DISCUSSION

Synthesis of New Fluorescent-Glycan. The first synthetic approach to obtain the fluorescent lactoside was via reductive amination (Scheme 1). On a first step, peracetylated lactoside **1** was activated via bromide derivative **2** (90% of yield), and finally, allyl alcohol was attached to the anomeric position in the presence of mercury oxide and mercury bromide (*16*), affording the desired allyl-lactoside **3** with the specific β-configuration and with 50% yield. Afterward, the functionalization of the allyl end was carried out by ozonolysis at −78 °C in CH_2Cl_2 to yield derivative **4** in 75% yield (*33*). This lactoside **4** is suitable for fluorescent labeling while keeping the naphthalene rings intact.

The fluorescent tag chosen for the labeling of the functionalized lactoside **4** was 1,5-diaminonaphthalene (maximum excitation at 320 nm, and maximum emission at 410 nm) (*34*). Reductive amination of compound **4** and DN was carried out in slightly acid conditions, and further reduction with $NaBH_3CN$ led to the formation of the desired fluorescent compound **7** in 50% yield. The overall yield of the synthesis of compound **7** via reductive amidation was 17%. Other authors have described access to fluorescent glycan derivatives from monoaminated pyridines in moderate yields of 29% (*35*). In our case, we introduced a diamine derivative with an improved yield, and in addition, the structure maintains a free amino group suitable for immobilization on activated surfaces.

Despite the fair yield of the overall process (17%), an alternative approach was explored to reduce the number of synthetic steps (Scheme 2). First, peracetylated lactose was functionalized with 2-bromoethanol to generate compound **5** in a yield, 40%, similar to that described in the literature (*35*). Bromine was then easily exchanged by iodine, passing after 2 h from **5** into the iodine derivative **6** in quantitative yield (*36*). With these two easy steps, the building block for the synthesis of fluorescent glycans was obtained. Consequently, the nuchleophilic substitution reaction was carried out with excess of DN (compound **6**/DN, 1:5) and in reflux of toluene to afford compound **7** in 70% yield. The overall yield of compound **7** via nucleophilic subtitution was 28%. In the final step, the protected compound **7** was deprotected using standard procedures in a basic milieu. In this way, the fluorescent glycan **8**, LacDN was obtained in quantitative yield.

Immobilization of the New Fluorescent-Glycoconjugates on Different Biochip Surfaces and Interaction Studies of *Viscum album* Agglutinin (VAA) by SPR. The new fluorescent-glycoconjugate (LacDN) has been synthesized with a fluorescent linker ending with an amino group that enables the immobilization of LacDN on a gold surface of a SPR biosensor chip functionalized with carboxylic groups (Figure 1).

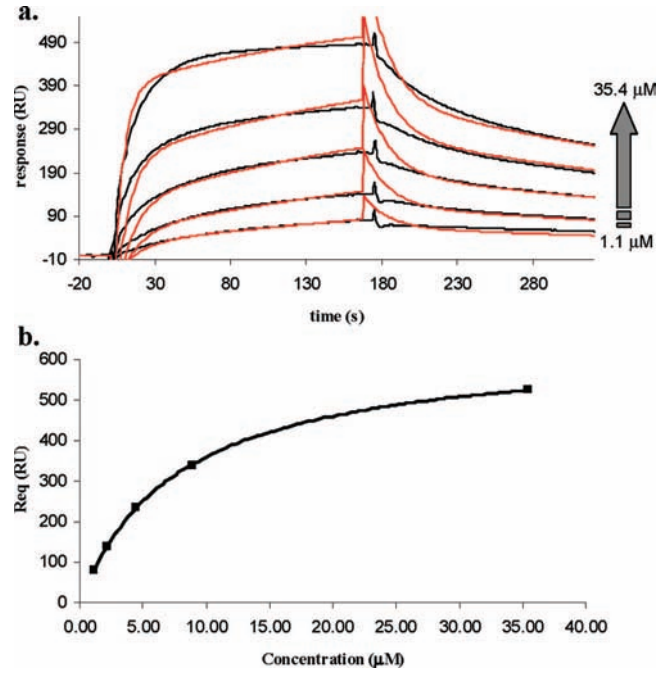

Figure 5. (a) Sensorgrams recorded for the interaction of VAA with LacDN immobilized on a SAM. (b) Steady state affinity study between VAA and LacDN immobilized on a SAM functionalized chip.

The first strategy was the immobilization of compound **8** (LacDN) on a C1 biosensor chip. The gold surface of the sensor chip C1 is directly functionalized with carboxymethyl groups, without the presence of a dextran matrix, and also has a low binding capacity. This surface is also useful for those interactions that may be affected by the presence of the matrix.

For that purpose, LacDN was immobilized in one of the flow cells of a C1 sensor chip, and an untreated flow cell was used as the reference surface for interactions studies. The optimal buffer for the immobilization was 10 mM sodium acetate, pH 4.5. After the immobilization and blocking with ethanolamine procedures, a response of 111 RU was reached. As model lectin, *Viscum album* agglutinin (VAA), a potent toxin and thus a potential biohazard, was tested to address the issues of whether the surface is bioactive. The K_D of VAA binding to LacDN was determined by titration of the surface with various VAA concentrations (1.2−17.7 μM) (data not shown). The K_D value was obtained from a nonlinear fit of the data in a plot of R_{eq} (response at equilibrium) versus the VAA concentration (Figure 2), and the data obtained afforded an apparent K_D value of 11.9 μM (Table 1).

The second strategy was the immobilization of compound **8** (LacDN) on a CM5 chip. The amino functionalized compound is covalently bound to the carboxymethylated dextran matrix that lays on the gold surface of the CM5 chip. The optimal buffer for the immobilization was 10 mM sodium acetate, pH 4.5. In order to evaluate the interaction, LacDN was immobilized on two different flow cells at different degrees of immobilization in the same sensor chip, to minimize the differences due to the dextran matrix. Finally, a third flow cell was activated, blocked, and used as negative control. In one flow cell, a very high density of LacDN was reached (660 Response Unit, RU). In a second flow cell, LacDN was injected to reach a comparatively low response (96 RU) to evaluate possible modifications in the behavior of the interaction due to the density of ligand immobilized.

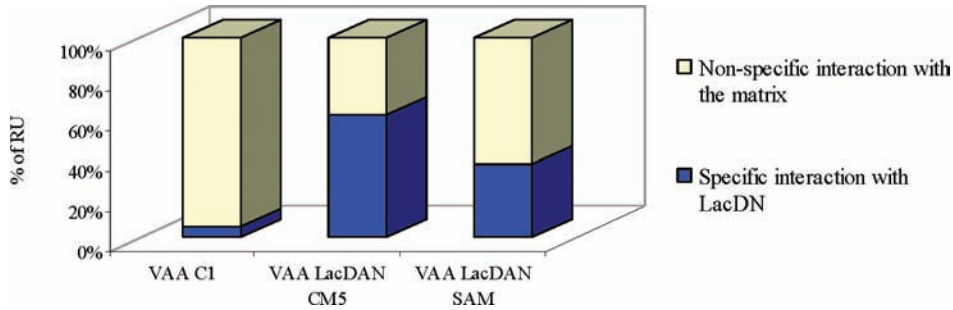

Figure 6. Percentage of specific binding compared to the nonspecific interaction of the lectin to the surfaces: C1, SAM and CM5.

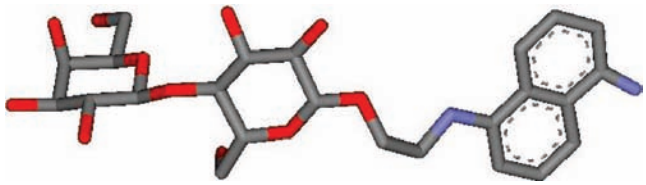

Figure 7. The major conformer of Lact-DN in solution as deduced from NMR experimental data and MD similations.

Afterward, the same VAA was tested to address the issues of whether the surface is bioactive and whether the density change may alter the kinetics. Figure 3 shows the binding of VAA to the sensor chip immobilized with two different densities of LacDN. Under both density surfaces (Figure 3), VAA associated relatively slowly, and the dissociation also proceeded gradually. Primarily, the binding curves obtained using concentrations of VAA from 0.4 μM to 11.8 μM were analyzed assuming a 1:1 (Langmuir) binding model. As shown in Figure 3, the absolute response in RU is drastically different in the two surfaces with different densities, but when data are fitted to a 1:1 kinetics, the apparent K_D is in the same micromolar range (Table 1). Thus, the surface is bioactive with an effect of density on k_{on}. It was found that the χ^2 values, which measure the closeness of the model fits and the experimental data, were consistently <10, indicative of a good curve fit (Table 1).

VAA has potentially two or more sugar binding sites (*37*, *38*), and for that reason the same data set was analyzed assuming bivalent binding. The bivalent binding model assumes that the analyte having two independent binding sites interacts with two receptor sites with identical binding properties. Detailed analysis of the bivalent analyte model of the interaction of the two surface densities of LacDN with VAA is summarized in Table 2. The kinetic analysis showed that the bivalent analyte model provides χ^2 values >10, indicative of a nonoptimal curve fit.

The fact that VAA has more than one binding site suggests that VAA makes more that one contact with the immobilized LacDN molecules on the chip surface. Althought the affinity of a multivalent interaction cannot be directly calculated from Biacore data, the apparent K_D value of the system was obtained from a nonlinear fit of the data in a plot of R_{eq} (response at equilibrium) versus the VAA concentration (data not shown), and the data obtained afforded an apparent K_D value of 11.3 μM for the low density surface and 11.8 μM for the high density surface (Table 1).

Finally, glycoconjugate **8** LacDN was immobilized on a chip where a self-assembled monolayer (SAM) was created by the injection of compound **11** over the gold surface of a commercial Au chip (Biacore).

This thiol-reactive heterobifunctional linker **11** was synthesized as described in Experimental Procedures (Figure 4). Tetra(ethylene glycol) reacted with 1,8-dibromooctane to afford compound **9** in 40% yield. Compound **9** was then oxidized with Jones reagent to afford **10** in good yield (70%). Finally, reaction with thiourea followed by base catalyzed hydrolysis afforded a thiol group and carboxyl containing compound **11** in 60%. The resulting monolayer was very homogeneous judging from the similar RU values obtained for both flow cells. The SAM was formed quickly and was quite stable due to the avidity of the thiol group for the gold. Several washings with 50% aqueous MeOH were required to eliminate the noncovalently bound linker.

In addition, the linker chains that form the SAM are functionalized at the free end with a carboxylic group to allow the covalent coupling of the desired compound to the surface. Therefore, a solution of LacDN (1 mM) in 10 mM AcONa/AcOH buffer, pH 4.5, was injected on this surface, and after the blocking procedure with ethanolamine, a final response of 530 RU was reached. VAA was chosen to perform interaction studies with the glycoconjugate immobilized on a SAM (Figure 5). For that purpose, different concentrations of VAA were injected, and the sensorgrams obtained were further analyzed. We analyzed these sensograms using two binding models in Bioevaluations sofwere. On a first attempt, we tried to adjust the data to a 1:1 kinetic model, and it was found that χ^2 values were <10, indicative of a good curve fit. We observed a k_{on} and k_{off} comparable to that observed for the CM5 surface giving a similar apparent K_D of 3.2 μM (Table 1). The same data set was analyzed assuming a bivalent binding model (Table 2). In this case, it was found that the χ^2 values were >10, indicative of a nonoptimal curve fit; for that reason, the sensograms of the SAM surface could not be analyzed with the bivalent model. In order to consider a multivalent binding model, only the results of the steady-state affinity determination were available. The apparent K_D value obtained by this methodology was 8.0 μM (Table 1).

Kinetic parameters obtained in the three surfaces studied (Table 1) are in the micromolar range, similar to those reported by André et al. (*39*) for the binding of VAA to galactose in the solid-phase assay in microplate wells.

The compound LacDN was immobilized on different surfaces (C1, CM5, and SAM) and an untreated flow cell was used as a blank surface for VAA lectin. The values of RU were obtained from the sensorgrams when VAA was injected over each sort of surface and were used to calculate the contribution (%RU) of nonspecific interaction of VAA lectin with the matrix and the contribution of the specific interaction of this lectin with the compound LacDN. As can be seen from Figure 6, the surface C1 showed stronger nonspecific interaction with the lectin (95%) than SAM (45%) and CM5 (33%). Of interest, CM5 is the one that showed the least nonspecific interaction with VAA lectin. Therefore, this is the surface of election to carry out carbohydrate−VAA lectin interaction through SPR when the glycoconjugate is the one immobilized on the chip.

Conformational Properties in the Free and Lectin-Bound States. The newly synthesized glycan carries a new group at the reducing end of the Glc moiety of lactose, which may affect

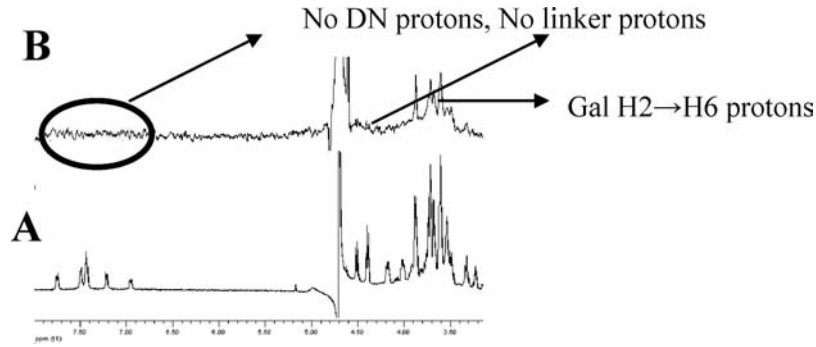

Figure 8. Interaction of LacDN with VAA. Trace A shows the regular 500 MHz ^{1}HNMR spectrum of LacDN at 300 K in the presence of VAA (30:1). Trace B shows the STD spectrum (saturation time 600 ms, on resonance irradiation at $\delta = -1$ ppm), showing only the Gal protons, especially H2, H3, H4, H5, and H6. Minor transfer to the Glc moiety and no transfer to the DN moiety is observed at this saturation time. When increasing the saturation time to 2 s, the Glc protons are also observed, as well as additional saturation transfer to the linker protons and even to the DN protons (not shown). In any case, the binding epitope clearly belongs to the Gal moiety.

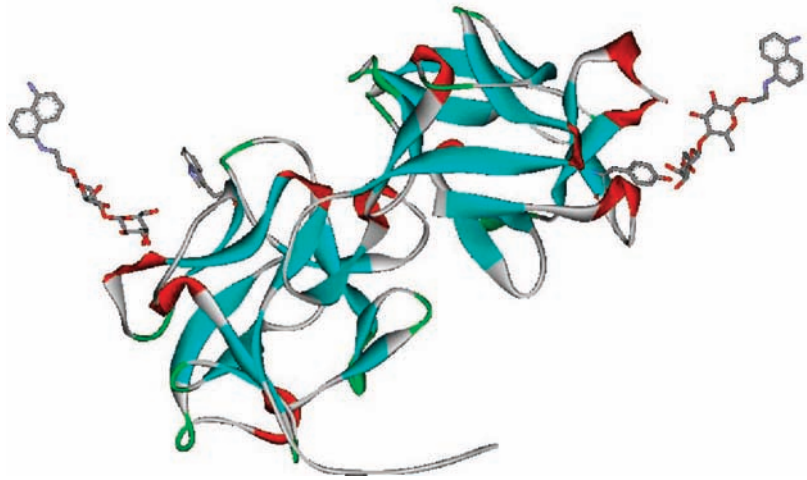

Figure 9. Three-dimensional model of the complex of VAA (coordinates taken from the Protein Data Bank, code 1PUM) with Lact-DN. Independent AUTODOCK simulations were performed with the Trp38 (top figure) and Tyr249 (bottom figure) binding sites as described in Experimental Procedures. The figures show the best result for both cases. No contacts between the linker or the DN moiety and the protein are observed. Key contacts are highlighted.

conformational or binding properties, when in contact to the protein surface.

To determine the free-state conformational space of LacDN, a combination of NMR experiments and molecular mechanics and dynamics calculations was performed. The ^{1}H NMR chemical shifts and coupling constants, as obtained at 500 MHz and 300 K, are given in the Supporting Information. The analysis of the coupling constants permitted us to assess whether the Glc and Gal rings keep the natural $^4C_1$(D) conformation. Then, the conformational preferences around the glycosidic linkage were assessed by NOE experiments. Only the expected inter-residue GalH1 to GlcH4 (overlapping with Glc H3) and GlcH6 NOEs were observed, indicating that LacDN adopts the natural exoanomeric syn-$\Phi\Psi$ geometry of lactose around the glycosidic linkage (*40, 41*). No intramolecular aromatic-sugar NOEs were observed, indicating that no stacking of the aromatic moiety onto the sugar faces takes place (*42*−*44*).

Thus, the pendant DN group stands away of the lactose moiety. A view of the major conformer, originating from the molecular mechanics calculations, is given in Figure 7. Moreover, MD simulations (3 ns, 300 K) that were performed rearrange the relative clause that the lateral chain, although flexible, only accesses a well-defined area of the available conformational space in terms of Φ/Ψ torsion angles (Figure S1, Supporting Information). The global minimum within this Φ/Ψ region is able to explain all of the NMR data (NOE contacts) in a satisfactory manner.

Having determined the free-state conformational behavior, we next studied binding and contact sites to the lectin, using saturation transfer difference (STD) experiments, and the bound-state conformation, using trNOE experiments.

The STD experiments demonstrated that the lectin recognizes LacDN. Clear STD signals for the sugar protons in the ligand were observed (Figure 8). The maximum enhancements were observed for the protons at the Gal moiety, followed by the contiguous protons at the Glc fragment and the linker and DN moieties, but only when the saturation time was increased. Smaller enhancements were evident at the linker, especially the CH_2 moiety contiguous to the Glc unit, while the DN protons showed moderate enhancements, indicating a minor interaction of this moiety with VAA. Additional experiments were performed with concanavalin A (ConA) as the receptor for the negative control. ConA binds glucose or mannose moieties and displays no binding activity for galactose derivatives. No STD or trNOE signals were observed, thus indicating the specificity of the synthetic probe for galactose-binding proteins.

The trNOE technique will answer the question on the conformation of the bound-state of the ligand, especially whether the derivatization may affect the selection of the low-energy conformer (*45*). At a 20:1 molar ratio of ligand/receptor, negative NOE cross-peaks, indicating binding, were only observed for the Gal and Glc moieties, whereas the linker protons only provide very weak (almost zero) cross-peaks. This result indicates that different degrees of mobility (different

effective correlation times) exist in the VAA-bound state for the different portions of the molecule. The Gal moiety is recognized by the lectin, and the lactose part increases the correlation time passing to the negative-NOE regime. In contrast, the linker and the DN moieties are less affected by the recognition of the Gal entity and are still in the weakly positive- or zero-NOE regimes. The observed NOEs for the Gal moiety are in agreement with those observed in the free state for LacDN (with positive NOEs for all the Gal, Glc, linker, and DN moieties; see Supporting Information) and lactose. Overall, cross-peak pattern indicates that the low-energy conformer is accommodated as the ligand (see Supporting Information).

To rationalize the interaction on the molecular level, the low-energy conformer, as observed by NMR, was docked into the binding sites by the program AUTODOCK. Two sites with different degrees of accessibility in the dimmer, i.e., the sites characterized by Trp38 in the 1α subdomain and by Tyr249 in the 2γ subdomain, are known (*46*). The conformer fit was very good in both cases (Figure 9). For both sites, the major interactions take place for the galactose moiety with very minor contacts for the remote glucose. In particular, for the Trp38 binding site, there is a clear stacking interaction between the indol moiety of Trp38 with H3, H4, and H5 of the galactose reisude, while Asp27, Asn47, and Lys41 provide polar contacts with the hydroxyl groups of Gal. Asp 27 provides a bidentate hydrogen bond to OH2 and OH3, and one additional hydrogen bond from the backbone carbonyl group to OH4, while Asn47 forms hydrogen bonds with OH3 and OH4. Lys41 also makes polar contacts with OH2 and OH3. Thus, the galactose moiety is fairly well bound by these aminoacid residues. In contrast, the glucose unit is only bound by two polar contacts between its OH2 and OH3 hydroxyl groups and the lateral chain of Asp26. For this site, no contacts between the DN moiety and the lectin were predicted in this model. For the Tyr249 binding site, now is the phenol ring, which provides stacking interactions to the galactose moiety, which is in turn involved in hydrogen bonds to the phenol hydroxyl through OH6. In addition, polar contacts between OH2, OH3, and OH4 to Asn235, Asn256, Asn256, and Glc257 are also observed in this model. Again, the Glc moiety is only involved in polar contacts with Glc238 through OH2 and OH3. Also, for this Tyr249 binding site, no contacts between the DN moiety and the protein were observed. This should be the case, unless drastic variations of the torsion angles around the Glc glycosidic torsion and the linker were considered, far from their low-energy regions. Thus, docking analysis was in accordance with the NMR-derived observations. The Gal moiety is the major contact site for VAA, the Glc gives tiny contacts, and the linker and the DN moieties remain in solution with distinct effective correlation time, which, in turn, produced different signs for the NOE cross-peaks of the different parts of the molecule. The predicted contacts by AUTODOCK are basically identical to those observed for the interaction with lactose in pdb entry 1PUM.

In conclusion, no major modifications of the presentation of lactose to a lectin takes place by attaching the DN moiety through a 2-carbon linker.

CONCLUSIONS

A new fluorescent glycan **8** has been prepared, and it can readily be conjugated to different surfaces. Three different matrices on a gold surface have been analyzed, plain surface, SAM, and dextran surface (CM5 Biacore chip), resulting in the CM5 chips showing the least nonspecific interaction in a carbohydrate-presenting surface, which are valuable probes for detecting lectins. Its fluorescent tag entails sensitive detection without affecting the ligand properties of the bioactive part.

ACKNOWLEDGMENT

This work was supported by Spanish MEC (CTQ2006-09052/BQU) and EU grant (FP-62003-NMP-SMF-3, proposal 011774-2), an EC Marie Curie Research Training Network grant (MRTN-CT-2005-019561), the research initiative LMUexcellent, and MEC-FPU predoctoral fellowship (AP2003-4820).

Supporting Information Available: Correct ^{1}H NMR assignment for LacDN, as well as the scattered Φ/Ψ map of LacDN and the cross-peak pattern obtained by trNOESY for the interaction of VAA and LacDN, 3D models of the complex of VAA with LacDN. This material is available free of charge via the Internet at http://pubs.acs.org.

LITERATURE CITED

(1) Hackenberger, C. P. R., O′Reilly, M. K., and Imperiali, B. (2005) Improving glycopeptide synthesis: A convenient protocol for the preparation of β-glycosylamines and the synthesis of glycopeptides. *J. Org. Chem. 70*, 3574–3578.

(2) Likhosherstov, L. M., Novikova, V. A., Dervitskaya, V. A., and Kochetkov, N. K. (1986) A new simple synthesis of amino sugar β-glycosylamines. *Carbohydr. Res. 146*, c1−c5.

(3) Vetter, D., and Gallop, M. A. (1995) Strategies for the synthesis and screening of glycoconjugates. 1. A library of glycosylamines. *Bioconjugate Chem. 6*, 316–318.

(4) Bigge, J. C., Patel, T. P., Bruce, J. A., Goulding, P. N., Charles, S. M., and Parekh, R. B. (1995) Nonselective and efficient fluorescent labelling of glycans using 2-amino benzamide and anthranilic acid. *Anal. Biochem. 230*, 229–238.

(5) Locke, D., Bevans, C. G., Wang, L.-X., Zhang, Y., Harris, A. L., and Lee, Y. C. (2004) Neutral, acidic, and basic derivatives of anthranilamide that confer different formal charge to reducing oligosaccharides. *Carbohydr. Res. 339*, 221–231.

(6) Rothenberg, B. E., Hayes, B. H., Toomre, D., Manzi, A. E., and Varki, A. (1993) Biotinylated diaminopyridine: An approach to tagging oligosaccharides and exploring their biology. *Proc. Natl. Acad. Sci. U.S.A. 90*, 11939–11943.

(7) Toomre, D., and Varki, A. (1994) Advances in the use of biotinylated diaminopyridine (BAP) as a versatile fluorescent tag for oligosaccharides. *Glycobiology 4*, 653–663.

(8) Xia, B., Kawar, Z. S., Ju, T., Alvarez, R. A., Sachdev, G. P., and Cummings, R. D. (2005) Versatile fluorescent derivatization of glycans for glycomic analysis. *Nat. Methods 2*, 845–850.

(9) Duverger, E., Frison, N., Roche, A. C., and Monsigny, M. (2003) Carbohydrate-lectin interactions assessed by surface plasmon resonance. *Biochimie 85*, 167–179.

(10) Mann, A. D., Kanai, M., Maly, D. J., and Kiessling, L. L. (1998) Probing low affinity and multivalent interactions with surface plasmon resonance: ligands for concanavalin A. *J. Am. Chem. Soc. 120*, 10575–10582.

(11) Gutiérrez Gallego, R., Haseley, S. R., van Miegem, V. F., Vliegenthart, J. F., and Kamerling, J. P. (2004) Identification of carbohydrates binding to lectins by using surface plasmon resonance in combination with HPLC profiling. *Glycobiology 14*, 373–386.

(12) Larsen, K., Thygesen, M. B., Guillaumie, F., Willats, W. G. T., and Jensen, K. J. (2006) Solid-phase chemical tolls for glycobiology. *Carbohydr. Res. 341*, 1209–1234.

(13) Houseman, B. T., and Mrksich, M. (2002) Carbohydrate arrays for the evaluation of protein binding and enzymatic modification. *Chem. Biol. 9*, 443–454.

(14) Love, K. R., and Seeberger, P. H. (2002) Carbohydrate arrays as tools for glycomics. *Angew. Chem., Int. Ed. 41*, 3583–3586.

(15) Bradford, M. M. (1976) A rapid and sensitive method for the quantitation of micrograms quantities of protein using the principle of protein-dye binding. *Anal. Biochem. 72*, 248–254.

(16) Dasgupta, F., and Anderson, L. (1994) Efficient preparation of allyl 2,3,6,2′,3′,6′-hexa-O-benzyl-β-lactoside and its use as a glycosyl acceptor for chain extension at *O*-4′. *Carbohydr. Res. 264*, 155–160.

(17) Gabius, H.-J. (1990) Influence of type of linkage and spacer on the interaction of β-galactoside-binding proteins with immobilized affinity ligands. *Anal. Biochem. 189*, 91–94.

(18) Gabius, H.-J., Darro, F., Remmelink, M., Andre, S., Kopitz, J., Danguy, A., Gabius, S., Salmon, I., and Kiss, R. (2001) Evidence for stimulation of tumor proliferation in cell lines and histotypic cultures by clinically relevant low doses of the galactoside-binding mistletoe lectin, a component of proprietary extracts. *Cancer Invest. 19*, 114–26.

(19) André, S., Kojima, S., Prahl, I., Lensch, M., Unverzagt, C., and Gabius, H.-J. (2005) Introduction of extended LEC14-type branching into core-fucosylated biantennary N-glycan. *FEBS J. 272*, 1986–1998.

(20) André, S., Pei, Z., Siebert, H.-C., Ramström, O., and Gabius, H.-J. (2006) Glycosyldisulfides from dynamic combinatorial libraries as *O*-glycoside mimetics for plant and endogenous lectins: Their reactivities in solid-phase and cell assays and conformational analysis by molecular dynamics simulations. *Bioorg. Med. Chem. 14*, 6314–6326.

(21) Jimenez, M., Saiz, J. L., Andre, S., Gabius, H.-J., and Solis, D. (2005) Monomer/dimer equilibrium of the AB-type lectin from mistletoe enables combination of toxin/agglutinin activities in one protein: analysis of native and citraconylated proteins by ultracentrifugation/gel filtration and cell biological consequences of dimer destabilization. *Glycobiology 15*, 1386–1395.

(22) Jiménez, M., André, S., Siebert, H.-C., Gabius, H.-J., and Solís, D. (2006) AB-type lectin (toxin/agglutinin) from mistletoe: differences in affinity of the two galactoside-binding Trp/Tyr-sites and regulation of their functionality by monomer/dimer equilibrium. *Glycobiology 16*, 926–937.

(23) Asensio, J. L., Cañada, F. J., Khan, N., Mootoo, D. A., and Jiménez-Barbero, J. (2000) Conformational differences between O- and C-glycosides: The alpha-O-Man-(1,1)-beta-Gal/alpha-C-Man-(1,1)-β-Gal case-A decisive demonstration of the importance of the exo-anomeric effect on the conformation of glycosides. *Chem.—Eur. J. 6*, 1035–1041.

(24) Mayer, M., and Meyer, B. (2001) Group epitope mapping by saturation transfer difference NMR to identify segments of a ligand in direct contact with a protein receptor. *J. Am. Chem. Soc. 123*, 6108–6117.

(25) Asensio, J. L., Espinosa, J. F., Dietrich, H., Cañada, F. J., Schmidt, R. R., Martin-Lomas, M., André, S., Gabius, H.-J., and Jiménez-Barbero, J. (1999) Bovine heart galectin-1 selects a unique (Syn) conformation of C-lactose, a flexible lactose analogue. *J. Am. Chem. Soc. 121*, 8995–9000.

(26) Asensio, J. L., Martin-Pastor, M., and Jiménez-Barbero, J. (1995) The use of cvff and cff91 force-fields in conformational-analysis of carbohydrate molecules. Comparison with amber molecular mechanics and dynamics calculations for methyl alpha-lactoside. *Int. J. Biol. Macromol. 17*, 137–148.

(27) Kogelberg, H., Solis, D., and Jiménez-Barbero, J. (2003) New structural insights into carbohydrate-protein interactions from NMR spectroscopy. *Curr. Opin. Struct. Biol. 13*, 1–8.

(28) Allinger, N. L., Yuh, Y. H., and Lii, J. H. (1989) Molecular mechanics. The MM3 force field for hydrocarbons. Vibrational frequencies and thermodynamics. *J. Am. Chem. Soc. 111*, 8551–8566.

(29) Still, W. C., Tempzyk, A., Hawley, R., and Hendrickson, T. (1990) Semianalytical treatment of solvation for molecular mechanics and dynamics. *J. Am. Chem. Soc. 112*, 6127–6129.

(30) Asensio, J. L., Martin-Pastor, M., and Jiménez-Barbero, J. (1995) The use of cvff and cff91 force-fields in conformational-analysis of carbohydrate molecules. Comparison with amber molecular mechanics and dynamics calculations for methyl alpha-lactoside. *Int. J. Biol. Macromol. 17*, 137–148.

(31) Corzana, F., Cuesta, I., Freire, F., Revuelta, J., Bastida, A., Jiménez-Barbero, J., and Asensio, J. L. (2007) The pattern of distribution of amino groups modulates the structure and dynamics of natural aminoglycosides: implications for RNA recognition. *J. Am. Chem. Soc. 129*, 2849–2865.

(32) Morris, G. M., Goodsell, D. S., Halliday, R. S., Huey, R., Hart, W. E., Belew, R. K., and Olson, A. J. (1998) Automated docking using a Lamarckian genetic algorithm and empirical binding free energy function. *J. Comput. Chem. 19*, 1639–1647.

(33) Kajihara, Y., Kamiyama, D., Yamamoto, N., Sakakibara, T., Izumi, M., and Hashimoto, H. (2004) Synthesis of 2-[(2-pyridyl)amino]ethyl β-D-lactosaminide and evaluation of its acceptor ability for sialyltransferase: a comparision with 4-methylumbelliferyl and dansyl β-D-lactosaminide. *Carbohydr. Res. 339*, 1545–1550.

(34) Paul, A., Sarpal, R. S., and Dogra, S. K. (1990) Effects of solvent and acid concentration on the absorption and fluorescence spectra of α,α-diaminonaphthalenes. *J. Chem. Soc., Faraday Trans. 86*, 2095–2101.

(35) Dahmen, J., Frejd, T., Grönberg, G., Lave, T., Magnusson, G., and Noori, G. (1983) 2-Bromoethyl glycosides: synthesis and characterisation. *Carbohydr. Res. 116*, 303–307.

(36) Jochum, A., Schlienger, N., Egron, D., Peyrottes, S., and Périgaud, C. (2005) Biolabile constructs for pronucleotide design. *J. Organomet. Chem. 690*, 2614–2625.

(37) Sweeney, E. C., Tonevitsky, A. G., Palmer, R. A., Niwa, H., Pfueller, U., Eck, J., Lentzen, H., Agapov, I. I., and Kirpichnikov, M. P. (1998) Mistletoe lectin I forms a double trefoil structure. *FEBS Lett. 431*, 367–370.

(38) Niwa, H., Tonevitsky, A. G., Agapov, I. I., Saward, S., Pfuller, U., and Palmer, R. A. (2003) Crystal structure at 3 Å of mistletoe lectin I, a dimeric type-II ribosome-inantivating protein, complexd with galactose. *Eur. J. Biochem. 270*, 2739–2749.

(39) André, A., Cejas-Ortega, P. J., Alamino-Perez, M., Roy, R., and Gabius, H.-J. (1999) Lactose-containing starburst dendrimers: influence of dendrimer generation and binding-site orientation of receptors (plant/animal lectins and immunoglobulins) on binding properties. *Glycobiology 9*, 1253–1261.

(40) Poveda, A., Asensio, J. L., Martin-Pastor, M., and Jiménez-Barbero, J. (1997) Solution conformation and dynamics of a tetrasaccharide related to the Lewis(x) antigen deduced by NMR relaxation measurements. *J. Biomol. NMR 10*, 29–43.

(41) Asensio, J. L., Cañada, F. J., García-Herrero, A., Murillo, M. T., Fernández-Mayoralas, A., Johns, B. A., Kozak, J., Zhu, Z., Johnson, C. R., and Jiménez-Barbero, J. (1999) Conformational behaviour of aza-C-glycosides: Experimental demonstration of the relative role of the exo-anomeric effect and 1,3-type interactions in controlling the conformation of regular glycosides. *J. Am. Chem. Soc. 121*, 11318–11329.

(42) Fernández-Alonso, M. C., Cañada, F. J., Jiménez-Barbero, J., and Cuevas, G. (2005) Molecular recognition of saccharides by proteins. Insights on the origin of the carbohydrate-aromatic interactions. *J. Am. Chem. Soc. 127*, 7379–7386.

(43) Martin, J. N., Munoz, E. M., Schwergold, C., Souard, F., Asensio, J. L., Jimenez-Barbero, J., Canada, J., and Vicent, C. (2005) Carbohydrate-based DNA ligands: sugar-oligoamides as a tool to study carbohydrate-nucleic acid interactions. *J. Am. Chem. Soc. 127*, 9518–9533.

(44) Heaton, N. J., Bello, P., Herradón, B., del Campo, A., and Jiménez-Barbero, J. (1998) NMR study of intramolecular interactions between aromatic groups: Van der Waals, charge-transfer, or quadrupolar interactions? *J. Am. Chem. Soc. 120*, 9632–9645.

(45) Alonso-Plaza, J. M., Canales, M. A., Jiménez, M., Roldán, J. L., García-Herrero, A., Iturrino, L., Asensio, J. L., Cañada, F. J., Romero, A., Siebert, H.-C., André, S., Solís, D., Gabius, H.-J., and Jiménez-Barbero, J. (2001) NMR investigations of protein-carbohydrate interactions: insights into the topology of the bound conformation of a lactose isomer and β-galactosyl xyloses to mistletoe lectin and galectin-1. *Biochim. Biophys. Acta 1568*, 225–236.

(46) Jiménez, M., André, S., Siebert, H.-C., Gabius, H.-J., and Solís, D. (2006) AB-type lectin (toxin/agglutinin) from mistletoe: differences in affinity of the two galactoside-binding Trp/Tyr-sites and regulation of their functionality by monomer/dimer equilibrium. *Glycobiology 16*, 926–937.

BC800350Q

Supporting Information for:

Glycan tagging to produce bioactive ligands for Surface Plasmon Resonance (SPR) study via immobilization on different surfaces.

F. Javier Muñoz, [†,‡], **José Pérez,** [†,‡], **Ángel Rumbero,** [§] **J. Ignacio Santos,** [⊥] **F. Javier Cañada,** [⊥] **Sabine André,** [#] **Hans-Joachim Gabius,** [#] **Jesús Jiménez-Barbero,** [⊥] **José V. Sinisterra,** [†,‡] **and María J. Hernáiz**[†,‡,▽,*]

Table of contents

1. Table 1 Supporting Information. ^{1}H NMR chemical shifts for the LacDN and the DN moiety.

2. Figure 1 Supporting Information. A) Scattered Φ1/Ψ1 map of LacDN, according to MD simulations. B) Scattered Φ/Ψ map for the Glc-O-CH_2 moiety.

3. Figure 2 Supporting Information. Bottom panel. Key section of the trNOESY (mixing time, 200 ms) for the LacDN/VAA complex (20:1 molar ratio) at 500 MHz and 300 K.

4. Figure 3 Supporting Information. A 3D model of the complex of VAA with LacDN at the Trp38 binding site.

5. Figure 4 Supporting Information A 3D model of the complex of VAA with LacDN at the Tyr249 binding site.

1. Table 1. Supporting information. ^{1}H NMR (500 MHz, 300 K) chemical shifts for the LacDN protons and the DN moiety, as deduced from TOCSY/HSQC analysis.

βGAL		βGLC	
δ (PPM)		δ (PPM)	
H1	4.39	**H1**	4.52
H2	3.50	**H2**	3.33
H3	3.61	**H3**	3.61
H4	3.88	**H4**	3.68
H5	3.66	**H5**	3.55
H6A	3.71	**H6A**	3.89
H6B	3.71	**H6B**	3.73

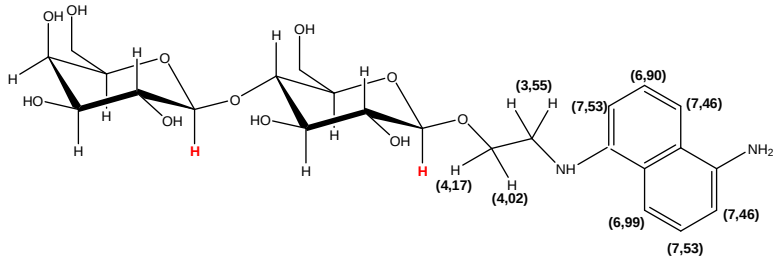

2. Figure 1 Supporting information,

A) Scattered Φ1/Ψ1 map of LacDN, according to MD simularions (3 ns, 300 K, MM3* force field, GB/SA solvent model for water). Φ1/Ψ1 are defined as described in the experimental section. The map is basically identical to that calculated for lactose with major exo-anomeric syn Φ/Ψ geometry. **B)** Scattered Φ/Ψ map for the Glc-O-CH_2 moiety. Φ is defined as H1Glc-C1Glc-O-CH_2 and Ψ as C1Glc-O-CH_2-CH_2. The most stable geometry (with Ψ close 180º) places the linker away from the disaccharide moiety (see below).

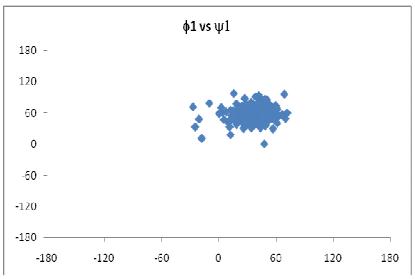

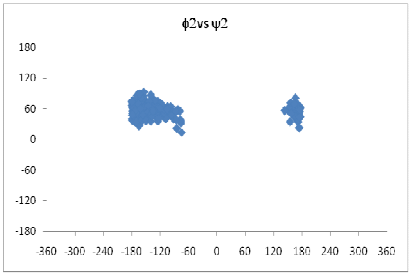

3. Figure 2 Supporting information. Bottom panel. Key section of the trNOESY (mixing time, 200 ms) for the LacDN/VAA complex (20:1 molar ratio) at 500 MHz and 300 K. Negative NOE cross peaks indicating binding are only observed for the Gal and Glc moieties. Indeed, the linker protons only provide very weak (almost zero) cross peaks. This fact indicates that different mobility (different effective correlation times) exists in the VAA-bound state for the different moieties of the molecule. The Gal moiety is recognized by the lectin and the lactose part increases the correlation time passing to the negative-NOE regime. In contrast, the linker and the DN moieties are less affected by the recognition of the Gal entity and are still in the weakly positive- or zero-NOE regimes. The observed NOEs for the Gal moiety are in agreement with those observed in the free state (top panel).

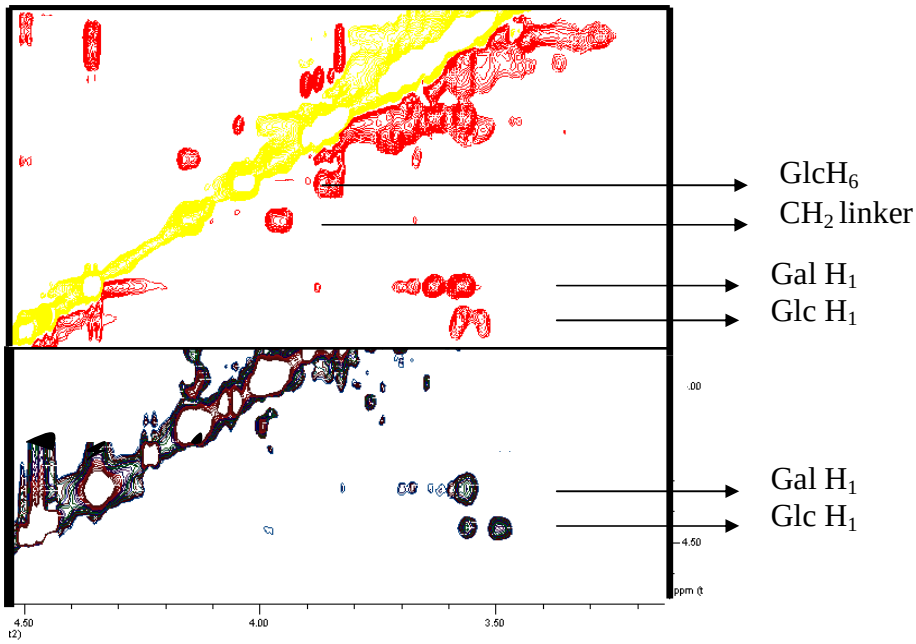

4. Figure 3 Supporting information. A 3D model of the complex of VAA with LacDN at the Trp38 binding site. No contacts between the linker or the DN moiety and the protein are observed. In the bottom view, a surface representation of the protein is given.

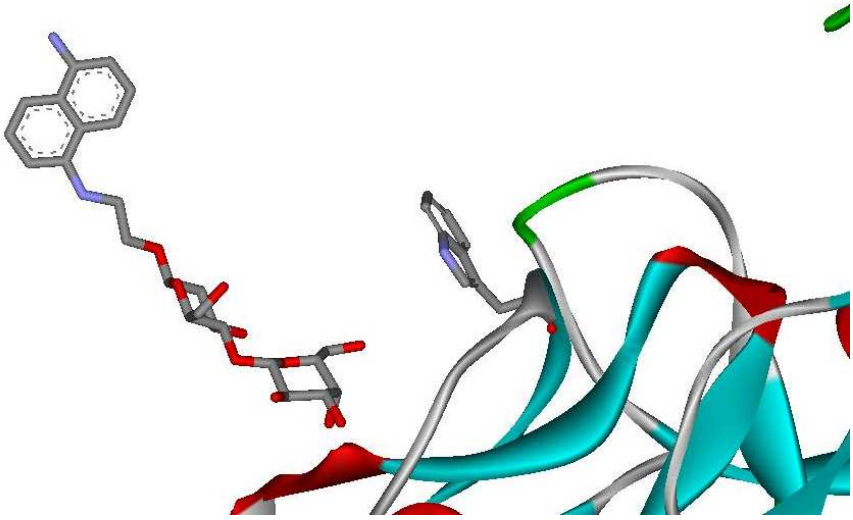

.

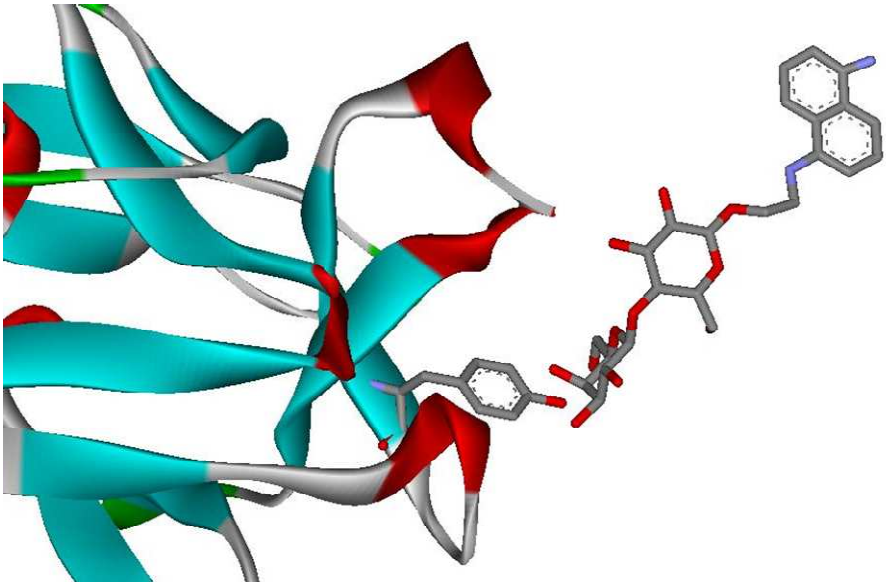

5. Figure 4 Supporting information. A 3D model of the complex of VAA with LacDN at the Tyr249 binding site. No contacts between the linker or the DN moiety and the protein are observed. In the bottom view, a surface representation of the protein is given.

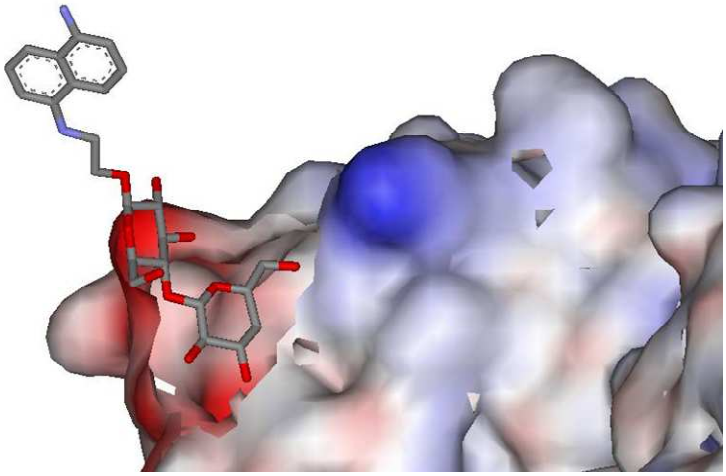

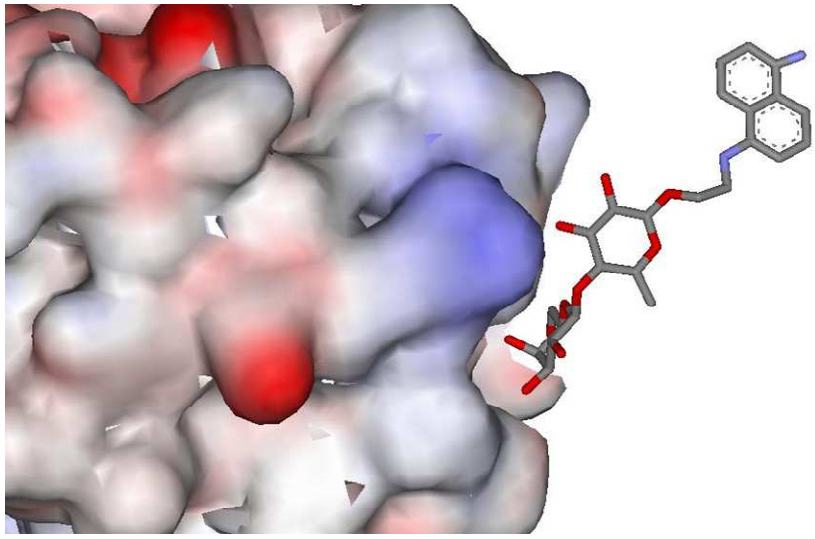

Subscriber access provided by SHEMYAKIN-OVCHINNIKOV INST

Article

Synthesis and Antibody Recognition of Cyclic Epitope Peptides, Together with Their Dimer and Conjugated Derivatives Based on Residues 9#22 of Herpes Simplex Virus Type 1 Glycoprotein D

Annama#ria Jakab, Gitta Schlosser, Matty Feijlbrief, Sytske Welling-Wester, Marilena Manea, Miquel Vila-Perello, David Andreu, Ferenc Hudecz, and Ga#bor Mezo#

Bioconjugate Chem., **2009**, 20 (4), 683-692• DOI: 10.1021/bc800324g • Publication Date (Web): 09 March 2009

Downloaded from http://pubs.acs.org on May 15, 2009

More About This Article

Additional resources and features associated with this article are available within the HTML version:

- Supporting Information
- Access to high resolution figures
- Links to articles and content related to this article
- Copyright permission to reproduce figures and/or text from this article

View the Full Text HTML

ACS Publications
High quality. High impact.

Bioconjugate Chemistry is published by the American Chemical Society. 1155 Sixteenth Street N.W., Washington, DC 20036

Synthesis and Antibody Recognition of Cyclic Epitope Peptides, Together with Their Dimer and Conjugated Derivatives Based on Residues 9−22 of Herpes Simplex Virus Type 1 Glycoprotein D

Annamária Jakab,[†] Gitta Schlosser,[†] Matty Feijlbrief,[§] Sytske Welling-Wester,[§] Marilena Manea,[||] Miquel Vila-Perello,[⊥] David Andreu,[⊥] Ferenc Hudecz,[†,‡] and Gábor Mező*[,†]

Research Group of Peptide Chemistry, Hungarian Academy of Sciences, and Department of Organic Chemistry, Eötvös L. University, P.O. Box 32, 1518 Budapest 112, Hungary, Laboratory for Medical Microbiology, Universiteit Groningen, 9713 GZ Groningen, The Netherlands, Laboratory of Analytical Chemistry and Biopolymer Structure Analysis, and Zukunftskolleg, University of Konstanz, 78457 Konstanz, Germany, and Department of Experimental and Health Sciences, Pompeu Fabra University, 08028 Barcelona, Spain. Received July 29, 2008; Revised Manuscript Received February 3, 2009

The synthesis of new cyclic peptides comprising the 9−22 epitope ^{9}LKMADPNRFRGKDL^{22} sequence derived from HSV gD-1 is reported. In addition, we describe procedures for the preparation of cyclic peptide dimers and conjugates with an oligotuftsin derivative carrier. The binding of a monoclonal antibody, Mab A16, to the synthesized compounds was determined by enzyme-linked immunosorbent assay. It was demonstrated that cyclization decreased the binding activity of the antibody to the epitope. However, dimerization and conjugation could significantly increase the binding capacity of the cyclic epitope peptides. The attachment site in dimers and conjugates, as well as the topology of the construct, had a significant influence on the antibody recognition, while replacement of Met in position 11 by Nle had no marked effect.

INTRODUCTION

The application in human therapy of conventional vaccines consisting of either killed or live attenuated disease-causing organisms has some limitations such as the loss of efficacy due to the genetic variation of many viruses; difficulties in the production and storage of many vaccine preparations; and biohazard in both production and use of vaccines against lethal infections. To overcome these drawbacks, synthetic peptide-based vaccines have been developed; and they have advantages of being selective, chemically defined, and safe and can be prepared in large quantities (*1, 2*). However, it is known that the administration of a synthetic epitope peptide rarely elicits an appropriate immune response. Peptide epitopes are generally short and are not able to adopt the same conformation as in the native protein; in addition, they are subjected to fast in vivo degradation by proteases (*3*). In many cases, antibodies to synthetic peptides react strongly with the homologous peptides, but weakly or not at all with the original protein or the intact infectious agents (*4*). Several approaches have been developed in order to modify the immunorecognition of synthetic epitope peptides such as (i) incorporation in the same construct of both B- and helper T-cell epitopes (*5*); (ii) cyclization (*6*); (iii) conjugation of multiple copies of epitopes to synthetic or natural carriers (*7*); and (iv) dimerization or controlled polymerization of the peptide epitope (*8, 9*).

Herpes simplex virus, with two closely related serotypes (HSV-1 and HSV-2), is one of the most common infectious agents in humans. Glycoprotein D (gD) represents a major immunogenic component of the virion envelope (*10*), able to induce high titers of virus-neutralizing antibodies (*11, 12*). The *N*-terminal region of HSV gD-1, comprising residues 1−21 of mature gD, is known to be a strong antigenic site, and peptides from this domain are able to induce both B- and T-cell responses (*13*). In addition, gD is required for viral entry into the cells. gD can bind to at least three distinct cellular receptor proteins. These three receptors are herpes virus entry mediator (HVEM), nectin 1 and 2, and a modified form of heparan sulfate. The *N*-terminal domain of gD is the binding site to the HVEM receptor. The crystal structure of the gD-HveA complex revealed that, upon binding to the cellular receptor HVEM, the flexible *N*-terminal region of gD is folded into a fixed hairpin structure that contains the residues of gD required for binding to HVEM. Monoclonal antibody (Mab) A16 can inhibit the binding of gD to the cellular receptor HVEM. A16 monoclonal antibody was also used for selection of peptides from a random peptide library (RPL) displayed on the surface of a filamentous bacteriophage. The selected RPL-derived peptide and peptide 9−19 of gD-1 had approximately the same affinity for Mab A16. Immunization of mice with the phage-derived RPL-peptide as well as the gD-1 derived peptide (after conjugation to BSA) protected against a challenge with a lethal dose of herpes simplex virus type 1 (*14*).

Peptide 9−21 (LKMADPNRFRGKD) was shown to be the optimal epitope of the *N*-terminal part of gD for Mab A16, in which amino acids ^{13}Asp, ^{16}Arg, and ^{17}Phe are essential for Mab A16 recognition (*15*). The 9−21 peptide exhibited good antibody recognition in linear form, either free or conjugated to carriers. It was further demonstrated that the peptide could adopt a β-turn-like structure at residues ^{14}Pro and ^{15}Asn under appropriate conditions (*16*−*18*), leading to the hypothesis that cyclization might stabilize the bioactive conformation of the peptide and thus increase its antibody recognition. Cyclization might also mimic the fixed hairpin structure of gD needed for

* Address correspondence to Gábor Mező, Research Group of Peptide Chemistry, Hungarian Academy of Sciences, Eötvös L. University, 1518 Budapest 112, P.O. Box 32, Hungary. E-mail: gmezo@elte.hu; Tel.: (+36)-1-209-0555/1433; Fax: (+36)-1-372-2620.

[†] Research Group of Peptide Chemistry, Hungarian Academy of Sciences.

[‡] Department of Organic Chemistry, Eötvös L. University.

[§] Universiteit Groningen.

[||] University of Konstanz.

[⊥] Pompeu Fabra University.

10.1021/bc800324g CCC: $40.75 © 2009 American Chemical Society
Published on Web 03/09/2009

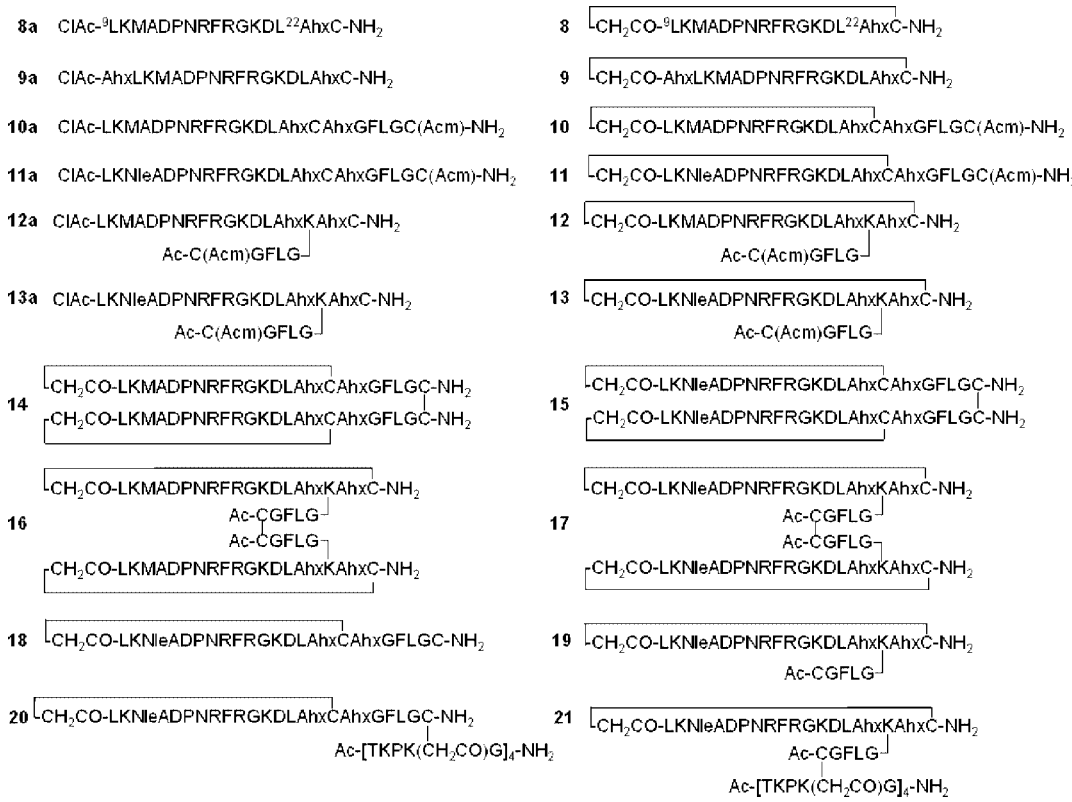

Figure 1. Chemical structure of cyclic epitope peptides (**8**−**13**, **18**, and **19**) derived from HSV gD-1, their precursors (**8a**−**13a**), dimer (**14**−**17**), and conjugated (**20**, **21**) derivatives.

binding to the HVEM receptor. In addition, cyclization might enhance the stability of the peptide against enzymatic degradation. However, for peptide 9−21 no effective cyclic version has yet been described (*19*).

In previous studies, we demonstrated that replacement of ^{11}Met in peptide 9−22 by homocysteine (Hcy) or cysteine (Cys) and replacement of ^{18}Arg by Lys made cyclization possible through a thioether bond between a chloroacetyl group at the ε-amino group of Lys and the thiol group of Cys or Hcy. The cyclic peptides (H-LK[XADPNRFK(CH_2CO)]GKDL-NH_2, where X = Cys or Hcy) thus obtained bound to the Mab A16 with three magnitudes lower efficiency than the linear analogues (*19*) and the Hcy cyclic peptide was more potent in competition ELISA than the Cys-containing version. In another study (*20*), the conjugation of linear (^{11}Nle)-9−22 peptides (replacement of Met by norleucine (Nle) in position 11 is permitted (*21*)) to carriers such as MAP-type lysine dendrimer (*22*), sequential oligopeptide carrier (SOC) (*23*), oligotuftsin derivative (OT20) (*24*), branched-chain SAK polypeptide with polylysine backbone (*25*), or the widely used protein keyhole limpet hemocyanine (KLH) (*26*) was performed. Results showed that the conjugates bound to Mab A16 by 1 order of magnitude more strongly than the linear epitope peptides, regardless of the carrier used. The disulfide dimers of peptide 9−22, either *C*- or *N*-terminally linked, also showed improved binding compared to the linear peptide, similarly to peptide 9−22 conjugated to oligotuftsin (*27*).

In line with the above-mentioned results, we describe here a new series of linear, cyclic, dimeric, and conjugated derivatives of the HSV gD-1 9−22 epitope. Large ring-size cyclic peptides (16 instead of 8 residues) derived from 9−22 epitope peptide of HSV gD-1 and their dimeric versions, as well as conjugates to OT20 carrier, were prepared, and their antigenicity was determined by enzyme-linked immunosorbent assay using Mab A16.

EXPERIMENTAL PROCEDURES

Materials. All amino acid derivatives were purchased from Senn Chemicals AG (Dielsdorf, Switzerland) or NovaBiochem (Läufelfingen, Switzerland). Rink-amide MBHA and 4-methylbenzhydrylamine (MBHA) resins were from NovaBiochem. Coupling agents (*N*,*N*′-diisopropylcarbodiimide (DIPCDI), 1-hydroxybenzotriazole (HOBt), *N*-ethyldiisopropylamine (DIPEA)), cleavage reagents (trifluoroacetic acid (TFA), hydrogenfluoride (HF), piperidine, 1,8-diazabicyclo[5.4.0]undec-7-ene (DBU)), and scavengers (triisopropylsilane (TIS), *m*-cresol, *p*-thiocresol) were from Fluka (Buchs, Switzerland) or SDS (Peypin, France), except for *O*-benzotriazole-*N*,*N*,*N*′,*N*′-tetramethyluronium hexafluorophosphate (HBTU), which was from Matrix Innovation (Montreal, Canada). Tallium(III) trifluoroacetate ($Tl(tfa)_3$)) and 1,4-DL-dithiothreitol (DTT) were Fluka products, while acetic anhydride (Ac_2O) was purchased from Reanal (Budapest, Hungary). Solvents (dichloromethane (DCM), *N*,*N*-dimethylformamide (DMF), diethyl ether, methanol (MeOH), and acetic acid (AcOH)) for synthesis were obtained from SDS and Reanal. Acetonitrile for HPLC was from SDS or Sigma (Sigma-Aldrich Kft., Budapest, Hungary). Peptides **1**−**7** were synthesized as previously reported (*19*, *20*, *27*).

Synthesis of Linear Precursor Peptides (Peptides 8a−**11a; Figure 1).** Linear precursor peptides **8a**−**11a** were synthesized by solid-phase methodology on Rink amide MBHA resin using an ABI 433A synthesizer (FAST-MOC, 0.1 mmol scale chemistry). Eight molar excess of Fmoc-amino acids were used in HBTU-HOBt-DIPEA-mediated coupling reactions. Fmoc-Arg(Pbf)-OH, Fmoc-Lys(Boc)-OH, Fmoc-Asp(O^{t}Bu)-OH, and Fmoc-Asn(Trt)-OH were applied as side chain protected deriva-

Scheme 1. Outline of the Synthesis of Cyclic Epitope Peptides with Spacer in the Branch

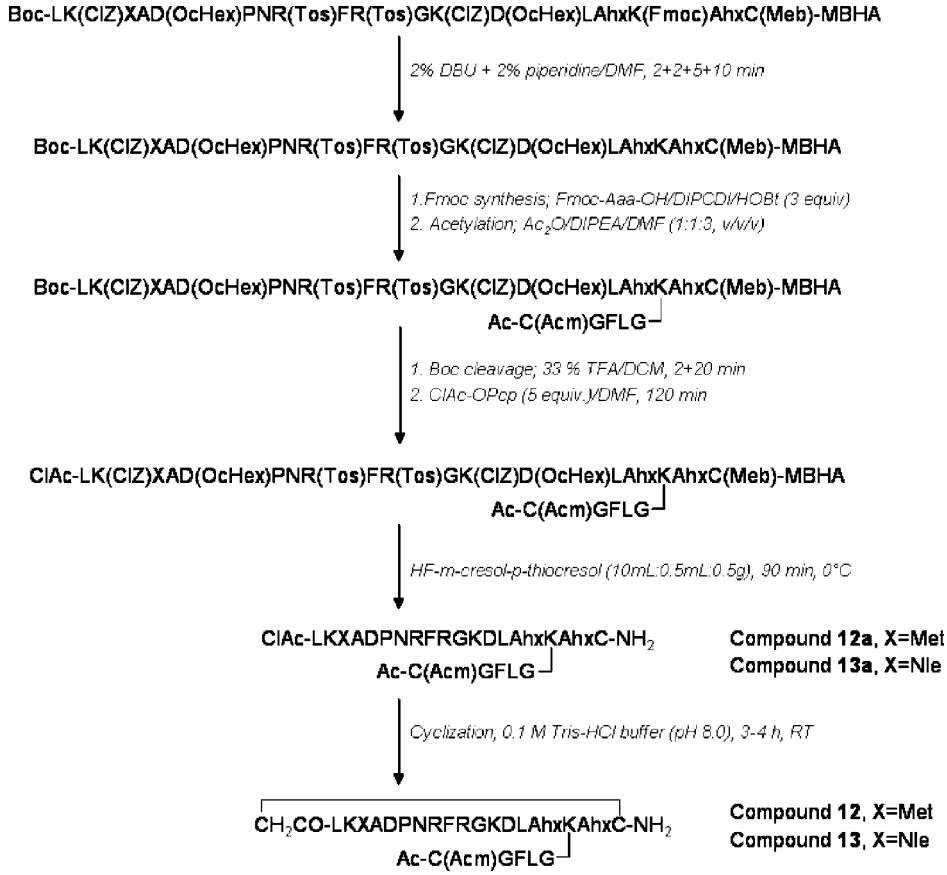

Table 1. ESI-MS Characteristics and RP-HPLC Retention Times of Derivatives of the Epitope Peptide 9−22 of HSV gD-1

	ESI-MS[b]		HPLC[c]
compound[a]	calcd	exp	R_t [min]
8	1914.99	1914.8	24.1
9	2028.08	2028.3	24.8
10	2578.12	2578.0	27.3
11	2560.08	2560.1	27.7
12	2748.33	2748.2	27.5
13	2730.29	2730.0	27.8
14	5012.07	5012.4	30.1
15	4976.00	4976.0	30.4
16	5352.50	5352.1	29.1
17	5316.42	5315.8	29.4
18	2489.05	2489.2	29.3
19	2659.22	2658.6	28.4
20	12222.25	12222.3	28.8
21	12902.52	12902.2	27.8

[a] The numbers of the compounds correspond to the structures presented in Figure 1. [b] Experimental MWs were calculated from the multiple charged ions measured by a Bruker Daltonics Esquire 3000+ mass spectrometer. [c] RP-HPLC conditions: Column, Phenomenex Jupiter C_{18} (250 × 4.6 mm, 5 μm, 300 Å); gradient, 0 min 0% B; 5 min 0% B; 50 min 90% B; eluents, 0.1% TFA in water (A) and 0.1% TFA in acetonitrile−water (80:20, v/v) (B); flow rate, 1 mL/min; detection, λ = 214 nm.

tives. The side chain of the Cys residue involved in the cyclization was protected by a trityl group (Trt). In peptides **10a** and **11a**, the thiol group of the additional (*C*-terminal) Cys used for dimerization or conjugation was protected by acetamidomethyl group (Acm). After chain assembly and removal of the *N*-terminal Fmoc protecting group, the free amino terminus was chloroacetylated with 5 equiv of chloroacetic acid pentachlorophenyl ester (ClAc-OPcp) (*20*). The peptides were cleaved from the resin with TFA-TIS-water (95:2.5:2.5, v/v/v) at room temperature for 2 h. The crude peptides were precipitated with chilled anhydrous diethyl ether, isolated by centrifugation, redissolved in 10% acetic acid, and freeze−dried. Prior to cyclization, they were purified by semipreparative RP-HPLC and characterized by analytical RP-HPLC and ESI-MS.

Synthesis of Branched Precursor Peptides (Peptides 12a and 13a; Figure 1 and Scheme 1). The branched peptides were prepared on MBHA resin (0.62 mmol/g) by manual SPPS applying a mixed Boc-Fmoc strategy. Linear peptides with Met or Nle in position 11, elongated with the Ahx-Lys-Ahx-Cys tetrapeptide (where Ahx is ε-aminohexanoic acid) at the *C*-terminus, were built up by Boc chemistry using Boc-Arg(Tos)-OH, Boc-Lys(ClZ)-OH, Boc-Asp(OcHex)-OH, and Boc-Cys(Meb)-OH as side chain protected derivatives. The ε-amino group of Lys in the *C*-terminal extension as a future branching site was blocked with an Fmoc group. The protocol of the Boc synthetic cycle was the following: (i) deprotection with 40% TFA/DCM (2 + 20 min); (ii) DCM washing (5 × 0.5 min); (iii) neutralization with 5% DIPEA/DCM (4 × 1 min); (iv) DCM washing (4 × 0.5 min); (v) coupling of 3 equiv Boc-amino acid derivative/DIPCDI/HOBt in DCM-DMF 4:1 (v/v) solvent mixture (60 min); (vi) DMF washing (2 × 0.5 min); (vii) DCM washing (2 × 0.5 min); and (viii) monitoring by ninhydrin (*28*) or isatin assay (*29*). After completion of the synthesis of the linear peptide and prior to the Boc cleavage from the *N*-terminus, the peptide was further developed in the branch by Fmoc strategy. Fmoc-Gly-OH, Fmoc-Leu-OH, Fmoc-Phe-OH, Fmoc-Gly-OH, and Fmoc-Cys(Acm)-OH were built in step by step, manually. The protocol of Fmoc chemistry was the following: (i) DMF washing (3 × 1 min); deprotection with 2% DBU + 2% piperidine in DMF (4 times for 2 + 2 + 5 + 10 min); (iii) DMF washing (8 × 0.5 min); (iv) coupling of 3 equiv Fmoc-amino acid derivative-DIPCDI-HOBt in DMF; (v) DMF washing (3 × 0.5 min); (vi) DCM washing (2 × 0.5 min);

Scheme 2. Outline of the Synthesis of Dimer and Conjugated Derivatives of Cyclic Epitope Peptide of 9−22 Sequence of HSV gD-1

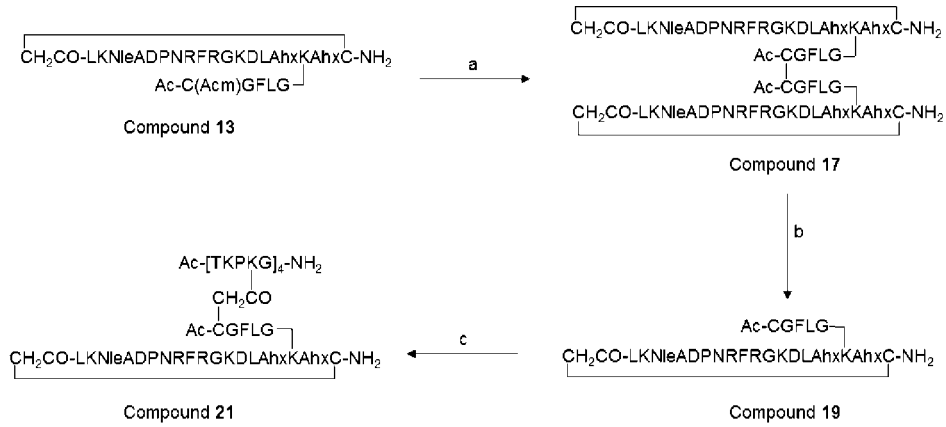

a: 0.6 eq Tl(tfa)$_3$ in TFA-anisole (98:2, v/v), 0°C, 90 min; b: 20 eq DTT in 0.1M Tris buffer (pH 8.2), RT, 2h;
c: Ac-OT20(ClAc)$_4$ (1 eq), Compound **19** (12 eq) in 0.1M Tris buffer (pH 8.2), RT, 16h.

Table 2. Binding of Derivatives of Epitope Peptide 9−22 of HSV gD-1 to Mab A16

code[a]	compound	competition ELISA[b]
1[d]	H-LKMADPNRFRGKDL-NH_2	4.2
2[d]	H-LKNleADPNRFRGKDL-NH_2	3.4[c] ± 1.8
3[e]	H-LK[CADPNRFK(CH_2CO)]GKDL-NH_2	7900
4[e]	H-LK[HcyADPNRFK(CH_2CO)]GKDL-NH_2	2300
5[d]	H-[TKPK(H-LKNleADPNRFRGKDLC{CH_2CO}-NH_2)G]$_4$-NH_2	0.72
6[d]	{H-LKNleADPNRFRGKDLC-NH_2}$_2$	0.74
7[f]	{H-CLKNleADPNRFRGKDL-NH_2}$_2$	0.66
8	c[CH_2CO-LKMADPNRFRGKDLAhxC]-NH_2	28.6
9	c[CH_2CO-AhxLKMADPNRFRGKDLAhxC]-NH_2	28.0
10	c[CH_2CO-LKMADPNRFRGKDLAhxC]AhxGFLGC(Acm)-NH_2	79.1
11	c[CH_2CO-LKNleADPNRFRGKDLAhxC]AhxGFLGC(Acm)-NH_2	75.6
12	c[CH_2CO-LKMADPNRFRGKDLAhxK(Ac−C(Acm)GFLG)AhxC]-NH_2	88.8
13	c[CH_2CO-LKNleADPNRFRGKDLAhxK(Ac−C(Acm)GFLG)AhxC]-NH_2	92.3
14	{c[CH_2CO-LKMADPNRFRGKDLAhxC]AhxGFLGC-NH_2}$_2$	11.8
15	{c[CH_2CO-LKNleADPNRFRGKDLAhxC]AhxGFLGC-NH_2}$_2$	11.1
16	{c[CH_2CO-LKMADPNRFRGKDLAhxK(Ac-CGFLG)AhxC]-NH_2}$_2$	57.7
17	{c[CH_2CO-LKNleADPNRFRGKDLAhxK(Ac-CGFLG)AhxC]-NH_2}$_2$	41.4
18	c[CH_2CO-LKNleADPNRFRGKDLAhxC]AhxGFLGC-NH_2	nt
19	c[CH_2CO-LKNleADPNRFRGKDLAhxK(Ac-CGFLG)AhxC]-NH_2	nt
20	Ac-[TKPK(**18**-CH_2CO)G]$_4$-NH_2	249.3
21	Ac-[TKPK(**19**-CH_2CO)G]$_4$-NH_2	7.2

[a] Compound numbers in the Table correspond to the compounds presented in Figure 1. [b] Pmol of the compound required to obtain a residual OD_{490} of 1.0 at a coat of peptide 9−22 (Arg), after preincubation of serial dilutions of the compounds and Mab A16 (at "optimal" dilution). nt; not tested. [c] Peptide (^{11}Nle) 9−22 (code 2) was included in all the competition ELISA assays performed. The amount required to obtain an OD_{490} of 1.00 was 3.4 ± 1.8 pmol. [d] Ref *20*. [e] Ref *19*. [f] Ref *27*.

and (vii) monitoring by ninhydrin assay. In the end, the Fmoc group was detached and the *N*-terminus of the branch was acetylated with Ac_2O/DIPEA/DMF (1:1:3, v/v/v) mixture. Finally, the Boc group was removed, and the free α-amino group was chloroacetylated with 5 equiv ClAc-OPcp in DMF. The peptide was cleaved from the dried resin simultaneously with the removal of the side chain protecting groups with liquid HF in the presence of *m*-cresol and *p*-thiocresol as scavengers (10 mL HF, 0.5 mL *m*-cresol, and 0.5 g *p*-thiocresol) at 0 °C for 90 min. The crude product was precipitated with dry diethyl ether. The solid material was filtered off, washed three times with diethyl ether, and then dissolved in 10% acetic acid prior to freeze−drying. The target peptide was obtained after purification by semipreparative RP-HPLC and characterized by analytical HPLC and mass spectrometry (MS) before cyclization.

Synthesis of Cyclic Epitope Peptides (Compounds 8−13; Figure 1 and Scheme 1). Cyclization of chloroacetylated linear epitope peptides by thioether bond formation was performed in 0.1 M Tris-HCl buffer, pH 8.0. The lyophilized solid material was added to the buffer solution (20 mL, 5 mg/mL final peptide concentration, in each case) in portions over 1 h. Then, the reaction was continued in a closed tube at RT for 3 h, and the cyclization reaction was monitored by analytical RP-HPLC. The reaction mixture was acidified with TFA and purified directly by semipreparative RP-HPLC. The yield of the cyclization was over 90% for each construct. The compounds were characterized by analytical RP-HPLC and ESI-MS (Table 1).

Dimerization of Cyclic Epitope Peptides (Compounds 14−17; Figure 1 and Scheme 2). Intermolecular disulfide bond formation was performed with Tl(tfa)$_3$ in TFA (*30*). The cleavage mixture contained 98% TFA, 2% anisole as a scavenger, and 0.6 equiv Tl(tfa)$_3$ (calculated for the cyclic epitope peptide). This mixture was cooled to 0 °C, and then the cyclic epitope peptide was dissolved at a concentration of 10 mg/mL. The reaction mixture was stirred at 0 °C for 90 min, and then the product was precipitated with dry diethyl ether, centrifuged, redissolved in 10% acetic acid, and freeze−dried. The crude peptide was purified by semipreparative RP-HPLC and characterized by analytical RP-HPLC and ESI-MS. Yields of the Met containing peptides were in the 50−55% range, while the Nle containing compounds were prepared with slightly better yields (58−65%).

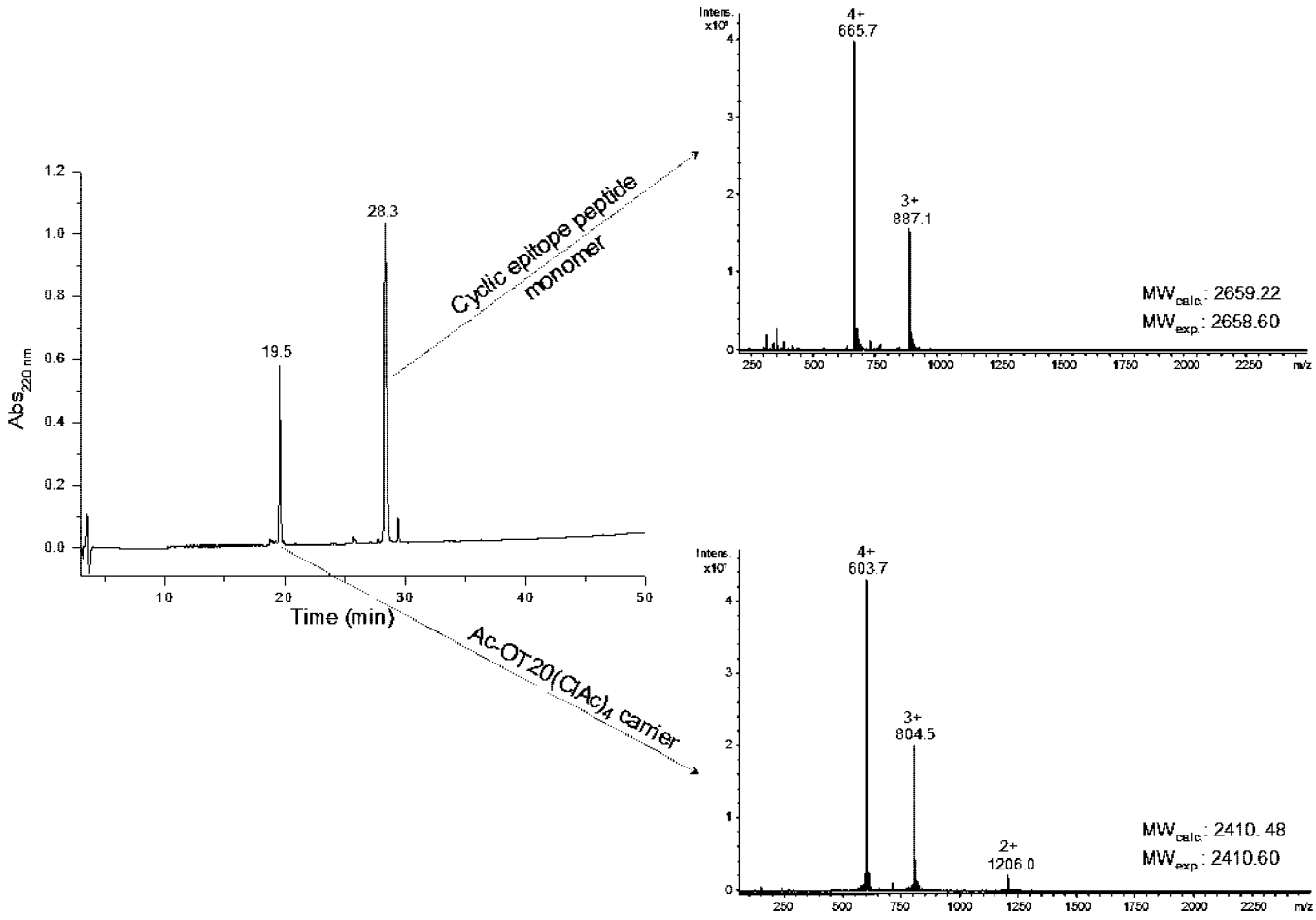

Figure 2. Conjugation of Ac-OT20(ClAc)$_4$ carrier with c[CH_2COLKNleADPNRFRGKDLAhxK(Ac-CGFLG)AhxC]-NH_2 (**19**) epitope peptide followed by RP-HPLC and mass spectrometry: 5 min reaction time.

Conjugation of Cyclic Epitope Peptides to Chloroacetylated Oligotuftsin Derivative (Compounds 20 and 21; Figure 1 and Scheme 2). Chloroacetylated oligotuftsin derivative (4 mg, 1.6 μmol) was dissolved in 0.1 M Tris−HCl buffer (pH 8.2) at a concentration of 1 mg/mL. The cyclic epitope peptide with the free SH-group (compounds **18** and **19** prepared by the reduction of dimer peptides **15** and **17**, respectively, Scheme 2) was added to the solution in small portions over an 8 to 12 h period. A 3-fold excess of epitope peptide derivative (calculated for each chloroacetyl group) was necessary for the complete alkylation reaction. The conjugation was monitored by RP-HPLC. As soon as only the conjugate with four copies of the epitope was observed beside the cyclic epitope peptide and its dimer, the reaction was terminated by acidification and then the mixture was purified by semipreparative RP-HPLC. The conjugate was characterized by analytical RP-HPLC and ESI-MS. The yield of the conjugation was in the range 70−75%.

Reverse-Phase High-Performance Liquid Chromatography (RP-HPLC). Analytical RP-HPLC was performed with a Knauer system (H. Knauer, Bad Homburg, Germany) using a Phenomenex Jupiter C_{18} column (250 × 4.6 mm I.D.) with a 5 μm silica (300 Å pore size) (Torrance, CA) as a stationary phase. Linear gradient elution (0 min 0% B; 5 min 0% B; 50 min 90% B) with eluent A (0.1% TFA in water) and eluent B (0.1% TFA in acetonitrile−water (80:20, v/v)) was used at a flow rate of 1 mL/min at room temperature. Peaks were detected at $\lambda = 214$ nm. The crude products were purified on a semipreparative Phenomenex Jupiter C_{18} column (250 × 10 mm I.D.) with 10 μm silica (300 Å pore size) (Torrance, CA). The flow rate was 4 mL/min. The same eluents with a linear gradient of 15−70% B over 40 min were applied.

Electrospray Ionization Mass Spectrometry (ESI-MS). Electrospray ionization mass spectrometry was performed with a Bruker Daltonics Esquire 3000+ mass spectrometer (Bremen, Germany), operating in continuous sample injection mode at 4 μL/min flow rate. Samples were dissolved either in a mixture of acetonitrile−water (1:1, v/v) or 50% MeOH, 1% AcOH in water. Mass spectra were recorded in positive ion mode in the *m*/*z* 50−3000 range.

Enzyme-Linked Immunosorbent Assay (ELISA). Throughout the ELISA studies, culture medium of the hybridoma cell line Mab A16 was used. The preparation of Mab A16 has been described earlier (*21*). Mab A16 was isolated after immunization of mice with extracts of HSV-1 infected cells. Hybridomas reactive only with HSV were isolated. The isolated hybridomas were screened for reactivity with HSV specific proteins and for unspecific reactivity according to the standard procedures for monoclonal antibodies. Mab A16 is reactive with glycoprotein D. It is a conformation-independent monoclonal antibody, classified together with Mabs LP14, ID3 as a group VII monoclonal antibody of gD (*21*). The core residues of the epitope of group VII Mabs is located within residues 9−19 of mature gD.

The competition ELISA was performed as previously described (*15*). Briefly, dilution series of linear peptide (^{11}Nle)-9−22 of gD and the different constructs of the epitope peptide were preincubated for 2 h at room temperature with "optimal" dilutions of Mab A16. After preincubation, the residual binding capacity of Mab A16 in the preincubation mixture was determined by ELISA in microtiter plate wells (Greiner Labortechnik, Germany) coated with the linear peptide (^{11}Nle)-9−22 (0.5 μg/well). As standard, a serial dilution of the peptide

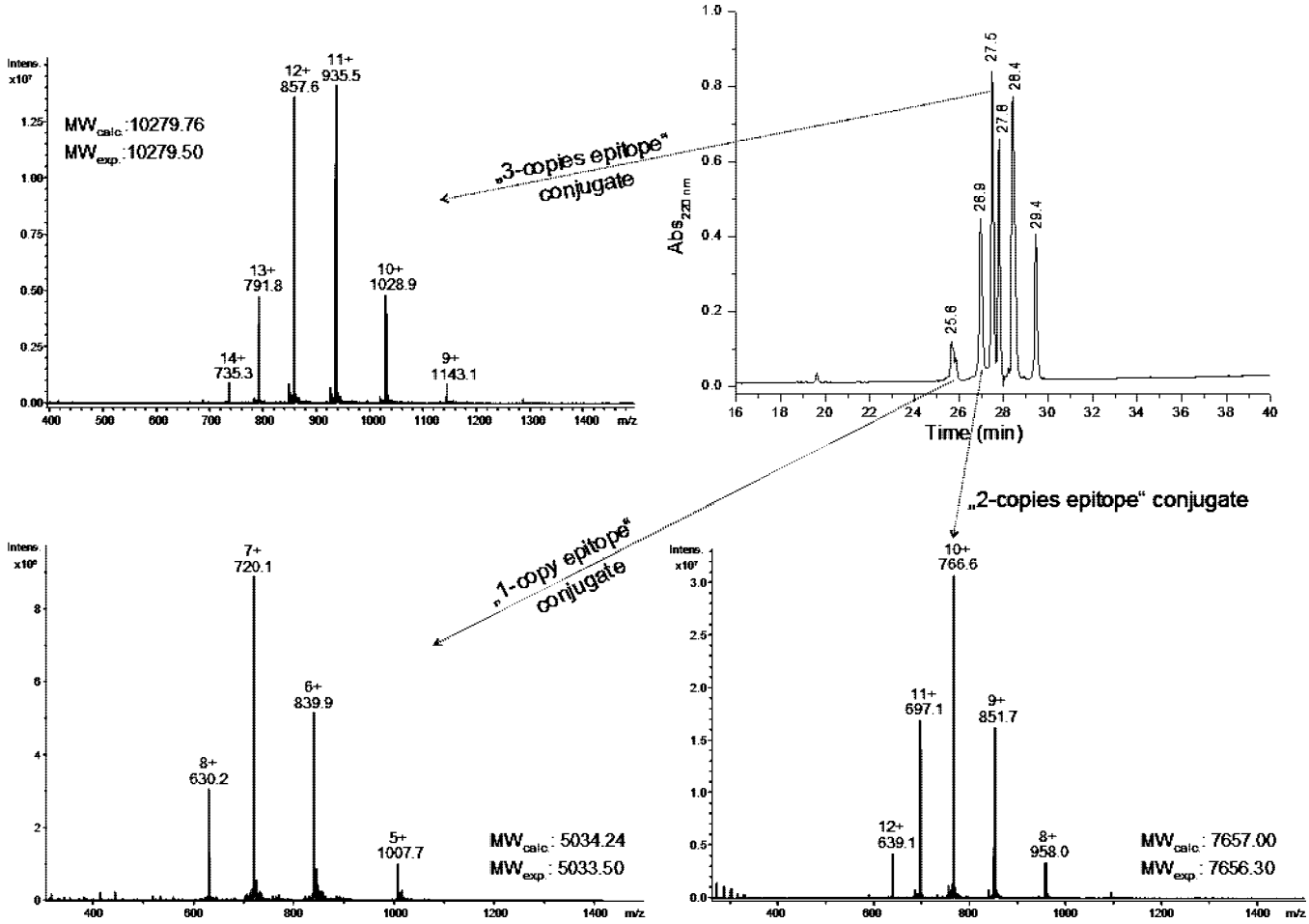

Figure 3. Conjugation of Ac-OT20(ClAc)$_4$ carrier with c[CH_2COLKNleADPNRFRGKDLAhxK(Ac-CGFLG)AhxC]-NH_2 (**19**) epitope peptide followed by RP-HPLC and mass spectrometry: 3 h reaction time.

(^{11}Nle)-9−22 with a fixed dilution of Mab A16 was always included: approximately 3 pmol peptide (^{11}Nle)-9−22 per 100 μL in the preincubation mixture resulted in a residual Mab A16, which gave an optical density of 1.0 at 490 nm (OD_{490}) on the coated peptide (^{11}Nle)-9−22. The relative amount of the epitope peptide constructs in the preincubation mixture required to give an OD_{490} of 1.0 was estimated graphically from plots of OD vs peptide concentrations. Data represent the average of at least three independent experiments for each compound.

RESULTS AND DISCUSSION

Here, we report on the synthesis, chemical characterization, and antibody binding of a new set of antigens derived from the sequence 9−22 of HSV gD-1. We investigated whether dimerization of the cyclic peptides and conjugation to an oligotuftsin derivative carrier influenced the binding to Mab A16 as compared to the monomeric form. Peptide 9−22, containing the sequence of 9−19 recognized by monoclonal antibody A16, was used. It is known that the binding activity of peptide 9−21 is higher than that of 9−19 and the addition of Leu at position 22 has no significant effect on antibody binding, but it is important to avoid the potential succinimide formation of a *C*-terminal Asp-amide or Asp-Ahx. For both the cyclization and the conjugation, we employed the thioether bond formation, which is known to provide a chemically and biologically stable linkage and allows the use of unprotected precursors (*31*). The fast intramolecular (cyclization) or intermolecular (conjugation) reaction between the haloacetyl group (in our experiments, chloroacetyl group) and the thiol group of Cys under slightly alkaline conditions provided the appropriate products with good yields and no significant side reactions.

Synthesis of Cyclic Derivatives of 9−22 Epitope Peptide of HSV gD-1. The 9−22 epitope peptide was elongated with ε-aminohexanoic acid (Ahx) either at the *C*-terminus of peptide **8a** or at both termini of the 9−22 sequence as in peptide **9a** (Figure 1). The cyclization of the peptides occurred between the chloroacetylated *N*-terminus and the thiol group of Cys attached to the *C*-terminus (compounds **8a** and **9a**). Thus, cyclic peptides **8** and **9** were obtained with a ring size of 55 and 62 atoms, respectively. These two cyclic derivatives were prepared with Met in position 11. However, peptides designed for dimerization and conjugation as well were synthesized either with Met (**10a**) or Nle (**11a**) in position 11 in order to analyze the effect of substitution of Met by Nle on the antibody recognition of the compounds.

Linear peptides **10a** and **11a**, similarly to peptides **8a** and **9a**, were synthesized by Fmoc chemistry, while their branched derivatives **12a** and **13a** were prepared by applying a mixed methodology of Boc and Fmoc chemistries (Scheme 1). In this case, the linear part containing the 9−22 epitope was built up using Boc amino acid derivatives, while for the synthesis of the branch, Fmoc strategy was utilized. Chloroacetylation of the *N*-terminus of the peptides was achieved by the use of chloroacetic acid pentachlorophenyl ester which provided products of higher purity than the chloroacetic anhydride. In the case of peptide **10a**, incorporation of a bromoacetyl (BrAc) moiety using bromoacetic anhydride was also attempted (data not shown). However, after cleavage of the peptide from the

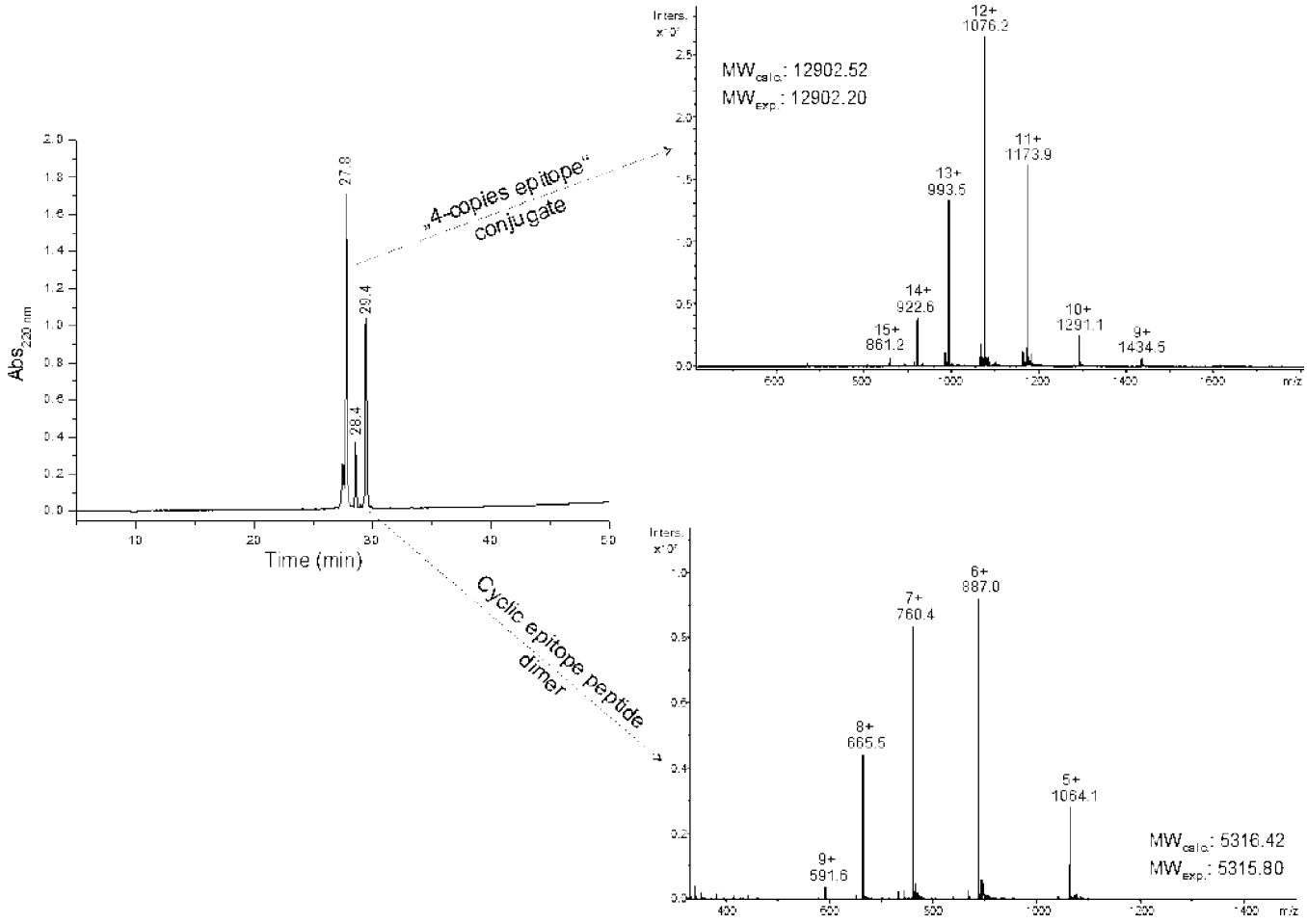

Figure 4. Conjugation of Ac-OT20(ClAc)$_4$ carrier with c[CH_2 COLKNleADPNRFRGKDLAhxK(Ac-CGFLG)AhxC]-NH_2 (**19**) epitope peptide followed by RP-HPLC and mass spectrometry: 24 h reaction time.

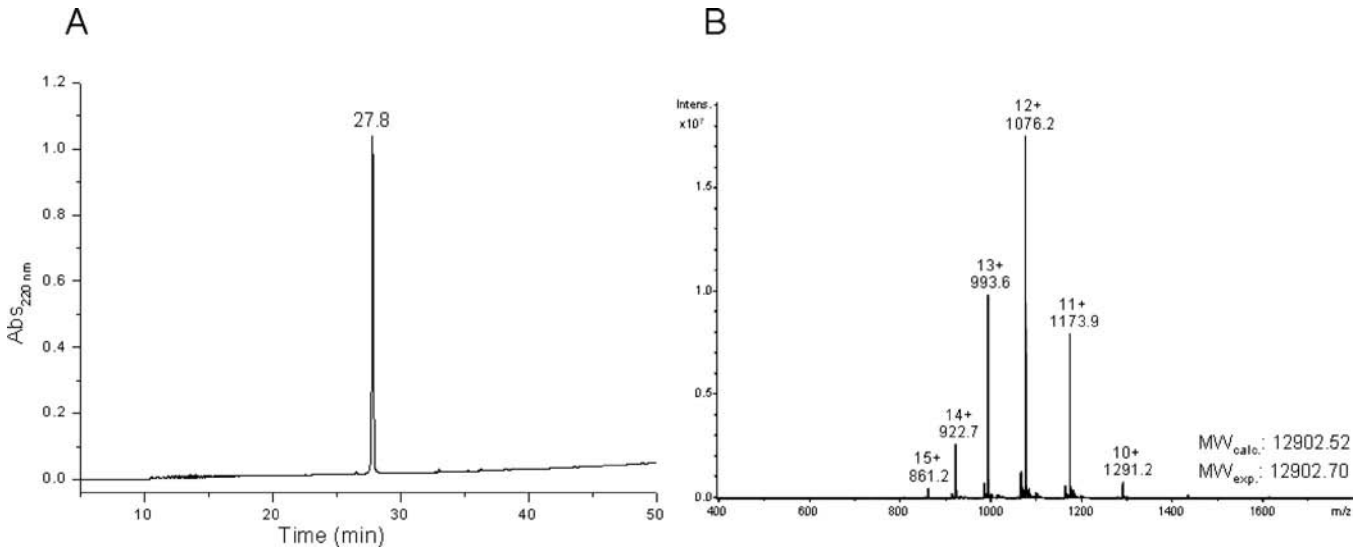

Figure 5. RP-HPLC profile (A) and ESI-ion trap mass spectrum (B) of purified conjugate **21**.

resin, a very complex crude product was detected by RP-HPLC. It was not stable even in freeze−dried form; a large number of byproducts were observed probably due to the reactivity of the BrAc group toward nucleophilic groups in the peptide (not only the thiol group) as well as to cross-linkage of peptide chains. On the basis of this observation, only chloroacetylated peptides were used in the further studies. In the linear peptide **10a**, the sequence at the *N*-terminal part was identical to the sequence in the peptide **8a**. The *C*-terminus was elongated by a hexapeptide consisting of an enzyme-labile sequence GFLG (*32*), with Cys and Ahx as spacer units. This Cys residue protected by Acm, which is stable under the acidic cleavage conditions as well as under the conditions of the cyclization procedure, provided the conjugation site in the dimerization reaction. In peptide **11a**, which is similar to peptide **10a**, Met was replaced with Nle. The cyclization of peptides **10a** and **11a** via thioether

bond formation yielded compounds **10** and **11**, respectively, each with a 55-atom ring. In linear peptides **12a** (^{11}Met) and **13a** (^{11}Nle), the Ahx-Lys-Ahx-Cys sequence was added to the *C*-terminus of the 9−22 epitope peptide. The *C*-terminal Cys was involved in a thioether cyclization with the *N*-terminal ClAc-group that yielded a 65-atom ring, while an additional Cys residue to be used for conjugation was included in an enzyme-labile (Ac-CGFLG) pentapeptide chain branching on the ε-amino group of the Lys near the *C*-terminus. The α-amino group of the Cys in this branch sequence was acetylated in order to prevent the fast formation of undesired disulfide bridge (*33*). Cyclization of peptides **12a** and **13a** provided **12** and **13**, respectively, with good yields. Compounds **10**−**13** were dimerized using $Tl(tfa)_3$ in a TFA solution. The disulfide bond formation was carried out at 0 °C for 90 min using 0.6 equiv of $Tl(tfa)_3$/Cys(Acm). Dimerization of compounds **10** and **12** with Met at residue 11 gave slightly lower yields, but no significant amount of methionine sulfoxide was detected. Cyclic dimers (compounds **14**−**17**) were isolated with fairly good yields (50−60%). Because the binding studies with Mab A16 (Table 2) indicated no significant differences between the recognition of cyclic dimer epitopes containing either ^{11}Met (11.8 pmol/100 μL (compound **14**) and 57.7 pmol/100 μL (compound **16**)) or ^{11}Nle (11.1 pmol/100 μL (compound **15**) and 41.4 pmol/100 μL (compound **17**)), only the Nle derivatives were used for further conjugation experiments. The dimers (compounds **15** and **17**) were reduced to their monomers with DTT (Scheme 2). The Cys connected to the spacer sequence (compounds **18** and **19**) was the conjugation site of the cyclic peptides in their coupling to the chloroacetylated oligotuftsin derivative carrier (Ac-[TKPK(ClAc)G]$_4$-NH_2). The conjugation was carried out in 0.1 M Tris−HCl buffer at pH 8.2 and monitored by RP-HPLC (Figures 2−4). After attachment of four copies of the cyclic epitope peptides to the carrier, the reaction was terminated by acidifying the solution with TFA. The conjugates (compounds **20** and **21**) were purified by semi-preparative RP-HPLC. The excess of Cys peptides was recovered after reduction with DTT. All cyclic peptides, their dimers, and conjugated derivatives were characterized by analytical RP-HPLC and ESI-MS (Figure 5). Data are summarized in Table 1.

Binding of Cyclic Derivatives of 9−22 Epitope Peptide of HSV gD-1 to Mab A16. Direct ELISA studies are often hampered by the different coating properties of the peptide constructs, which makes binding determination somehow unreliable. In our case, none of the dimers and conjugates of the cyclic peptides (compounds **14**−**17**) were able to bind to the ELISA plates. Therefore, competition ELISA was used to compare the antibody recognition of the compounds. Mab A16, which recognizes the 9−22 sequence in native gD (*9*), was used in this experiment. In a competition ELISA, only the binding properties of the compounds with Mab A16 in solution are measured, which gives more information on the binding properties of the peptide constructs.

Effect of Cyclization on Mab A16 Binding. No significant differences in binding were detected for various constructs with either Met or Nle at position 11 [79.1 (compound **10**, Met^{11}) vs 75.6 (compound **11**, Nle^{11}) and 88.0 (compound **12**, Met^{11}) vs 92.3 (compound **13**, Nle^{11}) pmol/100 μL]. This is in agreement with our previous results concerning linear peptides **1** and **2** (Table 2). Comparison between 16- and 8-residue cyclic peptides (e.g., **8** and **9** vs **3** and **4**, Table 2) showed that the larger ring clearly improved the antibody binding (79- and 273-fold, respectively). Whether this was due to less amino acids in the 8-residue cyclic peptides (compounds **8** and **9**) or to the modification of Arg at residue 18, it cannot be concluded. The cyclic peptides with hexapeptide spacer at the *C*-terminus (compounds **10**, **11**) or the branched ones (compounds **12**, **13**) had an approximately 2−3-fold lower binding activity to the Mab A16 than **8** and **9**. The binding activities of compounds **10** and **11** with the hexapeptide spacers were only slightly better than the binding of branched ones (compounds **12**, **13**).

Effect of Dimerization on Mab A16 Binding. Dimerization of the cyclic peptides **10**, **11**, **12**, and **13** resulting in compounds **14**, **15**, **16**, and **17**, respectively, increased the binding activity to Mab A16 in all cases. However, the disulfide bond formation at the *C*-terminus of the peptides (compounds **14**, **15**) led to higher antibody recognition of the cyclic dimer peptides than in the case of dimerization through the branching (compounds **16** and **17**). Both the Met and Nle containing derivatives (compounds **14** and **15**; 11.8 and 11.1 pmol/100 μL, respectively) had a higher binding activity to Mab A16 than the monomeric cyclic peptide without spacer sequences (compounds **8**, **9**; 28.6 and 28.0 pmol/100 μL, respectively). The binding capacity of dimers (57.7 (compound **16**) and 41.4 (compound **17**) pmol/100 μL), which had a disulfide bond between the branches, was better than that of their cyclic monomers (88.8 (compound **12**) and 92.3 (compound **13**) pmol/100 μL).

Effect of Conjugation on Mab A16 Binding. The binding data of the conjugates (compounds **20** and **21**) to the Mab A16 were surprising. In case of the conjugate (compound **20**) with the cyclic peptide containing a spacer and a Cys at the *C*-terminus (compound **18**) as the conjugation site, the binding affinity was dramatically decreased as compared to the monomer or dimer having the identical cyclic peptide (249.3 vs 75.6 (compound **11**) pmol/100 μL). In contrast, the other conjugate (compound **21**) in which the cyclic peptide was attached to the carrier through the branch showed excellent binding activity to the Mab A16 (7.2 vs 92.3 (compound **13**) pmol/100 μL). This binding capacity is comparable to the results of the linear epitope peptides as measured earlier (epitope construct **1** and **2**; Table 2). However, it is still 1 order of magnitude weaker than the binding of the OT20 conjugate containing the (^{11}Nle)-9−22C linear epitope peptide (**5**) and that of simple dimers of the linear peptide (**6**, **7**) (0.72, 0.74, and 0.66 pmol/100 μL, respectively; Table 2) (*25*).

CONCLUSION

The synthesis of cyclic forms of the epitope peptide 9−22 of gD-1, their dimers, and conjugates was carried out in this study. Dimers of cyclic peptides (without branches) and the cyclic peptide conjugated to an oligotuftsin derivative through the peptide spacer in the branch showed the highest binding activity to the Mab A16. Although a large variety of cyclic peptides and dimers of cyclic peptides were synthesized, a simple linear peptide 9−22 conjugated to OT20 and dimers of the linear peptide had the highest binding activity to the Mab A16. We hypothesize that only an accurate conformation of the cyclic constructs may result in higher binding activity than a linear construct with a potential to adopt the appropriate conformation. The strong binding activities of the dimers of the linear peptide are interesting. These results might be explained by binding of one peptide dimer molecule to both binding sites of one IgG or by cross-linking of IgG molecules. Mab A16 is directed against the native gD, as it is present in a cell infected by HSV. Therefore, another possible explanation of the strong binding of the dimer peptide 9−22 could be that gD in the native form during the virus infection has a dimer structure (*34*−*36*). We expected higher binding activity by cyclization of the epitope peptide 9−22, but our results showed that this was not the case. In addition, cyclization might enhance the stability of the peptide against enzymatic degradation. According to other results (*37, 38*) by our group, one can assume that conjugated cyclic peptides might have increased stability

in human serum compared to their linear versions. For this reason, in addition to compound **5** containing the linear epitope in the conjugate, compound **21** in which cyclic epitope was conjugated to OT20 carrier on its branch was selected for further development for the investigation of their immune response inducing potential. The results of these studies will be reported elsewhere.

ACKNOWLEDGMENT

This work was supported by the Hungarian Research Fund (OTKA T 049814, K68285) and the Hungarian-Spanish Intergovernmental Program.

LITERATURE CITED

(1) Ben-Yedidia, T., and Arnon, R. (1997) Design of peptide and polypeptide vaccines. *Curr. Opin. Biotechnol. 8*, 442–448.
(2) Arnon, R., and van Regenmortel, M. H. V. (1992) Structural basis of antigenic specificity and design of new vaccines. *FASEB J. 6*, 3265–3274.
(3) Purcell, A. W., Zeng, W., Mifsud, N. A., Ely, L. K., MacDonald, W. A., and Jackson, D. C. (2003) Dissecting the role of peptides in the immune response: Theory, practice and the application to vaccine design. *J. Pept. Sci. 9*, 255–281.
(4) van Regenmortel, M. H. V. (1999) Synthetic peptides as antigens. In *Laboratory Techniques in Biochemistry and Molecular Biology* (Pillai, S., and van der Vliet, P. C., Eds.) pp 281−374, Vol *28*, Elsevier, Amsterdam.
(5) Jackson, D. C., Fitzmaurice, C. J., Brown, L. E., and Zeng, W. (1999) Preparation and properties of totally synthetic immunogens. *Vaccine 18*, 355–361.
(6) Kaumaya, P. T. P., van Buskirk, A. M., Goldberg, E., and Pierce, S. K. (1992) Design and immunological properties of topographic immunogenic determinants of a protein antigen ($LDH\text{-}C_4$) as a vaccine. *J. Biol. Chem. 267*, 6338–6346.
(7) Hudecz, F. (2001) Manipulation of epitope function by modification of peptide structure: A minireview. *Biologicals 29*, 197–207.
(8) Francis, M. J., Fry, C. M., Rowlands, D. J., Bittle, J. L., Houghten, R. A., Lerner, R. A., and Brown, F. (1987) Immune response to uncouple peptides of foot-and-mouth disease virus. *Immunology 61*, 1–6.
(9) Van der Ploeg, J. R., Drijfhout, J. W., Feijlbrief, M., Bloemhoff, W., Welling, G. W., and Welling-Wester, S. (1989) Immunological properties of multiple repeats of a linear epitope of herpes simplex virus type 1 glycoprotein D. *J. Immunol. Methods 124*, 211–217.
(10) Hall, M. J., and Katrak, K. (1986) The quest for a herpes simplex virus vaccine: Background and recent developments. *Vaccine 4*, 138–150.
(11) Berman, P. W., Dowbenko, D., Lasky, L. A., and Simonsen, C. C. (1983) Detection of antibodies to herpes simplex virus with continuous cell lines expressing cloned glycoprotein D. *Science 222*, 524–527.
(12) Long, D., Madara, T. J., Ponce de Leon, M., Cohen, G. H., Montgomery, P. C., and Eisenberg, R. J. (1984) Glycoprotein D protects mice against lethal challenge with herpes simplex virus type 1 and 2. *Infect. Immun. 37*, 761–764.
(13) Welling-Wester, S., Scheffer, A. J., and Welling, G. W. (1991) B- and T- cell epitopes of glycoprotein D of herpes simplex virus type I. *Microbiol. Immunol. 76*, 59–68.
(14) Schellekens, G. A., Lasonder, E., Feijlbrief, M., Koedijk, D. G., Drijfhout, J. W., Scheffer, A. J., Welling-Wester, S., and Welling, G. W. (1994) Identification of the core residues of the epitope of a monoclonal antibody raised against glycoprotein D of herpes simplex virus type 1 by screening of a random peptide library. *Eur. J. Immunol. 24*, 3188–3193.
(15) Welling-Wester, S., Feijlbrief, M., Koedijk, D. G., Drijfhout, J. W., Weijer, W. J., Scheffer, A. J., and Welling, G. W. (1994) Analogues of peptide 9−21 of herpes simplex virus type I glycoprotein D and their binding to group VII monoclonal antibodies. *Arch. Virol. 138*, 331–340.
(16) Williamson, M. P., Handa, B. K., and Hall, M. J. (1986) Secondary structure of a herpes simplex virus glycoprotein D antigenic domain. *Int. J. Pept. Protein Res. 27*, 562–568.
(17) Williamson, M. P., Hall, M. J., and Handa, B. K. (1986) ^{1}H-NMR assignment and secondary structure of a herpes simplex virus glycoprotein D-1 antigenic domain. *Eur. J. Biochem. 158*, 527–536.
(18) Heber-Katz, E., Hollósi, M., Dietzschold, B., Hudecz, F., and Fasman, G. D. (1985) The T-cell response to the glycoprotein D of herpes simplex virus: The significance of antigen conformation. *J. Immunol. 135*, 1385–1390.
(19) Schlosser, G., Mező, G., Kiss, R., Vass, E., Majer, Zs., Feijlbrief, M., Perczel, A., Bõsze, Sz., Welling-Wester, S., and Hudecz, F. (2003) Synthesis, solution structure analysis and antibody binding of cyclic epitope peptides from glycoprotein D of herpes simplex virus type I. *Biophys. Chem. 106*, 155–171.
(20) Mező, G., de Oliviera, E., Krikorian, D., Feijlbrief, M., Jakab, A., Tsikaris, V., Sakarellos, C., Welling-Wester, S., Andreu, D., and Hudecz, F. (2003) Synthesis and comparision of antibody recognition of conjugates containing herpes simplex virus type I glycoprotein D epitope VII. *Bioconjugate Chem. 14*, 1260–1269.
(21) Weijer, W. J., Drijfhout, J. W., Geerlings, J., Bloemhoff, M., Feijlbrief, M., Bos, C. A., Hoogerhout, P., Kerling, K. E. T., Popken-Boer, T., Slopsema, K., Wilterdink, J. B., Welling, G. W., and Welling-Wester, S. (1988) Antibodies against synthetic peptide of herpes simplex virus type 1 glycoprotein D and their capability to neutralize viral infectivity in vitro. *J. Virol 62*, 501–510.
(22) Tam, J. P. (1988) Synthetic peptide vaccine design: Synthesis and properties of a high-density multiple antigenic peptide system. *Proc. Natl. Acad. Sci. U.S.A. 85*, 5409–5413.
(23) Tsikaris, V., Sakarellos, C., Cung, M. T., Marraud, M., and Sakarellos-Daitiotis, M. (1996) Concept and design of a new class of sequential oligopeptide carriers (SOC) for covalent attachment of multiple antigenic peptides. *Biopolymers 38*, 291–293.
(24) Mező, G., Kalászi, A., Reményi, J., Majer, Zs., Hilbert, Á., Láng, O., Kõhidai, L., Barna, K., Gaál, D., and Hudecz, F. (2004) Synthesis, conformation and immunoreactivity of new carrier molecules based on repeated tuftsin-like sequence. *Biopolymers 73*, 645–656.
(25) Mező, G., Kajtár, J., Nagy, I., Szekerke, M., and Hudecz, F. (1997) Carrier design: Synthesis and conformational studies of poly(L-lysine) based branched polypeptides with hydroxyl groups. *Biopolymers 42*, 719–730.
(26) Bartel, A., and Campbell, D. (1959) Some immunochemical differences between associated and dissociated hemocyanin. *Arch. Biochem. Biophys. 82*, 2332–2336.
(27) Mező, G., Jakab, A., Schlosser, G., Feijlbrief, M., Welling-Wester, S., Vila-Perello, M., Andreu, D., and Hudecz, F. (2006) Synthesis and characterization of cyclic epitope peptide dimers, conjugates from glycoprotein D of herpes simplex virus type 1. In *Peptide Science 2005* (Wakayima, T., Ed.) pp 53−56, Japanes Peptide Society, Osaka.
(28) Kaiser, E., Colescott, R. L., Bossinger, C. D., and Cook, P. I. (1970) Color test for detection of free terminal amino groups in the solid-phase synthesis of peptides. *Anal. Biochem. 34*, 595–598.
(29) Kaiser, E, Bossinger, C. D., Colescott, R. L., and Olser, D. B. (1980) Color test for terminal prolyl residues in the solid-phase synthesis of peptides. *Anal. Chem. Acta 118*, 149–151.
(30) Fujii, N., Otaka, A., Funakoshi, S., Bessho, K., and Yajima, H. (1987) New procedure for the synthesis of cystine-peptides by oxidation of S-substituted cysteine-peptides with thallium(III) trifluoroacetate. *J. Chem. Soc., Chem. Commun. 3*, 163–164.
(31) Robey, F. A., and Fields, R. L. (1989) Automated synthesis of N-bromoacetyl-modified peptides for the preparation of synthetic peptide polymers, peptide-protein conjugates and cyclic peptides. *Anal. Biochem. 177*, 373–377.

(32) Omelyanenko, V., Kopecková, P., Gentry, C., and Kopecek, J. (1998) Targetable HPMA copolymer-adriamycin conjugates. Recognition, internalization, and subcellular fate. *J. Controlled Release 53*, 25–37.

(33) Mező, G., Manea, M., Jakab, A., Kapuvári, B., Bõsze, S., Schlosser, G., Przybylski, M., and Hudecz, F. (2004) Synthesis and structural characterization of bioactive peptide conjugates using thioether linkage approaches. *J. Pept. Sci. 10*, 701–713.

(34) Eisenberg, R. J., Ponce de Leon, M., Pereira, L., Long, D., and Cohen, G. H. (1982) Purification of glycoprotein gD of herpes simplex virus types 1 and 2 by use of monoclonal antibody. *J. Virol. 41*, 1099–1104.

(35) Handler, C. G., Eisenberg, R. J., and Cohen, G. H. (1996) Oligomeric structure of glycoproteins in herpes simplex virus type 1. *J. Virol. 70*, 6067–6075.

(36) Willis, S. H., Rux, A. H., Peng, C., Whitebeck, J. C., Nicola, A. V., Lou, H., Hou, W., Salvador, L., Eisenberg, R. J., and Cohen, G. H. (1998) Examination of the kinetics of herpes simplex virus glycoprotein D binding to the herpesvirus entry mediator, using surface plasmon resonance. *J. Virol. 72*, 5937–5947.

(37) Tugyi, R., Mező, G., Fellinger, E., Andreu, D., and Hudecz, F. (2005) The effect of cyclization on the enzymatic degradation of herpes simplex virus glycoprotein D derived epitope peptide. *J. Pept. Sci. 11*, 642–649.

(38) Tugyi, R., Mező, G., Schlosser, G., Fellinger, E., Andreu, D., and Hudecz, F. (2008) The effect of conjugation with polypeptide carrier on the enzymatic degradation of herpes simplex virus glycoprotein D derived epitope peptide. *Bioconjugate Chem. 19*, 1652–1659.

BC800324G

Bioconjugate Chemistry 20th Anniversary

Subscriber access provided by SHEMYAKIN-OVCHINNIKOV INST

Article

Surface Modification of PAMAM Dendrimers Modulates the Mechanism of Cellular Internalization

Angkana Saovapakhiran, Antony D'Emanuele, David Attwood, and Jeffrey Penny

Bioconjugate Chem., **2009**, 20 (4), 693-701• DOI: 10.1021/bc8002343 • Publication Date (Web): 09 March 2009

Downloaded from http://pubs.acs.org on May 15, 2009

More About This Article

Additional resources and features associated with this article are available within the HTML version:

- Supporting Information
- Access to high resolution figures
- Links to articles and content related to this article
- Copyright permission to reproduce figures and/or text from this article

View the Full Text HTML

ACS Publications
High quality. High impact.

Bioconjugate Chemistry is published by the American Chemical Society. 1155 Sixteenth Street N.W., Washington, DC 20036

Surface Modification of PAMAM Dendrimers Modulates the Mechanism of Cellular Internalization

Angkana Saovapakhiran,[†] Antony D'Emanuele,[‡] David Attwood,[†] and Jeffrey Penny*[,†]

School of Pharmacy and Pharmaceutical Sciences, The University of Manchester, Oxford Road, Manchester M13 9PT, and School of Pharmacy and Pharmaceutical Sciences, University of Central Lancashire, Preston, Lancashire PR1 2HE, United Kingdom.
Received June 13, 2008; Revised Manuscript Received January 27, 2009

The aim of this study was to investigate the influence of dendrimer surface properties on cellular internalization and intracellular trafficking in the human colon adenocarcinoma HT-29 cell line. Third-generation (G3) polyamidoamine (PAMAM) dendrimers were modified to contain either two lauroyl chains (G3L2), two propranolol molecules (G3P2), or two lauroyl and two propranolol molecules (G3L2P2) at the dendrimer surface. Surface-modified and unmodified dendrimers were labeled with fluorescein isothiocyanate (FITC) at an average molar ratio of 1:1. The mechanisms of cellular internalization and intracellular trafficking of dendrimers were analyzed by confocal laser scanning microscopy and flow cytometry. The internalization of G3 and G3P2 dendrimers involved both caveolae-dependent endocytosis and macropinocytosis pathways; internalization of G3L2P2 dendrimer appeared to involve caveolae-dependent, and possibly clathrin-dependent, endocytosis pathways; and internalization of G3L2 dendrimer occurred via caveolae-dependent, clathrin-dependent, and macropinocytosis pathways. Subcellular colocalization data indicated that unmodified and all surface-modified G3 PAMAM dendrimers were internalized and trafficked to endosomes and lysosomes. It is therefore apparent that the initial mode of dendrimer internalization into HT-29 cells is influenced by the surface properties of G3 PAMAM dendrimer.

INTRODUCTION

Due to their highly branched nature and the presence of multivalent surface groups that can be conjugated with drugs, polyamidoamine (PAMAM) dendrimers offer significant potential as versatile carriers for drug delivery (*1*). Our previous studies have established that the conjugation of propranolol, a P-glycoprotein substrate with poor bioavailability, to cationic PAMAM dendrimer increased drug solubility and enhanced the permeation of propranolol across Caco-2 cell monolayers (*2*). Numerous studies have reported that surface modification of dendrimers can cause significant changes in their biological properties, including cytoxicity and permeation through cell monolayers (*2*−*6*). Addition of lauroyl moieties to cationic PAMAM dendrimers has been reported to increase transcellular apical-to-basal transport of both dendrimer and dendrimer−drug conjugates in Caco-2 cells (*2*−*4, 7, 8*). Addition of FITC onto cationic G4 PAMAM dendrimer at a ratio of 8:1 resulted in a decrease in dendrimer cytotoxicity and significant increase in permeation through Caco-2 cell monolayers (*5*). A study of the influence of surface acetylation of cationic G2 and G4 PAMAM dendrimer on the viability of Caco-2 cells revealed that acetylation resulted in a significant decrease in cytotoxicity. Cytotoxicity decreased as the number of surface acetyl groups increased while the permeability across cell monolayers was maintained (*6*). These findings reveal that PAMAM dendrimers offer potential as nanoparticulate drug delivery systems. However, although surface modification is able to enhance transcellular dendrimer permeation, little is known of the precise influence of surface modification on the mechanism(s) of dendrimer cellular internalization and intracellular trafficking.

PAMAM dendrimers are able to traverse cell monolayers via paracellular and transcellular pathways (*2, 4, 5, 9, 10*), and the endocytosis pathway is believed to be an important route for dendrimer internalization. Kitchens et al. (*11, 12*) reported that uptake of cationic and anionic (G2, G4, and G1.5) PAMAM dendrimers into Caco-2 cells was via clathrin-dependent endocytosis, whereas cationic G4 PAMAM dendrimer were predominately internalized via a cholesterol-dependent route in B16F10 melanoma cells (*13*).

In this study, we investigated the effect of conjugating lauroyl and/or propranolol groups onto the surface of G3 PAMAM dendrimers on the mechanism of cellular internalization and subsequent intracellular trafficking in HT-29 cells, which are capable of clathrin-mediated endocytosis, caveolae-mediated endocytosis, and macropinocytosis (*14*−*19*).

G3 PAMAM dendrimers were employed since they are less cytotoxic than both G4 and G5 PAMAM dendrimers (*3, 4*) and were chosen in preference to G2 dendrimers, because the latter possess significantly fewer surface groups available for attachment of surface moieties. In addition, G2 and anionic dendrimers, e.g., G2.5, G3.5, demonstrate less apparent permeation through cell monolayers than G3 dendrimer (*4*).

A better understanding of the influence of the surface properties of dendrimers on their internalization mechanisms is important in the development of dendrimer-mediated drug delivery systems.

EXPERIMENTAL PROCEDURES

Materials. G3 PAMAM dendrimer was purchased from Dendritech Inc. (Michigan, USA). Sephadex G-25, fluorescein isothiocyanate (FITC), chlorpromazine hydrochloride, filipin III, 5-(*N*-ethyl-*N*-isopropyl) amiloride, nystatin, trypan blue, formaldehyde, and bovine serum albumin were purchased from Sigma-Aldrich Co. Ltd. (Gillingham, Dorset, UK). Saponin was obtained from Fluka (Steinheim, Germany). Cell culture materials, Lysotracker Red DND-99, Alexa Fluor 555 rabbit antigoat

* Corresponding author. E-mail: jeff.penny@manchester.ac.uk; Telephone: +44 (0)161 275 8344; Fax: 0161 275 8349.
[†] The University of Manchester.
[‡] University of Central Lancashire.

10.1021/bc8002343 CCC: $40.75 © 2009 American Chemical Society
Published on Web 03/09/2009

IgG (heavy and light chains), Alexa Fluor 555 goat antirabbit IgG (heavy and light chains), and Alexa Fluor 555 conjugated transferrin (from human serum) were obtained from Invitrogen (Paisley, UK). Caveolin-1 (N-20) rabbit polyclonal IgG and tetramethylrhodamine-5-isothiocyanate (TRITC)-clathrin HC (C-20) goat polyclonal IgG were obtained from Santa Cruz Biotechnology (Heidelberg, Germany). Cytotoxicity detection kit (lactate dehydrogenase, LDH) was purchased from Roche Applied Science (Mannheim, Germany). All other chemicals were purchased from BDH Laboratory Supplier (Poole, Dorset, UK).

Synthesis of Surface-Modified G3 PAMAM Dendrimers. The synthesis of surface-modified PAMAM dendrimers containing two lauroyl chains (G3L2) was performed using 4-nitrophenyl chloroformate as a linker (*7*). Lauroyl alcohol, 200 mg (1 mmol), was dissolved in 5 mL of anhydrous tetrahydrofuran (THF), and triethylamine (TEA) 0.3 mL (2.1 mmol) was added. 4-Nitrophenylchloroformate, 417 mg (2 mmol), was dissolved in 1.5 mL of anhydrous THF, added dropwise to the mixture, and stirred for 24 h under nitrogen at room temperature. Following evaporation of solvent, the residue was dissolved in hexane/diethylacetate (85:15), filtered (Whatman No. 1), and purified by silica gel column chromatography using a hexane/diethylacetate (85:15) mobile phase. The mobile phase was applied with a flow rate of 120 mL per h, and 5 mL fractions were collected and analyzed by TLC (using the same mobile phase) to identify the purified compound. Purified lauroyl 4-(nitrophenyl carbonate) was characterized by ^{1}H NMR as described previously ($CDCl_3$): 0.88 (3H, t, J = 6.8, CH_3), 1.27−1.42 (18H, m, (CH_2)$_8$), 1.76 (2H, pentet, J = 7.0, CH_2), 4.29 (2H, t, J = 6.6, CH_2COO), 7.32−7.39 (2H, m, Ar-H_2 + Ar-H_6), 8.27−8.30 (2H, m, Ar-H_3 + Ar-H_5) (*7*). G3 PAMAM dendrimer, 0.21 mg (0.03 mmol), was dissolved in 20 mL of anhydrous *N*,*N*-dimethylformamide (DMF). Lauroyl (4-nitrophenyl carbonate), 0.06 mmol (2 lauroyl molecules/1 G3 PAMAM dendrimer), was dissolved in 5 mL of anhydrous DMF and added dropwise to the reaction mixture (Figure 1). The reaction was carried out, with stirring, at room temperature for 5 days. Lauroyl−G3 PAMAM conjugate (G3L2) (Figure 1-(1)) was purified by chromatography using Sephadex LH20 with a methanol/water (4:1) mobile phase applied at a flow rate of 90 mL per h. 1.5 mL samples were collected and absorbance measured at 230 nm. The ratio of lauroyl to G3 PAMAM dendrimer was verified by using ^{1}H NMR. The yield of G3L2 was 66.23% (w/w). ^{1}H NMR (d_4-MeOD): 0.89 (6H, CH_3), 1.29 (36H, (CH_2)$_9$), 1.43 (4H, CH_2), 2.38 (120H, CH_2C═ONH), 2.58 (120H, CH_2NH + CH_2N), 2.80 (124H, NCH_2), 3.31 (120H, *O*═CNHCH_2), 4.00 (4H, CH_2COO).

Synthesis of G3 PAMAM dendrimer conjugates containing either two propranolol molecules (G3P2) (Figure 1-(2)) or two propranolol molecules and two lauroyl molecules (G3L2P2) (Figure 1-(3)) employed chloroacetyl chloride as a linker (*2*). Propranolol base, 7.6 mmol, was dissolved in 20 mL of anhydrous dichloromethane (DCM) and TEA, 22.8 mmol, was added. Chloroacetyl chloride, 7.6 mmol, was added slowly and the reaction stirred for 1 h on ice. The dark brown solution obtained was sequentially washed once with equal volumes of saturated solutions of sodium bicarbonate and then sodium chloride. The organic layer was dried over anhydrous magnesium sulfate and evaporated to dryness. The crude residue was dissolved in mobile phase (hexane/diethylacetate (1:1)) and purified by silica gel column chromatography. The mobile phase was applied with a flow rate of 120 mL per h and 5 mL fractions collected and analyzed by TLC to identify fractions containing purified propranolol-*N*-chloroacetyl. Characterization of propranolol-*N*-chloroacetyl was by ^{1}H NMR and ^{13}C NMR. The yield of propranolol-*N*-chloroacetyl was 70.05% (w/w). ^{1}H NMR

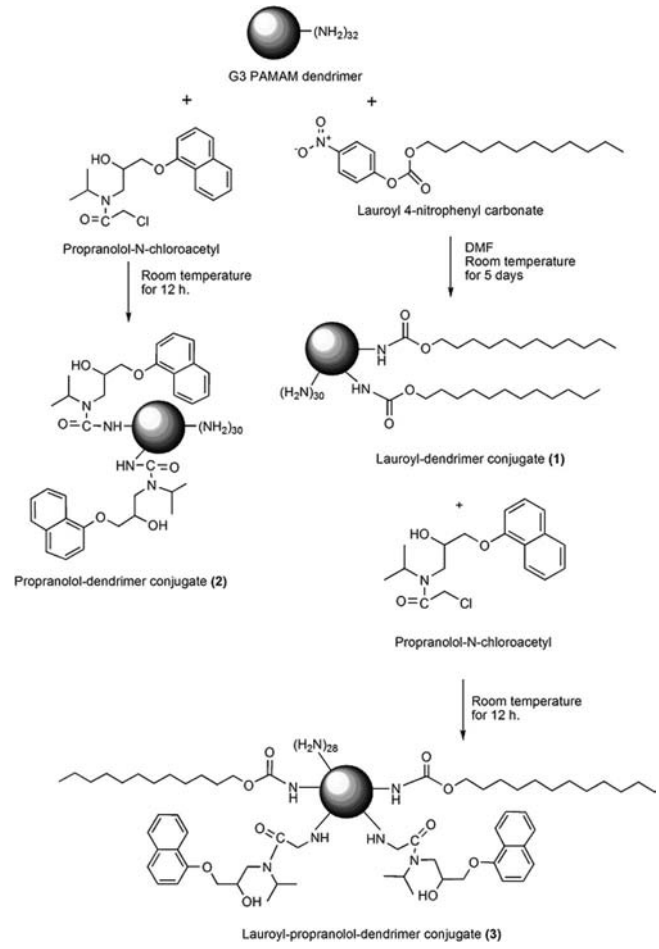

Figure 1. Synthetic scheme for surface modification of G3 PAMAM dendrimers.

($CDCl_3$): 1.30 (6H, dd J = 26.06 Hz, J = 6.71 Hz, (CH_3)CH), 3.66 (1H, dd, J = 14.6 Hz, J = 1.9 Hz (CH$_3$)CH), 3.72 (1H, dd, J = 14.6 Hz, J = 7.8 Hz (CH$_3$)CH), 4.09 (1H, m, CHN), 4.17 (2H, s, CH_2Cl), 4.21 (2H, m, CH_2O), 4.26 (1H, m, CHO), 6.84 (1H, d, J = 7.47 Hz, 1H, Ar-H_2), 7.45 (4H, m, Ar-H_3 + Ar-H_4 + Ar-H_7 + Ar-H_8), 7.79 (1H, m, Ar-H_6), 8.20 (1H, m, Ar-H_9). ^{13}C NMR: 21.0 (2 × CH_3), 41.0 (CH_2Cl), 46.1 (CH_2NCH), 49.8 ((CH$_3$)$_2$CHN), 69.4 (CHOH), 71.3 (CHCH_2O), 104.4 (CH, Ar), 120.3 (CH, Ar), 121.1 (CH, Ar), 124.8 (CH, Ar), 125.5 (CH, Ar), 126.0 (CH, Ar), 126.1 (C, Ar), 127.6 (CH, Ar), 134.0 (C, Ar), 153.5 (C, Ar), 168.9 (ONCCH$_2$).

In order to conjugate propranolol to dendrimer, either G3 PAMAM dendrimer, 0.21 mg (0.03 mmol), or G3L2 PAMAM dendrimer, 0.22 mg (0.03 mmol), was dissolved in 15−20 mL of anhydrous DMF. Propranolol-*N*-chloroacetyl, 0.06 mmol (1 propranolol molecules/1 G3 PAMAM dendrimer or 1 G3L2 PAMAM dendrimer), was dissolved in 5 mL of anhydrous DMF, added dropwise to the mixture, and stirred at room temperature for 12 h. Propranolol−G3 PAMAM conjugate (G3P2) was purified by column chromatography using Sephadex LH20 with methanol/water (4:1) mobile phase. The latter was applied at a flow rate of 90 mL per h. A series of 1.5 mL samples were collected and absorbance measured at 230 nm. The number of propranolol molecules attached was confirmed by using ^{1}H NMR. The yields of G3P2 and G3L2P2 were 31.01% and 54.37% (w/w), respectively. G3P2 (d_4-MeOD): 1.286−1.308 (12H, (CH_3)$_2$CH), 2.372 (120H, CH_2C═ONH), 2.583 (120H, CH_2NH + CH_2N), 2.789 (124H, NCH_2), 3.272−3.346 (120H, *O*═CNHCH_2), 3.593−4.695 (16H, CH_2NCH + CHN + CH_2O + HNCH_2C═ON + CHO), 6.878−7.046 (2H, Ar-H_2), 7.376−7.483 (8H, Ar-H_3 + Ar-H_4 + Ar-H_7 + Ar-H_8), 7.803−7.814 (2H,

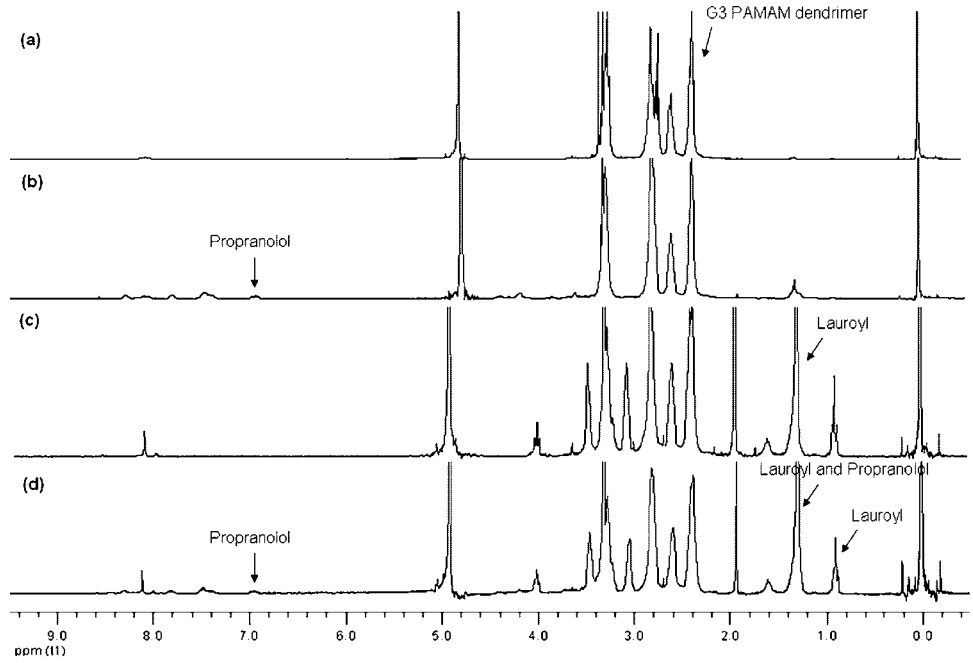

Figure 2. ^{1}H NMR spectra (270 MHz) of (a) G3, (b) G3P2, (c) G3L2, and (d) G3L2P2 PAMAM dendrimers (d_4-MeOD).

Ar-H_6), 8.293 (2H, Ar-H_9). G3L2P2 (d_4-MeOD): 0.89 (6H, CH_3), 1.23 (48H, (CH_2)$_9$ + (CH_3)$_2$CH), 1.54−1.67 (4H, CH_2), 2.46−2.53 (120H, CH_2C═ONH), 2.60 (120H, CH_2NH + CH_2N), 2.87 (124H, NCH_2), 3.05−3.06 (120H, *O*═CNHCH_2), 3.36−3.53 (16H, CH_2NCH + C*H*N + CH_2O + NHCH_2C═ON + C*H*O), 3.94−4.19 (4H, CH_2COO), 7.43−7.58 (8H, Ar-H_3 + Ar-H_4 + Ar-H_7 + Ar-H_8), 7.85 (2H, Ar-H_6), 8.23 (2H, Ar-H_9).

Preparation and Characterization of FITC-Labeled G3 PAMAM Dendrimers. G3 PAMAM dendrimer and surface-modified dendrimers were labeled with FITC via a thiourea bond between the isothiocyanate group of FITC and an amine group of PAMAM dendrimer, as described previously (*4*). Briefly, 15 mL of a methanolic solution of FITC containing 0.036 mmol was slowly added to 0.030 mmol of G3 PAMAM dendrimer (a molar ratio 1.2:1 of PAMAM dendrimer to FITC) in 15 mL PBS and stirred at room temperature for 24 h in the dark. FITC-labeled G3 PAMAM dendrimer was purified by size exclusion chromatography on a Sephadex G-25 column (mobile phase: phosphate buffered saline (PBS)). One milliliter fractions were collected and those containing FITC−dendrimer conjugate identified using TLC (mobile phase: chloroform/methanol/ammonia, 5:4:1). Fractions containing FITC−dendrimer were pooled and dialyzed against distilled water for 24 h to remove salts. Manipulations involving FITC-labeled dendrimers were carried out in a low-light environment. The ratio of FITC to dendrimer was confirmed using ^{1}H NMR.

Analysis of size distribution of FITC-labeled G3 dendrimer and surface-modified dendrimers was performed using dynamic light scattering (Zetasizer Nano, Malvern Instruments, UK) (*4, 20*). Samples were dissolved in PBS (10 mg/mL) and filtered through a Nalgene filter (0.2 μm pore size) into the scattering cell. All measurements were carried out at 37 °C. Diameters are represented as mean ± standard deviation of triplicate measurements.

Cell Culture. HT-29 cells (passage number 36−67) were maintained in Dulbecco's Modified Eagles Medium (DMEM) containing 10% (v/v) fetal calf serum, 2 mM L-glutamine, 10 mM nonessential amino acids, 50 IU/mL penicillin, and 50 μg/mL streptomycin at 37 °C in an atmosphere of 5% CO_2.

LDH Assay. Approximately 1×10^4 HT-29 cells/well were cultured in 96-well plates overnight. The cells were treated with chlorpromazine (5−50 μM), filipin (0.25−5 μg/mL), nystatin (5−50 μM), and EIPA (50−250 μM) for 4 h. To measure dendrimer cytotoxicity, 100 μL of supernatant was transferred into an optically clear 96-well plate. The LDH reaction mixture was freshly prepared according to the manufacturer's instruction (Roche Diagnostics), 100 μL added to each well, and the plate incubated for 30 min at 25 °C. The absorbances at 450 and 650 nm were measured using a multiplate reader (MRX, Dynatech Laboratories, Guernsey, UK).

Determination of the Effect of Endocytosis Inhibitors on Uptake of G3 PAMAM Dendrimers. Chlorpromazine (inhibitor of clathrin-dependent endocytosis) (*21, 22*), nystatin and filipin (inhibitors of caveolae-dependent endocytosis) (*23*−*25*), and ethyl isopropyl amiloride (inhibitor of macropinocytosis) (*26, 27*) were dissolved in Opti-MEM I medium containing 12.5 mM HEPES, pH 7.4. Approximately 1×10^6 HT-29 cells/well were seeded in 6-well plates and incubated at 37 °C in an atmosphere of 5% CO_2 until cells reached 80% confluency. Cells were washed twice with PBS and pretreated with Opti-MEM I medium with 12.5 mM HEPES pH 7.4 containing inhibitor (at the concentrations indicated in Figure 4) for 30 min at 37 °C in an atmosphere of 5% CO_2. FITC-labeled G3 PAMAM dendrimer and FITC-labeled surface-modified PAMAM dendrimers were added at a final concentration of 2.5 μM and cells incubated for 1 h. Following a 1 h incubation, cells were washed three times with ice-cold PBS and incubated with FITC-quench solution (PBS containing 0.4% w/v trypan blue) for 10 min to quench extracellular fluorescence. Cells were washed three times with ice-cold PBS and treated with 0.25% (v/v) trypsin−EDTA solution for 5 min at 37 °C. The cell suspension was centrifuged at 12 000 *g* for 3 min, the pellet resuspended in PBS, and intracellular fluorescence analyzed immediately by flow cytometry (Dako Cytomation, Glostrup, Denmark). A flow rate of less than 200 events/s and an excitation wavelength of 488 nm (530/40 bandpass filter) were employed.

Subcellular Localization of FITC-Labeled G3 PAMAM Dendrimers. HT-29 cells were seeded onto collagen-coated coverslips and grown to 70% confluency. DMEM growth medium was replaced with Opti-MEM I medium with 12.5 mM HEPES, pH 7.4, containing 2.5 μM FITC-labeled G3 PAMAM dendrimer or FITC-labeled surface-modified PAMAM den-

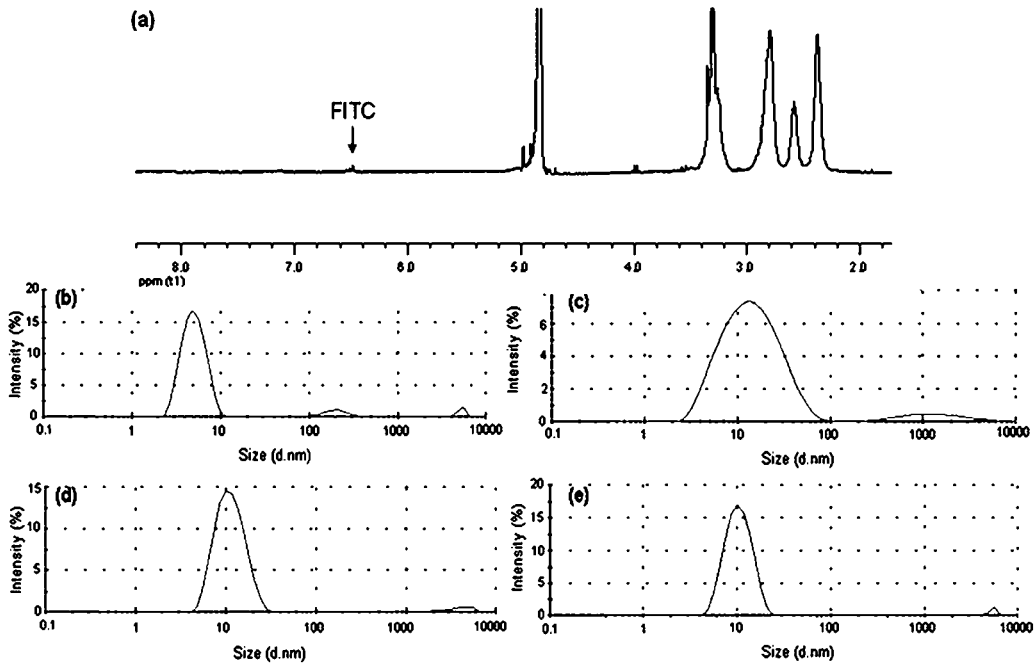

Figure 3. [1]H NMR spectra (270 MHz) of (a) FITC-labeled G3 PAMAM dendrimer and size distribution of (b) FITC-labeled G3, (c) FITC-labeled G3P2, (d) FITC-labeled G3L2, and (e) FITC-labeled G3L2P2 PAMAM dendrimers.

drimers. In immunofluorescence studies, cells were incubated for 1.5 h with dendrimer. In endosome localization studies, cells were incubated for 1 h, while in lysosome localization studies, cells were incubated for 12 h (G3), 3 h (G3P2), 6 h (G3L2), or 12 h (G3L2P2). Growth medium was removed, and cells were washed three times with ice-cold PBS.

For detection of clathrin and caveolin-1, HT-29 cells were fixed with 4% (v/v) formaldehyde in PBS for 10 min. Free aldehyde groups were quenched by incubating with 50 mM NH_4Cl for 10 min, and cells were then permeabilized by treatment with 0.1% (w/v) saponin in PBS. After three washes with PBS, permeabilized cells were incubated with PBS containing 5% (w/v) BSA to reduce nonspecific antibody binding and then incubated with either anticlathrin heavy-chain goat polyclonal IgG or anticaveolin-1 rabbit polyclonal IgG (1:100) for 2 h. Cells were washed three times with PBS and incubated with either Alexa Fluor 555 rabbit antigoat IgG or Alexa Fluor 555 goat antirabbit IgG (1:100) for 1 h. After thorough washing with PBS, coverslips were mounted onto microscope slides using mounting medium. Cell-associated fluorescence was analyzed by confocal laser scanning microscope.

Transferrin was used as a positive control of receptor-mediated endocytosis and trafficking into endosomes. Cells were incubated with Alexa Fluor 555-transferrin (50 μg/mL) in Opti-MEM I medium at 37 °C in an atmosphere of 5% CO_2 for either 10 min (G3P2, G3L2, G3L2P2) or 60 min (G3). Cells were washed with ice-cold PBS containing 0.5% w/v BSA and then with ice-cold PBS. Cells were fixed immediately with 4% w/v formaldehyde in PBS and treated with 50 mM NH_4Cl to quench residual formaldehyde fluorescence. Following further washing with PBS, coverslips were mounted onto microscope slides using mounting medium. Alexa Fluor 555-transferrin was visualized using confocal laser scanning microscopy.

For detection of lysosomes, HT-29 cells were incubated in Opti-MEM I medium containing Lysotracker Red DND-99 for 45 min at 37 °C. Cells were washed three times with PBS prior to confocal laser scanning microscopy.

Confocal Laser Scanning Microscopic Analysis and Image Processing. Cells were examined with a Zeiss LSM 510 Meta ConfoCor 2 using 63× oil immersion objective. FITC-labeled G3 PAMAM dendrimer or FITC-surface-modified PAMAM dendrimers were analyzed using an argon laser (excitation 488 nm; emission 505−550 nm). Lysotracker Red DND-99 or Alexa Fluor 555 labeled antibodies and Alexa Fluor 555−transferrin were analyzed using a helium/neon laser (excitation 543 nm; emission 560 nm). Images and a gallery of 30 optical sections (0.5 μm) through the *z* plane were collected and processed using Combi LSM-FCS and LSM Image Browser v4.0 software (Germany). Colocalization studies were carried out on three discrete regions of the microscope slide (with between 3 and 6 individual cells analyzed per slide). Data were analyzed using *ImageJ* v 1.410 (National Institutes of Health, USA). Channel overlap was determined by calculation of Pearson's coefficient and the true extent of three-dimensional colocalization defined by the Overlap Coefficient.

Statistical Analysis. Statistical analysis was carried out using one-way analysis of variance (ANOVA) followed by Dunnett's test (SPSS for Windows version 10.0). Probability values of $P < 0.05$ were considered to be significant.

RESULTS

Conjugation of Dendrimers with Lauroyl and Propranolol Molecules. [1]H NMR studies revealed that, on average, G3 PAMAM dendrimer (Figure 2a) was successfully conjugated with two propranolol molecules (Figure 2b), with two lauroyl chains (Figure 2c), and with both two lauroyl chains and two propranolol molecules (Figure 2d). The successful conjugation of lauroyl chains to the G3 PAMAM dendrimer is indicated by the additional peaks at the chemical shift 0.89−1.43 ppm, which confirmed the attachment of lauroyl chain onto G3 PAMAM dendrimer (Figure 2b). The number of lipid chains was calculated by comparing the peak integrations of the chemical shift at 1.29 ppm of lauroyl and at 2.38 ppm of PAMAM dendrimer (Figure 2b). Attachment of propranolol molecules to dendrimer is indicated by the additional peaks at the chemical shifts 1.29−1.31 ppm, 3.59−4.70 ppm, and 6.88−8.29 ppm. The integration of the peak between 7.43 and 7.49 ppm of propranolol and 2.38 ppm of PAMAM dendrimer revealed that two propranolol molecules were attached to G3 PAMAM

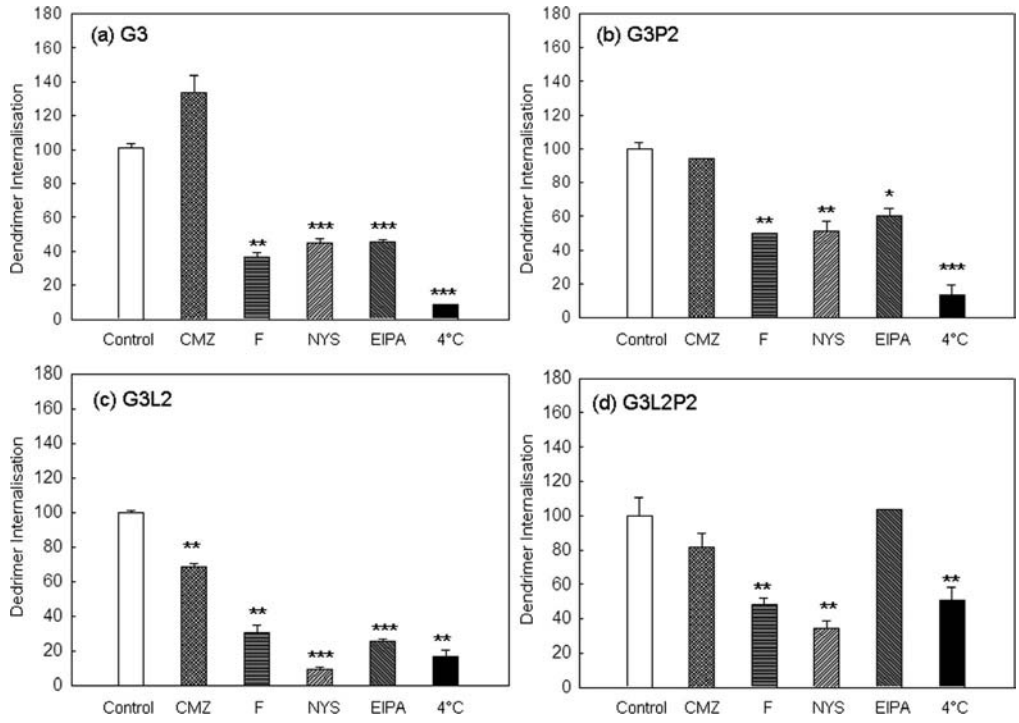

Figure 4. Effect of endocytosis and macropinocytosis inhibitors chlorpromazine 50 μM (CMZ), filipin 1 μg/mL (F), nystatin 50 μM (NYS), 5-(*N*-ethyl-*N*-isopropyl) amiloride 150 μM (EIPA), and low-temperature (4 °C) treatment on dendrimer internalization into HT-29 cells. Dendrimer accumulation in untreated cells was set at 100%. Data are given as mean ± SD of triplicate experiments. Statistical analysis was carried out using one-way analysis of variance (ANOVA) followed by Dunnett's test (* $p < 0.05$, ** $p < 0.01$, *** $p < 0.001$).

dendrimer (Figure 2c). However, there was an overlap between propranolol molecules and lauroyl moieties at a chemical shift of 1.23 ppm (Figure 2d). Therefore, the integration of peaks at chemical shift 0.89 of lauroyl moieties, 2.39−2.43 ppm of G3 dendrimer, and 6.90−7.01 ppm of propranolol were used to establish the presence of two lauroyl moieties and two propranolol molecules on the G3 dendrimer (Figure 2d).

Synthesis and Characterization of FITC-Labeled G3 PAMAM Dendrimers. ^{1}H NMR analyses indicated parent G3 PAMAM dendrimer (Figure 3a) and surface-modified dendrimers (data not shown) were successfully labeled with FITC at an average ratio of 1:1. Size distribution curves from dynamic light scattering for FITC-labeled G3 (Figure 3b), -G3P2 (Figure 3c), -G3L2 (Figure 3d), and -G3L2P2 (Figure 3e) PAMAM dendrimers yielded mean diameters of 5.18 ± 0.24, 17.00 ± 2.28, 11.81 ± 1.50, and 10.73 ± 0.01 nm, respectively. The data show that addition of the FITC label to the G3 dendrimer caused an increase of hydrodynamic diameter of approximately 1−2 nm. Addition of the lauroyl and/or propranolol groups to G3 PAMAM dendrimers resulted in an increase in hydrodynamic diameter of between 5.6 and 11.8 nm indicating successful attachment of moieties, with possible dimer and trimer formation due to chain entanglement (G3L2) and π-stacking of aromatic rings (G3P2). We also noted that the hydrodynamic diameter of G3L2P2 appeared to be less than that of G3P2, possibly a consequence of differing extents of dendrimer aggregation.

Effect of Dendrimers on Cell Viability. Studies were initially carried out to measure the viability of HT-29 cells exposed to dendrimer (2.5 μM). Viability of cells incubated with G3 was set at 100%, with viabilities of 100 ± 4.65%, 100 ± 4.65%, and 87.90 ± 2.60% observed for cells incubated with G3L2, G3P2, and G3L2P2, respectively.

Effect of Surface Modification on the Rate of Internalization of Dendrimers. The effect of surface modification on the rate of intracellular internalization of dendrimer into HT-29 cells was analyzed by flow cytometry. The rate of internalization of unmodified parent G3 dendrimer was 118.64 ± 0.22 absorbance units/hour (au/h). Addition of, on average, two lauroyl molecules to the parent dendrimer, to yield G3L2, significantly ($P < 0.05$) increased the rate of internalization to 235.74 ± 11.47 au/h. In contrast, the rate of uptake of parent dendrimer modified to possess, on average, two propranolol molecules (G3P2) at 49.10 ± 4.38 au/h, was significantly ($P < 0.001$) less than the uptake rate of G3 dendrimer. Addition of, on average, two lauroyl and two propranolol molecules to the parent dendrimer (G3L2P2) had no significant effect on the rate of internalization of modified dendrimer, 144.68 ± 6.64 au/h, compared to unmodified G3.

Effect of Endocytosis Inhibitors on the Internalization of Dendrimers. Studies were carried out using endocytosis inhibitors in order to examine the possible mechanisms of dendrimer internalization in HT-29 cells. Initial measurement of the cytotoxicity of endocytosis inhibitors showed that exposure of cells to chlorpromazine (50 μM) (*21*, *28*), filipin (1 μg/mL) (*12*), nystatin (50 μM) (*28*), and EIPA (150 μM) (*26*) resulted in cell viabilities of 74.22 ± 7.38% (compared to untreated cells at 100% viability), 78.23 ± 5.20%, 81.11 ± 6.01%, and 98.31 ± 0.61%, respectively. Confocal analyses of cells treated with endocytosis inhibitors at these concentrations revealed that cells possessed a healthy morphology, and subsequent inhibition studies were carried out using these inhibitor concentrations.

Flow cytometry studies were carried out to investigate the effects of endocytosis inhibitors on dendrimer internalization. Treatment of HT-29 cells with chlorpromazine (50 μM), an inhibitor of clathrin-dependent endocytosis, had no significant effect on the intracellular accumulation of FITC-labeled unmodified G3 dendrimer (Figure 4a), G3P2 (Figure 4b), or G3L2P2 (Figure 4d) but significantly reduced intracellular accumulation of lauroyl-modified (G3L2) dendrimer (Figure 4c). Treatment of cells with filipin (1 μg/mL) and nystatin (50 μM) (inhibitors of caveolae-dependent endocytosis) and incubation at reduced temperature (4 °C) significantly reduced intracellular accumulation of FITC-labeled unmodified G3 dendrimer and all of the dendrimer conjugates. EIPA (150 μM) (inhibitor of

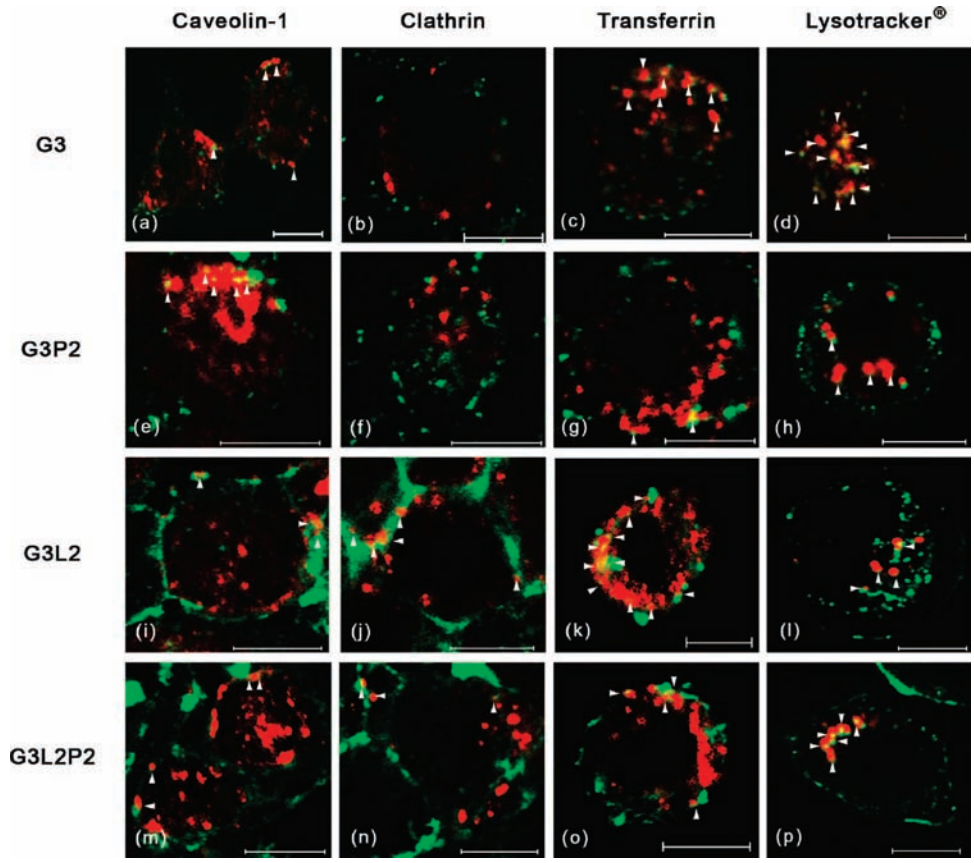

Figure 5. Subcellular localization of FITC-labeled G3 PAMAM dendrimers in HT-29 cells. HT-29 cells were incubated with the G3 dendrimers then either subjected to indirect immunostaining for caveolin-1 or clathrin or incubated with Alexa Fluor 555-transferrin or Lysotracker Red DND. Arrows indicate regions of colocalization of FITC-labeled dendrimers and endosome or lysosome marker.

macropinocytosis) significantly reduced intracellular accumulation of unmodified parent G3, G3P2, and G3L2 but had no significant effect on G3L2P2.

These findings suggest that cellular internalization of unmodified G3 dendrimer and G3P2 dendrimer conjugate occurs via both caveolae-dependent and macropinocytosis pathways. G3L2 dendrimer conjugate is internalized via clathrin-dependent, caveolae-dependent, and macropinocytosis pathways. However, internalization of G3L2P2 dendrimer conjugate appears to involve a caveolae-dependent endocytosis pathway.

Subcellular Localization of FITC Labeled-Unmodified and Surface-Modified G3 PAMAM Dendrimer in HT-29 Cells. To clarify further both the mechanism of internalization and the intracellular trafficking routes of dendrimers in HT-29 cells, subcellular colocalization of G3 PAMAM dendrimer and key endocytosis markers was investigated using confocal laser scanning microscopy. Clathrin was used as a marker of clathrin-dependent endocytosis and caveolin-1 as a marker of cavelae-dependent endocytosis. Transferrin undergoes receptor-mediated endocytosis and trafficks via the endosome pathway; therefore, Alexa Fluor 555-transferrin was used as an endosome marker. Lysotracker Red DND-99 was employed to identify lysosomes.

Unmodified FITC-labeled G3 dendrimer was localized both in the plasma membrane and intracellularly (Figure 5a,b,c,d, green). Indirect immunostaining of these cells with Alexa Fluor 555-caveolin-1 antibody showed caveolin-1 to be located predominantly in the plasma membrane, with some cytoplasmic localization (Figure 5a, red). Combining FITC and Alexa Fluor fluorescence revealed colocalization of G3 PAMAM dendrimer and caveolin-1 within the plasma membrane of HT-29 cells (Figure 5a, yellow). Confocal analyses of HT-29 cells indirectly immunostained with anticlathrin antibody showed fluorescence to be predominantly located at the plasma membrane (Figure 5b, red). However, negligible colocalization between FITC-labeled G3 dendrimer and clathrin were observed (Figure 5b). Alexa Fluor 555−transferrin was located both within the plasma membrane and intracellularly (Figure 5c, red). Areas of colocalization between G3 dendrimer and transferrin were observed both intracellularly and within the plasma membrane (Figure 5c, yellow). When HT-29 cells were incubated with FITC-labeled G3 dendrimer, sectioning in the *z*-plane indicated that fluorescence was associated with intracellular vesicle-like structures. Lysotracker Red DND was localized intracellularly (Figure 5d, red). Combining FITC and Alexa Fluor fluorescence of HT-29 cells incubated with FITC-labeled unmodified G3 dendrimer and Lysotracker Red DND-99 clearly revealed overlapping fluorescence of dendrimer and lysosome probe (Figure 5d, yellow).

The confocal images of HT-29 cells incubated with FITC-labeled G3P2 dendrimer revealed that fluorescence was associated both with the plasma membrane and with intracellular vesicle-like structures (Figure 5e, f, g, h, green), as was observed for FITC-labeled unmodified G3 dendrimer. FITC-labeled G3P2 dendrimer was found to colocalize with caveolin-1 (Figure 5e, yellow). There was negligible colocalization between this surface-modified G3 dendrimer and clathrin (Figure 5f), but colocalization with Alexa Fluor 555-transferrin (Figure 5g, yellow) and with Lysotracker Red DND (Figure 5h, yellow) was observed.

FITC-labeled G3L2 dendrimer localized at the plasma membrane, with some intracellular fluorescence observed (Figure 5i, j, k, l, green). This modified dendrimer colocalized with caveolin-1 (Figure 5i, yellow) and with clathrin (Figure 5j, yellow). These subcellular colocalization results are in

agreement with our finding that nystatin, filipin, and chlorpromazine reduce intracellular internalization (Figure 4c). FITC-labeled G3L2 dendrimer colocalized with Alexa Fluor 555−transferrin (Figure 5k, yellow) and was also observed to colocalize with Lysotracker Red DND (Figure 5l, yellow).

Incubation of HT-29 cells with FITC-labeled G3L2P2 dendrimer revealed FITC-associated fluorescence at the plasma membrane (Figure 5m, n, o, p, green). This modified dendrimer colocalized with caveolin-1 (Figure 5m, yellow) and with clathrin (Figure 5n yellow). Our studies revealed that FITC-labeled G3L2P2 dendrimer also colocalized with Alexa Fluor 555−transferrin (Figure 5o, yellow) and Lysotracker Red DND (Figure 5p, yellow).

All dendrimers and dendrimer conjugates studied are trafficked to lysosomes. In order to determine the effect of surface modification on the extent of dendrimer accumulation in lysosomes, semiquantitative analysis was carried out using *ImageJ* to obtain the overlap coefficient, which defines the extent of true 3-dimensional colocalization. The level of colocalization of G3 dendrimer with the lysosomal marker Lysotracker Red DND (overlap coefficient 0.8 ± 0.05) was significantly ($P < 0.0001$) higher than the colocalization levels observed with Lysotracker Red DND and G3P2 (0.5 ± 0.04), G3L2 (0.4 ± 0.07), or G2L2P2 (0.6 ± 0.08), suggesting that surface modification influences the extent of dendrimer trafficking to lysosomes.

DISCUSSION

Dendrimers are an attractive nanoparticulate drug delivery system which have been shown to significantly enhance delivery of several drugs such as propranolol, naproxen, terfenadine, 5-aminosalicylic acid, 5-fluorouracil, cisplatin, and doxorubicin (*2, 7, 8, 29*−*32*). However, little is known about the precise cellular mechanisms of dendrimer uptake and how modification of the dendrimer surface affect the internalization mechanism(s).

Cellular dendrimer internalization has been reported to involve both caveolae- and clathrin-mediated endocytosis (*11*−*13, 33*). In the HT-29 human intestinal adenocarcinoma cell line, confocal laser scanning microscopy revealed that caveolae and clathrin-1 were expressed in a manner consistent with the distribution patterns reported previously in HT-29 cells (*19*). All dendrimers studied colocalized with caveolin-1, as has been observed with the dendrimer−DNA complex in EAhy 926 cells (*33*), while G3L2 and G3L2P2 were found to colocalize with clathrin-1, consistent with our flow cytometry findings. The dendrimers used in the present study are cationic in nature, and several studies suggest that clathrin-dependent endocytosis may represent one of the most important pathways of internalization for several cationic lipoplexes in COS7, A549, and HeLa cells (*34*−*36*).

Subcellular colocalization studies revealed that all dendrimers colocalized with transferrin, consistent with studies that report that both FITC-labeled cationic and anionic PAMAM dendrimers (G2 and G1.5) colocalized with early endosomal antigen-1 (EEA-1) in Caco-2 cells (*11*) and with studies showing gold-labeled G3 PAMAM dendrimer localized into endosomes in Caco-2 cells (*37*).

To establish the effects of surface modification on the rate of intracellular internalization of dendrimers into HT-29 cells, flow cytometry studies were carried out. Associated with surface modification is a change in the size of dendrimer nanoparticles. These studies revealed no correlation between dendrimer size and either the rate or internalization mechanism of dendrimer uptake into HT-29 cells. These findings can be explained by the fact that linked with a change in size is a concomitant change in physicochemical characteristics, including charge and hydrophobicity, which have important roles in influencing interaction of nanoparticles with the cell surface.

Surface modification by the addition of, on average, two lauroyl molecules to G3 dendrimer significantly increased the rate of internalization. In addition, these studies revealed that G3 is taken up by both caveolae-mediated endocytosis and macropinocytosis. These results are in agreement with a reduction in cell-associated Orgeon green labeled G4 PAMAM dendrimer fluorescence observed in B16F10 murine melanoma cells in the presence of methyl-β-cyclodextrin (*13*) and the significant inhibition of uptake of second-generation dendrimer modified with 18 aminolaevulinic acid uptake in the presence of EIPA in PAM 212 cells (*27*). However, modification of G3 to G3L2 resulted in dendrimer internalization via clathrin-mediated endocytosis, as well as via caveolae-mediated endocytosis and macropinocytosis. These findings are consistent with those reported in Caco-2 cells in which the apparent permeability of G3 dendrimer modified with nine lauroyl moieties was reduced by inhibitors of clathrin-mediated endocytosis and caveolae-mediated endocytosis (Rachaneekorn Jevprasaphant, Antony D'Emanuele, David Attwood, Jeffrey Penny, unpublished results). Thus, modification of parent dendrimer with lauroyl moieties appears to offer an additional internalization pathway for G3 dendrimer uptake into HT-29 cells, and it is feasible that cellular uptake via an additional pathway has the potential to increase the rate of nanoparticle delivery.

The rate of intracellular internalization of G3 dendrimer possessing, on average, two propranolol molecules into HT-29 cells was significantly lower than that of unmodified G3 dendrimer. Furthermore, the rate-enhancing effect of lauroyl moieties on dendrimer uptake appeared to be negated in dendrimer possessing both lauroyl and propranolol moieties (G3L2P2). Multiple pathways are involved in the uptake of dendrimer and modified dendrimers into HT-29 cells, and the precise mechanism by which propranolol reduces the rate of dendrimer internalization is unknown. The plasma membrane is an extremely heterogeneous environment, possessing microenvironments with lipid, protein, and receptor profiles that differ significantly compared to the bulk of the plasma membrane. It is likely that the rate of dendrimer internalization is influenced by the physicochemical characteristics of the nanoparticles and the differential abilities of dendrimers to interact with the heterogeneous domains and microenvironments of the plasma membrane.

All dendrimers and dendrimer conjugates studied are trafficked into lysosomes, acidic organelles rich in hydrolytic enzymes. These findings are consistent with colocalization of FITC-labeled G1.5 and G2 PAMAM dendrimers with lysosome-associated membrane protein (LAMP-1) in Caco-2 cells (*11*). It is important to determine the relationship between surface modification and the extent of lysosome accumulation, since exposure to a hydrolytic environment may impact on the efficacy of dendrimer-mediated drug delivery. Semiquantitative colocalization studies revealed addition of lauroyl moieties to G3, to yield G3L2, resulting in significantly less modified dendrimer being trafficked into lysosomes. Similarly, semiquantitative colocalization studies revealed that, as with G3L2, significantly less G3P2 and G3L2P2 were associated with lysosomes compared to unmodified G3. It therefore appears that surface modification of G3 dendrimer influences not only the rate of intracellular accumulation in HT-29 cells, but also the extent of dendrimer accumulation within lysosomes.

CONCLUSION

Studies to elucidate the mechanisms and pathways of dendrimer internalization and trafficking are important, as they may

help define how surface modification may enhance cellular uptake of nanoparticulate dendrimer−drug complexes and potentially increase drug delivery across physiological cell barriers. The present study provides evidence that the surface properties of dendrimers influence the initial mode of dendrimer internalization in HT-29 cells. Modification of parent G3 dendrimer with lauroyl moieties increases the rate of intracellular uptake, a finding that could be exploited to increase the rate of oral drug delivery. In addition, modification of the nanoparticles with lauroyl moieties appears to reduce the extent of lysosomal accumulation, suggesting potentially less exposure of the dendrimer conjugate to the highly acidic lysosomal environment and hydrolytic enzymes, a potentially important issue when considering delivery of acid-labile drugs or drug conjugates. Thus, dendrimer modification with lauroyl chains is attractive, since it enhances the internalization kinetics of modified dendrimer into human intestinal epithelial cells and may have the potential for improving drug delivery via the oral route.

ACKNOWLEDGMENT

The authors would like to thank the Ministry of Science and Technology in Thailand for its financial support and Lesley Wright for secretarial assistance.

LITERATURE CITED

(1) D'Emanuele, A., Attwood, D., Abu-Rmaileh, R. (2003) Dendrimers, in *Encyclopaedia of Pharmaceutical Technology*, pp 1−21, Marcel Dekker, New York.

(2) D'Emanuele, A., Jevprasesphant, R., Penny, J., and Attwood, D. (2004) The use of a dendrimer-propranolol prodrug to bypass efflux transporters and enhance oral bioavailability. *J. Controlled Release 95*, 447–453.

(3) Jevprasesphant, R., Penny, J., Jalal, R., Attwood, D., McKeown, N. B., and D'Emanuele, A. (2003) The influence of surface modification on the cytotoxicity of PAMAM dendrimers. *Int. J. Pharm. 252*, 263–6.

(4) Jevprasesphant, R., Penny, J., Attwood, D., McKeown, N. B., and D'Emanuele, A. (2003) Engineering of dendrimer surfaces to enhance transepithelial transport and reduce cytotoxicity. *Pharm. Res. 20*, 1543–50.

(5) Kitchens, K. M., Kolhatkar, R. B., Swaan, P. W., Eddington, N. D., and Ghandehari, H. (2006) Transport of poly(amidoamine) dendrimers across Caco-2 cell monolayers: influence of size, charge and fluorescent labeling. *Pharm. Res. 23*, 2818–26.

(6) Kolhatkar, R. B., Kitchens, K. M., Swaan, P. W., and Ghandehari, H. (2007) Surface acetylation of polyamidoamine (PAMAM) dendrimers decreases cytotoxicity while maintaining membrane permeability. *Bioconjugate Chem. 18*, 2054–2060.

(7) Najlah, M., Freeman, S., Attwood, D., and D'Emanuele, A. (2007) In vitro evaluation of dendrimer prodrugs for oral drug delivery. *Int. J. Pharm. 336*, 183–90.

(8) Najlah, M., Freeman, S., Attwood, D., and D'Emanuele, A. (2007) Synthesis and assessment of first-generation polyamidoamine dendrimer prodrugs to enhance the cellular permeability of P-gp substrates. *Bioconjugate Chem. 18*, 937–46.

(9) El-Sayed, M., Rhodes, C. A., Ginski, M., and Ghandehari, H. (2003) Transport mechanism(s) of poly (amidoamine) dendrimers across Caco-2 cell monolayers. *Int. J. Pharm. 265*, 151–7.

(10) El-Sayed, M., Ginski, M., Rhodes, C., and Ghandehari, H. (2002) Transepithelial transport of poly(amidoamine) dendrimers across Caco-2 cell monolayers. *J. Controlled Release 81*, 355–65.

(11) Kitchens, K. M., Foraker, A. B., Kolhatkar, R. B., Swaan, P. W., and Ghandehari, H. (2007) Endocytosis and interaction of poly (amidoamine) dendrimers with Caco-2 cells. *Pharm. Res. 24*, 2138–45.

(12) Kitchens, K. M., Kolhatkar, R. B., Swaan, P. W., and Ghandehari, H. (2008) Endocytosis inhibitors prevent poly(amidoamine) dendrimer internalization and permeability across Caco-2 cells. *Mol. Pharm. 5*, 364–9.

(13) Seib, F. P., Jones, A. T., and Duncan, R. (2007) Comparison of the endocytic properties of linear and branched PEIs, and cationic PAMAM dendrimers in B16f10 melanoma cells. *J. Controlled Release 117*, 291–300.

(14) Maziere, J. C., Maziere, C., Emami, S., Noel, B., Poumay, Y., Ronveaux, M. F., Chastre, E., Porte, H., Barbu, V., Biade, S., et al. (1992) Processing and characterization of the low density lipoprotein receptor in the human colonic carcinoma cell subclone HT29−18: a potential pathway for delivering therapeutic drugs and genes. *Biosci. Rep. 12*, 483–94.

(15) Wirth, M., Hamilton, G., and Gabor, F. (1998) Lectin-mediated drug targeting: quantification of binding and internalization of Wheat germ agglutinin and Solanum tuberosum lectin using Caco-2 and HT-29 cells. *J. Drug Targeting 6*, 95–104.

(16) Phan, H. H., Barakat, A., Lefevre, C., Boissard, C., and Rosselin, G. (1992) Processing of vasoactive intestinal peptide and transferrin in human cancerous colonic cells. *Peptides 13*, 53–61.

(17) Sonne, O. (1985) Receptor-mediated degradation and internalization of insulin in the adenocarcinoma cell line HT-29 from human colon. *Mol. Cell. Endocrinol. 39*, 39–48.

(18) Waters, C. M., Wells, C. L., and Dunny, G. M. (2003) The aggregation domain of aggregation substance, not the RGD motifs, is critical for efficient internalization by HT-29 enterocytes. *Infect. Immun. 71*, 5682–9.

(19) Uotsu, N., Nishikawa, A., Watanabe, T., Ohyama, T., Tonozuka, T., Sakano, Y., and Oguma, K. (2006) Cell internalization and traffic pathway of Clostridium botulinum type C neurotoxin in HT-29 cells. *Biochim. Biophys. Acta 1763*, 120–8.

(20) Zhang, Y., Hu, Z., Ye, M., Pan, Y., Chen, J., Luo, Y., He, L., and Wang, J. (2007) Effect of poly(ethylene glycol)-block-polylactide nanoparticles on hepatic cells of mouse: low cytotoxicity, but efflux of the nanoparticles by ATP-binding cassette transporters. *Eur. J. Pharm. Biopharm. 66*, 268–80.

(21) Wang, L. H., Rothberg, K. G., and Anderson, R. G. (1993) Mis-assembly of clathrin lattices on endosomes reveals a regulatory switch for coated pit formation. *J. Cell Biol. 123*, 1107–17.

(22) Takahashi, Y., and Smith, J. D. (1999) Cholesterol efflux to apolipoprotein AI involves endocytosis and resecretion in a calcium-dependent pathway. *Proc. Natl. Acad. Sci. U.S.A. 96*, 11358–63.

(23) Lobie, P. E., Sadir, R., Graichen, R., Mertani, H. C., and Morel, G. (1999) Caveolar internalization of growth hormone. *Exp. Cell Res. 246*, 47–55.

(24) Orlandi, P. A., and Fishman, P. H. (1998) Filipin-dependent inhibition of cholera toxin: evidence for toxin internalization and activation through caveolae-like domains. *J. Cell Biol. 141*, 905–15.

(25) Manunta, M., Tan, P. H., Sagoo, P., Kashefi, K., and George, A. J. (2004) Gene delivery by dendrimers operates via a cholesterol dependent pathway. *Nucleic Acids Res. 32*, 2730–9.

(26) Huth, U. S., Schubert, R., and Peschka-Suss, R. (2006) Investigating the uptake and intracellular fate of pH-sensitive liposomes by flow cytometry and spectral bio-imaging. *J. Controlled Release 110*, 490–504.

(27) Battah, S., Balaratnam, S., Casas, A., O'Neill, S., Edwards, C., Batlle, A., Dobbin, P., and MacRobert, A. J. (2007) Macromolecular delivery of 5-aminolaevulinic acid for photodynamic therapy using dendrimer conjugates. *Mol. Cancer Ther. 6*, 876–85.

(28) Inal, J., Miot, S., and Schifferli, J. A. (2005) The complement inhibitor, CRIT, undergoes clathrin-dependent endocytosis. *Exp. Cell Res. 310*, 54–65.

(29) Najlah, M., Freeman, S., Attwood, D., and D'Emanuele, A. (2006) Synthesis, characterization and stability of dendrimer prodrugs. *Int. J. Pharm. 308*, 175–82.

(30) Wiwattanapatapee, R., Lomlim, L., and Saramunee, K. (2003) Dendrimers conjugates for colonic delivery of 5-aminosalicylic acid. *J. Controlled Release 88*, 1–9.

(31) Zhuo, R. X., Du, B., and Lu, Z. R. (1999) In vitro release of 5-fluorouracil with cyclic core dendritic polymer. *J. Controlled Release 57*, 249–57.

(32) Malik, N., Evagorou, E. G., and Duncan, R. (1999) Dendrimer-platinate: a novel approach to cancer chemotherapy. *Anticancer Drugs 10*, 767–76.

(33) Manunta, M., Nichols, B. J., Tan, P. H., Sagoo, P., Harper, J., and George, A. J. (2006) Gene delivery by dendrimers operates via different pathways in different cells, but is enhanced by the presence of caveolin. *J. Immunol. Methods 314*, 134–46.

(34) Zuhorn, I. S., Kalicharan, R., and Hoekstra, D. (2002) Lipoplex-mediated transfection of mammalian cells occurs through the cholesterol-dependent clathrin-mediated pathway of endocytosis. *J. Biol. Chem. 277*, 18021–8.

(35) Rejman, J., Bragonzi, A., and Conese, M. (2005) Role of clathrin- and caveolae-mediated endocytosis in gene transfer mediated by lipo- and polyplexes. *Mol. Ther. 12*, 468–74.

(36) Rejman, J., Conese, M., and Hoekstra, D. (2006) Gene transfer by means of lipo- and polyplexes: role of clathrin and caveolae-mediated endocytosis. *J. Liposome Res. 16*, 237–47.

(37) Jevprasesphant, R., Penny, J., Attwood, D., and D'Emanuele, A. (2004) Transport of dendrimer nanocarriers through epithelial cells via the transcellular route. *J. Controlled Release 97*, 259–67.

BC8002343

Bioconjugate Chemistry 20th Anniversary

Subscriber access provided by SHEMYAKIN-OVCHINNIKOV INST

Article

An Improved Cell-Penetrating, Caspase-Activatable, Near-Infrared Fluorescent Peptide for Apoptosis Imaging

Dustin Maxwell, Qing Chang, Xu Zhang, Edward M. Barnett, and David Piwnica-Worms

Bioconjugate Chem., **2009**, 20 (4), 702-709• DOI: 10.1021/bc800516n • Publication Date (Web): 30 March 2009

Downloaded from http://pubs.acs.org on May 15, 2009

More About This Article

Additional resources and features associated with this article are available within the HTML version:

- Supporting Information
- Access to high resolution figures
- Links to articles and content related to this article
- Copyright permission to reproduce figures and/or text from this article

View the Full Text HTML

ACS Publications
High quality. High impact.

Bioconjugate Chemistry is published by the American Chemical Society. 1155 Sixteenth Street N.W., Washington, DC 20036

An Improved Cell-Penetrating, Caspase-Activatable, Near-Infrared Fluorescent Peptide for Apoptosis Imaging

Dustin Maxwell,[†] Qing Chang,[‡] Xu Zhang,[‡] Edward M. Barnett,[‡] and David Piwnica-Worms*[,†,§]

Molecular Imaging Center, Mallinckrodt Institute of Radiology, Department of Ophthalmology and Visual Sciences, Department of Developmental Biology, Washington University Medical School, St. Louis, Missouri 63110. Received July 14, 2008

Apoptosis is required for normal cellular homeostasis, and deregulation of the apoptotic process is implicated in various diseases. Previously, we developed a cell-penetrating near-infrared fluorescence (NIRF) probe based on an activatable strategy to detect apoptosis-associated caspase activity in vivo. This probe consisted of a cell-penetrating Tat peptide conjugated to an effector recognition sequence (DEVD) that was flanked by a fluorophore−quencher pair (Alexa Fluor 647 and QSY 21). Once exposed to effector caspases, the recognition sequence was cleaved, resulting in separation of the fluorophore−quencher pair and signal generation. Herein, we present biochemical analysis of a second generation probe, KcapQ, with a modified cell-penetrating peptide sequence (KKKRKV). This modification resulted in a probe that was more sensitive to effector caspase enzymes, displayed an unexpectedly higher quenching efficiency between the fluorophore−quencher pair, and was potentially less toxic to cells. Assays using recombinant caspase enzymes revealed that the probe was specific for effector caspases (caspase 3 > 7 > 6). Analysis of apoptosis in HeLa cells treated with doxorubicin showed probe activation specific to apoptotic cells. In a rat model of retinal neuronal excitotoxicity, intravitreal injection of *N*-methyl-D-aspartate (NMDA) induced apoptosis of retinal ganglion cells (RGCs). Eyecup and retinal flat-mount images of NMDA-pretreated animals injected intravitreally with KcapQ using a clinically applicable protocol showed specific and widely distributed cell-associated fluorescence signals compared to untreated control animals. Fluorescence microscopy images of vertical retinal sections from NMDA-pretreated animals confirmed that activated probe was predominantly localized to RGCs and colocalized with TUNEL labeling. Thus, KcapQ represents an improved effector caspase-activatable NIRF probe for enhanced noninvasive analysis of apoptosis in whole cells and live animals.

INTRODUCTION

Apoptosis is a mode of programmed cell death critical for maintaining tissue homeostasis in multicellular organisms (*1, 2*). Deregulation of the apoptosis pathway can lead to a variety of debilitating diseases including cancer. Cells undergoing apoptosis show characteristic morphological and biochemical features, including membrane blebbing, chromatin and nuclear condensation, and formation of membrane bound bodies (apoptotic bodies) (*3, 4*). Biochemical changes include DNA fragmentation, translocation of phosphatidylserine (PS) from the cytoplasmic to the extracellular leaflet of the plasma membrane, and protease activation.

Several strategies have been attempted to monitor the early stages of apoptosis (*5*−*8*). One common approach is to target exposed PS on the outer leaflet of the plasma membrane with annexin V (*5, 9*). Annexin V is a phospholipid binding protein with a high affinity toward PS. Conjugated radionuclides, magnetic nanoparticles, or fluorescent reporters to annexin V have been developed to monitor apoptosis. However, annexin V alone cannot distinguish apoptotic (membrane intact) from necrotic (membrane damaged) tissues in vivo. This problem is resolved in cellulo by using a secondary marker of membrane integrity, e.g., propidium iodide, but this strategy is rarely implemented properly in vivo. An alternative approach is to target a more specific mediator of the apoptotic process, such as caspase activation (*2, 10*−*12*). Caspases are a family of intracellular cysteine proteases pivotal for the initiation and execution of apoptosis. To date, 13 caspases have been identified in mammals, which can be divided into 2 groups, initiator and effector caspases, based on the lengths of their N-terminal prodomains. Initiator caspases contain prodomains of over 100 amino acids compared to the shorter prodomains of 30 amino acids found in effector caspases. Canonically, caspases exist as inactive zymogens in cells until pro-apoptotic signals activate initiator caspases. Once activated, the initiator caspases cleave downstream effector caspases, resulting in a proteolytic cascade that leads to cell death.

All caspases cleave the peptide bond C-terminal to aspartic acid residues. Initiator caspase recognize the WEHD/(L/V)EXD sequences, whereas effector caspases (caspase 3, 6, and 7) recognize the DEXD motif (*13, 14*). Several imaging probes have been developed that detect caspase activity, including examples of imaging probes that incorporate fluorescence resonance energy transfer (FRET) or self-quenching strategies, which result in fluorescence following activation by caspases (*15*−*19*). While these strategies minimize fluorescence in the native quenched state and amplify signal upon the enzyme-mediated release of the fluorophore, further improvements in delivery to the cell interior and pharmacokinetic properties of the agents are desired.

Recently, we reported the chemical and biochemical characterization of a first in class, small cell-penetrating apoptosis imaging probe, TcapQ (*20, 21*). Herein, we describe a second-

* Correspondence to David Piwnica-Worms, M.D., Ph.D., Mallinckrodt Institute of Radiology, Washington University Medical School, 510 S. Kingshighway Blvd., Box 8225, St. Louis, MO 63110, Tel: 314-362-9356, Fax: 314-362-0152, Email: piwnica-wormsd@mir.wustl.edu.

[†] Molecular Imaging Center, Mallinckrodt Institute of Radiology.

[‡] Department of Ophthalmology and Visual Sciences.

[§] Department of Developmental Biology.

10.1021/bc800516n CCC: $40.75 © 2009 American Chemical Society
Published on Web 03/30/2009

generation apoptosis imaging probe, KcapQ, that contains a modified all D-amino acid cell-penetrating peptide sequence and an L-amino acid cleavable domain. A lysine-arginine-rich cell-penetrating sequence (KKKRKV) is now responsible for cellular uptake, likely through macropinocytosis and/or a non-receptor-mediated endocytosis pathway (*22*−*28*). Flanked by a fluorophore (Alexa Fluor 647) and quencher (QSY 21) pair, the cleavable domain of this probe, DEVD, is specifically designed to recognize effector caspases. Upon recognition of effector caspases, the probe is internally cleaved, separating the fluorophore from the quencher. In this study, we examined the chemical/biochemical characteristics of KcapQ and evaluated its potential as an imaging agent to monitor retinal neuronal apoptosis in an animal model.

EXPERIMENTAL PROCEDURES

Synthesis and Characterization. Standard solid-phase N-α-Fmoc chemistry was used to synthesize the apoptosis probe KcapQ and the noncleavable probe D-KcapQ (Tufts University Peptide Synthesis Core, Boston, MA). Each probe contained an all-D cell-penetrating peptide comprising the SV40 TAg nuclear localization signal (KKKRKV) (*23*) linked to a cleavage sequence consisting of L- or D-amino acids (GKDEVDAPC) for the KcapQ and D-KcapQ, respectively. The N-terminus was acetylated and resin coupling afforded C-terminus amidation of the final product. For conjugation, in a small reaction vial, 1 mL of 2% hydrazine in DMF was added to 20 mg of peptide on resin to selectively remove the single Dde group protecting the lysine N-terminal of the DEVD sequence (*20*). After 20 min, the supernatant was decanted and analyzed by UV−vis spectroscopy to confirm removal of the Dde protecting group. This step was repeated until selective deprotection of the peptide was confirmed. To deprotected resin, 2 mol equiv of QSY21 succimidyl ester in DMF was added and the conjugation reaction allowed to proceed for 4−5 h. Peptide was cleaved and deprotected from resin using a trifluoroacetic acid (TFA) cleavage mixture [stock solution: 10 mL trifluoroacetic acid, phenol (0.75 g), thioanisole (0.5 mL), deionized water (0.5 mL), and ethanedithiol (0.25 mL)] followed by precipitation in cold ether. QSY21-labeled peptide was then isolated by centrifuging the sample (2000 *g*) and the collected pellet dried under argon (Ac-KKKRKVGK(QSY21)DEVDAPC-NH_2; *m*/*z* 2404.1; calcd 2404.2). Alexa Fluor 647 maleimide (Invitrogen) was dissolved in 1 mL of 0.5 M PBS buffer and added to the QSY21-labeled peptide. Conjugation to the C-terminal cysteine residue was allowed to proceed for 2 h. The final product, KcapQ, was purified using reverse-phase HPLC using a flow rate of 1 mL/min and a 5%/95% to 40%/60% acetonitrile/0.1% TFA/water/0.1% TFA gradient over 40 min (t_R = 17.3 min). KcapQ was collected by measuring absorbance at 214 and 600 nm to obtain >98% purity (KcapQ: Ac-KKKRKVGK(QSY21)DEVDAPC(AF647)-NH_2) and characterized by MALDI mass spectrometry (*m*/*z* 3384.6; calcd 3386.0). KcapQ was then lyophilized, dissolved in water, and stored at −20 °C.

Quantitative amino acid analysis (Texas A&M University Protein Chemistry Laboratory, College Station, TX) was used to calculate the stock concentration of KcapQ (203 μM). UV−vis spectra were acquired by diluting KcapQ in water and scanning from 500 to 900 nm. KcapQ molecular extinction coefficient was calculated using the pronounced blue-shifted peak at 605 nm (112 000 M^{-1}). All KcapQ and D-KcapQ working concentrations were prepared using this molecular extinction coefficient.

Toxicity Studies. HeLa cells were grown at 37 °C in an atmosphere of 5% CO_2 in DMEM (GIBCO, Grand Island, NY) supplemented with L-glutamine (1%) and heat-inactivated fetal bovine serum (10%). Cells were seeded into a 96-well plate at a concentration of 1×10^5 HeLa cells per well. KcapQ or TcapQ was added at concentrations of 0.01 μM, 0.1 μM, 1 μM, 5 μM, 10 μM, and 25 μM in triplicate. Background samples of culture medium and wells with cells in medium only served as controls. Toxicity assays were performed using cellTiter 96 AQueous nonradioactive cell proliferation assay (Promega, Madison, WI). At 24 and 48 h, 20 μL of a 1:20 dilution of MTS [3-(4,5-dimethylthiazol-2-yl)-5-(3-carboxymethoxyphenyl)-2-(4-sulfophenyl)-2*H*-tetrazolium] solution was added to each well and placed in an incubator for 1 h at 37 °C in a humidified, 5% CO_2 atmosphere. After 1 h, the absorbance at 490 nm was recorded using a colorimetric plate reader. Absorbance values from background control wells containing media only were subtracted from the all other absorbance values. Cell viability was calculated as percent untreated cells.

Biochemical Analysis of KcapQ. Enzyme assays were performed utilizing a fluorescence spectrophotometer (Cary Eclipse, Varian, Palo Alto, CA). KcapQ (0.5 μM, final concentration) was added to 450 μL of caspase buffer (100 mM NaCl, 50 mM HEPES, 10 mM DTT, 1 mM EDTA, 10% glycerol, and 0.1% CHAPS, pH 7.4) in a cuvette at 37 °C. Recombinant caspases 1−10 (CalBiochem, San Diego, CA) (5 U caspases 1−2, 4−10, and 50 U of caspase 3) were incubated in buffer for 20 min at 37 °C. Fluorescence intensity was monitored over time with measurements recorded every 15 s using a 5 nm slit width at 647 nm (excitation) and a 5 nm slit width at 665 nm (emission). Background fluorescence of probe alone was subtracted from assay fluorescence units, and all data were normalized to milligram of protein for each enzyme.

Kinetic Analysis of KcapQ Cleavage. Inhibition assays were performed using the reversible inhibitor DEVD-CHO (Calbiochem, LeJolla, CA). Caspase 3 (50 U) and caspase 7 (1 U) were incubated at 37 °C in 450 μL of caspase buffer with increasing inhibitor concentrations for 40 min. After 40 min, KcapQ (0.5 μM) was added to the mixture, and fluorescence intensity at 665 nm was monitored over 20 min at 37 °C. Linear regression analysis was used to calculate the cleavage rates at each inhibitor concentration. $EC_{50(i)}$ values were determined by nonlinear regression analysis. Apparent K_m values for KcapQ for each enzyme were calculated using the Cheng-Pruschoff relationship: $EC_{50(i)} = K_i(1 + [S])/K_m)$, where [S] is concentration of the KcapQ substrate (*29*). K_i values were calculated by determining the $EC_{50(i)}$ values of the fluorogenic substrate SUBII (Calbiochem) with 10 U of caspase-3 ($K_{i,cas3} = 0.08$) or 1 U of Caspase-7 ($K_{i,cas7} = 0.23$) (*21*). Apparent K_{cat} values were calculated using the equation $K_{cat} = V(K_m + [S]/[E][S])$, where V is the initial rate of cleavage, [S] is the concentration of substrate, and [E] is the concentration of enzyme.

Microscopy Images. HeLa cells were added to a 96-well plate at a concentration of 10 000 cells per well. After 24 h, culture media were replaced with media containing doxorubicin (10 μM final concentration) for 6 h. The cells were gently washed with PBS buffer, and KcapQ or D-KcapQ in MEBSS at a final concentration of 0.5 μM were added to wells for 20 min at 37 °C. All fluorescence images were captured using the InCell fluorescence microscopy imaging system (GE Healthcare) using a CY5 filter set at 20× magnification. Each condition was performed in triplicate, and 10 fields of view were captured for each well. All images were set to the same background level and brightness/contrast setting for analysis using *Image J* software.

Intravitreal Injections. Protocols for all experiments involving animals were approved by the Washington University in St. Louis Institutional Animal Care and Use Committee. Norway rats were anesthetized by intraperitoneal injection of 1 mL/kg of a solution containing 1 mL ketamine (100 mg/mL) and 0.15

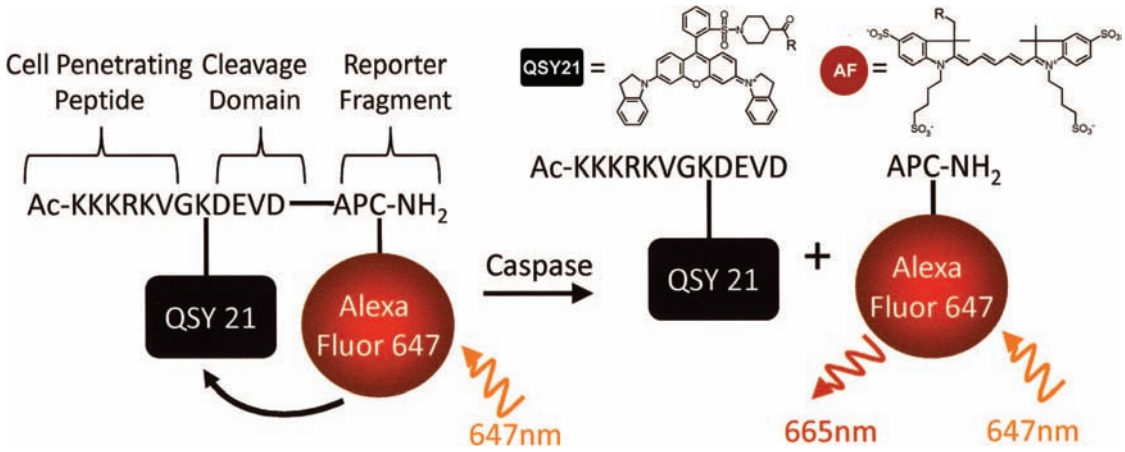

Figure 1. Schematic of KcapQ activation following cleavage by effector caspases. The DEVD cleavable sequence is flanked by an absorber (QSY21) and fluorophore (Alexa Fluor 647), which silence the reporter through intramolecular quenching. The cell-penetrating peptide sequence enables transport into the cell interior. Upon activation by caspase, the fluorophore is released inside target cells. The putative structure of Alexa Fluor 647 is from ref 45.

mL xylazine (100 mg/mL). The pupil was dilated with 1% tropicamide drops and intravitreal injections were performed using a 10 μL Hamilton syringe. To induce apoptosis in retinal ganglion cells, a 30 gauge syringe needle penetrated the sclera 2 mm posterior to the limbus and 5 μL of a 10 μM solution of *N*-methyl-D-aspartate (NMDA) was injected into the vitreous of the left eye. PBS injected into the right eye of each animal served as a control. After 16 h, 5 μL of a 200 μM solution of KcapQ or D-KcapQ in PBS was injected into the vitreous humor of each eye. At 2 h postinjection, the animals were euthanized and the globes enucleated. Experiments were performed in triplicate.

Preparation of Retina Tissue Sections. Eye cups were prepared from the harvested eye globes by removing the anterior segment (cornea and lens). Fluorescence images of the intact eye cups were collected using an Olympus macroscope equipped with a CY5 filter set. Images were acquired for 8 s. Immediately after fluorescence imaging, flat mounts were prepared by mounting the detached retina on a coverslip. Fresh retinal flat mounts were analyzed using an inverted Zeiss Axiovert 200 laser scanning confocal microscope equipped with a 633 nm He/Ne laser and a 650 nm long-pass filter to localize KcapQ. All images were recorded and target cells counted using a 40× objective.

TUNEL Labeling. Posterior ocular segments were fixed in 4% paraformaldehyde and paraffin embedded using standard techniques performed by the Tissue Support Center, Washington University. For TUNEL staining and confocal microscopy, vertical retinal sections (4 μm thick) were cut, deparaffinized, rehydrated, and then blocked with 10% normal donkey serum for 30 min. Tissue sections were washed three times with TBST (Tris-buffered saline with 0.1% Tween 20). Ethanol (70% v/v) was added to the sections and allowed to sit at −20 °C for 1 h. After 1 h, the sections were again washed with TBST and incubated with DNA-labeling solution (APO-BrdU TUNEL Assay Kit, Invitrogen) overnight at 37 °C. At the end of the incubation period, samples were rinsed with TBST and Alexa Fluor 488 dye-labeled anti-BrdU antibody was added to the tissue section. Samples were incubated overnight before analysis using confocal microscopy. TUNEL staining was detected with a Zeiss Axiovert 200 laser scanning confocal microscope with a 488 nm argon laser and a 520−560 nm bandpass filter. KcapQ localization was detected on the same sections with the 633 nm He/Ne laser and a 650 nm long-pass filter. All images were recorded using a 40× objective.

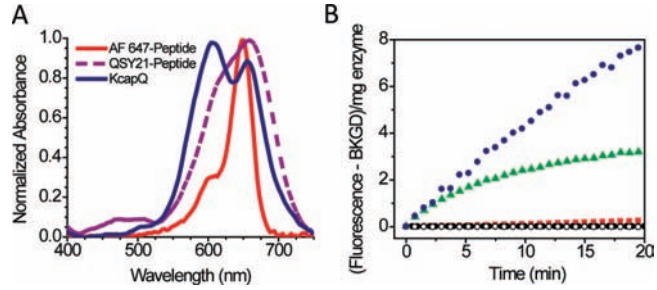

Figure 2. Chemical and biochemical characterization of KcapQ. (A) UV−vis spectra of KcapQ (blue line), QSY21-peptide (dash line), and Alexa Fluor 647-peptide (red line). Notice the increase in absorbance at 605 nm. (B) Recombinant enzyme assays of KcapQ normalized to milligrams of caspase for each enzyme (blue • caspase 3; green ▲ caspase 7; red ■ caspase 6; black • caspase 9; ○ D-KcapQ). Assays with effector caspases resulted in KcapQ activation, whereas assays with initiator caspases showed no proteolytic activity toward KcapQ.

RESULTS

KcapQ is a small, cationic cell-penetrating peptide that was designed to specifically recognize effector caspases (Figure 1). The caspase recognition sequence, DEVD, was flanked by a near-infrared emitting fluorophore (Alexa Fluor 647) and a quencher (QSY21) whose broad absorbance spectrum overlapped with the fluorophore emission spectrum (Figure 2A). Conjugation of the fluorophore and quencher to the peptide backbone was monitored by UV−vis spectroscopy. The absorption spectrum of the purified final product, KcapQ, revealed a substantial increase in the 605 nm peak compared to peptide conjugated to Alexa Fluor 647 alone. In its native state, the calculated quenching efficiency of the purified product in media was ∼96%.

To examine the selectivity of KcapQ, recombinant enzyme assays were performed by monitoring fluorescence intensity at 665 nm over time (Figure 2B). All data were normalized to milligram of enzyme. Data showed that KcapQ was highly selective toward the effector caspases 3, 6, and 7. In particular, KcapQ was cleaved at the highest rate by caspase 3, followed by caspase 7 and then caspase 6. In contrast, all initiator caspases showed essentially no activity (Table 1). Increasing the concentration of initiator caspases did not result in increased probe

Table 1. Cleavage Rate of KcapQ Incubated with Various Caspases

caspase	FU min^{-1} mg^{-1}
1	$<1.0 \times 10^{-3}$
2	$<1.0 \times 10^{-3}$
3[a]	4.0×10^{5}
4	$<1.0 \times 10^{-3}$
5	$<1.0 \times 10^{-3}$
6[a]	1.2×10^{4}
7[a]	1.0×10^{5}
8	$<1.0 \times 10^{-3}$
9	1.4×10^{2}
10	$<1.0 \times 10^{-3}$

[a] Effector caspase.

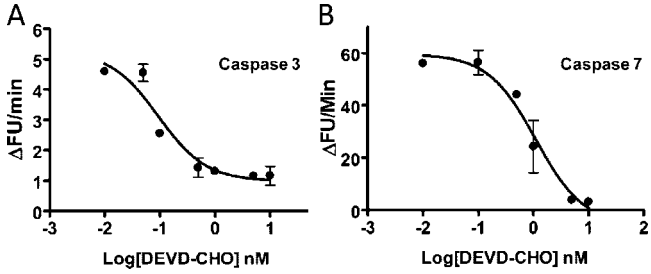

Figure 3. Inhibition curves of effector caspases interrogated with KcapQ. Increasing concentrations of the reversible inhibitor, DEVD-CHO, were incubated with 50 U caspase 3 (A) or 1 U caspase 7 (B) before the addition of KcapQ (0.5 μM). $EC_{50(i)}$ values were determined from analysis of cleavage rates (ΔFU min^{-1}) of KcapQ using nonlinear regression curve fitting. Data are presented as mean values $\pm$ SEM ($n = 2-3$ each).

Table 2. Kinetic Parameters of KcapQ Cleavage

caspase	$EC_{50(i)}$ (nM)	K_i (nM)	K_m (nM)	K_{cat} (FU min^{-1} μM^{-1})	K_{cat}/K_m (FU min^{-1} μM^{-1})/nM
3	0.09	0.08	3100	270 000	90
7	1.1	0.23	130	25 000	190

activation. To confirm the specificity of the probe, we tested D-KcapQ, a noncleavable version of the probe. D-KcapQ contained the identical amino acid sequence; however, the DEVD sequence consisted of noncleavable D-amino acid residues. No evidence of fluorescence activation was observed. To further characterize this probe, KcapQ was incubated with the caspase inhibitor DEVD-CHO, a highly specific reversible inhibitor of caspase 3, 6, and 7 (*30*). Inhibition studies were performed by preincubating each effector caspase with increasing concentrations of inhibitor (Figure 3). At each inhibitor concentration, the cleavage rate was calculated using a linear curve fit of the fluorescence−time data and plotted against inhibitor concentration. Using nonlinear regression analysis, single-site titration curves were determined to calculate the $EC_{50(i)}$ values for each effector caspase. From the $EC_{50(i)}$ values and the K_i values of DEVD-CHO, apparent K_m and k_{cat} values were calculated using the Cheng-Prusoff relationship (Table 2). From the k_{cat} data, we confirmed that KcapQ is preferentially cleaved by caspase 3 over caspase 7.

Following enzymatic characterization of KcapQ, live cell assays were performed to demonstrate intracellular delivery and apoptosis-induced probe activation. HeLa cells were pretreated for 6 h with 10 μM doxorubicin in culture medium (*31*), while cells incubated in culture medium alone served as a control. After pretreatment, KcapQ or its stereoisomer D-KcapQ (0.5 μM each) were incubated with the cells for 20 min prior to imaging. Figure 4 shows that KcapQ detected caspase activation in living cells. No fluorescence was observed with noncleavable D-KcapQ in doxorubicin-treated cells. The measured fluorescence emission for treated cells exposed to D-KcapQ was comparable to the fluorescence background observed with untreated cells, thus confirming the specificity of KcapQ.

To characterize any potential toxicity of KcapQ, we performed 24 and 48 h MTS assays to monitor cell viability in the continued presence of KcapQ (Figure 5). Increasing concentrations of KcapQ were added to a 96-well plate containing HeLa cells that were 50% confluent. Wells consisting of untreated cells and media only served as a control. Under these conditions, KcapQ showed no toxicity up to 25 μM concentration at 48 h. As a comparison, we tested TcapQ (*21*), a first-generation probe differing in cell-penetrating peptide sequence, under the same conditions. TcapQ produced a 50% loss of cell viability at 10 μM and a 90% loss of viability at 25 μM.

To determine if KcapQ could detect apoptosis in an in vivo model, apoptosis was induced in retinal ganglion cells (RGCs) using *N*-methyl-D-aspartate (NMDA). NMDA binds to and activates neuronal glutamate receptors, inducing excitotoxicity and subsequent apoptosis (*32*). The concentration of NMDA injected intravitreally, and the duration of exposure can be adjusted to restrict this effect predominantly to RGCs, thus serving as a model of RGC degeneration (*33, 34*). We recently reported that modified Tat-peptides enable robust uptake of conjugated fluorophore by RGCs (*35*). To stimulate RGC apoptosis in our animal model, NMDA was injected into the vitreous humor of the left eye. An identical injection of PBS into the right eye of each animal served as a control. After overnight pretreatment, KcapQ was injected into both the NMDA- and PBS-pretreated eyes. After 2 h, animals were euthanized and eyecups were immediately prepared by removing the lens and anterior segments. Figure 6A shows fluorescence images of fresh, intact eye cups. A significant amount of fluorescence signal could be observed in eye cups pretreated with NMDA and subsequently exposed to KcapQ. No fluorescence was observed in PBS-pretreated eyes injected with KcapQ or in NMDA-pretreated eyes injected with the control peptide D-KcapQ.

To more closely examine the pattern of probe activation, fresh retinal flat mounts were prepared from the harvested eye cups. Fluorescence microscopy confirmed a pattern of fluorescence in the NMDA-pretreated retina consistent with KcapQ activation in large cell bodies in the inner retina (Figure 6B). Minimal fluorescence was observed in the NMDA-pretreated eyes imaged with D-KcapQ or PBS-pretreated eyes imaged with KcapQ under identical conditions. Quantitatively, three different high-powered-fields showed 19 ± 5.5 and 2.3 ± 1.2 (mean $\pm$ SEM) labeled cells for NMDA-pretreated eyes imaged with KcapQ and D-KcapQ, respectively. Finally, vertical retinal paraffin sections were prepared from intact eye globes to enable localization of the fluorescent signal to specific retinal layers by confocal fluorescence microscopy. Examination of these retinal sections confirmed that the vast majority of probe activation was localized to large cell bodies in the RGC layer, consistent with RGCs (Figure 7). The pattern of fluorescent staining in the retina was consistent for all KcapQ samples. In a few sections, we observed sparse labeling of inner nuclear layer (INL) cells and small glial cells lining the nerve fiber layer (NFL), as would be anticipated with the NMDA-model, but no fluorescence was observed in any other retinal layers. Importantly, confocal fluorescence microscopy following TUNEL labeling of the same sections revealed colabeling of KcapQ positive cell bodies in the inner retina (Figure 7D, asterisks).

DISCUSSION

This study chemically and biochemically characterized a new self-quenching, caspase-activatable, near-infrared apoptosis imaging probe, KcapQ, and a noncleavable stereoisomer, D-KcapQ. Full chemical analysis of these probes showed that

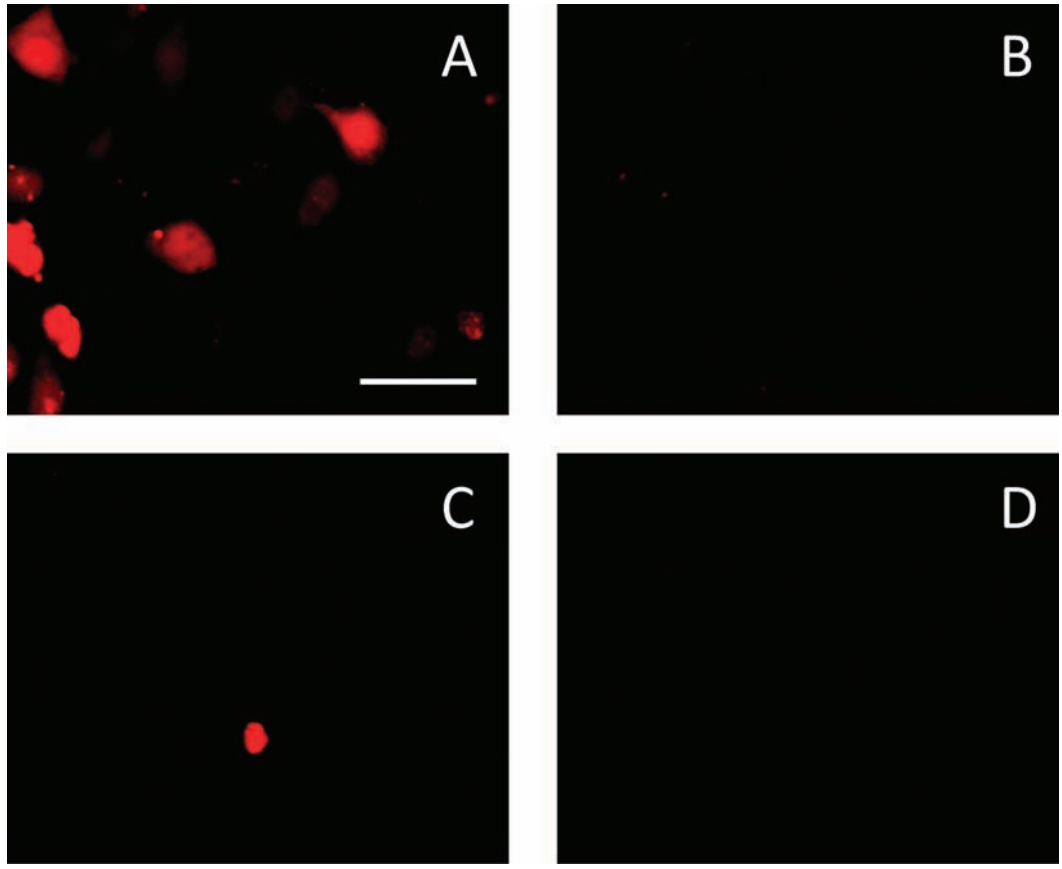

Figure 4. Representative fluorescence images of KcapQ activation during apoptosis in live cells. (A) Doxorubicin-treated (10 μM; 6 h) HeLa cells incubated with KcapQ (0.5 μM). (B) Untreated HeLa cells incubated with KcapQ (0.5 μM). (C) Doxorubicin-treated HeLa cells incubated with control D-KcapQ (0.5 μM). (D) Untreated HeLa cells incubated with control D-KcapQ (0.5 μM). Scale = 50 μm.

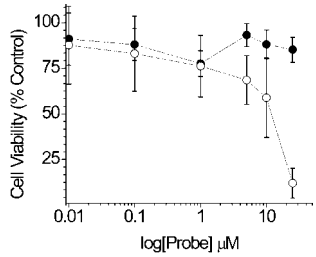

Figure 5. MTS cytotoxicity assays of KcapQ. Increasing concentrations of KcapQ (solid circles) and TcapQ (open circles) were incubated with HeLa cells for 48 h before the addition of MTS for analysis of cell viable mass. Data are presented as mean values ± SEM (n = 3 each).

they have identical mass, HPLC retention times, and UV−vis spectra. The absorbance spectrum of KcapQ displayed a striking increase in the 605 nm peak compared to the basic peptide conjugated to fluorophore alone, consistent with strong Coulombic intramolecular interactions in the quencher−fluorophore pair. The data suggested that the quenching mechanism occurred through n−π or π−π stacking rather than classical energy-transfer mechanisms, which rely strongly on spectral overlap in the fluorophore−quencher pair (*36, 37*). Preliminary studies replacing the Alexa Fluor 647 with a longer wavelength emitting fluorophore possessing no spectral overlap with QSY21 supported this hypothesis (data not shown). Indeed, there is precedence with other agents in which the proximity of the fluorophore and quencher pair to each other has been shown to quench a variety of fluorophores with no overlap in emission spectrum, as, for example, molecular beacons in which a single quencher was shown to quench numerous fluorophores spanning the visible region (*38*−*40*).

Biochemical studies showed that KcapQ was highly specific for effector caspases. KcapQ incubated with initiator caspases showed no increase in fluorescence intensity, demonstrating the selectivity of KcapQ toward effector caspases. Inhibition studies with the reversible inhibitor, DEVD-CHO, were performed to experimentally determine $EC_{50(i)}$ values for inhibition of caspase 3 and caspase 7 in the presence of KcapQ. This strategy allowed accurate spectrophotometric determination of cleavage rates independent of concentration-dependent artifacts produced by high concentrations of KcapQ (e.g., inner filter effects) and was used to derive apparent K_{cat} values (a measure of enzyme turnover rate). The data indicated that caspase 3 more readily cleaved KcapQ than caspase 7 by 11-fold, with K_{cat} values of 275 000 FU min^{-1} μM^{-1} and 25 000 FU min^{-1} μM^{-1}, respectively. However, a direct comparison of K_{cat}/K_m ratios, a measure of enzyme efficiency toward a specific substrate, revealed that KcapQ slightly preferred caspase 7, in part due to the high affinity of the peptide toward caspase 7. These findings were concordant with previously reported data from TcapQ (K_{cat}/K_m ratio: caspase 3, 7 = 60, 180, respectively) and provided evidence that the cell-penetrating peptide sequence of this class of probes had little effect on the overall resolved enzyme kinetics (*21*).

Live cell assays demonstrated that KcapQ could detect chemotherapy-induced apoptosis in HeLa cells. No activation was observed in treated cells with the noncleavable probe, D-KcapQ, or in untreated cells with KcapQ, confirming cleavage specificity. It should be noted that all assays were performed using live cells; fixing cells with 4% paraformaldehyde resulted in numerous false-positive fluorescence signals in both treated and untreated specimens as previously reported (*41*).

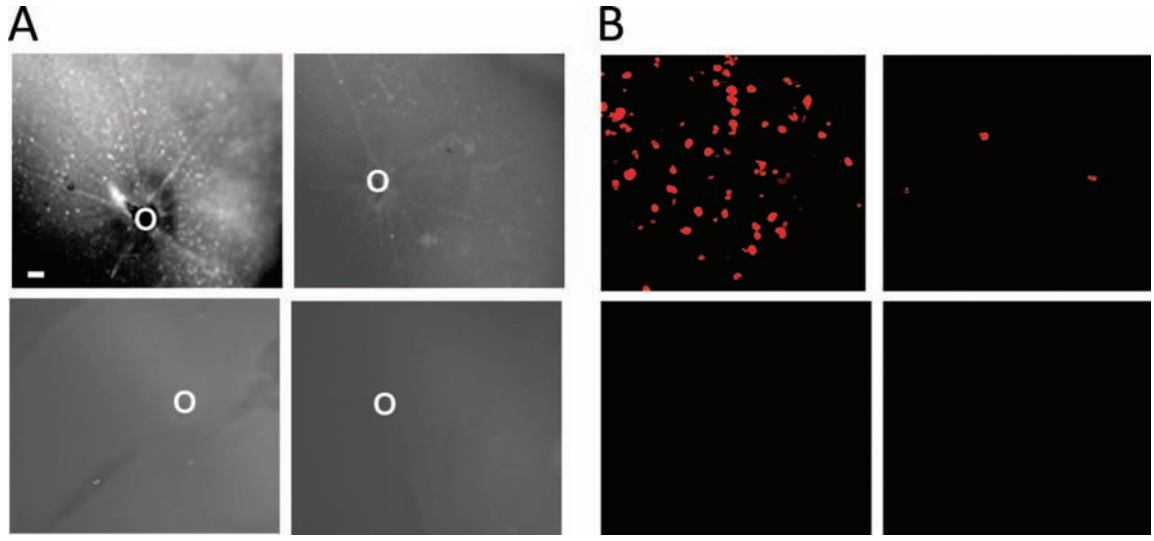

Figure 6. Fluorescence images of activated KcapQ in retinal ganglion cells in an in vivo model of induced neuronal apoptosis. (A) Fresh eye cup images of animals pretreated with NMDA for 16 h and imaged 2 h later with KcapQ or noncleavable-D-KcapQ. Top Left: NMDA-pretreated eye imaged with KcapQ. Top Right: PBS-pretreated eye imaged with KcapQ. Bottom Left: NMDA-pretreated eye imaged with D-KcapQ. Bottom Right: PBS-pretreated eye imaged with D-KcapQ. (B) Corresponding retinal flat mounts of eye cup samples. *T*op Left: NMDA-pretreated eye imaged with KcapQ. Top Right: PBS-pretreated eye imaged with KcapQ. Bottom Left: NMDA-pretreated eye imaged with D-KcapQ. Bottom Right: PBS-pretreated eye imaged with D-KcapQ. Scale = 100 μm. O, optic disk.

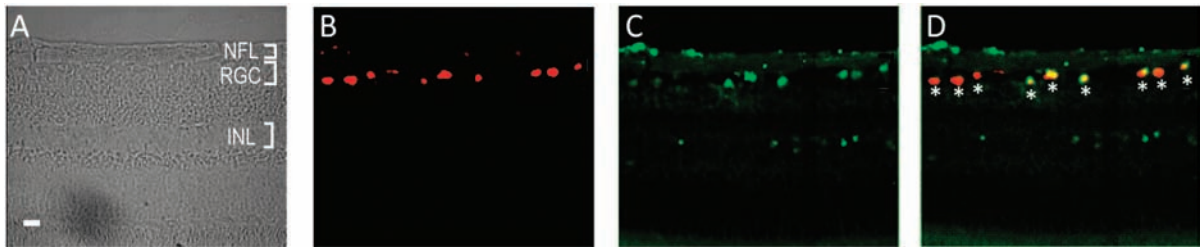

Figure 7. Colocalization of TUNEL staining and KcapQ to RGCs by confocal fluorescence microscopy of vertical retinal sections from NMDA-pretreated eyes. (A) Differential interference contrast image of retinal cell layers. (B) Fluorescence image showing KcapQ activation predominantly in large cell bodies in the retinal ganglion cell (RGC) layer. (C) Fluorescence immunohistochemistry showing TUNEL staining, again predominantly in the RGC layer. (D) Merged KcapQ fluorescence and TUNEL staining image. Brackets (]) indicate the nerve fiber layer (NFL), RGC layer, and inner nuclear layer (INL); asterisks indicate areas of colocalization of KcapQ and TUNEL positive signals in the RGC layer. Scale = 100 μm.

To characterize the "diagnostic index" of KcapQ (half-maximal toxic concentration (TC_{50}) divided by half-maximal diagnostically useful concentration), MTS assays were performed to measure HeLa cell viability after incubations with KcapQ for 24 and 48 h. KcapQ was shown to be nontoxic at doses as high as 25 μM. Because typical imaging experiments with KcapQ were performed at 0.5 μM, the "diagnostic index" of KcapQ would appear to be high ($\gg$50). By comparison, TcapQ, our first generation probe, was found to be toxic at higher concentrations, with a 90% reduction in cell viability at 25 μM. The difference between these probes is in the cell-penetrating peptide sequence. Whereas the KcapQ penetrating sequence is lysine-rich, the TcapQ penetrating sequence is composed of numerous arginine residues. Arginine residues contain positively charged guanidinium groups that have been shown to facilitate uptake of conjugated compounds into cells (*22, 25, 42*−*44*). Further supporting the argument that guanidinium moieties enhance cellular uptake, we have observed that TcapQ is more efficient in accumulating in apoptotic cells as judged by the relative intensity of fluorescent cells under identical conditions. While the TC_{50} for TcapQ was $\sim$10 μM, note that, at the concentrations of TcapQ useful in prior studies (0.5−1 μM), the diagnostic index would still be 10−20. There may be a coupling between high cell uptake and toxicity of cell-penetrating peptides, which requires a balanced approach to optimize the utility of these types of imaging agents. In this regard, because of the reduced toxicity, KcapQ may provide a reasonable compromise among diagnostic efficacy, signal intensity, and toxicity at diagnostically relevant concentrations of probe.

Examination of fresh eye cups and retinal flat mounts by epifluorescence imaging in a rat model of RGC degeneration showed that KcapQ could efficiently label RCGs that were undergoing apoptosis. Control samples showed minimal probe activation in the PBS-pretreated animals. Further examination of vertical retinal sections by confocal fluorescence microscopy confirmed that KcapQ activation was primarily localized to RGCs, as anticipated. Colocalization of TUNEL and KcapQ signals further confirmed that labeling was restricted to RGCs and occasional inner retinal cells undergoing apoptosis. The minimal fluorescence signal observed with KcapQ in PBS-pretreated samples was likely related to apoptosis due to the trauma of intravitreal injection itself. While we cannot exclude occasional false-positive signals from random probe activation, in each experiment, great precautions were taken to inject NMDA or PBS into the vitreous humor in a manner to minimize mechanical damage and subsequent elevation in intraocular pressure. To determine if the injection method caused apoptosis, mock-injections into the vitreous humor followed by KcapQ injection using a clinically applicable protocol, showed little probe activation in these tissue specimens (data not shown).

In conclusion, KcapQ, a new apoptosis imaging probe, is highly specific for effector caspases, preferentially cleaving caspase 3 over caspases 7 and 6. In our rat model of retinal

ganglion cell excitotoxicity, KcapQ specifically detects RGCs undergoing apoptosis. The near-infrared emission of KcapQ in combination with the accessibility and optimal optical properties of the mammalian eye makes this an attractive strategy to monitor neuronal loss in vivo. Future experiments developing KcapQ as a molecular imaging agent may aid the ability to diagnose and monitor treatment of many diseases, including neurodegenerative diseases of the eye, such as glaucoma.

ACKNOWLEDGMENT

Special thanks to Seth Gammon, Jayne Marasa, and Scott Harpstrite for valuable discussions, and the Hope Center for Neurological Diseases as well as the High-Throughput Core of the Molecular Imaging Center at Washington University for microscopy use and support. This work was supported by NIH grants CA82841, and P50 CA94056, EY017636, and P30 EY02687, a Horncrest Physician Scientist Award, and a Career Development Award from Research to Prevent Blindness (E.M.B.).

LITERATURE CITED

(1) Chang, H., and Yang, X. (2000) Proteases for cell suicide: functions and regulation of caspases. *Microbiol. Mol. Biol. Rev. 64*, 821–846.

(2) Grutter, M. (2000) Caspases: key players in programmed cell death. *Curr. Opin. Struct. Biol. 10*, 649–655.

(3) Shi, Y. (2001) A structural view of mitochondria-mediated apoptosis. *Nat. Struct. Biol. 8*, 394–401.

(4) Kroemer, G., and Martin, S. (2005) Caspase-independent cell death. *Nat. Med. 11*, 725–730.

(5) Ran, S., and Thorpe, P. E. (2002) Phosphatidylserine is a marker of tumor vasculature and a potential target for cancer imaging and therapy. *Int. J. Radiat. Oncol. Biol. Phys. 54*, 1479–1484.

(6) Petrovsky, A., Schellenberger, E., Josephson, L., Weissleder, R., and Bogdanov, A. J. (2003) Near-infrared fluorescent imaging of tumor apoptosis. *Cancer Res. 63*, 1936–1942.

(7) Schellenberger, E., Bogdanov, A. J., Hogemann, D., Tait, J., Weissleder, R., and Josephson, L. (2002) Annexin V-CLIO: a nanoparticle for detecting apoptosis by MRI. *Mol. Imaging 1*, 102–107.

(8) Schellenberger, E., Bogdanov, A. J., Petrovsky, A., Ntziachristos, V., Weissleder, R., and Josephson, L. (2003) Optical imaging of apoptosis as a biomarker of tumor response to chemotherapy. *Neoplasia 5*, 187–192.

(9) Blankenberg, F. G., Katsikis, P. D., Tait, J. F., Davis, R. E., Naumovski, L., Ohtsuki, K., Kopiwoda, S., Abrams, M. J., Darkes, M., Robbins, R. C., Maecker, H. T., and Strauss, H. W. (1998) In vivo detection and imaging of phosphatidylserine expression during programmed cell death. *Proc. Natl. Acad. Sci. U.S.A. 95*, 6349–6354.

(10) Chang, Y. H., and Yang, X. (2000) Proteases for cell suicide: functions and regulation of caspases. *Microbiol. Mol. Biol. Rev. 64*, 821–846.

(11) Shi, Y. (2002) Mechanisms of caspase activation and inhibition during apoptosis. *Mol. Cell 9*, 459–470.

(12) Shi, Y. (2004) Caspase activation, inhibition, and reactivation: a mechanistic view. *Protein Sci. 13*, 1979–1987.

(13) Thornberry, N. A., Rano, T. A., Peterson, E. P., Rasperi, D. M., Timkey, T., Garcia-Calvo, M., Houtzageri, V. M., Nordstromi, P. A., Royi, S., Vaillancourti, J. P., Chapman, K. T., and Nicholsoni, D. W. (1997) A combinatorial approach defines specificities of members of the caspase family and granzyme B: functional relationships established for key mediators of apoptosis. *J. Biol. Chem. 272*, 17907–17911.

(14) Lien, S., Pastor, R., Sutherlin, R., and Lowman, H. (2004) A substrate-phage approach for investigating caspase specificity. *The Protein J. 23*, 413–425.

(15) Takemoto, K., Kuranaga, E., Tonoki, A., Nagai, T., Miyawaki, A., and Miura, M. (2007) Local initiation of caspase activation in *Drosophila* salivary gland programmed cell death *in vivo*. *Proc. Natl. Acad. Sci. U.S.A. 104*, 13367–13372.

(16) Kim, K., Lee, M., Park, H., Kim, J. H., Kim, S., Chung, H., Cho, I. K., Kim, I. S., Seong, B. L., and Kwon, I. C. (2006) Cell-permeable and biocompatible polymeric nanoparticles for apoptosis imaging. *J. Am. Chem. Soc. 128*, 3490–1.

(17) Bullok, K., Gammon, S., Violini, S., Prantner, A., Villalobos, V., Sharma, S., and Piwnica-Worms, D. (2006) Permeation peptide conjugates for in vivo molecular imaging applications. *Mol. Imaging 5*, 1–15.

(18) Messerli, S., Prabhakar, S., Tang, Y., Shah, K., Cortes, M., Murthy, V., Weissleder, R., Breakefield, X., and Tung, C. (2004) A novel method for imaging apoptosis using a caspase-1 near-infrared fluorescent probe. *Neoplasia 6*, 95–105.

(19) Frangioni, J. V. (2003) In vivo near-infrared fluorescence imaging. *Curr. Opin. Chem. Biol. 7*, 626–34.

(20) Bullok, K., and Piwnica-Worms, D. (2005) Synthesis and characterization of a small, membrane-permeant, caspase-activatable far-red fluorescent peptide for imaging apoptosis. *J. Med. Chem. 48*, 5404–5407.

(21) Bullok, K. E., Maxwell, D., Kesarwala, A. H., Gammon, S., Prior, J. L., Snow, M., Stanley, S., and Piwnica-Worms, D. (2007) Biochemical and in vivo characterization of a small, membrane-permeant, caspase-activatable far-red fluorescent peptide for imaging apoptosis. *Biochemistry 46*, 4055–4065.

(22) Snyder, E. L., and Dowdy, S. F. (2004) Cell penetrating peptides in drug delivery. *Pharm. Res. 21*, 389–393.

(23) Fischer, R., Fotin-Mleczek, M., Hufnagel, H., and Brock, R. (2005) Break on through to the other side - biophysics and cell biology shed light on cell-penetrating peptides. *ChemBioChem 6*, 2126–2142.

(24) Nakase, I., Niwa, M., Takeuchi, T., Sonomura, K., Kawabata, N., Koike, Y., Takehashi, M., Tanaka, S., Ueda, K., Simpson, J. C., Jones, A. T., Sugiura, Y., and Futaki, S. (2004) Cellular uptake of arginine-rich peptides: roles for macropinocytosis and actin rearrangement. *Mol. Ther. 10*, 1011–1022.

(25) Gump, J. M., and Dowdy, S. F. (2007) TAT transduction: the molecular mechanism and therapeutic prospects. *Trends Mol. Med. 13*, 443–448.

(26) Kaplan, I. M., Wadia, J. S., and Dowdy, S. F. (2005) Cationic TAT peptide transduction domain enters cells by macropinocytosis. *J. Conrolled Release 102*, 247–253.

(27) Fischer, R., Köhler, K., Fotin-Mleczek, M., and Brock, R. (2004) A stepwise dissection of the intracellular fate of cationic cell-penetrating peptides. *J. Biol. Chem. 279*, 12625–12635.

(28) Khalil, I. A., Kogure, K., Futaki, S., and Harashima, H. (2006) High density of octaarginine stimulates macropinocytosis leading to efficient intracellular trafficking for gene expression. *J. Biol. Chem. 281*, 3544–3551.

(29) Burlingham, B. T., and Widlanski, T. S. (2003) An intuitive look at the relationship of K_i and IC_{50}: a more general use for the Dixon Plot. *J. Chem. Educ. 80*, 214–218.

(30) Garcia-Calvo, M., Peterson, E. P., Leiting, B., Ruel, R., Nicholson, D. W., and Thornberry, N. A. (1998) Inhibition of human caspases by peptide-based and macromolecular inhibitors. *J. Biol. Chem. 273*, 32608–32613.

(31) Dimanche-Boitrel, M., Meurette, O., Rebillard, A., and Lacour, S. (2005) Role of early plasma membrane events in chemotherapy-induced cell death. *Drug Resist. Update 8*, 5–14.

(32) Siliprandi, R., Canella, R., Carmignoto, G., Schiavo, N., Zanellato, A., Zanoni, R., and Vantini, G. (1992) N-methyl-D-aspartate-induced neurotoxicity in the adult rat retina. *Vis. Neurosci. 8*, 567–573.

(33) Lam, T. T., Abler, A. S., Kwong, J. M., and Tso, M. O. (1999) N-methyl-D-aspartate (NMDA)--induced apoptosis in rat retina. *Invest. Ophthalmol. Vis. Sci. 40*, 2391–2397.

(34) Manabe, S., and Lipton, S. A. (2003) Divergent NMDA signals leading to proapoptotic and antiapoptotic pathways in the rat retina. *Invest. Ophthalmol. Vis. Sci. 44*, 385–392.

(35) Barnett, E. M., Elangovan, B., Bullok, K. E., and Piwnica-Worms, D. (2006) Selective cell uptake of modified Tat peptide-fluorophore conjugates in rat retina in ex vivo and in vivo models. *Invest. Ophthalmol. Vis. Sci. 47*, 2589–2595.

(36) Johansson, M., Fidder, H., Dick, D., and Cook, R. (2002) Intramolecular dimers: a new strategy to fluorescence quenching in dual-labeled oligonucleotide probes. *J. Am. Chem. Soc. 124*, 6950–6956.

(37) Packard, B., Toptygin, D., Komoriya, A., and Brand, L. (1996) Profluorescent protease substrates: intramolecular dimers described by the exciton model. *Proc. Natl. Acad. Sci. U.S.A. 93*, 11640–5.

(38) Bernacchi, S., and Mély, Y. (2001) Exciton interaction in molecular beacons: a sensitive sensor for short range modifications of the nucleic acid structure. *Nucleic Acids Res. 29*, e62.

(39) Tyagi, S., Bratu, D., and Kramer, F. (1998) Multicolor molecular beacons for allele discrimination. *Nat. Biotechnol. 16*, 49–53.

(40) Marras, S., Kramer, F., and Tyagi, S. (1999) Efficiencies of fluorescence resonance energy transfer and contact-mediated quenching in oligonucleotide probes. *Nucleic Acids Res. 30*, e122.

(41) Richard, J., Melikov, K., Vives, E., Ramos, C., Verbeure, B., Gait, M., Chernomordik, L., and Lebleu, B. (2003) Cell-penetrating peptides. *J. Biol. Chem. 278*, 585–590.

(42) Jiang, T., Olson, E., Nguyen, Q., Roy, M., Jennings, P., and Tsien, R. (2004) Tumor imaging by means of proteolytic activation of cell-penetrating peptides. *Proc. Natl. Acad. Sci. U.S.A. 101*, 17867–17872.

(43) Kawamura, K. S., Sung, M., Bolewska-Pedyczak, E., and Gariépy, J. (2006) Probing the impact of valency on the routing of arginine-rich peptides into eukaryotic cells. *Biochemistry 45*, 1116–27.

(44) Wender, P. A., Galliher, W. C., Goun, E. A., Jones, L. R., and Pillow, T. H. (2008) The design of guanidinium-rich transporters and their internalization mechanisms. *Adv. Drug Delivery Rev. 60*, 452–472.

(45) Bates, M., Huang, B., Dempsey, G. T., and Zhuang, X. (2007) Multicolor super-resolution imaging with photo-switchable fluorescent probes. *Science 317*, 1749–1753.

BC800516N

Bioconjugate Chemistry 20th Anniversary

Subscriber access provided by SHEMYAKIN-OVCHINNIKOV INST

Article

Oligonucleotide#RGD Peptide Conjugates for Surface Modification of Titanium Implants and Improvement of Osteoblast Adhesion

Jan Michael, Lena Scho#nzart, Ina Israel, Rene# Beutner, Dieter Scharnweber, Hartmut Worch, Ute Hempel, and Bernd Schwenzer

Bioconjugate Chem., **2009**, 20 (4), 710-718• DOI: 10.1021/bc800372e • Publication Date (Web): 13 March 2009

Downloaded from http://pubs.acs.org on May 15, 2009

More About This Article

Additional resources and features associated with this article are available within the HTML version:

- Supporting Information
- Access to high resolution figures
- Links to articles and content related to this article
- Copyright permission to reproduce figures and/or text from this article

View the Full Text HTML

ACS Publications
High quality. High impact.

Bioconjugate Chemistry is published by the American Chemical Society. 1155 Sixteenth Street N.W., Washington, DC 20036

Oligonucleotide−RGD Peptide Conjugates for Surface Modification of Titanium Implants and Improvement of Osteoblast Adhesion

Jan Michael,[†] Lena Schönzart,[†] Ina Israel,[†] René Beutner,[‡] Dieter Scharnweber,[‡] Hartmut Worch,[‡] Ute Hempel,[§] and Bernd Schwenzer*[,†]

Lehrstuhl für Allgemeine Biochemie, Technische Universität Dresden, Bergstr. 66, 01069 Dresden, Max-Bergmann-Zentrum für Biomaterialien, Technische Universität Dresden, Budapester Str. 27, 01069 Dresden, and Institut für Physiologische Chemie, Medizinische Fakultät Carl Gustav Carus, Technische Universität Dresden, Fiedlerstr. 42, 01307 Dresden, Germany. Received September 2, 2008; Revised Manuscript Received February 12, 2009

A new concept for modular biosurface engineering of titanium implants based on the self-assembly of complementary oligonucleotides was biochemically investigated and optimized. This study describes the synthesis and characterization (RP-HPLC and Sakaguchi assay) of oligodeoxyribonucleotide (ODN) conjugates of the hexapeptide GRGDSP containing the RGD sequence as the recognition motif for cellular adhesion receptors (integrins). The peptide was chosen exemplarily as a model molecule, because it is a simple but potent bioactive molecule and relatively well investigated. The conjugation products must fulfill two main requirements: (I) the ability to hybridize and (II) the preservation of biological activity of the RGD peptide for the enhancement of osteoblast adhesion. In the following text, the term "hybridization" is generally used for Watson−Crick base pairing. The ability of the conjugates to hybridize to surface-immobilized complementary ODN was verified by competitive hybridization with radiolabeled (^{32}P) complementary strands and by hybridization experiments using a quartz crystal microbalance (QCM). Surface hybridization was further characterized using different adsorption isotherms (e.g., Freundlich and Frumkin types), since the type of isotherm and the derived thermodynamic parameters may reveal characteristic differences between ODN and conjugates thereof. Biological activity of the conjugates was examined in vitro with osteoblasts. The cells were either cultured directly on the ODN-GRGDSP modified titanium implants or used for competition adhesion studies with dissolved ODN-GRGDSP conjugates. All results support the successful establishment of the new surface modification system. Hybridization of RGD peptide-modified nucleic acids to ODN-modified titanium implant materials is thus a promising method for osteoblast attachment in a modular and self-organizing system on implant surfaces.

INTRODUCTION

Titanium and its alloys are widely used in implantology because of their good biocompatibility. These materials show high corrosion resistance in vivo and toxicological harmlessness (*1*−*3*). An outstanding aim is the fast and stable integration of metallic implants into the surrounding bone tissue. Integration and healing problems, occurring in the cases of systemic diseases (diabetes, osteoporosis, etc.) or smokers or after previous radiation treatment, led to a call for implants with osseoconductive or even osseoinductive surfaces (*4*−*7*).

One of several approaches for creating bioactive surfaces is the immobilization of smaller fragments of proteins or artificial peptides containing certain recognition sequences, e.g., RGD peptides promoting specific cell adhesion (*8*−*13*).

Widely used immobilization procedures such as covalent attachment (*8*−*11*, *14*) and adsorption (*12*, *15*, *16*) suffer from certain disadvantages. These are predominantly the need for additional chemical surface modification with potentially toxic properties and weak interaction, respectively.

Furthermore, recently used methods for biosurface modification are restricted to one or a few substances introduced early during surface treatment. Therefore, we have developed a new method for modular and flexible biosurface engineering (*17*) that overcomes the aforementioned disadvantages. The presented new procedure consists of the following steps:

1. Nucleic acid anchor strands or functional nucleic acids such as aptamers (*18*) adsorb on the native oxide layer of the titanium material (Figure 1a).

2. Adsorbed nucleic acids are partially entrapped during anodic growth of the TiO_2 layer (Figure 1b).

3. Such fixed nucleic acid anchor strands (AS) hybridize either with complementary strands (CS) that are conjugated to biomolecules (e.g., RGD peptides, growth factors) and drugs (e.g., antibiotics, antiphlogistics), or with functional nucleic acids. Favorably, this is done according to the patients' needs prior to implantation during surgery (Figure 1c).

4. After implantation, specific tissue reactions can be induced by biomolecules (immobilized and/or released in a defined way) (Figure 1d).

Along with the favorable electrochemical immobilization procedure of anchor strands, the use of molecular self-organization via nucleic acid hybridization with various conjugates and functional nucleic acids allows a wide range of targeted surface modification. The great advantage of this system of biosurface engineering is thus characterized by its high modularity and flexibility.

After the proof of principle (*17*) and further optimization (*19*) of the anchor part of the immobilization system, synthesis and characterization of bioactive conjugates of nucleic acids was crucial for the advancement of the system. The hexapeptide GRGDSP was chosen as a biological active model substance for the conjugation with ODN, since the RGD sequence is a

* Corresponding author. E-mail: Bernd.Schwenzer@chemie.tu-dresden.de; Phone: +49-351-46336447; Fax: +49-351-46335506.
[†] Lehrstuhl für Allgemeine Biochemie.
[‡] Max-Bergmann-Zentrum für Biomaterialien.
[§] Institut für Physiologische Chemie.

10.1021/bc800372e CCC: $40.75 © 2009 American Chemical Society
Published on Web 03/13/2009

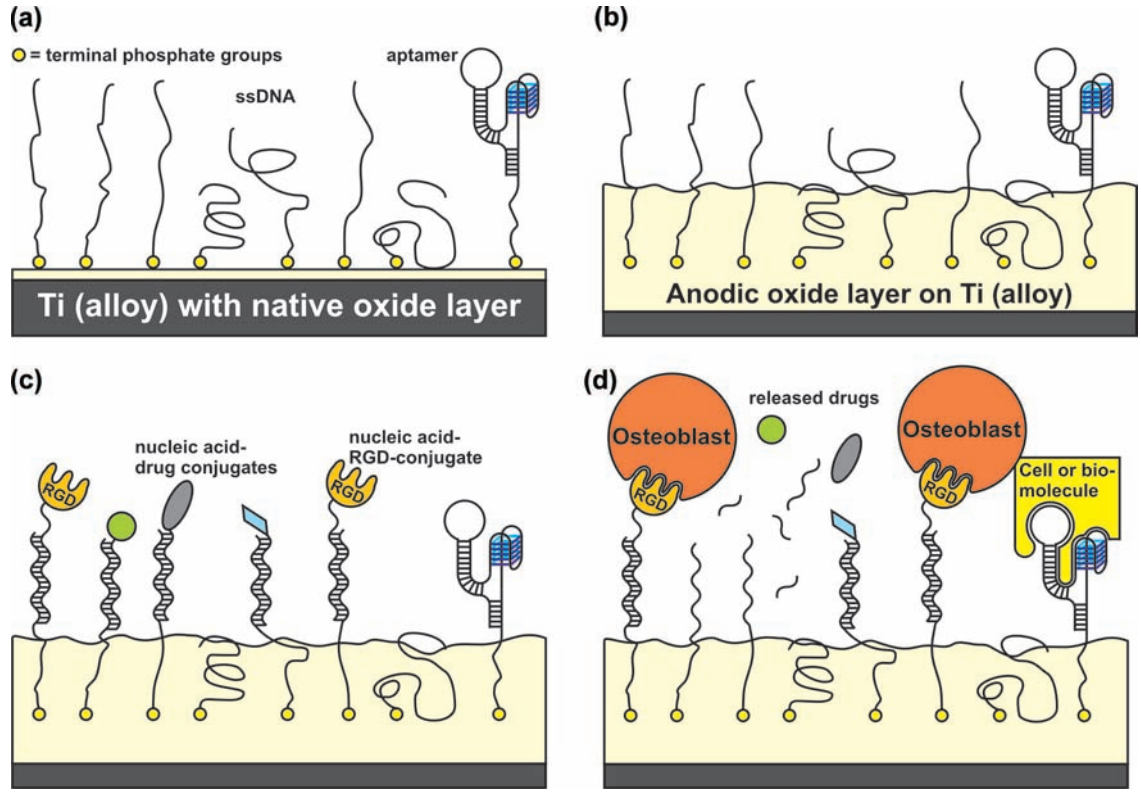

Figure 1. (a) Single-stranded anchors or functional nucleic acids (e.g., aptamers) are adsorbed via their terminal phosphate groups on the native oxide layer of titanium materials. (b) Anodic polarization leads to a partial entrapment of afore adsorbed nucleic acids in the thickened oxide layer. (c) Nucleic acid conjugates of bioactive molecules are hybridized to the single-stranded "anchor strands" (AS) fixed on the surface. (d) In the mammalian organism, osteoblasts can bind to RGD peptides on the surface. Aptamers can also bind cells or certain molecules. Both lead to faster integration into the surrounding bone. Released drugs from the surface-bound conjugates may be antibiotics, antiphlogistics, or growth factors.

ubiquitous adhesive motif in extracellular matrix proteins of bone cells and relatively well investigated. RGD peptides are widely used for surface modification and binding of osteoblasts (*8*−*13*).

In the course of synthesis and characterization of these GRGDSP conjugates, principal insight should be gained for the work with various more specific and potent bioactive molecules. To reach this aim, syntheses of conjugates were followed by analysis (RP-HPLC, Sakaguchi assay), hybridization experiments with the conjugates on titanium and using a QCM applying adsorption isotherms, and cell tests for biological activity in cell suspension and on titanium surfaces.

EXPERIMENTAL PROCEDURES

Oligodeoxyribonucleotides (ODN). Names/ synonyms, sequences, modifications, and suppliers:

Anchor Strand (AS). 5′ $^{2-}O_3$PO-CCA AAC CCG TCA ATC AAG TCT ACA CTG TTC CCA AAC CCG TCA ATC AAG TCT ACA CTG TTC-3′.

Thiolated Anchor Strand (HS-AS). 5′-HS-$(CH_2)_6$-CCA AAC CCG TCA ATC AAG TCT ACA CTG TTC CCA AAC CCG TCA ATC AAG TCT ACA CTG TTC-3′.

Complementary Strand (CS). 5′-CAG TGT AGA CTT GAT TGA CGG GTT T-3′.

Precursor for Radiolabeling of CS. 5′-CAG TGT AGA CTT GAT TGA CGG GTT-3′.

Noncomplementary Strand (NS). 5′-GCC ATA GTT TTT ATT AGG AGG TCG G-3′. Synthesis of the abovementioned strands: Thermo Scientific, Ulm, Germany. Radiolabeling using 3′-elongation with ^{32}P-dNTPs: Hartmann Analytic GmbH, Braunschweig, Germany.

Aminopropylated Complementary Strand (CS_C3). 5′-H_2N-C_3H_6-CAG TGT AGA CTT GAT TGA CGG GTT TGG GAA T-3′.

Aminohexylated Complementary Strand (CS_C6). 5′-H_2N-C_6H_{12}-CAG TGT AGA CTT GAT TGA CGG GTT TGG GAA T-3′.

Aminopropylated Noncomplementary Strand (NS_C3). 5′-H_2N-C_3H_6-GTC ATG TTG TGG TGA GCT AAT TCG GAA AGG C-3′.

Aminohexylated Noncomplementary Strand (NS_C6). 5′-H_2N-C_6H_{12}-GTC ATG TTG TGG TGA GCT AAT TCG GAA AGG C-3′. Synthesis of the abovementioned strands: Biozym Scientific GmbH, Germany.

Conjugate Synthesis. Substances, solutions, buffers, and devices: Sephadex G-25 Fine (Pharmacia Fine Chemicals AB, Sweden) swollen in sodium acetate buffer I, GRGDSP (Bachem AG, Switzerland), dimethyl sulfoxide (DMSO), disuccinimidyl suberate (DSS), disuccinimidyl tartrate (DST) (both Pierce Perbio Science, Germany), TRIS, $MgCl_2 \cdot 6H_2O$. Reaction buffer: 3 M NaCl, 1 mM $MgCl_2$, 0.1 M $NaHCO_3$, pH 8.3. Sodium acetate buffer I: 0.1 M $NaOOCCH_3$, pH 4.0. Sodium acetate buffer II: 1 mM $NaOOCCH_3$, pH 4.0. TRIS−NaCl: 100 mM NaCl, 50 mM TRIS, pH 8.5. Bicarbonate solution: 1 mM $NaHCO_3$, pH 8.5. DSS and DST: 27.15 mM in dry DMSO. ODN: 1 mM in sterile deionized H_2O (SDI H_2O). GRGDSP: 10 mM in reaction buffer. Chromatographic column: 0.7 × 50 cm, Econo System (BioRad Laboratories GmbH, Germany). Centrifugal filter devices: Centricon-3, exclusion size: 3000 Da (Millipore Corp.).

Conjugation was carried out according to Ruth (*20*). A chromatographic column with Sephadex G25 Fine was equilibrated with sodium acetate buffer II at 4 °C. A mixture of 40 μL ODN solution, 12 μL bicarbonate, and 40 μL DSS or DST

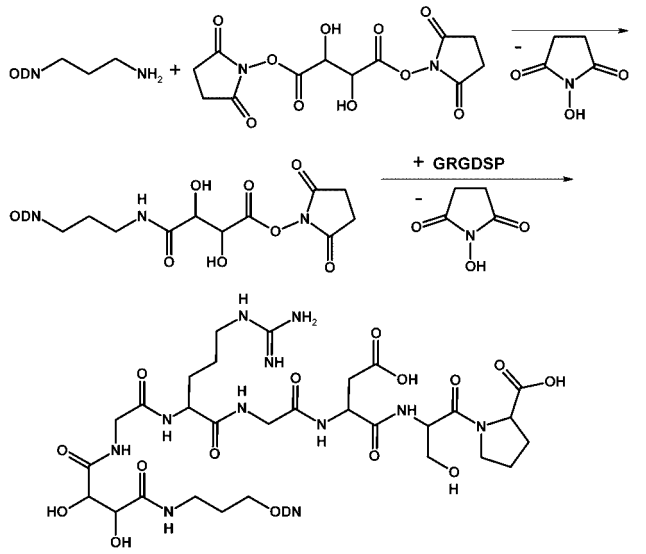

Figure 2. The conjugation reaction is exemplarily given for the aminopropylated ODN and disuccinimidyl tartrate (DST). In the other case, aminohexylated ODNs are coupled with disuccinimidyl suberate (DSS).

solutions, respectively, was mixed for 1−2 min, immediately dropped on the column, and eluted with sodium acetate buffer II at 4 °C and 0.5 mL/min. Absorbance of the collected fractions was determined at 260 nm to find those with activated ODN (first peak) which were then merged and concentrated in centrifugal filter devices at 5500 g. 100 μL of the concentrate were taken off for later analysis. Remaining activated ODNs were mixed with 40 μL of GRGDSP solution and adjusted at pH 8 with reaction buffer. Coupling took place for 18 h in the dark at room temperature and was followed by centrifugal filtration at 5500 *g* down to a volume of 0.5−1.0 mL that was then applied to a Sephadex G25 Fine column and eluted with TRIS−NaCl (pH 8.5) at 4 °C at 0.5 mL/min. Absorbance of the collected fractions was determined at 260 nm to find those with the conjugate. The merged product solutions were concentrated in centrifugal filter devices at 5500 *g*. To remove most of TRIS−NaCl, the concentrated conjugates were washed with SDI H_2O and concentrated in a centrifugal filter three times. Concentration determination by extinction measurements at 260 nm was based on calculated extinction coefficients of the ODN according to Puglisi (*21*).

Two coupling variants for conjugate synthesis were chosen: The aminopropylated ODN (CS_C3 and NS_C3) were activated with DST and the aminohexylated ODN (CS_C6 and NS_C6) with DSS before coupling with GRGDSP. Reaction equations are given in Figure 2 for the ODN_C3-DST coupling as example. The basic intention to use these two combinations was to realize (I) a different distance between the hybridizing ODN-domain and the adhesion peptide that might influence the biological activity and (II) a different hydrophobicity that might influence the separation using RP-HPLC.

RP-HPLC. HPLC column: C-18 monomeric reversed phase (150 mm × 4.6 mm, 5 μm; Grace Vydac). Precolumn: C-18; 5 μm; Grace Vydac. HPLC device: degasser, HPLC pump K-1001 (Wellchrom), solvent unit K-1500, dynamic mixing chamber, Wellchrom diode array detector K2800 (Knauer), autosampler (Holland Spark Midas (DataApex Comp.)). Software: *Knauer Eurochrom 2000 Basic Edition for Windows*, v 1.2. HPLC solvents: HPLC pure acetonitrile, triethylamine (TEA).

Sakaguchi Assay. The assay is based on Sakaguchi's original work (*22*) and later advancements thereof (*23*−*25*). Solutions: Reagent A: 1.25 g urea and 12.5 mg 1-naphthol in 25 mL 95% ethanol. Reagent B: 175 μL bromine in 25 mL 1.25 M NaOH. Arginine stock solution (1.435 M): 25 mg arginine in 100 mL SDI H_2O. Arginine working solution (0.359 M): 5 mL arginine stock solution and 15 mL SDI H_2O. Assay procedure: 25 μL of sample solution was mixed with 25 μL reagent A and 50 μL reagent B, then centrifuged. Reaction time allowed: 10 min. Immediately afterward, the spectrum was determined twice for each sample between 250 and 750 nm.

Electrochemical Immobilization of AS. Preparation of titanium samples: Discs (16 mm × 2 mm) were turned from round bar stocks of c.p. Ti (99.6 mass %) and ground down to a grain size of 26 μm (P600) with SiC abrasive paper. Subsequent sample etching was carried out in a mixture of 0.4 M hydrofluoric acid and 1 M nitric acid at room temperature (RT) for 2 min. After ultrasonic rinsing in SDI H_2O, samples were stored for 1 day in SDI H_2O in sterile bottles before use. Electrochemical cell: Custom product from acrylic glass in a conical shape with a gold wire acting as counter electrode. Reference electrode: Ag/AgCl. Salt bridge: buffer-agarose-filled plastic hose. Sample contact area to electrolyte: 1.8 cm^2. Potentiostat/Galvanostat: electrochemical system Voltalab 4.0 combined with a high-voltage booster HVB100 (Radiometer Analytical, Copenhagen). Ethanolic acetate buffer: 0.5 M acetate containing 5 M ethanol, pH 4.0. Anchor strand (AS): 400 nM in ethanolic acetate buffer. PBS (desorption) buffer: 200 mL 10× stock solution: 18 g NaCl, 0.462 g KH_2PO_4, 1.78 g Na_2HPO_4 in SDI H_2O, pH 6.85; pH of dilution 7.4−7.5. Immobilization procedure: 800 μL of the AS solution were put on the sample in the cell and left there 15 min for adsorption. After adding 2.2 mL of ethanolic acetate buffer, the cover with the gold electrode and the salt bridge was applied. Galvanostatic polarization at 7 mA/cm^2 was performed until a potential of 8 $V_{Ag/AgCl}$ was reached. The circuit was opened, and the salt bridge and gold electrode were removed. Ethanolic acetate buffer was used to rinse the cell three times. The sample was then dunked in SDI H_2O and immediately put in a well (12-well cell culture plate, NUNC Corp., Denmark) with 3 mL PBS. Desorption took place for 23 h in the dark.

Competitive Hybridization. Stock solutions: CS*: inactive CS and radiolabeled CS were mixed in a defined ratio (>99.5% nonlabeled) and filled up with SDI H_2O to give a 4 μM CS* stock solution. Competitor stock solutions (conjugates, GRGDSP, CS, and NS (both nonlabeled)): 4 μM solutions in SDI H_2O. Hybridization solutions: For each 3-fold experiment, 35 μL of CS* stock solution, 35 μL of competitor stock solution, 35 μL PBS (10×), and 245 μL SDI H_2O were mixed in a tube. Hybridization procedure: Tubes with hybridization solution were heated up to 95 °C for 2 min in a thermomixer and immediately shock-cooled for 5 min on ice (denaturation of possible secondary structures). Each sample carrying AS was placed in the center of a well in a 12-well cell culture plate. Empty wells and interstices between all wells were filled with SDI H_2O to prevent evaporation from samples. 100 μL of the hybridization solution was dropped and homogeneously spread on each sample. The 12-well plates were immediately placed in the dark. After 1 h, each sample was rinsed 4 times with 3 mL PBS and momentarily dunked into 300 mL SDI H_2O. Samples were dried in the dark and measured under a semiconductor radiation detector (PIPS, Canberra Ortec, Inc.). The determined count rate was used to calculate the amount of substance of CS* on the surface.

QCM Hybridization. Device: Q-Sense D300 (LOT-Oriel GmbH & Co. KG, Darmstadt, Germany): complete system with measurement chambers, electronics unit, and PC software for acquisition and analyzing. Sensor crystals: QSX 301 Standard Gold (LOT-Oriel), gold-coated quartz crystals with a sensing area of 1.13 cm^2. Substances: SDI H_2O, 6-mercapto-hexan-1-ol (MCH), PBS 10× stock solution, ethanol (undenatured)

(EtOH). Solutions: 70% EtOH in SDI H_2O, 400 nM thiolated anchor strand (HS-AS) in PBS, 1 mM MCH in PBS, 400 nM conjugate, CS or NS in PBS. Procedure: Loop and cell were disinfected with 70% EtOH and thoroughly rinsed with PBS. Frequency was observed in the third overtone (14.85 MHz). Further PBS was added to the cell until a stable frequency was reached. 1.5 mL HS-AS solution was filled into the loop and tempered for at least 10 min, and 0.5 mL HS-AS was then injected into the cell. Frequency change was observed until a stable value was reached and a further 0.5 mL HS-AS was added. After reaching the stable state, again the cell was rinsed and filled with PBS until frequency stability. 1.5 mL MCH was filled into the loop and tempered for at least 10 min, and 0.5 mL MCH was then injected into the cell. Frequency change was observed until a stable value was reached and a further 0.5 mL MCH added. After reaching the stable state again, the cell was rinsed and filled with PBS until frequency stability. Subsequently, the same procedure was carried out for the conjugates, CS, or NS. Obtained data were analyzed using the Sauerbrey equation (*26*) and adsorption isotherms. Fitting of adsorption isotherms: All tested isotherms were linearized, and processed data were checked for a linear dependence. For the tested isotherms, the following plots were analyzed by linear regression: Langmuir, $1/n_{ads}$ vs $1/c$; Freundlich, $\ln(n_{ads})$ vs $\ln(c)$; Temkin, $\ln(n_{ads})$ vs $\ln(c)$; Frumkin, $\ln(1/c)$ vs n_{ads}; own exponential type, n_{ads} vs e^c.

Osteoblast Adhesion. Substances: Cycloheximid (CHX), trichloroacetic acid (TCAA), [^{3}H]-thymidine (GE Healthcare Europe GmbH), HI (heat inactivated)-FCS (Th. Geyer Hamburg GmbH & Co. KG), McCoy's 5A medium (BioConcept GmbH), $Na_2HPO_4 \cdot 2H_2O$, KCl, KH_2PO_4, $CaCl_2$, $MgCl_2$, NaCl. Cell culture medium: McCoy's 5A w/o serum with 15% HI-FCS and 1 μCi [^{3}H]-thymidine/mL. Assay medium: McCoy's 5A with 100 μM CHX. PBS: 0.136 M NaCl, 2.7 mM KCl, 8.1 mM Na_2HPO_4, 1.5 mM KH_2PO_4, 1.1 mM $MgCl_2$, 0.9 mM $CaCl_2$. Lysis buffer: 100 mM NaOH, 22 mM Na_2CO_3, 1% sodium dodecylsulfate. Functionality of ODN-GRGDSP conjugates in adhesion competition assay: Human osteosarcoma cells (cell line SAOS-2) were prelabeled with 1 μCi [^{3}H]-thymidine/mL of culture medium for 24 h and incubated for the last 3 h with 100 μM CHX. Cells were trypsinized, resuspended in assay medium, and incubated with 20 μM of conjugates or 10−40 μM GRGDSP peptide as a reference substance for 20 min at 25 °C. 25 000 cells/cm^2 were plated onto 24-well culture plates. After 2 h of incubation at 37 °C in 5% CO_2 atmosphere, the culture medium was removed and adherent cells were washed three times with PBS. During the last rinsing step, the cell culture dish was shaken for 5 min at 100 rpm. The cells were then fixed with 10% TCAA and rinsed with 96% ethanol. After cell lysis, the amount of incorporated [^{3}H]-thymidine that corresponds to the number of adherent cells was determined by liquid scintillation counting. Functionality of immobilized ODN-GRGDSP conjugates: Radiolabeling and harvesting of the SAOS-2 osteoblasts was done as described above. 25 000 cells/cm^2 were plated in 200 μL of assay medium onto the modified titanium samples. Two hours after incubation at 37 °C in 5% CO_2 atmosphere, the culture medium was removed and adherent cells were washed three times with PBS. All further experimental steps and analysis are performed as described before.

RESULTS

RP-HPLC. The chromatograms of the product fractions of the four synthesized conjugates are shown in Figure 3. All of them have a clear peak. To ensure that these peaks represent the conjugate, the arginine within the peptide was assayed via the Sakaguchi reaction.

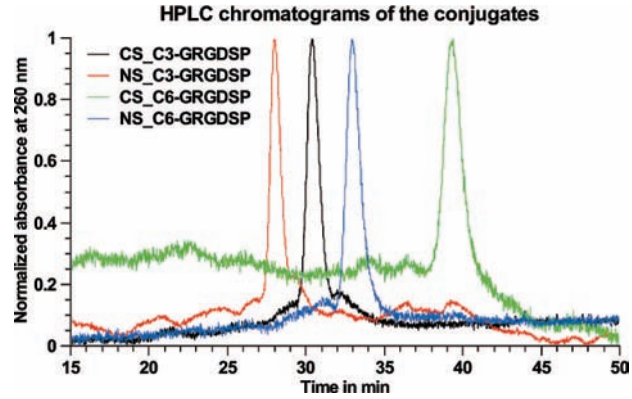

Figure 3. RP-HPLC chromatograms of the four conjugates.

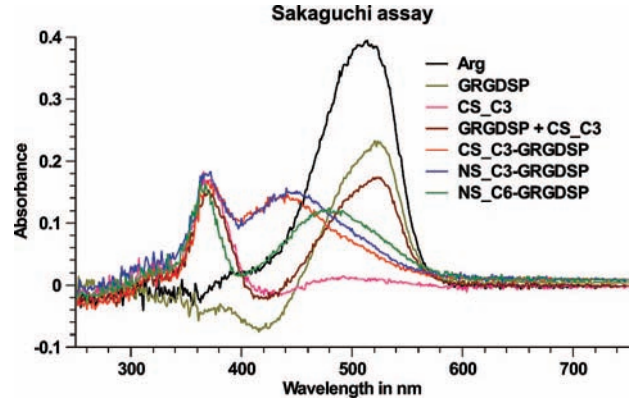

Figure 4. Selected absorption spectra of Sakaguchi products. Arginine, GRGDSP, and a mixture of GRGDSP and a modified nucleic acid precursor of the conjugate (CS_C3) show the expected absorption maximum at approximately 520 nm. The conjugates show a maximum shifted to shorter wavelengths.

Sakaguchi Assay. For verifying GRGDSP in the resulting conjugates, the arginine residue was derivatized and thus detected by Sakaguchi assay. The conjugates, their precursors as mixtures, and single components were treated with Sakaguchi reagents, and UV−vis spectra were obtained for each reaction product. Precursors and mixtures thereof were used as reference substances for the conjugates, and as visible in Figure 4, they show the expected absorption maximum at approximately 520 nm. Conjugates also exhibit a color after the Sakaguchi reaction but their absorption maximum is shifted to shorter wavelengths between 450 and 500 nm (Figure 4). Since these spectra only occur for the conjugates, one has to take into account that this shift is characteristic for such conjugates. Altogether, the Sakaguchi assay proves the presence of arginine and thus of GRGDSP in the conjugate. The observed shift in absorption maxima seems to be characteristic for the conjugates.

Competitive Hybridization. This key experiment should prove the mandatory ability of the conjugates to hybridize with surface-immobilized AS. For surface hybridization, we used radiolabel signaling in a procedure called "competitive hybridization": A mixture of a radiolabeled complementary strand (CS*) and the particular sample (conjugate, GRGDSP, etc.) was applied to the surface. In the case of a noncomplementary sample, all available anchor strands (AS) on the surface should hybridize with CS*. If the sample contains a complementary sequence, it competes with CS* for the AS. Thus, the amount of surface-bound CS* should be distinctly lower and a less intensive radioactive signal from the surface is proof for sample hybridization.

Results obtained using competitive hybridization with 1:1 mixtures of CS* and the analyte show that conjugates of

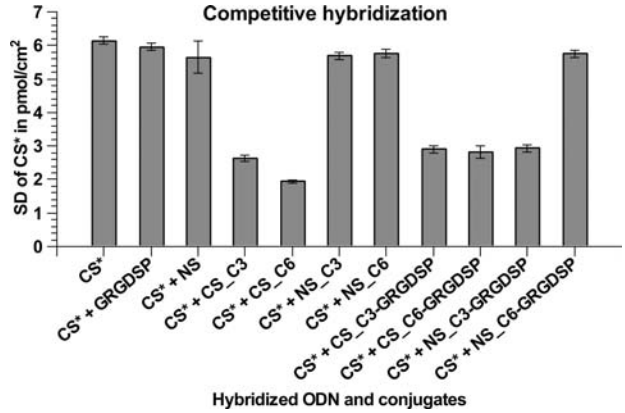

Figure 5. Competitive hybridization. Clearly declined amounts of radiolabeled CS* in the case of modified complementary strands and their conjugates prove their hybridizability. Noncomplementary strands, NS_C6-GRGDSP, and GRGDSP do not show an inhibitory effect on CS* binding, while NS_C3_GRGDSP caused a clear decline indicating nonspecific inhibitory effects on CS* hybridization. (SD - surface density).

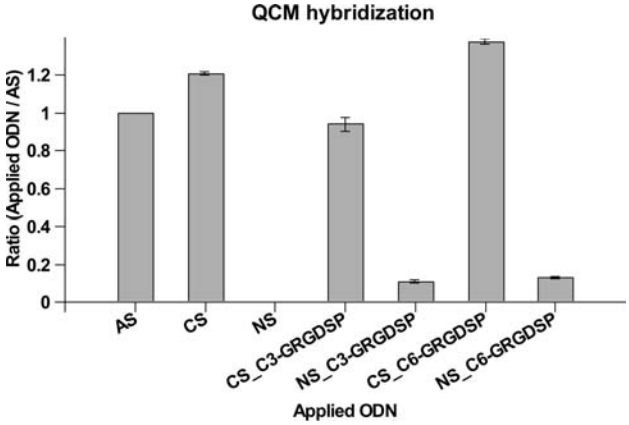

Figure 6. QCM hybridization experiments. The extent of binding of complementary conjugates (approximately 100% related to AS) to gold-coated quartz crystals modified with thiolated anchor strand (HS-AS) proves the ability to hybridize to surface-bound HS-AS, while non-complementary conjugates only show week nonspecific binding.

complementary strands are able to hybridize with anchor strands fixed in the anodic oxide layer, since the radioactive signal of CS* declined significantly (Figure 5). No difference was observed for the two spacer regions used for the CS conjugates.

QCM Hybridization. Gold-coated quartz crystals modified with thiolated anchor strands (HS-AS) as the approved system (*27*−*31*) were used to examine the surface hybridization of the conjugates and nonconjugated ODN, since the adaptation of our immobilization system to QCM measurements requiring anodic polarization of titanium-coated quartz crystals is still in progress. These experiments prove the preservation of hybridization ability of the complementary conjugates, since surface densities of up to 32 pmol·cm^{-2} were obtained. Noncomplementary conjugates show a small extent of binding with 2−3 pmol·cm^{-2}. These results are given in Figure 6 as relative numbers with respect to immobilized AS. Related to immobilized anchor strand, CS_C3-GRGDSP does not hybridize for 100%, while CS_C6_GRGDSP shows a higher extent of binding (>100%).

Surface hybridization was further examined in real time using adsorption isotherms. Fitted isotherms included the following types: Langmuir, Freundlich, Temkin, Frumkin (*41*, *43*, *44*), and an own exponential equation. A summary is given in Table 1.

Table 1. Summary of Suitable Hybridization Adsorption Isotherms for QCM Hybridization[a]

	type of isotherm				
strand	Langmuir	Freundlich	Temkin	Frumkin	own exponential
CS-C3-GRGDSP	N	N	Y	Y	Y
CS-C6-GRGDSP	N	N	N	N	Y
CS	N	Y	N	Y	Y

[a] Possibility to fit selected isotherm: Y - yes, N - no.

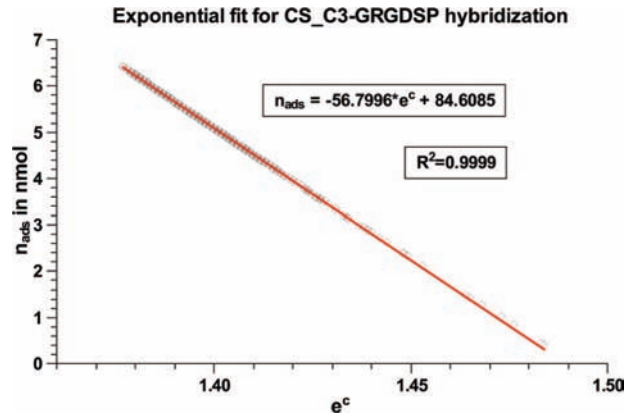

Figure 7. Empirically found exponential adsorption isotherm shown for CS_C3-GRGDSP as example. The fit shows excellent linearity.

Hybridization is analyzed for CS, CS_C3_GRGDSP, and CS_C6_GRGDSP. Neither of the species followed the Langmuir isotherm. Data for CS could perfectly be fit to the Freundlich model, but the conjugates could not. The Temkin isotherm could only be applied for CS_C3-GRGDSP, the Frumkin isotherm for CS_C3-GRGDSP and CS. However, all of the hybridization combinations can be fit by an empirically found exponential adsorption isotherm (*1*)

$$n_{ads} = k_1 \cdot e^c + k_2 \quad (1)$$

This empiric exponential isotherm for CS_C3-GRGDSP is exemplarily given in Figure 7. The term n_{ads} is the hybridized amount of substance, k_1 and k_2 are constants, and c is the concentration of the adsorbate.

Osteoblast Adhesion. For testing the functionality of dissolved and immobilized ODN-GRGDSP conjugates, two sets of in vitro experiments with osteoblasts were performed. The cells were (i) preincubated with the ODN-GRGDSP conjugates in order to occupy potential binding sites at the cell surface integrin receptors and inhibit their adhesion to cell culture plates (competition assay). (ii) Osteoblasts were plated onto ODN-GRGDSP modified titanium samples in order to promote adhesion by presentation of RGD binding sites to the cells (adhesion assay).

The results of the competition assay are shown in Figure 8a,b. The conjugates were able to suppress adhesion to the same or slightly higher extent than the GRGDSP control peptide. No differences in integrin blocking were observed for the two spacers of the conjugates.

Aminoalkylated ODNs were also able to suppress adhesion of osteoblasts on tissue culture polystyrene surfaces (Figure 8a). However, the conjugates always showed a higher suppression, indicating a specific effect of GRGDSP within the conjugate molecule. This is highlighted in Figure 8b where the effect of each aminoalkylated ODN is defined as 100% and the effect of the corresponding conjugate is shown relative to it. The only exception is NS_C6 and its conjugate, both exhibiting a similar effect.

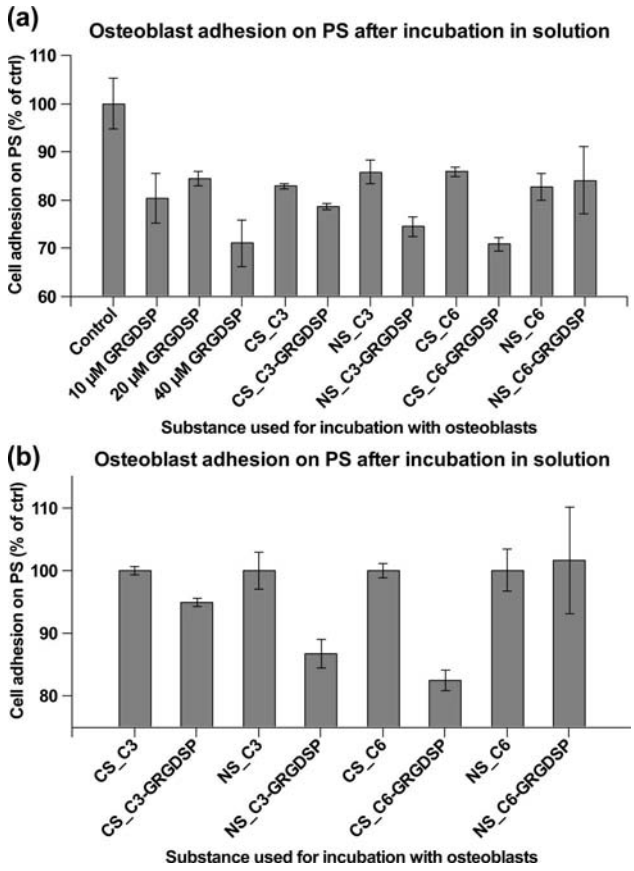

Figure 8. (a) Adhesion of SAOS-2 cells on polystyrene (PS) wells after incubation with different additives (competition assay). If no concentration is given, 20 μM were used. In the case of the control (ctrl), no additives were used. (b) Spotlighted results of part a. Adhesion of SAOS-2 cells on polystyrene (PS) wells after incubation with aminoalkylated ODN and their conjugates. Each ODN is normalized (100%), and the effect of its corresponding conjugate is given relative to it.

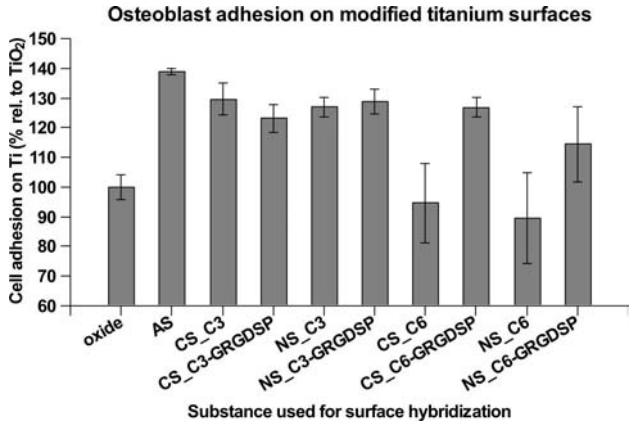

Figure 9. Adhesion of SAOS-2 cells on modified titanium surfaces. All samples were anodically oxidized to immobilize AS and later hybridized with the stated substances. Mere oxide layer and immobilized AS served as control.

Figure 9 shows osteoblast adhesion on titanium surfaces modified with AS and conjugates compared to merely anodically oxidized titanium (100%). Surfaces with immobilized AS exhibit the highest number of adherent cells, which indicates nonspecific interaction between AS and compartments of the cell membranes ("Specific binding" in this case only means interaction between integrins and the RGD peptide. All other interactions are regarded as "nonspecific".). In the case of treating AS-modified titanium with aminopropylated ODN and their conjugates, binding of the osteoblasts is lower than for AS alone and no clear difference between ODN and conjugates can be seen. If the AS-modified surface is treated with the aminohexylated ODN, there is a distinct decline in osteoblast binding compared to the other ODN species. However, their conjugates with GRGDSP show nearly the same adhesion behavior as the other ODN and conjugates. As already observed in suspension, different spacer properties do not affect the binding capacity of the RGD domain toward integrins of osteoblasts.

DISCUSSION

The aim of this work is the modular biosurface engineering of implants using nucleic acid self-organization in order to modify an implant surface according to special patients' needs. Therefore, full functionality of the conjugates must be assured for all stages of the immobilization and the implantation process. Storage conditions of the anchor strand modified implants have to ensure their hybridizability. The nucleic acid domain of the conjugate must retain its ability to hybridize when applied to AS-modified surfaces prior to implantation. Functional domains of the conjugates have to act properly in the body. We consider a working functional group in all stages of the production and application as crucial for its later functionality in the body. The obtained results must therefore be discussed from this point of view.

Analytical Characterization of the Conjugates. Successful conjugation had to be proven first. This was achieved combining RP-HPLC and the Sakaguchi reaction for assaying the conjugate fractions. RP-HPLC charts show single product peaks without major byproduct. The existence of arginine and thus of GRGDSP in the product fraction was successfully demonstrated using the Sakaguchi assay for arginine. Furthermore, the availability of the arginine for the reaction with 1-naphthol reinforces that the conjugation takes place via the amino terminus of glycine as intended and not accidentally via the guanidinium group of arginine. Thus, the integrin-binding domain RGD keeps its conformation and functionality. An interesting point for further scrutiny is the observed shift in the absorption maxima of the Sakaguchi products of the conjugates. This shift is presumed to be characteristic for ODN-GRGDSP conjugates. Possibly, the formed adduct interacts with the bases of the ODN. It must be a noncovalent interaction that is only possible in close proximity within a molecule, since the shift effect is not seen if mixtures of activated ODN and GRGDSP are subject to Sakaguchi assay. The different behavior of the more hydrophilic conjugates (CS_C3- and NS_C3-GRGDSP coupled with DST) and the more hydrophobic NS_C6-GRGDSP coupled with DSS supports the assumption of intramolecular interaction. The ODN_C3-DST conjugates have a shorter linkage domain, and therefore, the 1-naphthol adduct (λ_{max} = 450 nm) is closer to the nucleobases. In the case of NS_C6-GRGDSP (DSS), the longer linkage domain allows higher intramolecular flexibility and distances. This state is closer to the mere mixture and thus exhibits a shift that is not as high (λ_{max} = 485 nm). All these assumptions have to be subject to further examination, which might be the basis for the establishment of a special test for conjugates of RGD peptides and nucleic acids.

Hybridization Ability of the Conjugates. The experiments using competitive and QCM hybridization proved that our conjugates are able to hybridize to AS immobilized on titanium and gold surfaces. This highlights the retention of hybridizability under different conditions, which is the main functional prerequisite of the whole system for implant surface modification. Furthermore, the different spacer structure within the conjugate molecules does not affect the general ability to

hybridize but might slightly influence nonspecific binding on gold (QCM).

During competitive hybridization, the radioactive signal dropped to about 50% for equally concentrated mixtures of the competing strands. Noncomplementary strands (NS, NS_C3, NS_C6), the hexapeptide GRGDSP, and the NS_C6-GRGDSP conjugate do not interfere with CS* hybridization to surface-bound AS (Figure 5), since there is almost no loss in radioactive signal. In the case of NS_C3-GRGDSP, a competition with CS* occurred, although the conjugate is unable to hybridize specifically due to its noncomplementarity. Thus, the interaction must be based on other principles than hybridization. The conjugate may bind nonspecifically to the AS-modified titanium surface via hydrogen bonds of the bases, the sugar−phosphate backbone, or the peptide to AS and/or TiO_2, and/or via hydrophobic interactions between the bases of the strands ("Nonspecific" with respect to nucleic acids always means other interaction than Watson−Crick base pairing.). The conjugate might also interact with CS*, thus interfering with hybridization. The extent of nonspecific interaction might be very different for various conjugates, since they differ with respect to sequence, length, aminoalkylation, and linker molecule. Thus, certain noncomplementary conjugates might interact with ODN-modified surfaces. However, even if nonspecific interaction can occur hybridization is always more stable, predictable, and controllable, and therefore to be preferred.

The discrimination between CS and different conjugates thereof should also be reached using adsorption isotherms. Hybridization at surfaces is distinctly different from solution hybridization. The limited sites for hybridization and molecular interaction between the single strands and/or hybrids led to the treatment of surface hybridization as a special case of the adsorption process often called "adsorption hybridization". Therefore, adsorption isotherms are widely used for the characterization of surface hybridization (*32*−*40*). Mostly, the Langmuir isotherm (*41*) or modifications thereof are applied. Especially in the case of mismatched hybrids, the Sips isotherm (*42*) is observed (*32, 39*). Discrimination of perfectly matched and mismatched strands using adsorption isotherms was already achieved when surface hybridizations were characterized using Langmuir and Sips isotherms as reported by Peterson et al. and Stoermer et al. (*32, 39*). The Langmuir model is based on the assumption that there is a maximum surface density that can be reached and that all sites are energetically equivalent. However, the Sips isotherm deals with a distribution of energetically different sites. Since we do not assume such a distribution, the Langmuir isotherm as a special case of the Sips isotherm was applied first, also because the immobilized anchor strands represent a limited number of sites (N_{max}). Intermolecular forces and mutual interference are expected for the negatively charged nucleic acids hybridizing to the surface. The Frumkin isotherm (*43, 44*) describes such adsorption processes and was therefore applied to our system, too. Further applied isotherms included an own empirical exponential isotherm, the empirical Freundlich isotherm, and the Temkin isotherm that assumes a linear decline of adsorption heat with rising surface density (*44*).

As our results show, the Langmuir isotherm is not suitable to describe the surface hybridization of CS and their conjugates. This is reasonable, since one can expect an increase in intermolecular interaction with proceeding hybridization, which is not consistent with the Langmuir thermodynamic identity of all surface sites. The Temkin isotherm indicating a linear decline in adsorption heat could be fitted for CS_C3-GRGDSP hybridization, and CS hybridization could excellently be fitted with the empirical Freundlich isotherm. CS and CS_C3-GRGDSP hybridization could also be characterized using a Frumkin isotherm that takes intermolecular interaction into account. All hybridizations of the complementary species could be fitted by the empirically found exponential isotherm though the thermodynamic fundamentals are not yet clear. Even though the statistical basis is not yet broad enough, the different isotherms to fit hybridization indicate their potential for discrimination among different complementary species. Furthermore, kinetic and thermodynamic parameters can be obtained when the isotherms are analyzed. Thus, a clear discrimination between hybridization and nonspecific binding is possible. If the Frumkin isotherm (*2*) is suitable, data such as the energy of interaction of the molecules (E_i) (*3*) and the Gibbs free energy of surface hybridization (ΔG^0_{SH}) (*4*) can be calculated (*43, 44*) from the slope ($2a$) and the intercept ($\ln b$):

$$\ln \frac{\Theta}{(1-\Theta)c} = 2a\Theta + \ln b \tag{2}$$

$$E_i = -a2\Theta RT \tag{3}$$

$$\Delta G^0_{SH} = -2.3025RT \lg(55.5b) \tag{4}$$

In particular, the magnitude of ΔG^0_{SH} can give important information on the kind of binding (hybridization vs nonspecific binding).

These investigations will be broadened and extended to titanium-coated quartz crystals.

Biological Functionality of the Conjugates. The developed system for modular biosurface engineering must demonstrate its feasibility above all in the living system. The first experiments were done in vitro with osteoblast cell cultures. All conjugates were able to interact with osteoblasts in suspension, resulting in diminished cell adhesion on polystyrene even in a higher scale than with GRGDSP alone. However, the aminoalkylated ODNs also lead to a decline in cell adhesion after incubation. Obviously, ODNs can bind to osteoblasts, too, and subsequently reduce nonspecific binding on polystyrene. The principles of that interaction remain yet unclear. An explanation might be that our anchor strand has a kind of an aptamer functionality that might also be supported or induced by the substrate (induced fit) or that bases of a distinct sequence interact with RGD−peptides.

One must assume that the conjugates bind specifically to integrins via their RGD domain but also nonspecifically via their ODN compartment, while aminoalkylated ODNs only bind nonspecifically. This might explain why binding of the conjugates is even stronger than that of GRGDSP alone. In spite of the positive results, efforts have to be made to discriminate (specific) integrin binding and nonspecific binding in order to enable the evaluation of the specific effect of the conjugates.

Similar effects to the abovementioned were observed when osteoblasts were seeded on modified titanium surfaces. The conjugates hybridized to anodically immobilized AS increased osteoblast binding up to 125% compared to anodically thickened TiO_2. As in solution, the aminopropylated ODNs exhibit a nonspecific effect leading to increased osteoblast binding on modified Ti/TiO_2 in the same range as with conjugates. Thus, a clear discrimination between specific interaction with integrins and nonspecific interaction with ODN remains a problem for a proper evaluation of enhanced osteoblast adhesion. Beneficial biological effects of DNA immobilized on titanium have already been discussed by van den Beucken et al. (*45, 46*) earlier and might lead to enhanced osteoblast adhesion here, too. Only in the case of aminohexylated ODN and their conjugates can a clear difference be seen. However, the reason for the effect of NS_C6-GRGDSP is still dubious, since this conjugate is unable to hybridize to AS on the surface. As discussed above, this might be seen as a consequence of aptamer-like interaction. Future discrimination experiments for evaluation of the actual effect of GRGDSP within the conjugates should include the following:

more stringent adhesion/ desorption conditions using modified culture media with respect to parameters such as ionic strength and/or pH value; the use of different ODN sequences, thus reducing indefinable interactions (since different sequences are assumed to have different nonspecific effects).

Different properties of the conjugates (length, hydrophobicity) caused by the varied spacer molecule structures did not have an influence on biological activity. Such independence could be advantageous for further conjugations using other biomolecules and different linkers and linkage reactions.

CONCLUSIONS

As part of an ODN-based modular system for biosurface engineering in the field of implantology, conjugates of ODN and GRGDSP as recognition sequence for integrins were investigated in vitro. Successful conjugation could be proven using the Sakaguchi assay. The conjugates kept their ability to hybridize to different surfaces (Au, Ti) with immobilized anchor strands as shown with competitive and QCM hybridization on titanium and gold, respectively.

The comparison of the bound amounts of radiolabeled strands for different mixtures of conjugates (with respect to ratio and kind) in future experiments is expected to give information on the kind of interaction—hybridization or nonspecific binding.

First QCM experiments proved the applicability of adsorption isotherms for hybridization characterization. Experiments using the QCM will be extended to titanium-coated quartz crystals on which AS will be immobilized by anodic oxidation. For all QCM experiments (Au and Ti coating), the applicability of adsorption isotherms has to be scrutinized thoroughly, since surface densities of AS differ for gold (up to 32 pmol·cm^{-2}) and titanium (up to 7 pmol·cm^{-2}). Furthermore, the nonspecific interaction is different for both materials, which can influence the behavior. Types of isotherm and derived thermodynamic and kinetic data will be used for strand and conjugate discrimination. Again, the knowledge of surface hybridization kinetics is crucial for the planned patient-specific implant modification shortly before surgery.

Our future goal—an enhanced binding of osteoblasts on titanium implant materials within a modular and flexible system of surface modification—is achievable, since the in vitro experiments showed increased binding of osteoblasts on the conjugate-modified titanium surfaces. The nonspecific binding effects on merely anchor strand-modified surfaces suggest that osteoblasts may also bind to ODN or at least to certain ODN sequences. This effect has to be further scrutinized and might be used for cell attachment, too. Experiments in the near future, however, must focus on better discrimination between interactions of osteoblasts with conjugates or with ODN on surfaces, respectively. This is the prerequisite for a clear evaluation of the biological activity of the system if RGD is used. The analysis and separation of the conjugation products using chromatographic methods must be improved with respect to later in vivo experiments. Further interesting biomolecules such as VEGF (vascular endothelial growth factor) and BMP-2 (bone morphogenic protein) and antibiotics such as gentamycin have recently been conjugated to ODN to broaden the modularity and flexibility of the system and to study interactions if several conjugates are immobilized. This advanced system is under scrutiny at the moment.

ACKNOWLEDGMENT

Financial Support of the Deutsche Forschungsgemeinschaft (DFG), contract grant numbers WO494/14 and SCHW638/3-1, is greatly acknowledged. J. Michael would like to thank the Free State of Saxony and the Studentenwerk Dresden for their Graduate Grant. The authors would like to thank Dr. S. Taut and his staff of TU Dresden Central Radionuclide Laboratory for providing the analysis facilities and methodical support. We thank Dr. L. Renner of the Leibniz Institute of Polymer Research Dresden for supplying the QCM device and giving advice.

LITERATURE CITED

(1) Ratner, B. D. (2001) A perspective on titanium biocompatibility, In *Titanium in Medicine* (Brunette D. M., Tengvall P., Textor M., and Thomsen P., Eds.) pp 1−12, Springer, Berlin.

(2) Okazaki, Y., and Gotoh, E. (2005) Comparison of metal release from various metallic biomaterials in vitro. *Biomaterials 26*, 11–21.

(3) Gasser, B. (2001) Design and engineering criteria for titanium devices, In *Titanium in Medicine* (Brunette D. M., Tengvall P., Textor M., and Thomsen, P., Eds.) pp 673−746, Springer, Berlin.

(4) Jones, J. D., Lupori, J., Van Sickels, J. E., and Gardner, W. (1999) A 5-year comparison of hydroxyapatite-coated titanium plasma-sprayed and titanium plasma-sprayed cylinder dental implants. *Oral Surg. Oral Med. Oral Pathol. Oral Radiol. Endod. 87*, 649–652.

(5) van Steenberghe, D., Jacobs, R., Desnyder, M., Maffei, G., and Quirynen, M. (2002) The relative impact of local and endogenous patient-related factors on implant failure up to the abutment stage. *Clin. Oral Implants Res. 13*, 617–622.

(6) van Steenberghe, D., Quirynen, M., Molly, L., and Jacobs, R. (2003) Impact of systemic diseases and medication on osseointegration. *Periodontol. 2000 33*, 163–171.

(7) Cooper, L. F. (1998) Biologic determinants of bone formation for osseointegration: clues for future clinical improvements. *J. Prosthet. Dent. 80*, 439–449.

(8) Massia, S. P., and Stark, J. (2001) Immobilized RGD peptides on surface-grafted dextran promote biospecific cell attachment. *J. Biomed. Mater. Res. 56*, 390–399.

(9) Zreiqat, H., Akin, F. A., Howlett, C. R., Markovic, B., Haynes, D., Lateef, S., and Hanley, L. (2003) Differentiation of human bone-derived cells grown on GRGDSP-peptide bound titanium surfaces. *J. Biomed. Mater. Res., Part A 64*, 105–113.

(10) Davis, D. H., Giannoulis, C. S., Johnson, R. W., and Desai, T. A. (2002) Immobilization of RGD to 1 1 1 silicon surfaces for enhanced cell adhesion and proliferation. *Biomaterials 23*, 4019–4027.

(11) Porte-Durrieu, M. C., Labrugere, C., Villars, F., Lefebvre, F., Dutoya, S., Guette, A., Bordenave, L., and Baquey, C. (1999) Development of RGD peptides grafted onto silica surfaces: XPS characterization and human endothelial cell interactions. *J. Biomed. Mater. Res. 46*, 368–375.

(12) Tosatti, S., Schwartz, Z., Campbell, C., Cochran, D. L., VandeVondele, S., Hubbell, J. A., Denzer, A., Simpson, J., Wieland, M., Lohmann, C. H., Textor, M., and Boyan, B. D. (2004) RGD containing peptide GCRGYGRGDSPG reduces enhancement of osteoblast differentiation by poly(L-lysine)-graft-poly(ethylene glycol)-coated titanium surfaces. *J. Biomed. Mater. Res., Part A 68*, 458–472.

(13) Beutner, R., and Sewing, A. (2007) Electrochemically supported immobilization of a cyclic peptide containing the RGD sequence on Ti6Al4V. *Biomaterialien 8*, 25–31.

(14) Mikulec, L. J., and Puleo, D. A. (1996) Use of p-nitrophenyl chloroformate chemistry to immobilize protein on orthopedic biomaterials. *J. Biomed. Mater. Res. 32*, 203–208.

(15) Ishihara, M., Saito, Y., Yura, H., Ono, K., Ishikawa, K., Hattori, H., Akaike, T., and Kurita, A. (2000) Heparin-carrying polystyrene to mediate cellular attachment and growth via interaction with growth factors. *J. Biomed. Mater. Res. 50*, 144–152.

(16) Rö*β*ler, S., Scharnweber, D., Wolf, C., and Worch, H. (2000) Investigation of the adsorption of tropocollagen type I on titanium and Ti6Al4V. *J. Adhes. Sci. Technol. 14*, 453–465.

(17) Michael, J., Beutner, R., Hempel, U., Scharnweber, D., Worch, H., and Schwenzer, B. (2007) Surface modification of titanium-based alloys with bioactive molecules using electrochemically

fixed nucleic acids. *J. Biomed. Mater. Res., Part B 80*, 146–155.
(18) Guo, K., Scharnweber, D., Schwenzer, B., Ziemer, G., and Wendel, H. P. (2007) The effect of electrochemical functionalization of Ti-alloy surfaces by aptamer-based capture molecules on cell adhesion. *Biomaterials 28*, 468–474.
(19) Beutner, R., Michael, J., Förster, A., Schwenzer, B., and Scharnweber, D. Immobilization of oligonucleotides on titanium based materials by partial incorporation in anodic oxide layers *Biomaterials* (accepted), DOI: 10.1016/j.biomaterials.2009.01.047.
(20) Ruth, J. (1991) Conjugation of enzymes to linker arm oligodeoxynucleotides, In *Oligonucleotides and analogues. A practical approach* (Eckstein, F.) pp 270−274, IRL Press, New York.
(21) Puglisi, J. D., and Tinoco, I. J. (1989). Absorbance melting curves of RNA, In *Methods in Enzymology 180: RNA Processing Part A: General Methods* (Dahlberg, J., Abelson, J., and Simon, M.) pp 304−325, Academic Press, New York.
(22) Sakaguchi, S. (1925) Über eine neue Farbenreaktion von Protein und Arginin. *J. Biochem. (Tokyo) 5*, 24–31.
(23) Kleber, H., Schlee, D., and Schöpp, W. (1997) Biochemisches Praktium. Methoden für Studium, Praxis, Forschung. Gustav Fischer Verlag, Jena.
(24) Weber, C. J. (1930) A modification of Sakaguchi's reaction for the quantitative determination of arginine. *J. Biol. Chem. 86*, 217–222.
(25) Chinard, R. P. (1948) Use of the hypobromite reaction for the estimation of ammonia plus urea nitrogen in urines containing large amounts of protein; the reaction of alkaline hypobromite with proteins. *J. Biol. Chem. 176*, 1449–1457.
(26) Sauerbrey, G. (1959) Verwendung von Schwingquarzen zur Wägung dünner Schichten und zur Mikrowägung. *Z. Phys. 155*, 206–222.
(27) Okahata, Y., Matsunobu, Y., Ijiro, K., Mukae, M., Murakami, A., and Makino, K. (1992) Hybridization of nucleic acids immobilized on a quartz crystal microbalance. *J. Am. Chem. Soc. 114*, 8299–8300.
(28) Patolsky, F., Lichtenstein, A., and Willner, I. (2000) Amplified microgravimetric quartz-crystal-microbalance assay of DNA using oligonucleotide-functionalized liposomes or biotinylated liposomes. *J. Am. Chem. Soc. 122*, 418–419.
(29) Huang, E., Satjapipat, M., Han, S., and Zhou, F. (2001) Surface structure and coverage of an oligonucleotide probe tethered onto a gold substrate and its hybridization efficiency for a polynucleotide target. *Langmuir 17*, 1215–1224.
(30) Patolsky, F., Weizmann, Y., and Willner, I. (2002) Redox-active nucleic-acid replica for the amplified bioelectrocatalytic detection of viral DNA. *J. Am. Chem. Soc. 124*, 770–772.
(31) Cho, Y., Kim, S., Kim, Y. A., Lim, H. K., Lee, K., Yoon, D., Lim, G., Pak, Y. E., Ha, T. H., and Kim, K. (2004) Characterization of DNA immobilization and subsequent hybridization using in situ quartz crystal microbalance, fluorescence spectroscopy, and surface plasmon resonance. *J. Colloid Interface Sci. 278*, 44–52.
(32) Peterson, A. W., Wolf, L. K., and Georgiadis, R. M. (2002) Hybridization of mismatched or partially matched DNA at surfaces. *J. Am. Chem. Soc. 124*, 14601–14607.
(33) Binder, H., Preibisch, S., and Kirsten, T. (2005) Base pair interactions and hybridization isotherms of matched and mismatched oligonucleotide probes on microarrays. *Langmuir 21*, 9287–302.
(34) Binder, H. (2006) Thermodynamics of competitive surface adsorption on DNA microarrays. *J. Phys.: Condens. Matter 18*, 491–523.
(35) Halperin, A., Buhot, A., and Zhulina, E. B. (2004) Sensitivity, specificity, and the hybridization isotherms of DNA chips. *Biophys. J. 86*, 718–730.
(36) Glazer, M., Fidanza, J. A., McGall, G. H., Trulson, M. O., Forman, J. E., Suseno, A., and Frank, C. W. (2006) Kinetics of oligonucleotide hybridization to photolithographically patterned DNA arrays. *Anal. Biochem. 358*, 225–238.
(37) Knoll, W., Yu, F., Neumann, T., Schiller, S., and Naumann, R. (2003) Supramolecular functional interfacial architectures for biosensor applications. *Phys. Chem. Chem. Phys. 5*, 5169–5175.
(38) Tawa, K., Yao, D., and Knoll, W. (2005) Matching base-pair number dependence of the kinetics of DNA-DNA hybridization studied by surface plasmon fluorescence spectroscopy. *Biosens. Bioelectron. 21*, 322–329.
(39) Stoermer, R. L., Cederquist, K. B., McFarland, S. K., Sha, M. Y., Penn, S. G., and Keating, C. D. (2006) Coupling molecular beacons to barcoded metal nanowires for multiplexed, sealed chamber DNA bioassays. *J. Am. Chem. Soc. 128*, 16892–16903.
(40) Vainrub, A., and Pettitt, B. M. (2002) Coulomb blockage of hybridization in two-dimensional DNA arrays. *Phys. Rev. E 66*, 041905/1–4.
(41) Langmuir, I. (1918) The adsorption of gases on plane surfaces of glass, mica and platinum. *J. Am. Chem. Soc. 40*, 1361–1403.
(42) Sips, R. (1948) On the structure of a catalyst surface. *J. Chem. Phys. 16*, 490–495.
(43) Frumkin, A. (1926) Über die Beeinflussung der Adsorption von Neutralmolekülen durch ein elektrisches Feld. *Z. Phys. 35*, 792–802.
(44) Dörfler, H.-D. (1994) *Grenzflächen- und Kolloidchemie*, pp 143−155, VCH, Weinheim.
(45) van den Beucken, J. J. J. P., Vos, M. R. J., Thune, P. C., Hayakawa, T., Fukushima, T., Okahata, Y., Walboomers, X. F., Sommerdijk, N. A. J. M., Nolte, R. J. M., and Jansen, J. A. (2006) Fabrication, characterization, and biological assessment of multilayered DNA-coatings for biomaterial purposes. *Biomaterials 27*, 691–701.
(46) van den Beucken, J. J. J. P. (2007) DNA-based coatings in implantology - Utilization of the structural properties of the DNA-molecule to modulate cell and tissue response. Dissertation, Radboud Universiteit Nijmegen, Medische Wetenschappen.

BC800372E

Bioconjugate Chemistry 20th Anniversary

Subscriber access provided by SHEMYAKIN-OVCHINNIKOV INST

Article

Biotin-Tagged Probes for MMP Expression and Activation: Design, Synthesis, and Binding Properties

Elisa Dragoni, Vito Calderone, Marco Fragai, Rahul Jaiswal, Claudio Luchinat, and Cristina Nativi

Bioconjugate Chem., **2009**, 20 (4), 719-727• DOI: 10.1021/bc8003827 • Publication Date (Web): 10 March 2009

Downloaded from http://pubs.acs.org on May 15, 2009

More About This Article

Additional resources and features associated with this article are available within the HTML version:

- Supporting Information
- Access to high resolution figures
- Links to articles and content related to this article
- Copyright permission to reproduce figures and/or text from this article

View the Full Text HTML

ACS Publications
High quality. High impact.

Bioconjugate Chemistry is published by the American Chemical Society. 1155 Sixteenth Street N.W., Washington, DC 20036

Biotin-Tagged Probes for MMP Expression and Activation: Design, Synthesis, and Binding Properties

Elisa Dragoni, Vito Calderone, Marco Fragai, Rahul Jaiswal, Claudio Luchinat,* and Cristina Nativi*

Magnetic Resonance Center (CERM) - University of Florence, Via L. Sacconi 6, 50019 Sesto Fiorentino, Italy, Department of Organic Chemistry, University of Florence, Via della Lastruccia 13, 50019 Sesto Fiorentino, and Department of Agricultural Biotechnology, University of Florence, Via Maragliano, 75-77, 50144 Florence, Italy. Received September 8, 2008; Revised Manuscript Received January 24, 2009

The design and synthesis of biotin chain-terminated inhibitors (BTI) showing high affinity for matrix metalloproteinases (MMPs) on one side and high affinity for avidin through the biotinylated tag on the other are reported. The affinity of the designed BTI toward five different MMPs has been evaluated and the simultaneous formation of a highly stable ternary system Avidin-BTI-MMP clearly assessed. This system will permit the development of new approaches to detect, quantify, or collect MMPs in biological samples, with potential applications in vivo.

INTRODUCTION

The design of molecular probes able to selectively bind biomolecular targets is gaining importance not only for their applications in molecular biology, but also for the development of new techniques for the early stage diagnosis and therapy of several pathologies (*1*). Rational drug design driven by structural data is currently applied to speed up the design of new candidate drugs in pharmaceutical research (*2*−*5*). The same approach is even more important to design molecular probes where, besides classical requirements, additive structural and functional features are required.

Matrix metalloproteinases (MMPs), also known as matrixins, are proteinases that participate in extracellular matrix (ECM) degradation (*6*) and in several extracellular processes (*7*−*10*). Under normal physiological conditions, the activity of MMPs is strictly regulated by transcription/activation of zymogens precursors, interaction with specific ECM components, and inhibition by endogenous inhibitors (TIMPs) (*11*−*14*). An imbalance of these activities may results in diseases such as atherosclerosis, thrombosis, or heart failure (*15, 16*). As a matter of fact, expression and activation of MMPs are increased in these pathologies, as well as in almost all human cancers, compared to physiological conditions (*17*). Indeed, ECM degradation by MMPs does promote tumor invasiveness. Furthermore, it has been recently demonstrated that MMPs carry out functions other than promotion of invasion, and that they likely take part in the development of cancer even before invasion. Noteworthy, the degree of overexpression of MMPs in cancer tissues is strictly associated with the level of tumor invasiveness and with its tendency to form metastasis. It is therefore apparent that the development of efficient molecular devices designed to reveal the overexpression of MMPs may be a powerful tool for the early detection of tumors and the assessment of their aggressiveness, as well as of cardiocirculatory problems (*18*).

* Prof. Claudio Luchinat, Magnetic Resonance Center (CERM), University of Florence, Via L. Sacconi 6, 50019 Sesto Fiorentino, Italy, e-mail: luchinat@cerm.unifi.it, Tel.: +390554574262, Fax: +390554574253; Prof. Cristina Nativi, Department of Organic Chemistry, University of Florence, Via della Lastruccia 13, 50019 Sesto Fiorentino, Italy, e-mail: cristina.nativi@unifi.it, Tel.: +390554573540, Fax: +390554573531.

Studies focused on the detection of overexpression of MMPs have already been reported (*19*) and probes to profile MMPs in tissues synthesized and tested (*20, 21*). In particular, hydrolyzable, near-infrared fluorescent molecules have been successfully tested in mice to detect fibrosarcoma (*22*). Unfortunately, this innovative technique suffers from the serious limitation represented by the limited penetration of light (a few millimeters); such a degree of penetration is only sufficient for the readout of superficial subcutaneous tumors (<10 mm).

An interesting approach to detect overexpression of MMP in atherosclerosis has also been published. Low molecular weight inhibitors, able to interact with the active site of MMPs involved in atherosclerotic plaque disruption, have been targeted with nuclear agents and tested in vivo (*23*−*25*). Although the results reported were extremely encouraging, the approach presented a scarce flexibility, due to experimental difficulties in preparing the targeted inhibitors and to limited availability of suitable nuclear agents.

A significant improvement in the development of MMP-conjugated probes to detect pathological events may be the rational design of biotin-labeled inhibitors (*26*), capable of binding to MMPs exclusively and with high affinity. These tagged molecules rely on the well-known avidin−biotin molecular recognition system and could be used in conjunction with commercially available biotin-labeled probes (i.e., radionuclide chelates) to efficiently detect pathological tissues by imaging the local overexpression of MMPs. The use of such molecules is not limited to in vivo imaging but can be extended to in vitro applications such as MMP purification by using avidin columns or devices.

Capitalizing on our expertise on expression and structural characterization of MMPs (*27*−*29*) and on the rational design and synthesis of MMP inhibitors (*30*−*35*), in the present paper we report the design and synthesis of carboxylic-containing, biotinylated inhibitors able to show high affinity for MMPs and at the same time able to strongly interact with avidin through the biotinylated tag.

In clinical therapy, selectivity of inhibitors for a specific MMP is dramatically important, so much so that the lack of selectivity is believed to have been the main reason for failures of clinical trials in the past. Often, the failure of clinical trials, due to the severity of the side-effects, was related to the chronic adverse

10.1021/bc8003827 CCC: $40.75 © 2009 American Chemical Society
Published on Web 03/10/2009

effects of nonselective inhibitors. On the other hand, for the molecules proposed here, selectivity is not an issue as chronic use is not required. Indeed, ideal probes to detect overexpression of MMPs must not be selective inhibitors vs a specific MMP, but they should instead selectively recognize MMPs among other proteins. These new biotinylated molecules designed to bind to MMPs and to be recognized by avidin might therefore be successfully used in the in vitro collection/purification of MMPs, in the visualization of pathological tissues where MMPs are overexpressed, and to evaluate the aggressiveness of the pathology by monitoring, e.g., radioactivity. Moreover, it might be possible to test in vivo the efficacy of clinical treatments against a specific disease by just monitoring the level of MMPs produced during the therapy. In addition, such molecules can be easily employed for collecting and purifying MMPs from biological samples.

EXPERIMENTAL PROCEDURES

General. All reagents were commercially available and used as received. Dry solvents were prepared before use. The catalytic domain of the MMP-12 (G106-G263) was cloned into the pET21a (Novagen) using the restriction enzymes *Nde I* and *Xho I* (New England BioLabs). NMR spectra were recorded using a Varian Gemini 200, Varian Mercury 400 spectrometer, and a Brucker 700 spectrometer (HSQC). HPLC purification was performed using Althech Ultrasphere C-18 column (250 × 10 mm) and monitored with a Dionex photodiode array detector. SPR data were obtained using a BioRad ProteOn XPR36.

(*R*)-Methyl 2-(*N*-(bromomethyl)biphenyl-4-ylsulfonamido)-4-methylpentanoate (8). To a solution of **3** (600 mg, 1.66 mmol), 6-bromo-1-hexanol (450 mg, 2.49 mmol), and triphenylphosphine (872 mg, 3.32 mmol) in 17 mL of dry THF, 0.65 mL of DIAD (1.66 mmol) was added dropwise, in 1 h. The reaction was stirred at rt for 43 h, and then the solvent was removed in vacuo to give a yellow oil. After crystallization of the betainic side product (EtOAc/cyclohexane 1:8), the filtrate was concentrated in vacuum and the residue (3.20 g) was purified twice by flash column chromatography on silica gel (hexane/EtOAc 6:1, then CH_2Cl_2) to give pure **8** as a white solid (515 mg, 60% yield).

$[\alpha]^{25}_D$ +47.4 (c 1.13, $CHCl_3$). MP: 59−61 °C. ^{1}H NMR (200 MHz, $CDCl_3$) δ 7.90−7.86 (part AA′ of an AA′MM′ system, J_{AM} = 8.8 Hz, 2H), 7.72−7.68 (part MM′ of an AA′MM′ system, J_{AM} = 8.8 Hz, 2H), 7.65−7.40 (m, 5H), 4.63−4.55 (dd, 1H, J = 5.6 Hz, J = 6.0 Hz), 3.46 (s, 3H), 3.40 (t, J = 6.8 Hz, 2H), 3.30−3.06 (m, 2H), 1.97−1.17 (m, 11H), 0.99−0.94 (m, 6H). ^{13}C NMR (50 MHz, $CDCl_3$) δ 171.66, 145.27, 139.23, 138.26, 128.97, 128.38, 127.88, 127.26, 127.20, 58.09, 51.96, 45.95, 39.59, 33.86, 32.75, 31.19, 27.86, 26.36, 24.63, 22.99, 21.73. ESI-MS $[M + H]^+$ calcd 524.14. Found 524.11.

***tert*-Butyl (5-((4*S*)-2-oxohexahydro-1*H*-thieno[3,4-*d*]imidazol-4-yl)pentanamido)methylcarbamate (6).** A suspension of *N*-Boc-1,6-diaminohexane hydrochloride **5** (310 mg, 1.23 mmol) and NMM (0.14 mL, 1.23 mmol) in dry DMF (3 mL) was added to a slurry of D-biotin (300 mg, 1.23 mmol) and NMM (0.14 mL, 1.23 mmol) in dry DMF (10 mL), and the mixture was stirred at rt for 10 min. A solution of HATU (468 mg, 1.23 mmol) in dry DMF (3 mL) was added, and the mixture was stirred for 3.5 h. The reaction mixture was diluted with 20 mL of CH_2Cl_2 and washed with water: the organic layer was dried over anhydrous Na_2SO_4, and the solvent was removed in vacuo to give a yellow pale oil. Part of DMF was removed in vacuum to give 2.20 g of a yellow solid. The crude material was purified by flash column chromatography on silica gel (CH_2Cl_2/CH_3OH 6:1) to give **6** as a white solid (500 mg, 92% yield).

MP: 174−175 °C. ^{1}H NMR (200 MHz, $CDCl_3$) δ 6.17−6.07 (m, 2H), 4.70−4.56 (m, 1H), 4.55−4.49 (part A of an ABMN system, J_{AB} = 8.0 Hz, J_{AM} = 4.4 Hz, 1H), 4.36−4.29 (part B of ABX system, J_{AB} = 8.0 Hz, J_{BX} = 4.6 Hz, 1H), 3.24−3.10 (m, 5H), 2.97−2.71 (part MN of an AMN system, J_{MN} = 12.4 Hz, J_{AM} = 4.4 Hz, 2H), 2.22 (t, J = 7.0 Hz, 2H), 1.48−1.25 (m, 23H). ^{13}C NMR (50 MHz, $CDCl_3$) δ 173.80, 163.62, 155.91, 62.11, 60.56, 55.56, 40.56, 39.70, 35.65, 30.06, 29.87, 29.27, 28.61, 28.18, 28.09, 26.39, 26.25, 25.84. Anal. ($C_{16}H_{28}N_4O_4S$) C, 51.69; H, 7.62; N, 15.00.

(5-((4*S*)-2-Oxohexahydro-1*H*-thieno[3,4-*d*]imidazol-4-yl)pentanamido)methanaminium (7). A solution of CF_3COOH (1.9 mL, 23.8 mmol) in dry CH_2Cl_2 (6.2 mL) was added to a suspension of **6** (480 mg, 1.08 mmol) in dry CH_2Cl_2 (4.6 mL). After 1.5 h, 10 mL of toluene was added and solvent was removed under vacuum to give a pale yellow oil. The oil was repeatedly washed with CH_3OH and $CHCl_3$; the compound **7** (490 mg, >90%) so obtained was used without any further purification.

^{1}H NMR (200 MHz, CD_3OD) δ 4.53−4.47 (part A of an ABMN system, J_{AB} = 8.0 Hz, 1H), 4.33−4.27 (part B of an ABX system, J_{AB} = 8.0 Hz, J_{BX} = 4.4 Hz, 1H), 3.23−3.14 (m, 3H), 3.00−2.87 (m, 5H), 2.73−2.67 (part M of an AMN system, J_{MN} = 12.4 Hz, 1H), 2.20 (t, J = 7.2 Hz, 2H), 1.72−1.40 (m, 12H). ^{13}C NMR (50 MHz, CD_3OD): 174.45, 164.54, 159.90, 62.07, 60.32, 55.74, 39.77, 39.40, 38.79, 35.54, 28.87, 28.53, 28.27, 27.24, 26.12, 25.75, 25.69.

(2*R*)-Methyl-4-methyl-2-(*N*-(((5-((4*S*)-2-oxohexahydro-1*H*-thieno[3,4-*d*]imidazol-4-yl)pentanamido)methylamino)methyl)biphenyl-4-ylsulfonamido)pentanoate (9). To a solution of **7** (236 mg, 0.69 mmol) in dry DMF (4 mL) were added 4 Å activated pellets molecular sieves (400 mg). The mixture was stirred at rt for 1 h. Cesium hydroxide monohydrate previously dried at 120 °C for 24 h (116 mg, 0.69 mmol) was added, and the solution was allowed to stir for 30 min. TBAI (250 mg, 0.69 mmol) and compoud **8** (360 mg, 0.69 mmol) was finally added and the mixture was stirred for 48 h. The crude material was purified by flash column chromatography on silica gel (CH_2Cl_2/CH_3OH 6:1) to give **9** (300 mg, 55%) as a pale yellow solid.

MP: 129−131 °C. ^{1}H NMR (200 MHz, CD_3OD) δ 7.91−7.41 (m, 9H), 4.58−4.48 (m, 2H), 4.34−4.28 (part B of an ABX syst, J_{AB} = 7.8 Hz, J_{BX} = 4.4 Hz, 1H), 3.43 (s, 3H), 3.26−3.14 (m, 4H), 3.04−2.74 (m, 6H), 2.21 (t, J = 7.0 Hz, 2H), 1.73−1.29 (m, 25H), 0.95 (ad, 6H, J = 5.4 Hz). ^{13}C NMR (50 MHz, $CDCl_3$) δ 174.45, 171.45, 164.47, 145.45, 138.97, 138.03, 128.71, 128.15, 127.70, 127.05, 126.80, 62.07, 60.32, 58.13, 55.72, 51.14, 47.60, 45.71, 39.79, 39.26, 38.73, 35.54, 30.97, 28.94, 28.50, 28.27, 26.18, 26.06, 25.94, 25.84, 25.69, 24.42, 21.93, 20.58. ESI-MS $[M + H]^+$ calcd 786.42. Found 786.50.

(2*R*)-4-Methyl-2-(*N*-(((5-((4*S*)-2-oxohexahydro-1*H*-thieno[3,4-*d*]imidazol-4yl)pentanamido)methylamino)methyl)biphenyl-4-ylsulfonamido)pentanoic acid (4). To a solution of **9** (143 mg, 0.18 mmol) in 2.8 mL of THF/H_2O (1:1 v/v) LiOH·H_2O (15.1 mg, 0.36 mmol) was added and the mixture was stirred for 6 h at rt, then H_3PO_4 1 M was added (pH = 5); the solvent was removed in vacuum, and the solution was lyophilized. The solid obtained was redissolved in AcCN/H_2O 3:1 and purified by a reversed-phase semipreparative HPLC to give compound **4** (76 mg, 55%).

$[\alpha]^{25}_D$ +38.19 (c 0.33, CH_3OH). MP: 119−121 °C. ^{1}H NMR (400 MHz, CD_3OD) δ 7.96−7.38 (m, 9H), 4.49−4.46 (part A of an ABMN system, J_{AB} = 8.0 Hz, J_{AM} = 4.4 Hz, 1H), 4.41−4.37 (m, 1H), 4.30−4.27 (part B of an ABX system, J_{AB} = 8.0 Hz, J_{BX} = 4.6 Hz, 1H), 3.49−3.38 (m, 1H), 3.29−3.14 (m, 4H), 2.93−2.88 (m, 5H), 2.71−2.68 (part N of an AMN system, J_{MN} = 12.8 Hz, 1H), 2.19 (t, J = 7.2 Hz, 2H), 1.88−1.22 (m, 25H), 0.93 (at, J = 6.4 Hz, 6H). ^{13}C NMR (50 MHz, CD_3OD) δ 176.04, 174.39, 164.51, 144.75, 139.22,

128.64, 127.94, 127.79, 126.80, 126.76, 62.07, 61.02, 60.31, 55.72, 47.51, 45.04, 40.31, 39.77, 38.79, 35.54, 30.38, 28.96, 28.51, 28.27, 26.12, 25.92, 25.68, 25.56, 24.81, 22.17, 21.16. ESI-MS $[M + H]^+$ calcd 772.41. Found 772.54. Anal. ($C_{31}H_{45}N_5O_6S_2$) C, 57.43; H,7.08; N, 10.61.

(2*R*)-Methyl-2-(4-methoxy-*N*-(((5-((4*S*)-2-oxohexahydro-1*H*-thieno[3,4-*d*]imidazol-4-yl) pentanamido)methylamino)methyl)phenylsulfonamido)propanoate (12). To a solution of **7** (170 mg, 0.50 mmol) in dry DMF (2 mL), 4 Å activated pellets molecular sieves (280 mg) were added, and the mixture was gently stirred at rt for 1 h. Cesium hydroxide monohydrate, previously dried at 120 °C for 24 h, (84 mg, 0.50 mmol) was added, and the reaction mixture was stirred for 30 min. A solution of **11** (218 mg, 0.50 mmol) and TBAI (182 mg, 0.50 mmol) in DMF (1 mL) were finally added, and the mixture was stirred for 48 h at rt. The crude material obtained was purified by flash column chromatography on silica gel (CH_2Cl_2/CH_3OH 6:1) to give **12** (200 mg, 58%) as a pale yellow solid.

MP: 93−94 °C. ^{1}H NMR (200 MHz, CD_3OD) δ 7.78−7.70 (part AA′ of an AA′MM′ system, $J_{AM} = 9.2$ Hz, 2H), 6.95−6.94 (part MM′ of an AA′MM′ system, $J_{AM} = 9.2$ Hz, 2H), 4.58−4.47 (m, 2H), 4.38−4.32 (part B of an ABX system, $J_{AB} = 7.8$ Hz, $J_{BX} = 4.4$ Hz, 1H), 3.88 (s, 3H), 3.55 (s, 3H), 3.26−3.14 (m, 5H), 3.03−2.87 (m, 5H), 2.72−2.69 (part N of an AMN system, $J_{MN} = 12.6$ Hz, 1H), 2.20 (t, $J = 7.0$ Hz, 2H), 1.72−1.29 (m, 25 H). ^{13}C NMR (50 MHz, CD_3OD) δ 173.27, 171.80, 163.50, 162.71, 131.39, 129.28, 114.03, 68.21, 61.99, 60.22, 55.72, 55.18, 52.49, 52.26, 45.45, 40.70, 38.06, 35.78, 30.84, 29.85, 28.94, 28.15, 28.07, 26.33, 26.25, 26.03, 25.80, 23.16, 16.83. ESI-MS $[M + H]^+$ calcd 698.35. Found 698.30.

(2*R*)-2-(4-Methoxy-*N*-(((5-((4*S*)-2-oxohexahydro-1*H*-thieno[3,4-*d*]imidazol-4-yl)pentanamido)methylamino)methyl)phenylsulfonamido)propanoic Acid (10). To a solution of **12** (229 mg, 0.33 mmol) in 4.8 mL of CH_3OH/H_2O 1:1, $LiOH \cdot H_2O$ (28.0 mg, 0.66 mmol) was added and the mixture was stirred for 19 h at rt. A solution of H_3PO_4 (1 M, H_2O) was added (pH = 5), the solvent was removed under vacuum, and the crude product was lyophilized. The solid obtained was redissolved in AcCN/ H_2O 3:1 and purified by a reversed-phase semipreparative HPLC to give compound **10** (53 mg, 23%) as a white solid.

MP: 70−72 °C. ^{1}H NMR (400 MHz, CD_3OD) δ 7.80−7.77 (part AA′ of an AA′MM′, $J_{AM} = 9.2$ Hz, 2H), 7.04−7.02 (part MM′ of an AA′MM′ system, $J_{AM} = 9.2$ Hz, 2H), 4.50−4.47 (m, 1H), 4.36 (q, $J = 7.2$ Hz, 1H), 4.31−4.28 (m, 1H), 3.86 (s, 3H), 3.32−3.26 (m, 1H), 3.21−3.15 (m, 4H), 2.98−2.90 (m, 5H), 2.72−2.68 (part N of an AMN system, $J_{MN} = 12.4$ Hz, 1H), 2.19 (t, $J = 7.2$ Hz, 2H), 1.70−1.30 (m, 22H), 1.20 (d, $J = 7.2$ Hz, 3H). ^{13}C NMR (50 MHz, CD_3OD) δ 176.67, 174.39, 164.51, 162.68, 132.33, 129.02, 113.65, 62.07, 60.31, 57.73, 55.74, 54.83, 47.60, 44.68, 39.80, 38.80, 35.54, 29.84, 29.00, 28.51, 28.29, 26.13, 25.95, 25.70, 25.59, 25.53, 25.37, 16.16. ESI-MS: $[M + H]^+$ calcd 684.34. Found 684.30. Anal. ($C_{23}H_{37}N_5O_7S_2$) C, 49.47; H, 6.60; N, 12.70.

RESULTS AND DISCUSSION

Aryl-sulfonamide derivatives have been largely exploited to synthesize broad-spectrum MMP inhibitors. These scaffolds present different positions which can be easily functionalized by introducing new functional groups. This feature and their easy synthetic accessibility make sulfonamide derivatives suitable candidates to design biotin-tagged probes for MMPs. As zinc binding groups (ZBG), the carboxylic acid was selected despite its relatively weak affinity for the metal ion (*36*−*38*). The choice of a carboxylic acid to replace the most commonly used hydroxamic acid warrants higher stability of the inhibitor under physiological conditions (*39*) and provides better bioavailability (*40*).

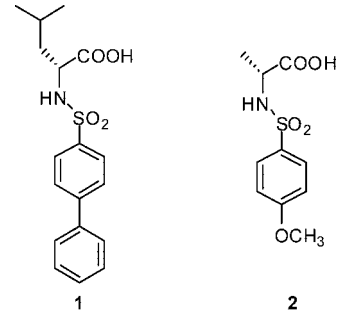

1 2

Figure 1. Structure of the selected scaffolds **1** and **2**.

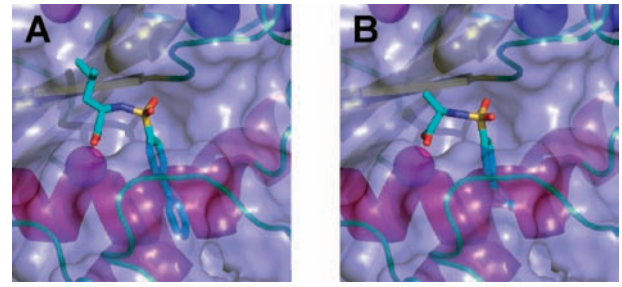

Figure 2. X-ray structure of the catalytic domain of MMP-12 complexed with **1** (A) and with **2** (B). Only the ligand binding site is shown for clarity.

In all MMPs, the flexibility of the protein loops forming the active site makes these enzymes able to modify the shape of the catalytic pocket to accommodate ligands with different structures (*41*−*44*). In particular, analyzing the structures available on the protein data bank, it is apparent that the volume of the S_1' cavity can be changed to host ligands bearing lipophilic groups of different size. However, in MMP-1 and MMP-7 the S_1' cavity is narrow as well as short "trucked" (MMP-7) such that bulky groups generally do not fit. Therefore, in order to probe all members of the MMP family, two scaffolds, bearing either a linear biphenyl moiety or a shorter methoxyphenyl group, were considered as possible bases for the synthesis of BTIs.

Among all the scaffolds evaluated, molecules **1** and **2** (Figure 1) were selected for their low K_i values against five different MMPs (see Table 1). Noteworthy, the two scaffolds exhibit a sizably different selectivity and affinity for the MMPs chosen. In particular, inhibitor **1**, due to the presence of a biphenyl moiety on the sulfonamide sulfur, showed inhibition constants in the nanomolar range. Only for MMP-1 and MMP-7 was the affinity in the low-micromolar range due to the relatively slim size of the S_1' pocket (*45*). Although still good, **2** is a weaker MMP inhibitor with micromolar values of K_i for all the MMPs tested.

Matrix metalloproteinase 12 (MMP-12) performs proteolysis of several ECM components including elastin, laminin, and type IV collagen. The stability of the active MMP-12 catalytic domain in the presence of weak inhibitors, the relatively large S_1' pockets, and the high yield of the ^{15}N-enriched protein in minimal medium make this enzyme an ideal model to evaluate BTI candidates.

To explore the binding mode of the two scaffolds and to properly design the biotin tag derivatives, the two inhibitors were soaked in crystals of MMP-12 and the structure of the complexes solved by X-ray crystallography. Analysis of the crystal structures (see Figure 2) revealed that the inhibitors share a similar binding mode, with the catalytic zinc ion coordinated by the oxygens of the free carboxylate, the sulfonyl oxygen H-bonded with the NH of the Ala 182, and the liphophilic

Table 1. Inhibition Constants (K_i) of the Considered Compounds toward the Considered MMPs

compound	MMP-1	MMP-7	MMP-8	MMP-12	MMP-13
1	18 ± 2 μM	56 ± 6 μM	31 ± 4 nM	25 ± 2 nM	108 ± 12 nM
2	302 ± 25 μM	80 ± 9 μM	4.6 ± 5 μM	1.4 ± 0.2 μM	2.6 ± 0.3 μM
4	25 ± 3 μM	450 ± 50 nM	4 ± 0.5 nM	5 ± 0.6 nM	0.7 ± 0.2 nM
10	295 ± 40 μM	73 ± 7 μM	8 ± 1 μM	1.6 ± 0.2 μM	1.2 ± 0.1 μM

Scheme 1. Synthesis of BTI 4 and Bromosulfenamide 8

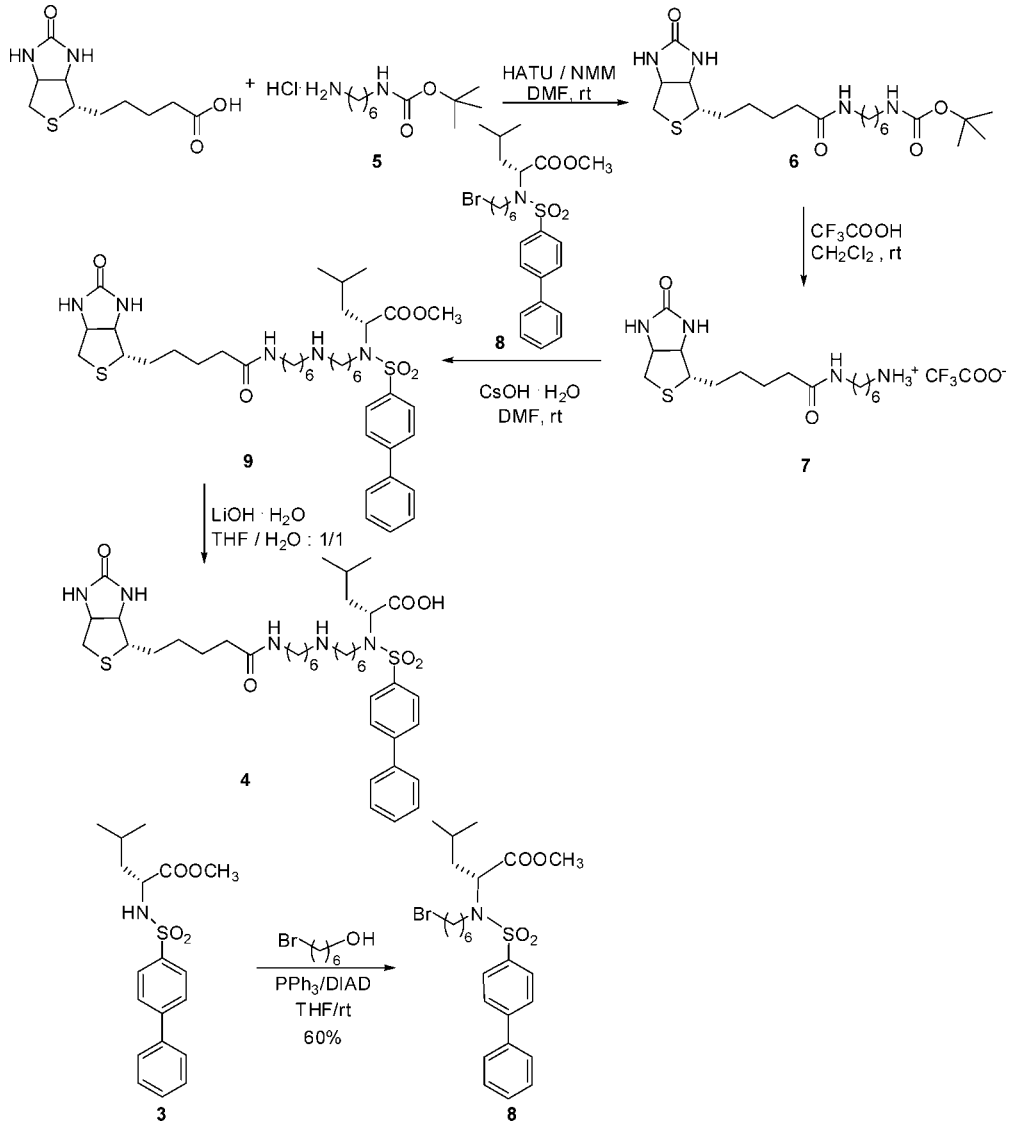

groups nested inside the S_1' pocket. The structural analysis accounts for the larger affinity of **1** for MMP-12 with respect to scaffold **2**, as observed in the enzymatic assays. Indeed, in the MMP-12−**1** complex, larger hydrophobic interactions result from the larger surface-to-surface contact area due to the presence of the biphenyl moiety. More important for the biotin tag inhibitor design was the solvent exposure of the sulfonamide nitrogen revealed by the crystal structures for both ligands. These structural data address the question related to the identification of the position where the tag can be inserted without spoiling the binding affinity.

A further critical point in developing efficient biotinylated probes for in vivo and in vitro applications is represented by the choice of a suitable linker able to prevent any steric clashes between avidin and the target biomolecule. While a too-short spacer may impair the ability of the probe to bind both MMP and avidin, the use of a too-long spacer could affect the bioavailability, stability, and solubility of the whole molecule. In particular, a too-long linker can increase the susceptibility of the probe to be split by enzymes such as the biotinidase that can degrade the molecule in vivo (*46*). Once more, the availability of the three-dimensional structure of both avidin−biotin complex (present in protein data bank, PDB code: 2avi) and **1**−MMP-12 complex has provided the background information needed for a rational molecular design of the biotin-tagged inhibitors we conceived (see Supporting Information).

A fourteen-membered spacer was designed to link the biotin residue to the carboxylic-methyl ester sulfonamide **3** (Scheme 1), that is the shorter, synthetically convenient linker allowing the probe to bind both MMP and avidin binding sites.

The biotinylated inhibitor **4** was obtained as shown in Scheme 1. Biotin was first reacted under known procedures (*46*) with the N-Boc-1,6-diaminohexane **5** to give the amido derivative **6** which, after removal of *tert*-butyloxy carbonyl protecting group, gave the trifluoroacetylammonium salt **7**. Compound **7** was treated with the bromosulfonamide **8** in the presence of cesium

Scheme 2. Synthesis of BTI 10

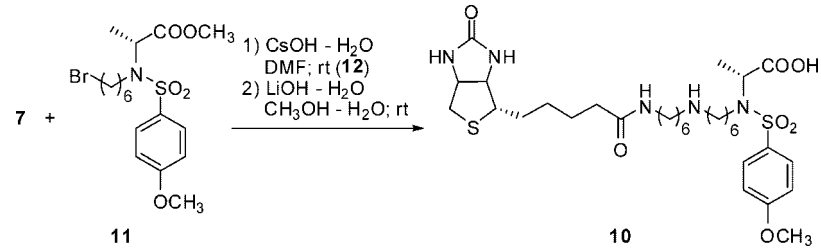

hydroxide, in dimethylformamide as solvent, to give the diastereomerically pure ester **9** in 55% yield. Removal of the methyl ester with lithium hydroxide/water from the latter afforded BTI **4** as a diastereomerically pure compound in 55% yield (Scheme 1). Following the synthetic pathway reported for **4**, the biotin-tagged MMP-12 inhibitor **10** was also prepared from **7** and bromosulfonamide **11**, as a diasteromerically pure compound (Scheme 2).

The affinity properties of the two BTI derivatives toward the selected MMPs were first evaluated by fluorimetric assay (see Supporting Information). The K_i values are reported in Table 1. While BTI **4** had lower K_i values as compared to the corresponding precursor **1**, BTI **10** exhibited comparable affinity with respect to its precursor **2**. The micromolar K_i of BTI **10** for all the tested MMPs unambiguously demonstrated that the latter is less interesting as a probe to detect these enzymes in vivo, though it might be suitable to collect and purify MMPs from biological samples. Conversely, BTI **4** exhibited a nanomolar affinity for all the MMPs considered (including MMP-7) except for MMP-1, for which the K_i was, however, still in the low micromolar range. The molecular details for the observed improved affinity were analyzed by investigating the BTI **4** -MMP-12 complex.

Several attempts aimed at obtaining the X-ray structure of the biotin tag inhibitors in complex with MMP-12, either by soaking or cocrystallization, failed, probably for steric reasons owing to the tag. Therefore, interaction of compound **1** and of its biotin tag derivative **4** with the catalytic domain of MMP-12 was further investigated following the chemical shift perturbations on $^{15}N-^{1}H$ HSQC spectra using ^{15}N-labeled protein samples. The chemical shift is a sensitive indicator of protein−ligand interactions and can be used to identify the binding site when the resonance assignment is available (*47*). The complete assignment of the catalytic domain of MMP-12 complexed with the weak inhibitor acetohydroxamic acid is available in our laboratory. Increasing amounts of **1** and **4** were added to 200 μM solutions of the protein up to an equimolar concentration. Although several NH signals were shifted by adding the inhibitors, as many as 134 and 129 cross-peaks belonging to protein adducts with **1** and **4**, respectively, were easily reassigned. The intensity of signals belonging to NH groups perturbed by the addition of the ligands decreased linearly, while new cross-peaks corresponding to the BTI-bound form of the protein appeared and gradually increased their intensity, in agreement with the effect produced by a slow-exchanging ligand.

The binding mode of ligands **1** and **4**, respectively, was analyzed and compared by reporting Garrett values [$\Delta\delta$(NH)] on a surface representation of the MMP-12 structure (Figure 3). As is evident from Figure 3, for both inhibitors, the region with significant $^{15}N-^{1}H$ HSQC spectral perturbations involves the catalytic pocket. The analysis of Garrett values rules out relevant additive interactions of the biotinylated tail present in BTI **4** with protein regions outside the catalytic pocket, suggesting a different origin for the observed improved affinity. In addition, a hypothetical binding mode with the biotinylated tail of BTI **4** fitting in the S_1' cavity can be completely excluded by the chemical shift perturbations on the $^{15}N-^{1}H$ HSQC spectra that are similar for **1** and **4** as well as by the K_i values of the BTI **10**, which, although biotinylated, showed a low affinity for the enzyme. Likely, extra interactions related to a better fit of **4** into the active site of the enzyme become possible when the fourteen-membered spacer is introduced on BTI **4**. These extra interactions are particularly evident for MMP-7 (Table 1) where the affinity increases by 2 orders of magnitude upon the introduction of the linker.

Although a high affinity for the target protein is a basic requirement for the proposed bifunctional ligand to play its role, only the ability of the latter to bind MMP and avidin simultaneously could prove its real efficacy as effective BTI.

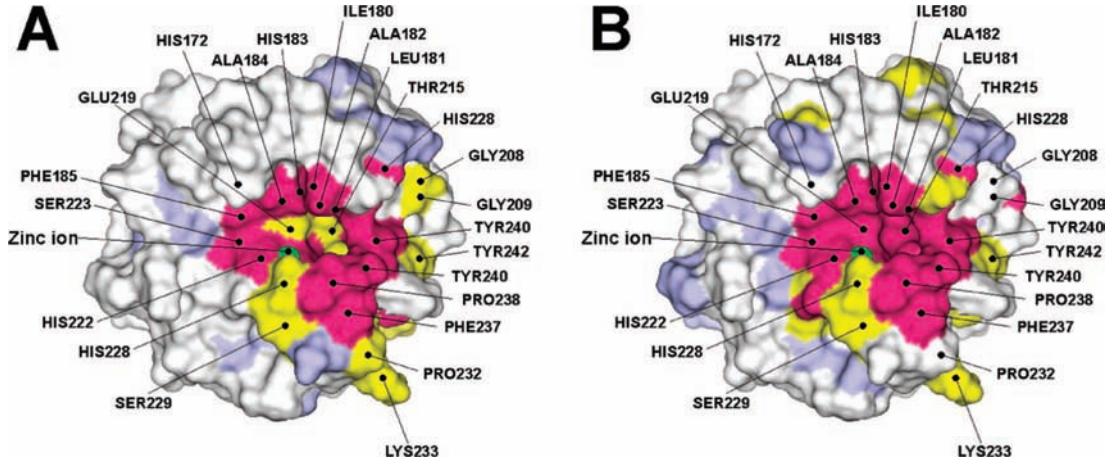

Figure 3. Surface representation of the residues of the catalytic domain of MMP-12 affected by chemical shift perturbation upon the addition of **1** (A) and of **4** (B). Areas of interaction with significant $^{15}N-^{1}H$ HSQC spectra perturbations are colored-coded according to the Garret values. Magenta, $\Delta\delta$(NH) > 0.1 ppm; Yellow, 0.1 > $\Delta\delta$(NH) > 0.05; Cyan, 0.05 > $\Delta\delta$(NH) > 0.03.

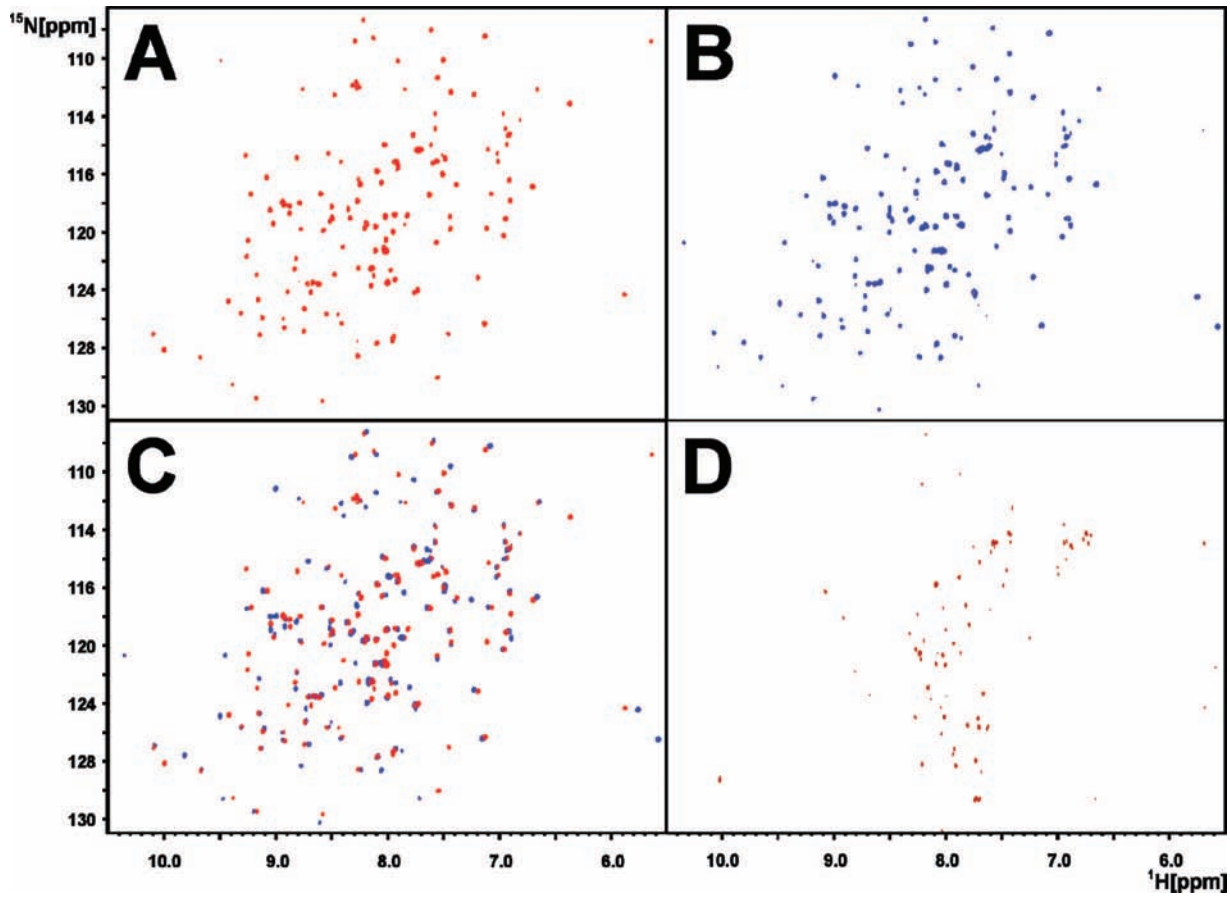

Figure 4. ^{15}N−^{1}H HSQC spectrum of MMP-12 catalytic domain in the absence (A) and in the presence (B) of compound **4** (equimolar concentration). The two spectra are superimposed to highlight the cross-peak shifts (C). The ternary complex formation Avidin-BTI-MMP is seen in panel D where most of the cross-peaks disappeared.

Two different approaches based on NMR spectroscopy and on surface plasmon resonance (SPR) were followed to demonstrate the ternary Avidin-BTI-MMP interaction. Several NMR parameters are strongly influenced by the molecular weight and by the dynamical properties of the investigated macromolecules. Classical NMR experiments such as ^{15}N−^{1}H HSQC usually performed to investigate biomolecules up to 30−40 kDa are inefficient for larger systems due to the fast transverse relaxation rate that broaden the signals beyond the detection threshold (*48*). Therefore, NH resonances can act as probes to investigate the formation of large protein−protein complexes (*49*). In the present case, the evolution of the NH signals of the ^{15}N MMP-12 catalytic domain complexed with the BTI **4** in ^{15}N−^{1}H HSQC spectra was exploited to monitor the interaction with nonlabeled avidin, given that the binding of the biotin moiety to one of the four binding sites on the tetrameric avidin should provide a 87 kDa complex. Since multiple binding for each avidin molecule may occur, even larger protein complexes are expected in solution. As shown in Figure 4 (panel D), the addition of an equimolar solution of the 65 kDa avidin to a solution of the ^{15}N-labeled catalytic domain of MMP-12 complexed with the BTI **4** caused the complete disappearance of all NH cross-peaks without any precipitation of the sample.

To exclude the presence of aspecific protein−protein interactions, avidin was added to a solution containing 200 μM of NNGH-inhibited-MMP-12 catalytic domain: in this case, no changes were detected in the HSQC spectra. Therefore, we can reasonably conclude that the strong protein−protein interaction, monitored by the ^{15}N−^{1}H HSQC experiments, is mediated by the BTI **4** which is able to bind MMP-12 and avidin and to prevent, at the same time, an extensive reciprocal reorientation of the complex subunits. Although NMR data allowed us to ascertain that **4** does bind both avidin and MMP-12 simultaneously, the micromolar concentrations used for these experiments do not provide information on how this simultaneous interaction may affect the nanomolar affinity of the inhibitor to MMP-12. Indeed, possible steric effects related to the presence of the hemopexin domain need to be evaluated to understand the real binding capability of the probe toward functionally active enzymes (*50*). In this respect, the availability of the active full-length MMP-12 allowed us to ascertain the efficiency of the biotinylated inhibitor to bind simultaneously avidin and the physiologically active enzyme and to quantify the effect of the hemopexin domain on the affinity constant.

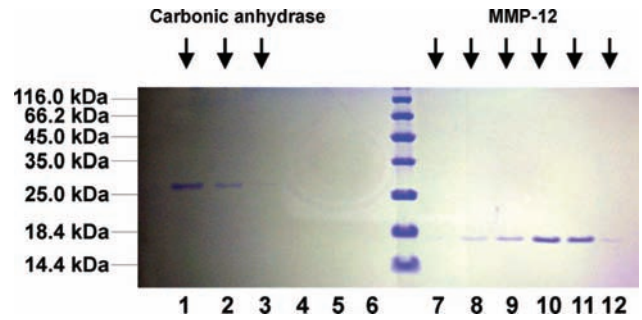

Figure 5. SDS PAGE analysis of the fractions shows an effective chromatographic separation of MMP-12 and carbonic anhydrase loaded on a monomeric avidin-bound column.

Surface plasmon resonance (SPR) is widely applied to investigate protein−protein and protein−ligand interactions. Information on affinity constant, on binding kinetics, as well as on binding enthalpy can be quickly obtained by using small

amounts of protein samples. In particular, the sensitivity of the SPR technique permits the investigation of high-affinity interactions and monitoring the formation of ternary complexes. SPR analysis was carried out using a ProteOn XPR36 parallel array biosensor equipped with avidin sensor chips (NLC). This chip has an avidin-coated surface that can be used to immobilize biotinylated molecules and macromolecules (*51*). In our study, BTI **4** was immobilized on channels 1−5 of the chip by injecting PBS-T buffered solutions of the biotinylated molecule at different concentrations. The sixth channel was left blank. The assay was performed by injecting solutions of the full-length MMP-12 on the chip channels and fitting the sensorgrams at four different concentrations. The measured K_D (4.6 ± 0.3 nM) (Supporting Information Figure S2) was comparable to the fluorimetric K_i measured for **4** vs the isolated catalytic domain of MMP-12 (BTI **4**−MMP-12 complex).

The employment of bifuctional ligand BTI **4** for the selective collection of matrix metalloproteinases from biological fluids has been evaluated by using a monomeric avidin-bound column (Pierce). An amount of 2.5 mg of BTI **4** was dissolved in 8.1 mL of Tris-buffer, and the solution (50 uL) was mixed with the same volume of an equimolar sample of MMP-12 (0.4 mM) dissolved into Tris buffer; 25 uL of the mixture so obtained was added to 50 uL of a solution of carbonic anhydrase from erythrocytes (0.1 mM in Tris-buffer). A monomeric avidin-bound column (0.6 mL of settled gel) was loaded with the solution of BTI **4**, MMP-12, and carbonic anhydrase; then, it was first eluted with 1.4 mL of Tris-buffer and subsequently with a solution of NNGH (1 mM, Tris buffer). Relying on the strong avidin−biotin interaction, the column blocked BTI **4**−MMP-12 complex, while carbonic anhydrase was completely washed out. Addition of nanomolar inhibitor NNGH displaced BTI **4** complexed to MMP-12, and the latter was so eluted and separated from carbonic anhydrase (Figure 5).

In summary, the present structure-based design led to the development of a potent biotin probe to bind matrix metalloproteinases for possible application in vitro and in vivo. The structural requirements defined through the analysis of the X-ray structures allowed selection of the position on the scaffold where the linker could be introduced and the correct length of the biotinylated tag. As defined by NMR analysis, the origin of the larger affinity observed for BTI **4** is a better fit of the selected scaffold in the catalytic pocket rather than additive interactions of the linker on the protein surface. The enzymatic assay demonstrated a nanomolar to low micromolar (MMP-1) affinity of **4** not only for MMP-12 but also for all the MMPs investigated. Furthermore, the evolution of the $^{15}N-^{1}H$ HSQC spectra upon the addition of unlabeled avidin to solution of ^{15}N MMP-12 clearly showed that the fourteen-member spacer used to link the biotin unit to carboxylic aryl sulfonamide inhibitor **1** ensures the simultaneous binding of the two proteins without permitting large interprotein mobility. SPR analyses clearly showed the ability of **4** to bind the functional active enzyme MMP-12 and avidin side-by-side. This simultaneous interaction did not affect negatively the nanomolar affinity of inhibitor **4** for MMP-12, given that the SPR data nicely reproduced the fluorimetric values measured for the BTI **4**−MMP-12 complex.

ACKNOWLEDGMENT

This work was supported by EC (Projects: MEST-CT-2004-504391, Integrated Project - SPINE2-COMPLEXES no 031220, Nano4Drugs no LSHB-CT-2005-019102; SFMET no 201640), by MIUR (FIRB Prot. RBLA032ZM7; FIRB Prot. RBIP06LSS2), Ente Cassa di Risparmio di Firenze, Genexpress.

Supporting Information Available: Protein cloning, expression and purification, X-ray data, details of fluorimetric assays and synthesis and characterization of compounds **1**−**3** and **11** are included. This material is available free of charge via the Internet at http://pubs.acs.org.

LITERATURE CITED

(1) Giepmans, B. N. G., Adams, S. R., Ellisman, M. H., and Tsien, R. Y. (2006) The fluorescent toolbox for assessing protein location and function. *Science 312*, 217–224.

(2) Blundell, T. L., Jhoti, H., and Abell, C. (2002) High-throughput crystallography for lead discovery in drug design. *Nat. Rev. Drug Discoery 1*, 45–54.

(3) Johnson, S. L., and Pellecchia, M. (2006) Structure- and fragment-based approaches to protease inhibition. *Curr. Top. Med. Chem. 6*, 317–329.

(4) Heckmann, D., Meyer, A., Marinelli, L., Zahn, G., Stragies, R., and Kessler, H. (2007) Probing integrin selectivity: rational design of highly active and selective ligands for the α 5β1 and α5β3 integrin receptor. *Angew. Chem., Int. Ed. 46*, 3571–3574.

(5) Jahnke, W., Blommers, M. J., Fernandez, C., Zwingelstein, C., and Amstutz, R. (2005) Strategies for the NMR-based identification and optimization of allosteric protein kinase inhibitors. *ChemBioChem 6*, 1607–1610.

(6) Page-McCaw, A., Ewald, A. J., and Werb, Z. (2007) Matrix metalloproteinases and the regulation of tissue remodelling. *Nat. Rev. Mol. Cell Biol. 8*, 221–233.

(7) Parks, W. C., Wilson, C. L., and Lopez-Boado, Y. S. (2004) Matrix metalloproteinases as modulators of inflammation and innate immunity. *Nat. Rev. Immunol. 4*, 617–629.

(8) D'Alessio, S., Fibbi, G., Cinelli, M., Guiducci, S., Del Rosso, A., Margheri, F., Serrati, S., Pucci, M., Kahaleh, B., Fan, P. S., Annunziato, F., Cosmi, L., Liotta, F., Matucci-Cerinic, M., and Del Rosso, M. (2004) Matrix metalloproteinase 12-dependent cleavage of urokinase receptor in systemic sclerosis microvascular endothelial cells results in impaired angiogenesis. *Arthritis Rheum. 50*, 3275–3285.

(9) Boire, A., Covic, L., Agarwal, A., Jacques, S., Sherifl, S., and Kuliopulos, A. (2005) PAR1 is a matrix metalloprotease-1 receptor that promotes invasion and tumorigenesis of breast cancer cells. *Cell 120*, 303–313.

(10) Fragai, M., and Nesi, A. (2007) Substrate specificities of matrix metalloproteinase 1 in PAR-1 exodomain proteolysis. *ChemBioChem 8*, 1367–1369.

(11) Knauper, V., Will, H., Lopez-Otin, C., Smith, B., Atkinson, S. J., Stanton, H., Hembry, R. M., and Murphy, G. (1996) Cellular mechanisms for human procollagenase-3 (MMP-13) activation. Evidence that MT1-MMP (MMP-14) and gelatinase a (MMP-2) are able to generate active enzyme. *J. Biol. Chem. 271*, 17124–17131.

(12) Morrison, C. J., and Overall, C. M. (2006) TIMP Independence of matrix metalloproteinase (MMP)-2 activation by membrane type 2 (MT2)-MMP is determined by contributions of both the MT2-MMP catalytic and hemopexin C domains. *J. Biol. Chem. 281*, 26528–26539.

(13) Ra, H. J., and Parks, W. C. (2007) Control of matrix metalloproteinase catalytic activity. *Matrix Biol. 26*, 587–596.

(14) Overall, C. M., Tam, E., McQuibban, G. A., Morrison, C., Wallon, U. M., Bigg, H. F., King, A. E., and Roberts, C. R. (2000) Domain interactions in the gelatinase A· TIMP-2· MT1-MMP activation complex: the ectodomain of the 44-kDa form of membrane type-1 matrix metalloproteinase does not modulate gelatinase A activation. *J. Biol. Chem. 275*, 39497–39506.

(15) Fingleton, B. (2007) Matrix metalloproteinases as valid clinical targets. *Curr. Pharm. Des. 13*, 333–346.

(16) Skiles, J. W., Gonnella, N. C., and Jeng, A. Y. (2004) The design, structure, and clinical update of small molecular weight matrix metalloproteinase inhibitors. *Curr. Med. Chem. 11*, 2911–2977.

(17) Egeblad, M., and Werb, Z. (2002) New functions for the matrix metalloproteinases in cancer progression. *Nat. Rev. Cancer 2*, 161–174.

(18) Bremer, C., Tung, C. H., Bogdanov, A., and Weissleder, R. (2002) Imaging of differential protease expression in breast cancers for detection of aggressive tumor phenotypes. *Radiology 222*, 814–818.

(19) Lepage, M., Dow, W. C., Melchior, M., You, Y., Fingleton, B., Quarles, C. C., Pepin, C., Gore, J. C., Matrisian, L. M., and McIntyre, J. O. (2007) Non invasive detection of matrix metalloproteinase activity in vivo using a novel magnetic resonance imaging contrast agent with a solubility switch. *Mol. Imaging 6*, 393–403.

(20) David, A., Steer, D., Bregant, S., Devel, L., Makaritis, A., Beau, F., Yiotakis, A., and Dive, V. (2007) Cross-linking yield variation of a potent matrix metalloproteinase photoaffinity probe and consequences for functional proteomics. *Angew. Chem., Int. Ed. 46*, 3275–3277.

(21) Saghatelian, A., Jessani, N., Joseph, A., Humphrey, M., and Cravatt, B. F. (2004) Activity-based probes for the proteomic profiling of metalloproteases. *Proc. Natl. Acad. Sci. U.S.A. 101*, 10000–10005.

(22) Bremer, C., Tung, C. H., and Weissleder, R. (2001) In vivo molecular target assessment of matrix metalloproteinase inhibition. *Nat. Med. 7*, 743–748.

(23) Faust, A., Waschkau, B., Waldeck, J., Holtke, C., Breyholz, H. J., Wagner, S., Kopka, K., Heindel, W., Schafers, M., and Bremer, C. (2008) Synthesis and evaluation of a novel fluorescent photoprobe for imaging matrix metalloproteinases. *Bioconjugate Chem. 19*, 1001–1008.

(24) Wagner, S., Breyholz, H. J., Law, M. P., Faust, A., Holtke, C., Schroer, S., Haufe, G., Levkau, B., Schober, O., Schafers, M., and Kopka, K. (2007) Novel fluorinated derivatives of the broad-spectrum MMP inhibitors N-hydroxy-2(R)-[[(4-methoxyphenyl)sulfonyl](benzyl)- and (3-picolyl)-amino]-3-methyl-butanamide as potential tools for the molecular imaging of activated MMPs with PET. *J. Med. Chem. 50*, 5752–5764.

(25) Wagner, S., Breyholz, H. J., Faust, A., Holtke, C., Levkau, B., Schober, O., Schafers, M., and Kopka, K. (2006) Molecular imaging of matrix metalloproteinases in vivo using small molecule inhibitors for SPECT and PET. *Curr. Med. Chem. 13*, 2819–2838.

(26) Uttamchandani, M., Wang, J., Li, J. Q., Hu, M. Y., Sun, H. Y., Chen, K. Y. T., Liu, K., and Yao, S. Q. (2007) Inhibitor fingerprinting of matrix metalloproteases using a combinatorial peptide hydroxamate library. *J. Am. Chem. Soc. 129*, 7848–7858.

(27) Bertini, I., Calderone, V., Fragai, M., Luchinat, C., and Maletta, M. (2006) Snapshots of the reaction mechanism of matrix metalloproteinases. *Angew. Chem., Int. Ed. 45*, 7952–7955.

(28) Bertini, I., Calderone, V., Fragai, M., Luchinat, C., Mangani, S., and Terni, B. (2003) X-ray structures of binary and ternary enzyme-product-inhibitor complexes of matrix metalloproteinases. *Angew. Chem., Int. Ed. 42*, 2673–2676.

(29) Bertini, I., Calderone, V., Fragai, M., Luchinat, C., Mangani, S., and Terni, B. (2004) Crystal structure of the catalytic domain of human matrix metalloproteinase 10. *J. Mol. Biol. 336*, 707–716.

(30) Bertini, I., Calderone, V., Fragai, M., Giachetti, A., Loconte, M., Luchinat, C., Maletta, M., Nativi, C., and Yeo, K. (2007) Exploring the subtleties of drug-receptor interactions: the case of matrix metalloproteinases. *J. Am. Chem. Soc. 129*, 2466–2475.

(31) Bertini, I., Fragai, M., Lee, Y.-M., Luchinat, C., and Terni, B. (2004) Paramagnetic metal ions in ligand screening: The CoII matrix metalloproteinase 12. *Angew. Chem., Int. Ed. 43*, 2254–2256.

(32) Calderone, V., Fragai, M., Luchinat, C., Nativi, C., Richichi, B., and Roelens, S. (2006) A high-affinity carbohydrate-containing inhibitor of matrix metalloproteinases. *ChemMedChem 1*, 598–601.

(33) Bertini, I., Fragai, M., Giachetti, A., Luchinat, C., Maletta, M., Parigi, G., and Yeo, K. J. (2005) Combining in silico tools and NMR data to validate protein−ligand structural models: application to matrix metalloproteinases. *J. Med. Chem. 48*, 7544–7559.

(34) Fragai, M., Nativi, C., Richichi, B., and Venturi, C. (2005) Design in silico, synthesis and binding evaluation of a carbohydrate-based scaffold for structurally novel inhibitors of matrix metalloproteinases. *ChemBioChem 6*, 1345–1349.

(35) Mannino, C., Nievo, M., Machetti, F., Papakyriakou, A., Fragai, M., and Guarna, A. (2006) Synthesis of bicyclic molecular scaffolds (BTAa): An investigation towards new selective MMP-12 inhibitors. *Bioorg. Med. Chem. 14*, 7392–7403.

(36) Agrawal, A., Romero-Perez, D., Jacobsen, J. A., Villarreal, F. J., and Cohen, S. M. (2008) Zinc-binding groups modulate selective inhibition of MMPs. *ChemMedChem 3*, 812–820.

(37) Puerta, D. T., and Cohen, S. M. (2004) A bioinorganic perspective on matrix metalloproteinase inhibition. *Curr. Top. Med. Chem. 4*, 1551–1573.

(38) Pikul, S., Ohler, N. E., Ciszewski, G., Laufersweiler, M. C., Almstead, N. G., De, B., Natchus, M. G., Hsieh, L. C., Janusz, M. J., Peng, S. X., Branch, T. M., King, S. L., Taiwo, Y. O., and Mieling, G. E. (2001) Potent and selective carboxylic acid-based inhibitors of matrix metalloproteinases. *J. Med. Chem. 44*, 2499–2502.

(39) Wang, X. Q., Choe, Y. C., Craik, C. S., and Ellman, J. A. (2002) Design and synthesis of novel inhibitors of gelatinase B. *Bioorg. Med. Chem. Lett. 12*, 2201–2204.

(40) Auge, F., Hornebeck, W., Decarme, M., and Laronze, J. Y. (2003) Improved gelatinase a selectivity by novel zinc binding groups containing galardin derivatives. *Bioorg. Med. Chem. Lett. 13*, 1783–1786.

(41) Bertini, I., Calderone, V., Cosenza, M., Fragai, M., Lee, Y.-M., Luchinat, C., Mangani, S., Terni, B., and Turano, P. (2007) Solution structure of inhibitor-free human metalloelastase (MMP-12) indicates an internal conformational adjustment. *J. Mol. Biol. 374*, 1333–1344.

(42) Bhaskaran, R., Palmier, M. O., Bagegni, N. A., Liang, X. Y., and Van Doren, S. R. (2007) Solution structure of inhibitor-free human metalloelastase (MMP-12) indicates an internal conformational adjustment. *J. Mol. Biol. 374*, 1333–1344.

(43) Devel, L., Rogakos, V., David, A., Makaritis, A., Beau, F., Cuniasse, P., Yiotakis, A., and Dive, V. (2006) Development of selective inhibitors and substrate of matrix metalloproteinase-12. *J. Biol. Chem. 281*, 11152–11160.

(44) Tochowicz, A., Maskos, K., Huber, R., Oltenfreiter, R., Dive, V., Yiotakis, A., Zanda, M., Bode, W., and Goettig, P. (2007) Crystal structures of MMP-9 complexes with five inhibitors: contribution of the flexible Arg424 side-chain to selectivity. *J. Mol. Biol. 371*, 989–1006.

(45) Lovejoy, B., Welch, A. R., Carr, S., Luong, C., Broka, C., Hendricks, R. T., Campbell, J. A., Walker, K. A. M., Martin, R., Van Wart, H., and Browner, M. F. (1999) Crystal structures of MMP-1 and -13 reveal the structural basis for selectivity of collagenase inhibitors. *Nat. Struct. Biol. 6*, 217–221.

(46) Sabatino, G., Chinol, M., Paganelli, G., Papi, S., Chelli, M., Leone, G., Papini, A. M., De Luca, A., and Ginanneschi, M. (2003) A new biotin derivative-DOTA conjugate as a candidate for pretargeted diagnosis and therapy of tumors. *J. Med. Chem. 46*, 3170–3173.

(47) Canales-Mayordomo, A., Fayos, R., Angulo, J., Ojeda, R., Martin-Pastor, M., Nieto, P. M., Martin-Lomas, M., Lozano, R., Gimenez-Gallego, G., and Jimenez-Barbero, J. (2006) Backbone dynamics of a biologically active human FGF-1 monomer, complexed to a hexasaccharide heparin-analogue, by 15N NMR relaxation methods. *J. Biomol. NMR 35*, 225–239.

(48) Pellecchia, M., Sebbel, P., Hermanns, U., Wuthrich, K., and Glockshuber, R. (1999) Pilus chaperone FimC-adhesin FimH interactions mapped by TROSY-NMR. *Nat. Struct. Biol. 6*, 336–339.

(49) D'Silva, L., Ozdowy, P., Krajewski, M., Rothweiler, U., Singh, M., and Holak, T. A. (2005) Monitoring the effects of antagonists

on protein-protein interactions with NMR spectroscopy. *J. Am. Chem. Soc. 127*13220–13226.
(50) Bertini, I., Calderone, V., Fragai, M., Jaiswal, R., Luchinat, C., Melikian, M., Mylonas, E., and Svergun, D. (2008) Evidence of reciprocal reorientation of the catalytic and hemopexin-like domains of full-length MMP-12. *J. Am. Chem. Soc. 130*, 7011–7021.
(51) Bravman, T., Bronner, V., Lavie, K., Notcovich, A., Papalia, G. A., and Myszka, D. G. (2006) Exploring "one-shot" kinetics and small molecule analysis using the ProteOn XPR36 array biosensor. *Anal. Biochem. 358*, 281–288.

BC8003827

Supporting Information

Biotin-Tagged Probes for Profiling of MMPs Expression and Activation: Design, Synthesis and Binding Properties

Elisa Dragoni,[1,2] *Vito Calderone,*[1] *Marco Fragai* [1,3] *Rahul Jaiswal*[1] *Claudio Luchinat,*[*,2,3]

Cristina Nativi[*,1,2]

[1] Magnetic Resonance Center (CERM) – University of Florence, Via L. Sacconi 6, 50019 Sesto Fiorentino, Italy

[2] Department of Organic Chemistry, University of Florence, Via della Lastruccia 13, 50019 Sesto Fiorentino (Italy)

[3] Department of Agricultural Biotechnology, University of Florence, Via Maragliano, 75-77, 50144 Florence, Italy.

[*] Prof. Claudio Luchinat
Magnetic Resonance Center (CERM)
University of Florence
Via L. Sacconi 6
50019 Sesto Fiorentino, Italy
e-mail: luchinat@cerm.unifi.it;
Tel.: +390554574262

[*] Prof. Cristina Nativi
Department of Organic Chemistry
University of Florence
Via della Lastruccia 13
50019 Sesto Fiorentino, Italy
e-mail: cristina.nativi@unifi.it;
Tel.: +390554573540

Protein Cloning, Expression and Purification Pag. S3

Crystallization, Data Collection and

X-ray Structure Determination S4

Fluorimetric Assays S5

Synthesis of compound **3** S5

Synthesis of compound **1** S6

Synthesis of compound **13** S7

Synthesis of compound **11** S7

Synthesis of compound **2** S8

Table S1 S9

Table S2 S10

Figure S1 S11

References S12

Protein Cloning, Expression and Purification

The cDNA encoding the catalytic domain of the MMP-12 (G106-G263) was cloned into the pET21a (Novagen) using the restriction enzymes *Nde I* and *Xho I* (New England BioLabs). One additional Methionine at position 105 was present in the final expression product. The expression vector encoding for the protein was transformed into competent *Escherichia coli* BL21 (DE3) Gold strain and colonies were selected for Ampicillin resistance. Bacteria were grown in LB medium containing 50 µg/ml Ampicillin in a shaker flask at 37°C. Protein expression was induced with 0.5 mM IPTG at an OD_{600} = 0.6 and cell growth was continued for a further 5 hours. For expression of ^{15}N and ^{13}C-enriched protein, the bacteria were grown in minimal medium containing ^{15}N enriched $(NH_4)_2SO_4$ and ^{13}C enriched glucose (Cambridge Isotope Laboratories). Cells were harvested by centrifugation, resuspended in a buffer containing 25% Sucrose, 50 mM Tris-HCl (pH 8), 0.1 M NaCl, 0.2 M EDTA, 1 mM DTT. 5-10 mg. Lysozyme was added to the resulting suspension and stirred for 15-20 min. at 4°C. A buffer containing 2% Triton, 50 mM Tris-HCl (pH 8), 0.1 M NaCl, 0.2 M EDTA, 1 mM DTT was added and sonicated (7-8 30-seconds cycles) and centrifuged at 40000 rpm for 20 min. at 4°C. The pellets were washed with 50 mM Tris, 5mM EDTA, 1mM DTT (pH 8) and centrifuged. The resulting inclusion bodies were solublized in 8 M Urea, 20 mM Sodium Acetate (pH 5). The insoluble material was removed by centrifuging at 9000 rpm for 10 min. Protein molecular weight and purity was checked on 15% Gel by SDS-PAGE.

Protein was purified with Ion Exchange chromatography using HiTrap SP column using a gradient of NaCl up to 350mM (6M Urea, 20mM Sodium Acetate, pH 5). The purified protein was refolded by serial dilution method. The protein was diluted to a final concentration of 0.10 mg/ml in 4 M Urea, 20 mM Tris-HCl, 10 mM $CaCl_2$, 0.1 mM $ZnCl_2$, 0.3 M NaCl (pH 7.2), dialysed overnight against same buffer (4 M Urea, 20 mM Tris-HCl, pH 7.2, 10mM $CaCl_2$, 0.1mM $ZnCl_2$, 0.3M NaCl) successively followed by two steps with Buffer B (2 M Urea, 20 mM Tris pH 7.2, 10 mM $CaCl_2$, 0.1 mM $ZnCl_2$, 0.3 M NaCl) for 8 hours, then finally 3 step of 8 hours each with Buffer C (20mM Tris pH 7.2, 10mM $CaCl_2$, 0.1mM $ZnCl_2$, 0.3M NaCl,). The protein solution was concentrated up to 5 ml and purified by size exclusion chromatography using High Load™ 16/60 Superdex™ 75 (Amersham Biosciences) and eluted with 20 mM Tris pH 7.2, 10 mM

$CaCl_2$, 0.1 mM $ZnCl_2$, 0.3 M NaCl and 0.2 M AHA. The eluted fractions were checked for purity on 15% Gel by SDS-PAGE and elution fractions containing protein were pooled and concentrated.

Crystallization, Data Collection and X-ray Structure Determination

Crystals of human MMP12, already containing AHA from the refolding process, grew at 20° C from a 0.1 M Tris-HCl, 30% PEG 8000, 200 mM AHA, solution at pH 8.0 using the vapor diffusion technique. The final protein concentration was about 14 mg/ml. The complexes have been obtained through soaking MMP12-AHA crystals with a solution containing the inhibitor itself.

The data were measured in-house, using a PX-Ultra copper sealed tube source (Oxford Diffraction). All the datasets were collected at 100 K and the crystals used for data collection were cryo-cooled without any cryo-protectant treatment. The crystals of all complexes had a mosaicity ranging from 0.6° to 0.8° and diffracted to a maximum resolution of 1.7 Å.

All the soaked adducts crystallize in the C2 space group with one molecule in the asymmetric unit.

The data were processed in all cases using the program MOSFLM[1] and scaled using the program SCALA[2] with the TAILS and SECONDARY corrections on (the latter restrained with a TIE SURFACE command) to achieve an empirical absorption correction. Table 1 shows the data collection and processing statistics for all datasets.

The structures of the all adducts were solved using the molecular replacement technique; the model used was that of a molecule of human MMP12 (1Y93) from where the inhibitor, all water molecules and ions were omitted. The correct orientation and translation of the molecule within the crystallographic unit cell was determined with standard Patterson search techniques[3;4] as implemented in the program MOLREP.[5;6] The refinement was carried out using REFMAC[7] and for the metal ions anisotropic B-factors were also refined. In between the refinement cycles the models were subjected to manual rebuilding by using XtalView.[8] The same program has been used to fit the two inhibitors in the electron density. Water molecules have been added by using the standard procedures within the ARP/wARP suite.[9]

The stereochemical quality of the refined models was assessed using the program Procheck.[10] The Ramachandran plot for all structures is of very good quality.

Fluorimetric Assays: To assess the binding properties of compounds **1, 2**, **4** and **10** their abilities to inhibit the hydrolysis of fluorescence-quenched peptide substrate Mca-Pro-Leu-Gly-Leu-Dpa-Ala-Arg-NH_2 (Biomol, Inc.)[11] were tested. The analyses were carried out at 298 K in 50 mM HEPES buffer, containing 10 mM $CaCl_2$, 0.05% Brij-35, at pH 7, using 1 nM of MMP catalytic domains and 1 μM of peptide. The experiments were performed with peptide concentration much lower than K_i. The fluorescence (excitation$_{max}$ 328 nm; emission$_{max}$ 393 nm) was measured for 3 minutes after the addition of the substrate using a Varian Eclipse fluorimeter. Fitting of rates as a function of inhibitor concentration provided the K_i values.

Synthesis of compound 3:

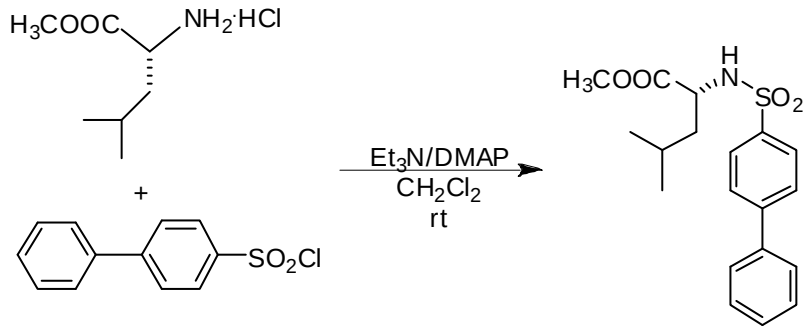

3

A solution of D-leucine methyl ester hydrochloride (3.00 g, 16.5 mmol) in CH_2Cl_2 (80 mL) was cooled to 0°C, triethylamine (6.85 mL, 49.5 mmol) and a catalytic amount of DMAP were added. The mixture was stirred at room temperature for 10 min, then biphenyl-4-sulfonyl chloride (4.17 g, 16.5 mmol) was added. The reaction was stirred at room temperature for 4.5 h. The mixture was neutralized with HCl (3%, H_2O) and washed with brine (3x). The organic layer was dried over anhydrous Na_2SO_4 and the

solvent was removed in vacuo to give 8.00 g of a pale yellow solid. The crude material was purified by flash chromatography on silica gel (hexane/$CHCl_3$/EtOAc 2:5:1) to give **3** as a white solid (5.38 g, 90% yield).

M.p. 135-137 °C

[α]$^{25}_{D}$ +1.85 (c 0.87, $CHCl_3$)

Anal. for $C_{19}H_{23}NO_4S$ Calcd: C, 63.13; H, 6.41; N, 3.88. Found: C, 63.23; H, 6.11; N, 3.84.

^{1}H NMR (200 MHz, $CDCl_3$) δ 7.93-7.89 (part AA' of an AA'MM' system, J_{AM} = 8.4 Hz, 2H), 7.73-7.69 (part MM' of an AA'MM' system, J_{AM} = 8.4 Hz, 2H), 7.64-7.44 (m, 5H), 5.07 (d, *J* = 10.2 Hz, 1H), 4.05-3.93 (m, 1H), 3.43 (s, 3H), 1.89-1.72 (m, 1H), 1.59-1.48 (m, 2H), 0.93 (d, *J* = 3.2 Hz, 3H); 0.90 (d, *J* = 2.8 Hz, 3H) ppm.

^{13}C NMR (50 MHz,$CDCl_3$): 172.49, 145.64, 139.09, 138.03, 129.02, 128.49, 127.80, 127.47, 127.20, 54.52, 52.43, 42.52, 24.51, 22.90, 21.63 ppm.

Synthesis of compound 1:

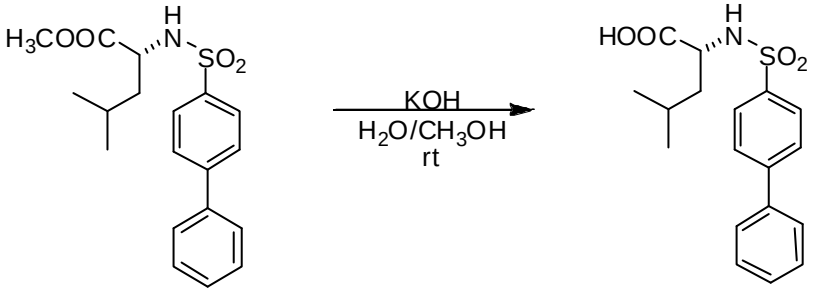

3 **1**

To a solution of **3** (500 mg, 1.38 mmol) in 15 mL of CH_3OH a solution of KOH (1.00 g, 17.90 mmol) in 7 mL of H_2O was added. After 72 h at room temperature, HCl (36%, H_2O) was added (pH=1); the precipitate formed was filtered and washed several times with water to give **1** (463mg, 97%) as a crystalline white solid.

M.p. 129-130 °C

Anal. Calcd for $C_{18}H_{21}NO_4S$: C, 62.23; H, 6.09; N, 4.03. Found: C, 61.61; H, 6.10; N, 3.99

[α]$^{25}_{D}$ -15.6 (c 1.13, CH_3OH).

^{1}H NMR (200 MHz, $CDCl_3$); δ 7.93-7.88 (part AA' of an AA'MM' system, J_{AM} = 8.4 Hz, 2H), 7.79-7.75 (part MM' of an AA'MM' system, J_{AM} = 8.4 Hz, 2H), 7.68-7.34 (m, 5H), 3.90-3.82 (m, 1H), 1.81-1.68 (m, 1H), 1.54-1.46 (m, 2H), 0.90 (d, *J* = 7.0 Hz, 3H), 0.83 (d, *J* = 6.2 Hz, 3H) ppm.

^{13}C NMR (50 MHz, CD_3OD): δ 173.97, 145.04, 139.34, 139.17, 128.62, 127.97, 127.33; 126.94; 126.79, 54.46, 41.84, 24.31, 22.02, 20.44 ppm.

Synthesis of compound 13:

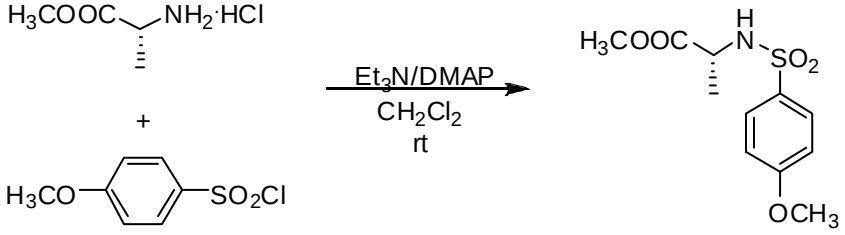

13

To a slurry of D-alanine methyl ester hydrochloride (1.00 g, 7.16 mmol) in 35 mL di CH_2Cl_2 at 0 °C triethylamine (2.95 mL, 21.48 mmol) and a catalytic amount of DMAP were added. The mixture was stirred at room temperature for 15 min, and p-metoxybenzensulfonyl chloride was added. After 2 h, 20 mL of CH_2Cl_2 were added, and the mixture was neutralized with HCl (3%, H_2O) and washed with brine (3 x). The organic layer was dried over anhydrous Na_2SO_4 and the solvent was removed in vacuo to give **13** (1.88 g, 96%) of pale yellow solid which was used without further purification.

M.p. 49-50 °C

[α]$^{25}_{D}$ -27.70 (c 1, $CHCl_3$).

Anal. Calcd for $C_{11}H_{15}NO_5S$: C, 48.34; H, 5.53; N, 5.12. Found: C, 48.44; H, 5.69; N, 5.21.

^{1}H NMR (200 MHz, $CDCl_3$); δ 7.79-7.75 (part AA' of an AA'MM' system, J_{AM} = 9.0 Hz, 2H), 6.98-6.93 (part MM' of an AA'MM' system, J_{AM} = 9.0 Hz, 2H), 5.20 (d, *J* = 8.0 Hz), 4.03-3.87 (m, 1H), 3.86 (s, 3H), 3.55 (s, 3H), 1.37 (d, *J* = 7.0 Hz) ppm.

^{13}C NMR (50 MHz, $CDCl_3$) δ 172.51, 162.84, 131.27, 129.27, 114.15, 55.74, 52.69, 51.52, 19.88 ppm.

Synthesis of compound 11:

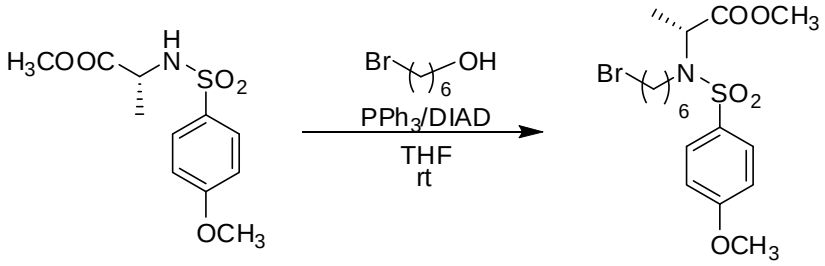

13 **11**

To a solution of **13** (1.00 g, 3.60 mmol), 6-bromo-1-hexanol (0.99 g, 3.60 mmol) and triphenilphosphine (1.93 g, 7.32 mmol) in 37 mL of dry THF, DIAD (1.44 mL, 7.32 mmol) were added dropwise in 1 h. The reaction was stirred at room temperature for 16.5 h, then the solvent was removed in vacuo to give 5 g of a yellow oil. After removal of crystalin betain (EtOAc/cyclohexane 1:8) the filtrate was concentrated in vacuo and the residue (4.10 g) was purified by flash chromatography on silica gel (CH_2Cl_2/CH_3OH 30:1) to give **11** (1.03 g, 64%) as a colourless oil.

$[\alpha]^{25}_D$ +37.5 (c 0.41, $CHCl_3$).

Anal. Calcd for $C_{17}H_{26}BrNO_5S$: C, 46.79; H, 6.01; N, 3.21. Found: C, 46.83; H, 5.84; N, 3.32.

^{1}H NMR (200 MHz, $CDCl_3$); δ 7.78-7.73 (part AA' of an AA'MM' system, J_{AM} = 8.8 Hz, 2H), 6.98-6.94 (part MM' of an AA'MM' system, J_{AM} = 8.8 Hz, 2H), 4.62 (q, *J* = 7.0 Hz, 1H), 3.87 (s, 3H), 3.57 (s, 3H), 3.39 (t, *J* = 6.6 Hz, 2H), 3.31-3.01 (m, 2H), 1.90-1.21 (m, 8H), 1.41 (d, *J* = 7.0 Hz, 3H) ppm.

^{13}C NMR (50 MHz, $CDCl_3$) δ 171.87, 162.63, 131.64, 129.32, 113.92, 55.71, 55.13, 52.25, 45.66, 33.92, 32.75, 30.85, 27.85, 26.21, 16.80 ppm.

Synthesis of compound 2:

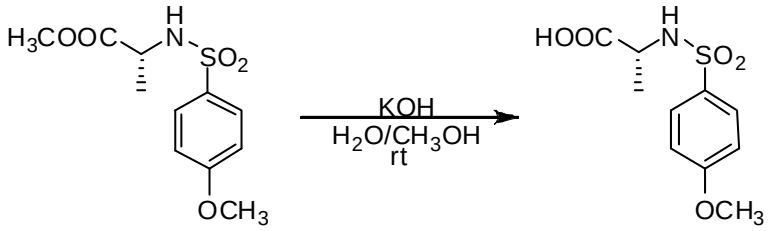

13 **2**

To a solution of **13** (500 mg, 1.18 mmol) in 1 mL of CH_3OH a solution of KOH (1M, H_2O; 304 mg, 5.43 mmol) was added. After 72 h, HCl (25%, H_2O) was added (pH=1). The CH_3OH was removed in vacuo and the acqueous phase was extracted with AcOEt (2 x). The organic layer was dried over anhydrous Na_2SO_4 and the solvent was removed in vacuo to give **2** (426 mg, 90%) as a white solid.

M.p. 90-92 °C

$[\alpha]^{25}_D$ +17.0 (c 0.34, CH_3OH).

Anal. Calcd for $C_{10}H_{13}NO_5S$: C, 46.32; H, 5.05; 5.40. Found; C, 46.67; H, 5.51; N, 5.77.

^{1}H NMR (200 MHz, CD_3OD) δ 7.83-7.78 (part AA' of an AA'MM' system, J_{AM} = 8.8 Hz, 2H), 7.08-7.04 (part MM' of an AA'MM' system, J_{AM} = 8.8 Hz, 2H), 3.88 (s, 3H), 3.62 (q, J = 7.4 Hz, 1H), 1.31 (d, J = 7.4 Hz, 3H) ppm.

^{13}C NMR (50 MHz, CD_3OD) δ 176.68, 162.81, 132.02, 128.82, 113.81, 54.91, 52.54, 19.08 ppm

Table S1. X-ray data collection and refinement statistics.

	EDR52	EDR55
Space group	C2	
Cell dimensions (Å, °)	a= 51.18 b= 60.55 c= 54.43 β = 115.90	a= 51.15 b= 60.58 c= 54.38 β = 115.76
Resolution (Å)	30.2 – 1.9	30.2 – 1.9
Unique reflections	11585 (1553)	11350 (1226)
Overall completeness (%)	98.0 (91.3)	95.7 (71.6)
R_{sym}	0.06 (0.17)	0.07 (0.17)
Multiplicity	6.5 (3.4)	5.2 (2.0)
I/(σI)	11.2 (4.6)	12.2 (5.2)
B-factor from Wilson plot (Å^2)	8.73	7.87

R_{cryst} / R_{free}	0.16 / 0.20	0.22 / 0.27
Protein atoms	1238	1238
Ions	5	5
Ligand atoms	23	17
Water molecules	163	123
RMSD bonds (Å)	0.01	0.02
RMSD angles (°)	1.61	2.30
Average B-factor (Å^2)	9.04	6.48

Numbers in parenthesis refer to high resolution shell

Table S2. SPR Sensorgram of BTI 4 vs. MMP-12 and Plot of Residuals

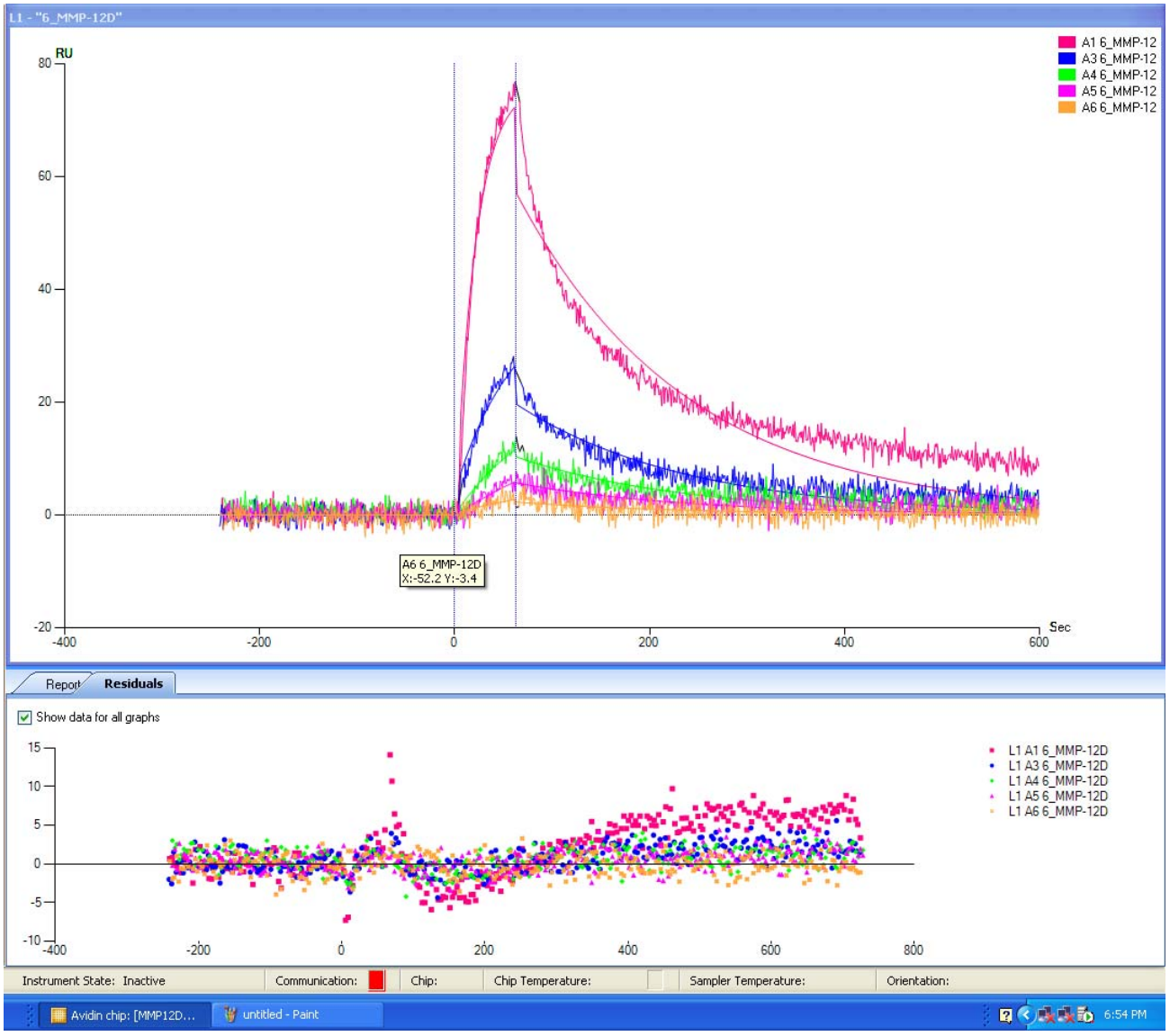

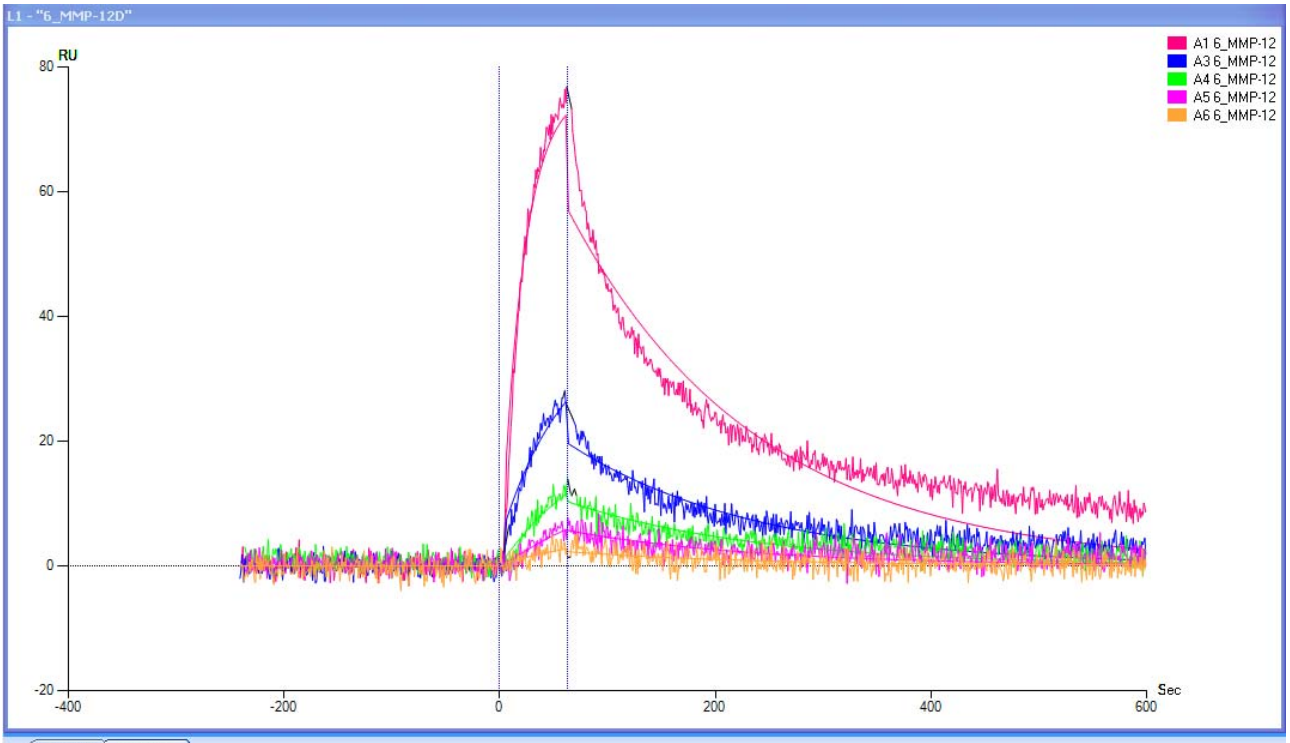

Report | Residuals

Parameter Units Scope Type	ka 1/Ms Global Fitted	kd 1/s Global Fitted	KD Auto Defined Fitted	Rmax RU Local Fitted	Concentration M Local Constant	t0 Association s Local Constant	t0 Dissociation s Local Constant	RI RU Local Fitted	Chi2 RU Constant
Kinetic - Langmuir 1	1.21E+06	5.75E-03	4.76E-09						4.3
⊟–L1 - "6_MMP-12D"									
–A1 6_MMP-12D				69.19	3.50E-08	5.33	63	15.42	
–A3 6_MMP-12D				49.71	8.75E-09	5.33	63	6.99	
–A4 6_MMP-12D				45.59	4.38E-09	5.33	63	1.41	
–A5 6_MMP-12D				47.1	2.18E-09	5.33	63	0.27	
└A6 6_MMP-12D				36.25	1.09E-09	5.33	63	0.5	

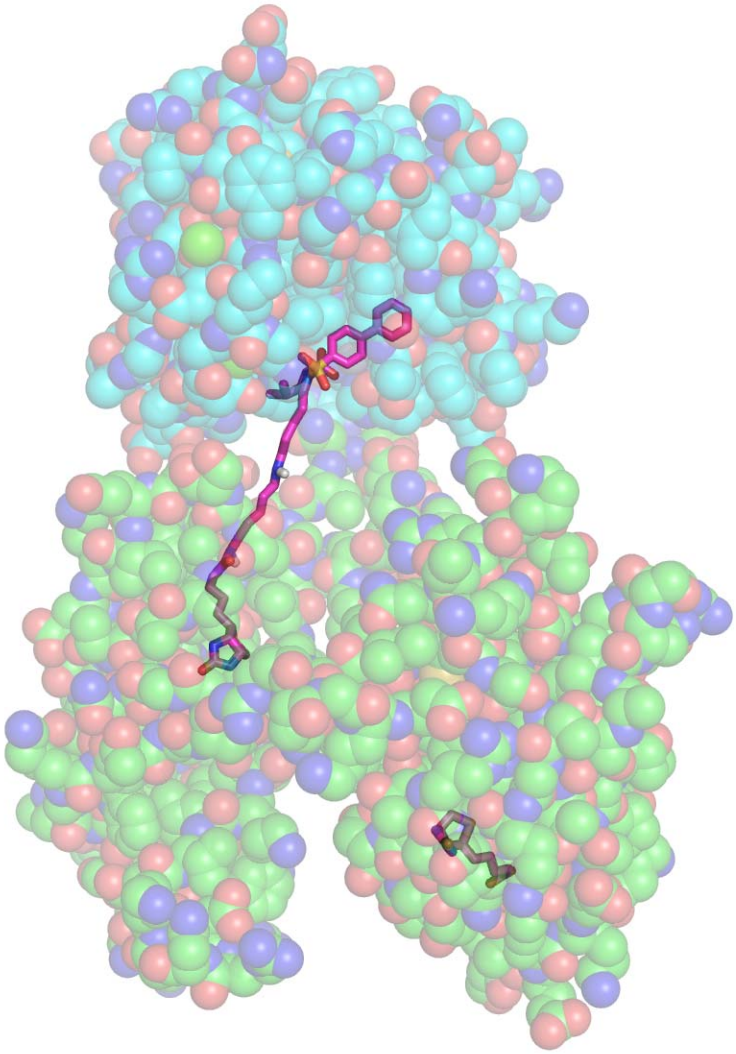

Figure S1. Model of the ternary system Avidin-BTI **4** -MMP generated starting from the avidin-biotin complex (pdb code: 2avi) and the BTI **1** -MMP-12 adduct, and obtained by linking the biotin moiety to the BTI **1** ligand with the fourteen-membered spacer. Such model, generated by using the program Pymol, was useful in the rational design of linker's length.[12]

References

1. Leslie, A. G. W. (**1991**) in *Molecular data processing* (Moras, D., Podjarny, A. D., and Thierry, J.-C., Eds.) pp 50-61, Oxford University Press, Oxford.

2. Evans, P. R. (**1997**) SCALA, *Joint CCP4 and ESF-EACBM Newsletter 33*, 22-24.

3. Rossmann, M. G.; Blow, D. M. *Acta Cryst.* **1962**, *15*, 24.

4. Crowther, R. A. The Molecular Replacement Method; Rossmann, M. G., ed. Gordon & Breach: New York, **1972**.

5. Vagin, A.; Teplyakov, A. *J.Appl.Crystallogr.* **1997**, *30*, 1022-1025.

6. Vagin, A.; Teplyakov, A. *Acta Crystallogr.D Biol.Crystallogr.* **2000**, *56*, 1622-1624.

7. Murshudov, G. N.; Vagin, A. A.; Dodson, E. J. *Acta Cryst.* **1997**, *D53*, 240-255.

8. McRee, D. E. *J.Mol.Graphics* **1992**, *10*, 44-47.

9. Lamzin, V. S. *Acta Crystallogr.D Biol.Crystallogr.* **1993**, *49*, 129-147.

10. Laskowski, R. A., MacArthur, M. W., Moss, D. S., and Thornton, J. M. *J. Appl. Crystallogr.* **1993**, *26*, 283-291.

11. Lukacova, V.; Zhang, Y.; Mackov, M.; Baricic, P.; Raha, S.; Calvo, J.A. and Balaz, S. *J. Biol. Chem.* **2004**, *279*, 14194

12. W. L. DeLano, The PyMOL Molecular Graphics System (**2002**)

Subscriber access provided by SHEMYAKIN-OVCHINNIKOV INST

Article

Comparative Methods for Analysis of Protein Covalent Modification by Electrophilic Quinoids Formed from Xenobiotics

Bolan Yu, Zhihui Qin, Gihani T. Wijewickrama, Praneeth Edirisinghe, Judy L. Bolton, and Gregory R. J. Thatcher

Bioconjugate Chem., **2009**, 20 (4), 728-741• DOI: 10.1021/bc800435m • Publication Date (Web): 20 March 2009

Downloaded from http://pubs.acs.org on May 15, 2009

More About This Article

Additional resources and features associated with this article are available within the HTML version:

- Supporting Information
- Access to high resolution figures
- Links to articles and content related to this article
- Copyright permission to reproduce figures and/or text from this article

View the Full Text HTML

ACS Publications
High quality. High impact.

Bioconjugate Chemistry is published by the American Chemical Society. 1155 Sixteenth Street N.W., Washington, DC 20036

Comparative Methods for Analysis of Protein Covalent Modification by Electrophilic Quinoids Formed from Xenobiotics

Bolan Yu, Zhihui Qin, Gihani T. Wijewickrama, Praneeth Edirisinghe, Judy L. Bolton, and Gregory R. J. Thatcher*

Department of Medicinal Chemistry and Pharmacognosy, College of Pharmacy, University of Illinois at Chicago, 833 S Wood Street, Chicago, Illinois 60612. Received October 13, 2008; Revised Manuscript Received February 14, 2009

Conjugation of biotin and fluorophore tags is useful for assaying covalent protein modification. Oxidative bioactivation of selective estrogen receptor modulators (SERMs) yields reactive quinoid electrophiles that covalently modify proteins, and bioactivation is associated with carcinogenic and chemopreventive effects. Identification of the protein targets of electrophilic metabolites is of general importance for xenobiotics. Four methodologies using SERM derivatized biotin/fluorophore tags were compared for purification and quantification: (1) covert oxidatively activated tags (COATags; SERM conjugated to biotin); (2) dansylTags (SERM conjugated to fluorophore); and azidoTags (SERM azide derivatives) in a two-step conjugation to biotin, using either (3) Staudinger ligation or (4) click chemistry. All synthetic derivatives retained the estrogen receptor ligand characteristics of the parent SERMs. Model proteins with bioactivation by tyrosinase in buffer or cell lysates and liver proteins with *in situ* bioactivation in rat primary hepatocytes were studied by immunoassay and fluorescence. Comparison showed that the azidoTag/Staudinger method was sensitive but nonspecific, the azidoTag/click methodology had low sensitivity, and the dansylTag methodology failed to detect modified proteins in hepatocytes. The COATag methodology was judged superior, detecting 5 ng of modified protein *in vitro* and identifying protein targets in hepatocytes. In metabolism studies in rat liver microsomes, the azide group was metabolically labile, which was a contributing factor in not selecting the azidoTag methodology in the oxidative environments required for bioactivation. For study of the protein targets of electrophilic metabolites formed by *in situ* oxidative bioactivation, the COATag is both sensitive and specific and does not appear to suffer from poor cell permeability.

INTRODUCTION

Selective estrogen receptor modulators (SERMs[1]) are widely used in the clinic for the treatment and prevention of breast cancer, osteoporosis, and other indications in postmenopausal women (*1*). All SERMs and their active metabolites share common polyaromatic phenolic scaffolds that are redox active *in vitro* and *in vivo* (*2, 3*). Formation of *o*-quinones, quinone methides, and diquinone methides has been reported from the oxidative metabolism of SERMs (*4*−*7*). As reactive electrophiles, SERM quinoids can potentially covalently modify cellular proteins with varied selectivity. Protein families that are involved in estrogen metabolism, ER signaling pathways, and redox sensing are theoretically susceptible to modification by SERM quinoids. It has been reported that metabolic enzymes, such as GST-P1 and P450 isoforms, can be inhibited by raloxifene and other SERMs (*7*−*9*); modification of ER and histone H3 by estrogens and quinoids has been reported (*10*−*13*); and sensor proteins such as Keap1 involved in cellular defense are also likely targets (*14*). It is increasingly clear that damage or covalent modification of cellular proteins is related to both toxicity and cytoprotective mechanisms, which impacts the balance between carcinogenesis and chemoprevention for a variety of small molecules that form electrophilic, reactive intermediates (*14*). The correlation between the structural properties of these electrophiles and their biological targets is not yet clear; however, it is important to identify cellular targets of xenobiotics to understand the long-term biological consequences of exposure.

Identification of protein targets of electrophiles remains a technical challenge that is limited by a lack of efficient strategies for labeling targets in a physiological environment. Previous studies have widely used isotopically labeled electrophiles to analyze modified proteins (*15*−*18*); animals or cells were treated with radioactive electrophiles and were further analyzed by 1D/2D-PAGE and/or LC-MS/MS (*17, 19*). Antibodies that can recognize adducts formed from electrophiles such as 4-hydroxynonenal (4-HNE) and butylated hydroxytoluene (BHT) have also been used for protein identification (*15, 16, 18*); however, these techniques suffer from low coverage of adducted proteins and cross-reactivity. A more recent approach using tagged electrophiles is highlighted by the use of 4-HNE tagged with biotin to identify protein targets of 4-HNE (*20*). Whereas 4-HNE and commercially available tagged electrophiles (i.e., iodoacetamide) are inherently reactive, SERMs require oxidative bioactivation. Therefore, a novel methodology was developed, coined the covert oxidatively activated tag (COATag), in which a biotin linker is tagged to the partial structure of the xenobiotic. A COATag is not inherently reactive toward cellular proteins but requires bioactivation. The proof of principle study used a

* Correspondence to Greg Thatcher, Department of Medicinal Chemistry and Pharmacognosy, University of Illinois at Chicago, 833 S. Wood Street, Chicago, IL, 60612; Phone: 312-355-5282; Fax: 312-996-7107; E-mail: thatcher@uic.edu.

[1]Abbreviations: BHT, 2,6-ditert-butyl-4-methylphenol; BSA, bovine serum albumin; COATag, covert oxidatively activated tag; 1DGE, 1-dimensional gel electrophoresis; 2DGE, 2-dimensional gel electrophoresis; DMA, desmethylarzoxifene; DMSO, dimethyl sulfoxide; DTT, dithiothreitol; ER, estrogen receptor; GST-P1, human glutathione S-transferase P1−1; KHB, Krebs-Henseleit Buffer; 4-HNE, 4-hydroxynonenal; LC-MS/MS, liquid chromatography with electrospray ionization tandem MS; PBS, phosphate buffered saline; Ral, raloxifene; r.t., room temperature; SDS-PAGE, sodium dodecyl sufate polyacrylamide gel electrophoresis; SERM, selective estrogen receptor modulator; TFA, trifluoroacetic acid; RalN3, azido raloxifene; DiQM-CG, diquinone methide CysGly conjugates; DiQM-GSH: diquinone methide GSH conjugates; *o*-QGSH, *o*-quinone GSH conjugates.

10.1021/bc800435m CCC: $40.75 © 2009 American Chemical Society
Published on Web 03/20/2009

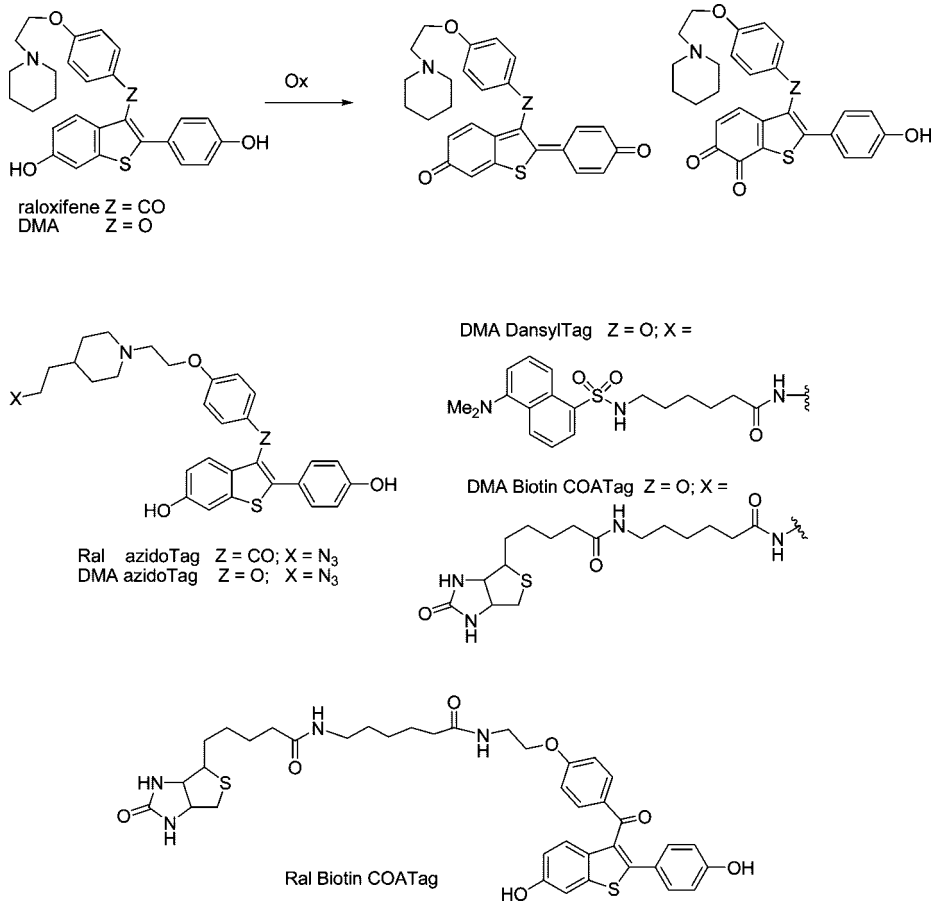

Figure 1. Diquinone methide and *o*-quinone metabolites formed by bioactivation of raloxifene/DMA: COATag, azidoTag, and dansylTag conjugates used in this study.

COATag of the clinical benzothiophene SERM raloxifene (Figure 1) and oxidative enzymes to activate the SERM to a reactive electrophile (*7*). In combination with mass spectroscopy, the COATag methodology revealed the selective modification of protein targets in liver microsomes (*7*); furthermore, raloxifene and desmethylarzoxifene (DMA) COATags were employed in uterine microsomes to demonstrate bioactivation by peroxidases (*21*). Of the potential problems with the use of COATags *in vivo* or in intact cell systems, the potential cell impermeability caused by the hydrophilic biotin linker is common to all biotin conjugates (*22*−*24*).

Progress in chemical biology has offered new approaches for identifying the protein targets of reactive electrophiles in intact cells, using azide or alkyne tags, followed by conjugation with the complementary biotin linker (*20*). These techniques exploit the so-called bioorthogonal reactivity of the azide functionality to conjugate with biotin or with a fluorophore using the mild reaction conditions of the modified Staudinger ligation or click chemistry (*25, 26*). Wide usage has been reported in cellular protein labeling (*26*), activity-based protein profiling (*27*), and, recently, identification of cellular targets of electrophiles (*20*). In addition to biotin conjugation, fluorophore conjugates including dansyl, BODIPY, and rhodamine have been reported (*28, 29*). However, in a few papers problems have been highlighted, such as high background response, poor enrichment of modified proteins, and cellular impermeability (*20, 22, 23, 30*).

The objective is to identify cellular targets of electrophiles formed by metabolic bioactivation. In this paper, the scope and limitations of different SERM tagging strategies are explored using raloxifene or DMA as the drugs of interest, comparing preformed COATags and fluorophore tags with conjugation methodologies based upon the bioorthogonal azide group subject to either Staudinger ligation or click chemistry. Perhaps surprisingly, the original COATag methodology was seen as superior, at least in part because of the influence on chemical conjugation of the oxidative environment required for bioactivation.

MATERIALS AND METHODS

Reagents and Materials. All solvents and chemicals were purchased from Fisher Scientific (Itasca, IL) or Sigma-Aldrich Chemical (St. Louis, MO) unless stated otherwise. UltraLink Immobilized Monomeric Avidin, MagnaBind streptavidin beads, HRP-streptavidin, ECL Western blotting substrate, and Imperial protein stain kit were obtained from Pierce (Rockford, IL). Click-iT biotinylation kit for click chemistry and all 1D and 2D gel electrophorosis instruments and reagents including NuPAGE precast gels, XCell SureLock Mini-Cell, ZOOM IPGRunner System, and ZOOM strips were purchased from Invitrogen (Carlsbad, CA). [1,5-Bis [2-(dimethylamino)ethyl]amino]-4,8-dihydroxyanthracene-9,10 -dione] (DRAQ5) was purchased from Axxora (San Diego, CA). Rat liver microsomes were prepared according to an existing procedure (*6*). Phosphinyl biotin for Staudinger ligation, compound **9** for the synthesis of dansyl DMA, and dansyl alkyne **11** for the study of click chemistry model reaction were prepared according to published procedures (*21, 31, 32*).

Instrumentation. LC-MS/MS was carried out using an Agilent (Palo Alto, CA) ion trap mass spectrometer equipped with a model 1100 HPLC system and electrospray ionization source. Proteomic MS analysis used a Dionex Ultimate 3000 HPLC system linked to a Thermo Finnigan LTQ-FT mass spectrometer equipped with a nanospray interface. ^{1}H NMR and ^{13}C NMR spectra were obtained with Bruker AVANCE 300, UltraShield 400, spectrometers.

Synthesis of Azido Raloxifene and Dansyl DMA. *2-[1-(tert-Butoxycarbonyl)piperidin-4-yl]ethyl Methanesulfonate (***2***).* Mesyl chloride (2.5 mL, 32.7 mmol) was added dropwise to compound **1** (5.0 g, 21.8 mmol) and NEt_3 (6.0 mL, 43.6 mmol) in anhydrous THF (100 mL) cooled in an ice−water bath. The reaction mixture was stirred overnight at r.t. Most of the solvent was removed; residue was diluted with dichloromethane (200 mL), washed with brine, and dried with anhydrous $MgSO_4$. After filtration and concentration, the product was obtained as a white solid (5.2 g, 78%). ^{1}H NMR ($CDCl_3$, 300 MHz): δ 4.28 (t, 2H, J = 6.1 Hz), 4.07−4.11 (m, 2H), 3.01 (s, 3H) 2.64−2.73 (m, 2H), 1.66−1.71 (m, 5H), 1.45 (s, 9H), 1.11−1.19 (m, 2H). ^{13}C NMR ($CDCl_3$, 75 MHz): δ 154.97, 79.57, 67.64, 43.93, 37.61, 35.79, 32.56, 31.92, 28.63.

*2-(N-tert-Butoxycarbonyl-4-piperidinyl)ethyl Azide (***3***).* Compound **2** (5.0 g, 16.3 mmol) dissolved in anhydrous acetonitrile (150 mL) and NaN_3 (4.3 g, 66 mmol) was added. The reaction mixture was refluxed overnight. Solvent was removed; the residue was diluted with dichloromethane (200 mL), washed with brine, and dried with anhydrous $MgSO_4$. After filtration and concentration, the product was obtained as a syrup with slight brown color (2.8 g, 80%). ^{1}H NMR ($CDCl_3$, 300 MHz): δ 4.04−4.09 (m, 2H), 3.30 (t, 2H, J = 6.4 Hz), 2.62−2.70 (m, 2H), 1.49−1.66 (m, 5H), 1.43 (s, 9H), 1.05−1.14 (m, 2H). ^{13}C NMR ($CDCl_3$, 75 MHz): δ 154.91, 79.41, 48.90, 43.94, 35.34, 33.46, 31.94, 28.57.

*4-(2-Azidoethyl)piperidine Trifluoroacetate (***4***).* Compound **3** (1.2 g, 4.7 mmol) was dissolved in dichloromethane (10 mL), TFA (3.0 mL) was added, and the reaction was stirred at r.t. for 1 h. Most of the solvent was removed, and a mixture of ether and water (v/v 1:1, 100 mL) was added. The aqueous phase was separated and washed with ether (30 mL). The aqueous solution was isolated and concentrated to give the product as white solid (890 mg, 70%). ^{1}H NMR (DMSO-d_6, 300 MHz): δ 8.91 (bs, 1H), 8.61 (bs, 1H), 3.38 (t, 2H, J = 6.8 Hz), 3.22−3.26 (m, 2H), 2.75−2.92 (m, 2H), 1.77−1.81 (m, 2H), 1.55−1.71 (m, 1H), 1.44−1.51 (m, 2H), 1.20−1.36 (m,2H). ^{13}C NMR (DMSO-d_6, 75 MHz): δ 158.82, 158.40, 47.96, 43.01, 34.12, 30.57, 28.07.

*[4-(2-Azidoethyl)-1-piperidinyl]ethanol (***5***).* Compound **4** (1.2 g, 4.4 mmol) and 2-bromoethanol (333 μL, 4.5 mmol) were dissolved in anhydrous acetonitrile (20 mL), followed by addition of anhydrous K_2CO_3 (1.85 g, 13.5 mmol). The reaction mixture was refluxed overnight. After filtration and concentration, the residue was dissolved in ethyl acetate (100 mL) and washed with saturated NaCl aqueous solution. The organic phase was separated and concentrated to give a residue which was used in the subsequent step without further purification (610 mg, 68%). A small amount of sample was taken for proton NMR analysis to confirm the product identity. ^{1}H NMR (Acetone-d_6, 400 MHz): δ 3.55 (t, 2H, J = 5.9 Hz), 3.37 (t, 2H, J = 7.1 Hz), 2.88−2.91 (m, 2H), 2.43 (t, 2H, J = 5.9 Hz), 1.95−2.01 (m, 2H), 1.66−1.69 (m, 2H), 1.50−1.55 (m, 2H), 1.33−1.45 (m, 1H), 1.18−1.28 (m, 2H).

*(4-Fluorophenyl)[6-hydroxy-2-(4-hydroxyphenyl)benzo[b]thien-3-yl] Methanone (***7***).* Compound **6** (2.1 g, 7.7 mmol) and 4-fluorobenzoyl chloride (0.92 mL, 7.8 mmol) were dissolved in anhydrous dichloromethane (50 mL) and cooled in an ice−water bath, followed by addition of $AlCl_3$ (1.1 g). The reaction mixture was stirred at r.t. overnight. The reaction was cooled in an ice−water bath, ethanethiol (2.8 mL, 38.5 mmol) was added, and the mixture stirred at r.t. for 6 h. The reaction mixture was diluted with dichloromethane (200 mL) followed by addition of 20% HCl (5 mL) and H_2O (50 mL) with vigorous stirring. The organic phase was separated and further washed carefully with saturated aqueous $NaHCO_3$ and brine. After concentration, the product was purified by column chromatography (hexanes/ethyl acetate 1:1) to give a slightly orange solid (2.5 g, 88%). ^{1}H NMR (Acetone-d_6, 400 MHz): δ 7.77−7.81 (m, 2H), 7.55 (d, 1H, J = 8.8 Hz), 7.41 (d, 1H, J = 2.0 Hz), 7.21 (d, 2H, J = 8.4 Hz), 7.06 (t, 2H, J = 8.8 Hz), 7.69 (dd, 1H, J = 8.8 Hz, 2.0 Hz), 6.73 (d, 2H, J = 8.8 Hz). ^{13}C NMR (Acetone-d_6, 100 MHz): δ 192.99, 167.49, 164.98, 158.86, 156.43, 144.30, 140.83, 135.16, 133.74, 133.28, 133.18, 131.25, 130.45, 125.46, 124.72, 116.34, 116.21, 115.99, 107.82.

*[4-[2-[4-(2-Azidoethyl)-1-piperidinyl]ethoxy]phenyl][6-hydroxy-2-(4-hyroxyphenyl)benzo[b]thien-3-yl] Methanone (***8***).* Compound **5** (590 mg, 2.9 mol) was dissolved in anhydrous DMF (5 mL), 60% NaH (120 mg) was added, and the mixture was stirred at r.t. for 10 min. Compound **7** (150 mg, 0.4 mmol) was added, and the reaction mixture was stirred at r.t. overnight. The reaction was quenched by adding MeOH (0.5 mL) and diluted with ethyl acetate (30 mL) containing 5% MeOH, then washed with saturated aqueous $NaHCO_3$. The organic phase was separated and concentrated to give crude product, which was purified by column chromatography (CH_2Cl_2/MeOH 10:1) to give the product as a yellow foam (55 mg, 25%). ^{1}H NMR (Acetone-d_6, 400 MHz): δ 8.67 (bs), 7.73 (d, 2H, J = 8.8 Hz), 7.39−7.42 (m, 2H), 7.28 (d, 2H, J = 8.8 Hz), 6.94 (dd, 1H, J = 2.4 Hz, 8.8 Hz), 6.89 (d, 2H, J = 8.8 Hz), 6.75 (d, 2H, J = 8.4 Hz), 4.13 (t, 2H, J = 5.8 Hz), 3.37 (t, 2H, J = 7.2 Hz), 2.93−2.96 (m,2H), 2.71 (t, 2H, J = 6.0 Hz), 1.65−1.69 (m, 2H), 1.49−1.54 (m, 2H), 1.33−1.43 (m,1H), 1.17−1.26 (m, 2H). ^{13}C NMR (Acetone-d_6, 100 MHz): δ 193.30, 164.04, 158.70, 156.34, 141.93, 140.81, 134.13, 132.77, 131.41, 131.30, 130.97, 125.84, 124.64, 116.43, 115.83, 115.12, 107.85, 67.27, 57.92, 54.89, 49.57, 35.96, 33.89, 32.86.

*[4-[2-[4-(2-(Dansyl-ε-aminocapronamide)ethyl)-1-piperidinyl]ethoxy]phenyl] [6-Hydroxy-2-(4-hyroxy phenyl)benzo[b]thien-3-yl] Methanone (***10***).* Compound **9** (50 mg, 0.09 mmol) and Ph_3P (42 mg, 0.15 mmol) were dissolved in the mixture of THF (1 mL) and H_2O (20 μL) and stirred at r.t. overnight (solution A). Dansyl-ε-aminocaproic acid (93 mg, 0.17 mmol), *N*-hydroxyl succinimide (23 mg, 0.20 mmol), and DCC (46 mg, 0.22 mmol) were dissolved in anhydrous DMF (1 mL) and stirred at r.t. overnight (solution B). Solution A was concentrated to dryness, dissolved in DMF (300 μL), and added to solution B. The reaction mixture was stirred at r.t. overnight. After filtration, the solvent was removed under high vacuum. The residue was purified by column chromatography (CH_2Cl_2/MeOH 10:1 and 0.2% $NH_3 \cdot H_2O$) to give the product as a foam with slight green coloration (38 mg, 49%). ^{1}H NMR (Acetone-d_6, 400 MHz): δ 8.54 (d, 1H, J = 8.5 Hz), 8.40 (d, 1H, J = 8.7 Hz), 8.20 (dd, 1H, J = 7.2 Hz, 1.0 Hz), 7.52−7.61 (m, 4H), 7.30 (d, 1H, J = 1.9 Hz), 7.25 (d, 1H, J = 7.5 Hz), 7.18 (d, 1H, J = 8.6 Hz), 6.99 (t, 1H, SO_2NH), 6.82−6.88 (m, 7H), 6.73 (t, 1H, CONH), 4.00 (t, 2H, J = 5.8 Hz), 3.16−3.21 (m, 2H), 2.85−2.92 (m, 10H), 2.65 (t, 2H, J = 5.8 Hz), 1.98−2.01 (m, 2H), 1.61−1.64 (m, 2H), 1.14−1.41 (m, 13H). ^{13}C NMR (Acetone-d_6, 100 MHz): δ 172.94, 158.18, 156.66, 155.19, 152.71, 152.49, 140.38, 137.50, 137.36, 130.69, 130.58, 130.48, 129.61, 129.44, 128.59, 128.12, 126.61, 124.64, 124.15, 122.71, 120.41, 116.99, 116.55, 116.40, 115.99, 115.45, 108.80, 67.26, 58.33, 55.00, 45.59, 43.62, 37.26, 37.19, 36.46, 34.27, 33.95, 32.98, 26.73, 25.33.

*5-(Dimethylamino)-N-((1-(2-(piperidin-4-yl) ethyl)-1H-1,2,3-triazol-4-yl)methyl)naphthalene-1-sulfonamide (***12***).* Azide **4** (250 μM), alkyne **11** (50 μM), $CuSO_4$ (500 μM), Na ascorbate (1.0 M), and tris[(1-benzyl-1*H*-1,2,3-triazol-4-yl)methyl]amine (100 μM) were stirred at room temperature for 1 h. The reaction product was identified by LC-MS and was quantified using as internal standard, 5-(dimethylamino)naphthalene-1-sulfonamide. The reaction yield in the presence of H_2O_2 (0, 100, 500, 1000 μM) was quantified in this way.

Rat Liver Microsomal Incubation of Azido Raloxifene. A solution containing azido raloxifene (10 μM), rat liver microsomes (1.0 mg/mL), GSH (500 μM), and NADPH (1 mM) in 50 mM phosphate buffer (pH 7.4, 500 μL total volume) was incubated for 30 min at 37 °C. For comparison, GSH was omitted and/or raloxifene was used as substrate. The reactions were terminated by chilling in an ice bath followed by the addition of a mixture of methanol/acetonitrile (100 μL, 1:1 v/v) and perchloric acid (50 μL/mL). The reaction mixtures were centrifuged at 13 000 rpm for 10 min; aliquots (80 μL) of supernatant were analyzed using LC-MS/MS. The HPLC analysis of the microsomal incubation was performed using an Agilent Eclipse XDB-C18 column (4.6 × 250 mm, 5 μm) with UV absorbance detection at 316 nm. The composition of HPLC mobile phase was a mixture of two solutions: solution A, water with 10% methanol and 0.1% formic acid; solution B, acetonitrile with 0.1% formic acid. The mobile phase consisted of a linear gradient of solution B from 10% to 30% over 20 min, 20 min gradient of solution B from 30% to 60%, and then 60% to 90% of solution B over 5 min at a flow rate of 1.0 mL/min.

ER Competitive Binding Assays. Competitive displacement of [^{3}H] estradiol (E_2) radioligand (Amersham Biosciences, Piscataway, NJ) from full-length recombinant human hERα and hERβ (PanVera/Invitrogen, Carlsbad, CA) was assayed as described (*33*, *34*). The reaction mixture consisted of 5 μL of compound in DMSO, 5 μL of hERα (0.5 pmol) in ER binding buffer (consisting of 10 mM Tris-HCl (pH 7.5), 10% glycerol, 2 mM dithiothrietol, 1 mg/mL BSA), 5 μL of "Hot Mix" [400 nM, prepared fresh using 95 Ci/mmol [^{3}H] estradiol, diluted in 1:1 ethanol/ER binding buffer (NEN Life Science Products; Boston, MA)] and 85 μL of ER binding buffer. The incubation was carried out at room temperature for 2 h before 50% hydroxyapatite slurry (100 μL; HAPS) was added. The tubes were incubated on ice for 15 min with vortexing every 5 min. The appropriate ER wash buffer was added (1 mL), and the tubes were vortexed before centrifuging at 10 000 *g* for 1 min. The supernatant was discarded, and this wash step was repeated three times. The HAPS pellet containing the ligand−receptor complex was resuspended in 200 μL of ethanol and transferred to scintillation vials. An additional 200 μL of ethanol was used to rinse the centrifuge tube. Cytoscint (4 mL/vial; ICN, Costa Mesa, CA) was added, and the radioactivity was counted using a Beckman LS 5801 liquid scintillation counter (Schaumburg, IL).

Induction of Alkaline Phosphatase in Cultured Ishikawa Cells. The Ishikawa cell line was provided by R. B. Hochberg (Yale University, New Haven, CT) and was maintained in Dulbecco's modified Eagle medium (DMEM/F12) containing 1% sodium pyruvate, 1% nonessential amino acids (NEAA), 1% glutamax-1, 0.05% insulin, and 10% heat-inactivated FBS. The procedure of Liu et al. was used as described previously (*33*). Ishikawa cells (1.5×10^4 cells/190 μL/well) were preincubated in 96-well plates overnight in estrogen-free medium. Test samples (10 μL at varying concentrations in DMSO) were added to determine EC_{50} values, and the cells in a total volume of 200 μL media/well were incubated at 37 °C for 4 days. For the determination of antiestrogenic activity, 2×10^{-8} M estradiol was added to the 10 mL of media used to dilute the test samples. The induction plates were processed by washing the plates with PBS and adding 50 μL of 0.01% Triton X100 in 0.1 M Tris buffer (pH 9.8). Plates were subjected to a freeze−thaw (−80 °C for at least 24 h before warming on a plate warmer to 37 °C). An aliquot (150 μL) of 1 mg/mL *p*-nitrophenylphosphate (phosphatase substrate) in 0.1 M Tris buffer (pH. 9.8) was added to each well. The enzyme activity was measured by reading the release of *p*-nitrophenol at 405 nm every 15 s with a 10 s shake between readings for 16 readings using a Power Wave 200 microplate scanning spectrophotometer (Bio-Tek Instruments, Winooski, VT). The maximal slopes of the lines generated by the kinetic readings were calculated. For antiestrogenic determination, the percent induction as compared with the background induction control was calculated using % antiestrogenic induction $= 100 \times [1 - ((\text{slope}_{\text{sample}} - \text{slope}_{\text{cells}})/(\text{slope}_{\text{estrogen}} - \text{slope}_{\text{cells}}))]$.

Modification of Model Proteins. Model protein GST-P1 (0.3 mg/mL) or BSA (0.2 mg/mL) and tyrosinase (5000 units/mL) were incubated with 50 μM tags (25 mM stock in DMSO) in PBS (pH 7.4), at 37 °C for 1 h. The azidoTag modified proteins were subsequently biotinylated via the modified Staudinger ligation by reaction with 500 μM phosphinyl biotin reagent (P-biotin; 50 mM stock in DMSO) at 47 °C for 2 h or via click chemistry using Click-iT kit according to the manufacturer's instructions. Reaction mixtures were chilled on ice, and 20 μL aliquots were separated in MOPS running buffer on 4−12% NuPAGE gels (Invitrogen) and run on 200 V, 1 h, and detected with HRP-streptavidin (Pierce, 1:5000) after transblotting onto PDVF membrane and blocking overnight (5% nonfat milk). For studying modified proteins in whole cell lysate, azidoTag was incubated with GST-P1 and tyrosinase as described above, and unreacted tag was removed by 5000 MWCM microcon to yield modified protein ("azido GST-P1"). The azido GST-P1 was then added to MDA-MB-231 breast cancer cell lysates (1 mg/mL) prepared with detergent or sonication, in a w/w ratio of GST-P1 to cell lysate proteins of 1:10. Ligation efficiency and background response were compared via chemiluminescence (for azidoTag and COATag) or in-gel fluorescence (for dansylTag) using 300 nm UV illumination.

Modification of Proteins in Rat Primary Hepatocytes. The cryo-preserved rat hepatocytes were thawed according to the protocol (Celsis Technologies). On the day of assay, the vials containing the rat cryopreserved hepatocytes were removed from liquid nitrogen storage. The cells were thawed by gently shaking the vials in a 37 °C water bath. The hepatocyte suspension was transferred into the prewarmed 50 mL thaw medium, the cells were centrifuged at 50 *g* for 3 min, and the resulting pellet was resuspended in Krebs-Hensleit buffer (KHB) at the appropriate cell density for further experiments. Viability was determined using the trypan blue exclusion assay. Tags dissolved in DMSO were added to the hepatocyte cultures to give a final concentration of 50 μM, and the DMSO concentration was 0.1% (v/v). After incubation at 37 °C, 5% CO_2, in the dark for 2 h, the hepatocytes were washed three times with cold PBS, collected by centrifuge, and immediately frozen at −75 °C and stored for future analysis. For the azidoTag-treated hepatocytes, the whole cell proteins were harvested, lysed using 1% NP40/PBS, and endogenous biotinylated proteins were pulled down using 1 mg/mL MagnaBind streptavidin beads. The supernatants were collected, and biotin conjugation was performed via Staudinger ligation or click chemistry as described above. Ligation efficiency and background response were compared via chemiluminescence (for azidoTag and COATag) or in-gel fluorescence (for dansylTag).

Avidin Affinity Concentration. The separation of biotinylated proteins from the unbiotinylated proteins was performed on an Ultralink Immobilized Monomeric Avidin column according to the manufacturer's instructions. Briefly, a monovalent avidin column was washed sequentially with 12 mL PBS (pH 7.2), 10 mL biotin buffer (2 mM D-biotin in PBS) to block any nonreversible biotin binding sites, 10 mL glycine buffer (0.1 M glycine, pH 2.8), and finally 12 mL PBS again. The protein mixture (1 mL) was incubated on the column at room temperature for 1 h and then washed extensively with 18 mL PBS to remove unbiotinylated proteins, followed by 12 mL biotin buffer to elute biotinylated proteins, and finally 10 mL glycine buffer

to regenerate the column. The biotinylated protein eluate was concentrated to 250 uL by ultrafiltration through a 5000 MWCM centricon at 4000 *g* for 1 h, and aliquots were stored at −75 °C until analysis.

Confocal Microscopy. ER-positive MCF-7 cells were grown (1×10^6 cells/mL) on each of eight wells on a sterile Nunc chambered cover glass and incubated for 48 h at 37 °C with 5% CO_2 in phenol red free RPMI medium supplemented with 10% stripped FBS. MCF-7 cells were treated with 1 μM dansyl DMA for 18 h. Before imaging, cells were rinsed two times with PBS to remove the unincorporated dye and 1 μM of DRAQ5 stain was added to the cells to see nuclear staining. In separate experiments, MCF-7 cells were treated with 1 μM dansyl DMA, and confocal imaging was performed in 1 min intervals to see the time-dependent localization of dansyl DMA. Imaging was performed with a Zeiss LSM510 laser-scanning confocal microscope with the detector gain adjusted to eliminate the background autofluorescence. The fluorescence signal from dansyl DMA was monitored with a 345 nm UV laser and a 420 nm band-pass filter. DRAQ5 nuclear staining signal was monitored with 568 nm argon/krypton laser and a 650 nm line pass filter. A 63× (1.2 numerical aperture) water immersion objective was used for all experiments. Images were analyzed using the analysis tool provided in Zeiss biophysical software package.

Two-Dimensional PAGE. 2DGE was performed at room temperature using ZOOM stripes and ZOOM IPG Runner System according to the manufacturer's instructions with minor modifications. Total 140 μL loading sample contains 10 μL cell lysate enriched using the Monomeric Avidin column (400 ng/μL), 128 μL ZOOM 2D protein solubilizer 1, 1.4 μL DTT (1 M), 0.7 μL ZOOM Carrier ampholytes (pH 3−10), trace bromophenol blue, and deionized water. The mixture was loaded into ZOOM IPGRunner cassettes and rehydrated in ZOOM pH 3−10 NL strips at room temperature. Isoelectric focusing was conducted using the following voltage gradient: 175 V for 15 min, 175−2000 V ramp for 45 min, and 2000 V for 30 min. After focusing, the strips were equilibrated with 10 mL NuPAGE LDS sample buffer with sample reducing agent for 15 min, followed by incubation for 15 min with the same sample buffer supplemented with iodoacetamide (125 mM). In the second dimension, focused strips were then applied to the ZOOM 4−20% IPG gel, and the proteins were further separated by SDS-PAGE at 200 V for 60 min. Proteins were transferred to PVDF, probed with HRP-streptavidin, and visualized by chemiluminescence. In all separation experiments, broad-range 2D protein markers (Pierce) and dual color precision plus protein markers (Bio-Rad) were used for calibration of the first and second dimension gels, respectively. The figures represented results from multiple experiments.

Mass Spectrometic Anaylsis of Tryptic Digests. The concentrated biotinylated proteins from rat hepatocytes were separated by 1D gel electrophoresis as described above. The gel was stained by Coomassie blue, excised, and digested with trypsin as described previously (*23*). The peptide mixture (30 μL, 10 μg enriched proteins) was injected onto a reversed-phase column (75 μm × 150 mm Zorbax SB300 C-18, Agilent Technologies) connected to a Dionex Ultimate 3000 HPLC system and a Thermo Finnigan LTQ-FT mass spectrometer equipped with a nanospray interface. The samples were chromatographed using a binary solvent system consisting of A, 0.1% formic acid and 5% acetonitrile, and B, 0.1% formic acid and 95% acetonitrile, at a flow rate of 200 nL/min. A gradient was run from 15% B to 55% B over 60 min. The mass spectrometer was operated in positive ion mode with the trap set to data dependent MS/MS acquisition mode. The instrument was set to complete a mass scan from 400 to 1800 Da in 1 s. Peaks eluting from the LC column that had ions above 1000 arbitrary intensity units triggered the ion trap to isolate the ion and perform an MS/MS experiment scan after the MS full scan. After every MS scan in the ion trap, ions were then transferred to the isolation cell of the 7 T magnet in the FT where a high-resolution (up to 500 000 at *m/z* 400) and high mass accuracy (1 ppm) mass spectrum of the precursor ions was obtained. Data analysis was carried out using the Mascot software platform (Matrix Science, UK) *Bioworks 3.2* (Thermo Instruments, CA) and the *X!tandem* software platform. The library searching and denovo interpretation identified the detected proteins from the individual peptides. The results for all proteins detected were collected and listed by protein name, detected peptide sequence(s), and search score. The reports were exported to an XML file for inclusion in a result database that was finally analyzed using *Scaffold 2.1.0*. Identifications were accepted only for proteins with three unique peptide identifications matching high-quality MS/MS spectra.

RESULTS

Synthesis of SERM Tags and Labeling Reagents. Azido raloxifene is an analogue of raloxifene with close structural similarity. It was synthesized by a nucleophilic aromatic substitution reaction between intermediates **5** and **7** (Figure 2A). To prepare **5**, compound **4** was obtained according to the literature with minor modifications (*35*); the subsequent N-alkylation of **4** gave the desired product. Intermediate **7** was conveniently synthesized by a one-pot, two-step procedure that has been used for the preparation of raloxifene (*36*). The synthesis of azido DMA has been reported previously (*21*); in this study, the azide group was reduced to an amino group prior to acylation to give dansyl DMA (Figure 2B).

ER Ligand Binding and Antiestrogenic Activity. Radioligand displacement competitive binding to full-length recombinant ERα and ERβ was assayed to determine the ability of tags to retain the molecular recognition characteristics of the parent molecule. For the DMA tags and parent drugs, nanomolar binding affinity was maintained despite the addition of substantial molecular baggage to the 3-position piperidine side chain (Table 1). Thus, the tags retain high affinity for binding to ERα relative to the parent molecule, DMA, and to the drug molecule, arzoxifene. Expectedly, given the greater steric requirement for binding to ERβ, the tags performed somewhat less favorably compared to DMA, but still retained nanomolar binding affinity.

The Ishikawa endometrial cancer cell line, used as a reporter for ERα-mediated classical estrogenic activity, also reveals antiestrogenic activity in intact cells in the presence of competing estradiol. All tags retained antiestrogenic activity in Ishikawa cells (Table 1) and were devoid of estrogenic activity (data not shown). Complete correspondence of isolated ER binding with cellular activity is not guaranteed, because classical antiestrogenic activity is thought to require ligand binding to the ER, receptor dimerization, and translocation to the nucleus to form a nonproductive transcriptional complex at the ER response element (ERE). Therefore, in cell culture for an antiestrogen to retain the potency indicated from simple binding assays, it must freely enter the cytoplasm, and as part of a liganded ER complex translocate through the nuclear membrane, permitting binding at the ERE. The data suggest that all the SERM tags under study manifest this ability in Ishikawa cells.

Having determined that the synthetic probes retain ER binding capacity in cell culture, protein modification by these probes was examined.

Model Protein Modification by SERMs with COATag, AzidoTag, and DansylTag. To compare modification by SERMs of isolated proteins, using different tag and conjugation strategies, GST-P1 and BSA were chosen as model proteins. GST-P1 is a key detoxification enzyme in phase II metabolism,

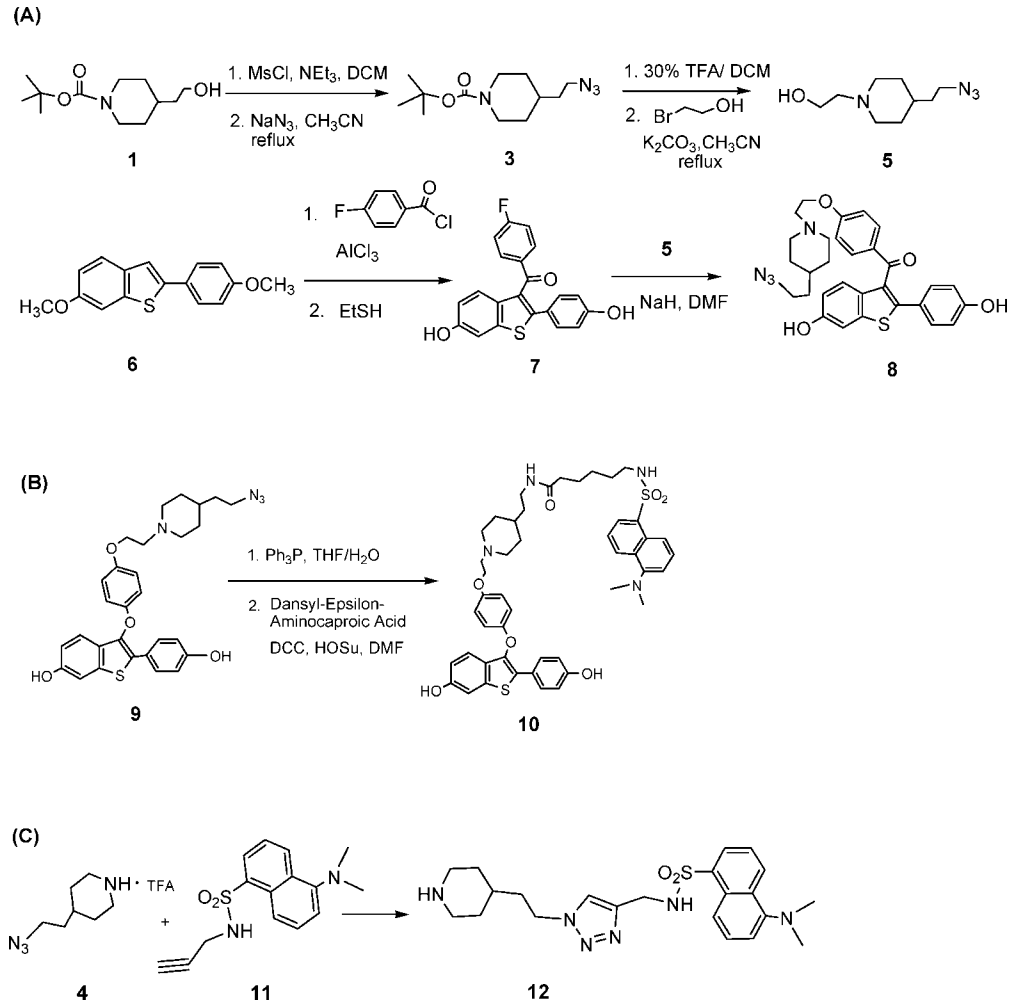

Figure 2. Synthesis of Ral AzidoTag (A), DMA DansylTag (B), and click ligation between model azide **4** and dansyl-tagged alkyne **11** (C).

Table 1. ER Binding Data and Antiestrogenic Activity in Cell Culture for COATag, dansylTag, and azidoTag Compared to Parent SERMs[a]

	ER IC_{50} (nM)[b]		Ishikawa cell IC_{50} (nM)[c]
compounds	ER-α	ER-β	ER-α
DMA COATag	9.37 ± 2.0	24.5 ± 4.7	6.7 ± 3.2
Ral COATag	37.7 ± 6.5	n.s.[d]	17.8 ± 2.5
DMA DansylTag	28.7 ± 4.0	49.2 ± 9.9	22.5 ± 1.9
DMA AzidoTag	14.8 ± 0.9	23.5 ± 4.4	6.5 ± 2.6
Ral AzidoTag	27.3 ± 7.6	n.s.	4.7 ± 0.5
DMA	16.5 ± 0.7	19.6 ± 3.6	0.4 ± 0.1
Arzoxifene	21.5 ± 6.5	66.3 ± 3.1	1.3 ± 0.3
Raloxifene	24.1 ± 1.9	399 ± 26	3.4 ± 0.4

[a] Data show mean ± SD for at least triplicate measurements. [b] Competitive binding assay with recombinant ER. [c] Estrogen antagonist activity. [d] Not studied.

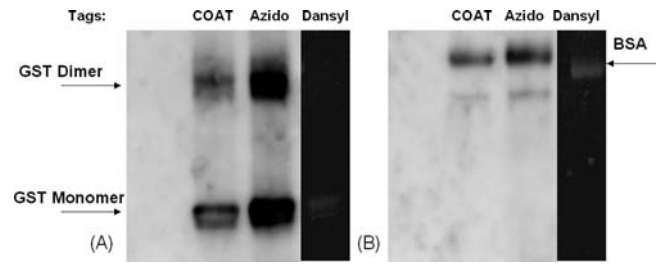

Figure 3. Modification of model proteins GST-P1 (A) and BSA (B) by COATag, azidoTag, and dansylTag. GST-P1 (0.3 mg/mL) and BSA (0.2 mg/mL) were incubated with tags (50 μM) and tyrosinase (5000 units/mL) in PBS (100 μL, pH 7.4) at 37 °C for 1 h. AzidoTag was further reacted with P-biotin (500 μM) at 47 °C for 2 h. Biotin tagged protein was visualized by Western blots using HRP-streptavidin; dansylTag was visualized by in-gel fluorescence (300 nm UV).

which has been reported previously to be a target for the raloxifene COATag, SERM quinoid metabolites, and *o*-quinones formed by oxidation of estrogens. GST-P1 contains four cysteine residues (Cys-14, Cys-47, Cys-101, and Cys-169); of these, Cys-47 and Cys-101 are highly susceptible to modification by quinoids derived from SERMs and estrogens (*7*, *9*, *37*). Alternately, BSA is a widely used model for study of protein modification by drugs (*38*). In model protein studies, tyrosinase was used to bioactivate the benzothiophene SERM moiety, since tyrosinase is not itself susceptible to covalent modification (*7*).

COATag, azidoTag, or dansylTag (50 μM) were incubated with either BSA or GST-P1 in the presence of tyrosinase, with solvent (DMSO) as vehicle control. The azidoTag modified proteins were subsequently labeled with biotin via the modified Staudinger ligation by reaction with phosphinyl biotin (P-biotin; 500 μM) at 37 °C for 2 h. Protein modification was detected by Western blots using HRP-streptavidin (for COATag and azidoTag) or in-gel fluoroscence (for dansylTag). Both GST-P1 and BSA were modified after incubation with tags for 1 h (Figure 3). GST-P1 readily oxidizes to form an intermolecular disulfide at Cys-47, leaving Cys-101 available for covalent modification (Figure 3A). Modification of GST-P1 dimer was not detected in the dansylTag incubation (Figure 3A). Densitometry indicated that the azidoTag appeared to give more protein modification than the COATag after incubation with GST-P1 for 1 h (Figure 3A). Explanations could rest on lower

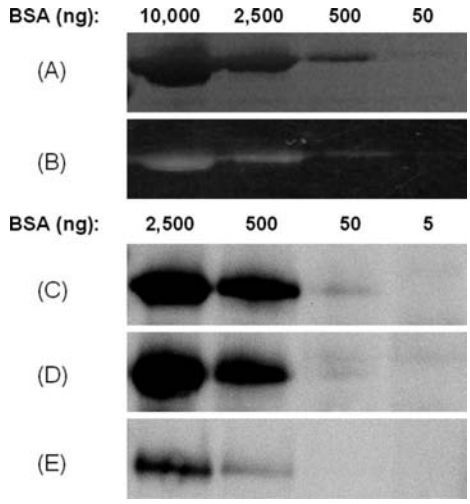

Figure 4. Comparison of sensitivity of different tag methodologies toward BSA (5 −10,000 ng per lane) after bioactivation of tags (50 μM) by tyrosinase (5,000 units/ml) in PBS (pH 7.4) at 37 °C for 1 h. AzidoTag was further conjugated with biotin via modified Staudinger ligation or click chemistry. The sensitivity was measured by Western blots using HRP-streptavidin (for COATag and azidoTag) or by in-gel fluorescence (for dansylTag). (A) Coomassie blue staining of BSA in the presence of dansylTag showing comparative sensitivity of protein dye staining. (B) In-gel fluorescence of BSA modified by dansylTag. (C−E) Western blots of BSA modified by COATag (C) and azidoTag/Staudinger (D) and azidoTag/click methodology (E).

reactivity of the COATag or on decreased tyrosinase oxidation rates for the COATag. In PBS, BSA was modified by all three tags (Figure 3B).

Sensitivity Comparison Using a Model Protein. From the study of the two model proteins, using tyrosinase as an oxidizing system, it was seen that protein modification can be observed using all three methodologies. However, it is critical to be able to detect low abundance proteins both in whole cell lysates and in future experiments with tissues. Therefore, the sensitivity of the four conjugation strategies was tested using BSA as model protein (avoiding the ambiguity resulting from GST-P1 dimerization). Varied amounts of BSA (5−10 000 ng) were incubated with tags, followed by workup. Electrophoresis on 1D gels visualized by immunoassay (for biotin-linked tags), in-gel fluorosence (for dansylTag), or Coomassie blue staining (for dansylTag) was used to quantify the relative response and sensitivity to the four methodologies: (1) COATag; (2) azidoTag/Staudinger; (3) azidoTag/click; (4) dansylTag.

The results showed that both COATag and azidoTag/Staudinger ligation methodologies were able to detect BSA modified in incubations with only 5 ng protein and quantify protein modification in incubations with 50 ng protein (Figure 4C,D). AzidoTag/click chemistry and dansylTag methodologies were 10-fold less sensitive (Figure 4B,E) and were comparable in sensitivity to Coomasie blue staining (Figure 4A).

The ability of oxidant systems to perturb the efficiency of conjugation by click chemistry was studied by the use of the click ligation between a model azide (*4*) and a dansyl tagged alkyne (*11*) (Figure 2B). As might be expected in the presence of H_2O_2 (0, 100, 500, 1000 μM), the efficiency of ligation was attenuated: 100%, 93%, 82%, and 52%, respectively. A solution of H_2O_2 does not fully mirror the oxidation potential of the catalytic oxidant systems under study, but the observations are in accord with the observed lower sensitivity of the azidoTag/click methodology. Although additional workup procedures could be used to mitigate against the oxidation of cuprous ion in click ligation, the addition of an extra step in the conjugation procedure is a disadvantage.

Application of Modified Staudinger Ligation and Click Chemistry in Cell Lysates. The conditions used for modified Staudinger ligation of azides with phosphinyl biotin (P-biotin) after cellular incubation are widely variable in the literature (*29*, *31*, *39*, *40*). Accordingly, time, temperature, and reactant concentrations were varied, in addition to variation of the common reagents used in cell lysis and SDS-PAGE. The model system selected to test the efficiency of each method in detecting modified protein in cell lysates was modified GST-P1 in MDA-MB-231 breast cancer cell lysates. AzidoTag was incubated with recombinant GST-P1 in the presence of tyrosinase and unreacted tag was removed by filtration to yield a protein mixture enriched in modified protein ("azido-GST"). Azido-GST was added to cell lysates, which contain no detectable endogenous biotinylated proteins (Figure 5A, lane 12), in a w/w ratio of GST-P1 to cell lysate proteins of 1:10. Modified Staudinger ligation and click chemistry were subsequently performed in the azido-GST cell lysate system, and ligation efficiency and background response were compared using Western blot.

The results showed that many variables influenced the azidoTag/Staudinger methodology, but most prominent was the high background response in the control experiment in the absence of azidoTag and presence of the P-Biotin (Figure 5A; lane 1). The concentration of P-biotin was critical for Staudinger ligation, with ligation being inefficient at lower P-biotin concentrations (Figure 5A; lane 4). Thus, reducing P-biotin concentration was not useful in reducing the nonspecific background. Increasing P-biotin concentration, incubation time, and temperature all enhanced ligation, but concomitantly increased the background signal (Figure 5A, Lanes 5−10). The reducing reagent DTT, commonly used to maintain reduced thiols, did not affect Staudinger ligation (Figure 5A, lanes 2,3), but detergents (i.e., NP40) interfered with the reaction (data not shown), consistent with previous reports (*39*). Even under optimal conditions, nonspecific labeling was observed (Figure 5A, lanes 5 and 8). Comparison reaction systems without azido-GST or P-biotin (Figure 5A, lanes 1 and 11) indicated that these nonspecific bands resulted from the reaction of proteins with P-biotin, which contains a benzoate ester moiety.

The azidoTag/click methodology was compared in the same model system consisting of cell lysate containing azido-GST, but in this case, using a commercial click labeling kit from Invitrogen requiring 1 h reaction at room temperature. The relative specificity of the azidoTag/click methodology was immediately apparent; both modified GST-P1 monomer and dimer were readily detected (Figure 5B, lane 1). Although modified GST-P1 dimer was also almost certainly present in the Western blots resulting from use of the azidoTag/Staudinger methodology, this band was obfuscated by the high nonspecific background of Staudinger ligation (Figure 5A, Lanes 2−10). The azidoTag/click methodology was specific and sensitive in this model system; no biotinylated proteins were detectable in the control incubation of unmodified GST-P1 in cell lysates after reaction with the click chemistry reagents (Figure 5B, lane 2).

Application of COATag and AzidoTag in Hepatocytes. The next step from assay of model proteins in cell lysates was to compare methodologies in intact cells. Hepatocytes contain high levels of metabolic enzymes that can oxidatively bioactivate SERMs to electrophilic quinoids. Primary rat hepatocytes were treated with either solvent control or the various tags (50−250 μM). The concentration and incubation time were optimized to give extensive protein modification in the absence of cell toxicity. The COATag was able to modify cellular proteins as shown by the concentration dependence of the immunoassay response, suggesting that the hepatocyte cell membrane is permeable to the COATag and confirming the high metabolic capacity of hepatocytes (Figure 5C). Major modification bands

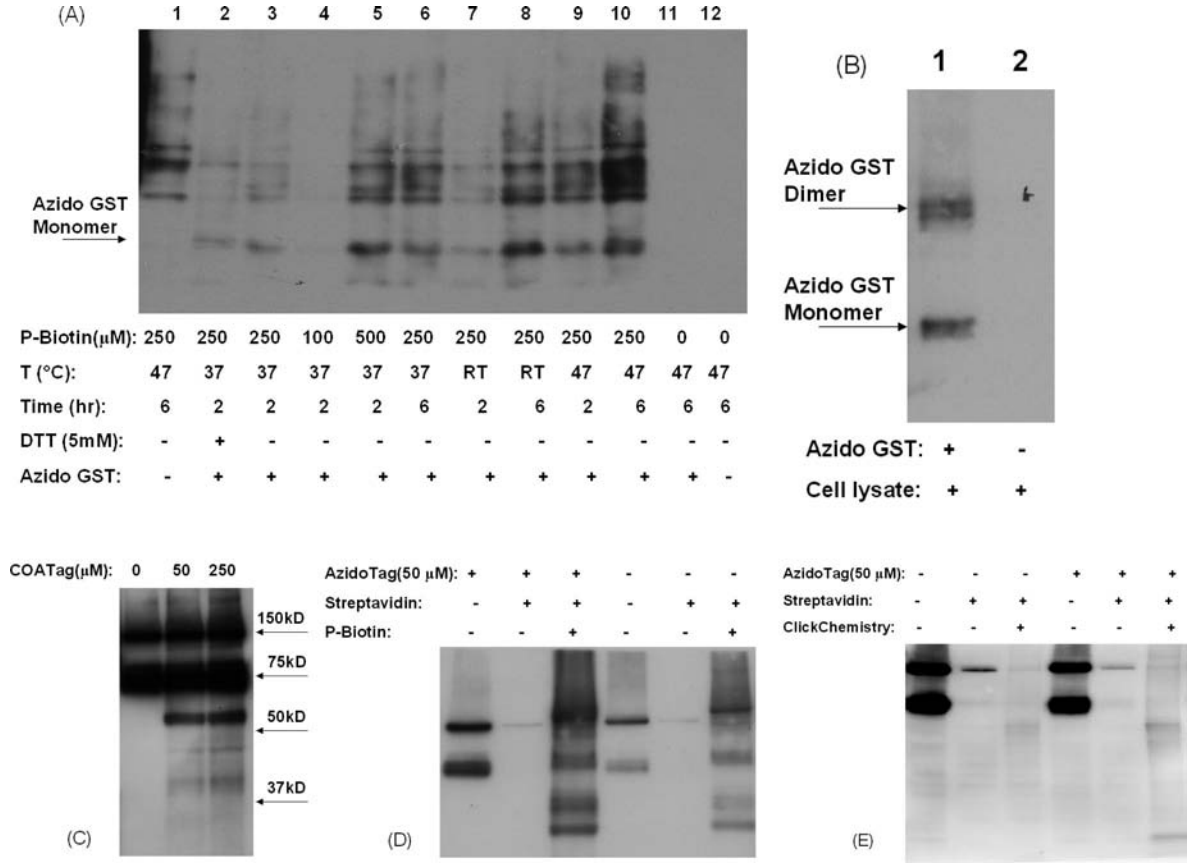

Figure 5. Comparison of protein tagging methodologies in rat primary hepatocytes. Upper: Application of modified Staudinger ligation and click chemistry for detecting modified protein targets in cell lysates. Biotin conjugation via modified Staudinger ligation or click chemistry is described in Materials and Methods. (A) Modified Staudinger ligation. Lane 1: cell lysate without azido GST-P1. Lanes 2−11: cell lysate with azido GST-P1 under varied conditions. Lane 12: cell lysate only. (B) Click chemistry. Lane 1: cell lysate + azido GST-P1. Lane 2: cell lysate only. Lower: Comparison of protein tagging methodologies in rat primary hepatocytes. Cells were incubated with COATag (C) or azidoTag (D,E) (50 μM) in KHB buffer for 2 h and then labeled via modified Staudinger ligation (D) or click chemistry (E).

were observed at about 60 kDa, 45 kDa, and 40 kDa, but low abundance proteins modified by SERM quinoids ranged from 15 kDa to 150 kDa (Figure 5C, lanes 2 and 3). A drawback in the COATag methodology is seen in the obfuscation of modification of proteins at 75 kDa and 150 kDa because of large amounts of endogenous biotinylated proteins (Figure 5C).

In the azidoTag treated hepatocytes, proteins were harvested and endogenous biotinylated proteins were pulled down using MagnaBind streptavidin beads (1 mg/mL). The supernatants were subsequently reacted with modified Staudinger ligation or click chemistry reagents. The capability to remove endogenous biotinylated proteins efficiently using streptavidin beads before conjugation of the tag using either Staudinger or click reactions represents an advantage of the azidoTag methodologies (Figure 5D,E). However, the azidoTag/Staudinger methodology again suffered from high nonspecific background response (Figure 5D, lane 6). Varying of the concentration of P-biotin was not effective in attenuating background (Figure 5A and Supporting Information). Using the azidoTag/click methodology, very minimal nonspecific background signal was observed; however, the ligation efficiency was lower than the COATag as reflected by the relatively weak visualization of only two bands of modified proteins (Figure 5E). The high nonspecific labeling associated with modified Staudinger ligation and low ligation efficiency of the azidoTag/click chemistry in hepatocytes led to abandonment of these methodologies.

Application of Dansyl Tag in Breast Cancer Cells and Hepatocytes. A major incentive for exploration beyond the COATag methodology was the anticipated poor cell membrane permeability of the large COATag, which must contain a relatively polar linker−biotin moiety to allow solubility at high micromolar concentrations. However, the hepatocyte experiments, where extensive protein modification was observed, suggest that the COATag is not inherently membrane impermeable (Figure 5C). A remote possibility was that the COATag was simply modifying extracellular proteins expressed by hepatocytes, but this was ruled out by study of cell culture supernatants prior to cell lysis (Supporting Information). The dansylTag (λ_{ex}337nm, λ_{em}492nm), which may share similar size and hyphophilicity with biotin tags, was studied in both hepatocytes and in ERα positive MCF-7 breast cancer cells, in order to visualize cell permeability using confocal fluorescence microscopy. In MCF-7 cells, the dansylTag rapidly penetrated the outer cell membrane in a time-dependent manner leading to relatively rapid accumulation in the cytoplasm (Figure 6A), but penetrated the nuclear membrane more slowly (after approximately 18 h incubation; Figure 6B). In hepatocytes, localization in the cytoplasm was also observed by fluorescence microscopy (data not shown); however, bands corresponding to modified proteins in hepatocyte lysates treated with dansylTag were not detectable by in-gel fluorescence (Supporting Information), indicating that the dansylTag methodology is not sufficiently sensitive for proteomic studies in intact cells.

Two-Dimensional Resolution of COATagged Proteins. As seen above, a drawback to the use of the COATag methodology is obfuscation of modified proteins by endogenous biotinylated proteins. The use of 2D gels to overcome this obstacle was explored in hepatocytes treated with COATag (50 μM). After incubation, cells were lysed, enriched, desalted, and concentrated; approximately 1 million hepatocytes yielded about 1 mg

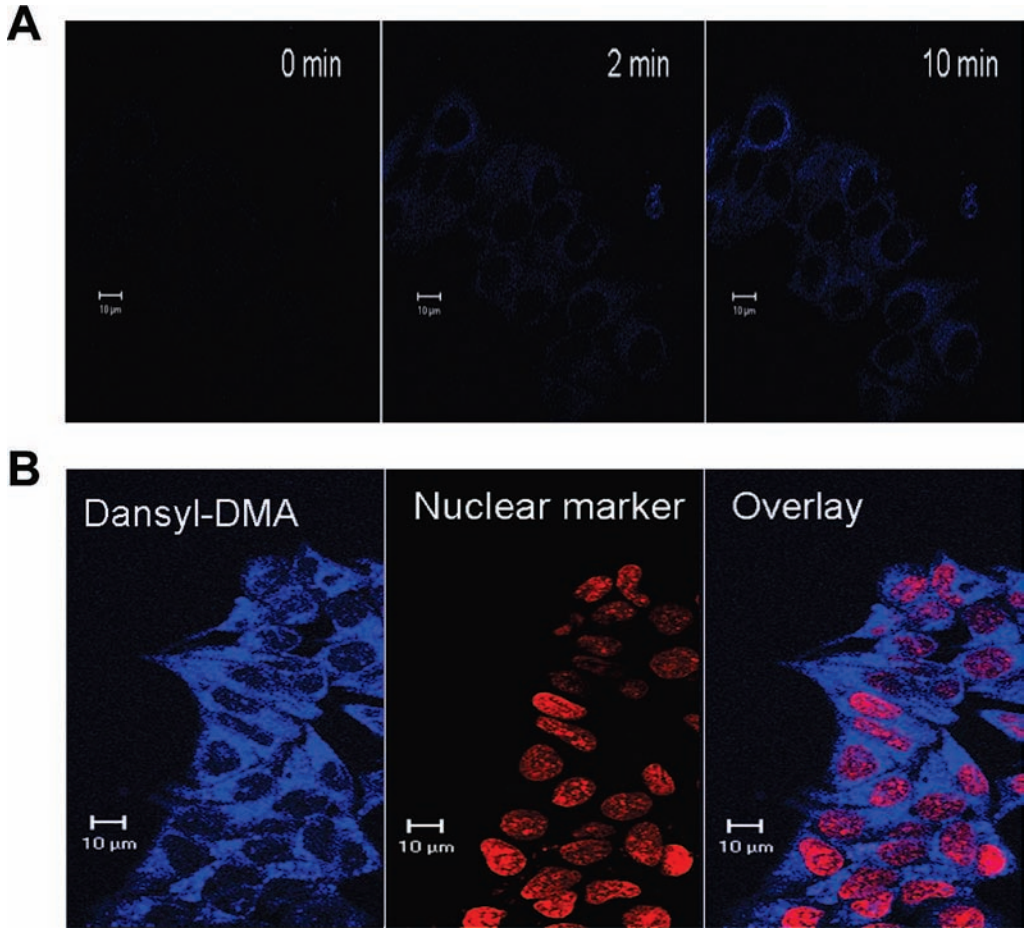

Figure 6. Localization of dansyl DMA in ERα positive MCF-7 cells. (A) Time-dependent localization of dansyl DMA (1 μM) in MCF-7 cells. (B) Localization of dansyl DMA (1 μM) in MCF-7 cells after 18 h treatment. The nuclear marker staining defines the location of the nucleus, and the overlay indicates the colocalization of dansyl DMA and the nuclear marker.

total protein; and after enrichment and purification, the yield was approximately 40 μg. Enriched proteins (4 μg aliquots) were separated by electrophoresis on 1D and 2D gels, followed by transfer and Western blot using HRP-streptavidin. 2D protein markers and solvent-treated hepatocytes provided controls and calibration.

Endogenous biotinylated proteins were observed at high concentration in hepatocytes (Figure 7A; lane 1). The COATag clearly modified a large number of lower molecular weight proteins that could be readily isolated by in gel digest and subsequent analysis and identification by mass spectroscopy (Figure 7A; lane 2), but several spots in the 2D gel were localized close to the bands of endogenous biotinylated proteins (Figure 7B), suggesting that proteomic methods would be required for definitive classification of endogenous and COAT-agged proteins. A large fraction of the COATag modified proteins were detected at pI 4−7, MW 20−75 kDa; these proteins were studied further by 2D electrophoresis and the comparison between COATag and vehicle treated hepatocytes revealed COATagged and endogenous biotinylated proteins. Approximately 30 spots were observed reproducibly in the COATag treated hepatocytes, in contrast to vehicle treated cells (Figure 7C,D).

Mass Spectroscopic Identification. Full proteomic analysis is not reported herein; however, in order to validate the use of the COATag methodology, several liver proteins were identified by MS analysis of in-gel digests. In addition to three modified proteins previously reported from rat liver microsomes, cytosolic glucose regulated protein, protein disulfide isomerase, and glutathione S-transferase, certain postulated target proteins such as peroxiredoxin-1 and heat shock proteins were also identified (Table 2).

Metabolism of AzidoTags. Several successful examples of the use of azidoTags have appeared in the literature, in particular using click chemistry for conjugation to various chemical "handles" including biotin. The reactions of azide and alkynyl functionalities are generally viewed as bioorthogonal and therefore inert to reactions in biological systems, which might confound analysis. However, since the purpose of the COATag methodology, and by extension the azidoTag, is to study electrophilic metabolites generated by oxidative bioactivation, examination of the metabolic stability of the azidoTag was warranted. As has been previously reported, raloxifene in liver microsomes is oxidized substantially and predominantly to the diquinone methide that is efficiently trapped by GSH. In this oxidative environment dominated by P450 3A4, the *o*-quinone and its GSH conjugate are minor products. The raloxifene azidoTag was observed to yield metabolites that were observed in the presence or absence of GSH (Figure 8A). These metabolites were further investigated by MS/MS and proven to be oxidative metabolites resulting from reaction and loss of the "bioorthoganol" azide moiety (Figure 8B). In addition to metabolism of the aliphatic azide, a spectrum of GSH conjugates of quinoid metabolites was observed to be qualitatively comparable to those observed for raloxifene itself (Figure 8A). Thus, the azidoTag was oxidized to quinoids, largely mirroring the parent drug, supporting its use as a probe for target proteins. However, the loss of the azido functionality in this same

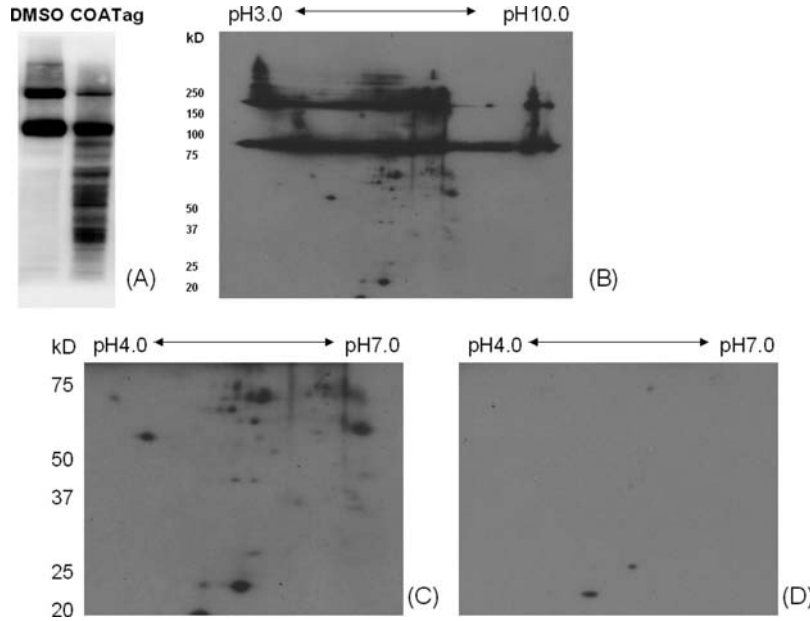

Figure 7. Two-dimensional resolution of COATag modified cellular proteins. Hepatocytes were incubated with COATag (50 μM) or DMSO in KHB buffer at 37 °C for 2 h. Approximately 4 μg of enriched modified proteins were analyzed using 1D (A) and 2D (B) gel electrophoresis and visualized using HRP-streptavidin. An expanded section of the 2D analysis of COATag modified proteins (C) is compared with the similar vehicle control experiment (D).

Table 2. Percent Coverage of Select Proteins Modified by Ral COATag in Rat Hepatocytes[a]

		Ral COATag[b]			
protein	accession#	ctrl.	rep. 1	rep. 2	rep. 3
78 kDa glucose-regulated protein precursor	IPI00206624	-	30.00	30.90	36.70
Protein disulfide-isomerase precursor	IPI00198887	-	14.10	7.27	12.40
Microsomal glutathione S-transferase 1	IPI00230889	-	-	26.50	
Glutathione S-transferase kappa 1	IPI00327079	-	-	-	27.40
Predicted Stress-70 protein, mitochondrial precursor	IPI00363265	-	9.72	25.90	11.60
Heat shock cognate 71 kDa protein	IPI00208205	-	12.70	10.50	-
Peroxiredoxin-1	IPI00211779	-	29.60	24.60	-

[a] This table presents select proteins identified from three independent experiments, in which rat primary hepatocytes were treated with raloxifene COATag (50 μM) or vehicle control. [b] The number value indicates the percent amino acid coverage of each protein identified by peptide fragmentation using LC-MS/MS analysis.

oxidative bioactivation process will inevitably decrease the sensitivity of the azidoTag methodology.

DISCUSSION

The COATag methodology was developed to study and identify the protein targets of electrophilic oxidative metabolites of small molecules (*7*). The proof-of-principle study focused on a clinical drug, the benzothiophene SERM raloxifene, which is oxidatively bioactivated to electrophilic quinoid metabolites (*4, 6*). The COATag technique was effective in identifying protein targets in microsomal incubations; including the abundant cytoplasmic disulfide isomerase proteins, chaperone proteins, and a detoxifying GST enzyme (*7*). In combination with protein-specific antibodies and mass spectroscopy, the COATag technique is transferable to other small molecules subject to bioactivation to electrophiles, including endogenous molecules such as estrogens and catecholamines. The technique has also been applied to assessment of the extent of protein modification and dependence on cofactors in microsomes (*21*). In order to proceed to identification of protein targets in intact cell incubations, the use of azidoTags was explored in anticipation of increased cell permeability relative to the larger more hydrophilic COATag.

The requirements for an effective tagging methodology are that the tagged small molecule must retain characteristics of the parent molecule including cell permeability and receptor binding characteristics. SERMs represent attractive subjects for study because side chain modification in COATags, azidoTags, and dansylTags does not significantly perturb binding to receptors that recognize the parent molecule; as demonstrated by the measured ER binding affinities and antiestrogenic activity in cell culture (Table 1). In contrast to tagging methodologies for inherently electrophilic biomolecules such as 9-HNE, the COATags and related tags studied herein require bioactivation to generate the electrophilic metabolites that target protein nucleophiles. Therefore, additionally, the tag must retain a similar metabolic profile to the parent molecule. Beyond these characteristics, tagging methodologies should provide sensitivity and specificity.

The use of biotin in affinity tags and the high-affinity binding of biotin by immobilized avidin provides effective systems for protein purification and enrichment. Biotin affinity tags and comparable fluorophore affinity tags have both been subject to widespread study and usage (*23*); however, it was not certain that tagging with biotin or fluorophore plus the required linker moieties would limit cell permeability and thus limit the use of these tagging approaches. An alternative approach is provided by the recent development of bioorthogonal reporter strategies in which azide-bearing molecules are labeled with biotin or a fluorophore via modified Staudinger ligation or click chemistry (*26, 27, 30, 31*). Azide is a small functional group assumed not to interfere with the properties of the parent molecule, including

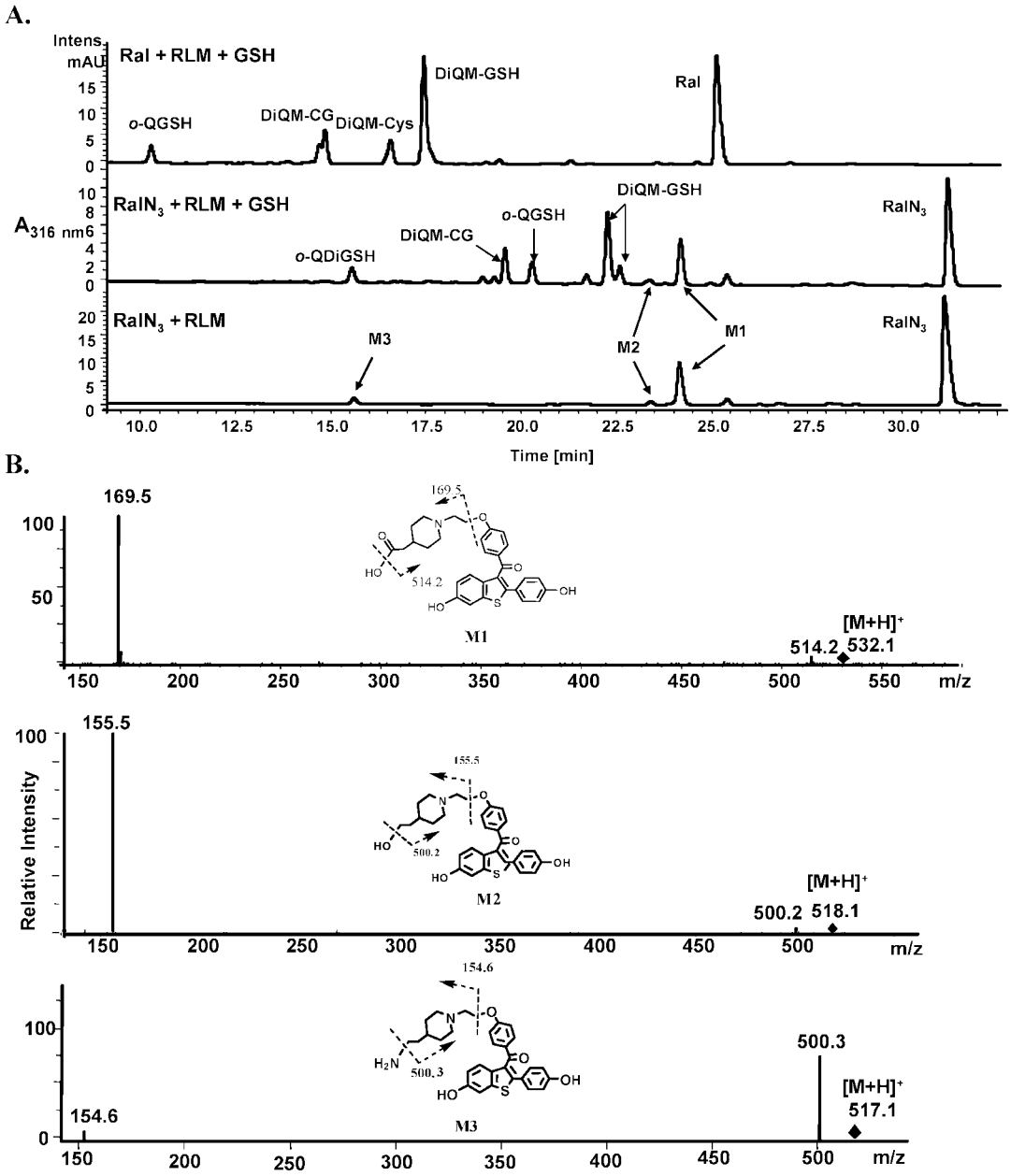

Figure 8. Metabolism of raloxifene azidoTag compared to raloxifene in induced rat liver microsomes. (A) Chromatograms of raloxifene and raloxifene azidoTag in microsomal incubations with and without GSH present to trap quinoid species. (B) MS/MS spectra and identification of azido raloxifene metabolites M1, M2, and M3 corresponding to annotations in (A). MS/MS spectra of GSH conjugates are presented in Supporting Information.

receptor binding, metabolism, and cell permeability, and is assumed to be biologically inert. In addition, a two-step labeling strategy offers multiple methods for downstream protein detection and purification.

Four tagging methodologies were compared as depicted in Figure 9: two one-step methods: method 1, COATag; and method 2, dansylTag; and two two-step methods: method 3, azidoTag/Staudinger; and method 4, azidoTag/click. The model systems employed were purified proteins (BSA and GST-P1), cell culture lysate, and primary cell cultures of rat liver hepatocytes. Both BSA, a highly abundant protein, and GST-P1, a known target of quinoid metabolites (*7*), contain thiol groups, which are susceptible to modification by SERM quinoids formed from bioactivation by oxidase/oxygenase enzymes such as tyrosinase. Hepatocytes are major cell mediators of metabolism *in vivo* including SERM metabolism and have been implicated in liver carcinogenesis caused by the archetypal SERM, tamoxifen (*41*). Hence, hepatocytes represent cells rich in both metabolic enzymes and cellular targets for SERM quinoid electrophiles. Previously, protein modification by COATags was observed to be time and concentration dependent (*7*). In this study, concentrations of tags employed (50 μM) were comparable with similar studies using tagged electrophiles. This concentration is suprapharmacological; however, the purpose of these studies is to identify cellular target proteins. It should also be noted that exposure time (1 h for model proteins and 2 h for hepatocytes) is much shorter than the long-term clinical exposure typical for SERMs.

In this study, the azidoTag/Staudinger methodology was found to offer high sensitivity but low specificity (Table 3). The modified Staudinger ligation reaction between triarylphosphine and azide functionalities produces an aza-ylide that is further stabilized by an electrophilic methyl ester via intramolecular cyclization (*31*). First introduced by Bertozzi, this ligation has been utilized for tagging and labeling surface proteins, expressed proteins, and engineered proteins in cells (*29*, *31*, *42*).

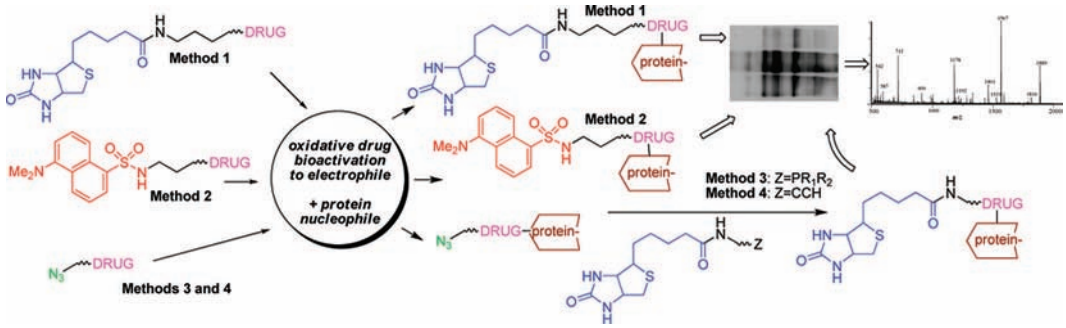

Figure 9. Schematic depiction of the four methodologies explored in this work culminating in proteomic analysis.

Table 3. Comparison of Tagging Methodologies[a]

tagging methodology	tag is ER ligand and active in cells?	sensitivity	specificity
Method 1 (COATag)	yes	higher	high[b]
Method 2 (dansylTag)	yes	lower	low
Method 3 (azidoTag)	yes	higher	N/A[c]
Method 4 (azidoTag)	yes	lower	high

[a] See Figure 9 for depiction of details of each method. [b] With the exception of natively biotinylated proteins. [c] Modified proteins not detectable from hepatocyte incubations.

The reaction is rapid in a physiological environment and is reported as compatible with living systems (*25*, *43*). Correspondingly, in this study, the azidoTag/Staudinger methodology efficiently labeled protein targets and detected nanogram level of modified proteins *in vitro* (Figures 3 and 4). Compared to the alternative methodologies studied, this methodology was highly sensitive.

Using purified proteins, the azidoTag/Staudinger methodology appeared superior; however, when applied to the more complex cell lysates and whole cell treatments, a high background from modified Staudinger ligation was observed (Figure 5A). Attempts to attenuate the nonspecific background reactivity, including optimization of Staudinger reaction conditions and reagents, failed (Figure 5A). Control experiments in cell lysates showed that the nonspecific background is linked to the second labeling reagent, P-biotin (Figure 5A), for which there is precedent in the literature (*20*). The nonspecific labeling of abundant proteins is possibly associated with reaction of the methyl benzoate group of P-biotin with protein amino groups. The nonspecific background obscures the detection of low-abundance protein targets of bioactivated metabolites limiting use of this method for analysis of protein modification by electrophilic metabolites in cells.

The azidoTag/click methodology was highly specific but suffered from low sensitivity. Click chemistry was first reported for activity-based protein profiling by Cravatt, in which the [2 + 3] cycloaddition of an alkyne and azide functional group was catalyzed by cuprous ion (*26*, *30*). In comparison to labeling via Staudinger ligation, click chemistry was considered to produce lower background (*20*). However, in the present study click chemistry both in model proteins and in cells was observed to have ligation efficiency much less than that of Staudinger ligation (Figures 4 and 5), and the methodology was observed to have lower detection sensitivity than either the COATag or azidoTag/Staudinger methodologies (Figures 4 and 5). Several studies have compared the efficiency of Staudinger ligation and click chemistry, describing varied time dependence for ligation efficiency and shorter reaction times for click ligation, but these studies have not reported the click methodology as having low sensitivity (*20*, *43*). A possible explanation for observed low sensitivity rests on the high oxidative capacity of the systems under study, containing either oxygenase (tyrosinase) or cytochrome P450 oxidase at high levels. Click ligation is catalyzed by Cu(I), which is attenuated by the oxidative environment that is essential for study of protein modification by the azidoTags. The attenuated efficiency of click ligation observed in the presence of H_2O_2 is compatible with the proposal. High ascorbate concentrations are used to maintain sufficient reduced copper ion for click ligation, but this is apparently not sufficient in highly oxidizing systems.

Metabolism studies in induced rat liver microsomes also reduced confidence in the use of the azidoTag methodologies, because the azide group was observed to be susceptible to metabolism to an amino group and subsequent oxidative metabolism normal for a primary amine. Although the oxidative loss of the conjugating azide group may be at acceptable levels for many applications, the focus of these studies is oxidative bioactivation; therefore, this is undesirable.

Fluorophore tagging is useful to provide an alternative or additional visualization method to biotin−avidin immunoassay, but the dansylTag methodology was the least sensitive of the methodologies compared herein. The most significant advantage of fluorophore tags is their use for direct imaging under fluorescence microscopy and by in-gel readouts (*24*). Fluorophore tags may be of comparable size and hydrophilicity to biotin tags limiting cell impermeability (*29*); however, the dansylTag proved invaluable in visualization of the cell permeability of tagged SERMs, rapidly accumulating in the cytoplasm in intact cells (Figure 6). The use of dansylTags and related fluorophore tagged SERMs in this regard is clear, but no detectable protein modification was observed by dansylTag in hepatocytes (Supporting Information). The in-gel fluorescence readout cannot be amplified in the same way as immunoassay signals. Important, cellular protein targets may be in low abundance; therefore, dansylTag is insufficiently sensitive for detection of protein targets in cells.

Biotin is a commonly used affinity tag for affinity labeling; the high affinity of avidin/streptavidin makes it a powerful tool for both detection and enrichment of probe-labeled targets (*23*). However, cell impermeability caused by biotin and its linker was a major concern for the generalized application of COATags to cells (*22*−*24*). The COATag used herein was observed to modify a large number of cellular protein targets in hepatocytes suggesting that the COATag is cell permeable. Cell permeability for the dansylTag in MDA-MB-231 cells was readily visualized, showing rapid access to the cytoplasm. The COATag was also observed to be a potent antiestrogen similar to the parent drug molecule in Ishikawa cells. Given the four-day incubation with Ishikawa cells, it cannot be ascertained if the COATag manifests slow nuclear membrane penetration as was observed with the dansylTag in MBA-MB-231 cells. Nevertheless, the COATag methodology appears applicable for whole cell and tissue studies. Given that SERMs are good ER ligands, their binding with and transportation by ER may assist transport of these COATags into the cytoplasm and nucleus in ER positive cells.

The COATag methodology also demonstrated high sensitivity and specificity and, furthermore, has the advantage of being a one-step labeling method, preventing sample loss during multistep experimental processing.

One inevitable limitation of COATags was the presence of endogenous biotinylated proteins, observed in high abundance in hepatocytes at 75 kDa and 150 kDa (Figure 5C). Biotin-dependent carboxylases are especially abundant in liver tissues (*44*). In many other cells, such as MDA-MB-231 cells (Figure 5A), endogenous biotinylated proteins may not present a problem; however, for generalization of the use of COATags, further separation and discrimination is required. Exploration of the COATag in primary hepatocytes followed by further separation using 2D PAGE illustrated one such approach. Interestingly, COATag modified proteins clustered at low molecular weight (20−75 kDa) and acidic pI (pH 4−7) (Figure 7); thiol-rich protein targets such as GST-P1 (MW, 23 kDa; PI, 6.9), Keap1 (MW, 69 kDa; pI, 6.0), and HSP70 (MW, 70 kDa; pI, 5.5) all occur within this range. The previous study of COATags in rat liver microsomes showed that the methodology is compatible with MS/MS analysis (*7*); therefore, antibodies specific for these potential targets and MS analysis can be used in combination, as a preferred methodology for future protein identification in cells treated with COATags. Preliminary MS-MS analysis was performed on gel digests using the COATag methodology, identifying modified cytosolic proteins previously described in liver microsomes (glucose regulated protein, protein disulfide isomerase, and glutathione S-transferase) (*7*) and certain proteins that were anticipated targets for quinoid electrophiles, such as peroxiredoxin-1 and heat shock proteins (Table 2), which were reported as targets for other electrophiles such as 4-HNE (*20*).

CONCLUSION

Endogenous small molecules, drugs, and xenobiotics are subject to oxidative bioactivation to electrophilic metabolites. SERMs are bioactivated to quinoids, implicated in carcinogenesis and chemoprevention, which illustrates the importance of understanding the cellular targets of such metabolites (*14, 45, 46*). Methodology development for detection and identification of cellular targets of electrophilic metabolites is therefore of importance in understanding and predicting the balance between cytotoxic and chemopreventive effects. In this study, four methodologies were studied and compared using purified protein targets and rat primary hepatocytes (Figure 9 and Table 3). Importantly, the azidoTag/click methodology, using the currently preferred combination of azide-tagged molecules with click chemistry ligation, was limited in this application by the high oxidative capacity of the systems under study, leading to both metabolic loss of the azide group and reduced sensitivity. The COATag methodology, introduced in 2005, demonstrated superior characteristics in this application. The presence of endogenous biotinylated proteins in hepatocytes was overcome by application of 2D gel separation and proteomic analysis.

ACKNOWLEDGMENT

This work was supported by NIH grants CA 102590, CA 79870, and CA 121107.

Supporting Information Available: Experiments of modified Staudinger ligation, COATag, and dansyl DMA in hepatocytes, and MS/MS spectra of GSH conjugates of azidoTag. This material is available free of charge via the Internet at http://pubs.acs.org.

LITERATURE CITED

(1) McMeekin, D. S., Gordon, A., Fowler, J., Melemed, A., Buller, R., Burke, T., Bloss, J., and Sabbatini, P. (2003) A phase II trial of arzoxifene, a selective estrogen response modulator, in patients with recurrent or advanced endometrial cancer. *Gynecol. Oncol. 90*, 64–69.

(2) Dowers, T. S., Qin, Z. H., Thatcher, G. R., and Bolton, J. L. (2006) Bioactivation of selective estrogen receptor modulators (SERMs). *Chem. Res. Toxicol. 19*, 1125–1137.

(3) Ariazi, E. A., Ariazi, J. L., Cordera, F., and Jordan, V. C. (2006) Estrogen receptors as therapeutic targets in breast cancer. *Curr. Top. Med. Chem. 6*, 181–202.

(4) Yu, L., Liu, H., Li, W., Zhang, F., Luckie, C., van Breemen, R. B., Thatcher, G. R., and Bolton, J. L. (2004) Oxidation of raloxifene to quinoids: potential toxic pathways via a diquinone methide and o-quinones. *Chem. Res. Toxicol. 17*, 879–888.

(5) Liu, H., Bolton, J. L., and Thatcher, G. R. (2006) Chemical modification modulates estrogenic activity, oxidative reactivity, and metabolic stability in 4'F-DMA, a new benzothiophene selective estrogen receptor modulator. *Chem. Res. Toxicol. 19*, 779–787.

(6) Liu, H., Liu, J., van Breemen, R. B., Thatcher, G. R., and Bolton, J. L. (2005) Bioactivation of the selective estrogen receptor modulator desmethylated arzoxifene to quinoids: 4′-fluoro substitution prevents quinoid formation. *Chem. Res. Toxicol. 18*, 162–173.

(7) Liu, J., Li, Q., Yang, X., van Breemen, R. B., Bolton, J. L., and Thatcher, G. R. (2005) Analysis of protein covalent modification by xenobiotics using a covert oxidatively activated tag: raloxifene proof-of-principle study. *Chem. Res. Toxicol. 18*, 1485–1496.

(8) Chen, Q., Ngui, J. S., Doss, G. A., Wang, R. W., Cai, X., DiNinno, F. P., Blizzard, T. A., Hammond, M. L., Stearns, R. A., Evans, D. C., Baillie, T. A., and Tang, W. (2002) Cytochrome P450 3A4-mediated bioactivation of raloxifene: irreversible enzyme inhibition and thiol adduct formation. *Chem. Res. Toxicol. 15*, 907–914.

(9) Chang, M., Zhang, F., Shen, L., Pauss, N., Alam, I., van Breemen, R. B., Blond, S. Y., and Bolton, J. L. (1998) Inhibition of glutathione S-transferase activity by the quinoid metabolites of equine estrogens. *Chem. Res. Toxicol. 11*, 758–765.

(10) Aliau, S., Delettre, G., Mattras, H., El Garrouj, D., Nique, F., Teutsch, G., and Borgna, J. L. (2000) Steroidal affinity labels of the estrogen receptor α. 4. Electrophilic 11β-aryl derivatives of estradiol. *J. Med. Chem. 43*, 613–628.

(11) Aliau, S., El Garrouj, D., Yasri, A., Katzenellenbogen, B. S., and Borgna, J. L. (1997) 17 α (haloacetamidoalkyl) estradiols alkylate the human estrogen receptor at cysteine residues 417 and 530. *Biochemistry 36*, 5861–5867.

(12) el Garrouj, D., Aliau, S., Aumelas, A., and Borgna, J. L. (1995) Steroidal affinity labels of the estrogen receptor. 2. 17 α-[(Haloacetamido)alkyl]estradiols. *J. Med. Chem. 38*, 2339–2348.

(13) Scott, G. K., Atsriku, C., Kaminker, P., Held, J., Gibson, B., Baldwin, M. A., and Benz, C. C. (2005) Vitamin K3 (menadione)-induced oncosis associated with keratin 8 phosphorylation and histone H3 arylation. *Mol. Pharmacol. 68*, 606–615.

(14) Yu, B., Dietz, B. M., Dunlap, T., Kastrati, I., Lantvit, D. D., Overk, C. R., Yao, P., Qin, Z., Bolton, J. L., and Thatcher, G. R. (2007) Structural modulation of reactivity/activity in design of improved benzothiophene selective estrogen receptor modulators: induction of chemopreventive mechanisms. *Mol. Cancer Ther. 6*, 2418–2428.

(15) Meier, B. W., Gomez, J. D., Kirichenko, O. V., and Thompson, J. A. (2007) Mechanistic basis for inflammation and tumor promotion in lungs of 2,6-di-*tert*-butyl-4-methylphenol-treated mice: electrophilic metabolites alkylate and inactivate antioxidant enzymes. *Chem. Res. Toxicol. 20*, 199–207.

(16) Meier, B. W., Gomez, J. D., Zhou, A., and Thompson, J. A. (2005) Immunochemical and proteomic analysis of covalent adducts formed by quinone methide tumor promoters in mouse lung epithelial cell lines. *Chem. Res. Toxicol. 18*, 1575–1585.
(17) Koen, Y. M., Gogichaeva, N. V., Alterman, M. A., and Hanzlik, R. P. (2007) A proteomic analysis of bromobenzene reactive metabolite targets in rat liver cytosol in vivo. *Chem. Res. Toxicol. 20*, 511–519.
(18) Carbone, D. L., Doorn, J. A., Kiebler, Z., and Petersen, D. R. (2005) Cysteine modification by lipid peroxidation products inhibits protein disulfide isomerase. *Chem. Res. Toxicol. 18*, 1324–1331.
(19) Bogyo, M., Verhelst, S., Bellingard-Dubouchaud, V., Toba, S., and Greenbaum, D. (2000) Selective targeting of lysosomal cysteine proteases with radiolabeled electrophilic substrate analogs. *Chem. Biol. 7*, 27–38.
(20) Vila, A., Tallman, K. A., Jacobs, A. T., Liebler, D. C., Porter, N. A., and Marnett, L. J. (2008) Identification of protein targets of 4-hydroxynonenal using click chemistry for ex vivo biotinylation of azido and alkynyl derivatives. *Chem. Res. Toxicol. 21*, 432–444.
(21) Liu, H., Qin, Z., Thatcher, G. R., and Bolton, J. L. (2007) Uterine peroxidase-catalyzed formation of diquinone methides from the selective estrogen receptor modulators raloxifene and desmethylated arzoxifene. *Chem. Res. Toxicol. 20*, 1676–1684.
(22) Greenbaum, D., Medzihradszky, K. F., Burlingame, A., and Bogyo, M. (2000) Epoxide electrophiles as activity-dependent cysteine protease profiling and discovery tools. *Chem. Biol. 7*, 569–581.
(23) Lennon-Dumenil, A. M., Bakker, A. H., Maehr, R., Fiebiger, E., Overkleeft, H. S., Rosemblatt, M., Ploegh, H. L., and Lagaudriere-Gesbert, C. (2002) Analysis of protease activity in live antigen-presenting cells shows regulation of the phagosomal proteolytic contents during dendritic cell activation. *J. Exp. Med. 196*, 529–540.
(24) Sadaghiani, A. M., Verhelst, S. H., and Bogyo, M. (2007) Tagging and detection strategies for activity-based proteomics. *Curr. Opin. Chem. Biol. 11*, 20–28.
(25) Prescher, J. A., and Bertozzi, C. R. (2005) Chemistry in living systems. *Nat. Chem. Biol. 1*, 13–21.
(26) Speers, A. E., Adam, G. C., and Cravatt, B. F. (2003) Activity-based protein profiling in vivo using a copper(i)-catalyzed azide-alkyne [3 + 2] cycloaddition. *J. Am. Chem. Soc. 125*, 4686–4687.
(27) Prescher, J. A., Dube, D. H., and Bertozzi, C. R. (2004) Chemical remodelling of cell surfaces in living animals. *Nature 430*, 873–877.
(28) Jessani, N., Niessen, S., Wei, B. Q., Nicolau, M., Humphrey, M., Ji, Y., Han, W., Noh, D. Y., Yates, J. R., 3rd, Jeffrey, S. S., and Cravatt, B. F. (2005) A streamlined platform for high-content functional proteomics of primary human specimens. *Nat. Methods 2*, 691–697.
(29) Hang, H. C., Loureiro, J., Spooner, E., van der Velden, A. W., Kim, Y. M., Pollington, A. M., Maehr, R., Starnbach, M. N., and Ploegh, H. L. (2006) Mechanism-based probe for the analysis of cathepsin cysteine proteases in living cells. *ACS Chem. Biol. 1*, 713–723.
(30) Speers, A. E., and Cravatt, B. F. (2004) Profiling enzyme activities in vivo using click chemistry methods. *Chem. Biol. 11*, 535–546.
(31) Saxon, E., and Bertozzi, C. R. (2000) Cell surface engineering by a modified Staudinger reaction. *Science 287*, 2007–2010.
(32) Bolletta, F., Fabbri, D., Lombardo, M., Prodi, L., Trombini, C., and Zaccheroni, N. (1996) Synthesis and photophysical properties of fluorescent derivatives of methylmercury. *Organometalllics 15*, 2415–2417.
(33) Liu, J., Burdette, J. E., Xu, H., Gu, C., van Breemen, R. B., Bhat, K. P., Booth, N., Constantinou, A. I., Pezzuto, J. M., Fong, H. H., Farnsworth, N. R., and Bolton, J. L. (2001) Evaluation of estrogenic activity of plant extracts for the potential treatment of menopausal symptoms. *J. Agric. Food Chem. 49*, 2472–2479.
(34) Obourn, J. D., Koszewski, N. J., and Notides, A. C. (1993) Hormone- and DNA-binding mechanisms of the recombinant human estrogen receptor. *Biochemistry 32*, 6229–6236.
(35) Ogino, Y., Ohtake, N., Kobayashi, K., Kimura, T., Fujikawa, T., Hasegawa, T., Noguchi, K., and Mase, T. (2003) Muscarinic M(3) receptor antagonists with (2R)-2-[(1R)-3,3-difluorocyclopentyl]-2-hydroxyphenylacetamide Structures. Part 2. *Bioorg. Med. Chem. Lett. 13*, 2167–2172.
(36) Jones, C. D., Jevnikar, M. G., Pike, A. J., Peters, M. K., Black, L. J., Thompson, A. R., Falcone, J. F., and Clemens, J. A. (1984) Antiestrogens. 2. Structure-activity studies in a series of 3-aroyl-2-arylbenzo[b]thiophene derivatives leading to [6-hydroxy-2-(4-hydroxyphenyl)benzo[b]thien-3-yl] [4-[2-(1-piperidinyl)ethoxy]-phenyl]methanone hydrochloride (LY156758), a remarkably effective estrogen antagonist with only minimal intrinsic estrogenicity. *J. Med. Chem. 27*, 1057–1066.
(37) Chandrasena, R. E., Edirisinghe, P. D., Bolton, J. L., and Thatcher, G. R. (2008) Problematic detoxification of estrogen quinones by NAD(P)H-dependent quinone oxidoreductase and glutathione-S-transferase. *Chem. Res. Toxicol. 21*, 1324–1329.
(38) Hoffmann, K. J., Streeter, A. J., Axworthy, D. B., and Baillie, T. A. (1985) Structural characterization of the major covalent adduct formed in vitro between acetaminophen and bovine serum albumin. *Chem. Biol. Interact. 53*, 155–172.
(39) Kho, Y., Kim, S. C., Jiang, C., Barma, D., Kwon, S. W., Cheng, J., Jaunbergs, J., Weinbaum, C., Tamanoi, F., Falck, J., and Zhao, Y. (2004) A tagging-via-substrate technology for detection and proteomics of farnesylated proteins. *Proc. Natl. Acad. Sci. U.S.A. 101*, 12479–12484.
(40) Sawa, M., Hsu, T. L., Itoh, T., Sugiyama, M., Hanson, S. R., Vogt, P. K., and Wong, C. H. (2006) Glycoproteomic probes for fluorescent imaging of fucosylated glycans in vivo. *Proc. Natl. Acad. Sci. U.S.A. 103*, 12371–12376.
(41) Tryndyak, V. P., Muskhelishvili, L., Kovalchuk, O., Rodriguez-Juarez, R., Montgomery, B., Churchwell, M. I., Ross, S. A., Beland, F. A., and Pogribny, I. P. (2006) Effect of long-term tamoxifen exposure on genotoxic and epigenetic changes in rat liver: implications for tamoxifen-induced hepatocarcinogenesis. *Carcinogenesis 27*, 1713–1720.
(42) Sprung, R., Nandi, A., Chen, Y., Kim, S. C., Barma, D., Falck, J. R., and Zhao, Y. (2005) Tagging-via-substrate strategy for probing O-GlcNAc modified proteins. *J. Proteome Res. 4*, 950–957.
(43) Agard, N. J., Baskin, J. M., Prescher, J. A., Lo, A., and Bertozzi, C. R. (2006) A comparative study of bioorthogonal reactions with azides. *ACS Chem. Biol. 1*, 644–648.
(44) Lewis, B., Rathman, S., and McMahon, R. (2001) Dietary biotin intake modulates the pool of free and protein-bound biotin in rat liver. *J. Nutr. 131*, 2310–2315.
(45) Dunlap, T., Chandrasena, R. E., Wang, Z., Sinha, V., and Thatcher, G. R. (2007) Quinone formation as a chemoprevention strategy for hybrid drugs: balancing cytotoxicity and cytoprotection. *Chem. Res. Toxicol. 20*, 1903–1912.
(46) Hagos, G. K., Carroll, R. E., Kouznetsova, T., Li, Q., Toader, V., Fernandez, P. A., Swanson, S. M., and Thatcher, G. R. (2007) Colon cancer chemoprevention by a novel NO chimera that shows anti-inflammatory and antiproliferative activity in vitro and in vivo. *Mol. Cancer Ther. 6*, 2230–2239.

BC800435M

Comparative methods for analysis of protein covalent modification by electrophilic quinoids formed from xenobiotics

Bolan Yu, Zhihui Qin, Gihani T. Wijewickrama, Praneeth Edirisinghe, Judy L. Bolton and Gregory R. J. Thatcher* [*]

Department of Medicinal Chemistry & Pharmacognosy, College of Pharmacy, University of Illinois at Chicago, 833 S Wood St, Chicago, IL 60612

*Correspondence: Greg Thatcher, Department of Medicinal Chemistry and Pharmacognosy, University of Illinois at Chicago, 833 S. Wood Street, Chicago, IL, 60612; Phone: 312-355-5282; Fax: 312-996-7107; E-mail: thatcher@uic.edu or judyb@uic.edu

Supporting Information

Supplemental Figure 1. The effects of varied concentration of P-biotin on modified Staudinger ligation in hepatocytes.

Supplemental Figure 2. Modification of proteins in cell medium and cell lysates.

Supplemental Figure 3. Application of dansyl DMA in hepatocytes for the detection of modified proteins.

Supplemental Figure 4. MS-MS spectra of GSH conjugates of raloxifene azidoTag in induced rat liver microsomes.

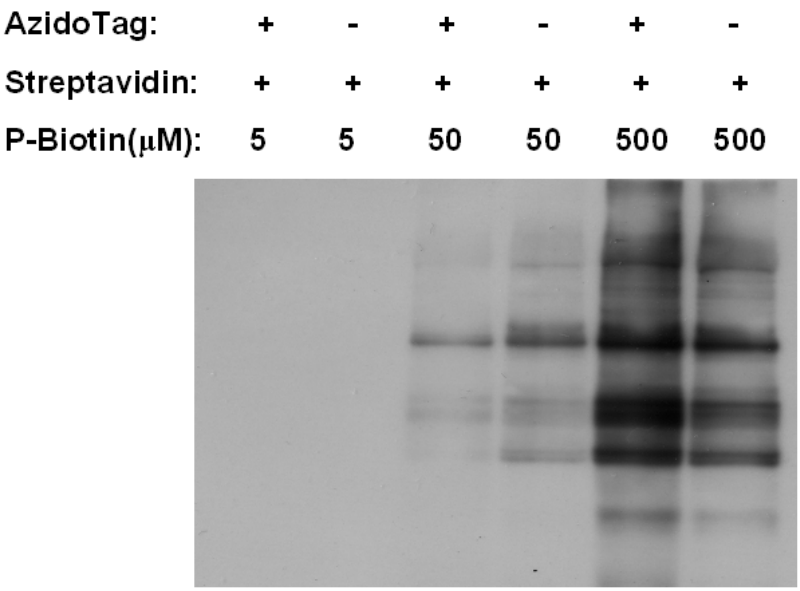

Supplemental Figure 1. The effects of varied concentration of P-biotin on modified Staudinger ligation in hepatocytes. Hepatocytes were treated with 50 μM azidoTag in KHB at 37□ for 2 h and endogenous biotinylated proteins in cell lysate were removed using streptavidin beads (1 mg/ml). Following biotinylation and western blotting were performed with varied concentration of P-biotin in PBS at 37□ overnight.

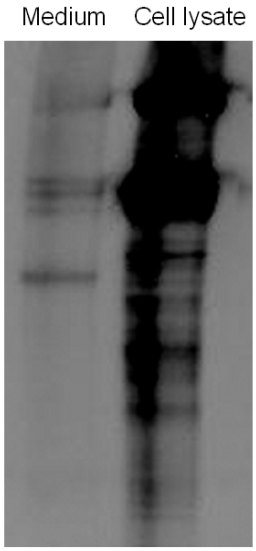

Supplemental Figure 2. Modification of proteins in cell medium and cell lysates. Hepatocytes were treated with 50 μM COATag in KHB for 2 h. Identical volume of supernatant medium and cell lysate were collected for western blotting.

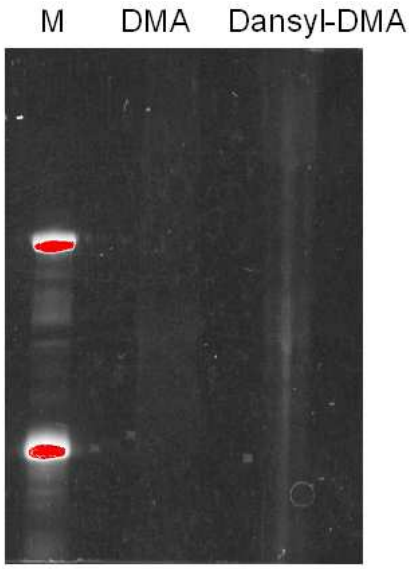

Supplemental Figure 3. Application of dansyl DMA in hepatocytes for the detection of modified proteins. Hepatocytes treated with 50 μM DMA or dansyl DMA were lysed and detected using 300 nm UV. Lane1: protein marker. Lane 2: hepatocyte lysates treated with DMA. Lane 3: hepatocyte lysates treated with dansyl DMA.

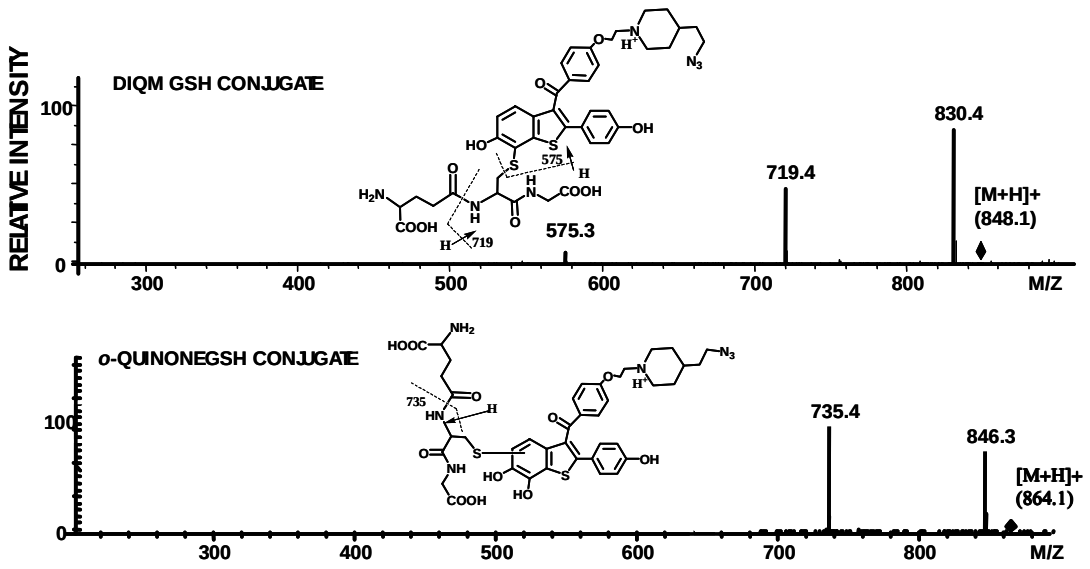

Supplemental Figure 4. MS-MS spectra of GSH conjugates of raloxifene azidoTag in induced rat liver microsomes.

SPECT and PET Imaging of EGF Receptors with Site-Specifically Labeled EGF and Dimeric EGF

Zoya Levashova,[†] Marina V. Backer,[‡] George Horng,[§] Dean Felsher,[§] Joseph M. Backer,[‡] and Francis G. Blankenberg*,[†]

Department of Radiology/MIPS, Stanford University School of Medicine, Stanford, California 94305, Sibtech, Inc., Brookfield, Connecticut 06804, and Department of Medicine/Oncology, Stanford University School of Medicine, Stanford, California 94305.
Received October 15, 2008; Revised Manuscript Received February 25, 2009

We describe a new generation of tracers for molecular imaging of the cell surface receptors for epidermal growth factor (EGF). These receptors play a key role in the progression of many tumors and are major drug development targets. Our tracers are based on a recombinant human EGF expressed with a cysteine-containing tag that enables facile site-specific radiolabeling with ^{99m}Tc for single photon emission computed tomography or site-specific conjugation of ^{64}Cu PEGylated chelators for positron emission tomography. These tracers retain EGF activities *in vitro* and display selective and highly specific focal uptake in tumors *in vivo*. We expect that nuclear imaging of EGF receptors with these tracers will be useful for clinical diagnosis, therapeutic monitoring, and development of new drugs and treatment regimens.

INTRODUCTION

Tumor growth critically depends on growth factors, and epidermal growth factor (EGF) appears to be of particular significance for the progression of many tumors (*1*). EGF acts via transmembrane tyrosine kinase receptors (EGFR) and promotes cell proliferation, motility, and survival by activating STAT, MAPK, and PI3K/Akt pathways. Receptors for EGF are the major drug development targets, and several EGFR-directed therapeutics, including anti-EGFR antibodies and EGFR tyrosine kinase inhibitors, are entering the clinic. Currently, EGFR expression in individual patients is determined by immunohistochemical analysis of tumor biopsies. Clinical experience, however, revealed that only 10−25% of patients that are defined as EGFR-positive by immunohistochemical analysis respond to EGFR-directed therapeutics (*1*−*3*), and there is a poor correlation between EGFR immunohistochemistry and treatment outcome (*4*−*6*). Such poor predictive power is not particularly surprising because immunohistochemical analysis does not discriminate between active and inactive EGFR, while functional activity of the receptors appears to be critical for the prediction of response to EGFR-targeting therapeutics (*7*). Therefore, for more efficacious use of EGFR-targeting therapeutics, there is a need for information on EGFR activity in patients. In this respect, molecular imaging of functionally active EGFR could provide such information and might allow for (1) rational patient stratification, (2) rapid monitoring of responses to therapy, and (3) development of personalized treatment regimens.

Since ultimate proof of EGFR activity is binding and internalization of EGF, we consider EGF-based tracers the most suited for imaging of functionally active EGFR. To develop uniform EGF-based tracers, we have expressed EGF with an N-terminal Cys-tag, a 15-aa cysteine-containing fusion tag for site-specific conjugation of therapeutic and diagnostic payloads (*8*−*10*). Furthermore, since a functional EGF/EGFR complex contains two EGF molecules and two EGFR molecules, for this study we have also engineered a Cys-tagged dimeric EGF (dEGF) containing two genetically fused EGF moieties. We report here that EGF- and dEGF-based SPECT tracers can be prepared by direct radiolabeling of Cys-tag with ^{99m}Tc, while the corresponding PET tracers can be prepared by conjugating a PEGylated DOTA chelator to Cys-tag, followed by radiolabeling with ^{64}Cu. The favorable imaging and biodistribution characteristics of new EGF-based tracers, as well as the simplicity of their preparation, open the possibilities for further development.

EXPERIMENTAL PROCEDURES

Production of Cys-Tagged EGF and dEGF. The construction, expression, and purification of Cys-tagged EGF have been described recently (*8*). Briefly, EGF without a stop-codon was amplified by PCR from a DNA fragment encoding codon-optimized human EGF (kindly provided by Dr. P. T. Pienkos, Molecular Logix, Woodlands, TX), introducing NcoI sites to both termini of the PCR fragment, and cloned into an NcoI site of the pET/Hu-R4C(G_4S) vector for bacterial expression of proteins with Cys-tag (*10*). Clones with correct orientation of EGF were selected by colony PCR using T7-promoter-based sense and EGF-based antisense primers. The second copy of EGF including a stop-codon was cloned in-frame with the first EGF using the *Bam*HI site. The resulting plasmid encodes a 147-aa fusion protein comprising an N-terminal Cys-tag, a $(G_4S)_3$MG-linker, and EGF without a stop-codon connected to a second copy of EGF via a 9-aa linker SMAAIGSGF.

EGF and dEGF were refolded in red-ox buffer containing glutathione, and therefore, Cys-tag C4 thiol groups were protected in a mixed disulfide bond with glutathione in at least 90% of the protein. Prior to radiolabeling with ^{99m}Tc or conjugation of chelator, C4 thiol groups were deprotected by incubating the proteins with equimolar amounts of DTT at 25 °C for 20 min in 0.1 M Tris-HCl at pH 8.0 (*8*−*10*).

* Corresponding author. 725 Welch Road, Room #1673, Stanford, CA 94304-1601. Phone: 650-497-8601. Fax: 650-497-8745. E-mail: blankenb@stanford.edu.

[†] Department of Radiology/MIPS, Stanford University School of Medicine.

[‡] Sibtech, Inc.

[§] Department of Medicine/Oncology, Stanford University School of Medicine.

10.1021/bc800443w CCC: $40.75 © 2009 American Chemical Society
Published on Web 03/25/2009

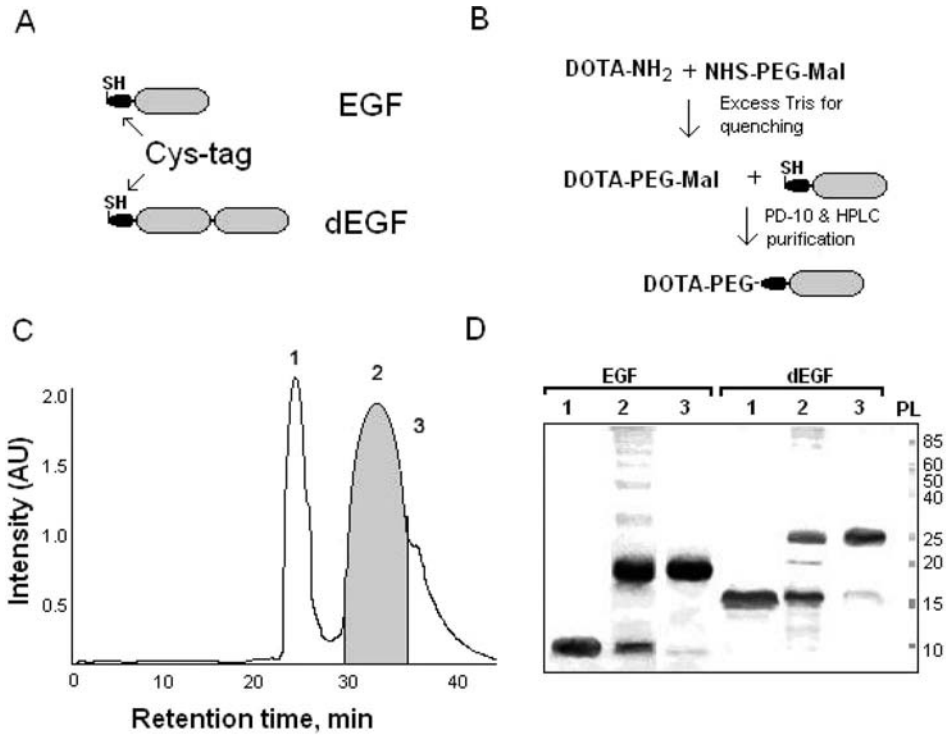

Figure 1. EGF and dEGF based conjugates. (A) Single or doubled copy of human EGF was cloned in-frame with the N-terminal Cys-tag (*9, 11*). Both proteins were expressed in *E.coli*, refolded into functionally active conformations in red-ox buffers, and purified via ion-exchange chromatography. (B) Flow chart of synthesis. (C) Separation of unmodified EGF (peak 1), EGF-PEG-DOTA (peak 2), and overmodified EGF-PEG-DOTA (peak 3) by RP-HPLC. Peak 2 (shown in gray) was collected, buffer-exchanged on a PD-10 column, and concentrated to 1−2 mg/mL. (D) Samples of unmodified EGF or dEGF (lanes 1), modification reaction mixtures (lanes 2), and RP-HPLC-purified products (lanes 3) were analyzed by reducing SDS−PAGE on 20% gels. PL, protein ladder (BioRad). Molecular weights are indicated in kDa.

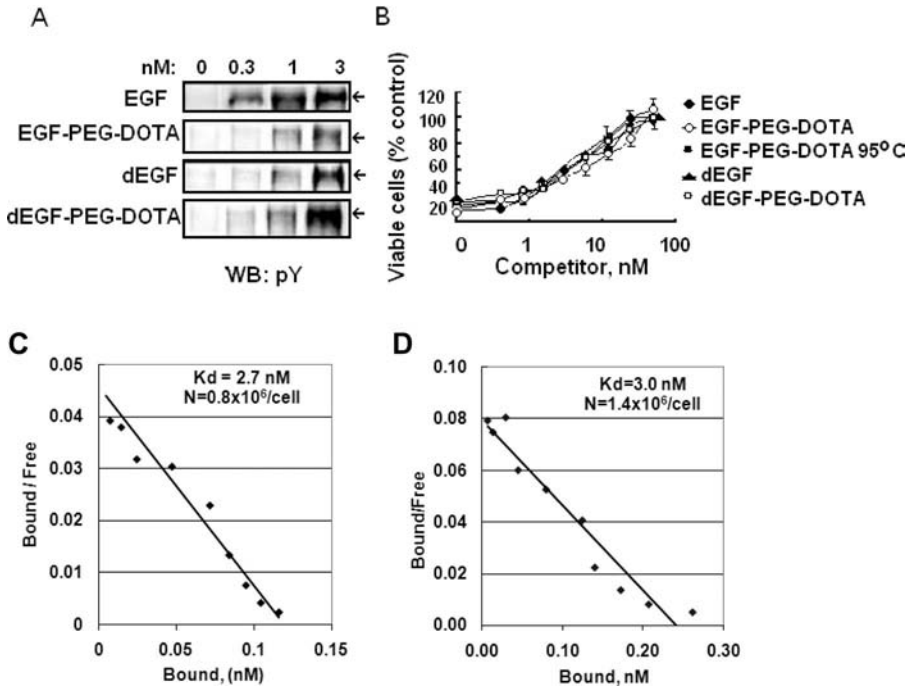

Figure 2. EGF- and dEGF-based conjugates are functionally active. (A) Induction of EGFR tyrosine autophosphorylation in rat F98/EGFR glioma cells. Arrows indicate positions of EGFR. 3.6×10^3 cell equivalents were loaded per one lane. (B) Competition with EGF-SLT fusion protein for binding to EGFR on human breast cancer cells MDA231luc. (C) Scatchard's analysis of EGF/Tc binding was undertaken with F98/EGFR cells. The values of K_d and N, the number of EGFR/cell, are indicated. (D) Scatchard's analysis of EGF-PEG-DOTA/Cu binding was undertaken with F98/EGFR cells. The values of K_d and N, the number of EGFR/cell, are indicated.

EGF and dEGF Direct Radiolabeling with ^{99m}Tc. Deprotected EGF or dEGF were radiolabeled, using a precursor complex [^{99m}Tc]-tricine, as described elsewhere for Cys-tagged single-chain VEGF (*9, 10*). Briefly, lyophilized tin-tricine reagent (a gift from Dr. J.-L. Vanderhyden, GE Healthcare, Piscataway, NJ) was reconstituted with 1.0 mL of degassed saline to give a final $SnCl_2 \cdot 2H_2O$ concentration of 0.6 mg/mL and a final tricine concentration of 20 mg/mL, pH 7.1. The

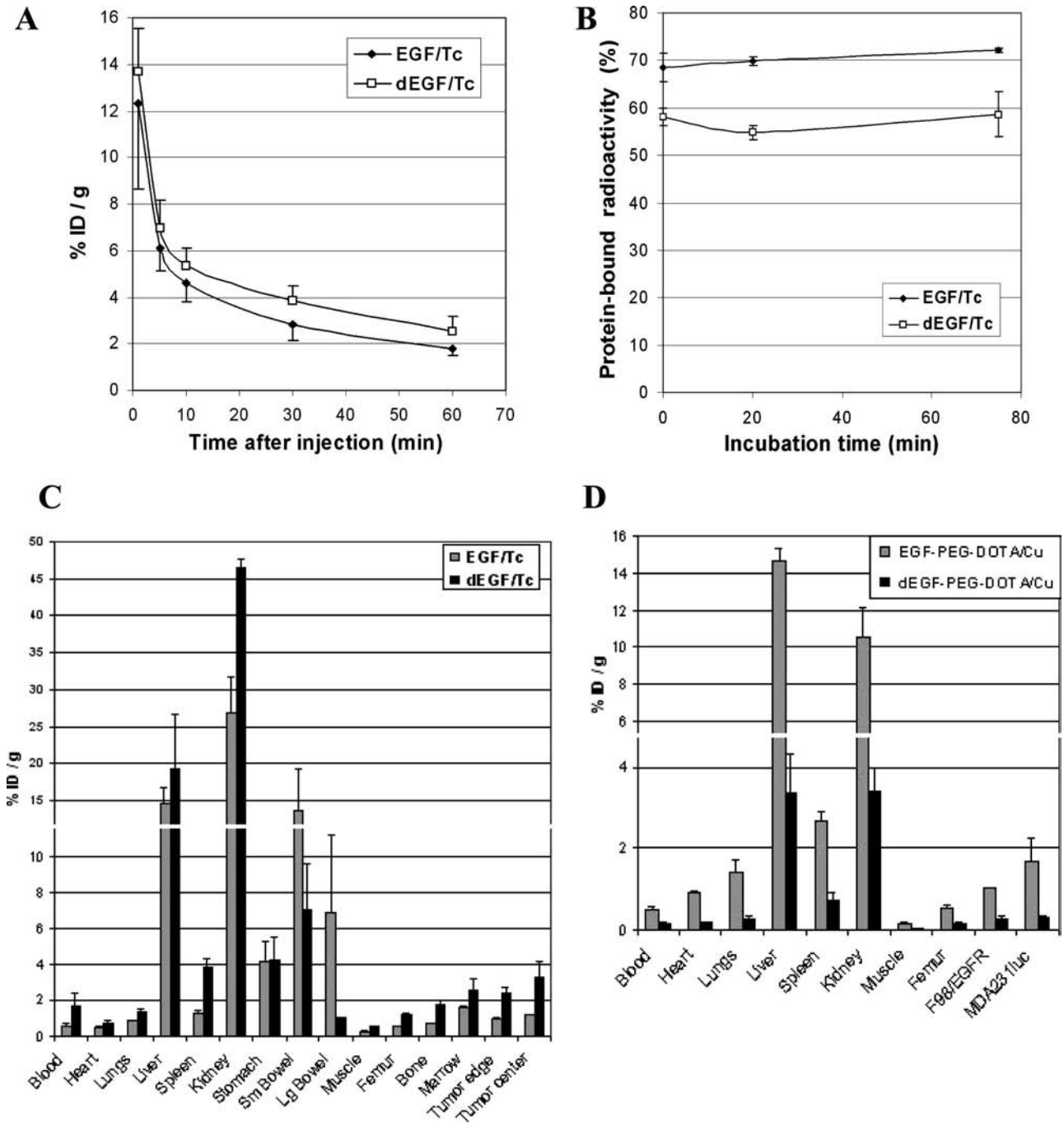

Figure 3. Tracer clearance, stability, and biodistribution. (A) Blood clearance of EGF/Tc and dEGF/Tc. (B) EGF/Tc and dEGF/Tc stability in murine plasma *ex vivo*. (C) Biodistribution of EGF/Tc (3.1 mCi/10 μg per mouse) and dEGF/Tc (0.81 mCi/13 μg per mouse) ($n = 4$ for every tracer) in 4 h after injection. (D) Biodistribution of EGF-PEG-DOTA/Cu (95 μCi/0.75 μg per mouse) and dEGF-PEG-DOTA/Cu (95 μCi/1.25 μg per mouse) in 22 h after injection ($n = 4$ for every tracer). Data for major organs are averaged for all tumor-bearing mice. Tumor uptake is averaged for specific tumors.

Table 1. Major Organ Uptake (%ID/g) for EGF-Based ^{99m}Tc Tracers

	EGF/Tc 3 h	dEGF/Tc 3 h	EGF-HYNIC/Tc/EDDA 4 h (*14*)	EGF-HYNIC/Tc 3 h (*13*)
kidney	27.0 ± 4.8	45.5 ± 1.4	96.3 ± 45.4	28.9 ± 14.0
liver	14.6 ± 2.3	24.5 ± 7.4	32.6 ± 13.2	29.2 ± 7.6

reaction mixture containing 10.0 μL of tin-tricine, 34 μg of deprotected protein, and 10 mCi of ^{99m}Tc-pertechnetate in a final volume of 50−100 μL was incubated for 30 min at 37 °C. Radiolabeled proteins, named EGF/Tc or dEGF/Tc, were purified by size-exclusion on PD-10 columns (GE Healthcare, Piscataway, NJ) equilibrated with phosphate-buffered saline (PBS). Specific activities ranged from 130 to 280 μCi/μg protein. The average purity before PD-10 purification was 45 ± 13% ($n = 13$), as judged by the amount of ^{99m}Tc eluted from PD-10 after the protein peak. Radiopurity after PD-10 was determined by ITLC using PBS as a solvent. We observed ^{99m}Tc batch-dependent variations of radiopurity in the range of 90−95%. The impurities migrated with the solvent front and appeared to arise from small and variable amounts of colloidal forms of ^{99m}Tc that were coeluted with radiolabeled protein from the PD-10 column but yielded migrating ^{99m}Tc under TLC conditions.

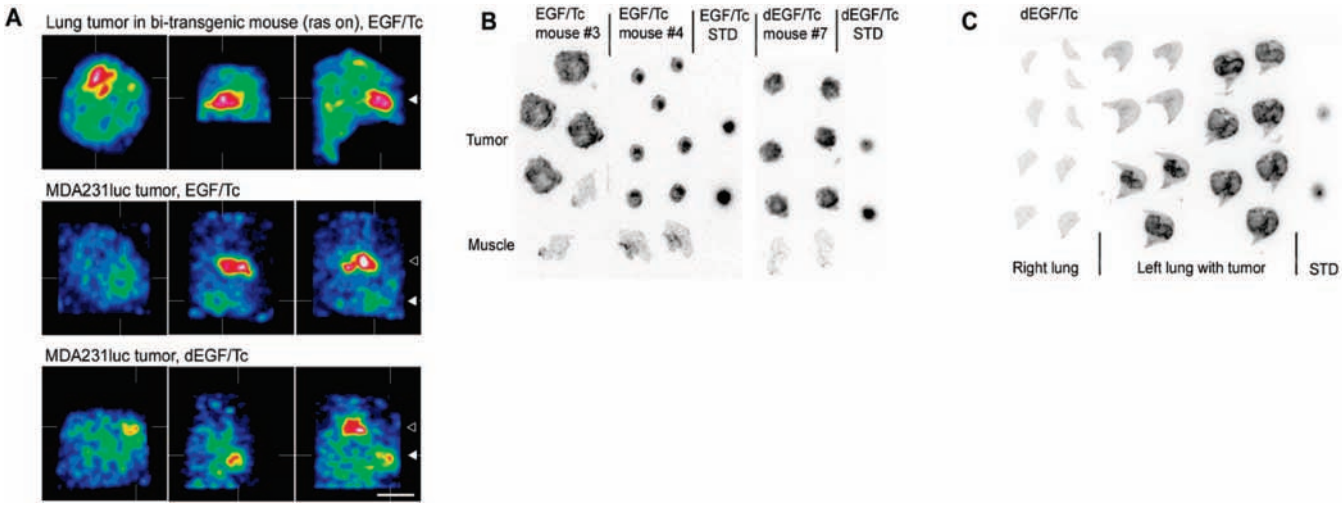

Figure 4. SPECT imaging and autoradiography. (A) SPECT images of mice injected with 3.1 mCi/10 μg of EGF/Tc or 1.7 mCi/13 μg dEGF/Tc per mouse. Representative transverse, sagittal, and frontal images are shown. Upper row: spontaneous lung tumor in bitransgenic mouse with ras-oncogene expression, EGF/Tc tracer. Middle row: orthotopic MDA231luc tumor, EGF/Tc tracer. Lower row: orthotopic MDA231luc tumor, dEGF/Tc tracer. The largest lung tumor and MDA231luc tumors are shown by white arrowheads. Open arrowheads show submandibular glands with nonspecific tracer uptake. The scale bar is 10 mm. (B) Autoradiographs of orthotopic MDA231luc tumors (25 days after cell injection). 3.1 mCi/10 μg per mouse of EGF/Tc or 1.7 mCi/13 μg of dEGF/Tc has been i.v. injected. STD is two spots of radioactivity equal 0.0016 and 0.0032% of injected dose. (C) Right (healthy) and left (tumor-invaded) lungs of a myc-on bitransgenic mouse injected with 4.5 mCi/20 μg of dEGF/Tc. STD is two spots of radioactivity equal to 0.0007 and 0.0014% of ID.

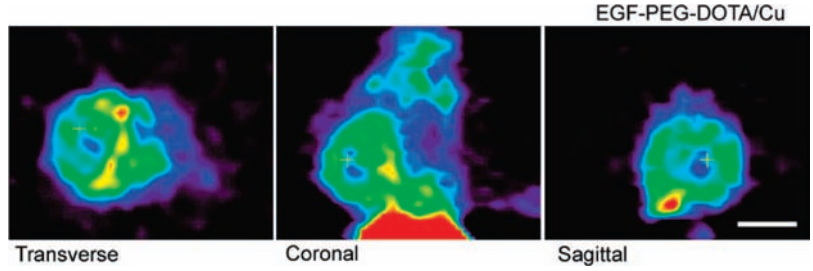

Figure 5. PET imaging. PET imaging of MDA231luc tumor (36 days after implantation). Representative transverse, coronal, and sagittal tomographic slices through the left mouse mammary fat pad tumor taken 3 h after an injection of 300 μCi of EGF-PEG-DOTA/^{64}Cu. The scale bar is 10 mm.

Radiolabeling of protected EGF and dEGF yielded ~20-fold less radioactivity in collected protein peaks, as compared with deprotected proteins. This low-level labeling is most likely due to the small amount of nonprotected C4 thiol groups generally present in preparations of Cys-tagged proteins.

Conjugation of DOTA to EGF or dEGF. DOTA was conjugated to EGF and to dEGF through a two-step procedure described elsewhere (*8, 10*), with minor modifications. Briefly, in step 1, functionalized DOTA was prepared by derivatization of *p*-NH_2-Bn-DOTA (2-(4-aminobenzyl)-1,4,7,10-tetraazacyclododecane-1,4,7,10-tetraacetic acid) (Macrocyclics, Dallas, TX) with 5 kDa of NHS-PEG-Mal, polyethylenglycol (PEG) containing an amino-reactive NHS group on the one end and a thiol-reactive maleimide on the other end of each PEG molecule (NOF America, Terrytown, NY). The reaction was performed at 2:1 DOTA to PEG molar ratio in a buffer containing 15 mM NaOAc, 50 mM Na_2CO_3, and 115 mM NaCl, pH 8.0. The reaction was incubated for 1 h at room temperature. Residual NHS was hydrolyzed by the addition of 1 M Tris HCl at pH 8.0 to a final concentration of 100 mM and incubated for 30 min. Functionalized DOTA-PEG-Mal was stored at −70 °C in small aliquots.

In step 2, the DOTA-PEG-Mal conjugate was added to freshly prepared deprotected protein at 2:1 maleimide to protein ratio and incubated for 1 h at room temperature. The reaction mixture was passed through PD-10 and then fractionated by RP-HPLC on a C4 column, which provided for a good separation of unmodified and PEGylated proteins. RP-HPLC purification was followed by solvent exchange on PD-10 to a buffer containing 0.1 M NaOAc at pH 5.5 and concentration of purified conjugates via reverse dialysis using Aquacide III powder (Calbiochem, San Diego, CA). Final preparations of EGF-PEG-DOTA and dEGF-PEG-DOTA were stored at °70 °C in small aliquots.

Radiolabeling of EGF-PEG-DOTA and dEGF-PEG-DOTA with ^{64}Cu. Conjugates were radiolabeled with ^{64}Cu, using a procedure developed previously for scVEGF-PEG-DOTA (*8, 10*). In a typical radiolabeling reaction, 20 μg of EGF-PEG-DOTA or dEGF-PEG-DOTA conjugate were mixed with 3.0−3.8 mCi of ^{64}Cu (Washington University Medical School, Saint Louis, MO) in 0.1 M NaOAc at pH 5.3−5.5 in the presence of DMSO (20% for EGF-PEG-DOTA and 30% for dEGF-PEG-DOTA) and incubated for 1 h at 55^o C. Residual free ^{64}Cu was sequestered by 1 mM EDTA. The reaction mixtures were passed through NAP-5 gel-filtration columns (GE Healthcare, Piscataway, NJ), yielding tracers with a specific activity of ~125 μCi/μg, for EGF-PEG-DOTA, and ~75 μCi/μg, for dEGF-PEG-DOTA.

Tissue Culture. F98/EGFR(F) rat glioma cells engineered to overexpress human EGFR were a kind gift from Dr. R. Barth (The Ohio State University, Columbus, OH). The high level of EGFR in these cells was supported by Scatchard analysis of radioligand binding, as described in the Results section. F98/EGFR(F) cells were grown in a 1:1 mixture of DMEM and F-12 nutrient mixture (Invitrogen, Carlsbad, CA), 5% FBS, and

2 mM L-glutamine. For prolonged cultivation, cells were maintained in 0.5 mg/mL of G418. For tumor implantation, cells were grown for 2−3 passages in complete medium without G418. MDA231luc cells expressing firefly luciferase were developed as described (*8*) from MDA-MB-231 mammary gland adenocarcinoma cells (ATCC # HTB-26) expressing a moderate level of EGFR, an average of 2×10^5 EGFR per cell (*11*). Approximately 5-fold difference in EGFR expression in MDA231luc and F98/EGFR(F) cells was supported by Western blot analysis of EGFR in cell lysates (data not shown). MDA231luc were cultured in high glucose DMEM (Invitrogen, Carlsbad, CA), 10% heat inactivated fetal bovine serum (FBS, HyClone, Logan, UT), and 2 mM L-glutamine. All cells were maintained at 37 °C and 5% CO_2.

Animals and Tumor Models. SCID mice (male, 5−6 week old) were purchased from Charles River Laboratories (Wilmington, MA). MDA231luc human breast carcinoma cells (*8, 9*) were implanted into the left axillary fat pad at 10^6 cells per mouse. F98/EGFR(F) rat glioma cells were implanted subcutaneously onto the right shoulder at 4.5×10^6 cells per mouse. The generation of spontaneous mouse lung adenocarcinomas in bitransgenic mice (FVBN original strain carrying *myc* or *ras* transgenes regulated by a tetracycline-inducible lung-specific promoter) has been described previously (*12*). The protocol for the animal studies was approved by the Stanford University Institutional Animal Care and Use Committee.

Stimulation of EGFR Phosphorylation in F98/EGFR(F) Cells. The EGFR tyrosine phosphorylation assay was performed as reported elsewhere (*8*). Briefly, near-confluent F98/EGFR(F) cells grown in 24-well plates were incubated overnight in serum-free DMEM, then shifted to serum-free DMEM with 0.5 mM sodium vanadate for 15 min at 37 °C. To stimulate EGFR tyrosine phosphorylation, proteins were added to cells to final concentrations in the range from 0 to 50 nM. After 10-min stimulation at 37 °C, cells were lyzed, separated by SDS−PAGE, and analyzed by Western blotting using phosphotyrosine-specific antibody PY clone PT-66 (Sigma, St Louis, MO). In these experiments, 3.6×10^3 cell equivalents were loaded per one lane.

Competition with EGF-SLT Fusion Cytotoxin for Binding to Cellular EGFR in MDA231luc Cells. MDA231luc cells were plated on 96-well plates 20 h before the experiment (1000 cells/well). Proteins were serially diluted in complete culture medium supplemented with EGF-SLT fusion cytotoxin (SibTech, Brookfield, CT) and added to cells in triplicate wells to a final EGF-SLT concentration of 1 nM and competitors ranging from 0 to 25 nM. EGF-SLT is highly toxic for MDA-231luc cells (IC_{50} of 50 pM); therefore, the ability of proteins to compete with EGF-SLT for binding to cellular EGFR can be readily measured by the numbers of surviving cells after a 72-h exposure. Viable cells were quantitated by CellTiter 96 AQ_{ueous} One Solution Cell Proliferation Assay kit (Promega, Madison, WI).

Scatchard's Analysis of Tracer Binding to Cellular EGFR. F98/EGFR(F) cells grown on 12-well plates were shifted to serum-free medium at room temperature for 45 min. Varying amounts of EGF/Tc or EGF-PEG-DOTA/Cu were added to cells in triplicate wells for 90 min, followed by two PBS and one high-salt (0.5 M NaCl in PBS) wash. Cells were lyzed in PBS containing 1% Triton X-100 and assayed for ^{99m}Tc or ^{64}Cu activity in a gamma counter (140 and 511 keV level, respectively, 20% window). Nonspecific binding was determined for the same amounts of labeled EGF supplemented with a 200-fold molar excess of cold EGF.

Stability of EGF/Tc and dEGF/Tc. For *in vivo* stability testing, Balb/c mice ($n = 2$) were injected via the tail vein with EGF/Tc (60 μCi/0.25 μg per mouse) or with dEGF/Tc (60 uCi/0.22 μg) and sacrificed 2 min later. Blood was collected and clarified by centrifugation. Plasma samples were incubated at 37 °C for 10, 20, and 75 min. Rough estimation of protein-bound radioactivity in 1-μL plasma aliquots was done by ITLC. Stability was also tested *in vitro* by incubating the tracers in PBS at room temperature followed by ITLC and SDS−PAGE analyses.

Blood Clearance and Biodistribution Studies. For blood clearance and biodistribution studies, tracers were injected via the tail vein, and serial ~50-μL blood samples were taken via the supraorbital sinus at various time points after injection. Tissue samples taken at specified time points were counted in a gamma counter along with three samples of standard activity (1/100 of injected dose). Results were calculated as the average of the percentage of injected dose (ID) or %ID per gram (g) of tissue ± one standard deviation of the mean.

SPECT Imaging and Autoradiography. For SPECT imaging, 1.7−4.5 mCi of tracer per mouse ($n = 4$) was injected via the tail vein. SPECT images were obtained 1 h after injection with the following parameters: 360° rotation, 64 steps, 30 s per step, 0.5 mm pinhole aperture, a 64 × 64 image matrix, and a 3.4 cm FOV using a small animal SPECT imaging gamma camera (A-SPECT, LumaGEM, Gamma Medica, Los Angeles). For autoradiography, tumors and pectoralis muscle from the healthy chest side were snap-frozen immediately after imaging, cryosectioned (60-μm thickness), and exposed to a phosphor storage screen for 16 h. For autoradiography of lung tumors, before freezing lungs have been perfused with 1% PFA in PBS followed by 20% sucrose in PBS. The phosphor screen images were read out with a laser digitizer at a resolution of 50 μm per pixel. Region of interest (ROI) analysis of radiotracer activity was performed using ImageQuant TL Software. The maximal cts/pixel of the rim and the average cts/pixel of the center of the tumor were normalized to corresponding contralateral pectoral muscle uptake (minimum cts/pixel).

PET Imaging. Two groups of tumor-bearing mice ($n = 8$) intravenously received 95 μCi of EGF-PEG-DOTA/Cu or dEGF-PEG-DOTA/Cu. Ten-minute static scans of mice in prone position were obtained on a microPET R4 rodent model scanner (Concorde Microsystems, Knoxville, TN) equipped with computer-controlled vertical and horizontal bed motion, with an effective axial field of view (FOV) of 7.8 cm and a transaxial FOV of 10 cm. Mice anesthetized with 2% isoflurane were placed near the center of the FOV to ensure the highest image resolution and sensitivity. The images were reconstructed by a two-dimensional ordered-subsets expectation maximum algorithm. No correction was necessary for attenuation and scattering. We obtained relative tumor or organ radioactivity concentrations from mean pixel values within the multiple ROI volumes. For biodistribution, tissue samples were taken at 22 h after injection and counted in a gamma counter along with three samples of standard activity (1/100 of injected dose). Results were calculated as the average of the percentage of injected dose per gram (%ID /g) of tissue ± one standard deviation of the mean.

RESULTS

Cys-Tagged EGF and dEGF and Site-Specific Conjugation of PEGylated DOTA Chelator. To make tracers for imaging EGF receptors, we used a previously described Cys-tagged EGF (*8*) and a newly engineered Cys-tagged head-to-tail EGF dimer (dEGF) (Figure 1A). We reasoned that since functional ligand/receptor complexes include two EGF molecules, dEGF might provide certain advantages in binding and/or internalization of tracers. EGF and dEGF were expressed in *E.coli*, recovered from inclusion bodies, refolded in red-ox buffer containing glutathione, and purified via ion-exchange chromatography (*8*). As

other Cys-tagged proteins refolded in red-ox buffer, EGF and dEGF proteins were recovered with the C4-thiol group in Cys-tag protected in a form of a mixed disulfide with glutathione. For direct radiolabeling with ^{99m}Tc or for conjugation of the DOTA chelator, the C4-thiol group was readily deprotected upon incubation with equimolar amounts of DTT.

The DOTA chelator was conjugated to the C4-thiol group in EGF or dEGF via a 5 kDa NHS-PEG-Mal linker, using a previously developed (*8*) two-step procedure (Figure 1B). First, NHS chemistry was used for conjugation of NHS-PEG-Mal to *p*-NH_2-Bn-DOTA, followed by quenching of unreacted NHS with excess of Tris HCl at pH 8.0. At the next step, the quenched reaction mixture, without further purification, was added to deprotected EGF or dEGF, and the resulting EGF-PEG-DOTA or dEGF-PEG-DOTA were purified by RP HPLC (Figure 1C). A typical preparation of RP HPLC purified EGF-PEG-DOTA or dEGF-PEG-DOTA contains less than 10% of unmodified or overmodified starting protein (Figure 1D).

Functional Activities of Proteins and Conjugates. Functional activities of EGF, dEGF, and the corresponding conjugates were tested in several cell-based assays. In a short-term assay (10 min), conjugates were tested for the ability to bind to EGFR and induce its tyrosine autophosphorylation. In this assay, both proteins and their conjugates displayed dose-dependent activities in a similar range (Figure 2A). Interestingly, EGF-PEG-DOTA was less active than EGF, while dEGF-PEG-DOTA was more active than dEGF. The latter data suggested that the presence of two PEG-DOTA moieties in the functional (EGF-PEG-DOTA)$_2$/EGFR$_2$ complex might be somewhat more detrimental for receptor binding than a single PEG-DOTA in the dEGF-PEG-DOTA/EGFR$_2$ complex.

In a long-term competition assay (3 days), conjugates were tested for their ability to protect EGFR-positive cells from EGF-SLT, a fusion cytotoxin, combining EGF and catalytic subunit A of Shiga-like toxin (Backer et al., submitted for publication). We reasoned that in this assay binding of EGF-based constructs to EGFR reaches equilibrium and therefore eliminates any kinetic effects that might affect short-term assays. We found that in this assay both parental proteins and corresponding EGF-PEG-DOTA and dEGF-PEG-DOTA displayed very similar activities (Figure 2B).

Since loading of the DOTA chelator with radionuclides takes place at elevated temperature, we also tested if such treatment would affect EGF activity. We found that incubation of EGF-PEG-DOTA conjugates in radiolabeling buffer at 95 °C for 30 min did not decrease its functional activity in the protection assay (Figure 2B).

Radiolabeling of Cys-Tagged EGF and dEGF with ^{99m}Tc. We have recently reported that Cys-tag in scVEGF can be directly radiolabeled with ^{99m}Tc using tin-tricine as a precursor complex and hypothesized that a similar radiolabeling can be undertaken with any Cys-tagged protein (*9*). Indeed, we found that deprotected EGF and dEGF, but not parental protected molecules, were readily radiolabeled with [^{99m}Tc]pertechnetate. After purification via size-exclusion chromatography on PD-10, we obtained EGF/Tc and dEGF/Tc tracers with specific activity in the range of 160−300 and 130−280 μCi/μg, respectively, and radiopurity in the range of 90−95%. The specific activity obtained through direct radiolabeling was compared favorably to the reported values 15−30 μCi/μg (*13*) or 82 μCi/μg (*14*) obtained after radiolabeling of the EGF-HYNIC conjugates with tin-tricin as a coligand, and 68 μCi/μg for EGF-HYNIC conjugates with EDDA as a coligand (*14*). As judged by a Scatchard analysis of EGF/Tc binding to F98/EGFR(F) cells, the procedure resulted in tracers with the expected low nanomolar affinity to EGFR (K_d = 2.7 nM) and indicated the presence of 0.8 × 10^6 EGFR/cell (Figure 2C). Notably, site-specifically radiolabeled EGF/Tc displayed 2−3-fold higher affinity to EGFR than that reported for EGF-HYNIC-Tc tracers obtained by random conjugation of the chelator, despite the fact that only one HYNIC molecule was conjugated per one EGF protein (*13*).

Radiolabeling of EGF- and dEGF-PEG-DOTA Conjugates with ^{64}Cu. The ^{64}Cu radiolabeling protocol was initially developed for scVEGF-PEG-DOTA conjugates (*8, 10*). As applied to EGF-PEG-DOTA and dEGF-PEG-DOTA, this procedure routinely resulted in a specific activity of ∼125 μCi/μg for EGF-PEG-DOTA and of ∼75 μCi/μg for dEGF-PEG-DOTA. As judged by Scatchard's analysis of binding of EGF-PEG-DOTA/Cu to F98/EGFR cells (Figure 2D), the K_d value of 3 nM and 1.4 × 10^6 of EGFR/cell for this tracer were close to that for the EGF/Tc tracer (see Figure 2C).

Stability, Blood Clearance, and Biodistribution Studies. ^{99m}Tc and ^{64}Cu radiolabeled tracers cleared rapidly from the circulation, with more than 95% of tracer cleared within 1 h after intravenous injection (Figure 3A for EGF/Tc). We found that these tracers are stable for at least 3 h at room temperature in PBS (not shown) and that radionuclides were protein-associated for at least 75 min at 37 °C in plasma (Figure 3B).

Biodistribution experiments with EGF/Tc and dEGF/Tc were performed on MDA231luc tumor-bearing mice (n = 4) with well-formed tumors at 25-day post implantation. At 3 h after intravenous injection, we found that uptake of dEGF/Tc in most organs, including tumors, was higher than that of EGF/Tc (Figure 3C). Interestingly, for both tracers, uptake at the edge of the tumor was very similar to uptake in the central tumor areas, suggesting that tracers are distributed throughout the tumor mass (Figure 3C). As summarized in Table 1, kidney uptake of EGF/Tc was ∼3-fold lower than that of EGF-HYNIC/Tc with EDDA as coligand (*14*), and comparable to that of EGF-HYNIC/Tc (*13*) with tricin as coligand. However, liver uptake of EGF/Tc was 2-fold lower than that for both EGF-HYNIC/Tc tracers (Table 1).

For biodistribution studies with EGF-PEG-DOTA/Cu and dEGF-PEG-DOTA/Cu, 95 μCi of either tracer were intravenously injected into mice (n = 4) 9 days after either MDA231luc or F98/EGFR tumor cell implantation, when tumors were just palpable (3−5 mm in diameter). We found that 22 h postinjection uptake of EGF-PEG-DOTA/Cu in all organs, including tumors, was ∼3-fold higher than that of dEGF-PEG-DOTA/Cu (Figure 3D). Interestingly, the uptake of both tracers in F98/EGFR(F) tumors was somewhat lower than in MDA231luc, despite the fact that the latter cells express ∼5-fold less EGFR in tissue culture (data not shown). We found this result very instructive since it indicated that only functional in vivo tests could provide meaningful information on the receptor activity *in vivo*.

SPECT Imaging and Autoradiographic Studies. SPECT tracers were tested in two tumor models: orthotopic MDA231luc breast carcinoma (*8*) and spontaneous mouse lung carcinoma in bitransgenic mice (*11*). In both models, the tracers readily accumulated in the tumors (Figure 4A).

We further explored EGF-based ^{99m}Tc tracers by autoradiography of cryosections prepared from two MDA231luc tumor-bearing mice immediately after whole-body SPECT imaging. As shown in Figure 4B, radioactivity in tumors was significantly higher as compared with that from contralateral muscles. For autoradiography analysis of a spontaneous lung tumor, we selected a mouse with only a left lung tumor, as detected by SPECT with dEGF/Tc tracer. As shown in Figure 4C, autoradiography confirmed that radioactivity was significantly higher in left lung cryosections, as compared with that in the right lung.

PET Imaging. PET tracers were tested in orthotopic MDA231luc breast carcinoma. The tracers readily accumulated in large (10−15 mm) MDA231luc tumors, as imaged at 3 h

after tracer injection (Figure 5A). In separate experiments, we observed a selective uptake of EGF-based PET tracers in barely palpable MDA231luc tumors, whose presence was validated by bioluminescent imaging after intraperitoneal injection of luciferine (data not shown).

DISCUSSION

We describe here a family of EGF-based tracers for SPECT and PET imaging of EGF receptors. The tracers are based on natural monomeric and on engineered dimeric EGF, expressed with cysteine-containing Cys-tag for site-specific conjugation of various payloads (*10*). To obtain SPECT tracers, C4 in Cys-tag is directly radiolabeled with ^{99m}Tc, while PET tracers are prepared by site-specific conjugation of a PEGylated chelator DOTA to C4, followed by radiolabeling with ^{64}Cu. Both procedures avoid random conjugation of chelating moieties to targeting proteins, thus yielding uniform functionally active tracers with high specific activities. Importantly, direct radiolabeling with ^{99m}Tc yields a stable SPECT tracer with specific activity higher than that reported for the tracers based on EGF-chelator conjugates (*12, 13*). Rather similar tumor uptake is obtained with tracers based on monomeric and dimeric Cys-tagged EGF, although there are differences in biodistribution patterns that need to be further explored.

Over the years, several groups reported SPECT, PET, and fluorescent tracers for imaging EGF receptors, based on EGF (*8, 11, 13*−*21*), anti-EGFR antibodies (*21*−*27*), and low-molecular weight EGFR inhibitors (*28*−*33*). Since all of these tracers invariably imaged EGFR-positive tumors in mouse models, the eventual selection of the best candidate for further development would be based on relative advantages in terms of production, specific activity, biodistribution, and specific, receptor-mediated tumor uptake. Taking into account these criteria, we reasoned that using EGF, a natural EGFR ligand, as a targeting vector would be particularly advantageous. First, only functionally active and therefore critical for disease progression EGFRs will bind and internalize an EGF-based tracer. In contrast, tracers based on low-molecular weight kinase inhibitors or anti-EGFR antibodies would bind to all EGFRs, regardless of their functional status, providing, in this respect, information similar to that derived from immunohistochemistry. Second, continuous internalization of EGF-based tracers by recyclable EGFR would lead to intracellular accumulation of a radionuclide, thereby improving a signal-to-background ratio. Third, the small size of EGF, relative to that of antibodies, would facilitate tumor penetration with vastly better nonspecific soft tissue and blood clearance rates. Finally as a human protein, EGF is not expected to be immunogenic.

Although several EGF-based tracers have been described previously (*11, 13*−*21*), we expect that functionally active and uniform tracers based on Cys-tagged EGF would provide major advantages because they eliminate heterogeneity associated with random conjugation of contrast agents to the protein. Furthermore, comparison of biodistribution data for various EGF-based SPECT tracers suggests that our tracers provide a lower liver uptake and a similar or a lower kidney uptake (Table 1). Furthermore, kidney and liver uptake for our EGF-based SPECT tracers are in the range of those found for Annexin-HYNIC/^{99m}Tc tracer (*34*), which was approved for clinical trials (*35*). However, detailed preclinical dosimetry studies would be required for assessing the developmental potential of tracers based on Cys-tagged EGF or dEGF.

It should be noted that, similar to the other tracers based on physiologically active molecules, there are reasonable concerns of potential harmful pharmacological effects of EGF-based tracers. To begin addressing such concerns, we can compare the anticipated doses of EGF-based tracers with the dose of recombinant EGF used in a recent clinical trial. The tracer dose can be estimated based on the clinical experience with another protein-based SPECT tracer, annexin-HYNIC/Tc, that was injected at an average dose of 6.9 mCi per 77 kg patient or approximately 90 μCi/kg (*35*). Considering that EGF/Tc is readily labeled to a specific activity of 200 μCi/μg, a similar dose of EGF/Tc would require an injection of the tracer at a level of only 0.45 μg/kg. However, a recent clinical study of recombinant EGF for the treatment of neonatal necrotizing enterocolitis (*36*) concluded that a dose of 0.1 μg/hour/kg may be safely given via continuous infusion for 6 days, leading to a cumulative dose well above the anticipated EGF-tracer dose. Thus, although a definitive answer to safety concerns regarding EGF-based tracers requires extensive experimentation, we expect that injection of tracer amounts of EGF for diagnostic imaging will have no adverse effects.

LITERATURE CITED

(1) Baselga, J., and Arteaga, C. L. (2005) Critical update and emerging trends in epidermal growth factor receptor targeting in cancer. *J. Clin. Oncol. 23*, 2445–2459.

(2) Hann, C. L., and Brahmer, J. R. (2007) Who should receive epidermal growth factor receptor inhibitors for non-small cell lung cancer and when? *Curr. Treat. Opt. Oncol. 8*, 28–37.

(3) Bonomi, P. D., Buckingham, L., and Coon, J. (2007) Selecting patients for treatment with epidermal growth factor tyrosine kinase inhibitors. *Clin. Cancer Res. 13* (15 Pt 2), s4606–4612.

(4) Scagliotti, G. V., Selvaggi, G., Novello, S., and Hirsch, F. R. (2004) The biology of epidermal growth factor receptor in lung cancer. *Clin. Cancer Res. 10*, s4227–4232.

(5) Chung, K. Y., Shia, J., Kemeny, N. E., Shah, M., Schwartz, G. K., Tse, A., Hamilton, A., Pan, D., Schrag, D., Schwartz, L., Klimstra, D. S., Fridman, D., Kelsen, D. P., and Saltz, L. B. (2005 Cetuximab shows activity in colorectal cancer patients with tumors that do not express the epidermal growth factor receptor by immunohistochemistry. *J. Clin. Oncol. 23*, 1803–1810.

(6) Bell, D. W., Lynch, T. J., Haserlat, S. M., Harris, P. L., Okimoto, R. A., Brannigan, B. W., Sgroi, D. C., Muir, B., Riemenschneider, M. J., Iacona, R. B., Krebs, A. D., Johnson, D. H., Giaccone, G., Herbst, R. S., Manegold, C., Fukuoka, M., Kris, M. G., Baselga, J., Ochs, J. S., and Haber, D. A. (2005) Epidermal growth factor receptor mutations and gene amplification in non-small-cell lung cancer. Molecular analysis of the IDEAL/INTACT gefitinib trials. *J. Clin. Oncol. 23*, 8081–8092.

(7) Johns, T. G., Perera, R. M., Vernes, S. C., Vitali, A. A., Cao, D. X., Cavenee, W. K., Scott, A. M., and Furnari, F. B. (2007) The efficacy of epidermal growth factor receptor-specific antibodies against glioma xenografts is influenced by receptor levels, activation status, and heterodimerization. *Clin. Cancer. Res. 13*, 1911–1925.

(8) Backer, M. V., Levashova, Z., Patel, V., Jehning, B. T., Claffey, K., Blankenberg, F. G., and Backer, J. M. (2007) Molecular Imaging of VEGF receptors in angiogenic vasculature with single-chain VEGF based probes. *Nature Med. 13*, 509–514.

(9) Levashova, Z., Backer, M., Backer, J. M., and Blankenberg, F. G. (2008) Direct site-specific labeling of the Cys-tag moiety in scVEGF with Technetium 99m. *Bioconjugate Chem. 19*, 1049–1054.

(10) Backer, M. V., Levashova, Z., Levenson, R., Blankenberg, F. G., and Backer, J. M. (2008) Cysteine-Containing Fusion Tag for Site-Specific Conjugation of Therapeutic and Imaging Agents to Targeting Proteins. *Methods in Molecular Medicine. Volume 494: Peptide-Based Drug Design* (Otvos, L. Ed.) pp 275−294, Humana Press, New York.

(11) Hu, M., Scollard, D., Chan, C., Chen, P., Vallis, K., and Reilly, R. M. (2007) Effect of the EGFR density of breast cancer cells on nuclear importation, in vitro cytotoxicity, and tumor and normal-tissue uptake of [111In]DTPA-hEGF. *Nucl. Med. Biol. 34*, 887–896.

(12) Tran, T. P., Fan, A. C., Bendapudi, P. K., Koh, S., Komatsubara, K., Chen, J., Horng, G., Bellovin, D. I., Giuriato, S., Wang, C. S., Whitsett, J. A., and Felsher, D. W. (2008) Combined inactivation of MYC and K-Ras oncogenes reverses tumorigenesis in lung adenocarcinomas and lymphomas. *PLoS ONE 3*, e2125.

(13) Cornelissen, B., Kersemans, V., Burvenich, I., Oltenfreiter, R., Vanderheyden, J-L., Boerman, O., Vandewiele, C., and Slegers, G. (2005) Synthesis, biodistribution and effects of farnesyltransferase inhibitor therapy on tumour uptake in mice of 99mTc labelled epidermal growth factor. *Nucl. Med. Commun. 26*, 147–153.

(14) Babaei, M. H., Almqvist, Y., Orlova, A., Shafii, M., Kairemo, K., and Tolmachev, V. (2005) [99mTc]HYNIC-hEGF, a potential agent for imaging of EGF receptors in vivo: preparation and preclinical evaluation. *Oncol. Rep. 13*, 1169–1175.

(15) Capala, J., Barth, R. F., Bailey, M. Q., Fenstermaker, R. A., Marek, M. J., and Rhodes, B. A. (1997) Radiolabeling of epidermal growth factor with 99mTc and in vivo localization following intracerebral injection into normal and glioma-bearing rats. *Bioconjugate Chem. 8*, 289–925.

(16) Hnatowich, D. J., Qu, T., Chang, F., Ley, A. C., Ladner, R. C., and Rusckowski, M. Labeling peptides with technetium-99m using a bifunctional chelator of a N-hydroxysuccinimide ester of mercaptoacetyltriglycine. *J. Nucl. Med. 39*, 56–64.

(17) Ke, S., Wen, X., Gurfinkel, M., Charnsangavej, C., Wallace, S., Sevick-Muraca, E. M., and Li, C. (2003) Near-infrared optical imaging of epidermal growth factor receptor in breast cancer xenografts. *Cancer Res. 63*, 7870–7875.

(18) Adams, K. E., Ke, S., Kwon, S., Liang, F., Fan, Z., Lu, Y., Hirschi, K., Mawad, M. E., Barry, M. A., and Sevick-Muraca, E. M. (2007) Comparison of visible and near-infrared wavelength-excitable fluorescent dyes for molecular imaging of cancer. *J. Biomed. Optics. 12*, 024017.

(19) Kovar, J. L., Volcheck, W. M., Chen, J., and Simpson, M. A. (2007) Purification method directly influences effectiveness of an epidermal growth factor-coupled targeting agent for noninvasive tumor detection in mice. *Anal. Biochem. 361*, 47–54.

(20) Diagaradjane, P., Orenstein-Cardona, J. M., Colon-Casasnovas, N. E., Deorukhkar, A., Shentu, S., Kuno, N., Schwartz, D. L., Gelovani, J. G., and Krishnan, S. (2008) Imaging epidermal growth factor receptor expression in vivo: pharmacokinetic and biodistribution characterization of a bioconjugated quantum dot nanoprobe. *Clin. Cancer Res. 14*, 731–741.

(21) Reilly, R. M., Kiarash, R., Sandhu, J., Lee, Y. W., Cameron, R. G., Hendler, A., Vallis, K., and Gariepy, J. (2000) A comparison of EGF and MAb 528 labeled with 111In for imaging human breast cancer. *J. Nucl. Med. 41*, 903–911.

(22) Rosenthal, E. L., Kulbersh, B. D., Duncan, R. D., Zhang, W., Magnuson, J. S., Carroll, W. R., and Zinn, K. (2006) In vivo detection of head and neck cancer orthotopic xenografts by immunofluorescence. *Laryngoscope 116*, 1636–1641.

(23) Rahman, M., Abd-El-Barr, M., Mack, V., Tkaczyk, T., Sokolov, K., Richards-Kortum, R., and Descour, M. (2005) Optical imaging of cervical pre-cancers with structured illumination: an integrated approach. *Gyn. Oncol. 99* (3, Suppl 1), S112–S115.

(24) Dadparvar, S., Krishna, L., Miyamoto, C., Brady, L. W., Brown, S. J., Bender, H., Slizofski, W. J., Eshleman, J., Chevres, A., and Woo, D. V. (1994) Indium-111-labeled anti-EGFr-425 scintigraphy in the detection of malignant gliomas. *Cancer. 73*, 884–889.

(25) Vallis, K. A., Reilly, R. M., Chen, P., Oza, A., Hendler, A., Cameron, R., Hershkop, M., Iznaga-Escobar, N., Ramos-Suzarte, M., and Keane, P. (2002) A phase I study of 99mTc-hR3 (DiaCIM), a humanized immunoconjugate directed towards the epidermal growth factor receptor. *Nucl. Med. Commun. 23*, 1155–1164.

(26) Schechter, N. R., Yang, D. J., Azhdarinia, A., Kohanim, S., III., Oh, C. S., Hu, M., Yu, D. F., Bryant, J., Ang, K. K., Forster, K. M., Kim, E. E., and Podoloff, D. A. (2003) Assessment of epidermal growth factor receptor with 99mTc-ethylenedicysteine-C225 monoclonal antibody. *Anti-Cancer Drugs 14*, 49–56.

(27) Hsu, E. R., Anslyn, E. V., Dharmawardhane, S., Alizadeh-Naderi, R., Aaron, J. S., Sokolov, K. V., El-Naggar, A. K., Gillenwater, A. M., and Richards-Kortum, R. R. (2004) A far-red fluorescent contrast agent to image epidermal growth factor receptor expression. *Photochem. Photobiol. 79*, 272–279.

(28) Mishani, E., Abourbeh, G., Rozen, Y., Jacobson, O., Laky, D., Ben David, I., Levitzki, A., and Shaul, M. (2004) Novel carbon-11 labeled 4-dimethylamino-but-2-enoic acid [4-(phenylamino)-quinazoline-6-yl]-amides: potential PET bioprobes for molecular imaging of EGFR-positive tumors. *Nucl. Med. Biol. 31*, 469–476.

(29) Shaul, M., Abourbeh, G., Jacobson, O., Rozen, Y., Laky, D., Levitzki, A., and Mishani, E. (2004) Novel iodine-124 labeled EGFR inhibitors as potential PET agents for molecular imaging in cancer. *Bioorg. Med. Chem. 12*, 3421–3429.

(30) Mishani, E., Abourbeh, G., Jacobson, O., Dissoki, S., Ben Daniel, R., Rozen, Y., Shaul, M., and Levitzki, A. (2005) High-affinity epidermal growth factor receptor (EGFR) irreversible inhibitors with diminished chemical reactivities as positron emission tomography (PET)-imaging agent candidates of EGFR overexpressing tumors. *J. Med. Chem. 48*, 5337–5348.

(31) Bonasera, T. A., Ortu, G., Rozen, Y., Krais, R., Freedman, N. M., Chisin, R., Gazit, A., Levitzki, A., and Mishani, E. (2001) (18)F-labeled biomarkers for epidermal growth factor receptor tyrosine kinase. *Nucl. Med. Biol. 28*, 359–374.

(32) Wang, J. Q., Gao, M., Miller, K. D., Sledge, G. W., and Zheng, Q. H. (2006) Synthesis of [11C]Iressa as a new potential PET cancer imaging agent for epidermal growth factor receptor tyrosine kinase. *Bioorg. Med. Chem. Lett. 16*, 4102–416.

(33) Gelovani, J. G. (2008) Molecular imaging of epidermal growth factor receptor expression-activity at the kinase level in tumors with positron emission tomography. *Cancer Metast. Rev. 27*, 645–653.

(34) Fonge, H., de Saint, H. M., Vunckx, K., Rattat, D., Nuyts, J., Bormans, G., Ni, Y., Reutelingsperger, C., and Verbruggen, A. (2008) Preliminary in vivo evaluation of a novel 99mTc-labeled HYNIC-cys-annexin A5 as an apoptosis imaging agent. *Bioorg. Med. Chem. Lett. 18*, 3794–3798.

(35) Kemerink, G. J., Liu, X., Kieffer, D., Ceyssens, S., Mortelmans, L., Verbruggen, A. M., Steinmetz, N. D., Vanderheyden, J. -L., Green, A. M., and Verbeke, K. (2003) Safety, biodistribution, and dosimetry of 99mTc-HYNIC-annexin V, a novel human recombinant annexin V for human application. *J. Nucl. Med. 44*, 947–952.

(36) Sullivan, P. B., Lewindon, P. J., Cheng, C., Lenehan, P. F., Kuo, B. S., Haskins, J. R., Goodlad, R. A., Wright, N. A., and de la Iglesia, F. A. (2007) Intestinal mucosa remodeling by recombinant human epidermal growth factor (1−48) in neonates with severe necrotizing enterocolitis. *J. Pediatr. Surg. 42*, 462–469.

BC800443W

Improving Tumor Uptake and Pharmacokinetics of ^{64}Cu-Labeled Cyclic RGD Peptide Dimers with Gly_3 and PEG_4 Linkers

Jiyun Shi,[†] Young-Seung Kim,[†] Shizhen Zhai,[†] Zhaofei Liu,[‡] Xiaoyuan Chen,[‡] and Shuang Liu*[,†]

School of Health Sciences, Purdue University, West Lafayette, Indiana 47907, and Molecular Imaging Program at Stanford (MIPS), Department of Radiology & Bio-X, Stanford University, Stanford, California 94305-5484. Received October 22, 2008; Revised Manuscript Received February 16, 2009

Radiolabeled cyclic RGD (Arg-Gly-Asp) peptides represent a new class of radiotracers with potential for early tumor detection and noninvasive monitoring of tumor metastasis and therapeutic response in cancer patients. This article describes the synthesis of two cyclic RGD peptide dimer conjugates, DOTA-PEG_4-E[PEG_4-c(RGDfK)]$_2$ (DOTA-3PEG_4-dimer: DOTA = 1,4,7,10-tetraazacyclododecane-1,4,7,10-tetraacetic acid; PEG_4 = 15-amino-4,7,10,13-tetraoxapentadecanoic acid) and DOTA-G_3-E[G_3-c(RGDfK)]$_2$ (DOTA-3G_3-dimer: G_3 = Gly-Gly-Gly). Integrin $\alpha_v\beta_3$ binding affinities of cyclic RGD peptides were determined by competitive displacement of ^{125}I-echistatin bound to U87MG human glioma cells and follow the order of DOTA-E{E[c(RGDfK)]$_2$}$_2$ (DOTA-tetramer: IC_{50} = 10 ± 2 nM) > DOTA-3G_3-dimer (IC_{50} = 62 ± 6 nM) ~ DOTA-3PEG_4-dimer (IC_{50} = 74 ± 3 nM) > DOTA-E[c(RGDfK)]$_2$ (DOTA-dimer: IC_{50} = 102 ± 5 nM). The addition of PEG_4 and G_3 linkers between two cyclic RGD motifs in DOTA-3G_3-dimer and DOTA-3PEG_4-dimer makes it possible for them to achieve the simultaneous integrin $\alpha_v\beta_3$ binding in a bivalent fashion. Both ^{64}Cu(DOTA-3PEG_4-dimer) and ^{64}Cu(DOTA-3G_3-dimer) were prepared in high yield with specific activity being >50 Ci/mmol. Biodistribution and imaging studies were performed in athymic nude mice bearing U87MG human glioma xenografts. The results from those studies show that PEG_4 and G_3 linkers are particularly useful for improving tumor uptake and clearance kinetics of ^{64}Cu radiotracers from the nontumor organs, such as kidneys, liver, and lungs. There is a linear relationship between the tumor size and %ID tumor uptake, suggesting that ^{64}Cu(DOTA-3PEG_4-dimer) and ^{64}Cu(DOTA-3PEG_4-dimer) might be useful for noninvasive monitoring of tumor growth or shrinkage during antiangiogenic therapy. MicroPET imaging data clearly demonstrate the utility of ^{64}Cu(DOTA-3G_3-dimer) as a new PET radiotracer for imaging integrin $\alpha_v\beta_3$-positive tumors.

INTRODUCTION

Angiogenesis is a requirement for tumor growth and metastasis (*1*−*10*). Without neovasculature to provide oxygen and nutrients, tumors cannot grow beyond 1−2 mm in size. Once vascularized, previously dormant tumors begin to grow rapidly, and their volumes increase exponentially. Recent clinical and experimental evidence suggests that tumor growth and progression are dependent on angiogenesis and invasion, which share common regulatory mechanisms (*2, 5*). Angiogenesis is an invasive process characterized by endothelial cell proliferation and is regulated by cell adhesion receptors. Integrins are such a family of proteins that facilitate cellular adhesion to and migration on extracellular matrix proteins found in intercellular spaces and basement membranes, and regulate cellular entry and withdraw from the cell cycle (*5*−*13*). Integrin $\alpha_v\beta_3$ is a receptor for the extracellular matrix proteins with an exposed arginine−glycine−aspartic (RGD) tripeptide sequence (*5, 6, 9*). Integrin $\alpha_v\beta_3$ is normally expressed at low levels on epithelial cells and mature endothelial cells; but it is highly expressed on the activated endothelial cells in neovasculature of tumors, including osteosarcomas, glioblastomas, melanomas, lung carcinomas, and breast cancer (*11*−*19*). It has been demonstrated that integrin $\alpha_v\beta_3$ is overexpressed on both endothelial and tumor cells in human breast cancer xenografts (*20*). The integrin $\alpha_v\beta_3$ expression correlates well with tumor progression and invasiveness of melanoma, glioma, and breast cancers (*13*−*16, 18*−*20*). The highly restricted expression of integrin $\alpha_v\beta_3$ during tumor growth, invasion, and metastasis presents an interesting molecular target for the early detection of rapidly growing and metastatic tumors (*21*−*33*). In addition, it would be highly advantageous to develop an integrin $\alpha_v\beta_3$-specific radiotracer that could be used to noninvasively visualize and quantify the integrin $\alpha_v\beta_3$ expression level before, during, or after antiangiogenic therapy (*34*).

Over the last several years, many radiolabeled cyclic RGD peptides have been evaluated as potential radiotracers for imaging the integrin $\alpha_v\beta_3$-positive tumors by single photon emission computed tomography (SPECT) or positron emission tomography (PET) (*35*−*68*). The integrin $\alpha_v\beta_3$-targeted radiotracers have recently been reviewed extensively (*21*−*33*). Among the radiotracers evaluated in different preclinical tumor-bearing animal models, [^{18}F]-AH111585, the core peptide sequence originally discovered from a phage display library (such as ACDRGDCFCG), and [^{18}F]Galacto-RGD (2-[^{18}F]fluoropropanamide c(RGDfK(SAA); SAA = 7-amino-L-glyero-L-galacto-2,6-anhydro-7-deoxyheptanamide) are under clinical investigations for noninvasive visualization of integrin $\alpha_v\beta_3$ expression in cancer patients (*69*−*71*). The imaging studies in cancer patients show that the ^{18}F-labeled cyclic RGD peptides are able to target integrin $\alpha_v\beta_3$-positive tumors. However, the low tumor uptake, high cost, and lack of preparation modules for the ^{18}F-labeled monomeric cyclic RGD peptides impose a significant challenge for their continued clinical applications.

* To whom correspondence should be addressed. School of Health Sciences, Purdue University, 550 Stadium Mall Drive, West Lafayette, IN 47907. Phone: 765-494-0236. Fax 765-496-1377. E-mail: lius@pharmacy.purdue.edu.

[†] Purdue University.

[‡] Stanford University.

10.1021/bc800455p CCC: $40.75 © 2009 American Chemical Society
Published on Web 03/25/2009

To improve integrin $\alpha_v\beta_3$ binding, multimeric cyclic RGD peptides, such as E[c(RGDfK)]$_2$ (dimer) and E{E[c-(RGDfK)]$_2$}$_2$ (tetramer), were used as targeting biomolecules to carry the radionuclide (e.g., ^{99m}Tc, ^{18}F, ^{64}Cu, and ^{111}In) to the integrin $\alpha_v\beta_3$ on tumor cells and endothelial cells of the tumor neovasculature (*41*−*43*, *47*−*68*). The results from the in vitro assays, ex-vivo biodistribution, and in vivo imaging studies clearly demonstrate that the radiolabeled (^{99m}Tc, ^{18}F, ^{64}Cu, and ^{111}In) multimeric cyclic RGD peptides, such as E{E[c(RGDxK)]$_2$}$_2$ and E[c(RGDxK)]$_2$ (x = f and y), have much better tumor targeting capability as evidenced by their higher tumor uptake with longer tumor retention times as compared to their monomeric RGD peptide counterparts (*47*−*68*). However, it remains unclear if the cyclic RGD motifs in E{E[c(RGDxK)]$_2$}$_2$ and E[c(RGDxK)]$_2$ (x = f and y) are indeed able to achieve simultaneous integrin $\alpha_v\beta_3$ binding in a bivalent fashion. In addition, the uptake of the radiolabeled (^{99m}Tc, ^{18}F, ^{64}Cu, and ^{111}In) multimeric cyclic RGD peptides in the kidneys and liver is also increased as the peptide multiplicity increases (*51*−*54*, *60*−*68*).

We recently reported the evaluation of two ^{99m}Tc-labeled cyclic RGD dimers, [^{99m}Tc(HYNIC-3PEG$_4$-dimer)(tricine)-(TPPTS)] (^{99m}Tc-3PEG$_4$-dimer: HYNIC = 6-hydrazinonicotinyl, 3PEG$_4$-dimer = PEG$_4$-E[PEG$_4$-c(RGDfK)]$_2$, PEG$_4$ = 15-amino-4,7,10,13-tetraoxapentadecanoic acid, and TPPTS = trisodium triphenylphosphine-3,3′,3″-trisulfonate) and [^{99m}Tc(HYNIC-3G$_3$-dimer)(tricine)(TPPTS)] (^{99m}Tc-3G$_3$-dimer: 3G$_3$-dimer = G$_3$-E[G$_3$-c(RGDfK)]$_2$ and G$_3$ = Gly-Gly-Gly), as new radiotracers for imaging integrin $\alpha_v\beta_3$ expression in the athymic nude mice bearing U87MG glioma and MDA-MB-435 breast cancer xenografts (*72*, *73*). The PEG$_4$ and G$_3$ linkers are used to increase the distance between two cyclic RGDfK motifs from 6 bonds (excluding the side arms of K-residues) in E[c(RGD-fK)]$_2$ to 26 bonds in 3G$_3$-dimer and 38 bonds in 3PEG$_4$-dimer so that they are able to achieve simultaneous integrin $\alpha_v\beta_3$ binding in a bivalent fashion and to improve the radiotracer excretion kinetics from noncancerous organs. Results from the $\alpha_v\beta_3$ integrin binding assay show that the addition of two PEG$_4$ or G$_3$ linkers between two cyclic RGD motifs makes 3PEG$_4$-dimer and 3G$_3$-dimer bivalent in binding to the integrin $\alpha_v\beta_3$. The results from ex-vivo biodistribution studies clearly demonstrate that PEG$_4$ and G$_3$ linkers are useful for improving the tumor uptake and clearance of ^{99m}Tc-3PEG$_4$-dimer and ^{99m}Tc-3G$_3$-dimer from the kidneys and liver. These promising results led us to prepare DOTA-3PEG$_4$-dimer and DOTA-3G$_3$-dimer (DOTA = 1,4,7,10-tetraazacyclododecane-1,4,7,10-tetraacetic acid) and their corresponding ^{64}Cu complexes, ^{64}Cu(DOTA-3PEG$_4$-dimer) and ^{64}Cu(DOTA-3G$_3$-dimer).

In this article, we present the synthesis and evaluation of ^{64}Cu(DOTA-3PEG$_4$-dimer) and ^{64}Cu(DOTA-3G$_3$-dimer) as PET radiotracers for imaging integrin $\alpha_v\beta_3$ expression in athymic nude mice bearing the U87MG glioma xenografts. We are particularly interested in ^{64}Cu because of its longer half-life ($t_{1/2}$ = 12.7 h) compared to that of ^{18}F ($t_{1/2}$ = 110 min). ^{64}Cu decays by β^+ emission (18% abundance, maximum β^+ energy of 0.655 MeV). It can be produced with high specific activity (*74*). All these factors make the ^{64}Cu-labeled cyclic RGD peptides very attractive as PET radiotracers. DOTA was chosen because it forms a highly stable ^{64}Cu chelate (*75*−*77*). The main objective of this study is to assess the impact of PEG$_4$ and G$_3$ linkers on integrin $\alpha_v\beta_3$ binding affinity of DOTA-conjugated cyclic RGD peptide dimers and on the tumor uptake and excretion kinetics of their ^{64}Cu radiotracers from noncancerous organs, particularly the kidneys and liver. The results from the integrin $\alpha_v\beta_3$ binding assay and biodistribution studies may also allow us to compare them with ^{64}Cu(DOTA-dimer) and ^{64}Cu(DOTA-tetramer).

EXPERIMENTAL SECTION

Materials. Chemicals were purchased from Sigma-Aldrich (St. Louis, MO). DOTA-NHS (1,4,7,10-tetraazacyclododecane-1-(*N*-hydroxysuccinimide acetate)-4,7,10-triacetic acid) was obtained from Macrocyclics Inc. (Dallas, TX). Peptide dimers, PEG$_4$-E[PEG$_4$-c(RGDfK)]$_2$ (3PEG$_4$-dimer) and G$_3$-E[G$_3$-c(RGDfK)]$_2$ (3G$_3$-dimer), were custom-made by Peptides International, Inc. (Louisville, KY). The ESI (electrospray ionization) mass spectral data were collected on a Finnigan LCQ classic mass spectrometer at School of Pharmacy, Purdue University. ^{64}CuCl$_2$ was produced using a CS-15 biomedical cyclotron at Washington University School of Medicine by the ^{64}Ni(p,n)^{64}Cu nuclear reaction.

HPLC Methods. HPLC Method 1 used a LabAlliance semiprep HPLC system (State College, PA) equipped with an UV/vis detector (λ = 254 nm) and Zorbax C$_{18}$ semiprep column (9.4 mm × 250 mm, 100 Å pore size). The flow rate was 2.5 mL/min. The gradient mobile phase started with 90% solvent A (0.1% TFA in water) and 10% solvent B (0.1% TFA in acetonitrile) to 85% solvent A and 15% solvent B at 5 min to 65% solvent A and 35% solvent B at 30 min, followed by an isocratic mobile phase with 50% solvent A and 50% solvent B at 32−36 min. The radio-HPLC method (Method 2) used the LabAlliance semiprep HPLC system equipped with a β-ram IN/US detector (Tampa, FL) and Zorbax C$_{18}$ column (4.6 mm × 250 mm, 300 Å pore size; Agilent Technologies, Santa Clara, CA). The flow rate was 1 mL/min. The mobile phase was isocratic with 90% solvent A (25 mM ammonium acetate buffer, pH 5.0) and 10% solvent B (acetonitrile) at 0−2 min, followed by a gradient mobile phase going from 10% solvent B at 2 min to 15% solvent B at 5 min and to 20% solvent B at 20 min.

DOTA-PEG$_4$-E[PEG$_4$-c(RGDfK)]$_2$ (DOTA-3PEG$_4$-Dimer). DOTA-NHS (4.6 mg, 11 μmol) and PEG$_4$-E[PEG$_4$-c(RGDfK)]$_2$ (5 mg, 2.8 μmol) were dissolved in DMF (2 mL). After the addition of triethylamine (10 mg, 10 μmol), the reaction mixture was stirred at room temperature overnight. The product was isolated from the mixture by HPLC purification (Method 1). The fraction at 19.5 min was collected. Lyophilization of the collected fractions afforded DOTA-3PEG$_4$-dimer as a white powder. The yield was 2.0 mg (∼34%) with >95% HPLC purity. ESI-MS (positive mode): m/z = 1058.59 for [M + H]$^+$ (1058.99 calcd. for [C$_{77}$H$_{103}$N$_{23}$O$_{23}$S]$^+$).

DOTA-G$_3$-E[G$_3$-c(RGDfK)]$_2$ (DOTA-3G$_3$-Dimer). DOTA-3G$_3$-monomer was prepared using the same procedure using DOTA-NHS (4.4 mg, 10.6 μmol) and G$_3$-E[G$_3$-c(RGDfK)]$_2$ (3 mg, 3.53 μmol). Lyophilization of the combined collections at ∼19.5 min (Method 1) afforded the expected product DOTA-3G$_3$-monomer. The yield was 1.6 mg (∼40%) with HPLC purity >95%. ESI-MS: m/z = 1154.17 for [M + H]$^+$ (1154.49 calcd. For [C$_{51}$H$_{72}$N$_{13}$O$_{16}$S]$^+$).

^{64}Cu-Labeling. To a 5 mL vial were added 50 μg of the DOTA-RGD conjugate (RGD = 3PEG$_4$-dimer or 3G$_3$-dimer) in 0.3 mL of 0.1 M NaOAc buffer (pH = 6.9) and 0.12 mL of ^{64}CuCl$_2$ solution (∼ 2.0 mCi) in 0.05 N HCl. The reaction mixture was heated at 100 °C for 30 min. After cooling to room temperature, a sample of the resulting solution was analyzed by radio-HPLC (Method 2). The radiochemical purity (RCP) for ^{64}Cu(DOTA-3PEG$_4$-dimer) and ^{64}Cu(DOTA-3G$_3$-dimer) was >95% with the specific activity of 300−400 mCi/μmol.

Dose Preparation. For biodistribution studies, ^{64}Cu(DOTA-3PEG$_4$-dimer) and ^{64}Cu(DOTA-3G$_3$-dimer) were prepared and then purified by HPLC (Method 2). Volatiles in the HPLC mobile phases were removed by rotary evaporation. The dose solution was prepared by dissolving the HPLC-purified ra-

diotracer in saline to a concentration of 10−25 μCi/mL. In the blocking experiment, E[c(RGDfK)]$_2$ was dissolved in the solution containing the radiotracer to give a concentration of 1.75 mg/mL. For microPET imaging studies, ^{64}Cu(DOTA-3G$_3$-dimer) was prepared by using 12 μg of DOTA-3G$_3$-dimer to react with about 2 mCi of ^{64}CuCl$_2$ in 0.3 mL of 0.1 M NaOAc buffer. After radiolabeling, ^{64}Cu(DOTA-3G$_3$-dimer) was purified with HPLC (Method 2). Volatiles in the HPLC mobile phases were removed by rotary evaporation. The residue was reconstituted in PBS to a concentration of ∼1 mCi/mL. The resulting solution was filtered with a 0.20 μm Millex-LG filter before being injected into animals. Each tumor-bearing mouse was injected with 0.1−0.2 mL of the filtered dose solution.

Solution Stability. For solution stability studies, ^{64}Cu(DOTA-3PEG$_4$-dimer) and ^{64}Cu(DOTA-3G$_3$-dimer) were prepared and purified by HPLC (Method 2). Volatiles in the HPLC mobile phase were removed by rotary evaporation. The HPLC purified ^{64}Cu radiotracers were dissolved in 25 mM phosphate buffer (pH 7.4) containing EDTA (1 mg/mL) to 1 mCi/mL. Samples of the resulting solution were analyzed by radio-HPLC (Method 2) at 0, 1, 2, 4, and 12 h post-purification.

Determination of Log *P* Values. Log *P* values of were determined using the following procedure: the ^{64}Cu radiotracer was purified by HPLC. Volatiles were removed completely under vacuum. The residue was dissolved in an equal volume (3 mL/3 mL) mixture of *n*-octanol and 25 mM phosphate buffer (pH 7.4). After stirring vigorously for ∼20 min, the mixture was centrifuged at a speed of 8,000 rpm for 5 min. Samples (in triplets) from *n*-octanol and aqueous layers were counted in a Perkin-Elmer Wizard-1480 γ-counter (Shelton, CT). The log *P* value was measured three different times and reported as an average of three independent measurements plus the standard deviation.

In Vitro Whole-Cell Integrin $\alpha_v\beta_3$ Binding Assay. The in vitro integrin binding affinity and specificity of cyclic RGD peptides were assessed via a cellular displacement assay using ^{125}I-echistatin as the integrin-specific radioligand. Experiments were performed on a U87MG glioma cell line by slight modification of a method previously described (*50, 52*). Briefly, the U87MG glioma cells were grown in Gibco's Dulbecco's medium supplemented with 10% fetal bovine serum (FBS), 100 IU/mL penicillin, and 100 μg/mL streptomycin (Invitrogen Co, Carlsbad, CA), at 37 °C in humidified atmosphere containing 5% CO_2. Filter multiscreen DV plates were seeded with 10^5 cells in binding buffer and incubated with ^{125}I-echistatin in the presence of increasing concentrations of cyclic RGD peptides. After removing the unbound ^{125}I-echistatin, hydrophilic PVDF filters were collected, and the radioactivity was determined using a gamma counter (Packard, Meriden, CT). The IC_{50} values were calculated by fitting the data by nonlinear regression using GraphPad Prism (GraphPad Software, Inc., San Diego, CA) and reported as an average of these samples plus the standard deviation.

Animal Model and Biodistribution Protocol. Biodistribution studies were performed using the athymic nude mice bearing U87MG human glioma xenografts in compliance the NIH animal experiment guidelines (Principles of Laboratory Animal Care, NIH Publication No. 86−23, revised 1985). The protocol was approved by Purdue University Animal Care and Use Committee (PACUC). Female athymic nu/nu mice were purchased from Harlan (Charles River, MA) at 4−5 weeks of age. The mice were implanted with 5×10^6 the U87MG human glioma cells into the upper left flank. Two to three weeks after inoculation, the tumor size was 0.2−0.5 g, and animals were used for biodistribution and imaging studies. Sixteen tumor-bearing mice (20−25 g) were randomly divided into four groups. The ^{64}Cu radiotracer (∼2.5 μCi in 0.1 mL saline) was administered into each animal via the tail vein. Four animals were euthanized by sodium pentobarbital overdose (100−200 mg/kg), exsanguinations, and opening of thoracic cavity at 5, 30, 60, and 120 min postinjection (p.i.). Blood samples were withdrawn from the heart through a syringe. Organs were excised, washed with saline, dried with absorbent tissue, weighed, and counted on a γ-counter (Perkin-Elmer Wizard-1480). Organs of interest included the tumor, brain, spleen, lungs, liver, kidneys, muscle, and intestine. Organ uptake was calculated as a percentage of the injected dose per gram of organ tissue (%ID/g). For the blocking experiment, each animal was administered with ∼2.5 μCi of ^{64}Cu(DOTA-3PEG$_4$-dimer) along with ∼350 μg of E[c(RGDfK)]$_2$ (∼14 mg/kg). At 1 h p.i., four animals were sacrificed by sodium pentobarbital overdose (100−200 mg/kg) for organ biodistribution. The organ uptake (%ID/g) was compared to that obtained in the absence of excess E[c(RGDfK)]$_2$ at the same time point. The biodistribution data and target-to-background (T/B) ratios are reported as an average plus the standard variation based on results from four animals at each time point. Comparison between two different radiotracers was made using the two-way ANOVA test (GraphPad Prim 5.0, San Diego, CA). The level of significance was set at $p < 0.05$.

MicroPET Imaging. MicroPET imaging was performed using a microPET R4 rodent model scanner (Concorde Microsystems, Knoxville, TN). The U87MG glioma-bearing mice ($n = 3$) were injected with ∼100 μCi of ^{64}Cu(DOTA-3G$_3$-dimer) via the tail vein, were then anesthetized with 2% isoflurane, and placed near the center of the FOV where the highest resolution and sensitivity are obtained. The 5-min static PET images were obtained at 60 min p.i. For the blocking experiment, a mouse bearing a U87MG tumor was injected with 100 μCi of ^{64}Cu(DOTA-3G$_3$-dimer) along with c(RGDyK) at the dose of 10 mg/kg. The 5-min static PET images were then acquired at 1 h p.i.

Metabolism. Normal athymic nude mice ($n = 2$) were used to evaluate the metabolic stability of ^{64}Cu(DOTA-3PEG$_4$-dimer) and ^{64}Cu(DOTA-3G$_3$-dimer). Each mouse was injected with the ^{64}Cu radiotracer at a dose of ∼100 μCi in 0.2 mL of saline via the tail vein. The urine samples were collected at 30 and 120 min p.i. by manual void and were mixed with equal volume of 20% acetonitrile aqueous solution. The mixture was centrifuged at 8,000 rpm. The supernatant was collected, counted on a Perkin-Elmer Wizard-1480 γ-counter, and filtered through a 0.20 μm Millex-LG filter unit. The filtrate was analyzed by radio-HPLC (Method 2). The feces samples were collected at 120 min p.i. and were suspended in a 20% acetonitrile aqueous solution. The mixture was vortexed for 5−10 min. After centrifuging at 8,000 rpm for 5 min, the supernatant was collected, counted on a Perkin-Elmer Wizard-1480 γ-counter, and passed through a 0.20 μm Millex-LG filter unit. The filtrate was then analyzed by radio-HPLC (Method 2). The percentage radioactivity recovery was >95% (by γ-counting) for both urine and feces samples.

RESULTS

Synthesis of DOTA-RGD Conjugates. DOTA-3PEG$_4$-dimer and DOTA-3G$_3$-dimer were prepared by direct conjugation of 3PEG$_4$-dimer and 3G$_3$-dimer, respectively, with excess DOTA-NHS in DMF in the presence of a base, such as triethylamine. DOTA-3PEG$_4$-dimer and DOTA-3G$_3$-dimer were purified by HPLC (Method 1) and characterized by ESI-MS. The mass spectral data were completely consistent with the proposed formula. Their HPLC purity was >95% before being used for the integrin $\alpha_v\beta_3$ binding assay and ^{64}Cu-labeling.

Integrin $\alpha_v\beta_3$ Binding Affinity. The integrin $\alpha_v\beta_3$-positive U87MG human glioma cells were used for the integrin $\alpha_v\beta_3$-

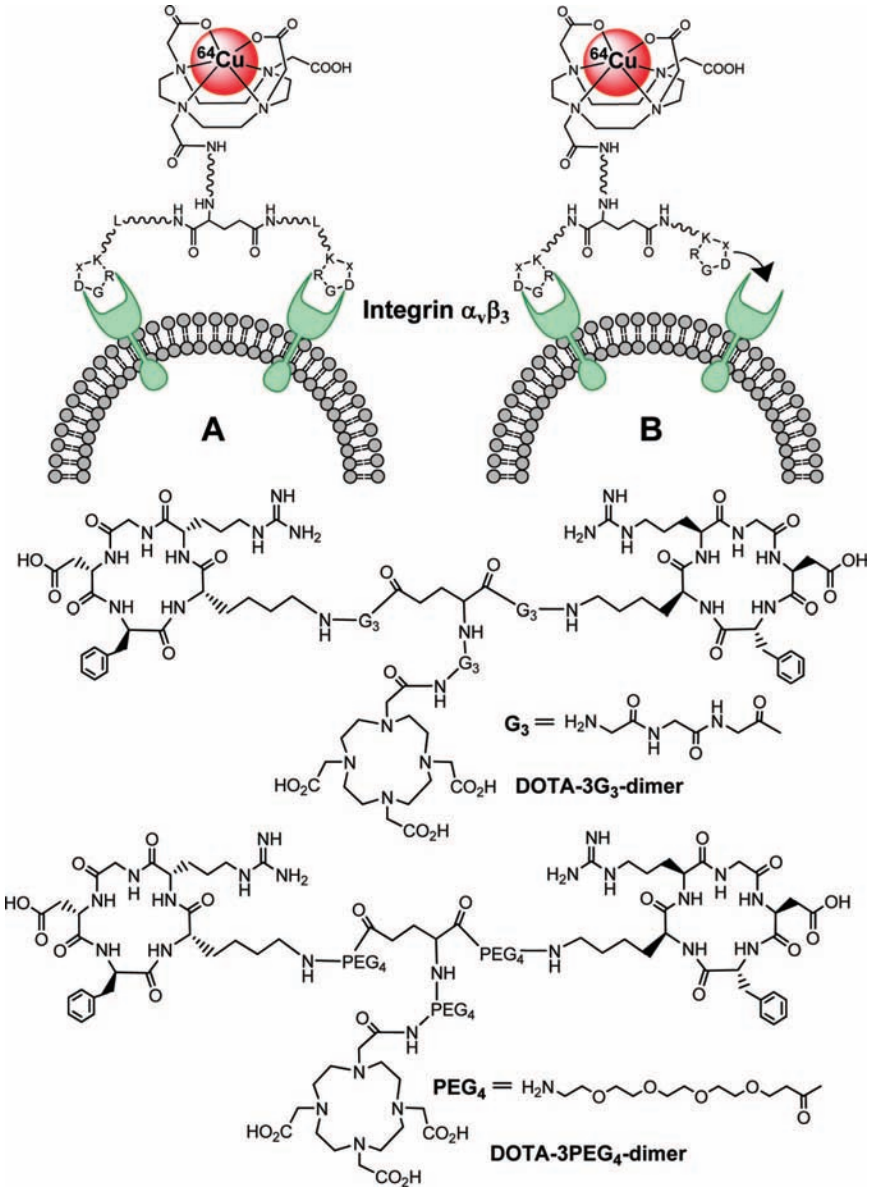

Figure 1. Novel DOTA-conjugated cyclic RGD dimers (DOTA-3G_3-dimer and DOTA-3PEG$_4$-dimer) and schematic illustration of interactions between cyclic RGD dimers and integrin $\alpha_v\beta_3$. (A) The distance between two RGD motifs is long, and the cyclic RGD dimer is able to bind integrin $\alpha_v\beta_3$ in a bivalent fashion. (B) The distance between two RGD motifs is not long enough for simultaneous integrin $\alpha_v\beta_3$ binding, but the RGD concentration is locally enriched in the vicinity of neighboring integrin $\alpha_v\beta_3$ once the first RGD motif is bound. In both cases, the result would be higher integrin $\alpha_v\beta_3$ binding affinity for the multimeric cyclic RGD peptides.

binding studies. We determined the integrin $\alpha_v\beta_3$ binding affinity of DOTA-3PEG$_4$-dimer and DOTA-3G_3-dimer by competitive displacement of ^{125}I-echistatin bound to U87MG glioma cells. For comparison purposes, we also evaluated DOTA-dimer and DOTA-tetramer using the same in vitro competition assay. The IC_{50} values for DOTA-dimer, DOTA-3PEG$_4$-dimer, DOTA-3G_3-dimer, and DOTA-tetramer were obtained from curve fitting from Figure 2 and were calculated to be 102 ± 5, 62 ± 6, 74 ± 3, and 10 ± 2 nM, respectively.

Radiochemistry. ^{64}Cu(DOTA-3PEG$_4$-dimer) and ^{64}Cu(DOTA-3G_3-dimer) were prepared by reacting DOTA-3PEG$_4$-dimer and DOTA-3G_3-dimer, respectively, with $^{64}CuCl_2$ in the 0.1 M NaOAc buffer (pH 5.0). ^{64}Cu-labeling could be accomplished by heating the reaction mixture at 100 °C for 20−30 min. Both ^{64}Cu(DOTA-3PEG$_4$-dimer) and ^{64}Cu(DOTA-3G_3-dimer) were analyzed using same radio-HPLC method (Method 2). Their HPLC retention times were 19.5 and 14.2 min, respectively. The RCP was >95% with the specific activity of 300−400 mCi/μmol for both ^{64}Cu(DOTA-3G_3-dimer) and ^{64}Cu(DOTA-3PEG$_4$-dimer). Their partition coefficients (*P* values) were determined in an equal volume mixture of *n*-octanol and 25 mM phosphate buffer (pH 7.4). The log *P* values were calculated to be −4.23 ± 0.21 and −4.84 ± 0.15, respectively, for ^{64}Cu(DOTA-3PEG$_4$-dimer) and ^{64}Cu(DOTA-3G_3-dimer). ^{64}Cu(DOTA-3PEG$_4$-dimer) and ^{64}Cu(DOTA-3G_3-dimer) were stable for >6 h after HPLC purification and remained intact for >6 h without any decomposition in the presence of EDTA (1 mg/mL in 25 mM phosphate buffer, pH 7.4).

Biodistribution Characteristics. Athymic nude mice bearing U87MG glioma xenografts were used to evaluate the biodistribution characteristics and excretion kinetics of ^{64}Cu(DOTA-3PEG$_4$-dimer) and ^{64}Cu(DOTA-3G_3-dimer). Figure 3 illustrates the %ID/g organ uptake for ^{64}Cu(DOTA-3G_3-dimer) and ^{64}Cu-(DOTA-3PEG$_4$-dimer). In general, ^{64}Cu(DOTA-3G_3-dimer) had a rapid and very high tumor uptake at an early time point (8.50 ± 1.44%ID/g at 30 min p.i.). The tumor radioactivity washout of ^{64}Cu(DOTA-3G_3-dimer) was slow (7.55 ± 0.49%ID/g, 7.43 ± 2.41%ID/g and 6.79 ± 1.36%ID/g at 60, 120, and 240 min

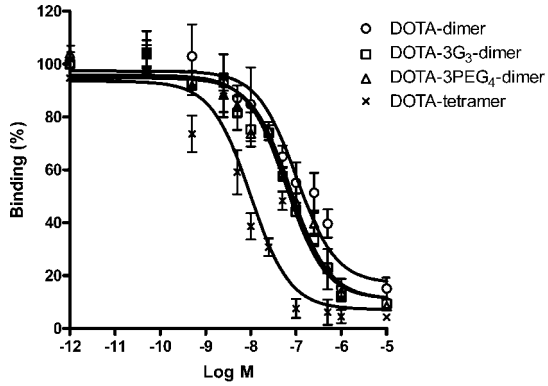

Figure 2. In vitro inhibition of ^{125}I-echistatin bound to integrin $\alpha_v\beta_3$ on U87MG glioma cells by DOTA-dimer, DOTA-3G$_3$-dimer, DOTA-3PEG$_4$-dimer, and DOTA-tetramer. Their IC$_{50}$ values were calculated to be 102 ± 5, 62 ± 6, 74 ± 3, and 10 ± 2 nM, respectively.

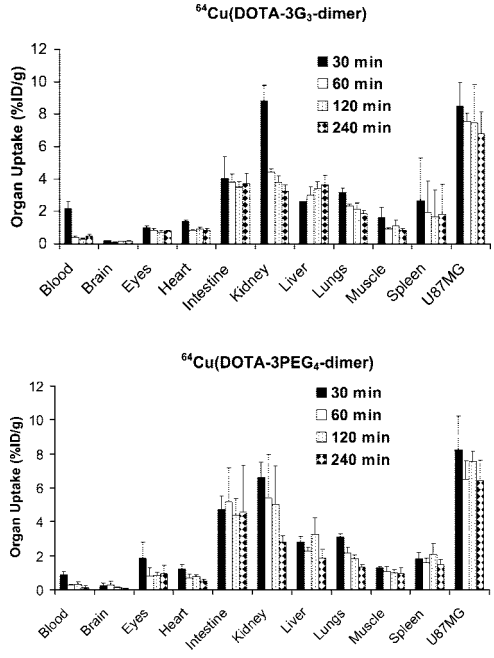

Figure 3. Biodistribution data for ^{64}Cu(DOTA-3G$_3$-dimer) and ^{64}Cu-(DOTA-3PEG$_4$-dimer) in athymic nude mice (n = 4) bearing U87MG glioma xenografts.

p.i., respectively). Its blood clearance was very fast (2.17 ± 0.45%ID/g at 30 min p.i. and 0.46 ± 0.15%ID/g at 240 min p.i.) with the tumor/blood ratios increasing from 4.01 ± 1.13 at 30 min p.i. to 24.31 ± 2.20%ID/g at 240 min p.i. The muscle uptake of ^{64}Cu(DOTA-3G$_3$-dimer) decreased steadily from 1.61 ± 0.66%ID/g at 30 min p.i. to 0.86 ± 0.08%ID/g at 240 min p.i., while the tumor/muscle ratios increased from 5.84 ± 2.49 at 30 min p.i. to 7.84 ± 1.15 at 240 min p.i. ^{64}Cu(DOTA-3G$_3$-dimer) also had a moderately high kidney uptake (8.83 ± 0.96%ID/g) at 30 min p.i.; but its kidney clearance was very fast (3.23 ± 0.40% ID/g at 240 min p.i.). The liver uptake of ^{64}Cu(DOTA-3G$_3$-dimer) was relatively low (2.60 ± 0.01%ID/g) at 30 min p.i. To our surprise, its liver uptake increased over the 4 h study period (3.01 ± 0.51%ID/g at 60 min and 3.62 ± 0.62%ID/g at 240 min p.i.). As a result, its tumor/liver ratio slowly decreased from 3.27 ± 0.56 at 30 min to 1.93 ± 0.56 at 120 min p.i.

^{64}Cu(DOTA-3PEG$_4$-dimer) also had very high tumor uptake (8.23 ± 1.97%ID/g, 6.49 ± 1.10%ID/g, 7.55 ± 0.62%ID/g, and 6.43 ± 1.22%ID/g at 30, 60, 120, and 240 min p.i., respectively) with fast blood clearance (0.87 ± 0.22%ID/g at 30 min p.i.

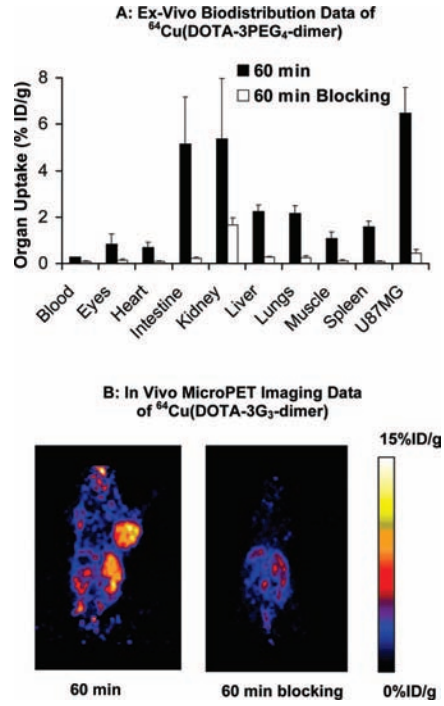

Figure 4. Biodistribution for ^{64}Cu(DOTA-3PEG$_4$-dimer) (n = 4) and in vivo microPET imaging data for ^{64}Cu(DOTA-3G$_3$-dimer) (n = 3) in athymic nude mice bearing U87MG glioma xenografts in the absence/presence of excess E[c(RGDfK)]$_2$ at 60 min p.i.

and 0.15 ± 0.07%ID/g at 240 min p.i.). As a result, its tumor/blood ratios increased steadily from 9.8 ± 3.3 at 30 min p.i. to 46.3 ± 15.1 at 120 min p.i.. ^{64}Cu(DOTA-3PEG$_4$-dimer) had a relatively low initial kidney uptake (6.59 ± 0.93%ID/g) at 30 min p.i. Its kidney uptake was 2.81 ± 0.36% ID/g at 240 min p.i., and the tumor/kidney ratio was 2.28 ± 0.31. The liver uptake of ^{64}Cu(DOTA-3G$_3$-dimer) was also low (2.80 ± 0.35%ID/g at 30 min p.i. and 1.87 ± 0.51%ID/g at 240 min p.i.); but its tumor/liver ratio remained relatively unchanged over the 4 h study period (2.98 ± 0.86 at 30 min to 3.52 ± 0.61 at 240 min p.i.). The muscle uptake of ^{64}Cu(DOTA-3PEG$_4$-dimer) (1.28 ± 0.11 and 0.95 ± 0.34%ID/g at 30 and 240 min p.i., respectively) was comparable to that of ^{64}Cu(DOTA-3G$_3$-dimer) (1.61 ± 0.66 and 0.86 ± 0.08%ID/g at 30 and 240 min p.i., respectively). The tumor/muscle ratio of ^{64}Cu(DOTA-3PEG$_4$-dimer) increased steadily from 6.48 ± 1.54 at 30 min p.i. to 7.24 ± 2.08 at 240 min p.i.

Blocking Experiment. The integrin $\alpha_v\beta_3$ specificity was demonstrated by coinjection of excess E[c(RGDfK)]$_2$ as the blocking agent (~14 mg/kg or ~350 μg per mouse) with ^{64}Cu(DOTA-3G$_3$-dimer). Such a high dose was used to ensure that the integrin $\alpha_v\beta_3$ is almost completely blocked. Figure 4A shows organ uptake of ^{64}Cu(DOTA-3G$_3$-dimer) at 60 min p.i. in the absence/presence of E[c(RGDfK)]$_2$. Coinjection of excess E[c(RGDfK)]$_2$ resulted in almost complete blockage of tumor uptake for ^{64}Cu(DOTA-3G$_3$-dimer) (0.43 ± 0.07%ID/g with E[c(RGDfK)]$_2$ vs 7.43 ± 2.41%ID/g without E[c(RGDfK)]$_2$). There was also a significant reduction in organ uptake of ^{64}Cu(DOTA-3G$_3$-dimer) in the eyes, heart, intestine, kidneys, lungs, liver, and spleen (Figure 4A).

MicroPET Imaging. Figure 4B illustrates the representative microPET images of the glioma-bearing mice at 1 h after administration of ~100 μCi of ^{64}Cu(DOTA-3G$_3$-dimer) in the absence or presence of excess E[c(RGDfK)]$_2$. We found that the tumor was clearly visualized with excellent contrast, suggesting that ^{64}Cu(DOTA-3G$_3$-dimer) is useful for imaging integrin $\alpha_v\beta_3$-positive tumors. In the presence of excess E[c(RGD-

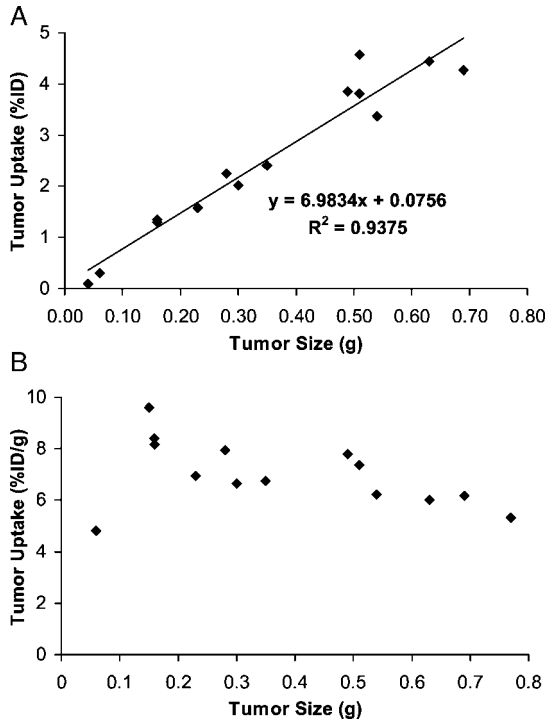

Figure 5. Relationship between tumor size and tumor uptake for ^{64}Cu(DOTA-3PEG$_4$-dimer) at 120 min p.i. in athymic nude mice (n = 7 with 14 tumors) bearing the U87MG glioma xenografts.

fK)]$_2$, the tumor uptake of ^{64}Cu(DOTA-3G$_3$-dimer) was almost completely blocked. The uptake of ^{64}Cu(DOTA-3G$_3$-dimer) was also blocked in many normal organs, in accordance with the biodistribution results shown in Figure 4A.

Tumor Size versus Tumor Uptake. During the biodistribution studies, we noticed that smaller tumors (<0.5 g) often have higher radiotracer uptake than large tumors. To further clarify the relationship between tumor uptake and tumor size, we added five extra glioma-bearing mice into the 120 min group for ^{64}Cu(DOTA-3PEG$_4$-dimer). The 120-min time point was chosen to avoid potential interference from the blood radioactivity and nonspecific radioactivity accumulation in the tumors. As illustrated in Figure 5A, there was a linear relationship between the %ID tumor uptake of ^{64}Cu(DOTA-3PEG$_4$-dimer) and tumor size (0.03−0.8 g; n = 7; tumor number = 14) with R^2 = 0.9375. The radiotracer %ID tumor uptake increases when tumor size increases. If the tumor uptake is expressed as %/ID/g (Figure 5B), ^{64}Cu(DOTA-3PEG$_4$-dimer) had a %ID/g tumor uptake of 6.5−10.0%ID/g with the tumor size in the range of 0.09 g−0.25 g. When the tumor size is >0.30 g, the tumor uptake of ^{64}Cu(DOTA-3PEG$_4$-dimer) was in the range of 6.0−7.0%ID/g. When the tumor size was <0.05 g, its tumor uptake was <5.0%ID/g.

Metabolic Properties. Figure 6 shows HPLC chromatograms of ^{64}Cu(DOTA-3PEG$_4$-dimer) (left) and ^{64}Cu(DOTA-3G$_3$-dimer) (right) in saline before injection, in urine at 30 min p.i. and 120 min p.i., and in feces at 120 min p.i. There were no metabolites detected in either urine and or feces samples from the mouse administered with ^{64}Cu(DOTA-3PEG$_4$-dimer). No metabolites were detected in the urine samples of the mouse administered with ^{64}Cu(DOTA-3G$_3$-dimer); but there was no intact ^{64}Cu(DOTA-3G$_3$-dimer) in the feces sample.

DISCUSSION

Previously, we reported the evaluation of ^{64}Cu-DOTA-dimer and ^{64}Cu-DOTA-tetramer as PET radiotracers for imaging integrin $\alpha_v\beta_3$ expression in athymic nude mice bearing MDA-MB-435 breast cancer and U87MG glioma xenografts (*50, 52*). The biodistribution studies clearly demonstrate that ^{64}Cu(DOTA-dimer) and ^{64}Cu(DOTA-tetramer) have better tumor uptake with longer tumor retention time than their monomeric counterparts. In this study, we prepared two new RGD dimer DOTA conjugates (DOTA-3PEG$_4$-dimer and DOTA-3G$_3$-dimer) and their ^{64}Cu complexes, ^{64}Cu(DOTA-3PEG$_4$-dimer) and ^{64}Cu-(DOTA-3G$_3$-dimer). The in vitro competition assay shows that the integrin $\alpha_v\beta_3$ binding affinities of cyclic RGD peptide conjugates follow the order of DOTA-tetramer > DOTA-3G$_3$-dimer ~ DOTA-3PEG$_4$-dimer > DOTA-dimer. DOTA-3G$_3$-dimer (IC$_{50}$ = 62 ± 6 nM) and DOTA-3PEG$_4$-dimer (IC$_{50}$ = 74 ± 3 nM) share very similar integrin $\alpha_v\beta_3$ binding affinity with HYNIC-3G$_3$-dimer (IC$_{50}$ = 61 ± 2 nM) and HYNIC-3PEG$_4$-dimer (IC$_{50}$ = 51 ± 7 nM) (*72, 73*). Apparently, replacing HYNIC with DOTA does not have a significant impact on their integrin $\alpha_v\beta_3$ binding affinity and the radiotracer tumor uptake. This may explain why ^{64}Cu(DOTA-3PEG$_4$-dimer) and ^{64}Cu(DOTA-3G$_3$-dimer) have a tumor uptake very similar to that of ^{99m}Tc-3PEG$_4$-dimer and ^{99m}Tc-3G$_3$-dimer (*72, 73*).

There are two factors contributing to their high integrin $\alpha_v\beta_3$ binding affinity (Figure 1). The key for bivalency is that the distance between two RGD motifs in multimeric cyclic RGD peptides must be long enough to achieve simultaneous integrin $\alpha_v\beta_3$ binding. The distance between two cyclic RGD motifs is 6 bonds in E[c(RGDfK)]$_2$, 26 bonds in 3G$_3$-dimer, and 38 bonds in 3PEG$_4$-dimer (excluding the side arms of K-residues). The higher integrin $\alpha_v\beta_3$ binding affinity of DOTA-3G$_3$-dimer (IC$_{50}$ = 62 ± 6 nM) and DOTA-3PEG$_3$-dimer (IC$_{50}$ = 74 ± 3 nM) than that of DOTA-dimer (IC$_{50}$ = 102 ± 5 nM) strongly suggests that 2G$_3$-dimer and 3PEG$_3$-dimer are bivalent in binding to integrin $\alpha_v\beta_3$ (Figure 1A) and that the distance between the two cyclic RGD motifs in E[c(RGDfK)]$_2$ is probably too short for simultaneous integrin $\alpha_v\beta_3$ binding. This conclusion is well supported by the significantly higher tumor uptake of ^{64}Cu(DOTA-3PEG$_4$-dimer) (8.50 ± 1.44%ID/g and 6.79 ± 1.36%ID/g at 30 and 240 min p.i., respectively) and ^{64}Cu(DOTA-3G$_3$-dimer) (8.23 ± 1.97%ID/g and 6.43 ± 1.22%ID/g at 30 and 240 min p.i., respectively) as compared to that of ^{64}Cu(DOTA-dimer) (3.23 ± 0.57%ID/g at 30 min and 3.83 ± 0.22%ID/g at 240 min p.i.) in the same tumor-bearing animal model (*50*). If DOTA-dimer were able to bind to integrin $\alpha_v\beta_3$ in a bivalent fashion as DOTA-2G$_3$-dimer and DOTA-3PEG$_3$-dimer, they would have shared a similar integrin $\alpha_v\beta_3$ binding affinity, and ^{64}Cu(DOTA-dimer) would have had a tumor uptake similar to that of ^{64}Cu(DOTA-3PEG$_4$-dimer) and ^{64}Cu(DOTA-3G$_3$-dimer). Even though DOTA-dimer is not bivalent, the binding of one cyclic RGD motif in E[c(RGDfK)]$_2$ may significantly increase local RGD concentration in the vicinity of neighboring integrin $\alpha_v\beta_3$ sites (Figure 1B). This may explain why ^{64}Cu(DOTA-dimer) has better tumor uptake than its monomeric counterpart (*50*).

The longest distance between the two adjacent cyclic RGD motifs in E[E[c(RGDfK)]$_2$]$_2$ is 16 bonds (excluding the side arms of K-residues). The integrin $\alpha_v\beta_3$ binding affinity of DOTA-tetramer (IC$_{50}$ = 10 ± 2 nM) is higher than that of DOTA-3G$_3$-dimer (IC$_{50}$ = 62 ± 6 nM) and DOTA-3PEG$_3$-dimer (IC$_{50}$ = 74 ± 3 nM), suggesting that DOTA-tetramer is also bivalent in binding to integrin $\alpha_v\beta_3$. The higher integrin $\alpha_v\beta_3$ binding affinity of DOTA-tetramer as compared to that of DOTA-3G$_3$-dimer and DOTA-3PEG$_3$-dimer is probably caused by the presence of two extra RGD motifs. This conclusion seems to be consistent with the fact that ^{64}Cu(DOTA-tetramer) has higher initial tumor uptake (9.93 ± 1.05%ID/g at 30 min p.i.) as compared to that of ^{64}Cu(DOTA-3PEG$_4$-dimer) (8.50 ±

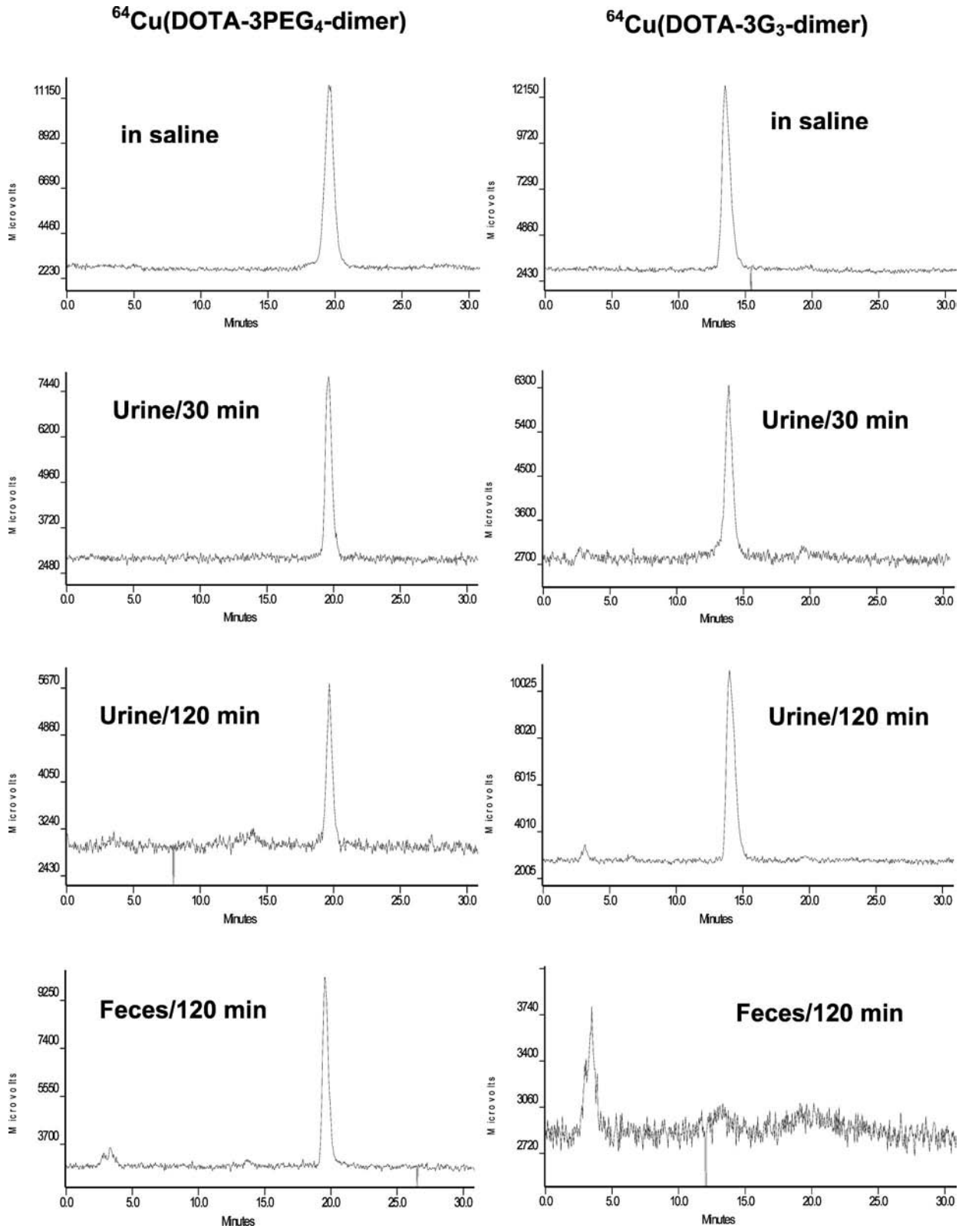

Figure 6. Typical radio-HPLC chromatograms (Method 2) for ^{64}Cu(DOTA-3PEG$_4$-dimer) (left) and ^{64}Cu(DOTA-3G$_3$-dimer) (right) in saline before injection, in urine at 30 and 120 min p.i., and in feces at 120 min p.i.

1.44%ID/g at 30 min p.i.) and ^{64}Cu(DOTA-3G$_3$-dimer) (8.23 ± 1.97%ID/g at 30 min p.i.) in the same tumor-bearing animal model.

However, ^{64}Cu(DOTA-3PEG$_4$-dimer) and ^{64}Cu(DOTA-3G$_3$-dimer) have significant advantages over ^{64}Cu(DOTA-tetramer) with respect to their uptake in noncancerous organs. For example, the liver uptake of ^{64}Cu(DOTA-3PEG$_4$-dimer) (2.25 ± 0.26%ID/g at 60 min p.i. and 1.87 ± 0.51%ID/g at 240 min p.i.) was significantly lower ($p < 0.01$) than that of ^{64}Cu(DOTA-tetramer) (4.38 ± 0.39%ID/g at 60 min p.i. and 3.57 ± 0.45%ID/g at 240 min p.i.) (*52*). As a result, the tumor/liver ratios of ^{64}Cu(DOTA-3PEG$_4$-dimer) (2.93 ± 0.66 at 60 min and 3.52 ± 0.61 at 240 min p.i.) were significantly better ($p < 0.01$) than that of ^{64}Cu(DOTA-tetramer) (1.98 ±

0.15 at 60 min p.i. and 2.35 ± 0.33 at 240 min p.i.). ^{64}Cu(DOTA-3PEG$_4$-dimer) has significantly ($p < 0.01$) lower kidney uptake (6.59 ± 0.93%ID/g at 30 min p.i. and 2.81 ± 0.36%ID/g at 240 min p.i.) than ^{64}Cu(DOTA-tetramer) (9.02 ± 0.56%ID/g at 30 min p.i. and 4.17 ± 0.35%ID/g at 240 min p.i.). The higher kidney uptake of ^{64}Cu(DOTA-tetramer) is probably caused by the presence of four R-residues, which are positively charged under physiological conditions, in E{E[c(RGDfK)]$_2$}$_2$ as compared to only two R-residues in both ^{64}Cu(DOTA-3PEG$_4$-dimer) and ^{64}Cu(DOTA-3G$_3$-dimer). On the basis of both tumor uptake and T/B ratios of ^{64}Cu radiotracers, we believe that 3PEG$_4$-dimer and 3G$_3$-dimer are better targeting biomolecules than E{E[c(RGDfK)]$_2$}$_2$. In addition, the synthesis of E{E[c(RGDfK)]$_2$}$_2$ is much more challenging than that of either 3PEG$_4$-dimer or 3G$_3$-dimer. The cost for successful isolation of pure multimeric cyclic RGDfK peptides increases dramatically as peptide multiplicity increases. Therefore, 3PEG$_4$-dimer and 3G$_3$-dimer are better suited for future development of the integrin $\alpha_v\beta_3$-targeted radiotracers for imaging purposes.

Since the tumor uptake of ^{64}Cu(DOTA-3PEG$_4$-dimer) is almost completely blocked by coinjection of E[c(RGDfK)]$_2$, we believe that its tumor localization is indeed integrin $\alpha_v\beta_3$-mediated. Similar results were obtained for ^{64}Cu(DOTA-dimer) in athymic nude mice bearing MDA-MB-435 human breast cancer xenografts (*50*) and ^{64}Cu(DOTA-tetramer) in athymic nude mice bearing U87MG human glioma xenografts (*52*). The uptake blockage in the eyes, heart, intestine, lungs, liver, and spleen suggests that major parts of the uptake of ^{64}Cu(DOTA-3PEG$_4$-dimer) in these organs is also integrin $\alpha_v\beta_3$-mediated. This conclusion is supported by the immunohistopathological studies (*53, 54*), which showed a strong positive staining of endothelial cells of the small glomeruli vessels in the kidneys and weak staining in the branches of the hepatic portal vein.

The ability to noninvasively quantify integrin $\alpha_v\beta_3$ level in vivo will provide new opportunities to more appropriately select patients for antiangiogenic treatment and more effectively monitor the therapeutic efficacy in integrin $\alpha_v\beta_3$-positive cancer patients (*34*). The %ID tumor uptake reflects the total integrin $\alpha_v\beta_3$ expression level, while the %ID/g tumor uptake reflects the integrin $\alpha_v\beta_3$ density. When the tumor is very small (<0.01 g or 100 m^3), there is little angiogenesis with very low blood flow. As a result, ^{64}Cu(DOTA-3PEG$_4$-dimer) has low %ID and %ID/g tumor uptake (Figure 5A and B). When tumors are in the range of 0.1−0.35 g (100−350 m^3), the microvessel and integrin $\alpha_v\beta_3$ density is high. The radiotracer %ID/g tumor uptake is high (Figure 5B) even though the %ID tumor uptake is relatively low (Figure 5A). As tumors grow, the total integrin $\alpha_v\beta_3$ level on tumor cells becomes larger, the microvessel density decreases due to maturity of blood vessels, and the integrin $\alpha_v\beta_3$ density also decreases due to larger interstitial space/pressure and higher collagen concentrations (*78*). Parts of the tumor may become necrotic, which also leads to lower integrin $\alpha_v\beta_3$ density in larger tumors. As a result, the %ID/g tumor uptake of ^{64}Cu(DOTA-3PEG$_4$-dimer) in larger tumors is lower than that of smaller ones (Figure 5B) even though its total %ID tumor uptake is higher (Figure 5A). The linear relationship between tumor size and %ID tumor uptake suggests that ^{64}Cu(DOTA-3PEG$_4$-dimer) might be useful for noninvasive monitoring of integrin $\alpha_v\beta_3$ expression in cancer patients. This assumption is supported by recent results obtained for the radiolabeled (^{18}F and ^{64}Cu) multimeric cyclic RGDyK peptides, which clearly showed that the %ID/g radiotracer tumor uptake was well correlated with the integrin $\alpha_v\beta_3$ density on the xenografted tumors of different origin (*52, 53*).

Metabolic degradation has been observed for ^{64}Cu(DOTA-dimer) and ^{64}Cu(DOTA-tetramer) in kidneys and urine samples (*50, 52*). In contrast, ^{64}Cu(DOTA-3PEG$_4$-dimer) has high metabolic stability during its excretion from the renal and hepatobiliary routes (Figure 6). Similar metabolic stability is also observed for ^{64}Cu(DOTA-3G$_3$-dimer) during its renal excretion; but it is completely metabolized during excretion from the hepatobiliary route. The PEG$_4$ and G$_3$ linkers have significant impact on the metabolic stability of ^{64}Cu-labeled RGD dimers probably due to the in vivo stability PEG$_4$ and G$_3$ linkers. It is important to note that the radioactivity detected in urine and feces samples represents only the portion of ^{64}Cu radiotracers excreted from renal and hepatobiliary routes. The remaining radioactivity is still trapped in normal tissues. Since the normal organ uptake of ^{64}Cu(DOTA-3PEG$_4$-dimer) can be blocked by the presence of excess E[c(RGDfK)]$_2$, it is reasonable to believe that the radioactivity accumulation inside normal organs is partially integrin $\alpha_v\beta_3$-mediated.

CONCLUSIONS

In this study, we prepared two novel cyclic RGD dimer conjugates: DOTA-3PEG$_4$-dimer and DOTA-3G$_3$-dimer. The integrin $\alpha_v\beta_3$ binding affinities follow the order of DOTA-tetramer > DOTA-3G$_3$-dimer ~ DOTA-3PEG$_4$-dimer > DOTA-dimer. Both DOTA-3G$_3$-dimer and DOTA-3PEG$_4$-dimer are bivalent in binding to integrin $\alpha_v\beta_3$, as evidenced by their higher integrin $\alpha_v\beta_3$ binding affinity as compared to that of DOTA-dimer and the higher tumor uptake of ^{64}Cu(DOTA-3PEG$_4$-dimer) and ^{64}Cu(DOTA-3G$_3$-dimer) than that of ^{64}Cu(DOTA-dimer). The PEG$_4$ and G$_3$ linkers are also useful for improving the radiotracer clearance from normal organs, such as kidneys, the liver, and lungs. The ex-vivo biodistribution studies show that there is a linear relationship between the %ID tumor uptake and tumor size, suggesting that ^{64}Cu(DOTA-3PEG$_4$-dimer) and ^{64}Cu(DOTA-3G$_3$-dimer) might be useful for noninvasive monitoring of tumor growth or shrinkage during antiangiogenic therapy. MicroPET imaging data clearly demonstrate the utility of ^{64}Cu(DOTA-3G$_3$-dimer) as a new PET radiotracer for imaging integrin $\alpha_v\beta_3$-positive tumors.

ACKNOWLEDGMENT

We thank Dr. Sulma I. Mohammed, the Director of Purdue Cancer Center Drug Discovery Shared Resource, for her assistance with tumor-bearing animal models. This work is supported, in part, by research grants R01 CA115883 A2 (to S.L.) from the National Cancer Institute (NCI), R21 HL083961-01 from National Heart, Lung, and Blood Institute (NHLBI), and DE-FG02-08ER64684 from the Department of Energy. The research performed at Stanford University is supported, in part, by NCI R01 CA119053, R21 CA121842, P50 CA114747, U54 CA119367, and R24 CA93862.

LITERATURE CITED

(1) Folkman, J. (1995) Angiogenesis in cancer, vascular, rheumatoid and other disease. *Nat. Med. 1*, 27–31.
(2) Folkman, J. (2002) Role of angiogenesis in tumor growth and metastasis. *Semin. Oncol. 29*, 15–18.
(3) Mousa, S. A. (1998) Mechanisms of angiogenesis in vascular disorders: potential therapeutic targets. *Drugs Future 23*, 51–60.
(4) Mousa, S. A. (2000) Integrins as novel drug discovery targets: potential therapeutic and diagnostic implications. *Emerging Ther. Targets 4*, 143–153.
(5) Carmeliet, P. (2000) Mechanism of angiogenesis and atheriogenesis. *Nat. Med. 6*, 389–395.
(6) Devita, V., Hellman, S., Bögler, O., and Mikkelsen, T. (2003) Angiogenesis in Glioma: molecular mechanisms and roadblocks to translation. *Cancer J. 9*, 205–213.

(7) Hwang, R., and Varner, J. V. (2004) The role of integrins in tumor angiogenesis. *Hematol. Oncol. Clin. North Am. 18*, 991–1006.

(8) Jin, H., and Varner, J. (2004) Integrins: roles in cancer development and as treatment targets. *Br. J. Cancer 90*, 561–565.

(9) Kumar, C. C. (2003) Integrin $\alpha_v\beta_3$ as a therapeutic target for blocking tumor-induced angiogenesis. *Curr. Drug Targets 4*, 123–131.

(10) Brooks, P. C., Clark, R. A. F., and Cheresh, D. A. (1994) Requirement of vascular integrin $\alpha_v\beta_3$ for angiogenesis. *Science 264*, 569–571.

(11) Friedlander, M., Brooks, P. C., Shatter, R. W., Kincaid, C. M., Varner, J. A., and Cheresh, D. A. (1995) Definition of two angiogenic pathways by distinct α_v integrin. *Science 270*, 1500–1502.

(12) Horton, M. A. (1997) The $\alpha_v\beta_3$ integrin "vitronectin receptor". *Int. J. Biochem. Cell Biol. 29*, 721–725.

(13) Bello, L., Francolini, M., Marthyn, P., Zhang, J. P., Carroll, R. S., Nikas, D. C., Strasser, J. F., Villani, R., Cheresh, D. A., and Black, P. M. (2001) Alpha(v)beta3 and alpha(v)beta5 integrin expression in glioma periphery. *Neurosurgery 49*, 380–389.

(14) Meitar, D., Crawford, S. E., Rademaker, A. W., and Cohn, S. L. (1996) Tumor angiogenesis correlates with metastatic disease, N-myc-amplification, and poor outcome in human neuroblastoma. *J. Clinical. Oncol. 14*, 405–414.

(15) Gasparini, G., Brooks, P. C., Biganzoli, E., Vermeulen, P. B., Bonoldi, E., Dirix, L. Y., Ranieri, G., Miceli, R., and Cheresh, D. A. (1998) Vascular integrin $\alpha_v\beta_3$: a new prognostic indicator in breast cancer. *Clin. Cancer Res. 4*, 2625–2634.

(16) Albelda, S. M., Mette, S. A., Elder, D. E., Stewart, R. M., Damjanovich, L., Herlyn, M., and Buck, C. A. (1990) Integrin distribution in maliganant melanoma: association of the beta3 subunit with tumor progression. *Cancer Res. 50*, 6757–6764.

(17) Falcioni, R., Cimino, L., Gentileschi, M. P., D'Agnano, I., Zupi, G., Kennel, S. J., and Sacchi, A. (1994) Expression of beta 1, beta 3, beta 4, and beta 5 integrins by human lung carcinoma cells of different histotypes. *Exp. Cell Res. 210*, 113–122.

(18) Sengupta, S., Chattopadhyay, N., Mitra, A., Ray, S., Dasgupta, S., and Chatterjee, A. (2001) Role of $\alpha_v\beta_3$ integrin receptors in breast tumor. *J. Exp. Clin. Cancer Res. 20*, 585–590.

(19) Felding-Habermann, B., Mueller, B. M., Romerdahl, C. A., and Cheresh, D. A. (1992) Involvement of integrin alpha V gene expression in human melanoma tumorigenicity. *J. Clin. Invest. 89*, 2018–2022.

(20) Zitzmann, S., Ehemann, V., and Schwab, M. (2002) Arginine-Glycine-Aspartic acid (RGD)-peptide binds to both tumor and tumor endothelial cells in vivo. *Cancer Res. 62*, 5139–5143.

(21) Weber, W. A., Haubner, R., Vabuliene, E., Kuhnast, B., Webster, H. J., and Schwaiger, M. (2001) Tumor angiogenesis targeting using imaging agents. *Q. J. Nucl. Med. 45*, 179–182.

(22) Costouros, N. G., Diehn, F. E., and Libutti, S. K. (2002) Molecular imaging of tumor angiogenesis. *J. Cell. Biochem. Suppl. 39*, 72–78.

(23) Liu, S., and Edwards, D. S. (2002) Fundamentals of receptor-based diagnostic metalloradiopharmaceuticals. *Top. Curr. Chem. 222*, 259–278.

(24) Van de Wiele, C., Oltenfreiter, R., De Winter, O., Signore, A., Slegers, G., and Dieckx, R. A. (2002) Tumor angiogenesis pathways: related clinical issues and implications for nuclear medicine imaging. *Eur. J. Nucl. Med. 29*, 699–709.

(25) Liu, S., Robinson, S. P., and Edwards, D. S. (2003) Integrin $\alpha_v\beta_3$ directed radiopharmaceuticals for tumor imaging. *Drugs Future 28*, 551–564.

(26) McDonald, D. M., and Choyke, P. (2003) Imaging of Angiogenesis: from microscope to clinic. *Nature Med. 9*, 713–725.

(27) Haubner, R., and Wester, H. R. (2004) Radiolabeled tracers for imaging of tumor angiogenesis and evaluation of anti-angiogenic therapies. *Curr. Pharm. Des. 10*, 1439–1455.

(28) Liu, S., Robinson, S. P., and Edwards, D. S. (2005) Radiolabeled integrin $\alpha_v\beta_3$ antagonists as radiopharmaceuticals for tumor radiotherapy. *Top. Curr. Chem. 252*, 193–216.

(29) Chen, X. (2006) Multimodality imaging of tumor integrin $\alpha_v\beta_3$ expression. *Mini-Rev. Med. Chem. 6*, 227–234.

(30) D'Andrea, L. D., Del Gatto, A., Pedone, C., and Benedetti, E. (2006) Peptide-based molecules in angiogenesis. *Chem. Biol. Drug Des. 67*, 115–126.

(31) Meyer, A., Auremheimer, J., Modlinger, A., and Kessler, H. (2006) Targeting RGD recognizing integrins: drug development, biomaterial research, tumor imaging and targeting. *Curr. Pharm. Design 12*, 2723–2747.

(32) Liu, S. (2006) Radiolabeled multimeric cyclic RGD peptides as integrin $\alpha_v\beta_3$-targeted radiotracers for tumor imaging. *Mol. Pharm. 3*, 472–487.

(33) Cai, W., and Chen, X. (2008) Multimodality Molecular imaging of tumor angiogenesis. *J. Nucl. Med. 49*, 113S–128S.

(34) Cai, W., Rao, J., Gambhir, S. S., and Chen, X. (2006) How molecular imaging is speeding up antiangiogenic drug development. *Mol. Cancer Ther. 5*, 2624–2633.

(35) Haubner, R., Wester, H. J., Senekowitsch-Schmidtke, R., Diefenbach, B., Kessler, H., Stöcklin, G., and Schwaiger, M. (1997) RGD-peptides for tumor targeting: biological evaluation of radioiodinated analogs and introduction of a novel glycosylated peptide with improved biokinetics. *J. Labelled Compd. Radiopharm. 40*, 383–385.

(36) Haubner, R., Bruchertseifer, F., Bock, M., Schwaiger, M., and Wester, H. J. (2004) Synthesis and biological evaluation of ^{99m}Tc-labeled cyclic RGD peptide for imaging integrin $\alpha_v\beta_3$ expression. *Nuklearmedizin 43*, 26–32.

(37) Haubner, R., Wester, H. J., Reuning, U., Senekowitsch-Schmidtke, R., Diefenbach, B., Kessler, H., Stöcklin, G., and Schwaiger, M. (1999) Radiolabeled $\alpha_v\beta_3$ integrin antagonists: a new class of tracers for tumor imaging. *J. Nucl. Med. 40*, 1061–1071.

(38) Sivolapenko, G. B., Skarlos, D., Pectasides, D., Stathopoulou, E., Milonakis, A., Sirmalis, G., Stuttle, A., Courtenay-Luck, N. S., Konstantinides, K., and Epenetos, A. A. (1998) Imaging of metastatic melanoma utilizing a technetium-99m labeled RGD-containing synthetic peptide. *Eur. J. Nucl. Med. 25*, 1383–1389.

(39) Haubner, R., Wester, H. J., Burkhart, F., Senekowitsch-Schmidtke, R., Weber, W., Goodman, S. L., Kessler, H., and Schwaiger, M. (2001) Glycosylated RGD-containing peptides: tracer for tumor targeting and angiogenesis imaging with improved biokinetics. *J. Nucl. Med. 42*, 326–336.

(40) Haubner, R., Wester, H. J., Weber, W. A., Mang, C., Ziegler, S. I., Goodman, S. L., Senekowitsch-Schmidtke, R., Kessler, H., and Schwaiger, M. (2001) Noninvasive imaging of $\alpha_v\beta_3$ integrin expression using ^{18}F-labeled RGD-containing glycopeptide and positron emission tomography. *Cancer Res. 61*, 1781–1785.

(41) Thumshirn, G., Hersel, U., Goodman, S. L., and Kessler, H. (2003) Multimeric cyclic RGD peptides as potential tools for tumor targeting: solid-phase peptide synthesis and chemoselective oxime ligation. *Chem.—Eur. J. 9*, 2717–2725.

(42) Poethko, T., Schottelius, M., Thumshirn, G., Herz, M., Haubner, R., Henriksen, G., Kessler, H., Schwaiger, M., and Wester, H. J. (2004) Chemoselective pre-conjugate radiohalogenation of unprotected mono- and multimeric peptides via oxime formation. *Radiochim. Acta 92*, 317–327.

(43) Poethko, T., Schottelius, M., Thumshirn, G., Hersel, U., Herz, M., Henriksen, G., Kessler, H., Schwaiger, M., and Wester, H. J. (2004) Two-step methodology for high yield routine radiohalogenation of peptides: ^{18}F-labeled RGD and octreotide analogs. *J. Nucl. Med. 45*, 892–902.

(44) Alves, S., Correia, J. D. G., Gano, L., Rold, T. L., Prasanphanich, A., Haubner, R., Rupprich, M., Alberto, R., Decristoforo, C., Snatos, I., and Smith, C. J. (2007) In vitro and in vivo evaluation of a novel ^{99m}Tc(CO)$_3$-pyrazolyl conjugate of *cyclo*-(Arg-Gly-Asp-D-Tyr-Lys). *Bioconjugate Chem. 18*, 530–537.

(45) Su, Z. F., Liu, G., Gupta, S., Zhu, Z., Rusckowski, M., and Hnatowich, D. J. (2002) In vitro and in vivo evaluation of a technetium-99m-labeled cyclic RGD peptide as specific marker of $\alpha_v\beta_3$ integrin for tumor imaging. *Bioconjugate Chem. 13*, 561–570.

(46) Decristoforo, C., Faintuch-Linkowski, B., Rey, A., vo Guggenberg, E., Rupprich, M., Hernandez-Gonzales, I., Rodrigo, T., and Haubner, R. (2006) [^{99m}Tc]HYNIC-RGD for imaging integrin $\alpha_v\beta_3$ expression. *Nucl. Med. Biol. 33*, 945–952.

(47) Chen, X., Park, R., Tohme, M., Shahinian, A. H., Bading, J. R., and Conti, P. S. (2004) MicroPET and autoradiographic imaging of breast cancer α_v-integrin expression using ^{18}F- and ^{64}Cu-labeled RGD peptide. *Bioconjugate Chem. 15*, 41–49.

(48) Chen, X., Park, R., Shahinian, A. H., Tohme, M., Khankaldyyan, V., Bozorgzadeh, M. H., Bading, J. R., Moats, R., Laug, W. E., and Conti, P. S. (2004) ^{18}F-labeled RGD peptide: initial evaluation for imaging brain tumor angiogenesis. *Nucl. Med. Biol. 31*, 179–189.

(49) Chen, X., Park, R., Shahinian, A. H., Bading, J. R., and Conti, P. S. (2004) Pharmacokinetics and tumor retention of ^{125}I-labeled RGD peptide are improved by PEGylation. *Nucl. Med. Biol. 31*, 11–19.

(50) Chen, X., Liu, S., Hou, Y., Tohme, M., Park, R., Bading, J. R., and Conti, P. S. (2004) MicroPET imaging of breast cancer α_v-integrin expression with ^{64}Cu-labeled dimeric RGD peptides. *Mol. Imaging Biol. 6*, 350–359.

(51) Chen, X., Tohme, M., Park, R., Hou, Y., Bading, J. R., and Conti, P. S. (2004) MicroPET imaging of breast cancer $\alpha_v\beta_3$-integrin expression with ^{18}F-labeled dimeric RGD peptide. *Mol. Imaging 3*, 96–104.

(52) Wu, Y., Zhang, X., Xiong, Z., Cheng, Z., Fisher, D. R., Liu, S., Gambhir, S. S., and Chen, X. (2005) MicroPET imaging of glioma integrin $\alpha_v\beta_3$ expression using ^{64}Cu-labeled tetrameric RGD peptide. *J. Nucl. Med. 46*, 1707–1718.

(53) Zhang, X., Xiong, Z., Wu, Y., Cai, W., Tseng, J. R., Gambhir, S. S., and Chen, X. (2006) Quantitative PET imaging of tumor integrin $\alpha_v\beta_3$ expression with ^{18}F-FPRGD2. *J. Nucl. Med. 47*, 113–121.

(54) Wu, Z., Li, Z., Chen, K., Cai, W., He, L., Chin, F. T., Li, F., and Chen, X. (2007) Micro-PET of tumor integrin $\alpha_v\beta_3$ expression using ^{18}F-labeled PEGylated tetrameric RGD peptide (^{18}F-FPRGD4). *J. Nucl. Med. 48*, 1536–1544.

(55) Zhang, X., and Chen, X. (2007) Preparation and characterization of ^{99m}Tc(CO)$_3$-BPy-RGD complex as $\alpha_v\beta_3$ integrin receptor-targeted imaging agent. *Appl. Radiat. Isot. 65*, 70–78.

(56) Liu, S., Edwards, D. S., Ziegler, M. C., Harris, A. R., Hemingway, S. J., and Barrett, J. A. (2001) ^{99m}Tc-Labeling of a hydrazinonictotinamide-conjugated vitronectin receptor antagonist for imaging tumors. *Bioconjugate Chem. 12*, 624–629.

(57) Liu, S., Hsieh, W. Y., Kim, Y. S., and Mohammed, S. I. (2005) Effect of coligands on biodistribution characteristics of ternary ligand ^{99m}Tc complexes of a HYNIC-conjugated cyclic RGDfK dimer. *Bioconjugate Chem. 16*, 1580–1588.

(58) Jia, B., Shi, J., Yang, Z., Xu, B., Liu, Z., Zhao, H., Liu, S., and Wang, F. (2006) ^{99m}Tc-labeled cyclic RGDfK dimer: initial evaluation for SPECT imaging of glioma integrin $\alpha_v\beta_3$ expression. *Bioconjugate Chem. 17*, 1069–1076.

(59) Liu, S., He, Z., Hsieh, W. Y., Kim, Y. S., and Jiang, Y. (2006) Impact of PKM linkers on biodistribution characteristics of the ^{99m}Tc-labeled cyclic RGDfK dimer. *Bioconjugate Chem. 17*, 1499–1507.

(60) Liu, S., Hsieh, W. Y., Jiang, Y., Kim, Y. S., Sreerama, S. G., Chen, X., Jia, B., and Wang, F. (2007) Evaluation of a ^{99m}Tc-labeled cyclic RGD tetramer for non-invasive imaging integrin $\alpha_v\beta_3$-positive breast cancer. *Bioconjugate Chem. 18*, 438–446.

(61) Liu, S., Kim, Y. S., Hsieh, W. Y., and Sreerama, S. G. (2008) Coligand effects on solution stability, biodistribution and metabolism of ^{99m}Tc-labeled cyclic RGDfK tetramer. *Nucl. Med. Biol. 35*, 111–121.

(62) Jia, B., Liu, Z., Liu, Z. F., Yu, Z. L., Yang, Z., Zhao, H. Y., He, Z. J., Liu, S., and Wang, F. (2008) Linker effects on biological properties of ^{111}In-labeled DTPA conjugates of a cyclic RGDfK dimer. *Bioconjugate Chem. 19*, 201–210.

(63) Wang, J. J., Kim, Y. S., and Liu, S. (2008) ^{99m}Tc-labeling of HYNIC-conjugated cyclic RGDfK dimer and tetramer using EDDA as coligand. *Bioconjugate Chem. 19*, 634–642.

(64) Janssen, M. L., Oyen, W. J. G., Dijkgraaf, I., Massuger, L. F., Frielink, C., Edwards, D. S., Rajopadhye, M., Boonstra, H., Corstens, F. H., and Boerman, O. C. (2002) Tumor targeting with radiolabeled $\alpha_v\beta_3$ integrin binding peptides in a nude mouse model. *Cancer Res. 62*, 6146–6151.

(65) Janssen, M., Oyen, W. J. G., Massuger, L. F. A. G., Frielink, C., Dijkgraaf, I., Edwards, D. S., Rajopadhye, M., Corsten, F. H. M., and Boerman, O. C. (2002) Comparison of a monomeric and dimeric radiolabeled RGD-peptide for tumor targeting. *Cancer Biother. Radiopharm. 17*, 641–646.

(66) Dijkgraaf, I., John, A. W., Kruijtzer, J. A. W., Liu, S., Soede, A., Oyezn, W. J. G., Corstens, F. H. M., Liskamp, R. M. J., and Boerman, O. C. (2007) Improved targeting of the $\alpha_v\beta_3$ integrin by multimerization of RGD peptides. *Eur. J. Nucl. Med. Mol. Imaging 2007 34*, 267–273.

(67) Dijkgraaf, I., Liu, S., Kruijtzer, J. A. W., Soede, A. C., Oyen, W. J. G., Liskamp, R. M. J., Corstens, F. H. M., and Boerman, O. C. (2007) Effect of linker variation on the in vitro and in vivo characteristics of an ^{111}In-labeled RGD Peptide. *Nucl. Med. Biol. 34*, 29–35.

(68) Line, B. R., Mitra, A., Nan, A., and Ghandehari, H. (2005) Targeting tumor angiogenesis: comparison of peptide and polymer-peptide conjugates. *J. Nucl. Med. 46*, 1552–1560.

(69) Beer, A. J., Haubner, R., Goebel, M., Luderschmidt, S., Spilker, M. E., Webster, H. J., Weber, W. A., and Schwaiger, M. (2005) Biodistribution and pharmacokinetics of the $\alpha_v\beta_3$-selective tracer ^{18}F-Galacto-RGD in cancer patients. *J. Nucl. Med. 46*, 1333–1341.

(70) Haubner, R., Weber, W. A., Beer, A. J., Vabulience, E., Reim, D., Sarbia, M., Becker, K. F., Goebel, M., Hein, R., Wester, H. J., Kessler, H., and Schwaiger, M. (2005) Noninvasive visuallization of the activiated $\alpha_v\beta_3$ integrin in cancer patients by positron emission tomography and [^{18}F]Galacto-RGD. *PLOS Med. 2 e70*, 244–252.

(71) Kenny, L. M., Coombes, R. C., Oulie, I., Contractor, K. B., Miller, M., Spinks, T. J., McParland, B., Cohen, P. S., Hui, A., Palmieri, C., Osman, S., Glaser, M., Turton, D., Al-Nahhas, A., and Aboagye, E. O. (2008) Phase I trial of the positron-emitting Arg-Gly-Asp (RGD) peptide radioligand ^{18}F-AH111585 in breast cancer patients. *J. Nucl. Med. 49*, 879–886.

(72) Shi, J., Wang, L., Kim, Y. S., Zhai, S., Liu, Z., Chen, X., and Liu, S. (2008) Improving tumor uptake and excretion kinetics of ^{99m}Tc-labeled cyclic arginine-glycine-aspartic (RGD) dimers with triglycine linkers. *J. Med. Chem. 51*, 7980–7990.

(73) Wang, L., Kim, Y. S., Shi, J., Zhai, S., Jia, B., Liu, Z., Wang, F., Chen, X., and Liu, S. (2009) Improving tumor targeting capability and pharmacokinetics of ^{99m}Tc-labeled cyclic RGD dimers with PEG$_4$ linkers. *Mol. Pharm. 6*, 231–245.

(74) Anderson, C. J., Green, M. A., and Fujibayashi, Y. (2003) Chemistry of copper radionuclides and radiopharmaceutical products. *Handb. Radiopharm.* 401–422.

(75) Blower, P. J., Lewis, J. S., and Zweit, J. (1996) Copper radionuclides and radiopharmaceuticals in nuclear medicine. *Nucl. Med. Biol. 23*, 957–980.

(76) Reichert, D. E., Lewis, J. S., and Anderson, C. J. (1999) Metal complexes as diagnostic tools. *Coord. Chem. Rev. 184*, 3–66.

(77) Liu, S. (2008) Bifunctional coupling agents for target-specific delivery of metallic radionuclides. *Adv. Drug Delivery Rev. 60*, 1347–1370.

(78) Jain, R. K. (1987) Transport of molecules in the tumor interstitium: a review. *Cancer Res. 47*, 3039–3051.

BC800455P

Development of a Dendritic Manganese-Enhanced Magnetic Resonance Imaging (MEMRI) Contrast Agent: Synthesis, Toxicity (in Vitro) and Relaxivity (in Vitro, in Vivo) Studies

Annabelle Bertin,[†] Jérôme Steibel,[‡] Anne-Isabelle Michou-Gallani,[§] Jean-Louis Gallani,[†] and Delphine Felder-Flesch*[,†]

Institut de Physique et Chimie des Matériaux de Strasbourg, UMR CNRS/ULP 7504, 23 rue du Lœss BP 43, 67034 Strasbourg Cedex 2, France, Laboratoire d'Imagerie et de Neurosciences Cognitives, UMR CNRS/ULP 7191, 12 rue Goethe, 67000 Strasbourg, France, and siRNA Therapeutics, NIBR Biologics Center, Novartis Institutes for Biomedical Research, Inc., 4002 Basel, Switzerland. Received October 28, 2008; Revised Manuscript Received January 26, 2009

A new dendritic manganese(II) chelate **1** has been evaluated by in vivo (relaxivity) and in vitro (toxicity and relaxivity) experiments as a manganese enhanced magnetic resonance imaging (MEMRI) contrast agent. Also, a comparison with its corresponding gadolinium(III) homologue **2** and the commercially available MEMRI agent MnDPDP (Teslascan, Amersham Health) was achieved in order to determine respectively the real influence of the paramagnetic ion in terms of toxicity and relaxivity for this precise treelike structure and the potential of **1** to be a favorable candidate for brain-targeting MRI. Complexes **1** and **2** displayed high hydrosolubility (0.1 M) and revealed no in vitro neuronal toxicity at concentrations as high as 1 mM. Considering manganese(II) complex **1**, the in vivo nontoxicity at 20 mM (100% rats survival) is very likely due to a slow diffusion of the compound, meaning a controlled release of the paramagnetic ions. Finally, T_1 relaxivity of 4.2 $mM^{-1}.s^{-1}$ for **2** and T_2 relaxivity of 17.4 $mM^{-1}.s^{-1}$ for **1** at 4.7 T were measured and are higher than that of the commercial MRI contrast agents GdDTPA and MnDPDP, respectively.

INTRODUCTION

The development of the current scientific techniques improves day by day the quality of human health and life. The field of medicine, in particular, has brought considerable improvement. Indeed, magnetic resonance imaging (MRI) is one of the most powerful diagnostic imaging tools in medicine, since it provides not only images with excellent anatomical details based on soft-tissue contrast, but also functional information in a noninvasive and real-time monitoring manner (*1*).

An MR image contrast is the result of a complex interplay of numerous factors, including the longitudinal (T_1) and transverse (T_2) relaxation times, proton density of the imaged tissues, and instrumental parameters. However, such contrast can be further improved by the administration of suitable paramagnetic species which affect longitudinal and transverse relaxation rates of the surrounding nuclei, mainly the water solvent protons (*2*).

Shortly after the development and market introduction of magnetic resonance imaging contrast media in 1988, their use became a worldwide established tool for improved medical diagnosis, and nowadays, developing effective, nontoxic, and organ-specific contrast agents (CAs) for in vivo image enhancement is a great current area of research (*3*−*10*). Indeed, today, contrast media are applied in approximately 30% of all MRI procedures.

Although most CAs are based on extracellular, low molecular weight gadolinium(III) chelates due to the seven unpaired electrons and relatively slow electronic relaxation of Gd(III) (*11*), a number of novel and more specific MRI contrast media (MRI-CM) containing other metals (Mn(II) chelates or iron oxide nanoparticles) (*12*−*14*) have been introduced. Notably, Mn(II) based MRI-CM are of great interest and especially in neuroscience research (*15*), since manganese (five unpaired electrons) has a natural human biochemistry, which may allow the design of target-specific CAs as a result of known biochemical uptake mechanisms.

CAs for manganese enhanced MRI (MEMRI) (*16*) have been investigated over the past decade, but so far, only two agents, the liver-specific manganese(II)-dipyridoxal diphosphate (MnDPDP, Teslascan, Amersham Health) and an oral agent containing manganese(II) chloride (LumenHance), have been available clinically for human use (*17*).

The present work describes the synthesis, toxicity (in vitro) studies, and relaxivity (in vitro and in vivo) measurements of a novel hydrophilic dendritic Mn(II) complex **1** (Figure 1) derived from diethylenetriamine pentaacetic acid (DTPA) with regard to its potential application in MEMRI dedicated to brain imaging. A dendritic approach to the preparation of such specific contrast agents appears promising, as the diversity of functionalization brought by the well-defined (on the opposite to polymers) and hyperbranched structure answers simultaneously all the criteria of biocompatibility, low toxicity, and specificity. Moreover, in addition to the multifunctionalization of a low molecular weight molecule, the dendrimer chemistry allows a versatility of size (according to the generation) and of physicochemical properties (hydrophilic, lipophilic). The resulting effects on stability (dendrimer effect), contrast qualities, and biodistribution of the contrast agents can then also clearly be identified.

EXPERIMENTAL PROCEDURES

Chemistry. GdDTPA was provided by Aldrich and Mangafodipir (MnDPDP or Teslascan) was purchased from Amer-

* Corresponding author. Tel.: + 33 3 88 10 71 63; fax: + 33 3 88 10 72 46; e-mail: Delphine.Felder@ipcms.u-strasbg.fr.
[†] UMR CNRS/ULP 7504.
[‡] UMR CNRS/ULP 7191.
[§] Novartis Institutes for Biomedical Research, Inc.

10.1021/bc8004683 CCC: $40.75 © 2009 American Chemical Society
Published on Web 03/09/2009

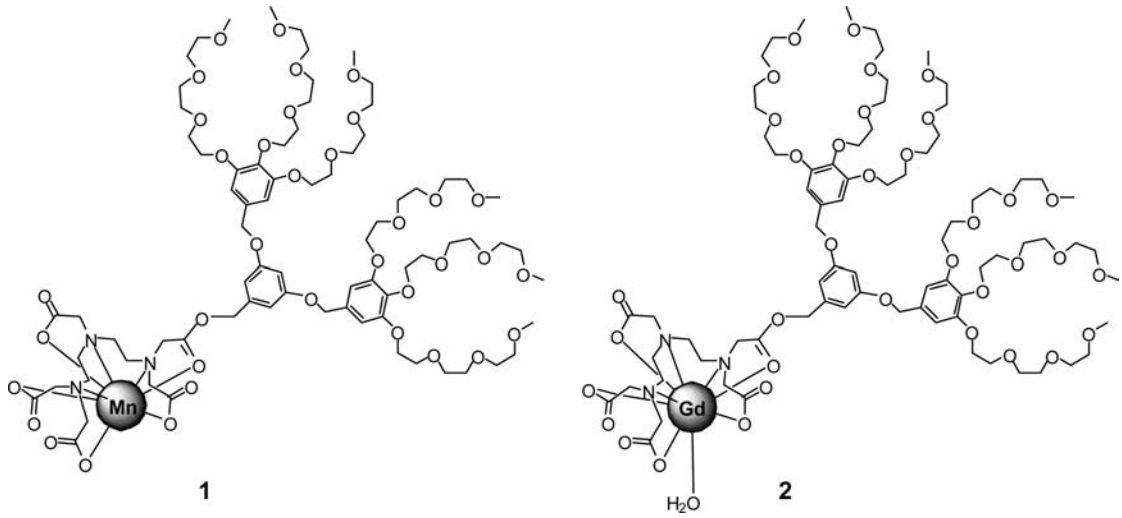

Figure 1. Structures of dendritic Mn(II) and Gd(III) DTPA complexes **1** and **2**, respectively.

sham Health. Reagents and solvents were purchased reagent-grade from Sigma Aldrich and Alfa Aesar and used without further purification. Bromide **3** was prepared according to literature procedures (*18*). All reactions were performed in standard glassware under Ar, and solvents were, if necessary, purified by standard procedures prior to use. Evaporation and concentration were done at water-aspirator pressure and drying in vacuo at 10^{-2} Torr. Column chromatography: silica gel 60 (230−400 mesh, 0.040−0.063 mm) from E. Merck. NMR spectra: Bruker AM-300 (300 MHz), solvent peaks as reference, δ in ppm.

4: A mixture of methyl-3,5-dihydroxybenzoate (372 mg, 2.21 mmol), **3** (3.20 g, 4.87 mmol), and K_2CO_3 (1.53 g,11.06 mmol) in acetone (25 mL) was stirred at 65 °C for 68 h. The reaction mixture was filtered (celite), and the solvent was evaporated. The residue was taken up in a mixture of $CH_2Cl_2/H_2O_{sat.NaCl}$ (1:1) (600 mL). The organic layer was isolated, washed with $H_2O_{sat.NaCl}$ (2 × 300 mL), dried ($MgSO_4$), filtered, and evaporated to dryness. Column chromatography (SiO_2, acetone) afforded **4** (2.07 g, 1.56 mmol) in 71% yield. Yellow oil. ^{1}H NMR ($CDCl_3$): 3.38 (s, 18H), 3.53−3.87 (m, 60H), 3.91 (s, 3H), 4.13−4.19 (m, 12H), 4.96 (s, 4H), 6.67 (s, 4H), 6.79 (t, ^4J = 2 Hz, 1H), 7.28 (d, ^4J = 2 Hz, 2H). ^{13}C NMR ($CDCl_3$): 52.28, 59.00, 68.91, 69.72, 70.36, 70.53, 70.55, 70.68, 70.81, 71.93, 71.95, 72.32, 107.16, 107.29, 108.34, 131.78, 132.07, 138.30, 152.81, 159.71, 166.69. $C_{64}H_{104}O_{28}\cdot 1/2\ H_2O$: calc. C 57.72, H 7.89, O 34.27; found C 57.74, H 7.92, O 34.34.

5: 7.81 mL of $LiAlH_4$ (1 M in THF) was added dropwise to a solution of methyl ester **4** (7.38 g, 5.58 mmol) in THF (100 mL). After 20 h stirring at room temperature, the reaction mixture was neutralized by careful addition of MeOH (50 mL) and H_2O (50 mL), filtered (celite), and evaporated to dryness. Column chromatography (SiO_2, CH_2Cl_2/10% MeOH) afforded **5** (6.50 g, 5.03 mmol) in 90% yield. Yellow oil. ^{1}H NMR ($CDCl_3$): 1.72 (s, 1H OH), 3.38 (s, 18H), 3.53−3.87 (m, 60H), 4.13−4.19 (m, 12H), 4.63 (s, 2H), 4.93 (s, 4H), 6.52 (t, ^4J = 2 Hz, 1H), 6.62 (d, ^4J = 2 Hz, 2H), 6.67 (s, 4H). ^{13}C NMR ($CDCl_3$): 58.98, 61.72, 65.1, 68.85, 69.68, 70.46, 70.49, 70.51, 70.64, 70.76, 71.88, 71.91,72.26, 101.25, 105.66, 107.23, 132.17, 138.17, 143.61, 152.73, 160.00. $C_{63}H_{104}O_{27}\cdot H_2O$: calc. C 57.70, H 8.15, O 34.16; found C 57.81, H 8.16, O 34.03.

6: Triethylamine (TEA) (3.23 mL, 23.10 mmol)) was added dropwise to a stirred solution of diethylenetriaminepentaacetic dianhydride (0.84 g, 2.31 mmol) and **5** (3.00 g, 2.31 mmol) in dry CH_2Cl_2 (100 mL) heated to 50 °C. After 70 h stirring, the reaction mixture was concentrated to 10 mL and hexane (50 mL) was added. The resulting suspension was cooled to 6 °C for 24 h. The white precipitate obtained was filtered off, washed with hexane (3 × 50 mL), and dried. No further purification was necessary to yield pure ligand **6** (3.50 g, 2.10 mmol) with 91% yield. ^{1}H NMR ($CDCl_3$): 1.29 (t, ^4J = 7.2 Hz, 8H), 3.05 (m, 10H), 3.32 (s, 18H), 3.46−3.85 (m, 60H), 4.07−4.13 (m, 12H), 4.88 (s, 2H), 4.90 (s, 4H), 6.61 (s, 4H), 6.73 (t, ^4J = 2.4 Hz, 1H), 7.22 (d, ^4J = 2.4 Hz, 2H). ^{13}C NMR ($CDCl_3$):45.56, 49.73, 52.63, 55.59, 56.76, 59.03, 68.89, 69.73, 70.50, 70.53, 70.55, 70.69, 71.92, 72.30, 101.29, 105.70, 107.28, 132.22, 138.22, 143.66, 152.78, 160.03, 168.79, 169.96, 170.62, 173.05. Elemental analysis: calc. C 55.40, H 7.55, O 34.53, N 2.52; found C 55.37, H 7.55, O 34.50, N 2.52. Maldi-MS (negative mode): $[M]^-$ 1666.85 obtained for $C_{77}H_{125}N_3O_{36}$ (1667.80).

1: An equimolar solution of **6** (0.50 g, 0.30 mmol) and $MnCl_2\cdot 4H_2O$ (0.06 g, 0.30 mmol) in H_2O (30 mL) was stirred at room temperature for 12 h while maintaining pH at 6.5 by addition of 1 M aqueous solution of NaOH. The reaction mixture is then lyophilized. Impure complex **1** (presence of inorganic salts like NaCl) is then diluted in CH_2Cl_2 (30 mL). The organic phase obtained is washed with H_2O (2 mL) (decreasing reaction yield), dried ($MgSO_4$), filtered, and evaporated to dryness. Complex **1** is obtained as a yellow solid (0.47 g, 0.27 mmol) with 90% yield. Maldi-MS (negative mode): $[M\ Na]^{2-}$ 1741.77 obtained for $MnC_{77}H_{121}N_3O_{36}Na$ (1741.70).

2: An equimolar solution of **6** (0.50 g, 0.30 mmol) and $Gd(ClO_4)_3$ (0.25 g of a 50% solution in H_2O, 0.30 mmol) in H_2O (30 mL) was stirred at room temperature for 12 h while maintaining pH at 6.5 by addition of a 1 M aqueous solution of NaOH. The solution is then treated with Chelex resin (2 g) for 2 h before filtration and lyophilization. The absence of free gadolinium is checked by the Xylenol orange test (*19*). Complex **2** is obtained as a white solid (0.47 g, 0.25 mmol) with 89% yield (taking into account remaining perchlorates). Maldi-MS (negative mode): $[M\ Na]^-$ 1861.75 obtained for $GdC_{77}H_{123}N_3O_{37}Na$ (1862.69).

In Vitro Toxicity Studies. Rat pups were sacrificed by decapitation at 7 days of age, and neurons were isolated from the cerebellum and plated in multiwell plates coated with poly(D-lysine). The plates were incubated for 3 days to allow cell maturation to continue to some extend. At DIV 3 (day in vitro 3), the cells were exposed to 0.001 to 10 mM of the test products or to 0.001 to 100 nM of β-bungarotoxin. β-Bungarotoxin is a known neurotoxin that is not expected to decrease cell counts but has a striking negative effect on neuron-specific parameters. The cells were treated with the compounds for 2 days and then

analyzed as follows: Measure of the cell leakage resulting from membrane damage: lactate deshydrogenase is normally a cytoplasmic enzyme. When the integrity of the plasma membrane is compromised, it leaks into the culture medium, where it can be measured by a colorimetric assay (Roche, LDH Assay). As a positive control for the test, a few test wells in the plate were exposed to a strong detergent, 1% Triton X100, for 30 min (thus causing immediate and measurable release of LDH); then, 120 μL of culture media was collected from all the wells and analyzed. Immunostaining of the cells*:* the cells were fixed with 4% paraformaldehyde, permeabilized with 0.5% Triton X100, blocked with 5% BSA (bovine serum albumine), and incubated with an antibody for neuron-specific beta III tubulin (RandD). The secondary antibody used was a TRIC-labeled mouse antibody. The nuclei were stained with DAPI or Hoechst 33342. High cell content analysis (ArrayScan system, Cellomics Thermofisher): The ArrayScan system is an imaging approach that uses fluorescent probes and automated microscopy to quantify multiple cellular markers at the single-cell level. Fluorescence microscopy coupled to electronic imaging allows quantification of many cell-specific parameters, such as nucleus counts, intensity, size or shape of nuclei, quantification of signals in the cytoplasma, or specific organelles (e.g., neurites). The ArrayScan system consists of an optical system with a spatial resolution of 0.68 μm (Carl Zeiss), a triple band fluorescence emission filter set with matched single band excitation filters for selectively imaging Hoechst, FITC, or TRITC (model XF93, Omega Optical), and a CDD camera. The system is used to scan multiple fields in each well (images acquisition). In our studies, the images acquired were analyzed with an algorithm specialized for neurons, "neuronal profiling".

Commercial MnDPDP (Teslascan, Amersham Health) and **6** were suspended in 5% DMSO at a stock concentration of 500 mM (yellow solution for commercial Mangafodipir, white−yellow solution for **6**). A 10-fold serial working dilution down to 0.05 mM was done in 5% DMSO. **1**, **2**, and commercial GdDTPA were suspended in water at a stock concentration of 500 mM (orange tainted solution for **1**, yellow solution for **2**) and stored at −20 °C. A fresh 10-fold serial working dilution down to 0.05 mM was done in water. Four microliter aliquots of each working dilution were applied to the cells covered by 200 μL culture medium, i.e., a 50× further dilution step. In summary, the cells were exposed to the following final concentrations of product: 10, 1, 0.1, 0.01, and 0.001 mM. As a control, β-bungarotoxin, was included on each plate of cells at concentrations ranging from 100 nM (because of its neurotoxicity, 10^4 times less concentrated than the test compounds) down to 0.001 nM.

Relaxivity Studies. In vitro: All MRI experiments were carried out at 4.7-T using an MR magnet (Magnex Sci. Ltd., Oxford, United Kingdom). T_1 and T_2 values were determined for each complex at pH 6.5−7 as a function of concentrations and at various temperature. In vivo: all studies were performed in accordance with French animal protection laws and approved by the responsible governmental authority. The animals (rats and mice) were kept under anesthesia using a mixture of isoflurane and oxygen. After being relaxed, the animals were intubated and artificially ventilated with an animal respirator. Rats and mice were placed in a stereostatic device to immobilize the head, with an integrated facility to maintain the body temperature at 37 °C. An anatomically shaped ^{1}H surface coil for small animals (Rapid Biomedical GmbH, Würzburg, Germany) was positioned on the head to serve as a receiver for the MR signal. The system was then placed into a ^{1}H resonator for rats and mice, with an inner diameter of 69 mm that fits into the −20 cm MR magnet. Brain saggital and coronal slices were acquired with a repetition time (T_R) of 3.8 s (T_2-weighted) and 0.5 s (T_1-weighted), spin−echo time (T_E) of 40 ms (T_2-weighted) and 21 ms (T_1-weighted). Image acquisitions were based on a T_1-weighted spin−echo MRI sequence or T_2-weighted sequence, using CPMG sequence. All data were analyzed with *Matlab* software.

As physicochemical properties like pH must be taken into account for potential clinical applications, intraperitoneal (i.p.) or intraveinous (i.v.) injections were performed at physiological pH (7.4) using a saline solution of the tested compound at [10 mM].

RESULTS AND DISCUSSION

Chemistry. The Mn(II) and Gd(III) DTPA-derived complexes **1** and **2** were synthesized starting from the previously described bromo derivative **3** (*18*) as depicted in Scheme 1. The bromide **3**, in the presence of methyl 3,5-dihydroxybenzoate and potassium carbonate in acetone under reflux, led to the formation of methyl ester **4** with 71% yield. Then, reduction of ester **4** by $LiAlH_4$ in THF allowed the preparation of the corresponding benzyl alcohol **5** with 90% yield. Finally, the ligand **6** is obtained by reaction of benzyl alcohol **5** with commercial diethylenetriaminepentaacetic dianhydride in the presence of triethylamine in dichloromethane. After precipitation in hexane, the pure dendritic ligand **6** is obtained with 91% yield. Then, preparing the manganese(II) complex, an equimolar solution of ligand **6** and $MnCl_2$ in water is stirred at room temperature while maintaining the pH of the solution at 6.5. After workup, the manganese complex **1** is then obtained with 90% yield. The same procedure is followed to prepare the gadolinium complex (III) using $Gd(ClO_4)_3$. After treatment with Chelex resin, the lack of free gadolinium is checked by the Xylenol orange test (*19*). After lyophilization, the complex **2** is obtained with 93% yield.

Solubility and log *P*. The distribution of a molecule between aqueous and organic phases (partition coefficient P) determines in part its biological properties such as transport, membrane crossing, and bioavailability (distribution and accumulation). We measured the log *P* of our contrast agents by the so-called "shake flask" method recommended by the European Union (*20*). The results are presented in Table 1, as well as their hydrosolubility estimated by the turbidimetric method (*21*). As it can be noticed, the DTPA complexation induces a huge variation of the partition coefficient: indeed, if the log *P* is −0.47 for ligand **6**, it increases to −2.66 and −3.27 for gadolinium(III) and manganese(II) complexes **1** and **2**, respectively. Complexation therefore increases hydrophilicity, which is confirmed by hydrosolubility measurements: concentrations as high as 0.1 M in water can be reached for complexes **1** and **2**. Such values are extremely important and encouraging, knowing that the contrast is function of the paramagnetic species concentration. Moreover, as will be explained in the following, our compounds are still nontoxic in vitro and in vivo at such concentrations.

In Vitro Toxicity. Toxicity, which is primarily due to the action of manganese as a calcium channel blocker with effects on muscle electrophysiology and contractility, has limited the use of manganese salts as paramagnetic contrast agents (*22, 23*). Early research in MR imaging employed the use of $MnCl_2$ in dogs (*24*) and rats (*25*) as well as in vitro systems involving human blood (*26*). Nevertheless, $MnCl_2$ is the active component of Lumenhance, a commercial contrast agent used for gastrointestinal imaging (*27*).

Manganese complexes are relatively unstable in vivo and are dissociated in biological media. Indeed, manganese can be displaced by other divalent cations such as calcium, magnesium, or zinc. Due to this release, some concern exists about the potential long-term toxicity associated with the development and use of Mn-based contrast agents (*28*). Free manganese was shown to be teratogenic and mutagenic in several models (*29*).

Scheme 1[a]

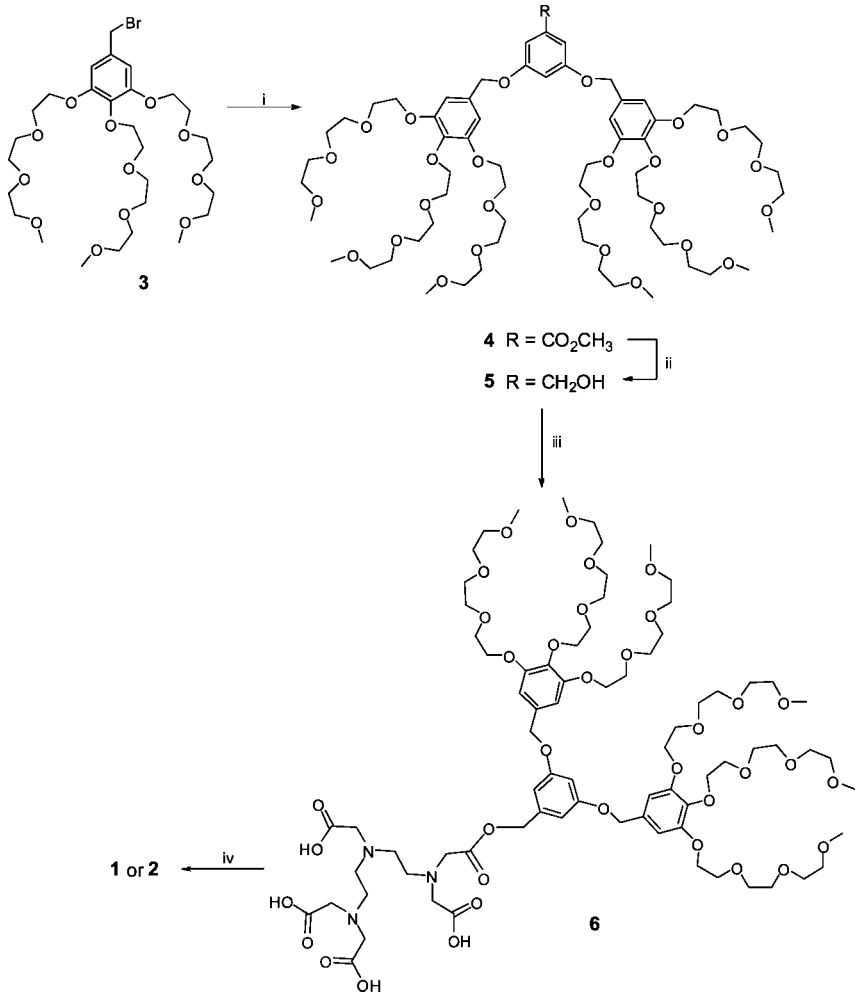

[a] Reagents: (i) Methyl-3,5-dihydroxybenzoate, K_2CO_3, acetone, 60 °C; (ii) $LiAlH_4$, THF, Ar, 0 °C; (iii) diethylenetriamine pentaacetic dianhydride, CH_2Cl_2, TEA; (iv) for Mn complex **1**: $MnCl_2 \cdot 4H_2O$, pH 7; for Gd complex **2**: $Gd(ClO_4)_3$, H_20, pH 7.

Table 1. Hydrosolubility and Log *P* Values of the Dendritic Ligand 6 and Its Corresponding Mn(II) and Gd(III) Complexes 1 and 2, Respectively

compound	dendritic ligand **6**	Mn(II) complex **1**	Gd(III complex **2**
hydrosolubility ($mg.mL^{-1}$)	62 ± 7	172 ± 17	182 ± 18
hydrosolubility ($mmol.L^{-1}$)	37 ± 4	98 ± 10	97 ± 10
log *P*	−0.47	−3.27	−2.66

The teratogenic effect was also demonstrated after commercial MnDPDP injection (*30*, *31*). It was thus of great importance to show that our MEMRI complex **1** is nontoxic both in vitro and in vivo at concentrations as high as 1 to 10 mM, knowing that commonly used concentrations for MRI studies and in vivo experiments are 0.5 mM.

Cells used in this test were rat cerebellar neurons isolated from 7-day-old pups. These cells are useful tools for toxicity tests as they are primary cells, unmodified and without any genomic aberration. They represent a great intermediate between cell lines and tests on tissue sections or in vivo tests. Since our final aim is to target the brain and perform chemical engineering to increase such percentage of contrast agents reaching the brain, it appeared important to perform the in vitro toxicity tests on cerebellar neurons. Moreover, as those cells are the most sensitive cells, it becomes possible to conclude that if they are not affected then other less sensitive cells will also not be affected.

Neurons used in our in vitro assay are exposed to the complexed entities and to an unknown fraction of free ions released from the complexes, while in vivo neurons may be exposed to free ions released from the complexes. However, despite its limitations, the use of a cellular model based on functional primary cells has the advantage to allow monitoring of alterations on various levels: cell death, loss of cells, alteration of cellular membranes, alteration of the ability to form an healthy neuritic network. All these alterations can be quantified, thus allowing a direct comparison of the contrast agents and a basic characterization.

The assay is used for analyzing compounds in case of possible brain penetration and can be proposed more generally if there is a concern about potential neurotoxic effects. Cells were stained in order to visualize nuclei (DAPI), cytoplasm, and neurites (anti β-tubulin III): thus, alteration of the neuron-specific parameters such as nuclei number, number of neurons, mean neurite count, mean total neurite length, and mean neurite width and area reflects neurotoxicity.

Influence of the Paramagnetic Ion and Comparison with Commercial Products. From the selected images shown Figure 2, it can be seen that the higher concentration (10 mM) of all four tested compounds disrupts the neuritic network. At 1 mM, disruption remains strong in the corresponding selected image for MnDPDP and gadolinium complex **2**, while **1** and GdDTPA are better tolerated. In order to better apprehend, and in a quantitative manner, the potential toxicity of these compounds,

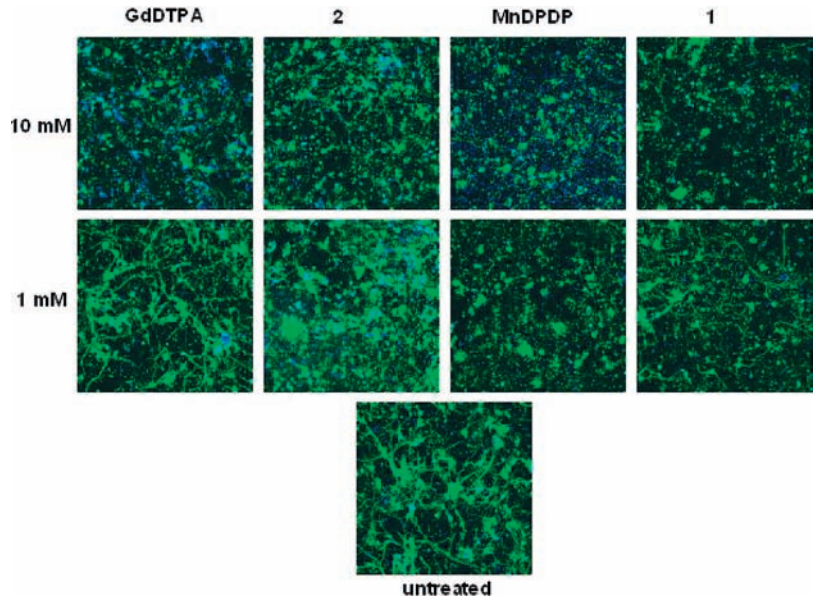

Figure 2. Pictures of treated neurons after staining for complexes **1** and **2** compared to commercial GdDTPA (Magnevist, Schering) and MnDPDP (Teslascan, Amersham Health) at 1 and 10 mM, together with untreated neurons.

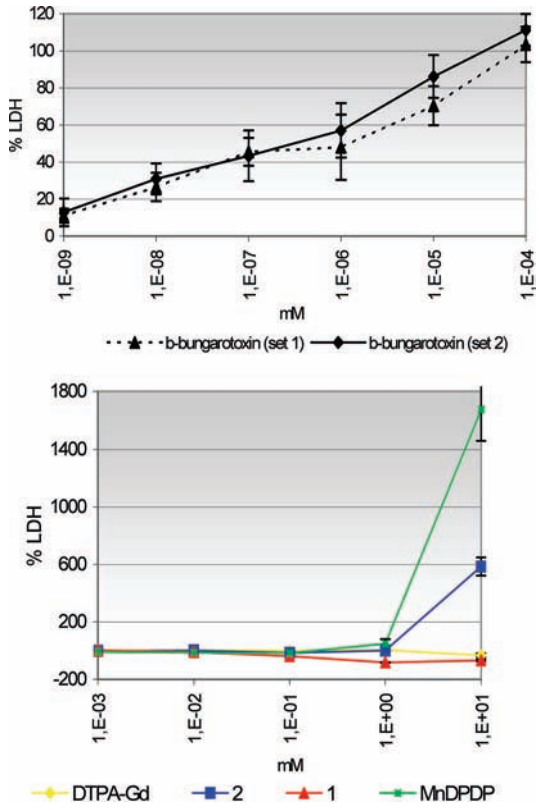

Figure 3. LDH efflux. Measurements of the cell leakage resulting from membrane damage of neuronal cells treated with increasing concentrations of dendritic complexes **1**, **2**, and commercial GdDTPA (Magnevist, Schering) and MnDPDP (Teslascan, Amersham Health).

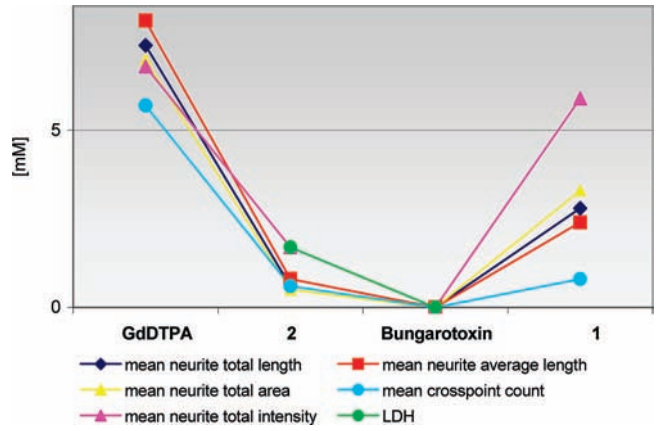

Figure 4. EC50 (mM) of all studied compounds.

we conducted a LDH release test (Figure 3). Indeed, the LDH measurement in the culture medium is a classical test for detection of overall toxicity: if the cell membranes lose their integrity, LDH, which is an enzyme present in the cytoplasm, is released in the supernatant culture, where it can be measured by a colorimetric test. Cells that have been exposed to the venom β-bungarotoxin also show dose-dependent membrane damage. **2** elicits a striking LDH release at 10 mM, confirming that this compounds compromises the membrane integrity at high concentration. MnDPDP is also strongly membrane damaging at 10 mM. Supernatants from wells with neurons treated with increasing concentrations of **1** show a loss in LDH activity. LDH release is a parameter that is proportional to cell number. In parallel, we observe that increasing the concentration of **1** induces loss of nuclei (data not shown). We can suggest that these two observations are linked. Nevertheless, the LDH test has shown that our complex **1** does not damage the cell membrane up to a concentration of 10 mM.

Thus, our in vitro neurotoxicity studies evidenced qualitatively (Figure 2) and quantitatively (Figures 3 and 4) that the manganese(II) dendritic complex **1** is no more toxic than the commercial GdDTPA at concentration up to 1 mM and is much less toxic than MnDPDP.

In Vitro Relaxivity Studies. *Influence of the Paramagnetic Ion and Comparison with Commercial Products.* The in vitro relaxivity measurements of dendritic complexes **1** and **2** allowed one to draw the linear relationships $r_{1,2} = f([M])$ (Figure 5), which where compared to the those recorded for one Gd-DTPA, $GdCl_3$, and the two principal MEMRI contrast agents, namely, $MnCl_2$ (only for animal experiments) and MnDPDP.

The observed relaxivities measured at 37 °C under 4.7 T are summarized in Table 2. The relaxation theory predicts that higher relaxation rates are obtained upon increase of the

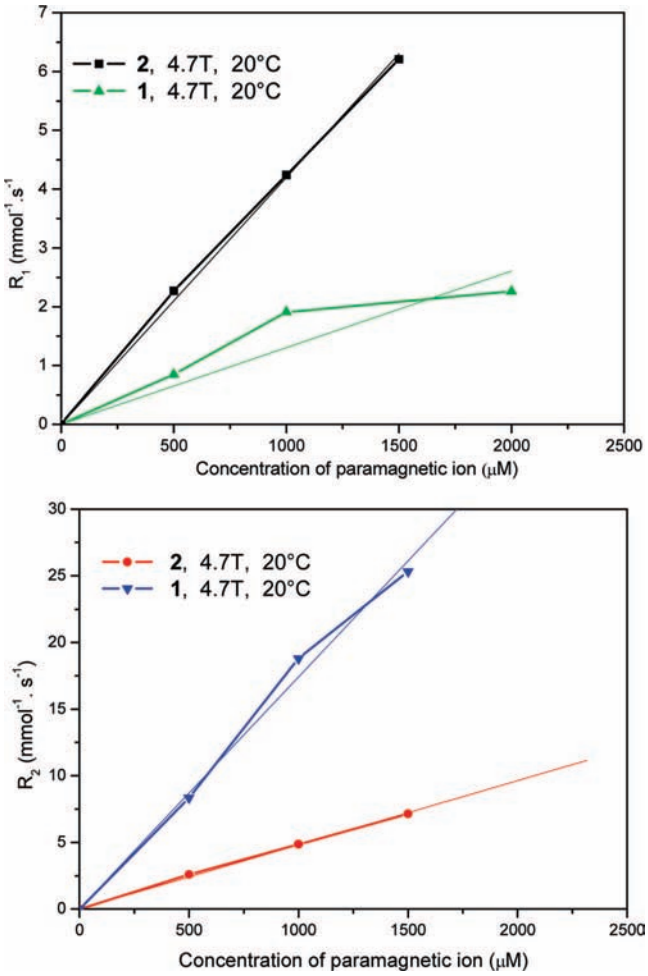

Figure 5. In vitro dose−response relaxivity studies of Mn(II) complex **1** and Gd(III) complex **2** at 4.7 T and 20 °C.

Table 2. r_1 and r_2 Relaxivities of 1, 2, GdDTPA, and MnDPDP in H_2O at 20 °C under 4.7 T

metal complexes	r_1 (mM^{-1}. s^{-1})	r_2 (mM^{-1}. s^{-1})
1	1.3	17.41
MnDPDP[a]	1.5 (1.3−1.7)	2.7 (2.6−2.8)
$MnCl_2$	3.59	48.42
2	4.2	4.82
GdDTPA[a]	3.2 (3.0−3.4)	4.0 (3.8−4.2)
$GdCl_3 \cdot 6H_2O$	18.63	28.2

[a] According to M. Rohrer, H. Bauer, J. Mintorovitch, M. Requardt, H.-J. Weinmann, *Invest. Radiol.* 40(*11*), **2005**, 715−724 for the 4.7 T values.

rotational correlation time of complexes (*32*). Since the molecular rotation correlation time (τ_R) is proportional to the molecular size, the attachment of low molecular weight paramagnetic gadolinium chelate to macromolecules can considerably enhance the relaxivity of the chelate unit and can extend the residence time in the cardiovascular system, with potential applications in MRI angiography (MRA) (*33*, *34*). However, macromolecular contrast agents tend to have less complete body elimination. In order for the complex to be excreted by kidneys and cleared from the blood pool quickly after being injected, the complex should have a molecular mass lower than 3.5 kD and also be hydrophilic. Thus, our PEG-based dendritic contrast agents may meet the satisfying conditions of both high relaxivity and low toxicity as confirmed by the following results.

In the case of the Mn(II)−DTPA complex, no water molecule is directly bound to the metal ion, which makes the outer-sphere relaxivity become the only relaxivity component. The in vitro relaxivities measured for **1** at 4.7 T are extremely encouraging: $r_1 = 1.3$ $(mM.s)^{-1}$ and $r_2 = 17.41$ $(mM.s)^{-1}$. One can see in Table 2 that, as expected, the highest relaxivities are obtained for $MnCl_2$ ($r_1 = 6.9$ $(mM.s)^{-1}$ and $r_2 = 37.5$ $(mM.s)^{-1}$), but the important point is that our dendritic Mn(II)-based complex **1** shows higher r_2 relaxivity (4 times higher) than that of the relative small molecular complex Mn-DPDP.

One can also point out that r_2 values measured at 4.7 T for the dendritic Gd(III)-based complex **2** are much lower than that of the corresponding Mn(II)-based complex **1** and r_1 and r_2 are of the same range as (as predicted by theory) and very close to the values recorded for Gd-DTPA. Thus, the dendritic architecture seems to have no substantial beneficial effect on the relaxivities.

In Vivo Relaxivity Studies. Given the fact that for a great number of MRI examinations the sensitivity is too low, the use of synthetic contrast agents is not only paramount but even mandatory. However, with the aim of rendering MRI an even more powerful technique, these contrast agents are confronted by the improvement of three factors: the spatial accuracy, the contrast resolution, and the examination time. The manganese(II) complex **1** has been synthesized in order to develop a nontoxic Mn^{2+} ion vehicle, knowing that these ions are highly toxic but for which the highest intracellular contrasts can be obtained. Moreover, as manganese is an essential nutrient for mammals and organisms, they have developed special carrier systems and selective cellular uptake mechanisms.

A possible strategy to reduce the in vivo toxicity of manganese(II) is to deliver Mn^{2+} to a specific site at an appropriate concentration (greatly reduce its concentration) and via a time-efficient manner (maintain a long diffusion). However, even if the MRI studies conducted on Gd(III) complex **2** showed the inability of the product to cross the healthy blood−brain barrier (BBB), they also highlighted a high vascular remanence (the contrast agent is circulating in the blood flow for at least 72 h), which is a behavior of good omen for use in functional imaging or for monitoring treatment.

The ability of Mn^{2+} to accumulate in active regions of the brain was first demonstrated in MRI by activity-induced manganese-enhanced MRI (AIM-MRI) (*35*). Unfortunately, AIM-MRI is a quite invasive method, as the contrast agent is infused after BBB opening with an hyperosmolar agent. Here, we chose a simple intraperitoneal (i.p) administration of **1** leading to interesting and useful anatomical contrast (Figure 6).

An aqueous isotonic saline solution (0.9% NaCl) of dendritic complex **1** was administered to a Long Evans male rat of 300 g via intraperitoneal injection (ip) at a 0.4 mmol/kg scale. As shown Figure 6, this injection led to a contrast increase in the rat brain on both the T_1- and T_2-weighted images. At 24 h after administration, the contrast is improved throughout the brain but heterogeneously, and details of the cytoarchitecture can be visualized as a result of the presence of Mn^{2+}. Similarly to other studies, on the T_1-weighted images, the contrast in the parenchyma is better at 24 h (b) while the contrast in the ventricle is maximal at 15 h (a) and gradually decreases after 48 h (c). The concentration of Mn^{2+} is minimal in the corpus callosum (a,b,d,e). The maximum concentration of Mn^{2+} is observed in the hippocampus region, the thalamus, and the cerebellum center (b,e). These results are consistent with previous studies performed on rats using intravenously injected $MnCl_2$ and would mean that Mn^{2+} ions enter the brain by release. However, on the opposite to $MnCl_2$, manganese chelation and probably the presence of the dendritic structure abolish the cardiovascular adverse side effects and effectively eliminate the problem of the Mn^{2+} retention in the tissues. In the case of our complex **1**, the toxicity disappearance is very likely due to a slow diffusion

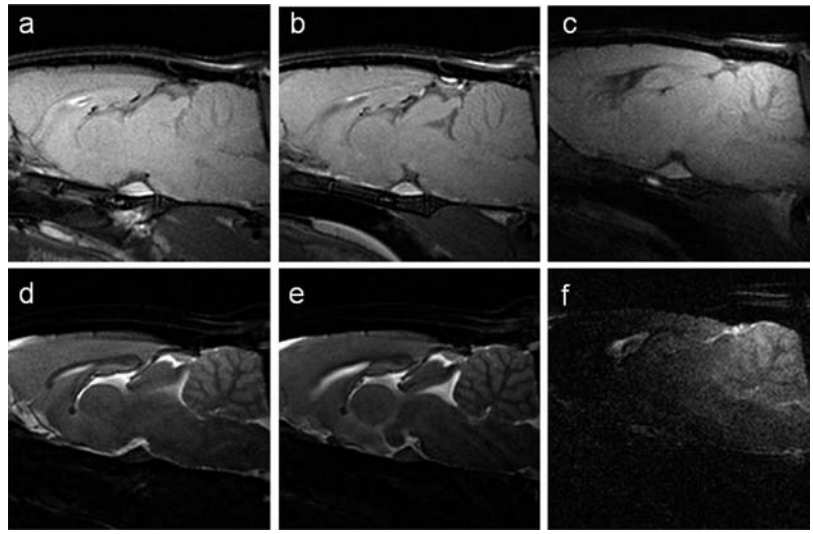

Figure 6. T_1 (a,b,c) and T_2 (d,e,f) MEMRI images obtained with complex **1**. (a,d) 15 h; (b,e) 24 h; (c,f) 72 h. Rat brain, at 0.4 mmol/kg, IP of a 20 mM solution of **1** in NaCl (150 mM); SMIS 4.7 T, 1 mm thickness, resolution 256 × 256, field of view 20 mm.

of the product, meaning a controlled release of the paramagnetic ions. In return, this follows a major loss of the relaxivity compared to $MnCl_2$. But still, the measured relaxivities for **1** are comparable to those obtained for commercial MnDPDP.

All these data support the view that, in spite of the lower effective magnetic moment of manganese, complex **1** and well-designed Mn(II) complexes can therefore be considered as viable alternatives to the currently used gadolinium(III) complexes as contrast agents for (ME)MRI. Considering brain imaging, this is mainly due to the rich biochemistry of manganese allowing absorption and transport of Mn^{2+} to the brain: the uptake of extracellular Mn^{2+} by a neuron is directly coupled to its physiological activity and function. This suggests potential applications not only for basic neurosciences but also for managing clinical neurological diseases such as Alzheimer or Parkinson, as well as other diseases showing disturbances in neuronal cell structures without disturbing the BBB.

ACKNOWLEDGMENT

We thank the French Ministry of Research for a fellowship to A. Bertin and CNRS for financial support. Pr. D. Grucker is warmly acknowledged for the in vitro relaxivity measurements. We also thanck E. Couzigné and B. Guignard for technical assistance.

Supporting Information Available: ^1H and ^{13}C NMR spectra of compound **6**, mass-spectrometry spectra (Maldi-MS, negative mode) of complexes **1** and **2**, in vitro relaxivity theory. This material is available free of charge via the Internet at http://pubs.acs.org.

LITERATURE CITED

(1) Mansson, S., Bjornerud, A. in: Merbach, A. E., Toth, E., Eds. (2001) *The Chemistry of contrast agents in medical magnetic resonance imaging*, pp 1−44, Wiley, New York.

(2) Aime, S., Frullano, L., and Crich, S. G. (2002) Compartmentalization of a gadolinium complex in the apoferritin cavity: a route to obtain high relaxivity contrast agents for MRI. *Angew. Chem., Int. Ed. Engl. 41*, 1018–1019.

(3) Reynolds, C. H., Annan, N., Beshah, K., Huber, J. H., Shaber, S. H., and Lenkinski, R. E. (2000) Gadolinium-loaded nanoparticles: new contrast agents for MRI. *J. Am. Chem. Soc. 122*, 8940–8945.

(4) Rodriguez, E., Roig, A., Molins, E., Arus, C., Quintero, M. R., Cabanas, M. E., Cerdan, S., Lopez-Larrubia, P., and Sanfeliu, C. (2005) In vitro characterization of an Fe_8 cluster as potential MRI contrast agent. *NMR Biomed. 18*, 300–307.

(5) Parmelee, D. J., Walovitch, R. C., Ouellet, H. S., Lauffer, R. B. (2001) *Invest. Radiol. 32*, 741−747.

(6) Lokling, K. E., Fossheim, S. L., Skurtveit, R., Bjornerud, A., and Klaveness, J. (2001) pH-sensitive paramagnetic liposomes as MRI contrast agents: *in vitro* feasibility studies. *Magn. Reson. Imaging 19*, 731–738.

(7) Wolfgang, S., Sanjay, S., Jan, P., Ralph, W., Mukesh, H., William, M.-S., and Peter, F. H. (1999) MR imaging of the liver with Gd-BOPTA: quantitative analysis of T_1-weighted images at two different doses. *J. Magn. Reson. Imaging 10*, 80–83.

(8) Langereis, S., de Lussanet, Q. G., van Genderen, M. H. P., Meijer, E. W., Beets-Tan, R. G. H., Griffioen, A. W., Engelshoven, J. M. A., and Backes, W. H. (2006) Evaluation of Gd(III)DTPA-terminated poly(propylene imine) dendrimers as contrast agents for MR imaging. *NMR Biomed. 19*, 133–141.

(9) Aime, S., Gianolio, E., Uggeri, F., Tagliapietra, S., Barge, A., and Cravotto, G. (2006) New paramagnetic supramolecular adducts for MRI applications based on non-covalent interactions between Gd(III) complexes and β- or γ-cyclodextrin units anchored to chitosan. *J. Inorg. Biochem. 100*, 931–938.

(10) Shu, C. Y., Gan, L. H., Wang, C. R., Pei, X. L., and Han, H. B. (2006) Synthesis and characterization of a new water-soluble endohedral metallofullerene. *Carbon 44*, 496–500.

(11) Comet, M., and Vidal, M. (1998) Radiopharmaceutiques. Chimie des radiotraceurs et applications biologiques. *In Presses Universitaires de Grenoble* 206–246.

(12) Laurent, S., Forge, D., Port, M., Roch, A., Robic, C., Vander Elst, L., and Muller, R. N. (2008) Magnetic iron oxide nanoparticles: synthesis, stabilization, vectorization, physicochemical characterizations and biological applications. *Chem. Rev. 108*, 2064–2110.

(13) Li, Z., Li, W., Li, X., Pei, F., Wang, X., and Lei, H. (2007) Mn(II)-monosubstituted polyoxometalates as candidates for contrast agents in magnetic resonance imaging. *J. Inorg. Biochem. 101*, 1036–1042.

(14) Na, H. B., Lee, J. H., An, K., Park, Y. I., Park, M., Lee, I. S., Nam, D.-H., Kim, S. T., Kim, S.-H., Kim, S.-W., Lim, K.-H., Kim, K.-S., Kim, S.-O., and Hyeon, T. (2007) Development of a T_1 contrast agent for magnetic resonance imaging using MnO nanoparticles. *Angew. Chem., Int. Ed. Engl. 46*, 1–6.

(15) Yu, X., Wadghiri, Y. Z., Sanes, D. H., and Turnbull, D. H. (2005) In vivo auditory brain mapping in mice with Mn-enhanced MRI. *Nat. Neurosci. 8* (7), 961–966.

(16) Koretsky, A. P., Silva, A. C (2004) Manganese-enhanced magnetic resonance imaging (MEMRI). *NMR Biomed, 17*, 527−531, special issue of NMR in biomedicine on manganese-enhanced magnetic resonance imaging.

(17) Elizondo, G., Fretz, C. J., Stark, D. D., Rocklage, S. M., Quay, S. C., Worah, D., Tsang, Y., Chen, M. C., and Ferrucci, J. T. (1991) Preclinical evaluation of MnDPDP: new paramagnetic hepatobiliary contrast agent for MR imaging. *Radiology 178*, 73–78.

(18) Hayek, A., Bolze, F., Nicoud, J.-F., Baldeck, P. L., and Mély, Y. (2006) Synthesis and characterization of water-soluble two-photon excited blue fluorescent chromophores for bioimaging. *Photochem. Photobiol. Sci. 5*, 102–106.

(19) Laurent, S., Parac-Vogt, T. N., Kimpe, K., Thirifays, C., Binnemans, K., Muller, R. N., and Vander Elst, L. (2007) Bis(phenylethylamide) derivatives of Gd-DTPA as potential receptor-specific MRI contrast agents. *Eur. J. Inorg. Chem.* 2061–2067.

(20) Simeonov, A., Matsushita, M., Juban, E. A., Thompson, E. H. Z., Hoffman, T. Z., Beusher, A. E., Taylor, M. J., Wirshing, P., Rettig, W., McCusker, J. K., Stevens, R. C., Millar, D. P., Schultz, P. G., Lerner, R. A., and Janda, K. D. (2000) Blue-fluorescent antibodies. *Science 290*, 307–313.

(21) Avdeef, A., and Testa, B. (2002) Physicochemical profiling in drug research: a brief survey of the state-of-the-art of experimental techniques. *Cell. Mol. Life Sci. 59*, 1681–1689.

(22) Langer, G. A., Serena, S. D., and Nudd, L. M. (1975) Localization of contractile-dependent calcium. Comparison of manganese and verapamil in cardiac and skeletal muscle. *Am. J. Physiol. 229*, 1003–1007.

(23) Haworth, R. A., Goknur, A. B., and Berkoff, H. A. (1989) Measurement of calcium channel activity of isolated adult rat heart cells using ^{54}Mn. *Arch. Biochem. Biophys. 268*, 594–604.

(24) Lauterbur, P. C., Mendoca-Dias, M. H., and Rudin, A. M. (1978) Augmentation of tissue water proton spin-lattice relaxation rates by in vivo addition of paramagnetic ions, In *Frontiers of Biological Energetics* (Dutton, P. L., Leigh, L. S., and Scarpa, A., Eds.) Vol *1*, pp 752−759, Academic Press, New York.

(25) Mamourian, A. C., Burnett, K. R., Goldstein, E. J., Wolf, G. L., Kressel, H. Y., and Baum, S. (1984) Proton relaxation enhancement in tissue due to ingested manganese chloride: time course and dose response in the rat. *Physiol. Chem. Phys. Med. NMR 16*, 123–128.

(26) Kang, Y. S., Gore, J. C., and Armitage, I. M. (1984) Studies of factors affecting the design of NMR contrast agents: manganese in blood as a model system. *Magn. Res. Med. 1*, 396–409.

(27) Small, W. C., DeSimone-Macchi, D., Parker, J. R., Sukerkar, A., Hahn, P. F., Rubin, D. L., Zelch, J. V., Kuhlman, J. E., Outwater, E. K., Weinreb, J. C., Brown, J. J., De Lange, E. E., Woodward, P. J., Arildsen, R., Foster, G. S., Runge, V. M., Aisen, A. M., Muroff, L. R., Thoeni, R. F., Parisky, Y. R., Tanenbaum, L. N., Totterman, S., Herfkens, R. J., Knudsen, J., Laster, R. E., Duerinckx, A., Stillman, A. E., Spritzer, C. E., Saini, S., Rofsky, N. M., and Bernardino, M. E. (1999) A multisite phase III study of the safety and efficacy of a new manganese chloride-based gastrointestinal contrast agent for MRI of the abdomen and pelvis. *J. Magn. Res. Imaging 10*, 15–24.

(28) Crossgrove, J., and Zheng, W. (2004) Manganese toxicity upon overexposure. *NMR Biomed. 17*, 544–553.

(29) Wolf, G. L., and Baum, L. (1983) Cardiovascular toxicity and tissue proton T1 response to manganese injection in the dog and raddit. *AJR Am. J. Roentgenol. 141*, 193–197.

(30) Gallez, B., Bacic, G. G., and Schwartz, H. M. (1996) Evidence for the dissociation of the hepatobiliary MRI contrast agent MnDPDP. *Magn. Reson. Med. 35*, 14–19.

(31) Federle, M. P., Chezmar, J. L., Rubin, D. L., Weinreb, J. C., Freeny, P. C., Semelka, R. C., Brown, J. J., Borello, J. A., Lee, J. K., Mattrey, R., Dachman, A. H., Saini, S., Harmon, B., Fenstermacher, M., Pelsang, R. E., Harms, S. E., Mitchell, D. G., Halford, H. H., Anderson, M. W., Johnson, C. D., Francis, I. R., Bova, J. G., Kenney, P. J., Klippenstein, D. L., Foster, G. S., and Turner, D. A. (2000) Safety and efficacy of mangafodipir trisodium (MnDPDP) injection for hepatic MRI in adults: results of the U.S. multicenter phase III clinical trials. *J. Magn. Reson. Imaging 12*, 186–197.

(32) Aime, S., Botta, M., Fasano, M., and Terreno, E. (1998) Lanthanide III chelates for NMR biomedical applications. *Chem. Soc. Rev. 27*, 19–29.

(33) Vander Elst, L., Maton, F., Laurent, S., Seghi, F., Chapelle, F., and Muller, R. N. (1997) A multinuclear MR study of Gd-EOB-DTPA: comprehensive preclinical characterization of an organ specific MRI contrast agent. *Magn. Res. Med. 38*, 604–614.

(34) Muller, R. N., Raduchel, B., Laurent, S., Platzek, J., Pierart, C., Mareski, P., and Vander Elst, L. (1999) Physicochemical characterization of MS-325, a new gadolinium complex, by multinuclear relaxometry. *Eur. J. Inorg. Chem.* 1949–1955.

(35) Lin, Y. J., and Koretsky, A. P. (1997) Manganese ion enhances T_1-weighted MRI during brain activation: an approach to direct imaging of brain function. *Magn. Reson. Med. 38*, 378–388.

BC8004683

ESI for

Development of a Dendritic Manganese-Enhanced Magnetic Resonance Imaging (MEMRI) Contrast Agent: Synthesis, Toxicity *(in vitro)* and Relaxivity (*in vitro, in vivo)* Studies.

Annabelle Bertin,[†] Jérôme Steibel,[‡] Anne-Isabelle Michou-Gallani,[§] Jean-Louis Gallani,[†] and Delphine Felder-Flesch[†]*

[†] Institut de Physique et Chimie des Matériaux de Strasbourg, UMR CNRS/ULP 7504, 23 rue du Lœss BP 43, 67034 Strasbourg Cedex 2, France

* Corresponding author. Tel. : + 33 3 88 10 71 63 ; fax : + 33 3 88 10 72 46 ; e-mail : Delphine.Felder@ipcms.u-strasbg.fr

[‡] Laboratoire d'Imagerie et de Neurosciences Cognitives, UMR CNRS/ULP 7191, 12 rue Goethe, 67000 Strasbourg, France

[§] siRNA Therapeutics, NIBR Biologics Center, Novartis Institutes for Biomedical Research, Inc. 4002 Basel, Switzerland

- ^{1}H spectrum of compound **6**
- Mass spectra (MALDI-MS, negative mode) of compounds **1** and **2**
- *In vitro* relaxivity discussion

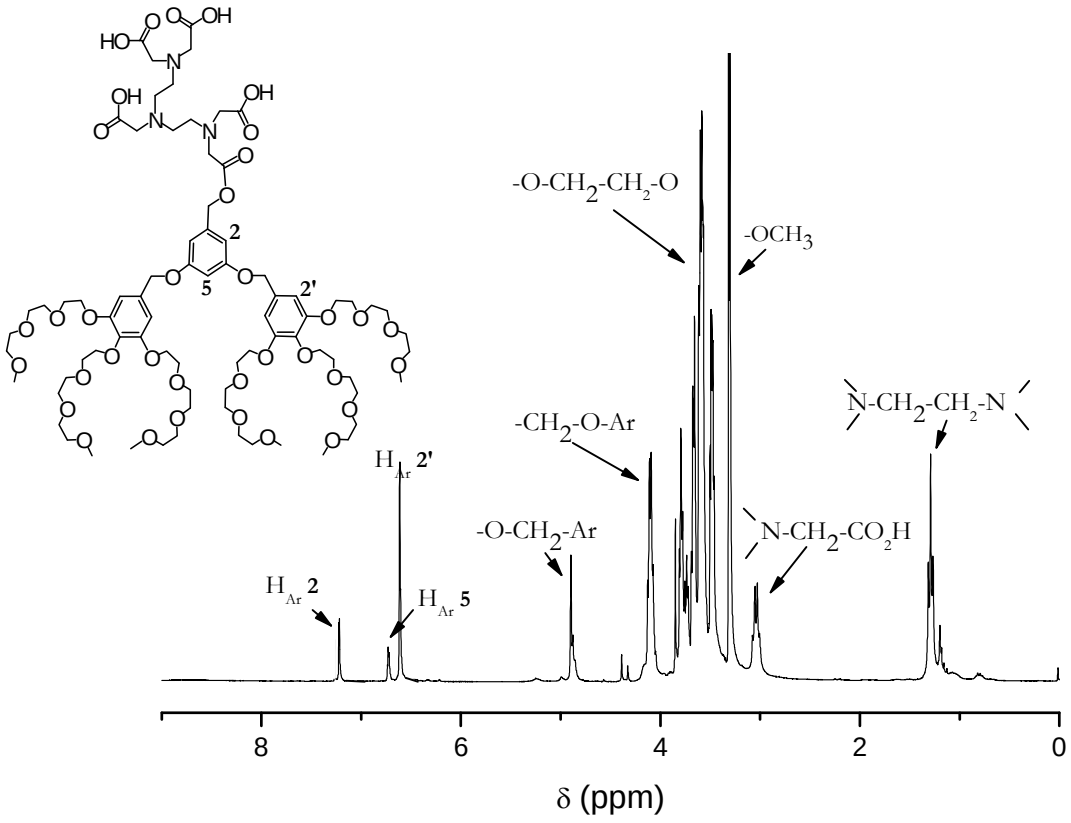

Figure 1. ^{1}H NMR ($CDCl_3$, 300 MHz) of compound **6**.

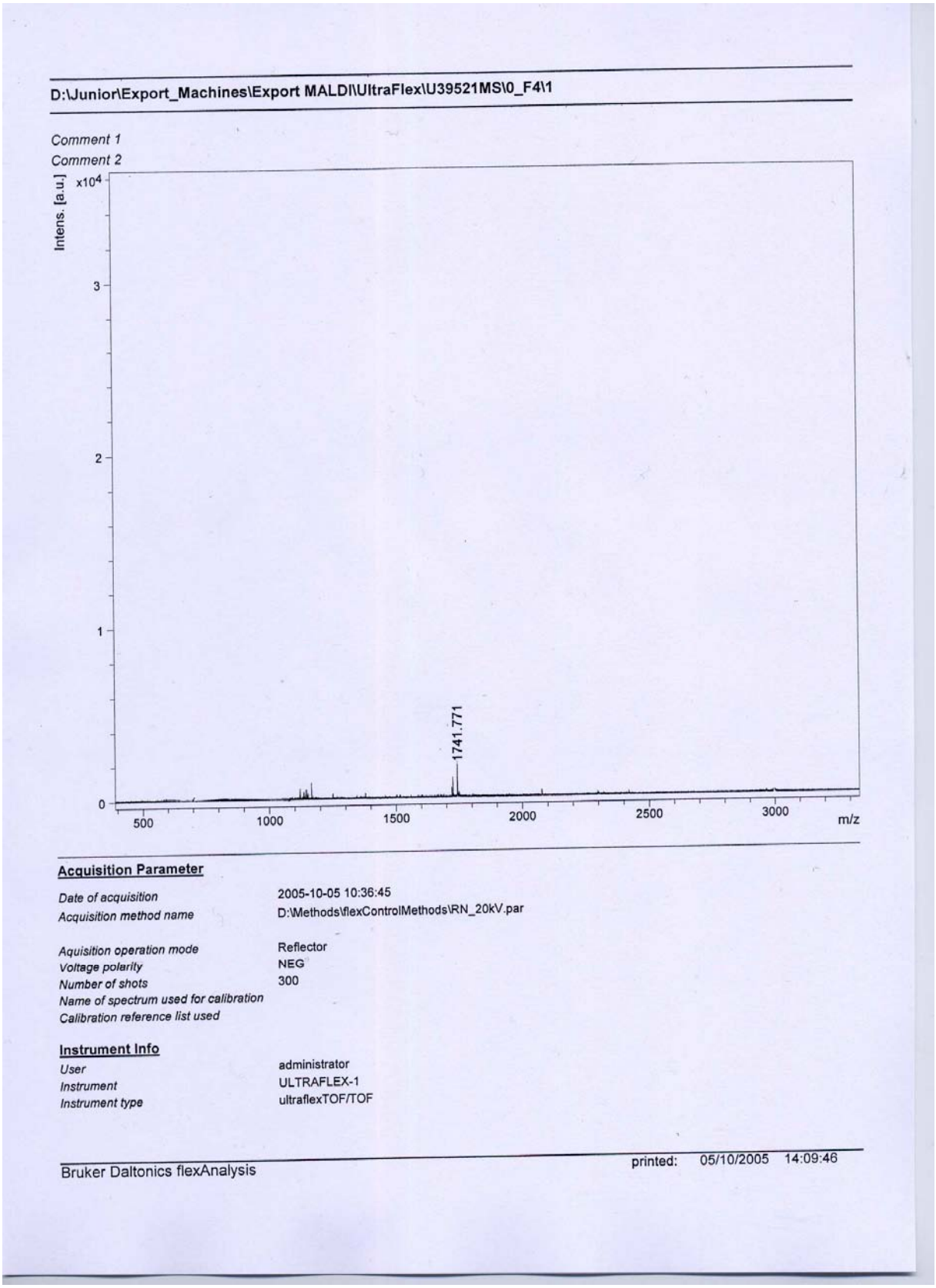

Figure 2. Mass spectrum (Maldi-MS, negative mode) of Mn(II)-complex **1**.

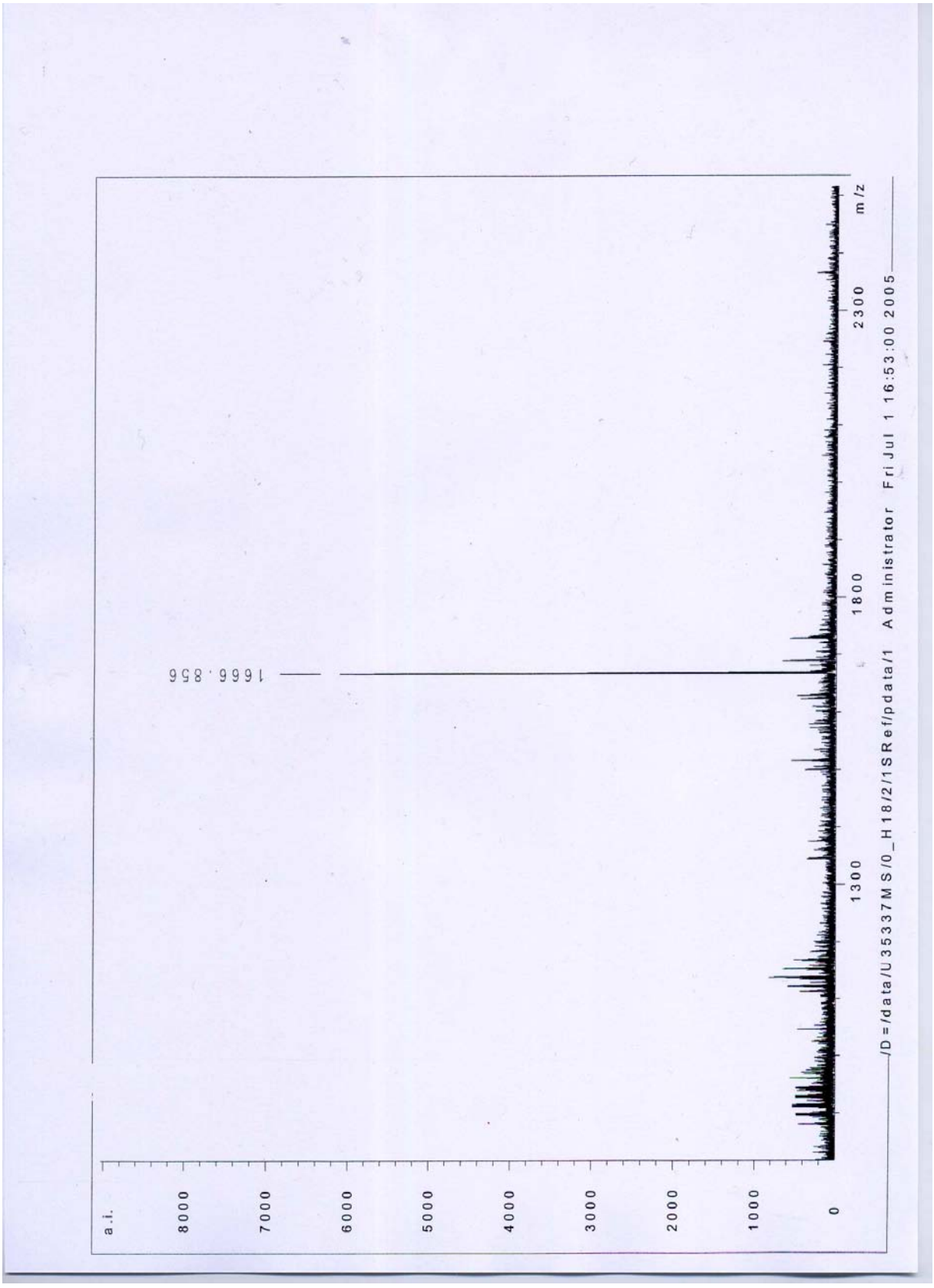

Figure 3. Mass spectrum (Maldi-MS, negative mode) of compound **6**.

***In vitro* relaxivity**

The contrast agent (CA) reduces locally the proton relaxation times. In the classic theory of NMR relaxation by Bloembergen et al. (*1*), it is predicted that the change in proton relaxation rate upon addition of paramagnetic ions to water is proportional to both the concentration and the square of the ion magnetic moment. But except gadolinium, all the lanthanides produce much smaller changes in relaxation rates than would be predicted by the magnetic moment of the alone ion (*2*, *3*). So other parameters should be taken into account.

The internal coordination sphere contribution to relaxivity can be described by the Solomon-Bloembergen-Morgan equation (Equation 1) (*4*-*6*):

$$\frac{1}{T_1} = \frac{3}{10}\frac{\gamma^4 \bar{h}^2}{b^6} r_0 \left[\frac{1}{1+\omega_0^2\tau_0^2} + \frac{4}{1+4\omega_0^2\tau_0^2} \right]$$

$$\frac{1}{T_2} = \frac{3}{20}\frac{\gamma^4 \bar{h}^2}{b^6} r_0 \left[3 + \frac{5}{1+\omega_0^2\tau_0^2} + \frac{2}{1+4\omega_0^2\tau_0^2} \right]$$

Equation (1)

where T_1 is the longitudinal relaxation time and T_2 the transverse relaxation time; τ_0 is the correlation time, ω_0 is the resonance pulse = $2\pi\nu_0$ where ν_0 is the resonance frequency. It is important to note that the dominant parameter in the Solomon-Bloembergen equations is the dipolar correlation time τ_C, defined in Equation (2) as

$$1 / \tau_C = l/\tau_R + l/\tau_S + 1 / \tau_M \qquad \text{Equation (2)}$$

where τ_R is the rotational correlation time, τ_S the electron-spin relaxation time and τ_M the residence lifetime of the water molecule in the inner coordination sphere of the paramagnetic ion. In principle all of these times can contribute to the value of τ_C, and thereby influence enhancement. In practice, τ_C will be determined by the term with the shortest time. Another feature to note is that T_1/T_2 is close to unity for most ions except for Mn^{2+}. This is explained by the fact that for this ion the scalar term in the Solomon-Bloembergen equation is an important contribution to R_2 (=1/ T_2) but not R_1 (=1/ T_1) (*7*).

The effect of one CA on the longitudinal and transverse relaxation times T_1 and T_2 is determined experimentally and measured as relaxivity r_1 and r_2 respectively) normalized to 1 mM concentration at a given magnetic field strength and is used to evaluate the CA efficiency

(*8-11*). So the enhanced relaxation ability of a paramagnetic solution is expressed by the relaxivity (r_i) defined as the slope of Equation (3) in $mM^{-1}. s^{-1}$:

$$(1/T_{1,2})_{observed} = (1/T_{1,2})_{diamagnetic} + r_{1,2}[M] \qquad \text{Equation (3)}$$

where $(1/T_{1,2})_{observed}$ and $(1/T_{1,2})_{diamagnetic}$ are water proton relaxation rates in the presence and absence of paramagnetic species, respectively, [M] is a concentration of a paramagnetic species (in this study [*M*] is either [Mn] or [Gd]), and $r_{1,2}$ is the specific relaxivity.

References

(*1*) Bloembergen, N., Purcell, E. M., Pound, R. V. (1948). Relaxation effects in nuclear magnetic resonance absorption. *Phys. Rev. 73,* 679-712.

(*2*) Solomon, I. (1955). Relaxation processes in a system of two spins. *Phys. Rev. 99,* 559-565.

(*3*) Bloembergen, N. (1957). Proton relaxation times in paramagnetic solutions. *J. Chem. Phys. 27,* 572-573.

(*4*) Bloembergen, N., Morgan, L. O. (1961). Proton relaxation times in paramagnetic solutions. Effects of electron spin relaxation. *J. Chem. Phys. 34,* 842-850.

(*5*) Comblin, V., Gilsoul, D., Hermann, M., Humblet, V., Jacques, V., Mesbahi, M., Sauvage, C., Desreux, J.-F. (1999). Designing new MRI contrast agents : a coordination chemistry challenge. *Coord. Chem. Rev. 185-186,* 451-470.

(*6*) Carrington, A., McLachlan, A. (1967). Introduction to magnetic resonance: with applications to chemistry and chemical physics. Chapman & Hall, London.

(*7*) Toth, E., Helm, L., Merbach, A. E. (2002). Relaxivity of MRI contrast agents. *Top. Curr. Chem. 221*, 61-101.

(*8*) Toth, E., Helm, L., Merbach, A. E. (2001). The chemistry of contrast agents in medical magnetic resonance imaging. In. Merbach, A. E., Toth, E. Editions, Wiley, Chichester, 45-119.

(*9*) Caravan, P., Ellison, J. J., McMurry, T. J., Lauffer, R. B. (1999). Gadolinium(III) chelates as MRI contrast agents :structure, dynamics and applications. *Chem. Rev. 99,* 2293-2352.

(*10*) Lauffer, R. B. (1987). Paramagnetic metal complexes as water proton relaxation agents for NMR imaging: theory and design. *Chem. Rev. 87,* 901-927.

(*11*) Peters, J. A., Huskens, J., Raber, D. J. (1996). Lanthanide induced shifts and relaxation rate enhancements. *Prog. Magn. Res. Spect. 28*, 283-350.

Nuclear Targeted Nanoprobe for Single Living Cell Detection by Surface-Enhanced Raman Scattering

Wei Xie,[†] Li Wang,[‡] Yuying Zhang,[§] Le Su,[†] Aiguo Shen,*[,†] Jinquan Tan,[‡] and Jiming Hu*[,†]

College of Chemistry and Molecular Sciences, School of Basic Medical Science, Wuhan University, Wuhan 430072, People's Republic of China, and Department of Polymer Science and Engineering, Zhejiang University, Hangzhou 310027, People's Republic of China. Received October 29, 2008; Revised Manuscript Received January 7, 2009

We present a novel nuclear targeting nanoprobe based on peptide functionalized gold nanoparticles and its surface-enhanced Raman scattering (SERS) in living cells. For the first time, we probe an original SERS signal from the living cell nucleus by using high-selectivity functionalized gold nanoparticles. The gold nanoparticles conjugated with SV-40 large T nuclear localization signal (NLS) peptide successfully enter the cell nucleus after the incubation with Hela cells and deliver the spatially localized chemical information of the nucleus, as well as the signature of chemicals that intruded subsequently. This new targeted nanoprobe is a nontoxic, biocompatible method for biological research, provided with multiple functions comprising subcellular targeting, intracellular imaging, and real-time SERS detection.

INTRODUCTION

Raman spectroscopy has long been regarded as a valuable tool for the identification of chemicals and biological samples (*1*−*3*). Within the past decade, this novel diagnostic method has attracted more and more interest because of its nondestructivity and low aqueous interference (*4*). At the same time, also along with the development of biomedical science, chemists and biologists have paid more attention to the components present in very low absolute amounts in living organisms. While the small cross sections required for Raman scattering have limited its use to the analysis of relatively concentrated samples, surface-enhanced Raman scattering (SERS) enables its advantage in the detection of very low concentration analytes, even single molecules (*5*−*7*). Generally, the Raman scattering in SERS takes place in the high local optical fields of noble metallic nanostructures, and this is the most important factor of the targeted study within a complex biological environment. As an effectual SERS substrate, gold nanoparticles are easily dispersed and are chemically stabler than silver nanoparticles, which enable them to be widely used for SERS in biomedical research (*8*−*10*).

Studying single living cells by SERS based on gold nanoparticles was first reported by Kneipp et al. (*11*). From then on, probing structural information of intracellular components using this biocompatible substrate was always a major purpose of such studies (*12*−*14*). In fact, there is an unarguable fact that the distribution of bare gold nanoparticles in cells is not under control. In recent years, purposeful SERS applications have been performed by functionalizing the nanoparticles with antibodies or other biomolecules that have a special receptor (*15,16*). The functionalized nanoparticles that also can be described as SERS targeting nanoprobes always contain Raman reporter molecules to highlight the positions of themselves by their high spectral specificity (*16*−*18*). More recently, this method has been successfully used in tumor detection on living animals (*8*). However, the Raman reporter modified targeting nanoprobe provides only the signature of the reporters and tends to be an imaging instrument rather than a detection probe, like the role of a fluorescent reagent or quantum dot; the application of the latter in targeting research is already proving to be excellent (*19*). In fact, delivering molecular structural information from the target analyte is the most important characteristic or advantage of SERS, which until now has not been possible by any other technique. The cell nucleus is a desirable target because the genetic information of the cell and transcription machinery reside there (*20*). Although many methods have succeeded in the nuclear targeted studies using gold nanoparticles, SERS has not been involved, because the functionalization might have blocked the metallic surface or imposed influence on the SERS spectra (*20*−*22*). Oyelere et al. (*23*) recently reported their nuclear targeting method by using gold nanorods, which has been shown to provide SERS information from the local biological environment together with significant influences originating from the functional molecules on the nanorods. Moreover, the targeting effect of the nanorods is not comparable to those using gold nanoparticles (*20*−*22*). The nanorods are distributed into both nucleus and cytoplasm, which is very similar to the distribution of bare gold nanoparticles in living cells observed in other work (*13*). Thus, developing a SERS probe for the detection of special targets remains urgent and will open a window for SERS application in the biomedical field.

In this paper, we show that the nuclear localization signal (NLS) peptide functionalized gold nanoparticles can locate effectively at the cell nucleus and deliver the molecular structural information from the nucleus without notable influence arising from the functionalization. By staining the cell nucleus with DNA intercalator, we are able to evaluate the ability of the nanoprobe to monitor the chemical changes in the nuclear environment.

EXPERIMENTAL PROCEDURES

Preparation of Nuclear Targeted SERS Probe. Gold nanoparticles with a diameter of ∼20 nm for SERS studies were prepared by reduction of gold (III) chloride hydrate using sodium

* Corresponding author. E-mail: jmhu@whu.edu.cn and agshen@whu.edu.cn, Tel: 0086-27-62258931, Fax: 0086-27-68754067, Address: College of Chemistry and Molecular Sciences, Wuhan University, Wuhan 430072, P. R. China.

[†] College of Chemistry and Molecular Sciences, Wuhan University.

[‡] School of Basic Medical Science, Wuhan University.

[§] Department of Polymer Science and Engineering, Zhejiang University.

10.1021/bc800469g CCC: $40.75 © 2009 American Chemical Society
Published on Web 03/06/2009

citrate. After centrifugation, the nanoparticles were resuspended in pH 7.3 borate buffer solution by ultrasonication. The concentrated suspension was then diluted in deionized water to a concentration of $\sim 10^{12}$ particles/mL. The nanoparticles were subsequently modified with 11-mercaptoundecanoic acid (11-MUA) (Aldrich) by adding a 30 μL aliquot of a 1 mM ethanol solution of 11-MUT to 3 mL of the aqueous nanoparticle suspension. Five microliters of 1 mM 1-ethyl-3-[3-dimethylaminopropyl]carbodiimide hydrochloride (EDC) (Sigma) and 2 μL of 1 mM *N*-hydroxysuccinimide (NHS) (Sigma) were added to the modified nanoparticle solution. After that, a 5 μL aliquot of a 0.75 mM SV-40 large T NLS peptide (GL Biochem Ltd.) aqueous solution was added, and the mixture was stirred for 24 h. At last, the product was centrifuged and resuspended in pH 7.4 PBS to a final concentration of $10^{10}-10^{11}$ particles/mL. The supernatant fluid after centrifugation was tested by HPLC (high performance liquid chromatography) to determine the number of NLS molecules on each nanoparticle. A control experiment was performed by using a NLS mutant peptide (KGGGPKKGRKVGG, GL Biochem Ltd.) connected to gold nanoparticles prepared in the same way as the nuclear targeted SERS probe.

Cell Culture and Targeting. Human cervix carcinoma cell line (HeLa) was purchased from China Center for Typical Culture Collection (CCTCC), and all reagents for the cell culture were purchased from Gibco. Cells were cultured in RPMI 1640 medium supplemented with 10% newborn bovine serum, 1% (w/v) glutamine, 100 U/mL penicillin, and 100 μg/mL streptomycin. After incubation at 37 °C in a humidified atmosphere containing 5% CO_2, the cells were resuspended for plating by removing the medium, rinsing three times with PBS, and rinsing the cells with fresh 0.25% trypsin, 1 mM EDTA-Na. Then, after incubation for another 3 min, the activity of trypsin was stopped by adding an equal volume of culture medium, and the cells were diluted to a concentration of 2×10^4 cells/mL. The resuspended cells (3 mL) were placed in a 35 mm Petri dish, permitted to adhere for 24 h, and then the functionalized nanoparticles (200 μL) were added in. After the mixture was incubated overnight at 37 °C, the culture medium was removed and 3 mL fresh medium was added to incubate for another 6 h. Additionally, the cells for DNA intercalator detection were incubated for 5 min with 10 μM 4′,6-diamidino-2-phenylindole (DAPI). Immediately before SERS mapping, the medium was removed, and the cells were rinsed three times in PBS. The cells involved in the SERS mapping (without DAPI staining) were fixed with paraformaldehyde (4% in PBS, pH 7.4) after the point by point scan and incubated subsequently for 40 min in the dark with 5 μM Hoechst 33258 (here, the fixed cells were only for fluorescence imaging). Then, the morphology of the cell nucleus was imaged by a fluorescence microscope (Leica).

Viability of the cells after incubation with the nanoprobe was tested by flow cytometric (FCM) analysis. In this experiment, the cells were incubated with the nanoprobe for 12 h and cultured subsequently for 12 h in fresh medium. After incubation, the cells were collected and washed three times with PBS and then suspended in 75% ethanol at 20 °C overnight. Fixed cells were centrifuged and washed with PBS twice. For detecting DNA content, cells were stained in the dark with propidium iodide (PI) (50 μg/mL) and 0.1% RNase A in PBS at 25 °C for 30 min. Stained cells were applied to a flow cytometer (Becton Dickinson). For each analysis, 10 000 events were recorded.

Raman Measurement. SERS spectra were obtained using a Jobin Yvon Raman microspectrometer (HR 800) with a 632.8 nm helium−neon laser at 13.6 mW with a 1 μm spot size. The objective used was an Olympus 50× long working distance lens (NA = 0.5) for both focusing the excitation beam on the sample and collecting the back-scattering light onto an air-cooled charge-coupled device detector. The collection time of each SERS spectrum was 1 s over a spectral range from 600 to 1700 cm^{-1}. Cells for the measurement adhered to a CaF_2 slide in the culture medium. When Raman mapping was performed, the scan over a single living cell was carried out on a computer-controlled *x*,*y* stage in 1 μm steps at a laser spot size of $\sim 1 \times 10^{-8}$ cm^2. Excitation intensities in the experiments of living cells were less than 1×10^5 W/cm^2, which ensures the safety of the living cells within the measurements. Peak frequencies and rapid checking of instrumental performance were calibrated with the silicon phonon line at 520 cm^{-1}.

Scheme 1. Preparation of the Nuclear Targeted Nanoprobe

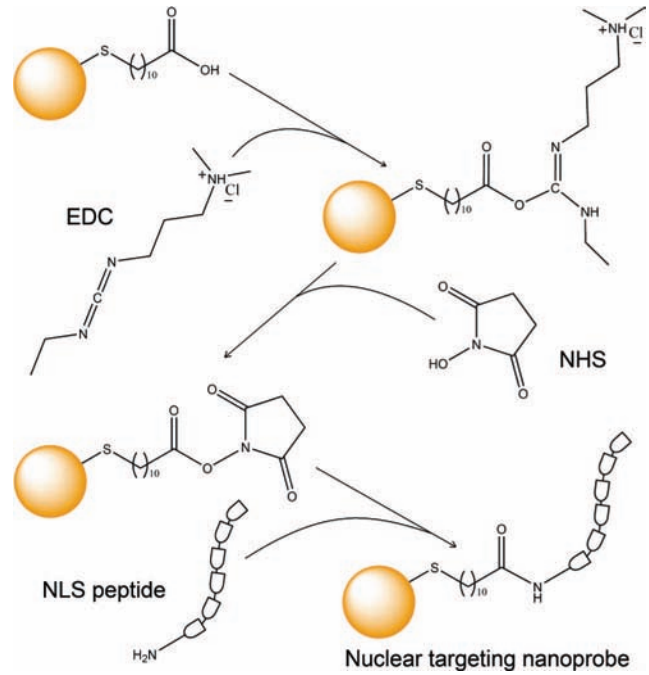

Transmission Electron Micrograph (TEM). Cells incubated with the targeting probe for the TEM experiment were prepared by staining in 1% OsO_4, dehydrating in ethanol gradient, immersing in LR white embedding resin, and curing under UV light. Microtomed sections were then placed on grids and poststained with uranyl acetate and lead acetate. TEM measurements for the cells were performed on a JEOL JEM-100CXII microscope, and high-resolution TEM for the probe was performed on a JEOL JEM-2010 microscope.

RESULTS AND DISCUSSION

Scheme 1 shows the illustration of preparation of the nucleus targeted nanoprobe. EDC reacts with the carboxyl group on the modified nanoparticles, forming an amine-reactive O-acylisourea intermediate. This intermediate reacts with an amine on the peptide, yielding a conjugate of the two molecules joined by a stable amide bond (*24*). In our experiment, HPLC was employed to detect the NLS peptides, which were not conjugated to the gold nanoparticles and remained in the solution after the reaction. The result shown in the Supporting Information indicates that only a very small amount of the peptide molecules were detected and almost all of the peptide were immobilized on the gold surface because of the superfluous carboxyl group. Thus, the number of the peptide molecules per nanoparticle is ~700. More peptide coverage will lead to an increase of nuclear uptake (*25*) but may also influence Raman signal collection, as we have mentioned in the Introduction. High-resolution TEM images of the nanoprobe and naked nanoparticles are shown in Figure 1a,b, respectively. The functionalization resulted in a

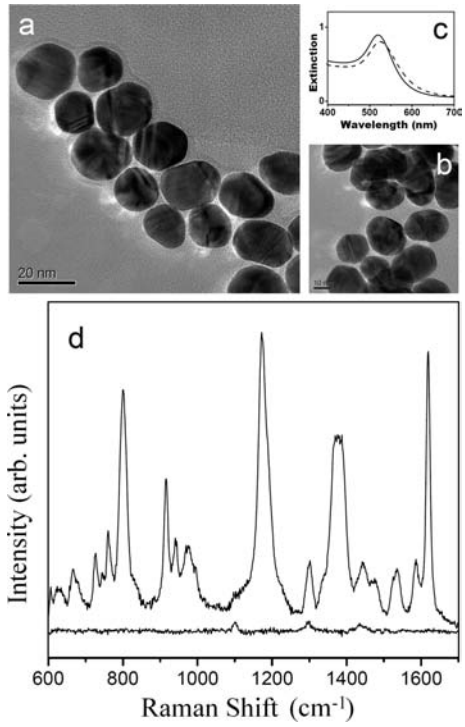

Figure 1. Transmission electron micrographs of the NLS peptide conjugated nanoparticle (nanoprobe) (a) and naked gold nanoparticles (b). (c) Extinction spectra of the nanoprobe and gold nanoparticles (dashed and solid line, respectively). (d) SERS spectra of the nanoprobe (lower spectrum) and CV (10^{-6} M) enhanced by the nanoprobe (upper spectrum).

low-contrast layer surrounding the metal and contributed a ~1.5 nm increment to the radius of the sphere. Figure 1c is the extinction spectra of the nanoparticles before and after the peptide modifying, obtained by using a Varian Cary 100 UV−vis spectrometer. The chemical change on the gold surface resulted in a 5 nm red shift of the surface plasmon because the citrate layer of the nanoparticles was disturbed by the conjugation. Also shown are the SERS spectra of the nanoprobe and its mixture together with 1×10^{-6} mM crystal violet (CV) (Figure 1d) obtained at an acquisition time of 1 s. The concentraton of the nanoprobe here is $10^{10}-10^{11}$ particles/mL, which is 15 times more than that of the nanoprobe used in the cell incubation. Although the signature of the nanoprobe is obtained at that condition, the relatively low SERS intensity of NLS peptide conjugated 11-MUA on the surface of the gold nanoparticles does not impose any notable influence on the SERS detection of CV. Theoretically, either chemical enhancement or electromagnetic enhancement emphasizes the adsorption or compact adjacency of the analyte and the metal surface (*26, 27*). The enhancement of CV by the nanoprobe indicates that the functionalization leads to a partial surface coverage of the gold nanoparticles and the product is capable of vibrational information delivery in aqueous solution.

Cultured cells were incubated with the nanoprobe as described in the Experimental Procedures, and the cell viability was tested by using FCM analysis in a broad concentration range of nanoprobe. The result shown in Figure 2 indicates that no evident apoptosis was caused by the nanoprobe even at a rather high concentration. Generally, after entry into the cell the NLS peptide will bring the particle to the nucleus by interaction with the pore complex and then cross the nuclear membrane (*20*). Raman mapping of living HeLa cells incubated with the targeting and control probe performed by the Jobon-Yvon system using a 50× long working distance objective is shown in Figure 3A. The mapping automatically merged by the

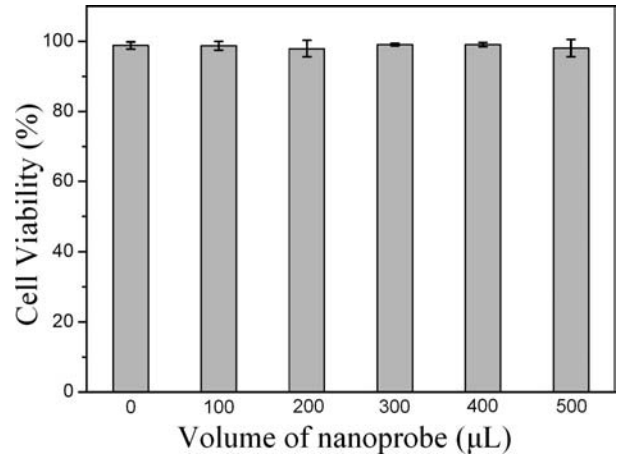

Figure 2. Cell viability after the addition of varying volumes of nanoprobe into 3 mL aliquots of culture medium. Error bars represent standard deviation of the measurements.

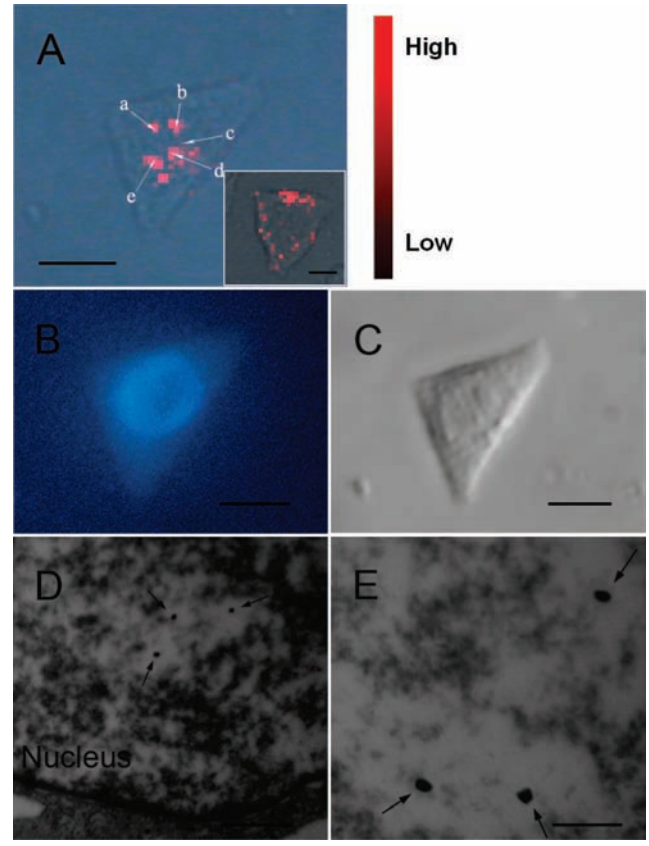

Figure 3. (A) Merged SERS image made up of a SERS map by the intensity from 600 to 1700 cm^{-1} and an optical transmission image. The arrows indicate the positions where the spectra in Figure 4 were collected. Scale bar: 10 μm. The insert is the cell incubated with NLS mutant functionalized nanoparticles as the control experiment. Scale bar: 5 μm. (B) Fluorescent image of the cell after nuclear staining by Hoechst 33258. Scale bar: 10 μm. (C) Differential interference contrast micrograph of the cell. Scale bar: 10 μm. (D) Transmission electron micrograph showing the entry of the nanoprobe to the cell nucleus. Scale bar: 400 nm. (E) Transmission electron micrograph of the nanoprobe inside the cell nucleus. Scale bar: 100 nm.

detection system contains an optical transmission image and a SERS image constructed by the total SERS intensity between 600 and 1700 cm^{-1}. These images only give the spatial information of the SERS. Several spectra which are selected as examples from 812 spectra (indicated by white arrows) in the mapping of the targeted cell will be discussed later. As shown

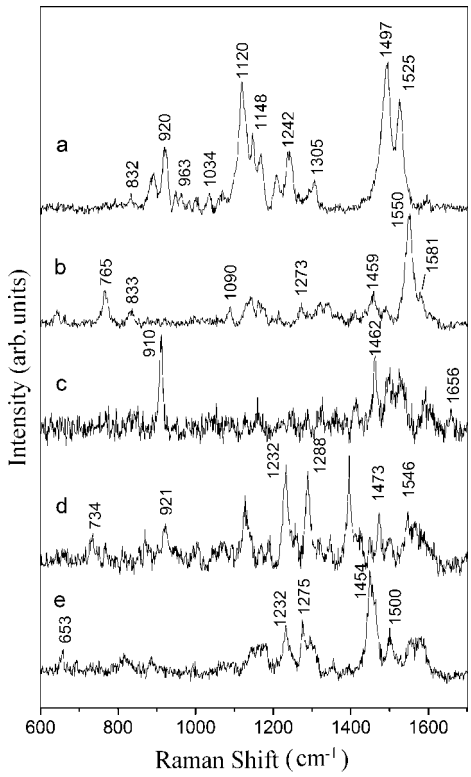

Figure 4. SERS spectra obtained from the nucleus of a single living cell incubated with the targeting nanoprobe at points 359, 334, 450, 506 and 532, respectively.

in the mapping, the SERS signals provided by the targeted probe tend to be in the center of the cell. In order to determine the distribution of the probe in the cell, or the position of the cell where the SERS signals come from, immediately after the SERS detection the cell was stained by Hoechst 33258, a bisbenzimide DNA intercalator which can highlight the nucleus by producing fluorescent emission at 461 nm while bound with DNA. The fluorescent image together with a differential interference contrast micrograph of the stained cell is presented in Figure 3 (B and C, respectively). It clearly shows in the figure that most of the SERS signals in the targeted mapping are generated in the location of cell nucleus and the signals in the control experiment are mainly from the cytoplasm. Additionally, in the electron micrograph (see Figure 3D) the nanoparticles were found inside the nucleus, which proves again that the nanoprobe is able to cross the nuclear membrane. Figure 3E is a typical electron micrograph of the nanoparticles inside the nucleus, and no evidence of membrane structure was found close by, which indicates that these nanoparticles were not in a special chemical environment inside the nucleus.

If this nanoprobe is to be a useful intracellular targeting tool, then one would expect to see the ability of chemical probing in the nucleus. Figure 4 shows the typical SERS spectra obtained from the cell nucleus at points 359, 334, 450, 506, and 532 of the mapping. Each of the spectra has received contributions originating from DNA backbone and bases. Deformations and rocking vibrations of CH_2 groups in deoxyribose appear at 1455−1462 cm^{-1} and 992−996 cm^{-1}, respectively. Spectrum a contains signatures of adenine base at 1305 cm^{-1} and of DNA backbone phosphate at 832 cm^{-1}, the frequency of both suggesting that the DNA molecule investigated has a right-handed double helix conformation, also known as the B form. Similar bands can also be found in spectra b and e, but no evidence of other DNA conformations (A and Z) was obtained during the experiment, which confirms that DNA of B form dominates

Table 1. Raman Frequencies Observed in Nuclear SERS Spectra of a Living HeLa Cell and Their Tentative Assignments

Raman bands (cm^{-1})	assignments[a,b]
642	Tyr: ν(CS)
653	Tyr: γ(CC)
734	A
832, 833	phosphate: ν(OPO)
868	deoxyribose: ν(CC)
891	saccharides
910, 920, 921	Pro: ring ν(CC)
963	proteins: ν(CC)
982	Phe: ω(CH)
996	deoxyribose: $\rho(CH_2)$
1000, 1003	Phe: ring breath
1034	deoxyribose: ν(CO)
1069, 1090, 1093	phosphate: $\nu(PO_2^-)$, ν(COC)
1120	proteins: ν(CN)
1134	Pro
1148	deoxyribose-phosphate
1159, 1160, 1164, 1167, 1168	proteins: ν(CN), ν(CC); $\rho(CH_3)$
1180, 1189	nucleotides: base ν(CN)
1207	Tyr, Phe
1215	T, A
1232, 1273, 1275, 1288	proteins: amide III
1242	A, T, ring ν
1297, 1305	A, $\gamma(CH_2)$
1320	G
1342, 1345, 1355	proteins: $\delta(CH_2)$
1410	$\nu_s(COO^-)$
1454, 1459	deoxyribose: $\delta(CH_2)$
1473	lipids, proteins: $\delta(CH_2, CH_3)$
1490, 1497, 1500, 1501	G, A
1530	G, C
1546, 1550, 1554	proteins: amide II; Trp
1580, 1581	G, A
1589	G, A, Phe, Tyr
1656	proteins: amide I

[a] Based on *refs* 12−14, 28, 29. [b] Abbreviations: ν, stretching; δ, deformation; ρ, rocking; γ, twisting; ω, wagging; s, symmetrical; Tyr, tyrosine; Phe, phenylalanine; Pro, proline; A, adenine; T, thymine; C, cytosine; G, guanine.

the cell nucleus. On the other hand, the SERS spectra also give conformational information on proteins, another main component of the nucleus. Spectrum c shows an amide I band at 1656 cm^{-1}, which indicates a protein α-helix. In spectra d and e, both characteristics of α-helix and β-sheet conformations are found according to amide III contributions at 1275 (α-helix) and 1232 cm^{-1} (β-sheet). The detailed SERS band assignments for these spectra are given in Table 1.

In addition to the detection of the original components in the nucleus, the nanoprobe is also propitious to deliver vibrational information from molecules intruded. The living cells were stained with DAPI, a DNA intercalator with great SERS activity, immediately after incubation with the nanoprobe, and SERS mapping was performed subsequently. Figure 5 shows the image recorded based on the band intensity at 1615 cm^{-1}, which is assigned to C═N stretching of DAPI in the nucleus. Characteristic DAPI signatures acquired outside using the nanoprobe are presented as trace A together with the SERS spectrum of DAPI obtained inside the stained nucleus at mapping point 510 for comparison. Both spectra show very similar SERS features of DAPI except for some band shifting due to the minor-groove binding at adenine−thymine sites of DNA. Typically, the C═N stretching vibration at 1607 cm^{-1} (spectrum A) shifted to 1615 cm^{-1} in spectrum B, which is very likely associated with the formation of conjugated systems between DAPI and DNA bases. Besides DAPI signatures, spectrum A also shows various contributions from cellular components. For example, the band at 1405 cm^{-1} can be assigned to symmetrical stretching vibration of COO^- in protein, and band 735 cm^{-1}

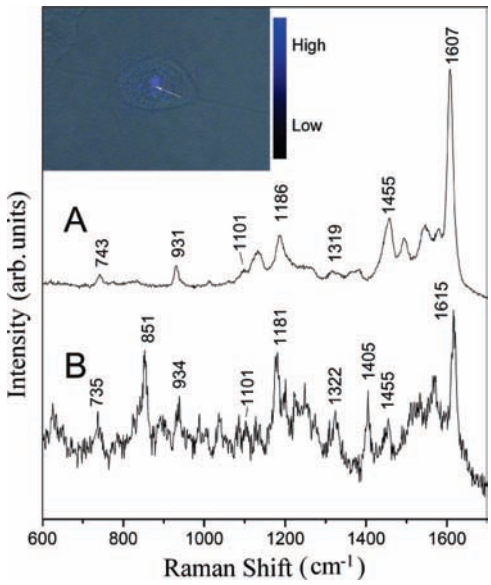

Figure 5. SERS spectra of DAPI obtained in solution (10 μg/mL) mixed with the NLS functionalized gold nanoparticles (A) and in a living cell nucleus (stained by DAPI) (B). The inset shows the SERS image which was collected according to the Raman intensity at 1615 cm^{-1}. The arrow indicates point 510 where spectrum B was obtained. Acquisition time: 1 s.

is a SERS characteristic of adenine. The targeting nanoprobe entered the cell before DAPI did, and the gold surface was still available for DAPI vibration to be enhanced. This result indicates that the gold surface has not been blocked even inside nucleus and the nanoprobe is capable of delivering real-time chemical changes in its vicinity.

CONCLUSIONS

We have demonstrated a targeting probing method for nucleus detection in living cells. The SV-40 large T NLS peptide functionalized gold nanoparticles can locate effectively at the cell nucleus after incubation with the cultured cells, allowing molecular probing of the nuclear components in vivo. Our SERS data provide abundant structural information for both nucleic acids and proteins without notable disturbance attributed to the functionalization. Moreover, by using DAPI as a test sample, we show that the targeting probe can also deliver the vibrations from molecules intruded subsequently, which enables this method to be a real-time targeting detection technique. The nanoprobe described in this study has the potential to be used in the research of drug delivery and cancer therapy.

ACKNOWLEDGMENT

W. Xie thanks the National Science Foundation of China (grants no. 30772058 and no. 20705025) for ongoing financial support of our work.

Supporting Information Available: HPLC result of the supernatant fluid after centrifugation in the preparation process of the nuclear targeted nanoprobe. This material is available free of charge via the Internet at http://pubs.acs.org.

LITERATURE CITED

(1) Tenne, D. A., Bruchhausen, A., Lanzillotti-Kimura, N. D., Fainstein, A., Katiyar, R. S., Cantarero, A., Soukiassian, A., Vaithyanathan, V., Haeni, J. H., Tian, W., Schlom, D. G., Choi, K. J., Kim, D. M., Eom, C. B., Sun, H. P., Pan, X. Q., Li, Y. L., Chen, L. Q., Jia, Q. X., Nakhmanson, S. M., Rabe, K. M., and Xi, X. X. (2006) Probing nanoscale ferroelectricity by ultraviolet Raman spectroscopy. *Science 313*, 1614–1616.

(2) Jayaraman, V., Rodgers, K. R., Mukerji, I., and Spiro, T. G. (1995) Hemoglobin allostery: resonance Raman spectroscopy of kinetic intermediates. *Science 269*, 1843–1848.

(3) Puppels, G. J., de Mul, F. F., Otto, C., Greve, J., Robert-Nicoud, M., Arndt-Jovin, D. J., and Jovin, T. M. (1990) Studying single living cells and chromosomes by confocal Raman microspectroscopy. *Nature 347*, 301–303.

(4) Haka, A. S., Shafer-Peltier, K. E., Fitzmaurice, M., Crowe, J., Dasari, R. R., and Feld, M. S. (2005) Diagnosing breast cancer by using Raman spectroscopy. *Proc. Natl. Acad. Sci. U.S.A. 102*, 12371–12376.

(5) Nie, S., and Emory, S. R. (1997) Probing single molecules and single nanoparticles by surface-enhanced Raman scattering. *Science 275*, 1102–1106.

(6) Kneipp, K., Kneipp, H., Itzkan, I., Dasari, R. R., and Feld, M. S. (1999) Ultrasensitive chemical analysis by Raman spectroscopy. *Chem. Rev. 99*, 2957–2976.

(7) Kneipp, K., and Kneipp, H. (2006) Single molecule Raman scattering. *Appl. Spectrosc. 60*, 322A–334A.

(8) Qian, X., Peng, X. H., Ansari, D. O., Yin-Goen, Q., Chen, G. Z., Shin, D. M., Yang, L., Young, A. N., Wang, M. D., and Nie, S. (2008) In vivo tumor targeting and spectroscopic detection with surface-enhanced Raman nanoparticle tags. *Nat. Biotechnol. 26*, 83–90.

(9) Driskell, J. D., Kwarta, K. M., Lipert, R. J., Porter, M. D., Neill, J. D., and Ridpath, J. F. (2005) Low-level detection of viral pathogens by a surface-enhanced Raman scattering based immunoassay. *Anal. Chem. 77*, 6147–6154.

(10) Souza, G. R., Levin, C. S., Hajitou, A., Pasqualini, R., Arap, W., and Miller, J. H. (2006) In vivo detection of gold-imidazole self-assembly complexes: NIR-SERS signal reporters. *Anal. Chem. 78*, 6232–6237.

(11) Kneipp, K., Haka, A. S., Kneipp, H., Badizadegan, K., Yoshizawa, N., Boone, C., Shafer-Peltier, K. E., Motz, J. T., Dasari, R. R., and Feld, M. S. (2002) Surface-enhanced Raman spectroscopy in single living cells using gold nanoparticles. *Appl. Spectrosc. 56*, 150–154.

(12) Kneipp, J., Kneipp, H., Rice, W. L., and Kneipp, K. (2005) Optical probes for biological applications based on surface enhanced Raman scattering from indocyanine green on gold nanoparticles. *Anal. Chem. 77*, 2381–2385.

(13) Tang, H. W., Yang, X. B., Kirkham, J., and Smith, D. A. (2007) Probing intrinsic and extrinsic components in single osteosarcoma cells by near-infrared surface-enhanced Raman scattering. *Anal. Chem. 79*, 3646–3653.

(14) Kneipp, J., Kneipp, H., McLaughlin, M., Brown, D., and Kneipp, K. (2006) In vivo molecular probing of cellular compartments with gold nanoparticles and nanoaggregates. *Nano Lett. 6*, 2225–2231.

(15) Souza, G. R., Christianson, D. R., Staquicini, F. I., Ozawa, M. G., Snyder, E. Y., Sidman, R. L., Miller, J. H., Arap, W., and Pasqualini, R. (2006) Networks of gold nanoparticles and bacteriophage as biological sensors and cell-targeting agents. *Proc. Natl. Acad. Sci. U.S.A. 103*, 1215–1220.

(16) Kim, J. H., Kim, J. S., Choi, H., Lee, S. M., Jun, B. H., Yu, K. N., Kuk, E., Kim, Y. K., Jeong, D. H., Cho, M. H., and Lee, Y. S. (2006) Nanoparticle probes with surface enhanced Raman spectroscopic tags for cellular cancer targeting. *Anal. Chem. 78*, 6967–6973.

(17) Cao, Y. C., Jin, R., and Mirkin, C. A. (2002) Nanoparticles with Raman spectroscopic fingerprints for DNA and RNA detection. *Science 297*, 1536–1540.

(18) Vo-Dinh, T., Yan, F., and Wabuyele, M. B. (2005) Surface-enhanced Raman scattering for medical diagnostics and biological imaging. *J. Raman Spectrosc. 36*, 640–647.

(19) Wu, X., Liu, H., Liu, J., Haley, K. N., Treadway, J. A., Larson, J. P., Ge, N., Peale, F., and Bruchez, M. P. (2003) Immunofluorescent labeling of cancer marker Her2 and other cellular

targets with semiconductor quantum dots. *Nat. Biotechnol. 21*, 41–46.

(20) Tkachenko, A. G., Xie, H., Coleman, D., Glomm, W., Ryan, J., Anderson, M. F., Franzen, S., and Feldheim, D. L. (2003) Multifunctional gold nanoparticle-peptide complexes for nuclear targeting. *J. Am. Chem. Soc. 125*, 4700–4701.

(21) Tkachenko, A. G., Xie, H., Liu, Y., Coleman, D., Ryan, J., Glomm, W. R., Shipton, M. K., Franzen, S., and Feldheim, D. L. (2004) Cellular trajectories of peptide-modified gold particle complexes: Comparison of nuclear localization signals and peptide transduction domains. *Bioconjugate Chem. 15*, 482–490.

(22) de la Fuente, J. M., and Berry, C. C. (2005) Tat peptide as an efficient molecule to translocate cold nanoparticles into the cell nucleus. *Bioconjugate Chem. 16*, 1176–1180.

(23) Oyelere, A. K., Chen, P. C., Huang, X., El-Sayed, I. H., and El-Sayed, M. A. (2007) Peptide-conjugated gold nanorods for nuclear targeting. *Bioconjugate Chem. 18*, 1490–1497.

(24) Staros, J. V., Wright, R. W., and Swingle, D. M. (1986) Enhancement by N-hydroxysulfosuccinimide of water-soluble carbodiimide-mediated coupling reactions. *Anal. Biochem. 156*, 220–222.

(25) Dworetzky, S. I., Lanford, R. E., and Feldherr, C. M. (1988) The effects of variations in the number and sequence of targeting signals on nuclear uptake. *J. Cell Biol. 107*, 1279–1287.

(26) Haynes, C. L., McFarland, A. D., and Van Duyne, R. P. (2005) Surface-enhanced Raman spectroscopy. *Anal. Chem. 77*, 338A–346A.

(27) Aroca, R. (2006) Electromagnetic enhancement mechanism. *Surface-Enhanced Vibrational Spectroscopy*, pp 76−96, John Wiley & Sons, Ltd., Chichester, England.

(28) Thomas, G., Jr., and Kyogoku, Y. (1977) Biological science. In *Infrared and Raman spectroscopy, Part C* (Bram, E., Jr., and Grasselli, J. G., Eds.) pp 717−872, Marcel Dekker, Inc., New York.

(29) Peticolas, W. L., Patapoff, T. W., Thomas, G. A., Postlewait, J., and Powell, J. W. (1996) Laser Raman microscopy of chromosomes in living eukaryotic cells: DNA polymorphism in vivo. *J. Raman Spectrosc. 27*, 571–587.

BC800469G

HPLC (High Performance Liquid Chromatography) was employed to test the supernatant fluid after centrifugation in the preparation process of the nuclear targeted nanoprobe. This experiment was aimed at detecting the NLS peptides which were not conjugated to the gold nanoparticles and thus to determine the average number of NLS molecules on each nanoparticle.

Experimental Information

Column: 250*4.6 mm, Kromasil Normal phase C18-5 μm.

Mobile Phase A: 0.1% trifluoroacetic in water.

Mobile Phase B: 0.1% trifluoroacetic in acetonitrile.

Gradient:

Time(min)	A	B
0.1	90%	10%
15	80%	20%
15.01	0	100%
20	STOP	

Flow rate: 1.0 ml/min.

Wavelength: Sig=220 nm, Ref=399 nm.

Volume: 10 μL (The samples, including the supernatant fluid and the control, are lyophilized and redissolved to achieve a proper concentration for the detection).

Result

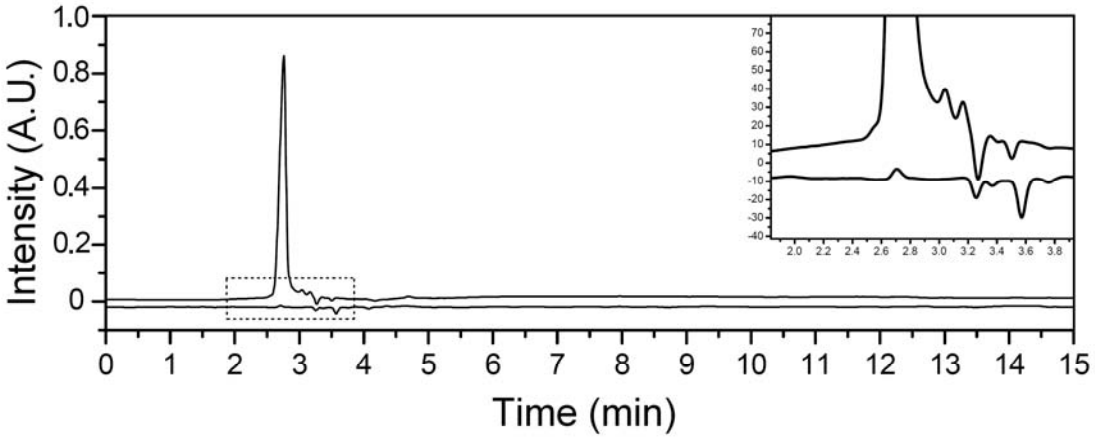

Figure 1. HPLC elution data of NLS peptide in the supernatant fluid after conjugating with 11-mercaptoundecanoic acid modified gold nanoparticles (lower line) and control experiment by using water instead of modified gold nanoparticles (upper line). The insert illustrates the data within the dashed pane.

Synthesis and Characterizations of New Lysine-Based Biodegradable Cationic Poly(urethane-co-ester) and Study on Self-Assembled Nanoparticles with DNA

Zheng-Yan Jian,[†] Jiunn-Kae Chang,[‡] and Min-Da Shau*[,‡]

Department of Chemical Engineering, National Cheng Kung University, Tainan 70101, Taiwan, and Department of Biotechnology, Chia-Nan University of Pharmacy and Science, Tainan 71710, Taiwan. Received November 19, 2008; Revised Manuscript Received February 16, 2009

To improve the self-assembly efficiency of nanoparticles with DNA, we synthesized lysine-based poly(urethane-co-ester) PMMD (**6**) and polyester PDMA (**8**) bearing ester linkages in the backbone and tertiary amines in the side chain. Both poly(urethane-co-ester) PMMD (**6**) and polyester PDMA (**8**), readily self-assembled with plasmid DNA (pCMV-β-gal) in HEPES buffer, were characterized by dynamic light scattering and zeta-potential. The results reveal that PMMD (**6**) and PDMA (**8**) were able to self-assemble particles with DNA and yield complexes with positive charges of 80−115 nm and 170−180 nm in size at mass ratios (W/W) of 2/1 and 20/1, respectively. The degradation studies indicate that the half-life of PMMD (**6**) in the HEPES buffer was 20 h at pH 7.4. Titration studies were performed to determine the buffering capacities of the polymers. In addition, the COS-7 cell viabilities in the presence of PMMD/DNA, PDMA/DNA, and PEI/DNA were studied. The results indicate that PMMD (**6**) is an attractive cationic poly(urethane-co-ester) for gene delivery and an interesting candidate for further study.

INTRODUCTION

Plasmid DNA has great potential as a therapeutic agent and in new vaccines (*1*). DNA-based pharmaceuticals largely depend on the characteristics of the delivery systems (*2*). To achieve controlled delivery of DNA to the target, vectors have been substantially developed. Because viral vectors have drawbacks such as the random insertion of viral sequences into the host chromosomes, indication of immunological responses, and limitations associated with DNA size, considerable attention has been given to nonviral vectors. Polycations (*3*−*9*) have been widely investigated in nonviral gene delivery in a variety of materials. Cationic polymers condense DNA into nanoparticles small enough to enter a cell, and protect negatively charged strands of DNA from nuclease degradation. Cytotoxicity and nonbiodegradability are concerns for long-term safety. Several amine-containing polymers, such as poly(urethane) (*4*, *10*), poly(2-(dimethylamino)ethyl methacrylate) (PDMAEMA) (*11*), poly(amido-amine) (*12*, *13*), poly(ethylene imine) (PEI) (*14*), poly(*N*-methyldietheneamine sebacate) (*15*), poly(amido ethylenimine) (*16*), PAMAM-PEG (*17*), and poly(ethylene glycol)s (*18*), have been synthesized. Release of the delivery vehicle from these sections into the cytoplasm is believed to be the limiting step in the transfection mediated by many cationic polymers (*19*). Molecular weights of polymers and the polymer/DNA ratio have been shown to be important for transfection efficiency. The molecular weight of a polymer affects the affinity between the cation-chain of the polymer and the anion-strand of DNA (*20*, *21*). Polyesters are biodegradable biomaterials that are used in a wide range of applications, including the controlled release of DNA-based therapeutic agents. These include the controlled degradation of the polymer and a great diversity of side groups and backbones. In this study, amine-containing polyester (PDMA) and poly(urethane-co-ester) (PMMD) were designed and synthesized. Their structures in correlation to DNA condensation capacity, biodegradability, and cytotoxicity are discussed in this article.

MATERIALS AND METHODS

Materials. 1,4-Butanediol diacrylate was purchased from Lancaster. L-Lysine methyl ester diisocyanate was from LDI, Kyowa Hakko Kogyo, Japan. 2-Hydroxyethyl acrylate (HEA), *n*-hexane, 2-dimethyaminoethylamine (DMAE), and glutaraldehyde were obtained from Fluka Co. (Switzerland). The solvent of *N*,*N*-dimethylformamide (DMF, Tedia co., USA) was dried over calcium hydride and distilled just before use. *N*-[2-Hydroxyethyl] piperazine-*N*′-[2-ethanesulfonic acid] (HEPES) was obtained from Sigma Co. (USA). *N*-Methyl dibenzopyrazine methyl sulfate (electron-coupling reagent) and sodium (2,3-bis(2-methoxy-4-nitro-5-sulfophenyl)-2*H*-tetrazolium-5-carboxanilide) (XTT) were purchased from Roche Co. (USA). The plasmid pCMV-LacZ (pCMV-βgal) (*4*, *22*) contained a CMV promoter to drive β-galactosidase (LacZ) gene expression (*4*, *14*, *23*). The plasmid DNA was amplified in *Escherichia coli* (DH5α strain) and purified using column chromatography (Qiagen Plasmid Mega kit, Germany). The purified plasmid DNA was dissolved in a tris(hydroxymethyl) methylamine-ethyldiaminetetraacetic acid (Tris-EDTA) buffer (pH 8.0) and determined using the ratio of UV absorbance at 260 nm/280 nm. Monkey SV40 transformed kidney fibroblast COS-7 cells were obtained from American type Culture Collection (ATCC, CRL-1651). The cells were cultured in Dulbecco's modified Eagle's medium (DMEM, GibcoBRL Co., Ltd.) supplemented with 10% FBS, 4.5 g/L glucose, 1.5 g/L sodium bicarbonate, and 4 mM L-glutamine, and maintained at 37 °C in a humidified 5% CO_2-containing atmosphere.

Polymer Characterizations. The structures of the polymers were characterized by nuclear magnetic resonance (NMR, Bruker AMX-400 spectrometer) and Fourier transform infrared (FT-IR, Mattson Galaxy Series 5000 spectroscope). The molecular weight and distribution of the polymer was determined

* Corresponding author. Tel: 886-6-2664911ext. 2505. Fax: +886-6-266-2132. E-mail: minda.shau@msa.hinet.net.
[†] National Cheng Kung University.
[‡] Chia-Nan University of Pharmacy and Science.

10.1021/bc800499w CCC: $40.75 © 2009 American Chemical Society
Published on Web 03/26/2009

Scheme 1. Synthesis Scheme of PMMD

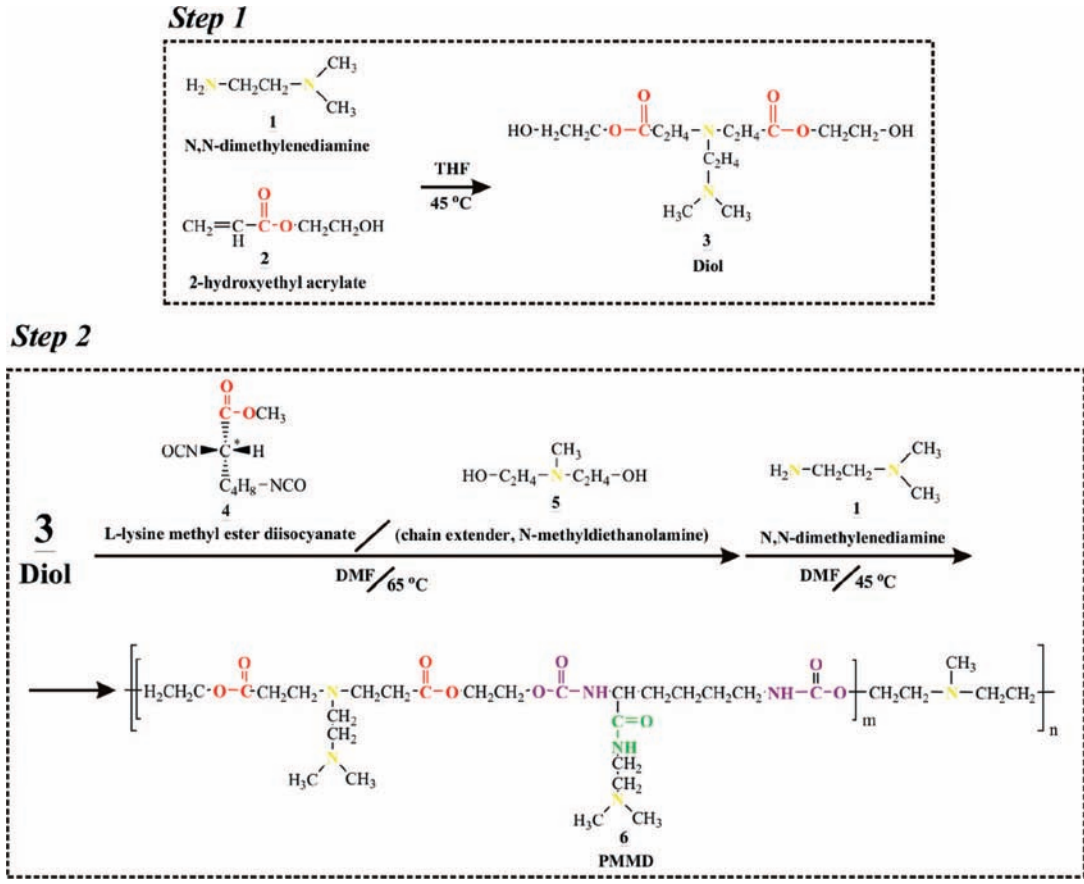

by gel permeation chromatography analysis (GPC, Waters Model LC-2410) based on polystyrene standards in THF.

Synthesis of PMMD (6). PMMD (**6**) was synthesized as shown in Scheme 1. HEA (**2**) and DMAE (**1**) with a molar ratio of 2/1 (-C═C/-NH_2) were mixed in THF in a three-necked reaction flask under a dry nitrogen purge and then heated to 45 °C to react for 24 h. The product was precipitated in anhydrous ethyl ether and vacuum-dried at 40 °C. The purity of diol (**3**) was about 98%. The diol (**3**) and polymers were characterized by FT-IR, ^{1}H NMR, and ^{13}C NMR.

Diol (3). ^{1}H NMR (400 MHz, d_6-DMSO, ppm) δ: 4.6 (1H, -$CH_2CH_2O\underline{H}$), 2.3−2.5 (6H, -$C\underline{H}_2C\underline{H}_2$-, -$C\underline{H}_2CH_2COO$-), 3.1 (2H, -$C\underline{H}_2COO$-), 4.1 (2H, -$COOC\underline{H}_2$-), 3.7 (2H, -$C\underline{H}_2OH$), 2.2 (6H, -$N(C\underline{H}_3)_2$). ^{13}C NMR (400 MHz, d_6-DMSO, ppm) δ: 57.5 (-$COOCH_2\underline{C}H_2$-), 60.2 (-$COO\underline{C}H_2CH_2$-), 53.9 (-$\underline{C}H_2COO$-), 59.3 ($N\underline{C}H_2CH_2$-), 58.9 ($N\underline{C}H_2CH_2N(CH_3)_2$), 59.1 ($NCH_2$-$\underline{C}H_2N(CH_3)_2$), 44.2 (-$N(\underline{C}H_3)_2$), 174.5 (-$\underline{C}OO$-).

The monomers of diol (**3**) and LDI (**4**) with an -OH/-NCO molar ratio of 2/1 were mixed and then heated to 70 °C to react using 0.5 wt % dibutyltin dilaurate as a catalyst. The chain extension was carried out by slowly adding MDEA (*N*-methyldiethanolamine) (**5**) to the isocyanate-terminated prepolymer until the -NCO/-OH molar ratio was 1/1. PMMD (**6**) was synthesized through the aminolysis reaction as previously reported (*4*).

PMMD (6). ^{1}H NMR (400 MHz, d_6-DMSO, ppm) δ: 2.0−2.2 (3H, $NC\underline{H}_3$), 2.3−2.5 (4H, -$C\underline{H}_2C\underline{H}_2N$), 3.1 (2H, -$C\underline{H}_2COO$-), 3.7−4.2 (4H, -$OC\underline{H}_2C\underline{H}_2O$-), 3.0 (1H, -$C\underline{H}CONH$-), 1.3−1.8 (6H, -$C\underline{H}_2C\underline{H}_2C\underline{H}_2$-), 3.6 (2H, -$C\underline{H}_2NHCOO$-), 3.7−4.2 (2H, -$NHCOOC\underline{H}_2$-), 3.6 (2H, -$CONHC\underline{H}_2$-), 5.3 (1H, -$CH_2N\underline{H}$-COO-), 5.7 (1H, -$COON\underline{H}CH$-), 7.0 (1H, -$CON\underline{H}CH_2$-). ^{13}C NMR (400 MHz, d_6-DMSO, ppm) δ: 43.7 ($N\underline{C}H_3$), 56.1 (-$CH_2\underline{C}H_2N$), 40.3 (-$\underline{C}H_2NHCOO$-), 22.3 (-$CH_2CH_2\underline{C}H_2CH_2NH$-COO-), 29.2 (-$CH_2\underline{C}H_2CH_2CH_2NHCOO$-), 31.8 (-$\underline{C}H_2CH_2$-$CH_2CH_2NHCOO$-), 53.6 (-$OOCNHC\underline{H}$), 36.5 (-$CONH$-$\underline{C}H_2CH_2N$), 58.6 (-$CONHCH_2\underline{C}H_2N(CH_3)_2$), 44.6 (-$CONH$-$CH_2CH_2N(\underline{C}H_3)_2$), 57.5 (-$CH_2COOCH_2\underline{C}H_2OOCNH$-), 60.2 (-$CH_2COO\underline{C}H_2CH_2OOCNH$-), 53.9 ($NCH_2\underline{C}H_2COO$-), 59.3 ($N\underline{C}H_2CH_2COO$-), 58.9 ($N\underline{C}H_2CH_2N(CH_3)_2$), 59.1 ($NCH_2$-$\underline{C}H_2N(CH_3)_2$), 44.2 ($NCH_2CH_2N(\underline{C}H_3)_2$), 156.1 (-$NH\underline{C}OO$-), 156.7 (-$OO\underline{C}NH$-), 162.5 (-$\underline{C}ONH$-),174.5 (-$\underline{C}OO$-).

Synthesis of PDMA (8). PDMA (**8**) was synthesized via standard steps as shown in Scheme 2. 1,4-Butanediol diacrylate was added to (DMAE) (**1**) according to the method of Ferruti et al. (*3*, *24*, *25*).

PDMA (8). ^{1}H NMR (400 MHz, d_6-DMSO, ppm) δ: 3.7 (2H, -$COOCH_2C\underline{H}_2$-), 4.1 (2H, -$COOC\underline{H}_2CH_2$-), 3.1 (2H, -$C\underline{H}_2$-COO-), 2.3−2.5 (6H, -$C\underline{H}_2C\underline{H}_2$-, -$C\underline{H}_2CH_2COO$-), 2.2 (6H, -$N(CH_3)_2$). ^{13}C NMR (400 MHz, d_6-DMSO, ppm) δ: 57.5 (-$COOCH_2\underline{C}H_2$-), 60.2 (-$COO\underline{C}H_2CH_2$-), 53.9 (-$\underline{C}H_2COO$-), 59.3 ($N\underline{C}H_2CH_2$-), 58.9 ($N\underline{C}H_2CH_2N(CH_3)_2$), 59.1 ($NCH_2$-$\underline{C}H_2N(CH_3)_2$), 44.2 (-$N(\underline{C}H_3)_2$), 174.5 (-$\underline{C}OO$-).

Acid−Base Titration Assay of Polymers. Acid−base titration was used to evaluate the buffering capacity of synthesized cationic polymers. In this assay, 10 mg of PMMD (**6**) was dissolved in 10 mL of 150 mM NaCl. One hundred microliters of 1 N NaOH was then added to the solution to adjust the PH to 11.6 before it was titrated with acid. The solution was titrated with increasing volumes of 0.1 N HCl solutions, and the results were measured using a pH meter. The pH range of PDMA (**8**) was determined using the same procedure.

Hydrolytic Degradation of Polymers. PDMA (**8**) and PMMD (**6**) were dissolved in a buffer solution (pH 7.4 and pH 5.1) with a concentration of 10 mg/mL and then incubated in a water bath at 37 °C for various durations. After hydrolysis for various durations, the solution was dried in vacuum for several

Scheme 2. Synthesis Scheme of PDMA

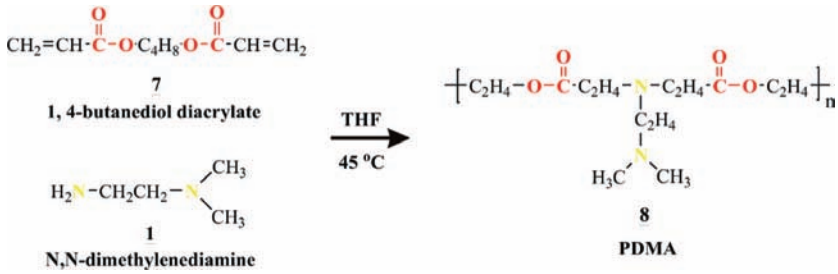

hours to remove water. The molecular weight of the polymer was determined using gel permeation chromatography (GPC).

XTT Assay. The influence of the polymer concentration on cell viability was evaluated in a cell culture for various polymers. The cytotoxicities of PDMA (**8**)/DNA and PMMD (**6**)/DNA for comparison with that of PEI/DNA were evaluated using the XTT assay (*4*, *22*). In a 96-well plate, COS-7 cells were cultured in complete DMEM and then seeded at a density of 1.0×10^4 cells/well. The cells were incubated at 37 °C and 5% CO_2 in a humidified atmosphere for 24 h. Subsequently, the cells were incubated for 1 h in 200 μL of FBS-free DMEM containing polymer with various concentrations. The cells were incubated in DMEM as a negative control. After 1 h, the cells were washed with 200 μL of PBS solution and replaced by complete DMEM for a further 48 h of incubation. Then, 50 μL of XTT labeling mixture was added to each well, and the cells were further incubated at 37 °C for 1 h. Results are expressed as the relative cell viability (%) with respect to control wells containing culture medium.

Formation of Polymer/DNA Complexes. The polymer (10.0 mg/mL) was dissolved in 20 mM HEPES buffer (pH7.4), and its serial dilutions were made with the mass ratio of PMMD (**6**)/DNA (w/w) from 1/2 to 50/1. The complexes were then allowed to self-assemble in the HEPES buffer. They were incubated at room temperature for 30 min before measurements.

Characterizations of Polymer/DNA Complexes. The particle sizes and surface charges of the polymer/DNA complexes were determined by dynamic light scattering (Nicomp 380 system, USA) and electrophoretic mobility at 25 °C with a Zeta-potential system (Nicomp Instrument, USA).

DNA Gel Retardation Assay of Polymer/DNA Complexes. PDMA (**8**)/DNA complexes and PMMD (**6**)/DNA complexes were loaded into a 0.7% agarose gel containing ethidium bromide (0.3 μg/mL) in a tris-acetate-EDTA (TAE) buffer and electrophoresis performed at 100 V for 45 min. After electrophoresis, the DNA bands were visualized using UV-irradiation. PDMA (**8**)/DNA complexes and PMMD (**6**)/DNA complexes with ratios of 0.5/1, 1/1, 2/1, 3/1, 4/1, 5/1, 6/1, 20/1, and 50/1 (w/w) were prepared.

RESULTS AND DISCUSSION

Structural Characterizations of Diol (3), PMMD (6), and PDMA (8). Diol ($C_{14}H_{28}O_6N_2$), PMMD ($(C_{26}H_{48}O_9N_6)_m$-$C_5H_{11}N_1)_n$, and PDMA ($(C_{14}H_{26}O_4N_2)_n$ were synthesized as shown in Schemes 1 and 2. The synthesis of diol (**3**) containing tertiary amine in the backbone, in accordance with the synthesis of poly(amido amine), was reported by Ferruti et al. (*3*, *24*, *25*). Figure 1 shows the FT-IR spectra of the synthesized diol (**3**) and starting materials. The peaks at 3400 cm^{-1} (-OH, stretching, hydrogen bond), 1650 cm^{-1} (-C = C, stretching, alkene), and 1640 cm^{-1} (-NH_2, amide) disappeared from the starting materials, and a peak at 1740 cm^{-1} (C═O, stretching, ester) of diol (**3**) was observed. Figure 2 shows the FT-IR spectra of the synthesized PMMD and PDMA. The peaks at 1720 cm^{-1} (C═O, stretching, urethane), 1668 cm^{-1} (C═O, stretching, amide), 1537 cm^{-1} (N−H, bending, amide), and 3340 cm^{-1} (N−H, stretching, urethane) represent the absorptions of urethane groups in PMMD (**6**), as shown at the top of Figure 2. The peak at 1740 cm^{-1} (C═O, stretching, ester) represents the absorption of ester induced from PDMA (**8**), as shown at the bottom of Figure 2. The chemical shifts of characterized protons and carbons of diol, PMMD, and PDMA are shown in the Materials and Methods section. In addition, the GPC data of PMMD (**6**) and PDMA (**8**) show that the weight-averaged molecular weights were 17600 and 16800 with polydispersities of 1.8 and 1.7, respectively, relative to polystyrene standards in THF.

Size and Zeta-Potential analysis of Polymer/DNA Complexes. Figures 3 and 4 show the size and zeta-potential of PMMD (**6**)/DNA and PDMA (**8**)/DNA complexes at various mass ratios, determined using dynamic light scattering (DLS) and electrophoretic mobility at 25 °C with zeta-potential analysis. The size of complexes decreased with an increase of the mass content of the polymers until the mass ratio of PMMD (**6**)/DNA reached 2/1 and that of PDMA (**8**)/DNA reached 20/1. The results show that the average diameters (80−115 nm) of PMMD (**6**)/DNA and the average diameters (170−180 nm) of PDMA (**8**)/DNA fall within the optimal range (40nm−200nm) required for cellular endocytosis (*26*). The above data demon-

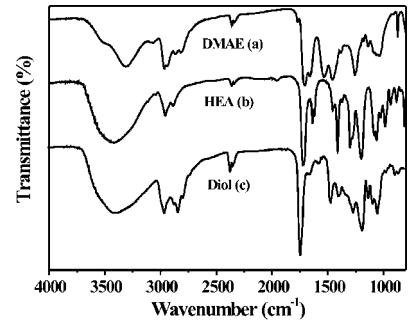

Figure 1. FT-IR spectra of (a) DMAE, (b) HEA, and (c) the synthesized diol.

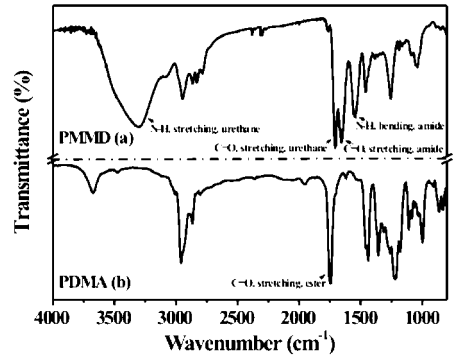

Figure 2. FT-IR spectra of (a) PMMD and (b) PDMA.

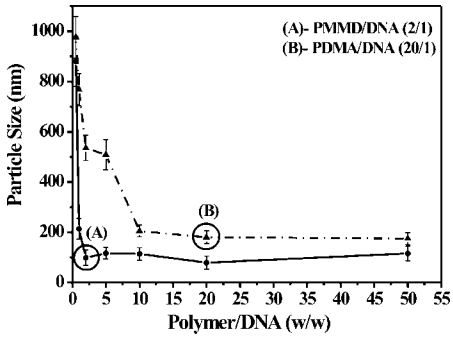

Figure 3. Sizes of PMMD/DNA and PDMA/DNA complexes prepared at various mass ratios. Results are presented as the mean ± SD (n = 3).

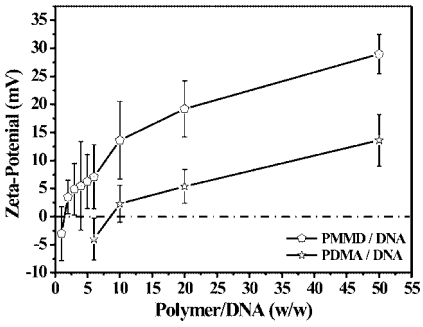

Figure 4. Zeta-potential of PMMD/DNA and PDMA/DNA complexes prepared at various mass ratios. Results are presented as the mean ± SD (n = 3).

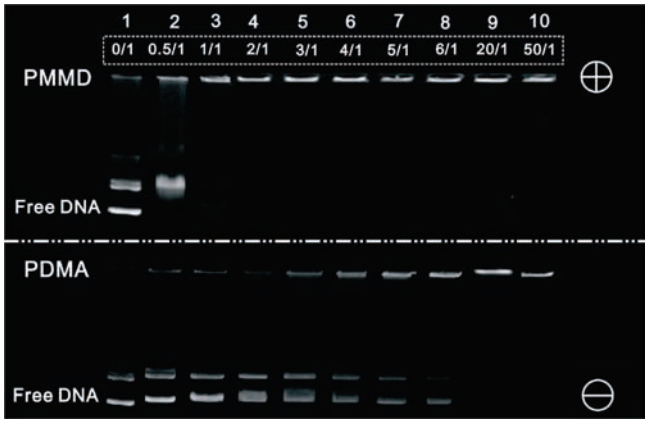

Figure 5. DNA gel retardation assay of PMMD and PDMA. Lanes: (1) 400 ng DNA; (2) PMMD/DNA and PDMA/DNA (w/w) 0.5/1; (3) PMMD/DNA and PDMA/DNA (w/w) 1/1; (4) PMMD/DNA and PDMA/DNA (w/w) 2/1; (5) PMMD/DNA and PDMA/DNA (w/w) 3/1; (6) PMMD/DNA and PDMA/DNA (w/w) 4/1; (7) PMMD/DNA and PDMA/DNA (w/w) 5/1; (8) PMMD/DNA and PDMA/DNA (w/w) 6/1; (9) PMMD/DNA and PDMA /DNA (w/w) 20/1; (9) PMMD/DNA and PDMA/DNA (w/w) 50/1.

strates that PMMD (**6**) bearing urethane groups in the backbone condenses DNA better than PDMA (**8**) without the urethane group.

The zeta-potential of the resulting complex changed from negative charge to positive charge when the amounts of PMMD (**6**) and PDMA (**8**) increased. When the mass ratio of PMMD (**6**)/DNA complexes was higher than 2/1, the surface of pCMV-β-gal was fully occupied with the PMMD (**6**) molecules, forming positive charge complexes. When the mass ratio of PDMA (**8**)/DNA complexes was higher than 10/1, positive zeta-potentials of the complexes formed. Complexes with extra

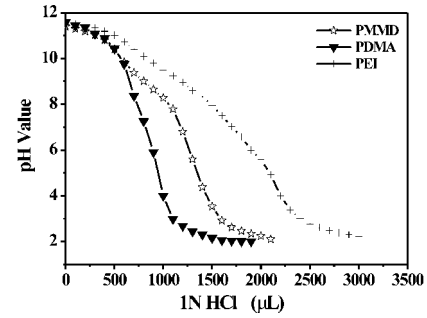

Figure 6. Acid−base titration profile of various polymers with 1 N HCl. Ten milligrams of various polymers was dissolved in 10 mL of 150 mM NaCl, the polymeric solution was added to 100 μL of 1 N NaOH, and the pH was recorded.

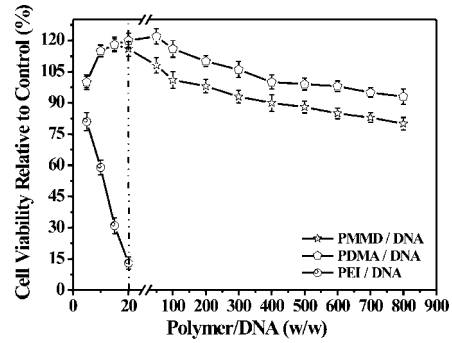

Figure 7. Cytotoxicity of polymer/DNA complexes in COS-7 cells. Results are presented as the mean ± SD (n = 3).

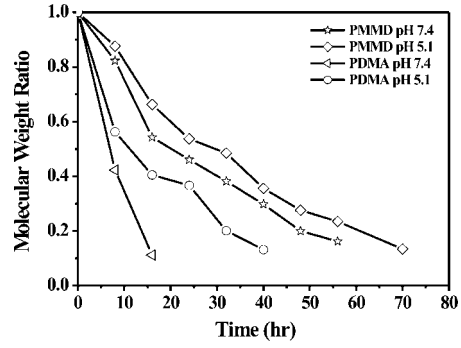

Figure 8. Hydrolytic degradation of PDMA (**8**) and PMMD (**6**), which were dissolved in a buffer solution (pH 7.4 and pH 5.1) with a concentration of 10 mg/mL and then incubated in a water bath at 37 °C for various durations. Degradation is expressed over time based on GPC data. (Molecular weight ratio: M_w after degradation/M_w before degradation).

positive charges on their surfaces had better interaction with the target cell membrane, resulting in an enhanced uptake.

DNA Gel Retardation Assay. The electrophoretic mobility behavior of free DNA, PMMD (**6**)/DNA, and PDMA (**8**)/DNA is shown in Figure 5. Increasing amounts of PMMD (**6**) and PDMA (**8**) led to the neutralization of DNA negative charges, as shown by gel retardation. The DNA mobility on agarose gel was influenced by the presence of PMMD (**6**) and PDMA (**8**). With a low mass ratio of PMMD (**6**) (2/1), plasmid DNA was totally retained, as indicated in lane 4. Plasmid DNA was partially retained by the presence of PDMA (**8**) at a mass ratio of 6/1 (lane 8) and totally retained at a mass ratio of 20/1 (lane 9). These results suggest that DNA was fully completed with PMMD (**6**) and PDMA (**8**) to form complexes, showing that amine groups of PMMD (**6**) and PDMA (**8**) with positive charges could interact with the charge of negative phosphate groups of DNA strands to form complexes.

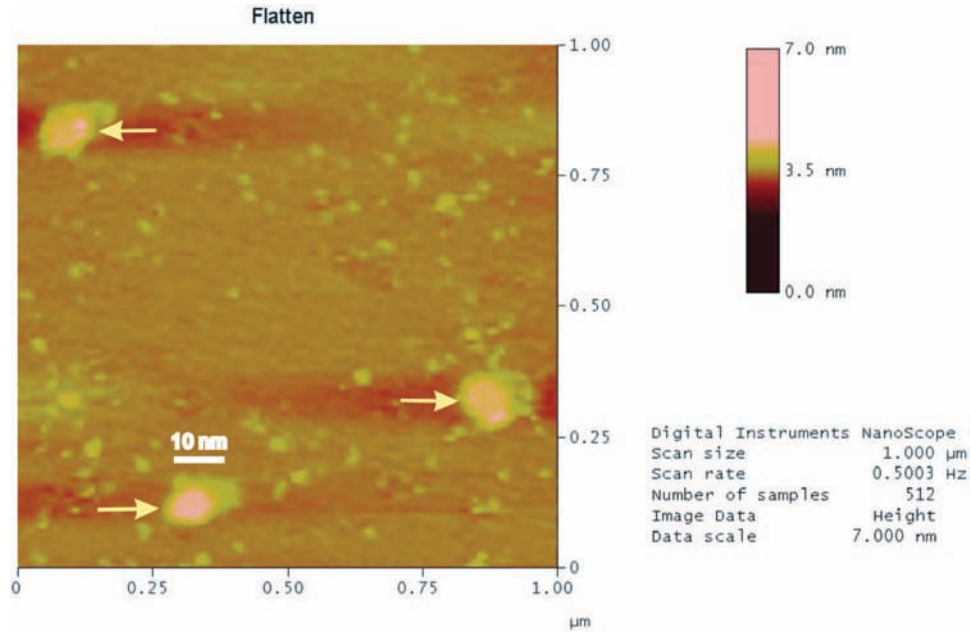

Figure 9. AFM (atomic force microscopy) of PMMD/DNA complexes at a mass ratio of 20/1.

Buffering Capacity of Polymers. Titration studies were performed to determine the buffering capacities of the various polymers regarding a proton buffering effect within the endosomal/lysosomal compartments of the cell (Figure 6). All of the polycation solutions had a pH of 11.5 to 11.8 after the addition of 1.0 N NaOH. The nonviral vector PEI showed a buffering capacity over a wide pH range, which is probably due to the high amount of amine functions present in the polymeric chain. The incorporation of tertiary amine content changed the buffering region of the polycation. PMMD (**6**) has more tertiary amine than PDMA (**8**) in the backbone and side chain. The data show the pH range of PMMD (**6**) to be between 11.5 and 5.4 and that of PDMA (**8**) to be between 11.5 and 7.5. It was found that the polymers with high tertiary amine content have a high buffering capacity.

Cytotoxicity of Polymer/DNA. A critical element for the gene delivery system is cytotoxicity. Cell damage resulting from a cytotoxic delivery system is deleterious because cells must be capable of supporting translation and transcription. To determine the cytotoxicity of PMMD (**6**)/DNA and PDMA (**8**)/DNA for comparison with that of PEI/DNA, we performed an XTT assay using the COS-7 cell line. Cells were incubated with increasing amounts of PMMD (**6**)/DNA and PDMA (**8**)/DNA (ranging from 5 μg/mL to 800 μg/mL) and PEI/DNA (ranging from 5 μg/mL to 20 μg/mL). The results show that PMMD (**6**)/DNA and PDMA (**8**)/DNA exhibited substantially lower toxicity on COS-7 cells than did PEI/DNA, as shown in Figure 7.

IC_{50} (defined as the concentration resulting in 50% inhibitory activity (cell death)) for PEI/DNA was around 15 μg/mL, whereas PMMD (**6**)/DNA and PDMA (**8**)/DNA had more than 75% viable cells even at a higher dose (800 μg/mL) with no significant change in cell morphology and proliferation relative to controls. We infer that poly(urethane-co-ester)/DNA can provide better cytotoxicity profiles than these presently used for PEI/DNA due to the introduction of amino groups and urethane units in the polycation backbone, which reduces the high charge density of the polycation.

In Vitro Hydrolysis of Polymers. Figure 8 shows the degradation profiles of polymers, which were monitored at 37 °C at buffer pH values of 5.1 and 7.4 in order to approximate the environments within endosmal vesicles and lysosome, respectively. The polymers generally degraded faster at pH 7.4 than at pH 5.1. PMMD (**6**) at pH 5.1 had a half-life of 32−33 h. In contrast, PDMA (**8**) was completely degraded in less than 16 h at pH 5.1. These results show that PDMA (**8**) exhibited a higher hydrolytic degradation rate than did PMMD (**6**) at pH 7.4 and 5.1.

AFM (Atomic Force Microscopy) Images of PMMD/DNA Nanoparticles. Figure 9 shows the atomic force microscopy (AFM) images of PMMD/DNA complexes at a mass ratio of 20/1. At a mass ratio of PMMD/DNA (20/1), nearly all complexes condensed to a roughly spherical shape. The discretely spherical images verify the very efficient DNA condensation obtained using PMMD. The AFM images of complexes were captured after the complexes were coated on mica and dried with compressed air. The observed dimensions, therefore, are different from the ones determined in aqueous media using DLS.

CONCLUSIONS

Poly(urethane-co-ester) (PMMD) with low cytotoxicity and high biodegradability was synthesized and then characterized using FT-IR, NMR, and GPC in this study. PMMD and DNA had a strong electrostatic interaction to self-assemble nanoparticles. The positive charges in the backbone and side chain of PMMD condense DNA to form DNA−polycation complexes. The complex efficiency was better than that of the polyester of PDMA, which resulted in numerous amine groups of PMMD with two tertiary amines in the backbone and two tertiary amines in the side chain. Biodegradable PMMD could potentially be used in a nonviral gene delivery system.

LITERATURE CITED

(1) Shroff, K. E., Smith, L. R., Bain, T., and Higgins, T. T. (1999) Potential for plasmid DNAs as vaccines for the new millennium. *Pharm. Sci. Technol. Today 5*, 205–212.
(2) Friedman, T. (1997) Overcoming obstacles in gene therapy. *Sci. Am. 6*, 96–101.
(3) Ferruti, P., Manzoni, S., Richardson, S. C. W., Duncan, R., Pattrick, N. G., Mendichi, R., and Casolaro, M. (2000) Amphoteric linear poly(amido-amine)s as endosomolytic polymers: Correlation between physicochemical and biological properties. *Macromolecules 33*, 7793–7800.

(4) Shau, M. D., Tseng, S. J., Yang, T. F., Cherng, J. Y., and Chin, W. J. (2006) Effect of molecular weight on the transfection efficiency of novel polyurethane as a biodegradable gene vector. *J. Biomed. Mater. Res., Part A 77A*, 736–746.
(5) Akinc, A., Lynn, D. M., Anderson, D. G., and Langer, R. (2003) Parallel synthesis and biophysical characterization of a degradable polymer library for gene delivery. *J. Am. Chem. Soc. 125*, 5316–5323.
(6) Buchanan, S. A., Balogh, N. L. P., and Meyerhoff, M. E. (2004) Potentiometric response characteristics of polycation-sensitive membrane electrodes toward poly(amidoamine) and poly(propylenimine) dendrimers. *Anal. Chem. 76*, 1474–1482.
(7) Zugates, G. T., Anderson, G. D., Little, S. R., Lawhorn, I. E. B., and Langer, R. (2006) Synthesis of poly(β-amino ester)s with thiol-reactive side chains for DNA delivery. *J. Am. Chem. Soc. 128*, 12726–12734.
(8) Choi, M. K., Arote, R., Kim, S. Y., Chung, S. J., Shim, C. K., Cho, C. S., and Kim, D. D. (2007) Transfection of primary human nasal epithelial cells using a biodegradable poly (ester amine) based on polycaprolactone and polyethylenimine as a gene carrier. *J. Drug Targeting 15*, 684–690.
(9) Wu, C. B., Hao, J. Y., Deng, X. M., and Li, X. H. (2008) Copolymer of tetraethylenepentamine and ethylene glycol diacrylate: Synthesis and degradation. *Polym. Degrad. Stab. 93*, 932–940.
(10) Boussif, O., Lezoualc'h, F., Zanta, M. A., Mergny, M. D., Scheman, D., Demeneix, B., and Behr, J. P. (1995) A versatile vector for gene and oligouncleotide transfer into cells in culture and in-vivo-polyethylenimine. *Proc. Natl. Acad. Sci. U.S.A. 92*, 7297–7301.
(11) Cherng, J. Y., Wetering, P. V., Talsma, H., Crommelin, D. J. A., and Hennink, W. E. (1996) Effect of size and serum proteins on transfection efficiency of poly((2-dimethylamino)ethyl methacrylate)-plasmid nanoparticles. *Pharm. Res. 13*, 1038–1042.
(12) Anderson, W. F. (1998) Human gene therapy. *Nature (London) 392*, 25–30.
(13) Friedman, J. M. (2004) Modern science versus the stigma of obesity. *Nature Med. 10*, 116.
(14) Crystal, R. G. (1995) Transfer of genes to humans: early lessons and obstacles to success. *Science 270*, 404–410.
(15) Wang, Y., Ke, C. Y., Beh, C. W., Liu, S. Q., Goh, S. H., and Yang, Y. Y. (2007) The self-assembly of biodegradable cationic polymer micelles as vectors for gene transfection. *Biomaterials 28*, 5358–5368.
(16) Christensen, L. V., Chang, C. W., Kim, W. J., and Kim, S. W. (2006) Reducible poly(amido ethylenimine)s designed for triggered intracellular gene delivery. *Bioconjugate Chem. 17*, 1233–1240.
(17) Kim, Y., Klutz, A. M., and Jacobson, K. A. (2008) Systematic investigation of polyamidoamine dendrimers surface-modified with poly(ethylene glycol) for drug delivery applications: Synthesis, characterization, and evaluation of cytotoxicity. *Bioconjugate Chem. 19*, 1660–1672.
(18) Braunova, A., Pechar, M., Laga, R., and Ulbrich, K. (2007) Hydrolytically and reductively degradable high-molecular-weight poly (ethylene glycol) s. *Macromol. Chem. Phys. 208*, 2642–2653.
(19) Deshmukh, H. M., and Huang, L. (1997) Cationic liposome-mediated DNA delivery to the lung endothelium. *New J. Chem. 21*, 113–124.
(20) Sanford, J. C. (1988) The biolistic process. *Trends Biotechnol. 6*, 299–302.
(21) Bieber, H., Meissner, W., and Kostin, S. (2002) Non-viral gene therapy: polycation-mediated DNA delivery. *J. Controlled Release 82*, 441–454.
(22) Cherng, J. Y., van de Wetering, P., Talsma, H., Crom-melin, D. J. A., and Hennink, W. E. (1996) Effect of size and serum proteins on transfection efficiency of poly((2-dimethylamino)ethyl methacrylate)-plasmid nanoparticles. *Pharm. Res. 13*, 1038–1042.
(23) Lim, K., and Chae, C. B. (1989) A simple assay for DNA transfection by incubation of the cells in culture dishes with substrates for beta-galactosidase. *Biotechnol. 7*, 576–579.
(24) Barbucci, R., Ferruti, P., Improta, C., Delfini, M., Segre, A. L., and Conti, F. (1978) Protonation studies of multifunctional polymers with a poly(amido-amine) structure. *Polymer 19*, 1329–1334.
(25) Ranucci, E., and Ferruti, P. (1991) Block copolymers containing poly(ethylene glycol) and poly(amido- amine) or poly(amido thioether amine) segments. *Macromolecules 24*, 3747–3752.
(26) Kabanov, A. V., and Kabanov, V. A. (1995) DNA complexes with polycations for the delivery of genetic material into cells. *Bioconjugate Chem. 6*, 7–20.

BC800499W

Synthesis of Linear Polyether Polyol Derivatives As New Materials for Bioconjugation

Zhongyu Li and Ying Chau*

Department of Chemical and Biomolecular Engineering, the Hong Kong University of Science and Technology, Clear Water Bay, Hong Kong SAR, China. Received December 3, 2008

Linear polyether polyol (PEP) consisting of glycidol as repeating units is a flexible hydrophilic aliphatic polymer. The polyether main chain is similar to the widely used, biocompatible polymer poly(ethylene glycol) (PEG). While linear PEG has one or two terminal hydroxyl group(s), linear PEP distinguishes itself by the large number of pendant hydroxyl groups along the polyether main chain. We propose that this property of PEP represents a major advantage over PEG, namely, by providing multiple anchorage points and increasing the possibility for introducing different functional groups. As a first step to establishing PEP as a bioconjugation material, we modified the pendant hydroxyl groups on PEP and prepared a series of mono- and heterobifunctional derivatives with the potential to join various drug entities and biomolecules. The synthesis methods and the results of characterization are reported here.

INTRODUCTION

Poly(ethylene glycol) (PEG) is one of the most widely used bioconjugation materials nowadays in pharmaceutical and biomedical applications (*1*−*10*). It consists of ethylene oxide as repeating units, with one terminal hydroxyl group in the monomethoxy form (mPEG) or two in the unmodified form of PEG. PEG is useful for bioconjugation due to the following reasons: (i) lack of immunogenicity, antigenicity, and toxicity; (ii) high solubility in water and most organic solvents; (iii) extensive hydration and high flexibility of the main chain, which is at the basis of its antifouling property; and (iv) approval by FDA for human use. However, the presence of only one or two reactive groups at the ends of PEG chain means that only one or two entities (drug, peptide, protein, nucleic acid, and other biomolecules) can be attached onto PEG. This severely limits not only the loading capacity of such conjugate but also the design options for PEG-based drug-carrier systems. One solution is to arrange PEG chains into a branched architecture, such as star-like, hyperbranched, arborescent, and dendrimeric PEG (*11*−*16*). Alternating polyurethanes have also been prepared by polymerization of bis-succinate-PEG with amino acid containing three functional groups, such as lysine (*17*−*19*). However, these strategies require complicated synthesis procedures, and the number of reactive groups are still low.

Here, we take a different approach and start with linear polyether polyol (PEP). Composed of glycidol (and possibly ethylene oxide) as monomeric units, PEP is a flexible hydrophilic aliphatic polymer with multiple pendant hydroxyl groups along the main chain (Figure 1). The similarity in the polymer backbone with the extensively used PEG suggests that these two polymers may share the same characteristics of being hydrophilic, water-soluble, biocompatible, and resistant to protein adsorption (*2, 18*). In fact, it has been shown that both linear and hyperbranched polyglycidol are nontoxic and safe in vitro and in vivo (*20*−*22*).

From the point of chemical synthesis, PEP with low polydispersity and well-defined structure can be readily synthesized by anionic polymerization (*23*−*25*). By adapting existing methods of hydroxyl group modification, we convert the pendant hydroxyl groups into different functional groups to increase their reactivity (*2*). Since the number of hydroxyl groups can be controlled by the ratio of monomers during polymerization, we can readily vary the drug loading density on PEP at will. We also use orthogonal chemistry to synthesize a number of heterobifunctional PEPs to further increase the versatility of this polymer. The chemical varieties of the derivatives mean that different chemical agents and biomolecules including peptides and nucleic acids are amenable for attaching to PEP. The increased number of functional groups along the main chain enables this polymer to be more effective as a bioconjugation carrier than PEG, since (i) the payload is higher; (ii) multivalency is possible; (iii) colocalized delivery of different drugs and simultaneous presentation of biospecific ligands are allowed.

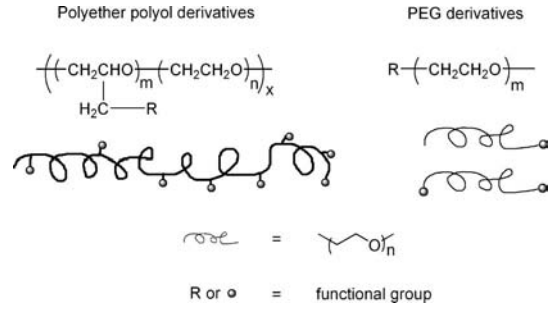

Figure 1. Polyether polyol derivatives and PEG derivatives.

MATERIALS AND METHODS

Materials. All starting compounds were used as received without additional purification except for those specified. Chemicals were purchased from Aldrich unless otherwise indicated. THF (Merck, 99%) was refluxed over sodium wire and distilled from sodium naphthalenide solution. Diethylene glycol monomethyl ether (Fluka, 99%) and DMSO (Merck, 98%) were distilled over CaH_2 under reduced pressure just before use. Ethylene oxide (EO, 99.7%) was purchased from Hong Kong Special Gas Company. Ethoxyethyl glycidyl ether (EEGE) and diphenylmethylpotassium (DPMK) were prepared

* Corresponding author. Tel.: +852-2358 8935; Fax: +852-2358 0054; E-mail address: keychau@ust.hk.

10.1021/bc900036f CCC: $40.75 © 2009 American Chemical Society
Published on Web 03/10/2009

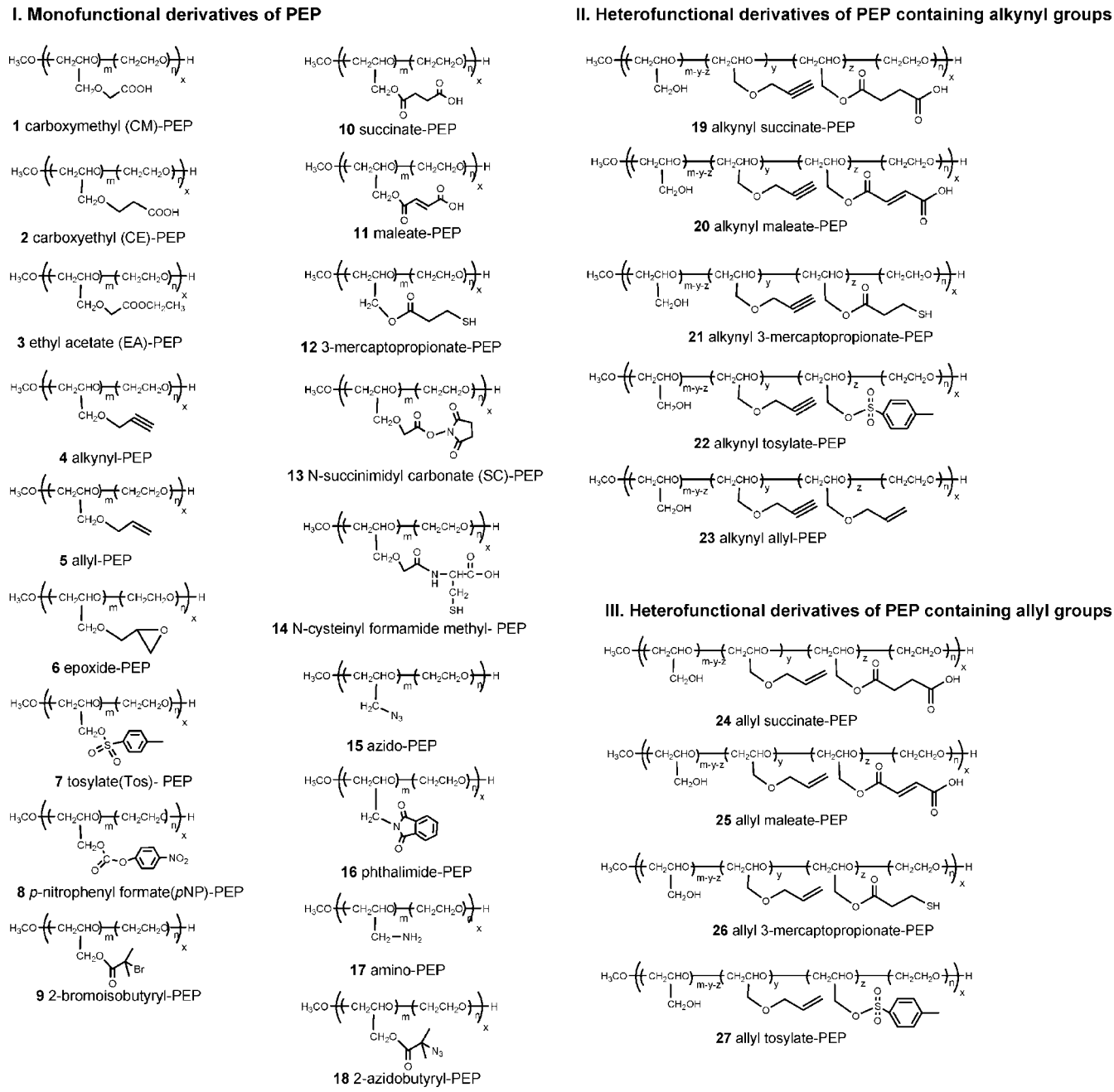

Figure 2. Structures and names of PEP derivatives that have been successfully synthesized and characterized.

as described elsewhere (*24*−*26*). An ultrafiltration separator and poly(ether sulfone) (PES) membranes with molar mass cutoff at 10k, 20k, 30k, and 50k g/mol as calibrated by globular proteins were purchased from the Shanghai Institute of Applied Physics, Chinese Academy of Sciences.

Methods. ^{1}H NMR and ^{13}C NMR spectra were obtained on a DMX 500 MHz spectrometer with tetramethylsilane (TMS) as the internal standard and $CDCl_3$ as the solvent. For poly(EEGE) and poly(EEGE-*co*-EO), gel permeation chromatography (GPC) was performed on a Waters HPLC system with a G1310A pump and a G1362A refractive index detector, using tetrahydrofuran (THF) as eluent at 35 °C with an elution rate of 1.0 mL/min. Two Styragel columns (HR 3 THF and HR4E THF, Waters) were calibrated by polystyrene standards (Polymer Source). For poly(Gly-*co*-EO), polyglycidol, and their derivatives, size exclusion chromatography (SEC) was performed in 0.1 M $NaNO_3$ at 40 °C with an elution rate of 0.5 mL/min on the same HPLC system. Ultrahydrogel 250 (Waters) and Ultrahydrogel 1000 (Waters) columns in series were calibrated by PEG standards (Polymer Source).

Synthesis of Polyether Polyol. Polyether polyol was synthesized in two steps similar to the published methods (*23*−*25*), except that EEGE molecules were used as monomers in addition to EO. PEEGE and poly(EEGE-*co*-EO) were first prepared using anionic polymerization. Acid deprotection of the precursor macromolecule afforded the homopolymer polyglycidol and the random copolymer poly(Gly-*co*-EO).

Poly(EEGE-co-EO). ^{1}H NMR (ppm) ($CDCl_3$): 1.19 (m, C**H**$_3$-CH_2-), 1.33 (d, -O-CH(C**H**$_3$)-O-), 3.38 (s, C**H**$_3$-O-), 3.45−3.85 (m, -C**H**$_2$C**H**$_2$O- and -C**H**$_2$C**H**O- of polyether polyol main chain and -C**H**$_2$-O-CH(CH_3)-), 4.69 (q, -O-C**H**(CH_3)-O-).

Poly(Gly-co-EO). ^{1}H NMR (ppm) ($CDCl_3$): 3.38 (s, C**H**$_3$-O-), 3.45−3.85 (m, -C**H**$_2$C**H**$_2$O- and -C**H**$_2$C**H**O- of polyether polyol main chain and the pendant -C**H**$_2$-OH groups). ^{13}C NMR (ppm) ($CDCl_3$): 58.3 **C**H_3-O-, 70.5−71.3 -**C**$H_2$$CH_2$O- and -**C**$H_2$CHO-, 80.4-$CH_2$**C**HO-, 60.7 and 63.9 -**C**H_2-OH.

Synthesis of Monofunctional Derivatives of Polyether Polyol. PEP derivatives are numbered according to Figure 2. Synthesis of the monofunctional derivatives of polyether polyol

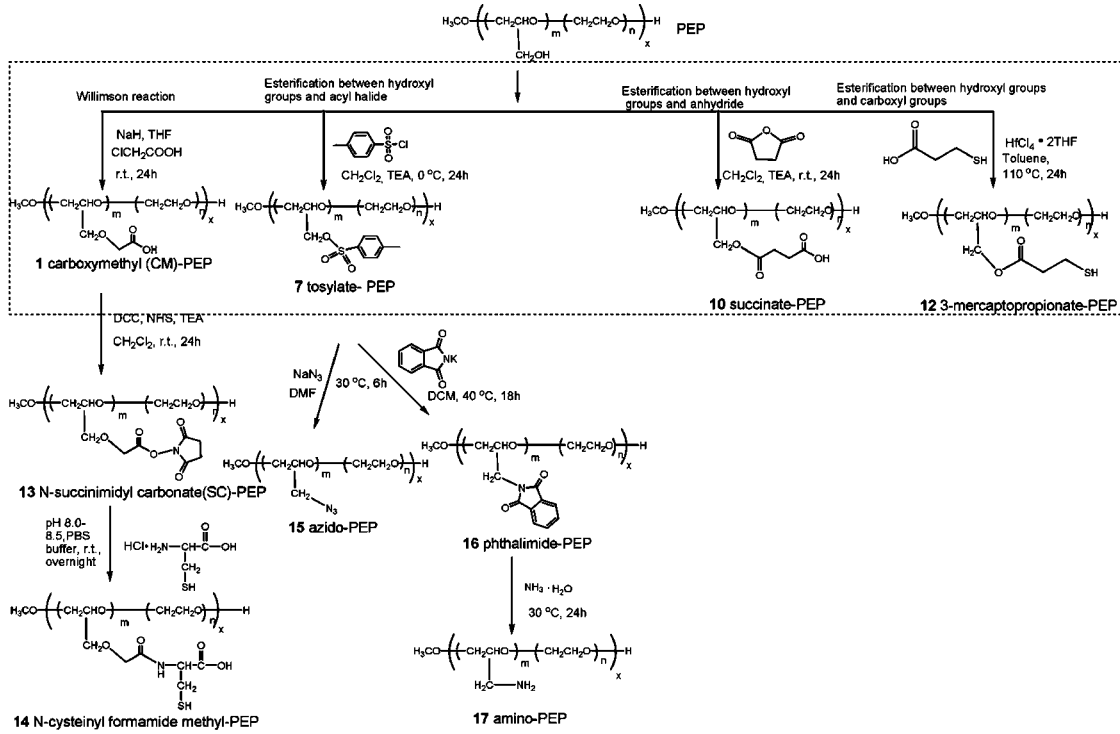

Figure 3. Chemical reactions and structures of the critical intermediate and final products resulting from the synthesis of monofunctional derivatives PEP. Representative PEP derivatives of each reaction type are shown as examples. Besides what is shown above, polyether polyol derivatives **2**−**6** were also synthesized by Williamson reaction, **8** and **9** by esterification between hydroxyl groups and acyl halide, and **11** by esterification between hydroxyl groups and anhydride groups.

(**1**−**18**) are summarized in Figure 3. The synthesis routes for PEP derivatives **1**−**12** can be classified into four categories: (1) Williamson reaction, (2) esterification between hydroxyl groups and acyl halide, (3) esterification between hydroxyl groups and anhydride, and (4) esterification between hydroxyl groups and carboxyl groups. PEP derivatives **13**−**18** are obtained by further reactions of PEP derivatives **1**, **7**, and **9**, respectively.

Williamson Reaction. Carboxymethyl (CM)-PEP (**1**), carboxyethyl(CE)-PEP (**2**), ethyl acetate (EA)-PEP (**3**), alkynyl-PEP (**4**), allyl-PEP (**5**), and epoxide-PEP (**6**) were synthesized by Williamson reaction to form ether bonds between the polymer and the residues (*27*−*31*). PEP derivatives **1**−**5** were synthesized in a homophase system, in which PEP reacted with 2-chloroacetic acid, 3-bromopropionic acid, ethyl bromoacetate, propargyl bromide, and allyl chloride respectively in THF with NaH (*27*). Synthesis of CM-PEP (**1**) shown in Figure 3, is described in detail here as a typical example. One gram PEP (M_n = 15.4 × 10^3 g/mol, 1.25 mmol hydroxyl groups) with moisture removed by azeotropic distillation with toluene just before use was reacted with 0.6 g NaH (2.5 mmol) in 10 mL anhydrous tetrahydrofuran (THF) at room temperature for 20 min, and then 0.43 g 2-chloroacetic acid (4.6 mmol) was added under vigorous stirring at room temperature for 24 h. After neutralization by hydrochloride solution, the solvent was removed by rotary evaporation. The product was purified by ultrafiltration. Filtered aqueous solution was concentrated to dryness, dissolved in dichloromethane (DCM), and dried over anhydrous $MgSO_4$. The filtrate was distilled under vacuum to remove DCM and dried in vacuo at 50 °C for 2 days, and a white product was obtained.

Epoxide-PEP (**6**) was synthesized in a heterophase system using tetrabutylammonium bromide (TBAB) as a phase transfer catalyst (PTC) (*29*). 0.5 g polyether polyol (M_n = 15.4 × 10^3 g/mol, 0.62 mmol hydroxyl groups), 0.018 g TBAB (0.055 mmol), and 0.248 g sodium hydroxide (6.2 mmol) in 5 mL of distilled water were mixed and reacted with 0.23 g epichlorohydrin (2.2 mmol) under vigorous stirring at 50 °C for 48 h. After the addition of 30 mL DCM, the organic phase was separated from the aqueous phase, dried over $MgSO_4$, filtered, and concentrated. The polymer was dissolved in water and purified by ultrafiltration. The filtered aqueous solution was concentrated to dryness, dissolved in DCM, and dried over anhydrous $MgSO_4$. The filtrate was distilled under vacuum to remove DCM and dried under vacuum at 50 °C for 2 days to afford a white product.

Esterification between Hydroxyl Groups and Acyl Halide. Tosylate (Tos)-PEP (**7**), *p*-nitrophenyl formate (*p*NP)-PEP (**8**), and 2-bromoisobutyryl-PEP (**9**) were synthesized by the esterification between PEP and *p*-toluenesulfonyl chloride(TsCl), *p*-nitrophenyl chloroformate, and 2-bromoisobutyryl bromide, respectively, in DCM with triethylamine (TEA) as a catalyst (*24*, *32*−*34*). Synthesis of Tos-PEP, as shown in Figure 3, is described here in detail as a typical example. Two grams of PEP (M_n = 15.4 × 10^3 g/mol, 2.5 mmol hydroxyl groups) with moisture removed by azeotropic distillation with toluene was reacted with 0.629 g *p*-toluenesulfonyl chloride (3.3 mmol) in the presence of 0.3 mL TEA in 10 mL anhydrous DCM at 0 °C for 24 h. The solvent was removed by rotary evaporation. The product was purified by ultrafiltration. The white precipitate of triethylamine hydrochloride was filtered off and washed with DCM. Filtered aqueous solution was concentrated to dryness, dissolved in DCM, and dried over anhydrous $MgSO_4$. The filtrate was distilled under vacuum to remove DCM and dried in vacuo at 50 °C for 2 days to yield a white product.

Esterification between Hydroxyl Groups and Anhydride Groups. Succinate-PEP (**10**) and maleate-PEP (**11**) were synthesized by the esterification (*35*−*37*) between PEP and succinic anhydride and maleic anhydride, respectively, in DCM with TEA as a catalyst. Synthesis of Succinate-PEP, as shown in Figure 3, is described here in detail as a typical example (*35*). 0.5 g PEP (M_n = 15.4 × 10^3 g/mol, 0.62 mmol hydroxyl groups) with moisture first removed by azeotropic distillation with toluene was reacted with 0.177 g succinic anhydride (1.77 mmol) in the presence of 0.1 mL TEA in 10 mL DCM at room temperature or 24 h. The solvent was removed by rotary evaporation. The product was purified by ultrafiltration. Filtered aqueous solution was concentrated to dryness, dissolved in

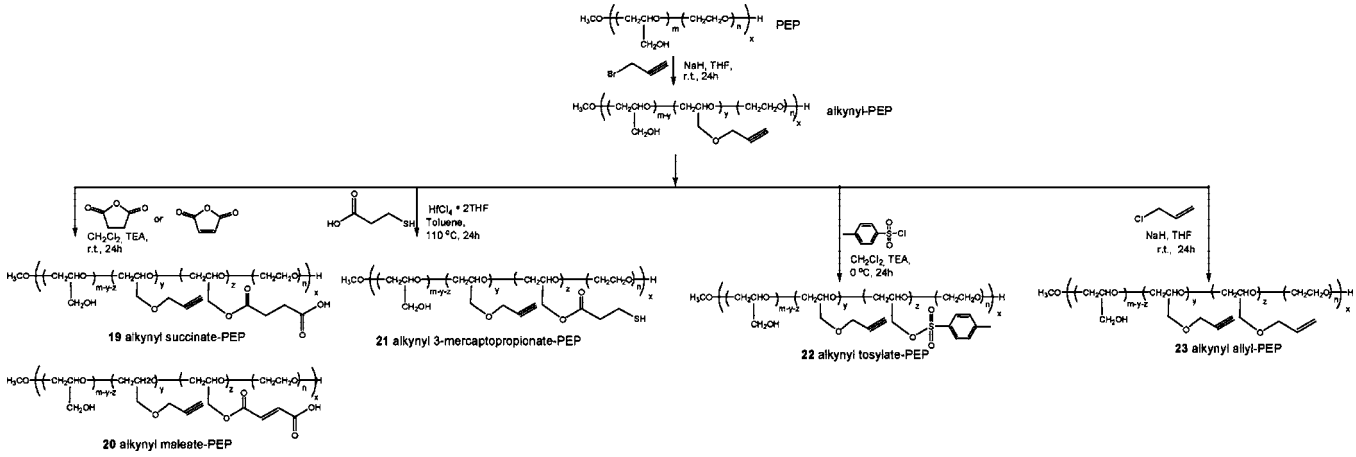

Figure 4. Synthesis of heterobifunctional polyether polyol derivatives containing alkynyl groups. (Similar methods are fit for synthesis of heterobifucntional PEP derivatives containing allyl groups).

DCM, and dried over anhydrous $MgSO_4$. The filtrate was distilled under vacuum to remove DCM and dried in vacuo at 50 °C to yield a white product.

Esterification between Hydroxyl Groups and Carboxyl Group. 3-Mercaptopropionate-PEP (**12**) was synthesized by the esterification (*38, 39*) between PEP and 3-mercaptopropionic acid. A typical experiment (Figure 3) was as follows: 2 g PEP ($M_n = 15.4 \times 10^3$ g/mol, 2.5 mmol hydroxyl groups) was dissolved in 20 mL toluene; then, 0.318 g 3-mercaptopropionic acid (MPA) (3 mmol) along with $HfCl_4 \cdot 2THF$ (2 mg, 0.004 mmol) were added and stirred at 50 °C under nitrogen. The reaction flask was equipped with an azeotropic distillation apparatus, and the mixture was refluxed at 110 °C under nitrogen for 24 h. Toluene was removed under reduced pressure. The crude product was dissolved in ethanol and was purified by an ultrafiltration membrane to remove low molar mass impurities under the pressure of nitrogen. Finally, ethanol was removed from the product by distillation and the remains were dried in vacuo at 50 °C for 2 days to afford a white product.

Other Reactions. N-Succinimidyl carbonate (SC)-PEP (**13**) was derived from CM-PEP (**1**) using a procedure adapted from Zalipsky et al. (*40*) Two grams CM-PEP ($M_n = 16.5 \times 10^3$ g/mol, 2.3 mmol carboxyl groups) was reacted with 0.824 g *N*,*N*′-dicyclohexylcarbodiimide (DCC, 4 mmol) and 0.46 g *N*-hydroxysuccinimide (NHS, 4 mmol) in the presence of 0.2 mL TEA in 10 mL DCM at room temperature for 24 h. The crude product was concentrated and filtered to remove the byproduct 1,3-dicyclohexylurea (DCU). The filtered solution was precipitated in diethyl ether. The product was redissolved in DCM and precipitated again in diethyl ether. This step was repeated twice, and the final product was dried in vacuo at 50 °C.

N-Cysteinyl formamide methyl-PEP (**14**) was derived from SC-PEP (**13**) using a procedure adapted from Zalipsky et al. (*40*) 0.39 g cystine hydrochloride (2.5 mmol) dissolved in 20 mL pH 8.0 phosphate buffer was reacted with 0.5 g SC-PEP ($M_n = 19.3 \times 10^3$ g/mol, 0.497 mmol SC groups), which was added in small aliquots. The solution was stirred vigorously at room temperature overnight. The product was purified by ultrafiltration. Filtered aqueous solution was concentrated to dryness, dissolved in DCM, and dried over anhydrous $MgSO_4$. The filtrate was distilled under vacuum to remove DCM and dried in vacuo at 50 °C.

Amino-PEP (**17**) was derived from Tos-PEP (**7**) via the formation of phthalimide-PEP (**16**). The method is modified from the synthesis route of amino PEG by Mutter et al. (*41*) 4 g PEP ($M_n = 15.4 \times 10^3$ g/mol, 5.0 mmol -OH groups) and 3.1 g phthalimide potassium (16.7 mmol) were dissolved in 50 mL DMF and heated at 40 °C with stirring for 18 h. The mixture was cooled and evaporated and dissolved in 200 mL DCM. The organic solution was washed with water (2 × 50 mL) and dried over magnesium sulfate. After filtration and evaporation under reduced pressure, phthalimide-PEP was precipitated in diethyl ether and dried in vacuo at 50 °C. 0.5 g phthalimide-PEP (**16**) ($M_n = 17.5 \times 10^3$ g/mol, 0.55 mmol phthalimide groups) was dissolved in ethanol (200 mL), and ammonia hydrate (40 mL) was added. The mixture was stirred at 30 °C for 24 h and then evaporated under reduced pressure. The crude product was dissolved in DCM and stirred for 24 h at room temperature. The solution was filtered and washed with water (2 × 50 mL) and dried over magnesium sulfate. The product, amino-PEP, was precipitated in diethyl ether and dried in vacuo at 50 °C.

Azido-PEP (**15**) and 2-azidobutyryl-PEP (**18**) were derived using similar methods from Tos-PEP (**7**) and 2-bromoisobutyryl-PEP (**9**), respectively. Synthesis of azido-PEP (**15**) illustrated in Figure 3 follows a method adapted from Mutter (*41*). 0.5 g Tos-PEP ($M_n = 20.1 \times 10^3$ g/mol, 0.478 mmol tosylate groups) was dissolved in 10 mL DMF, and then sodium azide was added under vigorous stirring at room temperature for 6 h. The product was purified by ultrafiltration. Filtered aqueous solution was concentrated to dryness, dissolved in DCM, and dried over anhydrous $MgSO_4$. The filtrate was distilled under vacuum to remove DCM and dried in vacuo at 50 °C to yield a white product.

Synthesis of Heterobifunctional Derivatives of Polyether Polyol. Synthesis of heterobifunctional derivatives **19**−**23** containing alkynyl groups is illustrated in Figure 4. As an example, the synthesis of alkynyl succinate-PEP is described here in detail. Alkynyl-PEP was obtained by Williamson reaction: 0.5 g alkynyl-PEP ($M_n = 16.2 \times 10^3$ g/mol, containing 0.25 mmol alkynyl groups and 0.59 mmol hydroxyl groups) with moisture removed was then reacted with 0.177 g succinic anhydride (1.77 mmol) in the presence of 0.1 mL TEA in 10 mL DCM at room temperature for 24 h. The solvent was removed by rotary evaporation. The product was purified by ultrafiltration. Filtered aqueous solution was concentrated to dryness, dissolved in DCM, and dried over anhydrous $MgSO_4$. The filtrate was distilled under vacuum to remove DCM and dried in vacuo at 50 °C to obtain a white product.

Synthesis methods for heterobifunctional derivatives **24**−**27** containing allyl groups follows similar routes, except that allyl chloride was first used to react with PEP to obtain allyl-PEP.

RESULTS AND DISCUSION

Synthesis and Characterization of Polyether Polyol (PEP). We have synthesized a number of polyether polyols which vary in their molar mass (from 6k to 20k g/mol) and

Table 1. Characterization of Polyether Polyol and Their Precursors

	feed ratio[a] EEGE:/EO	measured ratio[b] on copolymer EEGE/EO	M_n ($\times 10^{-3}$) designed[c] (g/mol)	precursor[d] M_n ($\times 10^{-3}$) (g/mol), [polydispersity]	PEP[e] M_n ($\times 10^{-3}$) (g/mol), [polydispersity]	N_{OH}[f]
A	1:0	1:0	5	4.95 [1.06]	2.23 [1.08]	34.2
B	1:0	1:0	10	10.1 [1.08]	5.01 [1.11]	69.5
C	1:0	1:0	20	19.6 [1.05]	9.76 [1.09]	134
D	1:19	1:18.4	20	17.4 [1.06]	15.4 [1.09]	19.2
E	1:19	1:19.2	15	13.5 [1.08]	11.1 [1.10]	14.5
F	1:9	1:8.6	10	11.7 [1.05]	10.3 [1.08]	23.1
G	1:5	1:5.3	5	5.8 [1.07]	4.7 [1.12]	16.5

[a] The feed ratio of EEGE to EO. [b] The molar ratio of EEGE to EO in copolymer poly(EEGE-*co*-EO) measured by ^{1}H NMR. [c] The designed number-average molar mass of precursor polymer. [d] Number-average molecular weight and polydispersity of precursor polymer are determined by GPC. Polydispersity is equal to the ratio of weight-average molar mass and number-average molar mass. [e] Number-average molar mass and polydispersity of PEP are determined by SEC. [f] The number of hydroxyl groups in polyether polyol: $N_{OH} = N_{EEGE} + 1$, in which N_{EEGE} was calculated by the integration of the peak in shift 1.19 ppm (m, C**H**$_3$CH$_2$-) and the integration of the peak in shift 3.38 ppm (s, C**H**$_3$-O-) of ^{1}H NMR data of poly(EEGE-*co*-EO).

ratio Gly/EO (from 1:0 to 1:19) (Table 1). The molar mass of these polymers can be well controlled by the input amount of initiator and monomer, and the resulting polymers are uniform in size. This feature is essential for bioconjugation materials. The polymer size influences the pharmacokinetics and biodistribution (*42, 43*). We expect PEP to behave similarly to PEG: the small molar mass PEG is cleared rapidly from the body, while PEG larger than 20k g/mol exhibits prolonged circulation in the body. The size also affects the extravasation into tissues and the uptake by the reticuloendothelial system (*44*).

The number of hydroxyl groups present on PEP dictates the number of anchorage points for drug conjugation. This can be designed by the ratio Gly/EO, which is in turn controlled by the feed ratio EEGE/EO in making the precursor of PEP (Table 1). Compared to linear PEG, which has one or two linkage points, PEP is a more efficient carrier in terms of higher number of drug molecules per polymer. The ability to control the hydroxyl density means that we can optimize the drug loading density in the polymer design stage, and this will introduce more opportunities to improve drug potency by taking advantage of the multivalency effects (*45, 46*).

Polyether polyol has a main chain similar to that of PEG and pendant hydroxyl groups similar to those on polyvinyl alcohol (PVA). It therefore possesses the same advantage of high water solubility as these two polymers. Each oxygen atom on the polyether main chain is a good hydrogen bond acceptor capable of interacting with two water molecules, while the pendant hydroxyl groups act as hydrogen donors for the surrounding water molecules. This property of polyether polyol means that it is a good drug delivery carrier of normally water-insoluble drug molecules (*47*). In addition to confirming the good solubility of PEP in water, we have also assessed the solubility of polyether polyol in common organic solvents, since these properties influence the choice of reaction types, conditions, and purification methods in the subsequent preparation of PEP derivatives. While the solubility in polar solvent such as methanol is not greatly affected by the Gly/EO ratio, the solubility in nonpolar solvents such as THF, toluene, and DCM increases with decreasing Gly/EO ratio. This is expected from the decreasing hydrophilicity due to hydroxyl groups on the polymer. When the ratio Gly/EO is 1:19.2 or lower, PEP has the same solubility as PEG in these nonpolar solvents.. A simple procedure very often used to isolate PEG is ether precipitation. The efficiency of precipitating PEP in diethyl ether decreases with increasing Gly/EO ratio: a viscous gum was observed when Gly/EO > 1:5, sparing precipitate when Gly/EO = 1:9, and white powder precipitate when Gly/EO < 1:19.

Synthesis and Characterization of Derivatives of PEP. We have successfully prepared a series of PEP derivatives: 18 monofunctional derivatives and 9 heterobifunctional derivatives (Figure 2, Tables 2 and 3). They cover a variety of chemical reactivities commonly used for bioconjugation. The derivatives have been analyzed by NMR to confirm the identity of the functional groups (Supporting Information Tables S1 and S2). The most appropriate synthesis route for each type of derivative was identified and adapted from existing methods on hydroxyl group modification. Most of the reaction yield and conversion efficiency (from hydroxyl groups to the indicated functional groups) were satisfactory (Table 2).

Carboxyl-PEP and Its Active Esters. Amines commonly found on peptides and drug molecules are available for covalent attachment to a polymeric carrier (*2, 5*). The widely used chemistry is via the formation of amide linkage with carboxyl or an active ester. We have prepared a number of derivatives in this group, which vary in the strength of chemical reactivity, length of linker, stability in water, and the presence of an additional functional group (Table 2).

Although oxidation of hydroxyl groups on PEP by permanganate can easily generate carboxyl groups (*30*), we chose not to use this method due to the likelihood of polyether chain degradation. We have produced carboxyl-PEP via Williamson reaction (**1** and **2**) (Figure 3 and Table 2). For example, CM-PEP was generated with 2-chloroacetic acid. The conversion efficiency of this type of reaction, however, only reached 88%. This is because the carboxyl group on 2-chloroacetic acid depletes the anionic ion in the reactive chain, and the anionic carboxyl group lowers the activity of the neighboring halogen atom. This disadvantage was overcome by first preparing ethyl acetate-PEP (**3**), and CM-PEP was produced by subsequent saponification. The conversion efficiency improved to 99% (Table 2 and Supporting Information Table S1).

Modification of the polymer with succinic, glutaric, or maleic anhydride is a straightforward way to synthesize carboxyl polymer. The reaction can be readily driven to completion using an excess of anhydride as confirmed by ^{1}H NMR (Supporting Information Table S1). Unlike the Williamson reaction, this route produces carboxyl-PEP with a hydrolyzable ester linkage instead of the noncleavable ether linkage. Depending on whether the therapeutic molecules to be attached to PEP need to be released in an aqueous environment, one can choose the linkage of desired stability.

The reactivity toward amino group is higher for active ester than carboxyl group. SC-PEG (**13**) was prepared by condensing NHS with CM-PEP using DCC as the coupling agent. The conversion efficiency was only about 80%. A more efficient approach we found was by esterification with acyl halide. Easy and quantitative conversion was achieved by transforming hydroxyl groups into *p*-nitrophenyl formate groups (**8**) and tosylate groups (**14**). It should be pointed out that tosylate-PEP is also an important intermediate for producing azido-PEP (Figure 2).

Mercapto-PEP and Epoxide-PEP. This group of PEP derivatives can join covalently with the thiol groups on biomolecules or small drugs. The thiol linkage has been widely adopted in

Table 2. Summary of Reaction Yield, Conversion Efficiency, and Reactivity of Monofunctional PEP Derivatives

PEP derivative	Chemical structure (-R group)	(%) Yield[a]	(%) Conversion efficiency[b]	Possible reactivity (opposite group) and comments
1[c]		91%	88%	
1[d]		94%	99%	
2		93%	85-87%	
6		86%	87%	
7		95%	98%	
8	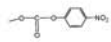	95%	99%	amino group
9		95%	98-99%	
10		96%	96-100%	
11		94%	95%	
13		79%	78-84%	
14		87%	62%	
14		87%	62%	thiol group
5		90%	94-96%	
6		86%	87%	
11		94%	95%	
12		94%	91%	
17	-NH_2	85%	34%	carboxyl, epoxide, halogen
4		87%	90-93%	azido group
15	-N_3	93%	93%	alkynyl group
18		91%	98%	alkynyl group
5		87%	99%	for synthesis of CM-PEP
17		64%	46%	for synthesis of amino group

[a] Yield (%) = $W_{product}/W_{precursor} \times 100\%$. [b] Conversion efficiency (%) = $[\text{functional group}]_{product}/[OH]_{precursor} \times 100\%$. [c] CM-PEP is synthesized by PEP reacting with 2-chloroacetic acid directly. [d] CM-PEP is synthesized by hydrolysis of ethyl acetate (EA)-PEP **5**.

attaching PEG to therapeutic molecules and proteins (*48, 49*). Epoxide-PEP is an electrophile of mild reactivity toward hydroxyl groups and amino groups and better reactivity toward thiols (*50*).

In our early attempts, 3-mercaptopropionate-PEP was prepared by esterification between hydroxyl groups and 3-mercaptopropionic acid in the presence of concentrated sulfuric acid as catalyst (*51*). We also tried to catalyze this reaction with DCC and DMAP. Both methods resulted in conversion efficiency of less than 10% according to ^{1}H NMR. The successful reaction reported in this paper used $HfCl_4 \cdot 2THF$, a recently developed and highly efficient catalyst, for the esterification between carboxyl groups and hydroxyl groups (*38, 39*).A gel was formed as a result of cross-linking between thiol groups in 3-mercaptopropionate-PEP. When the gel was treated with DL-dithiothreitol (DTT), sodium borohydride, or lithium aluminum anhydride, the disulfide bonds were reduced to thiol groups.

Amino-PEP. Compared with hydroxyl groups, primary amino groups have higher reactivity in nucleophilic substitution reactions, making them useful for conjugating with carboxyl groups and halide (*2*). The transformation of hydroxyl groups to amino groups was difficult, and the conversion efficiency was the lowest among all PEP derivatives. The reaction involved three steps: the conversion of hydroxyl group to tosylate group, followed by the formation of phthalimide, and finally the transformation of phthalimide into amino group. While the efficiency of the first step was

Table 3. Summary of Reaction Yield, Conversion Efficiency, and Reactivity of Heterobifunctional PEP Derivatives

Alkynyl-PEP derivative[a]	(%) Yield	Chemical structure (-R_2 group)	(%) Conversion efficiency[b]	Possible reactivity (opposite group) and comments
19	94%		50%	amino group
20	95%		53%	amino group, thiol group
21	94%		58%	thiol group
22	92%		47%	amino group, for synthesis of azido group, or as a leaving group
23	79%		36%	thiol group
Allyl-PEP derivative[c]	(%) Yield	Chemical structure (-R_2 group)	(%) Conversion efficiency	Possible reactivity (opposite group) and comments
24	94%		48%	amino group
25	91%		52%	amino group, thiol group
26	92%		41%	thiol group
27	93%		53%	amino group, for synthesis of azido group, or as a leaving group

[a] R_1functional group is -OCH_2CCH, the conversion efficiency is 30%. [b] The conversion efficiency here is the [R_2]/[OH]; therein, [R_2] is the number of -R_2 group in heterobifunctional PEP; [OH] is the total number of the -OH group in the original PEP. [c] R_1 functional group is -OCH_2CHCH_2; the conversion efficiency is 41%.

close to 100% according to ^{1}H NMR, the efficiency of subsequent steps suffered from the generation of a large amount of salt and high viscosity as a result of excess phthalimide potassium insoluble in methanol.

Azido-PEP and Alkynyl-PEP. Azido groups are able to react with alkynyl groups in cycloaddition to form a stable triazole linkage (*52, 53*). Since this "click chemistry" occurs in mild conditions, and the reaction is highly specific, it has found many applications in bioconjugation (*53*−*57*). This group of derivatives was prepared with high yield and conversion efficiency.

Dual Reactivities. The maleate and *N*-cysteinyl formamide methyl pendant groups provide dual reactivities, which make the PEP derivatives useful for conjugating with two different entities. This feature may be useful for developing drug carriers for combination therapy. The carboxyl groups and double bonds on maleate-PEP are reactive toward amino- and thiol-containing compounds, while the thiol and carboxyl groups on *N*-cysteinyl formamide methyl-PEP are reactive toward thiol- and amino-containing compounds. Although both *N*-cysteinyl formamide methyl-PEP and 3-mercapto-propionate-PEP are thiol-reactive, the former has a more stable linker (comprising an amide bond) than the latter (comprising an ester bond).

Heterobifunctional Polyether Polyol Derivatives. Heterobifunctional polymers provide more options for designing drug carriers. They are also useful spacers between surfaces and various ligands (*58*−*61*). Compared to heterobifunctional PEG, the synthesis and purification of heterobifunctional PEP derivatives are much simpler. Furthermore, controlling the ratio of the different functional groups is feasible. If PEG diol is modified to generate heterobifunctional groups, the separation among the modified PEG, the macromolecular intermediates, and the starting PEG is challenging, owing to the similarity in physical properties including size (*62*−*64*). Thus, heterobifunctional PEG is mostly prepared starting from anionic polymerization using a heterofunctional initiator (*65*−*72*). Since PEP carries multiple hydroxyl groups, they can be transformed into heterofunctional derivatives by successive modification steps. Separation between PEP derivatives and the small chemical reagents for modification can be readily achieved, for example, by membrane purification. We have demonstrated this approach by synthesizing two groups of heterobifunctional polyether polyol derivatives, one containing alkynyl groups and the other containing allyl groups (Figure 2, Table 3). The presence and the amount of different functional groups were characterized using NMR (Supporting Information Tables S1 and S2), which were tunable by the number of hydroxyl groups on PEP and the feeding amount of the modifying chemicals.

These heterobifunctional derivatives of polyether polyol are potentially useful as drug carriers for two different drugs. They can also be used to bind to a surface or coat a particle with one type of functional groups, leaving the other type of functional groups to couple with drugs, peptides, proteins, DNA, or imaging probes. The alkynyl series were designed to conjugate with azide-containing drugs or azide-modified peptides and proteins, and the allyl series to conjugate with thiol-containing compounds by the radical addition reaction in the presence of 2,2′-azobisiosobutyronitrile (AIBN) (*66, 67*).

CONCLUSION

A series of polyether polyol derivatives have been successfully prepared as materials for conjugating with drugs and biomolecules. The number of functional groups can be well-controlled. Heterobifunctional derivatives of polyether polyol can be readily prepared, and they should offer more flexibility in designing the next generation of polymer−drug conjugates.

LIST OF ABBREVIATIONS

AIBN	2,2′-azobisiosobutyronitrile
CM	carboxymethyl
CE	carboxyethyl
DCC	dicyclohexylcarbodiimide
DCM	dichloromethane
DCU	1,3-dicyclohexylurea

DMSO	dimethyl sulfoxide
DMAP	(dimethylamino) pyridine
DMF	*N*,*N*-dimethylformamide
DTT	DL-dithiothreitol
EA	ethyl acetate
EEGE	ethoxyethyl glycidyl ether
EO	ethylene oxide
Gly	glycidol
$HfCl_4 \cdot 2THF$	hafnium chloride·tetrahydrofuran
PEG	poly(ethylene glycol)
mPEG	monomethoxyl poly(ethylene glycol)
mTEG	triethylene glycol monomethyl
MPA	3-mercaptopropionic acid
NHS	*N*-hydroxysuccinimide
PG	polyglycidol
PEP	polyether polyol
Poly(Gly-*co*-EO)	poly(glycidol-*co*-ethylene glycol)
PBS	phosphate buffered saline
*p*NP	*p*-nitrophenyl formate
PTC	phase transfer catalyst
SC	succinimidyl carbonate
SEC	size exclusion chromatography
GPC	gel permeation chromatography
TEA	triethylamine
THF	tetrahydrofuran
TMS	tetramethylsilane
TsCl	*p*-toluenesulfonyl chloride
Tos	tosylate

ACKNOWLEDGMENT

The authors gratefully acknowledge financial support from the Hong Kong Research Grant Council (Earmarked Research Grant HKUST 6407/06M).

Supporting Information Available: Table S1 and Table S2 are ^1H NMR and ^{13}C NMR data of synthetic PEP derivatives and their precursors. This material is available free of charge via the Internet at http://pubs.acs.org.

LITERATURE CITED

(1) Duncan, R. (2003) The dawning era of polymer therapeutics. *Nat. Rev. Drug Discovery 2*, 347–360.
(2) Zalipsky, S. (1995) Chemistry of polyethylene-glycol conjugates with biologically-active molecules. *Adv. Drug Delivery Rev. 16*, 157–182.
(3) Zalipsky, S. (1995) Functionalized poly(ethylene glycol) for preparation of biologically relevant conjugates. *Bioconjugate Chem. 6*, 150–165.
(4) Kodera, Y., Matsushima, A., Hiroto, M., Nishimura, H., Ishii, A., Ueno, T., and Inada, Y. (1998) Pegylation of proteins and bioactive substances for medical and technical applications. *Prog. Polym. Sci. 23*, 1233–1271.
(5) Veronese, F. M. (2001) Peptide and protein PEGylation: a review of problems and solutions. *Biomaterials 22*, 405–417.
(6) Veronese, F. M., and Pasut, G. (2005) PEGylation, successful approach to drug delivery. *Drug Discovery Today 10*, 1451–1458.
(7) Pasut, G., and Veronese, F. M. (2007) Polymer-drug conjugation, recent achievements and general strategies. *Prog. Polym. Sci. 32*, 933–961.
(8) Roberts, M. J., Bentley, M. D., and Harris, J. M. (2002) Chemistry for peptide and protein PEGylation. *Adv. Drug Delivery Rev. 54*, 459–476.
(9) Harris, J. M., and Chess, R. B. (2003) Effect of pegylation on pharmaceuticals. *Nat. Rev. Drug Discovery 2*, 214–221.
(10) Harris, J. M., Martin, N. E., and Modi, M. (2001) Pegylation - A novel process for modifying pharmacokinetics. *Clin. Pharmacokinet. 40*, 539–551.
(11) Feng, X. S., Taton, D., Chaikof, E. L., and Gnanou, Y. (2005) Toward an easy access to dendrimer-like poly(ethylene oxide)s. *J. Am. Chem. Soc. 127*, 10956–10966.
(12) Gnanou, Y., Lutz, P., and Rempp, P. (1988) Synthesis of star-shaped poly(ethylene oxide). *Makromol. Chem. 189*, 2885–2892.
(13) Six, J. L., and Gnanou, Y. (1995) From star-shaped to dendritic poly(ethylene oxide)s - toward increasingly branched architectures by anionic-polymerization. *Macromol. Symp. 95*, 137–150.
(14) Lapienis, G., and Penczek, S. (2005) One-pot synthesis of star-shaped macromolecules containing polyglycidol and poly(ethylene oxide) arms. *Biomacromolecules 6*, 752–762.
(15) Lapienis, G., and Penczek, S. (2004) Reaction of oligoalcohol with diepoxides: An easy, one-pot way to star-shaped, multibranched polymers. II. Poly(ethylene oxide) Stars - Synthesis and analysis by size exclusion chromatography triple-detection method. *J. Polym. Sci., Part A: Polym. Chem. 42*, 1576–1598.
(16) Lapienis, G., and Penczek, S. (2003) Multibranched star-shaped polyethers. *Macromol. Symp. 195*, 317–327.
(17) Nathan, A., Bolikal, D., Vyavahare, N., Zalipsky, S., and Kohn, J. (1992) Hydrogels based on water-soluble poly(ether urethanes) derived from L-lysine and poly(ethylene glycol). *Macromolecules 25*, 4476–4484.
(18) Nathan, A., Zalipsky, S., Ertel, S. I., Agathos, S. N., Yarmush, M. L., and Kohn, J. (1993) Copolymers of lysine and polyethyleneglycol - a new family of functionalized drug carriers. *Bioconjugate Chem. 4*, 54–62.
(19) Nathan, A., Zalipsky, S., and Kohn, J. (1994) Strategies for covalent attachment of doxorubicin to poly(Peg-Lys), a new water-soluble poly(ether urethane). *J. Bioact. Compat. Polym. 9*, 239–251.
(20) Kainthan, R. K., and Brooks, D. E. (2007) In vivo biological evaluation of high molecular weight hyperbranched polyglycerols. *Biomaterials 28*, 4779–4787.
(21) Kainthan, R. K., Hester, S. R., Levin, E., Devine, D. V., and Brooks, D. E. (2007) In vitro biological evaluation of high molecular weight hyperbranched polyglycerols. *Biomaterials 28*, 4581–4590.
(22) Kainthan, R. K., Janzen, J., Levin, E., Devine, D. V., and Brooks, D. E. (2006) Biocompatibility testing of branched and linear polyglycidol. *Biomacromolecules 7*, 703–709.
(23) Taton, D., Leborgne, A., Sepulchre, M., and Spassky, N. (1994) Synthesis of chiral and racemic functional polymers from glycidol and thioglycidol. *Macromol. Chem. Phys. 195*, 139–148.
(24) Li, Z. Y., Li, P. P., and Huang, J. L. (2006) Synthesis of amphiphilic copolymer brushes: Poly(ethylene oxide)-graft-polystyrene. *J. Polym. Sci., Part A: Polym. Chem. 44*, 4361–4371.
(25) Li, Z. Y., Li, P. P., and Huang, J. L. (2006) Synthesis and characterization of amphiphilic graft copolymer poly(ethylene oxide)-graft-poly(methyl acrylate). *Polymer 47*, 5791–5798.
(26) Fitton, A. O., Hill, J., Jane, D. E., and Millar, R. (1987) Synthesis of simple oxetanes carrying reactive 2-substituents. *Synthesis* 1140–1142.
(27) Aggour, Y. A., Tomita, I., and Endo, T. (1995) Synthesis and radical polymerization of end-allenoxy polyoxyethylene macromonomer. *React. Funct. Polym. 28*, 81–87.
(28) Park, J. Y., Acar, M. H., Akthakul, A., Kuhlman, W., and Mayes, A. M. (2006) Polysulfone-graft-poly(ethylene glycol) graft copolymers for surface modification of polysulfone membranes. *Biomaterials 27*, 856–865.
(29) Bergstrom, K., Holmberg, K., Safranj, A., Hoffman, A. S., Edgell, M. J., Kozlowski, A., Hovanes, B. A., and Harris, J. M. (1992) Reduction of fibrinogen adsorption on peg-coated polystyrene surfaces. *J. Biomed. Mater. Res. 26*, 779–790.

(30) Buckmann, A. F., Morr, M., and Johansson, G. (1981) Functionalization of poly(ethylene glycol) and monomethoxy-poly(ethylene glycol). *Makromol. Chem. 182*, 1379–1384.
(31) Wang, Y., Lu, C. Q., and Huang, J. L. (2004) Copolymerization of the macromonomer poly(ethylene oxide) with styryl end group and styrene in the presence of poly(ε-caprolactone) with 2,2,6,6-tetramethylpiperidinyl-1-oxy end group by controlled radical mechanism. *J. Polym. Sci., Part A: Polym. Chem. 42*, 2093–2099.
(32) Swamikannu, A. X., and Litt, M. H. (1984) Preparation and characterization of para-toluene sulfonyl ester and amino derivatives of tri(ethylene glycol) and poly(ethylene glycol). *J. Polym. Sci., Part A: Polym. Chem 22*, 1623–1632.
(33) Devos, R. J., and Goethals, E. J. (1985) Convenient synthesis of α-tosyl-ω-tosyloxypoly(oxyethylene). *Makromol. Chem., Rapid Commun. 6*, 53–56.
(34) Veronese, F. M., Largajolli, R., Boccu, E., Benassi, C. A., and Schiavon, O. (1985) Surface modification of proteins - activation of monomethoxy-polyethylene glycols by phenylchloroformates and modification of ribonuclease and superoxide-dismutase. *Appl. Biochem. Biotechnol. 11*, 141–152.
(35) Geckeler, K., and Bayer, E. (1980) Functionalization of soluble polymers 0.3. preparation of carboxy-telechelic polymers. *Polym. Bull. 3*, 347–352.
(36) Treethammathurot, B., Ovartlarnporn, C., Wungsintaweekul, J., Duncan, R., and Wiwattanapatapee, R. (2008) Effect of PEG molecular weight and linking chemistry on the biological activity and thermal stability of PEGylated trypsin. *Int. J. Pharm. 357*, 252–259.
(37) Biswas, A., Shogren, R. L., Kim, S., and Willett, J. L. (2006) Rapid preparation of starch maleate half-esters. *Carbohydr. Polym. 64*, 484–487.
(38) Wan, D. C., Pu, H. T., and Yang, G. J. (2008) Highly efficient condensation of hydroxyl-terminated polyethylene oxide with 3-mercaptopropionic acid catalyzed by hafnium salt. *React. Funct. Polym. 68*, 431–435.
(39) Ishihara, K., Ohara, S., and Yamamoto, H. (2000) Direct condensation of carboxylic acids with alcohols catalyzed by hafnium(IV) salts. *Science 290*, 1140–1142.
(40) Zalipsky, S., Gilon, C., and Zilkha, A. (1983) Attachment of drugs to polyethylene glycols. *Eur. Polym. J. 19*, 1177–1183.
(41) Pillai, V. N. R., Mutter, M., Bayer, E., and Gatfield, I. (1980) New, easily removable poly(ethylene glycol) supports for the liquid-phase method of peptide-synthesis. *J. Org. Chem. 45*, 5364–5370.
(42) Yamaoka, T., Tabata, Y., and Ikada, Y. (1994) Distribution and tissue uptake of poly(ethylene glycol) with different molecular-weights after intravenous administration to mice. *J. Pharm. Sci. 83*, 601–606.
(43) Yamaoka, T., Tabata, Y., and Ikada, Y. (1995) Fate of water-soluble polymers administered via different routes. *J. Pharm. Sci. 84*, 349–354.
(44) Caliceti, P., and Veronese, F. M. (2003) Pharmacokinetic and biodistribution properties of poly(ethylene glycol)-protein conjugates. *Adv. Drug Delivery Rev. 55*, 1261–1277.
(45) De Jesus, O. L. P., Ihre, H. R., Gagne, L., Frechet, J. M. J., and Szoka, F. C. (2002) Polyester dendritic systems for drug delivery applications: In vitro and in vivo evaluation. *Bioconjugate Chem. 13*, 453–461.
(46) Liu, Z. G., Deshazer, H., Rice, A. J., Chen, K., Zhou, C. H., and Kallenbach, N. R. (2006) Multivalent antimicrobial peptides from a reactive polymer scaffold. *J. Med. Chem. 49*, 3436–3439.
(47) Duncan, R., and Kopecek, J. (1984) Soluble synthetic-polymers as potential-drug carriers. *Adv. Polym. Sci. 57*, 51–101.
(48) Brocchini, S., Godwin, A., Balan, S., Choi, J. W., Zloh, M., and Shaunak, S. (2008) Disulfide bridge based PEGylation of proteins. *Adv. Drug Delivery Rev. 60*, 3–12.
(49) Brocchini, S., Balan, S., Godwin, A., Choi, J. W., Zloh, M., and Shaunak, S. (2006) PEGylation of native disulfide bonds in proteins. *Nat. Protoc. 1*, 2241–2252.
(50) Elling, L., and Kula, M. R. (1991) Immunoaffinity partitioning-synthesis and use of polyethylene-glycol oxirane for coupling to bovine serum-albumin and monoclonal-antibodies. *Biotechnol. Appl. Biochem. 13*, 354–362.
(51) Du, Y. J., and Brash, J. L. (2003) Synthesis and characterization of thiol-terminated poly(ethylene oxide) for chemisorption to gold surface. *J. Appl. Polym. Sci. 90*, 594–607.
(52) Kolb, H. C., and Sharpless, K. B. (2003) The growing impact of click chemistry on drug discovery. *Drug Discovery Today 8*, 1128–1137.
(53) Lutz, J. F. (2007) 1,3-Dipolar cycloadditions of azides and alkynes: A universal ligation tool in polymer and materials science. *Angew. Chem., Int. Ed. 46*, 1018–1025.
(54) Parrish, B., Breitenkamp, R. B., and Emrick, T. (2005) PEG- and peptide-grafted aliphatic polyesters by click chemistry. *J. Am. Chem. Soc. 127*, 7404–7410.
(55) Liu, X. M., Lee, H. T., Reinhardt, R. A., Marky, L. A., and Wang, D. (2007) Novel biomineral-binding cyclodextrins for controlled drug delivery in the oral cavity. *J. Controlled Release 122*, 54–62.
(56) Lutz, J. F., and Zarafshani, Z. (2008) Efficient construction of therapeutics, bioconjugates, biomaterials and bioactive surfaces using azide-alkyne "click" chemistry. *Adv. Drug Delivery Rev. 60*, 958–970.
(57) Liu, X. M., Lee, H. T., Reinhardt, R. A., Marky, L. A., and Wang, D. (2007) Novel biomineral-binding cyclodextrins for controlled drug delivery in the oral cavity. *J. Controlled Release 122*, 54–62.
(58) Harris, J. M., Herati, M. T. S., Sather, P. J., Brooks, D. E., and Fyles, T. M. (1992) *Synthesis of new poly(ethylene glycol) derivatives.* pp 371−381. Plenum Publishing Corporation, New York.
(59) Diamente, P. R., Burke, R. D., and van Veggel, F. (2006) Bioconjugation of Ln(3+)-doped LaF_3 nanoparticles to avidin. *Langmuir 22*, 1782–1788.
(60) Zhang, Z. P., Yoo, R., Wells, M., Beebe, T. P., Biran, R., and Tresco, P. (2005) Neurite outgrowth on well-characterized surfaces: preparation and characterization of chemically and spatially controlled fibronectin and RGD substrates with good bioactivity. *Biomaterials 26*, 47–61.
(61) Zalipsky, S., Mullah, N., Harding, J. A., Gittelman, J., Guo, L., and DeFrees, S. A. (1997) Poly(ethylene glycol)-grafted liposomes with oligopeptide or oligosaccharide ligands appended to the termini of the polymer chains. *Bioconjugate Chem. 8*, 111–118.
(62) Huang, Y. H., Li, Z. M., and Morawetz, H. (1985) The kinetics of the attachment of polymer-chains to reactive latex-particles and the resulting latex stabilization. *J. Polym. Sci., Part A: Polym. Chem. 23*, 795–799.
(63) Li, J., and Kao, W. J. (2003) Synthesis of polyethylene glycol (PEG) derivatives and PEGylated-peptide blopolymer conjugates. *Biomacromolecules 4*, 1055–1067.
(64) Warnecke, A., and Kratz, F. (2003) Maleimide-oligo(ethylene glycol) derivatives of camptothecin as albumin-binding prodrugs: Synthesis and antitumor efficacy. *Bioconjugate Chem. 14*, 377–387.
(65) Otsuka, H., Akiyama, Y., Nagasaki, Y., and Kataoka, K. (2001) Quantitative and reversible lectin-induced association of gold nanoparticles modified with α-lactosyl-ω-mercapto-poly-(ethylene glycol). *J. Am. Chem. Soc. 123*, 8226–8230.
(66) Cammas, S., Nagasaki, Y., and Kataoka, K. (1995) Hetero-bifunctional poly(ethylene oxide) - synthesis of α-methoxy-ω-amino and α-hydroxy-ω-amino PEOs with the same molecular-weights. *Bioconjugate Chem. 6*, 226–230.
(67) Hiki, S., and Kataoka, K. (2007) A facile synthesis of azido-terminated heterobifunctional poly(ethylene glycol)s for "click" conjugation. *Bioconjugate Chem. 18*, 2191–2196.
(68) Jaturanpinyo, M., Harada, A., Yuan, X. F., and Kataoka, K. (2004) Preparation of bionanoreactor based on core-shell structured polyion complex micelles entrapping trypsin in the core cross-linked with glutaraldehyde. *Bioconjugate Chem. 15*, 344–348.

(69) Nagasaki, Y., Iijima, M., Kato, M., and Kataoka, K. (1995) Primary amino-terminal heterobifunctional poly(ethylene oxide)-facile synthesis of poly(ethylene oxide) with a primary amino group at one end and a hydroxyl group at the other end. *Bioconjugate Chem. 6*, 702–704.

(70) Nagasaki, Y., Kutsuna, T., Iijima, M., Kato, M., Kataoka, K., Kitano, S., and Kadoma, Y. (1995) Formyl-ended heterobifunctional poly(ethylene oxide) - synthesis of poly(ethylene oxide) with a formyl group at one end and a hydroxyl group at the other end. *Bioconjugate Chem. 6*, 231–233.

(71) Nakamura, T., Nagasaki, Y., and Kataoka, K. (1998) Synthesis of heterobifunctional poly(ethylene glycol) with a reducing monosaccharide residue at one end. *Bioconjugate Chem. 9*, 300–303.

(72) Yokoyama, M., Okano, T., Sakurai, Y., Kikuchi, A., Ohsako, N., Nagasaki, Y., and Kataoka, K. (1992) Synthesis of poly-(ethylene oxide) with heterobifunctional reactive groups at its terminals by an anionic initiator. *Bioconjugate Chem. 3*, 275–276.

BC900036F

Synthesis of linear polyether polyol derivatives as new materials for bioconjugation

Zhongyu Li, Ying Chau*

Department of Chemical and Biomolecular Engineering, the Hong Kong University of Science and Technology, Clear Water Bay, Hong Kong SAR, China

*Corresponding author. Tel.: +852-2358 8935; Fax: +852-2358 0054

Email address: keychau@ust.hk

Supporting Information

Table S1. ^{1}H NMR Chemical shifts (ppm) for PEP derivatives.

Chemical shifts of designated hydrogen (in superscript) for PEP derivatives of the following general structure:

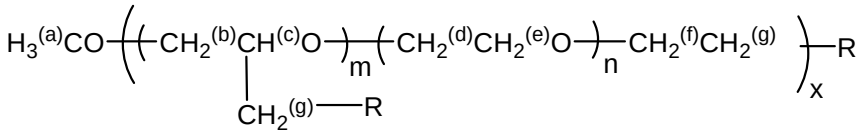

PEP derivative	H^{a}	$H^{(b)+(c)+(d)+(e)+(f)}$	$H^{(g)}$	$H^{(1)}$	$H^{(2)}$	$H^{(3)}$	$H^{(4)}$	$H^{(5)}$	$H^{(6)}$	Chemical group of pendant R
PEP		3.45-3.85	3.68							-OH$^{(1)}$
1	3.38	3.45-3.85	3.65	4.27						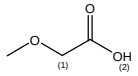
2	3.38	3.45-3.85	3.65	3.58	2.54					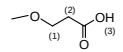
3	3.38	3.45-3.85	3.65	4.28	4.14-4.18	1.27				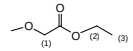
4	3.38	3.45-3.85	3.67	4.27	2.45					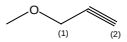
5	3.38	3.45-3.85	3.65	3.71	5.81	5.16				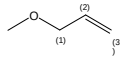
6	3.38	3.45-3.85	3.65	3.45-3.65	2.96	2.45, 2.57				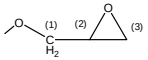
7	3.38	3.45-3.85	4.12-4.17	7.78	7.42	2.43				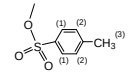
8	3.38	3.45-3.85	4.27	7.35	8.06					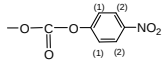
9	3.38	3.45-3.85	4.30, 4.13	1.92						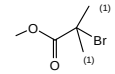
10	3.38	3.45-3.85	4.28, 4.16	2.65	2.65					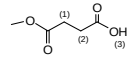
11	3.38	3.45-3.85	4.29, 4.16	7.03	7.03					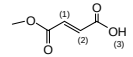
12	3.38	3.45-3.85	4.24, 4.14	2.58	2.66	1.68				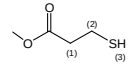
13	3.38	3.45-3.85	3.65	4.27	2.79					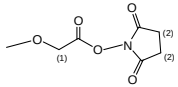
14	3.38	3.45-3.85	3.65	4.26		4.80	3.01	1.68		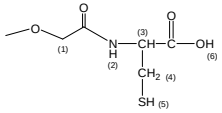
15	3.38	3.45-3.85	3.65	3.51						-N_3

16	3.38	3.45-3.85	3.65	7.94	7.65					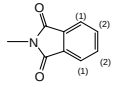
17	3.38	3.45-3.85	3.04							-NH_2
18	3.38	3.45-3.85	4.29, 4.15	1.92						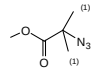
19	3.38	3.45-3.85	4.27	4.26	2.45	2.65				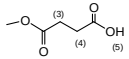
20	3.38	3.45-3.85	4.27	4.26	2.45	7.03	7.03			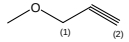 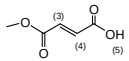
21	3.38	3.45-3.85	4.26,	2.45	2.58	2.66	1.59			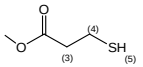 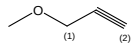
22	3.38	3.45-3.85	4.26	2.47	7.78	7.35	2.45			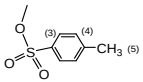 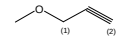
23	3.38	3.45-3.85	3.65	4.27	2.46	3.68	5.81	5.16		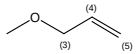
24	3.38	3.45-3.85	4.27, 4.14	3.71	5.81	5.17	2.66	2.66		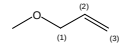 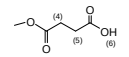
25	3.38	3.45-3.85	4.25, 4.16	3.70	5.81	5.16	7.05	7.05		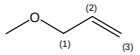 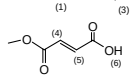
26	3.38	3.45-3.85	4.26, 4.15	3.70	5.80	5.15	2.57	2.67	1.67	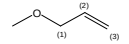 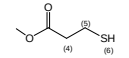
27	3.38	3.45-3.85	3.70	3.70	5.82	5.17	7.82	7.41	2.43	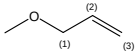 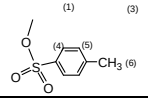

Table S2. ^{13}C NMR Chemical shifts (ppm) for PEP derivatives.

Chemical shifts of designated carbon (in superscript) for PEP derivatives of the following general structure:

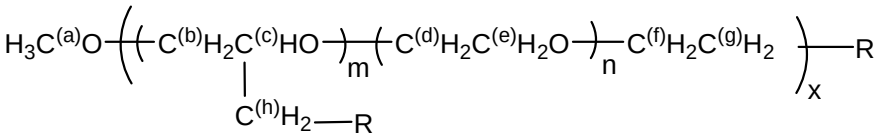

PEP derivative	$C^{(a)}$	$C^{(b)+(d)+(e)+(f)}$	$C^{(c)}$	$C^{(g)}$	$C^{(h)}$	$C^{(1)}$	$C^{(2)}$	$C^{(3)}$	$C^{(4)}$	$C^{(5)}$	$C^{(6)}$	$C^{(7)}$	$C^{(8)}$	Chemical group of pendant R
PEP	58.3	70.5-71.3	80.4	60.7	63.9									-OH
1	58.3	70.4-71.4	80.6	69.5	70.8	53.8	170.5							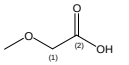
2	58.3	70.4-71.5	80.6	70.8	71.0.	66.1	32.5	173.5						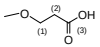
3	58.3	70.3-71.5	80.5	70.6	71.3	68.5	167.8	61.1	13.8					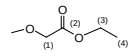
4	58.2	70.4-71.5	80.4	69.5	70.1	60.2	78.2	75.9						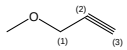
5	58.3	70.4-71.4	80.5	70.4	71.5	73.7	130.8	115.1						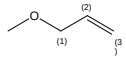
6	58.3	70.3-71.5	80.1	70.5	71.6	73.5	48.7	43.9						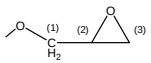
7	58.3	70.5-71.5	80.5	66.7	67.0	128.5	130.6	137.8	144.0	21.1				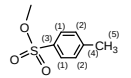
8	58.3	70.5-71.4	80.6	67.5	68.4	156.1	122.0	121.5	144.8	152.1				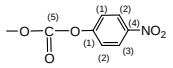
9	58.2	70.4-71.5	80.6	63.7	64.2	171.1	51.2	33.2						
10	58.2	70.4-71.5	80.6	66.5	66.4	173.2	29.6	31.9	174.4					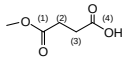
11	58.3	70.5-71.5	80.5	66.4.	66.1	165.7	134.8	134.1	169.5					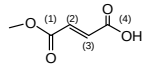

12	58.3	70.4-71.5	80.6	63.1	63.5	171.1	33.7	19.4					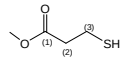
13	58.3	70.5-71.5	80.6	69.5	70.8	64.7	173.5	168.7	23.9				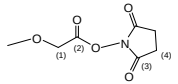
14	58.3	70.5-71.4	80.7	69.4	70.8	70.0	168.5	57.1	26.4	137.7			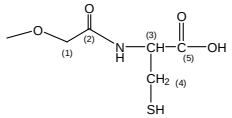
15	58.3	70.5-71.5	80.7	50.2	50.7								$-N_3$
16	58.3	70.5-71.4	80.7	64.8	65.0	160.6	131.8	127.1	132.0				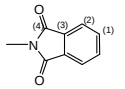
17	58.3	70.5-71.5	81.5	40.1	41.7								$-NH_2$
18	58.2	70.5-71.4	80.7	64.8	65.1	170.2	58.3	26.2					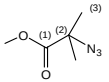
19	58.3	70.5-71.5	80.5	69.4, 66.3	70.0, 66.7	60.1	78.2	76.0	173.2	29.5	31.7	174.1	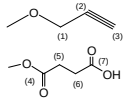
20	58.3	70.4-71.4	80.7	69.5, 65.8	70.0, 66.2	60.2	78.1	75.8	165.5	134.9	134.2	169.6	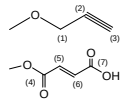
21	58.2	70.4-71.4	80.5	69.5, 63.0	70.1, 63.5	60.2	78.2	75.9	171.1	33.7	19.4		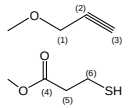
22	58.3	70.4-71.4	80.5	69.6, 66.3	70.2, 67.1	60.3	78.4	76.1	128.1	130.2	137.5	143.8	21.4 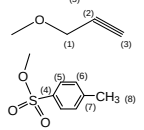
23	58.3	70.5-71.5	80.6	69.5, 70.6	70.1, 71.8	60.1	78.1	76.0	73.7	130.8	115.1		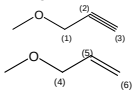

24	58.3	70.5-71.5	80.6	70.4, 66.0	71.5, 66.8	73.7	130.6	115.4	173.4	29.7	31.7	174.2		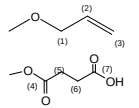
25	58.3	70.5-71.5	80.6	70.5, 65.9	71.7, 66.5	73.9	130.9	115.3	165.4	134.7	134.0	169.3		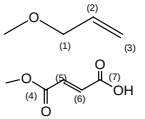
26	58.3	70.5-71.5	80.7	70.5, 63.1	71.7, 63.7	73.4	130.6	115.0	171.1	33.8	19.5			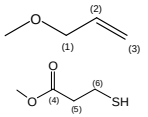
27	58.3	70.4-71.4	80.6	70.3, 66.7	71.5, 67.2	73.5	130.4	114.8	128.0	130.1	137.2	143.5	21.2	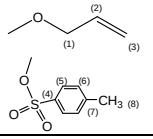

Evaluation of ^{64}Cu(DO3A-xy-TPEP) as a Potential PET Radiotracer for Monitoring Tumor Multidrug Resistance

Shuang Liu,* Young-Seung Kim, Shizhen Zhai, Jiyun Shi, and Guihua Hou

School of Health Sciences, Purdue University, West Lafayette, Indiana. Received December 16, 2008; Revised Manuscript Received February 1, 2009

In this study, we evaluated the potential of ^{64}Cu(DO3A-xy-TPEP) (DO3A-xy-TPEP = (2-(diphenylphosphoryl)-ethyl)diphenyl(4-((4,7,10-tris(carboxymethyl)-1,4,7,10-tetraazacyclododecan-1-yl)methyl)benzyl)phosphonium) as a PET (positron emission tomography) radiotracer for noninvasive monitoring of multidrug resistance (MDR) transport function in several xenografted tumor models (MDR-negative: U87MG; MDR-positive: MDA-MB-435, MDA-MB-231, KB-3-1, and KB-v-1). It was found that ^{64}Cu(DO3A-xy-TPEP) has a high initial tumor uptake (5.27 ± 1.2%ID/g at 5 min p.i.) and shows a steady uptake increase between 30 and 120 min p.i. (2.09 ± 0.53 and 3.35 ± 1.27%ID/g at 30 and 120 min p.i., respectively) in the MDR-negative U87MG glioma tumors. ^{64}Cu(DO3A-xy-TPEP) has a greater uptake difference between U87MG glioma and MDR-positive tumors (MDA-MB-231: 1.57 ± 0.04, 1.00 ± 0.17, and 0.93 ± 0.15; MDA-MB-435: 1.15 ± 0.19, 1.12 ± 0.20, and 0.81 ± 0.11; KB-3-1: 1.45 ± 0.31, 1.43 ± 0.16, and 1.08 ± 0.19; and KB-v-1: 1.63 ± 0.47, 1.81 ± 0.31, and 1.14 ± 0.22%ID/g at 30, 60, and 120 min p.i., respectively) than ^{99m}Tc-Sestamibi. Regardless of the source of MDR, the overall net effect is the rapid efflux of ^{64}Cu(DO3A-xy-TPEP) from tumor cells, which leads to a significant reduction of its tumor uptake. It was concluded that ^{64}Cu(DO3A-xy-TPEP) is more efficient than ^{99m}Tc-Sestamibi as the substrate for MDR P-glycoproteins (MDR Pgps) and multidrug resistance-associated proteins (MRPs), and might be a more efficient radiotracer for noninvasive monitoring of the tumor MDR transport function. ^{64}Cu(DO3A-xy-TPEP) and ^{99m}Tc-Sestamibi share almost identical subcellular distribution patterns in U87MG glioma tumors. Thus, it is reasonable to believe that ^{64}Cu(DO3A-xy-TPEP), like ^{99m}Tc-Sestamibi, is able to localize in mitochondria due to the increased plasma and mitochondrial transmembrane potentials in tumor cells.

INTRODUCTION

Cancer is the second leading cause of death worldwide. The most prevalent forms of the disease are solid tumors of the lung, breast, prostate, colon, and rectum. Although the exact cause of cancer remains unknown, most cancer patients will survive after surgery, radiation therapy, and chemotherapy or a combination thereof if it can be detected at an early stage. Therefore, accurate early detection is highly desirable so that various therapeutic regiments can be given before the tumors become widespread.

Multidrug resistance (MDR) remains a major obstacle in the treatment of cancer. The overexpression of multidrug resistance P-glycoproteins (MDR Pgps) and multidrug resistance-associated proteins (MRPs) in tumor cells has been shown to confer MDR onto drug-sensitive cells (*1*−*3*). Both MDR Pgps and MRPs belong to a large family of ATP-trafficking proteins that mediate the transport of a large number of drug molecules (*3*−*6*). Although the molecular mechanism is not entirely clear, the net effect of MDR Pgp and MRP overexpression is the reduced intracellular drug accumulation through an energy-dependent drug efflux in the MDR-positive cancer cells as compared with the drug-sensitive tumor cells (*5, 6*). While several different genes are associated with the MDR phenotype (*6, 7*), the MDR mediated by overexpression of MDR1 Pgp is one of the best characterized barriers to chemotherapeutics treatment. High levels of MDR1 Pgp expression have been detected in more than 50% of tumors (*8*−*11*). A correlation between the MDR1 Pgp expression and failure of chemotherapy or poor survival rates has been established (*11*). However, the lack of MDR1 Pgp in other MDR-positive tumors indicates that additional cellular changes also confer resistance to anticancer drugs (*12*−*15*). For example, MRP1 expression in retinoblastoma correlated well with the rare failure of chemotherapy (*16*). The lung resistance protein (LRP) and breast cancer resistance protein (BCRP) have also been observed in tumor cells (*17, 18*). More recently, the overexpression of a 40 kDa protein (P-40 or Annexin I) was reported in tumor cell lines without MDR1 Pgp (*19, 20*). Since MDR is a major obstacle in chemotherapy of cancer patients, there has been a continuing demand for radiotracers that are able to monitor the tumor MDR transport function in a noninvasive fashion (*21*−*27*).

Cationic radiotracers, such as ^{99m}Tc-Sestamibi and ^{99m}Tc-Tetrofosmin, tend to localize in tumor cells due to the increased negative mitochondrial potentials (*28*−*35*). ^{99m}Tc-Sestamibi and ^{99m}Tc-Tetrofosmin have been clinically used for both cancer early detection and noninvasive monitoring of the tumor MDR transport function by single photon emission computed tomography (SPECT) (*21*−*27, 30*). However, their diagnostic and prognostic values are often limited due to their insufficient tumor localization and high uptake in the heart, liver, and muscle, which makes it very difficult to detect small lesions in the chest and abdominal regions. Thus, there is an unmet medical need for radiotracers that are able to monitor noninvasively the MDR transport function in tumors.

Previously, we reported ^{64}Cu-labeled organic phosphonium cations, such as ^{64}Cu(DO3A-xy-TPEP) (Figure 1: DO3A-xy-TPEP = (2-(diphenylphosphoryl)ethyl)diphenyl(4-((4,7,10-tris(carboxymethyl)-1,4,7,10-tetraazacyclododecan-1-yl)methyl)benzyl)phosphonium), as a potential PET (positron emission

* To whom correspondence should be addressed. School of Health Sciences, Purdue University, 500 Stadium Mall Dr., West Lafayette, IN 47907. Phone: 765-494-0236; Fax 765-496-1377; E-mail: lius@pharmacy.purdue.edu.

10.1021/bc800545e CCC: $40.75 © 2009 American Chemical Society
Published on Web 03/13/2009

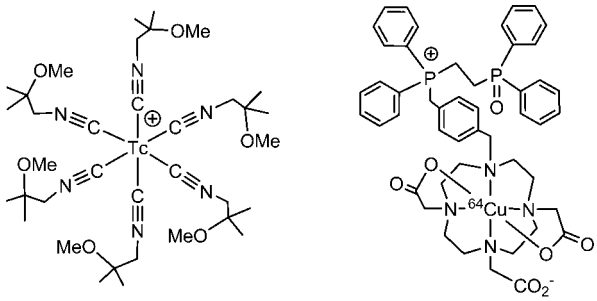

Figure 1. Structures of ^{99m}Tc-Sestamibi and ^{64}Cu(DO3A-xy-TPEP).

tomography) radiotracer in the athymic nude mice bearing U87MG human glioma xenografts (*36*−*39*). Both biodistribution and in vivo microPET imaging studies demonstrated that ^{64}Cu(DO3A-xy-TPEP) has higher tumor uptake with better tumor selectivity (as defined by their tumor/heart and tumor/muscle ratios) than ^{99m}Tc-Sestamibi (Figure 1). These promising results lead us to explore the potential of ^{64}Cu(DO3A-xy-TPEP) as a PET radiotracer for noninvasive monitoring of the MDR transport function in athymic nude mice bearing MDR-positive tumor xenografts.

The tumor cell lines used in this study include U87MG human glioma, MDA-MB-231, and MDA-MB-435 human breast cancer, KB-3-1 and KB-v-1. The U87MG glioma cell line was chosen because it has no overexpression of MDR1 Pgp (*40*−*42*). The U87MG cell line has been used for evaluation of the cellular uptake kinetics of ^{99m}Tc-Sestamibi and ^{99m}Tc-Tetrofosmin (*43*). MDA-MB-435 is the estrogen-independent human breast cancer cell line (metastatic ductal adenocarcinoma) and has a low level of MDR1 expression (*44*−*47*) and a high level expression of MRP2 and MRP4 (*47*, *48*). MDA-MB-231 is also an estrogen-independent human breast cancer cell line and is often considered "drug-sensitive" because it has little MDR1, MRP1, and BCRP overexpression (*47*, *48*). However, recent studies have clearly demonstrated that the MDA-MB-231 breast tumor cell line has a high level expression of P-40, a 40 kDa protein (*19*, *20*). The athymic nude mice bearing KB-3-1 and KB-v-1 tumor xenografts have been successfully used to evaluate cationic ^{99m}Tc and ^{68}Ga radiotracers (*49*−*56*), as well as luminescent probes (*57*). High level expression of MDR Pgps or/and MRPs will result in a rapid efflux of the cationic radiotracer from tumor cells and the significant reduction in tumor localization of the radiotracer. Since it has been used for imaging the tumor MDR transport function by SPECT (*21*−*27*), ^{99m}Tc-Sestamibi was the "control". We are interested in ^{64}Cu(DO3A-xy-TPEP) because of its high tumor uptake and rapid liver clearance in nude mice bearing the MDR-negative U87MG human glioma xenografts (*39*). The main objective of this study is to evaluate the potential of ^{64}Cu(DO3A-xy-TPEP) as a new PET radiotracer for noninvasive monitoring of MDR transport function in several xenografted tumor models. It is important to note that MDR is often mediated by a combination of MDR Pgps (particularly MDR1 Pgp) and MRPs. In addition, MDR Pgps and MRPs are also overexpressed in several normal organs involved in excretory functions, including kidneys and liver (*58*−*60*).

EXPERIMENTAL SECTION

Materials. Chemicals were purchase from Sigma/Aldrich (St. Louis, MO). ^{64}Cu was produced using a CS-15 biomedical cyclotron at Washington University School of Medicine by the ^{64}Ni(p,n)^{64}Cu nuclear reaction. Na^{99m}TcO$_4$ was obtained from a commercial DuPont Pharma ^{99}Mo/^{99m}Tc generator. Cardiolite vials were obtained as a gift from Bristol Myers Squibb Medical Imaging (N. Billerica, MA) and were reconstituted according to the manufacturer's package insert.

Methods. Radio-HPLC method used the LabAlliance HPLC system equipped with a UV/vis detector ($\lambda = 254$ nm), a β-ram IN-US detector, and Zorbax C_{18} analytical column (4.6 mm × 250 mm, 300 Å pore size). The flow rate was 1 mL/min with the mobile phase being isocratic with 90% solvent A (10 mM ammonium acetate) and 10% solvent B (acetonitrile) at 0−5 min, followed by a gradient mobile phase going from 10% B at 5 min to 60% B at 20 min.

Doses Preparation. ^{64}Cu(DO3A-xy-TPEP) was prepared according to the procedure described in our previous report (*39*) and was purified by HPLC. Volatiles in the HPLC mobile phases were evaporated under reduced pressure at room temperature. Doses were prepared by dissolving the residue to 20−30 μCi/mL in saline. The resulting solution was filtered with a 0.20 μm filter unit before being injected into animals. The injection volume for each animal was 0.1 mL.

Animal Models. Biodistribution studies were performed in compliance the NIH animal experiment guidelines (*Principles of Laboratory Animal Care*, NIH Publication No. 86−23, revised 1985). The animal protocol has been approved by the Purdue University Animal Care and Use Committee (PACUC). Female athymic nu/nu mice (5−6 weeks) were purchased from Harlan (Charles River, MA). The mice were implanted with 5 × 10^6 tumor cells into the mammary fat pad (MDA-MB-231 and MDA-MB-435 breast tumor cells) or shoulder flank (U87MG glioma, KB-3-1 and KB-v-1). U87MG glioma cells were cultured in the Minimum Essential Medium, Eagle with Earle's Balanced Salt Solution (nonessential amino acids sodium pyruvate) (ATCC, Manassas, VA). The MDA-MB-435 and MDA-MB-231 breast cancer cells were grown in the RPMI medium 1640 with L-glutamine (GIBCO, Grand Island, NY). The DMEM medium with 4.5 g/L D-glucose, L-glutamine, and 110 mg/L sodium pyruvate (GIBCO, Grand Island, NY) was used for KB-v-1 and KB-3-1 tumor cells. In all cases, 10% FBS (Sigma, St. Louis, MO) and 5% penicillin streptomycin (GIBCO, Grand Island, NY) were added into the medium just before use. All cell lines were grown in humidified atmosphere of 5% carbon dioxide. All procedures will be performed in a laminar flow cabinet using the aseptic technique. Two to four weeks after inoculation, the tumor size was in the range 0.1−0.5 g, and animals were used for biodistribution studies.

Biodistribution Protocol. Twelve tumor-bearing mice (20−25 g) were divided into four groups. Each animal was administered with ^{64}Cu(DO3A-xy-TPEP) (2−3 μCi) via tail vein. Three animals were euthanized by sodium pentobarbital overdose (100 mg/kg) at 5, 30, 60, and 120 min postinjection (p.i.). Blood samples were withdrawn from the heart. The tumor and normal organs (brain, eyes, heart, intestine, kidneys, liver, lungs, muscle, and spleen) were excised, washed with saline, dried with absorbent tissue, weighed, and counted on a Perkin-Elmer Wizard - 1480 γ-counter (Shelton, CT). The organ uptake was calculated as a percentage of the injected dose per organ (%ID/organ). The tumor uptake values are reported as an average ± standard deviation based on the results from three tumor-bearing mice, unless specified, at each time point. The normal organ uptake values are reported as an average ± standard deviation based on the results from fifteen tumor-bearing mice (three animals for each tumor type, and a total of five different tumor types) at each time point, unless specified. For comparison purposes,^{99m}Tc-Sestamibi was evaluated using the same protocol. Comparison between ^{64}Cu(DO3A-xy-TPEP) and ^{99m}Tc-Sestamibi was made using the one-way ANOVA test (GraphPad *Prism 5.0*, San Diego, CA). The level of significance was set at $p < 0.05$.

Table 1. Biodistribution Data for ^{64}Cu(DO3A-xy-TPEP) in Xenografted Tumor-Bearing Athymic Nude Mice[a]

organ	5 min	30 min	60 min	120 min
blood	9.52 ± 1.19 (n = 9)	2.09 ± 0.90 (n = 15)	1.30 ± 1.10 (n = 15)	0.84 ± 0.62 (n = 15)
brain	0.22 ± 0.06 (n = 9)	0.10 ± 0.09 (n = 15)	0.06 ± 0.05 (n = 15)	0.02 ± 0.02 (n = 15)
heart	4.04 ± 0.70 (n = 9)	1.25 ± 0.48 (n = 15)	0.92 ± 0.43 (n = 15)	0.55 ± 0.09 (n = 15)
intestine	4.06 ± 0.78 (n = 9)	3.23 ± 1.22 (n = 15)	2.87 ± 1.28 (n = 15)	2.61 ± 1.26 (n = 15)
kidney	31.79 ± 8.02 (n = 9)	6.77 ± 1.63 (n = 15)	4.11 ± 1.11 (n = 15)	2.98 ± 0.53 (n = 15)
liver	8.03 ± 1.33 (n = 9)	8.74 ± 3.30 (n = 15)	8.66 ± 4.85 (n = 15)	5.59 ± 1.39 (n = 15)
lungs	7.72 ± 0.74 (n = 9)	2.50 ± 0.61 (n = 15)	2.19 ± 0.91 (n = 15)	1.51 ± 0.18 (n = 15)
muscle	3.07 ± 0.45 (n = 9)	0.82 ± 0.39 (n = 15)	0.81 ± 0.98 (n = 15)	0.10 ± 0.06 (n = 15)
spleen	2.73 ± 0.31 (n = 9)	1.14 ± 0.37 (n = 15)	0.84 ± 0.40 (n = 15)	0.56 ± 0.17 (n = 15)
U87MG	5.27 ± 0.99 (n = 3)	2.09 ± 0.53 (n = 3)	2.58 ± 0.31 (n = 3)	3.35 ± 1.27 (n = 3)
MDA-MB-435	2.73 ± 0.55 (n = 3)	1.05 ± 0.19 (n = 3)	1.12 ± 0.20 (n = 3)	0.81 ± 0.11 (n = 3)
MDA-MB-231	3.54 ± 0.15 (n = 3)	1.57 ± 0.04 (n = 3)	1.10 ± 0.17 (n = 3)	0.93 ± 0.15 (n = 3)
KB-v-1		2.00 ± 0.48 (n = 6)	1.58 ± 0.47 (n = 6)	0.93 ± 0.22 (n = 3)
KB-3-1		1.97 ± 0.61 (n = 6)	1.46 ± 0.26 (n = 6)	1.16 ± 0.19 (n = 3)

[a] The tumor uptake is reported as an average ± standard deviation based on the results from three tumor-bearing mice, unless specified, at each time point. The normal organ uptake values are reported as an average ± standard deviation based on the results from fifteen tumor-bearing mice (three animals for each tumor type, and a total of five different tumor types) at each time point.

Blocking Experiment with Cyclosporin-A (Cys-A). In this experiment, each tumor-bearing mouse (n = 4) was treated with intraperitoneal injection of 0.1 mL DMSO solution containing 0.35 mg Cys-A (14 mg/kg) at 30 min before administration of radiotracer. In the "control" group (n = 4), each tumor-bearing mouse was treated with the same volume of DMSO solution without Cys-A. Four animals were euthanized by sodium pentobarbital overdose (100−200 mg/kg) at 30 min p.i. The ex vivo biodistribution was performed according to the procedure described above. The organ of uptake was calculated as a percentage of the injected dose per gram (%ID/g).

Subcelluar Distribution Characteristics. Subcellular distribution studies were performed using the athymic nude mice bearing U87MG glioma (n = 3) and MDA-MB-435 breast cancer (n = 3) xenografts according to literature method (*61*−*66*). Each tumor-bearing mouse was administered ∼30 μCi of ^{64}Cu(DO3A-xy-TPEP) via tail vein. Animals were sacrificed by intraperitoneal administration of sodium pentobarbital overdose (100−200 mg/kg) at 1 h p.i. The tumor was rapidly removed and placed immediately in ice−cold (4 °C) Buffer I, containing 230 mM mannitol, 70 mM sucrose, 3 mM 3-(*N*-morpholino)propanesulfonic acid (MOPS), 2 mM ethylene glycol tetraacetic acid (EGTA), and 0.2% bovine serum albumin (BSA) (w/v) with pH 7.2. The tumor tissue was then minced into 1−2 mm pieces and homogenized using a tissue grinder (Wheaton, NJ). The resulting mixture was centrifuged at 500*g* for 10 min at 4 °C. The supernatant (blood, extracellular components, and debris) was discarded, and the pellet was resuspended in 2 mL of ice−cold (4 °C) Buffer II (containing 110 mM KCl, 20 mM MOPS, 46 mM mannitol, 14 mM sucrose, 2 mM EGTA, pH 7.5). To the mixture was added 0.5 mg/mL of Trypsin protease (Gibco, Ground Island, NY). After 3 min homogenization, the protease reaction was terminated by adding 4 mL of Buffer II (4 °C) containing 0.2% BSA. The homogenate was centrifuged at 5000*g* for 5 min at 4 °C. Supernatant I was collected, and the pellet was resuspended in 5 mL of ice−cold (4 °C) Buffer II with 0.2% BSA. After centrifugation at 500*g* for 10 min (4 °C), pellet I (containing cellular fragments) was obtained. The supernatant was transferred and centrifuged at 3000*g* for 10 min (4 °C) to obtain the membrane fragment (supernatant II) and mitochondrial component (pellet II), respectively. Supernatant I, supernatant II, pellet I, and pellet II were counted by a Perkin-Elmer Wizard - 1480 automatic γ-counter (Shelton, CT). The percentage of radioactivity was calculated on the basis of the radioactivity counts in each subcellular component over the total radioactivity count before homogenization. The percentage of radioactivity recovery was calculated by the total radioactivity counts in supernatant I, supernatant II, pellet I, and pellet II over the total radioactivity count before homogenization. All data were reported as an average of three independent measurements. ^{99m}Tc-Sestamibi was evaluated using the same protocol for comparison purposes.

Western Blot Experiment. Western blot experiments were performed to demonstrate the presence or absence of MDR1 Pgp, MRP2, and MRP4 in different tumor tissues (U87MG glioma, MDA-MB-231, MDA-MB-435, KB-3-1 and KB-v-1). The tumor tissues (U87MG, MDA-MB-231, MDA-MB-435, KB-3-1, and KB-v-1) were harvested directly from the tumor-bearing nude mice. After homogenization, the tumor tissues (10−20 mg) were incubated with 500 μL of cell lysis buffer (Cell Signaling Technology, Danvers, MA) on ice for 5 min. The homogenates were centrifuged at 14 000*g* for 10 min. The supernatants were removed for further use. For tumor cells, MDA-MB-231 and MDA-MB-435, medium was removed at first. After washing with PBS, cells were incubated with cell lysis buffer (Cell Signaling Technology, Danvers, MA) on ice for 5 min. The tumor cells were scraped, and the mixture was sonicated briefly. The homogenates were centrifuged at 14 000*g* for 10 min. The supernatant was removed for further use. The protein content was determined by using the BCA Protein Assay Kit (Pierce, Rockford, IL). The protein (15 μg per lane) was subjected to electrophoresis on SDS-polyacrylamide gel at 160 V for 60 min and transferred electrophoretically on polyvinylidene difluoride membranes at 70 mA for 120 min. The blots were blocked with TBS-T containing 5% nonfat dry milk powder for 1 h. Then, the blotting membranes were incubated with 1 mL of the primary antibody (1:200) against MDR1 (JSB-1, mouse IgG_1 supernatant, Santa Cruz Biotechnology, CA), MRP2 (M2II-12, mouse IgG2a supernatant, Santa Cruz Biotechnology, CA), or MRP4 (M4I-10, rat IgG2a supernatant, Santa Cruz Biotechnology, CA) separately overnight. Primary antibody solution was removed, and the membranes were incubated for 1 h with secondary antibody (goat antimouse IgG-HRP, Santa Cruz Biotechnology, CA) diluted 1:5000. Finally, membranes were developed using the ECL Western Blotting Substrate (Pierce, Rockford, IL) according to the manufacturer's instructions. The positive control for MDR1 was Human PGP Membrane from BD Gentest (San Jose, CA). Human MRP2 Membrane (BD Gentest, San Jose, CA) was used as the positive control of MRP2.

RESULTS

Biodistribution Characteristics. The athymic nude mice bearing U87MG, MDA-MB-231, MDA-MB-435, KB-3-1, and KB-v-1 tumor xenografts were used to evaluate tumor uptake and biodistribution characteristics of ^{64}Cu(DO3A-xy-TPEP). For comparison purpose, ^{99m}Tc-Sestamibi was also evaluated in the

Table 2. Biodistribution Data for ^{99m}Tc-Sestamibi in Xenografted Tumor-Bearing Athymic Nude Mice[a]

organ	5 min	30 min	60 min	120 min
blood	0.87 ± 0.44 (n = 6)	0.26 ± 0.28 (n = 9)	0.28 ± 0.34 (n = 9)	0.08 ± 0.03 (n = 9)
brain	0.22 ± 0.05 (n = 6)	0.15 ± 0.05 (n = 9)	0.11 ± 0.02 (n = 9)	0.08 ± 0.02 (n = 9)
heart	19.22 ± 6.96 (n = 6)	20.52 ± 1.11 (n = 9)	20.07 ± 3.99 (n = 9)	20.88 ± 4.55 (n = 9)
intestine	9.80 ± 2.74 (n = 6)	11.13 ± 1.62 (n = 9)	11.11 ± 4.54 (n = 9)	5.29 ± 2.52 (n = 9)
kidney	37.45 ± 12.0 (n = 6)	25.50 ± 5.56 (n = 9)	20.24 ± 4.59 (n = 9)	12.47 ± 3.90 (n = 9)
liver	14.37 ± 0.92 (n = 6)	9.82 ± 2.12 (n = 9)	8.37 ± 1.90 (n = 9)	5.40 ± 0.42 (n = 9)
lungs	6.20 ± 2.36 (n = 6)	3.03 ± 1.04 (n = 9)	2.17 ± 0.80 (n = 9)	1.72 ± 0.47 (n = 9)
muscle	4.84 ± 1.12 (n = 6)	5.02 ± 1.01 (n = 9)	5.25 ± 1.67 (n = 9)	5.22 ± 1.22 (n = 9)
spleen	3.21 ± 1.27 (n = 6)	1.77 ± 0.554 (n = 9)	1.32 ± 0.33 (n = 9)	1.32 ± 0.90 (n = 9)
U87MG	3.06 ± 0.94 (n = 3)	2.11 ± 0.38 (n = 3)	1.47 ± 0.54 (n = 3)	1.55 ± 0.36 (n = 3)
MDA-MB-435	1.18 ± 0.17 (n = 3)	1.09 ± 0.20 (n = 3)	0.96 ± 0.42 (n = 3)	0.94 ± 0.21 (n = 3)
KB-v-1		0.92 ± 0.61 (n = 3)	1.05 ± 0.86 (n = 3)	0.95 ± 0.47 (n = 3)
KB-3−1		0.53 ± 0.09 (n = 3)	0.31 ± 0.09 (n = 3)	0.22 ± 0.03 (n = 3)

[a] The tumor uptake is reported as an average ± standard deviation based on the results from three tumor-bearing mice at each time point, unless specified. The normal organ uptake values are reported as an average ± standard deviation based on the results from nine tumor-bearing mice (three animals for each tumor type, and a total of three different tumor types) at each time point.

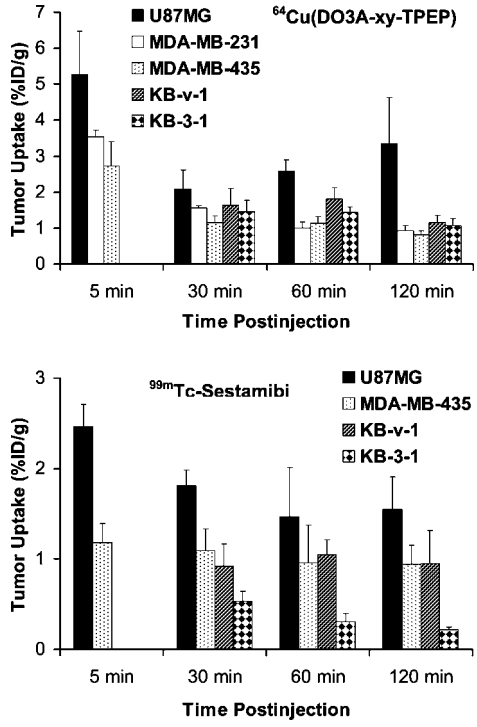

Figure 2. Comparison of tumor uptake for ^{64}Cu(DO3A-xy-TPEP) (top) and ^{99m}Tc-Sestamibi (bottom) in athymic nude mice bearing different tumor xenografts (U87MG glioma, MDA-MB-231, and MDA-MB-435 breast cancer, KB-3-1, and KB-v-1).

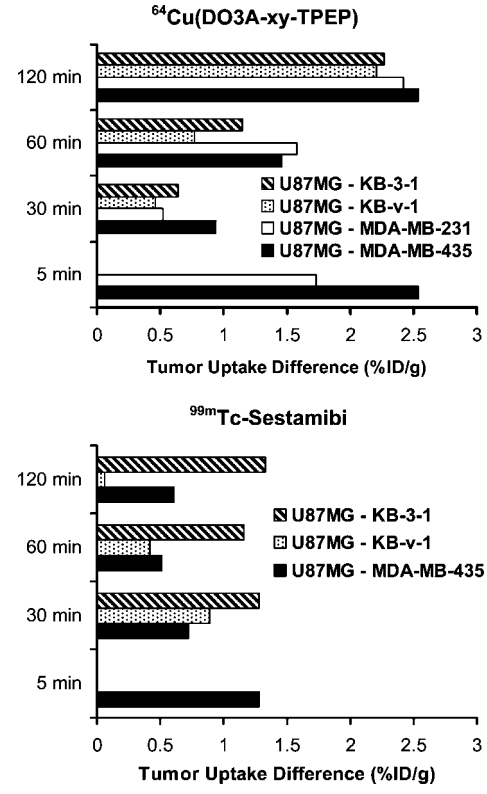

Figure 3. Tumor uptake difference between the MDR-negative U87MG glioma and the MDR-positive tumors (MDA-MB-231, MDA-MB-435, KB-3-1, and KB-v-1) for ^{64}Cu(DO3A-xy-TPEP) (top) and ^{99m}Tc-Sestamibi (bottom).

same animal model, since it has been clinically used for early cancer detection and for imaging MDR transport function in cancer patients (*21*−*27, 30*). Biodistribution data for ^{64}Cu(DO3A-xy-TPEP) and ^{99m}Tc-Sestamibi are summarized in Tables 1 and 2, respectively. Figure 2 compares the tumor uptake (%ID/g) of ^{64}Cu(DO3A-xy-TPEP) and ^{99m}Tc-Sestamibi. Figure 3 illustrates the tumor uptake differences between U87MG glioma and the MDR-positive tumors (MDA-MB-231, MDA-MB-435, KB-3-1, and KB-v-1) for ^{64}Cu(DO3A-xy-TPEP) and ^{99m}Tc-Sestamibi.

In general, the biodistribution of ^{64}Cu(DO3A-xy-TPEP) in noncancerous organs of the MDR-positive tumor-bearing mice was almost identical to that obtained from the mice bearing U87MG human glioma xenografts. There was no size dependence for the tumor uptake of ^{64}Cu(DO3A-xy-TPEP) and ^{99m}Tc-Sestamibi. However, ^{64}Cu(DO3A-xy-TPEP) and ^{99m}Tc-Sestamibi showed significant differences in their uptake in both tumors and normal organs. For example, ^{64}Cu(DO3A-xy-TPEP) had a rapid tumor washout in the MDR-negative glioma model between 5 min (5.27 ± 1.21%ID/g) and 30 min (2.09 ± 0.53%ID/g) p.i. due to its fast blood clearance, and a steady tumor uptake increase between 30 min (2.09 ± 0.53%ID/g) and 120 min (3.35 ± 1.27%ID/g) p.i. probably due to its slow kinetics to penetrate the cellular and mitochondrial transmembranes (*39*). In the MDR-positive tumor-bearing mice, ^{64}Cu(DO3A-xy-TPEP) showed a rapid tumor washout between 5 and 30 min p.i. (Figure 3: top), and its tumor uptake was relatively unchanged (ranging from 1.0%ID/g to 1.5%ID/g depending on the tumor type) in between 30 and 120 min p.i. The tumor uptake of ^{99m}Tc-Sestamibi decreased steadily in all four tumor-bearing animal models over the 2 h period (Figure 3: bottom). The most striking difference between ^{64}Cu(DO3A-xy-TPEP) (Table 1) and ^{99m}Tc-Sestamibi (Table 2) was their uptake in heart and muscle. For example, the heart uptake was <1% ID/g for ^{64}Cu(DO3A-xy-TPEP) at >30 min p.i., whereas ^{99m}Tc-Sestamibi had the heart uptake of 19.22 ± 7.62% ID/g at 5

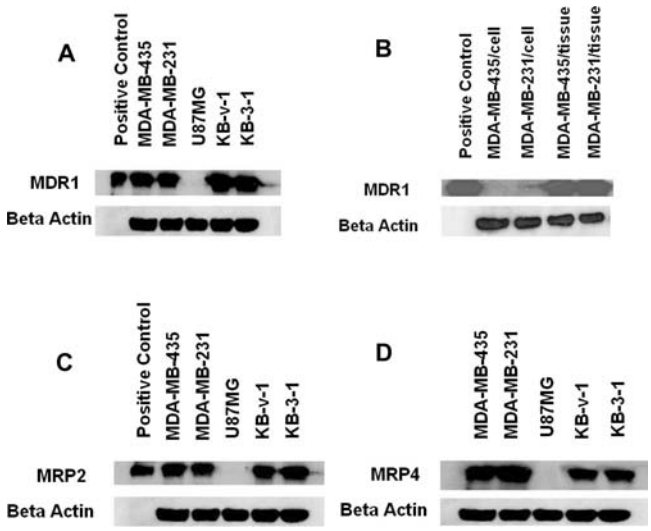

Figure 4. Western blot data to demonstrate the presence/absence of MDR1 (A,B), MRP2 (C), and MRP4 (D) in U87MG (MDR1, MRP2, and MRP4-negative), MDA-MB-435 (MDR1-negative in tumor cells but MDR1-positive in tumor tissue, MRP2 and MRP4-positive), MDA-MB-231 (MDR1-negative in tumor cells but MDR1-positive in tumor tissue, MRP2 and MRP4-positive), KB-v-1, and KB-3-1 (MDR1, MRP2, and MRP4-positive).

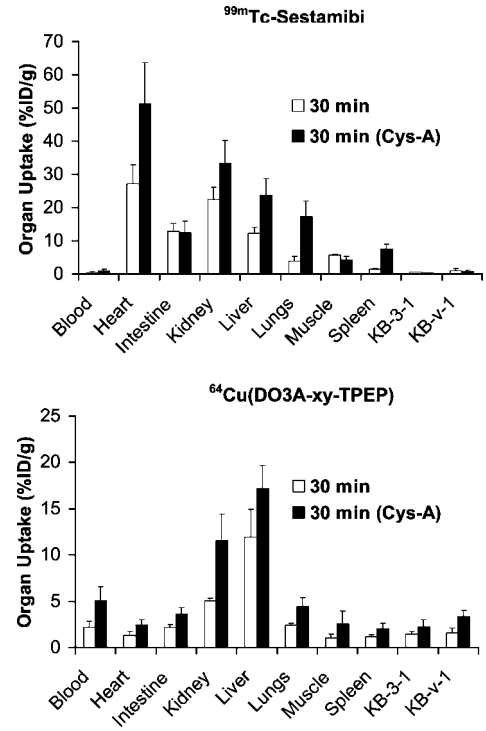

Figure 5. Impact of Cys-A on the uptake of ^{64}Cu(DO3A-xy-TPEP) and ^{99m}Tc-Sestamibi in selected organs of the athymic nude mice bearing KB-v-1 and KB-3-1 tumor xenografts.

min p.i. and 19.19 ± 5.32%ID/g at 120 min p.i. The muscle uptake of ^{64}Cu(DO3A-xy-TPEP) was undetectable at >30 min p.i. In contrast, ^{99m}Tc-Sestamibi had a high muscle uptake over the 2 h study period (4.84 ± 1.22 and 5.45 ± 1.24%ID/g at 5 and 120 min p.i., respectively). Another significant difference was their tumor uptake in the MDR-negative U87MG glioma and the MDR-positive tumor xenografts. For example, ^{64}Cu(DO3A-xy-TPEP) had the tumor uptake of 5.27 ± 0.99, 2.09 ± 0.53, 2.58 ± 0.31, and 3.35 ± 1.27%ID/g at 5, 30, 60, and 120 min p.i., respectively, in U87MG glioma. Its tumor uptake values in the MDR-positive tumors were significantly lower than that in glioma (Figure 2). The glioma uptake values of ^{99m}Tc-Sestamibi were 3.06 ± 0.94, 2.11 ± 0.38, 1.47 ± 0.54, and 1.55 ± 0.36%ID/g at 5, 30, 60, and 120 min p.i., respectively, and its uptake values in the MDA-MB-435 breast tumor were 1.18 ± 0.17, 1.09 ± 0.20, 0.96 ± 0.42, and 0.94 ± 0.21%ID/g at 5, 30, 60, and 120 min p.i., respectively.

Western Blot Experiments. Western blot experiments were performed to demonstrate the presence or absence of MDR1 Pgp, MRP2 and MRP4 in the U87MG, MDA-MB-231, MDA-MB-435, KB-3−1 and KB-v-1 tumor xenografts. Tumor cells were directly isolated from the tumor tissues. The total protein concentration was determined to be 4.5 ± 0.4, 4.0 ± 0.2, 3.3 ± 0.2, 4.3 ± 0.3, and 4.1 ± 0.2 mg/mL for the xenografted MDA-MB-435, MDA-MB-231, U87MG, KB-v-1, and KB-3-1 tumors, respectively. Figure 4 illustrates the Western blotting data for the U87MG, MDA-MB-231, MDA-MB-435, KB-3-1, and KB-v-1 tumor xenografts. The positive control was the Human PGP Membrane for MDR1 Pgp. The positive control for MPR2 was human MRP2 membrane. No positive control is commercially available for MRP4. The blotting data clearly demonstrated that there was very little or no expression of MDR1 Pgp, MRP2, and MRP4 in the U87MG glioma xenografts. However, there is a high expression of MDR1 Pgp, MRP2, and MRP4 in the MDA-MB-231, MDA-MB-435, KB-3-1, and KB-v-1 tumors.

It is important to note that MDA-MB-435 and MDA-MB-231 are often known "drug sensitive" or MDR1-negative breast cancer cell lines (*47, 48*). The results from Western blotting studies also showed that the MDA-MB-435 and MDA-MB-231 human breast cancer cell lines have little expression of MDR1 Pgp (Figure 4B). However, the MDA-MB-435 and MDA-MB-231 breast cancer cells isolated from the xenografted MDA-MB-435 and MDA-MB-231 breast tumors are MDR1-positive (Figure 4B). They also show a significant expression of MRP2 and MRP4.

Impact of Cys-A on Tumor Uptake and Radiotracer Liver Clearance Kinetics. To further demonstrate that the tumor washout is caused by the tumor MDR transport function, we performed blocking experiments using ^{64}Cu(DO3A-xy-TPEP) and ^{99m}Tc-Sestamibi as radiotracers in the athymic nude mice bearing KB-3-1 and KB-v-1 tumor xenografts. Cys-A, a well-known wide-spectrum MDR modulator (*67*), was injected as the blocking agent 1 h prior administration of ^{64}Cu(DO3A-xy-TPEP) or ^{99m}Tc-Sestamibi. The ex vivo biodistribution was performed at 30 min p.i. Figure 5 compares uptake of ^{64}Cu(DO3A-xy-TPEP) and ^{99m}Tc-Sestamibi in the tumor and selected normal organs in the absence/presence of Cys-A. As expected, pretreatment of the tumor-bearing mice with excess Cys-A resulted in a significant increase in tumor uptake of both ^{64}Cu(DO3A-xy-TPEP) (Figure 5: bottom) and ^{99m}Tc-Sestamibi (Figure 5: top). The tumor uptake difference was 0.83%ID/g in KB-3-1 and 1.70 KB-v-1%ID/g w/o Cys-A for ^{64}Cu(DO3A-xy-TPEP), while there was no significant difference for ^{99m}Tc-Sestamibi within experimental error, suggesting that ^{64}Cu(DO3A-xy-TPEP) might be a more efficient radiotracer for noninvasive monitoring of the MDR transport function.

In addition, the uptake of ^{64}Cu(DO3A-xy-TPEP) and ^{99m}Tc-Sestamibi in kidneys, liver, and lungs was also significantly increased, and the radioactivity excretion was delayed in the presence of Cys-A. For example, the liver uptake was 8.03 ± 1.33%ID/g for ^{64}Cu(DO3A-xy-TPEP) and 9.82 ± 2.12%ID/g for ^{99m}Tc-Sestamibi in the absence of Cys-A at 30 min p.i. In presence of Cys-A, however, the liver uptake values increased to 17.18 ± 2.47%ID/g for ^{64}Cu(DO3A-xy-TPEP) and 23.68 ± 5.08%ID/g for ^{99m}Tc-Sestamibi at the same time point. A similar increase (Figure 5) was also observed in the heart, kidneys, lungs, and spleen. The increase of muscle uptake of ^{64}Cu(DO3A-

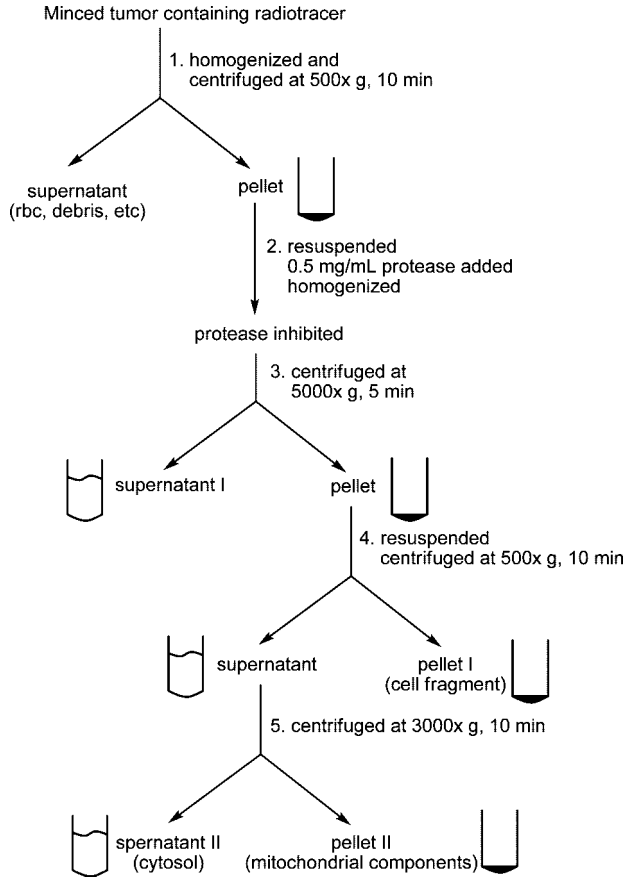

Figure 6. Schematic presentation of the standard differential centrifugation process.

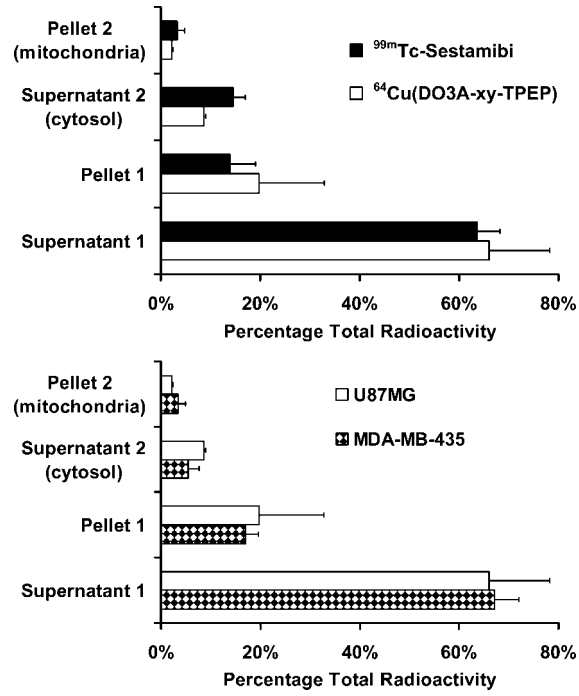

Figure 7. Top: subcellular distribution properties of ^{64}Cu(DO3A-xy-TPEP) and ^{99m}Tc-Sestamibi in U87MG human glioma xenografts. Bottom: direct comparison of subcellular distribution patterns of ^{64}Cu(DO3A-xy-TPEP) in the U87MG glioma and MDA-MB-435 breast tumor xenografts.

xy-TPEP) is probably caused by its high blood radioactivity accumulation in the presence of excess Cys-A. The impact of Cys-A on the excretion kinetics of ^{64}Cu(DO3A-xy-TPEP) was more significant than that of ^{99m}Tc-Sestamibi.

Subcellular Distribution Characteristics. We performed the subcellular distribution studies on ^{64}Cu(DO3A-xy-TPEP) and ^{99m}Tc-Sestamibi using the standard differential centrifugation method (Figure 6) according to the literature (*61*−*65*). The main objective of these studies is to elucidate the tumor localization mechanism of ^{64}Cu(DO3A-xy-TPEP). Figure 7 illustrates the subcellular distribution characteristics of ^{64}Cu(DO3A-xy-TPEP) and ^{99m}Tc-Sestamibi in the xenografted U87MG glioma and MDA-MB-435 tumors. The radioactivity recovery was >95% for both ^{64}Cu(DO3A-xy-TPEP) and ^{99m}Tc-Sestamibi. After cellular fractionation, the majority of the radioactivity was found in supernatants I (66.5 ± 12.5% for ^{64}Cu(DO3A-xy-TPEP) and 63.5 ± 4.7% for^{99m}Tc-Sestamibi) and II (8.5 ± 0.5% for ^{64}Cu(DO3A-xy-TPEP) and 14.5 ± 2.6% for^{99m}Tc-Sestamibi). Only a small portion of the radioactivity was found in the mitochondrial fraction (Figure 7: top) for ^{64}Cu(DO3A-xy-TPEP) (2.25 ± 0.21%) and ^{99m}Tc-Sestamibi (3.33 ± 1.50%). It is clear that ^{64}Cu(DO3A-xy-TPEP) and ^{99m}Tc-Sestamibi share almost identical subcellular distribution patterns in the U87MG glioma tumors. In addition, the subcellular distribution characteristics of ^{64}Cu(DO3A-xy-TPEP) are very similar in the xenografted U87MG glioma and MDA-MB-435 breast tumors (Figure 7: bottom).

DISCUSSION

During last two decades, cationic radiotracers, such as ^{99m}Tc-Sestamibi, have been widely used for early cancer detection and for noninvasive monitoring of the tumor MDR transport function by SPECT (*21*−*35*). The overwhelming emphasis of the prior literature has been focused on the tumor MDR transport function mediated by MDR1 Pgp most likely due to the fact that MDR1 Pgp is one of the best biologically characterized barriers to chemotherapy. It is very important to emphasize that the tumor MDR transport function can be mediated by MDR Pgps and MRPs (*1*−*11*), as well as other drug transporting proteins, such as LRP (*17*) and BCRP (*18*). Regardless of the source of MDR, the overall net effect is the rapid efflux of cationic radiotracers from tumor cells, which often leads to a significant reduction of the radiotracer tumor uptake. There is an inverse relationship between the radiotracer tumor uptake and the MDR transport function. If there is no MDR Pgps and/or MRPs in tumor cells, cationic radiotracers will have relatively high tumor uptake with no significant tumor washout. If there is a high level expression of MDR Pgps and/or MRPs, cationic radiotracers are expected to show a rapid tumor radioactivity washout with low tumor uptake. If the radiotracer is efficient as a substrate for MDR Pgps and MRPs, there would be less radiotracer uptake in the MDR-positive tumors. The ideal radiotracers useful for noninvasive monitoring of the tumor MDR transport function would be those which provide the largest uptake difference between the MDR-negative and MDR-positive tumors and have low uptake in noncancerous organs, such as the heart, liver, lungs, and muscle.

Since the uptake of ^{64}Cu(DO3A-xy-TPEP) in normal organs is almost identical in different xenografted tumor-bearing models, their tumor uptake difference should, in theory, reflect the MDR transport function in the MDR-negative vs MDR-positive tumors. For example, the U87MG glioma tumors have no significant expression of MDR1 Pgp and MRPs, as demonstrated by Western blot experiment (Figure 4). As a result, ^{64}Cu(DO3A-xy-TPEP) has a high initial tumor uptake and shows a steady uptake increase between 30 and 120 min p.i. (Figure 2: top). Similar results are obtained for ^{99m}Tc-Sestamibi (Figure 2: bottom). The xenografted MDA-MB-435, MDA-MB-231, KB-3-1, and KB-v-1 tumors all have high levels of MDR1 Pgp,

MRP2, and MRP4 expression (Figure 4A). As a result, both ^{64}Cu(DO3A-xy-TPEP) and ^{99m}Tc-Sestamibi show a significant washout from tumor over the 2 h period. Since ^{64}Cu(DO3A-xy-TPEP) has a greater tumor uptake difference between U87MG glioma and MDA-MB-231, MDA-MB-435, KB-3-1, and KB-v-1 than ^{99m}Tc-Sestamibi, it is reasonable to believe that ^{64}Cu(DO3A-xy-TPEP) is more efficient than ^{99m}Tc-Sestamibi as the substrate for MDR Pgps and MRPs and might be more efficient for noninvasive monitoring of the tumor MDR transport function. This conclusion is supported by the blocking experiments, which show a significant tumor uptake increase for ^{64}Cu(DO3A-xy-TPEP) and ^{99m}Tc-Sestamibi in the presence of excess Cys-A (Figure 5).

Both^{99m}Tc-Sestamibi and ^{99m}Tc-Tetrafosmin have been studied for their potential to monitor the tumor MDR in preclinical animal models and in clinical studies (*28*−*35*). The MDR1 Pgp and MRPs are also overexpressed in normal organs, such as kidneys and liver (*58*−*60*). As demonstrated in the blocking study (Figure 5), the preadministration of tumor bearing mice with excess Cys-A resulted in a significant increase of radioactivity accumulation in noncancerous organs, such as kidneys, liver, and lungs, and the delayed radioactivity excretion. Therefore, the MDR Pgp transport function is at least partially responsible of the fast efflux of ^{64}Cu(DO3A-xy-TPEP) from the kidneys, liver, and lungs.

The subcellular distribution characteristics of ^{64}Cu(DO3A-xy-TPEP) was compared with those of ^{99m}Tc-Sestamibi, a well-know radiotracer clinically useful for cancer detection by SPECT. The standard differential centrifugation technique has been successfully used to study the myocardial localization mechanism of cationic ^{99m}Tc radiotracers (*61*−*66*), such as ^{99m}Tc-Sestamibi. As expected, only a small fraction (3−4%) of ^{64}Cu radioactivity is found in the mitochondrial fraction, and the majority of the ^{64}Cu radioactivity is found in supernatants I and II. Almost identical distribution patterns were observed for ^{99m}Tc-Sestamibi. It has been suggested that tissue homogenization and differential centrifugation techniques may damage the mitochondrial structure (*61*−*66*), which allows the leakage of cationic radiotracers, such as ^{64}Cu(DO3A-xy-TPEP) and ^{99m}Tc-Sestamibi, from tumor mitochondria. Since ^{64}Cu(DO3A-xy-TPEP) and ^{99m}Tc-Sestamibi share almost identical subcellular distribution patterns in the U87MG glioma, we believe that ^{64}Cu(DO3A-xy-TPEP), like ^{99m}Tc-Sestamibi, is able to localize in the tumor mitochondria due to the increased plasma and mitochondrial transmembrane potentials in tumor cells as compared to normal epithelial cells (*68*−*72*). This conclusion is supported by the results from in vitro cellular assays, which showed that ^{64}Cu(DO3A-xy-TPP) (DO3A-xy-TPP: triphenyl(4-((4,7,10-tris(carboxymethyl)-1,4,7,10-tetraazacyclododecan-1-yl)methyl)benzyl)phosphonium) was able to localize in U87MG human glioma cells (*36*).

CONCLUSION

In this study, we evaluated the potential of ^{64}Cu(DO3A-xy-TPEP) as a new PET radiotracer for noninvasive monitoring of MDR transport function in several xenografted tumor models. It is important to note that MDR is often mediated by a combination of MDR Pgps (particularly MDR1 Pgp) and MRPs. ^{64}Cu(DO3A-xy-TPEP) has a high initial tumor uptake and shows a steady uptake increase between 30 and 120 min p.i. in the MDR-negative U87MG glioma, which has little expression of MDR1 Pgp and MRPs. In the xenografted MDA-MB-435, MDA-MB-231, KB-3-1, and KB-v-1 tumors, which have high levels of MDR1 Pgp, MRP2, and MRP4, ^{64}Cu(DO3A-xy-TPEP) and ^{99m}Tc-Sestamibi show a significant tumor washout over the 2 h period. Since ^{64}Cu(DO3A-xy-TPEP) has a greater tumor uptake difference between the MDR-negative U87MG glioma and MDR-positive tumors (MDA-MB-231, MDA-MB-435, KB-3-1, and KB-v-1) than ^{99m}Tc-Sestamibi, we believe that ^{64}Cu(DO3A-xy-TPEP) is more efficient than ^{99m}Tc-Sestamibi as the substrate for MDR Pgps and MRPs and might be a more efficient radiotracer for noninvasive monitoring of the MDR transport function in tumors of different origin. Regardless of the source of MDR, the overall net effect is the rapid efflux of cationic radiotracers from tumor cells, which often leads to a significant reduction of the radiotracer tumor uptake.

ACKNOWLEDGMENT

Authors would like to thank Dr. Sulma I. Muhammed, the Director of Purdue Cancer Center Drug Discovery Shared Resource, Purdue University, for her assistance with the tumor-bearing animal model. This work is supported, in part, by research grants: R01 CA115883 A2 (S.L.) from National Cancer Institute (NCI), R21 EB003419-02 (S.L.) from National Institute of Biomedical Imaging and Bioengineering (NIBIB) and R21 HL083961-01 from National Heart, Lung, and Blood Institute (NHLBI).

LITERATURE CITED

(1) Ling, V. (1997) Multidrug resistance: molecular mechanisms and clinical relevance. *Cancer Chemother. Pharmacol. 40*, S3–S8.

(2) Gros, P., Benneriah, Y. B., Croop, J. M., and Housman, D. E. (1986) Isolation and expression of a complementary DNA that confers multidrug resistance. *Nature 323*, 728–731.

(3) Zaman, G. J. R., Flens, M. J., Vanleusden, M. R., Dehaas, M., Mulder, H. S., Lankelma, J., Pinedo, H. M., Scheper, R. J., Baas, F., Broxterman, H. J., and Borst, P. (1994) The human multidrug resistance-associated-protein MRP is a plasma-membrane drug-efflux pump. *Proc. Natl. Acad. Sci. U.S.A. 91*, 8822–8826.

(4) Klein, I., Sarkadi, B., and Varadi, A. (1999) An inventory of the human ABC proteins. *Biochim. Biophys. Acta 1461*, 237–262.

(5) Shapiro, A. B., and Ling, V. (1995) Reconstitution of drug transport by purified P-glycoprotein. *J. Biol. Chem. 270*, 16167–16175.

(6) Mao, Q., Deeley, R. G., and Cole, S. P. (2000) Functional reconstitution of substrate transport by purified multidrug resistance protein MRP1 (ABCC1) in phospholipid vesicles. *J. Biol. Chem. 275*, 34166–34172.

(7) Ferté, J. (2000) Analysis of the tangled relationships between P-glycoprotein-mediated multidrug resistance and the lipid phase of the cell membrane. *Eur. J. Biochem. 267*, 277–294.

(8) Thomas, G. A., Barrand, M. A., Stewart, S., Rabbitts, P. H., Williams, E. D., and Tweentyman, P. R. (1994) Expression of the multidrug resistance-associated protein (MRP) gene in human lung tumors and normal tissue as determined by in situ hybridization. *Eur. J. Cancer 30*, 1705–1709.

(9) Charpin, C., Vielh, P., Duffaud, F., Devictor, B., Andrac, L., Lavaut, M. N., Allasia, C., Horschowski, N., and Piana, L. (1994) Quantitative immunocytochemical assays of P-glycoprotein in breast carcinoma-correlation to messenger-RNA expression and to immunohistochemical prognostic indicators. *J. Natl. Cancer Inst. 86*, 1539–1545.

(10) Hijazi, Y. M., Axiotis, C. A., Navarro, S., Steinberg, S. M., Horowitz, M. E., and Tsokos, M. (1994) Immunohistochemical detection of P-glycoprotein in Ewing's sarcoma and peripheral primitive neuroectodermal tumors before and after chemotherapy. *Am. J. Clin. Pathol. 102*, 61–67.

(11) Chan, H., Grogan, T., Haddad, G., DeBoer, G., and Ling, V. (1997) P-glycoprotein expression: critical determinant in the response to osteosarcoma chemotherapy. *J. Natl. Cancer Inst. 89*, 1706–1715.

(12) Lee, J. S., Scala, S., Matsumoto, Y., Dickstein, B., Robey, R., Zhan, Z., Altenberg, G., and Bates, S. E. (1997) Reduced drug accumulation and multidrug resistance in human breast cancer cells

without associated P-glycoprotein or MRP overexpression. *J. Cell Biol. 65*, 513–526.

(13) Linn, S. C., van Kalken, C. K., van Tellingen, O., van der Valk, P., van Groeningen, C. J., Kuiper, C. M., Pinedo, H. M., and Giaccone, G. (1994) Clinical and pharmacologic study of multidrug resistance reversal with vinblastine and bepridil. *J. Clin. Oncol. 12*, 812–819.

(14) Lonn, U., Lonn, S., Nilsson, B., and Stenkvist, B. (1994) Intratumoral heterogeneity for amplified genes in human breast carcinoma. *Int. J. Cancer 58*, 40–45.

(15) Sognier, M. A., Zhang, Y., Eberle, R. L., Sweet, K. M., Altenberg, G. A., and Belli, J. A. (1994) Sequestration of doxorubicin in vesciles in a multidrug-resistant cell line (LZ-100). *Biochem. Pharmacol. 48*, 391–401.

(16) Chan, H., Lu, Y., Grogan, T., Haddad, G., Hipfner, D., Cole, S., Deeley, R., Ling, V., and Gallie, B. (1997) Multidrug resistance protein (MRP) expression in retinoblastoma correlates with the rare failure of chemotherapy despite cyclosporine for reversal of P-glycoprotein. *Cancer Res. 57*, 2325–2330.

(17) Scheffer, G. L., Wijngaard, P. L., Flens, M. J., Izquierdo, M. A., Slovak, M. L., Pinedo, H. M., Meijor, C. J., Clevers, H. C., and Scheper, A. J. (1995) The drug resistance-related protein LRP is the human major vault protein. *Nat. Med. 1*, 578–582.

(18) Litman, T., Brangi, M., Hudson, E., Fetsch, P., Abati, A., Ross, D. D., Miyake, K., Resau, J. H., and Bates, S. E. (2000) The multidrug-resistant phenotype associated with overexpression of the new ABC half-transporter, MXR (ABCG2). *J. Cell Sci. 113*, 2011–2021.

(19) Wang, Y., Pan, X. Q., L'Heureux, F., and Georges, E. (1997) Overexpression of 40-kDa protein in human multidrug resistant cells. *Biochem. Biophys. Res. Commun. 236*, 483–488.

(20) Wang, Y., Serfass, L., Roy, M. O., Wong, J., Bonneau, A. M., and Georges, E. (2004) Annexi-I expression modulate drug resistance in tumors cells. *Biochem. Biophys. Res. Commun. 314*, 565–570.

(21) Del Vecchio, S., and Salvatore, M. R. (2004) ^{99m}Tc-MIBI in the evaluation of breast cancer biology. *Eur. J. Nucl. Med. Mol. Imaging 31*, S88–S96.

(22) Schomäcker, K., and Schicha, H. (2000) Use of myocardial imaging agents for tumor diagnosis- a success story? *Eur. J. Nucl. Med. 27*, 1845–1863.

(23) Sharma, V. (2004) Radiopharmaceuticals for assessment of multidrug resistance P-glycoprotein-mediated drug transport activity. *Bioconjugate Chem. 15*, 1464–1474.

(24) Sharma, V., and Piwnica-Worms, D. (2005) Monitoring multidrug resistance P-glycoprotein drug transport activity with single-photon emission computed tomography and positron emission tomography radiopharmaceuticals. *Top. Curr. Chem. 252* (Contrast Agents III), 155–178.

(25) Vaidyanathan, G., and Zalutsky, M. R. (2004) Imaging drug resistance with radiolabeled molecules. *Curr. Pharm. Des. 10*, 2965–2979.

(26) Mazzammil, T., Ballinger, J. R., and Moore, M. J. (1999) ^{99}Tc^{m}-sestamibi imaging of inhibition of the multidrug resistance transporter in a mouse xenograft model of human breast cancer. *Nucl. Med. Commun. 20*, 115–122.

(27) Filippi, L., Santoni, R., Manni, C., Danieli, R., Floris, R., and Schillaci, O. (2005) Imaging primary brain tumor by single-photon emission computed tomography (SPECT) with technetium-99m Sestamibi (MIBI) and Tetrofosmin. *Curr. Med. Imaging Rev. 1*, 61–66.

(28) Herman, L. W., Sharma, V., Kronauge, J. F., Barbarics, E., Herman, L. A., and Piwnica-Worms, D. (1995) Novel hexakis(areneisonitrile)technetium(I) complexes as radioligands targeted to the multidrug resistance P-glycoprotein. *J. Med. Chem. 38*, 2955–2963.

(29) Muzzammil, T., Ballinger, J. R., and Moore, M. J. (1999) ^{99m}Tc-sestamibi imaging of inhibition of the multidrug resistance transporter in a mouse xenograft model of human breast cancer. *Nucl. Med. Commun. 20*, 115–122.

(30) Agrawal, M., Abraham, J., Balis, F. M., Edgerly, M., Stein, W. D., Bates, S., Fojo, T., and Chen, C. C. (2003) Increased ^{99m}Tc-Sestamibi accumulation in normal liver and drug resistant-tumors after the administration of the glycoprotein inhibitor, XR9576. *Clin. Cancer Res. 9*, 650–656.

(31) Liu, Z. L., Stevenson, G. D., Barrett, H. H., Kastis, G. A., Bettan, M., Furenlid, L. R., Wilson, D. W., and Woolfenden, J. M. (2004) Imaging recognition of drug resistance in human breast tumors using ^{99m}Tc-labeled monocationic agents and a high-resolution stationary SPECT system. *Nucl. Med. Biol. 31*, 53–65.

(32) Liu, Z. L., Stevenson, G. D., Barrett, H. H., Furenlid, L. R., Wilson, D. W., Kastis, G. A., Bettan, M., and Woolfenden, J. M. (2005) Imaging recognition of inhibition of drug resistance in human breast cancer xenografts using ^{99m}Tc-labeled sestamibi and tetrofosmin. *Nucl. Med. Biol. 32*, 573–583.

(33) Luker, G. D., Francisco, P. M., Dobkin, J., and Piwbica-Worms, D. (1997) Modulation of the multidrug resistance P-glycoprotein: Detection with technetium-99m sestamibi in vivo. *J. Nucl. Med. 38*, 369–372.

(34) Márián, T., Szabó, G., Nagy, H., Szincsák, N., Juhász, I., Galuska, L., Balkay, L., Mikecz, P., Trón, L., and Krasznai, Z. (2003) In vivo and in vitro multitracer analysis of P-glycoprotein expression-related multidrug resistance. *Eur. J. Nucl. Med. Mol. Imaging 30*, 1147–1154.

(35) Lorker, D. E., Krüger, M., Buchert, R., Bohuslavizki, K. H., Clausen, M., and Schumacker, U. (2001) In vitro and in vivo tracer characteristics of an established multidrug-resistant human colon cancer cell line. *J. Nucl. Med. 42*, 646–654.

(36) Wang, J., Yang, C. T., Kim, Y. S., Sreerama, S. G., Cao, Q., Li, Z., He, Z., Chen, X., and Liu, S. (2007) ^{64}Cu-Labeled triphenylphosphonium and triphenylarsonium cations as highly tumor-selective PET imaging agents. *J. Med. Chem. 50*, 5057–5069.

(37) Kim, Y. S., Yang, C. T., Wang, J. J., Sreerama, S. G., Cao, Q., Li, Z., He, Z., Chen, X., and Liu, S. (2008) Radiolabeled triphenylphosphonium cations as highly tumor-selective imaging agents: Effects of radiometals, bifunctional chelators and molecular charge. *J. Med. Chem. 51*, 2971–2984.

(38) Yang, C. T., Li, Y. X., and Liu, S. (2007) Synthesis and structural characterization of complexes of a DO3A-conjugated triphenylphosphonium cation with diagnostically important metal ions. *Inorg. Chem. 46*, 8988–8997.

(39) Yang, C. T., Kim, Y. S., Wang, J., Wang, L., Shi, J., Li, Z., Chen, X., Fan, M., Li, J. J., and Liu, S. (2008) ^{64}Cu-labeled 2-(diphenylphosphoryl)ethyldiphenylphosphonium cations as highly selective tumor imaging agents: effects of linkers and chelates on biodistribution characteristics. *Bioconjugate Chem. 19*, 2008–2022.

(40) Bähr, O., Wick, W., and Weller, M. (2001) Modulation of MDR/MRP by wild-type and mutant p53. *J. Clin. Invest. 107*, 643–645.

(41) Bähr, O., Rieger, J., Duffner, F., Meyermann, R., Wller, M., and Wick, W. (2003) P-glycoprotein and multidrug resistance-associated protein mediate specific patterns of multidrug resistance in malignant glioma cell lines, but not in primary glioma cells. *Brain Pathol. 13*, 482–494.

(42) Nakatsu, S., Kondo, S., Kondo, Y., Yin, D., Peterson, J. W., Kaakaji, R., Morinura, T., Kikuchi, H., and Takeuchi, J. (1977) Induction of apoptosis in multi-drug resistant (MDR) human glioblastoma cells by SN38, a metabolite of the camptothecin derivative CPT-11. *Cancer Chemother. Pharmacol. 39*, 417–423.

(43) Le Jeune, N., Perek, N., Denoyer, D., and Dubois, F. (2004) Influence of gluthione depletion on plasma membrane cholesterol esterification and on Tc-99m-Sestamibi and Tc-99m-Tetrofosmin uptakes; a comparative study in sensitive U87MG and multidrug-resistant MRP1 human glioma cells. *Cancer Biother. Radiopharm. 19*, 411–421.

(44) Ihnat, M. A., Lariviere, J. P., Warren, A. J., Ronde, N. L., Blaxall, J. R. N., Pierre, K. M., Turpie, B. W., and Hamilton, J. W. (1997) Suppression of P-glycoprotein expression and

multidrug resistance by DNA cross-linking agents. *Clin. Cancer Res. 3*, 1339–1346.
(45) Matsumoto, Y., Takano, H., Kunishio, K., Nagao, S., and Fojo, T. (2001) Expression of drug resistance genes in VP-16 and mAMSA-selected human carcinoma cells. *Jpn. J. Cancer Res. 92*, 778–784.
(46) Liu, B. L., Sun, D. T., Xia, W. Y., Hung, M. C., and Yu, D. H. (1997) Cross-reactivity of C219 anti-p170^{mdr-1} antibody with p185$^{c\text{-}erbB2}$ in breast cancer cells: cautions on evaluating p170^{mdr-1}. *J. Natl. Cancer Inst. 89*, 1524–1529.
(47) Engel, J. B., Schally, A. V., Halmos, G., Baker, B., Nagy, A., and Keller, G. (2005) Targeted cytotoxic bombesin analog AN-215 effectively inhibits experimental human breast cancer with low induction of multi-drug resistance proteins. *Endocrine-Related Cancer 12*, 999–1009.
(48) Savas, B., Kerr, P. E., and Pross, H. F. (2006) Lymphokine-activated killer cell susceptibility and adhesion molecule expression of multidrug resistant breast carcinoma. *Cancer Cell Int.*, http:www.cancerci.
com/content/6/1/24.
(49) Sharma, V., Prior, J. L., Belinsky, M. G., Kruh, G. D., and Piwnica-Worms, D. (2005) Characterization of a ^{67}Ga/^{68}Ga radiopharmaceutical for SPECT and PET of MDR1 P-glycoprotein transport activity in vivo: validation in multidrug-resistant tumors and at the blood-brain barrier. *J. Nucl. Med. 46*, 354–364.
(50) Ocheskey, J. A., Polyakov, V. R., Harpstrite, S. E., Oksman, A., Goldberg, D. E., Piwnica-Worms, D., and Sharma, V. (2003) Synthesis, characterization, and molecular structure of a gallium(III) complex of an amine-phenol ligand with activity against chloroquine-sensitive *Plasmodium falciparum* strains. *J. Inorg. Biochem. 93*, 265–270.
(51) Dyszlewski, M., Blake, H. M., Dahlheimer, J. L., Pica, C. M., and Piwnica-Worms, D. (2002) Characterization of a novel ^{99m}Tc-carbonyl complex as a functional probe of MDR1 P-glycoprotein transport activity. *Mol. Imaging 1*, 24–35.
(52) Luker, G. D., Flagg, T. P., Sha, Q., Luker, K. E., Pica, C. M., Nichols, C. G., and Piwnica-Worms, D. (2001) MDR1 P-glycoprotein reduces influx of substrates without affecting membrane potential. *J. Biol. Chem. 276*, 49053–49060.
(53) Slapak, C. A., Dahlheimer, J., and Piwnica-Worms, D. (2001) Reversal of multidrug resistance with LY335979. *J. Clin. Pharmacol. 41*, 29S–38S.
(54) Rao, V. V., Herman, L. W., Kronauge, J. F., and Piwnica-Worms, D. (1998) A novel areneisonitrile Tc complex inhibits the transport activity of MDR P-glycoprotein. *Nucl. Med. Biol. 25*, 225–232.
(55) Crankshaw, C. L., Marmion, M., Luker, G. D., Rao, V., Dahlheimer, J., Burleigh, B. D., Webb, E., Deutsch, K. F., and Piwnica-Worms, D. (1998) Novel technetium (III)-Q complexes for functional imaging of multidrug resistance (MDR1) P-glycoprotein. *J. Nucl. Med. 39*, 77–86.
(56) Luker, G. D., Rao, V. V., Crankshaw, C. L., Dahlheimer, J., and Piwnica-Worms, D. (1997) Characterization of phosphine complexes of technetium(III) as transport substrates of the multidrug resistance P-glycoprotein and functional markers of P-glycoprotein at the blood-brain barrier. *Biochemistry 36*, 14218–14227.
(57) Pichler, A., Prior, J. L., and Piwnica-Worms, D. (2004) Imaging reversal of multidrug resistance in living mice with bioluminescence: MDR1 P-glycoprotein transports coelenterazine. *Proc. Natl. Acad. Sci. U.S.A. 101*, 1702–1707.
(58) Gatmaitan, Z. C., and Arias, I. M. (1993) Structure and function of P-glycoprotein in normal liver and small intestine. *Adv. Pharmacol. 24*, 77–97.
(59) Lee, C. H., Bradley, G., Zhang, J. T., and Ling, V. (1993) Differential expression of P-glycoprotein genes in primary rat hepatocytes culture. *J. Cell Physiol. 157*, 392–402.
(60) Mayer, R., Kartenbeck, J., Buchler, M., Jedlitschky, G., Leier, I., and Keppler, D. (1995) Expression of the MRP gene-encoded conjugate export pump in liver and its selective absence from the canalicular membrane in transport deficient mutant hepatocytes. *J. Cell Biol. 131*, 137–150.
(61) Carvalho, P. A., Chiu, M. L., Kronauge, J. F., Kawamura, M., Jones, A. G., Holman, B. L., and Piwnica-Worms, D. (1992) Subcellular distribution and analysis of technetium-99m-MIBI in isolated perfused rat hearts. *J. Nucl. Med. 33*, 1516–1521.
(62) Bolzati1, C., Cavazza-Ceccato, M., Agostini, S., Tokunaga, S., Casara, D., and Bandoli, G. (2008) Subcellular distribution and metabolism studies of the potential myocardial imaging agent [^{99m}Tc(N)(DBODC)(PNP5)]$^{+}$. *J. Nucl. Med. 49*, 1336–1344.
(63) Kim, Y. S., Shi, J., Hou, G. H., and Liu, S. Mechanism for myocardial localization and rapid liver clearance of ^{99m}TcN-MPO: a new heart imaging agent. *J. Nucl. Cardiol.* Submitted.
(64) Ochoa, S. (1955) Malic dehydrogenase from pig heart. *Methods Enzymol. 1*, 735–739.
(65) Platts, E. A., North, T. L., Pickett, R. D., and Kelly, J. D. (1995) Mechanism of uptake of technetium-tetrofosmin I: uptake into isolated adult rat ventricular myocytes and subcellular localization. *J. Nucl. Cardiol. 2*, 317–326.
(66) Younes, A., Songadele, J. A., Maublant, J., Platts, E., Pickett, R., and Veyre, A. (1995) Mechanism of uptake of technetium-tetrofosmin II: uptake into isolated adult rat heart mitochondria. *J. Nucl. Cardiol. 2*, 327–333.
(67) Qadir, M., O'Loughlin, K. L., Fricke, S. M., Williamson, N. A., Greco, W. R., Minderman, H., and Baer, M. (2005) Cyclosporin A is a broad-spectrum multidrug resistance modulator. *Clin. Cancer Res. 11*, 2320–2326.
(68) Kroemer, G., Dallaporta, B., and Resche-Rigon, M. (1998) The mitochondrial death/life regulator in apoptosis and necrosis. *Annu. Rev. Physiol. 60*, 619–642.
(69) Modica-Napolitano, J. S., and Aprille, J. R. (2001) Delocalized lipophilic cations selectively target the mitochondria of carcinoma cells. *Adv. Drug Delivery Rev. 49*, 63–70.
(70) Duchen, M. R. (2004) Mitochondria in health and disease: perspectives on a new mitochondrial biology. *Mol. Aspects Med. 25*, 365–451.
(71) Gottlieb, E., and Thompson, C. B. (2002) Targeting the mitochondria to enhance tumor suppression. *Methods Mol. Biol. 223*, 543–554.
(72) Mannella, C. A. (2006) The relevance of mitochondrial membrane topology to mitochondrial function. *Biochem. Biophys. Acta 1762*, 140–147.

BC800545E

Site-Specific Covalent Modification of RNA Guided by Functionality-Transfer Oligodeoxynucleotides

Kazumitsu Onizuka, Yosuke Taniguchi, and Shigeki Sasaki*

Graduate School of Pharmaceutical Sciences, Kyushu University, 3-1-1 Maidashi, Higashi-ku, Fukuoka 812-8582, Japan, and CREST, Japan Science and Technology Agency, 4-1-8 Motomachi, Kagaguchi, Saitama 332-0012, Japan. Received January 13, 2009; Revised Manuscript Received February 2, 2009

Efficient methods for the covalent modification of large RNA molecules should find significance utility as innovative biological tools as well as therapeutic methods. In this study, the development of a general method for site-specific RNA modification guided by the functional ODN template has been investigated. The ODN probe containing 6-thioguanosine was modified by the methylenediketone derivative to form the *S*-functionalized ODN. Site-specific and cytosine-selective RNA modifications were achieved by the functionality-transfer reaction from the sulfur atom of the functionalized probe to the amino group of the cytosine base of the target strand. It was shown that the base and site selectivity were due to the close proximity of the reactants in the DNA-RNA duplexes.

INTRODUCTION

A number of non-natural covalent modifications have been done for the structural and mechanistic studies of RNA (*1, 2*), manipulation of the gene expression at the single nucleoside level (*3*), single-molecule imaging (*4*), and so forth. Non-natural modifications are achieved by chemical synthesis, enzyme-mediated reactions, and combinations of both (*1*). The site-specific incorporation of a non-natural nucleoside into RNA by chemical reactions is a well-established method, but its drawback is that it cannot be directly applied to generate large, specifically modified RNAs. RNA fragments with natural and/or modified nucleotides can be joined by ligation with a ligase forming a large RNA. If the non-natural covalent modifications can be site-specifically made to RNA, the potential applications are numerous. However, only a limited number of methods showed potentials for use under physiological conditions. For example, DNA template-directed photoligation to the terminal site of RNAs was achieved through the 5-vinyl-2′-deoxyuridine, and is expected to allow the modification of small RNAs (*5*). The internal modification of large RNAs was made by a catalytic DNA molecule with a ligation ability (*6*). However, these methods have limitations because of the photoirradiation necessity in the former method or the large molecular size of the catalytic DNAs and the sequence dependency in the latter case. In this study, we have attempted to develop a general method for the site-specific RNA modification guided by the functionalized oligodeoxynucleotides.

Oligonucleotides and related oligomers with an attached chemically reactive accessory molecule have been used to perform chemical modification to RNA in a sequence-specific manner (*7*). Ideally, the accessory molecule needs to be stable under physiological conditions, and its reactivity should be induced on demand. UV irradiation is frequently used as an exogenous activation signal (*8*). The target strand itself was used for the generation of an active agent for alkylation (*9*). We have been developing an original strategy for the reactivity induction of the accessory molecules by taking advantage of minute environmental changes accompanied by nucleic acid hybridization. The first example was demonstrated by the hybridization-promoted cytosine-selective alkylation using the sulfide derivative of 2-amino-6-vinylpurine nucleoside, in which the stable sulfide precursor was spontaneously activated to the active vinyl species within the complementary duplex having the cytosine base at the target site (*10, 11*). The usefulness of this inducible alkylating agent was confirmed by enhancement of the intracellular antisense inhibition (*3*). Although the induction mechanism is not yet fully understood, the close proximity to the target cytosine base within the duplex is responsible for the selective activation of the sulfide precursor. This strategy was then expanded to the nitrosyl group transfer from the sulfur atom of 6-thioguanosine to the amino group of the cytosine base (*12*). Interesting results were that *S*-nitroso-6-thioguanosine in the ODN was much more stable than the corresponding monomer and that its reactivity was induced in close proximity to the cytosine base in the complementary duplex that affected the nitrosyl transfer to the amino group of the cytosine base. Cytosine deamination following the nitrosyl transfer reaction suggested a potential application as an artificial tool for RNA editing.

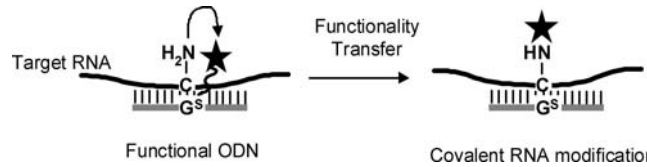

Figure 1. General strategy for site-specific RNA modification through the functionality transfer reaction from the *S*-functionalized 6-thioguanosine (Gs) to the amino group cytosine base.

These two early examples have demonstrated the validity of our strategy for the specific induction of reactivity in close proximity to the target cytosine base only by intrinsic changes in the microenvironment around the reactants. For further expansion of this strategy, we designed a new functionality-transfer reaction to the amino group of the cytosine base using the ODN incorporating *S*-functionalized 6-thioguanine, which may permit the site-specific covalent modification of RNAs with a variety of functional molecules for editing, tagging, fluorescence labeling, and so forth (Figure 1) (*13*). We now describe

* Corresponding author: 3-1-1 Maidashi, Higashi-ku, Fukuoka 812-8582, Japan, TEL: +81-92-642-6615, FAX: +81-92-642-6786, e-mail: sasaki@phar.kyushu-u.ac.jp.

10.1021/bc900009p CCC: $40.75 © 2009 American Chemical Society
Published on Web 03/06/2009

in detail the design of the new functionality-transfer reaction and site-specific modification of RNA.

EXPERIMENTAL PROCEDURES

Synthesis of Oligodeoxynucleotides and Oligonucleotides. All oligonucleotides were synthesized by by the automated DNA synthesizer according to the conventional amidite chemistry. The cleaved oligonucleotides were purified by HPLC equipped with a ODS column using a linear gradient between the 0.1 M TEAA buffer and CH_3CN. The MALDI-TOF/MS data are summarized in Supporting Information Table S2.

3-Chloromethylene-4-phenylbutane-2,4-dione (5a) as a General Procedure for the Synthesis of 5b and 5c. A mixture of benzoylacetone (977 mg, 6.02 mmol), ethyl *ortho*-formate (2 mL, 12.02 mmol), and acetic anhydride (2 mL, 21.16 mmol) was heated at 130 °C for 2.5 h, then cooled to rt. The solvents were evaporated under vacuum to give the residue, which was purified by column chromatography (silica gel, hexane/AcOEt = 4:1) to afford 3-ethoxymethylene-3-benzolyacetone (1.09 g, 83%). IR (cm^{-1}): 1669, 1624, 1210. ^1H NMR (400 MHz, $CDCl_3$) δ ppm: 7.86 (2H, d, J = 7.9 Hz), 7.70 (1H, s), 7.55 (1H, tt, J = 7.5, 1.5 Hz), 7.44 (2H, t, J = 7.5 Hz), 4.06 (2H, q, J = 7.0 Hz), 2.20 (3H, s), 1.19 (3H, t, J = 7.0 Hz). ESI-MS (m/z): 219.1 ($[M + H]^+$).

A solution of the above compound (250 mg, 1.15 mmol) in 10% aqueous HCl−THF (0.2 mL−2 mL) was stirred at rt for 1 h and diluted with AcOEt (10 mL). The mixture was washed with H_2O, and the aqueous layer was extracted with AcOEt (6 mL × 2). The combined organic layers were washed with brine, dried over Na_2SO_4, and evaporated to dryness to give 3-hydroxymethylene-3-benzoylacetone as a crude oil (205 mg, 94%), which was used for the next reaction without further purification.

$SOCl_2$ (50 mL, 0.685 mmol) was added dropwise to a solution of the above oil (120 mg, 0.63 mmol) in dry toluene (1 mL) at rt, and the mixture was heated under reflux. After 5 h, $SOCl_2$ (50 mL, 0.685 mmol) was added to the reaction mixture, and the mixture was heated for an additional 4 h. The mixture was evaporated under vacuum, and the remaining reagent was removed by azeotropic evaporation with toluene to give brown solids, which were purified by column chromatography (silica gel, $CHCl_3$/hexane = 3:1) to give 3-chloromethylene-3-benzoylacetone as white needles (108 mg, 82%). mp 85−87 °C. IR (cm^{-1}): 3094, 1678, 1662, 1596, 1234. ^1H NMR (400 MHz, $CDCl_3$) δ ppm: 7.88 (2H, dd, J = 8.2, 1.4 Hz), 7.62 (1H, tt, J = 7.6, 1.2 Hz), 7.54 (1H, s), 7.49 (2H, t, J = 7.9 Hz), 2.20 (3H, s). ESI-MS (m/z): 231.0, 233.0 ($[M + Na]^+$).

2-Benzoyl-2-chloromethylene Acetic Acid Ethyl Ester (5b). This compound was synthesized from ethyl benzoyl acetate. ^1H NMR (400 MHz, $CDCl_3$) δ ppm: 7.89 (2H, d, J = 7.1 Hz), 7.63 (1H, s), 7.59 (1H, t, J = 7.1 Hz), 7.48 (2H, t, J = 7.6 Hz), 4.20 (2H, q, J = 7.2 Hz), 1.18 (3H, t, J = 7.2 Hz). IR (cm^{-1}): 1720, 1679, 1598, 1243, 1227. ESI-MS (m/z): 239.1 ($[M + H]^+$).

2-(Chloromethylene)-1,3-diphenylpropane-1,3-dione (5c). This compound was synthesized from dibenzoylmethane. ^1H NMR (400 MHz, $CDCl_3$) δ ppm: 7.95 (2H, d, J = 7.3 Hz), 7.83 (2H, d, J = 7.3 Hz), 7.61−7.55 (2H, m), 7.49−7.44 (4H, m), 7.28 (1H, s). IR (cm^{-1}): 1681, 1648, 1596, 1330, 1229. ESI-MS (m/z): 271.2, 273.2 ($[M + H]^+$).

Synthesis of DNA2a as the General Procedure of the Synthesis of DNA2b−2d. A solution of **5a** (25 mM in CH_3CN, 0.3 μL, 7.5 nmol) was added to a solution of DNA**1** (750 μM, 2 μL, 1.5 nmol) in a carbonate buffer (50 mM, 2.7 μL, pH 10). After 5 min, DNA**2a** was purified by HPLC for the MALDIMS measurement. The crude reaction mixture containing DNA**2a** was used for the functionality transfer reaction without HPLC purification.

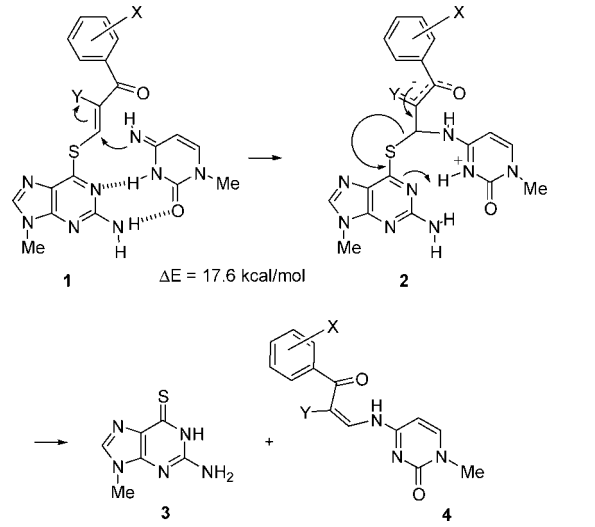

Figure 2. Design of the functionality-transfer reaction of the 6-thioguanine derivative modified with α,β-unsaturated carbonyl unit (**1**) to form the amino-modified cytosine (**4**) via the intermediate **2**. The hypothesized pathway using the imino tautomer of cytosine and diketone derivative (X = H, Y = $COCH_3$) was simulated by MOPAC (PM5).

Evaluation of the Stability of DNA2a as the General Procedure of the Evaluation of the Stability of DNA2b−2d. A solution of **5a** (25 mM in CH_3CN, 0.15 μL, 3.75 nmol) was added to a solution of DNA**1** (750 μM, 1 μL, 0.75 nmol) in a carbonate buffer (50 mM, 1.35 μL, pH 10). After 5 min, the mixture was diluted with ultrapurified water (24.5 μL) and neutralized with MES buffer (0.5 M MES and 1 M NaCl, 3 μL, pH 6.9). The formation of DNA**1** from DNA**2** (25 μM, pH 7.0) was analyzed by HPLC (column: SHISEIDO C18, 4.6 × 250 mm; solvent: A: 0.1 M TEAA buffer, B: CH_3CN, B: 10% to 30%/20 min, linear gradient; flow rate: 1.0 mL/min; monitored by UV detector at 254 nm).

Functionality Transfer Reaction From DNA2a to RNA3 to form RNA4 as the General Procedure for the Functionality Transfer Reaction. DNA**2a** (300 μM, 0.2 μL, 60 pmol), RNA**3** (50 μM, 1.0 uL, 50 pmol), and RNase OUT (40 u/μL, 0.75 μL, 30 u) were mixed in MES buffer (1 M NaCl, 0.5 M MES, 5 μL, pH 7), and the mixture was kept at rt. The reaction mixture was analyzed by HPLC (column: SHISEIDO C18, 4.6 × 250 mm; solvent: A: 0.1 M TEAA buffer, B: CH_3CN, B: 10% to 30%/20 min, linear gradient; flow rate: 1.0 mL/min; monitored by UV detector at 254 nm (Figures 3 and 4) or by monitoring the fluorescence at 518 nm with emission at 494 nm (Figures 5 and 6)).

RESULTS AND DISCUSSION

The design of the functionality-transfer reaction is shown in Figure 2. The conjugate addition of the amino group of the cytosine base to the α,β-unsaturated carbonyl group of the *S*-functionalized 6-thioguanine and the following elimination of 6-thioguanine might produce the *S* to *N* transfer reaction of the functional group. Prior to the synthetic investigation, the reactions within the complex resembling the natural G-C pair were simulated by MO calculations (MOPAC, PM5) using the diketone derivative (**1**, X = H, Y = $COCH_3$) as the starting material. A hypothesized transition state of the addition reaction from **1** to an intermediate **2** was simulated to have a relatively low activation energy with the imino tautomer of the cytosine base, similar to the NO-transfer reaction from the *S*-nitorosylated 6-thioguanine to the amino group of cytosine (Supporting Information Figure S1) (*12*). Also, a low activation energy was estimated for the elimination of 6-thioguanine (**3**) to form the

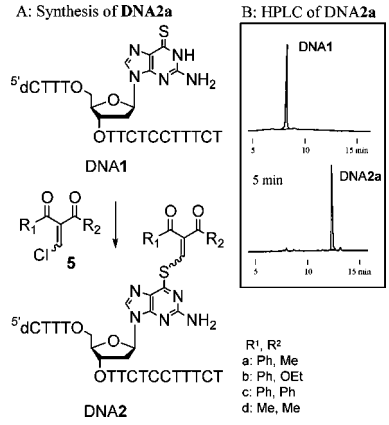

Figure 3. Formation of *S*-functionalized DNA**2** by the reaction of the diketone derivative (**5**) with DNA**1**. Panel A, the reaction scheme. Panel B, the HPLC chart. The reactions were performed by using 0.3 mM of DNA**1** and 1.5 mM of **5** in carbonate buffer at pH 10, followed by HPLC. HPLC: ODS Column. Solvent: A: 0.1 M TEAA Buffer, B: CH_3CN, B: 10% to 30%/20 min, 30% to 100%/25 min, linear gradient. Flow rate: 1.0 mL/min. UV: 254 nm.

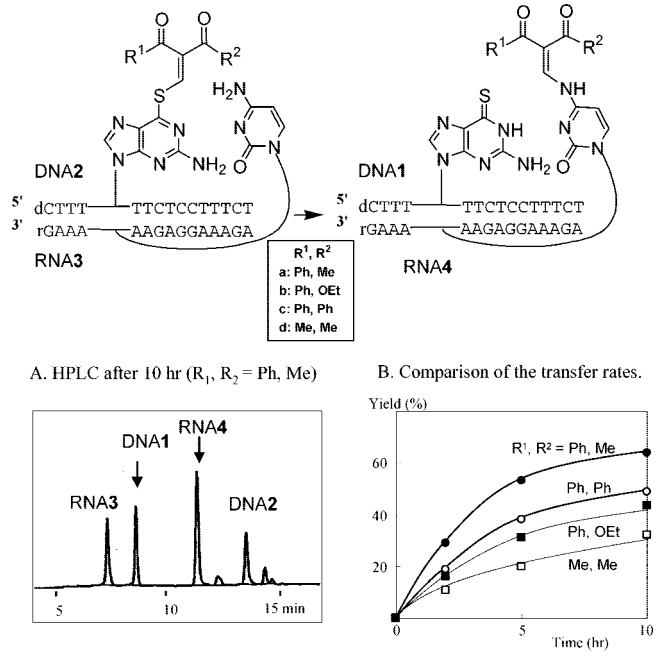

Figure 4. Comparison of the efficiency of the diketone structure for the functionality-transfer reaction. Panel A, HPLC Change during the functionality-transfer reaction from DNA**2a** (R^1, R^2 = Ph, Me) to RNA(**3**) to form RNA(**4a**). Panel B, comparison of the transfer rates of four dicarbonyl compounds. Arrows indicate the new peaks at 10 h after the reaction. The transfer reactions were performed using 30 μM of DNA**2** and 25 μM of RNA**3** in MES buffer at pH 7.0. HPLC: Column: SHISEIDO C18, 4.6 × 250 mm. Solvent: A: 0.1 M TEAA Buffer, B: CH_3CN, B: 10% to 30%/20 min, 30% to 100%/25 min, linear gradient. Flow rate: 1.0 mL/min. UV: 254 nm.

transformed product (**4**). It was expected that functional groups (X and Y) would be useful to adjust the reactivity of the α,β-unsaturated carbonyl group.

The investigation was started by a search of suitable α,β-unsaturated carbonyl compounds with different X and Y groups. It was shown in the preliminary experiments with monomers in organic solvents that the 2′-deoxy-6-thioguanosine derivative resembling **1** (X = $COCH_3$ or COOEt, Y = H) gave rise to the corresponding transferred product of the cytidine monomer, although the reaction slowly proceeded even at high concentrations (74% yield after 7 days at 0.1 M) (*13*). With the

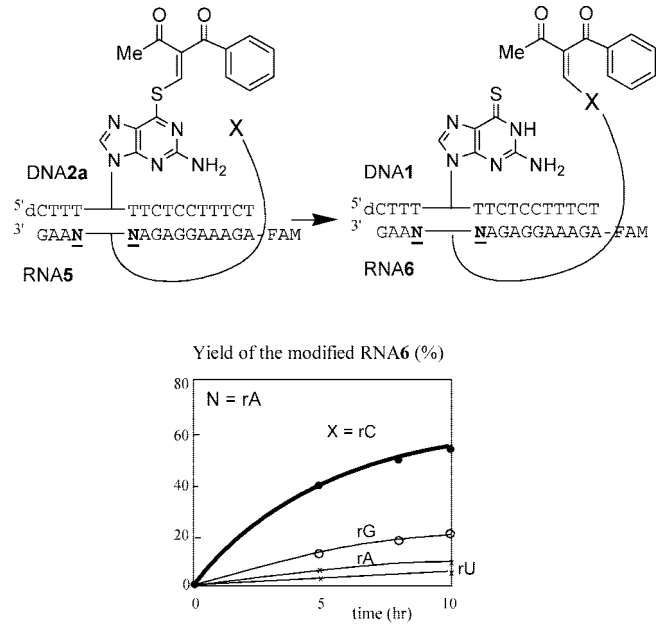

Figure 5. Selectivity to the cytosine base in the RNA substrates with *N* = rA or rC. The transfer reactions were performed at 25 °C using 1.2 μM of DNA**2** and 1 μM of RNA**5** in MES buffer at pH 7.0, followed by HPLC. The RNA**5** having the cytosine base next to the complementary position of 3′ rA-rU-rC or 3′ rC-rU-rA in the sequence of N-X-N produced no significant transferred product. HPLC: Column: SHISEIDO C18, 4.6 × 250 mm. Solvent: A: 0.1 M TEAA Buffer, B: CH_3CN, B: 10% to 30%/20 min, 30% to 100%/25 min, linear gradient. Flow rate: 1.0 mL/min; monitoring the fluorescence at 518 nm with emission at 494 nm.

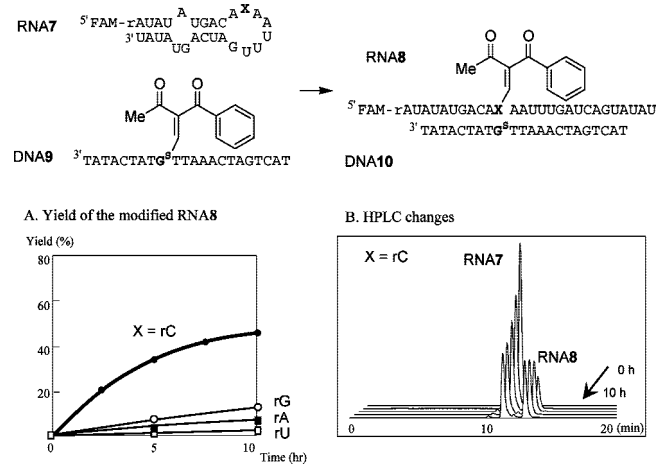

Figure 6. Selectivity to the cytosine base in the RNA substrates with the hairpin-loop structure. Panel A, yield of the modified RNA**8**. Panel B, HPLC Change during the functionality-transfer reaction from DNA**9** to RNA**7** to form RNA**8**. The transfer reactions were performed at 25 °C using 1.2 μM of DNA**9** and 1 μM of RNA**7** in MES buffer at pH 7.0, followed by HPLC. HPLC: Column: SHISEIDO C18, 4.6 × 250 mm. Solvent: A: 0.1 M TEAA Buffer, B: CH_3CN, B: 10% to 30%/20 min, 30% to 100%/25 min, linear gradient. Flow rate: 1.0 mL/min; monitoring the fluorescence at 518 nm with emission at 494 nm.

expectation that the reaction of the reactants would be enhanced due to proximity effect in the duplex, we selected the dicarbonyl derivative as a potential candidate for the interstrand transfer reaction in this study. 6-Thioguanosine containing DNA**1** was synthesized as previously reported (*12*). The 1,3-dicarbonyl compounds were transformed into the corresponding 2-chloromethyldene derivatives (**5**) (Scheme 1), which were then mixed with DNA**1** in a carbonate buffer at pH 10 to rapidly produce the corresponding *S*-functionalized DNA**2** as the single

Scheme 1[a]

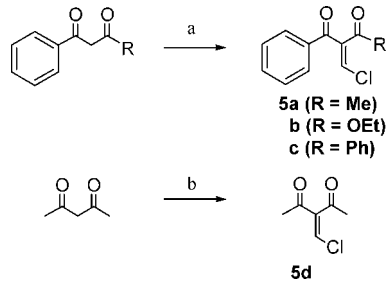

[a] (a) (1) $CH(OEt)_3$, Ac_2O, 120 °C, (2) 10% aq HCl, THF for **5a, c**, or 10 % aq NaOH for **5b**, (3) $SOCl_2$, toluene, reflux, (b) (1) $CH(OEt)_3$, Ac_2O, 120 °C, then H_2O, reflux, (2) $SOCl_2$, toluene, reflux.

peak (Figure 3). Structures of the modified DNA**2** were confirmed by MALDI-TOF/MS and UV spectral changes (Supporting Information Figure S2 and Table S2). The modified DNA**2** was relatively stable, and slowly regenerated DNA**1** in the MES buffer at pH 7.0 with a half-life of ca. 350 h (DNA**2b**), 100 h (DNA**2c**), or 70 h (DNA**2a**), except for DNA**2d** with a half-life of 14 h.

An interstrand functionality-transfer reaction was carried out using DNA**2** and its complementary RNA substrates (Figure 4). The reaction progress was followed by HPLC (panel A in Figure 4), in which the peaks marked by arrows indicated the newly formed products, DNA**1** and RNA**4**. The transferred product RNA**4** was isolated and the structure was determined by MALDI-TOF/MS measurements. The effects of the diketone structure on the efficiency of the functionality transfer were compared using DNA**2a**−**d** with a different dicarbonyl unit (panel B in Figure 2). The transfer reactivity decreased in the order of R_1, R_2 = Ph, Me > Ph, Ph > Ph, OEt > Me, Me. In the aromatic series (R^1 = Ph), the reactivity was in the same order as the intrinsic reactivity as suggested by their half-lives in the buffer. Interestingly, DNA**2d** with the shortest half-life gave the lowest reactivity compared to the other aromatic series. As the dicarbonyl structure with R_1, R_2 = Ph, Me (DNA**2a**) possessed a moderate stability and the highest transfer reactivity, a further investigation was performed using this dicarbonyl functional group.

The base selectivity in the transfer reaction was investigated using DNA**2a** and RNA substrates. Selective transfer to the cytosine base was observed (Figure 5), and the transfer rates were much slower to the adenine, guanine, or thymine base (RNA**5** with N = dA; X = dT, dA, or dG). The RNA substrates (RNA**5**) having the cytosine base next to the complementary position (3′ N-X-N = rA-rU-rC or rC-rU-rA) showed a very slow reaction at the background rates, proving that only the cytosine base at the complementary position exhibited a high reactivity during the functionality-transfer reaction. The generality of this functionality-transfer reaction was investigated using DNA probe **9** and RNA substrates **7**. As well as the transfer reaction in the DNA**2a**−RNA**5** duplex, selective transfer to the cytosine base was confirmed (Figure 6). Thus, a new functionality-transfer reaction with a site selectivity to the cytosine base has been established using the *S*-functionalized 6-thioguanosine containing DNA.

In order to confirm that the transfer reaction takes place within the duplex, the CD spectra and the melting temperatures of the duplexes were measured by using nonreactive DNA**11**, **12**, which were prepared by the addition of 1-phenyl-2-propyn-1-one (*14*) to DNA**1**, **10**, respectively, under the same conditions described in Figure 3. The duplex formed with DNA**11** and RNA**5** (N = rA, X = rC) showed the T_m value of 49 °C (panel A in Figure 7). The T_m values of the duplexes of all the other combinations were in the range 43−49 °C (Supporting Information Table S1). The CD spectra of the DNA**11**−RNA**5** (N = rA, X = rC) duplex suggested that the duplex had a conformation between A and B types (panel B in Figure 7) (*15*). It is shown from the melting curve and CD spectra (panels A and C in Figure 7) that the RNA**7** has a hairpin-loop structure in an A-type conformation. Similarly, DNA**12** was shown to have a hairpin-loop structure in a B-type conformation (panel C in Figure 7). The changes of the CD spectra indicated that the hairpin-loop structure of RNA**7** was transformed to the duplex with DNA**12** in a conformation between A-type and B-type (panel C in Figure 7). It was also observed that the functionality-transfer rates from DNA**2a** to RNA**4** were independent of the duplex concentrations between 25 μM and 1 μM. These results have supported that site specificity and cytosine selectivity are made possible due to the close proximity between *S*-vinylated thioguanosine and the amino group of cytosine at the target site of the complementary strand within the duplex.

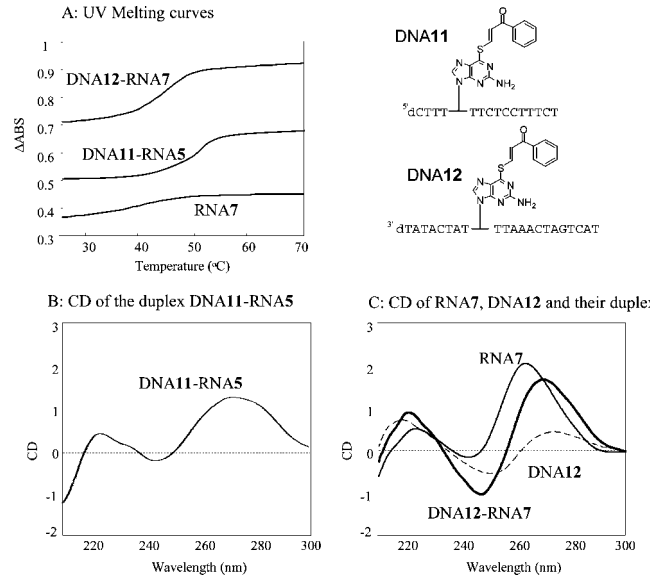

Figure 7. UV melting curves (panel A) and CD spectra (panels B and C). (A) Melting curves were measured using 1.3 μM of each DNA and RNA strands in 50 mM MES buffer at pH 7.0 containing 100 mM NaCl by monitoring at 260 nm. (B,C) CD spectra were measured by using 2.5 μM each DNA and RNA strands in 50 mM MES buffer containing 100 mM NaCl at pH 7.0.

CONCLUSIONS

In this study, the base- and site-selective modifications of the cytosine base of RNA have been successfully achieved using the newly designed functionality-transfer oligodeoxynucleotides. Experimental results have proven that the selectivity and efficiency arise due to the close proximity of the reactants in the DNA-RNA duplexes. As a variety of molecules such as fluorescent labeling groups and tagging molecules may be potentially transferred site-specifically to RNAs, this strategy will be useful for the development of a unique tool for the study of RNAs. If this functionality-transfer reaction is performed with the ODN with resistance to biological degradation, such a reactive ODN may be useful for covalent modification of RNAs under physiological conditions. A further study is now ongoing along this line.

ACKNOWLEDGMENT

This work was supported by a Grant-in-Aid for Scientific Research (A) from the Japan Society for the Promotion of Science (JSPS), and CREST from the Japan Science and Technology Agency. We thank Research Fellowships of the Japan Society for the Promotion of Science for Young Scientists (K.O.).

Supporting Information Available: UV melting temperatures, UV and NMR spectra, MALDI-TOF/MS of DNA, HPLC analysis of the transfer reactions. This material is available free of charge via the Internet at http://pubs.acs.org.

LITERATURE CITED

(1) Chow, C. S., Mahto, S. K., and Lamichhane, T. N. (2008) Combined approaches to site-specific modification of RNA. *ACS Chem. Biol. 3*, 30–37, and references cited therein.

(2) Kawai, R., Kimoto, M., Ikeda, S., Mitsui, T., Endo, M., Yokoyama, S., and Hirao, I. (2005) Site-specific fluorescent labeling of RNA molecules by specific transcription using unnatural base pairs. *J. Am. Chem. Soc. 127*, 17286–17295, and references cited therein.

(3) Ali, M. M., Oishi, M., Nagatsugi, F., Mori, K., Nagasaki, Y., Kataoka, K., and Sasaki, S. (2006) Intracellular inducible alkylation system that exhibits antisense effects with greater potency and selectivity than the natural oligonucleotide. *Angew. Chem., Int. Ed. 45*, 3136–3140.

(4) A review: Weiss, S. (1999) Fluorescence spectroscopy of single biomolecules. *Science 283*, 1676–1683.

(5) Yoshimura, Y., Noguchi, Y., and Fujimoto, K. (2007) Highly sequence specific RNA terminal labeling by DNA photoligation. *Org. Biomol. Chem. 5*, 139–142.

(6) Baum, D. A., and Silverman, S. K. (2007) Deoxyribozyme-catalyzed labeling of RNA. *Angew. Chem., Int. Ed. 46*, 3502–3504.

(7) Sasaki, S., and Nagatsugi, F. (2006) Application of unnatural oligonucleotides to chemical modification of gene expression. *Curr. Opin. Chem. Biol. 10*, 615–621, and references cited therein.

(8) (a) Lee, B. L., Murakami, A., Blake, K. R., Lin, S.-B., and Miller, P. S. (1988) Interaction of psoralen-derivatized oligodeoxyribonucleoside methylphosphonates with single-stranded DNA. *Biochemistry 27*, 3197–3203. (b) Kang, H., and Rokita, S. E. (1996) Site-specific and photo-induced alkylation of DNA by a dimethylanthraquinone-oligodeoxynucleotide conjugate. *Nucleic Acids Res. 24*, 3896–3902, and references cited therein.

(9) Zhou, Q., and Rokita, S. E. (2003) A general strategy for target-promoted alkylation in biological systems. *Proc. Natl. Acad. Sci. U.S.A. 100*, 15452–15457, and references cited therein.

(10) Nagatsugi, F., Kawasaki, T., Usui, D., Maeda, M., and Sasaki, S. (1999) Highly efficient and selective cross-linking to cytidine based on a new strategy for auto-activation within a duplex. *J. Am. Chem. Soc. 121*, 6753–6754.

(11) Kawasaki, T., Nagatsugi, F., Ali, Md. M., Maeda, M., Sugiyama, K., Hori, K., and Sasaki, S. (2005) Hybridization-promoted and cytidine-selective activation for cross-linking with the use of 2-amino-6-vinylpurine derivatives. *J. Org. Chem. 70*, 14–23.

(12) Ali, M. M., Alam, M. R., Kawasaki, T., Nakayama, S., Nagatsugi, F., and Sasaki, S. (2004) Sequence- and base-specific delivery of nitric oxide to cytidine and 5-methylcytidine leading to efficient deamination. *J. Am. Chem. Soc. 126*, 8864–8865.

(13) A preliminary report in the symposium: Onizuka, K., Taniguchi, Y., and Sasaki, S. (2007) Development of novel thioguanosine analogs with the ability of specific modification of cytidine. *Nucleic Acids Symp. Ser. 51*, 5–6.

(14) Maeda, Y., Kakiuchi, N., Matsumura, S., Nishimura, T., Kawamura, T., and Uemura, S. (2002) Oxovanadium complex-catalyzed aerobic oxidation of propargylic alcohols. *J. Org. Chem. 67*, 6718–6724.

(15) Hung, S.-H., Yu, Q., Gray, D. M., and Ratliff, R. L. (1994) Evidence from CD spectra that d(purine)-r(pyrimidine) and r(purine)-d(pyrimidine) hybrids are in different structural classes. *Nucleic Acids Res. 22*, 4326–4334.

BC900009P

Supporting Information

Site-Specific Covalent Modification of Nucleic Acids Guided by Functionality-Transfer Oligodeoxynucleotides

Kazumitsu Onizuka,Yosuke Taniguchi, Shigeki Sasaki,*

Graduate School of Pharmaceutical Sciences, Kyushu University, 3-1-1 Maidashi, Higashi-ku, Fukuoka 812-8582, Japan, and CREST, Japan Science and Technology Agency.

sasaki@phar.kyushu-u.ac.jp

Figure S1. MO Calculations S-2
Figure S2. UV of DNA**1** S-3
Figure S3. UV of DNA**2a** S-3
Figure S4. MALDI-TOF/MS of DNA**2a** and RNA**4a** S-3
Figure S5 ^{1}H-NMR of 5a S-4
Figure S6 ^{1}H-NMR of 5b S-4
Figure S7 ^{1}H-NMR of 5c S-5
Figure S8 ^{1}H-NMR of 5d S-5
Table S1. UV Melting temperatures S-6
Table S2. MALDI-TOF/MS data of all DNA and RNA S-6

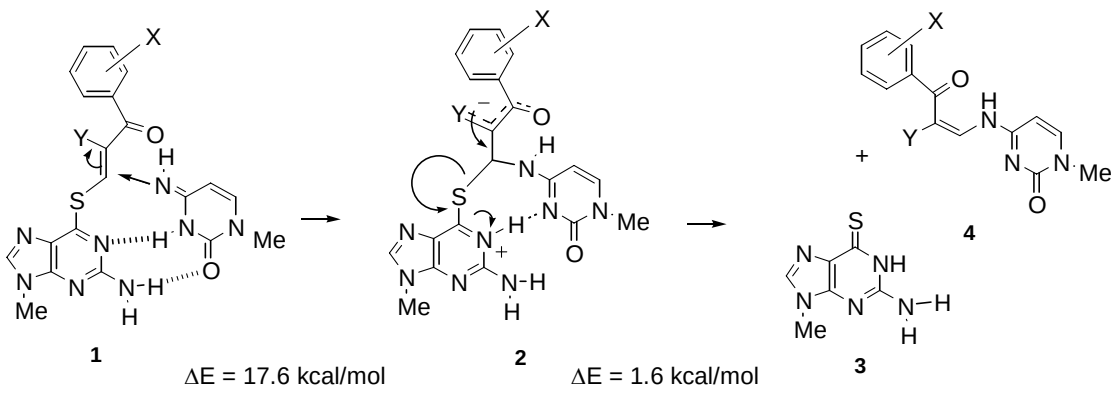

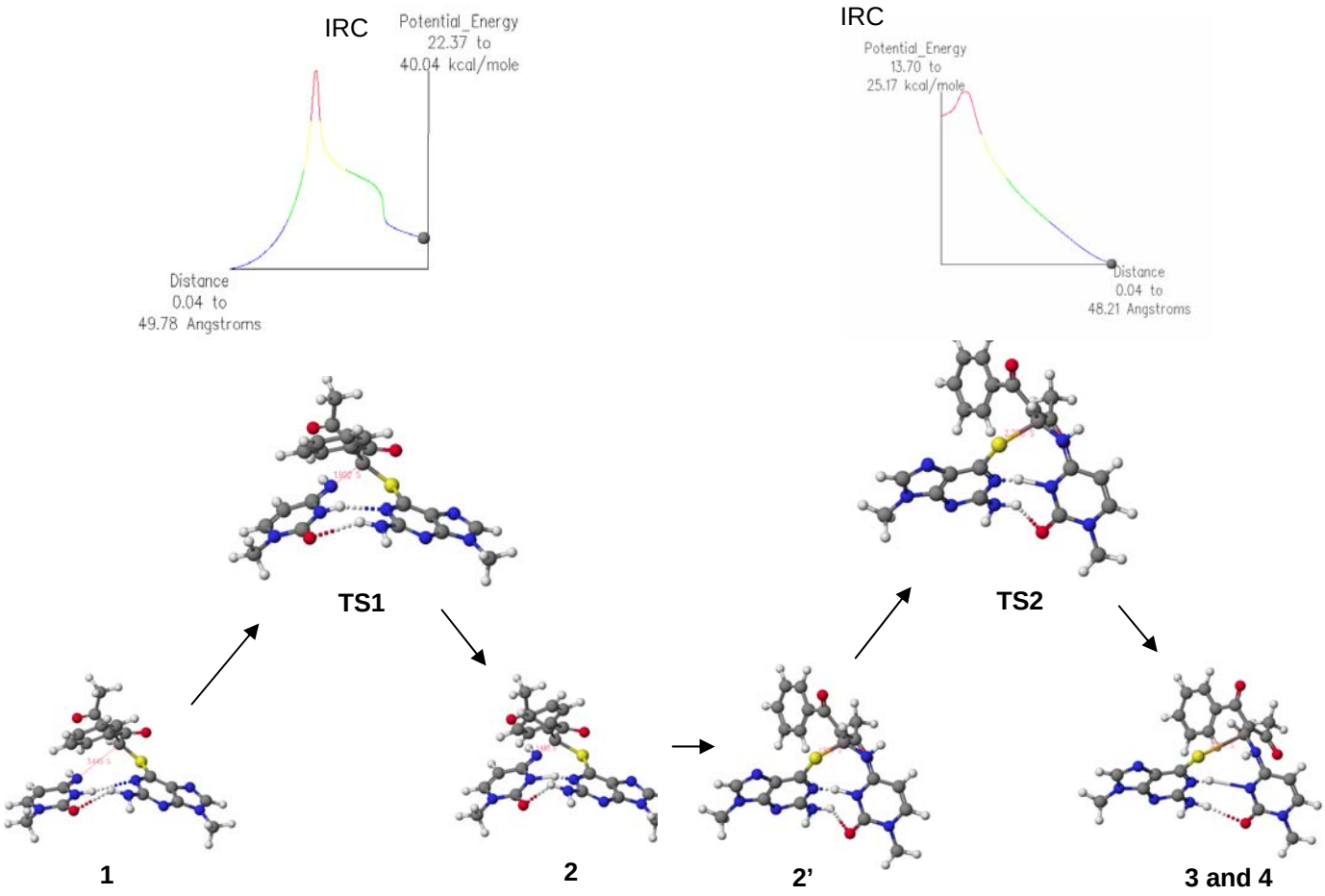

Figure S1. The hypothesized pathway between the imino tautomer of cytosine and the diketone derivative (X = H, Y = $COCH_3$) was simulated by MOPAC(PM5). IRC calculations of the transition states gave TS1 with the activation energy of 17.6 kcal/mol for the formation of an intermediate **2** and TS2 with 1.7 kcal/mol for the following elimination of **3**. Calculation of MOPAC (PM5) was performed by CAChe 6.1 on Windows XP. Although there is no experimental evidence of the intermediary of the imino tautomer in the complex **1**, only the imino tautomer produced the transition state (TS1) from **1** to the intermediate **2**.

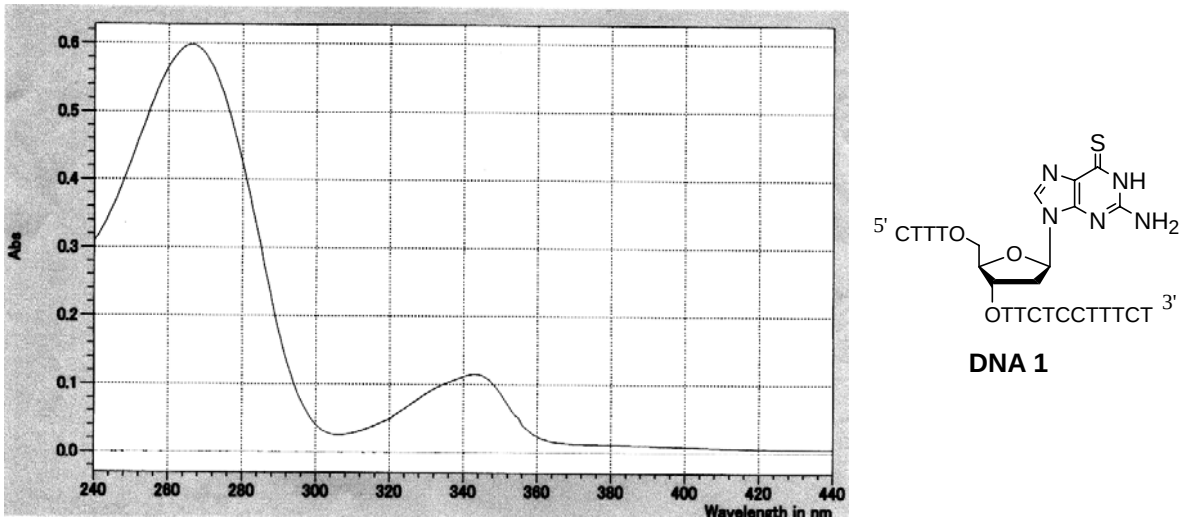

Figure S2. UV Spectra of DNA**1** (4.4 μM in H_2O at 25 °C).

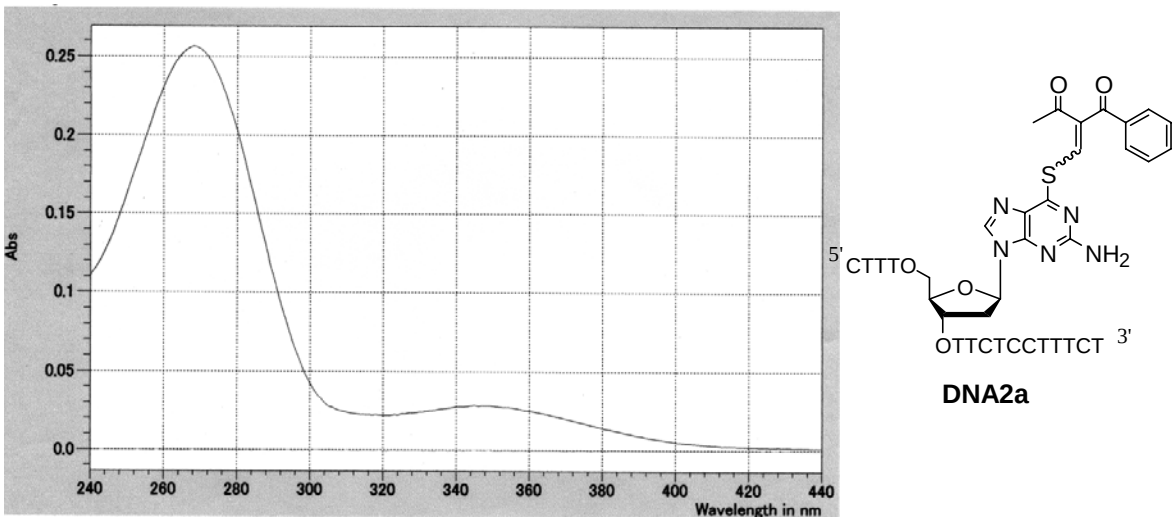

Figure S3. UV Spectra of DNA**2a** (1.8 μM in H_2O at 25 °C).

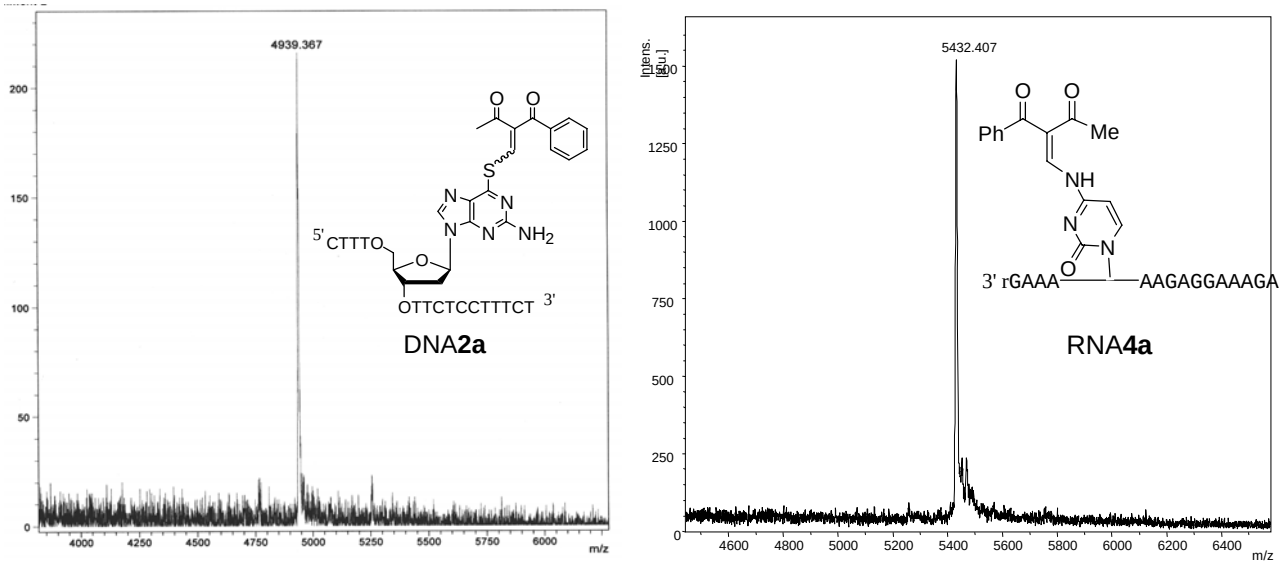

Figure S4. Examples of MALDI-TOF/MS Spectra of DNA**2a** and the modified RNA**4a**.

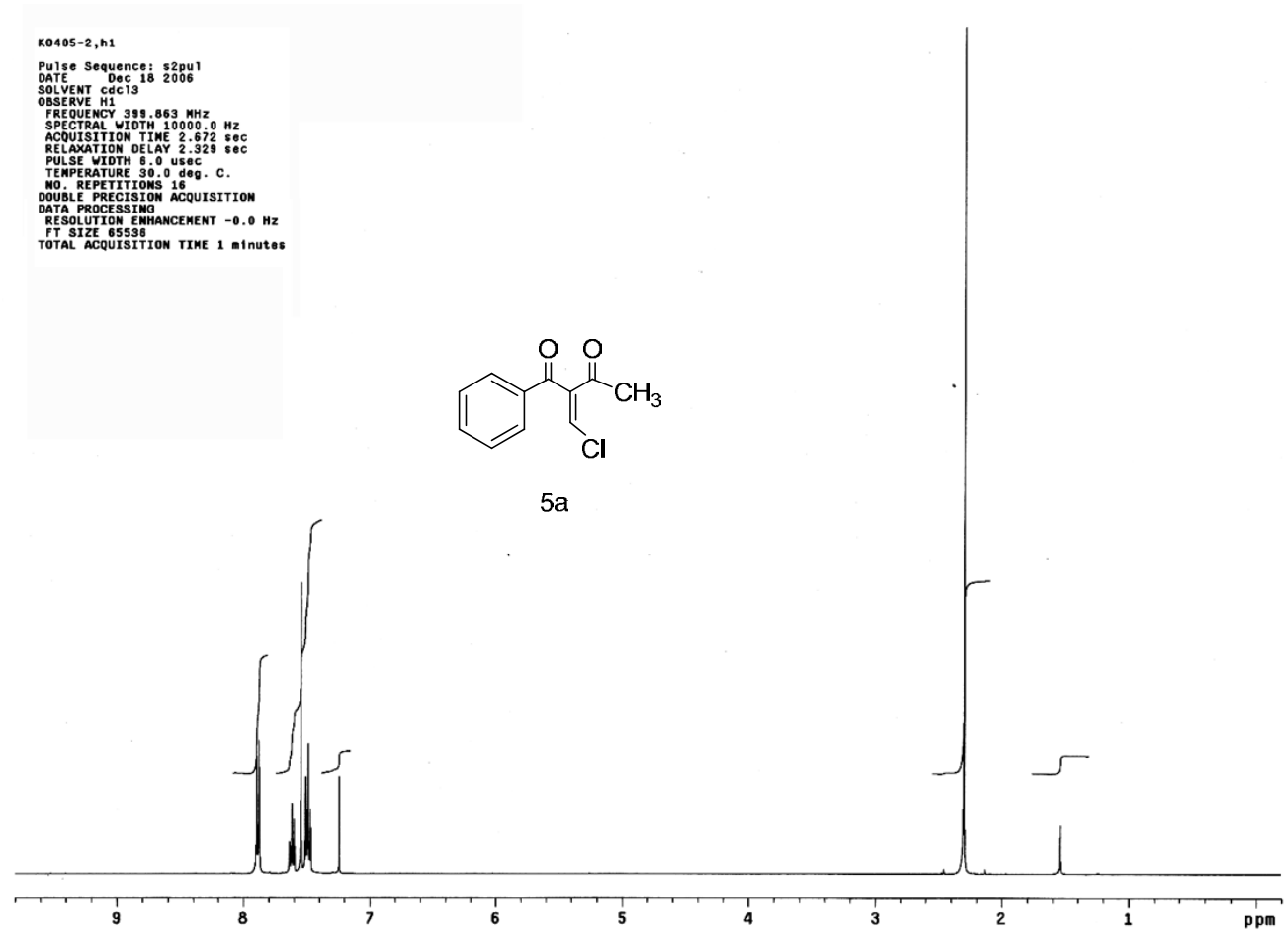

Figure S5. ^{1}H-NMR of 5a.

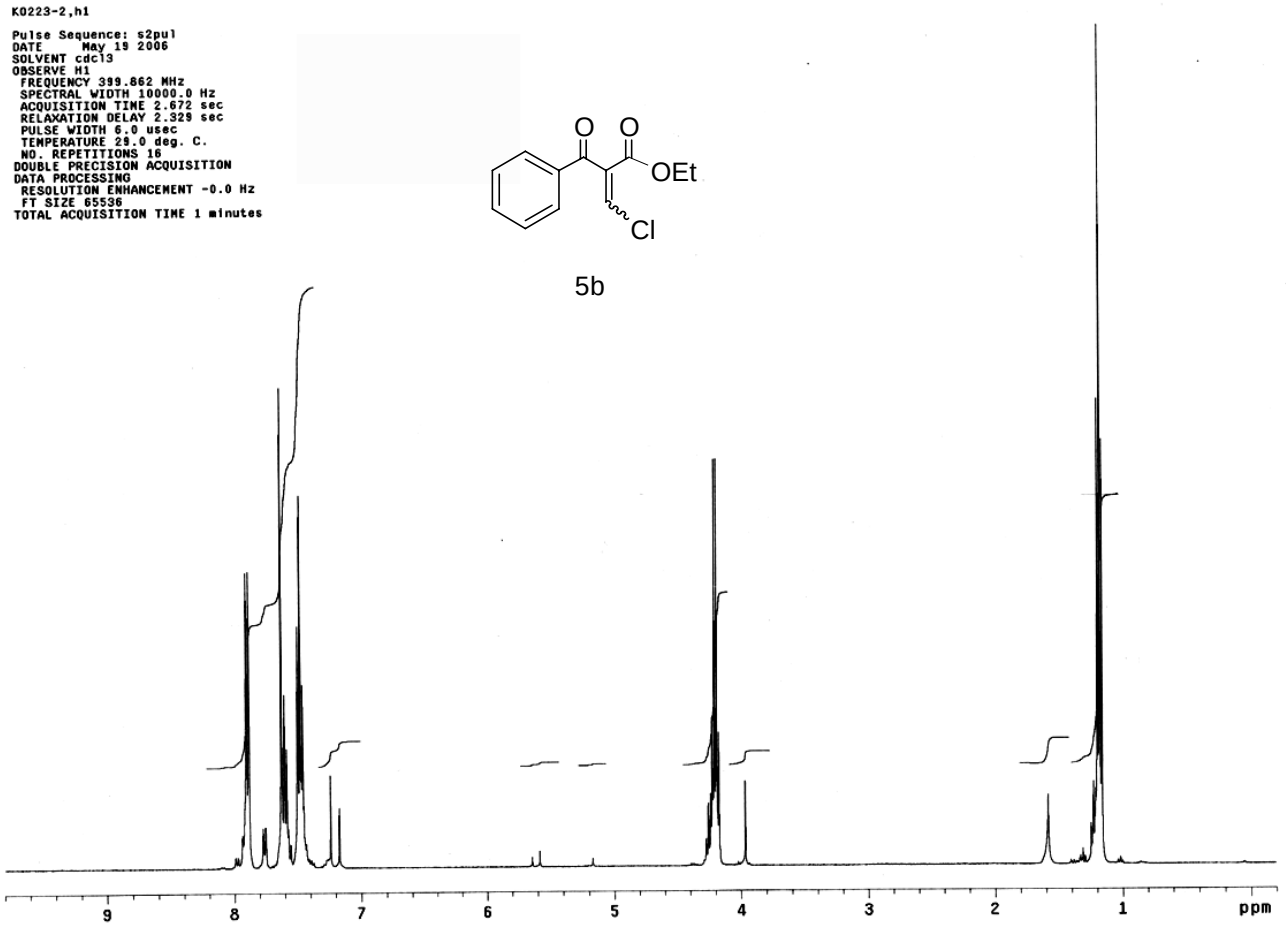

Figure S6. ^{1}H-NMR of 5b.

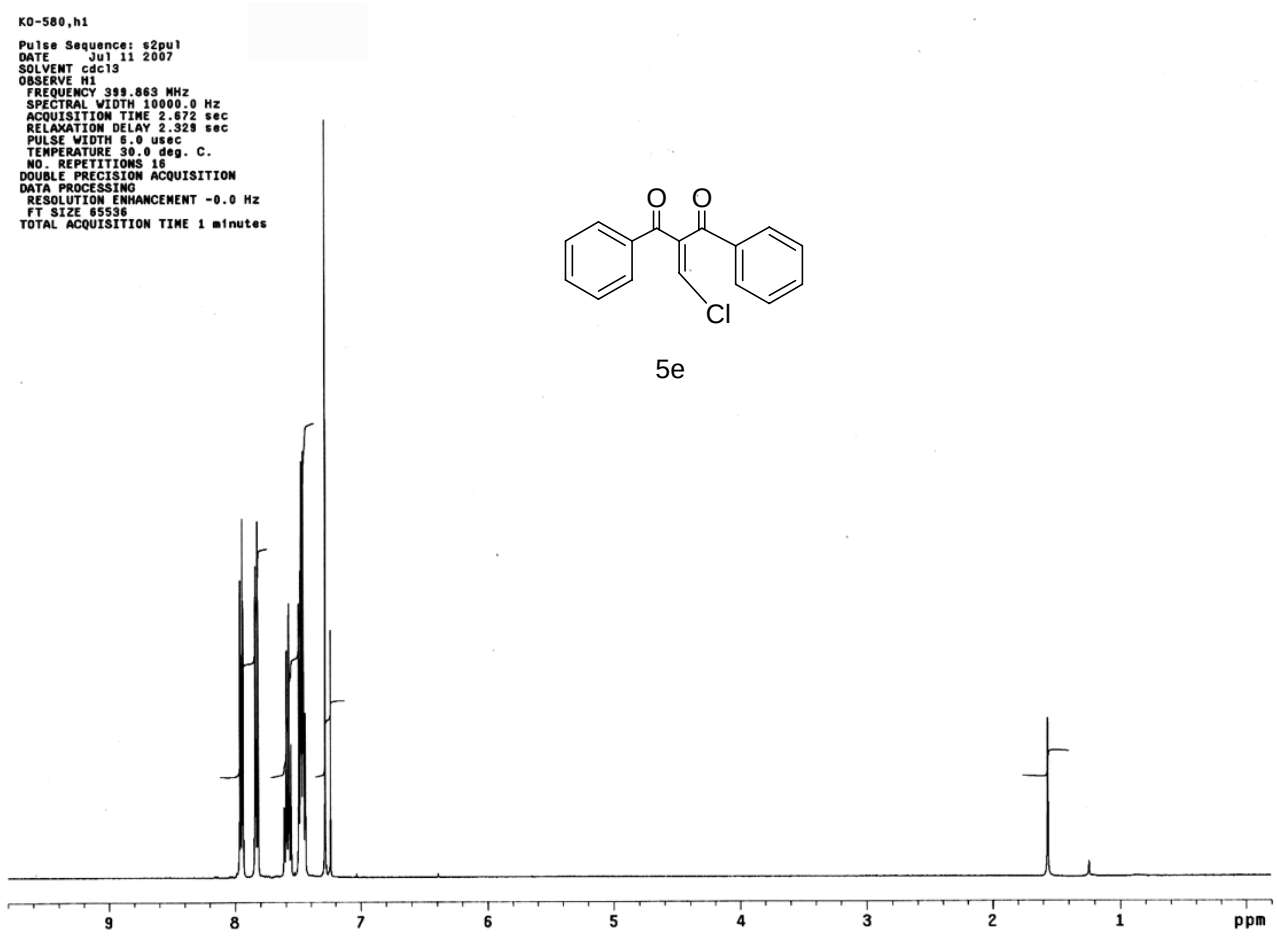

5e

Figure S7. ^{1}H-NMR of 5c.

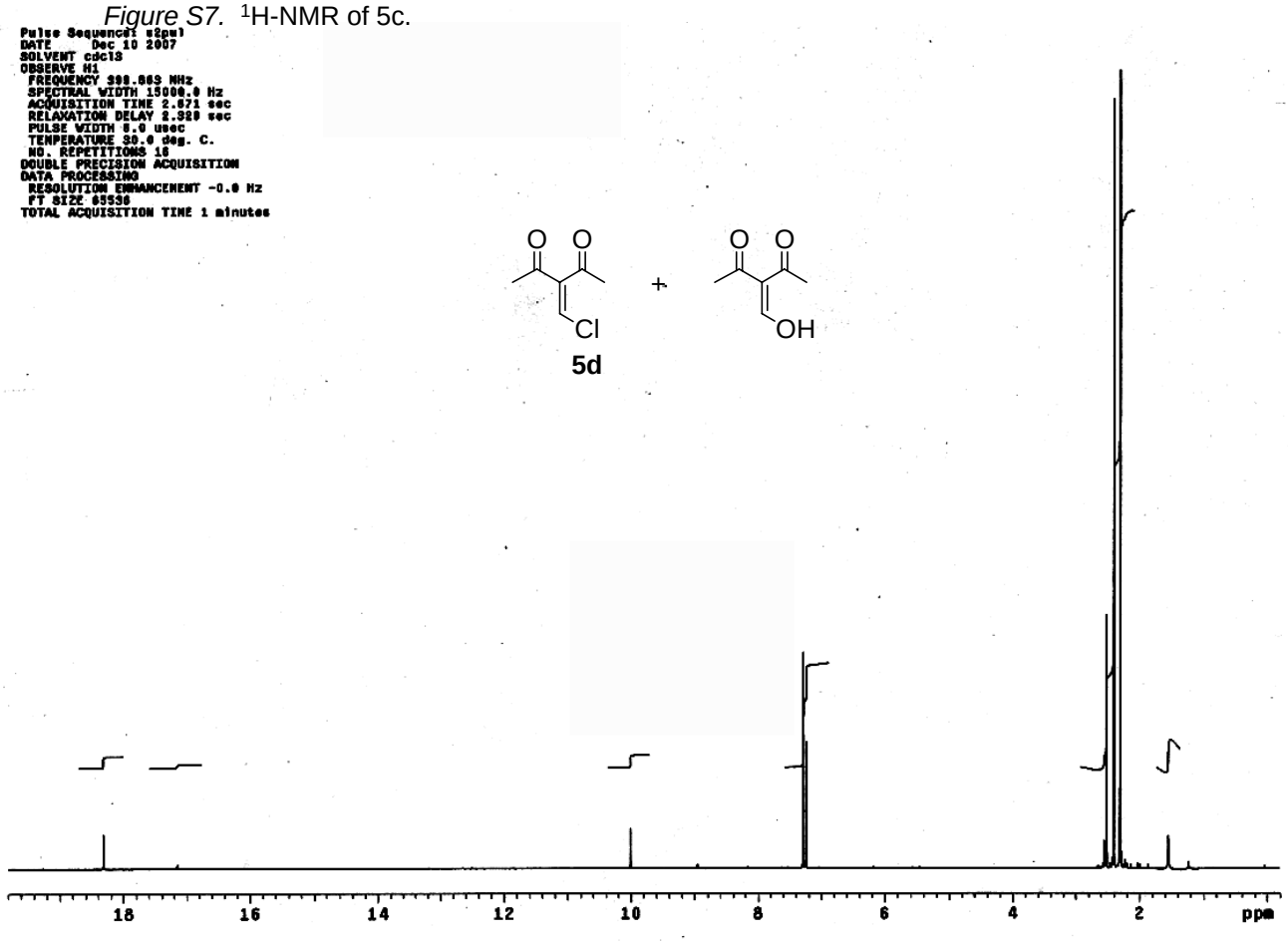

5d

Figure S8. ^{1}H-NMR of 5d.

Table S1. UV Melting temperatures of the duplexes formed with.

DNA	Complementary strand	X= , N=	Tm (^{o}C)
DNA**1**	RNA**7**	X = dC, N = rA	53
DNA**11**	RNA**7**	X = rC, N = rA	49
DNA**11**	RNA**7**	X = rG, N = rA	49
DNA**11**	RNA**7**	X = rA, N = rA	49
DNA**11**	RNA**7**	X = rT, N = rA	48
DNA**11**	RNA**7**	N-X-N = rA-rU-rC	46
DNA**11**	RNA**7**	N-X-N = rC-rU-rA	43
DNA**12**	RNA**8**	X = rC	45
-	RNA**8**	X = rC	40
DNA**12**	**-**	-	33

Table S2. MADI-TOF.MS Data of all DNA and RNA compounds used in this study.

DNA or RNA	5' Label	X, N or X, Y	Calcd ([M-H]$^{-}$)	Found
DNA**1**			4767.79	4766.53
DNA**2 a**		Ph, Me	4939.72	4941.53
DNA**2 b**		Ph, OEt	4969.87	4971.49
DNA**2 c**		Ph, Ph	5000.84	5000.61
DNA**2 d**		Me, Me	4876.81	4878.20
RNA**3**		X = rC	5795.90	5795.12
RNA**4 a**		Ph, Me	5429.82	5432.41
RNA**4b**		Ph, OEt	5459.83	5457.17
RNA**4 c**		Ph, Ph	5491.83	5492.58
RNA**4d**		Me, Me	5367.80	5368.63
RNA**5**	FAM	N-X-N = rA-rC-A, = RNA**3**	5795.90	5795.12
RNA**5**	FAM	N-X-N = rA-rG-rA	5835.91	5835.94
RNA**5**	FAM	N-X-N = rA-rA-rA	5819.92	5819.50
RNA**5**	FAM	N-X-N = rA-rU-rA	5796.88	5796.46
RNA**5**	FAM	N-X-N =r A-rU-rC	5772.86	5772.35
RNA**5**	FAM	N-X-N = rC-rU-rA	5772.86	5772.55
RNA**7**	FAM	X = rC	9105.12	9105.90
RNA**7**	FAM	X = rG	9145.12	9145.44
RNA**7**	FAM	X = rA	9129.13	9129.00
RNA**7**	FAM	X = rU	9106.10	9106.31
DNA**9**		Ph, Me	6891.13	6890.54
DNA**10**			6719.08	6719.10
DNA**11**			4897.83	4898.80
DNA**12**			6849.12	6849.00

Detection of Protein Phosphorylation on SDS-PAGE Using Probes with a Phosphate-Sensitive Emission Response

Alexander Riechers, Florian Schmidt, Stefan Stadlbauer, and Burkhard König*

Institute for Organic Chemistry, University of Regensburg, Regensburg, Germany. Received January 27, 2009

Fluorescent probes for the detection of protein phosphorylation on SDS-PAGE are presented. The probes were designed using a dinuclear metal-chelate phosphate recognition unit and an environmentally sensitive fluorophore. The specificity of the probes is determined by their binding site selectivity toward phosphate ions and the emission response induced by the change in the electrostatic environment of the fluorophore upon binding to a phosphorylated amino acid residue. The staining is fully reversible due to the noncovalent binding of the probe. Gel bands with less than 100 ng of phosphorylated α-casein are detectable with the new probes on a normal UV-table without specialized equipment like a laser-based gel scanner or a cooled camera detector.

INTRODUCTION

Staining of SDS gels is a standard technique in molecular biology. While silver and Coomassie staining are widely used for total protein staining, a number of stains selective for certain functional groups have emerged. Glycosylation (*1, 2*), His-tags (*3*), and phosphorylation (*4, 5*) are typical protein modifications targeted by selective gel stains reported so far. With respect to its biological importance, phosphorylation (*6, 7*) is widely regarded as the most significant post-translational modification. Phosphorylation plays an important part in signaling pathways, and it is estimated that 30% of the entire proteome becomes phosphorylated at some point (*8*). While there are phospho-specific antibodies available (*9, 10*), they require blotting of the proteins onto a polyvinyldifluoride (PVDF) or nitrocellulose membrane and may also be specific for additional epitopes in proximity to the phosphorylation site. Alternatively, ^{32}P-labeling of the proteins provides a very sensitive tool for detection of phosphorylation (*11, 12*); however, the handling and disposal of radioactive material are costly, potentially hazardous, and increasingly regulated. When staining for substoichiometric features such as phosphorylation, fluorescence detection is the method of choice due to its inherent sensitivity. The reported (*13*) and commercially available (*4, 5*) fluorescent phospho-specific stains gain their sensitivity from their binding site specificity. While other fluorescent probes for phosphorylated amino acids have been reported (*14*), their selectivity has only been demonstrated for peptides without other metal-chelating amino acids like histidine, tryptophan, or cysteine.

Herein, we report two novel phospho-specific gel stains based on the interaction of a metal-chelate binding site and a covalently attached fluorophore. We have previously described the binding of a bis-zinc(II)-cyclen triazine to phosphorylated serine and histidine (*15*). Since these artificial receptors showed high affinity under physiological conditions, we set about using this interaction in molecular biology. On the basis of these findings and a previously reported monozinc(II)-cyclen coumarin receptor (*16*), which changes its emission wavelength when bound to inorganic phosphate in solution, we designed fluorescently labeled bis-zinc(II)-cyclen triazine complexes for staining of phosphorylated proteins in SDS gels. Bis-zinc(II)-cyclen triazine was found to have a higher affinity toward phosphate than mononuclear zinc(II)-cyclen complexes and was therefore used as the recognition moiety. As fluorophores, we selected the widely employed carboxyfluorescein and 7-(diethylamino) coumarin, since a similar fluorophore has shown large solvatochromic emission shifts (*17*), which we associate to its sensitivity to the environment (*18*). The resulting probes **1** and **2** are depicted in Figure 1, while the emission response concept is shown in Scheme 1.

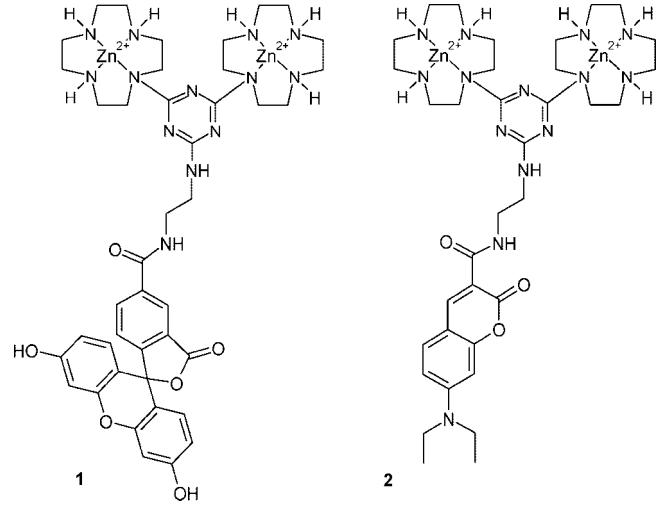

Figure 1. Probes **1** and **2** used for staining of phosphoproteins. Counterions are not shown.

MATERIALS AND METHODS

Synthesis. Detailed information on the synthetic procedures and compound characterization data are provided in the Supporting Information.

Dephosphorylation by *λ*-PPase Treatment. Bovine α-casein (40 μg, purchased from Sigma-Aldrich) was treated with 400 U of *λ*-PPase (purchased from New England Biolabs) in Tris-HCl (50 mM), NaCl (100 mM), dithiothreitol (2 mM), $MnCl_2$ (2 mM), EGTA (0.1 mM), 0.01% Brij 35, pH 7.5, at 30 °C for 6 h.

SDS-PAGE. Proteins were resolved on minigels under denaturating and reducing Laemmli conditions on a PeqLab 45−1010-i apparatus. The gels consisted of a 4% acrylamide (w/v), 120 mM Tris-HCl (pH 6.8), 0.1% SDS (w/v) stacking

* burkhard.koenig@chemie.uni-regensburg.de.

10.1021/bc9000307 CCC: $40.75 © 2009 American Chemical Society
Published on Web 03/27/2009

Scheme 1. Probes 1 and 2 Discriminate Phosphorylated from Nonphosphorylated Proteins on SDS Gels via Emission Intensity and Wavelength Shift, Respectively

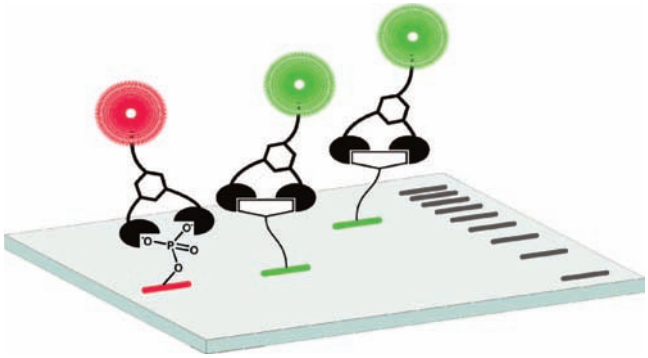

gel, and a 15% acrylamide (w/v), 375 mM Tris-HCl (pH 8.8), 0.1% SDS (w/v) running gel. A 25 mM Tris, 192 mM glycine, 0.1% SDS (w/v) running buffer (pH 8.3) was used. Protein samples were heated to 70 °C for 10 min with reducing and denaturating RotiLoad 1 sample buffer (purchased from Carl Roth, Germany) before being loaded onto the gel. The gels were run at 150 V until the proteins entered the running gel, and then the voltage was increased to 250 V. Water cooling was used during the entire run. Fixation was accomplished by treating the gels with 50% MeOH/10% AcOH twice, for 30 min and overnight, respectively.

Staining and Imaging. The gels were soaked in deionized water (4 × 10 min) before being treated with a solution of probe **1** or **2** in deionized water for 1 h with a probe concentration of 10^{-7} M. We found that destaining was not strictly necessary at this concentration; however, when the probes were used at higher concentrations, the gels could be destained by washing with deionized water until a nonfluorescent background was obtained. Due to their noncovalent binding mode (*19*), the probes could be completely removed by repeated washing of the gel with water. Conveniently, removal of the probes was not necessary for Coomassie restaining.

The gels were wrapped in cling film to prevent them from drying out and placed on a PeqLab Superbright UV table (λ_{ex} = 316 nm). Images were taken using either a Pentax K10D or a Traveler DC 8500. Emission spectra of individual protein bands were obtained using the same UV table and a Hamamatsu PMA-11 photonic multichannel analyzer. Data were acquired using the supplied PMA Optic software. A 455 nm long-pass filter was placed on top of the gel to prevent the UV light saturating the detector. Long-pass filters with a shorter cutoff proved unsuitable as they showed a strong fluorescence when subjected to the UV light.

After fluorescence imaging, a restain for total protein was accomplished with 0.1% Coomassie R-250, 50% MeOH, 10% AcOH for 1 h. Destaining was accomplished in 7% AcOH, 10% MeOH overnight. The gels were again wrapped in cling film and scanned using an office scanner.

RESULTS AND DISCUSSION

To evaluate the phospho-staining selectivity and sensitivity of our probes, a dilution series of phosphorylated bovine α-casein was electrophoretically resolved from the non-phosphorylated protein BSA. In addition, a sample of α-casein was de-phosphorylated using λ-PPase and used as a control to ensure the emission response would not depend on the amino acid composition of the protein. After fixation, the gels were stained and destained when necessary until little or no background was visible.

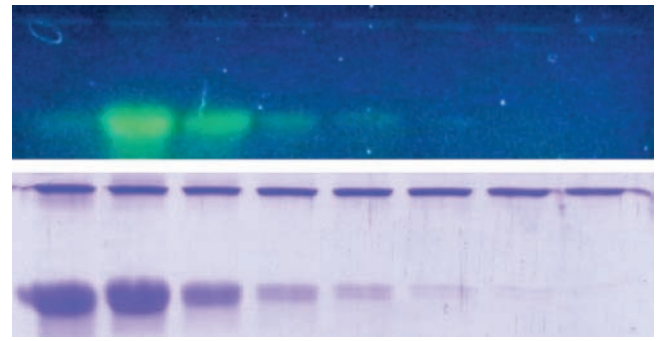

Figure 2. Gel stained with probe **1**. Each lane contains 1 μg BSA (66 kDa). From left to right: lane 1, 1 μg α-casein (23 kDa) dephosphorylated; lanes 2−8, 1 μg, 500 ng, 250 ng, 125 ng, 62 ng, 31 ng, 15 ng α-casein. Top image was taken on a UV table (λ_{ex} = 316 nm), lower image shows CBB R-250 total protein restain.

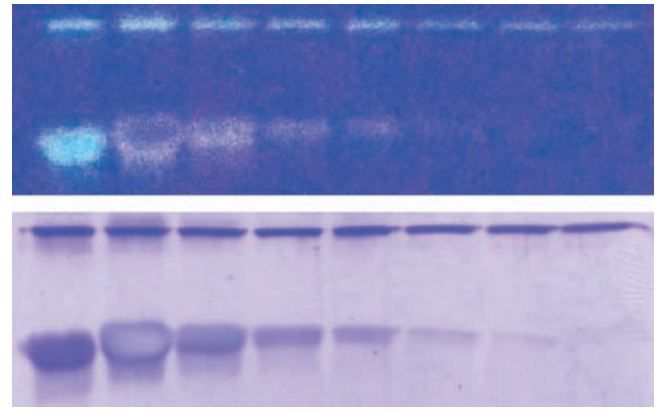

Figure 3. Gel stained with probe **2**. Each lane contains 1 μg BSA (66 kDa). From left to right: lane 1, 1 μg α-casein (23 kDa) dephosphorylated; lanes 2−8, 1 μg, 500 ng, 250 ng, 125 ng, 62 ng, 31 ng, 15 ng α-casein. Top image was taken on a UV table (λ_{ex} = 316 nm); lower image shows CBB R-250 total protein restain.

Probe **1** showed a distinct emission in the bands of phosphorylated α-casein, whereas the bands of de-phosphorylated α-casein and BSA are barely visible (Figure 2). Bis-zinc(II)-cyclen triazine complexes coordinate phosphate groups strongly, but we also expect an affinity of the probe to non-phosphorylated proteins due to the coordination of histidine by the bis-zinc(II)-cyclen triazine (*15*, *20*) or further unspecific interactions. However, these interactions do not interfere with the specific detection of phosphorylation: The emission of the probe is quenched, when bound to non-phosphorylated amino acid residues and the emission remains, when bound to phosphorylated amino acid residues. Similar emission quenching effects have been previously reported for the interaction of riboflavin with a zinc(II)-imidazole complex (*21*) and for zinc(II)-porphyrin with histidine (*22*). To prove that the observed effects originate from the coordination of the bis-zinc(II)-cyclen triazine complex and not from the binding of the fluorophore itself, a control gel was prepared and treated with carboxyfluorescein. No staining could be observed in this experiment.

When bound to phosphorylated α-casein, probe **2** showed a strong red-shift in the emission compared to unphosphorylated α-casein and BSA (Figure 3). We attribute this spectral change to the different electronic environments when the probe molecule is either unspecifically interacting with non-phosphorylated amino acid residues, such as histidine (unphosphorylated α-casein and BSA) or coordinating a negatively charged phosphorylated amino acid residue (phosphorylated α-casein). These findings are in agreement with the reported red-shift in emission of a monozinc(II)-cyclen coumarin complex upon

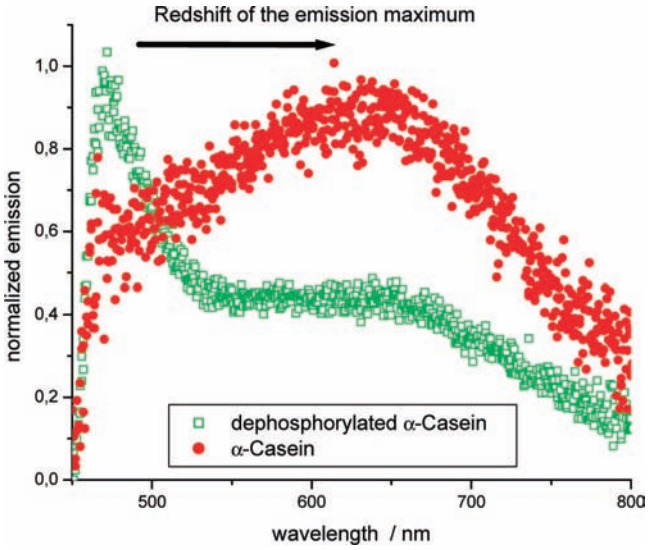

Figure 4. Normalized emission spectra of gel bands stained with probe **2** acquired through a 455 nm long-pass filter (λ_{ex} = 316 nm). BSA band showed the same spectrum as dephosphorylated α-casein (data not shown).

coordination to inorganic phosphate ions (*16*) To quantify this change in emission, fluorescence spectra of the gel bands were obtained using a photonic multichannel analyzer equipped with a fiber optic (Figure 4). As with probe **1**, a control gel was treated with the fluorophore itself, and again no staining was observed.

With both probes, the dilution series proved that 62 ng of phosphorylated α-casein is still detectable on a normal UV-table by the unaided eye (which was protected from UV light) while imaging was performed with common digital cameras. Hence, even without the use of specialized equipment like laser-illuminated gel scanners or cooled camera detectors as described in the protocols of commercially available phosphoprotein gel stains our probes reach similar limits of detection.

CONCLUSION

We have demonstrated the application of two new noncovalent, reversible, and fluorescent SDS-PAGE probes capable of indicating protein phosphorylation. The probes show different fluorescence responses discriminating phosphorylated from non-phosphorylated proteins. While probe **1** signals binding to a phosphorylated protein by a significant increase of emission intensity, probe **2** is the first phosphoprotein gel stain to change its emission spectrum upon binding to a phosphorylated protein. The probes achieve their selectivity through a combination of the specificity of the dinuclear metal chelate binding site toward phosphate oxoanions and a modulation of the chromophore emission due to the proximity of the phosphorylated amino acid. The environmentally sensitive fluorophore allows a clear distinction between phosphorylated and non-phosphorylated proteins on SDS-PAGE and allows the detection of 62 ng of phosphorylated α-casein on a normal UV-table. Evaluations of other metal-chelate fluorophore conjugates and applications of the existing probes to monitor signaling pathways are currently underway.

ACKNOWLEDGMENT

We thank Lorenz Fischer for help with the Hamamatsu PMA-11 analyzer and Andreas Grauer for help with the imaging. We are grateful to Jennifer Schmidt, Silke Kuphal, and Anja Katrin Bosserhoff for valuable discussions.

Supporting Information Available: Synthesis of probes **1** and **2** as well as compound characterization data. This material is available free of charge via the Internet at http://pubs.acs.org.

LITERATURE CITED

(1) Pío, R., Martínez, A., Unsworth, E. J., Kowalak, J. A., Bengoechea, J. A., Zipfel, P. F., Elsasser, T. H., and Cuttitta, F. (2001) Complement factor H is a serum-binding protein for adrenomedullin, and the resulting complex modulates the bioactivities of both partners. *J. Biol. Chem. 276*, 12292–12300.

(2) Misenheimer, T. M., Hahr, A. J., Harms, A. C., Annis, D. S., and Mosher, D. F. (2001) Disulfide connectivity of recombinant C-terminal region of human thrombospondin 2. *J. Biol. Chem. 276*, 45882–45887.

(3) Williams, N. K., Prosselkov, P., Liepinsh, E., Line, I., Sharipo, A., Littler, D. R., Curmi, P. M. G., Otting, G., and Dixon, N. E. (2002) In vivo protein cyclization promoted by a circularly permuted *Synechocystis* sp. PCC6803 DnaB mini-intein. *J. Biol. Chem. 277*, 7790–7798.

(4) Schulenberg, B., Goodman, T. N., Aggeler, R., Capaldi, R. A., and Patton, W. F. (2004) Characterization of dynamic and steady-state protein phosphorylation using a fluorescent phosphoprotein gel stain and mass spectrometry. *Electrophoresis 24*, 2526–2532.

(5) Kinoshita, E., Kinoshita-Kikuta, E., Takiyama, K., and Koike, T. (2006) Phosphate-binding tag, a new tool to visualize phosphorylated proteins. *Mol. Cell. Proteomics 5*, 749–757.

(6) Hunter, T. (1995) Protein kinases and phosphatases: The yin and yang of protein phosphorylation and signalling. *Cell 80*, 225–236.

(7) Hunter, T. (2000) Signaling—2000 and beyond. *Cell 100*, 113–127.

(8) Manning, G., Whyte, D. B., Martinez, R., Hunter, T., and Sudarsanam, S. (2002) The protein kinase complement of the human genome. *Science 298* 1912–1934.

(9) Salomon, A. R., Ficarro, S. B., Brill, L. M., Brinker, A., Phung, Q. T., Ericson, C., Sauer, K., Brock, A., Horn, D. M., Schultz, P. G., and Peters, E. C. (2003) Profiling of tyrosine phosphorylation pathways in human cells using mass spectrometry. *Proc. Natl. Acad. Sci. U.S.A. 100*, 443–448.

(10) Conrads, T. P., and Veenstra, T. D. (2005) An enriched look at tyrosine phosphorylation. *Nat. Biotechnol. 23*, 36–37.

(11) Larsen, M. R., Sorensen, G. L., Fey, S. J., Larsen, P. M., and Roepstorff, P. (2001) Phospho-proteomics: Evaluation of the use of enzymatic de-phosphorylation and differential mass spectrometric peptide mass mapping for site specific phosphorylation assignment in proteins separated by gel electrophoresis. *Proteomics 1*, 223–238.

(12) Immler, D., Gremm, D., Kirsch, D., Spengler, B., Presek, P., and Meyer, H. E. (1998) Identification of phosphorylated proteins from thrombin-activated human platelets isolated by two-dimensional gel electrophoresis by electrospray ionization-tandem mass spectrometry (ESI-MS/MS) and liquid chromatography-electrospray ionization-mass spectrometry (LC-ESI-MS). *Electrophoresis 19*, 1015–1023.

(13) Ojida, A., Kohira, T., and Hamachi, I. (2004) Phosphoprotein-selective recognition and staining in SDS-PAGE by bis-Zn(II)-dipycolylamine-appended anthracene. *Chem. Lett. 33*, 1024–1025.

(14) Ojida, A., Mito-oka, Y., Inoue, M., and Hamachi, I. (2002) First artificial receptors and chemosensors toward phosphorylated peptide in aqueous solution. *J. Am. Chem. Soc. 124*, 6256–6258.

(15) Grauer, A., Riechers, A., Ritter, S., and König, B. (2008) Synthetic receptors for the differentiation of phosphorylated peptides with nanomolar affinities. *Chem. Eur. J. 14*, 8922–8927.

(16) Mizukami, S., Nagano, T., Urano, N., Odani, Y., and Kikuchi, K. (2002) A fluorescent anion sensor that works in neutral aqueous solution for bioanalytical application. *J. Am. Chem. Soc. 124*, 3920–3925.

(17) Wolfbeis, O. S., and Uray, G. (1978) Fluoreszenzspektren, Photodissoziation und Phototautomerie einiger 4-Hydroxycumarine. *Monatsh. Chem. 109*, 123–136.
(18) To assess the influence of the fluorophore further, we also prepared the same type of probe with pyrene and dansyl fluorophores. Neither of these probes exhibited any distinction between phosphorylated and nonphosphorylated proteins (data not shown).
(19) Kruppa, M., and König, B. (2006) Reversible coordinative bonds in molecular recognition. *Chem. Rev. 106*, 3520–3560.
(20) Kruppa, M., Frank, D., Leffler-Schuster, H., and König, B. (2006) Screening of metal complex−amino acid side chain interactions by potentiometric titration. *Inorg. Chim. Acta 359*, 1159–1168.
(21) Lugina, L. N., Davidenko, N. K., and Gavrish, S. P. (1985) Quenching of the fluorescence of riboflavin by the histidinates and alaninates of nickel, copper, and zinc. *Theor. Exp. Chem. 21*, 466–470.
(22) Hou, J. L., Yi, H. P., Shao, X.-B., Li, C., Wu, Z.-Q., Jiang, X.-K., Wu, L.-Z., Tung, C.-H., and Li, Z.-T. (2004) In situ click chemistry: enzyme-generated inhibitors of carbonic anhydrase II. *Angew. Chem. 117*, 118–122.

BC9000307

DETECTION OF PROTEIN PHOSPHORYLATION ON SDS-PAGE USING PROBES WITH A PHOSPHATE-SENSITIVE EMISSION RESPONSE

Alexander Riechers, Florian Schmidt, Stefan Stadlbauer and Burkhard König

Institute for Organic Chemistry, University of Regensburg,

D-93040 Regensburg, Germany

SUPPORTING INFORMATION

Synthesis of probes **1** and **2** S-2

References S-12

1. SYNTHESIS OF PROBES 1 AND 2

GENERAL

All reactions were performed under an inert atmosphere of N_2 using standard Schlenk techniques if not otherwise stated. A Varian Cary BIO 50 UV/VIS/NIR Spectrometer was used. A 1 cm quartz cell was purchased from Hellma and Uvasol solvents from Merck or Baker. Absorption and emission maxima are given in nm, molar absorptivities (ε) are given in M^{-1} cm^{-1}. IR spectra were recorded on a Bio-Rad FT-IR FTS 155 and a Bio-Rad FTS 2000 MX FT-IR using a Specac Golden Gate Mk II ATR accessory where stated. NMR spectrometers used were: Bruker Avance 600 (^{1}H: 600.1 MHz, ^{13}C: 150.1 MHz, T = 300 K), Bruker Avance 400 (^{1}H: 400.1 MHz, ^{13}C: 100.6 MHz, T = 300 K) and Bruker Avance 300 (^{1}H: 300.1 MHz, ^{13}C: 75.5 MHz, T = 300 K). The chemical shifts are reported in δ [ppm] relative to external standards (solvent residual peak). The spectra were analyzed by first order, the coupling constants are given in Hertz [Hz]. Characterization of the signals: s = singlet, d = doublet, t = triplet, q = quartet, m = multiplet, bs = broad singlet, psq = pseudo quintet, dd = double doublet, dt = double triplet, ddd = double double doublet. Integration is determined as the relative number of atoms. Assignment of signals in ^{13}C-spectra was determined with DEPT-technique (pulse angle: 135 °) and given as (+) for CH_3 or CH, (-) for CH_2 and (C_{quat}) for quaternary C. Error of reported values: chemical shift: 0.01 ppm for ^{1}H-NMR, 0.1 ppm for ^{13}C-NMR and 0.1 Hz for coupling constants. The solvent used is reported for each spectrum. Mass spectra were recorded on Varian CH-5 (EI), Finnigan MAT 95 (CI; FAB and FD) and Finnigan MAT TSQ 7000 (ESI). Xenon served as the ionization gas for FAB. Melting Points were determined on a Büchi SMP-20 melting point apparatus and are uncorrected. TLC analyses were performed on silica gel 60 F-254 with a 0.2 mm layer thickness. Detection was via UV light at 254 nm / 366 nm or by staining with ninhydrin in EtOH. For preparative column-chromatography, Merck Geduran SI 60 silica gel was used. Commercially available solvents of standard quality were used. Unless otherwise stated, purification and drying was done according to accepted general procedures (*1, 2*). Compounds **3** (*3*) and **5** (*4*) were synthesized according to literature known procedures.

SYNTHESIS OF PROBES 1 AND 2

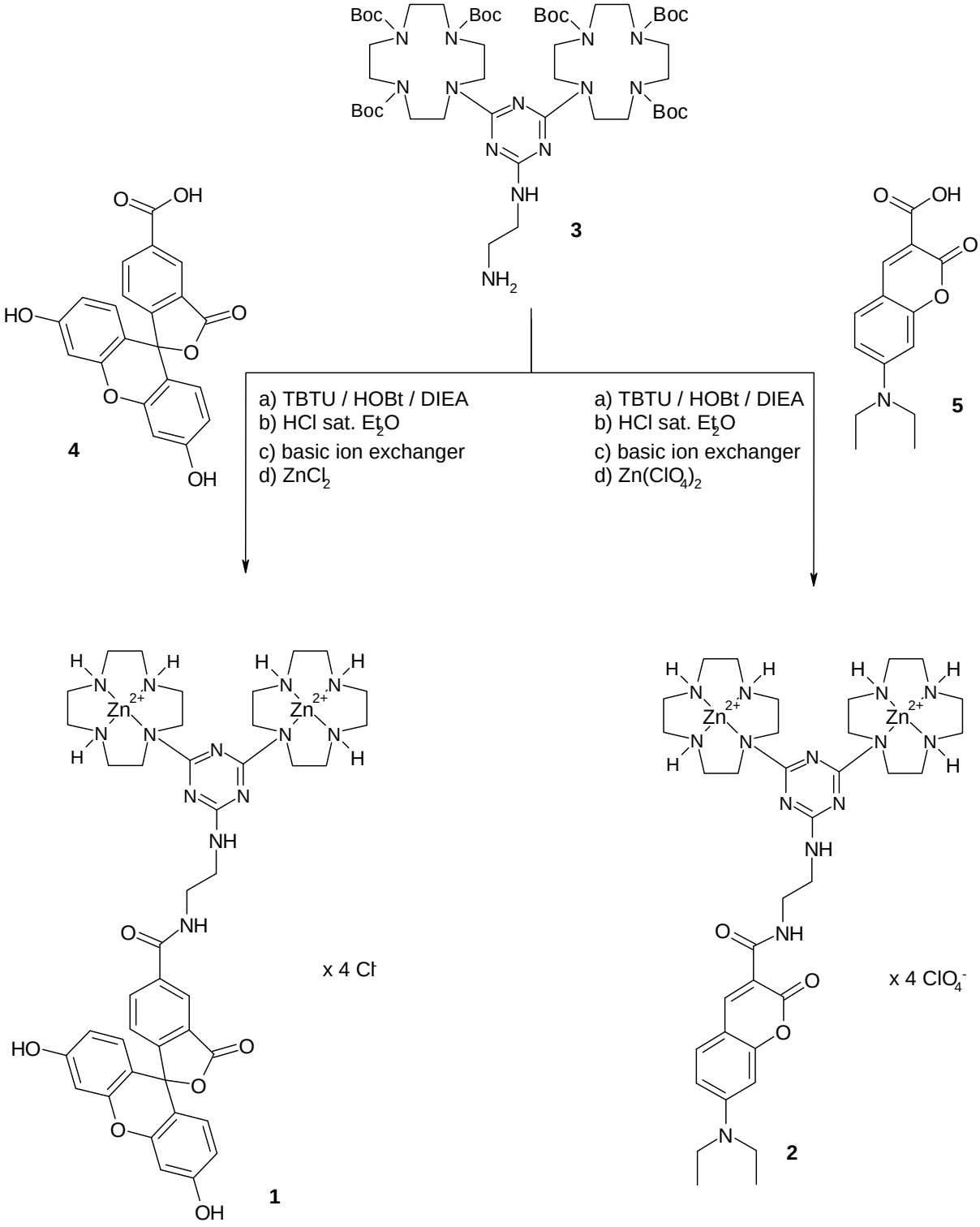

FIGURE S-1 Preparation of probes **1** and **2**

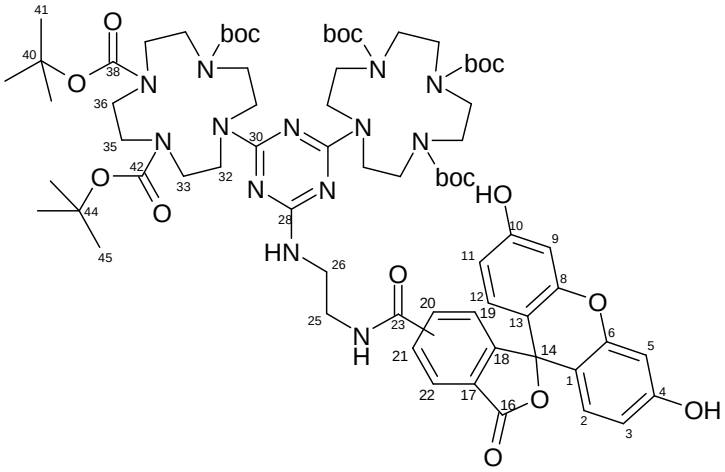

Regioisomeric 1,4,7-tri-tert-butyl 10,10'-{6-[2-(3',6'-dihydroxy-3-oxo-3H-spiro[isobenzofuran-1,9'-xanthene]-5/6-ylcarboxamido)ethylamino]-1,3,5-triazine-2,4-diyl}bis(1,4,7,10-tetraazacyclododecane-1,4,7-tricarboxylate) (**6**):

In a nitrogen flushed round bottom flask, regioisomeric 5-,6-carboxyfluorescein (0.15 g, 0.40 mmol) was dissolved in 10 mL of a mixture of dichloromethane and DMF (2:1), then DIPEA (0.17 g, 180 µL, 1.32 mmol) and HOBt monohydrate (0.07 g, 0.48 mmol) were added. While stirring, the mixture was cooled to 0°C in an ice water bath to add TBTU (0.15 g, 0.48 mmol). After 30 min, 1,4,7-tri-tert-butyl 10,10'-(6-(2-aminoethylamino)-1,3,5-triazine-2,4-diyl) bis (1,4,7,10-tetraazacyclo-dodecane-1,4,7-tricarboxylate) (**3**) (0.47 g, 0.44 mmol) was added in portions to the flask and the reaction mixture was heated to 40°C for 2h. Subsequently, the solvents were evaporated and the crude product was purified by column chromatography ($CHCl_3$: MeOH = 15 : 1) on flash-silica-gel yielding compound **6** as an orange amorphous solid (0.34 g, 0.23 mmol, 59%).

MP: 207°C

^{1}H-NMR (600 MHz, MeOD, COSY, ROESY, HSQC, HMBC): δ [ppm] = 8.36 (s, 0.7H, 22a), 8.13 (d, $^3J_{H,H}$ = 7.91 Hz, 0.7H, 20a), 8.07 (d, $^3J_{H,H}$ = 8.08 Hz, 0.3H, 21b), 8.03 (d, $^3J_{H,H}$ = 8.04 Hz, 0.3H, 22b), 7.61 (s, 0.3H, 19b), 7.24 (d, $^3J_{H,H}$ = 8.02 Hz, 0.7H, 19a), 6.68 (dd, $^3J_{H,H}$ = 1.75 Hz, $^5J_{H,H}$ = 1.75 Hz, 2H, 2+12), 6.57 (dd, $^4J_{H,H}$ = 8.71 Hz, $^5J_{H,H}$ = 8.71 Hz, 2H, 5+9), 6.52 (dd, $^3J_{H,H}$ = 8.72 Hz, $^4J_{H,H}$ = 2.31 Hz, 2H, 3+19), 3.99-3.20 (m, 36H, 25a/b, 26a/b, 32+33+35+36), 1.45-1.37 (m, 54H, 41+45)

^{13}C-NMR (150 MHz, MeOD, COSY, ROESY, HSQC, HMBC): δ [ppm] = 170.4 ($C_{quat.}$, 0.3C, 16b), 170.3 ($C_{quat.}$, 0.7C, 16a), 168.5 ($C_{quat.}$, 0.7C, 23a), 168.3 ($C_{quat.}$, 0.3C, 23b), 167.8 ($C_{quat.}$, 2C, 30), 167.5 ($C_{quat.}$, 0.7C, 28a), 167.3 ($C_{quat.}$, 0.3C, 28b), 161.3 ($C_{quat.}$, 2C, 4+10), 158.0 ($C_{quat.}$, 6C, 38+42), 156.7 ($C_{quat.}$, 0.7C, 18a), 1#54.4 ($C_{quat.}$, 0.3C, 18b), 153.9 ($C_{quat.}$, 2C, 6+8), 142.4 ($C_{quat.}$, 0.3C, 20b), 138.0 ($C_{quat.}$, 0.7C, 21a), 135.5 (+, 0.7C, 20a), 130.2 (+, 0.3C, 21b), 130.1 (+, 2C, 5+9), 128.5 ($C_{quat.}$, 1C, 17a/b), 126.1 (+, 0.3C, 22b), 125.6 (+, 0.7C, 19a), 124.8 (+, 0.7C, 22a), 124.0 (+, 0.3C, 19b), 113.7 (+, 2C, 3+11), 110.8 ($C_{quat.}$, 2C, 1+13), 103.7 (+, 2C, 2+12), 81.5 ($C_{quat.}$, 2C, 38), 81.4 ($C_{quat.}$, 4C, 42), 79.4 ($C_{quat.}$, 1C, 14), 51.4 (-, 16C, 32+33+35+36), 41.7 (-, 0.7C, 25a), 41.5 (-, 0.3C, 25b), 40.9 (-, 0.7C, 26a), 40.8 (-, 0.3C, 26b), 29.9 (+, 6C, 41), 28.8 (+, 12C, 45)

IR (ATR) [cm^{-1}]: ν = 3318, 2971, 2935, 1766, 1689, 1665, 1539, 1466, 1410, 1365, 1247, 1157, 1024, 852, 811, 751, 665

ES-MS (H_2O/MeOH + 10 mmol/L NH_4Ac): *m/z* (%) = 720.0 (100) [M + $2H^+$], 1439.0 (5) [MH^+]

UV (MeCN): λ (ε) = 454 (2175), 481 (1876)

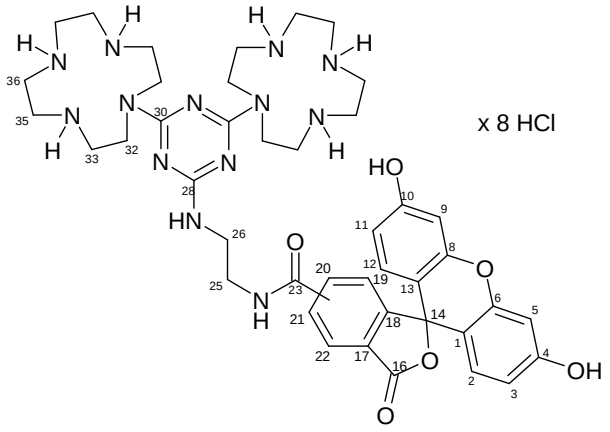

Regioisomeric N-{2-[4,6-di(1,4,7,10-tetraazacyclododecan-1-yl)-1,3,5-triazin-2-ylamino]ethyl}-3',6'-dihydroxy-3-oxo-3H-spiro[isobenzofuran-1,9'-xanthene]-5-carboxamide octachloride (**7**):

Compound **6** (80 mg, 0.05 mmol) was dissolved in as little dichloromethane as possible and cooled to 0°C before hydrochloric acid saturated diethyl ether (1.06 mL)

was added slowly to this solution. Stirring was continued for 16h while the reaction mixture was allowed to reach rt. Formation of a yellowish precipitate was observed. The desired product was obtained by evaporation of the solvent in vacuum as a red amorphous solid (50 mg, 0.05 mmol, quant.), which was deprotonated by ion exchange column on weakly basic anion exchanger resin.

^{1}H-NMR (600 MHz, D_2O, COSY, HSQC, HMBC): δ [ppm] = 8.43 (s, 2H, 24), 7.97 (s, 0.6H, 22a), 7.93-7.86 (d, $^{3}J_{H,H}$ = 7.37 Hz, 0.4H, 21b), 7.85-7.79 (d, $^{3}J_{H,H}$ = 7.40 Hz, 0.4H, 22b), 7.74 (bs, 0.6H, 20a), 7.44 (s, 0.4H, 19b), 7.02 (bs, 0.6H, 19a), 6.99-6.70 (m, 2H, 2+12), 6.61-6.41 (m, 2H, 3+11), 6.41-6.13 (m, 2H, 5+9), 3.87-3.39 (m, 12H, 25+26+36), 3.27-2.88 (m, 24H, 32+33+35)

^{13}C-NMR (150 MHz, D_2O, COSY, HSQC, HMBC): δ [ppm] = 179.9 ($C_{quat.}$, 2C, 30), 174.2 ($C_{quat.}$, 0.4C, 16b), 173.2 ($C_{quat.}$, 0.6C, 16a), 171.5 ($C_{quat.}$, 1C, 28), 170.1 ($C_{quat.}$, 0.4C, 23b), 169.5 ($C_{quat.}$, 0.6C, 23a), 167.2-166.3 ($C_{quat.}$, 2C, 4+10), 158.6-158.4 ($C_{quat.}$, 2C, 6+8), 157.9 ($C_{quat.}$, 0.6C, 18a), 157.2 ($C_{quat.}$, 0.4C, 18b), 143.7 ($C_{quat.}$, 0.4C, 20b), 140.7 ($C_{quat.}$, 0.6C, 21a), 135.6 ($C_{quat.}$, 0.4C, 17b), 135.2 ($C_{quat.}$, 0.6C, 17a), 131.9-131.5 (+, 2C, 2+12), 130.7 (+, 0.6C, 19a), 129.5 (+, 0.4C, 22b), 129.2 (+, 0.4C, 21b), 128.7 (+, 0.4C, 19b), 128.4 (+, 1.2C, 20a+22a), 123.3 (+, 2C, 3+11), 104.4 (+, 2C, 5+9), 46.5-45.2 (-, 12C, 33+35+36), 43.9 (-, 4C, 32), 40.8-40.6 (-, 1C, 25a/b), 39.9 (-, 1C, 26)

ES-MS (MeCN/TFA): *m/z* (%) = 280.1 (100) [M + 3H^{+}], 419.8 (63) [M + 2H^{+}], 838.5 (4) [MH^{+}], 874.4 (3) [MH^{+} + HCl]

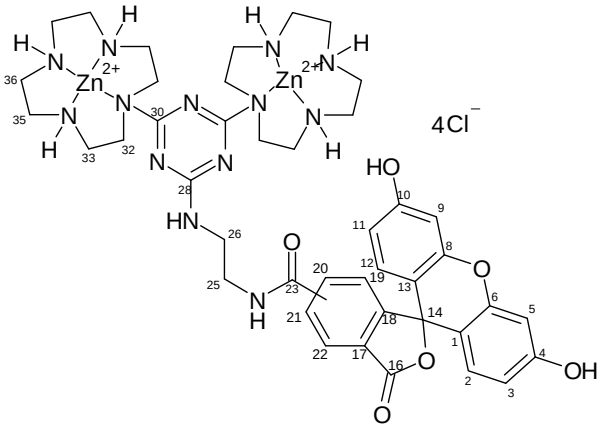

Probe **1***:*

Deprotonated compound **7** (48 mg, 0.06 mmol) was dissolved in 2 mL of warm water, then zinc(II)-chloride (16 mg, 0.12 mmol) was added. After pH-adjustment to 7-8 with saturated $NaHCO_{3,\ aqu.}$, the mixture was heated to 100°C for 2h while stirring. The desired product was isolated by lyophilisation of the reaction mixture as a dark orange, amorphous solid (48 mg, 0.04 mmol, 75%).

^{1}H-NMR (600 MHz, D_2O, COSY, HSQC, HMBC): δ [ppm] = 8.14-6.06 (m, 9H, *aryl*), 4.25-2.62 (m, 35H, *amide-NH+CH_2*)

^{13}C-NMR (150 MHz, D_2O, COSY, HSQC, HMBC): δ [ppm] = 174.1-103.2 ($C_{quat.}$&-, 24C, 1-23+28+30), 46.3-38.7 (-, 18C, 25+26+32-36)

ES-MS (H_2O/MeOH + 10 mmol/L NH_4Ac): *m/z* (%) = 511.4 (70) [M^{4+} - H^+ + CH_3COO^-], 481.8 (37) [M^{4+} - $2H^+$]

UV (40 mM TRIS-buffer, 10 mM $MgCl_2$, 2 mM DTE, pH 7.6): λ (ε) = 321 (6430), 497 (56320)

FLUORESCENCE (40 mM TRIS-buffer, 10 mM $MgCl_2$, 2 mM DTE, pH 7.6): exc. 494 nm, emission max. 526 nm

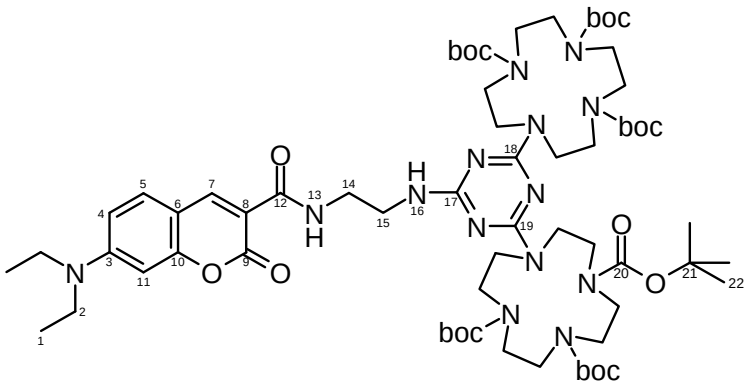

7-Diethylamino-2-oxo-2H-chromene-3-carboxylic acid {2-[4,6-bis-(1,4,7,10-tetraaza-cyclododec-1-yl)-[1,3,5]triazin-2-yl]-ethyl}-1,4,7-tricarboxylic acid tri-tert-butyl ester (**8**):

7-Diethylamino-2-oxo-2H-chromene-3-carboxylic acid (150 mg, 0.56 mmol), DIPEA (386 µL, 2.24 mmol), TBTU (203 mg, 0.63 mmol), and HOBt (97 mg, 0.63 mmol) were dissolved under nitrogen atmosphere in dry DMF (4 mL) under ice cooling and stirred for 1 h. Subsequently amine **3** (635 mg, 0.59 mmol) dissolved in DMF (2 mL) was added drop wise. The reaction was allowed to warm to room temperature and was stirred 30 min at room temperature and 3 h at 40 °C. The reaction progress was

monitored by TLC (chloroform/MeOH 97.5/2.5). After completion of the reaction the solvent was removed and the crude product was purified by flash column chromatography on flash silica gel (chloroform/MeOH 97.5/2.5; R_f (EE) = 0.60) yielding compound **8** (684 mg, 0.52 mmol, 93 %) as a yellow solid.

MP: 147 °C

^{1}H-NMR (400 MHz; $CDCl_3$): δ (ppm) = 1.21 (t, ^{3}J = 7.1 Hz, 6 H, HSQC, COSY: $C^{1}H_3$), 1.40 (s, 18 H, HSQC, COSY: $C^{22}H_3$), 1.42 (s, 36 H, HSQC, COSY: $C^{22}H_3$), 3.11-3.76 (m, 36 H, $C^{14}H_2$, $C^{15}H_2$, cyclen-CH_2), 3.42 (q, ^{3}J = 7.1 Hz, 4 H, HSQC, HMBC, COSY: $C^{2}H_2$), 5.02 (bs, 1 H, NH^{16}), 6.46 (d, ^{4}J = 2.3 Hz, 1 H, HSQC, HMBC, COSY: $C^{5}H$), 6.82 (dd, ^{3}J = 8.9 Hz, ^{4}J = 2.4 Hz, 1 H, HSQC, HMBC, COSY: $C^{4}H$), 7.39 (d, ^{3}J = 8.9 Hz, 1 H, HSQC, HMBC, COSY: $C^{11}H$), 8.65 (s, 1 H, HSQC, HMBC, COSY: $C^{7}H$), 8.90 (m, 1 H, HSQC, COSY: NH^{13}).

^{13}C-NMR (100 MHz; $CDCl_3$): δ (ppm) = 12.4 (+, 2 C, HSQC, HMBC: $C^{1}H_3$), 28.41, 28.46 (+, 18 C, HSQC, HMBC: $C^{22}H_3$), 39.6 (–, 1 C, HSQC, HMBC: $C^{14}H_2$), 40.8 (–, 1 C, HSQC, HMBC: $C^{15}H_2$), 45.0 (–, 2 C, HSQC, HMBC, COSY: $C^{2}H_2$), 50.2 (–, 16 C, HSQC, HMBC: cyclen-CH_2), 79.6 (C_q, 6 C, HSQC, HMBC: C^{21}), 96.5 (+, 1 C, HSQC, HMBC, COSY: $C^{5}H$), 108.3 (C_q, 1 C, HSQC, HMBC: C^{6}), 109.9 (+, 1 C, HSQC, HMBC, COSY: $C^{4}H$), 110.1 (C_q, 1 C, HSQC, HMBC: C^{8}), 131.1 (+, 1 C, HSQC, HMBC, COSY: $C^{11}H$), 148.0 (+, 1 C, HSQC, HMBC, COSY: $C^{11}H$), 152.5 (C_q, 1 C, HSQC, HMBC: C^{3}), 156.2 (C_q, 6 C, HSQC, HMBC: C^{20}), 157.6 (C_q, 1 C, HSQC, HMBC: C^{10}), 162.5 (C_q, 1 C, HSQC, HMBC: C^{9}), 163.7 (C_q, 1 C, HSQC, HMBC: C^{12}), 165.8 (C_q, 3 C, HSQC, HMBC: C^{17}, C^{18}, C^{19}).

IR (ATR) [cm^{-1}]: $\tilde{\nu}$ = 2974, 2933, 1686, 1619, 1584, 1532, 1512, 1466, 1409, 1364, 1246, 1158, 971, 751.

UV ($CHCl_3$): λ_{max} (ε) = 419 (41020)

MS (ESI(+), DCM/MeOH + 10 mmol/L NH_4Ac): m/z (%) = 1324.0 (100) [MH^+), 612.5 (12) [M + 2 H^+]$^{2+}$, 562.5 (25) [M + 2 H^+ - boc]$^{2+}$, 512.4 (51) [M + 2 H^+ - 2 boc]$^{2+}$, 462.3 (55) [M + 2 H^+ - 3 boc]$^{2+}$, 412.3 (34) [M + 2 H^+ - 4 boc]$^{2+}$, 362.2 (17) [M + 2 H^+ - 5 boc]$^{2+}$.

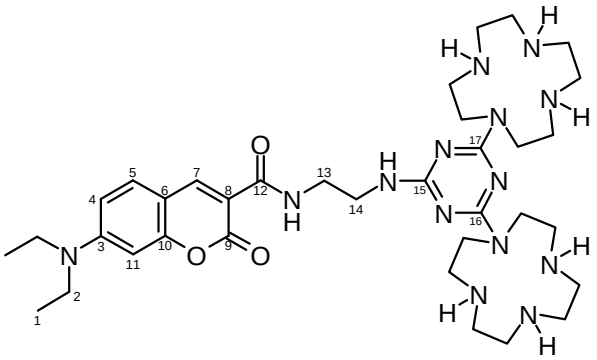

7-Diethylamino-2-oxo-2H-chromene-3-carboxylic acid {2-[4,6-bis-(1,4,7,10-tetraaza-cyclododec-1-yl)-[1,3,5]triazin-2-ylamino]-ethyl}-amide (**9**):

Compound **8** (275 mg, 0.21 mmol) was dissolved in dichloromethane (4 mL) and cooled to 0 °C. Subsequently 4.5 mL of HCl saturated diethylether were added. The solution was stirred 15 min at 0 °C and an additional 20 h at room temperature. The solvent was removed in vacuo, the residue was redissolved in water and extracted with dichloromethane (3x). Subsequently the combined organic layers were dried over $MgSO_4$ and the solvent was evaporated yielding the protonated hydrochloride of compound **9** as a yellow solid in quantitative yield (213 mg, 0.21 mmol).

^{1}H-NMR (400 MHz; $CDCl_3$): δ (ppm) = 1.13 (t, ^{3}J = 7.3 Hz, 6 H, HSQC, COSY: $C^{1}H_3$), 2.97-3.54 (m, 24 H, HSQC, HMBC, COSY: cyclen-CH_2), 3.57-3.72 (m, 6 H, HSQC, HMBC: $C^{13}H_2$; HSQC, HMBC, COSY: $C^{2}H_2$), 3.75 (t, ^{3}J = 5.6 Hz, 2 H, HSQC, COSY: $C^{14}H_2$), 3.89 (bs, 8 H, HSQC, HMBC, COSY: cyclen-CH_2), 7.37-7.56 (m, 2 H, HSQC, HMBC: $C^{4}H$, HSQC, HMBC: $C^{5}H$), 7.96 (d, ^{3}J = 8.4 Hz, 1 H, HSQC, HMBC: $C^{11}H$), 8.72 (s, 1 H, HSQC, HMBC: $C^{7}H$).

^{13}C-NMR (100 MHz; $CDCl_3$): δ (ppm) = 10.1 (+, 2 C, HSQC, COSY: $C^{1}H_3$), 39.0 (–, 1 C, HSQC, HMBC: $C^{13}H_2$), 39.9 (–, 1 C, HSQC, HMBC: $C^{14}H_2$), 44.0 (–, 2 C, HSQC, HMBC, COSY: cyclen-CH_2), 44.3 (–, 6 C, HSQC, HMBC, COSY: cyclen-CH_2), 46.1 (–, 4 C, HSQC, HMBC, COSY: cyclen-CH_2), 47.7 (–, 2 C, HSQC, HMBC, COSY: cyclen-CH_2), 48.3 (–, 2 C, HSQC, HMBC, COSY: cyclen-CH_2), 52.6 (–, 2 C, HSQC, HMBC, COSY: $C^{2}H_2$), 108.8 (+, 1 C, HSQC, HMBC: $C^{5}H$), 117.6 (C_q, 1 C, HSQC, HMBC: C^{6}), 117.9 (C_q, 1 C, HSQC, HMBC: C^{8}), 118.1 (+, 1 C, HSQC, HMBC: $C^{4}H$), 132.5 (+, 1 C, HSQC, HMBC: $C^{11}H$), 143.2 (C_q, 1 C, HSQC, HMBC: C^{3}), 147.6 (+, 1 C, HSQC, HMBC: $C^{7}H$), 154.9 (C_q, 1 C, HSQC, HMBC: C^{10}), 155.2 (C_q, 1 C, HSQC, HMBC: C^{16}), 155.8 (C_q, 1 C, HSQC, HMBC: C^{15}), 161.4 (C_q, 1 C, HSQC, HMBC: C^{9}), 163.6 (C_q, 1 C, HSQC, HMBC: C^{17}), 164.1 (C_q, 1 C, HSQC, HMBC: C^{8}).

MS (ESI(+), MeCN/TFA): m/z (%) = 362.3 (100) $[M + 2\ H^+]^{2+}$, 723.5 (10) $[MH^+]$.

To obtain the free base of compound **9** a weakly basic ion exchanger resin was swollen for 15 min in water and washed neutral with water. A column was charged with resin (473 mg, 40.0 mmol hydroxy equivalents at a given capacity of 5 mmol/g). The hydrochloride salt (60 mg, 59 µmol) was dissolved in water, put onto the column and eluated with water. The elution of the product was controlled by pH indicator paper (pH > 10) and was completed when pH was again neutral. The eluate was concentrated and lyophilised to yield 43 mg (59 µmol, 100 %) of free base **9** as a yellow solid.

MP: 169 °C

^{1}H-NMR (600 MHz; D_2O): δ (ppm) = 1.04 (t, ^{3}J = 7.1 Hz, 6 H, HSQC, COSY: $C^{1}H_3$), 3.02 (bs, 8 H, cyclen-CH_2), 3.12 (bs, 16 H, cyclen-CH_2), 3.27 (q, ^{3}J = 7.0 Hz, 4 H, HSQC, HMBC: $C^{2}H_2$), 3.38 (t, ^{3}J = 4.6 Hz, 2 H, HSQC, HMBC: $C^{13}H_2$), 3.48 (t, ^{3}J = 5.2 Hz, 2 H, HSQC, HMBC: $C^{14}H_2$), 3.62 (bs, 8 H, cyclen-CH_2), 6.13 (d, ^{4}J = 1.8 Hz, 1 H, HSQC, HMBC, ROESY: $C^{11}H$), 6.58 (d, ^{3}J = 9.0 Hz, 1 H, HSQC, HMBC, ROESY: $C^{4}H$), 7.24 (d, ^{3}J = 9.2 Hz, 1 H, HSQC, HMBC, ROESY: $C^{5}H$), 8.09 (s, ^{4}J = 1.8 Hz, 1 H, HSQC, HMBC, ROESY: $C^{7}H$), 8.28 (bs, 1 H, HSQC, NH).

^{13}C-NMR (150 MHz; D_2O): δ (ppm) = 11.8 (+, 2 C, HSQC, HMBC: $C^{1}H_3$), 39.4 (–, 1 C, HSQC, HMBC: $C^{14}H_2$), 40.1 (–, 1 C, HSQC, HMBC: $C^{13}H_2$), 42.4 (–, 2 C, HSQC, HMBC: cyclen-CH_2), 42.8 (–, 2 C, HSQC, HMBC: cyclen-CH_2), 44.7 (–, 4 C, HSQC, HMBC: cyclen-CH_2), 45.1 (–, 2 C, HSQC, HMBC: $C^{2}H_2$), 45.7 (–, 4 C, HSQC, HMBC: cyclen-CH_2), 46.1 (–, 4 C, HSQC, HMBC: cyclen-CH_2), 95.5 (+, 1 C, HSQC, HMBC, ROESY: $C^{11}H$), 106.0 (C_q, 1 C, HSQC, HMBC: C^{8}), 107.6 (C_q, 1 C, HSQC, HMBC: C^{8}), 111.4 (+, 1 C, HSQC, HMBC, ROESY: $C^{4}H$), 131.7 (+, 1 C, HSQC, HMBC, ROESY: $C^{5}H$), 148.1 (+, 1 C, HSQC, HMBC, ROESY: $C^{7}H$), 153.6 (C_q, 1 C, HSQC, HMBC: C^{3}), 157.0 (C_q, 1 C, HSQC, HMBC: C^{10}), 163.1 (C_q, 1 C, HSQC, HMBC: C^{8}), 165.3 (C_q, 1 C, HSQC, HMBC: C^{9}), 166.7 (C_q, 1 C, HSQC, HMBC: C^{15}), 166.8 (C_q, 2 C, HSQC, HMBC: C^{16}, C^{17}).

IR (ATR) [cm^{-1}]: $\tilde{\nu}$ = 3382, 3315, 2968, 2732, 1694, 1576, 1537, 1506, 1417, 1350, 1231, 1134, 1079, 809.

UV ($CHCl_3$): λ (ε) = 260 nm (12474), 426 (43341).

MS (ESI(+), TFA/MeCN): m/z (%) = 362.2 (100) $[M + 2\ H^+]^{2+}$, 241.7 (10) $[M + 3\ H^+]^{3+}$, 723.5 (6) $[MH^+]$, 837.4 (3.0) $[MH^+ + TFA]$.

HRMS Calcd for $C_{35}H_{58}N_{14}O_3$ 723.4895; Found: 723.4915.

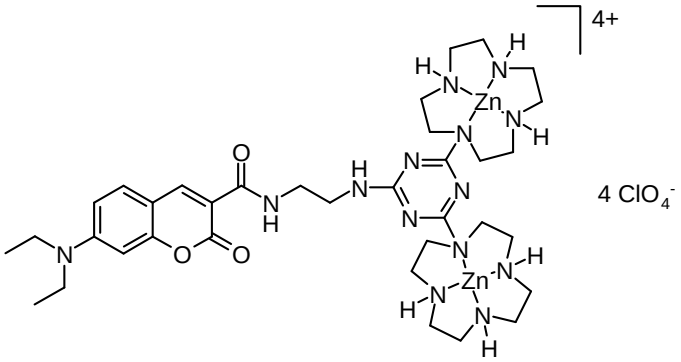

Probe **2**:

Compound **9** (43 mg, 59 µmol) was dissolved in 1 mL of water and heated to 65 °C to get a clear yellow solution. Subsequently zinc(II)-perchlorate (44 mg, 119 µmol) dissolved in 1 ml of water was added slowly. The reaction mixture was stirred for an additional 28 h at 65 °C. The solvent was removed in vacuo and the residue was redissolved in water and lyophilized. Probe **2** (74 mg, 59 µmol, 100 %) was obtained as a yellow solid.

MP: 166 °C

^{1}H-NMR (300 MHz; CD_3CN): δ (ppm) =1.19 (t, ^3J = 7.0 Hz, 6 H, ethyl-CH_3), 2.45 (bs, 4 H, cyclen-CH_2), 3.02 (bs, 8 H, cyclen-CH_2), 3.26 (bs, 12 H, cyclen-CH_2), 3.37 (bs, 2 H, ethylene diamine-CH_2), 3.49 (q, ^3J = 7.0 Hz, 6 H, ethyl-CH_2, ethylene diamine-CH_2), 3.71-4.50 (m, 8 H, cyclen-CH_2), 5.35-6.65 (m, 6 H, cyclen-NH), 6.55 (s, 1 H, CH), 6.80 (d, ^3J = 9.1 Hz, 1 H, CH), 7.58 (d, ^3J = 9.1 Hz, 1 H, CH), 8.72 (s, 1 H, CH), 9.23 (bs, 1 H, NH).

IR (ATR) [cm^{-1}]: $\tilde{\nu}$ = 3246, 2938, 2864, 1558, 1457, 1421, 1342, 1287, 1083, 968, 793.

UV (HEPES pH 7.4, 25 mM): λ (ε) = 432 (25177).

MS (ESI(+), TFA/MeCN): m/z (%) = 485.5 (100) $[M^{4+} + 2\ CH_3COO^-]^{2+}$, 455.7 (50) $[M^{4+} - H^+ + CH_3COO^-]^{2+}$, 425.1 (28) $[M^{4+} - 2\ H^+]^{2+}$,

REFERENCES

(1) Hünig, S., Märkl, G., Sauer, J. (1994) *Einführung in die apparativen Methoden in der Organischen Chemie*, 2nd Edition, Würzburg, Regensburg.

(2) Schwetlick, K. (2001) *Organikum*, 21st Edition, Wiley-VCH, Weinheim.

(3) Grauer, A., Riechers, A., Ritter, S., König, B. (2008) Synthetic Receptors for the Differentiation of Phosphorylated Peptides with Nanomolar Affinities. *Chem. Eur. J. 14,* 8922-8927.

(4) Berthelot, T., Talbot, J.-C., Laïn, G., Déleris, G., Latxague L. (2005) Synthesis of N^{ε}-(7-diethylaminocoumarin-3-carboxyl)- and N^{ε}-(7-methoxycoumarin-3-carboxyl)-L-fmoc lysine as tools for protease cleavage detection by fluorescence. *J. Pep. Sci. 11,* 153-160.

TECHNICAL NOTES

Bromination from the Macroscopic Level to the Tracer Radiochemical Level: ^{76}Br Radiolabeling of Aromatic Compounds via Electrophilic Substitution

Dong Zhou,*[,†] Haibing Zhou,[‡,§] Carl C. Jenks,[†] Jason S. Lewis,[†,||] John A. Katzenellenbogen,[‡] and Michael J. Welch[†]

Mallinckrodt Institute of Radiology, Washington University School of Medicine, St. Louis, Missouri 63110, and Department of Chemistry, University of Illinois, Urbana, Illinois 61801. Received July 22, 2008; Revised Manuscript Received February 11, 2009

No-carrier-added (NCA) ^{76}Br labeling of 4-(5-acetoxy-7-bromobenzoxazol-2-yl)phenyl acetate, a diacetate-protected estrogen-receptor beta (ERβ) selective ligand, was carried out successfully using [^{76}Br]bromide ion. The labeling was achieved via oxidative electrophilic destannylation of an organotin precursor molecule by modification of the leaving group (from Bu_3Sn to Me_3Sn) and the addition of methanol to the reaction mixture. The differences between the oxidative bromination reaction under small-scale macroscopic vs tracer level radiochemical conditions were explored in terms of effective brominating agents, which depend greatly on the nature of the solvent during the radiochemical bromination, and the potential interference by trace levels of highly reactive impurities in the reaction that compete for the desired bromination at the NCA level. Our observations, and our development of experimental protocols for successful radiobromination at the tracer NCA-scale, should be applicable to the synthesis of other radiobromine-labeled organic compounds of potential interest as PET radiopharmaceuticals and radiotherapy agents.

INTRODUCTION

Radiohalogenated organic compounds are commonly used in basic research and in the clinic as radiopharmaceutical probes for molecular imaging via positron emission tomography (PET[1]) or single photon emission computed tomography (SPECT). If labeled with a therapeutic nuclide, radiohalogenated compounds can be used for internal radiotherapy at the cellular level (*1*). Synthetic methods for radiofluorination and radioiodination have been extensively studied and reviewed (*2*−*5*). Radiobromination has been much less studied, especially regarding the effective brominating agents in radiobromination reactions (*6*, *7*).

Bromine-labeled compounds have some advantages over iodine-labeled compounds: the stronger C−Br bond results in less dehalogenation, and unlike iodide, bromide does not accumulate in the thyroid (*8*). Over the past two decades, interest in radiobromine has shifted from ^{77}Br and ^{82}Br to ^{76}Br (*8*). Radiopharmaceuticals labeled with ^{76}Br ($t_{1/2}$ = 16.2 h) are suitable for imaging slower physiologic processes than those labeled with ^{18}F ($t_{1/2}$ = 110 min). Furthermore, the decay scheme of ^{76}Br (57% positron and 43% electron capture) (*9*) gives it potential both for PET imaging and for radiotherapy. Finally, the ^{76}Br nuclide can be produced via the ^{76}Se(p,n)^{76}Br reaction on most medical cyclotrons (*10*).

Organic molecules often contain aromatic rings onto which ^{76}Br can be introduced by using very high specific activity [^{76}Br]bromide ion. Radiobromination at the tracer level produces products with the very high specific activities required for studying receptor-binding biological processes, but can differ from classical bromination and from radioiodination. Bromide is more difficult to oxidize than iodine, so harsher conditions are required for oxidative bromination. An effective brominating agent is also more reactive than an effective iodinating agent, so standard conditions for radioiodination might not be appropriate for radiobromination.

Major considerations for tracer-level synthesis are synthesis time (due to radioactive decay), specific activity (to achieve true tracer status), and relative stoichiometry. In classical electrophilic brominations, even those on a small scale, macroscopic amounts of the electrophilic brominating agent are used and are usually present in stoichiometric excess over the arene reactant. However, in true tracer-level, no-carrier-added electrophilic radiobromination reactions, the trace amount of "positive bromine" reacts with orders-of-magnitude excesses of a substrate in the presence of an excess of oxidizing agents. Because of this stoichiometric issue, the effective radiobrominating agent is likely to differ from that used in classical bromination. In addition, any highly reactive impurities present in tracer-scale

* Corresponding author. Mallinckrodt Institute of Radiology, Washington University School of Medicine, 510 S. Kingshighway Blvd., St. Louis, MO 63110, USA. Phone: 314-362-9072. Fax: 314-362-8399. E-mail address: zhoud@mir.wustl.edu.

† Washington University School of Medicine

‡ University of Illinois.

§ Current address: College of Pharmacy, Wuhan University, Wuhan, 430072, China.

|| Current address: Department of Radiology, Memorial Sloan-Kettering Cancer Center, New York, NY 10065.

[1]Abbreviations: AcOH, acetic acid; CAT or Chloramine-T, *N*-chloro-*p*-toluenesulfonamide sodium salt; ERα, estrogen receptor alpha; ERβ, estrogen receptor beta; IC, ion chromatography; NCA, no-carrier-added; PPA, peracetic acid; PET, positron emission tomography; SPECT, single photon emission computed tomography; TFA, trifluoroacetic acid.

10.1021/bc800313c CCC: $40.75 © 2009 American Chemical Society
Published on Web 03/05/2009

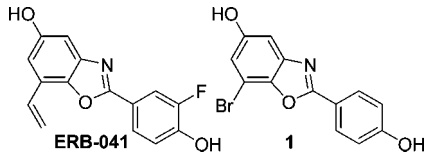

Figure 1. Structures of ERB-041 and **1**.

brominations might preferentially react with the "positive bromine", resulting in formation of bromine-substituted byproducts and reducing yield of the desired product. In contrast, in macroscopic scale reactions, the relatively tiny amounts of any highly reactive impurities compared to stoichiometric or excess bromine would produce chemically ignorable bromine-substituted byproducts. The lack of understanding and published information regarding effective agents for radiobromination of organic moieties has impeded development of some radiopharmaceuticals.

Compound **1** (Figure 1) (*11*), an analogue of ERB-041 (*11, 12*), is an estrogen receptor beta (ERβ) selective ligand with good binding affinity and excellent selectivity over estrogen receptor alpha (ERα) (*11, 12*). Once labeled with ^{76}Br, it is expected to have potential as a PET imaging agent for ERβ. Brominations of nonactivated organic compounds via electrophilic destannylation have been successful using unlabeled bromide and carrier-added [^{76}Br]bromide. However, no-carrier-added radiobrominations have been problematic. Difficulties in no-carrier-added radiolabeling of **1** with ^{76}Br led us to explore radiobrominations in greater detail.

Here, we report systematic exploration of reaction conditions leading to successful tracer-scale, no-carrier-added ^{76}Br radiobromination of aromatic compounds, most notably [^{76}Br]**2** (which can be deprotected to make [^{76}Br]**1**) via electrophilic destannylation. We also report investigation of other issues, including the effect of solvents, on ^{76}Br labeling of organic compounds including 5-bromo-2-furaldehyde **3**. These observations and the development of experimental protocols for successful tracer-scale radiobromination should find application for the radiobromination of other organic compounds.

EXPERIMENTAL PROCEDURES

General Information. All chemicals and solvents were obtained from commercial sources and used without further purification unless noted. The synthesis of compounds **2**, **4**, and **5** will be described elsewhere. Compound **6** was synthesized according to the literature (*13*). Bromine-76 was produced at the Washington University cyclotron facility on the Japanese Steel Works 16/8 cyclotron by the ^{76}Se(p,n)^{76}Br nuclear reaction on a ^{76}Se-enriched Cu_2Se target. Bromine-76 was recovered via a modified dry distillation method (*14*). Reversed-phase HPLC was performed with an ultraviolet detector and a radiation detector. Alltech Econosil or Altima C18 250 $\times$ 4.6 mm 10 μm or Agilent Zorbax SB-C18 250 $\times$ 4.6 mm 5 μm analytical columns were used for analysis. Acetonitrile and 0.1 M ammonium formate buffer (pH = 4.5) were used as the HPLC mobile phase. Ion chromatography (IC) was performed using a Dionex IonPac AS14A 250 $\times$ 4 mm column with UV at 210 nm and a radiation detector, with an elution solvent of 8 mM Na_2CO_3 and 1 mM $NaHCO_3$ aqueous solution. RadioTLC was performed using a Bioscan System 2000 imaging scanner.

Typical Procedure for Nonradioactive Synthesis of 4-(5-Acetoxy-7-bromobenzoxazol-2-yl)phenyl Acetate (2) from Precursor 4. Into a solution of **4** (100 μg) in acetic acid (100 μL), NH_4Br solution (3 μL, from a solution of 6 mg in 1000 μL water) and 3% peracetic acid in acetic acid (100 μL) were added. The reaction mixture was vortexed to homogeneity and allowed to react at ambient temperature. At 10 min, 10 μL of the reaction mixture was injected onto a reversed-phase HPLC (Alltech Altima C18 250 $\times$ 4.6 mm 10 μm), eluting with 60% acetonitrile 40% 0.1 M ammonium formate buffer (pH = 4.5) at a flow rate of 2 mL/min and UV detection at 285 nm. Compound **2** eluted at 8 min as the only product according to HPLC, and it was confirmed by comparison with authentic standard **2**.

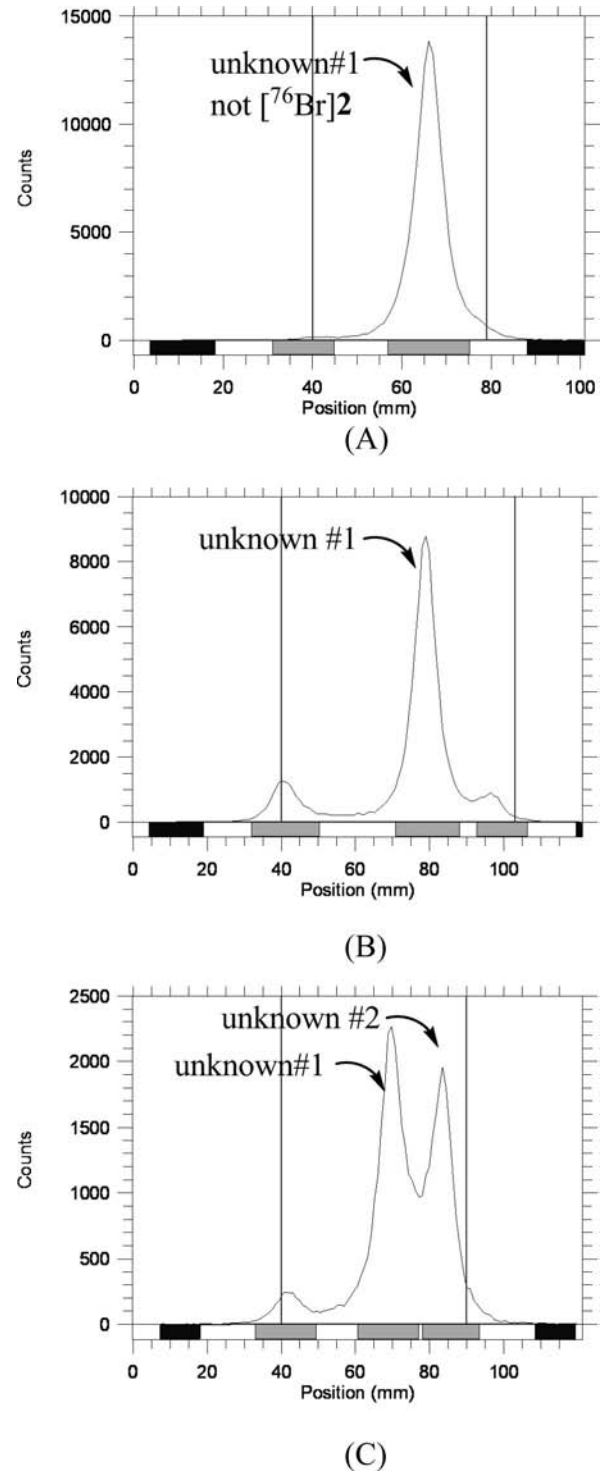

Figure 2. Radio-TLCs of attempted radiobrominations of **4** and a control reaction (performed in the absence of **4**), showing formation of unknown #1 and unknown #2. (A) Attempted radiobromination of **4**, using PAA. (B) Control reaction using PAA but no substrate **4**, (C) Attempted radiobromination of **4**, using CAT. Separations were on silica gel, 1:1 ethyl acetate/hexanes.

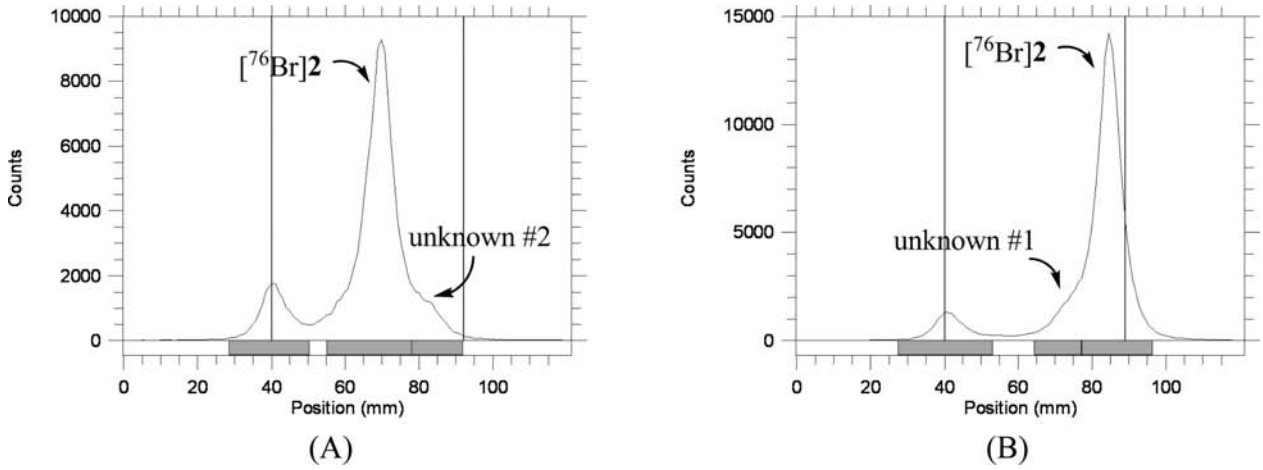

Figure 3. Radio-TLCs of successful synthesis of [^{76}Br]**2** developed in two TLC solvent systems (Silica gel). (A) 1:1 ethyl acetate/hexanes. (B) 10% methanol in dichloromethane.

Preparation of [^{76}Br]Bromide. A solution of [^{76}Br]bromide in 0.6 N ammonium hydroxide (up to 1 mL) was passed through a C18 SepPak (light) and a 0.45 μm nylon filter, which were conditioned by methanol (10 mL) and water (10 mL) beforehand and washed with water (100 μL) afterward. All collected activity was evaporated to dryness in a straight-sided shell vial (15 × 45 mm) in a heat block heated from ambient temperature to 130 °C and with a very gentle flow of N_2 over the top of the vial, which did not result in any loss of radioactivity; high gas flow can result in a significant loss of radioactivity. When the radioactivity was completely dry (less than 10 min), it was reconstituted in water, methanol, or acetic acid for the labeling reactions indicated below. Bromine-76 extracted in water or ethanol was used as is or dried directly at 130 °C.

Typical Procedure for Attempted No-Carrier-Added Synthesis of [^{76}Br]2 from 4 and Control Reactions. A solution of [^{76}Br]Bromide (20−100 μCi) in water, methanol, or acetic acid (10−50 μL) was added to a solution of **4** (no **4** for control reactions) (100 μL), and then acetic acid (100 μL) and a solution of peracetic acid in acetic acid or methanol (100 μL) were added to the solution. Reaction mixture was vortexed to achieve homogeneity and analyzed by radio-TLC.

No-Carrier-Added Synthesis of [^{76}Br]2 from Precursor 5. To [^{76}Br]bromide (1.5 mCi), dried as described above and reconstituted in MeOH (100 μL), was added a solution of trimethyltin precursor **5** (1 mg) in acetic acid (100 μL), and the reaction vessel was vortexed. After addition of 1% peracetic acid in methanol (100 μL), the reaction vessel was vortexed again and then allowed to react at ambient temperature. The reaction was checked by radio-TLC (silica); >80% [^{76}Br]bromide was consumed, and roughly 60% was obtained as [^{76}Br]**2** within 30 min. [^{76}Br]**2** was distinguished from unknown #1 by developing the plates in 1:1 ethyl acetate/hexanes and 10% methanol in dichloromethane (Figures 2 and 3). Reversed-phase HPLC purified [^{76}Br]**2** was confirmed by silica radio-TLC and HPLC coinjection with authentic standard **2** ([^{76}Br]**2**: R_f = 0.55, 0.91 for 1:1 ethyl acetate/hexanes and 10% methanol in dichloromethane, respectively; HPLC Agilent Zorbax SB-C18 250 × 4.6 mm 5 μm analytical column, 65% acetonitrile, 35% 0.1 M ammonium formate buffer (pH = 4.5), 2 mL/min, 285 nm, t_R = 5.2 min; Unknown #1, 0.54, 0.75, and unknown #2, 0.85, 0.99, on silica gel TLCs developed in 1:1 ethyl acetate/hexanes and in 10% methanol in dichloromethane, respectively. (For HPLC of unknown #1, see Supporting Information.)

RESULTS AND DISCUSSION

Oxidizing Agents and Precursors. The most commonly used oxidizing agent for radioiodination and radiobromination is *N*-chloro-*p*-toluenesulfonamide sodium salt (Chloramine-T or CAT). Conditions have been optimized for radiobromination of activated phenol analogues using CAT (*15*), and these conditions have been used to label organic compounds, antibodies, and nanoparticles and for the direct and indirect labeling of peptides. Chloramine-T is not ideal for tracer-scale radiosyntheses, however, because simultaneous chlorination can reduce final effective specific activity if chlorinated byproduct cannot be separated from the desired radiobrominated product (*16*). Furthermore, elevated temperatures may be necessary to promote labeling of electron-poor substrates. Premixed hydrogen peroxide/acetic acid (H_2O_2/AcOH), in which peracetic acid (PAA) is the effective oxidizing agent, also has been used to synthesize receptor-binding radiopharmaceuticals (*17*−*19*). Currently, the use of PAA as oxidizing agent is growing because reaction conditions are mild and labeling is cleaner compared to products obtained using CAT and H_2O_2. As a result, PAA was used for our radiobromination studies.

Scheme 1. Bromination of 4 Using NH_4Br and PAA in Acetic Acid

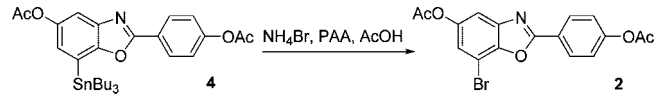

When small organic compounds of interest as potential radiopharmaceuticals do not contain an electron-rich aromatic ring activated for electrophilic aromatic substitution (e.g., tyrosine), electrophilic demetalation is an elegant approach to radiobromination (*7*). Among the metals used in these reactions (boron, silicon, germanium, and tin), the tin precursors ($SnMe_3$ and $SnBu_3$ substituted) generally give the best results (*20, 21*). This method often allows an aromatic compound to be labeled regiospecifically, quickly, and in high yields, and so the organic tin precursors **4**, **5**, and **6** were used for our investigations.

Non-Radioactive Bromination of Tributyltin Precursor 4. Nonradioactive electrophilic aromatic substitution of the tributyltin diacetate precursor **4** with bromine under classical macroscopic (but low-scale) reaction conditions was carried out in acetic acid using PAA as the oxidizing agent (Scheme 1; Table 1). Destannylation took place quickly, and the desired bromine-substituted compound **2** was the major product by HPLC analysis of the reaction mixture. The yield was not determined due to the small scale of the reactions and difficulty in determining the amount of starting material consumed, but investigations using nonradioactive bromine as the limiting reagent (see below and Table 3) suggest that yields were high. When the PAA was reduced from 200 to 1 equiv relative to

Table 1. Bromination of 4 Using NH_4Br and Different Concentrations of PAA in Acetic Acid[a]

#	**4**[b] (μmol)	NH_4Br[c] (μmol)	PAA[d] (μmol)	PAA/NH_4Br (in μmol)	reaction time (min)	relative yield[e] **2** (%)
1	0.17	0.18	39.4	21.9:1	10	(100)
2	0.17	0.18	13.1	73.0:1	10	84
3	0.17	0.18	4.4	24.3:1	10	80
					25	97
4	0.17	0.18	1.5	8.1:1	20	94
5	0.17	0.18	0.49	2.7:1	20	87
6	0.17	0.18	0.16	0.9:1	20	95

[a] Data from single experiment. [b] **4** (100 μg, 0.17 μmol) in AcOH (100 μL). [c] A solution of NH_4Br (18 μg, 0.18 μmol) in H_2O (3.0 μL). [d] PAA in AcOH (100 μL). [e] Yields are given relative to that obtained in reaction #1, based on HPLC integrations of **2**.

NH_4Br, the reaction slowed, but a similar amount of **2** was obtained within 30 min (Table 1, entry 6), suggesting that oxidation of bromide by PAA is highly efficient under these conditions.

Chloramine-T and hydrogen peroxide/acetic acid were also investigated for their effectiveness in the classical oxidative bromination reaction (Table 2). In general, reactions were slower and yields lower with CAT, probably due to slower oxidation of bromide, but addition of acetic acid as a proton source significantly accelerated the reaction at room temperature. This is consistent with the reported oxidative bromination of tyrosine using CAT (*15*). At elevated temperatures, the amount of product obtained was similar to using 3% PAA. Hydrogen peroxide/acetic acid, which produces small amounts of PAA, did not give any detectable product by HPLC analysis. Hence, for classical oxidative brominations, it appears that PAA is more efficient than CAT and H_2O_2/AcOH. The lack of reaction using H_2O_2/AcOH is not surprising, because H_2O_2 in the absence of strong acid is a much weaker oxidizing agent for bromide than PAA (*22, 23*). Apparently, H_2O_2/AcOH does not produce enough PAA to result in detectable bromination products in classical, macroscopic oxidative brominations.

When bromide (NH_4Br) was the limiting reagent and its concentration was varied, the yield of **2** in classical oxidative brominations using PAA was determined by HPLC (Table 3). When bromide concentration was above 10^{-5} M, the yield was high (74% after 10 min and 76% after 30 min). When bromide was reduced to 10^{-6} M, close to but still higher than in the NCA radiolabeling reaction, the yield of **2** was reduced dramatically to roughly 25% after 10 or 30 min. For 10^{-7} M bromide, yields were just 5% after 10 or 30 min. (Because the average specific activity of [^{76}Br]bromide is more than 1000 Ci/mmol, the concentration of bromide is less than 10^{-6} mol/L for 1 mCi radioactivity in 1 mL solution.) In this series of reactions, amounts of other brominated products were too small to allow their identification.

No-Carrier-Added Radiobromination of Precursor 4: Formation of Unexpected Byproducts. (Scheme 2) Conditions were the same as those used for nonradioactive bromination reactions, shown in Tables 1 and 2. When NH_4[^{76}Br]Br was used in 0.6 N ammonium hydroxide without drying, a single radioactive byproduct (unknown #1, Figure 2A) was formed within 15 min, according to radioactive detection using thin layer chromatography (radio-TLC). Unfortunately, the R_f value of this peak is almost the same as that of the nonradioactive standard **2** in the developing solvents (1:1 ethyl acetate/hexanes), which caused some confusion. After the reaction mixture was diluted with water, however, this radioactive byproduct was converted completely to a more polar product. This initial radioactive byproduct (unknown #1) was also observed in the labeling of other compounds via electrophilic destannylation (data not shown).

It initially was assumed that unknown #1 was actually the desired radioactive product **2**, and the more polar product formed after dilution with water was due to radiolysis from the high-energy radiation of ^{76}Br. However, unknown #1 also was found later in a control reaction, in which no precursor **4** was added (Figure 2B). Therefore, the initially observed radioactive byproduct clearly was not the desired product **2**, nor was it any radioactive form of the tributyltin precursor **4**. Unknown #1 was also observed when CAT (Figure 2C) or H_2O_2/AcOH was used as the oxidizing agent, although its formation was slow with CAT. A second unknown, a very lipophilic radioactive byproduct (unknown #2, Figure 2C) was observed with CAT and only in the presence of substrate **4** (Supporting Information Figure S1).

Effect of Carrier and Solvent on Radiobromination of Precursor 4. With carrier NH_4Br in water added to the radiolabeling reaction ([bromide] = 5×10^{-4} M) and PAA as the oxidizing agent, desired product **2** was formed exclusively. Its identity was confirmed by HPLC analysis by coeluting with nonradioactive standard **2**. These results are consistent with our experiments conducting nonradioactive bromination with various bromide concentrations (Table 3). Thus, sufficient carrier results in efficient radiobromination of **4**, but with no carrier added, it would appear that [^{76}Br]bromide in NH_4OH reacts first with some unidentified, more reactive species present at trace levels, rather than replacing the tributyltin moiety in precursor **4**. Thus at tracer scale, unknown #1 is produced rather than the desired product **2** under otherwise classical reaction conditions.

When [^{76}Br]bromide was produced in water or ethanol, and either PAA or CAT as the oxidizing agent, unknown #1 was only a minor product. However, under these conditions, unknown #2 was the major product observed. With H_2O_2/AcOH as the oxidizing agent, no reaction was observed for [^{76}Br]bromide produced in water or ethanol (Table 4).

Exploration for the Source of the Radioactive Byproducts Unknowns #1 and #2. Efforts were taken to identify unknown #1 and to remove its source. We found that formation of unknown #1 was dominant and fast when ^{76}Br in NH_4OH was used without drying. This was true even with activated 1-methoxy-4-tributylstannylbenzene analogues, where the desired radiolabeling reaction is expected to be prompt (data not shown). Ammonium ion is reported to react very rapidly ($k = 10^7$ M^{-1} s^{-1}) with HOBr to form NH_2Br (*24, 25*), a species that has relatively feeble brominating activity (*25*). However, addition of NH_4OH or NH_4NO_3 in solution to control reactions of PAA and [^{76}Br]bromide ion (produced in water) produced no additional unknown #1.

A solution of [^{76}Br]Bromide ion in 0.6 N NH_4OH was analyzed by ion chromatography (IC) to evaluate the possibility that trace selenium could have catalyzed oxidative halogenations (*26*) to form unknown #1. It is possible that trace amounts of O_2 leaked into the system during hours-long high-temperature distillation could have oxidized trace selenium to form SeO_2, which can be extracted as SeO_3^{2-} in aqueous solution but can be separated from the bromide after IC purification. In these experiments, NO_3^- and SeO_3^{2-} were observed, and identified by comparison to retention times of NH_4NO_3 and SeO_3^{2-} (a solution of SeO_2) in aqueous solutions (Supporting Information Figure S2). However, IC purified [^{76}Br]bromide and crude [^{76}Br]bromide in NH_4OH produced radiolabeled unknown #1 exclusively in control reactions. Therefore, SeO_3^{2-} cannot be responsible for the formation of unknown #1.

The high-energy radiation of ^{76}Br is likely to cause some radiolysis, and indeed, formation of NO_3^- was observed in our reaction mixtures but not in plain 0.6 N NH_4OH. We also observed that production of unknown #1 increased with the length of time [^{76}Br]bromide remained in a NH_4OH solution

Table 2. Bromination of 4 Using Different Oxidizing Agents[a]

#	**4**[b] (μmol)	NH_4Br[c] (μmol)	oxidizer (μmol)	reaction time (min)	temperature (°C)	relative yield[d] **2** (%)
1	0.17	0.06	PAA (39.4) AcOH (100 μL)	15	RT	(100)
2	0.17	0.06	CAT (0.44) MeOH (100 μL)	15	RT	3
3	0.17	0.06	2:1 H_2O_2/AcOH (1960) (100 μL)	15	RT	0
4	0.17	0.06	CAT (0.44) MeOH/AcOH (100 μL/100 μL)	15	RT	40
				30	RT	60
5	0.17	0.06	CAT (0.44) MeOH/AcOH (100 μL/100 μL)	10	88	89
				20	88	90

[a] Data from single experiment. [b] **4** (100 μg, 0.17 μmol) in MeOH (100 μL). [c] A solution of NH_4Br (6 μg, 0.06 μmol) in H_2O (10 μL). [d] Yields are given relative to that obtained in reaction #1, based on HPLC integrations of **2**.

Table 3. Bromination of 4 Using Different Concentrations of NH_4Br[a,b]

#	**4**[c] (μmol)	NH_4Br[d] (mol/L)	yield of **2** (%)[e] 10 min	30 min
1	0.33	6×10^{-4}	67	79
2	0.33	6×10^{-5}	74	76
3	0.33	6×10^{-6}	24	25
4	0.33	6×10^{-7}	5	5

[a] Data from single experiment. [b] Oxidant: PAA (3%, 39.4 μmol) in AcOH (100 μL). [c] **4** (200 μg, 0.33 μmol) in AcOH (200 μL). [d] Concentration of NH_4Br in the reaction mixture, added as a solution of NH_4Br in H_2O (3.0 μL). [e] Yields are based on bromide used as the limiting reagent and were determined by comparison with known concentrations of an authentic standard **2**.

and with the amount of radioactivity present. Although it has not been possible to identify unknown #1 or its source, its formation can be avoided by producing [^{76}Br]bromide in water or ethanol or by drying the activity immediately after its production in an NH_4OH solution.

Unknown #2, a radioactive, highly lipophilic compound, was also observed in radiolabeling reactions with the tributyltin precursor **4** when CAT was used as the oxidant (Figure 2C, Table 4, Supporting Information Figure S1). With [^{76}Br]bromide produced in water or ethanol, radiobromination of impurities present in the reaction mixture also contributed partially to the production of unknown lipophilic compounds (Supporting Information Figure S1). Furthermore, a solvent-related radioactive product was observed exclusively both in radiobromination of **4** and in its control reaction (no substrate **4**) when THF (inhibitor-free), DMF or acetonitrile was used in the experiments (Supporting Information Figure S3). These solvents have been documented in the literature as suitable for radiobromination.

We are unable to determine the chemical form of unknown #2, formed from the reaction with the tributyltin precursor **4**. It is more lipophilic than precursor **4** by silica gel TLC, and it is difficult to elute from a C18 Sep-Pak. It is resistant to 1 N LiOH treatment, but it can be converted to a polar product by treatment with trifluoroacetic acid (TFA). These characteristics suggest that unknown #2 still contains a tributyltin substituent.

Electrophilic substitution can take place at several sites on precursor **4** other than by *ipso* substitution of the tributyltin group, particularly on the aromatic rings, which are activated by several electron-donating substituents. Furthermore, the nitrogen of the benzoxazole could operate as a nucleophile to react with the electrophilic "positive bromine". Two examples from the literature support these possibilities. A similar highly lipophilic radiobrominated byproduct was produced by ^{76}Br radiobromination of 4-substituted-3,5-dimethoxytributylstannylbenzene (*27*), in which the benzene ring is activated by two methoxy groups. In that case, nonradioactive large-scale bromination produced the expected bromodestannylated product exclusively, while tracer-scale radiolabeling produced a radiobrominated product with the tributyltin substituent still present. In that reaction, the proton adjacent to the tributyltin on the benzene ring apparently was replaced by a radiobromine in preference to destannylation. Therefore, unknown #2 could be the product of electrophilic substitution of a proton on the activated benzene ring in **4**. Also, others have reported N-bromination as a byproduct, along with the desired product, in no-carrier-added bromination of a phenol analogue (*16*).

The low yield of the desired product **2** at low bromide concentrations (Table 3) is clearly due in part to competition with formation of unknowns #1 and #2, which are difficult to detect by HPLC in macroscopic-scale reactions using carrier-added or nonradiolabeled bromide but are readily apparent in tracer-scale radiobrominations.

Nature of the Active Electrophilic Brominating Agent in NCA Radiobromination Reactions: Dependence on Stoichiometry, Oxidant, and Solvent. If the reaction pathways for macroscopic nonradioactive (or carrier added) and tracer-scale NCA bromination are the same, both reactions should afford the same product. The differences we have observed could be due to differences in the nature of the effective brominating agents due to different levels of bromide in macroscopic versus tracer-scale reactions. Many effective brominating agents have been studied or suggested, including HOBr, H_2OBr^+, Br_2, BrCl, MeOBr, and AcOBr. Acetyl hypobromite was proposed as the effective brominating agent in acetic acid (*28*), and it is more reactive than Br_2 in electrophilic substitutions (*29*). Molecular bromine is about 10^3 times more reactive than HOBr in electrophilic substitution of *p*-xylene (*30*) and sodium *p*-anisate (*31*). Bromine chloride, about 2×10^3 times more reactive than Br_2 (*30*), has been proposed as an effective brominating agent under certain conditions (*32*) and is favored kinetically (*33*, *34*) and thermodynamically, especially in the presence of H^+ and Cl^- (*32*). When PPA or H_2O_2/AcOH is used as the oxidizing agent, HOBr is reported to form first (*23*). If the substrate does not react very rapidly with HOBr, HOBr will react further with excess of bromide to form Br_2. Formation of Br_2 is very fast ($k = 1.6 \times 10^{10}$ M^{-2} s^{-1}) (*35*, *36*) and thermodynamically favored ($K_{f(Br2)} = 2.53 \times 10^8$ M^{-2}) (Scheme 3) (*37*). However, formation of HOBr can be shifted depending on the solvent and pH of the solution (*22*, *23*, *30*, *38*). When CAT is the oxidizing agent, the mechanism is complicated, but BrCl has been proposed to be the effective brominating agent (Scheme 3) (*6*). However, BrCl can be converted to HOBr or its relatives easily by varying solvents and pH (*32*, *39*).

In the nonradioactive and carrier-added bromination of **4** (bromide $>10^{-5}$ M), the effective agent is most likely Br_2, which indeed was observed on TLC analysis ($R_f = 0.34$ in 1:1 ethyl acetate/hexanes, silica, visualized with I_2). In the no-carrier-added radiobromination, oxidation of bromide by peracetic acid is efficient, but bromide concentration is so low that formation of Br_2 is not likely. Therefore, at low bromide concentrations, the effective agent could be HOBr, AcOBr, H_2OBr^+, or MeOBr, depending on the solvent used and pH of the reaction solutions.

Molecular bromine and hypobromous acid may have different behavior in electrophilic substitution reactions. For example, HOBr has smaller steric requirements; HOBr afforded 38%

Scheme 2. Synthesis of [^{76}Br]2 from 4 or 5 Using [^{76}Br]Bromide and Various Oxidizing Agents[a]

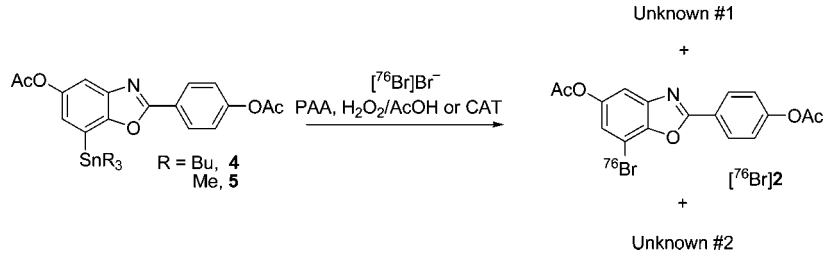

[a] Analyzed by radio-TLC.

Table 4. Byproducts Produced from Attempted Radiobromination of Tributyltin Precursor 4 Using [^{76}Br]bromide Produced in Ammonium Hydroxide and Water

		unknowns[a]	
^{76}Br/bromide	oxidizing agent	#1	#2
produced in 0.6 N NH_4OH or dried	PAA	major	none
	CAT	major	major
	2:1 H_2O_2/AcOH	major	none
produced in H_2O dried	PAA	minor	major
	CAT	minor	major
	2:1 H_2O_2/AcOH	none	none

[a] Determined by radioTLCs (silica gel).

Scheme 3. Reactions that Form Active Electrophilic Bromination Species

$$AcOOH + Br^- + H^+ \rightarrow AcOH + HOBr$$

$$HOBr + Br^- + H^+ \rightarrow Br_2 + H_2O$$

$$H^+ + HOCl + Br^- \rightarrow H_2O + BrCl$$

ortho-derivative on *t*-butylbenzene compared to 10% for Br_2 (*40*). Hypobromous acid and related sources of "positive bromine" can introduce a substituent adjacent to bulky groups in an aromatic ring (*40*). Trifluoroacetyl hypobromite (CF_3-COOBr), a relative of HOBr, also produced different electrophilic substituted products from those of Br_2 on phenol analogues (*41*).

Unified Consideration of the Nature and Activity of the Bromination Reagent and the Reactivity of the Substrate. Outcomes of radiobromination likely can be determined by altering the effective brominating agent. In a tracer-scale radiolabeling reaction with an only moderately reactive substrate, the effective brominating agent can be affected by solvent and pH. If AcOH is the solvent, the effective brominating agent might be the very reactive AcOBr, resulting in low selectivity and creating undesired radioactive byproducts. This is quite likely with no-carrier-added radiobromination of **4**. The effective brominating agent is also affected by concentration of bromine; in the carrier-added radiolabeling reactions, the effective brominating agent is Br_2, and the desired product **2** is formed exclusively, just as in the classical bromination.

The rate of aromatic bromination varies from very slow to diffusion-controlled, depending on the activation and steric effects of substituents on the aromatic rings. When the substrate is very reactive toward electrophilic substitution (such as tyrosine), it will out-compete reactive impurities in the reaction medium, and the exact chemical nature of the effective bromination agent may be less important. However, electronic and/or steric effects can render a substrate less reactive than impurities in the reaction mixture. A bulky leaving group like the tributyltin of **4** could be changed to reduce the steric effect and perhaps shift a reaction toward production of the desired product, particularly if attention also is paid to the likely effective brominating agent.

Successful Synthesis of [^{76}Br]2. As a result of these observations, NCA radiobromination on the trimethyltin precursor **5** was attempted in acetic acid using peracetic acid as an oxidizing agent. The reaction afforded slightly better yields of **2** than the corresponding reaction with tributyltin precursor **4**, but yields were still <5% because of formation of unknowns #1 and #2. This result does support the idea that altering the reactivity of the precursor can increase production of the desired radiobromo−destannylation product.

The solvent used also significantly affects the reaction. The reaction occurred quickly in acetic acid, but the most likely effective brominating agent, AcOBr, is very reactive and thus less selective. When radiobromination was carried out in a mixture of acetic acid and methanol, the reactivity of effective brominating agents was reduced by the addition of methanol. The desired bromination product **2** was the major radioactive product (61 ± 16%, $n = 5$, by radio-TLC) (Figure 3). After purification by reversed-phase HPLC, [^{76}Br]**2** was obtained in 30% yield (from 1.5 mCi [^{76}Br]bromide) with good specific activity (Once [^{76}Br]**2** was converted to [^{76}Br]**1** by the treatment of 1 M LiOH solution, the specific activity of [^{76}Br]**1** was determined by HPLC to be up to 1000 mCi/μmol). Reversed-phase HPLC analysis confirmed that [^{76}Br]**2** coeluted with an authentic sample of unlabeled **2** and that the radiochemical purity was >99% (Figure 4). Therefore, by increasing the reactivity of the precursor toward the desired substitution and decreasing the reactivity of effective brominating agent, we were able to obtain the desired radiolabeled product [^{76}Br]**2** consistently and in good yields.

Other Radiobromination Reactions. Peracetic acid is considered to be the effective oxidizing agent when a mixture of hydrogen peroxide and acetic acid is used, and it has been used in the radiobromination of steroid ligands (*10*). When premixed 2:1 H_2O_2/AcOH (up to 6 h) was used for radiobromination of precursors **4** or **5**; however, no desired product was obtained, only rapid formation of unknown #1 (Table 4). This implies that the effective brominating agent from 2:1 H_2O_2/AcOH is not reactive enough to effect electrophilic substitution with these precursors.

Hydrogen peroxide/acetic acid (2:1) was also used in the radiobromination of a 5-tributyltin substituted furfural **6**, in which the electron-rich furan ring is deactivated slightly by the aldehyde group, to make [^{76}Br]**3** (Scheme 4). [^{76}Br]**3** was used in the synthesis of a ^{76}Br-labeled progestin 16α,17α-dioxolane for breast tumor imaging and radiotherapy (*42*). Four hours of premixing of 2:1 H_2O_2/AcOH was necessary to make enough PAA to afford a high yield of bromination product **3** (Table 5). However, when 1% PPA was used as the oxidizing agent in a mixture of acetic acid and methanol, no-carrier-added radiobromination of the tributyltin precursor **6** produced only a very lipophilic product, which likely retained the tributyltin group (Supporting Information Figure S4).

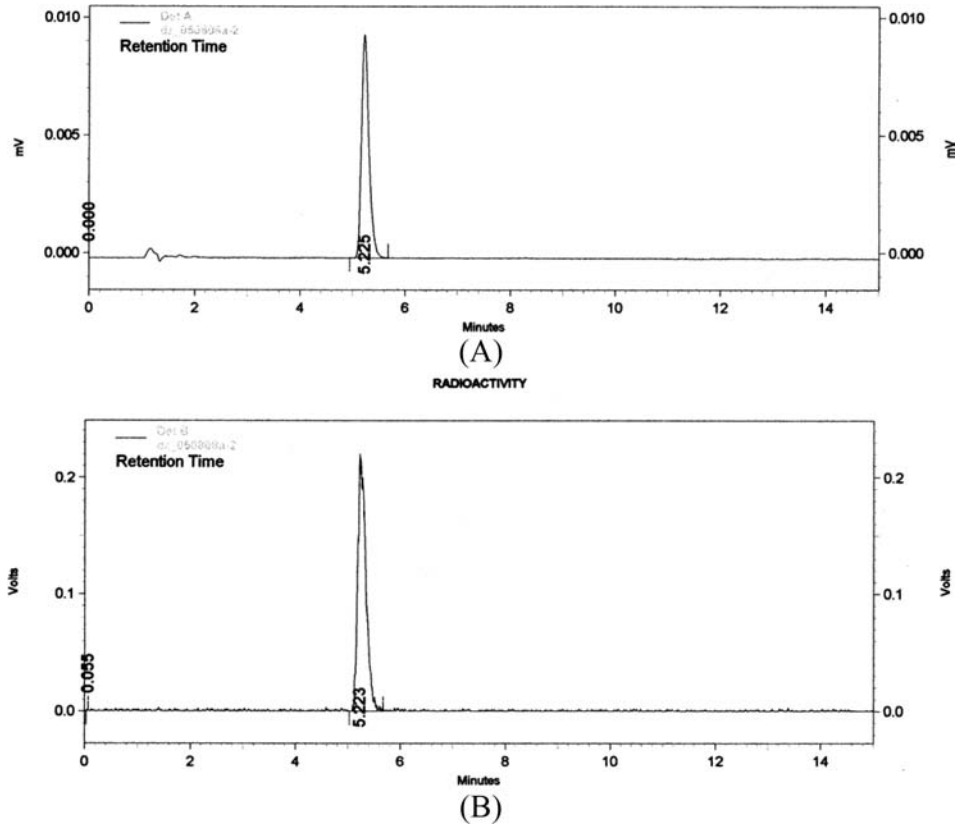

Figure 4. HPLC chromatographs of purified [^{76}Br]**2** coinjected with authentic **2**. (A) UV trace of **2** at 285 nm. (B) Radioactive trace of [^{76}Br]**2**. HPLC analysis was performed using Agilent Zorbax SB-C18 250 × 4.6 mm 5 μm analytical column and using 65% acetonitrile and 35% 0.1 M ammonium formate buffer (pH = 4.5) as mobile phase at a flow rate of 2 mL/min and UV at 285 nm.

Scheme 4. Radiobromination of 6

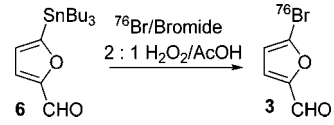

Table 5. Radiobromination of 6 Using 2:1 H_2O_2/AcOH

		premixing time (min) yield of **3** (%)[a]				
#	reaction time	0	30	60	120	240
1	15	8	30	39	62	84
2	30	11	41	53	70	84

[a] Radiochemical yield is determined by radioTLC.

As with unknown #2, this lipophilic product was not formed from a side reaction with solvents and is likely the product of electrophilic substitution other than by *ipso* substitution of the tributyltin on the furan ring under these reaction conditions, which provide a more reactive effective brominating agent than 2:1 H_2O_2/AcOH. When 1% PAA in freshly made 2:1 H_2O_2/AcOH was used, the radiobromo−destannylation product was formed exclusively, just as it was using premixed H_2O_2/AcOH. This observation is consistent with the proposed effective oxidizing agent PAA in the premixed H_2O_2/AcOH and suggests that solvent effects may contribute to the success of the radiobromination of **6**.

When this radiobromination was repeated using 1% PAA in 2:1 or 1:1 water/acetic acid to study the solvent effect, the desired product [^{76}Br]**3** was formed exclusively. Under these aqueous conditions, HOBr is probably the effective brominating agent. It is less reactive and more selective than the effective brominating agents present in acetic acid/methanol or the AcOBr in acetic acid alone. The reactivity of the effective brominating agent in different solvents increases in the order of water, methanol, and acetic acid.

In conclusion, tracer-scale NCA radiobromination differs from nonradioactive (or carrier-added) bromination and likely requires different effective brominating agents and careful attention to solvents. We suggest that the best results in tracer-scale NCA radiobromination can be achieved by considering the following:

(1) Removing highly reactive impurities that might consume the radiobromine in preference to the substrate. [Avoiding ammonium ions, carefully drying [^{76}Br]bromide and completely removing organic solvent residue from the substrate appeared to improve yields.]

(2) Increasing the specific reactivity of the precursor when possible. [Switching from the tributyltin precursor **4** to the trimethyltin precursor **5** improved yields.]

(3) Lowering the reactivity of the effective brominating agent. [Adding alcohols or water reduced side reactions and improved product yields.]

(4) Considering opportunities to reduce the number of steps. [We have shown that PAA very efficiently oxidizes bromide, and unlike CAT, PAA and solvents can be removed easily from the reaction mixture under a flow of N_2 or Ar (for nonvolatile substrate and products). This avoids extraction and/or drying in multistep reactions in which anhydrous conditions are needed, such as radiolabeling of steroids (*10*) and Bolton Hunter reagent (*43*).

SUMMARY AND CONCLUSION

Ipso substitution by electrophilic demetalation effectively introduces radiobromine regiospecifically into organic compounds containing aromatic rings, but competition can occur with other reactive sites, such as open positions on an activated aromatic ring and amine or amide groups. At the tracer level,

low reactivity of the substrate can result in competitive reactions with reactive impurities present in reagents or solvents, and this competition can be modulated by solvent and pH, which alter the effective brominating agent. Therefore, a clear understanding of the nature of effective brominating agents and the reactivity of the substrate is important in developing methods for radiobromination of organic compounds.

By considering these factors, we were able to label **2** and **3** from the two trialkyltin precursors **5** and **6** with ^{76}Br reliably and in good yield. We hope our strategy will help others achieve tracer-scale radiobromination of aromatic compounds of interest.

ACKNOWLEDGMENT

The authors thank Bill Margenau, Pat Margenau, Rajendra Singh, Lucie Tang, Grainne Biddlecombe, and Tom Voller for the production of [^{76}Br] isotope. In addition, special thanks go to Joanna B. Downer for excellent editorial assistance and helpful comments. This work was supported by grants from the National Cancer Institute (R24 CA086307 to M.J.W., and R01 CA25836 to J.A.K.).

Supporting Information Available: Synthesis of [^{76}Br]**3** using premixed 2:1 H_2O_2/AcOH and using PAA/H_2O; radio-TLCs of radiobromination of **4** and its control reaction; ion chromatographs of [^{76}Br]bromide extracted in 0.6 N NH_4OH; radio-TLCs of control reactions using solvents THF, acetonitrile, and DMF; radio-TLCs of radiobromination of **6** and its control reaction; HPLC chromatograph of nonradioactive synthesis of **2** from **4** using NH_4Br and PAA; and HPLC chromatographs of a reaction mixture from attempted synthesis of [^{76}Br]**2** from **4**. This material is available free of charge via the Internet at http://pubs.acs.org.

LITERATURE CITED

(1) For reviews, see: *Handbook of Radiopharmaceuticals* (2003) (Welch, M. J., and Redvanly, C. S., Eds.) John Wiley & Sons Ltd., New York.

(2) Lasne, M.-C., Perrio, C., Rouden, J., Barré, L., Roeda, D., Dolle, F., and Crouzel, C. (2002) Chemistry of β^+-emitting compounds based on fluorine-18. *Top. Curr. Chem. 222*, 201–258.

(3) Bolton, R. (2002) Radiohalogen incorporation into organic systems. *J. Label. Compd. Radiopharm. 45*, 485–528.

(4) Seevers, R. H., and Counsell, R. E. (1982) Radioiodination techniques for small organic molecules. *Chem. Rev. 82*, 575–590.

(5) Eisenhut, M., and Mier, W. (2004) *Radioiodination Chemistry and Radioiodinated Compounds. Handbook of Nuclear Chemistry. Volume 4: Radiochemistry and Radiopharmaceutical Chemistry in Life Sciences* (Vértes, A., Nagy, S., and Klencsár, Z., Eds.) pp 257−278, Chapter 7, Springer, New York.

(6) Coenen, H. H., Moerlein, S. M., and Stoecklin, G. (1983) No-carrier added radiohalogenation methods with heavy halogens. *Radiochim. Acta 34*, 47–68.

(7) Mazière, B., and Loc'h, C. (1986) Radiopharmaceuticals labelled with bromine isotopes. *Appl. Radiat. Isot. 37*, 703–713.

(8) Rowland, D. J., McCarthy, T. J., and Welch, M. J. (2003) *Radiobromine for imaging and therapy. Handbook of Radiopharmaceuticals* (Welch, M. J., and Redvanly, C. S., Eds.) pp 441−65, Chapter 14, John Wiley & Sons Ltd., New York.

(9) *Radiopharmaceuticals for Positron Emission Tomography* (1993) (Stöcklin, G., and Pike, V. W., Eds.) p 3, Springer, New York.

(10) Tolmachev, V., Lövqvist, A., Einarsson, L., Schultz, J., and Lundqvist, H. (1998) Production of ^{76}Br by a low-energy cyclotron. *Appl. Radiat. Isot. 49*, 1537–1540.

(11) Malamas, M. S., Manas, E. S., McDevitt, R. E., Gunawan, I., Xu, Z. B., Collini, M. D., Miller, C. P., Dinh, T., Henderson, R. A., Jr., and Harris, H. A. (2004) Design and synthesis of aryl diphenolic azoles as potent and selective estrogen receptor ligands. *J. Med. Chem. 47*, 5021–5040.

(12) Harris, H. A., Albert, L. M., Leathurby, Y., Malamas, M. S., Mewshaw, R. E., Miller, C. P., Kharode, Y. P., Marzolf, J., Komm, B. S., Winneker, R. C., Frail, D. E., Henderson, R. A., Zhu, Y., and Keith, J. C., Jr. (2003) Evaluation of an estrogen receptor-β agonist in animal models of human disease. *Endocrinology 144*, 4241–4249.

(13) Denat, F., Gaspard-Iloughmane, H., and Dubac, J. (1992) An easy one-pot synthesis of group 14 C-metallated 2(or 3)-furan- and thiophenecarbaldehydes. *Synthesis 10*, 954–956.

(14) Tang, L. (2008) Radionuclide production and yields at Washington University School of Medicine. *Q. J. Nucl. Med. Mol. Imaging 52*, 121–133.

(15) Petzold, G., and Coenen, H. H. (1981) Chloramine-T for no-carrier-added labelling of aromatic biomolecules with bromine-75, 77. *J. Label. Compd. Radiopharm. 18*, 1319–1336.

(16) Suehiro, M., Iwamoto, M., Arai, I., and Nozaki, T. (1990) Bromination, no-carrier-added radiobromination and simultaneously occurring chlorination by chloramine-T. *Appl. Radiat. Isot. 41*, 439–447.

(17) Katzenellenbogen, J. A., Senderoff, S. G., McElvany, K. D., Jr., and Welch, M. J. (1981) 16 alpha-[^{77}Br]bromoestradiol-17 beta: a high specific-activity, gamma-emitting tracer with uptake in rat uterus and uterus and induced mammary tumors. *J. Nucl. Med. 22*, 42–47.

(18) Senderoff, S. G., McElvany, K. D., Carlson, K. E., Heiman, D. F., Katzenellenbogen, J. A., and Welch, M. J. (1982) Methodology for the synthesis and specific activity determination of 16 alpha-[^{77}Br]-bromoestradiol-17 beta and 16 alpha-[^{77}Br]-11 beta-methoxyestradiol-17 beta, two estrogen receptor-binding radiopharmaceuticals. *Int. J. Appl. Radiat. Isot. 33*, 545–551.

(19) Katzenellenbogen, J. A., McElvany, K. D., Senderoff, S. G., Carlson, K. E., Landvatter, S. W., and Welch, M. J. (1982) 16 alpha-[^{77}Br]bromo-11 beta-methoxyestradiol-17 beta: a gamma-emitting estrogen imaging agent with high uptake and retention by target organs. *J. Nucl. Med. 23*, 411–419.

(20) Adam, M. J., Ruth, T. J., Homma, Y., and Pate, B. D. (1985) Radiobromination of aromatic compounds by cleavage of aryltin bonds. *Int. J. Appl. Radiat. Isot. 36*, 935–937.

(21) Moerlein, S. M., and Coenen, H. H. (1985) Regiospecific no-carrier-added radiobromination and radioiodination of aryltrimethyl group IVb organometallics. *J. Chem. Soc., Perkin Trans.* 1941–1947.

(22) Mohammad, A., and Liebhafsky, H. A. (1934) The kinetics of the reduction of hydrogen peroxide by the halides. *J. Am. Chem. Soc. 56*, 1680–1685.

(23) Fortnum, D. H., Battaglia, C. J., Cohen, S. R., and Edwards, J. O. (1960) The kinetics of the oxidation of halide ions by monosubstituted peroxides. *J. Am. Chem. Soc. 82*, 778–782.

(24) Wajon, J. E., and Morris, J. C. (1982) Rates of formation of N-bromo amines in aqueous solution. *Inorg. Chem. 21*, 4258–4263.

(25) Inman, G. W., Jr., and Johnson, J. D. (1984) Kinetics of monobromamine disproportionation-dibromamine formation in aqueous ammonia solutions. *Environ. Sci. Technol. 18*, 219–224.

(26) Mellegaard-Waetzig, S. R., Wang, C., and Tunge, J. A. (2006) Selenium-catalyzed oxidative halogenation. *Tetrahedron 62*, 7191–7198.

(27) Lang, L., Ma, Y., Jagoda, E. M., Kim, B. M., Rice, K. C., Szajek, L. P., Contoreggi, C., Eckelman, W. C., and Kiesewetter, D. O. (2007) [^{76}Br]BMK-152: a PET ligand for corticotropin-releasing hormone (CRH) type 1 receptor. *J. Label. Compd. Radiopharm. 50*, S56.

(28) Ogata, Y., and Aoki, K. (1966) Haloacyloxylation. II. addition of bromine or chlorine to propylene in the presence of peracetic acid. *J. Org. Chem. 31*, 4181–4183.

(29) Barnett, J. R., Andrews, L. J., and Keefer, R. M. (1972) Trifluoroacetyl hypohalites as aromatic halogenating agents. *J. Am. Chem. Soc. 94*, 6129–6134.

(30) Voudrias, E. A., and Reinhard, M. (1988) Reactivities of hypochlorous and hypobromous acid, chlorine monoxide, hypobromous acidium ion, chlorine, bromine, and bromine chloride in electrophilic aromatic substitution reactions with p-xylene in water. *Environ. Sci. Technol. 22*, 1049–1056.

(31) Derbyshire, D. H., and Waters, W. A. (1950) Significance of bromine cation in aromatic substitution. I. Kinetic evidence. *J. Chem. Soc.* 564–573.

(32) Wang, T. X., Kelley, M. D., Cooper, J. N., Beckwith, R. C., and Margerum, D. W. (1994) Equilibrium, kinetic, and UV-spectral characteristics of aqueous bromine chloride, bromine, and chlorine species. *Inorg. Chem. 33*, 5872–5878.

(33) Sander, R., and Crutzen, P. J. (1996) Model study indicating halogen activation and ozone destruction in polluted air masses transported to the sea. *J. Geophys. Res. 101*, 9121–9138.

(34) Farkas, L., Lewin, M., and Bloch, R. (1949) The reaction between hypochlorite and bromides. *J. Am. Chem. Soc. 71*, 1988–1991.

(35) Bielski, B. H. J., Cabelli, D. E., Arudi, R. L., and Ross, A. B. (1985) Reactivity of HO_2/O_2 radicals in aquesous solution. *J. Phys. Chem. Ref. Data 14*, 1041–1100.

(36) Eigen, M., and Kustin, K. (1962) The kinetics of halogen hydrolysis. *J. Am. Chem. Soc. 84*, 1355–1361.

(37) Liebhafsky, H. A. (1934) The equilibrium constant of the bromine hydrolysis and its variation with temperature. *J. Am. Chem. Soc. 56*, 1500–1505.

(38) Gilow, H. M., and Ridd, J. H. (1973) Mechanism of aromatic bromination by hypobromous acid in aqueous perchloric acid. Kinetic evidence against the prior formation of 'positive bromine'. *J. Chem. Soc., Perkin Trans. 2*, 1321–1327.

(39) Kumar, K., and Margerum, D. W. (1987) Kinetics and mechanism of general-acid-assisted oxidation of bromide by hypochlorite and hypochlorous acid. *Inorg. Chem. 26*, 2706–2711.

(40) De la Mare, P. B. D. (1976) *Electrophilic halogenation: reaction pathways involving attack by electrophilic halogens on unsaturated compounds*, p 125, Chapter 7, Cambridge University Press, London.

(41) Langer, O., Dollé, F., Loc'h, C., Halldin, C., Vaufrey, F., Coulon, C., Crouzel, C., Någren, K., and Mazière, B. (1997) Preparation of 4- and 6-[^{76}Br] bromometaraminol, two potential radiotracers for the study of the myocardial norepinephrine neuronal reuptake system with PET. *J. Label. Compd. Radiopharm. 39*, 803–816.

(42) Zhou, D., Sharp, T. L., Fettig, N. M., Lee, H., Lewis, J. S., Katzenellenbogen, J. A., and Welch, M. J. (2008) Evaluation of a bromine-76-labeled progestin 16α,17α-dioxolane for breast tumor imaging and radiotherapy: in vivo biodistribution and metabolic stability studies. *Nucl. Med. Biol. 35*, 655–663.

(43) Bolton, A. E., and Hunter, W. M. (1973) The labeling of proteins to high specific radioactivities by conjugation to a ^{125}I-containing acylating agent. *Biochem. J. 133*, 529–539.

BC800313C

Supporting Information

Bromination from the Macroscopic Level to the Tracer Radiochemical Level: ^{76}Br Radiolabeling of Aromatic Compounds via Electrophilic Substitution

Dong Zhou, Haibing Zhou, Carl C. Jenks, Jason S. Lewis, John A. Katzenellenbogen, and Michael J. Welch

Table of Contents:

1. Synthesis of [^{76}Br]5-bromo-2-furaldehyde [^{76}Br]**3**……..……..S2
2. Figure S1. Radio-TLCs of radiobromination of **4** and its control reaction showing the lipophilic byproducts…….……..…….S3
3. Figure S2. Chromatograph of [^{76}Br]bromide extracted in 0.6 N NH_4OH: UV and radioactive detection; and 0.6 N NH_4OH only……...…….……S4
4. Figure S3. Radio-TLCs of control reactions using different solvents THF, acetonitrile, and DMF…….…….…….S5
5. Figure S4. Radio-TLCs of radiobromination from **6** and its control reaction showing the formation of lipophilic byproducts……...……..…..S6
6. Figure S5. HPLC chromatograph of non-radioactive synthesis of **2** from **4** using NH_4Br and peracetic acid…….……S7
7. Figure S6. HPLC chromatographs of a reaction mixture from attempted synthesis of [^{76}Br]**2** from **4**, showing [^{76}Br]Bromide, unknown #1, and [^{76}Br]**2**…….S8

Synthesis of [^{76}Br]5-bromo-2-furaldehyde ([^{76}Br]3)

Using premixed 2:1 hydrogen peroxide/acetic acid: [^{76}Br]NH_4Br (~10 mCi) was dried in a 5 mL Wheaton V vial at 130 $^{\circ}$C under very gentle N_2 flow. At ambient temperature, acetic acid (20 µL) and a solution of **6** (0.5 mg) in methanol (50 µL) were added, and the solution was vortexed before addition of 2:1 hydrogen peroxide/acetic acid (100 µL, pre-mixed for at least 4 h). Then the reaction mixture was vortexed to homogeneity. Upon completion of the reaction in 30 min (> 80% incorporation according to radio-TLC analysis: silica gel plate, 1:1 ethyl acetate/hexanes, R_f = 0.8), the reaction was quenched by addition of water (2 mL). [^{76}Br]**3** was confirmed by silica radio-TLC and HPLC co-injection with authentic standard **3**. HPLC: Alltech Econosil C18 250×4.6 10µ, 55% acetonitrile, 45% water, 1.5 mL/min, 254 nm, T_R = 4.5 min.

Using peracetic acid: Into a 5 mL Wheaton V vial containing dried [^{76}Br]NH_4Br (~0.9 mCi) were added a solution of **6** (0.3 mg) in methanol (30 µL) and acetic acid (10 µL). The mixture was vortexed to homogeneity, then 1% PAA in 2:1 hydrogen peroxide(35% in water)/acetic acid (60 µL) and the mixture was vortexed again. According to radio-TLC, >90% incorporation of [^{76}Br]bromide was observed within 7 min.

Note: The same procedure for using PAA in 1:1 or 2:1 water/acetic acid mixture. However, organic compounds have better solubility in hydrogen peroxide/acetic acid.

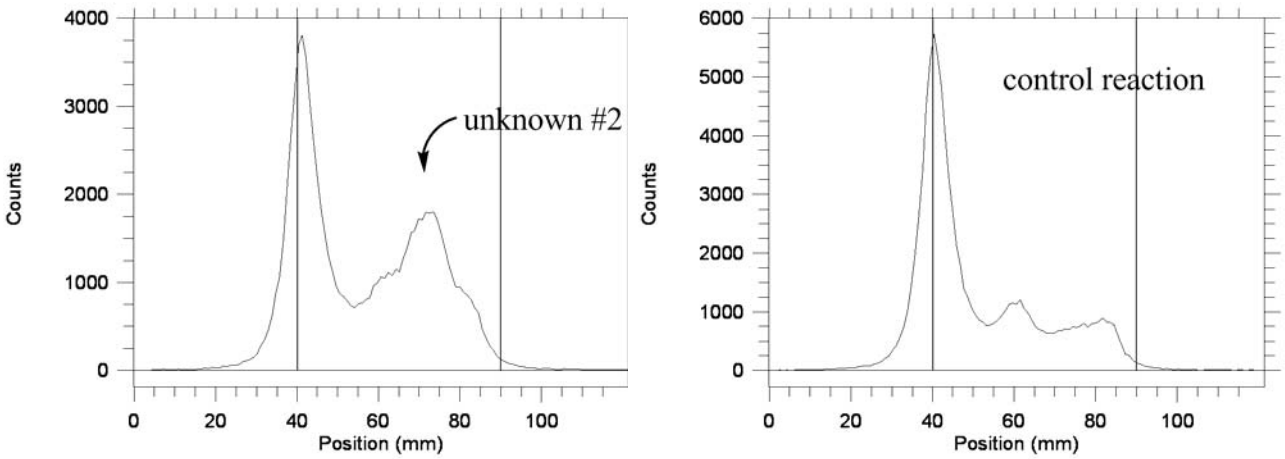

Figure S1. Radio-TLCs of radiobromination of **4** (a) and its control reaction (b) showing the lipophilic byproducts (Silica gel, 4:1 hexanes/ethyl acetate)

Reaction condition:

(a) ^{76}Br (produced in water, dried at 130 °C), acetic acid (100 µL), **4** (0.12 mg) in ethanol (20 µL), CAT (50 µL) from a solution of CAT (3.7 mg) in ethanol (2000 µL);

(b) ^{76}Br (produced in water, dried at 130 °C), acetic acid (100 µL), CAT (50 µL) from a solution of CAT (3.7 mg) in ethanol (2000 µL).

Note: Around 50% of the lipophilic byproducts was from the reaction with **4** (*panel a*), the rest was from the reaction with reactive species in the reaction mixture (*panel b*)

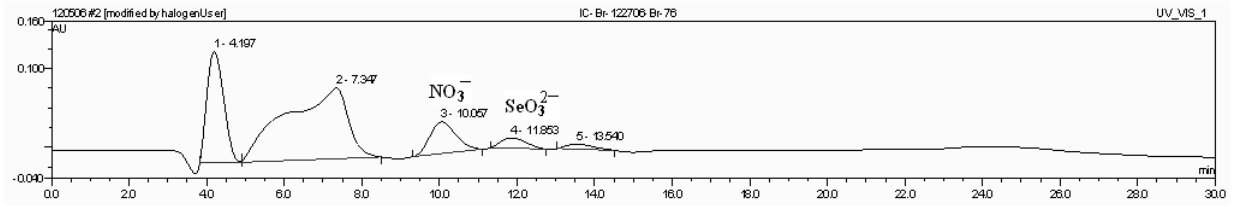

(a)

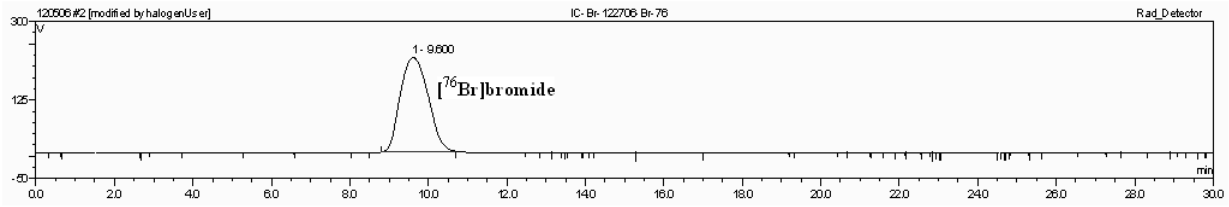

(b)

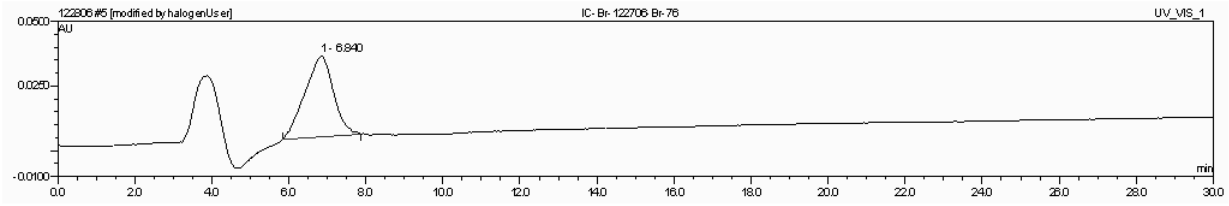

(c)

Figure S2. Ion Chromatography of [^{76}Br]bromide extracted in 0.6 N NH_4OH (a) UV trace at 210nm (b) radioactive trace (c) UV trace of 0.6 N NH_4OH only. (UV at 210 nm)

Note: Only [^{76}Br]bromide was observed in the IC, no other radioactive peaks were observed (*panel b*); no NO_3^- was observed in 0.6 N NH_4OH (*panel c*).

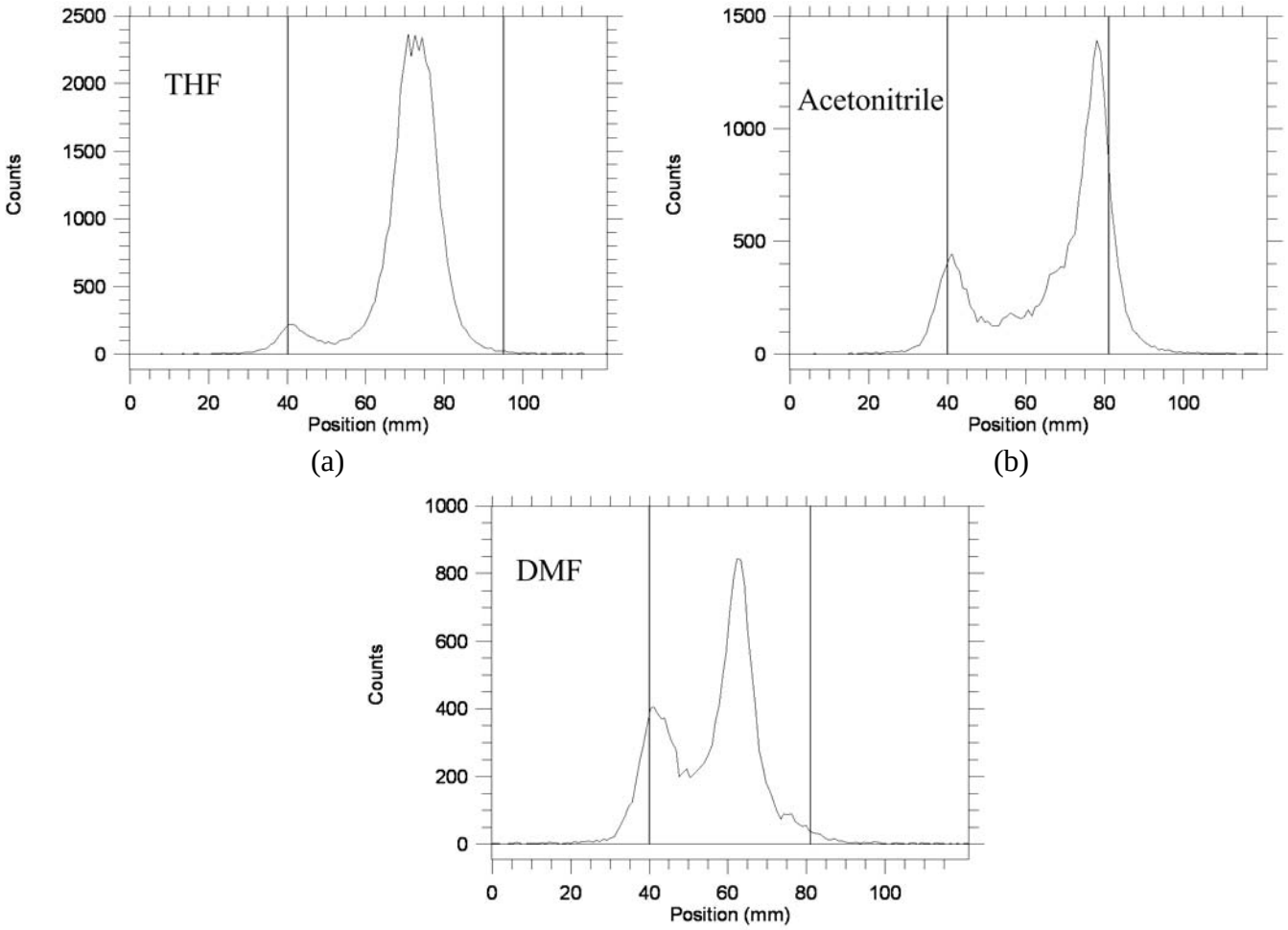

Figure S3. Radio-TLCs of control reactions using different solvents (a) THF (b) acetonitrile (c) DMF (Silica gel, 1:1 ethyl acetate/hexanes)

Reaction condition:

(a) ^{76}Br (dried, 20 µCi) in MeOH (10 µL), THF (200 µL), acetic acid (100 µL), PAA (1%) in MeOH (100 µL) (5 min);

(b) ^{76}Br (dried, 15 µCi) in MeOH (5 µL), MeCN (200 µL), acetic acid (50 µL), PAA (3%) in MeOH (100 µL) (10 min);

(c) ^{76}Br (dried, 15 µCi) in MeOH (5 µL), DMF (200 µL), acetic acid (50 µL), PAA (3%) in MeOH (100 µL) (10 min).

Note: A radioactive product was formed rapidly in the presence of THF, acetonitrile or DMF, respectively, in the above control reactions. These radioactive products were the same as those observed in the radiobromination of **4** or **5** when the above solvents were used.

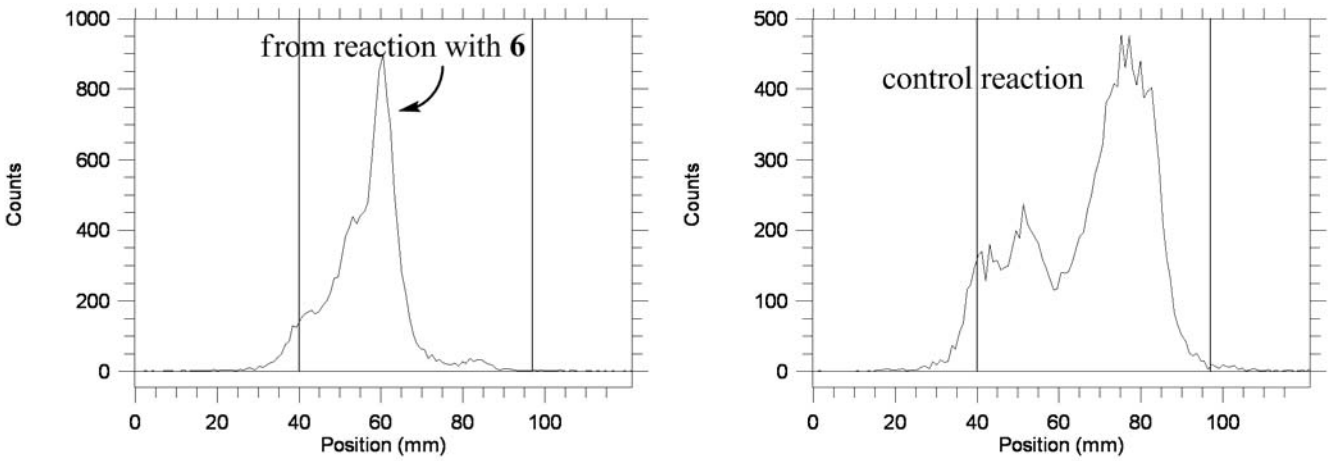

(a) (b)

Figure S4. Radio-TLCs of radiobromination of **6** (a) and its control reaction (b) showing the formation of lipophilic byproducts (Silica gel, 1:12 ethyl acetate/hexanes)

Reaction condition:

(a) ^{76}Br in MeOH (10 µL), **6** (1.0 mg) in MeOH (100 µL), acetic acid (100 µL), PAA (1%) in acetic acid (100 µL);

(b) ^{76}Br in MeOH (10 µL), MeOH (100 µL), acetic acid (100 µL), PAA (1%) in acetic acid (100 µL).

Note: A major radioactive product (*panel a*) was observed in the reaction with tributyl precursor **6**; however, this product was more lipophilic than **6** according to the radio-TLC; this peak was not observed in the control reaction (*panel b*).

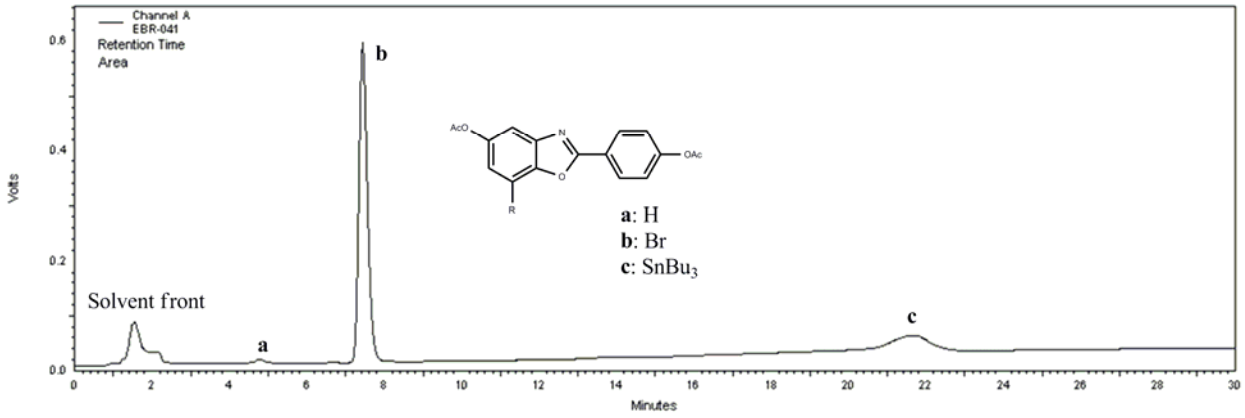

Figure S5. HPLC chromatograph of a non-radioactive synthesis of **2** from **4** using NH_4Br and PAA.

HPLC: Alltech Altima C18 250×4.6 mm 10µ, 285 nm, 2 mL/min; Gradient: Solvent A: Acetonitrile; Solvent B: ammonium formate buffer (0.1 M, pH = 4.5) A: 60%-90 % (0-20 min), 90% (20-30 min).

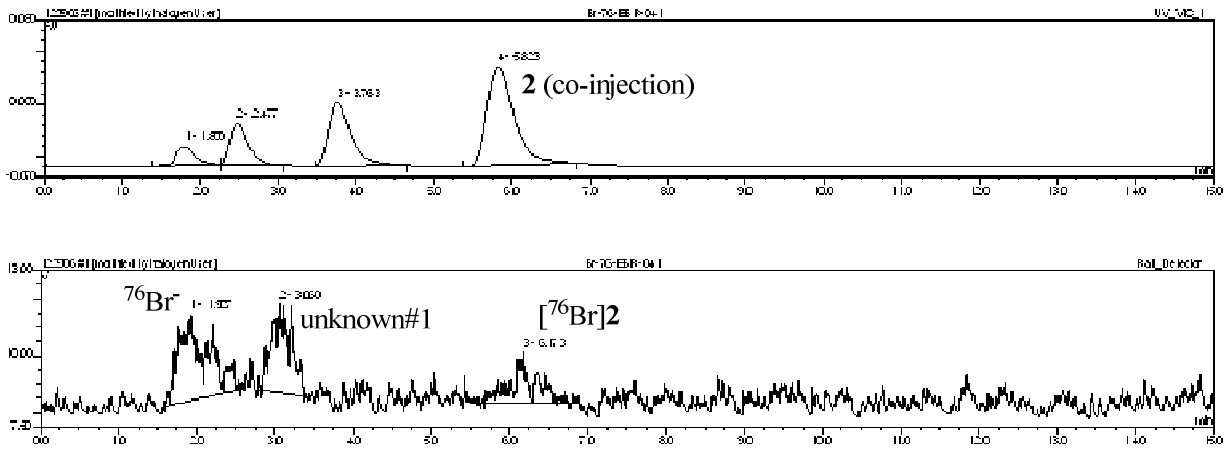

Figure S6. HPLC chromatographs of a reaction mixture from an attempted synthesis of [^{76}Br]**2** from **4**, showing [^{76}Br]Bromide, unknown #1, and [^{76}Br]**2** (co-injected with 2).

HPLC (Alltech Econosil, 250×4.6 mm, 10µ, 65% acetonitrile, 35% ammonium formate buffer (pH = 4.5), 2 mL/minun, 285 nm): [^{76}Br]bromide, t_R = 1.93 min, unknown #1, t_R = 3.06 min, [^{76}Br]**2**, t_R = 6.17 min, unknown #2 won't be eluted.

New Strategy for the Preparation of Clickable Peptides and Labeling with 1-(Azidomethyl)-4-[^{18}F]-fluorobenzene for PET

David Thonon,* Cécile Kech, Jérôme Paris, Christian Lemaire, and André Luxen

Cyclotron Research Center, Liege University, Sart-Tilman B.30, B-4000 Liege, Belgium. Received December 16, 2008; Revised Manuscript Received February 16, 2009

The alkyne-azide Cu(I)-catalyzed Huisgen cycloaddition, a click type reaction was used to label a peptide with fluorine-18. A novel solid phase synthesis approach for the preparation of clickable peptides has been developed and has also permitted the straightforward preparation of reference compounds. A complementary azide labeling agent (1-(azidomethyl)-4-[^{18}F]-fluorobenzene) has been produced in a four step procedure in 75 min with a 34% radiochemical yield (decay corrected). Conjugation of [^{18}F]fluoroazide with a model alkyne-neuropeptide produced the desired ^{18}F-radiolabeled peptide in less than 15 min with a yield of 90% and excellent radiochemical purity.

INTRODUCTION

Molecular imaging allows in vivo imaging of gene expression, optimizing drug therapy and imaging drug effect at the molecular and cellular level and may also be useful in detecting pathology at a predisease state (*1*). Thanks to its high sensitivity ($10^{-9}-10^{-12}$ M) and quantitative nature, positron emission tomography (PET[1]) is ideally suited to image molecular processes. Among a number of positron-emitting nuclides, fluorine-18 is particularly attractive for labeling biomolecules due to its favorable physical and nuclear properties.

The challenge for the radiochemist is to introduce a short half-life radioisotope (fluorine-18, $t_{1/2}$ 109.7 min) onto biomolecules that are specific to the biological process studied. As ^{18}F fluoride introduction onto organic compounds requires pretty harsh reaction conditions and is not compatible with H-acidic functions (*2*), biocompounds (e.g., peptides, proteins, antibodies, and oligonucleotides) are usually labeled with ^{18}F by means of prosthetic groups (*3*). A large number of ^{18}F labeled prosthetic groups have been developed (*4*), but none has emerged as a standard method because each has its own advantages and limitations (*5*). The main limitation of most advanced methods is that they are not site-specific as the labeling is accomplished through an amino group (N-terminus or lysine side chain), which is frequently contained in multiple copies in peptides. Therefore, the search for a rapid, selective, and generic method for radiolabeling biomolecules continues. Reactions defined as click reactions respond well to these criteria (*6, 7*). Moreover, these reactions are particularly well adapted to the preparation of radiopharmaceuticals as they require only benign reaction conditions and simple workup and purification procedures. Among these reactions, the Cu(I) catalyzed formation of 1,2,3-triazole using Huisgen 1,3-dipolar cycloaddition of alkynes with azides is the most explored reaction. In principle, this cycloaddition can be performed in the presence of water and oxygen and is orthogonal to any functional group and can thus be performed without the protection of other functional groups (*6, 7*).

For these reasons, our group and several other laboratories around the world have begun to evaluate this reaction to bind ^{18}F tagged molecules to biocompounds. In 2006, Marik and Sutcliffe reported the labeling of peptides bearing *N*-(3-azidopropionyl)-groups with volatile ω-[^{18}F]fluoroalkynes in 10 min with yields of 54−99% (coupling step) (*8*). Two other authors have recently reported the preparation of ^{18}F labeled synthons bearing both an alkyne function and a short polyethylene glycol linker to reduce volatility and obtain water solubility (*9, 10*). Various azido-containing molecules have been labeled with these bifunctional tracers. In particular, Li has labeled azido-RGD peptides in 20 min with a yield of 69% (coupling step). A more indirect approach has been followed by Ramenda and Wuest who have prepared a click building block by derivatizing the well-known *N*-succinimidyl-4-[^{18}F]fluorobenzoate [^{18}F]SFB with propargyl amine. This synthon has been used to label azido-neurotensin in 20 min with a yield of 66% (decay corrected, coupling step). Although a lot of effort has been applied to the preparation of an alkyne synthon, only one publication by Glaser and Årstad has described an azide synthon (*11*). After purification by distillation, 2-[^{18}F]fluoroethylazide was linked to a model peptide derivatized with propargylic acid in 15 min with a yield of 92% (decay corrected, coupling step).

In this technical note, we describe the radiosynthesis of a new azide synthon: 1-(azidomethyl)-4-[^{18}F]-fluorobenzene **[^{18}F]5** bearing an aromatic bound fluorine, which is known to be less susceptible to *in vivo* radiodefluorination (*12*). An original method to functionalize peptides with alkyne is also depicted. Finally, this new synthon has been used to label a model alkyne amino acid and an alkynylated neuropeptide by click chemistry (Figure 1).

EXPERIMENTAL PROCEDURES

General. All solvents and chemicals were of analytical grade and used without further purification. The [^{18}O]-enriched water was purchased from Cambridge Isotope Laboratories. Mass spectra were recorded with a Finnigan TSQ7000 mass spectrometer (ThermoElectronCorp.) operating in full-scan MS mode with an ESI+ source and with a Bruker Daltonics micrOTOF

* Corresponding author. Phone: +32 4 3662310. Fax: +32 4 3662946. E-mail: dthonon@ulg.ac.be.

[1]Abbreviations: DIEA, *N*,*N*-diisopropylethylamine; DMF, dimethylformamide; DMSO, dimethylsulfoxide; Enk, enkephalin (H-Tyr-Gly-Gly-Phe-Xxx-OH); [Leu^5]-Enk (Xxx=Leu); Fmoc, 9-fluorenylmethoxycarbonyl; HBTU, *O*-(benzotriazol-1-yl)-*N*,*N*,*N*′,*N*′-tetramethyluronium hexafluorophosphate; Kryptofix 222, 4,7,13,16,21,24-hexaoxa-1,10-diazabicyclo[8.8.8]-hexacosane; PET, positron emission tomography; pEPA and Phe (≡), *p*-ethynyl-L-phenylalanine; QMA, quaternary methyl ammonium; SPPS, solid-phase peptide synthesis; TBAF, tetrabutylammonium fluoride; TFA, trifluoracetic acid; THF, tetrahydrofuran; TMS, tetramethylsilane; TMS-≡, trimethylsilylacetylene.

10.1021/bc800544p CCC: $40.75 © 2009 American Chemical Society
Published on Web 03/26/2009

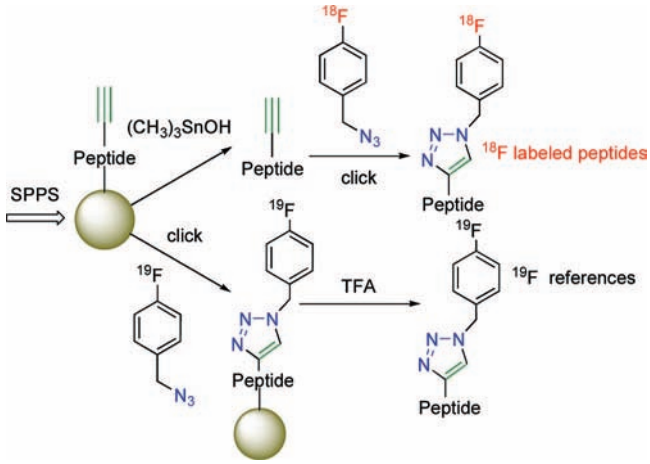

Figure 1. Synthetic strategies for the preparation of ^{18}F labeled peptides and ^{19}F references.

spectrometer (TOF-ES-MS). ^{1}H and ^{13}C NMR spectra were recorded on a Bruker AM 400 (^{1}H at 400 MHz and ^{13}C at 100 MHz). ^{1}H and ^{13}C spectra were referenced to TMS using the ^{13}C or residual proton signals of the deuterated solvents as internal standards. HPLC analyses were run on a Waters system (616 pump, a manual Rheodyne injector, 996 PDA detector,and NaI(Tl) scintillation detector from Eberline) controlled by the Empower program. Analyses were performed on an XTerra C18 column from Waters (150 × 4.6 mm, 3.5 μM) with CH_3CN and H_2O containing 0.1% TFA mixture (proportions given in parentheses) at 1 mL/min. Preparative HPLC was performed on a SymmetryPrep C18 column from Waters (300 × 7.8 mm, 7 μM). A Gilson model 233 XL reactarray automatic injection system was remotely controlled to achieve the radiosynthesis of **[^{18}F]5**. A Bioscan TLC scanner model AR2000 was used for analysis of the ^{18}F labeled compounds. Radiochemical yields are given decay corrected and take into account the losses due to transfer. *p*-Iodophenylalanine has been synthetized according to Ousmer (*13*), and Fmoc protection was carried out according to the standard procedure (*14*). 4-Ethynyl-L-phenylalanine (**6**) has been prepared according Zimmer (*15*). Peptide synthesis were carried out on an automated solid phase peptide synthesizer PS3 (Protein Technologies) by a Fmoc strategy employing HBTU as the coupling reagent. Enantiomerically pure L-amino acids were obtained from IRIS Biotech.

Chemistry. *(S)-2-Amino-3-(4-(1-(4-fluorobenzyl)-1H-1,2,3-triazol-4-yl)phenyl)propanoic Acid (**8**).* Twenty milligrams of 4-ethynyl-L-phenylalanine (**6**) (0.106 mmol), 40 mg of copper (I) iodide (2 equiv., 0.210 mmol), 55 mg of DIEA (4 equiv., 0.424mmol), and 16 mg of 1-(azidomethyl)-4-fluorobenzene (**5**) (0.106 mmol) were mixed in 3 mL of DMF. This solution was stirred for 4 h. The solvent was eliminated under vacuum. The residue obtained was suspended in acetonitrile and pre-purified by dry flash chromatography on silicagel (the column was washed by EtOAc and MeOH, and compound **8** was eluted by MeOH/NH_3 25% 3:1). The solid obtained was finally purified by HPLC (4 mL/min, CH_3CN/H_2O 25:75, 0.1% TFA) to furnish 13 mg (0.038 mmol, 36%) of the desired compound. TOF-ES-MS: *m/z* 341.1413 for $[MH]^+$ ($C_{18}H_{18}FN_4O_2$, calculated [MW] 341.1408). ^{1}H NMR (CD_3OD), δ: 8.36 (s, 1H, CH triazole), 7.84 (m, 2H, H_{Ar}, C_6H_4), 7.40 (m, 4H), 7.13 (m, 2H, H_{Ar}, C_6H_4F), 5.64 (s, 2H, $CH_2C_6H_4F$), 4.29 (m, 1H, $C_{\alpha,Phe}H$), 3.33−3.17 (m, 2H, $C_{\beta,Phe}H_2$) ppm.^{13}C NMR (CD_3OD) δ 178.6 (C═O), 166.75 (d, J = 246 Hz, C−F), 134.4, 131.4, 130.0, 129.9, 129.8, 129.7, 125.9, 121.0, 115.3 (d, ^3J = 22 Hz, $C_{ortho\text{-}F}$), 52.9 ($\underline{CH_2}C_6H_4F$), 47.6 ($C_{\alpha,Phe}$), 35.7 ($C_{\beta,Phe}$) ppm.

*[Ac-Tyr(tBu)^1, Phe (≡)^4, Leu^5)]-Enk bound to Wang Resin **11**.* Four hundred milligrams of peptide **10** (≤0.250 mmol) still bound to the resin was suspended in 4.5 mL of a degassed mixture of DMF/NEt_3 (2:1). Then 179 mg of trimethylsilylacetylene (1.82 mmol) was added to the reaction mixture followed by 15 min of degassing. Then 25 mg of CuI (0.13 mmol) and 50 mg of $Pd(PPh_3)_2Cl_2$ (0.071 mmol) were added, and the suspension was stirred overnight. The reaction mixture was filtered through a Büchner funnel, and the resin was successively rinsed with DMF, H_2O, EtOH, and CH_2Cl_2 and dried under reduced pressure.

Two hundred milligrams (≤0.125 mmol) of the obtained solid was suspended in 20 mL of THF at −78 °C. To this suspension was added 1600 μL of a solution 1 M of tetrabutylammonium fluoride in THF. This mixture was first stirred for 15 min at −78 °C then 30 min at RT. The reaction mixture was filtered through a Büchner funnel, and the resin was successively rinsed with THF, H_2O, EtOH, and CH_2Cl_2 and dried under reduced pressure.

[Ac-Tyr^1, Phe (1-(4-fluorobenzyl))-1H-1,2,3-triazol-4-yl)^4, Leu^5]-Enk **13.** Eighty milligrams of peptide **11** bound to the Wang resin (≤0.05 mmmol), 18 mg of copper (I) bromide (2 equiv., 0.126 mmol), 47 mg of DIEA (0.360 mmol), and 9 mg of 4-fluorobenzyle azide **5** (0.060 mmol) were mixed in 3 mL of DMF. The reaction medium was stirred under an inert atmosphere at RT overnight. The suspension was filtered through a Büchner funnel and the resin was successively rinsed with DMF, H_2O, EtOH, and CH_2Cl_2. Final deprotection and cleavage from the resin was performed with a TFA mixture (TFA/H_2O/anisole = 90:5:5, 5.5 mL, 3 h). The suspension was filtered and the resin washed once again with TFA. The filtrate was evaporated to dryness. The obtained oily residue was dissolved in a minimum of TFA, and ether was added to precipitate the peptide. This suspension was centrifuged (2500 rpm, 10 min). The supernatant was eliminated, and the obtained solid was washed with ether. The compound was purified by preparative HPLC (CH_3CN/H_2O 40:60 containing 0.1% TFA). Elimination of the solvent provided 10 mg of the targeted compound (0.013 mmol; yield starting from the commercial Wang resin, 26%). TOF-ES-MS: *m/z* 773.3397 for $[MH]^+$ ($C_{39}H_{46}FN_8O_8$, calculated [MW] 773.3417).^{1}H NMR (CD_3OD), δ: 8.29 (s, 1H, CH triazole), 7.73 (d, 2H, H_{Ar}), 7.40 (m, 4H, H_{Ar}), 7.10 (m, 4H, H_{Ar}), 6.70 (d, 2H, H_{Ar}), 5.63 (s, 2H, $CH_2C_6H_4F$), 4,70 (m, 1H) and 4,40 (m, 2H) Cα,Tyr, Leu, ethynylPheH, 3.68−3.86 (m, 4H, Cα,GlyH), 2.87−3.33 (m, 4H, Cβ,Tyr, EthynylPheH2), 1.95 (s, 3H, CH3, acetyl), 1.68 (m, 1H, $CH(CH_3)_2$), 1.65 (m, 2H, $C_{\beta,Leu}$), 0.93 (m, 6H, $CH(CH_3)_2$).^{13}C NMR (CD_3OD) 178.2, 173.8, 172.4, 170.8, 170.8, 170.0 (C═O), 169.7 (d, J = 240 Hz, C-F), 156.0 (C-OH_{tyr}), 137.4,131.8 129.8, 129.7, 129.6, 128.6, 128.1,127.4, 125.3, 120.7 (CH triazole), 115.5 (d, ^3J = 21 Hz, $C_{ortho\text{-}F}$), 114.8 ($C_{ortho\ C\text{-}OH\ Tyr}$), 56.9 ($\underline{CH_2}C_6H_4F$), 55.7, 54.3, 52.8 ($C_{\alpha,Tyr,\ Leu,\ ethynylPhe}$), 42.6, 41.9 ($C_{\alpha,Gly}$), 40.1, 37.0, 36.34 ($C_{\beta,Tyr,\ Leu,\ ethynylPhe}$), 24.5, 21.9, 21.1, 20.4 ($CH_{3,Leu,\ Acetyl}$, CH_{Leu}) δ ppm.

*[Ac-Tyr(tBu)^1, Phe (≡)^4, Leu^5]-Enk **14**.* Eighty milligrams of peptide **11** bound to the resin (≤0.05 mmmol) was suspended in 3 mL of $(CH_2Cl)_2$. Forty-five milligrams of trimethyltin hydroxide (0.16 mmol) was added to this suspension at RT under nitrogen. The reaction mixture was refluxed (83 °C) overnight under an inert atmosphere. The suspension was filtered through a Büchner funnel and washed with $(CH_2Cl)_2$, CH_2Cl_2, MeOH, and EtOAc. The filtrate was brought to dryness under reduced pressure, and the resulting residue was dissolved in EtOAc, washed with an aqueous solution of HCl (0.05 N), and extracted with a 5% $NaHCO_3$ solution. The pH of the combined aqueous solution was lowered to 3−4 with 2.5 N H_2SO_4 and extracted with EtOAc. The combined organic solution was dried (Na_2SO_4) and evaporated to dryness to yield 8 mg of a colorless solid (0.012 mmol; yield starting from the commercial Wang resin, 24%). TOF-ES-MS: *m/z* 678.3489 for $[MH]^+$ ($C_{36}H_{48}N_5O_8$, calculated [MW]

678.3497).^{1}H NMR (CD_3OD), δ: 7.48 (d, 2H, $H_{Ar,EthynylPhe}$), 7.37 (d, 2H, $H_{Ar,EthynylPhe}$), 7.25 (d, 2H, $H_{Ar,tBuTyr}$), 7.02 (d, 2H, $H_{Ar,tBuTyr}$), 4.78 (dd, 1H), 4.60 (dd, 1H), 4.51 (dd, 1H), $C_{\alpha,Tyr,\ Leu,\ EthynylPhe}H$, 3.77−3.97 (m, 4H, $C_{\alpha,Gly}H$), 3.42 (s, 1H, ≡CH), 3.00−3.30 (m, 4H, $C_{\beta,Tyr,\ EthynylPhe}H_2$), 1.95 (s, 3H, $CH_{3\ acetyl}$), 1.68 (m, 1H, $CH(CH_3)_2$), 1.65 (m, 2H, $C_{\beta,Leu}$), 1.29 (s, 9H, $CH_{3,\ t\text{-}Bu}$), 0.91 (m, 6H, $CH(CH_3)_2$) ppm.^{13}C NMR (CD_3OD) 174.6, 174.0, 173.1, 172.5, 171.4, 170.6 (C═O), 154.7 ($C_{Ar,\ tBuTyr}$), 138.8, 132.8, 132.4, 130.1, 130.0, 124.6, 121.4 ($C_{Ar,\ tBuTyr,\ EthynylPhe}$), 83.8 (C≡C), 79.2 ($C(CH_3)_3$, 77.7 (CH≡C), 56.3, 54.9, 51.5 ($C_{\alpha,Tyr,\ Leu,\ EthynylPhe}$), 43.3, 42.7 ($C_{\alpha,Gly}$), 40.9, 37.9, 37.3 ($C_{\beta,Tyr,\ Leu,\ EthynylPhe}$), 30.0 ($CH_{3,t\text{-}Bu}$), 30.0, 29.9, 28.5, 25.3 ($CH_{3Leu,\ Acetyl}$, CH_{Leu}) δ ppm.

[Ac-Tyr(tBu)[1], Phe (1-(4-fluorobenzyl))-1H-1,2,3-triazol-4-yl)[4], Leu[5]]-Enk ***15***. Protected peptide **15** was obtained by replacing the TFA treatment applied to **12** by a cleavage with trimethyltin hydroxide analogous to that applied to obtain peptide **14**. Compound **15** was isolated by preparative HPLC purification (CH_3CN/H_2O 40:60 containing 0.1% TFA) to give 5 mg of a colorless solid (0.006 mmol, 12% starting from the commercial Wang resin). TOF-ES-MS: *m/z* 829.4012 for $[MH]^+$ ($C_{43}H_{54}FN_8O_8$, calculated [MW] 829.4043).^{1}H NMR (CD_3OD), δ: 8.28 (s, 1H, CH triazole), 7.71 (d, 2H, H_{Ar}), 7.35 (m, 4H, H_{Ar}), 7.13 (m, 4H, H_{Ar}), 6.90 (d, 2H, H_{Ar}), 5.62 (s, 2H, $CH_2C_6H_4F$), 4,72 (m, 1H), 4,48 (m, 2H) $C_{\alpha,Tyr,\ Leu,\ EthynylPhe}H$, 3.70−3.87 (m, 4H, $C_{\alpha,Gly}H$), 2.82−3.28 (m, 4H, $C_{\beta,Tyr,\ EthynylPheH2}$), 1.93 (s, 3H, CH3, acetyl), 1.68 (m, 1H, CH(CH3)2), 1.65 (m, 2H, Cβ,Leu), 1.35 (s, 9H, (CH3, t-Bu), 0.94 (m, 6H, CH(CH3)2).^{13}C NMR (CD_3OD) 178.2, 173.8, 172.4, 170.8, 170.8, 170.0 (C═O), 169.7 (d, J = 240 Hz, C-F), 156.0 (C-OH,$_{tyr}$), 137.4,131.0 129.4, 129.7, 129.6, 128.6, 128.1,127.4, 123.3, 120.7 (CH triazole), 115.54 (d, ^3J = 21 Hz, $C_{ortho\text{-}F}$), 114.8 ($C_{ortho\ C\text{-}OH\ Tyr}$), 79.4 ($C(CH_3)_3$, 56.9 ($\underline{CH_2}C_6H_4F$), 55.7, 54.3, 52.8 ($C_{\alpha,Tyr,\ Leu,\ EthynylPhe}$), 42.6, 41.9 (C$\alpha$,Gly), 40.1, 37.0, 36.34 (Cβ,Tyr, Leu, EthynylPhe), 30.4 (CH3 t-Bu), 24.5, 21.9, 21.1, 20.4 (CH3Leu, Acetyl, CHLeu) δ ppm.

Radiochemistry. *4-[18F]-Fluorobenzaldehyde* ***[18F]2***. No-carrier-added [^{18}F] fluoride was obtained by proton bombardment of an [^{18}O]-enriched water target via the $^{18}O(p,n)^{18}F$ reaction. The activity was trapped by passing the target water through a Sep-Pak light QMA cartridge (Waters) previously conditioned under carbonate form. Then, 500 μL of a 50:50 CH_3CN/H_2O solution of K_2CO3 (6 mg) and Kryptofix 222 (20 mg) were used to elute the fluoride from the cartridge into a heated conical glass vial (120 °C). This eluate (110−740 MBq) was brought to dryness by azeotropic distillation after the addition of acetonitrile (3 × 250 μL) under a gentle stream of nitrogen gas. 4-*N*,*N*,*N*-Trimethylammonium benzaldehyde triflate (0.064 mmol) in DMSO (1 mL) was added to the dried residue, and the mixture was heated at 130 °C for 5 min. The reaction medium was then diluted with water (15 mL). Labeling efficiency was checked by radio-TLC (silica gel, CH_2Cl_2; R_f values: [^{18}F]fluoride = 0; **[18F]2** = 0.6). HPLC analysis: t_R = 3.9 min (CH_3CN/H_2O 50/50 0.1% TFA). Radiochemical yield (decay corrected) = 65%.

1-(Bromomethyl)-4-[18F]-fluorobenzene ***[18F]4***. The crude labeled compound **[18F]2** (250 MBq) diluted in H_2O was adsorbed onto a C_{18} environmental Sep-Pak cartridge. $NaBH_4$ (125 mg dissolved in 4 mL of H_2O) was passed with a flow rate of 3 mL/min through the cartridge then washed with water (5 mL). The 4-[^{18}F]-fluorobenzyl alcohol formed was not isolated but directly converted into the corresponding bromide derivative by heating the Sep-Pak (50 °C) with a stream of hot air while passing 48% aqueous HBr (vol = 2.8 mL; flow rate = 3 mL/min) through the cartridge. After a delay of 4 min, an additional portion of concentrated HBr (1.4 mL) was passed in the same manner. After 4 min, heating was stopped, and 6 mL of an ammonium formate solution (pH 4.0) was added to the Sep-Pak. The bromide compound **[18F]4** was finally eluted with DMF (3.5 mL) and was checked by radio-TLC (silica gel, CH_2Cl_2; R_f values: **[18F]4** = 1.0; in *n*-hexane, R_f **[18F]4** = 0.3). HPLC analysis: t_R = 9.0 min (CH_3CN/H_2O 40/60 0.1% TFA). Radiochemical yield (decay corrected) from **2** was 75%.

1-(Azidomethyl)-4-[18F]-fluorobenzene ***[18F]5***. Compound **[18F]4** (150 MBq) in DMF (3.5 mL) was transferred into a reaction vial containing 500 mg of azido resin (1.9 mmol). This suspension was agitated for 15 min by gentle N_2 bubbling and then filtered. The resin was washed with 1 mL of DMF, then filtered again. The filtrates were combined and analyzed by radio-TLC (silica gel, CH_2Cl_2; R_f values: **[18F]5** = 1.0; in *n*-hexane, R_f **[18F]5** = 0.1). HPLC analysis: $t_{R\ =}$ 7.8 min (CH_3CN/H_2O 40/60 0.1% TFA). Radiochemical yield (decay corrected) from **[18F]4** 70%.

(S)-2-Amino-3-(4-(1-(4-[18F]-fluorobenzyl)-1H-1,2,3-triazol-4-yl)phenyl)propanoic Acid ***[18F]8***. A solution of 1-(azidomethyl)-4-[^{18}F]-fluorobenzene **[18F]5** (20MBq) in DMF (1 mL) was added to (*S*)-2-amino-3-(4-ethynylphenyl) propanoic acid (**6**) (*p*EPA, 0.6 mg, 0.0032 mmol), CuI (3.2 mg, 0.017 mmol), sodium ascorbate (25 mg, 0.13mmol), and DIEA (50 μL, 0.28 mmol). The mixture was stirred at room temperature for 15 min. The reaction mixture was then diluted with water (15 mL) and passed through a Sep-Pak Plus Short tC18 cartridge. The cartridge was washed with water (9 mL), and activity was eluted with CH_3CN (1.5 mL).

Analysis by radio-TLC (silica gel, EtOAc; R_f values: **[18F]8** = 0; C_{18}, CH_3CN/H_2O 50/50, R_f values, **[18F]8** = 0.5). HPLC analysis: t_R = 3.1 min (CH_3CN/H_2O 40/60 0.1% TFA). Radiochemical yield (decay corrected) from **[18F]5** 90%.

[Ac-Tyr[1], Phe (1-(4-[18F] fluorobenzyl))-1H-1,2,3-triazol-4-yl)[4], Leu[5]] Enk ***[18F]13***. A solution of [^{18}F] fluoroazide **[18F]5** in DMF (1 mL) was added to peptide **14** (2 mg, 0.0032 mmol), CuI (3.2 mg, 0.017 mmol), sodium ascorbate (25 mg, 0.13 mmol), and DIEA (50 μL, 0.28 mmol). The mixture was stirred at room temperature for 15 min.

Analysis by radio-TLC (silica gel, CH_2Cl_2; R_f values: **[18F]15** = 0; C_{18}, CH_3CN/H_2O 60/40, R_f values, **[18F]15** = 0.6). HPLC analysis: $t_{R\ =}$ 6.3 min (CH_3CN/H_2O 50/50 0.1% TFA).

The reaction mixture was then diluted with water (15 mL) and passed through a Sep-Pak Plus Short tC18 cartridge. The column was washed with water (9 mL), and activity was directly eluted with TFA (1.5 mL) in the deprotection vial. Deprotection was finished under stirring in less than 3 min.

Analysis by radio-TLC (silica gel, CH_2Cl_2; R_f values: **[18F]13** = 0; C_{18}, CH_3CN/H_2O 50/50, R_f values, **[18F]13** = 0.30). HPLC analysis: $t_{R\ =}$ 5.6 min (CH_3CN/H_2O 40/60 0.1% TFA). Radiochemical yield (decay corrected) from **[18F]5** 90%. Radiochemical purity >95%.

RESULTS AND DISCUSSION

Synthesis. The strategy we have followed to functionalize peptides with alkynes was based on the Sonogashira reaction. This cross-coupling reaction between iodoaryl and alkyne is catalyzed by Pd^0 complexes in mild conditions and is insensitive to all side groups. Furthermore, functionalization through Sonogashira coupling generates regioselectively and quantitatively a very stable C-C bond (*16*). Therefore, we planned to introduce the residue *p*-iodophenylalanine, a non-natural amino acid, into the peptide chain and to convert it to *p*-ethynylphenylalanine through the Sonogashira coupling reaction of ethynyltrimethylsilane (Scheme 1). The direct introduction of an ethynyl group is also possible but is not compatible with trifluoroacetic acid (*17*), which is predominantly used in peptidic synthesis. Moreover, the synthesis of *p*-ethynylphenylalanine is more demanding than the simple preparation of *p*-iodophenylalanine (*13*, *18*). A similar approach has been described by Hoffmans who has used the Sonogashira coupling to label

Scheme 1. Synthesis of References (13, Deprotected, and 15, Protected) and Clickable Alkyne Peptide 14

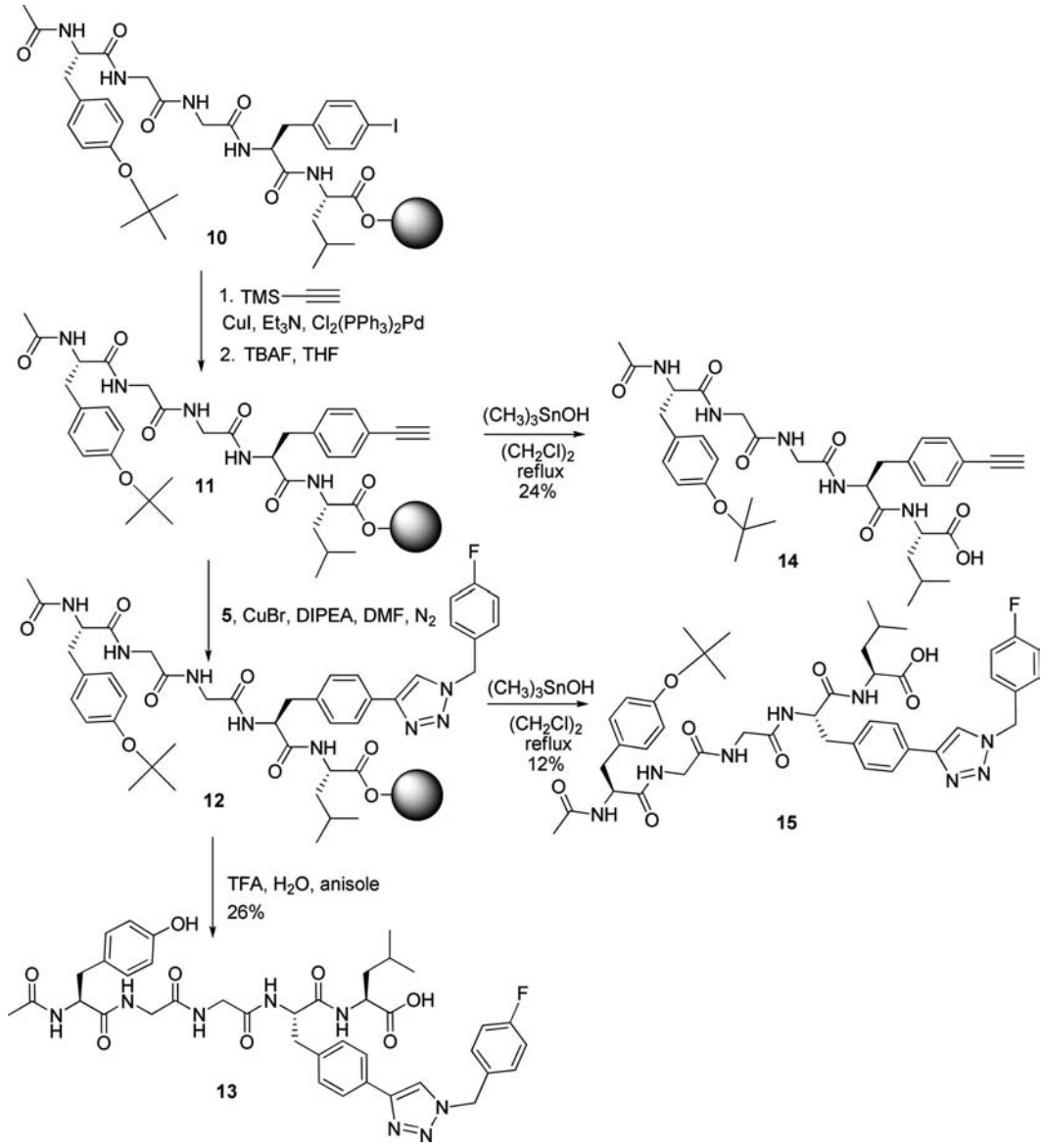

[Leu^5]Enkephalin (a neuropeptide that is a natural ligand of the opiate receptors) with ethynylferrocene (*19*). Thus, we have also chosen to use [Leu^5]Enkephalin as our model peptide because it is a small peptide, easy-to-handle to set up its labeling with fluorine-18 by click chemistry with 4-[^{18}F]fluorobenzyl azide. In the context of this work, no effort was made to preserve or improve the targeting ability or the in vivo stability of the labeled peptide. Readers interested in the imaging of the opiate receptors should read the following publications (*20*−*22*). Unlike Hoffmans, we decided to keep the [Leu^5]Enk peptide bound to the solid support (Wang resin) for the next steps to facilitate purification and isolation of the peptides **11**−**15**. The Sonogashira coupling between iodophenyl-derivatized peptide and trimethylsilylacetylene was carried out in conditions close to those described by Hoffmans. Excess reagents and catalysts were simply eliminated by filtration and washing. Completion of the reaction was checked by ES-MS after cleavage of small aliquots of the peptide by TFA. Deprotection of the alkyne group was achieved in the presence of TBAF in THF to furnish alkyne−peptide **11** still bound to the Wang resin.

Reference Compound Preparation. Conjugation of 4-ethynyl-L-phenylalanine (**6**) with 1-(azidomethyl)-4-fluorobenzene was conducted in DMF or acetonitrile, in the presence of DIEA and excess copper iodide (2 equiv.). When catalytic amounts of copper were used, the reaction did not start, possibly because of copper ion complexation by the amino acid (*23*). For cold chemistry, click conjugation of the peptide was carried out with the alkyne−peptide still bound to the resin support (Scheme 1). In the conditions used with 4-ethynyl-L-phenylalanine, compound **13** was obtained but iodo- and hydroxytriazole were also formed as secondary products. This problem was circumvented by replacing copper iodide with copper bromide and using an inert atmosphere. The reference peptide **13** was deprotected and removed from the resin by treatment with TFA. The protected reference peptide **15** was isolated by replacing the TFA treatment by a cleavage with trimethyltin hydroxide as described by Furlan (*24*). This solid phase method permits a rapid and easy preparation of reference peptides, which could be very valuable in a combinatorial approach.

Radiolabeling. The synthesis of 1-(azidomethyl)-4-[^{18}F]-fluorobenzene **[^{18}F]5**, a labeling agent for the subsequent click reaction, was carried out in four steps (Scheme 2) starting from the well-known nucleophilic fluorination of 4-formyl-*N*,*N*,*N*-trimethylanilinium triflate (**1**) (*25*−*28*). Radiofluorination was accomplished at 130 °C in DMSO for 5 min with an overall yield of 65%. This crude medium was diluted in

Scheme 2. Radiosynthesis of 1-(Azidomethyl)-4-[^{18}F]-fluorobenzene

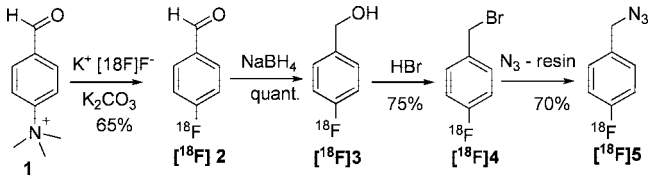

water, then passed on a Waters C_{18} environmental Sep-Pak cartdrige to trap compound **2[^{18}F]**. This compound was reduced to 4-[^{18}F]-fluorobenzyl alcohol **[^{18}F]3** by slowly passing a solution of $NaBH_4$ in water through the C_{18} cartridge following a procedure previously described (*29, 30*). The alcohol formed was not eluted from the cartridge but directly converted to the bromide **[^{18}F]4** by passing 48% aqueous HBr by small portions through the C_{18} cartdridge. At RT, less than 25% of the alcohol was converted into the bromide derivative. Fortunately, by heating the cartridge at 50 °C via a stream of hot air, the conversion was nearly quantitative. After neutralization of the medium by passing an ammonium formate buffer, the bromide **[^{18}F]4** was eluted by DMF (CH_3CN, toluene, and CH_2Cl_2 were also used). The bromide was obtained with a radiochemical yield of around 75% (decay corrected). Previously, this bromination was conducted in solution using PBr_3 or Ph_3PBr_2 (*29, 31*), $SOBr_2$ (*32, 33*), HBr 48% (*34*), or gaseous HBr (*35*). None of these methods is well suited for an easily automated routine production. Our method avoids using gas reagents, and excess reagents are readily and easily eliminated. This methodology may be extended beyond the present application as the fluorobenzyl bromide synthon is a common structure in some radiopharmaceuticals used for PET imaging (*30, 31, 34*). Finally, 1-(azidomethyl)-4-[^{18}F]-fluorobenzene **[^{18}F]5** was formed using a commercially available azide exchange resin (azide on Amberlite IRA-400) as described by Hassner (*36*). In DMF at RT, the reaction was completed in 15 min using 500 mg of the resin. In a less polar solvent such as acetonitrile, the reaction was slower (75% of conversion after 25 min). Tests conducted in the laboratory have shown that this reaction is insensitive to the presence of water and carbonate or formate salts. Nevertheless, acidic media inhibit the reaction. Resin is simply eliminated by filtration and the targeted azide collected in solution in DMF, ready to use for click reactions.

Hence, starting from 700 MBq [^{18}F]F^-, a total amount of 238 MBq (34%, decay corrected) of **[^{18}F]5** could be synthesized within 75 min.

Click Reactions with 1-(Azidomethyl)-4-[^{18}F]-fluorobenzene [^{18}F]5. Several catalytic systems have been described for Huisgen 1,3-dipolar cycloaddition (*6, 7*). In experiments to link [^{18}F]fluoroalkyne groups onto peptides, Marik and Sutcliffe have obtained better results using CuI than with Cu(I) generated *in situ* from copper sulfate and sodium ascorbate (*8*). Paradoxically, other teams have preferred *in situ* generation to click [^{18}F]fluoroprosthetic groups onto biomolecules. As we have obtained good results with copper (I) salts to prepare the cold references, we have chosen to follow the Marik and Sutcliffe approach. First, experiments with various conditions have been conducted on p-EPA (Table 1 and Scheme 3). The solvent greatly influences the reaction rate, which is much higher in DMF than in CH_3CN. This could be due at least partially to the better solubility of the alkyne in DMF. The reduction of the alkyne concentration also has a great impact on the reaction rate, which becomes insufficient at 0.003 M in the initial conditions (entry 4). Acceptable reaction rates were recovered by adding sodium ascorbate in the reaction medium (entry 5). Moreover, copper

Table 1. Influence of Reagent Concentration on the Radiochemical Yield for the Preparation of [^{18}F] 8 with 1-(Azidomethyl)-4-[^{18}F]-fluorobenzene [^{18}F]5 (RT, DMF)

alkyne (M)	CuI (M)	DIEA (M)	ascorbate (M)	solvent	reaction time (min)	yield (TLC)
0.050	0.105	0.600	0	AN	50	67%
0.050	0.105	0.600	0	AN:DMF 1:1	30	85%
0.05	0.105	0.600	0	DMF	7	90%
0.003	0.105	0.600	0	DMF	15	40%
0.003	0.017	0.280	0.130	DMF	15	95%

Scheme 3. 1,3-Dipolar Cycloaddition of 1-(Azidomethyl)-4-[^{18}F]-fluorobenzene with Alkyne Peptides or Amino Acid

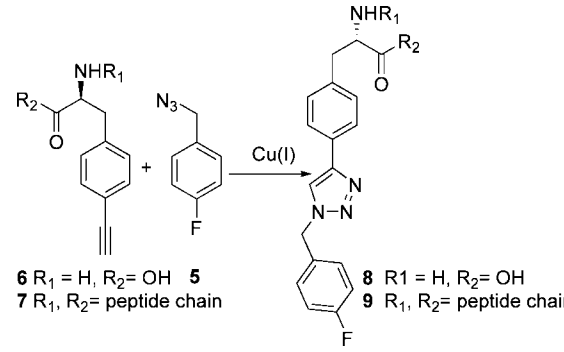

ions and base concentrations can also be diminished when ascorbate is used since the reaction still completes in less than 15 min at RT. Thus, similar conditions have been applied to conjugate alkyne−peptide **14** with 1-(azidomethyl)-4-[^{18}F]-fluorobenzene **[^{18}F]5.**

Fast coupling was also observed by radio-HPLC: labeling of the peptide was finished in less than 15 min. The radiolabeled peptide was trapped on a t-C18 cartridge, washed with water, and eluted with TFA. Deprotection of the tyrosine residue was accomplished in less than 3 min, and the targeted labeled peptide was obtained with a yield of 90% (coupling step + deprotection, decay corrected) and a radiochemical purity >95%. We would also like to point out that these results were obtained at room temperature with very diluted solutions of alkyne (0.003 mmol/mL), which is about 10 times less than that used by Sirion, Ramenda, or Glaser. Similar results have been reported by Marik and Sutcliffe who also used a copper (I) salt and not the $CuSO_4$/sodium ascorbate catalytic system used by the other groups. The low quantity of peptide required facilitates the HPLC separation of the labeled peptide from the unlabeled peptide precursor, which is essential to obtain suitable chemical purity.

CONCLUSIONS

A novel strategy for the preparation of clickable peptides has been developed. It can be applied to any peptides modified beforehand to contain a non-natural iodophenyl group. As demonstrated here on a model peptide, this moiety can be simply introduced during the synthesis of the peptide by substituting the modified amino acid 4-iodophenylalanine for a phenylalanine residue.

Furthermore, as the selective monoiodination of tyrosine residue in peptides with IPy_2BF_4 has been reported by Espuña et al., our approach can also been extended to directly label tyrosine containing peptides (*37*). In cases where the peptide does not contain any Phe or Tyr groups, 4-iodobenzoic acid can be used to N-terminally modify the peptide eventually through an appropriate linker (*19*).

A new labeling agent 1-(azidomethyl)-4-[^{18}F]-fluorobenzene **[^{18}F]5** has been produced in 75 min with a 34% radiochemical

yield (decay corrected). These satisfying results for a four-step procedure have been obtained thanks to the exploitation of solid phase supported reactions and the absence of the solvent evaporation process that allow one to minimize the losses of time and radioactivity during reaction workup and purification. Moreover, this radiosynthesis has been fully automated in our laboratory. Although all of these advantages are present, this click labeling agent is obtained in a less straightforward manner than others produced in a single step (*8*, *10*, *11*). However, the radiocompound **[^{18}F]5** is advantageous in that it is nonvolatile and bears an aromatic bound fluorine, which is known to be less susceptible to *in vivo* radiodefluorination. For these reasons, it will be very interesting to produce 1-(azidomethyl)-4-[^{18}F]-fluorobenzene **[^{18}F]5** in one or two fast steps. Work in this direction is in progress in our laboratory. Furthermore, this compound has been bound very rapidly (10 min), at room temperature, with a very diluted solution of alkyne (0.003M), in mild conditions and with an excellent yield to a model alkyne−peptide.

ACKNOWLEDGMENT

We acknowledge the financial support from the Biowin Project of the Walloon Region (NeoFor and KeyMarker).

LITERATURE CITED

(1) Massoud, T. F., and Gambhir, S. S. (2003) Molecular imaging in living subjects: seeing fundamental biological processes in a new light. *Genes Dev. 17*, 545–580.

(2) Wester, H.-J., Hamacher, K., and Stöcklin, G. (1996) A comparative study of N.C.A. Fluorine-18 labeling of proteins via acylation and photochemical conjugation. *Nucl. Med. Biol. 23*, 365–372.

(3) Olberg, D. E., Hjelstuen, O. K., Solbakken, M., Arukwe, J., Karlsen, H., and Cuthbertson, A. (2008) A novel prosthetic group for site-selective labeling of peptides for positron emission tomography. *Bioconjugate Chem. 19*, 1301–1308.

(4) Wester, H.-J., and Schottelius, M. (2007) Fluorine-18 Labeling of Peptides and Proteins. *Ernst Schering Research Foundation Workshop 62*, 79–111.

(5) Wuest, F., Berndt, M., Bergmann, R., van den Hoff, J., and Pietzsch, J. (2008) Synthesis and application of [18F]FDG-maleimidehexyloxime ([18F]FDG-MHO): A [18F]FDG-based prosthetic group for the chemoselective 18F-labeling of peptides and proteins. *Bioconjugate Chem. 19*, 1202–1210.

(6) Gil, M. V., Arévalo, M. J., and López, Ó. (2007) Click chemistry: What's in a name? Triazole synthesis and beyond. *Synthesis* 1589–1620.

(7) Victoria D. Bock, H. H. J. H. v. M. (2006) Cu^{I}-catalyzed alkyne-azide "click" cycloadditions from a mechanistic and synthetic perspective. *Eur. J. Org. Chem. 2006*, 51–68.

(8) Marik, J., and Sutcliffe, J. L. (2006) Click for PET: rapid preparation of [18F]fluoropeptides using CuI catalyzed 1,3-dipolar cycloaddition. *Tetrahedron Lett. 47*, 6681–6684.

(9) Li, Z.-B., Wu, Z., Chen, K., Chin, F. T., and Chen, X. (2007) Click chemistry for 18F-labeling of RGD peptides and microPET imaging of tumor Integrin $\alpha_v\beta_3$ expression. *Bioconjugate Chem. 18*, 1987–1994.

(10) Sirion, U., Kim, H. J., Lee, J. H., Seo, J. W., Lee, B. S., Lee, S. J., Oh, S. J., and Chi, D. Y. (2007) An efficient F-18 labeling method for PET study: Huisgen 1,3-dipolar cycloaddition of bioactive substances and F-18-labeled compounds. *Tetrahedron Lett. 48*, 3953–3957.

(11) Glaser, M., and Arstad, E. (2007) "Click labeling" with 2-[18F]fluoroethylazide for positron emission tomography. *Bioconjugate Chem. 18*, 989–993.

(12) Magata, Y., Lang, L., Kiesewetter, D. O., Jagoda, E. M., Channing, M. A., and Eckelman, W. C. (2000) Biologically stable [^{18}F]-labeled benzylfluoride derivatives. *Nucl. Med. Biol. 27*, 163–168.

(13) Ousmer, M., Boucard, V., Lubin-Germain, N., Uziel, J., and Augé, J. (2006) Gram-scale preparation of a *p*-(C-glucopyranosyl)-L-phenylalanine derivative by a Negishi cross-coupling reaction. *Eur. J. Org. Chem.* 1216–1221.

(14) Le Roy, I., Mouysset, D., Mignani, S., Vuilhorgne, M., and Stella, L. (2003) Solid phase [beta]-lactams synthesis using the Staudinger reaction, monitored by 19F NMR spectroscopy. *Tetrahedron 59*, 3719–3727.

(15) Zimmer, L., Luxen, A., Giacomelli, F., and Pujol, J.-F. (2002) Short- and long-term effects of p-ethynylphenylalanine on brain serotonin levels. *Neurochem. Res. 27*, 269–275.

(16) Sonogashira, K., Tohda, Y., and Hagihara, N. (1975) A convenient sytnhesis of acetylenes: catalytic substitutions of acetylenic hydrogen with bromoalkenes, iodoarenes and bromopyridines. *Tetrahedron Lett. 50*, 4467–4470.

(17) Walker, W. H., and Rokita, S. E. (2003) Use of a boroxazolidone complex of 3-iodo-L-tyrosine for palladium-catalyzed cross-coupling. *J. Org. Chem. 68*, 1563–1566.

(18) Kayser, B., Altman, J., and Beck, W. (1997) Alkyne bridged [alpha]- amino acids by palladium mediated coupling of alkynes with N-t-Boc-4-iodo-phenylalanine methyl ester. *Tetrahedron 53*, 2475–2484.

(19) Hoffmanns, U., and Metzler-Nolte, N. (2006) Use of the Sonogashira coupling reaction for the "two-step" labeling of phenylalanine peptide side chains with organometallic compounds. *Bioconjugate Chem. 17*, 204–213.

(20) Hartvig, P., Nagren, K., Lundberg, P. O., Muhr, C., Terenius, L., Lundqvist, H., Lärkfors, L., and Langström, B. (1986) Kinetics of four 11C-labelled enkephalin peptides in the brain, pituitary and plasma of Rhesus monkeys. *Regul. Pept. 16*, 1–13.

(21) Lever, J. R. (2007) PET and SPECT imaging of the opioid system: Receptors, radioligands and avenues for drug discovery and development. *Curr. Pharm. Des. 13*, 33–49.

(22) Malicka, J., Czaplewski, C., Groth, M., Wiczk, W., Oldziej, S., Lankiewicz, L., Ciarkowski, J., and Liwo, A. (2000) Use of NMR and fluorescence spectroscopy as well as theoretical conformational analysis in conformation-activity studies of cyclic enkephalin analogues. *Nucleic Acids Res. 28*, 15–18.

(23) Nowshuddin, S., and Reddy, A. R. (2006) Decomposition of copper-amino acid complexes by sodium sulfide. *Tetrahedron Lett. 47*, 5159–5161.

(24) Furlán, R. L. E., Mata, E. G., Mascaretti, O. A., Peña, C., and Coba, M. P. (1998) Selective detachment of Boc-protected amino acids and peptides from Merrifield, PAM and Wang resins by trimethyltin hydroxide. *Tetrahedron 54*, 13023–13034.

(25) Bruus-Jensen, K., Poethko, T., Schottelius, M., Hauser, A., Schwaiger, M., and Wester, H.-J. (2006) Chemoselective hydrazone formation between HYNIC-functionalized peptides and 18F-fluorinated aldehydes. *Nucl. Med. Biol. 33*, 173–183.

(26) Poethko, T., Schottelius, M., Thumshirn, G., Hersel, U., Herz, M., Henriksen, G., Kessler, H., Schwaiger, M., and Wester, H.-J. (2004) Two-step methodology for high-yield routine radiohalogenation of peptides: 18F-Labeled RGD and octreotide analogs. *J. Nucl. Med. 45*, 892–902.

(27) Vaidyanathan, G., Affleck, D. J., Cavazos, C. M., Johnson, S. P., Shankar, S., Friedman, H. S., Colvin, M. O., and Zalutsky, M. R. (2000) Radiolabeled guanine derivatives for the in vivo mapping of O6-alkylguanine-DNA alkyltransferase: 6-(4-[18F]Fluoro-benzyloxy)-9H-purin-2-ylamine and 6-(3-[131I]Iodobenzyloxy)-9H-purin-2-ylamine. *Bioconjugate Chem. 11*, 868–875.

(28) Lemaire, C., Guiillaume, M., Chrisitaens, L., Palmer, A. J., and Cantineau, R. (1987) A new route for the synthesis of [18F]fluoroaromatic substituted amino acids: no carrier added L-p-[18F]fluorophenylalanine. *Appl. Radiat. Isot. 38*, 1033–1038.

(29) Iwata, R., Horvath, G., Pascali, C., Bogni, A., Yanai, K., Kovács, Z., and Ido, T. (2000) Synthesis of 3-[1*H*-imidazol-4-yl]propyl 4-[^{18}F]fluorobenzyleyher ([^{18}F]fluoroproxyfan): A

potential radioligand for imaging histamine H_3 receptors. *Angew. Chem., Int. Ed. 43*, 873–882.

(30) Lemaire, C., Damhaut, P., Plenevaux, A., Cantineau, R., Christiaens, L., and Guillaume, M. (1992) Synthesis of fluorine-18 substituted aromatic aldehydes and benzyl bromides, new intermediates for n.c.a [^{18}F]fluorination. *Appl. Radiat. Isot. 43*, 485–494.

(31) Iwata, R., Pascali, C., Bogni, A., Horvath, G., Kovács, Z., Yanai, K., and Ido, T. (2000) A new, convenient method for the preparation of 4-[18F]fluorobenzyl halides. *Appl. Radiat. Isot. 52*, 87–92.

(32) Damhaut, P., Cantineau, R., Lemaire, C., Plenevaux, A., Christiaens, L., and Guillaume, M. (1992) 2- and 4-[^{18}F]fluorotropapride, two specific D_2 receptor ligands for positron emission tomography: N.C.A syntheses and animal studies. *Appl. Radiat. Isot. 43*, 1265–1274.

(33) Najafi, A., Peterson, A., Buchsbaum, M., O'Dell, S., and Weihmuller, F. (1993) Preparation and preliminary biological evaluation of [18F]NCQ-115: a new selective reversible dopamine D2 receptor ligand. *Nucl. Med. Biol. 20*, 549–555.

(34) Eyup Akgün, M. S. P. S. P. (2006) N1′-(p-[^{18}F]Fluorobenzyl)naltrindole (p-[^{18}F]BNTI) as a potential PET imaging agent for DOP receptors. *J. Labelled Compd. Radiopharm. 49*, 857–866.

(35) Hatano, K., Ido, T., and Iwata, R. (1990) The Synthesis of o- and p-[^{18}F]fluorobenzyl bromides and their application to the preparation of labeled neuroleptics. *J. Labelled Compd. Radiopharm. 29*, 373–380.

(36) Hassner, A., and Stern, M. (1986) Synthesis of Alkyl Azides with a Polymeric Reagent. *Angew. Chem., Int. Ed. Engl. 25*, 478–479.

(37) Espuña, G., Arsequell, G., Valencia, G., Barluenga, J., Pérez, M., and González, J. (2000) Control of the iodination reaction on activated aromatic residues in peptides. *Chem. Commun.* 1307–1308.

BC800544P

REVIEWS

Radioimmunoimaging with Longer-Lived Positron-Emitting Radionuclides: Potentials and Challenges

Tapan K. Nayak and Martin W. Brechbiel*

Radioimmune & Inorganic Chemistry Section, Radiation Oncology Branch, National Cancer Institute, National Institute of Health, Bethesda, Maryland 20892. Received July 15, 2008; Revised Manuscript Received October 12, 2008

Radioimmunoimaging and therapy has been an area of interest for several decades. Steady progress has been made toward clinical translation of radiolabeled monoclonal antibodies for diagnosis and treatment of diseases. Tremendous advances have been made in imaging technologies such as positron emission tomography (PET). However, these advances have so far eluded routine translation into clinical radioimmunoimaging applications due to the mismatch between the short half-lives of routinely used positron-emitting radionuclides such as ^{18}F versus the pharmacokinetics of most intact monoclonal antibodies of interest. The lack of suitable positron-emitting radionuclides that match the pharmacokinetics of intact antibodies has generated interest in exploring the use of longer-lived positron emitters that are more suitable for radioimmunoimaging and dosimetry applications with intact monoclonal antibodies. In this review, we examine the opportunities and challenges of radioimmunoimaging with select longer-lived positron-emitting radionuclides such as ^{124}I, ^{89}Zr, and ^{86}Y with respect to radionuclide production, ease of radiolabeling intact antibodies, imaging characteristics, radiation dosimetry, and clinical translation potential.

INTRODUCTION AND BACKGROUND

Applications of radiation in medicine have been described now for over 100 years. The use of radiation in medicine branches from many scientific discoveries, most notably the discovery of X-rays in 1895 and its use in surgery (*1*). Since that time frame, over the next 60 years critical advances in nuclear medicine technology and instrumentation have resulted in methodologies and technologies for the visualization of many of the body's organs, including liver and spleen scanning, brain tumor localization, and studies of the gastrointestinal tract by the injection of radionuclides (*2, 3*). The greatest potential use of radiation in medicine is its utility to provide diagnostic information of pathological processes before the outset of structural changes in an organ. In these applications, very small amounts of radioactive material most often labeled or conjugated to "smart" targeting agents such as antibodies, peptides, and small molecules are introduced into the body. These "smart" agents specifically target individual cells instead of just the general tissues or organs, and therefore provide more valuable information about actual pathology. One example of such "smart" targeting agents is the monoclonal antibody (mAb). Currently, 21 monoclonal antibodies (all intact) are approved by the U. S. Food and Drug Administration (U.S.F.D.A) for diagnosis and treatment of various illnesses.

Antibodies in Nuclear Medicine. Currently, radiolabeled antibodies are clinically used for numerous applications such as oncology and cardiology (*4, 5*). Use of radiolabeled antibodies for targeting specific organs in animals was explored almost half a century ago (*6, 7*). Radiolabeled antibodies have been used in the clinic for therapeutic and diagnostic purposes now for over 40 years (*8, 9*). In 1978, Goldenberg and colleagues successfully applied the principles of antibody−antigen binding by visualizing carcinoembryonic antigen (CEA) on tumors of patients with a history of cancer of diverse histopathology by injecting ^{131}I labeled goat IgG targeting CEA. However, the large-scale application of radiolabeled antibodies in the clinic was hindered due to low production yields and concerns of toxic immune reactions after injecting antibodies of animal origin into humans. The introduction of hybridoma technology for monoclonal antibody (mAb) production as developed by Kohler and colleagues along with the evolution of recombinant DNA technology has addressed many of these problems (*10*). Chimeric and humanized monoclonal antibodies and even completely human antibodies are now the standard. Numerous clinical studies have since been reported describing the use of radiolabeled intact antibodies for diagnosis of cancer using γ-scintigraphy and single photon emission tomography (SPECT) imaging (*4, 11*−*13*).

In spite of great successes in preclinical animal models, the promise of radioimmunoimaging by γ-scintigraphy has not fully lived up to expectations, mostly due to differences in biodistribution and pharmacokinetic characteristics between animals and humans, and limitations of γ-scintigraphy in terms of intrinsic spatial resolution (*14*). Radionuclides that decay with γ-energies lower than 100 keV produce too much scatter, while γ-energies over 250 keV are difficult to collimate and therefore pose a challenge for quantitative γ-scintigraphy. To overcome the disadvantages posed by γ-scintigraphy, attempts were made to exploit the superiorities of positron emission tomography (PET) for radioimmunoimaging. A single positron decay results in two 511 keV photons being emitted at 180°. Most

* Corresponding author. Dr. Martin W. Brechbiel, Building 10, Room 1B40, NCI-Bethesda, Bethesda, MD 20892, Fax: 301-402-192, E-Mail: martinwb@mail.nih.gov.

10.1021/bc800299f This article not subject to U.S. Copyright. Published 2009 by the American Chemical Society
Published on Web 01/06/2009

Table 1. Characteristics of Selected Longer-Lived Positron-Emitting Radionuclides for Radioimmunoimaging[a]

radionuclide	half-life	production	daughter (half-life)	β^+_{max} in MeV (β^+yields)	γ-energies in MeV (yields)	mean range (mm)	intrinsic spatial resolution loss (mm)	human studies
^{18}F	1.83 h	^{20}Ne(d, α)^{18}F ^{18}O(p, n)^{18}F	^{18}O (stable)	0.63 (97%)	0.14 (41%)	0.69	0.7	Yes
^{124}I	100.2 h	^{124}Te(p, n)^{124}I ^{124}Te(d, 2n)^{124}I ^{125}Te(p, 2n)^{124}I	^{124}Te (stable)	2.14 (24%)	0.60 (61%)	3.25	2.3	Yes
^{76}Br	16.0 h	^{76}Se(p, n)^{76}Br ^{75}As(^{3}He, 2n)^{76}Br	^{76}Se (stable)	3.98 (56%)	0.55 (74%)	5.07	5.3	Yes
^{52}Mn	134.2 h	^{52}Cr(p, n)^{52}Mn ^{51}V(^{3}He, 2n)^{52}Mn ^{52}Cr(^{3}He,t)^{52}Mn	^{52}Cr (stable)	0.58 (29%)	0.74 (90%)	5.00	0.6	Yes
^{55}Co	17.5 h	^{54}Fe(d, n)^{55}Co ^{56}Fe(p, 2n)^{55}Co	^{55}Fe (2.6 y)	1.50 (76%)	0.48 (20%)	5.74	1.6	Yes
^{7}Ga	9.4 h	^{66}Zn(p, n)^{66}Ga ^{63}Cu(4He,n)^{66}Ga	^{66}Zn (stable)	4.15 (56%)	1.03 (36.9%)	8.06	5.8	Yes
^{72}As	25.9 h	^{72}Ge(p, n)^{72}As	^{72}Ge (stable)	3.32 (88%)	0.83 (80%)	5.01	3.6	Yes
^{64}Cu	12.7 h	^{64}Ni(p, n)^{64}Cu ^{68}Zn(p, n)^{64}Cu ^{64}Ni(d,2 n)^{64}Cu	^{64}Ni,^{64}Zn (stable)	0.66 (18%)	-	0.70	0.7	Yes
^{86}Y	14.7 h	^{86}Sr(p, n)^{86}Y ^{nat}Rb(^{3}He, 2n)^{86}Y	^{86}Sr (stable)	3.15 (34%)	1.08 (83%)	2.46	1.8	Yes
^{89}Zr	78.4 h	^{89}Y(p, n)^{89}Zr ^{89}Y(d, 2n)^{89}Zr	^{89}mY (16 s)	0.90 (23%)	-	1.18	1.0	Yes

[a] Some of the data presented in the table were obtained from references (*4, 159*) and http://www.nndc.bnl.gov/nudat2/ (Nuclear Structure and Decay Data Searchable Database, National Nuclear Data Center, Brookhaven National Laboratory, USA) accessed on 03/07/2008.

PET cameras contain a circular array of detectors with coincidence circuits designed to capture 511 keV photons emitted in opposite direction and therefore offer much better resolution and counting efficiency as compared to conventional γ-scintigraphy and SPECT cameras (*15*). However, a major limitation challenging PET radioimmunoimaging was the half-lives of most of the routinely used PET radionuclides such as ^{18}F ($t_{1/2}$ = 1.8 h) and ^{11}C ($t_{1/2}$ = 0.3 h). The half-lives of routinely used PET radionuclides simply did not match well with the biological half-lives (up to several days) and pharmacokinetic parameters of slowly localizing intact antibodies. To overcome the initial blood pool uptake and slow localization of the intact antibody, antibody fragments (Fab) were labeled with ^{18}F for PET imaging. However, ^{18}F labeled antibody fragments failed to demonstrate high tumor localization as demonstrated by parent intact antibodies (*16, 17*). ^{18}F labeled antibody fragments were cleared from the tumor relatively more quickly than intact antibodies and then rapidly excreted through the urinary route delivering high radiation doses to the kidneys (*16, 17*). Numerous attempts have been made to modify intact antibodies to increase tumor uptake and residence time, and concomitantly decrease kidney uptake for successful PET with ^{18}F (*18, 19*). To date, results from these strategies have demonstrated low to moderate success. Another drawback of using ^{18}F as the choice of radionuclide for PET radioimmunoimaging is the cumbersome chemistry involved, which requires synthesis of ^{18}F labeled intermediate precursors for indirect labeling of antibodies with ^{18}F (*17, 20*).

As an alternative to the approach of modifying the antibody to match the physical characteristics of ^{18}F, the use of longer-lived positron emitters has been explored for radioimmunoimaging with intact antibodies (*21*−*23*). The half-lives of longer-lived positron emitters such as ^{124}I and ^{89}Zr (shown in Table 1) have a much closer match with the biological half-life of most intact antibodies. Antibodies labeled with longer-lived positron emitters can be imaged for 2−5 days after injection when the radioactivity in the blood pool has been cleared and target to background ratio is higher. In this report, we have examined the potentials and challenges of selected longer-lived positron-emitting radionuclides for radioimmunoimaging with intact antibodies. The criteria applied for selecting these longer-lived positron emitters (Table 1) includes previously published reports with antibodies or clinical studies, a potentially suitable half-life (10−140 h) versus biological half-life, an imageable positron emission, available or potentially available conjugation and radiolabeling chemistry, and reasonable or acceptable production logistics and radiation toxicity.

SELECTED LONGER-LIVED POSITRON-EMITTING RADIONUCLIDES FOR RADIOIMMUNOIMAGING

Numerous longer-lived positron-emitting radionuclides can be produced by cyclotrons, accelerators, and reactors. Selected longer-lived positron emitters ranging from halogens to metals are described below with respect to their production, feasibility of use in radiolabeling an intact antibody, biological applications, and imaging characteristics.

Iodine-124. Iodine (atomic radius of 1.3 Å and electronegativity of 2.66) belongs to Group VII of the periodic table. ^{124}I is a positron-emitting radionuclide with a complex decay scheme associated with numerous high-energy γ-emissions (0.6 MeV, 61% abundance) and high-energy positron emissions (2.14 MeV, 24% abundance) as shown in Table 1. ^{124}I ($t_{1/2}$ = 100.2 h) decays to a stable ^{124}Te daughter. The relatively longer half-life makes ^{124}I conducive for labeling intact antibodies for PET imaging over several days after administration. Additionally, the vast experience of radiolabeling proteins with the other Iodine radionuclides, i.e., ^{131}I, ^{125}I, and ^{123}I, promotes a significant level of confidence, since existing chemistry and protocols are directly applicable for use with ^{124}I.

Production of ^{124}I. ^{124}I can be produced by a conventional medical cyclotron using the ^{124}Te(p,n)^{124}I and ^{124}Te(d,2n)^{124}I reactions (Table 2). Typically, highly enriched tellurium dioxide is used as the target and ^{124}I is isolated using dry distillation with minimal impurities (*24*−*26*). The yield (<0.1 mCi/μAh) from the ^{124}Te(p,n)^{124}I reaction is low at 15 MeV (*27*). Alternatively, ^{124}I can be produced through a ^{125}Te(p,2n)^{124}I reaction with about four times higher yields than the commonly used ^{124}Te(p,n)^{124}I and ^{124}Te(d,2n)^{124}I reactions (*24, 27*). However, the production of ^{124}I through the ^{125}Te(p,2n)^{124}I reaction requires a medium−high-energy cyclotron, and impurities are relatively higher than the ^{124}Te(p,n)^{124}I reaction.

Table 2. Commonly Used Production Routes of Selected Longed-Lived Positron-Emitting Radioimmunoimaging and Corresponding Yields and Radionuclidic Impurities (adapted from ref 119)

radionuclide	commonly used production route	energy range (MeV)	calculated yield (MBq/μAh)	radionuclidic impurity
	^{124}Te(p, n)^{124}I	12 → 8	16	^{125}I (0.1%)
^{124}I	^{124}Te(d, 2n)^{124}I	14 → 10	17.5	^{125}I (1.7%)
	^{76}Se(p, n)^{76}Br	15 → 8	360	-
^{76}Br	^{75}As(^{3}He, 2n)^{76}Br	18 → 10	11	^{77}Br (1.6%)
	^{52}Cr(p, n)^{52}Mn	20 → 10	0.4	^{54}Mn (0.5%)
^{52}Mn	^{52}Cr(^{3}He, t)^{52}Mn	36 → 10	5.6	^{54}Mn (0.8%)
	^{54}Fe(d, n)^{55}Co	10 → 5	32	^{56}Co,^{57}Co (0.1%)
^{55}Co	^{58}Ni(p, n)^{55}Co	15 → 7	14	^{57}Co (0.5%)
^{66}Ga	^{66}Zn(p, n)^{66}Ga	13 → 8	433	-
^{72}As	^{72}Ge(p, n)^{72}As	18 → 8	93	^{71}As (10%)
	^{64}Ni(p,n)^{64}Cu	12 → 9	240	^{61}Cu (0.4%)
^{64}Cu	^{68}Zn(p, n)^{64}Cu	35 → 20	100	^{67}Cu (25%)
^{86}Y	^{86}Sr(p, n)^{86}Y	14 → 10	400	^{87}mY (3%)
^{89}Zr	^{89}Y(p, n)^{89}Zr	12 → 6	43	^{88}Zr (0.1%)

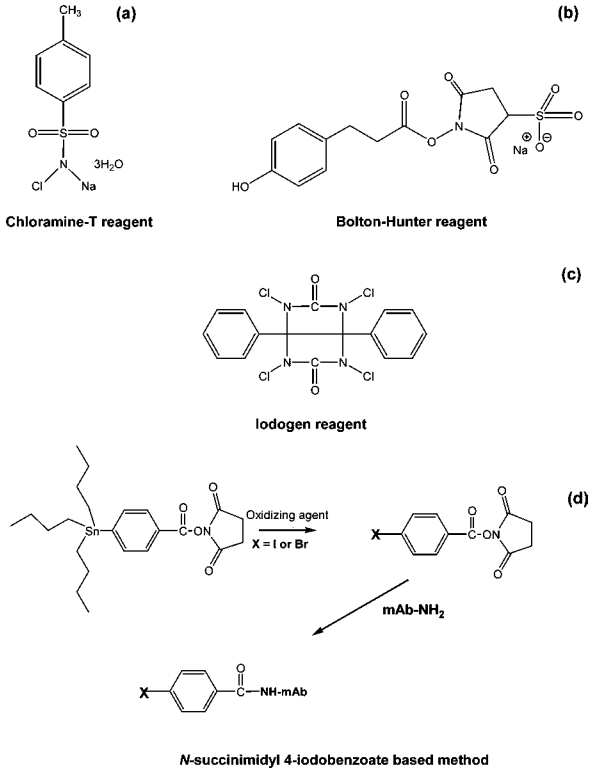

Figure 1. General scheme and reagents of radio-halogenation of intact antibodies using commonly used methods: (a) Chloramine-T method, (b) Bolton-Hunter method, (c) Iodogen method, and (d) *N*-succinimidyl 4-iodobenzoate based method.

Radiolabeling of Antibodies with ^{124}I. Radio-iodinated antibodies have been used for in vivo applications for more than 60 years (*6*, *7*, *28*, *29*). In the early 1960s, Hunter and co-workers described a method called the Chloramine-T method, to prepare high specific-activity radio-iodinated antibodies using *p*-toluene sulfonochloramide (Figure 1a) (*30*, *31*). Briefly, the Chloramine-T method is an oxidative method which involves exposure of the substrate to Chloramine-T in the presence of NaI for a short time, producing high specific activity proteins labeled with carrier-free radioiodine. However, the major disadvantage of the Choramine-T method is the risk of oxidation of thiol groups and protein denaturation due to the presence of high concentrations of strong oxidizing agent which can compromise the intended biological use of the antibody. As an alternative, an enzymatic method using lactoperoxidase as a catalyst was developed for iodination of antibodies (*32*, *33*). Lactoperoxidase catalyzes the oxidation of iodide using hydrogen peroxide as the enzyme substrate and is a milder oxidative agent than Chloramine-T. Due to the continuing concerns of protein denaturation and loss of biological activity by oxidizing agents, a newer technique (Bolton-Hunter method; Figure 1b) was later developed using iodinated 3-(4-hydroxyphenyl)propionic acid *N*-hydroxysuccinimide ester, which reacts with free amino groups in the protein molecule to attach the radioiodine-labeled groups by amide bonds (*34*, *35*). The Bolton-Hunter method is a nonoxidative technique that is less harsh on the proteins than alternative methods. Similarly, to avoid the interaction of oxidizing agent with the protein, an alternative solid-phase oxidation using 1,3,4,6-tetrachloro-3α,6α-biphenyl glycoluril (Figure 1c) was developed and is commonly called the Iodogen method (*36*). All of the above methods suffered from the drawback of in vivo deiodination in the presence of enzymes. To overcome in vivo deiodination, another method was developed using *N*-succinimidyl 4-iodobenzoate (PIB) (Figure 1d) to specifically label antibodies and proteins (*37*). This method produced a more stable radio-iodinated antibody as compared to methods like Bolton-Hunter, as PIB does not contain an *o*-phenol moiety, which protects PIB derivatives from the deiodinases that can act to delabel *o*-iodophenols that are formed with the other radio-iodination methods. As a result of increased in vivo stability, the uptake in the thyroid was dramatically reduced when a comparison was made between the same antibody radio-iodinated using the PIB and Chloramine-T methods (*37*). Many monoclonal antibodies are internalized via either clathrin-dependent or independent pathways. Antibodies rapidly internalized (within 2−4 h) via the clathrin-dependent endocytosis pathway are catabolized within lysosomes. Iodotyrosine is known to rapidly exit from the lysosome and the cell after catabolism, and as a result, target-to-background ratios are poor (*38*−*40*). In order to overcome the issue of catabolism of conventional radio-iodinated antibodies, dilactitol-tyramine (DLT) and radio-iodinated diethylenetriaminepentaacetic acid-appended peptides have successfully been used to residualize the radio-iodinated antibody within the cells (*41*−*44*). As a result of decreased catabolism, the tumor uptake of cell surface binding radio-iodinated antibodies was significantly higher than antibodies radiolabeled with the Chloramine-T method (*41*, *42*).

Detailed methodologies for radio-iodination of proteins can be found in a review article published in *Bioconjugate Chemistry* (*45*). Currently, most ^{124}I labeled antibodies are prepared using commercial iodination kits based on some of the above-described techniques.

Biological Studies with ^{124}I Labeled Antibodies. In the early 1990s, murine monoclonal antibody H17E2 recognizing placental alkaline phosphatase (PLAP) was radiolabeled with ^{124}I using the Iodogen method for targeting PLAP on HEp2 human tumor xenografts (*21*). The ^{124}I labeled H17E2 localized in the tumor for at least 7 days, demonstrating the feasibility of using monoclonal antibodies labeled with ^{124}I for tumor localization studies (*21*). The utility of antibodies labeled with ^{124}I for PET imaging, imaging feasibility, and quantification studies were studied by Pentlow and co-workers (*22*). In this study, when compared to ^{18}F, the spatial resolution was only slightly degraded while the linearity was the same (*22*). This technique was translated to in vivo application by measurements of human neuroblastoma tumors in rats which had been injected with ^{124}I labeled 3F8 antibody demonstrating that quantitative PET imaging of ^{124}I labeled antibodies was possible in biological systems. Use of ^{124}I in PET radioimmunoimaging was further demonstrated by c-erb B2 quantification and visualization in tumor xenografts for up to 160 h using ^{124}I labeled rat monoclonal antibody (ICR12) recognizing the external domain

of the human c-erb B2 proto-oncogene product (*23*). With advances in imaging instrumentation and technology, whole-animal PET studies were performed for noninvasive measurements of tumor vascular endothelial growth factor (VEGF) in animal model using ^{124}I-SHPP-VG76e (*46*). Similarly, ^{124}I labeled engineered antibodies have been evaluated for in vivo imaging (*47, 48*).

Numerous applications of ^{124}I in humans for PET imaging have since been reported (*49*−*51*). PET with anti-VEGF ^{124}I-HuMV833 was conducted on 20 patients with progressive solid tumors with moderate success (*52*). A recently published clinical study successfully used a carbonic anhydrase-IX targeted ^{124}I-cG250 antibody to accurately identify clear-cell renal carcinoma and to predict the aggressiveness of the disease, information that could be valuable in treatment decision-making (*53*).

Challenges. ^{124}I is available from numerous academic centers and is also available commercially through sources such as IBA Molecular, but it tends to be expensive. Current concerns remain high radiation dose and degraded image quality from high-energy γ-emissions and the loss of spatial resolution as a result of high-energy positrons (Table 1). The image quality is further degraded due to decrease in tumor/background ratio as a result of intracellular catabolism of ^{124}I. Typically, radioiodide localizes in the thyroid, delivering high radiation doses, and therefore, potassium iodide solution has to be infused before protein labeled with ^{124}I infusion to block thyroid uptake.

Bromine-76. Bromine (atomic radius of 1.1 Å and electronegativity of 2.96) also belongs to group VII of the periodic table.^{76}Br has a fairly high abundance (56%) of high-energy β^+ emission (3.9 MeV) and decays to a stable ^{76}Se daughter, as shown in Table 1. The half-life of 16.2 h also makes ^{76}Br one of the most attractive radionuclides for PET imaging using intact antibodies that exhibit slow clearance. The positron abundance of ^{76}Br is almost double that of ^{124}I (Table 1) and the C−Br bond is stronger than the C−I bond in organic compounds, therefore making it less susceptible to in vivo dehalogenation, thereby potentially minimizing concerns regarding background activity and associated toxicity (*54*). Due to the smaller atomic radius and greater electronegativity, ^{76}Br has greater polarity than ^{124}I. The increased polarity of ^{76}Br can alter biological properties and pharmacokinetics of the biomolecule, which can be either unfavorable or favorable depending upon the objective and purpose of the study (*55, 56*).

Production of ^{76}Br. ^{76}Br can be prepared using a low−intermediate energy medical cyclotron. Typically, ^{76}Br is produced through the ^{76}Se(p,n)^{76}Br reaction in which a highly enriched ^{76}Se target is bombarded with 15−16 MeV protons (*57*). Alternatively, ^{76}Br can also be prepared through the ^{75}As(^{3}He,2n)^{76}Br and ^{nat}Br(p, xn)^{76}Kr→^{76}Br reactions using high-energy (over 50 MeV) protons (*58, 59*). Purification and recovery of ^{76}Br is performed by dry distillation methods.^{76}Br produced through alternative routes contains other radionuclide impurities such as ^{77}Br and ^{75}Br, which may result in lower yields due to separation and purification. The calculated yield for ^{76}Br produced through the ^{76}Se(p,n)^{76}Br reaction is almost 32 times greater than ^{76}Br produced through the ^{75}As(^{3}He,2n)^{76}Br reaction (Table 2). Another disadvantage of ^{76}Br produced through the ^{75}As(^{3}He,2n)^{76}Br reaction is the ^{77}Br ($t_{1/2}$ = 57.03 h) impurity.

Radiolabeling of Antibodies with ^{76}Br. Numerous antibodies have been brominated using techniques and approaches similar to iodination such as Chloramine-T, enzymatic, *N*-succinimidyl *para*-(trimethylstannyl)benzoate (*60*−*62*). Bromination of antibodies by oxidative methods can be more difficult than iodination due to the lower oxidation potential of bromide. Therefore, more powerful oxidizing agents are used for sufficient yield of bromination, potentially proving deleterious to proteins. Recently, a method was described for indirect radiobromination of antibodies to prevent protein denaturation in the presence of strong oxidizing agents (*63*). In this method, indirect labeling was performed using the *p*-isothiocyanatobenzene derivative of the [^{76}Br]undecahydro-bromo-7,8-dicarba-*nido*-undecaborate-(1-) (^{76}Br-NBI) as a precursor molecule. ^{76}Br-NBI was prepared using the Chloramine-T method, and thereafter, the coupling was performed without intermediate purification in an "one-pot" reaction (*63*). This technique resulted in improved intracellular retention of the radiolabeled antibody and decreased the loss of biological activity caused by direct bromination with oxidizing agents. Similar indirect radio-bromination efforts have been reported using 4-hydroxyphenylethylmaleimide for site-specific bromination of a cysteine containing a variant of the anti-HER2 affibody (*64*).

Biological Studies with ^{76}Br Labeled Antibodies. Proteins have been brominated and evaluated in animals now for over 30 years (*60*). In the past decade, anti-CEA mAb 38S1 was radio-brominated and evaluated in animals (*65, 66*). A comparative study using ^{76}Br-38S1, ^{18}FDG, and ^{11}C-Met demonstrated the superiority of ^{76}Br-38S1 in successful identification and imaging of liver metastases in nude rats bearing human colon carcinoma (*67*). In recent years, more studies have been reported with ^{76}Br labeled intact antibodies and engineered antibodies for the purpose of PET imaging (*56, 63, 64, 68*). In a recent study, an ED-B fibronectin-binding human antibody derivative (L19-SIP) was labeled with ^{76}Br via an enzymatic approach using bromoperoxidase resulting in both radiolabeling yields and immunoreactivity of over 80% (*56*). This radio-brominated immunoconjugate with a standardized uptake value of over 2.4 enabled detailed small-animal PET imaging of tumor neovasculature in F9 tumor-bearing animals (*56*). However, long retention of radioactivity in blood and very slow renal excretion were also observed, and as a result, the background activity in nontarget organs was higher than that reported for the ^{125}I-labeled L19-SIP, illustrating the differences between iodinated and brominated antibody (*56*).

Clinically, small molecules labeled with ^{76}Br have been successfully used for *in vivo* quantitative PET neuroimaging (*69, 70*); although, few if any radio-brominated antibodies have been successfully used in the clinic.

Challenges. Besides the loss of intrinsic spatial resolution of about 5.3 mm due to high-energy positrons (3.98 MeV) (Table 1), one of the major problems with ^{76}Br is the availability and large-scale production. Enriched ^{76}Se is relatively expensive due to low natural abundance (1 mg/∼US $6), although target material recovery and recycling could obviate that aspect. This may be one of the contributing factors hindering commercialization of large quantities of ^{76}Br, although smaller quantities of ^{76}Br are available on request through MDS Nordion and Isotrace Technology. The β^+ energy of ^{76}Br is relatively higher than conventional PET radionuclides, which may pose concerns of radiation doses for diagnostic purposes; however, the same could be viewed as a potential advantage if actually used for therapeutic applications.

Manganese-52. Manganese (atomic radius of 1.8 Å and electronegativity of 1.55) belongs to group VIIB of the periodic table. ^{52}Mn ($t_{1/2}$ = 134.2 h) decays to a stable ^{52}Cr daughter. The half-life and suitable imaging characteristics as a result of optimum positron energy of 0.58 MeV (Table 1) makes ^{52}Mn one of the most attractive and under-utilized longer-lived positron emitters for PET imaging of intact antibodies.

Production. ^{52}Mn can be produced using the ^{52}Cr(p,n)^{52}Mn reaction by irradiating a high-purity Cr target with 16−17 MeV protons or by ^{51}V(^{3}He,2n)^{52}Mn using a high-energy cyclotron (*71*−*73*).

Radiolabeling of Antibodies with ^{52}Mn. Although ^{52}Mn seems to be a suitable candidate for radioimmunoimaging, relatively little effort has been made to label antibodies. Chelating agents such as dipyridoxyl diphosphate (*74*), macrocyclic Schiff-base ligands (*73*), cyclopentadienide (*74*), and porphyrin derivatives (*75*) have been suggested for Mn in different oxidation states. However, generation of stable^{52}Mn(II) labeled radioimmunoconjugates in aqueous conditions remains unclear due to complex redox chemistry.

To date, no peer-reviewed reports have been published describing the production or use of ^{52}Mn labeled antibodies.

Biological Studies with ^{52}Mn. Radio-manganese has mostly been used as a cationic perfusion tracer and as a tracer to study the involvement of manganese in degenerative neurological diseases (*71, 72, 75*).

Challenges. ^{52}Mn is one of the positron emitters that have been understudied in nuclear medicine. Therefore, production, chelation and conjugation chemistry, and biological effects of ^{52}Mn all need to be extensively studied prior to embarking on radioimmunoimaging application studies.

Cobalt-55. Cobalt belongs to group VIIIB of the periodic table. Cobalt has an atomic radius of 1.7 Å and electronegativity of 1.88. ^{55}Co decays to a longer-lived ^{55}Fe daughter ($t_{1/2} = 2.6$ y) mainly by positron emission of 1.5 MeV (76% abundant) with a half-life of 17.5 h [Table1].

Production of ^{55}Co. The ^{54}Fe(d,n)^{55}Co reaction has been used to obtain ^{55}Co in good yields (32 MBq/μAh) and acceptable purity of over 99% using a medical cyclotron (Table 2) (*76*). Alternatively, ^{55}Co can produced through ^{58}Ni(p,n)^{55}Co on a medical cyclotron but yields are less than half that of ^{54}Fe(d,n)^{55}Co reaction (Table 2). No-carrier-added ^{55}Co can be prepared using the ^{56}Fe(p,2n)^{55}Co reaction by bombardment with 28 MeV protons using a cyclotron or 40 MeV protons using a linear accelerator (*77, 78*). Better yields and decreased impurities of ^{56}Co are achieved when the reaction is carried out using 28 MeV protons and high-purity target material. Typically, radiochemical separation is performed by solvent extraction techniques (*78, 79*).

Radiolabeling of Antibodies with ^{55}Co. In studies performed at Brookhaven National Laboratory, an anti-CEA antibody fragment was labeled with ^{55}Co using cyclohexyl EDTA monoanhydride (CDTA-MA), 4-isothiocyanato-*trans*-1,2,-diaminocyclohexane *N,N,N′,N′*-tetraacetic acid (4-ICE) and diethylenetriamine pentaacetic acid dianhydride (DTPA-DA) as bifunctional chelating agents (*77*). The radiolabeling was carried out at pH 5.5 at room temperature with an incubation time ranging 2−4 h. All three of the immunoconjugates were obtained in high labeling yields and demonstrated good serum stability after 4 days (*77*).

Biological Studies with ^{55}Co Labeled Antibodies. ^{55}Co labeled anti-CEA F(ab′)$_2$ using DTPA-DA and 4-ICE as bifunctional chelating agents was evaluated in athymic mice bearing human colon carcinoma LS174T xenografts as a potential PET imaging agent (*77*). In the same study, to appraise the feasibility of the use of ^{55}Co as a PET tracer, a Jaszczak phantom study was performed on a whole body PET scanner, providing images of satisfactory resolution (*77*). In vivo biodistribution studies revealed the superiority of 4-ICE as a better ^{55}Co chelating agent as compared to DTPA-DA, as the tumor uptake of 4-ICE conjugated antibody was 2.8 times with greater conjugated antibody than that of DTPA-DA.

In the past,^{55}Co labeled bleomycin has been evaluated for imaging of tumors in preclinical and clinical settings (*76, 78, 80*). Other applications of ^{55}Co include evaluation of renal function (*79*). However, most applications of ^{55}Co in the clinic are in the field of neuro-imaging to assess neuronal damage in stroke and traumatic brain injury (*81, 82*).

Challenges. Since the initial reports of successful use of ^{55}Co in radioimmunoimaging in early 1990's, no peer-reviewed reports have been published in over 15 years that demonstrate the use of ^{55}Co in radioimmunoimaging. Issues surrounding appropriate chelation chemistry should be addressable extrapolation from the prior reports, and the use of 1,4,7,10-tetraaminocyclododecane-*N,N,N′,N′*-tetraacetic acid (DOTA) derivatives might also prove useful in this application. The dissociation kinetics of Co(II)-DOTA complexes has been suggested to be very slow at neutral and slightly acidic pH and therefore may offer better in vivo stability than DTPA complexes (*83, 84*). Cobalt has been used to determine the mean number of DOTA chelating groups conjugated per antibody using a metal-binding assay (*85, 86*). Size considerations might also direct one to investigate NOTA. This is an area of research that remains unsettled. Another potential challenge might be the radiation dose from the ^{56}Co impurity and the generated presence of the longer-lived ^{55}Fe daughter ($t_{1/2} = 2.6$ y) (*87*). It is known that uncomplexed cobalt localizes in the bone and liver, which could pose issues related to radiation toxicity in case the ^{55}Co complex is unstable in vivo (*88*).

Gallium-66. Gallium belongs to group III of the periodic table. Gallium has an atomic radius of 1.8 Å and electronegativity of 1.81. ^{66}Ga has one of the highest energies of the candidates considered here for PET imaging ($E_{max} = 4.15$ MeV, 56% abundant). Along with a complex spectrum of γ-rays, ^{66}Ga is one of the more difficult positron emitters for quantitative PET imaging. Although at the shorter end of this criterion, ^{66}Ga has a half-life of 9.4 h and has been explored for radioimmunoimaging in the past decade (*89, 90*).

Production of ^{66}Ga. ^{66}Ga can be produced using a medical cyclotron employing the ^{66}Zn(p,n)^{66}Ga reaction (Table 2) (*91*). Alternatively, ^{66}Ga can be produced by ^{4}He bombardment of natural copper targets by means of the ^{63}Cu (^{4}He, n) ^{66}Ga reaction (*89, 92, 93*). However, this method also yields an impurity in the form of ^{67}Ga ($t_{1/2} = 3.26$ d). Chemical purification of ^{66}Ga from the copper target using multiple techniques is described in detail in these published reports (*89, 92, 93*).

Radiolabeling of Antibodies with ^{66}Ga. The coordination chemistry of Ga(III) is well-established, as it is known that Ga(III) readily binds to the harder oxygen donor chelating agents (*94*). Initially, $GaCl_3$ is complexed as an acetate or a citrate, and this weak coordination complex is then used to prepare complexes of higher stability (*94*).

The monoclonal antimyosin antibody, Imciromab was labeled with ^{66}Ga in high yield (99%) by transcomplexation from an acetate buffer to the DTPA-conjugated protein (*89, 90*). One of the major concerns of using ^{66}Ga for labeling antibodies is the formation of the insoluble hydrolyzed $Ga(OH)_3$ species above pH 4.5. The radiolabeling had to be carried out in a pH range 3−4.5, which may potentially degrade intact antibodies. Suitable chelation chemistry for Ga(III) radionuclides that has been evaluated includes EDTA, DTPA derivatives, and DOTA, the latter of which may be adequately stable in vivo within the context of the half-lives of the positron emitting gallium radionuclides (*95*). A critical parameter for *in vivo* stability of the Ga(III)-complex is its relative stability to the Ga(III)-transferrin complex. The reported formation constant for Ga(III)-transferrin complex is $\log K_1 = 20.3$ (*96*), and the high plasma concentration of transferrin increases the risks of transchelation. The majority of the Ga(III) complexes used in nuclear medicine are thermodynamically stable and kinetically inert to exchange with transferrin in vivo. However, the complex formed with the chelator 1,4,7-triazacyclononane-*N,N′,N″*-triacetic acid (NOTA) is exceptionally stable and quite probably will emerge as the agent of choice for use with Ga(III) radionuclides (*97, 98*).

Moreover, NOTA is a more suitable chelating agent for Ga(III) labeled antibodies, as the Ga(III)-NOTA complex is formed at room temperature, and therefore, the protein is exposed to less harsh conditions as compared to heating as in the use of DOTA (*99*).

Biological Studies with ^{66}Ga Labeled Antibodies. ^{66}Ga-DTPA-antimyosin antibody was evaluated in dogs for imaging of myocardial necrosis by PET (*89*). Most biological applications of ^{66}Ga in molecular imaging have been with either peptides or small molecules, as the radiolabeling in acidic conditions is more favorable as compared to use with antibodies (*100*, *101*). The initial use of ^{66}Ga in humans dates back to 1954 (*102*), and in that study, ^{66}Ga was used to investigate bone disease. As compared to ^{66}Ga, short-lived positron emitter ^{68}Ga ($t_{1/2}$ = 1.1 h) obtained from a ^{68}Ge/^{68}Ga generator has gained immense popularity in recent years due to the availability of commercial ^{68}Ge/^{68}Ga generators and clinical successes with ^{68}Ga labeled somatostatin peptide (*103*, *104*). In spite of such a short half-life, excellent results have been obtained from a ^{68}Ga labeled trastuzumab fragment when studying the tumor response to the heat shock protein 90 (Hsp90) inhibitor 17-allylamino-17-demethoxygeldanamycin (17-AAG) (*105*, *106*). In these studies, a ^{68}Ga labeled Herceptin fragment was successfully used to image the pharmacodynamics of HER2 degradation in response to 17-AAG and was an earlier predictor of tumor response to 17-AAG therapy than ^{18}F-FDG PET (*105*, *106*). However, ^{68}Ga may not be a suitable candidate for imaging with intact antibodies because of their slower pharmacokinetics and tumor localization.

Challenges. Apart from unfavorable antibody radiolabeling procedures, the utility of ^{66}Ga in quantitative radioimmunoimaging is severely impaired by high positron energy (4.15 MeV), which results in the loss of intrinsic spatial resolution of about 5.8 mm and additional high-energy γ-emission (1.03 MeV) resulting to poor signal-to-noise ratio (Table 1). The half-life of 9.4 h may be relatively longer than existing radionuclides such as ^{18}F ($t_{1/2}$ = 1.83 h), but the half-life is shorter with respect to the blood clearance and tumor localization of an intact antibody. Traditionally, gallium (^{67}Ga) is used for bone scans, and therefore ^{66}Ga lost from the chelate (if any) will localize in the bones delivering high radiation dose.

Arsenic-72. Arsenic belongs to group III of the periodic table and has an atomic radius of 1.3 Å and electronegativity of 2.18. ^{72}As ($t_{1/2}$ = 25.9 h) decays to a stable ^{72}Ge daughter with 88% high-energy positron emission (Table 1). The longer half-life and positron abundance makes ^{72}As one of the more attractive potential candidates for PET radioimmunoimaging. ^{72}As can also serve as a potential imaging and dosimetry surrogate for the β^--emitting ^{77}As ($t_{1/2}$ = 38.4 h), which can be used for radioimmunotherapy.

Production of ^{72}As. ^{72}As can produced by irradiating an enriched germanium target using the ^{72}Ge(p,n)^{72}As reaction, but the radionuclidic purity is low due to the formation of ^{71}As (10%) as shown in Table 2 (*107*). The target material can be recovered by dry distillation for reprocessing. Alternatively, ^{72}As can be produced from ^{72}Se/^{72}As radionuclide generators based on solid-phase extraction and distillation in which ^{72}As can be eluted in aqueous solvents with over 40−70% yield with less than 0.1% contamination of ^{72}Se (*108*−*110*). Unfortunately, generator-based production of ^{72}As from ^{72}Se is tedious, as it requires over 35 MeV bombardment of natural germanium target with helium ions. Another limitation of the ^{72}Se/^{72}As radionuclide generator is the relatively short half-life of ^{72}Se (8.40 d).

Radiolabeling of Antibodies by ^{72}As. Radio-arsenic (^{74}As and ^{77}As) has been used to label the phosphatidylserine targeting chimeric monoclonal antibody Bavituximab (*111*). Bavituximab was first modified with *N*-succinimidyl *S*-acetylthioacetate (SATA) using a commercial kit. Direct labeling with radio-arsenic was performed after deprotection of the sulfhydryl groups using hydroxylamine (Figure 2). The resultant radioimmunoconjugate demonstrated good stability over 72 h during incubation in fetal bovine serum as determined by size-exclusion HPLC (*111*).

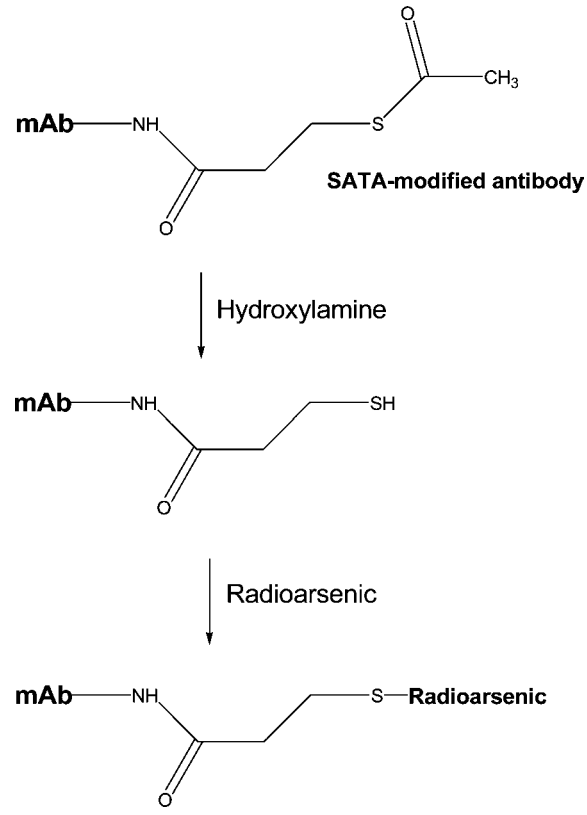

Figure 2. Representative scheme of radiolabeling intact antibodies with radio-arsenic using SATA approach.

Biological Studies with ^{72}As Labeled Antibodies. Bavituximab was labeled with ^{74}As ($t_{1/2}$ = 427 h, 30% positron emission) as a surrogate for ^{72}As for a proof of principle study and evaluated for PET imaging in rats bearing Dunning prostate R3327-AT1 tumors (*111*). Tumors were clearly visualized after 48 h with injection of 10 MBq of the radioimmunoconjugate with the highest tumor to background ratio being achieved at 72 h. Localization of the radio-arsenic labeled immunoconjugate was confirmed by autoradiography. This study demonstrated successful use of radio-arsenic in PET radioimmunoimaging. Although, it can be argued that ^{72}As is a better candidate for radioimmunoimaging with a more appropriate half-life and higher positron abundance. ^{72}As has been used in humans to study environmental toxicity caused by high doses of natural arsenic (*112*).

Challenges. Production of ^{72}As is limited to a few centers around the world, the issue of a steady supply of clinical grade ^{72}As remains unclear. There have been efforts by the United States Department of Energy to assist in the development of ^{72}As generators; yet, the availability of a commercial generator seems unlikely in the near future. Another drawback of ^{72}As is its association with a relatively high radiation dose that could restrict certain applications particularly when hematologic toxicity is a concern as the uncomplexed arsenic localizes in red blood cells (*88*).

Copper-64. Copper belongs to group IB of the periodic table and has an atomic radius of 1.6 Å, and an electronegativity of 1.90. ^{64}Cu has been a radionuclide of considerable interest for PET imaging due to its attractive physical and chemical

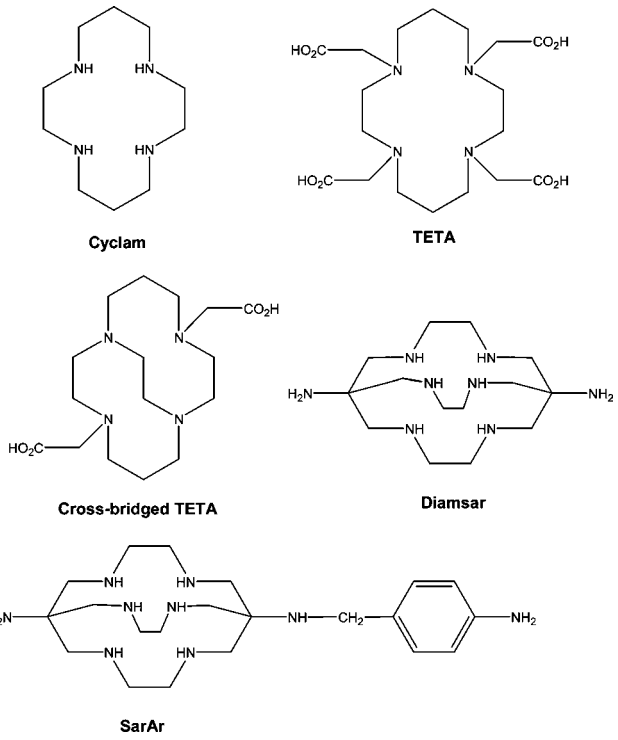

Figure 3. Selected chelating agents used for radiolabeling intact antibodies with ^{64}Cu.

properties. As compared to ^{18}F, ^{64}Cu has a longer half-life of 12.7 h and decays to stable ^{64}Ni and ^{64}Zn daughters. Besides the positron emission, ^{64}Cu also emits Auger electrons and has a β^--emission, and therefore could potentially be used for radioimmunotherapy (*113*). Imaging characteristics as a result of optimum positron energy (0.66 MeV) and no high-energy γ-emission are two of the biggest factors that make ^{64}Cu an attractive candidate for PET imaging (Table 1). The image quality and spatial resolution are equivalent to ^{18}F and require no major adjustments in data processing and analysis (*114*).

Production of ^{64}Cu. ^{64}Cu can be produced in numerous ways. Initially, ^{64}Cu was prepared by use of the ^{64}Zn(n,p)^{64}Cu reaction, but low yields and high contamination of ^{67}Cu, lead to the development of the ^{64}Ni(p,n)^{64}Cu reaction that was later employed to produce therapeutic quantities of ^{64}Cu (*115*−*117*). ^{64}Cu can also be produced through the ^{68}Zn(p,αn)^{64}Cu reaction using a high-energy instrument (*118*−*120*). ^{68}Zn(p,αn)^{64}Cu reaction gives a good yield, but the radionuclidic purity is as low as 75% and the final product contains around 25% of ^{67}Cu as shown in Table 2 (*118, 120*). High-yield production of good-quality ^{64}Cu has greatly improved over the past few years, and this radionuclide is now commercially available from several sources such as Trace Life Science, Isotrace Technologies, MDS Nordion, and IBA Molecular.

Radiolabeling of Antibodies with ^{64}Cu. Copper can exist in two primary oxidation states, Cu(I) and Cu(II). It has been demonstrated that kinetic inertness is more important than thermodynamic stability of Cu(II) complexes, as Cu(II) complexes of EDTA and DTPA rapidly dissociated in human serum and a Cu(II)-albumin complex was formed (*121*).

To improve the in vivo stability, antibodies have been labeled with ^{64}Cu using various bifunctional chelating agents (Figure 3) such as derivatives of 1,4,8,11-tetraazacyclotetradecane (cyclam) (*122*), 1,4,8,11-tetraazacyclotetradecane-*N, N′,N″,N‴*-tetraacetic acid (TETA) (*123, 124*), and DOTA (*125*). All these bifunctional chelates and their derivatives were unsuccessful in preventing metabolic processing of the ^{64}Cu complex, that is presumably a factor of the redox chemistry of Cu(II), causing elevated liver uptake. To overcome this *in vivo* instability of Cu(II) complexes, cross-bridged tetraamine chelating agents are currently being developed and evaluated (*126*). These cross-bridged chelating agents provide better geometric coordination and were inert in aqueous solutions (*126*). Most application of these chelating agents has been for labeling peptides (*127*). To the best of our knowledge, intact antibodies have not been labeled with ^{64}Cu using cross-bridged tetraamine chelating agents that required harsh radiolabeling conditions with high temperature and acidic pH that are not conducive for labeling heat- and acid-sensitive antibodies. To overcome these problems, a novel chelating agent SarAr 1-*N*-(4-aminobenzyl)-3,6,10,13,16,19-hexaazabicyclo[6.6.6]eicosane-1,8-diamine conjugated to anti-GD2 monoclonal murine antibody 14.G2a and the corresponding chimeric monoclonal antibody ch14.8 were evaluated recently (*128*). SarAr is based on the macrobicyclic sarcophagine cage structure and was modified to contain the reactive aminobenzyl group for conjugation with the antibody. At pH 5.0 and room-temperature conditions, the SarAr chelating agent forms a stable complex with Cu(II) within the multiple macrocyclic rings comprising the sarcophagine cage structure. Therefore, radiolabeling of SarAr-mAb was performed at less harsh conditions (*128*). The resulting radioimmunoconjugate was shown to be stable in the presence of liver proteins known to transchelate with ^{64}Cu (*128*). Alternately, attempts have been made to radiolabel antibodies with ^{64}Cu using porphyrin-based chelating agents (*129*).

Biological Studies with ^{64}Cu Labeled Antibodies. Numerous studies using ^{64}Cu labeled antibodies have been reported for PET radioimmunoimaging and radioimmunotherapy. Clinically approved antibodies such as Cetuximab and Abegrin have been labeled with ^{64}Cu for PET imaging in preclinical models (*130*−*132*). ^{64}Cu-DOTA-cetuximab was evaluated in mice bearing EGFR-positive and EGFR-negative tumors for quantitative PET imaging (*132*). In this study, ^{64}Cu-DOTA-cetuximab showed prominent uptake in EGFR-expressing tumors, but low accumulation in EGFR-negative tumors. A good linear correlation between the calculated %ID/g values as measured by PET imaging and the EGFR expression level as measured by Western blot was exhibited (*132*). Subcutaneous xenografts and peritoneal metastases were clearly visualized by PET imaging with an anti-L1-CAM antibody chCE7 labeled with ^{64}Cu in mice bearing L1-CAM tumors (*133, 134*). This PET study also revealed that radio-metabolites of the copper immunoconjugate nonspecifically localized in the lymph nodes through the reticuloendothelial system, which could be critical in imaging lymph node metastasis (*134*). Recent novel approaches for chelating agents and linkers have been used to decrease the liver uptake and increase the target/background ratio (*128, 135*). The evaluation of ^{64}Cu-SarAr-14.G2a demonstrated that the use of a better chelating agent could greatly improve the tumor/background ratio. MicroPET imaging confirmed significant uptake of the radioimmunoconjugate in GD-2-positive tumors, with minimal uptake in GD-2-negative tumors and nontarget tissues of interest such as the liver (*128*). Another use of ^{64}Cu labeled antibodies was to serve as a PET surrogate for ^{67}Cu-radioimmunotherapy (*13*). Compared with ^{67}Cu, it was found that the ^{64}Cu labeled antibody alone reduced tumor growth; however, a much higher dose (5 times higher) of ^{64}Cu was required to produce effects comparable to ^{67}Cu. Overall, the therapy with ^{64}Cu was largely ineffective in treating larger tumors (*136*). To date, there has been one clinical study that utilized ^{64}Cu-TETA-1A3 to evaluate 36 patients with suspected primary or advanced colorectal cancer (*137*). In this study, all patients had CT scans and PET scans 4 to 36 h after being injected with 370 MBq of ^{64}Cu-TETA-1A3 directed toward lipid antigens present in human colon carcinoma. The positive

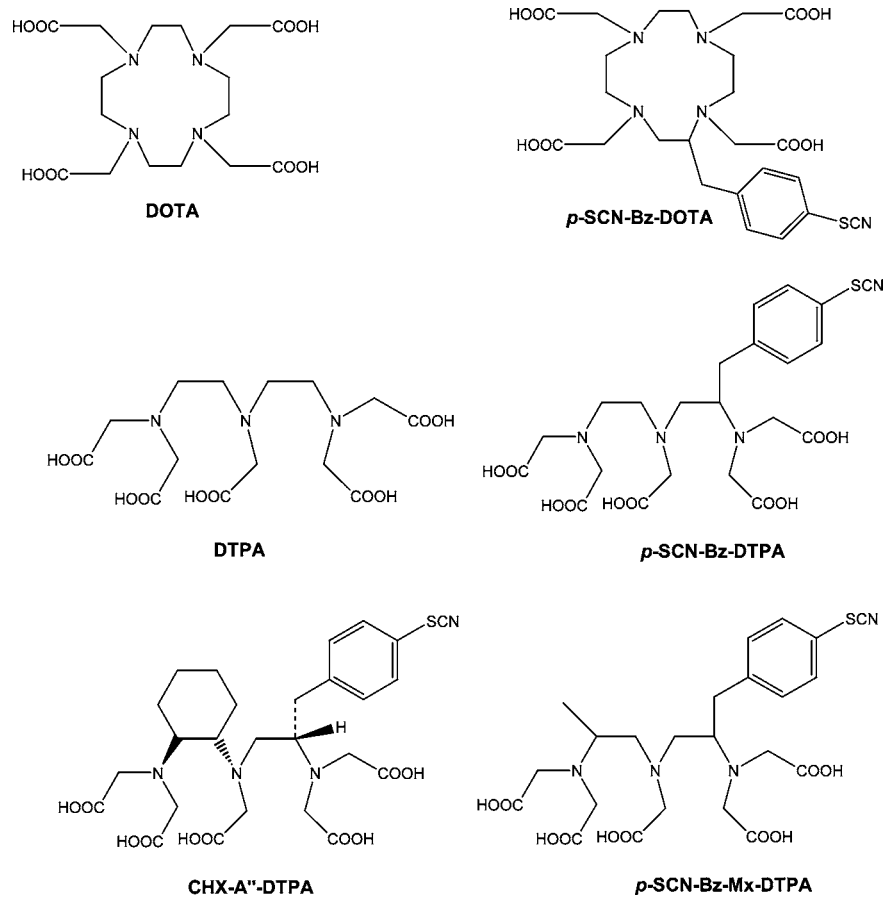

Figure 4. Selected chelating agents used for radiolabeling intact antibodies with $^{86}Y/^{90}Y$.

predictive value of ^{64}Cu-TETA-1A3 PET radioimmunoimaging was excellent, ranging from 89% (40/45) to 96% (43/45). The studies detected 11 new occult tumor sites including 9 small abdominopelvic foci less than 2.0 cm in diameter that were previously not detected by CT or MRI demonstrating that PET radioimmunoimaging with ^{64}Cu may have important applications in clinical oncology, particularly for detecting smaller lesions undetected by CT or MRI.

Challenges. Excellent results have been obtained while imaging intact antibodies with ^{64}Cu, but ^{64}Cu seems to be a more suitable candidate for imaging when applied to antibody fragments, diabodies, and other engineered targeting vectors which have faster localization and clearance (*124, 132*). Copper is a constituent of many metalloenzymes related to the cellular respiratory oxidation process (*88*). The release and accumulation of ^{64}Cu from most traditional radioimmunoconjugates in organs such as the liver remain a concern in spite of efforts to reduce the nonspecific uptake by developing better chelating agents and linkers.

Yttrium-86. Yttrium belongs to group IIIB of the periodic table. Yttrium has an atomic radius of 2.3 Å and electronegativity of 1.22. The primary purpose for exploring the viability of ^{86}Y for PET imaging was to use it as an imaging and dosimetry surrogate for the therapeutic radionuclide ^{90}Y, which has no imageable emission. ^{86}Y is an attractive candidate for studying ^{90}Y with its half-life of 14.2 h that allows imaging over several days.

Production of ^{86}Y. ^{86}Y can be produced on a medical cyclotron by irradiating $SrCO_3$ or SrO with 2−6 μA of beam current for <4 h applying the ^{86}Sr(p,n)^{86}Y reaction. As compared to $SrCO_3$, SrO is a superior target because it can withstand at least a 6 μA of beam current, which is a significant improvement over a maximum of 2 μA on the $SrCO_3$ target, resulting in yields that are almost doubled with minimum contaminants (*138*). At our own institution, we developed a simple and efficient semiautomated method to purify ^{86}Y, which does not compromise the biological properties of the ^{86}Y labeled antibody (*139, 140*).

Radiolabeling of Antibodies with ^{86}Y. In physiological conditions, the primary oxidation state of yttrium is Y(III). Chelation chemistry is well-established for Y(III) radionuclides, and several bifunctional derivatives of both DOTA and DTPA (Figure 4) have demonstrated their utility in this arena (*95*). The majority of the chelation chemistry for yttrium labeled antibodies was carried out with ^{90}Y and ^{88}Y. In 1976, ^{90}Y-DTPA was used for radionuclide therapy of brain tumors in patients (*141*), and since then, cyclic anhydride-DTPA was used to conjugate to antibodies for radiolabeling with ^{90}Y (*142*). However, when ^{90}Y-DTPA antibodies were evaluated in vivo, ^{90}Y was released from that DTPA and deposited in the bones, causing radiation toxicity (*143, 144*). In order to improve the in vivo stability of the radioimmunoconjugate, backbone-substituted DTPA derivatives such as *p*-isothiocyanatobenzyl-diethylenetriaminepentaacetic acid (SCN-Bz-DTPA) and a methyl derivative of *p*-isothiocyanatobenzyl-diethylenetriaminepentaacetic acid (SCN-Bz-Mx-DTPA also known as 1B4M-DTPA) (*143*−*145*) were evaluated. The 4-isothiocyanatobenzyl group (SCN-Bz) substituted onto the carbon backbone of DTPA for use in linkage to the antibody and the methyl groups were incorporated onto the backbone to sterically hinder the release of radiometal from the chelate. Comparative biological studies in mice demonstrated the superiority of backbone-substituted DTPA radioimmunoconjugates over cyclic anhydride DTPA radioimmunoconjugates (*143, 144*). With a better understanding of the coordination chemistry and geometry of DTPA derivatives, a cyclohexyl derivative of DTPA was developed,

which demonstrated excellent stability in vitro and in vivo (*146, 147*). Interestingly, stereochemistry of CHX-DTPA played a major role in in vivo stability of $^{90}Y/^{88}Y$ radioimmunoconjugate and subsequent bone uptake (*146, 148*). The single enantiomeric [(*R*)-2-amino-3-(4-isothiocyanatophenyl)propyl]-*trans*-(*S,S*)-cyclohexane-1,2-diamine-pentaacetic acid (CHX-A″-DTPA) radioimmunoconjugate was found to be more stable as compared to the corresponding diastereomeric pair of CHX-B-DTPA radioimmunoconjugates (*148*). After 7 days post-injection, bone uptake of the ^{88}Y labeled CHX-B′-DTPA or CHX-B″-DTPA radioimmunoconjugates was 5 times higher than that of the ^{88}Y labeled CHX-A″-DTPA radioimmunoconjugate (*148*). In order to further improve the stability, DOTA derivatives such as SCN-Bz-DOTA were explored for radiolabeling antibodies with ^{90}Y (*149, 150*). In a comparative study, it was found that DOTA conjugated antibody was more stable than the DTPA conjugated (*150*). Since then, numerous preclinical and clinical studies have been published reporting DTPA and DOTA based chelating agents for ^{90}Y radioimmunotherapy and thus extrapolating to ^{86}Y for PET imaging (*151*−*153*).

Biological Studies with ^{86}Y Labeled Antibodies. ^{86}Y labeled antibodies were most recently evaluated to perform dosimetry for ^{90}Y labeled antibodies used for radioimmunotherapy, as they were expected to be superior to ^{111}In labeled antibodies in terms of similarities in both chemical and biological behavior (*153*). Numerous studies have been reported with^{86}Y labeled antibodies including clinically approved trastuzumab (Herceptin) (*152, 154*) and cetuximab (Erbitux) (*154*). In a recent study, ^{86}Y-CHX-A″-DTPA-trastuzumab was evaluated in mice bearing intraperitoneal SKOV3 ovarian tumors (*152*). In this study, PET and MRI studies were performed to assess the therapeutic potential of ^{90}Y-CHX-A″-DTPA-trastuzumab using ^{86}Y-CHX-A″-DTPA-trastuzumab as an imaging surrogate for dosimetry. Intraperitoneal tumors were visualized by PET imaging 2 days after injecting ^{86}Y-CHX-A″-DTPA-trastuzumab, and the tumor localization was confirmed by MRI studies. ^{86}Y-CHX-A″-DTPA-trastuzumab localized to sites of disease with minimal normal organ uptake (*152*). In the study performed at our institution, we could clearly visualize LS-174T colon carcinoma xenografts in mice after 2 days of injecting ^{86}Y-CHX-A″-DTPA trastuzumab (tumor uptake was greater than 30% ID/g) (*154*). In the same study, the HER1-targeted ^{86}Y-CHX-A″-DTPA cetuximab was evaluated in mice bearing LS-174T colon carcinoma, SKOV3 ovarian carcinoma and DU-145 prostate carcinoma (*154*). All the tumors were clearly visualized at 1 day postinjection with the tumor uptake ranging from 20−30% ID/g.

Clinical use of ^{86}Y labeled agent used for dosimetry ^{90}Y labeled has been illustrated by the use of ^{86}Y-DOTA-Phe^1-Tyr^3-octreotide (SMT-487) for dosimetry of ^{90}Y-SMT-487 in patients with metastatic carcinoid tumors (*155*). The maximum dose that could be delivered to the tumor without exceeding the 23 Gy cutoff dose to kidneys was successfully calculated using PET imaging, and presumably reduced the incidence of potential renal toxicity caused by ^{90}Y-SMT-487 therapy.

Challenges. ^{86}Y is commercially available (Isotrace Technology) in a limited capacity and is also only available at centers capable of producing ^{86}Y on a regular basis. The high positron energy of 3.14 MeV (34% abundance) and additional γ-emission of 1.08 MeV (83% abundance) significantly affects the spatial resolution and image quality, respectively (Table 1). Uncomplexed ^{86}Y localizes in the bone and therefore can cause radiation toxicity in the events of "leakage" from the immunoconjugate and thus may be not a suitable candidate to image bone metastasis.

Zirconium-89. Zirconium belongs to group IVB of the periodic table and has an atomic radius of 2.2 Å and an electronegativity of 1.33. ^{89}Zr ($t_{1/2}$ = 78.4 h) decays to an ultrashort-lived daughter ^{89}mY ($t_{1/2}$ = 16 s) with a 23% β^+ emission and 77% electron capture (Table 1). Due to its appropriate half-life and imaging characteristics, ^{89}Zr labeled antibodies are currently being evaluated in the clinic as PET surrogates for both ^{90}Y and ^{177}Lu therapy studies despite the possibility of using the elementally matched ^{86}Y for ^{90}Y and ^{177}Lu possesses an imagable γ-emission (*156*).

Production of ^{89}Zr. ^{89}Zr can be produced through the $^{89}Y(p,n)^{89}Zr$ reaction in which inexpensive natural yttrium foil is irradiated with a 14−14.5 MeV proton beam and the target is separated by ion-exchange chromatography or solvent extraction (*26, 157, 158*). Alternatively, ^{89}Zr can also be produced through the $^{89}Y(d,2n)^{89}Zr$ reaction (*159*). A relatively high yield of 43 MBq/μAh is obtained with the $^{89}Y(p,n)^{89}Zr$ reaction with less than 0.2% impurity of ^{88}Zr ($t_{1/2}$ = 85 d and daughter ^{88}Y; $t_{1/2}$ = 105 d) (Table 2).

Radiolabeling of Antibodies with ^{89}Zr. Over the past 20 years, attempts have been made to label proteins and antibodies with ^{89}Zr using DTPA derivatives and porphyrins as chelating agents (*160, 161*). Proteins and antibodies were labeled with ^{89}Zr using desferal (Df) conjugates (*162, 163*). The process incorporates Df-groups onto monoclonal antibodies in a two-step procedure. Firstly, maleimide groups were incorporated into the protein with the assistance of succinimidyl-4-(*N*-maleimidomethyl)cyclohexane-1-carboxylate (SMCC). In the second step, the thioester of Df formed by conjugation to SATA was further converted to a free thiol with hydroxylamine to facilitate reaction with the maleimide groups of the antibody with subsequent radiolabeling with ^{89}Zr. The final purified product was obtained through gel filtration (*162, 163*). This protocol was further modified by formation of *N*-succinyldesferrioxamine B of Df (N-SucDf) as an intermediate (*164*). In this method, the hydroxamate groups of N-sucDf were temporarily blocked with formation of the Fe(III) complex. The N-sucDf-Fe complex was then esterified and coupled to antibodies. Thereafter, Fe(III) was removed by reduction to Fe(II) and transchelation to EDTA. Finally, the mAb-N-sucDf is radiolabeled with ^{89}Zr at pH 7.2−7.4 after a 30 min incubation at room temperature (*164*).

Biological Studies with ^{89}Zr Labeled Antibodies. Considering the success of ^{90}Y-labeled mAbs in clinical radioimmunotherapy (*12, 151, 165*), ^{86}Y-labeled mAbs are currently being developed in preclinical models for clinical dosimetry purposes (*139, 152, 153*). The half-life of ^{90}Y is nearly 4 times greater than that of ^{86}Y, and therefore, predicting ^{90}Y dosimetry of slowly clearing antibody may not be feasible or even appropriate. For these reasons, ^{89}Zr was explored as one of the possible radionuclides that could be used for dosimetry analysis of ^{90}Y-labeled mAbs (*166*). Clinically used antibodies such as HER1-targeted cetuximab (*156*), VEGF-targeted bevacizumab (*167*), and CD-20-targeted ibritumomab tiuxetan have been labeled with the ^{89}Zr-Df conjugate (*168*). All the above studies demonstrated the use of ^{89}Zr labeled antibodies in quantitative PET imaging. Additionally, the tumor localization of the ^{89}Zr-mAb was similar to that of the $^{111}In/^{90}Y$-mAb.

Due to the feasibility in production and purification of ^{89}Zr labeled mAb, clinical studies were performed with CD44V6-specific chimeric mAb, U36 labeled with ^{89}Zr (*169*). In this study, ^{89}Zr−U36 was evaluated in patients with squamous cell carcinoma of the head and neck (HNSCC), who were at high risk of having neck lymph node metastases. All primary tumors (n = 17) as well as lymph node metastases in 18 of 25 positive levels (sensitivity 72%) and in 11 of 15 positive sides (sensitivity 73%) were detected using PET radioimmunoimaging (*169*). Interpretation of PET was correct in 112 of 121 operated levels (accuracy 93%) and in 19 of 25 operated sides (accuracy 76%). For CT/MRI, sensitivities of 60% and 73% and accuracies of

90% and 80% were found per level and side, respectively. ^{89}Zr-immunoPET demonstrated a sensitivity of 85% and accuracy of 95% as compared to sensitivity of 62% and accuracy of 88% for^{18}F-FDG-PET (*169*). Thus, this study demonstrated the utility and advantages of ^{89}Zr PET radioimmunoimaging in a clinical setting in comparison with CT/MRI and ^{18}F-FDG (*169*). Similarly, all known tumor lesions previously identified by ^{18}F-FDG were successfully imaged by ^{89}Zr-Df-Zevalin in a pilot PET imaging study in a patient with Non-Hodgkin's lymphoma (*168*).

Challenges. Uncomplexed ^{89}Zr localizes in the bone and can deliver a high radiation dose to the bone marrow. The need for stable chelation chemistry remains an important consideration with this element (*88*). In spite of the recent success of ^{89}Zr PET imaging, clinical-grade ^{89}Zr is not commercially available yet (although ^{89}Zr can be obtained from IBA Molecular on request). Another major disadvantage is the currently used ^{89}Zr-mAb production scheme. The currently used conjugation and radiolabeling schemes are often tedious and time-consuming and involve numerous steps that increase the margin for error for the cGMP (current good manufacturing practice) production. In the currently used procedure, the Fe(III) complex is first formed with desferal, which is then activated for conjugation through extension of the terminal amine with succinic anhydride followed by the conversion of the formed carboxylate into an active ester. After conjugation of the antibody, the Fe(III) is then reduced and displaced with ^{89}Zr (*164*). Alternate, simpler conjugation and radiolabeling schemes that can be successfully carried out at local radiopharmacies are warranted to bolster the increased appeal of ^{89}Zr PET radioimmunoimaging. One of the suggested applications of ^{89}Zr has been to use it as a surrogate for ^{90}Y and ^{131}I labeled antibodies; however, ^{89}Zr labeled antibodies, while close, also do not exactly match the biodistribution and pharmacokinetics of ^{90}Y and ^{131}I labeled antibodies (*168, 170*).

OPPORTUNITIES AND CHALLENGES

Production. The reliable large-scale availability of the longer-lived positron emitting radionuclides that is suitable for clinical applications is critical for potential clinical translation. Many of the described radionuclides such as ^{64}Cu, ^{76}Br, ^{86}Y, and ^{72}As can be produced in good yields at low-energy medical cyclotrons (*26*). Most of the longer-lived positron-emitting radionuclides are currently produced by employing low-energy nuclear reactions such as (p, n) and (d, n), which may require isotopically enriched targets that are usually expensive. Alternatively, a higher-energy dual-particle cyclotron or a multiparticle intermediate-energy cyclotron could be used for production of some these radionuclides employing nuclear reactions such as (p, xn) and (^{3}He, xn). Two of the most important criteria in medical application of positron emitters are quality and yield; hence the target material is critical. It is absolutely essential to produce target material that is economical, may be efficiently recovered for reuse, can withstand high-energy beam fluxes of charged particles, and most importantly, also be easily isolated from the product to yield high-purity final product. One such example that meets these criteria has been the production of ^{64}Cu. Originally, ^{64}Cu was produced through the ^{64}Zn(n,p)^{64}Cu reaction resulting in low yields and a high contamination of ^{67}Cu, unless highly enriched pure ^{64}Zn was used. The low yields compounded with contamination of the β^--emitting therapeutic radionuclide ^{67}Cu were impediments to routine large-scale clinical applications of ^{64}Cu for PET imaging. As an alternative, the ^{64}Ni(p,n)^{64}Cu reaction was employed to obtain higher yields and better-quality ^{64}Cu (*115, 116*). However, the biggest drawback of this method remains the cost of the highly enriched ^{64}Ni target material, which can be a hindrance in large-scale production of ^{64}Cu at multiple centers across the world. With better understanding and characterization of cross-section data, integral yields, and chemical processing methods, it is possible to obtain good-quality positron emitters in large yields using a medical cyclotron that can be potentially used for radioimmunoimaging. Most commonly used production routes of selected longer-lived positron emitters for radioimmunoimaging with their corresponding yields and radionuclidic impurities are listed in Table 2.

Imaging Characteristics. Two of the major factors impacting image quality are the additional γ-emissions and the energy of the positron, which can contribute to the background noise and the loss of intrinsic spatial resolution respectively. Some of the longer-lived positron-emitting radionuclides such as ^{76}Br, ^{72}As, ^{124}I, and ^{66}Ga have high-energy positron emissions, which result in loss of intrinsic spatial resolution and poor signal-to-noise ratios (Table 1). In clinical settings, both radiation dosimetry and chemistry as a result of inadequate specific activity and stability may limit the amount of radioactivity injected, thereby further degrading image quality. Loss of spatial resolution could also limit the use of radioimmunoconjugates labeled with some of the described longer-lived positron-emitting radionuclides for the detection of metastasis and smaller lesions, which could be critical for their use in assessing or predicting clinical outcomes. Successful attempts have been made to improve the image characteristics of high-energy positron emitters by developing methods to correct for scatter fractions and spurious coincidences (*171*−*173*). Image reconstruction algorithms have been developed, which include models of the statistical nature of nuclear decays and tomography responses that improve the spatial resolution and at the same time reduce the image noise (*114, 171*−*173*). Further advances in instrumentation and image processing may additionally improve spatial resolution and the ability to perform more accurate quantitative analysis. However, implementing these improvements in the clinic may be complex, as new instruments and imaging software will require FDA approval.

Potential Therapeutic Applications and Radiation Toxicity. Tumor therapy using antibodies carrying radioactivity has been reported now for over 50 years (*174, 175*). In 1966, McCradle and co-workers reported the use of ^{131}I labeled antibody to human fibrinogen as a clinical diagnostic and therapeutic agent (*8*). In this study, 50 patients with reported neoplasm were imaged, and a high percentage of patients showed positive scans for metastases to the brain, which was a remarkable achievement during that period when targeted noninvasive radioimmunoimaging was still in its infancy. This study demonstrated the value of molecular imaging with radiolabeled antibodies for the assessment of primary and metastatic lesions (*8*). In this same study, two previously imaged patients were treated with higher doses of ^{131}I labeled antibody to human fibrinogen resulting in regression of their lesions (*8*). Since that time, numerous studies have been reported demonstrating the utility of antibodies labeled with radionuclides such as ^{111}In, ^{177}Lu, and ^{64}Cu, which could be used for diagnosis as well as therapy (*4, 176*). For better clinical acceptance, cost−benefit effectiveness and numerous other reasons including the need of a surrogate radionuclide, a radiolabeled antibody that could be used as a diagnostic as well as therapeutic becomes a desirable combination.

One of the major concerns in radioimmunotherapy is the nonuniform absorbed dose distribution in the tumor resulting in less effective therapy in spite of dose escalation (*177*). One possible solution might be the use of longer-lived radionuclides with longer emission ranges, which may increase the mean

absorbed dose to the tumor, as they are more likely to penetrate into the tumor before decaying in the body than shorter-lived radionuclides (*178*). Longer-lived positron-emitting radionuclides can deliver high absorbed doses to the target site, as the doses delivered by positrons are as high as negatrons of the same energy. Considering the success of negatron-emitting radioimmunotherapy in preclinical and clinical studies, longer-lived positron-emitting radioimmunoconjugates may potentially be used for therapeutic applications. The longer half-life may minimize the effects of nonuniformity up to an extent. However, the choice of radionuclide will be based upon the function of biological and pharmacokinetic properties of the targeting antibody (normal organs uptake and clearance), disease state, physical half-life of the radionuclide, abundance and energy of the positron emission, and additional γ-rays. For example, assuming a biological half-life of 100 h and whole-body uniform distribution in an adult human, based on the values given in the International Commission on Radiological Protection (ICRP) publications, the effective dose from ^{52}Mn ($t_{1/2} = 134.2$ h) will be approximately 0.9−1.1 mSv/MBq as compared to 0.02−0.04 mSv/MBq from ^{64}Cu ($t_{1/2} = 12.7$ h) and 0.2−0.3 mSv/MBq from ^{76}Br ($t_{1/2} = 16.2$ h) (*159*). Another important parameter in terms of therapeutic applications of longer-lived positron emitters is the positron abundance and the dose rate; a dose rate of 2−3 cGy/h has been suggested as being required to overcome the proliferation of most types of tumor cells (*179*). Therefore, the portion of the total dose that is delivered below this rate is essentially unnecessary and can potentially pose a hazard. Theoretically, high-specific-activity longer-lived positron-emitting radioimmunoconjugates could be used for therapy; however, toxicity and dose to the normal organs may pose a few challenges and will depend on whether the radioimmunoconjugate is delivered systemically or locally.

Economics, Regulatory Affairs, and Clinical Acceptance. Currently, the use of PET in the clinical setting revolves around ^{18}F-FDG, which has great clinical acceptance, as it can be used to image most metabolically active tumors and lesions, irrespective of any expression of cell surface molecular targets such as EGFR and HER2/μ. This characteristic of ^{18}F-FDG can also be disadvantageous, as it does not provide information regarding the status of cell surface targets that could be essential for patients about to undergo immunotherapy or radioimmunotherapy. Under those circumstances, PET radioimmunoimaging could play a critical role in risk stratification. In the past year, sales of Herceptin (trastuzumab), Avastin (Bevacizumab), Rituxan (Rituximab), and Erbitux (Cetuximab) each all exceeded one billion U.S. dollars (*180*). On the basis of previous results, not all patients may respond to immunotherapy due to low-density of target expression or changes in the target levels. In all likelihood, not all patients undergo some form of diagnostic scan to evaluate the status of target in the progression of illness. PET radioimmunoimaging could serve as one of the potential tools for screening patients that may or may not respond to therapy, thereby acting as a cost containment tool. Contrary to that positive aspect, a sizable financial investment and commitment is required to develop a clinically FDA approved radiopharmaceutical. In order to recover the cost spent in developing the PET radioimmunoconjugate, sales and use volumes have to be significantly high, which will be directly related to the clinical acceptance of PET radioimmunoimaging.

The number of radiopharmaceuticals approved by the U.S. FDA in the past decade has been limited due to more scrutiny and a tedious approval process. Radiation toxicity and required preapproval studies could potentially be a major obstacle for the approval of radioimmunoconjugates labeled with longer-lived positron emitters. Thus, one can question the rationale behind the objective of developing a novel PET radioimmunoconjugate considering the level of required investment and resources versus failure to acquire approval of the agent by the FDA.

Other regulatory barriers include waste disposal of large quantities of longer-lived high-energy positron emitters, decontamination, occupational hazards, and the radiation exposure to normal population by outpatients undergoing high-dose longer-lived positron-emitting radionuclide protocols.

Lack of Standards for Calibration, Decay Characteristics. A recent study has highlighted the differences in published values of decay data and energies of some of the described radionuclides (*119*). These differences in values could impact the overall biological and dosimetry results, as the same amount of radioactivity quantified from dose calibrator and PET image could vary from institution to institution depending on the values used. Therefore, there is a need to establish standards for calibration of instruments for these longer-lived positron emitters to avoid variances which could result in errors.

Future Perspective. It is clear from the selected examples cited in this report that efforts are continuing to develop radioimmunoconjugates labeled with longer-lived positron-emitting radionuclides for PET imaging. The superiority of PET in radioimmunoimaging was demonstrated by a recent clinical study in which a comparison was made among ^{131}I-G250, ^{124}I-cG250, and ^{18}F-FDG for detection of metastatic renal-cell carcinoma (*53*, *181*). ^{131}I-cG250 was able to detect 30% of metastatic lesions as compared to 69% for ^{18}F-FDG (*181*); however, the results were far better when ^{124}I-cG250 was used, as the sensitivity of detection of tumor was 94% (*53*, *181*). When compared to ^{124}I-cG250, ^{131}I-cG250 did not provide the same resolution, contrast, or the potential for quantification as ^{124}I-cG250 (*53*). Considering the advantages of PET radioimmunoimaging, further efforts are warranted to improve PET instrumentation and image processing, increase production of clinical-grade high-yield longer-lived positron emitters, and continue to create efficient radiolabeling methods to produce high-yield biologically active stable radioimmunoconjugates in the least amount of time and variability. Lastly, the most critical criterion for successful clinical translation is that continued efforts have to be applied toward making wise selections of the most appropriate antibody matched with the most appropriate radionuclide for the desired application within an appropriate patient population. Important questions still remain unanswered: how many positron-emitting radionuclides need to be evaluated that will fulfill the desired objectives of radioimmunoimaging? What are the alternatives in case of unexpected unreliable availability of the radionuclide? Is it worth the capital investments related to PET imaging if techniques such as biopsies and CT imaging are going to remain the mainstay of cancer diagnosis? Can future generation SPECT systems be as good as currently used PET (*182*, *183*)? If so, then why develop newer positron-emitting products if ^{111}In based SPECT can offer precise quantitation in future? And finally, should there be a common set of criteria and guidelines for choosing the radionuclide?

In conclusion, we believe that radioimmunoimaging with longer-lived positron-emitting radionuclides holds significant promises, but several scientific and nonscientific challenges have to be conquered before realizing the true potentials of PET radioimmunoimaging with intact antibodies.

ACKNOWLEDGMENT

This report was supported by the Intramural Research Program of the NIH, NCI, Center for Cancer Research, and the United States Department of Health and Human Services. Gratitude is expressed to Mike Slackenerny for constant encouragement and support.

LITERATURE CITED

(1) Cattell, H. W. (1896) Application of the X-rays to surgery. *Science 3*, 344–346.

(2) Wagner, H. N., Jr., and Bardfeld, P. A. (1967) Evaluation of structure and function of spleen with radioactive tracers. *JAMA 199*, 202–6.

(3) Wagner, H. N., Jr. (1963) The current status of nuclear medicine. *JAMA 183*, 500–3.

(4) Boswell, C. A., and Brechbiel, M. W. (2007) Development of radioimmunotherapeutic and diagnostic antibodies: an inside-out view. *Nucl. Med. Biol. 34*, 757–78.

(5) Khaw, B. A. (2005) Antibodies for molecular imaging in the cardiovascular system. *J. Nucl. Cardiol. 12*, 591–604.

(6) Melcher, L. R., and Masouredis, S. P. (1951) The in vivo stability of the I131 protein label of rabbit antibody in guinea pigs as determined by the quantitative precipitin reaction. *J. Immunol. 67*, 393–402.

(7) Pressman, D. (1949) The zone of localization of antibodies; the specific localization of antibodies to rat kidney. *Cancer 2*, 697–700.

(8) McCardle, R. J., Harper, P. V., Spar, I. L., Bale, W. F., Andros, G., and Jiminez, F. (1966) Studies with iodine-131-labeled antibody to human fibrinogen for diagnosis and therapy of tumors. *J. Nucl. Med. 7*, 837–47.

(9) Goldenberg, D. M., DeLand, F., Kim, E., Bennett, S., Primus, F. J., van Nagell, J. R., Jr., Estes, N., DeSimone, P., and Rayburn, P. (1978) Use of radiolabeled antibodies to carcinoembryonic antigen for the detection and localization of diverse cancers by external photoscanning. *N. Engl. J. Med. 298*, 1384–6.

(10) Kohler, G., and Milstein, C. (1975) Continuous cultures of fused cells secreting antibody of predefined specificity. *Nature 256*, 495–7.

(11) Goldenberg, D. M., Kim, E. E., Deland, F., Spremulli, E., Nelson, M. O., Gockerman, J. P., Primus, F. J., Corgan, R. L., and Alpert, E. (1980) Clinical studies on the radioimmunodetection of tumors containing alpha-fetoprotein. *Cancer 45*, 2500–5.

(12) O'Donnell, R. T., DeNardo, S. J., Yuan, A., Shen, S., Richman, C. M., Lara, P. N., Griffith, I. J., Goldstein, D. S., Kukis, D. L., Martinez, G. S., Mirick, G. R., DeNardo, G. L., and Meyers, F. J. (2001) Radioimmunotherapy with (111)In/(90)Y-2IT-BAD-m170 for metastatic prostate cancer. *Clin. Cancer Res. 7*, 1561–8.

(13) DeNardo, G. L., Kukis, D. L., Shen, S., DeNardo, D. A., Meares, C. F., and DeNardo, S. J. (1999) ^{67}Cu-versus ^{131}I-labeled Lym-1 antibody: comparative pharmacokinetics and dosimetry in patients with non-Hodgkin's lymphoma. *Clin. Cancer Res. 5*, 533–41.

(14) Mach, J. P., Carrel, S., Forni, M., Ritschard, J., Donath, A., and Alberto, P. (1980) Tumor localization of radiolabeled antibodies against carcinoembryonic antigen in patients with carcinoma: a critical evaluation. *N. Engl. J. Med. 303*, 5–10.

(15) Phelps, M. E. (2000) PET: the merging of biology and imaging into molecular imaging. *J. Nucl. Med. 41*, 661–81.

(16) Otsuka, F. L., Welch, M. J., Kilbourn, M. R., Dence, C. S., Dilley, W. G., and Wells, S. A., Jr. (1991) Antibody fragments labeled with fluorine-18 and gallium-68: in vivo comparison with indium-111 and iodine-125-labeled fragments. *Int. J. Rad. Appl. Instrum. B 18*, 813–6.

(17) Garg, P. K., Garg, S., Bigner, D. D., and Zalutsky, M. R. (1992) Localization of fluorine-18-labeled Mel-14 monoclonal antibody F(ab′)2 fragment in a subcutaneous xenograft model. *Cancer Res. 52*, 5054–60.

(18) Cai, W., Olafsen, T., Zhang, X., Cao, Q., Gambhir, S. S., Williams, L. E., Wu, A. M., and Chen, X. (2007) PET imaging of colorectal cancer in xenograft-bearing mice by use of an ^{18}F-labeled T84.66 anti-carcinoembryonic antigen diabody. *J. Nucl. Med. 48*, 304–10.

(19) Kramer-Marek, G., Kiesewetter, D. O., Martiniova, L., Jagoda, E., Lee, S. B., and Capala, J. (2008) [(18)F]FBEM-Z(HER2:342)-Affibody molecule-a new molecular tracer for in vivo monitoring of HER2 expression by positron emission tomography. *Eur. J. Nucl. Med. Mol. Imaging 35*, 1008–18.

(20) Vaidyanathan, G., Bigner, D. D., and Zalutsky, M. R. (1992) Fluorine-18-labeled monoclonal antibody fragments: a potential approach for combining radioimmunoscintigraphy and positron emission tomography. *J. Nucl. Med. 33*, 1535–41.

(21) Snook, D. E., Rowlinson-Busza, G., Sharma, H. L., and Epenetos, A. A. (1990) Preparation and in vivo study of ^{124}I-labelled monoclonal antibody H17E2 in a human tumour xenograft model. A prelude to positron emission tomography (PET). *Br. J. Cancer Suppl. 10*, 89–91.

(22) Pentlow, K. S., Graham, M. C., Lambrecht, R. M., Cheung, N. K., and Larson, S. M. (1991) Quantitative imaging of I-124 using positron emission tomography with applications to radioimmunodiagnosis and radioimmunotherapy. *Med. Phys. 18*, 357–66.

(23) Bakir, M. A., Eccles, S., Babich, J. W., Aftab, N., Styles, J., Dean, C. J., Lambrecht, R. M., and Ott, R. J. (1992) c-erbB2 protein overexpression in breast cancer as a target for PET using iodine-124-labeled monoclonal antibodies. *J. Nucl. Med. 33*, 2154–60.

(24) Hohn, A., Nortier, F. M., Scholten, B., van der Walt, T. N., Coenen, H. H., and Qaim, S. M. (2001) Excitation functions of ^{125}Te(p, xn)-reactions from their respective thresholds up to 100 MeV with special reference to the production of ^{124}I. *Appl. Radiat. Isot. 55*, 149–56.

(25) Sajjad, M., Bars, E., and Nabi, H. A. (2006) Optimization of ^{124}I production via ^{124}Te(p,n) ^{124}I reaction. *Appl. Radiat. Isot. 64*, 965–70.

(26) Tang, L. (2007) Radionuclide production and yields at Washington University School of Medicine. *Q. J. Nucl. Med. Mol. Imaging 52*, 122–33.

(27) Kondo, K., Lambrecht, R. M., and Wolf, A. P. (1977) Iodine-123 production for radiopharmaceuticals--XX excitation functions of the ^{124}Te(p, 2n) ^{123}I and ^{124}Te(p, n) ^{124}I reactions and the effect of target enrichment on radionuclidic purity. *Int. J. Appl. Radiat. Isot. 28*, 395–401.

(28) Pressman, D., Hill, R. F., and Foote, F. W. (1949) The zone of localization of anti-mouse-kidney serum as determined by radioautographs. *Science 109*, 65–66.

(29) Yalow, R. S., and Berson, S. A. (1959) Assay of plasma insulin in human subjects by immunological methods. *Nature 184*, 1648–9.

(30) Hunter, W. M., and Greenwood, F. C. (1962) Preparation of iodine-131 labelled human growth hormone of high specific activity. *Nature 194*, 495–6.

(31) Greenwood, F. C., Hunter, W. M., and Glover, J. S. (1963) The preparation of I-131-labelled human growth hormone of high specific radioactivity. *Biochem. J. 89*, 114–23.

(32) Marchalonis, J. J. (1969) An enzymic method for the trace iodination of immunoglobulins and other proteins. *Biochem. J. 113*, 299–305.

(33) David, G. S. (1972) Solid state lactoperoxidase: a highly stable enzyme for simple, gentle iodination of proteins. *Biochem. Biophys. Res. Commun. 48*, 464–71.

(34) Rudinger, J., and Ruegg, U. (1973) Appendix: Preparation of N-succinimidyl 3-(4-hydroxyphenyl)propionate. *Biochem. J. 133*, 538–539.

(35) Bolton, A. E., and Hunter, W. M. (1973) The labelling of proteins to high specific radioactivities by conjugation to a ^{125}I-containing acylating agent. *Biochem. J. 133*, 529–39.

(36) Salacinski, P. R., McLean, C., Sykes, J. E., Clement-Jones, V. V., and Lowry, P. J. (1981) Iodination of proteins, glycoproteins, and peptides using a solid-phase oxidizing agent, 1,3,4,6-tetrachloro-3α,6α-diphenyl glycoluril (Iodogen). *Anal. Biochem. 117*, 136–46.

(37) Wilbur, D. S., Hadley, S. W., Hylarides, M. D., Abrams, P. G., Beaumier, P. A., Morgan, A. C., Reno, J. M., and Fritzberg, A. R. (1989) Development of a stable radioiodinating reagent

to label monoclonal antibodies for radiotherapy of cancer. *J. Nucl. Med. 30*, 216–26.
(38) Press, O. W., DeSantes, K., Anderson, S. K., and Geissler, F. (1990) Inhibition of catabolism of radiolabeled antibodies by tumor cells using lysosomotropic amines and carboxylic ionophores. *Cancer Res. 50*, 1243–50.
(39) Geissler, F., Anderson, S. K., and Press, O. (1991) Intracellular catabolism of radiolabeled anti-CD3 antibodies by leukemic T cells. *Cell Immunol. 137*, 96–110.
(40) Geissler, F., Anderson, S. K., Venkatesan, P., and Press, O. (1992) Intracellular catabolism of radiolabeled anti-mu antibodies by malignant B-cells. *Cancer Res. 52*, 2907–15.
(41) Sharkey, R. M., Behr, T. M., Mattes, M. J., Stein, R., Griffiths, G. L., Shih, L. B., Hansen, H. J., Blumenthal, R. D., Dunn, R. M., Juweid, M. E., and Goldenberg, D. M. (1997) Advantage of residualizing radiolabels for an internalizing antibody against the B-cell lymphoma antigen, CD22. *Cancer Immunol. Immunother. 44*, 179–88.
(42) Mattes, M. J., Shih, L. B., Govindan, S. V., Sharkey, R. M., Ong, G. L., Xuan, H., and Goldenberg, D. M. (1997) The advantage of residualizing radiolabels for targeting B-cell lymphomas with a radiolabeled anti-CD22 monoclonal antibody. *Int. J. Cancer 71*, 429–35.
(43) Stein, R., Goldenberg, D. M., Thorpe, S. R., Basu, A., and Mattes, M. J. (1995) Effects of radiolabeling monoclonal antibodies with a residualizing iodine radiolabel on the accretion of radioisotope in tumors. *Cancer Res. 55*, 3132–9.
(44) Stein, R., Govindan, S. V., Mattes, M. J., Chen, S., Reed, L., Newsome, G., McBride, B. J., Griffiths, G. L., Hansen, H. J., and Goldenberg, D. M. (2003) Improved iodine radiolabels for monoclonal antibody therapy. *Cancer Res. 63*, 111–8.
(45) Wilbur, D. S. (1992) Radiohalogenation of proteins: an overview of radionuclides, labeling methods, and reagents for conjugate labeling. *Bioconjugate Chem. 3*, 433–70.
(46) Collingridge, D. R., Carroll, V. A., Glaser, M., Aboagye, E. O., Osman, S., Hutchinson, O. C., Barthel, H., Luthra, S. K., Brady, F., Bicknell, R., Price, P., and Harris, A. L. (2002) The development of [(^{124})I]iodinated-VG76e: a novel tracer for imaging vascular endothelial growth factor in vivo using positron emission tomography. *Cancer Res. 62*, 5912–9.
(47) Sundaresan, G., Yazaki, P. J., Shively, J. E., Finn, R. D., Larson, S. M., Raubitschek, A. A., Williams, L. E., Chatziioannou, A. F., Gambhir, S. S., and Wu, A. M. (2003) ^{124}I-labeled engineered anti-CEA minibodies and diabodies allow high-contrast, antigen-specific small-animal PET imaging of xenografts in athymic mice. *J. Nucl. Med. 44*, 1962–9.
(48) Fortin, M. A., Salnikov, A. V., Nestor, M., Heldin, N. E., Rubin, K., and Lundqvist, H. (2007) Immuno-PET of undifferentiated thyroid carcinoma with radioiodine-labelled antibody cMAb U36: application to antibody tumour uptake studies. *Eur. J. Nucl. Med. Mol. Imaging 34*, 1376–87.
(49) Phan, H. T., Jager, P. L., Paans, A. M., Plukker, J. T., Sturkenboom, M. G., Sluiter, W. J., Wolffenbuttel, B. H., Dierckx, R. A., and Links, T. P. (2008) The diagnostic value of (124)I-PET in patients with differentiated thyroid cancer. *Eur. J. Nucl. Med. Mol. Imaging*.
(50) Freudenberg, L. S., Antoch, G., Frilling, A., Jentzen, W., Rosenbaum, S. J., Kuhl, H., Bockisch, A., and Gorges, R. (2008) Combined metabolic and morphologic imaging in thyroid carcinoma patients with elevated serum thyroglobulin and negative cervical ultrasonography: role of (124)I-PET/CT and FDG-PET. *Eur. J. Nucl. Med. Mol. Imaging*.
(51) Kolbert, K. S., Pentlow, K. S., Pearson, J. R., Sheikh, A., Finn, R. D., Humm, J. L., and Larson, S. M. (2007) Prediction of absorbed dose to normal organs in thyroid cancer patients treated with ^{131}I by use of ^{124}I PET and 3-dimensional internal dosimetry software. *J. Nucl. Med. 48*, 143–9.
(52) Jayson, G. C., Zweit, J., Jackson, A., Mulatero, C., Julyan, P., Ranson, M., Broughton, L., Wagstaff, J., Hakannson, L., Groenewegen, G., Bailey, J., Smith, N., Hastings, D., Lawrance, J., Haroon, H., Ward, T., McGown, A. T., Tang, M., Levitt, D., Marreaud, S., Lehmann, F. F., Herold, M., and Zwierzina, H. (2002) Molecular imaging and biological evaluation of HuMV833 anti-VEGF antibody: implications for trial design of antiangiogenic antibodies. *J. Natl. Cancer Inst. 94*, 1484–93.
(53) Divgi, C. R., Pandit-Taskar, N., Jungbluth, A. A., Reuter, V. E., Gonen, M., Ruan, S., Pierre, C., Nagel, A., Pryma, D. A., Humm, J., Larson, S. M., Old, L. J., and Russo, P. (2007) Preoperative characterisation of clear-cell renal carcinoma using iodine-124-labelled antibody chimeric G250 (^{124}I-cG250) and PET in patients with renal masses: a phase I trial. *Lancet Oncol. 8*, 304–10.
(54) Vedeneyev, V. I. G., L.V.; Kondrat'YevV. N.; Medvedev, V. A. (1966) *Bond energies, ionization potentials and electron affinities*, Edward Arnold, London.
(55) Orlova, A., Hoglund, J., Lubberink, M., Lebeda, O., Gedda, L., Lundqvist, H., Tolmachev, V., and Sundin, A. (2002) Comparative biodistribution of the radiohalogenated (Br, I and At) antibody A33. Implications for in vivo dosimetry. *Cancer Biother. Radiopharm. 17*, 385–96.
(56) Rossin, R., Berndorff, D., Friebe, M., Dinkelborg, L. M., and Welch, M. J. (2007) Small-animal PET of tumor angiogenesis using a (76)Br-labeled human recombinant antibody fragment to the ED-B domain of fibronectin. *J. Nucl. Med. 48*, 1172–9.
(57) Bergstrom, M., Lu, L., Fasth, K. J., Wu, F., Bergstrom-Pettermann, E., Tolmachev, V., Hedberg, E., Cheng, A., and Langstrom, B. (1998) In vitro and animal validation of bromine-76-bromodeoxyuridine as a proliferation marker. *J. Nucl. Med. 39*, 1273–9.
(58) Loc'h, C., Mardon, K., Valette, H., Brutesco, C., Merlet, P., Syrota, A., and Maziere, B. (1994) Preparation and pharmacological characterization of [^{76}Br]-meta-bromobenzylguanidine ([^{76}Br]MBBG). *Nucl. Med. Biol. 21*, 49–55.
(59) Scott-Robson, S., Capala, J., Malmborg, P., and Lundqvist, H. (1991) Production of ^{76}Br and its use in labeling proteins. *Acta Radiol. Suppl. 376*, 64.
(60) Knight, L. C., Harwig, S. L., and Welch, M. J. (1977) In vitro stability and in vivo clearance of fibrinogen or serum albumin labeled with ^{77}Br, ^{131}I, or ^{125}I by direct or indirect synthetic methods. *J. Nucl. Med. 18*, 282–8.
(61) Wilbur, D. S., and Hylarides, M. D. (1991) Radiolabeling of a monoclonal antibody with N-succinimidyl para-[^{77}Br]bromobenzoate. *Int. J. Rad. Appl. Instrum. B 18*, 363–5.
(62) Lovqvist, A., Sundin, A., Ahlstrom, H., Carlsson, J., and Lundqvist, H. (1995) ^{76}Br-labeled monoclonal anti-CEA antibodies for radioimmuno positron emission tomography. *Nucl. Med. Biol. 22*, 125–31.
(63) Winberg, K. J., Persson, M., Malmstrom, P. U., Sjoberg, S., and Tolmachev, V. (2004) Radiobromination of anti-HER2/neu/ErbB-2 monoclonal antibody using the p-isothiocyanatobenzene derivative of the [^{76}Br]undecahydro-bromo-7,8-dicarba-nido-undecaborate(1-) ion. *Nucl. Med. Biol. 31*, 425–33.
(64) Mume, E., Orlova, A., Larsson, B., Nilsson, A. S., Nilsson, F. Y., Sjoberg, S., and Tolmachev, V. (2005) Evaluation of ((4-hydroxyphenyl)ethyl)maleimide for site-specific radiobromination of anti-HER2 affibody. *Bioconjugate Chem. 16*, 1547–55.
(65) Lovqvist, A., Sundin, A., Ahlstrom, H., Carlsson, J., and Lundqvist, H. (1997) Pharmacokinetics and experimental PET imaging of a bromine-76-labeled monoclonal anti-CEA antibody. *J. Nucl. Med. 38*, 395–401.
(66) Lovqvist, A., Lundqvist, H., Lubberink, M., Tolmachev, V., Carlsson, J., and Sundin, A. (1999) Kinetics of ^{76}Br-labeled anti-CEA antibodies in pigs; aspects of dosimetry and PET imaging properties. *Med. Phys. 26*, 249–58.
(67) Lovqvist, A., Sundin, A., Roberto, A., Ahlstrom, H., Carlsson, J., and Lundqvist, H. (1997) Comparative PET imaging of experimental tumors with bromine-76-labeled antibodies, fluorine-18-fluorodeoxyglucose and carbon-11-methionine. *J. Nucl. Med. 38*, 1029–35.
(68) Hoglund, J., Tolmachev, V., Orlova, A., Lundqvist, H., and Sundin, A. (2000) Optimized indirect (76)Br-bromination of

antibodies using N-succinimidyl para-[^{76}Br]bromobenzoate for radioimmuno PET. *Nucl. Med. Biol. 27*, 837–43.
(69) Maziere, B., Loc'h, C., Baron, J. C., Sgouropoulos, P., Duquesnoy, N., D'Antona, R., and Cambon, H. (1985) In vivo quantitative imaging of dopamine receptors in human brain using positron emission tomography and [^{76}Br]bromospiperone. *Eur. J. Pharmacol. 114*, 267–72.
(70) Martinot, J. L., Peron-Magnan, P., Huret, J. D., Mazoyer, B., Baron, J. C., Boulenger, J. P., Loc'h, C., Maziere, B., Caillard, V., Loo, H., et al. (1990) Striatal D2 dopaminergic receptors assessed with positron emission tomography and [^{76}Br]bromospiperone in untreated schizophrenic patients. *Am. J. Psychiatry 147*, 44–50.
(71) Davidsson, L., Cederblad, A., Hagebo, E., Lonnerdal, B., and Sandstrom, B. (1988) Intrinsic and extrinsic labeling for studies of manganese absorption in humans. *J. Nutr. 118*, 1517–21.
(72) Sastri, C. S., Petri, H., Kueppers, G., and Erdtmann, G. (1981) Production of manganese-52 of high isotopic purity by ^{3}He-activation of vanadium. *Int. J. Appl. Radiat. Isotopes 32*, 246–247.
(73) Lambrecht, R. M., and Wolf, A.P. (1979) The cyclotron production of ^{38}K, ^{51}Mn, ^{52}Mn, and ^{77}Kr for positron emission tomography. *J. Labelled Compd. Radiopharm. 16*, 129–130.
(74) Kong, G., Jackson, C., Koh, D. M., Lewington, V., Sharma, B., Brown, G., Cunningham, D., and Cook, G. J. R. (2008) The use of ^{18}F-FDG PET/CT in colorectal liver metastases-comparison with CT and liver MRI. *Eur. J. Nucl. Med. Mol. Imaging* 1–7.
(75) Cikrt, M. (1972) Biliary excretion of 203 Hg, 64 Cu, 52 Mn, and 210 Pb in the rat. *Br. J. Ind. Med. 29*, 74–80.
(76) Sharma, H, Z. J., Smith, A. M., and Downey, S. (1986) Production of cobalt-55, a short-lived, positron emitting radiolabel for bleomycin. *Int. J. Radiat. Instrum. [A] 37*, 105–109.
(77) Srivastava, S. C., M, L. F., Kolsky, K. L., Mease, R. C., Joshi, V., Meinken, G. E., Pyatt, B., Wolf, A. P., Schlyder, D. J., Levy, A. V., and Fowler, J. S. (1994) Production and use of cobalt-55 as an antibody label for PET imaging. *J. Labelled Compd. Radiopharm. 35*, 389–391.
(78) Lagunas-Solar, M. C., and Jungerman, J. A. (1979) Cyclotron production of carrier-free cobalt-55, a new positron-emitting label for bleomycin. *Int. J. Appl. Radiat. Isot. 30*, 25–32.
(79) Goethals, P., Volkaert, A., Vandewielle, C., Dierckx, R., and Lameire, N. (2000) ^{55}Co-EDTA for renal imaging using positron emission tomography (PET): a feasibility study. *Nucl. Med. Biol. 27*, 77–81.
(80) Nieweg, O. E., Beekhuis, H., Paans, A. M., Piers, D. A., Vaalburg, W., Welleweerd, J., Wiegman, T., and Woldring, M. G. (1982) Detection of lung cancer with ^{55}Co-bleomycin using a positron camera. A comparison with ^{57}Co-bleomycin and ^{55}Co-bleomycin single photon scintigraphy. *Eur. J. Nucl. Med. 7*, 104–7.
(81) Stevens, H., Jansen, H. M., De Reuck, J., Lemmerling, M., Strijckmans, K., Goethals, P., Lemahieu, I., de Jong, B. M., Willemsen, A. T., and Korf, J. (1999) ^{55}Cobalt (Co) as a PET-tracer in stroke, compared with blood flow, oxygen metabolism, blood volume and gadolinium-MRI. *J. Neurol. Sci. 171*, 11–8.
(82) Jansen, H. M., Paans, A. M., vd Vliet, A. M., Veenma-van der Duin, L., Bolwijn-Meijer, C. J., Pruim, J., Willemsen, A. T., Franssen, E. J., Minderhoud, J. M., and Korf, J. (1997) Cobalt-55 positron emission tomography in ischemic stroke. *Clin. Neurol. Neurosurg. 99*, 6–10.
(83) Byegård, J, S. G., and Skålberg, M. (1999) The stability of some metal EDTA, DTPA and DOTA complexes: Application as tracers in groundwater studies. *J. Radioanal. Nucl. Chem. 241*, 281–290.
(84) Heppeler, A., Andre, J. P., Buschmann, I., Wang, X., Reubi, J. C., Hennig, M., Kaden, T. A., and Maecke, H. R. (2008) Metal-ion-dependent biological properties of a chelator-derived somatostatin analogue for tumour targeting. *Chemistry 14*, 3026–34.
(85) Kukis, D. L., DeNardo, S. J., DeNardo, G. L., O'Donnell, R. T., and Meares, C. F. (1998) Optimized conditions for chelation of yttrium-90-DOTA immunoconjugates. *J. Nucl. Med. 39*, 2105–10.
(86) Kukis, D. L., DeNardo, G. L., DeNardo, S. J., Mirick, G. R., Miers, L. A., Greiner, D. P., and Meares, C. F. (1995) Effect of the extent of chelate substitution on the immunoreactivity and biodistribution of 2IT-BAT-Lym-1 immunoconjugates. *Cancer Res. 55*, 878–84.
(87) Beekhuis, H., and Nieweg, O. E. (1984) Radiation absorbed doses from Co-57- and Co-55 bleomycin. *J. Nucl. Med. 25*, 478–85.
(88) Bowen, H. (1966) The Biogeochemistry of the Elements, in *Trace Elements in Biochemistry*, pp 173−239, Academic Press, London.
(89) Goethals, P., Coene, M., Slegers, G., Vogelaers, D., Everaert, J., Lemahieu, I., Colardyn, F., and Heyndrickx, G. R. (1990) Production of carrier-free ^{66}Ga and labeling of antimyosin antibody for positron imaging of acute myocardial infarction. *Eur. J. Nucl. Med. 16*, 237–40.
(90) Graham, M. C., Pentlow, K. S., Mawlawi, O., Finn, R. D., Daghighian, F., and Larson, S. M. (1997) An investigation of the physical characteristics of ^{66}Ga as an isotope for PET imaging and quantification. *Med. Phys. 24*, 317–26.
(91) Szelecsenyi, F., Tarkanyi, F., Kovacs, Z., Bergman, J., Heselius, S. J., and Solin, O. (1991) Production of ^{66}Ga and ^{67}Ga at a compact cyclotron. *Acta Radiol. Suppl. 376*, 62–3.
(92) Goethals, P., Coene, M., Slegers, G., Agon, P., Deman, J., and Schelstraete, K. (1988) Cyclotron production of carrier-free ^{66}Ga as a positron emitting label of albumin colloids for clinical use. *Eur. J. Nucl. Med. 14*, 152–4.
(93) Zweit, J., Sharma, H., and Downey, S. (1987) Production of gallium-66, a short-lived, positron emitting radionuclide. *Int. J. Rad. Appl. Instrum. [A] 38*, 499–501.
(94) Green, M. A., and Welch, M. J. (1989) Gallium radiopharmaceutical chemistry. *Int. J. Rad. Appl. Instrum. B 16*, 435–48.
(95) Brechbiel, M. W. (2008) Bifunctional chelates for metal nuclides. *Q. J. Nucl. Med. Mol. Imaging 52*, 166–73.
(96) Harris, W. R., and Chen, Y. (1994) Electron paramagnetic resonance and difference ultraviolet studies of Mn^{2+} binding to serum transferrin. *J. Inorg. Biochem. 54*, 1–19.
(97) Eisenwiener, K. P., Prata, M. I., Buschmann, I., Zhang, H. W., Santos, A. C., Wenger, S., Reubi, J. C., and Macke, H. R. (2002) NODAGATOC, a new chelator-coupled somatostatin analogue labeled with [$^{67/68}$Ga] and [^{111}In] for SPECT, PET, and targeted therapeutic applications of somatostatin receptor (hsst2) expressing tumors. *Bioconjugate Chem. 13*, 530–41.
(98) Lee, J., Garmestani, K., Wu, C., Brechbiel, M. W., Chang, H. K., Choi, C. W., Gansow, O. A., Carrasquillo, J. A., and Paik, C. H. (1997) In vitro and in vivo evaluation of structure-stability relationship of ^{111}In- and ^{67}Ga-labeled antibody via 1B4M or C-NOTA chelates. *Nucl. Med. Biol. 24*, 225–30.
(99) Velikyan, I., Maecke, H., and Langstrom, B. (2008) Convenient preparation of ^{68}Ga-based PET-radiopharmaceuticals at room temperature. *Bioconjugate Chem. 19*, 569–73.
(100) Mathias, C. J., Lewis, M. R., Reichert, D. E., Laforest, R., Sharp, T. L., Lewis, J. S., Yang, Z. F., Waters, D. J., Snyder, P. W., Low, P. S., Welch, M. J., and Green, M. A. (2003) Preparation of ^{66}Ga- and ^{68}Ga-labeled Ga(III)-deferoxamine-folate as potential folate-receptor-targeted PET radiopharmaceuticals. *Nucl. Med. Biol. 30*, 725–31.
(101) Ugur, O., Kothari, P. J., Finn, R. D., Zanzonico, P., Ruan, S., Guenther, I., Maecke, H. R., and Larson, S. M. (2002) Ga-66 labeled somatostatin analogue DOTA-DPhe1-Tyr3-octreotide as a potential agent for positron emission tomography imaging and receptor mediated internal radiotherapy of somatostatin receptor positive tumors. *Nucl. Med. Biol. 29*, 147–57.
(102) Van Der Werff, J. T. (1954) Clinical investigations on the use of radioactive gallium (Ga66 and Ga67) in bone diseases. *Acta Radiol. 41*, 343–7.
(103) Henze, M., Dimitrakopoulou-Strauss, A., Milker-Zabel, S., Schuhmacher, J., Strauss, L. G., Doll, J., Macke, H. R., Eisenhut,

M., Debus, J., and Haberkorn, U. (2005) Characterization of ^{68}Ga-DOTA-D-Phe1-Tyr3-octreotide kinetics in patients with meningiomas. *J. Nucl. Med. 46*, 763–9.

(104) Koukouraki, S., Strauss, L. G., Georgoulias, V., Eisenhut, M., Haberkorn, U., and Dimitrakopoulou-Strauss, A. (2006) Comparison of the pharmacokinetics of ^{68}Ga-DOTATOC and [^{18}F]FDG in patients with metastatic neuroendocrine tumours scheduled for ^{90}Y-DOTATOC therapy. *Eur. J. Nucl. Med. Mol. Imaging 33*, 1115–22.

(105) Smith-Jones, P. M., Solit, D., Afroze, F., Rosen, N., and Larson, S. M. (2006) Early tumor response to Hsp90 therapy using HER2 PET: comparison with ^{18}F-FDG PET. *J. Nucl. Med. 47*, 793–6.

(106) Smith-Jones, P. M., Solit, D. B., Akhurst, T., Afroze, F., Rosen, N., and Larson, S. M. (2004) Imaging the pharmacodynamics of HER2 degradation in response to Hsp90 inhibitors. *Nat. Biotechnol. 22*, 701–6.

(107) Jennewein, M., Qaim, S. M., Hermanne, A., Jahn, M., Tsyganov, E., Slavine, N., Seliounine, S., Antich, P. A., Kulkarni, P. V., Thorpe, P. E., Mason, R. P., and Rösch, F. (2005) A new method for radiochemical separation of arsenic from irradiated germanium oxide. *Appl. Radiat. Isot. 63*, 343–351.

(108) Jennewein, M., Qaim, S. M., Kulkarni, P. V., Mason, R. P., Hermanne, A., and Ro?sch, F. (2005) A no-carrier-added ^{72}Se/^{72}As radionuclide generator based on solid phase extraction. *Radiochim. Acta 93*, 579–583.

(109) Jennewein, M., Schmidt, A., Novgorodov, A. F., Qaim, S. M., and Ro?sch, F. (2004) A no-carrier-added ^{72}Se/^{72}As radionuclide generator based on distillation. *Radiochim. Acta 92*, 245–249.

(110) Al-Kouraishi, S. H., and Boswell, G. G. J. (1978) An isotope generator for ^{72}As. *Int. J. Appl. Radiat. Isot. 29*, 607–609.

(111) Jennewein, M., Lewis, M. A., Zhao, D., Tsyganov, E., Slavine, N., He, J., Watkins, L., Kodibagkar, V. D., O'Kelly, S., Kulkarni, P., Antich, P. P., Hermanne, A., Rosch, F., Mason, R. P., and Thorpe, P. E. (2008) Vascular imaging of solid tumors in rats with a radioactive arsenic-labeled antibody that binds exposed phosphatidylserine. *Clin. Cancer Res. 14*, 1377–85.

(112) Turner, P. C. (1962) The calculation of absorbed tissue doses from arsenic-72. *Phys. Med. Biol. 7*, 329–34.

(113) Connett, J. M., Buettner, T. L., and Anderson, C. J. (1999) Maximum tolerated dose and large tumor radioimmunotherapy studies of ^{64}Cu-labeled monoclonal antibody 1A3 in a colon cancer model. *Clin. Cancer Res. 5*, 3207s–3212s.

(114) Ruangma, A., Bai, B., Lewis, J. S., Sun, X., Welch, M. J., Leahy, R., and Laforest, R. (2006) Three-dimensional maximum a posteriori (MAP) imaging with radiopharmaceuticals labeled with three Cu radionuclides. *Nucl. Med. Biol. 33*, 217–26.

(115) Obata, A., Kasamatsu, S., McCarthy, D. W., Welch, M. J., Saji, H., Yonekura, Y., and Fujibayashi, Y. (2003) Production of therapeutic quantities of (64)Cu using a 12 MeV cyclotron. *Nucl. Med. Biol. 30*, 535–9.

(116) McCarthy, D. W., Shefer, R. E., Klinkowstein, R. E., Bass, L. A., Margeneau, W. H., Cutler, C. S., Anderson, C. J., and Welch, M. J. (1997) Efficient production of high specific activity ^{64}Cu using a biomedical cyclotron. *Nucl. Med. Biol. 24*, 35–43.

(117) Zinn, K. R., Chaudhuri, T. R., Cheng, T. P., Morris, J. S., and Meyer, W. A., Jr. (1994) Production of no-carrier-added ^{64}Cu from zinc metal irradiated under boron shielding. *Cancer 73*, 774–8.

(118) Hilgers, K., Stoll, T., Skakun, Y., Coenen, H. H., and Qaim, S. M. (2003) Cross-section measurements of the nuclear reactions ^{nat}Zn(d,x) ^{64}Cu, ^{66}Zn(d,α) ^{64}Cu and ^{68}Zn(p,αn) ^{64}Cu for production of ^{64}Cu and technical developments for small-scale production of ^{67}Cu via the ^{70}Zn(p,α) ^{67}Cu process. *Appl. Radiat. Isot. 59*, 343–51.

(119) Qaim, S. M. (2008) Decay data and production yields of some non-standard positron emitters used in PET. *Q. J. Nucl. Med. Mol. Imaging 52*, 111–6.

(120) Szelecse?nyi, F., Steyn, G. F., Kova?cs, Z., Vermeulen, C., Van Der Meulen, N. P., Dolley, S. G., Van Der Walt, T. N., Suzuki, K., and Mukai, K. (2005) Investigation of the ^{66}Zn(p,2pn) ^{64}Cu and ^{68}Zn(p,x) ^{64}Cu nuclear processes up to 100 MeV: Production of ^{64}Cu. *Nucl. Instrum. Methods Phys. Res., Sect. B 240*, 625–637.

(121) Cole, W. C., DeNardo, S. J., Meares, C. F., McCall, M. J., DeNardo, G. L., Epstein, A. L., O'Brien, H. A., and Moi, M. K. (1986) Serum stability of ^{67}Cu chelates: comparison with ^{111}In and ^{57}Co. *Int. J. Rad. Appl. Instrum. B 13*, 363–8.

(122) Franz, J., Freeman, G. M., Barefield, E. K., Volkert, W. A., Ehrhardt, G. J., and Holmes, R. A. (1987) Labeling of antibodies with ^{64}Cu using a conjugate containing a macrocyclic amine chelating agent. *Int. J. Radiat. Appl. Instrum., Part B 14*, 479–484.

(123) Rogers, B. E., Anderson, C. J., Connett, J. M., Guo, L. W., Edwards, W. B., Sherman, E. L., Zinn, K. R., and Welch, M. J. (1996) Comparison of four bifunctional chelates for radiolabeling monoclonal antibodies with copper radioisotopes: biodistribution and metabolism. *Bioconjugate Chem. 7*, 511–22.

(124) Anderson, C. J., Connett, J. M., Schwarz, S. W., Rocque, P. A., Guo, L. W., Philpott, G. W., Zinn, K. R., Meares, C. F., and Welch, M. J. (1992) Copper-64-labeled antibodies for PET imaging. *J. Nucl. Med. 33*, 1685–91.

(125) Ping Li, W., Meyer, L. A., Capretto, D. A., Sherman, C. D., and Anderson, C. J. (2008) Receptor-binding, biodistribution, and metabolism studies of ^{64}Cu-DOTA-cetuximab, a PET-imaging agent for epidermal growth-factor receptor-positive tumors. *Cancer Biother. Radiopharm. 23*, 158–71.

(126) Anderson, C. J., Wadas, T. J., Wong, E. H., and Weisman, G. R. (2008) Cross-bridged macrocyclic chelators for stable complexation of copper radionuclides for PET imaging. *Q. J. Nucl. Med. Mol. Imaging 52*, 185–92.

(127) Sprague, J. E., Peng, Y., Sun, X., Weisman, G. R., Wong, E. H., Achilefu, S., and Anderson, C. J. (2004) Preparation and biological evaluation of copper-64-labeled tyr3-octreotate using a cross-bridged macrocyclic chelator. *Clin. Cancer Res. 10*, 8674–82.

(128) Voss, S. D., Smith, S. V., DiBartolo, N., McIntosh, L. J., Cyr, E. M., Bonab, A. A., Dearling, J. L., Carter, E. A., Fischman, A. J., Treves, S. T., Gillies, S. D., Sargeson, A. M., Huston, J. S., and Packard, A. B. (2007) Positron emission tomography (PET) imaging of neuroblastoma and melanoma with ^{64}Cu-SarAr immunoconjugates. *Proc. Natl. Acad. Sci. U.S.A. 104*, 17489–93.

(129) Bhalgat, M. K., Roberts, J. C., Mercer-Smith, J. A., Knotts, B. D., Vessella, R. L., and Lavallee, D. K. (1997) Preparation and biodistribution of copper-67-labeled porphyrins and porphyrin-A6H immunoconjugates. *Nucl. Med. Biol. 24*, 179–85.

(130) Ping Li, W., Meyer, L. A., Capretto, D. A., Sherman, C. D., and Anderson, C. J. (2008) Receptor-binding, biodistribution, and metabolism studies of (64)Cu-DOTA-Cetuximab, a PET-imaging agent for epidermal growth-factor receptor-positive tumors. *Cancer Biother. Radiopharm. 23*, 158–71.

(131) Cai, W., Wu, Y., Chen, K., Cao, Q., Tice, D. A., and Chen, X. (2006) In vitro and in vivo characterization of ^{64}Cu-labeled Abegrin, a humanized monoclonal antibody against integrin alpha v beta 3. *Cancer Res. 66*, 9673–81.

(132) Cai, W., Chen, K., He, L., Cao, Q., Koong, A., and Chen, X. (2007) Quantitative PET of EGFR expression in xenograft-bearing mice using ^{64}Cu-labeled cetuximab, a chimeric anti-EGFR monoclonal antibody. *Eur. J. Nucl. Med. Mol. Imaging 34*, 850–8.

(133) Grunberg, J., Novak-Hofer, I., Honer, M., Zimmermann, K., Knogler, K., Blauenstein, P., Ametamey, S., Maecke, H. R., and Schubiger, P. A. (2005) In vivo evaluation of ^{177}Lu- and $^{67/64}$Cu-labeled recombinant fragments of antibody chCE7 for radioimmunotherapy and PET imaging of L1-CAM-positive tumors. *Clin. Cancer Res. 11*, 5112–20.

(134) Novak-Hofer, I., Honer, M., Ametamey, S., Grunberg, J., Missimer, J., Zimmermann, K., and Schubiger, P. A. (2003) Imaging of renal carcinoma xenografts with ^{64}Cu-labelled anti-

L1-CAM antibody chCE7. *Eur. J. Nucl. Med. Mol. Imaging 30*, 1066.
(135) Li, L., Bading, J., Yazaki, P. J., Ahuja, A. H., Crow, D., Colcher, D., Williams, L. E., Wong, J. Y., Raubitschek, A., and Shively, J. E. (2008) A versatile bifunctional chelate for radiolabeling humanized anti-CEA antibody with In-111 and Cu-64 at either thiol or amino groups: PET imaging of CEA-positive tumors with whole antibodies. *Bioconjugate Chem. 19*, 89–96.
(136) Connett, J. M., Anderson, C. J., Guo, L. W., Schwarz, S. W., Zinn, K. R., Rogers, B. E., Siegel, B. A., Philpott, G. W., and Welch, M. J. (1996) Radioimmunotherapy with a ^{64}Cu-labeled monoclonal antibody: a comparison with ^{67}Cu. *Proc. Natl. Acad. Sci. U.S.A. 93*, 6814–8.
(137) Philpott, G. W., Schwarz, S. W., Anderson, C. J., Dehdashti, F., Connett, J. M., Zinn, K. R., Meares, C. F., Cutler, P. D., Welch, M. J., and Siegel, B. A. (1995) RadioimmunoPET: detection of colorectal carcinoma with positron-emitting copper-64-labeled monoclonal antibody. *J. Nucl. Med. 36*, 1818–24.
(138) Yoo, J., Tang, L., Perkins, T. A., Rowland, D. J., Laforest, R., Lewis, J. S., and Welch, M. J. (2005) Preparation of high specific activity (86)Y using a small biomedical cyclotron. *Nucl. Med. Biol. 32*, 891–7.
(139) Garmestani, K., Milenic, D. E., Plascjak, P. S., and Brechbiel, M. W. (2002) A new and convenient method for purification of ^{86}Y using a Sr(II) selective resin and comparison of biodistribution of ^{86}Y and ^{111}In labeled Herceptin. *Nucl. Med. Biol. 29*, 599–606.
(140) Park, L. S., Szajek, L. P., Wong, K. J., Plascjak, P. S., Garmestani, K., Googins, S., Eckelman, W. C., Carrasquillo, J. A., and Paik, C. H. (2004) Semi-automated ^{86}Y purification using a three-column system. *Nucl. Med. Biol. 31*, 297–301.
(141) Smith, S., Thomas, R. M., Steere, H. A., Beatty, H. E., Dawson, K. B., and Peckham, M. J. (1976) Therapeutic irradiation of the central nervous system using intrathecal 90Y--DTA. *Br. J. Radiol. 49*, 141–7.
(142) Hnatowich, D. J., Virzi, F., and Doherty, P. W. (1985) DTPA-coupled antibodies labeled with yttrium-90. *J. Nucl. Med. 26*, 503–9.
(143) Sharkey, R. M., Motta-Hennessy, C., Gansow, O. A., Brechbiel, M. W., Fand, I., Griffiths, G. L., Jones, A. L., and Goldenberg, D. M. (1990) Selection of a DTPA chelate conjugate for monoclonal antibody targeting to a human colonic tumor in nude mice. *Int. J. Cancer 46*, 79–85.
(144) Washburn, L. C., Sun, T. T., Lee, Y. C., Byrd, B. L., Holloway, E. C., Crook, J. E., Stubbs, J. B., Stabin, M. G., Brechbiel, M. W., Gansow, O. A., et al. (1991) Comparison of five bifunctional chelate techniques for ^{90}Y-labeled monoclonal antibody CO17−1A. *Int. J. Rad. Appl. Instrum. B 18*, 313–21.
(145) Brechbiel, M. W., and Gansow, O. A. (1991) Backbone-substituted DTPA ligands for ^{90}Y radioimmunotherapy. *Bioconjugate Chem. 2*, 187–94.
(146) Camera, L., Kinuya, S., Garmestani, K., Wu, C., Brechbiel, M. W., Pai, L. H., McMurry, T. J., Gansow, O. A., Pastan, I., Paik, C. H., et al. (1994) Evaluation of the serum stability and in vivo biodistribution of CHX-DTPA and other ligands for yttrium labeling of monoclonal antibodies. *J. Nucl. Med. 35*, 882–9.
(147) Camera, L., Kinuya, S., Garmestani, K., Pai, L. H., Brechbiel, M. W., Gansow, O. A., Paik, C. H., Pastan, I., and Carrasquillo, J. A. (1993) Evaluation of a new DTPA-derivative chelator: comparative biodistribution and imaging studies of ^{111}In-labeled B3 monoclonal antibody in athymic mice bearing human epidermoid carcinoma xenografts. *Nucl. Med. Biol. 20*, 955–62.
(148) Kobayashi, H., Wu, C., Yoo, T. M., Sun, B. F., Drumm, D., Pastan, I., Paik, C. H., Gansow, O. A., Carrasquillo, J. A., and Brechbiel, M. W. (1998) Evaluation of the in vivo biodistribution of yttrium-labeled isomers of CHX-DTPA-conjugated monoclonal antibodies. *J. Nucl. Med. 39*, 829–36.
(149) Deshpande, S. V., DeNardo, S. J., Kukis, D. L., Moi, M. K., McCall, M. J., DeNardo, G. L., and Meares, C. F. (1990) Yttrium-90-labeled monoclonal antibody for therapy: labeling by a new macrocyclic bifunctional chelating agent. *J. Nucl. Med. 31*, 473–9.
(150) Harrison, A., Walker, C. A., Parker, D., Jankowski, K. J., Cox, J. P., Craig, A. S., Sansom, J. M., Beeley, N. R., Boyce, R. A., Chaplin, L., et al. (1991) The in vivo release of ^{90}Y from cyclic and acyclic ligand-antibody conjugates. *Int. J. Rad. Appl. Instrum. B 18*, 469–76.
(151) Wong, J. Y., Chu, D. Z., Williams, L. E., Liu, A., Zhan, J., Yamauchi, D. M., Wilczynski, S., Wu, A. M., Yazaki, P. J., Shively, J. E., Leong, L., and Raubitschek, A. A. (2006) A phase I trial of (90)Y-DOTA-anti-CEA chimeric T84.66 (cT84.66) radioimmunotherapy in patients with metastatic CEA-producing malignancies. *Cancer Biother. Radiopharm. 21*, 88–100.
(152) Palm, S., Enmon, R. M., Jr., Matei, C., Kolbert, K. S., Xu, S., Zanzonico, P. B., Finn, R. L., Koutcher, J. A., Larson, S. M., and Sgouros, G. (2003) Pharmacokinetics and Biodistribution of (86)Y-Trastuzumab for (90)Y dosimetry in an ovarian carcinoma model: correlative MicroPET and MRI. *J. Nucl. Med. 44*, 1148–55.
(153) Lovqvist, A., Humm, J. L., Sheikh, A., Finn, R. D., Koziorowski, J., Ruan, S., Pentlow, K. S., Jungbluth, A., Welt, S., Lee, F. T., Brechbiel, M. W., and Larson, S. M. (2001) PET imaging of (86)Y-labeled anti-Lewis Y monoclonal antibodies in a nude mouse model: comparison between (86)Y and (111)In radiolabels. *J. Nucl. Med. 42*, 1281–7.
(154) Regino, C. M. D., Wong, K. , Garmestani, K. , Baidoo, K., Williams, M. , Seidel, J. , Green, M. , Choyke, P. , and Brechbiel, M. (2008) Abstract #3159 in *99th Annual Meeting of the American Association for Cancer Research*, American Association for Cancer Research, San Diego.
(155) Jamar, F., Barone, R., Mathieu, I., Walrand, S., Labar, D., Carlier, P., de Camps, J., Schran, H., Chen, T., Smith, M. C., Bouterfa, H., Valkema, R., Krenning, E. P., Kvols, L. K., and Pauwels, S. (2003) ^{86}Y-DOTA0)-D-Phe1-Tyr3-octreotide (SMT487)--a phase 1 clinical study: pharmacokinetics, biodistribution and renal protective effect of different regimens of amino acid co-infusion. *Eur. J. Nucl. Med. Mol. Imaging 30*, 510–8.
(156) Perk, L. R., Visser, G. W., Vosjan, M. J., Stigter-van Walsum, M., Tijink, B. M., Leemans, C. R., and van Dongen, G. A. (2005) (89)Zr as a PET surrogate radioisotope for scouting biodistribution of the therapeutic radiometals (90)Y and (177)Lu in tumor-bearing nude mice after coupling to the internalizing antibody cetuximab. *J. Nucl. Med. 46*, 1898–906.
(157) Hohn, A., Zimmermann, K., Schaub, E., Hirzel, W., Schubiger, P. A., and Schibli, R. (2008) Production and separation of "non-standard" positron emission tomography nuclides at a large cyclotron facility: the experiences at the Paul Scherrer Institute Switzerland. *Q. J. Nucl. Med. Mol. Imaging*.
(158) Meijs, W. E., Herscheid, J. D., Haisma, H. J., and Pinedo, H. M. (1992) Evaluation of desferal as a bifunctional chelating agent for labeling antibodies with Zr-89. *Int. J. Rad. Appl. Instrum. [A] 43*, 1443–7.
(159) Pagani, M., Stone-Elander, S., and Larsson, S. A. (1997) Alternative positron emission tomography with non-conventional positron emitters: effects of their physical properties on image quality and potential clinical applications. *Eur. J. Nucl. Med. 24*, 1301–27.
(160) Link, J. M., Krohn, K. A., and Eary, J. F. (1986) ^{89}Zr for antibody labeling and positron emission tomography. *J. Labelled Compd. Radiopharm. 23*, 1297–1298.
(161) Ali, S. A., and Shankland, E. G. (1991) Radiochemical synthesis of ^{89}Zr-porphyrin for positron label of monoclonal antibodies. *J. Labelled Compd. Radiopharm. 30*, 326.
(162) Meijs, W. E., Haisma, H. J., Klok, R. P., van Gog, F. B., Kievit, E., Pinedo, H. M., and Herscheid, J. D. (1997) Zirconium-labeled monoclonal antibodies and their distribution in tumor-bearing nude mice. *J. Nucl. Med. 38*, 112–8.
(163) Meijs, W. E., Haisma, H. J., Van der Schors, R., Wijbrandts, R., Van den Oever, K., Klok, R. P., Pinedo, H. M., and Herscheid, J. D. (1996) A facile method for the labeling of proteins with zirconium isotopes. *Nucl. Med. Biol. 23*, 439–48.

(164) Verel, I., Visser, G. W., Boellaard, R., Stigter-van Walsum, M., Snow, G. B., and van Dongen, G. A. (2003) ^{89}Zr immuno-PET: comprehensive procedures for the production of ^{89}Zr-labeled monoclonal antibodies. *J. Nucl. Med. 44*, 1271–81.

(165) Witzig, T. E., Gordon, L. I., Cabanillas, F., Czuczman, M. S., Emmanouilides, C., Joyce, R., Pohlman, B. L., Bartlett, N. L., Wiseman, G. A., Padre, N., Grillo-Lopez, A. J., Multani, P., and White, C. A. (2002) Randomized controlled trial of yttrium-90-labeled ibritumomab tiuxetan radioimmunotherapy versus rituximab immunotherapy for patients with relapsed or refractory low-grade, follicular, or transformed B-cell non-Hodgkin's lymphoma. *J. Clin. Oncol. 20*, 2453–63.

(166) Verel, I., Visser, G. W., and van Dongen, G. A. (2005) The promise of immuno-PET in radioimmunotherapy. *J. Nucl. Med. 46*, 164S–71S.

(167) Nagengast, W. B., de Vries, E. G., Hospers, G. A., Mulder, N. H., de Jong, J. R., Hollema, H., Brouwers, A. H., van Dongen, G. A., Perk, L. R., and Lub-de Hooge, M. N. (2007) In vivo VEGF imaging with radiolabeled bevacizumab in a human ovarian tumor xenograft. *J. Nucl. Med. 48*, 1313–9.

(168) Perk, L. R., Visser, O. J., Stigter-van Walsum, M., Vosjan, M. J., Visser, G. W., Zijlstra, J. M., Huijgens, P. C., and van Dongen, G. A. (2006) Preparation and evaluation of (89)Zr-Zevalin for monitoring of (90)Y-Zevalin biodistribution with positron emission tomography. *Eur. J. Nucl. Med. Mol. Imaging 33*, 1337–45.

(169) Borjesson, P. K., Jauw, Y. W., Boellaard, R., de Bree, R., Comans, E. F., Roos, J. C., Castelijns, J. A., Vosjan, M. J., Kummer, J. A., Leemans, C. R., Lammertsma, A. A., and van Dongen, G. A. (2006) Performance of immuno-positron emission tomography with zirconium-89-labeled chimeric monoclonal antibody U36 in the detection of lymph node metastases in head and neck cancer patients. *Clin. Cancer Res. 12*, 2133–40.

(170) Perk, L. R., Stigter-van Walsum, M., Visser, G. W., Kloet, R. W., Vosjan, M. J., Leemans, C. R., Giaccone, G., Albano, R., Comoglio, P. M., and van Dongen, G. A. (2008) Quantitative PET imaging of Met-expressing human cancer xenografts with (89)Zr-labelled monoclonal antibody DN30. *Eur. J. Nucl. Med. Mol. Imaging*.

(171) Laforest, R., and Liu, X. (2007) Image quality with non-standard nuclides in positron emission tomography. *Q. J. Nucl. Med. Mol. Imaging*.

(172) Beattie, B. J., Finn, R. D., Rowland, D. J., and Pentlow, K. S. (2003) Quantitative imaging of bromine-76 and yttrium-86 with PET: a method for the removal of spurious activity introduced by cascade γ rays. *Med. Phys. 30*, 2410–23.

(173) Vandenberghe, S. (2006) Three-dimensional positron emission tomography imaging with ^{124}I and ^{86}Y. *Nucl. Med. Commun. 27*, 237–45.

(174) Bale, W. F., and Spar, I. L. (1957) Studies directed toward the use of antibodies as carriers of radioactivity for therapy. *Adv. Biol. Med. Phys. 5*, 285–356.

(175) Bale, W. F., Spar, I. L., and Goodland, R. L. (1960) Experimental radiation therapy of tumors with I-131-carrying antibodies to fibrin. *Cancer Res. 20*, 1488–94.

(176) Milenic, D. E., Brady, E. D., and Brechbiel, M. W. (2004) Antibody-targeted radiation cancer therapy. *Nat. Rev. Drug Discovery 3*, 488–99.

(177) O'Donoghue, J. A. (1999) Implications of nonuniform tumor doses for radioimmunotherapy. *J. Nucl. Med. 40*, 1337–41.

(178) Howell, R. W., Goddu, S. M., and Rao, D. V. (1994) Application of the linear-quadratic model to radioimmunotherapy: further support for the advantage of longer-lived radionuclides. *J. Nucl. Med. 35*, 1861–9.

(179) Fowler, J. F. (1990) Radiobiological aspects of low dose rates in radioimmunotherapy. *Int. J. Radiat. Oncol. Biol. Phys. 18*, 1261–9.

(180) Nunn, A. D. (2007) Molecular imaging and personalized medicine: an uncertain future. *Cancer Biother. Radiopharm. 22*, 722–39.

(181) Brouwers, A. H., Dorr, U., Lang, O., Boerman, O. C., Oyen, W. J., Steffens, M. G., Oosterwijk, E., Mergenthaler, H. G., Bihl, H., and Corstens, F. H. (2002) 131 I-cG250 monoclonal antibody immunoscintigraphy versus [18 F]FDG-PET imaging in patients with metastatic renal cell carcinoma: a comparative study. *Nucl. Med. Commun. 23*, 229–36.

(182) Rahmim, A., and Zaidi, H. (2008) PET versus SPECT: strengths, limitations and challenges. *Nucl. Med. Commun. 29*, 193–207.

(183) Beekman, F., and van der Have, F. (2007) The pinhole: gateway to ultra-high-resolution three-dimensional radionuclide imaging. *Eur. J. Nucl. Med. Mol. Imaging 34*, 151–61.

BC800299F

COMMUNICATIONS

Effects of Branching Architecture and Linker on the Activity of Hyperbranched Polymer−Drug Conjugates

Omathanu Perumal,[#,†] Jayant Khandare,[‡] Parag Kolhe,[‡] Sujatha Kannan,*[,†] Mary Lieh-Lai,[†] and Rangaramanujam M. Kannan*[,‡]

Critical Care Medicine, Children's Hospital of Michigan, Wayne State University, Detroit, Michigan 48201, and Department of Chemical Engineering and Material Science, and Biomedical Engineering, Wayne State University, Detroit, Michigan 48202.
Received December 8, 2008; Revised Manuscript Received April 16, 2009

Drug release from hyperbranched polymer−drug conjugates and the subsequent activity are influenced by the branching architecture and the linker. To gain an understanding of these effects, we used hyperbranched polyol and G4-OH polyamidoamine (PAMAM) dendrimer with methyl prednisolone (MP) as the model drug. The drug was conjugated to dendrimer or polyol using a glutaric acid (GA) or a succinic acid (SA) spacer. Drug payload was the highest with polyol, while in the case of dendrimer, a higher payload was achieved with the GA than the SA spacer. Cell uptake of the polymer conjugates in A549 lung epithelial cells was higher than that of the free drug, and the conjugates largely localized in the cytosol. The anti-inflammatory activity of polymer conjugated MP, as measured by inhibition of prostaglandin synthesis, was the highest for MP-SA-dendrimer conjugate, followed by MP-GA-polyol conjugate, and then MP-GA-dendrimer conjugate. This study suggests that the branching architecture and spacer influence the drug payload and pharmacological activity of a drug−nanopolymer conjugate, which may significantly influence the in vivo efficacy of these nanodevices. This has key implications in the eventual in vivo efficacy of these nanodevices.

Polymer−drug conjugates are used to modulate drug pharmacokinetics and target the drug to the desired site (*1, 2*). Various linear polymer−drug conjugates have been investigated for improving the circulation half-life and intracellular targeting of drugs (*2*). However, linear polymers have limited drug payload capacity. Hyperbranched polymers (HBPs) can carry multiple copies of drug and/or targeting/imaging ligands (*3*). Depending on their branching architecture, these polymers are classified as "imperfectly branched" polymers or HBPs and "perfectly branched" polymers or dendrimers (*4*). Dendrimers are well-defined and monodisperse, with a controlled branching architecture. In comparison to dendrimers, HBPs are polydisperse, but their ease of synthesis (typically using one-pot reaction) makes them relatively cheaper to produce than dendrimers (*5, 6*). Both these polymers have core−shell architecture and can carry high drug payload due to the large number of tunable surface functional groups (*7, 8*). Earlier studies have shown that both HBPs and dendrimers can carry a high drug payload (*7, 8*). High drug payload polymeric conjugates were prepared with small molecules such as ibuprofen by directly conjugating the drug to the surface functional groups in HBPs and dendrimers (*7, 8*). However, the high density of surface functional groups poses steric hindrance, thus limiting the payload for large drug molecules such as steroids (*9*). Chemical spacers can be used to link the drug to the polymer to overcome the steric hindrance (*10*). Further, the spacers can also modulate the drug release from the polymer (*10*). In the present study, we investigated the conjugation of a model steroid drug, methylprednisolone (MP), to polyol and hydroxyl terminated polyamidoamine dendrimer (G4-OH) using glutaric acid (GA) and succinic acid (SA) as spacers. Comparative studies between linear and branched polymers have been reported in the literature (*11*).To our knowledge, this is the first report that compares the drug payload and pharmacological activity of drug−polymer conjugates between HBPs and dendrimers. The influence of the branching architecture of these two polymers and spacer on cell uptake and anti-inflammatory activity was tested in A549 human lung epithelial carcinoma cells.

Glutaric acid **2** (GA) was conjugated to C_{21} hydroxyl group of MP **1** using dicyclohexylcarbodiimide (DCC) as the coupling agent (Figure 1). This hydroxyl group is more favorable compared to C_9 (secondary) and C_{11} (tertiary) hydroxyl groups. The byproduct dicyclohexyl urea (DCU) was removed by filtration. In the next step, MP-GA conjugate **3** was dissolved in anhydrous dimethyl sulfoxide (DMSO) and conjugated with polyol **4** or G4-OH dendrimer in the presence of DCC to form polyol-GA-MP conjugate **5** or dendrimer-GA-MP conjugate (*9*). The solution was filtered to remove DCU and dialyzed against DMSO to remove unreacted components. The conjugate was characterized by ^{1}H NMR. A similar procedure was followed using succinic acid (SA) spacer where methyl prednisolone succinate (MPS) was conjugated to G4OH dendrimer. For cell uptake studies, both the free drug and the drug−polymer conjugate were further conjugated with fluoroisothiocyante (FITC) using DCC as the coupling agent (*9*). The absence of

* Corresponding authors. R.M. Kannan (rkannan@eng.wayne.edu) and Sujatha Kannan (skannan@med.wayne.edu).

[#] Present address: Department of Pharmaceutical Sciences, College of Pharmacy, South Dakota State University, Brookings, SD 57007.

[†] Children's Hospital of Michigan.

[‡] Wayne State University.

10.1021/bc800526z CCC: $40.75 © 2009 American Chemical Society
Published on Web 04/29/2009

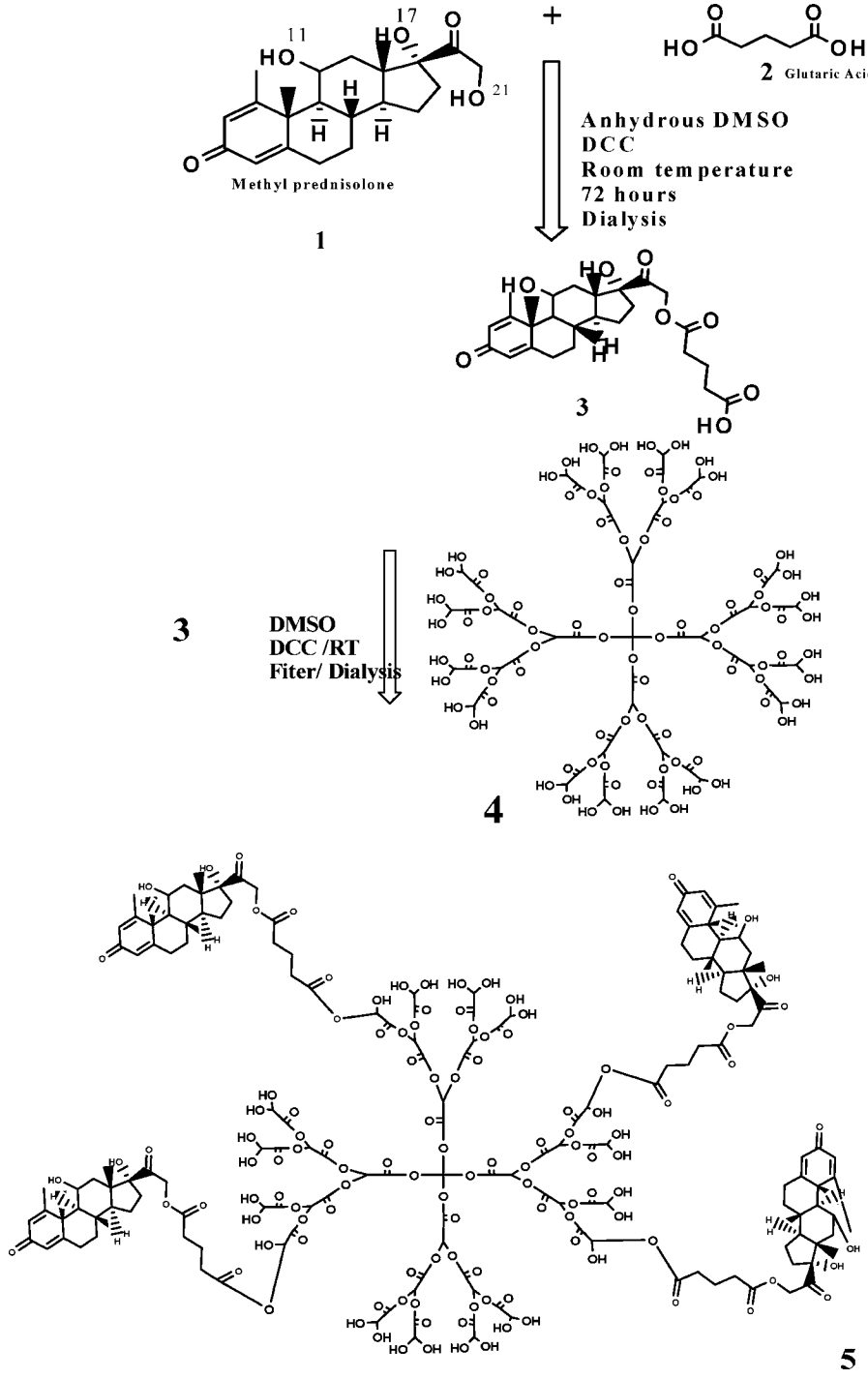

Figure 1. Synthetic scheme for methylprednisolone-glutaric acid-polyol conjugate.

free FITC was confirmed using TLC (*12*). Because of the use of homobifunctional spacers, there is a possibility of intermolecular cross-linking between dendrimers, leading to dimers and larger particles. Since we used low concentrations this was not observed and has been confirmed using HPLC and NMR spectroscopy previously (*9*).

Figure 2 shows the ^{1}H NMR spectrum of MP-GA-polyol conjugate. A broad singlet at δ 4.2 ppm corresponds to CH_2 protons of polyol, while the multiplets between δ 5.5 and 7.3 correspond to protons of MP. The NMR spectra for the other conjugates can be found in the Supporting Information. On an average, 25 molecules and 12 molecules of MP were conjugated to polyol and G4-OH dendrimer, respectively, using GA as the spacer (Table 1). On the other hand, 6 molecules of MP were conjugated to G4-OH using SA as the spacer. The polyol used in the present study has more functional groups than dendrimer (128 vs 64 groups), and this resulted in a higher drug loading in polyol. Furthermore, the "imperfect branching" architecture in polyol reduced the steric hindrance for conjugation of MP-GA to polyol. SA has a shorter alkyl chain than GA and this leads to a difference in drug payload between the two dendrimer conjugates. Further, MPS was used as the sodium salt, and therefore, the difference in acidity may also contribute to the difference in reactivity and lower drug payload with SA spacer. Nevertheless, the drug payload using MPS was higher than when free MP was directly conjugated to dendrimer (*9*). On average, 4−5 molecules of FITC were attached to the conjugates.

The cell uptake of FITC-labeled free drug and the conjugates was determined by measuring the intracellular fluorescence intensity using flow cytometry. Equivalent MP concentrations

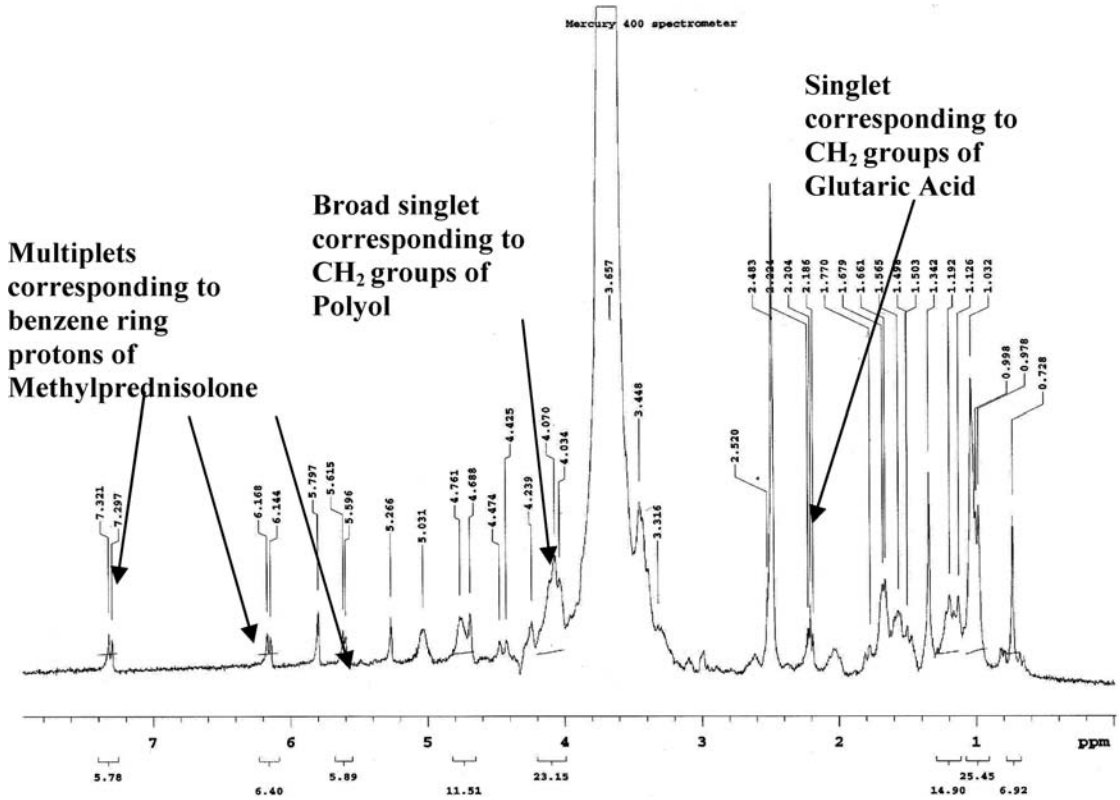

Figure 2. [1]H NMR spectrum of methylprednisolone-glutaric acid-polyol conjugate. The corresponding proton peaks are indicated in the spectrum. The spectra for the other conjugates were analyzed in a similar fashion and are not included for the sake of brevity. Proton integration method was used to calculate the drug payload.

Table 1. Comparison of Molecular Weight and Number of Molecules of Drug Conjugated to Polymers

polymer[a]	molecular weight (Da)	no. of groups	percent weight of MP in conjugate[b]	av. no. of MP per molecule of polymer[b]
G4-OH dendrimer	14 279	64		
Polyol	15 000[c]	128		
MP-GA-dendrimer	21 395		32	12
MP-SA-PAMAM dendrimer	16 790		17	06
MP-GA-polyol	27 550		45	25

[a] MP, methylprednisolone; SA, succinic acid; GA, glutaric acid. [b] Estimated from [1]H NMR. The molecular weights reported here are the approximations based on the number of molecules of MP conjugated to the polymer. [c] From Perstorp Polyol literature.

were used for uptake studies. With respect to the zero time point, the fluorescence intensity was found to increase with time for free MP and MP−polymer conjugates (Figure 3). However, the cell uptake of the conjugates appears to be significantly higher ($p < 0.05$) than the free MP. This is despite the fact that the FITC concentration is higher for free MP compared to the conjugates (each MP molecule had a FITC attached to it, whereas the conjugates have approximately half the FITC for equivalent MP concentration). The uptake profiles for the two glutaric acid spacer conjugates (MPGD and MPGP) are not appreciably different (Figure 3). However, the conjugate with succinic acid spacer (MPSG) showed higher cell uptake than the other two conjugates. Both free MP and polymer-conjugated MP were predominantly localized in the cytosol (Figure 4a−e). In the case of the conjugates, there was extensive fluorescence around the perinuclear region, indicative of endocytotic uptake of the conjugates as opposed to diffuse fluorescence distribution with the free drug. Free MP enters the cell by passive diffusion, and cell entry by passive diffusion is nonspecific, which is dictated by the concentration gradient between the extracellular

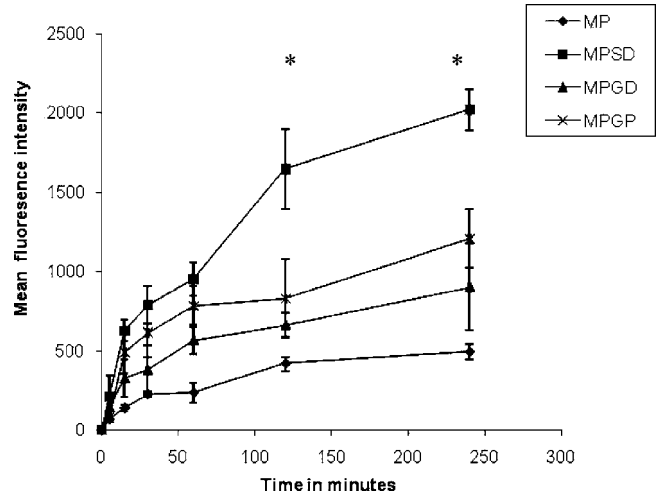

Figure 3. Cell uptake of free MP and polymer conjugated MP in A549 cells. The *y*-axis indicates the mean fluorescence intensity as measured by flow cytometry, after subtracting the autofluorescence at zero time. Each data point represents average of three measurements with standard error bars. Key: MP, methylprednisolone; MPSD, methylprednisolone-succinic acid-dendrimer; MPGD, methylprednisolone-glutaric acid-dendrimer; MPGP, methylprednisolone-glutaric acid-polyol. *Statistically significant ($p < 0.05$) for MPSD.

and intracellular milieu (*13*). Unlike the free drug, the polymer conjugates enter the cell by specific endocytosis processes. The rate of endocytosis of polymers is influenced by a number of factors including molecular weight, surface charge, and hydrophilicity of the polymer (*13, 14*). We have previously shown that, at the concentrations used in this study, the polymers were found to be nontoxic to A549 cells (*15*). The difference in the hydrophilicity of SA and GA can be attributed to the difference in uptake of the dendrimer conjugates. On the other hand, the

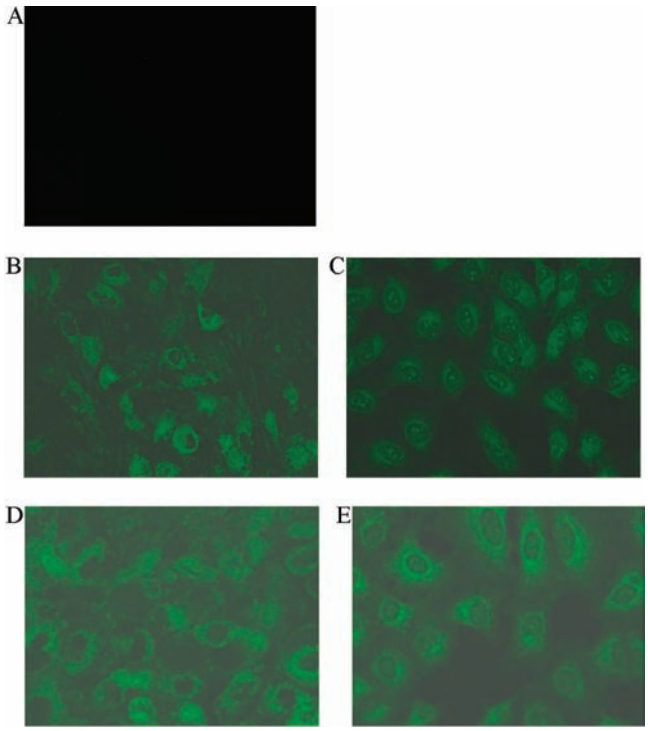

Figure 4. Fluorescent microscopic images (63 × 1.2) of A549 lung epithelial cells after 1 h of treatment with (A) control cells with no treatment, (B) MP-FITC, (C) MP-succinic acid-dendrimer-FITC, (D) MP-glutaric acid-dendrimer-FITC, (E) MP-glutaric acid-polyol-FITC.

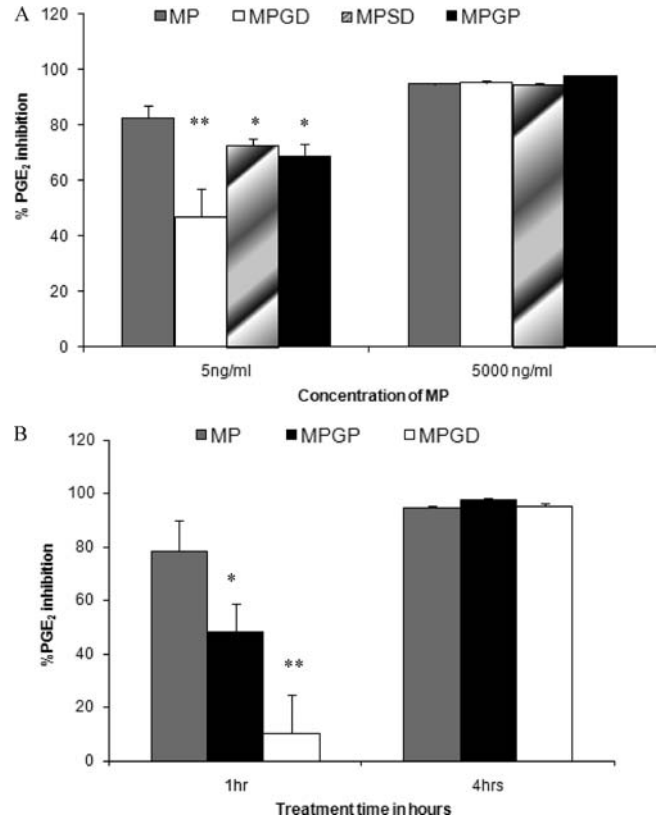

Figure 5. Inhibition of prostaglandin (PGE_2) synthesis after treatment with free drug and drug−polymer conjugates in A549 cells. (A) Percent inhibition of PGE_2 synthesis after treatment with two different concentrations of methyl prednisolone. The cells were treated with free drug or drug−polymer conjugates for 4 h. (B) Percent inhibition of PGE_2 synthesis after treating the cells for two different time periods with 5 μg/mL equivalent of methyl prednisolone. The percent inhibition represents the reduction in PGE_2 levels in comparison to control (A549 cells with prostaglandin induction but no treatment). Key: MP, free methyl prednisolone; MPSD, methylprednisolone-succinic acid-dendrimer; MPGD, methylprednisolone-glutaric acid-dendrimer; MPGP, methylprednisolone-glutaric acid-polyol. * Statistically significant ($p < 0.05$) when compared to the free MP treatment. ** Statistically significant when compared to other conjugates. All the values are mean of four measurements with standard error bars.

branching architecture did not appear to influence the cellular uptake of the conjugates, as the polyol and the dendrimer conjugates show a comparable uptake profile. This is not unexpected, as dendrimer and polyol do not differ much in their molecular weight and surface charge (Table 1). Both G4-OH dendrimer and polyol have no net surface charge and hence are expected to be transported by fluid-phase endocytosis through nonspecific interactions with the cell membrane (*15*).

The anti-inflammatory activity of conjugates was evaluated by their ability to inhibit cyclooxygenase enzyme (Cox-2) and suppress prostaglandin (PGE_2) synthesis in A549 cells. There was no significant difference in the activity of free and polymer conjugated drug at 5 μg/mL equivalent concentration of MP (Figure 5a). This is a significant result, since most polymer−drug conjugates show significantly less activity than the free drug in cells, even though they show better efficacy in vivo. The PGE_2 inhibition observed in the present study is consistent with the maximal inhibition reported for MP in A549 cells (*16*). When the activity was tested at a concentration (5 ng/mL) close to the IC_{50} of MP in A549 cells (*16*), the conjugates showed lower activity than free MP. Particularly, MP-GA-dendrimer conjugate showed significantly lower activity than the other two conjugates. Since an equivalent concentration of MP was used, the results show that the spacer has an influence on the release of free MP from the polymer. To further understand the influence of branching architecture, the activity was measured at shorter treatment time of 1 h. At short times, both the dendrimer and the polyol conjugates show lower activity than the free drug (Figure 5b). With time, the passive diffusion of free drug produces higher intracellular concentration, whereas the drug release from the conjugates is a much slower process. This may result in efficacies being comparable at the later time point.

As shown in Figure 5b, at shorter treatment time, there was a significant difference in the activity of polyol and dendrimer conjugates. The higher activity of polyol conjugates suggests that the imperfect branching architecture may allow easy access of the lysosomal enzymes to release the drug faster compared to the perfect branching architecture in dendrimer. At the same time, the polydispersity of polyol may also contribute to the difference in the activity of the conjugates.

Lysosomes in the cell are rich in enzymes that aid in releasing the free drug from the polymer conjugate (*17*). The release of free drug from the conjugate is influenced by many factors including the type of spacer, the stability of the chemical bond, distance of the spacer from the polymer backbone, the hydrophilicity of the surrounding medium, and steric overcrowding at the center of reaction (*18*). Both GA and SA have two ester bonds that connect the drug and polymer and can be cleaved by esterases. However, GA differs from SA by one carbon atom. This difference in the alkyl chain length seems to influence the enzymatic release of the free drug. Previously, Wiwattanapatapee et al. (*19*) have shown that the release of 5-amino salicylic acid from dendrimer conjugate is influenced by the carbon chain length in the spacer. Tang et al. (*20*) found that the DNA expression was enhanced when the dendrimer was scrambled by heat treatment. The authors attributed this effect to the increased conformational flexibility of dendrimer, which enabled DNA complexation and its subsequent release from the complex. Recently, Khandare et al. (*11*) reported that the release of paclitaxel in presence of esterase was faster from linear

polyethylene glycol (PEG) conjugate compared to dendrimer conjugate. On the other hand, the IC_{50} for antiproliferative activity of paclitaxel−dendrimer conjugate was 300 times lower than the paclitaxel−PEG conjugate. Since polyol has a higher drug payload, with the same given dose of the conjugate, polyol−MP conjugate will provide higher intracellular concentration when compared to the dendrimer−MP conjugate. Similarly, the drug loading and release of drug from the dendrimer−drug conjugate can be modulated by suitable choice of spacer. Further studies into the release kinetics of MP from the conjugates will provide better insights. However, the preliminary findings presented here show that drug payload and pharmacological activity of drug−polymer conjugates is influenced by the branching architecture and spacer chemistry, and these factors need to be considered in designing nanodevices for various therapies.

ACKNOWLEDGMENT

This research work was funded by the Wayne State University Nanotechnology initiative, Children's Research Center of Michigan (Children's Hospital of Michigan), and NIH−Pediatric pharmacology research unit supplement research funding (NIH 3U01HD-37261-04SI). We would like to thank Prof. David Bassett for the help with flow cytometry.

Supporting Information Available: Experimental procedures. This material is available free of charge via the Internet at http://pubs.acs.org.

LITERATURE CITED

(1) Veronese, F. M., and Morpurgo, M. (1999) Bioconjugation in pharmaceutical chemistry. *IL Farmaco 54*, 497–516.
(2) Duncan, R. (2003) The dawning era of polymer therapeutics. *Nat. Rev. Drug Discovery 2*, 347–360.
(3) Esfand, R., and Tomalia, D. A. (2001) Poly (amidoamine) (PAMAM) dendrimers: from biomimicry to drug delivery and biomedical application. *Drug Discovery Today 6*, 427–436.
(4) Kannan, R. M., Perumal, O. P., and Kannan, S. Dendrimers and hyperbranched polymers for drug delivery. In *Biomedical applications of nanotechnology* (Labhasetwar, V., Leslie-Pelecky, D. L., Eds.) pp 105−129, Chapter 5, John Wiley & Sons Inc., Hoboken, NJ.
(5) Voit, B. I. (2003) Hyperbranched polymers: a chance and a challenge. *C. R. Chim. 6*, 821–832.
(6) Jikei, M., and Kakimoto, M. A. (2001) Hyperbranched polymers: a promising new class of materials. *Prog. Polym. Sci. 26*, 1233–1285.
(7) Kolhe, P., Khandare, J., Pillai, O., Leih-Lai, M., Kannan, S., and Kannan, R. M. (2004) Hyperbranched polymer-drug conjugates with high drug payload for enhanced cellular delivery. *Pharm. Res. 21*, 2185–2195.
(8) Kolhe, P., Khandare, J., Pillai, O., Leih-Lai, M., Kannan, S., and Kannan, R. M. (2006) Preparation, cellular transport and activity of polyamidoamine based dendritic nanodevices with a high drug payload. *Biomaterials 27*, 660–669.
(9) Khandare, J., Kolhe, P., Pillai, O., Kannan, S., Lieh-Lai, M., and Kannan, R. M. (2005) Synthesis, cellular transport and activity of dendrimer-methylprednisolone conjugates. *Bioconjugate Chem. 16*, 330–337.
(10) Khandare, J., and Minko, T. (2006) Polymer-drug conjugates. *Prog. Polym. Sci. 31*, 359–397.
(11) Khandare, J., Jayant, S., Singh, A., Chandna, P., Wang, Y., Vorsa, N., and Minko, T. (2006) Dendrimer versus linear conjugate: influence of polymeric architecture on the delivery and anticancer effect of paclitaxel. *Bioconjugate Chem. 7*, 1464–1472.
(12) Jevprasesphant, R., Penny, J., Attwood, D., McKeown, N. B., and D'Emanuele, A. (2003) Engineering of dendrimer surfaces to enhance transepithelial transport and reduce cytotoxicity. *Pharm. Res. 20*, 1543–1550.
(13) Ouchi, T., and Ohya, Y. (1995) Macromolecular prodrugs. *Prog. Polym. Sci. 20*, 211–257.
(14) Mukherjee, S., Ghosh, R. N., and Maxfield, F. R. (1997) Endocytosis. *Physiol. Rev. 77*, 760–803.
(15) Kannan, S., Kolhe, P., Raykova, V., Glibatec, M., Kannan, R. M., Lieh-Lai, M., and Bassett, D. (2004) Dynamics of cellular entry and drug delivery by dendritic polymers into human lung epithelial carcinoma cells. *J. Biomater. Sci. Polym. Ed. 15*, 311–330.
(16) Croxtall, J. D., van Hal, P. T. W., Choudhury, Q., Gilory, D. W., and Flower, R. J. (2002) Different glucocorticoids vary in their genomic and non-genomic mechanism of action in A549 cells. *Br. J. Pharmacol. 135*, 511–519.
(17) Nori, A., and Kopecek, J. (2005) Intracellular targeting of polymer-bound drugs for cancer chemotherapy. *Adv. Drug Delivery Rev. 57*, 609–636.
(18) Joseph, A., Souza, M. D., and Topp, E. M. (2004) Release from polymeric prodrugs. Linkages and their degradation. *J. Pharm. Sci. 93*, 1962–1979.
(19) Wiwattanapatapee, R., Luelak, L., and Saramunee, K. (2003) Dendrimer conjugates for colonic delivery of 5-aminosalicylic acid. *J. Controlled Release 88*, 1–9.
(20) Tang, M. X., Redemann, C. T., and Szoka, F. C., Jr. (1996) In vitro gene delivery by degraded polyamidoamine dendrimers. *Bioconjugate. Chem. 7*, 703–714.

BC800526Z

Experimental Procedures

Materials

Methylprednisolone USP, Methylprednisolone hemisuccinate, PAMAM-G4-OH (Mw ~ 14,279 Da, 64 end groups) and dicyclohexylcarbodiimide (DCC) were purchased from Aldrich Chemical Company. Hyperbranched polymer, polyol was obtained from Perstorp (Sweden). Glutaric acid (M_w~132 Da) was purchased from Matheson Coleman and Bell Company (Norwood, Ohio). Fluorescent probe fluoroisothiocyanate (FITC) was purchased from Fluka Chemical Company. Interleukin (IL-1β) and lipopolysaccharide (LPS) were purchased from Sigma, USA. ELISA kit for prostaglandin estimation was purchased from Cayman Chemical Company and dialysis membrane of molecular weight cut off of 3500 Da was obtained from Spectrapor, USA. Dimethyl sulphoxide (DMSO), dimethyl formamide (DMF), methanol and diethyl ether were purchased from Fischer Scientific, USA.

Synthesis of spacer-MP conjugate

Glutaric acid-MP conjugate was synthesized by a method reported by our group earlier (9). Briefly, MP (0.1 g, 0.265 mmol) and GA (0.036 g, 0.26 mmol) were dissolved in anhydrous DMSO. Dicyclohexilcarbodiimide (DCC) (0.056 g, 0.26 mmol) was added as a coupling agent to the above solution. The reaction was carried out for 24 hrs at room temperature and filtered to remove dicyclohexyl urea (DCU) obtained as a by-product during this reaction. The filtrate was evaporated under vacuum to obtain MP-glutarate conjugate. In case of succinic acid methylprednisolone succinate (MPS) was used as the

starting material and the same procedure as described above was used to conjugate it to the dendrimer.

Conjugation of MP-spacer to polymer

A molar ratio equivalent to 1: 50 of MP-GA conjugate to polymer or 1:10 of MPS to PAMAM dendrimer was dissolved in anhydrous dimethyl sulfoxide (DMSO). To this mixture DCC was added as coupling agent and the reaction was stirred for 2-3 days and filtered to remove DCU. The filtrate was dialyzed against anhydrous DMSO for 24 hours (dialysis membrane of M_w cut off = 3,500 Da) to remove unreacted reaction components. The conjugate was evaporated under vacuum and was characterized by ^{1}H NMR. The presence of dendrimer

Conjugation of FITC to free MP and polymer conjugates

The reaction was carried out by dissolving FITC and free MP (molar ratio of 1:1) or the polymer conjugate (molar ratio of 10:1) for 24 hrs at room temperature. At the end of the reaction, the solution was filtered to remove DCU. The resultant filtrate was dialyzed against anhydrous DMSO for 24 hours (dialysis membrane of molecular weight cut off = 3500 Da) to remove unreacted FITC and DCC. Further, free FITC was removed by using excess acetone. The absence of free FITC in all conjugates was verified by thin layer chromatography (TLC), using chloroform and methanol (1:1) as solvents. The conjugates were dried under vacuum to obtain FITC labeled conjugates and were characterized by ^{1}H NMR.

Cell culture

Human lung carcinoma epithelial cell line, A549 was obtained from Children's Hospital of Michigan Cell Culture facility. Cells were seeded in RPMI 1640 (Gibco-BRL) cell culture medium supplemented with 10% fetal bovine serum (FBS) and 1% penicillin-streptomycin at 37°C with 5% CO_2 in a cell culture incubator. The cells were sub-cultured every 48 hours and harvested from sub-confluent (60 to 70%) cultures using 0.05% trypsin-EDTA.

Cell uptake of fluorescent-tagged conjugates

A549 cells (1.2×10^5 cells/ml) were seeded on 60 x 15 mm culture plates using RPMI 1640 cell culture medium supplemented with 10% FBS and 1% penicillin-streptomycin. When the cells were 60% confluent, they were treated separately with free MP and the polymer conjugated MP (10µg/ml) for varying time periods upto 4 hours. At the end of the study, the cells were washed with phosphate buffered saline (PBS; pH 7.4), trypsinized and centrifuged at 1500 rpm for 5 minutes to obtain a cell pellet. The cells were then rinsed with PBS buffer, spun down twice, and resuspended in PBS, and subsequently analyzed using a flow cytometer (FACS caliber, Becton Dickinson, USA) by counting 10,000 events. The viable cells were gated and the fluorescence intensity was computed from the histogram plot.

Fluorescence microscopy

The procedure for cell culture and drug treatment was same as described in previous section. After treatment with the conjugates for 1 hour, the cells were washed with PBS and were observed under confocal microscope (Zeiss LSM 310) using a magnification of 63X 1.2. The emission and excitation wavelengths were 488 and 518 nm respectively for FITC.

Pharmacological activity of conjugates

A549 lung epithelial cells (2 x 10^5 cells/ml) were seeded in 24 well plates in RPMI medium supplemented with 10% FBS and 1% penicillin-streptomycin. When the cells were 60% confluent, the medium was removed and washed with serum free medium (SFM). Each well was treated with 500 µl of SFM and prostaglandin (PGE_2) secretion was induced by addition of 1.5 µg/ml of lipopolysaccharide (LPS) and 1µg/ml of interleukin (IL- 1β). After 30 minutes, the medium was removed and fresh SFM was added. Free MP and its conjugate (5 ng/ml or 5 µg/ml equivalent of MP) in ethanol was added. Control treatments with solvent, polymers and positive control with no treatment and negative controls without any PGE_2 induction were also studied. The supernatant was removed after 1 or 4 hours and analyzed for PGE_2 using a commercial ELISA kit. Results were represented as percent inhibition of PGE_2 with respect to control. All the results were subjected to *one-way ANOVA* at a significance level of $p<0.05$.

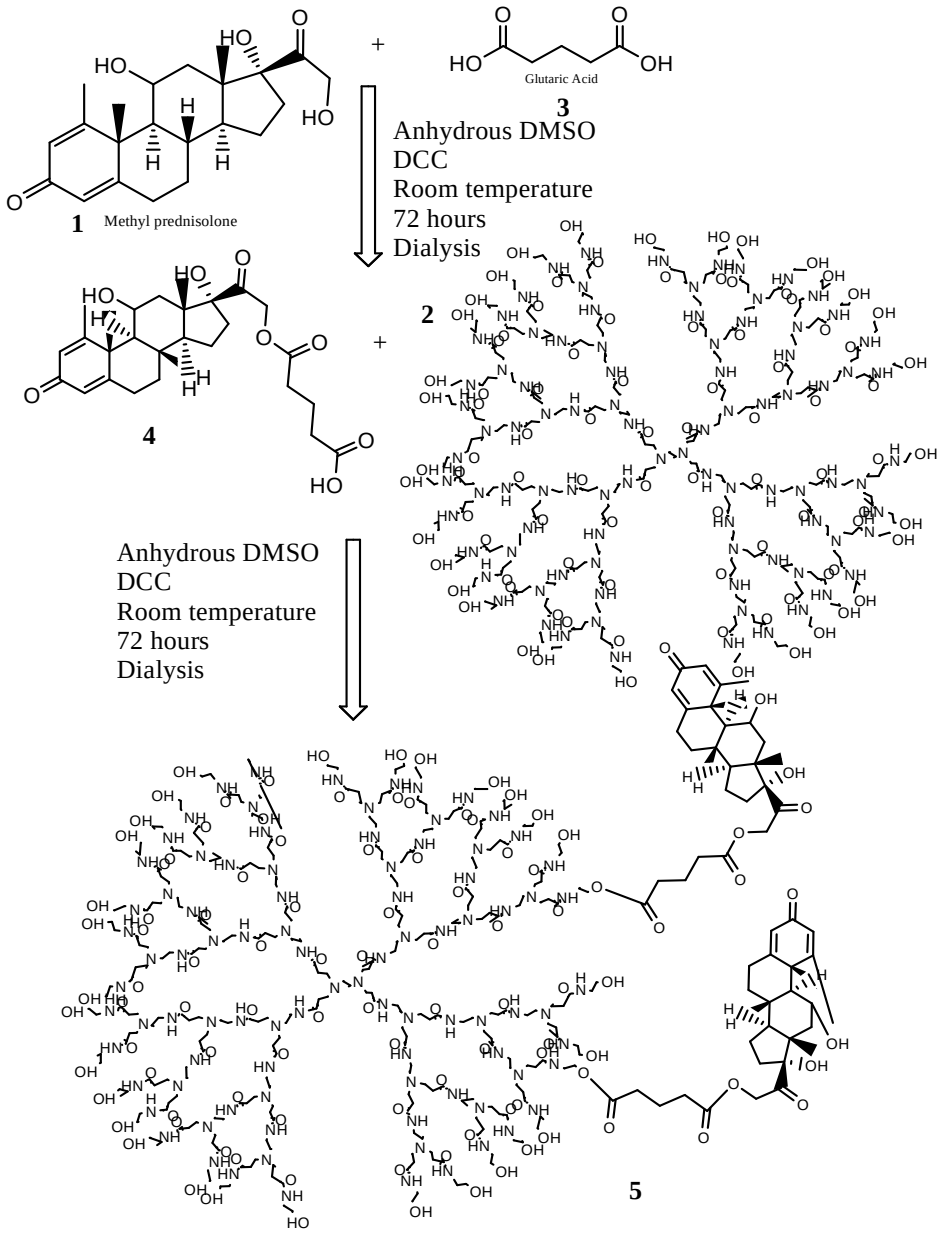

Figure S1. Schematic synthesis of glutaric acid-methylprednisolone- dendrimer conjugates.

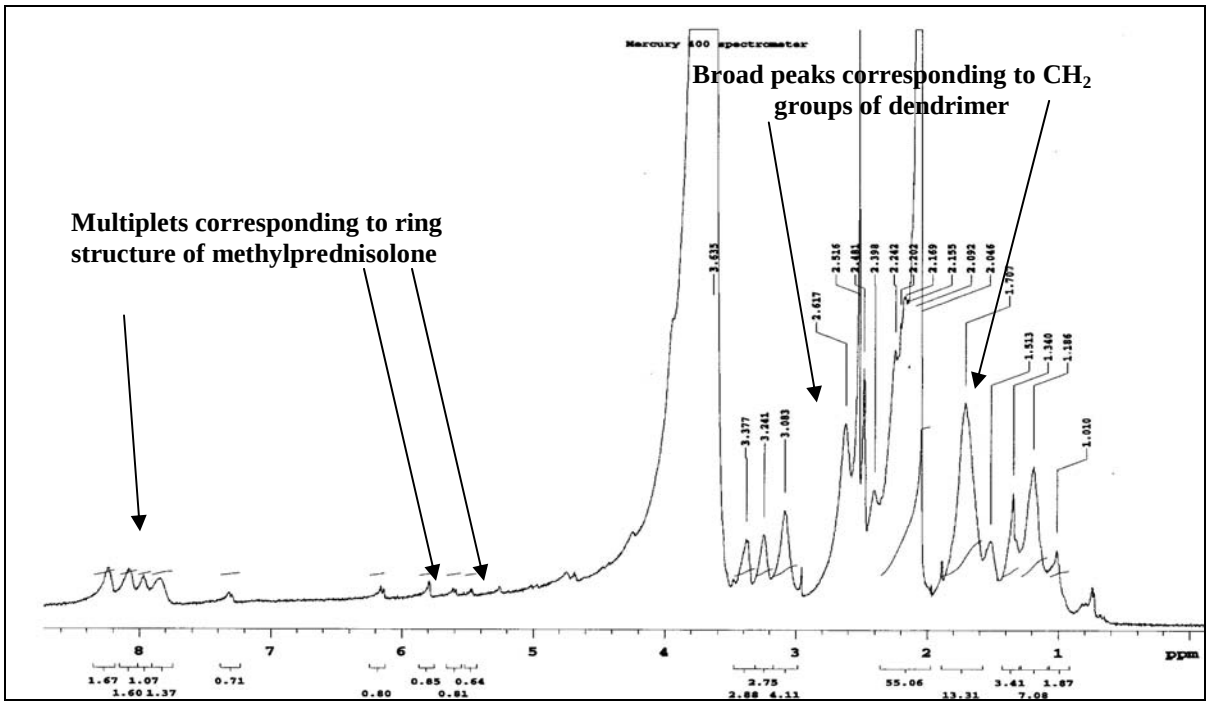

Figure S2. ^{1}H NMR spectrum of glutaric acid-methylprednisolone- dendrimer conjugates.

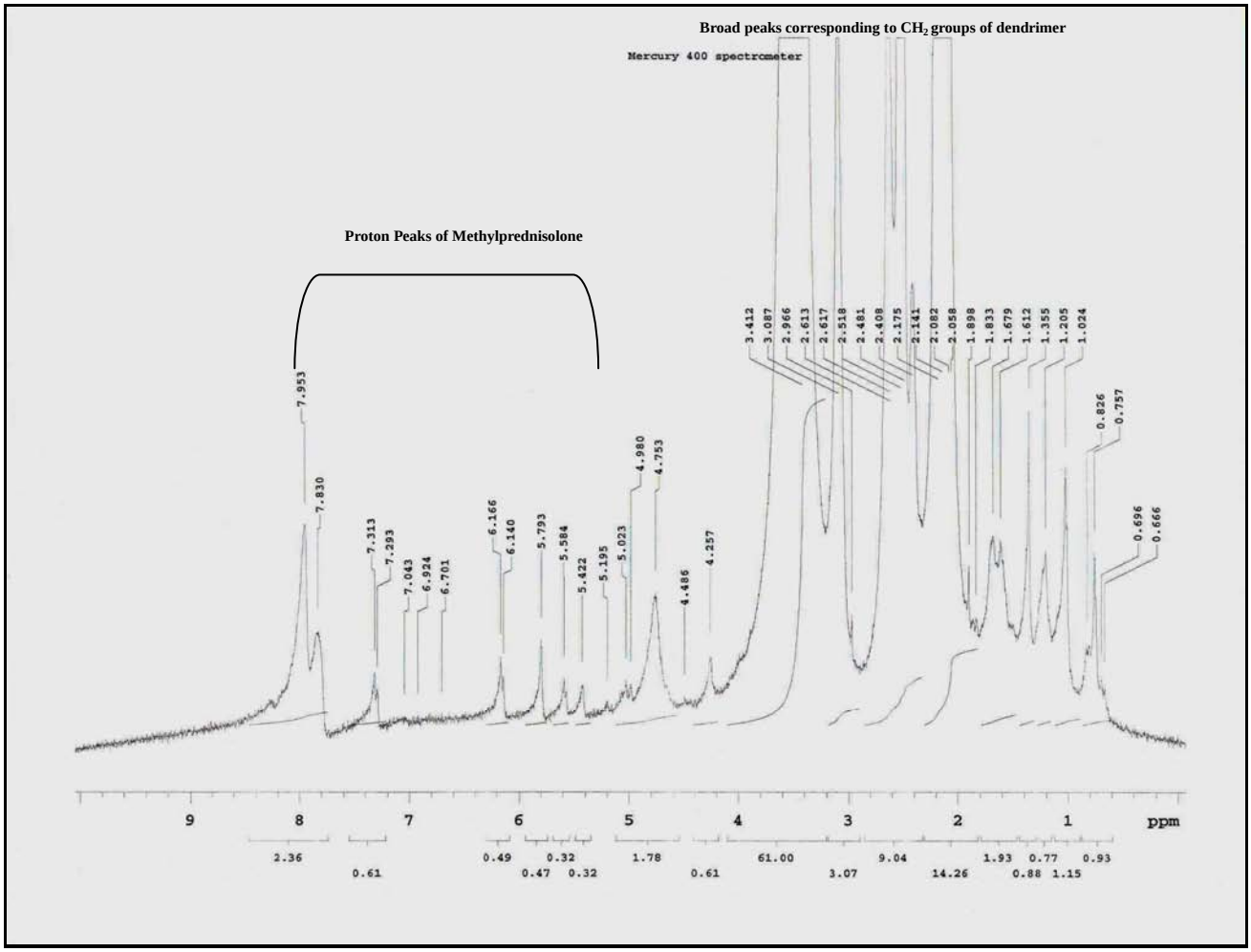

Figure S3. NMR spectrum of dendrimer-SA-MP conjugates

ARTICLES

Synthesis and Application of a N-1′ Fluorescent Biotinyl Derivative Inducing the Specific Carboxy-Terminal Dual Labeling of a Novel RhoB-Selective scFv

L. Chaisemartin,[†,§] P. Chinestra,[†,§] G. Favre,[†] C. Blonski,[‡] and J. C. Faye*[,†]

INSERM U563, Département Oncogénèse, Signalisation et Innovation Thérapeutique, Institut Claudius Regaud, 31052 Toulouse, France, and Groupe de Chimie Organique Biologique, Laboratoire LSPCMIB - UMR 5068 CNRS, Université Paul Sabatier, Toulouse cedex 9, France. Received July 3, 2008; Revised Manuscript Received March 3, 2009

The fluorescent site-specific labeling of protein would provide a new, easy-to-use alternative to biochemical and immunochemical methods. We used an intein-mediated strategy for covalent labeling of the carboxy-terminal amino acid of a RhoB-selective scFv previously isolated from a phage display library (a human synthetic V_H + V_L scFv phage library). The scFv fused to the Mxe intein was produced in *E. coli* and purified and was then labeled with a newly synthesized fluorescent biotinyl cysteine derivative capable of inducing scFv-Mxe intein splicing. In this study, we investigated the splicing and labeling properties of various amino acids in the hinge domain between scFv and Mxe under thiol activation. In this dual labeling system, the fluorescein is used for antibody detection and biotin is used for purification, resulting in a high specific activity for fluorescence. We then checked that the purified biotinylated fluorescent scFv retained its selectivity for RhoB without modification of its affinity.

INTRODUCTION

In the postgenomic era and beyond, the generation of monoclonal antibodies for proteome research and of recombinant antibody fragments will be essential for research, diagnosis, and treatment. These molecules can be selected from huge antibody gene libraries against any target, by an in vitro panning procedure (*1*−*5*). After phage display, scFv peptides are selected and produced in *E. coli*. Their recognition and purification are facilitated by the addition of various tags, such as the 6x histidine stretch and/or cmyc domains. Whatever the tag used, secondary antibodies carrying the detection system (enzymatic activity or fluorescence) are required to visualize the scFv. However, two methodologies described the direct selection and obtention of fluorescent antibodies (*6*, *7*). In the present study, we aimed to overcome the need for a secondary antibody, by generating dual-labeled scFv by chemical site-specific modification.

Various techniques have been used for chemical protein labeling to date, but most are inapplicable due to limitations to the reactivity of the amino acid in aqueous buffers. Other organic solvent-based methods frequently induce protein denaturation and do not provide specific single-site modification. Antos et al. (*8*) recently showed that an oxidative deamination reaction could be used to strip the N-terminal amino group from various proteins. This technique is of limited scope, being restricted to proteins meeting the requirements of N-terminal solvent accessibility. Moreover, the reaction is not quantitative and generates a pool containing singly labeled and unlabeled proteins. Biotechnology has led to the development of enzyme-mediated labeling (which would be used in vitro) for the same purpose, for the analysis of protein activities in vivo (*9*) (*10*−*16*) while others have developed Halo Tag (*17*−*19*). Various small peptides able to permit vizualization have been fused to the protein of interest inducing fluorescence in the presence of biarsenical ligands (*16*, *20*−*22*), lanthanide binding tag (*23*−*28*), and protein domains (*29*). The labeling strategy described here makes use of the properties of intein splicing (*30*−*34*) and the previously described N-1′ functionalization of biotin (*35*). This strategy should be applicable to any protein of known amino acid sequence but was used here with a previously isolated scFv against the native RhoB GTPase, selected by phage display in our laboratory. As part of this study, we synthesized a new N-1′ biotin derivative able to induce intein splicing (Schemes 1; 2).

Scheme 1. Synthesis of 1-(*N*-α-t-Boc-*S*-Trityl-L-cysteinamido)-11-amino-3,6,9-trioxaundecane, Compound 1′[a]

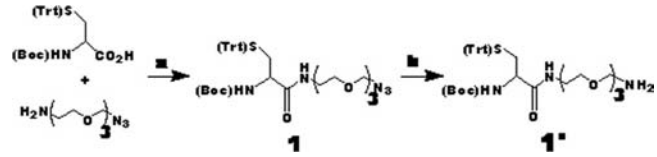

[a] (a) BOP + DIEA in CH_2Cl_2, one day at room temperature, 89%; (b) $P(Ph)_3$ in THF 12 h, then H_2O, with stirring for a further 12 h, 95%.

EXPERIMENTAL PROCEDURES

Materials and Methods. All chemical and biochemical reagents were purchased from Sigma-Aldrich, except for biotin

* To whom correspondence should be addressed. E-mail: jcfaye@hotmail.fr.

[†] Institut Claudius Regaud.

[‡] Université Paul Sabatier.

[§] L.C. and P.C. contributed equally to this work.

10.1021/bc800272r CCC: $40.75 © 2009 American Chemical Society
Published on Web 04/06/2009

Scheme 2. Synthesis of 1-(L-Cysteinamido)-11-[1′-*N*-(4-(thiourea fluorescein)-1-butoxycarbonyl)-D-biotinamido]-3,6,9-trioxaundecane, Compound 6[a]

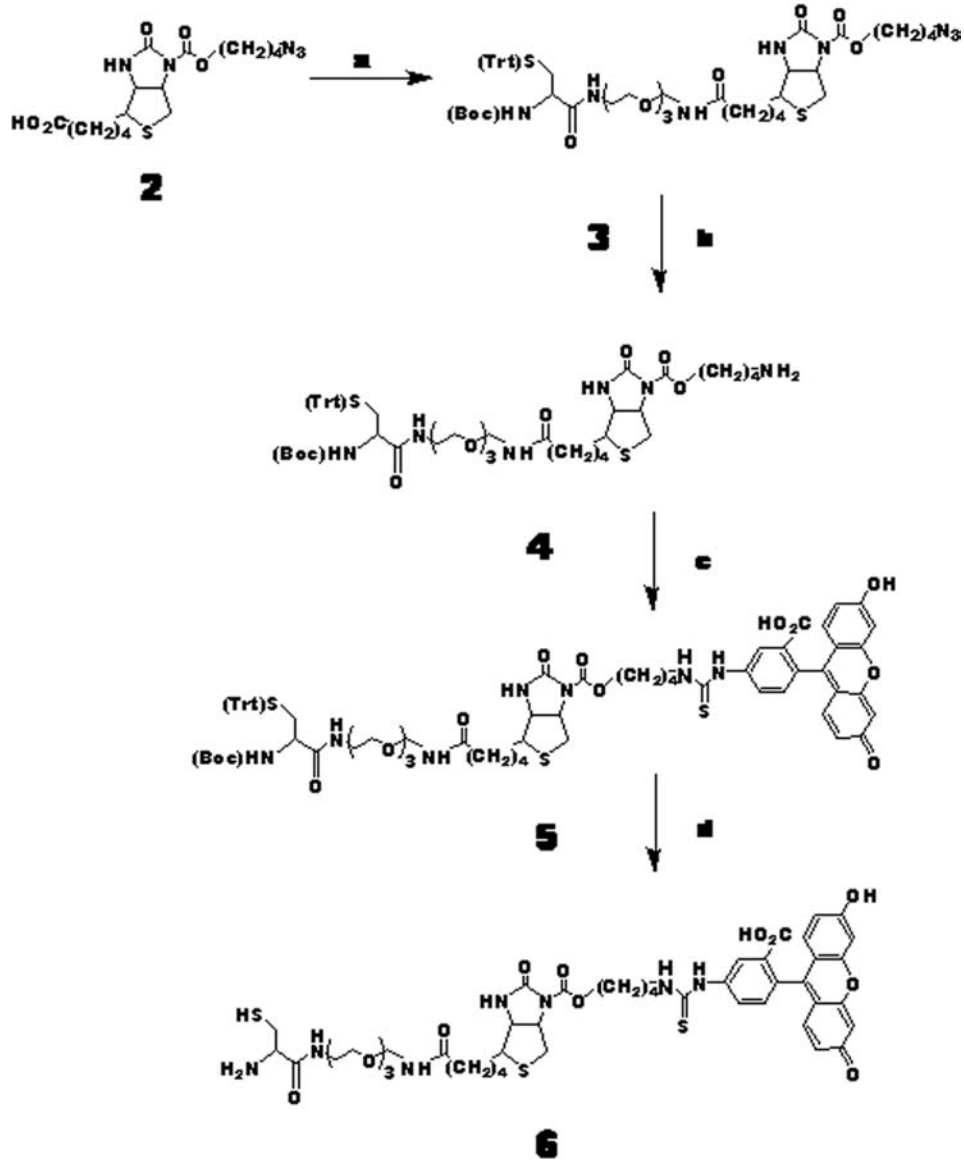

[a] (a) Under argon atmosphere, BOP + DIEA in CH_2Cl_2/DMF (3/2) at 0°C for 30 min, then **1′** added + DIEA, stirring for 24 h at room temperature, 93%; (b) $P(Ph)_3$ in THF with stirring for 12 h, then H_2O with stirring for a further 12 h, 68%; (c) CH_2Cl_2, $(Et)_3N$ at 0°C, then 12 h at room temperature; (d) CH_2Cl_2 TIS at room temperature for 5 h, 60%.

(Lancaster Synthesis), FITC (Molecular Probes), and amino acids and BOP (Novabiochem). All reactions involving nonaqueous solvents were carried out under a dry argon atmosphere. The progress of the reaction was monitored by analytical thin-layer chromatography (TLC) on silica gel Merck $60F_{254}$. Bands were visualized under UV (254 nm), with Pancaldi reagent (cerium IV, 5%), iodine, ninhydrin, or $KMnO_4$. Products were purified by flash chromatography on silica gel (Merck, 30−70 μm) or preparative reverse-phase HPLC (C18 Hyperprep, 250 × 21.2 mm, 8 μm). ^1H and ^{13}C NMR spectra were recorded on a Brücker AC 300 instrument, and chemical shift values (δ) are expressed in parts per million (ppm) with respect to the corresponding deuterated solvent. ESI mass spectra were recorded on a Nemag R10-10 machine. High-resolution FAB mass spectra were obtained from the Mass Spectrometry Service, CESAMO, Bordeaux.

Chemicals. *1-(N-α-t-Boc-S-Trityl-L-cysteinamido)-11-azido-3,6,9-trioxaundecane, Compound **1**.* We synthesized 1-amino-11-azido- 3,6,9-trioxaundecane as described by Schwabacher et al. (*36*, *37*). To a stirred solution of *N*-α-t-Boc-*S*-trityl-L-cysteine (1 g, 2.2 mmol) in CH_2Cl_2 (50 mL) were added BOP (954 mg, 2.2 mmol) and DIEA (420 μL, 2.4 mmol). Stirring was continued for 30 min at 0 °C. We added 1-amino-11-azido-3,6,9-trioxaundecane (520 mg, 2.4 mmol) in CH_2Cl_2 (25 mL) and DIEA (420 μL, 2.4 mmol) to the mixture, which was stirred for 1 day at room temperature. The reaction mixture was washed successively with 1 M HCl (150 mL), 1 M $NaHCO_3$ (150 mL), and a sodium chloride saturated solution (brine) (150 mL). The organic layer was dried ($MgSO_4$) and the solvent evaporated under reduced pressure. The resulting crude product was purified by flash chromatography, using a gradient of 95/5 to 80/20 dichloromethane/ethyl acetate, to give **1** (1.31 g, 89%) as a slightly yellow oil: R_f = 0.27 CH_2Cl_2/AcOEt (8/2); MS (ESI) *m/z*: $[M + H]^+$ = 664.7; ^1H NMR (300 MHz, $CDCl_3$) δ(ppm): 7.37−7.31 (m, 6H, CH), 7.25−7.10 (m, 9H, CH), 6.37 (t, J = 6 Hz, 1H, NH), 4.83 (d, J = 6 Hz, 1H, NH), 3.89−3.78 (m, 1H, CH), 3.61−3.48 (m, 10H, CH_2), 3.46−3.40 (m, 2H, CH_2), 3.36−3.26 (m, 4H, CH_2), 2.69−2.57 (m, 1H, CH), 2.50−2.38 (m, 1H, CH), 1.35 (s, 9H, CH_3); ^{13}C NMR (300 MHz, $CDCl_3$) δ(ppm): 2 × 170.38, 3 × 144.47, 6 × 129.60, 6 × 128.06, 3 ×

Scheme 3. pHEN2 Vector and scFvC5-(X)-Mxe Constructs[a]

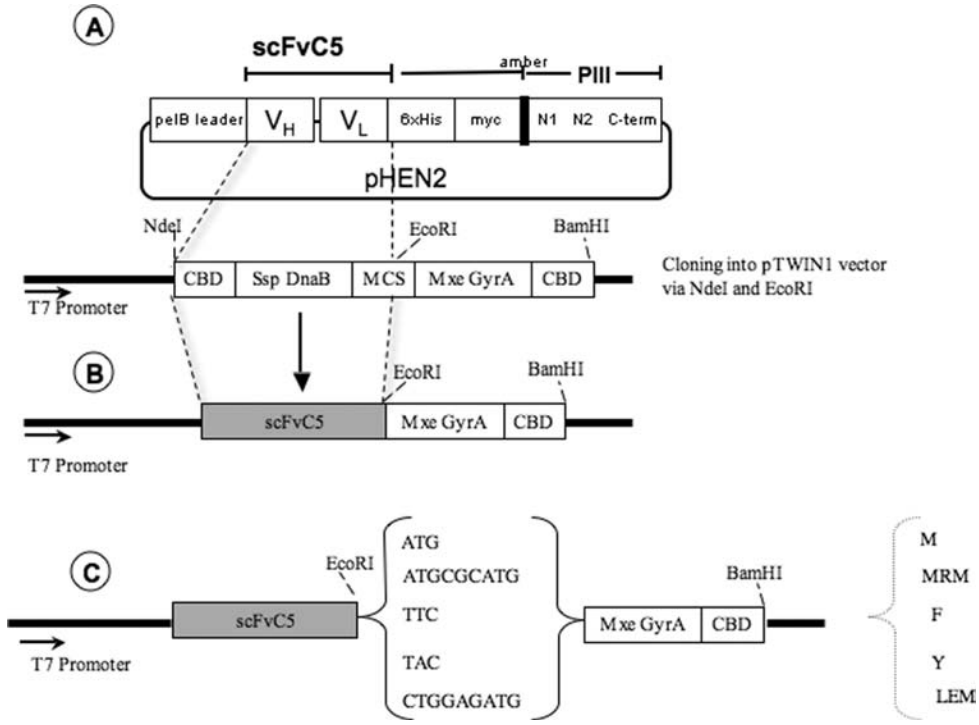

[a] A: Schematic representation of the pHEN2 phagemid vector (Griffin 1. library). pelB leader: signal peptide sequence of bacterial pectate lyase mediating secretion into the periplasmic space; V_H: variable fragment of the heavy chain; V_L: light chain; 6xHis: 6 histidine-tag; myc: myc-tag; amber: amber stop codon; N1, N2, C-term: portions of the N- and C-termini of phage capsid protein pIII. ScFvC5 (V_H V_L) amplified by PCR and inserted into the pTWIN 1 vector. B: Schematic representation of scFvC5 fused to the Mxe intein. C: Schematic representation of the various scFvC5-(X)-Mxe, constructed and checked for splicing efficiency.

Scheme 4. Splicing of scFvC5-(X)-Mxe[a]

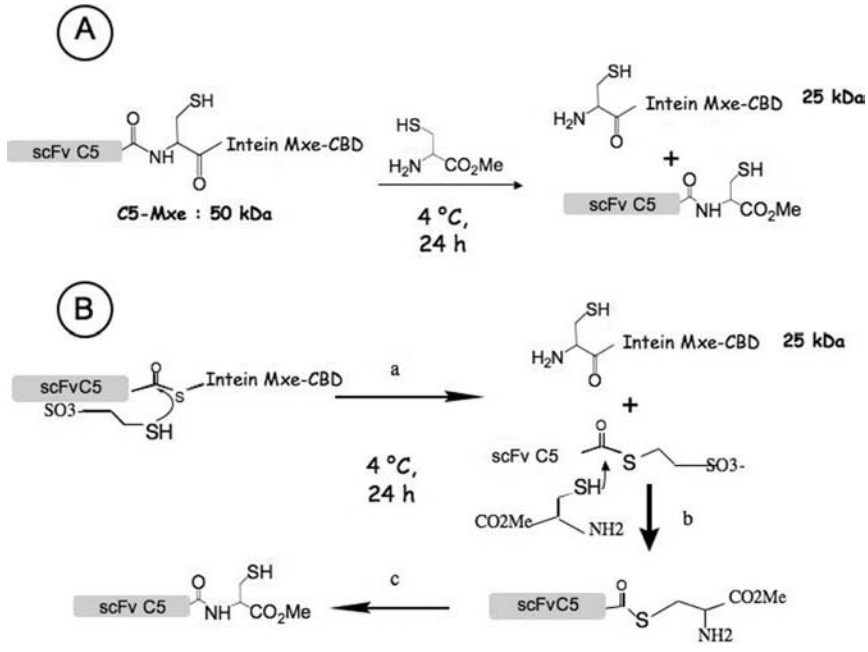

[a] A: Cysteine carboxymethyl ester induces the formation of two products with a molecular mass of 25 kDa. Only the product containing the chitin binding domain (CBD) is detected by the anti-CBD antibody on western blots. B: Mesna catalyzes the activity of the carboxymethyl ester of cysteine, generating an intermediate in addition to the two initial products. As in A, only the product containing the chitin binding domain (CBD) was detected with an anti-CBD antibody on western blots. (a) Mesna reacts with intein, producing mxeCBD plus scFvC5 linked to mesna. (b) Binding of cysteine carboxymethyl ester to scFvC5.

126.90, 80.12, 70.64, 70.61, 70.38, 70.12, 70.07, 69.73, 67.10, 53.53, 50.69, 39.38, 34.31, 3 × 28.32.

1-(N-α-t-Boc-S-Trityl-L-cysteinamido)-11-amino-3,6,9-trioxaundecane, Compound 1′. One equivalent of compound **1** (1 g, 1.5 mmol) was dissolved in anhydrous THF (15 mL); 4 equiv of triphenylphosphine, $P(Ph)_3$ (1.58 g), was added and activation was allowed to occur for 12 h at room temperature. We then added water (4 mL) and maintained stirring for a further 12 h.

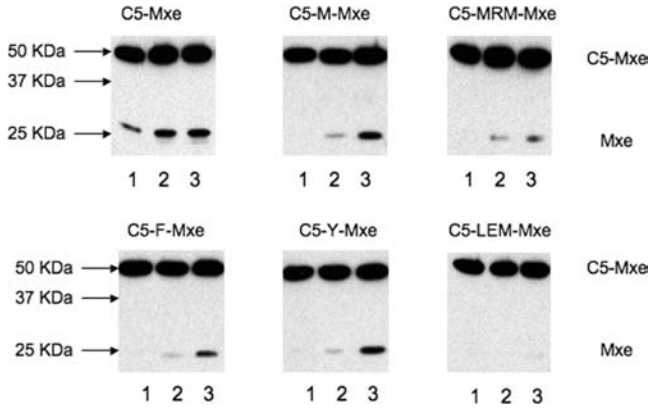

Figure 1. Western blot analyses, with anti-CBD antibody of the splicing induced by cysteine carboxymethyl ester alone. scFvC5-(X)-Mxe was generated and adsorbed onto chitin-coated plates, which were incubated with various concentrations of cysteine carboxymethyl ester: buffer alone (lane 1), 1 mM (lane 2), 10 mM (lane 3).

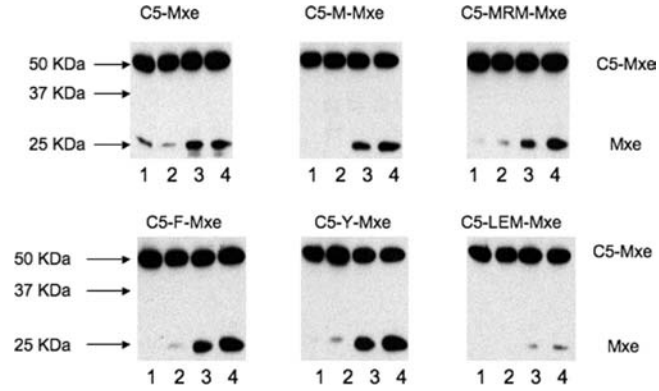

Figure 2. Western blot analyses, with antiCBD antibody, of the splicing induced by cysteine carboxymethyl ester in the presence of mesna (3 mM). scFvC5-(X)-Mxe was produced, adsorbed onto chitin-coated plates, and incubated with various concentrations of cysteine carboxymethyl ester in the presence of 3 mM mesna: buffer alone (lane 1), mesna (lane 2), mesna + 1 mM (lane 3), mesna + 10 mM (lane 4).

The mixture was concentrated under reduced pressure, diluted with 50 mL of water, and extracted with CH_2Cl_2 (10 × 50 mL). The resulting product was concentrated and purified by flash chromatography (dichloromethane/methanol, gradient 95/5 to 1/1), giving a pale yellow oil (0.91 g, 95%), **1′**: R_f = 0.15 CH_2Cl_2/MeOH (6/4); MS (ESI) *m/z*: $[M + H]^+$ = 638.6; ^{1}H NMR (300 MHz, $CDCl_3$) δ(ppm): 7.41−7.28 (m, 6H, CH), 7.28−7.01 (m, 10H, CH + NH), 5.19 (d, J = 9 Hz, 1H, NH), 4.01−3.86 (m, 1H, CH), 3.61−3.21 (m, 14H, CH_2), 2.75 (t, J = 6 Hz, 2H, CH_2), 2.61−2.36 (m, 2H, CH_2), 1.80 (s, 2H, NH_2), 1.35 (s, 9H, CH_3); ^{13}C NMR (300 MHz, $CDCl_3$) δ(ppm): 2 × 170.43, 3 × 144.50, 6 × 129.57, 6 × 127.98, 3 × 126.79, 79.86, 73.14, 2 × 70.51, 70.31, 70.09, 69.87, 66.85, 53.35, 41.52, 39.36, 34.62, 3 × 28.33).

1-(N-α-t-Boc-S-Trityl-L-cysteinamido)-11-[1′-N-(4-azido-1-butoxycarbonyl)-D-biotinamido]-3,6,9-trioxaundecane, Compound ***3.*** To a stirred solution of *N*-1′-(4-azido-1-butoxycarbonyl)-D-biotin **2** (*35*) (380 mg, 0.99 mmol) in CH_2Cl_2/DMF (3/2, 15 mL) at 0 °C were added BOP (436 mg, 0.99 mmol) and DIEA (190 μL, 1.1 equiv). After 30 min, a solution of **1′** (692 mg, 1.1 mmol) and DIEA (190 μL, 1.1 mmol) in CH_2Cl_2 (9 mL) was added dropwise, and the resulting mixture was stirred for 24 h at room temperature. The reaction mixture was concentrated under a vacuum and the residue dissolved in CH_2Cl_2 (50 mL). The resulting solution was washed successively with HCl (1 M, 150 mL), $NaHCO_3$ (1 M, 150 mL), and brine (150 mL) and then dried ($MgSO_4$) and the solvent evaporated off under a vacuum. The resulting crude product was purified by flash chromatography (CH_2Cl_2/MeOH, gradient 98/2 to 90/10) to give **3** as a pale yellow oil (0.93 g, 93%): R_f 0.2 (CH_2Cl_2/MeOH, 95/5); R_f = 0.2 CH_2Cl_2/MeOH (95/5); MS (ESI) *m/z*: $[M + H]^+$ = 1005.65 $[M + Na]^+$ = 1027.65; ^{1}H NMR (300 MHz, $CDCl_3$) $\delta\partial$ (ppm): 7.38−7.29 (m, 6H, CH), 7.29−7.10 (m, 9H, CH), 6.81 (s, 1H, NH), 6.66 (t, J = 6 Hz, 1H, NH), 6.55 (s, 1H) NHC_1O, 5.19 (s, 1H, NH), 4.76−4.68 (m, 1H, CH), 4.24−4.15 (m, 2H, CH_2), 4.15−4.04 (m, 1H, CH), 3.92−3.80 (m, 1H, CH), 3.60−3.20 (m, 18H, CH_2), 3.14−3.04 (m, 1H, CH), 3.04−2.87 (m, 2H, CH_2), 2.54−2.40 (m, 2H, CH_2), 2.10 (t, J = 6 Hz, 2H, CH_2), 1.80−1.45 (m, 8H, CH_2), 1.45−1.24 (m, 11H, CH_2, CH_3); ^{13}C NMR (300 MHz, $CDCl_3$) $\delta\partial$ (ppm): 1173.10, 2 × 170.78, 155.60, 151.85, 3 × 144.45, 6 × 129.58, 6 × 128.04, 3 × 126.87, 80.03, 70.48, 70.38, 70.34, 70.11, 69.83, 69.64, 67.03, 65.80, 62.65, 57.61, 55.21, 53.48, 50.95, 39.47, 39.18, 38.73, 35.51, 34.29, 3 × 28.34, 27.94, 27.87, 25.98, 25.48, 25.28;.

1-(N-α-t-Boc-S-Trityl-L-cysteinamido)-11-[1′-N-(4-amino-1-butoxycarbonyl)-D-biotinamido]-3,6,9-trioxaundecane, Compound ***4.*** To a solution of compound **3** (115 mg, 0.11 mmol) in dry THF (2 mL) was added triphenylphosphine (240 mg, 0.88 mmol). The resulting mixture was stirred for 12 h at room temperature. Water (2 mL) was then added, and the resulting mixture was stirred for a further 12 h. The solution was concentrated under reduced pressure, diluted with water (8 mL), and extracted 10 times with CH_2Cl_2 (20 mL). The combined organic layers were dried ($MgSO_4$) and evaporated under reduced pressure. The crude product was purified by flash chromatography (CH_2Cl_2/MeOH/Et_3N, 8/2/0.1). The resulting product was dissolved in CH_2Cl_2 (50 mL) and successively washed with HCl (1 N, 50 mL), $NaHCO_3$ (1 N, 50 mL), and brine (50 mL). The organic solution was dried ($MgSO_4$) and evaporated under reduced pressure to give **4** as a brown powder (73 mg, 68%): R_f = 0.17 CH_2Cl_2/MeOH (8/2 in the presence of 1% Et_3N); MS (ESI) *m/z*: $[M + H]^+$ = 979.65 $[M + Na]^+$ = 1001.75; ^{1}H NMR (300 MHz, $CDCl_3$) δ(ppm): 7.40−7.27 (m, 6H, CH), 7.27−7.09 (m, 9H, CH), 7.09−6.90 (m, 3H, NH, NH_2), 6.80−6.65 (m, 2H, NH × 2), 5.15−5.02 (m, 1H, NH), 4.77−4.60 (m, 1H, CH), 4.25−4.07 (m, 3H, CH, CH_2), 3.96−3.80 (m, 1H, CH), 3.60−3.25 (m, 16H, CH_2), 3.13−3.05 (m, 1H, CH), 3.01−2.80 (m, 4H, CH_2), 2.63−2.51 (m, 1H, CH), 2.51−2.40 (m, 1H, CH), 2.09 (t, J = 6 Hz, 2H, CH_2), 1.80−1.45 (m, 8H, CH_2), 1.45−1.25 (m, 11H, CH_2, CH_3); ^{13}C NMR (300 MHz, $CDCl_3$) δ(ppm): 173.25, 2 × 170.63, 156.31, 151.89, 3 × 144.44, 6 × 129.56, 6 × 128.03, 3 × 126.86, 80.04, 70.43, 70.36, 70.28, 70.08, 69.86, 69.67, 66.99, 66.24, 62.65, 58.06, 55.54, 53.45, 2 × 39,39, 39.13, 38.70, 35.72, 34.37, 28.54, 3 × 28.33 28.00, 3 × 25.42.

1-(N-α-t-Boc-S-Trityl-L-cysteinamido)-11-[1′-N-(4-(thiourea fluorescein)-1-butoxycarbonyl)-D-biotinamido]-3,6,9-trioxaundecane, Compound ***5.*** To a stirred mixture of compound **4** (220 mg, 0.23 mmol) and Et_3N (32 μL, 0.23 mmol) in dry CH_2Cl_2 (4 mL) at 0 °C was added dropwise a solution of FITC (87.4 mg, 0.23 mmol) in dry DMF (3 mL). The mixture was allowed to come up to room temperature, with stirring, over a period of 4 h and was then stirred for a further 20 h at room temperature. The reaction mixture was placed under low pressure to evaporate off the solvent, and the resulting crude residue was purified by flash chromatography (CH_2Cl_2/AcOEt/MeOH, 4/4/2), to give **5** as a yellow powder (240 mg, 78%): R_f = 0.32 CH_2Cl_2/AcOEt/MeOH (4/4/2); MS (ESI) *m/z*: $[M + Na]^+$ = 1390.50; ^{1}H NMR (300 MHz, DMSO) δ(ppm): 8.38−8.30 (m, 1H, CH), 7.96−7.68 (m, 4H, CH, NH × 3), 7.48−7.14 (m, 15H, CH, CH_2), 7.05−6.96 (m, 1H, CH), 6.77−6.61 (m, 6H, CH), 4.85−4.75

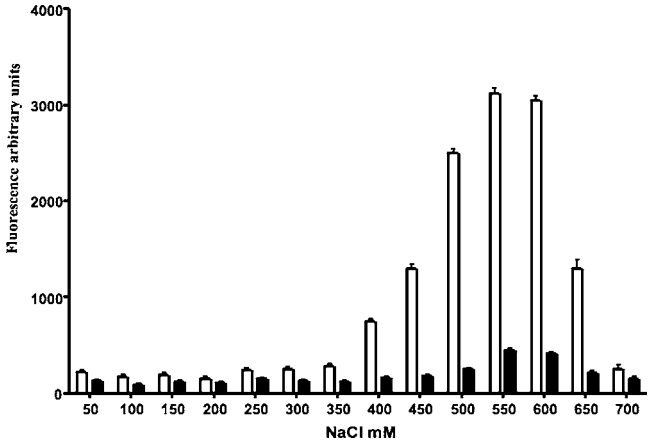

Figure 3. Fluorescence-linked immunosorbent assay of DEAE chromatography desorbed fractions. Labeled scFv C5 was loaded onto DEAE trisacryl and eluted with increasing concentrations of NaCl. Each fraction was then checked for binding to RhoA (white bars) and RhoB (black bars). The results shown are representative of a single experiment carried out in triplicate.

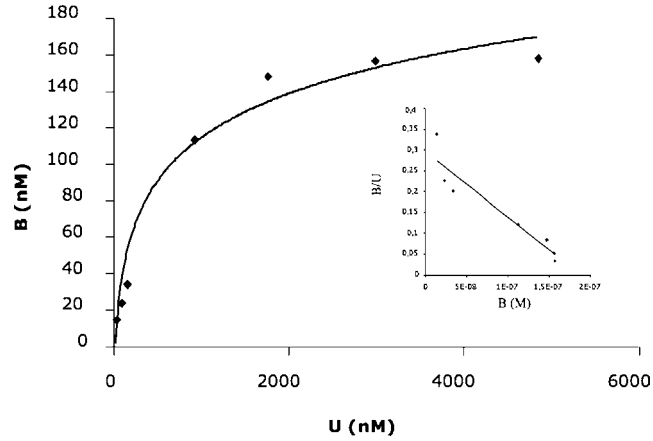

Figure 4. Binding study for compound **6**. Various concentrations of compound **6** (up to 6 μM) were loaded onto an avidin-coated plate, in the absence (total binding) or presence (nonspecific binding) of a large excess of biotin (1 mM). B was representative of the specific fluorescence (compound **6**) bound on avidin and U unbound. Representative data from one experiment of three performed in duplicate are shown. A Scatchard plot analysis is shown in the inset.

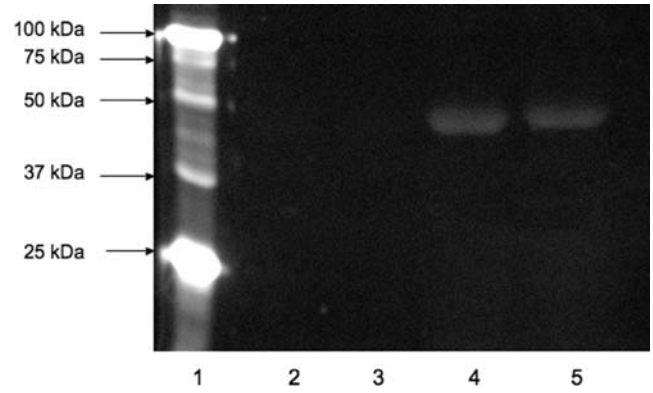

Figure 5. SDS- PAGE analysis of the eluate from streptavidin columns. The 500, 550, and 600 mM NaCl fractions from the DEAE column were pooled and loaded onto streptavidin beads. The beads were washed, and increasing concentrations were used for elution: 0.01 mM (lane 2), 0.1 mM (lane 3), 1 mM (lane 4), 10 mM (lane 5). The gel was illuminated under UV light (380 nm) for the detection of fluorescence.

(m, 1H, CH), 4.31−4.15 (m, 3H, CH, CH_2), 3.60−2.90 (m, 22H, CH, CH_2), 2.53 (m, 2H); 2.07 (t, 2H, CH_2), 1.70−1.20 (m, 10H, CH_2).

1-(L-Cysteinamido)-11-[1′-N-(4-(thiourea fluorescein)-1-butoxycarbonyl)-D-biotinamido]-3,6,9-trioxaundecane, Compound ***6.*** To a stirred solution of compound **5** (44 mg, 0.032 mmol) in CH_2Cl_2 (3 mL) at room temperature was added dropwise a solution of TIS (7 μL, 0.032 mmol) in CH_2Cl_2/TFA (2 mL, 75/25). After 5 h of stirring at room temperature, the reaction mixture was placed under low pressure conditions to evaporate off the solvent, and the resulting crude residue was purified by flash chromatography (CH_3CN/MeOH/H_2O; gradient 90/5/5 to 80/15/5) to yield **6** as an orange powder (20 mg, 60%): $R_f = 0.18$ CH_3CN/MeOH/H_2O (6/3/1); MS (ESI) *m/z*: $[M + H]^+ =$ 1026.3446 (theoretical mass: HRMS calculated for ($C_{47}H_{59}N_7O_{13}S_3$) ($[M + H]^+$), *m/z* 1026.3411); ^{1}H NMR (300 MHz, DMSO) δ(ppm): 8.28−8.19 (m, 1H, CH), 8.10−8.05 (m, 1H, NH), 7.90−7.82 (m, 1H, CH), 7.75−7.60 (m, 2H, NH), 7.15−7.05 (m, 1H, CH), 6.75−6.40 (m, 6H, CH), 4.80−4.70 (m, 1H, CH), 4.20−4.02 (m, 3H, CH, CH_2), 3.60−2.90 (m, 22H, CH, CH_2), 2.53 (m, 2H, CH_2), 2.07 (t, 2H, CH_2), 1.70−1.20 (m, 10H, CH_2).

Biological Agents. *Strains.* The bacterial strains used were *E. coli* DH5α for subcloning, BL 21 for Rho protein production, and ER 2566 (NEB) for scFvC5-intein chimeras.

ScFvC5 Selection and Production. The Griffin.1 library, a human synthetic V_H+V_L scFv phage library in a phagemid vector, and the positive control *E. coli* TG1 (TG1 containing an antityroglobulin clone) were generously provided by Fiona Sait of The Medical Research Council (Cambridge, England). We followed the protocol provided for the Griffin.1 library at http://www.mrc-cpe.cam.ac.uk (*38*), as previously described (*39*). Briefly, in the presence of GST-RhoA (to remove unspecific phages), phages were selected using recombinant GST-RhoB, coated on glutathione wells. After four rounds of selection/amplification, this led to the isolation of an scFv fragment subsequently referred to as C5. This fragment was then produced as a recombinant protein, from the PHEN plasmid (Scheme 3: A). This scFvC5 has not yet been completely characterized. Initial analyses have shown that it is selective for the native structure of RhoB, with a dissociation constant at equilibrium (K_D) of $5 \pm 3 \times 10^{-6}$ M.

Construction of ScFvC5-Mxe. This construction process was based on the prior work of L.-P. Tan et al. (*30, 31*) and C. Cui et al. (*40*) We used the pTWIN1 plasmid of the NEB IMPACT system as a vector and amplified the scFvC5 sequence by PCR with primers containing a 5′ *Nde*I site and a 3′ *Eco*RI site:

5′-GGAATTCCATATGCAGGTGCAGCTGCAGGAG-3′sense

3′-CGGAATTCTGCGGCCGCACCTAGGAC-5′ antisense

The amplified and digested DNA fragment was inserted (in place of the Ssp intein), between the *Nde*I and *Eco*RI sites of the pTWIN1 plasmid (Scheme 3B).

Construction of Mutated ScFvC5(-X)Mxe. Given the importance of the nature of the amino acids of the hinge domain between scFvC5 and intein for the induction of splicing, we generated five mutations in this hinge domain: methionine (scfvC5-MMxe), phenylalanine (scfvC5-Fmxe), tyrosine (scfvC5-YMxe), methionine-arginine-methionine (scfvC5-MRMMxe), and leucine-glutamic acid-methionine (scfvC5-LEMMxe). The various mutations were achieved by means of PCR using as the 3′ primer a common oligonucleotide, 5′-ACGATTGTT-TCGGGCTTT-3′, annealing the 3′ sequence of the *Bam*HI restriction site of pTWIN1, and, as the 5′ primer, sequences carrying the *Eco*RI site were used.

Amplified and digested DNA fragments were inserted between the *Eco*RI and *Bam*HI sites of the previously constructed scFvC5-pTWIN 1 plasmid (Scheme 3C). These plasmids were

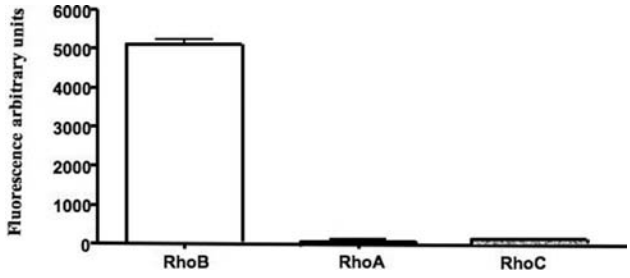

Figure 6. Fluorescence-linked immunosorbent assays of selectivity for RhoB. The streptavidin eluted with 1 mM biotin was diluted 1/20 and loaded onto Rho B (white bar), Rho A (black), or Rho C (gray)-coated plates.

constructed for the production in bacteria of an scFvC5 fragment fused to the mutated Mxe and tagged with a chitin-binding domain (CBD) from the pTWIN1 vector. This CBD was subsequently used to purify the protein of interest.

Production of scFvC5-X-Mxe Protein Chimeras. Transformed ER 2566 bacteria were grown at 37 °C in 50 mL of LB medium containing 100 μg/mL ampicillin to an OD_{600} of 0.6. Synthesis of the scFvC5-X-Mxe protein was then induced by incubation with IPTG (1 mM) for 18 h at 20 °C. Bacteria were harvested, centrifuged for 10 min at 4000*g*, resuspended in 5 mL of buffer A (HEPES (10 mM), NaCl (250 mM) pH 7.4), and subjected to six 10 s pulses of sonication on ice. The resulting lysate was centrifuged at 8500*g* for 30 min at 4 °C, and the supernatant was retained for subsequent experiments.

Induction of Splicing by the Carboxymethyl Ester of Cysteine. Supernatants were loaded on chitin-coated 96-well plates and incubated at 4 °C for 4 h. They were then washed three times with buffer A, and increasing concentrations of the carboxy methyl ester of cysteine were added. The mixture was then incubated at 4 °C for a further 24 h, or at 20 °C for 4 h. The plates were washed with buffer A, and 5 μL of 5% SDS at 80 °C was added to each well. Western blot analysis was then carried out with an antibody directed against the chitin binding domain (NEB Biolabs).

Induction of Splicing and Labeling with 1-(L-Cysteinamido)-11-[1′-N-(4-(thiourea fluorescein)-1-butoxycarbonyl)-D(+)-biotinamido]-3,6,9-trioxaundecane. We labeled only scFvC5-Y-Mxe using 100 mL of transformed bacteria. The bacteria were collected by centrifugation, and the pellet was resuspended in 10 mL of buffer A. The bacteria were lysed by sonication, and the 8500*g* supernatant was loaded at 4 °C onto 1 mL of chitin beads. The beads were washed with 4 × 5 mL of buffer A. We then added 2.5 mM of compound **6** in the presence of mesna (3 mM) in 300 μL of buffer A and incubated the beads at 4 °C for 24 h. The flow-through was salvaged and used in subsequent experiments.

*Partition of the Biotinylated Fluorescent scFVC5-Y (Biot-Fluo-scFvC5) from Unreacted Compound **6** and Unlabeled scfvC5-Y.* Anion exchange chromatography was carried out with 1 mL of DEAE Trisacryl resin from Pharmacia. The sample was diluted 1:5 in buffer B (HEPES 20 mM, pH 7.7) to adjust the NaCl concentration to 50 mM before loading. The column was then washed with 40 mL of buffer B supplemented with DTT (1 mM) and subjected to elution with buffer B plus DTT supplemented with increasing concentrations of NaCl (50 to 600 mM). Desorbed fractions were loaded, in the presence of BSA (10 mg/ml), onto 500 μL of streptavidin resin (Amersham). The resin was washed with 15 mL of buffer B supplemented with DTT and BSA and 15 mL of the same buffer without BSA. Elution was carried out with increasing concentrations of biotin (0−10 mM) in buffer B. The fraction eluted with 1 mM biotin (purified) was used in subsequent experiments.

Fluorescence-Linked Immunosorbent Assay (FLISA). The chimeric GST-RhoA, GST-RhoB, GST-RhoC proteins were produced in *E. coli*, as previously described (*41*). They were absorbed onto gluthatione-coated 96-well plates (Reacti-Bind Coated Black from Pierce). The plates were washed three times, with 200 μL of PBS each, and were then incubated with 100 μL of purified Biot-Fluo-scFvC5 (the 1 mM biotin fraction from streptavidin chromatography) for 1 h. The plates were washed was twice with 1 mM DTT in PBS, and the fluorescence of each well was determined with a spectrofluorimeter (Flite 2001 Fluorescence Reader from Perkin-Elmer).

Immunofluorescence. HeLa cells (ATCC, CCL-2) were grown on coverslips in Dulbecco's modified Eagle's medium (DMEM, Cambrex) supplemented with 5% fetal calf serum. They were fixed by incubation in paraformaldehyde (Cytofix) and permeabilized by incubation with Cytoperm (BD Biosciences). They were then incubated with 200 μL of Biot-Fluo-scFvC5 in the presence or absence of GST-RhoA (about 10 μg) or GST-RhoB (about 10 μg) for 1 h and washed twice with 500 μL of a 98/1/1 mixture of PBS/acetone/methanol. Control images were obtained with monoclonal anti-RhoB (sc8048) from Santa Cruz. Cell fluorescence was visualized with a Nikon Eclipse 90i microscope equipped with FITC fluorescence filters (Semrock) and a CoolsnapHQ^2 camera (Ropper). Images were acquired with NIS-Element Ar.

RESULTS

Synthesis of 1-(*N*-α-t-Boc-*S*-Trityl-L-cysteinamido)-11-amino-3,6,9-trioxaundecane 1′ (Scheme 1). With the aim of increasing the spacing between the biotin motif and the reacting cysteine and the scFv, we generated a poly(ethylene glycol) arm with a cysteine-reactive thiol at one end. This linker has been chosen in relation to Bucourt's work (*42*). Compound **1** was obtained with an 89% yield and was reduced in the presence of triphenylphosphine to obtain compound **1′** (95% yield). Boc and trityl protective groups were retained for subsequent experiments.

Synthesis of 1-(*N*-α-t-Boc-*S*-Trityl-L-cysteinamido)-11-[1′-*N*-(4-azido-1-butoxycarbonyl)-D-biotinamido]-3,6,9-trioxaundecane 3 (Scheme 2). The peptide bond between compounds **1′** and **2** generated in a previous study (*35*) was reproduced here by classical methods, yielding 93% purified product **3**.

Synthesis of 1-(L-Cysteinamido)-11-[1′-*N*-(4-(thiourea fluorescein)-1-butoxycarbonyl)-D-biotinamido]-3,6,9-trioxaundecane 6 (Scheme 2). A Staudinger reduction was used to generate **4**, the amino group of which was then reacted with FITC to give **5**.

Classical deprotection methods yielded 20 mg of an orange powder **6** with a final recovery rate of 29.6%. This final deprotection step was carried out three times to obtain the desired product with a good recovery rate. Given the small amount of compound **6** obtained, we checked product purity by a combination of NMR and high-resolution mass spectrometry, as elementary analysis would have consumed too much of the product.

Induction of Splicing by the Carboxymethyl Ester of Cysteine. Given the small amount of compound **6** available, we initiated the labeling study and defined the optimal conditions for splicing and labeling using a commercially available carboxymethyl ester of cysteine as the thiol reagent. Chimeric scFv-X-Mxe was produced and adsorbed onto a chitin plate. Splicing efficiency was assessed by Western blotting with an anti-CBD (fused to the Mxe intein) antibody (Scheme 4A). We aimed to select the sequence giving the lowest level of splicing in the absence of inducer and the highest level of splicing in the presence of inducer. As shown in Figure 1, the initial construct gave splicing in the absence of inducer (a; lane 1), and splicing levels increased with increasing concentrations of

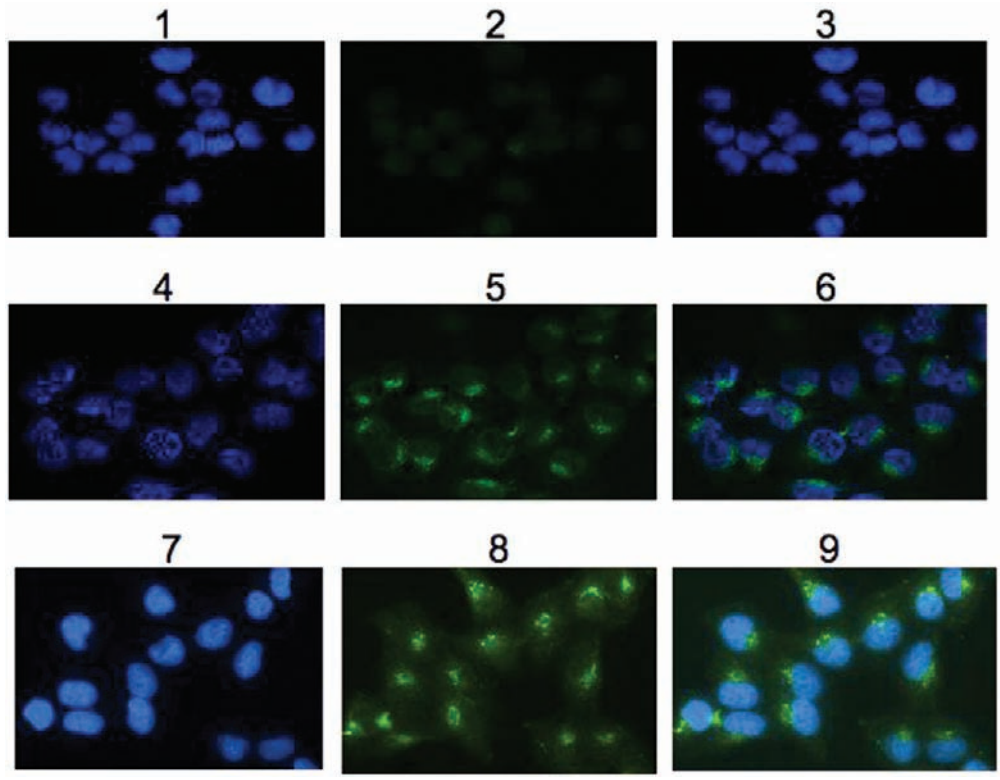

Figure 7. Immunofluorescence of RhoB in HeLa cells. The 1 μM biotin eluted fraction was diluted 1/10 and loaded onto HeLa cells in the presence of purified GST-RhoB (1, 2, 3) or in the presence of purified GST-RhoA (4, 5, 6). Nuclear DAPI labeling (1, 4) and (2, 5) fluorescence imaging. Merged image (3, 6). Control with commercial anti-RhoB (7, 8, 9).

Scheme 5. Labeling of scFvC5 with Biotin−Fluorescein

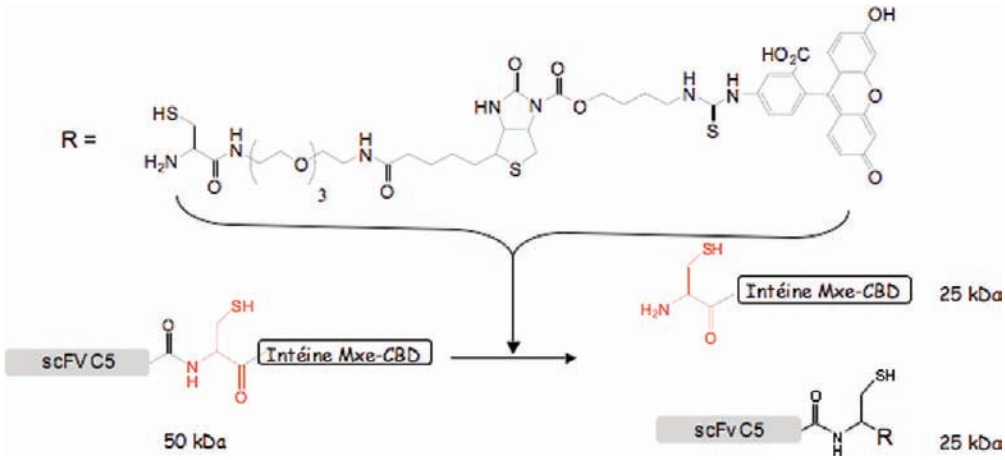

cysteine carboxymethyl ester. The other five constructs gave no detectable splicing in the presence of buffer alone (c, b, d, e, f, lanes 1) and higher levels of splicing with the thiol, with the exception of scFvC5-LEM-Mxe, for which no splicing was observed with these treatments (f, lanes 1, 2, 3). We tried to increase the low splicing efficiency of the cysteine derivative by adding TCEP up to a concentration of 20 mM to maintain the thiol group of the cysteine derivative in its reactive form: no increase in the splicing efficiency of cysteine carboxymethyl ester was observed (data not shown). We also used mesna, another widely used catalyst (*31*, *33*, *43*, *44*), for this reaction. The addition of mesna (3 mM) to the splicing buffer increased the effect of the cysteine derivative but had no effect alone, in the absence of the cysteine derivative (Figure 2a−f, lane 1). The largest increase was obtained with scFvC5-F-Mxe and scFvC5-Y-Mxe (Figure 2d,e), but, given the mechanism of action of mesna (Scheme 4B), splicing may occur without labeling of the desired protein. The effect of buffer pH was then assessed. Each construct had its own pattern of response to buffers of different pH (from 6.5 to 9), but for scFv−C5-Y-Mxe in the presence of 3 mM mesna, the best splicing effect was obtained at pH 7.4 (data not shown).

At this stage using GST-RhoB as ligand, we have not found a difference in K_D between the original scFv-C5-Hisx6-c.myc with the new scFv−C5-Y-Mxe: $K_D = 5 \pm 3 \times 10^{-6}$ M.

Experiments performed at 20 °C for 4 h showed an increase in the splicing in response to the thiol inducer as compared to 4 °C. However, at 20 °C, the splicing occurred even in the absence of the thiol inducer (data not shown). Because this methodology will be also used to label in vivo (on viable cells) membrane receptors, cellular labeling must be performed at 4 °C previously to follow the spatiotemporal changes of receptor in living cells at 37 °C.

ScFvC5 Labeling. In vitro labeling was carried out with scFvC5-Y-Mxe, which gave the highest splicing efficiency in the presence of the cysteine derivative. Compound **6** was used in the presence of mesna (3 mM), and temperature (4 °C) and pH (7.4) conditions were selected to minimize protease activity and the structural deformation of the scFv and to make it possible to extrapolate the system to in vivo studies, for membranous protein labeling. Bacterial culture (100 mL of ER 2566 transformed with scFvC5-Y-Mxe plasmid) was lysed as described in the Materials and Methods, and the lysate was loaded onto a 1 mL chitin bead column. The column was washed three times with 20 mL of buffer A, and 300 μL of compound **6** (2.5 mM), dissolved in buffer A (pH adjusted to 7.4), was mixed with the beads in the presence of mesna (3 mM). After 24 h of contact with the beads, the flow-through containing the labeled scFvC5 was collected.

Purification of Labeled scFvC5. Capture on chitin beads gave a high level of purification of scFvC5-Y-Mxe from protein lysate, but the splicing induced by compound **6** and mesna essentially gave three products in the flow-through: unreacted compound **6**, unlabeled scFvC5 (which had reacted with mesna only), and labeled scFvC5. The calculated pI of scFvC5-Y given by the EMBL WWW Gateway to Isoelectric Point Service site was 5.4. We therefore used an anionic purification step to separate the proteins from the unreacted compound **6**. The NaCl concentration of the flow-through was adjusted to 50 mM, and the flow-through was loaded onto a DEAE trisacryl column. We added dithiothreitol (1 mM) to each buffer to inhibit the formation of disulfide bridges (between compound **6** and other compounds with SH groups). Increasing concentrations of NaCl were used to elute the labeled scFv, which was obtained at NaCl concentrations of 400 to 600 mM (Figure 3). We have shown that N′1 modifications of D-biotin result in a major loss of affinity for avidin (*35*). We made use of this property in the purification of labeled scFv on streptavidin, by adding biotin to the elution buffer. Scatchard plot analysis of the affinity between streptavidin and compound **6** (Figure 4) showed a K_D of 0.6×10^{-6} M, suggesting competitive desorption with biotin ($K_D = 10^{-13}$ M).

We mixed the three fractions (500−550−600 mM) from the DEAE trisacryl column and loaded the resulting mixture onto streptavidin magnetic beads, to remove unlabeled scFv and increase the specific fluorescence activity of the labeled product. The beads were washed, and the labeled scFvC5 was eluted with increasing concentrations of biotin. Labeled scFvC5-Y(BF-scFvC5) was eluted with 1 and 10 mM biotin, with the dimeric form of scFv the principal form obtained (Figure 5). Because this technology would be useful for in vivo labeling of membranous protein and to involve the cell capture of the biotin derivate at 37 °C, we have opted to induce Mxe intein splicing at low temperature (4 °C). If this temperature has lowered the scFv labeling efficiency it has maintained a good stability of the scFv. Assuming that the fluorescence quantum yield of the labeled protein was similar to that for compound **6**, the labeling yield (in relation to the quantity of compound **6** used) of the purified scFVC5 was about 2%, since recovery of labeled scFvC5 was around 5%.

Fluorescence-Linked Immunoassay. Small Rho (ABC) GTPases fused with the glutathione-sulfonyl-transferase (GST) were produced in *E. coli* and adsorbed onto a glutathione-coated 96-well plate. BF-scFvC5-Y retained specificity for RhoB (Figure 6).

We used the same technique to determine the dissociation constant at equilibrium of the BF-scFvC5-Y. Using GST-RhoB in the presence of increasing concentrations of BF-scFvC5-Y, the bound fraction was determined on glutathione beads, we found a $K_D = 1 \pm 1 \times 10^{-6}$ M on the same order of value as for the original scFvC5.

Immunofluorescence. Fixed and permeabilized HeLa cells were incubated with BF-scFvC5-Y in the presence and absence of RhoA (4, 5, 6) or RhoB (1, 2, 3). A single wash with PBS supplemented with DTT plus acetone (1%) and methanol (1%) did not result in the clear visualization of specific binding (data not shown). However, two washes gave the results shown in Figure 7. The time required for the accumulation of fluorescence was identical for the three treatments. RhoB detection with BF-scFvC5-Y (5,6) in cells was essentially in endosomal vesicles and was consistent with published results and with our own observations obtained with a commercial antibody (7, 8, 9) (*41*).

CONCLUSION

Given the need for methods for selective protein labeling in biology and biochemistry, we aimed to design a strategy for the labeling and purification of scFv directed against the small GTPase RhoB selected by phage display techniques. It was essential for this labeling to be selective and to have no effect on antigen-scFv recognition. On the basis of previous work on the synthesis of functionalized biotin N-1′ derivatives (*35*), we synthesized a biotin N-1′ fluorescein derivative carrying a thiol inducer of intein splicing on its valeric chain. This molecule double-labeled the scFv, its biotin moiety facilitating purification of the labeled protein and its fluorescein moiety opening up opportunities for the use of fluorescence-based technology. This study demonstrated the dual activity of the cysteine-biotin N-1′ fluorescein, which selectively labeled a new scFv targeting RhoB by intein splicing, and made it possible to use this molecule for immunofluorescence studies.

LITERATURE CITED

(1) Griffiths, A. D. (1993) Production of human antibodies using bacteriophage. *Curr. Opin. Immunol. 5*, 263–7.
(2) Griffiths, A. D., Williams, S. C., Hartley, O., Tomlinson, I. M., Waterhouse, P., Crosby, W. L., Kontermann, R. E., Jones, P. T., Low, N. M., Allison, T. J., et al. (1994) Isolation of high affinity human antibodies directly from large synthetic repertoires. *EMBO J. 13*, 3245–60.
(3) Hayden, M. S., Gilliland, L. K., and Ledbetter, J. A. (1997) Antibody engineering. *Curr. Opin. Immunol. 9*, 201–12.
(4) Santamaria, H. (2003) [Phage display applications in clinical diagnosis]. *Rev. Invest. Clin. 55*, 711–8.
(5) Paschke, M. (2006) Phage display systems and their applications. *Appl. Microbiol. Biotechnol. 70*, 2–11.
(6) Olichon, A., and Surrey, T. (2007) Selection of genetically encoded fluorescent single domain antibodies engineered for efficient expression in Escherichia coli. *J. Biol. Chem. 282*, 36314–20.
(7) Ayriss, J., Woods, T., Bradbury, A., and Pavlik, P. (2007) High-throughput screening of single-chain antibodies using multiplexed flow cytometry. *J. Proteome Res. 6*, 1072–82.
(8) Antos, J. M., and Francis, M. B. (2006) Transition metal catalyzed methods for site-selective protein modification. *Curr. Opin. Chem. Biol. 10*, 253–62.
(9) Agard, N. J., Prescher, J. A., and Bertozzi, C. R. (2004) A strain-promoted [3 + 2] azide−alkyne cycloaddition for covalent modification of biomolecules in living systems. *J. Am. Chem. Soc. 126*, 15046–7.
(10) Bader, B., Kuhn, K., Owen, D. J., Waldmann, H., Wittinghofer, A., and Kuhlmann, J. (2000) Bioorganic synthesis of lipid-modified proteins for the study of signal transduction. *Nature (London) 403*, 223–6.
(11) Hofmann, R. M., and Muir, T. W. (2002) Recent advances in the application of expressed protein ligation to protein engineering. *Curr. Opin. Biotechnol. 13*, 297–303.

(12) Guignet, E. G., Segura, J. M., Hovius, R., and Vogel, H. (2007) Repetitive reversible labeling of proteins at polyhistidine sequences for single-molecule imaging in live cells. *ChemPhysChem 8*, 1221–7.

(13) Hauser, C. T., and Tsien, R. Y. (2007) A hexahistidine-Zn2+-dye label reveals STIM1 surface exposure. *Proc. Natl. Acad. Sci. U.S.A. 104*, 3693–7.

(14) Juillerat, A., Heinis, C., Sielaff, I., Barnikow, J., Jaccard, H., Kunz, B., Terskikh, A., and Johnsson, K. (2005) Engineering substrate specificity of O6-alkylguanine-DNA alkyltransferase for specific protein labeling in living cells. *Chembiochem 6*, 1263–9.

(15) Yin, J., Lin, A. J., Golan, D. E., and Walsh, C. T. (2006) Site-specific protein labeling by Sfp phosphopantetheinyl transferase. *Nat. Protoc. 1*, 280–5.

(16) Machleidt, T., Robers, M., and Hanson, G. T. (2007) Protein labeling with FlAsH and ReAsH. *Methods Mol. Biol. 356*, 209–20.

(17) Los, G. V., Encell, L. P., McDougall, M. G., Hartzell, D. D., Karassina, N., Zimprich, C., Wood, M. G., Learish, R., Ohana, R. F., Urh, M., Simpson, D., Mendez, J., Zimmerman, K., Otto, P., Vidugiris, G., Zhu, J., Darzins, A., Klaubert, D. H., Bulleit, R. F., and Wood, K. V. (2008) HaloTag: a novel protein labeling technology for cell imaging and protein analysis. *ACS Chem. Biol. 3*, 373–82.

(18) Los, G. V., and Wood, K. (2007) The HaloTag: a novel technology for cell imaging and protein analysis. *Methods Mol. Biol. 356*, 195–208.

(19) Zhang, Y., So, M. K., Loening, A. M., Yao, H., Gambhir, S. S., and Rao, J. (2006) HaloTag protein-mediated site-specific conjugation of bioluminescent proteins to quantum dots. *Angew. Chem., Int. Ed. 45*, 4936–40.

(20) Adams, S. R., Campbell, R. E., Gross, L. A., Martin, B. R., Walkup, G. K., Yao, Y., Llopis, J., and Tsien, R. Y. (2002) New biarsenical ligands and tetracysteine motifs for protein labeling in vitro and in vivo: synthesis and biological applications. *J. Am. Chem. Soc. 124*, 6063–76.

(21) Adams, S. R., and Tsien, R. Y. (2008) Preparation of the membrane-permeant biarsenicals FlAsH-EDT2 and ReAsH-EDT2 for fluorescent labeling of tetracysteine-tagged proteins. *Nat. Protoc. 3*, 1527–34.

(22) Chen, B., Cao, H., Yan, P., Mayer, M. U., and Squier, T. C. (2007) Identification of an orthogonal peptide binding motif for biarsenical multiuse affinity probes. *Bioconjugate Chem. 18*, 1259–65.

(23) Martin, L. J., Hahnke, M. J., Nitz, M., Wohnert, J., Silvaggi, N. R., Allen, K. N., Schwalbe, H., and Imperiali, B. (2007) Double-lanthanide-binding tags: design, photophysical properties, and NMR applications. *J. Am. Chem. Soc. 129*, 7106–13.

(24) Nitz, M., Franz, K. J., Maglathlin, R. L., and Imperiali, B. (2003) A powerful combinatorial screen to identify high-affinity terbium(III)-binding peptides. *Chembiochem 4*, 272–6.

(25) Reynolds, A. M., Sculimbrene, B. R., and Imperiali, B. (2008) Lanthanide-binding tags with unnatural amino acids: sensitizing Tb^{3+} and Eu^{3+} luminescence at longer wavelengths. *Bioconjugate Chem. 19*, 588–91.

(26) Sculimbrene, B. R., and Imperiali, B. (2006) Lanthanide-binding tags as luminescent probes for studying protein interactions. *J. Am. Chem. Soc. 128*, 7346–52.

(27) So, M. K., Yao, H., and Rao, J. (2008) HaloTag protein-mediated specific labeling of living cells with quantum dots. *Biochem. Biophys. Res. Commun. 374*, 419–23.

(28) Wohnert, J., Franz, K. J., Nitz, M., Imperiali, B., and Schwalbe, H. (2003) Protein alignment by a coexpressed lanthanide-binding tag for the measurement of residual dipolar couplings. *J. Am. Chem. Soc. 125*, 13338–9.

(29) Lin, M. Z., Glenn, J. S., and Tsien, R. Y. (2008) A drug-controllable tag for visualizing newly synthesized proteins in cells and whole animals. *Proc. Natl. Acad. Sci. U.S.A. 105*, 7744–9.

(30) Tan, L. P., Chen, G. Y., and Yao, S. Q. (2004) Expanding the scope of site-specific protein biotinylation strategies using small molecules. *Bioorg. Med. Chem. Lett. 14*, 5735–8.

(31) Tan, L. P., Lue, R. Y., Chen, G. Y., and Yao, S. Q. (2004) Improving the intein-mediated, site-specific protein biotinylation strategies both in vitro and in vivo. *Bioorg. Med. Chem. Lett. 14*, 6067–70.

(32) Wood, R. J., Pascoe, D. D., Brown, Z. K., Medlicott, E. M., Kriek, M., Neylon, C., and Roach, P. L. (2004) Optimized conjugation of a fluorescent label to proteins via intein-mediated activation and ligation. *Bioconjugate Chem. 15*, 366–72.

(33) Lue, R. Y., Chen, G. Y., Hu, Y., Zhu, Q., and Yao, S. Q. (2004) Versatile protein biotinylation strategies for potential high-throughput proteomics. *J. Am. Chem. Soc. 126*, 1055–62.

(34) Lesaicherre, M. L., Lue, R. Y., Chen, G. Y., Zhu, Q., and Yao, S. Q. (2002) Intein-mediated biotinylation of proteins and its application in a protein microarray. *J. Am. Chem. Soc. 124*, 8768–9.

(35) Inard, C., Fourcade, E., Baron, R., Tovar, D., Chaisemartin, L., Blonski, C., and Faye, J. C. (2006) Syntheses of functionalized biotin N-1′ derivatives: new tools for the control of gene expression with small molecules. *Bioconjugate Chem. 17*, 1030–5.

(36) Lee, J. W., and L. Fuchs, P. L. (1999) Reduction of Azides to Primary Amines in Substrates Bearing Labile Ester Functionality. Synthesis of a PEG-Solubilized, "Y"-Shaped Iminodiacetic Acid Reagent for Preparation of Folate-Tethered Drugs. *Org. Lett. 1*, 179–182.

(37) Schwabacher, A. W., Lane, J. W., Schiesher, M. W., Leigh, K. M., and Johnson, C. W. (1998) Desymmetrization Reactions: Efficient Preparation of Unsymmetrically Substituted Linker Molecules. *J. Org. Chem. 63*, 1727–1729.

(38) MRC Centre for Protein Engineering, [http://www.mrc-cpe.cam.ac.uk/]. Accessed April 1999.

(39) Goffinet, M., Chinestra, P., Lajoie-Mazenc, I., Medale-Giamarchi, C., Favre, G., and Faye, J. C. (2008) Identification of a GTP-bound Rho specific scFv molecular sensor by phage display selection. *BMC Biotechnol. 8*, 34.

(40) Cui, C., Zhao, W., Chen, J., Wang, J., and Li, Q. (2006) Elimination of in vivo cleavage between target protein and intein in the intein-mediated protein purification systems. *Protein Expr. Purif. 50*, 74–81.

(41) Lajoie-Mazenc, I., Tovar, D., Penary, M., Lortal, B., Allart, S., Favard, C., Brihoum, M., Pradines, A., and Favre, G. (2007) MAP1A light chain-2 interacts with GTP-RHOB to control EGF-dependent EGF-R signaling. *J. Biol. Chem. 283*, 4155–64.

(42) Bucourt, R., Vignau, M., and Torelli, V. (1978) New biospecific adsorbents for the purification of estradiol receptor. *J. Biol. Chem. 253*, 8221–8.

(43) Xu, M. Q., and Evans, T. C., Jr. (2001) Intein-mediated ligation and cyclization of expressed proteins. *Methods 24*, 257–77.

(44) Tolbert, T., and Wong, C. H. (2000) Intein-Mediated Synthesis of Proteins Containing Carbohydrates and Other Molecular Probes. *J. Am. Chem. Soc. 122*, 5421–5428.

BC800272R

Spacer Site Modifications for the Improvement of the *in Vitro* and *in Vivo* Binding Properties of ^{99m}Tc-N_3S-X-Bombesin[2−14] Derivatives

Eirini A. Fragogeorgi,[†] Christos Zikos,[†,‡] Eleni Gourni,[†] Penelope Bouziotis,[†] Maria Paravatou-Petsotas,[†] George Loudos,[§] Nikolaos Mitsokapas,[†] Stavros Xanthopoulos,[†] Mary Mavri-Vavayanni,[||] Evangelia Livaniou,[†] Alexandra D. Varvarigou,[†] and Spyridon C. Archimandritis*,[†]

Institute of Radioisotopes-Radiodiagnostic Products, National Center for Scientific Research "Demokritos", 15310 Aghia Paraskevi, Athens, Greece, Biomedica Life Sciences S.A. 15231, Athens, Greece, Technological Educational Institute of Athens, Athens, Greece, and Ethnikon kai Kapodistriakon Panepistimion Athinon, Greece. Received October 31, 2008; Revised Manuscript Received February 25, 2009

It has been shown that gastrin releasing peptide receptors (GRPRs) are overexpressed in various types of cancer cells. Bombesin is an analogue of the mammalian GRP that binds with high specificity and affinity to GRPRs. Significant research efforts have been lately devoted to the design of radiolabeled 8 or 14 aminoacid bombesin (BN) peptides for the detection (either with gamma or positron emitting radionuclides) and therapy (with β^- emitting radionuclides) of cancer. The specific aim of the present study was to further investigate the radiolabeled peptide structure and to determine whether the total absence of a linker or the use of a basic diverse amino acid linker could influence the biodistribution profile of the new compounds for specific targeting of human prostate cancer. Thus, two new derivatives with the structure Gly-Gly-Cys-X-BN[2−14], where linker X is either zero (I) or Orn-Orn-Orn (Orn: ornithine) (II) were designed and synthesized. The corresponding ^{99m}Tc-BN derivatives were obtained with high radiochemical yield (>98%) and had almost identical retention times in RP-HPLC with the $^{185/187}$Re complexes, which were also characterized by ESI-MS. Metabolic stability was found to be high in human plasma, moderate in PC-3 cells, and rather low in mouse liver and kidney homogenates for both BN derivatives studied. The BN derivative without the spacer was less stable in cell culture and liver homogenates. A satisfactory binding affinity to GRPRs, in the nanomolar range, was obtained for both BN derivatives as well as for their Re complexes, with BN (II) demonstrating the highest one. *In vitro* internalization/externalization assays indicated that ∼6% of BN (I) and ∼25% of BN (II) were internalized into PC-3 cells. *In vivo* evaluation in normal Swiss mice and in tumor bearing SCID mice showed that BN (II) presented higher tumor and pancreas uptake than BN (I). Small animal SPECT dynamic imaging, carried out after an injection of BN (II) in mice bearing PC-3 tumors, resulted in PC-3 tumor delineation with low background activity. Overall, this study performed for two new N_3S-X-BN[2−14] derivatives indicated that hydrophilicity and charge strongly affected the *in vitro* and *in vivo* binding properties and the biodistribution pattern. This finding is confirmed by SPECT imaging of BN (II), which is under further *in vivo* evaluation for detecting cancer-positive GRPRs.

INTRODUCTION

Bombesin, BN, is an active 14-amino acid neuropeptide (pGlu[1]-Gln[2]-Arg[3]-Leu[4]-Gly[5]-Asn[6]-Gln[7]-Trp[8]-Ala[9]-Val[10]-Gly[11]-His[12]-Leu[13]-Met[14]) originally isolated from the skin of the European frog *Bombina bombina* (*1*). Four bombesin receptors, for bombesin and its derivatives belonging to the G-protein receptor superfamily, have been cloned: NMB- receptor (NMBr or BB1), GRP receptor (GRPR or BB2), BN receptor (BRSr or BB3 or orphan), and BN receptor subtype 4 (BB4) (*2, 3*).

The bombesin mammalian counterpart, named gastrin-releasing peptide, GRP, is a 27-amino acid peptide sharing the same C-terminal heptapeptide with bombesin. This C-terminal BN 7−14 amino acid sequence (Gln[7]-Trp[8]-Ala[9]-Val[10]-Gly[11]-His[12]-Leu[13]-Met[14]) is considered to be essential for peptide biological activity and receptor binding affinity. Consequently, GRP and BN have essentially identical physiologic action (*4, 5*). The GRP receptor is widely expressed not only in the central nervous system and the gastrointestinal and respiratory tracts, where important physiologic functions take place, but is also found aberrantly in human malignancies including prostate, pancreatic, lung, breast, gastrointestinal, and colorectal carcinomas as well as in small cell lung cancer (*6, 7*). This overexpression in various neoplasias in reference to normal tissues, combined with the ability of GRPR agonists to be internalized, has led to the development of BN-based radiopharmaceuticals (*8*). In the majority of the studies, BN[7−14], which serves as a highly specific GRP-receptor binding motif, has been selected and radiolabeled with a variety of SPECT, PET, and therapeutical radionuclides (*9*). Most radiolabeled, BN-like peptides with substitutions or deletions at the 7−14 amino acid sequence (important for conferring agonistic or antagonistic properties) are N-terminally attached via various spacer arms or linkers to the radioisotope-chelating moiety.

Several peptide structures that provide stable ^{99m}Tc complexes attached on the N-terminal region of BN derivatives have been investigated. Garcia Garayoa et al. (*10−12*) reported the design and development of organometallic Re/^{99m}Tc$(CO)_3^{(I)}$ BN analogues by introducing non-natural amino acids and different spacers in the BN (7−14) sequence. It was concluded by the above study that the insertion of spacers had a clear influence on peptide uptake both in healthy organs and in tumors, leaving

* To whom correspondence should be addressed. Tel: +30(210) 6503685. Fax: +30(210) 6522661. E-mail: sarxim@rrp.demokritos.gr.
[†] National Center for Scientific Research "Demokritos".
[‡] Biomedica Life Sciences S.A. 15231.
[§] Technological Educational Institute of Athens.
[||] Ethnikon kai Kapodistriakon Panepistimion Athinon.

10.1021/bc800475k CCC: $40.75 © 2009 American Chemical Society
Published on Web 04/03/2009

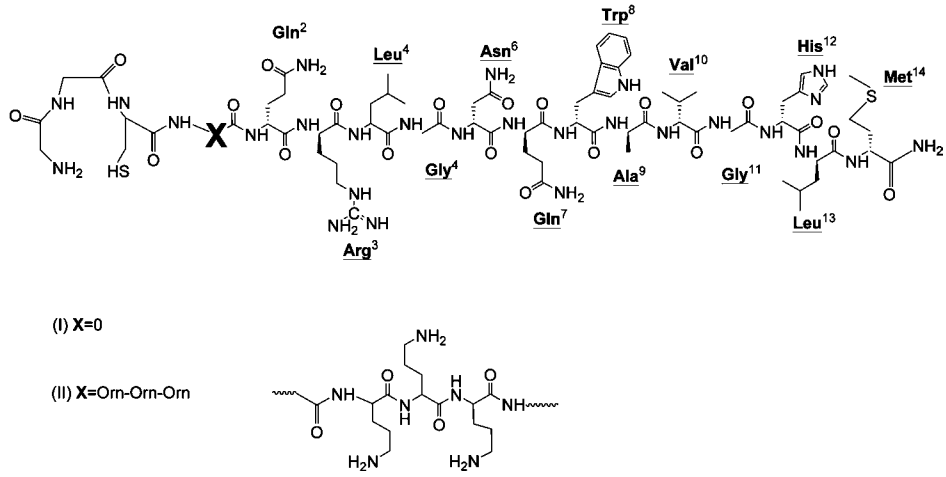

Figure 1. Structure and amino acid sequences of N_3S-X-BN[2−14] derivatives. BN(I): X = 0 (no spacer). BN(II): X = Orn-Orn-Orn.

the stability or receptor affinity unaffected. Smith et al. have studied ^{99m}Tc-complexes containing N_3S (*13*), tricarbonyl (*14, 15*), pyrazolyl (*16*), and "4 + 1" mixed ligand systems (*17*), N-terminally conjugated to BN(7−14) either directly or via spacer groups such as β-Ala, 5-Ava, 8-Aoc, 11-Aun, SSS, GGG, GSG, NNN, NNN-β-Ala, NNN-5-Ava, RRR, RRR- β-Ala, and RRR-5-Ava. Apart from ^{99m}Tc, which is among the most preferred radionuclides for imaging of the GRPR, for the design of BN-based radiopharmaceuticals labeled either with diagnostic [^{64}Cu (*18*−*21*), ^{68}Ga (*22*), ^{18}F (*23*), and ^{111}In (*24, 25*)] or therapeutic radioisotopes (^{64}Cu, ^{149}Pm, ^{153}Sm, ^{177}Lu, ^{90}Y, ^{111}In, and ^{188}Re) (*26*−*30*), BN structural modifications were also tried by the insertion of aliphatic, aminoacid, poly(ethyleneglycol), ether, and aromatic linking moieties. The main goal of all these efforts was to evaluate to what extent the length and the structure of the spacer or linking group would influence radiochemistry, metabolic stability, GRPR binding affinity, residualization of radioactivity in cancer cells, and pharmacokinetics of the labeled derivatives.

A traditional approach for radiolabeling BN derivatives with ^{99m}Tc is via stabilization of the $Tc^{(V)}O^{3+}$ metal core with ligands of the so-called N_3S type (*31*−*33*). Recently, our group (*34*) has focused on the design of BN derivatives in which the chelating moiety comprised a combination of amino acids X-Gly-Cys, where (X = Gly, methylglycine, dimethylglycine, and mercaptoacetic acid) N-terminally conjugated to the almost full length BN peptide, BN[2−14], through the hydrocarbon spacer arm Aca (6-aminohexanoic acid). A further comparative *in vivo* investigation (*35*) between the most promising derivative Gly-Gly-Cys-Aca-BN[2−14], resulting from the above study, and Gly-Gly-Cys-Aca-BN[7−14] showed that peptide chain length influenced the biodistribution of ^{99m}Tc-labeled derivatives. Taking into consideration the non-negligible liver uptake obtained with the peptides containing the six-carbon spacer, we further focused on the design of two novel BN[2−14]NH_2-like peptides. More specifically, the aliphatic spacer Aca was either eliminated or replaced by the non-natural basic amino acid sequence Orn-Orn-Orn (Orn = ornithine) (Figure 1). Previous studies of radiolabeled BN derivatives containing 3-, 5-, 8-, or 11-carbon spacers between the peptide and the chelator demonstrated that shortening the linker length liver uptake was reduced and pancreas was increased in nontumor bearing mice (*13*). Such considerations, together with an effort to make a full structure−activity relationship study, led us to the selection of a zero spacer in the case of BN (I) and of a more polar, charged linker in the case of BN (II). To the best of our knowledge, there are no other studies that have evaluated radiolabeled BN derivatives consisting of the BN[2−14] sequence conjugated to an N_3S chelator via no spacer or via a spacer containing the triaminoacid sequence of ornithines. The choice of three Orn as a spacer was made because we wanted to maximize the effect of the charge and thus to investigate whether, with the introduction of this polar linker in reference to no spacer, the hydrophilic character of the final compound dictates the biodistribution profile.

In the frame of the present study, the new BN derivatives were complexed with both ^{99m}Tc and $^{185/187}$Re(V) gluconate precursors. The nonradioactive rhenium complexes were characterized by liquid chromatography−electrospray ionization mass spectrometry (ESI-MS). Radiochemical identification, metabolic stability studies, *in vitro* assays including binding affinity, internalization/efflux studies as well as *in vivo* evaluation in normal Swiss mice and tumor (human prostate PC-3) bearing SCID mice are reported. The aim was to examine whether the modification of the spacer affected stability, affinity, lipophilicity, and the overall charge of the resulting ^{99m}Tc-BN derivatives and as a consequence the influence these changes exert on the *in vivo* profile of the resulting radiolabeled species.

EXPERIMENTAL PROCEDURES

Materials. The Fmoc-protected amino acids were purchased from the Chemical and Biopharmaceutical Laboratories (Patras, Greece), while the polystyrene resin was commercially available from Nova Biochem. Electrospray mass spectrum analyses were performed in the Mass Spectrometry and Dioxin Analysis Laboratory of NCSR "Demokritos". ^{99m}Tc, obtained in physiological saline as $Na^{99m}TcO_4$, was eluted from a commercial ^{99}Mo/^{99m}Tc generator (Mallinckrodt Medical, Petten, The Netherlands). The human prostate adenocarcinoma cell line was obtained from the American Type Culture Collection (ATCC). The product [^{125}I-Tyr^4]BN was purchased from Perkin-Elmer (Life Science Products, Boston MA, USA, Inc.; specific activity, 81.4 TBq/mmol, 10 μCi). Biodistribution studies were performed using female normal Swiss and SCID (severely compromised immunodeficient) mice (15−25 g) of the same colony and age, purchased from the Breeding Facilities of NCSR Demokritos. Reagents and media for cell culture were purchased from PAA Laboratories GmbH (Austria), and all other chemicals from Merck (Whitehouse Station, NJ 08889-0100 USA).

Instrumentation. Analytical reverse phase high performance liquid chromatography (RP-HPLCs) were performed on a Waters HPLC system (pump 616, detector 996 PDA) using a Hibar Pre-Packed Column RT 250−4, LiChrospher 100 RP-18 (5 μm) (250 mm, ID 4 mm, Merck). Semipreparative RP-HPLC was performed on a Waters (Milford, MA, USA) HPLC system

(pump 600E, detector UV-484). A 10 Nucleosil 7 C18 column [250 × 12.7 mm ID; Macherey-Nagel (Dueren, Germany)] was used. For (ESI-MS) mass spectral analysis, the test solution in 50% aqueous acetonitrile was infused into an electrospray interface mass spectrometer (AQA Navigator, Finnigan) at a flow rate of 0.1 mL/min, using a Harvant Syringe pump. Negative or positive ion ESI spectra were acquired by adjusting the needle and cone voltages accordingly. Hot nitrogen gas (Dominic-Hunter UHPLCMS-10) was used for desolvation at 170 °C. Instant thin layer chromatography (ITLC) measurements were made by electronic autoradiography (Instant Imager Packard-Canberra). Gamma decay detection of ^{125}I for the *in vitro* cell binding studies was performed on a γ counter (Model LB2111, Berthold detection system, Bad Wildbad, Germany). For internalization, efflux, and *in vivo* studies a multisample γ-counter system Packard Minaxi 5500 equipped with a 3″ NaI (Tl) crystal was used. Scintigraphic images were acquired on a pair of two square H8500 flat-panel PSPMT gently coupled to a NaI(Tl) crystal array (Bicron-St. Gobain), equipped with a parallel-hole lead collimator.

Solid Phase Peptide Synthesis. The BN derivatives were synthesized manually on a Rink-amide resin employing the Fmoc strategy as follows: Briefly, for coupling, an excess of Fmoc-protected amino acid and HOB*t* were dissolved in *N*,*N*′-dimethylformamide (DMF). The solution was cooled in ice, and then *N*,*N*′-diisopropylcarbodiimide (DIPC) was added. The reaction mixture was initially left for 10 min on ice, then for another 10 min at room temperature, and was finally added to the resin. The coupling efficiency was monitored by the Kaiser ninhydrin test (*36*). Removal of the N-terminal Fmoc group was achieved by repetitive treatment with 20% piperidine in DMF. The final product was cleaved from the resin using a cocktail of trifluoroacetic acid (TFA), thioanisol, ethanediol, phenol, H_2O, and triisopropylsilane (81.5/5/2.5/5/5/1, v/v/v/v/v/v). The crude product, obtained by precipitation with cold diethylether, was purified by semipreparative RP-HPLC. Elution was performed with a solvent system consisting of 0.05% TFA in water (solvent A) and 60% CH_3CN in solvent A (solvent B), by applying a linear gradient from 100% to 20% A in 47 min for BN (I) or from 100% to 50% A in 47 min for BN (II). The flow rate was 4.5 mL/min, and the peptide peaks were detected with a UV detector at 220 nm.

Conjugation of $^{185/187}$Re$^{(V)}$O-N$_3$S-BN Derivatives (Non-radioactive Complexes). Rhenium$^{(V)}$ oxo complexes of BN derivatives were prepared by ligand exchange reactions, starting from the preformed Re$^{(V)}$O gluconate precursor (*37*). An aqueous solution of both crude BN derivatives (10 and 20 mg, respectively) and a Re$^{(V)}$O gluconate solution were allowed to react at 60 °C for 2 h. The crude products were purified by semipreparative RP-HPLC. Elution was performed with a solvent system consisting of 0.05% TFA in water (solvent A) and 60% CH_3CN in solvent A (solvent B), by applying a linear gradient from 100% to 20% solvent A in 47 min for BN (I) and from 100% to 50% solvent A in 47 min for BN (II). The flow rate was 4 mL/min, and the peptide peaks were detected with a UV detector at 220 nm. The new Rhenium$^{(V)}$ oxo complexes of the BN derivatives were characterized by ESI-MS and RP-HPLC.

Conjugation of ^{99m}Tc$^{(V)}$O-N$_3$S-BN Derivatives (Radioactive Complexes). Radiolabeling of the BN derivatives was performed by radioisotope exchange from a ^{99m}Tc$^{(V)}$O gluconate precursor, (sodium gluconate being used as an intermediate exchange ligand for ^{99m}Tc, with stannous chloride as the reducing agent) (*38*). Thus, a solid mixture containing 1 g of sodium gluconate ($C_6H_{11}NaO_7$), 2 g of sodium bicarbonate ($NaHCO_3$), and 15 mg of stannous chloride ($SnCl_2$) was homogenized and kept dry. Three milligrams of the above mixture was dissolved in 1 mL of a sodium pertechnetate solution ($Na^{99m}TcO_4$), containing 370−555 MBq (10−15 mCi) of ^{99m}Tc. An aliquot of 200 μL of the above solution was added to 100 μL of an aqueous solution (pH 1−2) containing 75 ng of each BN derivative. The mixture (pH 6−7) was homogenized by vortexing and allowed to react at 37 °C for 20 min.

Radiochemical Analysis. The labeling efficiency of the radiolabeled products was followed for up to 6 h postlabeling and determined by analytical RP-HPLC. Elution was performed with a solvent system consisting of 0.1% TFA in water (solvent A) and 0.1% TFA in methanol (solvent B), by applying the following gradient: from 0% to 80% solvent B (1−20 min), 80% solvent B (20−23 min), 80% to 0% solvent B (23−25 min), and 0% solvent B (25−30 min) at a flow rate of 1 mL/min. The eluent was passed through a UV detector at 220 nm and through a sodium iodide scintillation detector, both connected to a computer for data analysis and storage.

The ^{99m}Tc$^{(V)}$O gluconate precursor and radioactive BN derivatives were also analyzed by ITLC on Silica Gel (ITLC-SG) strips. Briefly, 5 μL of the reaction mixtures were applied on two different strips (13 cm × 1 cm) of SG paper (application point: 2 cm from the bottom). The radiochromatographs were developed in saline (0.9% NaCl) and methylethyketone (MEK), respectively, over a distance of 10 cm. After drying, the radioactivity of the strips was measured by electronic autoradiography. When normal saline was used, the radioactive complexes migrated with the solvent front, while using MEK they remained at the application point.

Lipophilicity: log *D* Values. To a solution containing 500 μL of *n*-octanol and 500 μL of phosphate-buffered saline (PBS, pH 7.4), 10 μL of each radiolabeled BN derivative was added. The resulting solution was vortexed and centrifuged at 810*g* at 4 °C for 10 min. An aliquot of both saline and octanol layers was collected, and the activity was measured in a γ-counter. The log *D* value was calculated as the log ratio of the radioactivity in the organic and aqueous phases (mean of three samples).

Cell Culture. Human androgen-independent prostate cancer cells (PC-3) were grown in DMEM Glutamax-I, supplemented with 10% (v/v) fetal bovine serum (FBS), 1% L-glutamine, and 1% penicillin/streptomycin. Cells were incubated in a controlled humidified atmosphere containing 5% CO_2 at 37 °C and were subcultured weekly after being detached from the flask surface by trypsin/EDTA solution (0.25%).

Metabolic Stability. *(I) Human Plasma and PC-3 Cell Culture.* The metabolic stability of the radiolabeled BN derivatives was studied in human plasma as well as in PC-3 cell culture. A blood sample from healthy donors in heparinized polypropylene tubes was immediately centrifuged at 2240*g* at 4 °C for 10 min, and the supernatant (plasma) was collected. One hundred microliters (3.7−7.4 MBq or 100−200 μCi) of each radiolabeled BN derivative was incubated with 900 μL of plasma at 37 °C. Fractions were withdrawn at 5, 15, 30, and 120 min, treated with ethanol (2:1 EtOH/aliquot, v/v) (*39*), centrifuged at 16 000*g* at 4 °C for 20 min, filtered through a Millipore GV (0.22 μm) filter, and analyzed by RP-HPLC as described above. *In vitro* degradation in cell culture was studied by incubation of 450 μL of a PC-3 cell suspension (2−2.5 × 10^6/mL) with 50 μL (3.7−7.4 MBq or 100−200 μCi) of each radiolabeled BN derivative at 37 °C. After incubation, fractions were withdrawn at 5, 15, and 30 min and treated with 1:1 acetonitrile/ethanol containing TFA (0.01%) (3:1 CH_3CN/EtOH/aliquot, v/v) (*10*). The mixture was centrifuged at 16 000*g* at 4 °C for 20 min, filtered, and analyzed by RP-HPLC.

(II) Kidney and Liver Homogenates. The metabolic stability was evaluated by incubation of each radiolabeled BN derivative in homogenized mouse liver and kidney samples at 37 °C. Liver

or kidneys were extracted from mice, rapidly rinsed with cold water, and immersed in 500 μL of chilled 50 mM Tris/0.2 M sucrose buffer, pH 7.4, where they were homogenized. Aliquots of 50 μL of each radiolabeled BN derivative (3.7−7.4 MBq or 100−200 μCi) were added to ca. 450 μL of tissue homogenates, containing the same amount of protein as this was determined by a colorimetric method using a BCA protein assay reagent (Pierce, Rockford, IL). Fractions withdrawn at 5 and 15 min were treated with ethanol (2:1 EtOH/aliquot, v/v) (*40*), centrifuged at 16 000*g* at 4 °C for 20 min, filtered through Millipore GV (0.22 μm) filter, and analyzed by RP-HPLC.

In Vitro Cell Binding Studies. The IC_{50} values of the new BN derivatives were assessed by a competitive cell binding assay utilizing [^{125}I-Tyr^4]BN as the GRPR specific radioligand and [Tyr^4]BN as a control compound. PC-3 cells suspended in a medium containing 1% FBS, 0.125% BSA, 0.25 mM PMSF, 1 μg/mL aprotinin, and 50 μg/L bacitracin were distributed in 24-well plates and incubated at 37 °C for 1 h in the presence of 25 000 cpm ^{125}I-[Tyr^4]BN (2200 Ci/mmol) and increasing concentrations of each BN derivative or its complex with nonradioactive $^{185/187}$Re, ranging from 10^{-12} to 10^{-6} M. In this assay, [Tyr^4]BN was used as the control peptide. After incubation, the cells were washed twice with cold wash buffer and lysed with 1 N NaOH. Radioactivity bound to the cells was counted in a γ-counter. IC_{50} values were calculated by nonlinear regression analysis, using the GraphPad Software (San Diego, CA, USA) Prism 4 computer fitting program. Experiments were carried out three times in duplicate.

Internalization and Efflux Analysis. For the *in vitro* internalization analyses, PC-3 cells were distributed in six-well plates (1−1.5 × 10^6 cells per well) at 37 °C in 5%CO_2/air atmosphere overnight in culture medium (DMEM with 10% FBS, L-glutamine, and 1% penicillin/streptomycin). On the day of the experiment, the medium was removed, and the cells were washed twice with cold wash buffer and were incubated in 1.2 mL of internalization medium (DMEM containing 1% FBS) in the presence of 100 000−300 000 cpm of each radiolabeled BN derivative (in 150 μL of 0.5% BSA/PBS buffer corresponding to ∼200 fmol of total peptide) at 37 °C for 5, 15, 30, 60, 90, and 120 min. Specificity of internalization was evaluated in the presence of 1 μM unlabeled native BN. Upon completion of the incubation, cells were washed twice with cold PBS to discard unbound peptide. Surface bound activity was removed by washing the cells twice for 5 min each time with an acid wash (50 mM glycine−HCl/0.1 M NaCl buffer, pH 2.8). The amount of internalized peptides was recovered by solubilizing the cells with 1 N NaOH at 37 °C. The internalized radioactivity (% of total added) was determined using a multisample γ-counter system.

Externalization studies of the maximum internalized radioactivity were also performed after a 30 min internalization period. The medium was discarded, and the cells were washed three times with cold buffer. New medium was added, and the cells were incubated at 37 °C. Sampling at 0, 15, 30, 60, and 90 min postinternalization was performed by an initial cold buffer wash of the cells, followed by acid wash (for removal of surface bound activity), as previously described, and finally by treatment with 1 N NaOH to extract the radioactivity remaining trapped. Results are expressed as the percentage of total bound activity for each time point. Internalized and remaining radioactivity were calculated as a function of time by using a Microsoft Excel program.

Biodistribution Analysis in Normal Swiss Mice. The *in vivo* behavior was studied in normal female Swiss mice (average weight 20 ± 2 g) by injecting 100 μL (50−75 ng/100 μL) (5.5 MBq or ∼0.15 mCi) of each radiolabeled BN derivative, diluted in saline (pH 7.0), via the tail vein. Animals were sacrificed at predetermined time intervals of 15, 30, 60, and 120 min postinjection (p.i.), and the main organs were removed, weighed, and counted, together with samples of blood, muscle, and urine, in a γ-counter system. In comparison to a standard of the injected solution, results were expressed as a percentage of the injected dose (%ID) per organ and per gram of each organ or tissue. For total blood radioactivity calculation, blood is assumed to be 7% of the total body weight. Receptor blocking studies were also carried out with coadministration of an excess amount (100 μL, 1 mg/mL) of native BN. Animals were sacrificed 30 min postinjection, and the tissues were removed, weighed, and counted as previously described. *In vivo* studies were performed in compliance with the European legislation for animal welfare. All animal protocols have been approved by the Hellenic Authorities.

Biodistribution Analysis in PC-3 Tumor Bearing SCID Mice. For the implantation of tumors, PC-3 cells freshly suspended in medium were subcutaneously injected in the left front flank at a concentration of 10^7 cells/animal. Tumors were allowed to grow for two to three weeks. Animals were fed with autoclaved rodent food and water *ad libitum* before and during the time of tumor growth. On the day of assay, the mice were injected via the tail vein with 100 μL of a solution of each radiolabeled BN derivative in saline, pH 7.0 (7.4 MBq or ∼0.2 mCi corresponding to 100−125 ng of total peptide), and were sacrificed at 30 and 60 min p.i. [BN (I)] and at 30, 60, and 120 min p.i. [BN (II)]. For the determination of nonspecific uptake, blocking experiments were performed, in which three mice received excess amounts of native BN (100 μL, 1 mg/mL) along with the radiolabeled BN derivatives and sacrificed at 30 min postinjection.

Dynamic γ-Camera Imaging. Evaluation of the novel SPECT radiolabeled BN derivatives was performed by dynamic imaging studies using a high resolution dedicated small animal γ-camera. Tumor-bearing mice were anaesthetized with 100 μL of 10% xylazine and 5% ketamine, 10 mg/kg mouse body weight prior to scanning, and positioned to the animal bed. One hundred microliters of approximately 7.4 MBq (∼0.2 mCi) of BN (II) was administered through the tail-vein prior to anesthesia. These imaging studies of 10 min per frame were performed up to 120 min p.i.

Statistical Analysis. All data are expressed as the mean of values ± standard deviation (mean ± SD). Data comparison was performed by using Student's *t*-test. $P < 0.05$ was considered significantly different.

RESULTS

Synthesis and Characterization. Synthesis of the two new BN derivatives was performed following an Fmoc-based SPPS protocol. The BN derivative without spacer [BN (I)] was obtained at a yield of about 40%. The introduction of the spacer Orn-Orn-Orn [BN (II)] led to a significant reduction in the yield. Thus, <10% of [BN (II)] was obtained. The chemical purity was higher than 95% for both derivatives, as determined by analytical RP-HPLC. Both derivatives were characterized with MS-ESI (Table 1).

Conjugation of $^{185/187}$Re$^{(V)}$O-N$_3$S-BN Derivatives (Nonradioactive Complexes). The nonradioactive complexes of the two new crude BN derivatives obtained after the exchange ligand reaction were purified by semipreparative RP-HPLC and characterized by analytical RP-HPLC and ESI-MS (Table 1). The retention times of the $^{185/187}$Re-$^{(V)}$ON$_3$S-BN derivatives, compared to those of the respective radioactive complexes, were similar after their co-injection into RP-HPLC, confirming that $^{185/187}$Re and ^{99m}Tc form complexes of similar structure (Table 2).

Table 1. Mass Spectra Analysis of the Pure BN Derivatives and of Their Complexes with Nonradioactive $^{185/187}$Re

N_3S-**X**-BN[2−14] derivative	molecular mass (calcd.) (Da)	molecular mass (found) (Da)
(I)	1725.9	1725.8 (*m/z*: 863.9, $[M + 2H]^{2+}$)
(II)	2068.4	2068.8 (*m/z*: 690.6, 1035.4 $[M + 3H]^{3+}$, $[M + 2H]^{2+}$)
$^{185/187}Re^{(V)}ON_3S$-**X**-BN[2−14] derivative	molecular mass (calcd.) (Da)	molecular mass (found) (Da)
(I)	1924.9	1925.6 (*m/z*: 963.8, $[M + 2H]^{2+}$)
(II)	2267.6	2268.0 (*m/z*: 757.0, 1135.0 $[M + 3H]^{3+}$, $[M + 2H]^{2+}$)

Table 2. Analytical Data of N_3S-X-BN[2−14] and log $D_{(O/W)}$ for Their ^{99m}Tc Derivatives[a]

$^{185/187}Re^{(V)}ON_3S$-**X**-BN[2−14] derivative	R_T[b] (min)	$^{99m}Tc^{(V)}ON_3S$-**X**-BN[2−14] derivative	R_T[b] (min)	log $D_{(o/w)}$[c] ± SD
(I)	15.8	(I)	16.1	−1.60 ± 0.03[d]
(II)	13.9	(II)	14.2	−1.72 ± 0.03[d]

[a] Elution system: flow 1 mL/min; A, 0.1% TFA/H_20; B, 0.1% TFA/MeOH. [b] R_T: retention time. [c] log $D_{(o/w)}$ partition coefficient between *n*-octanol and PBS (pH 7.4). [d] Significant differences ($p < 0.05$) between BN derivatives (I) and (II).

Radiolabeling−Radiochemical Analysis. Radiolabeling of the two new BN derivatives with ^{99m}Tc was performed by the preconjugation approach using the $Tc^{(V)}O$ gluconate precursor as an intermediate exchange ligand. A two-strip ITLC-SG method for the analysis of a precursor showed that no amount of either pertechnetate $^{99m}TcO_4$ or of colloidal ^{99m}Tc was present. The radiochemical yield for both BN derivatives was higher than 98%, providing a single radioactive species, as detected by both RP-HPLC and paper chromatography (ITLC-SG). The stability of the new derivatives, tested up to 6.0 h postlabeling, remained high (>90%). The RP-HPLC retention time of BN (I) was 16.1 min, whereas that of BN (II) was lower, 14.2 min, indicative of its higher hydrophilic nature (Table 2). The lipophilicity of the two radiolabeled BN derivatives under study was evaluated by determining the log *D* partition coefficient values between *n*-octanol to PBS, at pH 7.4 (Table 2).

Metabolic Stability. *(I) Human Plasma and PC-3 Cell Culture.* The rate of catabolism of both new ^{99m}Tc-labeled BN derivatives was higher in cell culture than in human plasma. After 120 min of incubation, the radiolabeled BN derivatives remained intact in human plasma at a percentage of 60%. After 30 min of incubation with PC-3 cells, ∼30% of the radioactivity corresponded to the intact BN (I), while ∼50% of BN derivative (II) was found still intact at the same time period. Thus, the spacer group Orn-Orn-Orn did not greatly affect plasma stability, while it slightly increased cell stability.

(II) Kidney and Liver Homogenates. Enzymatic degradation tested in kidney and liver homogenates was found to occur after just 5 min of incubation. Thus, in kidney homogenates, BN derivatives (I) and (II) remained intact >40% and >45%, respectively, the rest being metabolized to more hydrophilic species of lower retention times. Further incubation for 15 min led to a percentage of 20−30% intact peptide for both BN derivatives. Catabolism in liver was much faster in the case of BN (I), which, within 5 min of incubation, was almost totally degraded, while degradation rates of BN (II) were found to be substantially slower (Figure 2).

In Vitro Cell Binding Studies. The binding affinity of N_3S-X-BN[2−14] and of their $^{185/187}$Re complexes for the GRPR was evaluated in the human prostate adenocarcinoma cell line PC-3. A typical sigmoid curve for displacement of ^{125}I-[Tyr^4]BN from PC-3 cells as a function of increasing concentration of all five different cold ligands used was obtained. The determined IC_{50} values are summarized in Table 3. BN derivative (I) (with or without Re) was less efficient in inhibiting the binding of ^{125}I-[Tyr^4]BN on PC-3 cells than [Tyr^4]BN (control). BN (II) (free of or complexed with Re) showed better affinity than BN (I).

Internalization and Efflux Analysis. The grade of uptake (internalization) and efflux (externalization) as a function of time of the two radiolabeled BN derivatives under study was assessed in human cancer PC-3 cells at 37 °C, in the presence (blocking experiments) or absence of native BN. Figure 3 reports the results of this study. Within the first 30 min of incubation, the proportion of radioactivity migrating into the cells increased significantly and remained at this level for 2 h.

More specifically, relative to the cell-associated activity after 5 min of incubation, 34% of BN (I) and 66% of BN (II) were internalized, attaining a value of 78% and 88% after 120 min, respectively. Although the membrane-bound activity was rather similar between the two radiolabeled BN derivatives, the internalized activity related to the total added substantially differed from one derivative to the other with the value for BN (II) being almost 5-fold higher than that for BN (I) (Figure 3A). To evaluate the externalization of ^{99m}Tc-conjugates from PC-3 cells after 30 min of incubation, cells were washed with acid wash buffer, for removal of surface-bound activity and then were further incubated in the medium. Measurements up to 90 min postincubation showed that around 53% of BN (I) and 63% of BN (II) remained trapped in the cells (Figure 3B).

Biodistribution Analysis in Normal Swiss Mice. Comparative *in vivo* studies in physiological experimental models at 15, 30, 60, and 120 min postinjection for both studied derivatives are summarized in Figure 4. Both ^{99m}Tc-Bombesin derivatives demonstrated fast blood clearance with the blood levels of BN (II) [0.51 ± 0.06 and 0.16 ± 0.06 (%)ID/g)] being lower than those of the BN (I) [1.00 ± 0.17 and 0.46 ± 0.05 (%)ID/g)], at 60 and 120 min p.i., respectively. Statistical evaluation (*t*-test) of the data sets of the two studied BN derivatives at 60 and 120 min demonstrated *p*-values <0.01 and <0.001. No significant uptake or retention in the stomach was observed, indicating that there is minimal, if any, release of free $^{99m}TcO_4^-$ derived from *in vivo* degradation of ^{99m}Tc of the N_3S complex. Liver activity values were relatively low, compared to the activity accumulated at the other normal tissues and seem to correlate with the log *D* values (Table 2). Similar to that in the liver, intestinal uptake was relatively low. The predominant excretion route for both studied derivatives was via the kidneys to urine. The higher kidney retention found for BN (II) is attributed to the increase of the overall positive charge of this derivative due to the presence of ornithine. The GRPR-positive pancreas also showed high uptake, significantly inhibited by the coadministration of an excess amount of blocking agent, while for BN (II), accumulation was significantly higher [27.89 ± 7.78, 16.72 ± 3.57, and 10.26 ± 1.64 (%)ID/g] at 15, 30, and 60 min p.i. as compared to [13.38 ± 3.99, 9.49 ± 3.31, and 5.20 ± 3.88 (%)ID/g] of BN (I). Statistical evaluation (*t*-test) of the data sets of the two studied BN derivatives at 15, 30, and 60 min demonstrated *p*-values <0.05.

Biodistribution Analysis in PC-3 Tumor-Bearing SCID Mice. Both ^{99m}Tc-bombesin derivatives were further tested *in vivo* in PC-3 tumor-bearing mice. The results are presented in Table 4. Tumor sizes in this study varied from 0.1 to 0.5 g. The greater portion of the ^{99m}Tc-Bombesin derivatives cleared efficiently from the bloodstream within 60 min p.i., with blood values being 0.52 ± 0.05 and 1.07 ± 0.12 (%)ID/g for radiolabeled BN (I) and BN (II) derivatives, respectively. They were mainly excreted into the urine via the kidneys. Both BN (I) and BN (II) were capable of rapidly targeting the GRP

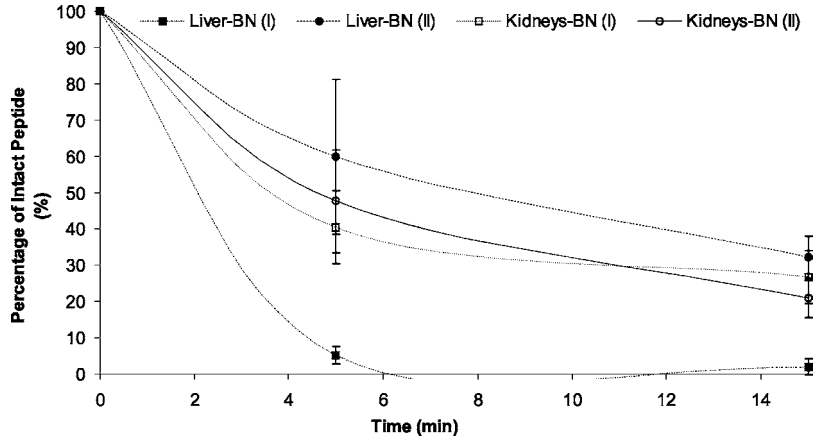

Figure 2. Degradation study of the two new $^{99m}Tc^{(V)}ON_3S$-**X**-BN[2−14] derivatives after incubation at 37 °C in liver [BN (I), ■; BN (II), ●] and kidney [BN (I), □; BN (II), ○] homogenates. Vertical bars indicate standard deviation (SD). Results are expressed as the mean of 3−5 experiments ± SD.

Table 3. IC_{50} Values of N_3S-X-BN[2−14] Derivatives and of Their Complexes with $^{185/187}Re$ Obtained by Displacement of ^{125}I-[Tyr^4]BN from PC-3 Cells

compound	IC_{50} ± SD
Tyr^4-BN (control)	1.6 ± 0.3
N_3S-X-BN[2−14] Derivatives	
(I)	3.2 ± 0.6
(II)	1.5 ± 0.2
$^{185/187}Re^{(V)}ON_3S$-**X**-BN[2−14] Derivatives	
(I)	3.0 ± 0.7
(II)	2.2 ± 0.1

receptor positive tissues, that is, the pancreas as well as the PC-3 tumor, within 30 min p.i. [(11.08 ± 2.76, 4.56 ± 0.95) (%)ID/g for BN (I) and (11.07 ± 4.2, 5.23 ± 2.10) (%)ID/g for BN (II)]. Specificity of *in vivo* delivery of the two novel BN derivatives was demonstrated with blocking by coadministration of an excess amount of the nonradiolabeled native BN at 30 min p.i.. In this case, uptake in the pancreas and PC-3 tumor was found to be significantly reduced ($p < 0.05$). Comparative studies between the radiolabeled derivatives BN (I) and BN (II) at 60 min p.i., indicated distinct differences in the uptake in both receptor-rich organs. In particular, BN (I) showed a significant reduction of accumulation in the tumor (1.02 ± 0.18%ID/g) and pancreas (4.17 ± 0.99%ID/g) related to 30 min p.i. BN (II) showed a more favorable, statistically different biodistribution ($p < 0.01$), in the tumor (7.14 ± 0.87%ID/g) and pancreas (27.59 ± 6.86%ID/g) than BN (I). Tumor-to-nontarget ratios of BN (II) were also significantly higher than those of BN (I) for the organs and tissues examined (blood, muscles, liver, and kidneys) ($p < 0.05$) at 60 min p.i. Tumor retention of BN (II) was also observed at 120 min p.i. (7.92 ± 0.79%ID/g) demonstrating even higher tumor/blood ratios than that for 60 min p.i. ($p < 0.05$). Moreover, intestinal uptake of BN (II) reached a maximum at 120 min p.i. (6.75 ± 0.91%ID/g) while liver accumulation was relatively low at the same time point (2.62 ± 0.17%ID/g).

Dynamic γ-Camera Imaging. The localization of ^{99m}Tc-labeled BN (II) in PC-3 tumor-bearing mice exhibited considerably higher tumor uptake than radiolabeled BN (I). This was further evaluated by γ-ray scintigraphy. The PC-3 tumor at the right front flank was visible with clear contrast from the adjacent background as early as 10 min after injection and remained observable up to 120 min p.i. Prominent uptake was also observed in the kidneys. Clearance of the radioactivity through the urinary bladder was evident as well (Figure 5). In contrast, the same tumor was not visualized in another SCID mouse, which had received a high dose of native BN along with the radiolabeled BN (II) derivative (Figure 6).

DISCUSSION

Much attention has been recently focused on radiolabeled BN-like peptides with different types of metal chelators, peptide sequences, and spacer groups (*9, 41*). As far as the spacer attaching the ^{99m}Tc-chelating moiety onto the peptide is concerned, this may be just an inactive moiety not affecting the properties of the parent molecule, but it may also be a pharmacokinetic modifier, able to improve stability, binding affinity, internalization into the tumor cells and biodistribution (*42*). Suitable spacer groups include peptides (amino acids linked together) alone (*18−22*), nonpeptide groups (for example a hydrocarbon chain from 3 to 9 carbon atoms) (*16, 24, 34, 35*) or a combination of an aminoacid sequence and a nonpeptide spacer (*17, 23, 25, 32*).

In the framework of the present study, the new BN derivatives were prepared by the well-established technique of solid-phase peptide synthesis (SPPS). The radiolabeling of BN derivatives was accomplished by a transchelation reaction. Prior to reaction with the selected amino acid chelator, Gly-Gly-Cys, ^{99m}Tc was reduced and complexed with the labile gluconate ligand. Nonradioactive $^{185/187}Re$ complexes of the BN derivatives, used for structural characterization, were prepared by the same method, as Re and Tc are both elements of the VIIB row of the periodic table and display the same complexation chemistry. The claim that $^{185/187}Re$- and ^{99m}Tc-BN derivatives have the same structure was verified by their similar retention times after their co-injection in a RP-HPLC column. The radiolabeled BN derivatives (I) and (II) were easily obtained in a yield higher than 98%. These results are consistent with previous studies, which demonstrated that N_3S ligand systems form stable peptide conjugates, obtained in high yield and high specific activity by transchelation from rhenium or technetium (V) gluconate precursors (*16, 31*).

Stability assays were performed in order to evaluate whether spacer modifications were sufficient for maintaining the stability of the ^{99m}Tc-BN derivatives (I) and (II) *in vivo* to ensure efficient delivery of radioactivity at the target. The stability of these new BN derivatives was determined *in vitro* in human plasma, human prostate cancer PC-3 cells, and in liver and kidney homogenates. After incubation at 37 °C, a higher stability was observed in plasma, where both derivatives remained intact at a level of 60% after 120 min. It is worthwhile to mention that during the first crucial 15 min of incubation the percentage of intact BN (I) and (II) was about 80 and 70%, respectively. In contrast,

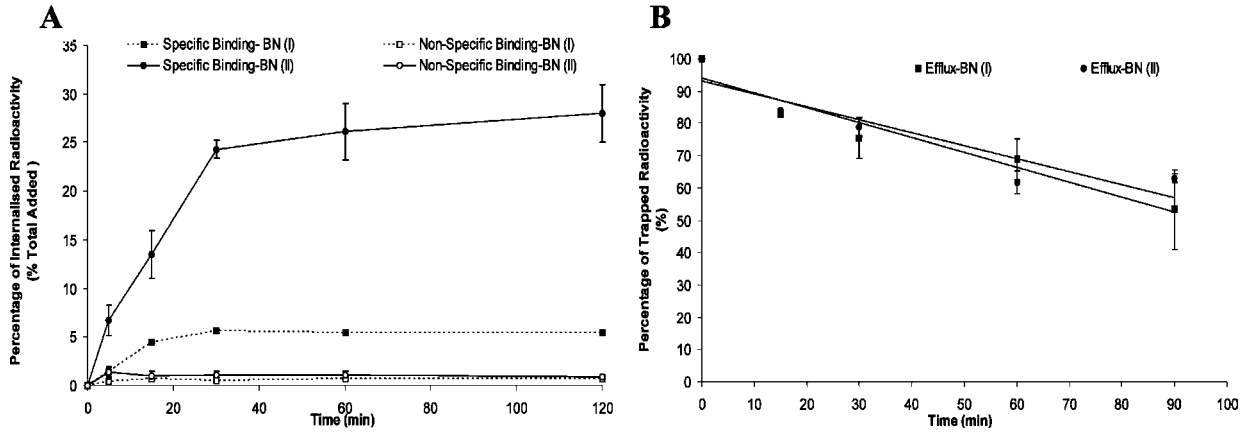

Figure 3. Internalization (A) and externalization (B) after maximum internalization (30 min of incubation at 37 °C) of the two $^{99m}Tc^{(V)}ON_3S$-**X**-BN[2−14] derivatives. Data represent the percentage of internalized and trapped radioactivity into the cells, in relation to the totally added radioactivity [BN (I), ■; BN (II), ●]. Vertical bars indicate standard deviation (SD). Results represent the mean of 2−3 experiments ± SD, each performed in triplicate.

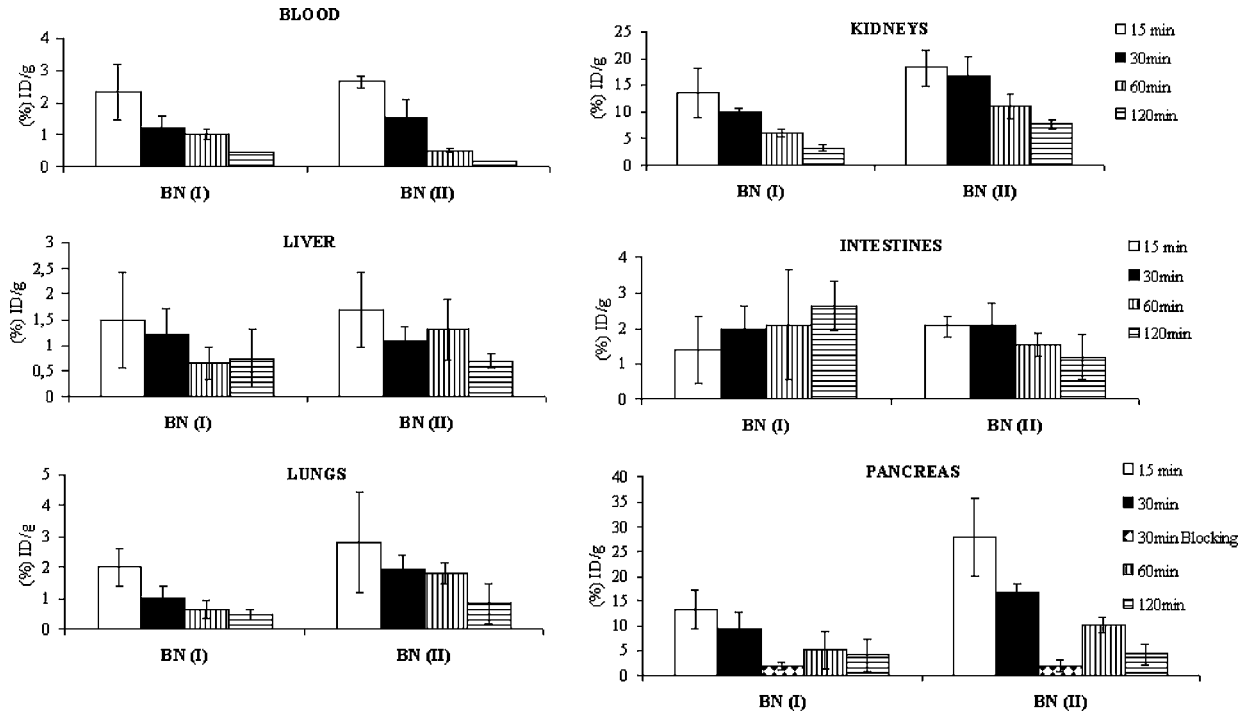

Figure 4. Comparative study of tissue or organ uptake for the two new $^{99m}Tc^{(V)}ON_3S$-X-BN[2−14] derivatives in normal Swiss mice at the time intervals of 15, 30, 60, and 120 min. Biodistribution values represent the mean ± standard deviation of %ID/g (3−5 animals were used per time point). Blocking studies were performed by coinjection of 3 animals with excess amounts of native BN.

the degradation was much faster in PC-3 cells, being more prominent for BN (I) than for BN (II). Nevertheless, a rapid catabolism in tumor cells would not necessarily be a problem, if the peptide is quickly internalized, and the metabolic products remain trapped inside the cell (*13*). However, even lower stability was found in liver and kidney homogenates with various metabolites of lower R_T values being formed, but in all cases, nondetectable technetium traces were released from the breakdown of the amino acid chelator ^{99m}Tc-Gly-Gly-Cys. Overall, results obtained during the metabolic stability study demonstrated that the insertion of the spacer group Orn-Orn-Orn seems to stabilize the resulting derivative (II) in cell culture and keep it more stable during exposure to the proteolytic action of liver enzymes. This is possibly due to the presence of the 3 nonnatural amino acids, which are not so easily recognized by the proteolytic liver enzymes.

The binding affinity of BN (I) and (II) for GRP receptors was in the nanomolar range, comparable to that of [Tyr^4]-BN and to those reported for Triaza-X-BBN (7−14) (X = SSS, GSG, GGG, and b-Ala) (*18*) and $Re(H_2O)(CO)_3$-Dpr-X-BBN (X = NNN, NNN-βAla, and NNN-5Ava) (*43*). The highest affinity among the tested BN derivatives was observed in the case of BN (II), while its complex with $^{185/187}$Re had the second better binding affinity for the GRPR. Once the radioactive BN derivative is residualized within cancer cells upon binding on the cell surface of GRPRs, then a specific delivery of diagnostic/therapeutic dose occurs. Experiments designed to determine the fraction of both studied ^{99m}Tc-derivatives internalized within the PC-3 cells showed that there were significant differences in the amount internalized for each of them at all time points. BN (II) showed a much higher degree and rate of internalization than BN (I). Even if the IC_{50} values of the unlabeled derivatives are similar, the internalization level of ^{99m}Tc-BN (I) is lower than ^{99m}Tc-BN (II). This discrepancy could be explained by the presence of the hydrophilic linker of Orn-Orn-Orn that leads to a final conformation of the whole complex of radioconjugate−

Table 4. Biodistribution Data of Radiolabeled BN (I) and (II) Derivatives in Female SCID Mice Bearing PC-3 Tumors[a]

	BN (I) derivative			BN (II) derivative	
organ/tissue	30 min ± SD	60 min ± SD	30 min ± SD	60 min ± SD	120 min ± SD
blood	2.57 ± 1.59	0.52 ± 0.05	3.33 ± 0.15	1.07 ± 0.12	0.24 ± 0.05
heart	1.86 ± 1.83	0.24 ± 0.01	1.45 ± 0.12	0.53 ± 0.05	0.42 ± 0.24
lung	2.23 ± 0.67	0.46 ± 0.08	2.40 ± 0.33	2.02 ± 0.83	1.39 ± 0.48
liver	2.81 ± 1.70	1.54 ± 0.08	1.57 ± 0.12	2.46 ± 0.63	2.62 ± 0.17
spleen	2.23 ± 1.39	0.64 ± 0.51	1.32 ± 0.06	1.06 ± 0.30	0.65 ± 0.36
stomach	1.86 ± 0.09	0.57 ± 0.04	0.46 ± 0.01	0.83 ± 0.80	2.61 ± 0.42
intestines	2.08 ± 1.55	1.74 ± 0.57	1.21 ± 0.41	2.69 ± 0.43	6.75 ± 0.91
kidneys	16.50 ± 1.42	5.56 ± 0.52	10.11 ± 2.78	25.49 ± 1.61	16.18 ± 2.17
pancreas	11.08 ± 2.76†	4.17 ± 0.99	11.07 ± 4.2*	27.59 ± 6.86	25.35 ± 5.95
blocked pancreas[b,c]	1.69 ± 1.42†	ND[d]	1.84 ± 0.22*	ND[d]	ND[d]
muscles	1.04 ± 0.91	0.11 ± 0.00	0.82 ± 0.14	0.51 ± 0.35	0.51 ± 0.38
PC3 tumor	4.56 ± 0.95§	1.02 ± 0.18	5.23 ± 2.10**	7.14 ± 0.87	7.92 ± 0.79
blocked tumor[b,c]	0.91 ± 0.60§	ND[d]	0.86 ± 0.17**	ND[d]	ND[d]
tumor to blood	1.77	1.96	1.57	6.67	33.32
tumor to muscles	4.38	9.27	6.38	14.00	15.53
tumor to liver	1.62	0.66	3.33	2.90	3.02
tumor to kidney	0.28	0.18	0.52	0.28	0.49

[a] Results are expressed as the mean ± standard deviation of %ID/g (3 animals were used per time point). [b] Blocking study was performed by co-injecting 3 animals with an excess amount of native BN along with the radiolabeled BN derivative. [c] Statistical analysis with †,§p values and *,**$p <$ 0.05 being considered significantly different versus unblocked. [d] ND = not determined.

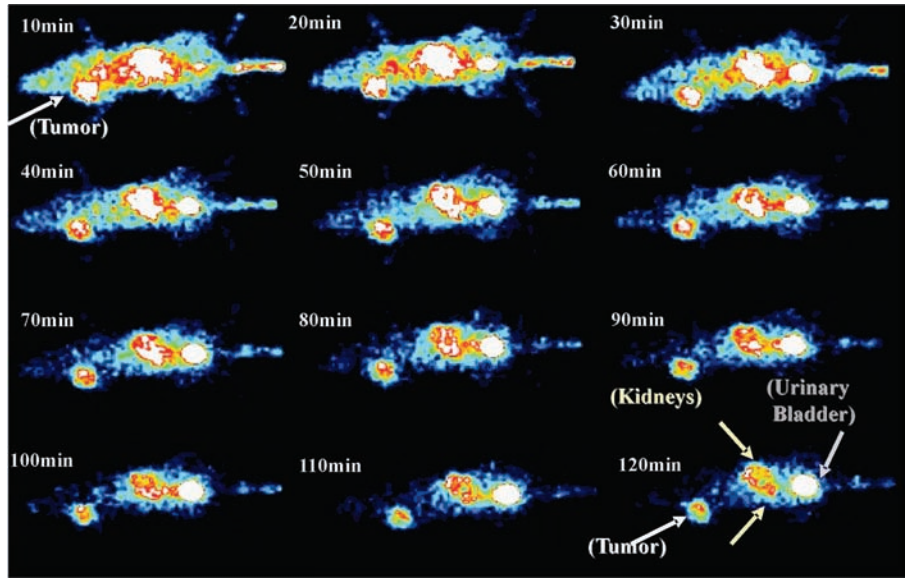

Figure 5. Gamma-ray dynamic images of 10 min per frame up to 120 min of a tumor bearing mouse for radiolabeled BN derivative (II). Arrows in white, yellow, and gray indicate the presence of the tumor, kidneys, and urinary bladder, respectively.

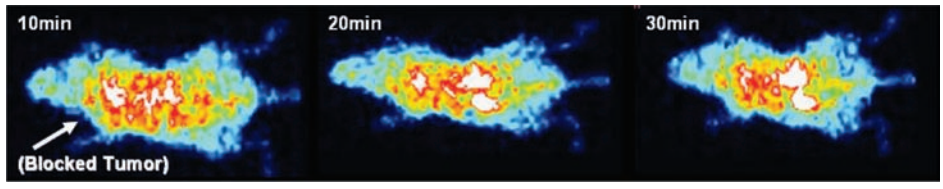

Figure 6. Gamma-ray dynamic images of 10 min per frame up to 30 min of a blocked tumor bearing mouse (PC-3 onto the right front flank) for radiolabeled BN (II). The arrow (in white) indicates the presence of the blocked tumor.

receptor, which probably induces penetration into the cells. This high level of internalization of BN (II) explains in part its superior *in vivo* properties compared to those of BN (I). Efflux studies indicated that the BN derivatives were rather rapidly released from PC-3 cells. Thus, about a half-for BN (I) and less than a half-for BN (II) of the internalized radioactivity was released in the first 90 min, probably due to the ability of functional intracellular proteases to degrade them. The rate of residualization of radioactivity inside cells is in accordance with other reports (*16*, *17*). In view of the design of radiolabeled BN peptides for therapy, new analogues should be developed with higher retention time into the cells.

An ideal pattern of biodistribution is one in which any radioactivity not bound to the receptive positive organ receptors or tumor is rapidly cleared from the blood and efficiently excreted without retention in any normal organ (*9*, *42*). In fact, during biodistribution studies in healthy mice, uptake in the pancreas of the derivative (II) from 15 to 60 min p.i. was higher than that of derivative (I). Clearance of radioactivity from the pancreas with time is probably due to excessive enzymatic

activity in this organ. Similar behavior has been reported for other ^{99m}Tc-labeled BN analogues such as ^{99m}Tc-Demobesin I (*39*) and [^{99m}Tc−P_2S_2]BN(7−14) (*44*). Specificity of the novel radiolabeled BN derivatives for the GRPR-rich healthy positive tissues (such as the pancreas) was confirmed by *in vivo* blocking after coadministration of native BN. The main clearance route of radioactivity for both derivatives was via the kidneys to urine. Although the changes in the linker sequence had a considerable effect on the reduction of liver accumulation, kidney values remained high enough, 7.73 ± 0.90% I.D./g, at 120 min p.i. for BN(II), while for the BN (I) derivative, they were 3.24 ± 0.57% I.D./g since more positively charged compounds are known to accumulate in the kidneys (*22*). However, an entirely renal route of excretion is preferable to a partly hepatobiliary clearance (*45*). Nonetheless, for prostate cancer radioimaging, there is high demand for achieving minimal accumulation of radioactivity in the abdominal area (intestines, stomach, liver, kidneys, and bladder). Thus, decreasing the lipophilicity of the radiolabeled BN derivatives serves to increase renal/urinary excretion, which is not preferable for detecting prostate tumors. Minimization of bladder interference can be achieved by several strategies such as differential timing of the images so as to highlight prostate gland and bladder drainage by means of an indwelling tube (*46*). In clinical practice, patients are asked to void the bladder before scintigraphy.

Results from the *in vivo* investigation in SCID mice, presented in Table 4 for BN (I) and (II), showed distinct differences in the biodistribution pattern of the two compounds in both receptor-positive and nontarget organs. Nevertheless, at the early time point of 30 min p.i., BN (I) showed tumor and pancreas uptake (4.56 ± 0.95 and 11.08 ± 2.76% I.D./g) values comparable to the corresponding values of BN (II) (5.23 ± 2.10 and 11.07 ± 4.2% I.D./g). The activity accumulated within the receptor-rich organs was quickly washed out at 60 min p.i. (1.02 ± 0.18 and 4.17 ± 0.99% I.D./g) for BN (I). However, a significant uptake of BN (II) in the GRPR-bearing tumor and pancreas was observed at 60 and 120 min p.i.. The greater accumulation of BN (II) in the pancreas may be explained by the higher receptor densities in this tissue in relation to the tumor and by the better penetration in the pancreatic acini cells in comparison to the weak vasculatory architecture of the PC-3 tumor (*47*). Receptor-bearing tissues, such as the tumor and pancreas present a relatively high uptake 30 to 60min p.i., with values remaining high up to 120 min p.i.. Pancreatic retention for BN (II) in SCID mice compared to that in normal mice is not fully understood. However, similar differences in the values of the pancreas concerning healthy animals and those with tumors have also been observed in a recent report by Faintuch et al., which compares ^{99m}Tc-HYNIC-BN with ^{99m}TcN(PNP6)-Cys-BN, and have been attributed to the different animal models used (*46*). Moreover, the washout of BN (II) from the PC-3 tumor is slow unlike its rate of externalization from PC-3 cells. This discrepancy may be due to the fact that the higher polarity of BN (II) probably favors pancreas and tumor penetration and retention (*48*). However, it should also be taken into consideration that the human tumor-bearing models are supported by murine vasculature architecture (*49*). It seems that the approach of using normal mice as a screening tool for GRPR targeted radiopharmaceuticals may be inadequate for predicting *in vivo* uptake in GRPR positive tumors (*25*). Furthermore, tumor to background ratios that are quite high at 60 min p.i. increased or remained constant at 120 min p.i. in the case of blood and muscles, respectively, illustrating a very good profile of BN (II) for GRPR targeted applications. GRPR specificity was confirmed by the receptor-blocking study at 30 min p.i. where the inhibition of uptake in these tissues was effective for both derivatives, by co-injection with a high dose of native bombesin. Similar trends were also observed for the other BN receptor positive organs, such as the intestines, where uptake of the radiolabeled BN derivatives was significantly reduced by coadministration of native bombesin (data not shown). It is also important to notice, as has already been mentioned in the case of healthy mice, that these modifications performed at the spacer site led to nonsignificant hepatic uptake and that the main clearance route of ^{99m}Tc radioactivity from the SCID mice is via the renal system. Nevertheless, the structure of spacer Orn-Orn-Orn did have an important effect on the retention of radioactivity in the kidneys of SCID mice, which was higher relative to what was observed with normal mice as also referred to by others (*25*). Obviously, this persistent kidney retention that the BN (II) derivative demonstrated is not optimal and is higher than that of BN (I). But as BN (II) has shown among the highest tumor and pancreas targeting efficacy of the ^{99m}Tc-BN conjugates of this type, following the Tc-labeled BN derivatives reported by Nock et al. (*39*) and Cescato et al. (*50*), this can be a problem only in the application of this compound for therapy due to potential nephrotoxicity (*25, 51*). To our knowledge, it may be possible to accelerate the wash out of BN (II) from kidneys by coadministration of polyornithine (more than 5 chain length), an approach that has been suggested in a previous report by Behe et al. (*52*), where uptake of ^{111}In-DTPA-DGlu^1-minigastrin in the kidneys was blocked by the use of polyglutamic acids.

A direct comparison of the tumor uptake observed for BN (I) and (II) with other publications using ^{99m}Tc-labeled bombesin derivatives is somehow difficult since in most of the reports, the C-terminal amidated BN(7−14) sequence or other stabilized forms of it were studied, while in the present study, the whole bombesin sequence is used. The full length sequence was proved by Gourni et al. (*35*) to lead to practically exclusive renal elimination. Radiochemical investigations of ^{99m}Tc(H_2O)(CO_3)-Dpr-SSS-BN(7−14) in PC-3 tumor-bearing mice by Smith et al. showed that tumor uptake was higher at 1 h p.i. (3.68 ± 0.92% I.D./g) than BN (I) and lower than BN (II) (*14*). The same group has also studied the pharmacokinetic properties of ^{99m}Tc(H_2O)(CO_3)-Dpr-NNN-βAla-BN(7−14) in PC-3 tumor-bearing mice, where two tumors were developed on the bilateral flank with accumulations of 2.79 ± 0.95% I.D./g and 3.28 ± 1.18% I.D./g at 1 h. p.i (*43*). Tumor uptake and retention were lower compared to ^{99m}Tc(H_2O)(CO_3)-Dpr-SSS-BN(7−14), which also seemed to be superior to ^{99m}Tc(H_2O)(CO_3)-Dpr-NNN-βAla-BN(7−14) for imaging prostate tumors. Results from the *in vivo* evaluation of ^{99m}Tc(CO_3)-pyrazolyl-X-BN(7−14) in SCID mice bearing xenografted human prostate PC-3 tumors by S. Alves et al. showed that maximum tumor uptake (1.76 ± 0.79% I.D./g and 1.76 ± 1.20% I.D./g) at 1 h p.i. for SSS and GGG linkers was higher when compared to that of BN (I) and lower than that of BN (II) (*16*). In a recent study with ^{99m}Tc(I)-BN derivatives consisting of different neutral or charged polar linkers (*53*), it was shown that by introducing a single negative charge in the form of β^3hGlu, the *in vivo* profile was improved exhibiting higher tumor uptake and retention. This general concept of inserting polar rather than lipophilic linkers, between the chelator and the binding sequence and ameliorating in this way the biodistribution pattern (higher tumor uptake and retention), has also been supported by our results as well as by a recent study of Garayoa et al. with ^{99m}Tc(CO)$_3$-glycated-BN derivatives (*48*). More specifically, ^{99m}Tc(I)-Ala(^{N}TG)-βAla-βAla-(Cha^{13}, Nle^{14})-BN(7−14) exhibited accumulation similar to that of BN (II) and higher than that of BN (I) at 30 min p.i. and a notable tumor localization at further studied time points.

The scintigraphic dynamic images obtained in SCID mice bearing human PC-prostate cancer tumors demonstrated an easy delineation of the neoplastic region by the BN (II) derivative

up to 120 min p.i.. At the same time, low background accumulation was observed, which is consistent with the biodistribution data and the tumor/tissue ratios reported.

CONCLUSIONS

Significant progress has been made over the past years in the development of new radiolabeled candidates for targeting peptide receptors, by separation of the radiolabeling area from the receptor-targeting peptide moiety. The structural tuning introduced in the N_3S-BN[2−14] derivatives, via the concept of modifications at the spacer site is very promising in order to visualize GRP receptors expressed at cell membranes of various tissues. Using Orn-Orn-Orn as a spacer compared to no spacer at all resulted in higher stability and greater internalization of the ^{99m}Tc-labeled species in cells, in a considerably better uptake in target-specific pancreatic and tumor tissue and finally in high-quality SPECT images. From previous studies, it is generally accepted that high and persistent localization of radioactivity in kidneys is caused by long residence times of radiometabolites generated after lysosomal degradation, following glomerular filtration and subsequent reabsorption into renal cells (*54*). On the basis of these findings, efforts are being made to inhibit tubular reabsorption of radiolabeled peptides by competitive blockage (*52*), charge modification with amino acid substitutions (*10*, *11*, *55*), and PEGylation (*22*, *56*). More wide-ranging modifications of the spacer are necessary to promote an efficient excretion of ^{99m}Tc-BN based radiopharmaceuticals of this type without significant retention in any normal organs such as the kidneys.

ACKNOWLEDGMENT

We thank Dr. Leondios Leondiadis for ESI-MS analyses performed at the Mass Spectrometry and Dioxin Analysis Lab, NCSR "Demokritos". The present work has been financially supported by the General Secretariat for Research and Technology.

LITERATURE CITED

(1) Anastasi, A., Erspamer, V., and Nucci, M. (1972) Isolation and aminoacid sequences of alytensin and bombesin, two analogous active tetradecapeptides from the skin of european discoglossid frogs. *Arch. Biochem. Biophys. 148*, 443–446.

(2) Nagalla, S. R., Barry, B. J., Falicks, A. M., Gibson, B. W., Taylor, J. E., Dong, J. Z., and Spindel, E. R. (1996) There are three distinct forms of bombesin. *J. Biol. Chem. 271*, 7731–7737.

(3) Ohki-Hamazaki, H., Iwabuchi, M., and Maekawa, F. (2005) Development and function of bombesin-like peptides and their receptors. *Int. J. Dev. Biol. 49*, 293–300.

(4) Cornelio, D. B., Roesler, R., and Schwartsmann, G. (2007) Gastrin-releasing peptide receptor as a molecule target in experimental anticancer therapy. *Ann. Oncol. 18*, 1457–1466.

(5) Dietrich, J. B. (1994) Neuropeptides, antagonists and cell proliferation: bombesin as an example. *Cell. Mol. Biol. 40*, 731–746.

(6) Patel, O., Shulkes, A., and Baldwin, G. S. (2006) Gastrin-releasing peptide and cancer. *Biochim. Biophys. Acta 1766*, 23–41.

(7) Qu, X., Xiao, D., and Weber, C. H. (2003) Biologic relevance of mammalian bombesin-like peptides and their receptors in human malignancies. *Curr. Opin. Endocrinol. Diabetes Obes. 10*, 60–71.

(8) Giblin, M. F., Veerendra, B., and Smith, C. J. (2005) Radiometallation of receptor-specific peptides for diagnosis and treatment of human cancer. *In Vivo 19*, 9–29.

(9) Smith, C. J., Volkert, W. A., and Hoffman, T. J. (2005) Radiolabeled peptide conjugates for targeting of the bombesin receptor superfamily subtypes. *Nucl. Med. Biol. 32*, 733–740.

(10) Garayoa, G. E., Ruegg, D., Blauenstein, P., Zwimpfer, M., Khan, I. A., Maes, V., Blanc, A., Beck-Sickinger, A., Tourwe, A. G., and Schubiger, P. A. (2007) Chemical and biological characterization of new $Re(CO)_3$/99m$Tc(CO)_3$ bombesin analogues. *Nucl. Med. Biol. 34*, 17–28.

(11) Garayoa, E. G., Schweinsberg, C., Maes, V., Ruegg, D., Blanc, A., Blauenstein, P., Tourwe, D. A., Beck-Sickinger, A. G., and Schubiger, P. A. (2007) New [^{99m}Tc]bombesin analogues with improved biodistribution for targeting gastrin releasing-peptide receptor-positive tumors. *Q. J. Nucl. Med. Mol. Imaging 51*, 42–50.

(12) La Bella, R., Garcia-Garayoa, E., Bahler, M., Blauenstein, P., Schibli, R., Conrath, P., Tourwe, D., and Schubiger, P. A. (2002) A ^{99m}Tc(I)-postlabeled high affinity bombesin analogue as a potential tumor imaging agent. *Bioconjugate Chem. 13*, 599–604.

(13) Smith, C. J., Gali, H., Sieckman, G. L., Higginbotham, C., Volkert, W. A., and Hoffman, T. J. (2003) Radiochemical investigations of ^{99m}Tc-N_3S-X-BBN[7−14]NH_2: An *in vitro*/*in vivo* structure-sctivity relationship study where X=0-, 3-, 5-, 8-, and 11-carbon tethering moieties. *Bioconjugate Chem. 14*, 93–102.

(14) Smith, C. J., Sieckman, G. L., Owen, N. K., Hayes, D. H., Mazuru, D. G., Kanna, R., Volkert, W. A., and Hoffman, T. J. (2003) Radiochemical investigations of gastrin-releasing peptide receptor specific [^{99m}Tc(X)(CO_3)-Dpr-Ser-Ser-Ser-Gln-Trp-Ala-Val-Gly-His-Leu-Met-(NH_2)] in PC-3, tumor-bearing, rodent models: syntheses, radiolabeling and *in vitro*/*vivo* studies where Dpr=2,3-diaminopropionic acid and X=H_2O or $P(CH_2OH)_3$. *Cancer Res. 63*, 4082–4088.

(15) Veerendra, B., Sieckman, G. L., Hoffman, T. J., Rold, T., Retzloff, L., and Smith, C. J. (2006) Synthesis, radiolabeling and in vitro GRP receptor targeting studies of ^{99m}Tc-Triaza-X-BBN[7−14]NH_2 (X=serylserylserine, glycylglycylglycine, glycylserylglycine, or beta alanine). *Synth. React. Inorg., Met.-Org., Nano-Met. Chem. 36*, 481–491.

(16) Alves, S., Paulo, A., Correia, J. D., Santos, I., Gano, L., Veerendra, B. C. J., Sieckman, G. L., Hoffman, T. J., Rold, T. L., Figueroa, S. D., Retzloff, L., McGrate, J., Prasanphanich, A., and Smith, C. J. (2006) Pyrazolyl conjugates of bombesin: a new tridentate ligand framework for the stabilization of fac-$[M(CO)_3]$+ moiety. *Nucl. Med. Biol. 33*, 625–634.

(17) Kunstler, J. U., Veerendra, B., Figueroa, S. D., Sieckman, G. L., Rold, T. L., Hoffman, T. J., Smith, L. C. J., and Pietzsch, H. J. (2007) Organometalic ^{99m}Tc(III) '4 + 1' bombesin(7−14) conjugates: synthesis, radiolabeling, and in vitro/in vivo studies. *Bioconjugate Chem. 18*, 1651–1661.

(18) Parry, J. J., Andrews, R., and Rogers, B. E. (2006) Micropet imaging of breast cancer using radiolabeled bombesin analogs targeting the gastrin-releasing peptide receptor. *Breast Cancer Res. Treat. 101*, 175–184.

(19) Parry, J. J., Kelly, T. S., Andrews, R., and Rogers, B. E. (2007) In vitro and in vivo evaluation of ^{64}Cu-labeled DOTA-linker-bombesin(7−14) analogues containing different amino acid linker moieties. *Bioconjugate Chem. 18*, 1110–1117.

(20) Rogers, B. E., Manna, D. D., and Savafy, A. (2004) In vitro and in vivo evaluation of a ^{64}Cu-labeled polyethylene glycol-bombesin conjugate. *Cancer Biother. Radiopharm. 19*, 25–34.

(21) Prasanphanich, A. F., Nanda, P. K., Rold, T. L., Ma, L., Lewis, M. R., Garrison, J. C., Hoffman, T. J., Sieckman, G. L., Figueroa, S. D., and Smith, C. J. (2007) [^{64}Cu-Nota-8-Aoc-BBN(7−14)NH_2] targeting vector for positron-emission tomography imaging of gastrin-releasing peptide receptor-expressing tissues. *Proc. Natl. Acad. Sci. U.S.A. 104*, 12462–12467.

(22) Schuhmacher, J., Zhang, H., Doll, J., Maecke, H. R., Matys, R., Hauser, H., Henze, M., Haberkorn, U., and Eisenhut, M. (2005) GRP receptor-targeted PET of a rat pancreas carcinoma xenograft in nude mice with a ^{68}Ga-labeled bombesin (6−14) analog. *J. Nucl. Med. 46*, 691–699.

(23) Zhang, X., Cai, W., Cao, F., Schreibmann, E., Wu, Y., Wu, J. C., Xing, L., and Chen, X. (2006) ^{18}F-Labeled bombesin analogs for targeting GRP receptor-expressing prostate cancer. *J. Nucl. Med. 47*, 492–501.

(24) Hoffman, T. J., Gali, H., Smith, C. J., Sieckman, G. L., Hayes, D. L., Owen, N. K., and Volkert, W. A. (2003) Novel series of ^{111}In-labeled

bombesin analogs as potential radiopharmaceuticals for specific targeting of gastrin-releasing peptide receptors expressed on human prostate cancer cells. *J. Nucl. Med. 44*, 823–831.

(25) Garrison, J. C., Rold, T. L., Sieckman, G. L., Naz, F., Sublett, S. V., Figueroa, S. D., Volkert, W. A., and Hoffman, T. J. (2008) Evaluation of the pharmacokinetic effects of various linking group using the ^{111}In-DOTA-X-BBN(7−14)NH_2 structural paradigm in a prostate cancer model. *Bioconjugate Chem. 19*, 1803–1812.

(26) Hu, F., Gutler, G. S., Hoffman, T. J., Sieckman, G. L., Volkert, W. A., and Jurisson, S. S. (2002) Pm-149 DOTA bombesin analogs for potential radiotherapy *In vivo* comparison with Sm-153 and Lu-177 labeled DO_3A-amide-β-Ala-BBN(7−14)NH_2. *Nucl. Med. Biol. 29*, 423–430.

(27) Zhang, H., Chen, J., Waldherr, C., Hinni, K., Waser, B., Reubi, J. C., and Maecke, H. R. (2004) Synthesis and evaluation of bombesin derivatives on the basis of pan-bombesin peptides labeled with indium-111, lutecium-177, and yttrium-90 for targeting bombesin receptor-expressing tumors. *Cancer Res. 64*, 6707–6715.

(28) Antunes, P., Ginj, M., Walter, M. A., Chen, J., Reubi, J. C., and Maecke, H. R. (2007) Influence of different spacers on the biological profile of a DOTA-somatostatin analogue. *Bioconjugate Chem. 18*, 84–92.

(29) Zhang, H., Schuhmacher, J., Waser, B., Wild, D., Eisenhut, M., Reubi, J. C., and Maecke, H. R. (2007) DOTA-PESIN, a DOTA-conjugated bombesin derivative designed for the imaging and targeted radionuclide treatment of bombesin receptor-positive tumors. *Eur. J. Nucl. Med. Mol. Imaging 34*, 1198–1208.

(30) Smith, C. J., Sieckman, G. L., Owen, N. K., Hayes, D. L., Mazuru, D. G., Volkert, W. A., and Hoffman, T. J. (2003) Radiochemical investigations of [^{188}Re(H_2O)$(CO)_3$-diamino propionic acid-SSS-bombesin(7−14)NH_2]: syntheses, radiolabeling and *in vitro*/*in vivo* GRP receptor targeting studies. *Anticancer Res. 23*, 63–70.

(31) Wong, E., Fauconnier, T., Bennett, S., Valliant, J., Nguyen, T., Lau, F., Lu, L. F. L., Pollak, A., Bell, R. A., and Thornback, J. R. (1997) Rhenium (V) and technetium (V) oxo complexes of an N_2NS peptidic chelator: evidence of interconversion between the syn and anti conformations. *Inorg. Chem. 36*, 5799–5808.

(32) Van de Wiele, C., Dumont, F., Vanden Broecke, R., Oosterlinck, W., Cocquyt, V., Serreyn, R., Peers, S., Thornback, J., Slegers, G., and Dierckx, R. A. (2000) Technetium-99m RP-527, a GRP analogue for visualization of GRP receptor-expressing malignancies: a feasibility study. *Eur. J. Nucl. Med. 27*, 1694–1699.

(33) Blok, D., Feitsma, H. I. J., Kooy, Y. M. C., Welling, M. M., Ossendorp, F., Vermeij, P., and Drijfhout, J. W. (2004) New chelation strategy allows for quick and clean ^{99m}Tc-labeling of synthetic peptides. *Nucl. Med. Biol. 31*, 815–820.

(34) Gourni, E., Paravatou, M., Bouziotis, P., Zikos, C., Fani, M., Xanthopoulos, S., Archimandritis, S. C., Livaniou, E., and Varvarigou, A. D. (2006) Evaluation of a series of new ^{99m}Tc-labeled bombesin-like peptides for early cancer detection. *Anticancer Res. 26*, 435–438.

(35) Gourni, E., Bouziotis, P., Zikos, C., Loudos, G., Xanthopoulos, S., Fani, M., Archimandritis, S. C., and Varvarigou, A. D. (2006) Comparative *in vivo* evaluation of two novel ^{99m}Tc-labeled bombesin derivatives. *Nucl. Instrum. Methods Phys. Res., Sect. A 569*, 518–521.

(36) Sarin, V. K., Kent, S. B. H., Tam, J. P., and Merrifield, R. B. (1981) Quantitative monitoring of solid phase peptide synthesis by the ninhydrin reaction. *Anal. Biochem. 117*, 147–157.

(37) Noll, B., Kniess, T., Friebe, M., Spies, H., and Johannsen, B. (1996) Rhenium $^{(V)}$ gluconate, a suitable precursor for the preparation of Rhenium$^{(V)}$ complexes. *Isot. Environ. Health Stud. 32*, 21–29.

(38) Varvarigou, A. D., Scopinaro, F., Leondiadis, L., Corleto, V., Schillaci, O., De Vincentis, G., Sourlingas, T. G., Sekeri-Pataryias, K. E., Enangelatos, G. P., Leonti, A., Xanthopoulos, S., Delle Fave, G., and Archimandritis, S. C. (2002) Synthesis, chemical, radiochemical and radiobiological evaluation of a new ^{99m}Tc-labeled bombesin-like peptide. *Cancer Biother. Radiopharm. 17*, 317–326.

(39) Nock, B., Nikolopoulou, A., Chiotellis, E., Loudos, G., Maintas, D., Reubi, J. C., and Maina, T. (2003) [^{99m}]Tc Demobesin 1, a novel potent bombesin analogue for GRP receptor-targeted tumor imaging. *Eur. J. Nucl. Med. 30*, 247–258.

(40) Alves, S., Paulo, A., Correia, J. D., Gano, L., Smith, C. J., Hoffman, T. J., and Santos, I. (2005) Pyrazolyl derivatives as bifunctional chelators for labeling tumor-seeking peptides with fac-[M(CO)3]+ Moiety (M=^{99m}Tc, Re): Synthesis, characterization, and biological behavior. *Bioconjugate Chem. 16*, 438–449.

(41) Okarvi, S. M. (2004) Peptide-based radiopharmaceuticals: future tools for diagnostic imaging of cancers and other diseases. *Med. Res. Rev. 24*, 357–397.

(42) Maecke, H. R. (2007) Radiolabeled peptides in Nuclear Oncology: Influence of Peptide Structure and Labeling Strategy on Pharmacology. *Molecular Imaging. Volume 49: An Essential Tool in Preclinical Research, Diagnostic Imaging and Therapy* (Bogdanor, A. A., Jr., Licha, K., Eds.) pp. 43−72, Chapter 10, Springer, Berlin, Germany.

(43) Prasanphanich, A. F., Lane, S. R., Figueroa, S. D., Ma, L., Rold, T. L., Sieckman, G. L., Hoffman, T. J., McCrate, J. M., and Smith, C. J. (2007) The effects of linking substituents on the *in vivo* behavior of site-directed, peptide-based, diagnostic radiopharmaceuticals. *In Vivo 21*, 1–16.

(44) Karra, S. R., Schibli, R., Gali, H., Katti, K. V., Hoffman, T. J., Higginbotham, C., Sieckman, G. L., and Volkert, W. A. (1999) ^{99m}Tc-Labeling and *in vivo* studies of a bombesin analogue with a novel water-soluble dithiaphosphine-based bifunctional chelating agent. *Bioconjugate Chem. 10*, 254–260.

(45) Dechristoforo, C., and Mather, S. J. (2002) The influence of chelator on the pharmacokinetics of ^{99m}Tc-labeled peptides. *Q. J. Nucl. Med. 46*, 195–205.

(46) Faintuch, B. L., Teodoro, R., Duatti, A., Muramoto, E., Faintuch, S., and Smith, C. J. (2008) Radiolabeled bombesin analogs for prostate cancer diagnosis: preclinical studies. *Nucl. Med. Biol. 35*, 401–411.

(47) Hohne, A., Mu, L., Honer, M., Schubiger, P. A., Ametamey, S. M., Graham, K., Stellfeld, T., Borkowski, S., Berndorff, D., Klar, U., Voigtmann, U., Cyr, J. E., Friebe, M., Dinkelborg, L., and Srinivasan, A. (2008) Synthesis, ^{18}F-labeling, and in vitro and in vivo studies of bombesin peptides modified with silicon-based building blocks. *Bioconjugate Chem. 19*, 1871–1879.

(48) Schweinsberg, C., Maes, V., Brans, L., Blauenstein, P., Tourwe, D. A., Schubiger, P. A., Schibli, R., and Garcia-Garayoa, E. (2008) Novel glycated [^{99m}Tc$(CO)_3$]-labeled bombesin analogues for improved targeting of Gastrin-releasing peptide receptor positive tumors. *Bioconjugate Chem. 19*, 2432–2439.

(49) Abd-Elgaliel, W. R., Gallazzi, F., Garrison, J. C., Rold, T. L., Sieckman, G. L., Figueroa, S. D., Hoffman, T. J., and Lever, S. Z. (2008) Design, synthesis and biological evaluation of an antagonist-bombesin analogue as targeting vector. *Bioconjugate Chem. 19*, 2040–2048.

(50) Cescato, R., Maina, T., Nock, B., Nikolopoulou, A., Charalambidis, D., Piccand, V., and Reubi, J. C. (2008) Bombesin receptor antagonists may be preferable to agonists for tumor imaging. *J. Nucl. Med. 49*, 318–326.

(51) Lambert, B., Cybulla, M., Weiner, S. M., Van De Wiele, C., Ham, H., Dierckx, R. A., and Otte, A. (2004) Renal toxicity after radionuclide therapy. *Radiat. Res. 161*, 607–611.

(52) Behe, M., Kluge, G., Becker, W., Gotthardt, M., and Behr, T. M. (2005) Use of polyglutamic acids to reduce uptake of radiometal-labeled minigastrin in the kidneys. *J. Nucl. Med. 46*, 1012–1015.

(53) Garcia-Garayoa, E., Schweinsberg, C., Maes, V., Brans, L., Blauenstein, P., Tourwe, D. A., Schibli, R., and Schubiger, P. A. (2008) Influence of molecular charge on the biodistribution of bombesin analogues labeled with the [^{99m}Tc$(CO)_3$]-core. *Bioconjugate Chem. 19*, 2409–2416.

(54) Akizawa, H., Uehara, T., and Arano, Y. (2008) Renal uptake and metabolism of radiopharmaceuticals derived from peptides and proteins. *Adv. Drug Delivery Rev. 60*, 1319–1328.

(55) Akizawa, H., Arano, Y., Mifune, M., Iwado, A., Saito, Y., Mukai, T., Uehara, T., Ono, M., Fujioka, Y., Ogawa, K., Kiso, Y., and Saji, H. (2001) Effect of molecular charges on renal uptake and metabolism of ^{111}In-DTPA-conjugated peptides. *Nucl. Med. Biol. 28*, 761–768.

(56) Chapman, A. P. (2002) PEGylated antibodies and antibody fragments for improved therapy: a review. *Adv. Drug Delivery Rev. 54*, 531–545.

BC800475K

Investigation of Novel Bis- and Tris-tetraazamacrocycles for Use in the Copper-64 (^{64}Cu) Radiolabeling of Antibodies with Potential To Increase the Therapeutic Index for Drug Targeting

Martalena Ramli,[§,†,‡] Suzanne V. Smith,*[,‡] and Leonard F. Lindoy[†]

Centre for Radioisotopes and Radiopharmaceuticals, Gd 11, Kawasan PUSPIPTEK, Serpong, Tangerang, Banten, 15314, Indonesia, School of Chemistry, F11, University of Sydney, 2006, Australia, and Australian Nuclear Science and Technology Organisation (ANSTO), PMB 1, Menai, NSW, 2234, Australia. Received August 6, 2008; Revised Manuscript Received April 3, 2009

The ^{64}Cu complexes of a series of mono-, bis-, and tris-tetraazamacrocycles have been prepared, and their stability in human sera has been assessed. The ligands forming the most stable Cu^{2+} complexes were then conjugated to the B72.3 antibody (mAb). Conditions for conjugation of the ligands to the mAb were optimized for the concentration of protein, ligand, pH, temperature, and time. The optimum moles of Cu^{2+} attached to the mAb were as high as 3.5 for **L2** and 5.5 or 2.7 for **L5**, and the immunoreactivity was ≥80%. Biodistribution of the radioimmunoconjugates showed good tumor localization and target-to-background ratios that were significantly enhanced compared to those achieved with monotetraazamacrocyclic derivatives.

INTRODUCTION

Over the years there has been considerable interest in the use of azamacrocycles and their derivatives for $^{67/64}$Cu-labeling of target agents, such as intact and fragmented antibodies and peptides (*1*−*15*). The tetraazamacrocycles and their polyaminocarboxylate and polyaminophosphonate derivatives are known to form thermodynamically stable complexes with Cu^{2+}. When radiolabeled with $^{64/67}Cu^{2+}$, serum stability studies and animal studies show that they are relatively stable under physiological conditions. Formation of their respective $^{64/67}Cu^{2+}$ complexes has been reported to be highly dependent on pH, temperature, ligand concentration, and reaction time. This variation is thought to be largely due to the concentrations of the radioisotopes being low (usually less than 10^{-6} M) and the pH (*5*). A comparison of the biodistribution behavior of selected $^{67/64}Cu^{2+}$ complexes of the tetraaza-, polyaminocarboxylate, and polyaminophosphonate ligand systems has shown that the charge and the lipophilicity of their respective Cu^{2+} complexes may also have an effect on their distribution in animals (*5, 16*).

The majority of the literature concerned with the use of azamacrocyclic derivatives for $^{64/67}Cu^{2+}$ radiolabeling of antibodies describe the use of polyaminocarboxylate macrocyclic derivatives, even though the unsubstituted tetraazamacrocycles have been reported to have a higher log *K* for Cu^{2+} and tend to show enhanced selectivity for Cu^{2+} over other biological cations (*9*). Zimmerman *et al*. compared a series of five bifunctional copper chelators, CPTA-*N*-hydroxysuccinimide, DO3A-L-*p*-isothiocyanatophenylalanine, DOTA-PA-L-*p*-isocyanatophenylalanine, DOTA-glycyl-L-*p*-isocyanatophenylalanine, and DOTA-triglycyl-L-*p*-isocyanatophenylalanine for $^{67/64}Cu^{2+}$ radiolabeling of the chimeric antibody, anti-L1-CAM antibody chCE7 (see Figure 1) (*17*). These workers found that the immunoreactivity and biodistribution of the final ^{67}Cu−mAb chCE7 conjugates were greatly affected by the type and number of ligands attached. Interestingly, they reported that the best tumor to normal tissue ratios were achieved using the unsubstituted azamacrocyclic system to form the ^{67}Cu-CPTA-labeled antibody.

Attempts to increase radioactivity at the target site in cancer therapy have involved various strategies that range from increasing the number of single metal-binding sites directly linked to a monoclonal antibody (mAb) (as mentioned above) to the deployment of streptavidin−biotin or "pre-targeting strategies" linking technologies (*18*−*21*). Unfortunately, increasing the number of ligands attached directly to the target agent often compromises the antibody immunoreactivity and the result of this approach can be highly variable from one antibody to another.

Two- and three-step linking strategies involving the streptavidin−biotin system can achieve faster blood clearance. Here the radiolabel is attached to either the streptavidin or the biotin. The smaller molecules clear more quickly compared to whole antibodies and can yield high target to background ratios more rapidly than the conventional approach. The design of such systems is also quite flexible and can be adapted to a wide range of diseases. However, the preferential clearance of the radiolabeled streptavidin via the kidney and of the biotin derivatives via the liver (due to the presence of biotin receptors) can result in undesirable high radiation dose to these organs.

We are interested in exploring the use of new multi-ligand systems for radiolabeling antibodies. Such systems provide an increased number of metal binding sites on the antibody without changing the number of attachment sites. A series of new mono-, bis-, and tris-ring macrocyclic bifunctional compounds of types **L1**−**L5** for use in radiolabeling monoclonal antibodies have been synthesized. (see Figure 2) (*22*). These new bis- and tris-cyclic ligands have the potential to yield radioimmunoconjugates with enhanced specific activities compared to corresponding single-ring systems, since two or three metal ions may potentially be attached via each linkage site on the mAb between the bifunctional compound and the mAb.

The present report describes the optimization of conditions for the formation of the 1:1 ^{64}Cu complexes of **L6**, **L7**, and

* To whom correspondence should be addressed. E-mail: svs@ansto.gov.au.

§ Centre for Radioisotopes and Radiopharmaceuticals.

‡ Australian Nuclear Science and Technology Organisation (ANSTO).

† University of Sydney.

10.1021/bc800337d CCC: $40.75 © 2009 American Chemical Society
Published on Web 04/27/2009

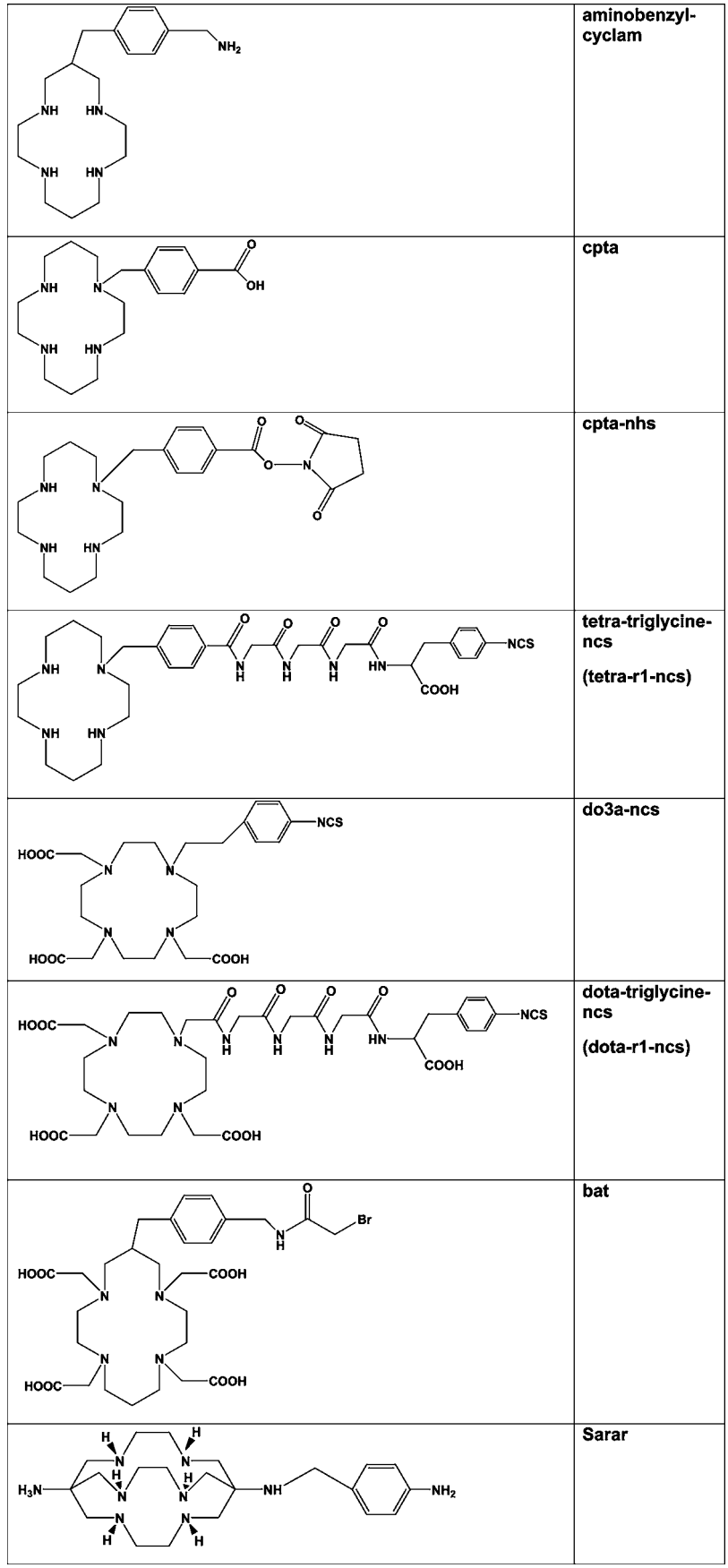

Figure 1. Selected bifunctional ligands used for $^{64}Cu^{2+}$ radiolabeling of antibodies (*3, 10, 11, 17*).

L8, 2:1 ^{64}Cu complexes of **L9**, and 3:1 ^{64}Cu complexes of **L10** and assessment of the stability in human serum. Ligands demonstrating suitable stability of their Cu^{2+} complexes were then selected for conjugation to the B72.3 mAb. The B72.3 antibody is well documented to target the Tag-72 antigen expressed by colorectal and ovarian cancers. The biodistri-

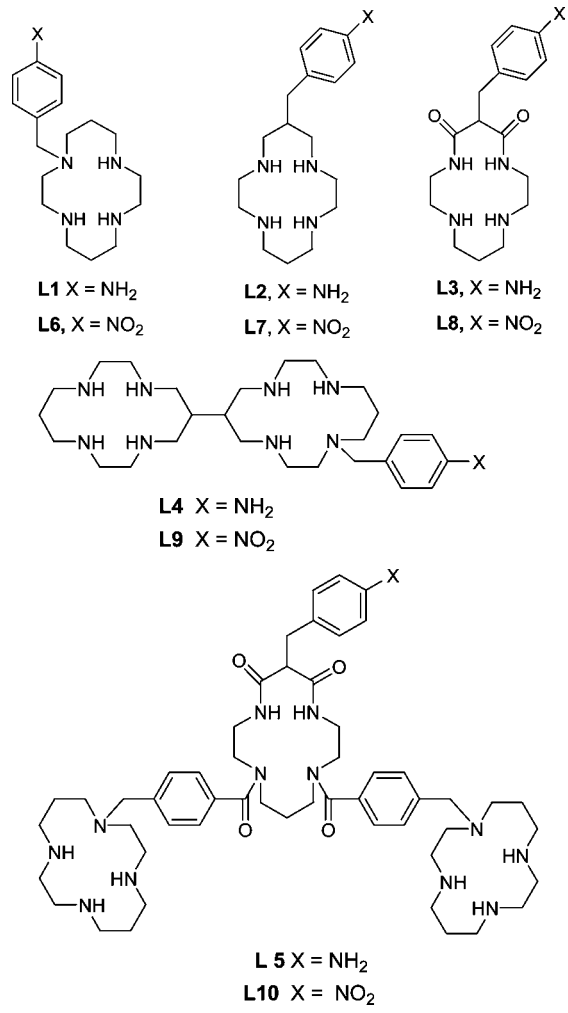

Figure 2. A series of mono-, bis- and tris-tetraazamacrocycles investigated for use in $^{64}Cu^{2+}$ radiolabeling of target agents.

bution of the resultant ^{64}Cu radioimmunoconjugates was investigated in nude mice bearing the colorectal LS174t tumors.

EXPERIMENTAL PROCEDURES

Materials and Equipment. Unless otherwise mentioned, all materials were of analytical grade and used without further purification. B72.3 mAb was obtained from Bioquest, Australia. All water used for experimental purposes was Milli-Q grade. Radioisotope ^{64}Cu was supplied by the National Medical Cyclotron (Sydney), with specific activity of up to 1.4×10^{11} MBq/g. The protein assay kit was obtained from Bio-Rad. Protein absorbance was measured on a Bio-Rad plate reader. Silica-gel impregnated glass fiber sheet for instant thin layer chromatography (ITLC-SG) was purchased from Gelman Science. Immulon 2, 1×12 strips used for measuring immunoreactivity were obtained from Dynatech. Freeze-dried immunoconjugate was prepared on a Dynavac freeze-dryer. The HPLC apparatus (Waters) consisted of a 625 pump, a 625 controller, 484 absorbance detector fitted with a 50 μL sample loop (Rheodyne), a Bio-Sep-Sec S3000 (75 mm $\times$ 7.8 mm) guard, and a Bio-Sep-Sec S3000 300 mm $\times$ 7.8 mm column (Phenomenex). Vivaspin 500 (MCO 5.000) protein filter was used for purification of both the immunoconjugates and radioimmunoconjugates (Viva Science-Sartorius).

Formation of Complexes of Type ^{64}Cu−L (L = L6, L7, L8, L9, or L10). The effect of pH on the complexation of Cu^{2+} with L was investigated. Buffers at pH 3−8 were employed: 0.1 M glycine in 0.1 M sodium chloride (pH 3.0), 0.1 M succinate (pH 4.0), 0.1 M acetate buffer (pH 5.0), 0.1 M sodium phosphate (pH 6.0, 7.0, and 8.0). A typical complexation study involved dissolving a known ligand concentration ($\sim 10^{-6}$ M) in the chosen buffer solution and a known concentration of Cu^{2+} (doped with $^{64}Cu^{2+}$) in the same buffer. The molar ratios of metal ($^{64}Cu^{2+}/Cu^{2+}$) to ligand were respectively **L2**, **L7**, **L8** = 1; **L9** = 2; **L10** = 3. The reaction mixtures were then heated at 37 °C for 30 min. The formation of each complex was monitored by ITLC-SG using a method similar to that described previously (*10*).

Table 1. Mobile Phases Used for Monitoring the Formation of ^{64}Cu−L Complexes (where L = L6, L7, L8, L9, or L10)

		R_f	
ligand	eluent	^{64}Cu−L	$^{64}Cu^{2+}$
7 and **6**	0.15 M ammonium acetate, pH 6.5	<0.3	>0.9
8	water/conc ammonium hydroxide, 65:1	>0.9	<0.1
9 and **10**	0.1 M acetate buffer (pH 4.5)/ethanol, 9:1	<0.1	>0.9

In order to monitor the formation of the $[^{64}Cu-\mathbf{L6}]^{2+}$, $[^{64}Cu-\mathbf{L7}]^{2+}$, $[^{64}Cu-\mathbf{L8}]^{2+}$, $[^{64}Cu_2\text{-}\mathbf{L9}]^{2+}$, and $[^{64}Cu_3\text{-}\mathbf{L10}]^{4+}$ complexes, various mobile phases were investigated for the separation of the complexes from free ^{64} Cu^{2+}. Table 1 lists the observed optimum mobile conditions.

Stability of the ^{64}Cu−L Complexes in Human Serum. The stability of each complex of type ^{64}Cu−L in human serum was investigated. Typically the complex was diluted (1/10 v/v, pH 7.5) in human serum (0.22 μm filtered) and incubated at 37 °C. At set intervals (2, 24, 48, and 72 h) a sample (0.1 mL) was withdrawn and loaded onto a Sephadex-G25 size exclusion column [0.6 cm $\times$ 50 cm, which had been previously equilibrated with 0.01 M PBS, pH 7.2, and preblocked with 10% bovine serum albumin (400 μL)]. The column was eluted with 0.01 M PBS, pH 7.2. The elution of serum protein was monitored by an UV monitor (at 280 nm), and fractions (1 mL) were collected and monitored for radioactivity by a γ counter. The UV and radioactivity elution profiles were then overlaid. The percentage of radioactivity was associated with the protein and radioisotope complex determined.

Formation of the Immunoconjugate of L5−mAb. The conditions for conjugation of **L5** to mAb were optimized for reaction time, pH, concentration of antibody, molar ratio of EDC and molar ratio of ligand.

Two strategies were employed in these studies: (i) post-conjugation, where the $^{64}Cu^{2+}$−L complex of the bifunctional ligand was initially formed and then this product was conjugated to the protein and the efficiency of reaction was monitored over time; (ii) pre-conjugation, where the ligand was initially conjugated to the protein under various conditions (e.g., pH, concentration of mAb, molar ratio of EDC, and molar ratio of ligand) and the resultant conjugate radiolabeled with $^{64}Cu^{2+}$.

The formation of the immunoconjugate of **L5**−mAb using EDC was carried out according to a procedure recommended by the commercial supplier (*23*). Typically a freshly prepared EDC solution (dissolved in 0.1 M (2-[*N*-morpholino]ethanesulfonic acid)-NaCl, MES buffer) was added to mAb (in 0.1 M MES buffer). A solution of **L5** (in 0.1 M MES, buffer) was subsequently added to the above mixture. The reaction mixture was incubated at 37 °C for 30 min, after which time the resultant mixture was purified by washing (4×500 μL of 0.2 M acetate, pH 4.0, and followed by 3×500 μL of 0.1 M phosphate buffer, pH 7.2) on a protein filter (MCO, 5000). The purified immunoconjugate was recovered, and its protein concentration was then measured. The purified immunoconjugate (100 μg) was transferred to 2.5 mL vials and then freeze-dried.

The freeze-dried immunoconjugate, **L5**−mAb, was dissolved in water (250 μL). An excess of $^{64}Cu^{2+}$ solution (of known

concentration and specific activity) in 0.2 M succinate buffer (1/10, v/v), pH 4.0, was added to a solution of **L5**−mAb. The reaction mixture was incubated at 37 °C for 30 min, after which time the radioimmunoconjugate that had formed was purified by washing (5 × 500 μL of 0.2 M acetate, pH 4.0, followed by 3 × 500 μL of 0.1 M phosphate buffer, pH 7.2) on a protein filter (MCO, 5000). The purified radioimmunoconjugate was then quality controlled by ITLC (mobile phase, 0.01 M EDTA in PBS, pH 7.2) or size exclusion chromatography on Sephadex G-25 (eluted with 0.01 M PBS, pH 7.2). Radioactivity associated with protein was determined using a γ counter or dose calibrator. Protein concentration was determined using Bio-Rad protein assay. The amount of cross-linking of protein was determined using a BioSep column 3000 (eluted with 0.1 M PBS, pH 7.2).

The relative immunoreactivity was determined by comparing the immunoreactivity of the new radioimmunoconjugates with that of the ^{125}I−mAb. The mAb (similar to the one radiolabeled with ^{64}Cu) was radiolabeled with ^{125}I according to Fracker and Speck (*24*), resulting in one iodide per mAb. Two plates (Immulon 2, consisting of 6 × 12 strips) were then prepared; the first measured specific binding and the second non-specific binding. Serially diluted mucin from 4 to 2 ng/mL in 0.05 M PBS, pH 7.2 (100 μL/well), was added to the first plate. Glycine (control for non-specific binding) was plated in parallel onto the second plate. The plates were covered and incubated overnight at 4 °C. Each well was then washed with 0.05% Tween-20 in 0.05 M PBS, pH 7.2 (2 × 200 μL). The wells were blocked with 0.05% Tween-20 in 0.05 M PBS, pH 7.2 (200 μL), for 2 h at 37 °C, then washed with 0.05% Tween in 0.05 M PBS, pH 7.2 (3 × 200 μL). Standard (^{125}I−mAb) and ^{64}Cu−L−mAb solutions (100 μL), 4 μg/mL in 0.05% Tween-20 in 0.05 M PBS, pH 7.2, were added to the first three rows and to the second three rows of wells of each plate, respectively. The plates were incubated for 1.5 h at 37 °C before washing with 0.05% Tween-20 in 0.05 M PBS, pH 7.2 (3 × 200 μL). Finally, the plates were washed with 0.05 M PBS, pH 7.2, and shaken dry. The strips were then removed, and each was counted using a γ counter. Specific binding of the antibody was determined by subtracting the average counts for glycine from the average counts for mucine strips at the same concentration. A saturation curve, correlating absorbance with antigen (in this study it was mucine) concentration, was plotted. A comparison of the saturation curve, generated for standard antibody and test antibody, was used to assess the relative immunoreactivity.

Effect of Reaction Time (Post-conjugation). Typically, **L5** was complexed with $^{64}Cu^{2+}$ [the molar ratio of Cu^{2+}:**L5** was 2] in 0.2 M succinate buffer, pH 4.0, and the resultant complex $[^{64}Cu_2-\mathbf{L5}]^{4+}$ was then conjugated to mAb (3.5 mg/mL at a molar ratio of 23) using EDC as the activating agent (molar ratio of EDC/mAb was 572) in pH 5.0 buffer. The reaction was monitored for up to 2 h, sampling at 15, 30, 60, 120 min. The percentage of $[^{64}Cu_2-\mathbf{L5}]^{4+}$ associated with mAb was determined by size exclusion chromatography (Sephadex-G25 column), eluting with 0.1 M PBS, pH 7.2.

Effect of pH, Concentration of mAb, Molar Ratio of EDC, and Molar Ratio of Ligand to mAb (Preconjugation). Typically, all reactions were allowed to continue for up to 30 min at 37 °C. The resultant conjugated **L5**−mAb was purified and then radiolabeled with $^{64}Cu^{2+}$, and the resultant product was purified as described above. The percentage of $[^{64}Cu_2-\mathbf{L5}]^{4+}$ associated with mAb was determined by size exclusion chromatography on a Sephadex-G25 column (eluted with 0.1 M PBS, pH 7.2). The range of reaction conditions employed is summarized as follows. (i) For effect of pH, **L5** was conjugated to mAb (3.5 mg/mL) (molar ratio **L5**:mAb = 114) at pH 4.5, 5.0, 5.5, or 6.0 using a molar ratio of EDC:mAb of 572. (ii) For effect of mAb concentration, **L5** was conjugated to mAb employing various concentrations of the latter (1.7, 2.6, 3.5, and 4.4 mg/mL; molar ratio **L5**−mAb of 114) at pH 5.0 with a molar ratio of EDC:mAb of 572. (iii) For effect of molar ratio of EDC:mAb, **L5** was conjugated to mAb (3.5 mg/mL; molar ratio **L5**:mAb of 114) at pH 5.0 with varying molar ratio of EDC:mAb of 114, 228, 572, 1145. (iv) For effect of molar ratio of **L5**:mAb, **L5** was conjugated to mAb (3.5 mg/mL) using molar ratios of 23, 57, 114, 229 at pH 5.0, with molar ratio of EDC:mAb of 572.

The $^{64}Cu^{2+}$−**L6**−mAb and $^{64}Cu^{2+}$−**L7**−mAb were prepared using the optimum conditions developed in the previous studies using **L5**.

Non-specific Binding of $^{64}Cu^{2+}$ to mAb. Non-specific binding of $^{64}Cu^{2+}$ to mAb was determined by incubating mAb (30 μg) in 0.1 M phosphate buffer, pH 7 (125 μL), and 10-fold molar excess of ^{64}Cu solution in succinate buffer, pH 4.0 (1/10, v/v). The reaction mixture was incubated at 37 °C for 30 min. Any ^{64}Cu−mAb that might have formed as a result of nonspecific binding of $^{64}Cu^{2+}$ with mAb was monitored by ITLC (mobile phase with 0.01 M EDTA in 0.01 M PBS, pH 7.2).

Animal Studies. Animal studies were carried out with the approval of the Animal Care and Ethics Committee (ACEC) at ANSTO under protocol numbers 2002/164. Nu/nu and Balb/C mice were purchased from the University New South Wales (Australia). LS174T cells (human colon adenocarcinoma cell line) were purchased from the American Type Culture Collection (ATCC) and cultured at ANSTO. Nude mice aged between 6 and 8 weeks (females) were subcutaneous injected with 100 μL of a 1 × 10^7 LS174t cell/mL suspension in PBS. Tumors were allowed to grow to approximately 0.7 × 0.7 cm (over 2 weeks).

Radioimmunoconjugates ^{64}Cu−**L2**−mAb and ^{64}Cu−**L5**−mAb were prepared according to the optimal conditions described above. Typical specific activities were 20.6 MBq/mg [corresponding to 3.5 Cu^{2+} or 3.5 ligands per antibody for the ^{64}Cu−**L2**−mAb] and 30.5 MBq/mg [corresponding to 5.5 Cu^{2+} or 2.7 ligands per antibody ^{64}Cu−**L5**−mAb]. The solutions were diluted to approximately 6 MBq/mL in 0.9% saline, and the solution was filtered (0.22 μm) prior to injection into nude mice bearing LS174T tumors. Nude mice bearing LS174T tumors were injected with 100 μL of 0.60 MBq (on 29 μg protein) for ^{64}Cu−**L2**−mAb or 0.64 MBq (on 21 μg of mAb protein) for ^{64}Cu−**L5**−mAb. At the required time interval each mouse was anaesthetized with CO_2 for cardiac puncture and then sacrificed by cervical dislocation (three mice per time point). Individual mice were dissected, and the organs and selected tissues were removed and weighed. Associated radioactivity was determined using a γ counter. The percentage of the injected dose in each organ as well as the percentage of the injected dose per gram was calculated.

RESULTS

Complexation of $^{64}Cu^{2+}$ by L6−L10. The effect of pH on the formation of the ^{64}Cu−L (L = **L6**−**L10**) complexes is shown in Figure 3.

The complexation of $^{64}Cu^{2+}$ at pH 3.0 and 37 °C over 30 min by the mono-rings **L6** and **L7** only reached 70% and 81%, respectively. However, raising the pH of the reaction mixture to ≥4.0 resulted in complete complexation of the available $^{64}Cu^{2+}$. In contrast to the above, complete formation of ^{64}Cu−**L8** was not achieved at pH ≤ 7.0. At pH 6.0 only 25% of this complex was formed. The complete formation of ^{64}Cu−**L8** was achieved only at a pH ≥ 8.0

Incomplete formation of $^{64}Cu_2$−**L9** occurred over the pH range investigated after 30 min at 37 °C. At pH ≥ 4.0 it was found that only between 65% and 68% of the above species had formed. In contrast, the related mononuclear complex of

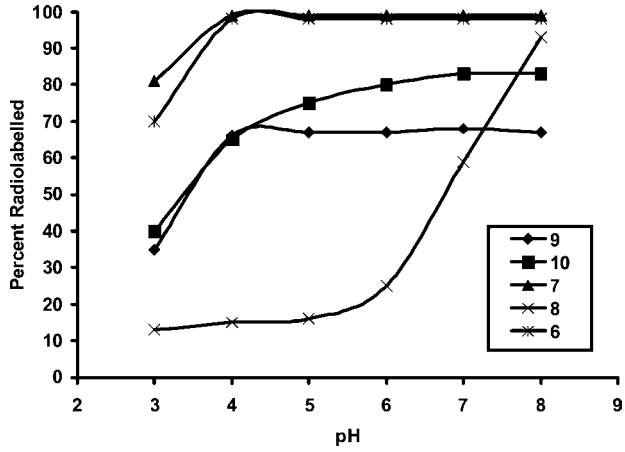

Figure 3. Percent of $^{64}Cu^{2+}$ complexed with various ligands at micromolar concentrations at 37 °C within 30 min. For additional information concerning copper-ligand loading under other conditions, see text.

the mono-ring ligand **L6** was formed in >95% under the same conditions. Complexation of $^{64}Cu_2$−**L9** at ≥95% was only achieved after the reaction mixture (pH 5.0) was heated at 50 °C for 1 h.

There was also no complete formation of $^{64}Cu_3$−**L10** when $^{64}Cu^{2+}$ was reacted with **L10** (at 37 °C for 30 min) in a 3:1 molar ratio over the range of pH values shown in Figure 3. At pH 3.0 only 40% of the metal is bound to **L10**. This percentage increased with increasing pH. By pH 4.0 the percentage of complex formed was 65. Nevertheless, by pH ≥ 8.0 complexation was still not complete, with only 83% of $^{64}Cu^{2+}$ bound.

Human Serum Stability Studies. The mono-ring complexes of types ^{64}Cu−**L6** and ^{64}Cu−**L7** were found to be stable in human serum over 72 h (≤0.5% loss of $^{64}Cu^{2+}$). However, the ^{64}Cu−**L8** complex was observed to break down rapidly in human serum. This is not surprising given that the formation constant (log K_1) for the complex of the unsubstituted parent of **L8,** dioxocyclam, is only 8.75 (*5*), whereas it is 27.2 for the Cu^{2+} complex of cyclam **(**1,4,8,11-tetraazacyclotetradecane), the parent compound for both **L6** and **L7**. Furthermore, the value for dioxocyclam with Cu^{2+} is significantly lower than for the Cu^{2+} complex of histidine (log K = 17.5). As a consequence, trans-metalation of $^{64}Cu^{2+}$ to serum protein is expected to proceed readily *in vivo*. Once complex is forced to >95% using the conditions described above, the resulting bis-Cu complex of **L9** is stable in serum. This stability was comparable to the complexes of the single ring systems **L6** and **L7** described above.

The behavior of the three-ring, ^{64}Cu complex of **L10** in human serum is not as straightforward as that of the above-mentioned complexes. As mentioned already, **L10** incorporates two different ring types (two "a" rings that are similar to the ring in **L6** and a "b" ring that is similar to the ring in **L8**) and only binds 83% of the $^{64}Cu^{2+}$ when reacted at pH 8.0 with **L10** in a 3:1 molar ratio. The complex formed can thus be expressed as $[^{64}Cu_n$−**L10**$]^{m+}$ where n is >2 but <3. As expected, the stability of this species in serum does appear to resemble that observed for a combination of ^{64}Cu−**L6** and ^{64}Cu−**L8**. Hence, for the reasons discussed above any loss of $^{64}Cu^{2+}$ from the complex is postulated to correspond to loss from ring "b".

When **L10** was reacted at pH 8.0 with 3 molar equivalents of $^{64}Cu^{2+}$, 83% of the $^{64}Cu^{2+}$ was taken up by this ligand. The complex formed can be expressed as $[^{64}Cu_n$−**L10**$]^{m+}$ where n is >2 and <3. The stability of this species in serum would be expected to resemble those for $[^{64}$Cu−**L8**$]^{2+}$ and $[^{64}$Cu−**L6**$]^{2+}$. For $[^{64}Cu_n$−**L10**$]^{m+}$ this seems to be the case. After 24 h of incubation, 20% of the $^{64}Cu^{2+}$ had been released from $[^{64}Cu_n$−**L10**$]^{m+}$. However, after 48 h, there was no further significant (within experimental error) amount of $^{64}Cu^{2+}$ released from this complex. Hence, any loss of total $^{64}Cu^{2+}$ from the complex is postulated to correspond to mainly loss of $^{64}Cu^{2+}$ originally bound to ring "b", again for the reasons discussed above (Table 2).

When **L10** was reacted with $^{64}Cu^{2+}$ (in 0.1 M succinate buffer, pH 4.0) in a 1:3 ratio, 65% of the $^{64}Cu^{2+}$ was taken up by **L10**, and it was assumed that the two "a" rings were the ones to participate in complex formation. When this complex was incubated in human serum there was only a nominal 2% of $^{64}Cu^{2+}$ released over the 24 h incubation time. Within experimental error, such a percentage is insignificant. No further release (≤0.5%) was observed to occur at the completion of the 72 h incubation time.

When $^{64}Cu^{2+}$ was reacted with **L10** in a 2:1 molar ratio, it was found that 98% of the $^{64}Cu^{2+}$ was bound to **L10** to form $[^{64}Cu_2$−**L10**$]^{4+}$ (in 0.1 M succinate buffer, pH 4.0). Again, within experimental error, this represents essentially complete uptake by two macrocyclic sites. When this complex was incubated in serum, it was found that there was no significant (≤0.5%) loss of $^{64}Cu^{2+}$ to the serum over 72 h. This is in accord with $^{64}Cu^{2+}$ binding to the two "a" rings, behavior that is in accord with that observed for **L6**.

Radiolabeling of Antibodies. *Effect of Reaction Time (Postconjugation).* Ligand **L5** was complexed with $^{64}Cu^{2+}$ in succinate buffer at pH 4.0, and the resultant complex was then conjugated to mAb using EDC in pH 5.0 buffer. The formation of **L5**−mAb conjugates was followed and analyzed at set intervals of 15, 30, 60, and 120 min. The percentage of $[^{64}Cu_2$−**L5**$]^{4+}$ associated with mAb reached 23% at 30 min, and no further significant change in the percentage of $[^{64}Cu_2$−**L5**$]^{4+}$ associated with mAb was noted after 120 min. Nakajima and Ikada (*27*) reported that EDC is stable at neutral and higher pH but will reduce to about 65% after 25 min in weakly acidic conditions (pH 4.0). This may explain why there was no increase in percentage of $[^{64}Cu_2$−**L5**$]^{4+}$ associated with the mAb after 30 min.

pH Employed for the Conjugation Reaction. The influence of pH on the formation of **L5**−mAb (subsequently quantified as the molar ratio of bound $^{64}Cu^{2+}$:mAb) is shown in Figure 4. The number of calculated ligands was based on the assumption that **L5** binds only two $^{64}Cu^{2+}$ ions. Over the pH range 4.0−6.0 no significant difference in the molar ratio of $^{64}Cu^{2+}$:mAb in the $^{64}Cu^{2+}$−**L5**−mAb conjugate occurred. The results also showed that there was no significant cross-linking of protein molecules.

The influence of mAb concentration on the formation of **L5**−mAb (subsequently quantified as the molar ratio of $^{64}Cu^{2+}$:mAb) (see Figure 5) and on any inter-antibody cross-linking

Table 2. Stabilities of the $[^{64}Cu_n$−L$]^{m+}$ Complexes in Human Serum (Indicated by the Percentage of $[^{64}Cu_n$−L$]^{m+}$ That Remains as an Intact Complex after the Listed Incubation Period)

molar ratio L/Cu			% $^{64}Cu^{2+}$−L complex remaining after the following incubation period				
L10	$^{64}Cu^{2+}$	pH	0 h	24 h	48 h	72 h	% ^{64}Cu lost from complex
1	3	8	83	63	63	63	20
1	3	4	65	62	62	62	3
1	2	4	98	98	98	98	0

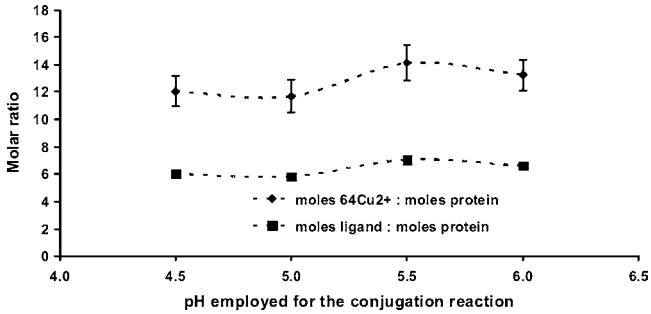

Figure 4. Effect of pH on the conjugation of **L5** to mAb. Reaction conditions are as follows: molar ratio mAb:EDC:**L5** = 1:572:114; [mAb] in the final reaction mixture, 3.5 mg/mL; 0.1 M MES buffer; reaction time, 30 min; temperature, 37 °C.

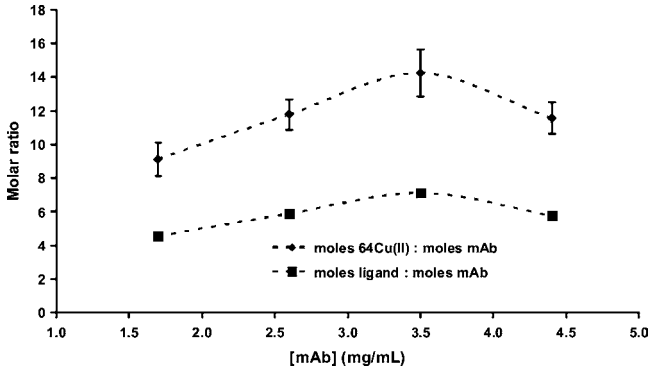

Figure 5. Effect of concentration of protein in the final reaction mixture on the formation of **L5**−mAb. Reaction conditions are as follows: molar ratio mAb:EDC:**L8** 71 = 1:572:114; reaction time, 30 min; 0.1 M MES buffer, pH 5.0; temperature, 37 °C.

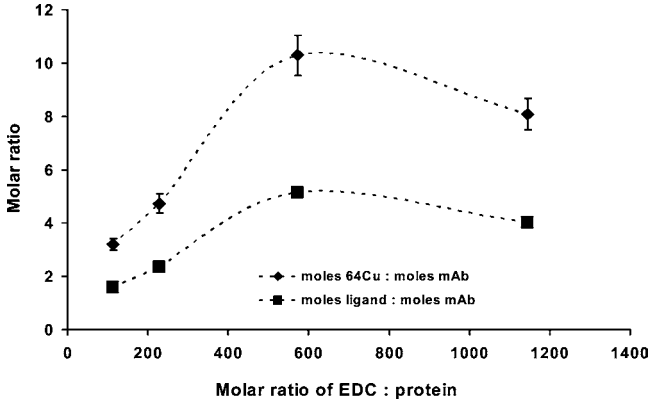

Figure 6. Effect of the molar ratio of EDC:mAb on the formation of **L5**−mAb. Reaction conditions are as follows: molar ratio mAb:**L5** = 1:114; [mAb] in the final reaction mixture, 3.5 mg/mL; reaction time, 30 min; 0.1 M MES buffer, pH 5.0.

was investigated by HPLC. Data show a slight increase in the molar ratio of $^{64}Cu^{2+}$:mAb when the mAb concentration was increased from 1.7 to 2.6 mg/mL but no further change at 3.5 mg/mL, and higher concentrations were observed. The inter-antibody cross-linking was <3% for all concentrations except at 4.4 mg/mL where it was ≤6%.

The influence of the molar ratio of EDC to mAb on the formation of **L5**−mAb is shown in Figure 6. Efficiency of radiolabeling increased significantly as the EDC molar ratio to protein increased from 114 to 572, with a slight decrease at 1145. Inter-antibody cross-linking remained low at <4% for all EDC:protein ratios except at 1145 where it increased (>5%), which explains the apparent decrease in radiolabeling efficiency at the higher EDC ratio.

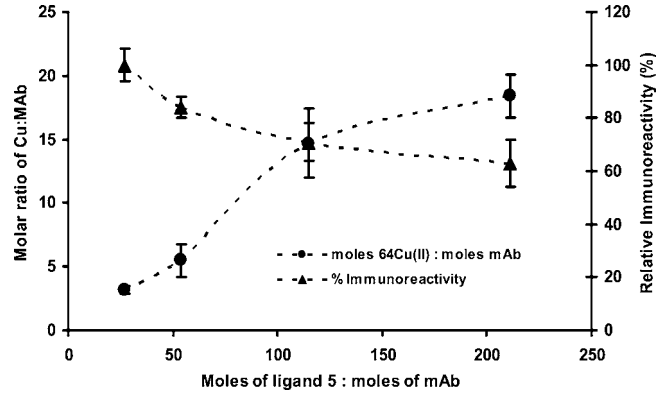

Figure 7. Influence of molar ratio of ligand **5**:moles of mAb on the formation of **L5**−mAb. Reaction conditions are as follows: molar ratio mAb:EDC = 1:572; [mAb] in the final reaction mixture, 3.5 mg/mL; reaction time, 30 min; 0.1 M MES buffer, pH 5 at 37 °C.

*Effect of Molar Ratio of Ligand **L5**:mAb on the Formation of **L5**−mAb.* Figure 7 summarizes the influence of the molar ratio of **L5**:mAb on the formation of **L5**−mAb. As expected, the molar ratio of $^{64}Cu^{2+}$:mAb increased with an increase in the moles of ligand **5**:moles of mAb ratio in the conjugation reaction. The immunoreactivity of ^{64}Cu−**L5**−mAb with a molar ratio of $^{64}Cu^{2+}$:mAb < 5.5 (corresponding to approximately 2.7 ligands per mAb) was found to be satisfactory (>80%). When the ratio of $^{64}Cu^{2+}$:mAb was >14 (corresponding to approximately 7 ligands:mAb), the immunoreactivity of ^{64}Cu−**L5**−mAb was substantially reduced (≤71%) and was not considered acceptable for *in vivo* studies.

Once the optimum conditions for the formation of **L5**−mAb were established, they were applied to the production of the **L1**−mAb and **L2**−mAb immunoconjugates. That is, **L1** and **L2** were reacted with the mAb at the molar ratio of mAb:ligand:EDC = 1:57:572. The concentration of mAb was fixed to 3.5 mg/mL, and the reaction was allowed to continue for 30 min in 0.1 M MES, pH 5.0 and 37 °C. The final products were isolated and characterized by HPLC; the ratios of purified $^{64}Cu^{2+}$:mAb were found to be 3.0 ± 0.3 and 3.4 ± 0.3 for **L1**−mAb and **L2**−mAb, respectively. Immunoreactivity for the radioimmunoconjugates was satisfactory (>80%), and as a result, they were selected for further evaluation in tumor bearing mice.

Biodistribution of Radioimmunoconjugates. The resultant specific activity for ^{64}Cu−**L2**−mAb was 20.6 MBq/mg which corresponds to 3.5 Cu^{2+} (or 3.5 ligands) per antibody. The specific activity for ^{64}Cu−**L5**−mAb was considerably higher at 30.5 MBq/mg, which corresponds to 5.5 Cu^{2+} (or 2.7 ligands) per antibody. Solutions of each ^{64}Cu radioimmunoconjugate were then diluted with 0.9% saline solution to approximately 6 MBq/mL, and 100 uL of this solution was injected into each nude mouse. The biodistribution of ^{64}Cu−**L2**−mAb and ^{64}Cu−**L5**−mAb in LS174T tumor-bearing nude mice is presented in Figure 8.

The primary objective of the animal studies was to assess whether the ^{64}Cu−**L5**−mAb containing less **L5** ligands per antibody molecule but more $^{64}Cu^{2+}$ binding sites would have similar uptake to the ^{64}Cu−**L2**−mAb. In fact, the biodistribution studies clearly illustrate that the uptake of ^{64}Cu−**L2**−mAb in the tumor over the time interval investigated appears broadly similar to that observed for ^{64}Cu−**L5**−mAb. The total accumulated radioactivity at 24 and 48 h was 23.7 ± 4.3% ID/g and 35.3 ± 11.2% ID/g, respectively, for ^{64}Cu−**L2**−mAb and 20.6 ± 2.2% ID/g and 29.6 ± 1.1% ID/g for ^{64}Cu−**L5**−mAb. While the total activity at the tumor site for ^{64}Cu−**L5**−mAb is similar to that for ^{64}Cu−**L2**−mAb, the former achieves this uptake with only 70% of the antibody conjugate.

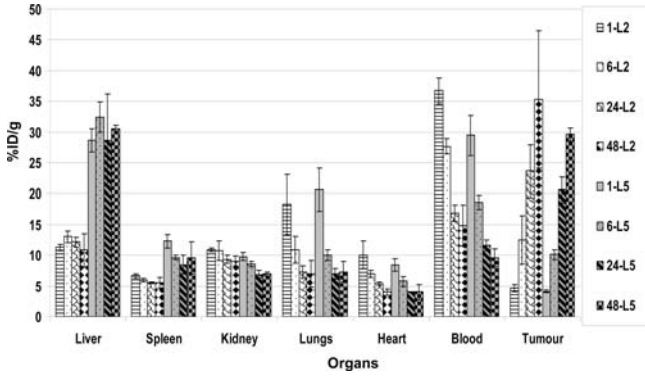

Figure 8. Biodistribution of ^{64}Cu−**L2**-mAB and ^{64}Cu−**L5**−mAb in nude mice bearing LS174T tumor.

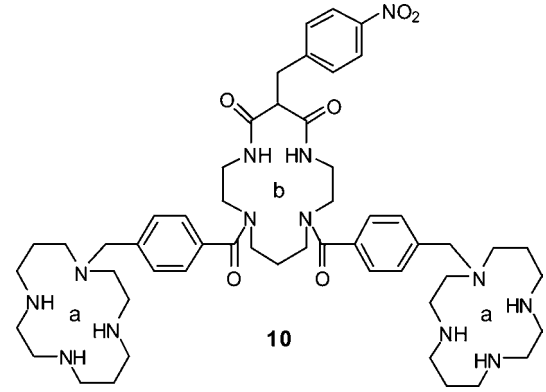

Figure 9. [13-(4-Nitrobenzyl)-4(11-(4-aminobenzoyl)-1,4,8,11-tetracyclotetradecane),8-(1-aminobenzoyl)-1,4,8,11-tetracyclotetradecane)]-1,4,8,11-tetracyclotetradecane-12,14-dione.

Examining the radioactivity remaining in the blood at 48 h indicates that the clearance of ^{64}Cu−**L5**−mAb (9.6 ± 1.5% ID/g) appears to be faster than that for ^{64}Cu−**L2**−mAb (14.6 ± 3.3% ID/g). The accumulation and retention of ^{64}Cu−**L5**−mAb (30.5 ± 0.6% ID/g at 48 h) in the liver were approximately 3-fold higher than for ^{64}Cu−**L2**−mAb (10.9 ± 2.7% ID/g at 48 h) over the time interval investigated.

DISCUSSION

The present study involves an investigation into whether tris- or bis-macrocyclic bifunctional ligands (i.e., **L5**, **L4**) are more efficient for radiolabeling an antibody compared to monomacrocyclic ligands (**L1**, **L2**, and **L3**). The complexation of the $^{64}Cu^{2+}$ with the ligands given in Figure 2 was investigated over a range of conditions (i.e., pH, buffer, and temperature) but all at equimolar concentration of M:L where L: represents the available binding site in the bifunctional ligand. The results showed that **L6** and **L7** complexed $^{64}Cu^{2+}$ efficiently (>95%) at >pH 4; however, complexation by **L8** was only efficient at >pH 8. This behavior is broadly similar to that observed for the (unsubstituted) parent compound of **L8** reported by Cutler *et al*. (*25*). Under related conditions these workers observed that only 25% complexation of the unsubstituted parent occurred at pH 5.5 at 37 °C after 1 h. This undoubtedly reflects the presence of the two amide groups in **L8**, since for strong complexation these groups need to be deprotonated. Thus, as found for the parent amide ligand, the formation of ^{64}Cu−**L8** in this study was found to be strongly pH dependent, with higher pH values required to promote complete complexation.

Complexation of $^{64}Cu_2$−**L9** was only achieved after the reaction mixture (pH 5.0) was heated at 50 °C for 1 h. Previous reports (*26*) have discussed the Cu^{2+} complexation behavior of the parent unsubstituted bis-macrocycle ligand **L9** and indicated that weak metal−metal communication is present that reflects the proximate locations of the Cu^{2+} ions. While statistical effects and charge repulsion considerations will result in weaker binding of copper in the second cavity of this ligand, these factors are likely to influence the non-complete complexation of two Cu^{2+} ions by **L9** under the conditions investigated in this study.

The three ring systems did not form the $^{64}Cu_3$−**L10** complex under any of the conditions investigated in this study. Maximum $^{64}Cu^{2+}$ labeling efficiency of 65% was achieved at pH 4, and at pH ≥ 8.0, 83% of **L10** was labeled. While statistical effects are expected to influence copper binding to the second and third rings in this case, inhibition of binding due to charge repulsion was expected to be negligible because of the considerably larger spacing of the three macrocyclic rings in **L10** compared to the two ring system in **L9**. By analogy with the formation of ^{64}Cu−**L6** and ^{64}Cu−**L8** (and the structures of the corresponding ligands) the two "a" rings in **L10** are expected to behave similarly to that in **L6** while the "b" ring is expected to be broadly similar to that in **L8** (see Figure 9). Hence, on the basis of the formation of ^{64}Cu−**L6**, it is expected that the two "a" rings of **L10** will dominate in binding $^{64}Cu^{2+}$ ions at lower pH values (such as at pH 4.0), and this was in accordance with the observed behavior. When **L10** was reacted with a 2 molar ratio of $^{64}Cu^{2+}$ (at pH 4.0, 37 °C for 30 min), it was found that 98% of the $^{64}Cu^{2+}$ bound under these conditions; that is, effectively complete binding had occurred. At higher pH values it is expected that the "b" ring might start to participate in coordinating $^{64}Cu^{2+}$. However, at pH ≥ 8.0 the percentage of $^{64}Cu^{2+}$ bound to **L10** had only increased marginally and, unlike the situation for **L8**, was found to be well short of the "ideal" value of ≥95%.

Collectively the complexation and serum stability results indicate that the mono-ring ligands **L6** and **L7** are suitable for use in radiolabeling mAbs with $^{64}Cu^{2+}$. Namely, these ligands bind $^{64}Cu^{2+}$ in a rapid manner at pH 4.0 and 37 °C (a pH value at which the formation of non-specific binding between $^{64}Cu^{2+}$ and mAb is not significant) as well as yielding stable $^{64}Cu^{2+}$ complexes in human serum. As the mono-ring complex of ^{64}Cu with **L8** was found to be rather unstable in human serum, its use was not pursued further for protein radiolabeling. While the double-ring **L9** yielded a ^{64}Cu complex that is stable in human serum, its formation was conducted at 50 °C. Such conditions were considered inappropriate for radiolabeling the mAb.

The complexation and serum stability collectively showed that only anilino derivatives **(L1**, **L2**, and **L5**) of **L4**, **L9**, and **L10** were appropriate for conjugating to the mAb. Hence, the conjugation of **L5** was optimized for a range of conditions (i.e., pH, concentration of EDC, mAb, and molar ratio of ligand to mAb). The optimum condition for the formation of **L5**−mAb was found to be a molar ratio of mAb:ligand:EDC = 1:57:572 and a mAb reaction concentration of 3.5 mg/mL. The reactions were conducted at pH 5.0 at 37 °C and found to be complete within 30 min. These conditions were also used for the production of the **L1**−mAb and **L2**−mAb immunoconjugates. Purified **L1**−mAb and **L2**−mAb were found (by HPLC) to have similar $^{64}Cu^{2+}$:mAb ratios ([3.0 and 3.4 (±0.3), respectively], and for **L5**−mAb they were ∼5.5 (corresponding to 2.7 ligands per mAb). Immunoreactivity for all radioimmunoconjugates was found to be satisfactory (>80%).

The primary objective of the animal studies was to assess whether the ^{64}Cu−**L5**−mAb containing less **L5** ligands per antibody molecule but more $^{64}Cu^{2+}$ binding sites would have similar uptake to the ^{64}Cu−**L2**−mAb. The biodistribution conducted over 48 h showed that the uptake of ^{64}Cu−**L2**−mAb in the tumor was similar to that observed for ^{64}Cu−**L5**−mAb.

The total accumulated radioactivity at 48 h was 35.3 ± 11.2% ID/g and 29.6 ± 1.1% ID/g, for ^{64}Cu−**L2**−mAb and ^{64}Cu−**L5**−mAb, respectively. While the total activity at the tumor site for ^{64}Cu−**L5**−mAb was similar to that for ^{64}Cu−**L2**−mAb, however, the former radioimmunoconjugate achieves this uptake with only 70% of the antibody conjugate. Clearance from all organs except the liver were comparable for these radioimmunoconjugates. The accumulation and retention of ^{64}Cu−**L5**−mAb in the liver were approximately 3-fold higher than for ^{64}Cu−**L2**−mAb over the time interval investigated. The clearance of ^{64}Cu−**L5**−mAb was found to be faster than that for ^{64}Cu−**L2**−mAb. There are a few factors that have been reported to influence the high uptake and slow clearance of radioabeled mAbs or peptides in organs such as the liver. These include the stability of the metal complex involved, the type of linker between the metal complex and the mAb, the charge on the metal complex, and the lipophilicity of the radioimmunoconjugate and/or radiometabolites (*5*, *28*−*33*). In this instance the high uptake and retention of radioactivity in the liver by the ^{64}Cu−**L5**−mAb is most probably a reflection of the increase in lipophilicity of **L5** compared to **L2**. The serum stability studies with the $[Cu_n-\mathbf{L5}]^{2n+}$ and $[Cu-\mathbf{L2}]^{2+}$ showed no significant breakdown (<0.5%) for both complexes over 72 h. The apparent stability of the ^{64}Cu−**L5**−mAb at the tumor site also supports the proposal that the ^{64}Cu−**L5** complex of this radioimmunconjugate is reasonably stable *in vivo*.

As the peptide bond generated in the synthesis of each of the radioimmunoconjugates, ^{64}Cu−**L5**−mAb and ^{64}Cu−**L2**−mAb, is the same, it is unlikely that the difference in the liver uptake reflects the presence of this linker type. The increased lipophilicity arising from the presence of phenyl group(s) has been suggested to aid a radioimmunoconjugate and/or a radiometabolite to be cleared preferentially via the liver (*32*). However, as the liver is also the natural site for bioaccumulation and metabolism of Cu^{2+}, it is the more likely rationale for the observed slow clearance of ^{64}Cu from the liver for both new radioimmunoconjugates.

Several classes of bifunctional chelators (from open chain to macrocyclic) have been used for radiolabeling mAbs with either ^{64}Cu or ^{67}Cu. A tetraazacarboxylate derivative, bat (Figure 1), has been used to radiolabel Lym-1 mAb with ^{67}Cu (*34*). While the animal models are quite different, the trends in behavior of the new ^{64}Cu radioimmunoconjugates relative to ^{67}Cu−bat lym-1 mAb *in vivo* are worth noting. For both ^{64}Cu−**L2**−mAb and ^{64}Cu−**L5**−mAb the tumor to blood ratios increased with time. The increases in this ratio for ^{64}Cu−**L2**−mAb and ^{64}Cu−**L5**−mAb at 24 and 48 h were found to be quite substantial (^{64}Cu−**L2**−mAb, 1.4 ± 0.4 at 24 h to 2.4 ± 1.3 at 48 h; ^{64}Cu−**L5**−mAb, 1.8 ± 0.3 at 24 h to 3.1 ± 0.6 at 48 h). Compared to the bat radioimmunoconjugate mentioned above, the present ^{64}Cu radioimmunoconjugates show greatly enhanced stability *in vivo*. This clearly reflects the increased kinetic stability of the tetraazamacrocyclic systems **L2** and **L5** compared to that of the tetraaza-substituted, tetraazacarboxylate derivative bat (*34*).

In summary, the results for the new ^{64}Cu radioimmunoconjugates, ^{64}Cu−**L2**−mAb and ^{64}Cu−**L5**−mAb, are in accord with greater uptake at the tumor site than occurs for the related systems mentioned above. They also show greater stability at the tumor site and higher tumor to blood ratios than those reported previously for the system incorporating the substituted tetraaza macrocycle, bat. Perhaps the most significant result of the present study is the similar uptake at the tumor site of ^{64}Cu−**L2**−mAb and of ^{64}Cu−**L5**−mAb. The latter achieved high tumor uptake with significantly less antibody and less chemical modification of the protein. This illustrates the potential of the new multiring tetraazamacrocycle system, **L5**, for generating higher specific radioimmunoconjugates.

LITERATURE CITED

(1) Liang, X. Y., and Sadler, P. J. (2004) Cyclam complexes and their applications in medicine. *Chem. Soc. Rev. 33*, 246–266.

(2) Reichert, J. M. (2002) Therapeutic monoclonal antibodies: trends in development and approval in the US. *Curr. Opin. Mol. Ther. 4*, 110–118.

(3) Anderson, C. J., Schwarz, S. W., Connett, J. M., Cutler, C., Guo, L. W., Germain, C. J., Philpott, G. W., Zinn, K. R., Greiner, D. P., Meares, C. F., and Welch, M. J. (1995) Preparation, biodistribution and dosimetry of copper-64-labeled anti-colorectal carcinoma monoclonal antibody fragments 1A3-F(ab′)2. *J. Nucl. Med. 36*, 850–858.

(4) Chen, X. Y., Hou, Y. P., Tohme, M., Park, R., Khankaldyyan, V., Gonzales-Gomex, I., Bading, J. R., Laug, W. E., and Conti, P. S. (2004) Pegylated Arg-Gly-Asp peptide: Cu-64 labeling and PET imaging of brain tumor alpha(v)beta(3)-integrin expression. *J. Nucl. Med. 45*, 1776–1783.

(5) Smith, S. V. (2004) Molecular imaging with copper-64. *J. Inorg. Biochem. 98*, 1874–1901.

(6) Smith, S. V. (2008) Sarar technology for the application of copper-64 in biology and materials science. *Q. J. Nucl. Med. Mol. Imaging. 52*, 193–202.

(7) Voss, S. D., Smith, S. V., DiBartolo, N., Mclntos, L. J., Cyr, E. M., Bonab, A. A., Dearling, J. L. J., Carter, E. A., Fischman, A. J., Treves, S. T., Gillies, S. D., Sargeson, A. M., Huston, J. S., and Packard, A. B. (2007) Positron emission tomography (PET) imaging of neuroblastoma and melanoma with Cu-64-SarAr immunoconjugates. *Proc. Natl. Acad. Sci. U.S.A. 104*, 17489–17493.

(8) Smith, A., Alberto, R., Blaeuenstein, P., Novakhofer, I., Maecke, H. R., and Schubiger, P. A. (1993) Preclinical evaluation of Cu-67 labeled intact and fragmented anti-colon carcinoma monoclonal antibody Mab35. *Cancer Res. 53*, 5727–5733.

(9) Kaden, T. A. (2006) Labeling monoclonal antibodies with macrocyclic radiometal complexes. A challenge for coordination chemists. *Dalton Trans.* 3617–3623.

(10) Morphy, J. R., Parker, D., Kataky, R., Eaton, M. A. W., Millican, A. T., Alexander, R., Harrison, A., and Walker, C. (1990) Towards tumor targetting with copper radiolabeled macrocycle antibody conjugates—synthesis, antibody linkage and complexation behavior. *J. Chem. Soc., Perkin Trans. 2* 573–585.

(11) Franz, J., Freeman, G. M., Barefield, E. K., Volkert, W. A., Ehrhardt, G. J., and Holmes, R. A. (1987) Labeling of antibodies with Cu-64 using a conjugated macrocyclic amine chelating agent. *Nucl. Med. Biol. 14*, 479–484.

(12) Liang, F., Wan, S. H., Li, Z., Xiong, X. Q., Yang, L., Zhou, X., and Wu, C. T. (2006) Medical applications of macrocyclic polyamines. *Curr. Med. Chem. 13*, 711–727.

(13) Boswell, C. A., Sun, X. K., Niu, W. J., Weisman, G. R., Wong, E. H., Rheingold, A. L., and Anderson, C. J. (2004) Comparative in vivo stability of copper-64-labeled cross-bridged and conventional tetraazamacrocyclic complexes. *J. Med. Chem. 47*, 1465–1474.

(14) Sun, X. K., Wuest, M., Weisman, G. R., Wong, E. H., Reed, D. P., Boswell, C. A., Motekaitis, R., Martell, A. E., Welch, M. J., and Anderson, C. J. (2002) Radiolabeling and in vivo behavior of copper-64-labeled cross-bridged cyclam ligands. *J. Med. Chem. 45*, 469–477.

(15) Anderson, C. J., Rogers, B. E., Connet, J. M., Guo, L. W., Swarz, S. W., Zinn, K. R., and Welch, M. J. (1994) Comparison of two bifunctional chelates for labeling Cu-64 to MAb 1A3 and 1A3-F(ab′)2: chemistry and animal biodistribution. *J. Labelled Compd. Radiopharm. 35*, 313–315.

(16) Jones-Wilson, T. M., Deal, K. A., Anderson, C. J., McCarthy, D. W., Kovacs, Z., Motekaitis, R. J., Sherry, A. D., Martell, A. E., and Welch, M. J. (1998) The in vivo behavior of copper-64-

labeled azamacrocyclic complexes. *Nucl. Med. Biol. 25*, 523–530.
(17) Zimmermann, K., Grunberg, J., Honer, M., Ametamey, S., Schubiger, P. A., and Novak-Hofer, I. (2003) Targeting of renal carcinoma with (Cu)-67/64-labeled anti-L1-CAM antibody chCE7: selection of copper ligands and PET imaging. *Nucl. Med. Biol. 30*, 417–427.
(18) Goodwin, D. A., and Meares, C. F. (1997) Pretargeting. General principles; October 10−12 1996. *Cancer 80*, 2675–2680.
(19) Janssen, M. L., Oyen, W. J., Dijkgraaf, I., Massuger, L. F., Frielink, C., Edwards, D. S., Rajopadhye, M., Boonstra, H., Corstens, F. H., and Boerman, O. C. (2002) Tumor targeting with radiolabeled alpha(v)beta(3) integrin binding peptides in a nude mouse model. *Cancer Res. 62*, 6146–6151.
(20) Goodwin, D. A., and Meares, C. F. (2001) Advances in pretargeting biotechnology. *Biotechnol. Adv. 19*, 435–450.
(21) Chinol, M., Grana, C., Gennari, R., Cremonesi, M., Geraghty, J. G., and Paganelli, G. (2000) Pretargeted radioimmunotherapy of cancer. *Radioimmunother. Cancer* 169–193.
(22) Ramli, M., Dong, Y., Lindoy, L. F., Smith, S. V., and Wilson, J. G. (2005) Synthesis of one-, two- and three-ring macrocyclic, bifunctional compounds for use in radiolabeling monoclonal antibodies. *J. Heterocycl. Chem. 42*, 77–83.
(23) Pierce Chemical Company. (6/2001) Instructions for EDC. Product Description Numbers 22980 and 22981.
(24) Fracker, P. J., and Speck, J. (1978) Protein and cell membrane iodinations with sparingly soluble chloroamide, 1,3,4,6-tetrachloro-3α-6-α-diphenyl-glycoluril. *Biochem. Biophys. Res. Commun. 80*, 849–857.
(25) Cutler, C. S., Wuest, M., Anderson, C. J., Reichert, D. E., Sun, Y. Z., Martell, A. E., and Welch, M. J. (2000) Labeling and in vivo evaluation of novel copper (II) dioxotetraazamacrocyclic complexes. *Nucl. Med. Biol. 27*, 375–380.
(26) Lindoy, L. F. (1998) The transition metal ion chemistry of linked macrocyclic ligands. *Adv. Inorg. Chem. 45*, 75–125.
(27) Nakajima, N., and Ikada, Y. (1995) Mechanism of amide formation by carboiimide for bioconjugation in aqueous media. *Bioconjugate Chem. 6*, 123–130.
(28) Cole, W. C., Denardo, S. J., Meares, C. F., McCall, M. J., Denardo, G. L., Epstein, A. L., Obrien, H. A., and Moi, M. K. (1987) Comparative serum stability of radiochelates for antibody radiopharmaceuticals. *J. Nucl. Med. 28*, 83–90.
(29) Anderson, C. J., Pajeau, T. S., Edwards, W. B., Sherman, E. L. C., Rogers, B. E., and Welch, M. J. (1995) In-vitro and in vivo evaluation of copper-64 octreotide conjugates. *J. Nucl. Med. 36*, 2315–2325.
(30) Rogers, B. E., Anderson, C. J., Connett, J. M., Guo, L. W., Edwards, W. B., Sherman, E. L. C., Zinn, K. R., and Welch, M. J. (1996) Comparison of four bifunctional chelates for radiolabeling monoclonal antibodies with copper radioisotopes: biodistribution and metabolism. *Bioconjugate Chem. 7*, 511–522.
(31) Duncan, J. R., and Welch, M. J. (1993) Intracellular metabolism of indium-111 DTPA labeled receptor targeted proteins. *J. Nucl. Med. 34*, 1728–1738.
(32) Arano, Y., Mukai, T., Uezono, T., Wakisaka, K., Motonari, H., Akizawa, H., Taoka, Y., and Yokoyama, A. (1994) A biological method to evaluate bi-functional chelating agents to label antibodies with metallic radionuclides. *J. Nucl. Med. 35*, 890–898.
(33) Kinuya, S., Jeong, J. M., Garmestani, K., Saga, T., Camera, L., Brechbiel, M. W., Gansow, O. A., Carrasquillo, J. A., Neumann, R. D., and Paik, C. H. (1994) Effect of metabolism on retention of indium-111 labeled monoclonal antibody in liver and blood. *J. Nucl. Med. 35*, 1851–1857.
(34) Deshpande, S. V., Denardo, S. J., Meares, C. F., McCall, M. J., Adams, G. P., Moi, M. K., and Denardo, G. L. (1988) Copper-67 labeled monoclonal antibody Lym-1 a potential radiopharmaceutical for cancer therapy labeling and biodistribution in Raji tumored mice. *J. Nucl. Med. 29*, 217–225.

BC800337D

Protein Delivery with Transportans Is Mediated by Caveolae Rather Than Flotillin-Dependent Pathways

Pille Säälik,[†,⊥] Kärt Padari,[†] Aira Niinep,[†] Annely Lorents,[†] Mats Hansen,[‡,||] Eija Jokitalo,[§] Ülo Langel,[‡,||] and Margus Pooga*[,†,⊥]

Institute of Molecular and Cell Biology, University of Tartu, Estonia, Department of Neurochemistry, Stockholm University, Sweden, Institute of Biotechnology, Electron Microscopy Unit, University of Helsinki, Finland, Institute of Technology, University of Tartu, Estonia, and Estonian Biocentre, Tartu, Estonia. Received September 30, 2008; Revised Manuscript Received March 3, 2009

Delivery of large bioactive cargoes into cells with the help of cell-penetrating peptides (CPPs) is mostly based on endocytic processes. Here we map the cellular pathways used by transportan and transportan 10 (TP10) for protein transduction in HeLa cells. CPP-mediated cellular delivery is often suggested to be lipid-raft-dependent; therefore, we used flotillin-1, caveolin, Rab5, and PI3P as markers to elucidate the involvement of these particular endosomal pathways in the protein uptake process. Confocal laser scanning and electron microscopy reveal only a negligible overlap of avidin/neutravidin conveyed into cells by transportans with the raft marker flotillin-1 or early endosomal markers Rab5 and PI3P. However, about 20% of protein−CPP complexes colocalize with the caveolar/caveosomal marker caveolin, and down-regulation of caveolin-1 by siRNA treatment leads to the inhibition of the CPP-mediated protein uptake by 30−50%. On the contrary, the lack of flotillin-1 increases rather than decreases the CPP-mediated protein transport. The participation of the caveolin-1-dependent pathway in CPP-mediated protein delivery was also corroborated by using caveolin-1 knockout mouse embryonic fibroblasts.

INTRODUCTION

The cellular transport of bioactive but low-permeable molecules using cell-penetrating peptides (CPPs) has been under intense investigation as an alternative mode for drug delivery for the past 15 years. During this period, the number of peptides with putative membrane-translocating abilities has grown dramatically and has also led to the broadening of the meaning of the term CPP toward less explicit characteristics (*1*). Currently CPP is considered a relatively short peptide being capable of gaining access to the cell interior by means of different mechanisms, including endocytosis, and having the capacity to promote the intracellular delivery of covalently or noncovalently attached bioactive cargoes. The main focus of CPP studies has now shifted to improving the specificity of targeting and characterization of the functionality of delivered cargo in cells. However, knowledge about the cell entry mechanism(s) is still of high importance, as the mode of internalization determines addressing of the cargo and thereby its residual activity.

Some CPPs are capable of using a nonvesicular cellular entry mechanism under certain conditions (*2*−*6*). However, in these studies the peptide was carrying a small cargo, a fluorescent tag (*2, 3, 6*) or a short peptide (*4, 5*), and the observed diffuse cellular staining, which is thought to reflect a nonvesicular internalization mode, was detected at high peptide concentrations or low temperature. Still, most peptide−cargo constructions, especially large ones, gain entry to the cell interior by inducing endocytic processes, i.e., within various types of plasma-membrane-derived vesicles (*7*−*9*). The rapidly accumulating knowledge about endocytosis mechanisms and intracellular targeting pathways also necessitates a more detailed analysis of routes involved in CPP-mediated cargo delivery and a better definition of the transport vesicles used.

CPPs as relatively unspecific ligands have been associated with many endocytosis routes. Clathrin-mediated endocytosis (CME[1]) is the most common for down-regulation of a variety of plasma membrane receptors. Although different receptors may utilize highly specifically regulated mechanisms, the CME seems to be the general route of uptake (*10*−*12*). Without the specification of the exact mode of CME, this pathway has been shown to be active in CPP-mediated cargo delivery in several experimental systems, although with different efficacy (*13, 14*). In addition, caveolae may participate in CPP-mediated cargo delivery. Caveolae are abundant in some cell types, and their functions extend from endocytosis to cell signaling (*15*). Interestingly, internalization of Tat-GFP fusion protein has been demonstrated to proceed using the caveolar pathway (*16, 17*) but has also been reported to use macropinocytosis (*7*). Macropinocytosis is initiated by certain stimuli (*18*), and it is reported that CPPs activate the cellular signaling cascades and subsequent macropinocytosis in analogy with growth factors as stimuli (*19, 20*). The least characterized/understood type of vesicular transport, clathrin- and caveolin-independent endocytic pathway, is active in pathogen internalization and also in some physiological processes. Simian virus 40 (SV40) has been shown to enter even caveolin-1 (Cav-1) knockout cells, which express dominant-negative Eps15 that interferes with the assembly of the clathrin-coated pits and the formation of caveolae. Accord-

* To whom correspondence should be addressed. Tel: (372)7 375 049, fax: (372)7 420 286, e-mail: mpooga@ut.ee.

[†] Institute of Molecular and Cell Biology, University of Tartu.

[⊥] Estonian Biocentre.

[‡] Stockholm University.

[||] Institute of Technology, University of Tartu.

[§] University of Helsinki.

[1] Abbreviations: AF, Alexa Fluor; Cav, caveolin; CLSM, confocal laser scanning microscopy; CME, clathrin-mediated endocytosis; CtxB, cholera toxin B subunit; FACS, fluorescence-activated cell sorter; Flot-1, flotillin-1; GFP, green fluorescent protein; PI3P, phosphatidyl inositol-3-phosphate; pTat, Tat peptide; siRNA, small interfering RNA; TEM, transmission electron microscopy; TxR, Texas Red; TP, transportan; TP10, transportan 10.

10.1021/bc800416f CCC: $40.75 © 2009 American Chemical Society
Published on Web 04/06/2009

ingly the internalization of SV40 is dependent on cholesterol, microtubules, and Arf1 (*21*). In addition, the internalization of cholera toxin B subunit (CtxB) is not inhibited in cells depleted of functional dynamin and Arf6, and it takes place by inducing formation of a tubular network that is not present in cells with active dynamin and Arf6 (*22*). The network formation was dependent on cholesterol (*22*), suggesting that lipid rafts play a significant role in this type of cellular trafficking. However, the lack of adequate methods for assessing the dynamics of lipids in membranes of living cells limits the studies to using mainly the raft-associated proteins (*23*). Recently, flotillin was suggested to be a membrane-organizing marker protein of lipid rafts. Endocytosis of CtxB subunit via flotillin-positive domains takes place independently of dynamin, and the formed vesicles do not contain proteins characteristic to CME or caveosomes (*24*).

We have described the cellular routing of complexes of transportan and TP10 with protein earlier based on morphological features of used endocytic vehicles (*8, 14*). However, we could not define the nature of a substantial fraction of vesicles that contained complexes of protein and transportan/TP10 by any of the used cellular markers and endocytic inhibitors (*8*). As the recently mapped flotillin-1-marked endocytic pathway and the CPP-mediated cellular delivery are both cholesterol-dependent and flotillin-1-defined membrane areas and endocytic vesicles do not overlap with the clathrin- or caveolin-dependent route (*24, 25*), we analyzed the cellular traffic of complexes of transportan/TP10 and avidin/neutravidin in relation to this novel lipid raft marker. We also included caveolin as a marker of specific type of membrane rafts in cells lacking the typical caveolae. The role of cholesterol rich membrane domains and the respective proteins in transportan/TP10-mediated protein was elucidated by down-regulation of flotillin-1 and caveolin-1 using siRNA. In addition, the cellular localization of complexes in relation to early endosomal markers Rab5 and phosphatidylinositol-3 phosphate (PI3P) was mapped in order to disclose the early steps of transportan-mediated delivery. Our data demonstrate that flotillin-containing lipid rafts do not participate in CPP-mediated delivery, and their absence rather increases translocation efficiency.

EXPERIMENTAL PROCEDURES

Reagents. For immunomicroscopy experiments, the following antibodies (Ab) were used: mouse monoclonal anti-PI3P (Echelon Biosciences, UT), rabbit polyclonal anticaveolin (cat no 610059, BD Transduction Laboratories, Belgium), anti-Rab5 (AbCam, UK), polyclonal antiflotillin-1 (Santa Cruz Biotechnology, Heidelberg, Germany), and mouse monoclonal anti-β1 integrin (anti-CD29, BD Transduction Laboratories). Alexa Fluor (AF) 488- or AF 594-conjugated antimouse and antirabbit antibodies, AF 594-conjugated transferrin and cholera toxin B subunit (CtxB), avidin−Texas Red, and Oligofectamine were bought from Invitrogen (UK). FITC-labeled avidin, saponin, and sodium thiosulfate pentahydrate were from Sigma-Aldrich and Nanogold-Fab′ fragments of goat antirabbit IgG and HQ Silver kit were purchased from Nanoprobes (Yaphank, NY). siRNA against flotillin-1 (sc-35391), caveolin-1 (sc-44202) and nonspecific siRNA (sc-37007) were acquired from Santa Cruz Biotechnology.

Peptide Synthesis. Transportan (GWTLNSAGYLLGKINLKALAALAKKIL-NH_2), TP10 (AGYLLGKINLKALAALAKKIL-NH_2), and pTat (GRKKRRQRRRPPQ-NH_2) were synthesized stepwise on a 0.1 mmol scale on an automated peptide synthesizer (Applied Biosystems Model 431A) using the *t*-Boc solid-phase peptide synthesis strategy. *tert*-Butyloxycarbonyl amino acids were coupled as hydroxybenzotriazole esters to a *p*-methylbenzylhydrylamine resin (Neosystem, Strasbourg, France) to obtain C-terminally amidated peptides. Biotin was coupled manually to the side chain of Lys13 or Lys7 in transportan and TP10, respectively, or to N-terminus of pTat. The final cleavage and purification of peptides was performed, as described earlier (*14*). The molecular weights of biotinylated peptides were determined by MALDI-TOF mass spectroscopy (prO-TOF 2000, PE Biosciences) and calculated molecular weights were obtained each time.

Cell Culture. Human cervical carcinoma cell line HeLa (ATCC CCL-2), wild type mouse (C57bl6/J) embryonic fibroblasts, and embryonic fibroblasts from caveolin-1 knockout 3T3 mouse (ATCC-CRL-2753) were cultured in a humidified atmosphere containing 5% CO_2 at 37 °C in Iscove's Modified Dulbecco's Medium (IMDM) (Gibco, Invitrogen, UK) supplemented with 10% fetal bovine serum (FBS) (PAA Laboratories, Austria), 100 IU/mL penicillin, and 100 μg/mL streptomycin (Gibco, Invitrogen, UK).

Confocal Laser Scanning Microscopy. An amount of 5×10^4 cells were seeded one day before experiments onto round glass coverslips (Ø 12 mm, Menzel-Glazer, Germany) on a 24-well plate. Cells were incubated with 0.15 μM Texas Red (TxR)- or FITC-labeled avidin and 0.5 μM biotinyl-CPP in 400 μL of serum-free IMDM at 37 °C for 30 min. Biotinylated transportan and TP10 were dissociated with 10 mg/mL leucine before formation of complexes with avidin in order to reduce the aggregation of peptides and the size of subsequently forming complexes. After incubation, the medium with CPP−avidin complexes was removed, the cells were rinsed twice with PBS and fixed for 2 h either with PLP fixative (2% paraformaldehyde, 75 mM lysine-HCl, and 10 mM sodium periodate in 75 mM phosphate buffer, pH 7.4) or with 4% paraformaldehyde for 30 min for staining with antibodies against flotillin-1/Rab5/β1-integrin or PI3P/caveolin, respectively. The cells were permeabilized either with 0.1% Triton X-100 (anticaveolin), 0.5% saponin (anti-PI3P) for 5 min, or with a solution of 0.01% saponin and 0.1% BSA in sodium phosphate buffer for 8 min, which also acted as a blocking solution (flotillin-1, Rab5, β1-integrin). Nonspecific binding sites were blocked with 10% w/v nonfat dry milk solution in PBS for 1 h (anticaveolin) or with 10% heat-inactivated goat serum (anti-PI3P). After treatment with the respective AF-labeled secondary antibodies, the coverslips were mounted in 30% glycerol in PBS.

For control experiments, AF 594-labeled transferrin and CtxB were applied to cells at 20 μg/mL and 3 μg/mL, respectively, for indicated time periods. For low temperature experiments, cells were precooled for 15 min followed by uptake of peptide−protein complexes/CtxB during 30 min on ice and treated for Flot-1 visualization as indicated above.

Images were obtained with Nikon EZ-Z1 confocal microscope using excitation at 488 nm (for Alexa Fluor 488) and 543 nm (for Texas Red, AF 594) or with Olympus IX81 inverted microscope equipped with FluoView 1000 confocal system using excitation at 488 nm (for AF 488) and 559 nm (for Texas Red, AF 594). In both cases the systems were run in sequential scanning mode, where only one laser was active at a time, to avoid spectral overlap. Obtained images were processed with Adobe Photoshop 7.0.

Down-Regulation of Flotillin-1 and Caveolin-1. An amount of 4×10^4 cells were seeded onto 12-well culture plates one day before siRNA transfections. Transfection was performed with duplex RNA oligonucleotides against flotillin-1 or caveolin-1, or nonspecific siRNA using Oligofectamine (Invitrogen), according to the manufacturer's instructions in two consecutive days. Concentrations of siRNA for single transfection were 0.1 μM for flotillin-1 (Flot-1) and nonspecific siRNA. Caveolin-1 (Cav-1) siRNA was applied at 0.1 and 0.2 μM on consecutive days. For the cotransfection of Flot-1 and Cav-1, the concentration of both siRNA was 0.1 μM per transfection. On day 4 the

cells were incubated 30 min in 700 μL of serum-free medium containing CPP−protein complexes at the same concentrations as in confocal microscopy experiments. The complex-treated cells were trypsinized (0.025% trypsin supplemented with 0.01% EDTA in PBS) for 10 min prior to FACS analysis to remove the membrane-bound but noninternalized avidin. The remaining extracellular fluorescence was quenched by addition of trypan blue into the cell suspension (final concentration 0.015%), and 3×10^4 cells were counted per sample. Measurements were performed in duplicates, and the results are presented as a mean of three separate experiments.

Western Blot. 10^5 HeLa cells were seeded onto six-well plates and treated with Flot-1 and/or Cav-1 siRNA at the same concentrations as described above. Forty eight hours after the second siRNA treatment, the cells were scraped off the dishes and pelleted by centrifugation, and the wet cell mass was weighed for determination of the protein amount. Cells were lysed in 2 × SDS sample buffer and sonicated, and 0.5 μg of protein per lane was separated on 15% SDS-PAGE. Proteins were transferred to polyvinyl difluoride (PVDF, Applied Biosystems) membrane, blocked in 5% solution of nonfat dry milk in PBS, and treated with primary antibodies against Cav, Flot-1 (0.5 and 0.4 μg/mL, respectively), or β-actin as internal control (0.6 μg/mL). After incubation with alkaline phosphatase (AP)-conjugated antirabbit (Flot-1, Cav) or antimouse (anti-β-actin) secondary antibody (1:2500), the protein bands were visualized with AP substrate BCIP/NBT treatment. Intensities of protein bands of specific size (47 kDa for Flot-1, 21−24 kDa for Cav, and 42 kDa for β-actin) were analyzed by Image J 1.38x.

Electron Microscopy. HeLa cells were seeded onto glass coverslips in 24-well plates and grown to 90−100% confluency. Cells were incubated with complexes of biotinylated transportan, TP10, or pTat and colloidal gold-labeled neutravidin at 37 °C for 1 h. CPP−protein complexes were preformed by incubating neutravidin−gold (*d* 10 nm, 1:100 or 1:200 dilution) (*8*) with biotinyl-CPP at room temperature in a minimal volume for 5 min. Solution with complexes was diluted with culture medium to a final peptide concentration of 1.5−3 μM according to experiment and applied to cells.

Pre-embedding Immunolabeling. The cells treated with CPP−neutravidin complexes were fixed for immunoelectron microscopy with PLP fixative at room temperature for 2 h and permeabilized with 0.01% saponin and 0.1% BSA in 0.1 M sodium phosphate buffer for 8 min. After permeabilization, the cells were incubated with anticaveolin (1:50) or antiflotillin-1 antibodies (1:30) for 1 h and treated with 1.4 nm nanogold-conjugated Fab′ fragments of secondary antibodies (1:60) for an additional 1 h. The nanogold label was magnified by silver enhancement according to manufacturer's protocol for 2−5 min, followed by gold-toning with 0.05% gold chloride (*26*). After postfixation with 1% osmium tetroxide in the 0.1 M sodium cacodylate buffer (pH 7.4), cells were dehydrated and embedded in epoxy resin. Ultrathin sections were cut parallel to the coverslip, poststained with uranyl acetate and lead citrate, and examined with a JEM-100S (JEOL, Japan) or FEI Tecnai 10 (Philips, Netherlands) transmission electron microscope at 80 kV. The scanned electron microphotos were analyzed and processed with Adobe Photoshop 7.0.

Statistical Analyses. Confocal fluorescence figures are representative of at least two independent experiments. Data from the FACS experiments and western band quantification are the mean ± SD ($n = 4-6$). The down-regulation of flotillin-1 was quantified in CLSM images by using FluoView10-ASW 1.6 software. Images of cells treated either with nonspecific or flotillin-1 specific siRNA were recorded with identical microscope settings. The regions of interest (ROI) that were chosen at the plasma membrane based on the β1-integrin staining and in the cytoplasmic areas were analyzed separately on 6−10 *z*-sections from seven cells (>40 sections for each pool). The results are shown as the percentage of flotillin-positive pixels of all pixels from the analyzed ROI. The colocalization of CPP−protein complexes with caveolin or flotillin-1 was quantified by counting vesicles in randomly selected 20 cells in thin sections by TEM. The number of vesicles containing respectively CPP−protein complexes, caveolin, or flotillin-1 or both, the CPP−protein complexes, and endocytic markers was counted and the percentage of colocalization of CPP−protein with Cav/Flot-1 was calculated (Table 1).

Table 1. Quantitative Analysis of Colocalization of Cell-Delivered Neutravidin and Lipid Raft Marker Proteins in TEM Images[a]

	flotillin-1		caveolin	
content of vesicle	TPb	TP10b	TPb	TP10b
CPP−protein complexes	158	242	467	183
Flot-1/Cav	522	644	942	1396
CPP−protein and Flot-1/Cav	23	33	93	28
% of colocalization	14.5[b]	13.6[b]	20	15.3

[a] The caveolin- or flotillin-1-positive and CPP−protein complex-containing vesicles were counted in 20 randomly selected cells, and colocalization is presented in percents. [b] Colocalization of CPP−protein complexes with flotillin-1 was detected almost exclusively in the perinuclear region. The degree of colocalization at the plasma membrane was lower than 5%.

RESULTS

Transportan and TP10 Do Not Direct the Cargo Protein to Flotillin-1-Dependent Endosomal Pathways. To unravel the internalization mode of transportan-mediated cargo delivery, we mapped the localization of the peptide−protein complexes in relation to flotillin-1, previously described as a marker of a specific type of lipid rafts (*24*). The flotillin-1 (Flot-1) positive areas showed almost no overlap with complexes of avidin and biotinylated transportan or TP10 when evaluated by confocal microscopy (Figure 1A,B). Almost no colocalization could be detected inside cells whereas some overlap was observed at the plasma membrane after 30 min incubation with peptide−protein complexes. At the plasma membrane, colocalization was mostly detected as smaller flotillin-marked focuses covered with a bigger irregular peptide−protein aggregate (Figure 1A−C). The loci of flotillin-1 were detected as a dense punctate staining on the plasma membrane, in the cytoplasm, and on the cellular projections while the majority of complexes assembled into larger structures, which were associated with the outer membrane, as detected by confocal microscopy (Figure 1A−C). As reported previously, cholera toxin B subunit uses (CtxB) uses flotillin-dependent endocytosis as one route for cell entry (*24*); therefore, we used CtxB for proving the relevance of this pathway in our system. After 30 min incubation of HeLa cells with the toxin, we detected CtxB in perinuclear structures showing partial overlap with Flot-1 (Figure 4A), confirming the functionality of this pathway in HeLa cells and corroborating the results published by Glebov et al. In parallel to confocal microscopy (CLSM) we used transmission electron microscopy (TEM), which allows identification of cellular structures by morphology at a higher resolution level. The complexes of biotinylated CPP and neutravidin (bigger gold particles) were detected as bigger aggregates, which localized mostly to the extracellular side of the plasma membrane, cell protrusions, and vesicular structures in the cytoplasm (arrows in Figure 1D−F). Flot-1 protein (smaller gold particles), on the contrary, was detected in specific loci at the cytoplasmic side of the plasma

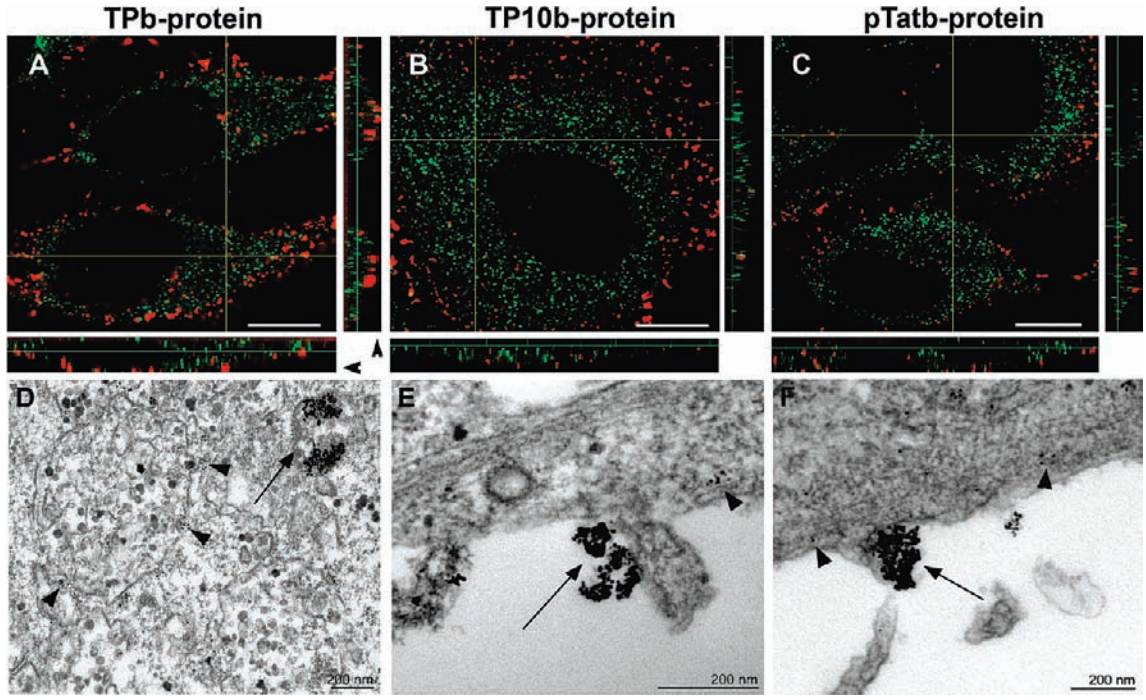

Figure 1. Localization of CPP−protein complexes in HeLa cells in relation to flotillin-1. For CLSM experiments, cells were incubated for 30 min with 0.5 μM biotinylated transportan (A), TP10 (B), or pTat (C) complexed with 0.15 μM avidin−Texas Red (red). Flotillin-1 was visualized with antiflotillin-1 pAb and AF 488-conjugated secondary Ab (green). A single optical section of cells is presented, which is indicated with a green line on the *z*-projections. Yellow lines in the *xy*-projection indicate the location of *z*-projections, and arrowheads indicate the apical part of cells in *z*-projections. (D−F) TEM images of cells incubated with complexes of neutravidin−gold (10 nm, arrows) and 1.5 μM biotinylated transportan (D), 3 μM TP10 (E), or pTat (F) for 1 h. Flotillin-1 is visualized with antiflotillin-1 pAb and secondary antibody tagged with nanogold (1.4 nm) particles (arrowheads in D−F). The bar in CLSM images represents 10 μM.

membrane (arrowheads in Figure 1E,F) but also on the membranes of multivesicular endosomes (arrowheads in Figure 1D) in the cytoplasm. Although the complexes of CPP−neutravidin were found close to the location sites of flotillin-1 protein, we could not detect colocalization between Flot-1 and CPP−protein complexes at the plasma membrane by TEM (Figure 1E,F). However, a small population of the intracellular vesicles containing TP/TP10−protein complexes also included Flot-1 protein. The same results were obtained with biotinylated Tat peptide complexed with avidin−Texas Red (CLSM) or neutravidin−gold (TEM) (Figure 1C,F). For transportan and TP10−protein complexes, overlapping structures with Flot-1 in TEM sections were estimated to remain around 14% of the total number of complex-containing vesicles (Table 1). Still, as revealed by quantitative analysis, the colocalization of TP/TP10−protein complexes with Flot-1 on the membrane areas and in the cortical cytoplasm was insignificant, only 1−5%, and the vesicles containing both markers were almost exclusively observed in the perinuclear region. We also performed CLSM experiments using a shorter incubation time, as peptide−protein complexes might pass the flotillin-positive vesicles earlier. However, after 10 min of incubation, very few complexes had internalized, and the colocalization between Flot-1 and TP/TP10−protein complexes was rarely detected on the plasma membrane (data not shown). In addition, we conducted experiments at a lower incubation temperature to assess the initial interaction of complexes with the plasma membrane. Although the peptide−protein complexes were not taken up by cells after 30 min incubation at 4 °C, the complexes interacted with the plasma membrane in a similar manner and colocalization with flotillin-1 was identical to that observed at physiological temperature (Supporting Information Figure 1A−C). CtxB interacted with the plasma membrane at 4 °C less avidly, but still colocalized with Flot-1 at certain loci, and no intracellular staining was detected (Supporting Information Figure 1D).

Transportan and TP10 Avoid the Early Endosomal Pathway Marked by Rab5 and PI3P in the Cellular Delivery of Cargo Protein. In order to assess whether the early endosomal pathway is exploited in peptide-mediated protein transport, we characterized the cellular localization of CPP−avidin complexes in comparison to Rab5 and PI3P, markers of early endosomes. The analogous rare intracellular colocalization of CPP−protein complexes as seen with flotillin-1 was also detected with PI3P (Figure 2A,B) and Rab5 (Figure 2D,E) as observed by CLSM after 30 min incubation. On the contrary, marked overlap was detected between PI3P/Rab5 and transferrin (Figure 2C,F), a marker of clathrin-dependent endocytosis, which passes early endosomes. Though both the CPP−protein complexes and PI3P/Rab5 were confined to punctate structures in cells and on the plasma membrane, they clearly represented different localization areas. Somewhat surprisingly the shorter (10 min) incubation time also revealed even less colocalization between the internalized CPP−protein complexes and Rab5 or PI3P at the plasma membrane, and a small amount of complexes was detected inside cells (Supporting Information Figure 2). Transferrin, on the contrary, entered the cell interior rapidly, already in 10 min (Supporting Information Figure 2). Again, in cases of rare overlap, the focuses stained by anti-Rab5 or anti-PI3P antibody were situated in the middle of large conglomerates of CPP−protein complexes. The negligible role of the PI3P-dependent pathway in CPP-mediated protein delivery (Figure 2A,B) correlates well with our unpublished results showing that internalization of TPb/TP10b−avidin complexes was not influenced in HeLa cells where the activity of PI3-kinase was inhibited by wortmannin treatment (data not shown).

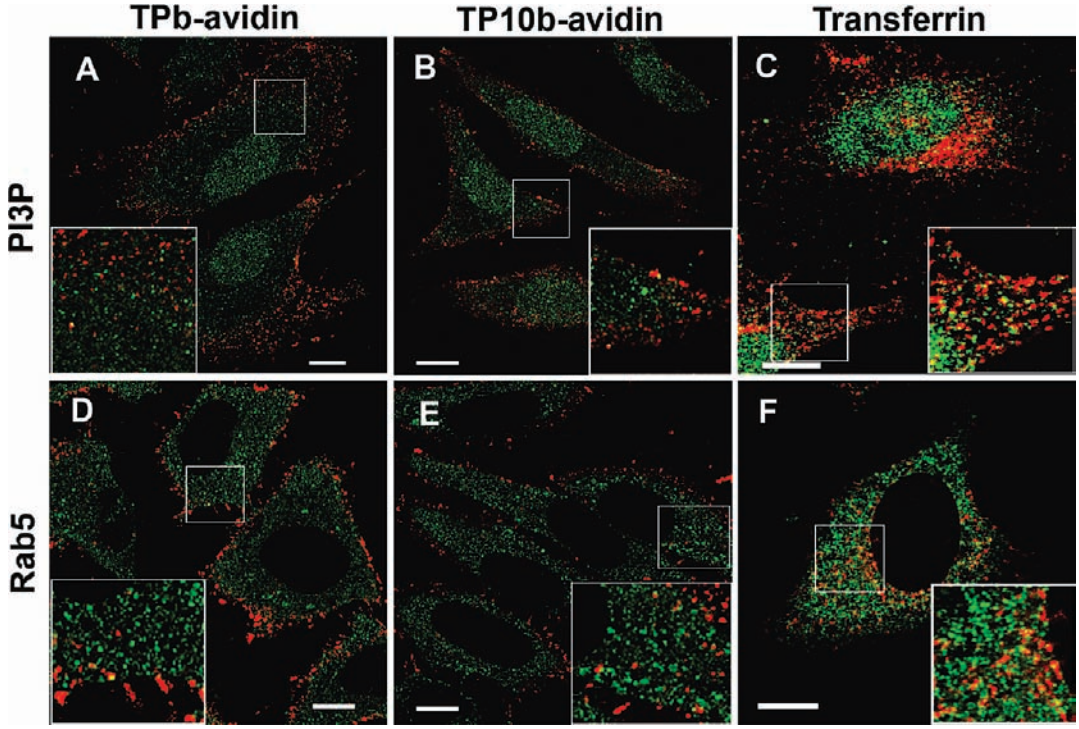

Figure 2. Localization of transportan- and TP10−protein complexes in HeLa cells in relation to Rab5 and PI3P. Cells were incubated for 30 min with 0.5 μM biotinylated transportan (A, D), TP10 (B, E) complexed with 0.15 μM avidin−Texas Red, or with AF 594-conjugated transferrin (20 μg/mL, C, F). To visualize PI3P and Rab5, cells were stained with anti-PI3P mAb (A, B) or anti-Rab5 pAb (D, E) and with appropriate AF 488-conjugated secondary Ab (green). A single optical section from the equatorial level of cells is presented. The bar represents 10 μM.

A Fraction of CPP−Protein Complexes Is Targeted to Caveolae. Earlier reports have demonstrated the involvement of caveolae-dependent endocytosis in both CPP internalization and the CPP-mediated cargo delivery (*16, 17*). Our results obtained by electron microscopy have shown that TP/TP10−protein complexes enter cells often in small (50−100 nm in diameter) morphologically caveosome-like or noncoated vesicles. Therefore, we looked for the presence of caveolin in these structures by both immunofluorescence and immunoelectron microscopy using antibody against all caveolin (Cav) isoforms. Indeed, a fraction of CPP−protein complexes colocalized with caveolin on the plasma membrane and in cells as observed by confocal microscopy. A higher number of colocalization could be detected on the plasma membrane than in the cytoplasm for all peptide−protein complexes. About 30% of CPP−avidin complexes on the membrane and 20% inside the HeLa cells exhibited similar localization to caveolin by visual estimation of CLSM images (Figure 3A−C). As expected, CtxB known to be also endocytosed via caveolae (*27*), exhibited a good overlap with caveolin-positive cell areas (Figure 4B). The results of electron microscopy revealed that most of the small vesicles or bigger rosette-like structures had caveolin on the cytosolic side (small gold particles in Figure 3D), and these structures were always located in close proximity to actin fibers. Although the caveosomes were abundant in the cortical cytoplasm, most of them did not contain the TP/TP10−neutravidin complexes (bigger gold particles). However, several of the TP/TP10−protein, as well as pTat−protein complexes, were found to reside in the Cav-positive vesicles in the perinuclear region (arrows in Figure 3G and 3H). The presence of both TP/TP10−neutravidin complexes and caveolin was also detected in bigger vesicles (0.4 μm), which had small caveosomes at close proximity or were connected to them (arrowheads in enlarged section of Figure 3E). Among complex-containing endosomal structures, about 20% for TP and 15% for TP10 were also marked by caveolin (Table 1) as revealed by the quantitative analysis of TEM results. The overlap of pTat−protein with caveolin-positive structures was comparable to that of TP−protein and caveolin, reaching about 20% (data not shown). About one-third of all CPP−protein complex-containing vesicles that did not contain caveolins were found in close proximity to caveosomes as shown in Figure 3F. It might have led to some overestimation of the degree of colocalization when using confocal microscopy (Figure 3A−C). In addition, from the analysis of TEM images we found that the overall number of caveosomes in control cells was about 2-fold lower than in cells incubated with CPP−protein complexes, indicating a triggering of caveolae internalization by CPPs.

Down-Regulation of Caveolin-1 Inhibits Transportan/TP10-Mediated Protein Delivery, but Down-Regulation of Flotillin-1 Has No Effect. In parallel with the colocalization experiments we down-regulated the Flot-1 with siRNA to see whether the lack of cellular Flot-1 interferes with the uptake of peptide−protein complexes. Surprisingly, the used siRNA decreased the Flot-1 concentration only moderately, to 40−50% as estimated by quantification of Western blot results (Figure 5A). Flotillin-1 seemed to be down-regulated differently in the plasma membrane and central cytoplasm; therefore, we visualized the plasma membrane with β1 integrin antibodies and analyzed the amount of Flot-1 at plasma membrane and in cytoplasm separately (see Experimental Procedures). The quantification corroborated that the down-regulation was more efficient at the plasma membrane compared to the cell interior, reaching 75−80% decrease of the Flot-1 signal in plasma membrane areas whereas the concentration of flotillin-1 in intracellular structures was reduced less than 2 times (Figure 5B). The uptake of TP/TP10−protein complexes by Flot-1 down-regulated cells, however, was not influenced (Figure 5C). Analogously to Flot-1, we checked whether depletion of Cav-1 from the plasma membrane influences the TP/TP10-mediated protein delivery. siRNA treatment yielded about 70−80% down-regulation of cellular Cav-1 protein expression as quantified by Western blot (Figure 5A). The decrease in Cav-1 concentration inhibited the uptake of TP10−protein complexes by 40−50%

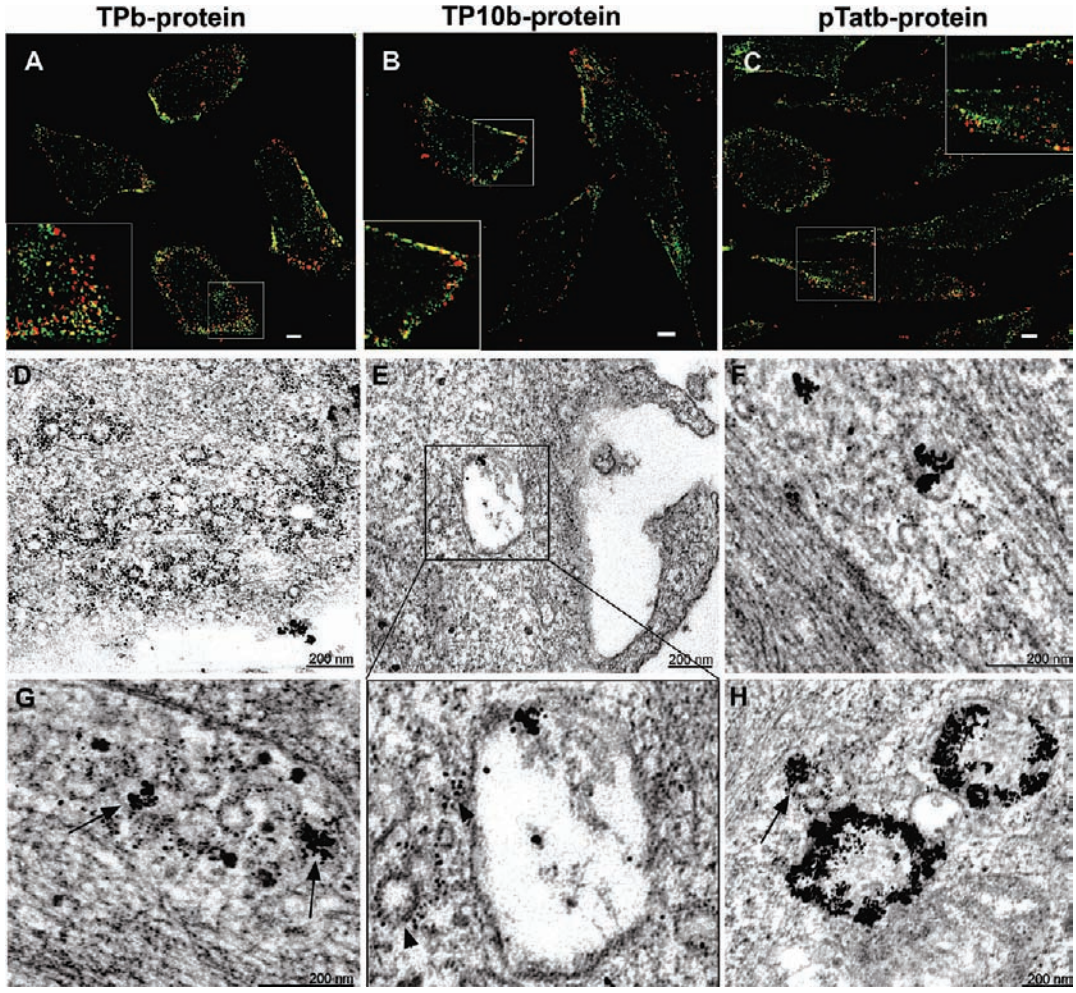

Figure 3. Localization of CPP−protein complexes in HeLa cells in relation to caveolin. Cells were incubated for 30 min with 0.5 μM biotinylated transportan (A), TP10 (B), or pTat (C) complexed with 0.15 μM avidin−Texas Red (red). To visualize the cellular caveolin, cells were stained with anticaveolin pAb and with appropriate AF 488-conjugated secondary Ab (green). A single optical section from the equatorial level of cells is presented. (D−H) TEM images of cells incubated with complexes of neutravidin−gold (10 nm, arrows) and 1.5 μM biotinylated transportan (D, G), TP10 (E), or pTat (F, H) for 1 h. Caveolin is visualized with anticaveolin pAb and 1.4 nm gold particle-conjugated secondary antibodies. The bar in CLSM images represents 10 μM.

while the TP-mediated transport was slightly less affected (Figure 5D). The coapplication of Flot-1 and Cav-1 siRNA did not lead to an additional inhibitory effect on the protein delivery as compared to Cav-1 knock-down (Figure 5E). In addition to the impaired protein uptake in caveolin-1 down-regulated cells by CLSM, the colocalization between the CPP−protein complexes and the remaining caveolin was markedly decreased for both peptides, most probably due to the lower amount of membranous caveolin (data not shown). However, by visual estimation the amount of membrane-associated complexes in Cav-1 down-regulated cells was on the same level with untreated control cells, indicating that the interaction with plasma membrane is not inhibited by a deficit of Cav-1. On the other hand, the extensive trypsin digestion and trypan blue quenching used in the FACS analysis helped to remove the loosely bound CPP−protein complexes from the cell surface and to diminish the extracellular signal, respectively. These treatments led to lower signal intensity and more correct estimation of the reduction in protein transduction in flow cytometry assays.

To completely exclude the induction of caveolin-1-dependent pathways by CPPs, we conducted analogous experiments in Cav-1 knockout mouse embryonic fibroblasts (MEFs). The results obtained by flow cytometry and confocal microscopy corroborated the high impact of Cav-1-dependent pathways on the uptake of avidin induced by peptides. The transduction yield of avidin into Cav-1 knockout MEFs was 60−70% lower than to wild-type fibroblasts for both TP10 and transportan. In analogy with the HeLa cells, the absence of caveolin-1 interfered with transportan-mediated delivery slightly less than that of TP10 (Figure 6A). Visualization of caveolins with anticaveolin antibody revealed its marked colocalization with TP/TP10−protein complexes in wild type MEFs (Figure 6B,D), which correlates well with the results obtained in HeLa cells. As expected, in Cav-1 knockout MEFs we detected the presence of caveolin-2 isoform at a very low level (*28*), which did not overlap with peptide−protein complexes (Figure 6C,E), corroborating the substantial role of membranous caveolin-1 in protein delivery with transportans.

DISCUSSION

The plasma membrane is a complex cellular organelle, being simultaneously a portal and a barrier for all metabolites. Cell-penetrating peptides are under intense study as carriers, which cross this barrier together with biologically active cargo. On the other hand, their ability to penetrate through membranes also represents an interesting scientific phenomenon per se. The endocytic processes have proven to mediate the CPP/CPP−cargo entry, and the role of pathways that originate from the lipid rafts and/or caveolae is often emphasized (*7, 16, 29*). Involvement of rafts is usually suggested based on the decreased cellular uptake of CPPs by cells depleted of cholesterol in the plasma membrane after treatment with methyl-β-cyclodextrin. However,

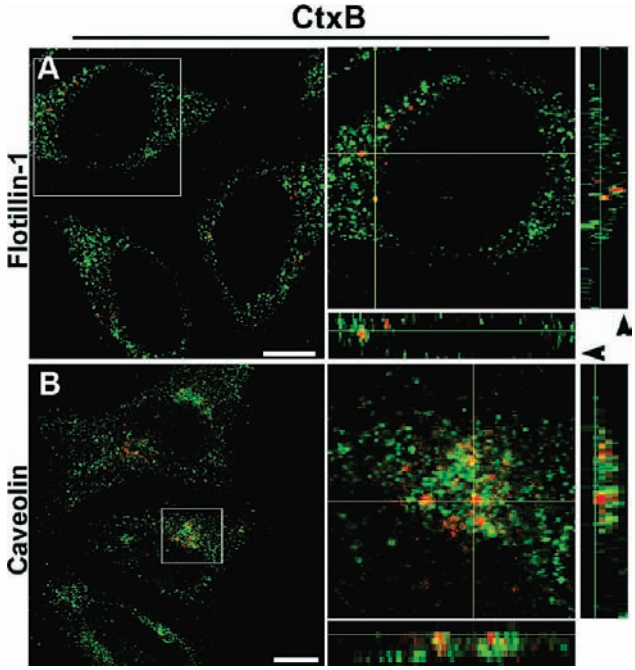

Figure 4. Localization of cholera toxin B subunit (CtxB) in relation to cellular flotillin-1 and caveolin. After incubation of HeLa cells with Alexa Fluor 594-conjugated CtxB (3 μg/mL, red) for 30 min, the cells were stained with antiflotillin-1 (A) or anticaveolin (B) polyclonal antibodies and with Alexa Fluor 488 conjugated secondary Ab (green). Enlarged sections of indicated areas are depicted on the right column with *z*-projections. Yellow lines in enlarged sections indicate the location of *z*-projections, and arrowheads indicate the apical part of cells in *z*-projections. Scale bar 10 μM.

it does not distinguish between the caveolar and raft-mediated pathways, which have different cellular destinations. Removal of cholesterol also influences other endocytic processes and might lead to changes in cell morphology (*30*). Moreover, very recently 60% of cellular cholesterol was demonstrated to localize in the inner leaflet of plasma membrane and endocytic recycling compartment in chinese hamster ovary cells (*31*), suggesting that cholesterol depletion might substantially interfere with the organization of lipids in the cytoplasmic leaflet of membranes and also endocytosis. Continuously accumulating data about the nature and complexity of endocytosis and involvement of its different types in CPP mechanisms prompted us to reassess the initial steps of CPP-mediated protein delivery. We chose flotillin-1 and caveolin as markers for two types of plasma membrane microdomains, and Rab5 and PI3P for characterization of early endosomal vesicles, to elucidate their involvement in TP/TP10-mediated protein delivery into HeLa cells. Cholesterol- and sphingolipid-rich rafts represent highly heterogeneous populations of functionally distinct membrane domains. The availability of caveolae-independent but morphologically similar endocytic pathways involved in the SV40 cell entry was recently demonstrated by two groups in parallel (*21, 22*). In analogy with CPP-mediated delivery into cells, this type of endocytosis is dependent on plasma membrane cholesterol and dynamin activity. Flotillins, in turn, are shown to be responsible for the assembly of a particular type of rafts, which participate in clathrin- and caveolin-independent endocytosis (*24*). Coassembly of flotillin-1 and flotillin-2 into microdomains induces formation of membrane invaginations that are morphologically reminiscent of caveolae and considered to be capable of forming intracellular vesicles, which localize in the cortical cytoplasm and look similar to caveosomes but lack caveolin-1 (*32*). According to our earlier electron microscopy results, the vesicular pathway of TP/TP10-mediated protein uptake also resembled by morphology the noncaveolar, flotillin-1-dependent internalization mode described by Frick and co-workers. Therefore, we assessed the putative involvement of a flotillin-1-dependent internalization pathway in the cellular translocation of TP/TP10−protein complexes. However, somewhat unexpectedly we could not find the colocalization of CPP−protein complexes with flotillin-1 on the plasma membrane or inside cells by immunocytochemical analysis either by confocal or by electron microscopy. In addition, efficient down-regulation of flotillin-1 in the plasma membrane, using siRNA silencing, increased rather than decreased the CPP−protein uptake, corroborating the microscopy results and suggesting that the flotillin-1-dependent pathway has a negligible, if any, role in CPP-mediated protein delivery. The cholera toxin B subunit, used in this study for assessing the activity of the flotillin-dependent pathway, can enter cells via several endosomal pathways (*22, 33*). Therefore, CtxB could only with great circumspection be considered a marker of the flotillin-dependent endocytic route. Unfortunately, no specific cargo has been characterized for the flotillin-mediated pathway yet, making the explicit evaluation of the role of this mechanism difficult. For the sake of clarity, we also checked the localization of cell-transduced protein in relation to flotillin-2, but in analogy with flotillin-1 no significant overlap was detected (data not shown). On the other hand, based on the experiments with flotillin-1 and -2, we could not exclude the participation of lipid rafts in delivery by CPPs, as the nature of lipid rafts is not unambiguously characterized yet. Moreover, the possibility that complexes indeed show equal or even better uptake in partially flotillin-1-depleted cells suggests that the phospholipids of nonraft areas of the plasma membrane might also play a role in CPP internalization mechanisms (*34, 35*), independently or in concert with the cell surface proteoglycans. Considering the ability of transportan to modulate the dynamics of the membrane lipids (*36*), and taking into account that the location and function of cell surface proteoglycans is probably interfered in flotillin-1-deficient cells, one can imagine that the changed properties of the plasma membrane could lead to the vesicular uptake mode(s) that is not common to cells with a properly organized membrane. The involvement of another cholesterol-dependent pathway, caveolar endocytosis, has been demonstrated in both the cellular uptake of Tat peptide and pTat-mediated cargo delivery (*16, 17*). Recent data about caveolae not just merely as a subtype of rafts but as an independent membrane structure (*37*−*39*), encouraged us to include it in the study. Our CLSM results demonstrated that approximately 30% of CPP−avidin complexes exhibited similar localization to caveolin, and a higher overlap was observed at the plasma membrane than inside cells. Still, electron microscopy revealed a somewhat lower degree of colocalization (15− 20%) of complexes with caveolin-positive vesicles, especially in the cortical cytoplasm where the main fraction of caveosomes was found. Electron microscopy results revealed that the CPP−neutravidin complexes and caveolin localized often in very close proximity, which might have led to the overestimation of the degree of colocalization by CLSM. However, we cannot exclude that the smaller ratio of colocalization detected in electron microscopy could be caused by different isoelectric points of avidin and neutravidin and by the higher affinity of avidin to negatively charged components of the plasma membrane. Still, after caveolin-1 down-regulation by 60−70%, a substantial inhibition of CPP-mediated protein uptake was detected by FACS analysis, which emphasizes the importance of caveolin-1-containing membrane areas in the internalization process. Moreover, the finding that the amount of caveosomes in cells incubated with CPP−protein complexes is about 2-fold higher than in untreated cells might suggest the induction of caveolae-dependent endocytosis, which contributes most to the TP/TP10-mediated protein delivery among the observed endosomal pathways. The

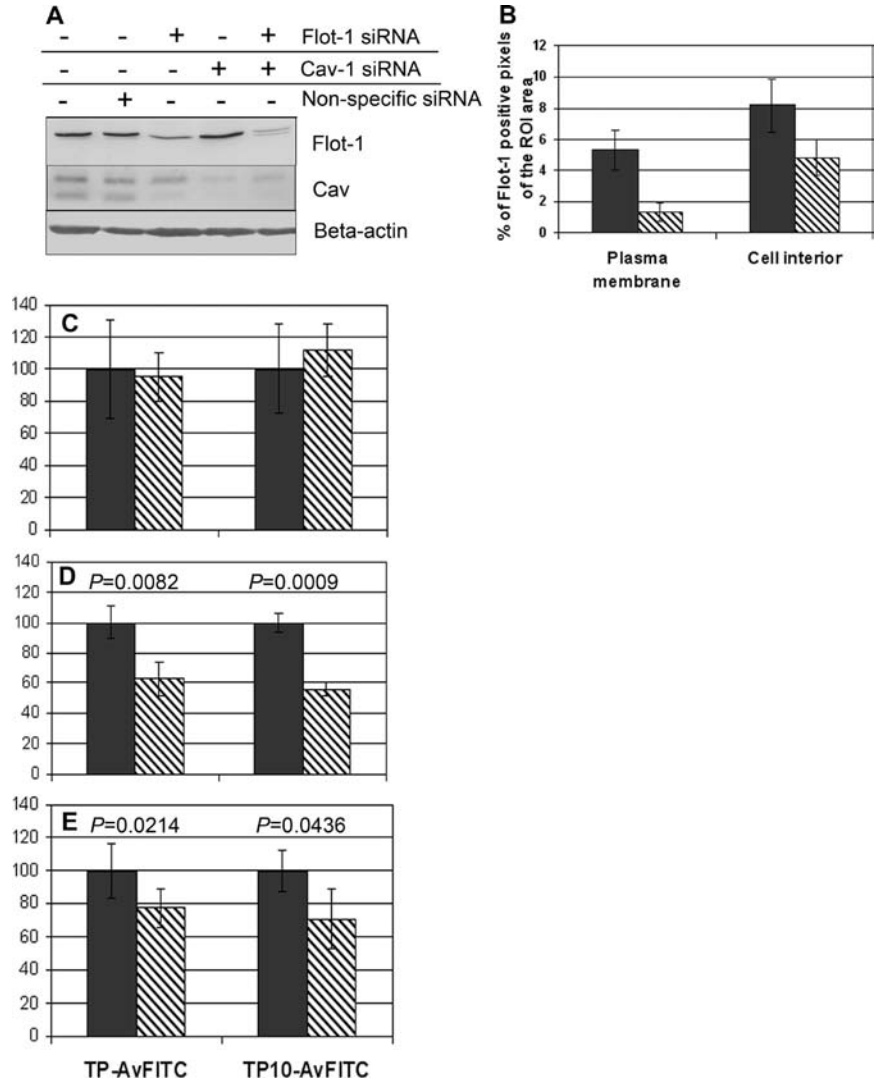

Figure 5. (A) Effect of down-regulation of flotillin-1 and caveolin-1 by siRNA on protein cellular delivery by transportan and TP10. (A) Estimation of protein concentration after siRNA treatment by Western blot. Characteristic result of three separate experiments is depicted. Proteins (0.5 μg per lane) were detected with anti-Flot-1 pAb (upper panel), anti-Cav pAb (middle panel), or anti-β-actin mAb as loading control (lower panel). (B) Quantification of the flotillin-1 in the plasma membrane and intracellular structures by the analysis of z-sections of CLSM images of cells treated with nonspecific (gray bars) or Flot-1 specific siRNA (striped bars) and stained for Flot-1 and β1-integrin to visualize the plasma membrane. Results show the percentage of Flot-1-positive pixels of all pixels from the analyzed areas. (C, D) The uptake of complexes by siRNA-treated cells. HeLa cells were treated with nonspecific (gray bars) or specific siRNAs (striped bars) against Flot-1 (C), Cav-1 (D), or both Flot-1 and Cav-1 siRNAs (E) and incubated with complexes of biotinylated TP/TP10 (0.5 μM) and avidin−FITC (0.15 μM) for 30 min prior to FACS analysis. Protein delivery efficiency into cells treated with nonspecific siRNA is represented as 100%. Error bars represent standard deviation, and statistical relevance is characterized with *P* values.

confocal micrographs reveal that siRNA treatment led to strong reduction of caveolin-positive areas from the plasma membrane and marked loss from intracellular structures. However, the lack of caveolin-1 in plasma membrane inhibits the TP10-induced protein uptake more strongly than that of transportan, and this trend is also observable when the protein delivery by transportans is compared in wild type and caveolin-1 knockout MEFs. CLSM shows rather comparable colocalization between caveolin and avidin complexed with both transportans in normal HeLa cells. Electron microscopy, on the contrary, revealed a slightly higher occupancy of caveolin-coated vesicles by TP−neutravidin than by TP10 complexes, which is in discrepancy with the cellular uptake data in Cav-1 siRNA-treated cells. The results might suggest that although transportan−protein complexes occupy more caveosomes in cells than TP10, it could more flexibly switch between different endosomal pathways. Our earlier results demonstrated that about 10−15% of TP/TP10−protein complexes localized in transferrin-containing vesicles showing the involvement of clathrin-mediated endocytosis in the uptake of complexes both by fluorescence and by electron microscopy (*8*). In addition, the hyperosmolar medium known to interfere with the clathrin-mediated endocytosis inhibited the avidin delivery in HeLa cells to the same extent, corroborating the proportion of the clathrin-dependent mechanism in transportan-mediated protein delivery (*14*). Assuming good concordance of results obtained by three above-mentioned methods and relatively low contribution of the clathrin-dependent pathway in the complexes' uptake, we did not apply a siRNA-included knock-down for evaluating the role of this pathway. The electron microphotos demonstrated that a substantial amount of cell-transduced protein was confined in macropinosome-like big vesicles (*8*), implicating that several endocytic pathways were active in CPP-mediated protein transduction. On the basis of this, we suggest that in conditions where the functioning of one entry route is restrained, TP/TP10 target the cargo into other/unimpaired endocytic pathways, although with smaller efficiency and depending on the features of the particular peptide. The further intracellular targeting of

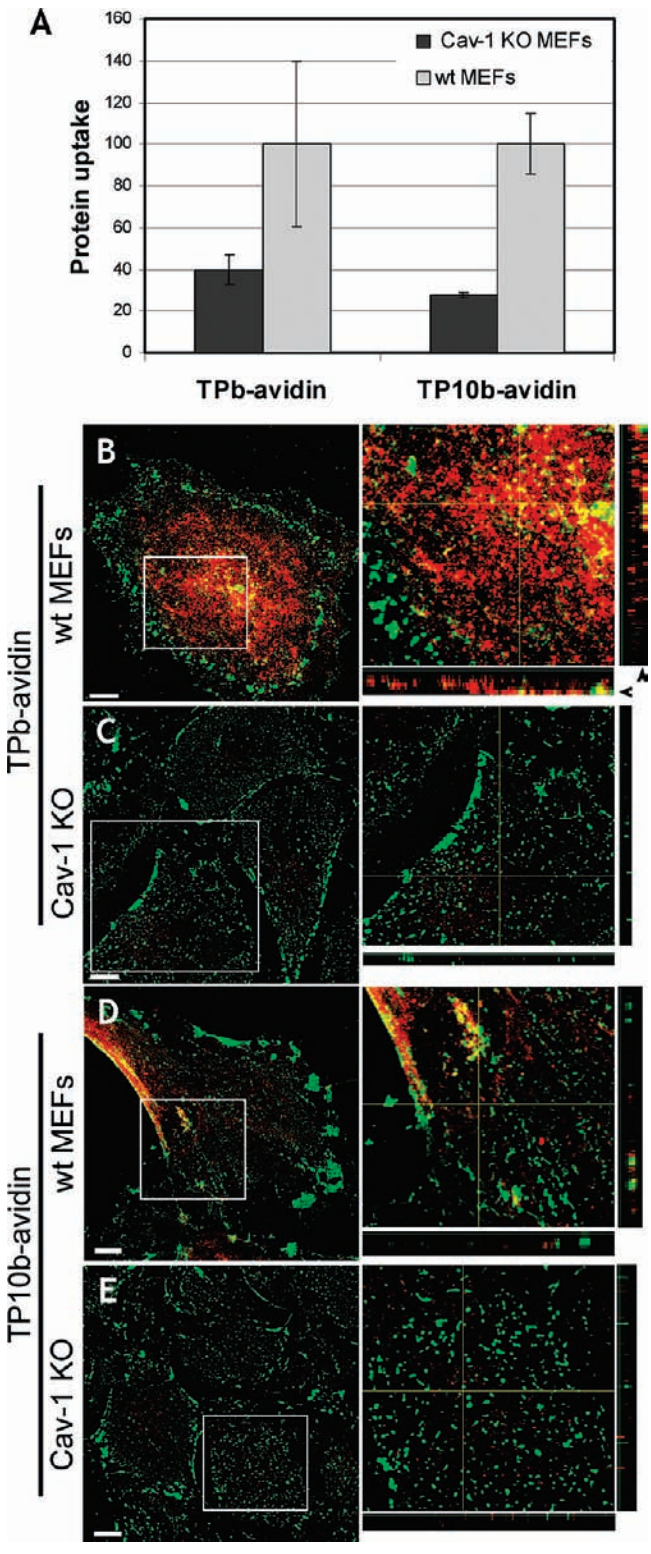

Figure 6. Internalization and localization of transportan/TP10−protein complexes in cells lacking caveolin-1. Wild-type or caveolin-1 knockout MEFs were incubated with complexes of biotinylated TP/TP10 (0.5 μM) and avidin−FITC (0.15 μM) for 30 min and analyzed by FACS (A) or confocal microscopy (B−E). The protein uptake into wt MEFs is presented as 100% in A. (B−E) Cells were stained with anticaveolin pAb and AF 594 conjugated secondary Ab (red) for visualizing caveolins. The caveolin signal in caveolin-1 knockout cells is very weak and rather diffuse, representing the localization of residual caveolin-2 (C, E). Images shown are merged from all optical slices, and the enlarged sections with *z*-projections are taken from indicated places and presented in the right column. Arrowheads indicate the apical part of cells in *z*-projections, and the bar represents 10 μM.

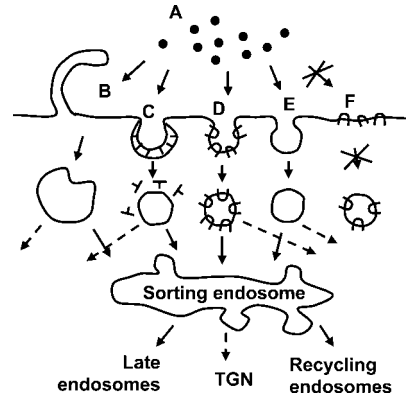

Figure 7. Endocytic pathways used for cellular entry by transportan/TP10−protein complexes. The scheme includes our earlier data (*8*). The complexes of peptide and protein (A) can enter cells via macropinocytosis (B), clathrin- (C) or caveolae (D)-mediated endocytosis, and clathrin- and caveolin-independent endocytosis (E). The flotillin-mediated pathway (F) is not utilized. Intracellular trafficking routes are indicated by solid arrows, putative directing is represented by dashed arrows. TGN-trans-Golgi network.

CPP-transduced cargos is even more important than the starting point. Upon long-time incubations, the majority of cargo protein delivered into cells by CPPs accumulates in LAMP2-containing structures in the perinuclear region (*8*) and is targeted to digestion (*3*). Therefore, mapping of the early steps of CPP-mediated delivery might provide valuable information for finding a way to induce liberation of cargo molecules from the endosomal structures before direction to degradation. The small GTPase Rab5 and PI3P are both typical constituents of early endosomes, and both of them are also reported to have role in macropinocytosis (*40*). In addition, the lateral transport between early endosomal vesicles and caveosomes has been shown to be Rab5-dependent (*38*). However, most of the CPP−protein complexes were observed to evade early endosomes since only a negligible fraction of complexes showed colocalization with Rab5 or PI3P after 10 or 30 min. Furthermore, the treatment of cells with wortmannin, a specific inhibitor of phosphoinositide 3-kinase, did not inhibit the CPP-induced protein transport into HeLa cells, which is in line with an earlier study by Payne et al. (*41*). Although early endosomes are reported to be capable of receiving contents from caveosomes (*38*), the fraction of TP/TP10 protein complexes that internalized in caveolin-positive vesicles might avoid early endosomes by using other transport route(s), probably analogous to SV40 (*42*). Still, the caveolar pathway is considered to lead to the Golgi complex, but only a minor part of TP/TP10−protein complexes is targeted there as we showed earlier (*8*). Although the CPP−protein complexes seem to avoid being trapped into early endosomal structures after translocation into HeLa cells, upon longer incubation they accumulate in vesicles containing endolysosomal marker protein LAMP2 (*8*). Recently, it has been reported that at least three endocytic pathways are used for cellular entry by CPPs: macropinocytosis, clathrin-mediated, and caveolar/lipid raft-mediated endocytosis (*5*). Our results on protein cellular delivery are well in line with this study suggesting analogous concurrently acting endocytic uptake mechanisms, and in our system the caveolin-dependent pathway but not the flotillin-1-mediated route is preferentially used. However, the intracellular targeting of complexes seems to avoid canonical trafficking pathways (schematic representation in Figure 7). Additionally, there is a fraction of small vesicles induced by CPPs and mediating the internalization of cargo molecules, which we have not been able to classify using markers of known endocytic pathways, and flotillin-1 did not help with filling this gap.

ACKNOWLEDGMENT

We thank M. Kure, T. Toivonen, M. Lindman, and A. Strandell for excellent technical assistance in electron microscopy, M. Ehandi for peptide synthesis, S. Ingerpuu for anti-β1-integrin antibody, and H. Räägel for critical reading of manuscript. The work was supported by grants from Estonian Science Foundation (ESF 5588 and 7058), European Community Program QLK3-CT-2002-01989, Swedish Research Council (VR-NT, VR-Med), Academy of Finland, and University of Tartu (PP1TI07902).

Supporting Information Available: Localization of CPP−avidin complexes (1) in relation to cellular flotillin-1 at low temperature, and (2) compared to cellular Rab5 and PI3P after short incubation time. This material is available free of charge via the Internet at http://pubs.acs.org

LITERATURE CITED

(1) Langel, Ü. (2007) Cell-penetrating peptides. In *Cell-penetrating peptides*, pp 1−600, CRC Press, Boca Raton.

(2) Ziegler, A., Nervi, P., Dürrenberger, M., and Seelig, J. (2005) The cationic cell-penetrating peptide CPP(TAT) derived from the HIV-1 protein TAT is rapidly transported into living fibroblasts: optical, biophysical, and metabolic evidence. *Biochemistry 44*, 138–48.

(3) Fretz, M. M., Penning, N. A., Al-Taei, S., Futaki, S., Takeuchi, T., Nakase, I., Storm, G., and Jones, A. T. (2007) Temperature-, concentration- and cholesterol-dependent translocation of L- and D-octa-arginine across the plasma and nuclear membrane of CD34+ leukaemia cells. *Biochem. J. 403*, 335–42.

(4) Tünnemann, G., Martin, R. M., Haupt, S., Patsch, C., Edenhofer, F., and Cardoso, M. C. (2006) Cargo-dependent mode of uptake and bioavailability of TAT-containing proteins and peptides in living cells. *FASEB J. 20*, 1775–84.

(5) Duchardt, F., Fotin-Mleczek, M., Schwarz, H., Fischer, R., and Brock, R. (2007) A comprehensive model for the cellular uptake of cationic cell-penetrating peptides. *Traffic 8*, 848–66.

(6) Ter-Avetisyan, G., Tünnemann, G., Nowak, D., Nitschke, M., Herrmann, A., Drab, M., and Cardoso, M. C. (2008) Cell entry of arginine-rich peptides is independent of endocytosis. *J. Biol. Chem. 284*, 3370−8.

(7) Wadia, J. S., Stan, R. V., and Dowdy, S. F. (2004) Transducible TAT-HA fusogenic peptide enhances escape of TAT-fusion proteins after lipid raft macropinocytosis. *Nat. Med. 10*, 310–315.

(8) Padari, K., Säälik, P., Hansen, M., Koppel, K., Raid, R., Langel, Ü., and Pooga, M. (2005) Cell transduction pathways of transportans. *Bioconjugate Chem. 16*, 1399–1410.

(9) El-Andaloussi, S., Johansson, H. J., Holm, T., and Langel, Ü. (2007) A Novel Cell-penetrating Peptide, M918, for Efficient Delivery of Proteins and Peptide Nucleic Acids. *Mol. Ther. 10*, 1820–6.

(10) Sigismund, S., Woelk, T., Puri, C., Maspero, E., Tacchetti, C., Transidico, P., Di Fiore, P. P., and Polo, S. (2005) Clathrin-independent endocytosis of ubiquitinated cargos. *Proc. Natl. Acad. Sci. U.S.A. 102*, 2760–5.

(11) Di Guglielmo, G. M., Le Roy, C., Goodfellow, A. F., and Wrana, J. L. (2003) Distinct endocytic pathways regulate TGF-beta receptor signalling and turnover. *Nat. Cell Biol. 5*, 410–21.

(12) Lakadamyali, M., Rust, M. J., and Zhuang, X. (2006) Ligands for clathrin-mediated endocytosis are differentially sorted into distinct populations of early endosomes. *Cell 124*, 997–1009.

(13) Richard, J. P., Melikov, K., Vivès, E., Ramos, C., Verbeure, B., Gait, M. J., Chernomordik, L. V., and Lebleu, B. (2003) Cell-penetrating peptides. A reevaluation of the mechanism of cellular uptake. *J. Biol. Chem. 278*, 585–90.

(14) Säälik, P., Elmquist, A., Hansen, M., Padari, K., Saar, K., Viht, K., Langel, Ü., and Pooga, M. (2004) Protein cargo delivery properties of cell-penetrating peptides. A comparative study. *Bioconjugate Chem. 15*, 1246–53.

(15) Parton, R. G., and Simons, K. (2007) The multiple faces of caveolae. *Nat. Rev. Mol. Cell Biol. 8*, 185–94.

(16) Fittipaldi, A., Ferrari, A., Zoppe, M., Arcangeli, C., Pellegrini, V., Beltram, F., and Giacca, M. (2003) Cell membrane lipid rafts mediate caveolar endocytosis of HIV-1 Tat fusion proteins. *J. Biol. Chem. 278*, 34141–34149.

(17) Ferrari, A., Pellegrini, V., Arcangeli, C., Fittipaldi, A., Giacca, M., and Beltram, F. (2003) Caveolae-mediated internalization of extracellular HIV-1 tat fusion proteins visualized in real time. *Mol. Ther. 8*, 284–294.

(18) Norbury, C. C. (2006) Drinking a lot is good for dendritic cells. *Immunology 117*, 443–51.

(19) Nakase, I., Tadokoro, A., Kawabata, N., Takeuchi, T., Katoh, H., Hiramoto, K., Negishi, M., Nomizu, M., Sugiura, Y., and Futaki, S. (2007) Interaction of arginine-rich peptides with membrane-associated proteoglycans is crucial for induction of Actin organization and macropinocytosis. *Biochemistry 46*, 492–501.

(20) Gerbal-Chaloin, S., Gondeau, C., Aldrian-Herrada, G., Heitz, F., Gauthier-Rouviere, C., and Divita, G. (2007) First step of the cell-penetrating peptide mechanism involves Rac1 GTPase-dependent Actin-network remodelling. *Biol. Cell 99*, 223–38.

(21) Damm, E. M., Pelkmans, L., Kartenbeck, J., Mezzacasa, A., Kurzchalia, T., and Helenius, A. (2005) Clathrin- and caveolin-1-independent endocytosis: entry of simian virus 40 into cells devoid of caveolae. *J. Cell Biol. 168*, 477–88.

(22) Kirkham, M., Fujita, A., Chadda, R., Nixon, S. J., Kurzchalia, T. V., Sharma, D. K., Pagano, R. E., Hancock, J. F., Mayor, S., and Parton, R. G. (2005) Ultrastructural identification of uncoated caveolin-independent early endocytic vehicles. *J. Cell Biol. 168*, 465–76.

(23) Janich, P., and Corbeil, D. (2007) GM1 and GM3 gangliosides highlight distinct lipid microdomains within the apical domain of epithelial cells. *FEBS Lett. 581*, 1783–7.

(24) Glebov, O. O., Bright, N. A., and Nichols, B. J. (2006) Flotillin-1 defines a clathrin-independent endocytic pathway in mammalian cells. *Nat. Cell Biol. 8*, 46–54.

(25) Rajendran, L., Le Lay, S., and Illges, H. (2007) Raft association and lipid droplet targeting of flotillins are independent of caveolin. *Biol. Chem. 388*, 307–14.

(26) Arai, R., Geffard, M., and Calas, A. (1992) Intensification of labelings of the immunogold silver staining method by gold toning. *Brain Res. Bull. 28*, 343–5.

(27) Nichols, B. J. (2002) A distinct class of endosome mediates clathrin-independent endocytosis to the Golgi complex. *Nat. Cell Biol. 4*, 374–8.

(28) Razani, B., Engelman, J. A., Wang, X. B., Schubert, W., Zhang, X. L., Marks, C. B., Macaluso, F., Russell, R. G., Li, M., Pestell, R. G., Di Vizio, D., Hou, H., Jr., Kneitz, B., Lagaud, G., Christ, G. J., Edelmann, W., and Lisanti, M. P. (2001) Caveolin-1 null mice are viable but show evidence of hyperproliferative and vascular abnormalities. *J. Biol. Chem. 276*, 38121–38.

(29) Foerg, C., Ziegler, U., Fernandez-Carneado, J., Giralt, E., Rennert, R., Beck-Sickinger, A. G., and Merkle, H. P. (2005) Decoding the entry of two novel cell-penetrating peptides in HeLa cells: lipid raft-mediated endocytosis and endosomal escape. *Biochemistry 44*, 72–81.

(30) Rodal, S. K., Skretting, G., Garred, O., Vilhardt, F., van Deurs, B., and Sandvig, K. (1999) Extraction of cholesterol with methyl-beta-cyclodextrin perturbs formation of clathrin-coated endocytic vesicles. *Mol. Biol. Cell 10*, 961–74.

(31) Mondal, M., Mesmin, B., Mukherjee, S., and Maxfield, F. R. (2009) Sterols are mainly in the cytoplasmic leaflet of the plasma membrane and the endocytic recycling compartment in CHO cells. *Mol. Biol. Cell 20*, 581–8.

(32) Frick, M., Schmidt, K., and Nichols, B. J. (2007) Modulation of lateral diffusion in the plasma membrane by protein density. *Curr. Biol. 17*, 462–7.

(33) Torgersen, M. L., Skretting, G., van Deurs, B., and Sandvig, K. (2001) Internalization of cholera toxin by different endocytic mechanisms. *J. Cell. Sci. 114*, 3737–3747.

(34) Lamaziere, A., Burlina, F., Wolf, C., Chassaing, G., Trugnan, G., and Ayala-Sanmartin, J. (2007) Non-metabolic membrane tubulation and permeability induced by bioactive peptides. *PLoS ONE 2*, e201.

(35) Yandek, L. E., Pokorny, A., Florén, A., Knoelke, K., Langel, Ü., and Almeida, P. F. (2007) Mechanism of the cell-penetrating peptide transportan 10 permeation of lipid bilayers. *Biophys. J. 92*, 2434–44.

(36) Barany-Wallje, E., Andersson, A., Gräslund, A., and Mäler, L. (2006) Dynamics of transportan in bicelles is surface charge dependent. *J. Biomol. NMR 35*, 137–47.

(37) Foster, L. J., De Hoog, C. L., and Mann, M. (2003) Unbiased quantitative proteomics of lipid rafts reveals high specificity for signaling factors. *Proc. Natl. Acad. Sci. U.S.A. 100*, 5813–8.

(38) Pelkmans, L., Burli, T., Zerial, M., and Helenius, A. (2004) Caveolin-stabilized membrane domains as multifunctional transport and sorting devices in endocytic membrane traffic. *Cell 118*, 767–80.

(39) Sprenger, R. R., Fontijn, R. D., van Marle, J., Pannekoek, H., and Horrevoets, A. J. (2006) Spatial segregation of transport and signalling functions between human endothelial caveolae and lipid raft proteomes. *Biochem. J. 400*, 401–10.

(40) Schnatwinkel, C., Christoforidis, S., Lindsay, M. R., Uttenweiler-Joseph, S., Wilm, M., Parton, R. G., and Zerial, M. (2004) The Rab5 effector Rabankyrin-5 regulates and coordinates different endocytic mechanisms. *PLoS Biol. 2*, E261.

(41) Payne, C. K., Jones, S. A., Chen, C., and Zhuang, X. (2007) Internalization and trafficking of cell surface proteoglycans and proteoglycan-binding ligands. *Traffic 8*, 389–401.

(42) Nichols, B. J., Kenworthy, A. K., Polishchuk, R. S., Lodge, R., Roberts, T. H., Hirschberg, K., Phair, R. D., and Lippincott-Schwartz, J. (2001) Rapid cycling of lipid raft markers between the cell surface and Golgi complex. *J. Cell Biol. 153*, 529–41.

BC800416F

PROTEIN DELIVERY WITH TRANSPORTANS IS MEDIATED BY CAVEOLAE RATHER THAN FLOTILLIN-DEPENDENT PATHWAYS

Pille Säälik[†,‖], Kärt Padari[†], Aira Niinep[†] Annely Lorents[†], Mats Hansen[‡,¤], Eija Jokitalo[§], Ülo Langel[‡,¤] and Margus Pooga[†,‖]

[†], Institute of Molecular and Cell Biology, University of Tartu, Estonia;

[‡] Department of Neurochemistry, Stockholm University, Sweden;

[§] Institute of Biotechnology, Electron Microscopy Unit, University of Helsinki, Finland

[¤] Institute of Technology, University of Tartu, Estonia

[‖] Estonian Biocentre, Tartu, Estonia

Supporting information

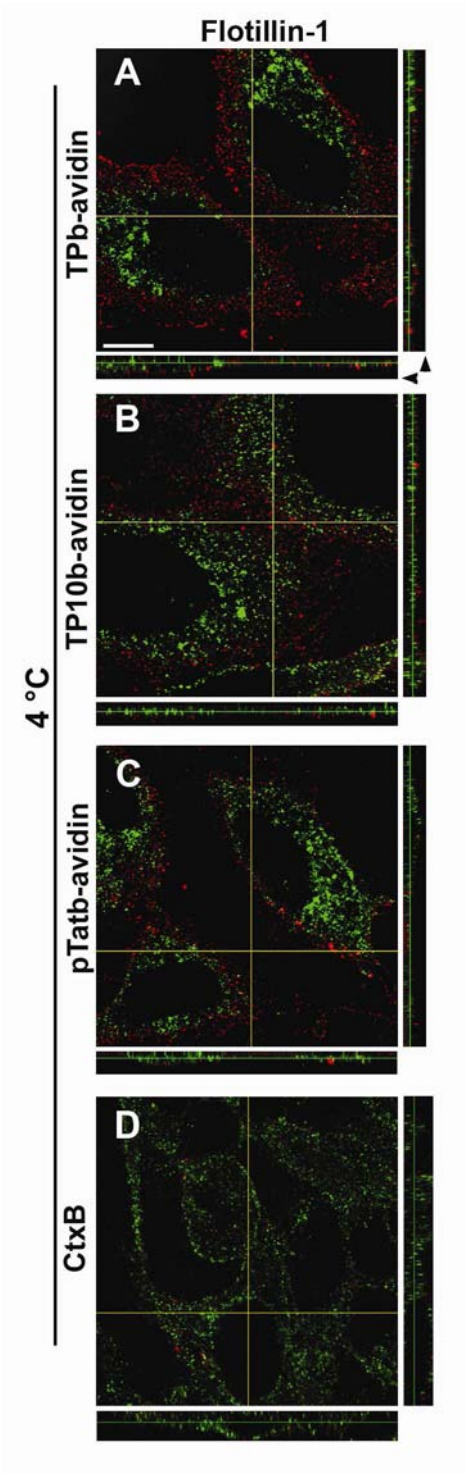

Figure S1. Localization of transportan-, TP10, pTat-protein complexes or cholera toxin B (CtxB) subunit in HeLa cells in relation to Flot-1 at low temperature. Cells were pre-cooled on ice for 15 min and incubated for 30 min with 0.5 μM biotinylated transportan (A), TP10 (B) or pTat (C) complexed with 0.15 μM avidin-Texas Red (red), or with 3 μg/mL of CtxB-AF 594 (D, red) in relation to Flot-1 at low temperature. To visualize Flot-1, the cells were stained with anti-Flot-1 polyclonal antibody and with anti rabbit Alexa Fluor 488-conjugated secondary Ab (green). A single optical section of cells is presented indicated with green line

on the z-projections and yellow lines in xy-projection indicate the location of z-projections. Arrowheads indicate the apical part of cells in z-projections. Scale bar 10 μM.

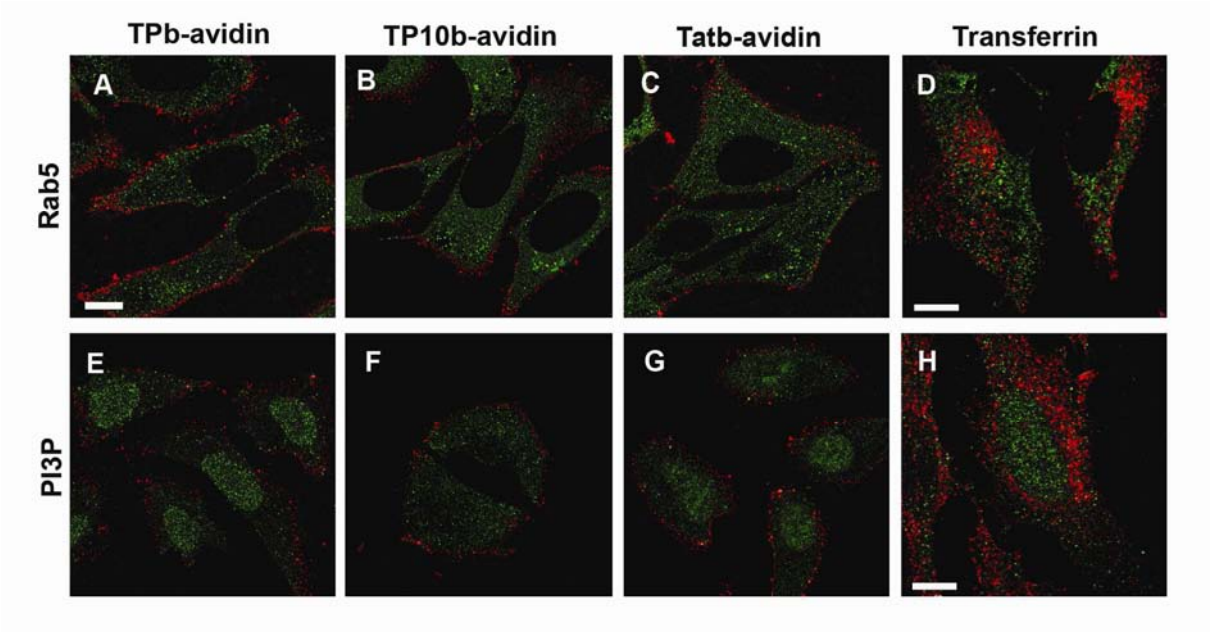

Figure S2. Localization of transportan-, TP10- and pTat-protein complexes in HeLa cells in relation to Rab5 and PI3P after short-time incubation. Cells were incubated at 37 ºC for 10 min with 0.5 μM biotinylated transportan (A, E), TP10 (B, F) or pTat (C, G) complexed with 0.15 μM avidin-Texas Red, or with 20 μg/mL transferrin-AF 594 (D, H, red). To visualize PI3P and Rab5, the cells were stained with anti-Rab5 pAb (A-D) or anti-PI3P mAb (E-H), respectively and with appropriate AF 488-conjugated secondary Ab (green).

Synthesis and Characterization of an ^{111}In-Labeled Peptide for the in Vivo Localization of Human Cancers Expressing the Urokinase-Type Plasminogen Activator Receptor (uPAR)

Dijie Liu,[†,§] Douglas Overbey,[†,§] Lisa Watkinson,[†,§] and Michael F. Giblin*[,†,‡,§]

Research Service, Harry S. Truman Memorial Veterans' Administration Hospital, Columbia, Missouri 65201, Department of Radiology, University of Missouri—Columbia School of Medicine, Columbia, Missouri 65211, and The Radiopharmaceutical Sciences Institute, University of Missouri—Columbia, Columbia, Missouri 65211. Received October 10, 2008; Revised Manuscript Received March 6, 2009

This study describes the synthesis and preliminary biologic evaluation of an ^{111}In-labeled peptide antagonist of the urokinase-type plasminogen activator receptor (uPAR) as a potential probe for assessing metastatic potential of human breast cancer in vivo. The peptide (NAc-dD-CHA-F-dS-dR-Y-L-W-S-βAla)$_2$-K-K(DOTA)-NH_2 was synthesized and conjugated with the DOTA chelating moiety via conventional solid-phase peptide synthesis (SPPS), purified by reversed-phase HPLC, and characterized by MALDI-TOF MS and receptor binding assay. In vitro receptor binding studies demonstrated an IC_{50} of 240 ± 125 nM for the peptide, compared with IC_{50} values of 0.44 ± 0.02 and 0.75 ± 0.01 nM for the amino terminal fragment (ATF) of the urokinase-type plasminogen activator (uPA) and full-length uPA, respectively. In vivo biodistribution studies were carried out using SCID mice bearing MDA-MB-231 human breast cancer xenografts. Biodistribution data was collected at 1, 4, and 24 h postinjection of ^{111}In-DOTA-peptide, and compared with data obtained using a scrambled control peptide as well as with data obtained using wild-type ATF radiolabeled with I-125. Biodistribution studies showed rapid elimination of the ^{111}-labeled peptide from the blood pool, with 0.12 ± 0.06% ID/g remaining in blood at 4 h pi. Elimination was seen primarily via the renal/urinary route, with 83.9 ± 2.2% ID in the urine at the same time point. Tumor uptake at this time was 0.53 ± 0.11% ID/g, resulting in tumor/blood and tumor/muscle ratios of 4.2 and 9.4, respectively. Uptake in tumor was significantly higher than that obtained using a scrambled control peptide that showed no specific binding to uPAR ($p < 0.05$). In vitro and ex vivo results both suggested that the magnitude of tumor-specific binding was reduced in this model by endogenous expression of uPA. The results indicate that radiolabeled peptide uPAR antagonists may find application in the imaging and therapy of uPAR-expressing breast cancers in vivo.

INTRODUCTION

The urokinase-type plasminogen activator (uPA) system plays an important role in the progression of many types of cancer (*1*−*4*). Binding of uPA to its receptor (uPAR) initiates a proteolytic cascade that ultimately results in degradation of extracellular matrix (ECM) components and activation of matrix metalloproteases (MMP's). These processes in turn lead to tumor invasion and metastasis. Components of the uPA system, including uPAR, are overexpressed in various cancers, including human breast, prostate, and colorectal cancer, and overexpression is correlated with poor prognosis due to increased rates of metastatic relapse (*5*−*11*). The proven correlation between uPAR expression and metastatic potential provides an opportunity to develop an *in vivo* imaging agent, which can both help define a subset of breast cancer patients at increased risk for metastatic disease and localize and ultimately treat metastatic disease.

Seminal research by Blasi, Ploug, and others (*1, 2, 4, 12*−*15*) has clarified the functional elements of uPAR that are required for its interaction with uPA and with other proteins, including integrins and fibrinogen. uPA is a 54 kDa glycosylated serine protease that catalyzes the conversion of plasminogen to plasmin. Binding of pro-uPA to uPAR (CD87) results in proteolytic activation, yielding two-chain high molecular weight uPA (tc-HMW-uPA). uPAR is a glycosylphosphatidylinositol (GPI)-anchored receptor for uPA and serves to concentrate uPA activity at the invasive front of tumor masses. Human uPAR is a 283 amino acid single chain protein, and is a member of the Ly-6/uPAR/α-neurotoxin family of proteins. In structure, it is arranged into three finger-like domains that enfold the uPA ligand within a central binding cavity. Binding of uPA to uPAR in this fashion serves to focalize uPA activity in such a way as to facilitate invasion of uPAR-expressing cancers by activation of a proteolytic cascade that breaks down extracellular matrix components and allows cancer cell migration into vasculature and lymphatics (*2*).

The aim of this study was to investigate the applicability of radiolabeled uPA antagonists to the detection of uPAR-expressing cancers in vivo. A series of small peptide inhibitors of the uPA−uPAR interaction have previously been developed (*15*), which demonstrate high affinity for uPAR. We have synthesized and characterized one such inhibitor, modified to contain a C-terminal DOTA chelating moiety, labeled the resulting compound with ^{111}In, and compared its in vivo

* To whom correspondence should be addressed. Research Service, A004 HSTMVH, 800 Hospital Dr., Columbia, MO 65201. Phone: 573-814-6000 ext. 53669. Fax: 573-882-6129. E-mail: GiblinM@health.missouri.edu.

† Harry S. Truman Memorial Veterans' Administration Hospital.

‡ University of Missouri—Columbia School of Medicine.

§ University of Missouri—Columbia.

10.1021/bc800433y CCC: $40.75 © 2009 American Chemical Society
Published on Web 04/08/2009

biodistribution profile to that of ^{125}I-ATF using SCID mice bearing MDA-MB-231 human breast cancer tumor xenografts.

MATERIALS AND METHODS

Materials. ATF was obtained from American Diagnostica, Inc. Na^{125}I was obtained from Perkin-Elmer. DOTA-mono-NHS-ester and Fmoc-L-Lys-monoamide-DOTA-tris (tBu ester) were obtained from Macrocyclics, Inc. Rink Amide MBHA peptide synthesis resin and protected Fmoc-amino acids were obtained from Novabiochem. MALDI-TOF mass spectral analyses were performed by the Proteomics Center at the University of Missouri—Columbia. $^{111}In_3$ was obtained from Mallinckrodt Medical, Inc. as a 0.05 N HCl solution. MDA-MB-231 cells were obtained from the American Type Culture Collection (ATCC). SiRNA's and antiurokinase antibodies were obtained from Santa Cruz Biotechnology. All solvents were either ACS certified or of HPLC grade, obtained from Fisher Scientific and used as received. Other reagents were purchased from Aldrich Chemical Co., Gibco, and Pierce.

Peptide Synthesis and Purification. Peptides were synthesized by standard solid phase peptide synthesis (SPPS) techniques, employing Fmoc protected amino acids and either DOTA-mono-NHS-ester or Fmoc-L-Lys-monoamide-DOTA-tris (tBu ester) as building blocks. Polypeptides were assembled on Rink Amide MBHA resin, acetylated via HoBT/DCC activation of 5-fold excess acetic acid in 3:1 NMP/DMSO, then cleaved from the resin and deprotected using a 36:2:1:1 mixture of TFA/thioanisole/water/ethanedithiol. The addition of DOTA-mono-NHS-ester to the ε-amino group of the C-terminal lysine residue of (NAc-dD-CHA-F-dS-dR-Y-L-W-S-βAla)$_2$-K-K-NH_2 was carried out with 0.1 M Na_2HPO_4, pH 8, for 3.5 h at room temperature, using a 10−20-fold excess of DOTA NHS ester.

DOTA-conjugated peptides were purified by high performance liquid chromatography (HPLC). HPLC was performed on a Shimadzu system equipped with an SPD-20A UV detector and an in-line sodium iodide crystal radiometric detector. HPLC solvents consisted of H_2O containing 0.1% trifluoroacetic acid (solvent A) and acetonitrile containing 0.1% trifluoroacetic acid (solvent B). Conditions: A Phenomenex Jupiter C-18 (5 μm, 300 Å, 4.6 × 250 mm) column was used with a flow rate of 1.5 mL/min. Gradient purification of all compounds was achieved during a linear 30 min ramp from 35% B to 45% B, followed by column rinse and reequilibration.

Radiolabeling. For the synthesis of ^{111}In-labeled compounds, aliquots of $^{111}In_3$ (0.2−2.5 mCi, 7.4−92.5 MBq, 4−50 μL) were added to solutions of (NAc-dD-CHA-F-dS-dR-YLWS-βAla)$_2$-K-K(DOTA)-NH_2 and scrambled negative control peptide (NAc-dD-W-dS-LY-dR-FS-CHA-βAla)$_2$-K-K(DOTA)-NH_2 (10−20 μg) in 0.4 M ammonium acetate (200 μL). The pH of the reaction mixture was adjusted to 6.0. The reaction mixture was incubated for 1 h at 80 °C. After 1 h, an aliquot of 0.002 M EDTA (50 μL) was added to the reaction mixture to complex unreacted $^{111}In^{3+}$. The resulting conjugates were purified to homogeneity by RP-HPLC. The ^{111}In-metalated conjugates eluted between 0.5−1.5 min after the associated nonmetalated species. Purified ^{111}In-DOTA conjugates were then concentrated by passing through a 3 M Empore C-18 HD high performance extraction disk (7 mm/3 mL) cartridge and eluting with 100% ethanol (400 μL). The concentrated fractions were immediately diluted 2-fold by the addition of 0.1 M NaH_2PO_4, then reduced in volume under a stream of $N_{2(g)}$, and finally diluted with 0.1 M NaH_2PO_4 buffer, pH 7.0, to a final activity of approximately 2 μCi/ 100 μL.

The amino terminal fragment of uPA was iodinated essentially according to a previously published protocol (*13*). Briefly, 2−10 μg of the Amino Terminal Fragment of uPA (ATF) was iodinated using 0.2−1 mCi Na^{125}I following ^{125}I activation using Iodogen precoated tubes (Pierce). After a 10-min incubation in 25 mM Tris and 0.4 M NaCl, pH 7.5, the reaction was quenched by the addition of excess free tyrosine and purified by fractionation on a D-Salt size exclusion cartridge (Pierce).

In Vitro/Ex Vivo Receptor Binding Assays. Binding affinity of urokinase antagonists was measured by competition against ^{125}I-ATF using whole MDA-MB-231 human breast cancer cells. Prior to incubations of peptide competitors and radiolabeled tracer with whole cells, cells were briefly rinsed with 50 mM glycine HCl and 100 mM NaCl, pH 3.0, then neutralized with 0.2 volume 0.5 M HEPES and 100 mM NaCl, pH 7.4, to strip away endogenous uPA. Cells were then rinsed and suspended in binding buffer, PBS/0.2% BSA, pH 7.4. Cells (3×10^6) suspended in binding buffer were incubated at 37 °C for 1 h in the presence of approximately 20−30,000 cpm ^{125}I-ATF and increasing concentrations of unlabeled peptide competitors. After the incubation, the reaction medium was aspirated, and cells were washed three times with binding buffer. The radioactivity bound to the cells was counted in a Packard Riastar gamma counting system. Experiments were performed in triplicate, and average values were used for the calculations. The specific activity of the tracer was 50−100 μCi/μg.

SiRNA Studies. MDA-MB-231 cells were maintained in RPMI 1640 supplemented with 10% FBS, 2 mM L-glutamine, 1 mM sodium pyruvate, 10 mM HEPES, 0.1 mM MEM nonessential amino acids, and 50 μg/mL gentamicin. SiRNA transfections were performed using lipofectamine 2000 (Invitrogen) according to the manufacturer's instructions. Briefly, 2×10^5 MDA-MB-231 cells were seeded in 6-well plates in antibiotic-free medium and reached 30−50% confluence by the time of transfection. Forty picomoles of uPA siRNA (Santa Cruz Biotechnology)/5 μL lipofectamine 2000 transfection complexes were added to each well and incubated at 37 °C for 4 h. Control siRNA (Santa Cruz Biotechnology) and no-transfection controls were run in parallel. Each assay was performed in triplicate. Forty-eight hours post-transfection, effectiveness of siRNA knockdown was assessed by receptor binding assay without acid stripping of endogenous uPA, Western blot, and RT-PCR.

Immunoblot Analysis. Whole cell MDA-MB-231 lysates were prepared 48 h post-transfection and separated by 10% SDS−PAGE, followed by transfer to a PVDF membrane. Loading volumes were normalized on the basis of cell number equivalents. After blocking in 5% nonfat milk, 0.1% Tween-20, and Tris-buffered saline (TTBS) at RT for 1 h, membranes were probed with primary antibodies in blocking solution for 1 h at RT, followed by extensive washing in TTBS. Goat antirabbit and goat antimouse IgG-HRP (Santa Cruz Biotechnology) were used for the detection of immunoreactive proteins by chemiluminescence. Primary antibodies used were rabbit anti-uPA and mouse anti-β-Actin (Santa Cruz Biotechnology).

Reverse Transcription-PCR Analysis. Total RNA from MDA-MB-231 cells 48 h post-siRNA transfection was extracted using Trireagent (Molecular Research Center) and the Qiagen RNeasy kit. Five micrograms of total RNA was applied to synthesize first-strand cDNA using SuperScript reverse transcriptase III (Invitrogen), and PCR was performed in a 25 μL total volume containing 12.5 pmol of primers. The following primers were used: uPA sense 5′-TGC GTC CTG GTC GTG AGC GC-3′ and uPA antisense 5′-CTA CAG CGC TGA CAC GCT TG-3′ to amplify a 780-bp uPA fragment after 35 cycles at 94 °C for 1 min, 55 °C for 1 min, 72 °C for 1 min (*31*). For control GAPDH, the following primers were used: sense 5′-CTT CAT TGA CCT CAACAT GGT TT-3′ and antisense 5′-GGC ATT GCT GAT GAT CTT GAG G-3′ to amplify a 346-bp GAPDH fragment after 23 cycles of 94 °C for 30 s, 63 °C for 30 s, and 72 °C for 1 min.

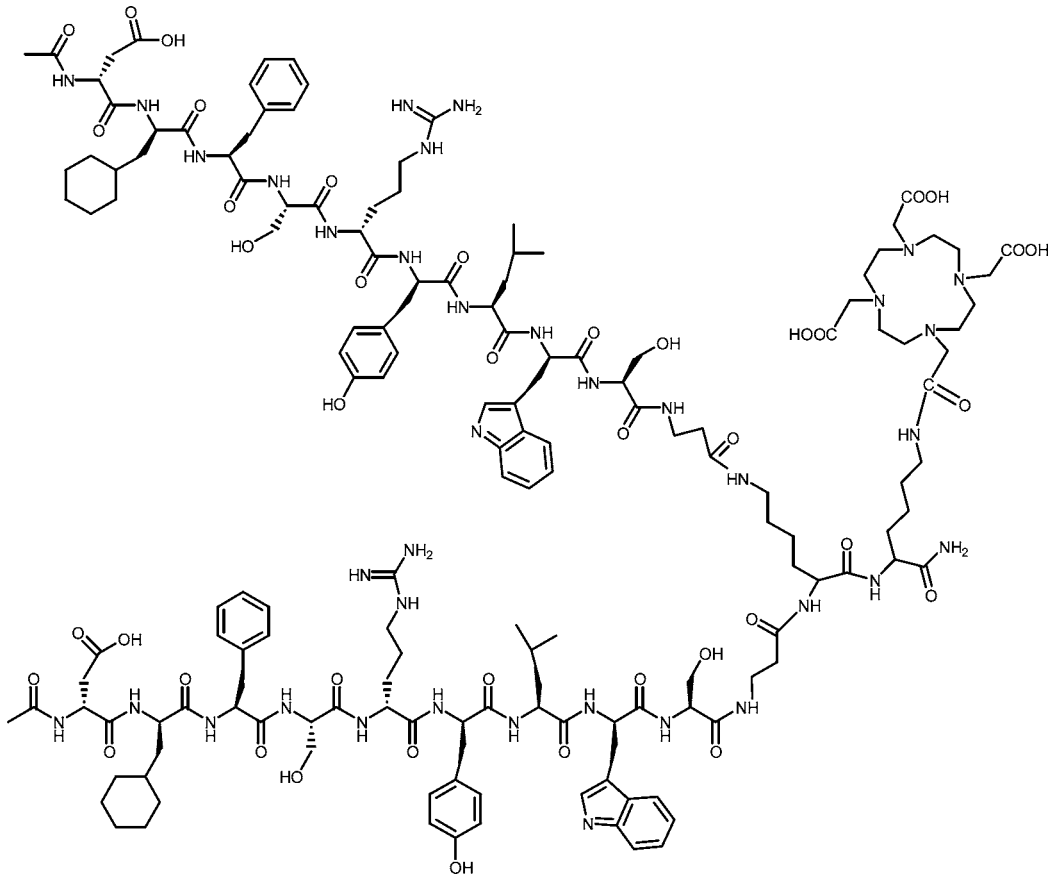

Figure 1. Structure of (NAc-dD-CHA-F-dS-dR-Y-L-W-S-βAla)$_2$-K-K(DOTA)-NH$_2$.

Biodistribution Studies. Four- to 5-week old female ICR SCID (severe combined immunodeficient) outbred mice were obtained from Taconic (Germantown, NY). The mice were housed four animals per cage in sterile microisolator cages in a temperature- and humidity-controlled room with a 12-h light/12-h dark schedule. The animals were fed sterile rodent chow (Ralston Purina Company, St. Louis, MO) and water *ad libitum*. Animals were housed one week prior to inoculation of tumor cells and anesthetized for injections with isoflurane (Baxter Healthcare Corp., Deerfield, IL) at a rate of 2.5% with 0.5 L/min oxygen through a nonrebreathing anesthesia vaporizer.

MDA-MB-231 human breast cancer cells were injected on the bilateral subcutaneous (s.c.) flank with $\sim 5 \times 10^6$ cells in a suspension of 100 μL 3:1 PBS/Matrigel per injection site. MDA-MB-231 cells were allowed to grow *in vivo* four to five weeks postinoculation, developing tumors ranging in size from 0.06−0.53 g. The biodistribution and uptake of (NAc-dD-CHA-F-dS-dR-YLWS-βAla)$_2$-K-K(^{111}In-DOTA)-NH$_2$, scrambled negative control peptide (NAc-dD-W-dS-LY-dR-FS-CHA-βAla)$_2$-K-K(^{111}In-DOTA)-NH$_2$, and ^{125}I-ATF in tumor bearing SCID mice was studied. The mice (average weight, 25 g) were injected with aliquots (50−100 μL) of the radiolabeled peptide solution (55−90 kBq) via the tail vein. Tissues, organs, and tumors were excised from animals sacrificed at 1, 4, and 24 h p.i., weighed, and counted. Radioactivity was measured in a Wallac 1480 automated gamma counter, and the percent-injected dose per gram tissue was calculated. Differences in organ uptake between the two ^{111}In-labeled peptides were analyzed by Student's *t*-test. Differences at the 95% confidence level ($P < 0.05$) were considered significant. Animal studies were conducted in accordance with the highest standards of care as outlined in the NIH Guide for Care and Use of Laboratory Animals and the Policy and Procedures for Animal Research at the Harry S. Truman Memorial Veterans' Hospital, and according to approved protocols.

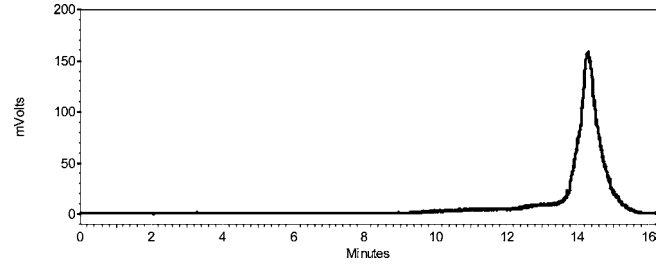

Figure 2. HPLC chromatogram of purified (NAc-dD-CHA-F-dS-dR-Y-L-W-S-βAla)$_2$-K-K(^{111}In-DOTA)-NH$_2$. The ^{111}In-peptide elutes at 14.1 min, while the unlabeled peptide has a retention time of 13.6 min.

RESULTS

Synthesis and in Vitro Characterization. The peptides (NAc-dD-CHA-F-dS-dR-Y-L-W-S-βAla)$_2$-K-K(DOTA)-NH$_2$ (Figure 1) and (NAc-dD-W-dS-L-Y-dR-F-S-CHA-βAla)$_2$-K-K(DOTA)-NH$_2$ were synthesized by standard solid phase peptide synthesis techniques, utilizing two distinct synthetic routes. In the first instance, (NAc-dD-CHA-F-dS-dR-Y-L-W-S-βAla)$_2$-K-K(DOTA)-NH$_2$ was synthesized using a Boc-protected ε-amino group on the C-terminal lysine residue. Following addition of the N-terminal D-aspartic acid residue, the Fmoc-peptide was acetylated on resin via HoBT/DCC activation of 5-fold excess acetic acid in 3:1 NMP/DMSO. Following acetylation, the peptide was cleaved from the resin in a standard deprotection/cleavage mixture, and the free amino group of the C-terminal lysine was conjugated to an activated NHS ester of DOTA. In the second route, the scrambled negative

Table 1. Calculated and Observed Molecular Weights and IC_{50} Values of DOTA-Peptides

peptide	$(M + H)^+$ calc.	$(M + H)^+$ obs.	IC_{50} (nM)
(NAc-dD-CHA-F-dS-dR-YLWS-βAla)$_2$-K-K(DOTA)-NH_2	3301.5	3301.7	240 ± 125
(NAc-dD-W-dS-LY-dR-FS-CHA-βAla)$_2$-K-K(DOTA)-NH_2	3301.5	3301.7	

control peptide (NAc-dD-W-dS-L-Y-dR-F-S-CHA-βAla)$_2$-K-K(DOTA)-NH_2 was synthesized using preconjugated Fmoc-L-Lys-monoamide-DOTA-tris(t-Bu ester), followed by acetylation with HoBT/DCC activated acetic acid, and cleavage from the resin. In each case, the final products were purified by C18 RP HPLC, and masses were confirmed by MALDI-TOF MS (Table 1 and Figure 2).

The peptide (NAc-dD-CHA-F-dS-dR-Y-L-W-S-βAla)$_2$-K-K(DOTA)-NH_2 contains a core uPAR-binding sequence (dD-CHA-F-dS-dR-Y-L-W-S) originally developed using phage display and combinatorial chemistry techniques (*14*, *15*). The affinity of this peptide construct for uPAR was measured using MDA-MB-231 human breast cancer cells and ^{125}I-labeled ATF. The ability of (NAc-dD-CHA-F-dS-dR-Y-L-W-S-βAla)$_2$-K-K(DOTA)-NH_2 to competitively displace ^{125}I-ATF from intact cells was 300−600-fold lower than that of either uPA or ATF, indicating that the dimeric peptide has relatively low affinity for uPAR (Figure 3 and Table 1). The effect of scrambling the peptide sequence was to completely abolish competitive displacement of ATF (Figure 3), demonstrating the specific nature of (NAc-dD-CHA-F-dS-dR-Y-L-W-S-βAla)$_2$-K-K(DOTA)-NH_2 binding to uPAR.

Biodistribution. In vivo biodistribution studies were carried out using SCID mice bearing MDA-MB-231 human breast cancer tumor xenografts. Animals were injected with ^{111}In-labeled peptides and sacrificed 1, 4, and 24 h postinjection (Table 2). Both the uPAR-targeting peptide and the scrambled control peptide cleared rapidly from the bloodstream, primarily via the renal/urinary route. At 4 h pi, uptake of (NAc-dD-CHA-F-dS-dR-Y-L-W-S-βAla)$_2$-K-K(^{111}In-DOTA)-NH_2 in blood and muscle were 0.12 ± 0.06% ID/g and 0.06 ± 0.02% ID/g, respectively, while uptake in tumor was 0.53 ± 0.11% ID/g. For comparison, uptake of the matched scrambled control peptide in blood and muscle were 0.15 ± 0.04% ID/g and 0.12 ± 0.02% ID/g, respectively, at this time point, while tumor uptake dropped significantly ($p < 0.05$) to 0.36 ± 0.05% ID/g.

In vivo results obtained using ^{111}In-labeled peptide uPA antagonists were compared to those obtained using ^{125}I-labeled ATF, a molecule with an approximately 600-fold higher affinity for uPAR. As shown in Table 3, tumor uptake of ^{125}I-ATF only exceeded blood levels at 24 h pi, although this did not reach significant levels. At this time point, however, tumor uptake was significantly lowered by coinjection of excess unlabeled ATF ($p < 0.05$), again demonstrating the specific nature of the tumor uptake observed.

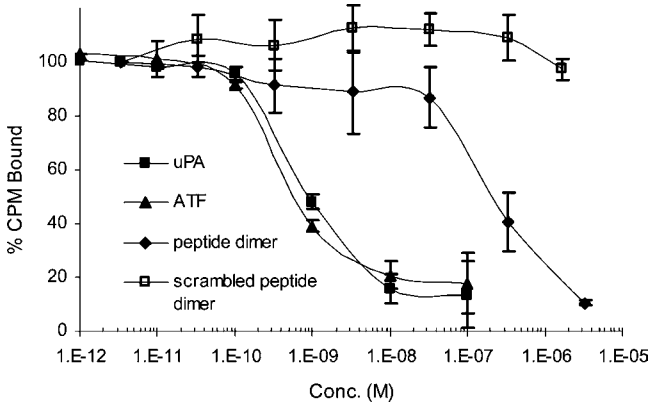

Figure 3. Competitive receptor binding assay using intact MDA-MB-231 human breast cancer cells and ^{125}I-ATF.

Table 2. In Vivo Biodistribution of (NAc-dD-CHA-F-dS-dR-Y-L-W-S-βAla)$_2$-K-K(^{111}In-DOTA)-NH_2 (Test) at 1, 4, and 24 h Postinjection and Scrambled Negative Control Peptide (NAc-dD-W-dS-L-Y-dR-F-S-CHA-βAla)$_2$-K-K(^{111}In-DOTA)-NH_2 (Control) at 4 h Postinjection in SCID Mice Bearing MDA-MB-231 Human Breast Cancer Tumor Xenografts ($N = 3$, mean % ID/g ± SD)

organ	test 1 h	test 4 h	control 4 h	test 24 h
blood	2.85 ± 0.57	0.12 ± 0.06	0.15 ± 0.04	0.07 ± 0.02
heart	0.93 ± 0.22	0.16 ± 0.02	0.55 ± 0.08	0.10 ± 0.03
lung	2.58 ± 0.51	0.42 ± 0.18	0.32 ± 0.06	0.32 ± 0.05
liver	7.97 ± 0.70	5.52 ± 0.95	13.44 ± 1.57	4.06 ± 0.34
spleen	0.72 ± 0.18	0.39 ± 0.34	0.37 ± 0.09	0.41 ± 0.04
intestines	1.07 ± 0.06	1.74 ± 1.09	1.71 ± 0.38	0.23 ± 0.07
kidney	19.09 ± 0.97	13.27 ± 2.61	13.19 ± 3.18	10.23 ± 2.29
muscle	0.30 ± 0.08	0.06 ± 0.02	0.12 ± 0.02	0.03 ± 0.01
bone	0.49 ± 0.22	0.06 ± 0.04	0.09 ± 0.02	0.06 ± 0.05
pancreas	0.83 ± 0.26	0.15 ± 0.07	0.25 ± 0.03	0.07 ± 0.06
tumor	1.48 ± 0.28	0.53 ± 0.11	0.36 ± 0.05	0.23 ± 0.07

Table 3. In Vivo Biodistribution ($N = 3$, mean % ID/g ± SD) of ^{125}I-ATF in SCID Mice Bearing MDA-MB-231 Human Breast Cancer Tumor Xenografts at 1, 4, and 24 h Postinjection

organ	1 h	4 h	24 h	24 h (blocked)
blood	7.75 ± 1.00	3.41 ± 0.86	0.26 ± 0.06	0.60 ± 0.69
heart	2.56 ± 0.12	1.19 ± 0.16	0.08 ± 0.02	0.06 ± 0.01
lung	5.39 ± 0.35	2.67 ± 0.51	0.16 ± 0.05	0.17 ± 0.02
liver	3.01 ± 0.45	1.81 ± 0.42	0.25 ± 0.06	0.23 ± 0.02
spleen	2.92 ± 0.39	1.72 ± 0.35	0.09 ± 0.02	0.10 ± 0.03
intestines	3.27 ± 0.40	2.53 ± 0.28	0.16 ± 0.03	0.13 ± 0.02
kidney	16.72 ± 1.59	4.65 ± 0.84	0.88 ± 0.21	0.81 ± 0.09
muscle	1.21 ± 0.08	0.61 ± 0.10	0.03 ± 0.01	0.02 ± 0.01
bone	1.55 ± 0.13	0.87 ± 0.11	0.04 ± 0.01	0.03 ± 0.001
pancreas	3.98 ± 0.77	2.18 ± 0.65	0.06 ± 0.03	0.05 ± 0.01
tumor	4.60 ± 0.63	3.09 ± 0.29	0.29 ± 0.06	0.19 ± 0.05

Ex Vivo/in Vitro Studies. To address the issue of uPAR binding capacity in the SCID/MDA-MB-231 model system used here, tumor xenografts were excised from SCID mice following 4−5 weeks of in vivo growth and assayed for ^{125}I-ATF binding with or without stripping of endogenous uPA. Figure 4 demonstrates that specific binding of uPAR-targeted ligands is decreased 4−5-fold due to receptor occupancy by endogenously produced uPA.

To further demonstrate that uPAR-targeted agents could be used to quantify uPA binding sites, we used a uPA-specific set

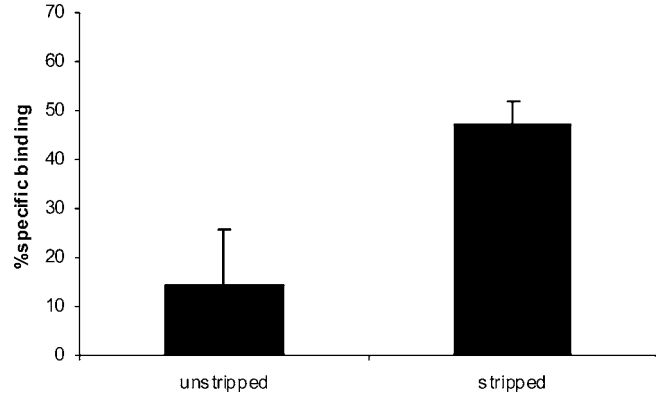

Figure 4. Specific binding of ^{125}I-ATF to MDA-MB-231 tumor cells ex vivo. MDA-MB-231 tumor xenografts were harvested from SCID mice following 4−6 weeks of in vivo growth. Tumors were physically dissociated in a buffered collagenase solution, and specific binding of ^{125}I-ATF was measured using either native preparations or cell preparations stripped of endogenous uPA with pH 3.0 buffer.

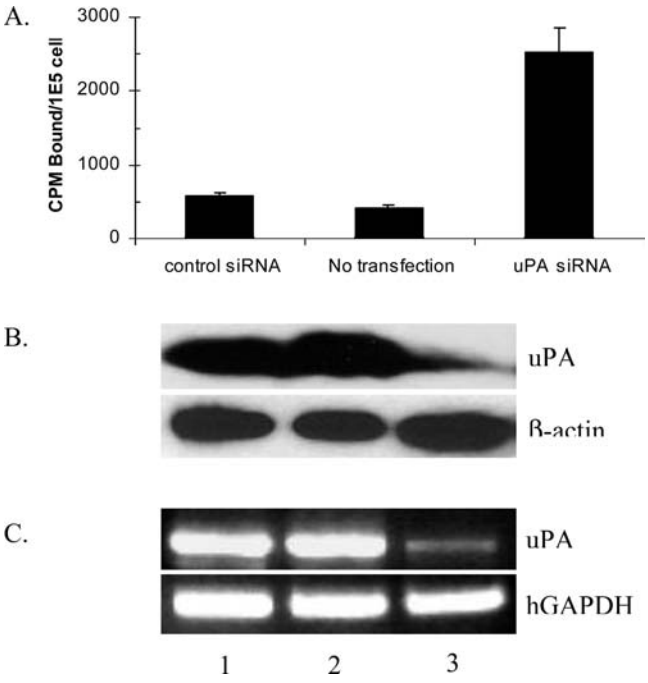

Figure 5. (A) Binding of ^{125}I-ATF to MDA MB-231 cells following knockdown of endogenous uPA production using a uPA-specific set of siRNA's. (B) Western blot demonstrating uPA knockdown 2 days post-transfection of MDA-MB-231 cells. (C) RT-PCR demonstrating decreased uPA message in siRNA transfected MDA-MB-231 cells. Lane 1, control siRNA; lane 2, no-transfection; lane 3, uPA siRNA.

of siRNAs to specifically knock down uPA expression in MDA-MB-231 cells. As seen in Figure 5, binding of ^{125}I-uPA to MDA-MB-231 cells is significantly increased ($p < 0.01$) approximately 4.4-fold following siRNA-mediated knockdown of endogenous uPA in an in vitro model system. This increase in specific binding is correlated with decreases in both uPA mRNA and protein expression as determined by RT-PCR and Western blot (Figure 5).

DISCUSSION

In this study, the synthesis and characterization of a low molecular weight peptide uPAR antagonist with an appended DOTA chelating moiety was described. This construct specifically displaced ^{125}I-labeled ATF with an IC_{50} of 240 ± 125 nM, a characteristic that was completely lost upon alteration of the primary peptide sequence employed. The affinity of (NAc-dD-CHA-F-dS-dR-Y-L-W-S-βAla)$_2$-K-K(DOTA)-NH_2 for uPAR was lower than expected from previously published data obtained for related constructs (*15*−*17*). This is due to a number of structural differences between these compounds. (NAc-dD-CHA-F-dS-dR-Y-L-W-S-βAla)$_2$-K-K(DOTA)-NH_2 is distinct from previously synthesized peptides in being N-terminally acetylated, C-terminally amidated, in the appended DOTA moiety C-terminal to the branching lysine residue, and in the chirality of the N-terminal aspartate residue.

The in vivo biodistribution of the ^{111}In-labeled peptide was compared with that of ^{125}I-labeled ATF and was significantly different at all time points examined. At 1 and 4 h pi, blood levels of each radiotracer were distinctly different, with the higher molecular weight ATF fragment demonstrating significantly slower clearance (Tables 2 and 3). ^{125}I-labeled ATF uptake was higher than (NAc-dD-CHA-F-dS-dR-Y-L-W-S-βAla)$_2$-K-K(^{111}In-DOTA)-NH_2 uptake in all normal tissues at these time points, with the exception of liver and kidney, which demonstrated higher levels of ^{111}In-peptide. Clearance of the ^{111}In-peptide occurs through both hepatobiliary and renal/urinary routes, and liver and kidney retention at 4 h pi was higher than is usually observed for peptides in this molecular weight range (*17*−*23*). Increased liver and kidney retention is still observed for the ^{111}In-labeled branched peptide relative to ^{125}I-ATF at 24 h pi, suggesting a structural mechanism of retention, perhaps due to the branched nature of this construct, distinct from normal residualization of ^{111}In-DOTA-amino acid conjugates.

With respect to specific retention of radiolabeled compounds in tumor tissue, significant ($p < 0.05$) blockade of ^{125}I-ATF uptake was only achieved at 24 h pi, when tumor uptake was 34% blocked by preinjection of 2 mg/kg unlabeled ATF 1 h prior to the injection of ^{125}I-ATF. Because of its more rapid clearance from blood and most normal tissues, (NAc-dD-CHA-F-dS-dR-Y-L-W-S-βAla)$_2$-K-K(^{111}In-DOTA)-NH_2 tumor uptake was significantly ($p < 0.05$) higher than that of the scrambled matched control peptide as early as 4 h pi, with 47% higher uptake at this time point.

The peptide uPAR antagonist discussed in this work was originally synthesized as part of a combinatorial library of peptides targeting uPAR (*15*). This combinatorial library was synthesized to further search conformational space for highest affinity uPAR binders, using lead peptides derived from earlier bacteriophage peptide display libraries (*14*). One of these peptides, termed AE105 in the original work (*15*), has served as the uPAR-targeting vector in two recent publications (*16*, *17*). In these studies, analogues of the AE105 parent peptide were N-terminally labeled with a DOTA moiety, with or without intervening linker residues, which served to coordinate imaging ^{64}Cu (*17*) or therapeutic ^{213}Bi (*16*). In the work described here, a dimeric peptide most closely related to AE120 in Ploug et al. (*15*) has been modified by the addition of DOTA C-terminal to a branching lysine residue.

In the report by Knör et al. (*16*), the assembly of a dimeric construct resulted in increased specific binding of radiolabeled peptide to uPAR-expressing cells in vitro relative to N-terminally labeled linear monomeric peptides. This is in agreement with increased binding affinities of dimeric peptides reported originally in the development of this class of uPAR antagonists (*15*), although the radiopharmaceutical construct was unique in having an N-terminal, rather than C-terminal, branchpoint. On the basis of the higher affinity of a dimeric construct, Knör et al. subsequently used it in an in vivo model of human ovarian cancer and demonstrated tumor uptake of the ^{213}Bi complex of 2.2 ± 0.4% ID/g at 1.5 h pi (*16*). This value is similar to the tumor uptake of 1.48 ± 0.28 at 1 h pi described in this article, although the values are not directly comparable due to differences in the model system, radioisotope, and experimental protocol. Additionally, the specificity of tumor uptake of the ^{213}Bi-labeled peptide in vivo was not addressed.

Li and co-workers have also recently published data relating to the use of radiolabeled uPAR antagonists for in vivo imaging of U87MG human glioma tumor xenografts (*17*). In this instance, an N-terminally DOTA-labeled AE105 analogue was used to deliver the PET radionuclide ^{64}Cu to uPAR-expressing cells. In this instance, the DOTA chelating group was directly linked to the amino group of the N-terminal L-aspartic acid residue of monomeric AE105. Tumor uptake in this model system was increased 2−5-fold relative to both the N-terminally modified dimeric construct of Knör et al. as well as the C-terminally modified dimeric construct described here (7.6 ± 0.9% ID/g at 1 h pi, as measured by PET imaging). Given the differences in experimental design among the three studies to date, more research will be required to directly compare these and similar analogues to define the optimal structure of uPAR-targeted molecular imaging agents.

One factor that could be responsible for differences in tumor uptake between different model cell lines is expression of

endogenous uPA, resulting in the blockade of available sites for binding of uPAR antagonists. The most widely used protocols for the measurement of binding of radiolabeled uPAR ligands in vitro typically employ an acid stripping step, during which endogenously produced uPA is removed, thereby unmasking previously blocked uPAR. Knör and co-workers spoke to this issue by demonstrating tracer binding to OV-MZ-6 cells without prior acid stripping (*16*), suggesting that this cell line produces lower amounts of uPA than does the MDA-MB-231 line employed in this study. As shown in Figures 4 and 5 in this work, binding of ^{125}I-ATF to MDA-MB-231 cells is increased when they have either had endogenous uPA removed by acid stripping (Figure 4) or have had endogenous expression of uPA reduced by the application of specific siRNAs (Figure 5). The fact that the increase in binding observed in Figure 4 was seen following excision of MDA-MB-231 human tumor xenografts from SCID mice following 4−5 weeks of in vivo growth suggests that autocrine saturation could be responsible for reduced tumor uptake in vivo using this model system. Additionally, the MDA-MB-231 human breast cancer cell line is known to produce high levels of uPA, which has been proposed to be correlated with its high degree of invasiveness in in vitro assays (*7, 24*). Last, the low specific tumor uptake of ^{125}I-ATF at 24 h pi provides further evidence that the similarly low uptake of the ^{111}In-DOTA-peptide at 4 h pi is not due solely to the lower affinity of the ^{111}In-labeled radiotracer but is primarily the result of occupancy of uPAR sites within the tumor by endogenously expressed uPA.

uPA is a 54 kDa glycoprotein with well-defined modular domains separated by a flexible linker region. Proteolysis of uPA yields a 36 kDa C-terminal domain that is catalytically active plus an 18.5 kDa amino terminal fragment (ATF) that is responsible for binding to uPAR. The structure of ATF has been solved both by NMR and crystallographic methods (*25, 28*). The ATF is itself composed of two independent domains, a C-terminal kringle domain attached via a flexible linker to an N-terminal growth factor-like domain (GFD). Receptor binding can be further localized within the ATF primarily to the GFD, within the N-terminal 45 amino acids of the ATF. The GFD shares significant homology to the epidermal growth factor (EGF), and binding of GFD to uPAR is mediated in large measure by a disulfide stabilized Ω loop region between residues 18−32 of the molecule. Numerous small peptides that behave as structural mimics of this receptor-binding region have been synthesized and characterized (*14−17, 26−29*), including the lead peptide composing the targeting moiety of the construct described here.

The development of low molecular weight uPAR antagonists as imaging agents for the detection of uPAR-expressing malignancies will potentially have relevance both to patient stratification and therapy monitoring. Several different approaches to cancer therapy have been described that target elements of the urokinase-type plasminogen activator system. These include inhibition of uPA enzymatic activity (*30*), blockade of uPA/uPAR binding (*14, 15*), targeted delivery of therapeutic radionuclides to uPAR-expressing tumors (*16*), and RNA interference (*31*). Targeted knockdown of uPA by a variety of methods, including delivery of siRNAs, shRNAs, or antisense RNAs, is currently under active investigation for cancer therapy (*24, 31, 32*). Such reductions in in vivo expression of uPA have been shown to reduce the metastatic potential of tumor cells and to reduce the rate of tumor growth. In the context of uPA-targeted RNA interference, imaging agents such as the type described here could provide a direct measure of treatment efficacy in vivo, by generating increasing signals proportional to the degree of uPA knockdown. With respect to the blockade of uPA/uPAR binding, such a probe could facilitate the delivery of inhibitors by enabling real-time monitoring of dosages required for inhibition of probe signal generation. Probes of the type illustrated here could ultimately provide a complementary imaging modality to optical sensors of uPA activity currently under development (*33, 34*). Further experiments are currently underway to develop the correlation suggested here between receptor occupancy and radiotracer uptake in vivo.

ACKNOWLEDGMENT

This material is the result of work supported with resources and the use of facilities at the Harry S. Truman Memorial Veterans' Hospital, Columbia, MO, 65201 and the Department of Radiology, University of Missouri—Columbia School of Medicine, Columbia, MO 65211. This work was funded by a United States Department of Veterans' Affairs Biomedical Laboratory Research and Development Service VA Merit Award, a National Cancer Institute Center grant (1 P50 CA103130-01), and a United States Department of Defense Concept Award (BC032697).

LITERATURE CITED

(1) Blasi, F., and Carmeliet, P. (2002) uPAR: a versatile signaling orchestrator. *Nat. Rev. Mol. Cell Biol. 3*, 932–943.

(2) Ploug, M. (2003) Structure-function relationships in the interaction between the urokinase-type plasminogen activator and its receptor. *Curr. Pharm. Des. 9*, 1499–1528.

(3) Romer, J., Nielsen, B. S., and Ploug, M. (2004) The urokinase receptor as a potential target in cancer therapy. *Curr. Pharm. Des. 10*, 2359–2376.

(4) Danø, K., Behrendt, N., Høyer-Hansen, G., Johnsen, M., Lund, L. R., Ploug, M., and Rømer, J. (2005) Plasminogen activation and cancer. *Thromb. Haemost. 93*, 676–681.

(5) Xue, A., Scarlett, C. J., Jackson, C. J., Allen, B. J., and Smith, R. C. (2008) Prognostic significance of growth factors and the urokinase-type plasminogen activator system in pancreatic ductal adenocarcinoma. *Pancreas 36*, 160–167.

(6) Beyer, B. C., Heiss, M. M., Simon, E. H., Gruetzner, K. U., Babic, R., Jauch, K. W., Schildberg, F. W., and Allgayer, H. (2006) Urokinase system expression in gastric carcinoma: prognostic impact in an independent patient series and first evidence of predictive value in preoperative biopsy and intestinal metaplasia specimens. *Cancer 106*, 1026–1035.

(7) Holst-Hansen, C., Johannessen, B., Hoyer-Hansen, G., Romer, J., Ellis, V., and Brunner, N. (1996) Urokinase-type plasminogen activation in three human breast cancer cell lines correlates with their in vitro invasiveness. *Clin. Exp. Metastasis 14*, 297–307.

(8) Boyd, D. D., Kim, S., Wang, H., Jones, T. R., and Gallick, G. E. (2003) A urokinase-derived peptide (A6) increases survival of mice bearing orthotopically grown prostate cancer and reduces lymph node metastasis. *Am. J. Pathol. 162*, 619–626.

(9) Boyd, D. D., Wang, H., Avila, H., Parikh, N. U., Kessler, H., Magdolen, V., and Gallick, G. E. (2004) Combination of an SRC kinase inhibitor with a novel pharmacological antagonist of the urokinase receptor diminishes in vitro colon cancer invasiveness. *Clin. Cancer Res. 10*, 1545–1555.

(10) Yang, L., Avila, H., Wang, H., Trevino, J., Gallick, G. E., Kitadai, Y., Sasaki, T., and Boyd, D. D. (2006) Plasticity in urokinase-type plasminogen activator receptor (uPAR) display in colon cancer yields metastable subpopulations oscillating in cell surface uPAR density--implications in tumor progression. *Cancer Res. 66*, 7957–7967.

(11) Foekens, J. A., Peters, H. A., Look, M. P., Portengen, H., Schmitt, M., Kramer, M. D., Brünner, N., Jänicke, F., Meijer-van Gelder, M. E., Henzen-Logmans, S. C., van Putten, W. L., and Klijn, J. G. (2000) The urokinase system of plasminogen activation and prognosis in 2780 breast cancer patients. *Cancer Res. 60*, 636–643.

(12) Reuning, U., Sperl, S., Kopitz, C., Kessler, H., Krüger, A., Schmitt, M., and Magdolen, V. (2003) Urokinase-type plasminogen activator (uPA) and its receptor (uPAR): development of antagonists of uPA/uPAR interaction and their effects in vitro and in vivo. *Curr. Pharm. Des. 9*, 1529–1543.

(13) Stoppelli, M. P., Corti, A., Soffientini, A., Cassani, G., Blasi, F., and Assoian, R. K. (1985) Differentiation-enhanced binding of the amino-terminal fragment of human urokinase plasminogen activator to a specific receptor on U937 monocytes. *Proc. Natl. Acad. Sci. U.S.A. 82*, 4939–4943.

(14) Goodson, R. J., Doyle, M. V., Kaufman, S. E., and Rosenberg, S. (1994) High-affinity urokinase receptor antagonists identified with bacteriophage peptide display. *Proc. Natl. Acad. Sci. U.S.A. 91*, 7129–7133.

(15) Ploug, M., Ostergaard, S., Gardsvoll, H., Kovalski, K., Holst-Hansen, C., Holm, A., Ossowski, L., and Dano, K. (2001) Peptide-derived antagonists of the urokinase receptor. affinity maturation by combinatorial chemistry, identification of functional epitopes, and inhibitory effect on cancer cell intravasation. *Biochemistry 40*, 12157–12168.

(16) Knör, S., Sato, S., Huber, T., Morgenstern, A., Bruchertseifer, F., Schmitt, M., Kessler, H., Senekowitsch-Schmidtke, R., Magdolen, V., and Seidl, C. (2008) Development and evaluation of peptidic ligands targeting tumour-associated urokinase plasminogen activator receptor (uPAR) for use in alpha-emitter therapy for disseminated ovarian cancer. *Eur. J. Nucl. Med. Mol. Imaging 35*, 53–64.

(17) Li, Z., Niu, G., He, L., Yang, L., Ploug, M., and Chen, X. (2008) Imaging of urokinase-type plasminogen activator receptor expression using a 64Cu-labeled linear peptide antagonist by microPET. *Clin. Cancer Res. 14*, 4758–4766.

(18) Thakur, M. L., Aruva, M. R., Gariepy, J., Acton, P., Rattan, S., Prasad, S., Wickstrom, E., and Alavi, A. (2004) PET imaging of oncogene overexpression using ^{64}Cu-vasoactive intestinal peptide (VIP) analog: comparison with 99mTc-VIP analog. *J. Nucl. Med. 45*, 1381–1389.

(19) Hoffman, T. J., Gali, H., Smith, C. J., Sieckman, G. L., Hayes, D. L., Owen, N. K., and Volkert, W. A. (2003) Novel series of 111In-labeled bombesin analogs as potential radiopharmaceuticals for specific targeting of gastrin-releasing peptide receptors expressed on human prostate cancer cells. *J. Nucl. Med. 44*, 823–831.

(20) Giblin, M. F., Gali, H., Sieckman, G. L., Owen, N. K., Hoffman, T. J., Forte, L. R., and Volkert, W. A. (2004) In vitro and in vivo comparison of human Escherichia coli heat-stable peptide analogues incorporating the 111In-DOTA group and distinct linker moieties. *Bioconjugate Chem. 15*, 872–880.

(21) Giblin, M. F., Wang, N., Hoffman, T. J., Jurisson, S. S., and Quinn, T. P. (1998) Design and characterization of alpha-melanotropin peptide analogs cyclized through rhenium and technetium metal coordination. *Proc. Natl. Acad. Sci. U.S.A. 95*, 12814–12818.

(22) Storch, D., Béhé, M., Walter, M. A., Chen, J., Powell, P., Mikolajczak, R., and Mäcke, H. R. (2005) Evaluation of [^{99m}Tc/EDDA/HYNIC0]octreotide derivatives compared with [^{111}In-DOTA0, Tyr3, Thr8]octreotide and [^{111}In-DTPA0]octreotide: does tumor or pancreas uptake correlate with the rate of internalization? *J. Nucl. Med. 46*, 1561–1569.

(23) Wu, Y., Zhang, X., Xiong, Z., Cheng, Z., Fisher, D. R., Liu, S., Gambhir, S. S., and Chen, X. (2005) microPET imaging of glioma integrin {alpha}v{beta}3 expression using (64)Cu-labeled tetrameric RGD peptide. *J. Nucl. Med. 46*, 1707–1718.

(24) Arens, N., Gandhari, M., Bleyl, U., and Hildenbrand, R. (2005) In vitro suppression of urokinase plasminogen activator in breast cancer cells--a comparison of two antisense strategies. *Int. J. Oncol. 26*, 113–119.

(25) Hansen, A. P., Petros, A. M., Meadows, R. P., Nettesheim, D. G., Mazar, A. P., Olejniczak, E. T., Xu, R. X., Pederson, T. M., Henkin, J., and Fesik, S. W. (1994) Solution structure of the amino-terminal fragment of urokinase-type plasminogen activator. *Biochemistry 33*, 4847–4864.

(26) Guthaus, E., Schmiedeberg, N., Burgle, M., Magdolen, V., Kessler, H., and Schmitt, M. (2003) The urokinase receptor (uPAR, CD87) as a target for tumor therapy: uPA-silica particles (SP-uPA) as a new tool for assessing synthetic peptides to interfere with uPA/uPA-receptor interaction. *Recent Results Cancer Res. 162*, 3–14.

(27) Appella, E., Robinson, E. A., Ullrich, S. J., Stoppelli, M. P., Corti, A., Cassani, G., and Blasi, F. (1987) The receptor-binding sequence of urokinase. A biological function for the growth-factor module of proteases. *J. Biol. Chem. 262*, 4437–4440.

(28) Huai, Q., Mazar, A. P., Kuo, A., Parry, G. C., Shaw, D. E., Callahan, J., Li, Y., Yuan, C., Bian, C., Chen, L., Furie, B., Furie, B. C., Cines, D. B., and Huang, M. (2006) Structure of human urokinase plasminogen activator in complex with its receptor. *Science 311*, 656–659.

(29) Llinas, P., Le Du, M. H., Gårdsvoll, H., Danø, K., Ploug, M., Gilquin, B., Stura, E. A., and Ménez, A. (2005) Crystal structure of the human urokinase plasminogen activator receptor bound to an antagonist peptide. *EMBO J. 24*, 1655–1663.

(30) Setyono-Han, B., Stürzebecher, J., Schmalix, W. A., Muehlenweg, B., Sieuwerts, A. M., Timmermans, M., Magdolen, V., Schmitt, M., Klijn, J. G., and Foekens, J. A. (2005) Suppression of rat breast cancer metastasis and reduction of primary tumour growth by the small synthetic urokinase inhibitor WX-UK1. *Thromb. Haemost. 93*, 779–786.

(31) Pulukuri, S. M., Gondi, C. S., Lakka, S. S., Jutla, A., Estes, N., Gujrati, M., and Rao, J. S. (2005) RNA interference-directed knockdown of urokinase plasminogen activator and urokinase plasminogen activator receptor inhibits prostate cancer cell invasion, survival, and tumorigenicity in vivo. *J. Biol. Chem. 280*, 36529–36540.

(32) Mohanam, S., Jasti, S. L., Kondraganti, S. R., Chandrasekar, N., Kin, Y., Fuller, G. N., Lakka, S. S., Kyritsis, A. P., Dinh, D. H., Olivero, W. C., Gujrati, M., Yung, W. K., and Rao, J. S. (2001) Stable transfection of urokinase-type plasminogen activator antisense construct modulates invasion of human glioblastoma cells. *Clin. Cancer Res. 7*, 2519–2526.

(33) Law, B., Curino, A., Bugge, T. H., Weissleder, R., and Tung, C. H. (2004) Design, synthesis, and characterization of urokinase plasminogen-activator-sensitive near-infrared reporter. *Chem. Biol. 11*, 99–106.

(34) Law, B., Weissleder, R., and Tung, C. H. (2007) Protease-sensitive fluorescent nanofibers. *Bioconjugate Chem. 18*, 1701–1704.

BC800433Y

Genetic Engineering of the S-Layer Protein SbpA of *Lysinibacillus sphaericus* CCM 2177 for the Generation of Functionalized Nanoarrays†

Helga Badelt-Lichtblau,‡ Birgit Kainz,‡ Christine Völlenkle,§ Eva-Maria Egelseer,‡ Uwe B. Sleytr,‡ Dietmar Pum,‡ and Nicola Ilk*,‡

Center for NanoBiotechnology, University of Natural Resources and Applied Life Sciences (BOKU), Vienna, Gregor Mendelstrasse 33, A-1180 Vienna, Austria, and Research Laboratories-Molecular Cardiology, I.R.CCS Policlinico San Donato, Via R. Morandi, 30, 20097 S. Donato M.se (MI), Italy. Received October 16, 2008; Revised Manuscript Received March 30, 2009

The mesophilic organism *Lysinibacillus sphaericus* CCM 2177 produces the surface (S)-layer protein SbpA, which after secretion completely covers the cell surface with a crystalline array exhibiting square lattice symmetry. Because of its excellent *in vitro* recrystallization properties on solid supports, SbpA represents a suitable candidate for genetically engineering to create a versatile self-assembly system for the development of a molecular construction kit for nanobiotechnological applications. The first goal of this study was to investigate the surface location of 3 different C-terminal amino acid positions within the S-layer lattice formed by SbpA. Therefore, three derivatives of SbpA were constructed, in which 90, 173, or 200 C-terminal amino acids were deleted, and the sequence encoding the short affinity tag *Strep*-tag II as well as a single cysteine residue were fused to their C-terminal end. Recrystallization studies of the rSbpA/STII/Cys fusion proteins indicated that C-terminal truncation and functionalization of the S-layer protein did not interfere with the self-assembly capability. Fluorescent labeling demonstrated that the orientation of the crystalline $rSbpA_{31-1178}$/STII/Cys lattice on solid supports was the same, like the orientation of wild-type S-layer protein SbpA on the bacterial cell. In soluble and recrystallized rSbpA/STII/Cys fusion proteins, *Strep*-tag II was used for prescreening of the surface accessibility, whereas the thiol group of the end-standing cysteine residue was exploited for site-directed chemical linkage of differently sized preactivated macromolecules via heterobifunctional cross-linkers. Finally, functionalized two-dimensional S-layer lattices formed by $rSbpA_{31-1178}$/STII/Cys exhibiting highly accessible cysteine residues in a well-defined arrangement on the surface were utilized for the template-assisted patterning of gold nanoparticles.

INTRODUCTION

Crystalline bacterial cell surface layer (S-layer) proteins form the outermost cell envelope component of prokaryotic organisms. They are composed of identical protein or glycoprotein subunits, which completely cover the cell surface during all stages of bacterial growth and division. Even after isolation from the cell wall, S-layer proteins have the intrinsic tendency to self-assemble into crystalline arrays in suspension or to recrystallize on solid supports, such as silicon wafers, gold chips, silanized glass, or plastic materials, on polyelectrolytic microcapsules, on Langmuir lipid films, on liposomes, and at the air−water interface (*1*−*5*). General aspects of the structure of S-layer proteins have been examined quite extensively, such as the ultrastructure of the lattice, and the binding and anchoring of S-layer proteins to the underlying cell envelope through the so-called S-layer-homology (SLH)-domains. Together with the high density and regular arrangement of functional groups in the S-layer lattice, this specific feature opens a broad application potential in biotechnology, molecular nanotechnology, and biomimetics (*3*). In previous studies, mainly carboxyl groups in the S-layer lattice were exploited for covalent binding of biologically active macromolecules, such as enzymes, antibodies, or ligands for the production of S-layer-based biosensors (*3*), solid-phase dipstick style immunoassays (*6*−*8*), or affinity matrices based on self-assembly products (*9*). The possibility to change the properties of S-layer proteins by genetic engineering offers new ways for tuning their functional and structural features as required in nanobiotechnology as well as in material sciences.

The S-layer protein SbpA of *Lysinibacillus sphaericus* CCM 2177 consists of a total of 1,268 amino acids (including a 30-amino-acid-long signal peptide). SbpA self-assembles into a square (p4) lattice structure with a center-to-center spacing of the morphological units of 13.1 nm. The self-assembly process is strongly dependent on the presence of bivalent cations (*10*). In their absence, SbpA stays in the water-soluble state, which means that the self-assembly process of this S-layer protein is dirigible (*11*). The N-terminal part of SbpA possesses 3 typical S-layer homologous (SLH) motifs and an additional 58 amino acid-long SLH-like motif that recognizes a distinct type of secondary cell wall polymer (SCWP), consisting of 8 to 9 disaccharide repeating units, as the proper anchoring structure in the rigid cell wall layer (*10*). These specific interactions can be exploited for an oriented binding of SbpA on solid supports precoated with SCWP to generate monomolecular protein lattices (*12*).

The gene *sbpA*, encoding this S-layer protein, has been sequenced, cloned, and expressed in *Eschericia coli* HMS174(DE3) (*13*). Studies on the structure−function relationship of SbpA revealed that deletions of up to 237 C-terminal amino acids do not interfere with the ability to self-assemble into the square lattice structure. However, the deletion of 350 amino acids was linked to a change from square (p4) to oblique (p1) lattice symmetry (*14*). An N- and C-terminally truncated form was capable of self-assembling into the square (p4) lattice structure with lattice parameters similar to that formed by the full-length SbpA. These findings indicated that the segment between amino acid 203 and 1,031 is responsible for the self-assembly process and for pore formation (*14*).

† This article is dedicated to the memory of Margit Sára.

* Corresponding author. Tel: + 43-1-47654-2233. Fax: + 43-1-4789-112. E-mail: nicola.ilk@boku.ac.at.

‡ University of Natural Resources and Applied Life Sciences.

§ I.R.CCS Policlinico San Donato.

10.1021/bc800445r CCC: $40.75 © 2009 American Chemical Society
Published on Web 04/29/2009

Table 1. Survey on the Three Genetically Engineered SbpA Derivatives

SbpA derivative	forward primer[a]	reverse primer[a]	cloning site	number of C-terminally truncated amino acids	C-terminally fusion of	theoretical molecular mass
rSbpA$_{31-1178}$/STII/Cys	*sbpA37* [5′-CG GAT T**CC ATG G**CG CAA GTA AAC GAC TAT AAC AAA ATC-3′]	*sbpAII/3* [5′-GGT TTA GTG GTT GCA TCA GCA TCT GGT GGT TGG TCT CAC CCG CAG TTC GAA AAA GGT GGT *TGC* TAA **CTC GAG** CGG TC 3′]	*Nco*I *Xho*I	90	*Strep*-tag II, cysteine	121,345 Da
rSbpA$_{31-1095}$/STII/Cys	*sbpA37* [5′-CG GAT T**CC ATG G**CG CAA GTA AAC GAC TAT AAC AAA ATC-3′]	*sbpAII/4* [5′-GCA GCA ACT ACT GCA TAT TCA GAA GGT GGT TGG TCT CAC CCG CAG TTC GAA AAA GGT GGT GGT *TGC* TAA **CTC GAG** CGG TC 3′]	*Nco*I *Xho*I	173	*Strep*-tag II, cysteine	113,720 Da
rSbpA$_{31-1068}$/STII/Cys	*sbpA37* [5′-CG GAT T**CC ATG G**CG CAA GTA AAC GAC TAT AAC AAA ATC-3′]	*sbpAII/5* [5′-GCA GCA ACT ACT GCA TAT TCA GAA GGT GGT TGG TCT CAC CCG CAG TTC GAA AAA GGT GGT GGT *TGC* TAA **CTC GAG** CGG TC 3′]	*Nco*I *Xho*I	200	*Strep*-tag II, cysteine	111,241 Da

[a] Cloning sites are in bold text (NcoI at the 5′-end and XhoI at the 3′-end of the coding sequence); Strep-tag II is underlined; and cysteine residue is in italic text and is underlined.

Recent studies have shown that bacterial S-layer proteins can be used for controlled deposition of inorganic material, which can be achieved by using the S-layer lattices as templates for direct precipitation of metals from solution or by binding preformed metallic and semiconductor nanoparticles (*15*−*18*). In this context, gold nanoparticles formed on cells and purified S-layer protein of *Bacillus sphaericus* JG-A12 after incubation with Gold(III) solution in the presence of H_2 as reducing agent were characterized by X-ray absorption spectroscopy, UV−vis spectroscopy, and X-ray powder diffraction (*19*). In another approach, the self-assembly of dendrimer-encapsulated platinum nanoparticles on S-layer proteins from the archaeon *Sulfolobus acidocaldarius* and the gram-positive *Deinococcus radiodurans* was used to create patterned nanoparticle arrays with potential technological applications (*20*).

In the present study, C-terminal functionalization of the S-layer protein SbpA combined with targeted chemical modification was used to identify amino acids that are located at the surface of the S-layer lattice and therefore accessible for binding of functional molecules or nanoparticles. A C-terminal cysteine residue was introduced with the aim to produce structured crystalline monolayers on solid supports offering free sulfhydryl groups for the activation with various heterobifunctional cross-linkers and covalent attachment of differently sized (macro)molecules. Binding of gold nanoparticles to the surface located cysteine residues should finally lead to the formation of regularly ordered nanoarrays.

MATERIAL AND METHODS

Cloning and Expression of the Genes Encoding the S-Layer Fusion Proteins rSbpA$_{31-1178}$STII/Cys, rSbpA$_{31-1095}$/STII/Cys, and rSbpA$_{31-1068}$/STII/Cys. For amplification of the genes encoding the C-terminally truncated forms rSbpA$_{31-1178}$, rSbpA$_{31-1095}$ and rSbpA$_{31-1068}$, chromosomal DNA of *Lysinibacillus sphaericus* CCM 2177 was used as a template. Isolation of chromosomal DNA and PCR amplifications were performed as described in ref 21. General procedures for DNA manipulations were carried out as reported in ref 22. The oligonucleotide forward primer *sbpA37* as well as the reverse primers *sbpA II/3*, *sbpA II/4*, and *sbpA II/5* (all listed in Table 1) introduced the cloning sites *NcoI* and *XhoI* at the 5′- and 3′-ends, respectively. In comparison to the wild-type S-layer protein, the reverse primers led to the C-terminal deletion of 90, 173, or 200 amino acids in the respective proteins, as well as to the fusion of *Strep*-tag II and a single cysteine residue to the C-terminal end. Cloning of pET28a (Invitrogen), carrying the genes *sbpA*$_{(93-3534)}$/*STII*/*Cys*, *sbpA*$_{(93-3285)}$/*STII*/*Cys*, and *sbpA*$_{(93-3204)}$/*STII*/*Cys* in *E. coli* TG1 (Stratagene), was done as described in ref 13. For the selection of positive transformants, kanamycin was added at a final concentration of 30 μg/mL. Heterologous expression of the genes *sbpA*$_{(93-3534)}$/*STII*/*Cys*, *sbpA*$_{(93-3285)}$/*STII*/*Cys*, and *sbpA*$_{(93-3204)}$/*STII*/*Cys* in *E. coli* BL21Star (DE3) One Shot (Invitrogen) was performed as described in ref 21. Samples of the *E. coli* BL21(DE3) cultures were taken before and 4 h after the induction of expression. For all three S-layer fusion proteins, preparation of samples for SDS−PAGE analysis was carried out as described by Laemmli (*23*). Immunoblotting with a polyclonal rabbit antiserum raised against the S-layer protein SbpA of *Ly. sphaericus* CCM 2177 was performed as described previously (*24*).

Isolation of the Three S-Layer/STII/Cys Fusion Proteins from the Host Cells and Purification. Isolation of the three different truncated SbpA fusion proteins carrying *Strep*-tag II and a cysteine residue at the C-terminal end was performed as previously described (*21*) except that only degassed buffers were

used, and additionally 1,4-dithio-D,L-threitol (DTT, GERBU) in a final concentration of 1 mM was added as reducing agent to all buffers to prevent the formation of disulfide bridges between the C-terminally located cysteine residues. Purification of the fusion proteins by gel permeation chromatography (GPC) using a Superdex 200 column (Pharmacia; Upsala, Sweden) in 2 M guanidine hydrochloride (GHCl) in 50 mM Tris-HCl/150 mM NaCl buffer (pH 7.2) and 1 mM DTT was done as described before (*25*). Fractions containing rSbpA$_{31-1178}$/STII/Cys, rSbpA$_{31-1095}$/STII/Cys, or rSbpA$_{31-1068}$/STII/Cys were pooled, dialyzed against degassed Milli-Q water containing 1 mM DTT for 18 h at 4 °C, analyzed by SDS−PAGE, lyophilized, and stored at −20 °C.

Investigation of the Self-Assembly and Recrystallization Properties of rSbpA$_{31-1178}$/STII/Cys, rSbpA$_{31-1095}$/STII/Cys, and rSbpA$_{31-1068}$/STII/Cys by Transmission Electron Microscopy (TEM) and Atomic Force Microscopy (AFM). To investigate the ability of the three rSbpA/STII/Cys fusion proteins to form self-assembly products in suspension, 2 mg of GPC-purified fusion protein were dissolved in 1 mL of 5 M GHCl in 50 mM Tris-HCl buffer (pH 7.2) with 1 mM DTT and dialyzed against degassed Milli-Q water containing 1 mM DTT and 10 mM $CaCl_2$ for 18 h at 4 °C. For recrystallization on solid supports, the fusion proteins dissolved as described above were dialyzed against degassed Milli-Q water containing 1 mM DTT. Then, 1 mg of lyophilized peptidoglycan-containing sacculi of *Ly. sphaericus* CCM 2177, prepared according to *refs* 10 *and* 13, was added to 1 mL of the solution containing the monomeric S-layer fusion protein. To induce the recrystallization process, 10 mM $CaCl_2$ was added, and the suspensions were stirred for 18 h at 4 °C.

To investigate the ability of monomeric rSbpA/Cys fusion proteins to recrystallize on poly-L-lysine coated copper grids, the GHCl-extracts were dialyzed against distilled water for 18 h at 4 °C. After centrifugation for 5 min at 16,000*g*, the clear supernatants containing nonassembled S-layer protein were incubated with poly-L-lysine (Sigma P2636) coated copper grids according to the procedures described in ref 26.

For electron microscopical examination, 30 μL of the solution containing self-assembly products or recrystallization products was transferred onto a carbon-coated electron microscope grid, which had been rendered hydrophilic by glow discharge. Negative staining of the samples with 2.5% uranyl acetate was performed as described in ref 26. Electron micrographs were taken with a Philips CM 12 transmission electron microscope (Philips Eindhoven, The Netherlands) operated at 80 kV in low-dose mode.

AFM measurements of rSbpA/STII/Cys fusion proteins recrystallized on silicon wafers were performed on a Digital Instruments Nanoscope IIIa (Santa Barbara, CA) with a J-scanner (nominal 130-μm scan size). Silicon wafers (100, p-type, boron-doped, resistivity 25−45 Ω cm; MEMC, Italy) were cut into pieces of 1 × 1 cm and precleaned as previously described in ref 27. The rSbpA/STII/Cys fusion proteins (0.1 mg/mL in recrystallization buffer: 0.5 mM Tris/HCl, pH 9, 10 mM $CaCl_2$) were recrystallized on the silicon wafers as reported in ref 16. The scanning was carried out in contact mode under fluid (100 mM NaCl, pH 7.5). For imaging, standard 200-μm-long oxide-sharpened silicon nitride cantilevers (NanoProbes, Digital Instruments, INC) with a nominal spring constant of 0.06 N/m were used. The scan speed was approximately 6 Hz, and the applied force was kept minimized during scanning to prevent the tip from modifying the sample surface.

Immunoblotting for Detection of the C-Terminally Fused *Strep*-tag II and Surface Accessibility Screens by Immuno Dot Assays. For immunoblotting, monomeric fusion proteins were subjected to SDS−PAGE and transferred to a nitrocellulose membrane by semidry-blotting as described previously (*24*). For detection of *Strep*-tag II, membranes were incubated with a monoclonal mouse anti-*Strep*-tag II antibody (IBA) diluted 1:350 in 2% Blocking Reagent GE in 0.1 M TBS (Tris-buffered saline) for 2 h at room temperature. After several washing steps and incubation with antimouse IgG-alkaline phosphatase (ALP) conjugate (Sigma), diluted 1:5,000 in 2% Blocking Reagent GE in 0.1 M TBS, for 1 h at room temperature, detection was accomplished by treatment with 5-bromo-4-chloro-3-indolyl phosphate and nitroblue tetrazolium chloride (BCIP/NBT, Roche).

To investigate the surface accessibility of *Strep*-tag II within the S-layer lattice, the three different SbpA fusion proteins were recrystallized on peptidoglycan-containing sacculi of *Ly. sphaericus* CCM 2177. Recrystallization products were dried onto a nitrocellulose membrane, and immuno dot assay using monoclonal mouse anti-*Strep*-tag II antibody and antimouse IgG-ALP conjugate was performed as described in ref 28.

Chemical Modification of the Cysteine Residues in Monomeric rSbpA$_{31-1178}$/STII/Cys Fusion Protein by Linkage of Differently Sized Preactivated Macromolecules. A monomeric solution of rSbpA$_{31-1178}$/STII/Cys was produced by dissolving 1 mg of S-layer fusion protein in 1 mL of 5 M GHCl in 50 mM Tris/HCl buffer (pH 7.2) with 1 mM DTT and dialyzing against degassed Milli-Q water containing 1 mM DTT. After removal of DTT by PD10 desalting columns, the protein solution was mixed with a 2-fold molar excess of methoxypoly(ethylene glycol)maleimide (m-PEG-mal, Nektar therapeutics) with a size of 5 or 20 kDa, respectively, overlaid with nitrogen and incubated overnight at 4 °C.

For modification of the cysteine residues with differently sized macromolecules via a heterobifunctional cross-linker, solutions containing momomers of rSbpA$_{31-1178}$/STII/Cys were mixed in a molar ratio of 1:2 with Protein A (Sigma), carbonic anhydrase (Sigma), or the major birch pollen allergen (rBet v1), which was preactivated with *m*-maleimidobenzoyl-*N*-hydroxysulfosuccinimide ester (Sulfo-MBS, Piercenet). For that purpose, 2 mg of Protein A, carbonic anhydrase, or Bet v1 was dissolved in conjugation buffer, PBS (0.1 M, pH 7.2), and Sulfo-MBS, prepared according to the manufacturer's recommendations, was added in a 10-fold molar excess. The mixture was incubated for 2 h at 4 °C. The excess unbound cross-linker was removed by using desalting columns (PD10, GE Healthcare) equilibrated with the conjugation buffer. Chemical modification was checked by SDS−PAGE analysis (gel shift assay).

Investigation of the Recrystallization Properties of the SbpA$_{31-1178}$/STII/Cys/Carbonic Anhydrase Conjugates by TEM and Detection of the Enzyme on the Surface of the S-Layer Lattice. For recrystallization, conjugates between carbonic anhydrase and rSbpA$_{31-1178}$/STII/Cys (1 mg/mL in recrystallization buffer: 0.5 mM Tris/HCl, pH 9, and 10 mM $CaCl_2$) were mixed with 1 mg of peptidoglycan-containing sacculi of *Ly. sphaericus* CCM 2177, and the solution was stirred at 4 °C overnight. The formation of recrystallization products was checked after negative staining by TEM. For detection of the preactivated carbonic anhydrase bound to the cysteine residues on the S-layer lattice, immuno dot assays were carried out. For this, recrystallization products were washed three times with Milli-Q water, and 10 μL of the sample solution was dried on a nitrocellulose membrane. The membrane was blocked with 2% Blocking Reagent GE (Applichem Biomedica) in 0.1 M TBS overnight at 4 °C followed by incubation with rabbit anticarbonic anhydrase antibody (Sigma), diluted 1:5,000 in 2% Blocking Reagent GE in 0.1 M TBS, for 2 h at room temperature. After several washing steps and incubation of the membrane with antirabbit IgG-ALP conjugate (Sigma), diluted

1:5,000 in 2% Blocking Reagent GE in 0.1 M TBS, for 1 h at room temperature, detection was accomplished by treatment with BCIP/NBT.

Binding of a Fluorescent Thiol-Reactive Dye to Crystalline Monolayers Formed by rSbpA$_{31-1178}$/STII/Cys. For site-specific-labeling, rSbpA$_{31-1178}$/STII/Cys was recrystallized overnight under rotation in recrystallization buffer (0.5 mM Tris/HCl, 10 mM $CaCl_2$, pH 9) on microparticles, which were based on silicon dioxide (SiO_2) in aqueous solution (3 μm SiO_2-particles; Fluka). Subsequently, the particles were incubated with 7-diethylamino-3-(4′-maleimidylphenyl)-4-methylcoumarine (CPM; Invitrogen) for 30 min at room temperature. The thiol-reactive coumarin, CPM is very weakly fluorescent until reacted with the thiol-group of the cysteine residue producing a conjugate with excitation and emission maxima of ~384/470 nm. The covered particles were washed three times with Milli-Q water and analyzed by using a fluorescence microscope (Nikon Eclipse TE 2000-S) with the filter DAPI. Wild-type S-layer protein SbpA recrystallized on SiO_2-particles as well as SiO_2-particles without S-layer protein, used as blanks, were measured under the same conditions. For measurement of excitation and emission spectra of the samples (protein concentration 0.1 mg/mL), the luminescence spectrometer LS 55 (PerkinElmer, Shelton CT, U.S.A.) was used. Fluorescence spectroscopy of the protein samples was carried out by wavelength scan with a scan speed of 500 nm/min in a quartz cuvette (1 cm). The band-pass for both the excitation and emission monochromators was 5 nm. Emission spectra were recorded at a fixed wavelength of the excitation maximum and excitation spectra at a fixed wavelength of the emission maximum. For the measurement of the emission and excitation spectra, 2 mL of 50 mM Tris/HCl buffer (pH 8) was mixed with 50 μL of SiO_2-particles covered with rSbpA$_{31-1178}$/STII/Cys or 10 μL of rSbpA$_{31-1178}$/STII/Cys solution (protein concentration 1 mg/mL) and stirred in a quartz cuvette with a magnetic stirring shaft. After 360 s, 100 μL of 2 mM fluorophore was added, and 1800 s later excitation and emission were measured. For reference studies, the sole fluorophore, soluble rSbpA$_{31-1178}$/STII/Cys without dye, soluble wild-type SbpA incubated with the dye, wild-type SbpA recrystallized on microparticles incubated with the fluorophore, and SiO_2-particles alone or incubated with the fluorophore were analyzed.

Chemical Modification of the Cysteine Residues of Recrystallized rSbpA$_{31-1178}$/STII/Cys with Carbonic Anhydrase via a Heterobifunctional Cross-Linker. Preactivation of carbonic anhydrase with Sulfo-MBS was carried out as described above. Recrystallization products consisting of rSbpA$_{31-1178}$/STII/Cys recrystallized on peptidoglycan-containing sacculi of *Ly. sphaericus* CCM 2177 were incubated with preactivated carbonic anhydrase for 2 h at 4 °C. To remove unbound preactivated carbonic anhydrase the recrystallization products were washed with Milli-Q water three times. For detection of the preactivated carbonic anhydrase bound to the cysteine residues on the S-layer lattice, immuno dot assays using rabbit anticarbonic anhydrase antibody (Sigma) and antirabbit IgG-ALP conjugate (Sigma) were carried out as described above.

Binding of Colloidal Gold Nanoparticles to Monolayers Formed by rSbpA$_{31-1178}$/STII/Cys on Peptidoglycan-Containing Sacculi of *Ly. sphaericus* CCM 2177. Recrystallization products consisting of rSbpA$_{31-1178}$/STII/Cys fusion protein recrystallized on peptidoglycan-containing sacculi of *Ly. sphaericus* CCM 2177 as well as self-assembly products of the fusion protein were incubated with 75 μL of colloidal gold (5 nm, $HAuCl_4$ in Tris/HCl, pH 7.2, Sigma) at room temperature for 20 min and then centrifuged for 10 min at 13,400 rpm. The procedure was repeated 2 times, then the pellet was washed three times with Milli-Q water and resuspended in 15 μL of Milli-Q water, and unstained samples were investigated by TEM. As a control, the same procedure was carried out with (a) self-assembly products formed by wild-type SbpA and (b) recrystallization products prepared with wild-type SbpA recrystallized on peptidoglycan-containing sacculi of *Ly. sphaericus* CCM 2177.

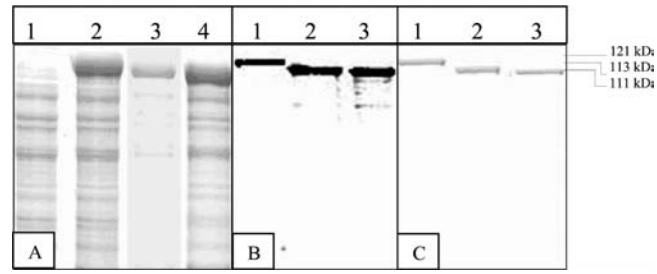

Figure 1. (A) SDS−PAGE analysis of SDS-extracted whole cells of *E. coli* BL21star(DE3) harboring plasmid pET28a/*sbpA*$_{(93-3534)}$/*STII*/*Cys* before the induction of expression (lane1); *E. coli* BL21star(DE3) harboring plasmid pET28a/*sbpA*$_{(93-3534)}$/*STII*/*Cys* (lane2); *E. coli* BL21star(DE3) harboring plasmid pET28a/*sbpA*$_{(93-3285)}$/*STII*/*Cys* (lane3), *E. coli* BL21star(DE3) harboring plasmid pET28a/*sbpA*$_{(93-3204)}$/*STII*/*Cys* (lane4), respectively, 4 h after the induction of expression. (B) Immunoblot analysis of rSbpA$_{31-1178}$STII/Cys (lane 1), rSbpA$_{31-1095}$/STII/Cys (lane 2), and rSbp$_{A31-1068}$/STII/Cys (lane 3) using a polyclonal rabbit antiserum raised against the S-layer protein SbpA of *Ly. sphaericus* CCM 2177. (C) GPC-purified fusion protein rSbpA$_{31-1178}$STII/Cys (lane 1), rSbpA$_{31-1095}$/STII/Cys (lane 2), and rSbpA$_{31-1068}$/STII/Cys (lane 3).

Image Processing. Electron microscopical images were recorded on 35 mm negative film (Kodak Fine Grain 5302, Eastman Kodak, Rochester, NY) and subsequently digitized with a Nikon Film Scanner (Model Super Cool Scan 4000 ED; Nikon Tokyo, Japan) at a resolution of 4000 dpi. Estimates of the lattice vectors of the gold nanoparticle superlattice were determined from digital diffraction patterns after Fourier transform of the image data. An accurate lattice fit, where gold nanoparticles at interlattice positions were also sorted out, was performed by using cross-correlation averaging (CCA) (*29*). Cross-correlation is a matched filtering image processing technique allowing reliable and almost fully automatic image averaging for near-periodic structures. First of all, a reference motif is cross-correlated with the image in order to indicate similar regions in the image. A superposition of small regions centered on each cross-correlation peak position lead to an improvement of the signal-to-noise ratio. Vectors pointing from positions on a least-squares fitted lattice toward actually found positions yield a graphical representation of the displacement field (*29*). The lattice parameters (two base vectors and a vector offset) were determined by minimizing the squared deviation between nanoparticle positions found in the course of CCA and ideal lattice sites. The root-mean-square deviation (r.m.s.) is a convenient measure of the degree of order in the superlattice of gold nanoparticles. Image processing software was developed in house.

RESULTS

Cloning and Expression of the Genes Encoding the Three S-Layer Fusion Proteins rSbpA$_{31-1178}$/STII/Cys, rSbpA$_{31-1095}$/STII/Cys, and rSbpA$_{31-1068}$/STII/Cys. PCR products were ligated into the pET28a vector, cloned in *E. coli* TG1, and then established in *E. coli* BL21(DE3) for expression. Biomass samples were harvested before and at 4 h after induction of expression and subjected to SDS−PAGE analysis. In comparison to noninduced *E. coli* BL21(DE3) cells (Figure 1A, lane 1), in samples from *E. coli* BL21(DE3) cultures induced to express the genes encoding rSbpA$_{31-1178}$/STII/Cys, rSbpA$_{31-1095}$/STII/Cys, and rSbpA$_{31-1068}$/STII/Cys, additional high molecular mass protein bands were observed on SDS-gels (Figure 1A,

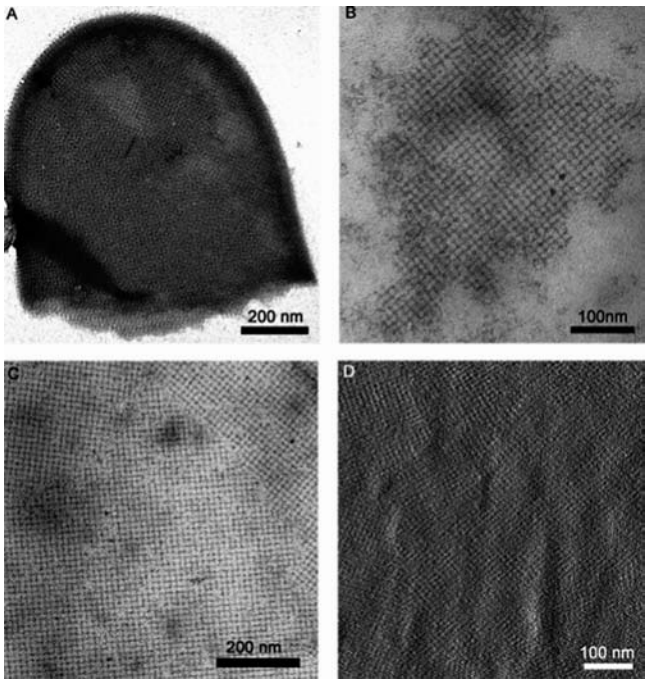

Figure 2. Electron micrograph of negatively stained preparations demonstrating the formation of the square S-layer lattice by the fusion protein rSbpA$_{31-1178}$STII/Cys on peptidoglycan-containing sacculi of *Ly. sphaericus* CCM 2177 (A); of rSbpA$_{31-1178}$STII/Cys self-assembly products in suspension (B); rSbpA$_{31-1178}$STII/Cys recrystallized into a closed monolayer consisting of numerous randomly oriented patches on poly-L-lysine coated EM-grids (C); and AFM image of rSbpA$_{31-1178}$STII/Cys recrystallized into a closed crystalline monolayer on a silicon chip (D).

lanes 2, 3, and 4). These additional protein bands had apparent molecular masses of 121,000 Da, 114,000 Da, and 111,000 Da, respectively, which corresponded to the theoretical molecular masses estimated for the three fusion proteins of 121,345 Da, 113,720 Da, and 111,241 Da, respectively. Immunoblotting using the polyclonal rabbit antiserum raised against the S-layer protein SbpA of *Ly. sphaericus* CCM 2177 revealed a strong cross-reaction with each of the three additional protein bands (Figure 1B, lanes 1, 2, and 3).

Isolation of the Three rSbpA/STII/Cys Proteins from the Host Cells and Purification and Investigation of the Recrystallization Properties. As derived from SDS−PAGE analysis of samples collected during the isolation procedure, all three fusion proteins had accumulated in the insoluble fraction of the lysed *E. coli* BL21(DE3) cells (data not shown). After purification by GPC, single protein bands with an apparent molecular mass of 121,000 Da, 114,000 Da, or 111,000 Da, respectively, were detected on SDS-gels (Figure 1C, lanes 1, 2, and 3). Recrystallization on peptidoglycan-containing sacculi of *Ly. sphaericus* CCM 2177 was induced by the addition of 10 mM $CaCl_2$ to monomeric solutions of the rSbpA fusion proteins. To avoid potential dimer formation caused by the C-terminally fused cysteine residue, which would disturb the recrystallization process, 1 mM DTT was added to the recrystallization buffer. As shown by transmission electron microscopy for the derivative rSbpA$_{31-1178}$/STII/Cys (Figure 2A), all three rSbpA derivatives recognized peptidoglycan-containing sacculi of *Ly. sphaericus* CCM 2177 as binding sites and recrystallized into the square lattice structure with a center-to-center spacing of the morphological units of 13.1 nm, which is typical for the S-layer protein SbpA. In this approach, the specific recognition mechanism between the N-terminal SLH-domain of the S-layer protein and the SCWP in the peptidoglycan-containing sacculi was used for oriented binding of the fusion proteins on the solid support. As shown by negative staining for rSbpA$_{31-1178}$/STII/Cys, all three

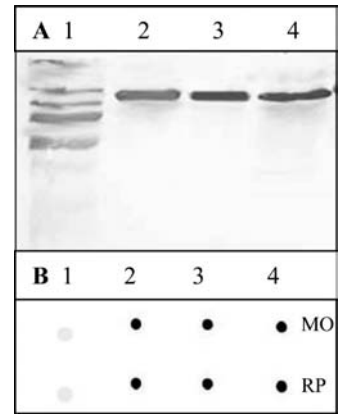

Figure 3. (A) Immunoblot analysis of rSbpA$_{31-1178}$STII/Cys (lane 2), rSbpA$_{31-1095}$/STII/Cys (lane 3), and rSbpA$_{31-1068}$/STII/Cys (lane 4) using monoclonal mouse anti-Strep-tag II antibody. Lane 1, bench mark ladder (All blue). (B) Immuno dot assay indicating the accessibility of the C-terminal Strep-tag II of rSbpA$_{31-1178}$STII/Cys (lane 2), rSbpA$_{31-1095}$/STII/Cys (lane 3), and rSbpA$_{31-1068}$/STII/Cys (lane 4) in a monomeric state (MO) or recrystallized on peptidoglycan-containing sacculi of *Ly. sphaericus* CCM 2177 (RP). In lane 1, corresponding samples prepared with wild-type SbpA showed no cross-reaction with the monoclonal mouse antibody raised against STII.

rSbpA/STII/Cys fusion proteins were able to reassemble in suspension into flat double layer sheets with a maximum size of 2 μm, clearly exhibiting the square lattice structure (Figure 2B). These results demonstrated that neither the C-terminal deletions nor the fusion of the *Strep*-tag II and the single cysteine residue interfered with the recrystallization and the cell wall binding properties of the S-layer protein. As shown for rSbpA$_{31-1178}$/STII/Cys in Figure 2C, all three rSbpA/STII/Cys fusion proteins were capable of recrystallizing into closed crystalline monolayers consisting of numerous randomly oriented patches on poly-L-lysine coated EM-grids. Additionally, AFM analysis of the three rSbpA/STII/Cys fusion proteins recrystallized on silicon chips clearly demonstrated the formation of closed monolayers displaying the square lattice structure (shown in Figure 2D for rSbpA$_{31-1178}$/STII/Cys). Comparison of the recrystallization behavior of the three differently truncated fusion proteins revealed that the derivative rSbpA$_{31-1178}$/STII/Cys was able to recrystallize into closed crystalline monolayers showing a good long-range order on solid supports (Figure 2A−D), whereas rSbpA$_{31-1095}$/STII/Cys and rSbpA$_{31-1068}$/STII/Cys showed a more patch-like recrystallization pattern (data not shown).

Investigation of the Accessibility of *Strep*-tag II in Water-Soluble and Recrystallized rSbpA/STII/Cys Fusion Proteins. The presence of *Strep*-tag II at the C-terminus of all three rSbpA/STII/Cys fusion proteins was confirmed by immunoblotting with a monoclonal mouse antibody raised against *Strep*-tag II. All three fusion proteins showed significant cross-reactions with the anti-*Strep*-tag II antibody (Figure 3A, lanes 2−4). Immuno dot assays of the three fusion proteins in a water-soluble state as well as those recrystallized on peptidoglycan-containing sacculi showed a good accessibility of *Strep*-tag II on the surface of the S-layer lattice (Figure 3B). These findings indicated that the accessibility of the *Strep*-tag II was not reduced in recrystallized S-layer fusion proteins. However, equal color-intensity of the dots indicated that minor differences in accessibility of the differently truncated C-termini of the three derivatives cannot be estimated with this method. Wild-type SbpA recrystallized on peptidoglycan-containing sacculi of *Ly. sphaericus* CCM 2177, used as a control, showed no reaction with the antibody against *Strep*-tag II (Figure 3B, lane 1).

Targeted Chemical Modification of the Cysteine Residue of Monomeric rSbpA$_{31-1178}$/STII/Cys with Differently Sized Preactivated Macromolecules. To assess the surface accessibility of the cysteine residue at the C-terminal end of folded monomers

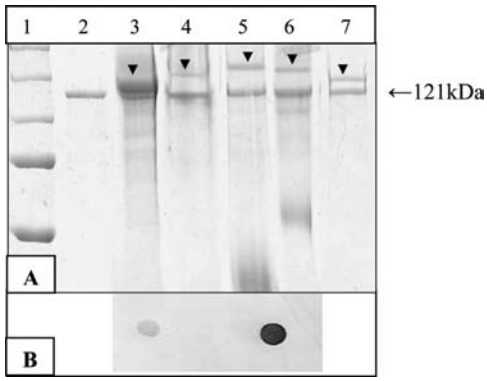

Figure 4. (A) Examination of the surface accessibility of the C-terminal cysteine residue of monomeric rSbpA$_{31-1178}$/STII/Cys fusion protein by targeted chemical modification with differently sized macromolecules. Bench mark ladder (All blue, Biorad laboratories, Hercules, CA) (lane 1); GPC-purified rSbpA$_{31-1178}$/STII/Cys (lane 2); rSbpA$_{31-1178}$/STII/Cys chemically modified with sulfhydryl-specific PEG-maleimide 5 kDa (lane 3) and 20 kDa (lane 4) as well as rSbpA$_{31-1178}$/STII/Cys modified with protein A (M_r = 42 kDa) (lane 5), carbonic anhydrase (M_r = 29 kDa) (lane 6), or rBet v1 (M_r = 17 kDa) (lane 7) preactivated with the heterobifunctional cross-linker Sulfo-MBS. The positions of modified (upshifted) bands are indicated by arrows. (B) Immuno dot assay using rabbit anticarbonic anhydrase antibody indicating the presence of carbonic anhydrase on the surface of the monolayer formed by recrystallization of rSbpA$_{31-1178}$/STII/Cys-Sulfo-MBS-carbonic anhydrase conjugate on peptidoglycan-containing sacculi of *Ly. sphaericus* CCM 2177 (right dot). Left dot: recrystallization products consisting of wild-type SbpA recrystallized on PGS of *Ly. sphaericus* CCM 2177 showed no signal.

of rSbpA$_{31-1178}$/STII/Cys in solution (Figure 4A, lane 2), sulfhydryl-specific PEG-maleimide modification was performed. The modification with m-PEG-mal, size 5 and 20 kDa, resulted in an increase of the molecular mass of the protein visible as a gel shift on SDS−PAGE corresponding to the molecular mass of the respective m-PEG-malemide (Figure 4A, lanes 3 and 4). By the addition of DTT, the upshift of the rSbpA$_{31-1178}$/STII/Cys-PEG conjugate could be reversed (data not shown), which indicated that the cysteine residues of the mutant were specifically PEGylated.

Consistently, chemical modification of the cysteine residues of monomeric SbpA$_{31-1178}$/STII/Cys fusion protein with the differently sized macromolecules Protein A, (M_r 42 kDa), carbonic anhydrase (M_r 29 kDa), or rBet v1 (M_r 17 kDa) via the heterobifunctional cross-linker Sulfo-MBS, resulted in an increase of the molecular mass as calculated for the sum of the theoretical masses of the truncated S-layer protein plus the respective macromolecules (Figure 4A, lanes 5, 6, and 7). The modification pattern of the mutant indicated the presence and accessibility of the cysteine residues in the monomeric fusion protein. Although during all stages of the experiment DTT was added, and the solutions and buffers were degassed, the monomeric mutant could not be completely modified, which indicated that maybe irreversible oxidation of the sulfhydryl groups of some of the cysteine residues has occurred. Increase of the molar ratio between rSbpA$_{31-1178}$/STII/Cys and the respective preactivated macromolecule (from 1:2 to 1:10) did not result in an increase in the modification rate.

Investigation of the Recrystallization Properties of rSbpA$_{31-1178}$/STII/Cys Conjugated with Carbonic Anhydrase via a Heterobifunctional Cross-Linker by TEM and Detection of the Enzyme on the Surface of the S-Layer Lattice. Electron microscopy of the recrystallization products showed that modification of the S-layer fusion protein with the preactivated carbonic anhydrase did not interfere with its recrystallization properties (data not shown). Immuno dot blots of recrystallization products with an antibody raised against carbonic

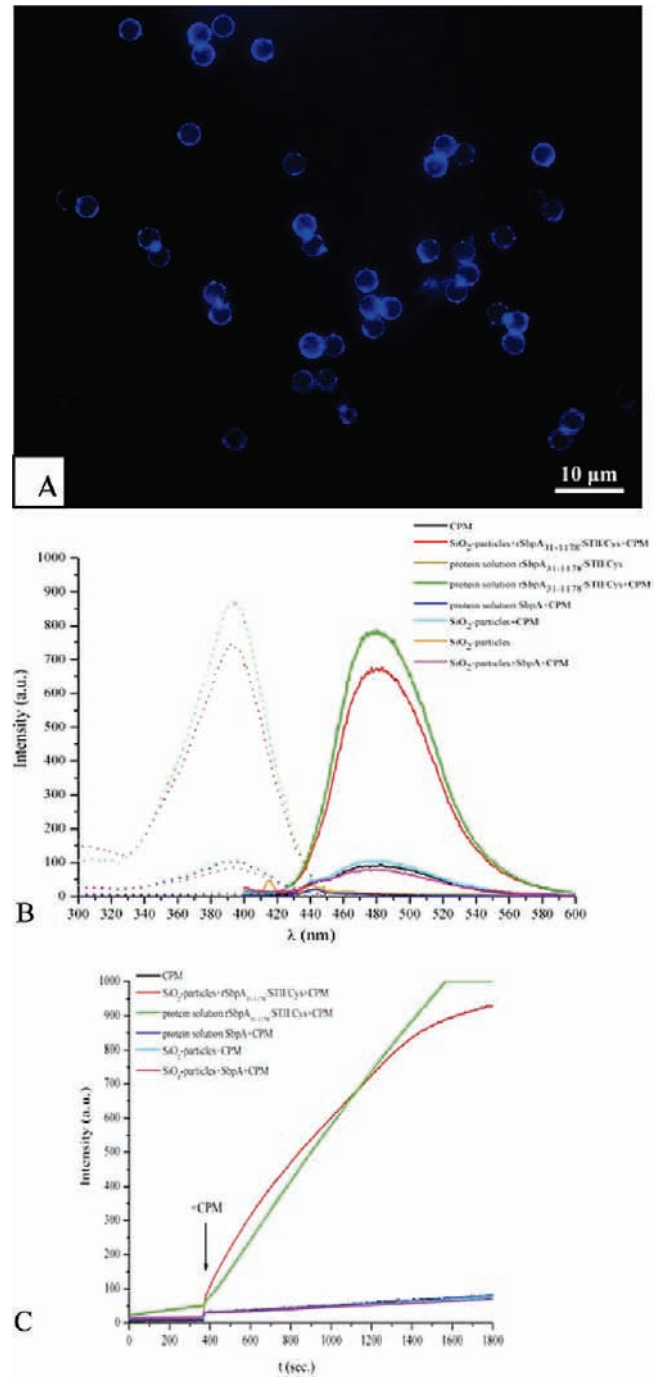

Figure 5. (A) Fluorescent micrograph of rSbpA$_{31-1178}$/STII/Cys recrystallized as a monolayer on SiO_2-microparticles and incubated with CPM indicating surface exposure of the C-terminally fused cysteine residue. (B) Fluorescent excitation and emission spectrum of the fusion protein rSbpA$_{31-1178}$/STII/Cys−CPM conjugate in solution or recrystallized on SiO_2-particles showing an excitation peak at 388 nm and an emission peak of 480 nm, which was in good accordance with the values (384 nm/470 nm) reported for the dye. As expected, the thiol-reactive coumarin, CPM alone, was very weakly fluorescent without reaction with a thiol group. Soluble rSbpA$_{31-1178}$/STII/Cys without dye, soluble wild-type SbpA incubated with the dye, wild-type SbpA recrystallized on microparticles incubated with the fluorophore, and the SiO_2-particles alone or incubated with the fluorophore, used as references, did not show a significant fluorescence intensity. (C) A time dependent increase of fluorescence was recorded for rSbpA$_{31-1178}$/STII/Cys−CPM conjugates in solution or recrystallized on SiO_2-particles, whereas soluble wild-type SbpA or SbpA recrystallized on SiO_2-particles as well as SiO_2-particles (all incubated with the dye for 30 min), used as a control for nonspecific interactions with CPM, reached no significant value.

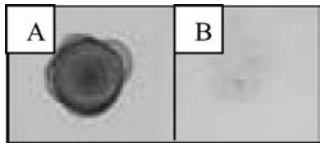

Figure 6. Immuno dot assay using rabbit anticarbonic anhydrase antibody demonstrating that carbonic anhydrase preactivated with the heterobifunctional cross-linker Sulfo-MBS could be successfully bound to rSbpA$_{31-1178}$/STII/Cys recrystallized on peptidoglycan-containing sacculi of *Ly. sphaericus* CCM 2177 (A). Wild-type SbpA recrystallized on peptidoglycan-containing sacculi of *Ly. sphaericus* CCM 2177, used as a control, showed no reaction with the antibody against carbonic anhydrase (B).

anhydrase, performed to confirm the presence of the carbonic anhydrase on the surface of the S-layers lattices, showed a clear signal (Figure 4B, right). Wild-type SbpA recrystallized on peptidoglycan-containing sacculi of *Ly. sphaericus* CCM 2177, used as a control, showed no reaction with the antibody against carbonic anhydrase (Figure 4B, left).

Fluorescent Labeling of the C-Terminal Cysteine Residue of Recrystallized rSbpA$_{31-1178}$/STII/Cys. To investigate the spatial accessibility of the C-terminal cysteine residue within the fusion protein lattice, rSbpA$_{31-1178}$/STII/Cys was recrystallized on SiO_2-particles and incubated with methylcoumarine (CPM), known as a thiol-reactive dye, which is only fluorescent if the binding between the thiol-group and the dye proceeds. As derived from former studies performed by using rSbpA (*10*, *13*), because of the specific physicochemical properties of its N-terminal part, the S-layer fusion protein was expected to recrystallize with its inner surface on the SiO_2-particles, thereby leaving the C-terminally fused cysteine residue exposed to the ambient environment. As shown by fluorescence microscopy, an oriented binding of rSbpA$_{31-1178}$/STII/Cys on SiO_2-particles could be demonstrated by obtaining a significant fluorescence signal after labeling the cysteine residues with methylcoumarine (Figure 5A). This led to the conclusion that the cysteine residues are located on the surface of the crystalline monolayer formed by rSbpA$_{31-1178}$/STII/Cys on SiO_2-particles and are accessible for modification with CPM. Compared to these data, wild-type protein SbpA recrystallized on SiO_2-particles or SiO_2-particles alone, used as blanks, showed no fluorescence signal (data not shown). Determination of the excitation and emission spectra of the rSbpA$_{31-1178}$/STII/Cys−CPM conjugates in solution or recrystallized on SiO_2-particles revealed an excitation peak at 388 nm and an emission peak at 480 nm (Figure 5B), which was in accordance with the reported values of E_x/E_m (nm) 384/470 for the dye. As described by the manufacturer, the thiol-reactive coumarin, CPM alone was very weakly fluorescent without reaction with a thiol group (Figure 5B). Soluble rSbpA$_{31-1178}$/STII/Cys without dye, soluble wild-type SbpA incubated with the dye, wild-type SbpA recrystallized on microparticles incubated with the fluorophore, and the SiO_2-particles alone or incubated with the fluorophore, used as references, did not show a significant fluorescence intensity (Figure 5B). A time dependent increase of fluorescence was recorded for rSbpA$_{31-1178}$/STII/Cys−CPM conjugates in solution or recrystallized on SiO_2-particles (Figure 5C), whereas soluble wild-type SbpA or SbpA recrystallized on SiO_2-particles as well as SiO_2-particles (all incubated with the dye for 30 min), used as a control for nonspecific interactions with CPM, reached no significant value (Figure 5C).

Chemical Modification of the Cysteine Residues of Recrystallized rSbpA$_{31-1178}$/STII/Cys. By performing immuno dot assays, it could also be shown that preactivated carbonic anhydrase could be successfully bound to rSbpA$_{31-1178}$/STII/Cys, which was recrystallized on peptidoglycan-containing sacculi of *Ly. sphaericus* CCM 2177 (Figure 6A). This result clearly indicated that the C-terminal cysteine residue at amino acid position 1,178 is surface exposed and accessible also in the recrystallized fusion protein rSbpA$_{31-1178}$/STII/Cys. Wild-type SbpA recrystallized on peptidoglycan-containing sacculi of *Ly. sphaericus* CCM 2177, used as a control, showed no reaction with the antibody against carbonic anhydrase (Figure 6B).

Formation of Gold Nanoparticle Arrays on Crystalline Monolayers Formed by rSbpA$_{31-1178}$/STII/Cys and Image Processing. Cysteine residues located on the surface of the S-layer lattice formed by rSbpA$_{31-1178}$/STII/Cys on peptidoglycan-containing sacculi of *Ly. sphaericus* CCM 2177 were used for covalent binding of gold nanoparticles with a diameter of 5 nm. A TEM image of the resulting regularly arranged gold nanoparticle array is shown in Figure 7A. Similar results could be obtained when self-assembly products formed by rSbpA$_{31-1178}$/STII/Cys were used as binding templates for a well-organized arrangement of gold nanoparticles (Figure 7B). The superlattice of the gold nanoparticles resembled the underlying square symmetry of the S-layer lattice formed by the fusion protein where every S-layer subunit carries one cysteine residue, and four subunits form one morphological unit. Base vector lengths were ~13.5 nm. An accurate lattice fit was obtained by cross-correlation averaging (CCA) where approximately 90% of the found nanoparticles in the image could be assigned to lattice

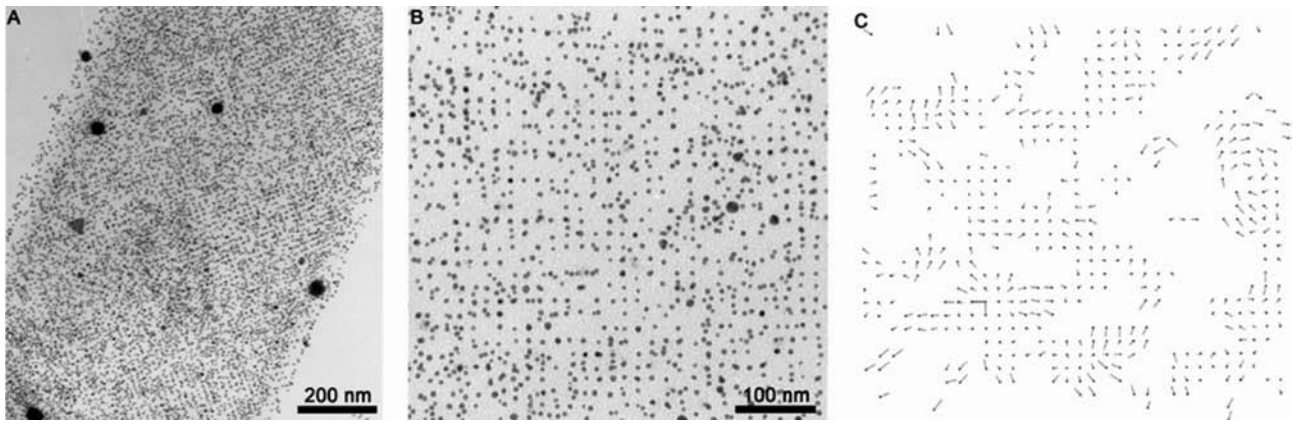

Figure 7. TEM micrograph of gold nanoparticles covalently bound to (A) recrystallization products consisting of rSbpA$_{31-1178}$/STII/Cys fusion protein recrystallized on peptidoglycan-containing sacculi of *Ly. sphaericus* CCM 2177 and (B) double-layered self-assembly products formed in suspension by rSbpA$_{31-1178}$/STII/Cys. (C) Cross-correlation averaging (CCA) of B. Bold dots mark positions at the nearest points on a least-squares fitted lattice. Small lines emanating from them indicate the direction and displacement (magnified 5 times) to the actually found positions, thus mapping the displacement field.

points (Figure 7C). The averaged root-mean-square deviation was found to be ~6% of the base vector lengths (~0.8 nm).

If recrystallization products consisting of wild-type SbpA recrystallized on PGS of *Ly. sphaericus* CCM 2177 were used, no binding of gold nanoparticles could be detected (data not shown). When double-layered self-assembly products formed by wild-type SbpA were used, gold nanoparticles were only found at incomplete regions of the double layer where the inner face of the S-layer lattice was accessible (data not shown). These findings led to the conclusion that the formation of regularly arranged gold nanoparticles on $rSbpA_{31-1178}$/STII/Cys monolayers is the result of specific binding of the nanoparticles to the sulfhydryl groups of the cysteine residues exposed on the outer face of the S-layer lattice.

DISCUSSION

In recent years, on the basis of the work on binding preactivated macromolecules, it has been demonstrated that metal and semiconducting nanoparticles can be bound in regular arrangements to native S-layer protein lattices by nonconvalent bonds (e.g., electrostatic interactions) or by covalent bounds after EDC activation (*15*−*17*). An alternative strategy for exploiting S-layer lattices as patterning elements for producing regularly ordered nanoparticle arrays in a much more controlled and specific way relates to genetically engineered S-layer proteins incorporating binding peptide domains.

The aim of the present study was to identify amino acid residues that are located on the surface of the S-layer lattice formed by the S-layer protein SbpA of *Ly. sphaericus* CCM 2177, which should serve as binding sites for functional macromolecules or for metal nanoparticles. Preliminary studies on the structure−function relationship of SbpA revealed that the N-terminal part of SbpA functions as a cell wall binding domain and that the truncated form $rSbpA_{31-1068}$, devoid of 200 C-terminal amino acids, was more surface accessible compared to the C-terminus of the full-length $rSbpA_{31-1268}$ (*13*). These results and the fact that various SbpA fusion proteins exhibit C-terminally fused functional domains (e.g., streptavidin (*30*), birch pollen allergen (*13, 31*), camel antibodies (*12, 32*), enhanced green fluorescent protein (*25*), and extremophilic enzymes (*33*)) on the surface of the S-layer lattice revealed that the SbpA-C-terminus must be exposed on the outer face of the S-layer lattice. Therefore, in the present study, for performing a refined surface accessibility screen in the domain between amino acid position 1,068 and 1,268, three different C-terminally truncated forms of SbpA carrying the short affinity tag *Strep-tag* II and a single cysteine residue at the C-terminal end were cloned and heterologously expressed in *E. coli*. Considering that the S-layer protein completely covers the cell surface of *Ly. sphaericus* CCM 2177 and that an aqueous environment is required for the diffusion of nutrients and metabolic degradation products, it can be expected that hydrophilic amino acid residues are exposed on the surface of the S-layer lattice. Therefore, three different hydrophilic amino acid residues within the C-terminally domain of SbpA were chosen as sites for the functionalization with STII and the cysteine residue. As S-layers usually do not possess sulfur-containing amino acids, the insertion of a single cysteine residue into the S-layer protein sequence is particularly attractive since the whole sulfur chemistry can be applied to covalently attach functional entities via the introduced cysteine residue. As reported in ref 34, a single cysteine residue has been inserted at various amino acid positions along the self-assembling domain of the S-layer proteins SbsB of *Geobacillus stearothermophilus* PV72/p2. In accordance with results from this study demonstrating that the replacement of selected amino acids by cysteine residues did not dramatically alter the structure of the S-layer protein SbsB (*34*), in the present work, electron microscopical examination revealed that all three rSbpA/STII/Cys fusion proteins retained their self-assembling and recrystallization ability. Recrystallization studies performed by TEM and AFM revealed that the SbpA derivative $rSbpA_{31-1178}$/STII/Cys (devoid of 90 C-terminal amino acids) turned out to be the best candidate for further modification experiments because of its ability to recrystallize into closed crystalline monolayers showing a long-range order on solid supports. This feature represents a prerequisite of regular nanoarrays used as templates for the organized arrangement of nanoparticles.

To conclude, one of the aims of current nanobiotechnological research is the bioinspired synthesis of nanostructured materials with novel mechanical or electrical properties. In the present study, for the first time, a natural self-assembly system based on a genetically engineered bacterial surface-layer protein was used for the bottom up fabrication of regularly arranged gold nanoparticles.

ACKNOWLEDGMENT

This work was supported by the FP6 EC-STREP project NASSAP 13523, by the Austrian Science Fund (FWF) Project P18510-B12 as well as by the US Air Force Office of Scientific Research (AFOSR) projects F49620-03-1-0222, FA9550-06-1-0208, and FA9550-07-0313. We thank Jacqueline Friedmann for performing the AFM studies and Manfred Tesarz for excellent technical support.

LITERATURE CITED

(1) Küpcü, S., Sara, M., and Sleytr, U. B. (1995) Liposomes coated with crystalline bacterial cells surface protein (S-layer) as immobilization structures for macromolecules. *Biochim. Biophys. Acta 1235*, 263–269.

(2) Moreno-Flores, S., Kasry, A., Butt, H. J., Vavilala, C., Schmittel, M., Pum, D., Sleytr, U. B., and Toca-Herrera, J. L. (2008) From native to non-native two-dimensional protein lattices through underlying hydrophilic/hydrophobic nanoprotrusions. *Angew. Chem., Int. Ed. 47*, 4707–4710.

(3) Sleytr, U. B., Messner, P., Pum, D., and Sára, M. (1999) Crystalline bacterial cell surface layers (S-layers): from supramolecular cell structure to biomimetics and nanotechnology. *Angew. Chem., Int. Ed. 38*, 1034–1054.

(4) Sleytr, U. B., Sára, M., Pum, D., Schuster, B., Messner, P., and Schäffer, C. (2003) Self Assembly Protein Systems: Microbial S-Layers, in *Biopolymers* (Steinbüchel, A., and Fahnestock, S., Eds.) pp 285−338, Wiley-VCH, Weinheim, Germany.

(5) Toca-Herrera, J. L., Krastev, R., Bosio, V., Küpcü, S., Pum, D., Fery, A., Sára, M., and Sleytr, U. B. (2005) Recrystallization of bacterial S-layers on flat polyelectrolyte surfaces and hollow polyelectrolyte capsules. *Small 1*, 339–348.

(6) Breitwieser, A., Kupcu, S., Howorka, S., Weigert, S., Langer, C., Hoffmann-Sommergruber, K., Scheiner, O., Sleytr, U. B., and Sára, M. (1996) 2-D protein crystals as an immobilization matrix for producing reaction zones in dipstick-style immunoassays. *Biotechniques 21*, 918–925.

(7) Breitwieser, A., Mader, C., Schocher, I., Hoffmann-Sommergruber, K., Aberer, W., Scheiner, O., Sleytr, U. B., and Sára, M. (1998) A novel dipstick developed for rapid Bet v 1-specific IgE detection: recombinant allergen immobilized via a monoclonal antibody to crystalline bacterial cell-surface layers. *Allergy 53*, 786–93.

(8) Sleytr, U. B., and Sára, M. (1997) Bacterial and archaeal S-layer proteins: structure-function relationships and their biotechnological applications. *Trends Biotechnol. 15*, 20–6.

(9) Weiner, C., Sára, M., and Sleytr, U. B. (1994) Novel protein A affinity matrix prepared from two-dimensional protein crystals. *Biotechnol. Bioeng. 43*, 321–330.

(10) Ilk, N., Kosma, P., Puchberger, M., Egelseer, E. M., Mayer, H. F., Sleytr, U. B., and Sára, M. (1999) Structural and functional analyses of the secondary cell wall polymer of *Bacillus sphaeri-*

cus CCM 2177 that serves as an S-layer-specific anchor. *J. Bacteriol. 181*, 7643–6.
(11) Sára, M., Pum, D., Huber, C., Ilk, N., Pleschberger, M., and Sleytr, U. (2006) Nanoscale Patterning of S-Layer Proteins As a Natural Self-Assembly System, in *Biological and Pharmaceutical Nanomaterials. Nanotechnologies for the Life Sciences* (Kumar, C., Ed.) pp 219−252, Wiley-VCH, Weinheim, Germany.
(12) Pleschberger, M., Neubauer, A., Egelseer, E. M., Weigert, S., Lindner, B., Sleytr, U. B., Muyldermans, S., and Sara, M. (2003) Generation of a functional monomolecular protein lattice consisting of an s-layer fusion protein comprising the variable domain of a camel heavy chain antibody. *Bioconjugate Chem. 14*, 440–8.
(13) Ilk, N., Völlenkle, C., Egelseer, E. M., Breitwieser, A., Sleytr, U. B., and Sára, M. (2002) Molecular characterization of the S-layer gene, sbpA, of *Bacillus sphaericus* CCM 2177 and production of a functional S-layer fusion protein with the ability to recrystallize in a defined orientation while presenting the fused allergen. *Appl. Environ. Microbiol. 68*, 3251–60.
(14) Huber, C., Ilk, N., Rünzler, D., Egelseer, E. M., Weigert, S., Sleytr, U. B., and Sára, M. (2005) The three S-layer-like homology motifs of the S-layer protein SbpA of *Bacillus sphaericus* CCM 2177 are not sufficient for binding to the pyruvylated secondary cell wall polymer. *Mol. Microbiol. 55*, 197–205.
(15) Bergkvist, M., Mark, S. S., Yang, X., Angert, E. R., and Batt, C. A. (2004) Bionanofabrication of ordered nanoparticle arrays: effect of particle properties and adsorption conditions. *J. Phys. Chem. B 108*, 8241–8248.
(16) Györvary, E., Schroedter, A., Talapin, D. V., Weller, H., Pum, D., and Sleytr, U. B. (2004) Formation of nanoparticle arrays on S-layer protein lattices. *J. Nanosci. Nanotechnol. 4*, 115–120.
(17) Hall, S. R., Shenton, W., Engelhardt, H., and Mann, S. (2001) Site-specific organization of gold nanoparticles by biomolecular templating. *Chem. Phys. Phys. Chem. 3*, 184–186.
(18) Mark, S. S., Bergkvist, M., Yang, X., Teixeira, L. M., Bhatnagar, P., Angert, E. R., and Batt, C. A. (2006) Bionanofabrication of metallic and semiconductor nanoparticle arrays using S-layer protein lattices with different lateral spacings and geometries. *Langmuir 22*, 3763–74.
(19) Merroun, M., Rossberg, A., Hennig, C., Scheinost, A. C., and Selenska-Pobell, S. (2007) Spectroscopic characterization of gold nanoparticles formed by cells and purified S-layer protein of *Bacillus sphaericus* JG-A12. *Mater. Sci. Eng. C 27*, 188–192.
(20) Mark, S. S., Bergkvist, M., Yang, X., Angert, E. R., and Batt, C. A. (2006) Self-assembly of dendrimer-encapsulated nanoparticle arrays using 2-D microbial S-layer protein biotemplates. *Biomacromolecules 7*, 1884–1897.
(21) Jarosch, M., Egelseer, E. M., Mattanovich, D., Sleytr, U. B., and Sára, M. (2000) S-layer gene *sbsC* of *Bacillus stearothermophilus* ATCC 12980: molecular characterization and heterologous expression in *Escherichia coli*. *Microbiology 146* (Pt 2), 273–281.
(22) Sambrook, J. F. E. F., and Maniatis, T. (1989) *Molecular Cloning: A Laboratory Manual*, 2nd ed., Cold Spring Habour Laboratory Press, Plainview, NY.
(23) Laemmli, U. K. (1970) Cleavage of structural proteins during the assembly of the head of bacteriophage T4. *Nature 227*, 680–685.
(24) Egelseer, E. M., Schocher, I., Sleytr, U. B., and Sára, M. (1996) Evidence that an N-terminal S-layer protein fragment triggers the release of a cell-associated high-molecular-weight amylase in *Bacillus stearothermophilus* ATCC 12980. *J. Bacteriol. 178*, 5602–5609.
(25) Ilk, N., Küpcü, S., Moncayo, G., Klimt, S., Ecker, R. C., Hofer-Warbinek, R., Egelseer, E. M., Sleytr, U. B., and Sára, M. (2004) A functional chimaeric S-layer-enhanced green fluorescent protein to follow the uptake of S-layer-coated liposomes into eukaryotic cells. *Biochem. J. 379*, 441–448.
(26) Pum, D., Sára, M., and Sleytr, U. B. (1989) Structure, surface charge, and self-assembly of the S-layer lattice from *Bacillus coagulans* E38−66. *J. Bacteriol. 171*, 5296–5303.
(27) Györvary, E. S., Stein, O., Pum, D., and Sleytr, U. B. (2003) Self-assembly and recrystallization of bacterial S-layer proteins at silicon supports imaged in real time by atomic force microscopy. *J. Microsc. (Oxford, U. K.) 212*, 300–306.
(28) Völlenkle, C., Weigert, S., Ilk, N., Egelseer, E., Weber, V., Loth, F., Falkenhagen, D., Sleytr, U. B., and Sára, M. (2004) Construction of a functional S-layer fusion protein comprising an immunoglobulin G-binding domain for development of specific adsorbents for extracorporeal blood purification. *Appl. Environ. Microbiol. 70*, 1514–1521; highlight in *Nat. Rev. Microbiol. 2*(5), 353.
(29) Saxton, W. O., and Baumeister, W. (1982) The correlation averaging of a regularly arranged bacterial cell envelope protein. *J. Microsc. 127*, 127–138.
(30) Moll, D., Huber, C., Schlegel, B., Pum, D., Sleytr, U. B., and Sára, M. (2002) S-layer-streptavidin fusion proteins as template for nanopatterned molecular arrays. *Proc. Natl. Acad. Sci. U.S.A. 99*, 14646–14651.
(31) Breitwieser, A., Egelseer, E. M., Moll, D., Ilk, N., Hotzy, C., Bohle, B., Ebner, C., Sleytr, U. B., and Sára, M. (2002) A recombinant bacterial cell surface (S-layer)-major birch pollen allergen-fusion protein (rSbsC/Bet v1) maintains the ability to self- assemble into regularly structured monomolecular lattices and the functionality of the allergen. *Protein Eng. 15*, 243–249.
(32) Pleschberger, M., Saerens, D., Weigert, S., Sleytr, U. B., Muyldermans, S., Sára, M., and Egelseer, E. M. (2004) An S-layer heavy chain camel antibody fusion protein for generation of a nanopatterned sensing layer to detect the prostate-specific antigen by surface plasmon resonance technology. *Bioconjug Chem 15*, 664–671.
(33) Tschiggerl, H., Breitwieser, A., de Roo, G., Verwoerd, T., Schaffer, C., and Sleytr, U. B. (2008) Exploitation of the S-layer self-assembly system for site directed immobilization of enzymes demonstrated for an extremophilic laminarinase from *Pyrococcus furiosus*. *J. Biotechnol. 133*, 403–411.
(34) Howorka, S., Sára, M., Wang, Y., Kuen, B., Sleytr, U. B., Lubitz, W., and Bayley, H. (2000) Surface-accessible residues in the monomeric and assembled forms of a bacterial surface layer protein. *J. Biol. Chem. 275*, 37876–37886.

BC800445R

Synthesis and Evaluation of a Novel Hydroxamate Based Fluorescent Photoprobe for Imaging of Matrix Metalloproteinases

Andreas Faust,*[,†,‡,||,⊥] Bianca Waschkau,[†,⊥] Jens Waldeck,[†] Carsten Höltke,[†,‡,||] Hans-Jörg Breyholz,[‡,||] Stefan Wagner,[‡,||] Klaus Kopka,[‡,||] Otmar Schober,[‡,||] Walter Heindel,[†] Michael Schäfers,[‡,§,||] and Christoph Bremer[†,§,||]

Department of Clinical Radiology, Albert-Schweitzer-Strasse 33, University Hospital Münster, 48149 Münster, Germany, Department of Nuclear Medicine, Albert-Schweitzer-Strasse 33, University Hospital Münster, 48149 Münster, Germany, Interdisciplinary Center for Clinical Research (IZKF Münster), Domagkstr. 3, University of Münster, 48149 Münster, Germany, and European Institute for Molecular Imaging (EIMI), University of Münster, Mendelstr. 11, 48149 Münster, Germany. Received October 20, 2008; Revised Manuscript Received March 11, 2009

The assessment of matrix metalloproteinase (MMP) activity in vivo is highly desirable in various human diseases such as cancers. Hydroxamic acids based on CGS27023A or CGS25966 are nonpeptidyl lead structures that specifically target activated MMPs in vivo. The aim of this study was the modification and fluorescent labeling of these lead structures to develop a highly affine, nonpeptide MMP inhibitor (MMPI)-ligand for molecular optical imaging of activated MMPs. An 11 step synthesis was developed involving a PEGylated benzyl derivative as a spacer to minimize the interactions between the activated MMP and the dye of conjugate **11** with an azide as a protected amino function. After reducing the azide (Staudinger reaction) and labeling with Cy5.5, we obtained a CGS-based MMP inhibitor **11** with a fluorescent signaling flag. To evaluate the biological properties of this photoprobe, three human cancer cell lines (A-673, HT-1080 and BT-20) were characterized with respect to their MMP-2 and -9 (gelatinases) expression levels (real-time PCR) and protein levels (Western blotting). Initially, fluorogenic inhibition assays were used to assess the MMP inhibition potential. The PEGylated CGS **10** showed complete inhibition of MMP-2 and MMP-9 activities in vitro both for purified MMP-2/-9 (active and pro-forms) and MMP-2/-9 containing cell culture supernatants. To test the imaging potential in biological tissues, gelatinase activity was measured on tumor cryostat sections of the above-mentioned tumor cells using FITC-labeled dye-quenched gelatin. Gelatinase positive tumors revealed strong binding of CGS-Cy5.5 **11**, while gelatinase negative tumors were not targeted. In conclusion, this new CGS-based MMP photoprobe has a high affinity for MMP-2 and -9 and is thus a promising candidate for sensitive imaging of MMP activity in various diseases in patients.

INTRODUCTION

Matrix metalloproteinases (MMPs) are a family of currently more than 24 known mammalian emzymes, which are able to degrade structural components of the extracellular matrix (ECM) and basement membranes with overlapping substrate specificities (*1*−*3*). On the basis of their specificity, the MMPs are classified into collagenases, gelatinases, stromelysins, and matrilysins. (*4*) MMPs are secreted as inactive pro-enzymes (zymogens). A mechanism termed cysteine switch (*5*) initiates the activation of the MMPs, which are subsequently tightly controlled by several endogenous inhibitors, e.g., the plasma inhibitor α2-macroglobulin and the four tissue inhibitors of metalloproteinases (TIMPs) (*6*). MMPs and TIMPs participate in physiological tissue remodelling processes that require the disruption of ECM barriers to allow cell migration and the modification of the matrix microenvironment. Elevated MMP expression and activity has been found in numerous human diseases, including inflammatory processes, cancer, and atherosclerosis (*7*, *8*). Especially, MMP-2 and -9 play a crucial role in local and metastatic invasion of cancer. One of the earliest events in the metastatic spread of cancer is the invasion through the basement membrane and proteolytic degradation of the extracellular matrix proteins, such as, collagens, laminin, elastin and fibronectin, etc., and nonmatrix proteins. MMPs are thus important regulators of tumor growth, both at the primary site and in distant metastases. Given that MMPs are clearly implicated in many human cancers, these represent important targets for imaging tumor biology (*9*, *10*).

Scheme 1. Structures of CGS25966 (A) and CGS27023A (B)

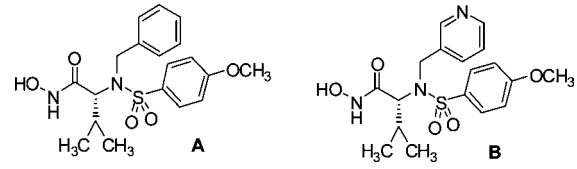

In this study, the synthesis of a MMP ligand based on the broad-spectrum inhibitor lead structures CGS27023A and CGS25966 (Scheme 1) is described. A polyethylene glycol (PEG) spacer group containing the amino functionality was successfully inserted to enable labeling with fluorescent dyes without significantly changing the MMP binding potential. The conjugation of the fluorescent dye Cy5.5 was accomplished by forming an amide bond under standard conditions. Enzyme activity assays, blocking experiments with the unlabeled CGS

* To whom correspondence should be addressed. Department of Clinical Radiology, Albert-Schweitzer-Str. 33, University Hospital Münster, 48149 Münster, Germany. Tel: +49-251-8347362. Fax: +49-251-8347363. E-mail: faustan@uni-muenster.de.

† Department of Clinical Radiology, University Hospital Münster.

‡ Department of Nuclear Medicine, University Hospital Münster.

§ Interdisciplinary Center for Clinical Research (IZKF Münster), University of Münster.

⊥ These authors contributed equally to this work.

|| European Institute for Molecular Imaging (EIMI), University of Münster.

10.1021/bc8004478 CCC: $40.75 © 2009 American Chemical Society
Published on Web 04/17/2009

10, and in vitro binding studies with CGS-Cy5.5 **11** confirmed a high binding potential of the probe to the target proteins.

EXPERIMENTAL PROCEDURES

Materials and Methods. All chemicals, reagents, and solvents for the synthesis of the compounds were of analytical grade and were purchased from commercial sources. For the labeling procedure, DNA-grade dimethylformamide was used. Melting points (uncorrected) were determined on a Stuart Scientific SMP3 capillary melting point apparatus. ^{1}H NMR and ^{13}C NMR spectra were recorded on a Bruker ARX 300 (Bruker BioSpin GmbH, Rheinstetten, Germany). Mass spectrometry was performed using a QUATTRO LCZ (Waters Micromass, Manchester, UK) spectrometer with a nanospray capillary inlet.

Synthetic Organic Chemistry. *Tetraethyleneglycol Dimethanesulfonate.* Methanesulfonyl chloride (317 mL, 470 g, 4.1 mol) was added dropwise over a period of 4 h to a solution of tetraethylene glycol (347 mL, 388 g, 2 mol) in dichloromethane (1.8 L) and triethyl amine (570 mL, 415 g, 4.1 mol) at 0 °C. The mixture was stirred at ambient temperature for an additional 16 h, and the resulting precipitate was filtered off. Concentration of the filtrate yielded an orange oil, which was used without further purification. Yield: 596 g (1.7 mol, 85%). ^{1}H NMR ($CDCl_3$, 300 MHz): δ (ppm) = 3.08 (s, 6H, SO_3CH_3), 3.65−3.68 (m, 8H, OCH_2CH_2O), 3.76−3.78 (m, 4H, $SO_3CH_2CH_2$), 4.37−4.40 (m, 4H, $SO_3CH_2CH_2$). ^{13}C NMR ($CDCl_3$, 75 MHz): δ (ppm) = 37.6 (SO_3CH_3), 68.9 ($SO_3CH_2CH_2$), 69.2 ($SO_3CH_2CH_2$), 70.4, 70.5 (OCH_2CH_2O). MS (ES^+) *m*/*e* = 373.1 $(M + Na)^+$, 351.1 $(M + H)^+$.

*2-(2-(2-(2-Azidoethoxy)ethoxy)ethoxy)ethyl Methanesulfonate (**1**).* To a solution of the dimesylate (83.4 g, 272 mmol) in dimethyl formamide (600 mL) sodium azide (10.6 g, 163 mmol) was added, and the reaction mixture was stirred at 120 °C for 5 h. Most of the dimethyl formamide was removed in vacuo. The crude product was dissolved in ethyl acetate (400 mL) and washed with water (5 × 200 mL) and brine (200 mL) and dried over magnesium sulfate. After removing the solvent, the resulting oil was chromatographed on a silica gel column (cyclohexane/EtOAc 2/1 to 1/1) to give a light yellow oil. Yield: 17.2 g (58 mmol, 36%). ^{1}H NMR ($CDCl_3$, 300 MHz): δ (ppm) = 3.08 (s, 3H, SO_3CH_3), 3.64−3.69 and 3.76−3.79 (m, 14H, OCH_2CH_2O and $OCH_2CH_2N_3$), 4.37−4.40 (m, 2H, $SO_3CH_2CH_2$). ^{13}C NMR ($CDCl_3$, 75 MHz): δ (ppm) = 37.6 (SO_3CH_3), 51.0 (CH_2N_3), 68.8 ($SO_3CH_2CH_2$), 69.3 ($SO_3CH_2CH_2$), 69.9, 70.4, 70.5 (OCH_2CH_2O). MS (ES^+) *m*/*e* = 319.1 $(M + Na)^+$, 297.1 $(M + H)^+$.

*4-(2-(2-(2-(2-Azidoethoxy)ethoxy)ethoxy)ethoxy)benzaldehyde (**2**).* To a solution of 14.2 g (47.8 mmol) of methansulfonate **1** and 9.16 g (75 mmol) of 4-hydroxybenzaldehyde in 200 mL of dimethyl formamide, 49 g (150 mmol) of cesium carbonate was added, and the resulting suspension was stirred at 100 °C for 2 h. After cooling to room temperature, 400 mL of ethyl acetate and 400 mL of water were added, and the organic layer was extracted with 1 N NaOH (150 mL) three times. After washing with water (3 × 150 mL) and brine, drying over magnesium sulfate, and removing the solvent, the crude product was chromatographed on a silica gel column (toluene/acetone 10/1) to give a yellow oil. Yield: 11.6 g (36 mmol; 75%). ^{1}H NMR ($CDCl_3$, 300 MHz): δ (ppm) = 3.36−3.39 (m, 2H, $OCH_2CH_2N_3$), 3.65−3.74 (m, 10H, OCH_2CH_2O), 3.87−3.90 (m, 2H, $PhOCH_2CH_2$), 4.20−4.23 (m, 2H, $PhOCH_2CH_2$), 7.02 (d, 2H, Ph*H*, $^3J_{HH}$ = 7.5 Hz), 7.82 (d, 2H, Ph*H*, $^3J_{HH}$ = 7.5 Hz). ^{13}C NMR ($CDCl_3$, 75 MHz): δ (ppm) = 50.5 (CH_2N_3), 67.6, 69.3, 69.9, 70.5, 70.6, 70.7 (OCH_2CH_2O), 114.7 (Ph*C*H), 125.2 (q-Ph*C*CHO), 131.8 (Ph*C*H), 163.7 (qPh*C*O), 190.7 (Ph*C*HO). HRMS (ES^+): calcd. ($C_{15}H_{21}N_3O_5Na$) = 346.1373; found = 346.1379.

*(4-(2-(2-(2-(2-Azidoethoxy)ethoxy)ethoxy)ethoxy)phenyl)methanol (**3**).* To a solution of 4-(2-(2-(2-(2-azidoethoxy)ethoxy)ethoxy)-ethoxy)benzaldehyde **2** (26.47 g, 82 mmol) in 300 mL of methanol, sodiumborhydride (4.65 g, 123 mmol) was carefully added at 0 °C. After stirring for 2 h at 0 °C, the excess sodiumborhydride was destroyed by adding 1 N HCl. The solvent was removed, and the resulting crude product was chromatographed on a silica gel column (cyclohexane/ethyl acetate 1/1) to give a colorless viscous oil. Yield: 23.66 g (73 mmol; 89%). ^{1}H NMR ($CDCl_3$, 300 MHz): δ (ppm) = 2.11 (bs, 1H, O*H*), 3.34−3.37 (m, 2H, $OCH_2CH_2N_3$), 3.63−3.72 (m, 10H, OCH_2CH_2O), 3.83−3.86 (m, 2H, $PhOCH_2CH_2$), 4.11−4.13 (m, 2H, $PhOCH_2CH_2$), 4.58 (s, 2H, CH_2OH), 6.87 (d, 2H, Ph*H*, $^3J_{HH}$ = 7.2 Hz), 7.26 (d, 2H, Ph*H*, $^3J_{HH}$ = 7.2 Hz). ^{13}C NMR ($CDCl_3$, 75 MHz): δ (ppm) = 50.5 (CH_2N_3), 64.7 ($PhCH_2OH$), 67.4, 69.6, 69.9, 70.5, 70.7 (OCH_2CH_2O), 114.5 (Ph*C*H), 128.4 (q-Ph*C*CHO), 133.3 (Ph*C*H), 158.2 (qPh*C*O). HRMS (ES^+): calcd. ($C_{15}H_{23}N_3O_5Na$) = 348.1530; found = 348.1522.

*4-(2-(2-(2-(2-Azidoethoxy)ethoxy)ethoxy)ethoxy)benzyl-2,2,2-trifluoro-acetate (**4**).* Benzylalcohol **3** (8.5 g, 26.2 mmol) was dissolved in dry tetrahydrofurane (50 mL), and trifluoroacetic acid anhydride (6.83 g, 4.5 mL, 32.5 mmol) was added slowly with stirring, and the mixture was heated to reflux for 30 min. After cooling to room temperature, the mixture was diluted with diethyl ether (150 mL) and washed with saturated $NaHCO_3$. The ether layer was dried with magnesium sulfate and concentrated to give a light yellow oil. Yield: 10.48 g (25 mmol, 95%). ^{1}H NMR ($CDCl_3$, 300 MHz): δ (ppm) = 3.35−3.38 (m, 2H, $OCH_2CH_2N_3$), 3.63−3.73 (m, 10H, OCH_2CH_2O), 3.85−3.88 (m, 2H, $PhOCH_2CH_2$), 4.14−4.16 (m, 2H, $PhOCH_2CH_2$), 5.28 (s, 2H, CH_2OCOCF_3), 6.93 (d, 2H, Ph*H*, $^3J_{HH}$ = 7.2 Hz), 7.31 (d, 2H, Ph*H*, $^3J_{HH}$ = 7.2 Hz). ^{13}C NMR ($CDCl_3$, 75 MHz): δ (ppm) = 50.5 (CH_2N_3), 67.4 ($PhCH_2O$), 69.5, 69.8, 70.5, 70.7 (OCH_2CH_2O), 114.4 ($COCF_3$, $^1J_{CF}$ = −284 Hz), 114.7 (Ph*C*H), 125.4 (q-Ph*C*CHO), 130.5 (Ph*C*H), 157.3 ($COCF_3$, $^2J_{CF}$ = −42 Hz), 159.5 (qPh*C*O). ^{19}F-NMR ($CDCl_3$, 282 MHz): δ (ppm) = −75.1 (CF_3). HRMS (ES^+): calcd. ($C_{17}H_{22}F_3N_3O_6Na$) = 444.1358; found = 444.1355.

*1-(2-(2-(2-(2-Azidoethoxy)ethoxy)ethoxy)ethoxy)-4-(bromomethyl)benzene (**5**).* Benzyl trifluoroacetate **4** (10.4 g, 25 mmol) was dissoled in dry tetrahydrofurane (50 mL), and dry lithium bromide (2.75 g, 32 mmol) was added with stirring. The mixture was heated to reflux for 20 h. After removing the solvent, the dark brown oil was chromatograhed on a silica gel column (cyclohexane/ethyl acetate 1/1) to give yellow oil. Yield: 8.4 g (21.6 mmol, 87%). ^{1}H NMR ($CDCl_3$, 300 MHz): δ (ppm) = 3.34−3.38 (m, 2H, $OCH_2CH_2N_3$), 3.62−3.71 (m, 10H, OCH_2CH_2O), 3.83−3.86 (m, 2H, $PhOCH_2CH_2$), 4.10−4.13 (m, 2H, $PhOCH_2CH_2$), 4.49 (s, 2H, CH_2Br), 6.87 (d, 2H, Ph*H*, $^3J_{HH}$ = 7.2 Hz), 7.30 (d, 2H, Ph*H*, $^3J_{HH}$ = 7.2 Hz). ^{13}C NMR ($CDCl_3$, 75 MHz): δ (ppm) = 50.5 (CH_2N_3), 33.8 ($PhCH_2Br$), 67.3, 69.5, 69.8, 70.3, 70.5, 70.7 (OCH_2CH_2O), 114.7 (Ph*C*H), 129.9 (q-Ph*C*CHO), 130.3 (Ph*C*H), 158.7 (qPh*C*O). HRMS (ES^+): calcd. ($C_{15}H_{22}BrN_3O_4Na$) = 410.0686, 411.0716, 412.0667, 413.0696; found = 410.0690, 411.0721, 412.0671, 413.0702.

*(R)-Methyl-2-(4-methoxyphenylsulfonamido)-3-methylbutanoate (**6**).* A solution of D-valine methylester (12.56 g, 75 mmol) in 35 mL of pyridine was cooled to 0 °C and 4-methoxybenzylsulfonyl chloride (15.5 g, 75 mmol) was slowly added. The resulting solution was stirred for 2 days at room temperature while a precipitate was formed. The suspension was diluted with 200 mL of dichloromethane and washed with 1 N HCl (200 mL), water (3 × 150 mL), and brine. After drying over magnesium sulfate, the solvent was removed to give the desired product with sufficient purity. Yield: 21.4 g (71 mmol, 95%). ^{1}H NMR ($CDCl_3$, 300 MHz): δ (ppm) = 0.87 (d, 3H, $CH(CH_3)_2$, $^3J_{HH}$ = 6.8 Hz), 0.94 (d, 3H, $CH(CH_3)_2$, $^3J_{HH}$ = 6.8

Hz), 1.97−2.08 (m, 1H, C*H*(CH_3)$_2$), 3.47 (s, 3H, COOCH_3), 3.70 (dd, 1H, (COO)C*H*, $^3J_{HH}$ = 5.2 Hz and 10.2 Hz), 3.86 (s, 3H, PhOCH_3), 5.20 (d, 1H, N*H*, $^3J_{HH}$ = 10.2 Hz), 6.96 (d, 2H, Ph*H*, $^3J_{HH}$ = 9 Hz), 7.76 (d, 2H, Ph*H*, $^3J_{HH}$ = 9 Hz). ^{13}C NMR ($CDCl_3$, 75 MHz): δ (ppm) = 17.4, 18.9 (CH(CH_3)$_2$), 31.5 (*C*H(CH_3)$_2$), 52.2 (COOCH_3), 55.6 (PhOCH_3), 60.9 (COO*C*H), 114.0 (Ph*C*H), 129.4 (Ph*C*H), 131.1 (qPhCSO_2), 162.9 (qPh-*C*OCH_3), 171.8 (*C*OOCH$_3$). HRMS (ES^+): calcd. ($C_{12}H_{17}NO_5SNa$) = 310.0720; found = 310.0721.

*(R)-Methyl-2-(N-(4-(2-(2-(2-(2-azidoethoxy)ethoxy)ethoxy)ethoxy)-benzyl)-4-methoxyphenyl-sulfonamido)-3-methylbutanoate (***7***).* To a solution of (*R*)-methyl-2-(4-methoxyphenyl-sulfonamido)-3-methyl-butanoate **6** (3.1 g, 10.1 mmol) and 1-(2-(2-(2-(2-azidoethoxy)-ethoxy)ethoxy)ethoxy)-4-(bromomethyl)benzene **5** (4 g, 10.3 mmol) in 100 mL of butanone potassium carbonate (7 g, 50 mmol) was added, and the resulting suspension was stirred for 4 h at 60 °C. After removing the solvent, the crude product was diluted with dichloromethane (150 mL) and washed with water (3 × 150 mL) and brine. The solution was dried over magnesium sulfate, filtered, and chromatographed on a silica gel column (cyclohexane/ethyl acetate 3/2) to give a colorless viscous oil. Yield: 4.56 g (7.5 mmol, 73%). ^{1}H NMR ($CDCl_3$, 300 MHz): δ (ppm) = 0.75 (d, 3H, CH(CH_3)$_2$, $^3J_{HH}$ = 6.5 Hz), 0.80 (d, 3H, CH(CH_3)$_2$, $^3J_{HH}$ = 6.5 Hz), 1.89−1.97 (m, 1H, C*H*(CH_3)$_2$), 3.41 (s, 3H, COOCH_3), 3.37−3.41 (m, 2H, OCH$_2$CH_2N$_3$), 3.66−3.73 (m, 11H, OCH_2CH_2O, COOC*H*), 3.84−3.88 (m, 5H, PhOCH$_2$CH_2, PhOCH_3), 4.09−4.12 (m, 2H, PhOCH_2CH$_2$), 4.33 (AB, 1H, $^2J_{HH}$ = 11.8 Hz, PhCH_2), 4.58 (AB, 1H, $^2J_{HH}$ = 11.8 Hz, PhCH_2), 6.80 (d, 2H, $^3J_{HH}$ = 8.6 Hz, Ph*H*), 6.91 (d, 2H, $^3J_{HH}$ = 8.9 Hz, Ph*H*), 7.30 (d, 2H, $^3J_{HH}$ = 8.6 Hz, Ph*H*), 7.69 (d, 2H, $^3J_{HH}$ = 8.9 Hz, Ph*H*). ^{13}C NMR ($CDCl_3$, 75 MHz): δ (ppm) = 19.6 (CH(*C*H$_3$)$_2$), 28.5 (*C*H-(CH_3)$_2$), 48.2 (N*C*H$_2$Ph), 50.7 (*C*H$_2$N$_3$), 51.4 (COO*C*H$_3$), 55.6 (PhO*C*H$_3$), 66.1 (COO*C*H), 67.4 (PhO*C*H$_2$), 69.8, 70.0, 70.7, 70.8, 70.9 (O*C*H$_2$*C*H$_2$O), 113.7, 114.1 (Ph*C*H), 129.4, 129.5, 130.1 (q-Ph*C*CH$_2$, Ph*C*H), 131.9 (q-Ph*C*SO$_2$), 158.1, 162.6 (qPh*C*O), 170.8 (*C*OO). HRMS (ES^+): calcd. ($C_{28}H_{40}N_4O_9SNa$) = 631.2414; found = 631.2416.

*(R)-2-(N-(4-(2-(2-(2-(2-Azidoethoxy)ethoxy)ethoxy)ethoxy)benzyl)-4-methoxyphenylsulfon-amido)-3-methylbutanoic acid (***8***).* To a solution of the methyl ester **7** in tetrahydrofuran, methanol and water (8:1:1, 100 mL) lithium hydroxide (2.4 g, 100 mmol) was added, and the resulting suspension was stirred at room temperature for 2 days. After removing the solvent, the crude product was purified on a silica gel column (cyclohexane/ethyl acetate 2/1 with 2.5% acetic acid) to give a colorless sticky oil. Yield: 9.1 g (15.3 mmol, 78%). ^{1}H NMR ($CDCl_3$, 300 MHz): δ (ppm) = 0.75 (d, 3H, CH(CH_3)$_2$, $^3J_{HH}$ = 6.5 Hz), 0.89 (d, 3H, CH(CH_3)$_2$, $^3J_{HH}$ = 6.5 Hz), 1.92−2.00 (m, 1H, C*H*(CH_3)$_2$), 3.36−3.40 (m, 2H, OCH$_2$CH_2N$_3$), 3.66−3.71 (m, 11H, OCH_2CH_2O, COOC*H*), 3.84−3.88 (m, 5H, PhOCH$_2$CH_2, PhOCH_3), 4.09−4.14 (m, 2H, PhOCH_2CH$_2$), 4.38 (AB, 1H, $^2J_{HH}$ = 15.7 Hz, PhCH_2), 4.58 (AB, 1H, $^2J_{HH}$ = 15.7 Hz, PhCH_2), 6.79 (d, 2H, $^3J_{HH}$ = 8.6 Hz, Ph*H*), 6.89 (d, 2H, $^3J_{HH}$ = 8.9 Hz, Ph*H*), 7.27 (d, 2H, $^3J_{HH}$ = 8.6 Hz, Ph*H*), 7.71 (d, 2H, $^3J_{HH}$ = 8.9 Hz, Ph*H*), 10.53 (bs, 1H, COO*H*). ^{13}C NMR ($CDCl_3$, 75 MHz): δ (ppm) = 19.7 (CH(*C*H$_3$)$_2$), 28.3 (*C*H(CH_3)$_2$), 48.4 (N*C*H$_2$Ph), 50.6 (*C*H$_2$N$_3$), 55.6 (PhO*C*H$_3$), 66.0 (COO*C*H), 67.3 (PhO*C*H$_2$), 69.7, 70.0, 70.6, 70.7, 70.8 (O*C*H$_2$*C*H$_2$O), 113.8, 114.1 (Ph*C*H), 129.1 (q-Ph*C*CH$_2$), 129.6, 130.2 (Ph*C*H), 131.6 (q-Ph*C*SO$_2$), 158.1, 162.7 (qPh*C*O), 175.1 (*C*OOH). HRMS (ES^+): calcd. ($C_{27}H_{38}N_4O_9SNa$) = 617.2252; found = 617.2259.

*(R)-2-(N-(4-(2-(2-(2-(2-Azidoethoxy)ethoxy)ethoxy)ethoxy)benzyl)-4-methoxyphenylsulfon-amido)-N-hydroxy-3-methylbutanamide (***9***).* A suspension of *N*-hydroxy-2-pyridone (500 mg, 4.5 mmol) in dichloromethane (25 mL) was subsequently treated at room temperature with acid **8** (1.8 g, 3 mmol) and 2-morpholinoethyl isocyanide (631 mg, 0.62 mL, 4.5 mmol). Stirring was continued for 19 h after which time the formation of the intermediate pyridine active ester was complete. The solution was treated at 0 °C with TMSO-NH_2 (473 mg, 0.56 mL, 4.5 mmol), and stirring was continued at 0 °C for 7 h. The solution was washed with saturated aqueous $NaHCO_3$ (75 mL) and water (3 × 75 mL). The aqueous layer was additionally washed with dichloromethane (100 mL), and the combined organic layers were dried over magnesium sulfate and subsequently filtered. The crude product was chromatographed on a silica gel column (cyclohexane/ethyl acetate 1/1 → 1/4) to give a colorless and highly viscous oil. Yield: 930 mg (1.53 mmol, 51%). ^{1}H NMR ($CDCl_3$, 300 MHz): δ (ppm) = 0.50 (d, 3H, CH(CH_3)$_2$, $^3J_{HH}$ = 6.5 Hz), 0.79 (d, 3H, CH(CH_3)$_2$, $^3J_{HH}$ = 6.5 Hz), 2.10−2.15 (m, 1H, C*H*(CH_3)$_2$), 3.37−3.40 (m, 2H, OCH$_2$CH_2N$_3$), 3.66−3.75 (m, 11H, OCH_2CH_2O, C*H*CON), 3.84−3.89 (m, 5H, PhOCH$_2$CH_2, PhOCH_3), 4.09−4.12 (m, 2H, PhOCH_2CH$_2$), 4.45 (AB, 1H, $^2J_{HH}$ = 15.4 Hz, PhCH_2), 4.57 (AB, 1H, $^2J_{HH}$ = 15.4 Hz, PhCH_2), 6.79 (d, 2H, $^3J_{HH}$ = 8.6 Hz, Ph*H*), 6.88 (d, 2H, $^3J_{HH}$ = 8.9 Hz, Ph*H*), 7.27 (d, 2H, $^3J_{HH}$ = 8.6 Hz, Ph*H*), 7.61 (d, 2H, $^3J_{HH}$ = 8.9 Hz, Ph*H*), 9.36 (bs, 1H, CON*H*OH). ^{13}C NMR ($CDCl_3$, 75 MHz): δ (ppm) = 19.2, 19.8 (CH(*C*H$_3$)$_2$), 27.3 (*C*H(CH_3)$_2$), 48.0 (N*C*H$_2$Ph), 50.7 (*C*H$_2$N$_3$), 55.6 (PhO*C*H$_3$), 63.7 (NHCO*C*H), 67.4 (PhO*C*H$_2$), 69.7, 70.0, 70.6, 70.7, 70.8 (O*C*H$_2$*C*H$_2$O), 114.1, 114.2 (Ph*C*H), 129.0 (q-Ph*C*CH$_2$), 129.4, 130.5 (Ph*C*H), 131.7 (q-Ph*C*SO$_2$), 158.2, 162.9 (qPh*C*O), 167.2 (*C*ONHOH). HRMS (ES^+): calcd. ($C_{27}H_{39}N_5O_9SNa$) = 632.2361; found = 632.2360.

*(R)-2-(N-(4-(2-(2-(2-(2-aminoethoxy)ethoxy)ethoxy)ethoxy)benzyl)-4-methoxyphenylsulfon-amido)-N-hydroxy-3-methylbutanamide (***10***).* To a solution of the hydroxamic acid **9** (900 mg, 1.48 mmol) in THF (50 mL) was added at room temperature triphenylphosphine (500 mg, 1.9 mmol), and stirring was continued for 16 h. The solution was treated with water (34 μL, 1.9 mmol), and after stirring for an additional 3 h, the solvent was removed. The crude product was chromatographed on a silica gel column (ethyl acetate/methanol 2/1 with 2% triethylamine) to give colorless foam. Yield: 410 mg (0.7 mmol, 47%). ^{1}H NMR ($CDCl_3$, 300 MHz): δ (ppm) = 0.54 (d, 3H, CH(CH_3)$_2$, $^3J_{HH}$ = 6.5 Hz), 0.81 (d, 3H, CH(CH_3)$_2$, $^3J_{HH}$ = 6.5 Hz), 2.16−2.18 (m, 1H, C*H*(CH_3)$_2$), 3.45−3.87 (m, 18H, PEG-CH_2, C*H*CON, PhOCH_3), 4.07−4.09 (m, 2H, PhOCH_2CH$_2$), 4.40 (AB, 1H, $^2J_{HH}$ = 15.4 Hz, PhCH_2), 4.65 (AB, 1H, $^2J_{HH}$ = 15.4 Hz, PhCH_2), 6.41 (bs, 2H, NH_2) 6.77 (d, 2H, $^3J_{HH}$ = 8.6 Hz, Ph*H*), 6.86 (d, 2H, $^3J_{HH}$ = 8.9 Hz, Ph*H*), 7.27 (m, 2H, Ph*H*), 7.63 (d, 2H, $^3J_{HH}$ = 8.9 Hz, Ph*H*). ^{13}C NMR ($CDCl_3$, 75 MHz): δ (ppm) = 19.1, 19.7 (CH(*C*H$_3$)$_2$), 27.1 (*C*H(CH_3)$_2$), 40.8 (*C*H$_2$NH$_2$), 47.6 (N*C*H$_2$Ph), 55.5 (PhO*C*H$_3$), 63.6 (NHCO*C*H), 67.4 (PhO*C*H$_2$), 69.6, 70.0, 70.2, 70.5, 70.6 (O*C*H$_2$*C*H$_2$O), 114.0, 114.1 (Ph*C*H), 129.3 (q-Ph*C*CH$_2$), 129.5, 130.3 (Ph*C*H), 132.2 (q-Ph*C*SO$_2$), 157.9, 162.7 (qPh*C*O), 166.7 (*C*ONHOH). HRMS (ES^+): calcd. ($C_{27}H_{41}N_3O_9SH$) = 584.2636; found = 584.2635.

Fluorochrome Conjugation. The amino-functionalized derivative 10 (1.0 mg, 1.71 μmol) was dissolved in 400 μL of dry dimethylformamide provided with 10 μL of triethylamine. To this solution, Cy5.5 NHS ester (Amersham Bioscience) (1 mg, 0.9 μmol) was added. The reaction mixture was vortexed for 2 h at room temperature in the dark. Purification of the Cy5.5-labeled derivative **6** was performed by gradient-HPLC using a Knauer system with two K-1800 pumps, an S-2500 UV detector, and a RP-HPLC Nucleosil 100−5 C_{18} column (250 mm × 4.6 mm). Eluent A was water (0.1% TFA). Eluent B was acetonitrile (0.1% TFA). The gradient was from 99% A to 40% A over 19 min, holding for 5 min, and back to 99% in 1 min at a flow rate of 5.5 mL/min, and detection was at λ = 254 nm. The appropriate fractions (t_R = 14.5 min) were collected, lyophilized, redissolved in 1 mL of water, and finally stored at

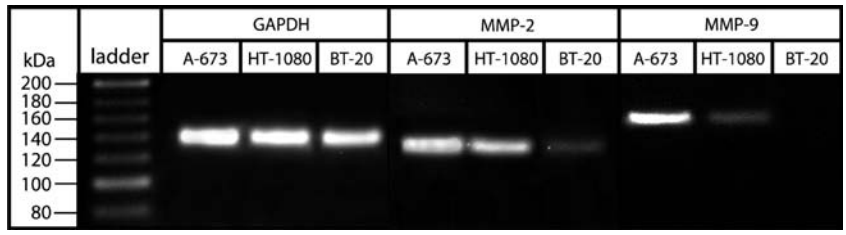

Figure 1. qRT-PCR was performed with primer pairs listed in Table 3, specific for MMP-2 and MMP-9, and normalized to the housekeeping gene GAPDH. After calculation of the RER for A-673, HT-1080, and BT-20, the amplified qRT-PCR products (GAPDH, 141 bp; MMP-2, 128 bp; and MMP-9, 160 bp) were analyzed by 2% gel electrophoresis.

−20 °C. The average content of **11** was 0.39 ± 0.02 μmol/mL (≈ 43%) as determined by fluorometer measurements with λ_{abs} = 678 nm and ε_{678} = 250000 $M^{-1}cm^{-1}$. MS (ES^-): *m*/*e* = 483.6 (100%), 484.0, 484.3, 484.6, 485.0 $[M]^{3-}$; 725.8, 726.3, 726.7, 727.4 $[M + H]^{2-}$.

Cell Culture. Three human carcinoma cell lines, purchased from ATCC (Manassas, VA, U.S.A.), were cultivated in the following media: fibrosarcoma HT-1080 (CCL-121) in RPMI-1640, mamma carcinoma BT-20 (HTB-19), and rhabdomyosarcoma A-673 (CRL-1598) in DMEM. Media (Invitrogen Corporation, San Diego, CA) were supplemented with 10% fetal calf serum (FCS), 1% penicillin and streptomycin (Biochrom AG, Berlin, Germany), 2 mM L-glutamine (Gibco BRL), and 13.5 mM sodium bicarbonate when using A-673 cells. Cells were grown routinely in T75 flasks, incubated at 37 °C in a 5% CO_2 humidified air atmosphere until the cultures were confluent (80−100%); medium was changed every 3−4 days. Cells were incubated with trypsin/EDTA, and cell numbers were determined in triplicate, counting only the viable cells able to exclude trypan blue (Sigma-Aldrich Chemie GmbH, Munich, Germany). For zymography, 107 cells were washed three times in serum-free medium and incubated in 3 mL of freshly FCS-free medium. After an incubation time of 48 h, the supernatant was collected and stored at −20 °C. For RNA isolation, 107 cells were incubated in FCS-containing media for further 24 h and washed with Dulbecco's phosphate-buffered saline (D-PBS) (Gibco BRL). Ten milliliters of medium was added to adherent cells, which were removed with a cell scraper and harvested by centrifugation (7 min, 1800*g*).

RNA Isolation and cDNA Synthesis. Total RNA was isolated from harvested cells (see above) using the PureLink Microto-Midi Total RNA Purification System (Invitrogen GmbH, Karlsruhe, Germany) according to the manufacturer's instructions with minor modifications. To remove possible genomic DNA contaminations, a DNase I digestion step was included between the washing steps. A reaction mix, consisting of OBI DNase I digestion buffer and RNase-free DNase I (20 units/μL), was added directly to the surface of the HiBind spin column for 15 min at room temperature. RNA was eluted with RNase-free DEPC-treated water and stored at −86 °C until use. The RNA quality was assessed on a 1% agarose gel, and its concentration was determined by UV spectroscopy at 260/280 nm with a NanoDrop photometer (Peqleb GmbH, Erlangen, Germany). First-strand cDNA was synthesized in a 20 μL reverse transciptase reaction mixture using the RevertAid First Strand cDNA Synthesis Kit (MBI Fermentas, St. Leon-Roth, Germany). Two micrograms of total RNA was denatured at 65 °C for 10 min and subsequently placed on ice. The no-template (NT)-control contained DEPC-treated water instead of RNA. Then, 5× reaction buffer, 1 mM of each nucleotide triphosphate, 20 units of RiboLock ribonuclease inhibitor, and 0.5 μg Oligo-(dT)18 primer were added and incubated at 25 °C for 5 min. After the addition of 200 units of RevertAid M-MuLV reverse transcriptase, the reaction mixtures were incubated according to the supplier's instructions. The no-reverse-transcription (NRT)-control contained DEPC-treated water instead of reverse transcriptase. Synthesized cDNA, the NT-, and NRT-control were stored at −20 °C until use.

Quantitative RT-PCR. All quantitative real-time polymerase chain reactions (qRT-PCR) were performed in a total volume of 20 μL, containing 5 μL of synthesized cDNA (or NTC or NRTC), 1 μL of SYBR Green I (1:600 diluted in DMSO) (Biozym Scientific GmbH, Oldendorf, Germany), 0.2 mM of each nucleotide triphosphate, 1× PCR-buffer, 50 μM of each primer (see Table 3), 1 mM $MgCl_2$, and 2.5 units of Taq DNA polymerase (New England Biolabs, Frankfurt a. M., Germany). To assess the accuracy of the procedures, triplicate aliquots of total RNA were used to produce cDNA in parallel reactions. QRT-PCR was accomplished using the Eppendorf Mastercycler EP Gradient (Eppendorf AG, Hamburg, Germany). The cycle conditions consisted of an initial step at 95 °C for 10 min followed by an amplification program for 40 cycles of 15 s at 95 °C, 30 s at 60 °C, 30 s at 72 °C, and 15 s at 78 °C with fluorescence acquisition. To distinguish primer dimers from the specific amplicon, the amplification program was followed immediately by a melting program consisting of 1 min at 95 °C, 1 min at 65 °C, and a gradual increase to 90 °C at a rate of 0.5 °C per second with fluorescence acquisition at each temperature transition. Linearity over the 20- to 40-cycle range and similar primer efficiencies were established by standard dilution curves (data not shown). The relative expression level of the target genes MMP-2 and -9 was normalized on the expression level of the internal housekeeping gene glycerinaldehyde-3-phosphate-dehydrogenase (GAPDH). All threshold cycle (*Ct*) values were determined in triplicate and obtained from the Eppendorf Mastercycler EP Gradient software. The relative expression ratio (RER) was determined with the comparative delta *Ct* (Δ*Ct*) method in addition to the kinetic PCR efficiency correction, using the relative expression software tool (REST). Amplified qRT-PCR products were separated by 2% agarose gel electrophoresis (Biozym Scientific GmbH, Oldendorf, Germany), stained with ethidium bromide, and visualized by UV transillumination. Fragment sizes were determined using the O'RangeRulerTM 20-bp DNA ladder (MBI Ferments, St. Leon-Rot, Germany).

Zymography. Gelatin zymography was performed in a sodium dodecyl sulfate (SDS)−polyacrylamide electrophoretic gel (PAGE) as described previously with minor modifications (*27*). Protein concentrations of collected FCS-free cell supernatants were derived with a Quant-iTTM Protein Assay Kit, using the Qubit fluorometer (Invitrogen GmbH, Karlsruhe, Germany). Thirty micrograms of total protein of each sample was mixed with (4×) SDS sample buffer without reducing agent and added to a 5% stacking and 7% separating SDS gel (containing 0.85 g/L gelatin). Positive controls included the following recombinant human enzymes: pro-MMP-2 (R & D Systems GmbH, Wiesbaden, Germany), active MMP-2 (Calbiochem, Wiesbaden, Germany), and pro/active MMP-9 (Sigma-Aldrich Chemie GmbH, Munich, Germany); the protein weight marker Precision Plus Dual Color (Bio-Rad Laboratories GmbH,

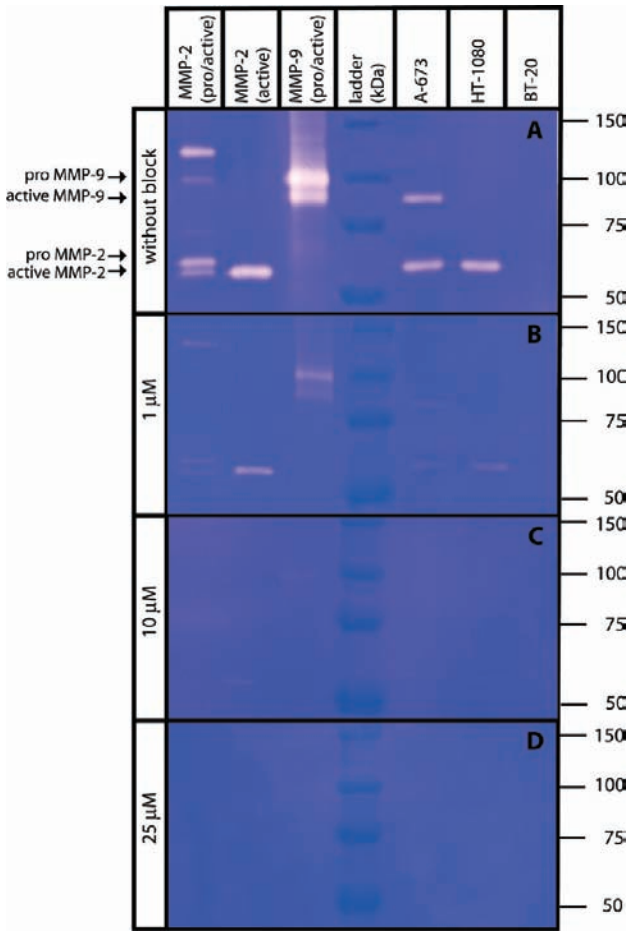

Figure 2. Gelatinolytic activities of purified MMP-2 (pro-form, 72 kDa; active form, 64 kDa) and MMP-9 (pro-form, 92 kDa; active form, 84 kDa) as well as that of collected supernatants of A-673, HT-1080, and BT-20 cells were assessed by zymography (A). Zymograms incubated overnight at 37 °C in buffers with varying concentrations of the unlabeled probe **10** show significant inhibition of MMP-2 and -9 by **10** (B−D). MMP-2 and -9 activities of purified enzymes and supernatants were completely inhibited by CGS concentrations ≥25 μM (D).

München, Germany) was also used. Gels were run for 120 min at 130 V and 4 °C in Tris-glycine SDS running buffer until the bromophenol blue front reached the bottom of the gel. After electrophoresis, the gels were washed with distilled water containing 2.5% Triton X-100 (30 min, room temperature) to renature proteins in the gel by the removal of SDS. Subsequently, the gels were incubated overnight at 37 °C with gentle shaking in incubation buffer (50 mM Tris-HCl at pH 7.8 and 10 mM $CaCl_2$). The incubation buffer contained 0 μM, 1 μM, 10 μM, or 25 μM unlabeled CGS-probe **10**. Zymograms were successively stained/destained with 1% Coomassie Brillant Blue G-250 dissolved in 10% ethanol and 5% acetic acid at room temperature for 120 min. Enzymatic activity was visualized through negative staining with Coomassie Brilliant Blue R-250 (Bio-Rad Laboratories GmbH, München, Germany). MMP-2/-9 activity was visible as clear zones of gelatin degradation against a dark blue background of stained gelatin. All gels were run under identical conditions with the same batch of reagents.

Routine Cryostat Sections and Fluorescence Microscopy. Three million cancer cells were injected subcutaneously into 7−9-week-old nude mice (nu/nu, Charles River, Germany). For in situ zymography and in vitro fluorescence binding assays, tumors with a size of approximately 7 × 10 mm were dissected, embedded into Tissue Freezing Medium (Leica Instruments, Nussloch, Germany), rapidly frozen by 2-methyl-butanol with cooled liquid nitrogen, and stored at −86 °C for sectioning. Embedded tumors were cut into 8 μm sections using a cryostat (Leica, Wetzler, Germany). For fluorescence microscopy, a Nikon TE 2000-S microscope (Tokyo, Japan) was employed, equipped with epifluorescence optics (AHF Analysentechnik AG, Tübingen, Germany). Images were recorded with a Nikon DXM1200F camera, using the NIS-Elements BR 2.30 software (Nikon, Tokyo, Japan). Fluorescence images, which had to be compared, were captured at identical illumination conditions with identical exposure time and system settings for digital image processing.

In Vitro Fluorescence Binding Assay and in Situ Zymography. Two hundred eighty picomoles of CGS-Cy5.5 (**11**), diluted in D-PBS (Gibco BRL), was given on unfixed air-dried cryostat sections and incubated, light protected, for 45 min at room temperature. Slides were washed in PBS (3 × 5 min) and air-dried for 5 min. Afterward, gelatinolytic activity of these cryostat sections was demonstrated using FITC-labeled dye-quenched (DQ)-gelatin, provided with the EnzCheck Gelatinase Assay Kit (EnzChek; Molecular Probes, Leiden, The Netherlands), as described previously with minor modifications (*26*). The DQ-gelatin, a specific enzymatic substrate detectable by fluorescence microscopy, is brought into close contact with cryostat sections of unfixed tissue. Proteolysis by gelatinases, such as MMP-2 and -9, yields cleaved gelatin-FITC peptides that are fluorescent so that green fluorescence indicates sites with gelatinolytic activity in tissue. At first, 1% low melting temperature agarose (Biozym Scientific GmbH, Oldendorf, Germany) was melted in D-PBS and cooled down to 37 °C, and DQ-gelatin (1 mg/mL) was added (1:200). Subsequently, a drop of the agarose−gelatin mixture was given to A-673 or BT-20 cryostat sections. All slides were incubated and light protected, at room temperature for 45 min. At the end of the incubation period, the DQ-gelatin was removed, and without fixation or wash steps, a drop of Fluoromont-GTM (Biozol Diagnostica GmbH, Eching, Germany) and a coverslip were added. Cleavage of DQ-gelatin was localized and photographed by fluorescence microscopy (emission, 535 nm; and excitation, 480 nm). Binding of CGS-Cy5.5 (**11**) to A-673 and BT-20 cryostat sections was assessed by emission of 700 nm and excitation of 620 nm.

RESULTS AND DISCUSSION

Since MMPs are involved in the regulation of the tumor microenvironment as well as expressed and activated in many types of human cancers, this distinct enzyme class appears to be a relevant molecular target for imaging of cancer. (*11*) MMP-2 and -9 are most consistently detected in malignant tissues in which they are associated with tumor aggressiveness, metastatic potential, and poor clinical prognosis *(12, 13)*.

Chemistry. The PEGylated benzyl derivative **5** was prepared as illustrated in Scheme 2. Mesylation of tetraethylene glycol and subsequent monosubstitution with sodium azide on a large scale gave the PEGylated azide derivative **1** in a satisfactory yield. Nucleophilic substitution of the mesyl moiety with 4-hydroxybenzaldehyde and subsequent reduc-

Scheme 2. Synthesis of the PEG-spacer 5[a]

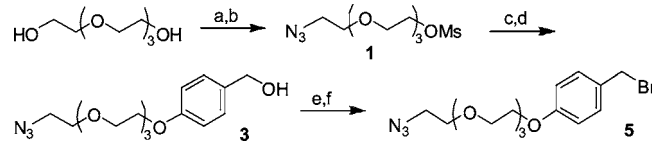

[a] (a) MsCl, NEt_3, CH_2Cl_2 (85%); (b) NaN_3, CH_3CN (36%); (c) 4-hydroxy-benzaldehyde, Cs_2CO_3, DMF (75%); (d) $NaBH_4$, MeOH (89%); (e) $(TFA)_2O$, THF (95%); (f) LiBr, THF (87%).

Scheme 3. Synthesis of the CGS-Cy5.5 11[a]

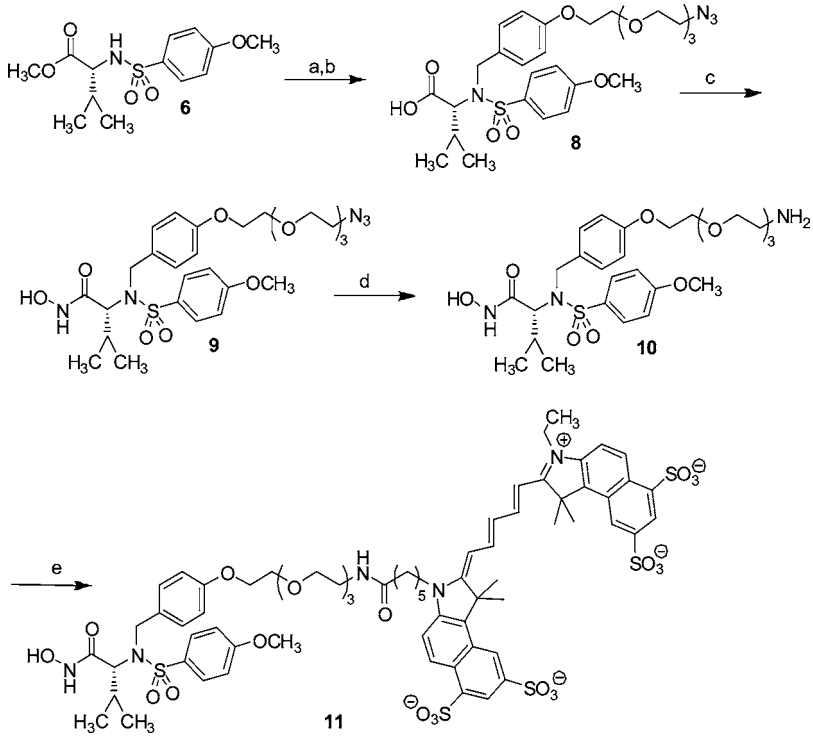

[a] (a) 5, K_2CO_3, butanone (73%); (b) LiOH, THF/MeOH/H_2O 8/1/1 (78%); (c) (1) *N*-hydroxy-2-pyridone, 2-morpholinoethylisocyanide, TMSO-NH_2, CH_2Cl_2; (2) aq. $NaHCO_3$ (51%); (d) PPh_3, H_2O, THF (47%); Cy5.5 NHS-ester, NEt_3, DMF (43%).

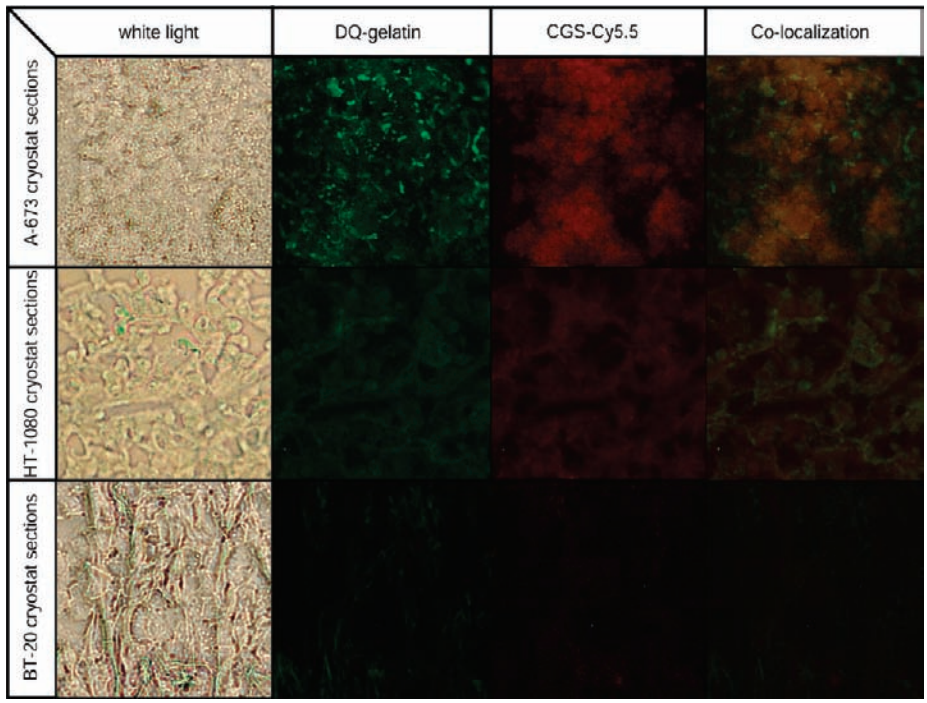

Figure 3. Gelatinolytic activity of A-673 (top), HT1080 (middle), and BT-20 (bottom) cryostat tumor sections was assessed by in situ zymography using FITC-labeled dye-quenched (DQ)-gelatin. In tissues with gelatinolytic activity, the DQ-gelatin was cleaved by MMP-2/-9 and resulted in green fluorescent signals. Binding of CGS-Cy5.5 (**11**) to MMP-2/-9 containing cryostat sections was demonstrated in an in vitro fluorescence binding assay. Incubation of the tumor sections with CGS-Cy5.5 resulted in high binding to A-673 sections (intense Cy5.5-based red fluorescence), a moderate binding to HT1080 sections, and low binding to BT-20 sections (low red fluorescence)). Additionally, FITC- and CGS-Cy5.5-based fluorescence was colocalized.

tion with sodium borhydride yielded the PEGylated benzyl alcohol **3**, which was converted into the benzyl bromide **5** in two steps (*14*).

On the basis of the known sulfonamide **6**, the secondary amine was benzylated and the ester hydrolyzed under mild conditions with lithium hydroxide in a THF/MeOH/water mixture (Scheme 3) Carboxylic acid **8** was directly converted into hydroxamic acid **9** with a silyl protected hydroxylamine and subsequent basic hydrolysis (*15*). For labeling with the NHS-ester of the commercially available cyanine dye Cy5.5, it

Table 1. MMP Inhibition Potencies of the CGS-Derivatives 9, 10, and 11 for Different MMPs Expressed in IC_{50} Values

	IC_{50} [μM][a]							
Cpd	MMP-1	MMP-2	MMP-3	MMP-8	MMP-9	MMP-13	*c* log *D*[b]	*c* log *P*[b]
9	0.300 ± 0.052	0.087 ± 0.020	0.058 ± 0.01	0.024 ± 0.005	0.036 ± 0.007	0.190 ± 0.027	2.96	2.96
10	0.034 ± 0.002	0.047 ± 0.005	0.007 ± 0.001	0.004 ± 0.001	0.065 ± 0.017	0.191 ± 0.010	0.37	2.10
11	n.d.[c]	16 ± 4	n.d.[c]	n.d.[c]	10 ± 0.7	n.d.[c]	n.c.[d]	n.c.[d]

[a] Values are the mean ± SD of three assays. [b] log *D* and log *P* values calculated by ACD/log *D* Suite at physiological pH. [c] Not determined. [d] Not calculated.

was necessary to reduce the azide function by a Staudinger reduction to get the precursor **10** in good yields.

The amino functionalized compound **10** was used for the conjugation of Cy5.5. The reaction was carried out in dry DMF with triethyl amine as the base (Scheme 3). Conjugate **11** was purified by reversed phase HPLC on an analytical column by collection of the appropriate fractions. After lyophilization and redissolving in PBS, the sample showed a purity of >97% (HPLC). The labeled ligand was verified by mass spectrometry with a triple negative charged ion emerging at 100% intensity.

With a molecular mass of 1,45 kDa, the resulting photoprobe belongs to the class of small molecule tracers. We and other groups are engaged in the development of MMP-targeted nonpeptide radiotracers for the in vivo detection of activated MMPs by positron emission tomography (PET) and single photon emission computed tomography (SPECT) (*16*−*20*). Recently, we successfully transferred the tracer concept to the optical imaging (OI) approach (*22*). A major advantage of OI is the opportunity to directly correlate signals in vivo with high resolution ex vivo techniques (e.g., fluorescence microscopy). A direct coregistration of biological expression patterns and the biodistribution of the tracer are thus feasible (see Figure 3). Moreover, the stability of the label and the lack of signal decay allow measurements over several days. With respect to clinical applications, small targeted probes could potentially allow endoscopic or laparoscopic tumor detection with high signal-to-noise ratios (SNRs). Imaging in the near-infrared spectrum (λ = 650−950 nm) shows very efficient tissue penetration as the absorption by water and hemoglobin is relatively low (diagnostic window) (*21*, *22*). Moreover, the tracer's excitation and emission spectra were identical to that of the Cy5.5 dye (ex, 678 nm; em, 692 nm).

Enzyme Studies in Vitro. A synthetic fluorogenic broad-spectrum MMP substrate was used in vitro to measure the activity of recombinant active human MMP-2 and -9 in the presence and absence of the unlabeled CGS **9** and **10**. The resulting inhibition potencies for several MMPs were determined as IC_{50} values and calculated from a nonlinear regression curve fit of the concentration-dependent reaction rates. This fluorogenic enzymatic activity assay yielded binding affinities of **9** and **10** to MMP-2 and -9 in the nanomolar range (Table 1).

MMP-2 and -9 Transcription, Translation, and Activity Tests. Three human cancer cell lines (rhabdomyosarcoma A-673, fibrosarcoma HT-1080 and breast carcinoma BT-20) were characterized regarding their genomic, proteomic, and functional MMP-2 and -9 expression levels. Cells were analyzed by quantitative real-time-PCR (qRT-PCR), secreted MMP proteins of collected supernatants were detected by Western blot analysis (data not shown), and MMP-2/-9 activities were verified by zymography.

In qRT-PCR analysis, the mRNA expression of the target genes MMP-2 and -9 was normalized by the internal housekeeping gene GAPDH since all three cancer cell lines (A-673, HT-1080, and BT-20) revealed nearly identical GAPDH mRNA levels. Using the software tool REST (*23*), the relative expression ratios (RER) of the target genes were determined as shown in Table 2. After determination of the RERs, amplified qRT-PCR products were analyzed in a 2% gelelectrophoresis as shown in Figure 1. Highest MMP-2 and -9 mRNA levels could be obtained for A-673, which therefore represented a MMP-2 and -9 positive cell line for the study of the binding affinity of CGS-Cy5.5 **11** to secreted gelatinases. HT-1080 cells showed high MMP-2 levels but weak MMP-9 mRNA levels. BT-20 cells expressed MMP-2 in very low amounts as compared to A-673 and HT-1080 cells. The MMP-9 mRNA level of BT-20 cells was lower than detectable levels; BT-20, therefore, was used as a cell line with very low gelatinase activity in our study.

Table 2. MMP-2 and -9 Expressions of the Carcinoma Cell Line A-673, HT-1080, and BT-20 Were Analyzed by qRT-PCR Analysis[a]

	A-673	HT-1080	BT-20
MMP-2 RER	23.0	12.7	1.0
MMP-9 RER	33.0	1.0	0

[a] The relative expression ratios (RER) for the target genes MMP-2 and -9 were determined by the software tool REST.

Table 3. Oligonucleotides Used As Primers

oligonucleotides	5′ → 3′-sequence	fragment size (bp)
GAPDH-for	CATTGCCCTCAACGACCAC	141
GAPDH-rev	CCTCTTGTGCTCTTGCTGGG	
MMP-2-for	GGAATGCCATCCCCGATAA	128
MMP-2-rev	TGCTTCCAAACTTCACGCTCT	
MMP-9-for	CCAAGTGGGCTACGTGACCTA	160
MMP-9-rev	CCTCCCTTTCCTCCAGAACAG	

Furthermore, gelatinolytic activities of collected supernatants from A-673, HT-1080, and BT-20 cells were analyzed by gelatin zymography. Purified MMP-2 and -9 (pro-/active forms) were used as controls (Figure 2A). Two prominent bands of gelatinolytic activity could be observed for the MMP-9 standard: the upper band exhibits the pro-form (92 kDa) and the lower band the active form (84 kDa). Purified pro-MMP-2 (72 kDa) and active MMP-2 (64 kDa) were identified accordingly. Furthermore, active MMP-2 was secreted by A-673 and HT-1080 cells. Active MMP-9 could only be detected in the supernatant of A-673 cells. Supernatants of BT-20 cells showed no detectable MMP-2 and -9 activities in zymography (Figure 2A). MMP-2 and -9 activities of the supernatants, analyzed with zymography, nicely correspond to the determined MMP-2-/9 relative expression ratios (RER) of the cells, analyzed by qRT-PCR. In following experiments, zymograms were incubated in buffers containing different amounts of the nonlabeled probe **10**. Varying the concentrations of the nonlabeled probe from 1 μM to 25 μM (Figure 2B−D) demonstrated its inhibition potential. Gelatinolytic activities of purified enzymes and cell supernatants were completely inhibited in the presence of 25 μM unlabeled CGS **10** as shown in Figure 2D, indicating efficient inhibition of MMP-2 and -9 by the probe.

Additionally, MMP-2 and -9 proteins in the collected supernatants were assessed by Western blotting with polyclonal antibodies, which recognize the latent and active MMP-2 and -9 forms. Western blot analysis and purified enzymes confirmed the results obtained with zymography (data not shown (*24*)).

Cellular Fluorescence MMP-Binding Assay of the Cy5.5-Labeled CGS (11) Using Cryostat Sections in Vitro. In situ zymography was used to proof high (A-673), weak (HT1080),

and low (BT-20) MMP-2 and -9 activities of respective tumor cryostat sections. Gelatinolytic activity was visualized in thin tissue sections by FITC-labeled dye-quenched (DQ)-gelatin, resulting in green fluorescence only in the case of enzymatic conversion. As expected, high extracellular and cellular green fluorescence was observed in the majority of regions of A-673 tumor sections (Figure 3) proving high MMP-2 and -9 activities of A-673 tumors suggested by the previous qRT-PCR and zymography experiments. Accordingly, BT-20 sections showed very low FITC-based fluorescence signals and only weak green fluorescence at the tumor border (Figure 3). In the fluorescence binding assay, MMP-2 and -9 containing A-673 tumor cryostat sections were treated with PBS containing 280 pmol of CGS-Cy5.5 **11**. High Cy5.5-based red fluorescence was obtained for A-673 sections as demonstrated in Figure 3. These results suggest high binding affinity of the labeled probe to gelatinases, secreted by the A673 tumor. In contrast, incubation of BT-20 sections showed only weak red fluorescence and revealed low binding of CGS-Cy5.5 **11** (Figure 3). CGS-Cy5.5- and FITC-based fluorescence signals were found colocalized, and further proof that activated MMPs can be detected with the newly developed photoprobe.

Alternative imaging approaches have been previously described in the literature (*25*). Large self-quenched molecules, e.g., allowed one to assess MMP expression in vivo via enzymatic activation of the probe. While this approach is a highly sensitive method for the detection of MMP activity, large molecule size (app. 400−500 kDa) and thus long blood half-life may be undesirable for translational imaging approaches.

CONCLUSIONS

The aim of this work was the development of a nonpeptide MMP inhibitor for optical imaging of MMP-2 and -9 activities. We have chosen CGS 25966 as the lead structure and developed a route for the synthesis of an amino-PEG-derivatized compound that can be used for the conjugation of common amino-reactive fluorescent markers such as Cy5.5. Thus, we obtained a near-infrared fluorescent photoprobe for the imaging of MMP-2 and -9. Using techniques such as qRT-PCR and zymography, the MMP-2 and -9 expressions of three human cancer cell lines was analyzed. The rhabdomyosarcoma cell line A-673 showed high MMP-2 and -9 levels, whereas the fibrosarcoma cell line HT-1080 exhibits lower levels and the breast carcinoma cell line BT-20 only marginal levels of MMP-2. MMP-2 and -9 activities of the three cell supernatants were verified by zymography. In subsequent blocking experiments, zymograms were incubated with different concentrations of unlabeled CGS **10**. Incubation with ≥ 25 μM unlabeled inhibitor revealed efficient binding and inhibition of MMP-2 and -9 activities. Additionally, gelatinolytic activity of A-673 and BT-20 cryostat sections was determined by in situ zymography using the DQ-gelatin technique. High binding affinity of CGS-Cy 5.5 **11** to MMP-2 and -9 containing A-673 tumor cryostat sections was demonstrated in an in vitro fluorescence binding assay. Thus, MMP-2 and -9 imaging with the fluorescent labeled probe **11** is feasible and should further be developed toward a molecular imaging approach to monitor disease processes such as invasion, metastasis, and angiogenesis in cancer in vivo being associated with activated MMP-2 and -9.

ACKNOWLEDGMENT

This work was supported by the Deutsche Forschungsgemeinschaft (SFB 656 projects A2/A4), the European Union Community (IP sixth framework; grant no. LSHG-CT-2003-503259 (Mol. Img) and MoldDiag-Paca LSHB- CT-2006-018771), the Interdisziplinary Centre of Clinical Research (FG3), and the European Institute for Molecular Imaging (EIMI). Thanks are due to Wiebke Gottschlich, Ulla Römer, and Sandra Schröer for technical assistance, and Professor Dr. H. Luftmann at the Organic Chemistry Department of the WWU Münster for mass spectrometry.

LITERATURE CITED

(1) Skiles, J. W., Gonnella, N. C., and Jeng, A. Y. (2004) The design, structure, and clinical update of small molecular weight matrix metalloproteinase inhibitors. *Curr. Med. Chem. 11*, 2911–2977.

(2) Tayebjee, M. H., Lip, G. Y. H., and MacFadyen, R. J. (2005) Matrix metalloproteinases in coronary artery disease: clinical and therapeutic implications and pathological significance. *Curr. Med. Chem. 12*, 917–925.

(3) Beaudeux, J. L., Giral, P., Bruckert, E., Foglietti, M. J., and Chapman, M. J. (2004) Matrix metalloproteinases, inflammation and atherosclerosis: therapeutic perspectives. *Clin. Chem. Lab. Med. 42*, 121–131.

(4) Whittaker, M., and Ayscough, A. (2000) Matrix metalloproteinases and their inhibitors - current status and future challenges. *Cell Transm. 17*, 3–14.

(5) Borkakoti, N. (2000) Structural studies of matrix metalloproteinases. *J. Mol. Med. 7*, 261–268.

(6) Stamenkovic, I. (2003) Extracellular matrix remodelling: the role of matrix metalloproteinases. *J. Pathol. 200*, 448–464.

(7) Galis, Z. S., and Khatri, J. J. (2002) Matrix metalloproteinases in vascular remodeling and atherogenesis: the good, the bad, and the ugly. *Circ. Res. 90*, 251–62.

(8) George, S. J. (2000) Therapeutic potential of matrix metalloproteinase inhibitors in atherosclerosis. *Exp. Opin. Invest. Drugs 9*, 993–1007.

(9) Katiyar, S. K. (2006) Matrix metalloproteinases in cancer metastasis: molecular targets for prostate cancer prevention by green tea polyphenols and grape seed proanthocyanidins. *Endocr., Metab. Immune Disord.: Drug Targets 6*, 17–24.

(10) Fridman, R. (2006) Metalloproteinases and cancer. *Cancer Metastasis Rev. 25*, 7–8.

(11) Vihinen, P., Ala-aho, R., and Kahari, V. M. (2005) Matrix metalloproteinases as therapeutic targets in cancer. *Curr. Cancer Drug Targets 5*, 203–20.

(12) Egeblad, M., and Werb, Z. (2002) New functions for the matrix metalloproteinases in cancer progression. *Nat. Rev. Cancer 2*, 161–74.

(13) Fingleton, B. (2003) Matrix metalloproteinase inhibitors for cancer therapy: the current situation and future prospects. *Expert Opin. Ther. Targets 7*, 385–397.

(14) Kopka, K., Faust, A., Keul, P., Wagner, S., Breyholz, H.-J., Höltke, C., Schober, O., Schäfers, M., and Levkau, B. (2006) 5-pyrrolidinylsulfonyl isatins as a potential tool for the molecular imaging of caspases in apoptosis. *J. Med. Chem. 49*, 6704–6715.

(15) Hilpert, H. (2001) Practical approaches to the matrix metalloproteinase inhibitor Trocade® (Ro 32-3555) and to the TNF-α converting enzyme inhibitor Ro 32-7315. *Tetrahedron 57*, 7675–7683. (a) Kopka, K., Breyholz, H.-J., Wagner, S., Law, M. P., Riemann, B., Schröer, S., Trub, M., Guilbert, B., Levkau, B., Schober, O., and Schäfers, M. (2004) Synthesis and preliminary biological evaluation of new radioiodinated MMP inhibitors for imaging MMP activity in vivo. *Nucl. Med. Biol. 31*, 257–267.

(16) Schäfers, M., Riemann, B., Kopka, K., Breyholz, H.-J., Wagner, S., Schäfers, K. P., Law, M. P., Schober, O., and Levkau, B. (2004) Scintigraphic imaging of matrix metalloproteinase activity in the arterial wall *in vivo*. *Circulation 109*, 2554–2559.

(17) Breyholz, H.-J., Wagner, S., Levkau, B., Schober, O., Schäfers, M., and Kopka, K. (2007) A 18F-radiolabeled analogue of CGS 27023A as a potential agent for assessment of matrix-metalloproteinase activity in vivo. *Q. J. Nucl. Med. Mol. Imaging 51*, 24–32.

(18) Wagner, S., Breyholz, H.-J., Law, M. P., Faust, A., Holtke, C., Schroer, S., Haufe, G., Levkau, B., Schober, O., Schafers, M., and Kopka, K. (2007) Novel fluorinated derivatives of the broad-spectrum MMP inhibitors N-hydroxy-2(*R*)-[[(4-methoxyphenyl)sulfonyl](benzyl)- and (3-picolyl)-amino]-3-methyl-butanamide as potential tools for the molecular imaging of activated MMPs with PET. *J. Med. Chem. 50*, 5752–5764.

(19) Su, H., Spinale, F. G., Dobrucki, L. W., Song, J., Hua, J., Sweterlitsch, S., Dione, D. P., Cavaliere, P., Chow, C., Bourke, B. N., Hu, X. Y., Azure, M., Yalamanchili, P., Liu, R., Cheesman, E. H., Robinson, S., Edwards, D. S., and Sinusas, A. J. (2005) Noninvasive targeted imaging of matrix metalloproteinase activation in a murine model of postinfarction remodeling. *Circulation 112*, 3157–3167.

(20) Chung, G., and Sinusas, A. J. (2007) Imaging of matrix metalloproteinase activation and left ventricular remodeling. *Curr. Cardiol. Rep. 9*, 136–142.

(21) Ntziachristos, V., Bremer, C., Graves, E. E., Ripoll, J., and Weissleder, R. (2002) In vivo tomographic imaging of near-infrared fluorescent probes. *Mol Imaging 1*, 82–88.

(22) Bremer, C., Ntziachristos, V., Weitkamp, B., Theilmeier, G., Heindel, W., and Weissleder, R. (2005) Optical imaging of spontaneous breast tumors using protease sensing 'smart' optical probes. *Invest. Radiol. 40*, 321–327.

(23) Pfaffl, M. W., Horgan, G. W., and Dempfle, L. (2002) Relative expression software tool (REST) for group-wise comparison and statistical analysis of relative expression results in real-time PCR. *Nucleic Acids Res. 26*, 509–515.

(24) Faust, A., Waschkau, B., Waldeck, J., Höltke, C., Breyholz, H.-J., Wagner, S., Kopka, K., Heindel, W., Schäfers, M., and Bremer, C. (2008) Synthesis and evaluation of a novel fluorescent photoprobe for imaging matrix metalloproteinases. *Bioconjugate Chem. 19*, 1001–1008.

(25) Bremer, C., Tung, C. H., and Weissleder, R. (2001) *In vivo* molecular target assessment of matrix metalloproteinase inhibition. *Nature Med. 7*, 743–748.

(26) Oh, L. Y., Larsen, P. H., Krekoski, C. A., Edwards, D. R., Donovan, F., Werb, Z., and Yong, V. W. (1999) Matrix metalloproteinase-9/gelatinase B is required for process outgrowth by oligodendrocytes. *J. Neurosci. 19*, 8464–8475.

(27) Heussen, C, and Dowdle, E. B. (1980) Electrophoretic analysis of plasminogen activators in polyacrylamide gels containing sodium dodecyl sulfate and copolymeri/ed substrates. *Anal. Biochem. 102*, 196–202.

BC8004478

Derivatized Mesoporous Silica Beads for MALDI-TOF MS Profiling of Human Plasma and Urine

Rosa Terracciano,*[,†] Luigi Pasqua,[‡] Francesca Casadonte,[†] Stella Frascà,[†] Mariaimmacolata Preianò,[†] Daniela Falcone,[†] and Rocco Savino[†]

Department of Experimental and Clinical Medicine, University of Catanzaro "Magna Graecia", School of Medicine, 88100 Catanzaro, Italy, and Department of Chemical Engineering and Materials, University of Calabria, 87036 Cosenza, Italy.
Received November 30, 2008; Revised Manuscript Received February 24, 2009

Matrix-assisted laser desorption/ionization-time-of-flight mass spectrometry (MALDI-TOF MS) is a promising tool for large-scale screening of body fluids for the early detection of human diseases. Proteins, peptides, and metabolites present in cells, tissues, or in body fluids constitute the molecular signatures of individuals. The design and generation of material-based platforms for capturing molecular signatures from body fluids has gained increasing interest in recent years. Highly selective materials are attractive candidates for a wide range of applications in biofluid proteomics. We have therefore developed a procedure based on mesoporous silica particles for the selective binding and enrichment of low molecular weight plasma/serum proteins by MALDI MS analysis (Terracciano, R., Gaspari, M., Testa, F., Pasqua, L., Cuda G., Tagliaferri, P., Cheng, M. C., Nijdam, A. J., Petricoin, E. F., Liotta, L. A., Ferrari, M., and Venuta, S. (2006) Selective binding and enrichment for low-molecular weight biomarker molecules in human plasma after exposure to nanoporous silica particles. *Proteomics 6,* 3243–3250). Mesoporous silica beads (MSB) are able to harvest peptides from plasma and serum by means of nanosized porous channels with high surface area, while excluding large size proteins. Moreover, the absorption properties can be modified since the pore walls can be functionalized with different chemical species due to the high concentration of silanol groups at the surface. In this study, we performed derivatization of MSB with different functionalities, and we evaluated the derivatized materials for plasma and urine peptidomic profiling. Aminopropyl, *N*-(2-aminoethyl)-3-aminopropyl, and *N*,*N*,*N*′ tris-carboxymethyl ethylene diamine, have been introduced onto the mesoporous silica surfaces in order to modulate selective peptide enrichment. We also explored various experimental conditions in order to optimize the performance of chemically modified MSB in the peptide profiling of human plasma and urine. These new derivatized mesoporous surfaces, in addition to the previous nonderivatized MSB, constitute an extended and reliable platform of five distinct chromatographic phases with defined surface functionality and porosity. Several plasma and urine peptides were extracted from derivatized MSB and then profiled by MALDI-TOF MS. The reproducibility of sample preparation by different functionalized beads was evaluated via three replicate analyses of plasma and urine samples. Lower coefficients of variation in the mass values and peak intensities resulted for plasma in comparison to those of urine samples; nevertheless, these where satisfactory for diagnostic purposes. For human urine, a linear correlation was found between spiked peptide concentrations and their peak areas ($R^2 > 0.98$) with a limit of detection in the low-nanogram per milliliter range, thus confirming the high sensitivity of the methodology, previously demonstrated for human plasma. Different panels of peptide repertoires have thus been collected from highly porous substrates chemically conjugated with different functional groups, and these may be used in biomarker discovery for disease diagnosis.

INTRODUCTION

The comparison of protein expression between healthy individuals and patients is one of the promising tools for biomarker identification. A fast and sensitive protein profiling method for biomarker discovery is an essential prerequisite for high-throughput and large-scale clinical studies. The establishment of proteomic approaches to biomarker discovery and disease profiling in recent years has tested the limits of existing tools for the capture and detection of low-abundance proteins in biological samples. The ability to isolate target proteins from complex protein mixtures, as well as improving the sensitivity toward peptides of low abundance, is a challenge for mass spectrometric analysis.

Proteomic pattern analysis by mass spectrometry (MS) is emerging as the preferred tool for robust and rapid expression profiling studies (*1*−*9*) and represents an alternative to the classical and laborious two-dimensional polyacrylamide gel electrophoresis (2D-PAGE) (*10*).

For biofluids, surface-enhanced laser desorption/ionization-time-of-flight (SELDI-TOF) or matrix-assisted laser desorption/ionization-time-of-flight (MALDI-TOF) MS are rapidly growing in popularity because of their ability to screen and discover multiple biomarkers simultaneously in clinical proteomics. In addition, SELDI-TOF MS and MALDI-TOF MS focus especially on the low molecular mass region analytes (1000−20000 Da), which include the small proteins, protein/peptide fragments, and peptides that constitute the peptidome or fragmentome, which are often overlooked by traditional techniques (*11, 12*).

Affinity binding reagents have played a crucial role in the translation of proteomic discoveries to clinical diagnostics due to their ability to isolate target proteins from complex protein mixtures (*13*). The design and generation of material-based

* Corresponding author. Tel: ++39/09613694080. Fax: ++39/09613694090. E-mail: terracciano@unicz.it.
[†] University of Catanzaro.
[‡] University of Calabria.

10.1021/bc800510f CCC: $40.75 © 2009 American Chemical Society
Published on Web 04/02/2009

platforms for capturing molecular signatures written in body fluids have also gained increasing interest in recent years (*14*−*17*). Additionally, novel bioconjugate materials, designed specifically for microscale genomic and proteomic analyses, are facilitating new separation techniques (*18, 19*). Mesoporous silica has captured considerable interest for a diverse range of applications, such as catalysis, filtration and separation, molecular collection and storage, nanofluidics, medical imaging, drug delivery, and sensors (*20*). Recently, our group has explored a new application of mesoporous silica. We have previously developed a strategy based on mesoporous silica beads (MSB) for profiling low molecular weight plasma peptides (*21*). In later correlated studies, nanoporous silicon and glass beads were used to harvest distinct subsets of the proteome from serum/plasma samples (*22, 23*).

According to IUPAC nomenclature, porous materials are divided into 3 classes: microporous material with a pore diameter below 2 nm, mesoporous material with a pore diameter between 2 and 50 nm, and macroporous material with a pore diameter above 50 nm. We speculated that mesopores would have the right dimensions for tunable peptide entrapment, while micropores might be too small and macropores too large for such a purpose. Given the high surface area, we demonstrated that mesoporous silica offered the desired adsorptive capacity for binding and enrichment of low molecular weight peptides present in human plasma (*21*). These results encouraged us to further investigate and explore the use of MSB as harvesting materials not only for human plasma but also for other clinically relevant body fluids such as human urine. The present study starts from the rationale that the absorption properties of mesoporous silica can be modified since the pore walls exhibit a high concentration of silanol groups on the surface, which can be functionalized with different chemical species. Aminopropyl, *N*-(2-aminoethyl)-3-aminopropyl, and *N*,*N*,*N*′-tris-carboxymethyl ethylene diamine (TED) have been introduced onto mesoporous silica surfaces in order to selectively modulate peptide enrichment. Plasma and urine peptides were extracted from derivatized mesoporous silica beads and then profiled by MALDI-TOF MS. The reproducibility of the method was also evaluated for the beads with different groups, both for plasma and urine samples. Depending on the chemical group and the chromatographic features, different subproteomes in plasma and urine were extracted and converted into reproducible MALDI profiles.

EXPERIMENTAL SECTION

Reagents and Materials. Reagents for sol−gel synthesis, sodium silicate solution, fumed silica, tetraethylorthosilicate (TEOS), 3-aminopropyltriethoxysilane (APTES), and hexadecyltrimethylammonium bromide [$C_{16}H_{25}N(CH_3)_3Br$] (CTABr), were purchased from Sigma Aldrich, (St. Louis, MO, USA). Polyoxyethylene(10)isononylphenylether (Nonfix10), was obtained from Condea (Houston, TX, USA), *n*-(Trimethoxysilylpropyl)ethylenediaminetriacetic acid and trisodium salt (EDA-TAS, 50 wt.% in water) were purchased from Gelest Inc. (Tullytown, PA, USA). Pluronic P123 (poly(ethylene oxide)-poly(propylene oxide)-poly(ethylene oxide) triblock copolymer, $PEO_{20}PPO_{70}PEO_{20}$) was obtained from BASF (Mount Olive, NJ, USA). Acetonitrile (ACN, HPLC grade) and trifluoroacetic acid (TFA, ACS grade) were purchased from Merck (Darmstadt, Germany).

The MALDI matrix *R*-cyano-4-hydroxycinnamic acid (CHCA) was purchased from Fluka (St. Louis, MO, USA). Peptide and protein standards, for mass spectrometer external calibration, were prepared from the Sequazime peptide mass standard kit (Applied Biosystems, Framingham, MA, USA). Angiotensin I and adrenocorticotropic hormone, ACTH (clip 1−17), for the spiking experiment were purchased from Sigma (St. Louis, MO, USA).

The water used was obtained from a Milli-Q water purification system (Millipore, Bedford, MA, USA).

Preparation of Materials. *MSB-A and MSB-B Preparation.* Mesoporous silica beads A and B were obtained according to two different synthetic procedures described elsewhere (*24, 25*).

Preparation of Material SBA-15 and Large Pore Mesoporous Silica Materials. *SBA-15 Mesoporous Material.* SBA-15 mesoporous material has been synthesized using a triblock-copolymer neutral surfactant PEO_{20}-PPO_{70}-PEO_{20} (Pluronic P123) in accordance with the procedure described by Zhao et al. (*26*). In a typical preparation, 4.0 g of Pluronic P123 was dissolved in 30 g of water and 120 g of 2 M HCl solution with stirring at 35 °C. Then 8.50 g of TEOS was added to the solution under vigorous stirring at 35 °C and maintained like this for 20 h. The mixture was aged at 80 °C overnight without stirring. The solid product was recovered, washed, and air-dried at room temperature.

Large Pore Mesoporous Silica Material. Large pore mesoporous silica spheres were synthesized by using TEOS as the silica source, P123 as the template, CTABr as the cosurfactant, and ethanol as the cosolvent. Typically, 0.3 g of triblock copolymer P123 and 0.05 g of CTABr were dissolved in a solution formed by mixing 6 mL of 2 M HCl, 3 mL of H_2O, and 2.5 mL of ethanol. Then, 1 mL of TEOS was added to the aqueous solution at room temperature under magnetic stirring. The reactant molar ratio TEOS/P123/CTAB/HCl/EtOH/H_2O in the final reaction mixture was 1:0.011:0.031:2.67:9.18:116. After 30 min of stirring, the solution was transferred to a Teflon-lined steel Parr autoclave and heated at 80 °C for 5 h and then kept at 120 °C for 12 h. The white precipitate was recovered by filtration, dried at 90 °C for 24 h, and calcined in air at 550 °C for 5 h to remove the templates.

Preparation of Functionalized MSB-C, MSB-D, and MSB-E. In the preparation of 3-aminopropyl mesoporous silica (MSB-C) 0.6 g of calcined mesoporous material SBA-15 were suspended and stirred for 40 h in a solution obtained by dissolving 2.5 mL of 3-aminopropyltriethoxysilane in 10 mL of ethanol at room temperature. The suspension had been filtered, washed, and dried.

In the preparation of *N*-(2-aminoethyl)-3-aminopropyl mesoporous silica (MSB-D), 0.6 g of calcined mesoporous material SBA-15 was suspended and stirred for 8 h in a solution obtained by dissolving 2.3 mL of *N*-(2-aminoethyl)-3-aminopropyltrimethoxysilane in 10 mL of ethanol under reflux. The suspension was filtered, washed, and dried.

In the preparation of *N*-(3-propyl) ethylenediaminetriacetic acid, trisodium salt mesoporous silica (MSB-E) and 0.4 g of calcined large pore mesoporous silica were suspended in a solution obtained by dissolving 1.0 mL of *N*-(trimethoxy silylpropyl)ethylenediaminetriacetic acid and trisodium salts 50% in water. The suspension was stirred under reflux for 6 h and then filtered, washed, and dried.

Material Characterization. All of the samples were characterized by X-ray diffraction on powder (XRD), thermogravimetrical analysis (TG), energy dispersive spectroscopy (EDS), X-ray microanalysis, and nitrogen adsorption−desorption isotherms. The XRD spectra were acquired on a Philips PW1710 diffractometer using Cu−Kα radiation (40 kV, 20 mA) over the range $1° < 2\theta < 15°$ with a rate scan of 0.005 2θ/s. TG analyses were carried out with a Netzsch STA 409 apparatus between 20 and 850 °C at a ramp of 10 °C/min in air with a flow rate of 5 cc/min. EDS chemical analyses were performed using a scanning electron microscope FEI Quanta 200.

Surface area of the samples was obtained by Brunauer-Emmet and Teller (BET) linearization in the pressure range 0.05−0.2 P/P_0. The nitrogen adsorption−desorption volumetric isotherms at 77 K were measured on a Micrometritics Asap 2010 apparatus. Average pore diameter was calculated according to the BJH (Barret−Joyner−Halenda) model applied to the desorption branch of the isotherm.

Plasma Collection. Venous blood samples were obtained from a total of 10 healthy adult males (age range 25−45 years) after they provided written informed consent.

Blood intended for plasma preparation was collected into the following tubes: BD Plus Plastic K2EDTA, 10 mL, # 367525 (BD Bioscience, Franklin Lake, NJ, USA). The samples were centrifuged at 1300*g* for 10 min under refrigerated conditions (2−6 °C). The resultant plasma was immediately transferred into 2 mL Eppendorf vials and frozen in aliquots at −80 °C.

Urine Collection. Midstream, first-void morning urine samples were collected from healthy consenting male volunteers after they provided written informed consent. For each participant, the urine sample (150 mL) collected in standard urine container flasks without additives or preservatives, was centrifuged at 1000*g* for 10 min at 4 °C. The supernatant was aliquoted and immediately stored at −80 °C.

Preparation of Samples. MSB were incubated with the plasma or urine sample for 1 h at room temperature. The beads were subsequently separated from the supernatant by centrifugation, and the washing step was performed according to the protocol optimized for each bead functionality (see the next subsections). The bound peptides were eluted using the appropriate CHCA solution, and 1 μL of this eluate was then deposited on the MALDI probe and analyzed by MALDI-TOF.

MSB Protocols for Human Plasma Peptidome Harvesting. For MSB-A and MSB-B, which have no functionalities, we used the following protocol. Briefly, aliquots (5 mg) of MSB were mixed with 500 μL of diluted human plasma sample (100 μL of plasma in 400 μL of deionized water) and shaken at room temperature for 1 h. The suspension was centrifuged at 2000*g* for 2 min, and then the MSB were separated from the supernatant and washed with deionized water (4 × 100 μL). After the last wash, bound species were directly extracted into 100 μL of a matrix solution, made up of 4 mg/mL CHCA in a 1:1 (v/v) mixture of acetonitrile and 0.1% TFA.

For MSB-C and MSB-D, with, respectively, the aminopropyl and *N*-(2-aminoethyl)-3-aminopropyl groups, two sets of experimental conditions for peptide harvesting were tested. In a first set of experimental conditions, aliquots (5 mg) of beads were preconditioned with 250 μL of 25 mM Tris HCl at pH 8.8 for 5 min. MSB were then mixed with 500 μL of diluted human plasma sample (100 μL of plasma in 400 μL of deionized water) and shaken at room temperature for 1 h. The suspension was centrifuged at 2000*g* for 2 min, and then the MSB were separated from the supernatant and washed with 25 mM Tris HCl at pH 8.8 (2 × 100 μL). In a second set of experimental conditions, aliquots (5 mg) of beads were directly mixed with 500 μL of diluted human plasma sample (100 μL of plasma in 400 μL of deionized water) and shaken at room temperature for 1 h. The suspension was centrifuged at 2000*g* for 2 min, and then the MSB were separated from the supernatant and washed with 25 mM Tris HCl at pH 8.8 (2 × 100 μL). In both cases, after the last wash, the bound species were directly extracted into 100 μL of a matrix solution, made up of 4 mg/mL CHCA in a 1:1(v/v) mixture of acetonitrile and ammonium formate (100 mM). To determine the pH value for optimal biomarker elution, the pH of the elution solution was adjusted to the values of 3, 4, and 5.

For MSB-E, a surface-derivatized with the TED group, we adopted the following protocol. Aliquots (5 mg) of beads were preconditioned with 60 μL of HCl 10 mM, followed by 60 μL of ammonium acetate buffer at pH 6.6; this process was repeated twice. The MSB were then mixed with 500 μL of diluted human plasma sample (100 μL of plasma in 400 μL of deionized water) and shaken at room temperature for 1 h. The suspension was centrifuged at 2000*g* for 2 min, and then the MSB were separated from the supernatant and washed twice with ammonium acetate buffer at pH 6.6, followed by a third washing step with 100 μL of deionized water. After the last wash, the bound species were directly extracted into 100 μL of a matrix solution, made up of 4 mg/mL CHCA in a 1:1 (v/v) mixture of acetonitrile and 0.5% TFA. Extraction conditions were also tested in a solution of CHCA in ACN and formic acid (70:30 v/v).

In all preparations, after centrifugation at 2000*g* for 2 min, 1 μL of supernatant CHCA solution with the extracted peptides was analyzed by MALDI-TOF MS. The samples were manually spotted by a pipettor onto the MALDI probe.

MSB Protocols for Human Urine Peptidome Harvesting. For nonderivatized MSB-A and MSB-B, the following protocol was adopted. Aliquots (2 mg) of MSB were mixed with 125 μL of 4-fold concentrated human urine sample and shaken at room temperature for 1 h. The suspension was centrifuged at 2000*g* for 2 min, and then the MSB were separated from the supernatant and washed with 0.1% TFA (4 × 100 μL). After the last wash, the bound species were directly extracted into 15 μL of a matrix solution, made up of 4 mg/mL CHCA in a 1:1 (v/v) mixture of acetonitrile and 0.1% TFA.

For MSB-C and MSB-D, derivatized, respectively, with the aminopropyl and *N*-(2-aminoethyl)-3-aminopropyl groups, two sets of experimental conditions for peptide harvesting were tested. In a first set of experimental conditions, aliquots (2 mg) of beads were preconditioned with 50 μL of 25 mM Tris HCl at pH 8.8 for 5 min. The MSB were then mixed with 125 μL of 4-fold concentrated human urine sample and shaken at room temperature for 1 h. The suspension was centrifuged at 2000*g* for 2 min, and then MSB were separated from the supernatant and washed with 25 mM Tris HCl at pH 8.8 (2 × 100 μL) and subsequently with deionized water (2 × 100 μL). In a second set of experimental conditions, aliquots (2 mg) of beads were directly mixed with 125 μL of 4-fold concentrated human urine sample and shaken at room temperature for 1 h. The suspension was centrifuged at 2000*g* for 2 min, and then the MSB were separated from the supernatant and washed with 25 mM Tris HCl at pH 8.8 (2 × 100 μL). In both cases, after the last wash, bound species were directly extracted into 40 μL of a matrix solution, made up of 4 mg/mL CHCA in a 1:1 (v/v) mixture of acetonitrile and ammonium formate (100 mM, pH 3).

For MSB-E, surface-derivatized TED, we adopted the following protocol. Aliquots (2 mg) of beads were preconditioned with 60 μL of 10 mM HCl, followed by 60 μL of ammonium acetate buffer at pH 6.6; this process was repeated twice. The MSB were then mixed with 120 μL of a 4-fold concentrated human urine sample, and the resulting slurry was shaken at room temperature for 1 h. To determine the pH value for optimal biomarker harvesting, the pH of the resulting slurry was also adjusted to pH 4.5. The suspension was centrifuged at 2000*g* for 2 min, and then the MSB were separated from the supernatant and washed twice with 100 μL of ammonium acetate buffer at pH 6.6, followed by a third washing step with 100 μL of deionized water. After the last wash, the bound species were directly extracted into 60 μL of a matrix solution, made up of 4 mg/mL CHCA in a 1:1(v/v) mixture of acetonitrile and 0.5% TFA.

In all preparations, after centrifugation at 2000*g* for 2 min, 1 μL of supernatant CHCA solution with the extracted peptides

Scheme 1. Functionalization of Mesoporous Silica

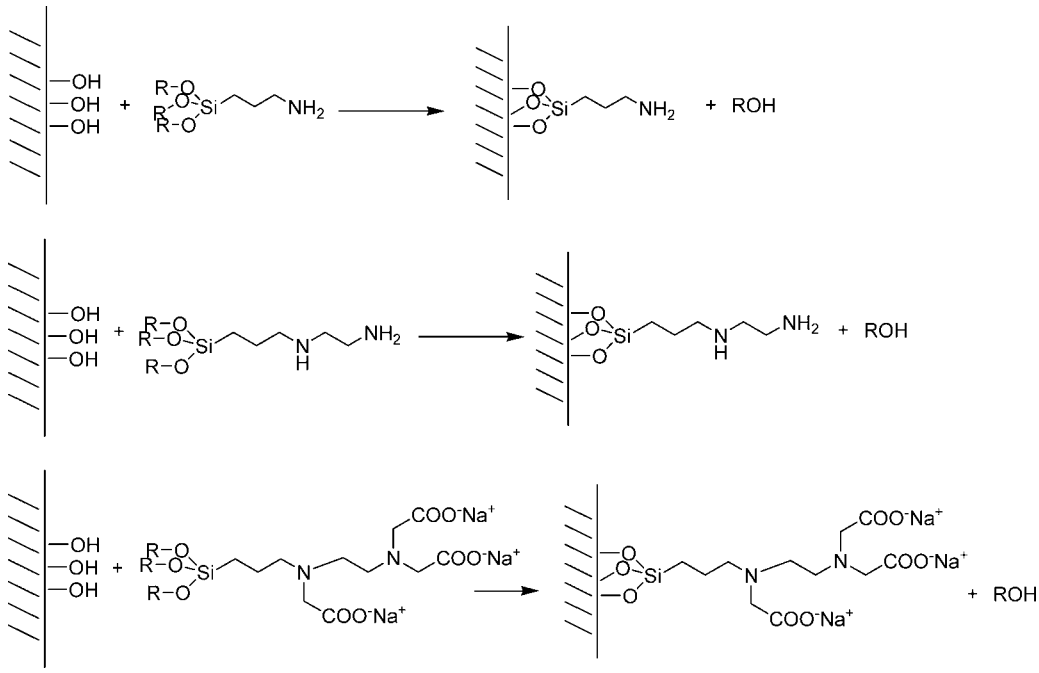

was analyzed by MALDI-TOF MS. The samples were manually spotted by a pipettor onto the MALDI probe.

Urine Sample Processing with Standard Peptides. Urine samples were spiked with angiotensin I and adrenocorticotropic hormone, ACTH (clip 1−17), at eight different concentrations: 1000, 500, 250, 125, 62.5, 26, 6.5, and 3.7 ng/mL for angiotensin I, and 1614, 807, 404, 202, 101, 42, 10.5, and 6 ng/mL for ACTH (clip 1−17). The samples were processed with MSB-C as described in the previous section in three independent assays.

MALDI MS Analysis. MALDI MS analysis was performed on a MALDI-TOF mass spectrometer (Voyager DE-STR, Applied Biosystems, Foster City, CA) equipped with a 337 nm nitrogen laser. Analyses were performed in linear positive-ion mode using delayed extraction. The acceleration voltage was 20 kV, the guide wire was 0.05% of the accelerating voltage, the grid voltage was 91.5%, and the delay time was 220 ns. Five 100-laser shots were averaged for each mass spectrum. All spectra were processed using Data Explorer Software (Applied Biosystems, Framingham, MA). All experiments were carried out at least in triplicate to ensure the reproducibility of the spectra. All signals with a signal-to-noise (S/N) ratio > 10 in a mass range of 1100−10000 for plasma and 1100−6000 for urine were collected in the Data Explorer Software. Peptide sequencing was carried out on a 4800 MALDI-TOF/TOF mass spectrometer (Applied Biosystems, Foster City, CA) equipped with a neodymium:yttrium−aluminum-garnet laser emitting at $\lambda = 355$ nm with a 200-Hz firing rate.

RESULTS AND DISCUSSION

The possibility of synthesizing mesoporous materials with regularly sized pores by means of the supramolecolar templating of a sol−gel process represents a starting point for the design of functional nanostructured materials. The MSB used in our approach belong to the class of ordered mesoporous silica synthesized for the first time in 1992 by the hydrolysis and condensation of inorganic precursors (the sol−gel process) in the presence of surfactant micelles (templates) (*27*).

The term ordered in this context means that the pores are ordered. It is widely accepted that when the mesopore diameter is sufficiently large for the comfortable entrapment of biomolecules, analytes penetrate deep into mesoporous networks rather than become adsorbed onto the external surface (*28*). The analytes entrapped by the mesoporous channels and consequently the resulting peptidomic profile of a given body fluid or complex protein mixture depend greatly on the size of the mesopores. Another way to modulate the selectivity of substrates may be by introducing functional groups. Indeed, it has been demonstrated that 17 and 70 nm pore sized aminopropyl-coated glass beads were able to adsorb serum peptides, but in a number ranging from one to a few dozens (*23*). On the contrary, hundreds of peptides were retained when mesoporous silica particles (MSB-A and MSB-B) containing pores with a size in the range of 2−3 nm were used (*21*). Therefore, we prepared a series of hybrid mesoporous silica in order to differentially modulate the selective binding and enrichment of low molecular weight proteins (LMWP) from plasma and urine, without significantly changing the physical properties (pore size, pore volume, and surface area) of the previously used MSB-A and MSB-B (*21*).

Briefly, hybrid inorganic−organic materials are produced when chemically active groups are covalently linked to the inorganic framework of mesoporous materials either by postsynthesis grafting or by the simultaneous condensation of siloxane and organic siloxane precursors, in which the latter contain a nonhydrolyzable Si−C bond (*29*).

In our case, three hybrid materials with different functional groups, namely, aminopropyl-, *N*-(2-aminoethyl)-3-aminopropyl-, and *N*-(3-propyl) ethylenediaminetriacetic acid, were prepared by postsynthesis modification of two different mesoporous silica obtained using Pluronic P-123, a triblock-copolymer neutral surfactant. The derivatization procedure is shown in Scheme 1. The derivatized particles MSB-C, MSB-D, and MSB-E were characterized according to analyses described in the Experimental Section to obtain information on the size, pore size, shape, surface area, and pore volume (more details on the materials are available in Supporting Information). The beads show an irregular shape, with the average pore size being approximately 4 nm for MSB-C and MSB-D, and 7 nm for MSB-E, and surface area in the order of 200 to 300 m^2/g. A more detailed description of textural properties of these new hybrid materials along with the previously used silica A and B is reported in Table 1. As briefly reported in the Experimental

Table 1. Textural Properties of Mesoporous Silica Bead Platforms

MSB	Functional group	Pore size diameter[(a)]	Pore volume[(b)]	BET Surface area[(c)]
MSB-A	-O-	2.6 and 4.2	0.30	406
MSB-B	-OH	2.7	0.78	848
MSB-C	$-(CH_2)_3-NH_2$	4.3	0.39	273
MSB-D	$-(CH_2)_3-NH-(CH_2)_2-NH_2$	4.6	0.41	310
MSB-E	$-(CH_2)_3-N(-(CH_2)_2-N(-COO^-Na^+)-COO^-Na^+)-COO^-Na^+$	7.0	0.41	171

[a] Pore size is expressed in nm. [b] Pore volume is expressed in cm^3/g. [c] Surface area is expressed in m^2/g.

Section under the paragraph on material preparation, MSB can be readily synthesized by a simple, inexpensive procedure. Additionally, given the good mechanical properties, (rigidity and stability), MSB can act as an excellent substrate for the pretreatment of body fluids.

Plasma and urine represent convenient diagnostic specimens for clinical analysis. Metabolites and peptides from these body fluids have the potential to serve as reliable indicators of the progression from a normal to a diseased state. Human urine contains the proteins filtered from blood within the glomerulus as well as the proteins secreted from the kidneys and the urogenital tract. Changes in kidney and urogenital tract function may be detected in the urine proteome. In addition, as a filtrate of blood, urine contains protein components that are similar to those found in the blood. Therefore, pathological changes in human organs, which could be found in blood, may also be reflected and detected in urine. In this sense, urine proteome analysis could be used in disease diagnostics (*30*).

In spite of multidimensional liquid chromatography-MS, which is usually unsuitable for clinical high-throughput screening, MALDI-TOF MS represents a key tool for rapidly analyzing clinical samples. Unfortunately, salts, lipids, and high concentrations of proteins in plasma as well as high concentrations of salts and metabolic wastes in urine make it difficult to detect and analyze peptides by MS. MSB represent a rapid procedure for reducing plasma and urine complexity prior to mass spectrometric analysis.

We have tested the new derivatized mesoporous silica beads for the generation of molecular signatures from plasma and urine samples. In MSB-A and MSB-B, previously tested on plasma only, peptide harvesting is largely regulated by the mesoporous properties and the electrostatic interactions of the silica (MSB-A) and the silanol groups (MSB-B) with the peptides (*21*). In the new hybrids, MSB-C, MSB-D, and MSB-E, weak basic and acid functionalities present on the surface differently modulate the electrostatic interactions toward a particular subset of negatively or positively charged peptides. In particular, in MSB-C, the aminopropyl group has one ion-exchange site with a pK_a of 9.8, while MSB-D, which contains both a primary and secondary amine (PSA), exhibits two ion-exchange sites (pK_a 10.1 and 10.9). MSB-E, derivatized with the chelating *N*,*N*,*N*′-triscarboxymethyl ethylene diamine group (TED), offers the possibility of forming pentadentate complexes when used in conjunction with specific metal ions used for the separation of proteins (*31*). Moreover, TED contains weak acid groups whose conjugate bases can act as weak cation exchangers; therefore, MSB-E also possesses cation exchange properties in addition to its chelating character. In this exploratory study, we tested this substrate as a weak cation exchanger. More detailed and additional investigations are planned by our group to study the feasibility of using this substrate as an immobilized metal affinity chromatography (IMAC) material (*32*).

In Scheme 2, we illustrate the workflow of the derivatized MSB for MALDI-TOF analysis of plasma and urine peptidome. It is divided into four main steps: adsorption, separation, washing, and extraction.

In the first step, a small amount of the particles are simply suspended in plasma or urine and left to act as sponges. During this step, only peptides and proteins with sizes smaller than or comparable to the pore size are adsorbed into the mesochannels. Moreover, given the specific chemical functionality present on the mesoporous surface, the adsorption process will also be driven by the electrostatic interactions of the positively (arginine, lysine, histidine) or negatively (glutamic and aspartic acids) charged residues of the peptides and proteins present in the plasma or urine, with the chemical groups conjugated to the mesoporous silica surface. Typically, the adsorption of body fluid peptides into MSB can often change with pH. Thus, in a neutral solution, MSB-C and MSB-D (pK_a around 10) retain a positively charged surface, which can adsorb negatively charged peptides. On the contrary, MSB-E possesses a negatively charged surface, which can adsorb positively charged peptides. From this point of view, our strategy in choosing the appropriate experimental conditions was driven by the chemical group conjugated to silica pore walls. In the Experimental Section, we report the detailed conditions used for each derivatized surface. Different pH values were tested in order to ensure that the maximum number of peptides were captured from plasma and urine. We found that for MSB-C, a primary amine phase, and MSB-D, a primary and secondary amine phase (PSA), better working conditions (in terms of plasma and urine peptide adsorption) were obtained in a pH range between 8 and 9, rather than under neutral conditions (data not shown). For MSB-E, containing the TED group, we also observed a strong pH dependence on the adsorption efficiency. In Figure 1, we report the comparison between the MALDI-TOF mass spectra of urinary peptides captured by MSB-E at two different pH values. When the (concentrated) urine sample was incubated with MSB-E at pH 6.6, we observed an increase in the number of peptides detected by MALDI-TOF mass spectrometry (Figure 1a) in comparison to that at pH 4.5 (Figure 1b).

In our experience with MSB, we found that the separation and washing steps were critical in order to ensure MALDI spectra of good quality. Separation of the beads from the supernatant requires gentle centrifugation and preferably a single pipettor aspiration, in order to avoid diffusion of adsorbed peptides into the mother liquor. At the same time, washing needs to be as fast as possible. The washing step is crucial in order to

Scheme 2. Workflow Diagram of Plasma and Urine Sample Preparation with Mesoporous Silica Beads (MSB)

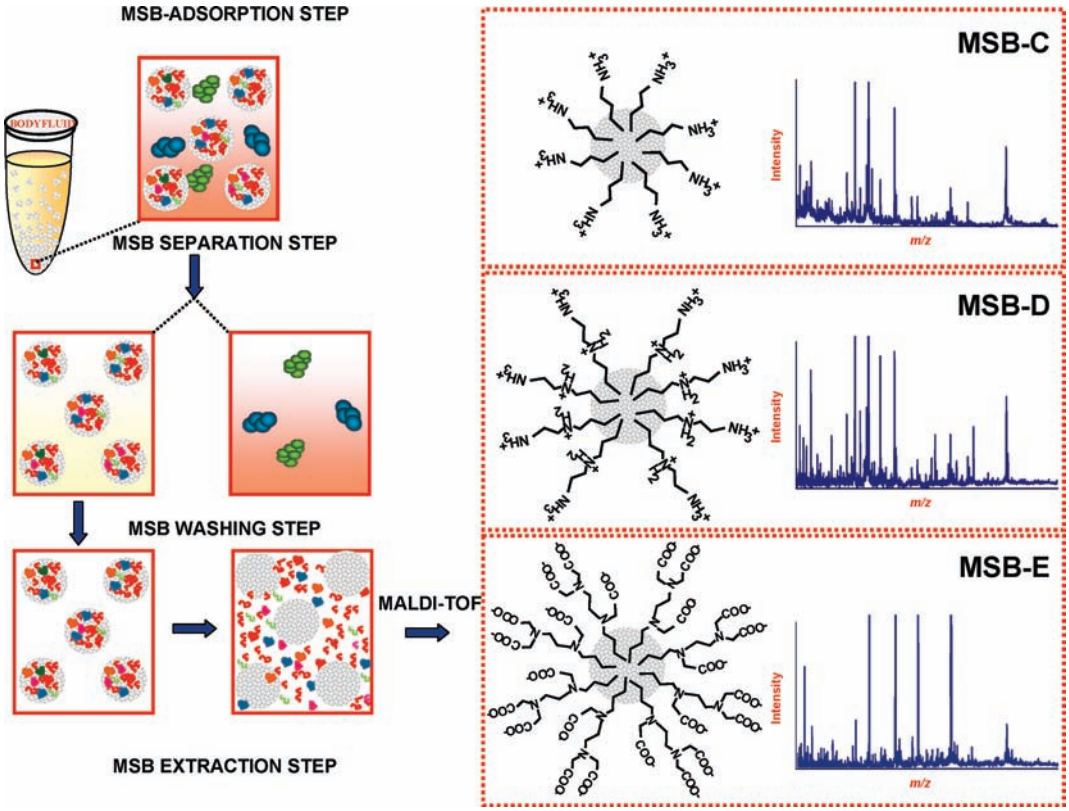

eliminate salts and other contaminants, which can interfere with MS analysis. Too many washes should be avoided due to the risk of sample loss. To overcome these problems, different washing conditions were tested, and the best compromise was found when the number of washes did not exceed three (data not shown).

Our derivatized beads have ionizable groups; therefore, the elution parameters are affected by a number of factors, and the ionic strength, temperature, and pH of the eluent may play a crucial role. In order to prevent the degradation of the human plasma and urine peptides harvested on the beads and to make

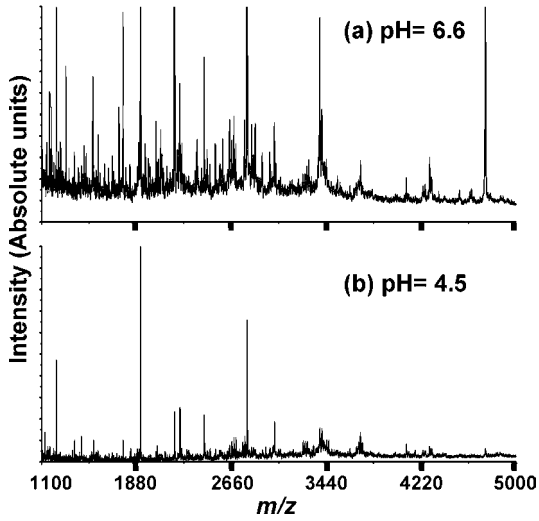

Figure 1. MALDI-TOF spectra of peptides extracted from a urine sample by weak cation mesoporous silica beads using two different pH values during the adsorption step. The resulting spectrum at pH 6.6 (a) reveals an increased number of peptide peaks compared to that in the spectrum at pH 4.5 (b).

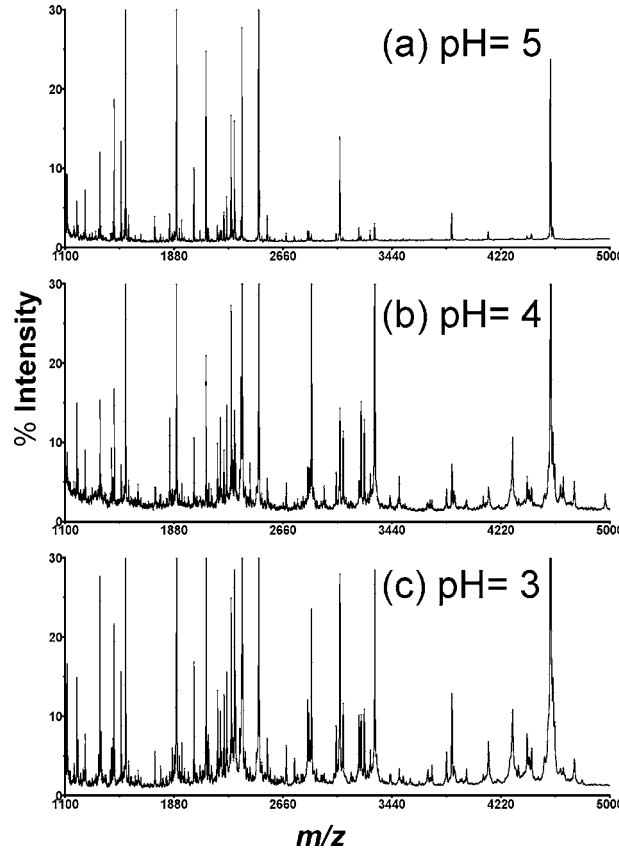

Figure 2. Effect of pH during the extraction step, on the mass spectral profiles of plasma processed with mesoporous silica beads derivatized with an aminopropyl group (MSB-C). The figure shows the change in the plasma profile when plasmatic peptides are extracted from the beads at pH 5 (a), pH 4 (b), and pH 3 (c). The optimal MS profile is obtained using a CHCA solution in ACN and 100 mM ammonium formate at pH 3 (c).

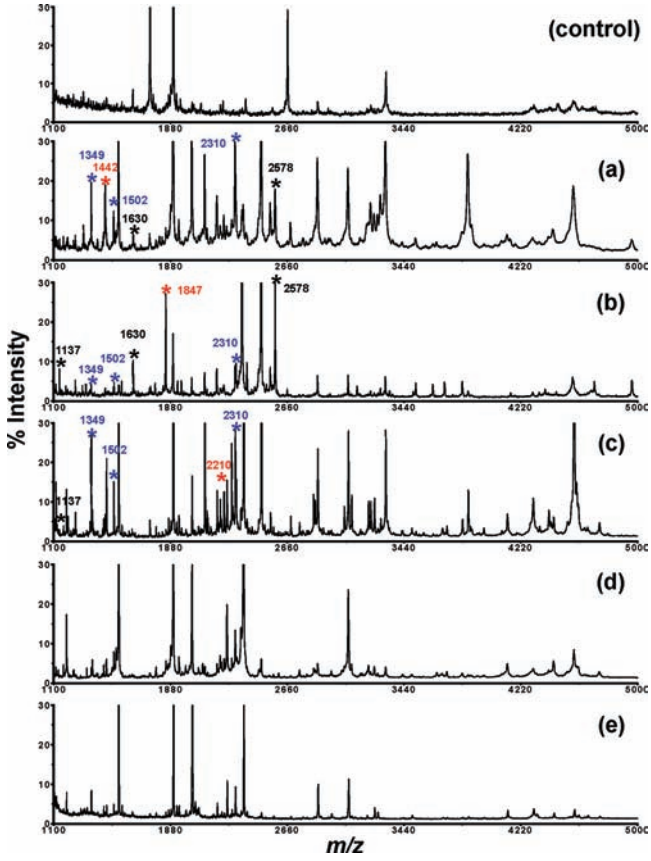

Figure 3. MALDI-TOF spectra of peptides extracted from human plasma using different mesoporous silica beads (MSB). Human plasma samples were incubated with mesoporous beads followed by washing and elution with a matrix CHCA solution. Eluates from MSB-A (a), MSB-B (b), MSB-C (c), MSB-D (d), and MSB-E (e) were analyzed by MALDI-TOF MS. The top panel (control) shows the MALDI spectrum of an unprocessed plasma sample. Asterisks mark peaks, sequenced by MS/MS experiments, which are retained by a single MSB (indicated in red), by two different MSB (indicated in black), or by all three MSB analyzed (indicated in blue).

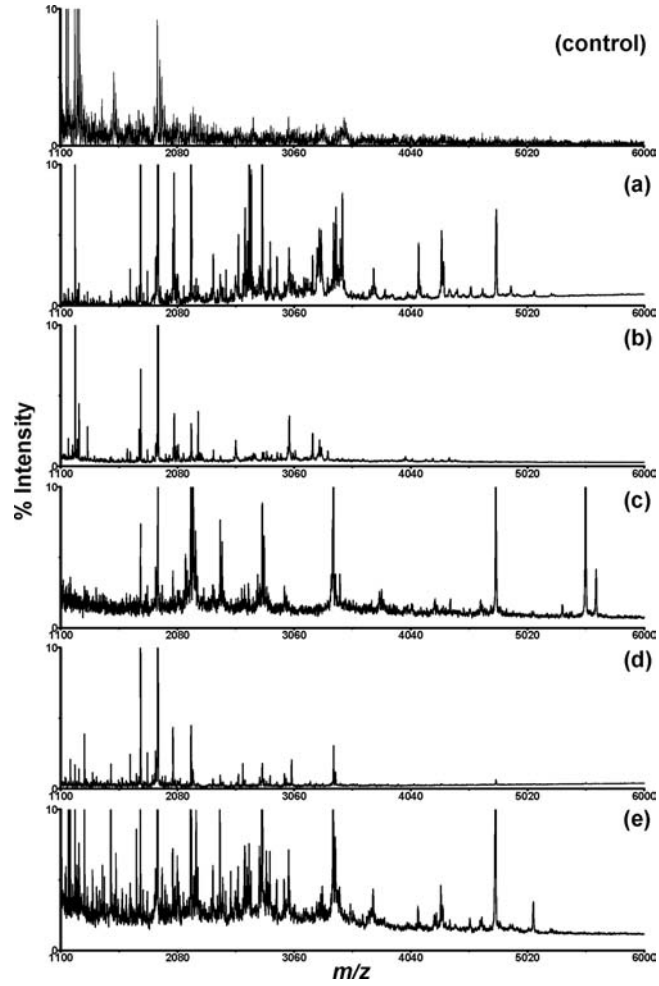

Figure 4. Processed MALDI spectra of peptides extracted from human urine samples using five different beads. The mass range from 1100 to 6000 Da is shown. Human urine was analyzed using MSB-A (a), MSB-B (b), MSB-C (c), MSB-D (d), and MSB-E (e). The top panel (control) shows the MALDI spectrum of an unprocessed urine sample.

the analysis more rapid, one elution step at room temperature was preferred to fractionation, which requires more time. Moreover, the extraction was performed directly with the matrix solution for MALDI-TOF analysis. CHCA was used as the matrix because it is more suitable for peptide analysis compared to other matrices used for MALDI-MS (sinapinic acid or DHB). Different elution parameters, in particular the eluent composition and pH, were assessed in order to maximize the elution of all of the adsorbed peptides in one step. We observed different MALDI MS spectra when plasma peptides were extracted from MSB-C at three different pH values (Figure 2). Comparing elution at pH 5 (Figure 2, panel a) and elution at pH 4 (Figure 2, panel b), the most significant differences were observed with increased mass signals in the *m/z* range between 2600 and 5000 at pH 4. The most efficient peptide extraction was accomplished at pH 3. We observed no substantial differences in peptide patterns when comparing the MALDI spectra at pH 4 and 3 (Figure 2, panels b and c) apart from a substantial variation in the relative signal intensities. Therefore, for anionic mesoporous beads, optimal elution conditions were obtained with a CHCA solution in ACN and 100 mM ammonium formate at pH 3. Plasmatic and urinary peptides bound to siloxane (MSB-A) and silanol (MSB-B) beads were eluted satisfactorily with a CHCA solution in ACN and 0.1% TFA 1:1 (v/v). For cationic beads, a solution of CHCA in ACN and 0.5% TFA (50:50, v/v) was more efficient compared to a solution of ACN and formic acid (70:30, v/v, data not shown).

Table 2. Mean Number of Peaks Detected by Each Bead Type from Human Plasma

	human plasma		
bead type	total peaks detected[a]	peaks detected range 1100−5000 Da	peaks detected range 5000−10000 Da
MSB-A	122	117	5
MSB-B	138	130	8
MSB-C	160	147	13
MSB-D	114	110	4
MSB-E	119	119	0

[a] The number of peaks detected in the range between 1100 and 10000 Da with a S/N > 10.

The working conditions used for capturing, washing, and eluting the plasma and urine peptides, in order to ensure the best MALDI-TOF profiling in terms of the number of peaks detected, reproducibility, signal-to-noise ratio, and signal intensity are summarized in Tables S1 and S2 of Supporting Information.

Representative examples of the profiles of human plasma and urine obtained with different bead types, using the experimentally determined optimal conditions, are shown in Figures 3 and 4.

The use of MSB appears to provide sufficiently rich fingerprints of plasma and urine, as revealed by comparing the mass spectra of unprocessed plasma (Figure 3, control) and urine

Table 3. Mean Number of Peaks Detected by Each Bead Type from Human Urine

	human urine
bead type	peaks detected[a] range 1100−6000 Da
MSB-A	92
MSB-B	40
MSB-C	82
MSB-D	44
MSB-E	199

[a] The number of peaks detected in the range between 1100 and 6000 Da with a S/N > 10.

(Figure 4, control) to mass spectra generated after MSB processing (Figure 3 and 4).

All MALDI spectra were generated using the same settings in the range from 800 to 10000 Da, imposing the stringent condition of a signal-to-noise ratio of higher than 10 for peak detection (see Experimental Section). Apart from some peak clusters related to the matrix CHCA used in MALDI analysis in the range between 800 and 1100 Da, most of the detected signals for all of the bead functionalities were in the range from 1100−5000 for plasma and 1100−6000 for urine, exhibiting some sporadic high intensity peaks outside this range. The numbers of peaks detected over the entire range from 1100 to 10000, in the case of plasma samples processed with the various kinds of silica, are reported in Table 2. Among all bead types, aminopropyl-derivatized MSB-C provided the best performance in resolving the plasma peptidome (160 peaks detected), thus indicating that mesoporous silica materials with a pore size of roughly 4 nm and with a surface area of around 270 m^2/g could be the starting point for future chemical tailoring aimed at increasing the affinity for plasma peptides. Our results extend the findings of Geho and co-workers, who used aminopropyl-coated 17 and 70 nm pore-sized glass beads from Sigma for serum fractionation, obtaining, however, only a few dozen peptides (*23*). The data presented here (Table 2) strongly suggest that, besides functionalization, tuning the pore size, pore volume, and the surface area of mesoporous silica may also be a viable approach to biomarker harvesting. Future development of our technology along this line will include surface functionalization with alkyl and aryl groups, which could increase the hydro-

Table 4. Peptides Identified by MALDI-MS/MS Fragmentation from Human Plasma after Processing on MSB-A, MSB-B, and MSB-C

observed mass	theoretical mass	mass error	MS/MS sequence	signal-to-noise ratio		
m/z	*m/z*	Da	peptide	MSB-A	MSB-B	MSB-C
1136.67	1136.61	0.06	MRDVVLFEK		68.30	11.66
1348.72	1348.66	0.06	RHDWGHEKQR	115.68	13.47	165.44
1441.84	1441.79	0.05	MKPVPDLVPGNFK	101.69		
1501.80	1501.74	0.06	MELERPGGNEITR	39.48	12.82	155.46
1629.89	1629.83	0.06	DSHSLTTNIMEILR	10.1	50.83	
1846.92	1846.87	0.05	ADSGEGDFLAEGGGVRGPR		224.25	
2209.65	2209.59	0.06	KHNLGHGHKHERDQGHGHQ			79.46
2310.21	2310.16	0.05	HTFMGVVSLGSPSGEVSHPRKT	115.44	40.33	231.00
2578.28	2578.23	0.05	DSHSLTTNIMEILRGDFSSANNR	63.05	257.95	

Table 5. Reproducibility Assessment for Peak *m/z* and Signal Intensity in Acquired MALDI TOF Spectra from Replicate Analyses ($n = 3$) of Human Plasma Samples Processed by Derivatized Mesoporous Silica Beads

Human Plasma								
MSB-C			MSB-D			MSB-E		
m/z	CV (%) on *m/z*	CV (%) on height	*m/z*	CV (%) on *m/z*	CV (%) on height	*m/z*	CV (%) on *m/z*	CV (%) on height
1350.70	0.0087	14.11	1515.63	0.049	8.42	1084.54	0.0023	6.41
1451.77	0.019	1.93	1532.29	0.022	4.63	1098.55	0.0018	21.77
1501.14	0.0094	17.30	1880.90	0.017	10.64	1184.94	0.0073	5.68
1896.31	0.012	9.20	1896.49	0.017	1.96	1921.70	0.015	11.09
2106.99	0.014	31.28	1936.06	0.015	6.06	2022.81	0.0023	4.11
2289.36	0.014	5.31	2210.97	0.017	10.57	2046.83	0.0064	9.84
2484.54	0.013	33.08	2256.66	0.014	9.80	2193.15	0.0023	5.37
3215.56	0.017	8.92	2349.95	0.013	9.45	2314.22	0.0022	4.10
3315.67	0.014	9.54	2366.77	0.012	10.29	2866.20	0.00092	3.31
4576.47	0.017	12.94	3066.33	0.0091	7.59	3113.44	0.00023	7.69
mean	0.014	14.36		0.018	7.94		0.0041	7.94

Table 6. Reproducibility Assessment for Peak *m/z* and Signal Intensity in Acquired MALDI TOF Spectra from Replicate Analyses ($n = 3$) of Human Urine Samples Processed by Derivatized Mesoporous Silica Beads

Human Urine								
MSB-C			MSB-D			MSB-E		
m/z	CV (%) on *m/z*	CV (%) on height	*m/z*	CV (%) on *m/z*	CV (%) on height	*m/z*	CV (%) on *m/z*	CV (%) on height
1181.33	0.028	16.83	1369.69	0.0054	17.49	1219.95	0.0094	23.69
1770.73	0.020	32.05	1656.70	0.0057	8.29	2238.03	0.0026	10.68
1897.32	0.0021	4.14	1770.27	0.0066	1.72	1520.92	0.011	27.32
1914.97	0.031	33.71	1914.54	0.0067	0.00	1914.19	0.015	2.68
2194.99	0.041	5.85	2067.57	0.0044	7.56	2080.66	0.031	18.59
2439.33	0.046	7.55	2194.74	0.0034	13.58	2193.91	0.017	6.79
2619.08	0.0066	8.62	2439.99	0.018	9.65	2438.26	0.022	5.68
2793.13	0.043	20.31	2774.59	0.0079	13.76	2791.65	0.020	0.00
2978.65	0.028	32.23	2924.64	0.011	12.56	4293.66	0.017	1.09
3391.03	0.026	10.61	3415.09	0.022	11.68	4752.78	0.021	28.56
mean	0.027	17.17		0.0091	9.63		0.017	12.51

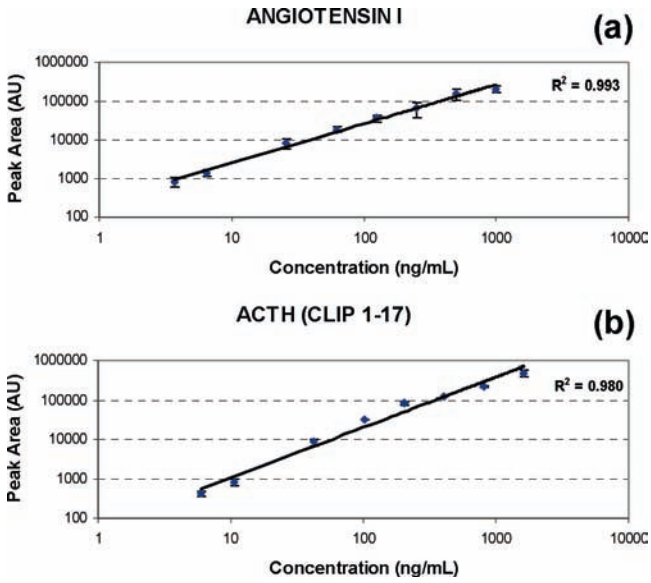

Figure 5. Peak areas of the tested peptides spiked in the urine sample, plotted against their concentrations. The assayed peptides are (a) angiotensin I (1297.51 *m*/*z*) and (b) adrenocorticotropic hormone (ACTH; clip 1−17; 2094.46 *m*/*z*). A linear equation is used in curve fitting. The error bars are the standard deviations of the mean peak areas.

phobicity of the mesoporous silica and allow the selective capture of hydrophobic peptides for mass spectrometric assays.

MSB-A and MSB-B, previously tested on plasma samples (*21*), have also been tested for urine in this investigation exhibiting very good mass coverage in the *m*/*z* range 1100−6000 (Figure 4, panels a and b). Urine analysis using MSB-A in fact produced 92 signals, while a lower number of peaks was generated in this range by MSB-B (40 peaks) (Table 3). MALDI spectra from anionic beads MSB-C and MSB-D show 82 and 44 peaks, respectively. Very high mass coverage is observed in the case of MSB-E with 199 peaks detected (Figure 4, panel e and Table 3). Mass profiles obtained from urine processed by MSB-C and MSB-D share many features in common as shown in Figure 4c and d, but closer examination and comparison of the *m*/*z* values and peak intensities reveal a higher efficiency for MSB-D at low *m*/*z*, ranging from 1100 to 1880 in comparison to that of MSB-C. In the case of plasma, a few common peaks are more abundant when MSB-D is used instead of MSB-C (Figure 3, panels c and d). One possible explanation for the lower efficiency of MSB-D in comparison to that of MSB-C is the different chemical functionalities present on the mesoporous surface. It may be speculated that the *N*-(2-aminoethyl)-3-aminopropyl groups of MSB-D possess higher selectivity toward plasma and urine components in comparison to that of the aminopropyl group of MSB-C.

For plasma samples, there are very few signals in the mass spectrum generated by MSB-E (Figure 3, panel e). Although valuable for selective binding studies, MSB-E does not provide the best choice for plasma peptidome profiling. On the contrary, this kind of beads significantly amplifies the peak detection of urine peptides as clearly shown in Figure 4e.

These results indicate that different mesoporous silica with unique surface characteristics produce different MALDI mass spectra for an identical plasma or urine sample; hence, these MSB could be used to obtain complementary proteomic information with high sample throughput.

To assess the selectivity of sample processing with MSB, as proof-of-principle we identified by MALDI-TOF/TOF some peaks, both from nonfunctionalized (MSB-A and MSB-B) and from functionalized (MSB-C) silicas. Therefore, in a preliminary analysis, we randomly selected for identification the following peaks, retained from plasma by MSB-A, MSB-B, and MSB-C: peak at *m*/*z* 1442, retained by MSB-A only; peak at *m*/*z* 1847, retained by MSB-B only; peak at *m*/*z* 2210, retained by MSB-C only; peaks at *m*/*z* 1630, and 2578, retained by MSB-A and MSB-B but not MSB-C; peak at *m*/*z* 1137, retained by MSB-B and MSB-C but not MSB-A; finally, peaks at *m*/*z* 1349, 1502, and 2310, retained by all three MSB examined. The selected peaks are marked with an asterisk in the mass spectra shown in Figure 3 panels a, b, and c. The amino acid sequences of each of the selected peptide are shown in Table 4, together with the corresponding mass errors and signal-to-noise ratios. Interestingly, peaks extracted selectively by a single MSB corresponded to specific peptides of unique sequence (Table 4), strongly suggesting that sample processing with MSB is compatible with peptidomic analysis. Moreover, even when the same peptide is extracted from plasma by more that one MSB, there is often a significant difference in the signal-to-noise ratio. For instance, the peptide at *m*/*z* 2578, retained by both MSB-A and MSB-B, is characterized by a signal-to-noise ratio of 63.05 in the mass spectrum of the MSB-A eluate and of 257.95 in the mass spectrum of MSB-B eluate, further suggesting that each MSB determines a significant increase in specific peptide components (Table 4).

Considering the stringent conditions used for peak detection, a signal-to-noise ratio of greater than 10, the MALDI spectra generated from plasma and urine, after MSB processing, resulted in a remarkable improvement in peak detection compared to that in the SELDI spectra reported in the literature (*23, 33*−*35*). In contrast to the SELDI chip arrays, MSB, with their greater surface area, can provide higher binding capacity, and moreover, the possibility of thoroughly washing the beads allows the effective removal of salts and other contaminants, which could negatively affect MALDI spectra quality. This particular limitation of SELDI, which resides in the small surface area of its flat chips directly used as MALDI targets, is also reported elsewhere (*36*). In a recent study, Tempst and co-workers specifically report that the use of porous particles for sample pretreatment is more sensitive than surface capture on chips because particles have a larger combined surface area than small-diameter spots (*14*).

Before peptidome analysis based on mass spectrometric screening can proceed from the bench to the bedside, a large number of important obstacles need to be overcome, among which are the valid and reproducible analyses of peptide patterns (*37, 38*). For this reason, we have investigated the reproducibility of the peptidome profiling of human plasma and urine by derivatized MSB in combination with MALDI-TOF MS. Plasma and urine samples were run in triplicate with all of the sample preparation methods, then the spectra obtained were used for data analysis. Triplicate MALDI spectral readouts of plasma and urine samples processed by the derivatized MSB are shown in Supporting Information (Figures S7 and S8).

The reproducibility of the mass spectra was evaluated with respect to the relative peak intensities and mass accuracy; variability was measured by coefficient of variance (CV). Tables 5 and 6 list CVs of the *m*/*z* values and the intensities of peaks randomly selected over a wide mass range for plasma and urine, respectively. In the plasma experiments, average CVs of 0.014%, 0.018%, and 0.0041% of the mean *m*/*z* values were obtained for MSB-C, MSB-D, and MSB-E, respectively. The average CV of the mean intensity values was 14.36% for MSB-C and 7.94% both for MSB-D and MSB-E (Table 5), ensuring good reproducibility for MALDI MS-based profiling studies. In the urine experiments, the average % CV corresponding to the mean *m*/*z* values was 0.027% for MSB-C, 0.0091% for MSB-D, and 0.017% for MSB-E. The mean CVs of the signal intensities for

Table 7. Accuracy and Precision Assessment of *m/z* Values for the Standard Peptides Spiked into Urine Sample and Processed by MSB-C MALDI-TOF MS

standard peptide				standard peptide			
angiotensin I (theoretical mass, MH^+ 1297.51)				ACTH (clip 1−17) (theoretical mass, MH^+ 2094.46)			
concentration (ng/mL)	mean[a] *m/z*	% error	CV (%) on *m/z*	concentration (ng/mL)	mean[a] *m/z*	% error	CV (%) on *m/z*
1000	1297.83	−0.025	0.06	1614	2094.83	−0.018	0.06
500	1297.82	−0.024	0.02	807	2094.90	−0.021	0.02
250	1297.09	0.032	0.02	404	2094.17	0.014	0.02
125	1297.38	0.010	0.02	202	2094.69	−0.011	0.01
62.5	1297.67	−0.012	0.02	101	2096.95	−0.023	0.02
26	1297.34	0.013	0.05	42	2097.18	0.013	0.03
6.5	1297.33	0.014	0.04	10.5	2096.06	0.019	0.04
3.7	1297.33	0.014	0.07	6.0	2097.11	0.017	0.04

[a] The *m/z* values are the means from three independent experiments.

10 urinary signals were 17.17% (ranging from 4% to 33%) for MSB-C, 9.63% (ranging from 0 to 17%) for MSB-D, and 12.51% (ranging from 0 to 28%) for MSB-E (Table 6).

In order to provide more information about the robustness, reproducibility, and linearity of the methodology, we added internal standards to urine before processing with MSB-C with a series of dilutions of angiotensin I (*m/z* 1297.51) and adrenocorticotropic hormone ACTH (clip 1−17) (*m/z* 2094.46). The analysis of 3 replicates of urine aliquots spiked with these two standard peptides at decreasing concentrations showed that there was a linear correlation between peak area and peptide concentration ($R^2 > 0.98$) in the range of 1 to 2000 ng/mL (Figure 5). We were able to detect these standard peptides in human urine with concentrations as low as 3.7 ng/mL for angiotensin I and 6.0 ng/mL for the fragment 1−17 of ACTH (Figure 5). Therefore, also for human urine, we confirmed the low-nanogram per milliliter sensitivity of the methodology, previously demonstrated for human plasma (*21*).

The precision and the accuracy of the MSB-MALDI-TOF MS methodology was evaluated as percentage error on the theoretical mass values, resulting for the tested standards with vaues <0.032% and 0.02% for *m/z* 1297.51 and 2094.46, respectively (Table 7).

Overall, these data with CVs obtained for both plasma and urine indicate that protein profiling by MSB, in combination with MALDI-TOF MS, is reliable and robust, in other words, reproducible and that valid peptide patterns are obtained, which ensure that the variations in the spectra reflect biological differences in protein concentration rather than systematic variability.

CONCLUSIONS

In summary, we have tested MSB with different surfaces for plasma and urine mass spectrometric profiling. Different conditions for adsorption/binding and elution of plasma and urine peptides have been accurately evaluated for each functionality to determine the best performances in terms of peptide extraction and MALDI data generations. MSB-A and MSB-B previously tested for plasma samples (*21*) have now been tested for urine, demonstrating a high efficiency in peptide enrichment. Aminopropyl derivatized MSB-C produced the highest number of peaks for plasma samples, whereas for urine, the largest number of peaks were obtained with TED functionalized MSB-E.

Derivatization of mesoporous silica materials with the aminopropyl group increases specific plasma peptide subset recognition in comparison to that of nonfunctionalized mesoporous silica materials. At the same time, TED groups on the mesoporous silica surface significantly amplify peak detection for urine peptides. These results indicate that different mesoporous silica with unique surface characteristics produce different MALDI mass spectra for identical plasma or urine samples; hence, these MSB could be used to obtain complementary proteomic information using high sample throughput. Predictably, robotic sample preparation will improve reproducibility compared to that of manual procedures; thus, we have plans to develop an automated sample procedure, starting from the sample incubation with the beads to spotting on the MALDI probe.

Finally, functionalized MSB can be readily prepared by a simple and low-cost procedure; the method described is fast and easy to perform for processing body fluids prior to MS analysis, thus minimizing the possible degradation of biological samples. We strongly believe that this platform is suitable for preliminary biomarker discovery studies.

ACKNOWLEDGMENT

We thank Dr. Christopher I. Fincham and Professor Susan Gerbi for critical reading of the manuscript and Dr. Marco Carbone for technical support. We are also indebted to Dr. Matthias Glükmann and Dr. Dietrich Merkel from Applied Biosystems (Darmstadt) for the skilled support in MS/MS sequencing. This work was supported in part by an AIRC 2005 grant, by a Ministero della Salute, Dipartimento dell' Innovazione (Direzione Generale della Ricerca Scientifica e Tecnologica) 2006 grant, and by a PRIN 2006 grant "Innovative approaches for the development of nanostructured devices for the analysis of plasma/tissue proteome in breast cancer" from the MIUR of Italy to R.T.

Supporting Information Available: Characterization of conjugated materials by nitrogen adsorption−desorption isotherms, average pore size distributions, and scanning electron microscopy; reproducibility studies on human plasma and urine peptidome profiling; and tables of working conditions used for plasma and urine processing. This material is available free of charge via the Internet at http://pubs.acs.org.

LITERATURE CITED

(1) Hortin, G. L., Jortani, S. A., Ritchie, J. C., Jr., Valdes, R., Jr., and Chan, D. W. (2006) Proteomics: a new diagnostic frontier. *Clin. Chem. 52*, 1218–22.

(2) Shen, Y., Kim, J., Strittmatter, E. F., Jacobs, J. M., Camp, D. G., II, Fang, R., Tolie, N., Moore, R. J., and Smith, R. D. (2005) Characterization of the human blood plasma proteome. *Proteomics 5*, 4034–4045.

(3) Villanueva, J., Philip, J., Chaparro, C. A., Li, Y., Toledo-Crow, R., DeNoyer, L., Fleisher, M., Robbins, R. J., and Tempst, P. (2005) Correcting common errors in identifying cancer-specific serum peptide signatures. *J. Proteome Res. 4*, 1060–1072.

(4) Xiao, Z., Luke, B. T., Izmirlian, G., Umar, A., Lynch, P. M., Phillips, R. K., Patterson, S., Conrads, T. P., Veenstra, T. D., Greenwald, P., Hawk, E. T., and Ali, I. U. (2004) Serum proteomic profiles suggest celecoxib-modulated targets and response predictors. *Cancer Res. 64*, 2904–2909.

(5) Conrads, T. P., Hood, B. L., Issaq, H. J., and Veenstra, T. D. (2004) Proteomic patterns as a diagnostic tool for early-stage cancer: a review of its progress to a clinically relevant tool. *Mol. Diagn. 8* (2), 77–85.

(6) Ekstrom, S., Wallman, L., Hok, D., Marko-Varga, G., and Laurell, T. (2006) Miniaturized solid-phase extraction and sample preparation for MALDI MS using a microfabricated integrated selective enrichment target. *J. Proteome Res. 5*, 1071–1081.

(7) Tirumalai, R. S., Chan, K. C., Prieto, D. A., Issaq, H. J., Conrads, T. P., and Veenstra, T. D. (2003) Characterization of the low molecular weight human serum proteome. *Mol. Cell. Proteomics 2*, 1096–1103.

(8) Gillette, M. A., Mani, D. R., and Carr, S. A. (2005) Place of pattern in proteomic biomarker discovery. *J. Proteome Res. 4* (4), 1143–1154.

(9) Ahmed, N., Oliva, K. T., Barker, G., Hoffmann, P., Reeve, S., Smith, I. A., Quinn, M. A., and Rice, G. E. (2005) Proteomic tracking of serum protein isoforms as screening biomarkers of ovarian cancer. *Proteomics 5*, 4625–4636.

(10) O'Farrel, P. H. (1975) High resolution two-dimensional electrophoresis of proteins. *J. Biol. Chem. 250*, 4007–21.

(11) Fiedler, G. M., Baumann, S., Leichtle, A., Oltmann, A., Kase, J., Thiery, J., and Ceglarek, U. (2007) Standardized peptidome profiling of human urine by magnetic bead separation and matrix-assisted laser desorption/ionization time-of-flight masss spectrometry. *Clin. Chem. 53*, 421–428.

(12) Hortin, G. L. (2006) The MALDI-TOF mass spectrometric view of the plasma proteome and peptidome. *Clin. Chem. 52*, 1223–1237.

(13) Cole, J. R., Dick, L. W., Jr., Morgan, E. J., and McGown, L. B. (2007) Affinity capture and detection of immunoglobulin E in human serum using an aptamer-modified surface in matrix-assisted laser desorption/ionization mass spectrometry. *Anal. Chem. 79*, 273–279.

(14) Villanueva, J., Philip, J., Entenberg, D., Chaparro, C. A., Tanwar, M. K., Holland, E. C., and Tempst, P. (2004) Serum peptide profiling by magnetic particle-assisted, automated sample processing and MALDI-TOF mass spectrometry. *Anal. Chem. 76*, 1560–1570.

(15) Liotta, L. A., Ferrari, M., and Petricoin, E. (2003) Clinical proteomics: written in blood. *Nature (London) 425*, 905.

(16) Navare, A., Zhou, M., McDonald, J., Noriega, F. G., Sullards, M. C., and Fernandez, F. M. (2008) Serum biomarker profiling by solid-phase extraction with particle-embedded micro tips and matrix-assisted laser desorption/ionization mass spectrometry. *Rapid Commun. Mass Spectrom. 22*, 997–1008.

(17) Feuerstein, I., Rainer, M., Bernardo, K., Stecher, G., Huck, C. W., Kofler, K., Pelzer, A., Horninger, W., Klocker, H., Bartsch, G., and Bonn, G. K. (2005) Derivatized cellulose combined with MALDI-TOF MS: a new tool for serum protein profiling. *J. Proteome Res. 4*, 2320–2336.

(18) Hobbs, S. K., Shi, G., and Bednarski, M. D. (2003) Synthesis of polymerized thin films for immobilized ligand display in proteomic analysis. *Bioconjugate Chem. 14*, 526–531.

(19) Vreeland, W. N., and Barron, A. E. (2002) Functional materials for microscale genomic and proteomic analyses. *Curr. Opin. Biotechnol. 13*, 87–94.

(20) Park, S. E., Ryoo, R., Ahn, W. S., Lee C. W., and Chang, R., Eds. (2003) *Nanotechnology in Mesostructured Materials*, Vol., 146, pp 1−815, Elsevier, Amsterdam.

(21) Terracciano, R., Gaspari, M., Testa, F., Pasqua, L., Cuda, G., Tagliaferri, P., Cheng, M. C., Nijdam, A. J., Petricoin, E. F., Liotta, L. A., Ferrari, M., and Venuta, S. (2006) Selective binding and enrichment for low-molecular weight biomarker molecules in human plasma after exposure to nanoporous silica particles. *Proteomics 6*, 3243–3250.

(22) Gaspari, M., Cheng, M. C., Terracciano, R., Liu, Nijdam, A. J., Vaccari, L., Di Fabrizio, E., Petricoin, E. F., Liotta, L. A., Cuda, G., Venuta, S., and Ferrari, M. (2006) Nanoporous surfaces as harvesting agents for mass spectrometric analysis of peptides in human plasma. *J. Proteome Res. 5*, 1261–1266.

(23) Geho, D., Cheng, M. M., Killian, K., Lowenthal, M., Ross, S., Frogale, K., Nijdam, J., Lahar, N., Johann, D., Herrmann, P., Whiteley, G., Ferrari, M., Petricoin, E., and Liotta, L. (2006) Fractionation of serum components using nanoporous substrates. *Bioconjugate Chem. 17*, 654–661.

(24) Pasqua, L., Testa, F., Aiello, R., Nagy, J. B., and Madeo, G. (2003) Surface properties of mesoporous silicate and alumino-silicate modified by reaction with benzoyl chloride. *Phys. Chem. Chem. Phys. 5*, 640–645.

(25) Pasqua, L., Testa, F., and Aiello, R. (2003) Reactivity of silica walls of mesoporous materials towards benzoyl chloride. *Stud. Surf. Sci. Catal. 146*, 497–500.

(26) Zhao, D. Y., Feng, J. L., Huo, Q. S., Melosh, N., Fredrickson, G. H., Chmelka, B. F., and Stucky, G. D. (1998) Triblock copolymer syntheses of mesoporous silica with periodic 50 to 300 angstrom pores. *Science 279*, 548–552.

(27) Kresge, C. T., Leonowicz, M. E., Roth, W. J., Vartuli, J. C., and Beck, J. S. (1992) Ordered mesoporous molecular sieves synthesized by a liquid-crystal template mechanism. *Nature (London) 359*, 710–712.

(28) Fan, J., Shui, W., Yang, P., Wang, X., Xu, Y., Wang, H., Chen, X., and Zhao, D. (2005) Mesoporous silica nanoreactors for highly efficient proteolysis. *Chem.—Eur. J. 11*, 5391–5396.

(29) Van Der Voort, P., Vercaemst, C., Schaubroeck, D., and Verpoort, F. (2008) Ordered mesoporous materials at the beginning of the third millennium: new strategies to create hybrid and non-siliceous variants. *Phys. Chem. Chem. Phys. 10*, 347–360.

(30) Sun, W., Li, F., Wu, S., Wang, X., Zheng, D., Wang, J., and Gao, Y. (2005) Human urine proteome analysis by three separation approaches. *Proteomics 5*, 4994–5001.

(31) Chaga, G. S. (2001) Twenty-five years of immobilized metal ion affinity chromatography: past, present and future. *J. Biochem. Biophys. Methods 49*, 313–334.

(32) Porath, J., Carlsson, J., Olsson, I., and Belfrage, G. (1975) Metal chelate affinity chromatography, a new approach to protein fractionation. *Nature (London) 258*, 598–599.

(33) Banks, R. E., Stanley, A. J., Cairns, D. A., Barrett, J. H., Clarke, P., Thompson, D., and Selby, P. J. (2005) Influences of blood sample processing on low-molecular-weight proteome identified by surface-enhanced laser desorption/ionization mass spectrometry. *Clin. Chem. 51*, 1637–1649.

(34) Papale, M., Pedicillo, M. C., Thatcher, B. J., Di Paolo, S., Lo Muzio, L., Bufo, P., Rocchetti, M. T., Centra, M., Ranieri, E., and Gesualdo, L. (2007) Urine profiling by SELDI-TOF/MS: monitoring of the critical steps in sample collection, handling and analysis. *J. Chromatogr., B 856*, 205–213.

(35) Roelofsen, H., Alvarez-Llamas, G., Schepers, M., Landman, K., and Vonk, R. J. (2007) Proteomics profiling of urine with surface enhanced laser desorption/ionization time of flight mass spectrometry. *Proteome Sci. 5*, 1–9.

(36) Tiss, A., Smith, C., Camuzeaux, S., Kabir, M., Gayther, S., Menon, U., Waterfield, M., Timms, J., Jacobs, I., and Cramer, R. (2007) Serum peptide profiling using MALDI mass spectrometry. *Pract. Proteomics 1*, 77–89.

(37) Diamandis, E. P. (2004) Mass spectrometry as diagnostic and a cancer biomarker discovery tool: opportunities and potential limitations. *Mol. Cell. Proteomics 3*, 367–378.

(38) Hortin, G. L. (2005) Can mass spectrometric protein profiling meet desired standards of clinical laboratory practice? *Clin. Chem. 51*, 3–5.

BC800510F

SUPPORTING INFORMATION

Derivatized Mesoporous Silica Beads for MALDI-TOF MS Profiling of Human Plasma and Urine

Rosa Terracciano,* Luigi Pasqua, Francesca Casadonte, Stella Frascà, Mariaimmacolata Preianò, Daniela Falcone, and Rocco Savino

Table of Contents

1. Figure S1: (A) Nitrogen adsorption-desorption isotherms and (B) Barret–Joyner–Halenda (BJH) pore size distribution of mesoporous silica beads bearing aminopropyl groups (MSB-C) used in proteomic experiments.
2. Figure S2: (A) Nitrogen adsorption-desorption isotherms and (B) Barret–Joyner–Halenda (BJH) pore size distribution of mesoporous silica beads bearing N-(2-aminoethyl)-3-aminopropyl groups (MSB-D) used in proteomic experiments.
3. Figure S3: (A) Nitrogen adsorption-desorption isotherms and (B) Barret–Joyner–Halenda (BJH) pore size distribution of mesoporous silica beads bearing and N, N, N' tris-carboxymethyl ethylene diamine groups (MSB-E) used in proteomic experiments.
4. Figure S4: Scanning electron micrographs of mesoporous silica materials derivatized with aminopropyl groups (MSB-C).
5. Figure S5: Scanning electron micrographs of mesoporous silica materials derivatized with N-(2-aminoethyl)-3-aminopropyl groups (MSB-D).
6. Figure S6: Scanning electron micrographs of mesoporous silica materials derivatized with N, N, N' tris-carboxymethyl ethylene diamine groups (MSB-E).
7. Figure S7: Reproducibility studies on human plasma peptidome profiling. MALDI-TOF spectra of the same plasma samples independently processed in triplicate with MSB-C (A), MSB-D. (B), MSB-E (C).
8. Figure S8: Reproducibility studies on human urine peptidome profiling. MALDI-TOF spectra of the same urine samples independently processed in triplicate with MSB-C (A), MSB-D. (B), MSB-E (C).
9. Table S1: working conditions used for processing plasma samples by derivatized MSB.
10. Table S2: working conditions used for processing urine samples by derivatized MSB.

Figure S1. (A) Nitrogen adsorption-desorption isotherms and (B) Barret–Joyner–Halenda (BJH) pore size distribution of mesoporous silica beads bearing aminopropyl groups (MSB-C) used in proteomic experiments.

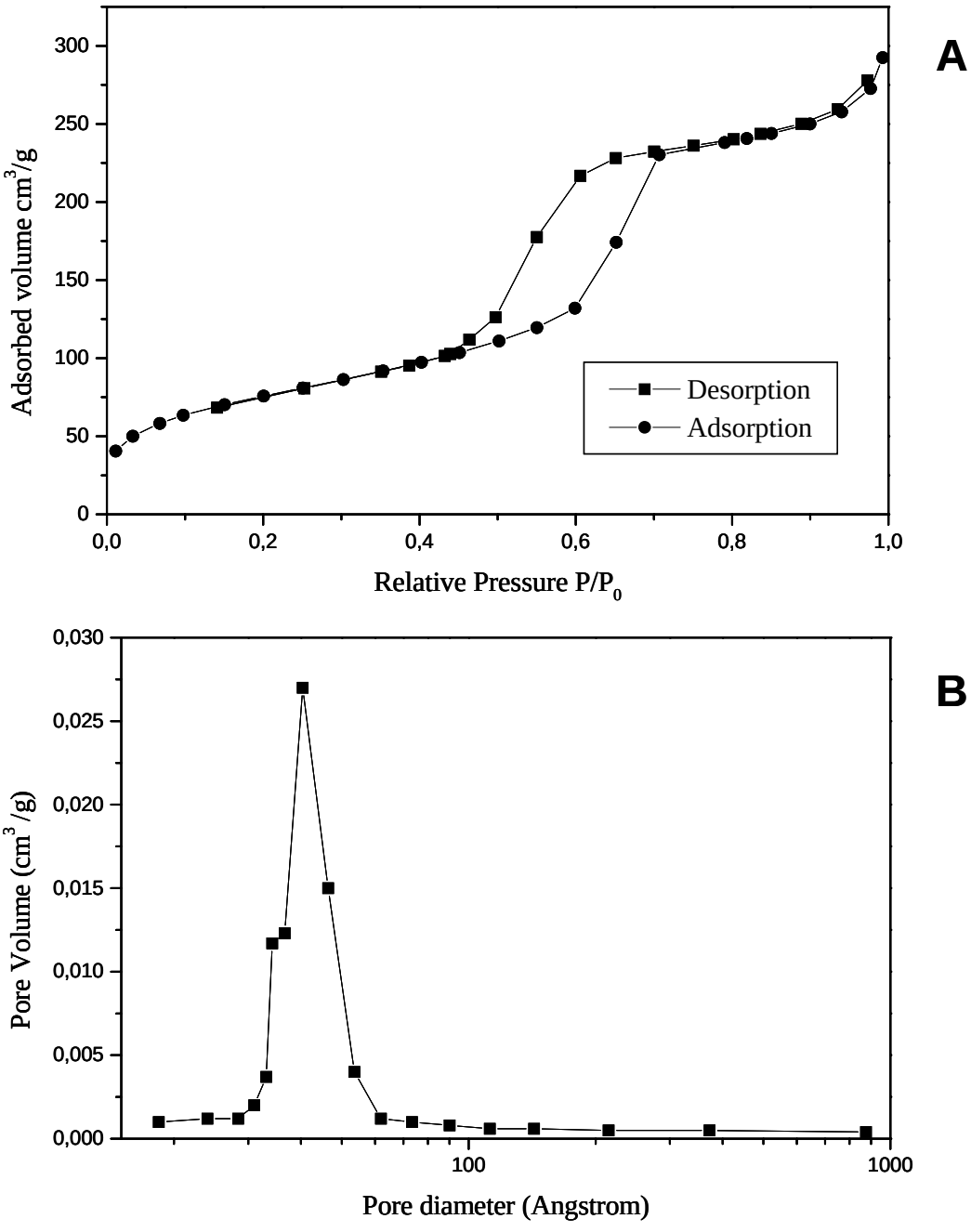

Figure S2. (A) Nitrogen adsorption-desorption isotherms and (B) Barret–Joyner–Halenda (BJH) pore size distribution of mesoporous silica beads bearing N-(2-Aminoethyl)-3-aminopropyl (MSB-D) groups used in proteomic experiments.

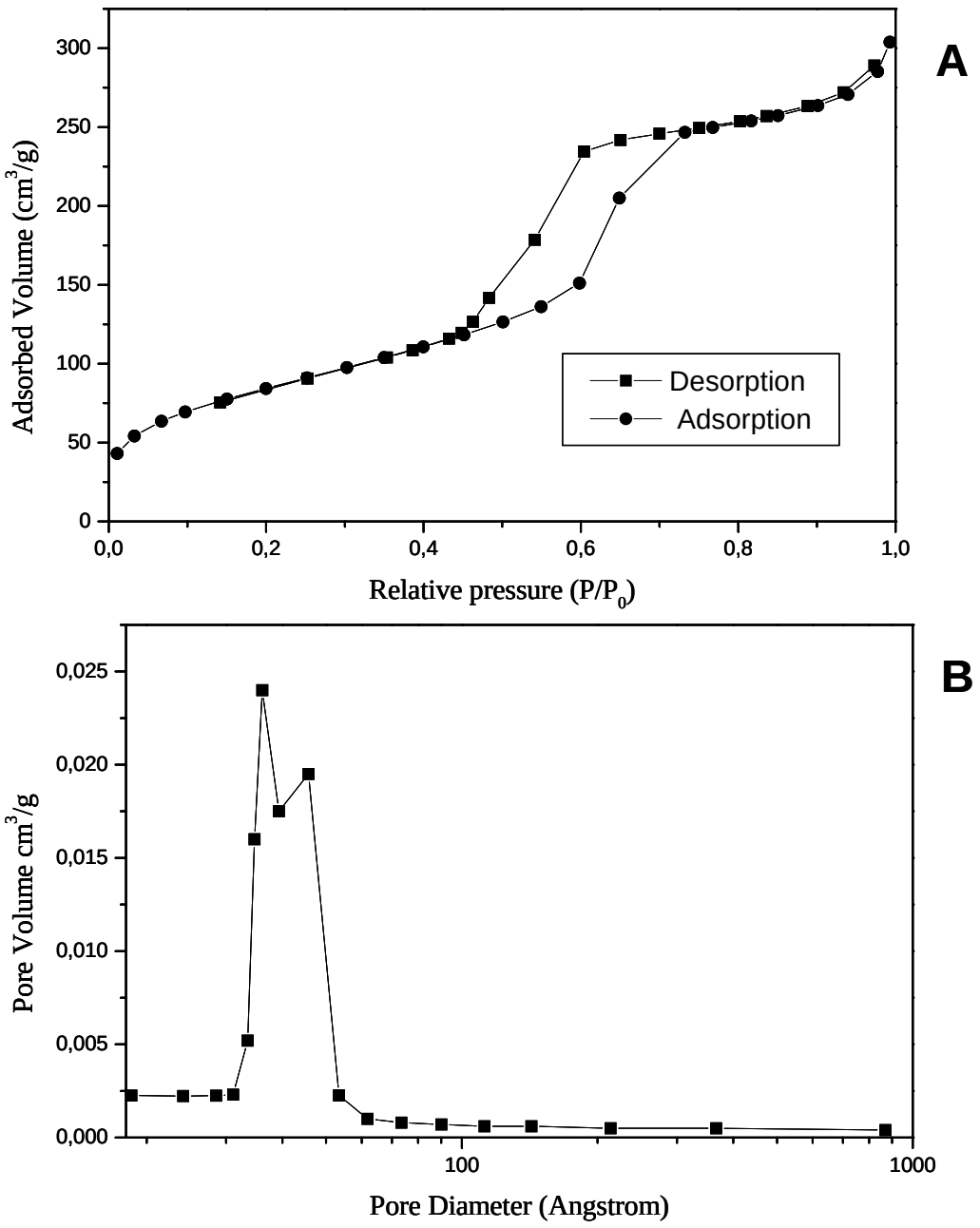

Figure S3. (A) Nitrogen adsorption-desorption isotherms and (B) Barret–Joyner–Halenda (BJH) pore size distribution of mesoporous silica beads bearing and N, N, N' tris-carboxymethyl ethylene diamine groups (MSB-E) used in proteomic experiments.

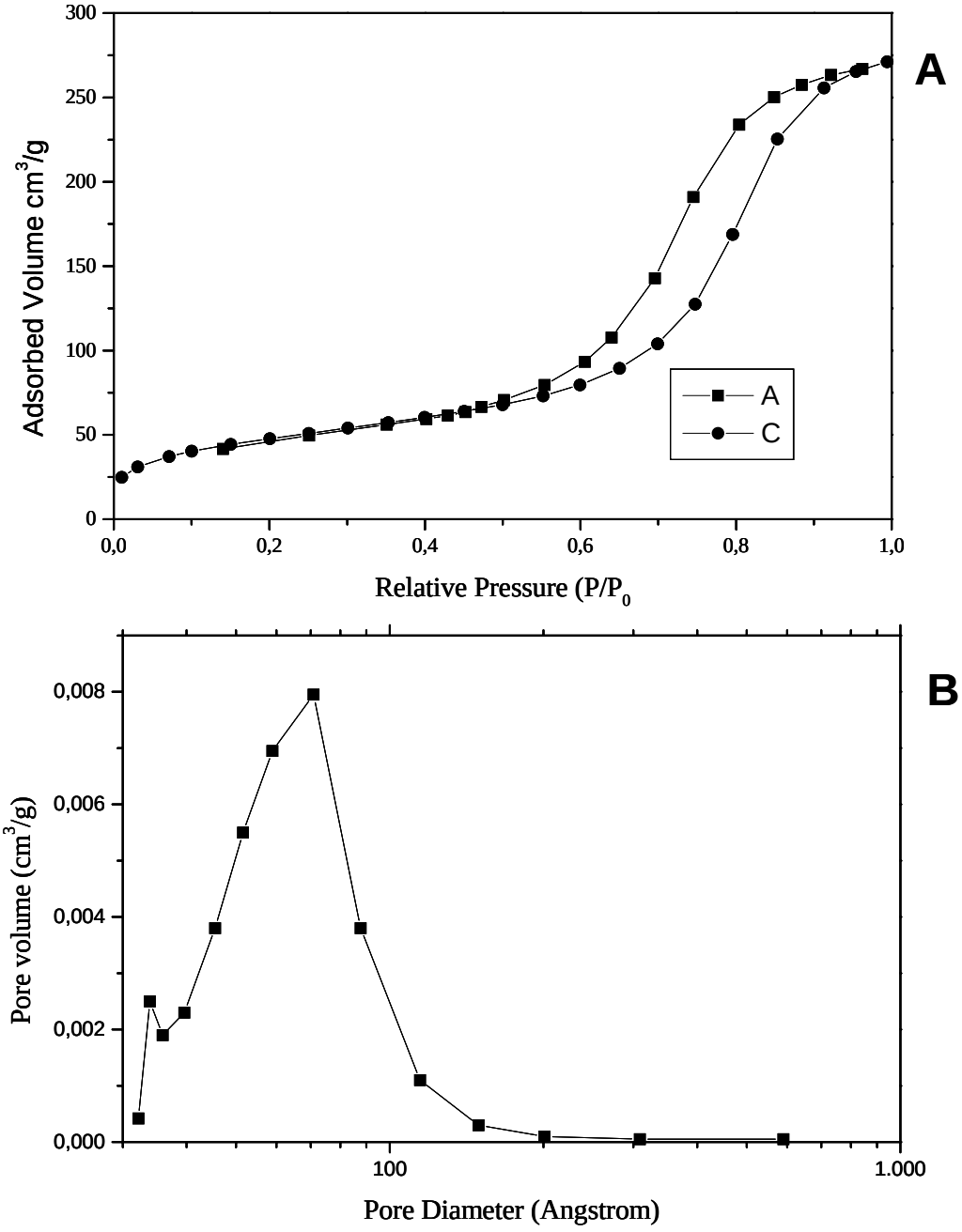

Figure S4. Scanning electron micrographs of mesoporous silica materials derivatized with aminopropyl groups (MSB-C).

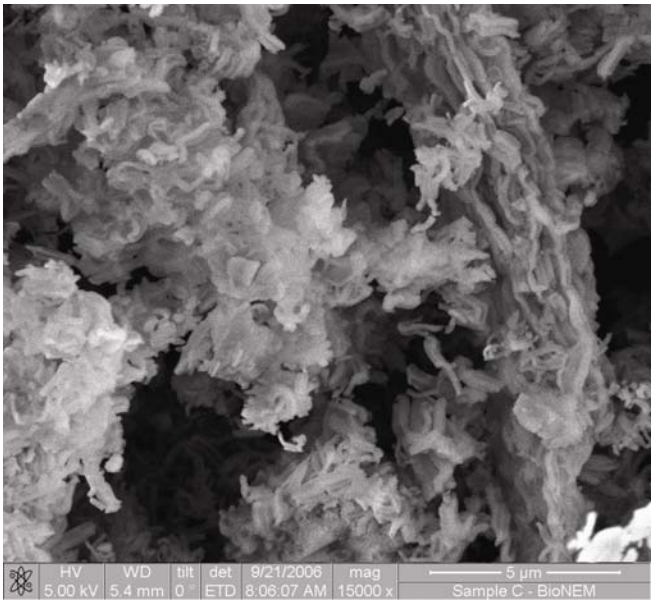

Figure S5. Scanning electron micrographs of mesoporous silica materials derivatized with N-(2-aminoethyl)-3-aminopropyl groups (MSB-D).

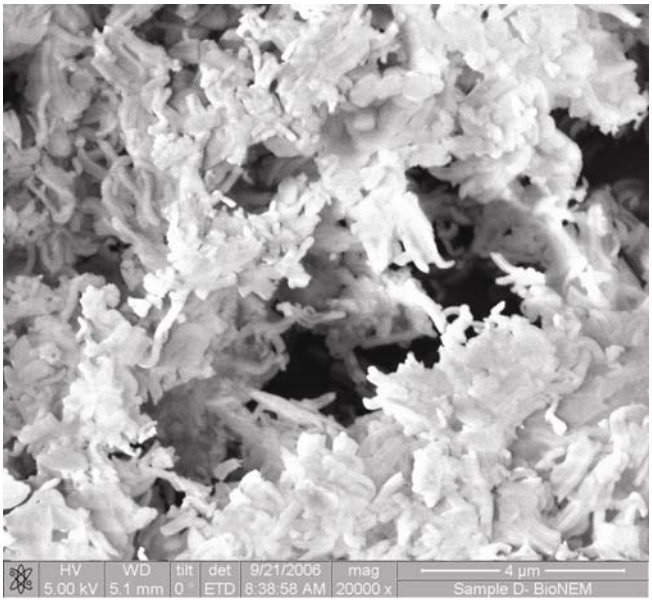

Figure S6. Scanning electron micrographs of mesoporous silica materials derivatized with N, N, N' tris-carboxymethyl ethylene diamine groups (MSB-E).

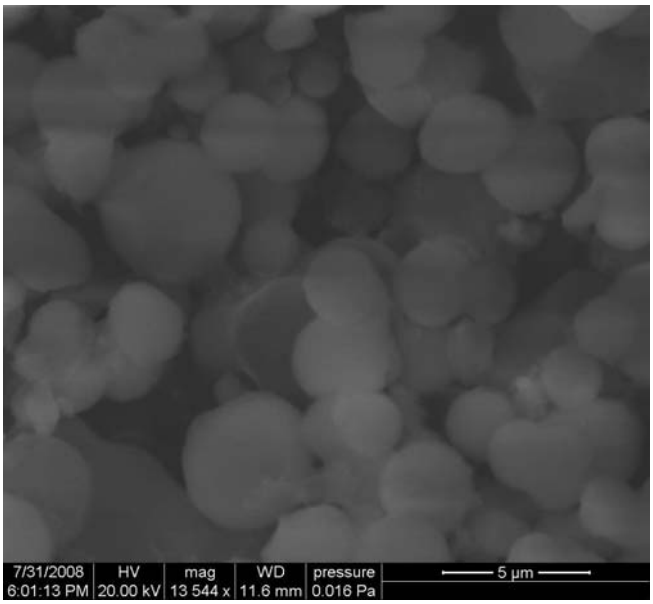

Figure S7. Reproducibility studies on human plasma peptidome profiling. MALDI-TOF spectra of the same plasma samples independently processed in triplicate with MSB-C (A), MSB-D. (B), MSB-E (C).

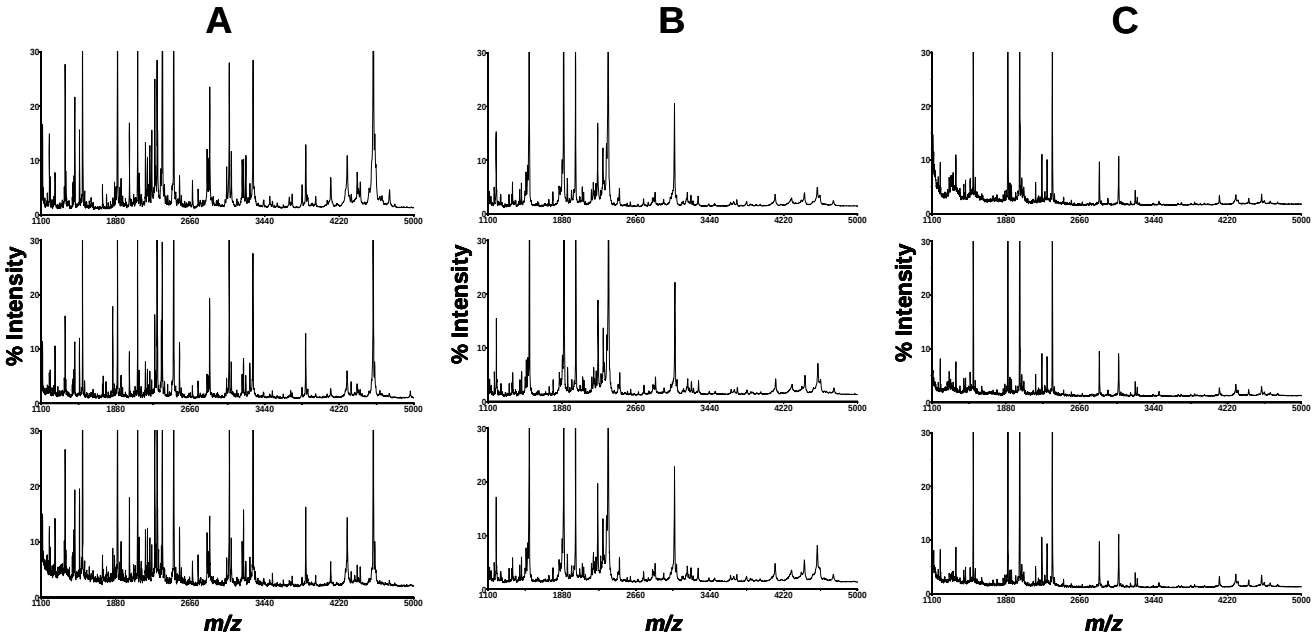

Figure S8. Reproducibility studies on human urine peptidome profiling. MALDI-TOF spectra of the same urine samples independently processed in triplicate with MSB-C (A), MSB-D. (B), MSB-E (C).

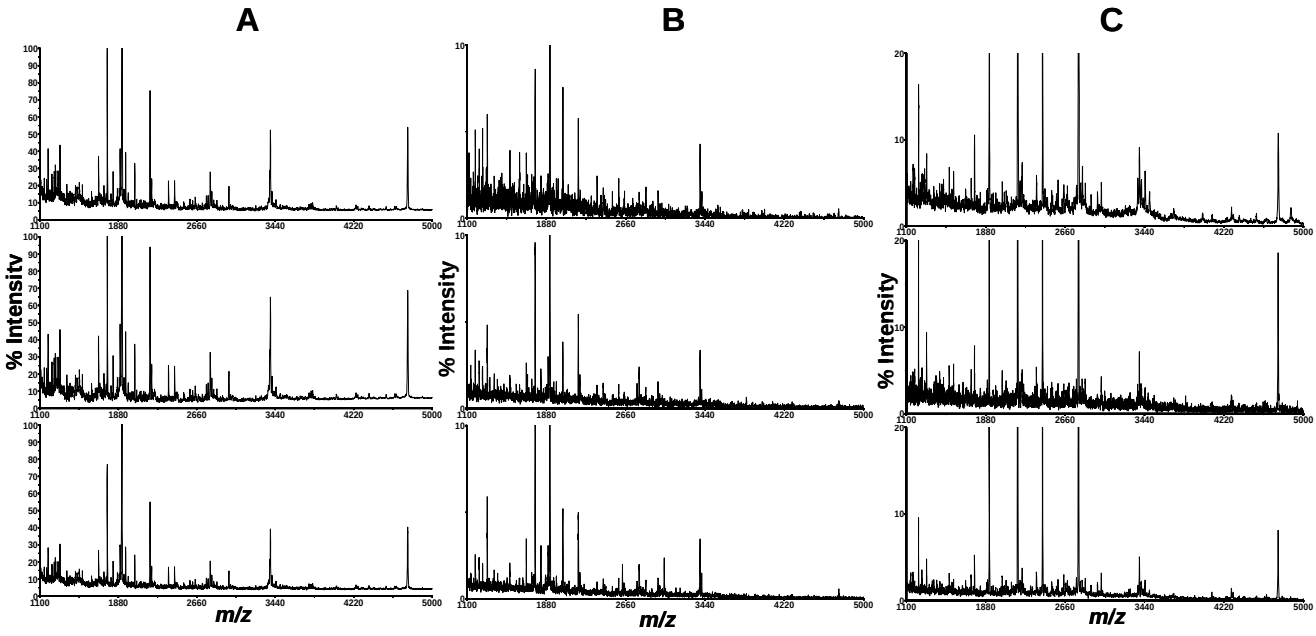

Table S1. Experimental conditions of the final protocol for plasma peptides enrichment by three differently derivatized mesoporous silica beads.

MSB	Pre-conditioning/Adsorption	Washes	Elution
MSB-C	Tris HCl 25 mM pH= 8.8	Tris HCl 25 mM pH= 8.8	CH_3CN/Ammonium formate 100 mM pH= 3 50/50
MSB-D	Tris HCl 25 mM pH= 8.8	Tris HCl 25 mM pH= 8.8	CH_3CN/Ammonium formate 100 mM pH= 3 50/50
MSB-E	Ammonium acetate pH= 6.6	Ammonium acetate pH= 6.6 followed by water	CH_3CN/0.5% TFA 50/50

Table S2. Experimental conditions of the final protocol for urine peptides enrichment by three differently derivatized mesoporous silica beads.

MSB	Pre-conditioning/Adsorption	Washes	Elution
MSB-C	Tris HCl 25 mM pH= 8.8	Tris HCl 25 mM pH= 8.8	CH_3CN/Ammonium formate 100 mM pH= 3 50/50
MSB-D	Tris HCl 25 mM pH= 8.8	Tris HCl 25 mM pH= 8.8	CH_3CN/Ammonium formate 100mM pH= 3 50/50
MSB-E	Ammonium acetate pH= 6.6	Ammonium acetate 100 mM pH= 6.6 followed by water	CH_3CN/0.5% TFA 50/50

Site-Specific Polysialylation of an Antitumor Single-Chain Fv Fragment

A. Constantinou,[†] A. A. Epenetos,[†] D. Hreczuk-Hirst,[⊥,‡] S. Jain,[‡] M. Wright,[#,†] K. A. Chester,[§] and M. P. Deonarain*[,†]

Division of Cell & Molecular Biology, Department of Life Sciences, Faculty of Natural Sciences, Imperial College London, Exhibition Road, London, SW7 2AZ, U.K., Lipoxen plc, 2 Royal College Street, London, U.K. NW1 0NH, and UCL Cancer Institute, University College London, 72 Huntley Street, London, U.K. WC1E 6BT. Received December 2, 2008; Revised Manuscript Received March 12, 2009

Protein pharmacokinetic modulation is becoming an important tool in the development of biotherapeutics. Proteins can be chemically or recombinantly modified to alter their half-lives and bioavailability to suit particular applications as well as improve side effect profiles. The most successful and clinically used approach to date is chemical conjugation with poly(ethylene glycol) polymers (PEGylation). Here, therapeutic protein half-life can be increased significantly while retaining biological function, reducing immunogenicity and cross-reaction. Naturally occurring alternatives to such synthetic polymers could have major advantages such as lower side effects due to biodegradability and metabolism. Polysialic acid (PSA) has been investigated as a pharmacokinetic modulatory biopolymer with many successful examples in preclinical and clinical development. Single-chain Fvs (scFvs) are a choice antibody format for human therapeutic antibody discovery. Because of their small size, they are rapidly eliminated from the circulation and often are rebuilt into larger proteins for drug development and a longer half-life. Here we show that chemical polysialylation can increase the half-life of an antiplacental alkaline (PLAP) and anticarcinoembryonic antigen (CEA) scFv (F1 and MFE-23, respectively) 3.4−4.9-fold, resulting in a 10.6−15.2-fold increase in blood exposure. Amine-directed coupling of the MFE-23 scFv reduced its immunoreactivity 20-fold which was resolved by site-specific polysialylation through an engineered C-terminal thiol residue. The site-specifically polysialylated MFE-23 scFv demonstrated up to 30-fold improved tumor uptake while displaying favorable tumor:normal tissue specificity. This suggests that engineering antibody fragments for site-specific polysialylation could be a useful approach to increase the half-life for a variety of therapeutic applications.

INTRODUCTION

Protein drugs are often compromised by limitations arising from their complex molecular structure. Factors such as proteolytic degradation, uptake by cells of the reticuloendothelial system, renal removal, and immunocomplex formation all lead to rapid elimination from the blood before effective concentrations are reached (*1*). This results in an undesirably short therapeutic window. The over-riding factors which contribute to these pharmacokinetic limitations are size, stability, and immunogenicity (*2*).

Polymer conjugation using poly(ethylene glycol) (PEGylation) has been one of the most successful approaches to improving protein pharmacokinetics (*3*). PEG is a neutral polymer that can bind water molecules, forming a 'watery cloud' around the protein (*4*). This gives the conjugate a larger hydrodynamic volume compared to its true molecular weight, affecting its pharmacokinetics and pharmacodynamics in the body (*4*). In addition to its size, the protein surface is modified and biological epitopes are shielded from potential immune responses or degradation. A number of PEGylated proteins have been approved for clinical use, e.g., PEGasys (PEG-interferon) for the treatment of chronic hepatitis C infections (*5*), and Cimzia (certolizumab pegol), a PEGylated anti-TNFα Fab for Crohn's disease (*6*). However, since PEG is a synthetic polymer, there are concerns about its metabolism and immunogenicity. Uptake by cells of the reticuloendothelial system has been reported, and PEG can accumulate in lysosomes, leading to toxicity (*7*). Repeated administration of PEG conjugates resulted in the production of anti-PEG antibodies (*8*). More recently it was shown that PEG-infusion-related side effects include unwanted complement activation (*9*). Taken together, the uncertainty in the metabolism and immune responses has led to the search for natural alternatives.

Molecules which are inconspicuous to the innate and adaptive immune systems are more likely to survive for prolonged periods in the circulation. Polysialic acid (PSA: polymers of *N*-acetylneuraminic (sialic) acid) (*10*) is one such molecule and offers a natural alternative to PEG. PSA is a human polymer found almost exclusively on NCAM (neural cell adhesion molecule) where it plays an antiadhesive function in brain development (*11*). The highly hydrophilic nature of PSA results in similar hydration properties to PEG, giving it a high apparent molecular weight in the blood. This increases circulation time since no receptors with PSA specificity have yet been identified (*12*).

PSA is also synthesized by bacteria such as *Neisseria meningitidis* and some *Escherichia coli* where it is synthesized as a capsule (*10*). Bacterial PSA is chemically and immunologically similar to human PSA and is naturally degraded by sialidases (e.g., neuraminidase); unlike PEG, it is metabolized as a natural sugar molecule by tissue sialidases (*13*). Pioneered by Gregoiadis et al. (*14*, *15*), PSA has been developed for

* Corresponding author. Tel: +44 207 594 5318; fax: +44 207 594 4560; e-mail: m.deonarain@imperial.ac.uk

[†] Imperial College London.

[‡] Lipoxen plc.

[§] University College London.

[⊥] Current address: Glycoform Ltd., Unit 44C, Milton Park, Abingdon, Oxon, OX14 4RU.

[#] Current address: UCB-Celltech, 208 Bath Rd., Slough, Berkshire, UK SL1 3WE.

10.1021/bc8005122 CCC: $40.75 © 2009 American Chemical Society
Published on Web 04/29/2009

clinical use. Reductive amination of the nonreducing end of the oxidized PSA allows chemical conjugation via primary amine groups on proteins, and the therapeutic benefits of PSA conjugation have been demonstrated with aspariginase (*16*) and insulin (*14*) for the treatment of leukemia and diabetes, respectively. Recent clinical data from trials with polysialylated insulin (SuliXen) and erythropoietin (ErepoXen) showed that these biopharmaceuticals were well tolerated and had improved pharmacokinetics [http://www.lipoxen.com/news.aspx]. More recently, we have shown that Fab fragments can be chemically polysialylated with a range of different lengths and ratios of linear PSA chains (*17*). Polysialylation of an antitumor Fab resulted in a 5-fold increase in blood exposure (bioavailability) with a corresponding 3-fold increase in tumor uptake compared to the unmodified Fab (*17*).

The use of recombinant antibody fragments has been increasingly investigated for therapeutic applications, as they are versatile and offer many advantages over current therapies using whole immunoglobulins (*18*). Because of their smaller size and lower molecular complexity, antibody fragments such as single-chain Fvs (scFvs) can be easily selected from combinatorial libraries and more readily expressed in a bacterial expression system, leading to rapid and inexpensive production (*19*). For therapy in vivo, the smaller size allows for faster tissue penetration; however, the targeted absolute uptake of such species may be limited by the subsequent faster clearance rate through glomerular filtration (*20*). We hypothesized that chemical polysialylation of a scFv would result in more favorable pharmacokinetic properties. The approach of modulating antibody pharmacokinetics by chemical polysialylation has not been applied to these molecules. Normally, antibody fragments are rebuilt into whole human immunoglobulins or constructed into fusion proteins which generally increases antibody size and hence decreases blood clearance (*20*). However, polysialylation may have advantages in terms of time and complexity as well as the advantages over chemical PEGylation already described.

The scFv used in our studies was MFE-23, a well characterized anti-CEA (carcinoembryonic antigen) scFv with a K_d of approximately 2 nM (*21, 22*). MFE-23 has been previously investigated in clinical trials for imaging (*23, 24*) and therapeutic use (*25, 26*). We compared the effectiveness of random, amine-directed chemical conjugation of PSA (*14, 17*) with site-specific, thiol-directed chemical conjugation. The latter method presents a number of advantages in the control of polymer attachment because it is distant from the antigen binding regions and limited only to hydrophilic and therefore normally surface-exposed thiol sites which generally are not involved with protein conformation and bioactivity.

Our results show that both amine-directed and site-specific polysialylation resulted in scFv-immunoconjugates with extended pharmacokinetic parameters, improved tumor uptake, and improved kidney to blood ratios. However, the amine-directed conjugation method resulted in reduced immunoreactivity. This problem was overcome by site-specific polysialylation on an engineered C-terminal thiol peptide.

EXPERIMENTAL PROCEDURES

Materials. Polysialic acid of 11 kDa was from Sigma. CEA antigen was supplied by Calbiochem; CEA-positive LS174T cell-line supplied by the EACC and grown in Dulbecco's modified Eagle medium (DMEM) supplemented with 10% fetal calf serum and 50 IU/mL of penicillin and streptomycin (Invitrogen). Unless stated, immunochemicals were from Sigma. Mouse anti-PSA-NCAM monoclonal IgM was from Chemicon. Carrier-free ^{125}I-NaCl was supplied by Amersham Pharmacia Biotech. Bacterial cultures were grown with 2TY media supplemented with 0.1 mg/mL ampicillin (Sigma) for selection purposes.

Cloning of MFE-23-cys scFv Construct. The pUC119 expression plasmid containing the scFv MFE-23 gene was used as a template to produce the mutant MFE-23-cys construct (*21*). Oligonucleotides incorporating restriction sites for recombinant subcloning, as well as mutations to include a C-terminal thiol group, were used to flank the scFv gene and allow PCR amplification of the mutant scFv MFE-23-cys. The forward primer was LMB3; 5′-CAGGAAACAGCTATGAC-3′, while the reverse primer cysMFE; 5′-GGCAGCAACGCCAAGT-GCGGCCG**CACAACCTCCGCCACC**CTGTTTC. AGCTC-CAGCTTGGTGCC-3′ contained a realigned *Nco* I site (underlined) and $(Gly)_4$Cys peptide (bold). The PCR product was subcloned into the pHEN2 vector as an *Nco* I/*Not* I fragment and DNA sequence verified.

Production and Purification of F1, MFE-23, and MFE-23-cys scFvs. F1 was used as a non-CEA binding negative control scFv. F1 binds to human placental alkaline phosphatase (PLAP) and was selected from a phage display library [Wright, Ph.D. thesis, University of London, 2003]. Protein expression of F1, MFE-23, and MFE-cys scFvs was initiated by growing single colonies of newly transformed *E.coli* HB2151 bacteria in 2TY media with 0.1 mg/mL ampicillin overnight shaking at 250 rpm and 37 °C. When a culture OD_{600nm} of 0.6−0.8 was reached, IPTG was added to a final concentration of 0.1 mM. The induced culture was then left to grow overnight at 30 °C and 250 rpm during which time protein expression occurred. Induced cultures were centrifuged at 10 000 rpm, and the supernatant from which protein was to be purified was supplemented with benzamidine (final concentration 2 mM) and kept on ice where possible to minimize protein degradation. The supernatant was concentrated 10-fold by ultrafiltration and dialyzed into phosphate-buffered saline (PBS). The scFv protein was purified by immobilized metal affinity chromatography using TALON according to the manufacturer's instructions. Pure protein was eluted with 200 mM imidazole and stored at 4 °C. ScFv proteins were further purified using a HiLoad 10/30 Superdex-75 HR gel filtration column equilibrated with PBS and compared to previously run protein standards. Samples were further analyzed for the presence of protein by Coomassie staining and Western blotting. The presence of a functional thiol in the MFE-23-cys scFv was confirmed by coupling a fluorescein maleimide (Pierce Chemicals) reporter group, electrophoresing by SDS-PAGE, and visualizing the protein band by fluorescence imaging compared to nonthiol containing MFE-23 scFv (data not shown) or by binding to CEA-positive LS174T cells and analyzing by flow cytometry (data not shown).

Chemical Polysialylation. The PSA used in this work was colominic acid (linear α-(2−8) linked *N*-acetylneuraminic acid) purified from the capsular coating of *E. coli* K1, supplied as a 11 kDa polymer (average molecular weight), which is equivalent to ∼35 units of sialic acid. The average molecular weight (nominal mass) of these polymers was determined by gas-phase chromatography by Viscotek Europe Ltd. (*14*). For the purpose of F1 and MFE scFvs-PSA conjugation by reductive amination, PSA (colominic acid) was oxidized with 0.1 M periodate as described (*14, 17*). The oxidized material was dialyzed extensively against a 0.01% ammonium carbonate buffer (pH 7.4) at 4 °C, concentrated by reverse dialysis on a bed of polyethylene glycol (8 kDa), lyophilized, and stored at −80 °C until required. Oxidized PSA was added to 5 mL of protein (0.2 mg/mL) to give a 2-fold molar excess in a glass tube. The sample was mixed gently and supplemented with 20 mg of $NaCNBH_4$. The tube was sealed and rotated at 37 °C for 48 h to allow the conjugation reaction to occur. For thiol conjugation, scFv samples were dialyzed extensively against 50 mM Tris-HCl buffer pH 7.0 concentrated to 0.5 mg/mL and made up to a final volume of 950 μL. Protein was reduced by addition of 50

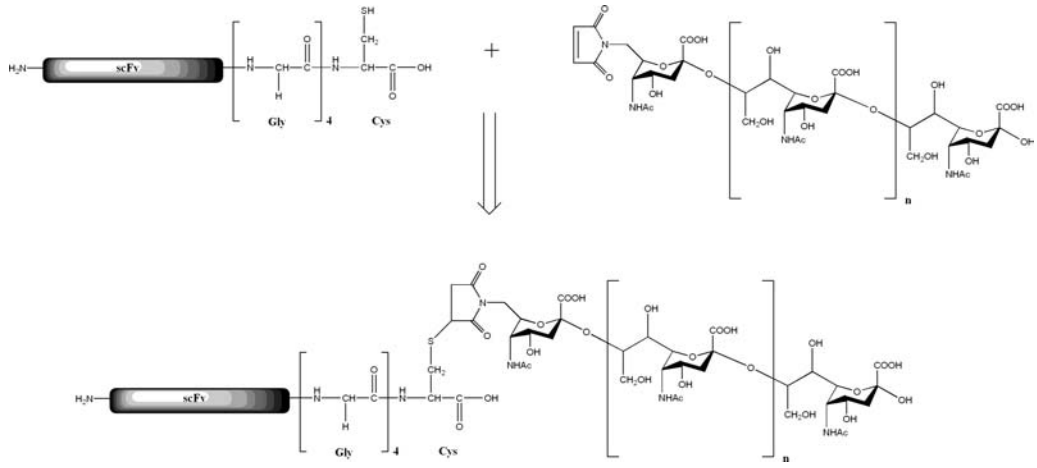

Figure 1. Schematic diagram of coupling. Showing the structure of the PSA maleimide and the scFv with a glycine-cysteine C-terminal peptide. The resulting chemical conjugate is shown.

μL of TCEP-HCl to give a final concentration of 2.5 mM and incubated for 90 min at room temperature. Reactive maleimide-PSA (made by the addition of 5-fold molar excess of N-[β-maleimidopropionic acid] hydrazide (Pierce) to colominic acid aldehyde dissolved in 0.1 M sodium acetate, vortex mixed, wrapped in foil and incubated at 37 °C for 2 h on a rotary mixer followed by ethanol precipitation) was added to the reduced protein sample to give a 25 molar excess of PSA/protein, mixed gently, and incubated at room temperature for 2 h. In both methods, the conjugated material was purified from free PSA by addition of $(NH_4)_2SO_4$ to give a 70% saturated solution. The sample was rotated for 5 min at room temperature followed by 30 min on ice. The mixture was then centrifuged at 5000 rpm for 5 min, and the resulting pellet resuspended in 1 mL of 100% saturated $(NH_4)_2SO_4$. The precipitation procedure was then repeated and the pellet dissolved in minimal PBS followed by extensive dialysis. Finally, the conjugated sample was analyzed by SDS-PAGE and characterized for polysialylation efficiency by resorcinol assay. A scheme of the coupling is shown in Figure 1.

Determination of PSA:Fab Ratios. The resorcinol assay was based on the method by Svennerholm (*27*) and allowed the amount of colominic acid present in a sample relative to known standards to be measured. The resorcinol agent (0.25 mM cupric sulfate, 0.2% resorcinol, 80% concentrated HCl made up with distilled water) was freshly prepared, and at least five colominic acid standards were prepared within the 40−400 μg/mL range were made. In triplicate, 100 μL of standard and test samples was added to 100 μL of resorcinol agent. The tubes were sealed, and the mixture was heated for 30 min at 95 °C. Once the tubes had cooled, 400 μL of ethanol was mixed in. Finally, the absorbance at 560 nm was measured for 250 μL of each sample and standards in a microplate assay. The standard values were used to construct a calibration curve from which the colominic acid content of the test samples could be determined. A molar value was determined according to the mean PSA length used in test samples, and similarly a protein concentration was determined for samples using the Coomassie Plus protein assay kit compared to protein standards. With these values, a PSA to protein molar ratio was calculated.

Western Blot Analyses. Protein gels for Western analysis were transferred to a nitrocellulose membrane, blocked in PBS/5% Marvel milk protein, and then incubated with either anti-His_6 specific (Qiagen) or anti-PSA specific (Chemicon) antibodies followed by antimouse HRPO conjugates (Sigma). The blot was developed using enhanced chemiluminescence and exposed to high performance autoradiography film.

Gel Filtration of Proteins and Conjugates. Gel filtration was carried out using a Superdex-200 column equilibrated with PBS run at 1.5 mL/min at 4 °C on a Biologic DuoFlow system. Native molecular weight standards were used to calibrate the column. Eluted protein were monitored at absorbencies of 280 nm (protein) and 214 nm (peptide bonds).

Protein Radioiodination. Protein samples were radioiodinated using Pierce iodination tubes. To precoated tubes, 100 μL of the Tris iodination buffer was added followed by 10 μL (1.0 mCi) $Na^{125}I$. The activated iodide was then removed and added directly to the protein solution (1 mL of 0.2−0.5 mg/mL) for iodination. The reaction was allowed to take place for 8 min. To end the reaction, 50 μL of scavenging buffer (10 mg/mL tyrosine in PBS) was added and mixed. After 5 min incubation, the iodinated sample was dialyzed against PBS.

Bioactivity by ELISA Analysis. Flat-bottom 96-well ELISA plates coated with CEA antigen at 2 μg/mL in PBS were used. After three washes with PBS/0.1% Tween-20 and three PBS washes, the plate was then blocked with 5% PBS/Marvel for 1 h at 37 °C and washed again. Binding activity of the anti-CEA scFvs and conjugates were established by serially diluting samples across test wells in 1% Marvel/PBS for 1 h at 37 °C. Following a repeat of the wash steps, detection of bound scFv was made by incubating with 'one-step' HRP conjugated anti-His antibody for 1 h at 37 °C. For the purpose of PSA detection, the plate was incubated first with primary anti-PSA IgM followed by secondary anti-IgM HRP for 1 h at 37 °C. In both cases, incubation with detection antibodies was terminated by washing the plates as described above and binding detected using BM Blue POD substrate. The development was stopped with 1 M H_2SO_4 and the absorbance measured at 450 nm. Sigmoidal curves were fitted to ELISA data to determine K_d values using SigmaPlot using the one-site saturation ligand-binding equation.

Pharmacokinetic and Biodistribution Studies. Female nude BALB/c mice, 6−8 weeks old (Harlan UK), were used for in vivo studies. All in vivo research was carried out under a UK Home Office project license PPL 70/5833. Human tumor xenografts were set up by injecting mice subcutaneously into the left flank with 0.1 mL containing up to 10 million LS174T cells. Tumour growth was monitored and took 3−4 weeks to reach the required 5−8 mm diameter for subsequent work. For tissue analyses, up to 100 μL radiolabeled samples (5−10 μg) were injected intravenously into the mouse tail vein. At the appropriate time points (typically 0.5, 2, 6, 24, and 48 h) mice were culled by exsanguination under terminal anesthesia. Immediately, blood was collected by cardiac puncture and

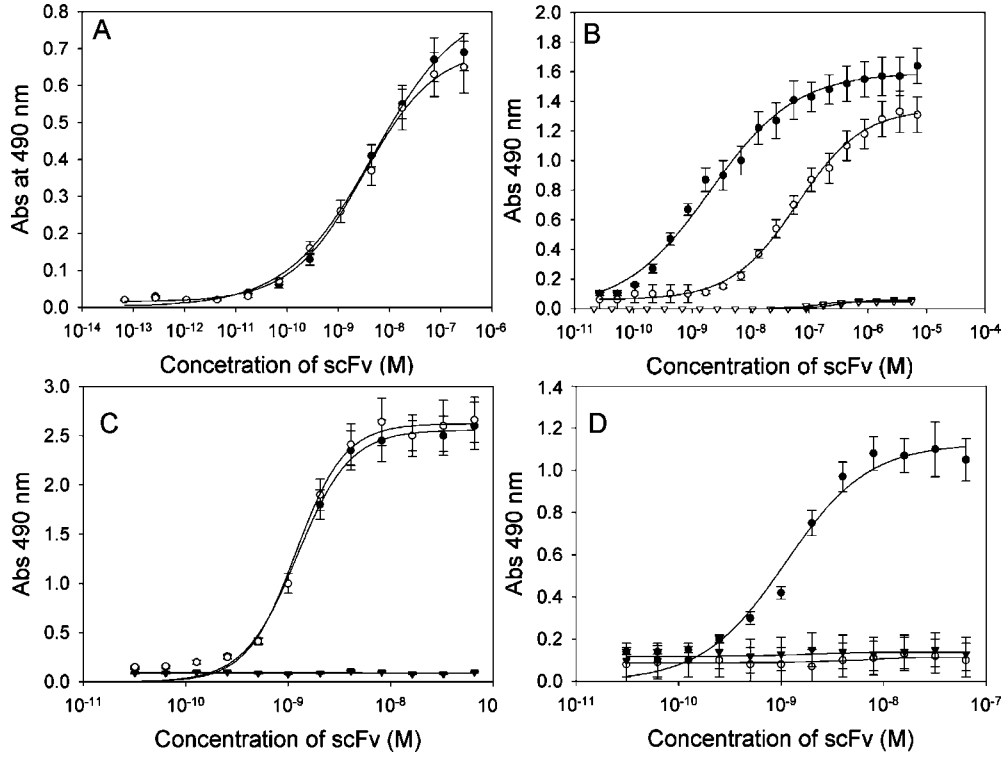

Figure 2. ELISAs of scFvs and scFv−PSA conjugates on immobilized CEA. (A) MFE-23 (○) and MFE-23-cys scFv (●) binding curves showing near identical affinities of 2.4 nM and 2.5 nM, respectively. (B) MFE-23 scFv binding curve before (●) and after (○) amine-directed coupling with PSA. F1 scFv binding curve before (▼) and after (▽) amine-directed PSA coupling. (C) MFE-23-cys (○) retains binding affinity after thiol-directed PSA coupling (●) detected with anti-His_6 antibody, whereas free PSA alone is not immunoreactive (▼). (D) The same experiment as (C), detected with an anti-PSA antibody, confirms binding and also polysialylation.

transferred to a sample tube. The mouse was then dissected, and tissues were collected for biodistribution analysis. Radioactivity was counted using a gamma counter. Values were expressed as a percentage of the initial injected dose per gram of tissue (% id/g). For studying in vivo blood clearance pharmacokinetics, data values were fitted using SigmaPlot to equations that conform to the two-compartmental intravenous model of clearance, which takes into account the biexponential clearance phases, distribution phase and elimination phase, of single intravenous doses. This is described by the exponential decay, double, four-parameter equation $y = ae^{-bx} + ce^{-dx}$, where the distribution phase clearance rate ($t_{1/2\alpha}$) can be determined by ln 2/*b*, and the elimination clearance rate ($t_{1/2\beta}$) can be determined by ln 2/*d*. The area under the curve values for blood clearance were determined using the macros available within SigmaPlot to represent protein blood bioavailability.

RESULTS

Purification and Characterization of scFv MFE-23-cys. The MFE-23-cys scFv constructed and expressed in *E. coli* showed a 5-fold lower level (∼1 mg/L) of protein expression than the parental scFv, probably because of the formation of incorrectly folded intermediates and mixed disulfides due to the unpaired cysteine as seen previously (*28*). As expected, the amount of monomeric MFE-cys scFv was even lower due to the presence of disulfide-linked scFv dimers and, additionally, noncovalent dimers (*29*) which were resolved by size-exclusion chromatography (see Supporting Information Figure S1). This led to a final yield of MFE-cys scFv monomer of around 0.5 mg/L of bacterial culture. The binding activity of the MFE-23-cys scFv relative to that of the unmodified scFv was determined by ELISA (Figure 2a). Similar K_d values were determined for the MFE-23-cys and MFE-23 scFvs of 2.5 and 2.4 nM, respectively (derived by fitting a curve using SigmaPlot) which implied that the additional thiol peptide in the MFE-23-cys scFv did not alter its antigen binding affinity. Fluorescein coupling confirmed the functionality and 1:1 stoichiometry of the C-terminal thiol and also demonstrated the ability for thiol conjugates to bind to live cells by FACS (data not shown).

Table 1. Mean PSA Coupling Ratio of the Three scFvs Used in This Study

ScFv species	mean PSA:scFv molar ratio
F1	1.5
MFE-23 (amine)	1.4
MFE-23-cys	1.1

Chemical Polysialylation of scFvs. F1 and MFE-23 were initially polysialylated by amine coupling at low (1:1 to 1:2) molar ratios. Resorcinol tests showed that the substitution ratios were approximately 1:1.5 (Table 1). However, the amine-coupled polysialylated MFE-23 scFv showed a 20-fold reduced immunoreactivity compared to the unmodified scFv (Figure 2b). This suggested that the process modified one or more key lysine residues in the MFE-23 scFv. Thiol coupling using the maleimide-activated PSA yielded a ratio of ∼1:1 with fully immunoreactive scFv (Figure 2c). Reducing/SDS-PAGE gel analysis compared amine- and thiol-coupled scFvs (Figures 3 and 4). Both the amine-coupled MFE-23 and F1 scFvs displayed a broad polydispersed migration pattern, characteristic for a protein conjugate of hetergenous mass composition (Figure 3). The thiol-coupled MFE-23-cys conjugate produced a less polydispersed immunoconjugate compared to the amine-coupled antibodies, suggesting a more defined molecular species. Both conjugates eluted from a gel filtration column in the excluded/void volume, indicating a larger apparent size (>300 kDa rather than the theoretical size of 41 kDa) or hydrodynamic radius. Proteins of molecular weight greater than 300 kDa are not resolved, and therefore it was not possible to determine the true apparent sizes of the scFv−PSA conjugates (see Supporting

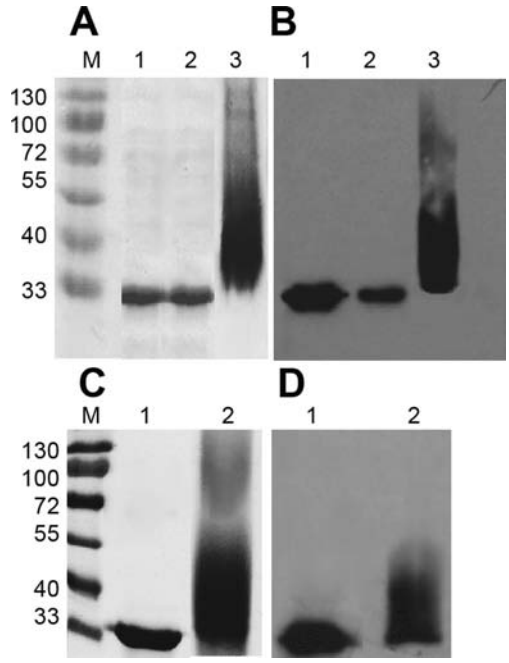

Figure 3. SDS-PAGE and blotting of amine-conjugated scFv. (A) Coomassie-stained gel of protein markers (M), MFE-23 scFv (1), MFE-23 scFv process control (2), and polysialylated MFE-23 scFv (3). (B) as in A, detected with anti-His_6 in a Western blot. (C) Coomassie-stained gel of protein markers (M), F1 scFv (1), and F1-PSA (2). (D) as in B, detected with anti-His_6 in a Western blot.

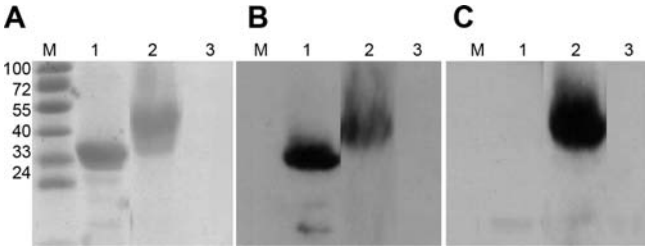

Figure 4. SDS-PAGE and blotting of thiol-conjugated scFv. (A) Coomassie-stained gel of protein markers (M), MFE-23 scFv (1), and polysialylated MFE-23-cys scFv (2), free PSA (3). (B) as in A, detected with anti-His_6 in a Western blot. (C) as in A, detected with anti-PSA in a Western blot.

Information Figure S1). Coomassie stained SDS-PAGE gels and Westerns blots of samples analyzed under reducing conditions showed that the amine-directed conjugates, despite being coupled at low molar ratios to obtain as close to 1:1 coupling as possible, had higher ratios and were much more dispersed in terms of molecular weight. The longer smear suggests high multiples of PSA conjugates even though the mean ratio was 1.4−1.5:1. This was in contrast to the 1.1:1 ratio seen with the site-specific coupled scFv and more importantly, the lower level of heterogeneity.

The presence of the PSA chain was confirmed by immunodetection of the PSA chain by ELISA (Figure 2d) or Western blotting (Figure 4c) as well as the resorcinol assay (Table 1). In each case, the PSA chain alone was undetectable by ELISA or Western blot unless conjugated to a protein.

MFE-23 scFv affinity was consistently in line with published values (around 2 nM) whether unmodified or thiol-coupled to PSA, detected using anti-HIS_6 or anti-PSA antibodies.

Anti-PSA detection by ELISA and Western blot confirmed that the scFvs had been chemically conjugated with the PSA polymer. Free PSA was unable to interact with the ELISA plates and migrated too rapidly on the SDS-PAGE gel (because of its high negative charge) for either to be detected by antibodies. This confirms that the PSA association was covalent and insignificant amounts of free PSA were present in the preparations.

Biodistribution and Pharmacokinetic Studies of MFE-cysPSA11 scFv in a Tumor-Bearing Murine Model. In vivo experiments showed that polysialylation conjugation of scFv led successfully to an increased blood half-life in all cases. We first assessed the effects of polysialylation on the F1 scFv which had no specificity for CEA-expressing LS174T human xenografts (Figure 5a). The blood half-life (beta elimination phase, $t_{1/2}\beta$) for F1-PSA increased almost 3.5-fold (Figure 5a and 5b, Figure 6, Table 2) from 5.6 h to 19.3 h with a 10-fold increase in blood exposure (bioavailability area under the blood clearance curve, Figure 6a, Table 2). Not unexpectedly, polysialylation conjugation also resulted in higher concentrations of scFv in normal tissues. However, this was observed in all tissues, and there was no specific effect on tumor uptake (Figure 5b). We next assessed the effect of polysialylation on biodistribution of MFE-23 (Figure 5c and 5d, Figure 6, Table 2). A greater increase in $t_{1/2}\beta$ was seen for the amine-coupled MFE-23 scFv (a 4.8-fold increase to 20.9 h) and bioavailability (15.2-fold increase). However, compared to the unmodified MFE-23 scFv which localized well and specifically (Figure 5c), the MFE-23-Lys-PSA conjugate was less effective in specifically targeting to the LS174T tumors (Figure 5d, Figure 6b). Consistent with previously published work, the MFE-23 scFv accumulates in this tumor model with a tumor:blood ratio of around 14:1 by 24 h, but the amine-coupled immunoconjugate had a ratio of 1.4 at this point. There was, however, some specificity for MFE-23-Lys-PSA for tumors compared to organs such as kidney, liver, spleen, and muscle.

The reduced immunoreactivity upon amine coupling was likely to account for these observations, and this was confirmed by analyzing the uptake and biodistribution of the fully active MFE-23 cys-PSA immunoconjugate (Figure 5e, Figure 6, Table 2). Once again, polysialylation led to an increased blood half-life but lower than that of the multiply substituted amine conjugates. The $t_{1/2}\beta$ increased 3.6-fold to 15.6 h and the bioavailability increased 9.8-fold Figure 6a. This increase led to increased tumor uptake compared to the faster-clearing unmodified MFE-23 scFv. Greater than 2-fold increase in tumor exposure was seen (Figures 5e and 6b) with the percentage uptake per gram of tumor increasing approximately 2-fold at 6 h (4% to 8.2%) and at 24 h (4.5% to 9.6%). There was 30-fold more scFv in the tumor by 48 h (0.1% to 3.3%). The higher tumor uptake caused by increased blood half-life was at the expense of lower tumor:tissue ratios (Figure 6c). However, there was still significant selectivity, with tumor:blood ratios of 4.4:1 at 24 h and 10.3:1 at 48 h. Throughout, it was observed that all tissue;blood ratios of polysialylated antibodies <1 indicating that polysialylation did not impart nonspecific binding.

DISCUSSION

We have employed chemical conjugation of PSA to scFv antibodies in order to extend their biological half-life. We have tested the immunoreactivity of the conjugates and investigated their biodisribution and ability to localize specifically to human tumors in murine models. All the scFvs showed an increase in apparent molecular weight as a result of conjugation. Although there was some heterogeneity of the immunoconjugates due to the polydisperse nature of naturally occurring PSA, this was consistent with previous observations (*14, 16, 17*).

Many researchers have previously used surface-exposed (*30, 31*) or engineered (*32, 33*) thiol groups for nondisruptive chemical conjugations. The use of mammalian systems often circumvents expression and yield problems (*32*). Furthermore, the incorporation of thiol sites for specific PSA conjugation

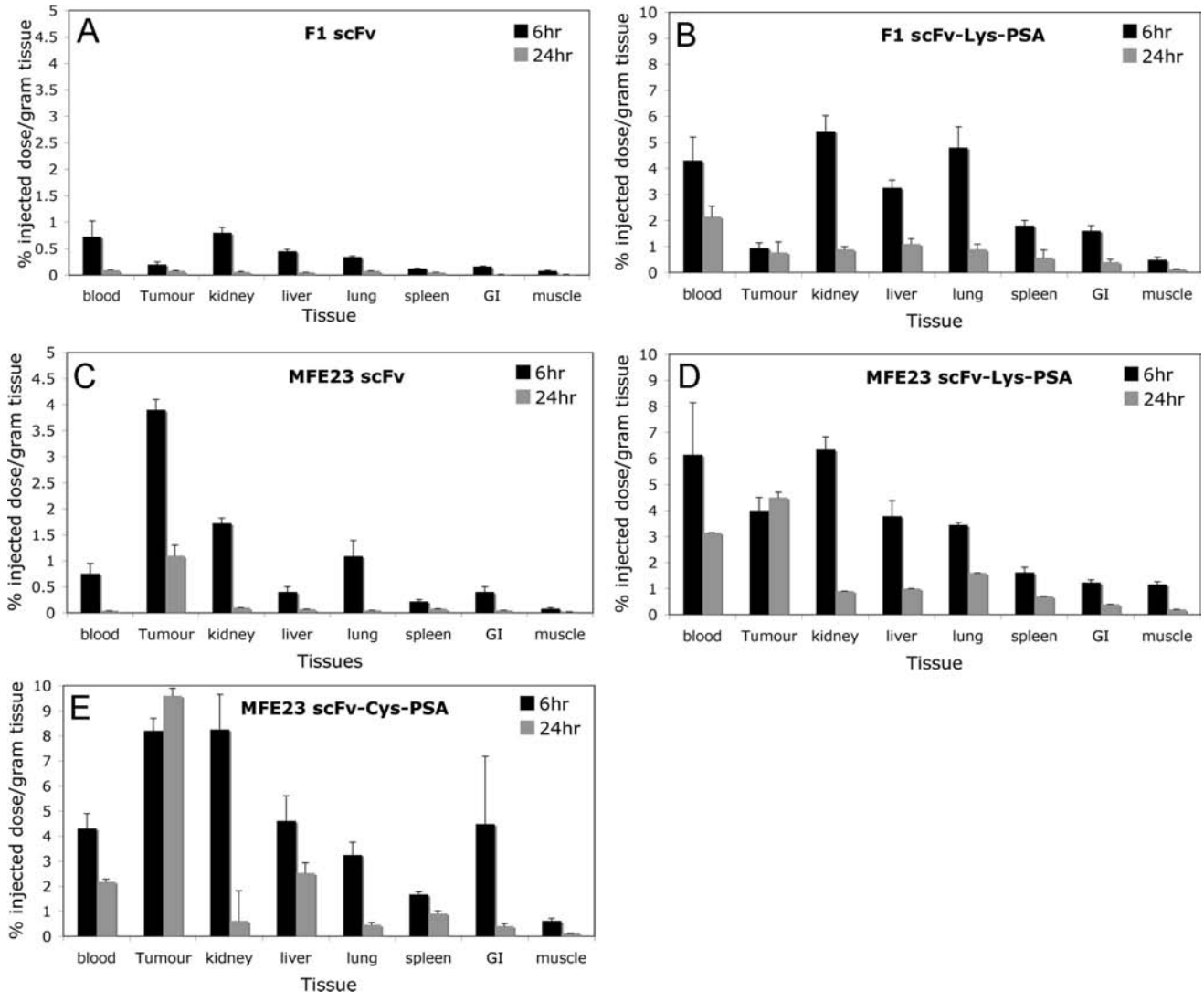

Figure 5. Biodistribution of scFvs and immunoconjugates in LS174T tumor model at 6 and 24 h time points. Percentage injected dose of radiolabeled protein per gram of tissue was determined for F1 scFv (A), amine-coupled F1 scFv-PSA (B), MFE-23 scFv (C), amine-coupled MFE-23 scFv-PSA (D), and thiol-coupled MFE-23-cys-PSA (E).

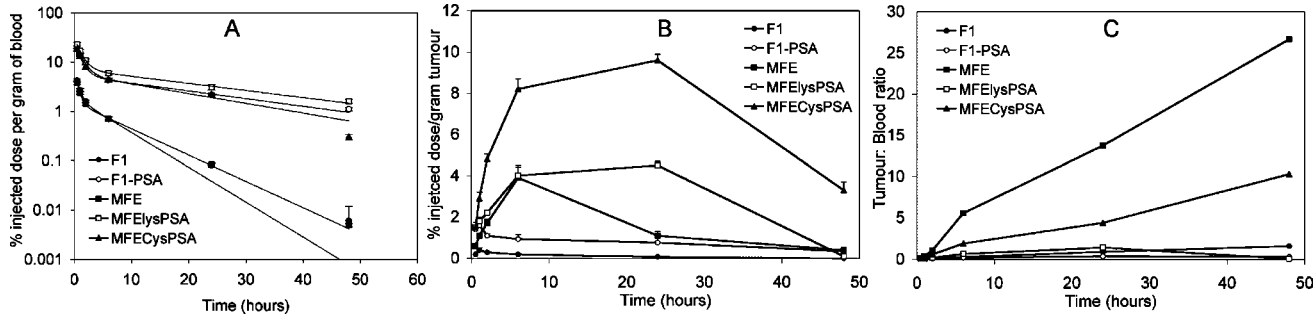

Figure 6. Pharmacokinetic profiles derived from full biodistribution study in LS174T tumor model over 48 h. (A) Blood clearance profile, (B) tumor uptake profile, and (C) tumor to blood ratio profile of F1 scFv (●), amine-coupled F1 scFv-PSA (○), MFE-23 scFv (■), amine-coupled MFE-23 scFv-PSA (□), and thiol-coupled MFE-23-cys-PSA (▲).

should result in a more reproducible, homogeneous product that can be more definitively characterized as has been shown for scFv−PEG immunoconjugates (*33*). This is of particular importance for any subsequent biopharmaceutical interest which requires definitive characterization to be determined for the purpose of therapeutic applications. By applying this methodology for PSA conjugation, it is believed that the longevity of antibodies in circulation can be improved without compromising its bioactivity or structural integrity.

Our immunoreactivity experiments with the PSA conjugations revealed that the thiol-specific conjugation method was superior to amine conjugation. The retention of protein bioactivity observed after thiol-specific PSA conjugation of the scFv MFE-23 has mirrored the success of other groups that have used thiols for chemical attachments. PEGylation of proteins, which represents the biggest contribution of polymer conjugates to the biopharmaceutical industry, has recently shown various successes in thiol-specific conjugation such as in the C-terminal

Table 2. Summary of Pharmacokinetic Parameters[a]

ScFv species	t1/2α (h)	t1/2β (h)	Area under blood clearance curve (bioavailability or blood exposure)
F1	0.43 ± 0.04	5.6 ± 0.12	13.03
F1-PSA	0.88 ± 0.19	19.3 ± 0.91	137.7
MFE-23	0.42 ± 0.01	4.3 ± 0.5	12.3
MFE-23-Lys-PSA	0.78 ± 0.03	20.9 ± 1.5	186.6
MFE-23-Cys-PSA	0.7 ± 0.07	15.6 ± 3.7	120.6

[a] The biodistribution experimental data are shown in Figures 4 and 5. The blood clearance profile was fitted to a biexponential decay model and $t_{1/2}\alpha$ and $t_{1/2}\beta$ determined. The bioavailability or blood exposure was determined by calculating the area under the blood clearance curve.

PEGylation of the thrombin cofactor thrombomodulin (*34*), modulating longevity of hemoglobin using different lengths of PEG (*35*), and PEGylation of an scFv (*33*), a *Pseudomonas*-derived immunotoxin (*36*) and a clinically approved antibody (*6*) have all been described using thiol-specific conjugation. However, increasing protein longevity through site-specific thiol PEGylation was demonstrated as early as 1990 with a 4-fold increased systemic exposure using conjugated interleulin-2 (*31*). The thioether linkage is well-characterized and used in many examples such as in the production of immunotoxins, suggesting that such bonds are stable and can lead to increased longevity in vivo (*37*).

Our study was concerned with investigating an alternative method to pharmacokinetic engineering as well as to illustrate the benefits of site-specific polysialylation over the more unpredictable amine coupling method. Reductive amine coupling was previously shown to work well for an antiplacental alkaline phosphatase (PLAP) Fab fragment with little loss in bioactivity; however, the similar approach used for the MFE-23 scFv led to a 20-fold reduction in affinity. By introducing a C-terminal cysteine residue on to the recombinantly expressed scFv it was anticipated that the free thiol group could be used to introduce a PSA chain through the formation of a thioether link, which would result in a more homogeneous coupled product that retained full bioactivity. The loss of reactivity could be explained by the chemical modification of the CDR-H1 loop in the scFv (*22*). A similar situation arose in the anti-HER2 scFv, C6.5 which had a undesirably situated lysine residue in the CDR-H3, which was not required for binding. This was subsequently replaced by mutagenesis to an alanine resulting in chemical conjugates which retained immunoreactivity (*38*).

The main reason for chemically modifying scFvs with PSA is to modulate their half-lives so that they clear more slowly, accumulate to higher levels in the target tissues (tumors in this case), but still retain some high degree of selectivity (e.g., high tumor:blood ratios). Whole immunoglobulins characteristically clear slowly with half-lives in the region of 3−5 days, resulting in tumor:blood ratios >1 after about 48 h (*20, 39*). Single-chain Fvs clear in a few hours but have tumor:blood ratios of >20:1 at this time. This research has shown that site-specific polysialylation can impart a blood clearance half-life (in murine models) slower than scFvs (4−5 h) or Fab (around 10 h), better blood bioavailability (2−3 fold better than some Fabs and only 2−3 lower than some whole IgGs), and specificity ratios much more favorable than whole immunoglobulins. Polysialylated scFvs, easily and inexpensively prepared, could represent a viable alternative to whole IgG without the concerns associated with the Fc-domain (*39, 40*). In vivo analyses confirmed the pharmacokinetic benefit of chemical polysialylation, but unlike the nonspecific approach shown to be successful with the H17E2 Fab (*17*), site-specific coupling was required to maintain scFv function. In all three examples shown here, polysialylation resulted in around 3- to 5-fold increase in blood clearance and around 10-fold increase in bioavailability. There was a less than 2-fold increase in the alpha-phase (distribution) blood clearance, suggesting that the main pharmacokinetic enhancement was in the systemic elimination phase. The pharmacokinetic extension observed here is likely due to the increase in apparent size, stabilizing the protein and excluding it from renal clearance. This is consistent with the increased size observed by size-exclusion chromatography (>300 kDa), due to the hydrophilic polymer binding noncovalently to a network of water molecules as has been proposed for PEG conjugates (*40*).

There have been many approaches to pharmacokinetic engineering (*20, 41*), with PEGylation being the most commonly used. The greatest potential for the present approach is in the modification of antibody fragments against blood-borne factors such as tissue necrosis factor (TNFα), interleukin-6 (IL-6), or vascular endothelial cell growth factor (VEGF). Longer bioavailability will lead to more pronounced inhibition, leading to an improved therapeutic potential. Although often problematic during expression in *E. coli*, but less so in mammalian systems, multiply appended C-terminal thiols will allow the coupling of defined numbers of PSA chains which could lead to pharmacokinetic refinement for a particular therapeutic purpose.

In conclusion, this work has shown that random amine-directed coupling of PSA to scFvs is successful but not optimal. Favorable conjugation is achieved by site-specific coupling of PSA to engineered C-terminal thiols. The latter approach leads to antibody fragments with full immunoreactivity and increased blood half-life leading to higher tumor uptake but with improved specificity ratios compared to other antibody formats.

ACKNOWLEDGMENT

This work was funded by a Lipoxen Technologies-BBSRC/CASE studentship to MPD and AC (ref. no. 01/A2/C/07249). We would like to thank Dr. Peter Laing and Prof. Gregory Gregoriadis for useful discussions and members of the Imperial College CBS Unit for advice and technical help with the in vivo experiments.

Supporting Information Available: The gel filtration chromatograms of the MFE scFv, MFE-Cys scFv, and MFE-Cys−PSA conjugate are shown in Figure S1. This material is available free of charge via the Internet at http://pubs.acs.org.

LITERATURE CITED

(1) Wang, W., Wang, E. Q., and Balthasar, J. P. (2008) Monoclonal antibody pharmacokinetics and pharmacodynamics. *Clin. Pharmacol. Ther. 84*, 548–58.

(2) Lobo, E. D., Hansen, R. J., and Balthasar, J. P. (2004) Antibody pharmacokinetics and pharmacodynamics. *Pharm. Sci. 93*, 2645–68.

(3) Harris, J. M., and Chess, R. B. (2003) Effect of pegylation on pharmaceuticals. *Nat. Rev. Drug Discovery 2*, 214–21.

(4) Veronese, F. M., and Pasut, G. (2005) PEGylation, successful approach to drug delivery. *Drug Discovery Today 10*, 1451–8.

(5) Hoofnagle, J. H., and Seeff, L. B. (2006) Peginterferon and ribavirin for chronic hepatitis. *N. Engl. J. Med. 355*, 2444–51.

(6) Dinesen, L., and Travis, S. (2007) Targeting nanomedicines in the treatment of Crohn's disease: focus on certolizumab pegol (CDP870). *Int. J. Nanomed. 2*, 39–47.

(7) Bendele, A., Seely, J., Richey, C., Sennello, G., and Shopp, G. (1998) Renal tubular vacuolation in animals treated with polyethyleneglycol-conjugated proteins. *Toxicol. Sci. 42*, 152–7.

(8) Srroda, K., Rydlewski, J., Langner, M., Kozubek, A., Grzybek, M., and Sikorski, A. F. (2005) Repeated injections of PEG-PE liposomes generate anti-PEG antibodies. *Cell Mol. Biol. Lett. 10*, 37–47.

(9) Hamad, I., Hunter, A. C., Szebeni, J., and Moghimi, S. M. (2008) Poly(ethylene glycol)s generate complement activation products in human serum through increased alternative pathway turnover and a MASP-2-dependent process. *Mol. Immunol. 46*, 225–32.
(10) Steenbergen, S. M., and Vimr, E. R. (2003) Functional relationships of the sialyltransferases involved in expression of the polysialic acid capsules of Escherichia coli K1 and K92 and Neisseria meningitidis groups B or C. *J. Biol. Chem. 278*, 15349–59.
(11) Durbec, P., and Cremer, H. (2001) Revisiting the function of PSA-NCAM in the nervous system. *Mol. Neurobiol. 24*, 53–64.
(12) Stockert, R. J. (1995) The asialoglycoprotein receptor: relationships between structure, function, and expression. *Physiol. Rev. 75*, 591–609.
(13) Muhlenhoff, M., Eckhardt, M., and Gerardy-Schahn, R. (1998) Polysialic acid: three-dimensional structure, biosynthesis and function. *Curr. Opin. Struct. Biol. 8*, 558–64.
(14) Jain, S., Hreczuk-Hirst, D. H., McCormack, B., Mital, M., Epenetos, A., Laing, P., and Gregoriadis, G. (2003) Polysialylated insulin: synthesis, characterization and biological activity in vivo. *Biochim. Biophys. Acta 1622*, 42–9.
(15) Gregoriadis, G., Jain, S., Papaioannou, I., and Laing, P. (2005) Improving the therapeutic efficacy of peptides and proteins: a role for polysialic acids. *Int. J. Pharm. 300*, 125–30.
(16) Fernandes, A. I., and Gregoriadis, G. (2001) The effect of polysialylation on the immunogenicity and antigenicity of asparaginase: implication in its pharmacokinetics. *Int. J. Pharm. 217*, 215–24.
(17) Constantinou, A., Epenetos, A. A., Hreczuk-Hirst, D., Jain, S., and Deonarain, M. P. (2008) Modulation of antibody pharmacokinetics by chemical polysialylation. *Bioconjugate Chem. 19*, 643–50.
(18) Holliger, P., and Hudson, P. J. (2005) Engineered antibody fragments and the rise of single domains. *Nat. Biotechnol. 23*, 1126–36.
(19) Schmidt, F. R. (2004) Recombinant expression systems in the pharmaceutical industry. *Appl. Microbiol. Biotechnol. 65*, 363–72.
(20) Beckman, R. A., Weiner, L. M., and Davis, H. M. (2007) Antibody constructs in cancer therapy: protein engineering strategies to improve exposure in solid tumors. *Cancer 109*, 170–9.
(21) Chester, K. A., Begent, R. H., Robson, L., Keep, P., Pedley, R. B., Boden, J. A., Boxer, G., Green, A., Winter, G., and Cochet, O. (1994) Phage libraries for generation of clinically useful antibodies. *Lancet 343*, 455–456.
(22) Boehm, M. K., Corper, A. L., Wan, T., Sohi, M. K., Sutton, B. J., Thornton, J. D., Keep, P. A., Chester, K. A., Begent, R. H., and Perkins, S. J. (2000) Crystal structure of the anti-(carcinoembryonic antigen) single-chain Fv antibody MFE-23 and a model for antigen binding based on intermolecular contacts. *Biochem. J. 346*, 519–528.
(23) Sainz-Pastor, N., Tolner, B., Huhalov, A., Kogelberg, H., Lee, Y. C., Zhu, D., Begent, R. H., and Chester, K. A. (2006) Deglycosylation to obtain stable and homogeneous Pichia pastoris-expressed N-A1 domains of carcinoembryonic antigen. *Int. J. Biol. Macromol. 39*, 141–150.
(24) Begent, R. H., Verhaar, M. J., Chester, K. A., Casey, J. L., Green, A. J., Napier, M. P., Hope-Stone, L. D., Cushen, N., Keep, P. A., Johnson, C. J., Hawkins, R. E., Hilson, A. J., and Robson, L. (1996) Clinical evidence of efficient tumor targeting based on single-chain Fv antibody selected from a combinatorial library. *Nat. Med. 2*, 979–984.
(25) Mayer, A., Tsiompanou, E., O'Malley, D., Boxer, G. M., Bhatia, J., Flynn, A. A., Chester, K. A., Davidson, B. R., Lewis, A. A., Winslet, M. C., Dhillon, A. P., Hilson, A. J., and Begent, R. H. (2000) Radioimmunoguided surgery in colorectal cancer using a genetically engineered anti-CEA single-chain Fv antibody. *Clin. Cancer Res. 6*, 1711–1719.
(26) Mayer, A., Francis, R. J., Sharma, S. K., Tolner, B., Springer, C. J., Martin, J., Boxer, G. M., Bell, J., Green, A. J., Hartley, J. A., Cruickshank, C., Wren, J., Chester, K. A., and Begent, R. H. (2006) A phase I study of single administration of antibody-directed enzyme prodrug therapy with the recombinant anti-carcinoembryonic antigen antibody-enzyme fusion protein MFECP1 and a bis-iodo phenol mustard prodrug. *Clin. Cancer Res. 12*, 6509–6516.
(27) Svennerholm, L. (1957) Quantitative estimation of sialic acids. II. A colorimetric resorcinol-hydrochloric acid method. *Biochim. Biophys. Acta 24*, 604–11.
(28) Schmiedl, A., Breitling, F., Winter, C. H., Queitsch, I., and Dübel, S. (2000) Effects of unpaired cysteines on yield, solubility and activity of different recombinant antibody constructs expressed in *E. coli*. *J. Immunol. Methods 242*, 101–14.
(29) Lee, Y. C., Boehm, M. K., Chester, K. A., Begent, R. H., and Perkins, S. J. (2002) Reversible dimer formation and stability of the anti-tumour single-chain Fv antibody MFE-23 by neutron scattering, analytical ultracentrifugation, and NMR and FT-IR spectroscopy. *J. Mol. Biol. 320*, 107–27.
(30) Antoniw, P., Farnsworth, A. P., Turner, A., Haines, A. M., Mountain, A., Mackintosh, J., Shochat, D., Humm, J., Welt, S., Old, L. J., Yarranton, G. T., and King, D. J. (1996) Radioimmunotherapy of colorectal carcinoma xenografts in nude mice with yttrium-90 A33 IgG and Tri-Fab (TFM). *Br. J. Cancer 74*, 513–24.
(31) Goodson, R. J., and Katre, N. V. (1990) Site-directed pegylation of recombinant interleukin-2 at its glycosylation site. *Bio/Technology 8*, 343–6.
(32) Fabbrini, M., Trachsel, E., Soldani, P., Bindi, S., Alessi, P., Bracci, L., Kosmehl, H., Zardi, L., Neri, D., and Neri, P. (2006) Selective occlusion of tumor blood vessels by targeted delivery of an antibody-photosensitizer conjugate. *Int. J. Cancer 118*, 1805–13.
(33) Natarajan, A., Xiong, C. Y., Albrecht, H., DeNardo, G. L., and DeNardo, S. J. (2005) Characterization of site-specific ScFv PEGylation for tumor-targeting pharmaceuticals. *Bioconjugate Chem. 16*, 113–21.
(34) Cazalis, C. S., Haller, C. A., Sease-Cargo, L., and Chaikof, E. L. (2004) C-terminal site-specific PEGylation of a truncated thrombomodulin mutant with retention of full bioactivity. *Bioconjugate Chem. 15*, 1005–9.
(35) Manjula, B. N., Tsai, A., Upadhya, R., Perumalsamy, K., Smith, P. K., Malavalli, A., Vandegriff, K., Winslow, R. M., Intaglietta, M., Prabhakaran, M., Friedman, J. M., and Acharya, A. S. (2003) Site-specific PEGylation of hemoglobin at Cys-93(beta): correlation between the colligative properties of the PEGylated protein and the length of the conjugated PEG chain. *Bioconjugate Chem. 14*, 464–72.
(36) Tsutsumi, Y., Onda, M., Nagata, S., Lee, B., Kreitman, R. J., and Pastan, I. (2000) Site-specific chemical modification with polyethylene glycol of recombinant immunotoxin anti-Tac(Fv)-PE38 (LMB-2) improves antitumor activity and reduces animal toxicity and immunogenicity. *Proc. Natl. Acad. Sci. U.S.A. 97*, 8548–53.
(37) Sanderson, R. J., Hering, M. A., James, S. F., Sun, M. M., Doronina, S. O., Siadak, A. W., Senter, P. D., and Wahl, A. F. (2005) In vivo drug-linker stability of an anti-CD30 dipeptide-linked auristatin immunoconjugate. *Clin. Cancer Res. 11*, 843–52.
(38) Adams, G. P., Shaller, C. C., Chappel, L. L., Wu, C., Horak, E. M., Simmons, H. H., Litwin, S., Marks, J. D., Weiner, L. M., and Brechbiel, M. W. (2000) Delivery of the alpha-emitting radioisotope bismuth-213 to solid tumors via single-chain Fv and diabody molecules. *Nucl. Med. Biol. 27*, 339–46.
(39) Deonarain, M. P. (2008) Recombinant antibodies for cancer therapy. *Expert Opin. Biol. Ther. 8*, 1123–41.
(40) Dhalluin, C., Ross, A., Leuthold, L. A., Foser, S., Gsell, B., Muller, F., Senn, H. (2005)Structural and biophysical characterization of the 40 kDa PEG-interferon-α_{2a} and its individual positional isomers*Bioconjugate Chem. 16*,504–17.
(41) Carter, P. (2006) Potent antibody therapeutics by design. *Nat. Rev. Immunol. 6*, 343–57.

BC8005122

SITE-SPECIFIC POLYSIALYLATION OF AN ANTI-TUMOR SINGLE-CHAIN FV FRAGMENT

[1]Constantinou, A, [1]Epenetos, AA, [2,3]Hreczuk-Hirst, D, [2]Jain S, [1,5]Wright, M, [4]Chester, KA. & [1*]Deonarain, MP.

SUPPORTING FIGURE S1

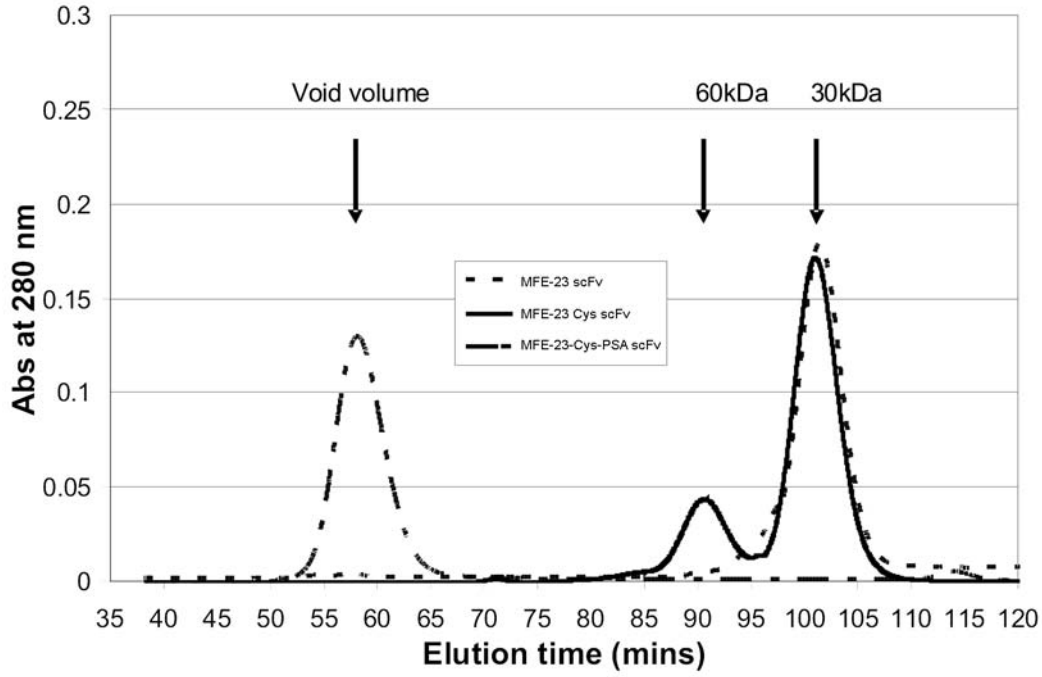

GEL FILTRATION PROFILES OF SCFVS AND SCFV-CYS-PSA CONJUGATE

Gel filtration on a Superdex-200 column shows that the scFvs migrate with native molecular weights as expected (scFv, dashed line, 30kDa; scFv-Cys, 60kDa, bold line). The size of the scFv-Cys-PSA conjugate (scFv-Cys-PSA, >300kDa, broken dashed line) was unable to be determined accurately.

Studies of Poly(ethylene glycol) Modification of HM-3 Polypeptides

Kang Zhou,† Xiaoqing Zheng,† Han-Mei Xu,* Jie Zhang, Yaqing Chen, Tao Xi, and Tingting Feng

Department of Life Science and Technology, China Pharmaceutical University, Nanjing, 210009, P. R. China. Received December 4, 2008; Revised Manuscript Received April 7, 2009

An RGD modified endostatin-derived synthetic peptide, named HM-3, is a polypeptide angiogenesis inhibitor previously synthesized in our laboratory. Its robust inhibitory effects on endothelial cell migration and tumor growth have been demonstrated by in vivo and in vitro activity assays. The RGD integrin recognition sequence enables the selective binding of HM-3 and its specific targeting to tumor cells that express high levels of integrin. However, the drug has relatively short half-life in vivo, thus requiring administration twice a day to achieve its optimal in vivo antitumor efficacy. In the current study designed to prolong HM-3 half-life, we used methoxy-poly(ethylene glycol)-aldehyde (mPEG-ALD) to specifically modify its N terminus and optimized the reaction condition via monitoring the modification by reverse-phase high-performance liquid chromatograph (RP-HPLC) under varying stoichiometric ratios ($n_{\text{mPEG10k-ALD}}$:$n_{\text{HM-3}}$), reaction times, and pH values. The maximal modification rate was achieved in a reaction when substrates mPEG10k-ALD and HM-3 were mixed at the molar ratio of 2:1 in a pH 6 phosphate buffer after 4 h incubation at room temperature. The reaction product of this optimal reaction was purified to 96% purity by RP-HPLC. Compared with HM-3, the newly modified PEG_{10k}-HM-3 was shown to be more active in the inhibition of angiogenesis in the chorioallantoic membrane of chick embryos (CAM), its rate of in vitro degradation in serum was markedly reduced, and its in vivo half-life was prolonged by 5.86-fold relative to unmodified HM-3 after intravenous injection into male SD rats.

INTRODUCTION

Endostatin, the C-terminal fragment of collagen XVIII, with a molecular weight of 20-kDa, can specifically inhibits endothelial cell proliferation and migration, and reduces vascularization and blood flow in gliosarcoma (*1*). It also dramatically inhibits growth of the various primary tumors in mice. Interaction of endostatin with integrin implicates its potential targets for function (*2, 3*). Endostatin binds one atom of zinc (Zn) per monomer via the three histidines in the NH_2 terminus of the molecule (histidines 1, 3, and 11) and aspartic acid 76 (*4*−*6*).

Numerous attempts have been made to produce biologically active endostatin via recombinant DNA technology (*7*). However, when expressed in *E. coli*, recombinant endostatin accumulated as inclusion bodies in the cytoplasm. During in vitro renaturation or the refolding process, the recovery of soluble and active endostatin was very low and most of the protein precipitated again during the refolding process owing to the renaturation of proteins containing multiple disulfide bonds (*8*−*10*). A highly efficient production of biologically active endostatin, with large quantity and low cost, urgently needs both further structure−function relationship investigation and its potential application as antitumor remedy. To achieve this goal, several groups have synthesized and studied the peptides that correspond to the partial sequence of endostatin (*11*−*16*).

Two groups have reported the activity of a peptide containing an 11 amino acid peptide (ES-2, IVRRADRAAVP) derived from the amino terminus of endostatin (*11, 12*). In our previous study, we found that the 11 amino acid peptide dramatically inhibited angiogenesis on the chorioallantoic membrane of chick embryo (CAM) in vivo but had no antitumor effect in tumor-bearing mice. We speculate that this difference might be caused by lesser distribution of the drug to tumor tissue in mouse models than that in chick embryos. In order to validate this hypothesis, a new strategy that increases the target delivery of the peptide to tumor is needed. In the past decade, many molecules with RGD peptide have been described as efficiently delivering drugs to tumor vasculature endothelium (*17, 18*). Therefore, in our previous study, we get a RGD-modified endostatin-derived synthetic peptide HM-3 (IRRADRAAVPG-GGGRGD); it displayed higher antitumor effects (*19*). Safety experiments were conducted to study the possible toxic effects of HM-3; there no evidence of toxicity in the treated animals. These results show that HM-3 is an effective and safe peptide as an anticancer drug.

However, in the in vivo pharmacokinetic studies, the half-life of HM-3 in male SD rats was measured at 27.66 ± 7.37 min. This indicates that, in any future clinical applications, higher doses or more frequent administration is required to maintain sufficient drug concentration in the blood, which in turn will exacerbate toxic effects on the patients.

Protein modification is an effective method to improve efficacy and prolong drug half-lives. PEG modification of drugs can enhance protein solubility and stability, slow down drug metabilization within the body, reduce or eliminate immunogenicity, increase circulation time in the bloodstream, and lengthen administration intervals (*20, 21*). Lee et al. (*16*) and Na et al. (*23, 24*) have successfully modified polypeptide drugs using PEG, prolonged in vivo clearance half-lives of glucagon-like peptide-1 and salmon calcitonin (sCT), and enhanced their pharmacokinetic properties and efficacy. This current study was aimed at identifying the appropriate PEG modifying reagents suitable for HM-3, to achieve the optimal combination of biological and pharmacokinetic properties following the specific

* Correspondence to: Center of Bitechnology, Department of Life Science and Technology, China Pharmaceutical University, 24 Tongjiaxiang, Nanjing, 210009, P. R. China; Tel: 86-25-83271007; Fax: 86-25-85438355; E-mail: xuhanmei@yahoo.com.cn.

† Kang Zhou and Xiaoqing Zheng are the first coauthor.

10.1021/bc900070r CCC: $40.75 © 2009 American Chemical Society
Published on Web 05/04/2009

modification, ultimately to provide a promising lead for development of new antitumor drugs.

MATERIALS AND METHODS

1. Materials. HM-3 (99% purity) was chemically synthesized. mPEG$_{10k}$-ALD (80% purity) was purchased from Beijing Kaizheng Biotech Development Co. Ltd., batch number 080540. Trifluoroacetate (TFA), acetonitrile (ACN), and sodium cyanoborohydride were purchased from TEDIA, ROE Scientific Inc., and Shanghai Darui Fine Chemicals Co. Ltd., respectively.

White leghorn chicken embryos and male SD rats were purchased from Nanjing Medical Instrument Factory and New Drug Screening Center at China Pharmaceutical University, respectively.

2. Methods. *2.1. PEG Modification of HM-3 and Purification.* A series of reactions were set up using varying stoichiometric ratios ($n_{\text{mPEG10k-ALD}}$:$n_{\text{HM-3}}$)of mPEG$_{10k}$-ALD and HM-3 (1 mg, 1 mg/mL) in phosphate buffers (0.1 mol/mL) at pH 5, 6, and 7. The final concentration of sodium cyanoborohydride was 0.05 mol/mL.

Sample aliquots were taken after 2, 3, and 4 h; then, glycine was added to terminate the reactions. The reaction mixtures were first analyzed for the modification rate by RP-HPLC on a C18 column (150 × 4.6 mm, 5 μm, YMC). The mobile phases contained 0.1% TFA in ACN (solution B) and 0.1% TFA in water (solution A), and was applied as a gradient of 10−100% solution B (or 90−10% solution A). Detection wavelength was set at 220 nm. The flow rate was at 1 mL/min, and the running time was 15 min.

The reaction products were further purified by a semipreparative RP-HPLC with a C18 column. The mobile phases were 0.1% TFA in ACN (solution B) and 0.1% TFA in water (solution A), and was applied as a gradient of 35−50% solution B (or 65−50% solution A). The detection wavelength was set at 220 nm; the flow rate was at 3 mL/min, and the running time was 20 min.

2.2. Validation of Reaction Products. Modification products were analyzed by RP-HPLC and SDS-PAGE electrophoresis. For the SDS-PAGE identification, reaction mixtures were separated on a SDS-PAGE gel comprising 5% stacking gel and 16% separation gel. The gel was stained with Coomassie brilliant blue, and destained until the background was washed off. For the HPLC identification, the polypeptide substrate and the reaction products were analyzed by RP-HPLC as described above in section 2.1, and their HPLC chromatograms were compared.

2.3. In Vitro Stability of PEG$_{10k}$-HM-3 in Serum. In aliquots of 0.9 mL SD rat serum, 0.1 mL of HM-3 (6 mol/mL), PEG$_{10k}$-HM-3 (6 mol/mL), and saline buffer were added into separate tubes and incubated in a 37 °C water bath. At 0, 2, 6, 10, 15, 20, 25, 50, and 60 min of incubation, 0.1 mL aliquots were taken and precipitated with perchloric acid. After centrifugation to obtain the supernatants, RP-HPLC analysis was carried out to measure the drug concentration in the supernatants, and retention percentages were calculated.

2.4. In Vivo Pharmacokinetics of PEG$_{10k}$-HM-3. Male SD rats weighing roughly 200 g were used, and blood samples were taken the day before the experiment as control. PEG$_{10k}$-HM-3 (35 mg/kg) was injected via tail vein, and blood samples were collected through the canthus at different time points and stored at −70 °C before use. Blood samples were precipitated with perchloric acid and centrifuged. The supernatants were analyzed by RP-HPLC to measure the drug concentration. The pharmacokinetic parameters in SD rats were calculated using the *DAS* v1.0 (Drug and Statistics for Windows) software and then subjected to statistical analyses.

2.5. CAM Angiogenesis Assays. In 7 day chick embryos, after the air chamber was opened, the shell membrane was removed and sealed by a transparent tape to form a pseudoair chamber which also serves as transparent observation windows. After a 1 day stabilization period, the transparent tape was cut open, and a drug carrier plate with a 5 mm diameter was placed in the chamber. Ten microliters of each test reagent was added onto the plate. The physiological saline and endostatin (8 mg/mL) were used as negative and positive controls, respectively. In the experimental groups, HM-3 (1 mg/mL) and PEG$_{10k}$-HM-3 (6.6 mg/mL) were used (1 mg/mL HM-3 and 6.6 mg/mL PEG-HM-3 yield equal molar concentrations). After 48 h incubation at 37 °C, the pseudoair chambers of chick embryos were opened and fixed in the fixative (formaldehyde−acetone, 1:1) for 5 min. The chick embryo was subsequently removed, and the CAM was carefully peeled off from the eggshell and laid out flat for photography. The medium−small blood vessels within a radius of 5 mm from the center of the carrier plate were counted and subjected to statistical analysis.

3. RESULTS

3.1. PEG Modification of HM-3 and Purification of the Modification Product. A series of modification reactions were set up by mixing mPEG-ALD and HM-3 at different molar ratios under conditions with varying buffer pH and reaction time. The reaction mixtures were analyzed by RP-HPLC to assess effects on the reactions by different conditions. The results (Figure 1A) showed that there was only one single peak for the modification product, and the maximal modification rate of 88.7% was achieved when the substrate molar ratio ($n_{\text{mPEG10k-ALD}}$:$n_{\text{HM-3}}$) was set at 2, and the reactions were incubated for 4 h at RT in a pH 6 phosphate buffer. The reaction time and substrate molar ratio have the most profound effects on the modification rate.

Reaction products were purified through semipreparative RP-HPLC. Analyses showed that the purity of the products was greater than 96% (Figure 1B).

3.2. Product Validation. After HM-3 modification by mPEG-ALD, the product was shown as a single band by electrophoresis analysis (Figure 2), and RP-HPLC chromatograms (Figure 1) also revealed the presence of a single peak, confirming that only one modification product was generated from the modification reaction.

3.3. In Vitro Serum Stability of PEG$_{10k}$-HM-3. Multiple enzymes are present in the blood that can degrade polypeptides and proteins. After the drug was mixed with serum and incubated at 37 °C, RP-HPLC analysis was performed to measure drug retention percentage in the serum at different time points. The degradation rate of HM-3 in serum was very high, as HM-3 became undetectable after only 15 min incubation. By contrast, 48.8% of PEG$_{10k}$-HM-3 remained intact after 15 min (Figure 3), and 16.5% could still be detected after 60 min. These results demonstrate that, after modification, the polypeptide became less susceptible to the degradative enzymes in the serum, and its stability was markedly enhanced.

3.4. In Vivo Pharmacokinetic Behaviors of PEG$_{10k}$-HM-3. After intravenous injection into male SD rats, the drugs before and after modification were tested for a panel of pharmacokinetic parameters. The results (Table 1 and Figure 4) showed significantly improved in vivo pharmacokinetic behavior of the drug after PEG modification. The half-life of HM-3 in the blood of these rats was 27.66 ± 7.37 min. After the modification, the half-life of PEG$_{10k}$-HM-3 was 162.08 ± 36.57 min, which was 5.86-fold longer than that of the unmodified drug, and the clearance rate was measured at 566.34 ± 56.68 L/min/kg, 141.59-fold slower relative to the unmodified HM-3. The area under the curve (AUC) was increased by 123.47-fold to reach

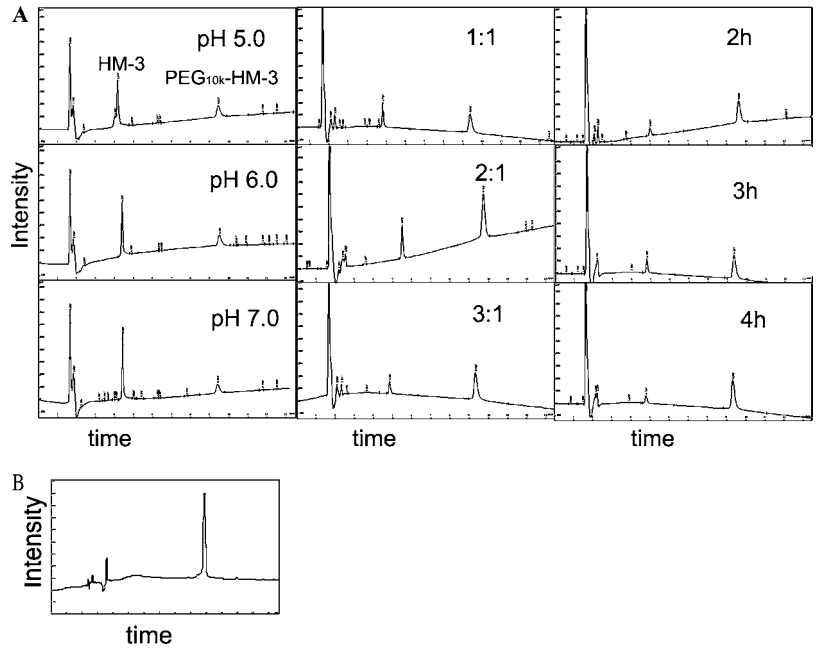

Figure 1. RP-HPLC analysis of reaction mixtures obtained by reaction of mPEG-ALD with HM-3 at different pHs, molar ratios ($n_{mPEG\text{-}ALD}$:$n_{HM\text{-}3}$), and reaction times as indicated. Analysis was performed on a C18 column with water/acetonitrile/TFA as eluent and a flow rate of 1 mL/min, and peaks were monitored at 220 nm (A). RP-HPLC analysis of the PEGylated HM-3 Purification (B).

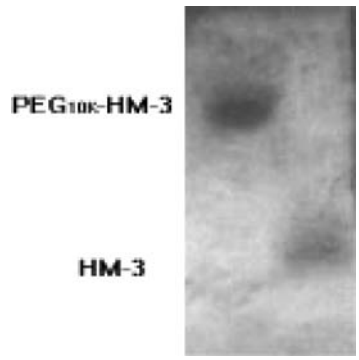

Figure 2. SDS-PAGE analysis of the PEGylated HM-3 purification and HM-3.

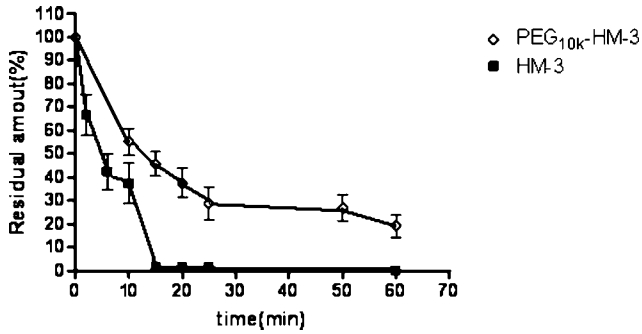

Figure 3. Residual amounts of equal molar HM-3 and PEG_{10k}-HM-3 in plasma in vitro at 37 °C. Values are mean ± SD (n = 3).

61 623.73 ± 4564.47 ng/L min. Finally, the average residence time of the modified PEG_{10k}-HM-3 was 69.39 ± 6.21 min.

3.5. Inhibitory Effects on Angiogenesis in the CAM Model. 48 h after drug administration into the chick embryos, medium and small blood vessels were counted within the 5 mm radius from the center of the drug carrier plate. The results demonstrated significant inhibitory effects of PEG_{10k}-HM-3 on angiogenesis. Compared with the negative control, both vessel number and branching were significantly reduced after treatment

Table 1. Pharmacokinetic Parameters after PEGylated HM-3 Administration to SD Rats[a]

	$T_{1/2}$ (min)	Cl (L/min/kg)	MRT (min)	AUC (ug/L min)
PEG_{10k}-HM-3	162.08 ± 36.57	566.34 ± 56.68	69.39 ± 6.21	61.62 ± 4.56
HM-3	27.66 ± 7.37	4.00 ± 0.80		0.49 ± 0.13

[a] Data are means ± SD (n = 3). $T_{1/2}$, half life; AUC, area under the curve; MRT, mean residence time; Cl, clearance; V_d, apparent distribution volume.

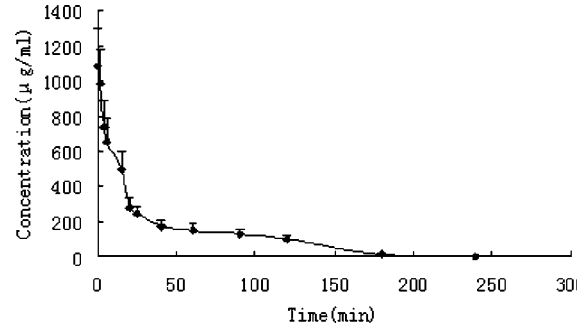

Figure 4. Plasma concentration of PEG_{10k}-HM-3(35 mg/kg) after injection via tail vein to SD rates. Values are mean ± SD (n = 3).

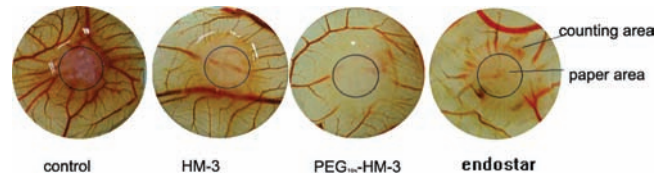

Figure 5. Chick chorioallantonic membranes treated with endostain (8 mg/mL), HM-3 (1 mg/mL), and PEG_{10k}-HM-3 (6.6 mg/mL) for 48 h.

with either PEG_{10k}-HM-3 or HM-3 (Figures 5 and 6). The blood vessels were as follows: endostatin 30 ± 5.0, HM-3 34.7 ± 7.3, and PEG10K-HM-3, 25.7 ± 5.6.

Moreover, PEG_{10k}-HM-3-treated CAMs showed much lower density of medium−small blood vessels and fewer to almost

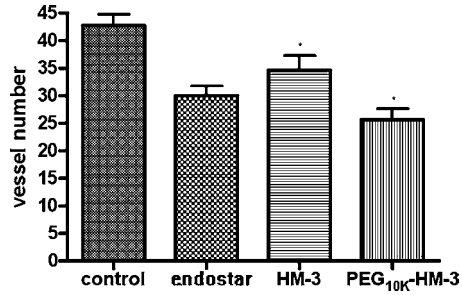

Figure 6. Blood vessels of chick chorioallantonic membrane treated with endostain (8 mg/mL), HM-3 (1 mg/mL), and PEG_{10k}-HM-3 (6.6 mg/mL) for 48 h. Values are represented as mean ± SD ($n = 8$). *$p < 0.05$ vs control group, $p < 0.05$ (HM-3 group vs PEG10k-HM-3 group).

no small vessels adjacent to the drug carrier plate compared with the control samples (Figure 6). The diameter of blood vessels in PEG_{10k}-HM-3-treated sample also seemed smaller. Together, these results indicate a more potent antiangiogenesis activity after HM-3 was modified.

4. DISCUSSION

HM-3 is an 18-amino-acid polypeptide synthesized in our laboratory. Previous studies found that it has robust antitumor activities, especially against liver and stomach tumors. HM-3 exhibits no overt toxic side effects and therefore may have great potential in cancer therapy. However, most protein and peptides have short half-lives in vivo, and the plasma half-life of HM-3 is only 10−27 min. In animal experiments, we had to administer the drug twice daily via tail intravenous injection to achieve significant antitumor activity. To improve HM-3 therapeutic potentials for future applications, this current study sought to increase its in vivo half-life using PEG modification.

Due to its nontoxic and nonimmunogenic properties, PEG has been widely used in drug modification to increase drug half-life without compromising activity. For polypeptides, many factors may affect modification reactions, including reaction time, temperature, substrate molar ratio, and so on. The current study reports a systematic optimization of these parameters.

mPEG-ALD is one group of modifying agents which can react with free amino groups, and the modifications typically occur at the N termini and lysine residues of proteins (*25*). The HM-3 polypeptide contains no lysine residue (*19*), therefore it could only be modified at its N terminus. The RP-HPLC chromatogram (Figure 1) showed only one peak for the modification product, and protein gel electrophoresis also confirmed the single identity. We have also tried to determine the precise molecular weight by MODI-TOF. However, this was not successful, possibly because the modification product was difficult to ionize.

A series of substrate molar ratios were tested. The maximal modification rate was obtained when the ratio of mPEG10k-ALD:HM-3 was 2 (Figure 1). The modification rate increased over time and reached the peak at 4 h. Different pH values were also tested and did not show significant effects on the reaction (Figure 1). Previously, Kinstler et al. documented an important characteristic of mPEG-ALD when they tried to modify G-CSF with PEG under acidic conditions (pH = 5); coupling of aldehyde and α-amino group was highly selective. This is because, under low pH, the N termini of proteins are susceptible to protonation (*25*−*27*), therefore conducive to site-specific modification. Given that HM-3 is a polypeptide with an isoelectric point greater than 11, optimal reaction conditions for mPEG-ALD should be a buffer system with a working range pH 6−9.5. For this reason, we selected pH 6 phosphate buffer as the final reaction system.

Previous in vivo studies have shown that HM-3 is mainly distributed in liver and kidney after administration (data not shown). Concerted action of various enzyme systems in the blood, liver, and kidney, as well as glomerular filtration, leads to in vivo fast degradation of HM-3 and short retention time in the body. However, after HM-3 was modified by PEG, its metabolic rate in the blood was reduced, and the half-life became longer. This could be due to several reasons. First, PEG may occupy the surface area of the drug, consequently blocking binding of degradative enzymes to the drug. Second, the size of the drug became larger after modification, which may reduce the loss due to glomerular filtration. As a result, the metabolic rate was decreased, and the circulation time in the body was increased. Our studies provide preliminary evidence for improved pharmacodynamic and pharmacokinetic behaviors of the drug. Future experiments are needed to validate these results.

After HM-3 modification and purification, the antiangiogenesis activity was shown to be significantly enhanced in the CAM experiment. CAM models are widely used models for angiogenesis study. In this isolated in vivo system, the drug can be directly delivered to the target site; since the chick embryos remain viable during the entire experiment, the drug metabolism is active. However, such metabolic activities are still largely different from the metabolic flux in live animals. Therefore, functional analysis of PEG_{10k}-HM-3 requires more detailed animal experiments under in vivo conditions. If PEG_{10k}-HM-3 can be administered only once a day and still achieve or exceed the antitumor activities we previously observed with HM-3 by twice-daily administration, our experimental approach would be considered a success. In addition, the immunogenicity of PEG_{10k}-HM-3 needs to be tested. Previously, we have attempted to generate mono- and polyclonal antibodies of HM-3 for radioimmunassays. The molecular weight of HM-3 is only 1788, which makes it difficult to generate antibodies. After it was coupled with a macromolecule (BSA), antibodies of high titer and specificity were obtained. It remains to be further investigated whether modification of HM-3 $mPEG_{10k}$-ALD might trigger immunogenic reaction in animals for antibody production. Furthermore, our previous experiments demonstrated that HM-3 had no overt toxic side effects on animals. Acute toxicity tests performed in mice showed that the maximum tolerable dose of HM-3 is 1926 mg/kg, more than 600-fold higher than its effective dose (3 mg/kg). Toxicological studies should also be carried out for $mPEG_{10k}$-ALD modified HM-3. Future therapeutic applications require that the modified product displays high antitumor activity while maintaining low immunogenicity and toxicity.

LITERATURE CITED

(1) Sorensen, D. R., Read, T.-A., and Porwol, T. (2002) Endostatin reduces vascularization, blood Xow and growth in a rat gliosarcoma. *Neuro-Oncology. 4*, 1–8.

(2) Sudhakar, A., Sugimoto, H., and Yang, C. (2003) Human tumstatin and human endostatin exhibit distinct antiangiogenic activities mediated by αVβ3 and α5β1 integrins. *Proc. Natl. Acad. Sci. U.S.A. 100*, 4766–71.

(3) Rehn, M., Veikkola, T., and Kukk-Valdre, E. (2001) Interaction of endostatin with integrins implicated in angiogenesis. *Proc. Natl. Acad. Sci. U.S.A. 98*, 1024–9.

(4) Ding, Y. H., Javaherian, K., and Lo., K. M. (1998) Zinc-dependent dimmers observed in crystals of human endostatin. *Proc. Natl. Acad. Sci. U.S.A. 95*, 10443–8.

(5) Boemhm, T., O'Reilly, M. S., Keough, K., Shiloach, J., Shapiro, R., and Folkman., J. (1998) Zinc-binding of endostatin is essential

for its antiangiogenic activity. *Biochem. Biophys. Res. Commun. 252*, 190–4.
(6) Sasaki, T., Fukai, N., Mann, K., Goring, W., Olsen, B. R., and Timpl, R. (1998) Structure, function and tissue forms of the C-terminal globular domain of collagen XVIII containing the angiogenesis inhibitor endostatin. *EMBO J. 17*, 4249–56.
(7) Dhanabal, M., Volk, R., Ramchandran, R., Simons, M., and Sukhatme, V. P. (1990) Cloning, expression, and in vitro activity of human endostatin. *Biochem. Biophys. Res. Commun. 258*, 345–352.
(8) O'Reilly, M. S., Boehm, T., and Folkman, J. (1997) Endostatin: an endogenous inhibitor of angiogenesis and tumor growth. *Cell 88*, 277–285.
(9) Dhanabal, M., Ramchandran, R., Volk, R., Stillman, E. I., Lombardo, M., Iruela-Arispe, M. L., Simons, M., and Sukhatme, P. V. (1999) Endostatin: yeast production, mutants, and anti-tumor eVect in renal cell carcinoma. *Cancer Res. 59*, 189−197.
(10) You, W. K., So, S. H., Lee, H., Park, S. Y., Yoon, M. R., Chang, S. L., Kim, H. K., Joe, Y. A., Hong, Y. K., and Chung, S. I. (1999) Purification and characterization of recombinant murine endostatin in *E. coli*. *Exp. Mol. Med. 31*, 197–202.
(11) Wickstrom, S. A., Alitalo, K., and Keski-Oja, J. (2004) An endostatin-derived peptide interacts with integrins and regulates actin cytoskeleton and migration of endothelial cells. *J. Biol. Chem. 279*, 20178–85.
(12) Robert, M., Sjin, T. T., Satchi-Fainaro, R., Birsner, A. E., Ramanujam, V. M. S., Folkman, J., and Javaherian, K. (2005) A 27-Amino-Acid synthetic peptide corresponding to the NH2-teminal zinc-binding domain of endostatin is responsible for its antitumor activity. *Cancer Res. 659*, 3656–63.
(13) Cattaneo, M. G., Pola, S., Francescato, P., Chillemi, F., and Vicentini, L. M. (2003) Human endostatin-derived synthetic peptides possess potent antiangiogenic properties *in vitro* and *in vivo*. *Exp. Cell Res. 283*, 230–6.
(14) Chillemi, F., Francescato, P., Ragg, E., Cattaneo, M. G., Pola, S., and Vicentini, L. (2003) Studies on the structure-activity relationship of endostatin: synthesis of human endostatin peptides exhibiting potent antiangiogenic activities. *J. Med. Chem. 46*, 4165–72.
(15) Morbidelli, L., Donnini, S., Chillemi, F., Giachetti, A., and Ziche, M. (2003) Angiosuppressive and angiostimulatory effects exerted by synthetic partial sequences of endostatin. *Clin. Cancer Res. 9*, 5358–69.
(16) Cho, H., Kim, W. J., Lee, Y. M., Kim., Y. M., Kwon, Y. G., Park, Y. S., Choi, E. Y., and Kim, K. W. (2004) N-/C-terminal deleted mutant of human endostatin efficiently acts as an anti-angiogenic and anti-tumorigenic agent. *Oncol. Rep. 11*, 191–5.
(17) Zitzmann, S., Ehemann, V., and Schwab, M. (2002) Arginine-Glycine-Aspartic Acid RGD;-peptide binds to both tumor and tumor-endothelial cells *in vivo*. *Cancer Res. 62*, 5139–43.
(18) Arap, W., Pasqualini, R., and Ruoslahti, E. (1998) Cancer treatment by targeted drug delivery to tumor vasculature in a mouse model. *Science 279*, 377–380.
(19) Xu, H. M., Yin, R. T., Chen, L. S., Siraj, S., Huang, X. F., Wang, M., Fang, H. S., and Wang, Y. (2008) An RGD-modified endostatin-derived synthetic peptide shows antitumor activity in vivo. *Bioconjugate Chem. 19*, 1980–6.
(20) Roberts, M. J., Bentley, M. D., and Harris, J. M. (2002) Chemistry for peptide and protein PEGylation. *Adv. Drug Delivery Rev. 54*, 459–476.
(21) Caliceti, P., and Veronese, F. M. (2003) Pharmacokinetic and biodistribution properties of poly(ethylene glycol)-protein conjugate. *Adv. Drug Delivery Rev. 55*, 1261–1277.
(22) Lee, S. H., Lee, S., Youn, Y. S., Na, D. H., Chae, S. Y., Byun, Y., and Lee, K. C. (2005) Synthesis, charaterization, and pharmacokinetic studies of PEGylated glucagon-like peptide-1. *Bioconjugate Chem 16*, 377–382.
(23) Na, D. H., Youn, Y. S., Park, E. J., Lee, J. M., Cho, O. R., Lee, K. R., Lee, S. D., Yoo, S. D., DeLuca, P. P., and Lee, K. C. (2004) Stability of PEGylated salmon calcitonin in nasal mucosa. *J. Pharm. Sci. 93*, 256–261.
(24) Na, D. H., Park, M. O., Choi, S. Y., Kim, Y. S., Lee, S. S., Yoo, S. D., Lee, H. S., and Lee, K. C. (2001) Identification of the modifying sites of mono-PEGylated salmon calcitonins by capillary electrophoresis and MALDI-TOF mass spectrometry. *J. Chromatogr., B 754*, 259–263.
(25) Roberts, M. J., Bentley, M. D., and Harris, J. M. (2002) Chemistry for peptide and protein PEGylation. *Adv. Drug Delivery Rev. 54*, 459–476.
(26) Kinstler, O. B., Brems, D. N., Lauren, S. L., Paige, A. G., Hamburger, J. B., and Treuheit, M. J. (1996) Characterization and stability of N-terminally PEGylated rhG-CSF. *Pharm. Res. 13*, 1724–34.
(27) Kinstler, O., Molineux, G., Treuheit, M., Ladd, D., and Gegg, C. (2002) Mono-N-terminal poly(ethylene glycol)-protein conjugates. *Adv. Drug Delivery Rev. 54*, 477–85.

BC900070R

Comparison of Synthetic High Density Lipoprotein (HDL) Contrast Agents for MR Imaging of Atherosclerosis

David P. Cormode,[†] Rohith Chandrasekar,[‡] Amanda Delshad,[†] Karen C. Briley-Saebo,[†] Claudia Calcagno,[†] Alessandra Barazza,[†,§] Willem J. M. Mulder,[†] Edward A. Fisher,*[,§] and Zahi A. Fayad*[,†]

Translational and Molecular Imaging Institute, Mount Sinai School of Medicine, One Gustave L. Levy Place, Box 1234, New York, New York 10029, The Cooper Union for the Advancement in Science and Art, 30 Cooper Square, New York, New York 10003, and Department of Medicine (Cardiology), Marc and Ruti Bell Vascular Biology and Disease Program and the NYU Center for the Prevention of Cardiovascular Disease, New York University School of Medicine, New York University, Smilow 8 522 First Avenue, New York, New York 10016. Received December 5, 2008; Revised Manuscript Received March 27, 2009

Determining arterial macrophage expression is an important goal in the molecular imaging of atherosclerosis. Here, we compare the efficacy of two synthetic, high density lipoprotein (HDL) based contrast agents for magnetic resonance imaging (MRI) of macrophage burden. Each form of HDL was labeled with gadolinium and rhodamine to allow MRI and fluorescence microscopy. Either the 37 or 18 amino acid peptide replaced the apolipoprotein A-I in these agents, which were termed 37pA-Gd or 18A-Gd. The diameters of 37pA-Gd and 18A-Gd are 7.6 and 8.0 nm, respectively, while the longitudinal relaxivities are 9.8 and 10.0 $(mM\ s)^{-1}$. 37pA has better lipid binding properties. In vitro tests with J774A.1 macrophages proved the particles possessed the functionality of HDL by eliciting cholesterol efflux and were taken up in a receptor-like fashion by the cells. Both agents produced enhancements in atherosclerotic plaques of apolipoprotein E knockout mice of ~90% ($n = 7$ per agent) and are macrophage specific as evidenced by confocal microscopy on aortic sections. The half-lives of 37pA-Gd and 18A-Gd are 2.6 and 2.1 h, respectively. Despite the more favorable lipid interactions of 37pA, both agents gave similar, excellent contrast for the detection of atherosclerotic macrophages using MRI.

Heart disease is now the primary cause of mortality in the world (*1*). The most common factor behind adverse cardiovascular events is rupture of vulnerable plaques caused by atherosclerosis (*2*). As such, there is a significant motivation to image atherosclerotic tissue for diagnosis, to characterize disease stage, and to monitor the effect of therapy (*3, 4*). One of the favored courses of action is to noninvasively image atherosclerotic plaques using magnetic resonance imaging (MRI) (*5, 6*), since this imaging modality has high spatial resolution and excellent soft tissue contrast and does not expose the patient to ionizing radiation. While MRI without contrast can determine plaque morphology and some features of plaque composition, targeted contrast agents are required to fully determine the cellular composition of the plaque.

Macrophages are key in the progression of atherosclerosis, entering the intima as monocytes and being activated to macrophages via interaction with and uptake of modified low density lipoprotein until they become foam cells and eventually forming the necrotic lipid core associated with unstable plaques (*7*). Furthermore, macrophage content has been identified as a key biological marker of vulnerable plaques. As a result, several methods have been proposed for molecular imaging of these cells in diseased arteries, for example, using targeted gadolinium-labeled micelles (*8, 9*) or dextran coated iron oxides (*10*) for MRI, iodine nanoparticles for computed tomography, (*11*) or ^{18}F-2-fluoro-2-deoxyglucose and ^{64}Cu labeled nanoparticles with positron emission tomography (*12, 13*).

We have previously reported the use of gadolinium (Gd^{3+}) and fluorophore modified high density lipoprotein (HDL), an endogenous nanoparticle naturally targeted to atherosclerotic plaques, to image macrophage burden in the abdominal aorta of a mouse model of atherosclerosis (*14, 15*). A restriction to the translation of this methodology to the clinic is the absence of a ready commercial source of apo A-I. Therefore, we recently reported preliminary data on a synthetic, MRI-active HDL formulation based on the amphiphatic peptide 37pA and gadolinium labeled phospholipids (*16*). 37pA, which mimics the properties of the major protein component of HDL, apoA-I (*18*), is composed of 37 amino acid residues and binds to lipidic particles strongly (*19*).

We report here the synthesis of an MRI-active HDL-based contrast agent formed using 18A, another apoA-I mimicking peptide composed of only 18 amino acid (*20*) residues, and an extensive comparison of this and the 37pA-based agent. The advantage of 18A over 37pA is that this shorter peptide is easier and less expensive to synthesize ($1584 for 18A vs $3541 for 37pA; both figures are for 100 mg, 95% purity, Global Peptide Services). The lipid binding properties of 18A, however, are inferior to those of 37pA, the peptides having an egg phosphatidylcholine exclusion pressure of 30 and 41 dyn/cm, respectively (*19*). The superior lipid binding properties of 37pA may result in a better MR enhancement of the arterial wall, since the gadolinium-labeled phospholipids in the HDL mimetic are held together more strongly and may be delivered to the atherosclerotic plaque with greater efficiency. Nevertheless, it is unclear if this would affect the efficacy of the agents for in vivo MR imaging studies. In this report we compare the 18A-based agent with the 37pA-based agent by investigating their physical properties, in vitro macrophage efflux, in vitro macrophage uptake, and MR imaging efficacy in apolipoprotein E knockout (apoE-KO) mice. In addition, the biodistribution and

* To whom correspondence should be addressed. For E.A.F.: phone, 212-263-6636; fax, 212-263-6632; e-mail, Edward.Fisher@nyumc.org. For Z.A.F.: phone, 212-241-6858; fax, 240-368-8096; e-mail, Zahi.Fayad@mssm.edu.

[†] Mount Sinai School of Medicine.

[‡] The Cooper Union for the Advancement in Science and Art.

[§] New York University School of Medicine.

10.1021/bc800520d CCC: $40.75 © 2009 American Chemical Society
Published on Web 04/20/2009

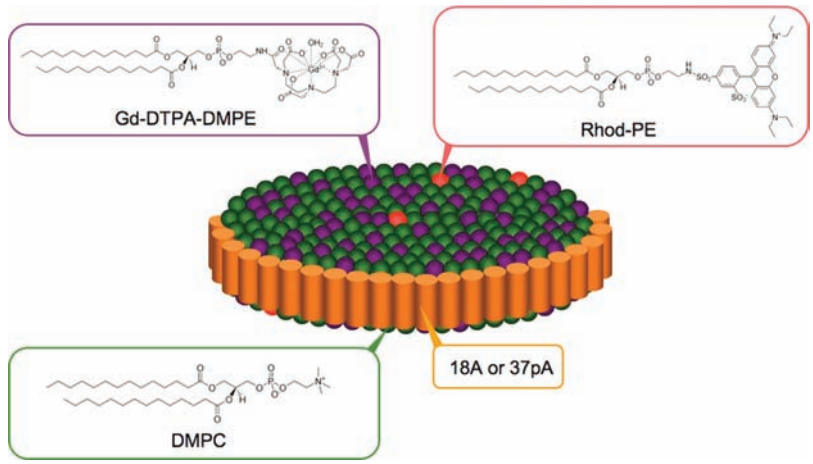

Figure 1. Schematic depiction of the agents used in this study. DMPC is dimyristoylphosphatidylcholine, Gd-DTPA-DMPE is gadolinium 1,2-dimyristoyl-*sn*-glycero-3-phosphoethanolamine diethylenetriamine pentaacetic acid, and Rhod-PE is 1,2-dimyristoyl-*sn*-glycero-3-phosphoethanolamine-*N*-(lissamine rhodamine B sulfonyl)ammonium salt.

pharmacokinetics of the agents were assessed. As will be shown, despite theoretical advantages of 37pA, comparable imaging efficacies were obtained with the 18A peptide.

EXPERIMENTAL PROCEDURES

Materials. Dimyristoylphosphatidylcholine (DMPC), gadolinium 1,2-dimyristoyl-*sn*-glycero-3-phosphoethanolamine diethylenetriamine pentaacetic acid (Gd-DTPA-DMPE), and 1,2-dimyristoyl-*sn*-glycero-3-phosphoethanolamine-*N*-(lissamine rhodamine B sulfonyl)ammonium salt (Rhod-PE) were all purchased from Avanti Polar Lipids and used as received. Cy5.5-labeled dimyristoylphosphoethanolamine (Cy5.5-PE) was synthesized as described below. The peptides 18A (sequence, DWL KAF YDK VAE KLK EAF) and 37pA (sequence, DWL KAF YDK VAE KLK EAF PDW LKA FYD KVA EKL KEA F) were synthesized by Global Peptide Services (Fort Collins, CO) at 95% purity. Cell culture supplies were purchased from Invitrogen (Carlsbad, CA).

Nanodisk Synthesis. To form synthetic, MRI-active HDL using 18A, a 200:200:1 mixture by mass of DMPC, Gd-DTPA-DMPE, and Rhod-PE (25 mg) was dissolved in a 1:4 mixture of methanol and chloroform. A lipid film was formed under vacuum from this solution, which was hydrated with a solution of 18A in 5 mL of 1× PBS such that there was 1 mg of peptide for each 2.5 mg of phospholipids used. The resulting mixture was heated at 65 °C for 45 min before being sonicated for 30 min on ice to form nanodisks, which were purified via centrifugation, filtration, and washing. This product was termed 18A-Gd and was characterized by dynamic light scattering (DLS), gel permeation, gel electrophoresis, relaxometry, gadolinium quantification, protein analysis, and phosphate quantification. Details of the characterization methodology may be found in ref 16. 37pA-Gd and Gd micelles (micelles forming using the same phospholipid mixture as for 18A-Gd and 37pA-Gd but without any peptide) were synthesized as previously described (*16*). A schematic depiction of 18A-Gd and 37pA-Gd is displayed in Figure 1. The disklike structure of such phospholipid−peptide aggregates has been established by ourselves (*16*) and others (*17*).

Cy5.5-PE Synthesis. For incorporation in the synthetic HDL nanoparticles, Cy5.5 monoreactive NHS esters were conjugated to dimyristoylphosphoethanolamine (DMPE). Typically, 50 μmol of DMPE and 50 μmol of stearoylhydroxyphosphatidylcholine (SHPC) was dissolved in 3 mL of a 4:1 chloroform/methanol solvent mixture. The solvents were removed from this solution to form a lipid film, which was subsequently hydrated for 30 min via agitation with 5 mL of a 0.1 M sodium bicarbonate aqueous solution (pH ∼8.4) at room temperature to form micelles. After this, 20 mg of Cy5.5 mono-NHS ester was dissolved in 250 μL of DMSO, which was added to the DMPE-SHPC micelle aqueous solution. The mixture was stirred overnight at 4 °C under nitrogen atmosphere to allow the conjugation of Cy5.5 to the lipids. A 50 kDa Vivaspin molecular weight cutoff tube was used to separate unconjugated Cy5.5 mono-NHS ester from Cy5.5 conjugated lipid micelles by washing 10 times with water until the residue was completely colorless. The Cy5.5 micelles were subsequently freeze-dried for 3 days to remove all water, after which they were dissolved in a 20:1 chloroform/methanol mixture.

Macrophage Uptake of Reconstituted HDL. J774A.1 murine macrophage cells were cultured in DMEM supplemented with 10% FBS and 1% streptomycin/penicillin. The cells were passaged 5 times before the incubations took place. The cells were grown to 70−80% confluency before being plated in black, nonfluorescent 96-well plates the day prior to incubation. For these studies agents labeled with Cy5.5-PE instead of Rhod-PE were used. 18A-Gd or 37pA-Gd was added to one row (12 wells) for each condition, with untreated cells and wells incubated with media only or Gd micelles as controls. The cells were incubated at a concentration of 0.02 mM Gd at time points from 1 to 24 h. Further experiments were carried out where the incubation time was held constant at 2 h and the concentration of the agent varied from 0.01 to 0.16 mM Gd. Incubations were performed where the agent uptake at 0.02 mM and 2 h was compared with macrophages also incubated with a 10-fold excess (by protein content) of non-Cy5.5 labeled 18A-Gd or 37pA-Gd. Last, the agent uptake of macrophages and smooth muscle cells (derived from Wistar rats as described below) was compared. After incubation, the medium was removed and the cells were washed with cold (4 °C) PBS three times and fixed with 4% paraformaldehyde. The cells were imaged in the plates using an IVIS imaging system 200 (Xenogen, Alameda, CA). The plates were illuminated for 5 s using a 150 W quartz halogen lamp filtered by the 615−665 nm Cy5.5 excitation band, while the emission was quantitatively recorded using the 695−770 nm Cy5.5 emission filter. Images were analyzed, and the fluorescence from each well was determined using the software supplied with the IVIS system.

Smooth Muscle Cell Isolation and Culture. Rat airway smooth muscle (ASM) cells were isolated from 10-week-old male Wistar rats. Rats were intraperitoneally injected with pentobarbital sodium (35 mg/kg), and the tracheas were asepti-

cally excised and placed in Ca^{2+}, Mg^{2+}-free Hanks balanced salt solution (HBSS) (Sigma). The isolated tracheas were cleaned of connective tissues, cut longitudinally through the cartilage, and enzymatically dissociated with filtered HBSS containing 0.2% collagenase type 2 (Worthington Biochemical Corporation, Lakewood, NJ) for 30 min in a shaking water bath at 37 °C. Dissociated cells in suspension were centrifuged and resuspended in Dulbecco's modified Eagle's medium (DMEM)−Ham's F12 medium (1:1 v/v) (Sigma) supplemented with 10% FCS (GIBCO) and 100 U/mL penicillin and 100 μg/mL streptomyocin (GIBCO). Cells were plated on Petri dishes and grown until confluence at 37 °C in humidified air containing 5% CO_2. The medium was changed every 48 h, and confluent cells were passaged with 0.25−0.02% EDTA solution (GIBCO). ASM cells in culture were elongated and spindle shaped, grew with typical hill and valley appearance, and stained positively for the smooth muscle specific protein α-Actin. Cells were used at the second passage.

Animal Model of Atherosclerosis. Both apoE-KO and wild type mice were used in this study. The apoE-KO mice were an average of 10 months old and fed a high cholesterol diet to induce plaque development for an average of 8 months prior to use in these experiments. The wild type mice were fed an ordinary chow diet and were the same average age. All mice were male and were housed and maintained at the Mount Sinai Animal Facility. The Mount Sinai School of Medicine Institute of Animal Care and Use Committee approved all experiments.

In Vivo MR Imaging. In vivo MRI was performed using a 9.4 T, 89 mm bore MRI system (Bruker Instruments, Billerica, MA). The imaging system and methodology are extensively described in ref 8. After a preinjection baseline MRI scan, mice were injected via a tail-vein catheter. Subsequent scans were carried out at 24, 48, 72, and 96 h postinjection. $n = 7$ apoE-KO mice and $n = 2$ wild type mice were injected with 18A-Gd, and the same group sizes were used as in the previous 37pA study. Use of the medical image analysis software package eFilm allowed the MR signal intensity of various tissues from the different time points to be ascertained and the percent change in normalized enhancement ratio (% NER) postinjection to be calculated. Normalization of the MR signal intensity in the aorta wall was performed by rebasing with the signal from the adjacent muscle to create the value *W*. The % NER was found from the difference between *W* from the postinjection scans and *W* from the prescan divided by *W* from the prescan and multiplied by 100, as per the method described in ref 8.

Confocal Microscopy. ApoE-KO mice were sacrificed 24 h after injection with contrast agent. The mice were perfused with saline at physiological pressure and their aortas removed. Then 3 mm pieces of the aorta were embedded in Tissue-Tek optimal cutting temperature media (Sakura Finetek, Torrance, CA), frozen, sectioned, and fixed in paraformaldehyde. These sections of aorta were stained with Alexa 647-CD68, a macrophage specific antibody conjugated to a fluorophore before the section was fixed in a DAPI (nuclei specific) containing agent and coverslipped. Confocal laser scanning microscopy on aortic sections was performed using a Zeiss LSM 510 META microscope (Carl Zeiss, Oberkochen, Germany) in an inverted configuration. Colocalization of rhodamine (contrast agent) and CD68 staining (macrophages) in the confocal microscopy images was quantified using an in-house developed image analysis software tool based in MatLab R2007b (Natick, MA).

Pharmacokinetics and Biodistribution. To determine the pharmacokinetics of 37pA-Gd, 18A-Gd, and Gd micelles, a 50 μmol/kg dose of the agent was injected into apoE-KO mice whose hair on their lower limbs had been removed to allow access to the saphenous veins. Blood (10−20 μL) was drawn from these veins at 5 min, 30 min, 1 h, 2 h, 3 h, 4 h, 24 h, and 48 h after injection and placed into preweighed vials containing 80 μL of heparin. The vials were weighed again to determine the volume of blood drawn, the density of blood being taken to be 1.05 g/mL (*21*). The gadolinium content of the blood for each time point was determined by inductively coupled plasma mass spectrometry (ICP-MS) performed on the blood−heparin mixture and adjusting for the blood volume. Half-lives were calculated from analysis of the variance of blood gadolinium content over time with the MatLab software package using a biexponential model.

The biodistribution was determined for 37pA-Gd and 18A-Gd at 48 h after injection of the agents into apoE-KO mice at a 50 μmol/kg dose. The animals were sacrificed by perfusion with saline administered via the left ventricle of the heart. The liver, kidneys, heart, spleen, and lungs were removed, weighed, and homogenized before analysis via ICP-MS for determination of Gd content. The per unit weight gadolinium content thus found was multiplied by the organ wet weight and divided by the injected dose to give the biodistribution. Cantest Ltd. (Burnaby, Canada) performed all ICP-MS analyses.

Statistical Analysis. Data populations were compared using Student's *t* test (two-tailed, heteroscedastic). Populations were considered to be significantly different if $p < 0.01$.

RESULTS

Characterization. The average diameter of the 18A-Gd particles was found via DLS to be 8.0 ± 0.3 nm. By use of gel electrophoresis, the size was found to be approximately 7.6 nm. The corresponding values for the 37pA-Gd complex are very similar, being 7.6 nm by both techniques. FPLC gave only one peak in a narrow size distribution, indicating high product purity. The longitudinal relaxivity was found to be 10.0 ± 0.2 mM^{-1} s^{-1}, which is not significantly different from relaxivities reported for previous HDL-based contrast agents that used the same gadolinium chelating phospholipid (*14, 16*). The gadolinium, phosphorus, and protein analyses gave a relative mass ratio of Gd-DTPA-DMPE/DMPC/18A of 1.18:1.10:1, which deviates somewhat from the input values of 1.25:1.25:1 and indicates a less efficient particle formation than for the 37pA-Gd agent (whose values were 1.23:1.23:1). This may be due to the lower lipid binding parameters of 18A compared to the dual domain peptide 37pA (*19*).

Macrophage Cholesterol Efflux. HDL-based particles have therapeutic properties in terms of their anti-inflammatory action as well as their ability to retrieve cholesterol from atherosclerotic plaques and transport it to the liver for excretion (*7*). A common measure of this latter property is macrophage cholesterol efflux, i.e., the quantity of cholesterol removed from macrophages by an agent (*22*). We performed such experiments using 18A-Gd and 37pA-Gd, while native HDL (CSL Behring, Bern, Switzerland) was used as a comparison and bovine serum albumin (BSA) was used as a control (phospholipid-only species are well established to give substantially lower macrophage cholesterol efflux than synthetic HDL nanoparticles (*22*)). Each agent was used with the same concentration of peptide/protein. The efflux produced by HDL after 4 h was 8.15 ± 0.27% of the total, for 18A-Gd 12.82 ± 0.29%, for 37pA-Gd 9.89 ± 0.20%, and for BSA 1.61 ± 0.19%. Thus, HDL, 18A-Gd, and 37pA-Gd produce significantly more cholesterol efflux than the control, BSA. Both 18A-Gd and 37pA-Gd removed more cholesterol than the native HDL used, which is unsurprising as the HDL used in this study was more highly lipidated than the peptide-based nanoparticle and so can accept a lesser amount of cholesterol from the macrophages. That this 18A complex produces a greater level of efflux than the 37pA complex is consistent with the results of investigations carried out by Davidson et al. (*22*).

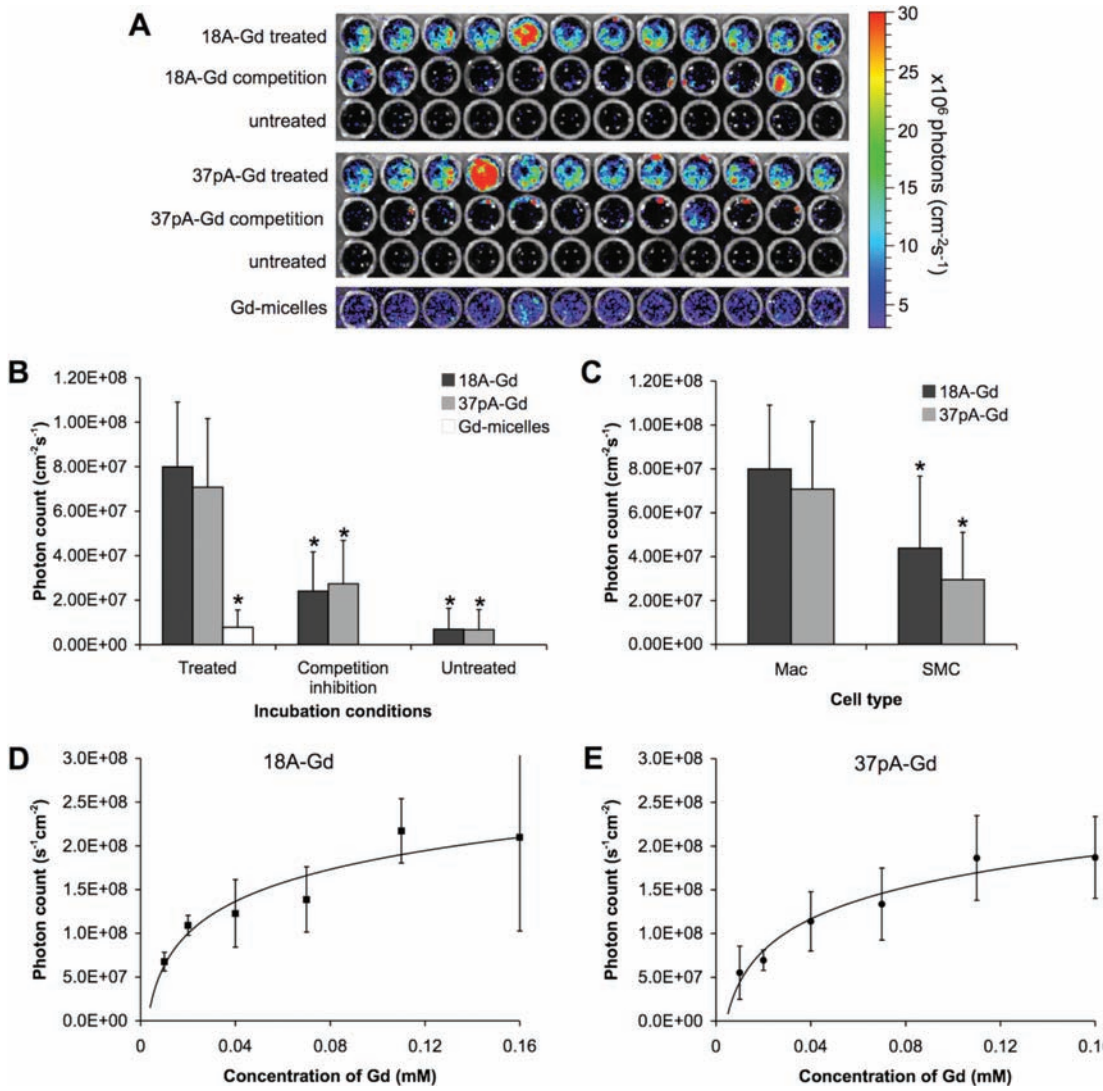

Figure 2. In vitro uptake of Cy5.5 labeled synthetic HDL agents in J774A.1 murine macrophages. Uptake was assessed using an IVIS 200 fluorescent imaging system. (A) Fluorescent images of cells treated with 18A-Gd or 37pA-Gd, with 18A-Gd or 37pA-Gd, and a 10-fold excess of agent without Cy5.5, untreated cells or treated with Gd-micelles. (B) Quantified fluorescence of macrophages compared with macrophages under competition−inhibition conditions and untreated macrophages. Incubation conditions were 2 h and 0.02 mM (by Gd) of agent. * indicates $p < 0.01$ compared to the treated macrophage cells. (C) Comparison of the uptake of 18A-Gd and 37pA-Gd in macrophages and smooth muscle cells. (D) and (E) show the quantified fluorescence of 18A-Gd and 37pA-Gd, respectively, when incubated for 2 h at the indicated concentrations (the solid lines are logarithmic lines of best fit generated by a Matlab program). Error bars are equal to 1 standard deviation, and $n = 12$ in all cases.

Macrophage Uptake of 18A-Gd and 37pA-Gd. To investigate in vitro effectiveness of 18A-Gd and 37pA-Gd and whether uptake was a receptor-like specific process, we performed extensive incubations of Cy5.5-labeled formulations of the agents with murine macrophages. Plates of incubated cells were analyzed using a fluorescence imaging system, resulting in images such as those shown in Figure 2A. We found that uptake increased over time until 4 h, after which increases in uptake were insubstantial (see Supporting Information Figures S1 and S2), suggesting a saturable process. Cy5.5 was used in these experiments because of the lower adsorption of light by biological components in the wavelengths in which this fluorophore emits compared to rhodamine, allowing better quantification of particle uptake (*23*). Macrophages incubated under competition-inhibition conditions (i.e., with a 10-fold excess of unlabeled agent in addition to the labeled agent) exhibited significantly less fluorescence than macrophages incubated with labeled agent only (Figure 2B), suggesting specificity. Furthermore, smooth muscle cells incubated with the agents took up significantly less agent than macrophages incubated under the same conditions (Figure 2C). Lastly, when macrophages were incubated with 18A-Gd and 37pA-Gd at concentrations ranging from 0.01 to 0.16 mM Gd, the uptake increased only slightly when the concentration increased from 0.04 to 0.16 mM Gd (parts D and E of Figure 2), again suggesting a saturable process. Taken together, these data strongly indicate that the uptake of these synthetic HDL particles is a specific, saturable process that is receptor-like in its characteristics. This would be compatible with interactions with HDL-interacting membrane proteins highly expressed by macrophages. The uptake of 18A-Gd and 37pA-Gd was not found to differ significantly. In comparison, macrophages took up Gd micelles to a much lesser extent than for 18A-Gd or 37pA-Gd, in the concentration range 0.01−0.16 mM Gd (parts A and B of Figure 2, Supporting Infomation Figure S3). Furthermore, the uptake was linear, indicating uptake through an aspecific pathway and confirming the need for the peptides to produce a macrophage specific agent.

In Vivo MR Imaging. Representative images of the aorta of an apoE-KO mouse preinjection and 24 h postinjection with 18A-Gd are displayed in Figure 3A (left panels, the enhanced structure below the aorta in the postimage for 18A-Gd is a lymph node, which typically accumulates injected nanoparticles sub-

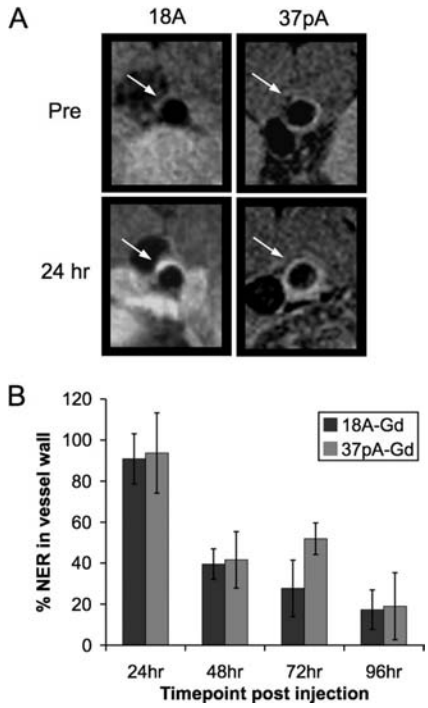

Figure 3. (A) Representative MR images of the aorta of apoE-KO mice preinjection and 24 h postinjection with 18A-Gd (left panels) and 37pA-Gd (right panels). (B) Summary of the mean normalized enhancement ratio (% NER) at 24, 48, 72, and 96 h in the aorta walls of apoE-KO mice injected with 18A-Gd or 37pA-Gd. Error bars are 1 standard deviation.

stantially). Visual inspection of the images indicates that there is significant enhancement of the image intensity in the aorta postinjection with 18A-Gd and that the enhancement is comparable to that observed postinjection with 37pA-Gd (Figure 3A, right panels). The results of analysis of the images from seven mice for each agent imaged preinjection and 24, 48, 72, and 96 h postinjection with each agent are displayed in Figure 3B.

18A-Gd gives an average enhancement in the aorta wall of 91% at 24 h before declining steadily to 17% at 96 h. Application of this agent to wild type mice gave only insignificant enhancements (<8%, data not shown) in the aorta wall. Injection of Gd micelles (composed of the same phospholipids as 18A-Gd and 37pA but without any peptide) into apoE-KO mice gave a maximum of 16% enhancement, which occurred at 24 h. This value was significantly less than that of 18A-Gd and 37pA-Gd, showing the importance of the peptides for targeting the particles to atherosclerosis. The enhancement for 37pA-Gd at the 24 h time point was slightly higher at 94%, but upon comparison of the data for 18A-Gd and 37pA-Gd using Student's *t* test, the difference in the average enhancement at this time point was not found to be significant. In addition, the differences were not significant at 48 or 96 h; however, for the 72 h time point the difference in the average enhancement produced by the two agents was found to be significant at the 1% level.

Confocal Microscopy. A typical confocal microscopy image of an aorta section excised from an apoE-KO mouse injected 24 h previously with 18A-Gd is displayed in Figure 4. As can be seen, there is a high level of rhodamine (red) signal in the plaque, in agreement with the MR imaging data that indicated plaque enhancement. The rhodamine colocalizes extensively with the macrophage staining (green), resulting in patches of yellow color in the merged image, indicative of macrophage specificity. Analysis of the confocal microscopy image using

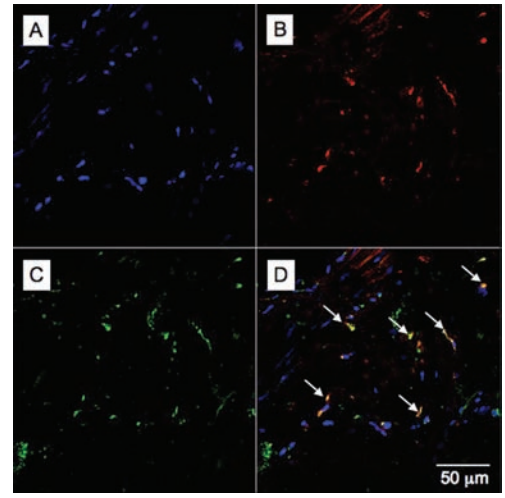

Figure 4. Confocal microscopy images of aortic tissue excised from an apoE-KO mouse injected with the 18A-Gd agent 24 h prior to excision: (A) DAPI staining for nuclei (blue); (B) rhodamine channel (red) indicating areas of 18A-Gd uptake; (C) Alexa 647:CD68 staining for macrophages (green). (D) Merging of the previous three images reveals the affinity of agent 18A-Gd for macrophages (yellow).

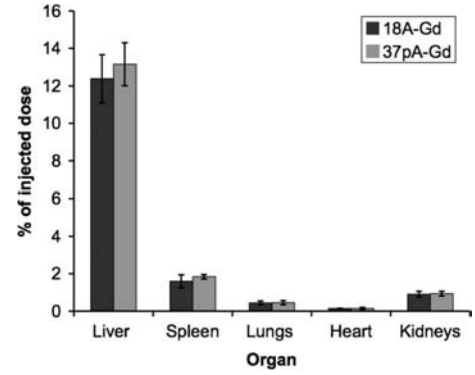

Figure 5. Biodistribution of 18A-Gd and 37pA-Gd between the liver, spleen, lungs, heart, and kidneys at 48 h given as the percentage of the injected dose. Error bars are equal to 1 standard deviation, and $n = 3$ in each case.

an in-house developed software tool revealed that 93% of the rhodamine signal colocalizes with CD68 positive regions, confirming the visual impression of macrophage specificity. In sections of the aorta that did not bear atherosclerotic plaques, no rhodamine signal could be observed (see Supporting Information Figure S4).

Pharmacokinetics and Biodistribution. The pharmacokinetics of 18A-Gd, 37pA-Gd, and Gd micelles were determined by analysis of blood drawn sequentially from mice injected with the agents. The half-life of 18A-Gd was found to be 2.1 ± 0.1 h and the half-life was 2.6 ± 0.3 h for 37pA-Gd and 2.4 ± 0.3 h for Gd-micelles, with no significant difference between them, meaning the agents can be directly compared. The biodistributions of 18A-Gd and 37pA-Gd at 48 h are displayed in Figure 5, given as the percentage of the injected dose. As can be seen, the vast majority of the retained dose is in the liver, with only a minor quantity in the spleen and negligible amounts in the lungs and heart. The levels of agent found in the kidneys are high compared to many contrast agents, but HDL is known to interact with these organs (*24*). The differences in biodistribution between the two agents are not statistically significant.

DISCUSSION

In this report, we compared the physical properties, in vitro macrophage interactions and in vivo imaging efficacy of two

different HDL-based MRI agents. Both contained apoA-I mimicking peptides, one being 37pA and the other being 18A. The physical properties of the two agents are very similar, excepting a superior efficiency of lipid binding in the case of 37pA-Gd. In terms of the in vitro properties, 18A-Gd appears to have a slight advantage. Macrophage efflux measurements show 18A-Gd to interact with these cells to a greater extent than 37pA-Gd, which is in agreement with previous studies by Davidson et al. (*22*). It could be the case that poor lipid binding properties are advantageous for interactions with macrophages, at least in the case of efflux, giving the particle the flexibility to distort to accept cholesterol. We have shown the agents 18A-Gd and 37pA-Gd to have receptor-like mediated uptake in vitro. 18A and 37pA have both been shown by others to bind to proteins highly expressed on macrophage cells (*18, 24*), while we have recently shown HDL particles whose core is modified to contain gold, iron oxide, or quantum dot nanoparticles to be internalized into macrophage cells (*25*). Taken together, the evidence suggests that membrane proteins highly expressed on macrophages allow the specific uptake of 18A-Gd and 37pA-Gd observed in vivo as part of a receptor-mediated endocytic process.

The in vivo imaging properties of the two contrast agents are not significantly different, both giving excellent enhancement in atherosclerotic plaque of apoE-KO mice at 24 h postinjection, compared to precontrast imaging. Immunofluorescence performed upon excised aortas of mice injected with 18A-Gd gave a similar level of colocalization with macrophages as 37pA-Gd. The pharmacokinetics of the agents are interesting, as they are relatively short and correspond more to those observed for micellar agents (*26*) than for lipoproteins ($t_{1/2} = 6$ h) (*27*). This could be due to enhanced rate of clearance due to the negative charge of the particles (*28*) (the gadolinium lipids have an overall negative charge). For studies of this sort, it is preferable to acquire postinjection images at time points at least 5 times the half-life of the contrast agent. As the half-life of the agents was around 2.5 h, it might be that better contrast in the aorta could occur in scans acquired at 12.5 h postinjection. In terms of biodistribution, both agents have very similar properties.

While increases in signal were observed in the aorta wall upon administration of the synthetic HDL agents, it is important to note that hyperintense areas were found, such as in the top left for both 18A-Gd and 37pA-Gd in Figure 3A. Additionally, there were sections of the aorta in both the animals depicted in this figure that bore atherosclerotic plaques, but the increase in signal was very small. As these agents are macrophage specific, this suggests that the hyperintense plaques are macrophage-rich and thus bear hallmarks of vulnerable plaques.

Molecular imaging of cardiovascular disease is critical for the early detection and monitoring of atherosclerosis. In the current study we present a low cost and potentially translatable agent for the in vivo MR imaging of intraplaque macrophages. Other groups have proposed iron oxide based MR agents, which are desirable from both a safety (liver cells safely excrete iron) and efficacy (strong T2* effects) point of view. However, clinical studies using Sinerem/Combidex (Guerbet, France) reveal that this ultrasmall iron oxide particle must be administered as an infusion to both increase efficacy and reduce toxic effects. Additionally, but importantly, there are some serious limitations to imaging negative contrast caused by iron oxide in the vessel wall (*29*). Therefore, we feel that our agent may offer some significant advantages over the alternatives that have been proposed. In addition, agents based on such peptides may be rerouted to other molecular targets (*30*), so this platform is not limited to macrophage imaging.

In summary, the HDL-based, MRI-active contrast agents 18A-Gd and 37pA-Gd have been extensively investigated as to their physical properties, in vitro macrophage interactions, potential as in vivo molecular imaging agents for macrophages in atherosclerosis, and their excretion. The two agents have similar effectiveness with respect to in vivo imaging; however, the 18A particles exhibit better cholesterol efflux. On the basis of these findings and because of the fact that the smaller 18A peptide is less expensive to manufacture, we recommend the 18A peptide be used for future investigations. We plan to continue to investigate 18A-Gd via testing in rabbit models of atherosclerosis using clinical scanners and to create new molecular imaging contrast agents based on this peptide.

ACKNOWLEDGMENT

We gratefully acknowledge Dr. Gustav Strijkers of the Eindhoven University of Technology for assisting with the MRI sequences. We thank Daniel Samber of Mount Sinai School of Medicine for developing the confocal image analysis software tool. We thank Joanne Stocks of Mount Sinai School of Medicine for providing the smooth muscle cells. We thank CSL Behring, Bern, Switzerland, for their kind gift of reconstituted HDL. Partial support was provided by NIH/NHLBI ROI HL71021, NIH/ NHLBI HL78667 (Z.A.F., E.A.F.). Confocal microscopy was performed at the MSSM-Microscopy Shared Resource Facility and supported by NIH-National Cancer Institute Grant 5R24 CA095823-04, National Science Foundation Grant DBI-9724504, and NIH Grant 1 S10 RR0 9145-01.

Supporting Information Available: Method for macrophage efflux determination and further details of the MRI scanning setup; figures displaying the uptake of 18A-Gd and 37pA-Gd in macrophages as a function of time (Figures S1 and S2), the uptake of Gd micelles in macrophages as a function of concentration (Figure S3), and a confocal microscopy image of the aorta of an apoE mouse where there are no macrophages (Figure S4). This material is available free of charge via the Internet at http://pubs.acs.org.

LITERATURE CITED

(1) Fuster, V., Voute, J., Hunn, M., and Smith, S. C. (2007) Low priority of cardiovascular and chronic diseases on the global health agenda: a cause for concern. *Circulation 116*, 1966–1970.

(2) Naghavi, M., Libby, P., Falk, E., Casscells, S. W., Litovsky, S., Rumberger, J., Badimon, J. J., Stefanadis, C., Moreno, P., Pasterkamp, G., Fayad, Z., Stone, P. H., Waxman, S., Raggi, P., Madjid, M., Zarrabi, A., Burke, A., Yuan, C., Fitzgerald, P. J., Siscovick, D. S., de Korte, C. L., Aikawa, M., Airaksinen, K. E. J., Assmann, G., Becker, C. R., Chesebro, J. H., Farb, A., Galis, Z. S., Jackson, C., Jang, I. K., Koenig, W., Lodder, R. A., March, K., Demirovic, J., Navab, M., Priori, S. G., Rekhter, M. D., Bahr, R., Grundy, S. M., Mehran, R., Colombo, A., Boerwinkle, E., Ballantyne, C., Insull, W., Schwartz, R. S., Vogel, R., Serruys, P. W., Hansson, G. K., Faxon, D. P., Kaul, S., Drexler, H., Greenland, P., Muller, J. E., Virmani, R., Ridker, P. M., Zipes, D. P., Shah, P. K., and Willerson, J. T. (2003) From vulnerable plaque to vulnerable patient. A call for new definitions and risk assessment strategies: Part I. *Circulation 108*, 1664–1672.

(3) Choudhury, R. P., Fuster, V., and Fayad, Z. A. (2004) Molecular, cellular and functional imaging of atherothrombosis. *Nat. Rev. Drug Discovery 3*, 913–925.

(4) Sanz, J., and Fayad, Z. A. (2008) Imaging of atherosclerotic cardiovascular disease. *Nature (London) 451*, 953–957.

(5) Jaffer, F. A., Libby, P., and Weissleder, R. (2007) Molecular imaging of cardiovascular disease. *Circulation 116*, 1052–1061.

(6) Leiner, T., Gerretsen, S., Botnar, R., Lutgens, E., Cappendijk, V., Kooi, E., and van Engelshoven, J. (2005) Magnetic resonance imaging of atherosclerosis. *Eur. Radiol. 15*, 1087–1099.

(7) Lusis, A. J. (2000) Atherosclerosis. *Nature (London) 407*, 233–241.
(8) Amirbekian, V., Lipinski, M. J., Briley-Saebo, K. C., Amirbekian, S., Aguinaldo, J. G., Weinreb, D. B., Vucic, E., Frias, J. C., Hyafil, F., Mani, V., Fisher, E. A., and Fayad, Z. A. (2007) Detecting and assessing macrophages in vivo to evaluate atherosclerosis noninvasively using molecular MRI. *Proc. Natl. Acad. Sci. U.S.A. 104*, 961–966.
(9) Lipinski, M. J., Amirbekian, V., Frias, J. C., Aguinaldo, J. G., Mani, V., Briley-Saebo, K. C., Fuster, V., Fallon, J. T., Fisher, E. A., and Fayad, Z. A. (2006) MRI to detect atherosclerosis with gadolinium-containing immunomicelles targeting the macrophage scavenger receptor. *Magn. Reson. Med. 56*, 601–610.
(10) Ruehm, S. G., Corot, C., Vogt, P., Kolb, S., and Debatin, J. F. (2001) Magnetic resonance imaging of atherosclerotic plaque with ultrasmall superparamagnetic particles of iron oxide in hyperlipidemic rabbits. *Circulation 103*, 415–422.
(11) Hyafil, F., Cornily, J. C., Feig, J. E., Gordon, R., Vucic, E., Amirbekian, V., Fisher, E. A., Fuster, V., Feldman, L. J., and Fayad, Z. A. (2007) Noninvasive detection of macrophages using a nanoparticulate contrast agent for computed tomography. *Nat. Med. 13*, 636–641.
(12) Rudd, J. H. F., Warburton, E. A., Fryer, T. D., Jones, H. A., Clark, J. C., Antoun, N., Johnstrom, P., Davenport, A. P., Kirkpatrick, P. J., Arch, B. N., Pickard, J. D., and Weissberg, P. L. (2002) Imaging atherosclerotic plaque inflammation with [F-18]-fluorodeoxyglucose positron emission tomography. *Circulation 105*, 2708–2711.
(13) Nahrendorf, M., Zhang, H., Hembrador, S., Panizzi, P., Sosnovik, D. E., Aikawa, E., Libby, P., Swirski, F. K., and Weissleder, R. (2008) Nanoparticle PET-CT imaging of macrophages in inflammatory atherosclerosis. *Circulation 117*, 379–387.
(14) Frias, J. C., Williams, K. J., Fisher, E. A., and Fayad, Z. A. (2004) Recombinant HDL-like nanoparticles: a specific contrast agent for MRI of atherosclerotic plaques. *J. Am. Chem. Soc. 126*, 16316–16317.
(15) Frias, J. C., Ma, Y., Williams, K. J., Fayad, Z. A., and Fisher, E. A. (2006) Properties of a versatile nanoparticle platform contrast agent to image and characterize atherosclerotic plaques by magnetic resonance imaging. *Nano Lett. 6*, 2220–2224.
(16) Cormode, D. P., Briley-Saebo, K. C., Mulder, W. J. M., Aguinaldo, J. G. S., Barazza, A., Ma, Y., Fisher, E. A., and Fayad, Z. A. (2008) An apoA-I mimetic peptide HDL-based MRI contrast agent for atherosclerotic plaque composition detection. *Small 4*, 1437–1444.
(17) Anantharamaiah, G. M., Jones, J. L., Brouillette, C. G., Schmidt, C. F., Chung, B. H., Hughes, T. A., Bhown, A. S., and Segrest, J. P. (1985) Studies of synthetic peptide analogs of the amphipathic helix. *J. Biol. Chem. 260*, 10248–10255.
(18) Tang, C., Vaughan, A. M., Anantharamaiah, G. M., and Oram, J. F. (2006) Janus kinase 2 modulates the lipid-removing but not protein-stabilizing interactions of amphipathic helices with ABCA1. *J. Lipid Res. 47*, 107–114.
(19) Anantharamaiah, G. M., Datta, G., and Garber, D. W. (2001) Toward the design of peptide mimics of antiatherogenic apolipoproteins A-I and E. *Curr. Sci. 81*, 53–65.
(20) Navab, M., Anantharamaiah, G. M., Reddy, S. T., and Fogelman, A. M. (2006) Apolipoprotein A-I mimetic peptides and their role in atherosclerosis prevention. *Nat. Clin. Pract. Cardiovasc. Med. 3*, 540–547.
(21) Marque, V., Kieffer, P., Gayraud, B., Lartaud-Idjouadiene, I., Ramirez, F., and Atkinson, J. (2001) Aortic wall mechanics and composition in a transgenic mouse model of Marfan syndrome. *Arterioscler., Thromb., Vasc. Biol. 21*, 1184–1189.
(22) Davidson, W. S., Lund-Katz, S., Johnson, W. J., Anantharamaiah, G. M., Palgunachari, M. N., Segrest, J. P., Rothblat, G. H., and Phillips, M. C. (1994) The influence of apolipoprotein structure on the efflux of cellular free cholesterol to high density lipoprotein. *J. Biol. Chem. 269*, 22975–22982.
(23) Sosnovik, D., and Weissleder, R. (2005) Magnetic resonance and fluorescence based molecular imaging technologies. *Prog. Drug Res. 62*, 86–114.
(24) Bocharov, A. V., Baranova, I. N., Vishnyakova, T. G., Remaley, A. T., Csako, G., Thomas, F., Patterson, A. P., and Eggerman, T. L. (2004) Targeting of scavenger receptor class B type I by synthetic amphipathic α-helical-containing peptides blocks lipopolysaccharide (LPS) uptake and LPS-induced proinflammatory cytokine responses in THP-1 monocyte cells. *J. Biol. Chem. 279*, 36072–36082.
(25) Cormode, D. P., Skajaa, T., van Schooneveld, M. M., Koole, R., Jarzyna, P., Lobatto, M. E., Calcagno, C., Barazza, A., Gordon, R. E., Zanzonico, P., Fisher, E. A., Fayad, Z. A., and Mulder, W. J. M. (2008) Nanocrystal core high-density lipoproteins: a multimodal molecular imaging contrast agent platform. *Nano Lett. 8*, 3715–3723.
(26) Liu, J. B., Zeng, F. Q., and Allen, C. (2007) In vivo fate of unimers and micelles of a poly(ethylene glycol)-block-poly(caprolactone) copolymer in mice following intravenous administration. *Eur. J. Pharm. Biopharm. 65*, 309–319.
(27) Hoffman, J. S., and Benditt, E. P. (1983) Plasma-clearance kinetics of the amyloid-related high density lipoprotein apoprotein, serum amyloid protein (ApoSAA), in the mouse—evidence for rapid ApoSAA clearance. *J. Clin. Invest. 71*, 926–934.
(28) Zahr, A. S., Davis, C. A., and Pishko, M. V. (2006) Macrophage uptake of core-shell nanoparticles surface modified with poly(ethylene glycol). *Langmuir 22*, 8178–8185.
(29) Kelly, K. A., Allport, J. R., Tsourkas, A., Shinde-Patil, V. R., Josephson, L., and Weissleder, R. (2005) Detection of vascular adhesion molecule-1 expression using a novel multimodal nanoparticle. *Circ. Res. 96*, 327–336.
(30) Nikanjam, M., Blakely, E. A., Bjornstad, K. A., Shu, X., Budinger, T. F., and Forte, T. M. (2006) Synthetic nano-low density lipoprotein as targeted drug delivery vehicle for glioblastoma multiforme. *Int. J. Pharm. 328*, 86–94.

BC800520D

SUPPORTING INFORMATION FOR: 'COMPARISON OF SYNTHETIC HDL CONTRAST AGENTS FOR MR IMAGING OF ATHEROSCLEROSIS'

David P. Cormode[1], Rohith Chandrasekar[2], Amanda Delshad[1], Karen C. Briley-Saebo[1], Claudia Calcagno[1], Alessandra Barazza[1,3], Willem J. M. Mulder[1], Edward A. Fisher[3*], and Zahi A. Fayad[1*].

METHODS

Macrophage cholesterol efflux

J774A.1 murine macrophages (ATCC, Manassas, VA) were incubated overnight with 15 μg/ml cholesterol and 0.5 μCi/ml [^{3}H]cholesterol in 0.2% BSA-DMEM. After an equilibration period of 3 h with 1 μg/ml of F-1394 in 0.2% BSA-DMEM, efflux was initiated by the addition of 50 μg/ml of acceptor agent (by protein mass). 100 μl aliquots of the medium were collected after 4 h, and the [^{3}H]cholesterol measured by liquid scintillation counting (LSC). In order to measure the [^{3}H]cholesterol present in the cells, cell lipids were then extracted by incubating the cell monolayers overnight in isopropanol. After lipid extraction, the total [^{3}H]cholesterol present in lipid extract was measured by LSC and the efflux calculated as percentage of total. Such efflux experiments were carried out with 18A-Gd, 37pA-Gd, HDL and bovine serum albumin.

MRI scanning

Mice were scanned using the following protocol. The abdominal aorta was identified in a coronal section on a localizing sequence. T1-weighted MRI was performed using a black blood sequence. Twenty-two contiguous 500 μm-thick slices with a microscale in-plane resolution of 101 μm were acquired using a spin echo sequence with a 256 × 256 matrix size. The repetition time (TR) and echo time (TE) for the T1W images were 800 and 8.6 ms, respectively. An inflow saturation band of 3 mm was used with a slice gap of 3 mm for additional luminal flow suppression. Sixteen signal averages were used for a total imaging time of 55 min per scan. A saturation pulse was used to eliminate signal from fat tissue and better delineate boundary of the aortic wall and minimize chemical shift artifacts. After a preinjection, baseline MRI scan, mice were injected, via a tail-vein catheter with a 50 μmol Gd/kg dose of the synthetic HDL contrast agents. The mice were scanned again at 24 hours post-injection. n=7 apoE-KO mice were injected with each agent. Use of the medical image analysis software package eFilm allowed the MR signal intensity of various tissues from the different time points to be ascertained and the percent change in normalized enhancement ratio (% NER) post-injection to be calculated. Normalization of the MR signal intensity in the aorta wall was performed by rebasing with the signal from muscle adjacent to the aorta.

ADDITIONAL FIGURES

Figure S1 Fluorescence of macrophages incubated with Cy5.5 labeled 18A-Gd for varying times ranging from 1 to 24 hours. Error bars are +/- one standard deviation.

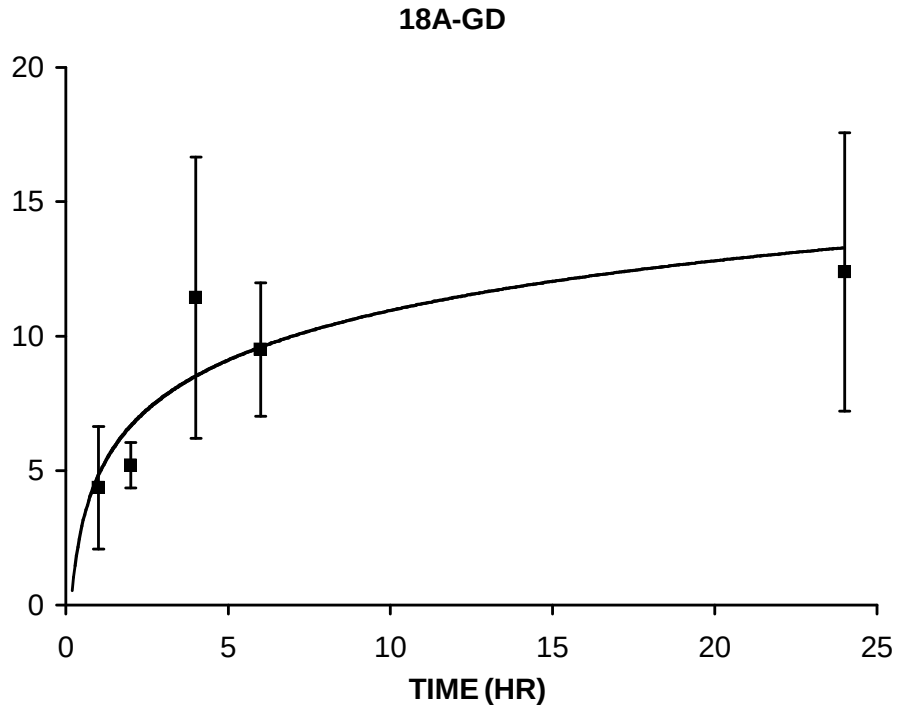

Figure S2 Fluorescence of macrophages incubated with Cy5.5 labeled 37pA-Gd for varying times ranging from 1 to 24 hours. Error bars are +/- one standard deviation.

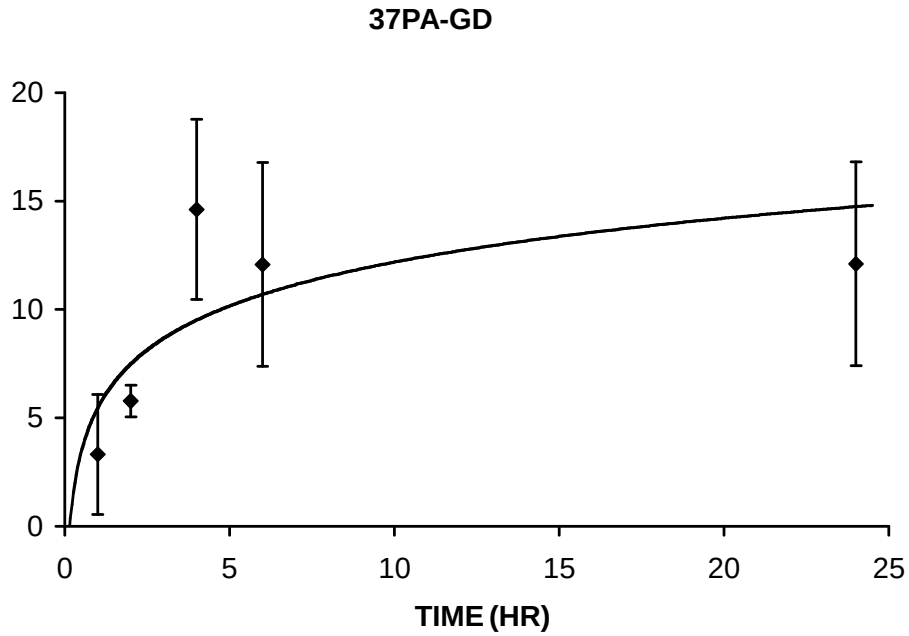

Figure S3 Uptake of cy5.5-labeled Gd-micelles in J774A.1 macrophages as determined by fluorescence imaging of cells. The data are displayed using the same scale as in Figure 2 D and E in order to allow comparison.

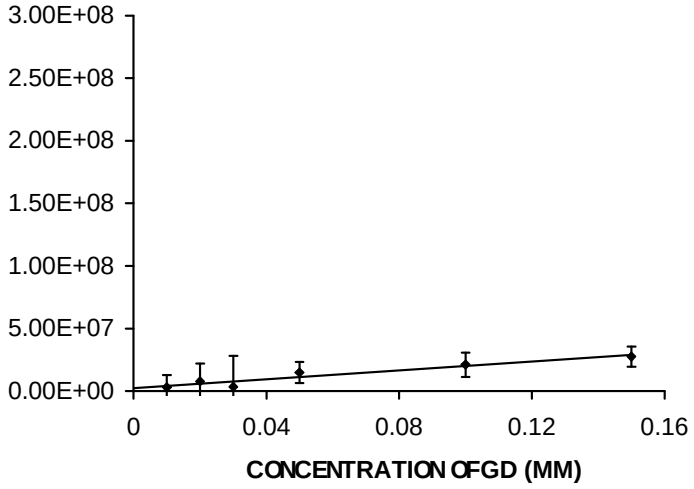

Figure S4 Confocal microscopy images of aortic tissue excised from an apoE-KO mouse injected with the 18A-Gd agent 24 hours prior to excision. A – DAPI staining for nuclei (blue), B – the rhodamine channel (red) indicating areas of 18A-Gd uptake, C – Alexa 647:CD68 staining for macrophages (green) and D – a merger of the previous 3 images. In this section there are no macrophages and no 18A-Gd uptake either.

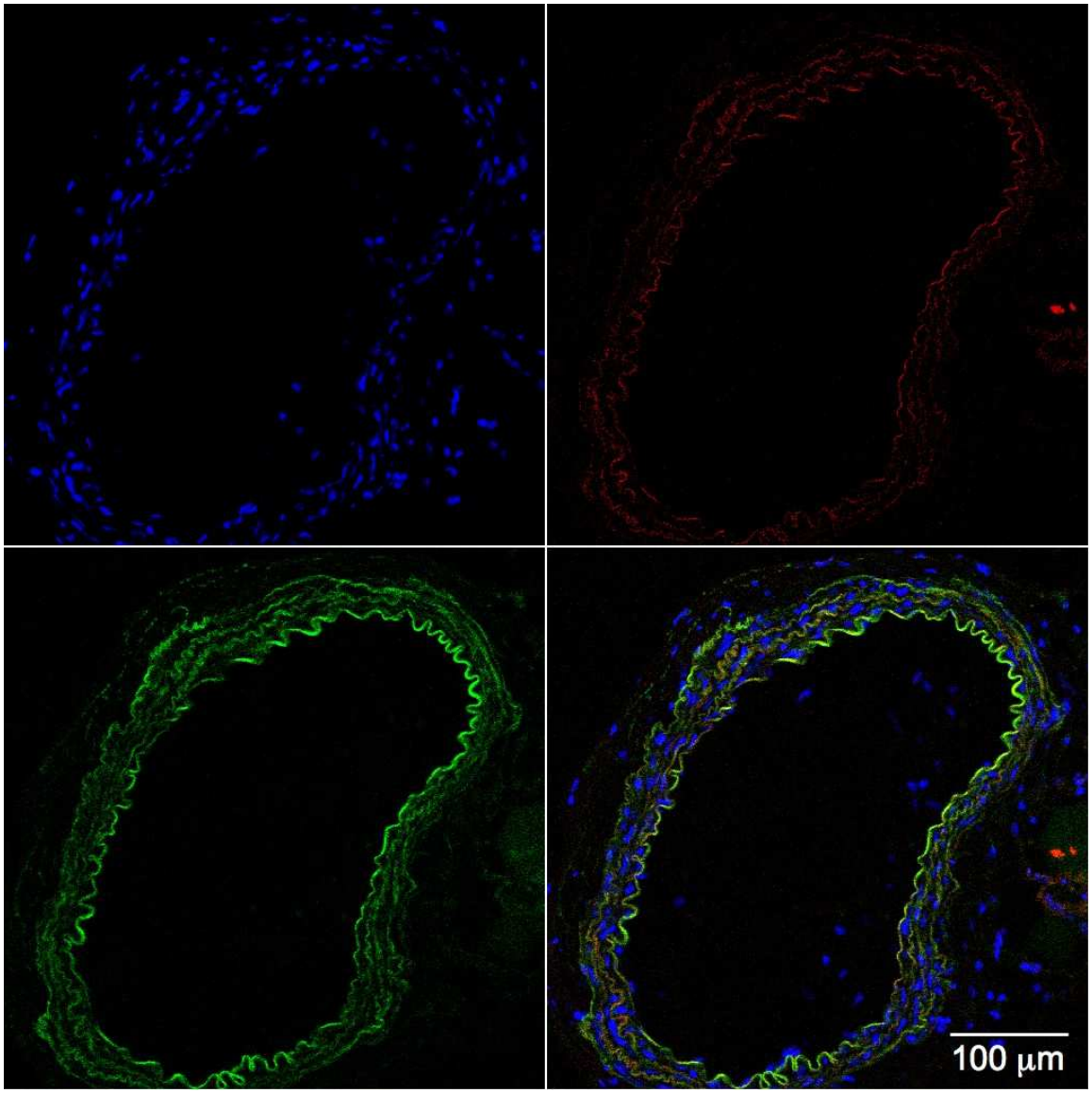

REFERENCES

1. Davidson WS, Lund-Katz S, Johnson WJ, Anantharamaiah GM, Palgunachari MN, Segrest JP, Rothblat GH, Phillips MC. The influence of apolipoprotein structure on the efflux of cellular free cholesterol to high density lipoprotein. *J. Biol. Chem.* 1994;269:22975-22982.
2. Marque V, Kieffer P, Gayraud B, Lartaud-Idjouadiene I, Ramirez F, Atkinson J. Aortic wall mechanics and composition in a transgenic mouse model of Marfan syndrome. *Arterioscler. Thromb. Vasc. Biol.* 2001;21:1184-1189.

Synthesis and Photocytotoxicity of S-Glucosylated 5,10,15,20-Tetrakis(tetrafluorophenyl)porphyrin Metal Complexes as Efficient $^1O_2$-Generating Glycoconjugates

Shiho Hirohara,*[,†] Makoto Obata,*[,‡] Hiroki Alitomo,[§] Kohei Sharyo,[†] Tsuyoshi Ando,[†] Shigenobu Yano,[⊥] and Masao Tanihara[†]

Graduate School of Materials Science, Nara Institute of Science and Technology, Takayama 8916-5, Ikoma, Nara 630-0192, Japan, Graduate School of Humanities and Sciences, Nara Women's University, Kitauoyanishimachi, Nara 630-8506, Japan, Department of Industrial Chemistry, Osaka Prefectural College of Technology, Osaka 572-8572, Japan, and Endowed Research Section, Photomedical Science, Innovative Collaboration Center, Kyoto University, Kyoto 615-8520, Japan. Received December 7, 2008; Revised Manuscript Received March 15, 2009

5,10,15,20-Tetrakis(4-(2,3,4,6-tetra-*O*-acetyl-*β*-D-glucopyranosylthio)-2,3,5,6-tetrafluorophenyl)porphyrin **2a** and its Zn(II), Pd(II), and Pt(II) complexes **2b**, **2c**, and **2d** were prepared in excellent yields by nucleophilic substitution of the corresponding free-base porphyrin and metalloporphyrins with acetyl 2,3,4,6-tetra-*O*-acetyl-1-thio-*β*-D-glucopyranoside. Deprotection of **2a**, **2b**, **2c**, and **2d** by alkaline hydrolysis afforded the corresponding S-glucosylated porphyrin **3a** and its metal complexes **3b**, **3c**, and **3d**. The structures and purity of all new photosensitizers were confirmed by elemental analysis and ^{1}H, ^{13}C, and ^{19}F NMR, UV−vis, and steady-state luminescence spectroscopy. The relative efficiency of singlet oxygen ($^1O_2$) production increased in the order of free-base fluoroporphyrins (**2a** and **3a**) < Zn(II) complexes (**2b** and **3b**) < Pd(II) complexes (**2c** and **3c**), which can be explained in terms of the heavy-atom effect, while the $^1O_2$-producing efficiency of Pt(II) complexes (**2d** and **3d**) were exceptionally low. In vitro photocytotoxicity of these eight S-glucosylated photosensitizers was examined in HeLa cells. Although all protected photosensitizers **2a**, **2b**, **2c**, and **2d** showed no photocytotoxicity, the photosensitizers **3a**, **3b**, and **3c** exerted potent photocytotoxicity. These results clearly indicated that the sugar moieties of **3a**, **3b**, and **3c** act as not only water-solubility-enhancing functionalities but also cellular-uptake-enhancing elements. Photocytotoxicity testing of **3a**, **3b**, and **3c** in the presence of reactive oxygen species inhibitors suggested that $^1O_2$ is the major mediator of cell death. Hence, the Zn(II) and Pd(II) complexes **3b** and **3c** are promising photosensitizers having cellular uptake-facilitating units (sugar moieties) and enhanced $^1O_2$ generation due to the heavy-atom effect.

INTRODUCTION

In photodynamic therapy (PDT[1]), an administered-photosensitizer is taken up by malignant cells and subsequent irradiation with light causes the generation of cytotoxic reactive oxygen species (ROS) that kill the cells (*1*−*7*). Thus, critical factors in PDT are the distribution of the photosensitizers and the site of photoirradiation. Tumor-specific accumulation of photosensitizers is extremely important, because ROS also attacks healthy cells, resulting in significant side effects. One promising approach is conjugation of a tumor-specific element to the photosensitizer. [2-^{18}F]2-Deoxy-2-fluoroglucose ([^{18}F]FDG) is a well-known diagnostic drug that is widely used in positron emission tomography (*8*). [^{18}F]FDG takes advantage of the enhanced uptake of glucose by malignant cells. Hence, much effort has been devoted to the development of photosensitizers incorporating biologically active sugar moieties in order to improve the water-solubility and to enhance uptake by tumor cells. Li et al. reported the synthesis and biological properties of glycoconjugated photosensitizers bearing galactose, lactose, galactosamine, and glucosamine (*9*). They demonstrated the sugar-dependent photocytotoxicity of glycosylated photosensitizers in radiation-induced fibrosarcoma tumors, which express galectin-3. Momenteau et al. reported the systematic synthesis of seventeen 5,10,15,20-tetraphenylporphyrin (H_2TPP) deriva-

* To whom correspondence should be addressed. (S.H.) Phone: +81 743726122. Fax: +81 743726129. E-mail: hirohara@ms.naist.jp. (M.O.) Phone: +81 742203622. Fax: +81 742203622. E-mail: mobata@cc.nara-wu.ac.jp.

† Nara Institute of Science and Technology.

‡ Nara Women's University.

§ Osaka Prefectural College of Technology.

⊥ Kyoto University.

[1]Abbreviations: DMF, *N*,*N*-dimethylformamide; DMEM, Dulbecco's modified Eagle's medium; Man, D-mannitol; DMSO, dimethyl sulfoxide; DPBF, 1,3-diphenylisobenzofuran; FCS, fetal calf serum; GPC, gel permeation chromatography; HPLC, high-performance liquid chromatography; PBS, Dulbecco's phosphate-buffered saline; PDT, photodynamic therapy; ROS, reactive oxygen species; TPPS, tetraphenylporphyrin tetrasulfonic acid; **1a**, 5,10,15,20-tetrakis(2,3,4,5,6-pentafluorophenyl)porphyrin; **1b**, 5,10,15,20-tetrakis(2,3,4,5,6-pentafluorophenyl)porphyrinato zinc(II); **1c**, 5,10,15,20-tetrakis(2,3,4,5,6-pentafluorophenyl)porphyrinato palladium(II); **1d**, 5,10,15,20-tetrakis(2,3,4,5,6-pentafluorophenyl)porphyrinato platinum(II); **2a**, 5,10,15,20-tetrakis(4-(2,3,4,6-tetra-*O*-acetyl-*β*-D-glucopyranosylthio)-2,3,5,6-tetrafluorophenyl)porphyrin; **2b**, 5,10,15,20-tetrakis(4-(2,3,4,6-tetra-*O*-acetyl-*β*-D-glucopyranosylthio)-2,3,5,6-tetrafluorophenyl)porphyrinato zinc(II); **2c**, 5,10,15,20-tetrakis(4-(2,3,4,6-tetra-*O*-acetyl-*β*-D-glucopyranosylthio)-2,3,5,6-tetrafluorophenyl)porphyrinato palladium(II); **2d**, 5,10,15,20-tetrakis(4-(2,3,4,6-tetra-*O*-acetyl-*β*-D-glucopyranosylthio)-2,3,5,6-tetrafluorophenyl)porphyrinato platinum(II); **3a**, 5,10,15,20-tetrakis(4-(*β*-D-glucopyranosylthio)-2,3,5,6-tetrafluorophenyl)porphyrin; **3b**, 5,10,15,20-tetrakis(4-(*β*-D-glucopyranosylthio)-2,3,5,6-tetrafluorophenyl)porphyrinato zinc(II); **3c**, 5,10,15,20-tetrakis(4-(*β*-D-glucopyranosylthio)-2,3,5,6-tetrafluorophenyl)porphyrinato palladium(II); **3d**, 5,10,15,20-tetrakis(4-(*β*-D-glucopyranosylthio)-2,3,5,6-tetrafluorophenyl)porphyrinato platinum(II); **4**, acetyl 2,3,4,6-tetra-*O*-acetyl-1-thio-*β*-D-glucopyranoside.

10.1021/bc800522y CCC: $40.75 © 2009 American Chemical Society
Published on Web 04/20/2009

Chart 1. Glycoconjugated Photosensitizers

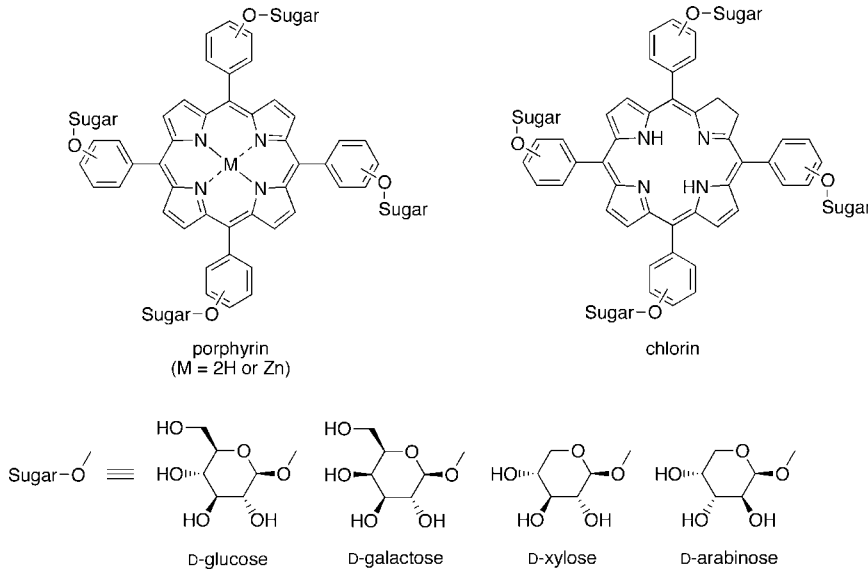

Chart 2. Photosensitizers Having Metal Ions

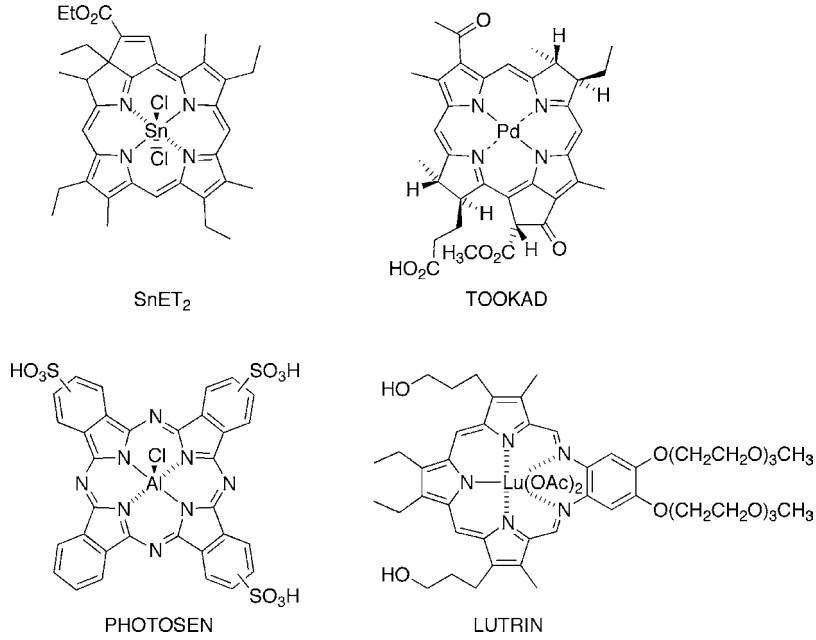

tives bearing glucose, galactose, maltose, and glucosamine (*10, 11*). They examined the efficiency of singlet oxygen ($^1O_2$) generation, partition coefficients, and photocytotoxicity in KB cells. While no differences were found in the photophysical properties of glycosylated porphyrins in organic solvents, the photocytotoxicity in KB cells depended on the sugar moiety. They suggested that the differences in photocytotoxicity might have arisen from differences in the sugar-dependent cellular uptake. Previously we have systematically synthesized porphyrin and chlorin derivatives having O-glycosylated phenyl groups at the meso positions (Chart 1) and demonstrated enhanced cellular uptake and sugar-dependent photocytotoxicity in HeLa cells (*12*−*16*).

In addition to the requirement for efficient cellular uptake, a photosensitizer must generate ROS efficiently for successful PDT. Since singlet oxygen ($^1O_2$) is thought to be involved in porphyrinoid-based PDT, the $^1O_2$ quantum yield (Φ_Δ) is likely to be a crucial factor for photocytotoxicity. In general, energy transfer from a photosensitizer to an oxygen molecule occurs in the excited triplet state. So, efficient intersystem crossing from the excited singlet state to the triplet state is a key process in $^1O_2$ generation. Because this spin-forbidden process is promoted by spin−orbit coupling, which is a function of Z^4 (Z is atomic number), heavy atoms should increase the $^1O_2$ quantum yield; this is the well-known heavy-atom effect (*17*). Several metalloporphyrin derivatives or analogues have been approved for PDT or are under clinical trial (Chart 2). For example, $SnET_2$ is a tin complex of etiopurpurin and is used in clinical treatment of cutaneous malignancies and age-related macular degeneration. The Φ_Δ value of $SnET_2$ is 0.71 ± 0.1 in acetonitrile (*18*). Bacteriochlorophyll is an attractive candidate due to the very large absorption bands in the near-infrared region but is photochemically unstable even in dim light. The introduction of palladium into bacteriopheophorbide, giving TOOKAD, improves the photostability and provides an excellent triplet yield of over 0.99 (*19*). Therefore, the combination of glycosylation and complexation with metal ion seems to be a promising design approach for PDT photosensitizers. However, relatively severe conditions are required for complexation, especially in the case of late transition metal complexes and are incompatible with porphyrins having delicate functional

groups, such as sugar moieties. Hence, complexation with the heavy metal ion should be done prior to introduction of sugar moieties. This strategy requires a selective and high-yield conjugation reaction between porphyrin and sugar units. Boyle et al. have developed nucleophilic substitution reaction of pentafluorophenyl groups of fluorinated porphyrin with thiolate anion (*20*), and Drain et al. applied this methodology to the synthesis of glycoconjugated fluorinated porphyrin using thioglycoside (*21*). We adopted this synthetic strategy, to design glycoconjugated metalloporphyrins that were expected to show both enhanced cellular uptake owing to glycosylation, and efficient $^1O_2$ generation owing to the heavy-atom (Zn, Pd, and Pt) effect. Here, we report the synthetic details and photophysical properties of these glycoconjugated metalloporphyrins and the results of evaluation of their in vitro photocytotoxicity in HeLa cells.

EXPERIMENTAL SECTION

Materials and Methods. All chemicals used were of analytical grade. Tetraphenylporphyrin tetrasulfonic acid (TPPS) and 1,3-diphenylisobenzofuran (DPBF) were purchased from Sigma-Aldrich Japan (Chiba, Japan). 5,10,15,20-Tetrakis(2,3,4,5,6-pentafluorophenyl)porphyrin (**1a**), 5,10,15,20-tetrakis(2,3,4,5,6-pentafluorophenyl)porphyrinato zinc(II) (**1b**), 5,10,15,20-tetrakis(2,3,4,5,6-pentafluorophenyl)porphyrinato palladium(II) (**1c**), 5,10,15,20-tetrakis(2,3,4,5,6-pentafluorophenyl)porphyrinato platinum(II) (**1d**), and acetyl 2,3,4,6-tetra-*O*-acetyl-1-thio-*β*-D-glucopyranoside (**4**) were prepared according to the literature (*22*−*24*). Preparative gel permeation chromatography (GPC) was performed on an LC-908 recycling preparative high-performance liquid chromatography (HPLC) system (Japan Analytical Industry Co., Ltd., Tokyo, Japan) equipped with two polystyrene columns (JAIGEL-2.5H and JAIGEL-2H), with $CHCl_3$ as an eluent. Preparative HPLC was carried out on octadecylsilyl-bound silica gel (Mightysil RP-18, 20 mm $\phi \times$ 250 mm, Kanto Chemical Co., Inc., Tokyo, Japan). ^{1}H, ^{13}C, and ^{19}F NMR spectra were recorded on JNM-EC600 (600 MHz, JEOL Ltd., Tokyo, Japan) and JNM-AL400 (400 MHz, JEOL Ltd., Tokyo, Japan) instruments. Electronic absorption spectra in DMSO were recorded on a V-570 spectrophotometer (JASCO Co., Ltd., Tokyo, Japan). Steady-state luminescence spectra in DMSO were recorded on a FP-6300 spectrofluorometer (JASCO Co., Ltd., Tokyo, Japan). Elemental analyses were performed on a Perkin-Elmer 2400 series II CHNS/O elemental analyzer (Perkin-Elmer. Inc., MA, USA).

Stock solutions of photosensitizers were prepared by weighing the dried photosensitizers and dissolving them in dimethyl sulfoxide (DMSO, Wako Pure Chemical Industries, Osaka, Japan) and kept in freezer (−30 °C) until use. The absorbance of each well was determined with a plate reader (Multiscan JX, Thermo Fisher Scientific Co., Yokohama, Japan).

5,10,15,20-Tetrakis(4-(2,3,4,6-tetra-*O*-acetyl-*β*-D-glucopyranosylthio)-2,3,5,6-tetrafluorophenyl)porphyrin (2a). S-Glucosylated porphyrin **2a** was prepared by a slight modification of the literature method (*21*) to prevent the formation of over-S-glucosylated porphyrins (vide infra). Porphyrin **1a** (64.9 mg, 66.6 μmol), S-glycoside **4** (113 mg, 278 μmol), and diethylamine (3.0 mL) were dissolved in *N*,*N*-dimethylformamide (DMF) (30 mL). The resulting mixture was stirred at ambient temperature for 24 h, diluted with $CHCl_3$ (30 mL), washed with water (30 mL × 5), and dried over Na_2SO_4. The solvent was removed under reduced pressure. The crude product was purified by column chromatography (silica gel, gradient from $CHCl_3$ to $CHCl_3$: AcOEt = 7: 3) followed by preparative GPC to give **2a** (116 mg, yield 74.0%) as a brown purple solid. Anal. Calcd for $C_{100}H_{86}O_{36}N_4F_{16}S_4 \cdot 2H_2O$: C, 50.30; H, 3.80; N, 2.35. Found: C, 50.24; H, 3.36; N, 2.19. ^{1}H NMR (600.07 MHz, $CDCl_3$, $Si(CH_3)_4$ = 0 ppm): δ (ppm) = 9.04 (8H, s, β-pyrrole*H*), 5.39 (4H, dd, ^3J = 9.3 and 9.3 Hz, 3-Glc*H*), 5.26 (8H, m, 2,4-Glc*H*), 5.19 (4H, d, ^3J = 10.0 Hz, 1-Glc*H*), 4.33 (8H, dd, ^3J = 3.0 Hz, ^2J = 1.6 Hz, 6-Glc*H*), 3.92 (4H, dt, ^3J = 10.1 Hz, ^3J = 3.1 Hz, 5-Glc*H*), 2.24 (3H, s, CH_3), 2.11 (3H, s, CH_3), 2.10 (3H, s, CH_3), 2.09 (3H, s, CH_3), −2.85 (2H, brs, N*H*). ^{13}C NMR (100.40 MHz, $CDCl_3$, *C*DCl_3 = 77 ppm): δ (ppm) = 170.37 (*C*═O), 169.91 (*C*═O), 169.22 (*C*═O), 169.14 (*C*═O), 147.76 (2,6-Ph*C*), 145.28 (3,5-Ph*C*, α-pyrrole*C*), 131.30 (β-pyrrole *C*), 121.95 (4-Ph*C*), 111.85 (1-Ph *C*), 104.24 (meso*C*), 84.43 (1-Glc *C*), 76.48 (5-Glc*C*), 73.96 (3-Glc *C*), 70.71 (2-Glc*C*), 68.18 (4-Glc *C*), 61.88 (6-Glc*C*), 20.75 (*C*H_3), 20.70 (*C*H_3). ^{19}F NMR (376 MHz, $CDCl_3$, CF_3CO_2H = −76.05 ppm): δ (ppm) = −132.13 (8F, dd, $^3J_{F-F}$ = 24 Hz, $^5J_{F-F}$ = 12 Hz, 3,5-Ph*F*), −136.43 (8F, dd, $^3J_{F-F}$ = 26 Hz, $^5J_{F-F}$ = 12 Hz, 2,6-Ph*F*). UV−vis (c = 2.30 μM, DMSO, path length = 1 cm, 25 °C): λ/nm ($\varepsilon \times 10^{-3}$ /M$^{-1}\cdot$cm^{-1}) = 416 (33.4), 507 (2.36), 539 (0.32), 580 (0.77), 634 (0.08). FL (c = 2.30 μM, DMSO, path length = 1 cm, λ_{ex} = 414.5 nm, 25 °C): λ/nm = 640, 705.

5,10,15,20-Tetrakis(4-(2,3,4,6-tetra-*O*-acetyl-*β*-D-glucopyranosylthio)-2,3,5,6-tetrafluorophenyl)porphyrinato Zinc(II) (2b). A procedure similar to that described for **2a** was applied to porphyrin **1b** (58.5 mg, 56.4 μmol) and S-glycoside **4** (93.4 mg, 230 μmol) to give **2b** (101 mg, yield 74.1%) as a pink red solid. Anal. Calcd for $C_{100}H_{84}O_{36}N_4F_{16}S_4Zn \cdot 4H_2O$: C, 48.29; H, 3.73; N, 2.25. Found: C, 48.19; H, 3.38; N, 2.24. ^{1}H NMR (600.17 MHz, $CDCl_3$, $Si(CH_3)_4$ = 0 ppm): δ (ppm) = 9.07 (8H, s, β-pyrrole*H*), 5.09 (4H, dd, ^3J = 9.0 and 9.0 Hz, 3-Glc*H*), 5.03 (4H, m, 2,4-Glc*H*), 4.99 (4H, d, ^3J = 9.7 Hz, 1-Glc*H*), 4.00 (8H, d, ^3J = 3.4 Hz, 6-Glc*H*), 3.73 (4H, dt, ^3J = 10.3 Hz, ^3J = 3.4 Hz, 5-Glc*H*), 2.04 (CH_3), 1.84 (CH_3). ^{13}C NMR (100.40 MHz, $CDCl_3$, *C*DCl_3 = 77 ppm): δ (ppm) = 170.31 (*C*═O), 169.79 (*C*═O), 169.13 (*C*═O), 168.97 (*C*═O), 149.65 (α-pyrrole*C*), 147.71 (2,6-Ph*C*), 145.24 (3,5-Ph*C*), 131.98 (β-pyrrole*C*), 122.98 (4-Ph*C*), 111.48 (1-Ph*C*), 104.59 (meso*C*), 84.54 (1-Glc*C*), 76.20 (5-Glc*C*), 73.76 (3-Glc*C*), 70.55 (2-Glc*C*), 67.91 (4-Glc*C*), 61.70 (6-Glc*C*), 20.50 (*C*H_3), 20.48 (*C*H_3), 20.38 (*C*H_3). ^{19}F NMR (376 MHz, $CDCl_3$, CF_3CO_2H = −76.05 ppm): δ (ppm) = −131.77 (8F, dd, $^3J_{F-F}$ = 26 Hz, $^5J_{F-F}$ = 12 Hz, 3,5-Ph*F*), −135.97 (8F, dd, $^3J_{F-F}$ = 26 Hz, $^5J_{F-F}$ = 12 Hz, 2,6-Ph*F*). UV−vis (c = 6.10 μM, DMSO, path length = 1 cm, 25 °C): λ/nm ($\varepsilon \times 10^{-3}$/M$^{-1}\cdot$cm^{-1}) = 425 (41.2), 515 (2.16), 587 (0.21). FL (c = 6.10 μM, DMSO, path length = 1 cm, λ_{ex} = 424.5 nm, 25 °C): λ/nm = 599, 651.

5,10,15,20-Tetrakis(4-(2,3,4,6-tetra-*O*-acetyl-*β*-D-glucopyranosylthio)-2,3,5,6-tetrafluorophenyl)porphyrinato Palladium(II) (2c). A procedure similar to that described for **2a** was applied to porphyrin **1c** (58.2 mg, 53.9 μmol) and S-glycoside **4** (87.3 mg, 215 μmol) to give **2c** (113 mg, yield 83.1%) as an orange solid. Anal. Calcd for $C_{100}H_{84}O_{36}N_4F_{16}S_4Pd \cdot 6H_2O$: C, 46.83; H, 3.77; N, 2.18. Found: C, 46.87; H, 3.41; N, 2.05. ^{1}H NMR (600.17 MHz, $CDCl_3$, $Si(CH_3)_4$ = 0 ppm): δ (ppm) = 8.99 (8H, s, β-pyrrole*H*), 5.38 (4H, dd, ^3J = 9.0 and 9.0 Hz, 3-Glc*H*), 5.25 (4H, m, 2,4-Glc*H*), 5.18 (4H, d, ^3J = 9.6 Hz, 1-Glc*H*), 4.32 (8H, m, 6-Glc*H*), 3.92 (4H, dt, ^3J = 10.3 and 3.3 Hz, 5-Glc*H*), 2.23 (CH_3), 2.10 (CH_3), 2.10 (CH_3), 2.09 (CH_3). ^{13}C NMR (100.40 MHz, $CDCl_3$, *C*DCl_3 = 77 ppm): δ (ppm) = 170.31 (*C*═O), 169.79 (*C*═O), 169.13 (*C*═O), 168.97 (*C*═O), 147.56 (2,6-Ph*C*), 145.07 (3,5-Ph*C*), 141.20 (α-pyrrole*C*), 131.18 (β-pyrrole*C*), 121.43 (4-Ph*C*), 111.78 (1-Ph*C*), 105.94 (meso*C*), 84.29 (1-Glc*C*), 76.33 (5-Glc*C*), 73.80 (3-Glc*C*), 70.57 (2-Glc*C*), 68.02 (4-Glc*C*), 61.73 (6-Glc*C*), 20.61 (*C*H_3), 20.56 (*C*H_3). ^{19}F NMR (376 MHz, $CDCl_3$, CF_3CO_2H = −76.05 ppm): δ (ppm) = −131.16 (8F, dd, $^3J_{F-F}$ = 25 Hz, $^5J_{F-F}$ = 11 Hz, 3,5-Ph*F*), −135.45 (8F, dd, $^3J_{F-F}$ = 25 Hz, $^5J_{F-F}$ = 12 Hz, 2,6-Ph*F*). UV−vis (c = 4.74 μM, DMSO, path length = 1 cm, 25 °C): λ/nm ($\varepsilon \times 10^{-3}$/M$^{-1}\cdot$cm^{-1}) = 409 (28.1), 519

(2.54), 552 (1.67). FL (c = 4.74 μM, DMSO, path length = 1 cm, λ_{ex} = 408.5 nm, 25 °C): λ/nm = 557, 607, 673.

5,10,15,20-Tetrakis(4-(2,3,4,6-tetra-*O*-acetyl-β-D-glucopyranosylthio)-2,3,5,6-tetrafluorophenyl)porphyrinato Platinum(II) (2d). A procedure similar to that described for **2a** was applied to porphyrin **1d** (99.9 mg, 85.6 μmol) and S-glycoside **4** (139 mg, 343 μmol) to give **2d** (107 mg, yield 85.3%) as a red orange solid. Anal. Calcd for $C_{100}H_{84}O_{36}N_4F_{16}S_4Pt\cdot 6H_2O$: C, 45.27; H, 3.65; N, 2.11. Found: C, 45.06; H, 3.08; N, 1.96. ^{1}H NMR (600.17 MHz, $CDCl_3$, Si(CH_3)$_4$ = 0 ppm): δ (ppm) = 8.93 (8H, s, β-pyrrole*H*), 5.38 (4H, dd, ^3J = 9.2 and 9.0 Hz, 3-Glc*H*), 5.25 (8H, dd, ^3J = 10.2 and 9.0 Hz, 2,4-Glc*H*), 5.18 (4H, d, ^3J = 10.2 Hz, 1-Glc*H*), 4.32 (8H, dd, ^3J = 3.9 Hz, ^2J = 1.7 Hz, 6-Glc*H*), 3.91 (4H, dt, ^3J = 10.2 and 4.4 Hz, 5-Glc*H*), 2.23 (CH_3), 2.10 (CH_3), 2.09 (CH_3), 2.09 (CH_3). ^{13}C NMR (150.92 MHz, $CDCl_3$, $CDCl_3$ = 77 ppm): δ (ppm) = 170.62 (*C*=O), 170.16 (*C*=O), 169.45 (*C*=O), 169.38 (*C*=O), 147.47 (2,6-Ph*C*), 146.08 (3,5-Ph*C*), 141.00 (α-pyrrole*C*), 131.24 (β-pyrrole*C*), 121.21 (4-Ph*C*), 112.06 (1-Ph*C*), 106.92 (meso*C*), 84.41 (1-Glc*C*), 76.44 (5-Glc*C*), 73.91 (3-Glc*C*), 70.64 (2-Glc*C*), 68.08 (4-Glc*C*), 61.79 (6-Glc*C*), 20.65 (CH_3), 20.64 (CH_3), 20.58 (CH_3), 20.57 (CH_3). ^{19}F NMR (376 MHz, $CDCl_3$, CF_3CO_2H = −76.05 ppm): δ (ppm) = −131.04 (8F, dd, $^3J_{F-F}$ = 25 Hz, $^5J_{F-F}$ = 12 Hz, 3,5-Ph*F*), −135.42 (8F, dd, $^3J_{F-F}$ = 24 Hz, $^5J_{F-F}$ = 12 Hz, 2,6-Ph*F*). IR (KBr): UV−vis (c = 4.29 μM, DMSO, path length = 1 cm, 25 °C): λ/nm ($\epsilon \times 10^{-3}$/$M^{-1}\cdot cm^{-1}$) = 394 (28.3), 507 (1.98), 539 (2.18). FL (c = 4.29 μM, DMSO, path length = 1 cm, λ_{ex} = 393.5 nm, 25 °C): λ/nm = 653, 702, 801.

5,10,15,20-Tetrakis(4-(β-D-glucopyranosylthio)-2,3,5,6-tetrafluorophenyl)porphyrin (3a). The synthesis of porphyrin **3a** reported in the literature (*21*) was modified as follows to obtain highly pure sample for in vitro photocytotoxicity testing. Porphyrin **2a** (51.1 mg, 21.7 μmol) was dissolved in CH_2Cl_2 (10 mL) and CH_3OH (10 mL). Sodium methoxide was added to adjust the pH to 9. This mixture was refluxed for 1 h at 45−50 °C. The reaction mixture was neutralized with acetic acid and evaporated to dryness. The crude product was purified by preparative HPLC (CH_3CN:H_2O = 1: 1). The collected fraction was desalted by dialysis using a cellulose ester membrane (molecular weight cutoff: 1000). Lyophilization of the desalted aqueous sample solution gave **3a** (24.9 mg, yield 68.8%) as a dark red powder. Anal. Calcd for $C_{68}H_{54}O_{20}N_4F_{16}S_4\cdot 6H_2O$: C, 45.69; H, 3.72; N, 3.13. Found: C, 45.57; H, 3.58; N, 3.14. ^{1}H NMR (600.07 MHz, CD_3OD, CHD_2OD = 3.30 ppm): δ (ppm) = 9.07 (8H, s, β-pyrrole*H*), 5.09 (4H, m, 1-Glc*H*), 3.92 (4H, m, 6-Glc*H*), 3.68 (4H, m, 6-Glc*H*), 3.44−3.22 (16H, m, 2,3,4,5-Glc*H*). ^{13}C NMR (100.40 MHz, CD_3OD, CD_3OD = 49.0 ppm): δ (ppm) = 149.70 (α-pyrrole*C*), 148.79 (α-pyrrole*C*), 147.18 (β-pyrrole*C*), 146.26 (β-pyrrole*C*), 125.00−135.00 (2,6-Ph*C* and 3,5-Ph*C*), 121.65 (4-Ph*C*), 115.02 (1-Ph*C*), 105.74 (meso*C*), 86.69 (1-Glc*C*), 82.73 (5-Glc*C*), 79.72 (3-Glc*C*), 75.96 (2-Glc*C*), 71.71 (4-Glc*C*), 63,10 (6-Glc*C*). ^{19}F NMR (376 MHz, CD_3OD, CF_3CO_2H = −76.05 ppm): δ (ppm) = −133.42 (8F, dd, $^3J_{F-F}$ = 25 Hz, $^5J_{F-F}$ = 12 Hz, 3,5-Ph*F*), −138.81 (8F, dd, $^3J_{F-F}$ = 24 Hz, $^5J_{F-F}$ = 12 Hz, 2,6-Ph*F*). UV−vis (c = 5.35 μM, DMSO, path length = 1 cm, 25 °C): λ/nm ($\epsilon \times 10^{-3}$/$M^{-1}\cdot cm^{-1}$) = 415 (33.4), 507 (2.32), 539 (0.35), 581 (0.76), 636 (0.07). FL (c = 5.35 μM, DMSO, path length = 1 cm, λ_{ex} = 415 nm, 25 °C): λ/nm = 640, 705.

5,10,15,20-Tetrakis(4-(β-D-glucopyranosylthio)-2,3,5,6-tetrafluorophenyl)porphyrinato Zinc(II) (3b). A procedure similar to that described for **3a** was applied to **2b** (143 mg, 99.2 μmol) to give **3b** (83.8 mg, yield 81.1%) as a pink red powder. Anal. Calcd for $C_{68}H_{52}O_{20}N_4F_{16}S_4Zn\cdot 10H_2O$: C, 42.47; H, 3.77; N, 2.91. Found: C, 42.50; H, 3.34; N, 2.85. ^{1}H NMR (600.07 MHz, CD_3OD, CHD_2OD = 3.30 ppm): δ (ppm) = 8.99 (8H, s, β-pyrrole*H*), 5.08 (4H, m, 1-Glc*H*), 3.91 (4H, m, 6-Glc*H*), 3.69 (4H, m, 6-Glc*H*), 3.44−3.22 (16H, m, 2,3,4,5-Glc*H*). ^{13}C NMR (100.40 MHz, CD_3OD, CD_3OD = 49.0 ppm): δ (ppm) = 151.20 (α-pyrrole*C*), 149.11 (2,6-Ph*C*), 146.67 (3,5-Ph*C*), 133.77−131.87 (β-pyrrole*C*), 132.82 (4-Ph*C*), 123.47 (1-Ph*C*), 114.00 (meso*C*), 86.69 (1-Glc*C*), 82.80 (5-Glc*C*), 79.25 (3-Glc*C*), 75.43 (2-Glc*C*), 71.07 (4-Glc*C*), 63.13 (6-Glc*C*). ^{19}F NMR (376 MHz, CD_3OD, CF_3CO_2H = −76.05 ppm): δ (ppm) = −134.06 (8F, dd, $^3J_{F-F}$ = 24 Hz, $^5J_{F-F}$ = 12 Hz, 3,5-Ph*F*), −138.57 (8F, dd, $^3J_{F-F}$ = 26 Hz, $^5J_{F-F}$ = 12 Hz, 2,6-Ph*F*). UV−vis (c = 5.16 μM, DMSO, path length = 1 cm, 25 °C): λ/nm ($\epsilon \times 10^{-3}$/$M^{-1}\cdot cm^{-1}$) = 425 (50.2), 554 (2.63), 597 (0.16). FL (c = 5.16 μM, DMSO, path length = 1 cm, λ_{ex} = 415 nm, 25 °C): λ/nm = 599, 650.

5,10,15,20-Tetrakis(4-(β-D-glucopyranosylthio)-2,3,5,6-tetrafluorophenyl)porphyrinato Palladium(II) (3c). A procedure similar to that described for **3a** was applied to **2c** (238 mg, 96.7 μmol) to give **3c** (117 mg, yield 67.9%) as an orange powder. Anal. Calcd for $C_{68}H_{52}O_{20}N_4F_{16}S_4Pd\cdot 6H_2O$: C, 43.17; H, 3.41; N, 2.96. Found: C, 43.04; H, 3.30; N, 2.71. ^{1}H NMR (600.07 MHz, CD_3OD, CHD_2OD = 3.30 ppm): δ (ppm) = 9.12 (8H, s, β-pyrrole*H*), 5.17 (4H, m, 1-Glc*H*), 3.99 (4H, m, 6-Glc*H*), 3.76 (4H, m, 6-Glc*H*), 3.52−3.30 (16H, m, 2,3,4,5-Glc*H*). ^{13}C NMR (100.40 MHz, CD_3OD, CD_3OD = 49.0 ppm): δ (ppm) = 149.13 (2,6-Ph*C*), 146.67 (3,5-Ph*C*), 142.97 (α-pyrrole*C*), 132.68 (β-pyrrole*C*), 121.29 (4-Ph*C*), 115.05 (1-Ph*C*), 107.68 (meso*C*), 86.67 (1-Glc*C*), 82.70 (5-Glc*C*), 79.70 (3-Glc*C*), 75.93 (2-Glc*C*), 71.69 (4-Glc*C*), 63.08 (6-Glc*C*). ^{19}F NMR (376 MHz, CD_3OD, CF_3CO_2H = −76.05 ppm): δ (ppm) = −133.28 (8F, dd, $^3J_{F-F}$ = 24 Hz, $^5J_{F-F}$ = 12 Hz, 3,5-Ph*F*), −138.74 (8F, dd, $^3J_{F-F}$ = 25 Hz, $^5J_{F-F}$ = 11 Hz, 2,6-Ph*F*). UV−vis (c = 5.45 μM, DMSO, path length = 1 cm, 25 °C): λ/nm ($\epsilon \times 10^{-3}$/$M^{-1}\cdot cm^{-1}$) = 409 (28.7), 519 (2.72), 552 (1.68). FL (c = 5.45 μM, DMSO, path length = 1 cm, λ_{ex} = 409 nm, 25 °C): λ/nm = 557, 606, 672.

5,10,15,20-Tetrakis(4-(β-D-glucopyranosylthio)-2,3,5,6-tetrafluorophenyl)porphyrinato Platinum(II) (3d). A procedure similar to that described for **3a** was applied to **2d** (171 mg, 67.1 μmol) to give **3d** (87.6 mg, yield 69.7%) as a red orange solid. Anal. Calcd for $C_{68}H_{52}O_{20}N_4F_{16}S_4Pt\cdot 7H_2O$: C, 40.87; H, 3.33; N, 2.80. Found: C, 40.57; H, 2.87; N, 3.00. ^{1}H NMR (600.07 MHz, CD_3OD, CHD_2OD = 3.30 ppm): δ (ppm) = 8.98 (8H, s, β-pyrrole*H*), 5.07 (4H, m, 1-Glc*H*), 3.91 (4H, m, 6-Glc*H*), 3.67 (4H, m, 6-Glc*H*), 3.43−3.22 (16H, m, 2,3,4,5-Glc*H*). ^{13}C NMR (100.40 MHz, CD_3OD, CD_3OD = 49.0 ppm): δ (ppm) = 149.09 (2,6-Ph*C*), 146.65 (3,5-Ph*C*), 132.44 (α-pyrrole*C*, β-pyrrole*C*), 120.84 (4-Ph*C*), 115.13 (1-Ph*C*), 108.38 (meso*C*), 86.65 (1-Glc*C*), 82.71 (5-Glc*C*), 79.69 (3-Glc*C*), 75.93 (2-Glc*C*), 71.69 (4-Glc*C*), 63.07 (6-Glc*C*). ^{19}F NMR (376 MHz, CD_3OD, CF_3CO_2H = −76.05 ppm): δ (ppm) = −133.20 (8F, dd, $^3J_{F-F}$ = 24 Hz, $^5J_{F-F}$ = 12 Hz, 3,5-Ph*F*), −138.83 (8F, dd, $^3J_{F-F}$ = 26 Hz, $^5J_{F-F}$ = 11 Hz, 2,6-Ph*F*). UV−vis (c = 4.65 μM, DMSO, path length = 1 cm, 25 °C): λ/nm ($\epsilon \times 10^{-3}$/$M^{-1}\cdot cm^{-1}$) = 394 (30.7), 507 (2.37), 539 (2.41). FL (c = 4.65 μM, DMSO, path length = 1 cm, λ_{ex} = 394 nm, 25 °C): λ/nm = 651, 698, 795.

Luminescence Quantum Yield. Photosensitzers were dissolved in DMSO to adjust the absorbance of 0.15 at the Soret band and placed in a square quart cell (1 cm). The luminescence intensity were determined by using spectrofluorometer. Luminescence quantum yield (Φ) was determined by a relative method using aqueous TPPS solution (Φ_{ref} = 0.1) as a standard (*25*).

Degradation Rate Measurement of DPBF. Photosensitizer (c = 3.7 μM) and DPBF (c = 102 μM) were dissolved in DMSO and placed in a square quartz cell (1 cm). Oxygen gas was introduced through the solution for 1 min in prior to photoirradiation. The solution was then exposed to light from

Scheme 1. Synthesis of S-Glucosylated Porphyrin and Its Metal Complexes

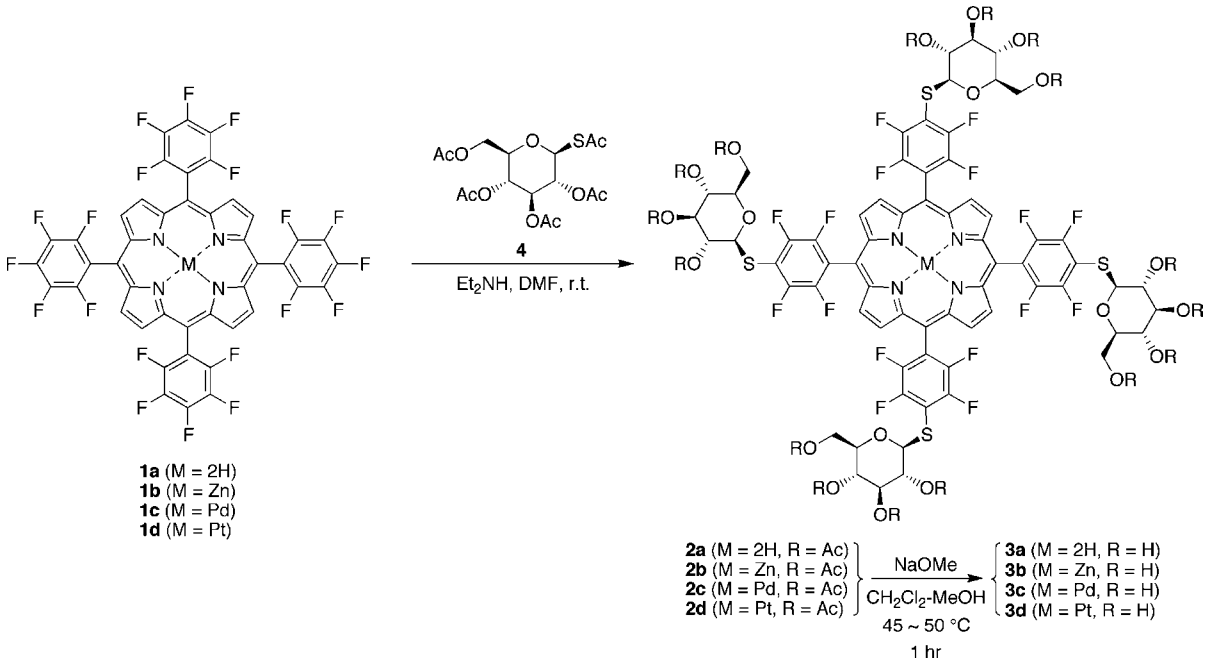

a 100 W halogen lamp (KBEX-102A, USHIO Inc., Tokyo, Japan) through a Y-50 cutoff filter ($\lambda > 500$ nm, Toshiba Co., Tokyo, Japan) at 37 °C. The concentration of DPBF was monitored by measuring the absorption at 418 nm. The rate constant k' (s^{-1}) was estimated by the first-order plot of the DPBF concentration as a function of the irradiation time.

In Vitro Cellular Uptake Measurement. HeLa cells (ATCC CCL-2) were obtained from Dainippon-Sumitomo Pharmaceutical (Osaka, Japan). They were grown in Dulbecco's modified Eagle's medium (DMEM) containing 10% fetal calf serum (FCS) (Hyclone Laboratories, Inc., Logan, UT). The cellular uptake of **3a** in HeLa cells was examined as follows: HeLa cells (3×10^4 cells/well) in 0.5 mL of DMEM containing 10% FCS were plated in a 24-well plate (Nalge Nunc International, Naperville, IL) and incubated for 24 h (37 °C, 5% CO_2). Five hundred microliters of 2 μM **3a** in DMEM containing 10% FCS and 2% DMSO was added to each well. The cells were then incubated from 1 to 24 h in the presence of the photosensitizer. The photosensitizer concentration in each well was 1 μM in DMEM containing 10% FCS (final DMSO content was 1% in all cases). The cells were washed twice with Dulbecco's phosphate-buffered saline (PBS) and lysed in 150 μL of DMSO to extract the photosensitizer. The fluorescence intensity of the extracts was measured with a plate reader using excitation and emission wavelengths of 430 and 635 nm, respectively. The fluorescence intensity of photosensitizers was estimated by subtracting the averaged background from the averaged fluorescence intensity of extracts. The cellular uptake amount of **3a** was determined by using a calibration plot obtained with the photosensitizer in DMSO. Each cellular uptake amount reported is mean value from by three replicate experiments.

In Vitro Photocytotoxicity Test. The photocytotoxicity of the eight S-glucosylated photosensitizers and TPPS in HeLa cells was examined as follows: HeLa cells (5×10^3 cells) in 100 μL of DMEM containing 10% FCS were plated in a 96-well plate (Nalge Nunc International, Naperville, IL) and incubated for 24 h (37 °C, 5% CO_2). One hundred microliters of a photosensitizer in DMEM containing 10% FCS and 2% DMSO was added to each well. The plate was then incubated for a period from 10 min to 24 h. The photosensitizer concentration was varied from 0.09 to 0.5 μM in DMEM containing 10% FCS (final DMSO content was 1% in all cases). After the irradiation, the cells were washed twice with PBS, and then 100 μL of DMEM containing 10% FCS was added to each well. The cells were exposed to light from a 100 W halogen lamp, equipped with a water jacket, through a Y-50 cutoff filter. The light intensity was adjusted by using a UV−vis power meter (ORION/TH, Ophir Optronics Ltd., Jerusalem, Israel). The light dose was calculated as the product of light intensity ($mW \cdot cm^{-2}$) and irradiation time, and the irradiation time was adjusted to obtain the desired light dose of 16 $J \cdot cm^{-2}$. The mitochondrial activity of NADH dehydrogenase of the cells in each well was measured at 24 h after photoirradiation using WST-8 reagent (10 μL) from Cell Counting Kit-8 (Dojindo, Tokyo, Japan) according to the manufacturer's instructions. Then, the absorbance at 450 nm

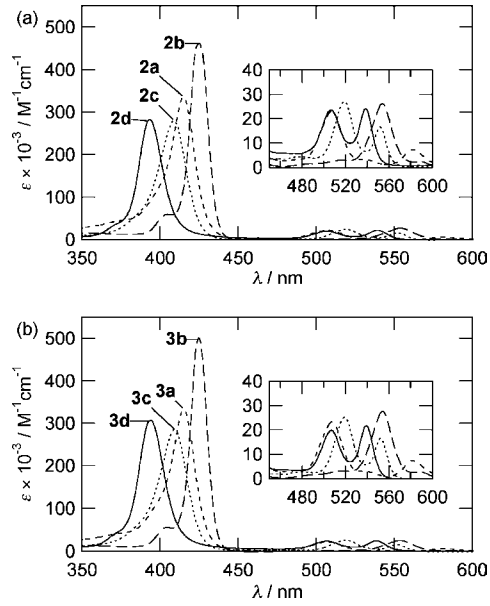

Figure 1. UV−vis spectra of S-glucosylated photosensitizers **2a**, **2b**, **2c**, and **2d** (a) and the deprotected compounds **3a**, **3b**, **3c**, and **3d** (b) in DMSO at 25 °C. Insets show the expanded spectra in the Q-band region.

Table 1. UV-vis Spectral Data of S-Glucosylated Photosensitizers 2a, 2b, 2c, 2d, 3a, 3b, 3c, and 3d in DMSO at 25 °C

	λ_{max}/nm ($\varepsilon \times 10^{-3}$/M^{-1}cm^{-1})					
	Soret band	Q bands				$f_{>500nm}$[a]
2a	415 (336)	507 (23.5)	539 (3.22)	580 (7.64)	634 (0.79)	0.11
2b	425 (464)	554 (27.9)				0.09
2c	409 (281)	519 (25.4)	552 (16.7)			0.13
2d	394 (283)	507 (19.8)	539 (21.8)			0.11
3a	415 (334)	507 (23.2)	539 (3.42)	581 (7.58)	636 (0.75)	0.11
3b	425 (502)	554 (26.3)				0.11
3c	409 (287)	519 (27.3)	552 (16.8)			0.14
3d	394 (307)	507 (23.7)	539 (24.1)			0.14

[a] Oscillator strength over 500 nm region.

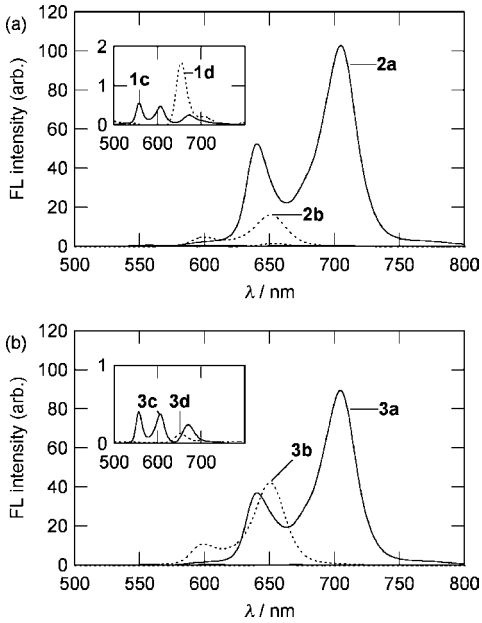

Figure 2. Steady-state luminescence spectra of S-glucosylated photosensitizers **2a** (2.30 μM), **2b** (6.10 μM), **2c** (4.74 μM), and **2d** (4.29 μM) (a) and the deprotected compounds **3a** (5.35 μM), **3b** (5.16 μM), **3c** (5.45 μM), and **3d** (4.65 μM) (b) in DMSO at 25 °C.

was measured using a plate reader. The percentage cell survival was calculated by normalization with respect to the value for no drug treatment.

In Vitro Photocytotoxicity Test in the Presence of Reactive Oxygen Species (ROS) Inhibitor. HeLa cells (5×10^3 cells) in 100 μL of DMEM containing 10% FCS were plated in a 96-well plate and incubated for 24 h (37 °C, 5% CO_2). One hundred microliters of a S-glucosylated photosensitizer (**3a**, **3b**, **3c** and **3d**) in DMEM containing 10% FCS and 2% DMSO was added to each well, and the plate was incubated for 24 h. The photosensitizer concentration was 0.1 μM (**3a**), 0.1 μM (**3b**), 0.1 μM (**3c**), and 2 μM (**3d**) in DMEM containing 10% FCS (the final concentration of DMSO was 1% in all cases). The cells were washed twice with PBS, and then 100 μL of DMEM containing 10% FCS (control) or 100 μL of ROS quencher (5 mM sodium azide (NaN_3) as a singlet oxygen ($^1O_2$) quencher or 40 mM D-mannitol (Man) as a hydroxyl radical (•OH) scavenger) in DMEM containing 10% FCS was added to each well. The plate was further incubated for 2 h (37 °C, 5% CO_2) and then exposed to light under the same conditions as described in the previous section. At 30 min after photoirradiation, the medium was replaced with fresh medium. Cell survival was determined by means of the same protocol as described in the previous section.

Table 2. Steady-State Luminescence Spectral Data of S-Glucosylated Photosensitizers 2a, 2b, 2c, 2d, 3a, 3b, 3c, and 3d in DMSO at 25 °C

	λ_{max}/nm			Φ
2a	640	705		0.081
2b	599	651		0.055
2c	557	607	673	0.003
2d	653	706	801	0.001
3a	640	705		0.063
3b	599	650		0.056
3c	557	606	670	0.002
3d	651	703	793	0.001

Statistical Analysis. All statistical evaluations were performed using Student's *t*-test. All values for cellular uptake and cytotoxicity are expressed as mean ± standard deviation.

RESULTS AND DISCUSSION

Synthesis of S-Glucosylated Photosensitizers. Porphyrin **1a** was prepared by condensation of pyrrole with pentafluorobenzaldehyde using a modification of the Lindsey method in 61.2% yield (*21*). Zn(II), Pd(II), and Pt(II) complexes (**1b**, **1c**, and **1d**, respectively) were prepared from **1a** by a conventional complexation method using $Zn(CH_3CO_2)_2$, $PdCl_2$, or $K_2[PtCl_4]$ as the metal source in 64.0, 69.4, and 76.4% yields, respectively (*22*, *23*). On the other hand, S-glycoside **4** was prepared by condensation of 1,2,3,4,6-penta-*O*-acetyl-1-thio-β-D-glucopyranose and thioacetic acid in the presence of $ZrCl_4$ as a Lewis acid catalyst in 76.8% yield (*24*). The S-glucosylated photosensitizers **2a**, **2b**, **2c**, and **2d** were synthesized by nucleophilic substitution at the para-position of the pentafluorophenyl groups of **1a**, **1b**, **1c**, and **1d** with S-glycoside **4** (Scheme 1). Drain et al. reported the synthesis of **2a** using 8 equiv of thioglucoside **4** in DMF (*21*). However, we observed the formation of penta-S-glucosylated porphyrins as a major product. Hence, we used 4 equiv of thioglucoside **4** with respect to the free-base porphyrin **1a** or metalloporphyrin **1b**, **1c**, or **1d** for the synthesis of S-glucosylated porphyrins **2a**, **2b**, **2c**, and **2d**. The reactions were conducted in DMF at ambient temperature using diethylamine as a base to yield **2a** (74.0%), **2b** (74.1%), **2c** (83.1%), and **2d** (85.3%). ^{1}H and ^{13}C NMR spectra of **2a**, **2b**, **2c**, and **2d** showed only one set of glucopyranosyl peaks owing to the C_4 symmetry of these molecules. ^{19}F NMR spectra of **2a**, **2b**, **2c**, and **2d** showed two peaks with equal intensities and an AA′XX′ splitting pattern ($^3J_{F-F}$ = 24 Hz and $^5J_{F-F}$ = 12 Hz), indicating para substitution of tetrafluorophenyl groups. Metal complexation, namely Zn(II), Pd(II) and Pt(II), caused a lower-field shift of the ^{19}F peak at the ortho position in the order of **2a** (−136.43) < **2b** (−135.97) < **2c** (−135.45) < **2d**, (−135.42), which is in good accordance with Pauling's electronegativity values (1.65, 2.20, and 2.28 for Zn(II), Pd(II), and Pt(II)) (*26*). This suggests that there is substantial electronic interaction between the porphyrin ring and the tetrafluorophenyl ring, even though these two rings are thought to be perpendicular to each other. Deprotection of the S-glucosylated photosensitizers **2a**, **2b**, **2c**,

Table 3. Relative Rate Constant *k* of DPBF Photodegradation in DMSO[a]

	1a	2a	2b	2c	2d	3a	3b	3c	3d
k	1.67	1.14	1.90	2.02	0.24	1.00	1.75	1.98	0.32

[a] Normalized to that of TPPS; condition: $[\text{photosensitizer}]_0 = 3.7\ \mu\text{M}$, $[\text{DPBF}]_0 = 102\ \mu\text{M}$, $\lambda > 500$ nm.

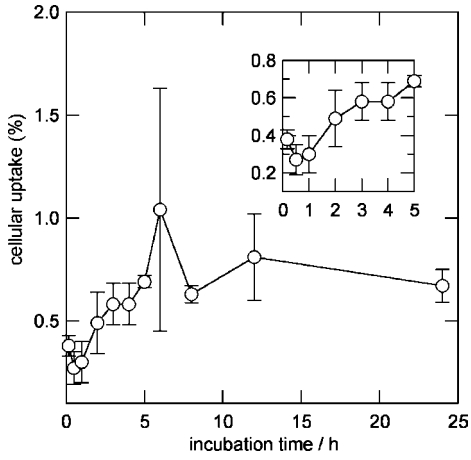

Figure 3. The cellular uptake amount of S-glucosylated porphyrin **3a** by HeLa cells as a function of incubation time. The cellular uptake amount represents the percentage of the total amount of photosensitizer added. Values are the mean ± standard deviation of three replicate experiments.

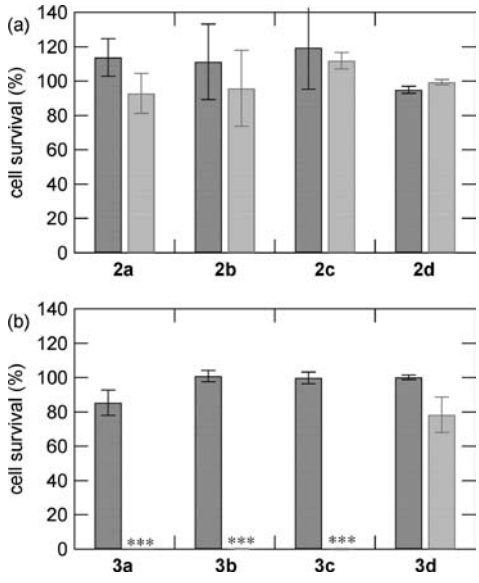

Figure 4. Dark cytotoxicity (left bar) and photocytotoxicity (right bar) of S-glucosylated photosensitizers **2a**, **2b**, **2c**, and **2d** (a) and the deprotected compounds **3a**, **3b**, **3c**, and **3d** (b) in HeLa cells. The concentration of photosensitizers was 0.5 μM. The light dose applied was 16 J·cm^{-2}. Values are the mean ± standard deviation of six replicate experiments. ***Significant difference, $p < 0.001$ vs dark.

and **2d** was carried out using sodium methoxide in a mixture of CH_3OH and CH_2Cl_2. A small amount of S-glycoside cleavage was detected by reverse-phase high-performance liquid chromatography (RP-HPLC) with an octadecylsilyl-bound silica gel column and electron-spray time-of-flight (ESI-TOF) mass spectrometry. The crude product was successfully purified by preparative RP-HPLC using a mixture of CH_3CN and H_2O (1:1). Eventually, four deprotected photosensitizers **3a**, **3b**, **3c**, and **3d** were obtained in 67.9−81.1% yield. The ^{1}H, ^{13}C and ^{19}F NMR spectra of **3a**, **3b**, **3c**, and **3d** supported the structures shown in Scheme 1, and all S-glucosylated photosensitizers were confirmed to be pure by elemental analysis.

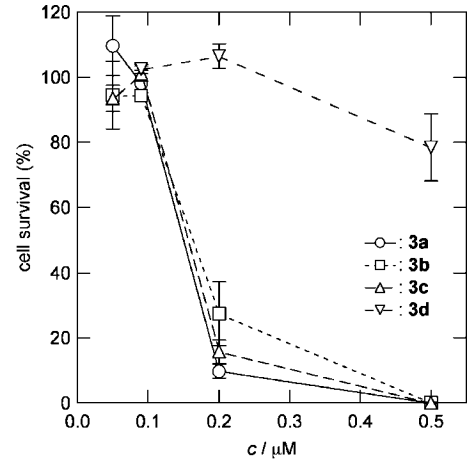

Figure 5. Plot of cell survival (%) as a function of the concentration (*c*) of S-glucosylated photosensitizers **3a**, **3b**, **3c**, and **3d**. The light dose applied was 16 J·cm^{-2}. Values are the mean ± standard deviation of six replicate experiments.

Photophysical and Photochemical Properties of S-Glucosylated Photosensitizers. Figure 1 shows UV−vis spectra of the S-glucosylated photosensitizers **2a**, **2b**, **2c**, **2d**, **3a**, **3b**, **3c**, and **3d** in DMSO at 25 °C and Table 1 lists the spectral data. There were no significant differences between photosensitizer **2** and the corresponding **3**. Free-base porphyrins **2a** and **3a** showed typical UV−vis spectra with one intense peak (Soret band) at ca. 415 nm and four vibronic peaks (Q bands) at ca. 507, 539, 580, and 635 nm. Zn(II) complexes **2b** and **3b** showed significantly red-shifted UV−vis spectra compared with those of **2a** and **3a**, while the UV−vis spectra of Pd(II) and Pt(II) complexes **2c**, **2d**, **3c**, and **3d** showed blue-shifted spectra. The disappearance of Q(0,0) of **2b** and **3b** is caused by axial ligation of DMSO to the Zn(II) ion; the intensity ratio of Q(0,0) to Q(1,0) of **1b** is known to be very sensitive to the axial ligand (*27*). Table 1 also lists the oscillator strength in the wavelength region over 500 nm ($f_{>500\text{nm}}$), which is a photophysical parameter used in our photocytotoxicity test (vide infra). The $f_{>500\text{nm}}$ values of S-glucosylated photosensitizers were substantially constant at around 0.09−0.14, despite the remarkable shift in maximum absorption wavelength upon complexation. Figure 2 shows steady-state luminescence spectra of the S-glucosylated photosensitizers **2a**, **2b**, **2c**, **2d**, **3a**, **3b**, **3c**, and **3d** in DMSO at 25 °C and Table 2 lists spectral data. While free-base porphyrins and Zn(II) complexes **2a**, **2b**, **3a**, and **3b** emitted light upon photoirradiation, Pd(II) and Pt(II) complexes **2c**, **2d**, **3c**, and **3d** were nonluminescent in DMSO.

The singlet oxygen ($^1O_2$)-producing ability of S-glucosylated photosensitizers **2a**, **2b**, **2c**, **2d**, **3a**, **3b**, **3c**, and **3d** was evaluated by measuring the degradation rate of 1,3-diphenylbenzofuran (DPBF) by $^1O_2$ generated upon photoirradiation using 100 W halogen lamp equipped with a Y-50 cutoff filter ($\lambda > 500$ nm) at 37 °C. The degradation of DPBF followed pseudo-first-order kinetics with an apparent rate constant k' s^{-1}, and we normalized the value to the k' value for TPPS under the same condition to give a relative scale of the rate constant *k* (Table 3). The *k* value for S-glucosylated porphyrin **2a** (1.14) is significantly lower than that for porphyrin **1a** (1.67). Hence, S-glucosylation of **1a** leads to a significant reduction of the $^1O_2$-producing efficiency. The introduction of Zn(II) and Pd(II) ions improves the $^1O_2$-producing efficiency of S-glucosylated porphyrin **2a**, presumably

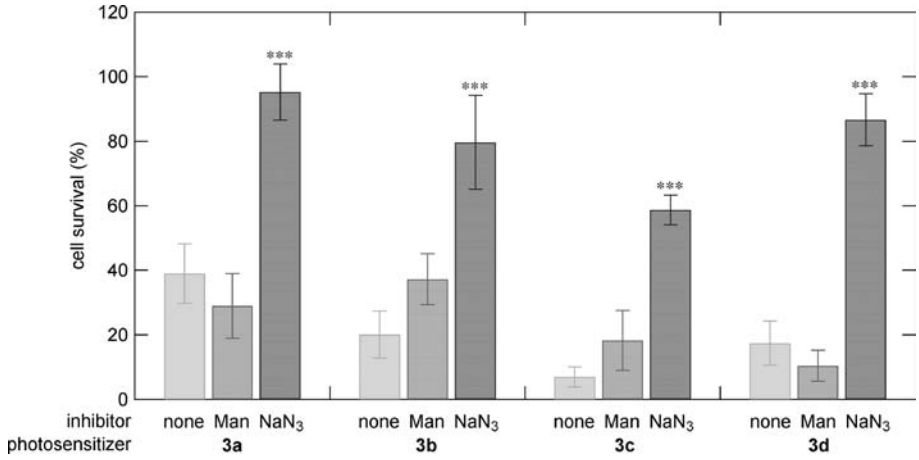

Figure 6. Cell survival (%) of HeLa cells treated with S-glucosylated photosensitizers **3a**, **3b**, **3c**, and **3d** in the absence of ROS quenchers and in the presence of 40 mM D-mannitol (Man, OH-scavenger), and 5 mM sodium azide (NaN_3, $^1O_2$-quencher). The light dose applied was 16 J·cm^{-2}. The concentrations of photosensitizers were 0.1 μM for **3a**, **3b**, and **3c** and 2 μM for **3d**. Values are the mean ± standard deviation of six replicate experiments. ***Significant difference, $p < 0.001$ vs none (without inhibitor).

due to heavy atom effect, while Pt(II) complexes **2d** and **3d** have essentially no photosensitizing ability. The exceptionally low efficiency in $^1O_2$ production of Pt(II) complexes was also found in the case of TPPS, which is a sulfur-containing porphyrin, as reported by Mosinger et al. (*28*). They reported that the $^1O_2$ quantum yield of TPPS and its Pt(II) complex in D_2O were determined to be 0.62 and 0.06, respectively. Although the photophysical mechanism is not fully understood, the introduction of Pt(II) ion into sulfur-containing porphyrins appears to reduce the $^1O_2$-producing efficiency.

In Vitro Photocytotoxicity in HeLa Cells. First, we examined the time course of the cellular uptake of **3a** in HeLa cells by using fluorometry, in order to determine an appropriate incubation time. Figure 3 shows the cellular uptake (percentage of the total amount of photosensitizer) of **3a** as a function of incubation time. The amount of cellular uptake reached a plateau level after 6 h. This result is similar to that reported for 5,10,15,20-tetrakis(3-hydroxyphenyl)chlorin (Foscan) by Leung et al. (*29*). In order to eliminate the influence of incubation time, we incubated HeLa cells in the presence of S-glucosylated photosensitizers for 24 h in the photocytotoxicity test (vide infra).

The cytotoxicity of eight S-glucosylated photosensitizers **2a**, **2b**, **2c**, **2d**, **3a**, **3b**, **3c**, **3d**, and TPPS was evaluated at the concentration of 0.5 μM without photoirradiation and under photoirradiation (16 J·cm^{-2}) in HeLa cells. The percent cell survival was determined after incubation for 24 h following photoirradiation (Figure 4). None of the S-glucosylated photosensitizers showed cytotoxicity without photoirradiation. S-Glucosylated photosensitizers **3a**, **3b**, and **3c** showed potent photocytotoxicity, and completely killed the HeLa cells, while the protected compounds **2a**, **2b**, **2c**, and **2d** and TPPS showed no photocytotoxicity. These results clearly demonstrate the importance of the sugar moieties, presumably for increasing cellular uptake. Despite the potent photocytotoxicity of the S-glucosylated photosensitizers **3a**, **3b**, and **3c**, as expected, the Pt(II) complex **3d** showed hardly any photocytotoxic effect. In order to explore the photocytotoxicity in more detail, the S-glucosylated photosensitizers **3a**, **3b**, **3c**, and **3d** were further examined in the concentration range from 0.5 μM to 0.09 μM (Figure 5). All of them showed similar plots, and the drug concentration inducing 90% cell death (EC_{90}) was estimated to be ca. 0.2 μM in each case. This EC_{90} value is much lower than that of the corresponding O-glucosylated tetraphenylporphyrin derivatives ($EC_{90} > 5$ μM) (Chart 1), which we have reported previously (*12*).

Upon photoirradiation in the presence of an S-glucosylated photosensitizer, two types of photochemical reactions, namely electron and/or proton transfer (type I reaction) and energy transfer (type II reaction), could be initiated. Type I reaction generates hydroxyl radical (·OH), superoxide anion (O^{2-}), and so on. On the other hand, type II reaction mainly forms $^1O_2$ which is thought to be a key species in the photodynamic effect because of its relatively long lifetime (ca. 2 μs in water) (*6*). In order to explore the origin of the photocytotoxicity, the photocytotoxicity of S-glucosylated photosensitizers **3a**, **3b**, **3c**, and **3d** was measured after a short (2 h) incubation of the cells with sodium azide (NaN_3) as a $^1O_2$-inhibitor or D-mannitol (Man) as a ·OH-scavenger prior to photoirradiation. Figure 6 shows the cell survival rate in the presence of **3a**, **3b**, **3c**, and **3d** in the absence and the presence of reactive oxygen species (ROS) inhibitors. Sodium azide dramatically reduced the photocytotoxicity of **3a**, **3b**, **3c**, and **3d**, while only a small increase of cell survival rate was found in the presence of Man. These results suggest that $^1O_2$ is a dominant species for the cytotoxic effect in **3a**, **3b**, **3c**, and **3d**. However, the photocytotoxicity of **3a**, **3b**, and **3c** in HeLa cells seemed to be insensitive to the $^1O_2$-producing ability in DMSO (the order was **3a** < **3b** < **3c**). This suggested that the $^1O_2$-producing ability of photosensitizers is not the limiting factor for in vitro photocytotoxicity, in which oxygen may be more abundant than in vivo. These findings support the idea that the Zn(II) and Pd(II) complexes of S-glucosylated porphyrin **3b** and **3c** act as efficient $^1O_2$-generators with enhanced cellular uptake owing to the sugar moieties.

In conclusion, S-glucosylated porphyrin and its metal complexes were prepared by means of a complexation-first approach. The $^1O_2$-producing ability increased in the order of free-base porphyrins < Zn(II) complexes < Pd(II) complexes, which is consistent with the well-known heavy-atom effect, but Pt(II) complexes showed unexpectedly low quantum yields for $^1O_2$ formation. Zn(II) and Pd(II) complexes of S-glucosylated porphyrin are promising photosensitizers having enhanced cellular uptake due to their glucosylation and high $^1O_2$-generating ability due to the heavy-atom effect.

ACKNOWLEDGMENT

This work was supported by the NAIST Presidential Special Fund, Grants-in-Aid for Scientific Research and Priority Areas from the Ministry of Education, Culture, Sport, Science and Technology (MEXT) of the Japanese Government, a grant from

the Japan-German exchange program supported by the Japan Society for the Promotion of Science (JSPS), Sasagawa Scientific Research Grants from The Japan Science Society, a Nara Women's University Intramural Grant for Project Research, and grants from The Kao Foundation for Arts and Sciences, OSAKA GAS, and San-EiGen Foundation for Chemical Research.

Supporting Information Available: Analytical data and ^{1}H, ^{13}C, and ^{19}F NMR spectra of S-glycosylated porphyrins. This material is available free of charge via the Internet at http://pubs.acs.org.

LITERATURE CITED

(1) Detty, M. R., Gibson, S. L., and Wagner, S. J. (2004) Current clinical and preclinical photosensitizers for use in photodynamic therapy. *J. Med. Chem. 47*, 3897–3915.

(2) MacDonald, I. J., and Dougherty, T. J. (2001) Basic principles of photodynamic therapy. *J. Porphyrins Phthalocyanines 5*, 105–129.

(3) Konan, Y. N., Gurny, R., and Allémann, E. (2002) State of art in the delivery of photosensitizers for photodynamic therapy. *J. Photochem. Photobiol. B Biol. 66*, 89–106.

(4) Moor, A. C. E. (2000) Signaling pathways in cell death and survival after photodynamic therapy. *J. Photochem. Photobiol. B 57*, 1–13.

(5) Tarak, D. M. (2000) Pharmaceutical development and medical applications of Porphyrin-type macrocycles. *J. Porphyrins Phthalocyanines 4*, 362–367.

(6) Bonnet R. (2000) *Chemical Aspects of Photodynamic Therapy*; Taylor and Francis, London.

(7) Okura I. (2000) *Photosensitization of Porphyrins and Phthalocyanines*; Kodansha, Tokyo.

(8) Som, P., Atkins, H. L., Bandoypadhyay, D., Fowler, J. S., MacGregor, R. R., Matsui, K., Oster, Z. H., Sacker, D. F., Shiue, C. Y., Turner, H., Wan, C.-N., Wolf, A. P., and Zabinski, S. V. (1980) A Fluorinated glucose analog, 2-fluoro-2-deoxy-d-glucose (F-18): Nontoxic tracer for rapid tumor detection. *J. Nucl. Med. 21*, 670–675.

(9) Li, G., Pandey, S. K., Graham, A., Dobhal, M. P., Mehta, R., Chen, Y., Gryshuk, A., Rittenhouse-Olson, K., Oseroff, A., and Pandey, R. K. (2004) Functionalization of OEP-based benzochlorins to develop carbohydrate-conjugated photosensitizers. Attempt to target β-galactoside-recognized proteins. *J. Org. Chem. 69*, 158–172.

(10) Momentreau, M., Oulmi, D., Maillard, P., and Croisy, A. (1994) In Vitro Photobiological Activity of a New Series of Photosensitizers: The Glycoconjugated Porphyrins. *Proc. Photodyn. Ther. Cancer II 2325*, 13–23.

(11) Momentreau, M., Maillard, P., de Bélinary, M.-A., Carrez, D., and Croisy, A. (1999) Tetrapyrrolic Glycosylated Macrocycles for an Application in PDT. *J. Biomed. Opt. 4*, 298–318.

(12) Obata, M., Hirohara, S., Sharyo, K., Alitomo, H., Kajiwara, K., Ogata, S., Tanihara, M., Ohtsuki, C., and Yano, S. (2007) Sugar-dependent photodynamic effect of glycoconjugated porphyrins: A study on photocytotoxicity, photophysical properties and binding behavior to bovine serum albumin (BSA). *Biochim. Biophys. Acta 1770*, 1204–1211.

(13) Hirohara, S., Obata, M., Ogata, S., Kajiwara, K., Ohtsuki, C., Tanihara, M., and Yano, S. (2006) Sugar-dependent aggregation of glycoconjugated chlorins and its effect on photocytotoxicity in HeLa cells. *J. Photochem. Photobiol. B 84*, 56–63.

(14) Hirohara, S., Obata, M., Ogata, S., Ohtsuki, C., Higashida, S., Ogura, S., Okura, I., Takenaka, M., Ono, H., Sugai, Y., Mikata, Y., Tanihara, M., and Yano, S. (2005) Cellular uptake and photocytotoxicity of glycoconjugated chlorins in HeLa cells. *J. Photochem. Photobiol. B 78*, 7–15.

(15) Hirohara, S., Obata, M., Saito, A., Ogata, S., Ohtsuki, C., Higashida, S., Ogura, S., Okura, I., Sugai, Y., Mikata, Y., Tanihara, M., and Yano, S. (2004) Cellular uptake and photocytotoxicity of glycoconjugated porphyrins in HeLa Cells. *Photochem. Photobiol. 80*, 301–308.

(16) Hirohara, S., Obata, M., Ogura, S., Okura, I., Higashida, S., Ohtsuki, C., Ogata, S., Nishikawa, Y., Takenaka, M., Ono, H., Mikata, Y., and Yano, S. (2004) Hydrophobicity parameters (Log *P*) of glycoconjugated porphyrins for photodynamic therapy evaluated by reversed phase HPLC. *J. Porphyrins Phthalocyanines 8*, 1289–1292.

(17) McGlynn, S. P., Azumi, T., Kinoshita, M. (1969) *Molecular Spectroscopy of the Triplet State*; Prentice-Hall, Englewood Cliffs, N.J.

(18) Pogue, B. W., Redmond, R. W., Trivedi, N., and Hasan, T. (1998) Photophysical properties of tin ethyl etiopurpurin I ($SnET_2$) and tin octaethylbenzochlorin (SnOEBC) in solution and bound to albumin. *Photochem. Photobiol. 68*, 809–815.

(19) Musewald, C., Hartwich, G., Pöllinger-Dammer, F., Lossau, H., Scheer, H., and Michel-Beyerle, M. E. (1998) Time-resolved spectral investigation of bacteriochlorophyll a and its transmetalated derivatives [Zn]-bacteriochlorophyll *a* and [Pd]-bacteriochlorophyll a. *J. Phys. Chem. 102*, 8336–8342.

(20) Shaw, S. J., Elgie, K. J., Edwards, C., and Boyle, R. W. (1999) Mono-(pentafluorophenyl)porphyrins - useful intermediates in the regioselective synthesis of multifunctionalised porphyrins. *Tetrahedron Lett. 40*, 1595–1596.

(21) Chen, X., Hui, L., Foster, D. A., and Drain, C. M. (2004) Efficient synthesis and photodynamic activity of porphyrin-saccharide conjugates: Targeting and incapacitating cancer cells. *Biochemistry 43*, 10918–10929.

(22) Kashiwagi, Y., Imahori, H., Araki, Y., Ito, O., Yamada, K., Sakata, Y., and Fukuzumi, S. (2003) Strong inhibition of singlet oxygen sensitization in pyridylferrocene-fluorinated zinc porphyrin supramolecular complexes. *J. Phys. Chem. A 107*, 5515–5522.

(23) Che, C.-M., Hou, Y.-J., Chan, M. C. W., Guo, J., Liu, Y., and Wang, Y. (2003) [*meso*-Tetrakis(pentafluorophenyl)porphyrinato]platinum(II) as an efficient, oxidation-resistant red phosphor: spectroscopic properties and applications in organic light-emitting diodes. *J. Mater. Chem. 13*, 1362–1366.

(24) Defaye, J., Driquez, H., Ohleyer, E., Orgeret, C., and Viet, C. (1984) Stereoselective synthesis of 1,2-trans-related 1-thioglycoses. *Carbohyd. Res. 130*, 317–321.

(25) Andrade, S. M., and Costa, S. M. B. (2002) Spectroscopic studies on the interaction of a water soluble porphyrin and two drug carrier proteins. *Biophys. J. 82*, 1607–1619.

(26) Pauling, L. (1932) The nature of the chemical bond. IV. The energy of single bonds and the relative electronegativity of atoms. *J. Am. Chem. Soc. 54*, 3570–3582.

(27) Spellane, P. J., Gouterman, M., Antipas, A., Kim, S., and Liu, Y. C. (1980) Porphyrins. 40. Electronic spectra and four-orbital energies of free-base, zinc, copper, and palladium tetrakis(perfluorophenyl)porphyrins. *Inorg. Chem. 19*, 386–391.

(28) Mosinger, J., and Mička, Z. (1997) Quantum yields of singlet oxygen of metal complexes of meso-tetrakis(sulphonatophenyl)porphine. *J. Photochem. Photobiol. A Chem. 107*, 77–82.

(29) Leung, W. N., Sun, X., Mak, N. K., and Yow, C. M. N. (2002) Photodynamic effects of mTHPC on human colon adenocarcinoma cells: photocytotoxicity, subcellular localization and apoptosis. *Photochem. Photobiol. 75*, 406–411.

BC800522Y

Supporting Information

Synthesis and Photocytotoxicity of *S*-Glucosylated 5,10,15,20-Tetrakis(tetrafluorophenyl)porphyrin Metal Complexes as Efficient $^1O_2$-Generating Glycoconjugates

Shiho Hirohara, Makoto Obata*, Hiroki Alitomo, Kohei Sharyo, Tsuyoshi Ando, Shigenobu Yano, Masao Taniharaa*

Contents

Table S1. Analytical Data for *S*-Glucosyalted Photosensitizers

Figures S1-3. ^{1}H, ^{13}C and ^{19}F NMR spectra of **2a** in $CDCl_3$.

Figures S4-6. ^{1}H, ^{13}C and ^{19}F NMR spectra of **2b** in $CDCl_3$.

Figures S7-9. ^{1}H, ^{13}C and ^{19}F NMR spectra of **2c** in $CDCl_3$.

Figures S10-12. ^{1}H, ^{13}C and ^{19}F NMR spectra of **2d** in $CDCl_3$.

Figures S13-15. ^{1}H, ^{13}C and ^{19}F NMR spectra of **3a** in CD_3OD.

Figures S16-18. ^{1}H, ^{13}C and ^{19}F NMR spectra of **3b** in CD_3OD.

Figures S19-21. ^{1}H, ^{13}C and ^{19}F NMR spectra of **3c** in CD_3OD.

Figures S22-24. ^{1}H, ^{13}C and ^{19}F NMR spectra of **3d** in CD_3OD.

Table S1. Analytical Data for *S*-Glucosylated Photosensitizers

Compound	Formula	Calcd. (%)			Found (%)		
		C	H	N	C	H	N
2a·2H_2O	$C_{100}H_{86}O_{36}N_4F_{16}S_4$·2$H_2O$	50.30	3.80	2.35	50.24	3.36	2.19
2b·4H_2O	$C_{100}H_{84}O_{36}N_4F_{16}S_4Zn$·4$H_2O$	48.29	3.73	2.25	48.19	3.38	2.24
2c·6H_2O	$C_{100}H_{84}O_{36}N_4F_{16}S_4Pd$·6$H_2O$	46.83	3.77	2.18	46.87	3.41	2.05
2d·6H_2O	$C_{100}H_{84}O_{36}N_4F_{16}S_4Pt$·6$H_2O$	45.27	3.65	2.11	45.06	3.08	1.96
3a·6H_2O	$C_{68}H_{54}O_{20}N_4F_{16}S_4$·6$H_2O$	45.69	3.72	3.13	45.57	3.58	3.14
3b·10H_2O	$C_{68}H_{52}O_{20}N_4F_{16}S_4Zn$·10$H_2O$	42.47	3.77	2.91	42.50	3.34	2.85
3c·6H_2O	$C_{68}H_{52}O_{20}N_4F_{16}S_4Pd$·6$H_2O$	43.17	3.41	2.96	43.04	3.30	2.71
3d·7H_2O	$C_{68}H_{52}O_{20}N_4F_{16}S_4Pt$·7$H_2O$	40.87	3.33	2.80	40.57	2.87	3.00

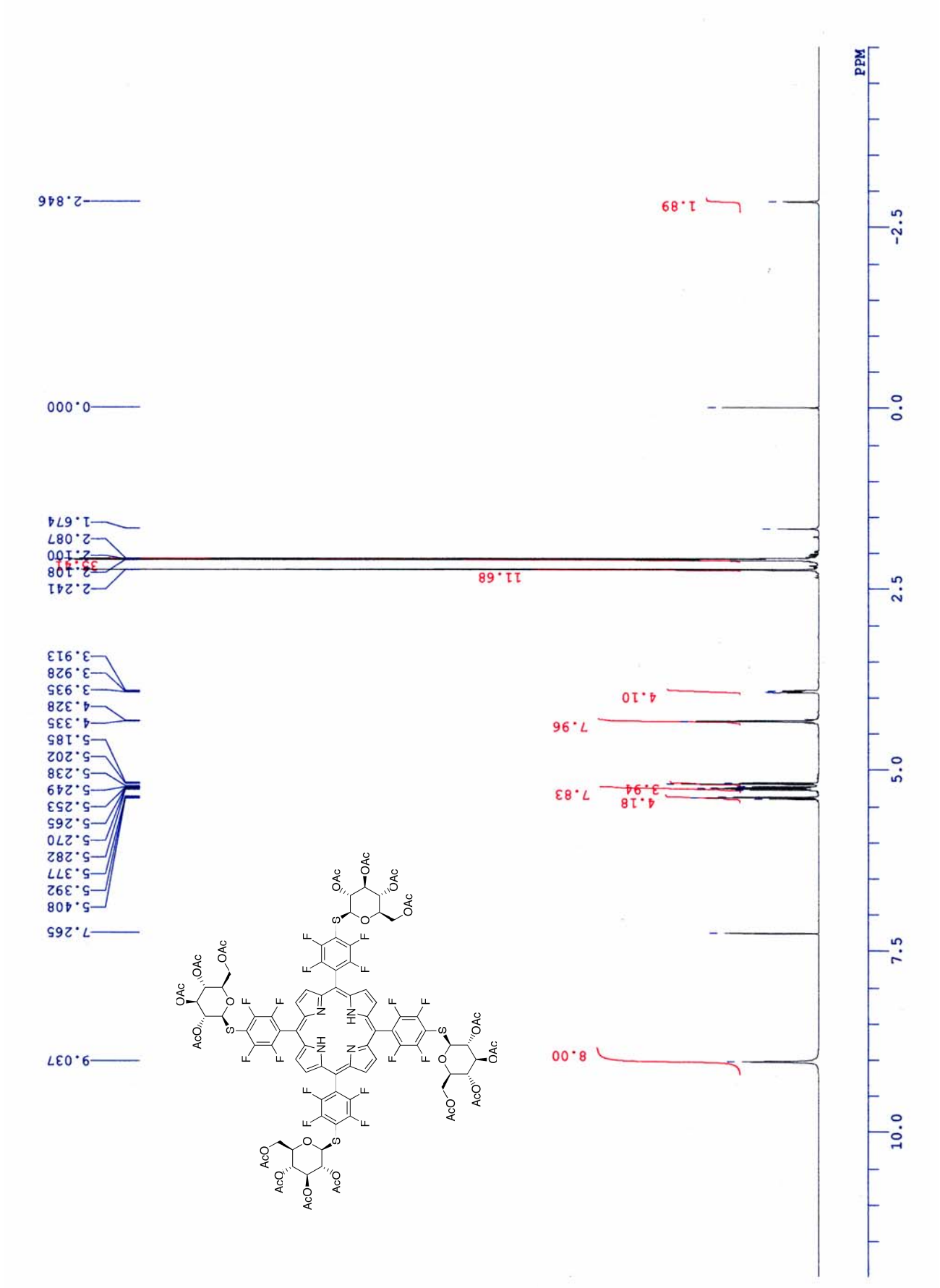

Figure S1 ^{1}H NMR spectrum of **2a** in $CDCl_3$

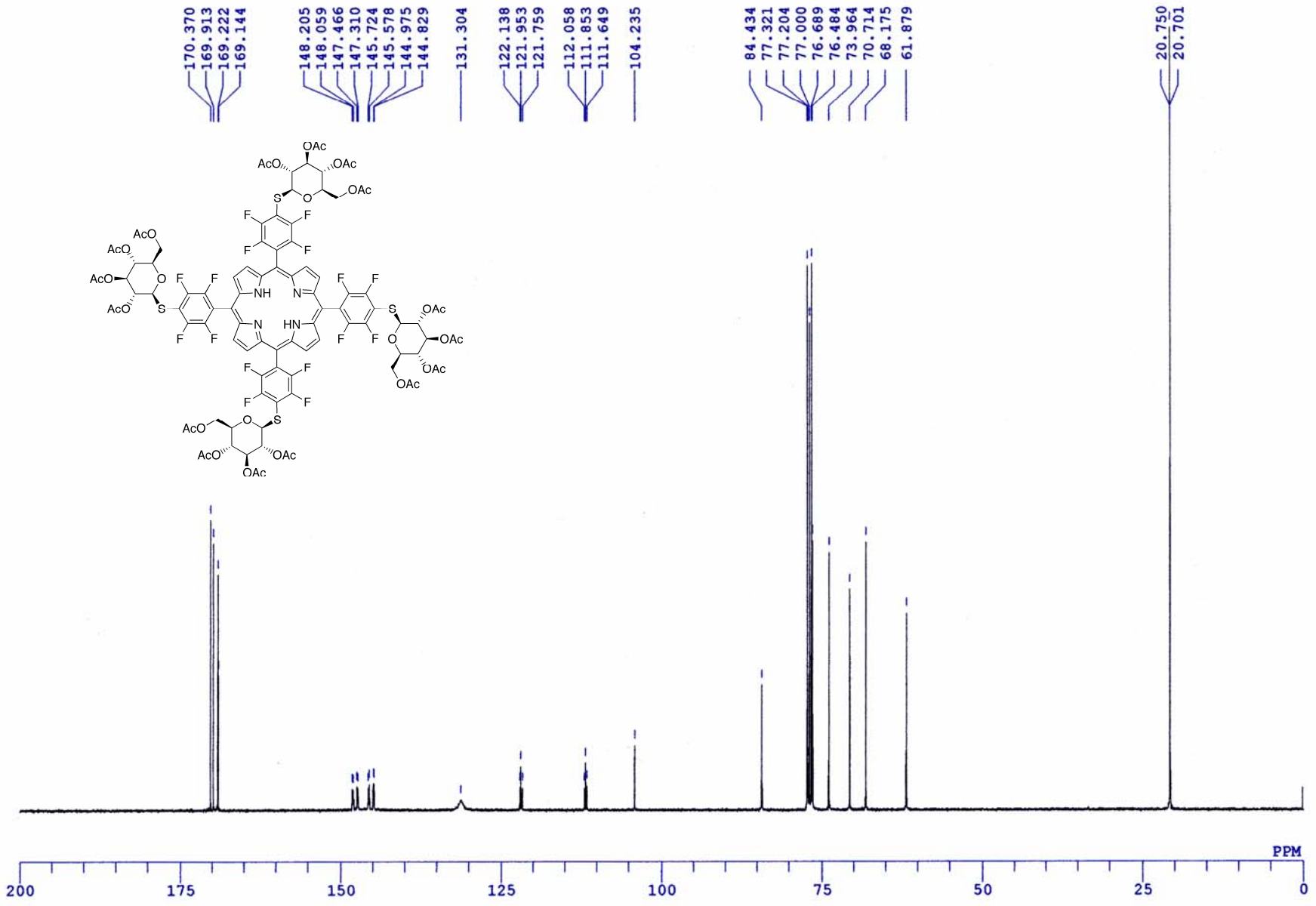

Figure S2 ^{13}C NMR spectrum of **2a** in $CDCl_3$

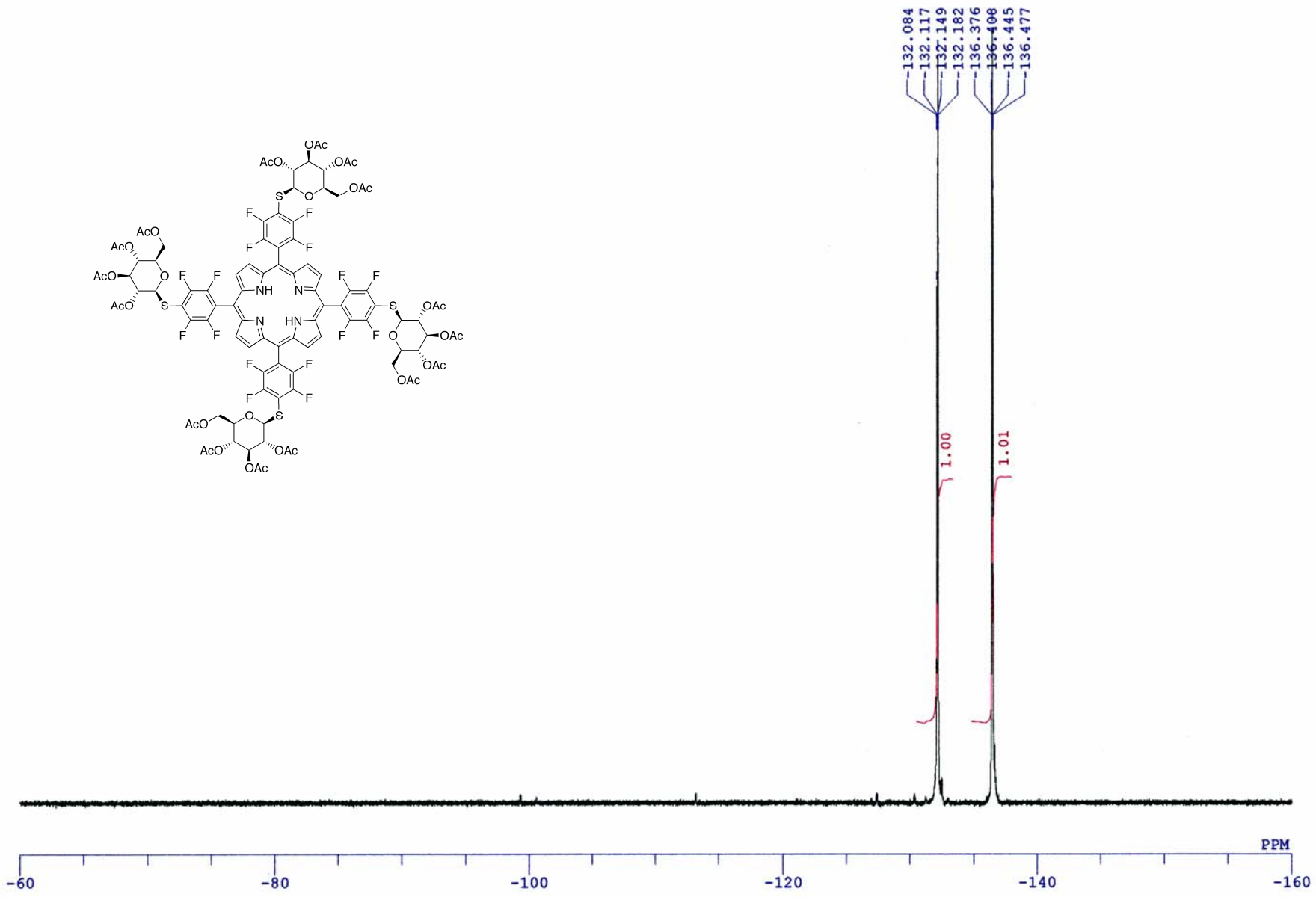

Figure S3 ^{19}F NMR spectrum of **2a** in $CDCl_3$

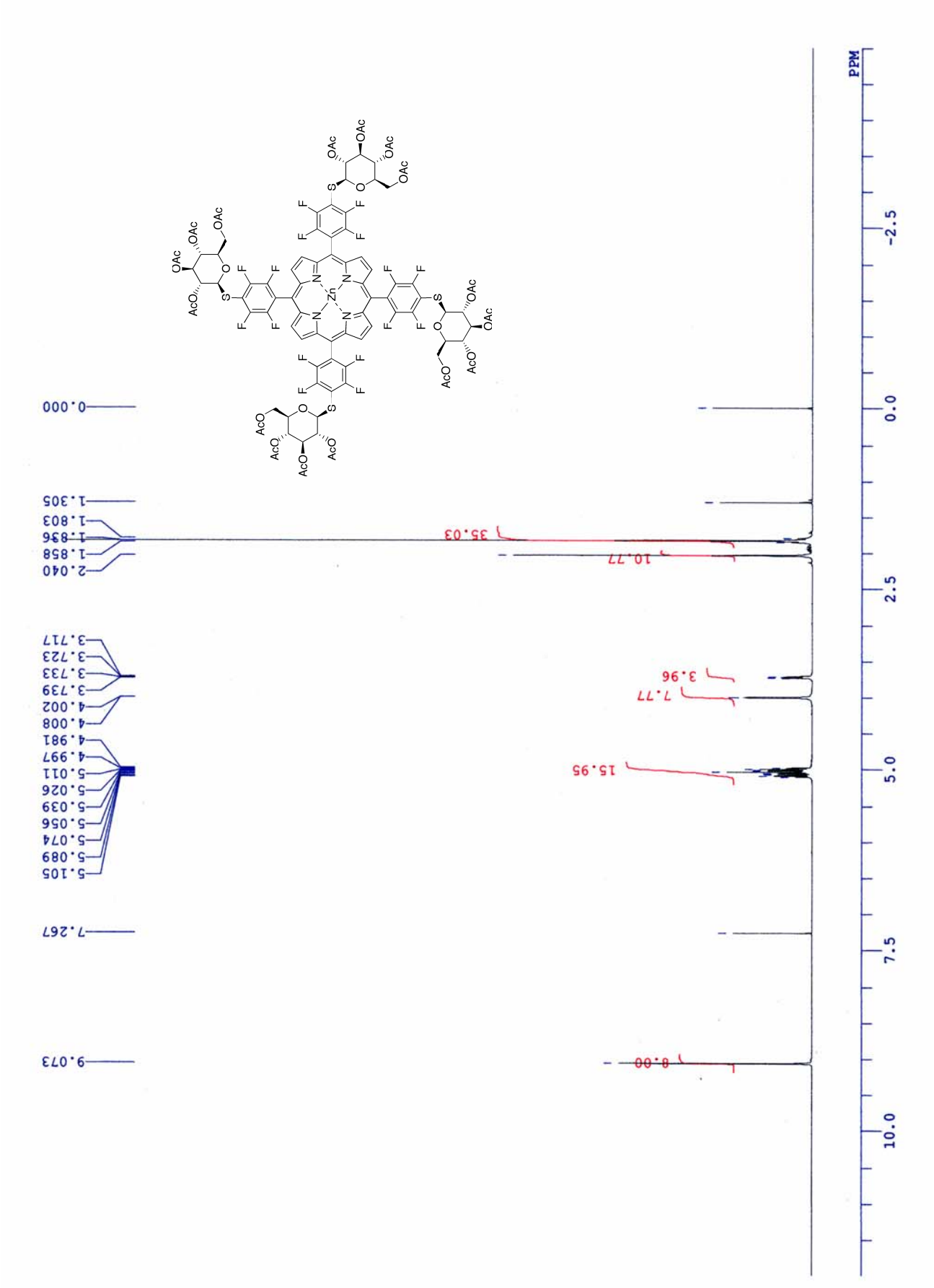

Figure S4 ^{1}H NMR spectrum of **2b** in $CDCl_3$

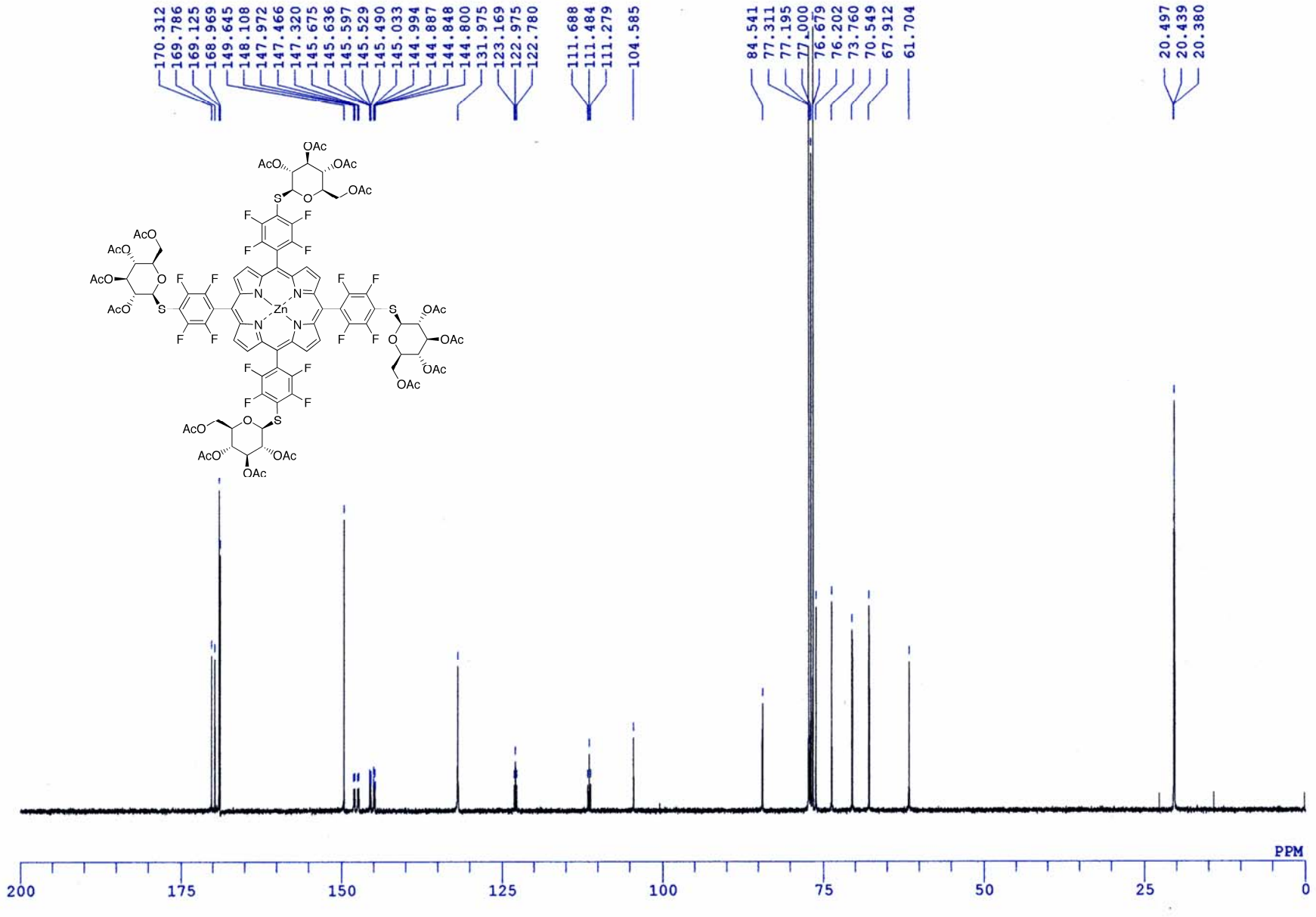

Figure S5 ^{13}C NMR spectrum of **2b** in $CDCl_3$

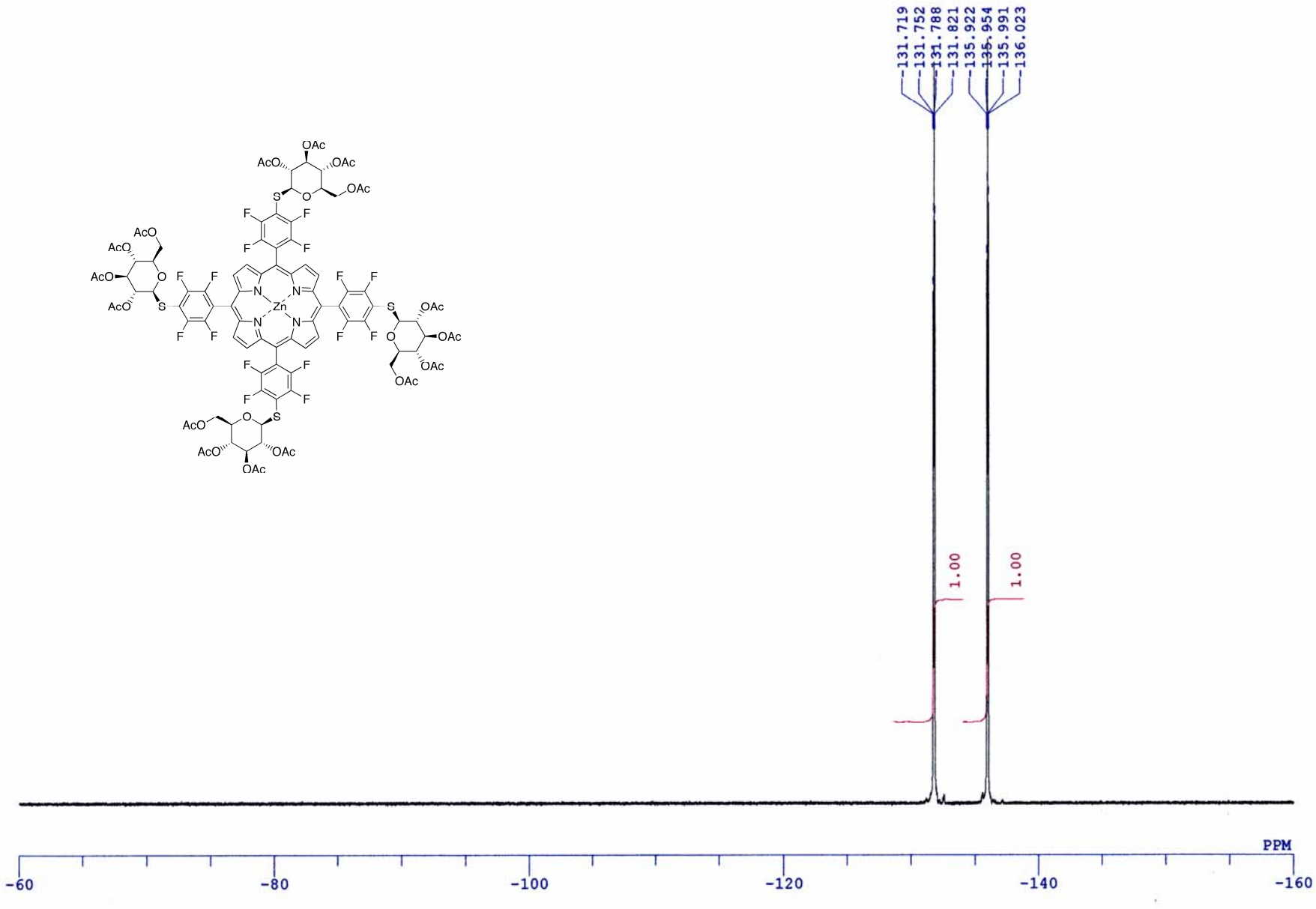

Figure S6 ^{19}F NMR spectrum of **2b** in $CDCl_3$

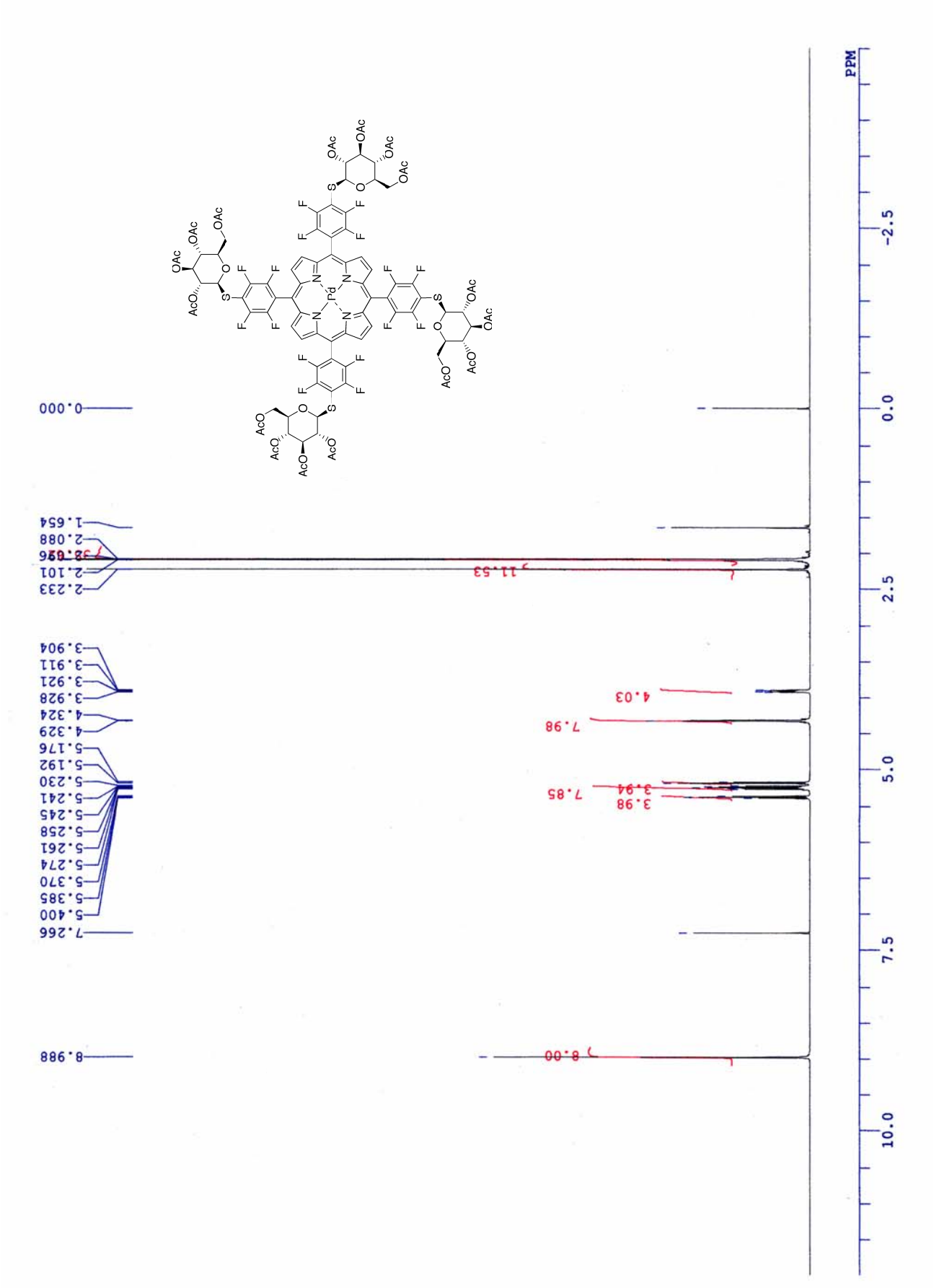

Figure S7 ^{1}H NMR spectrum of **2c** in $CDCl_3$

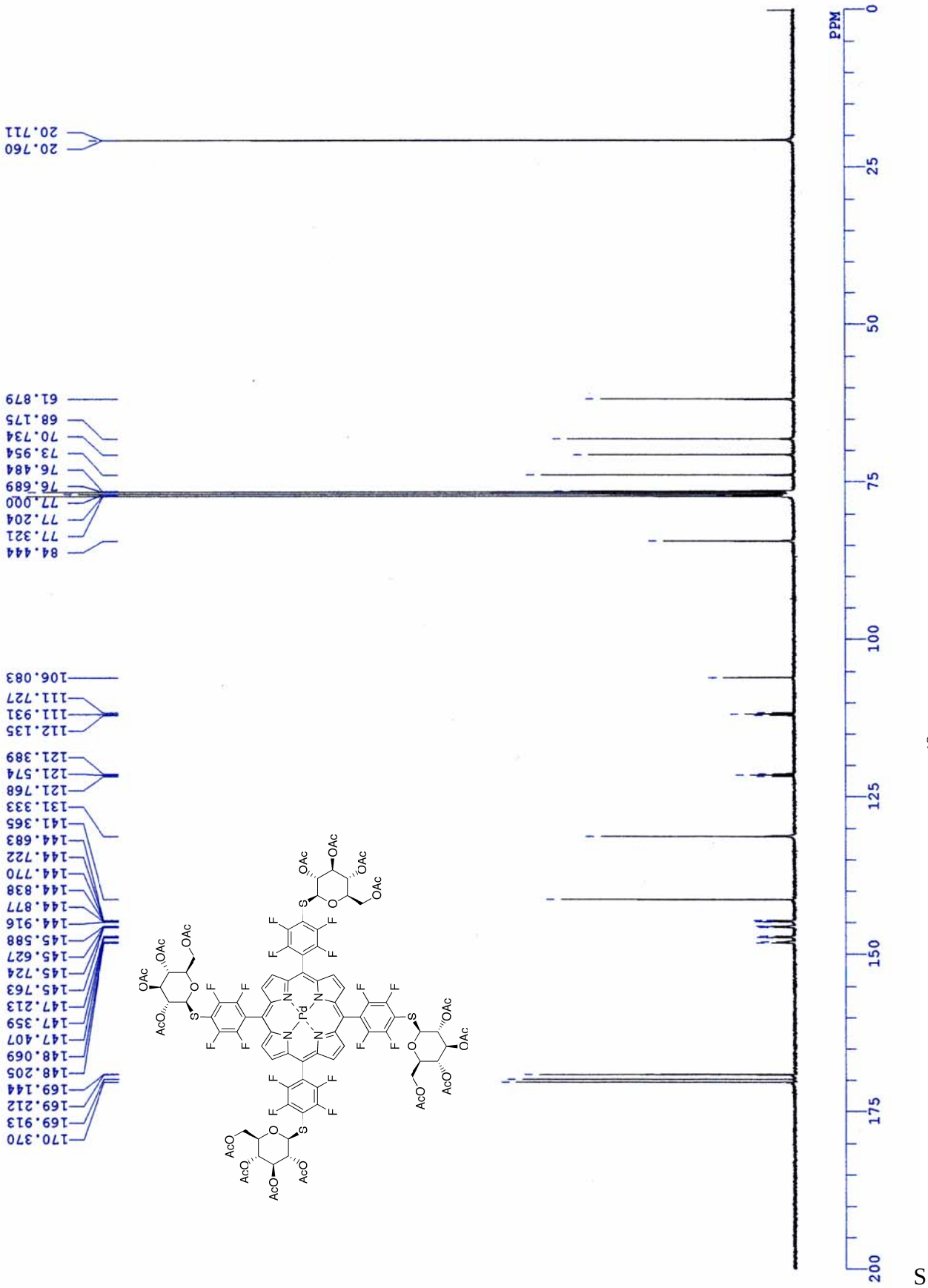

Figure S8 ^{13}C NMR spectrum of **2c** in $CDCl_3$

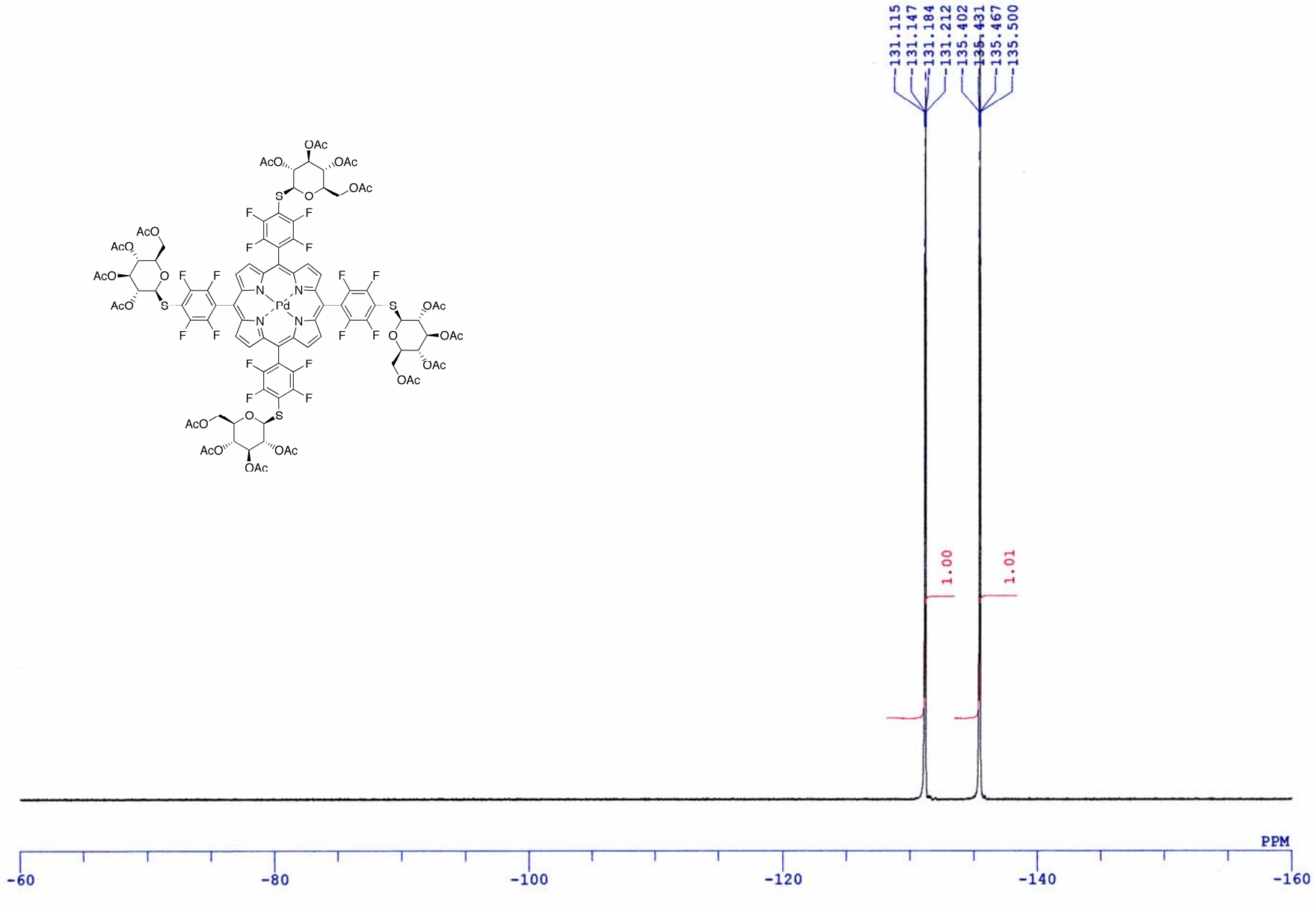

Figure S9 ^{19}F NMR spectrum of **2c** in $CDCl_3$

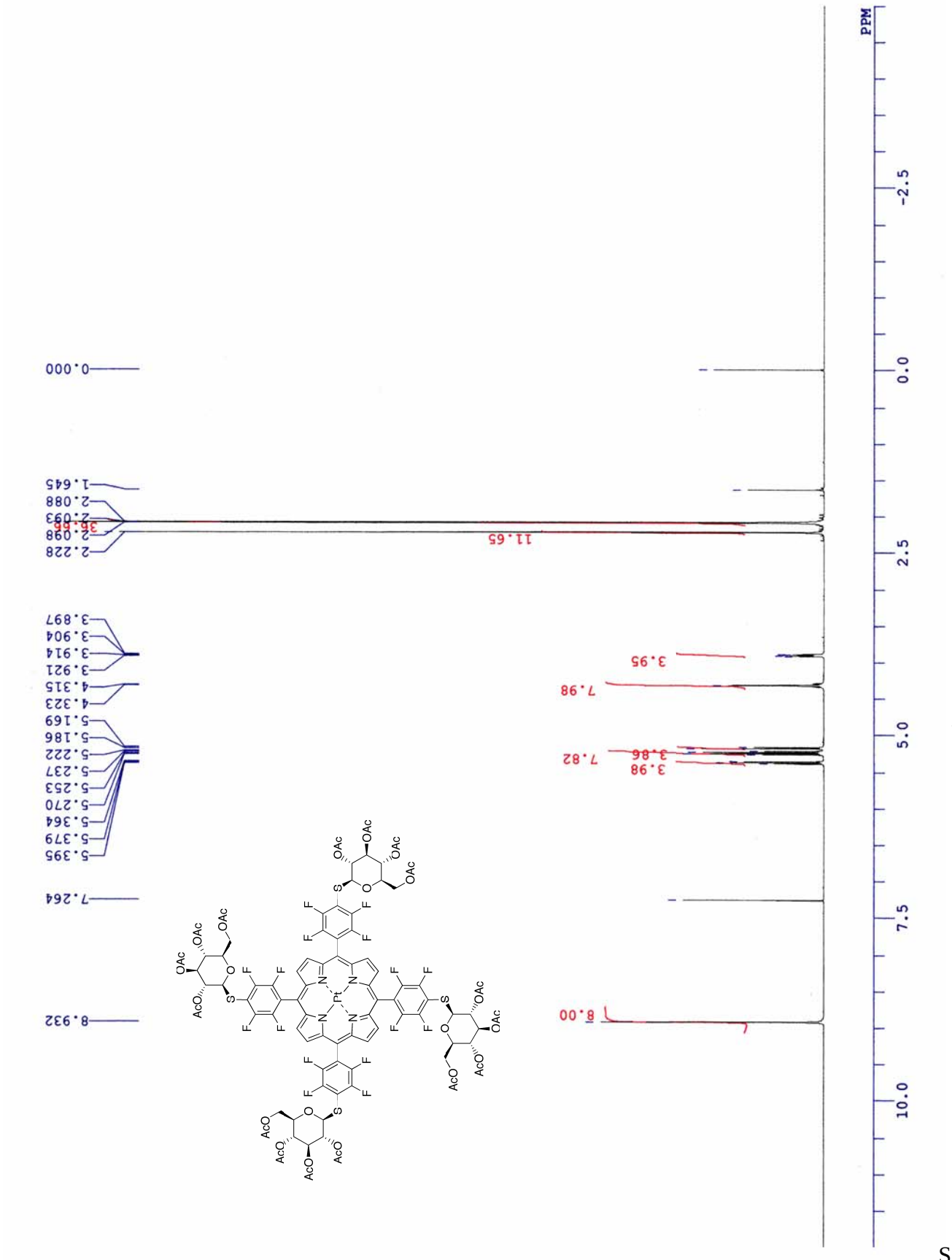

Figure S10 ^{1}H NMR spectrum of **2d** in $CDCl_3$

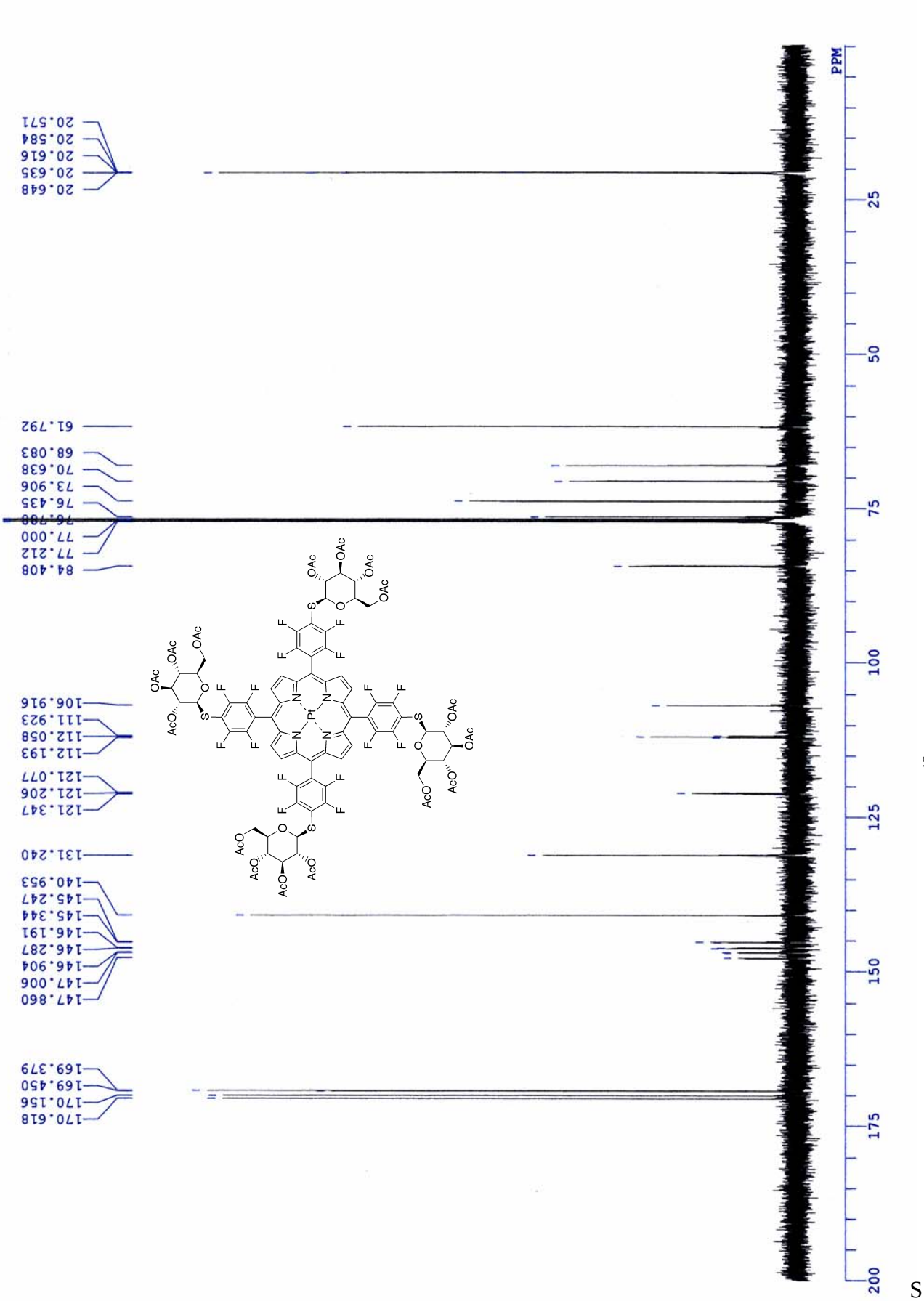

Figure S11 ^{13}C NMR spectrum of **2d** in $CDCl_3$

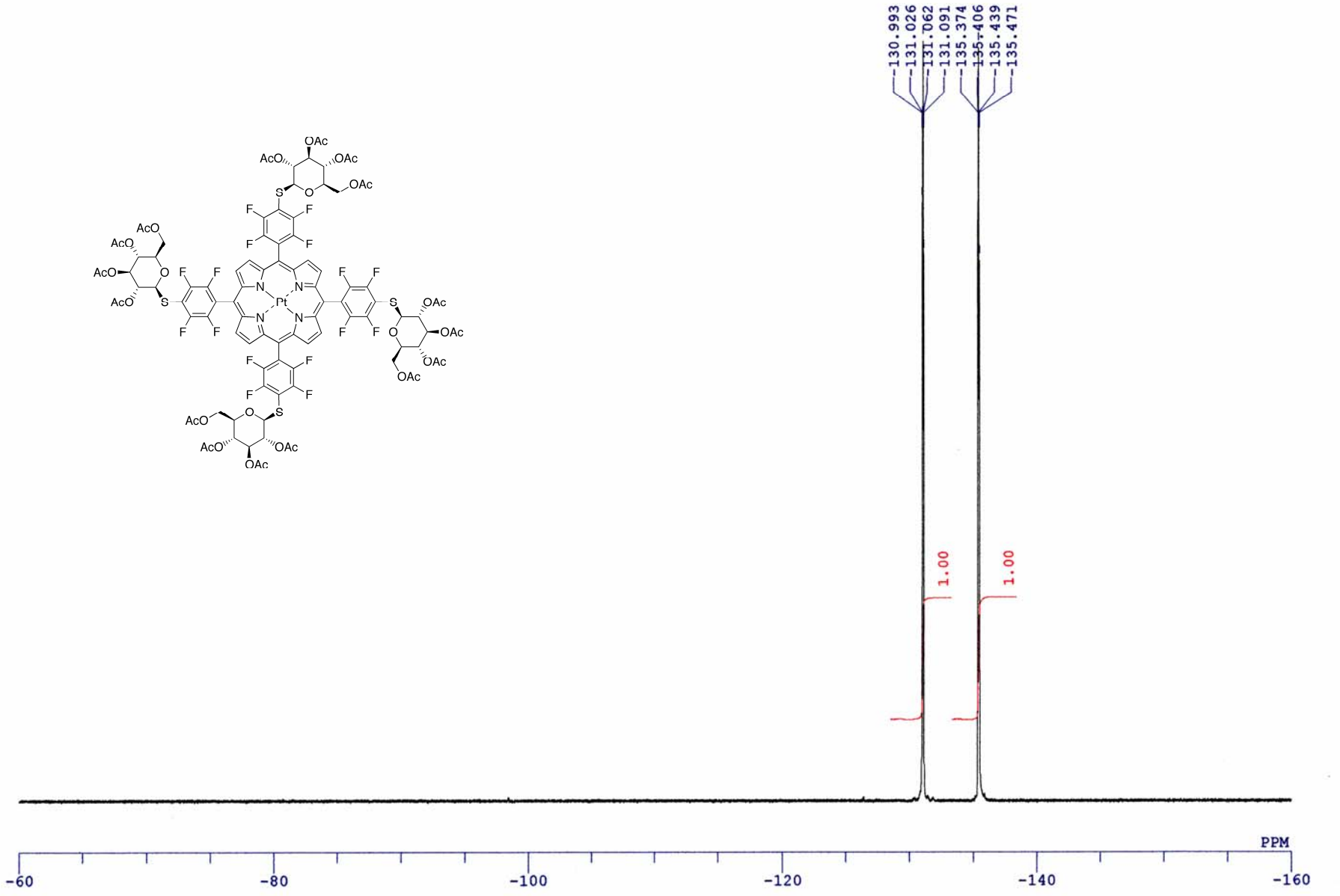

Figure S12 ^{19}F NMR spectrum of **2d** in $CDCl_3$

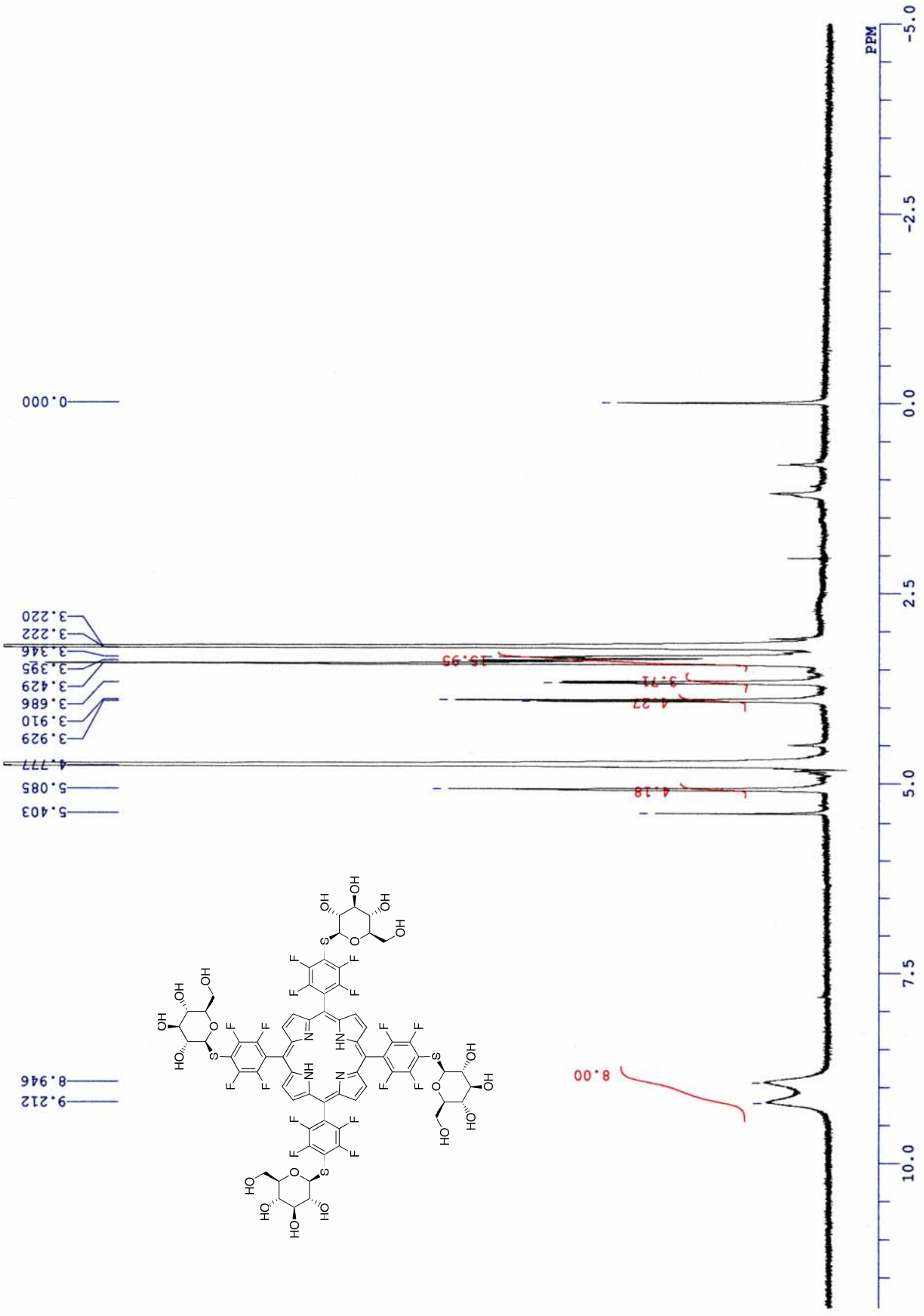

Figure S13 ^{1}H NMR spectrum of **3a** in CD_3OD

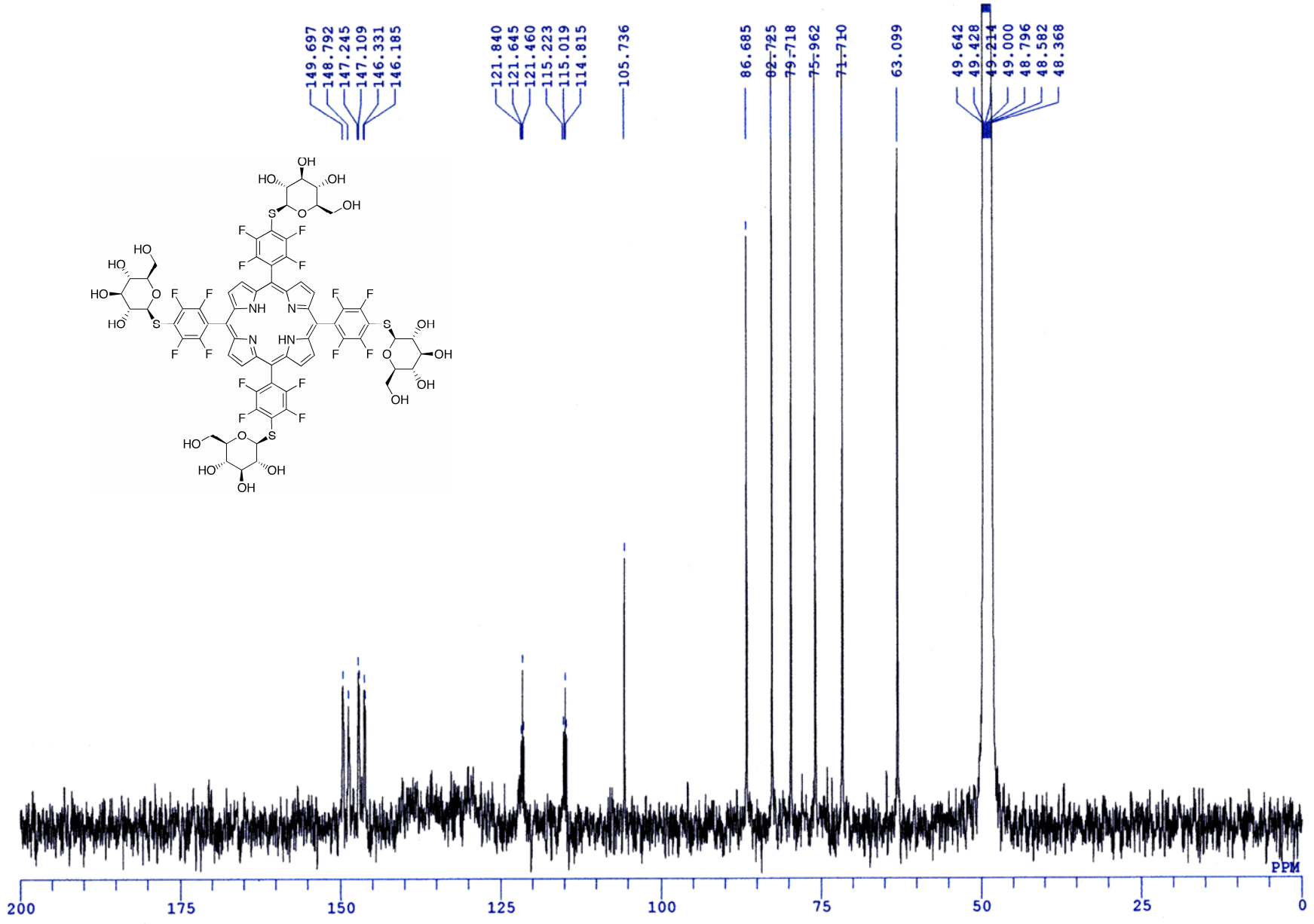

Figure S14 ^{13}C NMR spectrum of **3a** in CD_3OD

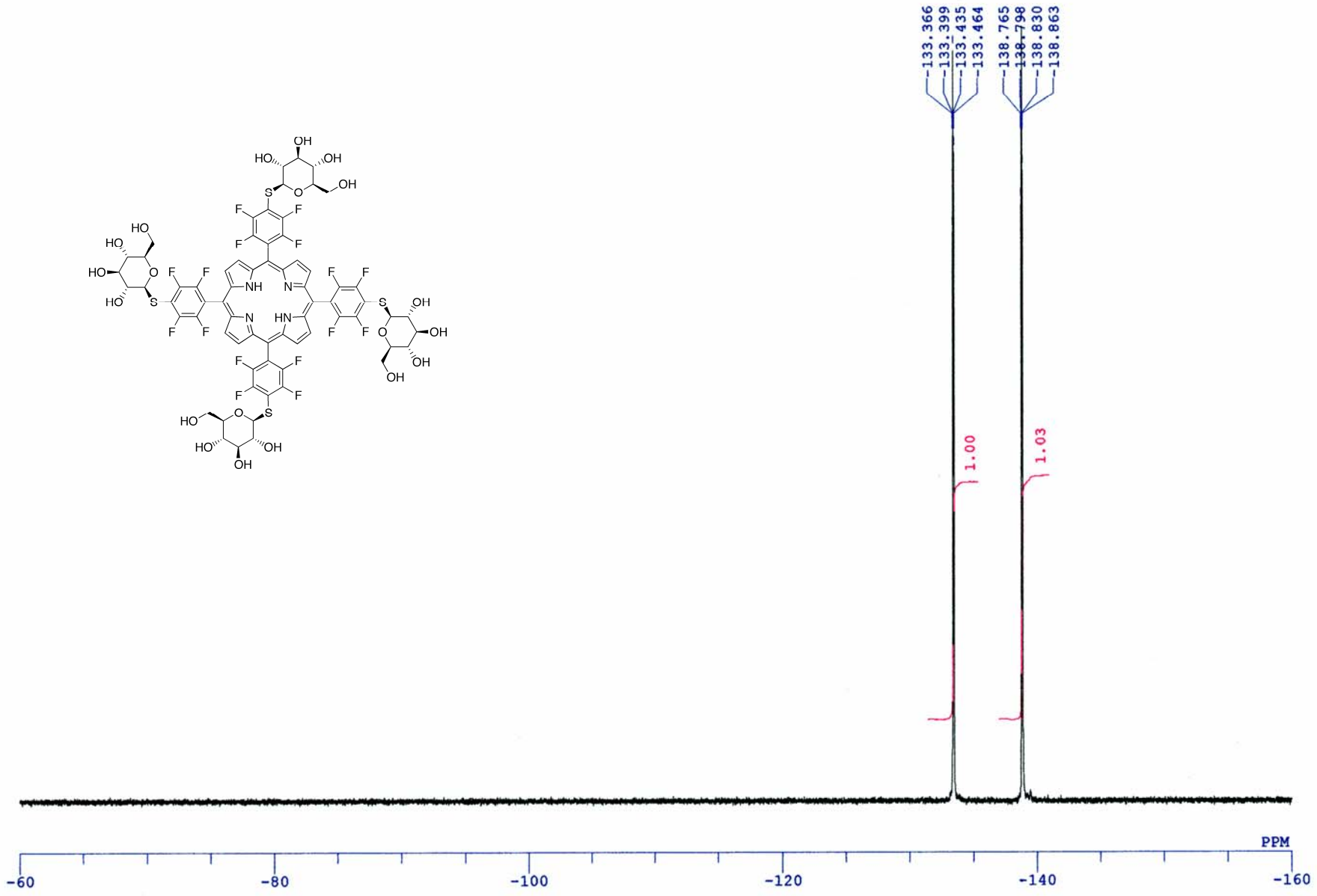

Figure S15 ^{19}F NMR spectrum of **3a** in CD_3OD

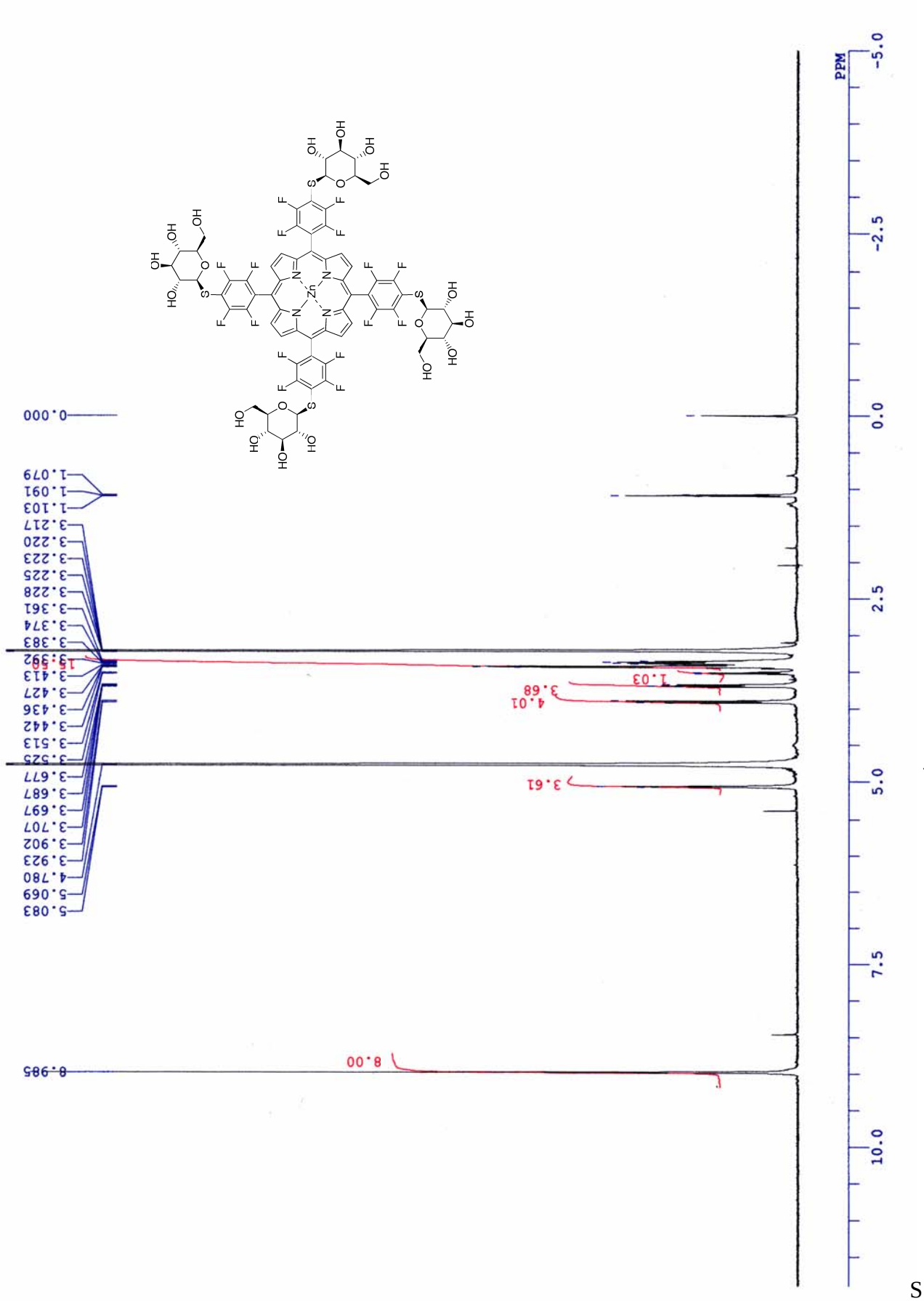

Figure S16 ^{1}H NMR spectrum of **3b** in CD_3OD

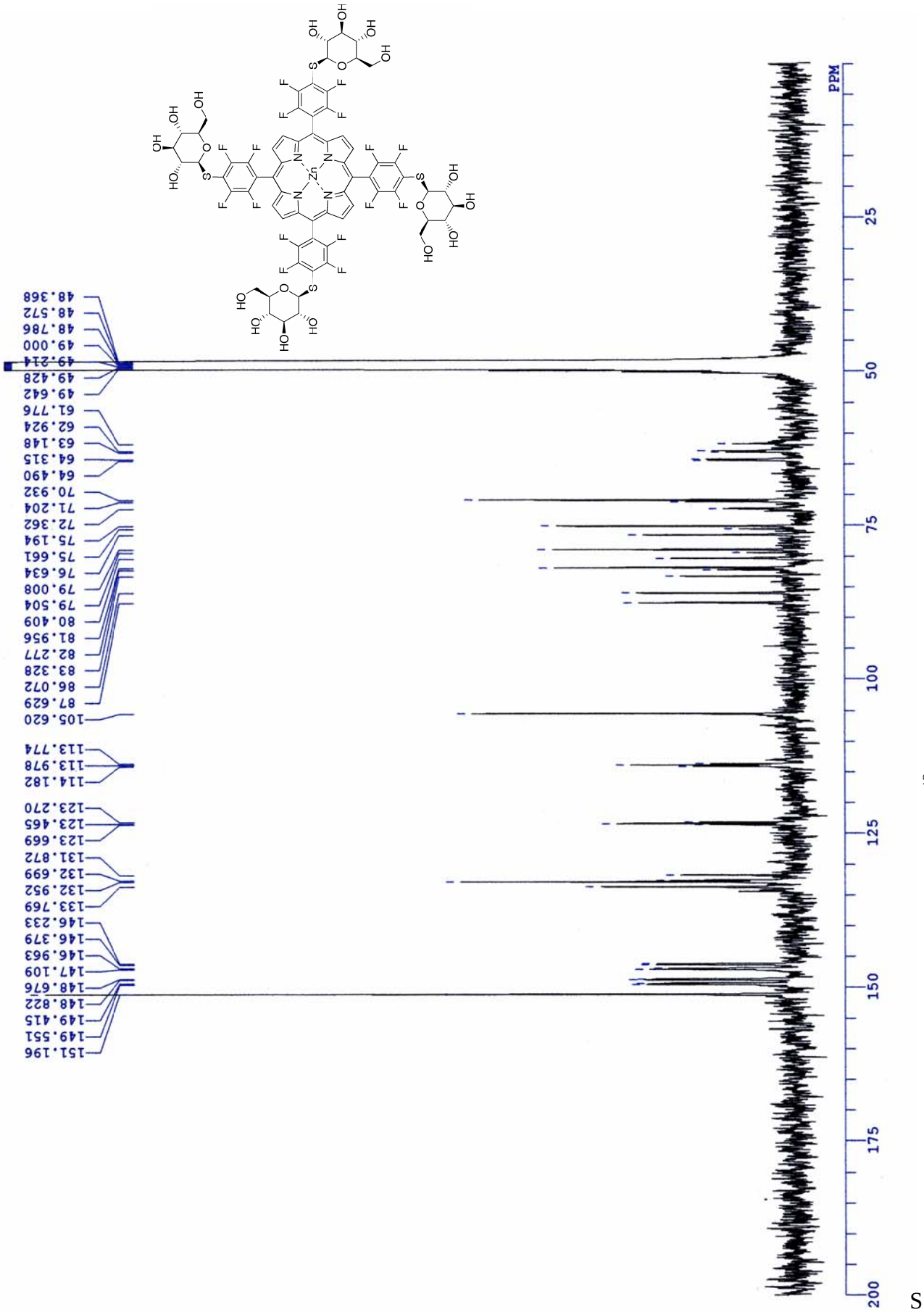

Figure S17 ^{13}C NMR spectrum of **3b** in CD_3OD

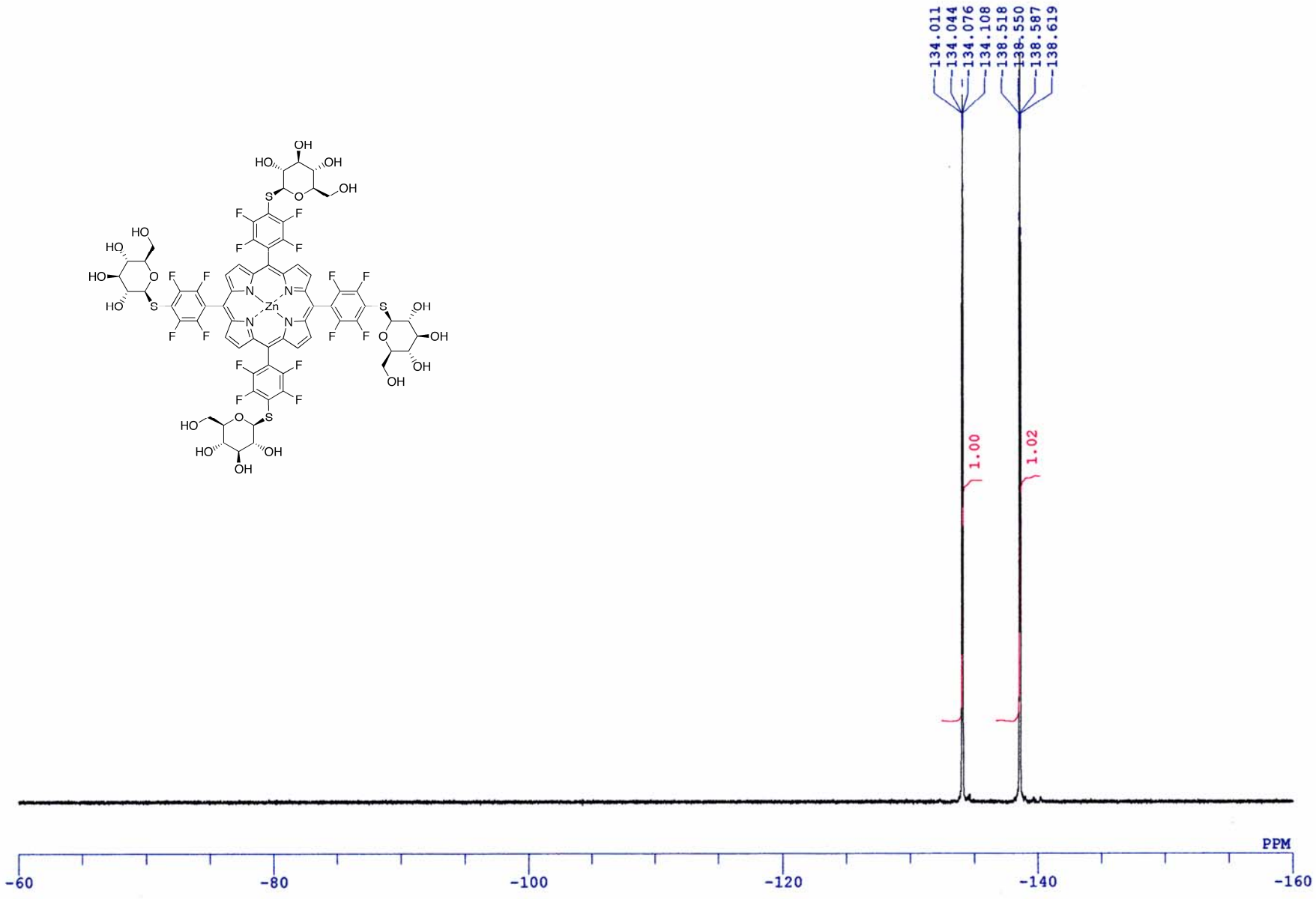

Figure S18 ^{19}F NMR spectrum of **3b** in CD_3OD

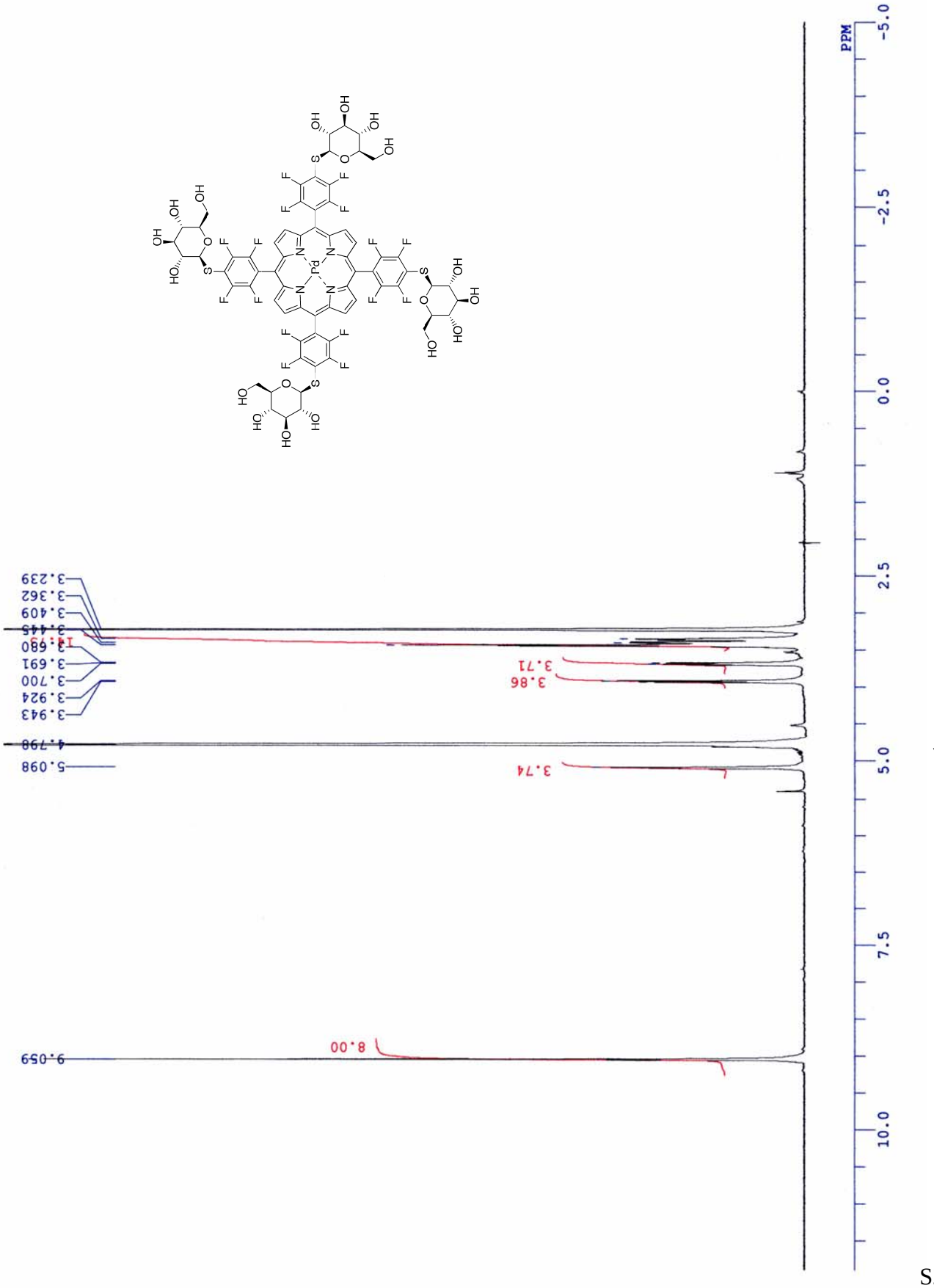

Figure S19 ^{1}H NMR spectrum of **3c** in CD_3OD

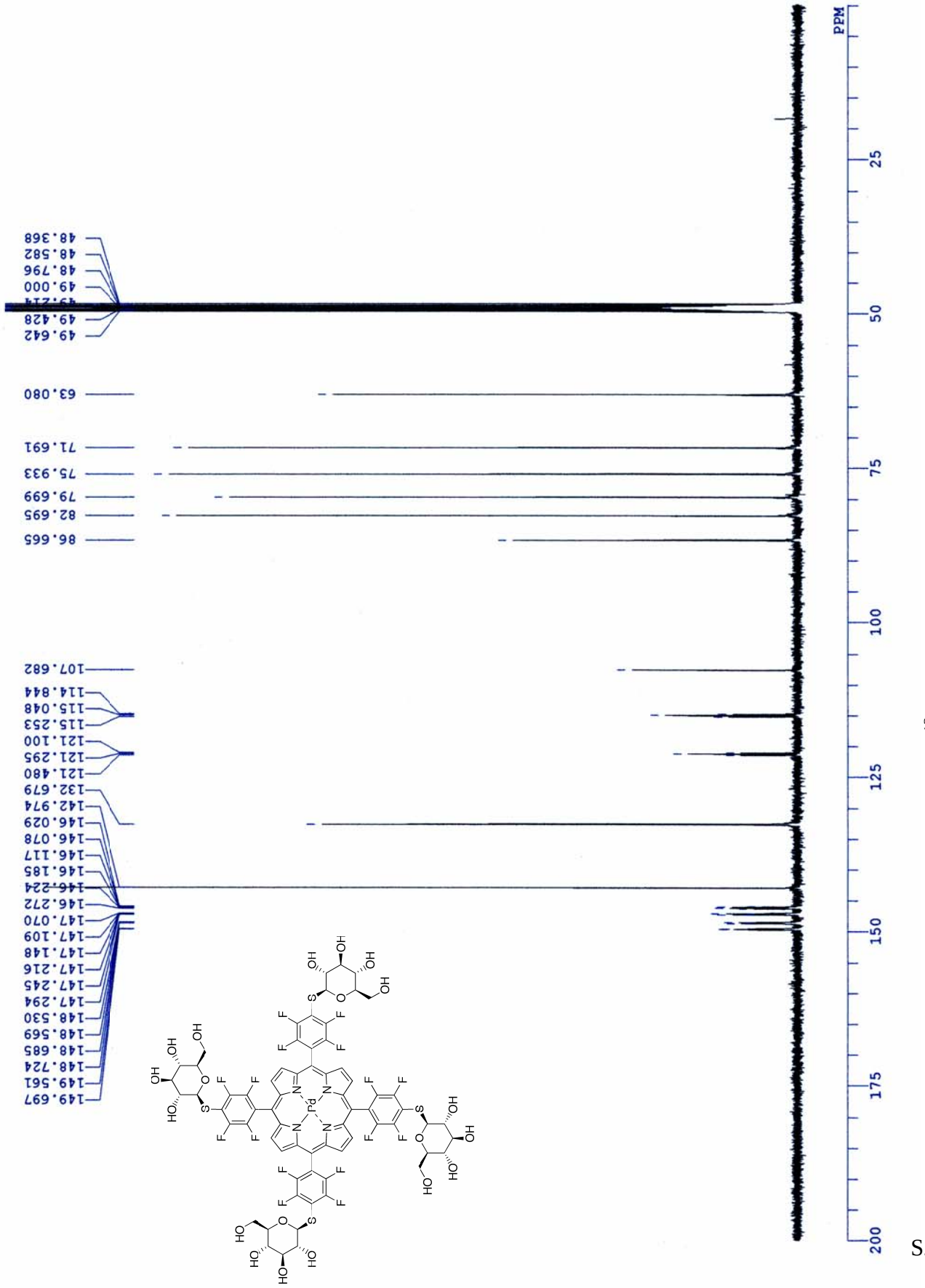

Figure S20 ^{13}C NMR spectrum of **3c** in CD_3OD

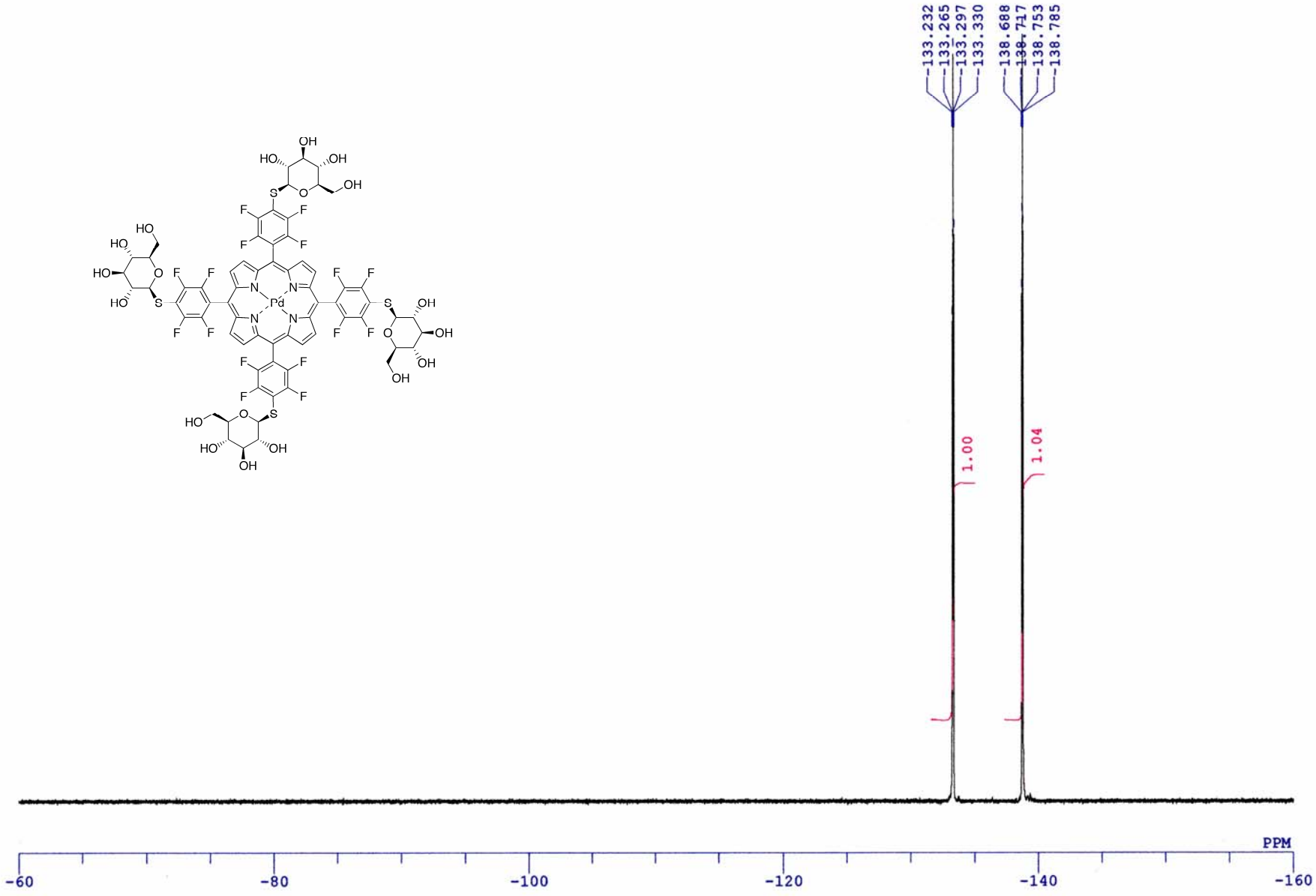

Figure S21 ^{19}F NMR spectrum of **3c** in CD_3OD

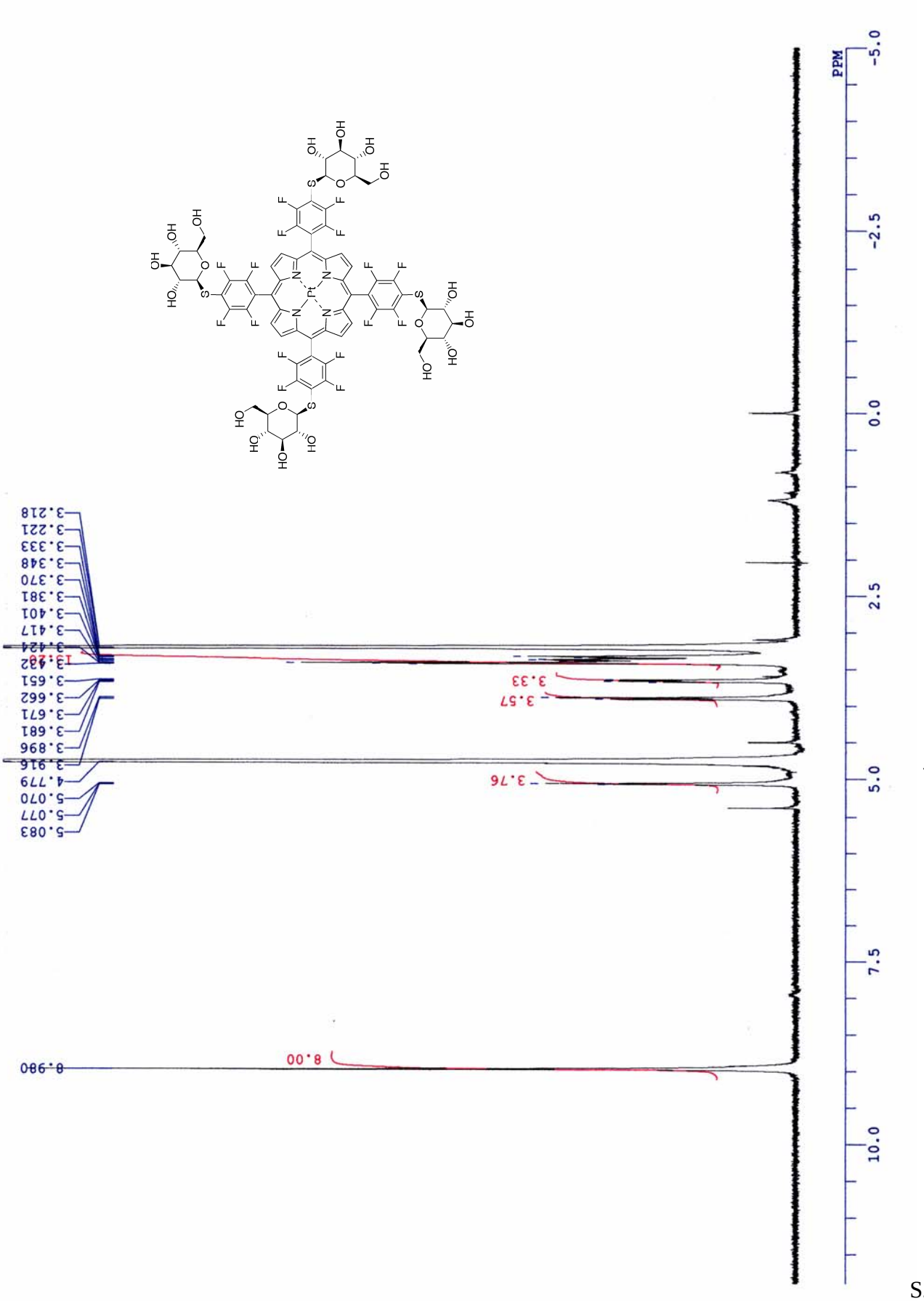

Figure S22 ^{1}H NMR spectrum of **3d** in CD_3OD

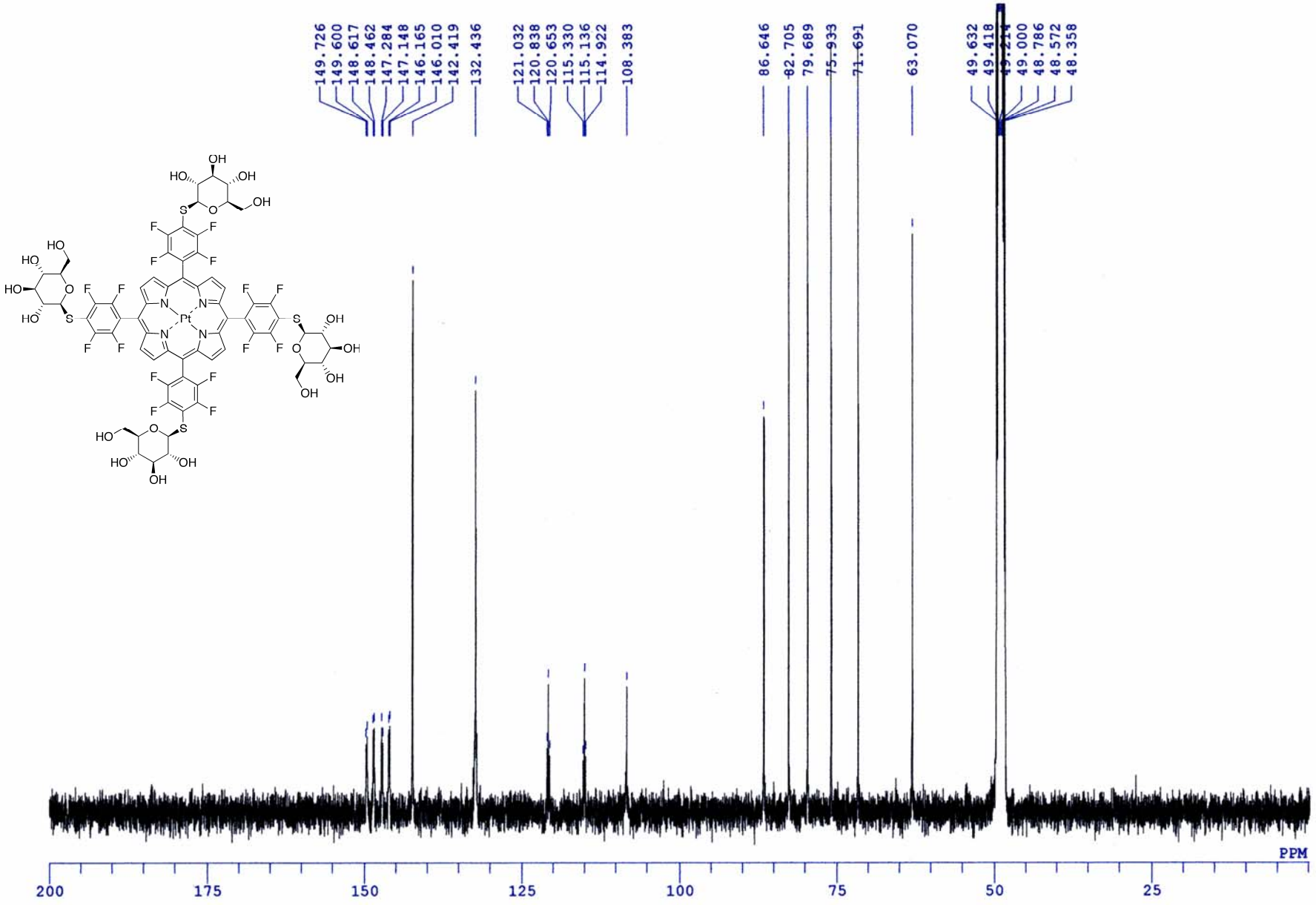

Figure S23 ^{13}C NMR spectrum of **3d** in CD_3OD

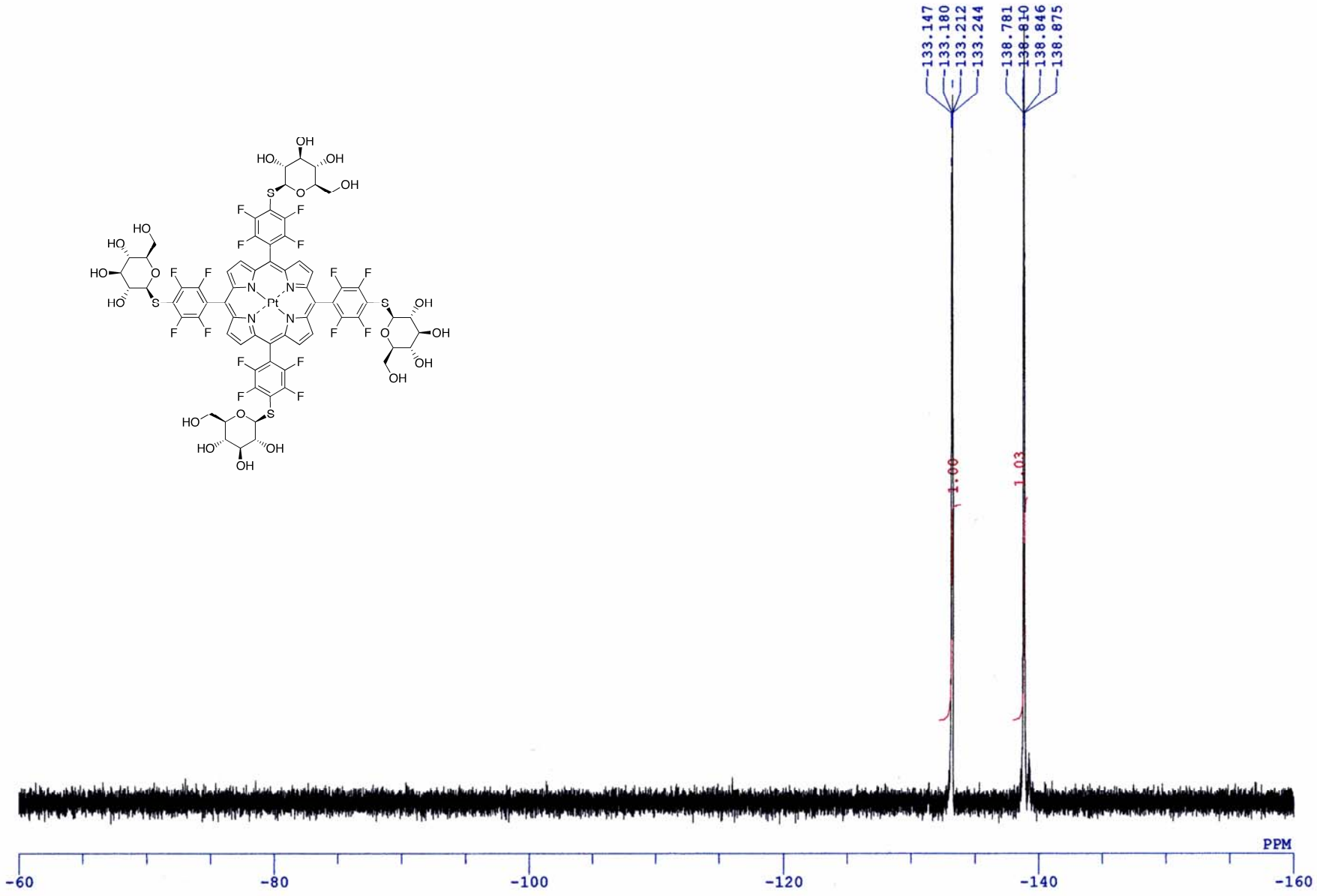

Figure S24 ^{19}F NMR spectrum of **3d** in CD_3OD

Cytosolic Targeting of Macromolecules Using a pH-Dependent Fusogenic Peptide in Combination with Cationic Liposomes

Sachiko Kobayashi,[†] Ikuhiko Nakase,[†] Noriko Kawabata,[†] Hao-Hsin Yu,[†] Sílvia Pujals,[§] Miki Imanishi,[†] Ernest Giralt,[§,#] and Shiroh Futaki*[,†]

Institute for Chemical Research, Kyoto University, Uji, Kyoto 611-0011, Japan, Institute for Research in Biomedicine, Barcelona Science Park, Baldiri Reixac 10, 08028 Barcelona, Spain, and Department of Organic Chemistry, University of Barcelona, Martí i Franquès 1-11, 08028 Barcelona, Spain. Received December 10, 2008; Revised Manuscript Received March 18, 2009

pH-Sensitive peptides and polymers have been employed as additives to enhance the cytosolic delivery of drugs and genes by facilitating their endosomal escape. However, little attention has been paid to the intracellular fate of these peptides and polymers. In this study, we explored the possibility of utilizing GALA, a pH-sensitive fusogenic peptide, as a cytosol-targeting vehicle. In combination with cationic liposomes, Lipofectamine 2000 (LF2000), the feasibility of this approach for the cytosolic targeting of proteins and nanoparticles was exemplified through the delivery of avidin (68 kDa) and streptavidin-coated quantum dots (15−20 nm) in serum-containing medium. The use of cationic liposomes is critical to enhance the cell-surface adhesion of the GALA conjugates and eventual endosomal uptake. Circular dichroism studies suggest that the GALA can be liberated from cationic liposomes at a reducing pH to form a helical structure and this may eventually lead to disruption of the endosomal membrane to achieve an efficient leakage of the GALA conjugates into the cytosol.

INTRODUCTION

Plasma membranes isolate the inside of cells from the outside and maintain cellular functions and homeostasis. These membranes also work as barriers to protect the cells against attack from outside the cells. Therefore, it is necessary to find a means to efficiently cross the membranes to allow cell entry of bioactive molecules with low membrane permeability. Certain classes of viruses have achieved this by using fusogenic peptides that often act at the level of the endosome once the virus is internalized. For example, influenza viruses adsorb on the cell surface by interaction with sialic acids expressed on the plasma membrane and gain access through endocytosis. The pH decrease in endosomes induces conformational changes in a viral coat protein hemagglutinin 2 (HA2), which leads to the fusion of endosomal membranes with viral membranes to allow leakage of the viral genes into the cytosol.

Studies have been reported describing efforts to mimic methods employed by viruses for intracellular delivery of membrane-impermeable macromolecules (*1, 2*). GALA is such a peptide that was developed by Szoka and co-workers (WEAALAEALAEALAEHLAEALAEALEALAA). This peptide is composed of repeating sequences of Glu-Ala-Leu-Ala and has an amphiphilic structure (*3*). A decrease in the endosomal pH leads to a decrease in negative charges of Glu residues and conversion of the structure from random to helical (*2*−*7*). This promotes its interaction with endosomal membranes, leading to their disruption. Therefore, GALA has been employed to facilitate endosomal escape of liposomes and polymers complexed with plasmid DNAs as a method to improve transfection efficiency (*1, 2, 8*−*14*).

In the course of our study assessing the capacity of GALA to enhance transfection, we observed that a FITC-labeled GALA peptide effectively diffused into the cytosol when administrated to cells as a plasmid DNA complex with cationic liposomes. By use of FITC as a model marker for cytosolic delivery, these results strongly support the potentyial of GALA as a vehicle to enhance the delivery of attached cargo to the cytosol (*11*).

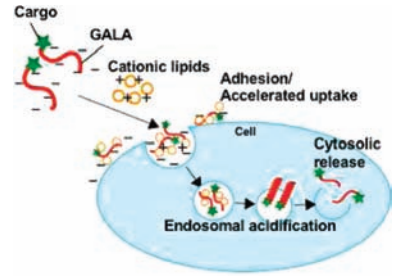

Figure 1. Concept of cytosolic targeting using GALA as an addressing vehicle in combination with cationic liposomes.

In this report, we explore the possibility of GALA as a cytosol-addressing vehicle with pH-sensitive fusogenic activity (Figure 1). Here, a high efficiency of cytosolic targeting using the GALA-based systems is not achieved without entrapment of GALA and the cytosol-targeting molecules in endosomes at a high concentration. Cationic liposomes are known to effectively adsorb onto cell surfaces and be endocytosed, and since GALA has negative charges, cationic liposomes can also form complexes with it. Conjugation or complex formation of cargo molecules with GALA was critical for it to be localized to endosomes where cytosolic escape would take place. The use of cationic liposomes further enhanced the cellular uptake of GALA/cargo molecules and increases the amount localized to endosomes (Figure 1).

EXPERIMENTAL PROCEDURES

Peptides. All the peptides in this report were chemically synthesized by Fmoc (9-fluorenylmethyloxycarbonyl) solid-

* To whom correspondence should be addressed. Phone: +81-774-38-3210. Fax: +81-774-32-3038. E-mail: futaki@scl.kyoto-u.ac.jp.
[†] Kyoto University.
[§] Institute for Research in Biomedicine.
[#] University of Barcelona.

10.1021/bc800530v CCC: $40.75 © 2009 American Chemical Society
Published on Web 04/23/2009

phase peptide synthesis as previously reported (*15*). Actual sequences of the synthesized peptides are as follows: GALA, WEAALAEALAEALAEHLAEALAEALEALAA-amide; scrambled GALA (sGALA), AAALHAALAAEAELLEEWLAAEEAELLAAA-amide; FITC-labeled GALA (FITC-GALA), FITC-NH-$(CH_2)_3$-CO-WEAALAEALAEALAEHLAEALAEALEALAA-amide; FITC-labeled scrambled GALA (FITC-sGALA), FITC-NH-$(CH_2)_3$-CO-AAALHAALAAEAELLEEWLAAEEAELLAAA-amide; biotinamidocaproyl-GALA peptide (biotin-GALA), biotin-amidocaproyl-NH-$(CH_2)_3$-CO-WEAALAEALAEALAEHLAEALAEALEALAA-amide; biotinamidocaproyl-GALA bearing SV40-derived nuclear localization signal (biotin-GALA-NLS), biotinamidocaproyl-NH-$(CH_2)_3$-CO-WEAALAEALAEALAEHLAEALAEALEALAA-GG-PKKKRKV-amide; biotinamidocaproyl-scrambled GALA peptide (biotin-sGALA), biotinamidocaproyl-NH-$(CH_2)_3$-CO-AAALHAALAAEAELLEEWLAAEEAELLAAA-amide; CG-GALA, CG-WEAALAEALAEALAEHLAEALAEALEALAA-amide. Details of the preparations of these peptides are described in the Supporting Information.

EGFP−GALA Fusion Protein. The enhanced green fluorescent protein (EGFP) fused with GALA at its C-terminus was prepared by expressed protein ligation (EPL) essentially as previously reported (*16*). Briefly, EGFP was bacterially expressed as a fusion protein with the C-terminal intein bearing the chitin-binding domain (CBD) tag in *E. coli*. Affinity purification was performed on chitin beads (IMPACT system, New England Biolabs) followed by subsequent intein cleavage by the addition of 100 mM 2-mercaptoethanesulfonic acid (MESNA), leading to thioester formation. Ligation of EGFP thioester with CG-GALA was conducted in 0.1 M Tris-HCl (pH 8.5) containing 500 mM NaCl at 4 °C for 24 h in the presence of 10 mM MESNA to yield the EGFP−GALA fusion protein.

Cell Culture. Human cervical-cancer-derived HeLa cells were cultured as exponentially growing subconfluent monolayers on 60 mm dishes in α-minimum essential medium (α-MEM) supplemented with 10% (v/v) heat-inactivated bovine serum (BS) (Invitrogen). Chinese hamster ovary (CHO) K1 cells were cultured in F-12 nutrient mixture (Ham's F-12) supplemented with 10% (v/v) heat-inactivated BS. Mouse fibroblast-derived NIH3T3 cells and human epidermoid carcinoma-derived A431 cells were cultured in Dulbecco's modified Eagle medium (D-MEM) supplemented with 10% (v/v) heat-inactivated BS. The respective cells were maintained at 37 °C in a humidified 5% CO_2 incubator, and a subculture was performed every 3−4 days.

Cellular Uptake Experiments and Microscopic Observation. The 1.5×10^5 HeLa cells were plated into 35 mm glass base dishes (Iwaki) and cultured for 24 h. Lipofectamine 2000 (LF2000, Invitrogen) (2 μL) diluted with serum-free α-minimum essential medium [α-MEM(−)] (18 μL) was added to a solution of the FITC-labeled GALA peptide (10 μM) in α-MEM(−) (20 μL), and the mixture was incubated for 15 min at room temperature. Heat-inactivated BS (13 % (v/v)) in α-MEM (160 μL) was then added to yield a solution of the GALA peptide (1 μM) containing LF2000 (2 μL) in α-MEM containing 10% (v/v) BS [α-MEM(+)] (200 μL). After the HeLa calls were incubated with this mixture at 37 °C under 5% CO_2 for 4 h, the cells were washed twice with PBS and fresh α-MEM(+) (1 mL) was added to the cells. Internalization of the peptides was analyzed in live cells using an FV300 Olympus confocal laser scanning microscope (CLSM) equipped with a 40× objective.

For the treatment of EGFP−GALA/LF2000 complex, EGFP−GALA (20 μM) in α-MEM(−) (20 μL) was mixed with LF2000 (8 μL) in α-MEM(−) (20 μL) and incubated for 15 min at room temperature. α-MEM (160 μL) containing 13% BS was then added to yield a solution of the EGFP−GALA (2 μM) in α-MEM(+) containing LF2000 (8 μL). HeLa cells were incubated with this mixture at 37 °C under 5% CO_2 for 8 h. The cells were then washed twice with PBS containing heparin sodium salt (0.5 mg/mL) (Sigma). Internalization of the EGFP was analyzed in a fresh medium using CLSM.

For assessment of the internalization of FITC-avidin/biotin-GALA complexes, biotinylated-GALA (10 μM) in α-MEM(−) (20 μL) was mixed with LF2000 (2 μL) in α-MEM(−) (20 μL) and incubated for 15 min at room temperature prior to adjustment of the total volume of the mixture to 200 μL with a solution of FITC-avidin (Sigma) in 13% BS-containing α-MEM to yield a solution of the FITC-avidin/biotin-GALA complex (FITC-avidin 0.25 μM; biotin-GALA 1 μM) in α-MEM(+) containing 2 μL of LF2000. HeLa cells were incubated with this mixture at 37 °C under 5% CO_2 for 6 h. The cells were then washed twice with PBS, and fresh medium (1 mL) was added prior to analysis of the internalization of the FITC-avidin by CLSM.

For the treatment of the streptavidin-coated quantum dot (QD-SA)/biotin-GALA complex, a solution of QD-SA (80 nM) (Invitrogen) in PBS (5 μL) was mixed with biotin-GALA (10 μM) in PBS (20 μL) and incubated for 20 min at room temperature. LF2000 (2 μL) diluted with PBS (18 μL) was then added to the mixture and incubated for 20 min at room temperature. The total volume of the mixture was then adjusted to 200 μL with 13% BS-containing α-MEM. HeLa cells were treated with this mixture for 24 h and washed twice with PBS. Internalization of the QD-SA was analyzed in a fresh medium using CLSM.

For FAST DiI staining, FAST DiI (1,1′-dihexadecyl-3,3,3′,3′-tetramethylindocarbocyamineperchlorate) (Invitrogen) was added to the described mixture of QD-SA/biotin-GALA/LF2000 in 200 μL of α-MEM(+) (final concentration of FAST DiI, 20 μM) prior to the addition to HeLa cells. Lysotracker staining was conducted after incubation of HeLa cells with the mixture of QD-SA/biotin-GALA/LF2000 followed by two PBS washings. The cells were incubated in α-MEM(+) (200 μL) containing Lysotracker (50 nM) (Invitrogen) for 1 min and washed twice with PBS prior to observation by CLSM.

Flow Cytometry. HeLa cells (5×10^4) were plated into 24-well microplates (Iwaki) and cultured for 48 h. The cells were incubated with the FITC-GALA/LF2000 complex (1 μM, 2 μL) in α-MEM(+) (200 μL), similarly prepared as for CLSM observation, for 4 h. The cells were then washed twice with PBS and treated with 0.01% trypsin for 10 min at 37 °C. The cells were harvested and centrifuged at 700*g* for 5 min. The cell pellets were suspended, washed twice with PBS, and finally resuspended in PBS (400 μL) for fluorescence analysis with a FACS Calibur flow cytometer (BD Biosciences) using 488 nm laser excitation and a 515−545 nm emission filter. Each sample was analyzed for 10 000 events.

Circular Dichroism. The circular dichroism (CD) spectra of the peptides were scanned by a JASCO J-820 spectrometer using a quartz optical cell with a 1 mm path length at 23 °C. All the spectra were obtained in the presence of egg yolk phosphatidylcholine (EPC) liposomes. The EPC liposomes were prepared similarly to that reported by Szoka and co-workers (*3*). Briefly, the dried film lipid of EPC (11 mg) was hydrated in 5 mM sodium acetate buffer (pH 5.0) containing 100 mM KCl [or in 5 mM sodium phosphate buffer (pH 7.5) containing 100 mM KCl] (2.5 mL) with gentle vortex mixing at room temperature. This emulsion was intermittently sonicated to obtain a clear solution in an ice bath for 40 min and diluted to 5.25 and 2.68 mL with the same buffer to yield 2.5 and 4.9 mM EPC liposome solutions for the CD measurements in the absence and the presence of LF2000, respectively. For the former measurement, 25 μM GALA in 50 mM sodium acetate buffer (pH 5.0) [or 50 mM sodium phosphate buffer (pH 7.5)] (200 μL) was added to the above 2.5 mM solution (100 μL) to

yield 17 μM GALA in the EPC liposomes (lipid concentration, 0.83 mM; lipid/peptide molar ratio, 50/1) in 35 mM sodium acetate buffer (pH 5.0) [or in 35 mM sodium phosphate buffer (pH 7.5)] containing 33 mM KCl. For the latter study, LF2000 (50 μL) was added to 25 μM GALA in 50 mM sodium acetate (pH 5.0) [or 50 mM sodium phosphate (pH 7.5)] (200 μL) and incubated for 15 min at room temperature prior to the addition of 4.9 mM EPC liposome (50 μL). The ratio peptide/LF2000 was the same as that in the cellular uptake experiments. To correct the base lines, spectra of the EPC liposomes in the absence and presence of LF2000 at the same concentrations in the respective buffers were subtracted from those with GALA.

Size Distribution and ζ-Potential Analysis. FITC-GALA (10 μM) in PBS (80 μL) was mixed with LF2000 (8 μL) in PBS (80 μL). The mixture was then diluted with PBS (640 μL) and subjected to size distribution and ζ-potential analysis using a Malvern Zetasizer Nano ZS. For the measurement of LF2000, a solution of PBS (800 μL) containing LF2000 (8 μL) was employed.

RESULTS AND DISCUSSION

Enhanced Cytosolic Diffusion of GALA Peptide by Coadministration with Cationic Liposomes. To assess the ability of GALA as a vehicle to target membrane impermeable bioactive molecules into the cytosol, the FITC-labeled GALA peptide (FITC-GALA) was synthesized and administered to cells. The FITC moiety can be regarded as a model of small molecular weight compounds impermeable to biological membranes, and the intracellular fate can be traced by microscopic observation. GALA has seven Glu residues in its sequence and is negatively charged at neutral pH. The administration of GALA to cells in the presence of cationic liposomes may enhance its adhesion on cell surfaces by increasing interactions with cell surface molecules and thus promoting its cellular uptake. We thus examined the internalization and localization of the GALA peptide in the presence of cationic liposomes. Commercially available Lipofectamine 2000 (LF2000), allowing its use in the presence of serum, was employed as a model of cationic liposomes.

To establish the optimum condition of this system, HeLa cells were treated with FITC-GALA (0.5, 1, 5, and 10 μM) and LF2000 [0.5, 1, and 2% (v/v)] in α-minimal essential medium containing 10% (v/v) BS [α-MEM(+)] at 37 °C for 4 h, as detailed in our previous study (*11*) (Figure 2A). As a result, 1 or 5 μM FITC-GALA in the presence of 1% (v/v) LF2000, and 5 μM FITC-GALA in the presence of 2% (v/v) LF2000 yielded more diffuse cytosolic labeling compared with other conditions. It seems likely that there may be optimum ranges in GALA/LF2000 ratios for efficient cellular uptake diffuse labeling of the cytosol. Excess amount of GALA and LF2000 did not necessarily yield higher cytosolic localization as witnessed by FITC signals. Dynamic light scattering and ζ potential analysis suggested that there was an increase in the averaged particle size of LF2000 and a positive-to-negative alternation in total charge by complex formation with the GALA peptide, respectively (Table 1). Therefore, excess amount of GALA peptide may increase the sizes and negative charges of the complexes to reduce the efficiency of cellular uptake of the complexes. A similar tendency was observed in other cell lines, including Chinese hamster ovary (CHO)-K1, mouse fibroblast-derived NIH3T3, and human epidermoid carcinoma-derived A431 cells (Supporting Information Figure S1), and another commercially available cationic liposome, Lipofectin (Supporting Information Figure S2). From the data it appears that a combination of 1−5 μM GALA with 1% (v/v) liposomes yielded effective cytosolic diffusion of GALA. To avoid possible cytotoxicity caused by the use of increasing amounts of cationic liposomes and GALA peptide, we predominantly employed a combination of 1 μM FITC-GALA and 1% (v/v) LF2000 for further studies.

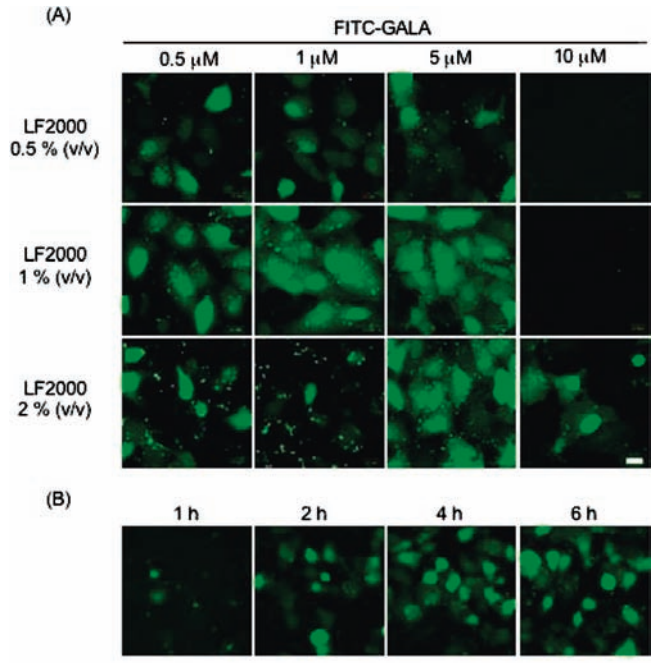

Figure 2. Cytosolic targeting of FITC as a model of membrane impermeable molecules using GALA in combination with Lipofectamine 2000 (LF2000). (A) Optimization of the ratios of GALA/Lipofectamine 2000 (LF2000). HeLa cells were treated with the GALA/LF2000 complexes in 10% serum-containing medium [α-MEM(+)] for 4 h. (B). Time course of cellular distribution of FITC-GALA (1 μM) treated with 1% (v/v) LF2000. Scale bars, 20 μm.

Table 1. Physicochemical Properties of the GALA/LF2000 Complex[a]

	average particle size, nm (PdI)	ζ potential value, mV
1% (v/v) LF2000	518 ± 51 (0.22 ± 0.04)	15.1 ± 2.9
1% (v/v) LF2000 + 1 μM FITC-GALA	745 ± 112 (0.48 ± 0.08)	−18.4 ± 1.5

[a] The particle size, ζ potential, and the polydispersion index (PdI) were determined using a Zetasizer Nano ZS instrument.

A time course study using 1 μM FITC-GALA and 1% (v/v) LF2000 demonstrated that diffuse FITC-GALA in the cytosol was observed within 2 h after the administration of FITC-GALA/LF2000 to the cells (Figure 2B). The signals then became more diffuse and intense in a time dependent fashion. The diffuse signal of FITC-GALA was observed in the cytosol of almost all cells after 6 h. These results suggested that the endosomal acidification stimulated disruption of the endosomal membranes by GALA even in the presence of cationic liposomes and that this led to efficient leakage of FITC-GALA into the cytosol. Additionally, no significant disruption of the plasma membrane or cytotoxicity was observed during these incubations and this was confirmed by propidium iodide costaining (*17*) and MTT [3-(4,5-dimethylthiazol-2-yl)-2,5-diphenyl-2*H*-tetrazolium bromide] assays (*18*), respectively (data not shown).

Covalent cross-linking between the GALA peptide and molecules targeted into the cytosol as well as co-incubation with cationic liposomes was necessary to achieve efficient cytosolic targeting (Figure 3A). No significant cytosolic spread of FITC was observed following FITC-GALA incubations in the absence of LF2000 or with a mixture of fluorescein and GALA (without covalent bonding) in the presence of LF2000 (Figure 3A). FACS analysis showed that the cellular uptake of FITC-GALA in the presence of LF2000 was about 30 times higher than that in the

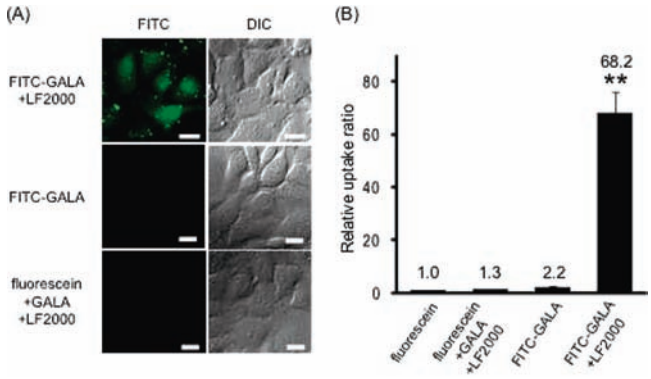

Figure 3. Necessities of conjugation with GALA and coadministration with LF2000 to attain effective cytosolic targeting. (A) HeLa cells were treated with (i) 1 μM FITC-GALA in the presence of 1% (v/v) LF2000 (top), (ii) 1 μM FITC-GALA in the absence of LF2000 (middle), and (iii) a mixture of 1 μM fluorescein and 1 μM GALA (without conjugation) in the presence of 1% (v/v) LF2000 (bottom) in α-MEM(+) for 4 h and analyzed by confocal microscopy. Scale bars, 20 μm. (B) FACS analysis of the FITC (fluorescein) uptake. HeLa cells were treated with (from the left) 1 μM fluorescein, 1 μM fluorescein/1 μM GALA (without conjugation)/1% (v/v) LF2000, 1 μM FITC-GALA, 1 μM FITC-GALA/1% (v/v) LF2000 for 4 h, respectively. The results were normalized by the fluorescein uptake (left). Error bars represent the mean ± standard deviation ($n = 3$). The statistical analysis was done using the Student t test. The symbol ** indicates statistical significance ($p < 0.01$).

absence of LF2000 (Figure 3B) and about 60 times higher than that of fluorescein in the presence or absence of LF2000. Therefore, the electrostatic interaction of the negatively charged GALA with cationic liposomes recruits the GALA-modified molecules onto the cell surface that leads to the efficient endocytic uptake and eventual leakage into the cytosol. The involvement of endocytosis was confirmed by inhibition of the cellular uptake at 4 °C where energy-driven processes including endocytosis are suppressed (Supporting Information Figure S3A). The importance of endosomal acidification in this targeting system was further ascertained by inhibition of the cellular uptake in the presence of nocodazole, a microtubule-disrupting agent that reversibly blocks the transport of endosomes to the lysosomes (*19*), and NH_4Cl, known to prevent endosomal acidification (*20*) (Supporting Information Figure S3B).

Dynamic pH-Dependent Structural Alteration of the GALA Peptide in the Presence of Cationic Liposomes. The results strongly suggest that GALA retains its ability to disrupt endosomal membranes at a reducing pH even when coadministered with cationic liposomes. The induction of the helical structure of the GALA peptide to increase membrane interaction is regarded as the key step that leads to the endosomal disruption by this peptide, and this was analyzed by the circular dichroism (CD) spectra of the GALA peptide in the presence of liposomes (Figure 4B). As reported by Szoka and co-workers (*3*), the GALA peptide (17 μM) took a modest helical structure at pH 7.5 in the presence of liposomes prepared from egg yolk phosphatidylcholine (EPC) (0.83 mM), and the helical content was about 60% [deduced on the basis of $[\theta]_{222}$ (*21*)]. The helical content increased to approximately 90% at pH 5.0 presumably because of the decrease in the electrostatic repulsion between the glutamic acid residues to yield a stronger membrane interaction. However, the GALA showed no typical secondary structure at pH 7.5 in the presence of EPC together with 1% (v/v) LF2000, suggesting a strong interaction between GALA and LF2000 (Figure 4B, right). Interestingly, GALA yielded a CD spectrum of a typical helical peptide at pH 5.0 even in the presence of 1% (v/v) LF2000 (Figure 4B, right), and the spectrum was very similar to that in the absence of LF2000

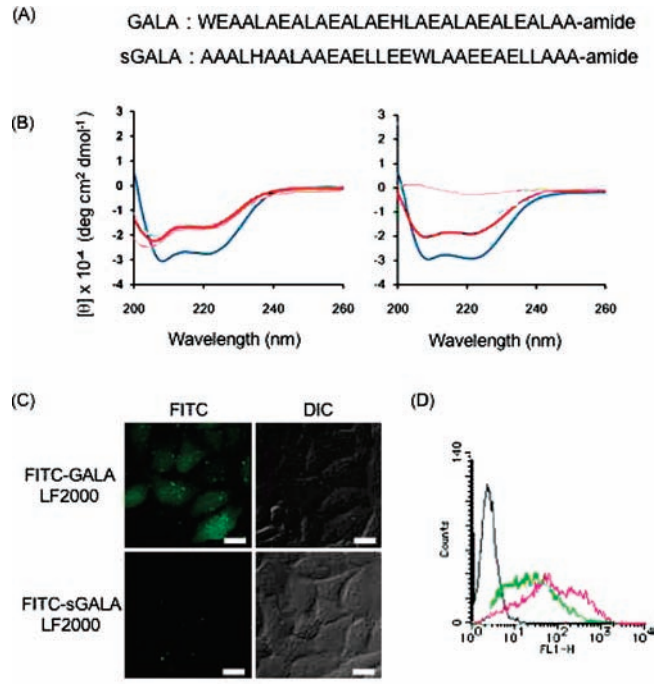

Figure 4. Importance of the GALA structure on cytosolic targeting. (A) Amino acid sequences of GALA peptide and scrambled GALA (sGALA) peptide. (B) The circular dichroism spectra of the peptides (17 μM) in the presence of egg yolk phosphatidylcholine vesicles (0.83 mM) and in the absence (left) and the presence (right) of 1% (v/v) LF2000: GALA at pH 7.5 (light blue) and pH 5.0 (dark blue); sGALA at pH 7.5 (light red) and pH 5.0 (dark red). (C) HeLa cells were incubated with these peptides and LF2000 in α-MEM(+) for 4 h and analyzed by confocal microscopy. Scale bars, 20 μm. (D) FACS analysis of the FITC uptake by the cells after treatment with 1 μM GALA peptides or fluorescein in the presence of 1% (v/v) LF2000 for 4 h: nontreated cells (control) (black); cells treated with FITC-sGALA/LF2000 (green) and FITC-GALA/LF2000 (magenta).

(Figure 4B, left). The decrease in the negative charges of GALA at the reducing pH may diminish its interaction with cationic liposomes, allowing it to form a helical structure that then interacts with the EPC membranes. The possible destabilization of LF2000 at the reducing pH (*22*) may also assist the liberation of GALA from the cationic liposomes.

To further confirm the importance of the induction of the helical structure at the reducing pH for endosomal membrane disruption, we designed an alterative peptide with a scrambled GALA sequence (designated as sGALA) (Figure 4A). Analysis by CD revealed that sGALA has the same degree of helical content as GALA at pH 7.5 in EPC liposomes. However, in marked contrast to GALA, sGALA yields no significant increase in helicity at the reducing pH (Figure 4B, left). In the presence of 1% (v/v) LF2000, no typical secondary structure was predicted for sGALA from its CD spectrum in EPC liposomes at pH 7.5 as in the case for GALA (Figure 4B, right). At pH 5.0, sGALA yielded a helical structure, but the helical content was about two-thirds of that of GALA under the same conditions. Additionally, the helical content of sGALA was similar in the presence (Figure 4B, right) and absence (Figure 4B, left) of LF2000 at pH 5.0. This suggests that this peptide, like GALA, is liberated from the cationic liposomes at pH 5.0.

A significant difference in fluorescence was observed between the cells treated with FITC-GALA and FITC-sGALA (Figure 4C). In contrast to the diffuse signals observed in FITC-GALA treated cells, FITC-sGALA gave predominantly punctate signals without showing any cytosolic diffusion, suggesting that the majority of the peptide was trapped in the endosomes, even when co-incubated with LF2000. The amount of cellular uptake

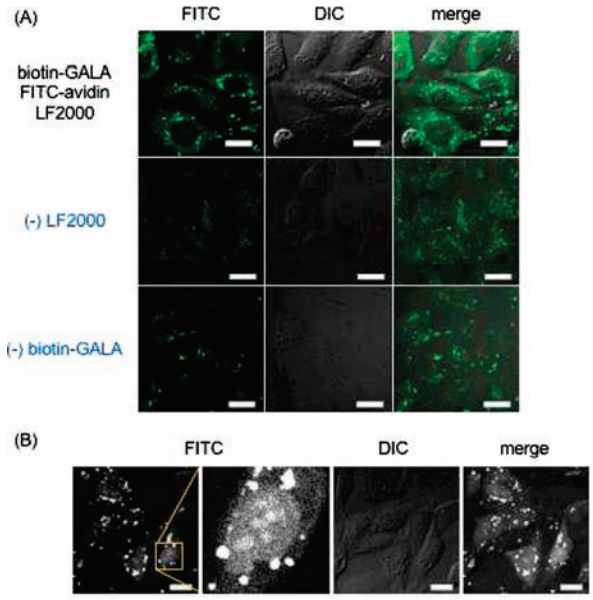

Figure 5. Application of GALA/LF2000 system to cytosolic targeting of avidin. (A) Confocal microscopic observation of HeLa cells treated with a mixture of 1 μM biotin-GALA, 0.25 μM FITC-avidin, and 1% (v/v) LF2000 for 6 h. Absence of LF2000 or biotin-GALA hampered the efficient cytosolic diffusion of FITC-avidin. (B) HeLa cells were incubated with a mixture of biotin-GALA-NLS (1 μM), FITC-avidin (0.25 μM), and 1% (v/v) LF2000 for 6 h. The nuclear translocation of FITC-avidin suggested that the complex structure with biotin-GALA-NLS was retained after its cytosolic release.

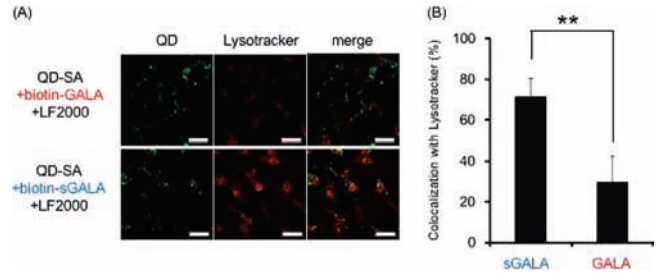

Figure 6. Application of GALA/LF2000 system to cytosolic targeting of QDs. (A) Confocal microscopic observation of HeLa cells treated with a complex of 2 nM streptavidin-conjugated QDs (QD-SA), 1% (v/v) LF2000 and biotin-GALA or biotin-sGALA (1 μM each) for 24 h in the presence of Lysotracker. Scale bars, 10 μm. (B) Statistical analysis of colocalization of the QD-SA signals with those of Lysotracker. HeLa cells were treated with biotin-sGALA/QD-SA/LF2000 (left column) or biotin-GALA/QD-SA/LF2000 (right column) for 24 h and then stained with Lysotracker after two washings with PBS. Total number of dots of QD-SA signal in the cells (775 and 1003 dots for the cells treated with biotin-GALA and biotin-sGALA containing QD-SA/LF2000 mixture, respectively), and the merged dots with the signal from Lysotracker were counted. Error bars represent the mean $\pm$ standard deviation. Statistical analysis was done using the Student *t* test. The symbol ** indicates statistical significance ($p < 0.01$).

of sGALA in the presence of LF2000 was 30% of that of GALA (Figure 4D). Considering the difference in the CD spectrum of sGALA from that of GALA, the conformational change in endosome-trapped sGALA may not be sufficient to induce its effective leakage into the cytosol. The negative charges of the GALA contribute to its endosomal packaging, but the induction of a highly helical structure at the reducing pH should also be an important criteria for efficient cytosolic targeting.

Cytosolic Targeting of Proteins Using the GALA in the Presence of Cationic Liposomes. The results shown indicated that this approach may be utilized for cytosolic targeting of bioactive molecules of relatively small molecular weights (<2000). Applicability of this approach to the cytosolic delivery of whole proteins was then assessed using avidin (68 kDa). Avidin is known to form a 1:4 complex with biotin with an apparent dissociation constant of 10^{-15} M (*23*, *24*). HeLa cells were treated with a mixture of FITC-avidin (0.25 μM), the N-terminal biotinylated GALA (biotin-GALA) (1 μM), and LF2000 [1% (v/v)] in α-MEM(+) for 6 h (Figure 5A). Although the large punctate signals of FITC-avidin were observed in the perinuclear area, significant diffuse signals were observed in the cytosol of most cells, suggesting that an acceleration of cytosolic targeting occurs for much larger molecules. In contrast, only punctate signals of lower intensities were observed in cells treated in the absence of LF2000 or biotin-GALA (Figure 5A). This also indicates the effectiveness of the GALA/LF2000 system to recruit exogenous molecules into endocytic pathways that then lead to endosomal escape.

Nuclear pores serve as gates on nuclear membranes to selectively separate the inside of the nucleus from the cytosol (*25*). Relatively small proteins (<30−40 kDa) can penetrate these pores by passive diffusion, whereas larger proteins cannot permeate unless they utilize the nuclear pore machinery whose function it is to allow access of selective macromolecules. Cellular traffic systems using importins achieve this by recognizing one of a number of different nuclear localization sequence (NLS). Addition of the NLS sequence (PKKKRKV) derived from the simian virus 40 (SV40) (*26*) to the GALA segments (biotin-GALA-NLS) significantly improved the nuclear localization of the FITC-avidin (Figure 5B). This suggests that certain portions of FITC-avidin/biotin-GALA-NLS retained its complex structure even after endosomal escape into the cytosol. Cytosolic and nuclear delivery using this system may therefore allow retention of complex structures comprising multiple components, thus offering a further advantage of this approach.

Applicability of this approach to intracellular delivery of proteins was also assessed using EGFP (27 kDa) as an alternative model. Presumably because of the increase in hydrophobicity and negative charges of EGFP when fused with the GALA segment, we noticed considerable amount of aggregation when it was added to LF2000, leading to a decrease in the cellular uptake of the protein. Although endosome-like, punctate signals of EGFP were observed in most of the cells; only 20−40% of the cells yielded diffuse signals of EGFP after an 8 h treatment with HeLa and CHO-K1 cells (Supporting Information Figure S4). Aggregate formation may be a drawback of this approach, and the physicochemical properties of cargo may affect this. However, since no significant signal was observed when cells were treated with EGFP−GALA in the absence of LF2000, the combination of GALA and cationic liposomes was still effective in promoting cytosolic delivery of the protein.

Application to the Cytosolic Targeting of Quantum Dots. Applicability of the GALA/LF2000 system for cytosolic targeting of nanoparticles was next evaluated using semiconductor quantum dots (QDs). QDs are a novel class of fluorescent probes with unique features that include tunable fluorescence emission, exceptional brightness, and photostability when compared to conventional organic dyes and fluorescent proteins (*27*). The efficient cytosolic delivery of QDs would open new avenues to cellular imaging and even some clinical applications for which the QDs hold the most promise (*28*−*30*). Streptavidin-conjugated QDs (QD-SA) (diameter, 15−20 nm; an average of 10 molecules of streptavidin are doped on one QD particle) were employed here to form complexes with biotin-GALA. HeLa cells were treated with a mixture of biotin-GALA (1 μM), QD-SA (2 nM), and 1% (v/v) LF2000 in α-MEM(+) for 24 h.

Unlike the treatment with FITC-avidin/biotin-GALA in the presence of LF2000 (Figure 5A), this treatment with QD-SA yielded only punctate signals in the cells (Figure 6A). However,

the majority of the signals of QD-SA did not show any colocalization with Lysotracker, a representative marker of late endosomes/lysosomes (*31*). A detailed analysis of the 775 spots of QD-SA signals in the former case showed that only about 30% of the fluorescent spots overlapped with those of Lysotracker. On the other hand, when the cells were treated with a mixtures of QD-SA (2 nM), biotinylated scrambled GALA (biotin-sGALA) (1 μM), and 1% (v/v) LF2000, a high degree of colocalization of the QD-SA signals with Lysotracker was observed (Figure 6). In addition, overlap of the signals of QD-SA with FAST DiI, an early/recycling endosome marker (*31, 32*), was about 20% (Supporting Information Figure S5). On the other hand, in the case when scrambled GALA was employed instead of GALA, as many as 70% of 1003 spots merged with those stained with Lysotracker (Figure 6B) and 20% of QD-SA spots showed colocalization with FAST DiI (Supporting Information Figure S5). The above results strongly suggested that the majority of the QD-SA escaped from the endosomes and reached the cytosol with the aid of GALA. Punctate signals from QD-SA may suggest possible aggregate formation in the cells. However, considering that no significant aggregates were extracellularly observed during these incubations and that QDs have a general tendency to aggregate, further studies are necessary to elucidate the structural characteristics that yield these punctate signals.

CONCLUSIONS

In this report, we have demonstrated the applicability of the GALA peptide as a cytosol-addressing vehicle having pH-sensitive fusogenic activity. In this system, the coadministration of cationic liposomes plays a critical role in enhancing the cell-surface adhesion and cellular uptake of molecules conjugated to GALA. The pH decrease in endosomes most probably alters the structure of GALA in the endosomes, and this liberates it from the cationic liposomes to achieve efficient endosomal escape. Cytosolic delivery of proteins (EGFP and avidin) and nanoparticle (QD) were also demonstrated. In this study we (i) employed direct conjugation of GALA with FITC (a model small molecular weight compound), (ii) expressed protein ligation for the preparation of EGFP−GALA fusion protein, and (iii) employed complex formation between QD-SA/biotin-GALA complex. Other methods to form chemical cross-linking and fusion proteins may also be employable for the tethering of the GALA peptide with the cargo of interest. Of special note is that this system can be employed in the presence of serum. A similar strategy may be applicable using other polycations including polyethyleneimine and polyarginine instead of cationic liposomes. There are, however, limitations to this approach including possible aggregation formation or incomplete cytosolic translocation especially in protein/large particle delivery, and these should be addressed in future studies. Despite these limitations, this system may serve as a prototype for a novel cytosol targeting strategy not only for chemical and biological studies of cell functions but also for diagnostic and therapeutic applications including in vivo bioimaging and the ex vivo treatment of cells for regenerative medicine.

ACKNOWLEDGMENT

This work was supported in part by Grant-in-Aid for Scientific Research on Priority Areas “Life Surveyor” from the Ministry of Education, Culture, Sports, Science and Technology of Japan. S.P. is grateful for a FPU fellowship and a temporary stay grant from the Ministerio de Ciencia e Innovación. The authors are grateful to Dr. Y. Higuchi and Prof. M. Hashida, Kyoto University, for their assistance in obtaining the size distribution and ζ-potential of the GALA/LF2000 complex.

Supporting Information Available: Details of peptide synthesis including HPLC retention times and MALDI-TOF MS results of the peptides synthesized in this study; confocal microscopy images. This material is available free of charge via the Internet at http://pubs.acs.org.

LITERATURE CITED

(1) Wagner, E. (1999) Application of membrane-active peptides for nonviral gene delivery. *Adv. Drug Delivery Rev. 38*, 279–289.

(2) Li, W. J., Nicol, F., and Szoka, F. C. (2004) GALA: a designed synthetic pH-responsive amphipathic peptide with applications in drug and gene delivery. *Adv. Drug Delivery Rev. 56*, 967–985.

(3) Subbarao, N. K., Parente, R. A., Szoka, F. C., Nadasdi, L., and Pongracz, K. (1987) pH-Dependent bilayer destabilization by an amphipathic peptide. *Biochemistry 26*, 2964–2972.

(4) Nicol, F., Nir, S., and Szoka, F. C. (2000) Effect of phospholipid composition on an amphipathic peptide-mediated pore formation in bilayer vesicles. *Biophys. J. 78*, 818–829.

(5) Simões, S., Slepushkin, V., Pires, P., Gaspar, R., de Lima, M. C. P., and Duzgunes, N. (1999) Mechanisms of gene transfer mediated by lipoplexes associated with targeting ligands or pH-sensitive peptides. *Gene Ther. 6*, 1798–1807.

(6) Nicol, F., Nir, S., and Szoka, F. C. (1996) Effect of cholesterol and charge on pore formation in bilayer vesicles by a pH-sensitive peptide. *Biophys. J. 71*, 3288–3301.

(7) Nir, S., and Nieva, J. L. (2000) Interactions of peptides with liposomes: pore formation and fusion. *Prog. Lipid Res. 39*, 181–206.

(8) Simões, S., Slepushkin, V., Pretzer, E., Dazin, P., Gaspar, R., de Lima, M. C. P., and Duzgunes, N. (1999) Transfection of human macrophages by lipoplexes via the combined use of transferrin and pH-sensitive peptides. *J. Leukocyte Biol. 65*, 270–279.

(9) Simões, S., Slepushkin, V., Gaspar, R., de Lima, M. C. P., and Duzgunes, N. (1998) Gene delivery by negatively charged ternary complexes of DNA, cationic liposomes and transferrin or fusigenic peptides. *Gene Ther. 5*, 955–964.

(10) Simões, S., Slepushkin, V., Pires, P., Gaspar, R., de Lima, M. C. P., and Duzgunes, N. (2000) Human serum albumin enhances DNA transfection by lipoplexes and confers resistance to inhibition by serum. *Biochim. Biophys. Acta 1463*, 459–469.

(11) Futaki, S., Masui, Y., Nakase, I., Sugiura, Y., Nakamura, T., Kogure, K., and Harashima, H. (2005) Unique features of a pH-sensitive fusogenic peptide that improves the transfection efficiency of cationic liposomes. *J. Gene Med. 7*, 1450–1458.

(12) Kakudo, T., Chaki, S., Futaki, S., Nakase, I., Akaji, K., Kawakami, T., Maruyama, K., Kamiya, H., and Harashima, H. (2004) Transferrin-modified liposomes equipped with a pH-sensitive fusogenic peptide: an artificial viral-like delivery system. *Biochemistry 43*, 5618–5628.

(13) Yamada, Y., Shinohara, Y., Kakudo, T., Chaki, S., Futaki, S., Kamiya, H., and Harashima, H. (2005) Mitochondrial delivery of mastoparan with transferrin liposomes equipped with a pH-sensitive fusogenic peptide for selective cancer therapy. *Int. J. Pharm. 303*, 1–7.

(14) Sasaki, K., Kogure, K., Chaki, S., Nakamura, Y., Moriguchi, R., Hamada, H., Danev, R., Nagayama, K., Futaki, S., and Harashima, H. (2008) An artificial virus-like nano carrier system: enhanced endosomal escape of nanoparticles via synergistic action of pH-sensitive fusogenic peptide derivatives. *Anal. Bioanal. Chem. 391*, 2717–2727.

(15) Futaki, S., Ishikawa, T., Niwa, M., Kitagawa, K., and Yagami, T. (1997) Embodying a stable alpha-helical protein structure through efficient chemical ligation via thioether formation. *Bioorg. Med. Chem. 5*, 1883–1891.

(16) Machova, Z., Mühle, C., Krauss, U., Tréhin, R., Koch, A., Merkle, H. P., and Beck-Sickinger, A. G. (2002) Cellular internalization of enhanced green fluorescent protein ligated to a human calcitonin-based carrier peptide. *ChemBioChem 3*, 672–677.

(17) Moore, A., Donahue, C. J., Bauer, K. D., and Mather, J. P. (1998) Simultaneous measurement of cell cycle and apoptotic cell death. *Methods Cell Biol. 57*, 265–278.

(18) Mosmann, T. (1983) Rapid colorimetric assay for cellular growth and survival: application to proliferation and cytotoxicity assays. *J. Immunol. Methods 65*, 55–63.

(19) Baravalle, G., Schober, D., Huber, M., Bayer, N., Murphy, R. F., and Fuchs, R. (2005) Transferrin recycling and dextran transport to lysosomes is differentially affected by bafilomycin, nocodazole, and low temperature. *Cell Tissue Res. 320*, 99–113.

(20) Puertollano, R., and Alonso, M. A. (1999) MAL, an integral element of the apical sorting machinery, is an itinerant protein that cycles between the trans-Golgi network and the plasma membrane. *Mol. Biol. Cell 10*, 3435–3447.

(21) Chen, Y. H., and Yang, J. T. (1971) A new approach to calculation of secondary structures of globular proteins by optical rotator dispersion and circular dichroism. *Biochem. Biophys. Res. Commun. 44*, 1285–1291.

(22) Dalby, B., Cates, S., Harris, A., Ohki, E. C., Tilkins, M. L., Price, P. J., and Ciccarone, V. C. (2004) Advanced transfection with Lipofectamine 2000 reagent: primary neurons, siRNA, and high-throughput applications. *Methods 33*, 95–103.

(23) Livnah, O., Bayer, E. A., Wilchek, M., and Sussman, J. L. (1993) Three-dimensional of avidin and the avidin−biotin complex. *Proc. Natl. Acad. Sci. U.S.A. 90*, 5076–5080.

(24) Hofmann, K., Finn, F. M., and Kiso, Y. (1978) Avidin−biotin affinity columns. General methods for attaching biotin to peptides and proteins. *J. Am. Chem. Soc. 100*, 3585–3590.

(25) Gorlich, D., and Kutay, U. (1999) Transport between the cell nucleus and the cytoplasm. *Annu. Rev. Cell Dev. Biol. 15*, 607–660.

(26) Yoneda, Y. (1997) How proteins are transported from cytoplasm to the nucleus. *J. Biochem. 121*, 811–817.

(27) Medintz, I. L., Uyeda, H. T., Goldman, E. R., and Mattoussi, H. (2005) Quantum dot bioconjugates for imaging, labelling and sensing. *Nat. Mater. 4*, 435–446.

(28) Chan, W. C. W., Maxwell, D. J., Gao, X. H., Bailey, R. E., Han, M. Y., and Nie, S. M. (2002) Luminescent quantum dots for multiplexed biological detection and imaging. *Curr. Opin. Biotechnol. 13*, 40–46.

(29) Michalet, X., Pinaud, F. F., Bentolila, L. A., Tsay, J. M., Doose, S., Li, J. J., Sundaresan, G., Wu, A. M., Gambhir, S. S., and Weiss, S. (2005) Quantum dots for live cells, in vivo imaging, and diagnostics. *Science 307*, 538–544.

(30) Chan, W. C. W., and Nie, S. M. (1998) Quantum dot bioconjugates for ultrasensitive nonisotopic detection. *Science 281*, 2016–2018.

(31) Hao, M. M., Mukherjee, S., Sun, Y., and Maxfield, F. R. (2004) Effects of cholesterol depletion and increased lipid unsaturation on the properties of endocytic membranes. *J. Biol. Chem. 279*, 14171–14178.

(32) Mukherjee, S., Soe, T. T., and Maxfield, F. R. (1999) Endocytic sorting of lipid analogues differing solely in the chemistry of their hydrophobic tails. *J. Cell Biol. 144*, 1271–1284.

BC800530V

Cytosolic targeting of macromolecules using a pH-dependent fusogenic peptide in combination with cationic liposomes

Sachiko Kobayashi,[†] Ikuhiko Nakase,[†] Noriko Kawabata,[†] Hao-hsin Yu,[†] Silvia Pujals,[§] Miki Imanishi,[†] Ernest Giralt,[§,#] and Shiroh Futaki[†,*]

[†]Institute for Chemical Research, Kyoto University, Uji, Kyoto 611-0011, Japan

[§]Institute for Research in Biomedicine, Barcelona Science Park, Baldiri Reixac 10, 08028 Barcelona, Spain

[#]Department of Organic Chemistry, University of Barcelona, Martí i Franquès 1-11, 08028 Barcelona, Spain

Supporting Information

Peptide Synthesis and Fluorescence Labeling.

All the peptides in this report were chemically synthesized by Fmoc (9-fluorenylmethyloxycarbonyl) solid-phase peptide synthesis on Rink amide resin using the standard protocol of a Shimadzu PSSM-8 peptide synthesizer as previously reported (*15*). For the coupling system, a combination of

benzotriazole-1-yloxytrispyrrolidinophos-phonium hexafluorophosphate (PyBOP), 1-hydroxy-benzotriazole (HOBt), and 4-methylmorpholine (NMM) was employed. Treatment of the peptide resin with trifluoroacetic acid (TFA)-ethanedithiol (EDT) (95:5) for the cleavage of the peptide from the resin and deprotection of the peptides at 25 °C for 3 h and high-performance liquid chromatography (HPLC) purification of the deprotected sample gave a pure peptide. The fidelity of the products was confirmed by matrix-assisted laser desorption ionization time-of-flight mass spectrometry (MALDI-TOFMS). Amino acid sequences and characterization of the synthesized peptides: GALA peptide, WEAALAEALAEALAEHLAEALAEALEALAA-amide, MALDI-TOFMS: 3032.5 [calcd. for $(M+H)^+$: 3032.4]; scrambled GALA (sGALA) peptide, AAALHAALAAEAELLEEWLAAEEAELLAAA-amide, MALDI-TOFMS: 3032.4 [calcd. for $(M+H)^+$: 3032.4]. CG-GALA, CG-WEAALAEALAEALAEHLAEALAEALEALAA-GG-PKKKRKV-amide, MALDI-TOFMS: 3192.4 [calcd. for $(M+H)^+$: 3192.6].

For the preparation of the fluorescently labeled peptides, a γ-aminobutyryl (GABA) residue was attached to the N-terminus of the peptide resin as a spacer for

connecting with a fluorescence label, and then the N-terminus of the resin was treated with fluorescein-5-isothiocyanate (Sigma) and N-ethyldiisopropylamine (DIEA) (3 eq. each to the peptide resin) in N, N-dimethylformamide (DMF) at 25 °C for 3 h. The fluorescein labeled peptide resin was treated with TFA-EDT (95:5), purified, and identified as stated above. Amino acid sequences and characterization of the synthesized peptides: FITC-GALA peptide, FITC-NH-$(CH_2)_3$-CO-WEAALAEALAEALAEHLAEALAEALEALAA-amide, MALDI-TOFMS: 3506.9 [calcd. for $(M+H)^+$: 3507.2]; FITC-scrambled GALA (FITC-sGALA) peptide, FITC-NH-$(CH_2)_3$-CO-AAALHAALAAEAELLEEWLAAEEAELLAAA-amide, MALDI-TOFMS: 3506.8 [calcd. for $(M+H)^+$: 3506.8].

For the preparation of biotinylated-GALA peptide (biotin-GALA) and biotinylated-scrambled GALA peptide (biotin-sGALA), the GABA residue was attached to the N-terminus of the peptide resin as a space followed by the treatment with biotinamidocaproate N-hydroxysuccinimide ester (Sigma) in the presence of DIEA (3 eq. each to the peptide resin) in DMF at 25 °C for 20 h. Biotinylated-GALA peptide

having the nuclear localization signal sequence, derived from SV40 T antigen, on its C-terminus (biotin-GALA-NLS) was similarly synthesized as stated; the Gly-Gly segment was inserted here between GALA sequences and NLS sequences as a spacer. The products were purified and analyzed as stated above. Amino acid sequences and characterization of the synthesized peptides: biotinylated-GALA peptide, biotinamidocaproyl-NH-$(CH_2)_3$-CO-WEAALAEALAEALAEHLAEALAEALEALAA-amide, MALDI-TOFMS: 3373.9 [Calcd. for $(M+H)^+$: 3373.9]; biotin-GALA-NLS, biotinamidocaproyl-NH-$(CH_2)_3$-CO-WEAALAEALAEALAEHLAEALAEALEALAA-GG-PKKKRKV-amide, MALDI-TOFMS: 4352.8 [calcd. for $(M+H)^+$: 4353.1]; biotinamidocaproyl-scrambled GALA peptide (biotin-sGALA), biotinamidocaproyl-NH-$(CH_2)_3$-CO-AAALHAALAAEAELLEEWLAAEEAELLAAA-amide, MALDI-TOFMS: 3371.9 [calcd. for $(M+H)^+$: 3373.9].

The conditions and the retention time for the synthesized peptides were following: column, Cosmosil Protein R (4.6 × 150 mm); gradient: 45-85% B in A over 40 min (A = H_2O containing 0.1% (v/v) CF_3COOH, B = CH_3CN containing 0.1% (v/v)

CF_3COOH); flow, 1.0 mL/min; detection, 215 nm. GALA, 17.2 min; sGALA, 5.3 min; GC-GALA, 20.1 min; FITC-GALA, 22.8 min; FITC-sGALA, 13.2 min; biotin-GALA, 21.5 min; biotin-GALA-NLS, 13.6 min, biotin-sGALA, 10.9 min.

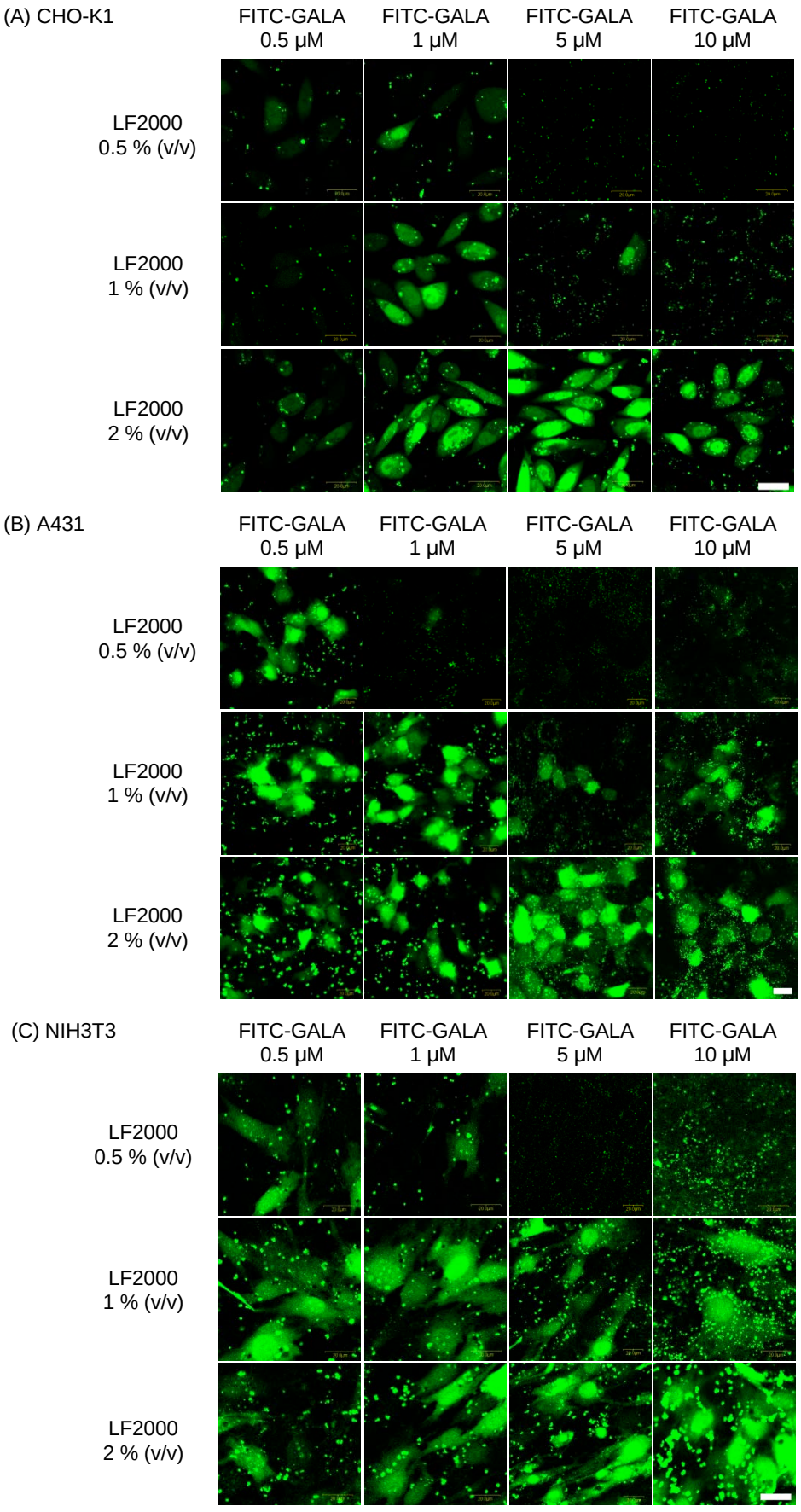

Figure S1. Effect of GALA/LF2000 ratios in cytosolic targeting of FITC as a model of membrane impermeable molecules. Cell, CHO-K1 (A), A431 (B), NIH3T3 (C). Scale bars, 20 μm. Incubation, 4 h.

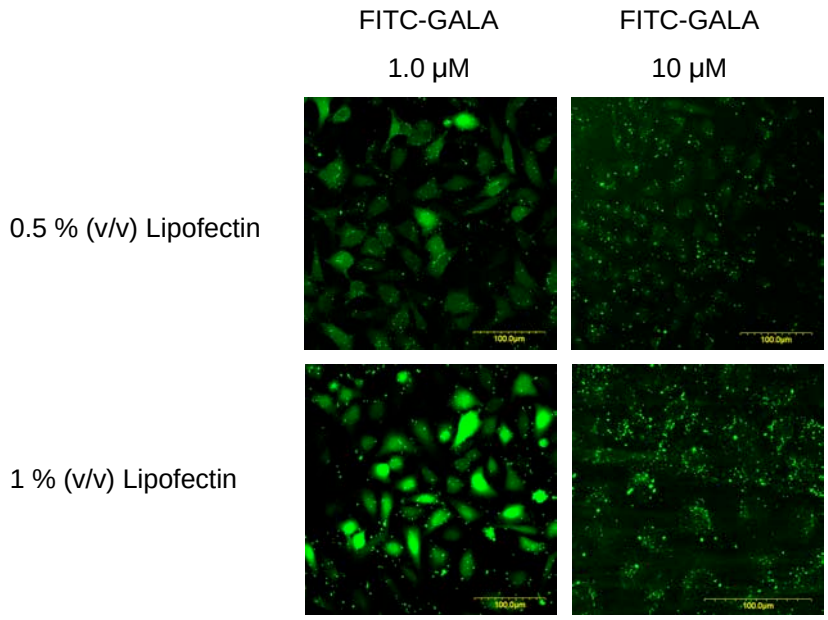

Figure S2. Effect of concentration of GALA and Lipofectin on the cellular distribution of the FITC signals. HeLa cells were treated with FITC-GALA in the presence of Lipofectin in α-MEM without containing serum for 6 h. Scale bars, 100 μm.

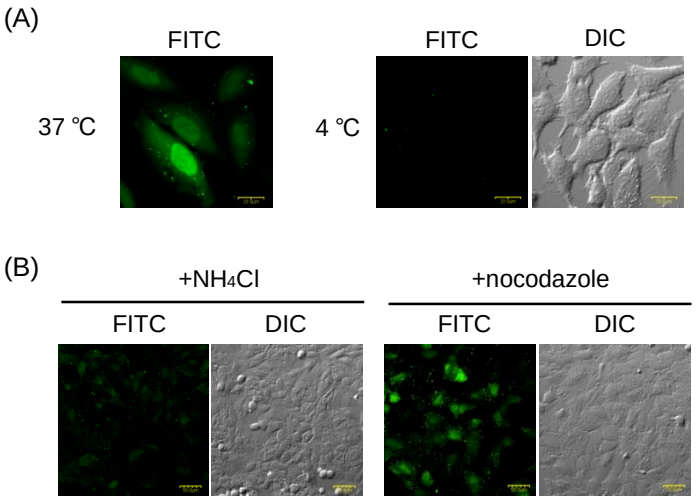

Figure S3. Involvement of endocytosis and importance of endosomal acidification for this cytosol targeting system. (A) HeLa cells were incubated with FITC-GALA (1 μM) in the presence of 1 % (v/v) LF2000 in α-MEM(+) at 37 °C or 4 °C for 2 h, respectively, and analyzed by confocal microscopy after PBS wash. Scale bars, 20 μm. (B) HeLa cells were incubated with 1 μM FITC-GALA/1%(v/v) LF2000 in the presence of NH_4Cl (50 mM) or nocodazole (20 μM) in α-MEM(+) at 37 °C for 2 h. Scale bars, 50 μm.

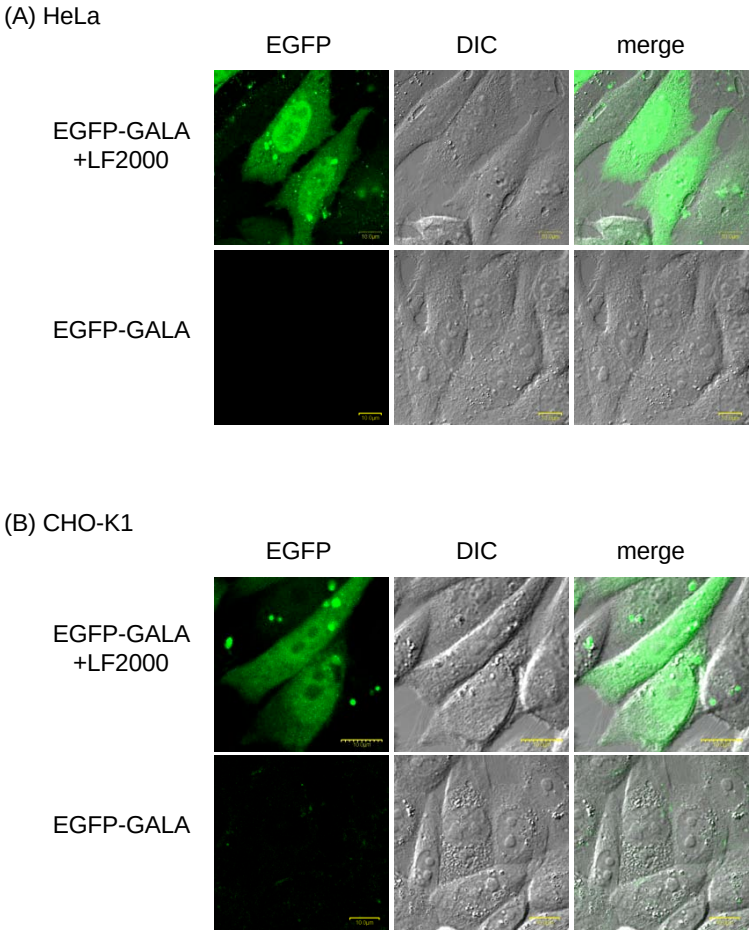

Figure S4. Application of GALA/LF2000 system to cytosolic targeting of EGFP. (A) Confocal microscopic observation of HeLa cells treated with 2 μM EGFP-GALA and 4% (v/v) LF2000 for 8 h. (B) CHO-K1 cells were treated with 0.5 μM EGFP-GALA and 1% (v/v) LF2000 for 8 h. Efficient cytosolic diffusion of EGFP-GALA was not observed in the absence of LF2000.

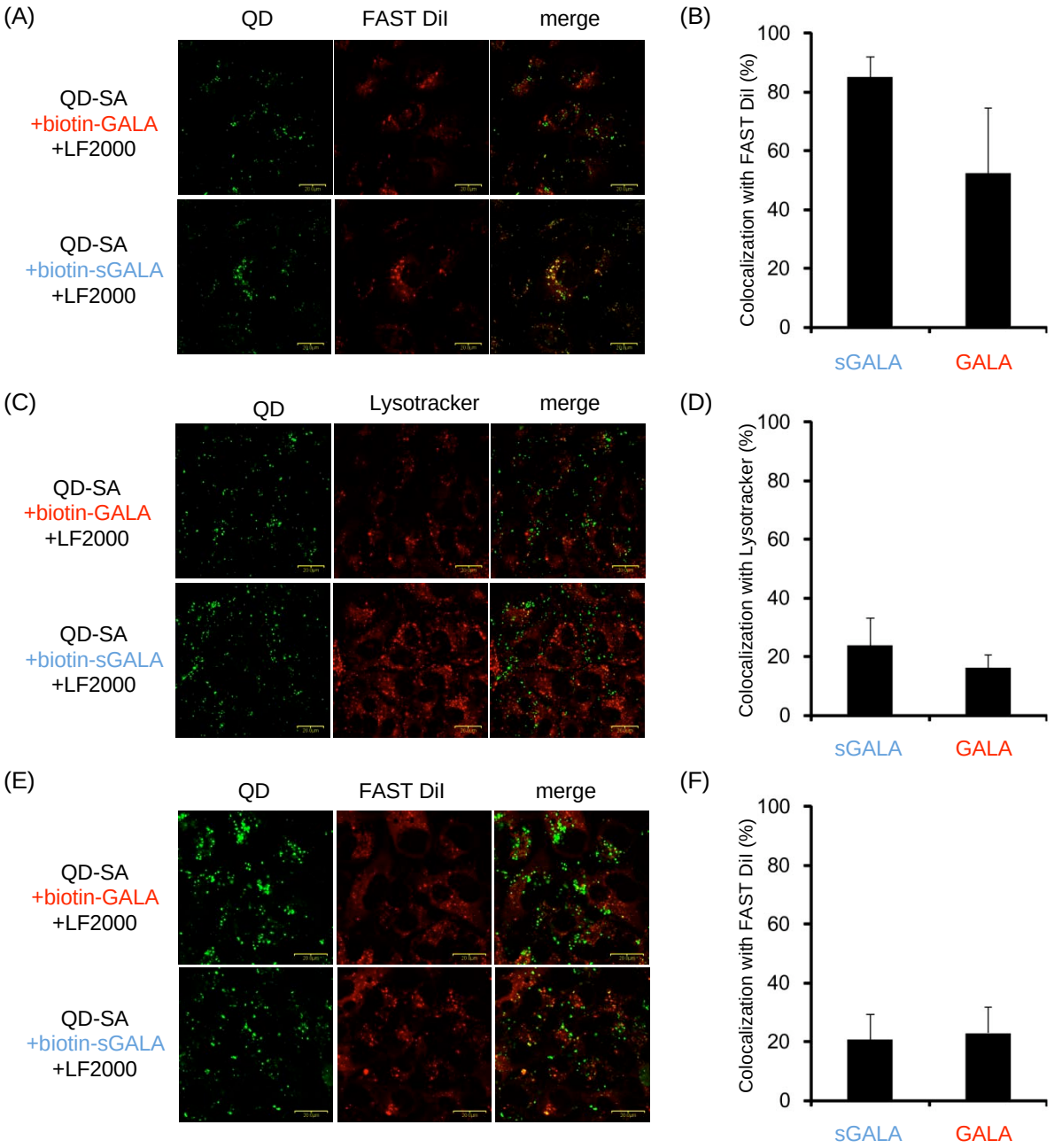

Figure S5. (A, C, E) Confocal microscopic observation of HeLa cells treated with the complex of QD-SA (2 nM), 1% (v/v) LF2000 and biotin-GALA or biotin-sGALA (1 μM each) for 6 h in the presence of FAST DiI (A) and Lysotracker (C), and 24 h in the presence of FAST DiI (E), respectively. FAST DiI was added to the medium 6 h prior to the microscopic observation. (B, D, F) Statistical analysis of colocalization of the QD-SA signal with that of FAST DiI or Lysotracker. HeLa cells were similarly treated with QD-SA/biotin-sGALA/LF2000 (left column) or QD-SA/biotin-GALA/LF2000 (right column) for 6 h (B, D) or 24 h (F). The total number of dots showing the QD-SA signal in the cells and the merged ones with the signals of Lysotraker or FAST DiI were manually counted (931, 1405, and 1210 counts for QD-SA/biotin-sGALA/LF2000-treated cells, and 1180, 632, and 883 counts for QD-SA/biotin-GALA/LF2000-treated cells, respectively). Scale bars, 20 μm. At 6 h, over 50% of QD-SA signals overlapped with those of FAST DiI, suggesting that a considerable portion of QD-SA were trapped in early endosomes (B), whereas only 20% of QD-SA localized in lysosomes (D). At 24 h, those overlapping with FAST DiI became 20%, suggesting the escape of QD-SA to cytosol or the shift to lysosomes.

Peptide-Functionalized Nanogels for Targeted siRNA Delivery

William H. Blackburn,[⊥,†,‡] Erin B. Dickerson,[⊥,‡,§,||] Michael H. Smith,[⊥,†,‡] John F. McDonald,[‡,§,||] and L. Andrew Lyon*[,†,‡]

School of Chemistry and Biochemistry, Petit Institute for Bioengineering and Bioscience, School of Biology, and Ovarian Cancer Institute, Georgia Institute of Technology, Atlanta, Georgia 30332. Received December 16, 2008; Revised Manuscript Received February 25, 2009

A major bottleneck in the development of siRNA therapies is their delivery to the desired cell type or tissue, followed by effective passage across the cell membrane with subsequent silencing of the targeted mRNA. To address this problem, we describe the synthesis of core/shell hydrogel nanoparticles (nanogels) with surface-localized peptides that specifically target ovarian carcinoma cell lines possessing high expression levels of the Eph2A receptor. These nanogels are also demonstrated to be highly effective in the noncovalent encapsulation of siRNA and enable cell-specific delivery of the oligonucleotides in serum-containing medium. Cell toxicity and viability assays reveal that the nanogel construct is nontoxic under the conditions studied, as no toxicity or decrease in cell proliferation is observed following delivery. Importantly, a preliminary investigation of gene silencing illustrates that nanogel-mediated delivery of siRNA targeted to the EGF receptor results in knockdown of that receptor. Excellent protection of siRNA during endosomal uptake and endosomal escape of the nanogels is suggested by these results since siRNA activity in the cytosol is required for gene silencing.

INTRODUCTION

Significant effort has been invested in the design of colloidal drug carriers in order to improve drug localization and bioavailability (*1*−*3*). Ideally, an actively targeted particulate drug carrier will increase the therapeutic efficacy of a drug by delivery to the diseased site, while reducing drug-associated side effects. Attainment of this goal would greatly advance treatment of diseases (e.g., cancer) where the toxic effects of therapeutics administered systemically may outweigh their benefit. To date, many types of delivery vehicles have been explored for in vitro and in vivo drug delivery applications, including inorganic nanoparticles (*4, 5*), polyelectrolyte complexes (*6*), liposomes (*7, 8*), block copolymer micelles (*9*−*11*), and polymeric nanoparticles (*12*−*15*).

A particularly compelling phenomenon from the standpoint of cancer therapy is RNA interference (RNAi). RNAi is a relatively new approach to gene silencing, which has been demonstrated effective both in vitro and in vivo (*16, 17*). This technique employs small 21−25 nucleotide long double stranded small interfering RNAs (or siRNAs) to inhibit gene expression through degradation of a targeted mRNA (*18*). Whereas the potential for therapeutic oncology applications exist where siRNA would be used to specifically shut down genes necessary for tumor growth, the lack of efficient methods for in vivo siRNA delivery prevent widespread therapeutic use (*16, 17*). In addition to the confounding issues associated with systemic, intraveneous delivery of siRNA, its polyanionic nature and high molecular weight (∼13 kDa) prevent transport across the cell membrane (*16, 17*). Thus, effective siRNA carriers must enable efficient transport through the vasculature to the tumor and then must additionally enable intracellular delivery of the cargo. A common method currently used for siRNA delivery in vitro employs cationic lipid-based carriers (*16, 17, 19*) or polyelectrolytes (*6*). These charged moieties form polyplexes with the siRNA, forming aggregates that can be taken up into the cells, thereby delivering the siRNA to the cytosol. However, these carriers can have notable drawbacks with respect to toxicity and difficulties in specific cell targeting (*16, 17, 20*), thereby giving rise to a need for alternative delivery methods. A number of new approaches have been reported that overcome some of the shortcomings of lipid-based approaches. For example, Schiffelers et al. used an RGD (Arg-Gly-Asp peptide ligand)−PEG−PEI complex to target siRNA to tumor neovasculature (*21*). Song et al. presented the use of a protamine−antibody fusion protein using the Fab fragment of HIV-1 envelope antibody for siRNA delivery (*22*). Another targeting motif has been the use of liposomes in the form of an immunoliposome complex reported by Pirollo et al. (*23*). A number of other similar approaches have been taken (*6, 20, 24*−*29*), and these siRNA carriers have enabled certain degrees of success. However, issues of toxicity, leakiness, and payload capacity still persist, especially in the context of in vivo gene silencing (*16, 17*).

Building upon many of the lessons learned from these approaches, we and others have developed drug delivery methods that employ the synthetic hydrogel nanoparticle (nanogel) (*13, 15, 30, 31*). Nanogels possess a high degree of porosity, permitting a high payload capacity, and can also be selectively surface-functionalized to enable tumor-specific targeting. Thus, we have developed straightforward, scalable syntheses of surface-functionalized, ∼100-nm diameter, core/shell nanogels composed of poly(*N*-isopropylmethacrylamide) (pNIPMAm) (*32, 33*), an amphiphilic polymer that is strongly hydrated at physiological temperature and is likely therefore to resist protein adsorption relative to more hydrophobic carriers. This polymer has also garnered interest because of its dramatic thermoresponsivity; it undergoes an entropically driven coil-to-globule (swollen-to-collapsed) transition at ∼43 °C, which may have utility for thermally triggered delivery (*32, 33*). However, in the present demonstration, this thermoresponsivity is only used to enable the synthesis of monodispersed core/

* To whom correspondence should be addressed. E-mail: lyon@gatech.edu.
† School of Chemistry and Biochemistry.
‡ Petit Institute for Bioengineering and Bioscience.
§ School of Biology.
|| Ovarian Cancer Institute.
⊥ W.H.B., E.B.D., and M.H.S. contributed equally to this work.

10.1021/bc800547c CCC: $40.75 © 2009 American Chemical Society
Published on Web 04/02/2009

Scheme 1. Noncovalent Encapsulation of siRNA in Peptide-Targeted Core/Shell Nanogels

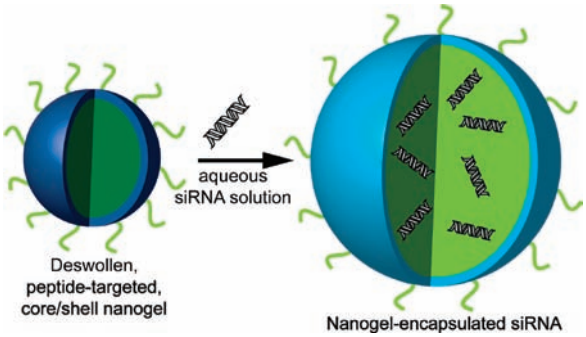

shell nanogels via precipitation polymerization, as we have discussed previously (*32*, *34*). The core/shell pNIPMAm nanogel construct used to encapsulate and deliver siRNA to ovarian cancer cells is illustrated in Scheme 1. A previously described 12 amino acid peptide (YSAYPDSVPMMS or YSA) (*35*) was coupled to the surface of ~100-nm diameter core/shell nanogels to permit cell-specific targeting and subsequent delivery of high concentrations of siRNA to the target cells. The YSA peptide mimics the ligand ephrin-A1, which binds to the erythropoietin-producing hepatocellular (Eph) A2 receptor. In addition to specific expression in neovasculature (*36*, *37*), EphA2 is highly expressed by a number of tumor cells including those derived from ovarian (*38*, *39*), prostate (*40*, *41*), breast (*42*, *43*), and colon (*44*, *45*) cancers, making it an excellent target for tumor-specific delivery. Thus, we demonstrate herein that pNIPMAm nanogels have a high loading capacity for siRNA, and that these nanogels are delivered to the cytoplasm of ovarian cancer cells via ligand−receptor binding mediated endocytosis. Importantly, overt cytotoxicity was not observed to arise from the nanocarrier, suggesting that this approach could be a highly efficacious one. In addition, delivery of siRNA to cells in culture can be performed in the presence of serum, suggesting that nanogels may be of particular advantage for in vivo delivery.

MATERIALS AND METHODS

All materials were purchased from Sigma-Aldrich (St Louis, MO) and used as received unless otherwise noted.

Nanogel Core Synthesis. Nanogel core particles were synthesized by free-radical precipitation polymerization, as previously reported (*32*). The use of thermally phase separating polymers enables the use of precipitation polymerization for the synthesis of highly monodispersed nanogels (*32*). The molar composition was 98% *N*-isopropylmethacrylamide (NIPMAm), 2% *N*,*N*′-methylenebis(acrylamide) (BIS), with a total monomer concentration of 140 mM. The solution also contained a small amount (~0.1 mM) of acrylamidofluorescein (AFA) to render the nanogels fluorescent for visualization via confocal microscopy (*30*, *32*). In a typical synthesis, 100 mL of a filtered, aqueous solution of NIPMAm, BIS, and sodium dodecyl sulfate (SDS, 8 mM total concentration) was added to the reaction flask, which was then heated to 70 °C. The solution was purged with N_2 gas and stirred vigorously until the temperature remained stable. The AFA was added, and after 10 min the reaction was initiated by the addition of a 1 mL solution of 800 mM ammonium persulfate (APS) to make the final concentration of APS in the reaction ~8 mM. The solution turned turbid, indicating successful initiation. The reaction was allowed to continue for 4 h under an N_2 blanket. After synthesis, the solution was filtered through Whatman filter paper to remove a small amount of coagulum.

Nanogel Shell Synthesis. The core nanogels described above were used as seeds for the addition of a hydrogel shell in a seeded precipitation polymerization scheme. The detailed procedure of the shell synthesis has been reported previously (*32*). Briefly, 10 mL of the core nanogel solution and 0.0577 g of SDS were first added to a three-neck round-bottom flask and heated under N_2 gas to 70 °C. A 50 mM monomer solution with molar ratios of 97.5% NIPMAm, 2% BIS, and 0.5% aminopropyl methacrylate (APMA, Polysciences, Warrington, PA) was prepared in 39.5 mL of dH_2O. The solution was added to the three-neck round-bottom flask, and the temperature was stabilized at 70 °C while continuously stirring. The reaction was initiated by a 0.5 mL aliquot of 0.05 M APS. The reaction proceeded for 4 h under N_2 gas. Following the synthesis, the solution was filtered through Whatman filter paper, and the nanogels were purified by centrifugation followed by resuspension in dH_2O.

Nanogel Characterization. Multiangle laser light scattering (MALLS) (Wyatt Technology Corporation, Santa Barbara, CA) detection following asymmetric field flow fractionation (AFFF) was used to determine the distribution of *z*-average radii (R_z) for all nanogels. For all separations, a cross-flow of 0.30 mL/min was used with a channel flow of 1.0 mL/min. The MALLS detector is equipped with a Peltier device to maintain a flow cell temperature of 25 °C and collects scattered light from 16 different fixed angles to determine the R_z of the nanogels. By measuring R_z as a function of elution time, we constructed a chromatogram that permits the determination of the weight fraction of nanogels as a function of radius, thereby providing a sample polydispersity. ASTRA 5.1.5.0 software was used to determine R_z values using the Debye fit method. The core/shell nanogels synthesized using the methods described above were determined to have R_z values of ~54 nm with size polydispersities of <10%, as described previously (*32*); representative AFFF/MALLS data are shown in Supporting Information.

Characterization of the refractive increment (d*n*/d*c*) of nanogels was performed to determine particle molecular weight by static light scattering. Differential refractive index analysis (dRI, OptiLab rEX, Wyatt Technologies, Inc.) was performed in batch mode. To ensure accurate data, the refractive index was calibrated prior to each measurement using sodium chloride concentrations ranging from 0.1 mg/mL to 15.0 mg/mL. All nanogel dilutions were prepared in dust-free vials, which were rinsed sequentially with deionized water, absolute ethanol, and HPLC-grade acetone. Nanogels were resuspended in distilled, deionized water over a concentration range from 2.5×10^{-6} g/mL to 3.75×10^{-4} g/mL. The use of MALLS in conjunction with the rEX differential refractometer permitted the measurement of the *z*-average molecular mass (M_z) from the determined d*n*/d*c* values and the angle-dependent light scattering data.

YSA Synthesis. The YSA peptide (YSAYPDSVPMMSC) was synthesized using standard Fmoc chemistry as described previously (*46*). Peptide synthesis was carried out by K. D. Clark, University of Georgia. Following synthesis, the peptide was cleaved from the resin and deprotected for 4 h in reagent K after air-drying. The peptide was purified using a series of 5 mL injections onto a preparatory HPLC column (10-m; particle size, 21.2 mm 25 cm, Jupiter C18; Phenomenex Inc., Torrance, CA) using HPLC-grade H_2O and a linear gradient of acetonitrile (0−70 min, 10−80%) at 5 mL per min. Both the acetonitrile and H_2O contained 0.05% trifluoroacetic acid. The desired peak was identified by matrix-assisted laser desorption ionization time-of-flight mass spectrometry, and the peaks from multiple runs were pooled, lyophilized, and stored at 4 °C in solid form. A scrambled form (SCR) of the YSA peptide (DYPSMAMYSPSVC) was also synthesized via this method for use as a control. On other occasions, the YSA and SCR peptides were purchased from GenScript Corp (Piscataway, NJ).

Peptide Conjugation. In this study we produced a maleimide-functionalized nanogel through the EDC coupling of ε-maleimidocaproic acid (EMCA) to the primary amines in the shell of the nanoparticle. As described in the nanogel shell synthesis, primary amines were introduced through the copolymerization of APMA (0.5% molar ratio). Given that APMA is efficiently incorporated at these low molar ratios, we can estimate the amine equivalents available for bioconjugation ($\sim 2.2 \times 10^{-6}$ amines per 88.3 mg of lyophilized particles). From this estimate, peptide coupling was performed by introducing YSA peptide in a 1:1 molar ratio with amine (YSA molecular weight = 1450.66 g/mol). The YSA peptide was then conjugated to the nanogels via maleimide coupling to the cysteine residue on the C-terminal end of the peptides.

First, 88.3 mg of nanogels ($\sim 2.2 \times 10^{-6}$ amine equivalents) was resuspended in 35.0 mL of pH 6.0 MES buffer and allowed to shake for 2 h. A second solution was prepared where 4.4×10^{-6} mol (0.68 mg) of 1-ethyl-3-methyl-(3-dimethylaminopropyl)carbodiimide (EDC, Pierce, Rockford, IL), 4.4×10^{-6} mol (0.96 mg) *N*-hydroxysulfosuccinimide (NHSS), and 2.2×10^{-6} mol (0.46 mg) of EMCA were dissolved in 3.0 mL of pH 6.0 MES buffer. This solution was reacted for 30 min at room temperature to activate the EMCA acid groups, which permits amide coupling to take place between the EMCA acid groups and the amines on the nanogel surface. This activated EMCA solution was then added to the nanogel solution and reacted for 2 h on a shaker table. The nanogels were centrifuged three times to remove any unreacted material, with resuspension in pH 6.0 MES buffer following each centrifugation. Finally, 3.2 mg of the appropriate peptide was added to the activated nanogels and reacted overnight. Peptide-functionalized nanogels were purified by centrifugation and resuspended in distilled, deionized water.

The number of bioconjugated YSA targeting peptides per particle was estimated by considering the number of primary amines available for conjugation and the number density of nanogels used during bioconjugation (as measured by static light scattering). Through differential refractometry, the nanogel refractive increment was determined to be 0.176 ± 0.002 mL/g. Measurement of *z*-average molecular weight through multi-angle static light scattering provided the *z*-average mass of nonconjugated particles, $M_z = 2.19 \times 10^7$ g/mol (1° Debye fitting, 0.1% fit error). Thus, a total mass of 88.3 mg of lyophilized particles used during conjugation is equivalent to 2.43×10^{15} particles. Assuming a 50% peptide conjugation efficiency (*47*) and 2.2×10^{-6} amine equivalents available for bioconjugation, we conservatively estimate a peptide density of ~225 YSA peptides/particle.

In Vitro siRNA Encapsulation and Release. Our group employs a "breathing-in" method for the encapsulation of various macromolecules within nanogels. In a typical method, lyophilized nanogels are resuspended in an aqueous solution containing the macromolecule to be loaded. Importantly, this is done using a loading solution volume that is almost completely imbibed by the swelling nanogels. In this fashion, the hydrogel network imbibes the payload with high efficiency and without relying on simple equilibrium partitioning to determine the maximum loading level. To determine the rate of siRNA release from nanogels loaded in this fashion, a mixture of oligonucleotide was prepared containing 0.250 mL of 20 μM siGLO red transfection indicator and 1.00 mL of 20 μM siGENOME Lamin A/C control siRNA (Dharmacon, Lafayette, CO). Particles were resuspended in this mixture at a concentration of 4 mg per 250 μL siRNA solution. This concentration of particles is near the solubility limit for the nanogels in PBS, ensuring a high degree of solvent and solute uptake into the hydrogel network. The particles were allowed to resuspend for 12 h at room temperature while shaking.

The encapsulation efficiency was determined via ultracentrifugation of the nanogel loading solution and measurement of supernatant siRNA concentration by UV−vis spectroscopy (Shimadzu UV-1601). The moles of siRNA in the loading solution ($m_{\text{siRNA,loading}}$) and in the supernatant ($m_{\text{siRNA,supernatant}}$) were determined via interpolation from a separately constructed standard curve of absorbance vs concentration ($R^2 > 0.99$). The encapsulation efficiency (EE) of the system could then be calculated through analysis of the amount of siRNA in the loading solution and the remaining moles of siRNA in the supernatant after nanogel swelling was complete, as illustrated by eq 1 and in similar encapsulation experiments (*48*).

$$\text{EE} = \frac{m_{\text{siRNA,loading}} - m_{\text{siRNA,supernatant}}}{m_{\text{siRNA,loading}}} \times 100 \qquad (1)$$

The release of solutes from nanogels was performed in 10% serum to simulate physiological conditions. Release experiments were performed by dispersing 200 μL of loaded nanogels in 2.20 mL of 0.01 M phosphate-buffered saline containing 10% fetal bovine serum (equilibrated at 37 °C) in 3.2 mL of polycarbonate centrifuge tubes (Beckman Coulter, Fullerton, CA). The nanogel suspension was allowed to incubate at 37 °C while being shaken. At specific time points, the tubes were centrifuged for 90 min at 687 000*g* (at 37 °C), and an aliquot of supernatant (0.75 mL) was removed for UV−vis analysis. This volume was replaced with fresh buffer. Upon centrifugation, the gel pellet had a homogenously distributed bright pink color, indicating significant retention of siRNA throughout the experiment. The cumulative siRNA released was calculated by calculating the total moles detected in the supernatant as a function of time, as described in eq 2.

$$\text{cumulative siRNA released} = \frac{m_{\text{TOTALsiRNA,supernatant}}}{m_{\text{siRNA,loading}}} \times 100 \qquad (2)$$

All release studies were performed in triplicate for statistical analysis, using identical nanogel loading and release conditions.

Zeta-Potential Determination. Excluding the 0.5 mol% APMA copolymerized into the shell of our nanogel particles, the nanogels are composed of largely nonionic monomers. To confirm their suspected electroneutrality, which should be critical for reducing nonspecific cell and protein interactions, we measured the zeta-potential of both YSA-conjugated and nonconjugated core/shell nanogels (Zeta-Sizer Nano, Malvern, U.K.). All nanoparticles used in this investigation demonstrated zeta-potential values $< +0.300$ mV, suggesting that they are only weakly charged and should therefore not interact strongly with serum proteins or cell surfaces via Coulombic forces.

Cell Culture. Hey cells were provided by Gordon B. Mills, Department of Systems Biology, the University of Texas, M. D. Anderson Cancer Center. Hey cells were cultured in RPMI 1640 (Mediatech, Manassas, VA) supplemented with 10% v/v heat-inactivated fetal calf serum (Invitrogen), 2 mM L-glutamine (Mediatech), 10 mM HEPES buffer (Mediatech), penicillin (100 U/mL), and streptomycin (100 μg/mL). The BG-1 cell line was provided by Julie M. Hall and Kenneth S. Korach, Receptor Biology Section, Laboratory of Reproductive and Developmental Toxicology, National Institute of Environmental Health Sciences, NIH, Division of Intramural Research, Environmental Disease and Medicine Program, Research Triangle Park, NC. BG-1 cells were propagated in DMEM:F12/50:50 (Mediatech) supplemented with 10% v/v heat-inactivated fetal calf serum, penicillin, and streptomycin.

siRNA Encapsulation for Cell Studies. Using the "breathing-in" method for encapsulation (as described above), dried

nanogels were reswollen in the presence of the siRNA, thereby imbibing the solute within the hydrogel network. In a typical procedure for in vitro cell delivery, a 20 μM solution (250 μL) of a fluorescent siRNA transfection indicator, siGLO (Dharmacon), or EGFR siRNA (Dharmacon, Lafayette, CO) was prepared in phosphate-buffered saline (PBS). Lyophilized nanogels were dissolved in the siRNA solution at a concentration of 4 mg in 250 μL and allowed to shake overnight at room temperature. Importantly, this nanogel concentration results in nearly all of the solvent being taken up by the nanogels. This volume-filling approach ensures a maximal uptake of siRNA within the nanogels. After being shaken, the nanogels were centrifuged to remove any free siRNA and resuspended in PBS. A standard curve for increasing concentrations of siRNA was made by measuring the absorbance at 260 nm using a Shimadzu UV 1601 spectrophotometer. After siRNA was encapsulated in the nanogels, they were centrifuged, and the absorbance of the supernatant was measured to determine the amount of incorporated siRNA.

Cell Transfection Using Nanogels. Hey or BG-1 cells were plated onto an eight-well chamber slide (5×10^3 cells/well) and the cells allowed to adhere overnight at 37 °C in a 5% CO_2 atmosphere. After the wells were washed with PBS and the media were replaced, siGLO-loaded/YSA-conjugated nanogels, unloaded YSA-conjugated nanogels, pNIPMAm nanogels, or siGLO only were added to wells. Cells were incubated in each case for 4 h. In experiments where preincubation of ephrin-A1 was used to initiate internalization and degradation of EphA2, ephrin-A1 was added to the media at a final concentration of the ligand of 2 μg/mL. After incubation, the cells were washed with PBS, and the medium replaced. For fixation prior to confocal imaging, the cells were incubated with 2% (v/v) paraformaldehyde for 30 min.

Immunoblotting. Hey cells were plated into six-well plates (5×10^5/well) and allowed to adhere overnight at 37 °C, 5% CO_2. The cells were lysed with 100 μL of lysis buffer (50 mM Tris-HCl, pH 7.5, 150 mM NaCl, 2 mM EDTA (Fisher), 2 mM EGTA (Fisher), 1 mM sodium orthovanadate, 2.5 mM sodium pyrophosphate, 1 mM β-gycerol phosphate, 1 mM phenylmethanesulfonyl fluoride, 10 μg/mL aprotinin, 10 μg/mL leupeptin, 1% Triton X-100, and 5% glycerol), and the cell lysates were sonicated four times for 5 s each. The lysates were cleared by centrifugation at 11 000*g* rcf for 15 min at 4 °C. Cell lysates were prepared for analysis by the addition of an equal volume of Laemmli 2X sample buffer. The samples were heated to 95 °C for 5 min to denature the proteins. The proteins were separated on a 10% SDS-PAGE gel and transferred onto nitrocellulose. The blots were blocked with either 5% nonfat dry milk (NFDM) or 5% bovine serum albumin (BSA) in 10 mM Tris-buffered saline, pH 7.5, plus 1% Tween 20 (TBST, BioRad), for 1 h at room temperature. The blots were probed with anti-EGFR antibody (Cell Signaling, Danvers, MA; cat. no. 4405) or with a β-actin antibody (Millipore, Billerica, MA; Mab1501) diluted in 5% NFDM or 5% BSA overnight, with shaking at 4 °C. For EphA2 detection, the blots were probed with an anti-EphA2 polyclonal antibody (Santa Cruz Biotechnology, Santa Cruz, CA; sc-294). The blots were washed three times with TBST and probed with goat antirabbit IgG (Santa Cruz, sc-2004) or with goat antimouse IgG (Santa Cruz, sc-2005) linked to horseradish peroxidase (HRP). Bands were visualized on film (Pierce) using the ECL reagent, SuperSignal West Pico (Pierce).

Confocal Microscopy. A Zeiss LSM510 confocal microscope was used to take cell images. Cells were incubated with nanogels for 4 h. After 4 h, the cells were washed and then fixed on the slide. An Ar^+ laser was used to excite the AFA-labeled nanogels, whereas a HeNe laser was used to excite the fluorescently labeled siGLO. LSM510 software was used to view the images.

Flow Cytometry. Hey cells were plated at 2.5×10^5 cells/well in a 12-well, cell culture plate. Cells were allowed to adhere overnight in an incubator at 37 °C in a 5% CO_2 atmosphere. Cells were washed, and fresh medium was added containing YSA-pNIPMAm or SCR-pNIPMAm nanogels at a concentration of 0.8 mg/mL and incubated for 4 h. Following incubation, the cells were washed with PBS and removed from the plate by trypsin−EDTA treatment. The cells were washed with PBS and fixed with 2% (v/v) paraformaldehyde. Cells were analyzed using a LSR Flow Cytometer (BD Biosciences). Data analysis was carried out using FlowJo software.

Toxicity Studies. *Trypan Blue Exclusion Assay.* Hey cells were plated onto an eight-well chamber slide (1×10^4 cells/well) and allowed to adhere overnight at 37 °C and 5% CO_2. The medium was removed, the wells were washed with PBS, and the medium was replaced. PNIPMAm nanogels, YSA-conjugated nanogels, and SCR-conjugated nanogels were added to cells and incubated for 72 h. Untreated cells were used as controls. After 72 h, the cells washed with PBS, and a 1:1 solution of trypan blue was added to each well. After 1 min, the trypan blue was removed, the cells were washed with PBS, fixed with 2% (v/v) paraformaldehyde, and air-dried. Each well was then viewed via bright field microscopy to determine the number of stained (dead) versus unstained cells. Five fields were viewed for each treatment. Representative images are shown in Supporting Information.

Tox 8 Assay. Hey cells were plated onto 96-well plates (1×10^4 cells/well) and allowed to adhere overnight at 37 °C and 5% CO_2. The media was removed, and the cells were washed with PBS followed by replacement of the medium. Cells incubated with EGFR siRNA-loaded YSA-labeled nanogels, unloaded YSA-labeled pNIPMAm nanogels, unlabeled pNIPMAm, or YSA peptide alone were tested using this assay. The cells were incubated under all conditions for 4 h. The cells were then washed with PBS, the medium was replaced, and the cells were incubated for an additional 72 h in medium. The Tox 8 reagent (Sigma) was added to the cells according to the manufacturer's instructions. The fluorescence at 590 nm was read after 1 h and the extent of cellular viability/proliferation determined.

RESULTS AND DISCUSSION

The nanogels described in this contribution were developed around two main design criteria, as depicted in Scheme 1. For this application, both peptide-based targeting of ovarian cancer and efficient encapsulation and delivery of RNA inhibitors (RNAi's) are required. The core/shell nanogels synthesized using the methods described above were determined to have R_z values of ~54 nm with size polydispersities of <10%, as described previously (*32*). Representative AFFF/MALLS chromatograms for both the core and core/shell nanogels are shown in Supporting Information. To determine the time scale for retention of siRNA within the pNIPMAm nanogels, we investigated siRNA leakage using simulated physiological conditions. As described above, nanogels were loaded using a model mixture of siRNA, containing both the siGLO red transfection indicator and the siGENOME Lamin control. The nanogel was observed to encapsulate the siRNA with high efficiency (93 ± 1%), which is equivalent to a loading level of 1.6 wt% or 16 μg siRNA/mg of nanogels. As shown in Figure 1, only ~33% of the siRNA is observed to leak from the nanogels within the first 12 h (67% retained). Indeed, this approximate level of retention persists out to 35 h, suggesting very efficient entrapment of the siRNA within the nanogel network. Retention of this magnitude is promising for intravenous oligonucleotide

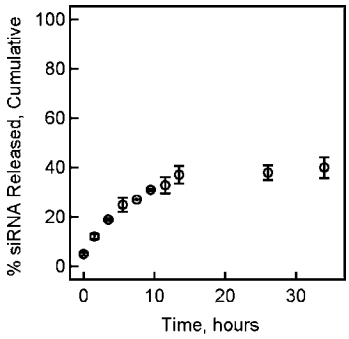

Figure 1. siRNA release profile from nanogels at 37 °C in PBS containing 10% fetal bovine serum. The error bars represent ±1 standard deviation about the mean value ($n = 3$).

delivery given previously determined time scales (~6 h) for extravasation via the enhanced permeability and retention effect (*49*).

To establish the efficacy of targeting in vitro, we determined the uptake of nanogels by two ovarian cancer cell lines, Hey and BG-1. We previously demonstrated high expression of EphA2 by Hey cells and low expression of the receptor by the BG-1 cell line (see Supporting Information) (*50*). Because of these differences in EphA2 expression, we expected to see higher levels of nanogel uptake via receptor-mediated endocytosis with Hey cells as compared to BG-1 cells. Furthermore, we expected that the degree of siRNA delivery to those cells would be dependent on the cell type and the presence of the peptide ligand. To load siRNA into the nanocarrier, lyophilized nanogels were loaded with siGLO (a fluorescently labeled siRNA delivery tracker) by reswelling them in a concentrated solution of the siRNA, as described above. To obtain a relative concentration of the siGLO taken up by the nanogels, absorbance measurements were compared to a standard curve of siGLO in solution ($R^2 > 0.99$). We determined in a series of three trials that 80−95% (by mass) of the siGLO was incorporated into the nanogels by this method, in agreement with the loading levels calculated in the release kinetics experiment described above.

Following loading with siGLO, nanogels were incubated with either Hey (high EphA2 expression) or BG-1 (low EphA2 expression) cells in order to compare the levels of targeted uptake by ovarian cancer cells. Uptake of the nanogels into the cells was followed using a fluorescent tag (AFA) incorporated into the nanogel core as well as by the fluorescence of the siGLO. In previous studies, we determined that high levels of nanogel uptake by cells occurred after 4 h (data not shown). As a result, cells were incubated for 4 h with siGLO-loaded/YSA-conjugated nanogels to monitor specific targeting to EphA2. Unloaded YSA-conjugated nanogels, nontargeted pNIPMAm nanogels, and siGLO only were used as controls, with identical 4-h incubation times. In all experiments described in this manuscript, we maintained a constant nanogel/cell ratio of 1 mg nanogels/5×10^5 cells. For siRNA-loaded nanogels, this corresponds to 16.6 μg siRNA/5×10^5 cells. After incubation, the cells were washed and the slides fixed for confocal microscopy imaging. Figure 2a shows that Hey cells targeted with YSA-conjugated nanogels have high levels of nanogel uptake as indicated by the presence of green fluorescence. At this time point, siGLO was retained at high levels within the internalized nanogels as indicated by the cell-localized red fluorescence. Merging of the two fluorescence channels showed strong overlap, further indicating delivery of the siGLO by the nanogels into the Hey cells. Hey cells incubated with YSA-targeted but unloaded nanogels showed strong green fluorescence, indicating cell uptake. A small amount of nontargeted uptake was observed for nanogels lacking the YSA peptide. Note that it was extremely difficult to find evidence of nonspecific uptake, and the fluorescence shown in the figure represents the appearance of the rare uptake event observed and does not represent the overall fluorescence from the entire population of cells. When Hey cells were incubated with siGLO alone, no cell-localized red fluorescence was detected; this is expected since RNA does not easily permeate the cell membrane in the absence of a carrier vehicle (*16, 17*).

Targeting experiments were also performed using low EphA2 expressing BG-1 cells (Figure 2b). Decreased levels of green fluorescence were observed in BG-1 cells when compared to the fluorescence observed in the Hey cell cultures. The lower amount of nanogel uptake by the BG-1 cells was most likely because of the reduced EphA2 receptor expression; we have demonstrated a ~2.5-fold difference in EphA2 expression levels between these two cell lines (Supporting Information). Control studies using nontargeted pNIPMAm nanogels or siGLO only showed no fluorescence in either the green or red fluorescent channels. These results indicate that the YSA peptide imparts targeting properties to the nanogels in the case of both the high (Hey) and low (BG-1) EphA2 expressing cells, and that the amount of nanogel uptake was dependent upon the level of EphA2 receptor expression. These results also indicate that nonspecific or nontargeted uptake of nanogels by cultured cells is low, and that the siRNA is unable to penetrate the cell membrane in the absence of a carrier vehicle. Together, these initial results illustrate the promise of the targeted nanogel construct for targeted delivery of oligonucleotide cargo.

To further establish the mechanism of nanogel targeting and uptake, we took advantage of the known receptor internalization properties of the EphA2 receptor. Specifically, it has been shown that binding of ephrin-A1, a ligand for EphA2, to EphA2 receptor causes internalization and degradation of the receptor−ligand complex (*51*). Figure 3 shows the results of studies wherein this receptor recycling process was used to establish the nanogel target by preincubating Hey cells with ephrin-A1 before YSA-targeted nanogel incubation. We hypothesized that if uptake of nanogels is EphA2 receptor-mediated, YSA-targeted uptake after cell exposure to ephrin-A1 should be reduced, as the EphA2 receptor will be internalized and less available for binding to the nanogels. Hey cells were incubated overnight in an eight-well chamber slide. Two μg/mL of ephrin-A1 was added, and the cells were incubated for 1 h at 37 °C. After ephrin-A1 incubation, siGLO-loaded/YSA-conjugated nanogels were added to both ephrin-A1 and control (PBS) treated wells. The cells were incubated for 4 h, washed, and processed for imaging. Figure 3 shows the nanogel uptake in Hey cells preincubated with ephrin-A1. Whereas these cells (top three panels) show some uptake of nanogels and encapsulated siGLO, the amount of uptake is greatly diminished compared with untreated cells (lower three panels). These results suggest that YSA-conjugated uptake by Hey cells is conducted to a large extent through EphA2; however, a small amount of uptake may occur through nonspecific mechanisms or via binding of YSA to other Eph receptors (*35*). This is not surprising, given the fact that ephrin and various small molecule ephrin mimics display binding affinities for multiple receptors of the Eph family (*52, 53*). Flow cytometry was also used to establish the EphA2-associated binding of the peptide-targeted nanogels. In this case, a scrambled (SCR) peptide sequence (DYPSMAMYSPSVC) possessing the same amino acid composition of the YSA peptide was tethered to the nanogels. The resultant nanogels should therefore possess the same physicochemical surface properties as the YSA-labeled nanogels but should not specifically bind to the EphA2 receptor. Figure 4 shows the results of these studies, where cells incubated with YSA-labeled

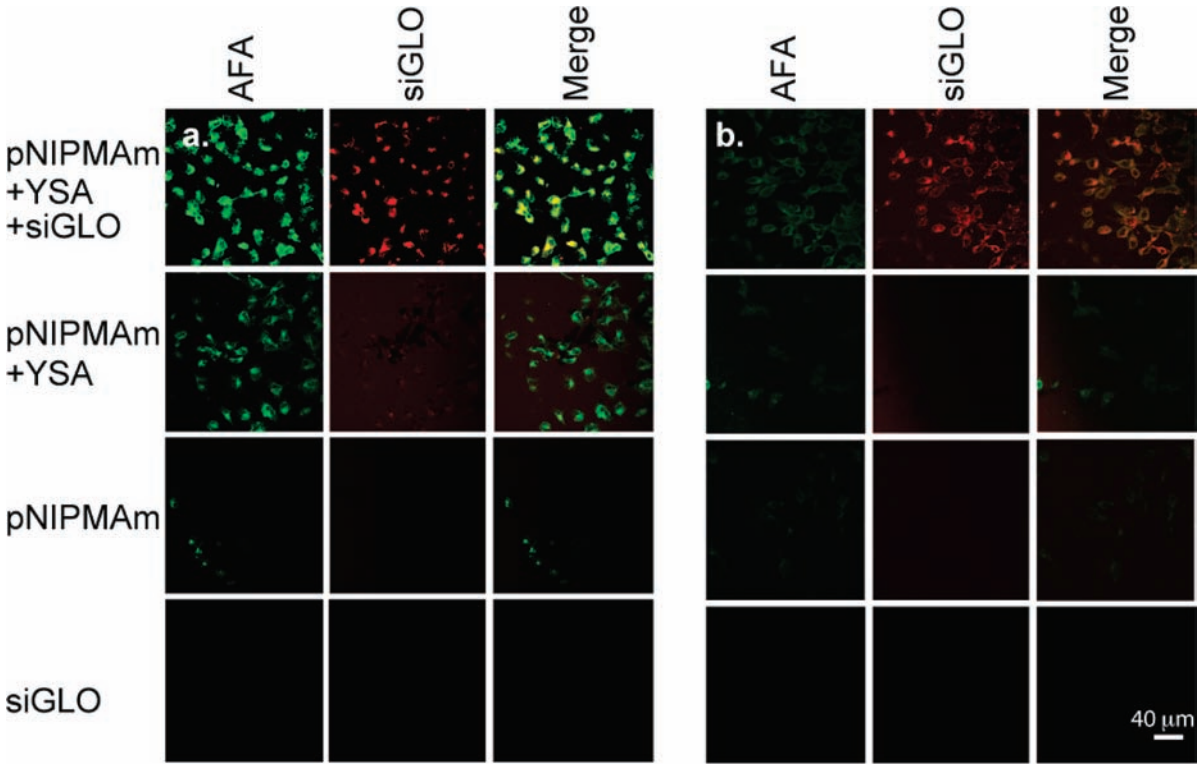

Figure 2. Confocal microscopy images of (a) Hey cells and (b) BG-1 cells following exposure to siGLO-loaded/YSA-conjugated pNIPAMAm nanogels, YSA-nanogels alone, unlabeled nanogels, and siGLO alone. The AFA and siGLO fluorescence channels are shown individually, along with a merge of the two channels. Scale bar = 40 μm.

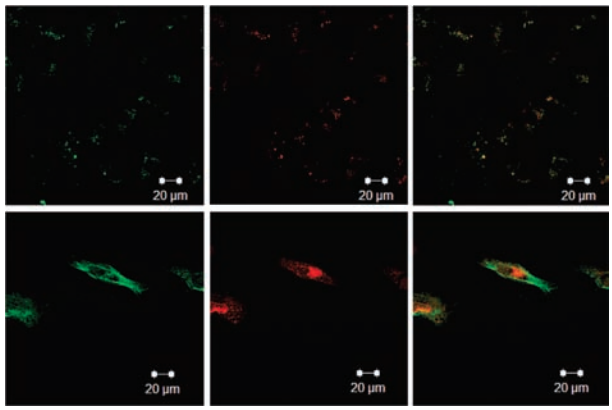

Figure 3. Confocal microscopy images of Hey cells (top) following exposure to siGLO-loaded/YSA-conjugated nanogels after 1 h ephrin-A1 incubation, and (bottom) following exposure to siGLO-loaded/YSA-conjugated nanogels alone. The fluorescence channels shown are as in Figure 2. Scale bar = 20 μm.

nanogels display ~10-fold greater fluorescence relative to those incubated with SCR-labeled nanogels. Furthermore, the fluorescence signal associated with cells incubated with SCR-labeled nanogels is only slightly greater than the cell autofluorescence background signal.

The effect of nanogels on tumor cell toxicity and proliferation was examined using two cell viability assays. For the trypan blue exclusion assay, Hey cells were incubated with pNIPMAm nanogels, YSA-conjugated nanogels, or SCR-conjugated nanogels for 72 h. The cells were then washed with PBS, and trypan blue was added to the cells. Five fields were observed via microscopy for each treatment group. Blue cells, indicating dead cells, were not observed in any of the fields examined for any of the treatment groups. Representative images are shown in the Supporting Information. To more precisely establish any negative effects associated with nanogel-based delivery, we used the Tox 8 viability proliferation assay. Hey cells were incubated in 96-well plates overnight, and nanogels were delivered and removed via the usual method. In the gene silencing data shown below, we chose siRNA targeting epidermal growth factor receptor (EGFR); knockdown of this receptor is nonlethal but has clinical relevance in the treatment of drug resistant ovarian carcinomas (*54*). This siRNA was therefore used in these toxicity studies as well. Again, we maintained a ratio of 1 mg nanogels/5 $\times$ 10^5 cells for all samples. For the EGFR siRNA-loaded nanogels, this corresponds to 16.6 μg siRNA/5 $\times$ 10^5 cells. Wells were washed with PBS, and 100 μL of cell culture medium was added to the wells. After 72 h, Tox 8 was added to the cells according to the manufacturer's instructions, and the cell viability was determined spectrophotometrically. This analysis (Figure 5) revealed no significant difference for any treatment when compared with control (untreated) cells, although exposure to nontargeted nanogels and siRNA-containing nanogels showed slight decreases in viability; the origin of this effect is currently under investigation. These results indicate that treatment of Hey cells with targeted nanogels does not greatly inhibit cell proliferation, indicating limited toxicity of the nanogels under these conditions.

These promising preliminary studies clearly illustrate the efficacy of peptide-targeted delivery of siRNA cargos via nanogel carriers. The lack of toxicity observed is of particular interest, given the high toxicity observed for some cationic lipid-based siRNA targeting methods, which limits the maximum doses that can be delivered, and also compromises the potential for in vivo delivery. In the present studies, a ratio of 16 μg siRNA or 1 mg nanogels/5 $\times$ 10^5 cells was used throughout without significant toxicity being observed. These concentrations are somewhat higher than those suggested for common commercial regents such as RNAiFect (Qiagen) or DharmaFECT

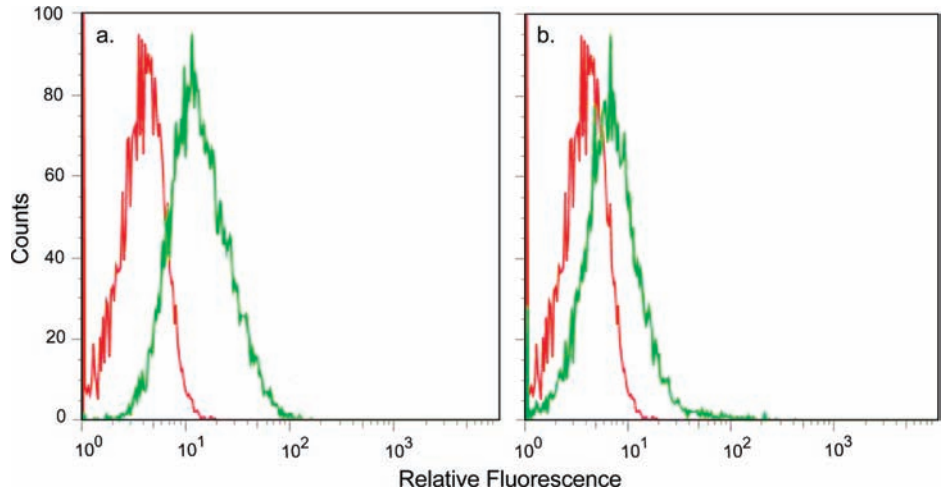

Figure 4. Flow cytometry data comparing (a) cell autofluorescence (red) vs cells incubated with YSA-pNIPMAm nanogels (green) and (b) cell autofluorescence (red) vs cells incubated with SCR-pNIPMAm nanogels (green). The differential uptake between the YSA- and SCR-labeled nanogels indicates the Eph2A receptor-specific binding and uptake pathway.

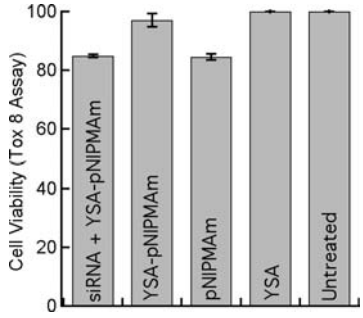

Figure 5. Cell viability as determined with a Tox 8 assay for untreated Hey cells and Hey cells following a 4 h incubation with EGFR siRNA-loaded YSA-labeled nanogels, YSA-labeled pNIPMAm nanogels, unlabeled pNIPMAm, or YSA peptide alone. Error bars represent ±1 standard deviation about the average value ($n = 3$).

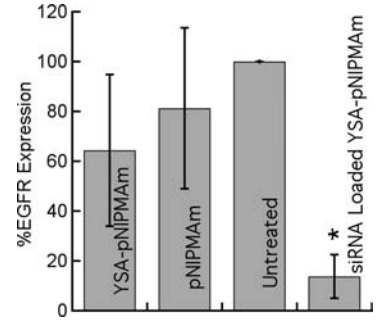

Figure 6. EGFR expression, as determined by immunoblot, in Hey cells following a 4 h incubation with either unloaded YSA-nanogels, unloaded nontargeted nanogels, or siRNA loaded YSA-nanogels. Untreated cells were set at 100% expression. All cells were harvested 48 h after removal of the nanogels. Error bars represent ±1 standard deviation about the average value ($n = 3$, $^*p < 0.01$ relative to untreated sample).

(Dharmacon), suggesting that the nanogel approach is capable of delivering siRNA amounts at or above those achievable by optimized commercial reagents. Another complicating factor in current methodologies is the frequent need for cellular delivery under serum free conditions; serum lipids and proteins compromise the stability of many liposomal formulations, making their efficacy significantly lower. In the studies described herein, we have illustrated that delivery of siGLO is excellent in serum-containing medium, further establishing the promise of this construct. As a final preliminary test of the efficacy of the approach, we performed a limited investigation of siRNA-based silencing. Clearly, any delivery approach must deliver *functional* siRNA to the cell interior in order for it to be truly useful. If the nanogel carrier were unable to protect the cargo against degradation in the endosomal or lysosomal compartments, or if the nanogels were unable to escape from endosomes in order to deliver the siRNA to the cytosol, the amount of RNAi would be very low. Thus, we have undertaken a preliminary study of gene silencing to illustrate a minimal requirement for siRNA delivery: the functional silencing of a target mRNA.

As described above, we chose siRNA targeting EGFR; knockdown of this receptor is nonlethal but has clinical relevance in the treatment of drug resistant ovarian carcinomas (*54*). To determine if we could effectively knockdown EGFR in vitro, EGFR siRNA was encapsulated at a concentration of 16.6 μg of EGFR siRNA/mg of nanogels, using the loading technique described above. Nanogels were then added to Hey cells (1 mg of nanogels or 16.6 μg siRNA/5 $\times$ 10^5 cells) and incubated at 37 °C for 4 h. The unincorporated nanogels were then removed by washing the cells, and the medium was replaced. Controls included cells incubated with unloaded YSA-targeted nanogels, pNIPMAm nanogels, and untreated cells. All cells were harvested at 48 h and assayed for EGFR expression by immunoblotting, as described in the Experimental Section. Figure 6 shows the results of this experiment; a significant reduction in EGFR expression is observed under these conditions relative to all controls ($p < 0.01$ relative to untreated sample by paired t test, $n = 3$). A small, statistically insignificant decrease in EGFR expression was noted in the unloaded, YSA-targeted nanogel control ($p > 0.1$). If this observation is indeed a real one, it may be due to cross talk between the EGFR and the EphA2 receptors, as described by Larsen and colleagues (*55*). In addition, a small decrease in EGFR expression was observed when cells were incubated with pNIPMAm nanogels alone, although the difference is not statistically significant ($p > 0.3$) in light of the large observed variability in expression.

These preliminary results illustrate that the targeted nanogels are capable of functional delivery of siRNA to ovarian carcinomas without overt toxic effects, and that the subsequently internalized siRNA is available for gene silencing. Whereas this preliminary demonstration is relatively focused in scope, it clearly shows the promise of the construct. We are currently exploring the generality of this approach in a detailed study of

silencing timecourse, persistence, cell type dependence, dose response, and applicability to other known silencing targets.

CONCLUSIONS

Peptide-labeled nanogels with a high loading capacity for siRNA have been developed and can be effectively targeted to ovarian carcinomas by receptor−peptide binding. The encapsulated siRNA is transported into the cell interior, where it is available for gene silencing, as illustrated in this case by EGFR knockdown. Since the locus of siRNA-mediated gene silencing is the cytosol, the results are suggestive of the surprising conclusion that endosomal uptake of the nanogels is followed by endosomal escape, resulting in efficient transport/release of the siRNA to the cytosol. Whereas we do not currently know the exact mechanism by which endosomal escape occurs. It is plausible that the nanogels respond to endosomal changes in osmotic pressure and ionic strength by undergoing a volume change. This phenomenon, called osmotic swelling/deswelling (*56*) is fundamental to the phase behavior of gel networks and may serendipitously be responsible for the excellent delivery properties described above. In addition to the gene-silencing efficacy, the nanocarriers are demonstrated to be nontoxic under the conditions investigated and are effective even when delivered in serum-containing medium. As a result of these studies, we are currently investigating the fundamental mechanisms of nanogel endosomal release. Additionally, the gene silencing results are being validated in a broader study of RNAi with plans to extend their use to in vivo delivery and silencing in animal models.

ACKNOWLEDGMENT

The authors acknowledge support from Emory−Georgia Tech Nanotechnology Center for Personalized and Predictive Oncology (5-40256-G11). L.A.L. acknowledges financial support from the DHHS (1 R21 EB006499-01). The ovarian cancer studies (E.B.D. and J.F.M.) were supported by the Georgia Cancer Coalition, The Debora Nash Harris Endowment Fund, and The Ovarian Cancer Institute. Thanks to Roman Mezencev for his help with the flow cytometry studies.

Supporting Information Available: Scanned immunoblot illustrating the expression levels of Eph2A receptor in Hey and BG-1 cells and representative AFFF/MALLS chromatograms showing the size and monodispersity of the core and core/shell nanogels, and representative trypan blue assay microscopy results. This material is available free of charge via the Internet at http://pubs.acs.org/BC.

LITERATURE CITED

(1) Saad, M., Garbuzenko, O. B., Ber, E., Chandna, P., Khandare, J. J., Pozharov, V. P., and Minko, T. (2008) Receptor targeted polymers, dendrimers, liposomes: Which nanocarrier is the most efficient for tumor-specific treatment and imaging? *J. Controlled Release 130*, 107–114.

(2) LaVan, D. A., McGuire, T., and Langer, R. (2003) Small-scale systems for in vivo drug delivery. *Nat. Biotechnol. 21*, 1184–1191.

(3) Moses, M. A., Brem, H., and Langer, R. (2003) Advancing the field of drug delivery: Taking aim at cancer. *Cancer Cell 4*, 337–341.

(4) Derfus, A. M., Chen, A. A., Min, D. H., Ruoslahti, E., and Bhatia, S. N. (2007) Targeted quantum dot conjugates for siRNA delivery. *Bioconjugate Chem. 18*, 1391–6.

(5) Lee, S. H., Bae, K. H., Kim, S. H., Lee, K. R., and Park, T. G. (2008) Amine-functionalized gold nanoparticles as non-cytotoxic and efficient intracellular siRNA delivery carriers. *Int. J. Pharm. 364*, 94–101.

(6) Kim, S., Jeong, J. H., Lee, S. H., Kim, S., and Park, T. G. (2008) LHRH Receptor-Mediated Delivery of siRNA Using Polyelectrolyte Complex Micelles Self-Assembled from siRNA−PEG−LHRH Conjugate and PEI. *Bioconjugate Chem. 19*, 2156–2162.

(7) Eavarone, D. A., Yu, X., and Bellamkonda, R. V. (2000) Targeted drug delivery to C6 glioma by transferrin-coupled liposomes. *J. Biomed. Mater. 51*, 10–14.

(8) Lee, R. J., and Low, P. S. (1994) Delivery of liposomes into cultured KB cells via folate receptor-mediated endocytosis. *J. Biol. Chem. 269*, 3198–204.

(9) van Nostrum, C. F. (2004) Polymeric micelles to deliver photosensitizers for photodynamic therapy. *Adv. Drug Delivery Rev. 56*, 9–16.

(10) Zhang, K., Fang, H., Wang, Z., Taylor, J. S., and Wooley, K. L. (2008) Cationic shell-crosslinked knedel-like nanoparticles for highly efficient gene and oligonucleotide transfection of mammalian cells. *Biomaterials. 30*, 968−977.

(11) Sun, T. M., Du, J. Z., Yan, L. F., Mao, H. Q., and Wang, J. (2008) Self-assembled biodegradable micellar nanoparticles of amphiphilic and cationic block copolymer for siRNA delivery. *Biomaterials 29*, 4348–55.

(12) Mao, H. Q., and Leong, K. W. (2005) Design of polyphosphoester-DNA nanoparticles for non-viral gene delivery. *Adv. Genet. 53*, 275–306.

(13) Vinogradov, S. V. (2006) Colloidal microgels in drug delivery applications. *Curr. Pharm. Des. 12*, 4703–4712.

(14) Cheng, J., Teply Benjamin, A., Sherifi, I., Sung, J., Luther, G., Gu Frank, X., Levy-Nissenbaum, E., Radovic-Moreno Aleksandar, F., Langer, R., and Farokhzad Omid, C. (2007) Formulation of functionalized PLGA-PEG nanoparticles for in vivo targeted drug delivery. *Biomaterials 28*, 869–76.

(15) Das, M., Mardyani, S., Chan, W. C. W., and Kumacheva, E. (2006) Biofunctionalized pH-responsive microgels for cancer cell targeting: Rational design. *Adv. Mater. (Weinheim, Ger.) 18*, 80–83.

(16) Akhtar, S., and Benter, I. F. (2007) Nonviral Delivery of synthetic siRNAs in vivo. *J. Clin. Invest. 117*, 3623–3632.

(17) Sepp-Lorenzino, L., and Ruddy, M. (2008) Challenges and Opportunities for Local and Systemic Delivery of siRNA and Antisense Oligonucleotides. *Clin. Pharmacol. Ther. 84*, 628–632.

(18) Martinez, J., Patkaniowska, A., Urlaub, H., Luhrmann, R., and Tuschl, T. (2002) Single-stranded antisense siRNAs guide target RNA cleavage in RNAi. *Cell 110*, 563–74.

(19) Spagnou, S., Miller, A. D., and Keller, M. (2004) Lipidic carriers of siRNA: Differences in the formulation, cellular uptake, and delivery with plasmid DNA. *Biochemistry 43*, 13348–13356.

(20) Jeong, J. H., Mok, H., Oh, Y. K., and Park, T. G. (2009) siRNA Conjugate Delivery Systems. *Bioconjugate Chem. 20*, 5−14.

(21) Schiffelers, R. M., Ansari, A., Xu, J., Zhou, Q., Tang, Q. Q., Storm, G., Molema, G., Lu, P. Y., Scaria, P. V., and Woodle, M. C. (2004) Cancer siRNA therapy by tumor selective delivery with ligand-targeted sterically stabilized nanoparticle. *Nucleic Acids Res. 32*, e149.

(22) Song, E., Zhu, P., Lee, S.-K., Chowdhury, D., Kussman, S., Dykxhoorn, D. M., Feng, Y., Palliser, D., Weiner, D. B., Shankar, P., Marasco, W. A., and Lieberman, J. (2005) Antibody mediated in vivo delivery of small interfering RNAs via cell-surface receptors. *Nat. Biotechnol. 23*, 709–717.

(23) Pirollo, K. F., Rait, A., Zhou, Q., Hwang, S. H., Dagata, J. A., Zon, G., Hogrefe, R. I., Palchik, G., and Chang, E. H. (2007) Materializing the Potential of Small Interfering RNA via a Tumor-Targeting Nanodelivery System. *Cancer Res. 67*, 2938–2943.

(24) Mok, H., and Park, T. G. (2008) Self-crosslinked and reducible fusogenic peptides for intracellular delivery of siRNA. *Biopolymers 89*, 881–8.

(25) Juliano, R. L. (2005) Peptide-oligonucleotide conjugates for the delivery of antisense and siRNA. *Curr. Opin. Mol. Ther. 7*, 132–136.

(26) Kang, H. M., DeLong, R., Fisher, M. H., and Juliano, R. L. (2005) Tat-conjugated PAMAM dendrimers as delivery agents for antisense and siRNA oligonucleotides. *Pharm. Res. 22*, 2099–2106.

(27) Simeoni, F., Morris, M. C., Heitz, F., and Divita, G. (2003) Insight into the mechanism of the peptide-based gene delivery system MPG: implications for delivery of siRNA into mammalian cells. *Nucleic Acids Res. 31*, 2717–2724.

(28) Zatsepin, T. S., Turner, J. J., Oretskaya, T. S., and Gait, M. J. (2005) Conjugates of oligonucleotides and analogues with cell penetrating peptides as gene silencing agents. *Curr. Pharm. Des. 11*, 3639–3654.

(29) Zhang, C. L., Tang, N., Liu, X. J., Liang, W., Xu, W., and Torchilin, V. P. (2006) siRNA-containing liposomes modified with polyarginine effectively silence the targeted gene. *J. Controlled Release 112*, 229–239.

(30) Nayak, S., Lee, H., Chmielewski, J., and Lyon, L. A. (2004) Folate-Mediated Cell Targeting and Cytotoxicity Using Thermoresponsive Microgels. *J. Am. Chem. Soc. 126*, 10258–10259.

(31) Shin, Y., Chang, J. H., Liu, J., Williford, R., Shin, Y. K., and Exarhos, G. J. (2001) Hybrid nanogels for sustainable positive thermosensitive drug release. *J. Controlled Release 73*, 1–6.

(32) Blackburn, W. H., and Lyon, L. A. (2008) Size-controlled synthesis of monodisperse core/shell nanogels. *Colloid Polym. Sci. 286*, 563–569.

(33) Berndt, I., Popescu, C., Wortmann, F.-J., and Richtering, W. (2006) Mechanics versus thermodynamics: swelling in multiple-temperature-sensitive core-shell microgels. *Angew. Chem., Int. Ed. 45*, 1081–1085.

(34) Jones, C. D., and Lyon, L. A. (2000) Synthesis and Characterization of Multiresponsive Core-Shell Microgels. *Macromolecules 33*, 8301–8306.

(35) Koolpe, M., Dail, M., and Pasquale, E. B. (2002) An ephrin mimetic peptide that selectively targets the EphA2 receptor. *J. Biol. Chem. 277*, 46974–9.

(36) Lin, Y. G., Han, L. Y., Kamat, A. A., Merritt, W. M., Landen, C. N., Deavers, M. T., Fletcher, M. S., Urbauer, D. L., Kinch, M. S., and Sood, A. K. (2007) EphA2 overexpression is associated with angiogenesis in ovarian cancer. *Cancer 109*, 332–40.

(37) Brantley-Sieders, D. M., Fang, W. B., Hicks, D. J., Zhuang, G., Shyr, Y., and Chen, J. (2005) Impaired tumor microenvironment in EphA2-deficient mice inhibits tumor angiogenesis and metastatic progression. *FASEB J. 19*, 1884–6.

(38) Han, L., Dong, Z., Qiao, Y., Kristensen, G. B., Holm, R., Nesland, J. M., and Suo, Z. (2005) The clinical significance of EphA2 and Ephrin A-1 in epithelial ovarian carcinomas. *Gynecol. Oncol. 99*, 278–86.

(39) Thaker, P. H., Deavers, M., Celestino, J., Thornton, A., Fletcher, M. S., Landen, C. N., Kinch, M. S., Kiener, P. A., and Sood, A. K. (2004) EphA2 expression is associated with aggressive features in ovarian carcinoma. *Clin. Cancer Res. 10*, 5145–50.

(40) Walker-Daniels, J., Coffman, K., Azimi, M., Rhim, J. S., Bostwick, D. G., Snyder, P., Kerns, B. J., Waters, D. J., and Kinch, M. S. (1999) Overexpression of the EphA2 tyrosine kinase in prostate cancer. *Prostate 41*, 275–80.

(41) Zeng, G., Hu, Z., Kinch, M. S., Pan, C. X., Flockhart, D. A., Kao, C., Gardner, T. A., Zhang, S., Li, L., Baldridge, L. A., Koch, M. O., Ulbright, T. M., Eble, J. N., and Cheng, L. (2003) High-level expression of EphA2 receptor tyrosine kinase in prostatic intraepithelial neoplasia. *Am. J. Pathol. 163*, 2271–6.

(42) Ogawa, K., Pasqualini, R., Lindberg, R. A., Kain, R., Freeman, A. L., and Pasquale, E. B. (2000) The ephrin-A1 ligand and its receptor, EphA2, are expressed during tumor neovascularization. *Oncogene 19*, 6043–52.

(43) Zelinski, D. P., Zantek, N. D., Stewart, J. C., Irizarry, A. R., and Kinch, M. S. (2001) EphA2 overexpression causes tumorigenesis of mammary epithelial cells. *Cancer Res. 61*, 2301–6.

(44) Kataoka, H., Igarashi, H., Kanamori, M., Ihara, M., Wang, J. D., Wang, Y. J., Li, Z. Y., Shimamura, T., Kobayashi, T., Maruyama, K., Nakamura, T., Arai, H., Kajimura, M., Hanai, H., Tanaka, M., and Sugimura, H. (2004) Correlation of EPHA2 overexpression with high microvessel count in human primary colorectal cancer. *Cancer Sci. 95*, 136–41.

(45) Saito, T., Masuda, N., Miyazaki, T., Kanoh, K., Suzuki, H., Shimura, T., Asao, T., and Kuwano, H. (2004) Expression of EphA2 and E-cadherin in colorectal cancer: correlation with cancer metastasis. *Oncol. Rep. 11*, 605–11.

(46) Clark, K. D., Volkman, B. F., Thoetkiattikul, H., King, D., Hayakawa, Y., and Strand, M. R. (2001) Alanine-scanning mutagenesis of plasmatocyte spreading peptide identifies critical residues for biological activity. *J. Biol. Chem. 276*, 18491–6.

(47) Hermanson, G. T. (1996) *Bioconjugate Techniques*, 1st ed., Vol. 1, Academic Press, San Diego.

(48) Betancourt, T., Shah, K., and Brannon-Peppas, L. (2009) Rhodamine-loaded poly(lactic-co-glycolic acid) nanoparticles for investigation of in vitro interactions with breast cancer cells. *J. Mater. Sci. Mater. Med. 20*, 387–395.

(49) Maeda, H. (2001) The enhanced permeability and retention (EPR) effect in tumor vasculature: The key role of tumor-selective macromolecular drug targeting. *Adv. Enzyme Regul. 41*, 189–207.

(50) Scarberry, K. E., Dickerson, E. B., McDonald, J. F., and Zhang, Z. J. (2008) Magnetic nanoparticle-peptide conjugates for in vitro and in vivo targeting and extraction of cancer cells. *J. Am. Chem. Soc. 130*, 10258–10262.

(51) Miao, H., Burnett, E., Kinch, M., Simon, E., and Wang, B. (2000) Activation of EphA2 kinase suppresses integrin function and causes focal-adhesion-kinase dephosphorylation. *Nat. Cell Biol. 2*, 62–9.

(52) Noberini, R., Koolpe, M., Peddibhotla, S., Dahl, R., Su, Y., Cosford, N. D., Roth, G. P., and Pasquale, E. B. (2008) Small molecules can selectively inhibit ephrin binding to the EphA4 and EphA2 receptors. *J. Biol. Chem. 283*, 29461–72.

(53) Surawska, H., Ma, P. C., and Salgia, R. (2004) The role of ephrins and Eph receptors in cancer. *Cytokine Growth Factor Rev. 15*, 419–33.

(54) Thaker, P. H., Yazici, S., Nilsson, M. B., Yokoi, K., Tsan, R. Z., He, J., Kim, S. J., Fidler, I. J., and Sood, A. K. (2005) Antivascular therapy for orthotopic human ovarian carcinoma through blockade of the vascular endothelial growth factor and epidermal growth factor receptors. *Clin. Cancer Res. 11*, 4923–33.

(55) Larsen, A. B., Pedersen, M. W., Stockhausen, M. T., Grandal, M. V., van Deurs, B., and Poulsen, H. S. (2007) Activation of the EGFR gene target EphA2 inhibits epidermal growth factor-induced cancer cell motility. *Mol. Cancer Res. 5*, 283–93.

(56) Saunders, B. R., and Vincent, B. (1997) Osmotic deswelling of microgel particles in the presence of free polymer. *Prog. Colloid Polym. Sci. 105*, 11–15.

BC800547C

Supporting Information for:

Peptide-Functionalized Nanogels for Targeted siRNA Delivery

William H. Blackburn,[1,2,†] Erin B. Dickerson,[2,3,4,†] Michael H. Smith,[1,2,†] John F. McDonald,[2,3,4] and L. Andrew Lyon*[1,2]

[1]*School of Chemistry and Biochemistry,* [2]*Petit Institute for Bioengineering and Bioscience,* [3]*School of Biology, and the* [4]*Ovarian Cancer Institute, Georgia Institute of Technology, Atlanta, Georgia, 30332*

[†]WHB, EBD, and MHS contributed equally to this work
*To whom correspondence should be addressed: lyon@gatech.edu

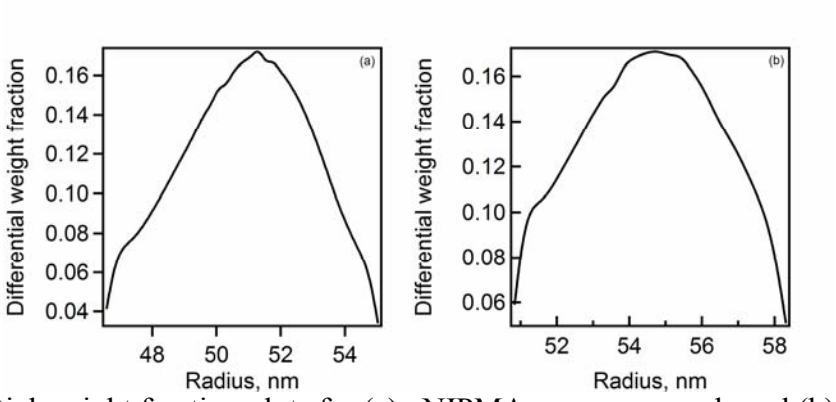

Figure S1. Differential weight fraction plots for (a) pNIPMAm core nanogels and (b) pNIPMAm core/shell nanogels, as determined by AFFF-MALLS.

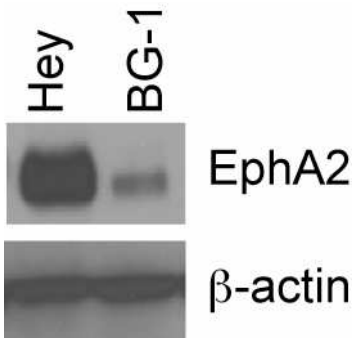

Figure S2. Immunoblot showing the differential expression levels between the Hey and BG-1 ovarian carcinoma cell lines. β-actin is included as a loading control.

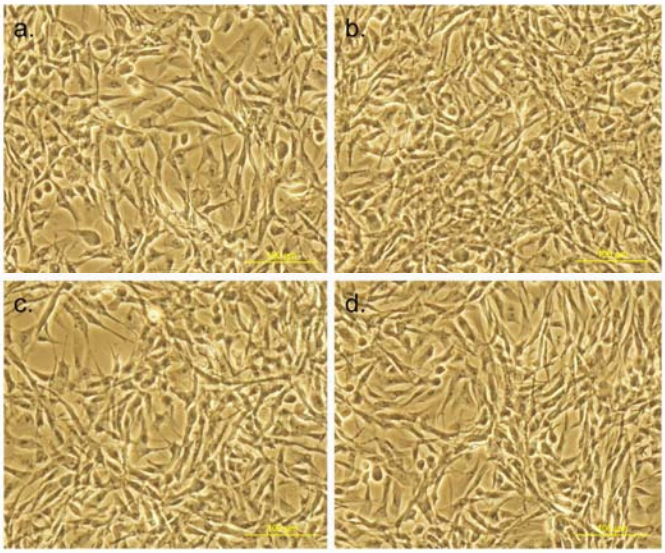

Figure S3. Representative bright field microscopy images of trypan blue-treated Hey cells. (a) Control (no nanogels), (b) pNIPMAm nanogels, (c) YSA-pNIPMAm nanogels, and (d) SCR-pNIPMAm.

Tuning of Peroxidase Activity by Covalently Tethered DNA Oligonucleotides

Maximilian Glettenberg and Christof M. Niemeyer*

Technische Universität Dortmund, Fakultät Chemie, Biologisch-Chemische Mikrostrukturtechnik, Otto-Hahn Strasse 6, D-44227 Dortmund, Germany. Received December 24, 2008; Revised Manuscript Received February 25, 2009

We report on the modulation of the peroxidase activity of hybrid catalysts, comprising short DNA oligonucleotides and heme enzymes by means of sequence variation of tethered oligonucleotides. In particular, binary mixtures of native heme (protophorphyrin IX) and single-stranded DNA oligonucleotides as well as the analogous covalent heme-oligonucleotide conjugates were compared with DNA−enzyme conjugates, prepared by reconstitution of apo-myoglobin or apo-horseradisch peroxidase, using the aforementioned covalent heme−oligonucleotide conjugates. In all systems, it was clearly evident that the implemented oligonucleotides markedly influence the catalytic activity in a sequence-dependent matter. Greater than 100-fold changes in catalytic constants were observed, depending on which oligonucleotide was incorporated in the hybrid catalyst. We also observed that the tethered oligomers affect the inhibition of HRP-mediated peroxidation by means of small molecule inhibitors. On the basis of the quantitative description of this phenomenon and consideration of the current state of knowledge, we hypothesize that distinct interactions, such as hydrogen bonding or electrostatic contacts, occur between the oligonucleotides and the heme-containing catalyst, which account for the effects observed.

INTRODUCTION

The design of biocatalysts is of major importance for many technical processes and commercial applications (*1*). Mainstream developments in this area focus on either the search for new enzymes in natural habitats or else the *a priori* design or *in vitro* evolutionary optimization of known enzymes. However, novel approaches are currently being explored, in which semiartificial bioinorganic hybrid catalysts are generated by a combination of natural biomacromolecules and synthetic building blocks (*2, 3*). For example, catalytically inactive molecules, such as streptavidin (*4*−*7*), papain (*8*−*10*), serum albumin (*11*), or double-stranded DNA (*12, 13*), have been modified with organometallic moieties to create catalysts for hydrogenation, alkylation, Diels−Alder, or other chemo- and stereoselective transformations. Moreover, naturally occurring enzymes have been modified with synthetic groups to alter existing catalytic reactivities and create novel ones. For instance, hemoenzymes have been modified with synthetic analogues of their native prosthetic group to change catalytic specificity (*14, 15*). Enzymes have also been attached to colloidal semiconductor nanoparticles to generate light-switchable photocalysts (*16*−*18*) or with gold nanoparticles to produce electrically addressable catalysts for biosensing (*19, 20*).

The reconstitution of apoenzymes, which are enzymes whose natural prosthetic group has been removed by chemical treatment, with artificial prosthetic group analogues represents a powerful approach to generate bioinorganic hybrid catalysts (*14, 15, 21*). We have previously applied this method to the synthesis of semisynthetic DNA oligonucleotide conjugates of myoglobin (Mb, in Figure 1) (*22, 23*) or horseraddish peroxidase (HRP) (*23, 24*). It should be noted that Mb, whose main physiological function concerns the reversible storage of oxygen in muscle tissue, under certain conditions can act as peroxidase (*25*−*27*); however, its peroxidase activity is several orders of magnitude lower than that of classical peroxidases, such as HRP. Owing to the highly specific binding capabilities of the DNA oligomers attached to Mb or HRP, these conjugates can be specifically immobilized at solid surfaces by means of DNA hybridization. Thus, they can be considered as programmable catalysts, useful for applications in biocatalysis or sensing (*24, 28*). Interestingly, the attachment of the oligonucleotide to the enzyme's active site leads to significant changes in catalytic activity. While HRP−DNA conjugates revealed a reduced peroxidase activity, the enzymatic activity was largely increased in the case of Mb (*23*). These effects were observed for both conjugates, containing either one or two DNA oligomers (MbD_1 and MbD_2, respectively, in Figure 1), and they may result from steric constraints of the DNA strands leading to an opening of the active site, thereby facilitating an increased accessibility for substrate molecules (*23*). We here report a novel phenomenon, observed in the course of kinetic analyses of the Mb- and HRP−DNA conjugates, that the catalytic activity of the enzyme can be significantly changed by alterations of the nucleotide sequence of the appended DNA moiety.

EXPERIMENTAL PROCEDURES

Syntheses of rMb−DNA (*22*), rHRP−DNA conjugates (*23*), and chemical HRP−DNA conjugates (*24*) were carried out as previously described. Kinetic measurements of the H_2O_2-mediated peroxidation of Amplex Red have also been described elsewhere (*23*). Full details on experimental protocols for conjugate synthesis, Michaelis−Menten kinetic measurements, data analysis, and controls are available in the Supporting Information.

RESULTS

In this work, we studied the influence of DNA oligonucleotide sequences on the enzymatic activity of covalent DNA−enzyme conjugates. As schematically depticted in Figure 1, semisynthetic DNA−heme enzyme conjugates were prepared in a two-step process (*22, 23*). Initially, covalent on-column coupling of aminoalkyl-modified DNA oligonucleotides with heme (protoporphyrin IX) was carried out to synthesize two DNA−heme

* Corresponding author. Tel/Fax: + 49 (0)231/755 7082. E-mail: christof.niemeyer@tu-dortmund.de.

10.1021/bc800558g CCC: $40.75 © 2009 American Chemical Society
Published on Web 04/01/2009

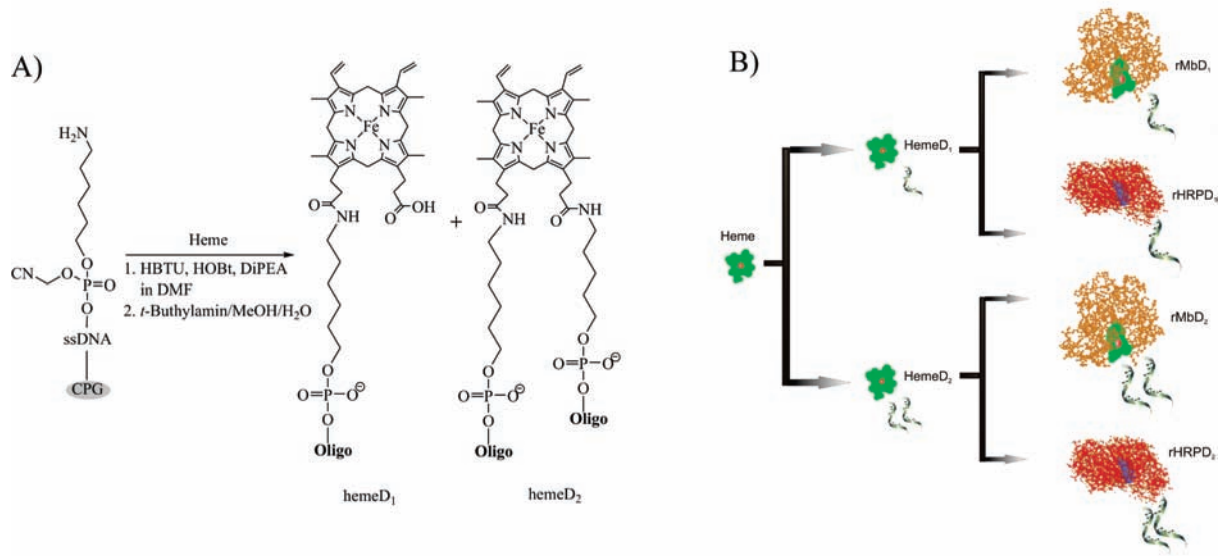

Figure 1. Overview on the preparation of semisynthetic DNA−heme enzyme conjugates. (A) Covalent on-column coupling of aminoalkyl-modified DNA oligonucleotides with heme (protoporphyrin IX) yields two DNA−heme conjugates, containing one (hemeD$_1$) or two (hemeD$_2$) single-stranded oligonucleotides, linked to the propionate chains of heme. (B) The two conjugates are separated by ion-exchange chromatography and used for the reconstitution of apo-myoglobin (Mb, orange) and apo-horseraddish peroxidase (HRP, red), respectively.

Table 1. Oligonucleotide Sequences Investigated in This Study

name	nt	sequence
F1	22	5′-CCT GCG TCG TTT AAG GAA GTA C-3′
F5	22	5′-GGT CCG GTC ATA AAG CGA TAA G-3′
F9	22	5′-GTG GAA AGT GGC AAT CGT GAA G-3′
F10	22	5′-GAA CGA ATA CAA AGG CTA CAC G-3′
A24	24	5′-TCC TGT GTG AAA TTG TTA TCC GCT-3′
B14	14	5′-CCT GTG TGA AAT TG-3′
A12	12	5′-AAG ACC ATC CTG-3′
C2b	12	5′-GAT CTC TTC ACC-3′
GA1	12	5′-GGG GGG GGG GGG-3′
GA2	12	5′-GGG GGG GGG CCC-3′
GA3	12	5′-GGG GGG CCC GGG-3′
GA4	12	5′-GGG CCC GGG GGG-3′
GA5	12	5′-CCC GGG GGG GGG-3′

conjugates, containing one (hemeD$_1$) or two (hemeD$_2$) single-stranded oligonucleotides, linked to the propionate chains of heme (Figure 1A). The two conjugates were separated by ion-exchange chromatography and then used for the reconstitution of apo-myoglobin and apo-horseraddish peroxidase, respectively, previously prepared by Teale's methylethylketone extraction method (*29*). The reconstitution of the apoenzymes led to the formation of the desired semisynthetic DNA−enzyme conjugates (rMbD$_1$, rMbD$_2$, rHRPD$_1$, and rHRPD$_2$ in Figure 1B), which were purified by FPLC and characterized spectrophotometrically (Figures S1 and S2, in the Supporting Information) (*30*).

In the course of Michaelis−Menten kinetic studies of the peroxidase activity of the DNA−enzyme conjugates in the H_2O_2-mediated conversion of the fluorogenic substrate Amplex Red to form the highly fluorescent product resorufin (*30*), we observed that hybrids, which contained different oligonucleotides, revealed significant differences in their enzymatic activity. For example, we investigated the reconstituion of apoMb with a set of 22-mer oligonucleotides, denominated as F1, F5, F9, and F10 (Table 1), which had previously been designed and selected for orthogonal and highly efficient hybridization characteristics in DNA-directed immobilization of oligonucleotide−protein conjugates (*31*). Typical Michealis−Menten kinetic curves of rMb conjugates, reconstituted with oligomers F1−F10, are shown in Figure 2. The kinetic curves of the conjugates revealed substrate inhibition characteristics, which was accounted for by using the appropriate two-parameter fit for the Michaelis−Menten kinetics fitting method (*30*, *32*). It was clearly evident from naked-eye inspection of the curves, that the activity of D$_1$-conjugates was highest when oligomer F10 was used (Figure 2a). In the case of the D$_2$-conjugates, however, greatest activity was observed when oligomer F5 was used (Figure 2b). More precisely, the order of enzyme activity was F10 > F5 > F9 > F1 in the case of D$_1$-conjugates (Figure 2a), while F5 ≫ F9 > F10 ≈ F1 was observed for D$_2$-conjugates (Figure 2b).

Since these results were rather unexpected, we repeated the kinetic measurements using entirely independent samples, prepared from different batches of oligonucleotides and apoenzymes, at least three times. The Michaelis−Menten parameters (K_M, k_{cat}, and k_{cat}/K_M) obtained from kinetic analyses of various hybrid conjugates were then calculated and listed in Table 2. Because of the large number of independent repetitions (n = 3−7), the data can be considered highly reproducible. To compare the reactivity of two enzymes acting on the same substrate, the so-called catalytic efficiency (k_{cat}/K_M) is frequently used (*33*). This k_{cat}/K_M value, also termed as specificity constant, is a useful index for comparing the relative rates of an enzyme acting on alternative, competing substrates. Since Eisenthal and collegues have recently emphasized that the use of k_{cat}/K_M as a quantitative index of catalytic power is at best misleading and at worst invalid (*33*), we here restrict our discussion on the comparison of k_{cat} values, which are the catalytic constants for the conversion of a substrate (Amplex Red) to a product (resorufin). Inspection of k_{cat} data obtained from the aforementioned eight rMb-oligonucleotide conjugates (entries 11−14, in Table 2) indeed confirmed the obove described order in activity, i.e., that F10- and F5-modification induced highest activity for the D$_1$- and D$_2$-conjugates, respectively. Moreover, comparison with native Mb (entry 10) confirmed our previous observation that the reconstitution of apoMb with oligonucleotide−heme conjugates leads to an increased peroxidase activity, as compared to the native enzyme (*22*, *23*).

Peroxidase Activity of Heme−DNA Conjugates. To systematically investigate the sequence-dependent peroxidase activity of the conjugates, we measured whether the *F*-oligonucleotides do influence the peroxidase activity of heme (entries 1−5, in Table 2) and of the respective heme−DNA conjugates (entries

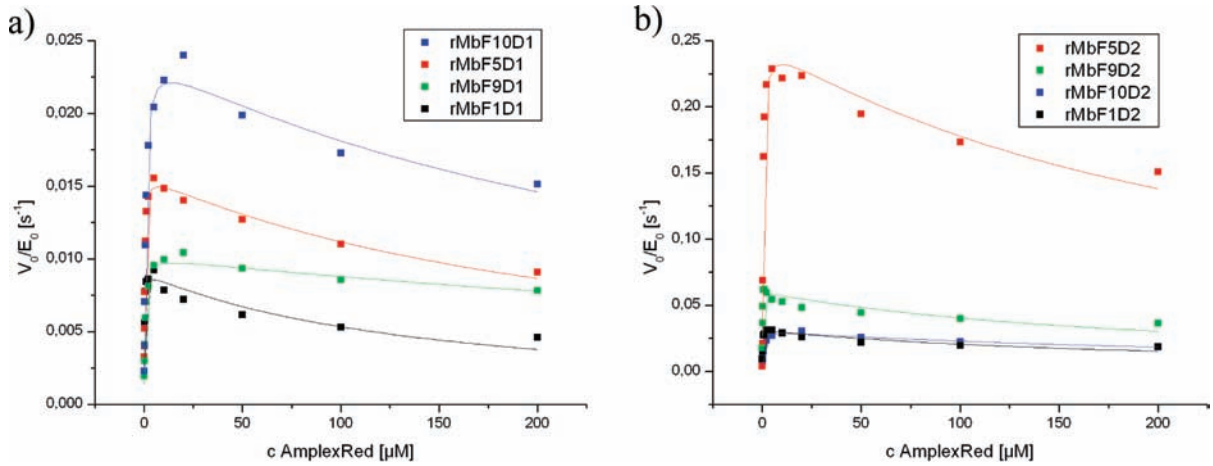

Figure 2. Representative kinetic curves obtained from myoglobin, reconstituted with four different 22-mer oligonucleotide−heme conjugates, synthesized from oligonucleotides F1 (black), F5 (red), F9 (green), and F10 (blue). Shown are the kinetic curves determined for the respective $rMbD_1$ (a) and $rMbD_2$ (b) conjugates.

Table 2. Kinetic Data Determined by Michaelis−Menten Measurements of Various Heme− and Myoglobin−Oligonucleotide Conjugates[a]

no.	nt	name	k_{cat} [10^{-3} s^{-1}]	K_M [μM]	k_{cat}/K_M [10^{-3} μM^{-1} s^{-1}]
1	0	native heme	34 ± 4	0.44 ± 0.08	78 ± 10
2	22	nheme + aF1[b]	1 to 1: 62 ± 28	1 to 1: 0.85 ± 0.04	1 to 1: 72 ± 30
			1 to 2: 17 ± 1	1 to 2: 0.63 ± 0.12	1 to 2: 28 ± 4
3	22	nheme + aF5[b]	1 to 1: 53 ± 1	1 to 1: 0.96 ± 0.01	1 to 1: 55 ± 1
			1 to 2: 12 ± 3	1 to 2: 0.56 ± 0.001	1 to 2: 22 ± 6
4	22	nheme + aF9[b]	1 to 1: 21 ± 1	1 to 1: 0.76 ± 0.13	1 to 1: 29 ± 6
			1 to 2: 9 ± 3	1 to 2: 0.46 ± 0.04	1 to 2: 19 ± 4
5	22	nheme + aF10[b]	1 to 1: 28 ± 18	1 to 1: 0.69 ± 0.07	1 to 1: 39 ± 22
			1 to 2: 12 ± 5	1 to 2: 0.58 ± 0.17	1 to 2: 20 ± 2
6	22	hemeF1	D_1: 48 ± 16	D_1: 0.23 ± 0.10	D_1: 252 ± 183
			D_2: 54 ± 13	D_2: 0.09 ± 0.01	D_2: 631 ± 39
7	22	hemeF5	D_1: 230 ± 28	D_1: 0.45 ± 0.12	D_1: 544 ± 183
			D_2: 1102 ± 39	D_2: 0.48 ± 0.09	D_2: 2316 ± 388
8	22	hemeF9	D_1: 201 ± 60	D_1: 0.63 ± 0.10	D_1: 330 ± 150
			D_2: 2 ± 0.3	D_2: 0.25 ± 0.03	D_2: 7 ± 2
9	22	hemeF10	D_1: 59 ± 8	D_1: 0.50 ± 0.11	D_1: 119 ± 8
			D_2: 30 ± 0.89	D_2: 0.45 ± 0.08	D_2: 68 ± 14
10	0	native Mb	1.41 ± 0.13	0.25 ± 0.14	7 ± 3
11	22	rMbF1	D_1: 9 ± 3	D_1: 0.11 ± 0.03	D_1: 84 ± 33
			D_2: 32 ± 3	D_2: 0.11 ± 0.01	D_2: 298 ± 40
12	22	rMbF5	D_1: 15 ± 3	D_1: 0.22 ± 0.05	D_1: 73 ± 25
			D_2: 282 ± 86	D_2: 0.49 ± 0.18	D_2: 597 ± 99
13	22	rMbF9	D_1: 10 ± 3	D_1: 0.33 ± 0.10	D_1: 33 ± 10
			D_2: 55 ± 17	D_2: 0.06 ± 0.02	D_2: 1050 ± 187
14	22	rMbF10	D_1: 33 ± 11	D_1: 0.59 ± 0.15	D_1: 57 ± 15
			D_2: 38 ± 3	D_2: 0.48 ± 0.04	D_2: 80 ± 9

[a] Conjugates with one or two DNA oligonucleotides are denoted as D_1 or D_2, respectively. [b] Native heme was mixed with 1 or 2 M equivalents of amino-modified DNA *F*-oligonucleotides, as indicated with 1:1 or 1:2, respectively.

6−9). In the case of two component mixtures containing native heme and the amino-modified *F*-oligonucleotides, the addition of F1 and F5 oligonucleotides increased the peroxidase activity of native heme about 2-fold (entries 2, 3, and 1, respectively), while the presence of oligomers F9 and F10 (entries 4, 5) did not reveal significant effects. Interestingly, the addition of two molar equivalents of the *F*-oligonucleotides led to an about 2-fold decrease in heme activity. In the case of covalent *F*-oligonucleotide−heme conjugates (entries 6−9), peroxidase activity of the monoadducts ($hemeD_1$), sequences F1 and F10, affected the activity only slightly (≤2-fold), while oligomers F5 and F9 significantly increased the peroxidase activity ≈7-fold. The bis-adducts ($hemeD_2$) containing oligomers F1 and F10 showed activity similar to that of the monoadducts; however, sequence F9 strongly decreased the activity, while the $hemeD_2$−F5 conjugate revealed a significant (>30-fold, entry 7) increase in activity, as compared to the native heme.

To ease the comparison of the above-described data, Figure 3A−C shows a graphical representation of k_{cat} values. It is evident that the oligonucleotides markedly influence the catalytic constants; however, no distinctive patterns or trends are evident in terms of which sequence increases or decreases the catalytic activity. For a discussion of the observed phenomena, one should initially take into account that it is well known that noncovalent adducts of folded nucleic acid motifs, such as G-quadrupletts or aptamer sequences, and heme can exhibit fairly strong peroxidase activity. For instance, Sen and collegues have previously reported on the selection of a catalytic DNA−heme complex, which reveals peroxidase activity substantially greater than those of heme proteins, such as catalase and Fe(III)-myoglobin (*34*−*37*). On the basis of these achievements, designed aptamer−heme adducts have already been employed in a variety of bioanalytical assays (*38*−*40*). Therefore, the changes in heme catalytic activity induced by covalent coupling (Figure 3A) or simple addition (Figure 3B) of oligonucleotides suggest the formation of folded secondary structures or even oligomeric aggregates, which interact with heme. Although the

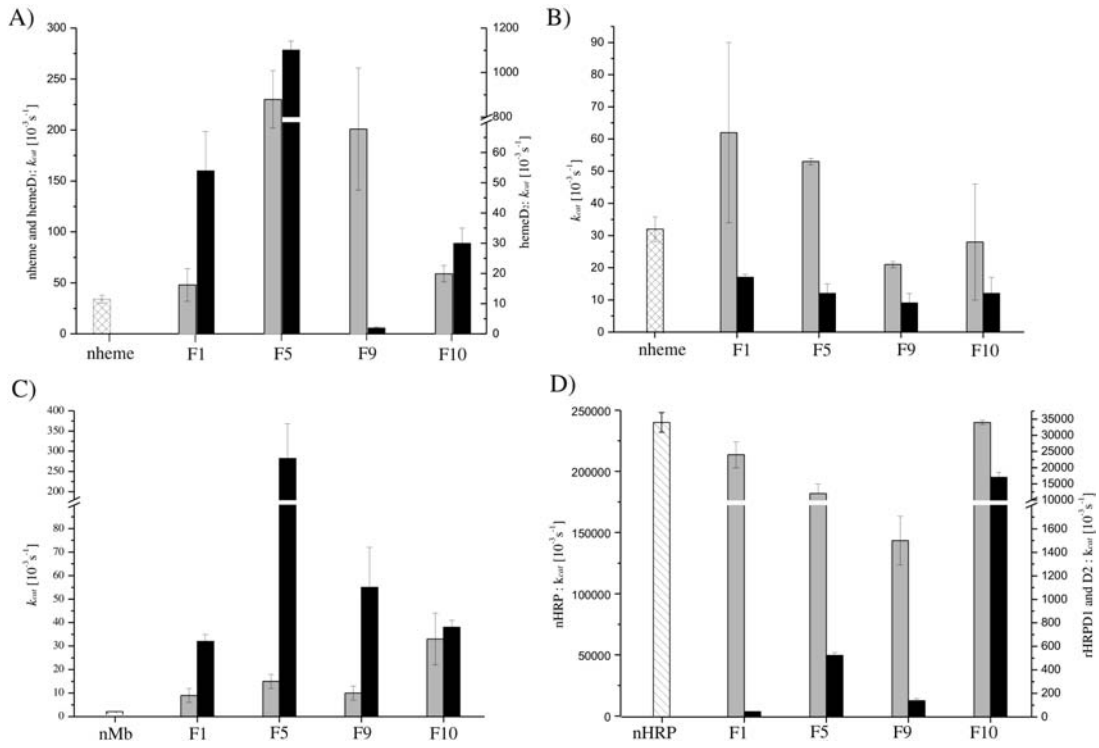

Figure 3. Column diagrams of the experimentally determined k_{cat} value of (A) covalent heme−DNA conjugates and native heme (hatched bar), (B) binary mixtures containing native heme, amino-modified *F*-oligonucleotides, and native heme (hatched bar), (C) reconstituted Mb−DNA conjugates and native Mb (hatched bar), and (D) reconstituted HRP−DNA conjugates and native HRP (hatched bar). The light gray and black bars represent the D_1- and D_2-conjugates, respectively. Note that the heme−D_2 conjugate of F5 in A revealed a strongly increased peroxidase activity, indicated by the differently scaled *y*-axis in A.

F-oligonucleotides had previously been designed by applying the criteria of minimized secondary structure and homodimer formation (*31*), we again analyzed these sequences *in silico*, using the DINAMelt web server (*41*), which also allows one to adjust sodium chloride concentration. Under the given peroxidase assay conditions ($T = 25$ °C, 300 mM NaCl), no appreciable secondary structure formation was detected. The most stable secondary and homodimer structures were detected for oligomers F5 ($\Delta G = -0.9$ or -6.1 kcal/mol, respectively) and F1 ($\Delta G = -0.76$ or -4.3 kcal/mol, respectively, see Figure S3, Supporting Information). Thus, *in silico* analysis did not provide any distinctive trends that helped to explain the observed reactivity patterns (Figure 3A,B).

Peroxidase Activity of Mb−DNA Conjugates. In the comparison of oligonucleotide-induced k_{cat} patterns observed for heme−DNA (Figure 3A) and the respective rMb−DNA conjugates (Figure 3C), it is evident that sequence F5 has the strongest activating effect in the D_2-conjugates; however, this trend is not consistent in the case of the D_1-conjugates. It is well known that native Mb is a relatively weak peroxidase (*14*). This fact is reflected by the data in Table 2, which indicate that the absolute k_{cat} value, and thus peroxidase activity, of native Mb (entry 10) is about 25-fold lower than that of native heme (entry 1). This suggests that the protein shell of native Mb in fact reduces the peroxidase activity of heme. Thus, it is most likely that this general effect also occurs in the reconstituted rMb−DNA conjugates. Monzani et al. have reported that the introduction of hydrogen donor and acceptor peptide groups to the heme influences the hydrogen bond network of the Mb, thereby leading to a slight rigidification of the active site and an increased stability of compound I (*42*). They also showed that the heme-binding pocket is not sufficiently large to entirely accommodate the peptide-modified heme derivatives, and therefore, the peptide-carrying propionate chains extend to the outside of the heme pocket. On the basis of these observations, we have previously hypothesized that the attachement of the bulky negatively charged DNA in close proximity to the enzyme's active site may lead to an opening of the active site, thereby facilitating an increased accessibility for substrate molecules (*23*). Unfortunately, this general steric model is not sufficient to explain the sequence-dependent data reported here.

To further investigate this phenomenon, we analyzed a number of analogous rMb−DNA conjugates containing longer or shorter DNA oligomers, which also included a set of GC-rich oligomers (Table S1, Supporting Information). The latter were chosen to investigate whether guanine or cytosine nucleobases might specifically contribute to the sequence-dependent peroxidase activity of rMb−DNA conjugates. Guanine has a lower redox potential than other nucleobases, and chemical oxidation of this base has been observed experimentally (*43*), while cytosine bases are known be to easily protonated and thus play an important role in RNA-based catalysis (*44*). Although we again observed sequence-dependent peroxidase activity, regrettably no distinct patterns could be deduced from the kinetic data summarized in Table S1 (Supporting Information).

Peroxidase Activity of HRP−DNA Conjugates. We then investigated whether sequence-dependent peroxidase activity can also be observed for other reconstituted heme enzymes. To this end, rHRP−DNA conjugates were prepared by using the *F*-oligomers. The resulting kinetic data are summarized in Table 3 and graphically depicted in Figure 3D. As expected from previous results (*23*), the peroxidase activity was significantly higher than that of the rMb−DNA conjugates. Specifically, native HRP showed an about 170.000-fold higher k_{cat} value than native Mb, while the rHRP−DNA conjugates revealed on average about a 500-fold increase, as compared to the rMb−DNA conjugates. Thus, the rHRP−DNA conjugates were significantly less active than native HRP. This was also observed for chemically linked conjugates (entries 6−9, in Tab. 3), which

Table 3. Kinetic Data Determined by Michaelis−Menten Measurements of Native Horseradish Peroxidase (HRP) and Respective Oligonucleotide Conjugates, Obtained by Reconstitution (rHRP) or Chemical Conjugation (cHRP)[a]

no.	nt	name	k_{cat} [10^{-3} s^{-1}]	K_M [μM]	k_{cat}/K_M [10^{-3} μM^{-1} s^{-1}]
1	0	native HRP	240000 ± 8000	81 ± 3	2974 ± 205
2	22	rHRP-F1	D_1: 24000 ± 4000	D_1: 213 ± 76	D_1: 118 ± 23
			D_2: 44 ± 2	D_2: 0.06 ± 0.01	D_2: 702 ± 96
3	22	rHRP-F5	D_1: 12000 ± 3000	D_1: 220 ± 58	D_1: 57 ± 20
			D_2: 523 ± 24	D_2: 0.52 ± 0.09	D_2: 1007 ± 106
4	22	rHRP-F9	D_1: 1500 ± 207	D_1: 53 ± 10	D_1: 30 ± 6
			D_2: 138 ± 18	D_2: 0.14 ± 0.01	D_2: 1012 ± 224
5	22	rHRP-F10	D_1: 34000 ± 667	D_1: 121 ± 9	D_1: 279 ± 21
			D_2: 17000 ± 1620	D_2: 199 ± 4	D_2: 85 ± 6
6	22	cHRP-F1[b]	D_1: 15500 ± 1100	D_1: 87 ± 15	D_1: 181 ± 18
7	22	cHRP-F5[b]	D_1: 17800 ± 700	D_1: 144 ± 1	D_1: 124 ± 6
8	22	cHRP-F9[b]	D_1: 16700 ± 400	D_1: 89 ± 8	D_1: 188 ± 14
9	22	cHRP-F10[b]	D_1: 16100 ± 1800	D_1: 71 ± 11	D_1: 226 ± 8

[a] Conjugates with one or two DNA oligonucleotides are denoted as D_1 or D_2, respectively. [b] The chemical conjugates were synthesized by coupling thiolated DNA oligonucleotides to accessible lysin residues of the protein's surface using the heterobifunctional cross-linker sSMCC.

Table 4. IC_{50} Values of Competitive Inhibitors Fluoranthene and 9-Methylanthracene for Native HRP and Reconstituted rHRP-D_1-Conjugates

no.	name	fluoranthene IC_{50} [μM]	9-methylanthracene IC_{50} [μM]
1	nHRP	98.6 ± 12.8	85.3 ± 7.3
2	rHRP-F1	24.1 ±4.7	27.5 ± 6.9
3	rHRP-F5	13.8 ± 1.8	5.2 ± 0.6
4	rHRP-F9	17.1 ± 7.1	10.4 ± 1.3
5	rHRP-F10	26.9 ± 7.7	26.8 ± 2.9

were synthesized by coupling 5′-alkylthiol-modified *F*-oligonucleotides to accessible lysin residues of the HRP's surface, using the heterobifunctional cross-linker sSMCC (*24*). Interestingly, the chemical conjugates revealed an almost identical k_{cat} value of about 17000 × 10^{-3} s^{-1}, regardless of the oligomer attached to the HRP. Since the chemical coupling occurs statistically at one of the 4 lysine residues of HRP, one can assume that mere synthetic manipulations decrease the activity of native HRP about 14-fold. In contrast, reconstitution of apoHRP with the various heme−DNA conjugates led to large variations in peroxidase activity (entries 6−9, in Table 3). In particular, k_{cat} values ranged from 1500 (F9) to 24.000 10^{-3} s^{-1} (F1) and 44 (F1) to 17.000 10^{-3} s^{-1} (F10) for the D_1- and D_2-conjugates, respectively. The observed activity pattern (Figure 3D) differed significantly from that observed for heme−DNA (Figure 3A) or heme−rMb conjugates (Figure 3C). Moreover, yet another pattern of DNA-dependent peroxidase activity was observed when the heme−rHRP-D_1 conjugates were allowed to hybridize with one molar equivalent of the complementary oligomer (cF1, cF5, cF9, or cF10; see Table S2, Supporting Information).

Small Molecule HRP Inhibitors. We also investigated whether the action of small-molecule inhibitors is affected by the tethered F-oligonucleotides attached to HRP's active site. In the course of another project, we had accidentally observed that fluoranthene and 9-methylanthracene act as strong inhibitors of native HRP in the peroxidation of Amplex Red (Rabe, K. S., and Niemeyer, C. M., unpublished results). We here followed up on this qualitative observation and determined the inhibitory concentrations (IC_{50}) of fluoranthene and 9-methylanthracene for native HRP and the respective rHRP-D_1 conjugates (Table 4). The IC_{50} values of both inhibitors were significantly decreased for the rHRP-D_1 conjugates, as compared to native HRP. This means that, for example, the IC_{50} value of 9-methylanthracene was almost 20-fold reduced when oligomer F5 was present in the rHRP-D_1 conjugate. Interestingly, the analogous chemical conjugates revealed no such strong dependence on the oligomer sequence attached (Table S3, Supporting Information). Since we determined that both fluoranthene and 9-methylanthracene act as competitive inhibitors (Figure S4, Supporting Information), the decrease in IC_{50} indicates that the sequence of the tethered DNA moiety increases the affinity of the inhibitor for the enzyme's active site to a different extent. The data thus provide a hint toward a changed geometry and/or conformational flexibility of the active site. However, no distinct correlation could be deduced between the inhibitor enhancement (Table 4) and peroxidase activity modulation (Table 3) by the various *F*-oligomers under investigation.

DISCUSSION

In conclusion, we here reported on the modulation of the activity of biomolecular peroxidation catalysts by means of sequence variation of tethered oligonucleotides. Five independent systems, i.e., binary heme/oligonucleotide mixtures, covalent heme−oligonucleotide conjugates, and rMb−DNA and rHRP−DNA conjugates as well as the inhibition of peroxidase activity of rHRP−DNA conjugates, were investigated. In all systems, it was clearly evident that the oligonucleotides involved in the system markedly influence the catalytic activity in a sequence-dependent matter. Regrettably, however, no distict patterns or trends were evident in terms of which sequences induce an increase or decrease in the catalytic activity. Thus, the present work is restricted to the phenomenological description of these effects and possible explanations are hypothetical. On the basis of (i) the *in silico* analysis of oligonucleotide sequences and (ii) the variability of reactivity patterns observed for the various systems, it seems safe to assume that the formation of stable oligonucleotide secondary structures or homodimers is not the predominant mode of action. In addition, since we used only one substrate (Amplex Red) throughout the entire study, the reactivity patterns observed cannot originate from interactions between the substrates and/or inhibitors with the nucleic acid or protein because this should bias all catalyst systems in a similar way. More likely, therefore, distinct interactions, such as hydrogen bonding or electrostatic contacts, between the oligonucleotides and the heme-containing catalyst may account for the effects observed. As discussed above, this hypothesis is supported by numerous previous studies of artificial heme enzymes, reconstituted with non-natural heme derivatives. It is clearly evident from these studies that the introduction of hydrogen donor and acceptor groups to the heme do influence the hydrogen bond network of the Mb. This can signficantly change the catalytic activity of the enzyme and also affect its secondary and tertiary structures (*42*, *45*). Similar effects have also been observed for other heme enzymes, such as hemoglobin (*46*). Therefore, we speculate that sequence-dependent, distinct contacts between the nucleic acid and the protein are responsible for the observed phenomenon. The detailed analysis of structural origins on the molecular level might be unraveled by NMR or X-ray crystallography, and efforts toward this challenging goal are currently underway.

Even without knowing the detailed mechanism of action, the present work has implications on the design and development of semiartificial biomolecular hybrid catalysts. On the one hand, catalysts containing only nucleic acids as the biomolecular component should be carefully analyzed for similar sequence-dependent secondary effects (*12*, *13*). On the other hand, hybrid catalysts comprising proteins as the biomolecular component (*4*−*11*) might be revisited to explore whether the synthetic appendix induces conformational changes in addition to providing the primary catalytic effect. Moreover, our study demonstrates that hybrid catalysts containing both nucleic acid and protein components have an intrinsic potential for tuning the catalytic activity by simply changing the base composition. As

demonstrated here, a weak catalyst, such as myoglobin, can be improved either 30-fold or even 280-fold by simply changing the oligonucleotide sequence. We therefore anticipate that current developments of nucleic acid−based hybrid catalysts will benefit from focusing on designed oligomer sequences, selected by either rational or evolutive methods, to facilitate the generation of novel powerful catalysts.

ACKNOWLEDGMENT

This work was supported through funding from Zentrum für Angewandte Chemische Genomik (ZACG), a joint research initiative funded by the European Union and the Ministry of Innovation and Research of the state Northrhine Westfalia. We thank Jens Reiber for experimental support and Dr. Ljiljana Fruk, Dr. Udo Feldkamp, and Kersten Rabe for valuable discussions.

Supporting Information Available: Full details on experimental protocols for conjugate synthesis, Michaelis−Menten kinetic measurements, data analysis, and controls. This material is available free of charge via the Internet at http://pubs.acs.org.

LITERATURE CITED

(1) Waldmann, H., and Drauz, K. *Enzymes Catalysis in Organic Synthesis*, Wiley-VCH, New York, 2002.
(2) Qi, D., Tann, C. M., Haring, D., and Distefano, M. D. (2001) Generation of new enzymes via covalent modification of existing proteins. *Chem. Rev. 101*, 3081–3111.
(3) Kramer, R. (2006) Supramolecular bioinorganic hybrid catalysts for enantioselective transformations. *Angew. Chem., Int. Ed. 45*, 858–860.
(4) Wilson, M. E., and Whitesides, G. M. (1978) Conversion of a Protein to a homogeneous asymmetric hydrogenation catalyst by site-specific modification with a diphosphinerhodium(I) moiety. *J. Am. Chem. Soc. 10*, 306–307.
(5) Letondor, C., Humbert, N., and Ward, T. R. (2005) Artificial metalloenzymes based on biotin-avidin technology for the enantioselective reduction of ketones by transfer hydrogenation. *Proc. Natl. Acad. Sci. U.S.A. 102*, 4683–4687.
(6) Klein, G., Humbert, N., Gradinaru, J., Ivanova, A., Gilardoni, F., Rusbandi, U. E., and Ward, T. R. (2005) Tailoring the active site of chemzymes by using a chemogenetic-optimization procedure: towards substrate-specific artificial hydrogenases based on the biotin-avidin technology. *Angew. Chem., Int. Ed. 44*, 7764–7767.
(7) Reetz, M. T., Peyralans, J. J., Maichele, A., Fu, Y., and Maywald, M. (2006) Directed evolution of hybrid enzymes: Evolving enantioselectivity of an achiral Rh-complex anchored to a protein. *Chem. Commun. (Cambridge, U. K.)* 4318–4320.
(8) Reetz, M. T., Rentzsch, M., Pletsch, A., and Maywald, M. (2002) Towards the directed evolution of hybrid catalysts. *Chimia 56*, 721–723.
(9) Panella, L., Broos, J., Jin, J., Fraaije, M. W., Janssen, D. B., Jeronimus-Stratingh, M., Feringa, B. L., Minnaard, A. J., and de Vries, J. G. (2005) Merging homogeneous catalysis with biocatalysis; papain as hydrogenation catalyst. *Chem. Commun. (Cambridge, U. K.)* 5656–5658.
(10) Haquette, P., Salmain, M., Svedlung, K., Martel, A., Rudolf, B., Zakrzewski, J., Cordier, S., Roisnel, T., Fosse, C., and Jaouen, G. (2007) Cysteine-specific, covalent anchoring of transition organometallic complexes to the protein papain from *Carica papaya*. *ChemBioChem 8*, 224–231.
(11) Reetz, M. T., and Jiao, N. (2006) Copper-phthalocyanine conjugates of serum albumins as enantioselective catalysts in Diels-Alder reactions. *Angew. Chem., Int. Ed. 45*, 2416–2419.
(12) Roelfes, G., and Feringa, B. L. (2005) DNA-based asymmetric catalysis. *Angew. Chem., Int. Ed. 44*, 3230–3232.
(13) Boersma, A. J., Klijn, J. E., Feringa, B. L., and Roelfes, G. (2008) DNA-based asymmetric catalysis: sequence-dependent rate acceleration and enantioselectivity. *J. Am. Chem. Soc. 130*, 11783–11790.
(14) Hayashi, T., and Hisaeda, Y. (2002) New functionalization of myoglobin by chemical modification of heme-propionates. *Acc. Chem. Res. 35*, 35–43.
(15) Lu, Y. (2005) Design and engineering of metalloproteins containing unnatural amino acids or non-native metal-containing cofactors. *Curr. Opin. Chem. Biol. 9*, 118–126.
(16) Ipe, B. I., and Niemeyer, C. M. (2006) Nanohybrids Composed of Quantum Dots and Cytochrome P450 as Photocatalysts. *Angew. Chem., Int. Ed. 45*, 504–507.
(17) Fruk, L., Rajendran, V., Spengler, M., and Niemeyer, C. M. (2007) Light-induced triggering of peroxidase activity using quantum dots. *ChemBioChem 8*, 2195–2198.
(18) Gandubert, V. J., Torres, E., and Niemeyer, C. M. (2008) Investigation of cytochrome P450-modified cadmium sulfide quantum dots as photocatalysts. *J. Mater. Chem. 18*, 3824–3830.
(19) Xiao, Y., Patolsky, F., Katz, E., Hainfeld, J. F., and Willner, I. (2003) "Plugging into Enzymes": nanowiring of redox enzymes by a gold nanoparticle. *Science 299*, 1877–1881.
(20) Willner, B., Katz, E., and Willner, I. (2006) Electrical contacting of redox proteins by nanotechnological means. *Curr. Opin. Biotechnol. 17*, 589–596.
(21) Fruk, L., Kuo, C.-H., Torres, E., and Niemeyer, C. M. (2009) Apoenzyme reconstitution as a chemical tool for structural enzymology and biotechnology. *Angew. Chem., Int. Ed. 48*, 1550–1574.
(22) Fruk, L., and Niemeyer, C. M. (2005) Covalent hemin-DNA adducts for generating a novel class of artifical heme enzymes. *Angew. Chem., Int. Ed. 44*, 2603–2606.
(23) Fruk, L., Müller, J., and Niemeyer, C. M. (2006) Kinetic analysis of semisynthetic peroxidase enzymes containing a covalent DNA−heme adduct as the cofactor. *Chem.—Eur. J. 12*, 7448–7457.
(24) Fruk, L., Müller, J., Weber, G., Narváez, A., Domínguez, E., and Niemeyer, C. M. (2007) DNA-directed immobilization of horseradish peroxidase-DNA conjugates on microelectrode arrays: towards electrochemical screening of enzyme libraries. *Chem.—Eur. J. 13*, 5223–5231.
(25) Keilin, D., and Hartree, E. F. (1955) Catalase, peroxidase and metmyoglobin as catalysts of coupled peroxidatic reactions. *Biochem. J. 60*, 310–325.
(26) George, P., and Irvine, D. H. (1952) The reaction between metmyoglobin and hydrogen peroxide. *Biochem. J. 52*, 511–517.
(27) Kalyanaraman, B., Mason, R. P., Tainer, B., and Eling, T. E. (1982) The free radical formed during the hydroperoxide-mediated deactivation of ram seminal vesicles is hemoprotein-derived. *J. Biol. Chem. 257*, 4764–4768.
(28) Fruk, L., Kuhlmann, J., and Niemeyer, C. M. (2009) Analysis of heme-reconstitution of apoenzymes by means of surface plasmon resonance. *Chem. Commun.* 230–232.
(29) Teale, F. W. (1959) Cleavage of the haem-protein link by acid methylethylketone. *Biochim. Biophys. Acta 35*, 543.
(30) Full details of experimental protocols for conjugate synthesis, Michaelis−Menten kinetic measurements, data analysis, and controls are available in the Supporting Information.
(31) Feldkamp, U., Wacker, R., Banzhaf, W., and Niemeyer, C. M. (2004) Microarray-based in vitro evaluation of DNA oligomer libraries designed in silico. *ChemPhysChem 5*, 367–372.
(32) Capeland, R. A. *Enzymes: A Practical Introduction to Structure, Mechanism and Data Analysis*, Wiley-VCH, New York, 2000.
(33) Eisenthal, R., Danson, M. J., and Hough, D. W. (2007) Catalytic efficiency and kcat/KM: a useful comparator? *Trends Biotechnol. 25*, 247–249.
(34) Witting, P. K., Travascio, P., Sen, D., and Mauk, A. G. (2001) A DNA oligonucleotide-hemin complex cleaves t-butyl hydroperoxide through a homolytic mechanism. *Inorg. Chem. 40*, 5017–5023.

(35) Travascio, P., Li, Y., and Sen, D. (1998) DNA-enhanced peroxidase activity of a DNA-aptamer-hemin complex. *Chem. Biol. 5*, 505–517.
(36) Travascio, P., Bennet, A. J., Wang, D. Y., and Sen, D. (1999) A ribozyme and a catalytic DNA with peroxidase activity: active sites versus cofactor-binding sites. *Chem. Biol. 6*, 779–787.
(37) Travascio, P., Witting, P. K., Mauk, A. G., and Sen, D. (2001) The peroxidase activity of a hemin--DNA oligonucleotide complex: free radical damage to specific guanine bases of the DNA. *J. Am. Chem. Soc. 123*, 1337–1348.
(38) Xiao, Y., Pavlov, V., Gill, R., Bourenko, T., and Willner, I. (2004) Lighting up biochemiluminescence by the surface self-assembly of DNA-hemin complexes. *ChemBioChem 5*, 374–379.
(39) Weizmann, Y., Cheglakov, Z., Pavlov, V., and Willner, I. (2006) Autonomous fueled mechanical replication of nucleic acid templates for the amplified optical detection of DNA. *Angew. Chem., Int. Ed. 45*, 2238–2242.
(40) Willner, I., Shlyahovsky, B., Zayats, M., and Willner, B. (2008) DNAzymes for sensing, nanobiotechnology and logic gate applications. *Chem. Soc. Rev. 37*, 1153–1165.
(41) Markham, N. R., and Zuker, M. (2005) DINAMelt web server for nucleic acid melting prediction. *Nucleic Acids Res. 33*, W577–W581; http://dinamelt.bioinfo.rpi.edu/twostate-fold.php.
(42) Monzani, E., Alzuet, G., Casella, L., Redaelli, C., Bassani, C., Sanangelantoni, A. M., Gullotti, M., de Gioia, L., Santagostini, L., and Chillemi, F. (2000) Properties and reactivity of myoglobin reconstituted with chemically modified protohemin complexes. *Biochemistry 39*, 9571–9582.
(43) Burrows, C. J., and Muller, J. G. (1998) Oxidative nucleobase modifications leading to strand scission. *Chem. Rev. 98*, 1109–1152.
(44) Bevilacqua, P. C., and Yajima, R. (2006) Nucleobase catalysis in ribozyme mechanism. *Curr. Opin. Chem. Biol. 10*, 455–464.
(45) Roncone, R., Monzani, E., Murtas, M., Battaini, G., Pennati, A., Sanangelantoni, A. M., Zuccotti, S., Bolognesi, M., and Casella, L. (2004) Engineering peroxidase activity in myoglobin: the haem cavity structure and peroxide activation in the T67R/S92D mutant and its derivative reconstituted with protohaemin-l-histidine. *Biochem. J. 377*, 717–724.
(46) Ishimori, K., and Morishima, I. (1986) NMR study of hybrid hemoglobins containing unnatural heme: effect of heme modification on their tertiary and quaternary structures. *Biochemistry 25*, 4892–4898.

BC800558G

Tuning of Peroxidase-Activity by Covalently Tethered DNA Oligonucleotides

Maximilian Glettenberg and Christof M. Niemeyer*

Supporting Information

List of contents

1. Experimental
2. Tables
3. Figures
4. References

1. Experimental

Chemicals and Materials. Horseradish peroxidase (HRP; purity number of 3), horse heart myoglobin (Mb), Hemin (Protoporphyrin IX), Fluoranthene, 2-Butanone, Dithiothreitol (DTT) and all used oligonucleotides with modifications or left on solid support (see Table 1) were purchased from Sigma-Aldrich. O-(benzotriazol-1-yl)-N,N,N',N'-tetramethyluronium hexafluorophosphate (HBTU), hydrogen peroxide (30%) and 3% dichloroacetic acid in dichloromethane were from Fluka. N,N-dimethylformide (DMF), *tert*-butylamine, N,N-Diisopropylethylamine (DIPEA) and 9-Methylanthracene was obtained from Acros. Acetonitrile (ACN) and Methanol (MeOH) were purchased from Roth. N-Hydroxybenzotriazole (HOBt) and AmplexRed were from Nova Biochem and Invitrogen, respectively. Bifunctional crosslinker Sulfosuccinimidyl 4-[N-maleimidomethyl]cyclohexane-1-carboxylate (sSMCC) was obtained from Pierce. VIVA-Spin columns (MWCO 10kDa) were purchased from VivaScience, untreated F96 microtiterplates and F16-maxisorp modules from NUNC and Sephadex NAP-5 and Sephadex NAP-10 size exclusion columns from Amersham Bioscience.

Buffers. Phosphate buffer (mix of 0.1 M KH_2PO_4 and K_2HPO_4 to obtain a pH of 7.4), PBS buffer (phosphate buffer + 300 mM NaCl), TE (10 mM Tris-Cl, 1 mM EDTA, pH 7.4), TRIS A (20 mM Tris-Cl, pH 8.3), TRIS B (20 mM Tris-Cl, 1.5 M NaCl, pH 8.3)

DNA-heme conjugates. Synthesis of the DNA-heme conjugates was carried out as reported before (*1, 2*). In brief, Hemin (Protoporphyrin IX) was activated in solution by using O-(benzotriazol-1-yl)-N,N,N',N'-tetramethyluronium hexafluorophosphate (HBTU), N-

Hydroxybenzotriazole (HOBt) and N,N-Diisopropylethylamine (DIPEA) in DMF and coupled to the 5'-alkylamino-modified oligonucleotides. The oligonucleotides were still attached the the controlled porous glass (CPG) solid support, while the trityl amino protecting group was removed by use of 3% dichloroacetic acid in methylcyanide (ACN) as deprotection solution. Coupling at room temperature (1.5 hours) yielded, after thorough washing with DMF, ACN and drying under Argon, heme-DNA conjugates with 1 ($hemeD_1$) or 2 ($hemeD_2$) DNA-oligonucleotides attached to the carboxylic groups of the heme. Subsequent to incubation of the CPG coupled products in a solution of *tert*-butylamine, MeOH, H_2O (1:2:1 v/v/v) and 65°C to cleave them from the solid support, the heme-DNA conjugates were purified with reversed-phase HPLC (A:Ammoniumacetate, B:Acetonitrile, linear gradient). For examplary chromatogram, see Figure S1A). Buffer exchange using NAP-5 and NAP-10 columns with water as solvent yielded the desired $hemeD_1$ and $hemeD_2$ which were subsequently analyzed by MALDI (see Figure S2A and B).

Apoenzyme reconstitution to generate DNA-enzyme conjugates. The apoenzymes apoMb and apoHRP, lacking their heme cofactor, were prepared by Teale's 2-butanone method (*3*). Briefly, 200 μL of a 50 μM aqueous solution of the enzyme was acidified to pH 2.3 (Mb) or 2.5 (HRP) using 0.1 M HCl and the heme was extracted by addition of ice cold 2-butanone. The colorless apoenzyme solution was then passed through a NAP-5 size exclusion column to remove the excess of 2-butanone. These freshly prepared apoenzymes were then reconstituted with DNA-heme conjugates (in phosphate buffer) at 4°C and incubated 24 to 48 hours, since the reconstitution of apoHRP with DNA-heme conjugates takes more time, as described before (*1*). The semisynthetic DNA-enzyme conjugates (rMbD1, rMbD2 and rHRPD1, rHRPD2, see Figure 1) were analyzed and purified by FPLC by using a linear gradient of 1.5 M NaCl in Tris buffer, pH 8.3 (TRIS B) over 25 min (for example, see Figure S1B) that followed centrifugation with VIVA-Spin columns (MWCO 10kDa) and rebuffering to PBS buffer. Concentrations were determined spectrophotometrically.

Chemical DNA-HRP conjugates. For the activation of the 5'-thiolated oligonucleotide (SHF1, SHF5, SHF9 or SHF10; oligonucleotide sequences are identical to those given for oligomers F1, F5, F9, and F10 in Table 1) in TE buffer, 60 μL of a 1 M dithiothreitol (DTT) solution in H_20 was added, briefly mixed and incubated overnight at 37°C. In the meantime, 2 mg of the bifunctional crosslinker sulfosuccinimidyl 4-[N-maleimidomethyl]cyclohexane-1-carboxylate (sSMCC) were dissolved in 60 μL of DMF. The sSMCC-solution was then combined with 200 μL of a 100 μM solution of HRP in phosphate buffer (0.1M, pH 7.4). This mixture was protected from light and incubated for 1 hour at room temperature. Prior to

combining the thiolated DNA and the HRP-crosslinker solutions, both solutions were purified by size exclusion chromatography using NAP-5 and NAP-10 columns, using phosphate buffer (0.1M, pH 7.4). The combined solutions were protected from light and incubated at room temperature for 2 hours. Subsequently, the reaction mixture was transferred to a VIVA-Spin column (MWCO 10kDa) for buffer exchange to TRIS A and to remove starting materials. Repeated centrifugation steps at 4500 rpm were used for concentration of the sample until a final volume of 200 – 300 μL was reached. The chemical DNA-HRP conjugates were then further purified via FPLC using MonoQ Anion Exchange Column and linear gradient (TRIS A and TRIS B). The DNA-HRP conjugates, containing only one oligonucleotide per HRP, were collected, concentrated and rebuffered in PBS using VIVA-Spin column. Concentration was determined spectrophotometrically and purity was analyzed by non-denaturing acrylamide gel-electrophoreses.

Peroxidase assays. Michaelis-Menten kinetic analyses of the various enzyme-DNA conjugates were carried out as previously described (*2*). Peroxidase assays were measured with the multiwellplate reader Synergy II from BioTek (Bad Friedrichshall, Germany) and carried out in black 96-well microtiterplates from NUNC. In one row of the plate the reaction mixture consisting of hydrogen peroxide and AmplexRed in phosphate buffer (0.1 M, pH 7.4, 300 mM NaCl) was prepared in sufficient amount to start the reaction in each well simoultaneously with a multichannel pipette. In the next rows of the plate the negative control and the enzyme solutions were present (each 50 μL). Subsequent 50 µL of the reaction mixture were added to each well to start the reaction. The final concentrations were 1 mM hydrogen peroxide, 10 nM rMb and 5 nM rHRP respectively. The AmplexRed concentrations varied from 0.05 to 200 µM. Determination of Michaelis-Menten-constants was carried out similar as described before (*2*). All the kinetic curves of the conjugates revealed substrate inhibition characteristics, which was accounted for by using the appropriate two parameter fit for Michaelis-Menten kinetics (*4*). To obtain Michaelis–Menten parameters Equation (1) was used, which takes into account the effects occurring from substrate inhibition.

$$\frac{v_0}{[\mathrm{E}]_0} = \frac{k_{\mathrm{cat}}[\mathrm{S}]}{K_{\mathrm{M}} + [\mathrm{S}]\left(1 + \frac{[\mathrm{S}]}{K_{\mathrm{S}}}\right)} \qquad (1)$$

Determination of competetive vs non-competetive inhibitor action. To determine the nature of inhibition of HRP by 9-Methylanthracene and Fluoranthene (Scheme S1), kinetic measurements of Amplex Red peroxidation were carried out as described above, however, in

presence of constant inhibitor concentrations. To prepare the Lineweaver-Burk-Plots, the data obtained were normalized and $1/v_0$ was plotted against 1/[S], depicting the reziprokal substrate concentration of Amplex Red (*5*). Exemplary figures are shown in Figure S4.

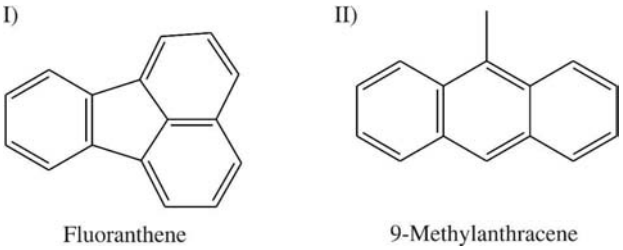

Scheme S1: Structures of the two inhibitors of HRP used in this study.

Determination of IC50 values. For the determination of the IC50 values the similar pippetting scheme was used, as described for Michaelis-Menten kinetics. However, various concentrations of the inhibitors 9-Methylanhracene and Fluoranthene were present in these measurements while Amplex Red concentration was fixed to 10 μM. The inhibitors were diluted in Acetonitrile and adjusted to a range of concentration (10^{-5} μM to 500 μM). This way the same volume of Acetonitrile was present in all samples. Enzyme concentrations were always 5 nM and the concentration of hydrogen peroxide was 1 mM. Analysis was carried out in 96-well microtiterplates from NUNC using the Synergy II microplate reader for fluorescence measurements. The resulting data are shown in Figures S5-S9.

2. Tables

Table S1: Kinetic data determined by Michaelis-Menten measurements of various myoglobin-oligonucleotide conjugates. Conjugates with one or two DNA oligonucleotides are denoted as D_1 or D_2, respectively.

No.	nt	Name	k_{cat} [10^{-3} s^{-1}]	K_M [μM]	k_{cat}/K_M [$10^{-3}\mu M^{-1}s^{-1}$]
15	24	rMbA24	D_1: 9 ± 2 D_2: 13 ± 2	D_1: 0.11 ± 0.04 D_2: 0.05 ± 0.02	D_1: 90 ± 44 D_2: 281 ± 100
16	14	rMbB14	D_1: 7 ± 3 D_2: 7 ± 1	D_1: 0.16 ± 0.06 D_2: 0.11 ± 0.01	D_1: 47 ± 15 D_2: 62 ± 12
17	12	rMbA12	D_1: 8 ± 2 D_2: 12 ± 4	D_1: 0.10 ± 0.02 D_2: 0.06 ± 0.01	D_1: 89 ± 20 D_2: 212 ± 71
18	12	rMbC2b	D_1: 6 ± 3 D_2: 18 ± 6	D_1: 0.17 ± 0.05 D_2: 0.34 ± 0.05	D_1: 34 ± 11 D_2: 55 ± 13
19	12	rMbGA1	D_1: 15 ± 5 D_2: 24 ± 8	D_1: 0.16 ± 0.02 D_2: 0.20 ± 0.03	D_1: 91 ± 23 D_2: 125 ± 33
20	12	rMbGA2	D_1: 31 ± 10 D_2: 30 ± 13	D_1: 0.36 ± 0.09 D_2: 0.15 ± 0.08	D_1: 86 ± 21 D_2: 211 ± 37
21	12	rMbGA3	D_1: 41 ± 2 D_2: 63 ± 1	D_1: 0.24 ± 0.04 D_2: 0.27 ± 0.02	D_1: 174 ± 34 D_2: 237 ± 26
22	12	rMbGA4	D_1: 31 ± 12 D_2: 42 ± 12	D_1: 0.33 ± 0.05 D_2: 0.23 ± 0.03	D_1: 96 ± 27 D_2: 182 ± 26
23	12	rMbGA5	D_1: 27 ± 8 D_2: 54 ± 10	D_1: 0.27 ± 0.04 D_2: 0.28 ± 0.03	D_1: 100 ± 28 D_2: 190 ± 27

Table S2: Kinetic data determined by Michaelis-Menten measurements of reconstituted rHRP-D_1 conjugates, hybridized with their Watson-Crick complements cF1, cF2, cF5, cF10

No.	nt	Name	k_{cat} [10^{-3} s^{-1}]	K_M [µM]	k_{cat}/K_M [$10^{-3}\mu M^{-1}s^{-1}$]
1	22	rHRP-F1_cF1	D_1: 14820 ± 6580	D_1: 354 ± 140	D_1: 41 ± 2
2	22	rHRP-F5_cF5	D_1: 1300 ± 570	D_1: 240 ± 150	D_1: 6 ± 1
3	22	rHRP-F9_cF9	D_1: 530 ± 180	D_1: 15 ± 2	D_1: 34 ± 7
4	22	rHRP-F10_cF10	D_1: 15160 ± 2150	D_1: 290 ± 10	D_1: 53 ± 6

Table S3: IC50 values of competitive inhibitors Fluoranthene and 9-Methylanthracene with chemically modified cHRP-D_1-conjugates.

No	Name	Fluoranthene IC50 [μM]	9-Methylanthracene IC50 [μM]
1	cHRP-F1	79.8 ± 1.7	86.8 ± 2.7
2	cHRP-F5	52.1 ± 12.1	41.6 ± 2.8
3	cHRP-F9	61.2 ± 7.3	73.7 ± 3.2
4	cHRP-F10	74.4 ± 3.4	80.8 ± 6.2

3. Figures

Figure S1

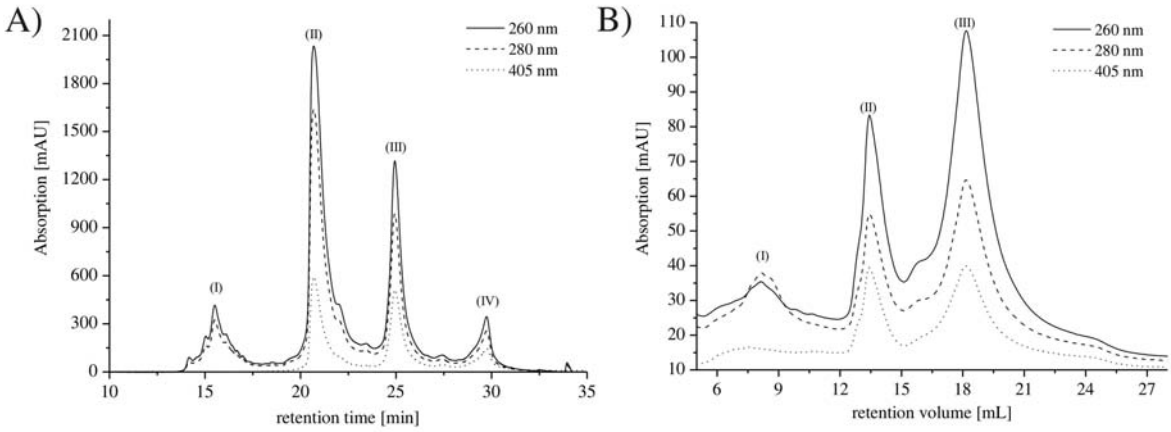

Figure S1 A) HPLC chromatogram of DNA-heme conjugate purification, examplified for conjugate hemeF1. The four peaks show I) uncoupled F1, II) hemeF1-D_2, III) hemeF1-D_1 and IV) free heme. B) FPLC chromatogram of DNA-HRP conjugate purification, examplified for conjugate rHRP-F5-D_1. The three different peaks represent I) apoHRP, II) rHRP-F5-D_1 and III) hemeF1-D_1.

Figure S2

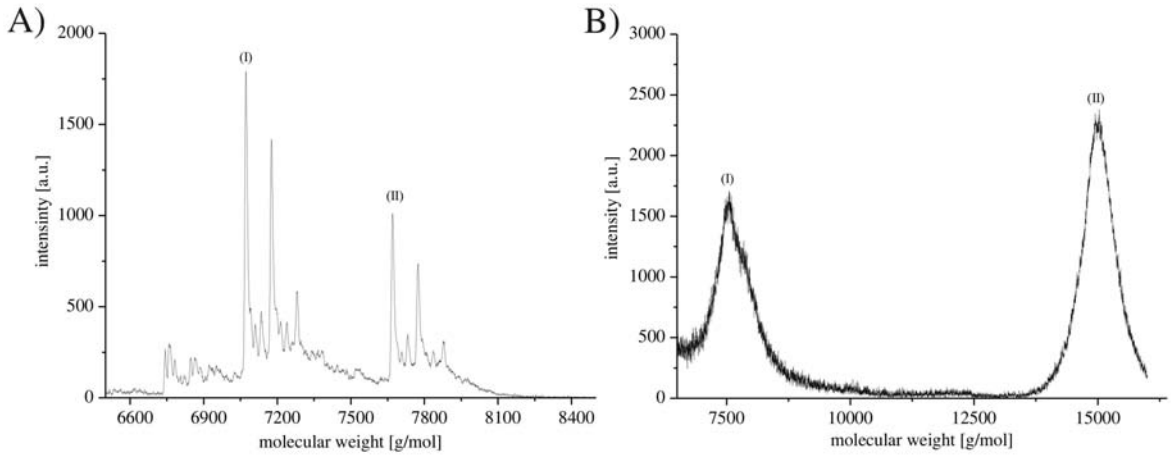

Figure S2 MALDI measurements of A) hemeF9-D1 with measured MW = 7671 g/mol (calculated MW = 7719 g/mol) and B) hemeF9-D_2 with measured MW = 14990 g/mol (calculated MW = 14788 g/mol)

Figure S3

Sequence	ssDNA-fold	homodimer
F1	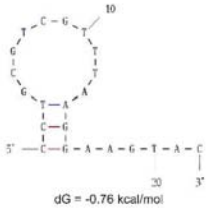	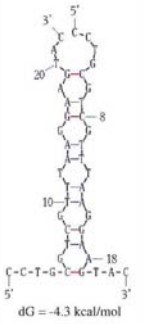
F5	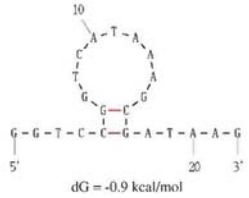	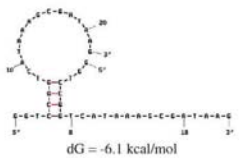
F9	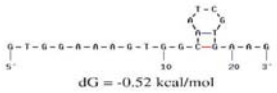	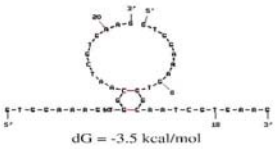
F10	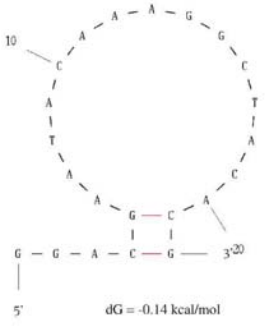	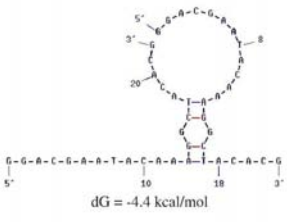

Figure S3 DINAMelt-Sever (*6*) *in silico* analysis of the F-oligonucleotide sequences; T = 25 °C, [Na^+] = 300 mM

Figure S4

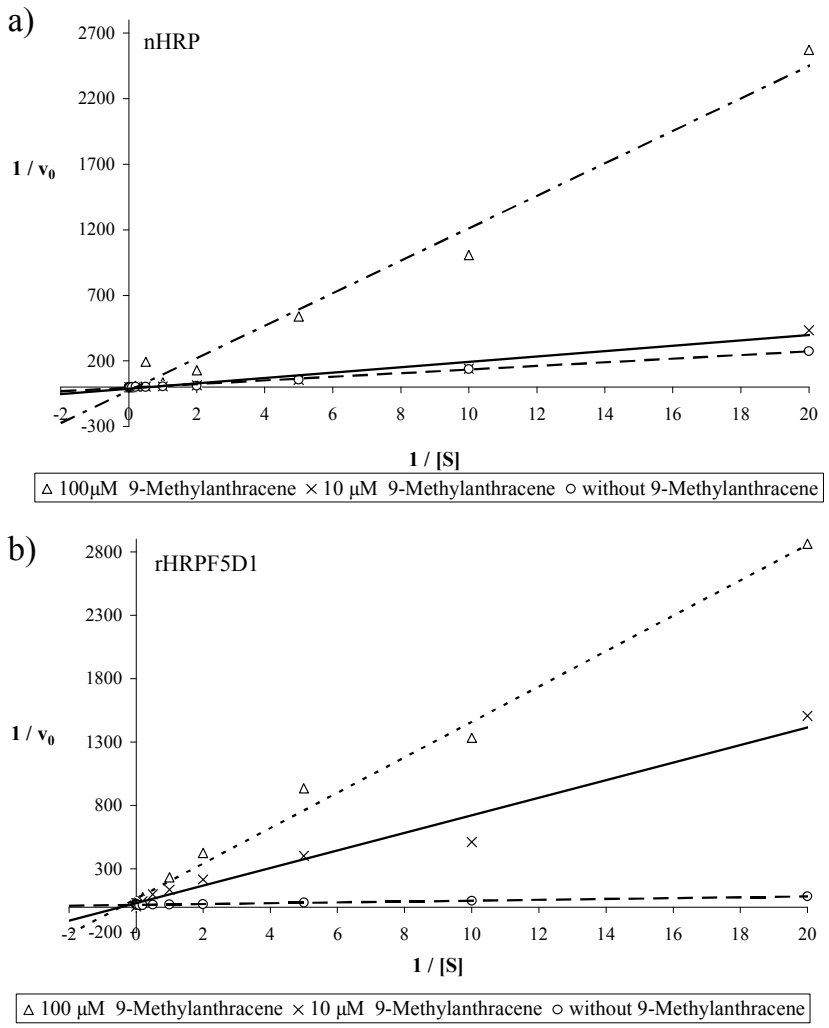

Figure S4 : Lineweaver-Burk-Plots of the a) nHRP and b) rHRPF5D1 with varying concentrations of 9-Methylanthracene. The plots clearly indicate that $1/V_{max}$ (intercept of y-axis) is constant, while K_M (calculated from slope of the curve and/or intercept of x-axis) is changed upon addition of the inhibitor. This characteristics is indicative for competitive inhibition.(*5*) Similar measurements with Fluoranthene gave comparable results.

Figure S5

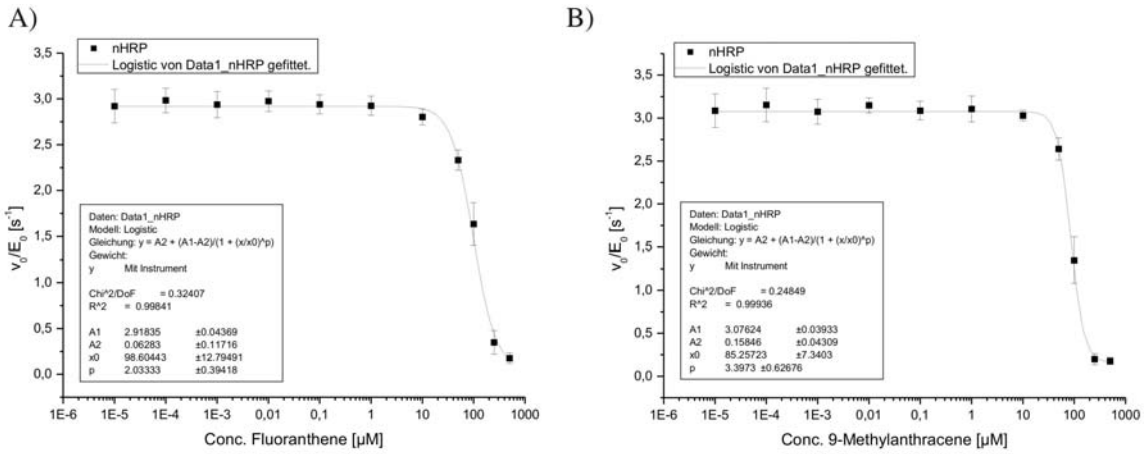

Figure S5 IC50 measurements of native HRP. Shown are plots of v_0/E_0 vs. the logarithmic Inhibitor concentration. A) nHRP with Fluoranthene; B) nHRP with 9-Methylanthracene. The concentration of the inhibitors was varied from 10^{-5} μM to 500 μM. Note that higher inhibitor concentrations were not applicable due to limited solubility in the buffer. The resulting curves were fitted sigmoidally to obtain the IC50 values.

Figure S6

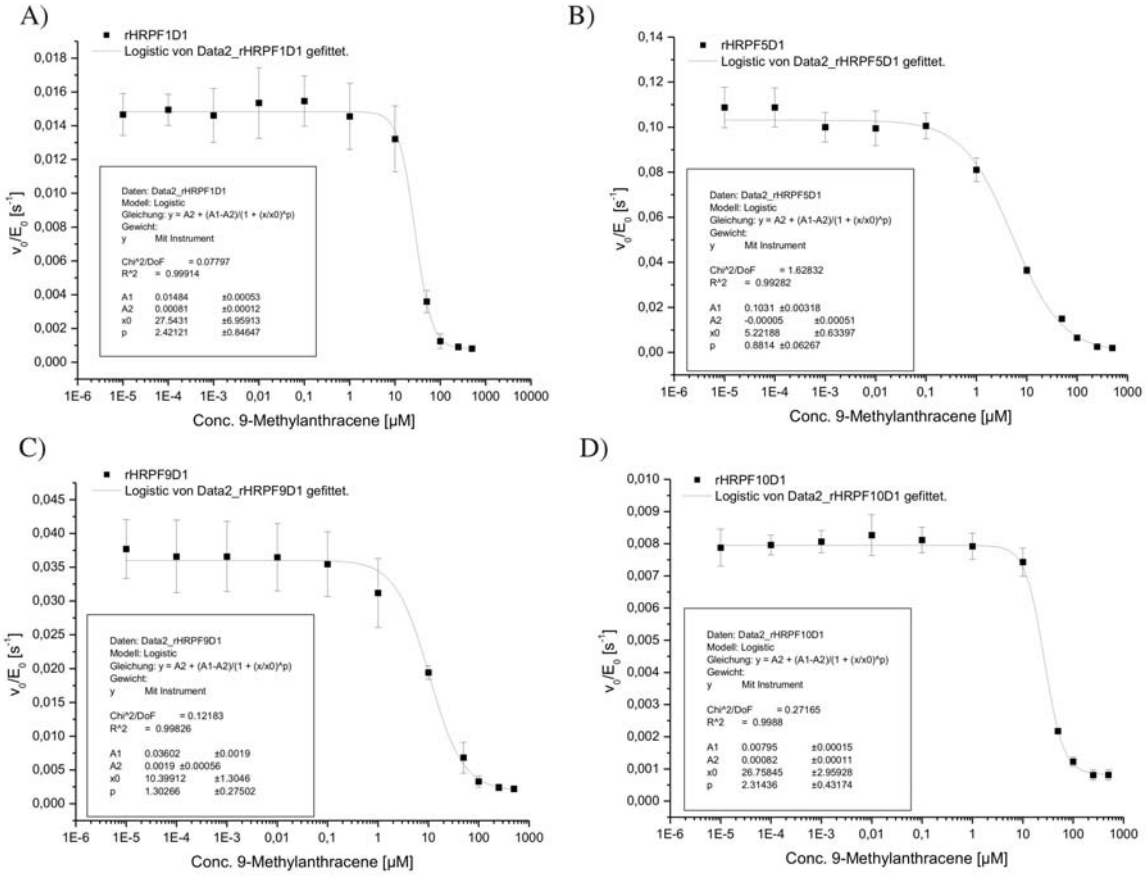

Figure S6 Plots of v_0/E_0 vs. the logarithmic Inhibitor concentration. In A) rHRPF1D1, B) rHRPF5D1, C) rHRPF9D1 and in D) rHRPF10D1. The concentration of 9-Methylanthracene varied from 10^{-5} μM to 500 μM. Note that higher inhibitor concentrations were not applicable due to limited solubility in the buffer. The resulting curves were fitted sigmoidally to obtain the IC50 values.

Figure S7

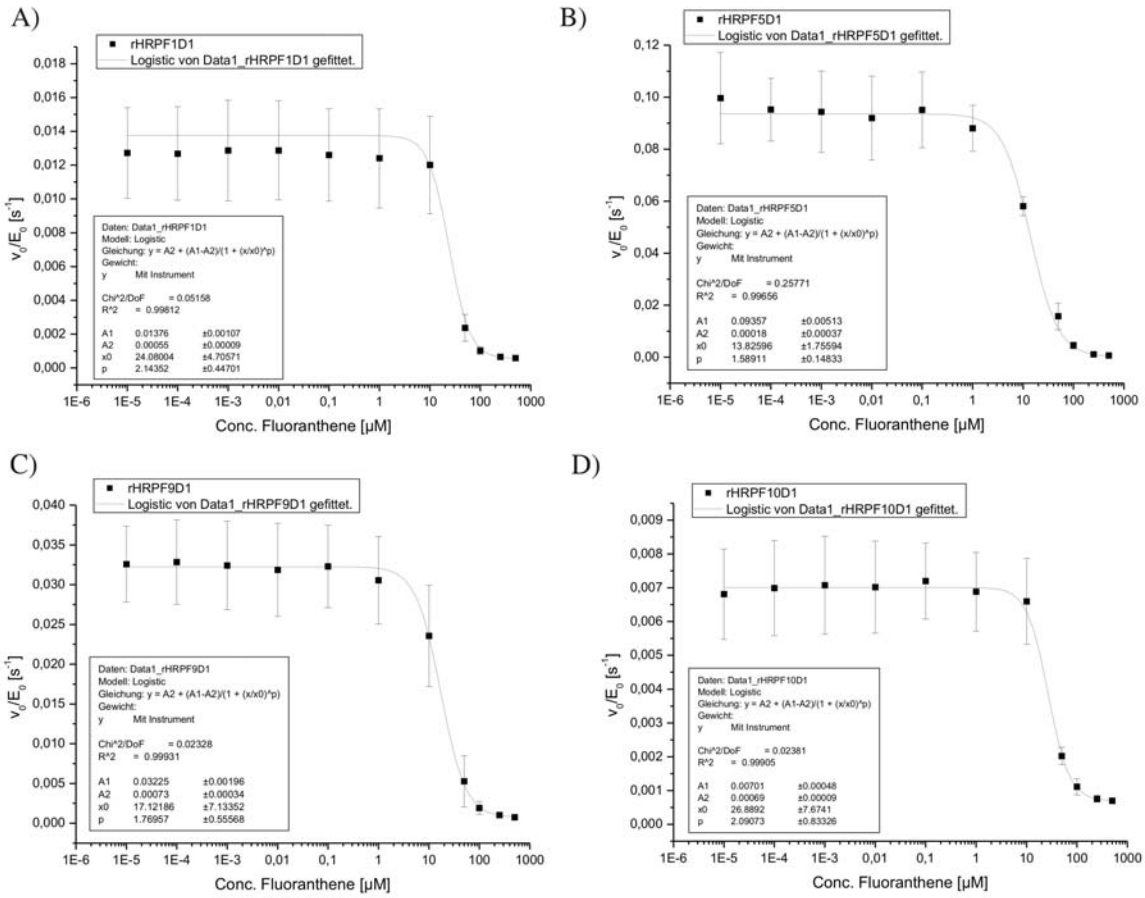

Figure S7 Plots of v_0/E_0 vs. the logarithmic Inhibitor concentration. In A) rHRPF1D1, B) rHRPF5D1, C) rHRPF9D1 and in D) rHRPF10D1. The concentration of Fluoranthene varied from 10^{-5} μM to 500 μM. Note that higher inhibitor concentrations were not applicable due to limited solubility in the buffer. The resulting curves were fitted sigmoidally to obtain the IC50 values.

Figure S8

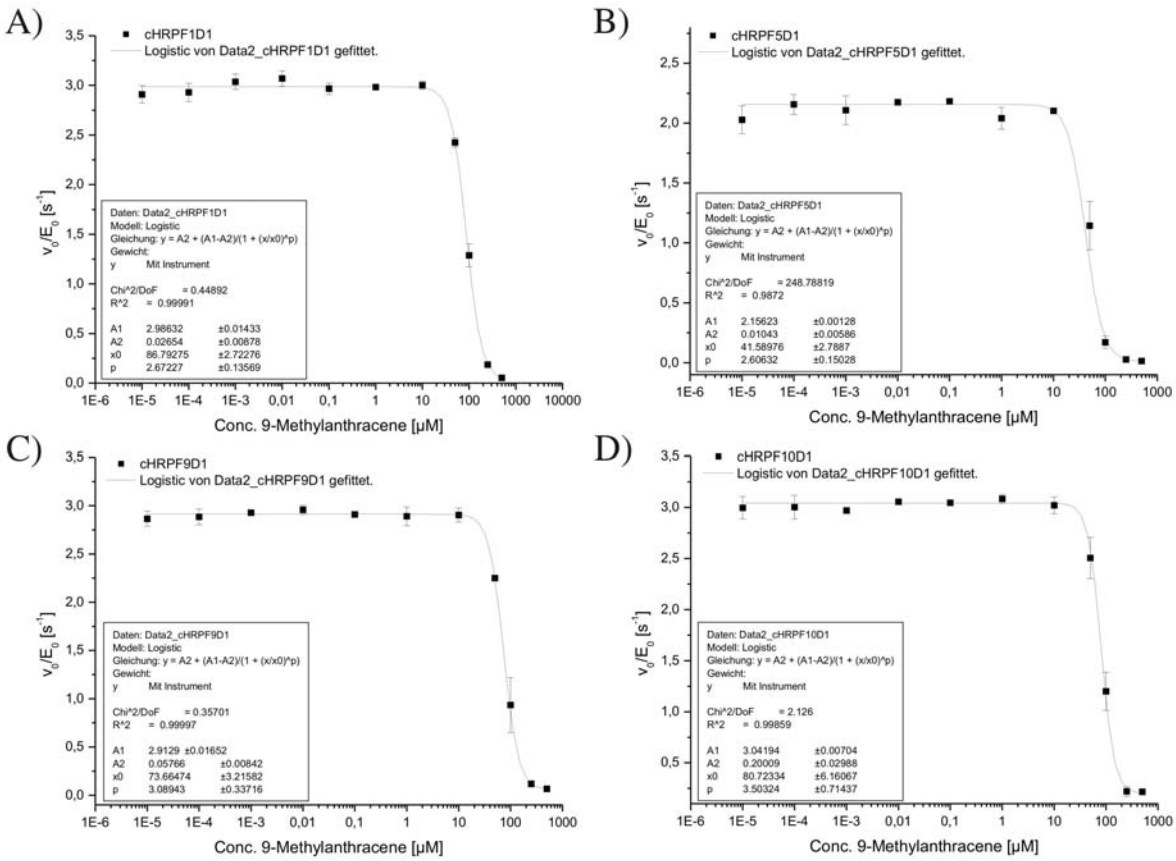

Figure S8 Plots of v_0/E_0 vs. the logarithmic Inhibitor concentration. In A) cHRPF1D1, B) cHRPF5D1, C) cHRPF9D1 and in D) cHRPF10D1. The concentration of 9-Methylanthracene varied from 10^{-5} μM to 500 μM. Note that higher inhibitor concentrations were not applicable due to limited solubility in the buffer. The resulting curves were fitted sigmoidally to obtain the IC50 values.

Figure S9

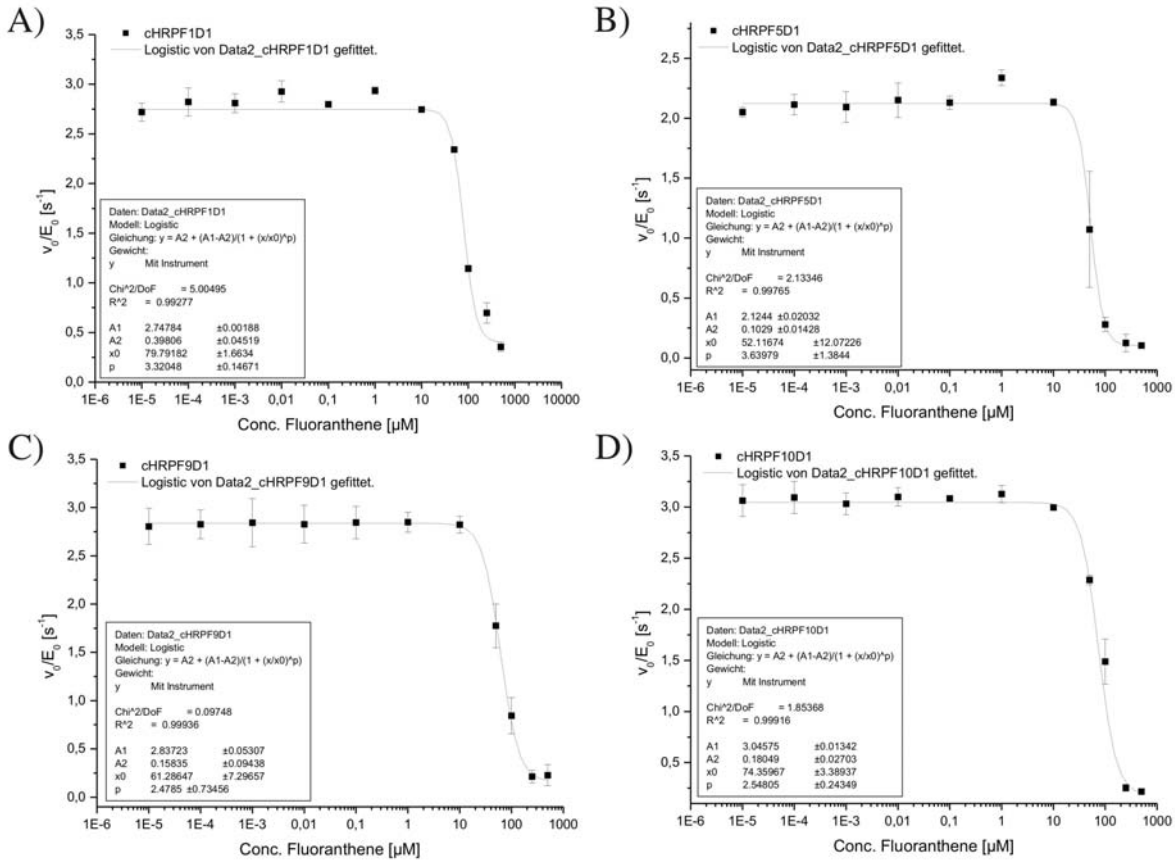

Figure S9 Plots of v_0/E_0 vs. the logarithmic Inhibitor concentration. In A) cHRPF1D1, B) cHRPF5D1, C) cHRPF9D1 and in D) cHRPF10D1. The concentration of Fluoranthene varied from 10^{-5} μM to 500 μM. Note that higher inhibitor concentrations were not applicable due to limited solubility in the buffer. The resulting curves were fitted sigmoidally to obtain the IC50 values.

4. References

(1) Fruk, L., and Niemeyer, C. M. (2005) Covalent Hemin-DNA Adducts for Generating a Novel Class of Artifical Heme Enzymes. *Angew. Chem. Int. Ed. 44*, 2603 –2606.

(2) Fruk, L., Müller, J., and Niemeyer, C. M. (2006) Kinetic analysis of semisynthetic peroxidase enzymes containing a covalent DNA-heme adduct as the cofactor. *Chem. Eur. J. 12*, 7448 – 7457.

(3) Teale, F. W. (1959) Cleavage of the haem-protein link by acid methylethylketone. *Biochim. Biophys. Acta 35*, 543.

(4) Capeland, R. A. *Enzymes- A Practical Introduction to Structure, Mechanism and Data Analysis*; Wiley -VCH: New York, 2000.

(5) Berg, J. M., Tymoczko, J. L., and Stryer, L. *Biochemistry, 5th Ed.*; W.H. Freeman: New York, 2002.

(6) Markham, N. R., and Zuker, M. (2005) DINAMelt web server for nucleic acid melting prediction. *Nucleic Acids Res. 33*, W577-W581; http://dinamelt.bioinfo.rpi.edu/twostate-fold.php.

Enhanced Survival of Neural Cells Embedded in Hydrogels Composed of Collagen and Laminin-Derived Cell Adhesive Peptide

Makiko Hiraoka, Koichi Kato, Tadashi Nakaji-Hirabayashi, and Hiroo Iwata*

Institute for Frontier Medical Sciences, Kyoto University, 53 Kawahara-cho, Shogoin, Sakyo-ku, Kyoto 606-8507, Japan.
Received January 7, 2009; Revised Manuscript Received February 20, 2009

To develop biomaterials that serve to improve the survival of neural cells transplanted into central nervous tissues, type I collagen-based hydrogels were prepared as a cell carrier. The hydrogels were modified with a laminin-derived peptide that is known to have an affinity for alpha3beta1 integrin, to transduce antiapoptotic signaling in embedded cells. For the modification of collagen, the peptide was fused to the N- or C-terminus, or both termini of a collagen-binding polypeptide domain by means of recombinant DNA technology. The chimeric proteins were characterized by polyacrylamide gel electrophoresis and circular dichroism spectroscopy, while binding of chimeric proteins to collagen-coated substrates was verified by surface plasmon resonance analysis under physiological conditions. Cell culture assays revealed that the adhesion of neurosphere-forming cells to collagen-coated polystyrene surfaces was significantly promoted by the incorporation of the chimeric proteins in a peptide-density dependent manner. The live/dead assays for cells cultured for 24 or 48 h in the hydrogels revealed that peptide incorporation improved the survival of cells embedded in collagen hydrogels. These results suggest that collagen hydrogel containing the laminin-derived peptide provides microenvironments suitable for the survival of neural cells.

INTRODUCTION

Recently, stem cell transplantation has received much attention as potential treatments for neurodegenerative diseases and traumatic injuries of the central nervous system (*1*). Neural stem/progenitor cells derived from brain tissues or embryonic stem cells have been transplanted after appropriate processing in vitro. Many studies demonstrated the engraftment of neural stem/progenitor cells directly infused into the brain of model animals (*2*). However, the number of cells surviving initial few days in the host tissues is limited, which reduces therapeutic effects of cell transplantation (*3*). One of the most critical causes of this problem may be cellular apoptosis that is triggered by disruption of cell−cell and cell−extracellular matrix interactions upon cell harvesting for transplantation (*4, 5*). In addition, infiltration of inflammatory microglia into transplanted sites is considered as another cause for limited engraftment (*6, 7*).

In an attempt to promote cell survival, we have studied the development of collagen-based hydrogels to be used as a carrier for neural cells (*8, 9*). We expect that the form of hydrogels serves as a temporal barrier against infiltrating microglia, reducing adverse effects due to acute inflammation. To enhance cell survival, attempts were made to incorporate epidermal growth factor to the collagen matrix (*8*). That study led us to suppose as well that, in addition to growth factor stimulation, signaling through cell adhesion molecules would have additional effects for promoting cell survival. In practice, hippocampus neurons were shown to adhere and extend neurites on collagen that incorporated a peptide mimetic of the neural cell adhesion molecule (*9*). In contrast, here we examined the effects of an integrin-binding peptide on the survival of neural cells.

It has been reported that neural stem cells express various integrin complexes (*10*) whose interactions with extracellular matrix play important roles in the development of the central nervous system (*11, 12*). Among integrins expressed on neural stem cells, $\alpha 3\beta 1$ integrin is known to interact with laminin-5 and has been implicated in brain development (*13*) through the modulation of neuronal migration and neuron-glial interactions (*14, 15*). In addition, cell adhesion to laminin-5 via $\alpha 3\beta 1$ integrin was reported to mediate survival signaling in a variety of epithelial cells (*16, 17*). For these reasons, we sought a peptide sequence capable of specific binding to $\alpha 3\beta 1$ integrin and incorporated such a peptide into collagen hydrogels to promote the survival of embedded neural cells on account of integrin signaling.

We employed here a small peptide, PPFLMLLKGSTR, derived from the G3 domain of a laminin $\alpha 3$ chain of laminin-5 (designated this peptide as G3P hereafter). Kim et al. (*18*) demonstrated that this sequence has a strong affinity for $\alpha 3\beta 1$ integrin expressed on epithelial cells. To incorporate the peptide into collagen hydrogels, we adopted a similar strategy as in our previous studies (*8, 9*): Chimeric proteins consisting of G3P and the A3 domain of von Willebrand factor (vWF) that has an affinity for collagen α chains (designated this domain as CBD hereafter) were prepared by recombinant DNA technology. It was shown that (*8*) CBD contained in the chimeric proteins specifically bound to type I collagen under physiological conditions, presenting its fusion partners on collagen.

In the present study, chimeric proteins with different domain structures were prepared. The G3P was fused to the C- or N-terminus, or both termini of CBD, which allows us to study the effects of molecular architecture. Another polypeptide that contained no G3P was prepared and used as a control. These proteins were bound to a collagen-coated polystyrene surface to evaluate the effect of chimeric proteins on the adhesion and neurite extension of the neural stem cell-containing population. Further investigation was conducted to determine the viability of neural cells embedded in collagen hydrogels that incorporated G3P-containing chimeric proteins. In this article, we report that the incorporation of G3P significantly promotes cell survival in collagen hydrogels.

EXPERIMENTAL PROCEDURES

Genetic Engineering. A bacterial expression system was used to synthesize three types of chimeric proteins consisting of G3P

* To whom correspondence should be addressed. E-mail: iwata@frontier.kyoto-u.ac.jp, tel and fax: +81-75-751-4119.

10.1021/bc9000068 CCC: $40.75 © 2009 American Chemical Society
Published on Web 04/07/2009

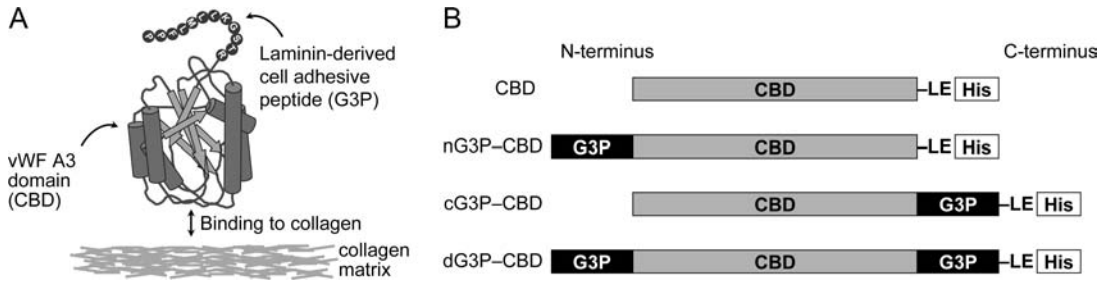

Figure 1. (A) Schematic representation of a chimeric protein consisting of a laminin-derived cell adhesive peptide (G3P) and a collagen binding domain (CBD) derived from vWF. (B) Structure of chimeric proteins synthesized in this study. His: hexahistidine sequence for affinity purification. The dipeptide, L-E, inserted upstream of His comes from the plasmid. The number of amino acid residues: CBD, 189; G3P, 12; His, 6.

and CBD. The structures of these proteins are shown in Figure 1. Chimeric proteins fused with G3P at the N-, C-, and both termini are designated as nG3P-CBD, cG3P-CBD, and dG3P-CBD, respectively. A control protein lacking G3P is designated as CBD. The complete sequence of chimeric proteins is provided in Supporting Information.

For the preparation of chimeric genes, polymerase chain reaction (PCR) was performed using primers shown in Table 1. A DNA sequence encoding GP3 was incorporated in forward and/or reverse primers depending on the structure of chimeric proteins. Forward primers contained an Nde I restriction site, while reverse primers contained an Xho I site. The chimeric genes for four proteins are separately amplified from the EGF-CBD expression vector (*8*). PCR was performed using a thermal cycler (Gene Amp PCR 9700G, Applied Biosystems) under the following conditions: 35 cycles, denaturation at 94 °C for 30 s, annealing at 62 °C for 30 s, and extension at 72 °C for 30 s. DNA fragments thus obtained were separated by agarose gel electrophoresis and digested with restriction enzymes, Nde I and Xho I. The fragments were inserted into the upstream of 6 × histadine-tag in pET-22b(+) plasmid (Novagen) and transformed to *Escherichia coli* (*E. coli*) DH5α. After overnight culture, colonies were randomly picked up, and the presence of the plasmid was verified by colony PCR using primers specific for T7 promoter and T7 terminator. The correctness of the plasmids was verified by sequencing. Cells harboring the correct plasmid were cultured in LB medium to prepare glycerol stocks.

Protein Expression. *E. coli* strain BL21-CodonPlus (Stratagene) was transformed with the plasmid and cultured in a medium (Overnight Express Autoinduction System, Novagen) at 37 °C for 12 h. Proteins expressed as inclusion bodies were extracted with 20 mM phosphate buffer (pH 7.4) containing 8 M urea and 5 mM 2-mercaptoethanol and purified by Ni-chelate affinity chromatography using a Prime ÄKTA system (GE Healthcare) equipped with a His Trap HP column (GE Healthcare). The purity and the molecular size of the proteins were analyzed by sodium dodecylsulfate−polyacrylamide gel electrophoresis (SDS-PAGE). The proteins were refolded by stepwise dialysis against the series of buffers (see Supporting Information for buffer compositions). Finally, the solutions of refolded proteins in 5 mM 2-amino-2-hydroxymethyl-1,3-propanediol (Tris)-HCl buffer were stored at −80 °C until use.

Circular Dichroism (CD) Spectroscopy. CD spectra were recorded using JASCO J-805 spectropolarimeter. Stock solutions of proteins were diluted with 5 mM Tris-HCl (pH 8.9 for CBD, nG3P-CBD, and cG3P-CBD; pH 9.5 for dG3P-CBD) to the final concentration of 150 μg/mL. Far-UV CD spectra were recorded in a 0.1 cm path length cell at 20 °C, a response time of 0.5 s, a bandwidth of 1 nm, and a scan speed of 100 nm/min with an accumulation of eight scans. Pure Tris-HCl buffer (5 mM, pH 8.9 or 9.5) was used as reference.

Surface Plasmon Resonance (SPR) Analysis. The binding of chimeric proteins to collagen was analyzed by SPR as reported before (*9, 19*). In brief, a glass plate bearing a thin gold layer and a carboxylic acid-terminated self-assembled monolayer was mounted to the hemicylinderical glass prism of an SPR sensor equipped with an He−Ne laser tube. Light reflectance was continuously monitored at a fixed incident angle, while protein or pure buffer solution was sequentially circulated over the surface of the plate in a flow cell at 37 °C and a flow rate of 3 mL/min. After equilibrating with phosphate-buffered saline (PBS), the surface was exposed to 100 μg/mL type I collagen solution (Sigma) in 0.1 M acetic acid buffer (pH 4.9) for 30 min, followed by circulation of PBS for 60 min to wash the surface. Then, chimeric protein solution (diluted with PBS to a final concentration of 50 μg/mL) was circulated for 60 min to bind the protein to preadsorbed collagen, followed by washing with pure PBS for 60 min. The reflectance changes were used to determine a resonance angular shift and then converted to the surface density of protein assuming the unit angular shift of 0.5 μg/cm^2/DA (*20*).

Cell Isolation and Adhesion Assay. Chimeric protein was diluted with PBS to a concentration of 50 μg/mL. The solution was added to a collagen-coated polystyrene dish (Asahi Techno Glass Corp., Tokyo, Japan) and incubated at room temperature for 2 h to bind chimeric protein onto collagen. The plate was washed with PBS to remove unbound protein and immediately used for cell adhesion assays. As reported previously (*21*), the striatum was isolated from rat fetuses (embryonic day 16) and dissociated into single cells, according to the guideline of the institutional Animal Welfare Committee. The cells were cultured in suspension to form neurospheres (*22*) that contained neural stem cells (50−60% of total cells) as well as more differentiated cells (*21*). Neurospheres at passage 2 were dissociated into single cells by trypsin treatment. This cell population is referred to as neurosphere-forming cells in this paper. The cells were suspended in DMEM/F12 (1:1) (Gibco) containing 2% B27 supplements (Gibco), 5 μg/mL heparin, 100 unit/mL penicillin, and 100 μg/mL streptomycin. The cells were seeded to the protein-bound dish at a density of 5.0 × 10^4 cells/cm^2 and incubated at 37 °C under 5% CO_2 atmosphere. In separate experiments, soluble peptide (PPFLMLLKGSTR, Invitrogen) was dissolved in a cell suspension to a concentration of 25 μg/mL, and the cells were incubated at 37 °C for 30 min prior to seeding. The cells were then cultured on the protein-bound dish under the same condition as described above to confirm the specific effect of surface-bound peptide on cell adhesion. After incubation for 6 h, cells were washed gently with the same medium as mentioned above to remove weakly attaching cells and observed with a phase-contrast optical microscope (DP51, Olympus Optical CO., Ltd., Tokyo, Japan). The number of cells that adhered to the dish was determined on the microphotographs acquired at five different sights (area: 0.33 mm^2) on the same sample and averaged. The data are expressed in this paper as mean ± standard deviation for four independent samples.

Cell Culture in Collagen Hydrogel. Type I collagen solution (3 mg/mL, Cellmatrix type I-A, Nitta Gelatin Inc., Osaka, Japan)

Table 1. Primers Used for PCR

chimeric proteins		DNA sequence of forward (FW) and reverse (RV) primers[a]
CBD	FW	5′-GGTCGTCATATG**GACTGCAGCCAGCCCCTGGAC**-3′
	RV	5′-TCCTCGAG***AGAGCACAGTTTGTGGAGGAAGG***-3′
nG3P-CBD	FW	5′-GGTCGTCATATG*CCACCTTTTCTAATGTTGCTTAAAGGTTCTACCAGG***GACTGCAGCCAGCCCCTGGAC***-3′
	RV	5′-TCCTCGAG***AGAGCACAGTTTGTGGAGGAAGG***-3′
cG3P-CBD	FW	5′-GGTCGTCATATG**GACTGCAGCCAGCCCCTGGAC**-3′
	RV	5′-TCCTCGAG*CCTGGTAGAACCTTTAAGCAACATTAGAAAAGGTGG***AGAGCACAGTTTGTGGAGGAAGG***-3′
dG3P-CBD	FW	5′-GGTCGTCATATG*CCACCTTTTCTAATGTTGCTTAAAGGTTCTACCAGG***GACTGCAGCCAGCCCCTGGAC***-3′
	RV	5′-TCCTCGAG*CCTGGTAGAACCTTTAAGCAACATTAGAAAAGGTGG***AGAGCACAGTTTGTGGAGGAAGG***-3′

[a] Restriction sites are underlined. Italics represent the sequence encoding G3P. Boldface represents the sequence encoding the 5′ or 3′ region of CBD.

was mixed on ice with 5-fold concentrated culture medium and reconstitution buffer (50 mM NaOH, 260 mM $NaHCO_3$, 200 mM HEPES) at a volume ratio of 7:2:1. Then, nG3P-CBD solution was added to the mixture to an nG3P-CBD concentration of 300 μg/mg collagen. An aliquot of the mixture (500 μL) was added into each well of a 12-well tissue culture plate and incubated at 37 °C for 90 min to allow formation of hydrogels with a thickness of approximately 1 mm. The neurosphere-forming cells obtained as above were seeded onto the collagen hydrogel at a density of 1.0×10^5 cells/cm^2 and incubated for 4 h at 37 °C under 5% CO_2 and subsequently overlaid with 500 μL of a chimeric protein-containing collagen hydrogel of the same composition as described above to embed the cells in a hydrogel. The embedded cells were additionally cultured for 24 and 48 h in an incubator at 37 °C under 5% CO_2 atmosphere.

Cell Viability. The live/dead assay (*23*) was performed by staining cells with 3′,6′-di(*O*-acetyl)-4′,5′-bis[*N*,*N*-bis(carboxymethyl)aminomethyl]fluorescein, tetraacetoxymethyl ester (calcein-AM), and propidium iodide (PI). Cells cultured in a collagen gel for 24 and 48 h were exposed to PBS containing 1 μg/mL calcein-AM, 1 μg/mL PI, 0.05 mM $MgCl_2$, and 0.9 mM $CaCl_2$ for 30 min and then washed with PBS containing 0.05 mM $MgCl_2$ and 0.9 mM $CaCl_2$. In this procedure, calcein-AM penetrates into the cytosol of living cells and fluorescently stains them in green, while PI fluorescently stains the nucleus of dead cells in red. The microphotographs of cells stained in green and red were recorded using the epifluorescent microscope (DP70, Olympus). For the quantification of living cells, the number of cells stained in red (dead cells) was determined on five different microphotographs (area: 0.54 mm^2) recorded for each sample, while total cell numbers were determined by Hoechst staining. Cell viability was determined as percent living cells to the total cells and presented as mean ± standard deviation for four independent samples.

Statistical Analysis. The results of cell proliferation and viability assays were statistically analyzed using a software (JMP5.0.1a, SAS Institute Inc., Cary, NC). One-way analysis of variance (ANOVA) was performed for assessing significant differences. Tukey's honestly significant difference (HSD) test was performed for multiple comparisons at a significance level set of $p < 0.05$.

RESULTS

Preparation of Chimeric Proteins. Figure 2 shows the result of SDS-PAGE analysis for the chimeric and control proteins. These proteins were separated as single bands. The molecular weight estimated from the mobility of protein bands are as follows: CBD 22 kDa, nG3P-CBD 23 kDa, cG3P-CBD 23 kDa, and dG3P-CBD 24 kDa. These results are consistent with the molecular weights predicted from their amino acid compositions.

As shown in Figure 3, all the proteins gave CD spectra with minima at 208 and 222 nm for the α-helix and at 216 nm for the β-sheet (*24*). Compared with CBD, nG3P-CBD and cG3P-CBD exhibited slightly decreased Cotton effects, indicating lower contents of secondary structure. dG3P-CBD exhibited much more reduction in negative Cotton effects at 208, 216, and 222 nm. The α-helix contents of these proteins were determined from mean residue molar ellipticity at 222 nm (*25*) and compared with those calculated based on crystallographic data (*26*). The results are shown in Table 2. The experimentally determined α-helix contents are in good agreement with predictions for CBD, nG3P-CBD, and cG3P-CBD, suggesting the structural integrity of these proteins. In the case of dG3P-CBD, a relatively large difference was observed between experimental and predicted values. This is probably due to the fact that proper refolding is hindered by hydrophobic amino

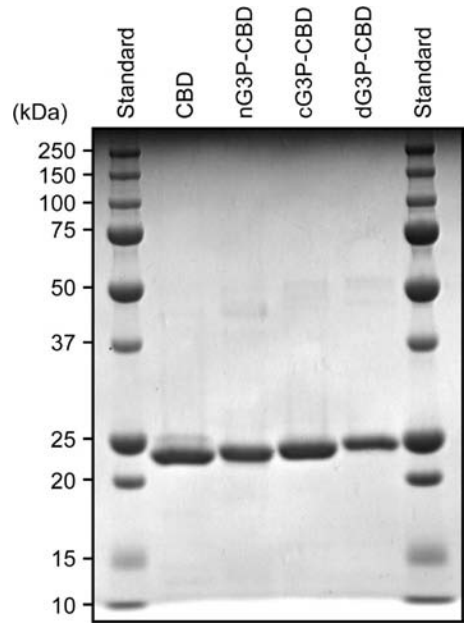

Figure 2. The result of SDS-PAGE analysis. Chimeric proteins were electrophoresed in 12.5% polyacrylamide gel and visualized by coomassie brilliant blue staining. Molecular weight standard was electrophoresed in two lanes at both sides.

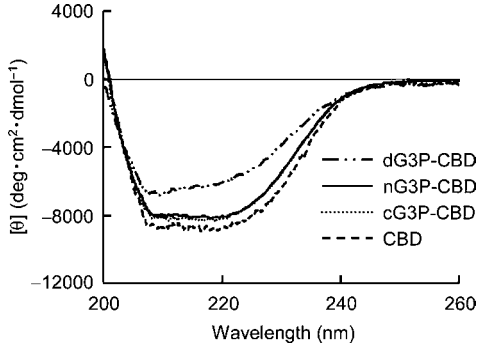

Figure 3. Far UV circular dichroism spectra of chimeric proteins recorded at 20 °C. Mean residue molar ellipticity [θ] is shown as a function of wavelength.

Table 2. α-Helix Content Determined from CD Spectra

protein	α-helix content (%) determined from CD spectra	α-helix content (%) predicted from structural data[a]
CBD	28.4	28.9
nG3P-CBD	26.2	27.3
cG3P-CBD	26.2	27.3
dG3P-CBD	19.5	25.8

[a] Calculated under the assumption that G3P, hexahistidine, and Leu-Glu sequence have no α-helical structure. α-Helix content of the wild-type A3 domain is 30.2% when calculated from structural data (*23*).

acids rich in G3P. In practice, dG3P-CBD had poor solubility in buffer solutions compared with other chimeric proteins. This appeared remarkably when the solutions at relatively high concentration were dialyzed against neutral buffer solutions.

Binding of Chemic Proteins to Collagen. Figure 4 shows SPR sensorgrams recorded for the binding of chimeric proteins to collagen. The amounts of bound proteins determined from these sensorgrams are shown in Table 3. As is seen, CBD, nG3P-CBD, and cG3P-CBD bound to collagen at a similar density to each other. On the other hand, more than 2-fold larger amount of dG3P-CBD bound to the collagen compared with

Table 3. Amount of Chimeric Proteins Bound to the Collagen-Coated Surface Determined by SPR Analysis[a]

chimeric protein	chimeric protein bound (ng/cm^2)[b]	surface density of G3P (10^4 molecules/μm^2)
CBD	47 ± 6	—
nG3P-CBD	57 ± 16	1.5 ± 0.4
cG3P-CBD	61 ± 11	1.6 ± 0.3
dG3P-CBD	131 ± 27	6.6 ± 1.4

[a] The amount of collagen preadsorbed to the substrate: 120 ± 30 ng/cm^2 (mean ± standard deviation for n = 12). [b] Mean ± standard deviation for n = 3.

nG3P-CBD and cG3P-CBD. Accordingly, the surface density of G3P is approximately 4-fold higher with dG3P-CBD than with nG3P-CBD and cG3P-CBD. It seems that the hydrophobic nature of dG3P-CBD has an additional contribution to collagen binding.

Cell Adhesion to Collagen-Coated Surfaces. Reverse transcriptase-PCR (RT-PCR) was performed to analyze the expression of mRNA for α3 and β1 integrins in neurosphere-forming cells. As shown in Supporting Information Figure S1, these cells certainly express both α3 and β1 integrins, although the presence of an α3β1 complex is not identified. These cells were cultured for 6 h on the collagen-coated surfaces bound with chimeric proteins. Figure 5 shows the phase-contrast images of these cells. It is clearly seen that few cells adhered to the collagen-coated dish bearing no chimeric proteins (Figure 5A). Similarly, poor cell adhesion was observed on a collagen-coated surface bound with CBD (Figure 5B). In contrast, a substantial number of cells are seen on surfaces with nG3P-CBD, cG3P-CBD, and dG3P-CBD (Figure 5C−E). These cells extended dendrites, producing cellular networks. The addition of soluble G3P to the medium largely blocked cell adhesion to the collagen-coated surface with chimeric proteins (Figure 5F), suggesting that the observed cell adhesion (Figure 5C−E) is mediated by specific interaction of cells with the surface-bound G3P. The number of adhering cells are shown in Figure 6. The data show that cell adhesion to collagen was significantly promoted by nG3P-CBD and cG3P-CBD, and much more by dG3P-CBD.

It seems that cell differentiation was not effectively induced by the chimeric proteins because of the short period (6 h) after seeding. The formation of dendrites (Figure 5C−E) is not indicative of cell differentiation. In fact, as shown in Supporting Information Figure S2, the fraction of neural stem cells was rather higher in the cells adhering to the G3P-bearing surface (70%) than that in neurosphere-forming cells (50−60%) (*21*), indicating somewhat preferential adhesion of neural stem cells to the G3P-bearing surface.

Cell Survival in Collagen Hydrogels. Figure 7 shows the phase-contrast images of cells cultured in a collagen hydrogel with or without incorporated nG3P-CBD. Although cell adhesion was most effectively promoted by dG3P-CBD on polystyrene-based substrates (Figures 5 and 6), we used nG3P-CBD in this experiment. This is because the handling of nG3P-CBD was much easier because of its moderate hydrophilicity. As shown in Figure 7, observation of cells with an optical microscope was difficult because cells were not distributed in the same plane. However, careful inspection of cells revealed that most of the cells had round shapes in a pure collagen hydrogel. On the other hand, many cells are seen to flatten and extend dendrites in the collagen hydrogel with incorporated nG3P-CBD. Compared to the cells on rigid polystyrene substrates (Figure 5), cell aggregation is noticeable in the hydrogels.

Figure 8 shows the results of live/dead assays performed for cells cultured in collagen hydrogels with or without incorporated nG3P-CBD. In pure collagen hydrogels, the fraction of living cells decreased rapidly likely due to an anoikis effect, and only

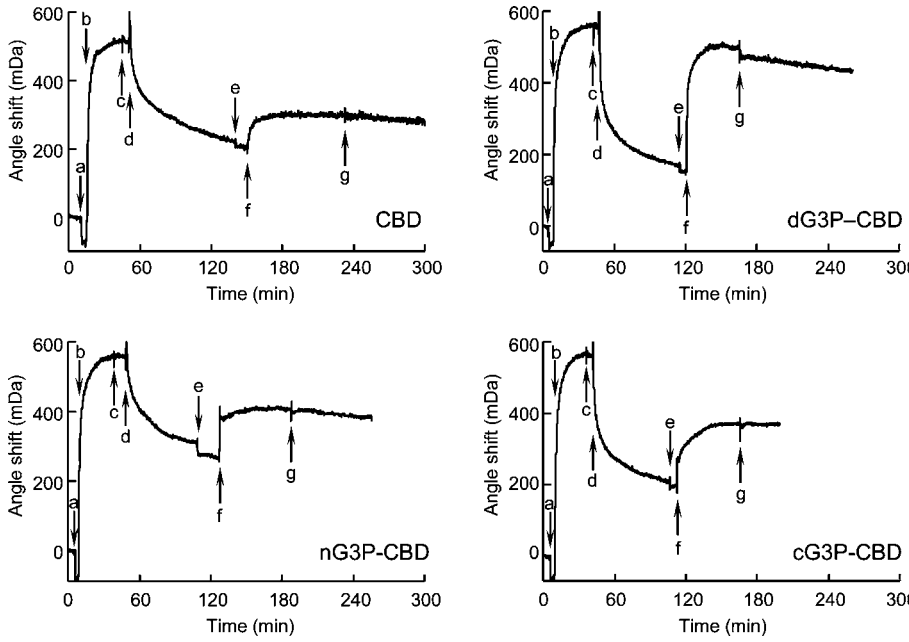

Figure 4. SPR sensorgrams for the binding of chimeric proteins onto collagen. a−g represent the times when the following solutions were injected to the gold surface bearing a self-assembled monolayer of COOH-terminated alkanethiol, initially equilibrated with PBS: a, acetic acid buffer (pH 4.9); b, 100 μg/mL collagen in sodium acetate buffer (pH 4.9); c, sodium acetate buffer (pH 4.9); d, PBS (pH 7.4); e, PBS (pH 7.4) mixed with pure Tris-HCl buffer at the same mixing ratio as in f; f, 50 μg/mL chimeric protein diluted with PBS (pH 7.4); g, PBS (pH 7.4) mixed with pure Tris-HCl buffer at the same mixing ratio as in f. All measurements were carried out at 37 °C.

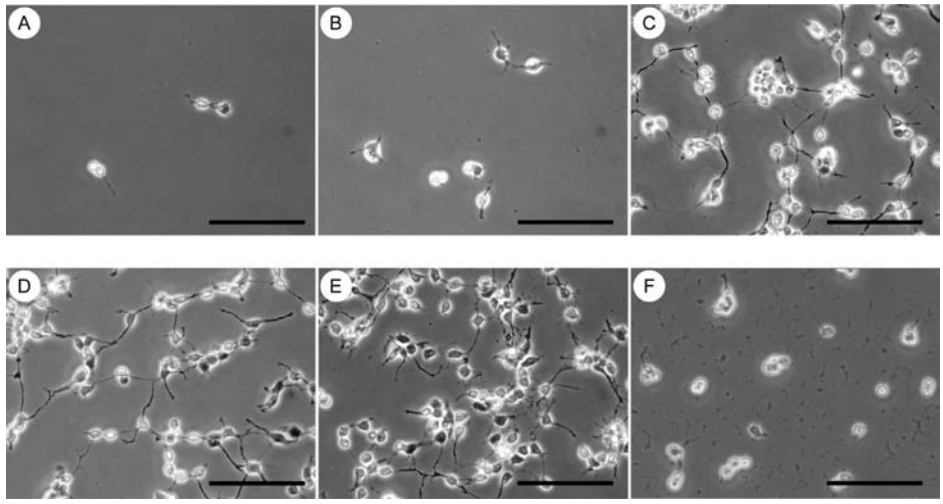

Figure 5. Phase-contrast microphotographs of cells cultured for 6 h on the collagen-coated polystyrene surfaces bound with or without chimeric proteins. (A) No chimeric proteins were bound (collagen-coated surface). (B−E) Collagen-coated surfaces bound with (B) CBD, (C) nG3P-CBD, (D) cG3P-CBD, and (E) dG3P-CBD. (F) Cells were cultured on the collagen-coated surface bound with dG3P-CBD in a medium containing 25 μg/mL soluble G3P. Bars: 100 μm.

21.0 ± 5.6% of cells survived 2 days. On the other hand, a significantly larger number of cells survived 24 h (54.0 ± 4.8%) or 48 h (45.5 ± 3.7%) in collagen hydrogels with incorporated nG3P-CBD. These results indicate that cell death was delayed by incorporating nG3P-CBD.

DISCUSSION

This study demonstrates that the viability of neurosphere-forming cells embedded in a collagen hydrogel is improved by incorporating G3P to the hydrogel (Figures 7 and 8). Because the viability of most cells largely relies on adhesion signaling (*27*), the improved viability is conceivably the consequence of enhanced cell adhesion in the hydrogel networks. In fact, neurosphere-forming cells cultured in the G3P-incorporating collagen hydrogel exhibited more extended forms than in the pure collagen hydrogel. The continued existence of an increased number of living cells for 2 days will be greatly beneficial to cell transplantation therapy in the brain.

In this study, the peptide G3P was attached to collagen networks through specific interactions of the fusion partner CBD with collagen. To date, a variety of conjugation methods have been reported for the modification of collagen with various peptides (*28, 29*) including G3P as well (*30*). These methods often require severe reaction conditions. In addition, it is not always straightforward to modulate the orientation and density of peptides with conventional chemical methods. Our approach using biospecific interactions allows us to densely immobilize a peptide on collagen under physiological conditions. This is exemplified by the data presented in Table 3 as well as our previous studies (*8, 9*). In addition, one can easily design

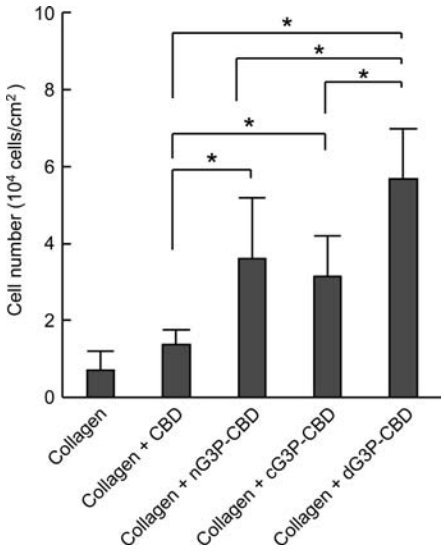

Figure 6. The number of cells adhered to collagen-coated polystyrene surfaces bound with chimeric proteins. Data are expressed as mean ± standard deviation for $n = 4$. *Statistically significant ($p < 0.05$, Tukey's HSD test).

collagen-binding chimeric proteins bearing different peptides using the CBD as a universal coupler.

The laminin-derived cell-adhesive peptide, G3P, was originally identified by Kim et al. as a ligand for $\alpha 3\beta 1$ integrin expressed on epithelial cells (*18*). This peptide is contained in a G3 domain of a laminin α3 chain, a component of a laminin-5 isoform. The interaction between laminin-5 and $\alpha 3\beta 1$ integrin was reported to have an antiapoptotic effect in a variety of epithelial cells (*16*, *17*). Laminin-5 is abundantly found in epithelial basement membranes (*31*) and also expressed in developing brain tissues (*32*). Therefore, the collagen matrix bound with G3P can be regarded as a biomaterial that mimics in part the native basement membrane.

We examined the effects of chimeric proteins with three different structures: G3P was fused at the N- or C-terminus, or both termini of CBD (Figure 1). It was shown that nG3P-CBD and cG3P-CBD had comparable properties with regard to solubility, collagen binding (Table 3), and cell adhesion (Figure 5). This finding suggests the structural and functional similarities between G3Ps in nG3P-CBD and cG3P-CBD. A CBD contains a disulfide bond between two cysteine residues located at the N- and C-terminal regions (*26*), forming a globular domain with both termini close each other. Accordingly, it is expected that G3Ps in nG3P-CBD and cG3P-CBD have minor differences with regard to their arrangements in the proteins, although the peptides are tethered to CBD in an opposite orientation.

Among chimeric proteins studied, dG3P-CBD having G3P at the both ends exhibited the highest binding capacity for collagen (Table 3). As described earlier, dG3P-CBD exhibited low solubility due in part to the high occupancy of amino acids with nonpolar side chains (P, F, M, L, and G). Presumably, two G3Ps raise the hydrophobicity of dG3P-CBD. In addition, the slightly disordered structure of this protein, as demonstrated by CD spectroscopy (Figure 3), suggests the enhanced exposure of hydrophobic amino acids that would be located in the core region in the native state. It is likely that such structural alteration enhances the nonspecific adsorption of dG3P-CBD to collagen and hence gives rise to elevated surface density.

The highest cell density observed for the dG3P-CBD-collagen surface (Figures 5 and 6) may be directly related to exceptionally high surface density of G3P (Table 3). The probability of interaction between G3P and integrin may be enhanced on this surface. The range of the G3P density that has influence on the number of adhering cells (15 000−66 000 molecules/μm^2) is similar to the dynamic range of ligand density reported by Maheshwari et al. (*33*) for the adhesion of fibroblasts via interaction between integrins and surface-immobilized RGD peptide. On the other hand, it may not be the case that two G3Ps in the same molecule simultaneously engage in binding to two proximal integrins, contributing to the clustering of

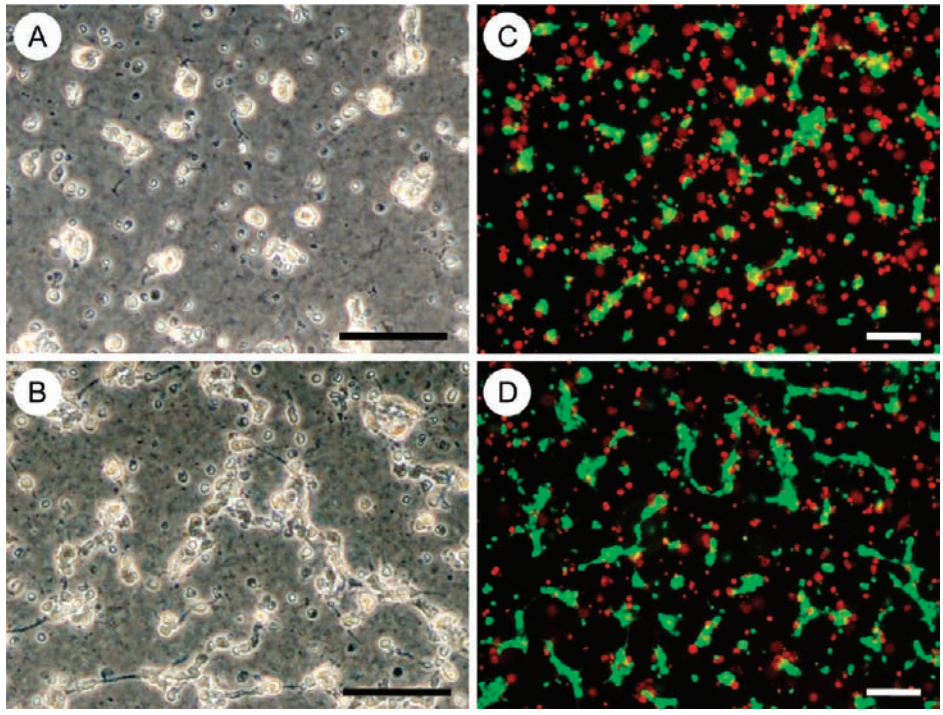

Figure 7. Results of cell culture assays in collagen hydrogels with or without incorporated nG3P-CBD. (A, B) Phase-contrast microphotographs of cells cultured for 48 h in (A) a pure collagen hydrogel and (B) a collagen hydrogel containing nG3P-CBD. Bars: 100 μm. (C, D) Fluorescent microphotographs of cells cultured for 48 h in (C) a pure collagen hydrogel and (D) a collagen hydrogel containing nG3P-CBD. Cells were stained with calcein-AM (live cells in green) and propidium iodide (dead cells in red). Bars: 100 μm.

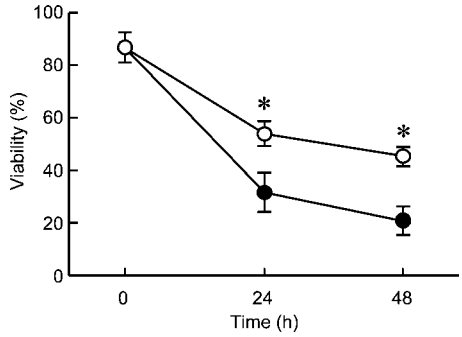

Figure 8. The viability of cells cultured for 24 and 48 h in (○) collagen hydrogels containing nG3P-CBD or (●) pure collagen hydrogels. Data are expressed as mean ± standard deviation for $n = 4$. *Statistically significant ($p < 0.05$, Tukey's HSD test).

integrins and the formation of focal contacts. This is because an $\alpha 3\beta 1$ integrin complex is much larger than the spun of two G3Ps contained in a single dG3P-CBD molecule.

As we observed in the live/dead assays (Figures 7 and 8), a larger number of neurosphere-forming cells survived in collagen hydrogels containing nG3P-CBD than in pure collagen hydrogels. We were unable to distinguish necrotic cells from apoptotic ones by PI staining alone, and possibly both mechanisms were involved in observed cell death. Regarding necrotic conditions, if any, cells were equally effected in both hydrogels, and cell viability may be improved by optimizing culture conditions such as oxygen and nutrient supply. For the observed difference in viability, we assume that this is due to antiapoptotic signaling cascades activated in the cells in consequence of an interaction between G3P and $\alpha 3\beta 1$ integrin. Actually, integrin subunits $\alpha 3$ and $\beta 1$ are both expressed on the neurosphere-forming cells (Supporting Information Figure S1), being in agreement with reports for neural stem cells (*10*), cerebral cortex neurons (*34*), and differentiating neuroblastoma cells (*35*). However, we need further mechanistic study on intracellular signaling to understand more deeply the effect of the incorporated G3P.

CONCLUSION

The chimeric proteins consisting of the laminin-derived G3P and the vWF-derived CBD bind to collagen under physiological conditions, providing collagen-based substrates to which neurosphere-forming cells are able to adhere. When incorporated in collagen hydrogels, the chimeric protein serves to enhance the survival of neurosphere-forming cells in the hydrogels. Although further mechanistic studies are needed, the promoted cell adhesion and survival may be ascribed to signaling mediated by the specific interaction of the G3P with $\alpha 3\beta 1$ integrin. The composite hydrogels reported here have the potential to improve the survival and engraftment of neural cells transplanted into central nervous tissues.

ACKNOWLEDGMENT

This work was supported by Grants-in-Aid for Scientific Research (No. 19659364), MEXT, Japan. T.N.-H. acknowledges JSPS for a research fellowship.

Supporting Information Available: Amino acid sequences of chimeric proteins, dialysis conditions, results of RT-PCR, and immunocytochemistry. This material is available free of charge via the Internet at http://pubs.acs.org.

LITERATURE CITED

(1) Björklund, A., and Lindvall, O. (2000) Cell replacement therapies for central nervous system disorders. *Nat. Neurosci. 3*, 537–544.

(2) Goldman, S. (2005) Stem and progenitor cell-based therapy of the human central nervous system. *Nat. Biotechnol. 23*, 862–871.

(3) Lepore, A. C., Neuhuber, B., Connors, T. M., Han, S. S. W., Liu, Y., Daniels, M. P., Rao, M. S., and Fischer, I. (2006) Long-term fate of neural precursor cells following transplantation into developing and adult CNS. *Neuroscience 142*, 287–304.

(4) Marchionini, D. M., Collier, T. J., Camargo, M., McGuire, S., Pitzer, M., and Sortwell, C. E. (2003) Interference with anoikis induced cell death of dopamine neurons: implications for augmenting embryonic graft survival in a rat model of Parkinson's disease. *J. Comp. Neurol. 464*, 172–179.

(5) Koyanagi, M., Tanahashi, J., Arakawa, Y., Doi, D., Fukuda, H., Hayashi, H., Narumiya, S., and Hashimoto, N. (2008) Inhibition of the Rho/ROCK pathway reduces apoptosis during transplantation of embryonic stem cell-derived neural precursors. *J. Neurosci. Res. 86*, 270–280.

(6) Imitola, J., Comabella, M., Chandraker, A. K., Dangond, F., Sayegh, M. H., Snyder, E. Y., and Khoury, S. J. (2004) Neural stem/progenitor cells express costimulatory molecules that are differentially regulated by inflammatory and apoptotic stimuli. *Am. J. Pathol. 164*, 1615–1625.

(7) Kim, D. E., Tsuji, K., Kim, Y. R., Mueller, F.-J., Eom, H.-S., Snyder, E. Y., Lo, E. H., Weissleder, R., and Schellingerhout, D. (2006) Neural stem cell transplant survival in brains of mice: assessing the effect of immunity and ischemia by using real-time bioluminescent imaging. *Radiology 241*, 822–830.

(8) Kato, K., Sato, H., and Iwata, H. (2007) Ultrastructural study on the specific binding genetically engineered epidermal growth factor to type I collagen fibrils. *Bioconjugate Chem. 18*, 2137–2143.

(9) Miyazaki, H., Kato, K., Teramura, Y., and Iwata, H. (2008) A collagen-binding mimetic of neural cell adhesion molecule. *Bioconjugate Chem. 19*, 1119–1123.

(10) Hall, P. E., Lathia, J. D., Miller, N. G., Caldwell, M. A., and ffrench-Constant, C. (2006) Integrins are markers of human neural stem cells. *Stem Cells 24*, 2078–2084.

(11) Lathia, J. D., Patton, B., Eckley, D. M., Magnus, T., Mughal, M. R., Sasaki, T., Caldwell, M. A., Rao, M. S., Mattson, M. P., and ffrench-Constant, C. (2007) Patterns of laminins and integrins in the embryonic ventricular zone of the CNS. *Comp. Neurol. 505*, 630–643.

(12) Flanagan, L. A., Rebaza, L. M., Derzic, S., Schwartz, P. H., and Monuki, E. S. (2006) Regulation of human neural precursor cells by laminin and integrins. *J. Neurosci. Res. 83*, 845–856.

(13) Kreidberg, J. A. (2000) Functions of $\alpha 3\beta 1$ integrin. *Curr. Opin. Cell Biol. 12*, 548–553.

(14) Anton, E. S., Kreidberg, J. A., and Rakic, P. (1999) Distinct functions of alpha3 and alpha(v) integrin receptors in neuronal migration and laminar organization of the cerebral cortex. *Neuron 22*, 277–289.

(15) Schmid, R. S., Shelton, S., Stanco, A., Yokota, Y., Kreidberg, J. A., and Anton, E. S. (2004) Alpha3beta1 integrin modulates neuronal migration and placement during early stages of cerebral cortical development. *Development 131*, 6023–6031.

(16) Edick, M. J., Tesfay, L., Lamb, L. E., Knudsen, B. S., and Miranti, C. K. (2007) Inhibition of integrin-mediated crosstalk with epidermal growth factor receptor/Erk or Src signaling pathways in autophagic prostate epithelial cells induces caspase-independent death. *Mol. Biol. Cell 18*, 2481–2490.

(17) Manohar, A., Shome, S. G., Lamar, J., Stirling, L., Iyer, V., Pumiglia, K., and DiPersio, C. M. (2004) Alpha 3 beta 1 integrin promotes keratinocyte cell survival through activation of a MEK/ERK signaling pathway. *J. Cell Sci. 117*, 4043–454.

(18) Kim, J.-M., Park, W. H., and Min, B.-M. (2005) The PPFLMLLKGSTR motif in globular domain 3 of the human laminin-5 alpha3 chain is crucial for integrin alpha3beta1 binding and cell adhesion. *Exp. Cell Res. 304*, 317–327.

(19) Hirata, I., Morimoto, Y., Murakami, Y., Iwata, H., Kitano, E., Kitamura, H., and Ikada, Y. (2000) Study of complement activation on well-defined surfaces using surface plasmon resonance. *Colloids Surf., B 18*, 285–292.

(20) Knoll, W. (1991) Polymer thin films and interfaces characterized with evanescent light. *Makromol. Chem. 192*, 2827–2856.
(21) Nakaji-Hirabayashi, T., Kato, K., Arima, Y., and Iwata, H. (2007) Oriented immobilization of epidermal growth factor onto culture substrates for the selective expansion of neural stem cells. *Biomaterials 28*, 3517–3529.
(22) Reynolds, B. A., Tetzlaff, W., and Weiss, S. A. (1992) Multipotent EGF-responsive striatal embryonic progenitor cell produces neuron and astrocytes. *J. Neurosci. 12*, 4565–4574.
(23) Fukuda, J., Khademhosseini, A., Yeo, Y., Yang, X., Yeh, J., Eng, G., Blumling, J., Wang, C. F., Kohane, D. S., and Langer, R. (2006) Micromolding of photocrosslinkable chitosan hydrogel for spheroid microarray and co-cultures. *Biomaterials 27*, 5259–5267.
(24) Auton, M., Cruz, M. A., and Moake, J. (2007) Conformational stability and domain unfolding of the von Willebrand factor A domains. *J. Mol. Biol. 366*, 986–1000.
(25) Kelly, S. M., Jess, T. J., and Price, N. C. (2005) How to study proteins by circular dichroism. *Biochim. Biophys. Acta 1751*, 119–139.
(26) Huizinga, E. G., Martijn van der Plas, R., Kroon, J., Sixma, J. J., and Gros, P. (1997) Crystal structure of the A3 domain of human von Willebrand factor: implications for collagen binding. *Structure 5*, 1147–1156.
(27) Grossmann, J. (2002) Molecular mechanisms of "detachment-induced apoptosis - Anoikis". *Apoptosis 7*, 247–260.
(28) Zhang, L., Hum, M., Wang, M., Li, Y., Chen, H., Chu, C., and Jiang, H. (2005) Evaluation of modifying collagen matrix with RGD peptide through periodate oxidation. *J. Biomed. Mater. Res. 73A*, 468–475.
(29) Myles, J. L., Burgess, B. T., and Dickinson, R. B. (2000) Modification of the adhesive properties of collagen by covalent grafting with RGD peptides. *J. Biomater. Sci. Polym. Ed. 11*, 69–86.
(30) Damodaran, G., Collighan, R., Griffin, M., and Pandit, A. Tethering a laminin peptide to a crosslinked collagen scaffold for biofunctionality. J. Biomed. Mater. Res., Part A, in press.
(31) Ekblom, M., Falk, M., Salmivirta, K., Durbeej, M., and Ekblom, P. (1998) Laminin isoforms and epithelial development. *Ann. N.Y. Acad. Sci. 857*, 194–211.
(32) Galliano, M. F., Aberdam, D., Aguzzi, A., Ortonne, J. P., and Meneguzzi, G. (1995) Cloning and complete primary structure of the mouse laminin alpha 3 chain. Distinct expression pattern of the laminin alpha 3A and alpha 3B chain isoforms. *J. Biol. Chem. 270*, 21820–21826.
(33) Maheshwari, G., Brown, G., Lauffenburger, D. A., Wells, A., and Griffith, L. G. (2000) Cell adhesion and motility depend on nanoscale RGD clustering. *J. Cell Sci. 113*, 1677–1686.
(34) Schmid, R. S., and Anton, E. S. (2003) Role of integrins in the development of the cerebral cortex. *Cereb. Cortex 13*, 219–224.
(35) Tarone, G., Hirsch, E., Brancaccio, M., De Acetis, M., Barberis, L., Balzac, F., Retta, S. F., Botta, C., Altruda, F., and Silengo, L. (2000) Integrin function and regulation in development. *Int. J. Dev. Biol. 44*, 725–731.

BC9000068

Supporting Information

Enhanced Survival of Neural Cells Embedded in Hydrogels Composed of Collagen and Engineered Cell Adhesive Peptide

Makiko Hiraoka, Koichi Kato, Tadashi Nakaji-Hirabayashi, and Hiroo Iwata*

Institute for Frontier Medical Sciences, Kyoto University, 53 Kawahara-cho, Shogoin, Sakyo-ku, Kyoto 606-8507, Japan

*Corresponding author: E-mail: iwata@frontier.kyoto-u.ac.jp

---

1. Amino acid sequences of chimeric proteins

Complete sequence of chimeric proteins are shown below. Characters in red represent the sequence of G3P.

CBD (control protein lacking G3P)

1	DCSQPLDVIL	LLDGSSSFPA	SYFDEMKSFA	KAFISKANIG	PRLTQVSVLQ	YGSITTIDVP
61	WNVVPEKAHL	LSLVDVMQRE	GGPSQIGDAL	GFAVRYLTSE	MHGARPGASK	AVVILVTDVS
121	VDSVDAAADA	ARSNRVTVFP	IGIGDRYDAA	QLRILAGPAG	DSNVVKLQRI	EDLPTMVTLG
181	NSFLHKLCSL	EHHHHHH				

nG3P-CBD (G3P at the N-terminus of CBD)

1	PPFLMLLKGS	TRDCSQPLDV	ILLLDGSSSF	PASYFDEMKS	FAKAFISKAN	IGPRLTQVSV
61	LQYGSITTID	VPWNVVPEKA	HLLSLVDVMQ	REGGPSQIGD	ALGFAVRYLT	SEMHGARPGA
121	SKAVVILVTD	VSVDSVDAAA	DAARSNRVTV	FPIGIGDRYD	AAQLRILAGP	AGDSNVVKLQ
181	RIEDLPTMVT	LGNSFLHKLC	SLEHHHHHH			

cG3P-CBD (G3P at the C-terminus of CBD)

1	DCSQPLDVIL	LLDGSSSFPA	SYFDEMKSFA	KAFISKANIG	PRLTQVSVLQ	YGSITTIDVP
61	WNVVPEKAHL	LSLVDVMQRE	GGPSQIGDAL	GFAVRYLTSE	MHGARPGASK	AVVILVTDVS
121	VDSVDAAADA	ARSNRVTVFP	IGIGDRYDAA	QLRILAGPAG	DSNVVKLQRI	EDLPTMVTLG
181	NSFLHKLCSP	PFLMLLKGST	RLEHHHHHH			

dG3P-CBD (G3P at both termini of CBD)

1	PPFLMLLKGS	TRDCSQPLDV	ILLLDGSSSF	PASYFDEMKS	FAKAFISKAN	IGPRLTQVSV
61	LQYGSITTID	VPWNVVPEKA	HLLSLVDVMQ	REGGPSQIGD	ALGFAVRYLT	SEMHGARPGA
121	SKAVVILVTD	VSVDSVDAAA	DAARSNRVTV	FPIGIGDRYD	AAQLRILAGP	AGDSNVVKLQ
181	RIEDLPTMVT	LGNSFLHKLC	SPPFLMLLKG	STRLEHHHHH	H	

2. Buffer solutions used for refolding of chimeric proteins

Chimeric proteins were sequentially dialyzed against the following buffer solutions:

(1) 50 mM Tris-HCl, 8 M urea, 10 mM NaCl, 0.2 M L-Arg, 0.2 mM DTT

(2) 50 mM Tris-HCl, 8 M urea, 10 mM NaCl, 0.2 M L-Arg

(3) 50 mM Tris-HCl, 2.5 M urea, 10 mM NaCl, 0.2 M L-Arg, 3.75 mM GSH, 0.375 mM GSSG

(4) 50 mM Tris-HCl, 2.5 M urea, 10 mM NaCl, 0.1 M L-Arg, 0.5 mM GSH, 0.3 mM GSSG

(5) 50 mM Tris-HCl, 10 mM NaCl, 0.1 M L-Arg

(6) 20 mM Tris-HCl

(7) 10 mM Tris-HCl

(8) 5 mM Tris-HCl

Abbreviations: Tris; 2-amino-2-hydroxymethyl-1,3-propanediol, L-Arg; L-arginine hydrochloride, DTT; dithiothreitol, GSH; the reduced form of glutathione, and GSSH; the oxidized form of glutathione.

3. Gene expression analysis

Total RNA was isolated from neurosphere-forming cells using SV Total RNA Isolation system (Promega). A hundred nanogram of RNA was used per reverse transcription (RT) reaction using Ready-to-Go You-Prime First-Strand Beads (Amersham) primed by oligo$(dT)_{15}$ (Promega). First-strand cDNA was then amplified by polymerase chain reaction (PCR) using specific primers: integrin α3, (sense) gtggccgtatgaagttacca and (antisense) cacggtctcagacttggctt; integrin β1, (sense) caacctgtgagacctgtcag and (antisense) caatgtccttctccttgcag; glyceraldehyde-3-phosphate dehydrogenase, (sense) tgaacgggaagctcactgg and (antisense) tccaccaccctgttgctgta. Thirty cycles of PCR was performed under the thermal cycling conditions of denaturation at 94 ^{o}C for 30 s, annealing at 55 ^{o}C for 30 s, and elongation at 72 ^{o}C for 30 s. All samples were run triplicate, and the products were analyzed by electrophoresis in 2% agarose gel with ethidium bromide staining. The electrophoresed DNA was imaged using Gel Doc 2000 (BioRad). As shown in Figure S1, neurosphere-forming cells express both α3 and β1 integrins.

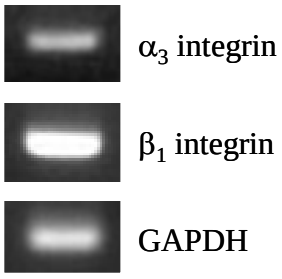

Figure S1. RT-PCR analysis for the expression of α_3 and β_1 integrin mRNA in neurosphere-forming cells. Glyceraldehyde-3-phosphate (GAPDH) was analyzed as an internal standard.

4. Immunocytochemistry

A neural stem cell marker (nestin) and differentiation markers of neuron (β-tubulin III; βIII) and astrocyte (glial fibrillary acidic protein; GFAP) were immunfluorescently stained as reported before (Nakaji-Hirabayashi, T., Kato, K., Arima, Y., and Iwata, H. *Biomaterials* **2007**, *28*, 3517–3529). In brief, after fixation with 4% paraformaldehyde and 0.1% glutaraldehyde, cells were permeabilized by treating with 0.5% TritonX-100 solution and subsequently treated with 2% skim milk solution to block non-specific adsorption of antibodies. Then, the cells were reacted with antibody against nestin (1:200, mouse monoclonal Rat 401, BD Pharmingen), GFAP (mouse monoclonal, MAB3402, Chemicon), or βIII (1:600, rabbit polyclonal, Covance, Princeton, NJ), followed by binding of fluorescently-active secondary antibodies (1:500, Alexa Fluor 594 anti-mouse immunoglobulin G and Alexa Fluor 488 anti-rabbit immunoglobulin G, both from Molecular Probes). Cell nuclei were counterstained with 1 mg/mL Hoechst33258. The localization of secondary antibodies and Hoechst dye was analyzed with an epifluorescent microscope. The results are shown in Figure S2.

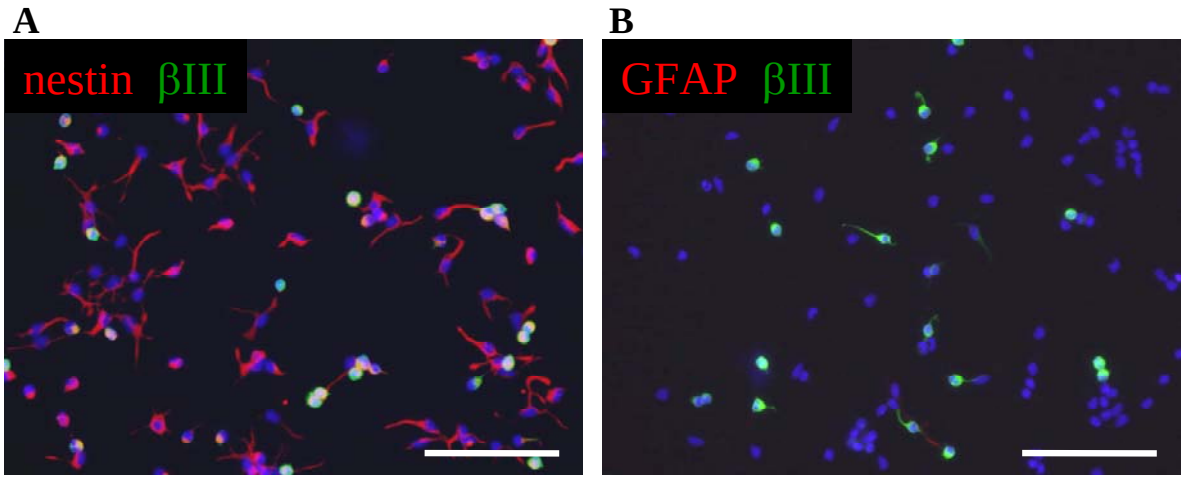

Figure S2. Immunofluorescent staining of neurosphere-forming cells cultured for 6 h on the collagen-coated surface with nG3P-CBD. Primary antibody used: A, nestin (red) and βIII (green); B, GFAP (red) and βIII (green). Nuclei were stained with Hoechst dye. Note that GFAP expression was negligible. The fraction of subpopulations: nestin^{+}βIII^{-}, 70%; nestin^{+}βIII^{+}, 20%; nestin^{-}βIII^{+}, 6%; nestin^{-}βIII^{-}, 4%. Bars: 100 μm.

Glycosylated DOTA−α-Melanocyte-Stimulating Hormone Analogues for Melanoma Targeting: Influence of the Site of Glycosylation on in Vivo Biodistribution

Jean-Philippe Bapst, Martine Calame, Heidi Tanner, and Alex N. Eberle*

Laboratory of Endocrinology, Department of Biomedicine, University Hospital and University Children's Hospital, Basel, Switzerland. Received January 8, 2009; Revised Manuscript Received March 9, 2009

α-Melanocyte-stimulating hormone (α-MSH) is known to bind to the melanocortin receptor 1 (MC1R) which is overexpressed on melanotic and amelanotic melanoma cells. α-MSH analogues are potential candidates for specific targeting of melanoma metastases. Several linear and cyclic radiolabeled MSH peptides have been designed and tested in the past, showing both high affinity for the MC1R in vitro and good incorporation in tumor xenografts in vivo. However, considerable kidney reabsorption of the radiopeptides could not be avoided. With the aim to increase the tumor-to-kidney ratio, we synthesized six glycosylated derivatives of NAPamide, an α-MSH octapeptide analogue with high tumor selectivity and coupled them to the chelator DOTA (1,4,7,10-tetraazacyclododecane-1,4,7,10-tetraacetic acid). The peptides were evaluated in vitro for MC1R binding and bioactivity and, after labeling with ^{111}In, for in vitro cellular uptake and in vivo tissue distribution in mice carrying B16F1 melanoma tumors. The glycopeptides showed excellent binding affinities in the low nanomolar to subnanomolar range using both murine and human melanoma cell lines. However, five glycopeptides displayed lower selectivity in vivo than the parent DOTA−NAPamide, because of either a lower tumor uptake or a higher kidney uptake. In particular C-terminal extension of the amide group by a galactosyl moiety increased the kidney retention dramatically. By contrast, an N-terminally positioned galactose residue in DOTA−Gal-NAPamide improved the tumor-to-kidney ratio (4−48 h AUC of 1.34) by a factor of about 1.2 as compared to the parent DOTA−NAPamide (4−48 h AUC of 1.11), thus serving as new lead compound for MC1R-targeting molecules.

INTRODUCTION

The melanocortin type-1 receptor (MC1R), which is overexpressed on the plasma membrane of melanoma cells, is a potential target for the diagnosis or therapy of metastases of malignant melanoma (*1*−*3*). Radiolabeled α-melanocyte-stimulating hormone (α-MSH), the natural ligand of MC1R, and various types of synthetic linear or cyclic analogues have been studied as candidates for MC1R targeting (*4*−*10*). These analogues not only showed excellent binding properties to both murine and human melanoma cells in vitro but also good tumor uptake in vivo (*4*−*10*). However, because of considerable unspecific retention of radioactivity in the kidneys, clinical studies with these compounds remained scarce (*11*).

Generally, renal toxicity of DOTA−containing radiopeptides remains one of the main dose-limiting factors for peptide-targeted radiotherapy (*12*, *13*), as demonstrated for somatostatin analogues (*14*, *15*) which are routinely used in the clinic for the diagnosis and therapy of various tumors expressing somatostatin receptors (*16*, *17*). To improve the in vitro and in vivo characteristics of peptide hormone analogues in general, and of radiolabeled somatostatin or α-MSH derivatives in particular, different types of modification of the chelator−peptide structures have been examined, such as structural stabilization of the peptide (*16*, *18*), reduction of the size of the peptide (*8*), chemical variation of the radiometal chelator (*19*−*21*), the use of different radiometals such as $^{67/68}$Ga, ^{111}In, ^{90}Y, ^{177}Lu, ^{99m}Tc, and ^{188}Re (*6*, *9*, *22*, *23*), the adjustment of the net charge of chelator−peptide complexes (*7*, *24*), the position of the chelator on the peptide (*7*), cyclization of the peptides via a rhenium core (*5*, *9*), and the synthesis of dimerized α-MSH analogues (*25*). Another approach to reduce nonspecific uptake of, for example, somatostatin (*26*) or α-MSH (*6*), by the kidneys is the coinjection of cationic amino acids. All these strategies improved melanoma targeting with radiolabeled α-MSH analogues in experimental models, but none of these lowered kidney uptake sufficiently to allow a broad clinical evaluation of diagnostic or therapeutic MSH radiopharmaceuticals.

Alternative approaches to obtain α-MSH compounds with improved pharmacokinetic properties are needed, yielding molecules with particularly high receptor affinity, low nontarget tissue retention, and an almost exclusively urinary excretion route with minimal kidney reabsorption and retention, in order to further minimize nephrotoxicity. Coupling of carbohydrate moieties to radiopeptides can strongly influence the pharmacokinetics of peptides, owing to the more hydrophilic character of glycosylated molecules (*27*). The excretion of glycosylated radiopeptides into the primary urine may be favored, and reuptake by the tubular system of the kidneys reduced, as shown for glycosylated peptides and proteins (*27*, *28*). It has been shown that carbohydrates, if properly positioned, preserve structure−activity relationships (SAR) of the peptides with their target receptors. For example, glycosylated enkephalin derivatives maintained their binding properties and exhibited prolonged bioavailability (*29*, *30*). The in vivo stability of renin inhibitors could also be improved by glycosylation (*31*), and carbohydrated somatostatin analogues displayed a more favorable pharmacokinetic profile with reduced liver uptake and biliary excretion (*32*−*34*), thus switching the excretion route from hepato-biliary to renal. Sugyama and colleagues (*27*, *28*, *35*) investigated numerous modifications of Arg-vasopressin by coupling a

* For correspondence or reprints contact Alex N. Eberle, Ph.D., Department of Biomedicine, University Hospital Basel, Klingelbergstrasse 23, CH-4031 Basel, Switzerland. Phone: +41-61-265-2382. Fax: +41-61-265-2706. E-mail: alex-n.eberle@unibas.ch.

10.1021/bc900007u CCC: $40.75 © 2009 American Chemical Society
Published on Web 04/23/2009

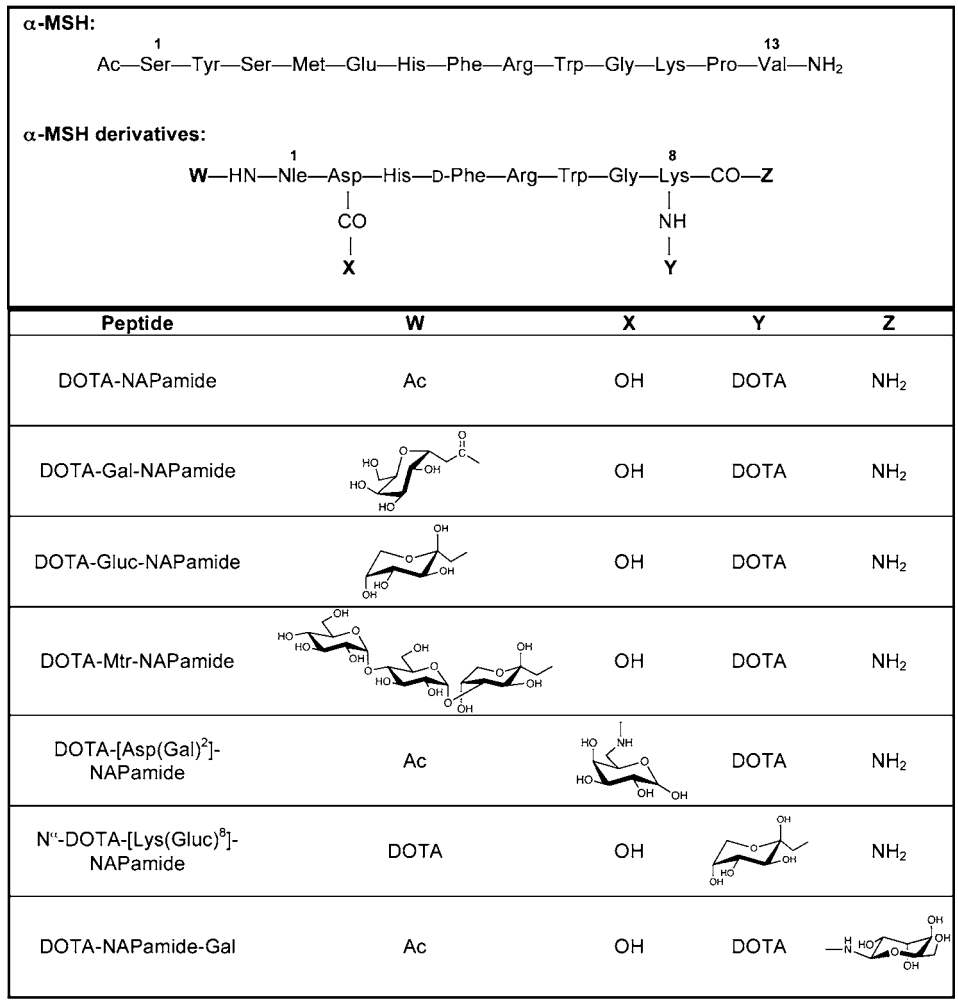

Peptide	W	X	Y	Z
DOTA-NAPamide	Ac	OH	DOTA	NH_2
DOTA-Gal-NAPamide		OH	DOTA	NH_2
DOTA-Gluc-NAPamide		OH	DOTA	NH_2
DOTA-Mtr-NAPamide		OH	DOTA	NH_2
DOTA-[Asp(Gal)^2]-NAPamide	Ac		DOTA	NH_2
N$^\alpha$-DOTA-[Lys(Gluc)^8]-NAPamide	DOTA	OH		NH_2
DOTA-NAPamide-Gal	Ac	OH	DOTA	

Figure 1. Structures of glycopeptides used in this study. W, N-terminal position; Z, C-terminal position; X, side chain of residue 2; Y, side chain of residue 8; Ac, acetyl group.

variety of different sugar moieties to the peptide in order to improve kidney targeting. Their investigations revealed that the affinity of the peptides for kidney tubular cell membranes could be influenced, depending on the type of sugar used (*27*, *28*, *35*).

In this study, we synthesized and evaluated, both in vitro with mouse and human melanoma cells and in vivo with biodistribution experiments using melanoma tumor-bearing mice, several radiolabeled carbohydrated α-MSH analogues whose structure was based on [^{111}In]DOTA−NAPamide previously synthesized in our laboratory and found to be one of the most efficient MSH targeting derivatives (*6*). The novel MSH peptides which contained different carbohydrate moieties inserted into the C-terminus and N-terminus as well as side chains of the NAPamide peptide, included DOTA−NAPamide-Gal, N$^\alpha$-DOTA−[Lys(Gluc)^8]-NAPamide, DOTA−[Asp(Gal)^2]-NAPamide, DOTA−Mtr-NAPamide, DOTA−Gluc-NAPamide, DOTA−Gal-NAPamide (Figure 1).

EXPERIMENTAL PROCEDURES

Peptides and Analytical Procedures. α-MSH was a gift from Novartis (Basel, Switzerland), and [Nle^4, D-Phe^7]-α-MSH (NDP-MSH) was purchased from Bachem (Bubendorf, Switzerland). The reference compound DOTA−NAPamide (*6*) and all other peptides were synthesized in our laboratory using a Pioneer peptide synthesizer (PerSeptive Biosystems Inc., Framingham, MA) and the continuous-flow strategy with Fmoc (9-fluorenylmethoxycarbonyl) protection of N$^\alpha$-amino groups (for recent details, see Bapst et al. (*25*)). Fmoc-amino acids were purchased from Novabiochem (Läufelfingen, Switzerland). Fmoc-PAL−PEG−PS polystyrene resin was from Applied Biosystems (Rotkreuz, Switzerland) and TentaGel S TRT-Lys(Boc)-Fmoc acid-labile resin from Fluka (Buchs, Switzerland). Fmoc-Asp(1,2:3,4-diisopropylidene-6-amino-α-D-galactosyl)-OH was a gift from SynphaBase AG (Muttenz, Switzerland). Other carbohydrates and organic reagents were purchased from Fluka or Sigma (Buchs, Switzerland).

NMR spectra were recorded on a Bruker Avance DMX-500 (500 MHz) spectrometer (Bruker, Fällanden, Switzerland). Assignment of ^{1}H and ^{13}C spectra was achieved using 2D methods (COSY, HSQC). Chemical shifts are expressed in ppm using residual $CDCl_3$ and CHD_2OD as references. Mass spectra (MS) were recorded on a Finnigan LCQ Deca (Thermo Fisher Scientific Inc., Waltham, MA) electrospray ion trap small molecules and proteomics MS system. Analytical reversed-phase high-performance liquid chromatography (RP-HPLC) of all peptides was performed on a Jasco PU-980 system (Jasco Inc., Easton, MD) usually with a Waters (Waters, Milford, MA) Symmetry C18 analytical column (5 μm, 3.9 × 150 mm), or a Vydac (Grace, Deerfield, IL) 218TP54 C18 analytical column (5 μm, 4.6 × 250 mm). Preparative RP-HPLC of peptides was performed on the same system but either with a Vydac 218TP510 C18 semipreparative column (5 μm, 10 × 250 mm) or a Waters SymmetryPrep C18 preparative column (7 μm, 19 × 150 mm). Peptides were eluted by applying a gradient of 5−95% solvent B (solvent A: 0.1% trifluoroacetic acid (TFA) in H_2O; solvent B: 0.1% TFA in 70:30 acetonitrile/H_2O; gradient

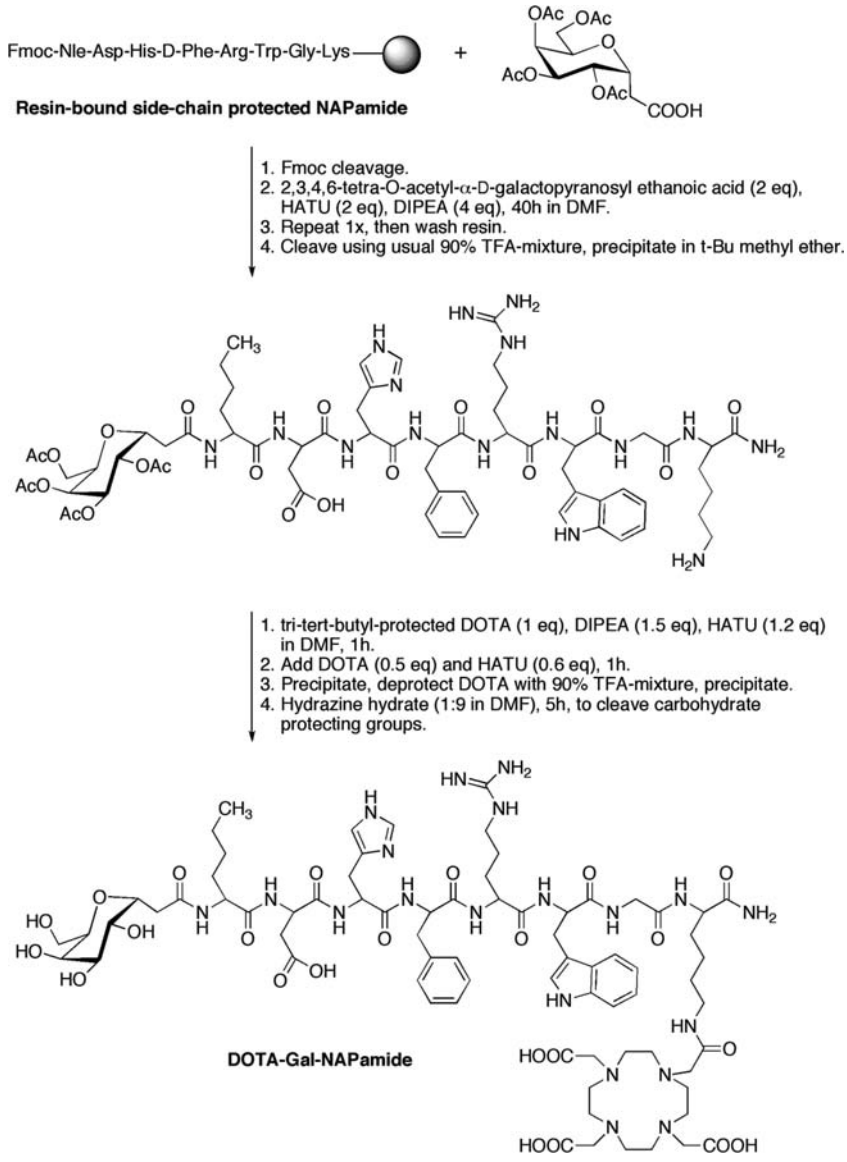

Figure 2. Summary of the synthesis and structures of Gal-NAPamide and DOTA−Gal-NAPamide.

cycle: 0−27 min, 95%−10% A; 27−30 min, 10%−95% A; 30−32 min, 95% A) in 32 min at constant flows of 1 mL/min for the analytical columns, 3 mL/min for the semipreparative column, and 5 mL/min for the preparative column. UV detection was performed at 280 nm on a Jasco UV-1570 UV−vis detector.

Preparation of Glycopeptides. *DOTA−Gal-NAPamide.* The peptide with an N-terminal Gal and DOTA on the Lys side chain (DOTA−Gal-NAPamide) was synthesized by first preparing a Gal-octanoic acid (*36*).

*Allyl-2,3,4,6-tetra-O-acetyl-*α*-D-galactopyranoside.* 1,2,3,4,6-Penta-*O*-acetyl-*β*-D-galactopyranose (10.24 mmol, 1 equiv) was dissolved in anhydrous acetonitrile (40 mL) and cooled to 0 °C. Allyltrimethylsilane (30.76 mmol, 3 equiv) and boron trifluoride diethyl etherate (58.4 mmol, 5.7 equiv) were carefully added under an N_2 atmosphere. The mixture was slowly warmed up to room temperature and stirred overnight under N_2. It was then neutralized by pouring the solution into an Erlenmeyer flask containing $NaHCO_3$ (40 mL). Once the bubbling was over, the reaction mixture was transferred to a separation funnel, extracted with dichloromethane (2 × 40 mL), and dried over Na_2SO_4. The crude product was purified by column chromatography (petroleum ether/ethyl acetate 3:1 to 2:1), resulting in a clear syrup. Yield: 6.96 mmol (68%).

^{1}H NMR ($CDCl_3$, 500.1 MHz) δ: 1.97 (s, 3H, CH_3), 1.98 (s, 3H, CH_3), 2.01 (s, 3H, CH_3), 2.06 (s, 3H, CH_3), 2.21 (m, 1H, CH_2CH=CH_2), 2.40 (m, 1H, CH_2CH=CH_2), 4.00−4.04 (m, 2H, H-5, H-6a), 4.14 (m, $^3J_{5,6b}$ = 9.1 Hz, $^2J_{6a,6b}$ = 12.9 Hz, 1H, H-6b), 4.24 (m, 1H, H-1), 5.03−5.08 (m, 2H, CH_2CH=CH_2), 5.15 (dd, $^3J_{3,4}$ =3.3 Hz, $^3J_{2,3}$ = 9.3 Hz, 1H, H-3), 5.21 (dd, $^3J_{1,2}$ = 5.0 Hz, $^3J_{2,3}$ = 9.3 Hz, 1H, H-2), 5.35 (m, 1H, H-4), 5.69 (m, 1H, CH_2C*H* = CH_2). ^{13}C NMR ($CDCl_3$, 125.8 MHz) δ: 20.67, 20.73, 20.74, 20.79 (4C, 4 CH_3), 30.92 (1C, CH_2CH=CH_2), 61.45 (C-6), 67.58 (C-4), 67.90 (C-3), 68.24 (2C, C-5, C-2), 71.43 (C-1), 117.67 (1C, CH_2CH=CH_2), 133.30 (1C, CH_2C*H*=CH_2), 169.81, 169.94, 170.09, 170.56 (4C=O).

*2,3,4,6-Tetra-O-acetyl-*α*-D-galactopyranosyl Aldehyde.* A solution of allyl-2,3,4,6-tetra-*O*-acetyl-α-D-galactopyranoside (6.96 mmol) was dissolved in anhydrous CH_2Cl_2 (100 mL) and cooled to −70 °C. Ozone (O_3) was bubbled through the solution for approximately 1 h, until the solution turned blue. The mixture was deozonized by bubbling N_2 through the solution until it was colorless. Acetic acid (10 mL) and zinc dust (7.5 g) were added to the solution, and the suspension was slowly warmed up to room temperature overnight under stirring. The suspension was filtered through Celite, and the filtrate was concentrated to dryness. The crude product was purified by column chroma-

Table 1. MC1R Affinity and Biological Activity of α-MSH Analogues on B16F1 and HBL Cells

α-MSH analogues	B16F1 IC_{50} (nmol/L)[a]	HBL IC_{50} (nmol/L)[a]	rEC_{50} (α-MSH = 1)[b]
α-MSH	1.50 ± 0.14	1.91 ± 0.26	1
DOTA−NAPamide	1.38 ± 0.35	3.09 ± 1.11	0.66 ± 0.35
DOTA−Gal-NAPamide	1.62 ± 0.20	5.08 ± 0.25	0.63 ± 0.13
DOTA−Gluc-NAPamide	1.90 ± 0.07	5.57 ± 0.58	0.34 ± 0.03
DOTA−Mtr-NAPamide	2.95 ± 0.17[c]	7.61 ± 0.66[c]	0.62 ± 0.37
DOTA−[Asp(Gal)^2]-NAPamide	0.45 ± 0.01[c]	0.88 ± 0.08	0.26 ± 0.03
N^{α}-DOTA−[Lys(Gluc)^8]-NAPamide	4.58 ± 0.42[c]	5.61 ± 2.17	1.02 ± 0.21
DOTA−NAPamide-Gal	1.24 ± 0.22	2.00 ± 0.13	0.48 ± 0.17

[a] MC1R affinity of α-MSH analogues was assessed by competition binding experiments with B16F1 or HBL cells and ^{125}I-NDP-MSH as radioligand (n = 3−16). [b] Biological activity of α-MSH analogues was determined by melanin assay with B16F1 cells, and results are expressed as relative concentration inducing half-maximal response (rEC_{50}, n = 3−10) normalized on α-MSH = 1. [c] $P < 0.05$ vs DOTA−NAPamide.

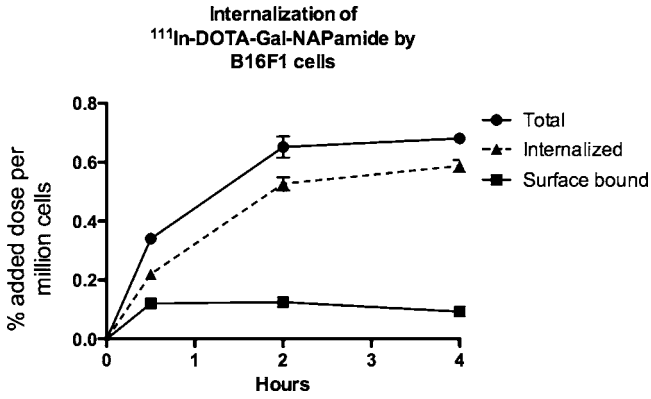

Figure 3. Internalization of ^{111}In-DOTA−Gal-NAPamide into B16-F1 mouse melanoma cells (exemplary experiment showing the means of n = 3 individual determinations).

tography (petroleum ether/ethyl acetate 1.5:1) and dried under high vacuum. Yield: 4.74 mmol (68%).

^{1}H NMR ($CDCl_3$, 500.1 MHz) δ: 2.05 (s, 6H, 2 CH_3), 2.06 (s, 3H, CH_3), 2.11 (s, 3H, CH_3), 2.65−2.76 (m, 2H, CH_2CHO), 4.05−4.11 (m, 2H, H-5, H-6a), 4.32 (m, 1H, H-6b), 4.86 (m, 1H, H-1), 5.17 (dd, $^3J_{3,4}$ = 3.2 Hz, $^3J_{2,3}$ = 8.5 Hz, 1H, H-3), 5.28 (dd, $^3J_{1,2}$ = 4.7 Hz, $^3J_{2,3}$ = 8.4 Hz, 1H, H-2), 5.41 (m, 1H, H-4), 9.72 (m, 1H, CHO). ^{13}C NMR ($CDCl_3$, 125.8 MHz) δ: 20.63, 20.67, 20.70 (4C, 4 CH_3), 41.94 (CH_2CHO), 60.82 (C-6), 66.62 (C-1), 66.88 (C-4), 67.72 (C-3), 67.84 (C-2), 69.67 (C-5), 169.61, 169.72, 169.88, 170.63 (4 C═O), 198.31 (CHO).

2,3,4,6-Tetra-O-acetyl-α-D-galactopyranosylethanoic Acid. A solution of 2,3,4,6-tetra-*O*-acetyl-α-D-galactopyranosyl aldehyde (4.74 mmol) in *tert*-butyl alcohol (20 mL) and a solution of KH_2PO_4 (1.25 M, 8 mL) were added to a vigorously stirred solution of $KMnO_4$ (1 M, 9 mL). The mixture was stirred for 20 min. A solution of saturated Na_2SO_3 was added dropwise until $KMnO_4$ was neutralized, yielding a brown precipitate of MnO_2 which was filtered through Celite and washed with ethanol (2 × 25 mL). Ethanol was then removed from the filtrate under reduced pressure, and the remaining solution was acidified to pH 3 using 1 N HCl and then extracted with dichloromethane (4 × 30 mL). The combined extracts were concentrated and dried under high vacuum to yield a white foam (4.31 mmol, 91%).

^{1}H NMR ($CDCl_3$, 500.1 MHz) δ: 2.04 (s, 6H, 2 CH_3), 2.07 (s, 3H, CH_3), 2.12 (s, 3H, CH_3), 2.63 (dd, ^3J = 5.6 Hz, ^2J = 15.7 Hz, 1H, CH_2CO_2H), 2.72 (dd, ^3J = 8.9 Hz, ^2J = 15.6 Hz, 1H, CH_2CO_2H), 4.10−4.17 (m, 2H, H-5, H-6a), 4.24 (dd, $^3J_{5,6b}$ = 6.9 Hz, $^2J_{6a,6b}$ = 10.7 Hz, 1H, H-6b), 4.70 (m, 1H, H-1), 5.17 (dd, $^3J_{3,4}$ = 3.3 Hz, $^3J_{2,3}$ = 8.9 Hz, 1H, H-3), 5.33 (dd, $^3J_{1,2}$ = 5.0 Hz, $^3J_{2,3}$ = 8.9 Hz, 1H, H-2), 5.43 (m, 1H, H-4). ^{13}C NMR ($CDCl_3$, 125.8 MHz) δ: 20.65, 20.65, 20.70 (4C, 4 CH_3), 33.02 (CH_2CO_2H), 61.04 (C-6), 67.04 (C-4), 67.56 (C-2), 67.77 (C-3), 68.73 (C-1), 69.45 (C-5), 169.57, 169.85, 169.98, 170.65 (4 C═O), 174.90 (CO_2H).

The Gal-octanoic acid was attached to the N-terminus of partially protected NAPamide: 2,3,4,6-tetra-*O*-acetyl-α-D-galactopyranosylethanoic acid (2 equiv) in DMF was preactivated with HATU (2 equiv) for 10 min and added to a suspension of solid-phase-bound, partially protected NAPamide (1 equiv) containing DIPEA (4 equiv). After 40 h at room temperature, the resin was washed (DMF, MeOH, DMF) and the coupling cycle repeated. After the resin was washed, the peptide was cleaved using a 90% TFA-mixture (*25*), precipitated in *t*-butyl methyl ether, and purified by RP-HPLC (t_R = 12.51 min). The DOTA moiety was then coupled to the ε-amino group of Lys^{11} and deprotected in acid-treated (2 N HCl; >1 h) glassware using the standard procedure (*25*). Deprotection of the acetyl groups of the carbohydrate moiety was carried out in liquid phase using hydrazine hydrate (diluted 1:9 in DMF, 1 mL/20 mg peptide) for 5 h and purified by RP-HPLC (Vydac semipreparative column, t_R = 14.8 min). Calculated monoisotopic mass: 1647.79 g mol^{-1}; measured: 1647.5 g mol^{-1}.

DOTA−Gluc-NAPamide. The glucose moiety was coupled to solid-phase bound NAPamide using the Maillard reaction which is a slow nonenzymatic chemical reaction of reducing sugars modifying amino groups of peptides, proteins, lipids, and nucleic acids (*37*), thus leading to the formation of Amadori products (*38*−*40*). The resin containing NAPamide (1 equiv) was stirred in the presence of β-D-glucose (10 equiv) under reflux in a mixture of MeOH/AcOH (95:5) at 60 °C for 72 h. After the mixture was washed with MeOH and 2-propanol, completion of the reaction was checked by the Kaiser test. The peptide was then cleaved from the resin, precipitated with *t*-butyl methyl ether, and purified by RP-HPLC (t_R = 8.94 min). Coupling and deprotection of DOTA followed standard procedures (see above), followed by purification using RP-HPLC (t_R = 9.1 min). Calculated monoisotopic mass: 1605.6 g mol^{-1}; measured: 1605.5 g mol^{-1}.

DOTA−Mtr-NAPamide. The maltotriose moiety was coupled to solid-phase-bound NAPamide using the Maillard reaction, followed by the addition and deprotection of DOTA, as described above for DOTA−Gluc-NAPamide. RP-HPLC yielded the product peak at t_R = 7.8 min. Calculated monoisotopic mass: 1930.03 g mol^{-1}; measured: 1930.1 g mol^{-1}.

DOTA−[Asp(Gal)^2]-NAPamide. To the solid-phase-bound partial NAPamide sequence His-D-Phe-Arg-Trp-Gly-Lys-resin (with side-chain protection), Fmoc-Asp(1,2:3,4-diisopropylidene-6-amino-α-D-galactosyl)-OH and, subsequently, Fmoc-Nle-OH were coupled manually using the HOBt-DIPC method. After cleavage of Fmoc, the N-terminal acetyl group was introduced to the peptide-resin (1 equiv, suspended in a very small amount of DMF) by the addition of *p*-nitrophenyl acetate (2 equiv) activated by HOBt (1 equiv). After 24 h, the resin was filtered and extensively washed with DMF and with 2-propanol. The peptide was cleaved from the resin using a 90% TFA-mixture, precipitated, and purified by RP-HPLC (Vydac analytical column, t_R = 13.71 min). The DOTA moiety was then coupled to the ε-amino group of Lys^{11} and deprotected as

Table 2. Pharmacokinetics of α-MSH Analogues 4, 24, and 48 h after Injection (mean ± SEM)

		%ID/g of tissue[b]												
α-MSH analog	time (h)	blood	tumor	stomach	kidney	liver	spleen	lung	small intestine	pancreas	heart	bone	muscle	skin
DOTA−NAPamide[a]	4	0.09 ± 0.02	7.77 ± 0.35	0.09 ± 0.01	4.77 ± 0.26	0.34 ± 0.05	0.14 ± 0.01	0.08 ± 0.01	0.07 ± 0.01	0.04 ± 0.00	0.05 ± 0.01	0.11 ± 0.02	0.05 ± 0.01	–
	24	0.02 ± 0.00	2.32 ± 0.15	0.12 ± 0.02	2.41 ± 0.20	0.31 ± 0.02	0.11 ± 0.01	0.05 ± 0.01	0.08 ± 0.01	0.03 ± 0.00	0.03 ± 0.00	0.14 ± 0.02	0.02 ± 0.00	–
	48	0.00 ± 0.00	1.41 ± 0.12	0.11 ± 0.05	1.55 ± 0.07	0.27 ± 0.02	0.10 ± 0.01	0.03 ± 0.00	0.05 ± 0.01	0.02 ± 0.00	0.01 ± 0.00	0.05 ± 0.01	0.01 ± 0.00	–
DOTA−Gal-NAPamide	4	0.04 ± 0.00	8.30 ± 1.22	0.06 ± 0.01	4.43 ± 0.34	0.26 ± 0.05	0.13 ± 0.01	0.26 ± 0.05[c]	0.06 ± 0.00	0.04 ± 0.00	0.05 ± 0.00	0.09 ± 0.01	0.03 ± 0.00	0.12 ± 0.01
	24	0.01 ± 0.00	2.00 ± 0.34	0.05 ± 0.00	2.06 ± 0.28	0.17 ± 0.03[c]	0.11 ± 0.02	0.12 ± 0.04	0.05 ± 0.01	0.03 ± 0.00	0.03 ± 0.00	0.09 ± 0.01	0.02 ± 0.00	0.09 ± 0.01
	48	0.01 ± 0.00[c]	0.88 ± 0.02[c]	0.06 ± 0.00	1.15 ± 0.05	0.16 ± 0.01[c]	0.15 ± 0.01[c]	0.15 ± 0.03[c]	0.06 ± 0.01	0.03 ± 0.00[c]	0.03 ± 0.00[c]	0.10 ± 0.02[c]	0.02 ± 0.00[c]	0.07 ± 0.00
DOTA−Gluc-NAPamide	4	0.09 ± 0.06	4.15 ± 0.18[c]	0.37 ± 0.13[c]	4.48 ± 0.39	0.29 ± 0.05	0.30 ± 0.15	0.11 ± 0.04	0.18 ± 0.09	0.22 ± 0.19	0.04 ± 0.01	0.09 ± 0.01	0.03 ± 0.01	0.08 ± 0.02
	24	0.01 ± 0.00	1.40 ± 0.08[c]	0.11 ± 0.01	2.92 ± 0.37	0.23 ± 0.02	0.15 ± 0.01	0.06 ± 0.01	0.05 ± 0.00	0.03 ± 0.00	0.03 ± 0.00	0.07 ± 0.01	0.02 ± 0.00	0.07 ± 0.01
	48	0.01 ± 0.00	0.62 ± 0.08[c]	0.05 ± 0.00	1.91 ± 0.19	0.15 ± 0.01[c]	0.12 ± 0.01	0.05 ± 0.01[c]	0.05 ± 0.01	0.02 ± 0.00	0.03 ± 0.00[c]	0.07 ± 0.01	0.02 ± 0.00[c]	0.06 ± 0.02
DOTA−Mtr-NAPamide	4	0.02 ± 0.00	7.82 ± 0.17	0.16 ± 0.03	5.01 ± 0.40	0.17 ± 0.01	0.10 ± 0.01	0.07 ± 0.01	0.06 ± 0.01	0.03 ± 0.00	0.03 ± 0.00	0.08 ± 0.01	0.02 ± 0.00	0.15 ± 0.02
	24	0.01 ± 0.00	1.02 ± 0.44	0.04 ± 0.02	1.72 ± 0.78	0.08 ± 0.03[c]	0.05 ± 0.02	0.02 ± 0.01	0.03 ± 0.01	0.02 ± 0.01	0.02 ± 0.01	0.04 ± 0.02	0.01 ± 0.00	0.05 ± 0.02
	48	0.01 ± 0.00	0.64 ± 0.10[c]	0.09 ± 0.03	1.33 ± 0.17	0.08 ± 0.01[c]	0.08 ± 0.01	0.03 ± 0.00	0.04 ± 0.00	0.02 ± 0.00	0.03 ± 0.00	0.05 ± 0.00	0.02 ± 0.00[c]	0.06 ± 0.02
DOTA−[Asp(Gal)^2]-NAPamide	4	0.06 ± 0.00	6.04 ± 0.39	0.32 ± 0.12[c]	5.93 ± 0.64	0.34 ± 0.03	0.31 ± 0.18	0.09 ± 0.01	0.14 ± 0.04	0.40 ± 0.35	0.05 ± 0.00	0.19 ± 0.06	0.04 ± 0.01	0.14 ± 0.02
	24	0.02 ± 0.00	1.67 ± 0.22	0.07 ± 0.00	2.92 ± 0.48	0.27 ± 0.03	0.12 ± 0.01	0.05 ± 0.00	0.06 ± 0.00	0.03 ± 0.00	0.03 ± 0.00	0.09 ± 0.02	0.02 ± 0.00	0.06 ± 0.02
	48	0.01 ± 0.00[c]	0.91 ± 0.05[c]	0.06 ± 0.00	1.93 ± 0.10	0.20 ± 0.01	0.11 ± 0.01	0.05 ± 0.01[c]	0.07 ± 0.01	0.03 ± 0.00	0.03 ± 0.00[c]	0.09 ± 0.01[c]	0.02 ± 0.00[c]	0.07 ± 0.00
N$^{\alpha}$-DOTA−[Lys(Gluc)^8]-NAPamide	4	0.04 ± 0.00	5.08 ± 0.25[c]	0.86 ± 0.42[c]	5.79 ± 0.25	0.21 ± 0.01	0.13 ± 0.00	0.11 ± 0.01	0.08 ± 0.01	0.05 ± 0.01	0.04 ± 0.00	0.11 ± 0.01	0.03 ± 0.00	0.12 ± 0.01
	24	0.01 ± 0.00	1.38 ± 0.15[c]	0.16 ± 0.05	3.81 ± 0.21	0.16 ± 0.01[c]	0.12 ± 0.01	0.05 ± 0.01	0.07 ± 0.01	0.04 ± 0.01	0.04 ± 0.00	0.09 ± 0.01	0.02 ± 0.00	0.10 ± 0.03
	48	0.01 ± 0.00[c]	0.70 ± 0.05[c]	0.13 ± 0.01	2.04 ± 0.23	0.12 ± 0.02[c]	0.15 ± 0.05	0.07 ± 0.02[c]	0.06 ± 0.00	0.03 ± 0.00	0.04 ± 0.00[c]	0.09 ± 0.01[c]	0.02 ± 0.00[c]	0.08 ± 0.02
DOTA−NAPamide-Gal	4	0.02 ± 0.00	6.33 ± 1.25	0.13 ± 0.02	5.94 ± 0.63	0.18 ± 0.03	0.10 ± 0.01	0.06 ± 0.01	0.14 ± 0.04	0.04 ± 0.00	0.03 ± 0.00	0.07 ± 0.01	0.03 ± 0.01	0.08 ± 0.02
	24	0.01 ± 0.00	1.74 ± 0.14	0.07 ± 0.02	5.90 ± 1.84	0.17 ± 0.03[c]	0.08 ± 0.01	0.04 ± 0.01	0.05 ± 0.00	0.03 ± 0.00	0.03 ± 0.00	0.07 ± 0.01	0.03 ± 0.01	0.07 ± 0.01
	48	0.01 ± 0.00	0.95 ± 0.17	0.05 ± 0.01	2.00 ± 0.09	0.11 ± 0.00[c]	0.09 ± 0.01	0.04 ± 0.00	0.05 ± 0.01	0.03 ± 0.00[c]	0.03 ± 0.00[c]	0.08 ± 0.01	0.02 ± 0.00[c]	0.06 ± 0.00

[a] Data for DOTA−NAPamide from Froidevaux et al. (2005) *J. Nucl. Med. 46*, 887−895. [b] Tissue radioactivity is expressed as mean ± SEM (n = 4−12). [c] $P < 0.05$ vs DOTA−NAPamide.

described above. RP-HPLC yielded the product peak at t_R = 10.68 min. Calculated monoisotopic mass: 1646.8 g mol^{-1}; measured: 1646.8 g mol^{-1}.

N$^{\alpha}$-DOTA−[Lys(Gluc)^8]-NAPamide. Solid-phase bound NAPamide was first N-terminally extended by DOTA and cleaved from the resin, and then Gluc was attached to the ε-amino group of Lys^{11}. DOTA was coupled using the standard procedure. The peptide was then cleaved from the resin, and the chelator complex was simultaneously deprotected using the standard 90% TFA-mixture. After precipitation, the peptide was purified by RP-HPLC (t_R = 9.5 min) and lyophilized. The carbohydrate moiety was coupled using a slightly modified Maillard reaction: N$^{\alpha}$-DOTA−NAPamide (1 equiv) and β-D-glucose (10 equiv) were stirred for only 45 h at 60 °C under reflux and an N_2 atmosphere using a mixture of MeOH/AcOH (95:5). After the mixture was washed with MeOH and 2-propanol, the completion of the reaction was checked by the Kaiser test. The peptide was directly purified by RP-HPLC (t_R = 8.59 min) and lyophilized. Calculated monoisotopic mass: 1605.75 g mol^{-1}; measured: 1605.8 g mol^{-1}.

DOTA−NAPamide-Gal. NAP (Nle-Asp-His-D-Phe-Arg-Trp-Gly-Lys) was assembled on TentaGel S TRT-Lys(Boc)-Fmoc resin containing an acid-labile linker producing a free C-terminal acid under very mild acid cleavage conditions, without deprotection of the side chains. The free N$^{\alpha}$ group of Nle was acetylated as described above and the peptide cleaved from the resin using DCM/TFE/AcOH 7:2:1 (1 mL/0.1 g of resin; 1 h). The solvent volume was reduced by careful evaporation, and the peptide was precipitated by the addition of 10 volumes of ice-cold diethyl ether and purified by RP-HPLC (t_R = 21.32 min). Calculated monoisotopic mass: 1851.21 g mol^{-1}; measured: 1850.69 g mol^{-1}. The peptide (1 equiv) was dissolved in DMF and its free C-terminal -COOH group preactivated with HATU (2 equiv) for 10 min. 1-Amino-1-deoxy-β-D-galactose (2 equiv) and DIPEA (4 equiv) were added, and the mixture was agitated for 1 h and then left at room temperature overnight. It was purified by RP-HPLC (t_R = 20.95 min) and lyophilized. Calculated monoisotopic mass: 1770.05 g mol^{-1}; measured: 1770.10 g mol^{-1}. Side-chain protecting groups were then cleaved using a 94% TFA-mixture (2 h) containing only 1% thioanisole, which kept the formation of side products minimal. Solvents were removed by careful evaporation with the help of added diethyl ether as solvent carrier. The peptide was dissolved by consecutive addition of 20% AcOH, H_2O and CH_3CN and purified by RP-HPLC (t_R = 9.9 min). Finally, the DOTA moiety was coupled to the ε-amino group of Lys^{11} and deprotected using standard procedures as described above. Purification was achieved by RP-HPLC (t_R = 10.12 min). Calculated monoisotopic mass: 1647.79 g mol^{-1}; measured: 1648.0 g mol^{-1}.

Radioligands. *^{111}In-Labeled Peptides.* Incorporation of ^{111}In into DOTA−peptides was performed by the addition of 55.5 MBq of ^{111}In-Cl_3 (Mallinckrodt, Petten, The Netherlands; stock concentration: 370 MBq/mL) to the DOTA−peptides (10 nmol) dissolved in 54 μL of acetate buffer (0.4 mol/L, pH 5) containing 2 mg of gentisic acid. After 10 min of incubation at 95 °C, the radiolabeled DOTA−peptides were purified on a small reversed-phase cartridge (Sep-Pak C18, Waters), using sodium acetate buffer (pH 7) for washing out unbound radioisotope, followed by elution of the radiopeptide with ethanol. The purity of the resulting radioligands was assessed by RP-HPLC on a Jasco PU-980 chromatography system, connected to a Radiomatic 500TR LB506C1 γ-detector (Packard) and a Waters Spherisorb ODS2/5-μm column under the following conditions: eluent A = 0.1% TFA in water; eluent B = 0.1% TFA in acetonitrile; gradient = 0−2 min, 96% A; 2−22 min, 96%−45% A; 22−30 min, 45%−25% A; 30−32 min, 25% A; 32−34 min, 25%−96% A; flow rate, 1.0 mL/min. The specific activity of the radioli-

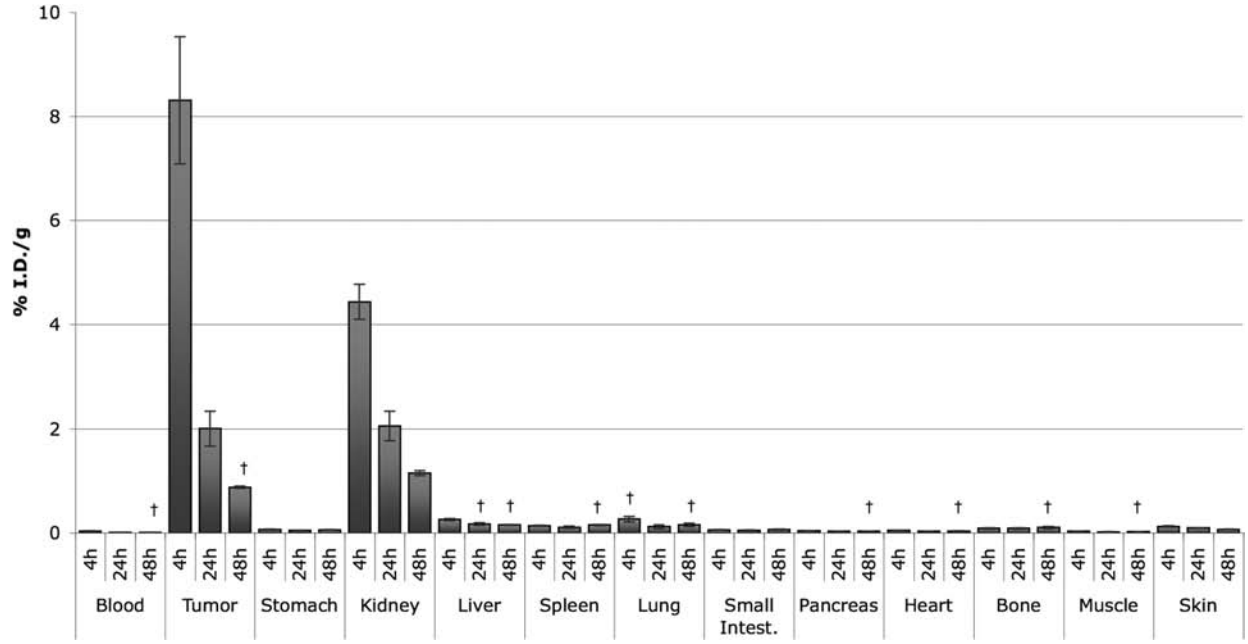

Figure 4. Tissue distribution of [^{111}In]DOTA−Gal-NAPamide at 4, 24, and 48 h postinjection. Results are expressed as % of injected dose per gram of tissue (%ID/g; means ± SEM; $n = 4$). $^{\dagger}P < 0.05$ vs [^{111}In]DOTA−NAPamide.

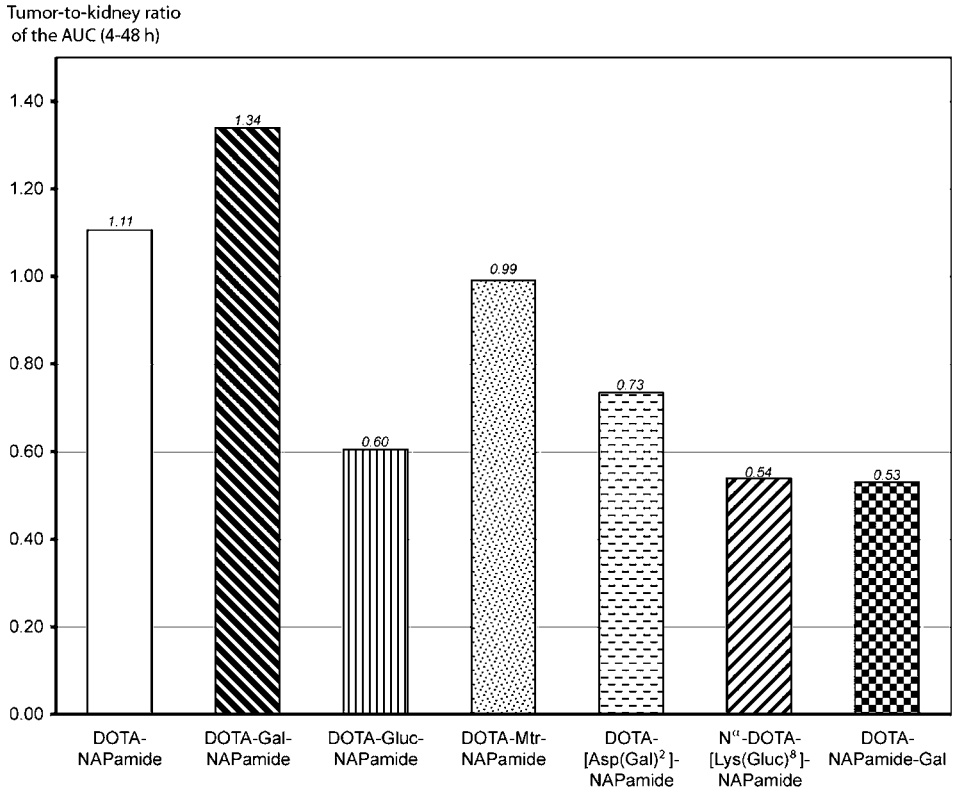

Figure 5. Tumor vs kidney ratio of the area under the curve (4−48 h) of the glycopeptides compared to DOTA−NAPamide in B16F1 melanoma-bearing mice.

gands was estimated by HPLC analysis of radioligand peaks in comparison with HPLC profiles of the parent radioligand DOTA−NAPamide whose specific activity had previously been determined in a competitive binding assay using an antibody which exhibited the same affinity to labeled and unlabeled peptide (for methodological details, see (*41*)). From these profiles, it was estimated that the specific activity of all ^{111}In-labeled peptides was ∼7.4 GBq/μmol.

^{125}I-Labeled Peptide. NDP-MSH was iodinated using the IODO-GEN method. NDP-MSH (12.14 nmol) was mixed with 37 MBq of Na^{125}I (Amersham Bioscience, Otelfingen, Switzerland; stock concentration: 3.7 GBq/mL) in 60 μL of phosphate buffer (0.3 M, pH 7.4) in IODO-GEN-precoated tubes (Pierce, Rockford, IL). After 15 min of incubation at room temperature under shaking, the mixture was loaded on a small reversed-phase cartridge (Sep-Pak C18, Waters) and washed

with water and acetic acid (0.5 M), and finally the peptide was eluted with methanol and collected. The fractions containing ^{125}I-NDP-MSH were supplemented with dithiothreitol (1.5 mg/mL) and stored at −20 °C. Before each binding experiment, an additional purification was performed by RP-HPLC using γ-detection.

Cell Culture. The mouse B16F1 melanoma cell line (*42*) was cultured in modified Eagle's medium (MEM; Biochrom AG, Germany) supplemented with 10% heat-inactivated fetal calf serum, 2 mmol/L L-glutamine, 1% nonessential amino acids, 1% vitamin solution, 50 IU/mL penicillin, and 50 μg/mL streptomycin (all from Gibco/Invitrogen, Carlsbad, CA) at 37 °C in an atmosphere of 95% air/5% CO_2. For expansion or experiments, the cells were detached with 0.02% ethylenediaminetetraacetic acid (EDTA) in PBS (150 mmol/L, pH 7.2−7.4).

The human HBL melanoma cell line was cultured in modified RPMI medium (Biochrom AG) supplemented with 10% heat-inactivated fetal calf serum, 2 mmol/L L-glutamine, 50 IU/mL penicillin, and 50 μg/mL streptomycin in the same culture and expansion conditions as B16F1 cells.

In Vitro Binding Assay with B16F1 or HBL Cells. Competition binding experiments were performed by incubating MC1R-expressing B16F1 or HBL cells in microplates with the radioligand ^{125}I-NDP-MSH and a series of dilutions of competitor peptides (from 1×10^{-6} to 1×10^{-12} mol/L) as described previously (*43*). Triplicates of 100 μL of B16F1 or HBL cell suspensions adjusted to 4×10^6/mL were incubated in 96-well U-bottom microplates (Falcon 3077) for 3 h at 15 °C (B16F1) or for 2 h at 37 °C (HBL) with 50 μL of ^{125}I-NDP-MSH (50 000 cpm). The binding medium consisted of MEM with Earle's salts (Biochrom AG), 0.2% bovine serum albumin, and 1,10-phenanthroline (0.3 mmol/L; Merck). The reaction was stopped by incubation on ice for 10 min, and the cell-bound radioactivity was collected on filters by use of a cell harvester (Packard, Meriden, CT). The radioactivity was counted by use of a TopCount microplate scintillation counter (Packard), and the 50% inhibitory concentration (IC_{50}) was calculated with the Prism 5.0 software (GraphPad Software, Inc.).

In Vitro Melanin Assay. The biological activity of the α-MSH derivatives was assessed with an in situ melanin assay (*44*). B16F1 cells (2500 per well, 100 μL) were distributed in cell culture flat bottom 96-well plates in medium consisting of MEM without phenol red and supplemented with 10% heat-inactivated fetal calf serum, 2 mmol/L L-glutamine, 0.31 mmol/L L-tyrosine, 1% nonessential amino acids, 1% vitamin solution, 50 IU/mL penicillin, and 50 μg/mL streptomycin. After overnight incubation in a cell incubator at 37 °C, serial concentrations of α-MSH derivatives, ranging from 1×10^{-8} to 1×10^{-12} in 100 μL volume, were added and incubation was prolonged for an additional 72 h. Melanin production was then monitored through measurement of the absorbance at 310 nm in a microplate reader (Spectra MAX 190, Molecular Devices, Menlo Park, CA).

In Vitro Internalization Assay. B16F1 cells were seeded in six-well plates and incubated overnight at 37 °C in B16F1 cell culture medium. For the experiments, B16F1 medium was removed and replaced by 1 mL of Mouse Binding Medium (MBM) internalization buffer, consisting of MEM with Earle's salts (Biochrom AG, Germany), 0.2% bovine serum albumin, and 1,10-phenanthroline (0.3 mmol/L; Merck). After 1 h of incubation at 37 °C, 74 kBq of radioligand (^{111}In-labeled peptides) was added, and the plates were incubated for different times. Nonspecific internalization was assessed by addition of 50 μL of a 1 μM nonradioactive α-MSH solution. Samples were taken from the supernatant after 0.5, 2, and 3.5 h to determine the total dose added, immediately followed by extensive washings of the cells (6×) using prewarmed (37 °C) MBM to remove the excess of radioligand. The cells were then incubated in 2 mL of ice-cold acid buffer (acetate-buffered HBSS, pH 5) for 10 min to dissociate surface-bound ligand. After collection of the acidic fraction, cells were rinsed once with MBM and the washing was pooled with the acid buffer fraction. The cells were washed once more with MBM (37 °C), lysed in 1% Triton X-100, and finally transferred to tubes for quantification. The radioactivity of all collected fractions was determined in a Cobra II Auto-Gamma γ-counter (Packard). One counting plate was subjected to the same treatment as the plate incubated for the longest time. Cells from this plate were not lysed but detached (EDTA) and counted. Results of the experiments are expressed as the percentage of added dose per million cells.

Biodistribution in B16F1 Tumor-Bearing Mice and Stability of Radioligands after Kidney Excretion. All animal experiments were performed in compliance with Swiss regulations for animal welfare. Female B6D2F1 mice (C57BL/6 × DBA/2 F1 hybrids; breeding pairs obtained from IFFA-CREDO) were implanted subcutaneously with 0.5 million B16F1 cells in phosphate-buffered saline (PBS) to generate a primary skin melanoma. One week later, 200 μL containing 185 kBq (25 pmol) of radioligand diluted in PBS/BSA (pH 7.4) was injected intravenously in the lateral tail vein of each mouse. To allow determination of nonspecific uptake, 50 μg of α-MSH (30 pmol) was coinjected with the radioligand in some mice. The animals were killed at the indicated time points; organs and tissues of interest were dissected and rinsed of excess blood and weighed, and the radioactivity measured in a γ-counter. The percentage of the injected dose per gram tissue (%ID/g) was calculated for each tissue. The total counts injected per animal were calculated by extrapolation from counts of a standard taken from the injected solution for each animal.

As part of the biodistribution experiments, samples of urine were collected from melanoma-bearing mice 10, 15, 20 min, and 4 h after injection of 185 kBq of ^{111}In-DOTA peptide and kept frozen at −80 °C until use. Urine (1 vol) was mixed with methanol (2 vol) to precipitate the proteins and was analyzed by RP-HPLC/γ-detection under the conditions mentioned above.

Analysis of Data. Unless otherwise stated, results are expressed as mean ± standard error of the mean (SEM). Statistical evaluation of the binding assays was performed by using Student's *t*-test. For the analysis of data collected during biodistribution experiments, the mean value obtained for each organ was compared individually to each DOTA−NAPamide organ values by using Student's *t*-test, and the results were corrected with the Bonferroni correction. A *P*-value of <0.05 was considered statistically significant. The area under the curve (AUC) was calculated for a particular time period (4−48 h) using the GraphPad Prism software; mean tissue uptake values at each time point were used for this calculation.

RESULTS

Synthetic Glycosylated DOTA−NAPamide Analogues. The preparation of glycosylated DOTA−NAPamide analogues followed four different strategies: (1) synthesis of a galactopyranosylethanoic acid for straightforward attachment to the N^{α}-terminal amino group of the peptide, as indicated for DOTA−Gal-NAPamide (Figures 1 and 2), requiring a three-step synthesis of the glyco derivative (allylation of its anomeric center, followed by ozonolysis and oxidation (*36*)); (2) Maillard reaction of β-D-glucose or maltotriose with the N^{α}-terminal or the N^{ε}-side-chain amino group, as exemplified for DOTA−Gluc-NAPamide, DOTA−Mtr-NAPamide, or N^{α}-DOTA−[Lys(Gluc)^8]-NAPamide (Figure 1); (3) use of the Fmoc-Asp(1,2:3,4-diisopropylidene-6-amino-α-D-galactosyl)-OH building block for a direct introduction of the carbohydrate during solid-phase

assembly into the side-chain position of residue 2 of DOTA−[Asp(Gal)^2]-NAPamide; (4) functionalization of the C-terminal amide as glycoamide, by attachment of 1-amino-1-deoxy-β-D-galactose to the free carboxy terminus of a side-chain-protected peptide, followed by deprotection and attachment of the DOTA group at the N$^\varepsilon$-side chain of Lys 8.

The glycopeptides were usually obtained in high purity (>99%) but in low yields. Indeed, if DOTA−Gal-NAPamide was obtained in a total yield of 7.4%, the total yields of other glycopeptides were 3% for DOTA−Gluc-NAPamide, 3.4% for DOTA−Mtr-NAPamide, 2% for DOTA−[Asp(Gal)^2]-NAPamide, 1% for N$^\alpha$-DOTA−[Lys(Gluc)^8]-NAPamide, and 3.1% for DOTA−NAPamide-Gal.

The retention times of ^{111}In-labeled peptides on analytical γ-detection RP-HPLC were found to be 18.6 min for DOTA−Gal-NAPamide, 19.2 min for DOTA−Gluc-NAPamide, 18.0 min for DOTA−Mtr-NAPamide, 20.6 min for DOTA−[Asp(Gal)^2]-NAPamide, 19.1 min for N$^\alpha$-DOTA−[Lys(Gluc)^8]-NAPamide, and 19.6 min for DOTA−NAPamide-Gal. Their level of radiochemical purity always exceeded 97%, and the specific activity did not appear to differ significantly between the different glycosylated peptides as deduced from HPLC analysis.

Receptor Binding. MC1R affinity of the glycosylated NAPamide analogues was assessed by competition binding assays against ^{125}I-NDP-MSH on both murine B16F1 and human HBL melanoma cell lines, using α-MSH and DOTA−NAPamide as reference compounds. All peptides showed very good binding affinities to mouse and human MC1R with IC_{50}s ranging from 0.45 to 7.61 nmol/L (Table 1). DOTA−[Asp(Gal)^2]-NAPamide displayed the highest affinity for the MC1R on both B16F1 and HBL cells and exceeded that of DOTA−NAPamide by a factor of 3 to 3.5. DOTA−NAPamide-Gal was also slightly more active than DOTA−NAPamide. DOTA−Gal-NAPamide and DOTA−Gluc-NAPamide displayed slightly lower IC_{50}s than DOTA−NAPamide, while the affinity of DOTA−Mtr-NAPamide and N$^\alpha$-DOTA−[Lys(Gluc)^8]-NAPamide was about 2- to 3.5-fold lower than that of DOTA−NAPamide. The glycopeptides without the DOTA chelator all showed markedly higher affinity (data not shown).

Biological Activity. In the melanin assay using B16F1 cells, all DOTA−glycopeptides, except for N$^\alpha$-DOTA−[Lys(Gluc)^8]-NAPamide, displayed higher biological (agonist) activity than DOTA−NAPamide, all in the picomolar range. In order to compare the EC_{50} of different experiments, these were normalized against the EC_{50} of the reference compound α-MSH whose rEC_{50} was defined as 1 (Table 1). DOTA−[Asp(Gal)^2]-NAPamide and DOTA−Gluc-NAPamide displayed the lowest rEC_{50}s with 0.26 and 0.34, respectively. The values of the other glycopeptides were comparable to that of DOTA−NAPamide. The induction of melanin synthesis by B16F1 cells started at doses matching their IC_{50}s and lower. Only DOTA−Mtr-NAPamide showed a slightly worse rEC_{50} but still matching that of α-MSH. Again, DOTA−[Asp(Gal)^2]-NAPamide exhibited the best agonist activity in vitro.

Internalization Assay. Internalization assays were carried out to determine if and how fast the glycopeptides were internalized by B16F1 cells. The results were excellent, all glycopeptides being almost totally internalized in 2 h or less. As an example, Figure 3 shows the internalization kinetics of DOTA−Gal-NAPamide, which reached a plateau after 2 h when internalization of the peptide was almost total. These data show that internalization of the peptide by tumor cells cannot be an issue regarding the in vivo tumor uptake.

Biodistribution in Melanoma-Bearing Mice. Table 2 shows the tissue distributions of the different ^{111}In-labeled, glycosylated DOTA−NAPamide peptides in comparison with [^{111}In]-DOTA−NAPamide at 4, 24, and 48 h after injection of the radioligand. Coinjection of an excess of α-MSH to block MC1R reduced the 4-h tumor uptake of DOTA−Gal-NAPamide by >90%, of DOTA−Mtr-NAPamide by 89%, of N$^\alpha$-DOTA−[Lys(Gluc)^8]-NAPamide by 86%, of DOTA−Gluc-NAPamide by 80%, of DOTA−NAPamide-Gal by 77%, and of DOTA−[Asp(Gal)^2]-NAPamide by 75%, indicating that all these derivatives are taken up by melanoma cells through receptor-mediated internalization. DOTA−Gal-NAPamide showed the highest tumor uptake among the glycopeptides, comparable to that of DOTA−NAPamide (Figure 4), followed by DOTA−Mtr-NAPamide, DOTA−NAPamide-Gal, DOTA−[Asp(Gal)^2]-NAPamide, N$^\alpha$-DOTA−[Lys(Gluc)^8]-NAPamide, and DOTA−Gluc-NAPamide. The ranking of melanoma uptake of the different glyco-NAPamide peptides did not correspond with the in vitro MC1R binding affinity.

Clearance of ^{111}In from the kidneys was found to be quite a slow process, as also reported for other peptides. Indeed, 46% of the radioactivity measured in the kidneys 4 h after injection of DOTA−Gal-NAPamide was still present after 24 h, and 26% after 48 h. For DOTA−[Asp(Gal)^2]-NAPamide the values were 49% and 33%, for DOTA−Mtr-NAPamide 34% and 27%, for DOTA−Gluc-NAPamide 65% and 43%, and for N$^\alpha$-DOTA−[Lys(Gluc)^8]-NAPamide 66% and 35%. The slowest clearance from the kidneys was observed for DOTA−NAPamide-Gal whose values were 99% and 34% and hence was opposed to the expectation that glycosylation of the C-terminal amide of Lys^8 may increase kidney clearance and reduce reuptake.

Radioactivity release from the tumor was faster than from the kidneys, with 25% of the radioactivity measured after 4 h still present after 24 h and 11% after 48 h for DOTA−Gal-NAPamide, and slightly higher but comparable values for DOTA−[Asp(Gal)^2]-NAPamide, DOTA−Gluc-NAPamide, N$^\alpha$-DOTA−[Lys(Gluc)^8]-NAPamide, and DOTA−NAPamide-Gal, in part due to their lower overall tumor uptake. Indeed, DOTA−Mtr-NAPamide, which displayed an almost similar tumor uptake as that of DOTA−Gal-NAPamide after 4 h, exhibited values of 22% and 8% at 24 and 48 h.

The glycopeptides with the highest in vitro binding affinity displayed a lower in vivo accumulation in melanoma than would have been predicted from their in vitro potency. DOTA−Gal-NAPamide, showing an average receptor binding affinity comparable to DOTA−NAPamide, delivered a more favorable biodistribution profile with higher tumor uptake after 4 h (8.30% ± 1.22%ID/g) and higher tumor-to-kidney ratio after 4 h (1.87 ± 0.15) than that for any other glycopeptide. Indeed, DOTA−Gal-NAPamide exhibited a 4−48 h AUC tumor-to-kidney ratio of 1.34 (Figure 5), which exceeds that of DOTA−NAPamide (1.11) by 17%. It was unfortunately impossible to compare directly the tumor-to-kidney ratio of the AUC of the peptides synthesized in this work with peptides synthesized by others, because of the lack of 48 h data in their work. Nevertheless, their 4 h tumor-to-kidney-ratio could be compared, and it appeared that DOTA−Gal-NAPamide was among the best radiolabeled α-MSH analogues synthesized so far. Indeed, as mentioned above, DOTA−Gal-NAPamide displayed a 4 h tumor-to-kidney ratio of 1.87 while, for instance, ^{111}In-DOTA−ReCCMSH (1.02) (*4*), ^{188}Re-(Arg^{11})CCMSH (0.32) (*10*), ^{111}In-DOTA−NAPamide (1.63) (*7*), [^{111}In-DOTA−Nle^4, Asp^5,D-Phe^7,Ac-Lys^{11}-NH$_2$]-α-MSH$_{4-11}$ (1.06) (*7*), ^{90}Y- or ^{177}Lu-DOTA−Re(Glu^2,Arg^{11})CCMSH (1.30 and 1.57) (*9*), ^{111}In-DOTA−Cyc-MSH (0.35) (*45*), or ^{111}In-DOTA−GlyGlu-Cyc-MSH (0.61) (*45*) exhibited lower tumor-to-kidney ratios after 4 h.

DISCUSSION

This study focused on the influence of introducing a few different types of carbohydrates at the N- or C-terminal end

and at side-chain positions of the α-MSH derivative DOTA−NAPamide. In view of the reports that glycosylation of peptides or proteins would reduce reuptake by the tubular system of the kidneys (*27*, *28*), our first attempt was to study a DOTA−NAPamide derivative whose C-terminal amide was glycosylated. Previous observations in our laboratory (unpublished data) demonstrated that an important metabolite of [^{111}In]DOTA−NAPamide was H-Lys([^{111}In]DOTA)-NH_2 which was regularly observed in the urine collected from mice treated with this peptide. However, DOTA−NAPamide-Gal showed a higher and much longer kidney retention than all other glycopeptides which we investigated. Most likely, the C-terminal carbohydration led to increased reuptake and trapping of the peptide or its metabolites in endosomes in tubular cells of the kidney.

Glycosylation of the amino acid side chains of Asp^2 or Lys^8 does not seem to be a good alternative either. DOTA−[$Asp(Gal)^2$]-NAPamide and N^{α}-DOTA−[$Lys(Gluc)^8$]-NAPamide both displayed slightly lower tumor uptake and higher kidney uptake than the other glycopeptides. Again, the increased kidney uptake may be the result of higher rate of internalization and marked retention by tubular cells. A precise molecular explanation would require a detailed analysis, particularly in view of the very high in vitro potency of DOTA−[$Asp(Gal)^2$]-NAPamide which would rule out steric hindrance by the side-chain galactosyl group for receptor binding.

Finally, three different glycopeptides bearing a glucose, galactose, or maltotriose moiety at their N-terminal end were then examined in order to assess the influence of the type of sugar on the pharmacokinetics. The derivative with a glucose residue showed poor pharmacokinetic properties, displaying an in vivo tumor-to-kidney ratio (4−48 h AUC) of only 0.60 (Figure 5), although it exhibited a similarly low kidney uptake after 4 h (4.48%ID/g) as the structurally similar [^{111}In]DOTA−Gal-NAPamide. The analogue with N-terminal maltotriose showed much better properties with a tumor-to-kidney ratio (4−48 h AUC) of 0.99. The tumor uptake was similar to that of [^{111}In]DOTA−NAPamide, but the higher kidney uptake led to a lower ratio as compared to DOTA−NAPamide. The most encouraging data were obtained with [^{111}In]DOTA−Gal-NAPamide which exhibited the relatively highest melanoma uptake and lowest kidney uptake in vivo, leading to a tumor-to-kidney ratio which exceeded that of [^{111}In]DOTA−NAPamide by a factor of about 1.2. This result is very valuable, as it shows the direction to follow in order to improve tumor-to-nontarget-tissue ratios which are fundamental for future therapeutic applications.

In conclusion, we demonstrated that introduction of different types of sugars at various positions along the sequence of ^{111}In-labeled NAPamide affect the in vitro binding affinity and the in vivo pharmacokinetic behavior. It is noteworthy that carbohydration generally did not reduce the binding affinity when compared to the nonglycosylated reference peptide. Also, the sugar moieties appeared to be without influence on the extent of ^{111}In-labeling of DOTA, owing to a rigidly standardized labeling protocol. Kidney reuptake and retention, however, were increased with side-chain and C-terminal sugar groups but decreased with an N-terminal galactosyl group. This compound, DOTA−Gal-NAPamide, exhibited favorable pharmacokinetic data. Its high melanoma uptake and lower kidney retention, and above all its improved tumor-to-kidney uptake ratio, opens the door to the development of novel glycosylated radiolabeled α-MSH derivatives for melanoma targeting with further reduced nephrotoxicity.

ACKNOWLEDGMENT

The authors thank the Swiss National Science Foundation and the Swiss Cancer League for financial support of this work.

LITERATURE CITED

(1) Ghanem, G. E., Comunale, G., Libert, A., Vercammen-Grandjean, A., and Lejeune, F. J. (1988) Evidence for α-melanocyte-stimulating hormone (α-MSH) receptors on human malignant melanoma cells. *Int. J. Cancer 41*, 248–55.

(2) Siegrist, W., Solca, F., Stutz, S., Giuffre, L., Carrel, S., Girard, J., and Eberle, A. N. (1989) Characterization of receptors for α-melanocyte-stimulating hormone on human melanoma cells. *Cancer Res. 49*, 6352–8.

(3) Bagutti, C., Oestreicher, M., Siegrist, W., Oberholzer, M., and Eberle, A. N. (1995) α-MSH receptor autoradiography on mouse and human melanoma tissue sections and biopsies. *J. Recept. Signal Transduction Res. 15*, 427–42.

(4) Chen, J., Cheng, Z., Owen, N. K., Hoffman, T. J., Miao, Y., Jurisson, S. S., and Quinn, T. P. (2001) Evaluation of an ^{111}In-DOTA−rhenium cyclized α-MSH analog: a novel cyclic-peptide analog with improved tumor-targeting properties. *J. Nucl. Med. 42*, 1847–55.

(5) Cheng, Z., Chen, J., Miao, Y., Owen, N. K., Quinn, T. P., and Jurisson, S. S. (2002) Modification of the structure of a metallopeptide: synthesis and biological evaluation of ^{111}In-labeled DOTA−conjugated rhenium-cyclized α-MSH analogues. *J. Med. Chem. 45*, 3048–56.

(6) Froidevaux, S., Calame-Christe, M., Schuhmacher, J., Tanner, H., Saffrich, R., Henze, M., and Eberle, A. N. (2004) A gallium-labeled DOTA−α-melanocyte- stimulating hormone analog for PET imaging of melanoma metastases. *J. Nucl. Med. 45*, 116–23.

(7) Froidevaux, S., Calame-Christe, M., Tanner, H., and Eberle, A. N. (2005) Melanoma targeting with DOTA−α-melanocyte-stimulating hormone analogs: structural parameters affecting tumor uptake and kidney uptake. *J. Nucl. Med. 46*, 887–95.

(8) Froidevaux, S., Calame-Christe, M., Tanner, H., Sumanovski, L., and Eberle, A. N. (2002) A novel DOTA−α-melanocyte-stimulating hormone analog for metastatic melanoma diagnosis. *J. Nucl. Med. 43*, 1699–706.

(9) Miao, Y., Fisher, D. R., and Quinn, T. P. (2006) Reducing renal uptake of ^{90}Y- and ^{177}Lu-labeled α-melanocyte stimulating hormone peptide analogues. *Nucl. Med. Biol. 33*, 723–33.

(10) Miao, Y., Whitener, D., Feng, W., Owen, N. K., Chen, J., and Quinn, T. P. (2003) Evaluation of the human melanoma targeting properties of radiolabeled α-melanocyte stimulating hormone peptide analogues. *Bioconjugate Chem. 14*, 1177–84.

(11) Miao, Y., and Quinn, T. P. (2008) Peptide-targeted radionuclide therapy for melanoma. *Crit. Rev. Oncol. Hematol. 67*, 213–28.

(12) Boerman, O., Oyen, W. J., and Corstens, F. H. (2001) Between the Scylla and Charybdis of peptide radionuclide therapy: hitting the tumor and saving the kidney. *Eur. J. Nucl. Med. 28*, 1447–9.

(13) Behr, T. M., Béhé, M., Kuge, G., Gotthardt, M., Schipper, M. L., and Gratz, S. (2002) Nephrotoxicity versus anti-tumour efficacy in radiopeptide therapy: facts and myths about the Scylla and Charybdis. *Eur. J. Nucl. Med. 29*, 277–9.

(14) Cybulla, M., Weiner, S. M., and Otte, A. (2001) End-stage renal disease after treatment with ^{90}Y-DOTATOC. *Eur. J. Nucl. Med. 28*, 1552–4.

(15) Moll, S., Nickeleit, V., Müller-Brand, J., Brunner, F. P., Mäcke, H. R., and Mihatsch, M. J. (2001) A new case of renal thrombotic microangiopathy: yttrium-90-DOTATOC internal radiotherapy. *Am. J. Kidney Dis. 37*, 847–51.

(16) Froidevaux, S., and Eberle, A. N. (2002) Somatostatin analogs and radiopeptides in cancer therapy. *Biopolymers 66*, 161–83.

(17) De Visser, M., Verwijnen, S. M., and De Jong, M. (2008) Improvement strategies for peptide receptor scintigraphy and radionuclide therapy. *Cancer Biother. Radiopharm. 23*, 137–57.

(18) Miao, Y., and Quinn, T. P. (2007) α-Melanocyte stimulating hormone peptide-targeted melanoma imaging. *Front. Biosci. 12*, 4514–24.

(19) Bakker, W. H., Albert, R., Bruns, C., Breeman, W. A., Hofland, L. J., Marbach, P., Pless, J., Pralet, D., Stolz, B., Koper, J. W., et al. (1991) [^{111}In-DTPA-D-Phe^{1}]-octreotide, a potential radiopharmaceutical for imaging of somatostatin receptor-positive tumors: synthesis, radiolabeling and in vitro validation. *Life Sci. 49*, 1583–91.

(20) Fritzberg, A. R., Abrams, P. G., Beaumier, P. L., Kasina, S., Morgan, A. C., Rao, T. N., Reno, J. M., Sanderson, J. A., Srinivasan, A., Wilbur, D. S., et al. (1988) Specific and stable labeling of antibodies with technetium-99m with a diamide dithiolate chelating agent. *Proc. Natl. Acad. Sci. U.S.A. 85*, 4025–9.

(21) Wraight, E. P., Bard, D. R., Maughan, T. S., Knight, C. G., and Page-Thomas, D. P. (1992) The use of a chelating derivative of alpha melanocyte stimulating hormone for the clinical imaging of malignant melanoma. *Br. J. Radiol. 65*, 112–8.

(22) Chen, J., Cheng, Z., Hoffman, T. J., Jurisson, S. S., and Quinn, T. P. (2000) Melanoma-targeting properties of ^{99m}technetium-labeled cyclic α-melanocyte-stimulating hormone peptide analogues. *Cancer Res. 60*, 5649–58.

(23) Miao, Y., Owen, N. K., Whitener, D., Gallazzi, F., Hoffman, T. J., and Quinn, T. P. (2002) In vivo evaluation of ^{188}Re-labeled alpha-melanocyte stimulating hormone peptide analogs for melanoma therapy. *Int. J. Cancer 101*, 480–7.

(24) Akizawa, H., Arano, Y., Mifune, M., Iwado, A., Saito, Y., Mukai, T., Uehara, T., Ono, M., Fujioka, Y., Ogawa, K., Kiso, Y., and Saji, H. (2001) Effect of molecular charges on renal uptake of ^{111}In-DTPA-conjugated peptides. *Nucl. Med. Biol. 28*, 761–8.

(25) Bapst, J. P., Froidevaux, S., Calame, M., Tanner, H., and Eberle, A. N. (2007) Dimeric DOTA−α-melanocyte-stimulating hormone analogs: synthesis and in vivo characteristics of radiopeptides with high in vitro activity. *J. Recept. Signal Transduction Res. 27*, 383–409.

(26) Behr, T. M., Goldenberg, D. M., and Becker, W. (1998) Reducing the renal uptake of radiolabeled antibody fragments and peptides for diagnosis and therapy: present status, future prospects and limitations. *Eur. J. Nucl. Med. 25*, 201–12.

(27) Suzuki, K., Susaki, H., Okuno, S., Yamada, H., Watanabe, H. K., and Sugiyama, Y. (1999) Specific renal delivery of sugar-modified low-molecular-weight peptides. *J. Pharmacol. Exp. Ther. 288*, 888–97.

(28) Shirota, K., Kato, Y., Suzuki, K., and Sugiyama, Y. (2001) Characterization of novel kidney-specific delivery system using an alkylglucoside vector. *J. Pharmacol. Exp. Ther. 299*, 459–67.

(29) Filippi, B., Biondi, L., Filira, F., Rocchi, R., Bellini, C., and Sarto, G. (1983) Synthesis and biological activity of D-Ala^{2}, Leu^{5}-enkephalins containing hydrophilic or hydrophobic moieties. *Biopolymers 22*, 575–8.

(30) Polt, R., Porreca, F., Szabo, L. Z., Bilsky, E. J., Davis, P., Abbruscato, T. J., Davis, T. P., Harvath, R., Yamamura, H. I., and Hruby, V. J. (1994) Glycopeptide enkephalin analogues produce analgesia in mice: evidence for penetration of the blood-brain barrier. *Proc. Natl. Acad. Sci. U.S.A. 91*, 7114–8.

(31) Fisher, J. F., Harrison, A. W., Bundy, G. L., Wilkinson, K. F., Rush, B. D., and Ruwart, M. J. (1991) Peptide to glycopeptide: glycosylated oligopeptide renin inhibitors with attenuated in vivo clearance properties. *J. Med. Chem. 34*, 3140–3.

(32) Schottelius, M., Wester, H. J., Reubi, J. C., Senekowitsch-Schmidtke, R., and Schwaiger, M. (2002) Improvement of pharmacokinetics of radioiodinated Tyr^{3}-octreotide by conjugation with carbohydrates. *Bioconjugate Chem. 13*, 1021–30.

(33) Wester, H. J., Schottelius, M., Poethko, T., Bruus-Jensen, K., and Schwaiger, M. (2004) Radiolabeled carbohydrated somatostatin analogs: a review of the current status. *Cancer Biother. Radiopharm. 19*, 231–44.

(34) Wester, H. J., Schottelius, M., Scheidhauer, K., Reubi, J. C., Wolf, I., and Schwaiger, M. (2002) Comparison of radioiodinated TOC, TOCA and Mtr-TOCA: the effect of carbohydration on the pharmacokinetics. *Eur. J. Nucl. Med. Mol. Imaging 29*, 28–38.

(35) Suzuki, K., Ando, T., Susaki, H., Mimori, K., Nakabayashi, S., and Sugiyama, Y. (1999) Structural requirements for alkyl-glycoside-type renal targeting vector. *Pharm. Res. 16*, 1026–34.

(36) Arya, P., Barkley, A., and Randell, K. D. (2002) Automated high-throughput synthesis of artificial glycopeptides. Small-molecule probes for chemical glycobiology. *J. Comb. Chem. 4*, 193–8.

(37) Ames, J. M. (1998) Applications of the Maillard reaction in the food industry. *Food Chem. 62*, 431–439.

(38) Albert, R., Marbach, P., Bauer, W., Briner, U., Fricker, G., Bruns, C., and Pless, J. (1993) SDZ CO 611: a highly potent glycated analog of somatostatin with improved oral activity. *Life Sci. 53*, 517–25.

(39) Frolov, A., Singer, D., and Hoffmann, R. (2006) Site-specific synthesis of Amadori-modified peptides on solid phase. *J. Pept. Sci. 12*, 389–95.

(40) Horvat, S., and Jakas, A. (2004) Peptide and amino acid glycation: new insights into the Maillard reaction. *J. Pept. Sci. 10*, 119–37.

(41) Eberle, A. N. (1988) *The Melanotropins: Chemistry, Physiology and Mechanisms of Action*; pp 77−78, Chapter 5, Karger, Basel.

(42) Fidler, I. J. (1973) Selection of successive tumour lines for metastasis. *Nat. New Biol. 242*, 148–9.

(43) Froidevaux, S., and Eberle, A. N. (2002) Homologous regulation of melanocortin-1 receptor (MC1R) expression in melanoma tumor cells in vivo. *J Recept. Signal Transduction Res. 22*, 111–21.

(44) Siegrist, W., and Eberle, A. N. (1986) In situ melanin assay for MSH using mouse B16 melanoma cells in culture. *Anal. Biochem. 159*, 191–7.

(45) Miao, Y., Gallazzi, F., Guo, H., and Quinn, T. P. (2008) ^{111}In-labeled lactam bridge-cyclized α-melanocyte stimulating hormone peptide analogues for melanoma imaging. *Bioconjugate Chem 19*, 539–47.

BC900007U

Biotinylated Glyco-Functionalized Quantum Dots: Synthesis, Characterization, and Cytotoxicity Studies

Xiaoze Jiang, Marya Ahmed, Zhicheng Deng, and Ravin Narain*

Department of Chemistry and Biochemistry, Biomolecular Sciences Program, Laurentian University, 935, Ramsey Lake Road, Sudbury, Ontario P3E 2C6, Canada. Received January 13, 2009; Revised Manuscript Received April 14, 2009

Quantum dots (QDs) containing surface carboxylic groups have been successfully modified using biotinylated glycopolymer and carbohydrate/biotin reagents via EDC coupling. The biotinylated glycopolymer was synthesized in controlled dimension via the reversible addition−fragmentation chain transfer (RAFT) polymerization of the three monomers containing biotin, sugar, and amine groups as pendent groups, respectively. The modified QDs were analyzed by dynamic light scattering and fluorescence spectrophotometry, and the data revealed no change in the physical properties of QDs after surface modification. Furthermore, the surface modified QDs showed excellent water solubility and colloidal stability. Subsequently, the availability of the biotin ligand on the surface of functionalized QDs was quantified using 4-hydroxyazobenzene 2-carboxylic acid (HABA)/avidin binding assay. Cell viability studies revealed that the cytotoxicity of QDs after surface functionalization is improved and that the biotinylated glycopolymer modified QDs showed an enhancement in biocompatibility as compared to that of the original QDs. The biotinylated glyco-functionalized quantum dots may act as new suitable fluorescent probes in biomedical applications.

INTRODUCTION

Semiconductor nanocrystals (usually called quantum dots, QDs) have been receiving enormous attention in recent years (*1*−*6*). QDs display unique size dependent optical properties for potential applications from electronic to biomedical fields. In the field of biomedicine, the high luminescence, single excitation narrow emission, and low photobleaching properties of high quality water-soluble QDs with low toxicity are exploited for *in vivo* labeling/imaging of cells (*7*−*11*), and their surfaces have been functionalized with DNA (*12*−*14*), peptides (*15, 16*), proteins (*5, 6, 17, 18*), and other small ligands (*19*−*21*) to realize their applications as a new class of size-tunable optical probes.

Several strategies have previously been reported in the surface functionalization of water-soluble QDs with surface functional groups (*22*−*27*). The promised method generally used for the functionalization of QDs is encapsulating the QDs with water-soluble polymer chains (*26, 27*) or charged proteins (*18*), which improve their solubility, reduce toxicity, and essentially preserve their initial optical properties in physiological conditions. As the main application of functionalized QDs concern the labeling of cells, specific ligands have to be incorporated for site specific binding of the functionalized QDs, and the cytotoxicity of QDs have to be considered as well.

Protein−carbohydrate interactions are involved in a wide variety of cellular recognition processes including cell growth regulation, differentiation, adhesion, cancer cell metastasis, cellular trafficking, inflammation by bacteria and viruses, and immune response (*28, 29*). However, individual carbohydrate−protein interactions are generally weak, and multivalent forms of carbohydrate ligands, such as glycopolymers (*30*−*34*), glycodendrimers (*35*−*37*), or glyconanoparticles (*38, 39*), have been used to enhance them through cooperative multiple interactions. Therefore, the functionalization of QDs with carbohydrates is of interest for the study of carbohydrate−cell interactions. The incorporation of carbohydrates on the surface of the QDs is also expected to improve the solubility and biocompatibility, and reduce the toxicity of fluorescent nanocrystals. Sun and co-workers (*20*) were the first to report glyco-functionalized QDs with biotin end-terminated glycopolymers synthesized via a cyanoxyl-mediated free radical polymerization. However, the glycopolymers with free hydroxyl groups were obtained via polymerization of the protected glycomonomer and deprotection after polymerization. Recently, Babu et al. (*19*) reported the functionalization of QDs with several carbohydrates bearing reactive thiol groups at the end chains in aqueous solution via the ligand exchange method, and the special binding of the fluorescent glyconanoparticles to glycoproteins was studied. However, in both of the reports, the biocompatibility of the carbohydrate functionalized QDs, which is important for potential biomedical applications, is still to be investigated.

Biotinylated QDs have also been synthesized for the study of site-specific biomolecular interactions of biotin and avidin as a ligand−receptor pair, which was widely used in the fields of biology and medicine (*40, 41*). Two new ligands consisting of thiol and biotin terminal groups were synthesized to functionalize the surface of QDs reported by Reiss et al. (*7*) Another new series of ligands comprising a poly(ethylene glycol) chain, a dihydrolipoic acid, and a potential biological functional group such as biotin were designed and prepared by Mattoussi and co-workers (*9*). However, both of the biotinylated QDs were prepared via the ligand exchange method, which usually changes the optical properties of original QDs, and the ligands used generally need complicated synthesis. Therefore, designing well-defined biotinylated glycopolymers bearing biotin and carbohydrates moieties as pendent groups is interesting for the fabrication of high quality water-soluble and bioactive QDs with low toxicity.

In order to maximize the biological functions of the QDs, we herein report two different strategies to prepare stable surface functionalized QDs with both biotin and carbohydrates moieties. Our motivation here is to incorporate carbohydrate and biotin moieties on the surface of QDs for improving biocompatibility

* Corresponding author. Tel: 1 705-6751151 (2186). Fax: 1 705-6754844. E-mail: rnarain@laurentian.ca.

10.1021/bc800566f CCC: $40.75 © 2009 American Chemical Society
Published on Web 04/29/2009

and cell viability of the original QDs. Two strategies are used to functionalize the surface of original carboxyl-capped QDs, and the bioavailability of the biotin ligands on the surface of functionalized QDs is quantified. The cytotoxicity of biotinylated glyco-functionalized QDs is clearly reduced as shown by MTT assay results.

EXPERIMENTAL SECTION

Materials. 2-Aminoethyl methacrylamide hydrochloride (AEMA) (*42, 43*), gluconamidoethyl methacrylamide hydrochloride (GAEMA) (*44*), and *S*,*S*′-bis(α,α′-dimethyl-α″-acetic acid) trithiocarbonate (CTA1) (*45*) were synthesized as previously described. 4,4′-Azobis(4-cyanovaleric acid) (ACVA, 97%) was purchased from Acros Organics and used as received. 1-Ethyl-3-[3-dimethylaminopropyl] carbodiimide hydrochloride (EDC) and *N*-hydroxysuccinimide (NHS) were purchased from Sigma-Aldrich and used as received. The synthesis and characterization of biotinyl-*N*-hydroxysuccinimide ester (biotin-NHS), *N*-(2-aminoethyl) biotinamide (biotin-NH_2), *N*-(2-aminoethyl) gluconamide hydrochloride (sugar-NH_2), and biotinyl-2-aminoethyl methacrylamide hydrochloride (BAEMA) are given in Supporting Information.

Quantum dots (yellow color, carboxy-functionalized CdS-capped CdTe nanoparticle solution, sodium as carboxyl counterion; 20 mg/mL in water, and emission maxima wavelength and full-width at half-maximum (FWHM) are 563 and 90 nm at 350 nm of excitation, respectively) with surface carboxylic groups were obtained from Northern Nanotechnologies Inc., and their detailed information could be checked at https://store.vivenano.com/library/Qdots_specs.pdf. Dulbecco's modified Eagle's medium (DMEM), fetal bovine serum, phosphate buffered solution at pH 7.4 (DPBS), trypsin, and a (3-(4,5-dimethylthiazol-2-yl)-2,5-diphenyltetrazolium bromide, a tetrazole) assay kit (MTT assay kit) were purchased from Sigma-Aldrich Chemicals.

Preparation of P(GAEMA-*stat*-AEMA-*stat*-BAEMA) Copolymer via RAFT Polymerization. The RAFT polymerization was achieved at 70 °C, employing ACVA as the initiator and CTA1 as the chain transfer agent. A typical protocol was as follows. In a 10 mL flask, GAEMA (0.5 g, 1.46 mmol) and BAEMA (0.21 g, 0.54 mmol) were dissolved in distilled water (3 mL) at 40 °C and then cooled to room temperature. AEMA (0.18 g, 1.09 mmol, dissolved in 1.0 mL water) and the mixture of ACVA (2.0 mg, 0.007 mmol) and CTA1 (10 mg, 0.035 mmol) dissolved into 2 mL of dioxane were added into the above solution. After degassing via three freeze-pump-thaw cycles, the flask was placed in an oil bath preheated at 70 °C to start the polymerization. After 18 h, the flask was placed into liquid nitrogen to quench the polymerization. The mixture was diluted with water and then precipitated into an excess of isopropanol. This purification cycle was repeated twice. The obtained slightly yellow powder (0.60 g, 67% yield) was dried in a vacuum oven overnight at room temperature.

EDC Coupling. Quantum dots solution (1 mL) was added to PBS buffer solution (pH 7.4, 4 mL) of EDC (2.6 mg) and NHS (1.5 mg). The reaction mixture was stirred for 30 min at room temperature. Then the P(GAEMA-*stat*-AEMA-*stat*-BAEMA) copolymer (10.0 mg in 35 mL of PBS buffer solution) or the mixture of sugar-NH_2 (2.6 mg, dissolved in 34 mL of PBS buffer solution) and biotin-NH_2 (1.1 mg in 1 mL of DMF) was added to the above PBS buffer solution. After stirring the reaction mixture overnight at room temperature, the mixture was purified by dialysis against distilled water for 2 days using the dialysis membrane molecular weight cut-off (MWCO) of 12,000−14,000. The desired QDs were freeze-dried under vacuum for 2 days.

Instrumentation. ^{1}H NMR spectra of the monomers and polymers were recorded on a Varian 200 MHz instrument. Aqueous gel permeation chromatography analysis was performed on a Viscotek Instrument using a 0.5 M sodium acetate/acetic acid buffer as eluent, two Waters WAT011545 columns, and a flow rate of 1.0 mL/min. Six near-monodisperse PEO standards (M_p = 1,010−101,200 g mol^{-1}) were used for calibration.

The products were analyzed by an Agilent HPLC 1100 interfaced with an Electro-Spray Ionization Agilent Mass Spectrometer Model 6120 with a Chemstation data system LC-MSD B.03.01.

Dynamic light scattering (DLS) was performed at room temperature using a Viscotek DLS instrument with an He−Ne laser at a wavelength of 632 nm and a Pelletier temperature controller. The surface functionalized quantum dot aqueous solutions (20 nM) were filtered through Millipore membranes (0.45 μm pore size). The data was recorded with OmniSize Software.

The 4-hydroxyazobenzene 2-carboxylic acid (HABA)/avidin binding assay was performed as described by Green group (*46, 47*). UV−visible absorption spectra were recorded on a Cary UV 100 spectrophotometer from the aqueous solution of surface functionalized quantum dots at room temperature. The absorbance values at 500 nm for the HABA/avidin reagent and for the solution after the addition of surface functionalized quantum dots were monitored. Before the samples were tested, the solutions were filtered through Millipore membranes (0.45 μm pore size) and then concentrated or diluted to the appropriate concentration. The change of absorbance at 500 nm of HABA/avidin and after HABA/avidin added surface functionalized quantum dots should be at 0.1−0.4.

Fluorescence measurements were performed on an OLISRSM-1000 (Desa rapid-scanning monochromator spectrophotometry system). The spectra were recorded in the wavelength range of 500−650 nm upon excitation at 490 nm; a 1.00 cm path length rectangular quartz cell was used for this study. Very dilute solutions of surface functionalized quantum dots (20 nM) were used in the experiment.

Cell viability/cytotoxicity of quantum dots was characterized using an MTT (3-(4,5-bimethylthiazol-2-yl)-2,5-diphenyltetrazolium bromide, a tetrazole) assay. HeLa cells were plated in a 96-well plate at a density of 15000 cells/well in 100 μL of growth medium consisting of Dulbecco's modified Eagle's medium (DMEM) with 5% fetal bovine serum and antibiotics (100U/mL penicillin and 100 μg/mL streptomycin). Cells were incubated for 24 h at 37 °C and 5% CO_2, after which time the growth medium was replaced with DMEM medium containing different concentrations of quantum dots. The preparation of QD stock solutions was as follows. All aqueous quantum dot solutions were dissolved into Dulbecco's phosphate buffer at a final concentration of 32 nM. The samples were autoclaved, and different volumes of prepared solution were added into different volumes of DMEM medium to obtain final concentrations of 2, 10, and 20 nM of QDs in the medium. The cells were further incubated for 24 h under the same conditions, after which 25 μL of MTT dye was added to each well, and the plate was incubated for 2 h. Next, 100 μL of MTT lysis solution was added to each well, and cells were incubated overnight. Absorbance was measured at 570 nm (Power wave X plate reader). Survival percentage was calculated by comparison to blank cells (100% survival).

Confocal microsocopy was performed to determine the uptake of QDs by HeLa cells. HeLa cells were grown in Dubelcco's modified Eagle's medium, DMEM, containing 10% fetal bovine serum, and 1% penicillin/streptomycin, in a humidified atmosphere with 5% CO_2 at 37 °C. Upon 80% confluency, cells were trypsinized and neutralized with an equal amount of medium. The cells were then reseeded in a 6 well plate, in which each

Scheme 1. Schematic Illustration of the Synthesis of *N*-(2-Aminoethyl)gluconamide Hydrochloride (Sugar-NH_2) and *N*-(2-Aminoethyl)biotinamide (Biotin-NH_2)

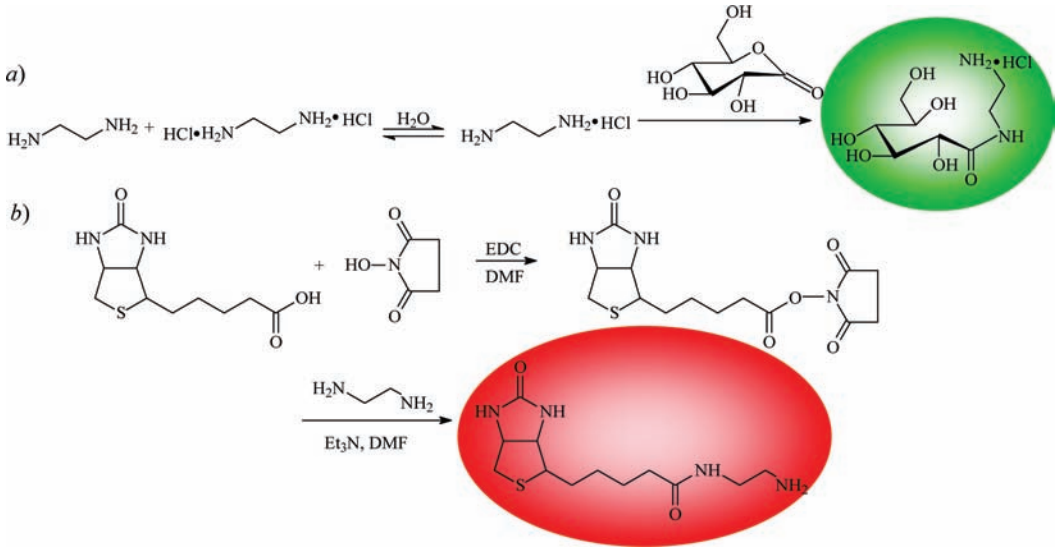

well contained sterile glass coverslips. The plate was incubated in a humidified atmosphere at 37 °C, and upon 80% confluency, 75 nM QDs containing medium was introduced in chambered cover glass. The cells were further incubated for 3 h at 37 °C. The growth medium was then removed, and the cells were washed several times with phosphate buffered saline. The cells were fixed with 4% paraformaldehyde solution at room temperature for 5 min, followed by washing with PBS. The cover glass was then mounted on a microscopic glass slide and was studied under a microscope. The fluorescent images were obtained using a Zeiss LSM 510 Meta confocal microscope with a 63× objective. The wavelengths of excitation and emission used were 490 and 510 nm, respectively.

RESULTS AND DISCUSSION

Quantum dots (QDs) have attracted tremendous interest because of their remarkable and unique properties such as photochemical stability, size dependent broad absorption, very high extinction coefficients, and high fluorescence quantum yield (*1, 2, 48, 49*). Such features make the QDs an indispensable tool for use in biomedical research, especially for biological assays and imaging. Recent advances in QD nanoparticles have led to the development of high-quality water-soluble biotin or sugar functionalized QDs to reduce the toxicity of QDs for biomedical applications (*7, 20*). To the best of our knowledge, there is only one report that describes the functionalization of QDs using both biotin and sugar groups (*20*). However, the reported method requires a multiple step synthetic process, and therefore, our goal was to find a simple method to fabricate biotin and sugar functionalized QDs without protecting group chemistry.

The original quantum dots (yellow color) used in this study were donated by Northern Nanotechnologies, which were carboxy-functionalized in CdS-capped CdTe nanoparticle solution, with sodium as carboxy counterion, and stabilized in aqueous solution by the carboxyl terminated polymer chains. The polymers improve their water solubility in basic conditions and provide the surface for further functionalization. In order to obtain the surface biotin and sugar functionalized QDs from the carboxyl-capped QDs, two methods could be used. The first approach is to modify the COOH groups with small biotin and carbohydrate molecules bearing amine groups. Alternatively, the QD surface could be modified with biotinylated glycopolymers bearing biotin, amine, and carbohydrate as pendent moieties.

Synthesis of Biotin-NH_2 and Sugar-NH_2. Although, various biotin functionalized QDs have been reported in the literature, very few studies deal with the direct functionalization of the QD surface. The general approach deals with the fabrication of QDs with avidin groups, which are then conjugated with biotin to form the desired QDs. Recently, biotinylated CdSe/ZnSe nanocrystals were directly synthesized by Reiss et al. (*7*) with two new ligands consisting of a thiolated diethylene glycol derivative and an alkylthiol substituted biotin molecule by the ligand exchange method. They further demonstrated that functionalized QDs could be used for special fluorescent labeling. However, the fabrication process of two ligands needs multistep synthetic pathways in their study, and the ligand exchange method usually changes the optical properties of original QDs. Therefore, we have aimed at the synthesis of biotin and sugar reagents via a simple and straightforward method to obtain the biotinylated glyco-functionalized QDs.

Herein, the biotin bearing terminal amino group was fabricated via a two-step synthesis to functionalize the carboxyl-capped QDs from D-biotin. The D-biotin was first activated by the NHS to form biotin-NHS and then reacted with ethylenediamine to obtain biotin-NH_2 as shown in Scheme 1a. In order to minimize side reactions in the fabrication process, the DMF solution of BNHS was added dropwise into the flask containing ethylenediamine to avoid any possible side reactions. The product was characterized by ^{1}H NMR in d_6-DMSO solvent and mass spectrometry to confirm the formation of the desired product (Figures S1 and S2, Supporting Information).

Similarly, the sugar bearing terminal amino group (sugar-NH_2) was synthesized by the reaction of D-(+)-gluconic acid δ-lactone with ethylenediamine as shown in Scheme 1b. A sticky yellow product was obtained in high yield (~90%), and the chemical structure was confirmed by mass spectrometry (as shown in Figure S3 in Supporting Information).

Synthesis of Monomers and RAFT Polymerization. Quantum dots were usually encapsulated with water-soluble polymer chains to improve their water solubility and reduce their toxicity. The polymers bearing the sugar or biotin groups were found to be ideal to enhance biocompatibility and for their potential use in biosensing applications. These new types of nanoparticles linked with bioactive groups will maintain the optical properties of original QDs and offer new opportunities for multicolor imaging of molecular targets in living cells. We have therefore synthesized the monomers bearing sugar or biotin moieties and

Scheme 2. Schematic Illustration of the Synthesis of the 2-Gluconamidoethyl Methacrylamide (GAMEA) Monomer and the P(GAEMA-*stat*-AEMA-*stat*-BAEMA) Copolymers

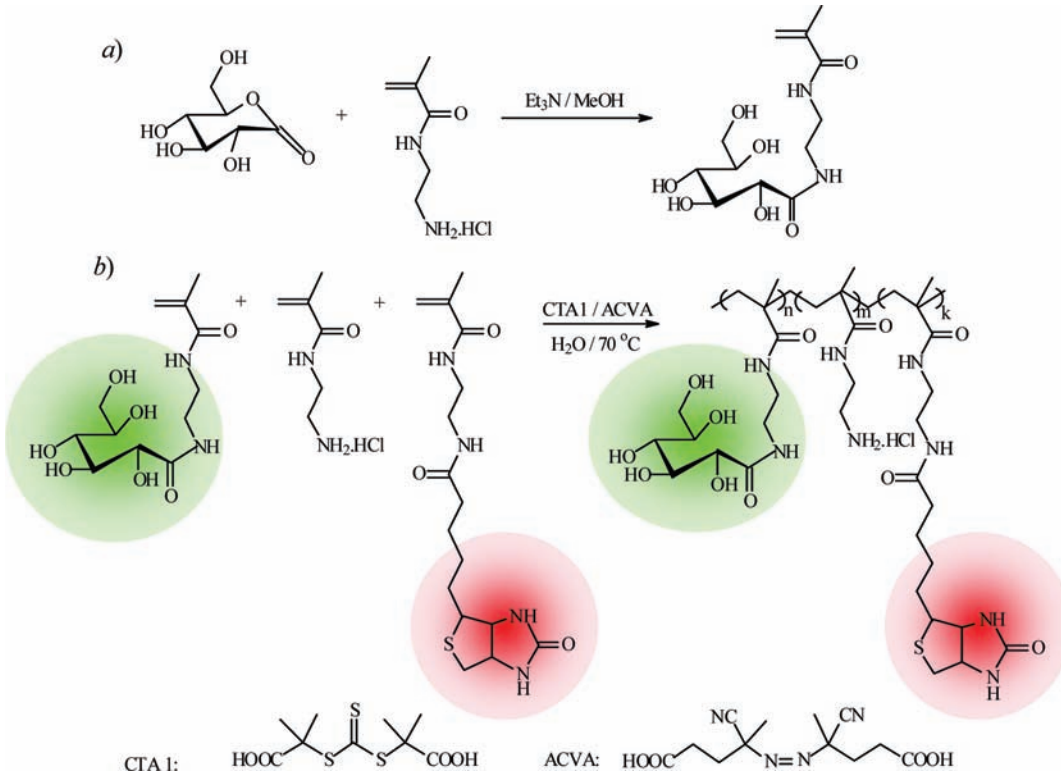

the monomer containing amino groups for realizing the possibility to link the polymer chain onto the surface of original QDs.

The detailed synthesis process of the amine-based monomer (AEMA) and carbohydrate-containing monomer (GAEMA) has been reported by our group (*42*−*44*). Similarly, a novel biotin-containing monomer, BAEMA, was prepared by the reaction of biotin-NHS with AEMA. The structure has been confirmed via ^{1}H NMR spectroscopy and mass spectrometry (as shown in Figures S1d and S4, Supporting Information).

Reversible addition−fragmentation chain transfer polymerization (RAFT) is a highly versatile method as it works well both in aqueous and organic media for the synthesis of polymers with controlled dimensions (*50*−*54*). The controlled RAFT polymerizations of AEMA and GAEMA monomers in aqueous media have been well documented in our group (*42, 44*). PBAEMA could also be obtained via RAFT polymerization for the characteristic RAFT processes. In preliminary experiments, RAFT polymerization of BAEMA was attempted in 1,4-dioxane and water (v/v = 1:2) at 70 °C using CTA 1 as the chain transfer agent. The PBAEMA homopolymer could be obtained with narrow polydispersity (less than 1.3), but the conversion is very low (about 30% calculated from ^{1}H NMR spectroscopy) even after 18 h. This may be related to the hindrance effect of the biotin group in the RAFT process. In our case, our aim is to obtain the copolymer-bearing biotin groups to functionalize desired QDs. As BAEMA was structurally similar to AEMA and GAEMA, the statistical RAFT copolymerization of AEMA, GAEMA, and BAEMA using CTA 1 as the RAFT agent was quite expected, leading to the formation of the P(GAEMA-*stat*-AEMA-*stat*-BAEMA) copolymer (Scheme 2).

Polymerization was carried out using CTA1 as the chain transfer agent and ACVA as the initiator. The ratio of CTA to initiator was set to 5. The AEMA monomer was used in the protonated form during polymerization to prevent any side reactions of the primary amino group to the chain transfer groups. Furthermore, it has been demonstrated in previous reports that the amine groups of the AEMA monomer in the protonated form have no influence on the RAFT process (*42, 43*). The carbohydrate monomer used, GAEMA, is a kind of acrylamide monomer and is very stable in aqueous solution. After polymerization for 18 h, the final statistical glycopolymer was obtained and denoted P(GAEMA$_{36}$-*stat*-AEMA$_{24}$-*stat*-BAEMA$_{4.4}$) from the ^{1}H NMR and HABA/avidin binding assay results, and the GPC trace in Figure S5b (Supporting Information) shows a monomodal peak with a very low polydispersity index (1.19), which has a M_n about 12,900 g/mol using polyethylene oxide as standards. The details are given in Supporting Information.

Bioconjugated Quantum Dots via Covalent Functionalization. Water-soluble QDs (yellow color) containing surface carboxylic groups were used in this study. The QDs are originally dispersed in basic aqueous solution, but they rapidly lost fluorescence below pH 6−6.5. Some of the carboxylic groups on the surface of the QDs are activated using the NHS/EDC coupling method once the pH of the QDs solution was fixed at 7.4 using PBS and subsequently reacted with the biotinylated glycopolymer or the mixture of biotin-NH_2 and sugar-NH_2 as shown in Figure 1. The primary amino group on the statistical copolymer or biotin and sugar reagents was targeted to react with the activated carboxylic groups on the QDs. Since we are only aiming at modifying the surface carboxyl groups of the QDs, we do not expect a significant change in the quantum yield of the original QDs. Fluorescence spectra were recorded on the original QDs, biotin and sugar functionalized QDs, and biotinylated glycopolymer functionalized QDs. Both surface functionalized QDs still show strong fluorescence indicating that the surface modification did not cause a significant change in the optical properties of the original QDs (Figure 2), which is as expected.

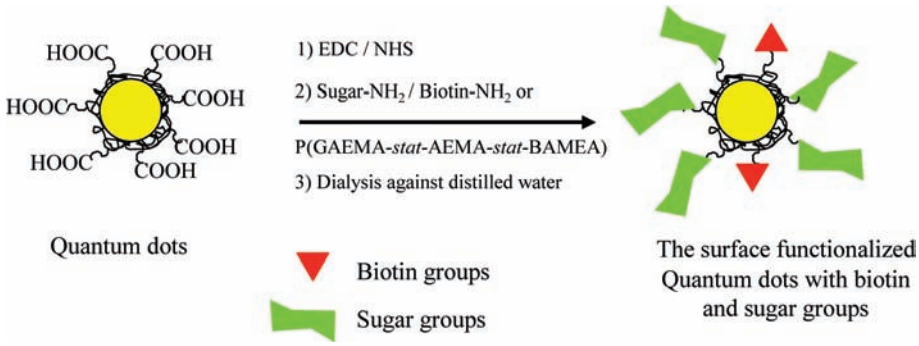

Figure 1. Schematic illustration of the fabrication of biotin and sugar surface functionalized or glycopolymer functionalized QDs.

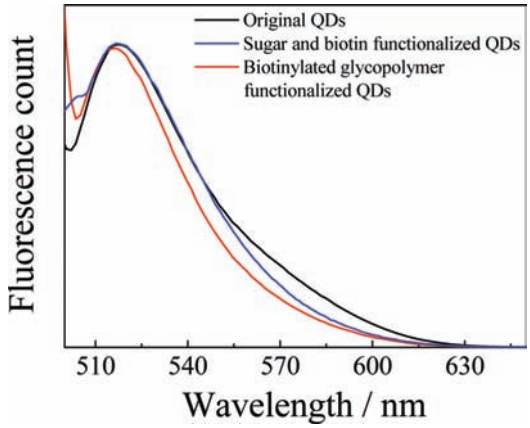

Figure 2. Emission spectra of original QDs, biotin and sugar functionalized QDs, and biotinylated glycopolymer functionalized QDs, where the excitation wavelength is at 490 nm.

After surface functionalization, the QDs were further investigated by dynamic light scattering (DLS). Figure 3 shows the number size distribution of original QDs, biotin and sugar functionalized QDs, and biotinylated glycopolymer functionalized QDs. The size distributions of both surface functionalized QDs are relatively narrow (less than 0.15), and the size of biotin and sugar functionalized QDs is similar to that of original QDs, which further confirms that surface functionalization has no influence on the physical states of original QDs. The glycopolymer functionalized QDs revealed a larger size (10−11 nm), which confirms the successful functionalization of the glycopolymer to the QDs. It should be noted that the covalent attachment of the RAFT copolymer to a carboxylated polymer chain coating already present on the surface of the original QDs causes a significant increase in the size of QDs. The DLS data and fluorescence spectra confirm that surface functionalization of QDs does not alter their optical properties.

The functionalized QDs are stable, and no precipitates were observed even after several weeks when dispersed in aqueous basic solution condition. This is not considered as a significant change in the water solubility of surface functionalized QDs, when compared to that of the original QDs. However, when the solution pH is changed to acidic conditions (pH 5−6) the surface functionalized QDs remain stable and maintain their fluorescence even after two weeks. It clearly shows that the QDs after surface modification have excellent water solubility and colloidal stability compared to those of the original QDs over a broad pH range.

HABA/Avidin Binding Assay. After EDC coupling, the surface of functionalized QDs must contain the biotin groups, but the amount of surface available biotin groups was difficult to calculate directly especially for the surface modification

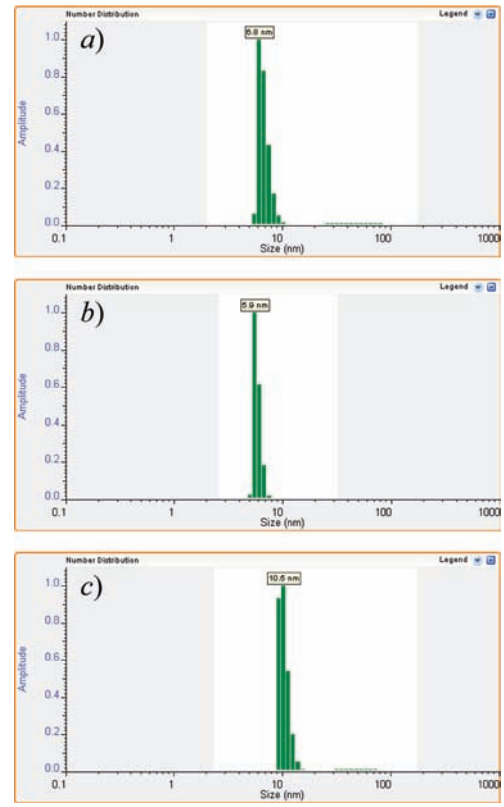

Figure 3. DLS number average distribution of original QDs, biotin and sugar functionalized QDs, and biotinylated glycopolymer functionalized QDs.

of QDs using the synthesized glycopolymer. To prevent possible flocculation of the QDs, the coupling reaction was carried out under high dilution to decrease the possibility of side reactions, and the amount and bioavailability of biotin presented from the functionalized QDs was evaluated and quantified using the HABA/avidin binding assay.

HABA is a dye that binds to avidin, and when HABA is complexed with avidin in water, the aqueous solution has a maximum absorbance at 500 nm. Upon addition of biotin or biotinylated reagents to the HABA/avidin solution, HABA is displaced quantitatively by available biotin, as avidin's affinity for biotin ($K_d = 10^{-15}$ M) is much higher than that of HABA ($K_d = 10^{-6}$ M). This displacement can be quantitatively monitored by the decrease in UV absorbance at a wavelength of 500 nm.

Upon addition of the functionalized QDs, the absorbance value at 500 nm of HABA clearly decreases, suggesting that HABA is displaced from the HABA/avidin complex by available biotin presented on the QD surface. The results of these analyses are shown in the overlaid UV−vis spectra

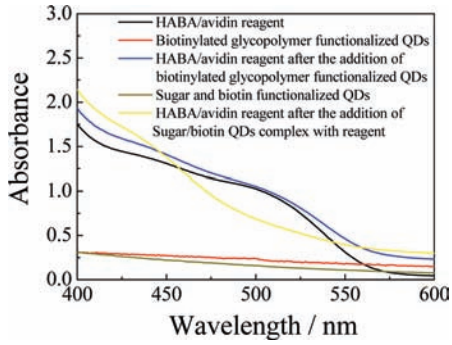

Figure 4. UV−vis spectra of the HABA/avidin reagent before and after the addition of surface functionalized QDs, biotinylated glycopolymer QDs, and sugar and biotin functionalized QDs, where the QDs concentrations were 0.02 μM and 0.1 μM for biotinylated glycopolymer QDs and sugar and biotin functionalized QDs, respectively.

(Figure 4). The amount of biotin in each biotinylated QD solution could be calculated by the following formula:

$$\Delta A_{500} = 0.9\ A_{\text{HABA / avidin}} + A_{\text{QDs}} - A_{\text{HABA / avidin+QDs}}$$

$$\mu\text{mol biotin/mL} = 10(\Delta A_{500}/34)$$

where the dilution factor of HABA/avidin is 0.9, the mM extinction coefficient of biotin at 500 nm is 34, and the dilution factor of QDs is 10.

The aqueous solution of QDs before or after surface functionalization is a colored solution and has an absorbance of about 0.238 at 500 nm after surface functionalization of QDs using polymer chains. So the total decreased absorbance of the HABA/avidin complex after the addition of surface functionalized QDs should be considered the initial absorbance of QDs. Although the absorbance of HABA/avidin complex solution seems to increase after the addition of the glycopolymer functionalized QDs solution as shown in Figure 4, the total absorbance after mixing actually decreases, and this decrease can be calculated by the above formula to be 0.11. The amounts of available biotin per mL of QDs solution were thus calculated to be 1.29 μmol and 0.93 μmol for the glycopolymer functionalized QDs and biotin and sugar functionalized QDs, respectively. According to the concentration of original QDs, which is about 0.8 μM, the quantity of available biotin per QD could be calculated to be ~1600 and ~1100 for biotinylated glycopolymer functionalized QDs and biotin and sugar functionalized QDs, respectively.

Cytotoxicity of the QD Solution. The actual application of QDs in biology needs to address the question about its toxicity. Many methods including polymer or silica encapsulation have been reported to reduce the toxicity of QDs, and it has been shown that the toxicity of QDs can be reduced by modifying the surface area of QDs (*55, 56*). In a recent study, biotin or carbohydrate coated QDs have been synthesized and are shown to be biocompatible. The main idea is to find new strategies that can encapsulate the QDs using biocompatible polymer chains to reduce toxicity. We have addressed this issue by surface functionalization of carboxylic acid coated QDs with polymer chains bearing a variety of biocompatible materials.

The *in vitro* cytotoxicity of the QDs is obtained using the MTT assay on the HeLa cell line. The assay determines the number of viable cells based on the mitochondrial activity of the cells. The MTT dye produces formazan crystals based on the mitochondrial activity of the cells. The MTT lysis buffer dissolves the formazan crystals produced, and their absorbance can be read at 570 nm, giving the approximate number of viable cells in each well. The wells that contained only the media were used as the negative control, and the wells containing untreated cells were used as the positive control. Each experiment was performed in triplicate and, % cell viability was obtained by QD treated cells/absorbance of positive control.

Confocal microsocopy was performed to determine the uptake of QDs by HeLa cells. The fluorescent images obtained were overlapped on bright field images to determine the site of localization of QDs in the cells shown in Figure 5. The images show the uptake of QDs by cells, after 3 h of incubation with cells. The images obtained confirm that MTT data provide the toxicity of QDs after their uptake by the cell line. The QDs are found to be mostly localized in the endosomes of the cells, thus indicating that the possible mechanism of uptake is receptor mediated endocytosis.

The cytotoxicity of QDs has been studied as a function of concentration. The biological and biomedical applications of QDs are highly dependent upon their biocompatibility. We therefore, studied the toxicity of QDs before and after surface functionalization at different concentrations. As shown in Figure 6, QDs were coated with sugar and biotin reagents, and glycopolymer P($GAEMA_{36}$-*stat*-$AEMA_{24}$-*stat*-$BAEMA_{4.4}$) individually, and their cytotoxicity values were compared to those of the original QDs. At very low concentration (2 nM), the cell viability of all QDs are found to be above 75%. Increasing the concentration of QDs up to 20 nM causes a significant increase in the toxicity of the original QDs, and the cell viability is only 59%. However, the cell viability for the glycopolymer functionalized QDs is 89% at this concentration. It is also apparent from the graph that biotin and sugar coated QDs also show

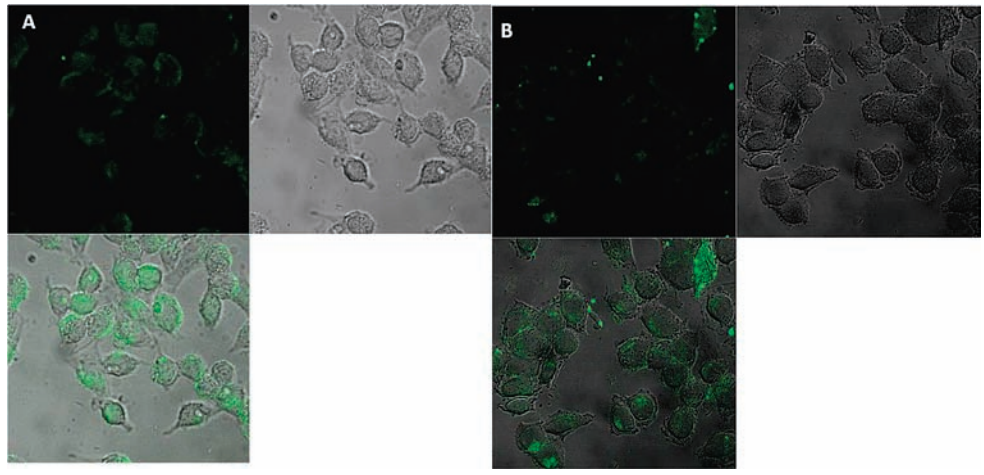

Figure 5. Representative fluorescent and white cell images of HELA cells incubated with (A) sugar and biotin functionalized QDs and (B) biotinylated glycopolymer functionalized QDs.

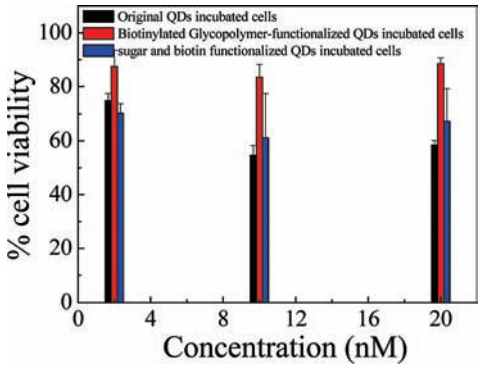

Figure 6. Percent cell viability/cytotoxicity as a function of different QD concentrations before and after surface functionalization.

concentration dependent cytotoxicity, which is comparable to that of the original QDs, whereas the cytotoxicity is negligible for glycopolymer stabilized QDs, regardless of concentration. Although, all of the molecules used for the surface functionalization of QDs are biocompatible, the 12.9 kDa glycopolymer seems to mask the surface of QDs more efficiently, thus accounting for the low toxicity, when compared to small molecules such as sugar and biotin coated QDs. The biotinylated glycopolymer functionalized QDs may be suitable for use in some potential biomedical applications.

It should also be noted that the original QDs have been functionalized by water-soluble polymer chains, which also prevent the release of metal and increase the cell viability of QDs.

CONCLUSIONS

We have successfully synthesized biotin and carbohydrate functionalized reagents for the surface functionalization of QDs. The modified QDs have a high affinity biotin ligand as well a high density of surface carbohydrate moieties. The surface modified QDs showed excellent optical properties and colloid stability compared to those of the original QDs at whole pH conditions. The amount of available biotin was quantified via the HABA/avidin binding assay, and surface functionalization using the glycopolymer chains bearing biocompatible biotin and carbohydrate moieties clearly reduces the cytotoxicity of original QDs. Therefore, the designed biotinylated glyco-functionalized QDs have high potential for applications in biodiagnostic devices or *in vivo* cellular imaging. In our current case, the amount of carbohydrate moieties and their interaction with protein have not been studied. We will study the bioavailability of the surface carbohydrate moieties on the QDs for various carbohydrate−protein interactions in our next work, which is of considerable interest in biomedicine.

ACKNOWLEDGMENT

This work was supported jointly by Ontario Centres of Excellence, Emerging Materials and Knowledge (OCE-EMK), and Northern Nanotechnologies Inc.

Supporting Information Available: Synthesis of biotin-NHS, biotin-NH_2, sugar-NH_2, BAEMA, and GAEMA as well as compound characterization data. This material is available free of charge via the Internet at http://pubs.acs.org.

LITERATURE CITED

(1) Murray, C. B., Norris, D. J., and Bawendi, M. G. (1993) Synthesis and characterization of nearly monodisperse CdE (*E* = sulfur, selenium, tellurium) semiconductor nanocrystallites. *J. Am. Chem. Soc. 115*, 8706–8715.

(2) Alivisatos, A. P. (1996) Semiconductor clusters, nanocrystals, and quantum dots. *Science 271*, 933–937.

(3) Moriarty, P. (2001) Nanostructured materials. *Rep. Prog. Phys. 64*, 297–381.

(4) Efros, A. L., and Rosen, M. (2000) The electronic structure of semiconductor nanocrystals. *Annu. Rev. Mater. Sci. 30*, 475–521.

(5) Bruchez, M., Moronne, M., Gin, P., Weiss, S., and Alivisatos, A. P. (1998) Semiconductor nanocrystals as fluorescent biological labels. *Science 281*, 2013–2016.

(6) Chan, W. C. W., and Nie, S. M. (1998) Quantum dot bioconjugates for ultrasensitive nonisotopic detection. *Science 281*, 2016–2018.

(7) Charvet, N., Reiss, P., Roget, A., Dupuis, A., Grünwald, D., Carayon, S., Chandezon, S., and Livache, T. (2004) Biotinylated CdSe/ZnSe nanocrystals for specific fluorescent labeling. *J. Mater. Chem. 14*, 2638–2642.

(8) Murray, C. B., Kagan, C. R., and Bawendi, M. G. (2000) Synthesis and characterization of monodisperse nanocrystals and close-packed nanocrystal assembles. *Annu. Rev. Mater. Sci. 30*, 545–610.

(9) Susumu, K., Uyeda, H. T., Medintz, I. L., Pons, T., Delehanty, J. B., and Mattoussi, H. (2007) Enhancing the stability and biological functionalities of quantum dots via compact multifunctional ligands. *J. Am. Chem. Soc. 129*, 13987–13996.

(10) Qi, L., and Gao, X. (2008) Emerging application of quantum dots for drug delivery and therapy. *Expert Opin. Drug Delivery 5*, 263–267.

(11) Gao, X., Chan, W. C. W., and Nie, S. (2002) Quantum-dot nanocrystals for ultrasensitive biological labeling and multicolor optical encoding. *J. Biomed. Opt. 7*, 532–537.

(12) Gill, R., Willner, I., Shweky, I., and Banin, U. (2005) Fluorescence resonance energy transfer in CdSe/ZnS-DNA conjugates: probing hybridization and DNA cleavage. *J. Phys. Chem. B 109*, 23715–23719.

(13) Peng, H., Zhang, L., Kjällman, T. H. M., Soeller, C., and Travas-Sejdic, J. (2007) DNA hybridization detection with blue luminescent quantum dots and dye-labeled single-stranded DNA. *J. Am. Chem. Soc. 129*, 3048–3049.

(14) Charkrabarti, R., and Klibanov, A. M. (2003) Nanocrystals modified with peptide nucleic acids (PNAs) for selective self-assembly and DNA detection. *J. Am. Chem. Soc. 125*, 2531–12540.

(15) Åkerman, M. E., Chan, W. C. W., Laakkonen, P., Bhatia, S. N., and Ruoslahti, E. (2002) Nanocrystal targeting in vivo. *Proc. Natl. Acad. Sci. U.S.A. 99*, 12617–12621.

(16) Pinaud, F., King, D., Moore, H.-P., and Weiss, S. (2004) Bioactivation and cell targeting of semiconductor CdSe/ZnS nanocrystals with phytochelatin-related peptides. *J. Am. Chem. Soc. 126*, 6115–6123.

(17) Winter, J. O., Liu, T. Y., Korgel, B. A., and Schmidt, C. E. (2001) Recognition molecule directed interfacing between semiconductor quantum dots and nerve cells. *Adv. Mater. 13*, 1673–1677.

(18) Mattoussi, H., Mauro, J. M., Goldman, E. M., Anderson, G. P., Sundar, V. C., Mikulec, F. V., and Bawendi, M. G. (2000) Self-assembly of CdSe-ZnS quantum dot bioconjugates using an engineered recombinant protein. *J. Am. Chem. Soc. 122*, 12142–12150.

(19) Babu, P., Sinha, S., and Surolia, A. (2007) Sugar-quantum dot conjugates for a selective and sensitive detection of lectins. *Bioconjugate Chem. 18*, 146–151.

(20) Sun, X.-L., Cui, W., Haller, C., and Chaikof, E. L. (2004) Site-specific multivalent carbohydrate labeling of quantum dots and magnetic beads. *ChemBioChem. 5*, 1593–1596.

(21) Rosenthal, S. J., Tomlinson, I., Adkins, E. M., Schroeter, S., Adams, S., Swafford, L., McBbride, J., Wang, Y., DeFelice, L. J., and Blakely, R. D. (2002) Targeting cell surface receptors with ligand-conjugated nanocrystals. *J. Am. Chem. Soc. 124*, 4586–4594.

(22) Wuister, S. F., Swart, I., Driel, F. V., Hickey, S. G., and Donega, C. D. M. (2003) Highly luminescent water-soluble CdTe quantum dots. *Nano Lett. 3*, 503–507.
(23) Aldana, J., Wang, Y. A., and Peng, X. (2001) Photochemical instability of CdSe nanocrystals coated by hydrophilic thiols. *J. Am. Chem. Soc. 123*, 8844–8850.
(24) Gerion, D., Pinaud, F., Williams, S. C., Parak, W. J., Zanchet, D., Weiss, S., and Alivisatos, A. P. (2001) Synthesis and properties of biocompatible water-soluble silica-coated CdSe/ZnS semiconductor quantum dots. *J. Phys. Chem. B 105*, 8861–8871.
(25) Tan, W., Wang, K., He, X., Zhao, X. J., Drake, T., Wang, L., and Bagwe, R. P. (2004) Bionanotechnology based on silica nanoparticles. *Med. Res. Rev. 24*, 621–638.
(26) Fan, H., Leve, E. M., Scullin, C., Gabaldon, J., Tallant, D., Bunge, S., Boyle, T., Wilson, M. C., and Brinker, C. J. (2005) Surfactant-assisted synthesis of water-soluble and biocompatible semiconductor quantum dot micelles. *Nano Lett. 5*, 645–648.
(27) Gao, X., Cui, Y., Levenson, R. M., Chung, L. W. K., and Nie, S. (2004) In vivo cancer targeting and imaging with semiconductor quantum dots. *Nat. Biotechnol. 22*, 969–976.
(28) Goldstein, I. J., Iyer, R. N., Smith, E. E., and So, L. L. (1967) Protein-carbohydrate cnteraction. XX. the Interaction of concanavalin A with sophorose and some of its derivatives. *Biochemistry. 6*, 2373–2377.
(29) Hong, C.-H. (2003) *Carbohydrate-Based Drug Discovery*, Wiley-VCH, Weinheim, Germany.
(30) Choi, S.-K., Mammen, M., and Whitesides, G. M. (1997) Generation and in situ evaluation of libraries of poly(acrylic acid) presenting sialosides as side chains as polyvalent inhibitors of influenza-mediated hemagglutination. *J. Am. Chem. Soc. 119*, 4103–4111.
(31) Bovin, N. V., and Gabius, H.-J. (1995) Polymer-immobilized carbohydrate ligands: versatile chemical tools for biochemistry and medical sciences. *Chem. Soc. Rev.* 413–421.
(32) Kiessling, L. L., Gestwicki, J. E., and Strong, L. E. (2000) Synthetic multivalent ligands in the exploration of cell-surface interactions. *Curr. Opin. Chem. Biol. 4*, 696–703.
(33) Bertozzi, C. R., and Kiessling, L. L. (2001) Chemical glycobiology. *Science 291*, 2357–2364.
(34) Gestwicki, J. E., and Kiessling, L. L. (2002) Inter-receptor communication through arrays of bacterial chemoreceptors. *Nature 415*, 81–84.
(35) Roy, R. (1996) Syntheses and some applications of chemically defined multivalent glycoconjugates. *Curr. Opin. Struct. Biol. 6*, 692–702.
(36) Rökendorf, N., and Lindhorst, T. K. (2001) Glycodendrimers. *Top. Curr. Chem. 217*, 201–238.
(37) Turnbull, W. B., Kalovidouris, S. A., and Stoddart, J. F. (2002) Large oligosaccharide-based glycodendrimers. *Chem. Eur. J. 8*, 2988–3000.
(38) Otsuka, H., Akiyama, Y., Nagasaki, Y., and Kataoka, K. (2001) Quantitative and reversible lectin-induced association of gold nanoparticles modified with α-lactosyl-ω-mercapto-poly(ethylene glycol). *J. Am. Chem. Soc. 123*, 8226–8230.
(39) Lin, C.-C., Yeh, Y.-C., Yang, C. Y., Chen, C.-L., Chen, G.-F., Chen, C.-C., and Wu, Y.-C. (2002) Selective binding of mannose-encapsulated gold nanoparticles to type 1 Pili in *Escherichia coli*. *J. Am. Chem. Soc. 124*, 3508–3509.
(40) Wilchek, M., and Bayer, E. A. (1988) The avidin-biotin complex in bioanalytical applications. *Anal. Biochem. 171*, 1–32.
(41) Wilchek, M., and Bayer, E. A. (1990) Introduction to avidin-biotin technology. *Methods Enzymol. 184*, 5–13.
(42) Deng, Z.-C., Bouchékif, H., Babooram, K., Housni, A., Choytun, N., and Narain, R. (2008) Facile synthesis of controlled-structure primary amine-based methacrylamide polymers via the reversible addition-fragmentation chain transfer process. *J. Polym. Sci., Part A: Polym. Chem. 46*, 4984–4996.
(43) Li, Y., Lokitz, B. S., and McCormick, C. L. (2006) Thermally responsive vesicles and their structural "locking" through polyelectrolyte complex formation. *Angew. Chem., Int. Ed. 118*, 5924–5927.
(44) Deng, Z.-C., Ahmed, M., and Narain, R. (2009) Novel well-defined glycopolymers synthesized via the reversible addition fragmentation chain transfer process in aqueous media. *J. Polym. Sci., Part A: Polym. Chem. 47*, 614–627.
(45) Lai, J. T., Filla, D., and Shea, R. (2002) Functional polymers from novel carboxyl-terminated trithiocarbonates as highly efficient RAFT agents. *Macromolecules 35*, 6754–6756.
(46) Green, N. M. (1965) A spectrophotometric assay for avidin and biotin based on binding of dyes by avidin. *Biochem. J. 94*, 23c–24c.
(47) Green, N. M. (1970) Spectrophotometric determination of avidin and biotin. *Methods Enzymol. 18*, 418–424.
(48) Chen, Y., and Rosenzweig, Z. (2002) Luminescent CdSe quantum dot doped stabilized micelles. *Nano Lett. 2*, 1299–1302.
(49) Farmer, S. C., and Patten, T. E. (2001) Photoluminescent polymer/quantum dot composite nanoparticles. *Chem. Mater. 13*, 3920–3926.
(50) Chiefari, J., Chong, Y. K., Ercole, F., Krstina, J., Jeffery, J., Le, T. P. T., Mayadunne, R. T. A., Meijs, G. F., Moad, C. L., Moad, G., Rizzardo, E., and Thang, S. H. (1998) Living free-radical polymerization by reversible addition-fragmentation chain transfer: the RAFT process. *Macromolecules 31*, 5559.
(51) Moad, G., Rizzardo, E., and Thang, S. H. (2005) Living radical polymerization by the RAFT process. *Aust. J. Chem. 58*, 379–410.
(52) Donovan, M. S., Lowe, A. B., Sumerlin, B. S., and McCormick, C. L. (2002) Raft polymerization of *N*,N-dimethylacrylamide utilizing novel chain transfer agents tailored for high reinitiation efficiency and structural control. *Macromolecules 35*, 4123–4132.
(53) Narain, R., Housni, A., Gody, G., Boulanger, P., Charreyre, M. T., and Delair, T. (2007) Preparation of biotinylated glyconanoparticles via a photochemical process and study of their bioconjugation to streptavidin. *Langmuir 23*, 12835–12841.
(54) Spain, S. G., Albertin, L., and Cameron, N. R. (2006) Facile in situ preparation of biologically active multivalent glyconanoparticles. *Chem. Commun.* 4198–4200.
(55) Hoshino, A., Fujioka, K., Oku, T., Suga, M., Sasaki, Y. F., Ohta, T., Yasuhara, M., Suzuki, K., and Yamamoto, K. (2004) Physicochemical properties and cellular toxicity of nanocrystal quantum dots depend on their surface modification. *Nano Lett. 4*, 2163–2169.
(56) Duan, H., and Nie, S. (2007) Cell-penetrating quantum dots based on multivalent and endosome-disrupting surface coatings. *J. Am. Chem. Soc. 129*, 3333–3338.

BC800566F

SUPPORTING INFORMATION

Biotinylated Glyco-Functionalized Quantum Dots: Synthesis, Characterization, and Cytotoxicity Studies

Xiaoze Jiang, Marya Ahmed, Zhicheng Deng, and Ravin Narain*

Department of Chemistry and Biochemistry, Biomolecular Sciences Program, Laurentian University, 935, Ramsey Lake Rd, Sudbury, ON, P3E 2C6, Canada

Experimental Section

Materials. D-Biotin, D-(+)-gluconic acid δ-lactone, *N*-hydroxysuccinimide (NHS), Ethylenediamine, 1-ethyl-3-[3-dimethylaminopropyl] carbodiimide hydrochloride (EDC), 1,3-Dicyclohexylcarbodiimide (DCC), and ethylenediamine dihydrochloride were purchased from Sigma-Aldrich and used as received. 2-Aminoethyl methacryl-amide hydrochloride (AEMA) was synthesized as previously described (1). 4,4'-Azobis(4-cyanovaleric acid) (ACVA, 97%) was purchased from Acros Organics and used as received. *N*,*N*'-Dimethylformamide (DMF), isopropanol, methanol, hydroquinone, 1,4-dioxane, and other chemical solvents were purchased from Caledon Chemicals and used as received. Doubly distilled de-ionized water was used in all experiments, and PBS buffer solution (pH 7.4) was used.

Synthesis of Biotinyl-*N*-hydroxysuccinimide Ester (Biotin-NHS)

D-Biotin (2.00 g, 8.19 mmol) and *N*-hydroxysuccinimide (0.94 g, 8.19 mmol) were dissolved into hot anhydrous DMF (60 mL, 70 ^{o}C) in a 100 mL round-bottom flask with

stirring. 1,3-Dicyclohexylcarbodiimide (DCC, 2.19 g, 10.65 mmol) was added, and the solution was stirred overnight at room temperature. The formed dicyclohexylurea was filtered off; most of the solvents were evaporated, and the residue precipitated into excess ether. The white precipitate was filtered and washed with isopropanol three times to give a white powder, and this solid was recrystallized in isopropanol. The final yield of the product is 85%. Finally, its structure was confirmed via ^{1}H NMR spectroscopy as shown in Figure S1b. ^{1}H NMR in d_6-DMSO, δ (ppm): 4.1 and 4.3 [m, 2H, (C*H*NH)$_2$CO], 3.1(m, 1H, SC*H*), 2.7-2.9 (d and s, 6H, SCH_2 and CH_2CON), 2.6(t, 2H, CH_2COO), 1.0-1.7(m, 6H, CHCH_2CH_2CH_2).

Synthesis of *N*-(2-Aminoethyl) Biotinamide (Biotin-NH$_2$)

Ethylenediamine (150 *u*L, 2.2 mmol), triethylamine (1.5 mL), and DMF (10 mL) were added into a round-bottom 50 mL flask fitted with a stirrer. A DMF solution (5 mL) of biotin-NHS (0.75 g, 2.2 mmol) was added dropwise at room temperature under nitrogen atmosphere and stirred overnight. The formed precipitate was filtered off, most of the solvents were evaporated, and the residue precipitated into excess hexane. The white precipitate was filtered and washed with isopropanol three times to give a white powder. The final yield of the product is 70%. ^{1}H NMR in d_6-DMSO as shown in Figure S1c, δ (ppm): 4.1 and 4.3 [m, 2H, (C*H*NH)$_2$CO], 2.9-3.2(m, 3H, SC*H* and CONHCH_2), 2.8(d and dd, 2H, SCH_2), 2.6(t, 2H, CH_2NH$_2$), 2.0(t, 2H, CH_2CONH), 1.0-1.7(m, 6H, CHCH_2CH_2CH_2). ESI-MS: calcd. For $(C_{12}H_{22}N_4O_2S + H)^+$: 287.4; found: 287.2.

Synthesis of *N*-(2-Aminoethyl) Gluconamide Hydrochloride (Sugar-NH$_2$)

Ethylenediamine (5.5 mL, 0.08 mol) was added to an ethylenediamine dihydro-

chloride solution (12.76 g, 96 mmol, in 100 mL distilled water) in a round-bottom flask fitted with a stirrer. After 1 h of stirring, aqueous solution (70 mL) of D-(+)-Gluconic acid δ-lactone (14.25 g, 0.08 mol) was added dropwise into the above solution cooled in an ice bath condition. The mixture was stirred at room temperature overnight. Finally, the solvent was removed under vacuum; the crude product was washed with isopropanol twice. The product was dissolved into methanol and precipitated into isopropanol twice; the viscous product was dried under vacuum. The final yield of the product is 90%. ^{1}H NMR in D_2O, δ (ppm): 4.35(d, 1H), 4.1(t, 1H), 3.5-3.85 (m,6H), 3.1-3.2(t, 2H). ESI-MS: calcd. For ($C_8H_{19}N_2O_6Cl$) : 274.7; found: 275.

Synthesis of Biotinyl-2-Aminoethyl Methacrylamide Hydrochloride (BAEMA)

Biotin-NHS (0.85 g, 2.5 mmol), hydroquinone (0.05 g), triethylamine (0.7 mL), and 2-aminoethyl methacrylamide hydrochloride (AEMA, 0.41g, 2.5 mmol) were dissolved in 15 mL anhydrous DMF. This solution was stirred overnight at room temperature, the solid formed was filtered off and DMF was evaporated under reduced pressure. The residue was precipitated into ether and was washed with isopropanol three times. The powder was dried overnight under vacuum. The yield is 70%. ^{1}H NMR in d_6-DMSO as shown in Figure S1d, δ (ppm): 5.3 and 5.6(s, 2H, CH_2CCH_3), 4.1 and 4.3 [m, 2H, (CHNH)$_2$CO], 2.9-3.2(m, 5H, SCH, CONHCH_2, and CH_2CH_2NH), 2.8(d and dd, 2H, SCH_2), , 2.0(t, 2H, CH_2CONH),, 1.7 (s, 3H, CH_2CCH_3), 1.0-1.7(m, 6H, CHCH_2CH_2CH_2). ESI-MS: calcd. For ($C_{16}H_{26}N_3O_4S$ + Na)$^+$: 377.5; found: 377.2.

Synthesis of Gluconamidoethyl Methacrylamide Hydrochloride (GAEMA)

D-(+)-Gluconic acid δ-lactone (1.77 g, 0.08 mol) and hydroquinone (0.05 g) were dissolved in methanol at 50 °C and then cooled to room temperature before the addition of 2-aminoethyl methacrylamide hydrochloride (AEMA) (2.0 g, 0.012 mmol) and triethylamine (10 mL). The mixture was stirred overnight at room temperature, concentrated by rotary evaporation, and precipitated into isopropanol. The white solid formed was filtered, washed with isopropanol three times, and dried under vacuum. The final yield of the product was 95%. ^{1}H NMR (D_2O, ppm): 5.7(s, 1H), 5.4(s, 1H), 4.35(d, 1H), 4.1(t, 1H), 3.6-3.85 (m, 4H), 3.4 (t, 4H).1.85 (s, 3H).

Characterization

1. Characterization of small reagents. The characteristic signals of biotin, biotin-NHS, and biotin-NH_2 were shown in Figure S1, and the characteristic signals of succinimide group at δ 2.8 ppm could be detected in the ^{1}H NMR spectrum of biotin-NHS (shown in Figure S1b), and subsequently disappear after reaction with ethylenediamine (shown in Figure S1c). From the peak integration, the purities of both desired products could be calculated to be above 95%. The purity of biotin-NH_2 was further confirmed by mass spectrum (shown in Figure S2 in supporting information).

Similarly, the sugar bearing terminal amino group (Sugar-NH_2) was synthesized by the reaction of D-(+)-Gluconic acid δ-lactone with ethylenediamine, and the chemical structure was confirmed by mass spectrum (shown in Figure S3).

BAEMA monomer was synthesized by the reaction of biotin-NHS with AEMA, it's structure was confirmed via ^{1}H NMR spectroscopy (shown in Figure S1c). The characteristic signals of double bond at δ 5-5.5 ppm of BAEMA are clearly evident, and the signal of succinimide group for biotin-NHS at δ 2.8 ppm also disappear after being replaced by AEMA. The purity of obtained BAEMA monomer could be calculated to be above 95% based on integration of the peaks at δ 5-5.5 ppm and δ 4.0 ppm, and the purity was further confirmed also by mass spectrum shown in Figure S4.

2. Characterization of biotinylated glycopolymer. The final statistical glycopolymer was obtained and analyzed by ^{1}H NMR in D_2O solvent. The GAEMA monomer conversion is about 80% in this polymerization condition, and the DP_n of GAEMA and AEMA could be calculated to be 36 and 24, respectively, from their characteristic signals at δ 3-4 ppm shown in Figure S5a. However, the signals of BAEMA could not be clearly detected or quantified by ^{1}H NMR as the characteristic peaks of BAEMA were masked. The amount of biotin contents in the glycopolymer was therefore further quantified to 4.4 using HABA/avidin binding assay. By dissolving the glycopolymer into water and adding into the HABA/avidin solution, the change of absorbance of HABA/avidin complex at 500 nm was monitored using UV-vis absorption spectra. The obtained glycopolymer was thus denoted P(GAEMA$_{36}$-*stat*-AEMA$_{24}$-*stat*-BAEMA$_{4.4}$). Aqueous gel permeation chromatography was used also to analyze the polymer, and a mono-modal peak with a very low polydispersity index was obtained as shown in Figure S5b. The M_n and M_w/M_n were determined to be 12,900 and 1.19, respectively. By comparing to the theoretical molecular weight

($M_{n,theo}$ = 18,130) calculated from the conversion using ^{1}H NMR spectroscopy, the experimental M_n is found to be smaller and this is attributed to the fact that a conversion GPC calibration was used using polyethylene oxide as standards.

Reference.

(1) Deng, Z-C., Bouchékif, H., Babooram, K., Housni, A., Choytun, N., and Narain, R. (2008) Facile synthesis of controlled-structure primary amine-based methacrylamide polymers via the reversible addition-fragmentation chain transfer process. *J. Polym. Sci., Part A: Polym. Chem. 46*, 4984-4996.

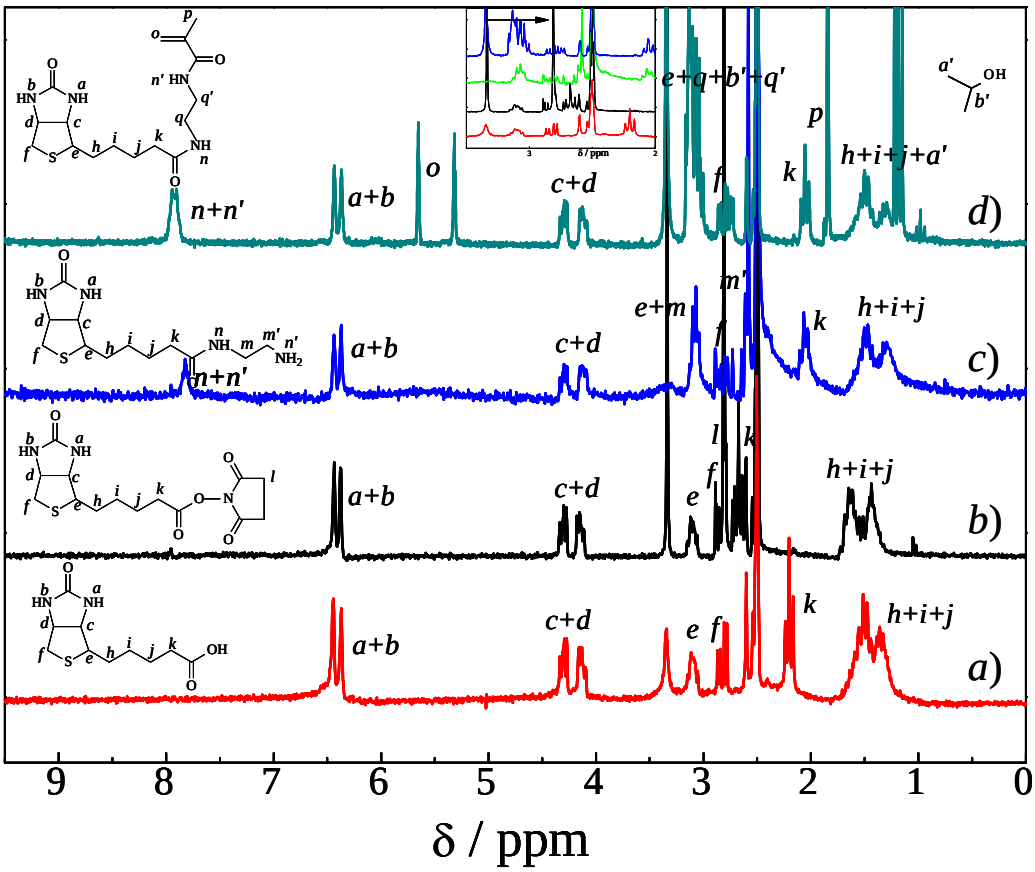

Figure S1. ^{1}H NMR spectra of biotin (a), Biotin-NHS (b), Biotin-NH_2 (c), and BAEMA (d) in d_6-DMSO solvent. The zoom region from δ 2-3.5 ppm is shown in subset.

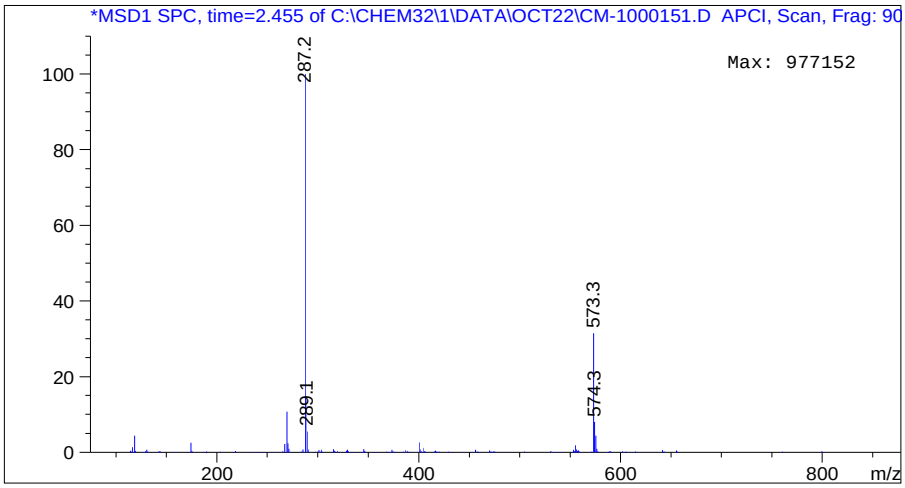

Figure S2. Mass spectrum for N-(2-Aminoethyl) Biotinamide (Biotin-NH_2).

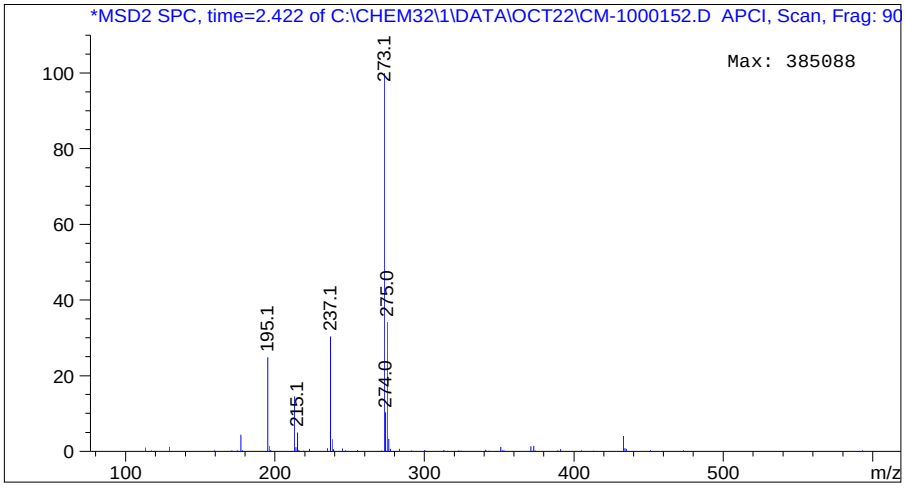

Figure S3. Mass spectrum for Gluconamidoethylamide Hydrochloride (Sugar-NH_2).

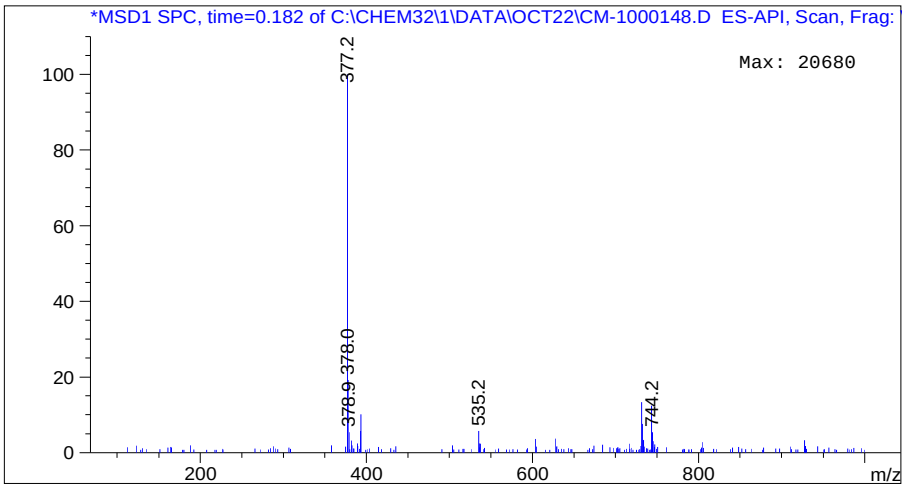

Figure S4. Mass spectrum for Biotinyl-2-Aminoethyl Methacrylamide Hydrochloride (BAEMA).

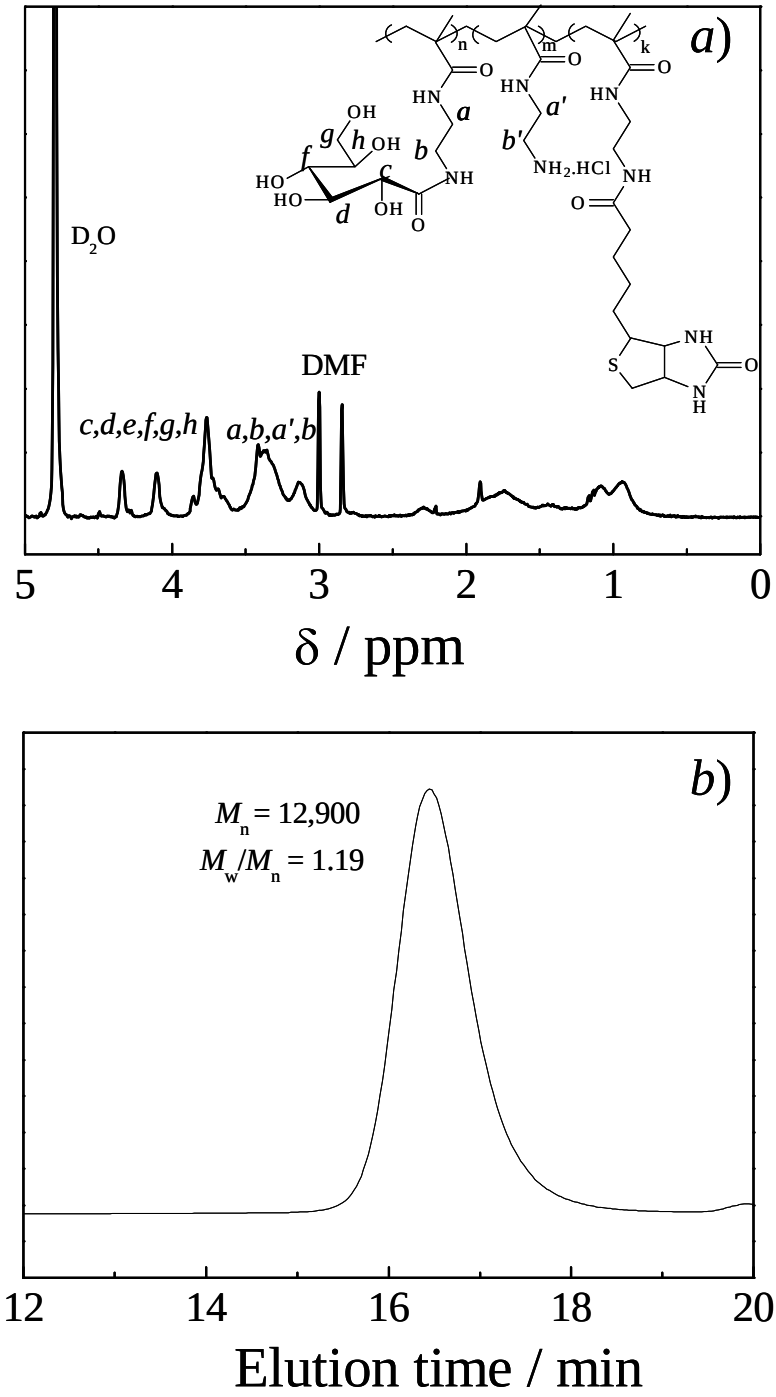

Figure S5. Assigned ^{1}H NMR spectrum (a) and aqueous GPC trace (b) of the P(GAEMA-*stat*-AEMA-*stat*-BAEMA) copolymer. It should be noted that the characteristic signals of BAEMA are undistinguishable for its very low contents in glycopolymer.

Design, Synthesis, and Imaging of Small Amphiphilic Rhenium and ^{99m}Technetium Tricarbonyl Complexes

Eszter Boros,[†,§] Urs O. Häfeli,[‡] Brian O. Patrick,[†] Michael J. Adam,*[,§] and Chris Orvig*[,†]

Medicinal Inorganic Chemistry Group, Department of Chemistry, University of British Columbia, 2036 Main Mall, Vancouver, British Columbia V6T 1Z1, Canada, Faculty of Pharmaceutical Sciences, University of British Columbia, 2146, East Mall, Vancouver, British Columbia, V6T 1Z3, Canada, and TRIUMF, 4004 Wesbrook Mall, Vancouver, British Columbia, V6T 2A3, Canada. Received January 20, 2009; Revised Manuscript Received March 9, 2009

The design, synthesis, radiolabeling, evaluation of stability, and in vivo investigation are presented of three variably charged, novel, short C_8 chain derivatized chelators for the $[M(CO)_3]^+$ core (M = ^{99m}Tc or Re). Labeling with $[^{99m}Tc(CO)_3]^+$ showed complex formation in under 1 h reaction time and high stability toward 24 h histidine and cysteine challenges, as well as distinctive log *P* values for each complex. Distinct localization of small amphiphilic molecules in in vivo systems depends on the charge of the polar moiety and was studied via biodistribution (4 h) and imaging (15 min, 1, 2, and 4 h) in female C57Bl/6 mice.

INTRODUCTION

Because of its low cost and availability, ^{99m}Tc has been a radionuclide of interest in radiopharmaceutical chemistry and nuclear medicine for the past four decades (*1*). Resulting from intensive research, the vast majority of nuclear medicine scans utilize this isotope, which displays the ideal physical properties $t_{1/2} = 6$ h and $\gamma = 141$ keV for imaging with single photon emission computed tomography (SPECT) (*2*). While today's imaging facilities still rely on high oxidation state Tc cores (*3*−*5*), much research has turned its focus toward the versatile and highly stable *fac*-$[^{99m}Tc(CO)_3(H_2O)_3]^+$ core developed by Alberto et al. (*6*). The *fac*-$[^{99m}Tc(CO)_3(H_2O)_3]^+$ complex has the metal center in a ^{99m}Tc(I)-d^6 low-spin electron configuration (inert toward a broad range of experimental conditions) and can be prepared in high yields via a commercially available kit (Isolink, Covidien, Mansfield, MA) under aqueous conditions using boranocarbonate anion as the reducing agent and in situ CO source (*6*). Simple exchange of the three water molecules can be achieved with suitable chelates in a *fac* coordination mode (*7*, *8*), shown previously on examples of bioconjugates such as derivatized amino acids, carbohydrates, peptides, and nucleosides (*9*−*11*).

Over the past decade, synthesis of novel imaging agents based on ^{99m}Tc has shifted toward target-specific peptide derivatives with one type of chelating entity for the $[^{99m}Tc(CO)_3]^+$ core, following the so-called "technetium-tagged" approach (*12*), In contrast to this, it was our aim in this work to obtain a simple, small, and nonspecific "technetium-based" complex with potential uptake in a large range of different tissues and also to explore the in vivo properties of novel, amphiphilic metal complexes of the $[Tc(CO)_3]^+$ core. In an attempt to achieve this, the synthesis incorporated a mimic of the charge distribution of molecules highly abundant and essential to cell membranes such as sphingosine (neutral), lysophosphatidic acid (negatively charged headgroup), and sphingomyelin (zwitterionic headgroup), aiming for an in vivo distribution of the resulting complexes comparable to other small amphiphilic molecules such as cocamidopropyl betaine (CAPB, zwitterionic), sodium dodecylsulfate (SDS, anionic), and octanol (neutral). These compounds, also known as surfactants, are known to integrate into the lipid bilayer, before their concentration (much larger than the concentration range imaging agents usually operate at) exceeds the saturation concentration and solubilizes the membrane (*13*). The synthesis was achieved by varying the tridentate chelator but attaching a short, saturated C8-chain in a consistent fashion via a simple ester bond; this differs strongly from the previously used tagged approach with long-chain fatty acids (*14*). The goal was also to investigate and compare the heart-specific uptake of these new compounds with strictly cationic conjugates (*15*, *16*). Therefore, the design of these molecules was such that the size of the polar and lipophilic entities are in the same size range but of strongly differing polarity (Figure 1). Exploring the in vivo behavior of these compounds, following the less investigated approach of nontarget-specific uptake of small amphiphilic molecules, was of major interest.

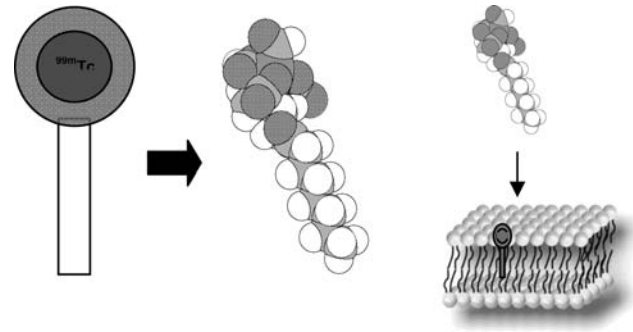

Figure 1. Envisioned biological pathway of the "integrated approach molecules".

EXPERIMENTAL DETAILS

Instruments and Materials. All solvents and reagents were used as received. $Re(CO)_5Br$ is commercially available (Strem). The analytical thin-layer chromatography (TLC) plates were aluminum-backed ultrapure silica gel 60, 250 μm; the flash column silica gel (standard grade, 60 Å, 32−63 mm) was from

* To whom correspondence should be addressed: adam@triumf.ca (M.J.A.); orvig@chem.ubc.ca (C.O.).
† Department of Chemistry, University of British Columbia.
‡ Faculty of Pharmaceutical Sciences, University of British Columbia.
§ TRIUMF.

10.1021/bc900022c CCC: $40.75 © 2009 American Chemical Society
Published on Web 04/02/2009

Scheme 1. Synthesis Pathway for Proligands HL1 and H_2L3

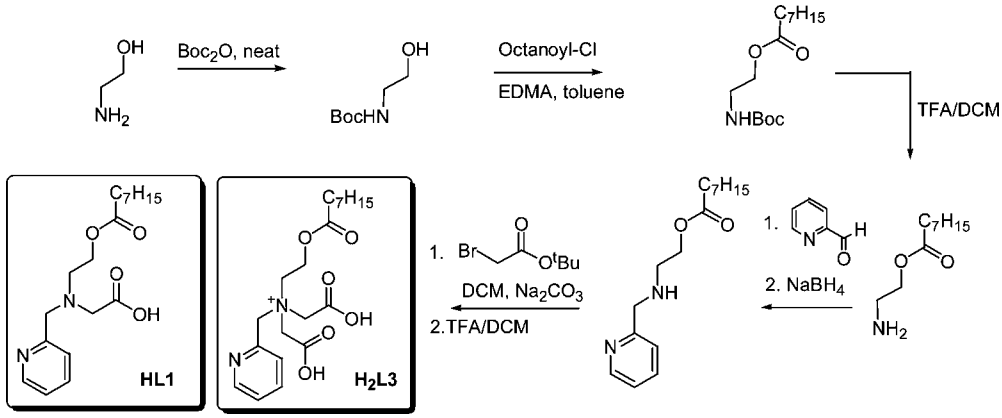

Scheme 2. Synthesis Pathway for Proligand HL2

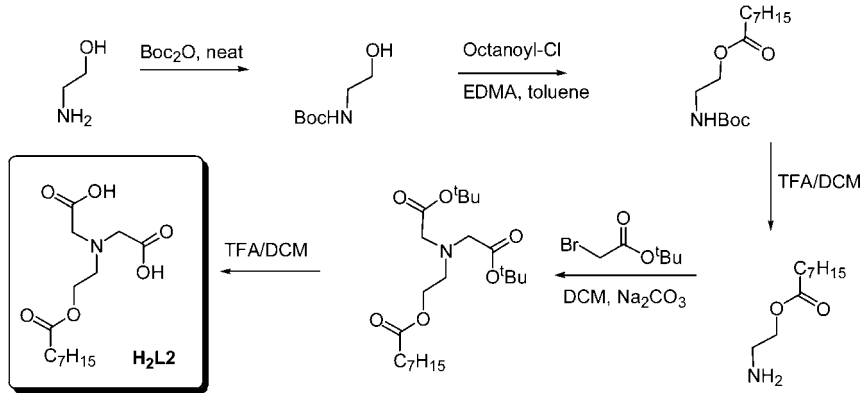

Scheme 3

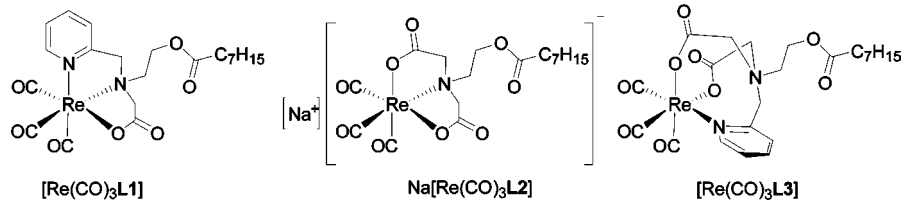

Silicycle. ^{1}H and ^{13}C NMR spectra were recorded on Bruker AV300 or AV400 instruments at ambient temperature; the NMR spectra are expressed on the δ scale and referenced to residual solvent peaks or internal tetramethylsilane. Electrospray ionization mass spectrometry (ESI-MS) spectra were recorded on a Micromass LCT instrument at the Department of Chemistry, University of British Columbia. High-performance liquid chromatography (HPLC) analysis of cold compounds was done on a Phenomenex Synergi 4 μm Hydro-RP 80A column (250 $\times$ 4.6 mm) in a Waters WE 600 HPLC system equipped with a 2478 dual-wavelength absorbance UV detector run using the Empower software package. IR spectra were collected neat in the solid or liquid state on a Thermo Nicolet 6700 FT-IR spectrometer. TLC analysis of radiolabeled compounds was performed on a Bioscan-System 200 Imaging scanner, equipped with a Bioscan-Autochanger 100. Radio-TLCs were prepared with acetonitrile as the mobile phase. HPLC analyses of radiolabeled complexes were performed on a Knauer Wellchrom K-1001 HPLC equipped with a K-2501 absorption detector and a Capintec radiometric well counter. A Phenomenex Hydro-Synergi 4 μm C18 RP analytical column with dimensions 250 $\times$ 4.6 mm was used. HPLC solvents consisted of 0.1% trifluoroacetic acid in water (solvent A) and methanol (solvent B). Samples were analyzed and purified with a linear gradient method (100% solvent A to 100% solvent B over 30 min). For biodistributions, organ samples were counted in a Packard Cobra II autogamma counter one to two days after administration. μSPECT and CT images were recorded on an XSPECT instrument from Gamma Medica (Northridge, CA).

Syntheses (Schemes 1 and 2). *N*-Boc-Ethanolamine. Boc_2O (2.18 g, 10 mmol) was added to ethanolamine (610 mg, 10 mmol) at 0 °C and allowed to stir for 1 h. A colorless precipitate formed immediately with the evolution of heat. Column chromatography (hexanes/ethyl acetate, silica, 6:1) with subsequent evaporation of the solvent yields 1.45 g of the desired product as a colorless oil (9.9 mmol, yield 90%, $R_f = 0.1$). ESI-MS (MeOH, 30 V): 184.1 $[M + Na]^+$. ^{1}H NMR ($CDCl_3$, 300 MHz, δ): 3.55 (t, CH_2-OH, 2H), 3.14 (t, CH_2-NH-Boc, 2H), 1.33 (s, (CH_3)$_3$, 9H), ^{13}C NMR ($CDCl_3$, 300 MHz, δ): 155.6 (carbonyl-*C*), 79.34 (*C*-(CH_3)$_3$), 61.6 (*C*H_2-OH), 42.98 (*C*H_2-NH-Boc), 28.17 ((*C*H_3)$_3$). IR (cm^{-1}): 1682 (m), 1517 (m), 1164 (m).

***N*-Boc-2-Aminoethyl Ester Octanoic Acid.** *N*-Boc-Ethanolamine (1.45 g, 9.9 mmol) was dissolved in toluene (50 mL) to afford a clear solution. EDMA (ethyldimethylamine, 20 mL) and octanoyl chloride (1.908 g,11.78 mmol, 1.3 equiv) were added dropwise simultaneously. A cloudy precipitate formed immediately, and the reaction solution was stirred at room

temperature for another 1.5 h, after which time the solvent and a large fraction of the added EDMA were evaporated under reduced pressure. The residue was redissolved in H_2O (30 mL) and extracted into ether (30 mL) twice. The organic phase was collected and the solvent evaporated under reduced pressure to afford the crude product as a yellow oil which was purified by column chromatography (hexanes/ethyl acetate, 1:1, $R_f = 0.6$) to yield *N*-Boc-2-aminoethyl ester octanoic acid (1.505 g, 5.45 mmol, yield 53%) after solvent evaporation. ESI-MS (MeOH, 30 V): 326.2 $[M + K]^+$. ^{1}H NMR ($CDCl_3$, 400 MHz, δ): 4.07 (t, CH_2-OCOR, 2H), 3.33 (t, CH$_2$-N*H*COR, 2H), 2.27 (t, ROCO-CH_2, 2H), 1.57 (m, ROCOCH$_2$-CH_2, 2H), 1.40 (s, (CH_3)$_3$, 9H), 1.24 (m, CH$_2$-CH_2-CH$_2$, 8H), 0.83 (t, CH_3, 3H). ^{13}C NMR ($CDCl_3$, 400 MHz, δ): 173.54 (carbonyl-*C*), 155.69 (carbamate-*C*), 79.55 (*C*-(CH$_3$)$_3$), 63.22 (*C*H$_2$-OCOR), 39.55 (*C*H$_2$-NH-Boc), 33.98, (ROCO-*C*H$_2$), 31.48, (ROCOCH$_2$-*C*H$_2$), 28.75 (ROCO(CH$_2$)$_2$-*C*H$_2$), 28.17 ((*C*H$_3$)$_3$), 24.72 (*C*H$_2$), 22.42 (*C*H$_2$-CH$_3$), 13.86 (*C*H$_3$). IR (cm^{-1}): 1684 (m), 1631 (m), 1482 (w).

2-Aminoethyl Ester Octanoic Acid. *N*-Boc-2-Aminoethyl ester octanoic acid (1.505 g, 5.45 mmol) was dissolved in dichloromethane (4 mL). Trifluoroacetic acid (4 mL) was added, and the reaction solution was stirred for 20 min after which time a slow change of color to light yellow was observed. TFA and DCM were removed in vacuo, and the oily residue was purified by column chromatography (DCM/MeOH, 4:1, R_f = 0.15) yielding 2-aminoethyl ester octanoic acid (444 mg, 2.37 mmol, yield 43%) after rotary evaporation as a colorless oil which solidifies upon standing. ESI-MS (MeOH, 30 V): 188.2 $[M + H]^+$, 210 $[M + Na]^+$. ^{1}H NMR (MeOD, 300 MHz, δ): 4.47 (s, NH_2, 2H), 3.55 (t, CH_2-OCOR, 2H), 3.25 (t, CH_2-NH$_2$, 2H), 2.15 (t, ROCO-CH_2, 2H), 1.57 (m, ROCOCH$_2$-CH_2, 2H), 1.28 (m, CH$_2$-CH_2-CH$_2$, 8H), 0.86 (t, CH_3, 3H). ^{13}C NMR (MeOD, 300 MHz, δ): 173.7 (carbonyl-*C*), 62.27 (*C*H$_2$-OCOR), 43.42(*C*H$_2$-NH$_2$), 37.61−23.95 (six signals, *C*H$_2$), 14.66 (*C*H$_3$). IR (cm^{-1}): 3312 (w), 2954 (s), 2924 (s), 2855 (s), 1637 (s), 1552 (m), 1464 (m).

***N*-Pyridinemethyl-2-aminoethyl Ester Octanoic Acid.** 2-Aminoethyl ester octanoic acid (0.51 g, 2.7 mmol) was dissolved in dry ethanol (15 mL). Na_2CO_3 (~10 equiv, 2.86 g) was added to afford a turbid solution. Pyridine-2-aldehyde (0.27 g, 237 μL, 0.95 equiv) was added, and the reaction mixture was stirred overnight at room temperature. After the formation of the intermediate imine was monitored by TLC, $NaBH_4$ (95 mg, 2.51 mmol, 0.98 equiv) was added and the reaction mixture was subsequently stirred for another 1 h. DCM (20 mL) was then added and extracted twice with a saturated solution of $NaHCO_3$ (20 mL). The organic fractions were collected, and the solvent was evaporated. The crude product was purified by column chromatography (DCM/MeOH, 85:15, R_f = 0.55) yielding *N*-pyridinemethyl-2-aminoethyl ester octanoic acid (361 mg, 1.3 mmol, yield 48%) as a colorless oil with low viscosity, after evaporation of the solvent. ESI-MS (MeOH, 30 V): 279 $[M + H]^+$, 301.2 $[M + Na]^+$. ^{1}H NMR ($CDCl_3$, 300 MHz, δ): 8.48 (d, *o*-pyridine-*H*, 1H), 7.66 (t, *p*-pyridine-*H*, 1H), 7.32 (d, *m*-pyridine-*H*, 1H), 7.17 (t, *m*-pyridine-*H*, 1H), 4.72 (s, N*H*, 1H), 3.91 (s, pyr-CH_2, 2H), 3.63 (t, CH_2-OCOR, 2H), 3.37 (t, CH_2-NH, 2H), 2.14 (t, ROCO-CH_2, 2H), 1.56 (m, ROCOCH$_2$-CH_2, 2H), 1.22 (m, CH$_2$-CH_2-CH$_2$, 8H), 0.82 (t, CH_3, 3H). ^{13}C NMR ($CDCl_3$, 300 MHz, δ): 174.54 (carbonyl-*C*), 149.03 (*o*-pyridine-*C*), 148.27 (*o*-pyridine-*C*), 136.84 (*m*-pyridine-*C*), 122.26 (*m*-pyridine-*C*), 120.71 (*p*-pyridine-*C*), 64.21 (pyr-*C*H$_2$), 61.60 (*C*H$_2$-NH$_2$), 54.06 (*C*H$_2$-OCOR), 42.12−22.46 (six signals, *C*H$_2$), 13.93 (*C*H$_3$). IR (cm^{-1}): 3294 (br), 2925 (s), 2855 (s), 1632 (s), 1595 (s), 1549 (m).

***N*-Bis(*tert*-Butylcarboxyethyl)-2-aminoethyl Ester Octanoic Acid.** 2-Aminoethyl ester octanoic acid (0.1 g, 0.53 mmol) was dissolved in dry DCM (10 mL). Na_2CO_3 (1 g) was added to afford a turbid solution. *tert*-Butyl bromoacetate (209 mg, 179 μL, 1.06 mmol, 2 equiv) was added, and the mixture was stirred for 2 days. After the presence of the product was confirmed by ESI-MS, the solvent was evaporated and the crude mixture was purified by column chromatography (silica, hexanes/ethyl acetate, 1:1, R_f = 0.8) to yield *N*-bis(*tert*-butylcarboxyethyl)-2-aminoethyl ester octanoic acid (60 mg, 0.144 mmol, yield 27%) after rotary evaporation of all solvents. ESI-MS (MeOH, 30 V): 438.3 $[M + Na]^+$. ^{1}H NMR ($CDCl_3$, 300 MHz, δ): 4.13 (t, CH_2-OCOR, 2H), 3.69 (s, ^{t}Bu-carbonyl-C-CH_2-N, 4H), 3.45 (t, CH_2-N, 2H), 2.95 (t, ROCO-CH_2, 2H), 1.55 (m, ROCOCH$_2$-CH_2, 2H),, 1.41 (s, (CH_3)$_3$, 18 H), 1.21 (m, CH$_2$-CH_2-CH$_2$, 8H), 0.84 (t, CH_3, 3H). ^{13}C NMR ($CDCl_3$, 300 MHz, δ): 170.18 (carbonyl-*C*), 166.03 (^{t}Bu-carbonyl-*C*), 62.68 (*C*H$_2$-OCOR), 58.19 (^{t}Bu-carbonyl-*C*-CH$_2$-N), 52.42 (*C*H$_2$-N), 34.06−22.40 (six signals, *C*H$_2$), 27.61 ((*C*H$_3$)$_3$), 13.88 (*C*H$_3$).

***N*-*N*-(*tert*-Butylcarboxyethyl)-pyridinemethyl-2-aminoethyl Ester Octanoic Acid.** *N*-Pyridinemethyl-2-aminoethyl ester octanoic acid (361 mg, 1.3 mmol) was dissolved in dry DCM (20 mL). Na_2CO_3 (~10 equiv, 2.86 g) was added to afford a turbid solution. *tert*-Butyl bromoacetate (1.4 equiv, 354 mg, 1.8 mmol) was added, and the mixture was stirred for 2 days. The solvent was evaporated after confirmation of product presence by ESI-MS, and the crude product was purified by column chromatography (silica, DCM/MeOH, 95:5, R_f = 0.8) yielding *N*-*N*-(*tert*-butylcarboxyethyl)-pyridinemethyl-2-aminoethyl ester octanoic acid (109 mg, 0.27 mmol, yield 21%), after rotary evaporation of all solvents, as a light yellow oil. ESI-MS (MeOH, 30 V): 415.3 $[M + Na]^+$. ^{1}H NMR ($CDCl_3$, 300 MHz, δ): 8.52 (d, *o*-pyridine-*H*, 1H), 7.68 (t, *p*-pyridine-*H*, 1H), 7.56 (d, *m*-pyridine-*H*, 1H), 7.17 (t, *m*-pyridine-*H*, 1H), 4.16 (t, CH_2-OCOR, 2H), 4.03 (s, pyr-CH_2, 2H), 3.40 (s, ^{t}Bu-carbonyl-C-CH_2-N, 2H), 3.00 (t, CH_2-N, 2H), 2.26 (t, ROCO-CH_2, 2H), 1.56 (m, ROCOCH$_2$-CH_2, 2H), 1.46 (s, (CH_3)$_3$, 9 H), 1.26 (m, CH$_2$-CH_2-CH$_2$, 8H), 0.87 (t, CH_3, 3H). ^{13}C NMR ($CDCl_3$, 300 MHz, δ): 184.65 (^{t}Bu-carbonyl-*C*), 173.66 (carbonyl-*C*), 148.64 (*o*-pyridine-*C*), 136.82 (*o*-pyridine-*C*), 122.91 (*m*-pyridine-*C*), 122.11(*m*-pyridine-*C*), 62.52 (pyr-*C*H$_2$), 60.30 (*C*H$_2$-N), 56.21 (^{t}Bu-carbonyl-C-*C*H$_2$-N), 52.53 (*C*H$_2$-OCOR), 34.24−22.54 (six signals, *C*H$_2$) 28.15 ((*C*H$_3$)$_3$), 14.02 (*C*H$_3$).

***N*-*N*-Bis(*tert*-Butylcarboxyethyl)-pyridinemethyl-2-aminoethyl Ester Octanoic Acid.** *N*-*N*-Bis(*tert*-Butylcarboxyethyl)-pyridinemethyl-2-aminoethyl ester octanoic acid is afforded as a side product of the synthesis of *N*-*N*-(*tert*-butylcarboxyethyl)-pyridinemethyl-2-aminoethyl ester octanoic acid and separated from the main product by column chromatography (silica, DCM/MeOH, 95:5, R_f of product: 0.35) yielding *N*-*N*-bis(*tert*-butylcarboxyethyl)-pyridinemethyl-2-aminoethyl ester octanoic acid (37 mg, 0.072 mmol, yield 5.6%) after solvent evaporation as a light orange oil. ESI-MS (MeOH, 30 V): 507.3 $[M]^+$. ^{1}H NMR ($CDCl_3$, 300 MHz, δ): 9.59 (d, *o*-pyridine-*H*, 1H), 8.48 (t, *p*-pyridine-*H*, 1H), 8.21 (d, *m*-pyridine-*H*, 1H), 8.05 (t, *m*-pyridine-*H*, 1H), 4.38 (t, CH_2-OCOR, 2H), 4.10 (s, pyr-CH_2, 2H), 3.71 (s, ^{t}Bu-carbonyl-C-CH_2-N, 2H), 3.92 (t, CH_2-N, 2H), 2.26 (t, ROCO-CH_2, 2H), 1.56 (m, ROCOCH$_2$-CH_2, 2H), 1.47 (s, (CH_3)$_3$, 18 H), 1.23 (m, CH$_2$-CH_2-CH$_2$, 8H), 0.83 (t, CH_3, 3H). ^{13}C NMR ($CDCl_3$, 300 MHz, δ): 169.48 (*o*-pyridine-*C*), 164.73 (*o*-pyridine-*C*), 155.39 (*m*-pyridine-*C*), 128.75 (*m*-pyridine-*C*), 64.74 (*C*H$_2$-N), 61.74, (pyr-*C*H$_2$) 55.21 (^{t}Bu-carbonyl-C-*C*H$_2$-N), 52.65 (*C*H$_2$-OCOR), 34.04−22.42 (six signals, *C*H$_2$) 27.25 ((*C*H$_3$)$_3$), 13.91 (*C*H$_3$).

***N*-*N*-Carboxyethyl-pyridinemethyl-2-aminoethyl Ester Octanoic Acid (HL1).** *N*-*N*-(*tert*-Butylcarboxyethyl)-pyridinemethyl-2-aminoethyl ester octanoic acid (109 mg, 0.27 mmol) was dissolved in dry DCM (1 mL). TFA (1 mL) was added, and the reaction mixture was stirred for 30 min at room temperature. Xylene (1 mL) was added, and all the solvents

were evaporated under reduced pressure to yield the crude product, which was purified by preparative HPLC to afford *N*-*N*-carboxyethyl-pyridinemethyl-2-aminoethyl ester octanoic acid (45 mg, 0.133 mmol, yield 49%) after solvent evaporation. ESI-MS (MeOH, 30 V): 337.2 $[M + H]^+$. ^{1}H NMR (MeOD, 400 MHz, δ): 8.76 (d, *o*-pyridine-*H*, 1H), 8.41 (t, *p*-pyridine-*H*, 1H), 7.93 (d, *m*-pyridine-*H*, 1H), 7.86 (t, *m*-pyridine-*H*, 1H), 4.48 (s, HOOC-CH_2-N, 2H), 4.22 (t, CH_2-OCOR, 2H), 3.78 (s, pyr-CH_2, 2H),, 3.23 (t, CH_2-N, 2H), 2.28 (t, ROCO-CH_2, 2H), 1.56 (m, ROCOCH$_2$-CH_2, 2H), 1.29 (m, CH$_2$-CH_2-CH$_2$, 8H), 0.9 (t, CH$_3$, 3H). ^{13}C NMR (MeOD, 400 MHz, δ): 184.22 (carboxyl-*C*), 171.35 (carbonyl-*C*), 156.08 (*o*-pyridine-*C*), 146.14 (*o*-pyridine-*C*), 144.42 (*m*-pyridine-*C*), 127.00 (*m*-pyridine-*C*), 84.15 (HOOC-*C*H$_2$-N), 63.06 (pyr-*C*H$_2$), 57.75 (*C*H$_2$-N), 55.30 (*C*H$_2$-OCOR), 35.22−23.97 (six signals, *C*H$_2$), 13.93 (*C*H$_3$). IR (cm^{-1}): 2929 (w), 2858 (w), 1727 (m), 1668 (m).

***N*-Bis(carboxyethyl)-2-aminoethyl Ester Octanoic Acid (H_2L2).** The exact same procedure as for H**L1** was followed with *N*-bis(*tert*-butylcarboxyethyl)-2-aminoethyl ester octanoic acid (120 mg, 0.288 mmol) to yield *N*-bis(carboxyethyl)-2-aminoethyl ester octanoic acid (56 mg, 0.184 mmol, yield 64%). ESI-MS (MeOH, 30 V): 304.2 $[M + H]^+$. ^{1}H NMR (MeOD, 400 MHz, δ): 4.60 (s, HOOC-CH_2-N, 4H), 3.86 (t, CH_2-OCOR, 2H), 3.44 (t, CH_2-N, 2H), 2.35 (t, ROCO-CH_2, 2H), 1.61 (m, ROCOCH$_2$-CH_2, 2H), 1.32 (m, CH$_2$-CH_2-CH$_2$, 8H), 0.91 (t, CH_3, 3H). ^{13}C NMR (MeOD, 400 MHz, δ): 183.61 (carboxyl-*C*), 177.18 (carbonyl-*C*), 62.45 (*C*H$_2$-OCOR), 57.55 (carboxyl-C-*C*H$_2$-N), 55.64 (*C*H$_2$-N), 38.33−24.10 (six signals, *C*H$_2$), 16.22 (*C*H$_3$). IR (cm^{-1}): 2928 (w), 2857 (w), 1737(m), 1682 (m).

***N*-*N*-Bis(carboxyethyl)-pyridinemethyl-2-aminoethyl Ester Octanoic Acid (H_2L3).** The exact same procedure as for H**L1** was followed with *N*-*N*-bis(*tert*-butylcarboxyethyl)-pyridinemethyl-2-aminoethyl ester octanoic acid (37 mg, 0.072 mmol) to afford *N*-*N*-bis(carboxyethyl)-pyridinemethyl-2-aminoethyl ester octanoic acid (12 mg, 0.0303 mmol, yield 42%). ESI-MS (MeOH, 30 V): 395.2 $[M]^+$. ^{1}H NMR (MeOD, 400 MHz, δ): 8.95 (d, *o*-pyridine-*H*, 1H), 8.65 (t, *p*-pyridine-*H*, 1H), 8.30 (d, *m*-pyridine-*H*, 1H), 8.11 (t, *m*-pyridine-*H*, 1H), 5.77 (s, HOOC-CH_2-N, 4H), 4.32 (t, CH_2-OCOR, 2H), 4.07 (s, pyr-CH_2, 2H), 3.91 (t, CH_2-N, 2H), 2.19 (t, ROCO-CH_2, 2H), 1.60 (m, ROCOCH$_2$-CH_2, 2H), 1.31 (m, CH$_2$-CH_2-CH$_2$, 8H), 0.90 (t, CH_3, 3H). ^{13}C NMR (MeOD, 400 MHz, δ): 186.22 (carboxyl-*C*), 169.48 (*o*-pyridine-*C*), 163.94 (*p*-pyridine-*C*), 128.20 (*m*-pyridine-*C*), 65.31 (*C*H$_2$-N), 61.79 (pyr-*C*H$_2$) 56.65 (HOOC-*C*H$_2$-N), 52.65 (*C*H$_2$-OCOR), 37.26−23.81 (six signals, *C*H$_2$), 14.54 (*C*H$_3$). IR (cm^{-1}): 2927(w), 2857(w), 1731(m), 1630 (m).

***N*-*N*-Carboxyethyl-pyridinemethyl-2-aminoethyl Ester Octanoic Acid Tricarbonylrhenium(I) [Re(L1)(CO)$_3$].** A solution of $[NEt_4]_2[ReBr_3(CO)_3]$ (0.040 g, 0.052 mmol) and H**L1** (0.017 g, 0.052 mmol) in MeOH (5 mL) was allowed to reflux overnight. The solution flask was placed into the freezer for 2 h to afford the product as a white solid (0.021 g, 0.034 mmol, yield 66%) after filtration. Small, colorless crystals were obtained by slow diffusion of the product dissolved in DCM into diethyl ether. ESI-MS (MeOH, 30 V): 605.1 $[^{185}Re + H]^+$, 607.1 $[^{187}Re + H]^+$. ^{1}H NMR ($CDCl_3$, 300 MHz, δ): 8.84 (d, *o*-pyridine-*H*, 1H), 7.79 (t, *p*-pyridine-*H*, 1H), 7.56 (d, *m*-pyridine-*H*, 1H), 7.46 (t, *m*-pyridine-*H*, 1H), 4.55 (s, HOOC-CH_2-N, 2H), 4.48 (t, CH_2-OCOR, 2H), 3.89 (s, pyr-CH_2, 2H), 3.78 (t, CH_2-N, 2H), 2.40 (t, ROCO-CH_2, 2H), 1.54 (m, ROCOCH$_2$-CH_2, 2H), 1.30 (m, CH$_2$-CH_2-CH$_2$, 8H), 0.89 (t, CH_3, 3H). IR (cm^{-1}): 2020 (m), 1905 (w), 1870 (m) ($\nu_{C=O}$).

Sodium *N*-Bis(carboxyethyl)-2-aminoethyl Ester Octanoic Acid Tricarbonylrhenate Na[Re(L2)(CO)$_3$]. A solution of $[NEt_4]_2[ReBr_3(CO)_3]$ (0.040 g, 0.052 mmol) and **L2** (0.016 g, 0.052 mmol) in MeOH (5 mL) was allowed to reflux overnight.

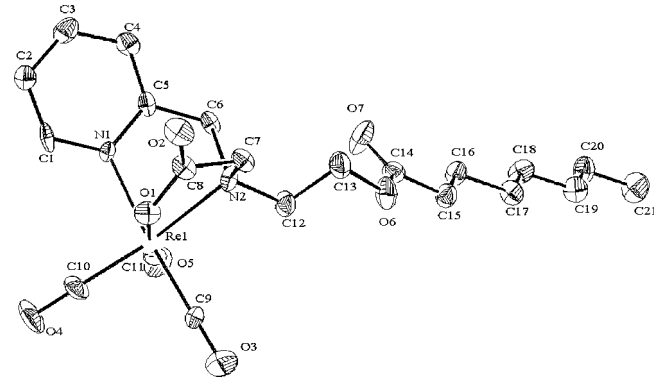

Figure 2. ORTEP view of complex Re(CO)$_3$**L1** (50% thermal probability ellipsoids).

The solvent was evaporated, and the oily residue was purified by preparative HPLC to afford the product as a white solid (0.005 g, 0.0087 mmol, yield 15%) after rotary evaporation of all solvents. ESI-MS (MeOH, 30 V): 570.1 $[^{185}Re]^-$, 572.1 $[^{187}Re]^-$. ^{1}H NMR (MeOD, 300 MHz, δ): 4.80 (s, HOOC-CH_2-N, 4H) 3.97 (t, CH_2-OCOR, 2H), 3.78 (t, CH_2-N, 2H), 2.35 (t, ROCO-CH_2, 2H), 1.62 (m, ROCOCH$_2$-CH_2, 2H), 1.31 (m, CH$_2$-CH_2-CH$_2$, 8H), 0.90 (t, CH_3, 3H). IR (cm^{-1}): 2017 (m), 1881 (m, br) ($\nu_{C=O}$), 1606 (w).

***N*-*N*-Bis(carboxyethyl)-pyridinemethyl-2-aminoethyl Ester Octanoic Acid Tricarbonylrhenium [Re(L3)(CO)$_3$].** A solution of $[NEt_4]_2[ReBr_3(CO)_3]$ (0.040 g, 0.052 mmol) and H_2**L3** (0.016 g, 0.052 mmol) in MeOH (5 mL) was allowed to reflux overnight. The solvent was evaporated, and the oily residue was purified by preparative HPLC to afford the product as a yellow solid (0.003 g, 0.0045 mmol, yield 8%). MALDI-MS: 663.1 $[^{185}Re + H]^+$, 665.1 $[^{187}Re + H]^+$. ^{1}H NMR (MeOD, 400 MHz, δ): 8.96 (d, *o*-pyridine-*H*, 1H), 8.66 (t, *p*-pyridine-*H*, 1H), 8.30 (d, *m*-pyridine-*H*, 1H), 8.08 (t, *m*-pyridine-*H*, 1H), 5.71 (s, HOOC-CH_2-N, 4H), 4.36 (t, CH_2-OCOR, 2H), 4.14 (s, pyr-CH$_2$, 2H),, 3.97 (t, CH_2-N, 2H), 2.32 (t, ROCO-CH_2, 2H), 1.54 (m, ROCOCH$_2$-CH_2, 2H), 1.30 (m, CH$_2$-CH_2-CH$_2$, 8H), 0.90 (t, CH_3, 3H). IR (cm^{-1}): 2018 (s), 1894 (m), 1874 (m) ($\nu_{C=O}$), 1661 (w).

[^{99m}Tc(H$_2$O)$_3$(CO)$_3$]$^+$ Labeling Studies. The organometallic precursor $[^{99m}Tc(H_2O)_3(CO)_3]^+$ was prepared from a saline solution of Na[^{99m}TcO$_4$] (1 mL, 200 MBq) using the Isolink kit. A solution of Na[^{99m}TcO$_4$] (1 mL) was added to the Isolink kit, and the vial was heated to reflux for 25 min. Upon cooling, 0.1 M HCl solution (1 mL) was added to adjust the pH to 7−8. Labeling was achieved by mixing an aliquot (0.2 mL) of the $[^{99m}Tc(H_2O)_3(CO)_3]^+$ precursor with a 0.1 mM solution of **L1**−**L3** (with the solution pH previously adjusted to 7−7.5 with an aqueous 0.1 M $NaHCO_3$ solution) at 90 °C for 25 (**L1**), 35 (**L2**), or 45 (**L3**) min. Analysis was performed by HPLC and TLC. HPLC solvents consisted of 0.1% trifluoroacetic acid in water (solvent A) or neat methanol (solvent B). Samples were analyzed with a linear gradient method (100% solvent A to 100% solvent B over 30 min). TLCs were analyzed with acetonitrile as mobile phase.

Cysteine and Histidine Challenge Experiments. To a solution of either cysteine (0.1 M, 0.9 mL) or histidine (0.1 M, 0.9 mL) in PBS (phosphate-buffered saline, 1 mM, pH 7.4) was added a solution of the ^{99m}Tc complex (final ligand concentration 10^{-5} M). The samples were incubated at 37 °C and aliquots analyzed after 24 h by analytical TLC and HPLC.

Octanol−Water-Distribution Coefficients. The log $P_{o/w}$ values of complexes [^{99m}Tc(CO)$_3$**L1**], Na[^{99m}Tc(CO)$_3$**L2**], and [^{99m}Tc(CO)$_3$**L3**] were determined by extraction with equivalent amounts of octanol and aqueous solutions of the ^{99m}Tc complex

Table 1. Experimental Conditions and log $P_{o/w}$ Data for All Complexes

complex	radio-chemical yield (%)	labeling time (min)	T (°C)	ligand concn	t_R (min)	log $P_{o/w}$	R_f
^{99m}Tc(CO)$_3$L1	>95	25	90	3×10^{-4}	20.5 (21.3)[a]	−0.034	0.49
[^{99m}Tc(CO)$_3$L2]$^-$	>95	35	90	3.3×10^{-4}	15.6 (14.01) [a]	−1.014	0.39
^{99m}Tc(CO)$_3$L3	~ 30	45	90	1×10^{-3}	18.1 (18.7) [a]	−0.38	0.46

[a] Retention time for the analogous cold-chemical Re complexes.

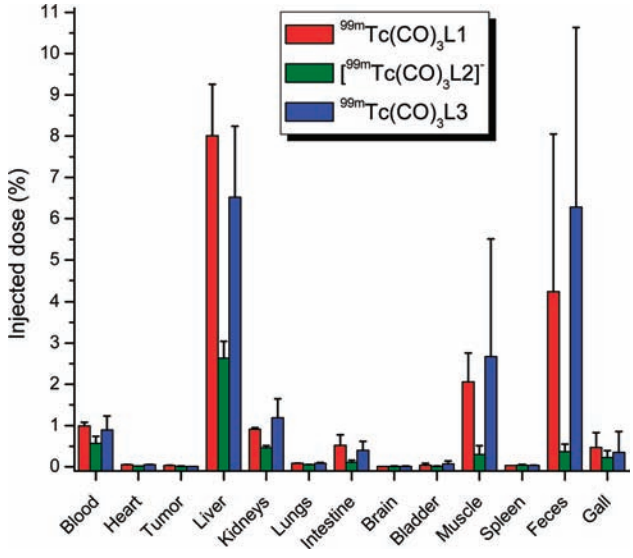

Figure 3. Biodistribution of ^{99m}Tc-labeled ligands at the 4 h time point ($n = 4$).

(*17*). Octanol (1 mL) was mixed with an equivalent amount of the aqueous reaction mixture and stirred for 1 min. Subsequently, the two phases were partitioned, and the activity of both was determined by the measurement of activity of 5 μL droplets of each solution on a radio-TLC-plate.

X-ray Diffraction Analysis of Re(CO)$_3$L1. The sample was mounted on a glass fiber and cooled to 173 K. X-ray data were collected and processed using a Bruker X8 APEX II diffractometer using graphite-monochromated Mo Kα radiation (λ = 0.71073 Å) to a maximum 2θ value of 48.0°. Data were collected and integrated using the Bruker SAINT software package (*18*) and corrected for Lorentz and polarization effects, as well as for absorption effects, using the multiscan technique (SADABS) (*19*). The X-ray structure was solved using direct methods (SIR92) (*20*) and expanded using Fourier techniques (*21*). All calculations were performed using the SHELXTL crystallographic software package (*22*).

Imaging and Biodistribution. Animals were used in accordance with the regulations on the protection of animals in Canada. Female C57Bl/6 mice were obtained from Sarah Reid, McMaster University. Each mouse had a 4 mm tumor in its neck, grown from a primary cell line at passage six derived from mammary tumors of a PyVMT transgenic mouse. ^{99m}Tc complexes were prepared as described above. While complexes [^{99m}Tc(CO)$_3$**L1**] and [^{99m}Tc(CO)$_3$**L2**]$^-$ were injected without any further purification because of their high yield in synthesis, [^{99m}Tc(CO)$_3$**L3**] was purified by preparative HPLC. The solvent was removed from the collected fraction in vacuo, and [^{99m}Tc(CO)$_3$**L3**] was redissolved in 0.9 M saline solution. Aliquots (100 μL) of complex solutions of [^{99m}Tc(CO)$_3$**L1**], [^{99m}Tc(CO)$_3$**L2**]$^-$, and [^{99m}Tc(CO)$_3$**L3**] were injected into groups of four mice via their tail vein. After injection of [^{99m}Tc(CO)$_3$**L1**] and [^{99m}Tc(CO)$_3$**L2**]$^-$, dynamic imaging was carried out during the first 15 min. All animals were imaged under isoflurane anesthesia in the supine position during the first 15 min, and then 1, 2, and 4 h after injection for 15 min each. After the last time point, animals were sacrificed by an overdose of pentobarbital, and samples of blood, liver, kidney, muscle, spleen, heart, brain, lung, gallbladder, intestine, stomach, bladder and tumor were removed, weighed, and counted in a gamma counter. Results are expressed as the percentage of the injected dose per gram of tissue (%ID/g). Tumor-to-organ ratios were calculated from %ID/g of the tumor and relevant organs.

RESULTS AND DISCUSSION

Proligand Synthesis. The tridentate chelator moieties of H**L1** and H$_2$**L2** were selected for this study since they were previously known for forming highly stable complexes with the metals of interest (*8*, *23*). The chelation entity of H$_2$**L3** is of a novel type arising from the synthesis of H**L1** where its *tert*-butyl-protected form appears as a byproduct in the synthesis of *tert*-butyl-protected H**L1**. All three ligand systems were synthesized via the free, C$_8$-chain-derivatized amine, which was subsequently converted by reductive amination and/or alkylation into the corresponding protected ligand system and in a final step was deprotected and purified by preparative HPLC. The identity of all ligands was confirmed by characterization through ^{1}H and ^{13}C NMR spectroscopy, as well as mass spectrometry and IR spectrophotometry. Elemental analysis was uninformative because of the oily consistency of the synthesized compounds.

Re Complexes. Re(CO)$_3$ complexes were synthesized as macroscopic models for the ^{99m}Tc(CO)$_3$ complexes by mixing a methanolic solution of ligand with [Re(CO)$_3$Br$_3$][NEt$_4$]$_2$ previously dissolved in H$_2$O and stirring the mixture at elevated temperatures overnight (*24*). While the neutral complex [Re(CO)$_3$**L1**] precipitates from the reaction solution, the solutions of the complexes Na[Re(CO)$_3$**L2**] or [Re(CO)$_3$**L3**] turn slightly yellow in color without precipitation of the product. Na[Re(CO)$_3$**L2**] and [Re(CO)$_3$**L3**] were isolated and purified via preparative HPLC. All complexes were characterized by ^{1}H and ^{13}C NMR spectroscopy, as well as mass spectrometry and IR spectrophotometry, where intense, diagnostic CO bands between 2020 and 1870 cm^{-1} can be assigned to the *fac*-[Re(CO)$_3$**L**]-products.

Solid-State Structure of [Re(CO)$_3$L1]. Colorless crystals of [Re(CO)$_3$**L1**] were obtained by slow diffusion of the product dissolved in DCM into diethyl ether. An ORTEP diagram is shown in Figure 2. The complex displays a nearly perfect octahedral coordination sphere. The Re−C bond lengths are all close to 1.9 Å and therefore shorter than the Re−O bond length (2.142 Å) and the Re−N bond lengths (2.184 Å, 2.227 Å). The Re−N2 bond proves to be the longest because of the nondirected lone pair on the tertiary amine nature of the nitrogen atom N2.

Synthesis, Stability, and Lipophilicity of ^{99m}Tc Complexes. The complexes [^{99m}Tc(CO)$_3$**L1**] and [^{99m}Tc(CO)$_3$**L2**]$^-$ were prepared in high radiochemical yield through reaction of *fac*-[^{99m}Tc(CO)$_3$(H$_2$O)$_3$]$^+$ with the ligands H**L1** and H$_2$**L2**. The ligands were initially deprotonated with NaHCO$_3$ (0.1 M solution, 2 equiv) and added to the technetium tricarbonyl solution with final concentrations of approximately 3×10^{-4} M.

After a reaction time of 25−35 min at 90 °C, the chelation reaction was 95% complete as verified by HPLC and radio-TLC analysis. No major byproducts were detected by HPLC. ^{99m}Tc(CO)$_3$**L3** was produced in only 30% yield after a 45 min reaction time. Several byproducts were visible in the γ-trace of

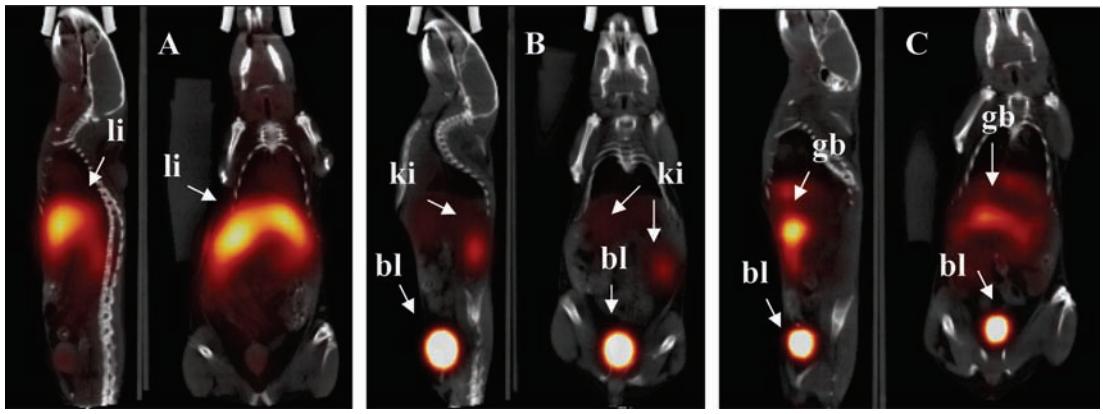

Figure 4. Representative μSPECT/CT pictures taken 15 min after injection of (A) [^{99m}Tc(CO)$_3$**L1**], (B) [^{99m}Tc(CO)$_3$**L2**]$^-$, and (C) [^{99m}Tc(CO)$_3$**L3**]. Abbreviations of organs: li: liver, ki:kidney, bl: bladder, gb: gallbladder.

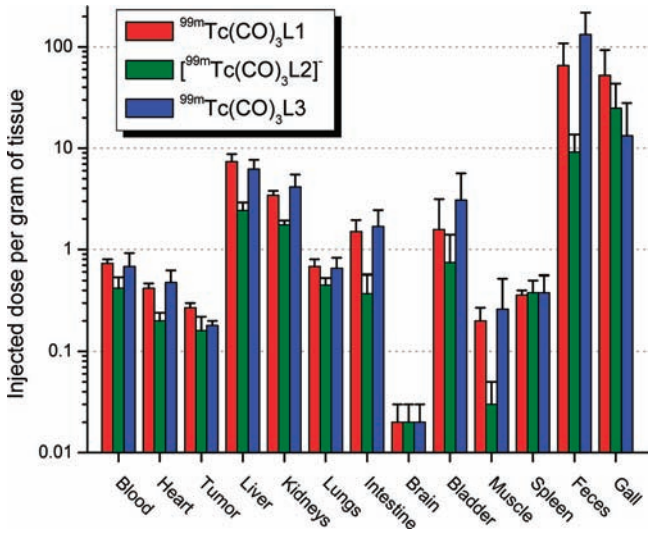

Figure 5. Logarithmic table of injected dose per gram of tissue (%ID/g) of ^{99m}Tc-labeled ligands at the 4 h time point ($n = 4$).

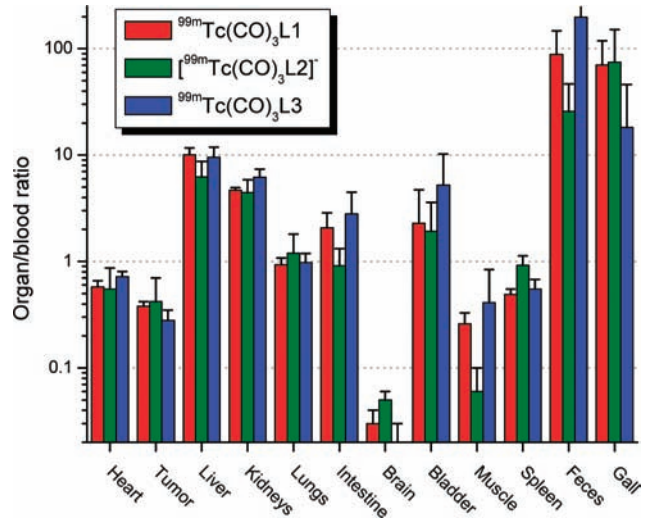

Figure 6. Logarithmic table of organ/blood ratio of ^{99m}Tc-labeled ligands at the 4 h time point ($n = 4$).

the HPLC spectrum, perhaps from coordination with decomposition fragments of **L3**.

The product peak was assigned by comparison of the retention time of the Re complex isolated by preparative HPLC. To investigate the complex stability toward the naturally occurring amino acids cysteine and histidine (both can act as potential tridentate ligands), the ^{99m}Tc-complexes were kept in 10^{-3} M cysteine/histidine solutions in PBS (pH = 7.4, 37 °C) for 24 h. In the subsequent HPLC analysis of the solution, no noticeable decomposition could be detected for any of the three complexes.

The lipophilicity of the complexes was determined by evaluation of water/octanol partition coefficients. [^{99m}Tc(CO)$_3$**L2**]$^-$ should be the most ionic compound by virtue of its full −1 charge, followed by the zwitterionic [^{99m}Tc(CO)$_3$**L3**] and the nonpolar [^{99m}Tc(CO)$_3$**L1**]; this was confirmed by the order of lipophilicity log P values ranging from [^{99m}Tc(CO)$_3$**L1**] > [^{99m}Tc(CO)$_3$**L3**] > [^{99m}Tc(CO)$_3$**L2**] (listed in the order from highest to lowest lipophilicity, Table 1).

Imaging and Biodistribution. Imaging of all three compounds was performed at 15 min, 1 h, 2 h, and 4 h after injection. Biodistribution studies were performed at the 4 h time point after injection (Figure 3). This tumor-bearing model was used to evaluate the imaging potential of [^{99m}Tc(CO)$_3$**L1**], [^{99m}Tc(CO)$_3$**L2**]$^-$, and [^{99m}Tc(CO)$_3$**L3**]. Data from the imaging is displayed in Figures S2, S3, and S4 (Supporting Information). Data from the biodistribution is displayed in Figures 5 and 6 as well as in Tables S3 and S4 (Supporting Information). Imaging screenshots of mice 15 min postinjection are shown in Figure 4.

All compounds show very distinct biodistribution behavior. The in vivo distribution of [^{99m}Tc(CO)$_3$**L1**] could be followed from the onset of injection. Very fast localization of the complex in the liver was observed, with clearance through the intestines, which is confirmed through the biodistribution data, showing large uptake of activity in liver, intestines, and feces. This behavior is not surprising considering that this complex has no overall charge and a very small log P value. [^{99m}Tc(CO)$_3$**L2**]$^-$ was also followed after injection with dynamic imaging. Here, fast processing of the compound through the kidneys, within the first 5−10 min after injection, and consequent localization in the bladder, followed by excretion was observable. The excretion of large portions of the dose is confirmed by the small fraction of the originally injected dose in the biodistribution measurements. The large log P value of this compound, plus its localized negative charge, determines its fate to be excreted through the renal tract. Finally, for [^{99m}Tc(CO)$_3$**L3**] after 1 h after injection, high localization in the gall bladder was observed, paired with slow clearance through the intestines. The biodistribution profile shows some similarity to the profile of [^{99m}Tc(CO)$_3$**L1**], but with faster excretion through the intestines and the renal system (high percentage of dose in the feces, elevated organ/blood ratio in kidneys), which can be a conse-

quence of the increased polarity of the complex (compared to [^{99m}Tc(CO)$_3$**L1**]). No significant heart, brain, or tumor uptake was observed for any of the investigated compounds.

CONCLUSION

For the first time, small amphiphilic ^{99m}Tc(CO)$_3$ complexes of which one bore a localized negative charge, one was a zwitterionic complex, and one was an entirely neutral molecule, have been synthesized, fully characterized, and investigated for their lipophilicity and behavior in vivo. Among the molecules, for the zwitterionic complex, a new type of chelation entity was incorporated, forming eight-membered rings between the metal center and the ligand sphere. This chelator proves to be slower coordinating but still high in stability toward cysteine and histidine challenges. Lower reaction yields arise from instability of the ligand toward prolonged heating at 90 °C. The products afforded by this decomposition are capable of coordinating to the metal center and make an additional purification step inevitable.

Unfortunately, none of the three investigated complexes showed significant brain, tumor, or heart uptake. The last confirms that negatively charged or zwitterionic complexes not do show the same potential for myocardial uptake as do other, cationic complexes for this very purpose. One way to confirm this would be the investigation of the corresponding cationic compound.

Also, for a more efficient mimicking of phospholipid-type molecules, a technetium-tagged approach might be more suitable, such as for example attachment of a small neutral ^{99m}Tc-complex to the aliphatic residue of the corresponding molecule. Changing the charge of a small amphiphilic molecule results in highly contrasting but still defined biodistribution behavior in an in vivo system. This is somewhat surprising and of potential importance for future applications.

ACKNOWLEDGMENT

The authors acknowledge UBC for a University Graduate Fellowship (E.B.), Troy Farncombe, Chantal Saab, and Rod Rhem for excellent imaging support at the McMaster Centre for Preclinical and Translational Imaging (MCPTI) and for use of their SPECT/CT scanner, Drs. Andrea Armstrong and John Valliant for advice and use of the radiochemistry facilities in the McMaster Institute of Applied Radiation Sciences (McIARS), MDS Nordion (Canada) for some financial support of this project, Covidien for the donation of Isolink Kits, Vancouver Coastal Health-UBC Hospital for [^{99m}TcO$_4$]$^-$, and the Natural Sciences and Engineering Research Council of Canada (NSERC) for a Strategic Grant.

Supporting Information Available: Crystal data for [Re(CO)$_3$L1], radio-HPLC traces of reaction mixtures of ^{99m}Tc-compounds, curves of all ^{99m}Tc-compounds' levels in selected organs taken from the SPECT/CT images. This information is available free of charge via the Internet at http://pubs.acs.org.

LITERATURE CITED

(1) Steigman, J., and Eckelman, W. C. (1992) *The Chemistry of Technetium in Medicine*, Nuclear Science Publication NAS-NS-3204, National Academy Press, Washington, DC.

(2) Dilworth, J. R., and Parrott, S. J. (1998) The biomedical chemistry of technetium and rhenium. *Chem. Soc. Rev. 27*, 43–55.

(3) Hom, R. K., and Katzenellenbogen, J. A. (1997) Technetium-99m-Labeled Receptor-Specific Small-Molecule Radiopharmaceuticals: Recent Developments and Encouraging Results. *Nucl. Med. Biol. 24*, 485–498.

(4) Jurisson, S. S., and Luxdon, J. D. (1999) Potential Technetium Small Molecule Radiopharmaceuticals. *Chem. Rev. 99*, 2205–2218.

(5) Bandoli, G., Dolmella, A., Porchia, M., Refosco, F., and Tisato, F. (2001) Structural Overview of Technetium Compounds (1993−1999). *Coord. Chem. Rev. 214*, 43–90.

(6) Alberto, R., Schibli, R., Egli, A., Schubiger, A. P., Abram, U., and Kaden, T. A. (1998) A novel organometallic aqua complex of Technetium for the labeling of biomolecules: Synthesis of [^{99m}Tc(OH$_2$)$_3$(CO)$_3$]$^+$ from [^{99m}TcO$_4$]$^-$ in aqueous solution and its reaction with a bifunctional ligand. *J. Am. Chem. Soc. 120*, 7987–7988.

(7) Rattat D., E. K., Cleynhens, B., Knight, H., Fonge, H., and Verbruggen, A. (2004) Comparison of tridentate ligands in competition experiments for their ability to form a [^{99m}Tc(CO)$_3$] complex. *Tetrahedron Lett. 45*, 2531–2534.

(8) Schibli, R., La Bella, R., Alberto, R., Garcia-Garayoa, E., Ortner, K., Abram, U., and Schubiger, P. A. (2000) Influence of the denticity of ligand systems on the in vitro and in vivo behavior of Tc-99m(I)-tricarbonyl complexes: A hint for the future functionalization of biomolecules. *Bioconjugate Chem. 11*, 345–351.

(9) Schibli, R., Schwarzbach, R., Alberto, R., Ortner, K., Schmalle, H., Dumas, C., Egli, A., and Schubiger, P. A. (2002) Steps toward high specific activity labeling of biomolecules for therapeutic application: Preparation of precursor [^{188}Re(H$_2$O)$_3$(CO)$_3$]$^+$ and synthesis of tailor-made bifunctional ligand systems. *Bioconjugate Chem. 13*, 750–756.

(10) Liu, Y., Pak, J.-K., Schmutz, P., Bauwens, M., Mertens, J., Knight, H., and Alberto, R. (2006) Amino Acids Labeled with [^{99m}Tc(CO)$_3$]+ and Recognized by the L-Type Amino Acid Transporter LAT1. *J. Am. Chem. Soc. 128*, 15996–15997.

(11) Ferreira, C. L., Ewart, C. B., Bayly, S. R., Patrick, B. O., Steele, J., Adam, M. J., and Orvig, C. (2006) Glucosamine Conjugates of Tricarbonylcyclopentadienyl Rhenium(I) and Technetium(I) Cores. *Inorg. Chem. 45*, 6979–6987.

(12) Hom, R. K., and Katzenellenbogen, J. A. (1997) Synthesis of a tetradentate oxorhenium(V) complex mimic of a steroidal estrogen. *J. Org. Chem. 62*, 6290–6297.

(13) Simons, A., and Helenius, K. (1975) Solubilization of membranes by detergents. *Biochim. Biophys. Acta 415*, 29–79.

(14) Saw, M. M., Kurz, P., Agorastos, N., Hor, T. S. A., Sundram, F. X., Yan, Y. K., and Alberto, R. (2006) Complexes with the *fac*-{M(CO)$_3$}$^+$ (M = ^{99m}Tc, Re) moiety and long alkyl chain ligands as Lipiodol surrogates. *Inorg. Chim. Acta 259*, 4087–4094.

(15) Maria, L., Cunha, S., Videira, M., Gano, L., Paulo, A., Santos, I. C., and Santos, I. (2007) Rhenium and technetium tricarbonyl complexes anchored by pyrazole-based tripods: novel lead structures for the design of myocardial imaging agents. *Dalton Trans.* 3010–3019.

(16) Cazzola, E., Benini, E., Pasquali, M., Mirtschink, P., Walther, M., Pietzsch, H.-J., Uccelli, L., Boschi, A., Bolzati, C., and Duatti, A. (2008) Labeling of Fatty Acid Ligands with the Strong Electrophilic Metal Fragment [^{99m}Tc(N)(PNP)]$^{+2}$ (PNP = diphosphane ligand). *Bioconjugate Chem. 19*, 450–460.

(17) Troutner, D. E., Volkert, W. A., Hoffman, T. J., and Holmes, R. A. (1984) A Neutral Lipophilic Complex of Tc-99m with a Multidentate Amine Oxime. *Int. J. Appl. Radiat. Isot. 35*, 467–470.

(18) SAINT, Bruker AXS Inc., Madison, WI, 1999.

(19) SADABS, Bruker AXS Inc., Madison, WI, 1999.

(20) Altomare, A., Burla, M. C., Camalli, M., Cascarano, G. L., Giocavazzo, C., Guagliardi, A., Moliterni, A. G. G., Polidori, G., and Spagna, R. (1999) SIR92: a new tool for crystal structure determination and refinement. *J. Appl. Crystallogr. 32*, 115–119.

(21) Beurskens, P. T., Admiraal, G., Beurskens, G., Bosman, W. P., Garcia-Granda, S., Gould, R. O., Smits, J. M. M., and Smykalla, C. (1992) PATTY, The DIR-DIF-94 program system. In *Technical Report of the Crystallography Laboratory*, 2nd ed., University of Nijmegen, The Netherlands.

(22) SHELXTL, Bruker AXS Inc., Madison, WI, 1999.
(23) Schibli, R., Bella, R. L., Alberto, R., Garcia-Garayoa, E., Ortner, K., Abram, U., and Schubiger, P. A. (2000) Influence of the denticity of ligand systems on the in vitro and in vivo behavior of ^{99m}Tc(I)-tricarbonyl complexes: A hint for the future functionalization of biomolecules. *Bioconjugate Chem. 3*, 345–351.
(24) Storr, T., Fisher, C. L., Mikata, Y., Yano, S., Adam, M. J., and Orvig, C. (2005) A glucosamine dipicolylamine conjugate of Tc-99m(I) and Re-186(I) for use in imaging and therapy. *Dalton Trans.* 654–655.

BC900022C

Supporting Information

Design, Synthesis and Imaging of Small Amphiphilic Rhenium and ^{99m}Technetium Tricarbonyl Complexes

Eszter Boros [†,‡], Urs O. Häfeli[§], Brian O. Patrick [†], Michael J. Adam[‡*] and Chris Orvig[†*]

Medicinal Inorganic Chemistry Group, Department of Chemistry, University of British Columbia, 2036 Main Mall, Vancouver, British Columbia V6T 1Z1, Canada,
Faculty of Pharmaceutical Sciences, University of British Columbia, 2146 East Mall, Vancouver, British Columbia, V6T 1Z3, Canada.
TRIUMF, 4004 Wesbrook Mall, Vancouver, British Columbia, V6T 2A3, Canada.

† University of British Columbia, Chemistry
[§] University of British Columbia, Pharmaceutical Sciences
‡ TRIUMF
* To whom correspondence should be addressed: adam@triumf.ca (M. J. A.); orvig@chem.ubc.ca (C. O.).

Table S1. Crystal Data for [$Re(CO)_3L1$]

Empirical Formula	$C_{21}H_{27}N_2O_7Re$
Formula Weight	605.65
Crystal Color, Habit	colourless, plate
Crystal Dimensions	0.05 X 0.12 X 0.45 mm
Crystal System	triclinic
Lattice Type	primitive
Lattice Parameters	a = 6.8109(11) b = 10.4134(19) Å c = 17.057(4) Å a = 102.114(8) o b = 94.058(13) o g = 102.511(9) o V = 1146.1(2) Å3
Space Group	*P* -1 (#2)
Z value	2
Dcalc	1.755 g/cm3
F000	596.00
m(MoKa)	53.44 cm-1
temp. (°C)	-100.0 $\pm$ 0.1oC
reflns collctd/ unique	9144/3421 (Rint = 0.053)
residuals (F^2, all data) R1; wR2 0.063; 0.142	0.063; 0.142
residuals (refined on F): R1; wR2	0.055; 0.135

Table S2. Bond lengths [Å] and angles [°] in [$Re(CO)_3L1$]

C(1)-N(1)	1.360(13)
C(1)-C(2)	1.373(14)
C(1)-H(1)	0.9500
C(2)-C(3)	1.373(15)
C(2)-H(2)	0.9500
C(3)-C(4)	1.398(15)
C(3)-H(3)	0.9500
C(4)-C(5)	1.370(13)
C(4)-H(4)	0.9500
C(5)-N(1)	1.380(13)
C(5)-C(6)	1.492(14)
C(6)-N(2)	1.518(12)
C(6)-H(6A)	0.9900
C(6)-H(6B)	0.9900
C(7)-N(2)	1.504(12)

C(7)-C(8)	1.535(14)
C(7)-H(7A)	0.9900
C(7)-H(7B)	0.9900
C(8)-O(1)	1.226(11)
C(8)-O(2)	1.287(12)
C(9)-O(3)	1.140(13)
C(9)-Re(1)	1.928(12)
C(10)-O(4)	1.158(13)
C(10)-Re(1)	1.909(12)
C(11)-O(5)	1.168(14)
C(11)-Re(1)	1.918(11)
C(12)-C(13)	1.494(15)
C(12)-N(2)	1.506(13)
C(12)-H(12A)	0.9900
C(12)-H(12B)	0.9900
C(13)-O(6)	1.448(13)
C(13)-H(13A)	0.9900
C(13)-H(13B)	0.9900
C(14)-O(7)	1.208(13)
C(14)-O(6)	1.335(13)
C(14)-C(15)	1.515(14)
C(15)-C(16)	1.524(14)
C(15)-H(15A)	0.9900
C(15)-H(15B)	0.9900
C(16)-C(17)	1.531(14)
C(16)-H(16A)	0.9900
C(16)-H(16B)	0.9900
C(17)-C(18)	1.548(14)
C(17)-H(17A)	0.9900
C(17)-H(17B)	0.9900
C(18)-C(19)	1.514(16)
C(18)-H(18A)	0.9900
C(18)-H(18B)	0.9900
C(19)-C(20)	1.526(15)
C(19)-H(19A)	0.9900
C(19)-H(19B)	0.9900
C(20)-C(21)	1.516(17)
C(20)-H(20A)	0.9900
C(20)-H(20B)	0.9900
C(21)-H(21A)	0.9800
C(21)-H(21B)	0.9800
C(21)-H(21C)	0.9800
N(1)-Re(1)	2.184(8)
N(2)-Re(1)	2.227(8)
O(2)-Re(1)	2.142(6)

N(1)-C(1)-C(2)	122.1(9)
N(1)-C(1)-H(1)	119.0
C(2)-C(1)-H(1)	119.0
C(1)-C(2)-C(3)	119.5(9)
C(1)-C(2)-H(2)	120.3
C(3)-C(2)-H(2)	120.3
C(2)-C(3)-C(4)	119.4(9)
C(2)-C(3)-H(3)	120.3
C(4)-C(3)-H(3)	120.3
C(5)-C(4)-C(3)	119.7(9)
C(5)-C(4)-H(4)	120.2
C(3)-C(4)-H(4)	120.2
C(4)-C(5)-N(1)	120.8(9)
C(4)-C(5)-C(6)	124.2(9)
N(1)-C(5)-C(6)	114.9(8)
C(5)-C(6)-N(2)	110.2(7)
C(5)-C(6)-H(6A)	109.6
N(2)-C(6)-H(6A)	109.6
C(5)-C(6)-H(6B)	109.6
N(2)-C(6)-H(6B)	109.6
H(6A)-C(6)-H(6B)	108.1
N(2)-C(7)-C(8)	112.3(8)
N(2)-C(7)-H(7A)	109.2
C(8)-C(7)-H(7A)	109.2
N(2)-C(7)-H(7B)	109.1
C(8)-C(7)-H(7B)	109.1
H(7A)-C(7)-H(7B)	107.9
O(1)-C(8)-O(2)	125.5(9)
O(1)-C(8)-C(7)	118.6(9)
O(2)-C(8)-C(7)	115.7(8)
O(3)-C(9)-Re(1)	179.1(10)
O(4)-C(10)-Re(1)	179.9(13)
O(5)-C(11)-Re(1)	179.3(11)
C(13)-C(12)-N(2)	115.2(9)
C(13)-C(12)-H(12A)	108.5
N(2)-C(12)-H(12A)	108.5
C(13)-C(12)-H(12B)	108.5
N(2)-C(12)-H(12B)	108.5
H(12A)-C(12)-H(12B)	107.5
O(6)-C(13)-C(12)	109.0(9)
O(6)-C(13)-H(13A)	109.9
C(12)-C(13)-H(13A)	109.9
O(6)-C(13)-H(13B)	109.9
C(12)-C(13)-H(13B)	109.9
H(13A)-C(13)-H(13B)	108.3
O(7)-C(14)-O(6)	123.6(10)

O(7)-C(14)-C(15)	124.6(10)
O(6)-C(14)-C(15)	111.7(9)
C(14)-C(15)-C(16)	114.4(9)
C(14)-C(15)-H(15A)	108.6
C(16)-C(15)-H(15A)	108.6
C(14)-C(15)-H(15B)	108.7
C(16)-C(15)-H(15B)	108.6
H(15A)-C(15)-H(15B)	107.6
C(15)-C(16)-C(17)	110.5(9)
C(15)-C(16)-H(16A)	109.5
C(17)-C(16)-H(16A)	109.6
C(15)-C(16)-H(16B)	109.6
C(17)-C(16)-H(16B)	109.5
H(16A)-C(16)-H(16B)	108.1
C(16)-C(17)-C(18)	113.3(9)
C(16)-C(17)-H(17A)	108.9
C(18)-C(17)-H(17A)	108.9
C(16)-C(17)-H(17B)	108.9
C(18)-C(17)-H(17B)	108.9
H(17A)-C(17)-H(17B)	107.7
C(19)-C(18)-C(17)	112.9(10)
C(19)-C(18)-H(18A)	109.0
C(17)-C(18)-H(18A)	109.0
C(19)-C(18)-H(18B)	109.0
C(17)-C(18)-H(18B)	109.0
H(18A)-C(18)-H(18B)	107.8
C(18)-C(19)-C(20)	113.3(10)
C(18)-C(19)-H(19A)	108.9
C(20)-C(19)-H(19A)	108.9
C(18)-C(19)-H(19B)	108.9
C(20)-C(19)-H(19B)	108.9
H(19A)-C(19)-H(19B)	107.7
C(21)-C(20)-C(19)	113.1(11)
C(21)-C(20)-H(20A)	109.0
C(19)-C(20)-H(20A)	109.0
C(21)-C(20)-H(20B)	109.0
C(19)-C(20)-H(20B)	109.0
H(20A)-C(20)-H(20B)	107.8
C(20)-C(21)-H(21A)	109.5
C(20)-C(21)-H(21B)	109.5
H(21A)-C(21)-H(21B)	109.5
C(20)-C(21)-H(21C)	109.5
H(21A)-C(21)-H(21C)	109.5
H(21B)-C(21)-H(21C)	109.5
C(1)-N(1)-C(5)	118.6(8)
C(1)-N(1)-Re(1)	125.2(7)

C(5)-N(1)-Re(1)	115.1(6)
C(7)-N(2)-C(12)	110.2(8)
C(7)-N(2)-C(6)	109.1(7)
C(12)-N(2)-C(6)	108.2(7)
C(7)-N(2)-Re(1)	108.8(5)
C(12)-N(2)-Re(1)	114.2(6)
C(6)-N(2)-Re(1)	106.2(6)
C(8)-O(2)-Re(1)	117.5(6)
C(14)-O(6)-C(13)	118.0(9)
C(10)-Re(1)-C(11)	88.8(5)
C(10)-Re(1)-C(9)	87.1(5)
C(11)-Re(1)-C(9)	88.6(5)
C(10)-Re(1)-O(2)	97.5(4)
C(11)-Re(1)-O(2)	96.4(4)
C(9)-Re(1)-O(2)	173.2(3)
C(10)-Re(1)-N(1)	96.8(4)
C(11)-Re(1)-N(1)	172.7(4)
C(9)-Re(1)-N(1)	96.3(4)
O(2)-Re(1)-N(1)	78.2(3)
C(10)-Re(1)-N(2)	173.2(3)
C(11)-Re(1)-N(2)	97.0(4)
C(9)-Re(1)-N(2)	96.6(4)
O(2)-Re(1)-N(2)	78.4(3)
N(1)-Re(1)-N(2)	77.2(3)

Table S3. Injected dose per gram of tissue (%ID/g) of ^{99m}Tc-labeled ligands at the 4 h time point (n=4).

Organ	**^{99m}Tc(CO)$_3$L1**		**[^{99m}Tc(CO)$_3$L2]$^-$**		**^{99m}Tc(CO)$_3$L3**	
	Average	**± S.D.**	**Average**	**± S.D.**	**Average**	**± S.D.**
Blood	0.73%	0.07%	0.42%	0.12%	0.68%	0.24%
Heart	0.42%	0.05%	0.20%	0.04%	0.48%	0.14%
Tumor	0.27%	0.03%	0.16%	0.06%	0.18%	0.02%
Liver	7.37%	1.35%	2.43%	0.49%	6.20%	1.46%
Kidneys	3.43%	0.37%	1.75%	0.18%	4.14%	1.34%
Lungs	0.68%	0.12%	0.45%	0.08%	0.65%	0.18%
Intestine	1.50%	0.49%	0.37%	0.20%	1.69%	0.75%
Brain	0.02%	0.01%	0.02%	0.01%	0.02%	0.01%
Bladder	1.57%	1.57%	0.74%	0.66%	3.07%	2.59%
Muscle	0.20%	0.07%	0.03%	0.02%	0.26%	0.26%
Spleen	0.36%	0.04%	0.38%	0.12%	0.38%	0.18%
Feces	65.34%	43.03%	9.14%	4.49%	132.37%	86.29%
Gall	52.52%	40.40%	24.83%	18.58%	13.28%	14.74%

Table S4. Organ/blood ratio of ^{99m}Tc-labeled ligands at the 4 h time point (n=4).

Organ	**^{99m}Tc(CO)$_3$L1**		**[^{99m}Tc(CO)$_3$L2]$^-$**		**^{99m}Tc(CO)$_3$L3**	
	Average	**± S.D.**	**Average**	**± S.D.**	**Average**	**± S.D.**
Blood	**1.00**	0.00	**1.00**	0.00	**1.00**	0.00
Heart	0.58	0.08	0.55	0.32	0.72	0.09
Tumor	0.38	0.04	0.42	0.28	0.28	0.07
Liver	10.07	1.63	6.23	2.50	9.51	2.35
Kidneys	4.68	0.26	4.43	1.43	6.19	1.18
Lungs	0.93	0.15	1.20	0.61	0.98	0.21
Intestine	2.07	0.79	0.91	0.41	2.80	1.68
Brain	0.03	0.01	0.05	0.01	0.02	0.01
Bladder	2.28	2.43	1.92	1.68	5.23	5.01
Muscle	0.26	0.07	0.06	0.04	0.41	0.43
Spleen	0.49	0.06	0.92	0.21	0.55	0.13
Feces	88.59	58.49	25.61	21.01	197.36	146.69
Gall	70.41	48.56	74.49	76.70	18.16	27.88

Figure S1. Radio-HPLC traces of reaction mixtures of [^{99m}Tc(CO)$_3$**L1**] (A), [^{99m}Tc(CO)$_3$**L2**]$^-$ (B) and[^{99m}Tc(CO)$_3$**L3**] (C).

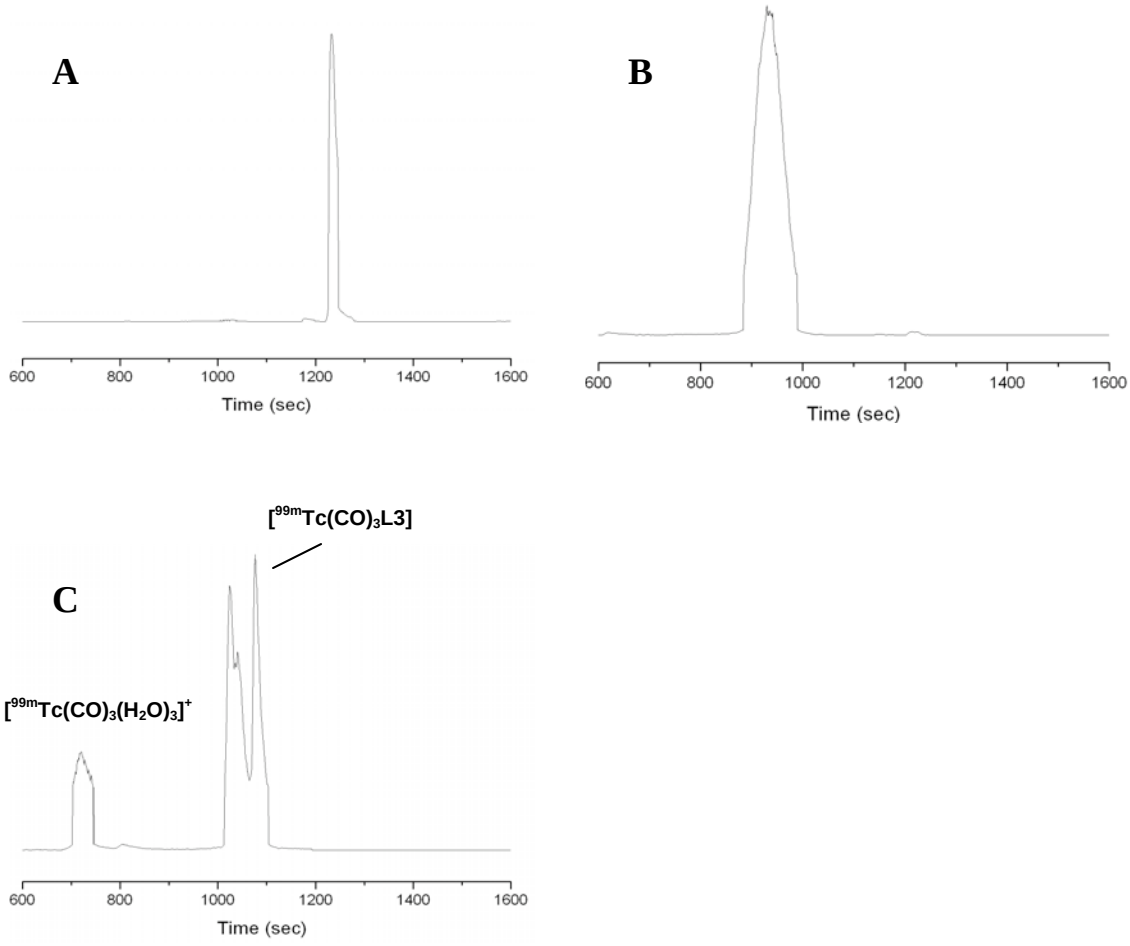

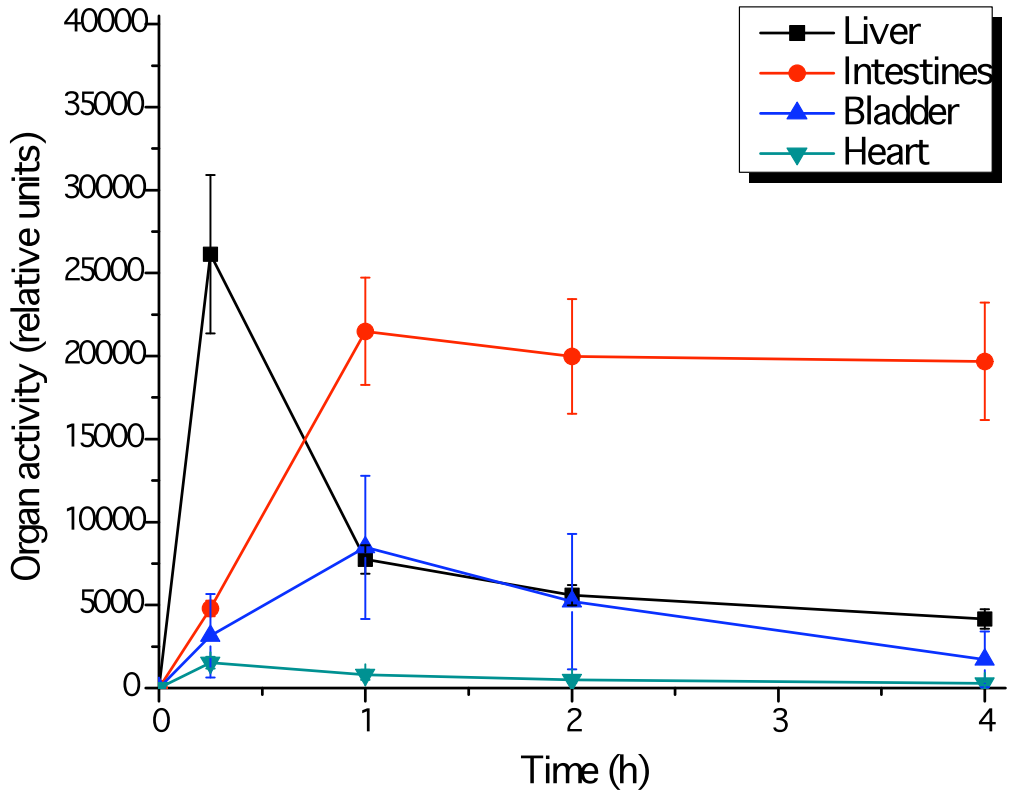

Figure S2. Curves of $^{99m}Tc(CO)_3L1$ levels in selected organs taken from the SPECT/CT images; the data points are the averaged value from 4 mice ± S.D.

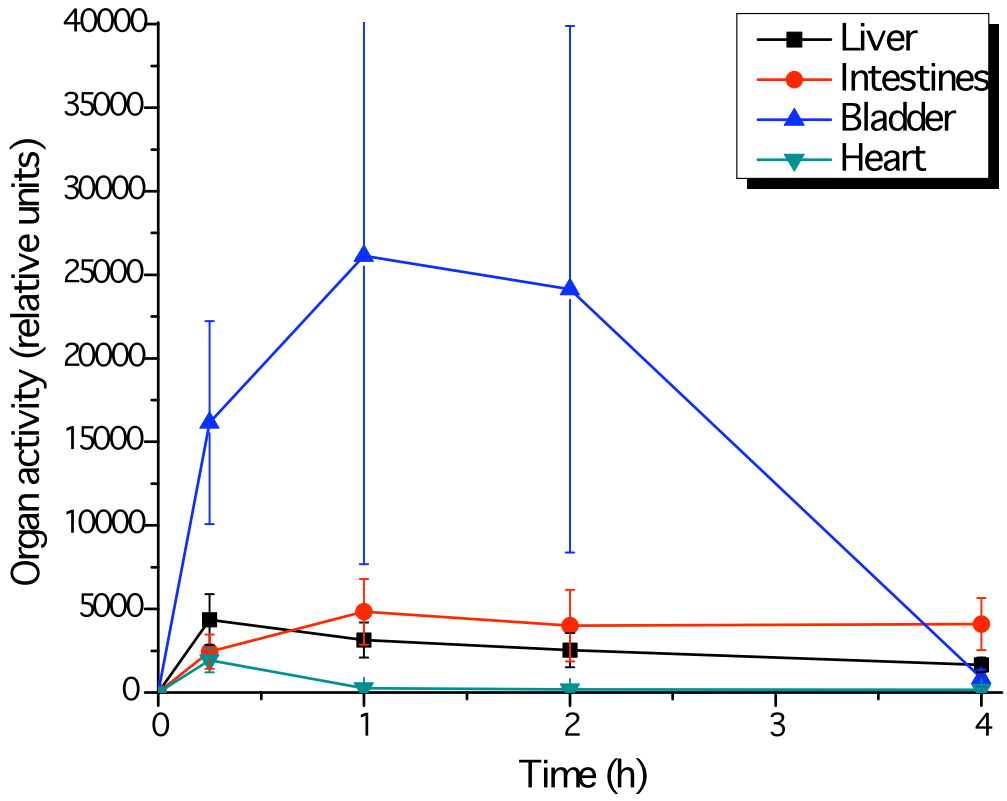

Figure S3. Curves of [^{99m}Tc(CO)$_3$L2]$^-$ levels in selected organs taken from the SPECT/CT images; the data points are the averaged value from 4 mice ± S.D.

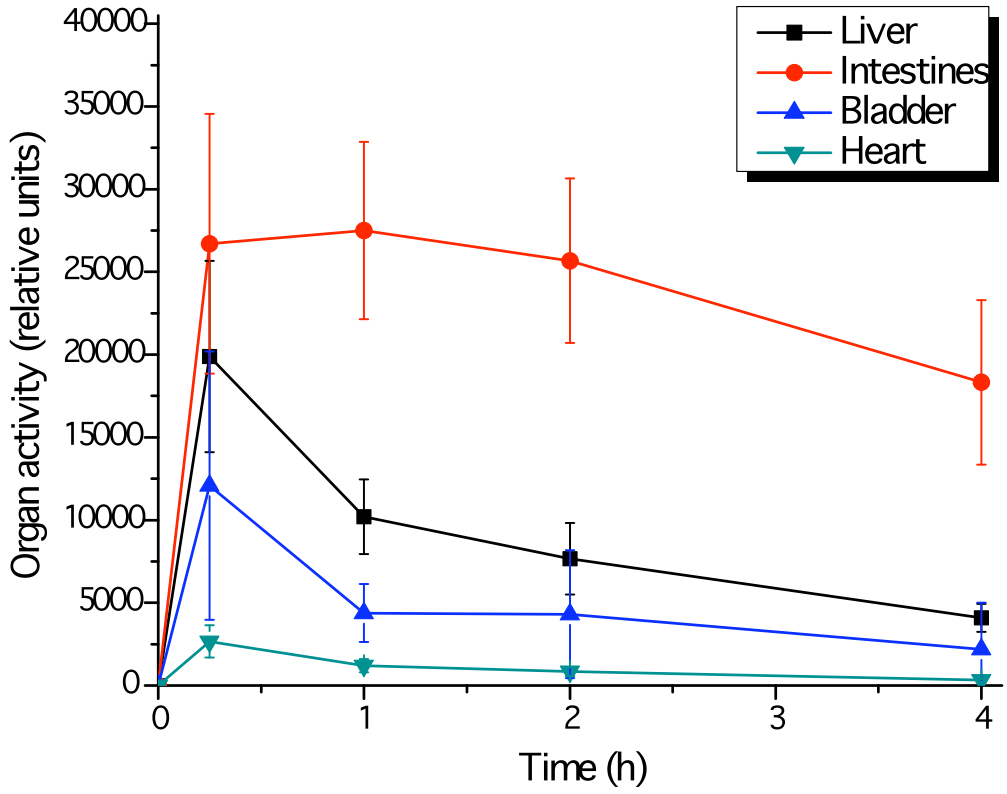

Figure S4. Curves of $^{99m}Tc(CO)_3L3$ levels in selected organs taken from the SPECT/CT images; the data points are the averaged value from 4 mice ± S.D.

Site-Specific, Covalent Labeling of Recombinant Antibody Fragments via Fusion to an Engineered Version of 6-*O*-Alkylguanine DNA Alkyltransferase

Florian Kampmeier,[†,#] Markus Ribbert,[†,#] Thomas Nachreiner,[‡] Sofia Dembski,[§] Florent Beaufils,[||] Andreas Brecht,[||] and Stefan Barth*[,†,⊥]

Fraunhofer Institute for Molecular Biology and Applied Ecology, Forckenbeckstrasse 6, 52074 Aachen, Germany, Institute for Neuropathology, University Hospital, RWTH Aachen University, Pauwelsstrasse 30, 52074 Aachen, Germany, Fraunhofer-Insitut für Silicatforschung ISC, 97082 Wuerzburg, Germany, Covalys Biosciences AG, Benkenstrasse 254, CH4108 Witterswil, Switzerland, and Department of Experimental Medicine and Immunotherapy, Helmholtz Institute for Biomedical Engineering, RWTH Aachen University, Pauwelsstrasse 20, 52074 Aachen, Germany. Received January 21, 2009; Revised Manuscript Received March 13, 2009

Recombinant antibodies are promising tools for a wide range of bioanalytical and medical applications. However, the chemical modification of such molecules can be challenging, which limits their broader utilization. Here we describe a universal method for the site-specific labeling of antibody fragments and protein ligands by genetically fusing them to an engineered version of the human DNA-repair enzyme *O*(6)-alkyllguanine DNA alkyltransferase (AGT), known as SNAP-Tag (*1*−*3*). Substrates containing *O*(6)-benzylguanine are covalently bound to the fusion proteins via a stable thioether bond in a rapid and highly specific self-labeling reaction. The coupling is site-directed, allowing the design and synthesis of antibody conjugates with predefined stoichiometry. We cloned a series of ligand SNAP-Tag fusion proteins and expressed them in HEK 293T cells. The antibody/ligand-fusions were characterized by labeling with different fluorophores, labeling with biotin, or by coupling them to fluorescent nanobeads, followed by analysis by flow cytometry and confocal microscopy. All ligands retained their original antigen-binding properties when fused to the SNAP-Tag. The combination of recombinant antibodies or protein ligands with the SNAP-Tag facilitates simple and efficient covalent modification with a broad range of substrates, thus providing a useful and advantageous alternative to existing coupling strategies.

INTRODUCTION

Recombinant antibodies and protein ligands have many applications in nanobiotechnology, analytical assays, diagnosis, and therapy, but there is an increasing demand for efficient strategies to further functionalize these proteins. Available methods often rely on the random modification of sulfhydryl, amine, or carboxyl groups and thus have unpredictable side effects on the stability, solubility, and affinity of the modified proteins. Directed coupling via carbohydrate residues works well for many full-size antibodies, but this approach is not easily transferred to other recombinant proteins, particularly antibody fragments that lack glycan chains. Genetic engineering can be used to introduce or remove additional reactive groups, such as cysteine residues, but this requires laborious screening procedures to identify suitable positions on the antibody for modification, and complex chemistry may be necessary to achieve site-specific coupling (*4*−*7*). An alternative method for the site-specific labeling of proteins is the introduction of short peptide tags that function as label acceptor sites. Here the label is attached either through an intrinsic activity of the tag or the activity of an enzyme supplied in trans. Site-specific biotinylation, as mediated by the biotin holoenzyme synthetase BirA, allows tagged proteins to be combined with a broad range of avidin/streptavidin reagents but does not allow direct labeling (*8*−*10*). Proteins fused to the LUMIO-tag (a hexapeptide containing a tetracysteine motif) can be stained directly with dyes containing two arsenic atoms, but the modification is noncovalent and thus far limited to a small number of fluorescent dyes (*11, 12*). In addition the significant toxicity of arsenic prevents the application of this technology in vivo. When using recombinant antibodies for analytical, diagnostic, or therapeutic applications, it is useful to have a broad range of modification options available, facilitating the adaptation of particular antibodies to suit diverse purposes. The SNAP-Tag technology allows us to equip a given fusion partner with many different dyes, with biotin, or with other effector molecules. It also facilitates coupling to nanoparticles and directed immobilization on chemically modified surfaces. The Tag is derived from the human DNA-repair enzyme *O*(6)-alkylguanine DNA alkyltransferase (AGT) (*1*). It rapidly, specifically, and covalently binds substrates that contain *O*(6)-benzylguanine. The SNAP-Tag reacts with para-substituted *O*(6)-benzylguanine (BG) derivatives by transferring the substituted benzyl group to its active site through a nucleophilic substitution reaction while releasing free guanine. The technology has been applied in a variety of experimental systems, ranging from in-cell labeling of tagged proteins to the immobilization of proteins on chip surfaces (*3, 13*). We cloned and expressed a series of single-chain antibodies (scFv) and natural protein ligands as SNAP-Tag fusions, to develop a platform for the directed modification of these molecules (Figure 1). The fusion proteins were expressed efficiently in 293T and CHO cells and retained the antigen-binding properties of their parent ligands. To demonstrate the versatility of the method, we present fluorescence-activated cell

* Corresponding author. Phone: +49-241-6085.11060; fax: +49-241-6085.10000; e-mail: stefan.barth@ime.fraunhofer.de.
[†] Fraunhofer Institute for Molecular Biology and Applied Ecology.
[‡] Institute for Neuropathology, RWTH Aachen University.
[§] Fraunhofer-Insitut für Silicatforschung ISC.
[||] Covalys Biosciences AG.
[⊥] Helmholtz Institute for Biomedical Engineering, RWTH Aachen University.
[#] These authors contributed equally to this work.

10.1021/bc9000257 CCC: $40.75 © 2009 American Chemical Society
Published on Web 04/23/2009

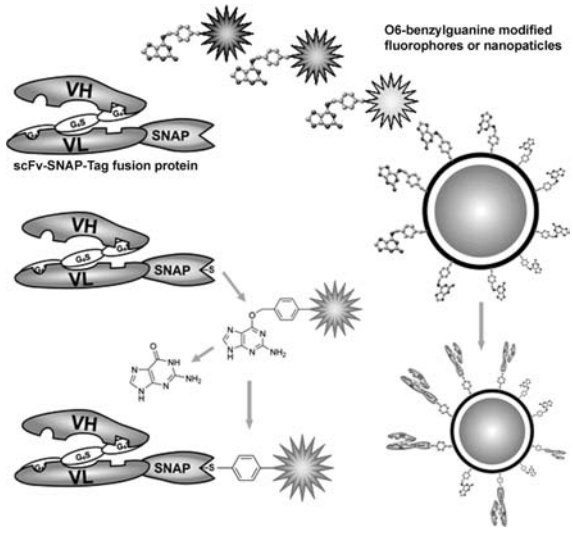

Figure 1. Site-directed modification of recombinant antibody fragments mediated by the SNAP-Tag. Para-substituted *O*(6)-benzylguanine (BG) derivatives are bound by transfer of the substituted benzyl group to the active site of the SNAP-Tag through a nucleophilic substitution reaction while releasing free guanine. Small compounds like fluorophores as well as nanometer- to micrometer-sized particles can be bound without affecting the antibody or protein ligand activity.

sorting (FACS) and confocal microscopy data for an anti-CD30 scFv and its natural ligand CD30L labeled with different dyes, labeled with biotin and coupled to fluorescent silica beads.

EXPERIMENTAL PROCEDURES

Bacterial Strains, Oligonucleotides, and Cloning. All plasmids were prepared using *E. coli* strain XL1-blue (*sup*E44 *hsd*R17 *rec*A1 *end*A1 *gyr*A46 *thi rel*A1 *lac*F0[*pro*AB$^+$ *lac*I^q *lac*ZDM15 Tn*10*(tet^r)]). Molecular cloning steps were performed by standard methods. Synthetic oligonucleotides were supplied by MWG (Martinsried, Germany). The source plasmid containing the SNAP-Tag sequence was provided by Covalys (Witterswil, Switzerland).

Single Chain Antibodies and Ligands. The ligands used to generate the SNAP-Tag fusions have been described (*14*−*18*). The CD30 receptor is highly overexpressed on Hodgkin Reed−Sternberg cells. The human CD30L as well as scFvKi4, a high affinity antibody fragment generated from a monoclonal anti-CD30 antibody, has been shown to target L540 Hodgkin lymphoma cells efficiently (*19*, *20*).

Construction of Mammalian Expression Vectors. We used a modified version of the pSecTac vector (*21*) and introduced the SNAP-Tag sequence to generate both N-terminal and C-terminal fusions. An internal SfiI restriction site was removed by using splice overlap PCR to introduce two silent mutations, allowing scFv fragments and other fusion partners to be introduced by standardized SfiI/NotI restriction.

Culture and Transfection of HEK-293T Cells. HEK-293T cells were transfected with RotiFect (Carl Roth GmbH; Karlsruhe, Germany) using 1 μg of plasmid DNA and 3 μL of RotiFect, according to the manufacturer's instructions. The expression and functionality of each fusion protein was tested 3 days after transfection by FACS analysis of the culture supernatant, using an antipenta-HisAlexa488 antibody (Qiagen). SNAP-Tag activity was tested by staining 10 μL of supernatant with a BG derivative modified with carboxyfluorescein (Vista-Green, Covalys) followed by sodium dodecyl sulfate polyacrylamide gel electrophoresis (SDS-PAGE) and visualization of the labeled protein with a UV-transilluminator. Further subcultivation of transfected cells and expression of the recombinant SNAP-Tag fusion proteins were carried out as previously described (*21*). Established transfected cultures were grown in RPMI 1640 medium supplemented with 10% (v/v) heat inactivated fetal calf serum (FCS), 50 μg/mL penicillin, 100 μg/mL streptomycin, 2 mM L-glutamine, and 100 μg/mL Zeocin (all components were obtained from Invitrogen, Carlsbad, CA). For the production of larger amounts of protein, triple flasks were inoculated and 500−1000 mL of supernatant was collected for purification.

Protein Purification. His-tagged proteins were purified from cell-free supernatants by Ni−NTA metal affinity chromatography as described (*21*). Larger volumes were purified on an Äkta FLPC system with a 5 mL Ni-NTA Superflow cartridge (Qiagen) after equilibration with 4× buffer (200 mM NaH_2PO_4, 1.2 M NaCl, 40 mM imidazole, pH 8). After elution, proteins were dialyzed against phosphate-buffered saline (PBS) containing 1 mM dithioerythritol. After concentration to 0.5−1 mg/mL (if necessary) with a 5 kDa MWCO VivaSpin Column (Sigma-Aldrich), ectoine was added as cryopreservative (*22*) to a final concentration of 50 mM and aliquots were stored at −20 °C until further use.

Protein Labeling with BG Derivatives of Organic Fluorophores or Biotin. Purified SNAP-Tag fusion proteins were conjugated with the BG-modified dyes (Covalys AG, Witterswil) by incubation in the dark with 1.5−3-fold molar excess of dye for 2 h at room temperature or overnight at 4 °C. Residual dye was removed by gel filtration chromatography using PD10 columns (GE) or dialysis. Alternatively, the conjugation was performed with the protein still bound to the Ni-NTA resin with one bed volume of a 2 μM dye solution in 1× Ni-NTA wash buffer (300 mM NaCl, 50 mM sodium phosphate, pH 7.5). The labeled protein was eluted with 500 mM imidazole after washing away residual dye.

Coupling efficacy was determined photometrically using the extinction coefficients of the corresponding dyes and the theoretical extinction coefficient of the fusion protein. Stained proteins were visualized after separation by SDS-PAGE with either a UV transilluminator (BioRad Gel Doc XR gel documentation) or with a CRi Maestro imaging system using the blue, red, and near-infrared filter sets. Biotinylation was performed by incubating the fusion proteins with a 2−5 fold molar excess of BG-Biotin using the same procedure described above.

Coupling SNAP-Tag Fusion Proteins to Luminescent Silica Beads. We used spherical silica nanoparticles labeled with carboxyrhodamine to demonstrate coupling of the antibodies. The particles were prepared using a modified Stöber synthesis method (*23*) and had an average diameter of 90 nm. Amine functions were introduced at the bead surface using bifunctional aminosilane (*24*). The average number of amino functionalities on the bead surface was determined with the fluorescamine test and adjusted to ∼320 functions per bead as described (*25*). To facilitate benzylguanine coupling, the beads were dispersed in dimethylformamide (DMF) and incubated with a 60-fold molar excess of BG-NHS (Covalys) over amino groups for 3 h at room temperature. The beads were washed three times with PBS (pH 7.4) and dispersed in the same buffer. For coupling, beads where dispersed in RPMI containing 10% FCS and 0.1% Tween 20 (R10-T) and sonicated to disrupt aggregates. Approximately 0.2 nmol of BG-beads was incubated with 50 μg of Ki4-SNAP (1 nmol) in 100 μL of R10-T for 2 h at room temperature. Coupled beads were washed four times with R10-T and dispersed in 200 μL of RPMI-10% FCS, and 60 μL of the bead preparation was used for analysis by flow cytometry and confocal microscopy. To block SNAP-Tag mediated coupling, Ki4-SNAP was incubated beforehand with a 3-fold molar excess of bromothenylpteridine (BTP, Covalys) for 1 h at room temperature.

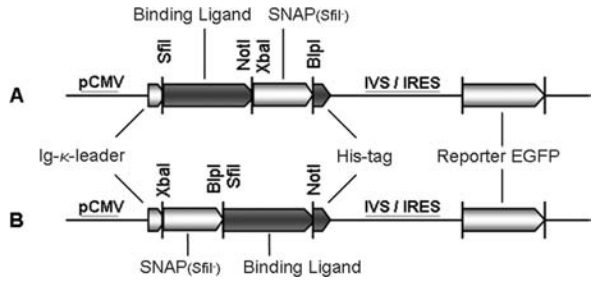

Figure 2. Expression cassettes for C-terminal (A) and N-terminal (B) SNAP-Tag fusions. The coding sequences for the protein ligands are introduced using SfiI/NotI either upstream or downstream of the *SNAP26m* gene, modified to delete an internal SfiI site. The fusion proteins are secreted into the culture supernatant of transfected cells and can be purified via the C-terminal His-tag.

Flow Cytometry. The labeled fusion-proteins were analyzed by flow cytometry with a FACSCalibur (Becton & Dickinson) and CellQuest software. The $CD30^+$ cell line L540 was used as the target for scFv Ki4-SNAP and SNAP-CD30L, whereas the $CD30^-$ histiocytic lymphoma cell line U937 was used as control. Approximately 4×10^5 cells were incubated in 300 μL of PBS containing 1 ng to 1 μg of labeled protein for 20 min on ice. For detection of biotinylated proteins, cells were washed and incubated with 1.5 μg/mL StreptavidinDyLight^{488} for 20 min on ice. The cells were then washed twice with 1.8 mL of PBS in a conventional cell washer.

Confocal Microscopy. All images were taken with a LEICA confocal microscope (TCS SP5). Cells were prepared as described above for flow cytometry. The cells were resuspended in 30 μL of PBS, and 10 μL of the cell suspension was incubated for 5 min with 2 μL of a 1:100 diluted Draq5 solution (Biostatus, Shepshed, UK) to counterstain the nucleus.

RESULTS

Expression of SNAP-Tag Fusion Proteins in HEK 293 Cells. We cloned and expressed several N- and C-terminal SNAP-fusion proteins by transfecting 293T cells and selecting transformants on the basis of Zeocin resistance and reporter GFP fluorescence. To facilitate cloning, the internal SfiI restriction site in the vector was removed by splice overlap PCR, and the modified SNAP-Tag sequence was inserted into different pMS vectors for the generation of C- and N-terminal fusions (Figure 2). A selection of the functionally expressed constructs is shown in Table 1. Ki4-SNAP and SNAP-EGF expression was also assessed in CHO-K1 cells. Active protein could be purified from the culture supernatant, but more intensive selection and screening was required and expression levels as achieved with the 293T cells were not reached. The SNAP-Tag was active irrespective of the position in the fusion protein. The single chain antibodies were usually used in the C-terminal position, in accordance with other fusion proteins based on these ligands. In contrast, the ligands CD30L and EGF were functional only with the SNAP-Tag at the N-terminal position. High expression levels were observed for most of the fusion proteins, e.g., up to

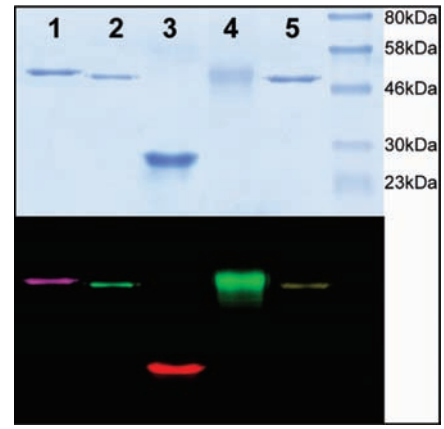

Figure 3. Purified SNAP-Tag fusion proteins labeled with different fluorophores. (1) scFv425-SNAP-782; (2) scFvKi4-SNAP-VistaGreen; (3) SNAP-EGF-Alexa Fluor647; (4) SNAP-CD30L-505 (glycosylation leads to band broadening and an increase in size); (5) scFvH22-SNAP-TMR-star. Approximately 1 μg of labeled protein was separated by SDS-PAGE and visualized with a CRi Maestro Imaging System (lower part) and then stained with coomassie brilliant blue (upper part). Different dye spectra were unmixed using Maestro software.

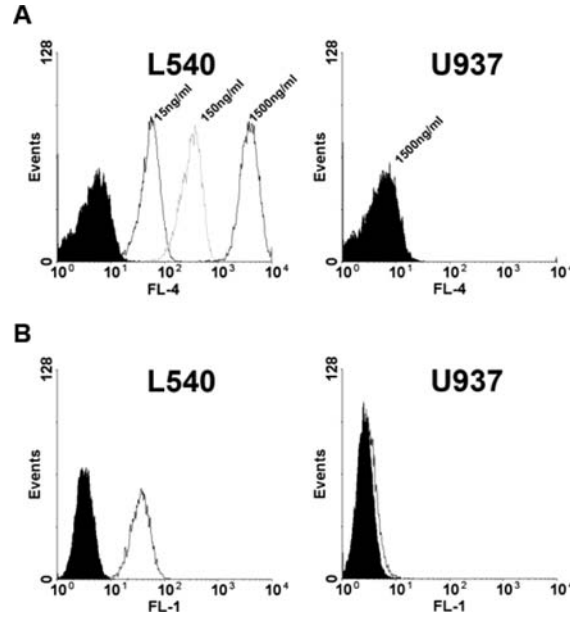

Figure 4. FACS analysis with Ki4-SNAP and SNAP-CD30L. (A) Increasing amounts of Ki4-SNAP labeled with BG-Alexa Fluor647 on L540 ($CD30^+$) and U937 ($CD30^-$) cells. (B) SNAP-CD30L labeled with BG-biotin and detected with StreptavidinDyLight488.

17.5 mg/L culture supernatant for scFv 425-SNAP, and 5−10 mg/L for the others (Table 1). Comparisons of the fusion proteins and their parental counterparts indicated that the SNAP-Tag did not have a negative impact on expression levels. Stability was not tested in detail for every fusion protein, but scFv Ki4-SNAP showed no significant loss of binding activity

Table 1. Selection of Successfully Expressed Ligand−SNAP-Tag Fusion Proteins

fusion protein	target	tag position	expression rate in 293T cells	binding confirmed on
scFv Ki4-SNAP (49 kDa)	CD30	N-term.	>10 mg/L	L540
SNAP-CD30L (41 kDa + glycosylation)	CD30	C-term.	~5 mg/L	L540
scFv 425-SNAP (48 kDa)	EGFR	N-term.	>15 mg/L	A431/L3.6pl
SNAP-EGF (28 kDa)	EGFR	C-term.	>10 mg/L	A431/L3.6pl
SNAP-Myelin Oligodendrocyte Glycoprotein (MOG) (38 kDa)	anti MOG Ig	N-term.	>10 mg/L	8.18-C5 murine hybridoma cells
Annexin V-SNAP (59 kDa)	Phosphatidyl-serine	N-term. or C-term.	nd	apoptotic L3.6pl cells
scFv H22-SNAP (48 kDa)	CD64	N-term.	~ 8 mg/L	U937
scFv RFT5-SNAP (48 kDa)	CD25	N-term.	nd	L540

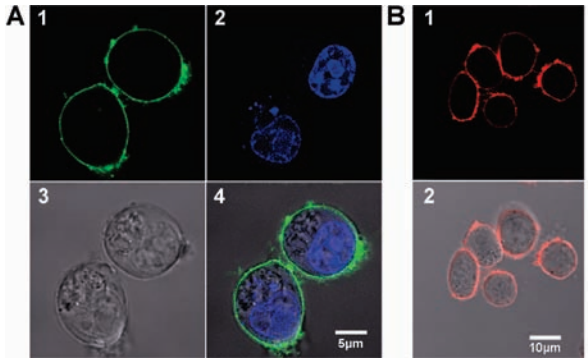

Figure 5. Confocal microscopy of Ki4-SNAP and SNAP-CD30L on $CD30^+$ L540 cells. (A) Ki4-SNAP labeled with BG-505. 1= 505 fluorescence signal, 2 = nucleus stained with Draq5, 3 = transmission light picture, 4 = overlay of 1−3. (B) SNAP-CD30L labeled with BG-Alexa Fluor 647. One = Alexa Fluor 647 fluorescence signal, 2 = overlay of fluorescence and transmission light picture. The high CD30 expression on the L540 cell surface results in a strong membrane staining mediated by the Ki4 single chain antibody, as well as the natural human CD30L, fusion protein.

or SNAP-Tag activity when concentrated at ∼1 mg/mL and stored at 4 °C for 4 weeks. All the constructs we tested were still active after at least 4 months when stored at −20 °C.

Labeling of SNAP-Tag Fusion Proteins with Organic Fluorophores. Figure 3 shows a selection of five fusion proteins labeled with different fluorophores and stained with Coomassie Brilliant Blue after separation by SDS-PAGE. Coupling efficiencies were independent of the SNAP-Tag fusion partner. We achieved rates of 90−100% efficiency after overnight incubation using different constructs and different dyes (BG-Alexa Fluor647, BG-TMR-star, BG-505 and BG-Vista-Green, BG-782), and in most cases 60−70% efficiency after 1 h at room temperature. A 1.5-fold molar excess of dye was sufficient to achieve these labeling efficiencies.

Confocal Microscopy and FACS Analysis. To evaluate the activities of the different fusion proteins, we carried out FACS analyses with proteins purified from the supernatant of transfected 293T cells and stained with various BG-modified fluorescent dyes. All the labeled proteins we tested gave a strong fluorescence signal on the corresponding target cell line but not on control cells. To exemplify these results, FACS and confocal microscopy data are shown for the anti-CD30 scFv Ki4-SNAP and the corresponding human ligand SNAP-CD30L. For Ki4-SNAP labeled with BG-Alexa Fluor647, less than 15 ng/mL was sufficient to detect binding to target cells by flow cytometry (Figure 4A). Confocal microscopy of Ki4-SNAP labeled with BG-505 confirmed homogeneous membrane staining on L540 cells (Figure 5A). A similar staining pattern was observed with the natural ligand of CD30, CD30L, labeled with Alexa Fluor647 (Figure 5B). We also used BG-biotin to label the fusion proteins, and FACS analysis of cells treated with biotinylated CD30L followed by StreptavidinDyLight 488 is shown in Figure 4B.

SNAP-Tag Coupling to Silica Beads. To test the versatility of the coupling procedure, we used carboxyrhodamine-labeled silica beads and modified them with an *N*-hydroxysuccinimide-ester derivativeof BG (BG-GLA-NHS) via surface amino groups. The anti-CD30 scFv Ki4 was coupled to these beads, and the labeling and binding properties were analyzed by FACS (data not shown) and confocal microscopy. The bead conjugates showed specific labeling of $CD30^+$ L540 cells (Figure 6 A) while only minimal background was observed when the SNAP-Tag was blocked with bromothenylpteridine (Figure 6 B). No binding of the beads was observed on $CD30^-$ U937 cells (not shown). The multivalency of the conjugated beads led to the

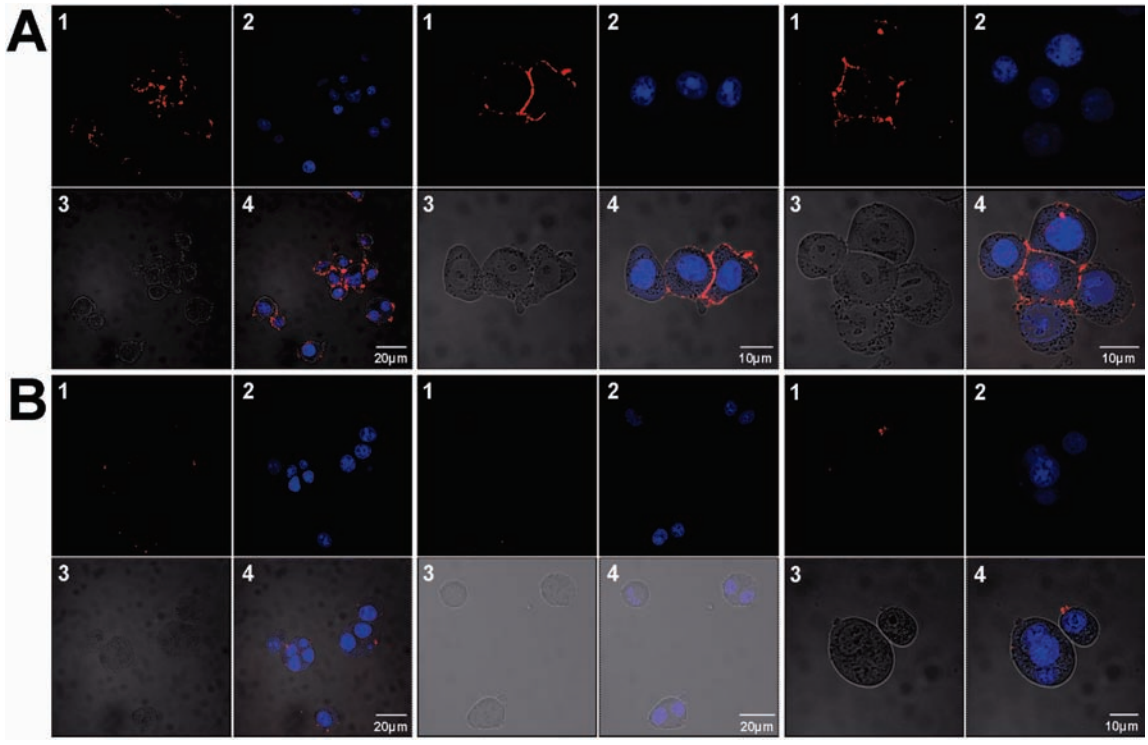

Figure 6. Confocal microscopy with Ki4-SNAP coupled to benzylguanine-modified fluorescent beads on L540 cells. (A) Ki4-SNAP-coupled beads. (B) Beads incubated with Ki4-SNAP with the SNAP-Tag previously blocked with bromothenylpteridine. In each panel, 1 = signal from carboxyrhodamine silica beads, 2 = nucleus stained with Draq5, 3 = transmission light picture, and 4 = overlay of 1−3. The Ki4-SNAP coupled beads bind to and lead to aggregation of the L540 target cells while only minimal attachment of bead aggregates is observed with the blocked Ki4-SNAP-Tag.

formation of cell aggregates, linking several cells via their surface receptors.

DISCUSSION

To demonstrate the feasibility of directed coupling of protein ligands and antibodies using the SNAP-Tag method, we cloned and expressed a series of SNAP-Tag fusion proteins containing either a single chain antibody fragment or a corresponding natural ligand directed against well-characterized tumor markers. All constructs listed in Table 1 retained both the binding activity of the parental molecule and SNAP-Tag activity. The fact that such activity could be demonstrated for a range of different ligand formats, the extracellular domains of membrane glycoproteins (CD30L, MOG), a secreted peptide ligand (EGF), and engineered antibody fragments, provides ample evidence for the broad applicability of this method. SNAP-Tag fusions have previously been expressed in *E. coli*, yeast, and mammalian cells (*13*, *26*) but never with the intention of producing large amounts of a reagent for further applications. Expression in 293T cells provides a convenient system that allows rapid screening of the fusion proteins, since 293T cells are easy to transfect and expression of the target protein can be assessed directly by correlation with eGFP expression levels (*21*). The average yield of purified fusion protein was 10 mg/L supernatant (Table 1), and this was achieved without further enrichment for high-performance clones, indicating that much higher yields should be possible.

Several different approaches have been used to engineer antibody fragments for site-specific coupling/labeling, including the introduction of additional cysteine residues at the C-terminus (*27*) or at the end of each linker connecting the V_H and V_L chains in a scFv diabody (*28*). The site-specific immobilization of a scFv fusion protein by transglutaminase has also been reported (*29*) as well as the directed biotinylation of different antibody fragments by coexpression with the bacterial biotin ligase BirA in HEK293 cells (*30*).

Despite these successes, it would be advantageous to increase the versatility of site-specific labeling systems to allow diverse labels to be used with the same parental protein. Labeling with the SNAP-tag is advantageous because large quantities of very pure ligands can be produced and made directly available for coupling, and the activity of the ligand is not affected by the fusion or by coupling to a substrate. Furthermore, conjugation is covalent, stable, is site-specific, and has a predefined stoichiometry. The approach is not limited to a single class of recombinant proteins but is applicable to a wide range of protein ligands.

The targeted delivery of nanoparticles for imaging and drug delivery has become a very active area of biomedical research. Quantum dots, iron oxide or gold nanoparticles, liposomes and polymers have all been equipped with antibodies for targeted delivery in vivo (*31*−*33*). The coupling strategy described here enables the efficient modification of such particles with recombinant proteins, as demonstrated for BG-functionalized silica nanobeads.

By genetically fusing antibody fragments and other targeting ligands to the SNAP-Tag, we have developed and evaluated a new platform for the directed modification of diverse protein molecules. A series of different ligands has been cloned, expressed, and successfully labeled with several fluorophores, biotin, and silica nanoparticles, showing the versatility of the approach. Experimental data is shown for a single chain antibody fragment directed against CD30 and the natural human ligand CD30L. This new platform could have a significant impact on the labeling of recombinant proteins used as reagents in nanobiotechnology, molecular biology, and cell biology, as well as proteins used in analytical assays, disease diagnosis, and therapy.

ACKNOWLEDGMENT

We would like to thank Dr. Richard Twyman for the critical reading of the manuscript.

LITERATURE CITED

(1) Gronemeyer, T., Chidley, C., Juillerat, A., Heinis, C., and Johnsson, K. (2006) Directed evolution of O6-alkylguanine-DNA alkyltransferase for applications in protein labeling. *Protein Eng. Des. Sel. 19*, 309–16.

(2) Juillerat, A., Heinis, C., Sielaff, I., Barnikow, J., Jaccard, H., Kunz, B., Terskikh, A., and Johnsson, K. (2005) Engineering substrate specificity of O6-alkylguanine-DNA alkyltransferase for specific protein labeling in living cells. *Chembiochem 6*, 1263–9.

(3) Keppler, A., Kindermann, M., Gendreizig, S., Pick, H., Vogel, H., and Johnsson, K. (2004) Labeling of fusion proteins of O6-alkylguanine-DNA alkyltransferase with small molecules in vivo and in vitro. *Methods 32*, 437–44.

(4) Junutula, J. R., Bhakta, S., Raab, H., Ervin, K. E., Eigenbrot, C., Vandlen, R., Scheller, R. H., and Lowman, H. B. (2008) Rapid identification of reactive cysteine residues for site-specific labeling of antibody-Fabs. *J. Immunol. Methods 332*, 41–52.

(5) McDonagh, C. F., Turcott, E., Westendorf, L., Webster, J. B., Alley, S. C., Kim, K., Andreyka, J., Stone, I., Hamblett, K. J., Francisco, J. A., and Carter, P. (2006) Engineered antibody-drug conjugates with defined sites and stoichiometries of drug attachment. *Protein Eng. Des. Sel. 19*, 299–307.

(6) Messerschmidt, S. K., Kolbe, A., Muller, D., Knoll, M., Pleiss, J., and Kontermann, R. E. (2008) Novel single-chain Fv′ formats for the generation of immunoliposomes by site-directed coupling. *Bioconjugate Chem. 19*, 362–9.

(7) Yamamoto, Y., Tsutsumi, Y., Yoshioka, Y., Nishibata, T., Kobayashi, K., Okamoto, T., Mukai, Y., Shimizu, T., Nakagawa, S., Nagata, S., and Mayumi, T. (2003) Site-specific PEGylation of a lysine-deficient TNF-alpha with full bioactivity. *Nat. Biotechnol. 21*, 546–52.

(8) Beckett, D., Kovaleva, E., and Schatz, P. J. (1999) A minimal peptide substrate in biotin holoenzyme synthetase-catalyzed biotinylation. *Protein Sci. 8*, 921–9.

(9) Chapman-Smith, A., and Cronan, J. E., Jr. (1999) In vivo enzymatic protein biotinylation. *Biomol. Eng. 16*, 119–25.

(10) Tirat, A., Freuler, F., Stettler, T., Mayr, L. M., and Leder, L. (2006) Evaluation of two novel tag-based labelling technologies for site-specific modification of proteins. *Int. J. Biol. Macromol. 39*, 66–76.

(11) Griffin, B. A., Adams, S. R., and Tsien, R. Y. (1998) Specific covalent labeling of recombinant protein molecules inside live cells. *Science 281*, 269–72.

(12) Hearps, A. C., Pryor, M. J., Kuusisto, H. V., Rawlinson, S. M., Piller, S. C., and Jans, D. A. (2007) The biarsenical dye Lumio exhibits a reduced ability to specifically detect tetracysteine-containing proteins within live cells. *J. Fluoresc. 17*, 593–7.

(13) Kindermann, M., George, N., Johnsson, N., and Johnsson, K. (2003) Covalent and selective immobilization of fusion proteins. *J. Am. Chem. Soc. 125*, 7810–1.

(14) Barth, S., Huhn, M., Wels, W., Diehl, V., and Engert, A. (1998) Construction and in vitro evaluation of RFT5(scFv)-ETA′, a new recombinant single-chain immunotoxin with specific cytotoxicity toward CD25+ Hodgkin-derived cell lines. *Int. J. Mol. Med. 1*, 249–56.

(15) Bruell, D., Bruns, C. J., Yezhelyev, M., Huhn, M., Muller, J., Ischenko, I., Fischer, R., Finnern, R., Jauch, K. W., and Barth, S. (2005) Recombinant anti-EGFR immunotoxin 425(scFv)-ETA′ demonstrates anti-tumor activity against disseminated human pancreatic cancer in nude mice. *Int. J. Mol. Med. 15*, 305–13.

(16) Nachreiner, T., Kampmeier, F., Thepen, T., Fischer, R., Barth, S., and Stocker, M. (2008) Depletion of autoreactive B-lymphocytes by a recombinant myelin oligodendrocyte glycoprotein-based immunotoxin. *J. Neuroimmunol. 195*, 28–35.
(17) Stahnke, B., Thepen, T., Stocker, M., Rosinke, R., Jost, E., Fischer, R., Tur, M. K., and Barth, S. (2008) Granzyme B-H22(scFv), a human immunotoxin targeting CD64 in acute myeloid leukemia of monocytic subtypes. *Mol. Cancer Ther. 7*, 2924–32.
(18) Stocker, M., Pardo, A., Hetzel, C., Reutelingsperger, C., Fischer, R., and Barth, S. (2008) Eukaryotic expression and secretion of EGFP-labeled annexin A5. *Protein Expr. Purif. 58*, 325–31.
(19) Huhn, M., Sasse, S., Tur, M. K., Matthey, B., Schinkothe, T., Rybak, S. M., Barth, S., and Engert, A. (2001) Human angiogenin fused to human CD30 ligand (Ang-CD30L) exhibits specific cytotoxicity against CD30-positive lymphoma. *Cancer Res. 61*, 8737–42.
(20) Klimka, A., Barth, S., Matthey, B., Roovers, R. C., Lemke, H., Hansen, H., Arends, J. W., Diehl, V., Hoogenboom, H. R., and Engert, A. (1999) An anti-CD30 single-chain Fv selected by phage display and fused to Pseudomonas exotoxin A (Ki-4(scFv)-ETA′) is a potent immunotoxin against a Hodgkin-derived cell line. *Br. J. Cancer 80*, 1214–22.
(21) Stocker, M., Tur, M. K., Sasse, S., Krussmann, A., Barth, S., and Engert, A. (2003) Secretion of functional anti-CD30-angiogenin immunotoxins into the supernatant of transfected 293T-cells. *Protein Expr. Purif. 28*, 211–9.
(22) Barth, S., Huhn, M., Matthey, B., Klimka, A., Galinski, E. A., and Engert, A. (2000) Compatible-solute-supported periplasmic expression of functional recombinant proteins under stress conditions. *Appl. Environ. Microbiol. 66*, 1572–9.
(23) Stöber, W., Fink, A., and Bohn, E. (1968) Controlled growth of monodisperse silica spheres in the micron size range. *J. Colloid Interface Sci.* 62–69.
(24) Gellermann, C., Storch, W., and Wolter, H. (1997) Synthesis and characterization of the organic surface modifications of monodisperse colloidal silica. *J. Sol-Gel Sci. Technol. 8*, 173–6.
(25) Shirahata, N., Furumi, S., Masuda, Y., Hozumi, A., and Sakka, Y. (2008) Fluorescence detection and imaging of amino-functionalized organic monolayer. *Thin Solid Films* 2541–2546.
(26) Keppler, A., Gendreizig, S., Gronemeyer, T., Pick, H., Vogel, H., and Johnsson, K. (2003) A general method for the covalent labeling of fusion proteins with small molecules in vivo. *Nat. Biotechnol. 21*, 86–9.
(27) Natarajan, A., Xiong, C. Y., Albrecht, H., DeNardo, G. L., and DeNardo, S. J. (2005) Characterization of site-specific ScFv PEGylation for tumor-targeting pharmaceuticals. *Bioconjugate Chem. 16*, 113–21.
(28) Sirk, S. J., Olafsen, T., Barat, B., Bauer, K. B., and Wu, A. M. (2008) Site-Specific, Thiol-mediated conjugation of fluorescent probes to cysteine-modified diabodies targeting CD20 or HER2. *Bioconjugate Chem. 19*, 2527–34.
(29) Sugimura, Y., Ueda, H., Maki, M., and Hitomi, K. (2007) Novel site-specific immobilization of a functional protein using a preferred substrate sequence for transglutaminase 2. *J. Biotechnol. 131*, 121–7.
(30) Predonzani, A., Arnoldi, F., Lopez-Requena, A., and Burrone, O. R. (2008) In vivo site-specific biotinylation of proteins within the secretory pathway using a single vector system. *BMC Biotechnol. 8*, 41.
(31) Cormode, D. P., Skajaa, T., Fayad, Z. A., and Mulder, W. J. (2009) Nanotechnology in Medical Imaging. Probe Design and Applications, *Arterioscler., Thromb., Vasc. Biol.*, in press.
(32) Smith, A. M., Duan, H., Mohs, A. M., and Nie, S. (2008) Bioconjugated quantum dots for in vivo molecular and cellular imaging. *Adv. Drug Delivery Rev. 60*, 1226–40.
(33) Sofou, S., and Sgouros, G. (2008) Antibody-targeted liposomes in cancer therapy and imaging. *Expert Opin. Drug. Delivery 5*, 189–204.

BC9000257

^{18}F, ^{64}Cu, and ^{68}Ga Labeled RGD-Bombesin Heterodimeric Peptides for PET Imaging of Breast Cancer

Zhaofei Liu,[†,‡] Yongjun Yan,[†] Shuanglong Liu,[†] Fan Wang,[‡] and Xiaoyuan Chen*[,†]

The Molecular Imaging Program at Stanford (MIPS), Department of Radiology, Biophysics, and Bio-X Program, Stanford University School of Medicine, 1201 Welch Road, Stanford, California 94305-5484, and Medical Isotopes Research Center, Peking University, Beijing, 100191, China. Received January 21, 2009; Revised Manuscript Received March 25, 2009

Radiolabeled RGD (Arg-Gly-Asp) and bombesin (BBN) radiotracers that specifically target integrin $\alpha_v\beta_3$ and gastrin releasing peptide receptor (GRPR) are both promising radiopharmaceuticals for tumor imaging. We recently designed and synthesized a RGD-BBN heterodimeric peptide with both RGD and BBN motifs in one single molecule. The ^{18}F-labeled RGD-BBN heterodimer exhibited dual integrin $\alpha_v\beta_3$ and GRPR targeting in a PC-3 prostate cancer model. In this study we investigated whether radiolabeled RGD-BBN tracers can be used to detect breast cancer by using microPET. Cell binding assay demonstrated that the high GRPR expressing breast cancer cells typically express low to moderate level of integrin $\alpha_v\beta_3$, while high integrin $\alpha_v\beta_3$ expressing breast cancer cells have negligible level of GRPR. We labeled RGD-BBN heterodimer with three positron emitting radionuclides ^{18}F, ^{64}Cu, and ^{68}Ga and investigated the corresponding PET radiotracers in both orthotopic T47D (GRPR$^+$/low integrin $\alpha_v\beta_3$) and MDA-MB-435 (GRPR$^-$/integrin $\alpha_v\beta_3^+$) breast cancer models. The three radiotracers all possessed in vitro dual integrin $\alpha_v\beta_3$ and GRPR binding affinity. The advantages of the RGD-BBN radiotracers over the corresponding BBN analogues are obvious for imaging MDA-MB-435 (GRPR$^-$/integrin $\alpha_v\beta_3^+$) tumor. ^{18}F-FB-PEG$_3$-RGD-BBN showed lower tumor uptake than ^{64}Cu-NOTA-RGD-BBN and ^{68}Ga-NOTA-RGD-BBN but was able to visualize breast cancer tumors with high contrast. Synthesis of ^{64}Cu-NOTA-RGD-BBN and ^{68}Ga-NOTA-RGD-BBN is much faster and easier than ^{18}F-FB-PEG$_3$-RGD-BBN. ^{64}Cu-NOTA-RGD-BBN showed prolonged tumor uptake but also higher liver retention and kidney uptake than ^{68}Ga-NOTA-RGD-BBN and ^{18}F-FB-PEG$_3$-RGD-BBN. ^{68}Ga-NOTA-RGD-BBN possessed high tumor signals but also relatively high background uptake compared with the other two radiotracers. In summary, the prosthetic labeling groups, chelators, and isotopes all have a profound effect on the tumor targeting efficacy and in vivo kinetics of the RGD-BBN tracers for dual integrin and GRPR recognition. Further development of suitably labeled RGD-BBN tracers for PET imaging of cancer is warranted.

INTRODUCTION

Breast cancer is the most frequently diagnosed malignancy among women in the Western world and the second leading cause of cancer-related deaths in women (*1*−*3*). Early detection of the primary breast cancer or its metastases at distant sites remains the best approach for improving the odds of curing or controlling this disease. The receptors overexpressed on the surface of cancer cells or uniquely expressed during the progress of cancer invasion and metastasis represent the promising targets for breast cancer diagnosis or therapy.

Gastrin-releasing peptide receptor (GRPR[1]) is one of the subtypes of the bombesin (BBN) receptors. GRPRs have been found to be massively overexpressed in several types of human cancers, such as lung cancer, colon cancer, gastric cancer, pancreas cancer, breast cancer, and prostate cancer (*4*, *5*). In the past decade, various bombesin and analogues were labeled with different isotopes like ^{99m}Tc, ^{111}In, ^{90}Y, ^{64}Cu, ^{177}Lu, ^{18}F, or ^{68}Ga and investigated for GRPR-positive tumor targeted imaging and therapy in both animal models and human trails (*6*−*18*). Several bombesin related radiotracers were also investigated for breast cancer imaging (*9*, *19*, *20*).

It is well documented that integrin $\alpha_v\beta_3$ plays an important role in the regulation of tumor growth, angiogenesis, local invasiveness, and metastatic potential (*21*−*23*). Integrin $\alpha_v\beta_3$ is up-regulated on the activated tumor endothelial cells and also highly expressed on some tumor cells such as glioblastoma, breast, and prostate tumors, malignant melanomas, and ovarian carcinomas (*24*). Radiolabeled RGD (Arg-Gly-Asp) peptides and analogues that specifically target integrin $\alpha_v\beta_3$ have been wildly tested for tumor imaging in preclinical and clinical studies (*25*−*32*). Most recently, two ^{18}F labeled RGD based tracers studied in breast cancer patients showed promising results (*28*, *33*).

For the one target based breast cancer imaging, the cell-surface receptor must be highly expressed in tumors relative to normal tissues, which may not occur during the whole process of tumor development and in all types of breast cancers. It is thus desirable to develop a new type of radiotracer that can target two types of receptors simultaneously, allowing tumor contrast when either or both receptor types are expressed. We recently designed and synthesized a RGD-BBN heterodimeric peptide that contain both the RGD and BBN motifs in one single molecule (Figure 1) (*34*, *35*). The ^{18}F labeled RGD-BBN heterodimer exhibited excellent in vivo kinetic and dual GRPR and integrin $\alpha_v\beta_3$-receptor targeting properties in a PC-3 prostate cancer xenograft model. Here, we test whether radiolabeled

* To whom correspondence should be addressed. Phone: 650-725-0950. Fax: 650-736-7925. E-mail: shawchen@stanford.edu.

† Stanford University School of Medicine.

‡ Peking University.

[1]Abbreviations: NOTA, 1,4,7-triazacyclononane-1,4,7-triacetic acid; GRPR, gastrin-releasing peptide receptor; PEG$_3$, 11-amino-3,6,9-trioxaundecanoic acid; Aca-BBN(7−14), Aca-Gln-Trp-Ala-Val-Gly-His-Leu-Met-NH$_2$; c(RGDyK), cyclo(Arg-Gly-Asp-D-Tyr-Lys); RGD-BBN, cyclo(Arg-Gly-Asp-D-Tyr-Lys)-Glu-(Aca-Gln-Trp-Ala-Val-Gly-His-Leu-Met-NH$_2$); SFB, *N*-succinimidyl-4-fluorobenzoate.

10.1021/bc9000245 CCC: $40.75 © 2009 American Chemical Society
Published on Web 04/20/2009

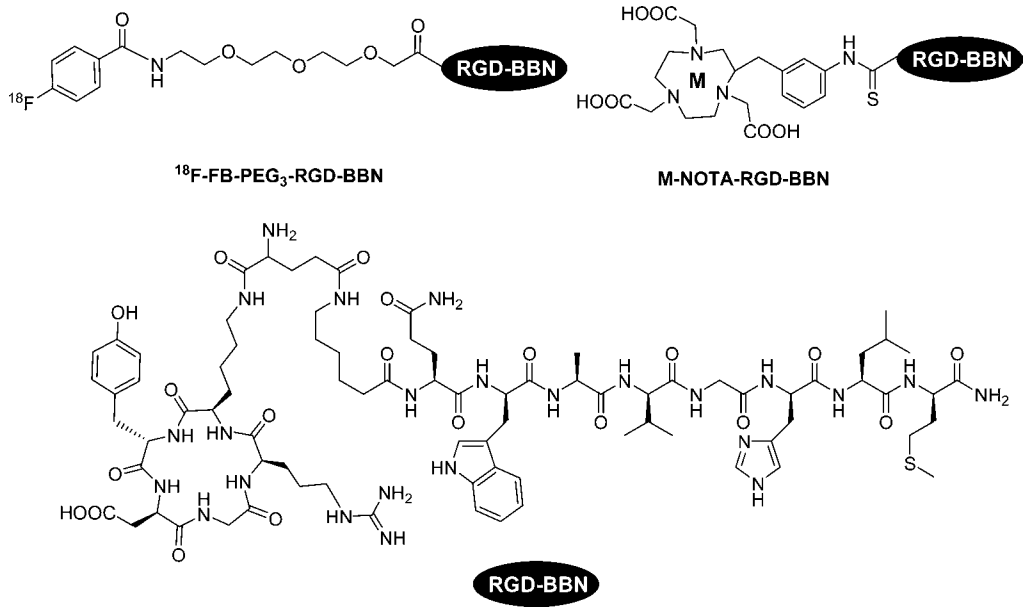

Figure 1. Chemical structures of ^{18}F-FB-PEG$_3$-RGD-BBN and NOTA-RGD-BBN with M corresponding to the chelated ^{64}Cu or ^{68}Ga. RGD-BBN: cyclo(Arg-Gly-Asp-D-Tyr-Lys)-Glu-(Aca-Gln-Trp-Ala-Val-Gly-His-Leu-Met-NH$_2$).

RGD-BBN heterodimers can be generally used for the diagnosis of breast cancers as well. In this study, we first screened the GRPR and integrin $\alpha_v\beta_3$ expression in various breast cancer cell lines. We found that among all the tested breast tumor cell lines, almost all the GRPR high expressing tumor cells (e.g., BT474 and T47D) have low to moderate level of integrin $\alpha_v\beta_3$, while the high integrin $\alpha_v\beta_3$ expressing tumor cells (e.g., MDA-MB-435 and MDA-MB-231) have low or undetectable level of GRPR. We thus chose two representative breast cancer models T47D (GRPR$^+$/low integrin $\alpha_v\beta_3$) and MDA-MB-435 (GRPR$^-$/integrin $\alpha_v\beta_3{}^+$) for in vivo test of ^{18}F-FB-PEG$_3$-RGD-BBN, ^{64}Cu-NOTA-RGD-BBN, and ^{68}Ga-NOTA-RGD-BBN (Figure 1).

EXPERIMENTAL PROCEDURES

All commercially obtained chemicals were of analytical grade and used without further purification. *p*-SCN-Bn-NOTA was purchased from Macrocyclics (Dallas, TX). Chelex 100 resin (50−100 mesh) was purchased from Sigma-Aldrich (St. Louis, MO). Water and all buffers were passed through Chelex 100 column before use in ^{64}Cu and ^{68}Ga labeling procedures to ensure that the aqueous buffer is heavy-metal-free. The syringe filter and polyethersulfone membranes (pore size, 0.22 μm; diameter, 13 mm) were obtained from Nalge Nunc International (Rochester, NY). The peptides Aca-BBN(7−14) and c(RGDyK) were synthesized by Peptides International (Louisville, KY). RGD-BBN heterodimer and PEG$_3$-Glu-RGD-BBN were synthesized from Aca-BBN and c(RGDyK) as we previously described (*35*). Na^{125}I was purchased from Perkin-Elmer (Waltham, MA). ^{125}I-[Tyr^4]BBN (2,000 Ci/mmol) was purchased from GE Healthcare (Piscataway, NJ). ^{64}Cu was obtained from University of Wisconsin (Madison, WI). No-carrier-added ^{18}F−F$^-$ was obtained from an in-house cyclotron (GE Healthcare). ^{68}Ga was obtained from a ^{68}Ge/^{68}Ga generator (Obninsk, Russia) and eluted with 0.1 N HCl. The reversed-phase high-performance liquid chromatography (HPLC) system was the same as previously reported (*27, 36*). For NOTA conjugates and ^{18}F-labeled peptides purification, a Vydac protein and peptide column (218TP510; 5 μm, 250 mm × 10 mm) was used with a flow rate of 5 mL/min. For analytical HPLC and ^{64}Cu or ^{68}Ga labeling purification, a Vydac 218TP54 column (5 μm, 250 mm × 4.6 mm) was used with a flow rate of 1 mL/min. The mobile phase was changed from 95% solvent A (0.1% trifluoroacetic acid [TFA] in water) and 5% solvent B (0.1% TFA in acetonitrile [ACN]) (0−2 min) to 35% solvent A and 65% solvent B at 32 min. The UV absorbance was monitored at 218 nm, and the identification of the peptides was confirmed on the basis of the UV spectrum acquired using a photodiode array (PDA) detector. The radioactivity was detected by model 105S single-channel radiation detector (Carroll and Ramsey Associates).

Synthesis of NOTA Conjugates. NOTA-BBN and NOTA-RGD-BBN conjugates were prepared as we previously described (*37*). In brief, a solution of 2 μmol of peptide (BBN or RGD-BBN) was mixed with 6 μmol of *p*-SCN-Bn-NOTA in 0.1 N $NaHCO_3$ solution (pH 9.0). After the mixture was stirred at room temperature for 5 h, the NOTA conjugates were isolated by semipreparative HPLC. The collected fractions were combined and lyophilized to afford the final product as a white powder. NOTA-bombesin (NOTA-BBN) was obtained in 72% yield with 22.1 min retention time on analytical HPLC. MALDI-TOF-MS was *m*/*z* 1504.0 for $[MH]^+$ ($C_{69}H_{102}N_{18}O_{16}S_2$, calculated molecular weight 1503.8). NOTA-RGD-BBN was obtained in 52% yield with 20.7 min retention time on analytical HPLC. MALDI-TOF-MS was *m*/*z* 2235.3 for $[MH]^+$ ($C_{102}H_{149}N_{27}O_{26}S_2$, calculated molecular weight 2234.6).

^{68}Ga Radiolabeling. The ^{68}Ga labeling procedure was conducted according to the methods we previously described (*37*). Briefly, 5 nmol of NOTA-BBN or NOTA-RGD-BBN peptide was dissolved in 500 μL of 0.1 M sodium acetate buffer and incubated with 4 mCi (148 MBq) of ^{68}Ga for 15 min at 40 °C. ^{68}Ga-NOTA-BBN or ^{68}Ga-NOTA-RGD-BBN product was then purified by analytical HPLC, and the radioactive peak containing the desired product was collected. After removal of the solvent by rotary evaporation, the activity was then reconstituted in PBS and passed through a 0.22 μm Millipore filter into a sterile multidose vial for in vitro and in vivo experiments. The labeling was done with 95% decay-corrected yield for NOTA-BBN (t_R = 21.8 min) and 90% for NOTA-RGD-BBN (t_R = 20.3 min).

^{64}Cu Radiolabeling. The ^{64}Cu labeling was performed as we previously described (*26, 38*). Briefly, 5 nmol of NOTA-BBN or NOTA-RGD-BBN dissolved in NaOAc buffer was labeled with 2 mCi (74 MBq) of ^{64}Cu for 15 min at 40 °C. The labeled

peptides were then purified by analytical HPLC. The radioactive peak containing the desired product was collected and rotary evaporated to remove the solvent. The products were then formulated in phosphate-buffered saline (PBS) and passed through a 0.22-μm Millipore filter into a sterile multidose vial for in vitro and in vivo experiments. The labeling was done with 94% decay-corrected yield for NOTA-BBN ($t_R = 21.4$ min) and 92% for NOTA-RGD-BBN ($t_R = 20.5$ min).

^{18}F-Radiolabeling. The detailed labeling procedure was reported previously (*35*). PEG_3-RGD-BBN or BBN was labeled with ^{18}F using *N*-succinimidyl-4-^{18}F-fluorobenzoate (^{18}F-SFB) as the synthon. The desired fractions containing ^{18}F-FB-PEG_3-RGD-BBN or ^{18}F-FB-BBN were combined and rotary evaporated to dryness, respectively. The products were then passed through a 0.22 μm Millipore filter into a sterile multidose vial for in vitro and in vivo experiments.

Cell Lines and Animal Models. The MDA-MB-231, MDA-MB-468, BT-474, BT-20, T47D, MCF-7, and MDA-MB-435 human breast cancer cell lines, U87MG human glioblastoma cell line, and PC-3 human prostate carcinoma cell line were all obtained from the American Type Culture Collection (ATCC, Manassas, VA) and maintained under standard conditions according to ATCC. Animal procedures were performed according to a protocol approved by the Stanford University Institutional Animal Care and Use Committee. The MDA-MB-435 tumor model was established by orthotopic injections of 5×10^6 cells into the right mammary fat pad of female athymic nude mice. For T47D tumor model establishment, the female nude mice were first subcutaneously implanted with 60-day release 17β-estradiol pellets (Innovative Research of America, Sarasota, FL) in the left neck. One day after the estradiol implantation, 1×10^7 T47D cells were orthotopically injected into the right mammary fat pad of the nude mice. The mice were subjected to microPET studies when the tumor volume reached 100−300 mm^3 (2−3 weeks for MDA-MB-435 and 4−5 weeks for T47D).

Cell Binding Assay. ^{125}I-[Tyr4]BBN and ^{125}I-c(RGDyK) were used as the radioligands to detect the GRPR and integrin $\alpha_v\beta_3$ receptor levels on the various breast cancer cells, respectively. We labeled c(RGDyK) with Na^{125}I and purified it with HPLC according to our previously described method (*39*). The ^{125}I-c(RGDyK) was prepared in high specific activity (~1200 Ci/mmol). Different breast cancer cells were seeded in the 96-well multiscreen DV plates (10^6 cells/well) and then incubated with ~30,000 cpm ^{125}I-[Tyr^4]BBN or ^{125}I-c(RGDyK) for 2 h at room temperature with or without excess doses of cold Acta-BBN(7−14) or c(RGDyK) as blocking agents. After the mixture was washed with PBS, hydrophilic PVDF filters were collected and the radioactivity was determined using a γ counter (Packard, Meriden, CT). Results were expressed as percent added dose per million cells (% AD/10^6 cells). Experiment was repeated twice with five parallel samples.

The integrin $\alpha_v\beta_3$ receptor-binding affinity of NOTA-RGD-BBN and FB-PEG_3-RGD-BBN was determined by competition binding assay using ^{125}I-c(RGDyK) as the radioligand on integrin $\alpha_v\beta_3$ high-expressing U87MG cells as we previously described (*26*). The GRPR receptor-binding affinity of NOTA-RGD-BBN and FB-PEG_3-RGD-BBN was determined by competition binding assay using ^{125}I-[Tyr^4]BBN as the radioligand on GRPR high-expressing PC-3 cells as we previously described (*10*). The best-fit 50% inhibitory concentration (IC_{50}) values were calculated by fitting the data with nonlinear regression using Graph-Pad Prism (GraphPad Software, Inc.). Experiments were performed twice with triplicate samples.

Immunofluorescent Staining. The expression of GRPR, human integrin $\alpha_v\beta_3$, and murine integrin β_3 on T47D and MDA-MB-435 tumor tissues was detected by immunofluorescent staining. Briefly, frozen T47D and MDA-MB-435 tumor slices (5 μm thickness) from the tumor-bearing nude mice were fixed with ice-cold acetone, rinsed with PBS, and blocked with 10% goat serum for 30 min at room temperature. The slices were incubated with goat anti-GRPR antibody (1:100; Santa Cruz Biotechnology, Santa Cruz, CA), humanized antihuman integrin $\alpha_v\beta_3$ antibody Abegrin (MedImmune, Gathersberg, MD, 20 μg/mL) (*40*) with FITC-conjugated donkey antigoat, Cy3-conjugated donkey antihuman, and FITC-conjugated goat antihamster secondary antibodies (1:200; Jackson Immuno-Research Laboratories, West Grove, PA), respectively.

Cell Uptake Studies. The cell uptake studies were performed as we previous described with some modifications (*10, 34, 35*) the day before experiment to allow adherence. Cells were incubated with ^{18}F-FB-PEG_3-RGD-BBN, ^{64}Cu-NOTA-RGD-BBN, or ^{68}Ga-NOTA-RGD-BBN (~18 kBq/well) at 37 °C for 15, 30, 60, and 120 min. Tumor cells were then washed three times with chilled PBS and harvested by trypsinization with 0.25% trypsin/0.02% EDTA (Invitrogen, Carlsbad, CA). The cells suspensions were collected and measured in a γ counter (Packard, Meriden, CT). The cell uptake was expressed as the percent added dose (% AD) after decay correction. Experiments were performed twice with triplicate wells.

MicroPET Imaging. PET scans and image analysis were performed using a microPET R4 rodent model scanner (Siemens Medical Solutions, Malvern, PA) as previously reported (*26, 27*). The microPET studies were performed by tail-vein injection of 3.7~5.6 MBq (100~150 μCi) ^{18}F-FB-PEG_3-RGD-BBN, ^{64}Cu-NOTA-RGD-BBN, or ^{68}Ga-NOTA-RGD-BBN into nude mice bearing T47D or MDA-MB-435 tumor xenografts under isoflurane anesthesia. Five-minute static PET images were acquired at 30 min, 1 h, and 2 h time points postinjection (p.i). Ten-minute static PET images were acquired at 4 and 24 h pi for ^{64}Cu-NOTA-RGD-BBN ($n = 4$/group). The images were reconstructed by a two-dimensional ordered-subsets expectation maximum (OSEM) algorithm, and no correction was necessary for attenuation or scatter correction. For control studies, each group of three mice bearing MDA-MB-435 tumors were injected via tail-vein with 3.7 MBq (100 μCi) of ^{18}F-FB-BBN, ^{64}Cu-NOTA-BBN, or ^{68}Ga-NOTA-BBN. Five-minute static PET scans were then acquired at 30 min pi ($n = 3$/group).

Serum Stability and Metabolism. ^{18}F-FB-PEG_3-RGD-BBN, ^{64}Cu-NOTA-RGD-BBN, or ^{68}Ga-NOTA-RGD-BBN was incubated in fetal bovine serum (FBS) for 2 h at room temperature to test the in vitro serum stability. After passing through a 0.22 μm Millipore filter, the samples were analyzed by radio-HPLC. For metabolism studies, female nude mice ($n = 2$/group) were injected with ^{18}F-FB-PEG_3-RGD-BBN, ^{64}Cu-NOTA-RGD-BBN, or ^{68}Ga-NOTA-RGD-BBN at a dose of 7.4 MBq (200 μCi) in 0.2 mL PBS via tail vein. At 60 min pi, the urine samples were collected and then centrifuged at 8000 rpm for 5 min. The supernatant was collected, filtered through a 0.22 μm Millipore filter, and then analyzed by radio-HPLC.

Statistical Analysis. Quantitative data were expressed as the mean ± SD. Mean values were compared using one-way analysis of variance (ANOVA) and Student's *t* test. *P* values of <0.05 were considered statistically significant.

RESULTS

Chemistry and Radiochemistry. The NOTA conjugates of BBN and RGD-BBN were analyzed by both HPLC and mass spectrometry to confirm the identity of the products. The characterizations of ^{18}F-FB-PEG_3-RGD-BBN, ^{64}Cu-NOTA-RGD-BBN, and ^{68}Ga-NOTA-RGD-BBN (Figure 1) are listed in Table 1. The decay-corrected labeling yield of ^{18}F-FB-PEG_3-RGD-BBN was 40−50% based on ^{18}F-SFB. The decay-corrected labeling yields of ^{64}Cu-NOTA-RGD-BBN and ^{68}Ga-

Table 1. Characterizations of ^{18}F-FB-PEG$_3$-RGD-BBN, ^{64}Cu-NOTA-RGD-BBN, and ^{68}Ga-NOTA-RGD-BBN[a]

	receptor affinity IC_{50} (nM)				
	integrin $\alpha_v\beta_3$	GRPR	labeling yield (%)	radiochemical purity (%)	preparation time (min)
^{18}F-FB-PEG$_3$-RGD-BBN	13.77 ± 1.82	73.28 ± 1.57	40−50	>98	~180
^{64}Cu-NOTA-RGD-BBN	16.15 ± 2.77	92.75 ± 3.53	>90	>98	~40
^{68}Ga-NOTA-RGD-BBN			>90	>98	~45

[a] The IC_{50} was determined by FB-PEG$_3$-RGD-BBN and NOTA-RGD-BBN. Labeling yield of ^{18}F-FB-PEG$_3$-RGD-BBN was based on ^{18}F-SFB. Preparation time of ^{18}F-FB-PEG$_3$-RGD-BBN was determined from ^{18}F−F.

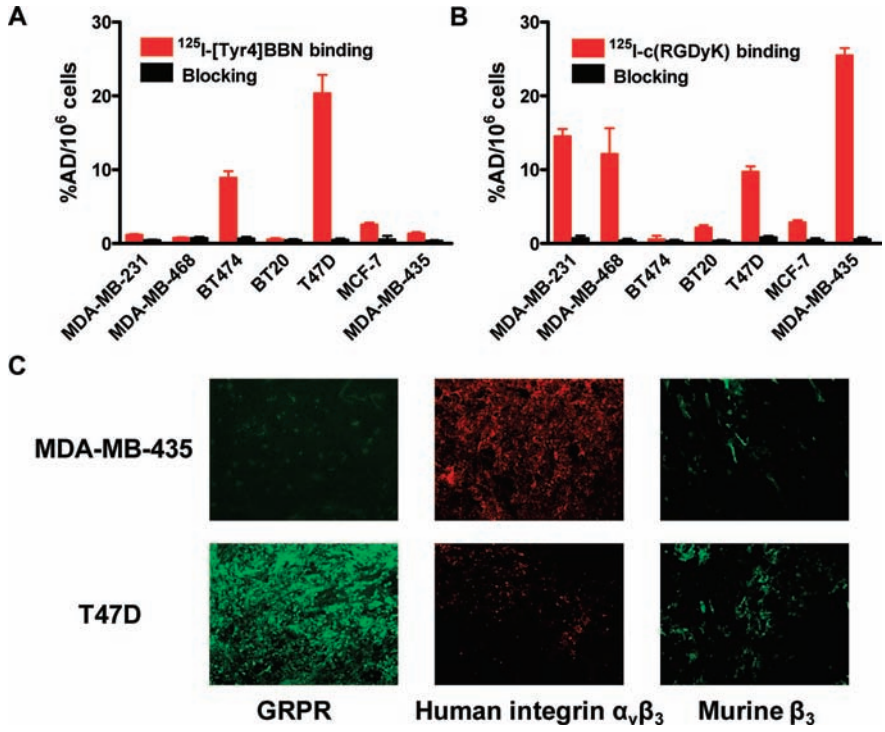

Figure 2. (A, B) GRPR and integrin $\alpha_v\beta_3$ levels in different breast cancer cell lines determined by cell binding assay using ^{125}I-[Tyr^4]BBN (A) or ^{125}I-c(RGDyK) (B) as the radioligand (mean ± SD, $n = 5$). (C) Immunofluorescent staining for GRPR, human integrin $\alpha_v\beta_3$, and murine integrin β_3 in MDA-MB-435 and T47D tumor tissues.

NOTA-RGD-BBN were both higher than 90% under the conditions of reaction at 40 °C for 15 min. After the purification with HPLC, the radiochemical purity of each tracer was higher than 98%. The overall preparation time was ~180 min for ^{18}F-FB-PEG$_3$-RGD-BBN starting from ^{18}F−F, ~40 min for ^{64}Cu-NOTA-RGD-BBN from $^{64}CuCl_2$, and ~45 min for ^{68}Ga-NOTA-RGD-BBN from $^{68}Ga^{3+}$ elution. The specific activity of ^{64}Cu-NOTA-RGD-BBN and ^{68}Ga-NOTA-RGD-BBN used in the in vitro and in vivo experiments was typically 7.4−14.8 MBq/nmol (0.2−0.4 Ci/μmol) at the end of synthesis.

Receptor Binding Affinity. The integrin $\alpha_v\beta_3$ receptor-binding affinities of NOTA-RGD-BBN and FB-PEG$_3$-RGD-BBN were determined by performing competitive binding assay with ^{125}I-c(RGDyK) as the radioligand on U87MG tumor cells. The IC_{50} values for NOTA-RGD-BBN and FB-PEG$_3$-RGD-BBN were 16.15 ± 2.77 and 13.77 ± 1.82 nM, respectively (mean ± SD, $n = 3$, Table 1). The binding affinities of NOTA-RGD-BBN and FB-PEG$_3$-RGD-BBN for GRPR were evaluated using GRPR-positive PC-3 cells with ^{125}I-[Tyr^4]BBN as the radioligand. The IC_{50} values were determined to be 92.75 ± 3.53 nM for NOTA-RGD-BBN and 73.28 ± 1.57 nM for FB-PEG$_3$-RGD-BBN (mean ± SD, $n = 3$, Table 1). The comparable IC_{50} values from these two sets of experiments suggest that NOTA-RGD-BBN and FB-PEG$_3$-RGD-BBN possessed comparable integrin $\alpha_v\beta_3$ binding affinities to c(RGDyK) and GRPR receptor-binding affinities to Aca-BBN(7−14).

GRPR and Integrin $\alpha_v\beta_3$ Expression on Breast Cancer Cells. The expression of GRPR and integrin $\alpha_v\beta_3$ on various breast cancer cells was determined by radioligand receptor-binding assay using ^{125}I-[Tyr^4]BBN and ^{125}I-c(RGDyK) as radioligands, respectively. As shown in Figure 2A, among all the breast cancer cells tested, T47D expressed the highest level of GRPR, as the cell binding percentage of ^{125}I-[Tyr^4]BBN was the highest. The binding specificity of ^{125}I-[Tyr^4]BBN with T47D cells was confirmed by blocking study with cold BBN. The expression of integrin $\alpha_v\beta_3$ on the breast cancer cell lines followed the order MDA-MB-435 > MDA-MB-231 > MDA-MB-468 > T47D > MCF-7 > BT20 > BT474 (Figure 2B). After blocking with cold c(RGDyK), the cell bound ^{125}I-c(RGDyK) all decreased to a background level, indicating the binding of ^{125}I-c(RGDyK) with the tumor cells was integrin $\alpha_v\beta_3$-mediated specific binding.

Immunofluorescent Staining. The expression of GRPR and integrin $\alpha_v\beta_3$ in the T47D and MDA-MB-435 tumor tissues was detected by immunofluorescent staining. As shown in Figure 2C, T47D tumor showed strong GRPR staining while MDA-MB-435 tumor had only weak background staining, which is consistent with the cell-based radioligand study (Figure 2A). The anti-integrin $\alpha_v\beta_3$ antibody Abegrin we used can only recognize the human integrin $\alpha_v\beta_3$, which does not cross-react with murine integrin $\alpha_v\beta_3$ of the tumor cells. MDA-MB-435 tumor tissue showed much higher human integrin $\alpha_v\beta_3$ expression than T47D tumor tissue. Besides human integrin $\alpha_v\beta_3$

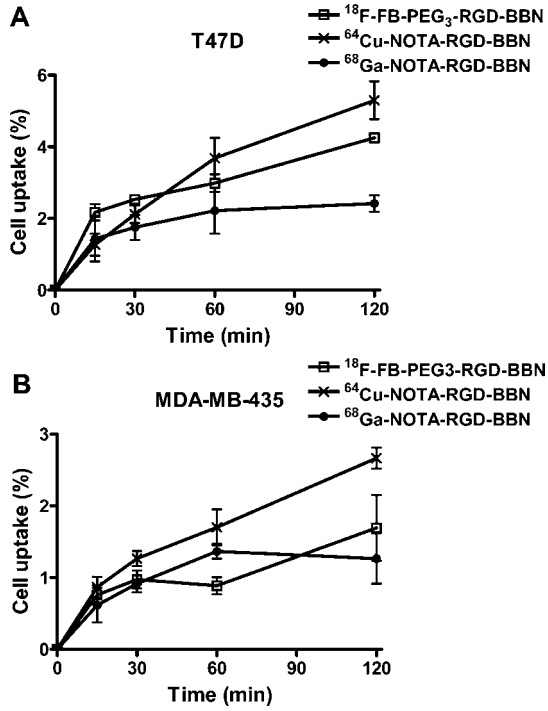

Figure 3. Cell uptake assay of ^{18}F-FB-PEG$_3$-RGD-BBN, ^{64}Cu-NOTA-RGD-BBN, and ^{68}Ga-NOTA-RGD-BBN on T47D (A) and MDA-MB-435 (B) tumor cells (mean ± SD, $n = 3$).

expressed by the tumor cells, the tumors grown in the nude mice also expressed murine integrin $\alpha_v\beta_3$ on the tumor vasculature. As shown in Figure 2C, both T47D and MDA-MB-435 tumors expressed murine integrin β_3, which can also be recognized by RGD.

Cell Uptake Studies. The cell uptake studies of ^{18}F-FB-PEG$_3$-RGD-BBN, ^{64}Cu-NOTA-RGD-BBN, and ^{68}Ga-NOTA-RGD-BBN were performed on T47D and MDA-MB-435 tumor cells. As shown in Figure 3, all the radiotracers exhibited an increased uptake with time on both tumor cell lines. Generally speaking, the cell uptake levels of the three tracers on the T47D cells were all higher than those on the MDA-MB-435 tumor cells, which may be due to the higher GRPR expression of the T47D cells, and the GRPR is more easily internalized into the cells than integrin. For both tumor cells, the uptake of ^{64}Cu-NOTA-RGD-BBN was significantly higher than that of ^{18}F-FB-PEG$_3$-RGD-BBN and ^{68}Ga-NOTA-RGD-BBN at late time points ($P < 0.05$). For example, the T47D cell uptake value at 120 min was 4.25 ± 0.13% AD for ^{18}F-FB-PEG$_3$-RGD-BBN, 5.30 ± 0.53% AD for ^{64}Cu-NOTA-RGD-BBN, and 2.42 ± 0.23% AD for ^{68}Ga-NOTA-RGD-BBN, respectively ($n = 3$).

MicroPET Imaging. Representative coronal microPET images of T47D and MDA-MB-435 tumor-bearing mice ($n = 4$/group) at different times after intravenous injection of 3.7−5.6 MBq (100−150 μCi) of ^{18}F-FB-PEG$_3$-RGD-BBN, ^{64}Cu-NOTA-RGD-BBN, or ^{68}Ga-NOTA-RGD-BBN are shown in Figure 4. The tumors after injection of the radiotracers were all clearly visible with high contrast to contralateral background at all time points measured beginning 30 min. The mice injected with ^{64}Cu-NOTA-RGD-BBN showed higher abdominal activity accumulation than those injected with ^{68}Ga-NOTA-RGD-BBN or ^{18}F-FB-PEG$_3$-RGD-BBN. Prominent uptake of ^{18}F-FB-PEG$_3$-RGD-BBN was observed in the kidneys and urinary bladder at early time points, suggesting that this radiotracer is mainly excreted through the renal route. Quantification of tumor and major organ activity accumulation in the microPET scans was realized by measuring the regions of interest (ROIs) that encompass the entire organ on the coronal images. The tumor and major organ uptake comparison of ^{18}F-FB-PEG$_3$-RGD-BBN, ^{64}Cu-NOTA-RGD-BBN, and ^{68}Ga-NOTA-RGD-BBN is depicted in Figure 5 and Table 2. The T47D and MDA-MB-435 tumor uptake was expressed as the average of each radiotracer in four mice, while the normal organ uptake was expressed as the average of each tracer in eight mice (four T47D tumor-bearing mice and four MDA-MB-435 tumor-bearing mice per tracer). As shown in Figure 5, for all three radiotracers, the uptake in T47D tumors was higher than that in MDA-MB-435 tumors at any time point examined, which is consistent with the in vitro cell uptake studies. For example, the tumor uptake comparison of ^{18}F-FB-PEG$_3$-RGD-BBN in T47D tumor and MDA-MB-435 was 2.96 ± 0.53 vs 2.72 ± 0.80, 1.81 ± 0.34 vs 1.59 ± 0.65, and 0.91 ± 0.12 vs 0.84 ± 0.22% ID/g at 30, 60, and 120 min pi, respectively (Figure 5A,B). The tumor uptake of ^{68}Ga-NOTA-RGD-BBN was higher than that of the ^{18}F- and ^{64}Cu-labeled RGD-BBN radiotracers from 30 to 120 min pi, and the differences were statistically significant compared with ^{18}F-FB-PEG$_3$-RGD-BBN at any time tested ($n = 4$, $P < 0.05$). ^{18}F-FB-PEG$_3$-RGD-BBN also showed rapid washout in the blood and normal organs. As can be seen from Figure 5, the uptake of the ^{18}F-labeled RGD-BBN decreased rapidly with time in the blood, kidneys, and liver. The uptake values of ^{18}F-FB-PEG$_3$-RGD-BBN in the blood and normal organs were all significantly lower than those of the ^{64}Cu and ^{68}Ga tracers at any time from 30 to

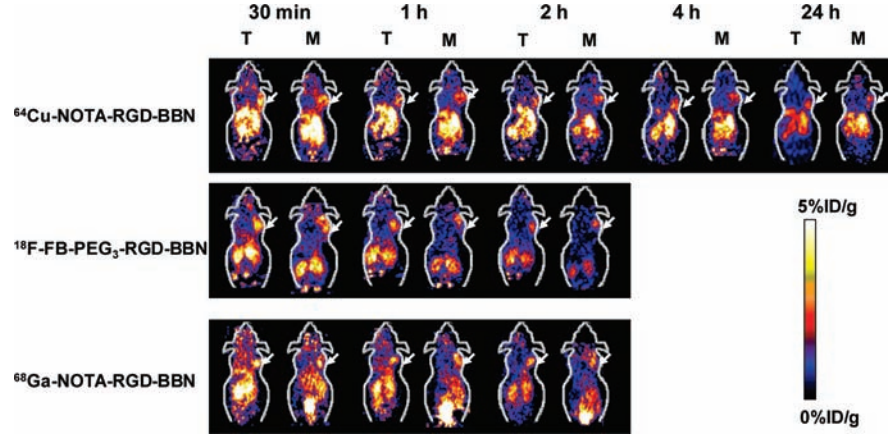

Figure 4. Decay-corrected whole-body coronal microPET images of T47D (T) and MDA-MB-435 (M) tumor-bearing mice at 30 min, 1 h, 2 h, 4 h, and 24 h after injecting 3.7−5.5 MBq (100−150 μCi) of ^{64}Cu-NOTA-RGD-BBN, ^{18}F-FB-PEG$_3$-RGD-BBN, or ^{68}Ga-NOTA-RGD-BBN. Images shown are static scans of a single mouse, which is representative of the four mice tested in each group. Arrows indicate the presence of T47D (T) or MDA-MB-435 (M) tumors.

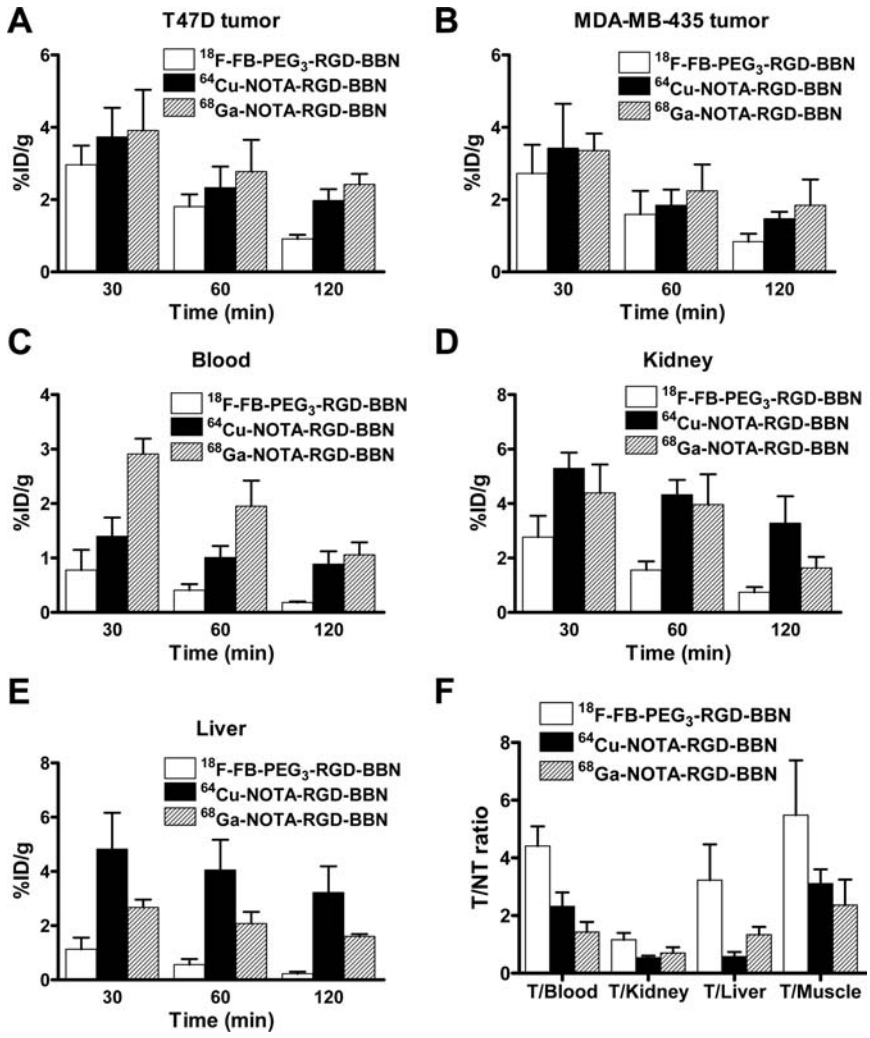

Figure 5. (A−E) Comparison between the uptake of ^{18}F-FB-PEG$_3$-RGD-BBN, ^{64}Cu-NOTA-RGD-BBN, and ^{68}Ga-NOTA-RGD-BBN in T47D tumor (A), MDA-MB-435 tumor (B), blood (C), kidneys (D), and liver (E) after injection of 3.7−5.5 MBq (100−150 μCi) tracer in T47D or MDA-MB-435 tumor-bearing mice (n = 4−8, mean ± SD). (F) Comparison of tumor (T) with blood, kidney, liver, and muscle ratio of ^{18}F-FB-PEG$_3$-RGD-BBN, ^{64}Cu-NOTA-RGD-BBN, and ^{68}Ga-NOTA-RGD-BBN at 60 min after injection of 3.7−5.5 MBq (100−150 μCi) tracer in T47D tumor-bearing mice (n = 4/group, mean ± SD).

120 min (n = 8, P < 0.05). ^{68}Ga-NOTA-RGD-BBN also showed higher blood retention compared to the ^{18}F and ^{64}Cu radiotracers (Figure 5C). The kidney uptake of ^{68}Ga-NOTA-RGD-BBN and ^{64}Cu-NOTA-RGD-BBN decreased with time, and ^{68}Ga-NOTA-RGD-BBN seemed to be cleared slightly more rapidly than ^{64}Cu-NOTA-RGD-BBN. At 120 min pi, the kidney uptake was 0.74 ± 0.19% ID/g for ^{18}F-FB-PEG$_3$-RGD-BBN, 1.64 ± 0.40% ID/g for ^{68}Ga-NOTA-RGD-BBN, and 3.28 ± 0.99% ID/g for ^{64}Cu-NOTA-RGD-BBN, respectively (n = 8, Figure 5D). The liver uptake of ^{64}Cu-NOTA-RGD-BBN was significantly higher than those of the ^{18}F- and ^{68}Ga-labeled RGD-BBN radiotracers at any time point examined (n = 8, P < 0.05). At 4 and 24 h pi, the liver uptake of ^{64}Cu-NOTA-RGD-BBN was still higher than that of the tumor uptake (Table 2). The liver uptake of ^{18}F-FB-PEG$_3$-RGD-BBN was very low with the highest uptake being 1.13 ± 0.43% ID/g at 30 min p.i., indicating that the ^{18}F labeled RGD-BBN was excreted predominantly through the renal route (Figure 5E). Although the absolute tumor uptake of ^{18}F-FB-PEG$_3$-RGD-BBN was lower than that of the other two radiotracers, the tumor-to-nontumor (T/NT) ratios of ^{18}F-FB-PEG$_3$-RGD-BBN were all significantly higher than those of ^{64}Cu-NOTA-RGD-BBN and ^{68}Ga-NOTA-RGD-BBN (P < 0.05), because of the rapid washout of the tracer in blood and normal organs (Figure 5F).

MDA-MB-435 tumor is integrin $\alpha_v\beta_3$-positive but GRPR-negative (Figure 2B). As shown in Figure 6A, the BBN radiotracers appeared to be more lipophilic than the corresponding RGD-BBN radiotracers, resulting in significant activity accumulation in the gallbladder and intestines. Because of the absence of GRPR, neither ^{18}F-FB-BBN, ^{64}Cu-NOTA-RGD-BBN, nor ^{68}Ga-NOTA-RGD-BBN was able to visualize the tumors. The MDA-MB-435 tumor uptake at 30 min pi was 0.45 ± 0.11% ID/g for ^{18}F-FB-BBN, 0.63 ± 0.17% ID/g for ^{64}Cu-NOTA-RGD-BBN, and 0.57 ± 0.13% ID/g for ^{68}Ga-NOTA-RGD-BBN, which was significantly lower than the corresponding RGD-BBN radiotracers (P < 0.01, Figure 6B).

Serum Stability and Metabolic Stability. The serum stability of ^{18}F-FB-PEG$_3$-RGD-BBN, ^{64}Cu-NOTA-RGD-BBN, and ^{68}Ga-NOTA-RGD-BBN was tested by incubating with FBS for 2 h at room temperature. As shown in Figure 7A, all three radiotracers showed good in vitro serum stability, with only minor peaks (t_R around 5 min) for ^{18}F-FB-PEG$_3$-RGD-BBN and ^{64}Cu-NOTA-RGD-BBN as detected by radio-HPLC. We also studied the metabolic stability of the three radiotracers in mice urine at 60 min after injection. As shown in Figure 7B, all three radiotracers showed detectable metabolites in the urine. Although we did not identify the composition of the metabolites, it was found that all metabolites eluted earlier from the HPLC

Table 2. Quantified MicroPET Imaging Data of ^{18}F-FB-PEG$_3$-RGD-BBN, ^{64}Cu-NOTA-RGD-BBN, and ^{68}Ga-NOTA-RGD-BBN in T47D and MDA-MB-435 Tumor-Bearing Nude Mice (Mean ± SD, n = 4−8)

	uptake (% ID/g)											
	^{18}F-FB-PEG$_3$-RGD-BBN			^{68}Ga-NOTA-RGD-BBN			^{64}Cu-NOTA-RGD-BBN					
	0.5 h	1 h	2 h	0.5 h	1 h	2 h	0.5 h	1 h	2 h	4 h	24 h	
blood	0.78 ± 0.37	0.41 ± 0.11	0.18 ± 0.02	2.91 ± 0.28	1.95 ± 0.47	1.06 ± 0.23	1.40 ± 0.34	1.01 ± 0.21	0.89 ± 0.23	0.54 ± 0.20	0.36 ± 0.04	
liver	1.13 ± 0.43	0.56 ± 0.21	0.23 ± 0.07	2.68 ± 0.29	2.08 ± 0.43	1.60 ± 0.09	4.82 ± 1.34	4.05 ± 1.12	3.22 ± 0.97	2.76 ± 0.81	2.24 ± 0.36	
kidney	2.77 ± 0.78	1.56 ± 0.32	0.74 ± 0.19	4.39 ± 1.05	3.96 ± 1.12	1.64 ± 0.40	5.29 ± 0.58	4.32 ± 0.55	3.28 ± 0.99	2.95 ± 0.26	2.10 ± 0.72	
muscle	0.81 ± 0.23	0.33 ± 0.17	0.15 ± 0.05	1.33 ± 0.28	1.18 ± 0.44	0.78 ± 0.07	0.91 ± 0.27	0.75 ± 0.12	0.56 ± 0.33	0.40 ± 0.07	0.21 ± 0.04	
T47D	2.96 ± 0.53	1.81 ± 0.34	0.91 ± 0.12	3.91 ± 1.13	2.78 ± 0.87	2.42 ± 0.29	3.73 ± 0.81	2.33 ± 0.59	1.97 ± 0.32	1.94 ± 0.22	1.38 ± 0.16	
MDA-MB-435	2.72 ± 0.80	1.59 ± 0.65	0.84 ± 0.22	3.36 ± 0.47	2.24 ± 0.73	1.84 ± 0.72	3.42 ± 1.23	1.84 ± 0.44	1.47 ± 0.19	1.79 ± 0.20	1.29 ± 0.09	

Figure 6. (A) Decay-corrected whole-body coronal microPET images of MDA-MB-435 tumor-bearing mice at 30 min after injection of 3.7 MBq (100 μCi) ^{18}F-FB-BBN, ^{64}Cu-NOTA-BBN, or ^{68}Ga-NOTA-BBN. Images shown are static scans of a single mouse, which is representative of the three mice tested in each group. Arrows indicate the presence of MDA-MB-435 tumors. (B) Comparison between the quantified uptake of ^{18}F/^{64}Cu/^{68}Ga labeled RGD-BBN tracers with ^{18}F/^{64}Cu/^{68}Ga labeled BBN tracers in MDA-MB-435 tumors (n = 3−4/group, mean ± SD).

column than the parent compounds. The major metabolite peaks were found at about 17 min for ^{68}Ga-NOTA-RGD-BBN and ^{18}F-FB-PEG$_3$-RGD-BBN and about 20 min for ^{64}Cu-NOTA-RGD-BBN. Because the RGD peptides seemed to be more metabolically stable than BBN peptides in urine (*11, 40*), we speculate that the metabolites of the RGD-BBN radiotracers were more likely to be from the BBN counterparts of the radiolabeled heterodimers.

DISCUSSION

In this study, we investigated whether radiolabeled RGD-BBN heterodimers can be used as probes for breast cancer PET imaging. The RGD-BBN was labeled with the three most commonly used positron emitters (^{18}F, ^{64}Cu, and ^{68}Ga), and the tumor targeting and in vivo kinetics of the corresponding radiotracers were compared in two orthotopic breast cancer models.

Breast cancers can be sorted into two categories, estrogen dependent (ER$^+$) and estrogen-independent (ER$^-$), based on the presence or absence of estrogen receptors (*41*). We screened the GRPR and integrin $\alpha_v\beta_3$ expression in both the ER$^+$ (T47D, BT474, MCF-7) and ER$^-$ (MDA-MB-231, MDA-MB-435, MDA-MB468, BT20) breast cancer cells (*42*−*45*). T47D and BT474 cells had high GRPR but low to moderate integrin $\alpha_v\beta_3$ expression. On the other hand, the estrogen-independent tumor cells such as MDA-MB-435, MDA-MB-231, and MDA-MB-468 had high integrin $\alpha_v\beta_3$ but undetectable GRPR expression (Figure 2A,B). It is of note that MDA-MB-435 cells were reported to express GRPR at the mRNA level (*43*), but our receptor binding assay using ^{125}I-[Tyr^4]BBN indicated low level of GRPR at the protein level. We selected the T47D and MDA-MB-435 tumor cells for further investigation, which represent the two typical types of breast cancers. The tumor tissues were investigated by immunohistochemical staining to confirm the receptor expression. The expression of GRPR and human integrin $\alpha_v\beta_3$ was consistent with the cell binding assay data. Although the tumor cells are of human origin, the tumor endothelial cells are of murine origin. We thus also checked integrin expression on the tumor vasculature murine integrn

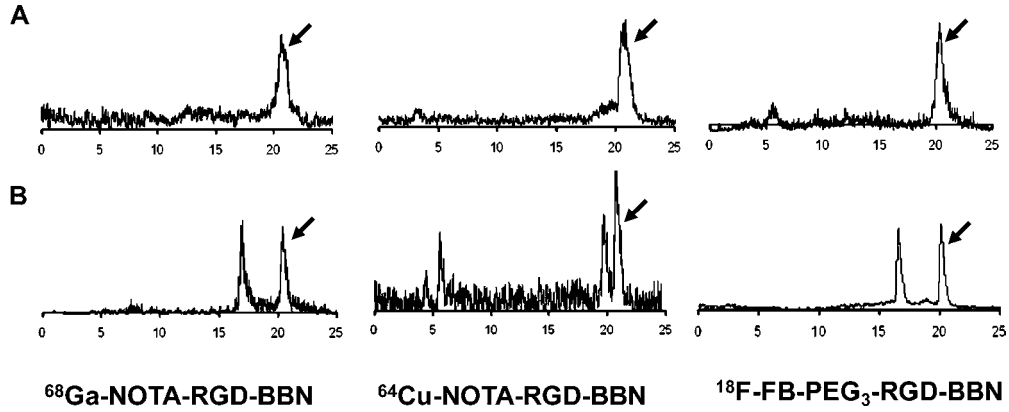

Figure 7. (A) In vitro serum stability of ^{68}Ga-NOTA-RGD-BBN, ^{64}Cu-NOTA-RGD-BBN, or ^{18}F-FB-PEG$_3$-RGD-BBN after incubating in fetal bovine serum (FBS) for 2 h at room temperature. (B) Metabolic stability of ^{68}Ga-NOTA-RGD-BBN, ^{64}Cu-NOTA-RGD-BBN, or ^{18}F-FB-PEG$_3$-RGD-BBN in mice urine at 1 h after injection ($n = 2$).

β_3 staining and found that both T47D and MDA-MB-435 tumor vasculatures were integrin positive (Figure 2C).

The RGD-BBN peptides were labeled with ^{18}F, ^{64}Cu, and ^{68}Ga, respectively. ^{18}F labeling of peptides typically require lengthy procedures because $^{18}F-F^-$ is cyclotron-dependent and a prosthetic group such as ^{18}F-SFB needs to be synthesized before peptide labeling. In contrast, the metal isotopes such as ^{64}Cu and ^{68}Ga can be easily labeled with the chelated RGD-BBN peptides. In particular, ^{68}Ga can be easily acquired from an in-house ^{68}Ge/^{68}Ga generator (^{68}Ge, $t_{1/2} = 270.8$ days) instead of from a medical cyclotron. All three radiotracers showed similar dual receptor binding affinity as determined by receptor binding assay, indicating that the radiotracers maintained comparable in vitro dual receptor-binding properties. Each radiotracer can be acquired in high radiochemical purity after being purified by HPLC, which is sufficient for both in vitro and in vivo experiments. The in vitro cell uptake studies demonstrated that the cell uptake values of the radiotracers on T47D tumor cells were higher than those on MDA-MB-435 tumor cells, which may be caused by the much higher GRPR expression on the T47D cells, leading to efficient internalization of the radiotracers.

The in vivo behaviors of the three radiotracers were tested by microPET in orthotopic T47D and MDA-MB-435 breast cancer models. The radiolabeled BBN was also tested in the non-GRPR expressing MDA-MB-435 tumor model as a control. The much higher tumor uptake of the ^{18}F, ^{64}Cu, and ^{68}Ga labeled RGD-BBN radiotracers than those of the corresponding BBN radiotracers indicates that the RGD-BBN tracers are more useful for imaging than BBN tracers in GRPR negative tumors. We did not compare the tumor imaging characteristics of RGD-BBN and RGD radiotracers in vivo, as we were unable to identify a breast cancer model that is completely integrin negative because all the integrin negative tumor cell lines when inoculated into mice develop integrin positive tumor vasculature. The metal isotopes labeled radiotracers showed higher background than ^{18}F tracers, and ^{18}F labeled RGD-BBN showed a more rapid washout than the ^{64}Cu- and ^{68}Ga-labeled peptides. The tumor uptake of ^{18}F-FB-PEG$_3$-RGD-BBN was also found to be lower than that of the ^{64}Cu and ^{68}Ga labeled RGD-BBN radiotracers. A similar trend has been previously found in both BBN and RGD peptide cases (*29*).

The selection of chelators for radiometal labeling is important. For ^{68}Ga labeling, NOTA is commonly used because the rapid reaction kinetics of NOTA can meet the short half-life of ^{68}Ga ($t_{1/2} = 68$ min). The NOTA conjugates can reach a higher yield when incubated with ^{68}Ga for 10 min at room temperature (*37*). For ^{64}Cu labeling, DOTA was previously reported as a widely used "universal" chelator, and we have reported a series of ^{64}Cu-DOTA peptide tracers for tumor imaging (*10, 26, 38, 46, 47*). The high and prolonged liver uptake is problematic for ^{64}Cu-DOTA radiotracers, which was suggested to be the slow dissociation of ^{64}Cu from the DOTA chelator (*48*−*51*). The instability of the ^{64}Cu-DOTA conjugates would result in demetalation and subsequent accumulation in nontarget tissues such as the liver (*49*). Recently, Prasanphanich et al. (*49*) reported ^{64}Cu-labeled bombesin analogues using NOTA as a chelator. Their results suggested high in vivo kinetic stability of ^{64}Cu-NOTA-BBN vectors with little or no dissociation of ^{64}Cu from NOTA. From the microPET data, the liver uptake of ^{64}Cu-NOTA-RGD-BBN was relatively lower than other ^{64}Cu-DOTA radiotracers (*18, 26*) but still higher than ^{68}Ga-NOTA-RGD-BBN, which may be caused by the ^{68}Ga chelating ability of NOTA being higher than ^{64}Cu (*52*).

ACKNOWLEDGMENT

This work was supported in part by the National Cancer Institute (NCI Grants R01 120188, R01 CA119053, R21 CA121842, R21 CA102123, P50 CA114747, U54 CA119367, and R24 CA93862). We thank the cyclotron team at Stanford University for $^{18}F-F^-$ production and thank the cyclotron team of University of Wisconsin-Madison for ^{64}Cu production. Z.L. acknowledges the China Scholarship Council (CSC) for partial financial support during his study at Stanford University.

LITERATURE CITED

(1) Greenlee, R. T., Hill-Harmon, M. B., Murray, T., and Thun, M. (2001) Cancer statistics, 2001. *Ca—Cancer J. Clin. 51*, 15–36.

(2) Veronesi, U., Boyle, P., Goldhirsch, A., Orecchia, R., and Viale, G. (2005) Breast cancer. *Lancet 365*, 1727–1741.

(3) Weigelt, B., Peterse, J. L., and van't Veer, L. J. (2005) Breast cancer metastasis: markers and models. *Nat. Rev. Cancer 5*, 591–602.

(4) Cornelio, D. B., Roesler, R., and Schwartsmann, G. (2007) Gastrin-releasing peptide receptor as a molecular target in experimental anticancer therapy. *Ann. Oncol. 18*, 1457–1466.

(5) Smith, C. J., Volkert, W. A., and Hoffman, T. J. (2005) Radiolabeled peptide conjugates for targeting of the bombesin receptor superfamily subtypes. *Nucl. Med. Biol. 32*, 733–740.

(6) Schweinsberg, C., Maes, V., Brans, L., Blauenstein, P., Tourwe, D. A., Schubiger, P. A., Schibli, R., and Garayoa, E. G. (2008)

Novel glycated [^{99m}Tc(CO)$_3$]-labeled bombesin analogues for improved targeting of gastrin-releasing peptide receptor-positive tumors. *Bioconjugate Chem. 19*, 2432–2439.

(7) Santos-Cuevas, C. L., Ferro-Flores, G., Arteaga de Murphy, C., and Pichardo-Romero, P. A. (2008) Targeted imaging of gastrin-releasing peptide receptors with ^{99m}Tc-EDDA/HYNIC-[Lys^3]-bombesin: biokinetics and dosimetry in women. *Nucl. Med. Commun. 29*, 741–747.

(8) Garrison, J. C., Rold, T. L., Sieckman, G. L., Naz, F., Sublett, S. V., Figueroa, S. D., Volkert, W. A., and Hoffman, T. J. (2008) Evaluation of the pharmacokinetic effects of various linking group using the ^{111}In-DOTA-X-BBN(7−14)NH$_2$ structural paradigm in a prostate cancer model. *Bioconjugate Chem. 19*, 1803–1812.

(9) Van de Wiele, C., Phonteyne, P., Pauwels, P., Goethals, I., Van den Broecke, R., Cocquyt, V., and Dierckx, R. A. (2008) Gastrin-releasing peptide receptor imaging in human breast carcinoma versus immunohistochemistry. *J. Nucl. Med. 49*, 260–264.

(10) Chen, X., Park, R., Hou, Y., Tohme, M., Shahinian, A. H., Bading, J. R., and Conti, P. S. (2004) microPET and autoradiographic imaging of GRP receptor expression with ^{64}Cu-DOTA-[Lys^3]bombesin in human prostate adenocarcinoma xenografts. *J. Nucl. Med. 45*, 1390–1397.

(11) Zhang, X., Cai, W., Cao, F., Schreibmann, E., Wu, Y., Wu, J. C., Xing, L., and Chen, X. (2006) ^{18}F-labeled bombesin analogs for targeting GRP receptor-expressing prostate cancer. *J. Nucl. Med. 47*, 492–501.

(12) Dimitrakopoulou-Strauss, A., Hohenberger, P., Haberkorn, U., Macke, H. R., Eisenhut, M., and Strauss, L. G. (2007) ^{68}Ga-labeled bombesin studies in patients with gastrointestinal stromal tumors: comparison with ^{18}F-FDG. *J. Nucl. Med. 48*, 1245–1250.

(13) Schuhmacher, J., Zhang, H., Doll, J., Macke, H. R., Matys, R., Hauser, H., Henze, M., Haberkorn, U., and Eisenhut, M. (2005) GRP receptor-targeted PET of a rat pancreas carcinoma xenograft in nude mice with a ^{68}Ga-labeled bombesin(6−14) analog. *J. Nucl. Med. 46*, 691–699.

(14) Waser, B., Eltschinger, V., Linder, K., Nunn, A., and Reubi, J. C. (2007) Selective in vitro targeting of GRP and NMB receptors in human tumours with the new bombesin tracer ^{177}Lu-AMBA. *Eur. J. Nucl. Med. Mol. Imaging 34*, 95–100.

(15) Lantry, L. E., Cappelletti, E., Maddalena, M. E., Fox, J. S., Feng, W., Chen, J., Thomas, R., Eaton, S. M., Bogdan, N. J., Arunachalam, T., Reubi, J. C., Raju, N., Metcalfe, E. C., Lattuada, L., Linder, K. E., Swenson, R. E., Tweedle, M. F., and Nunn, A. D. (2006) ^{177}Lu-AMBA: synthesis and characterization of a selective ^{177}Lu-labeled GRP-R agonist for systemic radiotherapy of prostate cancer. *J. Nucl. Med. 47*, 1144–1152.

(16) Zhang, H., Chen, J., Waldherr, C., Hinni, K., Waser, B., Reubi, J. C., and Maecke, H. R. (2004) Synthesis and evaluation of bombesin derivatives on the basis of pan-bombesin peptides labeled with indium-111, lutetium-177, and yttrium-90 for targeting bombesin receptor-expressing tumors. *Cancer Res. 64*, 6707–6715.

(17) Cai, W., Shin, D. W., Chen, K., Gheysens, O., Cao, Q., Wang, S. X., Gambhir, S. S., and Chen, X. (2006) Peptide-labeled near-infrared quantum dots for imaging tumor vasculature in living subjects. *Nano Lett. 6*, 669–676.

(18) Yang, Y. S., Zhang, X., Xiong, Z., and Chen, X. (2006) Comparative in vitro and in vivo evaluation of two ^{64}Cu-labeled bombesin analogs in a mouse model of human prostate adenocarcinoma. *Nucl. Med. Biol. 33*, 371–380.

(19) Scopinaro, F., Varvarigou, A. D., Ussof, W., De Vincentis, G., Sourlingas, T. G., Evangelatos, G. P., Datsteris, J., and Archimandritis, S. C. (2002) Technetium labeled bombesin-like peptide: preliminary report on breast cancer uptake in patients. *Cancer Biother. Radiopharm. 17*, 327–335.

(20) Parry, J. J., Andrews, R., and Rogers, B. E. (2007) MicroPET imaging of breast cancer using radiolabeled bombesin analogs targeting the gastrin-releasing peptide receptor. *Breast Cancer Res. Treat. 101*, 175–83.

(21) Hood, J. D., and Cheresh, D. A. (2002) Role of integrins in cell invasion and migration. *Nat. Rev. Cancer 2*, 91–100.

(22) Ruoslahti, E. (2002) Specialization of tumour vasculature. *Nat. Rev. Cancer 2*, 83–90.

(23) Brooks, P. C., Clark, R. A., and Cheresh, D. A. (1994) Requirement of vascular integrin $\alpha v\beta 3$ for angiogenesis. *Science 264*, 569–571.

(24) Hynes, R. O. (2002) Integrins: bidirectional, allosteric signaling machines. *Cell 110*, 673–687.

(25) Chen, X., Park, R., Shahinian, A. H., Tohme, M., Khankaldyyan, V., Bozorgzadeh, M. H., Bading, J. R., Moats, R., Laug, W. E., and Conti, P. S. (2004) ^{18}F-labeled RGD peptide: initial evaluation for imaging brain tumor angiogenesis. *Nucl. Med. Biol. 31*, 179–189.

(26) Wu, Y., Zhang, X., Xiong, Z., Cheng, Z., Fisher, D. R., Liu, S., Gambhir, S. S., and Chen, X. (2005) microPET imaging of glioma integrin $\alpha v\beta 3$ expression using ^{64}Cu-labeled tetrameric RGD peptide. *J. Nucl. Med. 46*, 1707–1718.

(27) Zhang, X., Xiong, Z., Wu, Y., Cai, W., Tseng, J. R., Gambhir, S. S., and Chen, X. (2006) Quantitative PET imaging of tumor integrin $\alpha v\beta 3$ expression with ^{18}F-FRGD2. *J. Nucl. Med. 47*, 113–121.

(28) Beer, A. J., Niemeyer, M., Carlsen, J., Sarbia, M., Nahrig, J., Watzlowik, P., Wester, H. J., Harbeck, N., and Schwaiger, M. (2008) Patterns of $\alpha v\beta 3$ expression in primary and metastatic human breast cancer as shown by ^{18}F-Galacto-RGD PET. *J. Nucl. Med. 49*, 255–259.

(29) Decristoforo, C., Hernandez Gonzalez, I., Carlsen, J., Rupprich, M., Huisman, M., Virgolini, I., Wester, H. J., and Haubner, R. (2008) ^{68}Ga- and ^{111}In-labelled DOTA-RGD peptides for imaging of $\alpha v\beta 3$ integrin expression. *Eur. J. Nucl. Med. Mol. Imaging 35*, 1507–1515.

(30) Cai, W., Niu, G., and Chen, X. (2008) Imaging of integrins as biomarkers for tumor angiogenesis. *Curr. Pharm. Des. 14*, 2943–2973.

(31) Cai, W., and Chen, X. (2008) Multimodality molecular imaging of tumor angiogenesis. *J. Nucl. Med. 49* (Suppl. 2), 113S–128S.

(32) Chen, X. (2006) Multimodality imaging of tumor integrin $\alpha v\beta 3$ expression. *Mini-Rev. Med. Chem. 6*, 227–234.

(33) Kenny, L. M., Coombes, R. C., Oulie, I., Contractor, K. B., Miller, M., Spinks, T. J., McParland, B., Cohen, P. S., Hui, A. M., Palmieri, C., Osman, S., Glaser, M., Turton, D., Al-Nahhas, A., and Aboagye, E. O. (2008) Phase I trial of the positron-emitting Arg-Gly-Asp (RGD) peptide radioligand ^{18}F-AH111585 in breast cancer patients. *J. Nucl. Med. 49*, 879–886.

(34) Li, Z. B., Wu, Z., Chen, K., Ryu, E. K., and Chen, X. (2008) ^{18}F-labeled BBN-RGD heterodimer for prostate cancer imaging. *J. Nucl. Med. 49*, 453–461.

(35) Liu, Z., Yan, Y., Chin, F. T., Wang, F., and Chen, X. (2009) Dual integrin and gastrin-releasing peptide receptor targeted tumor imaging using ^{18}F-labeled PEGylated RGD-bombesin heterodimer ^{18}F-FB-PEG$_3$-Glu-RGD-BBN. *J. Med. Chem. 52*, 425–432.

(36) Cai, W., Zhang, X., Wu, Y., and Chen, X. (2006) A thiol-reactive ^{18}F-labeling agent, *N*-[2-(4-^{18}F-fluorobenzamido)ethyl-]maleimide, and synthesis of RGD peptide-based tracer for PET imaging of $\alpha v\beta 3$ integrin expression. *J. Nucl. Med. 47*, 1172–1180.

(37) Li, Z. B., Chen, K., and Chen, X. (2008) ^{68}Ga-labeled multimeric RGD peptides for microPET imaging of integrin $\alpha v\beta 3$ expression. *Eur. J. Nucl. Med. Mol. Imaging 35*, 1100–1108.

(38) Li, Z. B., Cai, W., Cao, Q., Chen, K., Wu, Z., He, L., and Chen, X. (2007) ^{64}Cu-labeled tetrameric and octameric RGD peptides for small-animal PET of tumor $\alpha v\beta 3$ integrin expression. *J. Nucl. Med. 48*, 1162–1171.

(39) Chen, X., Park, R., Shahinian, A. H., Bading, J. R., and Conti, P. S. (2004) Pharmacokinetics and tumor retention of ^{125}I-labeled RGD peptide are improved by PEGylation. *Nucl. Med. Biol. 31*, 11–19.

(40) Wu, Z., Li, Z. B., Cai, W., He, L., Chin, F. T., Li, F., and Chen, X. (2007) ^{18}F-labeled mini-PEG spacered RGD dimer (^{18}F-FPRGD2): synthesis and microPET imaging of $\alpha v\beta 3$ integrin expression. *Eur. J. Nucl. Med. Mol. Imaging 34*, 1823–1831.

(41) Strande, V., Canelle, L., Tastet, C., Burlet-Schiltz, O., Monsarrat, B., and, and Hondermarck, H. (2009) The proteome of the human breast cancer cell line MDA-MB-231: analysis by LTQ-Orbitrap mass spectrometry. *Proteomics: Clin. Appl. 3*, 41–50.

(42) Cassoni, P., Papotti, M., Ghe, C., Catapano, F., Sapino, A., Graziani, A., Deghenghi, R., Reissmann, T., Ghigo, E., and Muccioli, G. (2001) Identification, characterization, and biological activity of specific receptors for natural (ghrelin) and synthetic growth hormone secretagogues and analogs in human breast carcinomas and cell lines. *J. Clin. Endocrinol. Metab. 86*, 1738–1745.

(43) Bajo, A. M., Schally, A. V., Krupa, M., Hebert, F., Groot, K., and Szepeshazi, K. (2002) Bombesin antagonists inhibit growth of MDA-MB-435 estrogen-independent breast cancers and decrease the expression of the ErbB-2/HER-2 oncoprotein and c-jun and c-fos oncogenes. *Proc. Natl. Acad. Sci. U.S.A. 99*, 3836–3841.

(44) Anzick, S. L., Kononen, J., Walker, R. L., Azorsa, D. O., Tanner, M. M., Guan, X.-Y., Sauter, G., Kallioniemi, O.-P., Trent, J. M., and Meltzer, P. S. (1997) AIB1, a steroid receptor coactivator amplified in breast and ovarian cancer. *Science 277*, 965–968.

(45) Brandi, G., Paiardini, M., Cervasi, B., Fiorucci, C., Filippone, P., De Marco, C., Zaffaroni, N., and Magnani, M. (2003) A new indole-3-carbinol tetrameric derivative inhibits cyclin-dependent kinase 6 expression, and induces G1 cell cycle arrest in both estrogen-dependent and estrogen-independent breast cancer cell lines. *Cancer Res. 63*, 4028–4036.

(46) Cai, W., Wu, Y., Chen, K., Cao, Q., Tice, D. A., and Chen, X. (2006) In vitro and in vivo characterization of ^{64}Cu-labeled Abegrin, a humanized monoclonal antibody against integrin alpha v beta 3. *Cancer Res. 66*, 9673–9681.

(47) Chen, X., Liu, S., Hou, Y., Tohme, M., Park, R., Bading, J. R., and Conti, P. S. (2004) MicroPET imaging of breast cancer alphav-integrin expression with ^{64}Cu-labeled dimeric RGD peptides. *Mol. Imaging Biol. 6*, 350–359.

(48) Wadas, T. J., Eiblmaier, M., Zheleznyak, A., Sherman, C. D., Ferdani, R., Liang, K., Achilefu, S., and Anderson, C. J. (2008) Preparation and biological evaluation of ^{64}Cu-CB-TE2A-sst2-ANT, a somatostatin antagonist for PET imaging of somatostatin receptor-positive tumors. *J. Nucl. Med. 49*, 1819–1827.

(49) Prasanphanich, A. F., Nanda, P. K., Rold, T. L., Ma, L., Lewis, M. R., Garrison, J. C., Hoffman, T. J., Sieckman, G. L., Figueroa, S. D., and Smith, C. J. (2007) [^{64}Cu-NOTA-8-Aoc-BBN-(7−14)NH_2] targeting vector for positron-emission tomography imaging of gastrin-releasing peptide receptor-expressing tissues. *Proc. Natl. Acad. Sci. U.S.A. 104*, 12462–12467.

(50) Boswell, C. A., Sun, X., Niu, W., Weisman, G. R., Wong, E. H., Rheingold, A. L., and Anderson, C. J. (2004) Comparative in vivo stability of copper-64-labeled cross-bridged and conventional tetraazamacrocyclic complexes. *J. Med. Chem. 47*, 1465–1474.

(51) Garrison, J. C., Rold, T. L., Sieckman, G. L., Figueroa, S. D., Volkert, W. A., Jurisson, S. S., and Hoffman, T. J. (2007) In vivo evaluation and small-animal PET/CT of a prostate cancer mouse model using ^{64}Cu bombesin analogs: side-by-side comparison of the CB-TE2A and DOTA chelation systems. *J. Nucl. Med. 48*, 1327–1337.

(52) Clarke, E., and Martell, A. E. (1991) Stabilities of the Fe(III), Ga(III) and In(III) chelates of *N*,*N*′,*N*″-triazacyclononanetriacetic acid. *Inorg. Chim. Acta 181*, 273–280.

BC9000245

Reduction-Triggered Fluorescent Amplification Probe for the Detection of Endogenous RNAs in Living Human Cells

Kazuhiro Furukawa,[†,§] Hiroshi Abe,*[,†] Kayo Hibino,[†] Yasushi Sako,[‡] Satoshi Tsuneda,[§] and Yoshihiro Ito*[,†]

Nano Medical Engineering Laboratory, RIKEN Advanced Science Institute, 2-1 Hirosawa, Wako-Shi, Saitama, 351-0198 Japan, Cellar Informatics Laboratory, RIKEN Advanced Science Institute, 2-1 Hirosawa, Wako-Shi, Saitama, 351-0198 Japan, and Department of Life Science and Medical Bio-Science, Waseda University, 2-2 Wakamatsu-cho, Shinjuku-ku, Tokyo 162-8480, Japan. Received January 29, 2009; Revised Manuscript Received February 22, 2009

Oligonucleotide-templated reactions are attracting attention as a method for RNA detection in living cells. Previously, a reduction-triggered fluorescence probe has been reported that is based on azide reduction to switch fluorescence on. In this article, we report a more advanced probe, a reduction-triggered fluorescent amplification probe that is capable of amplifying a target signal. Azidomethyl fluorescein was newly synthesized and introduced into a probe. Azido-masked fluorescein on the probe showed a strong turn-on fluorescence signal upon oligonucleotide-templated Staudinger reduction. The catalytic reaction of the probe offered a turnover number of 50 as fluorescence readout within 4 h. Finally, probes were introduced into human leukemia HL-60 cells by use of streptolysin O pore-forming peptide. We successfully detected and quantitated the 28S rRNA and β-Actin mRNA signal above the background by flow cytometry. In addition, the same RNA targets were imaged by fluorescence microscopy. The data suggest that a reduction-triggered amplification probe may be a powerful tool in analyzing the localization, transcription, or processing of RNA species in living eukaryotic cells.

INTRODUCTION

The detection and imaging of RNA species in native human cells have been gaining importance in the biological and biomedical research fields (*1*−*7*). Several approaches for imaging mRNAs in genetically engineered cells have been reported recently (*8*−*10*). Although such a strategy can be a useful tool for biological studies, it is not applicable for imaging native RNAs in unmodified cellular specimens. Our specific goal is the detection of RNA sequences in intact cells at single nucleotide resolution using a fluorescence signal as readout. This requires no extraction of RNA species from the cell; therefore, it should be a very rapid and simple method for disease-related RNAs as a biomedical application. Messenger RNAs are expected to be more difficult to detect than rRNAs because they exist in smaller quantities in living cells (*11*). Moreover, their sequences vary widely, and their structures are generally unknown; it is therefore very difficult to find an optimal target site (*12*−*14*). In addition, there is the issue of breaching the barrier of the cell membrane in live human cells. Finally, live cells also show numerous enzymatic activities that degrade oligonucleotide probes.

No method has yet been successful enough to gain wide application for the imaging and detection of mRNA in living cells. However, a small number of molecular approaches have been reported as potentially practical methods (*15*−*37*). Prominent among these approaches are quenched-probe strategies, including molecular beacon (MB) probes (*16*−*20, 28*) and quenched autoligation (QUAL) probes (*21*−*27*). The most important issue for detection in living cells is to keep a low background signal in the absence of the RNA target. These probes allow target-dependent fluorescence enhancement based on the resonance energy transfer (RET) mechanism, for which a pair of quencher and fluorescence dyes is normally used. Recent reports have shown evidence for detection by fluorescence microscopy of mRNAs by MB probes and QUAL probes in intact human cells (*19, 21*−*23, 35*−*40*). Moreover, QUAL probes have been used for flow cytometric detection of RNA species in native human cells (*23*). However, these approaches still need improvement in signal/background (S/B) ratio to become established methods.

Oligonucleotide-templated reactions (OTRs) have received attention as a potential approach for RNA detection in living cells (*21, 23*). This strategy exploits the target strand as a template between two functionalized DNAs or PNAs. For example, native chemical ligation (*41*−*43*), catalytic hydrolysis (*44*−*46*), the Staudinger reaction (*47*−*50*), transfer of a reporter group (*51*), DNAzyme (*52*), an S_N2 quencher displacement ligation reaction (QUAL probe) (*25*), and organomercury-activated reactions (*53*) have been applied to fluorescence nucleic acid reactions. However, few methods have been applied to RNA detection in living human cells (*23*). We considered two important issues to develop a highly sensitive RNA detection probe based on OTR. These are a new fluorogenic system to offer a higher S/B ratio and turnover of OTR to offer amplification of RNA signal.

The catalytic turnover reaction can provide signal amplification and enable sensitive oligonucleotide detection in living cells. Various chemistries for the catalytic turnover have been reported (*26, 41, 46, 47, 49*−*51, 54*). A few laboratories have reported that self-ligation reactions provide amplified products. However, theoretically, ligation reactions suffer from an increased affinity of the product for the oligonucleotide template (*41,54*). This causes product inhibition and prevents higher catalytic activity of the template. Therefore, to reduce product inhibition, a few other laboratories have recently investigated unligated

* To whom correspondence should be addressed. (H.A.) Tel: +81-(0)48-467-9303. Fax: +81-(0)48-467-9300. E-mail: h-abe@riken.jp. (Y.I.) Tel: +81-(0)48-467-9303. Fax: +81-(0)48-467-9300. E-mail: y-ito@riken.jp.

† Nano Medical Engineering Laboratory, RIKEN Advance Science Institute.

‡ Cellar Informatics Laboratory, RIKEN Advance Science Institute.

§ Waseda University.

10.1021/bc900040t CCC: $40.75 © 2009 American Chemical Society
Published on Web 04/17/2009

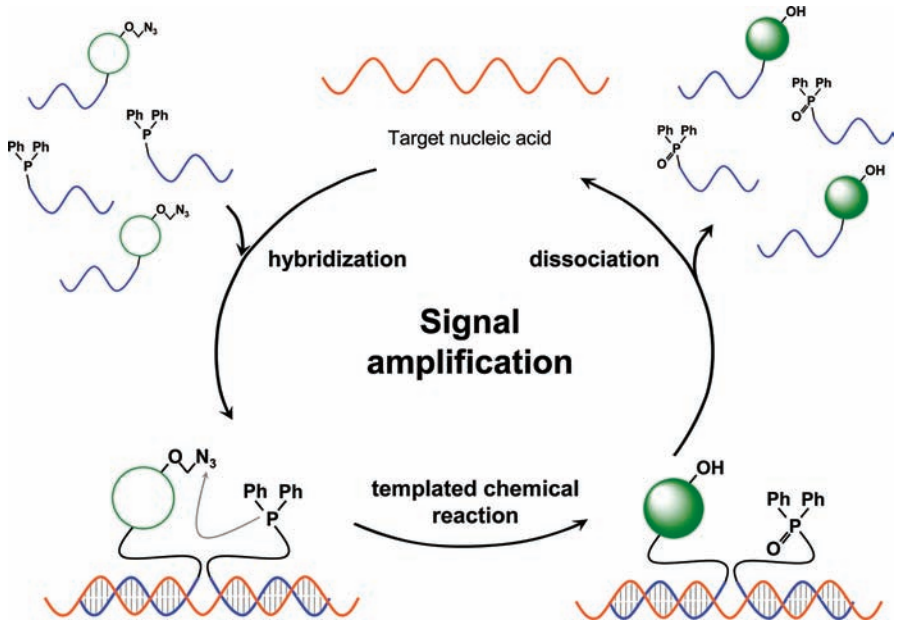

Figure 1. Illustration of the turnover of the azide reduction, which can generate multiple signals per target.

systems by using pairs of modified probes to generate an amplified signal. These approaches are catalytic ester hydrolysis (*46*), the Staudinger reaction (*47*, *49*, *50*), DNAzyme (*52*), and transfer of a reporter group (*51*). Even though they showed significant a turnover number up to 400 times in a test tube, application to living human cells has not been demonstrated. This implies that these methods still need to be improved in background fluorescence or sensitivity.

Recently, various fluorogenic compounds have been developed for the detection of small biological substances (*55*−*59*). Fluorescence modulation of these compounds is caused by photoinduced electron transfer or absorption change triggered by a chemical reaction accompanied with transformation of chemical structure. The S/B ratio for these types of molecules could exceed that of the RET mechanism (*60*). Combined with the catalytic turnover mechanism, this type of fluorogenic system could become a very powerful method for RNA detection in living cells. However, there are only a few reports that describe chemical reaction-triggered fluorogenic molecules for oligonucleotide sensing with amplification of signal in test tubes (*47*,*49*,*50*).

Recently, we reported a reduction-triggered fluorescence (RETF) probe having a rhodamine azide as the fluorogenic molecule that showed a response with a high S/B ratio (*48*). However, this probe did not offer a catalytic turnover because of an unexpected ligated intermediate on OTR. Here, we report another fluorogenic molecule using the azidomethyl protecting group (*61*, *62*) for the fluorescein compound, although Kool and co-workers very recently reported an azidomethyl-protected coumarin dye for OTR that has not been applied to RNA detection in living cells (*50*). The new reduction-triggered fluorescent amplification (RETFA) probe enables catalytic turnover under isothermal conditions without significant product inhibition (Figure 1). The turnover mechanism in the steady state was analyzed by fluorescence spectroscopy, and association and dissociation rate constants for the probe on a template were calculated by BIAcore technology. Finally, by using this RETFA probe design, we show that endogenous mRNA, as well as 28S rRNA in living human HL60 cells, could be imaged by fluorescence microcopy and detected by flow cytometry.

EXPERIMENTAL PROCEDURES

Monoalkyl Fluorescein (1). To a solution of fluorescein (3.00 g, 9.03 mmol) and sodium iodide (271 mg, 1.81 mmol) in DMF (50 mL) chilled via an external ice bath was added a THF (30 mL) solution of potassium *t*-butoxide (3.04 g, 27.1 mmol). After the solution was clear, methyl bromoacetate (944 μL, 9.94 mmol) was slowly added. The reaction was allowed to warm gradually to room temperature. After 2.5 h, the reaction mixture was diluted with AcOEt and washed with H_2O and brine. The combined organic extracts were pooled and dried over Na_2SO_4. Na_2SO_4 was removed by filtration and volatiles removed *in vacuo*. The residue was purified by flash column chromatography (silica, gradient elution 30:1 $CHCl_3$/MeOH to 20:1 $CHCl_3$/MeOH with 0.5% triethylamine) to afford a clear syrup on concentration (820 mg, 23%) (**1**). ^{1}H NMR (400 MHz, CD_3OD) δ7.91 (1H, d, J = 7.32 Hz), 7.62 (2H, dt, J = 16.40, 15.10 Hz), 7.10 (1H, d, J = 7.56 Hz), 6.79 (1H, d, J = 2.20 Hz), 6.67−6.55 (4H, m), 6.44 (1H, dd, J = 2.20, 2.44 Hz), 4.70 (2H, s), 3.69 (3H, s). ^{13}C NMR (100 MHz, CD_3OD) δ 180.6, 172.5, 169.9, 163.5, 159.4, 155.1, 138.8, 137.6, 129.6, 129.1, 124.9, 116.3, 116.0, 114.5, 104.7, 102.3, 66.1, 52.7. QSTAR (Applied Biosystems/MDS SCIEX) (ESI): *m*/*z* 404.0896 [MH+] $C_{23}H_{16}O_7$: 405.0974; found, 405.0987.

Monoalkyl Thiomethyl Fluorescein (2). Monoalkyl fluorescein (**1**) (720 mg, 1.78 mmol) was dissolved in dry CH_3CN (36 mL) under Ar (g). Silver oxide (620 mg, 2.67 mmol) and chloromethylmethylsulfide (223 μL, 2.67 mmol) were added followed by the addition of one drop of pyridine. After stirring for 15 h at room temperature, the remaining solid residue was removed by filtration. The filtrate was concentrated and subjected to flash column chromatography. Elution with a slow gradient of hexane/AcOEt from 6:1 to 2:1 (v/v) with 0.5% triethylamine gave monoalkyl thiomethyl fluorescein (**2**) as a pale yellow crystalline solid (206 mg, 25%). ^{1}H NMR (400 MHz, $CHCl_3$) δ8.01 (1H, d, J = 7.08 Hz), 7.64 (2H, dt, J = 16.10, 15.10 Hz), 7.15 (1H, d, J = 7.56 Hz), 6.83 (1H, d, J = 2.44 Hz), 6.83−6.62 (5H, m), 5.15 (2H, s), 4.66 (2H, s), 3.80 (3H, s), 2.24 (3H, s). ^{13}C NMR (100 MHz, CDCl3) δ 168.94, 168.43, 159.04, 152.64, 151.86, 134.80, 129.08, 128.87, 126.41, 124.75, 123.78, 112.66, 102.82, 101.65, 82.57, 72.34, 65.12, 52.27, 14.59. QSTAR (Applied Biosystems/MDS SCIEX) (ESI): *m*/*z* 464.0930 [MH+] $C_{25}H_{20}O_7S$: 465.1008; found, 465.1004.

Monoalkyl Azidomethyl Fluorescein (3). Monoalkyl thiomethyl fluorescein (**2**) (164 mg, 350 μmol) was dissolved in dichloromethane (7 mL). A dichloromethane (1 mL) solution of *N*-chlorosuccinimide (51.8 mg, 390 μmol) and trimethylsilyl

chloride (42.0 mg, 390 μmol) was added. The resulting solution was stirred at ambient for 1 h, and the reaction was quenched with saturated Na_2CO_3 aqueous. The aqueous layer was extracted with $CHCl_3$ ($\times$ 2), and the combined organic layers were concentrated in vacuum to give the crude, which was subjected to the next reaction. Sodium azide (34.4 mg, 530 mmol) was dissolved in H_2O (3.5 mL) and added to a solution of the crude in DMF (7 mL) in room temperature. After stirring for 1 h, the reaction was quenched with saturated aqueous Na_2CO_3. The aqueous layer was extracted with AcOEt ($\times$2), and the combined organic layers was concentrated in vacuum and subjected to flash column chromatography. Elution with a slow gradient of hexane/AcOEt from 5:1 to 3:2 (v/v) with 0.5% triethylamine gave monoalkyl azidomethyl fluorescein (**3**) as a pale yellow crystalline solid (71.3 mg, 44%). ^{1}H NMR (400 MHz, $CHCl_3$) δ8.02 (1H, d, J = 7.80 Hz), 7.65 (2H, dt, J = 15.2, 14.9 Hz), 7.16 (1H, d, J = 7.32 Hz), 6.90 (1H, d, J = 2.20 Hz), 6.76−6.63 (5H, m), 5.18 (2H, s), 4.66 (2H, s), 3.82 (3H, s). ^{13}C NMR (100 MHz, CDCl3) δ 169.02, 168.54, 157.87, 152.64, 152.76, 152.08, 134.95, 129.70, 129.27, 126.46, 124.95, 123.80, 111.79, 103.26, 101.80, 82.46, 79.43, 65.27, 52.42. QSTAR (Applied Biosystems/MDS SCIEX) (ESI): [MH^+] $C_{24}H_{17}N_3O_7$: 460.1145; found, 460.1134.

Azidomethyl Carboxyfluorescein (4). Monoalkyl azidomethyl fluorescein (**3**) (27.8 mg, 60 μmol) was dissolved in methanol (605 μL). An aqueous solution of 1 M NaOH (66.6 μL, 66.6 μmol) was added. The resulting solution was stirred at ambient for 1 h, and the reaction was quenched with 0.1 M HCl. The aqueous layer was extracted with AcOEt ($\times$2), and the combined organic layers were concentrated in vacuum and subjected to flash column chromatography. Elution with a slow gradient of $CHCl_3$/MeOH from 30:1 to 20:1 (v/v) with 0.5% triethylamine gave azidomethyl carboxyfluorescein (**4**) as a pale yellow crystalline solid (28.2 mg, 100%). ^{1}H NMR (400 MHz, $CHCl_3$) δ 8.01 (1H, d, J = 7.32 Hz), 7.64 (2H, dt, J = 14.9, 15.2 Hz), 7.16 (1H, d, J = 7.56 Hz), 6.88 (1H, d, J = 2.20 Hz), 6.82 (1H, d, J = 2.20 Hz), 6.73−6.63 (4H, m), 5.18 (2H, s), 4.51 (2H, s). ^{13}C NMR (100 MHz, CDCl3) δ 173.69, 169.17, 157.76, 152.79, 152.30, 134.83, 129.23, 128.61, 126.62, 124.82, 123.91, 112.30, 103.22, 101.74, 82.50, 79.41, 67.57. QSTAR (Applied Biosystems/MDS SCIEX) (ESI): *m*/*z* 445.0910 [MH+] $C_{23}H_{15}O_7N_3$: 446.0988; found, 468.0808.

Azidomethyl Fluorescein NHS Ester. Azidomethyl carboxyfluorescein (**4**) (4.60 mg, 10.3 μmol) and *N*-hydroxysuccinimide (1.30 mg, 11.4 μmol) were dissolved in DMF (205 μL). DCC (2.35 mg, 11.4 μmol) was added. After stirring for 2 days at room temperature, the remaining solid residue was removed by filtration. The filtrate was subjected to coupling with 3′-amino DNA without purification.

Synthesis of Unmodified Oligonucleotides. All oligonucleotides were synthesized on a 0.2 μmol scale on a DNA synthesizer (H-8-SE; Gene World) using standard phosphoroamidite coupling chemistry. Deprotection and cleavage from the CPG support was carried out by incubation in concentrated ammonia for 4 h at 55 °C. Following deprotection, the oligonucleotides were purified by reverse-phase column chromatography (MicroPure II column; Biosearch Technologies) and quantitated by UV absorbance using the nearest neighbor approximation to calculate molar absorptivities.

3′-Monoazidomethyl Fluorescein-Conjugated Oligonucleotide. The crude product of azidomethyl fluorescein NHS ester was reacted with 3′-amino-modified oligonucleotide. 3′-PT-amino-modifier C3 CPG (Glen Research) was used to prepare the 3′-amino-modified oligonucleotide. Fifty nanomoles of the 3′-amino-modified oligonucleotide in 50 μL of 80 mM sodium tetraborate (pH 8.5) was shaken for 5 h at room temperature with 0.75 μmol of the compound in 200 μL of dimethylformamide. The reacted products were collected by ethanol precipitation. Next, the collected products were purified by reverse-phase HPLC (0−80% acetonitrile/50 mM triethylammonium acetate gradient). The probe structure was confirmed by ESI-TOF mass spectrometry (Table S1, Supporting Information).

5′-Triphenylphosphine (TPP)-Linked Oligonucleotide. A carboxy-triphenylphosphine (TPP) NHS ester was reacted with a 5′-amino-modified oligonucleotide. 5′-Amino-modifier C6 (Glen Research) was used to prepare the 5′-amino-modified oligonucleotide. Fifty nanomoles of the 5′-amino-modified oligonucleotide in 135 μL of 93 mM sodium tetraborate (pH 8.5) was shaken for 5 h at room temperature with 2 μmol of TPP NHS ester in 115 μL of dimethylformamide. The reacted products were collected by ethanol precipitation. Next, the collected products were purified by reverse-phase HPLC (0−50% acetonitrile/50 mM triethylammonium acetate gradient). The probe structure was confirmed by ESI-TOF mass spectrometry (Table S1, Supporting Information).

3′-Bisazidomethyl Fluorescein-Conjugated Oligonucleotide. The bromoacetyl group of the bisazidomethyl fluorescein was reacted with the phosphorothioate group on the oligonucleotides. For 3′-phosphorothioate sequences, the 3′-phosphate CPG was sulfurized by the sulfrizing reagent (Glen Research) after the first nucleotide was added. Seventy-five nanomoles of the 3′-phosphorothioate oligonucleotide in 50 μL of 400 mM triethylammonium bicarbonate buffer was shaken for 5 h at room temperature with 750 nmol of compound **9** in 200 μL of dimethylformamide. The reacted products were collected by ethanol precipitation. Next, the products were purified by reverse-phase HPLC (0−80% acetonitrile/50 mM triethylammonium acetate gradient). The probe structure was confirmed by ESI-TOF mass spectrometry (Table S1, Supporting Information).

Measurement of Quantum Yield. A 1 mM DMF stock solution of each compound was prepared. Absorption spectra were obtained with a 20 mM tris-HCl buffer (pH 7.2) solution of each compound at the desired concentration, adjusted by appropriate dilution of the 1 mM DMF stock solution. For determination of the quantum efficiency of fluorescence (Φ_{fl}), fluorescein in 0.1 M NaOH was used as a fluorescence standard (Φ = 0.85). The quantum efficiency of fluorescence was obtained with the following equation (F denotes fluorescence intensity at each wavelength, and Σ [F] was calculated by summation of fluorescence intensity).

$$\Phi_{fl}^{sample} = \Phi_{fl}^{standard} Abs^{standard} \Sigma[F^{sample}]/Abs^{sample} \Sigma[F^{standard}]$$

DNA-Templated Reaction. Reactions on the DNA template were performed in 1.2 mL of tris-HCl buffer (20 mM, pH 7.2) containing 100 mM $MgCl_2$ and 0.01 mg/mL BSA with *bcr/abl*-1 or -2, probe 1 (50 nM), and probe 2 (50 nM) at 37 °C. The increase of fluorescence intensity produced by the reduction of probe 1 was continuously monitored at time intervals. Reactions were observed by fluorescence spectrometry (FP-6500; JASCO). For the time course of the azide reduction, the fluorescence intensity was measured for 0.5 s at 1 min intervals: excitation, 490 nm; emission, 520 nm.

Cell Culture and Streptolysin O (SLO) Permeabilization. HL60 cells (RIKEN BRC cell bank) were grown in DMEM without phenol red and containing 10% FCS, 50 units/mL penicillin, and 50 mg/mL streptomycin. They were passaged in 75-cm^2 culture flasks (Falcon). Cells were maintained at 37 °C in an atmosphere of 5% CO_2 at 1 $\times$ 10^5 cells/mL and within 0−20 passages after purchasing from the supplier.

SLO was purchased from BioAcademia (Japan). SLO was activated according to the procedure reported by Abe et al. (*23*). Briefly, SLO (10,000 units/mL) was incubated in Mg^{2+}/Ca^{2+}-

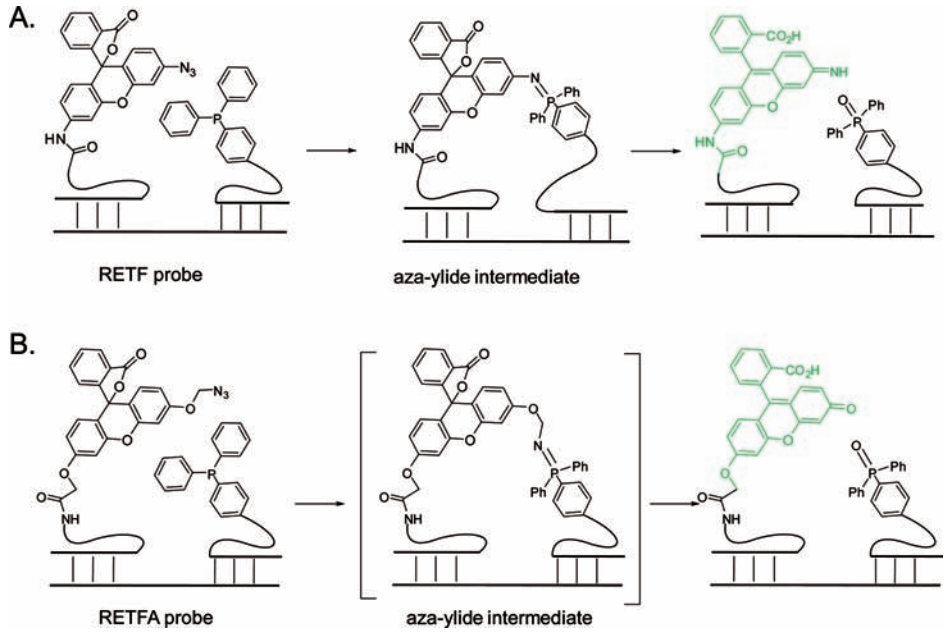

Figure 2. Fluorescence emission of an RETF probe (A) and RETFA probe (B) by triphenylphosphine as reducing reagents.

free PBS buffer solution containing 10 mM DTT and 0.05% BSA at 37 °C for 2 h. Small aliquots of activated SLO were stored at −20 °C. To introduce probes into cells, HL60 cells were washed with Mg^{2+}/Ca^{2+}-free PBS twice and then incubated with 300 mL of Mg^{2+}/Ca^{2+}-free PBS buffer solution containing SLO (50 units/mL), BSA (0.01 mg/mL), and calf thymus DNA (1 mg/mL). After 15 min, the 3′-bisazidomethyl fluorescein-conjugated probe (200 nM) and TPP-conjugated probe (200 nM) were added. After 30 min, cells were resealed by the addition of 1 mL of DMEM containing $CaCl_2$ (0.2 g/L) and incubated for 1 h at 4 °C.

Flow Cytometry. The live cell suspension was directly analyzed without any washing step with a Cytomics FC500 instrument (Beckman Coulter). Fluorescent signals were observed under the following conditions: excitation by argon laser, 488 nm; emission, 515−535 nm. Forward angle light scatter (FSC), side angle light scatter (SSC), and fluorescence data were recorded, and for each measurement, above 1,000 events were stored. Data were analyzed with the CXP analysis software (Beckman Coulter). Fluorescent intensity was determined as the mean of fluorescent value of single cells lying in a gate that were defined in a FSC versus SSC dot plot.

Microscopy and Data Processing. Intracellular distributions of 28S rRNA and β-Actin mRNA were observed using an inverted microscope (IX-81, Olympus). Specimens were illuminated with the 488-nm line of an Ar^+ laser (543-A-A03, Omnichrome) through a 60× oil-immersion objective (PlanApo, Olympus). Fluorescence images were acquired at 500−550 nm through the same objective using an image intensifier (C8600-05; Hamamatsu) and an EB-CCD camera (C7190-20; Hamamatsu) and recorded on a digital videotape. Bright field images of cells in the same field of view were recorded successively to the fluorescence images. Image processing was carried out using MetaMorph software (Molecular Devices). Experiments were performed at 27 °C.

Surface Plasmon Resonance Analysis. Kinetic parameters were assessed using BIAcore equipment with a Series S SensorChip SA (GE Healthcare bioscience). The central part of this equipment is the sensor chip consisting of a gold surface covered with a layer of dextran, which in our case contained streptavidin chemically coupled to dextran. The biotinylated DNA strands (target DNA: *bcr/abl-1*) were immobilized to the streptavidin chip. The association as well as dissociation kinetics of two probes, probe 1 and probe 2, were studied. All kinetics experiments were performed in 20 mM Tris-HCl buffer (pH 7.2) containing 100 mM $MgCl_2$ at 37 °C. To immobilize the biotinylated DNA strand to the streptavidin on the chip surface, 5′-biotin-labeled DNA was dissolved in Tris-HCl buffer at a concentration of 600 nM. The solution (15 μL) was injected with a flow rate of 5 μL/min, and the immobilization was followed in the corresponding sensorgram as a function of time. Probes were dissolved in running buffer at appropriate concentrations (15.6−150 nM). A volume of 75 μL (30 μL/min) was injected to measure the association kinetics, and immediately thereafter, the dissociation was followed by purging running buffer through the system. After an approximately 150 s buffer wash, the immobilized DNA surface was regenerated with 30 μL of 10 mM HCl (30 μL/min). The association and dissociation rate constants for each probe were calculated with BIAcore T100 evaluation software (GE Healthcare bioscience).

RESULTS

Design and Molecular Mechanism of the RETFA Probe. Our chief goal was to develop a new RNA detection probe having a chemical reaction-based fluorogenic compound that was capable of signal amplification under isothermal conditions. As one achievement, we recently reported a RETF system that uses a fluorogenic compound, rhodamine azide derivative, that is activated only by reducing reagents and enhanced 2100 times in fluorescence intensity (Figure 2A) (*48*). Reaction of the RETF probe on an oligonucleotide target proceeded without any enzymes or reagents, and offered high signal and very low background fluorescence under biological conditions. We successfully applied the probe to the detection of oligonucleotides in solution and endogenous RNA in bacterial cells. However, the reaction between the rhodamine azide probe and the TPP probe in the RETF system initially produces a ligated intermediate between the two halves of the probe connected with a stable aza-ylide bond, and then gradually gives half of the fluorescent rhodamine product through hydrolysis of the aza-ylide bond over 24 h (Figure 2A). Formation of a ligated product with an aza-ylide bond between the two probes prevents catalytic turnover because the long product binds the template with higher affinity than the reactant probe did before

Scheme 1[a]

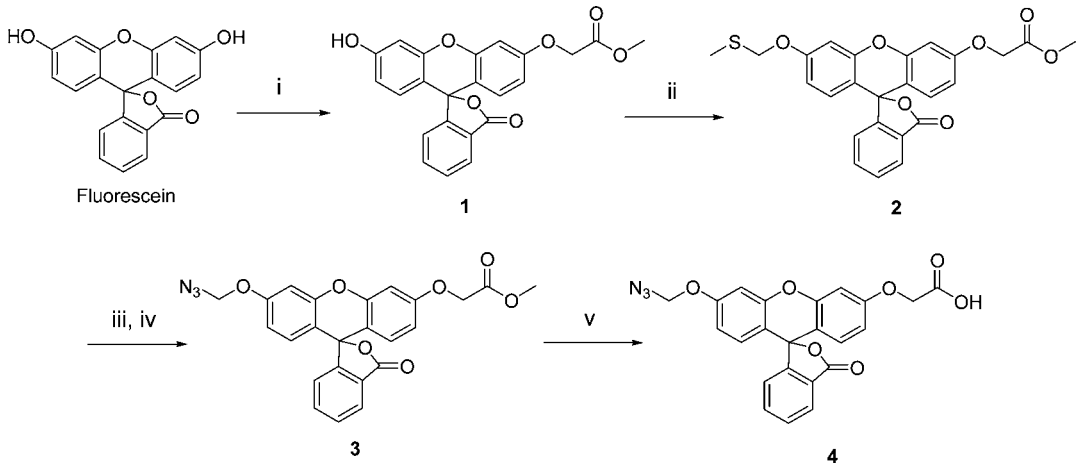

[a] (i) Methyl bromoacetate, sodium iodide, NaI, DMF, rt, 2.5 h, 23%; (ii) chloromethylmethylsulfide, Ag_2O, pyridine, CH_3CN, rt, 15 h, 25%; (iii) NCS, TMSCl, CH_2Cl_2, rt, 1 h; (iv) NaN_3, DMF, rt, 1 h, 44% over 2 steps from 2; (v) NaOH, MeOH, rt, 1 h, 100%. NCS = N-chlorosuccinimide, TMSCl = trimethylsilyl chloride.

Scheme 2[a]

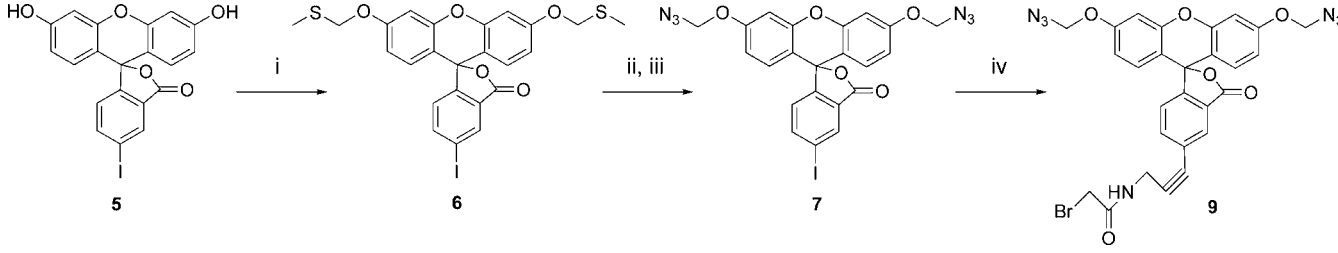

[a] (i) Chloromethylmethylsulfide, Ag_2O, pyridine, CH_3CN, 40 °C, 24 h, 25%; (ii) NCS, TMSCl, CH_2Cl_2, rt, 8 h; (iii) NaN_3, DMF, rt, 30 h, 21% over 2 steps from 2; (iv) 8, tetrakis (triphenylphosphine) palladium, CuI, TEA, THF, rt, 3 h, 37%. NCS = N-chlorosuccinimide, TMSCl = trimethylsilyl chloride, TEA = triethylamine, THF = tetrahydrofuran.

reaction. To achieve higher sensitivity for detecting less abundant RNA species such as intracellular mRNA, the RETF system still shows room for improvement to achieve efficient turnover.

To obtain a high turnover in the reaction mechanism of the RETF probe, the aza-ylide bond of the ligated intermediate must be quickly hydrolyzed to reduce product inhibition. We assumed that the aza-ylide bond in the RETF system is stabilized by long π-conjugation between rhodamine and triphenylphosphine (*63*). Therefore, it was suggested that to destabilize the aza-ylide bond, π-conjugation of the intermediate should be minimized. Here, we designed a fluorogenic molecule based on azidomethyl-protected fluorescein that was switched on by reduction (Figure 2B). In the first step of the reaction, the unstable aza-ylide bond is formed and quickly hydrolyzed. Consequently, the azide group is transformed to an amino group, and TPP is transformed to the corresponding phosphorus compound. The resulting amino-hemiacetal group is quickly hydrolyzed to give an unmasked phenol group, and the probe emits a fluorescence signal. A reduction-triggered fluorescence amplification (RETFA) system with azidomethyl-protected fluorescein is expected to offer efficient turnover because of the short life of the ligated intermediate (Figure 2B).

Synthesis of Azidomethyl Fluorescein. We designed two fluorogenic compounds, monoazidomethyl fluorescein (MAF) and bisazidomethyl fluorescein (BAF). MAF offers a quantitative fluorescence signal to give a single product after deprotection of the azidomethyl group. However, BAF offers a more potent fluorescent signal after deprotection of the two azidomethyl groups. The synthesis of MAF (**4**) is shown in Scheme 1. Mono-*O*-carboxymethyl fluorescein **1** was synthesized by treatment with one equivalent of methyl bromoacetate in the presence of potassium *tert*-butoxide and sodium iodide from commercially available fluorescein in 23% yield (*64*). The treatment of compound **1** with chloromethyl methyl sulfide and Ag_2O in pyridine gave methyl thioacetal **2** in 25% yield (*62*). Activation of *O,S*-acetal with *N*-chlorosuccinimide (NCS) in the presence of *tert*-butyldimethylsilyl chloride (TMS-Cl) provides the chloromethyl intermediate. The intermediate was unstable during purification by flash chromatography and was used for the next reaction without further purification. The transformation of the intermediate to azide **3** was carried out by treatment with sodium azide in 44% yield in two steps. Hydrolysis of methyl ester **3** with NaOH provided the desired azidomethyl carboxyfluorescein (**4**). The NHS ester was prepared by dicyclohexylcarbodiimide-mediated coupling of *N*-hydroxysuccinimide with compound **4**. This activated ester cannot be purified by flash chromatography because of hydrolysis; therefore, the crude product of the NHS ester was directly used for coupling with the DNA probe. Synthesis of BAF is shown in Scheme 2. 5-Iodofluorescein was protected with chloromethyl methyl sulfide to give bismethyl thioacetal **6** in 25% yield. Compound **6** was transformed to bisazidomethyl fluorescein **7** by treatment with NCS and NaN_3. Finally, the desired BAF **9** was obtained by Sonogashira coupling between **7** and 2-bromoacetyl propargylamide.

Spectrum Analysis of Azidomethyl Fluorescein. We tested the photochemical properties of azidomethyl fluorescein (Figure 3). MAF **3** showed no absorbance at wavelengths longer than 350 nm in 20 mM Tris-HCl (pH 7.2), whereas the corresponding monoalkyl fluorescein **1** showed absorption bands at 455 and 490 nm. When a high concentration of dithiothreitol (DTT) was added to a solution of MAF **3**, a

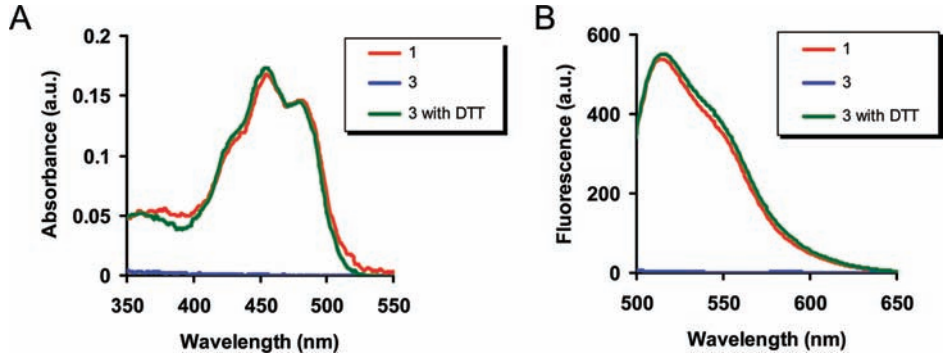

Figure 3. Spectrum analysis. (A) Absorption spectra of 100 μM **1** (red), **3** (blue), or **3** treatment with 100 mM DTT (green) in 20 mM Tris-HCl (pH 7.2) in 50% DMF/H_2O at 25 °C. (B) Fluorescent emission spectra with excitation at 490 nm of 500 nM **1** (red), **3** (blue), or **3** treatment with 100 mM DTT (green) in 20 mM Tris-HCl (pH 7.2) in 5% DMF/ H_2O at 25 °C.

peak having a maximum at 455 nm appeared, resulting from reduction followed by hydrolysis of the azidomethyl group (Figure 3A). The fluorescence properties of azidomethyl fluorescein (MAF) were also examined. No significant fluorescence with excitation at 490 nm was observed for MAF **3**. However, monoalkyl fluorescein **1** showed strong fluorescence emission at around 520 nm. After the addition of DTT to the solution of MAF **3**, a strong emission appeared around 515 nm; the emission was enhanced almost 300-fold (Figure 3B). Monoalkyl fluorescein **1** showed high fluorescence quantum yields (0.20) in contrast with the low yield of MAF **3** (<0.01) (Table 1). We also measured the quantum yields of BAF **7** and its deprotected form **5**. The quantum yields of **5** were 0.68, which is higher than monoalkyl fluorescein **1**, whereas BAF **7** also shows a low quantum yield (<0.01) (Table 1).

Reaction of the RETFA Probe *in Vitro.* We designed two DNA probes to test the utility of the RETFA system for fluorescence-based oligonucleotide detection (Figure 4). The probes and target sequences are shown in Figure 4A. Probe 1 was modified at the 3′-terminal with MAF, where the crude NHS-ester product derived from **4** was reacted with the amino group at the 3′-end of the DNA probe (Figure S1A, Supporting Information). Probe **2** was modified at the 5′-terminal with 2′-carboxytriphenylphosphine (TPP), which was conjugated with the 5′-amino linker of the DNA probe through amide bond formation (Figure S1B, Supporting Information). Two DNA templates originating from the human *bcr/abl* junction site sequence, which is related to chronic myelogenous leukemia, were designed containing *bcr/abl-1* with a full match sequence and also *bcr/abl-2* with a one-base mismatch to evaluate the ability for single-base discrimination that is important for diagnostic applications (*65*).

To prove whether the probes could function by emitting fluorescence, we tested the RETFA probe *in vitro*. The RETFA probe pairs consisted of an 8-mer MAF probe (probe 1) and a 10-mer TPP probe (probe 2). The T_m of two adjacent probes and target DNA was 46.7 °C (Figure S2, Supporting Information). When 50 nM probe 1 and probe 2 were incubated in Tris-HCl buffer (pH 7.2) at 37 °C, the increase in fluorescence at 520 nm was monitored. In the presence of target *bcr/abl-1*, the signal at 520 nm reached saturation within 3 min by deprotection of the azidomethyl group of probe 1 (Figure 4B). The signal

Table 1. Quantum Yields of the Compounds[a]

compound	**1**	**3**	**5**	**7**
Φ_F[b]	0.202	<0.001	0.683	0.002

[a] All measurements were performed in Tris-HCl buffer (20 mM, pH 7.2). Compounds were excited at 490 nm. [b] Quantum yields were determined using fluorescein in 0.1 M NaOH as a standard (Φ_F = 0.85).

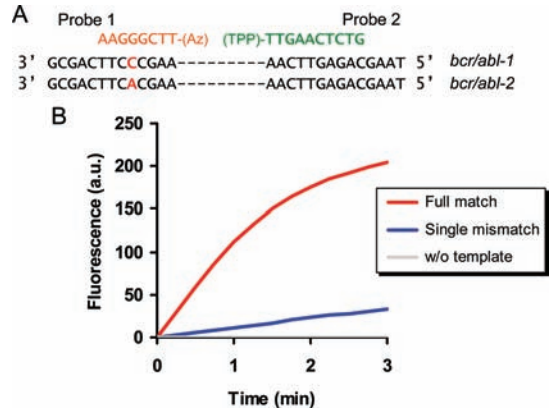

Figure 4. (A) Probe sequences for the *bcr/abl* gene. Designed 8- or 10-mer probes are azidomethyl fluorescein probe or TPP probe, respectively. The DNA targets are 27-mer ODNs with a full matched sequence *bcr/abl-1* and a single mismatched sequence *bcr/abl-2*. (B) Time course of the fluorescence intensity in the reaction between 50 nM probe 1 and 2 with 50 nM matched *bcr/abl-1* or mismatched DNA *bcr/abl-2* in pH 7.2 Tris-HCl buffer containing 100 mM $MgCl_2$ and 10 μg/mL BSA. The reaction was monitored by excitation at 490 nm and emission at 520 nm.

did not increase in the absence of target *bcr/abl-1* for 3 min. HPLC and MALDI-TOF mass analyses showed that 97.7% of probe 1 that reacted with probe 2 on the template after 5 min was converted to the deprotected product (Figure S3, Supporting Information). Next, the reaction of probe 1 and probe 2 in the presence of one-base-mismatched target *bcr/abl*-2 was tested and showed good single-base mismatch discrimination, dropping in initial rate by 9.5-fold, compared with fully matched *bcr/abl-1* (Figure 4B).

Turnover Measurements. The RETFA system was expected to cause multiple reactions with turnover using target oligonucleotide as a catalytic template. Thus, we tested the ability for fluorescent signal amplification. Catalytic turnover, and the associated signal amplification, is useful when target concentrations are low (*49, 51, 54*). Under these conditions, one would typically use a large excess of the probe relative to the number of targets. To measure turnover with the current probes, we compared the number of equivalents of fluorescent signal with moles of target. This required the development of a method for carefully quantitating the signal and confirming that the signal arises from true template-dependent intermolecular reactions rather than from background sources such as intermolecular reactions independent of the template strand or photolysis of the azidomethyl group by the excitation light.

To evaluate this, we performed DNA-templated reactions at various target concentrations and continuously monitored the

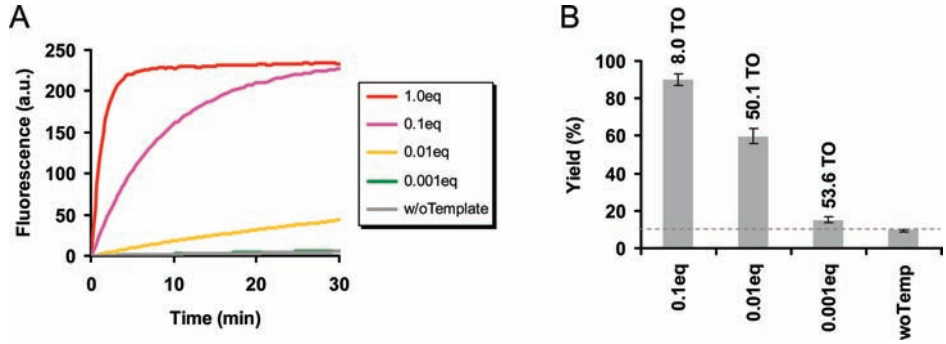

Figure 5. Turnover experiment. (A) Time course of fluorescence intensity in the reaction between 50 nM matched azidomethyl fluorescein and 50 nM matched TPP probe at shown target DNA concentrations in pH 7.2 Tris-HCl buffer containing 100 mM $MgCl_2$ and 10 μg/mL BSA. (B) Reaction yields after 4 h and turnover numbers (TO).

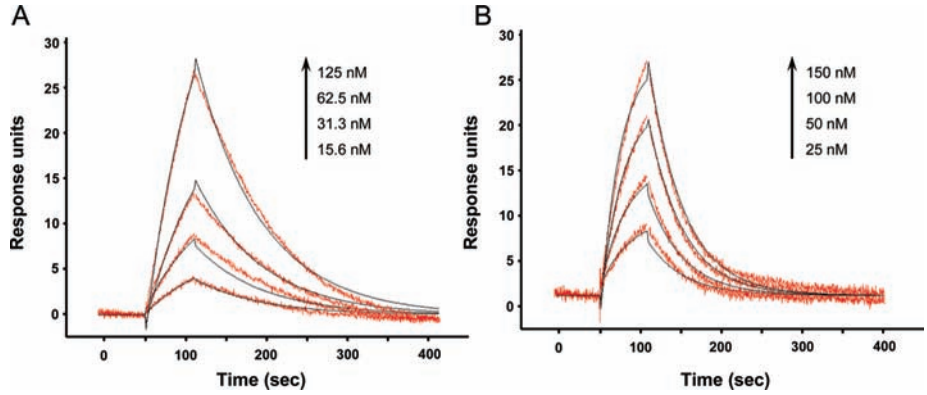

Figure 6. DNA hybridization sensorgrams (fully complementary duplex) analyzed by biacore with varying concentrations of the azidomethyl fluorescein probe (A) or TPP probe (B). The values inside the graphs indicate the probe concentrations.

fluorescent signals as a function of time (Figure 5A). We first prepared a standard dilution curve to make a calibration plot of fluorescent intensity as a function of the amount of the deprotected (= fluorescent) probe 1. This plot showed good linearity and allowed us to take a given signal and, from the plot, extract the number of moles of fluorescent product in solution. Turnover (TO) number was obtained by dividing the number of moles of fluorescent product by that of template DNA (Figure 5B). The turnover of reaction products from the target DNA is expected to increase as the concentration of target decreases. To test this, we varied target concentrations over the range from 50 nM to 50 pM. The probe concentrations were held constant at a considerable excess (50 nM). To ensure that the signal was not the result of template-independent reactions or hydrolysis, we subtracted background signals from identical reactions lacking templates.

The time course of the fluorescent signal at 520 nm showed a rapid signal increase in the presence of 1 equiv of matched DNA *bcr/abl-1* (Figure 5A, red line) within 5 min. Catalytic amounts of *bcr/abl-1* (0.1 equiv, 5 nM) also proved efficient in conferring a rapid signal increase, reaching a plateau within 30 min, which is the same level of fluorescence signal to the stoichiometric amount of *bcr/abl-1* (Figure 5A, pink line), and provided 90% yield of reaction product after 4 h calculated from the fluorescence standard curve (Figure 5B). In the absence of DNA, 50 nM probes 1 and 2 yielded 9.7% background reaction after 4 h (Figure 5A, gray line). When the background signal is subtracted, the RETFA probe achieved 8.0 TO in the case of 0.1 equiv *bcr/abl-1*. With a load of 0.01 equiv (500 pM) *bcr/abl-1*, the reaction showed slower fluorescence increase than in the case of 0.1 equiv *bcr/abl-1* (Figure 5A, yellow line) and furnished 69% of the fluorescent product with 50 TO after 4 h. The highest TO number of 54 was achieved with 0.001 equiv *bcr/abl-1* (50 pM; Figure 5A, green line). The speed of the DNA-catalyzed reaction is reduced at very low DNA/probe ratios to an extent that reaction yields are dominated by the off-template background reaction. However, the 15% reaction product obtained with 0.001 equiv *bcr/abl-1* (50 pM) demonstrates that the DNA-templated reaction (5.4%) proceeds more efficiently than the background reaction (9.7%), even with such a very low concentration of target.

Kinetic Analysis of the DNA-Templated Reaction. The mechanism of a DNA-catalyzed reaction gives important information for optimizing the RETFA probe and designing new probes. However, a study of the mechanism has not been carefully carried out. In particular, the rate-limiting step of the DNA-catalyzed reaction is still unclear. Thus, we evaluated the association and dissociation rate constants for the DNA hybridization between *bcr/abl-1* and the RETFA probe, and the rate constants of the azide reduction on DNA templates to obtain information on the rate-limiting step.

The kinetics of association (k_a) and dissociation (k_d) of probe 1 or probe 2 to the immobilized *bcr/abl-1* were successfully monitored using BIAcore technology (*66*). Figure 6 shows that BIAcore trajectories of *bcr/abl-1*/probe 1 or *bcr/abl-1*/probe 2 hybridization runs at different concentrations of each probe in solution. The k_a and k_d for each probe were calculated with BIAcore T100 evaluation software and are summarized in Table 2. The k_a for probes 1 and 2 are 3.1×10^4 M^{-1} s^{-1} (k_{a1}) and 1.3×10^4 M^{-1} s^{-1} (k_{a2}), respectively. The concentration of the DNA-templated reaction (C_0) was 50 nM. Therefore, the k_a' ($k_a \times C_0$) for probes 1 and 2 are calculated as 1.5×10^{-3} s^{-1} (k_{a1}') and 6.3×10^{-3} s^{-1} (k_{a2}'), respectively. However, the k_d for probes 1 and 2 showed about 10 times higher values, 2.2×10^{-2} s^{-1} (k_{d1}) and 1.2×10^{-2} s^{-1} (k_{d2}), than k_a'.

Next, to determine the rate constant of azide reduction on DNA templates, the plots of $\ln[\text{probe 1}]_t/[\text{probe 1}]_0$ versus time were analyzed by linear regression as simple first-order kinetics

Table 2. Kinetic Parameters for the Hybridization of Each Probe and DNA-Templated Reaction

	k_a ($\times 10^4$ M^{-1} s^{-1})	k_a' ($\times 10^{-3}$ s^{-1})	k_d ($\times 10^{-2}$ s^{-1})	k_{app} ($\times 10^{-3}$ s^{-1})
hybridization (probe 1)[a]	3.06	1.53	1.25	
hybridization (probe 2)[a]	1.26	6.29	2.24	
DNA-templated reaction[b]				5.91

[a] Analyzed by a BIAcore instrument. [b] Analyzed by linear regression as simple first-order kinetics by Microsoft Excel.

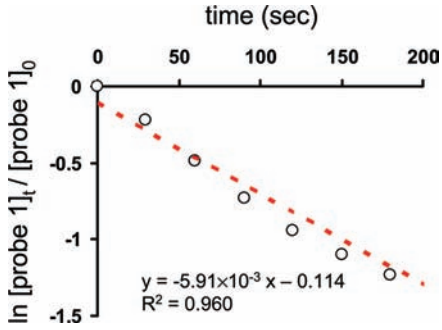

Figure 7. Plots of ln[probe 1]$_t$/[probe 1]$_0$ versus time for 50 nM azidomethyl fluorescein and TPP probe with 50 nM target in 20 mM Tris-HCl (pH 7.2) containing 100 mM $MgCl_2$ and 10 μg/mL BSA.

by Microsoft Excel (Figure 7). [probe 1]$_0$, [probe 1]$_t$, and [reduced probe 1]$_t$ correspond to initial concentration of probe 1, time dependent concentration of probe 1, and concentration of reduced product, respectively. [probe 1]$_t$ was calculated according to [probe 1]$_t$ = [probe 1]$_0$ − [reduced probe 1]$_t$, and [reduced probe 1]$_t$ was calculated from a standard curve. The apparent first-order rate constant, k_{app}, was obtained from the slope of this plot as 5.9×10^{-3} s^{-1}. The value of k_{app} is very close to the association rate constants k_{a1}' and k_{a2}', which is the slower step in the hybridization kinetics. This similarity suggests that the actual reaction rate of an azide reduction on DNA templates (k_{act}) is close to or even faster than the hybridization kinetics. Therefore, we assumed that the association of the probe to the DNA template might be the rate-limiting step for the DNA-catalyzed reaction for the RETFA probe.

Flow Cytometric Analysis of RNAs in HL60 Cells. So far, there has only been one example of quenched probes in living human cells. Flow cytometry (FC) offers the possibility of rapid analysis of a large number of cells and quantitative evaluation of an average over all RNA signals. Thus, we evaluated the feasibility of FC analysis of RNAs by the RETFA probe in HL60 cells. In the in-cell experiment, we used the bisazidomethyl-quenched fluorescein probe because the quantum yield for the deprotected form of **9**, 0.683, is higher than that of monoazide **3**, 0.202. As described above, our probes have a potential for catalytic turnover. Therefore, both azidomethyl groups on **9** should be deprotected. The targets we chose were 28S rRNA, which is abundant in cells, and β-Actin mRNA, which has relatively low copies in cells (~2500 molecules per cell) (*36*). To decide if the RETFA probe offers the desired fluorescent signal from the target and evaluate any undesired background fluorescence signal from the nontemplated reaction or decomposition of the probe, we carried out a series of control experiments by testing the following conditions: the scramble probes, only the profluorescent azide probe, and no probe (the cellular autofluorescence). The sequence of the scramble probe was designed so as not to hybridize next to each other on the target RNA. The probe and target site sequences for 28S rRNA and β-Actin mRNA are described in Figures S4A and S5A (Supporting Information), respectively. Prior to the FC analysis, we determined whether the probes could generate a target-dependent fluorescence signal *in vitro* using a short DNA target. As shown in Figure S4B (Supporting Information), no significant background fluorescence was observed in the absence of the short 28S rRNA target. In the case of targeting β-Actin mRNA, we used three sets of probes for multiple target sites to increase sensitivity (Figure S5A, Supporting Information). The three sets of probes for β-Actin mRNA (33.3 nM each) and DNA targets (33.3 nM each) were mixed to adjust the total concentrations to 100 nM. Reaction of the scramble probe was tested under the same conditions. The reaction with the β-Actin probe shows a strong fluorescence signal with the target and generated a slight background signal without the target, which was comparable with the background level in the case of the scramble probes (Figure S5B, Supporting Information).

The FC data are summarized in Figure 8. To introduce the probes into cells, the cells were permeabilized with streptolysin O (SLO) according to the previously reported method. The cells were incubated with SLO in the presence of the RETFA probe for 30 min, resealed with cell culture medium containing $CaCl_2$, and incubated for 1 h at 37 °C and analyzed by FC. The histogram data indicate cell populations with varied fluorescence intensity, which correspond to 28S rRNA, three sets of β-Actin mRNA, scramble probes, only azide probe, and no probe (Figure

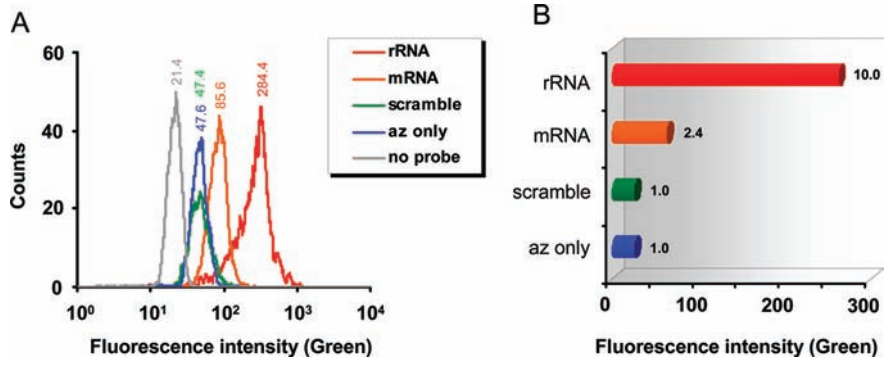

Figure 8. Detection of intracellular RNAs in HL60 cells by flow cytometry. (A) Flow cytometry histogram showing cell-count frequency vs fluorescence intensity for each probe. These histograms correspond to cells that were treated by no probe (negative control, gray); by azidomethyl fluorescein probe only (negative control, blue); by scramble probe (negative control, green); by β-Actin mRNA targeted probes (orange); and by 28S rRNA targeted probes (red). The values on each histogram indicate the mean fluorescent signals. (B) Means of fluorescence intensity and signal to background calculated from the histograms. The bars were corrected by cell autofluorescence background (no probe). The values next to the bars indicate the ratios between each probe and scramble probe as a signal to background.

8A). The median values of fluorescence intensity after subtraction of autofluorescence from cells (no probe) are plotted in Figure 8B. The values on the bars indicate signal to background (S/B) ratio, which is defined as the relative ratios of fluorescence intensity to background signal from the scramble probe. Both 28S rRNA and the three sets of β-Actin mRNA probes offered significantly higher fluorescence signals than did the controls, although each set of β-Actin mRNA probes did not produce a significant signal. The background value from the scramble probes was comparable with that from the azide probe alone, indicating that undesirable intermolecular reactions between the TPP probe and the azidomethyl probe did not occur in living cells. The S/B ratios were 10.0 and 2.4 for 28S rRNA and β-Actin mRNA, respectively. This result clearly showed that cellular endogenous 28S rRNA and β-Actin mRNA can be detected by our RETFA probes and is consistent with the notion that 28S rRNA is more abundant than β-Actin mRNA in the cells.

Fluorescence Microscopic Analysis of RNAs in HL60 Cells. To demonstrate that our approach can give a clear and detailed picture of intracellular localization in living cells, we carried out fluorescence microscopic analysis of RNA species. The imaging technique may reveal important information on mRNA processing, transport, and protein production. Fluorescence images of 28S rRNA and β-Actin mRNA in HL60 cells are shown in Figure 9. First, imaging 28S rRNA was performed using bisazidomethyl fluorescein and TPP probes as for the FC experiment. After the probes were introduced into cells using the SLO method, the cell suspension was directly spotted on glass slides without any washing step and was imaged by a fluorescence microscope. Specimens were illuminated with a 488 nm laser, and the specific fluorescence signal from the probe was directed at fluorescein emission 500−550 nm. Panels C and D in Figure 9 display the fluorescent signal of the scramble probes, showing that little or no signal was observed. However, a strong signal was observed in the nucleolus using target-specific probes (panels A and B), which is in fair agreement with previous results by FISH in fixed specimens (*67*).

Next, to confirm that our system can detect low-expression RNA in cells, β-Actin mRNA probes were delivered into HL60 cells using SLO. Again, the majority of the fluorescent signals was observed around the nucleus only from target-specific probes (panels E and F), whereas the scramble probes gave small signals (panels G and H). We conclude that signals from specific RNAs can be observed using the designed RETFA probe in human cells.

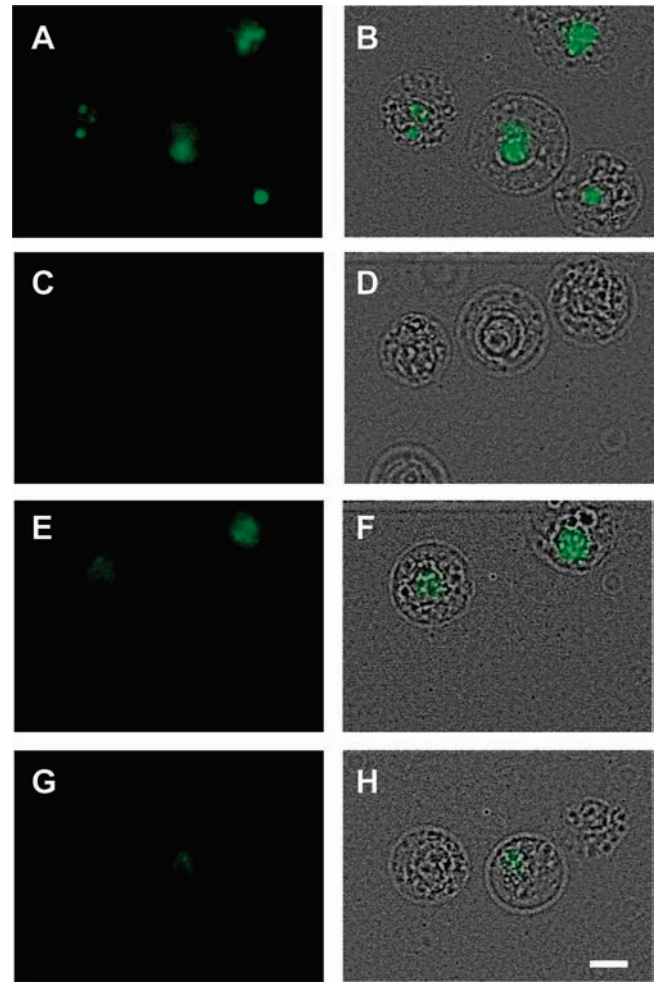

Figure 9. Detection of intracellular human 28S rRNA and β-Actin mRNA by fluorescence microscopy. (A−D) 28S rRNA probe (A and B) and scramble control (C and D). A and C show fluorescent signal only. B and D show its overlay with bright field image. (E−H) β-Actin mRNA probe (E and F) and scramble control (G and H). E and G show the fluorescent signal only. F and H show its overlay with bright field image. Bar: 10 μm.

DISCUSSION

The Staudinger reduction of organic azides by TPP holds promise for OTR because of its exceptional degree of bioorthogonality. Several ideas have been applied to link the Staudinger reaction to the fluorescence turn-on event for OTR. These strategies can be categorized into two types. One strategy involves the reaction step where the azide probe unmasks a 2-(diphenylphosphino)benzoate derivative of fluorescein (*47*). Alternatively, a TPP-probe activates the azide-masked fluorophores, which are 7-azidocoumarin (*49*) and azide-substituted rhodamines (RETF probe) (*48*). In addition, azidomethyl-protected coumarin has very recently been reported as a new fluorogenic molecule (*50*). These probes demonstrate excellent signal amplification with fluorescence readout except for the RETF probe. However, possible drawbacks limit the scope of in-cell applications because of increased undesired background fluorescence. This may be due to the hydrolysis of the phenolic ester or light decomposition of the azide group when azide-protected coumarin is irradiated with excitation light in the ultraviolet region. In general, oxidation of TPP in living cells was also involved. Consequently, these previous approaches have not been applied to imaging or detection of RNA in living cells (*47*−*50*).

In this article, we have demonstrated that the RETFA probe with azidomethyl-protected fluorescein can detect endogenous RNAs in living cells. Azidomethyl-protected fluorescein is quickly uncaged by reduction of the azide group and emits fluorescence at 520 nm with excitation at 490 nm, which is a suitable wavelength for in-cell detection. In addition, the RETFA probe completed the stoichiometric reaction within 3 min and can amplify fluorescence signals based on a catalytic OTR when the target is at a very low concentration compared with that of the probes (*26*, *41*, *46*, *47*, *49*−*51*). The TO number reached up to 50 when 100 times excess of probe was used. This amplification property is one of the great improvements compared with our previous RETF probe (*48*).

Quantitative detection of 28S rRNA and β-Actin mRNA was successfully carried out on the FC instrument. A single probe was sufficient for the detection of 28S rRNA. However, simultaneous introduction of three sets of probes offered significant signal for detection of β-Actin, although each individual probe offered no significant signal. Cellar mRNA is known to form complex secondary or tertiary structures. It is very hard to design an optimum probe with accessibility to target sites. This result indicates that introducing multiple sets of

probes might be one solution to achieve accessibility by opening up the complex mRNA structure. However, accessibility or turnover of RETFA probe is different on each RNA target. Therefore, further study is required to estimate the exact amount of RNA species in living cells.

Finally, development of an efficient catalytic reaction on the oligonucleotide template is still challenging. The RETFA probe is expected to moderate product inhibition on catalytic OTR because the T_m of unreacted probes or products to the target is almost same. Unreacted probes and products become exchangeable on the target to give turnover when the T_m is close to reaction temperature. Therefore, probe length was designed to give a T_m that is close to 37 °C at biological conditions. Next, we carried out a mechanistic study of the catalytic reaction on the RETFA probe to obtain clues for designing efficient turnover probes. Kinetic analysis by BIAcore technology showed that the association step of the probe (k_a') is 10 times slower than the dissociation step (k_d') on probe hybridization. The apparent rate constant of the fluorogenic chemical reaction (k_{app}) has a value similar to that of k_a'. Presumably, association might be the rate-limiting step for the amplification reaction from these results, although this experiment did not reflect an exact phenomenon in solution. We assume that new probe designs should enhance association speed to achieve more efficient turnover.

CONCLUSIONS

We have developed a reduction-triggered fluorescent amplification (RETFA) probe with a new azidomethyl-protected fluorescein. The RETFA probe completes the reaction within 3 min and can amplify the fluorescence signal from the target up to 50 times. The probe was successfully applied to the detection of endogenous RNA in living human cells using flow cytometry and fluorescence microscopy.

ACKNOWLEDGMENT

H.A. and Y.I. were financially supported by MEXT (Ministry of Education, Culture, Sports, Science, and Technology of Japan) and NEDO (New Energy and Industrial Technology Development Organization of Japan), and by MEXT, respectively. K.F. was supported by a Grant-in-Aid for JSPS Fellows. This work was also supported by a Grant-in-Aid for Scientific Research on Priority Areas "Lifesurveyor" from MEXT. We are grateful to the support of BSI's Research Resources Center for mass spectrum analysis.

Supporting Information Available: The scheme for synthesizing BAF, MALDI-TOF mass analysis of synthesized probes, the structures, sequences, and *Tm* of the probes, HPLC analysis of the reaction product, and ^{1}H-NMR and ^{13}C-NMR data. This material is available free of charge via the Internet at http://pubs.acs.org/BC.

LITERATURE CITED

(1) Shav-Tal, Y., Darzacq, X., and Singer, R. H. (2006) Gene expression within a dynamic nuclear landscape. *EMBO J. 25*, 3469–3479.
(2) Dirks, R. W., and Tanke, H. J. (2006) Advances in fluorescent tracking of nucleic acids in living cells. *Biotechniques 40*, 489–496.
(3) Behrens, S., Fuchs, B. M., Mueller, F., and Amann, R. (2003) Is the in situ accessibility of the 16S rRNA of *Escherichia coli* for Cy3-labeled oligonucleotide probes predicted by a three-dimensional structure model of the 30S ribosomal subunit? *Appl. Environ. Microbiol. 69*, 4935–4941.
(4) Dirks, R. W., Molenaar, C., and Tanke, H. J. (2001) Methods for visualizing RNA processing and transport pathways in living cells. *Histochem. Cell Biol. 115*, 3–11.
(5) Czaplinski, K., and Singer, R. H. (2006) Pathways for mRNA localization in the cytoplasm. *Trends Biochem. Sci. 31*, 687–693.
(6) Shav-Tal, Y., Darzacq, X., Shenoy, S. M., Fusco, D., Janicki, S. M., Spector, D. L., and Singer, R. H. (2004) Dynamics of single mRNPs in nuclei of living cells. *Science 304*, 1797–1800.
(7) Levsky, J. M., and Singer, R. H. (2003) Fluorescence in situ hybridization: past, present and future. *J. Cell Sci. 116*, 2833–2838.
(8) Isaacs, F. J., Dwyer, D. J., Ding, C. M., Pervouchine, D. D., Cantor, C. R., and Collins, J. J. (2004) Engineered riboregulators enable post-transcriptional control of gene expression. *Nat. Biotechnol. 22*, 841–847.
(9) Hasegawa, S., Jackson, W. C., Tsien, R. Y., and Rao, J. (2003) Imaging Tetrahymena ribozyme splicing activity in single live mammalian cells. *Proc. Natl. Acad. Sci. U.S.A. 100*, 14892–14896.
(10) Rodriguez, A. J., Condeelis, J., Singer, R. H., and Dictenberg, J. B. (2007) Imaging mRNA movement from transcription sites to translation sites. *Semin. Cell Dev. Biol. 18*, 202–208.
(11) Lewin, B. (1997) *Gene* VI ed., Oxford university press, Inc., New York.
(12) Giles, R. V., and Tidd, D. M. (1992) Increased specificity for antisense oligodeoxynucleotide targeting of RNA cleavage by RNaseH using chimeric methylphosphonodiester phosphodiester structures. *Nucleic Acids Res. 20*, 763–770.
(13) Tu, G. C., Cao, Q. N., Zhou, F., and Israel, Y. (1998) Tetranucleotide GGGA motif in primary RNA transcripts: Novel target site for antisense design. *J. Biol. Chem. 273*, 25125–25131.
(14) Sohail, M., and Southern, E. M. (2000) Selecting optimal antisense reagents. *Adv. Drug Delivery Rev. 44*, 23–34.
(15) Tyagi, S., Bratu, D. P., and Kramer, F. R. (1998) Multicolor molecular beacons for allele discrimination. *Nat. Biotechnol. 16*, 49–58.
(16) Tyagi, S., and Kramer, F. R. (1996) Molecular beacons: probes that fluoresce upon hybridization. *Nat. Biotechnol. 14*, 303–308.
(17) Piatek, A. S., Tyagi, S., Pol, A. C., Telenti, A., Miller, L. P., Kramer, F. R., and Alland, D. (1998) Molecular beacon sequence analysis for detecting drug resistance in *Mycobacterium tuberculosis*. *Nat. Biotechnol. 16*, 359–363.
(18) Tyagi, S., Marras, S. A., and Kramer, F. R. (2000) Wavelength-shifting molecular beacons. *Nat. Biotechnol. 18*, 1191–1196.
(19) Bratu, D. P., Cha, B. J., Mhlanga, M. M., Kramer, F. R., and Tyagi, S. (2003) Visualizing the distribution and transport of mRNAs in living cells. *Proc. Natl. Acad. Sci. U.S.A. 100*, 13308–13313.
(20) Vargas, D. Y., Raj, A., Marras, S. A. E., Kramer, F. R., and Tyagi, S. (2005) Mechanism of mRNA transport in the nucleus. *Proc. Natl. Acad. Sci. U.S.A. 102*, 17008–17013.
(21) Sando, S., and Kool, E. T. (2002) Imaging of RNA in bacteria with self-ligating quenched probes. *J. Am. Chem. Soc. 124*, 9686–9687.
(22) Silverman, A. P., and Kool, E. T. (2006) Detecting RNA and DNA with templated chemical reactions. *Chem. Rev. 106*, 3775–3789.
(23) Abe, H., and Kool, E. T. (2006) Flow cytometric detection of specific RNAs in native human cells with quenched autoligating FRET probes. *Proc. Natl. Acad. Sci. U.S.A. 103*, 263–268.
(24) Silverman, A. P., and Kool, E. T. (2007) Oligonucleotide probes for RNA-targeted fluorescence in situ hybridization. *Adv. Clin. Chem. 43*, 79–115.
(25) Sando, S., and Kool, E. T. (2002) Quencher as leaving group: efficient detection of DNA-joining reactions. *J. Am. Chem. Soc. 124*, 2096–2097.
(26) Abe, H., and Kool, E. T. (2004) Destabilizing universal linkers for signal amplification in self-ligating probes for RNA. *J. Am. Chem. Soc. 126*, 13980–13986.
(27) Sando, S., Abe, H., and Kool, E. T. (2004) Quenched autoligating DNAs: multicolor identification of nucleic acids at single nucleotide resolution. *J. Am. Chem. Soc. 126*, 1081–1087.

(28) Fang, X. H., Li, J. J., and Tan, W. H. (2000) Using molecular beacons to probe molecular interactions between lactate dehydrogenase and single-stranded DNA. *Anal. Chem. 72*, 3280–3285.
(29) Tsuji, A., Koshimoto, H., Sato, Y., Hirano, M., Sei-Iida, Y., Kondo, S., and Ishibashi, K. (2000) Direct observation of specific messenger RNA in a single living cell under a fluorescence microscope. *Biophys. J. 78*, 3260–3274.
(30) Molenaar, C., Marras, S. A., Slats, J. C. M., Truffert, J. C., Lemaitre, M., Raap, A. K., Dirks, R. W., and Tanke, H. J. (2001) Linear 2′ O-methyl RNA probes for the visualization of RNA in living cells. *Nucleic Acids Res. 29*, e89.
(31) Perlette, J., and Tan, W. (2001) Real-time monitoring of intracellular mRNA hybridization inside single living cells. *Anal. Chem. 73*, 5544–5550.
(32) Bratu, D. P., Cha, B. J., Mhlanga, M. M., Kramer, F. R., and Tyagi, S. (2003) Visualizing the distribution and transport of mRNAs in living cells. *Proc. Natl. Acad. Sci. U.S.A. 100*, 13308–13313.
(33) Santangelo, P. J., Nix, B., Tsourkas, A., and Bao, G. (2004) Dual FRET molecular beacons for mRNA detection in living cells. *Nucleic Acids Res. 32*, e57.
(34) Nitin, N., Santangelo, P. J., Kim, G., Nie, S., and Bao, G. (2004) Peptide-linked molecular beacons for efficient delivery and rapid mRNA detection in living cells. *Nucleic Acids Res. 32*, e58.
(35) Matsuo, T. (1998) In situ visualization of messenger RNA for basic fibroblast growth factor in living cells. *Biochim. Biophys. Acta 1379*, 178–184.
(36) Tyagi, S., and Alsmadi, O. (2004) Imaging native beta-Actin mRNA in motile fibroblasts. *Biophys. J. 87*, 4153–4162.
(37) Sokol, D. L., Zhang, X., Lu, P., and Gewirtz, A. M. (1998) Real time detection of DNA.RNA hybridization in living cells. *Proc. Natl. Acad. Sci. U.S.A. 95*, 11538–11543.
(38) Wang, W., Cui, Z. Q., Han, H., Zhang, Z. P., Wei, H. P., Zhou, Y. F., Chen, Z., and Zhang, X. E. (2008) Imaging and characterizing influenza A virus mRNA transport in living cells. *Nucleic Acids Res. 36*, 4913–4928.
(39) Chen, A. K., Behlke, M. A., and Tsourkas, A. (2007) Avoiding false-positive signals with nuclease-vulnerable molecular beacons in single living cells. *Nucleic Acids Res. 35*, e105.
(40) Kubota, T., Ikeda, S., and Okamoto, A. (2009) Doubly thiazole orange-labeled DNA for live cell RNA imaging. *Bull. Chem. Soc. Jpn. 82*, 110–117.
(41) Dose, C., Ficht, S., and Seitz, O. (2006) Reducing product inhibition in DNA-template-controlled ligation reactions. *Angew. Chem., Int. Ed. 45*, 5369–5373.
(42) Dose, C., and Seitz, O. (2008) Single nucleotide specific detection of DNA by native chemical ligation of fluorescence labeled PNA-probes. *Bioorg. Med. Chem. 16*, 65–77.
(43) Dose, C., and Seitz, O. (2005) Convergent synthesis of peptide nucleic acids by native chemical Ligation. *Org. Lett. 7*, 4365–4368.
(44) Ma, Z., and Taylor, J. S. (2003) PNA-based RNA-triggered drug-releasing system. *Bioconjugate Chem. 14*, 679–683.
(45) Ma, Z., and Taylor, J. S. (2001) Nucleic acid triggered catalytic drug and probe release: a new concept for the design of chemotherapeutic and diagnostic agents. *Bioorg. Med. Chem. 9*, 2501–2510.
(46) Ma, Z., and Taylor, J. S. (2000) Nucleic acid-triggered catalytic drug release. *Proc. Natl. Acad. Sci. U.S.A. 97*, 11159–11163.
(47) Cai, J., Li, X., Yue, X., and Taylor, J. S. (2004) Nucleic acid-triggered fluorescent probe activation by the Staudinger reaction. *J. Am. Chem. Soc. 126*, 16324–16325.
(48) Abe, H., Wang, J., Furukawa, K., Oki, K., Uda, M., Tsuneda, S., and Ito, Y. (2008) A reduction-triggered fluorescence probe for sensing nucleic acids. *Bioconjugate Chem. 19*, 1219–1226.
(49) Pianowski, Z. L., and Winssinger, N. (2007) Fluorescence-based detection of single nucleotide permutation in DNA via catalytically templated reaction. *Chem. Commun. 37*, 3820–3822.
(50) Franzini, R. M., and Kool, E. T. (2008) 7-azidomethoxy-coumarins as profluorophores for templated nucleic acid detection. *ChemBioChem 9*, 2981–2988.
(51) Grossmann, T. N., and Seitz, O. (2006) DNA-catalyzed transfer of a reporter group. *J. Am. Chem. Soc. 128*, 15596–15597.
(52) Sando, S., Sasaki, T., Kanatani, K., and Aoyama, Y. (2003) Amplified nucleic acid sensing using programmed self-cleaving DNAzyme. *J. Am. Chem. Soc. 125*, 15720–15721.
(53) Franzini, R. M., and Kool, E. T. (2008) Organometallic activation of a fluorogen for templated nucleic acid detection. *Org. Lett. 10*, 2935–2938.
(54) Abe, H., and Kool, E. T. (2005) Universal linkers for signal amplification in auto-ligating probes. *Nucleic Acids Symp. Ser. 49*, 37–38.
(55) Lemieux, G. A., de Graffenried, C. L., and Bertozzi, C. R. (2003) A fluorogenic dye activated by the Staudinger ligation. *J. Am. Chem. Soc. 125*, 4708–4709.
(56) Kojima, H., Nakatsubo, N., Kikuchi, K., Kawahara, S., Kirino, Y., Nagoshi, H., Hirata, Y., and Nagano, T. (1998) Detection and imaging of nitric oxide with novel fluorescent indicators: Diaminofluoresceins. *Anal. Chem. 70*, 2446–2453.
(57) Maeda, H., Fukuyasu, Y., Yoshida, S., Fukuda, M., Saeki, K., Matsuno, H., Yamauchi, Y., Yoshida, K., Hirata, K., and Miyamoto, K. (2004) Fluorescent probes for hydrogen peroxide based on a non-oxidative mechanism. *Angew. Chem., Int. Ed. 43*, 2389–2391.
(58) Miller, E. W., Tulyathan, O., Isacoff, E. Y., and Chang, C. J. (2007) Molecular imaging of hydrogen peroxide produced for cell signaling. *Nat. Chem. Biol. 3*, 263–267.
(59) Dale, T. J., and Rebek, J., Jr. (2006) Fluorescent sensors for organophosphorus nerve agent mimics. *J. Am. Chem. Soc. 128*, 4500–4501.
(60) Marras, S. A., Kramer, F. R., and Tyagi, S. (2002) Efficiencies of fluorescence resonance energy transfer and contact-mediated quenching in oligonucleotide probes. *Nucleic Acids Res. 30*, e122.
(61) Loubinoux, B., Tabbache, S., Gerardin, P., and Miazimbakana, J. (1988) Protection of phenols via the azidomethylene group: Application in the synthesis of unstable phenolic compounds. *Tetrahedron 44*, 6055–6064.
(62) Young, T., and Kiessling, L. L. (2002) A strategy for the synthesis of sulfated peptides. *Angew. Chem., Int. Ed. 41*, 3449–3451.
(63) Sakurai, K., Snyder, T. M., and Liu, D. R. (2005) DNA-templated functional group transformations enable sequence-programmed synthesis using small-molecule reagents. *J. Am. Chem. Soc. 127*, 1660–1661.
(64) Payne, R. J., Toscano, M. D., Bulloch, E. M., Abell, A. D., and Abell, C. (2005) Design and synthesis of aromatic inhibitors of anthranilate synthase. *Org. Biomol. Chem. 3*, 2271–2281.
(65) Pinnisi, E. (1998) A closer look at SNPs suggests difficulties. *Science 281*, 1787–1789.
(66) Jensen, K. K., Orum, H., Nielsen, P. E., and Norden, B. (1997) Kinetics for hybridization of peptide nucleic acids (PNA) with DNA and RNA studied with the BIAcore technique. *Biochemistry 36*, 5072–5077.
(67) Paillasson, S., Van De Corput, M., Dirks, R. W., Tanke, H. J., Robert-Nicoud, M., and Ronot, X. (1997) In situ hybridization in living cells: detection of RNA molecules. *Exp. Cell Res. 231*, 226–233.

BC900040T

Supporting Information

Reduction-triggered Fluorescent Amplification probe for detection of endogenous RNAs in living human cells

Kazuhiro Furukawa, [1,3] *Hiroshi Abe,* [*1] *Kayo Hibino,* [2] *Yasushi Sako,* [2] *Satoshi Tsuneda*[3] *and Yoshihiro Ito*[*1]

[1]Nano Medical Engineering Laboratory, RIKEN Advance Science Institute, 2-1, Hirosawa, Wako-Shi, Saitama, 351-0198 Japan.
[2]Cellar Informatics Laboratory, Advance Science Institute, RIKEN 2-1, Hirosawa, Wako-Shi, Saitama, 351-0198 Japan.
[3]Department of Life Science and Medical Bio-Science, Waseda University, 2-2 Wakamatsu-cho, Shinjuku-ku, Tokyo 162-8480, Japan
h-abe@riken and y-ito@riken.jp

CONTENTS:

Organic synthesis of bisazidomethyl fluorescein 3

Figure S1**.** Molecular structures of RETFA probe 6

Figure S2**.** Melting temperature measurement 7

Figure S3**.** HPLC analysis of the DNA-templated reaction mixture 8

Figure S4**.** Probe sequences and in vitro analysis for 28S rRNA 9

Figure S5**.** Probe sequences and in vitro analysis for β-actin mRNA 10

Table S1**.** ESI-MS analysis of synthesized probes 11

^{1}H-NMR and ^{13}C-NMR 12

Experimental section

Iodo fluorescein (5). (Reference 1) Fluorescein (1.60 g, 4.61 mmol) was dissolved in 12N HCl (16.4 ml) and 8.2 g of ice. An aqueous solution (8.2 ml) of sodium nitrite (397 mg, 5.76 mmol) was added slowly. After stirring for 2.5 hour, an aqueous solution (13.2 ml) of potassium iodide (15.3 g, 92.2 mmol) was added slowly. The reaction was allowed to warm gradually to room temperature. After stirring for 5 hour, the reaction mixture was diluted with $CHCl_3$ and washed with H_2O and brine. The combined organic extracts were pooled and dried over Na_2SO_4. The Na_2SO_4 was removed by filtration and volatiles removed *in vacuo.* The residue was purified by flash column chromatography (silica, gradient elution 10:1 hexane/AcOEt to 3:1 hexane/AcOEt (v/v) with 0.5% triethylamine) to afford a yellow solid (1 g, 47%) (**5**). ^{1}H NMR (400MHz, CD_3OD) δ8.33-8.31(1H, m), 8.08-8.04 (1H, m), 7.00-6.96 (1H, m), 6.67-6.50 (4H, m). ^{13}C NMR (100MHz, CD_3OD) δ 169.5, 161.3, 153.9, 145.1, 134.7, 130.3, 130.0, 127.1, 113.6, 110.7, 103.5, 95.6. QSTAR (Applied Biosystems/MDS SCIEX) (ESI): *m/z* 457.9651 [MH+] $C_{20}H_{11}IO_5$: 458.9729, found: 458.9721

Bisthiomethyl fluorescein (6). Iodo fluorescein (**5**) (1 g, 2.18 mmol) was dissolved in dry CH_3CN (36 ml) under Ar (g). Silver oxide (1.52 g, 6.55 mmol) and Chloromethylmethylsulfide (550 µl, 6.55 mmol) was added followed by addition of five drop of pyridine. After stirring for 24 hour at 40 °C, the remaining solid residue was removed by filtration. The filtrate was concentrated and subjected to flash column chromatography. Elution with a slow gradient of hexane/AcOEt from 10:1 to 3:1 (v/v) with 0.5% triethylamine gave thiomethyl fluorescein (**6**) as pale yellow crystalline solid (234 mg, 19%). ^{1}H NMR (400MHz, $CDCl_3$) δ 8.35 (1H, s), 7.96 (1H, d, J = 8.1Hz), 6.92 (1H, d, J = 8.3Hz), 6.83 (2H, d, J = 2.2Hz), 6.73-6.65 (4H, m), 5.16 (4H, s), 2.26 (6H, s). ^{13}C NMR (100MHz, $CDCl_3$) δ 167.3, 158.6, 152.2, 152.0, 143.6, 133.9, 128.9, 128.6, 125.6, 112.9, 111.3, 103.0, 94.9, 83.1, 72.5, 14.8. QSTAR (Applied Biosystems/MDS SCIEX) (ESI): *m/z* 577.9719 [MH+] $C_{24}H_{19}IO_5S_2$: 578.9797, found: 578.9775

Bisazidomethyl fluorescein (7). Thiomethyl fluorescein (**6**) (200 mg, 350 μmol) was dissolved in dichloromethane (7 ml). N-chlorosuccinimide (102 mg, 760 μmol) was added. After stirring for 2 hour at room temperature, trimethylsilyl chloride (97.3 μl, 760 μmol) was added. The resulting solution was stirred at ambient for 6 h and the reaction was quenched with saturated Na_2CO_3 aqueous. The aqueous layer was extracted with $CHCl_3$ (×2) and the combined organic layers was concentrated in vacuum to give the crude which was subjected to the next reaction. Sodium azide (67.5 mg, 1.04 mmol) was dissolved in H_2O (3.5 ml) and added to a solution of the crude in DMF (7 ml) in room temperature. After stirring for 30 hour, the reaction was quenched with saturated Na_2CO_3 aqueous. The aqueous layer was extracted with AcOEt (×2) and the combined organic layers was concentrated in vacuum and subjected to flash column chromatography. Elution with a slow gradient of hexane/AcOEt from 10:1 to 3:1 (v/v) with 0.5% triethylamine gave azidomethyl fluorescein (**7**) as pale yellow crystalline solid (41.0 mg, 21%). ^{1}H NMR (400MHz, $CDCl_3$) δ 8.36 (1H, s), 7.99-7.97 (1H, m), 6.94-6.90 (3H, m), 6.77-6.70 (4H, m), 5.19 (4H, s). ^{13}C NMR (100MHz, $CDCl_3$) δ 167.3, 158.1, 152.1, 152.0, 143.7, 134.0, 129.2, 128.5, 125.5, 112.7, 112.3, 103.4, 95.0, 82.6, 79.4. QSTAR (Applied Biosystems/MDS SCIEX) (ESI): *m/z* 567.9992 [MH+] $C_{22}H_{13}IN_6O_5$: 569.0070, found: 569.0065

Bromoacetyl acetylene linker (8). (Reference 2) To a solution of propargylamine (116.28 μl, 1.82 mmol) and potassium carbonate (251 mg, 1.82 mmol) in benzene (18.2 ml) chilled via an external ice bath was added bromoacetyl bromide (159μl, 1.82 mmol). After stirring for 20 h, the reaction mixture was diluted with ether and washed with H_2O. The combined organic extracts were pooled and dried over Na_2SO_4. The Na_2SO_4 was removed by filtration and volatiles removed *in vacuo*. The residue (**8**) (118 mg, 37.1%) was subjected to the coupling with azidomethyl fluorescein. QSTAR (Applied Biosystems/MDS SCIEX) (ESI): *m/z* 174.9633 [MH+] C5H6BrNO: 175.9711, found: 175.9703

Bisazidomethyl bromoacetyl linker fluorescein (9). Azidomethyl fluorescein (**7**) (50 mg, 88 μmol) was dissolved in THF (1.6 ml) under Ar (g). Tetrakis (triphenylphosphine) palladium (10.2

mg, 8.8 μmol), copper iodide (3.35 mg, 1.8 μmol) and triethylamine (61.9 μl, 440 μmol) were added followed by addition of bromoacetyl acetylene linker (**8**) (77.0 mg, 440 μmol). After stirring for 3 hour, the remaining solid residue was removed by filtration. The filtrate was concentrated and subjected to flash column chromatography. Elution with a slow gradient of hexane/AcOEt from 5:1 to 1:1 (v/v) with 0.5% triethylamine gave azidomethyl bromoacetyl linker fluorescein (**9**) as pale yellow crystalline solid (20 mg, 37%). ^{1}H NMR (400MHz, $CDCl_3$) δ 8.06 (1H, s), 7.70 (1H, d, J = 8.04), 7.27 (2H, s), 7.11 (1H, d, J = 8.1), 6.91 (2H, d, J = 2.2), 6.77-6.69 (4H, m), 5.19 (4H, s), 4.36 (2H, d, J = 5.6), 3.94 (1H, s), 3.76 (1H, s). ^{13}C NMR (100MHz, $CDCl_3$) δ 168.1, 166.6, 158.0, 152.3, 152.0, 138.2, 131.8, 129.2, 128.3, 123.9, 113.0, 112.6, 112.5, 103.4, 86.7, 82.5, 81.8, 79.4, 30.9, 28.8. QSTAR (Applied Biosystems/MDS SCIEX) (ESI): *m/z* 615.0502 [MH+] $C_{27}H_{18}BrN_7O_6$: 616.0580, found: 616.0578

Reference

1. Jiao, G. S., Han, J. W., and Burgess, K. (2003) Syntheses of regioisomerically pure 5- or 6-halogenated fluoresceins. *J. Org. Chem. 68,* 8264-8267.
2. Macmillan, D., and Blanc, J. (2006) A novel neoglycopeptide linkage compatible with native chemical ligation. *Org. Biomol. Chem. 4,* 2847–2850.

A

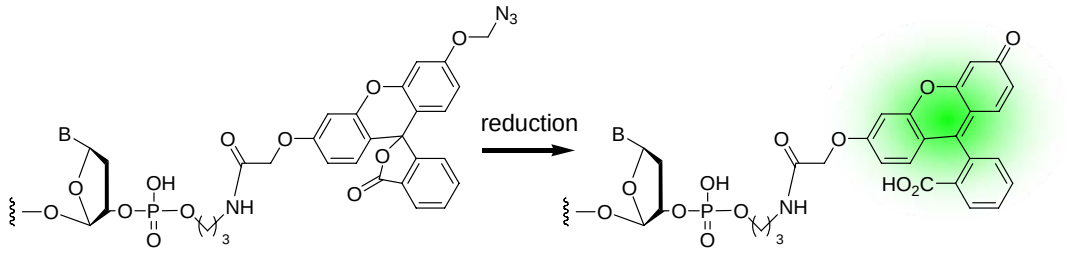

B

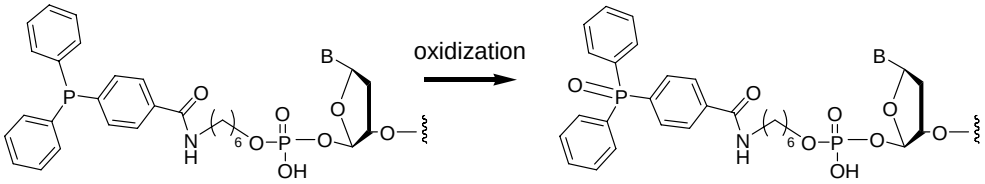

Figure S1. (A) Molecular structure of fluorogenic probe, which carry a fluorogenic molecule monoazidomethyl fluorescein at the 3’-end of the oligonucleotide. (B) Molecular structure of triphenylphosphine (TPP) probe as a reductant, which labelled at the 5’-end of the oligonucleotide.

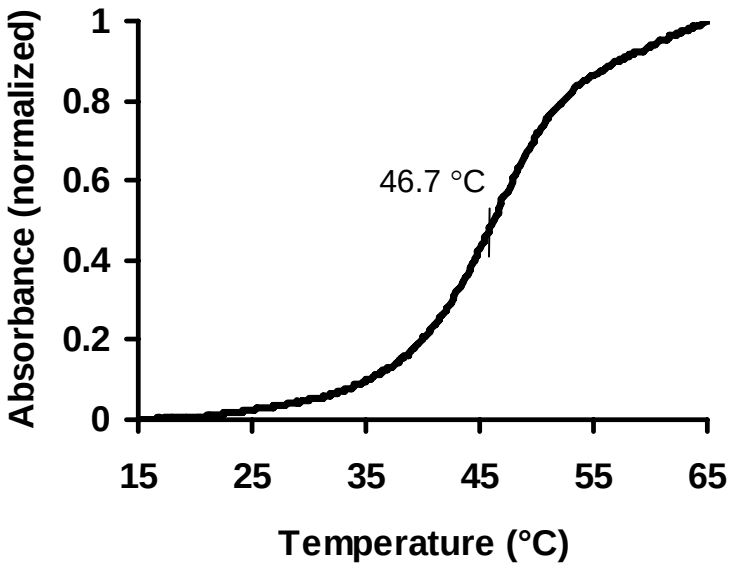

Figure S2. Melting temperature measurement. Conditions: 5 μM probes and target DNA, 100 mM $MgCl_2$ in 20 mM tris-HCl (pH 7.2) buffer. Absorbance changes were normalized.

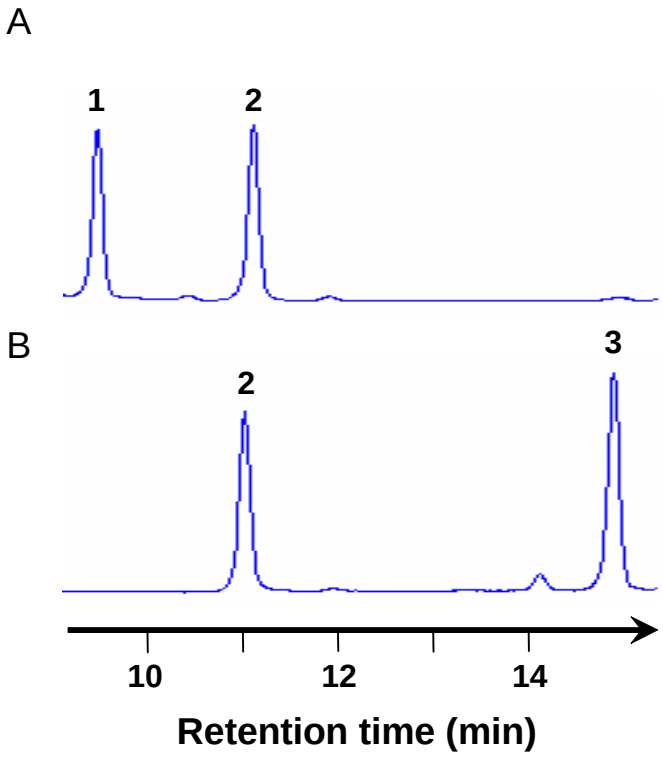

Figure S3. HPLC analysis of the DNA-templated reaction mixture. A) 5 min reaction with target DNA, B) 5 min reaction without target DNA. Peak 1, reduced azidomethyl fluorescein probe; Peak 2, derived from phosphine probe; Peak 3, azidomethyl fluorescein probe. The reaction products were analyzed by reverse-phase HPLC (0-80 % acetonitrile/50 mM triethylammonium acetate gradient) using hydrosphere C18 column (250×4.6 mm; YMC Co., Ltd, Japan). Each peak was characterized by ESI-mass spectrometry.

A

CCACATCAGGAGGGA-(Az) (TPP)-TCCGCTGCCCCCATT Scramble probe

TTTGAATATTTGCTA-(Az) (TPP)-CTACCACCAAGATCT Matched probe

3′ AAACUUAUAAACGAU----------GAUGGUGGUUCUAGA 5′ Target RNA

B

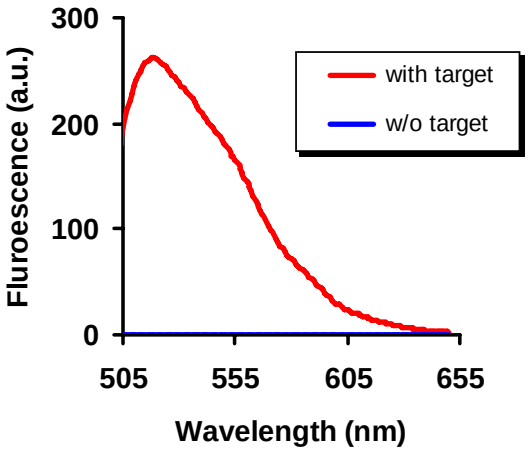

Figure S4. (A) Probe sequences for human 28S rRNA. Designed 15 mer probes are azidomethyl fluorescein probe or TPP probe. (B) Fluorescent emission spectra with excitation at 490 nm in the reaction between 50 nM azidomethyl fluorescein and TPP probe with or without 50 nM target in 20 mM Tris-HCl (pH 7.2) containing 100 mM $MgCl_2$ and 10 μg/ml BSA.

A

```
    CAGAGGCGTACAGGG-(Az)     (TPP)-ATAGCACAGCCTGGA
3′  GUCUCCGCAUGUCCC----------UAUCGUGUCGGACCU  5′   Target site 1

    GCGGCGATATCATCA-(Az)     (TPP)-TCCATGGTGAGCTGG
3′  CGCCGCUAUAGUAGU----------AGGUACCACUCGACC  5′   Target site 2

    TTCCCGCTCGGCCGT-(Az)     (TPP)-GGTGGTGAAGCTGTA
3′  AAGGGCGAGCCGGCA----------CCACCACUUCGACAU  5′   Target site 3
```

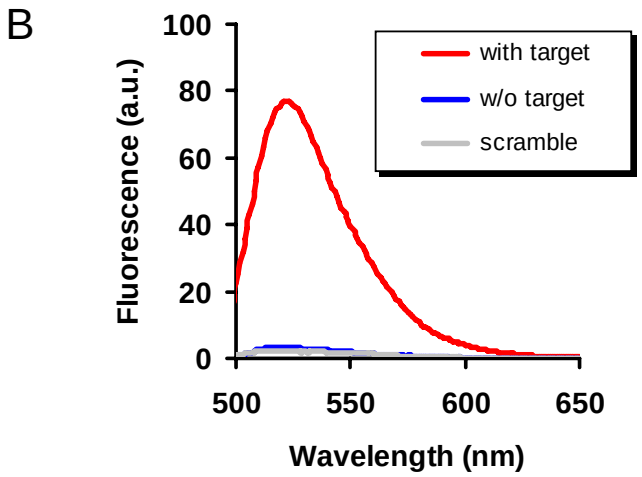

Figure S5. (A) Probe sequences for human β–actin mRNA. Designed 15 mer probes are azidomethyl fluorescein probe or TPP probe. (B) Fluorescent emission spectra with excitation at 490 nm in the reaction between 33.3 nM each azidomethyl fluorescein and TPP probe with or without 100 nM target in 20 mM Tris-HCl (pH 7.2) containing 100 mM $MgCl_2$ and 10 μg/ml BSA.

Table S1. Characterization of each probe by ESI-MS spectrometry.

	Calculated mass	Observed mass	Chemical formula
Probe 1	3012.56	3012.56	$C_{105}H_{120}N_{36}O_{55}P_{8}$
Probe 2	3483.68	3483.70	$C_{123}H_{152}N_{35}O_{64}P_{11}$
Probe 3	5239.89	5239.8	$C_{173}H_{200}N_{71}O_{92}P_{15}S$
Probe 4	4904.9	4904.8	$C_{167}H_{212}N_{48}O_{95}P_{16}$
Probe 5	5200.86	5200.8	$C_{176}H_{207}N_{56}O_{100}P_{15}S$
Probe 6	4945.94	4945.97	$C_{169}H_{211}N_{55}O_{90}P_{16}$
Probe 7	5295.89	5295.83	$C_{174}H_{200}N_{73}O_{93}P_{15}S$
Probe 8	5050.96	5050.96	$C_{171}H_{210}N_{62}O_{89}P_{16}$
Probe 9	5205.88	5205.8	$C_{173}H_{202}N_{65}O_{95}P_{15}S$
Probe 10	5088.94	5088.8	$C_{172}H_{212}N_{58}O_{94}P_{16}$
Probe 11	5124.83	5124.7	$C_{170}H_{203}N_{56}O_{100}P_{15}S$
Probe 12	5152.96	5152.9	$C_{174}H_{212}N_{62}O_{93}P_{16}$

C:¥Documents and Settings¥共通2¥デスクトップ¥furukawa NMR¥AzMe_paper¥1 1H.als

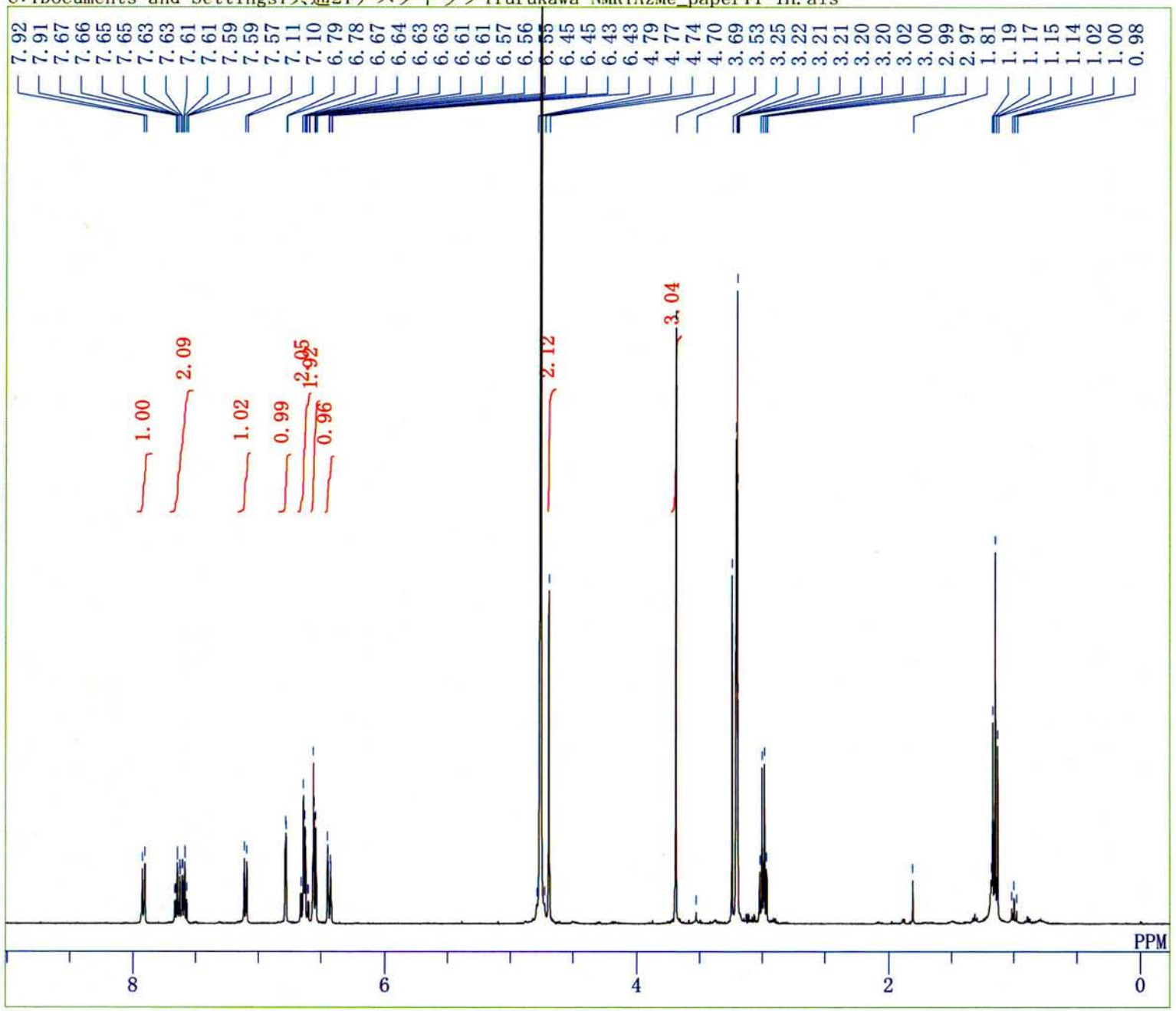

DFILE 1 1H.als
COMNT
DATIM Thu May 31 13:22:35 2007
OBNUC 1H
EXMOD NON
OBFRQ 395.75 MHz
OBSET 124.00 KHz
OBFIN 10277.00 Hz
POINT 32768
FREQU 7917.60 Hz
SCANS 32
ACQTM 4.1386 sec
PD 2.8610 sec
PW1 6.30 usec
IRNUC 1H
CTEMP 22.1 c
SLVNT CD3OD
EXREF 0.00 ppm
BF 0.12 Hz
RGAIN 17

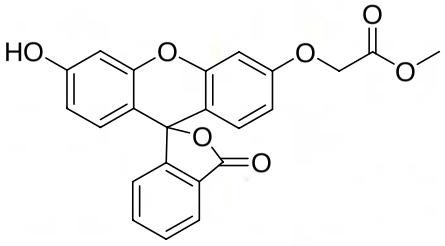

^{1}H NMR ($CDCl_3$), 400MHz

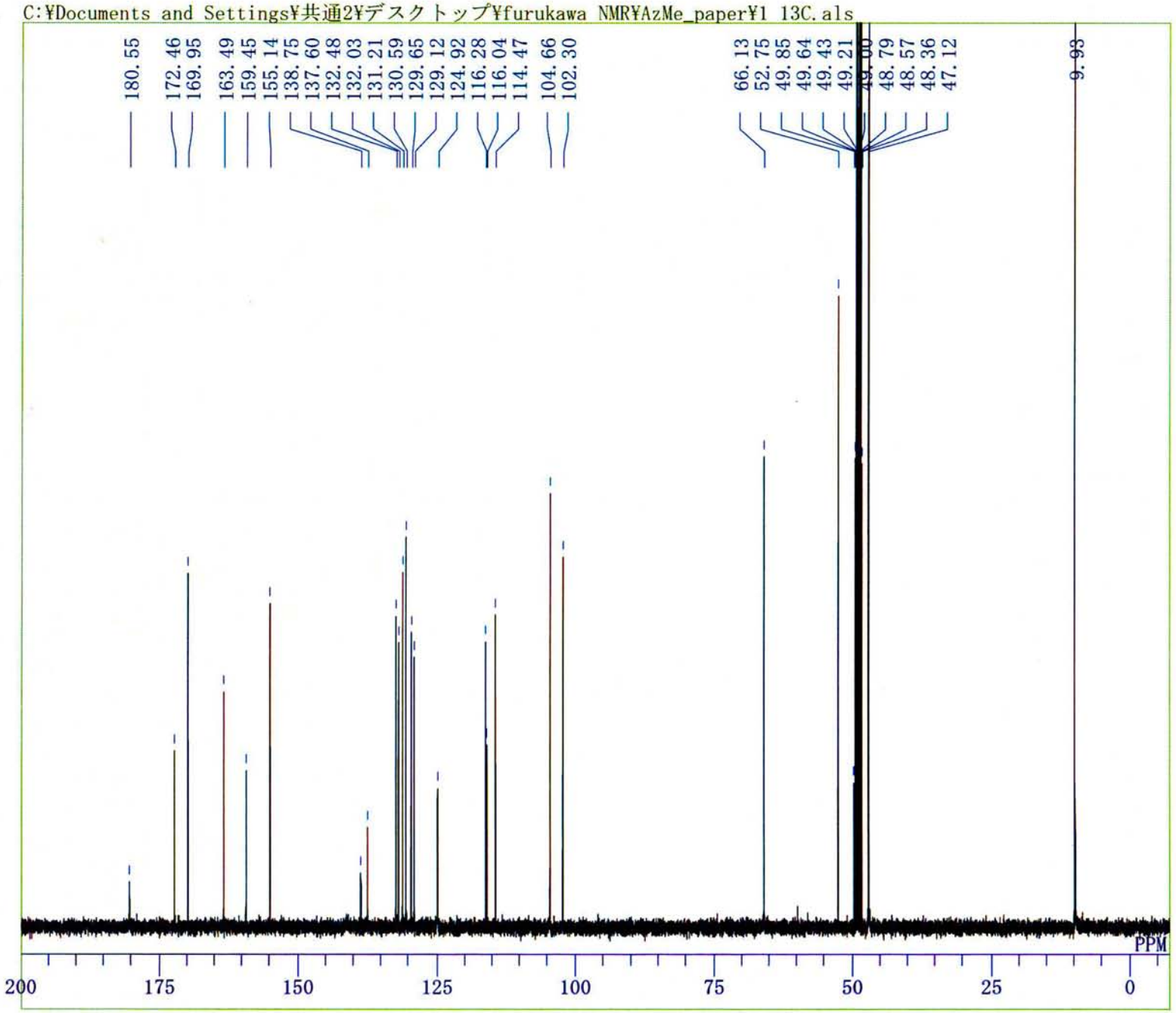

DFILE 1 13C.als
COMNT
DATIM Mon Jun 04 19:24:04 2007
OBNUC 13C
EXMOD BCM
OBFRQ 99.45 MHz
OBSET 94.00 KHz
OBFIN 10309.00 Hz
POINT 32768
FREQU 26881.70 Hz
SCANS 597
ACQTM 1.2190 sec
PD 1.7810 sec
PW1 6.20 usec
IRNUC 1H
CTEMP 22.6 c
SLVNT CD3OD
EXREF 49.00 ppm
BF 0.12 Hz
RGAIN 27

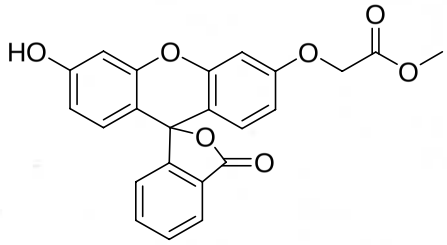

^{13}C NMR ($CDCl_3$), 100MHz

C:¥Documents and Settings¥共通2¥デスクトップ¥furukawa NMR¥AzMe_paper¥2 1H.als

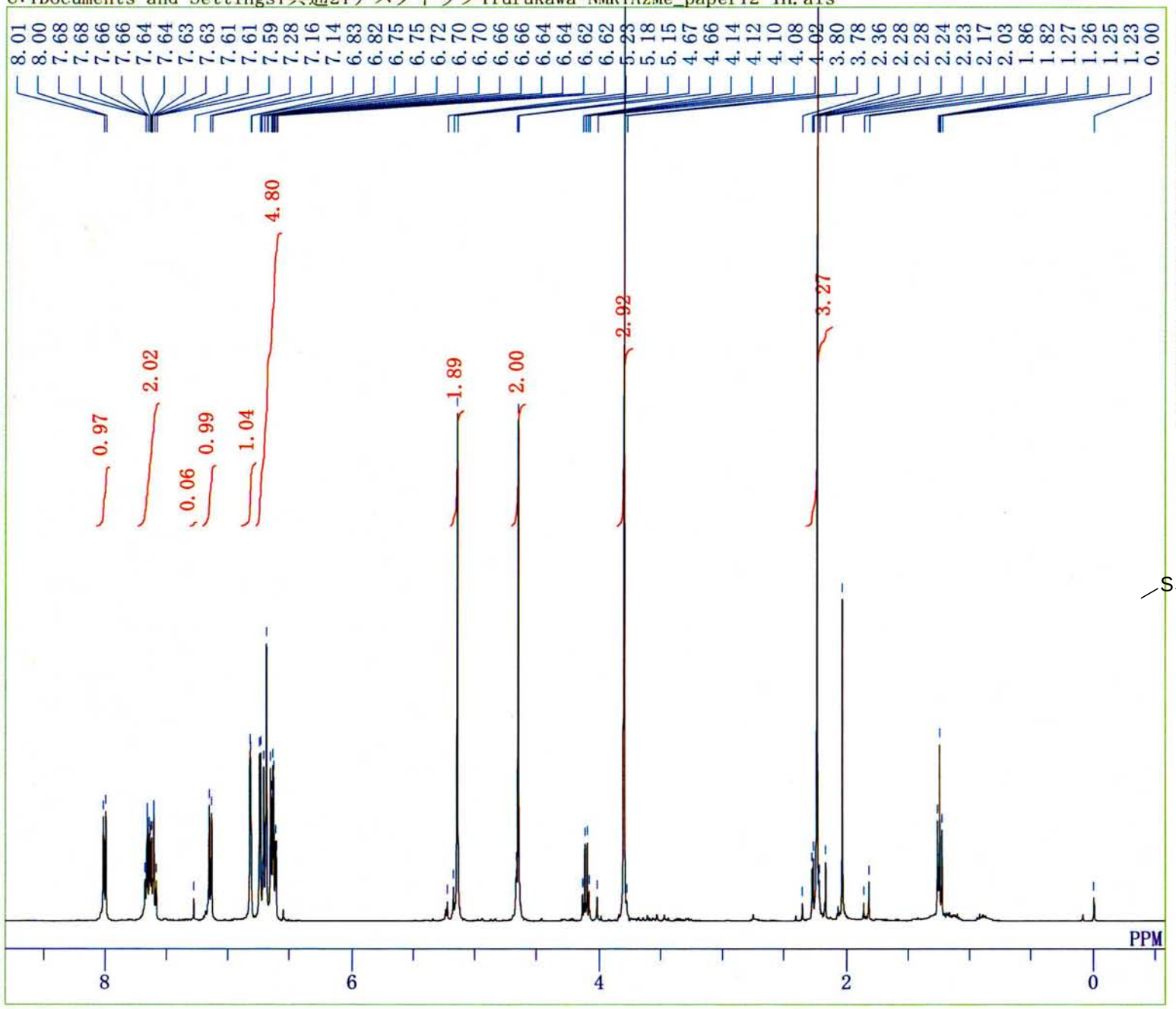

DFILE 2 1H.als
COMNT
DATIM Tue Jun 05 17:50:30 2007
OBNUC 1H
EXMOD NON
OBFRQ 395.75 MHz
OBSET 124.00 KHz
OBFIN 10277.00 Hz
POINT 32768
FREQU 7917.60 Hz
SCANS 8
ACQTM 4.1386 sec
PD 2.8610 sec
PW1 6.30 usec
IRNUC 1H
CTEMP 22.8 c
SLVNT CDCL3
EXREF 0.00 ppm
BF 0.12 Hz
RGAIN 10

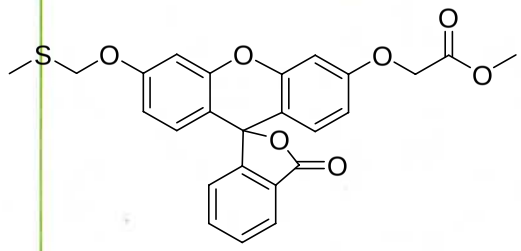

^{1}H NMR ($CDCl_3$), 400MHz

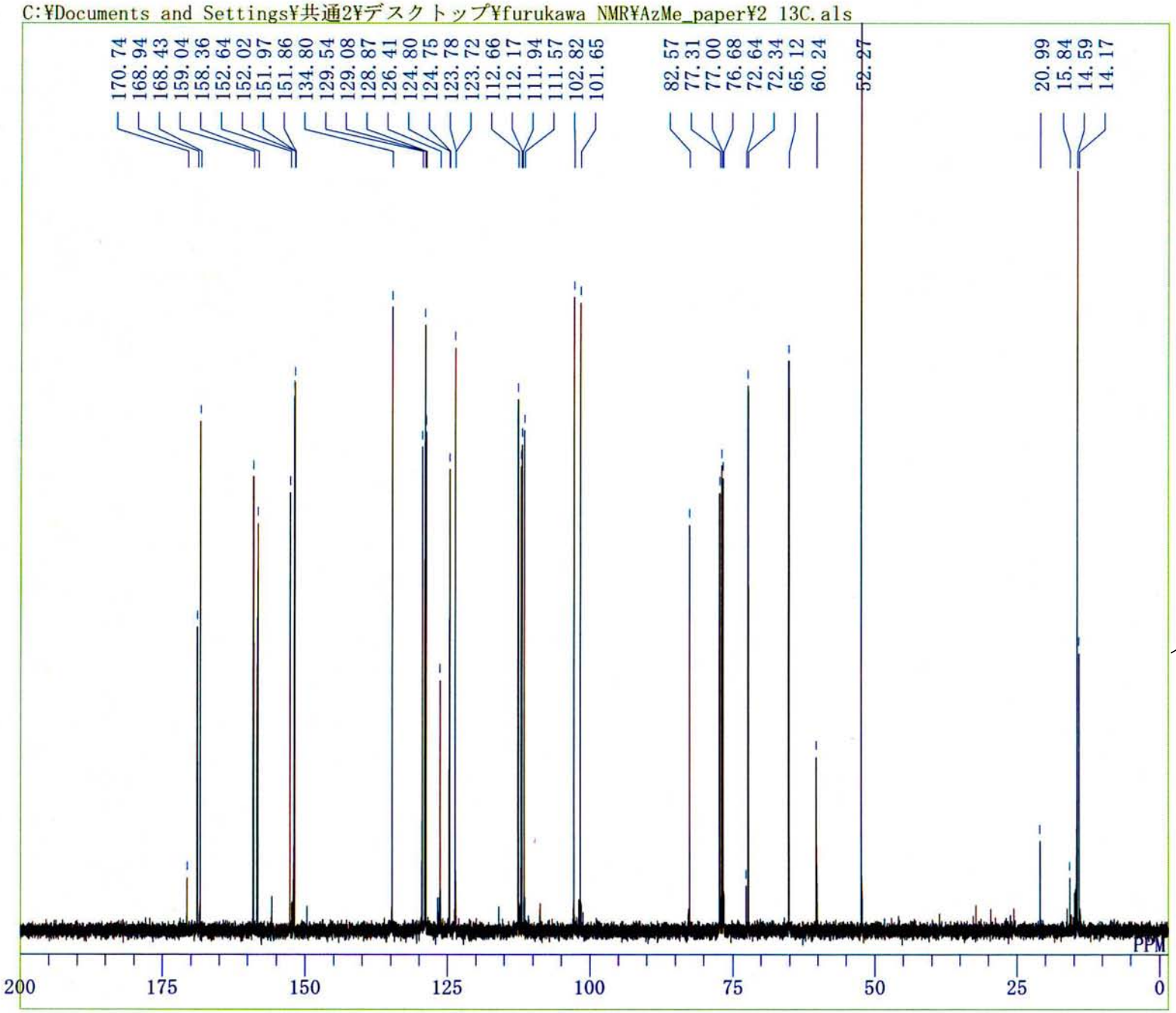

DFILE 2 13C.als
COMNT
DATIM Tue Jun 05 18:27:03 2007
OBNUC 13C
EXMOD BCM
OBFRQ 99.45 MHz
OBSET 94.00 KHz
OBFIN 10309.00 Hz
POINT 32768
FREQU 26881.70 Hz
SCANS 596
ACQTM 1.2190 sec
PD 1.7810 sec
PW1 6.20 usec
IRNUC 1H
CTEMP 22.7 c
SLVNT CDCL3
EXREF 77.00 ppm
BF 0.12 Hz
RGAIN 28

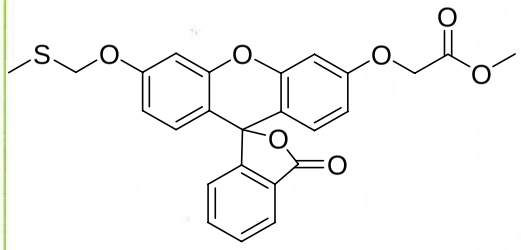

^{13}C NMR ($CDCl_3$), 100MHz

C:¥Documents and Settings¥共通2¥デスクトップ¥furukawa NMR¥AzMe_paper¥3 1H.als

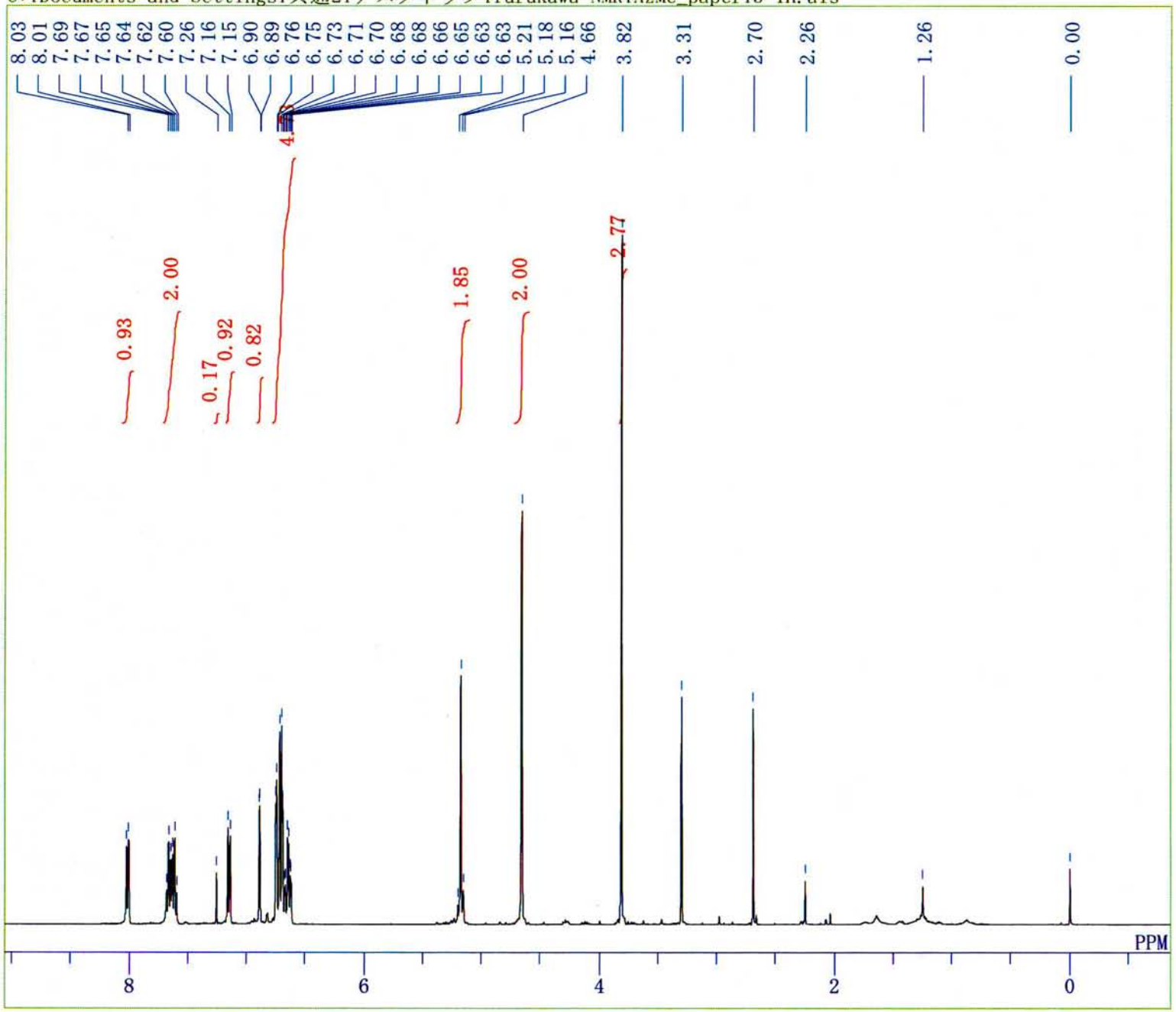

DFILE	3 1H.als	
COMNT		
DATIM	Thu Jun 07 17:34:48 2007	
OBNUC	1H	
EXMOD	NON	
OBFRQ	395.75	MHz
OBSET	124.00	KHz
OBFIN	10277.00	Hz
POINT	32768	
FREQU	7917.60	Hz
SCANS	16	
ACQTM	4.1386	sec
PD	2.8610	sec
PW1	6.30	usec
IRNUC	1H	
CTEMP	23.7	c
SLVNT	CDCL3	
EXREF	0.00	ppm
BF	0.12	Hz
RGAIN	14	

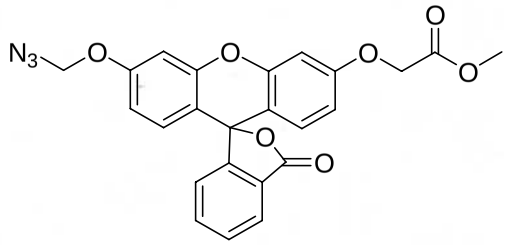

^{1}H NMR ($CDCl_3$), 400MHz

C:¥Documents and Settings¥共通2¥デスクトップ¥furukawa NMR¥AzMe_paper¥3 13C.als

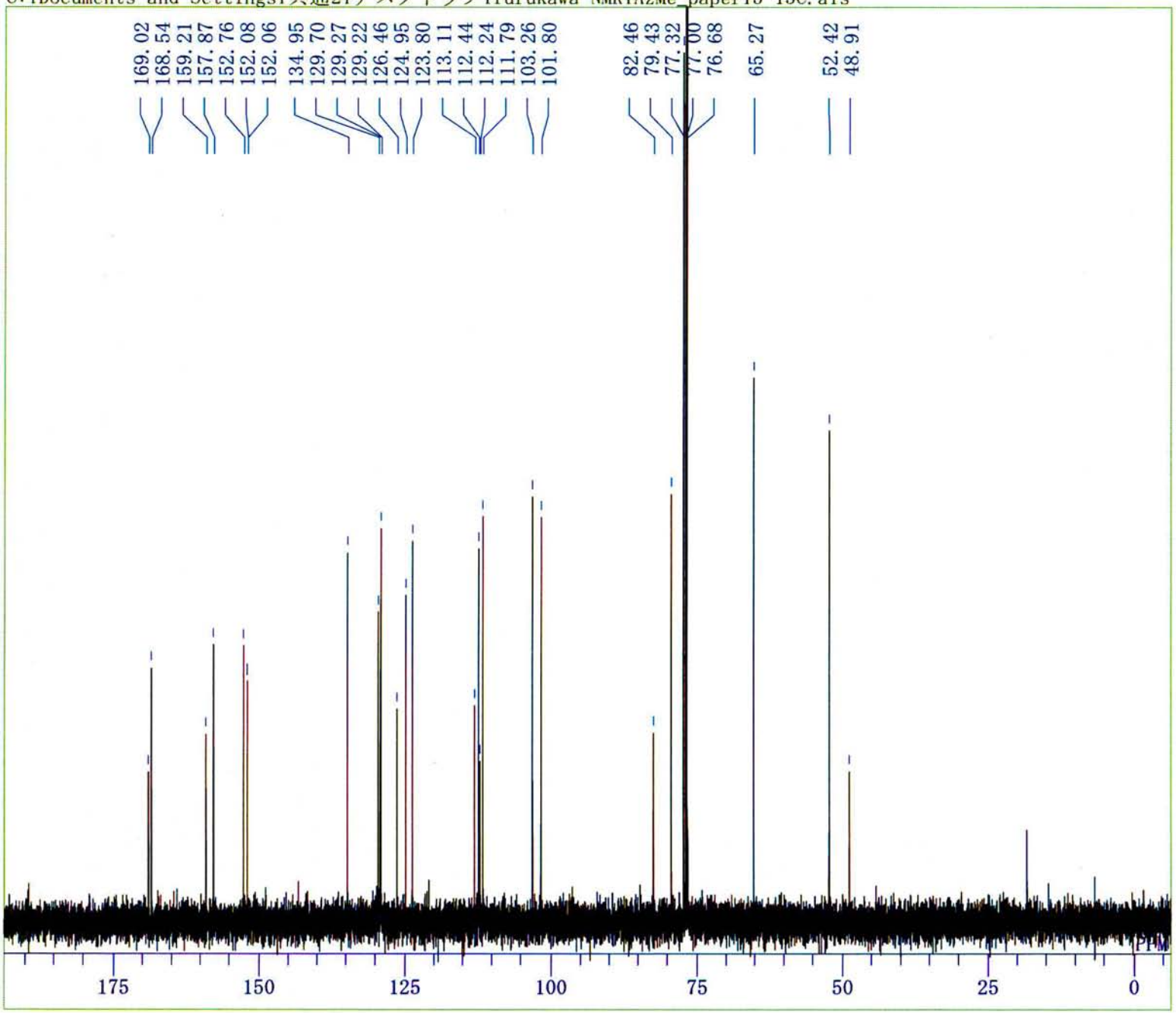

DFILE	3 13C.als	
COMNT		
DATIM	Thu Jun 07 17:55:00 2007	
OBNUC	13C	
EXMOD	BCM	
OBFRQ	99.45	MHz
OBSET	94.00	KHz
OBFIN	10309.00	Hz
POINT	32768	
FREQU	26881.70	Hz
SCANS	292	
ACQTM	1.2190	sec
PD	1.7810	sec
PW1	6.20	usec
IRNUC	1H	
CTEMP	23.4	c
SLVNT	CDCL3	
EXREF	77.00	ppm
BF	0.12	Hz
RGAIN	27	

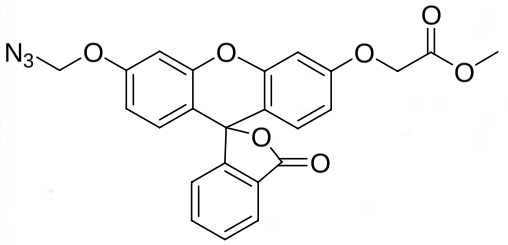

^{13}C NMR ($CDCl_3$), 100MHz

C:¥Documents and Settings¥共通2¥デスクトップ¥furukawa NMR¥AzMe_paper¥4 1H.als

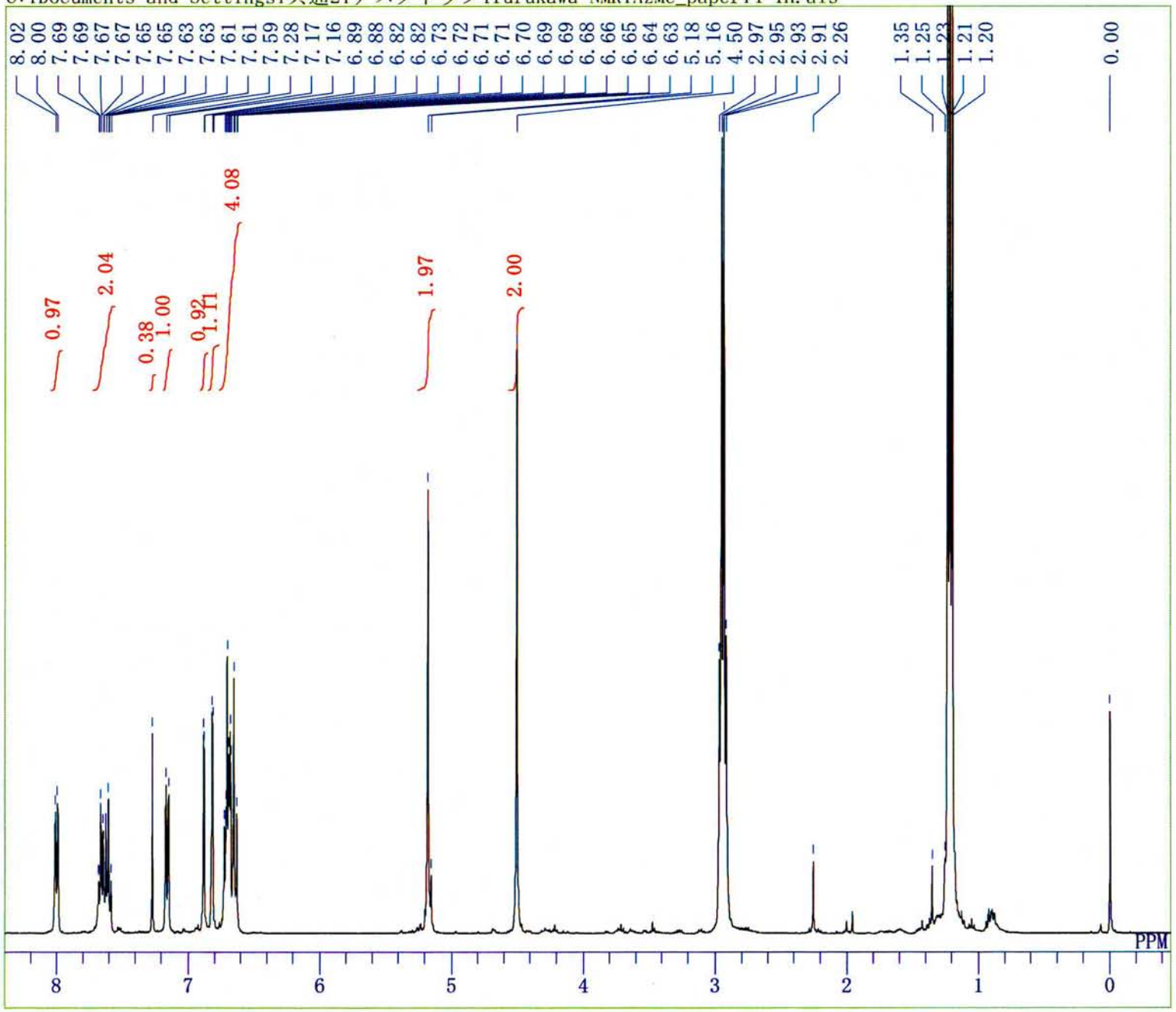


```
DFILE  4 1H.als
COMNT
DATIM  Mon Jun 11 17:18:41 2007
OBNUC  1H
EXMOD  NON
OBFRQ        395.75 MHz
OBSET        124.00 KHz
OBFIN      10277.00 Hz
POINT        32768
FREQU        7917.60 Hz
SCANS           16
ACQTM        4.1386 sec
PD           2.8610 sec
PW1             6.30 usec
IRNUC  1H
CTEMP           23.1 c
SLVNT  CDCL3
EXREF           0.00 ppm
BF              0.12 Hz
RGAIN           13
```

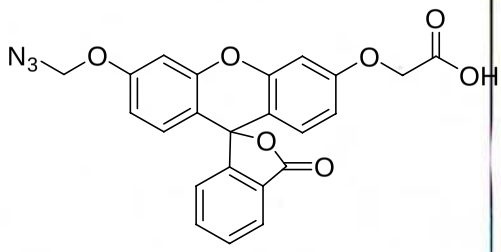

^{1}H NMR ($CDCl_3$), 400MHz

C:¥Documents and Settings¥共通2¥デスクトップ¥furukawa NMR¥AzMe_paper¥4 13C.als

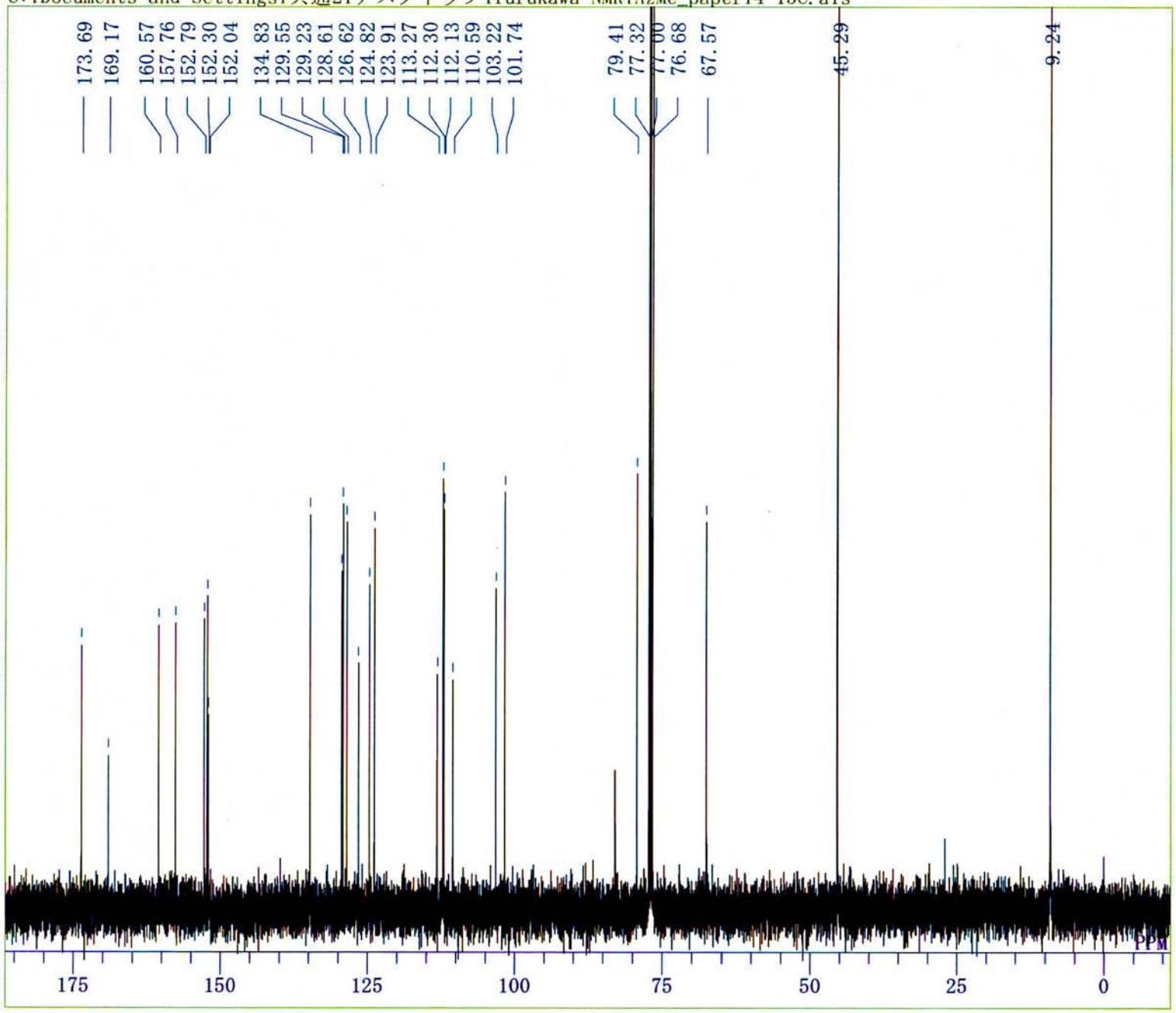


```
DFILE   4 13C.als
COMNT
DATIM   Mon Jun 11 17:59:13 2007
OBNUC   13C
EXMOD   BCM
OBFRQ         99.45 MHz
OBSET         94.00 KHz
OBFIN      10309.00 Hz
POINT         32768
FREQU      26881.70 Hz
SCANS           683
ACQTM         1.2190 sec
PD            1.7810 sec
PW1           6.20 usec
IRNUC   1H
CTEMP         22.7 c
SLVNT   CDCL3
EXREF         77.00 ppm
BF            0.12 Hz
RGAIN           27
```

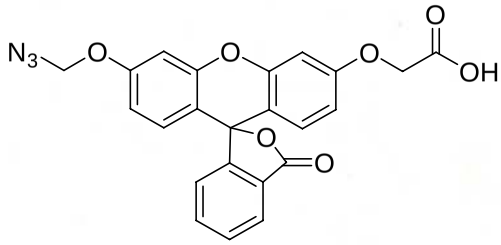

^{13}C NMR ($CDCl_3$), 100MHz

C:¥Documents and Settings¥共通2¥デスクトップ¥furukawa NMR¥AzMe_paper¥6 1H.als

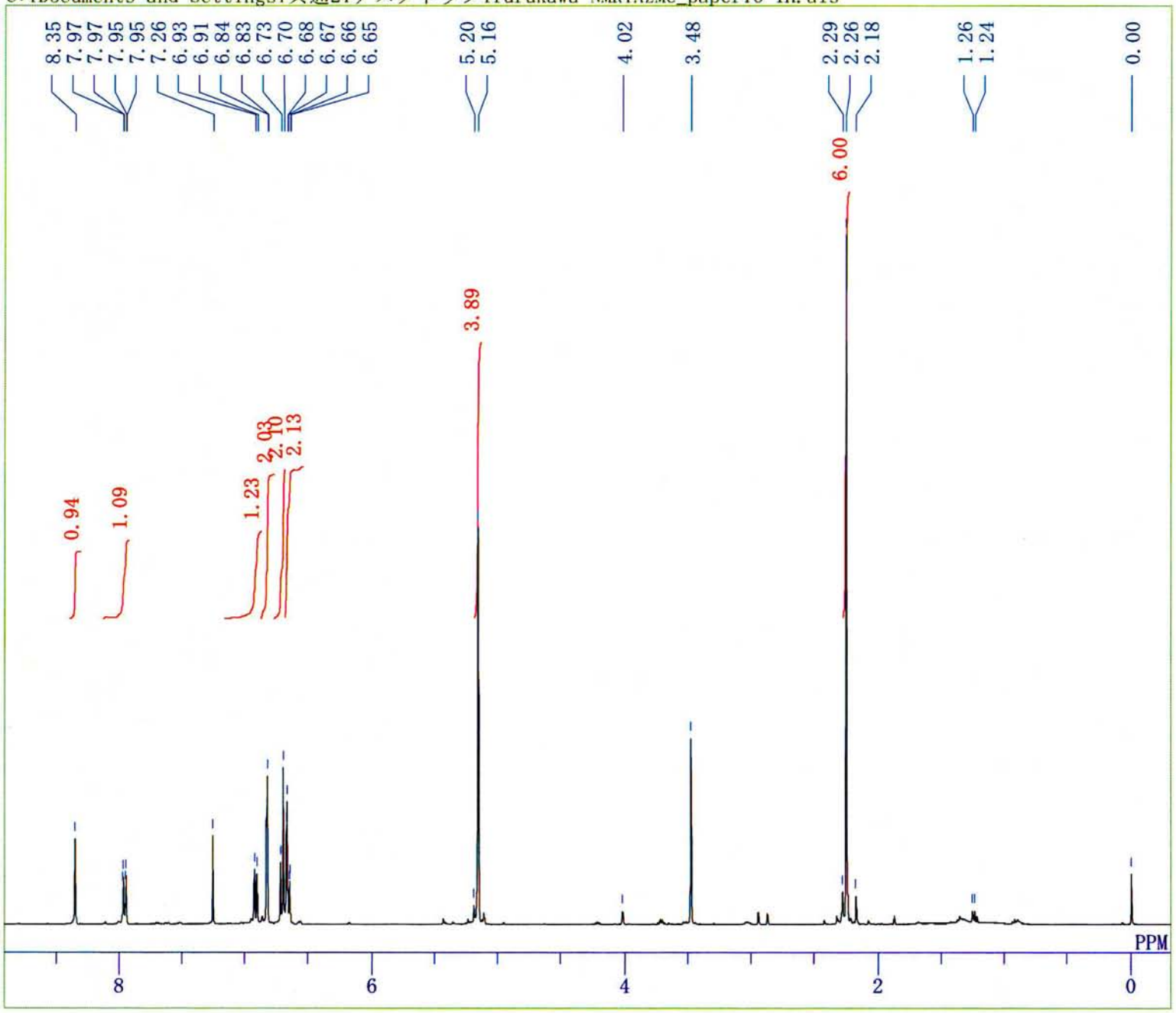

DFILE	6 1H.als	
COMNT		
DATIM	Mon Feb 05 15:14:06 2007	
OBNUC	1H	
EXMOD	NON	
OBFRQ	395.75	MHz
OBSET	124.00	KHz
OBFIN	10277.00	Hz
POINT	32768	
FREQU	7917.60	Hz
SCANS	8	
ACQTM	4.1386	sec
PD	2.8610	sec
PW1	6.30	usec
IRNUC	1H	
CTEMP	23.2	c
SLVNT	CDCL3	
EXREF	0.00	ppm
BF	0.12	Hz
RGAIN	15	

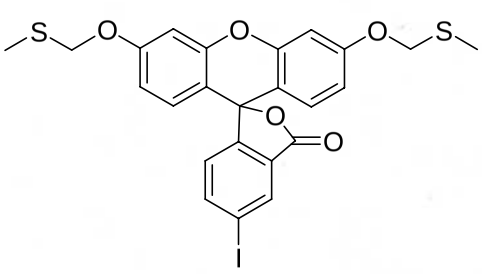

^{1}H NMR ($CDCl_3$), 400MHz

C:¥Documents and Settings¥共通2¥デスクトップ¥furukawa NMR¥AzMe_paper¥6 13C.als

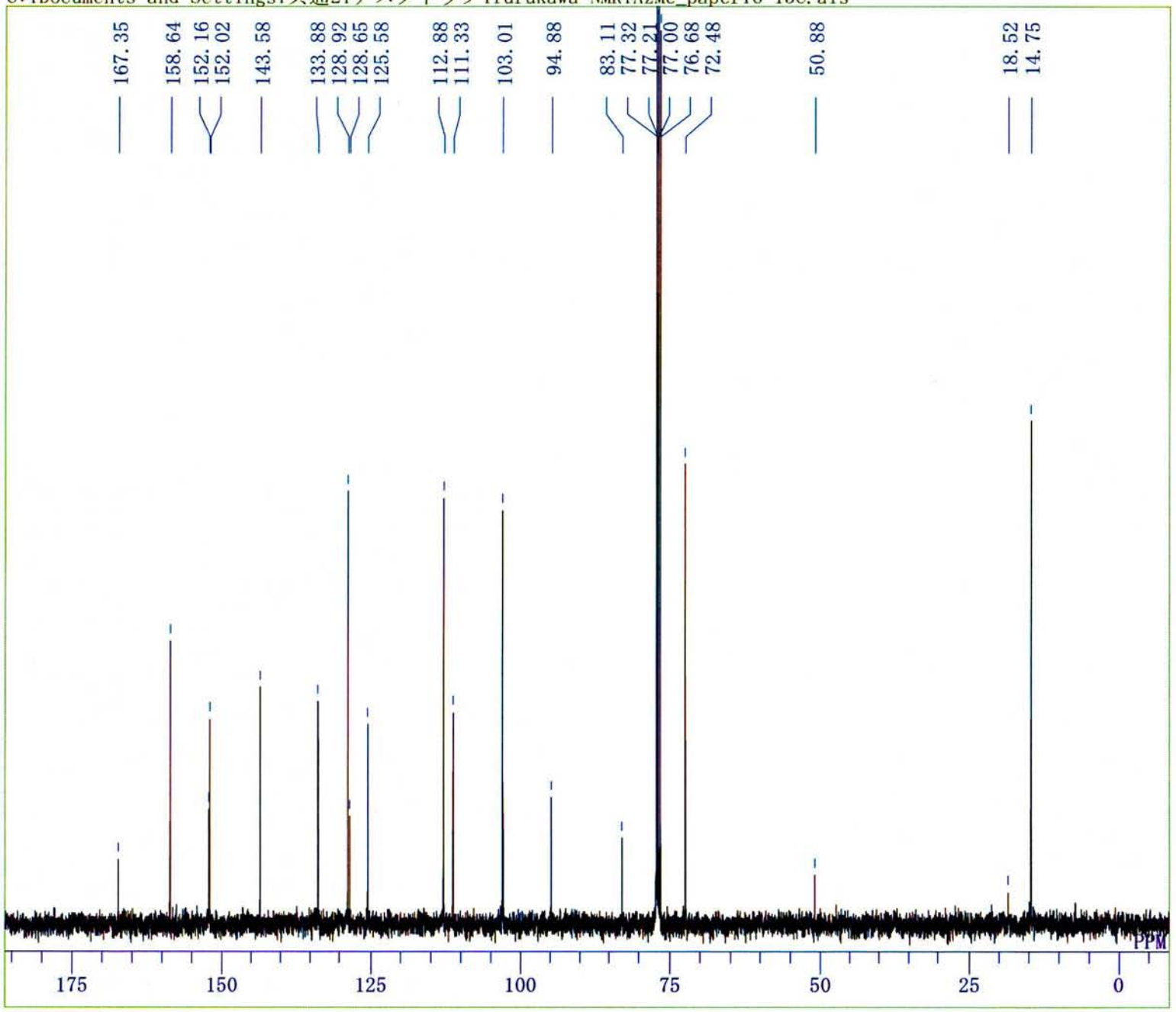


```
DFILE   6 13C.als
COMNT
DATIM   Mon Feb 05 15:38:53 2007
OBNUC   13C
EXMOD   BCM
OBFRQ         99.45 MHz
OBSET         94.00 KHz
OBFIN      10309.00 Hz
POINT         32768
FREQU      26881.70 Hz
SCANS           292
ACQTM         1.2190 sec
PD            1.7810 sec
PW1             6.20 usec
IRNUC   1H
CTEMP          22.1 c
SLVNT   CDCL3
EXREF         77.00 ppm
BF             1.20 Hz
RGAIN            27
```

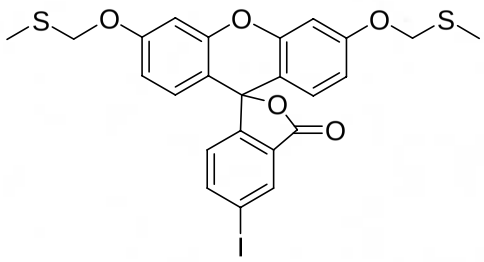

^{13}C NMR ($CDCl_3$), 100MHz

C:¥Documents and Settings¥共通2¥デスクトップ¥furukawa NMR¥AzMe_paper¥7 1H.als

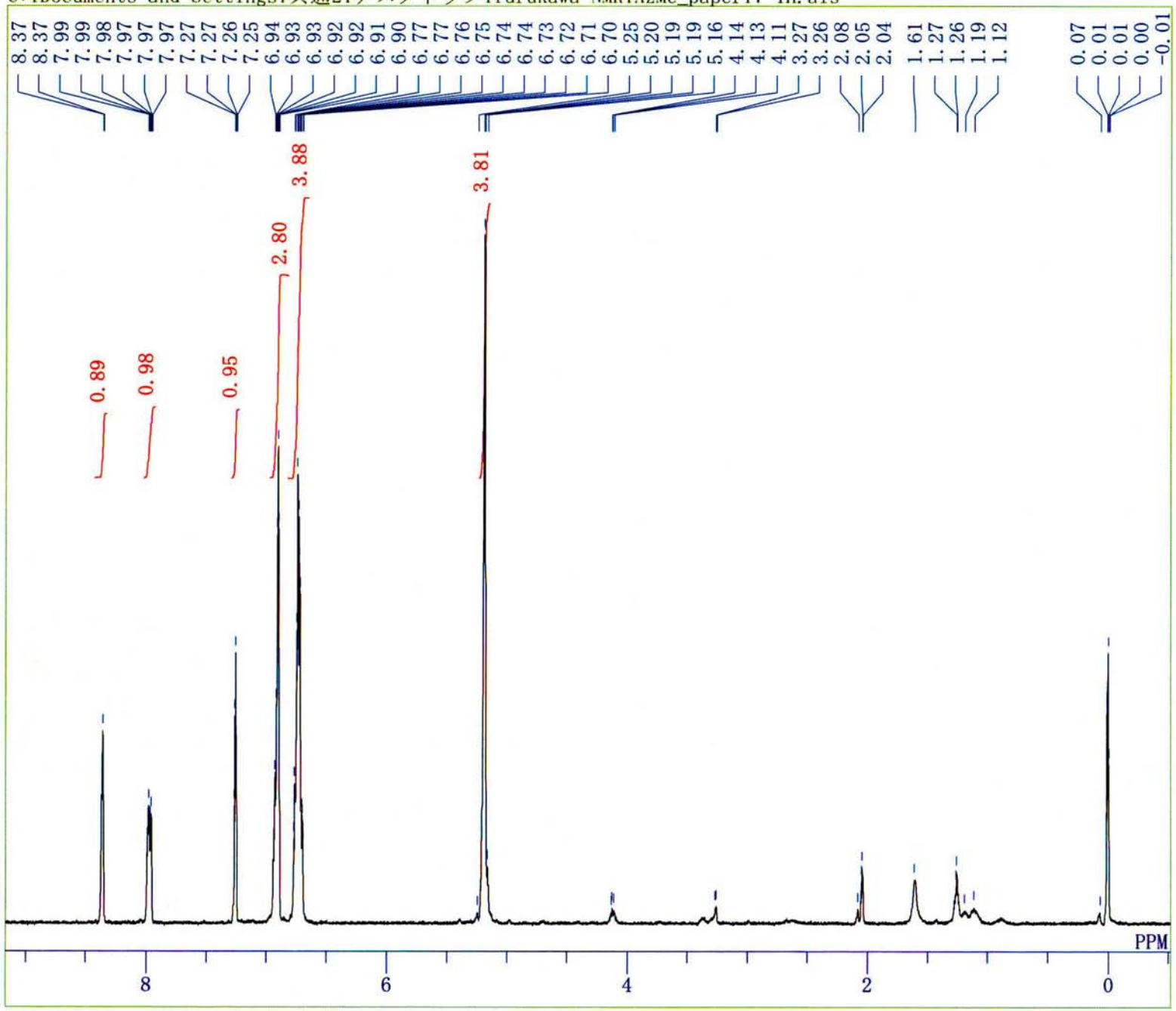


```
DFILE   7 1H.als
COMNT
DATIM   Thu Feb 15 17:05:00 2007
OBNUC   1H
EXMOD   NON
OBFRQ         395.75 MHz
OBSET         124.00 KHz
OBFIN       10277.00 Hz
POINT         32768
FREQU        7917.60 Hz
SCANS             8
ACQTM         4.1386 sec
PD            2.8610 sec
PW1             6.30 usec
IRNUC   1H
CTEMP           22.2 c
SLVNT   CDCL3
EXREF           0.00 ppm
BF              0.12 Hz
RGAIN             20
```

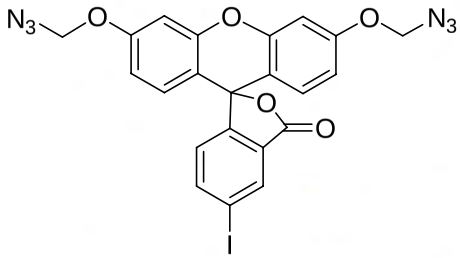

^{1}H NMR ($CDCl_3$), 400MHz

C:¥Documents and Settings¥共通2¥デスクトップ¥furukawa NMR¥AzMe_paper¥7 13C.als

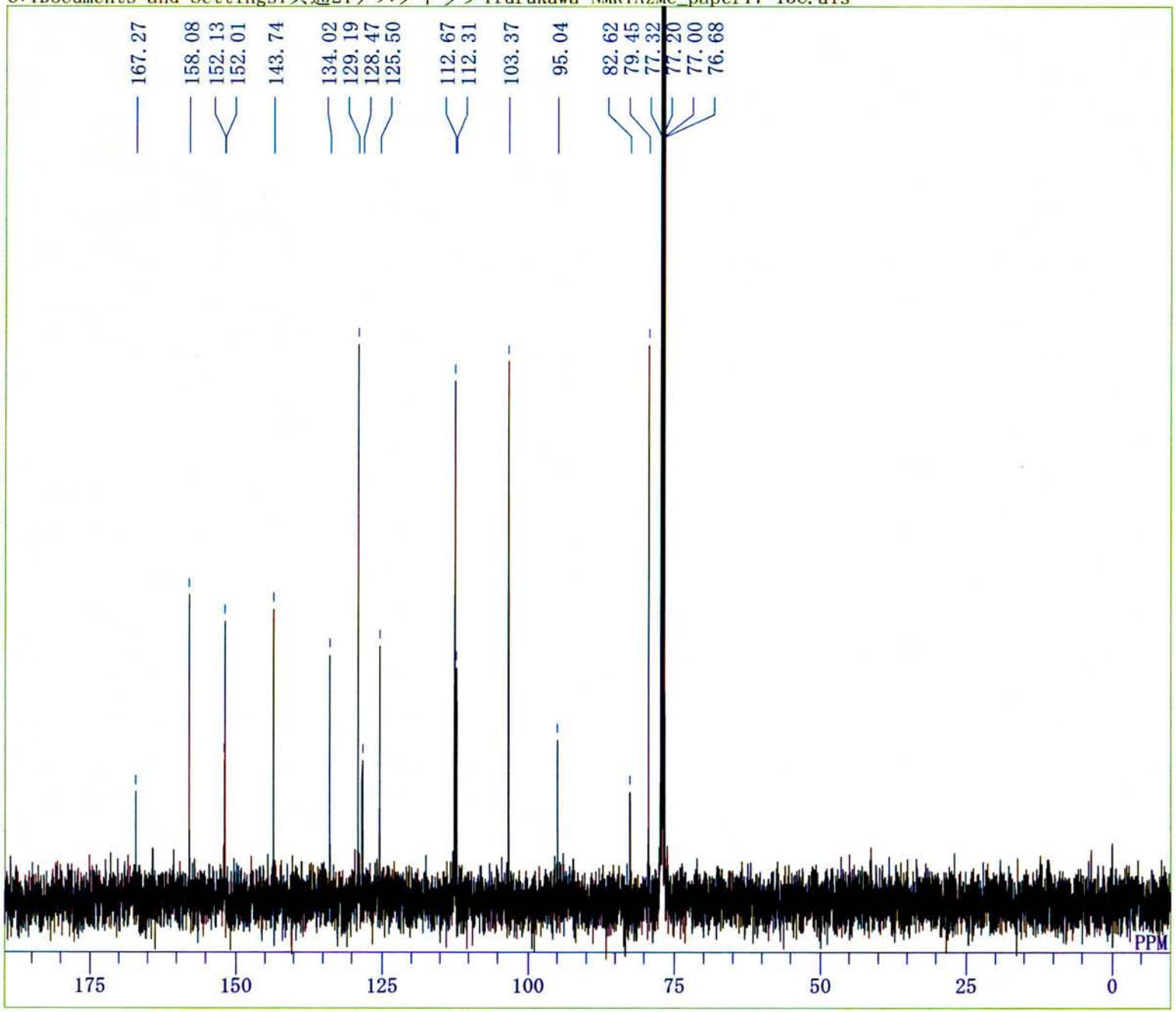


```
DFILE  7 13C.als
COMNT
DATIM  Thu Feb 15 17:44:02 2007
OBNUC  13C
EXMOD  BCM
OBFRQ        99.45 MHz
OBSET        94.00 KHz
OBFIN     10309.00 Hz
POINT        32768
FREQU     26881.70 Hz
SCANS          665
ACQTM       1.2190 sec
PD          1.7810 sec
PW1            6.20 usec
IRNUC  1H
CTEMP         22.0 c
SLVNT  CDCL3
EXREF        77.00 ppm
BF            1.20 Hz
RGAIN           28
```

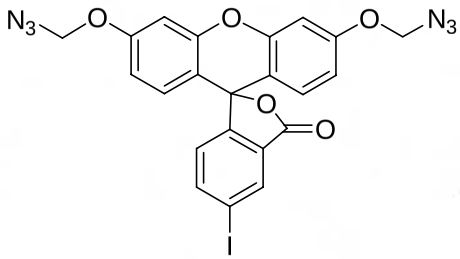

^{13}C NMR ($CDCl_3$), 100MHz

C:¥Documents and Settings¥共通2¥デスクトップ¥furukawa NMR¥AzMe_paper¥9 1H.als

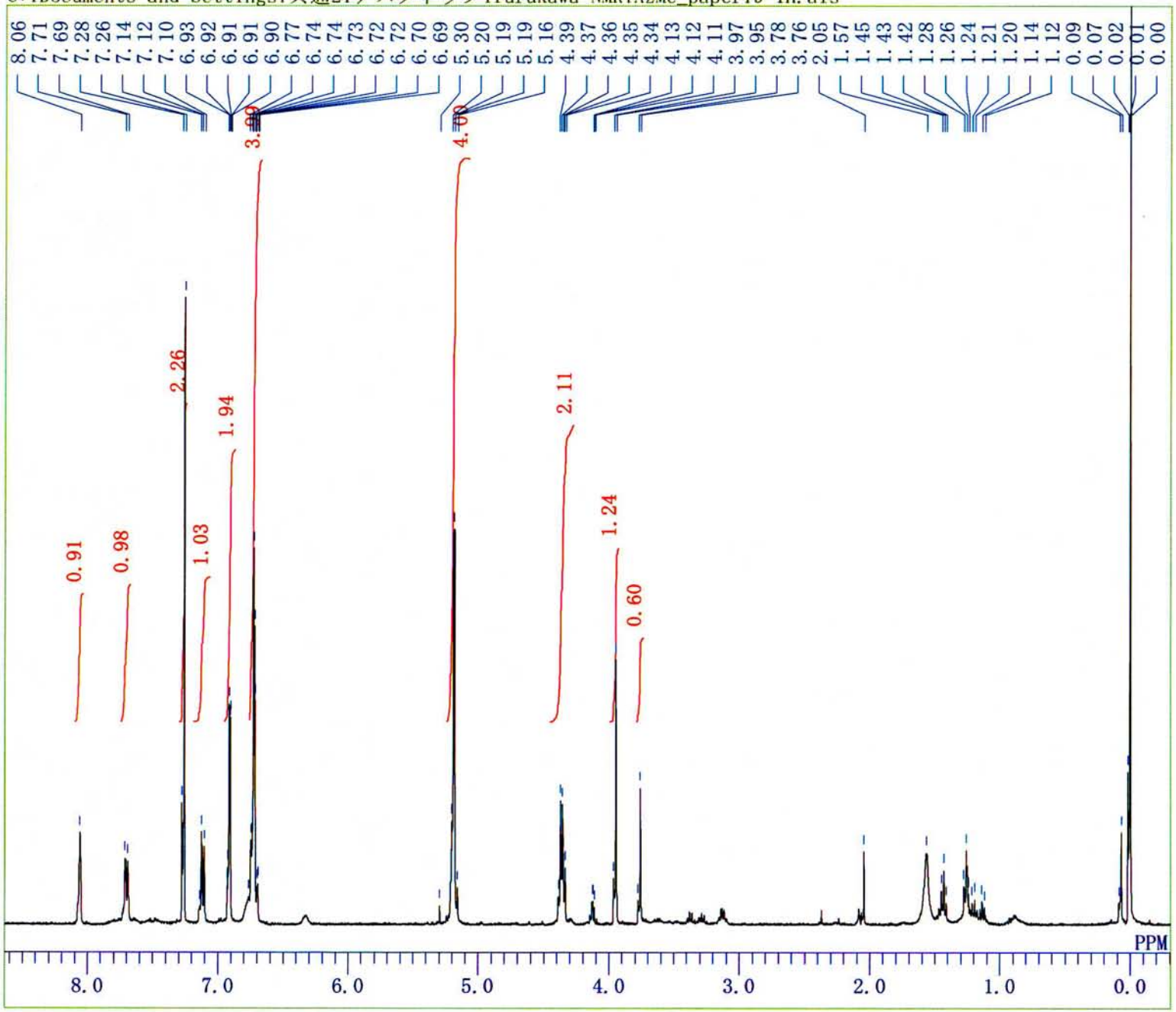

DFILE 9 1H.als
COMNT
DATIM Thu Feb 22 12:10:37 2007
OBNUC 1H
EXMOD NON
OBFRQ 395.75 MHz
OBSET 124.00 KHz
OBFIN 10277.00 Hz
POINT 32768
FREQU 7917.60 Hz
SCANS 27
ACQTM 4.1386 sec
PD 2.8610 sec
PW1 6.30 usec
IRNUC 1H
CTEMP 21.9 c
SLVNT CDCL3
EXREF 0.00 ppm
BF 0.12 Hz
RGAIN 22

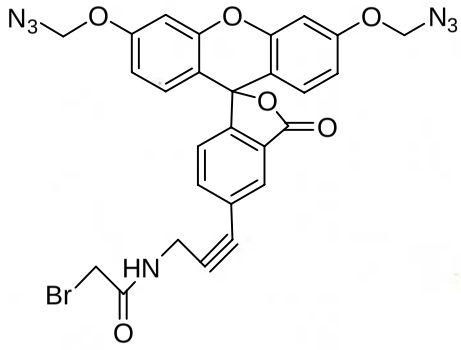

^{1}H NMR ($CDCl_3$), 400MHz

C:¥Documents and Settings¥共通2¥デスクトップ¥furukawa NMR¥AzMe_paper¥9 13C.als

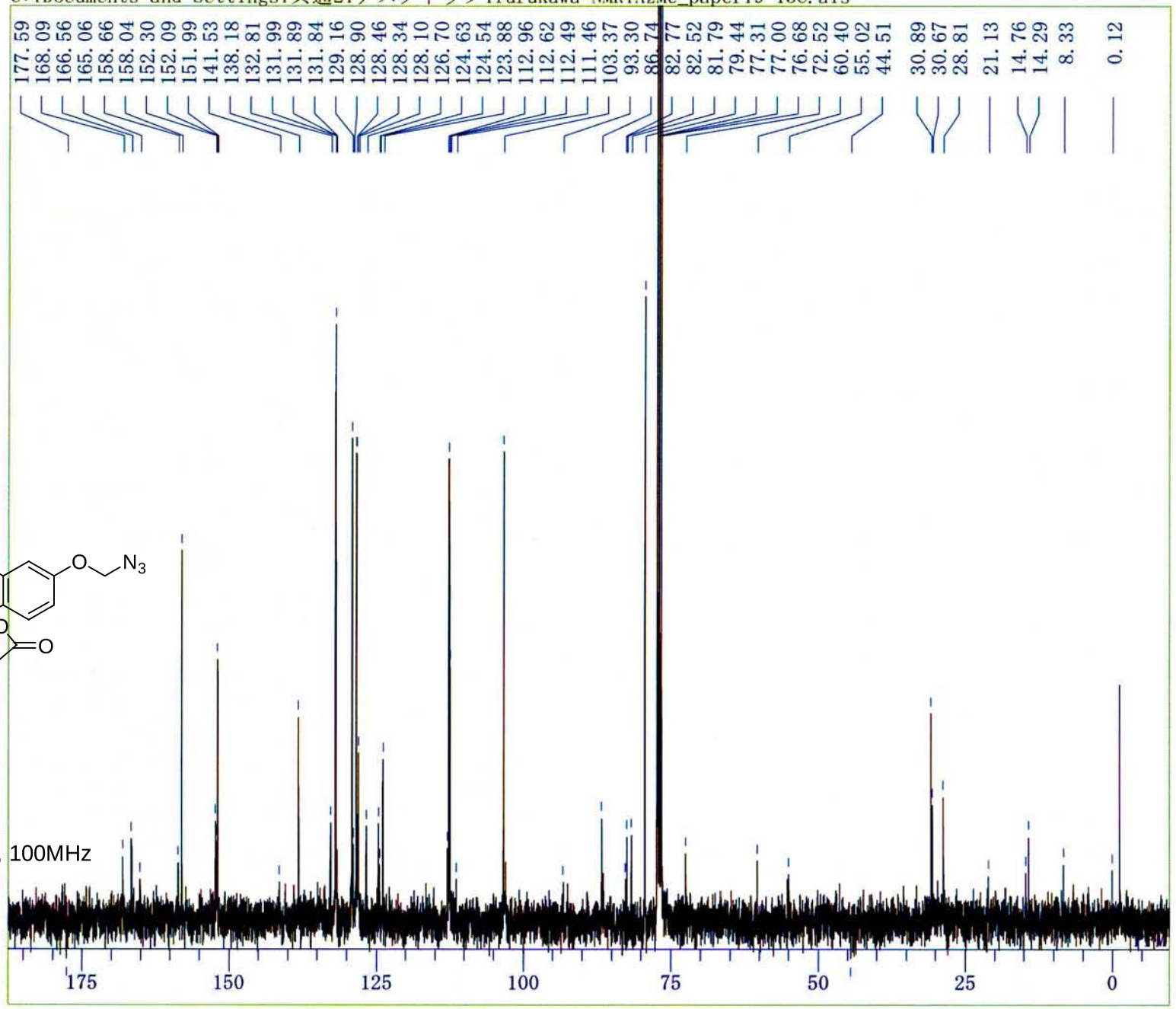

DFILE 9 13C.als
COMNT
DATIM Thu Jun 21 22:54:53 2007
OBNUC 13C
EXMOD BCM
OBFRQ 99.45 MHz
OBSET 94.00 KHz
OBFIN 10309.00 Hz
POINT 32768
FREQU 26881.70 Hz
SCANS 702
ACQTM 1.2190 sec
PD 1.7810 sec
PW1 6.20 usec
IRNUC 1H
CTEMP 23.6 c
SLVNT CDCL3
EXREF 77.00 ppm
BF 1.20 Hz
RGAIN 27

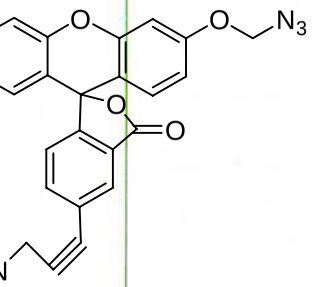

(CDCl3), 100MHz

Thermally Gated Liposomes: A Closer Look

Ravil R. Petrov, Wen-Hua Chen, and Steven L. Regen*

Department of Chemistry, Lehigh University, Bethlehem, Pennsylvania 18015. Received February 25, 2009; Revised Manuscript Received March 23, 2009

A homologous series of pore-forming amphiphiles (PFAs), derived from cholic acid, lysine, and spermine, have been used as "thermal gates" for releasing sucrose from liposomes made from 1,2-dipalmitoyl-*sn*-glycero-3-phosphocholine (DPPC) and 1,2-dipalmitoyl-*sn*-glycero-3-[phospho-*rac*-(1-glycerol)] (sodium salt) [DPPG]. Binding measurements have established that these PFAs are fully bound to these liposomes in their gel state and that their transfer to fluid phase membranes is negligible. Release experiments have shown that thermal gating is sensitive to both the size and the concentration of the PFA that are used. Increases in the extent of release of sucrose with increasing temperature that have been found in the gel/fluid coexistence region indicate the existence of heterogeneity among the liposomes.

INTRODUCTION

Finding ways to control the release of encapsulated agents from the aqueous interior of liposomes continues to attract broad interest from an applications standpoint (*1*−*22*). Although most of this interest has centered around drug delivery, a variety of other applications can be considered as well, e.g., the release of catalysts, reagents, cosmetics, flavors, dyes, fragrances, contrast agents, etc.

One well-established approach for controlling the release of liposome-encapsulated agents takes advantage of differences in membrane permeability between the gel (i.e., solid-like) and the liquid−crystalline (i.e., fluid-like) state. In particular, whereas gel-phase bilayers are characterized by tight lipid packing and low permeability, fluid phase analogues are loosely packed and have relatively high permeabilities (*23*−*26*). Thus, by increasing the temperature of liposomes beyond their gel to liquid−crystalline phase transition temperature (T_m), one can observe increased permeation rates (*24*−*26*). In some instances, it has been noted that maximum rates occur at or near the lipid's T_m, where half of the membrane has melted and gel and fluid phases coexist (*27*). Although the reason for this maximum has not been firmly established, it has been suggested that a mismatch in lipid packing between the two phases produces defects through which permeants can pass (*27*).

Previously, we introduced the concept of "thermally gated liposomes", whereby a pore-forming agent (PFA) derived from facially amphiphilic cholic acid is used to enhance thermally induced liposomal release (*28*). Our working hypothesis is that these PFAs assemble into pores either in the fluid phase or at gel/fluid interfaces (Figure 1).

In the work reported herein, we sought to gain insight into the interactions between PFAs and gel phase liposomes and to better characterize the thermally gated release process. Of particular interest was to determine whether PFAs are fully bound to gel phase liposomes, whether they are transferrable to fluid phase analogues, and whether thermally gated release is dependent on the size of the PFA that is used. We also sought to distinguish between thermally gated release occurring in the fluid phase versus gel/fluid interfaces.

In earlier studies, we showed that a nonfacially amphiphilic, ion conductor is "squeezed out" of liposomal membranes and released into the aqueous phase when the bilayer is converted from the fluid phase to the gel state (*29*). If PFAs derived from cholic acid were to behave similarly, this would limit their usefulness in drug delivery, since they would be expected to undergo competitive binding to cell membranes. For this same reason, transfer of a PFA from gel phase liposomes to fluid phase membranes via direct membrane−membrane contact would be a significant limitation. Thus, the inherent stability of thermally gated liposomes in the presence of fluid membranes has practical implications. Equally important from a drug delivery standpoint is the rate at which encapsulated agents are released from liposomes. Since release rates approaching "burst kinetics" are most suitable for drug targeting via localized hyperthermia, knowing whether release is faster in the fluid phase or in the gel/fluid coexistence region has practical relevance. In addition, knowing whether the size of a PFA significantly influences release rates is an important consideration. Although we have shown that the activity of a PFA for Na^+ transport increases exponentially with increasing size, whether the size of a PFA influences the rate of release of molecules from liposomes *under thermally gated conditions* remains to be determined (*28*).

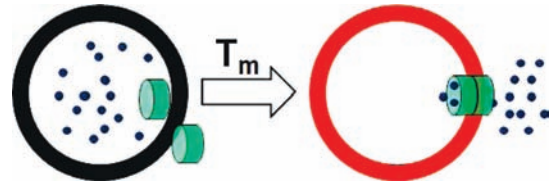

Figure 1. Stylized illustration showing two PFAs forming a pore in a melted bilayer.

RESULTS

Experimental Design. To examine these issues, we employed liposomal carriers (∼200 nm diameter, extrusion) made from 1,2-dipalmitoyl-*sn*-glycero-3-phosphocholine (DPPC) and a small amount (5 mol %) of the negatively charged analogue 1,2-dipalmitoyl-*sn*-glycero-*e*-[phospho-*rac*-(1-glycerol)] (sodium salt) [DPPG]. The latter was included in these dispersions to stabilize them by preventing aggregation. Extrusion procedures used in forming thermally gated liposomes (200 nm Nuclepore membranes) are described in the Supporting Information.

* To whom correspondence should be addressed. E-mail: slr0@lehigh.edu.

10.1021/bc9000849 CCC: $40.75 © 2009 American Chemical Society
Published on Web 04/17/2009

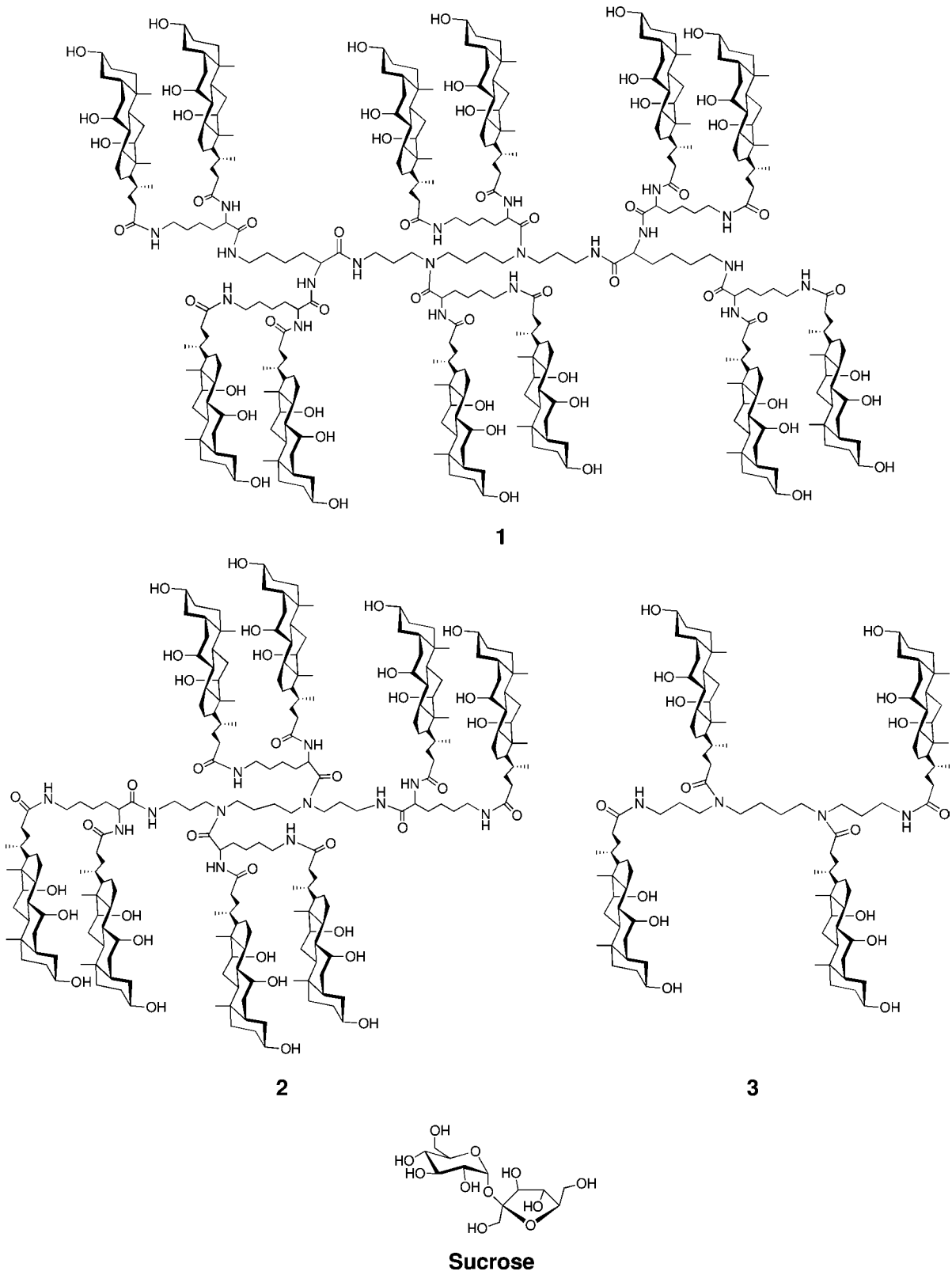

Figure 2. Structures of pore-forming amphiphiles and permeant (sucrose) used in this study.

Because DPPC and DPPG have a T_m of 41 °C, which is slightly above physiological 37 °C, these liposomes could be considered for drug delivery.

Three pore-forming agents that were chosen for this study were derived from cholic acid, lysine, and spermine (Figure 2). The largest one (i.e., **1**) contains 12 choloyl groups coupled to a spermine backbone that has been extended at each end by one lysine group (*30*). An intermediate-sized analogue (i.e., **2**) has a total of eight choloyl groups bound to this same framework (*30*). Finally, a relatively small analogue (i.e., **3**) has only four choloyl groups bound to spermine (*31*). In this work, sucrose was chosen as a model permeant because it is uncharged and highly water-soluble.

Thermotropic Properties. Before carrying out thermally gated release experiments, we first examined the melting properties of our liposomes in the absence and in the presence

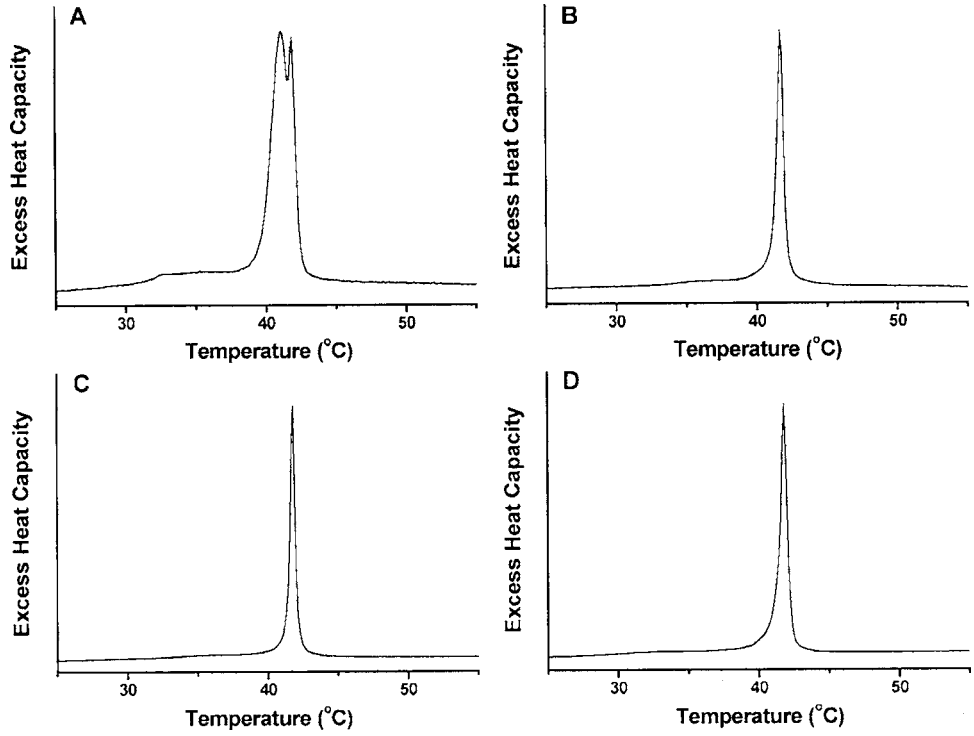

Figure 3. High-sensitivity differential scanning calorimetry data for extruded liposomes made from DPPC/DPPG (95/5, mol/mol) with (A) no PFA added, (B) 0.1 mol % of **1**, (C) 0.15 mol % of **2**, and (D) 0.3 mol % of **3**.

Table 1. Quantification of Liposome-Bound PFAs before and after Gel Filtration[a]

	integrated density of TLC spots					
	before gel filtration			after gel filtration		
PFA	PFA	DPPG	ratio of PFA/DPPG	PFA	DPPG	ratio of PFA/DPPG
1	107 423	401 666	0.27	79 194	315 235	0.25
2	197 958	919 363	0.22	203 264	885 709	0.23
3	125 934	755 700	0.17	75 604	470 334	0.16

[a] Integrated densities measured for PFAs and DPPG are in arbitrary units.

of **1**, **2**, and **3** by high-sensitivity differential scanning calorimetry (hs-DSC). For these measurements and for thermally gated release experiments, a low concentration of PFA was used, that is, 1.2 mol % choloyl groups, corresponding to 0.1, 0.15, and 0.3 mol % of **1**, **2**, and **3**, respectively.

In the absence of PFAs, a broad pretransition was observed at ~35 °C. In addition, the main gel to liquid−crystalline phase transition appeared as a doublet, centering at ~41 °C (Figure 3). It is noted that similar splitting has been reported for other phosphocholine-based liposomes when their diameters are less than ~200 nm (*32*). In the presence of each of these PFAs, the pretransition was essentially eliminated and the main phase transition was converted into a sharp single endotherm.

Binding of PFAs to Gel Phase Liposomes. To judge the extent of binding of each PFA by gel phase liposomes, we determined relative concentrations in dispersions before and after gel filtration by quantitative thin layer chromatography. For these analyses, the DPPG that was present in the liposomes was used as an internal standard. Since the ratio of PFA/DPPG was essentially the same before and after gel filtration in all cases, these results indicate that these PFAs are fully bound (about ±5%) to these gel phase liposomes at 23 °C (Table 1).

Attempted Transfer of a PFA from Gel to Fluid Phase Liposomes. In an attempt to transfer a PFA from gel phase liposomes to fluid analogues, we mixed an extruded dispersion made from DPPC/DPPG (95/5, mol/mol) containing 0.3 mol % of **3** with multilamellar vesicles (MLVs) made from 1-palmitoyl, 2-oleoyl-*sn*-glycero-3-phosphocholine (POPC, $T_m = -2.6$ °C) (*33*, *34*). After an incubation period of 16 h at 37 °C with 10 equiv of POPC, the resulting dispersion was cooled to room temperature and centrifuged to pellet the MLVs. Under these conditions, the extruded liposomes remain dispersed. Analysis of the ratio of **3**/DPPG in the supernatant by quantitative TLC indicated no loss of **3** from the gel phase liposomes.

Thermally Gated Release of Sucrose. To test for thermal gating, sucrose was encapsulated in liposomes containing **1**, **2**, or **3**. After gel filtration to remove external sucrose, the liposomes were then immediately heated to either 37 or 43 °C. Aliquots were withdrawn as a function of time and rapidly gel-filtered a second time to remove the sucrose that had been released. The amount of sucrose that was retained by the liposomes was quantified by spectrophotometry after digestion (see Supporting Information). In Figure 4 are shown the release profiles. In the absence of a PFA, the release of sucrose was negligible at both of these temperatures. When **1** was included in the liposomes, however, the release was rapid and complete at 43 °C. Somewhat unexpectedly, a similar release profile was observed at 37 °C. When **2** was used as the PFA, the extent of release was nearly complete at both temperatures but was apparently slower at 37 °C. In contrast to **1** and **2**, the use of **3** as the PFA resulted in thermal gating; that is, there was negligible release at 37 °C and rapid and substantial release at 43 °C.

The difference in release rates for **2** at 37 °C versus 43 °C suggested that an even greater difference might be observed using a lower concentration of the PFA. Consistent with this

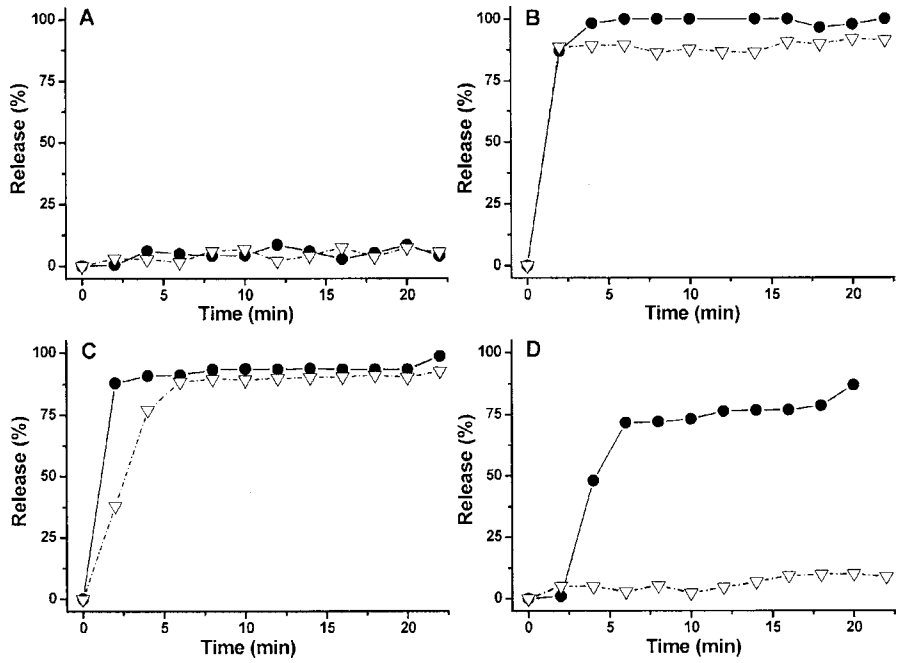

Figure 4. Plot of percent of sucrose released as a function of time from liposomes made from DPPC/DPPG (95/5, mol/mol) with (A) no PFA added, (B) 0.1 mol % of **1**, (C) 0.15 mol % of **2**, and (D) 0.3 mol % of **3** at (▽) 37 °C and (●) at 43 °C.

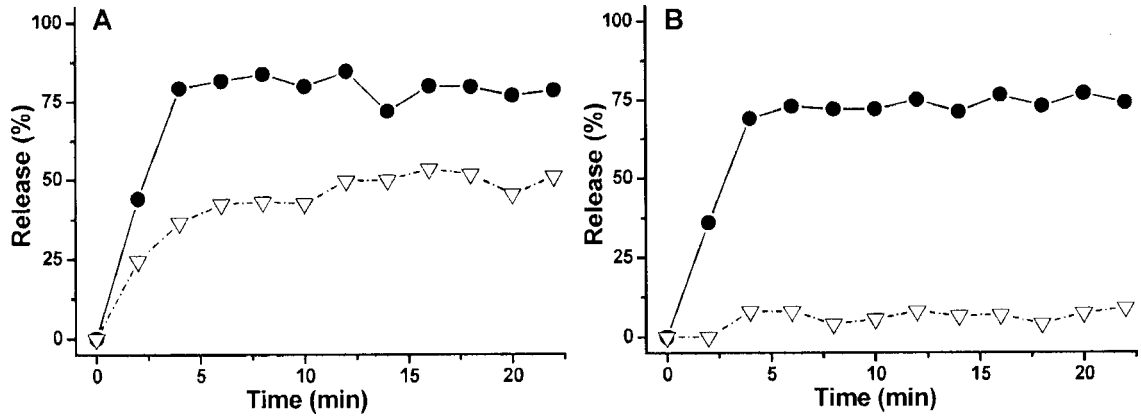

Figure 5. Release of sucrose as a function of time from liposomes made from DPPC/DPPG (95/5, mol/mol) containing (A) 0.010 mol % of **1** and (B) 0.015 mol % of **2** at (▽)37 °C and (●) 43 °C.

thinking, when only 0.015 mol % of **2** was used, the extent of release at 37 °C was negligible; however, at 43 °C, a rapid and significant release was observed (Figures 5). Qualitatively, similar behavior was observed when 0.010 mol % of **1** was used.

Dynamic light scattering measurements that were made for liposomes containing 0.10 mol % of **1**, 0.15 mol % of **2**, and 0.30 mol % of **3** showed diameters before (and after) thermally gated release that were 164 ± 59 nm (164 ± 62 nm), 150 ± 57 nm (150 ± 60 nm), and 148 ± 59 nm (148 ± 56 nm), respectively.

In an effort to determine whether thermally gated release is favored in the fluid phase or the gel/fluid coexistence region, a similar set of experiments was carried out using **3** at 41 °C and at 43 °C; that is, at the T_m of the bilayer and at a temperature in which the bilayer is fully melted. Thus, if release were favored in the gel/fluid coexistence region, the efflux rate should be greater at 41 °C than at 43 °C; if release were favored in the fluid phase, then a greater efflux rate should be observed at 43 °C. Although the release profiles at 41 °C showed a slight time lag for the onset of release, the similarity in the slopes at both temperatures does not allow a clear distinction to be made between preferred release in fluid phase versus the gel/fluid coexistence region (Figure 6). One interesting difference between these release profiles is *the lower extent of release* at the lower temperature. To confirm this behavior, we prepared a similar dispersion and divided it into 10 portions. Each portion was heated for 6 min at temperatures ranging between 36.5 and 43.5 °C, and the extent of release was determined. As shown in Figure 7, a maximum release was found when the membrane was fully melted.

Further evidence for greater release occurring when the liposomes were fully melted was obtained by dividing a dispersion containing 0.3 mol % of **3** into two portions. One portion was rapidly heated to 41.5 °C and held at that temperature for 6 min and cooled to room temperature. This heating/cooling cycle was then repeated five additional times, and the extent of sugar release was analyzed after each cycle. The second portion of liposomes was heated only once to 43 °C and held for 6 min before cooling to room temperature. As shown in Figure 8, only a modest increase in the amount of sucrose that was released was observed with additional heating/

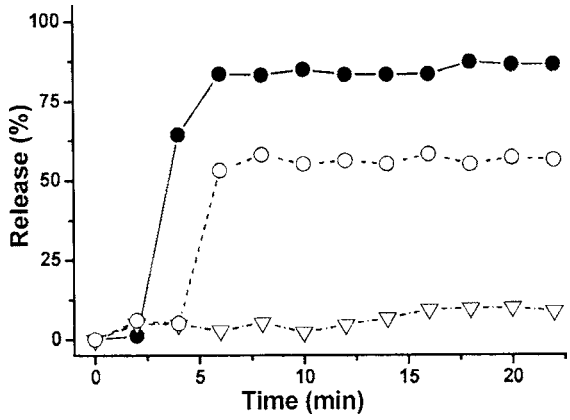

Figure 6. Release of sucrose as a function of time from liposomes made from DPPC/DPPG (95/5, mol/mol) containing 0.3 mol% of **3** at (▽) 37 °C, (○) 41 °C, and (●) 43 °C.

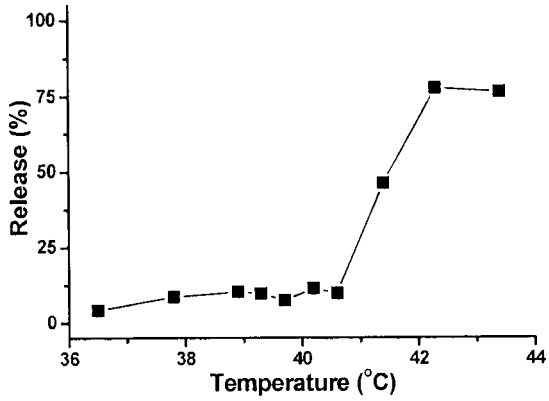

Figure 7. Release of sucrose from liposomes made from DPPC/DPPG (95/5, mol/mol) containing 0.3 mol % of **3** as a function of temperature using a 6 min incubation period.

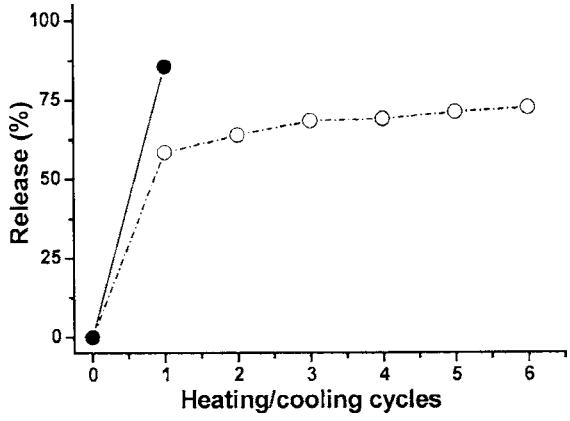

Figure 8. Release of sucrose from liposomes made from DPPC/DPPG (95/5, mol/mol) containing 0.3 mol % of **3** as a function of the number of heating/cooling cycles at 41.5 °C (○) and from one heating period at 43 °C (●). In all cases 6 min incubation periods were used.

cooling cycles at 41.5 °C. In contrast, the extent of release at 43 °C was significantly greater.

DISCUSSION

Analysis of the gel phase liposomes used in this study by hs-DSC, in the absence of PFAs, showed a main phase transition that appeared as a doublet, which is similar to observations that have been made by other researchers for highly curved phosphocholine-based liposomes (*32*). Although the basis for this splitting remains to be established, one possibility is that the inner-concave and outer-convex leaflets have distinct melting characteristics due to differences in packing. Regardless of its origin, the addition of very small amounts of **1**, **2**, and **3** was sufficient to promote greater cooperativity in the melting process and the conversion to a sharp single endotherm. We suspect that this effect may be due to a "filling in" of gaps within each of the leaflets by the PFA.

Binding measurements that were made for **1**, **2**, and **3** have shown that these PFAs are fully bound to gel phase liposomes made from DPPC/DPPG (95/5, mol/mol) and that the transfer of **3** to a fluid phase analogue is negligible. Thus, thermally gated liposomes would appear to be reasonably stable.

The dependency of thermally gated release on the size of the PFA that is used was found to be significant. The fact that **1** and **2** release almost all of the entrapped sucrose at 37 °C (when 0.10 and 0.15 mol % are used, respectively), but release very little when their concentration is reduced by 1 order of magnitude, suggests that aggregates may be responsible for release from gel phase liposomes. A previous study of **1** and **2** as agents for promoting the transport of Na^+ across fluid bilayers has shown that two PFAs combine to form a pore (*28*, *30*). If the release of sucrose is favored in fluid regions of the membrane under thermal-gating conditions, then a similar pore structure may be involved.

The fact that the maximum amount of sucrose, which is released under thermal gating conditions, is dependent on temperature and that repetitive heating/cooling cycles at a fixed temperature in the gel/fluid coexistence region barely increase the extent of this release indicates that there is heterogeneity among the liposomes; that is, some of liposomes release their contents at a given temperature while others do not. The origin of this heterogeneity is not presently clear. One model that can be considered is based on the following assumptions: (i) the PFAs are nonuniformly distributed among the liposomes; (ii) the effective concentration of a PFA within a liposome is determined by its total concentration in the membrane and by the fraction of the membrane that has been converted into the fluid phase; (iii) those PFAs that reside in gel regions of the membrane do not form pores at sufficiently low concentrations; (iv) small aggregates of PFAs are formed in fluid regions, and it is these pores that are responsible for thermally gated release. Thus, at a given temperature in the gel/fluid coexistence region, some of the liposomes have a sufficient concentration of PFA in fluid regions to form pores, which release sucrose. As the temperature is increased and a greater percentage of the membranes are melted, the concentration of PFAs in fluid regions is then increased and the release of sucrose from those liposomes containing lesser amounts of PFA is possible.

The finding that less than 100% of sucrose is released even at 43 °C (under thermal gating conditions) is consistent with a nonuniform distribution of PFAs among the liposomes. The fact that at 43 °C, 100% release was found using 0.1 mol % of **1**, slightly less than 100% release was found using 0.15 mol % of **2**, and significantly less than 100% release was observed using **3** suggests that the larger PFAs are more efficient in releasing sucrose, if one assumes that their distribution among the liposomes is similar. From an operational standpoint, the fact that 0.015 mol % of **2** shows thermal gating behavior that is very similar to that found with 0.3 mol% of **3** indicates that a main virtue of the use of larger PFAs is that much lower concentrations can be employed.

Studies that are currently in progress are aimed at determining (i) the size of the pores that are created under thermal gating conditions by examining the release of entrapped sugars of varying size and (ii) whether aggregates of such amphiphiles

produce pores when these membranes have been converted to the fluid phase by means of kinetic measurements (*30*).

CONCLUSIONS

Experimental evidence has been obtained showing that PFAs **1**, **2**, and **3** are fully bound to gel-phase liposomes made from DPPC/DPPG (95/5, mol/mol), that transfer of a PFA from gel phase liposomes to fluid phase analogues is negligible, and that thermally gated release is sensitive to both the size and the concentration of the PFA that is used. Relatively high concentrations of PFAs favor the release of entrapped sucrose from gel phase liposomes, suggesting that aggregates may be responsible. An increase in the extent of sucrose release with increasing temperatures within the gel/fluid coexistence region has also revealed heterogeneity among the liposomes. The question of whether thermally gated release is favored in the fluid phase or the gel/fluid coexistence region has not been answered unambiguously, although the present findings suggest that the fluid phase may be more likely.

ACKNOWLEDGMENT

We are grateful to the National Science Foundation (Grant CHE-0345248) and to the National Institutes of Health (PHS Grant GM51814) for support of this research.

Supporting Information Available: Experimental procedures and images of TLC plates. This material is available free of charge via the Internet at http://pubs.acs.org.

LITERATURE CITED

(1) Allen, T. M., and Cullis, P. R. (2004) Drug delivery systems: entering the mainstream. *Science 303*, 1818–1822.
(2) Dreher, M. R., and Chilkoti, A. (2007) Toward a systems engineering approach to cancer drug delivery. *J. Natl. Cancer Inst. 99*, 983–985.
(3) Guo, X., and Szoka, F. C. (2003) Chemical approaches to triggerable lipid vesicles for drug and gene delivery. *Acc. Chem. Res. 36*, 335–341.
(4) Sawant, R. M., Hurley, J. P., Salmaso, S., Kale, A., Tolcheva, E., Levchenko, T. S., and Torchilin, V. P. (2006) "SMART" drug delivery systems: double-targeted pH-responsive pharmaceutical nanocarriers. *Bioconjugate Chem. 17*, 943–949.
(5) Andresen, T. L., Jensen, S. S., Kaasgaard, T., and Jorgensen, K. (2005) Triggered activation and release of liposomal prodrugs and drugs in cancer tissue by secretory phospholipase A2. *Curr. Drug Delivery 2*, 353–362.
(6) Fattal, E., Couvreur, P., and Dubernet, C. (2004) "Smart" delivery of antisense oligonucleotides by anionic pH-sensitive liposomes. *Adv. Drug Delivery Rev. 56*, 931–946.
(7) Ong, W., Yang, Y., Cruciano, A. C., and McCarley, R. L. (2008) Redox-triggered contents release from liposomes. *J. Am. Chem. Soc. 130*, 14739–14744.
(8) Gerasimov, O. V., Boomer, J. A., Qualls, M. M., and Thompson, D. H. (1999) Cytosolic drug delivery using pH- and light-sensitive liposomes. *Adv. Drug Delivery Rev. 38*, 317–338.
(9) Davidsen, J., Jorgensen, K., Andresen, T. L., and Mouritsen, O. G. (2003) Secreted phospholipase A2 as a new enzymatic trigger mechanism for localized liposomal drug release and adsorption in diseased tissue. *Biochim. Biophys. Acta 1609*, 95–101.
(10) Meers, P. (2001) Enzyme-activated targeting of liposomes. *Adv. Drug Delivery Rev. 53*, 265–272.
(11) Huang, Z., and Szoka, F. C. (2006) *Liposome Technology*, 3rd ed. (Gregoriadis, G., Ed.) Vol. 3, pp 165−196, CRC Press, Boca Raton, FL.
(12) Sarkar, N., Banerjee, J., Hanson, A. J., Elegbede, A. I., Rosendahl, T., Krueger, A. B., Banerjee, A. L., Tobwala, S., Wang, R. Y., Lu, X. N., Mallik, S., and Srivastava, D. K. (2008) Matrix metalloproteinase-assisted triggered release of liposomal contents. *Bioconjugate Chem. 19*, 57–64.
(13) Chandra, B., Mallik, S., and Srivastava, D. K. (2005) Design of photo-cleavable lipids and their applications in liposomal "uncorking". *Chem. Commun.* 3021–3023.
(14) Eastoe, J., Vesperinas, A., Donnewirth, A. C., Wyatt, P., Grillo, I., Heenan, R. K., and Davis, S. (2006) Photodestructible vesicles. *Langmuir 22*, 851–853.
(15) Shum, P., Kim, J. M., and Thompson, D. H. (2001) Phototriggering of liposomal drug delivery systems. *Adv. Drug Delivery Rev. 53*, 273–284.
(16) Zhang, Z. Y., and Smith, B. D. (1999) Synthesis and characterization of NVOC-DOPE, a caged photoactivatable derivative of dioleoylphosphatidylethanolamine. *Bioconjugate Chem. 10*, 1150–1152.
(17) Kono, K., Murakami, T., Yoshida, T., Haba, Y., Kanaoka, S., Takagishi, T., and Aoshima, S. (2005) Temperature-sensitization of liposomes by use of thermosensitive block copolymers synthesized by living cationic polymerization. *Bioconjugate Chem. 16*, 1367–1374.
(18) Needham, D., and Dewhirst, M. W. (2001) The development and testing of a new temperature-sensitive drug delivery system for the treatment of solid tumors. *Adv. Drug Delivery Rev. 53*, 285–305.
(19) Boomer, J. A., Inerowicz, H. D., Zhang, Z. Y., Bergstrand, N., Edwards, K., Kim, J. M., and Thompson, D. H. (2003) Acid-triggered release from sterically stabilized fusogenic liposomes via a hydrolytic DePEGylation strategy. *Langmuir 19*, 6408–6415.
(20) Anyarambhatla, G. R., and Needham, D. (1999) Enhancement of the phase transition permeability of DPPC liposomes by incorporation of MPPC: a new temperature-sensitive liposome for use with mild hyperthermia. *J. Liposome Res. 9*, 491–506.
(21) Reisch, M. S. (2007) Ushering cosmetics to the right spots. *Chem. Eng. News 85*, 15–21.
(22) Langereis, S., Keupp, J., van Velthoven, J. L. J., II., de Roos, I. H. C., Burdinski, D., Pikkemaat, J. A., and Grull, H. (2009) A temperature-sensitive liposomal ^{1}H CEST and ^{19}F contrast agent for MR image-guided drug delivery. *J. Am. Chem. Soc., 131*, 1380–1381.
(23) Margin, R. L., and Weinstein, J. N. (2006) *Liposome Technology*, 3rd ed. (Gregoriadis, G., Ed.) Vol. 3, pp 137−155, CRC Press, Boca Raton, FL.
(24) Yatvin, M. B., Weinstein, J. M., Dennis, W. H., and Blumentahl, R. (1978) Design of liposomes for enhanced local release of drugs by hyperthermia. *Science 202*, 1290–1293.
(25) Kong, G., and Dewhirst, M. W. (1999) Hyperthermia and liposomes. *Int. J. Hyperthermia 15*, 345–370.
(26) Lindner, L. H., Eichorn, M. E., Eibl, H., Teichert, N., Schmitt-Sody, M., Issels, R. D., and Dellian, M. (2004) Novel temperature-sensitive liposomes with prolonged circulation time. *Clin. Cancer Res. 10*, 2168–2178.
(27) Papahadjopoulos, D., Jacobson, K., Nir, S., and Isac, T. (1973) Phase transitions in phospholipid vesicles. Fluorescence polarization and permeability measurements concerning the effect of temperature and cholesterol. *Biochim. Biophys. Acta 311*, 330–348.
(28) Chen, W.-H., and Regen, S. L. (2005) Thermally gated liposomes. *J. Am. Chem. Soc. 127*, 6538–6539.
(29) Otto, S., Osifchin, M., and Regen, S. L. (1999) Squeezing a synthetic ionophore and mechanistic insight out of a lipid bilayer. *J. Am. Chem. Soc. 121*, 10440–1014.
(30) Chen, W.-H., Shao, X.-B., and Regen, S. L. (2005) Poly(choloyl)-based amphiphiles as pore-forming agents. Transport-active monomers by design. *J. Am. Chem. Soc. 127*, 12727–12735.
(31) Bandyopadhyay, P., Janout, V., Zhang, L., and Regen, S. L. (2001) Ion conductors derived from cholic acid and spermine: importance of facial hydrophilicity on Na^{+} transport and membrane selectivity. *J. Am. Chem. Soc. 123*, 7691–7696.

(32) Brocca, P., Cantu, L., Corti, M., Del Favero, E., Motta, S., and Nodari, M. C. (2006) Curved single-bilayers in the region of the anomalous swelling: effect of curvature and chain length. *Colloids Surf., A 291*, 63–68.

(33) Kunneke, S., Kruger, D., and Janshoff, A. (2004) Scrutiny of the failure of lipid membranes as a function of headgroups, chain length and lamellarity measured by scanning force microscopy. *Biophys. J. 86*, 1545–1553.

(34) Ceppi, P., Colombo, S., Francolini, M., Raimondo, F., Borgese, N., and Masserini, M. (2005) Two tail-anchored protein variants, differing in transmembrane domain length and intracellular sorting, interact differently with lipids. *Proc. Natl. Acad. Sci. U.S.A. 102*, 16269–16274.

BC9000849

Thermally-Gated Liposomes: A Closer Look

Ravil R. Petrov, Wen-Hua Chen and Steven L. Regen

Departments of Chemistry, Lehigh University, Bethlehem, Pennsylvania 18015

SUPPORTING INFORMATION

Experimental Section

General Methods. Unless noted otherwise, all chemicals and reagents were obtained from Sigma-Aldrich (St. Louis, MO) and used as obtained. 1,2-Dipalmitoyl-*sn*-glycero-3-phosphocholine and 1,2-dipalmitoyl-*sn*-glycero-3-[phospho-*rac*-(1-glycerol)]) were purchased from Avanti Polar Lipids Inc. (Alabaster, AL) as dry powders and used directly. Stock solutions of DPPC (10 mg/mL) and DPPG (0.51 mg/mL) were prepared by dissolving DPPC (400 mg, 545 μmol) and DPPG (20.3 mg, 27 μmol) in 40 mL of chloroform/methanol (2:1, v/v). Conjugates **1**, **2** and **3** were synthesized using methods similar to those previously described (*1,2*). House-deionized water was purified using a Millipore Milli-Q filtering system containing one carbon and two ion-exchange stages. The PBS buffer that was used in all experiments (0.1 M NaCl and 0.01 M NaH_2PO_4, pH 7.4) was prepared by dissolving commercially available NaCl (23.4 g, 400 mmol) and NaH_2PO_4 (4.8 g, 40 mmol) in 4 L of deionized water, and adjusting the pH to 7.4 with 0.1 M HCl and 0.1 M NaOH solutions. An Orion Triode™ pH electrode that was purchased from Thermo Fisher Scientific (Beverly, MA) was used for pH adjustments. Thin layer chromatography (TLC) was performed on glass plates coated with 0.25 mm silica gel (60Å pore size, cat. no. 57457-100) obtained from VWR (West Chester, PA) (*3,4*). Osmotic pressures were measured using a Precision Systems Model 2007 Osmometer

from Thomas Scientific (cat. no. # 7180B10). Densitometry analyses were carried out using Scion Image software (*5*). A Digital 2-Block Model 125DQ Dry Bath Incubator (cat. no. 11-715-125DQ) that was used for thermal-gating was purchased from Fisher Scientific (Pittsburgh, PA). Particle sizes were determined by dynamic light scattering measurements using a Nicomp Model 270 Submicron Particle Sizer (Pacific Scientific, Santa Barbara, CA). The temperatures inside the tubes that were used for thermal-gating were monitored using a digital thermometer (VWR, cat. no. 12777-842) with 0.1 ºC readability.

Preparation of Liposomes. Typically, 2 mL of a stock solution of DPPC/DPPG (95:5, mol/mol) was transferred to a 10 mL glass tube, and the following amounts of pore-forming agents were added as methanol solutions: 1 mL of compound **1** (0.16 mg/mL, 0.1 mol%), 388.4 μL of compound **2** (0.404 mg/mL, 0.15 mol%), or 455 μL of compound **3** (0.317 mg/mL, 0.3 mol%). The solvents were then removed under a stream of nitrogen by rotating the test tube, and the resulting thin film of lipid dried for 12 h under reduced pressure (0.1 Torr). For thermally-gated release experiments, a 100 mM sucrose solution in PBS buffer was used to form multilamellar vesicles (MLVs) instead of pure PBS. Typically, 2 mL of PBS buffer was added to a given tube and the lipids dispersed by vortex mixing to give a final concentration of DPPC equalling 10 mg/mL. The MLVs were then frozen in liquid nitrogen and warmed to 65°C. This freeze/thaw cycle was repeated an additional four times. The dispersion was then extruded ten times through 400 nm Nucleopore membranes (Whatman Nuclepore; Clifton, NJ), followed by ten extrusions through 200 nm Nuclepore membrane using a gas pressure assisted extrusion devise with the temperature of the system that was maintained at 65 ºC.

Calorimetric Measurements. High-sensitivity differential scanning calorimetry (*hs*-DSC) measurements were made using a MC-2 calorimeter from MicroCal (Northampton, MA) in the heating scan mode with a 30ºC/h heating rate. This instrument was interfaced to a PC computer via the DA-2 digital system that was supplied by Microcal Inc. The sample cell was filled with ca. 1.3 mL of phospholipid dispersion with a lipid concentration of 1.6 mg/mL; the reference cell was filled with a corresponding buffer solution. Excess heat capacities, ΔC_p, are given with respect to the reference as evaluated by the software package provided by Microcal Inc. Each sample was scanned at least five times. No significant differences were noticed among each of the scans.

Phospholipid Analysis. Phospholipid concentrations were determined using methods similar to those described by Stewart (*6*). In a typical analysis, 50 µL of a given dispersion was added to a 1.5 mL Eppendorf safe-lock micro polypropylene tube followed by 200 µL of an ammonium ferrothiocyanate solution (containing 0.1 M ferric chloride hexahydrate and 0.4 M ammonium thiocyanate). After shaking for 10 min, 200 µl of chloroform was added followed by 20 s of vigorous vortexing. The chloroform layer was then carefully transferred to a glass optical cell and the absorbance measured at 485 nm. Control experiments showed that there was no interference by sucrose.

Analysis of Sucrose. Specific methods that were used for sugar analysis were similar to those described in the literature, using a freshly prepared stock of digestion solution for experiments carried out at 37°C and at 43°C (*7*).

Binding of PFAs to Gel Phase Liposomes. Liposomes that were used in these experiments were prepared as described above. Typtically, a 2 mL dispersion containing

a given PFA was divided into two equal portions. The first portion was frozen in liquid nitrogen and lyophilized to determine PFA/DPPG ratios before gel filtration. The second portion was gel-filtered using a disposable PD-10 column that was filled with 8.5 mL of Sephadex G-25 (VWR, cat. no. 95017-001), which had been equilibrated with PBS buffer. Before use, the PD-10 columns were allowed to drain until the flow was stopped by a polypropylene frit. Then, the second portion of liposomes (1 mL) was loaded onto the column, followed by addition of PBS buffer (9 mL, 3 mL at a time), and 2 mL-fractions were collected. The phospholipid dispersion that was recovered in the void volume was frozen in liquid nitrogen and lyophilized. To the lyophilized residue was added 200 µL of chloroform/methanol (2/2, v/v) and the sample then sonicated (bath-type) for 1 h, followed by centrifugation. The resulting solution was decanted, concentrated with a stream of nitrogen to approximately half of its original volume and centrifuged. Aliquots of the resulting clear solutions were deposited onto TLC plates using a 1 µL disposable Drummond micropipette (VWR; cat. no. 53440-001). The TLC plates were then developed with chloroform/methanol/water (6/4/1, v/v/v). Detection was made using a reagent that was prepared by adding, sequentially, $MnCl_2 \cdot 4H_2O$ (0.2 g) and concentrated H_2SO_4 (2 mL) to a solution made from 30 mL of water and 30 mL of methanol that was cooled by an ice-water bath. The thin layer chromatography plates were developed by immersing them into this solution and removing the excess solution with polyethylene sorbent pads (VWR, cat. no. 56616-380). The plates were then heated to 220°C for 2 min and cooled to room temperature. Analysis of DPPC, DPPG, and PFA was then made by densitometry. Images of the TLC plates were recorded with 300 dpi resolution in the grey scale mode (8 bits) using a digital scanner, and saved in the BMP

(bitmap) file format. The integrated densities of TLC chromatographic spots were analyzed by the Scion Image software by comparing integrated densities of the corresponding areas (5).

Attempted Transfer of 3 from Gel Phase to Fluid Phase Liposomes. A liposomal dispersion that was made from DPPC/DPPG (95/5, mol/mol) and 0.3 mol% **3** was centrifuged two times (10000 rpm, 5 min, rt) prior to use in this experiment. A separate batch of liposomes was prepared from POPC in PBS buffer in MLV form using methods similar to those described above for DPPC/DPPG. After a 1.5 mL portion of these MLVs (20 mg of total lipid/mL) was pelleted by centrifugation (10000 rpm, 5 min, rt), and the supernatant completely removed by careful decantation, 1.5 mL of the extruded liposomes made from DPPC, DPPG, and **3** were added. The mixed liposomal dispersion was stirred, gently, for 16 h at 37°C. After this incubation period, the MLVs were pelleted by centrifugation (10000 rpm, 20 min, rt), and the supernatant frozen in liquid nitrogen and lyophilized. The residue was dissolved in 200 μL of $CHCl_3$/MeOH (2:1, v/v) with bath sonication, centrifuged and decanted. The resulting solution was concentrated with a stream of nitrogen to approximately half of the original volume and centrifuged. The PFA content of the clear solution was then quantified by TLC with respect to the DPPG concentration as described above. Typical R_f values were DPPC (R_f 0.22), DPPG (R_f 0.31), **3** (R_f 0.33) using chloroform/methanol/water (6/4/1, v/v/v) as the eluent.

Thermally-Gated Release of Sucrose. In these experiments, sucrose was entrapped within extruded liposomes by including it in PBS buffer. Removal of non-entrapped sugar was carried out by gel filtration (Sephadex G-25) where the liposomes were

collected in the void volume (determined by the Blue Dexran). Prior to these filtrations, the columns were equilibrated and washed with four void volumes of osmotically-compensated PBS buffer, which took into account the increase in osmolarity due to the presence of sucrose. Specifically, 3.9 g (67 mmol) of NaCl was added per 1 L of PBS buffer. Following the gel-filtration step, the size of liposomes was monitored by dynamic light scattering.

Thermally-gated release experiments were carried out by rapidly heating 1.2 mL of a given dispersion from room temperature to a desired temperature (typically 37°C or 43°C) and withdrawing 90 μL aliquots using a single channel micropipettor at 2 min time intervals. These aliquots were immediately applied to the gel-media (analytical spin-columns; Handee,™ Mini-Spin Columns from Pierce Biotechnology, Rockford, IL), which were equilibrated with osmotically-balanced buffer. The spin-columns were then centrifuged two times (10000 rpm, rt), each with the duration of 1 min. For these gel filtrations, spin-columns columns were filled with Sephadex G-50. An Eppendorf 5415C Micro Centrifuge was used for these gel filtrations. The amount of sucrose that was retained by the liposomes was quantified by spectrophotometry after digestion using procedures described above. The percentage of sugar release was calculated according to the formula: % release = $(I_0\text{-}I_t)/I_0 \times 100$, where I_o is the sugar content of unheated samples that were gel filtered, and I_t is the sugar content of heated samples at the different time intervals. In all cases, the fractions that were collected were monitored for phospholipid recovery using a standard Stewart assay and were typically greater than 95%.[6] Specific values for the phospholipid recovery were used to correct for the extent of carbohydrate release.

LITERATURE CITED:

(1) Chen, W.-H., Shao, X.-B., Regen, S. L. (2005) Poly(choloyl)-based amphiphiles as pore-forming agents. Transport-active monomers by design, *J. Am. Chem. Soc.*, *127*, 12727-12735.

(2) Bandyopadhyay, P., Janout, V., Zhang, L., Regen, S. L. (2001) Ion conductors derived from cholic acid and spermine: importance of facial hydrophilicity on Na^+ transport and membrane selectivity, *J. Am. Chem. Soc.*, *123*, 7691-7696.

(3) Jork, H., Funk, W., Fischer, W., Wimmer, H. (1990) "Thin-Layer Chromatography: Reagents and Detection Methods", Vol. 1a: Physical and Chemical Detection Methods: Fundamentals, Reagents I; 464 pp.

(4) Jork, H., Funk, W., Fischer, W., Wimmer, H. (1994)"Thin-Layer Chromatography: Reagents and Detection Methods, Vol. 1b: Physical and Chemical Detection Methods: Activation Reactions, Reagents Sequences, Reagents II ; 496 pp.

(5) Sotanaphun, U., Phattanawasin, P., Sriphong, L. (2008) Application of Scion image software to the simultaneous determination of curcuminoids in turmeric (Curcuma longa), *Phytochemical Analysis, 20,* 19-23.

(6) Stewart, J. C. M. (1980) Colorimetric determination of phospholipids with ammonium ferrothiocyanate, *Anal. Biochem.*, *104*, 10-14.

(7) Laurentin, A., Edwards, C. A. (2003) A microtitre modification of the anthrone sulphuric acid colorimetric assay for glucose based carbohydrates, *Anal. Biochem., 315,* 143–145.

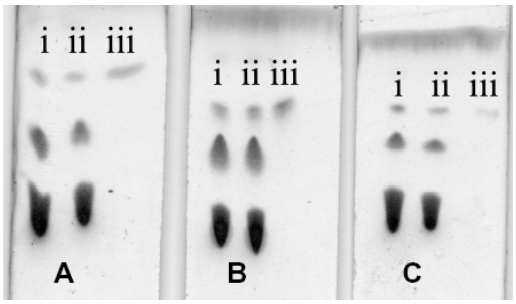

Figure S1. Photographs of TLC plates used for densitometry of PFAs (i) before and (ii) after gel filtration for (A) **1**, (B) **2** and (C) **3**, respectively; lane (iii) shows the migration of only the PFAs. The order of elution was PFA> DPPG > DPPC, using $CHCl_3/CH_3OH/H_2O$ (6/4/1) as the eluent.

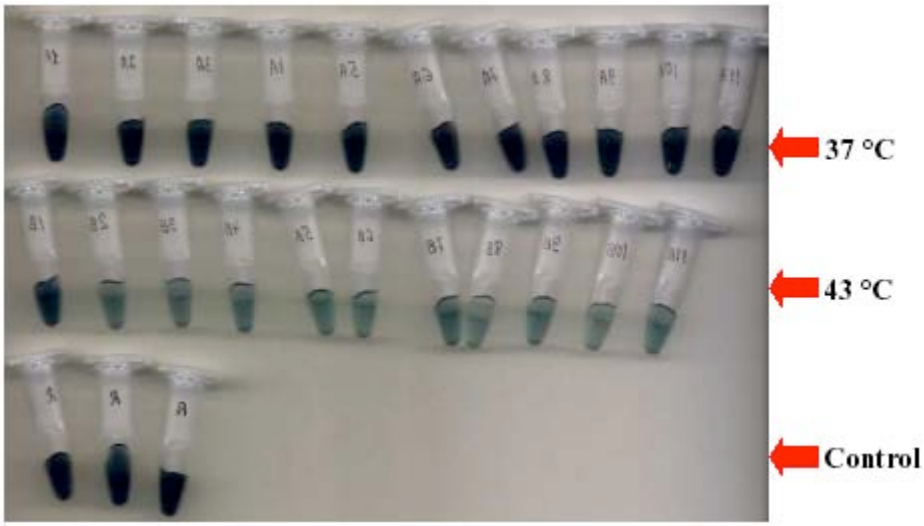

Figure S2. Release of sucrose as a function of time from liposomes made from DPPC/DPPG (95/5, mol/mol) containing 0.015 mol% of **2** at 37°C and at 43°C. Each microtube shows an aliquot of the dispersion that was taken after 2-minute intervals (starting from the left side of each row), gel filtered and digested using an anthrone-sulfuric acid reagent. The microtubes shown in the bottom row were samples that were not heated.

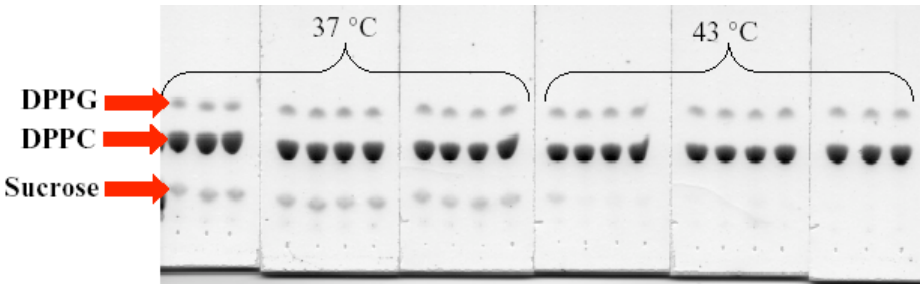

Figure S3. Release of sucrose as a function of time from liposomes made from DPPC/DPPG (95/5, mol/mol) containing 0.015 mol% of **2** at 37°C and at 43°C. Each lane shows an aliquot that was taken after 2-minute intervals (starting from the left side of the photograph), gel filtered, and developed on the TLC plate. The PFA is not readily visible in this photograph due to the very low concentration that was used.

Guanidinylated Polyethyleneimine−Polyoxypropylene−Polyoxyethylene Conjugates as Gene Transfection Agents

Lev Bromberg,[†] Svetlana Raduyk,[‡] T. Alan Hatton,[†] Angel Concheiro,[§] Cosme Rodriguez-Valencia,[§] Maite Silva,[||] and Carmen Alvarez-Lorenzo*[,§]

Department of Chemical Engineering, Massachusetts Institute of Technology, Cambridge, Massachusetts 02139, Department of Biological Sciences, Southern Methodist University, Dallas, Texas 75275-0376, and Departamento de Farmacia y Tecnología Farmacéutica, Facultad de Farmacia, and Instituto de Ortopedia y Banco de Tejidos Musculoesqueléticos, Universidad de Santiago de Compostela, 15872-Santiago de Compostela, Spain. Received March 17, 2009; Revised Manuscript Received April 14, 2009

Conjugates of linear and branched polyethyleneimine (PEI) and monoamine polyether Jeffamine M-2070 (PO/EO mol ratio 10/31, 2000 Da) were synthesized through polyether activation by cyanuric chloride followed by attachment to PEI and guanidinylation by 1*H*-pyrazole-carboxamidine hydrochloride. The resulting guanidinylated PEI−polyether conjugates (termed gPEI−Jeffamine) efficiently complexed plasmid DNA, and their polyplexes possessed enhanced colloidal stability in the presence of serum proteins. *In vitro* studies with mammalian CHO-1, 3T3, and Cos-7 cell lines demonstrated improved transfection efficiency of the pCMVβ-gal plasmid/gPEI−Jeffamine polyplexes. The guanidinylation of the amino groups of PEI and the conjugation of PEI with the Jeffamine polyether enhanced the conjugates' interaction with genetic material and reduced the cytotoxicity of the polyplexes in experiments with the L929 cell line.

INTRODUCTION

The polyethylenimine (PEI) family of polymers of varying molecular weight and branching has evolved into the polycations most frequently applied in the field of polymer-assisted gene transfer. Because of its high ion-exchange capacity and affinity toward protons, PEI can promote the escape of the genetic material to the cytosol from endosomes via the proton sponge effect, and significant DNA transfer efficiency can be observed *in vitro* and *in vivo* (*1*−*5*). Polyplexes based on high molecular weight PEI are typically much more potent as well as more toxic than those of low molecular weight PEI (*6*). In general, the transfection efficiency of PEI polyplexes remains rather low compared to that of viral vectors. Several recognized traits have been noted that could explain the deficiency of the polymer vectors versus viral ones. Polyplexes of high-molecular weight PEI have low colloidal stability and show considerable *in vivo* toxicity (*7*). Also, such polycations have a relatively weak affinity to DNA, resulting in the formation of polyplexes that are readily dissociated under physiological conditions. The buffer capacity of polycations may be hampered by their facilitated protonation due to the zipper effect of the neighboring group during the complexation process with DNA (*8*). An approach toward improvement of the PEI transfection efficiency and decrease in its cytotoxicity has been actively pursued that involves covalent attachment of hydrophilic and biocompatible polymers such as poly(ethylene glycol) or poly(ethylene oxide) (PEO) onto PEI (*9*−*11*). Polyplexes of PEO-modified high-MW PEI show decreased cytotoxicity and improved colloidal and serum stability. However, the steric repulsion and competition for water between PEO and other hydrophilic surfaces often result in a diminished transfection due to decreased cellular association and internalization (*6*). A variation of the PEI modification by PEO route is a recent trend toward the utilization of polycations modified by conjugation with self-assembling block copolymers of PEO and poly(propylene oxide) (PEO-PPO-PEO, trade name Pluronic) in gene delivery (*12*−*16*). Self-assembling, colloidal properties such as surface activity, micellization, ability to bind biological membranes, and favorable hydrophilic−lipophilic balance of the Pluronic-polycation conjugates enhance the transfection efficiency both *in vitro* and *in vivo* and provide a favorable biodistribution of the transfected DNA. The presence of the hydrophobic PPO block in Pluronics tends to enhance the stability of the complex between the polycation and the DNA. In the present study, we adopted an approach toward PEI modification similar to that with Pluronics, but chose a diblock PEO-PPO copolymer with a rather short PO_6 chain in the hope of stabilizing the polyplex with multiple PPO chains, yet without excessive association capability that could result in the binding of several polyplex particles together into large aggregates that would impede gene transfer. From a synthesis standpoint, the monoamine Jeffamine polyether is preferable over Pluronic, which needs to be additionally modified at its hydroxyl termini if multifunctional conjugates are to be obtained. Furthermore, in the present work the PEI−Jeffamine conjugates were guanidinylated with the goal of lowering conjugate cytotoxicity.

MATERIALS AND METHODS

Materials. Polyethyleneimine, end-capped by ethylenediamine (PEI1, average M_w ~800 by LS; average M_n ~600 by GPC), branched polyethyleneimine (PEI2, nominal M_n ~10 kDa by GPC; M_w ~25 kDa by LS), triethylamine (99.5%), 1-naphthol-4-sulfonic acid (sodium salt), L-arginine (98%), 2′-(4-hydroxyphenyl)-5-(4-methyl-1-piperazinyl)-2,5′-bi-1*H*-benzimidazole hydrate (Hoechst 33258 Dye), trihydrochloride 1*H*-pyrazole-carboxamidine hydrochloride (99%), 2,4,6-trichloro-1,3,5-triazine (99%, cyanuric chloride, or C-Cl), *o*-nitrophenyl-β-D-glucopyranoside (>99%), human male serum, fetal bovine serum

* Corresponding author. E-mail: carmen.alvarez.lorenzo@usc.es.
[†] Massachusetts Institute of Technology.
[‡] Southern Methodist University.
[§] Departamento de Farmacia y Tecnología Farmacéutica, Universidad de Santiago de Compostela.
[||] Instituto de Ortopedia y Banco de Tejidos Musculoesqueléticos, Universidad de Santiago de Compostela.

10.1021/bc900119t CCC: $40.75 © 2009 American Chemical Society
Published on Web 04/29/2009

Scheme 1. Activation of the Jeffamine Polyether by Cyanuric Chloride (C-Cl)

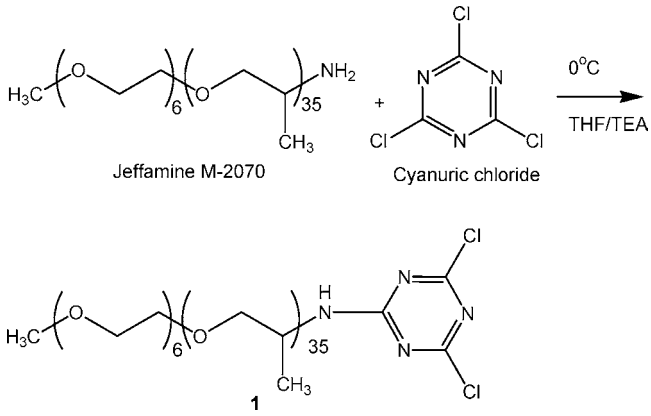

(FBS), 4-(2-hydroxyethyl)piperazine-1-ethanesulfonic acid, sodium salt (HEPES, 99%) and DNA, sodium salt from salmon testes were purchased from Sigma-Aldrich Co. (St. Louis, MO). PEI2 was dialyzed against DI water (12−14 kDa MW cutoff), and its solution pH was adjusted to 7.5. After dialysis, the solution was lyophilized and dry polymer stored at −20 °C. Polyether monoamine, Jeffamine M-2070 (PO/EO mole ratio 10/31, 2000 Da) was obtained from Huntsman Chemical Corp. (The Woodlands, TX) and used as received. Ethidium bromide (EB) solution (1% in water) was supplied by Fluka (Switzerland). Luminiscent β-galactosidase reporter system 3 and pβgal-control vector were obtained from Clontech Takara Bio, Inc. (Japan). Plasmid DNA encoding β-galactosidase (pCMV-β), double-stranded DNA of pUC18 plasmid (2.7 kb) isolated from *E. coli* strain DH5α, and Lipofectamine 2000 reagent were obtained from Invitrogen Corp. (Carlsbad, CA). SuperFect Transfection reagent was obtained from Qiagen Inc. (Valencia, CA). Deuterated solvents were obtained from Cambridge Isotope Laboratories (Andover, MA), and all other chemicals were received from commercial sources and were of the highest purity available.

Polymer Syntheses. *Jeffamine Activation by Cyanuric Chloride (Scheme 1) (17).* A solution of Jeffamine M2070 (30 g, 15 mmol) in 100 mL of dry tetrahydrofuran was charged to a three-neck, round-bottom flask equipped with a magnetic stirrer, nitrogen inlet−outlet lines, and a thermometer, and the mixture was stirred on ice at 0−4 °C under nitrogen atmosphere. Then a powder of C-Cl (2.77 g, 15 mmol) was added, and the mixture was continuously agitated at 0−4 °C for 5 min followed by the addition of triethylamine (1.5 g, 15 mmol). Cloudiness due to the formation of a quaternary ammonium salt was observed at this point. The reaction was allowed to proceed for 8 h at 0−4 °C while stirring under nitrogen atmosphere. The flask was allowed to equilibrate at ambient temperature, the products were filtered through Whatman #5 filter paper, and the filtrate was concentrated using a rotary evaporator. The product (yield, ∼95 wt %) was stored at −80 °C. For elemental analysis, the product was dialyzed against DI water (MWCO, 500 Da) and lyophilized. ^{1}H NMR (400 MHz, $CDCl_3$): $\delta = 1.1$ (3H, methyl, β to -N, β to -C-R), 1.9 (1H, methine), 3.3−3.1 (2H, methylene; 3H, methyl α to -O-C), 3.55 (2H, methylene α,β to −O-C, β to -N-CR). Calcd for $C_{62}H_{120}Cl_2N_4O_{41}$: C, 45.17; H, 7.34; Cl, 4.30; N, 3.40. Found: C, 46.55; H, 8.11; N, 3.22.

Guanidinylation of PEI (18). Guanidinylation of PEI1 and PEI2 was accomplished in 15 wt % aqueous solutions of PEI with a known concentration of primary amino groups, wherein an equimolar amount of 1*H*-pyrazole-carboxamidine hydrochloride was added. The reaction was allowed to proceed at neutral pH for 24 h at room temperature under stirring; the products were exhaustively dialyzed against DI water (MWCO, 1 kDa) and lyophilized. Titration of guanidine groups in the gPEI and gPEI−Jeffamine copolymers was accomplished spectrophotometrically using the Sakaguchi reaction of guanidine with 1-naphthol-2-sulfonic acid and hypobromite (1% Br_2 v/v in 1.25 M NaOH) (*19*). Calibration curves were developed using L-arginine as a standard (*20*). Approximately 5 meq/g of guanidine groups were detected in either gPEI1 or gPEI2.

Scheme 2. PEI−Jeffamine Conjugation and Guanidinylation

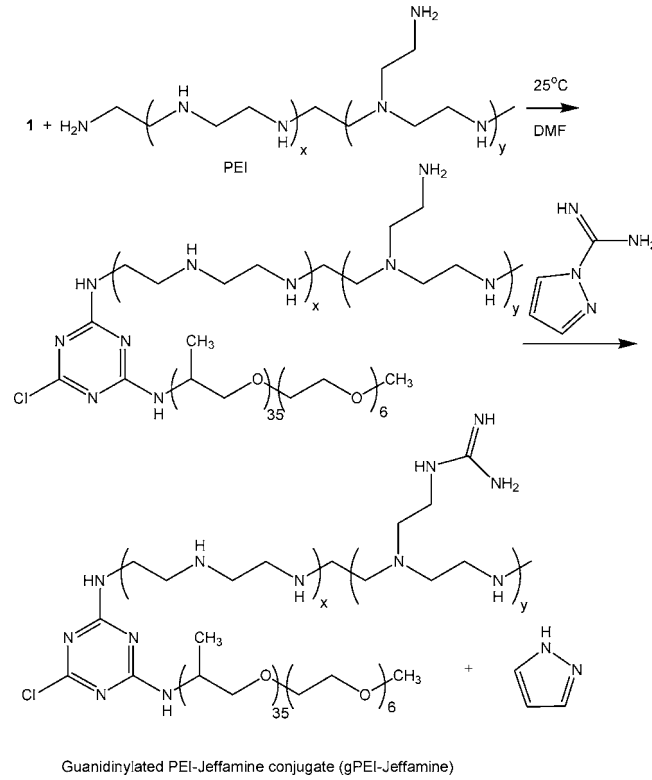

PEI−Jeffamine Conjugation and Guanidinylation (Scheme 2). A solution of Jeffamine activated by C-Cl (10 g, 6 mmol) and PEI (9 g) in 50 mL dry *N*,*N*-dimethylformamide was stirred at room temperature for 24 h. The mixture was then dissolved in 50 mL of deionized water, dialyzed against excess water (membrane MWCO, 1 kDa), and lyophilized. For guanidinylation, the PEI−Jeffamine conjugate (4 g) was dissolved in 50 mL of water, 1*H*-pyrazole-carboxamidine hydrochloride (2 g, 13.6 mmol) was added, and the solution was kept at room temperature for 24 h while stirring. The product was exhaustively dialyzed against DI water (MWCO 1 kDa) and lyophilized. Yield, 75%. Calculated, on the basis of a 1:1 mol ratio of gPEI1/Jeffamine ($C_{180}H_{378}Cl_2N_{44}O_{82}$; mol mass 4.53 kDa): C, 47.60; H, 8.39; Cl, 1.56; N, 13.57; O, 28.88. Found, %: C, 48.31; H, 8.72; N, 14.12. ^{1}H NMR (400 MHz, D_2O): $\delta = 1.06$ (3H, methyl), 2.48 (2H, methylene, α to -N(C)C, β to -N-C), 2,55 (2H, methylene, α,β to -N, β to -N(C)C, β to -N-C), 3.4 (2H, methylene, α to -O-C, β to -C). For gPEI2−Jeffamine, the obtained elemental analysis (found, %: C, 50.14; H, 9.15; Cl, 0.94; N, 16.86) indicated a PEI molecule of ∼15 kDa conjugated with 12 residues of activated Jeffamine, with primary amino groups guanidinylated. The total calculated, nominal MW was 34.4 kDa. Calcd ($C_{1412}H_{3076}Cl_{12}N_{432}O_{492}$): C, 49.29; H, 9.01; Cl, 1.24; N, 17.59; O, 22.88. The experimentally measured molecular weights of gPEI1−Jeffamine and gPEI2−Jeffamine were 4.04 (Pd ∼1.67) and 28.1 (Pd ∼1.92) kDa, respectively, which correlated with the elemental analyses. The main properties of the PEI−Jeffamine conjugates are collected in Table 1.

Methods. Proton NMR spectra of polymer solutions in D_2O or $CDCl_3$ were acquired on a Bruker AMX400 spectrometer.

Table 1. Properties of gPEI−Jeffamine Conjugates

species	MW (kDa)	pK_a	Jeffamine content (meq/g)	guanidine group content (meq/g)
gPEI1−Jeffamine	4.04	11.1	0.44	1.3
gPEI2−Jeffamine	28.1	11.6	0.35	1.9

The copolymer MW was measured in DMF using a Hewlett-Packard series 1100 HPLC system as described previously (*21*). Potentiometric titration was performed at 25 ± 1 °C using a 736 GP Titrino potentiometric titration system (Metrohm Ltd., Herisau, Switzerland) as described previously (*22*).

Preparation of DNA−Polymer Complexes. A stock solution of a cationic polymer of known concentration was added dropwise to a stock 10 μg/mL solution of double-stranded plasmid cloning vector pUC18 (2686 bp, 1.74 MDa) in 10 mM HEPES buffer (pH 7.4). Then the mixture was vortexed for 2−3 s and left at room temperature for 0.5 h for equilibration. Throughout this work, we used the total molar concentration ratio of nitrogen atoms in the polycation (N) to the phosphate groups (P) in the DNA as the metric characteristic of the complex formation. An average molecular weight per nucleotide of 324.5 g/mol PO_4^- (*23*) and the percentage in N of the copolymers obtained by elemental analysis were used to calculate the N/P molar ratio. Thus, suspensions of known concentrations and N/P ratios were obtained. To visualize complex formation, a fluorometric dye exclusion assay was performed using Hoechst 33258 dye. Fluorescence emission by DNA and dye solutions was measured using a TimeMaster Fluorescence Spectrometer (Photon Technology International, Inc.) before and after polymer solution addition.

Dynamic Light Scattering (DLS). Dynamic light scattering (DLS) experiments were performed with a Brookhaven BI-200SM light scattering system (Brookhaven Instruments Corp.) at a measurement angle of 90° and 37 °C. Number-average particle size distributions were obtained using the built-in software, and the reported particle mean hydrodynamic diameters are the average of five measurements, each conducted for 1 min. All samples dispersed in aqueous 10 mM HEPES buffer (pH 7.4) were filtered with a 0.45 μm syringe filter followed by equilibration at 37 °C prior to the DLS tests.

ζ-Potential Measurements. All ζ-potential measurements were performed using a Brookhaven ZetaPALS ζ-potential analyzer (Brookhaven Instruments Corp.). The Smoluchowski equation was used to calculate the ζ-potential from the electrophoretic mobility. The reported ζ-potential values are an average of 5 measurements, each of which was obtained over 25 electrode cycles. Measurements were conducted in triplicate at 25 °C in 10 mM HEPES buffer at pH 7.4. Standard deviations are shown.

Titration Microcalorimetry. Calorimetric experiments were performed in duplicate using a Tronac-450 isoperibol microcalorimeter equipped with Tronac FS101 calorimetry software (Tronac Inc., Orem, UT). In each experiment, a copolymer solution (0.16% w/w in pH 7.4 phosphate buffer, 47.5 mL) was placed in a Dewar reaction vessel, and a relatively concentrated salmon DNA solution (0.75% in pH 7.4 phosphate buffer) was loaded into a 2 mL calibrated buret. The entire assembly was then immersed in a water bath equilibrated at 310.0 K. After thermal equilibration, the DNA solution was delivered at a constant rate of 0.33 mL/min into the reaction vessel, wherein a stirrer rapidly mixed the two solutions. This approach leads to a minimum dilution of the copolymer and, thus, to the release of less ionization energy. In the experiments carried out in a reverse way, i.e., by adding a concentrated copolymer solution (4%) into the dewar containing 0.03% DNA, the ionization energy during the addition of the polycations was so high that it completely hindered the quantification of the energy of interaction between the copolymer and DNA. Previous studies of the interaction of branched and linear PEI with DNA using isothermal titration calorimetry (ITC) have reported similar difficulties (*24*). The temperature change in the system was monitored using a thermistor and later reproduced using a heating coil in the reaction vessel. The apparent enthalpy was calculated from the applied current and voltage, and heating time. A buffer solution was used as a blank instead of the DNA dispersion. The system was calibrated by titration of tris(hydroxymethyl)aminomethane with HCl. The integral binding heat for the polymer/DNA interaction (Q_{agg}) process was estimated by subtracting from the measured heat produced by the addition of DNA to the copolymer solution (Q_p) the heat effects due to the dilution/ionization of the copolymer in the buffer solutions used as a blank (Q_d) (*25*):

$$Q_{agg} = Q_p - Q_d$$

The enthalpies of DNA dilution and Jeffamine/DNA interaction were negligible.

Ethidium Bromide Displacement Assay. Aliquots of PEI or gPEI−Jeffamine solutions were added within a given range of N/P ratios to 5 mL of solutions of salmon DNA (0.06%) and EB (0.03%) in phosphate buffer (pH 7.4). The systems were diluted with buffer medium up to 10 mL. The final concentrations of cationic polymer ranged from 0.0024% to 0.010 wt %. The samples were stirred overnight in the dark and stored at 20 °C. The EB emission spectra were recorded with a Fluoro-Max2 spectrofluorometer (HORIBA Jobin Yvon, Irvine, CA). The excitation and emission wavelengths were 545 and 596 nm, respectively. Solutions of DNA (0.03%) and EB (0.015%) containing approximately 2 EB molecules per 5 base pairs were used as a blank (*26*).

Transfection Studies with CHO-K1 Cells. Chinese hamster ovary cells (CHO-K1) obtained from the American type Culture Collection (Manassas, VA) were grown in DMEM Ham's F-12 Nutrient Mixture supplemented by 10% FCS (both from Invitrogen). The cells were seeded in a 24-well plate (Nunc, Denmark) one day prior to the transfection at a density of 1×10^5 cells/cm^2 in 500 μL of the growth medium. The cells were 90−95% confluent at the time of transfection. Stock solutions of PEI2 and gPEI2−Jeffamine were prepared in Dulbecco's modified Eagle's medium (DMEM, D-2902, Sigma-Aldrich). The plasmid/copolymer complexes were prepared by diluting 1.6 μL of pβgal-control vector solution (500 ng/μL) in DMEM to 50 μL followed by dropwise addition of 50 μL of copolymer solution of appropriate concentration to obtain a N/P ratio of 4 or 6. The complexes were incubated at room temperature for 20 min. The cells were then transfected with pβgal-control vector for β-galactosidase expression following the manufacturer's protocol developed for Lipofectamine 2000. Solutions of either Lipofectamine/plasmid or copolymer/plasmid complexes (100 μL) were added to each well, containing cells with 500 μL of fresh growth medium supplemented by 10% FCS. After 5 h in contact with the polyplexes, the medium was replaced by DMEM Ham's F-12 Nutrient Mixture supplemented by 10% FCS and the cells further incubated at 37 °C in a CO_2 incubator (NuAire Inc., Plymouth, MN) for 48 h. Then, the cells were rinsed with PBS and lysed using a detergent solution according to the protocol described by the manufacturer. β-Galactosidase expression was quantified by chemiluminescent assay using a plate luminometer (ULTRA Evolution Multi-Detection Microplate Reader, Canada) recording light signals as 5-s integrals. Cell viability after transfection was confirmed by observation using an inverted microscope. Negative controls were prepared by adding pβgal-basic vector to the cell lysate from untransfected cells. The average value obtained for three negative controls was subtracted from each experimental result. Positive controls were prepared by adding bacterial β-galactosidase to the cell lysate obtained from intact cells.

Transfection Studies with 3T3 Cells. Cytomegalovirus-β-galactosidase plasmid (pCMVâ-gal, 7.2 kbp, Clontech, Mountain View, CA), which contains the human CMV promoter and the *E. coli* β-galactosidase gene, was utilized in the *in vitro* transfection study. *In vitro* transfection studies were conducted with 3T3-Swiss albino mouse embryo fibroblast cells (ATCC CCL-92) grown for 24 h in 24-well plates (2×10^4 cells/well) in DMEM supplemented with 10% fetal bovine serum, 100 mM L-glutamine, and 100 mM antibiotics (penicillin, streptomycine, and amphotericin B) at 37 °C and 5% CO_2. For complex preparation, the amount of DNA was kept constant at 0.6 μg, and the amount of polycation stock solution added was varied at the required N/P ratio. Plasmid DNA/polymer suspensions in the medium containing 10% human serum were added to the cells (100 μL/well). Transfection with polymers of the present study was compared to that using SuperFect cationic polyamidoamine dendrimer solution (*27*). The N/P ratio for SuperFect was calculated according to the manufacturer's protocols. The cells were incubated for 24 h, washed with PBS three times, and lysed by three freezing and thawing cycles. The β-galactosidase Enzyme Assay System kit (Promega, Madison, WI) combined with a BCA Protein Assay Reagent kit (Bio-Rad Laboratories, Inc., Richmond, CA) were used for assaying β-galactosidase activity in lysates prepared from the transfected cells following the assay protocol from the manufacturer. The β-galactosidase activity was determined against *o*-nitrophenyl-β-D-glucopyranoside (ONPG) as a substrate of the enzyme. The ONPG solution was added to the cells and incubated at 37 °C for 2 h; then the reaction was stopped by the addition of 1 M sodium carbonate solution. The enzyme activity was characterized by the appearance of the yellow-colored *o*-nitrophenol product assayed spectrophotometrically ($\lambda_{max} = 420$ nm, $n = 6$) (*21*). Untreated cells that did not undergo transfection were taken as a control.

Transfection Studies with Cos-7 Cells (28). African green monkey kidney fibroblast-like Cos-7 cells, SV40-transformed, ATCC CRL-1651 (Sigma-Aldrich Co.) were cultured in DMEM supplemented with HEPES (20 mM), penicillin (100 μU/mL), streptomycin (100 μg/mL), and FBS (0%). The day before transfection, cells were seeded in 12-well plates (2×10^4 cells/well) in complete culture medium. The cells were incubated with the polyplexes of tested polycations with the plasmid pCMV-LacZ (pCMV-βgal), which contained a CMV promoter to drive β-galactosidase (LacZ) gene expression, in the absence or presence of 10% FBS, at 37 °C and under a humidified 5% CO_2 atmosphere. After 3 h, the excess complexes were removed, and the cells were washed with DMEM and were further cultured for 24 h in culture medium with 5% serum. In order to evaluate β-galactosidase expression, cells were washed twice with PBS and lysed with the Mammalian Protein Extraction Reagent (Thermo Scientific Pierce, Rockford, IL). ONPG, the β-galactosidase substrate (100 μL, 4.4 mM) was mixed with 100 μL of cell lysates and incubated at 37 °C. After 30 min, absorbance (415 nm) was measured. For each sample, protein concentration was determined according to the Bio-Rad Protein Assay protocol using BSA as a standard. Positive control experiments were performed with the same plasmid and cell line using Lipofectamine 2000 according to the Invitrogen protocols. Results are expressed as relative transfection efficiency, i.e., absorbance units observed with a particular polyplex divided by absorbance observed with Lipofectamine (*21*). The results are presented as the mean ± standard deviation of quadruplicate determinations.

Cytotoxicity Assay with the Mammalian Cell Line. Cell line L929 (ATCC CCL-1) derived from normal subcutaneous areolar and adipose tissue of a male C3H/An mouse (Sigma-Aldrich) was used for the evaluation of polymer cytotoxicity. The cells were grown without the addition of antibiotics in Eagle's minimum essential medium supplemented by 10% fetal bovine serum (FBS, Invitrogen Corp). The MTT cytotoxicity assays (Mosmann's test) were performed as follows (*29*). The L929 cells were seeded onto 96-well cell culture plates, 0.1 mL/well, at a density of 10^6 cells/mL to reach >80% confluence. At 24 h after seeding, 0.1 mL of fresh medium and pUC18 plasmid DNA/polymer solutions of known concentrations (DNA content, 10 μg; N/P ratio maintained at 6.0 throughout) pre-equilibrated at 37 °C in the cell medium were added. Six replicate wells per concentration were tested. After 36 h of incubation in a humidified atmosphere of 5% CO_2/95% air at 37 °C, the medium was removed, and the wells were washed twice for 2−3 min with 0.2 mL of the fresh medium. Then, the fresh medium containing 0.5 mg of MTT (0.1 mL) was added at 37 °C and kept in the wells for another 4 h. The yellow tetrazolium salt is reduced in viable cells to a blue formazan product. After incubation, the media were completely removed, the cells were washed carefully with two washes of PBS (0.25 mL) for 3 min, and the solutions were aspirated. Cell-incorporated NR dye was extracted by adding 0.2 mL of 1% (v/v) acetic acid/50% (v/v) ethanol, and the blue formazan product was dissolved in 0.2 mL of 0.04 M HCl in 2-propanol. The plates were agitated on an orbital shaker for at least 1 h in order to ensure quantitative extraction and dissolution of the dyes. The optical density of each well was measured spectrophotometrically at 570 nm using a Bio-Rad Benchmark Plus Microplate Reader (Bio-Rad Laboratories, Hercules, CA), and the data were normalized by subtracting the background absorbance at 655 nm. The results were expressed as a percentage of the viability versus control (L929 cells not exposed to the test solution or dispersion). All experiments were performed three times in the independent measurements. The Student's statistical test (unpaired *t*-test) was used for statistical calculations. Probabilities of correlation using the Pearson coefficient (p) considered p values below 0.05 as a statistically significant threshold.

RESULTS AND DISCUSSION

The present work deals with the polycationic conjugates specifically designed for an effective complexation between polycations and DNA, with the resulting polyplexes, hopefully of reduced toxicity, enabling DNA transfection and enhanced stability in the presence of plasma proteins.

The synthetic route of PEI modification via polyether activation and conjugation to the primary amino groups of PEI followed by guanidinylation is simple and utilizes commercially available polyethers. Conjugation of one amino terminus of Jeffamine to C-Cl in the process of activation is ensured by the proper choice of temperature (0−5 °C) (*17, 30*). The attained yields of the gPEI−Jeffamine conjugates (≥75%) are acceptable, with the losses occurring primarily during purification. Importantly, since the polyether chains were activated and conjugated at one terminus only, it was possible to avoid byproduct conjugates with alternating structures typical of bifunctional polyether segments. Unmodified PEO or PEO-PPO-PEO blocks cannot be attached selectively via a single terminus, unless a monosubstituted diol such as monomethoxy PEG is used. In contrast to the design employed in the present work, the products of bifunctional polyether conjugation need to undergo preparative separation from the bisubstituted products attached at both termini using preparative chromatography and the like, if conjugates of a well-defined composition are desired (*31*).

We assessed mechanisms of the conjugate−DNA interactions using microcalorimetric titrations and ethidium bromide (EB) assays to see whether the polycation−DNA electrostatic interaction is preserved while the polycation structure provides charge shielding with pendant polyether chains.

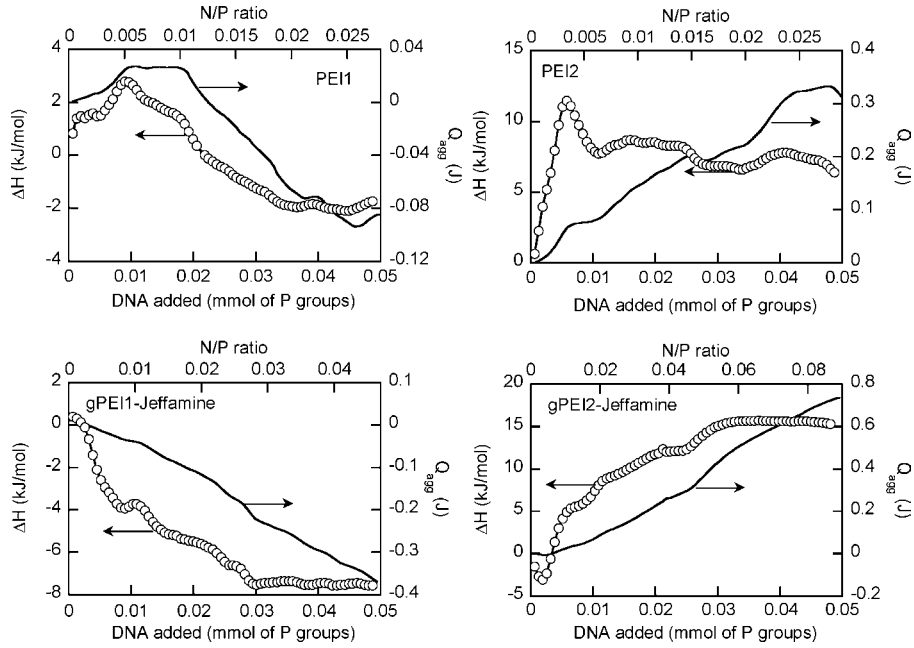

Figure 1. Calorimetric titration of 0.16% polycation solutions with 0.75% salmon DNA solution in 50 mM phosphate buffer at pH 7.4. The solid line and open points show the integral binding heat of the polymer/DNA interaction (Q_{agg}) and the interaction enthalpy of the copolymers, respectively.

Thermodynamics of Polycation−DNA Binding. Isoperibol titration calorimetry and EB fluorescence assay were used to compare the binding between the polycations under study and DNA. The energy plots shown in Figure 1 indicate that the binding of PEI1 to DNA is practically null; the enthalpy changes related to the process (+2.8 J/mmol and −2.0 J/mmol when 0.01 and 0.04 mmol DNA were added) are of the same magnitude as the thermal energy RT (2.6 kJ/mol). PEI1 is apparently too short for a cooperative binding with the DNA molecules. By contrast, guanidinylation and conjugation with Jeffamine rendered the resulting PEI1 conjugate (gPEI1−Jeffamine) capable of interacting exothermically with the DNA, the enthalpy of interaction being −7.6 kJ/mol. Binding of PEI2 and gPEI2−Jeffamine with DNA was an endothermic process accompanied by significant changes in enthalpy, 11.5 and 15.7 kJ/mol, respectively. In general, the energy of gPEI−Jeffamine interaction with DNA was greater, in absolute value, than that of the parent PEI. Condensation and aggregation above 0.04 mmol DNA (expressed via the phosphate group contents) led to a phase separation of the polyplexes from the solution. Both exothermic and endothermic interactions between polymers and DNA have been reported (*32*−*35*). The enthalpy values result from the combination of electrostatic interactions, protonation changes, and hydrogen bonding (*36*). ITC experiments carried out with 750 kDa PEI and plasmid DNA indicated that the binding process was exothermic and entropy-driven with an enthalpy of −2.7 kJ/mol (*37*). We have previously observed greater enthalpy changes with a block copolymer of poly[(2-dimethylaminoethyl)methacrylate] and PEO (−31 kJ/mol) or Pluronic P123 (45 kJ/mol) interacting with salmon DNA (*25*). Related, but neutral amphiphilic polyethers, such as tetrafunctional block copolymers of PEO-PPO bound to ethylenediamine (Tetronic), can also form polyplexes with DNA via hydrogen bonding as well as hydrophobic interactions (*38*). DNA and gPEI−Jeffamine act as hydrogen-bond donor and acceptor, respectively, and bind via hydrophobic, endothermic processes as well as via other (exothermic) events. The predominance of one or the other type of interactions, together with conformational changes that may accompany such interactions, determine whether the process is exo- or endothermic as a whole. The branched PEI2 is known to contain three different types of amino groups: secondary and tertiary amino groups in the main chain, and secondary and primary amino groups in the side chain. The ratio of primary-to-secondary-to-tertiary amino groups is 1:2:1 (*39*, *40*). However, PEI1 contains only secondary amino groups in the main chain, which is less sterically constrained than that of the branched PEI2 and readily undergoes conformational changes. Divergent exo- or endothermic processes have been recorded for branched and linear PEIs interacting with an anionic surfactant sodium dodecylsulfate, depending on the different conformations adopted by the PEI-surfactant mixed micelles (*41*). Analogously, the fact that gPEI1−Jeffamine led to an exothermic binding while gPEI2−Jeffamine led to an endothermic event may be explained, at least partially, to be due to different conformations adopted by the polyplexes. Furthermore, in the case of gPEI−Jeffamine polycations one should take into account the contribution of the guanidinium groups to the interaction with DNA. Titration experiments carried out with Jeffamine alone revealed no detectable binding with DNA. By contrast, it has been shown previously that positively charged guanidinium groups significantly enhance the capability of the imine-containing polymers to bind to the negatively charged DNA (*42*). The effect of guanidinylation is more significant for gPEI1−Jeffamine than for gPEI2−Jeffamine because the long PEI2 chains of the latter already bind DNA significantly even before guanidinylation. However, the unfavorable ΔH of PEI2 and of gPEI2−Jeffamine binding to DNA (endothermic process) is similar to the ΔH of +10 kJ/mol recorded for spermine and, as expected for electrostatic interactions, is compensated for by a favorable entropy change (*43*). It was not possible to achieve valid fits to common binding models for PEI and gPEI−Jeffamine because of the tendency for their complexes to aggregate. Therefore, neither an affinity constant nor the entropy change for the binding of PEI and gPEI−Jeffamine to DNA could be estimated. Analogous problems were reported previously with PEI and other strongly binding gene vectors (*24*, *43*). The enhancement of the binding observed with gPEI−Jeffamine compared to that of its parent PEI resembles the beneficial effect of the conjugation of Pluronic L92 to poly[(2-dimethylaminoethyl)methacrylate] (*21*, *25*). Similar to Pluronic, Jeffamine can facilitate the formation of polyplexes with a core−shell structure, in which

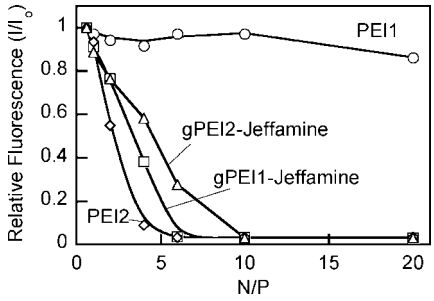

Figure 2. Ethidium bromide exclusion assay of 0.3 mg/mL salmon DNA solution in 50 mM phosphate buffer at pH 7.4.

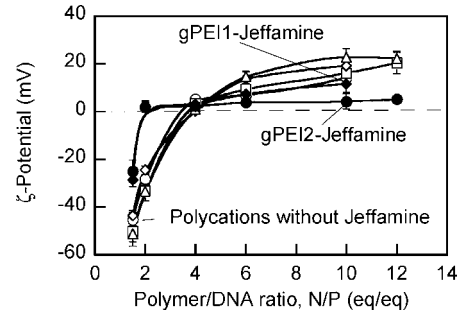

Figure 3. ζ-Potentials of the complexes formed between plasmid cloning vector pUC18 and polycationic copolymers as a function of the polymer/DNA (N/P) ratio at pH 7.4. Data points with PEI1, PEI2, gPEI1, gPEI2, gPEI1−Jeffamine, and gPEI2−Jeffamine are shown by open circles, open squares, open diamonds, open triangles, filled diamonds, and filled circles, respectively.

the shells are composed of PEO chains and ionized amino groups, while the cores comprise PPO blocks and neutralized DNA−PEI complexes (*25*). Such a notion is based on the P/N ratios at which the polyplex phase separation occurs and the Q_{agg} values level off (Figure 1). In the case of PEI2, a plateau was reached at a P/N ratio of 0.025. This ratio corresponds to 40 nitrogen atoms for each nucleotide, which means that most of the amine groups of PEI did not bind to the DNA effectively. In the case of the gPEI1−Jeffamine and gPEI2−Jeffamine copolymers, the plateau was observed at a P/N ratio of 0.03 (N/P = 33) and 0.06 (N/P = 16.7), respectively. These results indicate that the chemical modification of the PEI structure by the Jeffamine polyether facilitates the interaction with DNA, probably because of the enhanced solubility of the polyplexes that makes the amino groups of the copolymer more accessible to the nucleotides. This also explains the higher enthalpy values.

Ethidium Bromide Exclusion Assay. EB is a DNA intercalator that exhibits an increase in fluorescence intensity upon DNA intercalation. This fluorescence is reduced by EB competitors, such as polycations, via EB exclusion from its complex with DNA. Therefore, the ability of the polycation to reduce the EB fluorescence is used as a measure of the DNA−polycation binding strength. The results of the EB exclusion assay with the parent PEI1, PEI2, and their modified conjugates gPEI1−Jeffamine and gPEI2−Jeffamine are shown in Figure 2. The presence of PEI1 did not result in any appreciable change in the EB fluorescence, which is indicative of poor intercalation of the PEI1 and is in accord with the microcalorimetric results. In contrast, gPEI1−Jeffamine derived from the PEI1 polymer was quite effective in EB exclusion. The DNA binding strength, which is reported by the IC_{50} value (the N/P ratio of polymer necessary to inhibit 50% of the relative EB-DNA fluorescence) was estimated to be approximately 2.2, 3.5, and 4.5 for PEI2, gPEI1−Jeffamine, and gPEI2−Jeffamine, respectively. It is interesting to observe that the conjugation with Jeffamine slightly increased the IC_{50} for gPEI2−Jeffamine compared to that of its parent PEI2. Nevertheless, gPEI2−Jeffamine and all other polycations except for PEI1 quenched EB fluorescence completely at N/P = 10, indicating a strong polycation−DNA binding. The results of both the microcalorimetric experiments and EB fluorescence studies indicate that suitable N/P ratios for the polyplex formation with the polycations under study are in the range of 4 to 10 or higher. These ratios are in agreement with those previously found for polyplexes based on linear, 25 kDa PEI as well as branched 2 kDa, 25 kDa, and 750 kDa PEI (*24*).

Polyplex Stability in Water and in the Presence of Blood Components. Microcalorimetric titrations and the EB exclusion assays described above pointed to a strong complexation between the polycations under study (except for PEI1) and salmon DNA. In order to elucidate the effect of the PEI modifications on their ability to bind the plasmid DNA relevant for transfection, we conducted experiments with a double-stranded plasmid cloning vector pUC18 as a model, measuring the electrophoretic mobility and size of the polyplex particles. The effect of the polycation/DNA molar ratio (N/P value) on the polyplex ζ-potential in aqueous buffer (pH 7.4) is shown in Figure 3. At N/P ratios below 2, the polyplexes with polycations that were not modified with the polyether chains were strongly anionic, with ζ-potentials in the −45 to −35 mV range, whereas the presence of Jeffamine in the gPEI−Jeffamine conjugates reduced the charge somewhat (ζ-potential in the range of −30 to −25 mV). Pronounced aggregation and sedimentation of the polyplex particles was observed with PEI2, gPEI1, and gPEI2 in the N/P value range below 4. At N/P ranging from 6 to 12, where the polyplexes were positively charged, the polyplex particles were significantly more stable and possessed a number-average hydrodynamic diameter size in the 65−85 nm range. Modification of PEI with Jeffamine altered the colloidal behavior of the polyplexes. No precipitation of the gPEI−Jeffamine /DNA polyplexes was observed at a N/P ratio of 2, and a slight change of N/P from 1.5 to 2 afforded a dramatic shift from negatively charged (ζ-potential from −30 or −25 mV) to positively charged (ζ-potential approximately +2 mV) polyplex particles. The particles remained only slightly charged throughout the range of N/P ≤ 12, with the ζ-potential not exceeding +12 and +5 mV for gPEI1−Jeffamine and gPEI2−Jeffamine, respectively. This is in contrast to other polycations devoid of Jeffamine, polyplexes of which became significantly more charged at N/P > 6. These observations indicate the charge shielding by the PEO chains of Jeffamine, which probably comprise the hydrophilic, stabilizing shell of the polyplex. The sharp neutralization of the gPEI−Jeffamine chains by DNA (compare with the smooth negative-to-positive charge transition spanning 3.5 N/P units for all polycations devoid of Jeffamine) indicates enhanced cooperativity of the polycation−DNA binding. Overall, these observations are in agreement with the calorimetric results.

It has been demonstrated previously that the coagulation cascade proteins present in human serum can dramatically accelerate the aggregation of polycation−DNA polyplexes (*44*). Such an aggregation is highly undesirable for *in vivo* gene targeting and can be avoided through polycation conjugation with PEO chains of appropriate length and grafting density (*45*). It has been demonstrated that the presence of PEO-PPO-PEO triblock copolymer segments on the polycationic transfection vector provides polyplex stability in serum as well (*21, 46*). Herein, we extended an approach toward stabilization of the polyplexes by PEO-PPO polyethers by the use of Jeffamine, a $EO_{35}PO_6$ diblock. As is seen in Figure 4, the conjugation of gPEI with Jeffamine was effective in preventing polyplex aggregation in the presence of as much as 10% serum. Polyplexes of all polycations devoid of Jeffamine aggregated

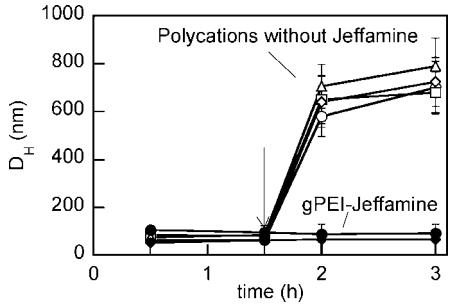

Figure 4. Effect of plasma on aggregation of DNA/polycation complexes at 37 °C. The complexes comprised double-stranded plasmid cloning vector pUC18 and a polycation at a fixed N/P ratio of 10 suspended in 10 mM HEPES buffer (pH 7.4). The number-average hydrodynamic diameter (D_H) was measured by dynamic light scattering following a 0.5-h equilibration at 37 °C. At a time point indicated by an arrow, human serum was added to each sample to result in a 10 vol% serum concentration. The samples were then incubated at 37 °C, and the D_H values were measured 1 and 2 h from the time of serum addition. Data with PEI1, PEI2, gPEI1, gPEI2, gPEI1−Jeffamine, and gPEI2−Jeffamine are shown by open circles, open squares, open diamonds, open triangles, filled diamonds, and filled circles, respectively.

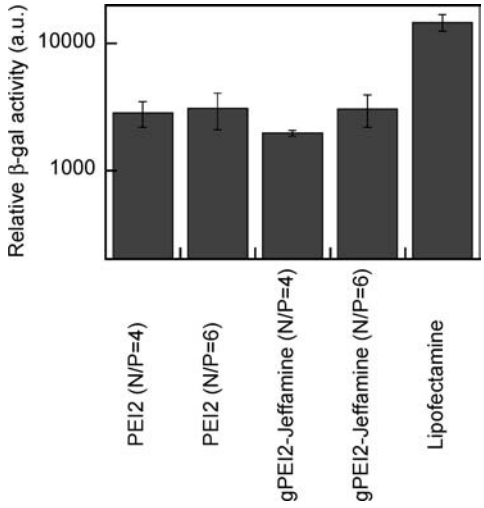

Figure 5. Transfection of Chinese hamster ovary (CHO-K1) cells with pCMVβ-gal plasmid DNA using polyplexes based on PEI2, gPEI2−Jeffamine, and Lipofectamine 2000 in medium supplemented with 10 vol % fetal bovine serum (FBS). Chemiluminiscent β-gal signal in arbitrary units was taken as a measure of β-galactosidase activity as a result of transfection.

when serum was present. These results are indicative of the steric repulsion of the serum proteins by the PEO segments of the Jeffamine in the outer shell of the DNA/gPEI−Jeffamine polyplex particles.

***In Vitro* DNA Transfection.** To test the *in vitro* gene transfer effectiveness of the polylexes, we used β-galactosidase expression in three mammalian cell lines (Figures 5, 6, and 7). gPEI−Jeffamine conjugates maintained the cell transfection efficiency in the CHO-K1 hamster ovary cell line comparable to that of the parent PEI, which was ~5-fold lower with gPEI2−Jeffamine at N/P = 6 than with the Lipofectamine 2000 cationic lipids used as a transfection standard (Figure 5). However, gPEI−Jeffamine enhanced the transfection in 3T3 fibroblast cells 2−3-fold, compared to that of their parent PEI species, throughout the polymer/DNA ratio range studied (Figure 6). Transfection of the pCMV-βgal plasmid with PEI1 polycation was inefficient because of its poor binding with DNA, which correlated well with the microcalorimetric and binding assays (compare with

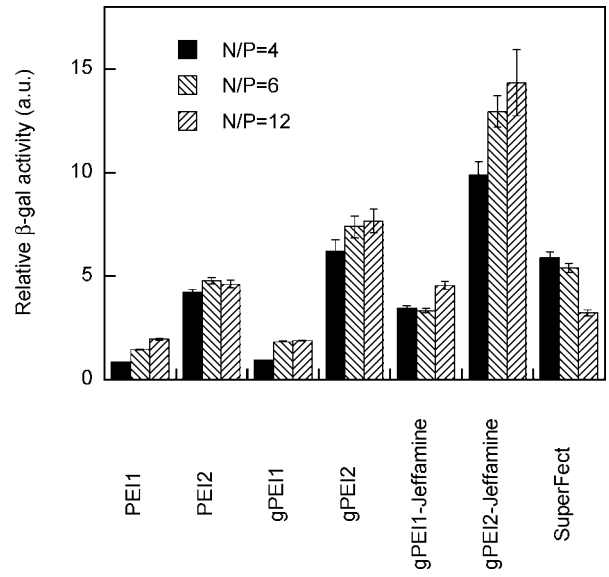

Figure 6. Transfection of 3T3 mouse embryo fibroblast cells with pCMVβ-gal plasmid DNA using the polycations of the present study and SuperFect in medium supplemented with 10% human serum. Relative β-galactosidase activity was expressed as the ratio of the spectrophotometric absorbance reading with a given transfection agent relative to the control readings with untreated cells that did not undergo transfection (see Materials and Methods).

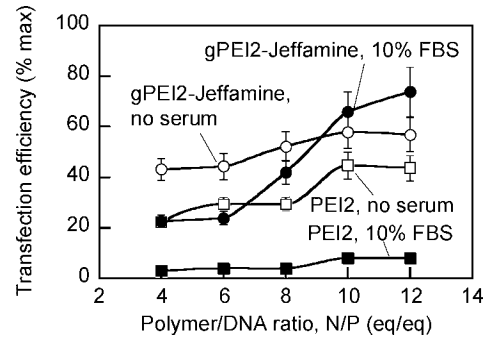

Figure 7. Transfection of Cos-7 green monkey kidney fibroblast cells with pCMVβ-gal plasmid DNA using PEI2 or gPEI2−Jeffamine in the presence of 10% FBS or in the absence of serum as a function of the polymer/DNA (N/P) ratio in the polyplexes. Relative transfection efficiency, was expressed via β-gal signal intensity (absorbance units) observed with a particular polyplex, divided by the absorbance observed with Lipofectamine 2000.

Figures 1 and 2). Interestingly, a notable improvement in the transfection efficiency was observed at higher N/P ratios in the case of gPEI2 and gPEI2−Jeffamine but not with cationic dendrimer formulation, SuperFect (Figure 6). At N/P = 12, polyplexes with the gPEI2−Jeffamine conjugate transfected the plasmid over 4-fold more efficiently than those with SuperFect. At N/P > 10, DNA/PEI or DNA/gPEI−Jeffamine complexes were positively charged, but in the case of gPEI−Jeffamine, the charges were substantially shielded by the polyether chains (compare with Figure 3), which contributed to the transfection efficiency with this polymer at higher N/P values. A more detailed study of the DNA transfection with gPEI2−Jeffamine and parent PEI2 polycations, without and in the presence of 10% serum using the Cos-7 cell line, revealed that without serum, plasmid transfection with gPEI2−Jeffamine was 1.3- to 1.9-fold more efficient than with the parent PEI2 throughout the N/P range of 4 to 12 studied (Figure 7). However, the presence of 10% serum lowered the efficiency of the PEI2 as a transfection agent due to the persistent aggregation but did not signifi-

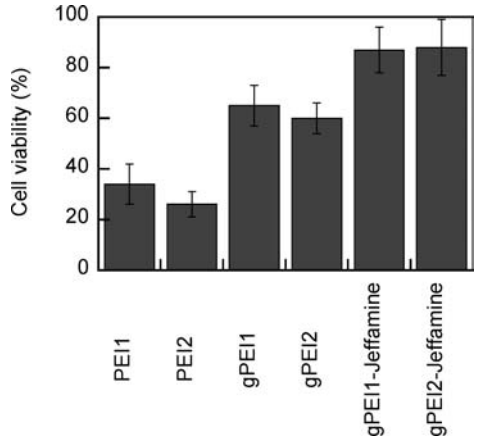

Figure 8. Viability of the L929 mouse fibroblast cells in the presence of plasmid DNA/polymer complexes measured by MTT assay in 10% fetal bovine serum. The N/P ratio of 10 was maintained in all experiments. Only statistically significant data and standard errors are shown.

cantly affect that of the gPEI2−Jeffamine so that the latter was 6- to 10-fold more efficient than the former when the serum was present. This result is in excellent accord with the observation of the gPEI−Jeffamine stability in the presence of serum proteins (see Figure 3). At N/P = 12, the efficiency of the transfection with gPEI2−Jeffamine reached over 70% of that with Lipofectamine 2000. Hence, the results with the 3T3 and Cos-7 cell lines indicate that gPEI2−Jeffamine is a rather effective transfection agent, with DNA transfection efficiency comparable to or exceeding that of the commercially available transfection agents, especially at N/P ratios of 10 or 12.

Cytotoxicity Study. The results of the cytotoxicity studies with the polycations of the present study are shown in Figure 8. The study was designed to compare the cytotoxicity of the polyplexes made with different polycations. A fixed N/P ratio of 10 was set throughout these experiments, as this ratio resulted in a significant binding of polycations (except for PEI1) and plasmid DNA and an efficient DNA transfection with gPEI−Jeffamine conjugates. The low-MW PEI1 (nominal MW 600) was less cytotoxic than PEI2 (MW 10 kDa), in agreement with the literature (*47*). Guanidinylation of either PEI1 or PEI2 lowered the cell morbidity approximately 2-fold. The positive effect of guanidinylation of the primary amino groups on polymer biocompatibility has been noted with branched PEI (*48*) and some poly(propylene imine) dendrimers (*42*). Although it has been suggested that guanidinylation of the primary amino group results in randomization of the cationic charges along the PEI chains (*48*), the mechanism of the lower cytotoxicity of the guanidinylated PEI vs original PEI is not well understood. However, it appeared that guanidinylation and Jeffamine conjugation afforded a synergistic effect of enhanced cell viability, i.e., the gPEI−Jeffamine conjugates were less cytotoxic than PEI or gPEI polycations (Figure 8). The plasmid cloning vector pUC18 DNA/gPEI−Jeffamine complexes were compatible with L929 fibroblast cells (viability, ∼90%) and demonstrated 200% and 25−30% higher cell viability than their parent PEI and gPEI counterparts, respectively. This interesting result indicates the enhancement of cell survival due to the presence of PEO chains of Jeffamine, which partially shield the positive charges of the polyplexes at N/P = 10. This effect is somewhat analogous to the previously reported effect of PEGylation of PEI, with the resulting PEGylated PEI−DNA complexes preventing the aggregation of mouse erythrocytes (*44*).

CONCLUDING REMARKS

The enhancement of polyplex transfection efficiency by polycation conjugation with PEO-PPO-PEO (Pluronic) triblock copolymers has been reported previously (*13*, *46*, *49*) and explained by the decreasing polyplex particle size through hydrophobic binding of poly(propylene oxide) chains of Pluronic with nonpolar sites in the polyplex. In the present work, we employed a monoamine diblock PEO-PPO copolymer (Jeffamine), which afforded a simple synthetic route toward polycation−polyether conjugates. *In vitro* studies demonstrated that guanidinylation of the amino groups of PEI and conjugation of PEI with Jeffamine polyether reduce the cytotoxicity of the polyplexes, enhance the conjugates' interaction with genetic material, protect the polyplexes from aggregation in the presence of serum proteins, and improve the transfection efficiency of the conjugates.

ACKNOWLEDGMENT

This work was supported by MICINN (SAF2008-01679), FEDER, Xunta de Galicia (PGIDIT07CSA002203PR), Spain.

LITERATURE CITED

(1) Lemkine, G. F., and Demeneix, B. A. (2001) Polyethylenimines for in vivo gene delivery. *Curr Opin. Mol. Ther. 3* (2), 178–182.

(2) Demeneix, B., and Behr, J. P. (2005) Polyethylenimine (PEI). *Adv. Genet. 53*, 217–230.

(3) Lungwitz, U., Breunig, M., Blunk, T., and Göpferich, A. (2005) Polyethylenimine-based non-viral gene delivery systems. *Eur. J. Pharm. Biopharm. 60* (2), 247–266.

(4) Neu, M., Fischer, D., and Kissel, T. (2005) Recent advances in rational gene transfer vector design based on poly(ethylene imine) and its derivatives. *J. Gene Med. 7* (8), 992–1009.

(5) Vicennati, P., Giuliano, A., Ortaggi, G., and Masotti, A. (2008) Polyethylenimine in medicinal chemistry. *Curr. Med. Chem. 15* (27), 2826–2839.

(6) Zhong, Z., Feijen, J., Lok, M. C., Hennink, W. E., Christensen, L. V., Yockman, J. W., Kim, Y.-H., and Kim, S. W. (2005) Low molecular weight linear polyethylenimine-b-poly(ethylene glycol)-b-polyethylenimine triblock copolymers: synthesis, characterization, and in vitro gene transfer properties. *Biomacromolecules 6* (6), 3440–3448.

(7) Kircheis, R., Wightman, L., and Wagner, E. (2001) Design and gene delivery activity of modified polyethylenimines. *Adv. Drug Delivery Rev. 53* (3), 341–358.

(8) Kabanov, A. V., Bronich, T. K., Kabanov, V. A., Yu, K., and Eisenberg, A. (1996) Soluble stoichiometric complexes from poly(N-ethyl-4-vinylpyridinium) cations and poly(ethylene oxide)-block-polymethacrylate anions. *Macromolecules 29* (21), 6797–6802.

(9) Lee, M., and Kim, S. W. (2005) Polyethylene glycol-conjugated copolymers for plasmid DNA delivery. *Pharm. Res. 22* (1), 1–9.

(10) Merdan, T., Kunath, K., Petersen, H., Bakowsky, U., Voigt, K. H., Kopecek, J., and Kissel, T. (2005) PEGylation of poly(ethylene imine) affects stability of complexes with plasmid DNA under in vivo conditions in a dose-dependent manner after intravenous injection into mice. *Bioconjugate Chem. 16* (4), 785–792.

(11) Kunath, K., von Harpe, A., Fischer, D., Petersen, H., Bickel, U., Voigt, K., and Kissel, T. (2003) Low-molecular-weight polyethylenimine as a non-viral vector for DNA delivery: comparison of physicochemical properties, transfection efficiency and in vivo distribution with high-molecular-weight polyethylenimine. *J. Controlled Release 89* (1), 113–125.

(12) Lemieux, P., Vinogradov, S. V., Gebhart, C. L., Guérin, N., Paradis, G., Nguyen, H. K., Ochietti, B., Suzdaltseva, Y. G., Bartakova, E. V., Bronich, T. K., St-Pierre, Y., Alakhov, V. Y., and Kabanov, A. V. (2000) Block and graft copolymers and NanoGel copolymer networks for DNA delivery into cell. *J. Drug Targeting 8* (2), 91–105.

(13) Gebhart, C. L., Sriadibhatla, S., Vinogradov, S., Lemieux, P., Alakhov, V., and Kabanov, A. V. (2002) Design and formulation of polyplexes based on pluronic-polyethyleneimine conjugates for gene transfer. *Bioconjugate Chem. 13* (5), 937–944.

(14) Ochietti, B., Lemieux, P., Kabanov, A. V., Vinogradov, S., St-Pierre, Y., and Alakhov, V. (2002) Inducing neutrophil recruitment in the liver of ICAM-1-deficient mice using polyethyleneimine grafted with Pluronic P123 as an organ-specific carrier for transgenic ICAM-1. *Gene Ther. 9* (14), 939–945.

(15) Ochietti, B., Guérin, N., Vinogradov, S. V., St-Pierre, Y., Lemieux, P., Kabanov, A. V., and Alakhov, V. Y. (2002) Altered organ accumulation of oligonucleotides using polyethyleneimine grafted with poly(ethylene oxide) or pluronic as carriers. *J. Drug Targeting 10* (2), 113–121.

(16) Bromberg, L., Alakhov, V. Yu., and Hatton, T. A. (2002) Self-assembling Pluronic®-modified polycations in gene delivery. *Curr. Opin. Colloid Interface Sci. 11* (4), 217–223.

(17) Jan, J. Z., Huang, B. H., and Lin, J.-J. (2003) Facile preparation of amphiphilic oxyethylene oxypropylene block copolymers by selective triazine coupling. *Polymer. 44* (4), 1003–1011.

(18) Bernatowicz, M. S., Wu, Y., and Matsueda, G. R. (1992) 1H-Pyrazole-1-carboxamidine hydrochloride an attractive reagent for guanylation of amines and its application to peptide synthesis. *J. Org. Chem. 57* (8), 2497–2502.

(19) Jorpes, E., and Thorén, S. (1932) The use of the Sakaguchi reaction for the quantitative determination of arginine. *Biochem. J. 26* (5), 1504–1506.

(20) Tomlinson, G., and Viswanatha, T. (1974) Determination of the arginine content of proteins by the Sakaguchi procedure. *Anal. Biochem. 60* (1), 15–24.

(21) Bromberg, L., Deshmukh, S., Temchenko, M., Iourtchenko, L., Alakhov, V., Alvarez-Lorenzo, C., Barreiro-Iglesias, R., Concheiro, A., and Hatton, T. A. (2005) Polycationic block copolymers of poly(ethylene oxide) and poly(propylene oxide) for cell transfection. *Bioconjugate Chem. 16* (3), 626–633.

(22) Bromberg, L., and Hatton, T. A. (2007) Poly(N-vinylguanidine): Characterization, and catalytic and bactericidal properties. *Polymer 48* (26), 7490–7498.

(23) Lobo, B. A., Davis, A., Koe, G., Smith, J. G., and Middaugh, C. R. (2001) Isothermal titration calorimetric analysis of the interaction between cationic lipids and plasmid DNA. *Arch. Biochem. Biophys. 386* (1), 95–105.

(24) Choosakoonkriang, S., Lobo, B. A., Koe, G. S., Koe, J. G., and Middaugh, C. R. (2003) Biophysical characterization of PEI/DNA complexes. *J. Pharm. Sci. 92* (8), 1710–1722.

(25) Alvarez-Lorenzo, C., Barreiro-Iglesias, R., Concheiro, A., Iourtchenko, L., Alakhov, V., Bromberg, L., Temchenko, M., Deshmukh, S., and Hatton, T. A. (2005) Biophysical characterization of complexation of DNA with block copolymers of poly(2-dimethylaminoethyl) methacrylate, poly(ethylene oxide), and poly(propylene oxide). *Langmuir 21*, 5142–5148.

(26) Bronich, T. K., Nguyen, H. K., Eisenberg, A., and Kabanov, A. V. (2000) Recognition of DNA topology in reactions between plasmid DNA and cationic copolymers. *J. Am. Chem. Soc. 122* (35), 8339–8343.

(27) Uchida, E., Mizuguchi, H., Ishii-Watabe, A., and Hayakawa, T. (2002) Comparison of the efficiency and safety of non-viral vector-mediated gene transfer into a wide range of human cells. *Biol. Pharm. Bull. 25* (7), 891–897.

(28) Pirotton, S., Muller, C., Pantoustier, N., Botteman, F., Collinet, S., Grandfils, C., Dandrifosse, G., Degée, P., Dubois, P., and Raes, M. (2004) Enhancement of transfection efficiency through rapid and noncovalent post-PEGylation of poly(dimethylaminoethyl methacrylate)/DNA complexes. *Pharm. Res. 21* (8), 1471–1479.

(29) Mosmann, T. J. (1983) Rapid colorimetric assay for cellular growth and survival: application to proliferation and cytotoxicity assays. *Immunol. Methods 65* (1−2), 55–63.

(30) Tigelaar, D. M., Meador, M. A. B., Kinder, J. D., and Bennett, W. R. (2006) APTES cross-linked polymers from poly(ethylene oxide)s and cyanuric chloride for lithium batteries. *Macromolecules. 39* (1), 120–127.

(31) Vinogradov, S. V., Bronich, T. K., and Kabanov, A. V. (1998) Self-assembly of polyamine-poly(ethylene glycol) copolymers with phosphorothioate oligonucleotides. *Bioconjugate Chem. 9* (6), 805–812.

(32) Rungsardthong, U., Ehtezazi, T., Bailey, L., Armes, S. P., Garnett, M. C., and Stolnik, S. (2003) Effect of polymer ionization on the interaction with DNA in nonviral gene delivery systems. *Biomacromolecules 4* (3), 683–690.

(33) Ehtezazi, T., Rungsardthong, U., and Stolnik, S. (2003) Thermodynamic analysis of polycation-DNA interaction applying titration microcalorimetry. *Langmuir 19* (22), 9387–9394.

(34) Matulis, D., Rouzina, I., and Bloomfield, V. A. (2000) Thermodynamics of DNA binding and condensation: isothermal titration calorimetry and electrostatic mechanism. *J. Mol. Biol. 296* (4), 1053–1063.

(35) Bronich, T., Kabanov, A. V., and Marky, A. L. (2001) A thermodynamic characterization of the interaction of a cationic copolymer with DNA. *J. Phys. Chem. B 105* (25), 6042–6050.

(36) Prevette, L. E., Kodger, T. E., Reineke, T. M., and Lynch, M. L. (2007) Deciphering the role of hydrogen bonding in enhancing pDNA-polycation interactions. *Langmuir 23* (19), 9773–9784.

(37) Ikonen, M., Murtomaki, L., and Kontturi, K. (2008) Controlled complexation of plasmid DNA with cationic polymers: Effect of surfactant on the complexation and stability of the complexes. *Colloids Surf., B 66* (1), 77–83.

(38) Mumper, R. J., Duguid, J. G., Anwer, K., Barron, M. K., Nitta, H., and Rolland, A. P. (1996) Polyvinyl derivatives as novel interactive polymers for controlled gene delivery to muscle. *Pharm. Res. 13* (5), 701–709.

(39) Winnik, M. A., Bystryak, S. M., Chassenieux, C., Strashko, V., Macdonald, P. M., and Siddiqui, J. (2000) Study of interaction of poly(ethylene imine) with sodium dodecyl sulfate in aqueous solution by light scattering, conductometry, NMR, and microcalorimetry. *Langmuir 16* (10), 4495–4510.

(40) Rivas, B. L., and Geckeler, K. E. (1992) Synthesis and metal complexation of poly(ethyleneimine) and derivatives. *Adv. Polym. Sci. 102*, 171–188.

(41) Wang, H., Wang, Y., Yan, H., Zhang, J., and Thomas, R. K. (2006) Binding of sodium dodecyl sulfate with linear and branched polyethyleneimines in aqueous solution at different pH values. *Langmuir 22* (4), 1526–1533.

(42) Tziveleka, L.-A., Psarra, A.-M. G., Tsiourvas, D., and Paleos, C. M. (2007) Synthesis and characterization of guanidinylated poly(propylene imine) dendrimers as gene transfection agents. *J. Controlled Release 117* (1), 137–146.

(43) Patel, M. M., and Anchordoquy, T. J. (2005) Contribution of hydrophobicity to thermodynamics of ligand-DNA binding and DNA collapse. *Biophys. J. 88* (3), 2089–2103.

(44) Ogris, M., Brunner, S., Schüller, S., Kircheis, R., and Wagner, E. (1999) PEGylated DNA/transferrin-PEI complexes: reduced interaction with blood components, extended circulation in blood and potential for systemic gene delivery. *Gene Ther. 6* (4), 595–605.

(45) Petersen, H., Fechner, P. M., Martin, A. L., Kunath, K., Stolnik, S., Roberts, C. J., Fischer, D., Davies, M. C., and Kissel, T. (2002) Polyethylenimine-graft-poly(ethylene glycol) copolymers: influence of copolymer block structure on DNA complexation and biological activities as gene delivery system. *Bioconjugate Chem. 13* (4), 845–854.

(46) Nguyen, H. K., Lemieux, P., Vinogradov, S. V., Gebhart, C. L., Guérin, N., Paradis, G., Bronich, T. K., Alakhov, V. Y., and Kabanov, A. V. (2000) Evaluation of polyether-polyethyleneimine graft copolymers as gene transfer agents. *Gene Ther. 7* (2), 126–138.

(47) Godbey, W. T., Wu, K. K., and Mikos, A. G. (1999) Size matters: Molecular weight affects the efficiency of poly(ethylenimine) as a gene delivery vehicle. *J. Biomed. Mater. Res. 45* (3), 268–275.

(48) Nimesh, S., and Chandra, R. (2008) Guanidium-grafted polyethyleneimine: an efficient transfecting agent for mammalian cells. *Eur. J. Pharm. Biopharm. 68* (3), 647–655.

(49) Yang, Z., Sahay, G., Sriadibhatla, S., and Kabanov, A. V. (2008) Amphiphilic block copolymers enhance cellular uptake and nuclear entry of polyplex-delivered DNA. *Bioconjugate Chem. 19* (10), 1987–1994.

BC900119T

TECHNICAL NOTES

Synthesis and Characterization of Hyperbranched Poly(glycidol) Modified with pH- and Temperature-Sensitive Groups

Chie Kojima,[§,†] Kohei Yoshimura,[†] Atsushi Harada,[†] Yuichi Sakanishi,[‡] and Kenji Kono*[,†]

Department of Applied Chemistry, Graduate School of Engineering, Osaka Prefecture University, Osaka, Japan, and Daicel Chemical Industries, Ltd., Osaka, Japan. Received January 15, 2009; Revised Manuscript Received March 3, 2009

Hyperbranched poly(glycidol)s with varying degrees of polymerization were modified by reaction with succinic anhydride and isopropylamine to obtain novel pH- and thermosensitive polymers. These polymers exhibited phase transitions in response to decreasing pH and/or increasing temperature, depending on the degree of polymerization and the ratio of succinyl group to *N*-isopropylamide. It was possible to harvest a bioactive molecule, rose bengal, from solution using the phase transition of thermosensitive hyperbranched poly(glycidol).

INTRODUCTION

Dendrimers and hyperbranched polymers have three-dimensional structures and unique properties that are different from those of linear polymers (*1, 2*). For example, various types of dendrimers have been shown to be capable of encapsulating guest molecules, and many researchers have investigated their potential as carriers of bioactive molecules (*3*−*5*). Despite the lower regularity of their branched backbone structures, hyperbranched polymers tend to have spherical structures and exhibit properties in common with dendrimers. In addition, hyperbranched polymers tend to be more easily prepared than dendrimers (*6*−*8*). Thus hyperbranched polymers may be more useful, from a practical viewpoint, than dendrimers. To increase the usefulness of hyperbranched polymers, it is crucial to impart desired functionality to target hyperbranched polymers with appropriate structure and properties. However, there have been only a few reports on the modification of hyperbranched polymers with functional groups (*9, 10*).

Stimuli-sensitive properties are among the most useful functions of polymers for various fields of application. In particular, temperature- and pH-responsiveness are of great importance for biomedical applications. The temperature of target sites, such as tumor tissues, in the body can be changed safely by hyperthermia. Also, it is known that some cellular compartments and tissues have lower pH environments than normal physiological pH. For those reasons many efforts have been made to develop polymers with temperature-sensitive and pH-sensitive properties for biomedical use (*11*−*15*).

To increase the potential usefulness of hyperbranched polymers in the biomedical and related fields, in the present study we have attempted to render biocompatible hyperbranched polymers sensitive to temperature and pH. We propose a novel method for imparting thermosensitivity to temperature-insensitive polymers, by which side-chain units of thermosensitive polymers are introduced to the target polymer as temperature-sensitive moieties. We have previously reported that temperature-insensitive poly(amidoamine) and poly(propyleneimine) dendrimers can exhibit lower critical solution temperatures in aqueous solution after incorporation of isobutylamide or *N*-isopropylamide in their chain terminal groups (*16*−*19*). In the present study, we have applied this method to biocompatible hyperbranched poly(glycidol) (HPG) and examined the effectiveness of the method for the temperature sensitization (*20*). We have also attempted to impart pH sensitivity to HPG by the introduction of carboxyl groups. We have succeeded in making biocompatible hyperbranched polymers that respond to temperature and pH in ranges around normal physiological conditions, by controlling the relative proportions of the temperature-sensitive and pH-sensitive units.

MATERIALS AND METHODS

Materials and General Characterization. HPG with DP 10, 20, and 40 (HPG10, HPG20 and HPG40) were provided by Daicel Chemical Industries, Ltd. (Osaka, Japan). Succinic anhydride and pyridine were purchased from Kishida Chemical (Osaka, Japan). Triethylamine (TEA) was purchased from Sigma-Aldrich Corp. (St. Louis, MO). Isopropylamine (IPA) and rose bengal (RB) were purchased from Wako Pure Chemical Industries Ltd. (Osaka, Japan), 2-(1*H*-benzotriazol-1-yl)-1,1,3,3-tetramethyluronium hexafluorophosphate (HBTU) was obtained from Watanabe Chemical Industries, Ltd. (Hiroshima, Japan). ^{1}H NMR spectra were recorded using a JEOL JNM-LA400 instrument (JEOL, Japan).

Synthesis of Succinylated Hyperbranched Poly(glycidol)-(Suc-HPG). HPG10 (5.7 g, 7.5 mmol), HPG20 (5.8 g, 3.9 mmol), or HPG40 (5.9 g, 2.0 mmol) was dissolved in pyridine (60 mL). Twenty-five grams (2.6×10^2 mmol) of succinic anhydride was added, and the solution was stirred at 60−65 °C for 7 h under argon in the dark. The reaction mixtures were filtered to remove the solid deposit and concentrated by evaporation. The precipitates produced by addition of diethyl ether were purified on a Sephadex LH-20 column (GE health-

* To whom correspondence should be addressed. Tel.: +81 72 254 9330; fax: +81 72 254 9330; e-mail: kono@chem.osakafu-u.ac.jp.

† Osaka Prefecture University.

‡ Daicel Chemical Industries, Ltd.

§ Present affiliation: Nanoscience and Nanotechnology Research Center, Research Institutes for the Twenty First Century, Osaka Prefecture University, Japan.

10.1021/bc900016x CCC: $40.75 © 2009 American Chemical Society
Published on Web 04/24/2009

Table 1. Synthesis Conditions, Yields, and Characterization of Various NIPAM-Suc-HPGs

	Suc-HPG							characterization by ^{1}H NMR		
									ratio in succinylation	
trial	DP	in feed [g(mmol)]	Et_3N (mmol)	HBTU (mmol)	IPA (nmol)	IPA equiv[a]	yield[(g%)]	succinilation(%)	-NIPAM	-COOH
1	10	0.94 (0.51)	15	7.11	15.20	2.5	0.88 (78)	87	0.96	0.04
2	10	1.19 (0.64)	19	4.16	3.20	0.4	1.02 (79)	91	0.37	0.63
3	20	1.00 (0.28)	18	11.86	11.78	1.9	0.97 (82)	91	0.94	0.06
4	20	1.01 (0.28)	18	7.14	9.14	0.8	1.04 (91)	88	0.79	0.21
5	20	1.22 (0.34)	20	6.38	4.79	0.6	1.18 (86)	94	0.60	0.40
6	20	1.23 (0.33)	19	3.21	3.21	0.4	1.02 (77)	97	0.34	0.66
7	40	1.02 (0.14)	17	8.18	9.30	1.6	1.14 (93)	95	0.96	0.04
8	40	1.09 (0.15)	26	8.28	5.09	0.8	1.12 (92)	98	0.80	0.20
9	40	1.24 (0.17)	21	6.91	5.18	0.7	1.27 (92)	95	0.60	0.40
10	40	1.26 (0.18)	21	3.35	3.35	0.4	1.20 (89)	98	0.33	0.67

[a] Per terminal group.

Scheme 1

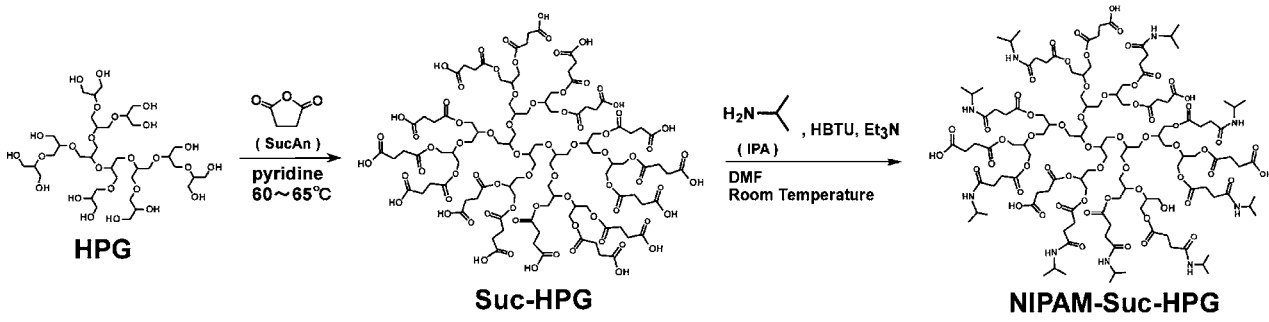

care) by elution with methanol to obtain Suc-HPG10, Suc-HPG20, and Suc-HPG40 with yields 5.2 g (37%), 8.3 g (59%), and 10.3 g (74%), respectively.

δ_H (Suc-HPG, 400 MHz, CD_3OD): 2.6 (br, OCOCH_2CH_2COOH), 3.4−4.1 (br, HPG-scaffold), 4.1−4.5 (br, CH_2OCO), 5.0−5.3 (br, >CHOCO).

Synthesis of *N*-Isopropylamination of Succinylated Hyperbranched Poly(glycidol) (NIPAM-Suc-HPG). Suc-HPG10, Suc-HPG20, and Suc-HPG40 were dispersed in water and evaporated. This treatment was repeated four times, and then the residues were lyophilized to completely remove methanol. The methanol-free Suc-HPG10, Suc-HPG20, and Suc-HPG40 were reacted with isopropylamine at different ratios (see reaction conditions given in Table 1). Because HBTU is an effective condensation reagent that can form ester bonds, it is necessary to take care to avoid contamination and addition of alcohol. In a typical preparation Suc-HPG20 was dissolved in distilled DMF (13 mL), triethylamine and HBTU were added, IPA diluted with distilled DMF (2.32 M) was added, and the mixture was stirred at 28−30 °C for 3 days under argon in the dark. After evaporation of the reaction mixture, the residue was purified by reprecipitation from acetic acid−1 N HCl and washed several times with diethyl ether. The crude product, dispersed in acetic buffer (pH 4−5) to adjust pH, was purified on a Sephadex LH-20 column (GE Healthcare) by elution with methanol. Other polymers were synthesized by varying the amounts of each material according to Table 1. The yields of the synthesized polymers are given in Table 1.

δ_H (400 MHz, CD_3OD): δ 1.1 (d, NHCH(CH_3)$_2$), 2.5 (br, OCOCH$_2$CH_2CONH-), 2.6 (br, OCOCH_2CH_2COOH and OCOCH_2CH$_2$CONH), 3.4−4.1 (br, HPG-scaffold), 3.9 (br, COONHCH(CH_3)$_2$), 4.1−4.5 (br, CH_2OCO), 5.0−5.3 (br, >CHOCO), 7.8 (br, CONH).

Measurement of Phase Transition. The turbidity of solutions of NIPAM-Suc-HPGs in 10 mM phosphate containing 150 mM NaCl buffer, pH 5.0−7.4, was measured at 700 nm using a Jasco Model V-560 spectrophotometer equipped with a Peltier type thermostatic cell holder coupled with an ETC-505T controller. The heating rate of the sample cell was maintained at 1.0 °C min^{-1}. The cloud points were taken as the initial break points in the resulting transmittance versus temperature curves.

Temperature-Dependent Separation of Rose Bengal. A solution of rose bengal (59 μM) containing NIPAM-Suc-HPG40 (5 mg mL^{-1}, 0.59 mM) or unmodified HPG40 (5 mg mL^{-1}, 1.7 mM) in phosphate buffer (10 mM phosphate containing 150 mM NaCl buffer, pH 7.4) was prepared. After 30 min incubation at 4 or 40 °C, the solution was centrifuged at 15 000 rpm for 30 min at 4 or 40 °C. The supernatants of rose bengal solutions without polymer were also prepared. The absorption spectra of the supernatants were obtained using a Jasco Model V-560 spectrophotometer equipped with a thermomodule (ETC-717T, Jasco Inc., Japan).

RESULTS AND DISCUSSION

Synthesis of NIPAM-Suc-HPGs. Stimuli-responsive polymers based on HPG were synthesized according to Scheme 1. HPGs with degree of polymerization (DP) 10, 20, and 40 were reacted with excess succinic anhydride to provide a pH sensitive unit for HPG (Suc-HPG). Suc-HPGs were then reacted with different amounts of isopropylamine. The experimental conditions for the polymers that were synthesized are shown in Table 1. The synthesized compounds were characterized by ^{1}H NMR. The NMR spectra of unmodified HPG20, Suc-HPG20, and NIPAM-Suc-HPG20 (#5) are shown in Figure 1. The spectrum of Suc-HPG20 reveals signals derived from HPG (3.4−4.0 ppm) and the succinyl unit (2.6 ppm). The signals at 5.0−5.3 ppm and 4.1−4.5 ppm were shifted from 3.4−4.0 ppm by making ester bonds in HPG20 (methine and methylene, respectively). The integral ratio of the succinyl unit signal (2.6 ppm) to the HPG20 signals (3.4−4.1, 4.1−4.5, and 5.0−5.3 ppm) indicates that virtually all terminal hydroxyl groups of HPG20 were succinylated. The same results were obtained for HPG10 and HPG40. The spectrum of NIPAM-Suc-HPG20 (#5) is shown in Figure 1C. Signals from the NIPAM unit (1.1 and 3.9 ppm) were observed in addition to the Suc-HPG signals. The signals

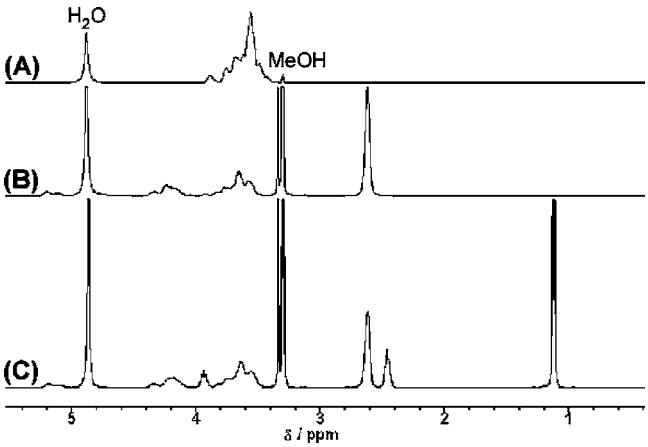

Figure 1. [1]H NMR spectra of HPG20 (A), Suc-HPG20 (B), and NIPAM-Suc-HPG20 (#5) (C) in CD_3OD.

at 2.6 ppm were shifted to 2.5 ppm by making amide bonds in Suc-HPG20. From the integral ratios of the succinyl and NIPAM unit signals to the HPG20 signals, we estimated the proportions of NIPAM and Suc in HPG. The results for all of the polymers that were synthesized are shown in Table 1. We found that the extent of succinylation slightly decreased after amidation with isopropylamine. This might be caused by the hydrolysis of ester bonds in the second reaction step and purification. We synthesized polymers with different DPs and with varying proportions of NIPAM groups and unreacted carboxyl groups.

Phase Transitions of NIPAM-Suc-HPGs. The phase transition of aqueous solutions containing the synthesized polymers was examined. We could not observe a phase transition for unmodified HPGs and Suc-HPGs in 10 mM phosphate buffer containing 150 mM sodium chloride (pH 5.0−7.4). However, NIPAM-Suc-HPGs exhibited thermosensitive behavior depending on the conditions of preparation. We examined first the influence of the DP on the thermosensitivity of the polymers. Figure 2A shows the optical transmittance of aqueous solutions (pH 5.0) of $NIPAM_{0.96}$-Suc-HPG10, $NIPAM_{0.94}$-Suc-HPG20, and $NIPAM_{0.96}$-Suc-HPG40, in which almost all of the hydroxy groups were replaced by NIPAM groups. The transmittance changed drastically at 16, 10, and 7 °C which are called cloud points. The decrease of cloud point with increasing DP of the HPG polymers is consistent with previously reported observations (*9*). It is thought that increase of the terminal group density and van der Waals interaction might result in the lower cloud point of polymer with higher DP. These cloud points are lower than the LCST of polyNIPAM (32 °C). The lower cloud point may be caused by the different structure of the polymer and hydrogen bonds between the main chain and the side chain of the polymer.

We also investigated the influence of the relative proportions of NIPAM groups and unreacted carboxyl groups on the thermosensitivity of the polymers. Figure 2B shows that the optical transmittance of aqueous solutions (pH 5.0) of $NIPAM_{0.94}$-Suc-HPG20, $NIPAM_{0.79}$-Suc-HPG20, and $NIPAM_{0.60}$-Suc-HPG20 drastically changed at 10, 13, and 25 °C, respectively, but that of $NIPAM_{0.33}$-Suc-HPG20 did not. Similar behavior was observed for solutions of a series of HPG40-based polymers (see Supporting Information), indicating that a larger proportion of NIPAM groups induced the phase transition because of the enhanced hydrophobicity.

Because the unreacted carboxyl groups of the NIPAM-Suc-HPG can act as a pH sensor, we investigated the influence of pH on the thermosensitivity of the polymers. The cloud points of $NIPAM_{0.60}$-Suc-HPG20 at pH 5.0, 5.2, and 5.4 were 28, 38, and 56 °C (Figure 2C), respectively, and a cloud point was not

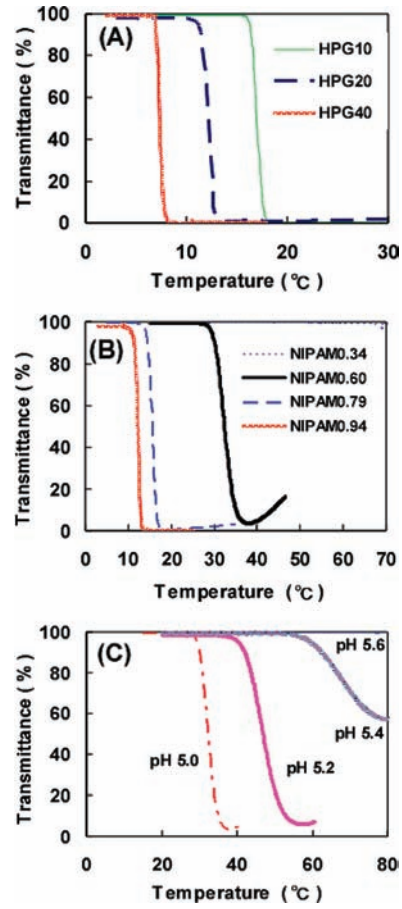

Figure 2. pH- and temperature sensitivity of various NIPAM-Suc-HPGs. (A) The influence of the DP of HPG on the thermosensitivity. Temperature dependence of transmittance for solutions of $NIPAM_{0.96}$-Suc-HPG10, $NIPAM_{0.94}$-Suc-HPG20, and $NIPAM_{0.96}$-Suc-HPG20 at pH 5.0. (B) The influence of the proportion of NIPAM on the thermosensitivity. Temperature dependence of transmittance for solutions of $NIPAM_{0.34}$-Suc-HPG20, $NIPAM_{0.60}$-Suc-HPG20, $NIPAM_{0.79}$-Suc-HPG20, and $NIPAM_{0.94}$-Suc-HPG20 at pH 5.0. (C) pH-sensitivity of $NIPAM_{0.60}$-Suc-HPG20. Temperature dependence of transmittance for solutions of $NIPAM_{0.60}$-Suc-HPG20 at pH 5.0, 5.2, 5.4, and 5.6.

detected at pH 5.6. Similar behavior was observed for solutions of a series of HPG40-based polymers (see Supporting Information). Since $NIPAM_{0.60}$-Suc-HPG20 contained 40% carboxyl group and 60% NIPAM group, this polymer was responsive to both pH and temperature, as we expected. Protonated carboxyl groups at lower pH may increase the hydrophobicity and induce hydrogen bond formation, leading to lower cloud point. The cloud points of $NIPAM_{0.94}$-Suc-HPG20 at pH 5.0 and 7.4 were the same temperature (see Supporting Information). Because this polymer contained few remaining carboxyl groups, it was not sensitive to pH. Consequently, polymers containing an appropriate amount of carboxyl groups can sense both pH and temperature, and it is possible to control pH- and thermosensitivity by tuning the DP, and the relative proportions of NIPAM and carboxyl groups.

Temperature-Dependent Separation of Rose Bengal by Using NIPAM-Suc-HPGs. Thermosensitive dendrimers can act as a nanocapsule for harvesting bioactive molecules (*5*). We investigated the temperature-dependent encapsulation ability of NIPAM-Suc-HPG to rose bengal (RB), which is a type of photosensitizer (*4, 21*). RB aqueous solution with and without NIPAM-Suc-HPG were prepared and heated to 40 °C. After centrifugation, the UV−vis spectra of the solutions were obtained. As shown in Figure 3, the absorption spectrum of RB in the presence of NIPAM-Suc-HPG almost disappeared after

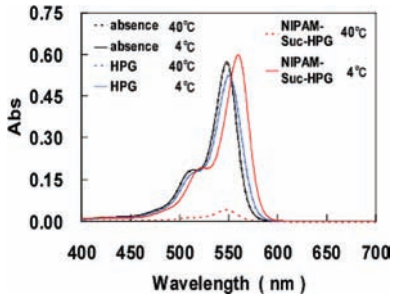

Figure 3. UV−vis spectra of RB in the absence (black) and the presence (red) of $NIPAM_{0.96}$-Suc-HPG40 at 4 °C (solid lines) and 40 °C (dotted lines). The spectrum in the presence of unmodified HPG40 (blue) is also shown.

heating, although the spectrum in the absence of NIPAM-Suc-HPG was unchanged. The spectrum at 40 °C in the presence of HPG, which is not thermosensitive, was the same as at 4 °C. Thus the thermosensitive hyperbranched polymer is a candidate as a temperature-dependent carrier of bioactive molecules. This property is of benefit for accumulation of drug molecules at the site of heated tissue.

In conclusion, we synthesized and characterized NIPAM-Suc-HPG, which contained both carboxyl groups as pH-sensing units and NIPAM groups as thermosensitive units. The pH- and thermosensitivity is dependent on the DP of based polymers and the relative proportions of pH- and thermosensing units. The pH- and thermosensitivity of the polymer can thus be adjusted and controlled by selecting the DP and tuning the reaction conditions. Shen et al. reported very recently a preparation of a type of thermosensitive HPG, by modification of *N*-isopropylacrylamide after the substitution of hydroxyl groups by amino groups. This polymer was sensitive to pH and temperature due to the tertiary amino groups and the NIPAM groups (*9*). However, the pH range of pH sensitivity was above pH 7, which is unlikely to occur in the body. By contrast, our polymers responded in the range from pH 5 to 7, a typical physiological pH range, and a photosensitizer, rose bengal, can be harvested by adding these polymers and heating. Consequently, NIPAM-Suc-HPG is a candidate as a functional material for biomedical applications.

ACKNOWLEDGMENT

We are grateful to Daicel Chemical Industries, Ltd. (Osaka, Japan) for the kind gift of HPGs and for financial support.

Supporting Information Available: Figures S1–S3. This material is available free of charge via the Internet at http://pubs.acs.org.

LITERATURE CITED

(1) Lee, C. C., MacKay, J. A., Frechet, J. M. J., and Szoka, F. C. (2005) Designing dendrimers for biological applications. *Nat. Biotechnol. 12*, 1517–1526.
(2) Boas, U., and Heegaad, P. M. H. (2004) Dendrimers in drug research. *Chem. Soc. Rev. 33*, 43–63.
(3) Kojima, C., Kono, K., Maruyama, K., and Takagishi, T. (2000) Synthesis of polyamidoamine dendrimers having poly(ethylene glycol) grafts and their ability to encapsulate anticancer drugs. *Bioconjugate Chem. 33*, 9169–9172.
(4) Kojima, C., Toi, Y., Harada, A., and Kono, K. (2007) Preparation of polyethylene glycol-attached dendrimers encapsulating photosensitizers for application to photodynamic therapy. *Bioconjugate Chem. 18*, 663–670.
(5) Kono, K., Miyoshi, T., Haba, Y., Murakami, E., Kojima, C., and Harada, A. (2004) Temperature sensitivity control of alkylamide-terminated poly(amidoamine) dendrimers induced by guest molecule binding. *J. Am. Chem. Soc. 129*, 7222–7223.
(6) Sunder, A., Mulhaupt, R., Haag, R., and Frey, H. (2000) Hyperbranched polyether polyols: a modular approach to complex polymer architectures. *Adv. Mater. 12*, 235–239.
(7) Sunder, A., Heinemann, J., and Frey, H. (2000) Controlling the growth of polymer trees: concepts nad perspectives for hyperbrnached polymers. *Chem.—Eur. J. 6*, 2499–2506.
(8) Frey, H., and Haag, R. (2002) Dendritic polyglycerol: a new versatile biocompatible material. *Rev. Mol. Biotechnol. 90*, 257–267.
(9) Shen, Y., Kuang, M., Shen, Z., Nieberle, J., Duan, H., and Frey, H. (2008) Gold nanoparticles coated with a thermosensitive hyperbranched polyelectrolyte: towards smart temperature and pH nanosensors. *Angew. Chem., Int. Ed. 47*, 2227–2230.
(10) Liu, H., Chen, Y., and Shen, Z. (2007) Thermoresponsive hyperbranched polyethylenimines with isobutyramide functional groups. *J. Polym. Sci., Part A 45*, 1177–1184.
(11) Rijcken, C. J. F., Soga, O., Hennink, W. E., and van Nostrum, C. F. J. (2007) Triggered destabilisation of polymeric micelles and vesicles by changing polymers polarity: An attractive tool for drug delivery. *Controlled Release 120*, 131–148.
(12) Alarcon, C. H., Pennadam, S., and Alexander, C. (2005) Stimuli responsive polymers for biomedical applications. *Chem. Soc. Rev. 34*, 276–285.
(13) Schmaljohann, D. (2006) Thermo- and pH-responsive polymers in drug delivery. *Adv. Drug Delivery Rev. 58*, 1655–1670.
(14) Kono, K., Zenitani, K., and Takagishi, T. (1994) Novel pH-sensitive liposomes: liposomes bearing a poly(ethylene glycol) derivative with carboxyl groups. *Biochim. Biophys. Acta 1193*, 1–9.
(15) Sakaguchi, N., Kojima, C., Harada, A., and Kono, K. (2008) Preparation of pH-sensitive poly(glycidol) derivatives with varying hydrophobicities: their ability to sensitize stable liposomes to pH. *Bioconjugate Chem. 19*, 1040–1048.
(16) Haba, Y., Harada, A., Takagishi, T., and Kono, K. (2004) Rendering poly(amidoamine) or poly(propylenimine) dendrimers temperature sensitive. *J. Am. Chem. Soc. 126*, 12760–12761.
(17) Haba, Y., Kojima, C., Harada, A., and Kono, K. (2006) Control of temperature-sensitive properties of poly(amidoamine) dendrimers using peripheral modification with various alkylamide groups. *Macromolecules 39*, 7451–7453.
(18) Tono, Y., Kojima, C., Haba, Y., Takahashi, T., Harada, A., Yagi, S., and Kono, K. (2006) Thermosensitive properties of poly (amidoamine) dendrimers with peripheral phenylalanine residues. *Langmuir 22*, 4920–4922.
(19) Haba, Y., Kojima, C., Harada, A., and Kono, K. (2007) Comparison of thermosensitive properties between poly(amidoamine) dendrimers having peripheral N-isopropylamide groups and linear polymers with the same groups. *Angew. Chem., Int. Ed. 46*, 234–237.
(20) Kainthan, R. K., Janzen, J., Levin, E., Devine, D. V., and Brooks, D. E. (2006) Biocompatibility testing of branched and linear polyglycidol. *Biomacromolecules 7*, 703–709.
(21) Detty, M. R., Gibson, S. L., and Wagner, S. J. (2004) Current clinical and preclinical photosensitizers for use in photodynamic therapy. *J. Med. Chem. 47*, 3897–3915.

BC900016X

Supporting Information

Synthesis and Characterization of Hyperbranched Poly(glycidol) Modified with pH- and Temperature-Sensitive Groups

Chie Kojima[1], Kohei Yoshimura[1], Atsushi Harada[1], Yuichi Sakanishi[2], Kenji Kono[1]*

[1]Department of Applied Chemistry, Graduate School of Engineering, Osaka Prefecture University, Osaka, Japan; [2]Daicel Chemical Industries, Ltd., Osaka, Japan;

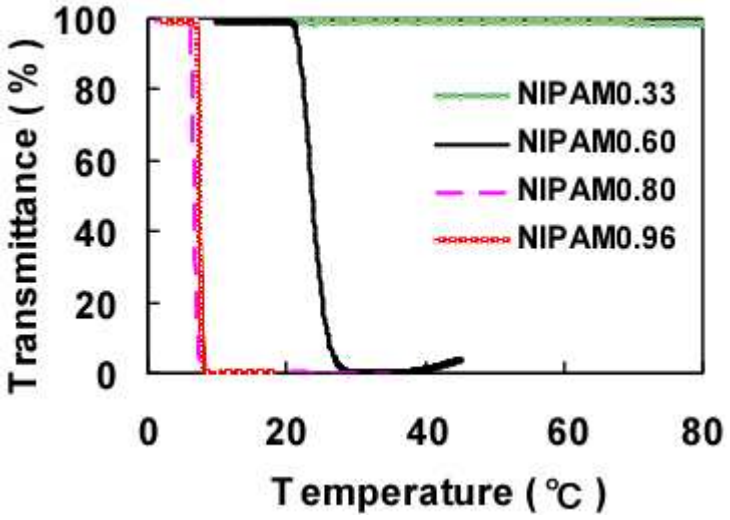

Figure S1. Influence of the proportion of NIPAM on the thermosensitivity. Temperature dependence of transmittance for solutions of $NIPAM_{0.33}$-Suc-HPG40, $NIPAM_{0.60}$-Suc-HPG40, $NIPAM_{0.80}$-Suc-HPG40 and $NIPAM_{0.96}$-Suc-HPG40 at pH 5.0.

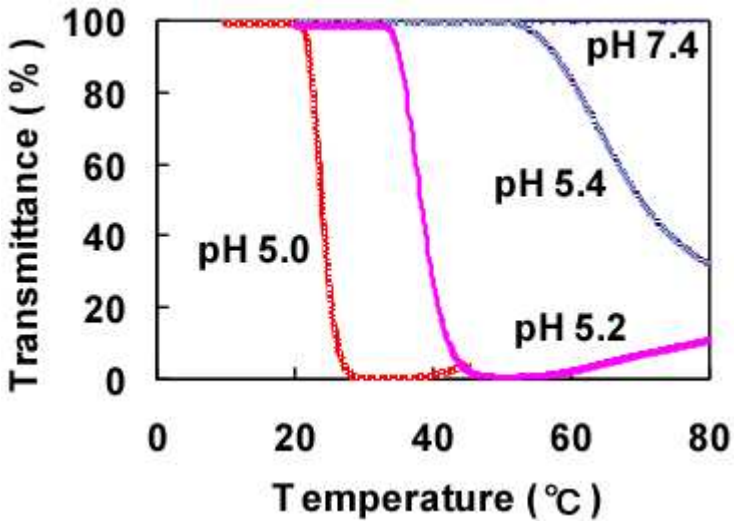

Figure S2. pH-sensitivity of $NIPAM_{0.60}$-Suc-HPG40. Temperature dependence of transmittance for solutions of $NIPAM_{0.60}$-Suc-HPG40 at pH 5.0, 5.2, 5.4, and 7.4.

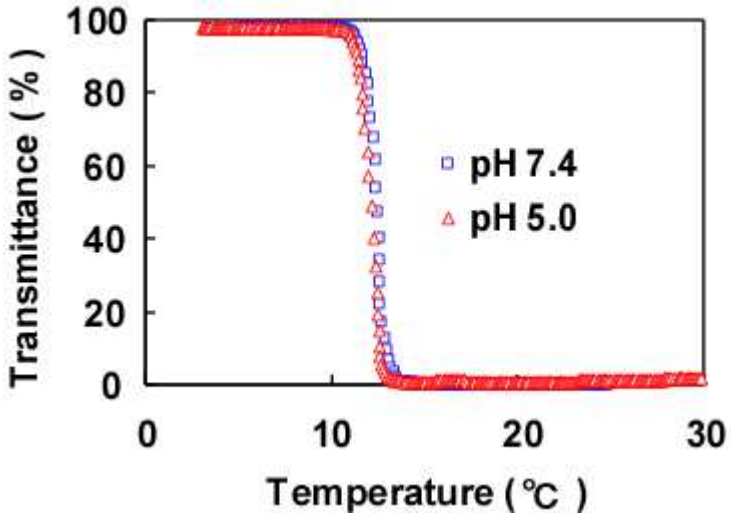

Figure S3. pH-sensitivity of $NIPAM_{0.94}$-Suc-HPG20. Temperature dependence of transmittance for solutions of $NIPAM_{0.94}$-Suc-HPG20 at pH 5.0 and 7.4.

Preparation of Mammalian Expression Vectors Incorporating Site-Specifically Platinated-DNA Lesions

Wee Han Ang, William Wesley Brown, and Stephen J. Lippard*

Department of Chemistry, Massachusetts Institute of Technology, Cambridge, Massachusetts 02139. Received January 26, 2009; Revised Manuscript Received February 26, 2009

FDA-approved platinum-based anticancer drugs, cisplatin, carboplatin, and oxaliplatin, are some of the most effective chemotherapies in clinical use. The cytotoxic action of these compounds against cancer requires a combination of processes including cell entry, drug activation, DNA binding, and transcription inhibition resulting in apoptotic cell death. The drugs form Pt lesions with nuclear DNA, leading to the arrest of key cellular functions and triggering a variety of cellular responses. DNA probes containing Pt−DNA conjugates are important tools for studying the molecular mechanisms of these processes. In order to facilitate investigation of specific Pt−DNA lesion processing within live cells, we devised a strategy for constructing plasmids containing a single site-specific Pt−DNA adduct. The method involves the use of nicking restriction enzymes to create closely spaced tandem gaps on the plasmid followed by removal of the intervening doubly nicked DNA strand to form a short single-stranded gap. Synthetic platinated oligonucleotides were incorporated into the gapped plasmid construct to generate a covalently closed circular platinated plasmid in good yield. We discuss the application of this methodology to prepare plasmids containing a platinum 1,2-d(G*pG*) or 1,3-d(G*pTpG*) intrastrand cross-link, two notable adducts formed by the three clinically approved drugs.

INTRODUCTION

The simple inorganic compound *cis*-diamminedichloroplatinum(II) or cisplatin confers one of the most remarkable treatments for cancer, particularly testicular germ-cell cancer (*1, 2*). The cytotoxic action of cisplatin occurs by a sequence of steps involving cell entry, drug activation, DNA binding, and transcription inhibition, resulting in apoptotic cell death (*3*). Formation of Pt−DNA adducts is an important determinant of the anticancer activity of platinum-based drugs, leading to the arrest of key cellular functions, including transcription (*4*−*7*), triggering a variety of cellular responses, including nucleotide excision repair (*8*−*11*). Cisplatin reacts with nuclear DNA to form predominantly 1,2-d(G*pG*), 1,2-d(A*pG*) intrastrand, and to a lesser extent, 1,3-d(G*pNpG*) intrastrand and interstrand cross-links, where the asterisks denote the platinated nucleosides (*12, 13*). Understanding how the cell processes these specific lesions is important in elucidating the mechanism of action and in forming a basis for the rational design of improved drugs.

Our group along with others have synthesized and utilized a variety of platinated DNA constructs as probes to investigate the action of platinum-based drugs in vitro and the processing of Pt−DNA adducts by cellular proteins (*14*−*17*). In particular, we are interested in preparing site-specifically platinated plasmids that can be used in live cells for application as in vitro transcription probes. A widely used method involves priming a single-stranded circular DNA template with a platinated oligonucleotide followed by extension around the template with a DNA polymerase (*18*−*20*). However, we require a more efficient means of preparation that can be applied to existing mammalian expression vectors with minimal modification to the construct and which can generate the platinated plasmid in good yield. In related work, plasmids containing site-specific mismatches as substrates for mismatch repair studies were prepared by treatment with nicking endonucleases followed by incorporation of synthetic oligonucleotides into the resulting gap (*21, 22*). This method, together with some special design elements devised during the present study, has the potential to generate plasmids containing specific Pt−DNA lesions for mechanistic work. In the present technical note, we demonstrate the power of this methodology to generate the desired constructs using commercial mammalian expression vectors as the host. Plasmids containing the most mechanistically important Pt−DNA adducts, 1,2-d(G*pG*)-Pt and 1,3-d(G*pTpG*)-Pt, formed by the clinically relevant cisplatin, carboplatin, and oxaliplatin anticancer drugs, were prepared and characterized. The key design features incorporated in our study ensure a high yield of the desired bioconjugates.

EXPERIMENTAL PROCEDURES

Materials. Restriction endonucleases (REases), Nt.BbvCI nicking enzyme, calf intestinal phosphatase (CIP), T4 polynucleotide kinase (T4 PNK), and T4 DNA ligase were obtained from New England Biolabs (NEB), and enzymatic reactions were carried out in the reaction buffers that were provided with the enzyme. Ethidium bromide (EtdBr) and nuclease S1 were purchased from Promega and supercompetent XL1BLUE *E. coli* cells, from Stratagene. K_2PtCl_4 was obtained as a gift from Engelhard Corporation. Cisplatin and [Pt(*R*,*R*-dach)Cl_2] were prepared according to literature procedures (*23, 24*). Desalted oligonucleotides were ordered from Integrated DNA Technologies (IDT, Coralville, Indiana, USA) unless otherwise stated.

Vector Construction and Preparation. A mammalian vector expressing *Gaussia* luciferase, pCMV-GLuc (NEB), was used as the vector construct. pCMV-GLuc (NEB) was treated sequentially with HindIII and BamHI to digest the vector between the *CMV* promoter and *GLuc* reporter genes. A synthetic insert designed for subsequent incorporation of the 1,2-d(G*pG*)-Pt DNA lesion was prepared by annealing 5′-AGCTGCTGAGGACCGGTGCTGAGG with 5′-GATCCCT-CAGCACCGGTCCTCAGC, which left 5′-AGCT/GATC noncohesive overhangs, and ligated to the HindIII/BamHI-digest

* To whom correspondence should be addressed. E-mail: lippard@mit.edu.

10.1021/bc900031a CCC: $40.75 © 2009 American Chemical Society
Published on Web 04/07/2009

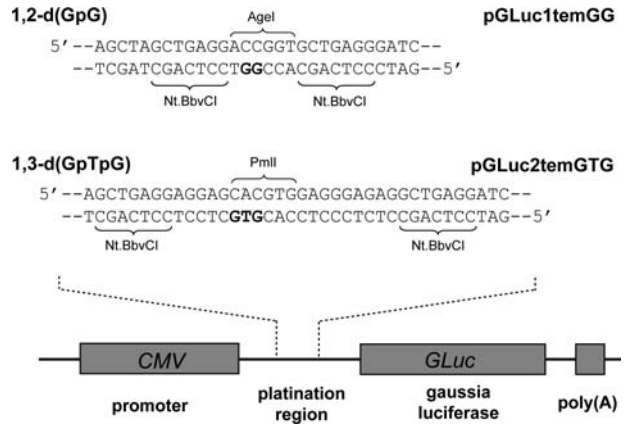

Figure 1. DNA sequence of the platination regions in pGLuc1temGG and pGLuc2temGTG vectors; the position of the intended platination sites are highlighted in bold text.

of pCMV-GLuc. Similarly, the synthetic insert for the 1,3-d(G*pTpG*)-Pt DNA lesion was prepared from 5′-AGCTGAGGAGGAGCACGTGGAGGGAGAGGCTGAG and 5′-GATCCTCAGCCTCTCCCTCCACGTGCTCCTCCTC. The ligation mixtures were transformed directly into XL1BLUE cells on LB agar plates supplemented with 100 mg/L of ampicillin. Colonies were randomly picked and plasmid extracted (Qiagen miniprep kit). Incorporation of synthetic inserts was confirmed by restriction analysis and sequencing (MWG Operon, Huntsville, Alabama, USA) prior to large scale plasmid preparation. The modified vectors for the 1,2-d(G*pG*)-Pt and 1,3-d(G*pTpG*)-Pt DNA lesions are designated as pGLuc1temGG and pGLuc2temGTG, respectively (Figure 1).

Preparation of 13-mer Insertion Strands Containing 1,2-d(G*pG*)-Pt Lesions. Desalted 5′-TCAGCACCGGTCC oligonucleotide was ordered from IDT (Chart 1). The 13-mer nonplatinated insertion strand (13-is) was obtained by purifying the desalted oligonucleotide using ion-exchange HPLC. To prepare the 13-mer insertion strand with the 1,2-d(G*pG*)-[$Pt(NH_3)_2$] lesion (13-is-Pt), desalted oligonucleotide (800 nmol) was allowed to react with *cis*-$[Pt(NH_3)_2(H_2O)_2]^{2+}$ (1200 nmol) in buffer (1 mL, 10 mM sodium phosphate at pH 6.0) for 2 h at 37 °C (*25*). The platinated oligonucleotide was purified twice by ion-exchange HPLC. The linear gradient was 10−45% B over 13.5 min, where solvent A contained 20 mM Tris·HCl at pH 8.0 and 20% acetonitrile, and solvent B contained solvent A supplemented with 1 M NaCl. The final yield was 120 nmol (15.0%). The 13-mer insertion strand with the 1,2-d(G*pG*)-[Pt(*R*,*R*-dach)] lesion (13-is-oxPt) was purified by the same method except that the conditions were 800 nmol of oligonucleotide and 1200 nmol of $[Pt(R,R\text{-dach})(H_2O)_2]^{2+}$ in buffer (1.5 mL, 10 mM sodium phosphate at pH 6.0) for 4 h at 37 °C. The final yield was 10.5 nmol (1.3%).

Preparation of 27-mer Insertion Strands Containing 1,3-d(G*pTpG*)-Pt Lesions. The 27-mer insertion strand (27-is) 5′-TCAGCCTCTCCCTCCACGTGCTCCTCC was prepared by using an Applied Biosystems 392 DNA/RNA synthesizer on a 1 μmol scale by standard phosphoramidite protocols and purified with PolyPak II reverse-phase cartridges (Glen Research) in accord with the manufacturer's instructions (Chart 1). The 27-mer insertion strand with the 1,3-d(G*pTpG*)-[$Pt(NH_3)_2$] lesion (27-is-Pt) was prepared by ligating a platinated 17-mer strand to a 10-mer in the presence of a 35-mer scaffold. The 10-mer 5′-TCAGCCTCTC and 17-mer 5′-CCTCCACGTGCTCCTCC strands were prepared on the DNA synthesizer and purified as described for 27-is. The 17-mer oligonucleotide (250 nmol) was allowed to react with *cis*-$[Pt(NH_3)_2(H_2O)_2]^{2+}$ (375 nmol) in buffer (1 mL, 10 mM sodium phosphate at pH 6.0) for 2 h at 37 °C and purified by ion-exchange HPLC (*25*). The linear gradient was 30% B for 3 min, 30−52.5% B over 13.5 min, where solvent A contained 20 mM Tris·HCl at pH 8.0, and 20% acetonitrile, and solvent B contained solvent A supplemented with 1 M NaCl.

The platinated 17-mer (25 nmol) was phosphorylated using T4 PNK (50 U) in buffer (250 μL, 70 mM Tris·HCl at pH 7.6, 10 mM $MgCl_2$, 5 mM DTT, and 1 mM ATP) for 6 h at 37 °C, treated with phenol/chloroform/isoamyl alcohol (25:24:1), and dialyzed against water for 4 h. The phosphorylated 17-mer, 10-mer (30 nmol), and the 35-mer scaffold 5′-TTTTGGAGGAGCACGTGGAGGGAGAGGCTGATTTT (37.5 nmol) were annealed and ligated using T4 DNA ligase (200 U) in buffer (200 μL, 50 mM Tris·HCl at pH 7.6, 10 mM $MgCl_2$, 10 mM DTT, and 1 mM ATP) at 16 °C for 36 h. The product was purified by 14% urea−PAGE, followed by ion-exchange HPLC. The linear gradient used was 60−77.5% B over 13 min, where solvent A contained 10 mM NaOH, and solvent B contained solvent A supplemented with 1 M NaCl. The yield obtained was 0.8 nmol (3.2%). The 27-mer insertion strand containing the 1,3-d(G*pTpG*)-[Pt(*R*,*R*-dach)] lesion (27-is-oxPt) was prepared using the same method, and the final yield was 1.5 nmol (6.0%).

Characterization of Platinated and Nonplatinated Insertion Strands. The insertion strands were characterized by MALDI-TOF MS to determine their molecular mass, which in all cases was within 0.1% of the calculated value. Mass spectra of the synthesized oligonucleotides were recorded on a Bruker OmniFlex instrument. The analyte was mixed with a matrix containing 10 mg/mL 2,4,6-trihydroxyacetophenone with 25 mM ammonium citrate in 50% MeCN solution and applied on the target using the dried droplet method. External calibration was performed using ABI Biosystems Calibration Mixture 2. The insertion strands were analyzed for nucleotide composition by enzymatic digestion. The oligonucleotide (500 pmol) was digested with nuclease S1 (10 U) for 12 h at 37 °C in buffer (100 μL, 50 mM NaOAc, 280 mM NaCl, and 4.5 mM $ZnSO_4$). Next, Tris·HCl buffer (1.5 M at pH 8.8) and calf intestinal phosphatase (10 U) were added, and the reaction was incubated for 4 h at 37 °C. The digests were analyzed by reverse-phase HPLC using a Supelcosil LC-18-S column. The method used was 5−15% B over 30 min, where solvent A contained 10 mM NaOAc, and solvent B contained 100% methanol.

Preparation of the Site-Specifically Gapped Plasmid. The plasmid (200 μg) was incubated with Nt.BbvCI (50 U) at 37 °C for 1.5 h. The enzyme was deactivated by heating the reaction at 80 °C for 20 min and removed by phenol/chloroform/isoamyl alcohol (25:24:1) treatment. The single-stranded gap was formed by trapping the nicked strand with its complement (Chart 2). Briefly, the plasmid solution was supplemented with synthetic cDNA (1:500 molar ratio) in annealing buffer (10 mM Tris·HCl at pH 8.0, 2 mM $MgCl_2$, and 0.4 M NaCl), and heated in a thermocycler (80 °C for 5 min then −10 °C/min to 20 °C for 5 cycles). The gapped plasmid was purified by repeated washing (6−8 times) through a diafiltration centrifugal device (Pall, MWCO 30 KDa or 100 KDa) and dissolved in buffer (10 mM Tris·HCl at pH 8.0).

Incorporation of Platinated/Nonplatinated Insertion Strands into the Gapped Plasmid. The insertion strands were phosphorylated by T4 PNK in buffer (70 mM Tris·HCl at pH 7.6, 10 mM $MgCl_2$, 5 mM DTT, and 1 mM ATP) at 37 °C for 1 h. The phosphorylated insertion strands were treated with phenol/chloroform/isoamyl alcohol (25:24:1), dialyzed against water, and dried in vacuo. The gapped plasmid (40 μg) was added at 1:10 to 1:100 molar ratio (vs the insertion strands), and the mixture was annealed in a thermocycler (80 °C for 10 min, then cooling to 4 °C at −1 °C/min). The reaction was supplemented with T4 DNA ligase (80 U) in buffer (50 mM Tris·HCl at pH

Chart 1. Sequences of Platinated and Unplatinated Insertion Strands

	1,2-d(G*pG*)-Pt lesion	1,3-d(G*pTpG*)-Pt lesion
unplatinated	5′-TCAGCACC**GG**TCC (13-is)	5′-TCAGCCTCTCCCTCCAC**GTG**CTCCTCC (27-is)
$[Pt(NH_3)_2]^{2+}$	5′-TCAGCACC**GG**TCC (13-is-Pt)	5′-TCAGCCTCTCCCTCCAC**GTG**CTCCTCC (27-is-Pt)
$[Pt(R,R\text{-dach})]^{2+}$	5′-TCAGCACC**GG**TCC (13-is-oxPt)	5′-TCAGCCTCTCCCTCCAC**GTG**CTCCTCC (27-is-oxPt)

Chart 2. DNA Sequence at the Gapping Site of pGLuc1temGG (Left) and pGLuc2temGTG (Right) with the Nicked Strand Annealed to Synthetic cDNA

pGLuc1temGG

```
                AgeI
        Nt.BbvCI------Nt.BbvCI
          =======      =======
5′--AGCTGCTGAGGACCGGTGCTGAGGGATC--
  --TCGACGACT               CCCTAG--5′

            CCTGGCCACGACT
            |||||||||||||
5′-TTTTGGACCGGTGCTGATTTT (cDNA)
```

pGLuc2temGTG

```
                    PmlI
Nt.BbvCI      ------          Nt.BbvCI
  =======                     =======
5′--AGCTGAGGAGGAGCACGTGGAGGGAGAGGCTGAGGATC--
  --TCGACT                              CCTAG--5′

          CCTCCTCGTGCACCTCCCTCTCCGACT
          |||||||||||||||||||||||||||
5′-TTTTGGAGGAGCACGTGGAGGGAGAGGCTGATTTT (cDNA)
```

7.6, 10 mM $MgCl_2$, 10 mM DTT, and 1 mM ATP) and incubated at 16 °C for 12 h. The mixture was supplemented with 6× loading buffer (NEB), heated at 75 °C for 15 min, and separated using preparative 0.8% w/v agarose gel electrophoresis containing 0.5 μg/mL EtdBr. The DNA bands were revealed using a hand-held UV lamp and the band with higher electrophoretic mobility, corresponding to the covalently closed circular product, was excised. Gel extraction was carried out using a commercial kit (Promega).

The platinated plasmids were purified further by treatment with AgeI (5 U) or PmlI (40 U) at 37 °C for 30 min. The enzyme was deactivated by heating the reaction at 75 °C for 15 min and separated using preparative 0.8% w/v agarose gel electrophoresis containing 0.5 μg/mL EtdBr. The DNA bands were revealed with a hand-held UV lamp and the band with higher electrophoretic mobility, corresponding to the covalently closed circular product, was excised. Gel extraction was carried out as described above (Qiagen). Quantitation of the platinated and nonplatinated plasmid was carried out using the picogreen assay (Molecular Probes). Overall yields range between 5−25%.

Restriction Analysis on Ligated Platinated/Nonplatinated Plasmids. pGLuc1temGG plasmid (100 ng) was incubated with AgeI (0.5 U) at 37 °C for 15 min, and the enzyme was inactivated by heating at 75 °C for 15 min. The plasmids were analyzed using 0.8% w/v agarose gel electrophoresis containing 0.5 μg/mL EtdBr. Pt−DNA lesions were chemically removed by treating the platinated plasmid (200 ng) with 0.2 M NaCN at 55 °C for 10 h, followed by dialysis against water for 4 h (*14*, *26*), prior to REase treatment. pGLuc2temGTG (100 ng) were treated with PmlI (2 U) in the same manner except that the mixture was incubated at 37 °C for 45 min. Control lanes containing untreated plasmids were also added for comparison. The gels were imaged using BioRad Fluor-S MultiImager.

RESULTS AND DISCUSSION

Vector Design Considerations. The strategy used to prepare platinated plasmids is to create single-stranded gaps within the DNA and to fill them in by using synthetic platinated insertion strands containing the precise complementary sequences (Figure 2). The single-stranded gap is created by removing the DNA strand positioned between two closely spaced nicks in the plasmid. Nicking enzymes were employed to introduce single-stranded scissions site-specifically into the plasmid. These enzymes were developed from REases that recognize asymmetric DNA sequences (Type IIA) but are engineered to cleave only one strand of the sequence (*27*). By designing their recognition sequences in tandem into the vector, we can use the nicking sites to predefine the sequence and position of the gap within the plasmid. In addition, the Pt−DNA lesion is intentionally situated within a REase recognition site on the plasmid. Platination at the recognition site

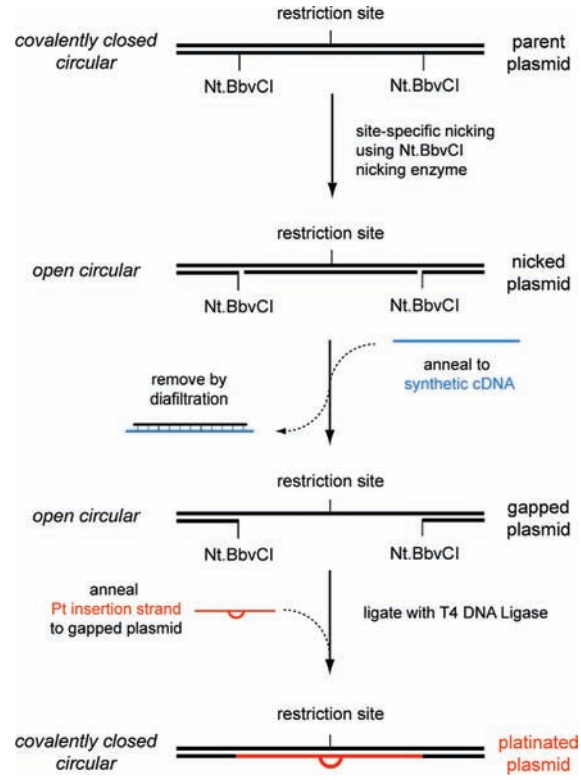

Figure 2. Overall scheme for preparing platinated plasmids.

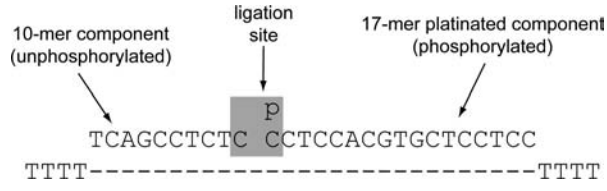

Figure 3. Preparation of platinated 27-mer insertion strands.

blocks REase cleavage and provides a facile method for discriminating between platinated and nonplatinated plasmids. In order to achieve a high level of control and specificity, both the nicking enzyme and the REase for the platination site must be unique and be noncutters of the parent vector. The design of these sequences must be such that they insert with noncohesive overhangs for directional ligation into the vector backbone (Figure 1).

An initial search for appropriate restriction sites was performed on pCMV-Gluc *in silico* to determine that the commercially available REases we selected have no restriction sites on the plasmid (*28*). Nt.BbvCI (CC↓TCAGC) was chosen as the nicking enzyme, and AgeI (A↓CCGGT) and PmlI (CAC↓GTG) as the REases for the platinated inserts for 1,2-d(G*pG*)-Pt and 1,3-d(G*pTpG*)-Pt lesions, respectively (Chart 2). Since platinated oligonucleotides are prepared by treating unplatinated single strands with the diaqua derivatives of cisplatin or oxaliplatin, the insertion strand sequence should ideally contain G bases only at the desired 1,2-d(GpG) or 1,3-d(GpNpG) platination site. In utilizing Nt.BbvCI for tandem nicking, the gap formed necessitates an insertion strand with a 5′-TCAGC starting and a 3′-CC terminal sequence. The presence of 1,2-d(ApG) in the starting sequence, in particular, complicates the preparation of insertion strands containing 1,3-d(G*pTpG*)-Pt lesions. Therefore, additional CT-rich sequences were designed into the insertion strands so that they could be constructed in a modular manner from separate component strands (see below).

Preparation of Platinated Insertion Strands. Platination of the 13-mer synthetic oligonucleotide 5′-TCAGCACCGGTCC was carried out with *cis*-$[Pt(NH_3)_2(H_2O)_2]^{2+}$ or $[Pt(R,R\text{-dach})(H_2O)_2]^{2+}$, in accordance with reported procedures (*7, 14, 16, 25*), to prepare oligonucleotides carrying the 1,2-d(G*pG*)-Pt lesions formed by anticancer drugs cisplatin/carboplatin and oxaliplatin (*12, 13*). The 1,2-d(ApG) sequence competed directly with the 1,2-d(GpG) sequence for platination and resulted in an additional peak overlapping with the abundant product peak in the HPLC chromatogram. We were able to separate the major 1,2-d(G*pG*)-Pt product by repeated HPLC runs, however (Figure S1, Supporting Information). The MALDI-TOF MS and enzymatic digestions with nuclease S1 and CIP were consistent with the formation of a single 1,2-d(G*pG*)-Pt lesion on the 13-mer insertion strand (Table S1, Supporting Information).

The 27-mer insertion strands containing 1,3-d(G*pTpG*)-$[Pt(NH_3)_2]$ or 1,3-d(G*pTpG*)-[Pt(*R,R*-dach)] lesions were constructed by ligating the platinated 17-mer fragment to the 10-mer fragment using a DNA scaffold (Figure 3). This strategy was adopted because direct platination of the 27-mer synthetic oligonucleotide 5′-TCAGCCTCTCCCTCCACGTGCTCCTCC might yield the 1,2-d(A*pG*)-Pt adduct as a major product rather than the desired 1,3-d(G*pTpG*)-Pt cross-link. The 17-mer 5′-CCTCCACGTGCTCCTCC synthetic oligonucleotide was therefore platinated with *cis*-$Pt(NH_3)_2(H_2O)_2]^{2+}$ or $[Pt(R,R\text{-dach})(H_2O)_2]^{2+}$. The 17-mers containing the 1,3-d(G*pTpG*)-$[Pt(NH_3)_2]$ or 1,3-d(G*pTpG*)-[Pt(*R,R*-dach)] lesion were readily isolated by ion-exchange HPLC (Figure S2, Supporting Information). Next, the platinated 17-mer was phosphorylated with T4 PNK and ligated, using T4 DNA ligase, to the 10-mer 5′-TCAGCCTCTC fragment using the 35-mer 5′-TTTTGGAGGAGCACGTGGAGGGAGAGGCTGATTTT DNA as a scaffold. Although the product was obtained in modest yield (3−6%), characterization of the ligated material using MALDI-TOF MS and nucleotide composition analysis was consistent with a 27-mer sequence with platination at the desired 1,3-d(G*pTpG*) site (Table S1, Supporting Information).

Preparation of Site-Specifically Platinated Plasmids. A gapped plasmid was prepared by tandem nicking with Nt.BbvCI at the predefined sites and removal of the intervening nicked strand by trapping with synthetic cDNA in large molar excess (Chart 2). The plasmid was purified quantitatively by repeated washings through diafiltration devices, which separate the gapped plasmid from excess cDNA and annealed duplexes.

In order to verify that the single-stranded gap was formed, a set of control ligation experiments were carried out on an analytical scale. The gapped plasmid was mixed with water, as a control, or with the various phosphorylated insertion strands at a 1:100 ratio, annealed, and treated with T4 DNA ligase. In the absence of the insertion strands, ligation of the gapped plasmid could not be achieved; only the open circular (oc) precursor was observed by agarose gel electrophoresis. This result confirmed that the gapping procedure was successful (Figure 4, lanes 1 and 5). In contrast, ligation of the gapped plasmid with both unplatinated and platinated insertion strands yielded significant quantities of covalently closed circular (cc) DNA products (Figure 4, lanes 2−4 and 6−8). Preparation of platinated and nonplatinated plasmids was carried out on a preparative scale. The phosphorylated insertion strands were annealed to the gapped plasmid by using a shallow thermal gradient of −1 °C/min. Ligation with T4 DNA ligase formed the desired covalently closed circular DNA product in good yield. Ligation efficiency was estimated by comparing the fluorescence intensity of the open and covalently closed circular bands on the gel by a BioRad Fluor-S MultiImager, typically ranges lying between 40−60%. The platinated plasmids were purified further by REase treatment, which linearizes nonplatinated plasmid contaminants. Purification of the plasmids was carried out by preparative agarose gel electrophoresis with commercial gel extraction kits at an efficiency of 50−70%. The overall yield from the entire procedure was typically 5−25%. Better yields were obtained on larger, preparative scales (results not shown), but purification of a greater amount of plasmid using agarose gel electrophoresis also becomes more challenging.

The incorporation of the Pt−DNA lesion site-specifically into the plasmid was verified by REase treatment of the synthesized plasmid and analytical agarose gel electrophoresis. In the absence of the Pt−DNA adduct, the plasmid was readily linearized by REase (Figures 5 and 6, lanes 1 and 2). In contrast, plasmids containing the site-specific Pt−DNA lesions were not linearized by the respective REases (Figures 5 and 6, lanes 3 and 4). The reagent NaCN is capable of chemically reversing Pt−DNA cross-links from platinated DNA as $[Pt(CN)_4]^{2-}$ (*14, 26*). Treatment of the platinated plasmids with NaCN at 55 °C for 10 h restored the susceptibility of the plasmids toward REase linearization (Figures 5 and 6, lanes 5 and 6), confirming that the Pt−DNA adducts were site-specifically incorporated into the REase recognition site of the plasmid.

CONCLUSIONS

The method of inserting platinated oligonucleotides into a single stranded gap provides ready access to large platinated DNA constructs, such as plasmids, in a controlled and selective fashion. The key advantage of the method is the high specificity involved in annealing the synthetic oligonucleotide into the gap since only the correct sequence length will result in successful ligation. Only two products are expected from the ligation, the unligated open

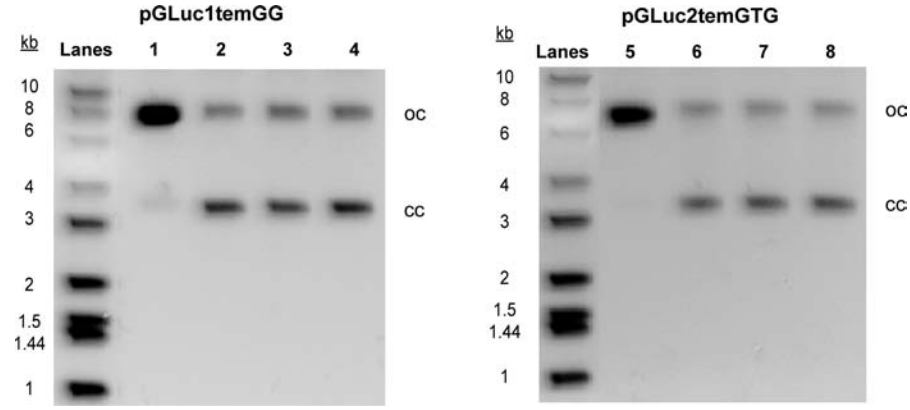

Figure 4. Ligation experiment of gapped pGLuc1temGG (left) and pGLuc2temGTG (right) in the presence of different insertion strands with T4 DNA ligase at 16 °C for 12 h; lane 1, gapped pGLuc1temGG alone; lane 2, plasmid + 13-is; lane 3, plasmid + 13-is-Pt; lane 4, plasmid + 13-is-oxPt; lane 5, gapped pGLuc2temGTG alone; lane 6, plasmid + 27-is; lane 7, plasmid + 27-is-Pt; lane 8, plasmid + 27-is-oxPt.

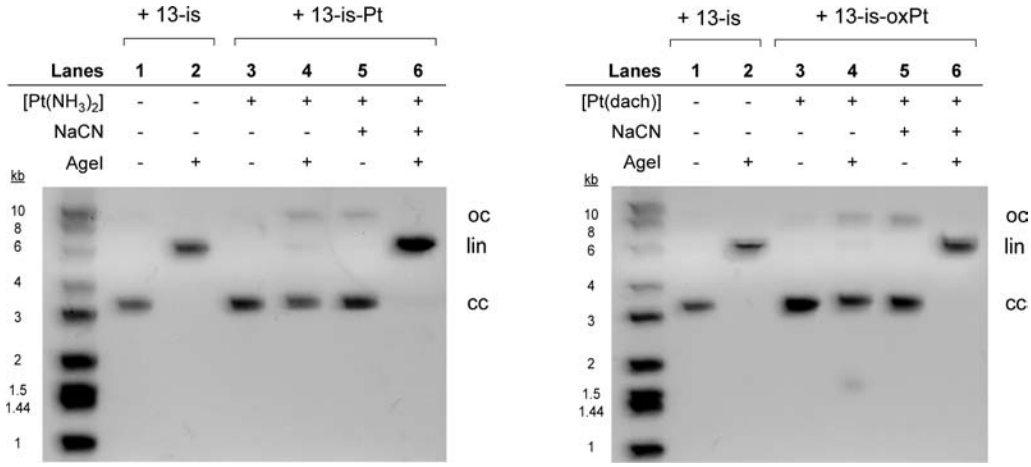

Figure 5. Restriction analysis of platinated/nonplatinated plasmids with AgeI; pGLuc1temGG + 13-is (lanes 1−2); pGLuc1temGG + 13-is-Pt (left, lanes 3−6); and pGLuc1temGG + 13-is-oxPt (right, lanes 3−6).

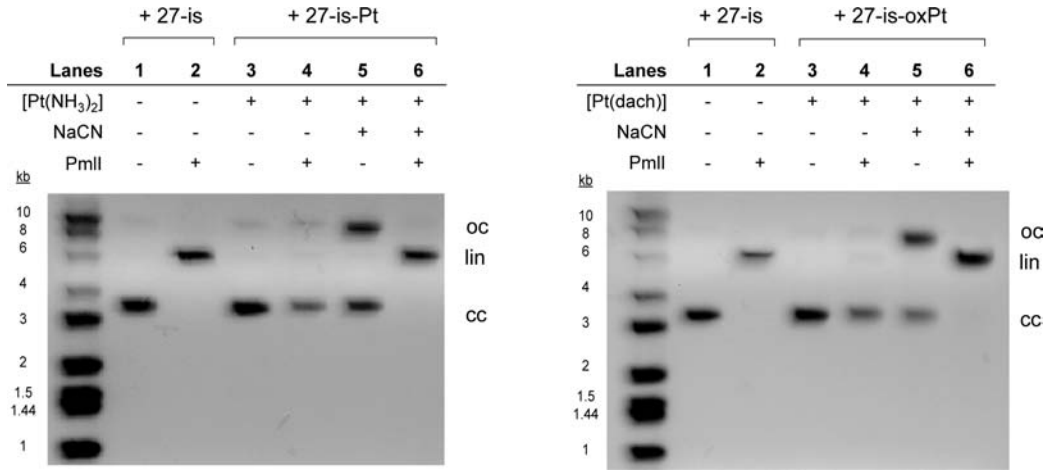

Figure 6. Restriction analysis of platinated/nonplatinated plasmids with PmlI; pGLuc2temGTG + 27-is (lanes 1−2); pGLuc2temGTG + 27-is-Pt (left, lanes 3−6); and pGLuc2temGTG + 27-is-oxPt (right, lanes 3−6).

circular form and the ligated covalently closed circular product, both of which are easily separated by conventional techniques. Good product yields are thus obtained, which is essential for the large-scale production of platinated plasmid for transfection studies in live cells. By comparison, the method of extending a platinated oligonucleotide primed on a single-stranded circular DNA, using DNA polymerase, can lead to the formation of multiple products due to nonspecific priming or incomplete extension, complicating product purification. In addition, the single-stranded circular DNA production from the plasmid template is accomplished using helper phages, and the strand of plasmid produced is dictated by the orientation of the f1 sequence on the plasmid. Since most expression vector systems contain the f1 sequence oriented to yield the template strand to facilitate DNA sequencing, the platinated oligonucleotide can only be extended on the coding strand.

The main challenge in applying the single-stranded gapping methodology in the production of platinated plasmid is that sequence of the gap is highly dependent on the nicking enzyme

used which, in turn, affects the design of the insertion strand. Ideally, the insertion strand should contain only G bases at the platination site, but due to the gap sequence, it may not be possible to exclude them entirely. Nevertheless, we have shown that it is possible to overcome these limitations through more extensive purification or by applying more innovative methods to produce the platinated oligonucleotides.

In summary, the methodology of incorporating platinated oligonucleotides into synthetically gapped plasmid constructs is a versatile way of accessing site-specifically platinated plasmids with different Pt−DNA lesions. Application of the platinated plasmids as in vitro transcription and other probes in mammalian cells is currently underway.

ACKNOWLEDGMENT

This work was supported by the US National Cancer Institute (CA34992 to S.J.L). W.H.A. thanks the National University of Singapore for the Overseas Postdoctoral Fellowship.

Supporting Information Available: HPLC chromatograms of the insertion strand purification (Figure S1 and S2) and their characterization (Table S1). This material is available free of charge via the Internet at http://pubs.acs.org.

LITERATURE CITED

(1) Horwich, A., Shipley, J., and Huddart, R. (2006) Testicular germ-cell cancer. *Lancet 367*, 754–765.
(2) Rosenberg, B., VanCamp, L., Trosko, J. E., and Mansour, V. H. (1969) Platinum compounds: a new class of potent antitumour agents. *Nature (London) 222*, 385–386.
(3) Wang, D., and Lippard, S. J. (2005) Cellular processing of platinum anticancer drugs. *Nat. Rev. Drug Discovery 4*, 307–320.
(4) Cullinane, C., Mazur, S. J., Essigmann, J. M., Phillips, D. R., and Bohr, V. A. (1999) Inhibition of RNA polymerase II transcription in human cell extracts by cisplatin DNA damage. *Biochemistry 38*, 6204–6212.
(5) Mello, J. A., Lippard, S. J., and Essigmann, J. M. (1995) DNA adducts of *cis*-diamminedichloroplatinum(II) and its trans isomer inhibit RNA polymerase II differentially in vivo. *Biochemistry 34*, 14783–14791.
(6) Tremeau-Bravard, A., Riedl, T., Egly, J. M., and Dahmus, M. E. (2004) Fate of RNA polymerase II stalled at a cisplatin lesion. *J. Biol. Chem. 279*, 7751–7759.
(7) Jung, Y., and Lippard, S. J. (2006) RNA polymerase II blockage by cisplatin-damaged DNA: Stability and polyubiquitylation of stalled polymerase. *J. Biol. Chem. 281*, 1361–1370.
(8) Jones, J. C., Zhen, W., Reed, E., Parker, R. J., Sancar, A., and Bohr, V. A. (1991) Gene-specific formation and repair of cisplatin intrastrand adducts and interstrand cross-links in chinese hamster ovary cells. *J. Biol. Chem. 266*, 7101–7107.
(9) Zamble, D. B., Mu, D., Reardon, J. T., Sancar, A., and Lippard, S. J. (1996) Repair of cisplatin-DNA adducts by the mammalian excision nuclease. *Biochemistry 35*, 10004–10013.
(10) Moggs, J. G., Szymkowski, D. E., Yamada, M., Karran, P., and Wood, R. D. (1997) Differential human nucleotide excision repair of paired and mispaired cisplatin-DNA adducts. *Nucleic Acids Res. 25*, 480–490.
(11) Lee, K. B., Wang, D., Lippard, S. J., and Sharp, P. A. (2002) Transcription-coupled and DNA damage-dependent ubiquitination of RNA polymerase II in vitro. *Proc. Natl. Acad. Sci. U.S.A. 99*, 4239–4244.
(12) Jamieson, E. R., and Lippard, S. J. (1999) Structure, recognition, and processing of cisplatin-DNA adducts. *Chem. Rev. 99*, 2467–2498.
(13) Jung, Y., and Lippard, S. J. (2007) Direct cellular responses to platinum-induced DNA damage. *Chem. Rev. 107*, 1387–1407.
(14) Jung, Y., and Lippard, S. J. (2003) Multiple states of stalled T7 RNA polymerase at DNA lesions generated by platinum anticancer agents. *J. Biol. Chem. 278*, 52084–52092.
(15) Malina, J., Novakova, O., Vojtiskova, M., Natile, G., and Brabec, V. (2007) Conformation of DNA GG intrastrand cross-link of antitumor oxaliplatin and its enantiomeric analog. *Biophys. J. 93*, 3950–3962.
(16) Guggenheim, E. R., Xu, D., Zhang, C. X., Chang, P. V., and Lippard, S. J. (2009) Photoaffinity isolation and identification of proteins in cancer cell extracts that bind to platinum-modified DNA. *ChemBioChem 10*, 141–157.
(17) Lovejoy, K. S., Todd, R. C., Zhang, S., McCormick, M. S., D'Aquino, J. A., Reardon, J. T., Sancar, A., Giacomini, K. M., and Lippard, S. J. (2008) cis-Diammine(pyridine)chloroplatinum(II), a monofunctional platinum(II) antitumor agent: Uptake, structure, function, and prospects. *Proc. Natl. Acad. Sci. U.S.A. 105*, 8902–8907.
(18) Moggs, J. G., Yarema, K. J., Essigmann, J. M., and Wood, R. D. (1996) Analysis of incision sites produced by human cell extracts and purified proteins during nucleotide excision repair of a 1,3-intrastrand d(GpTpG)-cisplatin adduct. *J. Biol. Chem. 271*, 7177–7186.
(19) Shivji, M. K. K., Moggs, J. G., Kuraoka, I., and Wood, R. D. (2006) Assaying for the dual incisions of nucleotide exicision repair using DNA with a lesion at a specific site. *Methods Mol. Biol. 314*, 435–456.
(20) Tornaletti, S., Patrick, S. M., Turchi, J. J., and Hanawalt, P. C. (2003) Behavior of T7 RNA polymerase and mammalian RNA polymerase II at site-specific cisplatin adducts in the template DNA. *J. Biol. Chem. 278*, 35791–35797.
(21) Wang, H., and Hays, J. B. (2001) Simple and rapid preparation of gapped plasmid DNA for incorporation of oligomers containing specific DNA lesions. *Mol. Biotechnol. 19*, 133–140.
(22) Wang, H., and Hays, J. B. (2002) Mismatch repair in human nuclear extracts. Quantitative analyses of excision of nicked circular mismatched DNA substrates, constructed by a new technique employing synthetic oligonucleotides. *J. Biol. Chem. 277*, 26136–26142.
(23) Dhara, S. C. (1970) A rapid method for the synthesis of *cis*-$[Pt(NH_3)_2Cl_2]$. *Indian J. Chem. 8*, 193–194.
(24) Kidani, Y., Inagaki, K., Iigo, M., Hoshi, A., and Kuretani, K. (1978) Antitumor activity of 1,2-diaminocyclohexaneplatinum complexes against Sarcoma-180 ascites form. *J. Med. Chem. 21*, 1315–1318.
(25) Wang, D., Hara, R., Singh, G., Sancar, A., and Lippard, S. J. (2003) Nucleotide excision repair from site-specifically platinum-modified nucleosomes. *Biochemistry 42*, 6747–6753.
(26) Bauer, W., Gonias, S. L., Kam, S. K., Wu, K. C., and Lippard, S. J. (1978) Binding of the antitumor drug platinum uracil blue to closed and nicked circular duplex DNAs. *Biochemistry 17*, 1060–1068.
(27) Roberts, R. J., Belfort, M., Bestor, T., Bhagwat, A. S., Bickle, T. A., Bitinaite, J., Blumenthal, R. M., Degtyarev, S. K., Dryden, D. T. F., Dybvig, K., Firman, K., Gromova, E. S., Gumport, R. I., Halford, S. E., Hattman, S., Heitman, J., Hornby, D. P., Janulaitis, A., Jeltsch, A., Josephsen, J., Kiss, A., Klaenhammer, T. R., Kobayashi, I., Kong, H., Krüger, D. H., Lacks, S., Marinus, M. G., Miyahara, M., Morgan, R. D., Murray, N. E., Nagaraja, V., Piekarowicz, A., Pingoud, A., Raleigh, E., Rao, D. N., Reich, N., Repin, V. E., Selker, E. U., Shaw, P.-C., Stein, D. C., Stoddard, B. L., Szybalski, W., Trautner, T. A., Van Etten, J. L., Vitor, J. M. B., Wilson, G. G., and Xu, S.-Y. (2003) A nomenclature for restriction enzymes, DNA methyltransferases, homing endonucleases and their genes. *Nucleic Acids Res. 31*, 1805–1812.
(28) Vincze, T., Posfai, J., and Roberts, R. J. (2003) NEBcutter: a program to cleave DNA with restriction enzymes. *Nucleic Acids Res. 31*, 3688–3691.

BC900031A

Supporting Information for

Preparation of Mammalian Expression Vectors Incorporating Site-Specifically Platinated-DNA Lesions

Wee Han Ang, William Wesley Brown, Stephen J. Lippard*

Department of Chemistry, Massachusetts Institute of Technology, 77 Massachusetts Ave., Cambridge, Massachusetts 02139.

*To whom correspondence should be addressed. E-mail: lippard@mit.edu

Running Title: Site-Specifically Platinated Mammalian Expression Vectors

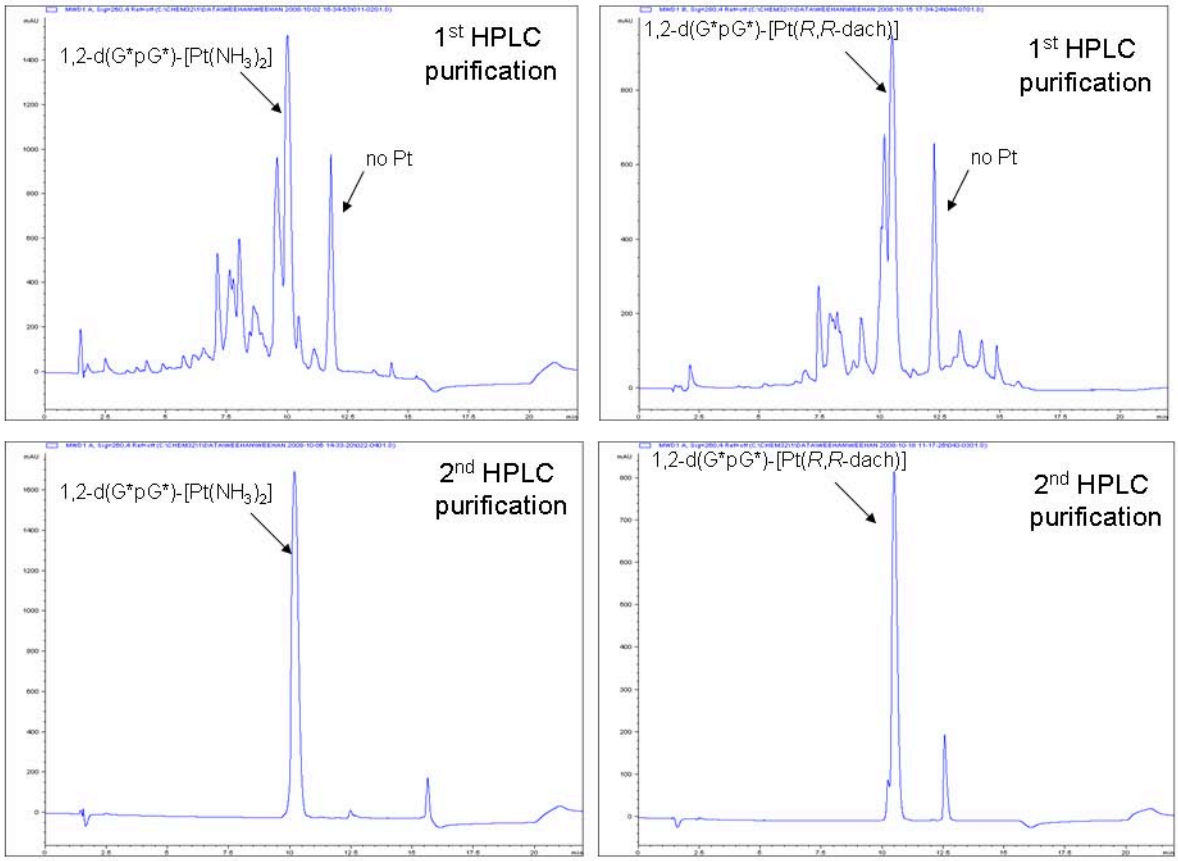

Figure S1. HPLC purification of platinated 13-mer insertion strands; 13-is-Pt (left panel) and 13-is-oxPt (right panel).

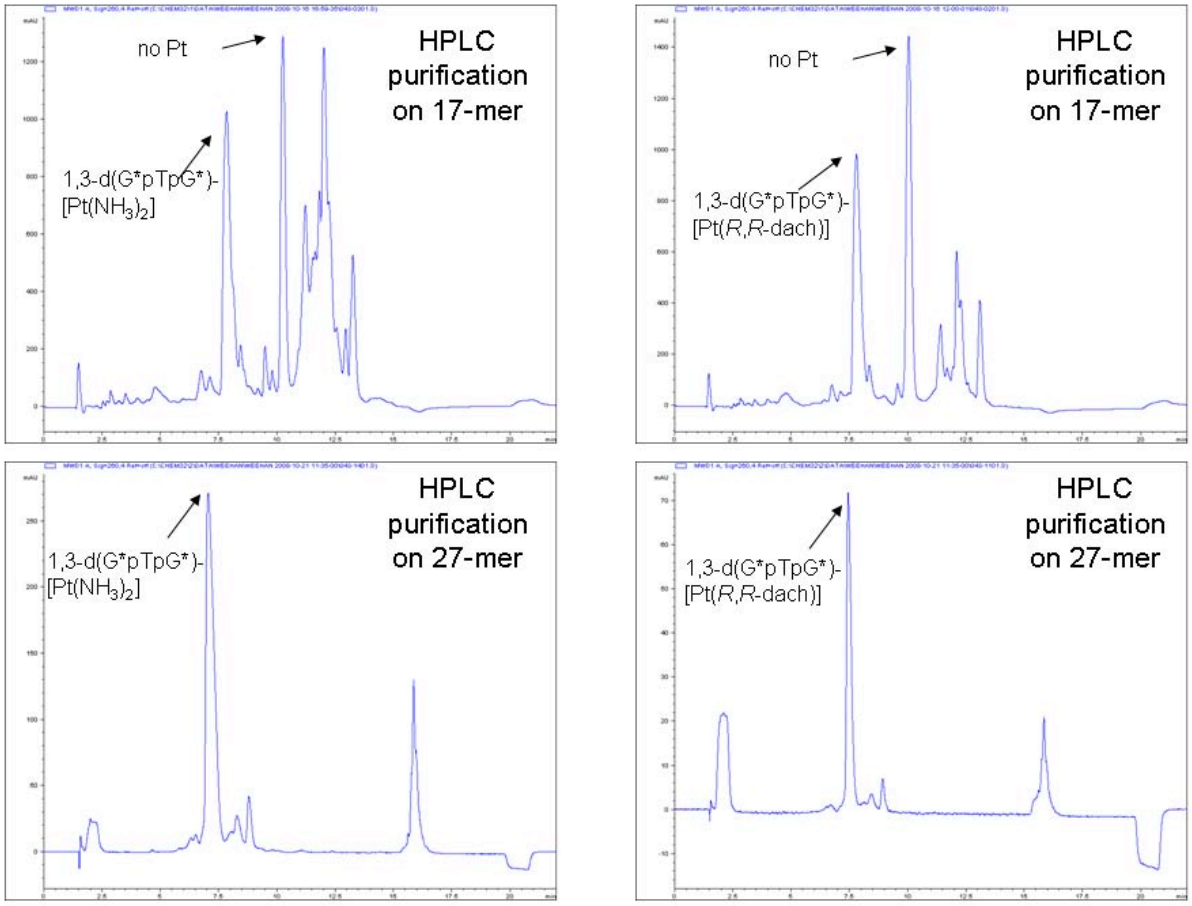

Figure S2. HPLC purification of platinated 27-mer insertion strands, 27-is-Pt (left panel) and 27-is-oxPt (right panel); top panel depicts HPLC purification of platinated 17-mer strand, bottom panel depicts denaturing HPLC purification of ligated 27-mer strands.

Table S1. Characterization of the Insertion Strand by Nucleotide Composition Analysis[a] and MALDI-TOF MS.

insertion strand	Nucleotide composition analysis								MALDI-TOF MS (m/z)	
	dC		dG		T		dA			
	obsd	calcd	obsd	calcd	obsd	calcd	obsd	calcd	obsd	calcd
13-is	6.2	6	3.0	3	2.0	2	1.8	2	3894	3895
13-is-Pt	6.1	6	1.1	1	2.0	2	1.7	2	4123	4124
13-is-oxPt	6.2	6	1.0	1	2.0	2	1.8	2	4204	4202
27-is	14.8	15	3.1	3	7.1	7	1.9	2	8022	8018
27-is-Pt	15.2	15	1.2	1	6.9	7	1.8	2	8245	8247
27-is-oxPt	15.3	15	1.0	1	7.1	7	1.6	2	8328	8325

[a]The insertion strand (500 pmol) was digested with nuclease S1 (10 U) for 12 h at 37 °C followed by calf intestinal phosphatase (10 U) for 4 h at 37 °C. Analyses of digests were carried out using reverse-phase HPLC with Supelcosil LC-18-S column; the gradient used was 5-15% B over 30 min, where solvent A contained 10 mM NaOAc and solvent B contained 100% methanol.

JUNE 2009
Volume 20, Number 6

© Copyright 2009 by the American Chemical Society

Bioconjugate Chemistry

REVIEWS

Solid-Phase Synthesis of Oligonucleotide Conjugates Useful for Delivery and Targeting of Potential Nucleic Acid Therapeutics

Harri Lönnberg*

Department of Chemistry, University of Turku, FIN-20014 Turku, Finland. Received September 23, 2008; Revised Manuscript Received November 13, 2008

Olignucleotide-based drugs show promise as a novel form of chemotherapy. Among the hurdles that have to be overcome on the way of applicable nucleic acid therapeutics, inefficient cellular uptake and subsequent release from endosomes to cytoplasm appear to be the most severe ones. Covalent conjugation of oligonucleotides to molecules that expectedly facilitate the internalization, targets the conjugate to a specific cell-type or improves the parmacokinetics offers a possible way to combat against these shortcomings. Since workable chemistry is a prerequisite for biological studies, development of efficient and reproducible methods for preparation of various types of oligonucleotide conjugates has become a subject of considerable importance. The present review summarizes the advances made in the solid-supported synthesis of oligonucleotide conjugates aimed at facilitating the delivery and targeting of nucleic acid drugs.

INTRODUCTION

Selective inhibition of gene expression by oligonucleotides, including single-stranded antisense oligonucleotides (*1*−*8*), ribozymes (*9*), and double-stranded siRNAs (*10*−*12*), shows promise as a novel form of chemotherapy, which instead of proteins uses nucleic acids as targets. In addition, aptamers (*13*) and immunostimulatory CpG-oligonucleotides (*14*) exhibit potential as therapeutic agents recognizing proteins. While some of these approaches, above all antisense and siRNA technology, are extensively used for target validation of conventional small molecule drugs, the pathway to exploitation of oligonucleotides themselves or their structural analogues as drugs has been long; despite considerable advances, several thresholds still remain to be overcome (*15*−*21*).

Among the existing problems, inefficient cellular uptake and subsequent release from endosomes to cytoplasm appear to be the most severe ones. In addition, cell type or organ specific targeting, proper intracellular distribution, and increased plasma half-lives are subjects that play a central role in development of oligonucleotide-based therapeutics.

* Corresponding author. Phone +358-2-333 6770, Fax +358-2-333 6776, E-mail: harlon@utu.fi.

[1]ABBREVIATIONS: Ac, Acetyl; All, Allyl; Alloc. Allyloxycarbonyl; Bhoc, Benzhydryloxycarbonyl; Bn, Benzyl; Boc, *tert*-Butoxycarbonyl; Bpoc, 2-(Biphen-4-yl)propan-2-yloxycarbonyl; Bz, Benzoyl; 2-ClTr, 2-Chlorotrityl; CPG, Controlled pore glass; DBU, 1,8-Diazabicyclo[5.4.0]undec-7-ene; DCM, Dichloromethane; DIPEA, *N*,*N*-Diisopropylethylamine; DMTr, 4,4′-Dimethoxytrityl; Dmab, 4-{*N*-[1-(4,4-Dimethyl-2,6-dioxocyclohexylidene)-3-methylbutyl]amino}-benzyl; Dnp, 2,4-Dinitrophenyl; Fm, 9-Fluorenylmethyl; Fmoc, 9-Fluorenylmethoxycarbonyl; HATU, *N*-[(dimethylamino)-1*H*-1,2,3-triazolo[4,5-b]pyridin-1-ylmethylene]-*N*-methylmethanium hexaflorophosphate *N*-oxide; HOBt, 1-Hydroxybenzotriazole; iBu, Isobutyryl; LDL, Low density lipoprotein; Lev, Levulinoyl; MBHA, Methylbenzhydrylamine; MMTr, 4-Methoxytrityl; MSNT, 1-(2-Mesitylenesulfonyl)-3-nitro-1*H*-1,2,4-triazolide; ODN, Oligodeoxyribonucleotide; ORN, Oligoribonucleotide; PEG, Poly(ethylene glycol); PhiPr, Phenylisopropyl (1-methyl-1-phenylethyl); Pix, 9-Phenylxanthen-9-yl; PNA, Peptide nucleic acid; PyBOP, benzotriazol-1-yloxytris(pyrrolidino)phosphonium hexafluorophosphate; RISC, RNA-induced silencing complex; TBDMS, *tert*-Butyldimethylsilyl; TBDPS, *tert*-Butyldiphenylsilyl; TBTU, *O*-(1*H*-benzotriazol-1-yl)-1,1,3,3-tetramethyluronium tetrafluoroborate; TCA, Trichloroacetic acid; TFA, Trifluoroacetic acid; Tfa, Trifluoroacetyl; THF, Tetrahydrofuran; Tol, Toluoyl; Tr, trityl.

10.1021/bc800406a CCC: $40.75 © 2009 American Chemical Society
Published on Web 01/28/2009

Scheme 1

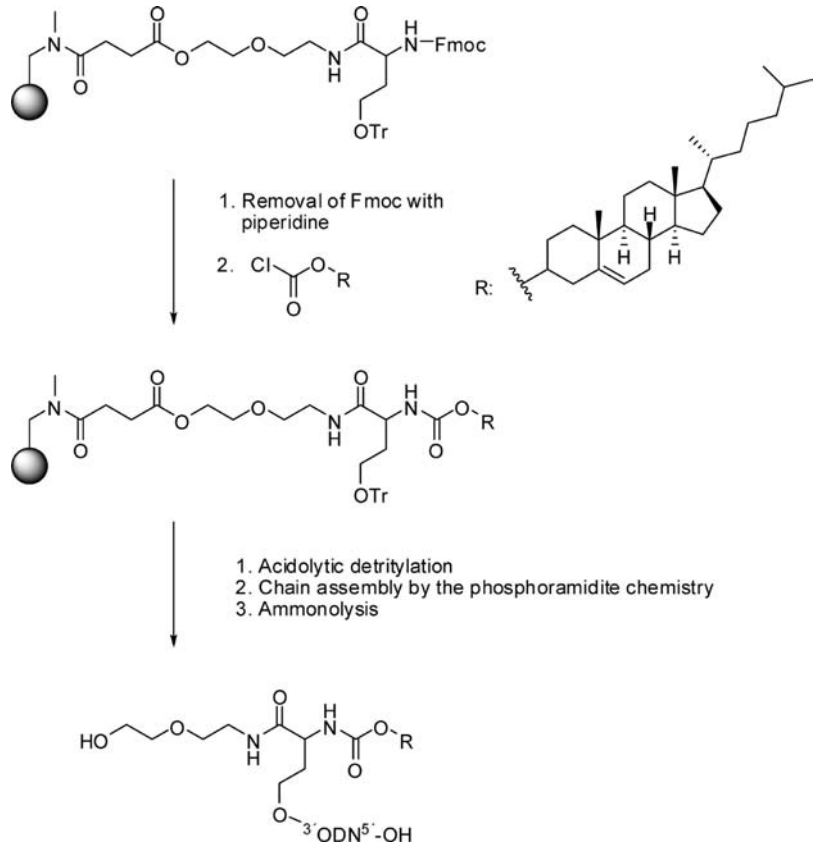

Chart 1

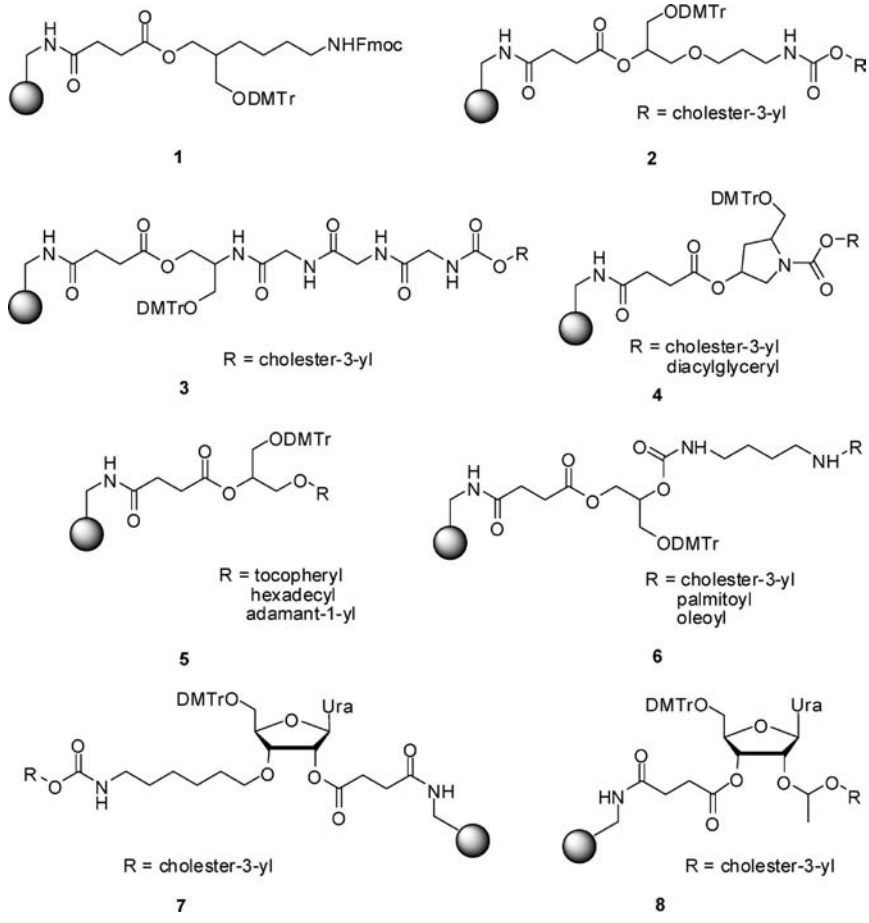

Chart 2

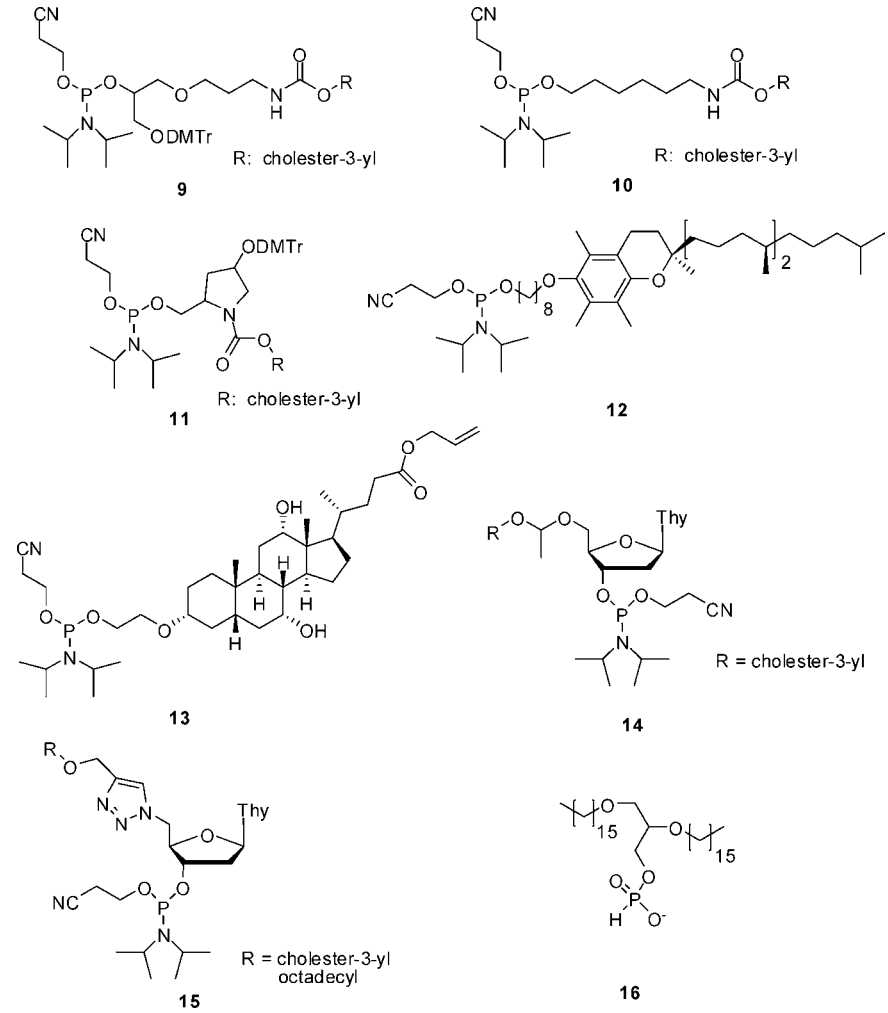

Scheme 2

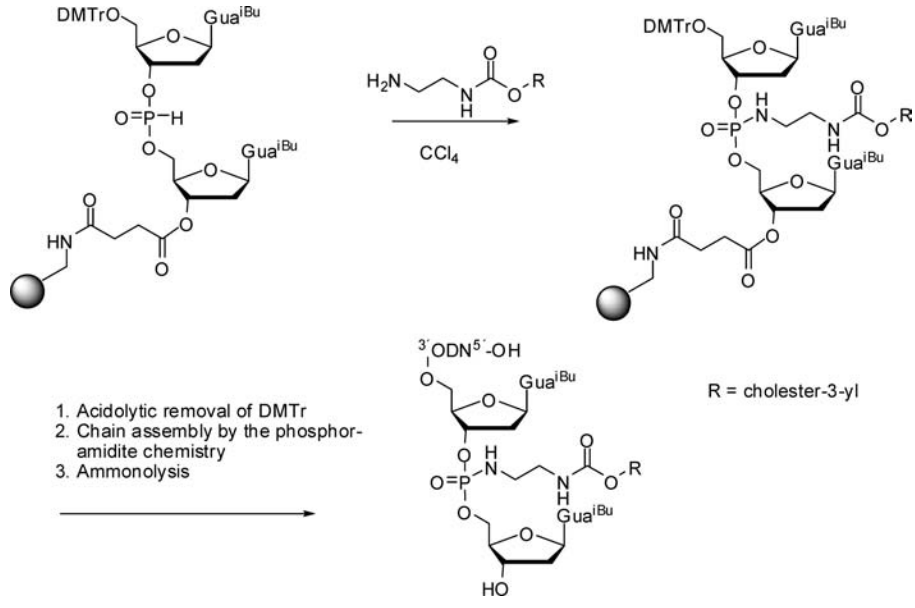

Conjugation of oligonucleotides with molecules that provide the conjugate with a desired novel property offers a feasible way to respond to these requirements. For example, oligonucleotides bearing a conjugate group known to be internalized by receptor-mediated active transport expectedly exhibit enhanced uptake compared to their nonconjugated counterparts (*22*−*24*). Cell-penetrating peptides, glycoclusters, lipids, polyamines, and numerous small molecules have all received interest as possible carriers of oligonucleotides. Although none of these approaches has so far led to a real breakthrough,

Chart 3

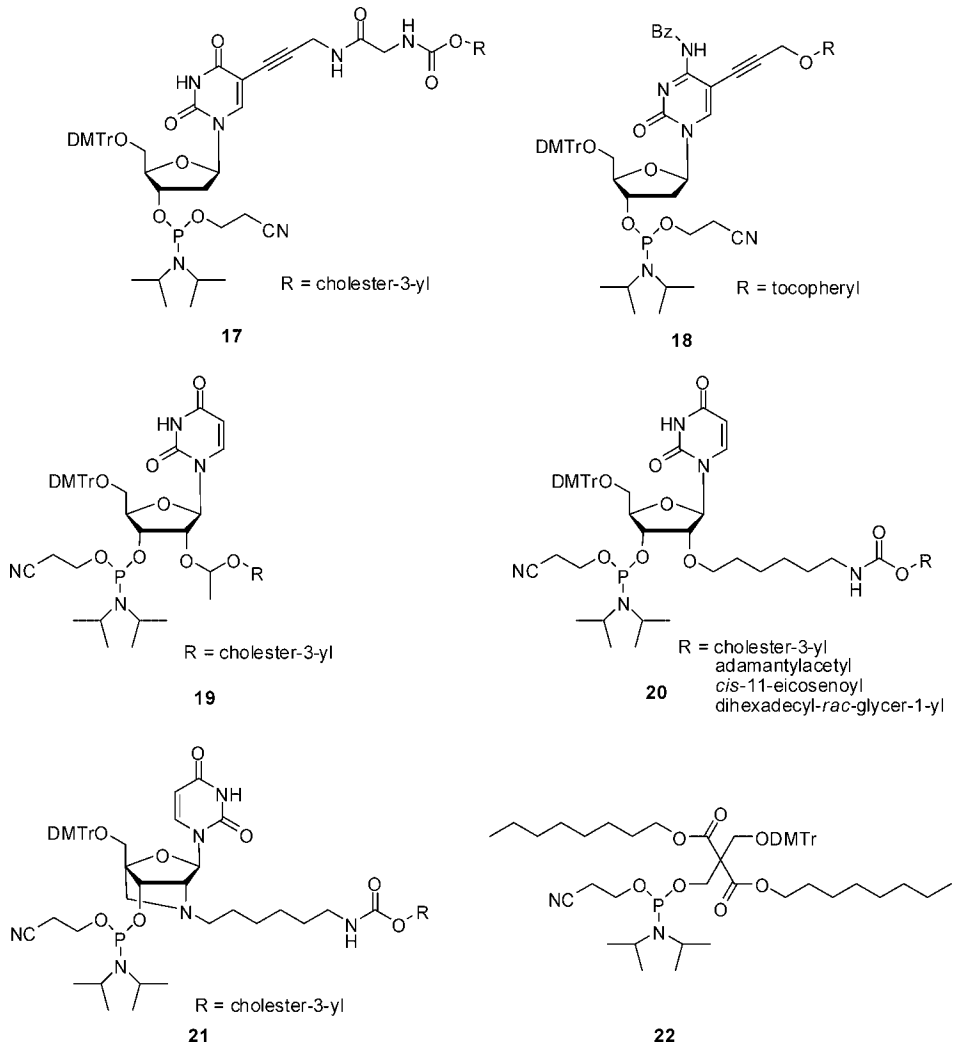

Scheme 3

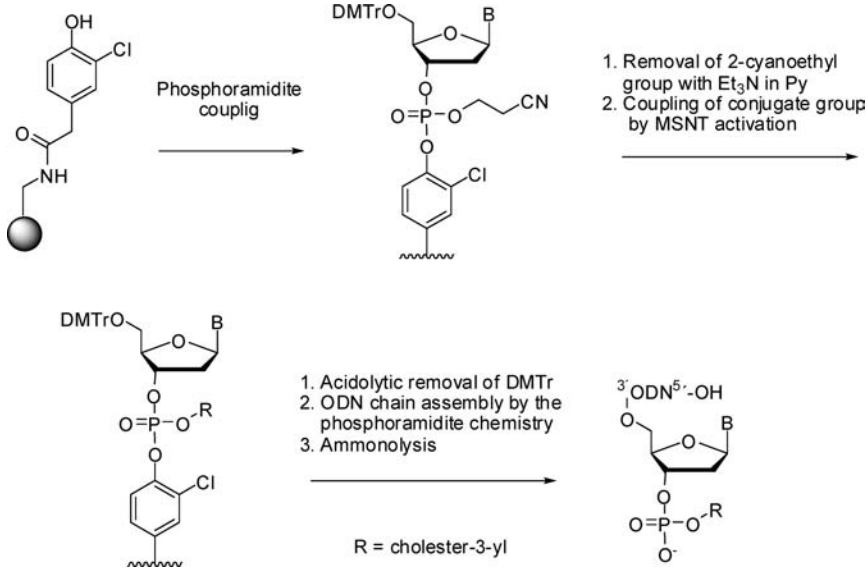

many encouraging observations have been made. Conjugation of neutral peptide nucleic acid (PNA[1]) or phosphoramidate morpholino analogues of oligonucleotides to arginine-rich peptides has been reported to significantly enhance their cellular uptake and strengthen their antisense effect (*25*−*29*). Galactosylated conjugates of oligodeoxyribonucleotide (ODN) phosphorothioates are internalized via the galactose-specific asialoglycoprotein receptor-mediated endycytosis (*30*). Poly(ethylene glycol) (PEG) conjugation has been shown to prolong the half-life in plasma (*31*), and conjugation with

Scheme 4

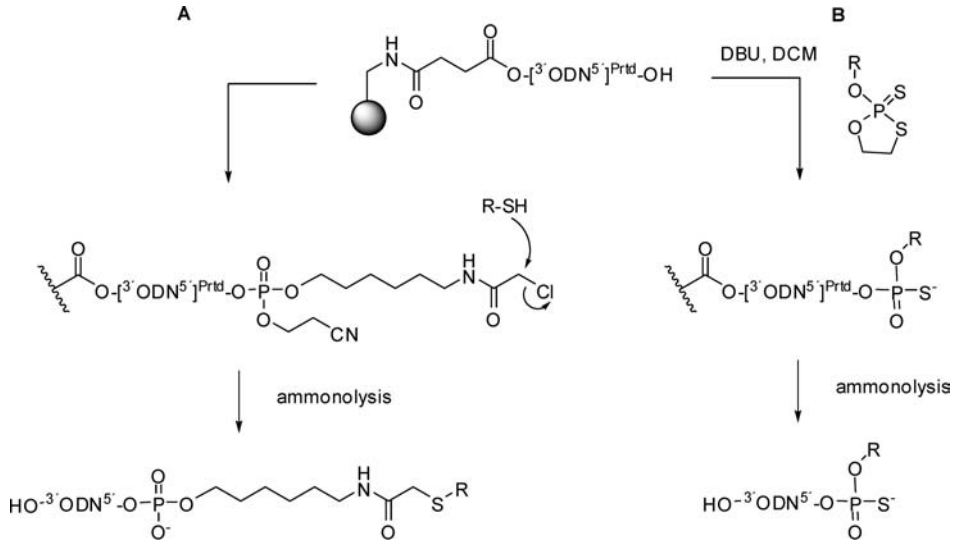

Chart 4

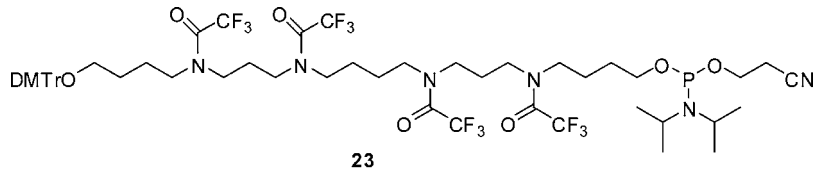

23

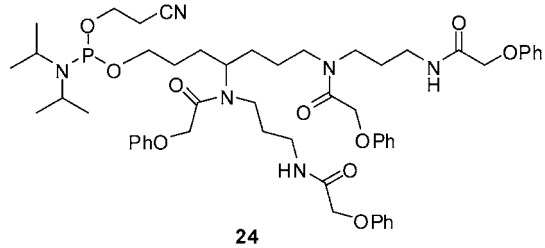

24

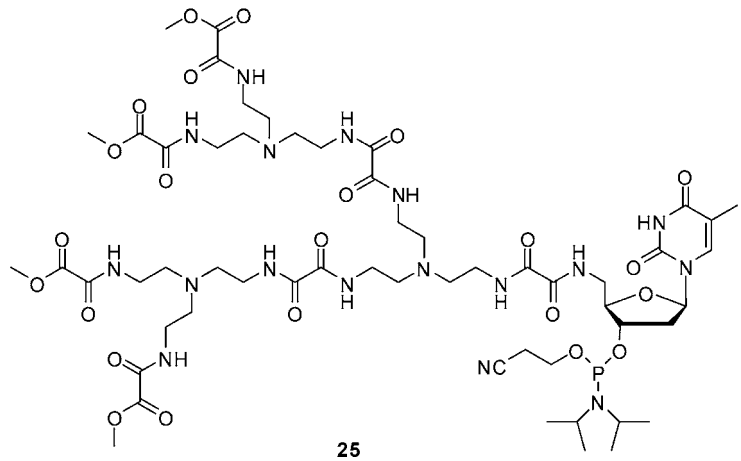

25

lipophilic groups (*32*−*34*) or aptamers (*35*) has increased the efficiency of siRNA-induced gene silencing in vivo. Owing to these and many other promising results, development of efficient and reproducible methods for convenient preparation of various types of oligonucleotide conjugates has become a subject of considerable importance. Workable chemistry is a prerequisite for extensive biological studies.

The methods used for the preparation of oligonucleotide conjugates fall in two major categories: solution- and solid-phase conjugation. On applying the solution-phase approach, the oligonucleotide is at some stage of its solid-phase synthesis equipped with an appropriate functionality, to which the conjugate group is coupled in solution after release and purification of the oligonucleotide. When the solid-phase methodology is used, the entire conjugate is assembled on a single support, either by conjugation of a prefabricated conjugate group or by assembling the conjugate moiety by a stepwise process prior to or after the oligonucleotide synthesis. The advantage of the solid-supported method compared to conjugation in solution is a less laborious

Chart 5

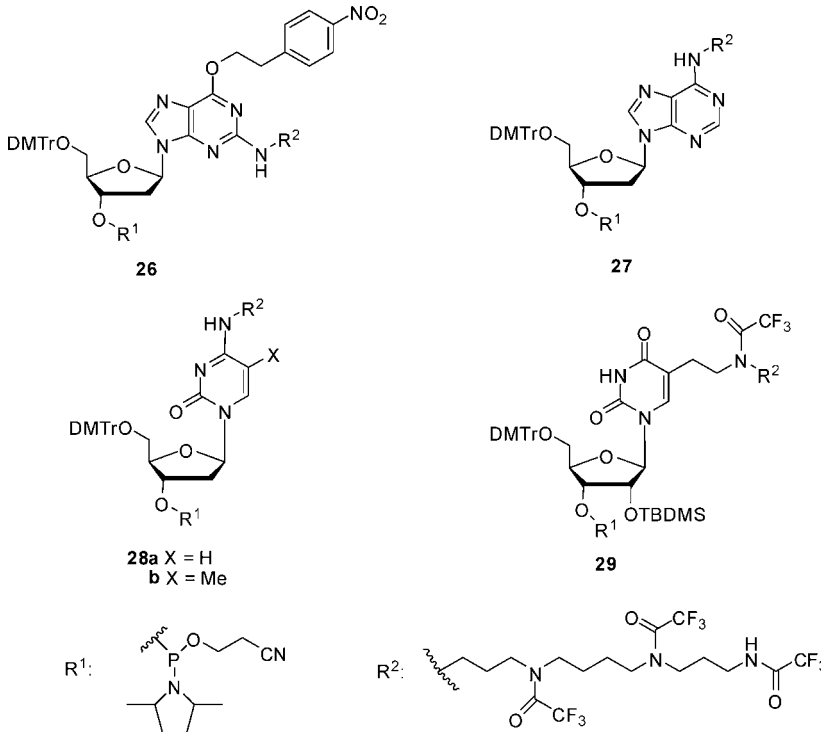

purification. To achieve high coupling efficiency, the conjugate group is usually used in considerable excess, which complicates the purification when the conjugation is carried out in solution. By contrast, on a solid support, the unreacted conjugate group and the possible side products may be removed by simple washing, which markedly facilitates the chromatographic purification after release from the support. The use of a solid support may also help to avoid the problems otherwise arising from limited solubility of one of the reactants.

The present paper reviews the methods described for the solid-supported synthesis of oligonucleotide conjugates useful for delivery and targeting of potential nucleic acid therapeutics. Accordingly, preparation of oligonucleotides conjugated with lipids, polyamines, peptides, carbohydrates, PEG, and some small molecules are discussed. In addition, synthetic procedures for oligonucleotides bearing biodegradable or thermolabile phosphate protecting groups are summarized.

HYDROPHOBIC CONJUGATES

Since the hydrophobic interior of the phospholipid bilayer forms the main obstacle to internalization of polyanionic oligonucleotides, it is quite natural that conversion of oligonucleotides to their lipid conjugates has long received interest as a possible method to enhance their cellular uptake (*36*). Reduction of the hydrophilic nature of the oligonucleotide is not, however, the only reason for lipid conjugation. Some hydrophobic pendants, above all cholesterol, are believed to bind to lipoproteins and particles of low-density lipoproteins (LDL), a cholesterol transporter in blood. Consequently, the cholesterol conjugate becomes recognized by hepatitic cells (*37*−*39*) and, hence, internalized by lipoprotein-mediated endocytosis. As mentioned above, conjugation with cholesterol has been shown to increase the efficacy of siRNA-induced silencing of the apoB mRNA gene in rodents' liver and jejunum (*32*).

The hydrophobic conjugates of oligonucleotides are usually obtained by one of the following solid-phase approaches: (i) 3′-conjugates by chain assembly on a support bearing the desired conjugate group, (ii) 5′-conjugates by introduction of the conjugate group as a phosphoramidite reagent, and (iii) intrachain conjugates by making use of prefabricated nucleosidic building blocks or their congeners incorporating the conjugate group. Scheme 1 shows an illustrative example of the preparation of the 3′-conjugates. A branched alcohol bearing orthogonally protected amino and hydroxyl groups is attached to the support via a succinyl linker. The conjugate group bearing a hydroxyl function is first attached to the deprotected amino group of this handle as a chloroformate ester, and the ODN is then assembled on the deprotected hydroxyl function (*40*). Support **1** (Chart 1) had earlier been used similarly (*41*). While in these cases a stepwise immobilization has been applied to obtain the cholesterol bearing support, related supports have more often been prepared by immobilization of a prefabricated linker−cholesterol conjugate (*34*, *42*−*48*). Among these, support **6** has been used for construction of oligoribonucleotide (ORN) conjugates (*34*) and **2**−**5** for the synthesis of ODN conjugates. Supports **4** derived from *trans*-L-hydroxyprolinol have additionally been used for the preparation of ODN conjugates of many other steroids and diacylated glycerols (*49*). 2′-*O*- (*50*) and 3′-*O*-succinylated uridine (*51*), **7** and **8**, conjugated with cholesterol via the remaining secondary hydroxyl function represent still another type of support utilized for preparation of the 3′-terminal conjugates.

Chart 2 shows the structures of the phosphoramidite (**9**−**15**) and H-phosphonate (**16**) reagents, both non-nucleosidic and nucleosidic ones, used to introduce hydrophobic conjugate groups into the 5′-terminus of ODNs (*46*, *47*, *49*, *51*−*55*). Building block **13** deserves special attention. This phosphoramidite reagent derived from the allyl ester of 3-α-(2-hydroxyethoxy)cholic acid is obtained by selective phosphitylation of the primary hydroxyl group with 1.1 equiv of 2-cyanoethyl-*N*,*N*-diisopropylphosphorochloridite without interference of the secondary hydroxyl functions (*54*). The allyl protection may then be removed on-support with $Pd[PPh_3]_4$. 5′-Palmitoyl ODNs have been obtained by using base-labile *t*-butylphenoxyacetyl protecting groups for base moiety amino functions and oxalyl

Scheme 5

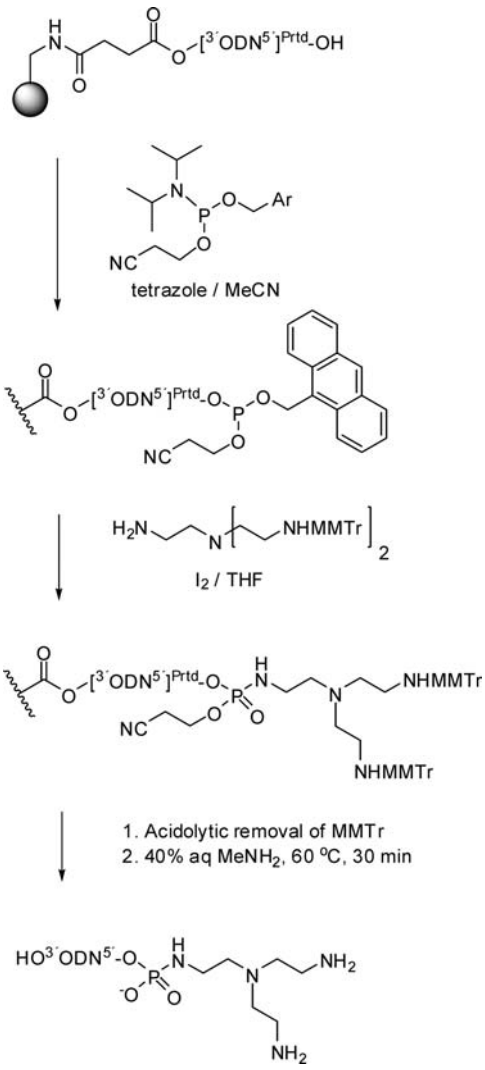

linker. These modifications to the standard phosphoramidite strategy allow mild deprotection with ethanolamine, and hence, the 5′-ester linkage remains intact (*56*).

Incorporation of hydrophobic groups into intrachain positions of the oligonucleotide chain is usually performed with the aid of prefabricated nucleosidic or non-nucleosidic building blocks. The nucleosidic building blocks exploited include the phosphoramidites of C5-derivatized pyrimidine 2′-deoxyribonucleosides (**17**, **18**) (*57, 58*), 2′-*O*-derivatized uridine (**19**, **20**) (*50, 51*), and a thymine amino-LNA monomer (**21**) (*59*). Several hydrophobic conjugate groups including cholesterol (*50, 57, 59*), α-tocopherol (*58*), adamantanylacetic acid (*50*), long chain fatty acids (*50*), and diacylglycerol (*50*) have been introduced in this manner (Chart 3). A prolonged coupling time is required to couple the lipidated block (*57, 58*). Octyl groups have been incorporated into ODNs using a phosphoramidite building block derived from dioctyl 2,2-bis(hydroxymethyl)malonate (*60*). Again, a prolonged coupling time (10 min) is required for high coupling yield (>98%) and the subsequent detritylation has to be carried out with TFA. Interestingly, the ester linkages at internucleosidic positions withstand normal ammonolysis.

Besides exploitation of prefabricated solid supports and phosphoramidite reagents bearing the conjugate group, several on-support conjugation procedures have been reported. In fact, the first solid-phase synthesis of a cholesterol conjugate is a nice example of such an approach, involving oxidative phosphoramidation of a support bound dinucleoside-3′,5′-(*H*-phosphonate) with CCl_4 in the presence of cholester-3-yloxycarbonylaminoethylamine and subsequent assembly of the ODN chain (Scheme 2) (*61*). Interestingly, one of the very recent approaches follows a related principle. Instead of conventional succinyl linker, an aminoalkyl support is acylated with 3-chloro-4-hydroxyphenylacetic acid, and the 3′-terminal nucleoside is coupled to the hydroxyl function by the normal phosphoramidite chemistry (Scheme 3) (*62*). The 2-cyanoethyl protection is then removed with triethylamine in pyridine (1 h, 50 °C) and the conjugate group, e.g., cholesterol, is coupled to the exposed phosphodiester linkage by the phosphotriester chemistry. On using MSNT as an activator, the coupling yield has been reported to range from 75% to 80%. The ODN chain is then assembled by phosphoramidite chemistry. Upon ammonolysis, only the ODN bearing the conjugate group is released from the support, since the phosphodiester linkage is not cleaved by ammonolysis, not even when aryl pohosphodiesters are concerned. It is also possible to remove the 2-cyanoethyl protection and assemble the ODN chain prior to the introduction of the conjugate group. In case one wishes to conjugate amines instead of alcohols, the phosphodiester linkage is first tosylated, and a nucleophilic displacement with the amine is then carried out.

Chart 6

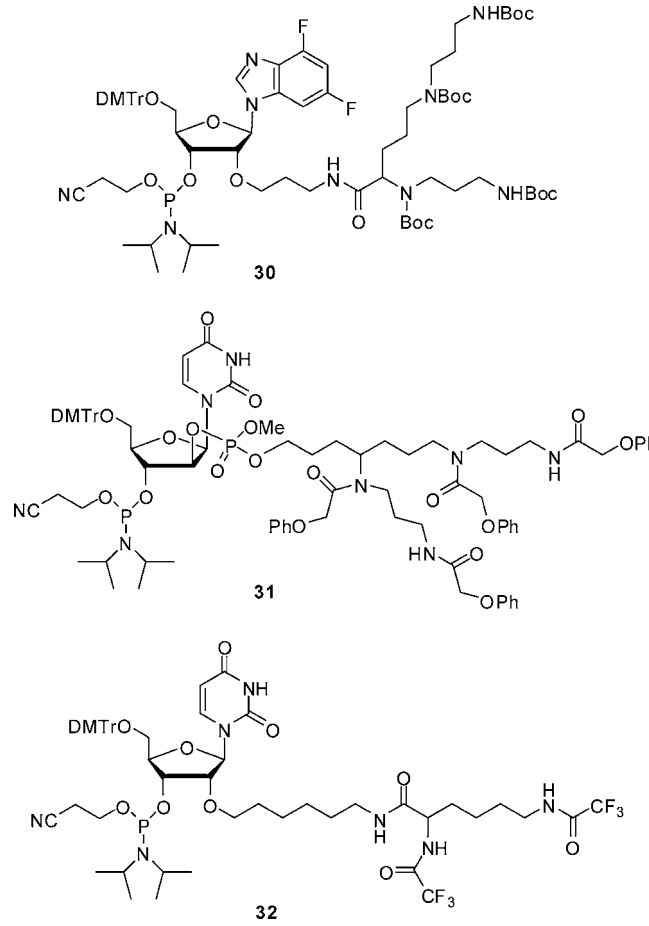

Thiocholesterol has been conjugated to the 5′-terminus of a support-bound ODN by elongation of the chain with 6-chloroacetamidohexanol phosphoramidite and displacing the chloro substituent with thiocholesterol in dioxane in the presence of DBU. Normal ammonolysis then releases the conjugate (Scheme 4A) (*63*). Long chain aliphatic alkyl groups and small aromatic groups have been introduced similarly. Several lipophilic alcohols, including cholesterol, borneol, menthol, and heptadecanol, have been converted to 2-alkoxy-2-thiono-1,3,2-oxathiaphospholane and reacted in DCM in the presence of DBU with

Chart 7

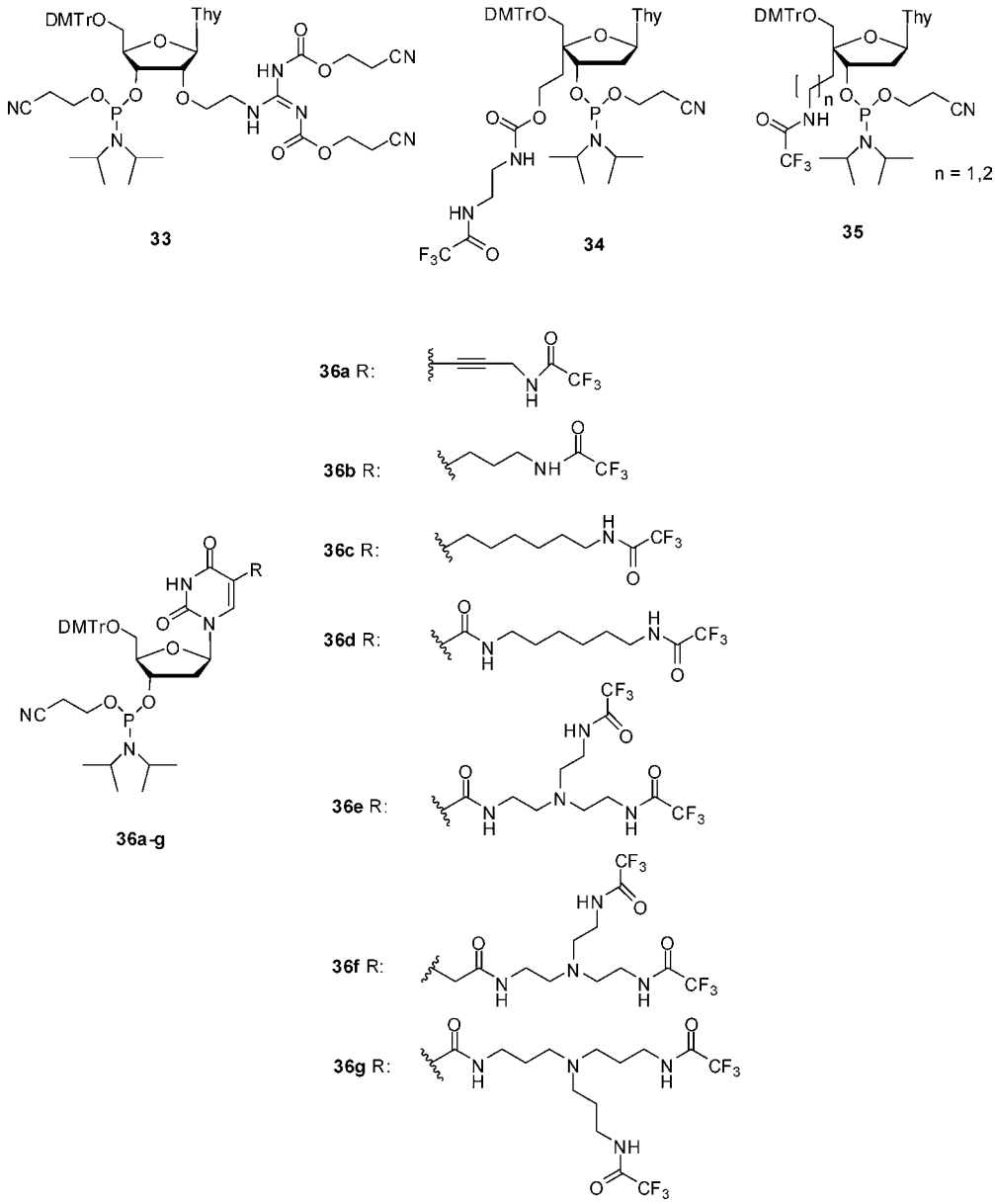

the 5′-hydroxy group of a support-bound ODN (Scheme 4B) (*64*). Again, a normal ammonolysis is finally carried out.

Masking of the internucleosidic phosphodiester bonds of an antisense oligonucleotide with biodegradable or thermolabile protecting groups represent another type of utilization of hydrophobic conjugate groups. The most extensively studied examples are *S*-acyl-2-mercaptoethyl and alkoxymethyl-protected ODNs. The former pro-oligonucleotides have been assembled by the phosphoramidite chemistry using *S-tert*-butyl-2-mercaptoethyl-*N*,*N*-diisopropylphosphoramidites instead of the 2-cyanoethyl protected ones (*65*). Since the phosphotriester linkages do not withstand ammonolysis, the base moiety acyl protecting groups have been replaced with photolabile 6-nitroveratryloxycarbonyl or 2,2′-bis(2-nitrophenyl)ethoxycarbonyl group, and the synthesis has been carried out on a photolabile 1-(2-nitrophenyl)-1,3-propanediol linker. For the *S*-acetyl-2-mercaptoethyl protected oligomers, three alternative strategies have been proposed. First, the chain assembly has been carried out on a photolabile linker, but the base moieties have been protected with a Pd(0)-labile allyloxycarbonyl group and those phosphodiester linkages that do not bear a 2-methylthioethyl group with an allyl group (*66*). Second, fluoride-ion-labile protections, viz., 4-(*tert*-butyldiphenylsilyloxymethyl)benzoyl group for the base moieties and 2-(trimethylsilyl)ethyl group for the phosphate moieties, have been used (*67*). When the oligomer is assembled on a phosphoramidate linker, it is released by the $Et_3N\cdot(HF)_3$ treatment used to remove the base and phosphate protections. The third alternative is chain assembly on a disulfide linker using building blocks that bear 2-(trimethylsilyl)ethoxycarbonyl protections on nucleobases and 2-(trimethylsilyl)ethyl protection on phosphate moieties (*68*). The base moiety and phosphate protections are removed by a single $ZnBr_2$-treatment on the support and the deprotected oligomer is released reductively into the solution. *O*-(4-Acyloxybenzyl)phosphorothioate linkages have also been site-specifically introduced into oligonucleotides by the phosphoramidite strategy using building blocks bearing a 4-acyloxybenzyl group instead of the 2-cyanoethyl group. *N*-Pent-4-enoyl group, cleaved upon release of the oligomer from the support with methanolic K_2CO_3, has been used for the base moiety protection (*69*). 3-Pivaloyloxy-2,2-bis(ethoxycarbonyl)propyl protections have been introduced into ODNs as prefabricated dimeric phosphoramidite reagents (*70*).

Scheme 6

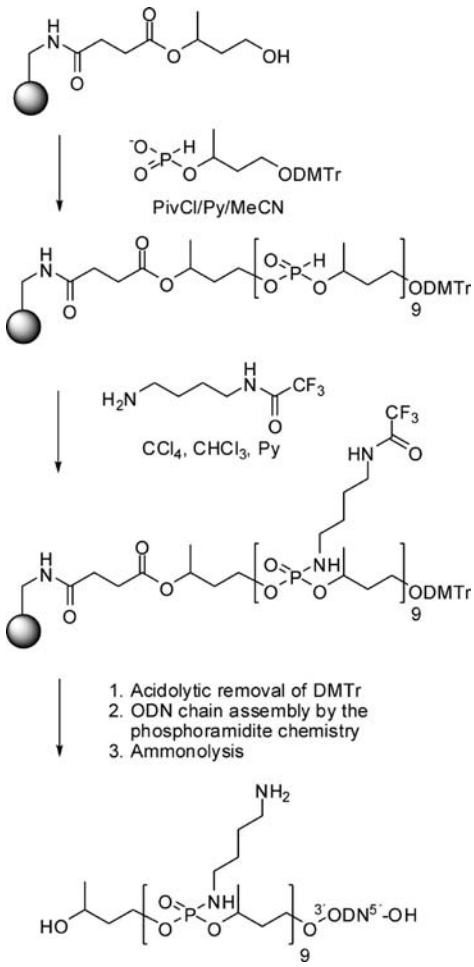

All the pro-oligonucleotides discussed above bear esterase-labile protecting groups. In addition, oligonucleotides bearing spontaneously cleavable phosphate protections have been suggested to be viable antisense prooligonucleotides. For this purpose, ODNs bearing 3-hydroxypropyl (*71*), 4-hydroxybutyl (*71*), or *N*-formyl-*N*-methyl-2-aminoethyl (*72*) protecting groups on selected internucleosidic phosphodiester linkages have been prepared. The departure of all these groups is based on thermolytic cyclization. For the synthesis, conventional phosphoramidite chemistry may be applied when nucleoside 3′-(*N*,*N*-diisopropylphosphoramidites) bearing the desired protecting groups are used and normal ammonolysis is replaced by treatment with pressurized ammonia at 25 °C.

POLYAMINE CONJUGATES

Polyamines, being positively charged at physiological pH, form complexes with negatively charged oligonucleotides. These complexes, known as polyplexes, interact with the negatively charged phospholipids of the cell membrane and, hence, enhance the cellular uptake (*73*). Dendrimeric polyamines, for example, are extensively used as transfection agents for plasmids, but also for siRNA and oligonucleotides. Accordingly, it is no surprise that covalent polyamine−oligonucleotide conjugates have received attention as potential facilitators of the delivery of therapeutic oligonucleotides. In addition, it is worth noting that some oligoamines, such as spermine and spermidine, are naturally occurring metabolites known to complex in cells with RNA (*74*), and they may, hence, affect the biodistribution of their oligonucleotide conjugates.

Oligoamines, either linear or branched, are usually attached to the 5′-terminal hydroxyl function of the chain, to a C5 site

Scheme 7

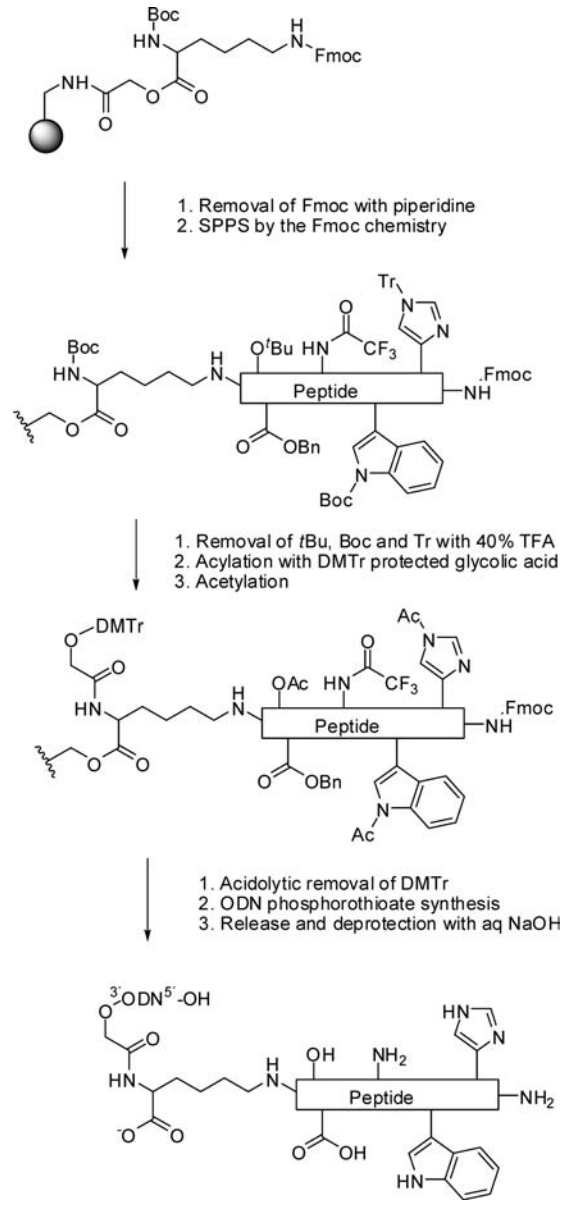

of a pyrimidine base or to 2′-*O* of a ribonucleoside unit. Up to 6 α,ω-bis(4-hydroxybutyl)spermine molecules have been incorporated as trifluoroacetyl protected phosphoramidite reagents (**23**; Chart 4) into the 5′-terminus of ODNs, giving a long linear spermine−phosphate tail (*75*). The coupling efficiency of these building blocks has been reported to be as high as 90−96%. Standard ammonolysis is adequate to remove all trifluoroacetyl protections. A single C-branched spermine has been incorporated as a phenoxyacetyl protected phosphoramidite reagent (**24**) (*76*, *77*). More complex 5′-terminal polyamine structures have been constructed by coupling a 5′-amino-5′-deoxythymidine phosphoramidite bearing a spruce-like methoxyoxalamido-functionalized polyamine (**25**) as the last building block of the chain assembly. Upon release and deprotection of the conjugate with a primary amine, e.g., spermidine or histidine, each branch becomes further derivatized with this amine by formation of oxalyldiamide linkages (*78*). Tetrazole activation with 15 min reaction time has been used for coupling of this highly branched block.

Several spermine moieties have been incorporated into ODNs with the aid of appropriately protected phosphoramidites of N^2-derivatized 2′-deoxyguanosine (**26**; Chart 5) (*79*, *80*), N^6-

Chart 8

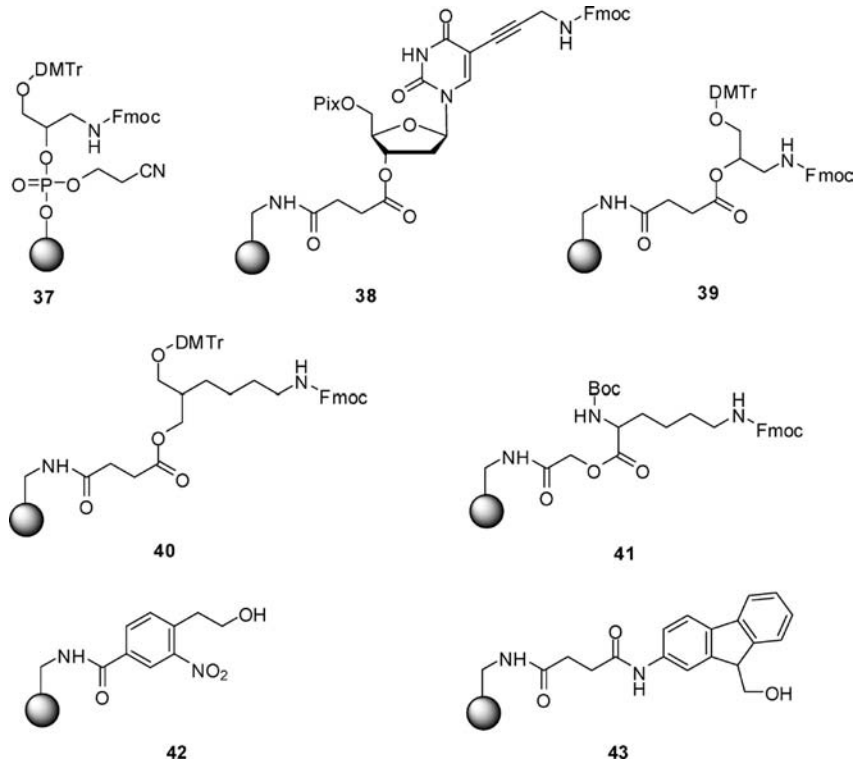

derivatized 2′-deoxyadenosine (**27**) (*80, 81*), and N^4-derivatized 2′-deoxycytidine (**28a**) (*82*) and its 5-methyl analogue (**28b**) (*83*). The cytidine derivative coupled as well as the unmodified 2′-deoxynucleoside building blocks, but for the guanosine derivative, repeated coupling and prolonged coupling time (10 min) had to be applied to obtain a coupling efficiency of 95%. Into ORNs, spermine moieties have been incorporated with a C5-modified 5′-*O*-DMTr-2′-*O*-TBDMS-uridine 3′-phosphoramidite building block (**29**) (*84*). A coupling efficiency of 96% has been achieved by using 5-benzylthiotetrazole as an activator.

Besides the phosphoramidite chemistry, oligoamines have been introduced into oligonucleotides by on-support nucleophilic displacement and oxidative amidation. 5-Methoxycarbonylmethyl-2′-deoxyuridine (*85*) or 2-fluoro-2′-deoxyinosine (*86*) has been incorporated into a desired site of the sequence, and treatment with sperimine has then resulted in conjugation by aminolysis of the methoxycarbonyl group upon release and deprotection of the conjugate. Similarly, treatment of the electrophilic conjugate depicted in Scheme 4A with spermine gives the desired oligoamine conjugate (*63*). Spermine can be used as a cleaving agent in an unprotected form, since the primary amino group is a much more efficient nucleophile than the secondary one. A branched oligoamine, N^1,N^1-bis(2-aminoethyl)ethane-1,2-diamine, has, in turn, been conjugated by oxidative amidation (*87*). For this purpose, the 5′-hydroxy function has been phosphitylated with (anthracen-9-yl)methyl 2-cyanoethyl *N*,*N*-diisopropylphosphoramidite and oxidation with I_2 in THF in the presence of the appropriately protected amine has then been carried out (Scheme 5). 98% of the (anthracen-9-yl)methyl group becomes oxidatively displaced with the amine. A special feature of this kind of conjugation is that the phosphoramidate linkage is acid-labile and may, hence, be cleaved, although expectedly quite slowly, at the relatively low pH of endosomes (pH 5).

Another possible way to introduce several aliphatic amino groups into an oligonucleotide is incorporation of several modified nucleosidic building blocks, each bearing a single amino group, into the chain along its entire length. 2′-*O* has been regarded as an appropriate site for tethering of aminoalkyl groups, since 2′-*O*-alkylated oligonucleotides hybrizide even better than their 2′-deoxy counterparts (*88*). In addition, the catalytic argounaut proteins within the RISC complex appear to tolerate well 2′-*O*-modifications of siRNA (*89*). All canonical ribonucleosides have been prepared as 2′-*O*-(*N*-phthaloyl-3-aminopropyl) derivatives and introduced into oligonucleotides as appropriately protected phosporamidites (*90*). The oligonucleotides prepared contained long, contiguous sequences of the aminoalkylated nucleosides. A coupling efficiency of 98.5% has been achieved by repeated coupling steps. In addition to normal ammonolysis, a treatment with 10% aq methylamine has been applied to remove the phthaloyl protections. Several contiguous 2′-*O*-(3-dimethylaminopropyl)- (*91*) and 2′-*O*-[2-(2-dimethylaminoethoxy)ethyl]-5-methyluridine (*92*) blocks have been introduced without any amino protection, whereas 2′-*O*-(6-aminohexyl)-adenosine and -uridine blocks have been inserted as trifluorocetamides (*93*).

The shortcoming of the attachment of bulky groups to 2′-*O*, however, is reduced coupling efficiency. For example, the phosphoramidite **30** (Chart 6) bearing a bulky Boc-protected carboxyspermine has been reported to couple only in 40% yield (*88*). By contrast, phosphoramidite **31**, having an *ara* configuration and bearing a branched phenoxyacetyl protected spermine attached to the 2′-*O* via a phosphotriester linkage, has been observed to couple without marked difficulty (*76*, *77*). Oligonucleotides bearing up to five contiguous 2′-*O*-(*N*-lysyl-6-aminohexyl)uridines (**32**), introduced in *N*-trifluoroacetylated form, have been successfully assembled on a solid support by using extended coupling times (*94*, *95*). Like amino groups, guanidinium groups remain protonated and, hence, positively charged at physiological pH. ODNs bearing 2′-*O*-[2-(guanidinium)ethyl] groups have been prepared by using phosphoramidite **33** (Chart 7), where the guanidinium moiety is protected with 2-cyanoethoxycarbonyl groups (*96*). *tert*-Butylhydroperoxide or 1-*S*-(+)-(10-camphorsulfonyl)oxaziridine has been used for the oxidation and the 2-cyanoethoxycarbonyl groups have been removed with piperidine before normal ammonolysis to

Scheme 8

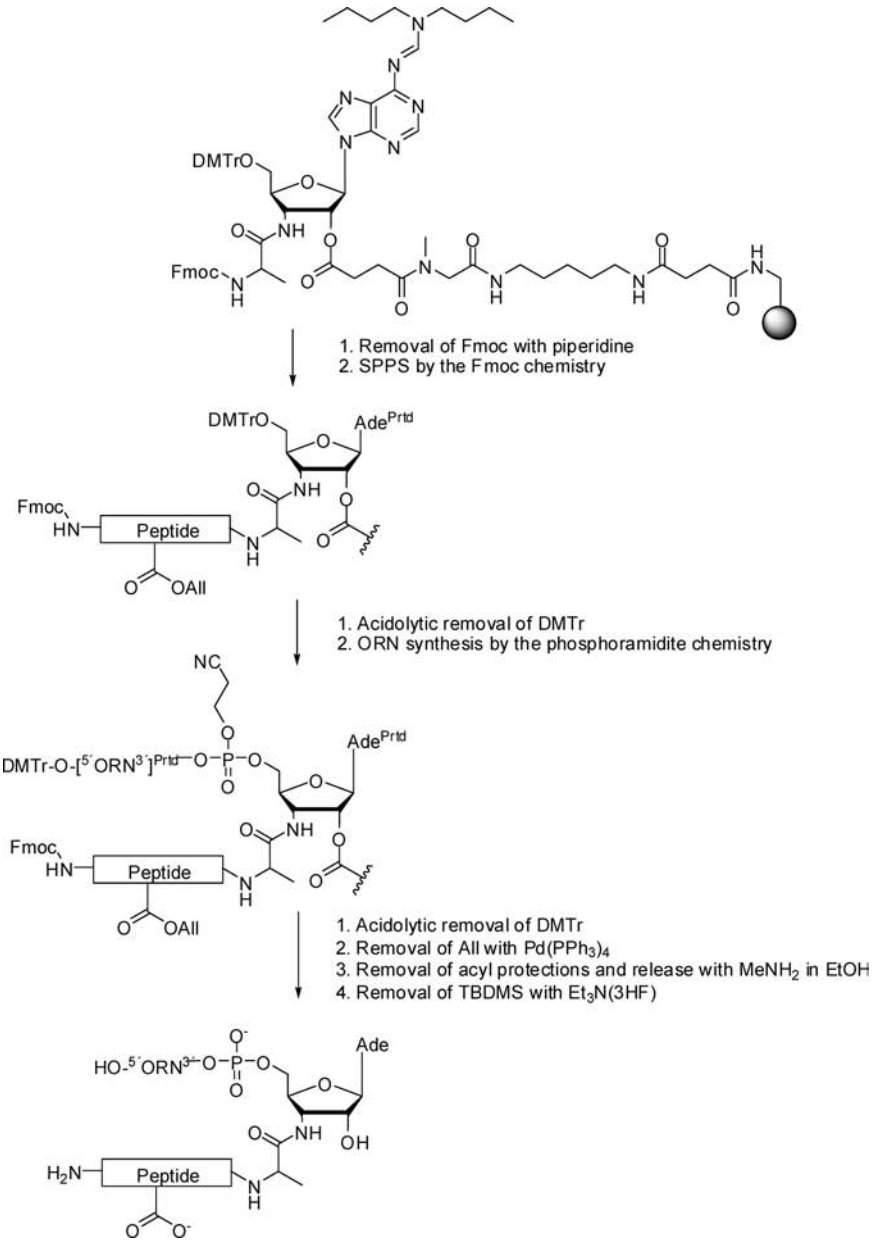

prevent cyclization of the guanidinium group to triazine. Aminoalkyl groups have also been tethered to C4′ of thymidine, and several such modified nucleosides (**34**, **35**) have been incorporated into ODNs by the phosphoramidite chemistry (*97, 98*). A 96% coupling efficiency has been achieved on using a prolonged coupling time (6 min) and a high phosphoramidite concentration (1.2 mol L^{-1}).

Besides the sugar hydroxyl functions, C5 of pyrimidine nucleosides has been used as a site for the attachment of aminoalkyl groups. Several 2′-deoxyuridines and 2′-deoxycytidines bearing linear (*99*−*102*) or branched (*103, 104*) aminoalkyl side chains at C5 have been incorporated into ODNs by normal phosphoramidite chemistry. Immobilization of the corresponding nucleosides to an aminoalkylated solid support via a succinyl linker has allowed synthesis of conjugates having the 3′-terminal nucleoside modified also (*100, 103, 105*). Additionally, a postsynthetic approach has been applied to obtain aminoalkyl-derivatized oligonucleotides. 5-(Methoxycarbonyl)-2′-deoxyuridine has first been introduced into the ODN chain, and treatment with ethane-1,2-diamine or hexane-1,6-diamine has then resulted in aminolysis of the methoxycarbonyl function to an ω-aminoalkylcarbamoyl function upon the release and deprotection of the conjugate (*106*).

ODNs bearing an aminoalkylated phosphoramidate tail at the 3′-terminus have been prepared by assembling first a non-nucleosidic backbone for the tail from 3-DMTrO-1-methylpropyl H-phosphonates and oxidizing the H-phosphonate diester linkages obtained with CCl_4 in the presence of *N*-trifluoroacetylbutane-1,4-diamine (Scheme 6). The oligonucleotide chain is then assembled by phosphoramidite chemistry (*107*). Similarly, ODNs bearing a 5′-polyimidazole tail have been prepared by consecutive coupling of several 4-DMTrO-butyl H-phosphonates to the 5′-terminus of an otherwise fully protected support-bound ODN and subsequent oxidation with CCl_4 in the presence of histamine (*108*).

PEPTIDE CONJUGATES

Some rather short peptides have been discovered to translocate across cell membranes, partly by endocytic processes but partly by endocytosis-independent cytoplasmic entry (*109*). Such peptides usually are Arg- or Lys-rich. The two naturally

Scheme 9

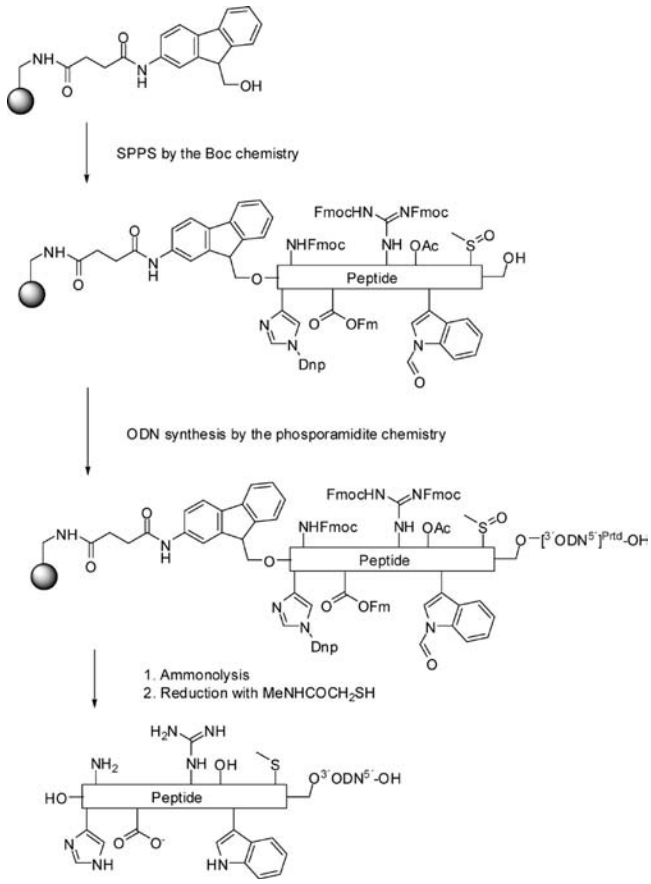

Scheme 10

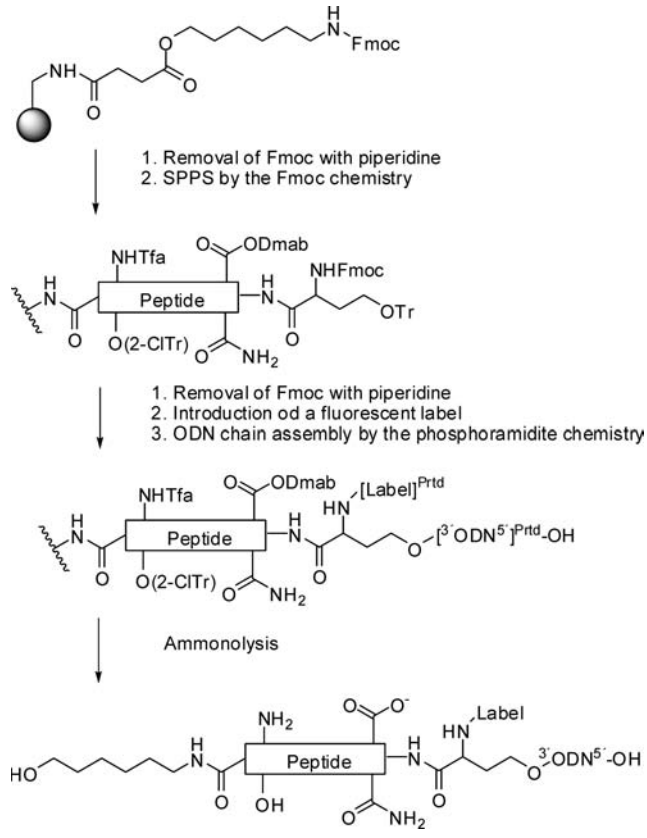

occurring sequences, Penetratin and Tat peptide, and a synthetic hybrid, Transportan, of two naturally occurring sequences are

Scheme 11

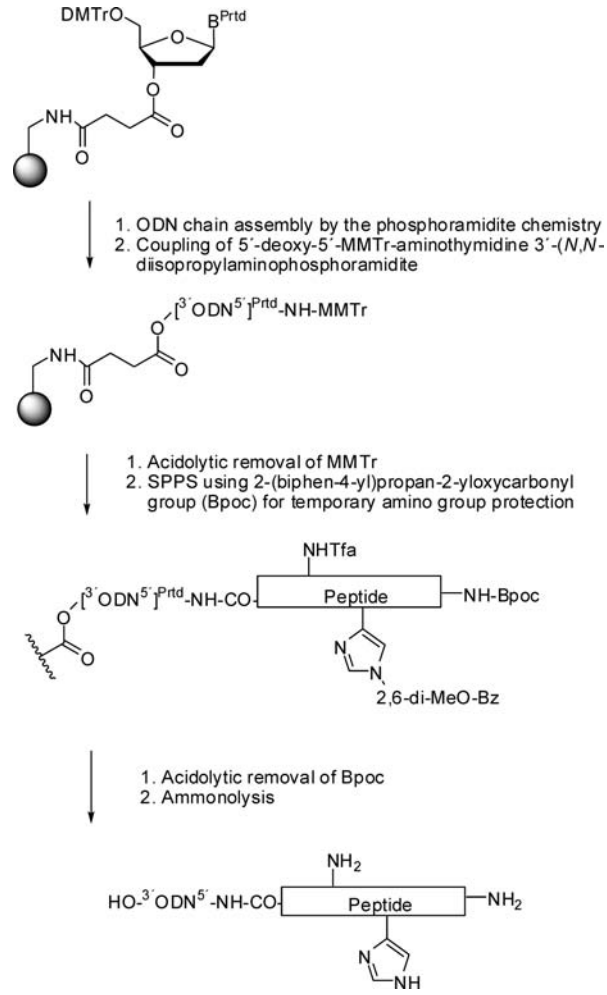

the best-known examples (*110*). Conjugation of antisense oligonucleotides with these cell-penetrating peptides has received wide interest as a possible way to enhance their delivery into cells (*111*−*113*). In addition, conjugation with nuclear localization signal peptides has been studied as a means to affect the intracellular distribution of oligonucleotides (*114*). It is not, hence, surprising that synthesis of peptide conjugates has been the subject of more intensive studies than any other category of oligonucleotide conjugates. The progress of the field has been reviewed every few years (*115*−*119*). In the present review, attention is only paid to alternative approaches of solid-supported synthesis and, in particular, to novel approaches applicable to preparation of reasonably long peptide conjugates. The solution-phase conjugation of prefabricated peptides and oligonucleotides bearing mutually reactive functionalities is not discussed, although such methods are often highly useful and still more extensively used than solid-phase syntheses (*116*−*118, 120*).

Although the solid-phase synthesis of both oligonucleotides and peptides is well-established, assembly of oligonucleotide−peptide conjugates from monomeric units on a single support still is a considerable challenge. The existing protocols of oligonucleotide synthesis are largely based on acid-labile temporary protection and base-labile global protection, whereas the opposite is true for the peptide synthesis, or alternatively, both the temporary and global protecting groups are acid-labile. Accordingly, at least one of the existing strategies must be considerably modified to enable a stepwise chain assembly. The stepwise strategies suggested so far fall into two major categories: either a branched linker bearing an amino group for peptide synthesis and a hydroxyl function for subsequent

Scheme 12

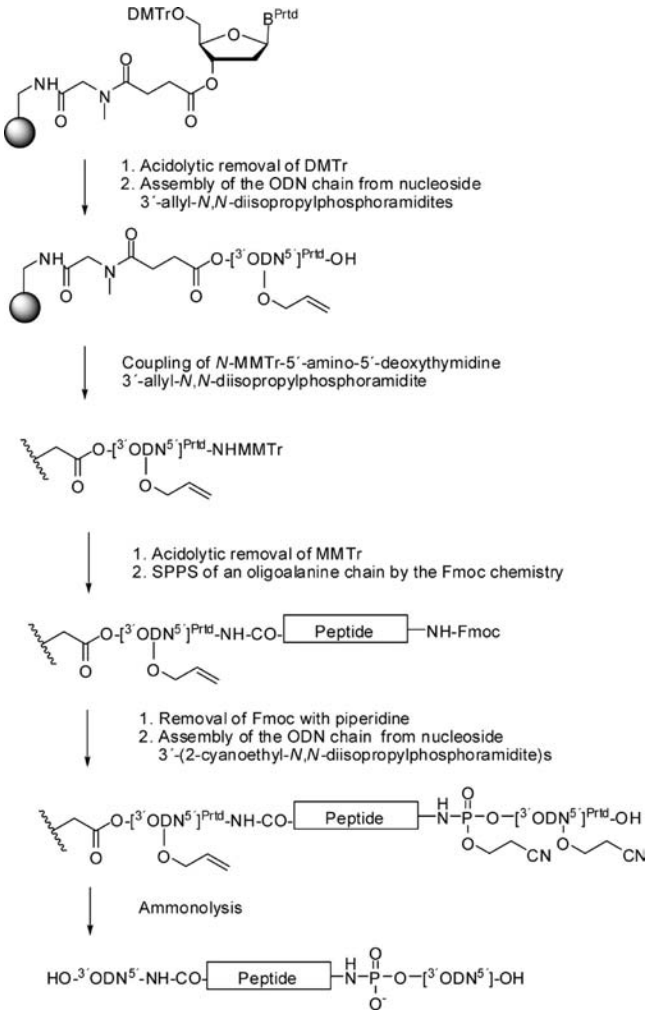

assembly of the oligonucleotide sequence is utilized, or a linker bearing a hydroxyl function is attached to the amino terminus of the support-bound peptide and used as a starting point for the oligonucleotide chain assembly. Both approaches face the same difficulty, viz., incompatibility of the protecting group strategies usually applied to oligonucleotide and peptide synthesis.

As far as the peptide moiety containing no side-chain fuctionalities, or only those that can be protected with orthogonally removable groups or such base-labile groups that withstand the Fmoc removal with piperidine, the situation is not very problematic. The synthesis may be carried out on a branched linker bearing an Fmoc-protected amino group and a DMTr-protected hydroxy function. The peptide moiety is first assembled on the amino group by the Fmoc chemistry and the ODN moiety then on the hydroxyl function by the phosphoramidite chemistry. The early examples of such an approach are offered by the synthesis of a conjugate of 17-mer ODN and a 3′-terminal tripeptide on linker **37** (Chart 8) (*121*) and a conjugate of a 23-mer ODN and a base moiety bound dipeptide on linker **38** (*122*). Among these, **37** may be cleaved by successive treatments with ethane-1,2-diamine in ethanol and IO_4^- in aqueous acetonitrile and **38** by normal ammonolysis. More recently, a branched linker strategy (**39**) has been applied to preparation of a 14-mer phosphorothioate ODN bearing a 16-mer membrane permeable peptide, viz., the hydrophobic region of the signal peptide sequence of the *Kaposi* fibroblast growth factor (*123*). While this sequence does not contain any trifunctional amino acids, incorporation of some such residues appears feasible. Linker **40** has been successfully used for

Scheme 13

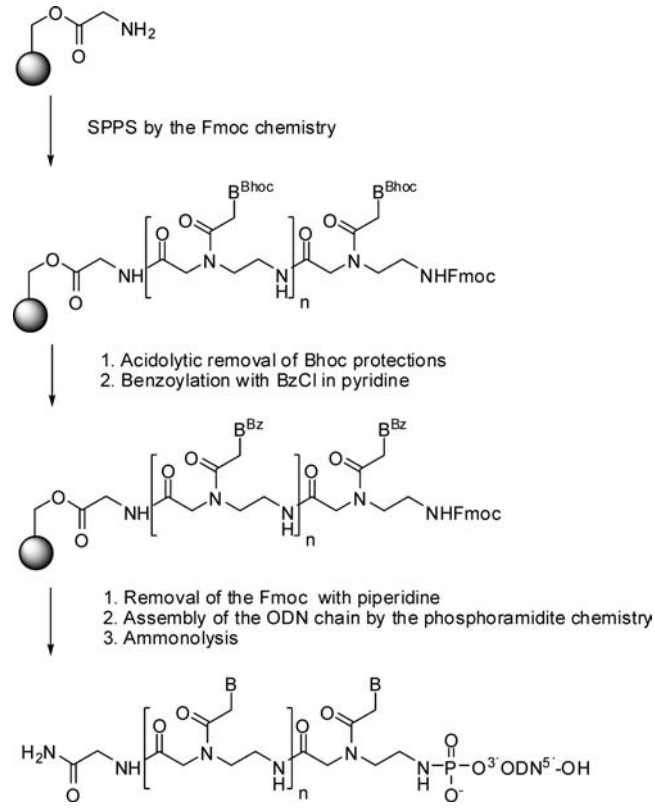

synthesis of peptide conjugates containing Cys, Lys, and Ser residues (*124*). Their side-chain functionalities have been protected with Tr, Boc, and TBDMS groups, respectively. Although these protecting groups are acid-labile, they have been reported to tolerate the repeated removal of DMTr protections during the assembly of a 15-mer ODN. They have been removed after the ODN assembly, but before the ammonolysis. When an even more generally applicable procedure is required, exchange of the acid-labile side-chain protecting groups of the peptide moiety to base-labile acetyl protections before assembly of the ODN chain appears to be an attractive alternative (*125*). The synthesis is carried out on linker **41**, the essential part of which is N^{α}-Fmoc-N^{ε}-Boc-lysine anchored to the support through an ester linkage (Scheme 7). The peptide moiety is assembled by the normal Fmoc chemistry on the α-amino group of this lysine handle. The acid-labile side-chain protections, including Tr on histidine, Boc on tryptophan, and *t*Bu on serine, are removed, as well as the Boc protection of the lysine handle. The exposed ε-amino group is acylated with DMTr-protected glycolic acid, and the side-chain functionalities of the peptide moiety are acetylated. The oligonucleotide chain is then assembled on the detritylated hydroxy function of the glycolic acid residue by the phosphoramidite strategy. The conjugate obtained is deprotected and cleaved from the support with aqueous sodium hydroxide. Apart from arginine, this protocol allows introduction of all trifunctional amino acids. Arginine residues have to be incorporated in the sequence as ornithines and converted postsynthetically to arginines by treatment with *N*,*N*′-bis-Fmoc-guanidine-*N*″-triflate (*126*).

Peptide conjugates of ORNs have been prepared by using an aminonucleoside as a branched linker (Scheme 8). An appropriately protected 3′-amino-3′-deoxyadenosine bearing a Fmoc protected alanyl group at 3′-*N* is immobilized to an amino-functionalized support via a 2′-*O*-succinyl linker (*127*). A peptide chain, containing only hydrophobic or allyl ester protected amino acids, is assembled on the alanyl residue by the Fmoc chemistry, after which the ORN sequence is assembled

Scheme 14

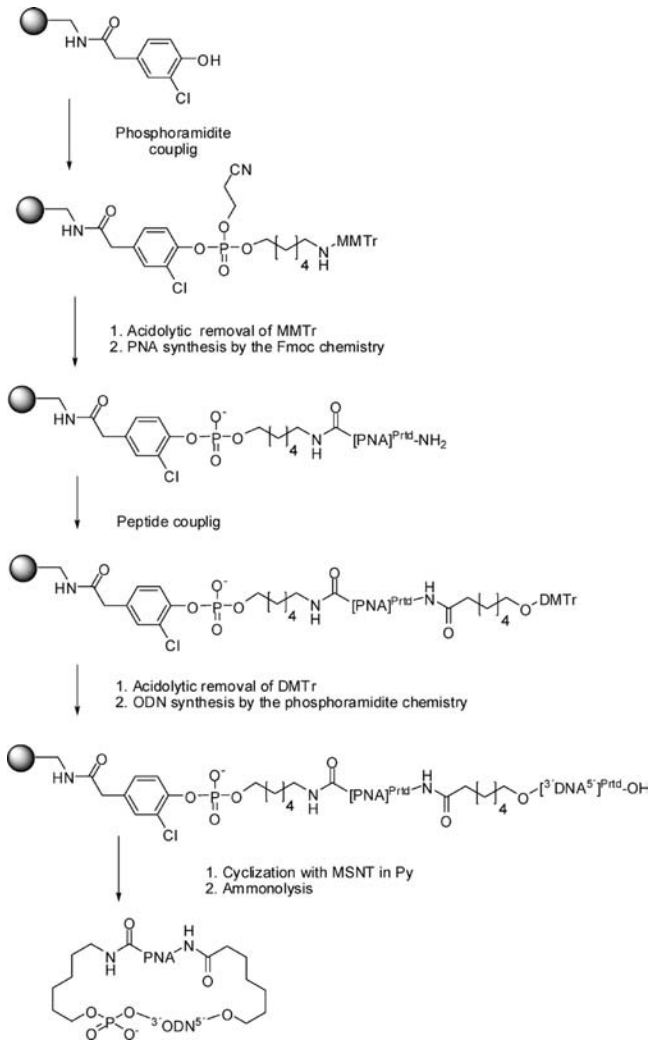

on the 5′-OH by the TBDMS/phosphoramidite chemistry. The allyl protections are removed with $Pd(PPh_3)_4$ on the support and the silyl protections in solution after ammonolysis. Another example of the utilization of an aminonucleoside as a branched linker is synthesis of ODN phosphorothioates bearing a 2′-*O*-trilysylsuccinyl tail on the 3′-terminal nucleoside. 2′-Deoxy-2′-(2-benzyloxy-1,2-dioxoethylamino)uridine has been immobilized to a PEG-grafted support via a 3′-succinyl linker (*128*). After the ODN chain assembly, the benzyl group is reductively removed and N^{ϵ}-trifluoroacetyllysine benzyl ester is coupled to the exposed carboxy function using carbodiimide activation. The procedure is repeated until the desired number of Lys residues have been coupled. Ammonolysis completes the synthesis.

Still, one possible way to use a nucleoside as a branched linker is to immobilize it through the base moiety to the support. 3′-*O*-TBDMS-5′-*O*-DMTr-2′-deoxycytidine has been immobilized through the N^4-atom via a succinyl linker to an aminoalkylated support (*129*). The ODN moiety is then assembled on the detritylated 5′-OH in an inverse direction using appropriately protected nucleoside 5′-phosphoramidites. After desilylation, the 3′-hydroxy group is phosphitylated with *N*-MMTr-6-aminohexylphosphoramidite, and the deprotected amino group is used as a starting point for the synthesis of the peptide moiety by the Fmoc chemistry.

Instead of a branched linker, the hydroxyl function serving as the starting point of the ODN synthesis may be provided by an *N*-terminal *ω*-hydroxyacyl group or by a side-chain hydroxyl function of an *N*-terminal amino acid. The limitations concerning

Scheme 15

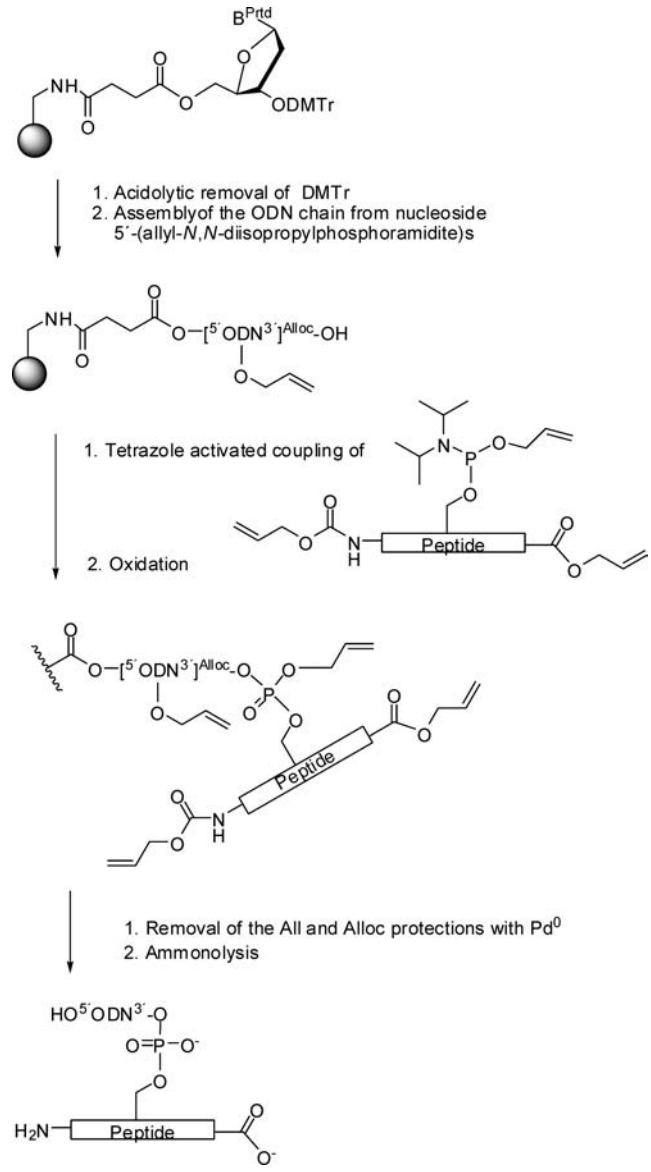

the side-chain protections of the peptide moiety are naturally similar to those using a branched linker. On applying this methodology, the peptide synthesis has often been carried out by the Boc chemistry on a base-labile 2-nitrophenylethanol (**42**) or 9-fluorenylmethanol linker (**43**) and the ODN chain is then assembled on a side-chain hydroxyl functionality of the *N*-terminal amino acid, viz., tyrosine, threonine, or serine (Scheme 9) (*130*−*137*). Use of homoserine instead of serine appears, however, preferable, since this increases the stability of the conjugate toward basic conditions (*138*, *139*). When desired, the ODN synthesis may also be initiated from a nonterminal amino acid, usually serine or homoserine (*138*, *140*). The side chains are protected with base-labile groups: Asp with Fm (*132*, *133*), His with Dnp (*138*), Lys with Fmoc or Tfa (*134*), Arg with Fmoc (*134*), Trp with formyl (*134*), and Ser, Thr, and Tyr with Ac (*134*). These groups expectedly withstand repeated acidolytic detritylations during the ODN synthesis and are removed by ammonolysis together with the nucleobase acyl protections. Met-containing conjugates are obtained by introducing methionine as a sulfoxide and reducing it back to methionine postsynthetically (*141*). Examples of the use of a hydroxyl-bearing linker between the ODN and peptide moieties include assembly of the peptide chain by the Boc chemistry on an ester linker and acylation of the *N*-terminus with 4-hydroxybenzoic

Scheme 16

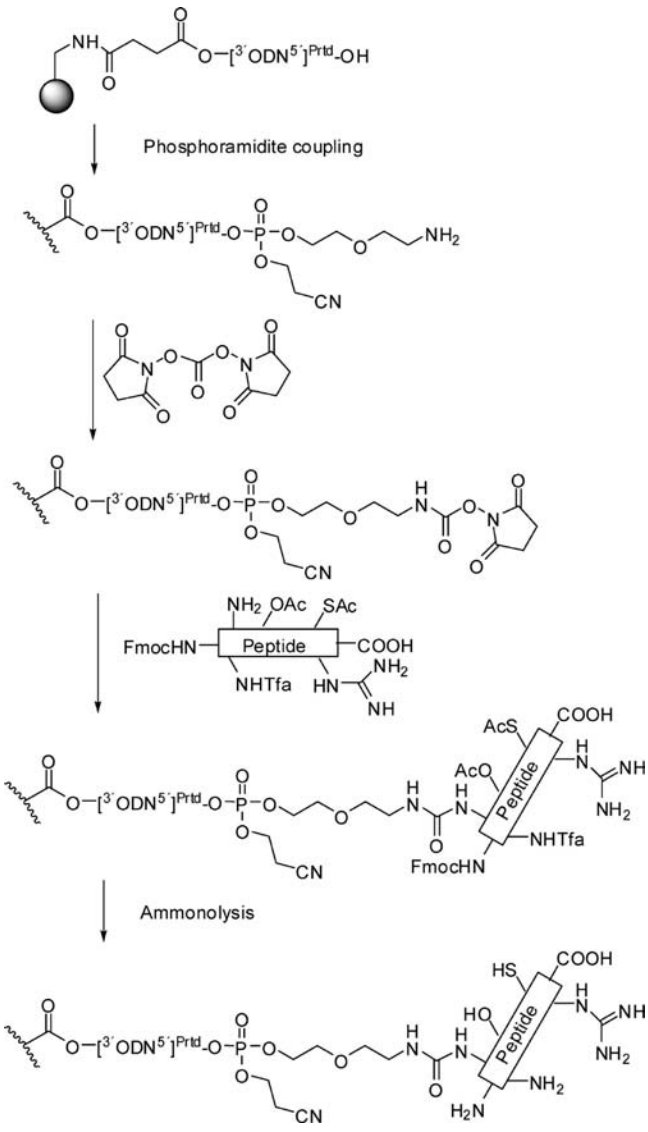

acid (*142*) or 2,2-dimethyl-3-hydroxypropionic acid (*143*), peptide synthesis on an *o*-nitrophenylethanol linker followed by *N*-terminal acylation with *N*-succinyl-6-aminohexanol (*144, 145*), peptide synthesis on a 4-hydroxybutanoyl linker followed by *N*-terminal acylation with 4-[(6-hydroxyhexyl)amino]-4-oxobutanoic acid (*146*), and use of 10-hydroxydecanoyl group both as a support-bound linker and as an intervening spacer (*147, 148*).

Alternatively, Fmoc chemistry may be applied to the initial assembly of the peptide chain. In a rather recent report exploiting this overall strategy, homoserine has been used as a connector between the peptide and ODN moieties (*149*). While the homoserine residue provides the hydroxyl function required as the starting point for the ODN chain assembly, it simultaneously offers an amino function to be used for fluorescent labeling. 6-Aminohexanol esterified to a succinyl linker has been used as a handle for the peptide synthesis, and the side chains have been protected with base-labile protecting groups: Tfa for Lys, Dmab for Asp, and 2-ClTr for Tyr (Scheme 10). N^{α}-Fmoc-asparagines have been coupled as pentafluorophenyl esters without amide protection to avoid the side reactions that the HATU activation induces. Coupling of N^{α}-Fmoc-*O*-Tr-homoserine to the *N*-terminus, fluorescent labeling of the deprotected amino group, and ODN chain assembly on the detritylated hydroxyl group, followed by conventional ammonolysis, complete the synthesis. Earlier, a related strategy involving normal Fmoc peptide synthesis on a hydroxy-functionalized support, followed by coupling of 10-hydroxydecanoyl (*150*), 4-hydroxybutanoyl (*151, 152*), or 4-(6-hydroxyhexylamino)-4-oxobutanoyl (*152*) group as an intervening linker between the peptide and ODN moiety, has been applied. Very recently, a 35-mer peptide containing 25 trifunctional residues has been synthesized on a Rink-MBHA amide resin by the normal Fmoc/*t*Bu chemistry and elongated with 3-trityloxypropionic acid. After acidolytic detritylation, an oligothymidylate sequence has been assembled by phosphoramidite chemistry. Consecutive treatments with piperidine in DMF and 95% TFA have then given the conjugate (*153*). The question that remains to be answered is whether a heterosequence withstands without depurination the acidolytic removal of the *t*Bu-derived side-chain protecting groups.

Although the stepwise synthesis of oligonucleotide−peptide conjugates is usually initiated by assembly of the peptide moiety, the opposite is also possible. The use of conventional Fmoc chemistry for the synthesis of the peptide moiety is, however, hampered by the fact that repeated removals of the Fmoc groups with organic bases also remove the 2-cyanoethyl protections from the internucleosidic phosphodiester linkages. To avoid this, an acid-labile 2-(biphen-4-yl)propan-2-yloxycarbonyl group (Bpoc) has been introduced for the α-amino protection (Scheme 11) (*154*). This group may be removed under the same conditions as used for removal of the 5′-*O*-DMTr groups during the ODN synthesis. MMTr protected 5′-amino-5′-deoxythymidine has been coupled as the last nucleoside to provide the amino group required for the peptide synthesis. Acyl protections can be used for both the amino acid side-chains and the nucleic acid bases, and hence, release from support and global deprotection is achieved by conventional ammonolysis. In spite of instability of the 2-cyanoethyl phosphate protections to Fmoc removal, Fmoc chemistry has been applied to the synthesis of 5′-peptide conjugates of ODNs on a single support (*155*). Up to octapeptide conjugates have been obtained by this approach. The acid-labile side-chain protections, viz., PhiPr for Asp and Glu, MMTr for Lys and Cys, Tr for Gln and His, and ClTrt for Tyr, are removed with TCA in DCM before ammonolysis. Compatibility with incorporation of arginine has not been tested. Previously, an essentially similar protocol has been applied to synthesis of up to tetrapeptide 5′-conjugates (*156*).

Another possible way to avoid the problems arising from incompatibility of the 2-cyanoethyl phosphate and N^{α}-Fmoc protections is the use Pd^0-labile allyl group instead of 2-cyanoethyl group for protection of the phosphodiester linkages. Peptide−ODN hybrids consisting of two terminal ODN sequences and an intervening peptide segment have been prepared by this strategy (*157*). The 3′-ODN segment is first assembled on a sarcosine linker by the phosphoramidite chemistry, using 5′-*N*-MMTr-5′-amino-5′-deoxythymidine 3′-allyl-*N*,*N*-diisopropylphosphoramidite as the last building block (Scheme 12). The peptide sequence is then assembled on the deprotected amino group by the Fmoc chemistry, and the 5′-terminal ODN sequence is assembled on the terminal amino group. The allyl protecting groups and sarcosine linker are compatible with the Fmoc peptide chemistry when DBU is used for the removal of the Fmoc group. It is, however, worth noting that the feasibility of the approach has not been demonstrated with trifunctional amino acids. 3′,5′-Dipeptidyl conjugates of ODNs bearing very short peptide segments have been synthesized similarly (*158, 159*).

Peptide nucleic acids (PNA), isosteric analogues of oligonucleotides where the nucleic acid bases are linked through *N*-(1-oxoethylene) bridges to a peptide-like backbone composed of *N*-(2-aminoethyl)glycine units (*160*), are biologically stable and hybridize more efficiently and selectively than oligonucleotides, and they, hence, show potential as therapeutic oligonucleotide analogues. Unfortunately, they exhibit low cellular uptake and

Scheme 17

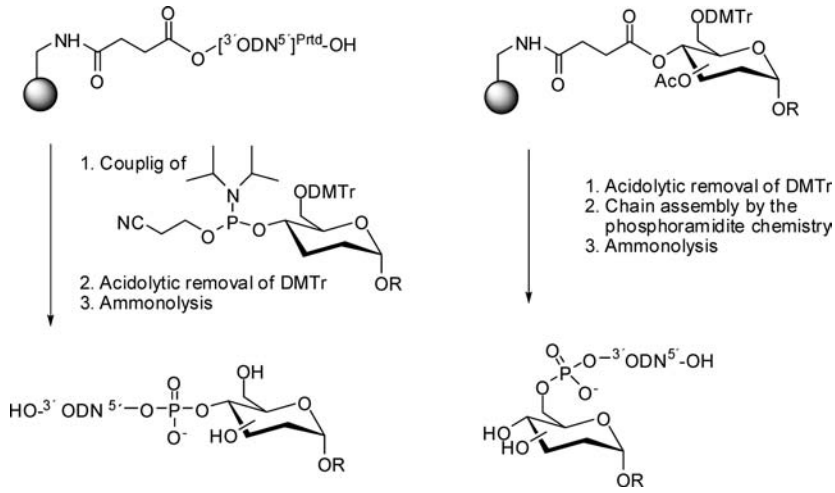

Chart 9

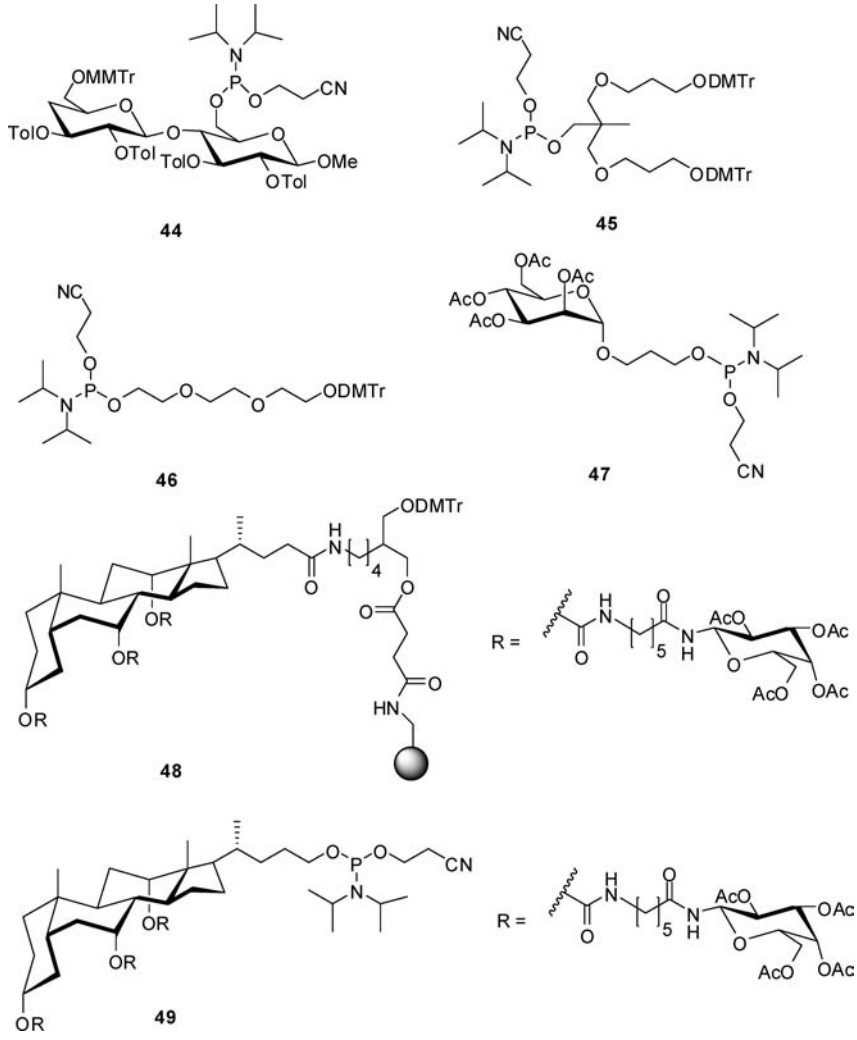

are unable to activate RNaseH, an enzyme that cleaves the RNA component of an mRNA/antisense oligomer duplex, providing the antisense oligomer with turnover (*161*). In addition, PNAs often suffer from solubility problems (*161*). Accordingly, conjugation of PNA with ODNs is not of any help for the targeting and internalization of ODNs. With PNA−ODN conjugates, the ODN moiety may rather be regarded as a conjugate group, which increases the solubility of PNA and provides it with the ability to activate RNaseH. 5′-Terminal PNA−ODN conjugates have been prepared as described above for 5′-peptide conjugates, viz., by introduction of 5′-amino-5′-deoxythymidine at the 5′-terminus of the support-anchored ODN and subsequent elongation of the chain by the PNA chain assembly (*162*). The 3′-conjugates have, in turn, been synthesized by using PNA building blocks bearing benzhydryloxycarbonyl (Bhoc) protection at the amino functions of the nucleic

Scheme 18

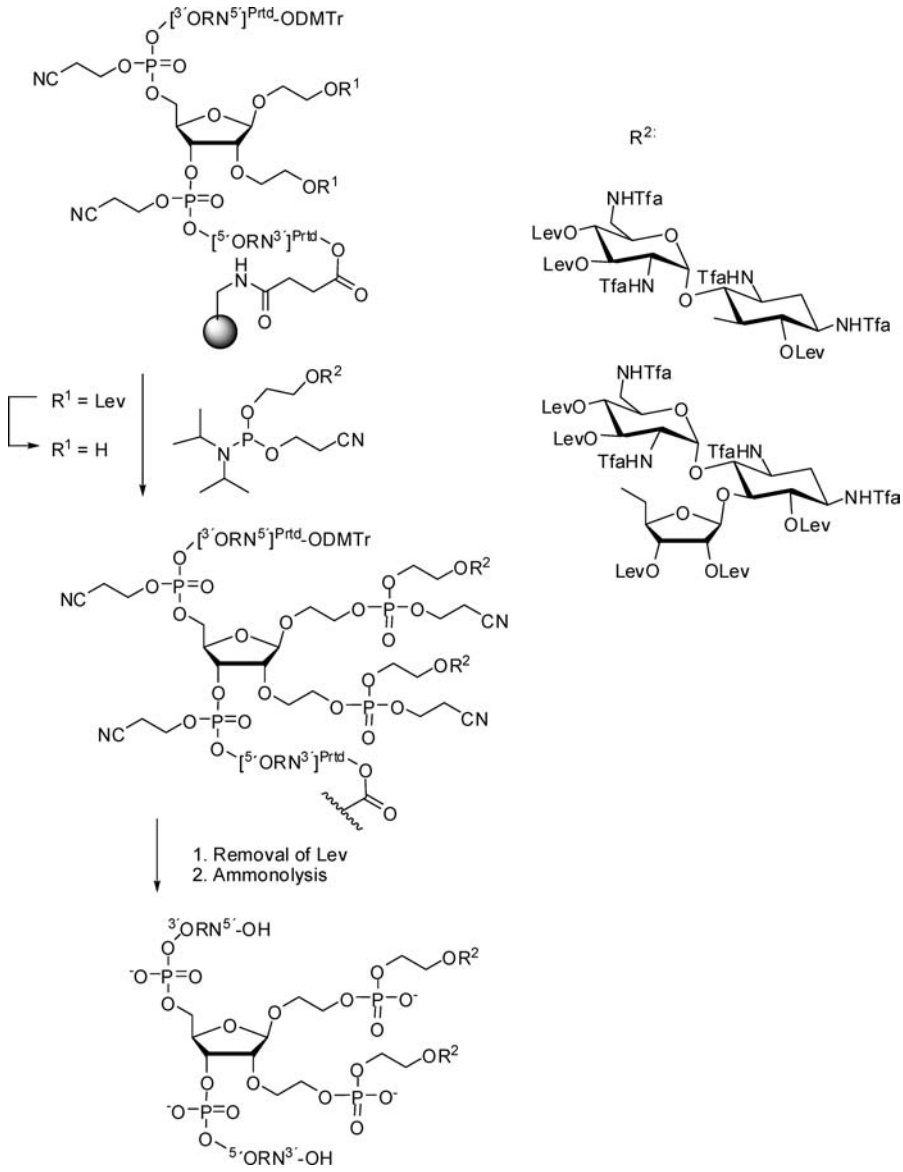

acid bases (*163*). The key point is that, after the assembly of the PNA sequence by the Fmoc chemistry, the Bhoc groups are removed with TFA and replaced with conventional benzoyl protections on the support (Scheme 13). Finally, the terminal Fmoc group is removed, and the ODN chain is assembled on the exposed amino group. Cyclic ODN−PNA chimeras have been synthesized on an *O*-(2-chlorophenyl)-*N*-(6-aminohexyl)-phosphoramidate linker (*164*). PNA is first assembled by Fmoc chemistry on the amino group of the linker and elongated with 6-DMTrO-hexanoic acid (Scheme 14). Owing to repeated removal of the Fmoc group with piperidine, the phosphodiester linkage becomes deprotected. The ODN moiety is then synthesized on the detritylated hydroxyl function, and the PNA−ODN hybrid is cyclized on support by treatment with MSNT in pyridine. Normal ammonolysis releases the cyclic conjugate and removes the base moiety protections.

Fragmental coupling offers an alternative for the stepwise synthesis on a single support: a prefabicated peptide bearing a single unprotected amino group and base-labile side-chain protecting groups is conjugated to a support-bound oligonucleotide. Usually, the oligonucleotide is first assembled on the support and an appropriately activated peptide is linked to the 5′-terminal hydroxyl function. One possible activation method is conversion of the peptide to a phosphoramidite ragent. Normal tetrazole activated coupling and subsequent oxidation to phosphoramidate is then carried out. The C-terminal amido nitrogen (*165*) and the side-chain hydroxyl group of a serine residue (*166*) have been used as a site of the phosphoramidite activation with 2-cyanoethyl-*N*,*N*-diisopropylphosphorochloridite. Both 3′- and 5′-conjugates have been prepared (*166*). 3′-Conjugates have been obtained by assembling the ODN chain in the inverse 5′→3′ direction and coupling the peptide phosphoramidite to the 3′-terminal hydroxy function of the support-bound chain (Scheme 15). On using conjugation through the serine side chain, deprotection under drastically basic conditions may result in elimination of the ODN as a 5′-phosphate or 3′-phosphate by concomitant conversion of the serinyl residue to dehydroalanine. To avoid this, the phosphate linkages and the C-terminal carboxy function of the peptide have been protected with allyl groups and the nucleoside amino groups and the *N*-terminal amino group with Alloc groups.

In an alternative approach, an α,ω-alkanediamine is tethered to the 5′-hydroxy function by 1,1′-carbonyldiimidazole activation and a preprepared protected peptide is coupled to the amino group by PyBOP/HOBt-promoted peptide bond formation (*167*). Up to dodecyl peptides have been successfully coupled. A long C12 spacer between the peptide and ODN and, interestingly, removal of the 2-cyanoethyl protections have improved the

Scheme 19

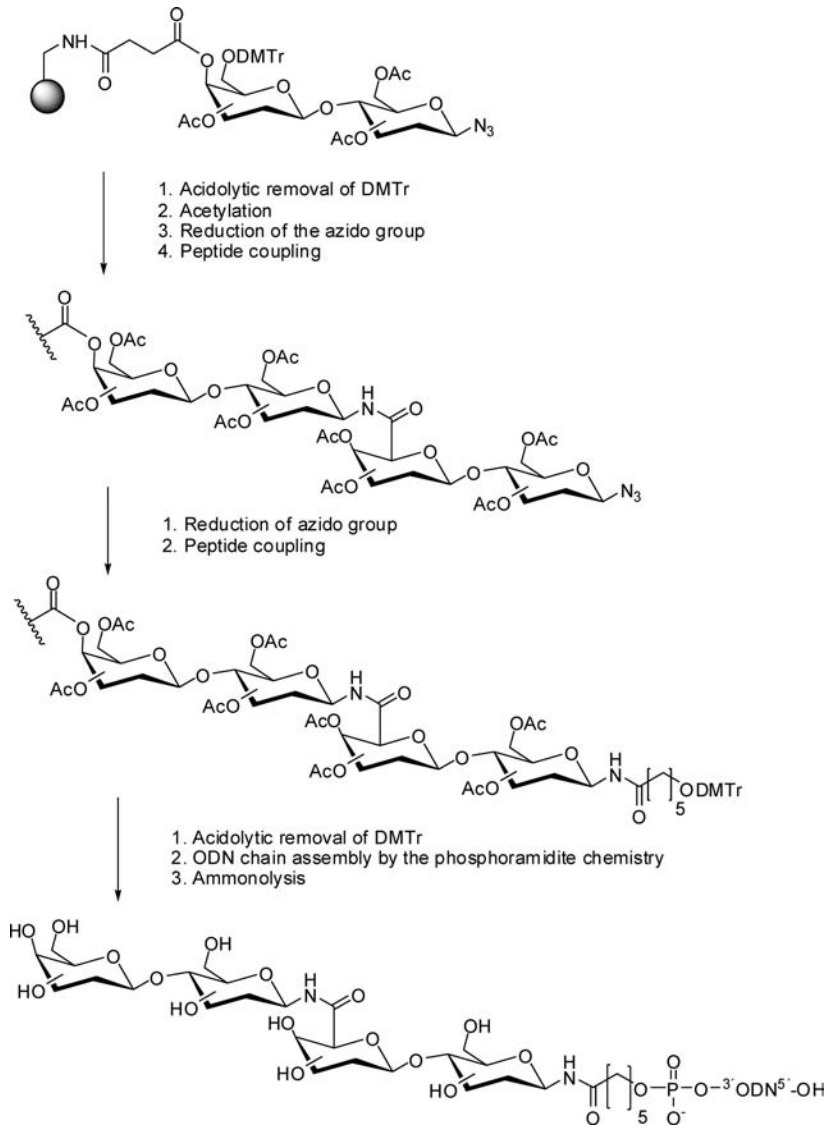

coupling yield (*168*). More recently, 1,6-diisocyanatohexane has been utilized to tether peptides bearing an *N*-terminal β-alanine to the 5-amino-3-oxapentyl tail of a protected support-bound ODN (*169*). The ε-amino functions of the peptides have to be protected with trifluoroacetyl groups, but no other side chain protections are necessary. On using the peptide in 10-fold excess, coupling yields up to 20% are achieved. Another feasible conjugation method depends on conversion of the 5′-aminoalkyl tail to an active urethane by reaction with bis(*N*-succinimidyl)-carbonate (*170*). Up to 18-mer peptides have been attached in this manner to ODN phosphorothioates (Scheme 16). Instead of a 5′-aminoalkyl tail, the *N*-(3-aminopropanoyl) sidearm of a 2′-amino-2′-deoxy-*arabino* nucleotide within an otherwise protected support-bound oligonucleotide has been used as the site of conjugation (*171*).

Unprotected peptides up to an heptamer have been conjugated by TBTU/HOBt coupling to solid-supported ODNs incorporating either a 2′-*O*-carboxymethyluridine unit (*172*) or a 5′-carboxyalkyl tail (*173*). 80% yields have been obtained using the peptide in 100-fold excess. The carboxymethylated unit can be introduced as a phosphoramidite having the carboxy group protected as an Pd^0-labile allyl ester and the 5′-carboxy group as a 1-methyl-4-oxo-4-trityloxybutyl phosphoramidite. An *N*-Fmoc-*O*-Tr-homoserinyl linker attached via an amide linkage to an amino-functionalized resin has been exploited in preparation of 3′-oligolysine conjugates by fragment coupling (*40*). The Fmoc group is first removed, and a trifluoroacetyl protected oligolysine is coupled. After that, the trityl protection is removed, and the ODN chain is assembled.

Reaction of an aldehyde with hydrazine or alkoxyamine is one of the conjugation methods most extensively applied in the solution phase (*120*). The same method has also been successfully applied to solid-supported conjugation. Laminin peptide (H-RSGIYGPD-OH) has been conjugated as a C-aminooxy or hydrazine derivative to an aldehyde-functionalized ODN on a solid support (*174*). For this purpose, an appropriately protected 2′-*O*-[2,3-bis(allyloxycarbonyloxy)propyl]cytidine phosphoramidite building block has been introduced into the ODN sequence, the Pd-labile Alloc groups have been removed on-support, and the resulting 2′-*O*-(2,3-dihydroxypropyl) group has been oxidized with periodate ion to a 2′-*O*-(2-oxoethyl) group. Treatment with a 1000-fold excess of the peptide conjugate and subsequent ammonolysis have given the conjugates in high yield.

GLYCOCONJUGATES

Carbohydrate−protein interactions play a central role in cellular recognition. Usually, multiantennary carbohydrates anchored to proteins or lipids of cell membranes recognize

Chart 10

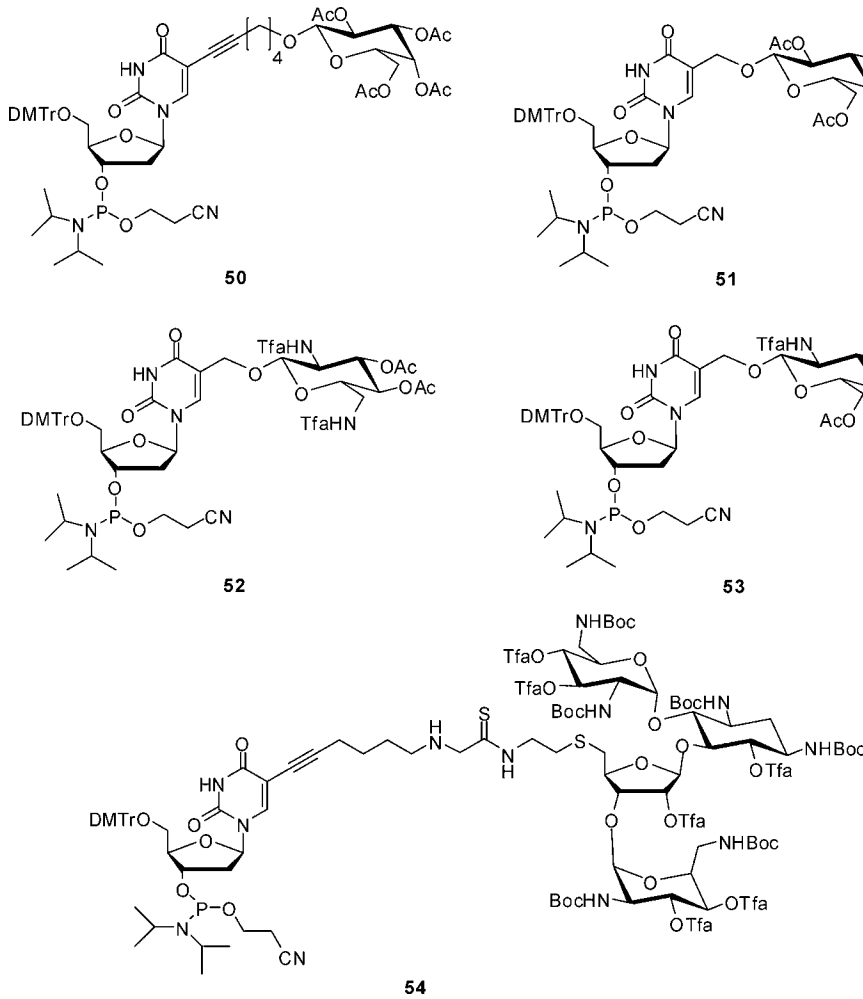

extracellular proteins, but the opposite is also possible (*175*−*177*). For example, hyaluronic acid, a linear polysaccharide composed of a repeating disaccharide unit of D-glucuronic acid and *N*-acetyl-D-glucosamine, [→3)-*β*-D-GlcNAc-(1→4)-*β*-D-GlcUA-(1→]$_n$, is the main ligand for a transmembrane glycoprotein CD44 that is overexpressed in many cancers (*178*), and hyaluronic acid conjugates of cancer drugs have been shown to exhibit increased uptake to cancer cells (*179*). Galactosylated PEG-conjugates of ODN phosphorothioates have, in turn, been reported to show enhanced uptake via the galactose-specific asialoglycoprotein receptor-mediated endycytosis (*30*), and antigenic peptides have been targeted to dendritic cells by an appropriate glycoconjugation (*180*). Additionally, it has been shown that galactosylated dendrimers are able to inhibit at nanomolar concentrations cellular binding of pathogens bearing galactose-binding membrane proteins (*181*). Accordingly, several lines of evidence suggest that glycotargeting may well be a viable method with which to enhance the delivery of therapeutic oligonucleotides (*182*). Preparation of oligonucleotide glycoconjugates has previously been reviewed in 2004 (*183*). In the present survey, attention is paid only to solid-phase methods and mainly to those published since 2004.

The protocols reported so far for the solid-phase synthesis of oligonucleotide glucoconjugates utilize phosphoramidite coupling, Cu(I) promoted 1,3-dipolar cycloaddition ("click reaction"), or oximation. Among these approaches, the phosphoramidite coupling is oldest, but still extensively applied. The simplest example is offered by introduction of a single mono- or disaccharide unit into a terminal position of a support-bound ODN. To obtain 5′-glycosylated conjugates, appropriately protected methyl glycosides have been converted to phosphoramidite reagents and introduced into the ODN by the last coupling cycle (Scheme 17) (*184, 185*). Besides sugar hydroxyl functions, the *ω*-hydroxy group of appropriately protected *ω*-hydroxyalkyl glycosides has been used as the site of phosphitylation (*186, 187*). 3′-Terminal sugar conjugates have, in turn, been prepared by assembling the ODN chain on the primary hydroxyl group of an *O*-acetyled glycoside immobilized to the support via a succinyl linker (*184, 185*). Conjugates bearing a sucrose moiety at both termini have been obtained by using these two approaches in combination (*188*). The 3′-terminal sugar tail has been elongated by coupling one O6-DMTr protected sugar phosphoramidite building block to the support-anchored sugar before the assembly of the ODN chain (*189*). A phosphoramidite building-block derived from methyl 4′-deoxy-*β*-D-lactoside (**44**; Chart 9) has been used to introduce a sugar moiety within the ODN chain (*190*). A spruce-like tetramannosyl conjugate has been prepared by using phosphoramidate **45** for branching, **46** for elongation of the branches, and **47** for the terminal mannosylation (*191*).

In addition to mono- and disaccharides, more complicated carbohydrate structures have been conjugated to oligonucleotides by the phosphoramidite chemistry. Very recently, solid-phase synthesis of aminoglycoside conjugates bearing two neamine or ribostamycin units at an intrachain position has been described (*192*). The procedure is outlined in Scheme 18. The oligonucleotide chain is assembled by conventional phosphoramidite chemistry. At the desired site of aminoglycoside conjugation, an abasic ribofuranose phosphoramidite bearing one or two levulinoyloxyalkyl side arms is introduced. The levulinoyl

Scheme 20

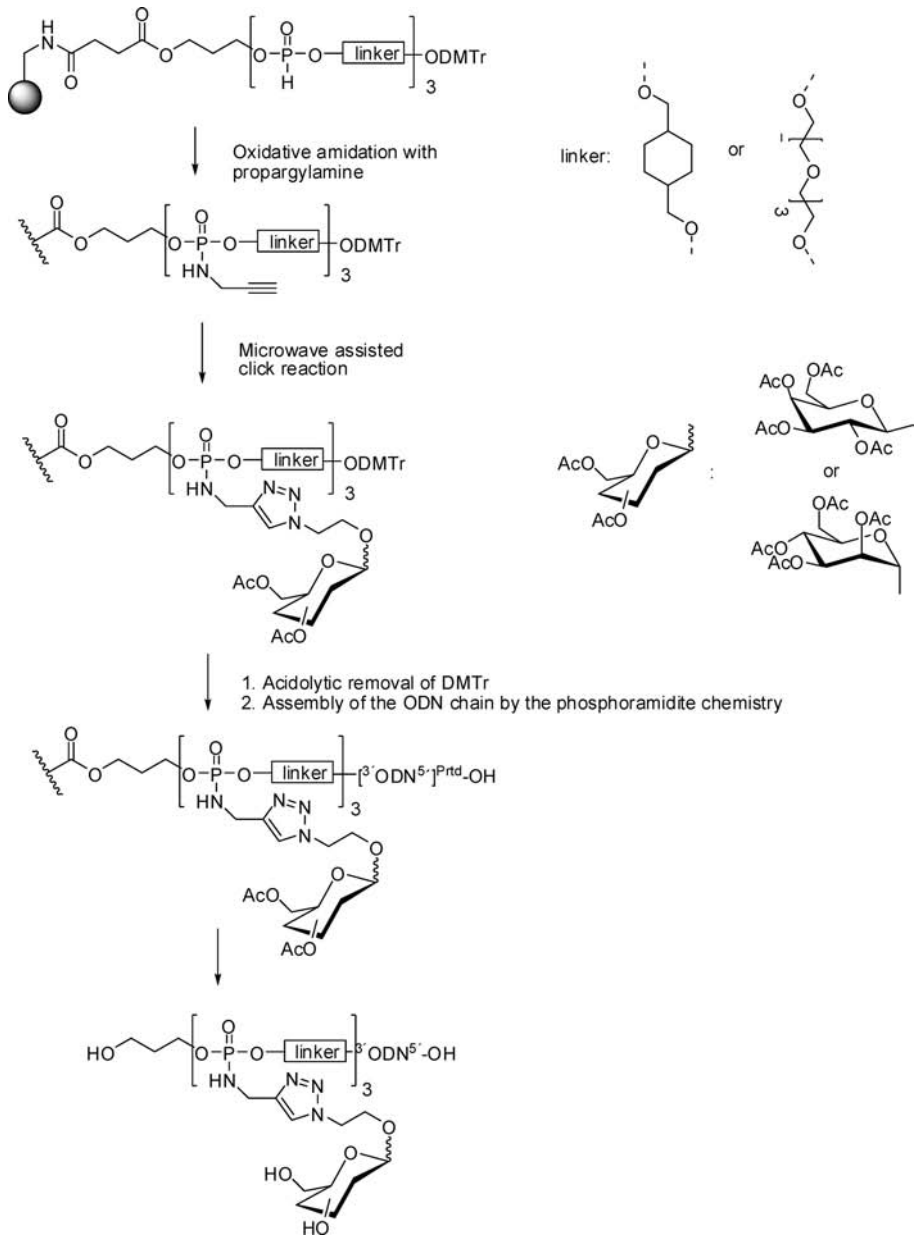

protecting groups are removed with hydrazinium acetate on support and the appropriately protected aminoglycosides are coupled to the exposed hydroxyl functions as phosphoramidite reagents. An important detail of the synthesis is the protection of the aminoglycoside building block. Acyl groups readily migrate from hydroxyl functions to amino groups under basic conditions. That is why removal of the acyl protections from hydroxyl groups, while keeping the amino groups still protected, is highly desirable. Therefore, levulinoyl groups have been used instead of more common acetyl groups for protection of the hydroxyl functions. These groups may be removed under conditions that leave trifluoroacetyl protections on the amino groups intact. The latter protections are then removed upon ammonolysis used for the global deprotection and release of the conjugate from the support.

Other complex structures conjugated to oligonucleotides by the solid-supported phosphoramidite chemistry include a triga-lactosylated tetrahydroxycholane, introduced into the 3′-terminus of oligonucleotides with the aid of a branched linker (**48**) and to the 5′-terminus as a phosphoramidite reagent (**49**) (*193*), and 3′-(*β*-cyclodextrin) conjugates obtained by assembling the ODN chain in the reversed 5′ → 3 ′ and conjugating an amino-functionalized cyclodextrin to the terminal 3′-hydroxy function activated as a 4-nitrophenyl carbonate (*44*). Cyclodextrin conjugates have also been obtained by applying the phospho-triester conjugation method outlined in Scheme 3 in the foregoing (*62*). 3′-Conjugates derived from a tetrasaccharide glycomimetic have been prepared by sequential peptide and phosphoramidite coupling on a single support (*194*). An example is outlined in Scheme 19. An acetylated 1-azido-1-deoxy-6′-*O*-DMTr-*β*-D-lactose is immobilized via a 4′-*O*-succinyl linker to an amino-functionalized support. The DMTr protection is converted to an acetyl protection and the azido group reduced with 1,3-propanedithiol. The resulting amino group is then subjected to peptide coupling with fully acetylated 1-azido-1-deoxy-*β*-D-lacturonic acid using HATU/HOBt/DIPEA activation. The azido function is again reduced to an amino group, and a DMTr protected 6-hydroxyheptanoic linker is coupled. The ODN chain is then assembled on the detritylated hydroxyl function of this linker. Conventional ammonolysis gives the fully deprotected glycoconjugate.

Scheme 21

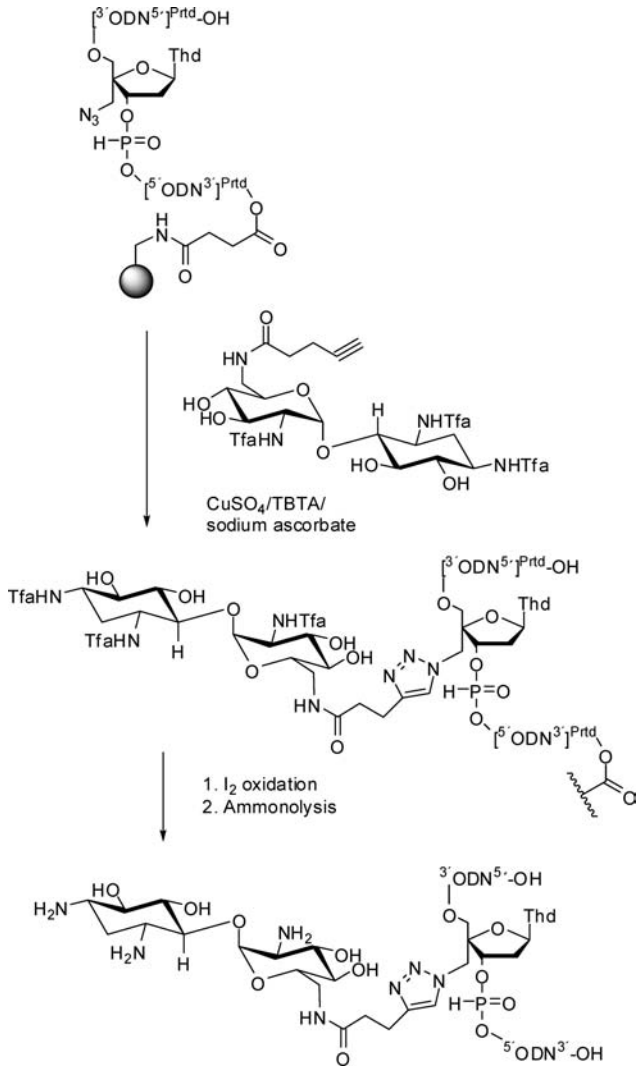

Chart 11

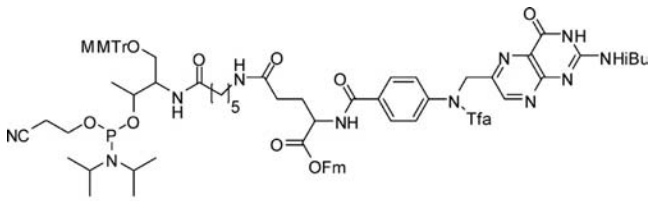

55

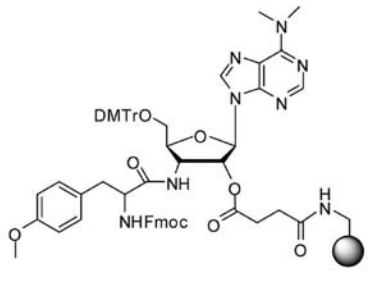

56

The most frequently used method for incorporation of sugars into intrachain positions of oligonucleotides is the use of phosphoramidites derived from prefabricated nucleoside conjugates. The building blocks successfully incorporated include 5′-*O*-DMTr protected 3′-(2-cyanoethyl-*N*,*N*-diisopropylphosphoramidite)s of 5-[6-(2,3,4,6-tetra-*O*-acetyl-*β*-D-galactopyranosyloxy)-1-hexynyl]-2′-deoxyuridine (**50**; Chart 10) (*195, 196*), 5-(2,3,4,6-tetra-*O*-acetyl-*β*-D-glucopyranosyloxy)methyl-2′-deoxyuridine (**51**) (*197*), 5-[2,6-bis(trifluoroacetamido)-3,4-di-*O*-acetyl-2,6-dideoxy-*β*-D-glucopyranosyloxy]methyl-2′-deoxyuridine (**52**) (*198*), and 5-(3,4,6-tri-*O*-acetyl-2-deoxy-2-trifluoroacetamido-*β*-D-glucopyranosyloxy)methyl-2′-deoxyuridine (**53**) (*199*). This approach has been applied to introduction of even very complex carbohydrate groups into ODNs. For example, an aminoglycoside antibiotic, neomycin, has been incorporated into oligonucleotides as a C5-tethered 2′-deoxyuridine 3′-phosphoramidite building block (**54**) (*200*). An exceptionally long reaction time (30 min) was, however, required to couple this modified block. The Boc protections were removed after ammonolytic release in solution phase with a mixture of 3% TFA and 1% *m*-cresol in dioxane. It should be noted that the ODN chain contained no purine nucleosides prone to acid-catalyzed cleavage of the *N*-glycosidic bond. Several contiguous *N*-acetyl-D-galactosamine groups have been introduced into ORNs with the aid of a phosphoramidite reagent derived from *N*-[12-(3,4,6-tri-*O*-acetyl-2-acetamido-2-deoxy-*β*-D-galactopyranosyl)dodecanoyl]threoninol (*201*).

Click chemistry has recently gained popularity in preparation of bioconjugates. Several applications concerning solid-supported synthesis of oligonucleotide glycoconjugates have also been reported. Usually, sugar azides are conjugated to support-anchored alkynylated oligonucleotides. ODNs bearing up to three *β*-D-galactopyranosyl or α-D-mannopyranosyl groups at the 3′-terminus have been obtained by consecutive application of oxidative amidation and microwave-assisted click chemistry (*202, 203*). Scheme 20 outlines the procedure. A non-nucleosidic tail consisting of cyclohexane-1,4-diyldimethanol or tetraethylene glycol units is first assembled by H-phosphonate chemistry, and the H-phosphonate diester linkages obtained are subjected to amination with propargylamine. Fully acetylated 8-azido-3,6-dioxaoctyl glycopyranosides are then attached by Cu(I)-promoted 1,3-dipolar cycloaddition under microwave irradiation. The ODN sequence is assembled by the phosphoramidate chemistry on the hydroxyl function of the last non-nucleosidic unit, and conventional ammonolysis completes the synthesis.

Another indication of the applicability of click chemistry to the solid-supported construction of oligonucleotide glycoconjugates is the synthesis of fucosylated pentaerythrityl phosphodiester oligomers (*204*). Very recently, an example of a reaction of an alkynylated sugar with a support-bound azido-functionalized oligonucleotide has been reported (*205*). A 5′-DMTr protected 3′-H-phosphonate monomer derived from 4′-*C*-azidomethylthymidine has been prepared and inserted into an ODN by the H-phosphonate chemistry (Scheme 21). The corresponding phosphoramidite building block cannot be prepared, owing to an intramolecular Staudinger reaction between the azido and phosphoramidite moieties. The unmodified nucleosides may, however, be coupled as phosphoramidites even though 4′-*C*-azidomethylthymidine blocks would have already been incorporated into the chain. While the click reaction has been observed to be virtually quantitative, removal of the copper complex of tris[(1-benzyl-1,2,3-triazol-4-yl)methyl]amine (TBTA) used as a promoter requires special attention, as indicated by capillary electrophoresis of the released product before and after HPLC purification.

Solid-phase oximation has been applied to preparation of ODN 5′-glycoconjugates bearing up to 6 identical monosaccharides (*206*) For this purpose, a non-nucleosidic phosphoramidite building block containing two phthaloyl protected aminooxy functions has been prepared and inserted into an ODN by the phosphoramidite chemistry. These protections may be easily removed on a solid support, and sugars may be introduced by oximation with alkyl glycosides bearing an aldehyde function on the aglycon (Scheme 22).

Scheme 22

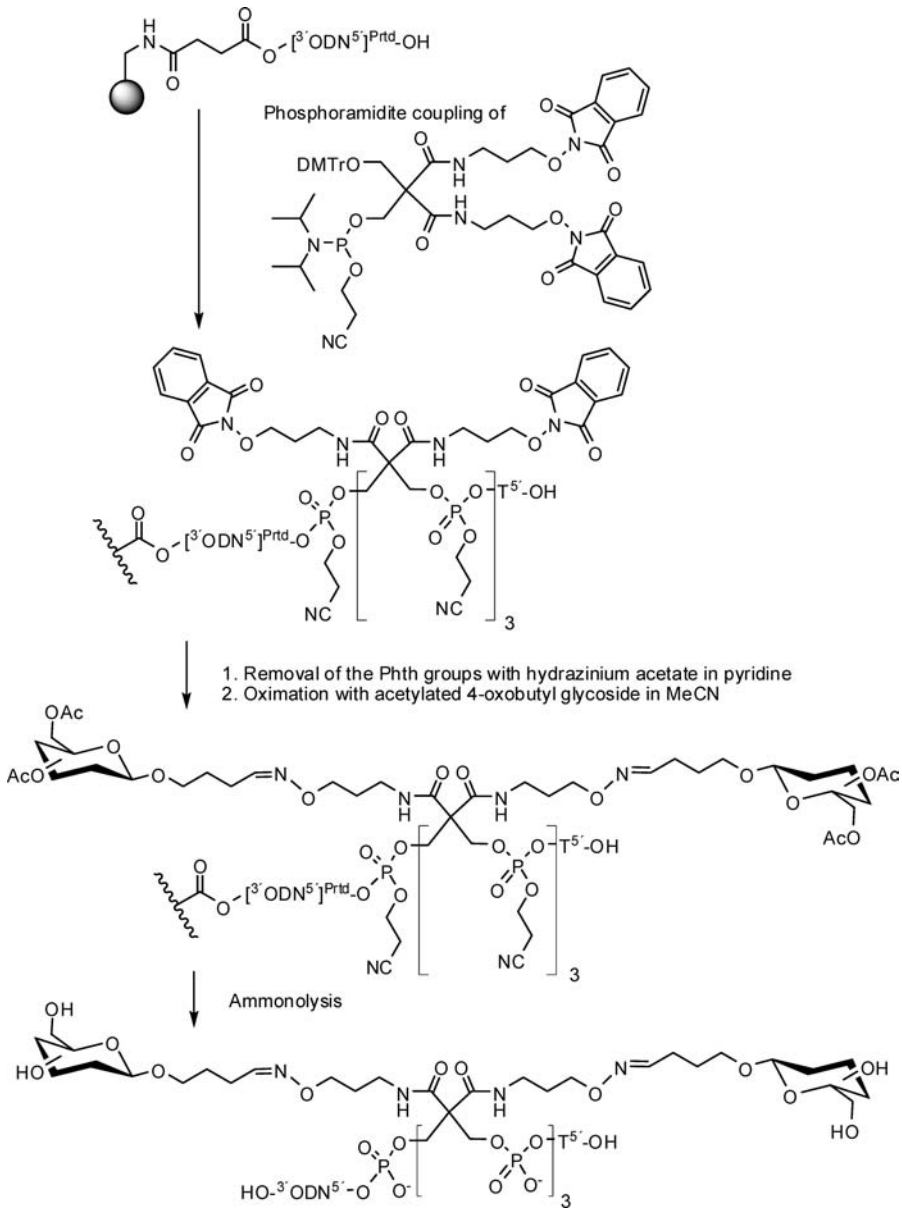

The oxime linkages withstand standard ammonolysis, which also quantitatively removes the acetyl protections from the sugar hydroxyl functions.

Usually, lectins bind only one type of sugar, and hence, homoclusters are considered to adequately guarantee high affinity binding (*175*, *177*). There are, however, some indications that in special cases heteroclusters containing more than one type of sugars bind more tightly than the corresponding homoclusters (*207*). For example, mixed-type α-Man, *β*-Glc and α-Man, *β*-Lac heteroglycoclusters exhibit 8 times higher affinity to Con A than α-Man homoclusters of identical valency (*208*). Accordingly, synthesis of oligonucleotide glycoconjugates containing more than one type of sugar ligands is of interest. To construct such conjugates on a solid support, a non-nucleosidic bis(hydroxymethyl)-malondiamide-based building block bearing three orthogonally removable hydroxy protections has been prepared and introduced into the 5′-terminus of a solid-supported ODN (*209*). The hydroxyl protections are removed in a stepwise manner, and the sugar units are introduced as phosphoramidite reagents. Methyl-protected phosphoramidites have to be used for the chain assembly, since the 2-cyanoethyl groups do not withstand removal of the fluoride ion labile TBDPS group. For the same reason, a polymer support has to be used instead of CPG. As depicted in Scheme 23, the first sugar unit is attached after detritylation. Then, the levulinoyl protection is removed and the second sugar phosphoramidite is coupled, and removal of TBDPS with triethylamine hydrogen fluoride followed by coupling of the last sugar completes the conjugation process. The phosphodiester likages are demethylated before normal ammonolysis.

Solid-supported glycosidation has very seldom used for the preparation of oligonucleotide glycoconjugates on a single solid support. Glycosidation usually depends on electrophilic activation, and this easily results in depurination of the ODN chain. Very short 5′-glycosylated conjugates of ODNs have, however, been obtained by glycosylating the 5′-terminal hydroxyl function of the support-bound ODN with fully benzoylated glycopyranosyl trichloroacetimidate using trimethylsilyl triflate as an activator (*210, 211*).

MISCELLANEOUS

Conjugation of ODN phosphorothioates with poly(ethylene glycol) polymers ranging from 6 to 20 kDa has been shown

Scheme 23

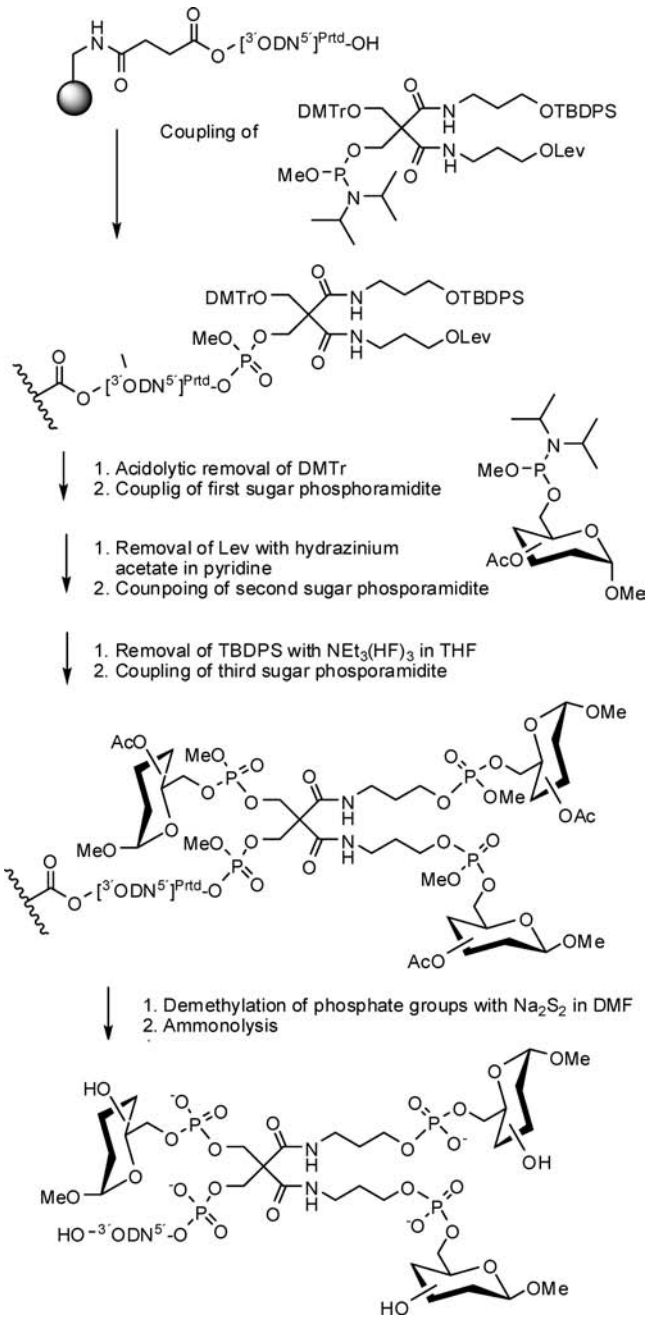

to increase their half-life in rat plasma, to enhance the stability against nucleases, and to improve the pharmacokinetics (*31*). 3′-Terminal ODN conjugates of poly(ethylene glycol)s with degrees of polymerization up to 150 have been prepared by immobilization of the PEG oligomer to an aminoalkylated support via a succinyl linker and subsequent synthesis of the ODN chain by the phosphoramidite (*212*−*214*) or H-phosphonate chemistry (*215*). *N*-Fmoc protected amino-poly(ethylene glycol)-900 (*216*) and PEG polymers up to the length of 120 units (*213*, *214*) have been conjugated as phosphoramidite reagents to the 5′-terminus of a support-bound oligonucleotide.

Among small molecules known to undergo receptor-mediated cellular uptake, folic acid has received interest as a potential carrier of oligonucleotides into cells. 3′-Terminal folic acid conjugates have been prepared with the aid of a branched linker, as depicted in Scheme 24 (*217*), and intrachain conjugates by insertion of an appropriately protected non-nucleosidic phosphoramidite reagent

Scheme 24

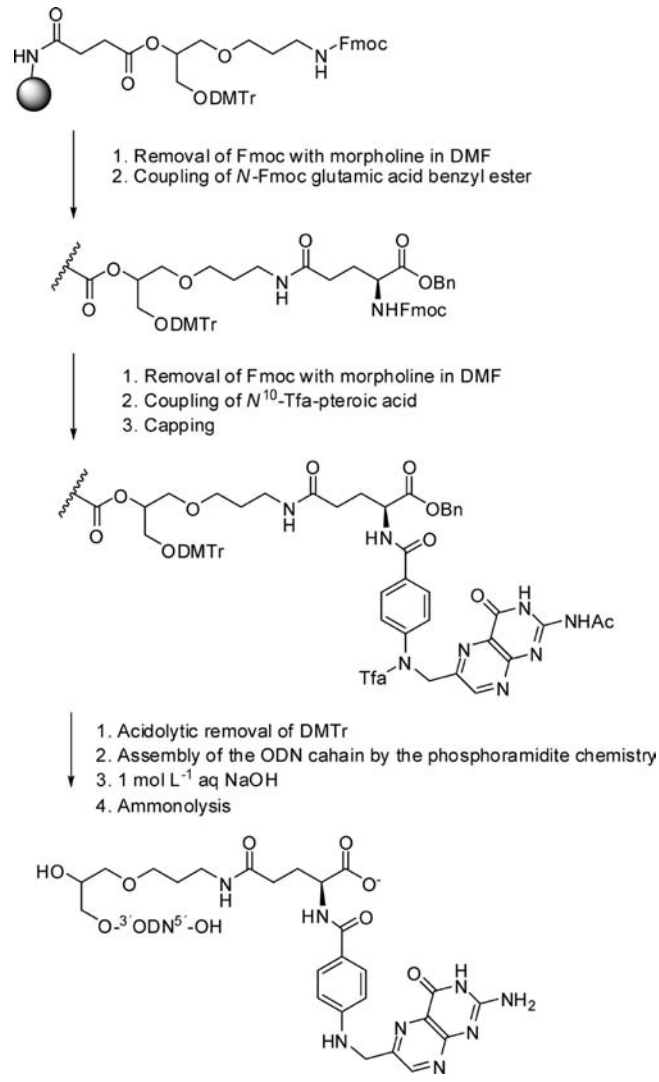

(**55**; Chart 11) into the desired place of the chain (*201*). Puromycin, porphyrins, groove binders, and intercalators have also received considerable interest as conjugate groups. Although these conjugates are not primarily aimed at exhibiting enhanced cellular uptake or cell-type specific targeting, their solid-phase synthesis is briefly discussed here. 3′-Conjugates of puromycin have been obtained by conventional ODN synthesis on puromycin-derived linker **56** (*218*, *219*). Porphyrins have been conjugated as nucleoside derived phosphoramidite (*220*) or hydrogen phosphonate (*221*) building blocks, as non-nucleosidic phosphoramidite (*222*) or hydrogen phosphonate (*223*, *224*) reagents, or as carboxy-functionalized derivatives to the 5′-amino group of a support-bound ODN (*225*). Groove binders have been coupled as pentafluorophenyl esters to a 5′-amino tail of a support-bound ODN (*226*, *227*) or to an amino group of a support-bound linker before the ODN chain assembly (*227*, *228*), or they have been coupled as an alcohol to the 5′-terminal OH activated as 2-cyanoethyl *N*,*N*-diisopropylphosphoramidite (*229*). Intercalators are introduced as non-nucleosidic phosphoramidite reagents (*230*, *231*) or prefabricated nucleoside-derived building blocks (*230*), or they are attached as an active ester to an amino group of a branched linker (*233*, *234*).

LITERATURE CITED

(1) Sasaki, S., and Nagatsuki, F. (2006) Application of unnatural oligonucleotides to chemical modification of gene expression. *Curr. Opin. Chem. Biol. 10*, 615–621.

(2) Aboul-Fadl, T. (2005) Antisense oligonucleotides: the state of the art. *Curr. Med. Chem. 12*, 2193–2214.
(3) Da Ros, T., Spalluto, G., Prato, M., Saison-Behmoaras, T., Boutorine, A., and Cacciari, B. (2005) Oligonucleotides and oligonucleotide conjugates: a new approach for cancer treatment. *Curr. Med. Chem. 12*, 71–78.
(4) Goodchild, J. (2004) Oligonucleotide therapeutics: 25 years growing. *Curr. Opin. Mol. Ther. 6*, 120–128.
(5) Crooke, S. T. (2004) Progress in antisense technology. *Annu. Rev. Med. 55*, 61–95.
(6) Dean, N. M., and Bennett, C. F. (2003) Antisense-oligonucleotide-based therapeutics for cancer. *Oncogene 22*, 9087–9096.
(7) Opalinska, J. B., and Gewirtz, A. M. (2002) Nucleic-acid therapeutics: basic principles and recent applications. *Nat. Rev. Drug Discovery 1*, 503–514.
(8) Uhlmann, E., and Peyman, A. (1990) Antisense oligonucleotides: a new therapeutic principle. *Chem. Rev. 90*, 543–584.
(9) Usman, N., and Blatt, L. M. (2000) Nuclease-resistant synthetic ribozymes: developing a new class of therapeutics. *J. Clin. Invest. 106*, 1197–1202.
(10) Grosshans, H., and Filipowicz, W. (2008) Molecular biology: The expanding world of small RNAs. *Nature 451*, 414–416.
(11) Corey, D. R. (2007) RNA learns from antisense. *Nat. Chem. Biol. 3*, 8–11.
(12) Mittal, V. (2004) Improving the efficiency of RNA interference in mammals. *Nat. Rev. Gen. 5*, 355–365.
(13) Lee, J. F., Stovall, G. M., and Ellington, A. D. (2006) Aptamer therapeutics advance. *Curr. Opin. Chem. Biol. 10*, 282–289.
(14) Uhlmann, E., and Vollmer, J. (2003) Recent advances in the development of immunostimulatory oligonucleotides. *Curr. Opin. Drug Discovery Dev. 6*, 204–217.
(15) Wilson, C., and Keefe, A. D. (2006) Building oligonucleotide therapeutics using non-natural chemistries. *Curr. Opin. Chem. Biol. 10*, 607–614.
(16) Haasnoot, J., Westerhout, E. M., and Berkhout, B. (2007) RNA interference against viruses: strike and counterstrike. *Nat. Biotechnol. 25*, 1435–1443.
(17) Kim, D. H., and Rossi, J. J. (2007) Strategies for silencing human disease using RNA interference. *Nat. Rev. Gen. 8*, 173–184.
(18) Bumcrot, D., Manoharan, M., Koteliansky, V., and Sah, D. W. Y. (2006) RNAi therapeutics: a potential new class of pharmaceutical drugs. *Nat. Chem. Biol. 2*, 711–719.
(19) Dykxhoorn, D. M., Palliser, D., and Lieberman, J. (2006) The silent treatment: siRNAs as small molecule drugs. *Gene Ther. 13*, 541–552.
(20) Leung, R. K. M., and Whittaker, P. A. (2005) RNA interference: from gene silencing to gene-specific therapeutics. *Pharm. Ther. 107*, 222–239.
(21) Dorsett, Y., and Tuschl, T. (2004) siRNA: applications in functional genomics and potential as therapeutics. *Nat. Rev. Drug Discovery 3*, 318–329.
(22) Manoharan, M. (2002) Oligonucleotide conjugates as potential antisense drugs with improved uptake, biodistribution, targeted delivery, and mechanism of action. *Antisense Nucleic Acids Drug Dev. 12*, 103–128.
(23) Akhtar, S., Hughes, M. D., Khan, A., Bibby, M., Hussain, M., Nawaz, Q., Double, J., and Sayyed, P. (2000) The delivery of antisense therapeutics. *Adv. Drug Delivery Rev. 44*, 3–21.
(24) de Fougerolles, A., Vornlocher, H.-P., Maraganore, J., and Lieberman, J. (2007) Interfering with disease: a progress report on siRNA-based therapeutics. *Nat. Rev. Drug Discovery 6*, 443–453.
(25) Bendifallah, N., Rasmussen, F. W., Zachar, V., Ebbesen, P., Nielsen, P. E., and Koppelhus, U. (2006) Evaluation of cell-penetrating peptides (CPPs) as vehicles for intracellular delivery of antisense peptide nucleic acid (PNA). *Bioconjugate Chem. 17*, 750–758.
(26) Turner, J. J., Ivanova, G. D., Verbreure, B., Williams, D., Arzumanov, A. A., Abes, S., Lebleu, B., and Gait, M. J. (2005) Cell-penetrating peptide conjugates of peptide nucleic acids (PNA) as inhibitors of HIV-1 Tat-dependent *trans*-activation in cells. *Nucleic Acids Res. 33*, 6837–6849.
(27) Moulton, H. M., Nelson, M. H., Hatlevig, S. A., Reddy, M. T., and Iversen, P. L. (2004) Cellular uptake of antisense morpholino oligomers conjugated to arginine rich peptides. *Bioconjugate Chem. 15*, 290–299.
(28) Youngblood, D. S., Hatlevig, S. A., Hassinger, J. N., Iversen, P. L., and Moulton, H. M. (2007) Stability of cell-penetrating peptide-morpholino oligomer conjugates in human serum and in cells. *Bioconjugate Chem. 18*, 50–60.
(29) Amantana, A., Moulton, H. M., Cate, M. L., Reddy, M. T., Whitehead, T., Hassinger, J. N., Youngblood, D. S., and Iversen, P. L. (2007) Pharmacokinetics, biodistribution, stability and toxicity of a cell-penetrating peptide-morpholino oligomer conjugate. *Bioconjugate Chem. 18*, 1325–1331.
(30) Zhu, L., Ye, Z., Cheng, K., Miller, D. D., and Mahato, R. I. (2008) Site-specific delivery of oligonucleotides to hepatocytes after systemic administration. *Bioconjugate Chem. 19*, 290–298.
(31) Zhao, H., Greenwald, R. B., Reddy, P., Xia, J., and Peng, P. (2005) A new platform for oligonucleotide delivery utilizing the PEG prodrug approach. *Bioconjugate Chem. 16*, 758–766.
(32) Soutschek, J., Akinc, A., Bramlage, B., Charisse, K., Constien, R., Donoghue, M., Elbashir, S., Geick, A., Hadwiger, P., Harborth, J., John, M., Kesavan, V., Lavine, G., Pandey, R. K., Racie, T., Rajeev, K. G., Röhl, I., Toudjarska, I., Wang, G., Wuschko, S., Bumcrot, D., Koteliansky, V., Limmer, S., Manoharan, M., and Vornlocher, H.-P. (2004) Therapeutic silencing of an endogenous gene by systemic administration of modified siRNAs. *Nature 432*, 173–178.
(33) Wolfrum, C., Shi, S., Jayaprakash, K. N., Jayraman, M., Wang, G., Pandey, R. K., Rajeev, K. G., Nakayama, T., Charrise, K., Ndungo, E. M., Zimmermann, T., Koteliansky, V., Manoharan, M., and Stoffel, M. (2007) Mechanisms and optimization of *in vivo* delivery of lipophilic siRNAs. *Nat. Biotechnol. 25*, 1149–1157.
(34) Ueno, Y., Kawada, K., Naito, T., Shibata, A., Yoshikawa, K., Kim, H.-S., Wataya, Y., and Kitade, Y. (2008) Synthesis and silencing properties of siRNAs possessing lipophilic groups at their 3′-termini. *Bioorg. Med. Chem. 16*, 7698–7704.
(35) McNamara, J. O., II, Andrechek, E. R., Wang, Y., Viles, K. D., Rempel, R. E., Gilboa, E., Sullenger, B. A., and Giangrande, P. H. (2006) Cell type-specific delivery of siRNAs with aptamer-siRNA chimeras. *Nat. Biotechnol. 24*, 1005–1015.
(36) For a recent review, see (a) Gissot, A., Camplo, M., Grinstaff, M. W., and Barthelemy, P. (2008) Nucleoside, nucleotide and oligonucleotide based amphiphiles: a successful marriage of nucleic acids with lipids. *Org. Biomol. Chem. 6*, 1324–1333.
(37) Bijsterbosch, M. K., Manoharan, M., Dorland, R., Waarlo, I. H. E., Biessen, E. A. L., and van Berkel, T. J. C. (2001) Delivery of cholesteryl-conjugated phosphorothioate oligodeoxynucleotides to Kupffer cells by lactosylated low-density lipoprotein. *Biochem. Pharmacol. 62*, 627–633.
(38) Manoharan, M., Tivel, K. L., Condon, T. P., Andrade, L. K., Barber-Peoch, I., Inamati, G., Shah, S., Mohan, V., Graham, M. J., Bennett, C. F., Crooke, S. T., and Cook, P. D. (1997) Conjugated antisense oligonucleotides. *Nucleosides Nucleotides 16*, 1129–1138.
(39) Krieg, A. M., Tonkinson, J., Matson, S., Zhao, Q., Saxon, M., Zhang, L. M., Bhanja, U., Yakubov, L., and Stein, C. A. (1993) Modification of antisense phosphodiester oligodeoxynucleotides by a 5′ cholesteryl moiety increases cellular association and improves efficacy. *Proc. Natl. Acad. Sci. U.S.A. 90*, 1048–1052.
(40) Stetsenko, D. A., and Gait, M. J. (2001) A convenient solid-phase method for synthesis of 3′-conjugates of oligonucleotides. *Bioconjugate Chem. 12*, 576–586.
(41) Marasco, C. J., Angekino, N. J., Paul, B., and Dolnick, B. J. (1994) A simplified synthesis of acridine and/or lipid containing oligodeoxynucleotides. *Tetrahedron Lett. 35*, 3029–3032.

(42) Manoharan, M. (2002) Oligonucleotide conjugates as potential antisense drugs with improved uptake, biodistribution, targeted delivery, and mechanism of action. *Antisense Nucleic Acids Drug Dev. 12*, 103–128.

(43) Rait, A., Pirollo, K., Will, D. W., Peyman, A., Rait, V., Uhlmann, E., and Chang, E. H. (2000) 3′-End conjugates of minimally phopshorothioate-protected oligonucleotides with 1-*O*-hexadecylglycerol: synthesis and anti-*ras*-activity in radiation-resistant cells. *Bioconjugate Chem. 11*, 153–160.

(44) Habus, I., Zhao, Q., and Agrawal, S. (1995) Synthesis, hybridization properties, nuclease stability and cellular uptake of the oligonucleotide-amino-β-cyclodextrins and adamantine conjugates. *Bioconjugate Chem. 6*, 327–331.

(45) Vu, H., Hill, T. S., and Jayaraman, K. (1994) Synthesis and properties of cholesteryl-modified triplex-forming oligonucleotides containing a triglycyl linker. *Bioconjugate Chem. 5*, 666–668.

(46) Vu, H., Singh, P., Lewis, L., Zendegui, J. G., and Jayaraman, K. (1993) Synthesis of cholesteryl supports and phosphoramidite for automated DNA synthesis of triple-helix forming oligonucleotides. *Nucleosides Nucleotides 12*, 853–864.

(47) Will, D. W., and Brown, T. (1992) Attachement of vitamin E derivatives to oligonucleotides during solid-phase synthesis. *Tetrahedron Lett. 33*, 2729–2732.

(48) Reed, M. W., Adams, A. D., Nelson, J. S., and Meyer, R. B., Jr. (1991) Acridine and cholesterol-derivatized solid supports for improved synthesis of 3′-modified oligonucleotides. *Bioconjugate Chem. 2*, 217–225.

(49) Reed, M. W., Lukhtanov, E. A., Gorn, V. V., Lucas, D. D., Zhou, J. H., Pai, S. B., Cheng, Y.-c., and Meyer, R. B., Jr. (1995) Structure-activity relationships of cytotoxic cholesterol-modified DNA duplexes. *J. Med. Chem. 38*, 4587–4596.

(50) Manoharan, M., Tivel, K. L., and Cook, P. D. (1995) Lipidic nucleic acids. *Tetrahedron Lett. 36*, 3651–3654.

(51) Matysiak, S., Frank, R., and Pfleiderer, W. (1997) Acetal oligonucleotide conjugates in antisense strategy. *Nucleosides Nucleotides 16*, 855–861.

(52) MacKellar, C., Graham, D., Will, D. W., Burgess, S., and Brown, T. (1992) Antisense oligonucleotides bearing terminal lipophilic groups. *Nucleic Acids Res. 20*, 3411–3417.

(53) Shea, R. G., Marsters, J. C., and Bischofberger, N. (1990) Synthesis, hybridization properties and antiviral activity of lipid-oligodeoxynucleotide conjugates. *Nucleic Acids Res. 18*, 3777–3783.

(54) Lehmann, T. J., and Engels, J. W. (2001) Synthesis and properties of bile acid phosphoramidites 5′-tethered to antisense oligodeoxynucleotides against HCV. *Bioorg. Med. Chem. 9*, 1827–1835.

(55) Godeau, G., Staedel, C., and Barthélémy, P. (2008) Lipid-conjugated oligonucleotides via "click chedmistry" efficiently inhibit Hepatitis C virus translation. *J. Med. Chem. 51*, 4374–4376.

(56) Polushin, N. N., and Cohen, J. S. (1994) Antisense pro-drugs: 5′-ester oligodeoxyribonucleotides. *Nucleic Acids Res. 22*, 5492–5496.

(57) Durand, A., and Brown, T. (2007) Synthesis and properties of oligonucleotides containing a cholesterol thymidine monomer. *Nucleosides Nucleotides Nucleic Acids 26*, 785–794.

(58) Kurz, A., Bunge, A., Windeck, A.-K., Rost, M., Flasche, W., Arbuzova, A., Strohbach, D., Müller, S., Liebscher, J., Huster, D., and Herrmann, A. (2006) Lipid-anchored oligonucleotides for stable double-helix formation in distinct membrane domains. *Angew. Chem., Int. Ed. 45*, 4440–4444.

(59) Bryld, T., and Lomholt, C. (2007) Attachment of cholesterol to amino-LNA: synthesis and hybridization properties. *Nucleosides Nucleotides Nucleic Acids 26*, 1645–1647.

(60) Guzaev, A., and Lönnberg, H. (1999) Solid support synthesis of ester linked hydrophobic conjugates of oligonucleotides. *Tetrahedron 55*, 9101–9116.

(61) Letsinger, R. L., Zhang, G., Sun, D. K., Ikeuchi, T., and Sarin, P. S. (1989) Cholesteryl-conjugated oligonucleotides: Synthesis, properties, and activity as inhibitors of replication of human immunodeficiency virus in cell culture. *Proc. Natl. Acad. Sci. U.S.A. 86*, 6553–6556.

(62) D′Onofrio, J., Montesarchio, D., De Napoli, L., and Di Fabio, G. (2005) An efficient and versatile solid-phase synthesis of 5′- and 3′-conjugated oligonucleotides. *Org. Lett. 7*, 4927–4930.

(63) Guzaev, A., and Manoharan, M. (1998) Conjugation of oligonucleotides via an electrophilic tether: *N*-chloroacetamidohexyl phosphoramidite reagent. *Bioorg. Med. Chem. Lett. 8*, 3671–3676.

(64) Kobyláska, A., Okruszek, A., and Stec, W. J. (1998) Application of oxathiaphospholane method for the synthesis of oligodeoxyribonucleotide 5′-*O*-conjugates. *Nucleosides Nucleotides Nucleic Acids 17*, 1977–1982.

(65) Alvarez, K., Vasseur, J.-J., Beltran, T., and Imbach, J.-L. (1999) Photocleavable protecting groups as nucleobase protections allowed the solid-phase synthesis of base-sensitive SATE-prooligonucleotides. *J. Org. Chem. 64*, 6319–6328.

(66) Spinelli, N., Meyer, A., Hayakawa, Y., Imbach, J.-L., and Vasseur, J.-J. (2002) Use of allylic protecting groups for the synthesis of base-sensitive prooligonucleotides. *Eur. J. Org. Chem.* 49–56.

(67) Guerlavais-Dagland, T., Meyer, A., Imbach, J.-L., and Morvan, F. (2003) Fluoride-labile protecting groups for the synthesis of base-sensitive methyl-SATE oligonucleotide prodrugs. *Eur. J. Org. Chem.* 2327–2335.

(68) Ferreira, F., Vasseur, J.-J., and Morvan, F. (2004) Lewis acid deprotection of silyl-protected oligonucleotides and base-sensitive oligonucleotide analogues. *Tetrahedron Lett. 45*, 6287–6290.

(69) Iyer, R. P., Ho, N.-H., Yu, D., and Agrawal, S. (1997) Bioreversible oligonucleotide conjugates by site-specific derivatization. *Bioorg. Med. Chem. Lett. 7*, 871–876.

(70) Poijärvi, P., Heinonen, P., Virta, P., and Lönnberg, H. (2005) 2,2-Bis(ethoxycarbonyl) and 2-(alkylaminocarbonyl)-2-cyano substituted 3-(pivaloyloxy)propyl groups as biodegradable phosphate protections of oligonucleotides. *Bioconjugate Chem. 16*, 1564–1571.

(71) Grajkowski, A., Ausin, C., Kauffman, J. S., Snyder, J., Hess, S., Lloyd, J. R., and Beaucage, S. L. (2007) Solid-phase synthesis of thermolytic DNA oligonucleotides functionalized with a single 4-hydroxy-1-butyl or 4-phosphato-/thiophosphato-1-butyl tiophosphate protecting group. *J. Org. Chem. 72*, 805–815.

(72) Grajkowski, A., Pedras-Vasconcelos, J., Wang, V., Ausin, C., Hess, S., Verthelyi, D., and Beaucage, S. L. (2005) Thermolytic CpG-containing DNA oligonucleotides as potential immunotherapeutic prodrugs. *Nucleic Acids Res. 33*, 3550–3560.

(73) Gilmore, I. R., Fox, S. P., Hollins, A. J., and Akhtar, S. (2006) Delivery strategies for siRNA-mediated gene silencing. *Curr. Drug Delivery 3*, 147–155.

(74) Watanabe, S., Kusama-Eguchi, K., Kobayashi, H., and Igarashi, K. (1991) Estimation of polyamine binding to macromolecules and ATP in bovine lymphocytes and rat liver. *J. Biol. Chem. 266*, 20803–20809.

(75) Pons, B., Kotera, M., Zuber, G., and Behr, J.-P. (2006) Online synthesis of diblock cationic oligonucleotides for enhanced hybridization to their complementary sequence. *ChemBioChem 7*, 1173–1176.

(76) Sund, C., Puri, N., and Chattopadhyaya, J. (1996) Synthesis of *C*-branched spermine tethered oligo-DNA and the thermal stability of the duplexes and triplexes. *Tetrahedron 52*, 12275–12290.

(77) Sund, C., Puri, N., and Chattopadhyaya, J. (1997) The chemistry of *C*-branched spermine tethered oligo-DNA and their properties in forming duplexes and triplexes. *Nucleosides Nucleotides 16*, 755–760.

(78) Polushin, N. N. (2000) The precursor strategy: terminus methoxyoxalamido modifiers for single and multiple funcgtionalizations of oligodeoxyribonucleotides. *Nucleic Acids Res. 28*, 3125–3133.

(79) Potier, P., Abdennaji, A., and Behr, J.-P. (2000) Synthesis and hybridization properties of oligonucleotides containing polyamines at the C2 position of purines: A pre-synthetic approach for the incorporation of spermine into oligodeoxynucleotides containing 2-(4,9,13-triazatridecyl)-2′-deoxuguanosine. *Chem. Eur. J. 6*, 4188–4194.

(80) Godzina, P., Adrych-Rozek, K., and Markiewicz, W. T. (1999) Synthetic oligonucleotide combinatorial libraries. 3. Synthesis of polyaminonucleosides. *Nucleosides Nucleotides 18*, 2397–2414.

(81) Markiewicz, W. T., Godzina, P., and Markiewicz, M. (1999) Synthesis of polyaminooligonucleotides and their combinatorial libraries. *Nucleosides Nucleotides 18*, 1449–1454.

(82) Markiewicz, W. T., Godzina, P., Markiewicz, M., and Astriab, A. (1998) Synthesis of a polyaminooligonucleotide combinatorial library. *Nucleosides Nucleotides 17*, 1871–1880.

(83) Prakash, T. P., Barawkar, D. A., Kumar, V., and Ganesh, K. N. (1994) Synthesis of site-specific oligonucleotide-polyamine conjugates. *Bioorg. Med. Chem. Lett. 4*, 1733–1738.

(84) Marsh, A. J., Williams, D. M., and Grasby, J. A. (2004) The synthesis and properties of oligoribonucleotide-spermine conjugates. *Org. Biomol. Chem. 2*, 2103–2112.

(85) Shinozuka, K., Umeda, A., Aoki, T., and Sawai, H. (1998) Facile post-synthetic derivatization of oligodeoxynucleotide containing 5-methoxycarbonylmethyl-2′-deoxyuridine. *Nucleosides Nucleotides 17*, 291–300.

(86) Diaz, A. R., Eritja, R., and Garcia, R. G. (1997) Synthesis of oligodeoxynucleotides containing 2-substituted guanine derivatives using 2-fluoro-2′-deoxyinosine as common nucleoside precursor. *Nucleosides Nucleotides 16*, 2035–2051.

(87) Cooke, L. A., Frauendorf, C., Gilea, M. A., Holmes, S. C., and Vyle, J. S. (2006) Solid-phase synthesis of terminal oligonucleotide phosphoramidate conjugates. *Tetrahedron Lett. 47*, 719–722.

(88) Haas, J., and Engels, J. W. (2007) A nevel entry to 2′-*O*-aminopropyl modified nucleosides amenable for further modifications. *Tetrahedron Lett. 48*, 8891–8894.

(89) Zhang, H.-Y., Du, Q., Wahlestedt, C., and Liang, Z. (2006) RNA interference with chemically modified siRNA. *Curr. Top. Med. Chem. 6*, 893–900.

(90) Griffey, R. H., Monia, B. P., Cummins, L. L., Freier, S., Greig, M. J., Guinosso, C. J., Lesnik, E., Manalili, S. M., Mohan, V., Owens, S., Ross, B. R., Sasmor, H., Wancewicz, E., Weiler, K., Wheeler, P. D., and Cook, P. D. (1996) 2′-*O*-Aminopropyl ribonucleotides: a zwitterionic modification that enhances the exonuclease resistance and biological activity of antisense oligonucleotides. *J. Med. Chem. 39*, 5100–5109.

(91) Prakash, T. P., Manoharan, M., Fraser, A. S., Kawasaki, A. M., Lesnik, E. A., and Owens, O. R. (2000) Zwitterionic oligonucleotides with 2′-*O*-[3-(*N*,*N*-dimethylamino)propyl]-RNA modification: synthesis and properties. *Tetrahedron Lett. 41*, 4855–4859.

(92) Prhavc, M., Prakash, T. P., Minasov, G., Cook, P. D., Egli, M., and Manoharan, M. (2003) 2′-*O*-{2-[2-(*N*,N-Dimethylamino)ethoxy]ethyl} modified oligonucleotides: symbiosis of charge interaction factors and stereoelectronic effects. *Org. Lett. 5*, 2017–2020.

(93) Noe, C. R., Winkler, J., Urban, E., Gilbert, M., Haberhauer, G., and Brunar, H. (2005) Zwitterionic oligonucleotides: a study on binding properties of 2′-*O*-aminohexyl modifications. *Nucleosides Nucleotides Nucleic Acids 24*, 1167–1185.

(94) Winkler, J., and Noe, C. R. (2007) Oligonucleotide charge reversal: 2′-*O*-lysylaminohexyl modified oligonucleotides. *Nucleosides Nucleotides Nucleic Acids 26*, 939–942.

(95) Wikler, J., Gilbert, M., Kocourkova, A., Stessl, M., and Noe, C. R. (2008) 2′-*O*-Lysylaminohexyl oligonucleotides: Modifications for antisense and siRNA. *ChemMedChem 3*, 102–110.

(96) Prakash, T. P., Puschl, A., Lesnik, E., Mohan, V., Tereshko, V., Egli, M., and Manoharan, M. (2004) 2′-*O*-[(2-Guanidinium)ethyl]-modified oligonucleotides: stabilizing effect on duplex and triplex structures. *Org. Lett. 6*, 1971–1974.

(97) Ueno, Y., Nagasawa, Y., Sugimoto, I., Kojima, N., Kanazaki, M., Shuto, S., and Matsuda, A. (1998) Synthesis of oligodeoxynucleotides containing 4′-*C*-[2-[[*N*-(2-Aminoethyl)carbamoyl]oxy]ethyl]thymidine and their thermal stability and nuclease-resistance properties. *J. Org. Chem. 63*, 1660–1667.

(98) Kanazaki, M., Ueno, Y., Shuto, S., and Matsuda, A. (2000) Highly nuclease-resistant phosphodiester-type oligodeoxynucleotides containing 4′α-*C*-aminoalkylthymidines form thermally stable duplexes with DNA and RNA. A candidate for potent antisense molecules. *J. Am. Chem. Soc. 122*, 2422.

(99) Heystek, L. E., Zhou, H.-q., Dande, P., and Gold, B. (1998) Control over the localization of positive charge in DNA: the effect on duplex DNA and RNA stability. *J. Am. Chem. Soc. 120*, 12165–12166.

(100) Ueno, Y., Kumagai, I., Haginoya, N., and Matsuda, A. (1997) Effects of 5-(*N*-aminohexyl)carbamoyl-2′-deoxyuridine on endonuclease stability and the ability of oligodeoxynucleotide to activate RNase H. *Nucleic Acids Res. 25*, 3777–3782.

(101) Hashimoto, H., Nelson, M. G., and Switzer, C. (1993) Zwitterionic DNA. *J. Am. Chem. Soc. 115*, 7128–7134.

(102) Ito, T., Ueno, Y., Komatsu, Y., and Matsuda, A. (2003) Synthesis, thermal stability and resistance to enzymatic hydrolysis of the oligonucleotides containing 5-(*N*-aminohexyl)carbamoyl-2-′-*O*-methyluridines. *Nucleic Acids Res. 31*, 2514–2523.

(103) Ueno, Y., Mikawa, M., and Matsuda, A. (1998) Synthesis and properties of oligoceoxynucleotides containing 5-[*N*-[2-[*N*,*N*-bis(2-aminoethyl)amino]ethylcarbamoyl-2′-deoxyuridine and 5-[*N*-[3-[*N*,*N*-bis(3-aminopropyl)amino]propyl]carbamoyl]-2′-deoxyuridine. *Bioconjugate Chem. 9*, 33–39.

(104) Shinozuka, K., Matsukura, M., Okamoto, T., and Sawai, H. (1998) Synthesis and anti-HIV property of novel oligo-DNA phosphorothioate analogs bearing an intercalative moiety and/or polyamine residues. *Nucleosides Nucleotides 17*, 2081–2084.

(105) Ito, T., Ueno, Y., Komatsu, Y., and Matsuda, A. (2003) Synthesis, thermal stability and resistance to enzymatic hydrolysis of the oligonucleotides containing 5-(*N*-aminohexyl)carbamoyl-2′-*O*-methyluridines. *Nucleic Acids Res. 31*, 2514–2523.

(106) Haginoya, N., Ono, A., Nomura, Y., Ueno, Y., and Matsuda, A. (1997) Synthesis of oligodeoxyribonucleotides containing 5-(*N*-aminoalkyl)carbamoyl-2′-deoxyuridines by a postsynthetic modification method and their thermal stability and nuclease-resistance properties. *Bioconjugate Chem. 8*, 271–280.

(107) Vinogradov, S. V., Suzdaltseva, Y. G., and Kabanov, A. V. (1996) Block polycationic oligonucleotide derivative: synthesis and inhibition of herpes virus reproduction. *Bioconjugate Chem. 7*, 3–6.

(108) Morvan, F., Castex, C., Vives, E., and Imbach, J.-L. (2001) Polyimidazole conjugated oligonucleotides reach the nucleus of HeLa cells. *Nucleosides Nucleotides Nucleic Acids 20*, 805–808.

(109) Stewart, K. M., Horton, K. L., and Kelley, S. O. (2008) Cell-penetrating peptides as delivery vehicles for biology and medicine. *Org. Biomol. Chem. 6*, 2242–2255.

(110) Hansen, M., Kilk, K., and Langel, U. (2008) Predicting cell-penetrating peptides. *Adv. Drug Delivery Rev. 60*, 572–579.

(111) Lebleu, B., Moulton, H. M., va, G. D., Abes, S., Stein, D. A., Iversen, P. L., Arzumanov, A. A., and Gait, M. J. (2008) Cell penetrating peptide conjugates of steric block oligonucleotides. *Adv. Drug Delivery Rev. 60*, 517–529.

(112) Zatsepin, T. S., Turner, J. J., Oretskaya, T. S., and Gait, M. J. (2005) Conjugates of oligonucleotides and analogues with cell penetrating peptides as gene silencing agents. *Curr. Pharmaceut. Design 11*, 3639–3654.

(113) Gait, M. J. (2003) Peptide-mediated cellular delivery of antisense oligonucleotides and their analogues. *Cell. Mol. Life Sci. 60*, 844–853.

(114) Kubo, T., Bakalova, R., Zhelev, Z., Ohba, H., and Fujii, M. (2005) Controlled intracellular localization of oligonucleotides by chemical conjugation, In *Non-Viral Gene Therapy* (Taira, K., Kataoka, K., and Niidome, T., Eds.) pp 187−197, Springer, Tokyo.

(115) Eritja, R. (2007) Solid-phase synthesis of modified oligonucleotides. *Int. J. Pept. Res. Therapeut. 13*, 53–68.
(116) Venkatesan, N., and Kim, B. H. (2006) Peptide conjugates of oligonucleotides: synthesis and applications. *Chem. Rev. 106*, 3712–3761.
(117) Zubin, E. M., Romanova, E. A., and Oretskaya, T. S. (2002) Modern methods for the synthesis of peptide-oligonucleotide conjugates. *Russ. Chem. Rev. 71*, 239–264.
(118) Tung, C.-H., and Stein, S. (2000) Preparation and applications of peptide-oligonucleotide conjugates. *Bioconjugate Chem. 11*, 605–618.
(119) Eritja, R. (2000) Synthesis of oligonucleotide-peptide conjugates and nucleopeptides, In *Solid-Phase Synthesis* (Kates, S. A. and Albericio, F., Eds.) pp 529−548, Marcel Dekker, New York.
(120) Singh, Y., Spinelli, N., and Defrancq, E. (2008) Chemical strategies for oligonucleotide-conjugate synthesis. *Curr. Org. Chem. 12*, 263–290.
(121) Juby, C. D., Richardsson, C. D., and Brousseau, R. (1991) Facile preparation of 3′-oligonucleotide-peptide conjugates. *Tetrahedron Lett. 32*, 879–882.
(122) Tung, G., Lawlor, J. M., Tregear, G. W., and Haralambidis, J. (1993) The synthesis of oligonucleotide-polyamide conjugate molecules suitable as PCR primers. *J. Org. Chem. 58*, 2223–2231.
(123) Antopolsky, M., and Azhayev, A. (1999) Stepwise solid-phase synthesis of peptide-oligonucleotide conjugates on new solid supports. *Helv. Chim. Acta 82*, 2130–2140.
(124) Basu, S., and Wickstrom, E. (1995) Solid phase synthesis of a D-peptide-phosphorothioate oligodeoxynucleotide conjugate from two arms of a polyethylene glycol-polystyrene support. *Tetrahedron Lett. 36*, 4943–4946.
(125) Antopolsky, M., Azhayeva, E., Tengvall, U., and Azhayev, A. (2002) Towards a general method for the stepwise solid-phase synthesis of peptide-oligonucleotide conjugates. *Tetrahedron Lett. 43*, 527–530.
(126) Antopolsky, M., and Azhayev, A. (2000) Stepwise solid-phase synthesis of peptide-oligonucleotide phosphorothioate conjugates employing Fmoc peptide chemistry. *Tetrahedron Lett. 41*, 9113–9117.
(127) Terenzi, S., Biala, E., Nguyen-Trung, N. Q., and Strazewski, P. (2003) Amphiphilic 3′-peptidyl-RNA conjugates. *Angew. Chem., Int. Ed. 42*, 2909–2912.
(128) Winkler, J., Urban, E., and Noe, C. R. (2005) Oligonucleotides conjugated to short lysine chains. *Bioconjugate Chem. 16*, 1038–1044.
(129) De Napoli, L., Messere, A., Montesarchio, D., Piccialli, G., Benedetti, E., Bucci, E., and Rossi, F. (1999) A new solid-phase synthesis of oligonucleotides 3′-conjugated with peptides. *Bioorg. Med. Chem. 7*, 395–400.
(130) Robles, J., Maseda, M., Beltran, M., Concernau, M., Pedroso, E., and Grandas, A. (1997) Synthesis and enzymatic stability of phosphodiester-linked peptide-oligonucleotide hybrids. *Bioconjugate Chem. 8*, 785–788.
(131) Debéthune, L., Marchán, V., Fàbregas, G., Pedroso, E., and Grandas, A. (2002) Towards nucleopeptides containing any trifunctional amino acid (II). *Tetrahedron 58*, 6965–6978.
(132) Robles, J., Pedroso, E., and Grandas, A. (1994) Stepwise solid-phase synthesis of nucleopeptide Phac-Ser(p$^{5'}$CATCAT)-Gly-Asp-OH from adenovirus-2 nucleoprotein. *Tetrahedron Lett. 35*, 4449–4452.
(133) Robles, J., Pedroso, E., and Grandas, A. (1995) Solid-phase synthesis of a nucleopeptide from the linking site of adenovirus-2 nucleoprotein, -Ser(p$^{5'}$CATCAT)-Gly-Asp-. Convergent versus stepwise strategy. *Nucleic Acids Res. 23*, 4151–4161.
(134) Robles, J., Beltran, M., Marchan, V., Perez, Y., Travesset, I., Pedroso, E., and Grandas, A. (1999) Towards nucleopeptides containing any trifunctional amino acid. *Tetrahedron 55*, 13251–13264.
(135) Gómez-Pinto, I., Marchán, V., Gago, F., Grandas, A., and González, C. (2003) Solution structure and stability of tryptophan-containing nucleopeptide duplexes. *ChemBioChem 4*, 40–49.
(136) Debéthune, L., Kohlhagen, G., Grandas, A., and Pommier, Y. (2002) Processing of nucleopeptides mimicking the topoisomerase I-DNA covalent complex by tyrosyl-DNA phosphodiesterase. *Nucleic Acids Res. 30*, 1198–1204.
(137) Frieden, M., Aviñó, A., Tarrasón, G., Escorihuela, M., Piulats, J., and Eritja, R. (2004) Synthesis of oligonucleotide-peptide conjugates carrying the c-*myc* peptide epitope as recognition system. *Chem. Biodiversity 1*, 930–938.
(138) Beltran, M., Pedroso, E., and Grandas, A. (1998) A comparison of histidine protecting groups in the synthesis of peptide-oligonucleotide conjugates. *Tetrahedron Lett. 39*, 4115–4118.
(139) Betran, M., Maseda, M., Perez, Y., Robles, J., Pedroso, E., and Grandas, A. (1997) Stepwise solid-phase synthesis of serine-, tyrosine- and homoserine-nucleopeptides. *Nucleosides Nucleotides 16*, 1487–1488.
(140) Robles, J., Pedroso, E., and Grandas, A. (1994) Stepwise solid-phase synthesis of the nucleopeptide Phac-Phe-Val-Ser(p$^{3'}$ACT)-Gly-OH. *J. Org. Chem. 59*, 2482–2486.
(141) Marchan, V., Rodriguez-Tanty, C., Estrada, M., Pedroso, E., and Grandas, A. (2000) Alternative procedures for the synthesis of methionine-containing peptide-oligonucleotide hybrids. *Eur. J. Org. Chem.* 2495–2500.
(142) Chen, C.-P., Li, X.-X., Zhang, L.-R., Min, J.-M., Chan, J. Y.-W., Fung, K.-P., Wang, S.-Q., and Zhang, L.-H. (2002) Synthesis of antisense oligonucleotide-peptide conjugate targeting to GLUT-1 in HepG-2 and MCF-7 cells. *Bioconjugate Chem. 13*, 525–529.
(143) Chen, C.-P., Zhang, L.-R., Peng, Y.-F., Wang, X.-B., Wang, S.-Q., and Zhang, L.-H. (2003) A concise method for the preparation of peptide and arginine-rich peptide-conjugated antisense oligonucleotide. *Bioconjugate Chem. 14*, 532–538.
(144) de laTorre, B. G., Avino, A., Tarrason, G., Piulats, J., Albericio, F., and Eritja, R. (1994) Stepwise solid-phase synthesis of oligonucleotide-peptide hybrids. *Tetrahedron Lett. 35*, 2733–2736.
(145) de la Torre, B. G., Albericio, F., Saison-Behmoaras, E., Bachi, A., and Eritja, R. (1999) Synthesis and binding properties of oligonucleotides carrying nuclear localization sequences. *Bioconjugate Chem. 10*, 1005–1012.
(146) Haralambidis, J., Duncan, L., and Tregear, G. W. (1987) The solid phase synthesis of oligonucleotides containing a 3′-peptide moiety. *Tetrahedron Lett. 28*, 5199–5202.
(147) Truffert, J.-C., Asseline, U., Brack, A., and Thuong, N. T. (1996) Synthesis, purification and characterization of two peptide-oligonucleotide conjugates as potential artificial nucleases. *Tetrahedron 52*, 3005–3016.
(148) Truffert, J.-C., Asseline, U., Thuong, N. T., and Brack, A. (1995) Synthesis, characterization and binding properties of peptide-oligonucleotide conjugates containing the SPKK peptide motif. *Protein Pept. Lett. 2*, 419–424.
(149) Stetsenko, D. A., Malakhov, A. D., and Gait, M. J. (2002) Total stepwise solid-phase synthesis of oligonucleotide-(3′→*N*)-peptide conjugates. *Org. Lett. 4*, 3259–3262.
(150) Truffert, J.-C., Lorthioir, O., Asseline, U., Thuong, N. T., and Brack, A. (1994) On-line solid phase synthesis of oligonucleotide-peptide hybrids using silica supports. *Tetrahedron Lett. 35*, 2353–2356.
(151) Soukchareun, S., Tregear, G. W., and Haralambidis, J. (1995) Preparation and characterization of antisense oligonucleotide-peptide hybrids containing viral fusion peptides. *Bioconjugate Chem. 6*, 43–53.
(152) Haralambidis, J., Duncan, L., Angus, K., and Tregear, G. W. (1990) The synthesis of polyamide-oligonucleotide conjugate molecules. *Nucleic Acids Res. 18*, 493–499.
(153) Portela, C., Mascarenas, J. L., Albericio, F., Mazzini, S., Caminal, C., Ramos, R., Ocampo, S. M., and Eritja, R. (2007) New developments in the synthesis of oligonucleotide-peptide conjugates. *Nucleosides Nucleotides Nucleic Acids 26*, 963–967.

(154) Zaramella, S., Yeheskiely, E., and Strömberg, R. (2004) A method for solid-phase synthesis of oligonucleotide 5′-peptide-conjugates using acid-labile α-amino protections. *J. Am. Chem. Soc. 126*, 14029–14035.

(155) Ocampo, S. M., Albericio, F., Fernandez, I., Vilaseca, M., and Eritja, R. (2005) A straightforward synthesis of 5′-peptide oligonucleotide conjugates using N^{α}-Fmoc-protected amino acids. *Org. Lett. 7*, 4349–4352.

(156) Tetzlaff, C. N., Schwope, I., Bleczinski, C. F., Steinberg, J. A., and Richert, C. (1998) A convenient synthesis of 5′-amino-5′-deoxythymidine and preparation of peptide-DNA hybrids. *Tetrahedron Lett. 39*, 4215–4218.

(157) Bergmann, F., and Bannwarth, W. (1995) Solid phase synthesis of directly linked peptide oligodeoxynucleotide hybrids using standard synthesis protocols. *Tetrahedron Lett. 36*, 1839–1842.

(158) Schwope, I., Bleczinski, C. F., and Richert, C. (1999) Synthesis of 3′,5′-dipeptidyl oligoribonucleotides. *J. Org. Chem. 64*, 4749–4761.

(159) Sarracino, D. A., and Richert, C. (2001) Synthesis and nuclease stability of trilysyl dendrimer-oligodeoxyribonucleotide hybrids. *Bioorg. Med. Chem. Lett. 11*, 1733–1736.

(160) Engholm, M., Buchardt, O., Nielsen, P. E., and Berg, R. H. (1992) Peptide nucleic acids (PNA). Oligonucleotide analogs with an achiral peptide backbone. *J. Am. Chem. Soc. 114*, 1895–1897.

(161) Nielsen, P. E., Koppelhus, U., and Beck, F. (2004) A pseudopeptide with DNA-like properties, In *Pseudo-peptides in drug discovery* (Nielsen, P. E., Ed.) pp 153−191, Wiley, Weinheim.

(162) van der Laan, A. C., Meeuwenoord, N. J., Kuyl-Yeheskiely, E., Oosting, R. S., Brands, R., and van Boom, J. (1995) Solid support synthesis of a PNA DNA hybrid. *Rec. Trav. Chim. Pays-Bas 114*, 295–297.

(163) Capasso, D., De Napoli, L., Di Fabio, G., Messere, A., Montesarchio, D., Pelone, C., Piccialli, G., and Saviano, M. (2001) Solid phase synthesis of DNA-3′-PNA chimeras by using Bhoc/Fmoc PNA monomers. *Tetrahedron 57*, 9481–9486.

(164) Moggio, L., De Napoli, L., Di Blasio, B., Di Fabio, G., D′Onofrio, J., Montesarchio, D., and Messere, A. (2006) Solid-phase synthesis of cyclic PNA and PNA-DNA chimeras. *Org. Lett. 8*, 2015–2018.

(165) Robles, J., Pedroso, E., and Grandas, A. (1995) Peptide-oligonucleotide hybrids with *N*-acylphosphoramidate linkages. *J. Org. Chem. 60*, 4856–4861.

(166) Sakakura, A., and Hayakawa, Y. (2000) A novel synthesis of oligonucleotide-peptide conjugates with a base-labile phosphate linker between the two components according to the allyl-protected phosphoramidite strategy. *Tetrahedron 56*, 4427–4435.

(167) Peyrottes, S., Mestre, B., Burlina, F., and Gait, M. J. (1998) The synthesis of peptide-oligonucleotide conjugates by a fragment coupling approach. *Tetrahedron 54*, 12513–12522.

(168) Peyrottes, S., Mestre, B., Burlina, F., and Gait, M. J. (1999) Studies towards the synthesis of peptide-oligonucleotide conjugates. *Nucleosides Nucleotides 18*, 1443–1448.

(169) Kubo, T., Morikawa, M., Ohba, H., and Fujii, M. (2003) Synthesis of DNA-peptide conjugates by solid-phase fragment condensation. *Org. Lett. 5*, 2623–2626.

(170) Diala, I., Osada, A., Maruoka, S., Imanisi, T., Murao, S., Ato, T., Ohba, H., and Fujii, M. (2007) Synthesis of phosphorothioate oligonucleotide-peptide conjugates by solid phase fragment condensation. *Bioorg. Med. Chem. Lett. 17*, 6576–6578.

(171) Zubin, E. M., Romanova, E. A., Volkov, E. M., Tashlitsky, V. N., Korshunova, G. A., Shabarova, Z. A., and Oretskaya, T. S. (1999) Oligonucleotide-peptide conjugates as potential antisense agents. *FEBS Lett. 456*, 59–62.

(172) Kachalova, A., Zubin, E., Stetsenko, D., Gait, M., and Oretskaya, T. (2004) Oligonucleotides with 2′-*O*-carboxymethyl group: synthesis and 2′-conjugation *via* amide bond formation on solid phase. *Org. Biomol.Chem. 2*, 2793–2797.

(173) Kachalova, A. V., Stetsenko, D. A., Romanova, E. A., Tashlitsky, V. N., Gait, M. J., and Oretskaya, T. S. (2002) A new and efficient method for synthesis of 5′-conjugates of oligonucleotides through amide-bond formation on solid phase. *Helv. Chim. Acta 85*, 2409–2416.

(174) Zatsepin, T. S., Stetsenko, D. A., Gait, M. J., and Oretskaya, T. S. (2005) Synthesis of DNA conjugates by solid-phase frament condensation via aldehyde-nucleophile coupling. *Tetrahedron Lett. 46*, 3191–3195.

(175) Doores, K. J., Gamblin, D. P., and Davis, B. G. (2006) Exploring and exploiting the therapeutic potential of glycoconjugates. *Chem. Eur. J. 12*, 656–665.

(176) Kiessling, L. L., Gestwicki, J. E., and Strong, L. E. (2006) Synthetic multivalent ligands as probes of signal transduction. *Angew. Chem., Int. Ed. 45*, 2348–2368.

(177) Gabius, H.-J., Siebert, H.-C., Andre, S., Jimenez-Barbero, J., and Rüdiger, H. (2004) Chemical biology of the sugar code. *ChemBioChem 5*, 740–764.

(178) Toole, B. P. (2004) Hyaluronan: From extracellular glue to pericellular cue. *Nat. Rev. Cancer 4*, 528–539.

(179) Luo, Y., Ziebell, M. R., and Prestwich, G. D. (2000) A hyaluronic acid-taxol antitumor bioconjugate targeted to cancer cells. *Biomacromolecules 1*, 208–218.

(180) Srinivas, O., Larrieu, P., Duverger, E., Boccaccio, C., Bousser, M.-T., Monsigny, M., Fonteneau, J.-F., Jotereau, F., and Roche, A.-C. (2007) Synthesis of glycocluster-tumor antigenic peptide conjugates for dendritic cell targeting. *Bioconjugate Chem. 18*, 1547–1554.

(181) Rendle, P. M., Seger, A., Rodrigues, J., Oldham, N. J., Bott, R. R., Jones, J. B., Cowan, M. M., and Davisv, B. G. (2004) Glycodendriproteins: a synthetic glycoprotein mimic enzyme with branched sugar-display potently inhibits bacterial aggregation. *J. Am. Chem. Soc. 126*, 4750–4751.

(182) Yan, H., and Tram, K. (2007) Glycotargeting to improve cellular delivery efficiency of nucleic acids. *Glycoconj. J. 24*, 107–123.

(183) Zatsepin, T. S., and Oretskaya, T. S. (2004) Synthesis and applications of oligonucleotide-carbohydrate conjugates. *Chem. Biodiversity 1*, 1401–1416.

(184) D′Onofrio, J., Petraccone, L., Martino, L., Di Fabio, G., Iadonisi, A., Balzarini, J., Giancola, C., and Montesarchio, D. (2008) Synthesis, biophysical characterization and anti-HIV activity of glycol-conjugated G-quadruplex-forming oligonucleotides. *Bioconjugate Chem. 19*, 607–616.

(185) D′Onofrio, J., Erra, E., Di Fabio, G., Iadonisi, A., Petraccone, L., De Napoli, L., Barone, G., Balzarini, J., Giancola, C., and Montesarchio, D. (2007) Synthesis and biophysical characterization of G-rich oligonucleotides conjugated with sugar-phosphate tails. *Nucleosides Nucleotides Nucleic Acids 26*, 1225–1229.

(186) Akhtar, S., Routledge, A., Patel, R., and Gardiner, J. M. (1995) Synthesis of mono- and dimannoside phosphoramidite derivatives for solid-phase conjugation to oligonucleotides. *Tetrahedron Lett. 36*, 7333–7336.

(187) Wang, Y., and Sheppard, T. L. (2003) Chemoenzymatic synthesis and antibody detection of DNA glycoconjugates. *Bioconjugate Chem. 14*, 1314–1322.

(188) Adinolfi, M., De Napoli, L., Di Fabio, G., Iadonisi, A., and Montesarchio, D. (2004) Modulating the activity of oligonucleotides by carbohydrate conjugation: solid phase synthesis of sucrose-oligonucleotide hybrids. *Org. Biomol. Chem. 2*, 1879–1886.

(189) Adinolfi, M., De Napoli, L., Di Fabio, G., Iadonisi, A., Montesarchio, D., and Piccialli, G. (2002) Solid phase synthesis of oligonucleotides tethered to oligo-glucose phosphate tail. *Tetrahedron 58*, 6697–6704.

(190) Sheppard, T. L., Wong, C.-H., and Joyce, G. F. (2000) Nucleoglycoconjugates: Design and synthesis of a new class of DNA-carbohydrate conjugates. *Angew. Chem., Int. Ed. 39*, 3660–3663.

(191) Dubber, M., and Fréchet, J. M. J. (2003) Solid-phase synthesis of multivalent glycoconjugates on a DNA synthesizer. *Bioconjugate Chem. 14*, 239–246.

(192) Ketomäki, K., and Virta, P. (2008) Synthesis of aminoglycoside conjugates of 2′-*O*-methyl oligoribonucleotides. *Bioconjugate Chem. 19*, 766–777.

(193) Maier, M. A., Yannopoulos, C. G., Mohamed, N., Roland, A., Fritz, H., Mohan, V., Just, G., and Manoharan, M. (2003) Synthesis of antisense oligonucleotides conjugated to a multilalent carbohydrate cluster for cellular targeting. *Bioconjugate Chem. 14*, 18–29.

(194) D′Onofrio, J., de Champdoré, M., De Napoli, L., Montesarchio, D., and Di Fabio, G. (2005) Glycomimetics as decorating motifs for oligonucleotides: solid-phase synthesis, stability, and hydridization properties of carbopeptoid-oligonucleotide conjugates. *Bioconjugate Chem. 16*, 1299–1309.

(195) Matsuura, K., Hibino, M., Ikeda, T., Yamada, Y., and Kobayashi, K. (2004) Self-organized glycoclusters along DNA: Effect of the spatial arrangement of galactoside residues on cooperative lectin recognition. *Chem. Eur. J. 10*, 352–359.

(196) Matsuura, K., Hibino, M., Yamada, Y., and Kobayashi, K. (2001) Construction of glycol-clusters by self-organization of site-specifically glycosylated oligonucleotides and their cooperative amplification of lectin recognition. *J. Am. Chem. Soc. 123*, 357–358.

(197) Turner, J. J., Meeuwenoord, N. J., Rood, A., Borst, P., van der Marel, G. A., and van Boom, J. H. (2003) Reinvestigation into the synthesis of oligonucleotides containing 5-(*β*-D-glucopyranosyloxymethyl)-2′-deoxyuridine. *Eur. J. Org. Chem.* 3832–3839.

(198) Tona, R., Bertolini, R., and Hunziker, J. (2000) Synthesis of aminoglycoside-modified oligonucleotides. *Org. Lett. 2*, 1693–1696.

(199) Hunzinker, J. (1999) Synthesis of 5-(2-amino-2-deoxy-*β*-D-glucopyranosyloxymethyl)-2′-deoxyuridine and its incorporation into oligothymidylates. *Bioorg. Med. Chem. Lett. 9*, 201–204.

(200) Charles, I., Xi, H., and Arya, D. P. (2007) Sequence-specific targeting of RNA with an oligonucleotide-neomycin conjugate. *Bioconjugate Chem. 18*, 160–169.

(201) Matulic-Adamic, J., Serebryany, V., Haeberli, P., Mokler, V. R., and Beigelman, L. (2002) Synthesis of *N*-acetyl-D-galactosamine and folic acid conjugated ribozymes. *Bioconjugate Chem. 13*, 1071–1078.

(202) Chevolot, Y., Bouillon, C., Vidal, S., Morvan, F., Meyer, A., Cloarec, J.-P., Jochum, A., Praly, J.-P., Vasseur, J.-J., and Souteyrand, E. (2007) DNA-based carbohydrate biochips: a platform for surface glycol-engineering. *Angew. Chem., Int. Ed. 46*, 2398–2402.

(203) Bouillon, C., Meyer, A., Vidal, S., Jochum, A., Chevolot, Y., Cloarec, J.-P., Praly, J.-P., Vasseur, J.-J., and Morvan, F. (2006) Microwave assisted click chemistry for the synthesis of multiple labeled-carbohydrate oligonucleotides on solid support. *J. Org. Chem. 71*, 4700–4702.

(204) Morvan, F., Meyer, A., Jochum, A., Sabin, C., Chevolot, Y., Imberty, A., Praly, J.-P., Vasseur, J.-J., Souteyrand, E., and Vidal, S. (2007) Fucosylated pentaerythrityl phosphodiester oligomers (PePOs): automated synthesis of DNA-based glycoclusters and binding to *Pseudomonas aeruginosa* lectin (PA-IIL). *Bioconjugate Chem. 18*, 1637–1643.

(205) Kiviniemi, A., Virta, P., and Lönnberg, H. (2008) Utilization of intrachain 4′-*C*-azidomethylthymidine for preparation of oligodeoxyribonucleotide conjugates by click chemistry in solution and on a solid support. *Bioconjugate Chem. 19*, 1726–1734.

(206) Katajisto, J., Virta, H., and Lönnberg, H. (2004) Solid-phase synthesis of multiantennary oligonucleotide glycoconjugates utilizing on-support oximation. *Bioconjugate Chem. 15*, 890–896.

(207) Ambrosi, M., Cameron, N. R., and Davis, B. G. (2005) Lectins: tools for the molecular understanding of the glycocode. *Org. Biomol. Chem. 3*, 1593–1608.

(208) Gomez-Garcia, M., Benito, J. M., Rodriguez-Lucena, D., Yu, J.-X., Chmurski, K., Ortiz Mellet, C., Gutierrez Gallego, R., Maestre, A., Defaye, J., and Garcia Fernandez, J. M. (2005) Probing secondary carbohydrate-protein interactions with highly dense cyclodextrin-centered heteroglycoclusters: the heterocluster effect. *J. Am. Chem. Soc. 127*, 7970–7971.

(209) Katajisto, J., Heinonen, P., and Lönnberg, H. (2004) Solid-phase synthesis of oligonucleotide glycoconjugates bearing three different glycosyl groups: Orthogonally protected bis(hydroxymethyl)-*NN*-bis(3-hydroxypropyl)malondiamide phosphoramidite as a key building block. *J. Org. Chem. 69*, 7609–7615.

(210) Adinolfi, M., De Napoli, L., Di Fabio, G., Guariniello, J., Iadonisi, A., Messere, A., Montesarchio, D., and Piccialli, G. (2001) Solid phase synthesis of glyco-oligonucleotide conjugates. *Synlett* 745–748.

(211) Adinolfi, M., Barone, G., De Napoli, L., Guariniello, L., Iadonisi, A., and Piccialli, G. (1999) Solid phase glycosidation of oligonucleotides. *Tetrahedron Lett. 40*, 2607–2610.

(212) Bayer, E., Maier, M., Bleicher, K., and Gaus, H.-J. (1995) Synthesis of 3′-PEG-modified oligonucleotides on PS-PEG Tentagel polymers. *Z. Naturforsch. 50b*, 671–676.

(213) Jäschke, A., Fürste, J. P., Nordhoff, E., Hillenkamp, F., Cech, D., and Erdmann, V. A. (1994) Synthesis and properties of oligodeoxyribonucleotide-polyethylene glycol conjugates. *Nucleic Acids Res. 22*, 4810–4817.

(214) Jäschke, A., Bald, R., Nordhoff, E., Hillenkamp, F., Cech, D., Erdmann, V. A., and Fürste, J. P. (1996) Synthesis and analytical characterization of RNA-polyethylene glycol conjugates. *Nucleosides Nucleotides 15*, 1519–1529.

(215) Efimov, V. A., Kalinkina, A. L., and Chakhmakhcheva, O. G. (1993) Dipentafluorophenyl carbonate - a reagent for the synthesis of oligonucleotides and their conjugates. *Nucleic Acids Res. 21*, 5337–5344.

(216) Chernov, B. K., Chandler, D. P., and Golova, J. B. (2005) Synthesis of α-amino-*ω*-hydroxy-polyethyleneglycol oligodeoxyribonucleotide conjugates. *Lett. Org. Chem. 2*, 690–693.

(217) Kazanova, E. V., Zubin, E. M., Kachalova, A. V., Volkov, E. M., Oretskaya, T. S., Stetsenko, D. A., and Gottikh, M. B. (2007) A convenient solid-phase method for the synthesis of novel oligonucleotide-folate conjugates. *Nucleosides Nucleotides Nucleic Acids 26*, 1273–1276.

(218) Ikeda, S., Saito, I., and Sugiyama, H. (1998) Facile synthesis of puromycin-tethered oligonucleotides at the 3′-end. *Tetrahedron Lett. 39*, 5975–5978.

(219) Nyilas, A., Agrawal, S., and Zamecnik, P. (1993) Solid phase synthesis of oligonucleotides carrying puromycin at 3′-terminal. *Bioorg. Med. Chem. Lett. 3*, 1371–1374.

(220) Balaz, M., Holmes, A. E., Benedetti, M., Proni, G., and Berova, N. (2005) Porphyrin substituted phosphoramidites: new building blocks for porphyrin-oligonucleotide syntheses. *Bioorg. Med. Chem. 13*, 2413–2421.

(221) Sitaula, S., and Reed, S. M. (2008) Porphyrin conjugated to DNA by a 2′-amido-2′-deoxyuridine linkage. *Bioorg. Med. Chem. Lett. 18*, 850–855.

(222) Murashima, T., Hayata, K., Saiki, Y., Matsui, J., Miyoshi, D., Yamada, T., Miyazawa, T., and Sugimoto, N. (2007) Synthesis, structure and thermal stability of fully hydrophobic porphyrin-DNA conjugates. *Tetrahedron Lett. 48* (2007), 8514–8517.

(223) Li, H., Fedorova, O. S., Trunmle, W. R., Fletcher, T. R., and Czuchajowski, L. (1997) Site-specific photomodification of DNA by porphyrin-oligonucleotide conjugates synthesized via a solid phase H-phosphonate approach. *Bioconjugate Chem. 8*, 49–56.

(224) Sessler, J. L., Sansom, P. I., Kral, V., O'Connor, D., and Iverson, B. L. (1996) Sapphyrin-oligonucleotide conjugates. *J. Am. Chem. Soc. 118*, 12322–12330.

(225) Mammana, A., Asakawa, T., Bitsch-Jensen, K., Wolfe, A., Chaturantabut, S., Otani, Y., Li, X., Li, Z., Nakanishi, K., Balaz, M., Ellestad, G. A., and Berova, N. (2008) Synthesis and characterization of water-soluble free-base, zinc and copper porphyrin-oligonucleotide conjugates. *Bioorg. Med. Chem. 16*, 6544–6551.

(226) Milesi, D., Kutyavin, I., Lukhtanov, E. A., Gorn, V. V., and Reed, M. W. (1999) Synthesis of oligonucleotide conjugates in anhydrous dimethyl sulfoxide. *Methods Enzymol. 313*, 164–173.

(227) Lukhtanov, E. A., Kutyavin, I. V., Gamper, H. B., and Meyer, R. B., Jr. (1995) Oligodeoxyribonucleotides with conjugated dihydropyrroloindole oligopeptides: preparation and hybridization properties. *Bioconjugate Chem. 6*, 418–426.

(228) Lukhtanov, E. A., Kutyavin, I. V., and Meyer, R. B., Jr. (1996) Direct, solid phase assembly of dihydropyrroloindole peptides with conjugated oligonucleotides. *Bioconjugate Chem. 7*, 564–567.

(229) Robles, J., Rajur, S. B., and McLaughlin, L. W. (1996) A parallel-stranded DNA triplex tethering a Hoechst 33258 analogue results in complex stabilization by simultaneous major groove and minor groove binding. *J. Am. Chem. Soc. 118*, 5820–5821.

(230) Moriguchi, T., Sekiguchi, H., Tachibana, M., and Shinozuka, K. (2006) Synthesis and duplex forming property of oligonucleotides bearing a novel polyamine modified intercalator at the terminal of the internal position. *Nucleosides Nucleotides Nucleic Acids 25*, 601–612.

(231) Chen, J.-k., Weith, H. L., Grewal, R. S., Wang, G., and Cushman, M. (1995) Synthesis of novel phosphoramidite reagents for the attachment of antisense oligonucleotides to various regions of the benzophenanthridine ring system. *Bioconjugate Chem. 6*, 473–482.

(232) Wamberg, M. C., Walczak, K., Andersen, L., Hassan, A. A., and Pedersen, E. B. (2006) Intercalating nucleic acids containing insertions of naphthalimide. *Helv. Chim. Acta 89*, 1826–1838.

(233) Casals, J., Debéthune, L., Alvarez, K., Risitano, A., Fox, K. R., Grandas, A., and Pedroso, E. (2006) Directing quadruplex-stabilizing drugs to the telomere: synthesis and properties of acridine-oligonucleotide conjugates. *Bioconjugate Chem. 17*, 1351–1359.

(234) Gianolio, D. A., Segismundo, J. M., and McLaughlin, L. W. (2000) Tethered naphthalene diimide-based intercalators for DNA triplex stabilization. *Nucleic Acids Res. 28*, 2128–2134.

BC800406A

COMMUNICATIONS

Shell-Detachable Micelles Based on Disulfide-Linked Block Copolymer As Potential Carrier for Intracellular Drug Delivery

Ling-Yan Tang,[†] Yu-Cai Wang,*[,‡] Yang Li,[†] Jin-Zhi Du,[‡] and Jun Wang*[,†]

Hefei National Laboratory for Physical Sciences at Microscale and School of Life Science, Hefei, Anhui 230027, People's Republic of China, and Department of Polymer Science and Engineering, University of Science and Technology of China, Hefei, Anhui 230026, People's Republic of China. Received April 2, 2009; Revised Manuscript Received April 28, 2009

Aiming at development of a micellar nanoparticle system for intracellular drug release triggered by glutathione in tumor cells, a disulfide-linked biodegradable diblock copolymer of poly(ε-caprolactone) and poly(ethyl ethylene phosphate) was synthesized. It formed biocompatible micelles loaded with doxorubicin in aqueous solution but detached the shell material under glutathione stimulus, resulting in rapid drug release with destruction of micellar structure. These glutathione-sensitive micelles also rapidly released the drug molecules intracellularly and led to enhanced growth inhibition to A549 tumor cells, suggesting that this nanoparticle system may have potential for improving drug delivery efficacy.

Despite the discovery of many anticancer drugs for cancer therapy, clinical outcomes have been disappointing due to the severe side effects. Various nanovehicles such as polymeric micelles and vesicles (*1*−*3*), liposomes (*4*), and nanogels (*5, 6*) have been developed to overcome the problems. Such nanoparticle-based vehicles can passively accumulated in solid tumor tissues owning to the enhanced permeation and retention effect and improve the therapeutic efficiency (*7*). However, the concentration of active anticancer drug within cancer cells is often insufficient due to the inefficient release of drug from the vehicle into the cytoplasm, resulting in a requirement for higher drug dosage. The promising approach to improving the efficacy is to develop carrier systems that can release the drug triggered by intracellular stimuli, such as pH (*8*−*11*), glutathione (*12*−*15*), and enzyme (*16*). Upon reaching the targeted tumor, such carriers can be rapidly localized intracellularly and subsequently provoked by the stimuli to release the drug, hence inducing aggressive activity within tumor cells and leading to maximal therapeutic efficacy with reduced side effects.

Chemical reaction involving the reductive degradation of disulfide bonds of polymers by intracellular glutathione (GSH) has been widely investigated for responsive drug and gene delivery (*17*−*19*). GSH is a thiol-containing tripeptide and reduces disulfide bonds in the cytoplasm. It has been demonstrated that the intracellular concentration of GSH (ca. 10 mM) is significantly higher than the level in the cell exterior (ca. 2 μM) (*17*). We have previously demonstrated that micellar nanoparticles assembled from diblock copolymer of poly(ε-caprolactone) (PCL) and hydrophilic poly(ethyl ethylene phosphate) (PEEP) is potential as a drug carrier (*20, 21*). In the present work, aiming at development of micellar nanoparticle system for intracellular drug release triggered by GSH in tumor cells, we synthesized a disulfide-linked diblock copolymer of PCL and PEEP (PCL-SS-PEEP), which formed biocompatible micelles in aqueous solution, and detached the shell material under GSH stimulus, resulting in rapid drug release with destruction of micellar structure (Scheme 1).

PCL-SS-PEEP was synthesized by a coupling reaction between the thiol end group functionalized poly(ε-caprolactone) (PCL-SH) with the pyridyldisulfide groups at the end of poly(ethyl ethylene phosphate). PCL-SH was obtained through polymerization of ε-caprolactone initiated by 2-(2,4-dinitrophenylthio)ethanol in the presence of stannous octoate ($Sn(Oct)_2$) to give a precursor polymer PCL-DNP, followed by deprotection of dinitrophylenyl groups with mercaptoethanol. As shown in Figure 1, the ^1H NMR spectrum of PCL-SH indicates that proton signals at δ 7.76, 8.37, and 9.05 from 2-(2,4-dinitrophenylthio) groups of PCL-DNP are no longer present, demonstrating the successful deprotection. The degree of polymerization (DP) of PCL-SH is 32, which is calculated from the integration ratio of resonance at δ 4.02 of PCL-DNP against those at δ 7.76, 8.37, and 9.05. In another aspect, the pyridyldisulfide end group functionalized poly(ethyl ethylene phosphate) (PEEP-Py) was synthesized through ring-opening polymerization of ethyl ethylene phosphate, initiated by 2-(2-pyridyldithio)-ethanol and $Sn(Oct)_2$. The ^1H NMR spectrum of PEEP-Py given in Figure 1 shows resonances at δ 7.13, 7.56, 7.70 and 8.50, assigned to protons of pyridyl end groups. The DP of PEEP is 22, calculated based on the integration ratio of resonances at δ 4.1−4.3 against those at δ 7.13, 7.56, 7.70 and 8.50. The molecular weights determined by gel permeation chromatography (GPC) analyses are summarized in Table 1.

* To whom correspondence should be addressed. Jun Wang, School of Life Science, University of Science and Technology of China; 443 Huangshan Road, Hefei, Anhui 230027, P.R. China. Fax: 86-551-3600402. E-mail: jwang699@ustc.edu.cn; Or Yu-Cai Wang, Department of Polymer Science and Engineering, University of Science and Technology of China; 96 Jinzhai Road, Hefei, Anhui 230026, P.R. China. E-mail: qingbo62@mail.ustc.edu.cn.

[†] Hefei National Laboratory for Physical Sciences at Microscale and School of Life Science.

[‡] Department of Polymer Science and Engineering.

10.1021/bc900144m CCC: $40.75 © 2009 American Chemical Society
Published on Web 05/13/2009

Scheme 1. Synthesis Pathway of the Disulfide-Linked PCL-SS-PEEP and Schematic Illustration of Intracellular Drug Release

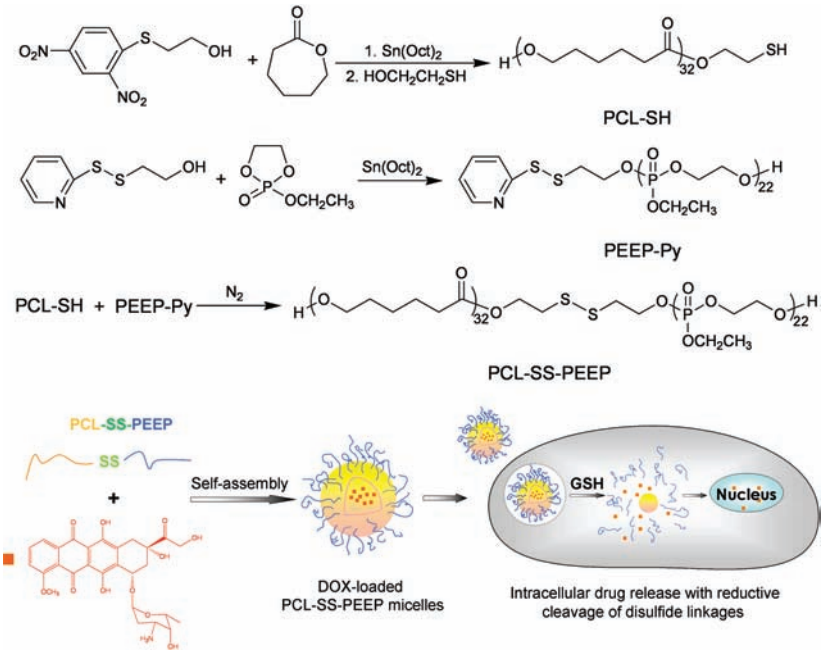

The coupling reaction of PCL-SH and PEEP-Py was carried out at room temperature under N_2 atmosphere carefully to minimize the air oxidation and homodimerization. The feed ratio of PEEP-Py to PCL-SH was set at 1.2:1. The excessive PEEP-Py was removed by precipitating the product in methanol, followed by thorough dialysis in water. GPC profile of the disulfide-linked diblock copolymer PCL-SS-PEEP compared with the precursor polymers PCL-SH and PEEP-Py (Supporting

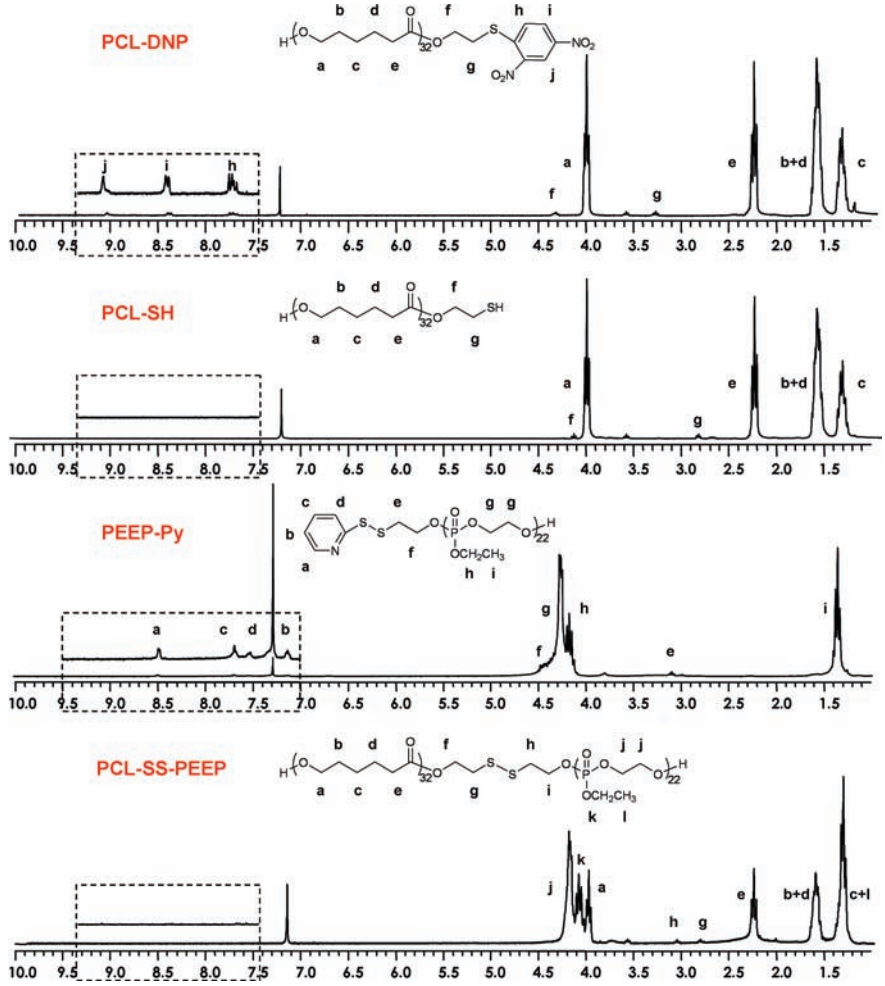

Figure 1. ^{1}H NMR spectra of diblock copolymer PCL-SS-PEEP and the precursors.

Table 1. Characterization of the Disulfide-Linked Block Copolymer and the Precursors

polymer	M_n[a]	M_w[a]	PDI[a]	M_n[b]
PCL-SH	4780	5500	1.15	3650
PEEP-Py	2900	3950	1.36	3480
PCL-SS-PEEP	6420	8670	1.35	6950

[a] Determined from GPC. [b] Determined from ^{1}H NMR.

Information Figure S1) shows a significant shift toward higher molecular weights, suggesting successful coupling. ^{1}H NMR of PCL-SS-PEEP in Figure 1 also shows the complete disappearance of pyridyl group resonances at δ 7.13, 7.56, 7.70 and 8.50, indicating successful conversion of PEEP-Py to the targeted copolymer.

Like previously reported diblock copolymer PCL-b-PEEP (*21*), PCL-SS-PEEP is amphiphilic and self-assembles into micelles in aqueous solution. The critical micellization concentration of PCL-SS-PEEP is 3.1×10^{-3} mg mL^{-1}, which was determined by fluorescent measurements with pyrene as the probe (*20*). Using the dialysis method, anticancer drug doxorubicin (DOX) was encapsulated into the core of the micelles with 2.8% drug loading content. Transmission electron microscopy image shown in Figure 2A exhibits the spherical morphology of DOX-loaded PCL-SS-PEEP micelles, with a diameter around 70 nm, which is consistent with that observed by dynamic light scattering (DLS) measurements.

The disulfide bridge linkage between PCL and PEEP block makes PCL-SS-PEEP micelles reductively breakable with response to GSH. To demonstrate the responsiveness, micelles were treated with 10 mM of GSH, and at different time intervals, the particle sizes were measured by DLS. As shown in Figure 2B, the average diameter of GSH-treated micelles immediately raised, reaching about 1000 nm within 10 min. Further incubation resulted in microsized particles and severe aggregations. However, without GSH treatment, PCL-SS-PEEP micelles showed negligible size variation within the same period of time. The variation of particle size in the presence of GSH was caused by the cleavage of disulfide linkages, which led to detachment of the PEEP shells from the micellar nanoparticles and resulted in enhanced hydrophobic PCL core material interaction.

The effect of PEEP shell detachment to the DOX release from the drug-loaded PCL-SS-PEEP micelles was directly observed by measuring DOX fluorescence of the micelle solution with treatment of 10 mM of DL-dithiothreitol (DTT). The relative fluorescence intensities of treated micelles to the nontreated micelles were plotted in Figure 2C. It has been reported that incorporation of DOX in the hydrophobic core of micelles decreases the fluorescent intensity of DOX when compared with free DOX at the same concentration (*22, 23*). The enhanced DOX fluorescence of DTT-treated DOX-loaded micelles therefore should be due to the rapid release of drug from the micelles. The drug release was also quantitatively studied by incubation of nanoparticles in GSH-containing medium. The DOX release profiles are displayed in Figure 2D. The DOX release from micelles was around 40% in 4 days in the absence of GSH, indicating lack of stability of micelles; however, in the presence of 10 mM of GSH corresponding to an intracellular level, the DOX release from the micelles was much faster, reaching almost complete drug release. These results demonstrate that cleavage of disulfide bridge linkages accelerated the drug release. It can be assumed that, under the stimulus of GSH, the disulfide bridge linkages of PCL-SS-PEEP are reduced and broken, which destabilizes the micellar nanoparticles and results in accelerated DOX release.

The intracellular behavior of DOX-loaded PCL-SS-PEEP micelles was evaluated in A549 cells to assess whether these GSH-responsive micelles function in the intracellular environment. Most tumor cells have an elevated GSH level compared with normal cells (*24*−*26*). As a model system, A549 cells were incubated with glutathione monoester (GSH-OEt) for 2 h to manipulate the intracellular GSH concentration. GSH-OEt can penetrate cellular membranes and rapidly generates high intracellular GSH concentration with ethyl ester hydrolyzation in cytoplasm (*13, 24*). After pretreatment with 10 mM of GSH-OEt, the cells were further incubated with DOX-loaded PCL-SS-PEEP micelles for 2 h. The DOX fluorescence of the cells

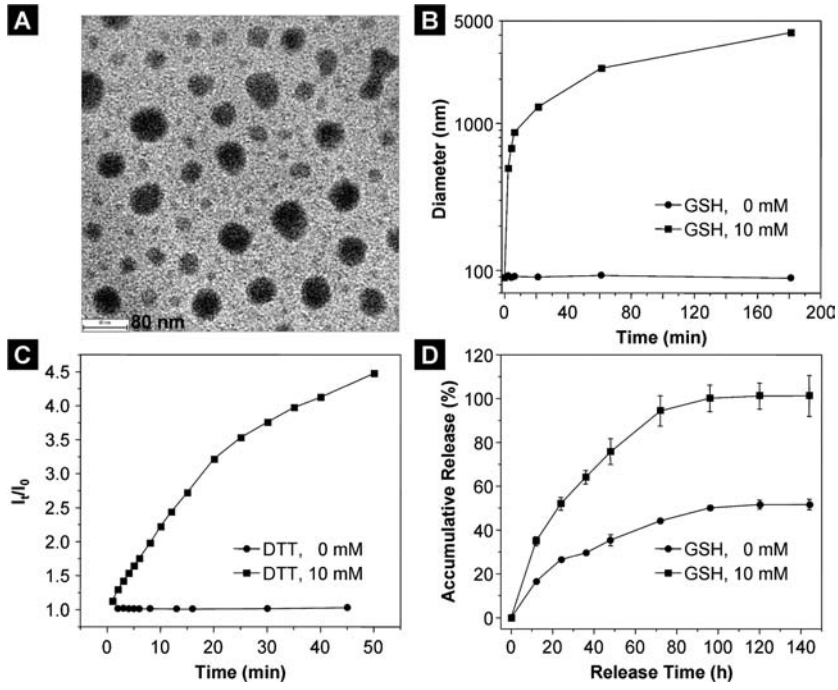

Figure 2. Transmission electron microscopy image of doxorubicin-loaded PCL-SS-PEEP micelles (A); dynamic light scattering measured PCL-SS-PEEP micelle size changes with glutathione (GSH) treatment (B); relative fluorescence intensity of doxorubicin-loaded PCL-SS-PEEP micelles with treatment of DL-dithiothreitol (DTT) (C); *in vitro* release of doxorubicin from PCL-SS-PEEP micelles in PBS (pH 7.4) at 37 °C with or without GSH treatment (D).

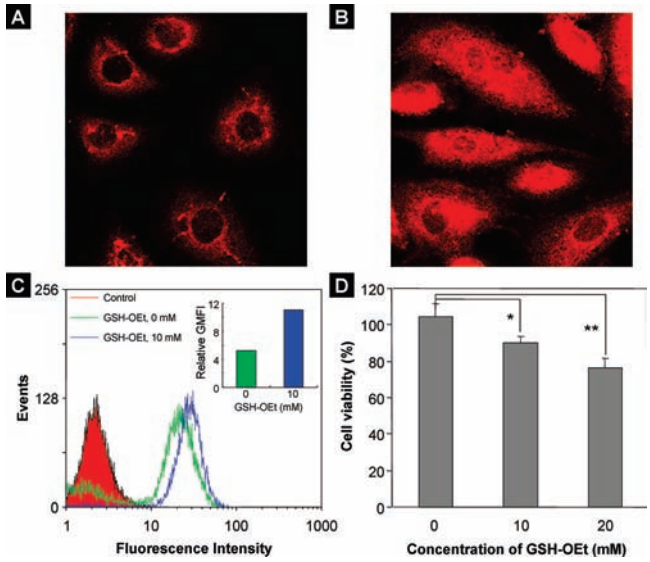

Figure 3. (A,B) Confocal laser scanning microscopy observation of nonpretreated (A) and GSH-OEt pretreated A549 cells (B) after 2 h incubation with DOX-loaded PCL-SS-PEEP micelles. (C) Flow cytometric analyses of nonpretreated and GSH-OEt pretreated A549 cells incubated with DOX-loaded PCL-SS-PEEP micelles for 2 h. Nonpretreated A549 cells without DOX-loaded micelle treatment was used as the control. The relative geometrical mean fluorescence intensities (GMFI) of cells are shown as an inset. (D) Viability of non-pretreated and pretreated A549 cells with either 10 or 20 mM of GSH-OEt incubated with DOX-loaded PCL-SS-PEEP micelles for 24 h. * $p < 0.05$, ** $p < 0.01$ by Student's *t*-test.

was observed under confocal laser scanning microscopy and analyzed by flow cytometric analyses. The results were compared with the A549 cells not pretreated with GSH-OEt but incubated for 2 h with the same dose of DOX-loaded PCL-SS-PEEP micelles. As shown in Figure 3A,B, stronger DOX fluorescence was observed in the cytoplasm of GSH-OEt pretreated cells. Flow cytometric analyses shown in Figure 3C also exhibit similar results, and relative geometrical mean fluorescence intensities (GMFI) of GSH-OEt pretreated cells are about 2-fold of nonpretreated cells. It is noteworthy that incubating DOX-loaded PCL-*b*-PEEP micelles without reducible disulfide bridges did not result in significant DOX fluorescence difference between non-pretreated and pretreated A549 cells, indicating that GSH-OEt pretreatment did not affect the endocytosis ability of A549 cells. On the other hand, broken disulfide linkages of PCL-SS-PEEP micelles enhanced the DOX fluorescence (Figure 2C). Therefore, the enhanced intracellular DOX fluorescence in GSH-OEt pretreated cells is due to the rapid intracellular DOX release from the DOX-loaded PCL-SS-PEEP micelles. Pretreatment of A549 cells with GSH-OEt up-regulated the intracellular GSH concentration, which subsequently accelerated the DOX release from the micelles owning to GSH-responsive disulfide bridge linkage degradation.

Such an enhanced intracellular release of DOX from PCL-SS-PEEP micelles led to improved cytotoxicity. DOX-loaded PCL-SS-PEEP micelles at the same dose were incubated with A549 cells, which were either non-pretreated or pretreated with GSH-OEt at 10 or 20 mM for 2 h. Cell viability measured by MTT assay shows significant differences between GSH-OEt pretreated and nonpretreated cells, as shown in Figure 3D. Incubation of DOX-loaded PCL-SS-PEEP micelles at a DOX dose of 3.4 μg mL^{-1} with non-pretreated A549 cells for 24 h did not exhibit significant inhibition to the cell proliferation, while the viability of GSH-OEt pretreated cells significantly decreased with increased GSH-OEt concentration for the pretreatments. However, proliferation of A549 cells incubated with free DOX was not affected by the treatment of GSH-OEt (Supporting Information Figure S2). On the other hand, treatments of both GSH-OEt and DOX free PCL-SS-PEEP micelles did not result in significant cytotoxicity to A549 cells under the same conditions (Supporting Information Figure S3). These results demonstrated that the destabilization of PCL-SS-PEEP micelles by intracellular GSH accelerated DOX release, and the cell proliferation inhibition was thus enhanced due to the faster intracellular DOX release. To further confirm such a response to intracellular GSH concentration, viability of incubation of A549 cells with DOX-loaded PCL-SS-PEEP micelles was examined after buthionine sulfoximine (BSO) pretreatments. BSO is an inhibitor of intracellular GSH synthesis (*27*) and does not affect the proliferation of A549 cells at the tested concentrations up to 0.5 mM (Supporting Information Figure S4). With the pretreatment of BSO at higher concentration, DOX-loaded PCL-SS-PEEP micelles exhibited lower cytotoxicity (Supporting Information Figure S4). This is due to that incubation of A549 cells with BSO lowered down the intracellular GSH concentration; therefore, destabilization of DOX-loaded PCL-SS-PEEP micelles was suppressed, resulting in less DOX release from the micelles.

In conclusion, micelle nanoparticles self-assembled from a disulfide-linked diblock copolymer PCL-SS-PEEP have been prepared for enhanced intracellular drug delivery. The micelles exhibit GSH-responsive structure change, and the intracellular DOX release is accelerated at higher GSH concentration. The enhanced intracellular DOX release leads to more significant growth inhibition to A549 cells. This GSH-triggered drug release system has the potential to maximize the delivery efficiency for cancer chemotherapy.

ACKNOWLEDGMENT

This work was supported by grants from the National Natural Science Foundation of China (50733003, 20774089), the Ministry of Sciences and Technology of the People's Republic of China (2006CB933300, 2009CB930300), and "Bairen" Program of Chinese Academy of Sciences.

Supporting Information Available: Experimental procedures, gel permeation chromatography analyses, and MTT assayed cytotoxicity. This material is available free of charge via the Internet at http://pubs.acs.org.

LITERATURE CITED

(1) Torchilin, V. P. (2007) Micellar nanocarriers: pharmaceutical perspectives. *Pharm. Res. 24*, 1–16.
(2) Savic, R., Luo, L. B., Eisenberg, A., and Maysinger, D. (2003) Micellar nanocontainers distribute to defined cytoplasmic organelles. *Science 300*, 615–8.
(3) Peer, D., Karp, J. M., Hong, S., FarokHzad, O. C., Margalit, R., and Langer, R. (2007) Nanocarriers as an emerging platform for cancer therapy. *Nat. Nanotechnol. 2*, 751–60.
(4) Gregoriadis, G. (2008) Liposome research in drug delivery: the early days. *J. Drug Targeting 16*, 520–4.
(5) Vinogradov, S. V., Zeman, A. D., Batrakova, E. V., and Kabanov, A. V. (2005) Polyplex Nanogel formulations for drug delivery of cytotoxic nucleoside analogs. *J. Controlled Release 107*, 143–57.
(6) Oh, J. K., Siegwart, D. J., Lee, H. I., Sherwood, G., Peteanu, L., Hollinger, J. O., Kataoka, K., and Matyjaszewski, K. (2007) Biodegradable nanogels prepared by atom transfer radical polymerization as potential drug delivery carriers: synthesis, biodegradation, in vitro release, and bioconjugation. *J. Am. Chem. Soc. 129*, 5939–45.
(7) Matsumura, Y., and Maeda, H. (1986) A new concept for macromolecular therapeutics in cancer chemotherapy: mechanism of tumoritropic accumulation of proteins and the antitumor agent smancs. *Cancer Res. 46*, 6387–92.

(8) Zhang, L. Y., Guo, R., Yang, M., Jiang, X. Q., and Liu, B. R. (2007) Thermo and pH dual-responsive nanoparticles for anticancer drug delivery. *Adv. Mater. 19*, 2988–92.
(9) Lee, Y., Fukushima, S., Bae, Y., Hiki, S., Ishii, T., and Kataoka, K. (2007) A protein nanocarrier from charge-conversion polymer in response to endosomal pH. *J. Am. Chem. Soc. 129*, 5362–3.
(10) Lee, E. S., Gao, Z., and Bae, Y. H. (2008) Recent progress in tumor pH targeting nanotechnology. *J. Controlled Release 132*, 164–70.
(11) Gillies, E. R., and Frechet, J. M. J. (2005) pH-responsive copolymer assemblies for controlled release of doxorubicin. *Bioconjugate Chem. 16*, 361–8.
(12) Takae, S., Miyata, K., Oba, M., Ishii, T., Nishiyama, N., Itaka, K., Yamasaki, Y., Koyama, H., and Kataoka, K. (2008) PEG-detachable polyplex micelles based on disulfide-linked block catiomers as bioresponsive nonviral gene vectors. *J. Am. Chem. Soc. 130*, 6001–9.
(13) Koo, A. N., Lee, H. J., Kim, S. E., Chang, J. H., Park, C., Kim, C., Park, J. H., and Lee, S. C. (2008) Disulfide-cross-linked PEG-poly(amino acid)s copolymer micelles for glutathione-mediated intracellular drug delivery. *Chem. Commun. (Cambridge)* 6570–2.
(14) Kim, S. H., Jeong, J. H., Lee, S. H., Kim, S. W., and Park, T. G. (2008) Local and systemic delivery of VEGF siRNA using polyelectrolyte complex micelles for effective treatment of cancer. *J. Controlled Release 129*, 107–16.
(15) Cerritelli, S., Velluto, D., and Hubbell, J. A. (2007) PEG-SS-PPS: reduction-sensitive disulfide block copolymer vesicles for intracellular drug delivery. *Biomacromolecules 8*, 1966–72.
(16) Thornton, P. D., Mart, R. J., and Ulijn, R. V. (2007) Enzyme-responsive polymer hydrogel particles for controlled release. *Adv. Mater. 19*, 1252–6.
(17) Saito, G., Swanson, J. A., and Lee, K. D. (2003) Drug delivery strategy utilizing conjugation via reversible disulfide linkages: role and site of cellular reducing activities. *Adv. Drug Delivery Rev. 55*, 199–215.
(18) Lin, C., Blaauboer, C. J., Timoneda, M. M., Lok, M. C., van Steenbergen, M., Hennink, W. E., Zhong, Z., Feijen, J., and Engbersen, J. F. (2008) Bioreducible poly(amido amine)s with oligoamine side chains: synthesis, characterization, and structural effects on gene delivery. *J. Controlled Release 126*, 166–74.
(19) Christensen, L. V., Chang, C. W., Kim, W. J., Kim, S. W., Zhong, Z., Lin, C., Engbersen, J. F., and Feijen, J. (2006) Reducible poly(amido ethylenimine)s designed for triggered intracellular gene delivery. *Bioconjugate Chem. 17*, 1233–40.
(20) Wang, Y. C., Tang, L. Y., Sun, T. M., Li, C. H., Xiong, M. H., and Wang, J. (2008) Self-assembled micelles of biodegradable triblock copolymers based on poly(ethyl ethylene phosphate) and poly(epsilon-caprolactone) as drug carriers. *Biomacromolecules 9*, 388–95.
(21) Wang, Y. C., Liu, X. Q., Sun, T. M., Xiong, M. H., and Wang, J. (2008) Functionalized micelles from block copolymer of polyphosphoester and poly(epsilon-caprolactone) for receptor-mediated drug delivery. *J. Controlled Release 128*, 32–40.
(22) Oishi, M., Hayashi, H., Michihiro, I. D., and Nagasaki, Y. (2007) Endosomal release and intracellular delivery of anticancer drugs using pH-sensitive PEGylated nanogels. *J. Mater. Chem. 17*, 3720–5.
(23) Bae, Y., Fukushima, S., Harada, A., and Kataoka, K. (2003) Design of environment-sensitive supramolecular assemblies for intracellular drug delivery: polymeric micelles that are responsive to intracellular pH change. *Angew. Chem., Int. Ed. Engl. 42*, 4640–3.
(24) Hong, R., Han, G., Fernandez, J. M., Kim, B. J., Forbes, N. S., and Rotello, V. M. (2006) Glutathione-mediated delivery and release using monolayer protected nanoparticle carriers. *J. Am. Chem. Soc. 128*, 1078–9.
(25) Coban, T., Mabsout, A., Eke, B. C., Bulbul, D., Berberoglu, U., and Iscan, M. (1998) Glutathione and lipid peroxidation levels in human breast tumors. *Neoplasma 45*, 151–6.
(26) Arrick, B. A., and Nathan, C. F. (1984) Glutathione metabolism as a determinant of therapeutic efficacy: a review. *Cancer Res. 44*, 4224–32.
(27) Liebmann, J. E., Hahn, S. M., Cook, J. A., Lipschultz, C., Mitchell, J. B., and Kaufman, D. C. (1993) Glutathione depletion by L-buthionine sulfoximine antagonizes taxol cytotoxicity. *Cancer Res. 53*, 2066–70.

BC900144M

Shell-detachable micelles based on disulfide-linked block copolymer as potential carrier for intracellular drug delivery

Ling-Yan Tang,[†] *Yu-Cai Wang,*[*‡] *Yang Li,*[†] *Jin-Zhi Du,*[‡] *and Jun Wang,*[*†]

[†] Hefei National Laboratory for Physical Sciences at Microscale and School of Life Science, Hefei, Anhui 230027, P.R. China.

[‡]Department of Polymer Science and Engineering, University of Science and Technology of China, Hefei, Anhui 230026, P.R. China.

*To whom correspondence should be addressed:
Jun Wang or Yu-Cai Wang
Hefei National Laboratory for Physical Sciences at Microscale and School of Life Science
University of Science and Technology of China
Hefei, Anhui 230027, P.R. China
Tel: 86-551-3600335
Fax: 86-551-3600402
E-mail: jwang699@ustc.edu.cn or qingbo62@mail.ustc.edu.cn

Experimental

Materials: Ethyl ethylene phosphate (EEP) was synthesized and purified as previously reported [1]. ε-Caprolactone was dried over CaH_2, distilled twice under reduced pressure and stored under a nitrogen atmosphere. 2-(2,4-Dinitrophenylthio)-ethanol and 2-(2-pyridyldithio)-ethanol were synthesized following previously reported procedures [2,3]. Stannous octoate was purified according to a method described in literature [1]. Tetrahydrofuran (THF) was refluxed over potassium–sodium alloy under N_2 atmosphere. 3-(4,5-Dimethylthiazol-2-yl)-2,5-diphenyltetrazolium bromide (MTT), glutathione (GSH), glutathione monoester (GSH-OEt) and buthionine sulfoximine (BSO) were purchased from Sigma-Aldrich Co. Doxorubicin (DOX) hydrochloride was purchased from Zhejiang Hisun Pharmaceutical Co. Ltd. Mercaptoethanol, Triethylamine and other solvents were analytical grade and used as received.

Characterization and Measurements: NMR spectra were recorded on a Bruker AV300 NMR spectrometer. Gel permeation chromatography (GPC) measurements were performed on a Waters 1515 HPLC system, equipped with a Waters 2414 refractive index detector. Chloroform was used as the eluent and delivered at 40 °C at a flow rate of 1.0 mL min^{-1}. Monodispersed polystyrene standards from Waters Co. were used to generate the calibration curve. Transmission electron microscopy observation was performed on a JEOL–2010 transmission electron microscopy with an accelerating voltage of 200 kV. The samples were prepared by pipetting a drop of the micelle solution (about 1 g L^{-1}) onto a 230 mesh copper grids coated with carbon

and allowing the sample to dry in air before measurements. Particle sizes were characterized on a Malvern Zetasizer Nano ZS90 with a He-Ne laser (633 nm) and 90° collecting optics. Fluorescence spectra were recorded on a Shimadzu RF-5301PC spectrofluorophotometer.

Synthesis of thiol-terminated Poly(ε-caprolactone) (PCL-SH): ε-Caprolactone (8.06 g, 70.7 mmol), 2-(2,4-dinitrophenylthio)-ethanol (0.493 g, 2.02 mmol), and $Sn(Oct)_2$ (0.036 g, 0.088 mmol) were added into a round flask stirred at 120 °C for 12 h in a glove box with water content less than 0.01 ppm. The resulted solution was dissolved in CH_2Cl_2 then precipitated into cold diethyl ether twice. The precipitate was collected after filtration and dried under vacuum to a constant weight. The obtained polymer was further dissolved in mercaptoethanol (100 equiv) with triethylamine at pH 8. After 15 h stirring the mixture was precipitated into cold methanol twice to give the thiol-terminated PCL (PCL-SH) with an overall yield of 82%. The Mw is 5500 with a polydispersity of 1.15 as determined by GPC analysis.

Synthesis of 2-pyridyldithio-termianted poly(ethyl ethylene phosphate) (PEEP-Py): In a nitrogen filled glove box with water content less than 0.01 ppm, to a solution of EEP (5.12 g, 33.6 mmol) and 2-(2-pyridyldithio)-ethanol (0.210 g, 1.12 mmol) in THF at 30 °C was added $Sn(Oct)_2$ (0.241 g, 0.60 mmol). After 3 h reaction, the mixture was concentrated and precipitated in cold diethyl ether twice. The polymer was collected and dried under vacuum to give PEEP-Py with a yield of 71%. The Mw is 3950 with a polydispersity of 1.36 as determined by GPC analysis.

Synthesis of disulfide-linked block copolymer PCL-SS-PEEP: PEEP-Py (1.1 g) was dissolved in THF, and the solution was freeze-thawn for three times. PCL-SH (0.97 g) was then added to this solution in a glove box filled with nitrogen. The mixture was allowed to react for 24 h, concentrated, and precipitated into diethyl ether/methanol (10:1 v/v) for three times. The precipitate was dried in vacuum and dialyzed against water at 4 °C for 3 days and freeze dried to obtain the product with a yield of 65%. The Mw is 8670 with a polydispersity of 1.35 as determined by GPC analysis.

Determination of critical micellization concentration (CMC) of PCL-SS-PEEP: A predetermined amount of pyrene in acetone was added into a series of ampoules, and the acetone was then removed by gently flowing N_2 and then by vacuum. Predetermined volume of PCL-SS-PEEP solutions and ultrapurified water (Millipore, 18.2 MΩ) were added into the ampoules consecutively to get solutions of different concentrations ranging from 1.0×10^{-4} to 0.1 g L^{-1} while the concentration of pyrene in each flask was fixed at 6.0×10^{-7} mol L^{-1}, slightly lower than the saturation solubility of pyrene in water. Fluorescence spectra were recorded at 373 nm excitation wavelength and 5 nm slit width. The intensity ratio of the bands at 338.0 and 335 nm (I_{338}/I_{335}) as a function of the logarithm of the concentration of PCL-SS-PEEP was plotted and the CMC value was taken as the intersection of the tangents to the horizontal line of intensity ratio with relatively constant values and the diagonal line with rapid increased intensity ratio.

Preparation of DOX-loaded PCL-SS-PEEP micelles: One milligram of DOX hydrochloride and 15 mg of PCL-SS-PEEP were dissolved in 1 mL of DMSO, and

then 1 μL of triethylamine was added. The mixture was stirred for 2 h at room temperature. Thereafter, the solution was added dropwise to 5 mL of ultrapurified water and transferred into a dialysis membrane tubing (MWCO=2000 Da, Spectrum®). It was dialyzed against water for 24 h to completely remove DMSO. After centrifugation at 3000 g for 3 min to remove possible free DOX, the DOX-loaded micelles were obtained. The DOX concentration and drug loading content were determined according to our previous method using HPLC analyses [4].

Destabilization of PCL-SS-PEEP micelles: GSH was added to the micelle solution (0.5 mg mL^{-1}) in N_2 bubbled ultrapurified water to achieve a final concentration at 10 mM. Immediately, the micelle solution was subjected to particle size measurements at 25 °C using Malvern Zetasizer Nano ZS90 with a He-Ne laser (633 nm) and 90° collecting optics. On the other hand, DOX-loaded PCL-SS-PEEP micelles with similar treatment of DL-dithiothreitol was immediately followed by fluorescence measurements with excitation wavelength at 479 nm and the emission spectra were recorded at different time intervals using a Shimadzu RF-5301PC spectrofluorophotometer.

Glutathione-mediated drug release: DOX-loaded PCL-SS-PEEP micelles prepared above was diluted to 1 mg mL^{-1} and transferred to a 1-mL dialysis membrane tubing (MWCO=14,000, Spectrum®). It was immersed in a tube containing 8 mL of phosphate buffered saline (PBS, 0.01 M, pH 7.4) or PBS with 10 mM GSH in a shaking water bath at 37 °C. At predetermined time intervals, 4 mL of the external buffer was withdrawn and it was replaced with 4 mL of fresh PBS or PBS with 10

mM GSH. The release medium was freeze-dried, dissolved in acetonitrile-water (50:50, v/v), and the concentration of DOX was analyzed by HPLC analysis.

Confocal laser scanning microscopy observation and flow cytometric analysis (FACS) of DOX-loaded PCL-SS-PEEP micelle treated A549 cells: A549 human lung carcinoma cells were seeded on coverslips in a 24-well plate at a density of 50,000 cells/well with complete Dulbecco's modified Eagle's medium (DMEM, Gibco) supplemented with 10% Hyclone fetal bovine serum (FBS) and 4 mM L-glutamine. The cells were incubated for 24 h in a humidified atmosphere with 5 % CO_2 at 37 °C, and then treated with GSH-OEt for 2 h. Cells were washed by PBS and incubated at 37 °C for additional 2 h with DOX-loaded PCL-SS-PEEP micelles at a final DOX concentration of 3.4 μg mL^{-1} in complete DMEM. Cells without GSH-OEt treatment was used as the control. The cells were washed with PBS twice and fixed with 4% formaldehyde. The slides were mounted and observed with a Zeiss LSM510 Laser Confocal Scanning Microscope imaging system (Germany) with an upright confocal microscope and a 40× objective. For FACS analyses, A549 cells were seeded onto 24-well tissue-culture plate at 150,000 cells/well and incubated for 24 h. Cells were either treated with GSH-OEt for 2 h or not, and washed with PBS. Cells were then incubated at 37 °C for additional 2 h with DOX-loaded PCL-SS-PEEP micelles in complete DMEM. Cells were washed with PBS twice and harvested, then suspended in 200 μL of PBS for FACS analyses using FACSCalibur flow cytometer (BD Biosciences, USA).

Cell growth inhibition measurements: A549 cells were seeded in 96-well plate at a density of 5000 cells/well and further incubated for 24 h. The cells were then treated with GSH-OEt for 2 h or BSO for 24 h. After washing off the GSH-OEt or BSO with PBS, DOX-loaded PCL-SS-PEEP micelles diluted in complete DMEM (100 μL) was added to cells to reach a final DOX concentration at 3.4 μg mL^{-1} and the cells were further incubated for 24 h or 48 h. The cytotoxicity was evaluated by a MTT assay as described previously [4].

[1] C. S. Xiao, Y. C. Wang, J. Z. Du, X. S. Chen, J. Wang, *Macromolecules* **2006**, *39*, 6825.

[2] G. Carrot, J. G. Hilborn, M. Trollsas, J. L. Hedrick, *Macromolecules* **1999**, *32*, 5264.

[3] S. Ghosh, S. Basu, S. Thayumanavan, *Macromolecules* **2006**, *39*, 5595.

[4] Y. C. Wang, X. Q. Liu, T. M. Sun, M. H. Xiong, J. Wang, *J Control. Rel.* **2008**, *128*, 32.

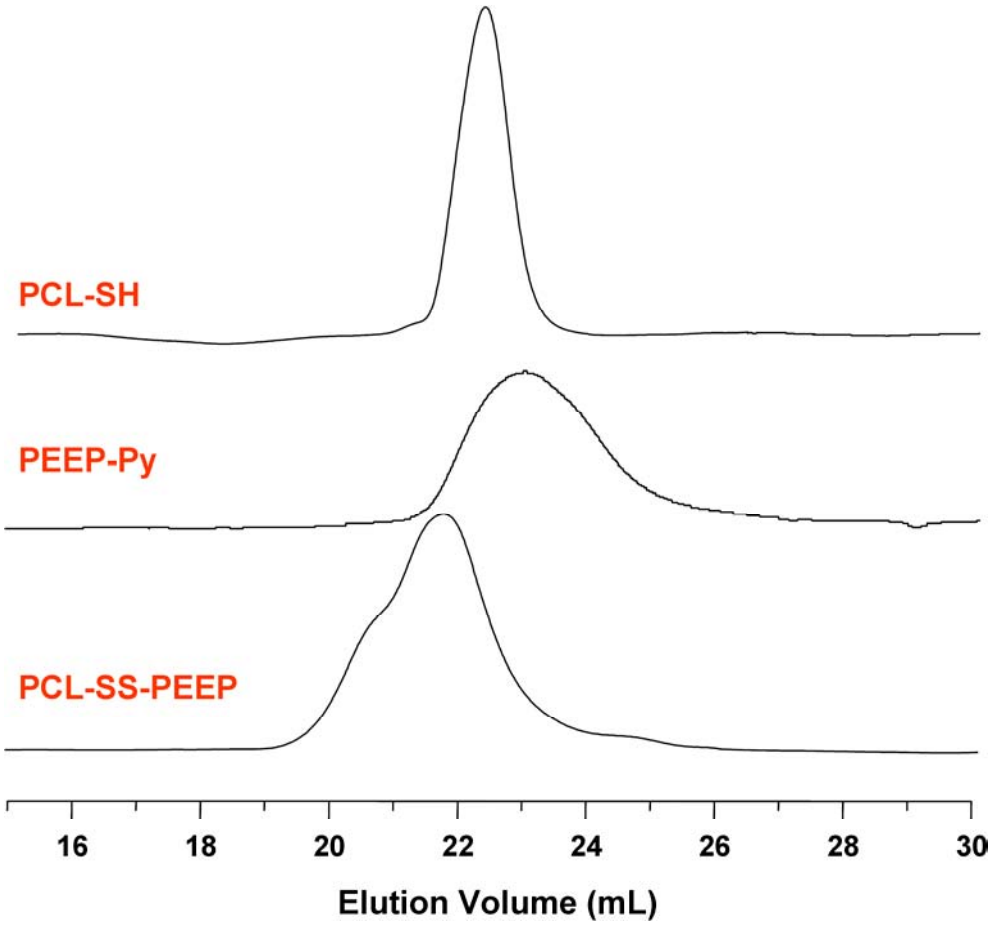

Figure S1. GPC chromatograms of PCL-SH, PEEP-Py and PCL-SS-PEEP.

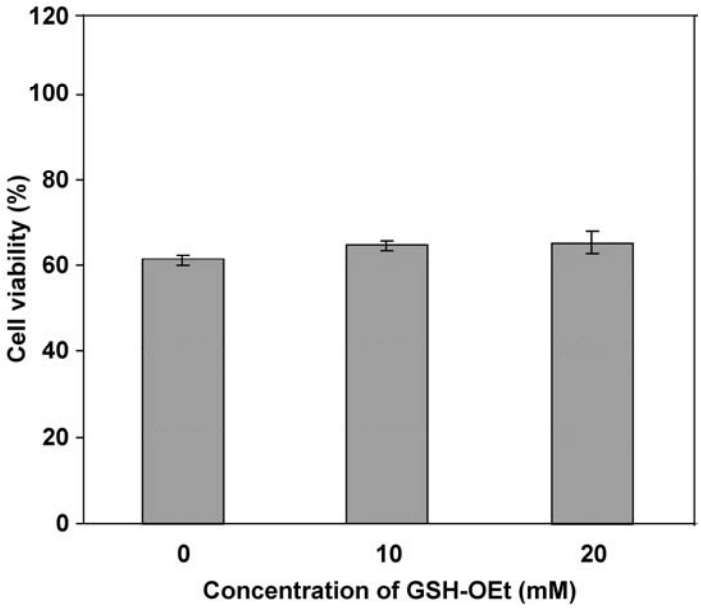

Figure S2. MTT assayed cytotoxicity of free DOX (3.4 μg mL^{-1}) after the pretreatment with GSH-OEt at different concentrations.

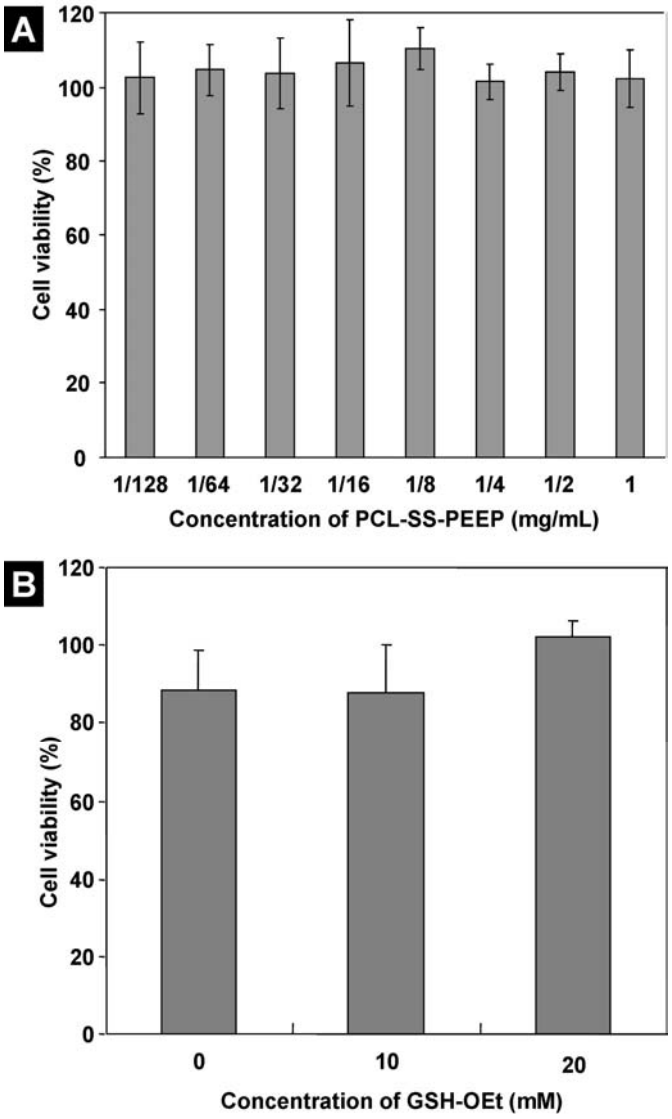

Figure S3. MTT assayed cytotoxicity of blank PCL-SS-PEEP micelles (up) and GSH-OEt at different concentrations (B).

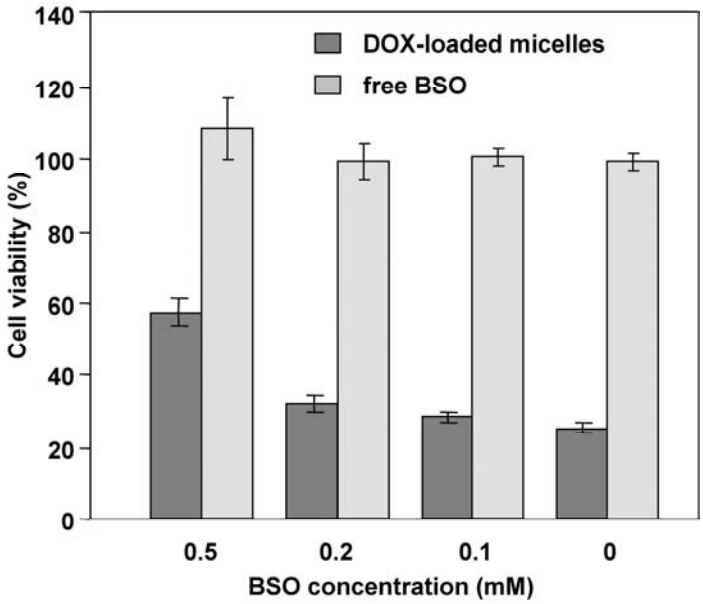

Figure S4. Viability of A549 cells incubated with DOX-loaded PCL-SS-PEEP micelles for 48 h after the pretreatment with BSO at different concentrations. A549 cells incubated with BSO at the same concentration were used as the control. The DOX concentration was fixed at 3.4 μg mL^{-1}.

ARTICLES

Lamellarin D Bioconjugates I: Synthesis and Cellular Internalization of PEG-Derivatives

Daniel Pla,[†,‡] Andrés Francesch,[§] Pilar Calvo,[§] Carmen Cuevas,[§] Rosa Aligué,[||] Fernando Albericio,*[,⊥,†,‡] and Mercedes Álvarez*[,#,†,‡]

Institute for Research in Biomedicine, Barcelona Science Park-University of Barcelona, and CIBER-BBN Networking Centre on Bioengineering, Biomaterials, and Nanomedicine, Baldiri Reixac 10, E-08028 Barcelona, Spain, Pharma Mar S. A., Avda de los Reyes 1, E-28770 Colmenar Viejo, Madrid, Spain, and Department of Cell Biology, Faculty of Medicine, University of Barcelona, Casanova 143, E-08036 Barcelona, Spain. Received November 24, 2008; Revised Manuscript Received March 24, 2009

Herein is reported the design and synthesis of poly(ethylene glycol) derivatives of Lamellarin D with the aim of modulating their physicochemical properties and improving the biological activity. Mono-, di-, and tri-PEG conjugates with improved solubility were obtained in 18−57% overall yields from the corresponding partially protected phenolic derivatives of Lamellarin D. Conjugates **1**−**9** were tested in a panel of three human tumor cell lines (MDA-MB-231 breast, A-549 lung, and HT-29 colon) to evaluate their cytotoxicity. Several compounds exhibited enhanced cellular internalization, and more than 85% of the derivatives showed a lower GI_{50} than Lam-D. Furthermore, cell cycle arrest at G2 phase and apoptotic cell-death pathways were determined for Lamellarin D and these derivatives.

INTRODUCTION

Compounds with a good therapeutic profile often do not reach the drug market because they show poor pharmacokinetics, mainly due to poor solubility. Attachment of well-defined, water-soluble, biocompatible, nontoxic, and non-immunogenic polymeric systems to drug candidates can overcome this limitation. Furthermore, these chemical modifications can significantly improve tumor targeting, in addition to therapeutic efficacy, by EPR[1] effect of the drug in tumor tissue. Advances in this field require robust and reliable chemical strategies for the preparation of such derivatives of key pharmacological lead compounds, because very often the polymeric backbone should be incorporated in the chemical structure in the middle of the synthetic strategy.

Lam-D (*1*−*6*) (**1**) is a marine alkaloid with a wide range of biological activities, such as antiproliferative activity against various tumor cell lines in the low nanomolar concentration. Lam-D inhibits the Topo I (*3*), thereby disrupting the potential of mitochondrial transmembrane (*4*), which promotes apoptosis (*7*). The conjugation of water-soluble biocompatible polymers to low molecular weight anticancer drugs has been reported to enhance the solubility of the drugs, enhance their accumulation in tumors, and prolong their retention in the circulatory system, thereby improving the drugs' pharmacodynamics and pharmacokinetics (*8*, *9*). Notwithstanding, further controlled drug delivery by means of a readily hydrolyzable conjugation bond is required for the appropriate release of the bioactive drug (*10*). Therefore, modulation of biopolymers that bind drugs is of paramount importance for preclinical research and developments with new lead compounds (*11*). Recently, PEGylated compounds used in cancer therapy have been shown to promote the EPR effect (*12*, *13*), raising the local concentration of drug accumulated in targeted solid tumors. It has been proposed that this effect is caused by vascular leakage in the tumor and a reduction in the tumor's lymphatic drainage (*14*).

Our group sought to modulate the physicochemical properties of Lam-D by creating a series of mono-, di-, and tri-PEG ester conjugates of this drug. Herein are described the syntheses using

* Corresponding authors. M.A. and F.A., Institute for Research in Biomedicine, Barcelona Science Park-University of Barcelona, Baldiri Reixac 10, E-08028 Barcelona, Spain. Tel.: +34934037086; Fax: +34934037126. E-mail mercedes.alvarez@irbbarcelona.org.

[†] Barcelona Science Park-University of Barcelona.

[‡] CIBER-BBN Networking Centre on Bioengineering, Biomaterials, and Nanomedicine.

[§] Pharma Mar S. A.

[||] Faculty of Medicine, University of Barcelona.

[⊥] Department of Organic Chemistry, University of Barcelona, E-08028 Barcelona.

[#] Laboratory of Organic Chemistry, Faculty of Pharmacy, University of Barcelona, E-08028 Barcelona.

[1]Abbreviations: AU, absorbance units; A-549, lung carcinoma cell line; BJ, skin fibroblast cell line; Bn, benzyl; Boc, *tert*-butoxycarbonyl; CIQ, cellular internalization quotient; DDQ, 2,3-dichloro-5,6-dicyano-*p*-benzoquinone; DMAP, 4-dimethylaminopyridine; DMEM, Dulbecco's modified Eagle's medium; DMF, dimethylformamide; DMSO, dimethylsulfoxide; DPE-Phos, (oxidi-2,1-phenylene)bis(diphenylphosphine); EDC·HCl, *N*-(3-dimethylaminopropyl)-*N*′-ethylcarbodiimide hydrochloride; EPR, enhance permeability and retention; FACS, fluorescence-activated cell sorting; FBS, fetal bovine serum; FITC, fluorescein isothiocyanate; HeLa, human cervix carcinoma cell line; HT-29, colon carcinoma cell line; GI_{50}, 50% growth inhibition; *i*Pr, isopropyl; Lam, Lamellarin; MDA-MB-231, breast adenocarcinoma cell line; MW, microwave; NBS, *N*-bromosuccinimide; PBS, phosphate buffered saline; PEG, poly(ethylene glycol); PEGylated, poly(ethylene glycol)ated; SAR, structure activity relationship; SRB, sulforhodamine B; WGA, wheat germ agglutinin; THF, tetrahydrofurane; Topo, topoisomerase.

10.1021/bc800503k CCC: $40.75 © 2009 American Chemical Society
Published on Web 05/27/2009

modified synthetic strategies of these conjugates, as well as their biological activity.

EXPERIMENTAL PROCEDURES

General Procedures and Product Characterization. *A. General Procedures for Cross-Coupling Reactions.* A solution of bromide derivative **14** (1.0 mmol) in DMF (20 mL) was purged with Ar for 10 min, and boronate **12** (1.0 mmol), $Pd(PPh_3)_4$ (10%) and 2 M K_3PO_4 (3.0 mmol) were then added. The reaction mixture was stirred at 115 °C, and then another portion of boronate **12** (2.0 mmol) was added dropwise using a syringe pump during the first hour of reaction. The solvent was removed, and the residue was dissolved in EtOAc. The organic solution was washed with water and brine, dried, and concentrated to give a crude material, which was later purified by column chromatography on silica gel. Elution with hexane/EtOAc (75:25 to 60:40) gave **15a**−**c** (69−77% yield).

B. General Procedure for Oxidation. Synthesis of Compounds **16.** A mixture of **15** (1.0 mmol) and DDQ (1.0 mmol) in dry $CHCl_3$ (15 mL) was purged with Ar in a sealed vessel and heated in a microwave at 120 °C for 10 min. The organic solution was washed with water and brine and then dried ($MgSO_4$), filtered, and evaporated in a vacuum. The crude material was purified by column chromatography on silica gel. Elution with hexane/EtOAc (85:15 to 60:40) gave **16a**−**c** (65−93% yield).

C. General Method for Benzyloxy Removal. Pd/C (10%) was added to a solution of **16** (1.0 mmol) in MeOH (50 mL). The suspension was purged with H_2 and stirred for 16 h. The reaction mixture was filtered through a Celite pad, which was washed with CH_2Cl_2. The solvent was removed under vacuum to provide the compounds **17a**−**c** (yield 70−95%).

D. General Method for Lactonization. NaH (60% dispersion, 1.1 equiv) was washed twice with dry THF and a solution of **17** (1 mmol) was added in THF (60 mL). The mixture was stirred for 3 h at r.t. The solvent was then removed under reduced pressure, and EtOAc was added to the residue. The organic solution was washed with saturated aq. NH_4Cl, water, and brine, then dried and concentrated to provide the compounds **18a**−**c** (86% quant. yield).

E. General Method for Esterification. EDC·HCl (4 mmol × free OH) was added in one solid portion to a solution of DMAP (0.6 equiv in SM) PEG-COOH (4 mmol × free OH), and either Lam-D (*15*) or **18** (1 mmol) in dry CH_2Cl_2 (45 mL). The resulting solution was stirred at r.t. for 3 h. The reaction mixture was diluted with CH_2Cl_2 and washed with sat. aq. $NaHCO_3$ and brine. The organic phase was dried over anhydrous $MgSO_4$, and the solvent was removed under vacuum. The residue was directly purified on silica gel to provide compounds **8**, **9**, **19a**−**f** (40% quant. yield).

F. General Method for Isopropoxy Deprotection. Anhydrous $AlCl_3$ (1.3 equiv) was added to a solution of compound **19** (1 mmol) in dry CH_2Cl_2 (1 mL). The mixture was sonicated for 10 min, quenched with sat. NH_4Cl, and then washed with water and brine. Compounds **19b** and **19d** were treated only with brine, and the aqueous solution was extracted with EtOAc. The organic extracts were dried and evaporated. The crude product was purified by flash chromatography to give compounds **2**−**7** (yield 19−59%).

Methyl 1-(4-Benzyloxy-3-methoxyphenyl)-8-isopropoxy-9-methoxy-5,6-dihydropyrrolo[2,1-*a*]isoquinoline-3-carboxylate (13a). A solution of methyl 1-bromo-8-isopropoxy-9-methoxy-5,6-dihydropyrrolo[2,1-*a*]isoquinoline-3-carboxylate (543 mg, 1.4 mmol) in DMF (40 mL) was purged with Ar, and 2-(4-benzyloxy-3-methoxyphenyl)-4,4,5,5-tetramethyl-1,3,2-dioxaborolane (**11a**) (703 mg, 2.1 mmol), $Pd(PPh_3)_4$ (159 mg, 0.1 mmol), and 2 M K_2CO_3 (2.8 mL, 5.5 mmol) were added. The reaction mixture was stirred at 125 °C for 16 h. The solvent was removed after cooling to r.t., and the residue was dissolved in EtOAc. The organic solution was washed with water and brine, dried ($MgSO_4$), and concentrated to give a crude material, which was later purified by column chromatography on silica gel. Elution with hexane/EtOAc (90:10 to 75:25) gave **13a** (543 mg, 1.38 mmol) as a yellow oil (727 mg, quant.). IR (film) ν 1670, 1464, 1440, 1242. ^{1}H NMR ($CDCl_3$, 400 MHz) δ 1.37 (d, J = 6.0 Hz, 6H); 2.98 (t, J = 6.4 Hz, 2H); 3.31 (s, 3H, OMe); 3.84 (s, 3H, OMe); 3.85 (s, 3H, OMe); 4.52 (h, J = 6.0 Hz, 1H, OCH); 4.60 (t, J = 6.4 Hz, 2H); 5.19 (s, 2H); 6.73 (s, 1H); 6.86 (s, 1H); 6.89 (s, 1H); 6.93 (dd, J = 8.0, 1.8 Hz, 1H); 6.96−7.00 (m, 2H); 7.31 (d, J = 7.2 Hz, 1H); 7.35 (dd, J = 7.2, 7.2 Hz, 2H); 7.44 (d, J = 7.2 Hz, 2H). ^{13}C NMR ($CDCl_3$, 50.3 MHz) δ 22.2 (2q); 29.0 (t); 42.6 (t); 51.1 (q); 55.4 (q); 56.1 (q); 71.0 (t); 71.4 (d); 109.1 (d); 113.1 (d); 114.1 (d); 114.7 (d); 119.2 (d); 121.1 (s); 121.47 (s); 121.54 (s); 125.6 (d); 127.1 (2d); 127.8 (d); 128.5 (2d); 129.8 (s); 137.2 (s); 146.5 (s); 146.8 (s); 148.5 (s); 149.5 (s); 161.7 (s). MS (ESI) 528 (M+1, 100); 529 (M+2, 37). HRMS *m*/*z* calcd for $C_{32}H_{34}NO_6$ 528.2381, found 528.2373.

Methyl 1-(4-Benzyloxy-3-methoxyphenyl)-2-bromo-8-isopropoxy-9-methoxy-5,6-dihydropyrrolo[2,1-*a*]isoquinoline-3-carboxylate (14a). NBS (82 mg, 0.46 mmol) was added in one portion to a solution of **13a** (245 mg, 0.46 mmol) in THF (10 mL). The mixture was stirred at 70 °C under Ar for 90 min. The solvent was removed under reduced pressure. The residue was dissolved in CH_2Cl_2 and filtered through a pad of neutral alumina. **14a** was obtained as a yellow oil (278 mg, 99%). IR (film) ν 1693, 1462, 1112 cm^{-1}. ^{1}H NMR ($CDCl_3$, 400 MHz) δ 1.35 (d, J = 6.0 Hz, 6H); 2.98 (t, J = 6.4 Hz, 2H); 3.20 (s, 3H, OMe); 3.86 (s, 3H, OMe); 3.90 (s, 3H, OMe); 4.51 (h, J = 6.0 Hz, 1H, OCH); 4.59 (t, J = 6.4 Hz, 2H); 5.20 (br, 2H); 6.54 (s, 1H); 6.70 (s, 1H); 6.85−7.00 (m, 3H); 7.28−7.47 (m, 5H). ^{13}C NMR ($CDCl_3$, 100 MHz) δ 22.0 (2q); 28.6 (t); 43.4 (t); 51.1 (q); 55.0 (q); 56.0 (q); 70.7 (t); 71.2 (d); 107.6 (s); 108.9 (d); 113.0 (s); 113.7 (d); 113.9 (s); 114.3 (d); 114.5 (d); 119.1 (s); 122.2 (s); 123.2 (d); 125.3 (s); 126.9 (2d); 127.6 (d); 128.4 (2d); 131.8 (s); 137.0 (s); 146.6 (s); 147.3 (s); 148.3 (s); 149.4 (s); 161.1 (s). MS (ESI) 606 (MBr^{79}+1, 100); 607 (MBr^{79}+2, 23); 608 (MBr^{81} + 1, 95). HRMS *m*/*z* calcd. for $C_{32}H_{33}NO_6Br$ 606.1486, found 606.1485.

Methyl 2-(2,4-Dibenzyloxy-5-methoxyphenyl)-8-isopropoxy-1-(4-isopropoxy-3-methoxyphenyl)-9-methoxy-5,6-dihydropyrrolo[2,1-*a*]isoquinoline-3-carboxylate (15a). Following the general procedure **A** and starting from **14b** (*16*) (674 mg, 1.21 mmol) and 2-(2,4-dibenzyloxy-5-methoxyphenyl)-4,4,5,5-tetramethyl-1,3,2-dioxaborolane (**12b**), a yellow oil (719 mg, 75%) was obtained. IR (film) ν 1691, 1254, 1212. ^{1}H NMR ($CDCl_3$, 200 MHz) δ 1.31 (d, J = 6.2 Hz, 6H); 1.35 (d, J = 6.0 Hz, 6H); 3.03 (t, J = 6.4 Hz, 2H); 3.32 (s, 3H, OMe); 3.47 (s, 3H, OMe); 3.53 (s, 3H, OMe); 3.59 (s, 3H, OMe); 4.35−4.65 (m, 4H, 2OCH); 4.74 (s, 2H); 5.01 (s, 2H); 6.46 (s, 1H); 6.55 (s, 1H); 6.61 (br, 1H); 6.69−6.79 (m, 4H); 7.08−7.13 (m, 2H); 7.17−7.26 (m, 4H); 7.27−7.35 (m, 4H). ^{13}C NMR ($CDCl_3$, 50.3 MHz) δ 21.8 (2q); 22.0 (2q); 28.9 (t); 42.8 (t); 50.7 (q); 54.9 (q); 55.5 (q); 56.2 (q); 71.0 (t); 71.2 (d, t); 71.5 (d); 102.8 (d); 109.1 (d); 114.6 (2d); 115.8 (d); 115.9 (d); 118.2 (s); 118.7 (s); 121.1 (s); 121.5 (s); 122.9 (d); 125.4 (s); 126.5 (2d); 127.1 (2d); 127.5 (2d); 128.0 (2d); 128.2 (2d); 128.6 (s); 130.8 (s); 136.8 (s); 137.6 (s); 143.3 (s); 145.4 (s); 146.0 (s); 146.8 (s); 148.2 (s); 149.8 (s); 150.3 (s); 162.2 (s). MS (MALDI-TOF) 797 (M, 100), 798 (M+1, 54).

Methyl 2-(2-Benzyloxy-4-isopropoxy-5-methoxyphenyl)-1-(4-benzyloxy-3-methoxyphenyl)-8-isopropoxy-9-methoxy-5,6-dihydropyrrolo[2,1-*a*]isoquinoline-3-carboxylate (15b). Following the general procedure **A** and starting from **14a** (277 mg, 0.46

mmol) and 2-(2-benzyloxy-4-isopropoxy-5-methoxyphenyl)-4,4,5,5-tetramethyl-1,3,2-dioxaborolane (**12a**), a yellow oil (282 mg, 77%) was obtained. IR (film) ν 1692, 1254, 1212. ^{1}H NMR ($CDCl_3$, 200 MHz) δ 1.26 (d, J = 6.0 Hz, 6H); 1.36 (d, J = 6.0 Hz, 6H); 3.03 (t, J = 6.0 Hz, 2H); 3.21 (s, 3H, OMe); 3.55 (s, 3H, OMe); 3.57 (s, 6H, 2OMe); 4.37 (h, J = 6.0 Hz, 1H, OCH); 4.52 (h, J = 6.0 Hz, 1H, OCH); 4.63 (br, 2H); 4.82 (s, 2H); 5.12 (s, 2H); 6.46 (s, 1H); 6.55 (s, 1H); 6.66 (s, 1H); 6.72 (br, 4H); 7.16−7.41 (m, 10H). ^{13}C NMR ($CDCl_3$, 50.3 MHz) δ 21.9 (2q); 22.0 (2q); 28.0 and 28.9 (t); 42.2 and 42.8 (t); 50.7 (q); 55.0 (q); 55.5 (q); 56.2 (q); 70.5 (t); 71.1 (d); 71.3 (d); 71.5 (t); 104.5 (d); 109.0 (d); 113.3 (d); 114.3 (d); 114.4 (d); 116.1 (d); 118.2 (s); 118.7 (s); 121.0 (s); 121.4 (s); 122.9 (d); 125.4 (s); 126.5 (2d); 126.8 (2d); 127.1 (d); 127.5 (d); 127.7 (s); 128.0 (2d); 128.2 (2d); 130.8 (s); 137.0 (s); 137.7 (s); 144.0 (s); 145.9 (s); 146.0 (s); 146.1 (s); 148.1 (s); 148.8 (s); 150.2 (s); 162.2 (s). MS (ESI-TOF) 798 (M+1, 100), 799 (M+2, 39), 800 (M+3, 7). HRMS *m/z* calcd. for $C_{49}H_{51}NO_9$ 798.3636, found 798.3621.

Methyl 2-(2,4-Dibenzyloxy-5-methoxyphenyl)-1-(4-benzyloxy-3-methoxyphenyl)-8-isopropoxy-9-methoxy-5,6-dihydropyrrolo[2,1-*a*]isoquinoline-3-carboxylate (15c). Following the general procedure **A** and starting from **14a** (255 mg, 0.42 mmol) and 2-(2,4-dibenzyloxy-5-methoxyphenyl)-4,4,5,5-tetramethyl-1,3,2-dioxaborolane (**12b**), a reddish oil (246 mg, 69%) was obtained. IR (film) ν 1692, 1438, 1252, 1212. ^{1}H NMR ($CDCl_3$, 400 MHz) δ 1.38 (d, J = 6.0 Hz, 6H); 3.04 (t, J = 6.0 Hz, 2H); 3.24 (s, 3H, OMe); 3.54 (s, 3H, OMe); 3.56 (s, 3H, OMe); 3.63 (s, 3H, OMe); 4.54 (h, J = 6.0 Hz, 1H, OCH); 4.64 (br, 2H); 4.77 (s, 2H); 5.05 (s, 2H); 5.14 (s, 2H); 6.50 (s, 1H); 6.59 (s, 1H); 6.67 (s, 1H); 6.71−6.77 (m, 4H); 7.11−7.14 (m, 2H); 7.21−7.42 (m, 13H). ^{13}C NMR ($CDCl_3$, 100 MHz) δ 22.0 (2q); 28.8 (t); 42.8 (t); 50.6 (q); 55.0 (q); 55.6 (q); 56.3 (q); 70.5 (t); 71.0 (t); 71.2 (d); 71.5 (t); 102.9 (d); 109.1 (d); 113.5 (d); 114.46 (d); 114.54 (d); 116.0 (d); 118.3 (s); 118.8 (s); 121.0 (s); 121.5 (s); 122.9 (d); 125.4 (s); 126.6 (2d); 126.8 (2d); 127.19 (d); 127.21 (2d); 127.6 (2d); 127.9 (s); 128.0 (2d); 128.3 (2d); 128.3 (2d); 128.6 (s); 130.8 (s); 136.9 (s); 137.1 (s); 137.7 (s); 143.4 (s); 146.1 (s); 146.3 (s); 146.9 (s); 148.3 (s); 149.0 (s); 150.4 (s); 162.2 (s). MS (ESI-TOF) 846 (M+1, 100), 847 (M+2, 49), 848 (M+3, 12). HRMS *m/z* calcd. for $C_{53}H_{52}NO_9$ 846.3636, found 846.3621.

Methyl 2-(2,4-Dibenzyloxy-5-methoxyphenyl)-8-isopropoxy-1-(4-isopropoxy-3-methoxyphenyl)-9-methoxypyrrolo[2,1-*a*]isoquinoline-3-carboxylate (16a). Following the general procedure **B** and starting from **15a** (686 mg, 0.86 mmol), a yellow oil (637 mg, 93%) was obtained. IR (film) ν 1682, 1380, 1121 cm^{-1}. ^{1}H NMR ($CDCl_3$, 100 MHz) δ 1.32 (d, J = 6.0 Hz, 6H); 1.37 (d, J = 6.0 Hz, 6H); 3.42 (s, 6H, 2OMe); 3.59 (s, 3H, OMe); 3.63 (s, 3H, OMe); 4.49 (h, J = 6.0 Hz, 1H, OCH); 4.64 (h, J = 6.0 Hz, 1H, OCH); 4.78 (br, 2H); 5.03 (s, 2H); 6.48 (s, 1H); 6.54−6.73 (m, 2H); 6.79−6.94 (m, 3H); 7.03−7.11 (m, 3H); 7.15−7.20 (m, 3H); 7.23−7.34 (m, 6H); 9.31 (d, J = 7.6 Hz, 1H). ^{13}C NMR ($CDCl_3$, 50.3 MHz) δ 21.7 (2q); 22.0 (2q); 50.6 (q); 54.9 (q); 55.5 (q); 56.3 (q); 70.9 (d); 71.1 (t); 71.2 (d); 71.3 (t); 102.5 (d); 105.4 (d); 110.3 (d); 111.7 (d); 112.7 (s); 115.2 (d); 115.6 (d); 115.7 (s); 115.9 (d); 118.0 (s); 118.4 (s); 119.5 (s); 123.2 (d); 123.6 (d); 126.4 (d); 127.1 (d); 127.2 (2d); 127.5 (2d); 128.0 (2d); 128.2 (2d); 129.0 (s); 130.0 (s); 131.6 (s); 136.8 (s); 137.5 (s); 143.1 (s); 145.7 (s); 147.0 (s); 147.2 (s); 149.6 (s); 149.9 (s); 150.3 (s); 162.3 (s). MS (MALDI-TOF) 795 (M, 100), 796 (M+1, 73).

Methyl 2-(2-Benzyloxy-4-isopropoxy-5-methoxyphenyl)-1-(4-benzyloxy-3-methoxyphenyl)-8-isopropoxy-9-methoxypyrrolo[2,1-*a*]isoquinoline-3-carboxylate (16b). Following the general procedure **B** and starting from **15b** (1.06 g, 1.32 mmol), a yellow oil (685 mg, 65%) was obtained. IR (film) ν 1704, 1377, 1214 cm^{-1}. ^{1}H NMR ($CDCl_3$, 400 MHz) δ 1.41 (2d, J = 6.0 Hz, 12H); 3.28 (s, 3H, OMe); 3.57 (br, 3H, OMe); 3.62 (s, 3H, OMe); 3.65 (br, 3H, OMe); 4.39 (h, J = 6.0 Hz, 1H, OCH); 4.65 (h, J = 6.0 Hz, 1H, OCH); 4.86 (br, 2H); 5.14−5.18 (m, 2H); 6.47 (br, 1H); 6.76−6.88 (m, 2H); 6.91 (d, J = 7.6 Hz, 1H); 7.03 (s, 1H); 7.14−7.21 (m, 3H); 7.27−7.49 (m, 10H); 9.31 (d, J = 7.6 Hz, 1H). ^{13}C NMR ($CDCl_3$, 100 MHz) δ 21.9 (2q); 22.0 (2q); 50.7 (q); 55.2 (q); 55.6 (q); 56.4 (q); 70.6 (t); 70.8 (t); 71.0 (d); 71.5 (d); 104.3 (d); 105.5 (d); 110.3 (d); 111.8 (d); 112.8 (s); 113.3 and 113.6 (d); 115.2 (d); 116.2 (d); 118.5 (s); 119.6 (s); 123.4 (d); 123.7 (d); 127.0 (2d); 127.4 (s); 127.75 (2d); 128.2 (2d); 128.5 (2d); 128.6 (d); 128.7 (s); 128.8 (d); 129.2 (s); 130.2 (s); 131.9 (s); 137.2 (s); 137.7 (s); 144.1 (s); 146.6 (s); 147.4 (s); 149.7 (s); 150.4 (s); 162.6 (s). MS (ESI-TOF) 796 (M+1, 100), 797 (M+2, 54). HRMS *m/z* calcd. for $C_{49}H_{50}NO_9$ 796.3480, found 796.3480.

Methyl 2-(2,4-Dibenzyloxy-5-methoxyphenyl)-1-(4-benzyloxy-3-methoxyphenyl)-8-isopropoxy-9-methoxypyrrolo[2,1-*a*]isoquinoline-3-carboxylate (16c). Following the general procedure **B** and starting from **15c** (244 mg, 0.29 mmol), a yellow oil (181 mg, 74%) was obtained. IR (film) ν 1681, 1374, 1212 cm^{-1}. ^{1}H NMR ($CDCl_3$, 100 MHz) δ 1.43 (d, J = 6.0 Hz, 6H); 3.30 (s, 3H, OMe); 3.52−3.65 (m, 9H, 3 OMe); 4.60−4.90 (m, 3H); 5.07 (s, 2H); 5.18−5.21 (m, 2H); 6.50 (s, 1H); 6.59 (br, 1H); 6.74 (br, 1H); 6.82−6.89 (m, 2H); 6.94 (d, J = 7.6 Hz, 1H); 7.06 (s, 1H); 7.09−7.15 (m, 2H); 7.20−7.23 (m, 4H); 7.30−7.46 (m, 10H); 9.33 (d, J = 7.6 Hz, 1H). ^{13}C NMR ($CDCl_3$, 50.3 MHz) δ 21.9 (2q); 50.7 (q); 55.1 (q); 55.7 (q); 56.4 (q); 70.6 (t); 70.9 (d); 71.2 (t); 71.4 (t); 102.5 (d); 105.4 (d); 110.2 (d); 111.8 (d); 112.8 (s); 113.3 (d); 115.1 (d); 116.0 (d); 118.1 (s); 118.4 (s); 119.5 (s); 123.3 (d); 123.6 (d); 126.5 (d); 126.9 (2d); 127.2 (2d); 127.3 (2d); 127.7 (2d); 128.1 (2d); 128.3 (2d); 128.4 (2d); 129.0 (s); 130.1 (s); 131.7 (s); 136.9 (s); 137.1 (s); 137.5 (s); 143.2 (s); 146.5 (s); 147.1 (s); 147.3 (s); 149.0 (s); 149.6 (s); 150.4 (s); 162.4 (s). MS (MALDI-TOF) 844 (M+1, 100), 845 (M+1, 52), 846 (M+3, 8). HRMS *m/z* calcd. for $C_{53}H_{50}NO_9$ 844.3480, found 844.3467.

Methyl 2-(2,4-Dihydroxy-5-methoxyphenyl)-8-isopropoxy-1-(4-isopropoxy-3-methoxyphenyl)-9-methoxypyrrolo[2,1-*a*]isoquinoline-3-carboxylate (17a). Following the general procedure **C** and starting from **16a** (637 mg, 0.80 mmol), a brown oil (433 mg, 88%) was obtained. IR (film) ν 1685, 1381, 1223 cm^{-1}. ^{1}H NMR ($CDCl_3$, 100 MHz) δ 1.32 and 1.35 (d, J = 6.0 Hz, 6H); 1.42 (d, J = 6.0 Hz, 6H); 3.43 (s, 3H, OMe); 3.54 (br, 3H, OMe); 3.60 (br, 3H, OMe); 3.75 (s, 3H, OMe); 4.50 (h, J = 6.0 Hz, 1H, OCH); 4.67 (h, J = 6.0 Hz, 1H, OCH); 6.33 and 6.45 (2br, 1H); 6.57 (s, 1H); 6.82−7.00 (m, 3H); 7.05 (s, 1H); 7.17 and 7.34 (2br, 1H); 7.26 (s, 1H); 9.23 (d, J = 7.4 Hz, 1H). ^{13}C NMR ($CDCl_3$, 50.3 MHz) δ 21.6 (2q); 21.8 (2q); 51.0 (q); 54.8 (q); 55.5 (q); 56.2 (q); 70.8 (d); 71.1 (d); 102.5 (d); 105.3 (d); 110.1 (d); 112.1 (d); 112.4 (s); 112.8 (s); 114.1 (s); 115.0 (d); 115.6 (d); 119.0 (s); 119.1 (d); 122.9 (s); 123.2 (d); 123.4 (d); 128.4 (s); 130.2 (s); 130.6 (s); 139.8 (s); 145.5 (s); 145.7 (s); 147.3 (s); 148.2 (s); 149.5 (s); 162.1 (s); 129.0 (s). MS (MALDI-TOF) 615 (M, 100), 616 (M+1, 27).

Methyl 2-(2-Hydroxy-4-isopropoxy-5-methoxyphenyl)-1-(4-hydroxy-3-methoxyphenyl)-8-isopropoxy-9-methoxypyrrolo[2,1-*a*]isoquinoline-3-carboxylate (17b). Following the general procedure **C** and starting from **16b** (680 mg, 0.85 mmol), a brown oil (365 mg, 70%) was obtained. IR (film) ν 3440, 1684, 1381, 1218, 1121 cm^{-1}. ^{1}H NMR ($CDCl_3$, 200 MHz) δ 1.32 (d, J = 6.0 Hz, 6H); 1.38 (d, J = 6.0 Hz, 6H); 3.41 (s, 3H, OMe); 3.48 and 3.55 (2s, 3H, OMe); 3.57 and 3.68 (2br, 3H, OMe); 3.72 (s, 3H, OMe); 4.50 (h, J = 6.0 Hz, 1H, OCH); 4.64 (h, J = 6.0 Hz, 1H, OCH); 5.82 (br, 1H, OH); 6.34 and 6.40 (2br, 1H); 6.52 (br, 1H); 6.73 (d, J = 7.2 Hz, 1H); 6.84−6.95 (m, 2H); 7.00 (s, 1H); 7.06 and 7.15 (2d, J = 2.4 Hz, 1H); 7.26 (br, 1H); 9.13 (d, J = 7.2 Hz, 1H). ^{13}C

NMR ($CDCl_3$, 50.3 MHz) δ 21.8 (2q); 22.0 (2q); 51.3 (q); 55.2 (q); 55.8 (q); 56.3 (q); 70.9 (d); 71.0 (d); 103.5 (d); 105.5 (d); 110.2 (d); 112.4 (d); 112.5 (s); 113.8 (s); 113.9 (d); 115.2 and 115.4 (d); 119.3 (s); 123.1 (d); 123.4 (d); 124.4 (s); 124.5 (d); 124.6 (s); 127.0 (s); 131.0 (s); 144.7 (s); 146.4 (s); 147.2 (s); 147.7 (s); 147.9 (s); 148.0 (s); 149.8 (s); 162.3 (s). MS (MALDI-TOF) 615 (M, 100), 616 (M+1, 16).

Methyl 2-(2,4-Dihydroxy-5-methoxyphenyl)-1-(4-hydroxy-3-methoxyphenyl)-8-isopropoxy-9-methoxypyrrolo[2,1-*a*]isoquinoline-3-carboxylate (17c). Following the general procedure **C** and starting from **16c** (122 mg, 0.14 mmol), a yellow oil (80 mg, 95%) was obtained. IR (film) ν 3425, 1683, 1219, 1122 cm^{-1}. ^1H NMR (acetone-d_6, 400 MHz) δ 1.33 (d, J = 6.0 Hz, 6H); 3.38 (s, 3H, OMe); 3.58 (s, 3H, OMe); 3.62 (s, 3H, OMe); 3.73 (br, 3H, OMe); 4.70 (h, J = 6.0 Hz, 1H, OCH); 5.60 (s, 1H, OH); 6.37 (s, 1H); 6.57 (br, 1H); 6.82−6.88 (m, 2H); 7.07 (d, J = 7.5 Hz, 1H); 7.21 (br, 1H); 7.26 (s, 1H); 7.56 (s, 1H); 9.26 (d, J = 7.5 Hz, 1H). ^{13}C NMR (acetone-d_6, 50.3 MHz) δ 21.9 (2q); 51.3 (q); 55.3 (q); 55.9 (q); 56.4 (q); 71.0 (d); 102.5 (d); 105.5 (d); 110.2 (d); 112.5 (d); 112.6 (s); 113.3 (s); 113.9 (d); 114.0 (d); 114.3 (d); 114.4 (s); 119.3 (s); 123.2 (d); 123.5 (s); 124.4 (d); 127.2 (s); 130.1 (s); 131.1 (s); 140.0 (s); 144.6 (s); 145.7 (s); 146.4 (s); 147.7 (s); 148.4 (s); 149.9 (s); 162.2 (s). MS (ESI-TOF) 574 (M+1, 100), 575 (M+2, 23). HRMS m/z calcd. for $C_{32}H_{32}NO_9$ 574.2072, found 574.2055.

4′,11-Diisopropyl-Lam-D (18a). Following the general procedure **D** and starting from **17a** (433 mg, 0.70 mmol), a white solid (410 mg, quant.) was obtained. mp (MeCN) 218−220 °C. IR (film) ν 3359, 1699, 1432, 1258, 1157 cm^{-1}. ^1H NMR ($CDCl_3$, 200 MHz) δ 1.44 (d, J = 6.0 Hz, 12H); 3.44 (s, 3H, OMe); 3.51 (s, 3H, OMe); 3.86 (s, 3H, OMe); 4.57−4.77 (m, 2H, 2OCH); 6.72 (s, 1H); 6.98 (br, 1H); 7.02 (s, 1H); 7.09 (s, 1H); 7.15 (s, 1H); 7.16−7.18 (m, 3H); 9.19 (d, J = 7.2 Hz, 1H). ^{13}C NMR ($CDCl_3$, 50.3 MHz) δ 21.9 (4q); 55.1 (q); 55.5 (q); 56.2 (q); 71.2 (d); 71.8 (d); 103.5 (d); 104.6 (d); 105.6 (d); 107.7 (s); 109.8 (s); 110.3 (d); 110.8 (s); 112.2 (d); 115.0 (d); 116.9 (d); 118.9 (s); 123.1 (d); 123.9 (d); 124.7 (s); 128.8 (s); 129.3 (s); 134.3 (s); 143.2 (s); 146.2 (s); 146.9 (s); 147.1 (s); 148.4 (s); 150.0 (s); 151.3 (s); 155.4 (s). MS (MALDI-TOF) 583 (M, 100), 584 (M+1, 62).

3,11-Diisopropyl-Lam-D (18b). Following the general procedure **D** and starting from **17b** (365 mg, 0.59 mmol), a yellow solid (346 mg, quant. yield) was obtained. mp (MeCN) 130−132 °C. IR (film) 3435, 1704, 1430, 1223 cm^{-1}. ^1H NMR ($CDCl_3$, 200 MHz) δ 1.35 (d, J = 6.0 Hz, 6H); 1.39 (d, J = 6.0 Hz, 6H); 3.42 (s, 3H, OMe); 3.44 (s, 3H, OMe); 3.85 (s, 3H, OMe); 4.49 (h, J = 6.0 Hz, 1H); 4.65 (h, J = 6.0 Hz, 1H); 6.73 (s, 1H); 6.87 (s, 1H); 6.94 (d, J = 7.2 Hz, 1H); 7.04 (s, 1H); 7.09 (s, 1H); 7.13−7.16 (m, 3H); 9.11 (d, J = 7.2 Hz, 1H). ^{13}C NMR ($CDCl_3$, 50.3 MHz) δ 21.7 (2q); 21.8 (2q); 55.1 (q); 55.4 (q); 56.1 (q); 71.0 (d); 71.3 (d); 103.2 (d); 105.4 (d); 105.5 (d); 107.5 (s); 109.7 (s); 110.2 (d); 110.9 (s); 112.1 (d); 113.9 (d); 115.2 (d); 118.8 (s); 122.8 (d); 124.5 (d); 127.1 (s); 129.2 (s); 134.3 (s); 145.7 (s); 146.3 (s); 147.3 (s); 147.6 (s); 148.2 (s); 149.9 (s); 155.3 (s). MS (MALDI-TOF) 583 (M, 100), 584 (M+1, 77).

11-Isopropyl-Lam-D (18c). Following the general procedure **D** and starting from **17c** (80 mg, 0.14 mmol), a yellow solid (65 mg, 86%) was obtained. IR (film) ν 3312, 1710, 1432, 1264 cm^{-1}. ^1H NMR (acetone-d_6, 400 MHz) δ 1.31 (d, J = 6.0 Hz, 6H); 3.35 (s, 3H, OMe); 3.39 (s, 3H, OMe); 3.77 (s, 3H, OMe); 4.75 (h, J = 6.0 Hz, 1H); 6.73 (s, 1H); 6.87 (s, 1H); 7.01 (dd, J = 8.0, 1.7 Hz, 1H); 7.10 (d, J = 8.0 Hz, 1H); 7.145 (s, 1H); 7.153 (d, J = 1.7 Hz, 1H); 7.29 (d, J = 7.4 Hz, 1H); 7.44 (s, 1H); 9.05 (d, J = 7.4 Hz, 1H); 9.33 (s, 1H, OH); 9.83 (s, 1H, OH). ^{13}C NMR (acetone-d_6, 100 MHz) δ 21.4 (2q); 54.1 (q); 54.8 (q); 55.7 (q); 69.9 (d); 103.4 (d); 104.9 (s); 105.4 (d); 106.2 (d); 108.0 (s); 110.1 (d); 110.8 (d); 112.4 (s); 114.7 (d); 116.1 (s); 118.0 (d); 121.8 (s); 123.5 (d); 124.1 (d); 125.0 (s); 128.7 (s); 133.5 (s); 144.3 (s); 146.0 (s); 146.5 (s); 147.7 (s); 148.4 (s); 149.4 (s); 154.1 (s). MS (ESI-TOF) 542 (M+1, 100), 543 (M+2, 26). HRMS m/z calcd. for $C_{31}H_{28}NO_8$ 542.1809, found 542.1793.

4′,11-Diisopropyl-3-(2-(2-(2-methoxyethoxy)ethoxy)acetyl)-Lam-D (19a). Following the general procedure **E** and starting from **18a** (190 mg, 0.33 mmol), a yellow oil (204 mg, 84%) was obtained. IR (film) ν 1781, 1707, 1485, 1138 cm^{-1}. ^1H NMR ($CDCl_3$, 400 MHz) δ 1.39 (d, J = 6.0 Hz, 12H); 3.35 (s, 3H, OMe); 3.39 (s, 3H, OMe); 3.40 (s, 3H, OMe); 3.52−3.54 (m, 2H); 3.62−3.65 (m, 2H); 3.68−3.71 (m, 2H); 3.78−3.81 (m, 2H); 3.83 (s, OMe); 4.40 (s, 2H); 4.56−4.67 (m, 2H); 6.820 (s, 1H); 6.93 (d, J = 7.2 Hz, 1H); 7.03 (s, 1H); 7.05 (s, 1H); 7.0−7.14 (m, 4H); 9.07 (d, J = 7.2 Hz, 1H). ^{13}C NMR ($CDCl_3$, 100 MHz) δ 21.69 (q); 21.73 (q); 55.0 (q); 55.3 (q); 56.1 (q); 58.8 (q); 68.1 (t); 70.4 (t); 70.5 (t); 70.8 (t); 71.0 (d); 71.65 (d); 71.72 (t); 105.4 (d); 106.2 (d); 108.0 (s); 110.3 (d); 111.5 (s); 111.7 (d); 112.7 (d); 114.8 (d); 116.1 (s); 116.8 (d); 118.8 (s); 122.7 (d); 123.6 (d); 124.5 (s); 128.0 (s); 128.2 (s); 134.2 (s); 138.8 (s); 145.3 (s); 147.1 (s); 147.1 (s); 148.4 (s); 150.1 (s); 151.3 (s); 154.7 (s); 168.2 (s). MS (MALDI-TOF) 743 (M, 100), 744 (M+1, 90), 745 (M+2, 29).

3-[3-(2-(2-(2-(2-(2-(2-*tert*-Butoxycarbonylaminoethoxy)ethoxy)ethoxy)ethoxy)ethoxy)propanoyl]-4′,11-diisopropyl-Lam-D (19b). Following the general procedure **E** and starting from **18a** (154 mg, 0.26 mmol), a brown oil (205 mg, 76%) was obtained. IR (film) ν 3355, 1709, 1256, 1111 cm^{-1}. ^1H NMR ($CDCl_3$, 400 MHz) δ 1.42 (d, J = 6.0 Hz, 6H); 1.43−1.45 (m, 15H, O*i*Pr, *t*BuOC); 2.88 (t, J = 6.5 Hz, 2H); 3.31 (br, 4H, $2CH_2$); 3.40 (s, 3H, OMe); 3.43 (s, 3H, OMe); 3.51−3.54 (m, 4H, $2CH_2$); 3.61−3.66 (m, 16H); 3.75−3.80 (m, 2H, CH_2); 3.88 (s, 3H, OMe); 4.63 (h, J = 6.0 Hz, 1H); 4.70 (h, J = 6.0 Hz, 1H); 5.16 (br, 1H); 6.86 (s, 1H); 7.06 (d, J = 7.6 Hz, 1H); 7.10 (s, 1H); 7.12 (s, 1H); 7.15−7.19 (m, 4H); 9.23 (d, J = 7.6 Hz, 1H). ^{13}C NMR ($CDCl_3$, 100 MHz) δ 21.66 (q); 21.69 (q); 28.2 (q); 34.5 (t); 40.1 (t); 54.9 (q); 55.3 (q); 56.0 (q); 66.2 (t); 69.9 (2t); 70.0 (2t); 70.2 (2t); 70.3 (7t); 71.0 (d); 71.6 (d); 105.4 (d); 106.2 (d); 110.3 (d); 111.4 (s); 111.5 (s); 111.8 (d); 111.9 (s); 112.7 (d); 114.7 (d); 115.9 (s); 116.8 (d); 118.8 (s); 122.7 (s); 122.8 (d); 123.6 (d); 124.5 (s); 128.2 (s); 139.3 (s); 147.1 (s); 147.2 (s); 148.4 (s); 150.1 (s); 151.3 (s); 154.8 (s); 156.0 (s); 169.2 (s); 174.7 (s). MS (MALDI-TOF) 919 ([M-Boc], 100), 920 ([M-Boc]+1, 55).

3,11-Diisopropyl-4′-(2-(2-(2-methoxyethoxy)ethoxy)acetyl)-Lam-D (19c). Following the general procedure **E** and starting from **18b** (104 mg, 0.18 mmol), a yellow oil (127 mg, 96%) was obtained. IR (film) ν 1781, 1704, 1113 cm^{-1}. ^1H NMR ($CDCl_3$, 400 MHz) δ 1.31 (d, J = 6.0 Hz, 6H); 1.35 (d, J = 6.0 Hz, 6H); 3.32 (s, 3H, OMe); 3.40 (2s, 6H, 2OMe); 3.45−3.52 (m, 2H); 3.55−3.63 (m, 2H); 3.65−3.71 (m, 2H); 3.74 (s, 3H, OMe); 3.78−3.82 (m, 2H); 4.40−4.49 (m, 3H, OCH, CH_2); 4.61 (h, J = 6.0 Hz, 1H); 6.62 (s, 1H); 6.85 (s, 1H); 6.93 (d, J = 7.2 Hz, 1H); 7.00−7.03 (m, 2H); 7.16−7.19 (m, 2H); 7.22 (d, J = 8.0 Hz, 1H); 9.11 (d, J = 7.2 Hz, 1H). ^{13}C NMR ($CDCl_3$, 100 MHz) δ 21.67 (q); 21.73 (q); 55.4 (q); 55.6 (q); 56.1 (q); 58.9 (q); 68.5 (t); 70.4 (t); 70.5 (t); 70.9 (t); 71.1 (d); 71.3 (d); 71.8 (t); 103.3 (d); 105.1 (d); 105.3 (d); 107.7 (s); 109.5 (s); 110.1 (s); 110.4 (d); 112.3 (d); 115.4 (d); 118.6 (s); 122.8 (d); 123.5 (d); 123.9 (d); 124.5 (s); 129.1 (s); 134.1 (s); 135.0 (s); 139.3 (s); 146.3 (s); 146.6 (s); 147.8 (s); 148.4 (s); 150.3 (s); 151.8 (s); 155.3 (s); 168.2 (s); 170.7 (s). MS (MALDI-TOF) 743 (M, 75), 744 (M+1, 100), 745 (M+2, 45).

4′-[3-(2-(2-(2-(2-(2-(2-*tert*-Butoxycarbonylaminoethoxy)ethoxy)ethoxy)ethoxy)ethoxy)propanoyl]-3,11-diisopropyl-

Lam-D (19d). Following the general procedure **E** and starting from **18b** (82 mg, 0.14 mmol), a brown oil (143 mg, quant. yield) was obtained. IR (film) ν 3362, 1764, 1707, 1268, 1113 cm^{-1}. ^1H NMR ($CDCl_3$, 400 MHz) δ 1.41 (d, $J = 6.0$ Hz, 6H); 1.42−1.44 (m, 15H, O*i*Pr, *t*BuOC); 2.94 (t, $J = 6.5$ Hz, 2H); 3.29−3.32 (m, 4H, $2CH_2$); 3.48 (s, 6H, 2OMe); 3.61−3.71 (m, 20H, $10CH_2$); 3.81 (s, 3H, OMe); 3.94 (t, $J = 6.6$ Hz, 2H, CH_2); 4.58 (h, $J = 6.0$ Hz, 1H); 4.70 (h, $J = 6.2$ Hz, 1H); 5.09 (br, 1H); 6.72 (s, 1H); 6.98 (s, 1H); 7.05 (d, $J = 7.4$ Hz, 1H); 7.11 (s, 1H); 7.13 (s, 1H); 7.21 (d, $J = 1.6$ Hz, 1H); 7.24 (dd, $J = 8.0$, 1.6 Hz, 1H); 7.30 (d, $J = 8.0$ Hz, 1H); 9.24 (d, $J = 7.4$ Hz, 1H). ^{13}C NMR ($CDCl_3$, 100 MHz) δ 21.6 (2q); 21.7 (2q); 28.3 (q); 34.6 (t); 40.2 (t); 55.4 (q); 55.5 (q); 56.1 (q); 66.3 (t); 70.0 (t); 70.1 (t); 70.2 (t); 70.3 (t); 70.4 (5t); 71.0 (t); 71.3 (t); 103.3 (d); 105.1 (d); 105.3 (d); 107.7 (s); 109.5 (s); 110.2 (s); 110.3 (d); 112.3 (d); 115.3 (d); 118.6 (s); 122.8 (d); 123.7 (d); 123.8 (d); 124.4 (s); 129.1 (s); 134.1 (s); 134.7 (s); 139.8 (s); 146.3 (s); 146.5 (s); 147.7 (s); 148.4 (s); 150.3 (s); 152.0 (s); 155.3 (s); 155.9 (s); 169.2 (s). MS (MALDI-TOF) 919 ([M-Boc], 100), 1018 (M, 35).

11-Isopropyl-3,4′-*bis*(2-(2-methoxyethoxy)acetyl)-Lam-D (19e). Following the general procedure **E** and starting from **18c** (32 mg, 0.06 mmol), a yellow solid (32 mg, 71%) was obtained. mp (MeCN) 173−175 °C. IR (film) ν 1781, 1707, 1274, 1116 cm^{-1}. ^1H NMR ($CDCl_3$, 200 MHz) δ 1.44 (d, $J = 6.0$ Hz, 6H); 3.41 (s, 3H, OMe); 3.45 (s, 3H, OMe); 3.46 (s, 3H, OMe); 3.49 (s, 3H, OMe); 3.61−3.70 (m, 4H, $2CH_2$); 3.76−3.90 (m, 7H, OMe, $2CH_2$); 4.45 (s, 2H); 4.53 (s, 2H); 4.71 (h, $J = 6.0$ Hz, 1H); 6.81 (s, 1H); 7.04 (d, $J = 7.4$ Hz, 1H); 7.11 (s, 1H); 7.12 (s, 1H); 7.14 (s, 1H); 7.23−7.28 (m, 2H); 7.33 (d, $J = 8.0$ Hz, 1H); 9.19 (d, $J = 7.4$ Hz, 1H). ^{13}C NMR ($CDCl_3$, 50.3 MHz) δ 21.9 (2q); 55.6 (q); 55.8 (q); 56.2 (q); 59.0 (2q); 68.3 (t); 68.4 (t); 70.8 (t); 70.9 (t); 71.2 (d); 71.9 (2t); 105.3 (d); 106.1 (d); 108.3 (s); 110.3 (d); 110.8 (s); 111.9 (d); 112.9 (d); 115.3 (d); 115.9 (s); 118.7 (s); 122.8 (d); 123.7 (d); 123.8 (d); 124.5 (s); 128.1 (s); 134.1 (s); 134.8 (s); 138.9 (s); 139.5 (s); 145.3 (s); 147.4 (s); 148.6 (s); 150.4 (s); 152.0 (s); 154.8 (s); 168.2 (s). MS (ESI-TOF) 774 (M+1, 100), 775 (M+2, 31), 776 (M+3, 7). HRMS *m*/*z* calcd. for $C_{41}H_{44}NO_{14}$ 774.2756, found 774.2744.

11-Isopropyl-3,4′-*bis*(2-(2-(2-methoxyethoxy)ethoxy)acetyl)-Lam-D (19f). Following the general procedure **E** and starting from **18c** (32 mg, 0.06 mmol), a yellow solid (50 mg, 97%) was obtained. mp (MeCN) 125−127 °C. IR (film) ν 1708, 1464, 1275, 1114 cm^{-1}. ^1H NMR ($CDCl_3$, 400 MHz) δ 1.44 (d, $J = 6.0$ Hz, 6H); 3.39 (s, 3H, OMe); 3.42 (s, 3H, OMe); 3.46 (s, 3H, OMe); 3.49 (s, 3H, OMe); 3.54−3.63 (m, 4H, $2CH_2$); 3.65−3.92 (m, 15H, OMe, $6CH_2$); 4.46 (s, 2H); 4.53 (s, 2H); 4.71 (h, $J = 6.0$ Hz, 1H); 6.82 (s, 1H); 7.06 (d, $J = 7.4$ Hz, 1H); 7.12 (s, 2H); 7.16 (s, 1H); 7.23−7.35 (m, 3H); 9.21 (d, $J = 7.4$ Hz, 1H). ^{13}C NMR ($CDCl_3$, 50.3 MHz) δ 21.9 (2q); 55.6 (q); 55.8 (q); 56.2 (q); 59.0 (2q); 68.3 (t); 68.4 (t); 70.5 (2t); 70.6 (t); 70.7 (t); 71.0 (2t); 71.2 (d); 71.9 (2t); 105.3 (d); 106.1 (d); 108.3 (s); 110.4 (d); 110.8 (s); 112.0 (d); 113.0 (d); 115.3 (d); 115.9 (s); 118.7 (s); 122.8 (d); 123.7 (2d); 124.5 (s); 124.6 (s); 128.1 (s); 134.2 (s); 134.8 (s); 139.0 (s); 139.5 (s); 145.4 (s); 147.4 (s); 148.6 (s); 150.5 (s); 152.0 (s); 154.9 (s); 168.2 (s). MS (ESI-TOF) 862 (M+1, 83), 863 (M+2, 20). HRMS *m*/*z* calcd. for $C_{45}H_{52}NO_{16}$ 862.3281, found 862.3266.

3,4′,11-*tris*(2-(2-Methoxyethoxy)acetyl)-Lam-D (8). Following the general procedure **E** and starting from Lam-D (*15*) (38 mg, 0.08 mmol), elution with hexane/THF (60:40 to 40:60) gave a white solid (26 mg, 40%). mp (MeCN) 148−149 °C. IR (film) ν 1779, 1707, 1117 cm^{-1}. ^1H NMR ($CDCl_3$, 400 MHz) δ 3.405 (s, 3H, OMe); 3.410 (s, 3H, OMe); 3.44 (s, 3H, OMe); 3.45 (s, 3H, OMe); 3.46 (s, 3H, OMe); 3.61−3.64 (m, 4H, $2CH_2$); 3.66−3.68 (m, 2H, CH_2); 3.80−3.88 (m, 9H, OMe, $3CH_2$); 4.45 (s, 2H); 4.48 (s, 2H); 4.52 (s, 2H); 6.80 (s, 1H); 7.05 (d, $J = 7.6$ Hz, 1H); 7.16 (s, 1H); 7.21 (s, 1H); 7.24 (d, $J = 1.6$ Hz, 1H); 7.25−7.28 (m, 1H); 7.33 (d, $J = 8.0$ Hz, 1H); 7.42 (s, 1H); 9.22 (d, $J = 7.6$ Hz, 1H). ^{13}C NMR ($CDCl_3$, 100 MHz) δ 55.7 (q); 55.8 (q); 56.3 (q); 58.99 (q); 59.02 (q); 59.03 (q) 68.32 (t); 68.34 (t); 68.4 (t); 70.9 (2t); 71.0 (t); 71.9 (2t); 72.0 (t); 106.1 (d); 106.4 (d); 109.1 (s); 112.1 (d); 112.3 (s); 112.8 (d); 115.1 (d); 115.8 (s); 120.7 (d); 123.2 (s); 123.6 (s); 123.8 (2d); 124.0 (d); 128.1 (s); 133.4 (s); 134.5 (s); 139.2 (s); 139.7 (s); 140.4 (s); 145.4 (s); 147.6 (s); 150.8 (s); 152.3 (s); 154.9 (s); 168.3 (s); 168.4 (s). MS (ESI-TOF) 848 (M+1, 100), 849 (M+2, 35). HRMS *m*/*z* calcd. for $C_{43}H_{46}NO_{17}$ 848.2760, found 848.2751.

3,4′,11-*tris*(2-(2-(2-Methoxyethoxy)ethoxy)acetyl)-Lam-D (9). Following the general procedure **E** and starting from Lam-D (*15*) (37 mg, 0.08 mmol), elution with hexane/THF (60:40 to 40:60) gave a pink solid (34 mg, 46%). mp (MeCN) 137−139 °C. IR (film) ν 1779, 1707, 1117 cm^{-1}. ^1H NMR ($CDCl_3$, 400 MHz) δ 3.39 (s, 6H, 2OMe); 3.41 (s, 3H, OMe); 3.447 (s, 3H, OMe); 3.451 (s, 3H, OMe); 3.54−3.61 (m, 6H, $3CH_2$); 3.66−3.79 (m, 12H, $6CH_2$); 3.82−3.89 (m, 9H, OMe, $3CH_2$); 4.45 (s, 2H); 4.48 (s, 2H); 4.52 (s, 2H); 6.80 (s, 1H); 7.04 (d, $J = 7.6$ Hz, 1H); 7.15 (s, 1H); 7.21 (s, 1H); 7.24−7.27 (m, 2H); 7.32 (d, $J = 8.0$ Hz, 1H); 7.42 (s, 1H); 9.21 (d, $J = 7.6$ Hz, 1H). ^{13}C NMR ($CDCl_3$, 100 MHz) δ 55.7 (q); 55.8 (q); 56.3 (q); 59.0 (3q); 68.29 (t); 68.33 (t); 68.4 (t); 70.53 (2t); 70.60 (t); 70.62 (2t); 70.67 (t); 71.00 (t); 71.01 (t); 71.04 (t); 71.88 (2t); 71.90 (t); 106.1 (d); 106.4 (d); 109.1 (s); 112.1 (d); 112.3 (s); 112.8 (d); 115.1 (d); 115.8 (s); 120.6 (d); 123.1 (s); 123.6 (d); 123.7 (s); 123.8 (d); 124.0 (d); 128.1 (s); 133.4 (s); 134.5 (s); 139.2 (s); 139.7 (s); 140.4 (s); 145.4 (s); 147.6 (s); 150.8 (s); 152.3 (s); 154.9 (s); 168.3 (s); 168.5 (s). MS (ESI-TOF) 980 (M+1, 100), 981 (M+2, 62). HRMS *m*/*z* calcd. for $C_{49}H_{58}NO_{20}$ 980.3547, found 980.3529.

3-(2-(2-(2-Methoxyethoxy)ethoxy)acetyl)-Lam-D (2). Following the general procedure **F** and starting from **19a** (187 mg, 0.26 mmol), elution with hexane/THF (60:40 to 40:60) gave a yellow solid (73 mg, 44%). mp (MeCN) 163−164 °C. IR (film) ν 3284, 1786, 1684, 1424 cm^{-1}. ^1H NMR ($CDCl_3$, 400 MHz) δ 3.38 (s, 3H, OMe); 3.42 (s, 3H, OMe); 3.50 (s, 3H, OMe); 3.54−3.58 (m, 2H); 3.64−3.69 (m, 2H); 3.70−3.75 (m, 2H); 3.80−3.84 (m, 2H); 3.91 (s, OMe); 4.43 (s, 2H); 6.04 (br, 1H, OH); 6.28 (br, 1H, OH); 6.82 (s, 1H); 6.88 (d, $J = 7.2$ Hz, 1H); 7.04 (s, 1H); 7.09 (s, 1H); 7.10−7.11 (m, 1H); 7.13 (s, 2H); 7.18 (d, $J = 7.6$ Hz, 1H); 9.02 (d, $J = 7.2$ Hz, 1H). ^{13}C NMR ($CDCl_3$, 100 MHz) δ 55.3 (q); 55.5 (q); 56.3 (q); 59.0 (q); 68.2 (t); 70.4 (t); 70.6 (t); 70.9 (t); 71.8 (t); 104.9 (d); 106.3 (d); 108.0 (s); 110.9 (d); 111.5 (s); 111.7 (d); 112.7 (d); 113.8 (d); 115.3 (d); 116.1 (s); 118.6 (s); 122.8 (d); 124.5 (d); 125.1 (s); 127.0 (s); 128.1 (s); 134.5 (s); 138.8 (s); 145.3 (s); 145.8 (s); 146.9 (s); 147.1 (s); 147.2 (s); 147.5 (s); 154.8 (s); 168.4 (s). MS (ESI-TOF) 660 (M+1, 100), 682 (M+Na, 80). HRMS *m*/*z* calcd. for $C_{35}H_{34}NO_{12}$ 660.2075, found 660.2062.

3-[3-(2-(2-(2-(2-(2-(2-Aminoethoxy)ethoxy)ethoxy)ethoxy)ethoxy)ethoxy)propanoyl]-Lam-D (3). Following the general procedure **F** and starting from **19b** (140 mg, 0.14 mmol), elution with CH_2Cl_2/MeOH (95:5 to 90:10) gave a yellow oil (68 mg, 59%). IR (film) ν 3127, 1702, 1420, 1278 cm^{-1}. ^1H NMR ($CDCl_3$, 400 MHz) δ 2.60 and 2.86 (2t, $J = 6.4$ Hz, 2H); 3.20 (br, 2H); 3.43 (s, 3H, OMe); 3.50 (s, 3H, OMe); 3.63−3.70 (m, 20H); 3.83−3.89 (m, 4H); 3.90 (s, 3H, OMe) 6.82 (s, 1H); 6.93 (d, $J = 7.5$ Hz, 1H); 7.01 (s, 1H); 7.10 (dd, $J = 8.0$, 1.6 Hz, 1H); 7.12 (2s, 2H); 7.22 (s, 1H); 7.24 (d, $J = 8.0$ Hz, 1H); 7.92 (br, 4H, NH_2, 2 OH); 9.10 (d, $J = 7.5$ Hz, 1H). ^{13}C NMR ($CDCl_3$, 100 MHz) δ 34.6 (t); 40.2 (t); 55.2 (q); 55.5 (q); 56.2 (q); 66.2 (t); 66.6 (t); 69.7 (t); 69.8 (t); 69.9 (t); 70.0 (2t); 70.1 (t); 70.2 (2t); 70.3 (t); 70.4 (t); 104.9 (d); 106.3 (d); 107.8 (s); 111.0 (d); 111.5 (s); 111.7 (d); 112.7 (d); 113.9 (d); 115.6 (d); 115.9 (s); 118.5 (s); 122.7 (d); 124.3 (d); 125.1 (s); 126.7 (s);

128.1 (s); 134.5 (s); 139.2 (s); 145.2 (s); 146.0 (s); 147.2 (s); 147.3 (s); 147.4 (s); 147.7 (s); 154.8 (s); 169.5 (s). MS (ESI-TOF) 835 (M+1, 100); 836 (M+2, 40), 837 (M+3, 8). HRMS *m*/*z* calcd. for $C_{43}H_{51}N_2O_{15}$ 835.3283, found 835.3277.

4′-(2-(2-(2-Methoxyethoxy)ethoxy)acetyl)-Lam-D (4). Following the general procedure **F** and starting from **19c** (111 mg, 0.15 mmol), elution with hexane/THF (60:40 to 40:60) gave a yellow solid (55 mg, 55%). mp (MeCN) 201−203 °C. IR (film) ν 3455, 1679, 1426 cm^{-1}. ^1H NMR ($CDCl_3$, 400 MHz) δ 3.41 (s, 3H, OMe); 3.54 (s, 3H, OMe); 3.55 (s, 3H, OMe); 3.58−3.62 (m, 2H); 3.68−3.75 (m, 2H); 3.76−3.81 (m, 2H); 3.83 (s, OMe); 3.86−3.91 (m, 2H); 4.53 (s, 2H); 5.88 (br, 1H, OH); 5.98 (br, 1H, OH); 6.66 (s, 1H); 6.93−7.10 (m, 2H); 7.07 (s, 1H); 7.18 (s, 1H); 7.23−7.28 (m, 2H); 7.32 (d, J = 8.0 Hz, 1H); 9.17 (d, J = 7.2 Hz, 1H). ^{13}C NMR ($CDCl_3$, 100 MHz) δ 55.8 (q); 55.9 (q); 56.3 (q); 59.1 (q); 68.5 (t); 70.6 (t); 70.7 (t); 71.1 (t); 71.9 (t); 103.6 (d); 104.4 (d); 104.7 (d); 109.6 (s); 110.0 (s); 110.8 (d); 115.5 (d); 118.6 (s); 123.3 (s); 123.7 (d); 124.0 (d); 125.5 (d); 125.6 (d); 128.2 (s); 129.3 (s); 134.3 (s); 135.4 (s); 135.8 (s); 139.5 (s); 143.5 (s); 146.4 (s); 146.9 (s); 147.0 (s); 147.2 (s); 152.1 (s); 168.5 (s). MS (ESI-TOF) 660 (M+1, 100), 682 (M+Na, 33). HRMS *m*/*z* calcd. for $C_{35}H_{34}NO_{12}$ 660.2075, found 660.2065.

4′-[3-(2-(2-(2-(2-(2-Aminoethoxy)ethoxy)ethoxy)ethoxy)ethoxy)propanoyl]-Lam-D (5). Following the general procedure **F** and starting from **19d** (130 mg, 0.13 mmol), elution with CH_2Cl_2/MeOH (95:15 to 85:15) gave a brown oil (61 mg, 57%). IR (film) ν 3133, 1700, 1425, 1277 cm^{-1}. ^1H NMR ($CDCl_3$, 400 MHz) δ 2.60 and 2.95 (2t, J = 6.4 Hz, 2H); 3.16−3.24 (m, 2H); 3.43 and 3.47 (s, 3H, OMe); 3.52 (s, 3H, OMe); 3.62−3.77 (m, 20H); 3.83 (s, 3H, OMe); 3.89−3.96 (m, 4H); 6.65 (s, 1H); 6.95 (d, J = 7.4 Hz, 1H); 6.99 (s, 1H); 7.06 (s, 1H); 7.19−7.24 (m, 2H); 7.25 (d, J = 1.6 Hz, 1H); 7.26−7.31 (m, 1H); 9.10 (d, J = 7.4 Hz, 1H). ^{13}C NMR ($CDCl_3$, 100 MHz) δ 34.7 (t); 40.2 (t); 55.6 (q); 55.8 (q); 56.3 (q); 66.4 (t); 66.7 (t); 69.7 (t); 69.8 (t); 69.9 (2t); 70.0 (2t); 70.1 (t); 70.2 (t); 70.3 (t); 70.4 (t); 103.7 (d); 104.6 (d); 104.8 (d); 107.7 (s); 109.4 and 109.9 (s); 111.0 (d); 112.3 (d); 115.5 (d); 118.4 (s); 123.0 (d); 123.9 (2d); 125.2 (s); 129.2 (s); 134.3 (s); 135.0 (s); 139.9 (s); 143.8 (s); 146.6 (s); 146.8 (s); 147.2 (s); 147.5 (s); 152.1 (s); 155.4 (s); 169.5 (s); 172.1 (s). MS (ESI-TOF) 835 (M+1, 100); 836 (M+2, 44), 837 (M+3, 23). HRMS *m*/*z* calcd. for $C_{43}H_{51}N_2O_{15}$ 835.3283, found 835.3277.

3,4′-*bis*(2-(2-Methoxyethoxy)acetyl)-Lam-D (6). Following the general procedure **F** and starting from **19e** (41 mg, 0.05 mmol), elution with hexane/THF (60:40 to 40:60) gave a yellow solid (19 mg, 48%). mp (MeCN) 162−164 °C. IR (film) ν 3170, 1780, 1681, 1425 cm^{-1}. ^1H NMR ($CDCl_3$, 400 MHz) δ 3.40 (s, 3H, OMe); 3.44 (s, 3H, OMe); 3.45 (s, 3H, OMe); 3.56 (s, 3H, OMe); 3.61−3.64 (m, 2H); 3.66−3.68 (m, 2H); 3.80−3.82 (m, 2H); 3.83 (s, 3H, OMe); 3.85−3.88 (m, 2H); 4.45 (s, 2H); 4.52 (s, 2H); 6.00 (br, 1H, OH); 6.82 (s, 1H); 6.95−6.99 (m, 1H); 7.02 (d, J = 7.2 Hz, 1H); 7.06 (s, 1H); 7.14 (s, 1H); 7.18 (s, 1H); 7.24 (d, J = 2.0 Hz, 1H); 7.32 (d, J = 8.0 Hz, 1H); 9.17 (d, J = 7.2 Hz, 1H). ^{13}C NMR ($CDCl_3$, 100 MHz) δ 55.76 (q); 55.80 (q); 56.3 (q); 58.99 (q); 59.04 (q); 68.3 (t); 68.4 (t); 70.9 (t); 71.0 (t); 71.9 (t); 72.0 (t); 104.7 (d); 106.2 (d); 108.4 (s); 110.7 (s); 110.9 (d); 112.0 (d); 113.0 (d); 115.3 (d); 116.0 (s); 118.6 (s); 123.1 (d); 123.8 (d); 125.2 (s); 125.5 (d); 128.1 (s); 134.4 (s); 134.9 (s); 139.1 (s); 139.6 (s); 145.5 (s); 147.0 (s); 147.3 (s); 147.5 (s); 152.2 (s); 154.9 (s); 168.3 (s); 168.4 (s). MS (ESI-TOF) 732 (M+1, 100), 733 (M+2, 32); 734 (M+3, 9). HRMS *m*/*z* calcd. for $C_{38}H_{38}NO_{14}$ 732.2287, found 732.2307.

3,4′-*bis*(2-(2-(2-Methoxyethoxy)ethoxy)acetyl)-Lam-D (7). Following the general procedure **F** and starting from **19f** (48 mg, 0.06 mmol), elution with hexane/THF (60:40 to 40:60) gave a white solid (8 mg, 19%). mp (MeCN) 151−152 °C. IR (film) ν 3204, 1780, 1681, 1425 cm^{-1}. ^1H NMR ($CDCl_3$, 400 MHz) δ 3.39 (s, 3H, OMe); 3.41 (s, 3H, OMe); 3.44 (s, 3H, OMe); 3.55−3.58 (m, 5H, OMe, CH_2); 3.59−3.62 (m, 4H, $2CH_2$); 3.66−3.75 (m, 6H, $3CH_2$); 3.77−3.79 (m, 2H, CH_2); 3.83 (br, 3H, OMe); 3.87−3.90 (m, 2H, CH_2); 4.45 (s, 2H); 4.53 (s, 2H); 5.97 (br, 1H); 6.82 (s, 1H); 6.97−7.08 (m, 2H); 7.15 (s, 1H); 7.20 (s, 1H); 7.23−7.25 (m, 2H); 7.32 (d, J = 8.0 Hz, 1H); 9.20 (d, J = 7.2 Hz, 1H). ^{13}C NMR ($CDCl_3$, 100 MHz) δ 55.76 (q); 55.82 (q); 56.3 (q); 59.1 (2q); 68.3 (t); 68.5 (t); 70.55 (t); 70.62 (t); 70.65 (t); 70.70 (t); 71.0 (t); 71.1 (t); 71.90 (t); 71.93 (t); 103.6 (s); 104.4 (s); 104.7 (d); 106.2 (d); 110.8 (s); 110.9 (d); 112.1 (d); 112.4 (s); 113.0 (d); 115.3 (d); 115.5 (s); 116.0 (s); 118.6 (s); 123.1 (s); 123.8 (d); 123.9 (d); 125.3 (s); 125.5 (d); 135.0 (s); 139.6 (s); 145.5 (s); 147.0 (s); 147.5 (s); 152.2 (s); 155.0 (s); 168.4 (s); 168.5 (s). MS (ESI-TOF) 820 (M+1, 100), 821 (M+2, 39); 822 (M+2, 14). HRMS *m*/*z* calcd. for $C_{42}H_{46}NO_{16}$ 820.2811, found 820.2797.

Cell Lines and Culture. Established human-derived cell lines used in this study were purchased from ATCC (American type Culture Collection): A-549, human lung carcinoma; BJ, Skin Fibroblast; HT-29, human colorectal adenocarcinoma; and MDA-MB-231, human breast adenocarcinoma. All cell lines were maintained in DMEM supplemented with 10% FBS and 100 units/mL penicillin and streptomycin at 37 °C and 5% CO_2.

GI_{50} Analysis. Triplicate cultures were incubated for 72 h in the presence or absence of test compounds **1**−**9** (at ten concentrations, typically ranging from 0.0026 to 10 μg/mL).

A colorimetric assay using SRB was adapted for a quantitative measurement of cell growth and viability, following a previously described method (*16*). Cells were plated in 96-well microtiter plates at a density of 5×10^3/well and incubated for 24 h. One plate from each different cell line was fixed, stained, and used for Tz reference (see next paragraph). The cells were then treated with vehicle alone (control) or the test compounds at the concentrations indicated. The treated cells were incubated for additional 72 h, and then assayed for cytotoxicity via colorimetric analysis.

The cells were washed twice with PBS, fixed for 15 min in 1% glutaraldehyde solution, rinsed twice in PBS, and stained in 0.4% SRB solution for 30 min at room temperature. The cells were then rinsed several times in 1% acetic acid solution and air-dried. SRB was then extracted in 10 mM trizma base solution, and the absorbance at 490 nm was then measured. Cell survival is expressed as a percentage of control cell growth.

Dose−response curves were obtained by using the NCI algorithm (*17*): Tz = number of control cells at time t_0, C = number of control cells at time t, and T = number of treated cells at time t.

If Tz < T < C (growth inhibition), then the result is 100 × ([T − Tz]/[C − Tz]).

If T < Tz (net cell death), then the result is 100 × ([T − Tz]/Tz).

After dose−curve generation, the results were expressed as GI_{50}.

General Treatments for Imaging. A-549, MDA-MB-231, and HT-29 cells were seeded onto MatTek (Ashland, USA) glass-bottomed microwell dishes at 30×10^3 cells/cm^2. After 24 h, the culture medium was discarded and then replaced by fresh DMEM medium containing compound **9** at 25 nM. A negative control (no compound) was also used. The cells were then incubated for 48 h at 37 °C.

The following dyes were used for colocalization experiments: WGA-FITC (Sigma, USA) and Mitotracker Red (Molecular Probes). Standard staining protocols were employed for live-cell imaging. Images were then subsequently acquired within the following 30 min.

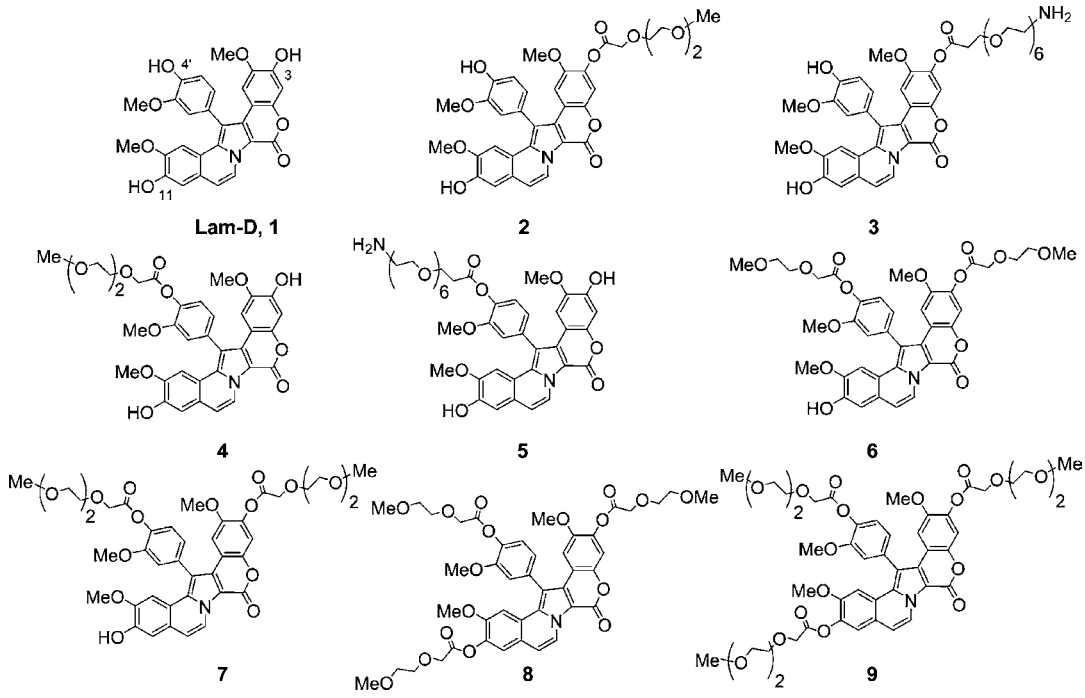

Figure 1. Structures of Lam-D 1 and PEG derivatives **2**−**9**.

Confocal Laser Scanning Microscopy. Confocal laser scanning microscopy was performed with a Leica TCS SPII spectral confocal laser scanning microscope (Leica Microsystems Heidelberg GmbH, Mannheim, Germany), using a 63× objective. FITC fluorescence was excited with an Ar laser at 488 nm. Lam-D and its derivatives were excited at 351 nm. Mitotracker was excited at 543 nm. The same microscope settings were maintained for each conjugate and concentration. To avoid crosstalk, two-fluorescence scanning was performed in a sequential mode.

Apoptosis Assay. The methodology used is based on fluorochrome inhibitors of caspases (FLICA; CaspaTag in situ caspase detection kits, Chemicon International, U.S. and Canada). The inhibitors are cell-permeable and non-cytotoxic. Once inside the cell, the inhibitor covalently binds to the active caspase. This kit uses a carboxyfluorescein-labeled fluoromethyl ketone peptide inhibitor of caspase-3 (FAM-DEVD-FMK), which fluoresces green. When added to a group of cells, the FAM-DEVD-FMK probe enters each cell and covalently binds to a reactive cysteine residue in the large subunit of the active caspase heterodimer, thereby inhibiting further enzymatic activity (*18*).

Cell cultures previously incubated with Lam-D for 48 h at a concentration of 25 nM were tested for apoptosis determination. After the latter drug treatments, 30 × FLICA reagent was added at 1:15 dilution in culture medium and then incubated for 1 h at 37 °C. The cells were then washed with PBS and subsequently analyzed by confocal scanning microscopy. The green fluorescence signal was a direct measure of the amount of active caspase-3/7 present in the cell at the time the reagent was added.

Uptake Measurements by FACS Flow Cytometry. 1×10^6 A-549, BJ, MDA-MB-231, and HT-29 cells were seeded onto 25 cm^2 cell culture flasks (Nalgene Nunc International, Naperville, USA) with 10 mL of DMEM. After 12 h, the culture medium was discarded and replaced by fresh DMEM medium containing compounds **1**−**9** at a concentration of 1 μM. A negative control (no compound) was also used. Cells were then incubated for 12 h at 37 °C. After incubation, cells were washed with 3 × PBS, detached with trypsin−EDTA 0.25%, and centrifuged at 1000× rpm. Finally, the medium was decanted, and the cellular pellet was resuspended in PBS and kept at 0 °C until measurements were performed. Fluorescence analysis was performed with a MoFlo cytometer (DakoCytomation, Colorado, USA), using the 351 nm excitation line of Ar laser (25 mW) and emission detection at 450 nm (tolerance range ±65 nm). CIQ is expressed as a percentage value in reference to Lam-D. It was calculated as a division of the fluorescence value obtained by the Lam-D fluorescence control under the same experimental conditions.

Cell Cycle Analysis. Cell cycle analysis were performed by DRAQ5 (Biostatus) staining to determine DNA content. DRAQ5 was added to the previous PBS cell culture suspensions (1 μL/4 × 10^5 cells), incubated for 15 min at 37 °C, and the cells were directly analyzed without any further treatment. Fluorescence analysis was performed with a MoFlo cytometer (DakoCytomation, Colorado, USA), using the 488 nm excitation line of an Ar laser (150 mW) and emission detection at 670 nm (tolerance range ±30 nm). Cell cycle profile was analyzed using *Cell Quest* software.

RESULTS

Lam-D contains three phenolic sites susceptible to modification. Despite previous SAR studies that highlighted the relevance of the phenolic residues at the C-3 and C-11 positions of Lam-D (*3*, *19*), and their essential role for cytotoxicity and topoisomerase I inhibition (*3*), in this study, the free OH groups were chosen for attachment the PEG moiety. As esters readily hydrolyze under physiological conditions, our group envisioned that these derivatives would enable gradual release of the drug. Use of Lam-D derivatives having differently protected phenols allowed selective deprotection and further conjugation with PEG-carboxylic acids to enable synthesis of mono-PEG (**2**−**5**), di-PEG (**6**, **7**), and tri-PEG (**8**, **9**) conjugates (Figure 1).

The derivatives prepared contain monodisperse PEG backbones with OMe (**2**, **4**, **6**, **7**, **8**, and **9**) and NH_2 (**3**, **5**) terminal moieties and vary in their chain length. The PEGs used for derivatization contain one, two, or six sequentially linked units of ethylene glycol. Another source of diversity introduced in the PEG carriers was a spacer; acetyl (**2**, **4**, **6**, **7**, **8**, and **9**) or propanoyl (**3**, **5**) moieties were used.

Scheme 1

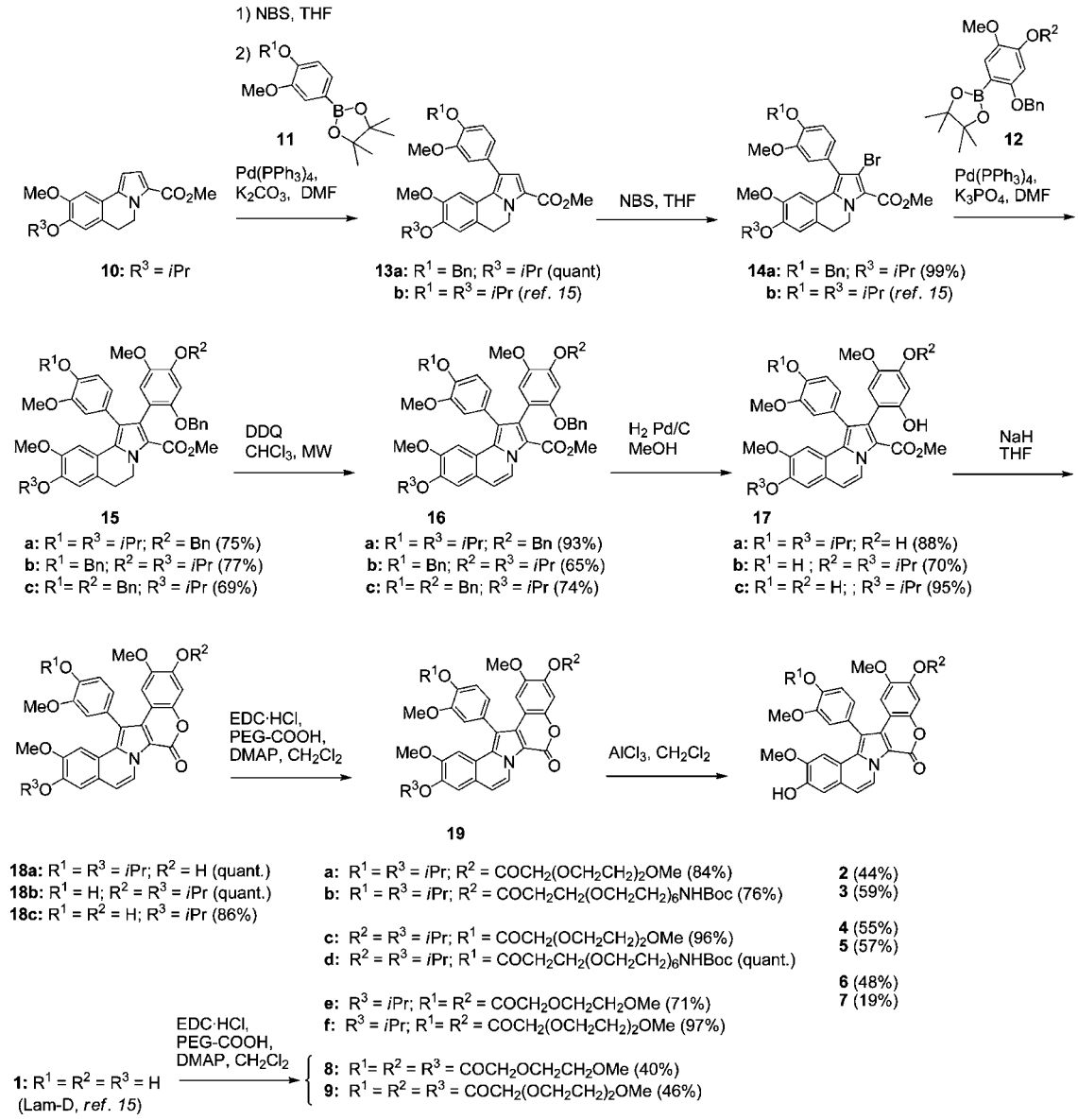

Table 1. Cytotoxicity of Compounds 1−9 in Three Human Cancer Cell Lines

	cytotoxicity (M)			
compound	HT-29 colon	A-549 lung	MDA-MB-231 breast	BJ skin fibroblast
Lam-D (1)	3.00×10^{-6}	1.22×10^{-7}	1.34×10^{-7}	6.37×10^{-9}
2	1.97×10^{-6}	7.13×10^{-8}	4.55×10^{-8}	6.28×10^{-7}
3	1.68×10^{-6}	8.86×10^{-8}	4.07×10^{-8}	6.51×10^{-9}
4	1.97×10^{-6}	5.46×10^{-8}	5.31×10^{-8}	2.90×10^{-6}
5	4.79×10^{-6}	3.47×10^{-7}	2.52×10^{-7}	3.51×10^{-6}
6	1.28×10^{-6}	6.29×10^{-8}	3.14×10^{-8}	1.81×10^{-9}
7	5.49×10^{-6}	5.37×10^{-8}	7.68×10^{-8}	3.17×10^{-9}
8	4.60×10^{-6}	7.31×10^{-8}	1.04×10^{-7}	4.90×10^{-8}
9	4.08×10^{-6}	4.69×10^{-8}	8.57×10^{-8}	2.67×10^{-8}

The methodology developed in our group for the total synthesis of Lam-D (*15*) was used for the preparation of conjugates **2**−**9**. The key steps of the synthesis comprise two successive processes of regioselective bromination and Pd(0)-catalyzed cross-coupling reactions starting from the scaffold **10**.

As shown in **Scheme 1**, several dialkoxy and trialkoxyphenylboronates **11a**,**b** and **12a**,**b** were required. These compounds were obtained with good yields by borylation of the corresponding aryl bromides with pinacolborane using $Pd(OAc)_2$ and DPE-Phos as catalysts (for details, see Supporting Information). The protected alkoxy-aryl bromides required were obtained by protection of commercially available phenols followed by mild bromination via NBS in THF at −78 °C (*20*).

Regioselective bromination of **10** (*21*) at position 1 using one equivalent of NBS in THF followed by Pd(0)-catalyzed cross-coupling reaction with the boronic ester **11a** or **11b** afforded the monoaryl scaffolds **13a** and **13b** (*15*), respectively, which were converted into the bromides **14a** and **14b** (*15*) by regioselective bromination at position 2. A second cross-

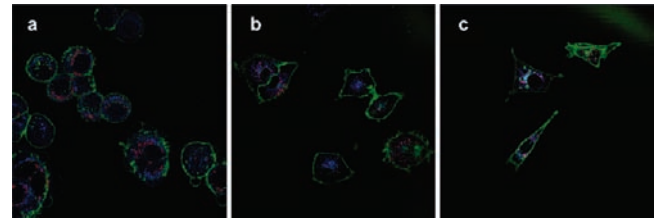

Figure 2. Cellular uptake of **9** and selective staining of mitochondria, Golgi apparatus, and cell membrane. The following cancer cell lines were used for the colocalization experiments. (a) HT-29, (b) A-549, and (c) MDA-MB-231.

Table 2. Cellular Internalization Uptake Measured by FACS

	cellular internalization uptake (AU)				cellular internalization quotient (CIQ)[a]			
compound	HT-29 colon	A-549 lung	MDA-MB-231 breast	BJ skin fibroblast	HT-29 colon	A-549 lung	MDA-MB-231 breast	BJ skin fibroblast
Lam-D (1)	82.7	328.5	443.8	259.4	100%[a]	100%[a]	100%[a]	100%[a]
2	41.1	463.1	266.6	321.0	50%	141%	60%	123.8%
3	88.0	393.0	527.5	333.4	106%	120%	119%	128.6%
4	59.8	500.6	364.8	501.5	72%	152%	82%	193.4%
5	84.4	373.7	328.1	371.4	102%	114%	74%	143.2%
6	90.3	407.2	535.0	317.7	109%	124%	121%	122.5%
7	49.3	379.3	432.1	279.3	60%	116%	97%	107.7%
8	78.7	532.6	414.8	352.0	95%	162%	94%	135.7%
9	143.3	514.8	529.7	371.0	173%	157%	119%	143.0%

[a] The CIQ has been calculated in reference to the cellular uptake of Lam-D.

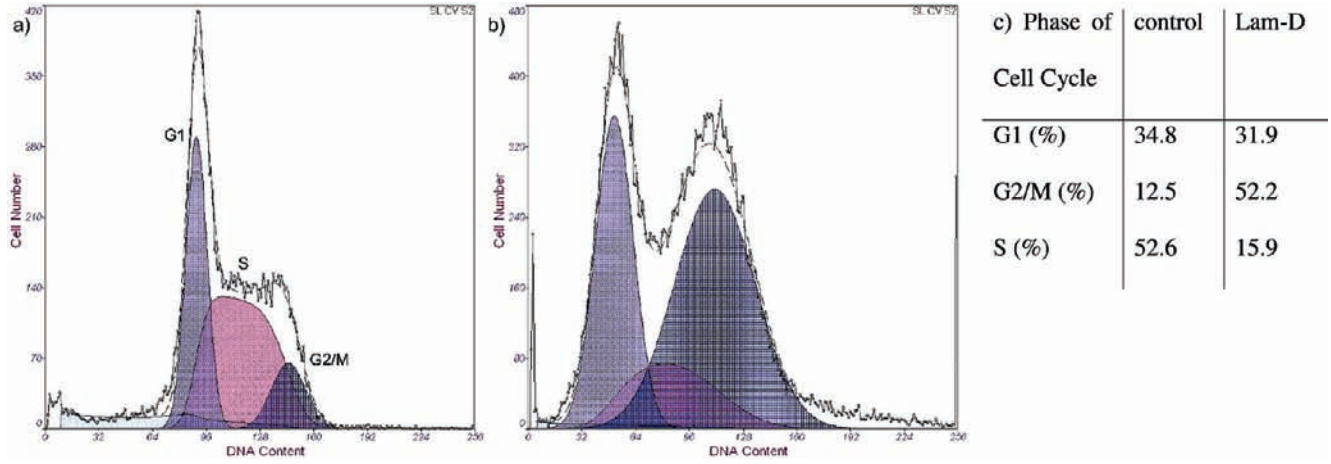

Figure 3. Cell cycle progression of Lam-D in HT-29 cancer cell line. (a) HT-29 asynchronous colon cell line; (b) HT-29 with 1 μM Lam-D for 12 h.

coupling reaction, using the trialkoxyphenylboronates **12a** or **12b**, gave the diaryl derivatives **15a**−**c** (with the desired orthogonal protected phenol groups as *i*Pr/Bn ethers) in 45−64% yields from the scaffold **10**.

Tight control of the oxidation of **15** using 1 equiv of DDQ and MW irradiation at 120 °C for 10 min gave **16a**−**c** (65−93% yield), avoiding the complex mixtures obtained by simultaneous *O*-Bn cleavage using other conditions (*22*).

The *O*Bn protecting group was successfully removed to give **17a**−**c** in 70−95% yields by hydrogenolysis over Pd−C in methanolic solution. Lactonization in excellent yields (86% to quant.) was achieved by direct treatment of the methyl esters **17a**−**c** with sodium hydride in THF. Lactonization was needed before PEGylation to protect the phenol required in the lactone formation and to prevent undesired PEG removal caused by the instability of the ester bond under the basic reaction conditions.[2] Compounds **18a** and **18b**, having only one free phenol group (each of which at a distinct position), and **18c**, with two free phenol groups, were then further conjugated. The PEG-groups were successfully introduced by esterification of the free phenols of **18a**−**c** to give compounds **19a**−**f** using EDC·HCl with a catalytic amount of DMAP in CH_2Cl_2 (*23*). The same reaction conditions were used for the conjugation of Lam-D, obtained by deprotection of two isopropyl groups of **18c** with $AlCl_3$, to give the triester derivatives **8** and **9**. The isopropyl-protecting groups of **19a**−**f** were eliminated using $AlCl_3$ in CH_2Cl_2 with moderate to good yields, with concomitant removal of the *N*-Boc-protecting groups of **19b** and **19d**.

High-polarity solvents such as DMSO and PEG-400 were required to dissolve Lam-D (**1**), which is insoluble in most common solvents. The solubility of monoPEG compounds **2**−**5**, with a single conjugation of one phenolic residue, is much better to that of Lam-D.[3] Conjugate **3**, bearing six units of ethylene glycol and a NH_2 termination, showed 80-fold greater solubility in water than Lam-D. The solubility of conjugates **3**, **7**, and **9** -mono-, di-, and triester, respectively- in PEG-400 solvent was in accordance with the increase of PEG conjugations. Final compounds **2**−**9** were prepared in 18% to 57% yields from the corresponding phenolic Lam-D precursors.

Lastly, the conjugates were further evaluated biologically, and in vitro drug delivery assays were carried out.

Cytotoxicity and Cellular Uptake. The cytotoxicity of Lam-D (**1**) and its analogues (**2**−**9**) was evaluated against BJ human skin fibroblasts, and a panel of three human tumor cell lines: HT-29, A-549, and MDA-MB-231. A conventional colorimetric assay was used to estimate values of GI_{50} (i.e., the drug concentration that causes 50% of cell growth inhibition after 72 h of continuous exposure to the test molecule (*17*)). The results are shown in Table 1.

Conjugates **2**−**9** are all active against the cell lines: HT-29, the cytotoxicity of **2**−**9** is similar to that of Lam-D; in A-549 and MDA-MB-231 cell lines, the activity of **2**−**4** and **6**−**9** is 1.4−4.3-fold better than that of Lam-D. Furthermore, BJ skin fibroblasts were used in the present study to evaluate the effects of the drug and its conjugates in normal cells. In this non-tumoral cellular culture, conjugates **3**, **6**, and **7** maintained the same order of magnitude of cytotoxicities than Lam-D. Besides,

[2]Lactonization of methyl 2-(2,4-dihydroxy-5-methoxyphenyl)-8-hydroxy-1-(4-(2-(2-(2-methoxyethoxy)ethoxy)acetoxy)-3-methoxyphenyl)-9-methoxypyrrolo[2,1-*a*]isoquinoline-3-carboxylate did not provide compound **4**; rather, it led exclusively to formation of Lam-D.

[3]The conjugates are more soluble in water, EtOH, and PEG-400 than Lam-D. See Table SI1 in the Supporting Information.

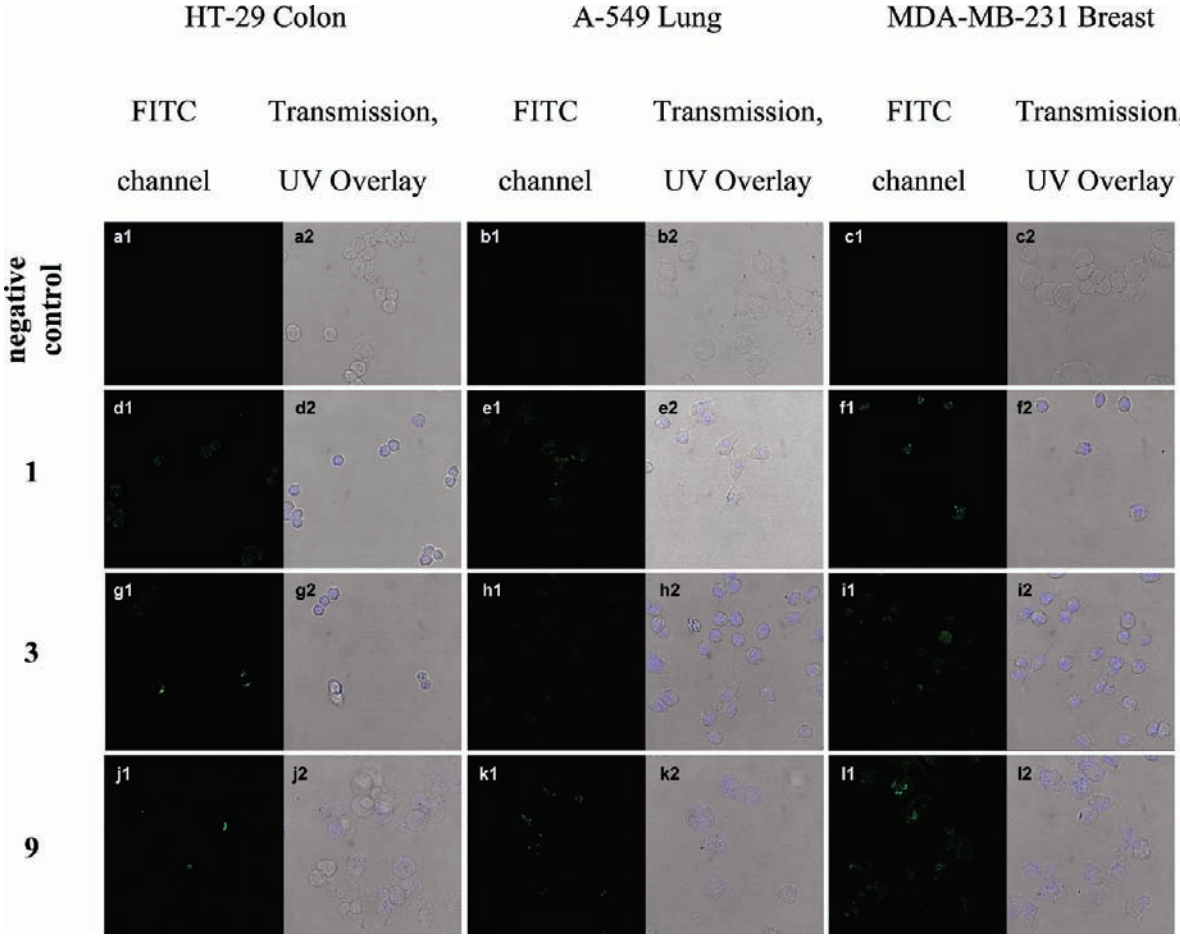

Figure 4. Detection of apoptosis by CaspaTag green fluorescence.

Chart 1. Cellular Internalization Quotient

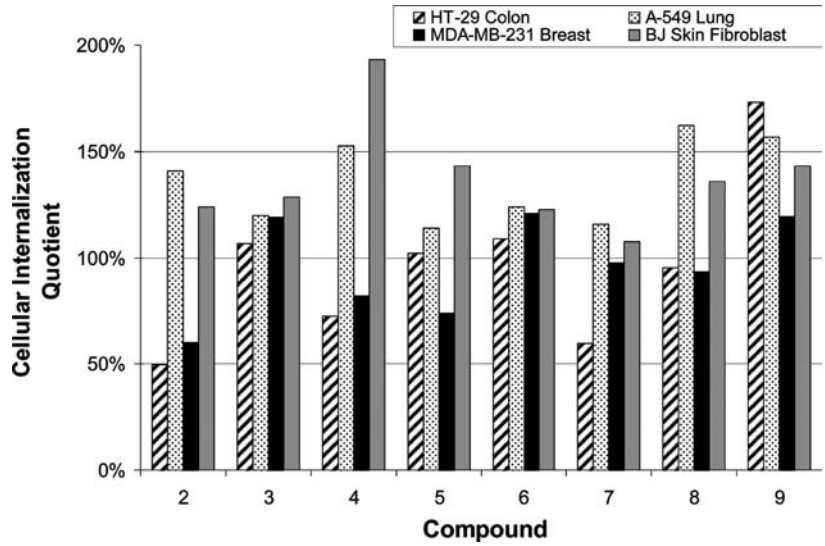

conjugates **2**, **4**, **5**, **8**, and **9** showed a decrease of 4- to 500-fold in their cytotoxic activity for BJ skin fibroblasts.

The results of initial cellular internalization experiments in HeLa cells at different compound concentrations and exposure times were encouraging for Lam-D and **7** (see Figure SI1 and Figure SI2 in the Supporting Information). Compound **9** was selected as one of the best compounds of the series for colocalization experiments. Cell cultures were incubated with compound **9** for 48 h. WGA-FITC and Mitotracker were then employed for the selective staining of cell membrane-Golgi apparatus (green fluorescence) and mitochondria (red fluorescence), respectively. Likewise, UV fluorescence corresponding to **9** was observed in the cytoplasm;[4] however, no fluorescence was observed in the nuclear region of any of the cells for compound **9** (Figure 2).

[4]The Lam-D UV spectrum presents four characteristic absorption maxima: 237, 267, 356, and 382 nm. Excitation at 267 nm of **1** led to three emission maximum wavelengths: 319, 430, and 490 nm. The authors assumed that any minor deviation in the molar extinction

The internalization of compounds **1**−**9** was measured by FACS flow cytometry (see Table 2). Conjugates **3**, **6**, and **9** underwent the greatest cellular uptake in HT-29 and MDA-MB-231. Furthermore, conjugates **2**−**9** all had higher internalization in A-549 than did Lam-D. Results were normalized in function of Lam-D uptake; thus, the CIQ was calculated relative to 100% internalization for Lam-D (**1**). The comparative study showed that all the PEG conjugation motifs introduced enabled greater internalization in A-549 and BJ cell lines. For compounds **4**, **8**, and **9**, the ratio was greater than 150%. Although compounds **3**, **6**, and **9** exhibited greater internalization than did Lam-D (**1**) in HT-29 and MDA-MB-231, the differences observed for these cell lines were not as dramatic. Likewise, as observed in the results for **3**, monoconjugation enables greater uptake. The introduction of the PEG-NH_2 backbone at phenolic position 3 of Lam-D (compound **3**) led to better GI_{50} cytotoxicity and internalization than at position 4′ (compound **5**).

Effects of 1 on Cell Cycle Progression of HT-29 Cells. Lam-D was tested for effects on cell cycle progression in HT-29 tumor cells (Figure 3). Cells were treated with the product (see Experimental Section) and then analyzed by flow cytometry to determine if the cell cycle had been arrested at a specific phase. A control set of untreated cells was also used.

Compared to the control cells (Figure 3, panels **1a**,**c**), the cells treated with **1** (Figure 3, panels **1b**,**c**) showed an arrest in G2/M progression. Hence, it was concluded that Lam-D inhibits cell cycle progression. Furthermore, conjugates **3** and **9** provoked cell cycle arrest in a greater extent. The results showed one single peak corresponding to the G2/M phase (see Figure SI3 in the Supporting Information).

Induction of Apoptosis by 1, 3, and 9 in HT-29, A-549, and MDA-MB-231 Cell Lines. Many anticancer drugs induce cell cycle arrest and apoptosis. Apoptotic cells undergo characteristic morphological changes. Among these, the cell surface often bends and breaks up into membrane-enclosed fragments called apoptotic bodies. This process depends on a cascade of proteolytic enzymes called caspases (*24*).

To analyze whether Lam-D induces apoptosis, HT-29, A-549, and MDA-MB-231 cell lines were incubated with a single compound and then qualitatively measured for apoptosis (Figure 4, see Experimental Section). The assay consists of detecting active caspases (caspase-3/7) using a commercially available colorimetric test.

All cell lines showed a high level of apoptotic cell death after treatment with compounds **1**, **3**, and **9** (Figure 4d−l). A negative control of the assay was performed by analyzing untreated cells under the same experimental conditions (Figure 4a−c). Altogether, these results indicate that Lam-D and derivatives **3** and **9** induce cell cycle arrest and apoptosis.

DISCUSSION

A procedure for preparing PEGylated Lam-D pro-drugs has been described for the first time. One, two, or three phenol groups were selectively conjugated to the Lam-D in mild reaction conditions employing selective orthogonal protection (benzyloxy and isopropoxy groups).

The feasibility of the selective modification of the phenolic moieties of Lam-D has been demonstrated with readily available and inexpensive PEG-carboxylic acid as starting material. Conjugates functionalized with only a single phenolic residue of **2**−**5** (C-3 or C-4′ OH groups) are much more soluble than Lam-D in various solvents. Notwithstanding, di- and tri-PEG conjugates were also synthesized. Di- and tri-PEG conjugates—which imply greater steric hindrance—were also synthesized, thereby demonstrating the robustness of our method. The pH-labile ester conjugates were prepared in 18% to 57% yields from the corresponding Lam-D phenolic precursors.

Conjugates (**2**−**9**), screened against normal BJ skin fibroblasts and three human cancer cell lines, exhibited better internalization than Lam-D (**1**) did. Conjugation provided cytotoxicity amelioration for the cancerous cell lines. Indeed, the GI_{50} of conjugates **2**−**4**, **6**, **7**, and **9** (bearing mono-, di-, and tri-PEG backbones) in MDA-MB-231 and A549 cancer cell lines were 1 order of magnitude lower than that of Lam-D (**1**). Comparison of cytotoxic activity in BJ skin fibroblast between Lam-D and compounds **2**−**9** shown that bioconjugates are equal or less toxic than Lam-D. Compounds **2**, **4**, and **9** with higher cytotoxycity than Lam-D in A-549 and MDA-MB-231 tumor cell lines displayed less cytotoxyc-activity in the BJ normal cell line. Although these compounds **2**, **4**, and **9** possess better internalization in normal cells. These results indicate that these compounds have better affinity to components of tumor cell lines. Confocal microscopy revealed that Lam-D (**1**) and the conjugates (**2**−**9**) were internalized in the cytoplasmatic region. Furthermore, Lam-D induces cell cycle arrest at the G2 phase. Lam-D, and derivatives **3** and **9**, produce caspase-3,7-dependent apoptosis in all cell lines tested.

ACKNOWLEDGMENT

This study was partially supported by CICYT (Grant BQU 2006-03794), *Generalitat de Catalunya*, and the Barcelona Science Park. We gratefully the Networking Centre on Bioengineering, Biomaterials and Nanomedicine (CIBER-BBN). This study was partially supported by the Industrial Consortium "NanoFarma" from the Spanish grants of CENIT program. We also thank Dr. J. Comas from Flow Cytometry Facility - SCT (UB) and M. Bosch from Confocal Microscopy Unit - SCT (UB) for their valuable discussions regarding this work. We also thank Ramon Eritja for recording Lam-D UV-emission spectra.

Supporting Information Available: Materials and methods, experimental procedures, characterization data of the precursor compounds. This material is available free of charge via the Internet at http://pubs.acs.org.

LITERATURE CITED

(1) Pla, D., Albericio, F., and Álvarez, M. (2008) Recent advances in lamellarin alkaloids: isolation, synthesis and activity. *Anti-Cancer Agents Med. Chem. 8*, 746–760.

(2) Facompré, M., Tardy, C., Bal-Mayeu, C., Colson, P., Pérez, C., Manzanares, I., Cuevas, C., and Bailly, C. (2003) Lamellarin D: a novel potent inhibitor of topoisomerase I. *Cancer Res. 63*, 7392–7399.

(3) Marco, E., Laine, W., Tardy, C., Lansiaux, A., Iwao, M., Ishibashi, F., Bailly, C., and Gago, F. (2005) Molecular determinants of topoisomerase I poisoning by lamellarins: comparison with camptothecin and structure-activity relationships. *J. Med. Chem. 48*, 3796–3807.

(4) Kluza, J., Gallego, M. A., Loyens, A., Beauvillain, J. C., Fernández Sousa-Faro, J. M., Cuevas, C., Marchetti, P., and Bailly, C. (2006) Cancer cell mitochondria are direct proapoptotic targets for the marine antitumor drug lamellarin D. *Cancer Res. 66*, 3177–3187.

(5) Bailly, C. (2004) Lamellarins, from A to Z: a family of anticancer marine pyrrole alkaloids. *Curr. Med. Chem.: Anti-Cancer Agents 4*, 363–378.

(6) IUPAC nomenclature of Lam-D: 3,11-dihydroxy-2,12-dimethoxy-14-(4-hydroxy-3-methoxyphenyl)-6*H*[1]benzopyrano[4′,3′:4,5]-pyrrolo[2,1-*a*]isoquinoline-6-one.

(7) Vanhuyse, M., Kluza, J., Tardy, C., Otero, G., Cuevas, C., Bailly, C., and Lansiaux, A. (2005) Lamellarin D: a novel pro-

coefficients of **2**−**9** due to ester conjugation of **1** with aliphatic PEG backbones was not important.

apoptotic agent from marine origin insensitive to p-glycoprotein-mediated drug efflux. *Cancer Lett. 221*, 165–175.
(8) Iyer, A. K., Khaled, G., Fang, J., and Maeda, H. (2006) Exploiting the enhanced permeability and retention effect for tumor targeting. *Drug Discovery Today 11*, 812–818.
(9) Vicent, M. J., and Duncan, R. (2006) Polymer conjugates: nanosized medicines for treating cancer. *Trends Biotechnol. 24*, 39–47.
(10) Duncan, R. (2006) Polymer conjugates as anticancer nanomedicines. *Nat. Rev. Cancer 6*, 688–701.
(11) Pasut, G., and Veronese, F. M. (2007) Polymer−drug conjugation, recent achievements and general strategies. *Prog. Polym. Sci. 32*, 933–961.
(12) Torchilin, V. P. (2005) Lipid-core micelles for targeted drug delivery. *Curr. Drug Delivery 2*, 319–327.
(13) Lukyanov, A. N., and Torchilin, V. P. (2004) Micelles from lipid derivatives of water-soluble polymers as delivery systems for poorly soluble drugs. *Adv. Drug Delivery Rev. 56*, 1273–1289.
(14) Greenwald, R. B., Pendri, A., Conover, C. D., Zhao, H., Choe, Y. H., Martínez, A., Shum, K., and Guan, S. (1999) Drug delivery systems employing 1,4- or 1,6-elimination: poly(ethylene glycol) prodrugs of amine-containing compounds. *J. Med. Chem. 42*, 3657–3667.
(15) Pla, D., Marchal, A., Olsen, C., Albericio, F., and Álvarez, M. (2005) Modular total synthesis of lamellarin D. *J. Org. Chem. 70*, 8231–8234.
(16) Skehan, P., Storeng, R., Scudiero, D., Monks, A., McMahon, J., Vistica, D., Waren, J. T., Bokesch, H., Kenney, S., and Boyd, M. R. (1990) New colorimetric cytotoxicity assay for anticancer drug screening. *J. Natl. Cancer Inst. 82*, 1107–1112.
(17) Boyd, M. R., and Paull, K. D. (1995) Some practical considerations and applications of the National Cancer Institute in vitro anticancer drug discovery screen. *Drug Dev. Res. 34*, 91–104.
(18) Rotonda, J., Nicholson, D. W., Fazil, K. M., Gallart, Y. G., Labelle, M., Peterson, E. P., Rasper, D. M., Ruel, R., Vaillancourt, J. P., Thornberry, N. A., and Becker, J. W. (1996) The three-dimensional structure of apopain/CPP32, a key mediator of apoptosis. *Nat. Struct. Biol. 3*, 619–625.
(19) Pla, D., Marchal, A., Olsen, C. A., Francesch, A., Cuevas, C., Albericio, F., and Álvarez, M. (2006) Synthesis and structure-activity relationship study of potent cytotoxic analogues of the marine alkaloid lamellarin D. *J. Med. Chem. 49*, 3257–3268.
(20) Pla, D., Albericio, F., and Álvarez, M. (2007) Regioselective monobromination of free and protected phenols. *Eur. J. Org. Chem.* 1921–1924.
(21) Olsen, C., Parera, N., Albericio, F., and Álvarez, M. (2005) 5,6-Dihydropyrrolo[2,1-*a*]isoquinolines as scaffolds for synthesis of lamellarin analogues. *Tetrahedron Lett. 46*, 2041–2044.
(22) Complex mixtures were obtained using DDQ as oxidating agent and following Weissman, S. A., and Zewge, D. (2005) Recent advances in ether dealkylation. *Tetrahedron 61*, 7833–7863.
(23) Tardy, C., Facompré, M., Laine, W., Baldeyrou, B., García-Gravalos, D., Francesch, A., Mateo, C., Pastor, A., Jiménez, J. A., Manzanares, I., Cuevas, C., and Bailly, C. (2004) Topoisomerase I-mediated DNA cleavage as a guide to the development of antitumor agents derived from the marine alkaloid lamellarin D: triester derivatives incorporating amino acid residues. *Bioorg. Med. Chem. 12*, 1697–1712.
(24) Ekert, P. G., Silke, J., and Vaux, D. L. (1999) Caspase inhibitors. *Cell Death Differ. 6*, 1081–1086.

BC800503K

SUPPLEMENTARY MATERIAL

Lamellarin D Bioconjugates I: Synthesis and Cellular Internalization of PEG-Derivatives

*Daniel Pla,[a, b] Andrés Francesch,[c] Pilar Calvo,[c] Carmen Cuevas,[c] Rosa Aligué,[d] Fernando Albericio,[a, b, ‡, *] and Mercedes Álvarez,[a, b, §, *]*

[a]Institute for Research in Biomedicine, Barcelona Science Park-University of Barcelona, Baldiri Reixac 10, E-08028 Barcelona, Spain. [b]CIBER-BBN Networking Centre on Bioengineering, Biomaterials and Nanomedicine, Baldiri Reixac 10, E-08028 Barcelona, Spain.

[c]Pharma Mar S. A., Avda de los Reyes 1, E-28770 Colmenar Viejo, Madrid, Spain.

[d]Department of Cell Biology, Faculty of Medicine, University of Barcelona, Casanova 143, E-08036 Barcelona, Spain.

mercedes.alvarez@irbbarcelona.org

* Corresponding author: Institute for Research in Biomedicine, Barcelona Science Park-University of Barcelona, Baldiri Reixac 10, E-08028 Barcelona, Spain Tel.: +34934037086; fax: +34934037126;

‡ Department of Organic Chemistry, University of Barcelona, E-08028 Barcelona

§ Laboratory of Organic Chemistry, Faculty of Pharmacy, University of Barcelona, E-08028 Barcelona

TABLE OF CONTENTS

SI3	General data.
SI4-SI6	General methods and characterization of precursor compounds.
SI7-SI14	^{1}H, ^{13}C-NMR spectra of final compounds **2-9**.
SI15	Table of solubility for compounds **1**, **3**, **7** and **9**.
SI16-SI17	Initial internalization assays in HeLa Cells.

General Data:

Reagents and solvents were purified according to *Purification of Laboratory Chemicals,* Armarego, W. and Chai C., Elsevier (2003). Melting points (mp) were determined in a Büchi Melting Point B540 in open capillaries and are uncorrected. Automatic flash chromatography was done in an Isco Combiflash medium pressure liquid chromatograph with Redisep silica gel columns (47-60 μm). A Branson ultrasound bath was used to perform sonication. ^{1}H NMR and ^{13}C NMR spectra were recorded on a Varian Mercury 400 MHz spectrometer and a Gemini 200 MHz spectrometer. Multiplicity of the carbons was assigned with DEPT and gHSQC experiments, although the usual abbreviations according to off-resonance decoupling are used: (s) singlet, (d) doublet, (t) triplet, and (q) quartet. The same abbreviations were used for the multiplicity of signals in H-NMR and also: (m) multiplet, (bs) broad singlet, (bd) broad doublet. Spectra were referenced to appropriate residual solvent peaks (d_6-acetone, d_6-DMSO, d_4-MeOH or $CDCl_3$). IR spectra were obtained on a Thermo Nicolet FT-IR spectrometer. HRMS were performed on a Bruker Autoflex high resolution mass spectometer by Unidad de Espectrometría de Masas (Universidad de Santiago de Compostela) and by Servei d'Espectrometria de Masses (Universitat de Barcelona). Microwave-assisted reactions were carried out in a CEM Discover microwave. The automatic syringe pump was used as specified for controlled addition of some reactants. Reversed phase analytical HPLC was performed on a Waters Alliance separation module 2695 using a Waters Xterra MS C_{18} column (150 x 4.6 mm, 5 μm) and a Waters 996 PDA detector at 254 nm.

General Methods and Characterization of Synthesized Precursor Compounds:

2-(4-Benzyloxy-5-methoxyphenyl)-4,4,5,5-tetramethyl-1,3,2-dioxaborolane (11a)

K_2CO_3 (2.49 g, 18.0 mmol) and BnBr (1.2 mL, 1.43 g/mL, 9.9 mmol) were added to a solution of 2-(4-hydroxy-5-methoxyphenyl)-4,4,5,5-tetramethyl-1,3,2-dioxaborolane (2.25 g, 9.0 mmol) in dry THF (25 mL) and DMF (0.5 mL). The mixture was stirred at 80 ºC under Ar for 16 h. The mixture was then cooled to r.t. and the solvent was removed *in vacuo*. EtOAc was added and the organic solution was washed with sat. aq. Na_2CO_3, water and brine. The organic layer was dried and concentrated, affording 3.06 g (quantitative yield) of the title compound as a white solid. mp (MeCN) 89-92 ºC. IR (film) ν 2977, 2931, 1598, 1410, 1354, 1138 cm^{-1}. ^1H NMR ($CDCl_3$, 200 MHz) δ 1.33 (s, 12H); 3.92 (s, 3H, OMe); 5.182 (s, 2H); 6.88 (d, J = 8.0 Hz, 1H); 7.27-7.44 (m, 7H). ^{13}C NMR ($CDCl_3$, 50.3 MHz) δ 24.9 (4q); 56.0 (q); 70.6 (t); 83.6 (s); 112.9 (d); 117.1 (d); 127.1 (2d); 127.7 (d); 128.4 (2d); 128.9 (s); 136.9 (s); 148.9 (s); 150.7 (s). MS (ESI) 341 (M+1, 100); 342 (M+2, 10).

General Procedure for Bromination of Polialcoxybenzenes. Solid NBS (1 mmol) was added to a cooled solution (–78 ºC) of the aromatic compound (1 mmol) in THF (5 mL), and the reaction mixture was stirred until complete consumption of starting material. The reaction mixture was allowed to reach r.t., and the solvent was then evaporated under reduced pressure. CH_2Cl_2 was added to the remaining residue, and the resulting solution was filtered through a pad of neutral alumina. After solvent removal, pure products were obtained (99%-quant. yield).

1-Bromo-2,4-dibenzyloxy-5-methoxybenzene

Starting from 1,3-dibenzyloxy-4-methoxybenzene (7.2 g, 22.4 mmol), a white solid (9.0 g, quant. yield) was obtained. mp (MeCN) 105-106 ºC. IR (film) ν 2929, 1505, 1382, 1212, 843 cm^{-1}. ^1H NMR (200 MHz, $CDCl_3$) δ 3.84 (s, 3H, OMe); 4.99 (s, 2H); 5.07 (s,

2H); 6.59 (s, 1H); 7.08 (s, 1H); 7.31-7.41 (m, 10H). ^{13}C NMR (50.3 MHz, $CDCl_3$) δ 56.7 (q); 71.5 (t); 72.2 (t); 103.1 (s); 104.1 (d); 116.7 (d); 127.2 (4d); 127.8 (d); 127.9 (d); 128.4 (2d); 128.5 (2d); 136.5 (s); 144.9 (s); 147.7 (s); 149.0 (s). MS (ESI) 399 (MBr^{79}+1, 97); 400 (MBr^{79}+2, 23); 401 (MBr^{81}+1, 100); 402 (MBr^{81}+2, 21).

1-Bromo-2-benzyloxy-4-isopropoxy-5-methoxybenzene

Starting from 1-benzyloxy-3-isopropoxy-4-methoxybenzene (11.3 g, 41.5 mmol), a white solid (14.4 g, 99%) was obtained. mp (MeCN) 73-75 ºC. IR (film) ν 2975, 2933, 1504, 1251, 844 cm^{-1}. ^{1}H NMR (200 MHz, $CDCl_3$) δ 1.28 (d, *J* = 6.2 Hz, 6H); 3.80 (s, 3H, OMe); 4.39 (h, *J* = 6.2 Hz, 1H); 5.08 (s, 2H); 6.58 (s, 1H); 7.05 (s, 1H); 7.30-7.49 (m, 5H). ^{13}C NMR (50.3 MHz, $CDCl_3$) δ 22.0 (2q); 56.7 (q); 72.1 (d); 72.3 (t); 103.2 (s); 106.0 (d); 117.0 (d); 127.3 (2d); 127.9 (d); 128.5 (2d); 145.8 (s); 147.0 (s); 149.0 (s). MS (ESI) 351 (MBr^{79}+1, 95); 352 (MBr^{79}+2, 15); 353 (MBr^{81}+1, 100); 354 (MBr^{81}+2, 12).

General Procedure for Pd (0) Catalyzed Borylations 3. A mixture of bromoalcoxybenzene (1 mmol), $Pd(OAc)_2$ (5%), DPEphos (0.1 mmol), and pinacolborane (3.0 mmol) in dry Et_3N-dioxane (83:17, 6 mL/mmol) was heated at 100 °C for 13.5 h. The cooled reaction mixture was quenched with saturated NH_4Cl, and the aq. solution was extracted with Et_2O. The organic solution was dried, filtered and concentrated. The resulting oil was purified by flash chromatography (SiO_2 previously deactivated with 5% Et_3N). Elution with hexane/EtOAc (70:30) afforded the title compounds **3a-3b** (62-88% yield).

2-(2-Benzyloxy-4-isopropoxy-5-methoxyphenyl)-4,4,5,5-tetramethyl-1,3,2-dioxaborolane (12a)

Starting from 1-bromo-2-benzyloxy-4-isopropoxy-5-methoxybenzene (7.37 g, 21.0 mmol), a white solid (7.31 g, 88%) was obtained. mp (MeCN) 98-99 ºC. IR (film) ν

2979, 2931, 1601, 1409, 1139, 1040 cm^{-1}. ^{1}H NMR ($CDCl_3$, 200 MHz) δ 1.33 (d, *J* = 6.0 Hz, 6H); 1.36 (s, 12H); 3.84 (s, 3H, OMe); 4.56 (h, *J* = 6.0 Hz, 1H); 5.07 (s, 2H); 6.59 (s, 1H); 7.28-7.40 (m, 4H); 7.61 (d, *J* = 7.5 Hz, 2H). ^{13}C NMR ($CDCl_3$, 50.3 MHz) δ 21.7 (2q); 24.6 (4q); 56.2 (s); 70.8 (d); 71.7 (t); 82.8 (2s); 103.1 (d); 119.5 (d); 126.7 (2d); 127.0 (d); 127.7 (2d); 137.4 (s); 144.2 (s); 150.4 (s); 158.6 (s). MS (ESI) 399 (M+1, 100); 400 (M+2, 12).

2-(2,4-Dibenzyloxy-5-methoxyphenyl)-4,4,5,5-tetramethyl-1,3,2-dioxaborolane (12b)

Starting from 1-bromo-2,4-dibenzyloxy-5-methoxybenzene (1.00 g, 2.5 mmol), a yellow syrup (694 mg, 62%) was obtained. IR (film) ν 2925, 2853, 1596, 1433, 1272, 1134 cm^{-1}. ^{1}H NMR ($CDCl_3$, 200 MHz) δ 1.33 (s, 12H); 1.35 (d, *J* = 6.0 Hz, 6H, 2Me); 3.89 (s, 3H, OMe); 4.95 (s, 2H); 5.15 (s, 2H); 6.54 (s, 1H); 7.22 (s, 1H); 7.30-7.39 (m, 8H); 7.50-7.54 (m, 2H). ^{13}C NMR ($CDCl_3$, 50.3 MHz) δ 25.0 (4q); 56.7 (q); 70.9 (t); 71.9 (t); 83.3 (s); 102.1 (d); 119.4 (d); 127.0 (2d); 127.2 (2d); 127.3 (d); 127.8 (d); 128.0 (2d); 128.5 (2d); 136.7 (s); 137.6 (s); 151.4 (s); 158.8 (s). MS (ESI) 447 (M+1, 100); 448 (M+2, 18).

^{1}H, ^{13}C-NMR spectra of final compounds

Compound **2**

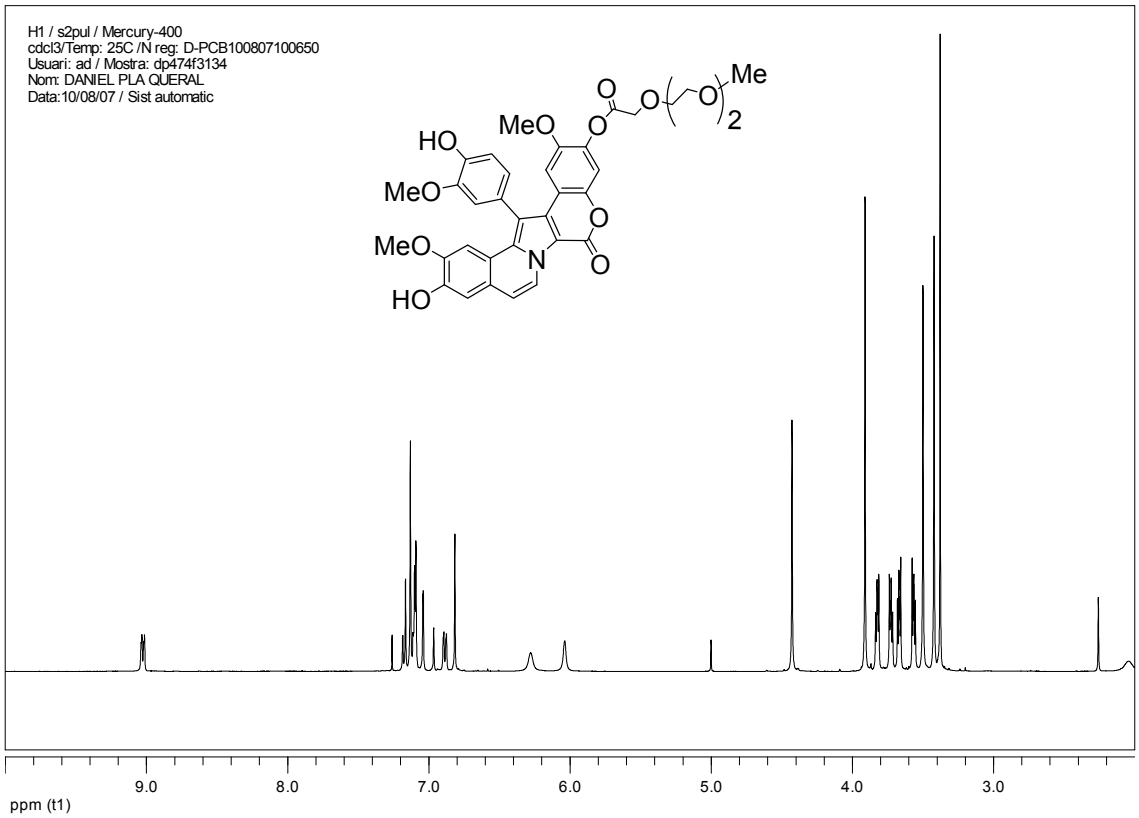

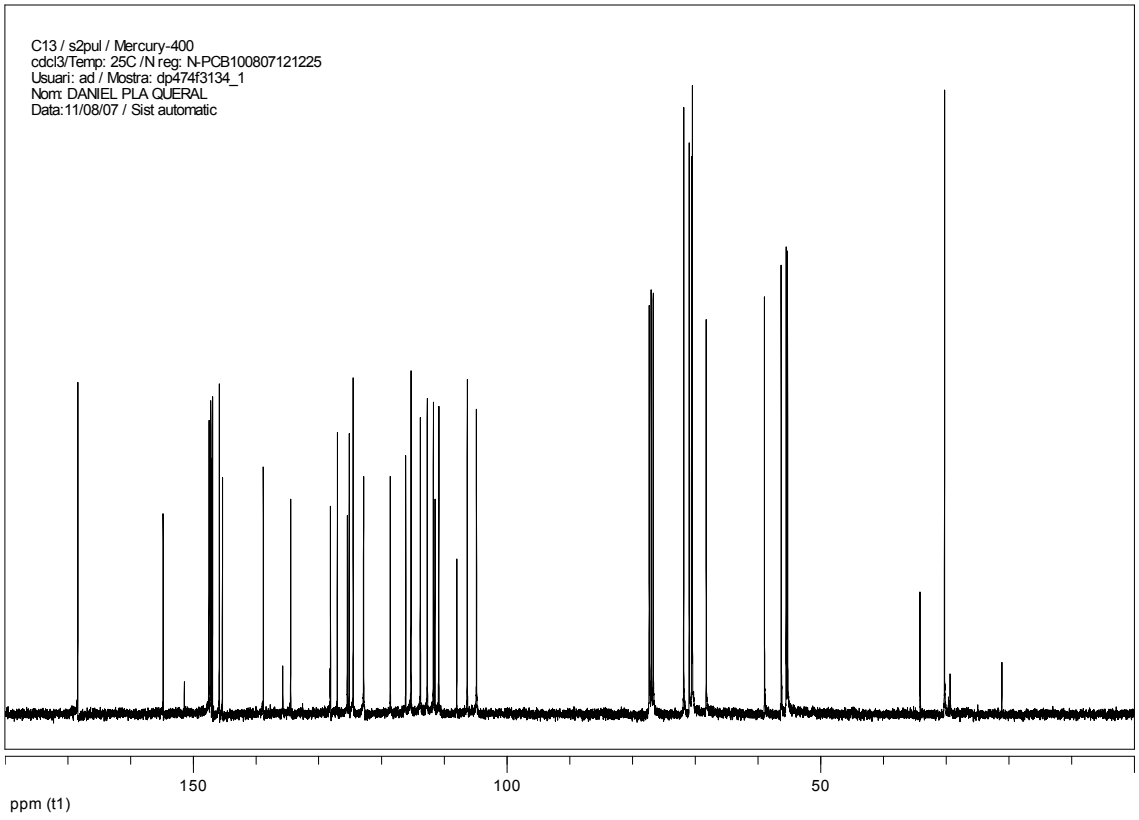

Compound **4**

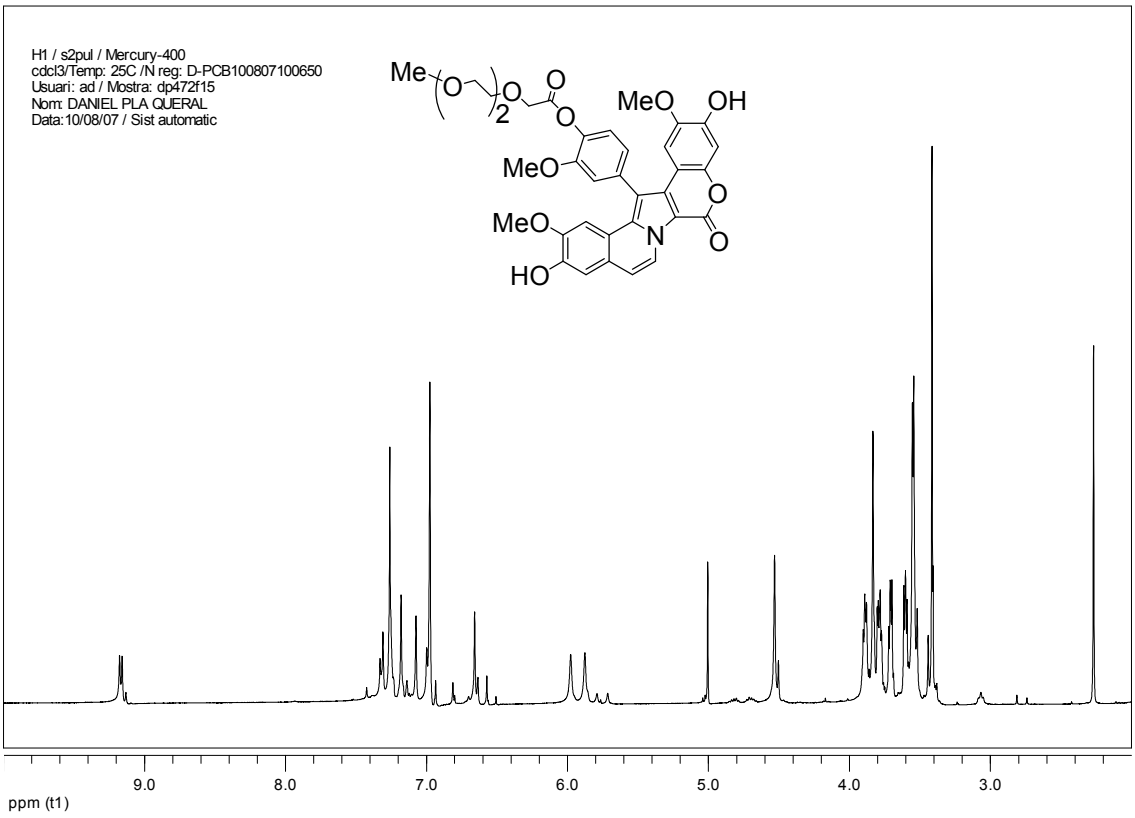
H1 / s2pul / Mercury-400
cdcl3/Temp: 25C /N reg: D-PCB100807100650
Usuari: ad / Mostra: dp472f15
Nom: DANIEL PLA QUERAL
Data: 10/08/07 / Sist automatic
Me
O
2
O
O
O
MeO
OH
MeO
O
MeO
N
O
HO
9.0
8.0
7.0
6.0
5.0
4.0
3.0
ppm (t1)

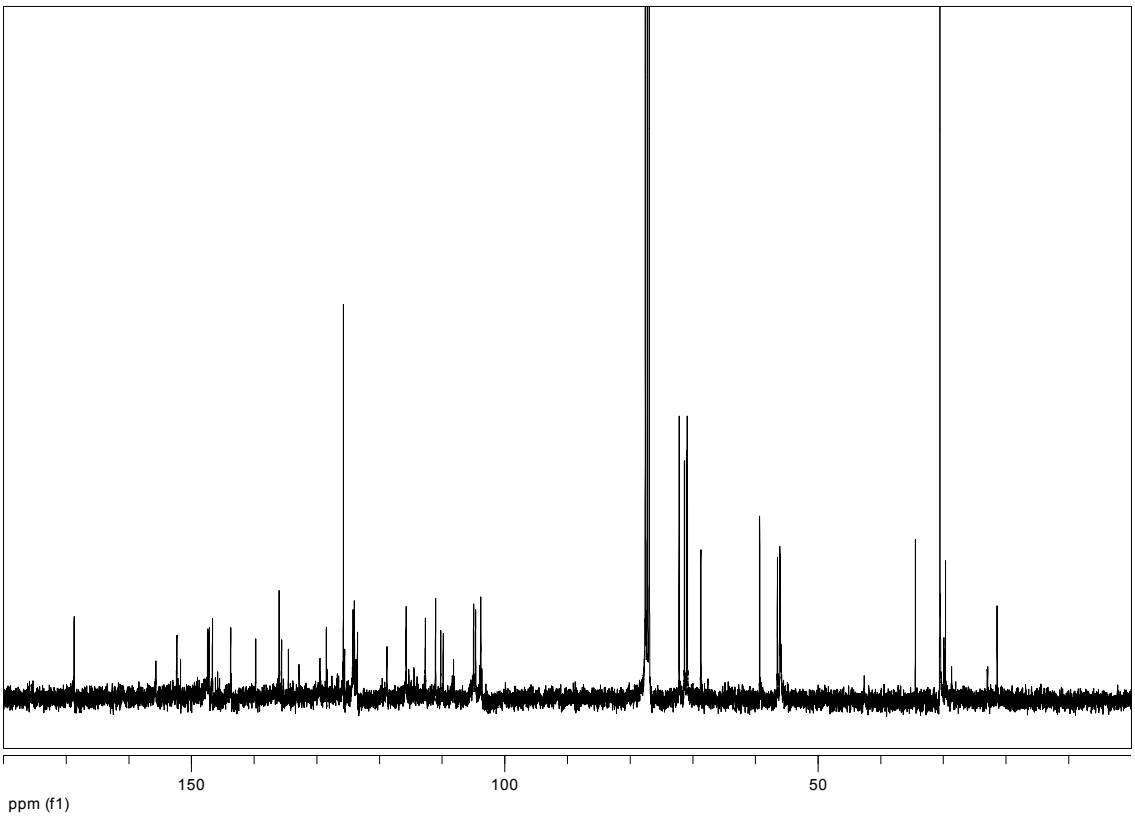
150
100
50
ppm (f1)

Compound **3**

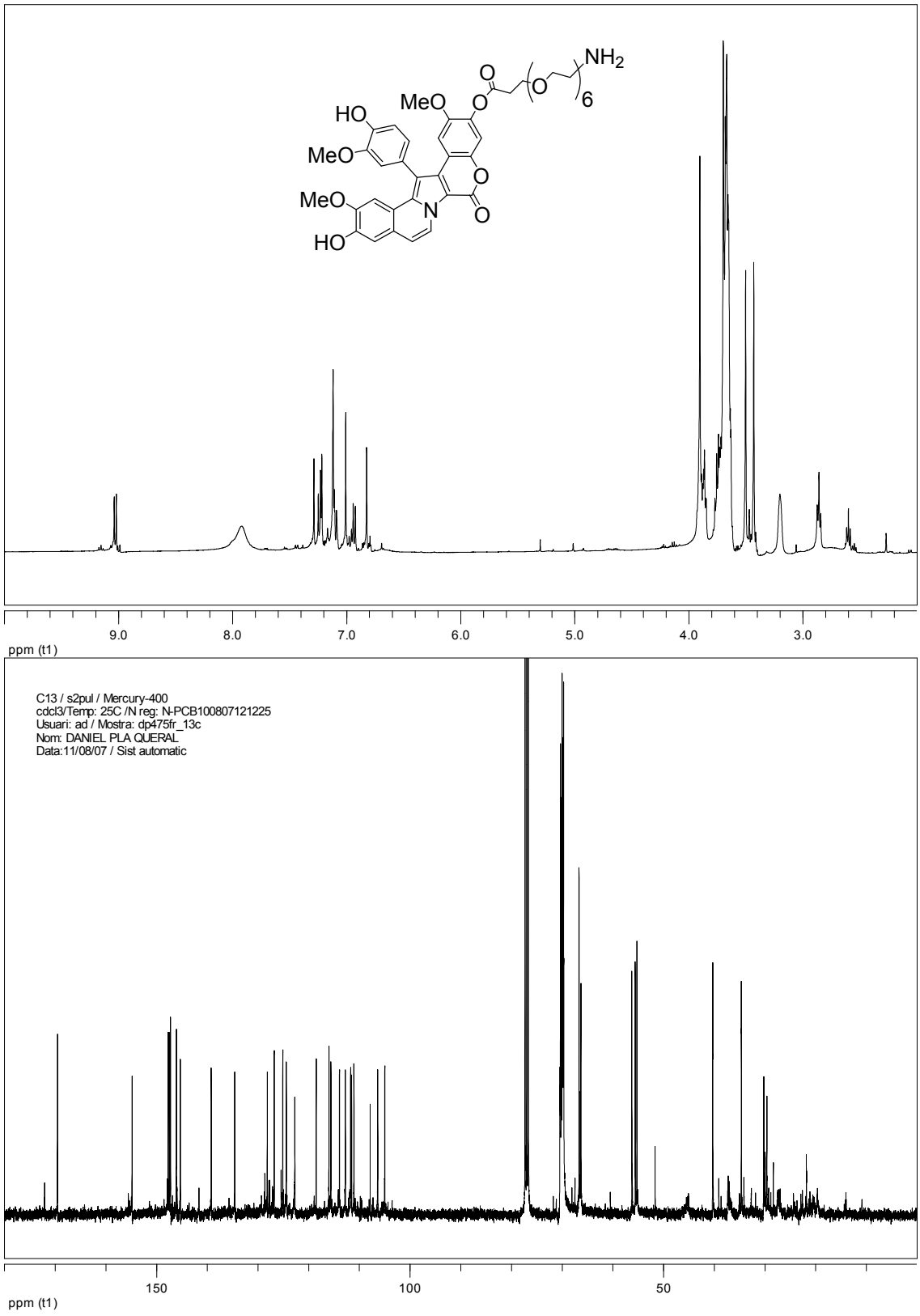
NH2
O
O
6
MeO
O
HO
MeO
O
MeO
N
O
HO
9.0
8.0
7.0
6.0
5.0
4.0
3.0
ppm (t1)
C13 / s2pul / Mercury-400
cdcl3/Temp: 25C /N reg: N-PCB100807121225
Usuari: ad / Mostra: dp475fr_13c
Nom: DANIEL PLA QUERAL
Data:11/08/07 / Sist automatic
150
100
50
ppm (t1)

Compound **5**

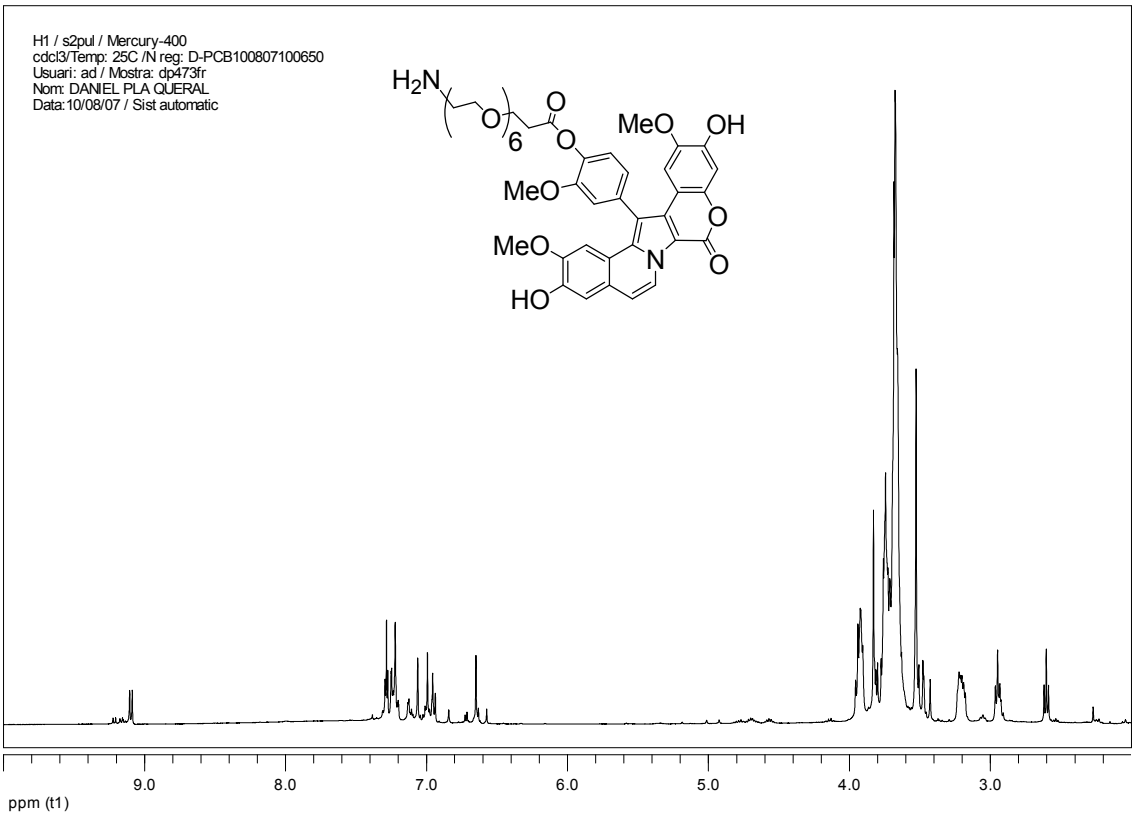
H1 / s2pul / Mercury-400
cdcl3/Temp: 25C /N reg: D-PCB100807100650
Usuari: ad / Mostra: dp473fr
Nom: DANIEL PLA QUERAL
Data:10/08/07 / Sist automatic
H2N
O
6
O
O
MeO
OH
MeO
O
MeO
N
O
HO
9.0
8.0
7.0
6.0
5.0
4.0
3.0
ppm (t1)

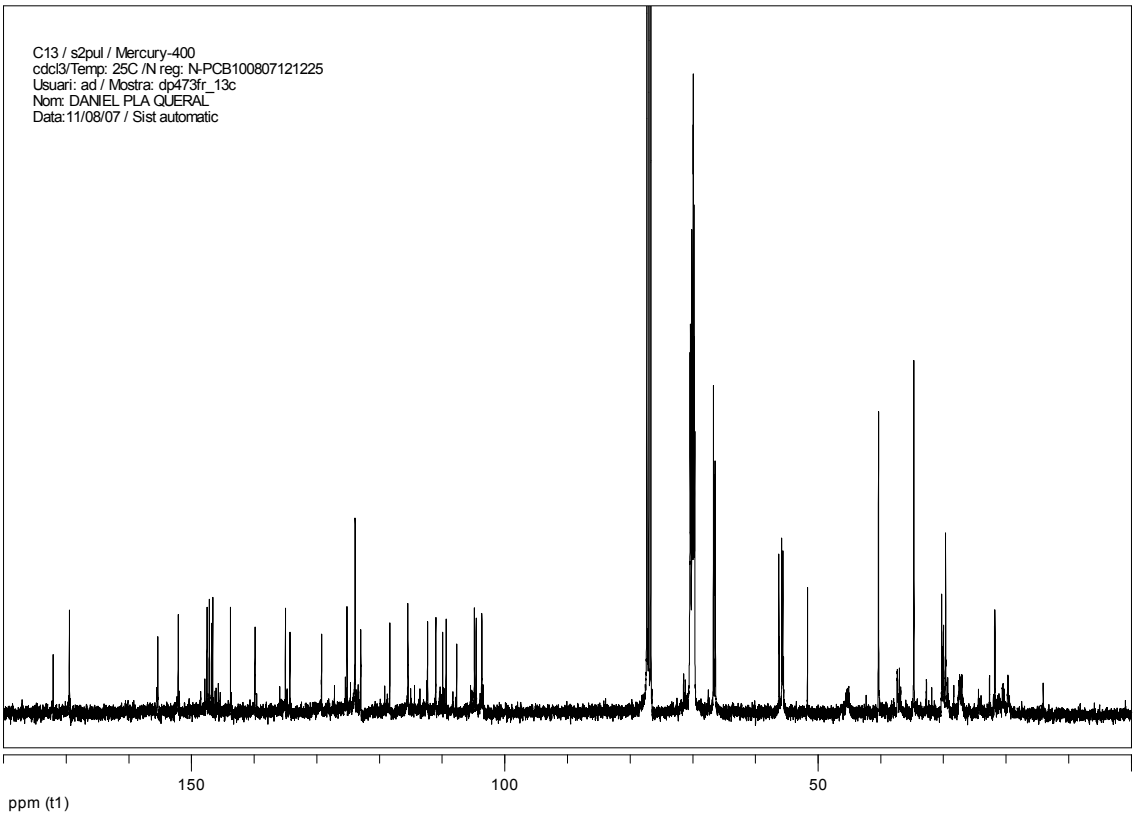
C13 / s2pul / Mercury-400
cdcl3/Temp: 25C /N reg: N-PCB100807121225
Usuari: ad / Mostra: dp473fr_13c
Nom: DANIEL PLA QUERAL
Data:11/08/07 / Sist automatic
150
100
50
ppm (t1)

Compound **6**

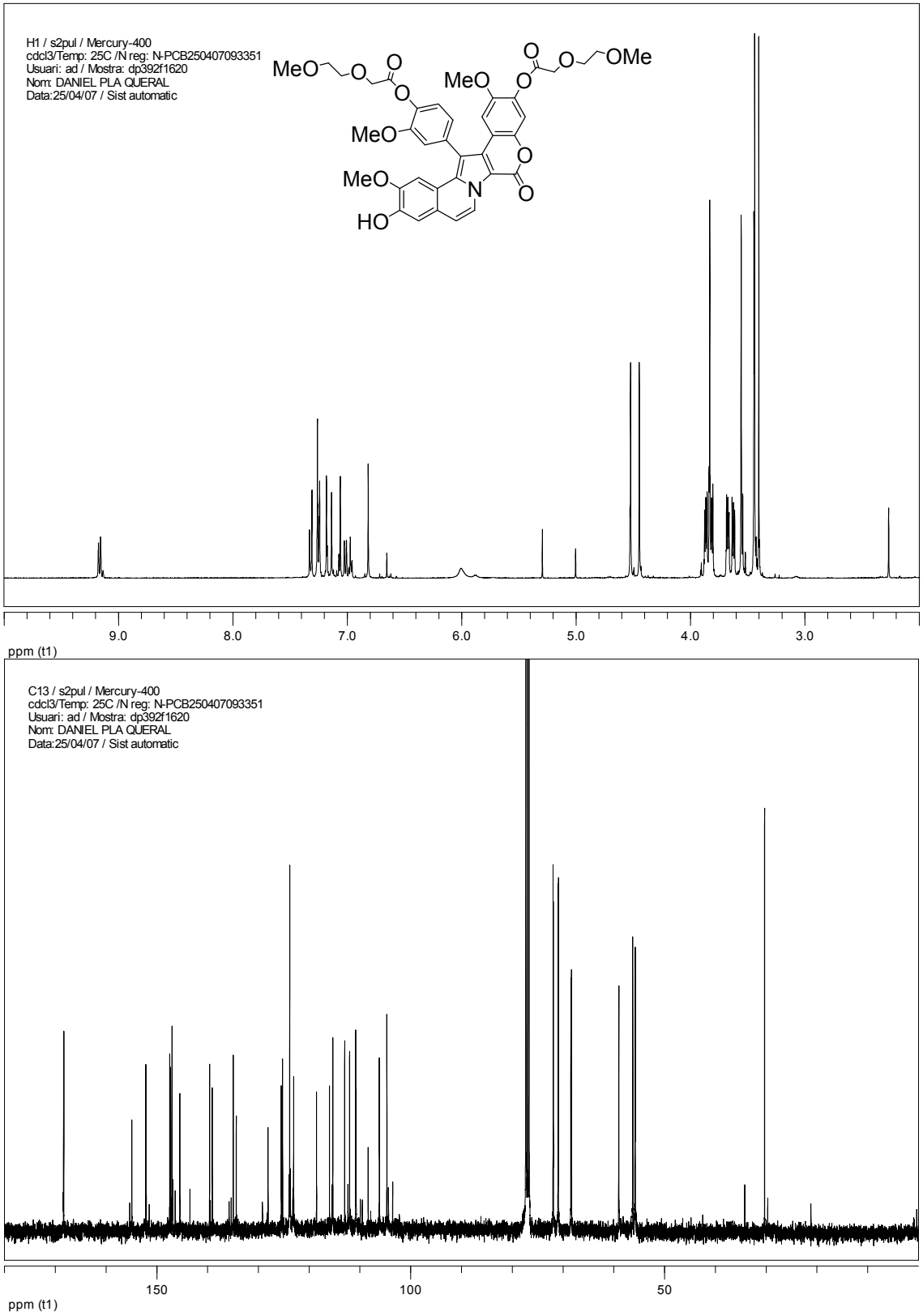
H1 / s2pul / Mercury-400
cdcl3/Temp: 25C /N reg: N-PCB250407093351
Usuari: ad / Mostra: dp392f1620
Nom: DANIEL PLA QUERAL
Data:25/04/07 / Sist automatic
MeO
O
O
MeO
O
O
O
OMe
MeO
O
MeO
N
O
O
HO
9.0
8.0
7.0
6.0
5.0
4.0
3.0
ppm (t1)
C13 / s2pul / Mercury-400
cdcl3/Temp: 25C /N reg: N-PCB250407093351
Usuari: ad / Mostra: dp392f1620
Nom: DANIEL PLA QUERAL
Data:25/04/07 / Sist automatic
150
100
50
ppm (t1)

Compound **7**

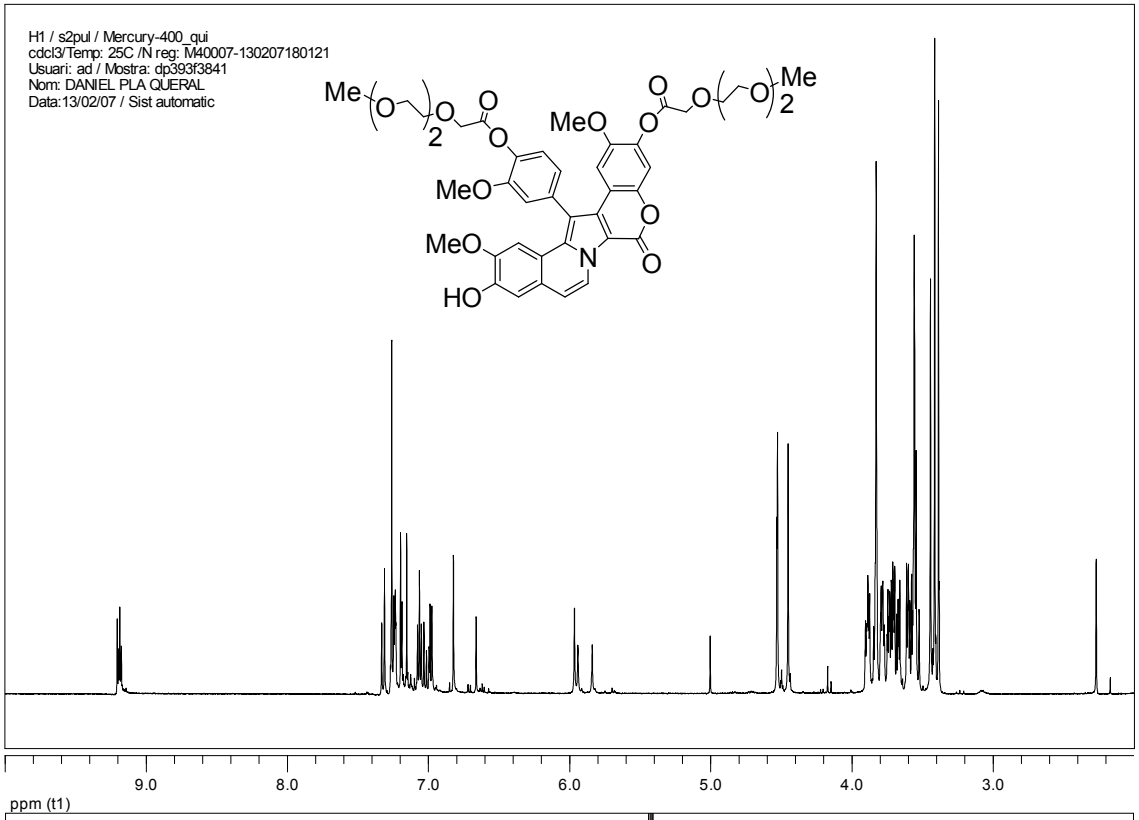
H1 / s2pul / Mercury-400_qui
cdcl3/Temp: 25C /N reg: M40007-130207180121
Usuari: ad / Mostra: dp393f3841
Nom: DANIEL PLA QUERAL
Data:13/02/07 / Sist automatic
Me
O
2
O
O
O
MeO
MeO
MeO
HO
N
O
O
O
O
O
Me
2
9.0
8.0
7.0
6.0
5.0
4.0
3.0
ppm (t1)

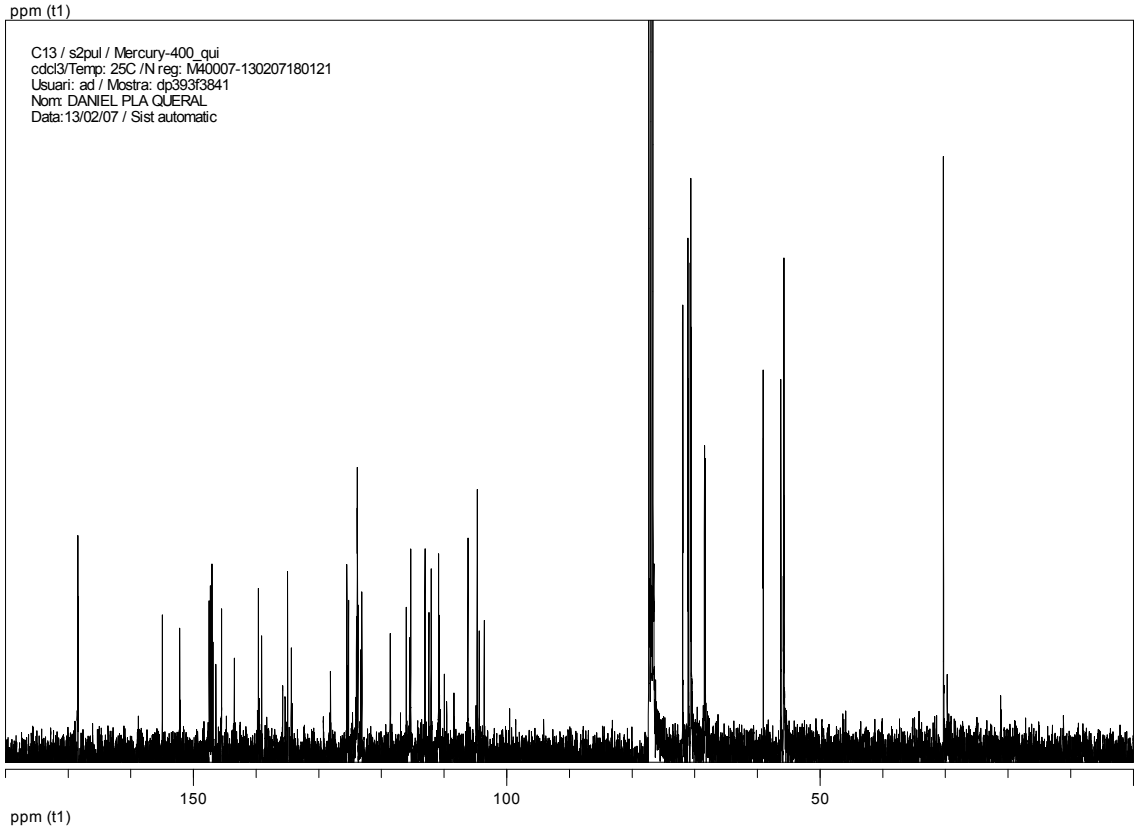
C13 / s2pul / Mercury-400_qui
cdcl3/Temp: 25C /N reg: M40007-130207180121
Usuari: ad / Mostra: dp393f3841
Nom: DANIEL PLA QUERAL
Data:13/02/07 / Sist automatic
150
100
50
ppm (t1)

Compound **8**

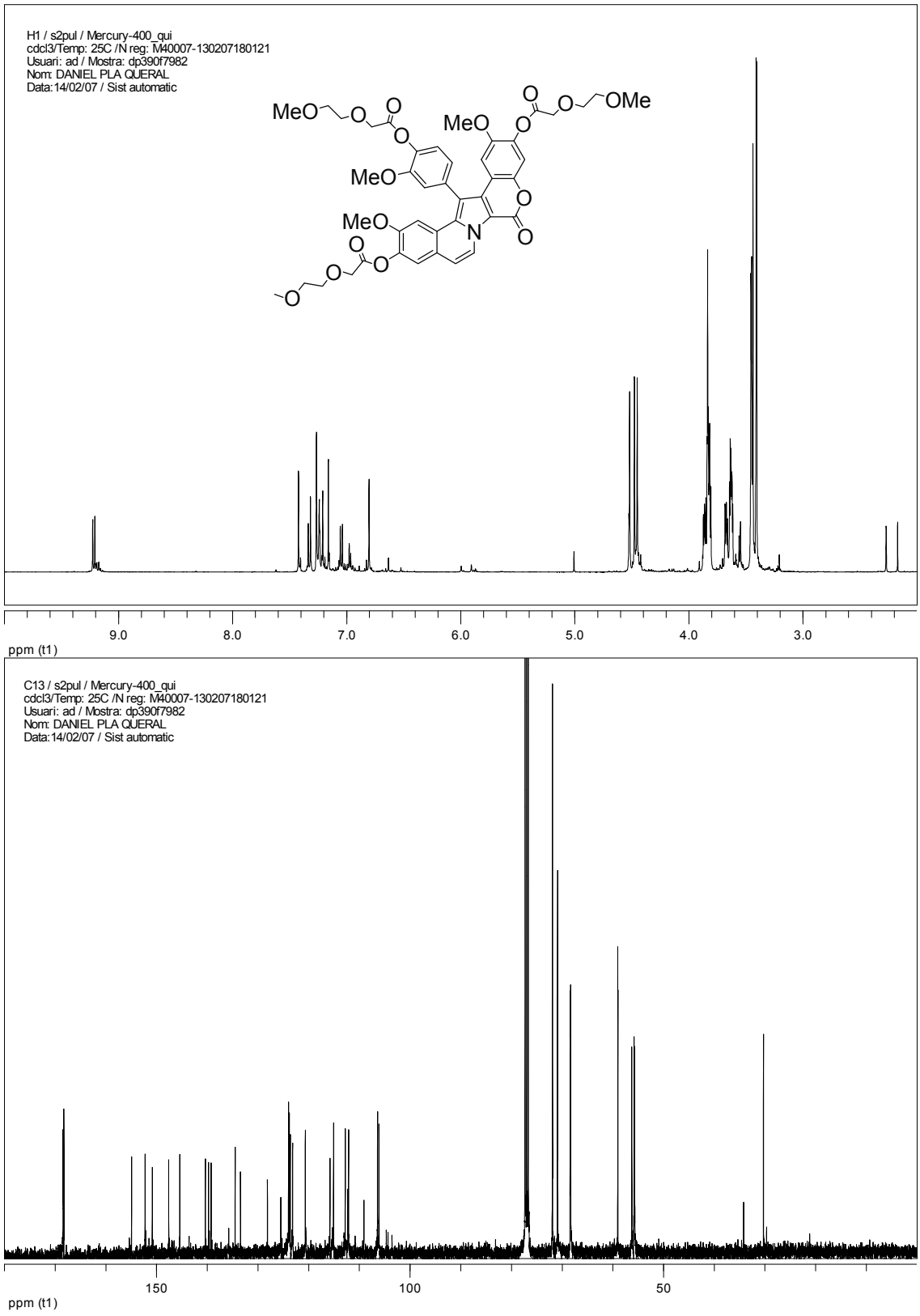
H1 / s2pul / Mercury-400_qui
cdcl3/Temp: 25C /N reg: M40007-130207180121
Usuari: ad / Mostra: dp390f7982
Nom: DANIEL PLA QUERAL
Data:14/02/07 / Sist automatic
MeO
MeO
MeO
MeO
OMe
N
9.0
8.0
7.0
6.0
5.0
4.0
3.0
ppm (t1)
C13 / s2pul / Mercury-400_qui
cdcl3/Temp: 25C /N reg: M40007-130207180121
Usuari: ad / Mostra: dp390f7982
Nom: DANIEL PLA QUERAL
Data:14/02/07 / Sist automatic
150
100
50
ppm (t1)

Compound **9**

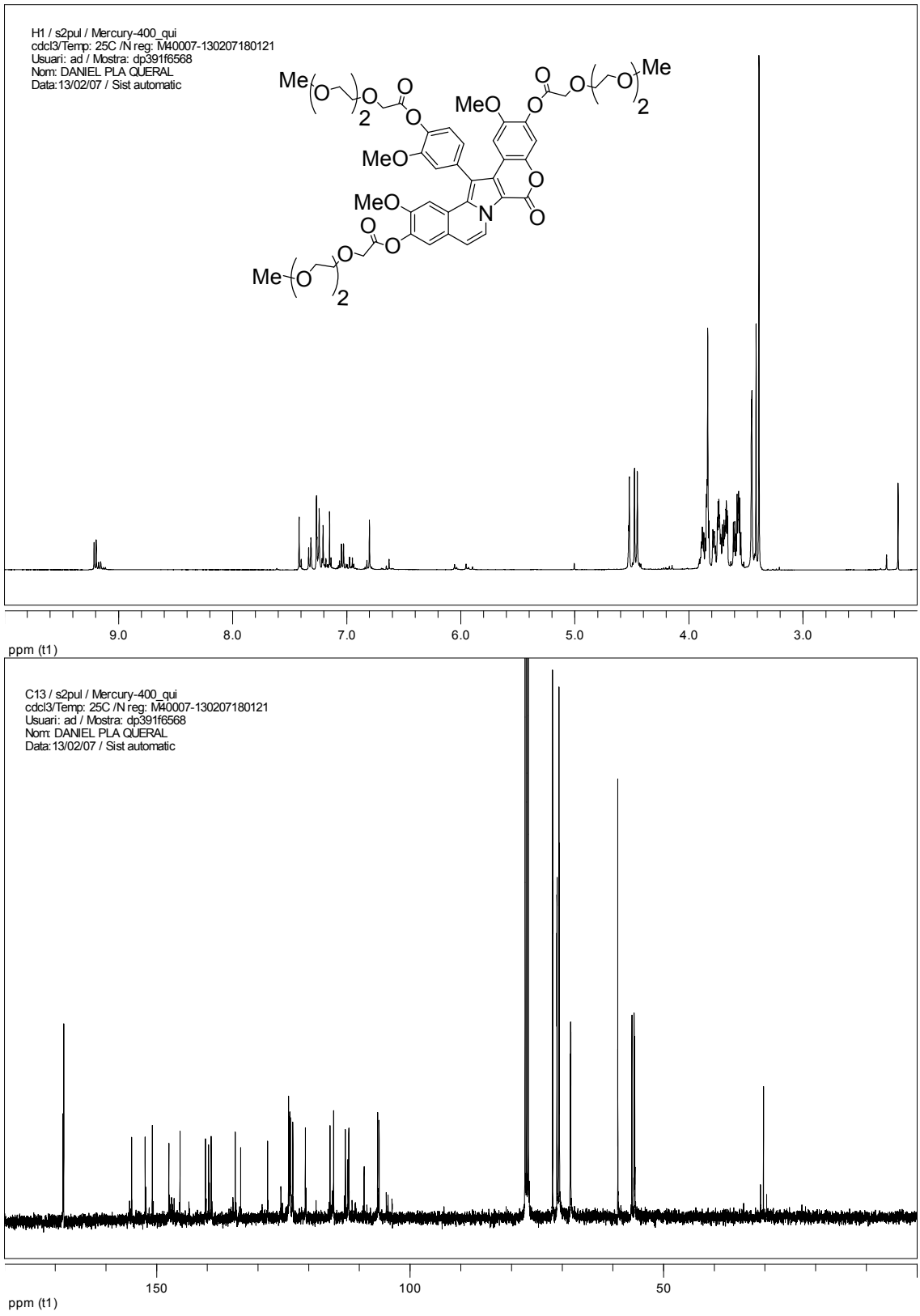
H1 / s2pul / Mercury-400_qui
cdcl3/Temp: 25C /N reg: M40007-130207180121
Usuari: ad / Mostra: dp391f6568
Nom: DANIEL PLA QUERAL
Data:13/02/07 / Sist automatic
9.0
8.0
7.0
6.0
5.0
4.0
3.0
ppm (t1)
C13 / s2pul / Mercury-400_qui
cdcl3/Temp: 25C /N reg: M40007-130207180121
Usuari: ad / Mostra: dp391f6568
Nom: DANIEL PLA QUERAL
Data:13/02/07 / Sist automatic
150
100
50
ppm (t1)

Table SI1. Solubilities of compounds **1**, **3**, **7** and **9** in H_2O, PEG-400 and EtOH.

Compound	Solubility [a] (mg/mL)		
	H_2O	PEG-400	EtOH
1	< 0.23	14.3	< 0.25
3	18.8	6.8	3.4
7	2.9	14.7	12.3
9	7.2	39.8	10.4

[a] All trials were carried out at r.t. and atmospheric pressure using 0.8 to 2.6 mg of product.

Figure SI1. Uptake of test compounds by HeLa cells.

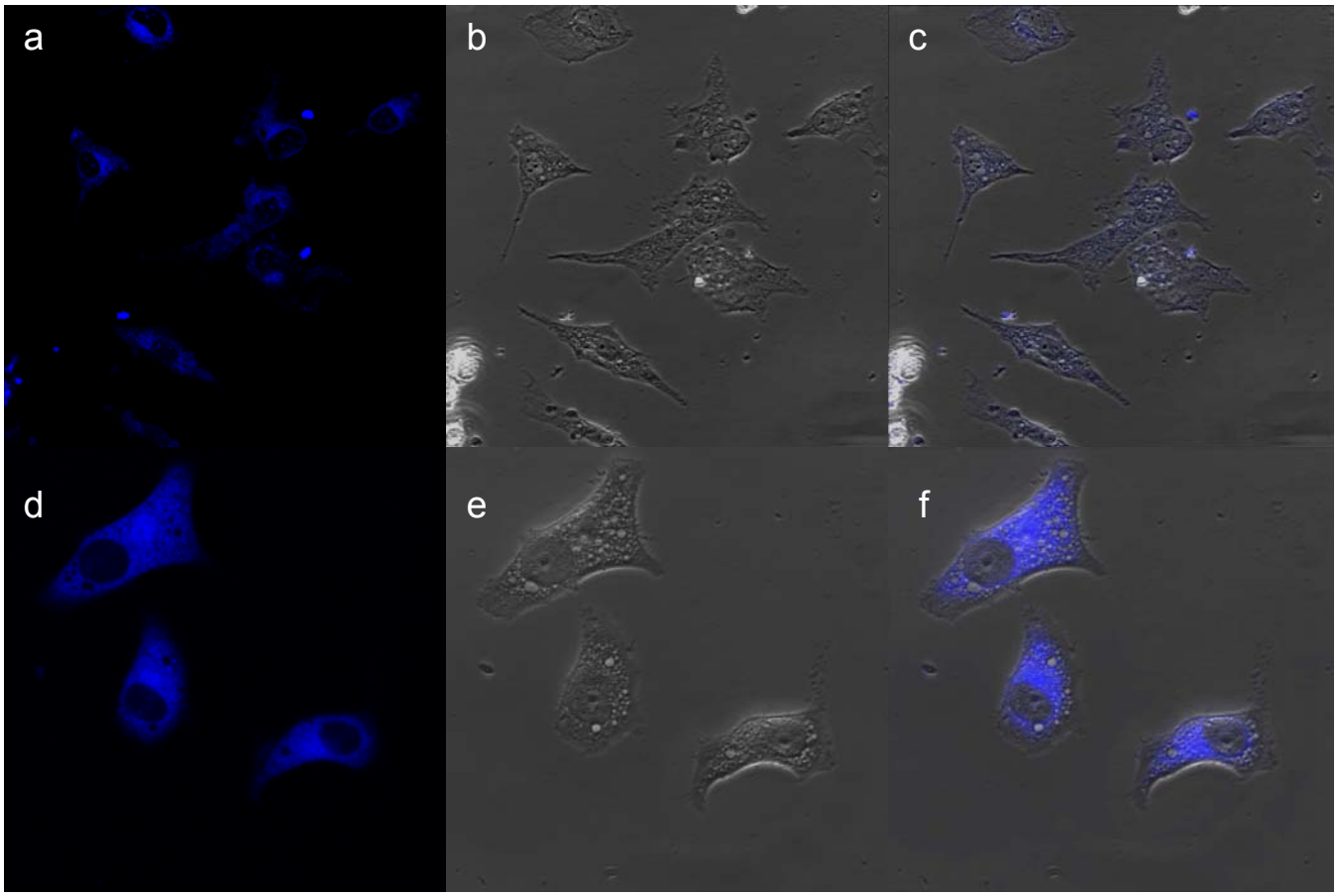

a-c) HeLa cells incubated with Lam-D at 1μM concentration for 24 h: **a)** UV image; **b)** transmission picture; and **c)** overlay picture. **d-f)** HeLa cells incubated with **7** at 1μM concentration for 24 h: **a)** UV image; **b)** transmission picture; and **c)** overlay picture.

Figure SI2. Uptake of Lam-D by HeLa cells.

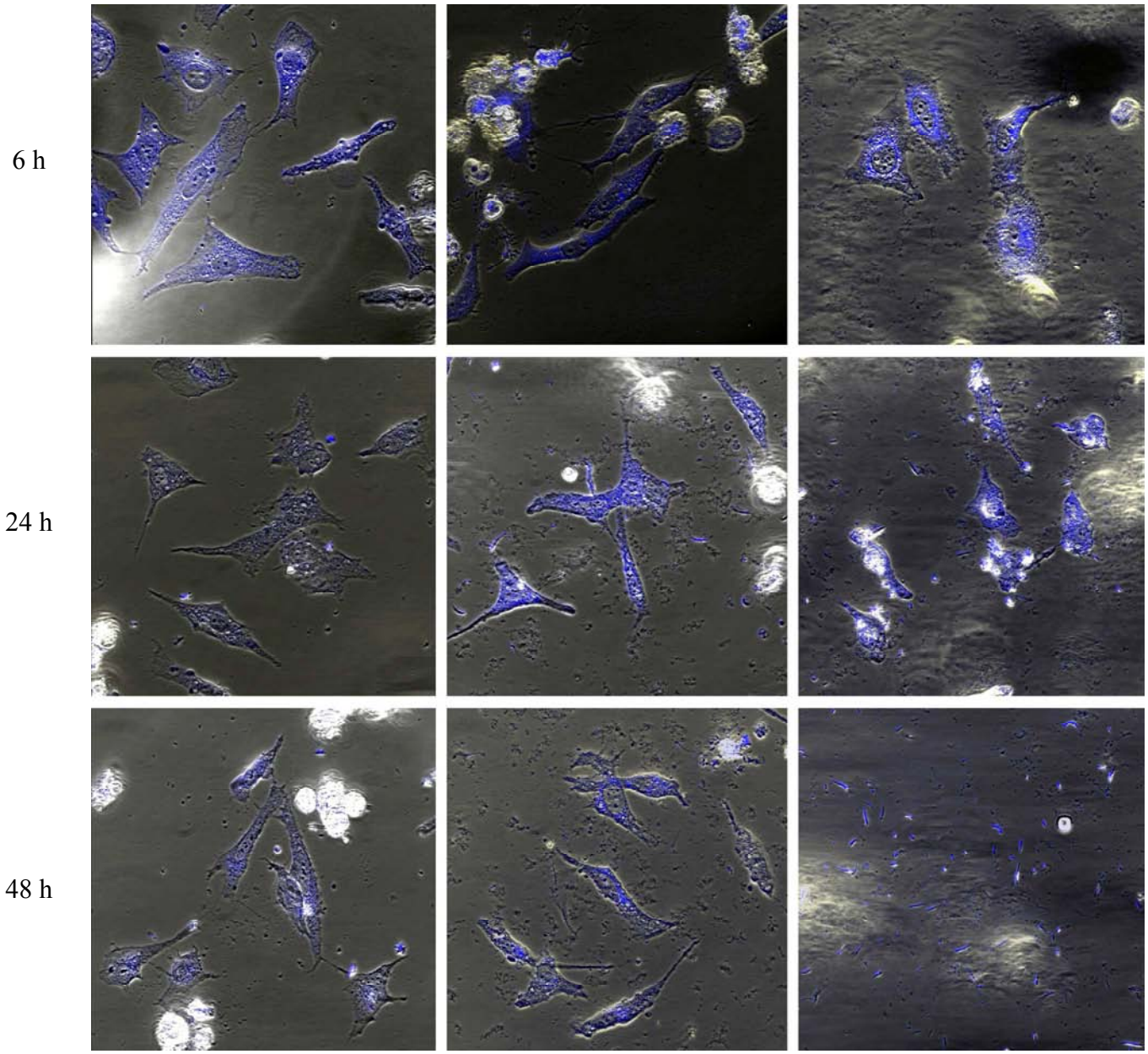

Figure SI3. Cell cycle progression of conjugates **3** and **9** in HT-29 cancer cell line

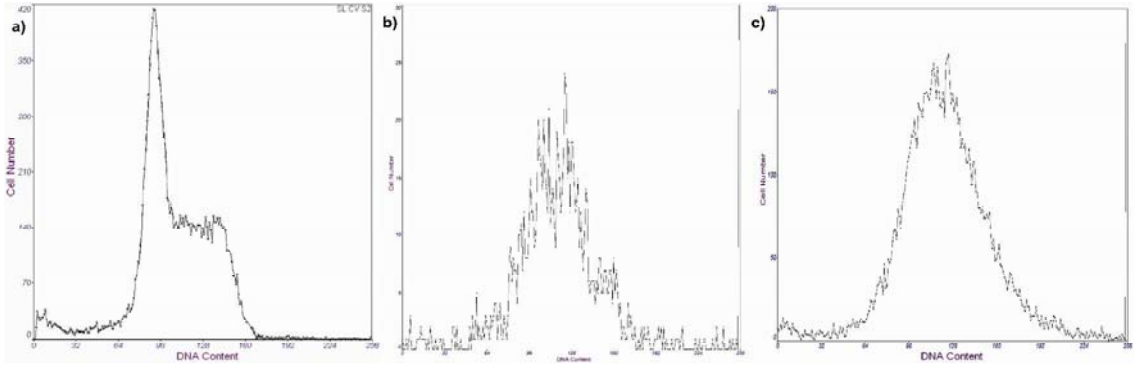

a) HT-29 asynchronous colon cell line.
b) HT-29 cell line treated with 1 μM conjugate **3** for 12 h.
c) HT-29 cell line treated with 1 μM conjugate **9** for 12 h.

Lamellarin D Bioconjugates II: Synthesis and Cellular Internalization of Dendrimer and Nuclear Location Signal Derivatives

Daniel Pla,[†,‡] Marc Martí,[†] Josep Farrera-Sinfreu,[†,§] Daniel Pulido,[‡,§] Andrés Francesch,[||] Pilar Calvo,[||] Carmen Cuevas,[||] Miriam Royo,[‡,§] Rosa Aligué,[⊥] Fernando Albericio,*[,#,†,‡] and Mercedes Álvarez*[,¶,†,‡]

Institute for Research in Biomedicine, Barcelona Science Park-University of Barcelona, Baldiri Reixac 10, E-08028 Barcelona, Spain, CIBER-BBN Networking Centre on Bioengineering, Biomaterials, and Nanomedicine, Combinatorial Chemistry Unit - Barcelona Science Park (UQC-PCB), Pharma Mar S. A., Avda de los Reyes 1, E-28770 Colmenar Viejo, Madrid, Spain, and Department of Cell Biology, Faculty of Medicine, University of Barcelona, Casanova 143, E-08036 Barcelona, Spain. Received November 24, 2008; Revised Manuscript Received March 24, 2009

The design and synthesis of Lamellarin D conjugates with a nuclear localization signal peptide and a poly(ethylene glycol)-based dendrimer are described. Conjugates **1**−**4** were obtained in 8−84% overall yields from the corresponding protected Lamellarin D. Conjugates **1** and **4** are 1.4- to 3.3-fold more cytotoxic than the parent compound against three human tumor cell lines (MDA-MB-231 breast, A-549 lung, and HT-29 colon). Besides, conjugates **3** and **4** showed a decrease in activity potency in BJ skin fibroblasts, a normal cell culture. Cellular internalization was analyzed, and a nuclear distribution pattern was observed for **4**, which contains a nuclear localization signaling sequence.

INTRODUCTION

Actively mediated cellular delivery of biomolecules (*1*) has garnered great interest as a strategy for delivering cancer chemotherapeutics (*2*−*5*). Conjugates of a drug and a macromolecular vehicle such as NLS[1] peptidic sequences (*5*−*8*), PEG carriers (*9*), and dendrimers (*10*) may have better cellular internalization than the drug alone and, in some cases, may produce passive accumulation of the drug in tumors by the EPR effect (*11*). In addition, the therapeutic activity of these conjugates is associated with their capacity to release the drug at a specific subcellular target. Thus, the suitability of macromolecules as vehicles also extends to their propensity to deliver the drug to a predetermined intracellular location.

The marine alkaloid Lam-D (*12*−*15*) is a promising drug candidate due to its Topo I inhibition activity. Topoisomerases are nuclear enzymes crucial in cellular replication. They change the topology of DNA before and after the replication and transcription processes. Therefore, they are especially attractive targets for cancer therapy (*16*−*19*). Lam-D is limited by its insolubility in common solvent media, especially in water. Therefore, it has been used to investigate its conjugation to macromolecules. In the previous paper, we have described the first generation of Lam D-bioconjugates based on PEG esters such as **1** (*9*). In this paper, we describe a second generation of Lam-D conjugates (Figure 1) based on esterification with either a poly(ethylene glycol)-based dendrimer (in **2**) or NLS oligopeptide sequences (in **3** and **4**). The peptide NLS H-Pro-Pro-Lys-Lys-Lys-Arg-Lys-Val-OH, which has been demonstrated (*20*) to shuttle compounds to the nucleus, was used in the present work.

The introduction of such oligomeric systems to Lam D demanded an integrated and robust synthetic scheme with a collection of suitable orthogonal protecting groups, in terms of selective removal and compatibility with the presence of other functional groups (*21*).

EXPERIMENTAL PROCEDURES

General Data. Reagents and solvents were purified according to *Purification of Laboratory Chemicals*, Armarego, W. and Chai C., Elsevier (2003). Melting points (m.p.) were determined

* Corresponding author. M.A. and F.A., Institute for Research in Biomedicine, Barcelona Science Park-University of Barcelona, Baldiri Reixac 10, E-08028 Barcelona, Spain. Tel.: +34934037086; Fax: +34934037126; E-mail mercedes.alvarez@irbbarcelona.org.

† Barcelona Science Park-University of Barcelona.

‡ CIBER-BBN Networking Centre on Bioengineering, Biomaterials, and Nanomedicine.

§ Combinatorial Chemistry Unit - Barcelona Science Park (UQC-PCB).

|| Pharma Mar S. A.

⊥ Faculty of Medicine, University of Barcelona.

Department of Organic Chemistry, University of Barcelona, E-08028 Barcelona.

¶ Laboratory of Organic Chemistry, Faculty of Pharmacy, University of Barcelona, E-08028 Barcelona.

[1] Abbreviations: AU, absorbance units; A-549, lung carcinoma cell line; Bn, benzyl; Boc, *tert*-butoxycarbonyl; Cbz, benzyloxycarbonyl; CIQ, cellular internalization quotient; DDQ, 2,3-dichloro-5,6-dicyano-*p*-benzoquinone; DIPCDI, *N*,*N*′-diisopropylcarbodiimide; DIPEA, diisopropylethylamine; DMAP, 4-dimethylaminopyridine; DMEM, Dulbecco's modified Eagle's medium; DMF, dimethylformamide; DMSO, dimethylsulfoxide; DTPA, diethylenetriamine-*N*,*N*,*N*′,*N*′,*N*″-pentaacetic acid; EDC·HCl, *N*-(3-dimethylaminopropyl)-*N*′-ethylcarbodiimide hydrochloride; EPR, enhance permeability and retention; FACS, fluorescence-activated cell sorting; FBS, fetal bovine serum; GFP, green fluorescent protein; HOAt, 1-hydroxy-7-azabenzotriazole; HOBt, 1-hydroxybenzotriazole; HT-29, colon carcinoma cell line; GI_{50}, 50% growth inhibition; *i*Pr, isopropyl; Lam, Lamellarin; MDA-MB-231, breast adenocarcinoma cell line; MOM, methoxymethyl; MSNT, 1-(mesitylene-2-sulfonyl)-3-nitro-1*H*-1,2,4-triazole; MW, microwave; NLS, nuclear location signal; NMI, *N*-methylimidazole; Pbf, (2,2,4,6,7-pentamethyldihydrobenzofuran-5-sulfonyl); PBS, phosphate buffered saline; PEG, poly(ethylene glycol); PS, polystyrene; PyBOP, (benzotriazol-1-yloxy)-tripyrrolidinophosphonium hexafluorophosphate, SRB, sulforhodamine B; TBAF, tetrabutylammonium fluoride; TBDPS, *tert*-butyldiphenylsilyl; TBME, *tert*-butyl methyl ether; *t*Bu, *tert*-butyl; TCFH, *N*,*N*,*N*′,*N*′-tetramethylchloroformamidinium hexafluorophosphate; TFFH, *N*,*N*,*N*′,*N*′-tetramethylfluoroformamidinium hexafluorophosphate; TFA, trifluoroacetic acid; THF, tetrahydrofurane; Topo, Topoisomerase.

10.1021/bc800504t CCC: $40.75 © 2009 American Chemical Society
Published on Web 05/27/2009

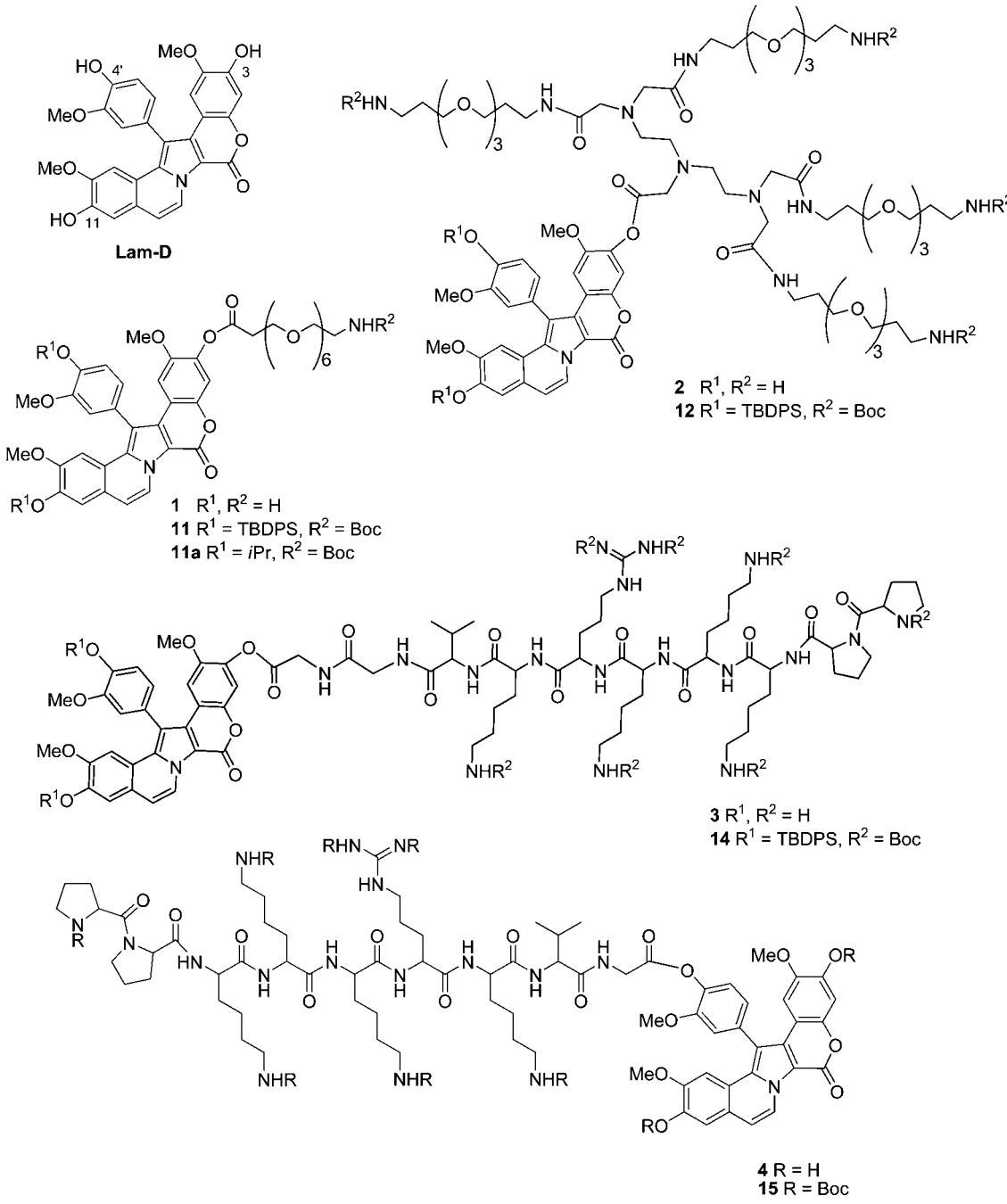

Figure 1. Structures of Lam-D conjugates.

in a Büchi Melting Point B540 in open capillaries and are uncorrected. Automatic flash chromatography was done in an Isco Combiflash medium-pressure liquid chromatograph with Redisep silica gel columns (47−60 μm). Sonication was performed in a Branson ultrasound bath. ^{1}H NMR and ^{13}C NMR spectra were recorded on a Varian Mercury 400 MHz spectrometer and a Gemini 200 MHz spectrometer. Multiplicity of the carbons was assigned with DEPT and gHSQC experiments, using standard abbreviations for off-resonance decoupling: (s) singlet, (d) doublet, (t) triplet, (q) quartet. The same abbreviations were also used for the multiplicity of signals in ^{1}H NMR, plus (m) multiplet, (bs) broad singlet, (bd) broad doublet. Spectra were referenced to appropriate residual solvent peaks (d_6-acetone, d_6-DMSO, d_4-MeOH, or $CDCl_3$). IR spectra were obtained on a Thermo Nicolet FT-IR spectrometer. HRMS were performed on a Bruker Autoflex high-resolution mass spectrometer by *Unidad de Espectrometría de Masas* (Universidad de Santiago de Compostela) and by *Servei d'Espectrometria de Masses* (Universitat de Barcelona). Microwave-assisted reactions were carried out in a CEM Discover microwave. The automatic syringe pump was used as specified for controlled addition of some reactants. Reversed-phase analytical HPLC was performed on a Waters Alliance separation module 2695 using a Waters Xterra MS C_{18} column (150 × 4.6 mm, 5 μm) and a Waters 996 PDA detector at 254 nm.

General Procedures. *A. General Method for Simultaneous Removal of TBDPSO and N-Boc.* HF (5 mL) at −196 °C was poured over solid **11**, **12**, or **14** (0.05−0.08 mmol). The solution was stirred for 1 min, and the solvent was immediately removed under vacuum at low temperature. MeCN was added to the crude, and the deprotected compound was precipitated by addition of MTBE, cooling to 0 °C and centrifugation (10 min, 2000 rpm). The residue was dried in vacuo to give the final Lam-D conjugates **1**−**3**.

B. General Method for MOMO Deprotection. Me_3SiI (142 μL, 3.00 mmol) was added at r.t. to a solution of **10a** or **10b** (1.00 mmol) in CH_2Cl_2 (225 mL), and the resulting orange solution was stirred at r.t. for 20 min. The solvent was removed in vacuo, and the residue was dissolved with EtOAc and then washed three times with sat NH_4Cl and brine. The organic phase was dried over anhydrous $MgSO_4$, and the solvent was removed in vacuo. Purification by column chromatography on silica gel by elution with hexane/EtOAc (80:20 to 60:40) gave the title compounds (84% quant yield).

C. General Method for Esterification. Synthesis of Conjugates. DMAP (0.6 mmol) and **5** (1 mmol) in dry CH_2Cl_2 (45 mL) were added to a solution of NHBocPEG$_6$-OH, or Boc-NLS-Gly-OH (4 mmol), and EDC·HCl (4 mmol) in dry CH_2Cl_2 (5 mL). The resulting solution was stirred at r.t. for 2 h. The reaction mixture was diluted with CH_2Cl_2 and washed with sat $NaHCO_3$ solution and brine. The organic phase was dried over anhydrous $MgSO_4$ and the solvent removed under vacuum, to provide the title compounds **11** and **13** (89% quant yield).

3-[3-(2-(2-(2-(2-(2-(2-Aminoethoxy)ethoxy)ethoxy)ethoxy)-ethoxy)ethoxy)propanoyloxy]Lam-D (*22*) (1). Following the general procedure **A** and starting from **11** (24, 23, and 23 mg, 0.05 mmol), a yellow solid (35 mg, 84%) was obtained. The spectroscopic data are in accordance with previous reports (*9*).

3-[2-(Bis(2-(bis(2-(3-(2-(2-(3-aminopropoxy)ethoxy)ethoxy)propylamino)-2-oxoethyl)amino)ethyl)amino)acetyl]Lam-D (*22*) (2). Following the general procedure **A** and starting from **12** (17 and 15 mg, 0.12 mmol), **2** as a yellow solid (8 mg, 36%) was obtained. ^{1}H NMR (D_2O, 400 MHz) δ 1.54 and 1.67 (2m, J = 6.6 Hz, 8H); 1.76 and 1.83 (2m, J = 6.6 Hz, 8H); 2.93 (2t, J = 7.2 Hz, 4H); 2.97 (2t, J = 7.2 Hz, 4H); 3.02−3.10 (m, 8H); 3.16−3.29 (m, 11H, OMe); 3.33−3.43 (m, 43H, OMe); 3.52−3.56 (m, 18H); 3.70 (br, 3H, OMe); 6.43 (s, 1H); 6.57 (br, 1H); 6.71 (br, 1H); 6.81−6.88 (m, 4H); 6.99 (br, 1H); 8.35 (br, 1H). ^{13}C NMR (D_2O, 100 MHz) δ 26.6 (t); 26.7 (t); 28.5 (t); 28.6 (t); 36.4 (t); 36.5 (t); 37.7 (t); 37.8 (t); 55.2 (q); 55.5 (q); 55.7 (q); 57.6 (t); 57.7 (t); 68.3 (t); 68.4 (t); 68.5 (t); 69.4 (t); 69.5 (t); 69.6 (t); 69.7 (t); 107.7 (d); 111.5 (d); 111.7 (d); 122.2 (d); 122.4 (d); 122.8 (d); 127.6 (d); 145.6 (d); 146.7 (d); 147.4 (s); 149.5 (s); 149.9 (s); 150.3 (s); 151.1 (s); 171.0 (s); 171.1 (s). MS (MALDI-TOF) 1684 (M+1, 100), 1685 (M+2, 93) 1686 (M+3, 49). HRMS *m*/*z* calcd for $C_{82}H_{131}N_{12}O_{25}$ 1683.9342, found 1683.9346. HPLC analysis: 6.9 min retention time (94% purity), with a gradient of 0% to 100% of eluent **B** over 15 min using the solvent system: H_2O/0.045% TFA (**A**) and MeCN/0.036% TFA (**B**).

3-[Gly-Gly-NLS]Lam-D (*22*) (3). Following the general procedure **A** and starting from **14** (28 and 17 mg, 0.16 mmol), **3** as a white solid (10 mg, 38%) was obtained. ^{1}H NMR (DMSO-d_6, 400 MHz) δ 0.83−0.88 (m, 6H, 2CH$_3$); 1.22−1.36 (m, 10H, 5CH$_2$); 1.42−1.54 (m, 8H, 4CH$_2$); 1.56−1.62 (m, 8H, 4CH$_2$); 1.88−1.93 (m, 4H, 2CH$_2$); 2.05 (br, 2H, CH$_2$); 2.07 (br, 2H, CH$_2$); 2.33 (t, J = 1.8 Hz, 2H, CH$_2$); 2.55 (br, 1H, CH); 2.67 (t, J = 1.8 Hz, 2H, CH$_2$); 2.69−2.75 (m, 16H, 3CH$_2$); 3.36 (2s, 6H, 2OMe); 3.75 (s, 3H, OMe); 3.99−4.05 (m, 3H, CH); 4.14−4.25 (m, 7H, 3CH, 2CH$_2$); 4.58 (br, 1H, CH); 5.93 (br, 1H); 5.76 (br, 1H); 5.47 (br, 1H); 6.70 (s, 1H); 6.87 (s, 1H); 7.01 (dd, J = 8.0, 1.7 Hz, 1H); 7.10 (d, J = 8.0 Hz, 1H); 7.12−7.13 (m, 2H); 7.19 (s, 1H); 7.21 (br, 1H); 9.00 (d, J = 7.4 Hz, 1H, H8). MS (MALDI-TOF) 1575 (M+1, 100), 1576 (M+2, 92). HRMS *m*/*z* calcd. for $C_{77}H_{111}N_{18}O_{18}$ 1575.8324, found 1575.8319. HPLC analysis: 1.8 min retention time (96.7% purity), with 15 min isocratic MeCN/0.036% TFA.

4′-[Gly-NLS]Lam-D (*22*) (4). Peptide **8** (392 mg, 0.23 mmol) was preactivated for 15 min at r.t. with TCFH (63 mg, 23 mmol) and NEt_3 (32 μL, 23 mmol) in dry CH_2Cl_2 (15 mL). Compound **6** (53 mg, 0.08 mmol) and DMAP (9 mg, 0.08 mmol) in dry CH_2Cl_2 (5 mL) were then added. The resulting solution was stirred at r.t. for 120 h. The reaction mixture was diluted with CH_2Cl_2 and washed with sat $NaHCO_3$ solution and brine. The organic phase was dried over anhydrous $MgSO_4$, and the solvent was removed under vacuum. The residue was purified by flash chromatography: elution with CH_2Cl_2/MeOH (99:1 to 95:5) gave **15** (45% yield based on 40% transformation of **6**). The Boc protected compound **15** was then treated with 40% TFA in CH_2Cl_2 (10 mL) at r.t. for 1 h. The solvent was removed under reduced pressure, and the residue was purified by reverse-phase chromatography. Elution with H_2O/MeCN (60:40 to 40:60) gave **4** as a yellow solid (3 mg, 17%). ^{1}H NMR (D_2O, 500 MHz) δ 1.04 (d, J = 6.5 Hz, 3H, CH$_3$); 1.16 (d, J = 6.5 Hz, 3H, CH$_3$); 1.39−1.56 (m, 8H, 4CH$_2$); 1.66−1.77 (m, 10H, 5CH$_2$); 1.78−1.88 (m, 8H, 4CH$_2$); 2.00−2.12 (m, 4H, 2CH$_2$); 2.17 and 2.36 (2br, 2H, CH$_2$); 2.44 and 2.58 (2br, 2H, CH$_2$); 2.84 (br, 1H, CH); 2.96−3.05 (m, 10H, 5CH$_2$); 3.40 (br, 3H, OMe); 3.44 (s, 3H, OMe); 3.45 (s, 3H, OMe); 3.22 (t, J = 7.5 Hz, 1H, CH$_2$); 3.59 (t, J = 7.0 Hz, 1H, CH$_2$); 3.81 (br, 2H, CH$_2$); 4.23−4.42 (m, 5H, 5CH); 4.51 (t, J = 8.3 Hz, 1H, CH); 4.65 (dd, J = 9.0, 8.4 Hz, 1H, CH); 6.38 (s, 1H); 6.64−6.87 (m, 4H); 6.99 (br, 1H); 7.01 (br, 1H); 7.32 (br, 1H); 8.54 (br, 1H). MS (MALDI-TOF) 1518 (M+1, 100), 1519 (M+2, 82). HRMS *m*/*z* calcd. for $C_{75}H_{108}N_{17}O_{17}$ 1518.8109, found 1518.8114. HPLC analysis: 6.9 min retention time (95% purity), with a gradient of 50% to 100% of eluent **B** over 15 min using the solvent system: H_2O/0.045% TFA (**A**) and MeCN/0.036% TFA (**B**).

4′,11-Bis(*tert*-butyldiphenylsilyl)Lam-D (*22*) (5). Following the general procedure **B** and starting from **10b** (1.06 g, 1.04 mmol), **5** as a yellow solid (856 mg, 84%) was obtained. mp (MeCN) 278−280 °C. IR (film) ν 1704, 1487, 1428, 1284, 1111 cm^{-1}. ^{1}H NMR ($CDCl_3$, 200 MHz) δ 1.15 (s, 9H); 1.17 (s, 9H); 3.18 (s, 3H, OMe); 3.47 (s, 3H, OMe); 3.64 (s, 3H, OMe); 5.89 (s, 1H); 6.68 (d, J = 7.4 Hz, 1H, H9); 6.69 (s, 1H); 6.91−6.93 (m, 3H); 6.95 (s, 1H); 7.05 (br, 1H); 7.06 (br, 1H); 7.37−7.48 (m, 10H); 7.71−7.79 (m, 10H); 9.04 (d, J = 7.4 Hz, 1H, H8). ^{13}C NMR ($CDCl_3$, 100 MHz) δ 19.9 (s); 26.6 (q); 26.7 (q); 54.5 (q); 55.5 (q); 55.7 (q); 103.4 (d); 104.7 (d); 105.9 (d); 107.6 (s); 109.8 (s); 111.0 (s); 112.1 (d); 115.4 (d); 116.5 (d); 119.7 (s); 120.3 (d); 122.7 (d); 123.7 (d); 124.4 (s); 127.5 (d); 127.6 (d); 128.5 (s); 129.1 (s); 129.7 (d); 129.9 (d); 132.9 (s); 133.0 (s); 133.4 (s); 134.1 (s); 135.0 (d); 135.1 (d); 143.1 (s); 144.9 (s); 146.1 (s); 146.8 (s); 150.7 (s); 151.1 (s); 155.3 (s). MS (MALDI-TOF) 976 (M+1, 100), 977 (M+1, 57), 978 (M+2, 38).

3,11-Di-*tert*-butoxycarbonyl-Lam-D (*22*) (6). A solution of TBAF in THF (1 M, 1.64 mmol) was added to a −78 °C solution of **10d** (771 mg, 0.82 mmol), in MeOH-THF (100 mL, 80:20). The mixture was stirred at −78 °C for 15 min. Solvents were removed under vacuum, and the residue was dissolved in CH_2Cl_2. The organic solution was washed with water and brine. The organic phase was dried over anhydrous $MgSO_4$ and the solvent removed under vacuum. The residue was purified by flash chromatography: elution with hexane/EtOAc (60:40 to 40:60) gave **6** as a white solid (491 mg, 85%). mp (MeCN) 149−150 °C. IR (film) ν 1760, 1709, 1275, 1255 cm^{-1}. ^{1}H NMR ($CDCl_3$, 400 MHz) δ 1.54 (s, 9H); 1.55 (s, 9H); 3.455 (s, 3H, OMe); 3.463 (s, 3H, OMe); 3.91 (s, 3H, OMe); 5.93 (br, 1H, OH); 6.83 (s, 1H); 6.97 (d, J = 7.4 Hz, 1H, H9); 7.11 (br, 1H); 7.15 (dd, J = 8.0, 1.8 Hz, 1H); 7.18 (br, 1H); 7.24−7.26 (m, 2H); 7.44 (br, 1H); 9.14 (d, J = 7.4 Hz, 1H, H8). ^{13}C NMR ($CDCl_3$, 100 MHz) δ 27.5 (q); 55.3 (q); 55.6 (q); 56.3 (q); 83.89 (s); 83.95 (s); 106.4 (d); 106.6 (d); 108.8 (s); 111.8 (d); 112.6 (d); 113.0 (s); 113.5 (d); 115.4 (d); 115.7 (s); 120.3 (d); 123.0 (d); 123.6 (s); 123.8 (s); 124.0 (s); 124.4 (d); 128.1 (s); 128.3 (s); 133.6 (s); 140.0 (s); 141.0 (s); 145.4 (s); 145.9 (s); 147.7

(s); 147.9 (s); 150.9 (s); 151.0 (s); 151.1 (s); 155.0 (s). MS (MALDI-TOF) 699 (M, 56), 700 (M+1, 100).

Boc-Pro-Pro-Lys(Boc)-Lys(Boc)-Lys(Boc)-Arg(Boc$_2$)-Lys-(Boc)-Val-Gly-OH (8). The Boc protected peptide was synthesized manually on solid phase in a polypropylene syringe fitted with a porous polyethylene disk. Solvents and soluble reagents were removed by suction. Washings between deprotection, coupling, and subsequent deprotection steps were carried out with DMF (5 × 1 min) and CH_2Cl_2 (5 × 1 min) using 10 mL solvent/g resin each time. Standard Fmoc/*t*Bu chemistry and chlorotrityl resin (0.5 g, 1.5 mmol/g) were used. The resin was preswollen in anhydrous CH_2Cl_2 and then in DMF. The first Fmoc-protected amino acid (Fmoc-L-Gly-OH) (155 mg, 0.7 equiv) was introduced in the presence of DIEA (635 μL, 5 equiv) in DMF. After 1 h, MeOH (0.5 mL) was added and the mixture was stirred for 30 min. The resin was then washed with DMF and CH_2Cl_2, and the synthesis continued as described below. The peptide was elongated through successive iterations of Fmoc removal and amino acid coupling. The Fmoc protecting group was removed with several treatments of 20% piperidine in DMF (1 × 1 min + 2 × 15 min). The resin was then washed with DMF and CH_2Cl_2. The corresponding Fmoc-protected amino acid (5 equiv) was introduced using DIPCDI (310 μL, 5 equiv) and HOBt (305 mg, 5 equiv) as coupling agents. After 2 h, the resin was washed with DMF and CH_2Cl_2, and the coupling was monitored using the Kaiser test. Recouplings were done when needed. Boc-L-Pro-OH (430 mg, 5 equiv) was used as a last amino acid. The peptide was finally cleaved from the resin using 3% TFA in CH_2Cl_2, (5 × 1 min). Washes were collected in a flask containing 50 mL of water. The CH_2Cl_2 was then evaporated under reduced pressure, MeCN (30 mL) was added to the aqueous solution, and the resulting mixture was then lyophilized. Peptide **8** (590 mg, 94%) was obtained as a white solid. HPLC analysis: 6.2 min retention time (92% purity), with a gradient of 50% to 100% of eluent **B** in 7 min using the solvent system: H_2O/0.045% TFA (**A**) and MeCN/0.036% TFA (**B**). HPLC ESI-MS calcd. for $C_{82}H_{144}N_{16}O_{24}$ $[M+H]^+$ 1738, found: $[M+2]^{2+}/2$, 870.

11-Benzyl-4′-*tert*-butyldiphenylsilyl-3-methoxymethyl-Lam-D (*22*) (10). A mixture of **9** (*27*) (1.54 g, 1.76 mmol) and DDQ (400 mg, 1.76 mmol) in dry $CHCl_3$ (25 mL) was purged with Ar in a sealed vessel and microwaved at 120 °C for 10 min. The organic solution was washed with water, and brine, dried over $MgSO_4$, filtered, and then concentrated in vacuo. Purification by column chromatography on silica gel by elution with hexane/EtOAc (80:20 to 60:40) gave **10** as a white solid (2.27 g, 81%). mp (MeCN) 144−145 °C. IR (film) ν 1705, 1429, 1267, 1223 cm^{-1}. ^{1}H NMR ($CDCl_3$, 200 MHz) δ 1.17 (s, 9H); 3.43 (s, 3H, OMe); 3.46 (s, 3H, OMe); 3.50 (s, 3H, OMe); 3.65 (s, 3H, OMe); 5.23 (s, 2H); 5.24 (s, 2H); 6.77 (s, 1H); 6.92−6.96 (m, 3H); 7.06−7.08 (m, 2H); 7.19 (s, 1H); 7.25 (d, J = 5.4 Hz, 1H); 7.32−7.47 (m, 11H); 7.75−7.79 (m, 4H); 9.16 (d, J = 7.2 Hz, 1H, H8). ^{13}C NMR ($CDCl_3$, 50.3 MHz) δ 19.9 (s); 26.7 (q); 55.2 (q); 55.5 (q); 55.7 (q); 56.3 (q); 70.7 (t); 95.4 (t); 105.1 (d); 105.5 (d); 105.6 (d); 109.4 (d); 111.3 (s); 111.4 (s); 112.3 (d); 115.4 (d); 119.3 (s); 120.3 (d); 123.1 (d); 123.7 (d); 124.5 (s); 127.2 (d); 127.7 (d); 128.0 (d); 128.4 (s); 128.5 (s); 128.6 (d); 128.9 (s); 129.9 (d); 133.3 (s); 134.1 (s); 135.1 (d); 136.2 (s); 145.0 (s); 146.0 (s); 146.2 (s); 146.6 (s); 149.0 (s); 149.5 (s); 151.2 (s); 155.3 (s). MS (MALDI-TOF) 871 (M, 18), 872 (M+1, 100).

4′-*tert*-Butyldiphenylsilyl-3-methoxymethyl-Lam-D (*22*) (10a). Pd/C (10%) was added to a solution of **10** (509 mg, 0.58 mmol) in MeOH/EtOAc (2:1, 58 mL), the mixture was purged with H_2, and the resulting suspension was stirred at r.t. for 16 h. The reaction mixture was filtered through a pad of Celite, which was then washed with CH_2Cl_2. The solvent was removed under vacuum to provide the **10a** as a brown solid (433 mg, 95%). mp (MeCN) 129−130 °C. IR (film) ν 3213, 1680, 1425, 1222 cm^{-1}. ^{1}H NMR ($CDCl_3$, 400 MHz) δ 1.16 (s, 9H); 3.44 (s, 3H, OMe); 3.47 (s, 3H, OMe); 3.51 (s, 3H, OMe); 3.65 (s, 3H, OMe); 5.24 (s, 2H); 5.92 (br, 1H, OH); 6.77 (s, 1H); 6.93−6.94 (m, 2H); 6.98 (d, J = 7.4 Hz, 1H, H9); 7.05 (br, 1H); 7.13 (s, 1H); 7.16 (s, 1H); 7.25 (d, J = 5.6 Hz, 2H); 7.38−7.47 (m, 5H); 7.75−7.78 (m, 4H); 9.18 (d, J = 7.4 Hz, 1H, H8). ^{13}C NMR ($CDCl_3$, 100 MHz) δ 19.8 (s); 26.7 (q); 55.3 (q); 55.5 (q); 55.7 (q); 56.3 (q); 95.5 (t); 105.0 (d); 105.3 (d); 105.6 (d); 110.8 (d); 111.2 (s); 111.5 (s); 112.4 (d); 115.4 (d); 118.8 (s); 120.4 (d); 123.3 (d); 123.7 (d); 125.3 (s); 127.7 (d); 128.6 (s); 129.0 (s); 129.96 (d); 129.98 (d); 133.37 (s); 133.43 (s); 134.4 (s); 135.2 (d); 135.3 (s); 145.1 (s); 146.1 (s); 146.3 (s); 146.66 (s); 146.69 (s); 146.8 (s); 151.3 (s); 155.4 (s). MS (MALDI-TOF) 781 (M, 60), 782 (M+1, 100).

4′,11-Bis(*tert*-butyldiphenylsilyl)-3-methoxymethyl-Lam-D (10b). TBDPSCl (389 μL, 1.07 g/mL, 1.47 mmol) was added to a solution of **10a** (768 mg, 0.98 mmol), imidazole (135 mg, 1.96 mmol), and DMAP (120 mg, 0.98 mmol) in dry DMF (30 mL). The mixture was stirred for 24 h under Ar. DMF was removed under reduced pressure, and the residue was dissolved in CH_2Cl_2. The organic phase was washed with water and brine, and then dried over anhydrous $MgSO_4$. The solvent was removed under vacuum, and the residue was purified by flash chromatography. Elution with hexane/CH_2Cl_2 (40:60 to 20:80) gave **10b** (584 mg, 58%) as a brown oil. IR (film) ν 1679, 1426, 1113 cm^{-1}. ^{1}H NMR ($CDCl_3$, 200 MHz) δ 1.13 (s, 9H); 1.15 (s, 9H); 3.17 (s, 3H, OMe); 3.42 (s, 3H, OMe); 3.49 (s, 3H, OMe); 3.61 (s, 3H, OMe); 5.21 (s, 2H); 6.71 (d, 1H, J = 7.4 Hz, H9); 6.74 (s, 1H); 6.90 (2s, 2H); 6.92 (s, 1H); 7.01−7.05 (m, 2H); 7.22 (br, 1H); 7.10−7.19 (m, 10H); 7.69−7.77 (m, 10H); 9.06 (d, J = 7.4 Hz, 1H, H8). ^{13}C NMR ($CDCl_3$, 100 MHz) δ 19.9 (s); 26.6 (q); 26.7 (q); 54.5 (q); 55.4 (q); 55.7 (q); 56.3 (q); 95.4 (t); 105.1 (d); 105.5 (d); 105.9 (d); 107.9 (s); 111.3 (s); 111.4 (s); 112.3 (d); 115.3 (d); 116.5 (d); 119.7 (s); 120.3 (d); 122.7 (d); 123.6 (d); 124.4 (s); 127.4 (d); 127.6 (d); 127.7 (d); 127.8 (d); 128.4 (s); 128.8 (s); 129.5 (d); 129.7 (d); 130.0 (d); 132.9 (s); 133.0 (s); 133.4 (s); 134.7 (d); 135.0 (d); 135.1 (d); 144.9 (s); 145.9 (s); 146.2 (s); 146.5 (s); 150.7 (s); 151.1 (s); 155.3 (s). MS (ESI) 1020 (M+1, 100).

4′-*tert*-Butyldiphenylsilyl-Lam-D (*22*) (10c). Following the general procedure **B** and starting from **10a** (639 mg, 0.81 mmol), **10c** as a white solid (603 mg, quant) was obtained. mp (MeCN) 275−276 °C. IR (film) ν 3415, 1679, 1429, 1271 cm^{-1}. ^{1}H NMR ($CDCl_3$, 400 MHz) δ 1.17 (s, 9H); 3.46 (s, 3H, OMe); 3.47 (s, 3H, OMe); 3.65 (s, 3H, OMe); 6.71 (s, 1H); 6.93−6.94 (m, 2H); 6.98−7.05 (m, 3H); 7.13 (s, 1H); 7.17 (s, 1H); 7.39−7.47 (m, 6H); 7.76−7.79 (m, 4H); 9.17 (d, J = 7.4 Hz, 1H, H8). ^{13}C NMR ($CDCl_3$, 100 MHz) δ 19.9 (s); 26.7 (q); 55.3 (q); 55.5 (q); 55.7 (q); 103.6 (d); 104.7 (s); 104.8 (d); 105.0 (d); 107.8 (s); 109.9 (s); 110.8 (d); 110.9 (s); 112.3 (d); 115.5 (d); 118.8 (s); 120.4 (d); 123.4 (d); 123.8 (d); 125.4 (s); 127.7 (s); 127.9 (d); 129.3 (s); 130.0 (d); 133.4 (s); 133.5 (s); 135.2 (d); 143.2 (s); 145.1 (s); 146.2 (s); 146.7 (s); 146.8 (s); 147.0 (s); 151.3 (s); 155.5 (s). MS (ESI-TOF) 737 (M, 73), 738 (M+1, 100).

4′-*tert*-Butyldiphenylsilyl-3,11-bis(*tert*-butoxycarbonyl)-Lam-D (*22*) (10d). $(Boc)_2O$ (536 mg, 2.45 mmol) and DMAP (30 mg, 0.25 mmol) were added to a solution of **10c** (605 mg, 0.82 mmol) in CH_2Cl_2 (130 mL). The reaction mixture was stirred at r.t. under Ar for 16 h. The mixture was washed with sat $NaHCO_3$ and brine. The organic layer was dried over anhydrous Na_2SO_4, filtered, and concentrated to dryness to give **10d** as a yellow solid (767 mg, quant). mp (MeCN) 188−189 °C. IR (film) ν 1760, 1710, 1486, 1430, 1274, 1255 cm^{-1}. ^{1}H NMR ($CDCl_3$, 400 MHz) δ 1.15 (s, 9H); 1.56 (s, 9H); 1.57 (s, 9H); 3.40 (s, 3H, OMe); 3.42 (s, 3H, OMe); 3.64 (s, 3H, OMe);

6.83 (s, 1H); 6.90−6.93 (m, 2H); 7.01 (br, 1H); 7.04 (d, J = 7.4 Hz, 1H, H9); 7.23 (s, 1H); 7.25 (d, J = 5.8 Hz, 2H); 7.38−7.46 (m, 6H); 7.74−7.77 (m, 4H); 9.22 (d, J = 7.4 Hz, 1H, H8). ^{13}C NMR ($CDCl_3$, 100 MHz) δ 19.9 (s); 26.7 (q); 27.6 (q); 55.3 (q); 55.6 (q); 55.7 (q); 83.96 (s); 84.02 (s); 106.5 (d); 106.7 (d); 108.9 (s); 111.9 (d); 112.7 (d); 113.1 (s); 115.0 (d); 115.8 (s); 120.3 (d); 120.5 (d); 123.3 (d); 123.4 (d); 123.7 (s); 123.9 (s); 127.7 (s); 127.9 (d); 128.3 (s); 130.0 (d); 133.4 (s); 133.6 (s); 135.1 (d); 140.0 (s); 141.0 (s); 145.3 (s); 145.5 (s); 147.7 (s); 150.8 (s); 151.0 (s); 151.2 (s); 151.5 (s); 155.1 (s). MS (MALDI-TOF) 938 (M+1, 100), 939 (M+2, 63).

4′,11-Bis(*tert*-butyldiphenylsilyl)-3-[3-(2-(2-(2-(2-(2-(2-(2-*tert*-butoxycarbonylaminoethoxy)ethoxy)ethoxy)ethoxy)ethoxy)-ethoxy)propanoyl]Lam-D (*22*) (11). Following the general procedure **C** and starting from **5** (78 mg, 0.80 mmol), **11** as a yellow oil (112 mg, quant) was obtained. IR (film) ν 1710, 1486, 1429, 1283, 1159, 1114 cm^{-1}. ^{1}H NMR ($CDCl_3$, 200 MHz) δ 1.04 (s, 9H); 1.06 (s, 9H); 1.36 (s, 9H); 2.81 (t, J = 6.5 Hz, 2H); 3.07 (s, 3H, OMe); 3.24 (br, 4H, $2CH_2$); 3.29 (s, 3H, OMe); 3.43−3.48 (m, 4H, $2CH_2$); 3.52−3.60 (m, 19H, $8CH_2$, OMe); 3.79 (t, J = 6.5 Hz, 2H); 5.05 (br, 1H); 6.68 (d, J = 7.4 Hz, 1H, H9); 6.75 (s, 1H); 6.81 (br, 2H); 6.85 (s, 1H); 6.91 (br, 1H); 6.95 (br, 1H); 7.03 (s, 1H); 7.24−7.38 (m, 10H); 7.61−7.68 (m, 10H); 9.00 (d, J = 7.4 Hz, 1H, H8). ^{13}C NMR ($CDCl_3$, 100 MHz) δ 19.8 (s); 26.5 (q); 26.7 (q); 28.4 (q); 34.7 (t); 40.3 (t); 54.4 (q); 55.4 (q); 55.6 (q); 66.3 (t); 70.1 (t); 70.5 (t); 105.8 (d); 106.3 (d); 108.1 (s); 111.8 (s); 111.9 (d); 112.6 (d); 115.1 (d); 116.0 (s); 116.5 (d); 119.6 (s); 120.3 (d); 122.5 (d); 123.5 (d); 124.3 (s); 127.4 (s); 127.5 (d); 127.6 (d); 128.0 (s); 128.1 (s); 129.7 (d); 129.8 (d); 132.8 (s); 132.9 (s); 133.3 (s); 134.2 (s); 134.9 (d); 135.1 (d); 139.2 (s); 144.9 (s); 145.3 (s); 146.2 (s); 147.2 (s); 150.8 (s); 151.1 (s); 154.9 (s); 169.2 (s). MS (MALDI-TOF) 1311 (M+1-Boc, 100), 1433 (M+Na, 45).

4′,11-Bis(*tert*-butyldiphenylsilyl)-3-[2-(bis(2-(bis(2-(3-(2-(2-(3-*tert*-butoxycarbonylamino-propoxy)ethoxy)ethoxy)propyl-amino)-2-oxoethyl)amino)ethyl)amino)acetyl]-Lam-D (*22*) (12). A mixture of polystyrene solid supported DMAP (6.0 mg, 19 mmol) and **5** (31 mg, 32 mmol) in dry CH_2Cl_2 (2 mL) was added to a solution of **7** (51 mg, 32 mmol) and EDC·HCl (6 mg, 32 mmol) in dry CH_2Cl_2 (2 mL). The resulting solution was stirred at r.t. for 16 h. The reaction mixture was filtered, and the solvent was removed under vacuum. The residue was purified by flash chromatography with neutral alumina. Elution with CH_2Cl_2/MeOH (99:1 to 98:2) gave **12** as a yellow oil (22 mg, 26%). IR (film) ν 3323, 1665, 1548, 1428, 1275, 1112 cm^{-1}. ^{1}H NMR ($CDCl_3$, 200 MHz) δ 1.11 (s, 9H); 1.13 (s, 9H); 1.41 (s, 18H); 1.42 (s, 18H); 1.61−1.77 (m, 16H); 2.34 (2t, 4H); 2.71−2.78 (m, 4H); 3.12 (s, 3H, OMe); 3.15−3.31 (m, 26H); 3.35 (s, 3H, OMe); 3.47−3.67 (m, 43H); 5.06 (br, 2H); 5.16 (br, 1H); 5.30 (br, 1H); 6.77 (d, J = 7.4 Hz, 1H, H9); 6.84 (s, 1H); 6.88 (br, 2H); 6.92 (s, 1H); 6.97 (br, 1H); 7.00 (br, 1H); 7.12 (s, 1H); 7.32−7.45 (m, 10H); 7.64−7.73 (m, 10H); 9.08 (d, J = 7.4 Hz, 1H, H8). ^{13}C NMR ($CDCl_3$, 100 MHz) δ 15.4 (q); 19.8 (s); 26.6 (q); 26.7 (q); 27.3 (t); 28.4 (q); 29.4 (t); 29.7 (t); 35.3 (t); 37.0 (t); 38.4 (t); 39.5 (t); 54.5 (q); 55.4 (q); 55.7 (q); 57.2 (t); 59.0 (t); 69.3 (t); 69.4 (t); 70.1 (t); 70.4 (t); 70.5 (t); 105.9 (d); 106.4 (d); 108.2 (s); 112.0 (d); 112.9 (d); 115.2 (d); 116.2 (s); 116.6 (d); 119.7 (s); 120.4 (d); 123.5 (d); 124.4 (s); 127.6 (d); 127.7 (d); 128.0 (s); 128.1(s); 129.8 (d); 129.9 (d); 130.0 (s); 132.9 (s); 133.0 (s); 133.4 (s); 134.4 (s); 135.1 (d); 135.2 (d); 138.9 (s); 145.2 (s); 145.4 (s); 146.4 (s); 147.2 (s); 150.9 (s); 151.3 (s); 154.9 (s); 156.1 (s); 159.1 (s); 169.2 (s); 170.7 (s). MS (ESI-TOF) 820 ([M-Boc+3]/3, 100).

4′,11-Bis(*tert*-butyldiphenylsilyl-3-(*tert*-butoxycarbonyl-aminoacetyl)-Lam-D (*22*) (13). Following the general procedure **C** and starting from **5** (99 mg, 1.02 mmol), **13** was obtained as a yellow solid (103 mg, 89%). mp (MeCN) 197−199 °C. IR (film) ν 1711, 1509, 1486, 1429, 1283, 1158 cm^{-1}. ^{1}H NMR ($CDCl_3$, 200 MHz) δ 1.14 (s, 9H); 1.15 (s, 9H); 1.49 (s, 9H); 3.17 (s, 3H, OMe); 3.37 (s, 3H, OMe); 3.62 (s, 3H, OMe); 4.23 (brd, J = 5.0 Hz, 2H); 5.13 (brt, J = 5.0 Hz, 1H); 6.73 (d, J = 7.4 Hz, 1H, H9); 6.85 (s, 1H); 6.91 (br, 2H); 6.93 (s, 1H); 7.02 (br, 1H); 7.05 (br, 1H); 7.12 (br, 1H); 7.36−7.48 (m, 10H); 7.70−7.77 (m, 10H); 9.05 (d, J = 7.4 Hz, 1H, H8). ^{13}C NMR ($CDCl_3$, 100 MHz) δ 19.9 (s); 26.6 (q); 26.7 (q); 28.3 (q); 42.3 (t); 54.5 (q); 55.5 (q); 55.6 (q); 105.8 (d); 106.4 (d); 108.1 (s); 111.7 (d); 111.9 (s); 112.7 (d); 115.2 (d); 116.3 (s); 116.6 (d); 119.7 (s); 120.3 (d); 122.5 (d); 123.5 (d); 124.3 (s); 127.5 (s); 127.6 (d); 127.7 (d); 127.9 (s); 128.1 (s); 129.6 (s); 129.7 (d); 129.9 (d); 132.9 (s); 133.3 (s); 134.2 (s); 135.0 (d); 135.2 (d); 135.4 (s); 138.8 (s); 145.0 (s); 145.3 (s); 146.3 (s); 147.0 (s); 150.8 (s); 151.2 (s); 154.8 (s); 168.3 (s). MS (MALDI-TOF) 1132 (M, 100), 1133 (M+1, 79), 1134 (M+2, 37).

4′,11-Bis(*tert*-butyldiphenylsilyl)-3-[Gly-Gly-Boc-NLS]-Lam-D (*22*) (14). Lamellarin **13** (32 mg, 29 mmol) was treated with 40% TFA in CH_2Cl_2 (10 mL) at 0 °C for 10 min. The solvent was removed under reduced pressure, and the crude was used without further purification. A solution of this residue and DIPEA (4.9 μL, 29 mmol) in dry CH_2Cl_2 (3 mL) was added to a solution of **8** (50 mg, 29 mmol), HOBt (5 mg, 34 mmol), DIPEA (4.9 μL, 29 mmol), and EDC·HCl (7 mg, 34 mmol) in dry CH_2Cl_2 (2 mL). The resulting solution was stirred at r.t. for 4 h. The reaction mixture was diluted with CH_2Cl_2 and washed with sat $NaHCO_3$ solution and brine. The organic phase was dried over anhydrous $MgSO_4$, and the solvent was removed under vacuum. The residue was purified by flash chromatography with neutral alumina: elution with CH_2Cl_2/MeOH (98:2 to 95:5) gave **14** as a yellow oil (46 mg, 58%). IR (film) 3328, 1650, 1534, 1429, 1365, 1281, 1166 cm^{-1}. ^{1}H NMR ($CDCl_3$, 200 MHz) δ 0.92−1.00 (m, 6H, $2CH_3$); 1.11 (s, 3H, CH_3); 1.13 (s, 3H, CH_3); 1.23−1.33 (m, 8H, $4CH_2$); 1.36−1.37 (m, 4H, $2CH_2$); 1.39 (s, 3H, CH_3); 1.41 (s, 18H, $6CH_3$); 1.44−1.50 (m, 4H, $2CH_2$); 1.46−1.50 (m, 8H, $4CH_2$); 1.84 (br, 4H, $2CH_2$); 2.07 (br, 4H, $2CH_2$); 2.43 (br, 4H, $2CH_2$); 2.71 (h, J = 6.8 Hz, 1H); 3.00 and 3.07 (2br, 8H, $4CH_2$); 3.14 (s, 3H, OMe); 3.34−3.41 (m, 2H, CH_2); 3.44 (s, 3H, OMe); 3.59 (s, 3H, OMe); 3.62−3.74 (m, 2H, CH_2); 3.92−4.23 (m, 5H, 5CH); 4.28 (br, 2H, CH_2); 4.47−4.53 (m, 2H, CH_2); 4.67−4.71 (m, 3H, 3CH); 4.77 (br, 1H); 4.86 (br, 1H); 6.67 (s, 1H); 6.71 (d, J = 7.4 Hz, 1H, H9); 6.80−6.89 (m, 2H); 6.91 (d, J = 1.8 Hz, 1H); 6.95−6.99 (m, 2H); 7.02 (d, J = 8.2 Hz, 1H); 7.32−7.47 (m, 10H); 7.56−7.75 (m, 10H); 8.2 (br, 1H); 8.3 (br, 1H); 8.4 (br, 1H); 8.5 (br, 1H); 9.07 (d, J = 7.4 Hz, 1H, H8). ^{13}C NMR ($CDCl_3$, 100 MHz) δ 19.8 (s); 23.6 (t); 23.7 (t); 24.6 (t); 26.2 (t); 26.6 (q); 26.7 (q); 28.0 (q); 28.3 (q); 28.4 (q); 29.5 (t); 29.7 (t); 30.2 (t); 40.4 (t); 47.1 (t); 54.4 (q); 55.48 (q); 55.53 (t); 55.6 (q); 56.4 (d); 56.5 (d); 56.6 (d); 56.7 (t); 63.1 (d); 63.6 (d); 83.2 (s); 103.5 (d); 104.8 (d); 105.9 (d); 109.8 (s); 111.1 (s); 112.2 (d); 115.4 (d); 116.6 (d); 119.7 (s); 120.3 (d); 122.7 (s); 123.7 (d); 124.4 (s); 127.5 (d); 127.6 (d); 127.7 (s); 128.6 (s); 129.2 (s); 129.8 (d); 129.9 (d); 130.0 (s); 132.9 (s); 133.0 (s); 133.4 (s); 135.0 (d); 135.2 (d); 143.3 (s); 145.0 (s); 146.2 (s); 146.3 (s); 146.9 (s); 150.8 (s); 151.2 (s); 153.4 (s); 155.2 (s); 155.9 (s); 156.0 (s); 156.1 (s); 157.4 (s); 170.4 (s); 171.9 (s); 173.1 (s); 174.7 (s); 175.3 (s). MS (ESI) 884 ([M-Boc+3]/3, 24), 1326 ([M-Boc+2]/2, 77).

Cell Lines and Culture. Human-derived established cell lines used in this study were purchased from ATCC (American type Culture Collection): A-549, human lung carcinoma (ATCC no. CCL-185); BJ, skin fibroblast (ATCC no. CRL-2522); HT-29, human colorectal adenocarcinoma (ATCC no. HTB-38); and MDA-MB 231, human breast adenocarcinoma (ATCC no. HTB-26). All cell lines were maintained in DMEM supplemented

with 10% FBS and 100 units/mL penicillin and streptomycin at 37 °C and 5% CO_2.

GI_{50} Analysis. Triplicate cultures were incubated for 72 h in the presence or absence of test compounds Lam-D, **1**, **2**, **4**, and **15** (at ten concentrations, typically ranging from 0.0026 to 10 μg/mL).

A colorimetric assay using SRB was adapted for quantitative measurement of cell growth and viability, following a previously described method (*23*). Cells were plated in 96-well microtiter plates at a density of 5×10^3/well and incubated for 24 h. One plate from each different cell line was fixed, stained, and used for Tz reference (see next paragraph). The cells were then treated with vehicle alone (control) or compounds at the concentrations indicated. Treated cells were incubated for an additional 72 h, and then evaluated for cytotoxicity via colorimetric analysis. The cells were washed twice with PBS, fixed for 15 min in 1% glutaraldehyde solution, rinsed twice in PBS, and stained in 0.4% SRB solution for 30 min at room temperature. The cells were then rinsed several times in 1% acetic acid solution and air-dried. SRB was then extracted in 10 mM trizma base solution and the absorbance measured at 490 nm. Cell survival is expressed as a percentage of control cell growth.

Dose−response curves were obtained by using the NCI algorithm (*24*): Tz = number of control cells at time t_0; C = number of control cells at time t; and T = number of treated cells at time t.

If $Tz < T < C$ (growth inhibition), then the result is $100 \times ([T - Tz]/[C - Tz])$.

If $T < Tz$ (net cell death), then the result is $100 \times ([T - Tz]/Tz)$.

After dose−curve generation, the results were expressed as GI_{50} (the concentration that causes 50% cell growth inhibition, compared to control cultures).

General Treatments for Imaging. A-549, MDA-MB-231, and HT-29 cells were seeded onto MatTek (Ashland, USA) glass-bottomed microwell dishes at 30×10^3 cells/cm^2. After 24 h, the culture medium was discarded and replaced by fresh DMEM medium containing Lam-D, **1**, or **4** at 1 μM. Absence of compound was used as a negative control. Cells were then incubated for 12 h at 37 °C.

Topo I-GFP Visualization. Procedure for a single microwell dish transfection: A-549, MDA-MB-231, and HT-29 cells were seeded onto a MatTek (Ashland, USA) glass-bottomed microwell dish at 30×10^3 cells/cm^2. Culture medium was discarded after 24 h, cells were washed 3 × PBS, and 1400 μL of reduced serum media Opti-MEM I (Invitrogen, USA) were added. The preparation of DNA for transfection required previous dilution of 3 μL FuGENE (Roche Molecular Biochemicals, Indianapolis, IN) in 100 μL of reduced serum media Opti-MEM I (Invitrogen, USA), and further addition of 6.7 μL of the plasmid solution encoding green fluorescent protein GFP with full-length Topo I (*25*). The mixture was mixed thoroughly and incubated for 30 min at r.t., before addition to the dish. Samples were incubated at 37 °C and 5% CO_2 for 10 h. Afterward, medium was discarded, cells were washed three times with PBS, and new DMEM solution containing 1 μM Lam-D, **1**, or **4** was added. Absence of compound was used as a negative control. The cells were incubated for an additional 12 h at 37 °C and then analyzed by confocal microscopy.

Confocal Laser Scanning Microscopy. Confocal laser scanning microscopy was performed with a Leica TCS SPII microscope (Leica Microsystems Heidelberg GmbH, Mannheim, Germany), using a 63× objective. GFP fluorescence was excited with an Ar laser excitation at 488 nm. Lam-D and its derivatives were excited at 351 nm. The same microscope settings were used for each conjugate and concentration. To avoid crosstalk, the two-fluorescence scanning was performed in a sequential mode.

Uptake Measurements by Fluorescence-Activated Cell Sorting Flow Cytometry. 1×10^6 A-549, BJ, MDA-MB-231, and HT-29 cells were seeded onto 25 cm^2 cell culture flasks (Nalgene Nunc International, Naperville, USA) with 10 mL of DMEM. After 12 h, the culture medium was discarded and replaced by fresh DMEM medium containing compounds 1 μM Lam-D, **1**, **2**, or **4**. Absence of compound was used as a negative control. The cells were then incubated for 12 h at 37 °C. After incubation, the cells were washed three times with PBS, detached with trypsin−EDTA 0.25%, and centrifuged at 1000× rpm. Finally, the medium was decanted, and the cellular pellet was resuspended in PBS and kept at 0 °C until measurements were performed. Fluorescence analysis was performed with a MoFlo cytometer (DakoCytomation, Colorado, USA), using the 351 nm excitation line of an Ar laser (25 mW) and emission detection at 450 nm (tolerance range ±65 nm). CIQ is expressed as a percentage value in reference to Lam-D. It was calculated by dividing the fluorescence value of the test compound by the fluorescence value obtained with the Lam-D control under the same experimental conditions.

RESULTS

Orthogonal protecting groups had to be used for the three phenol groups of Lam-D and for the functional groups presented into the conjugation building blocks. *N*-Boc was used to protect the amino and guanidino groups of the oligomeric building blocks **7** and **8**. Synthesis of compounds **2**−**4** required the preparation of different building blocks: the protected Lam-D derivatives **5** and **6**, the DTPA-PEG dendrimer **7**, and the peptide **8** (Figure 2). Compounds **5** and **6** are the precursors for the conjugates at positions 3 and 4′, respectively, and contain two phenolic groups protected as either TBDPS ethers or Boc esters, respectively. In the protected peptide **8**, a glycine was introduced as spacer at the C-terminal position to avoid the steric hindrance caused by the C-terminal Val residue during coupling.

Synthesis of Protected Lamellarins 5 and 6. The protecting groups *Oi*Pr/*O*Bn used in earlier strategies (*9*) required harsh deprotection conditions incompatible with the synthesis of more complex Lam-D conjugates such as **4**.[2] The previously described lamellarin **9** (*26*, *27*), for which three different and orthogonal protecting groups were employed (MOM, Bn, and TBDPS), was used as the precursor to Lam derivatives **5** and **6** (Scheme 1).[3] Lam **9** was prepared following Banwell's strategy for the total synthesis of Lam-K (*28*). Oxidation of **9** under MW irradiation using DDQ in $CHCl_3$ gave **10** with good yield. Compound **10** was subjected to changes of protecting groups (see Scheme 1). Catalytic hydrogenation of **10** over Pd−C in methanolic EtOAc gave **10a**, which was successfully converted into **10b** by TBDPS protection of the phenol. Removal of the MOM protecting group at position 3 of **10b** with trimethylsilyl iodide in $CHCl_2$ gave **5** in excellent yield. Moreover, compound **10a** was subjected to the latter conditions, which afforded the 4′-*O*TBDPS mono-protected Lam-D **10c** in quantitative yield. The free phenol groups of **10c** were protected as *tert*-butyl carbonates using Boc_2O, DMAP, and CH_2Cl_2 to give **10d** in quantitative yield. Finally, *O*TBDPS deprotection of **10d** with TBAF in MeOH gave the 4′-OH Lam-D intermediate **6** (85%).

As a side note, compounds **10a** and **10c** are privileged synthetic intermediates for the construction of additional mono-

[2]Conjugate **4** protected with *Oi*Pr on positions 3 and 11, and Boc-Lys, Boc-Pro and Pbf-Arg gave only mixtures on deprotection assays.

[3]The ester bonds of the protected Lam-D conjugates were labile; hence, to avoid problems with hydrolysis, we minimized the deprotection steps after condensation.

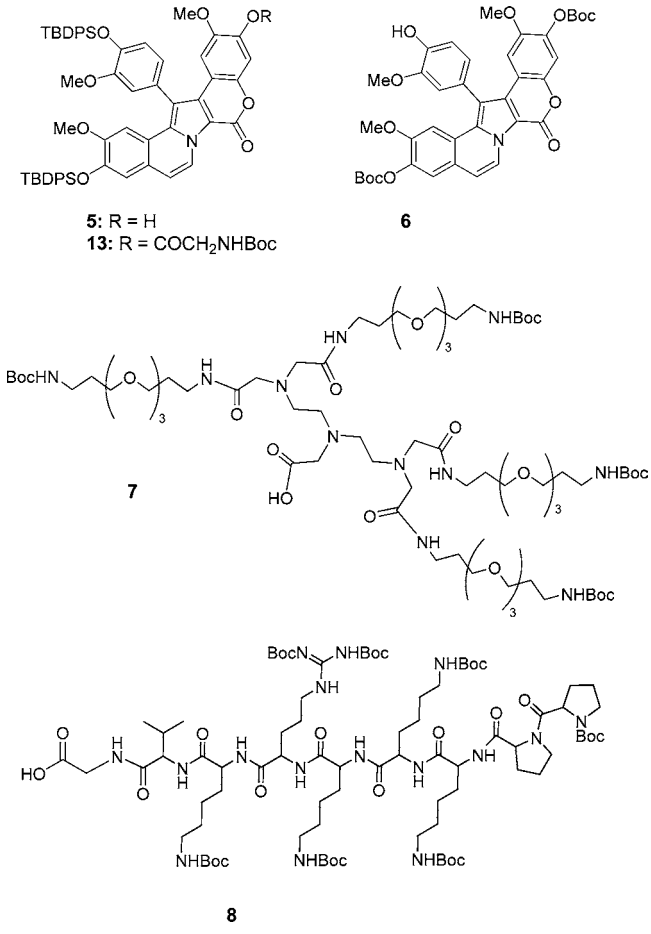

Figure 2. Building blocks for the synthesis. The UV emissions corresponding to Lam-D, **1**, and **4** are arbitrarily represented in red tones. The test compounds were seeded at a concentration of 1 μM and then incubated for 12 h.

and diconjugates at positions 11-OH and 3,11-OHs of Lam-D, respectively.

Synthesis of Poly(ethylene glycol)-Based Dendrimer 7. PEG-based dendrimer **7** was synthesized by coupling 1-(*tert*-butyloxycarbonylamino)-4,7,10-trioxa-13-tridecanamine to monobenzyl-protected diethylenetriamine pentaacetic acid with PyBOP and DIPEA. The tetracarboxylic moiety derivative was prepared from an orthogonally protected DTPA derivative (one benzyl and four *tert*-butyl protecting groups). The *t*Bu groups were eliminated using 4.0 M HCl in dioxane, and then, the benzyl group was eliminated by hydrogenolysis with Pd/C to render dendrimer **7** (*29*).

Synthesis of the Peptide NLS 8. The protected peptide **8** was synthesized on chlorotrityl resin following standard Fmoc/*t*Bu solid-phase chemistry, with 20% piperidine-DMF for the deprotection steps, and DIPCDI and HOBt as coupling reagents.

N-α-Fmoc-*N*-ω,*N*-ω′-bis-*tert*-butoxycarbonyl-L-arginine was used for the synthesis of the NLS peptide sequence. Attempts to use Fmoc-*N*-ω-Pbf-L-arginine resulted in harsher deprotection conditions and complex reaction crudes. The last amino acid used was Boc-L-Pro-OH (as the desired building block had to be completely protected). The peptide was cleaved from the resin using 3% TFA in CH_2Cl_2, and after solvent evaporation, it was lyophilized.

Esterification and Synthesis of Conjugates 1−4. To test the efficacy of the protecting scheme, the synthesis of bioconjugate **1** was repeated using the following strategy (*21*). An ester bond between **5** and BocNH-$CH_2(CH_2OCH_2)_6CH_2$COOH was formed using EDC·HCl with a catalytic amount of DMAP to afford compound **11** (Figure 1) in quantitative yield. Compound **11** was considered a good model for the deprotection assays, because it contains the critical protecting groups and the ester functional group. Hence, it was used for the optimization of procedures and to test the success of the deprotection steps. Initial assays of sequential TBAF-TFA, two-step deprotection led to complex crude products. Furthermore, purification on SiO_2 gave low yields of **1**. The best results were obtained via simultaneous deprotection of both groups, using liquid HF at low temperature. Highly pure final product was obtained from the reaction crude by precipitation with MTBE. Notwithstanding, the scope of the reaction was limited to small amounts of starting material.[4] Compound **1** was synthesized in 84% overall yield from its precursor **5**. This is a major improvement over previous *Oi*Pr/*O*Bn strategies (45% yield, from 4′,11-diisopropyl-Lam-D) (*9*).

Formation of an ester bond between **5** and **7** (*29*) afforded compound **12** (Figure 1) in 26% yield, using EDC·HCl with a catalytic amount of PS solid supported DMAP in CH_2Cl_2. Deprotection of compound **12** using HF provided **2** in 36% yield.

Ester bond formation between **8** and protected lamellarin **5** or **6** using EDC·HCl was unsuccessful. The inaccessibility of the carboxylic acid in the *N*-Boc protected oligopeptide sequence **8** or steric hindrance of the free phenolic group in Lam-D building blocks **5** and **6** may have been decisive to the lack of reaction. Various attempts at ester bond formation between **8** and the scaffold **5** were also unsuccessful.[5] Therefore, taking advantage of the relatively easy amide bond formation (i.e., compared to ester bonds), an *N*-Boc-Gly-OH spacer was introduced at position 3 of **5** (affording **13** in 89% yield, Figure 2) for subsequent amide bond formation with **8**. *N*-Boc deprotection of **13** with 40% TFA followed by reaction with **8** in EDC·HCl, HOBt, and DIPEA as base gave **14** (Figure 1, 58% yield). Deprotection of **14** with HF under standard conditions afforded the NLS peptidic conjugate **3** in 38% yield.

The NLS conjugate at position 4′ of Lam-D could not be formed using the same conditions employed for ester bond formation between **6** and **8**.[6,7] Instead, preactivation of **8** with TCFH (*30*) and NEt_3 followed by the addition of a solution of **6** and DMAP were required, affording **15** (Figure 1) in 45% yield (relative to 40% transformation of **6**). Elimination of the nine Boc protecting groups with 40% TFA in CH_2Cl_2 gave compound **4** in 17% yield.

The ester bond of compound **3**, which has a double Gly spacer, is more susceptible to nucleophilic attack by nucleophiles from the medium than that of compound **4**, which has a single Gly spacer. Thus, the final conjugate **3** (derived from **14**) was water-labile. The rapid degradation of **3** made biological tests with this compound impossible.[8]

Cytotoxicity and Cellular Uptake. The cytotoxicity of Lam-D and its analogues (**1**, **2**, **4**, and **15**) was evaluated against BJ human skin fibroblasts, and a panel of three human tumor

[4]The yield for the deprotection was 84% working on a 20−30 mg scale. However, the procedure could not be scaled up. The stability **1** was studied in DMEM supplemented with 10% FBS and 100 units/mL penicillin and streptomycin at 37 °C. HPLC analysis indicates 97% of Lam-D liberation after 360 min of incubation.

[5]Esterification of **5** was tested with EDC·HCl, TCFH, or *N*,*N*,*N*′,*N*′-tetramethylcholorformamidyl chloride as activating agent.

[6]*N*-Cbz-Gly-OH was anchored to **6** in quantitative yield. However, further Cbz deprotection could not be performed without concomitant hydrolysis of the conjugate ester bond.

[7]Other coupling reagents such as EDC·HCl, DIPCDI, TFFH, PyBOP with HOAt, and MSNT with NMI failed in ester bond formation.

[8]Compound **3** quickly hydrolyzes and liberates Lam-D into the medium, even on the time scale of an HPLC analysis.

Scheme 1[a]

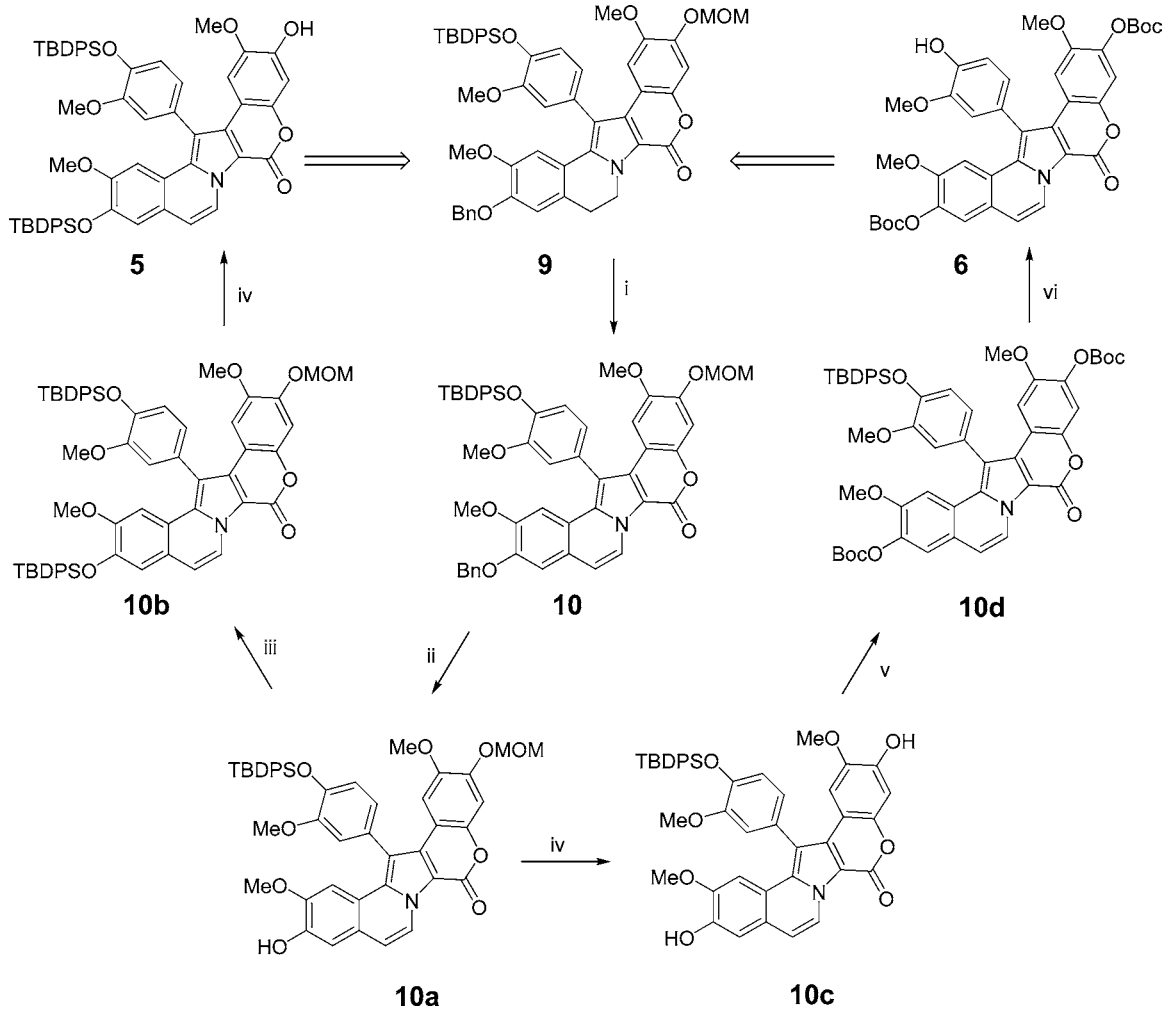

[a] Reagents and conditions: (i) DDQ, $CHCl_3$, MW, 120 °C, 10 min (81%); (ii) H_2, Pd−C, EtOAc, MeOH, r.t., 16 h (95%); (iii) TBDPSCl, Im, DMAP, DMF, r.t., 24 h (58%); (iv) Me_3SiI, CH_2Cl_2 r.t., 20 min (84% for **5**; quant. yield for **10c**); (v) Boc_2O, DMAP, CH_2Cl_2 r.t., 16 h (quant.); (vi) 1M TBAF in THF, MeOH, −78 °C, 15 min (85%).

Table 1. Cytotoxicity of Compounds 1, 2, 4, and 15 in Three Human Cancer Cell Lines

	cytotoxicity (M)			
compound	HT-29 colon	A-549 lung	MDA-MB-231 breast	BJ skin fibroblast
Lam-D	3.00×10^{-6}	1.22×10^{-7}	1.34×10^{-7}	6.37×10^{-9}
1	1.68×10^{-6}	8.86×10^{-8}	4.07×10^{-8}	6.51×10^{-9}
2	3.92×10^{-6}	2.20×10^{-7}	8.31×10^{-8}	1.54×10^{-8}
4	1.01×10^{-6}	4.79×10^{-8}	4.79×10^{-8}	3.14×10^{-8}
15	1.94×10^{-6}	n.d.	1.24×10^{-6}	–

cell lines: A-549, HT-29, and MDA-MB-231 (Table 1). A conventional colorimetric assay was used to estimate values of GI_{50} (defined here as the drug concentration that causes 50% of cell growth inhibition after 72 h of continuous exposure to the test molecule). Lam-D was included for comparison. The results are shown in Table 1. The tested compounds in the tumor cell lines exhibited cytotoxicities from 4 μM to 40.7 nM, except for the Boc protected derivative **15**, which only had micromolar activity for the HT-29 and MDA-MB-231 cell cultures. BJ skin fibroblasts were used in the present study to evaluate the effects of the drug and its conjugates in normal cells. In this non-tumoral cellular culture, conjugate **1** citotoxicity was similar to that of Lam-D, or even 2.4−4.9-fold less for **2** and **4**.

FACS flow cytometry was used to measure cellular uptake quantification (*9*). The results are shown in Table 2. Interestingly, the cellular internalization quotient for the PEGylated derivatives **1** and **2** were higher than that of Lam-D in all cancer cell lines. Indeed, compound **4**, with an NLS sequence, was 10 times more active than Lam-D in A-549 and MDA-MB-231 cell lines and retained CIQ, despite having the highly charged NLS peptide. CIQ of conjugates in BJ cellular culture were from 76.8% to 128.6%.

Table 2. Cellular Internalization as Measured by FACS

	cellular internalization (AU)				cellular internalization quotient (CIQ)[a]			
compound	HT-29 colon	A-549 lung	MDA-MB-231 breast	BJ skin fibroblast	HT-29 colon	A-549 lung	MDA-MB-231 breast	BJ skin fibroblast
Lam-D	82.7	328.5	443.8	259.4	100%[a]	100%[a]	100%[a]	100%[a]
1	88.0	393.0	527.5	333.4	106%	120%	119%	128.6%
2	83.7	374.9	455.3	199.2	101%	114%	103%	76.8%
4	88.5	377.7	434.9	240.6	107%	115%	98%	92.8%

[a] CIQ was calculated in reference to the cellular uptake of Lam-D.

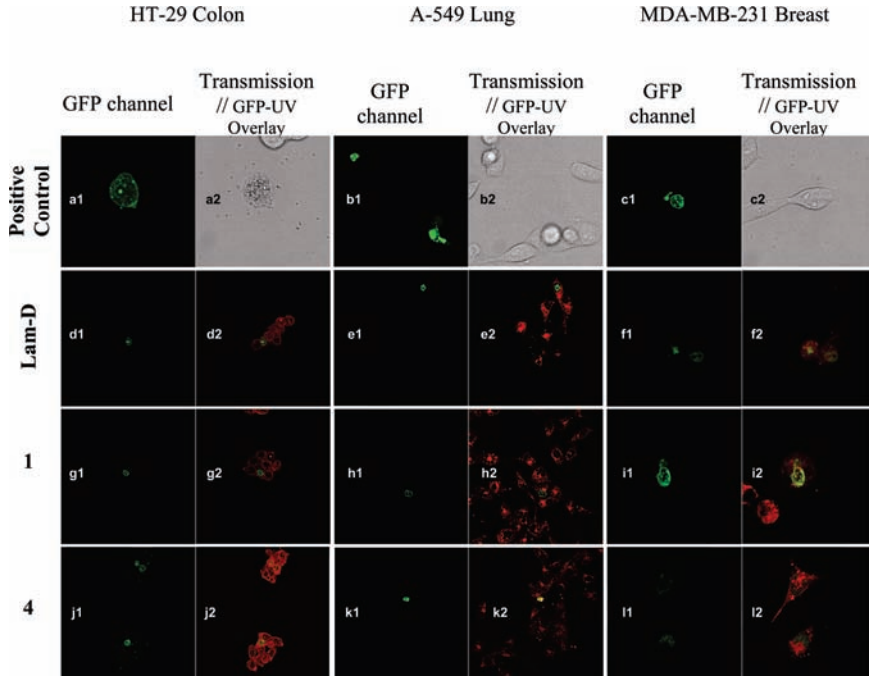

Figure 3. Internalization of Lam-D and conjugates **1** and **4** by Topo I-GFP transfected cells.

Cellular Distribution of Lam-D, 1 and 4. Tracking in GFP-Topo I Transfected Cell Cultures. Lam-D is a Topo I inhibitor. To determine whether Lam-D, **1**, and **4** localize to the same subcellular compartment as Topo I, a cellular localization assay was performed. A functional chimera of the green fluorescent protein EGFP with full-length Topo I (GFP-Topo I) was expressed in HT-29, A-549, and MDA-MD-231 cells, which were then treated with either Lam-D, **1**, or **4**. As described, GFP-Topo I was located in the nucleus (*25*) in all cell types (Figure 3, positive control). Conjugate **4**, carrying the NLS signal, was localized to the nucleus in HT-29 and A-549 cells (Figure 3, **j1**, **j2**, **k1**, and **k2**), suggesting that its higher activity could correlate to subcellular colocalization with its target, Topo I.

Interestingly, Lam-D and **1** showed both higher activity and greater nuclear localization in MDA-MB-231 cells than **4** did (Figure 3, **f1**, **f2**, **i1**, and **i2**).

DISCUSSION

We have described the synthesis of Lam-D conjugates with well-defined, water-soluble peptidic and dendritic systems as potential nontoxic drug delivery vehicles. Interestingly, the Lam-D conjugate containing a single backbone attached to a phenolic residue of Lam-D has very different solubility compared to Lam-D alone. Scaffold **10**, with three orthogonal protecting groups, has proven to be a good starting material, enabling synthesis of **5** and **6**, via protection group interchange, on a multigram scale and in good overall yield. New protected derivatives of Lam-D, which can be conjugated to one (C^{11}−OH, **10a**) or two (C^{3}−OH and C^{11}−OH, **10b**) phenol groups, have been isolated in good yields with this strategy. Compound **1** was synthesized in 84% overall yield from its precursor **5**; this constitutes an important improvement over previous strategies (45% yield, from 4′,11-diisopropyl-Lam-D) (*9*). Simultaneous removal of TBDPS*O* and *N*Boc with HF is a new and highly efficient deprotection scheme for compounds with labile ester bonds. The *O*Boc and TBDPS*O* protecting groups used in lamellarins **5** and **6** permitted optimization of the final deprotection conditions and represented adequate choices for total deprotection in the last step. Thus, single-step HF deprotection was the cleanest method for preparing Lam-D **1-3** (9−84% overall yields from **5**).

The new Lam-D conjugates reported here are excellent candidates for further biological evaluation. The evaluation of conjugates **3** and **4** in BJ skin fibroblasts as normal cells was used in the present study. In this cellular culture, no significant variation or even less cytotoxicity was obtained for conjugates **3** and **4** than the parent compound Lam-D. PEGylated conjugates **1** and **2** have much higher cytotoxicity to MDA-MB-231 cells than Lam-D alone. Surprisingly, compound **4** had nanomolar GI_{50} for MDA-MB-231 and A-549, representing 10-fold-lower GI_{50}, respectively, compared to Lam-D. These results in the A-549 cancer cell line could correlate to colocalization of **4** in nuclear regions where GFP−Topo I accumulated (Figure 3k). The NLS peptidic sequence is at least partly responsible for nuclear import of **4** in A-549 and HT-29 cell lines. In contrast, Lam-D and **1** were able to weakly reach the nucleus in only MDA-MB-231 cells. Altogether, we conclude that better cytotoxicity correlates with greater nuclear localization.

In summary, the use of a robust chemistry strategy, with a combination of solid-phase and solution strategies and a myriad of orthogonal and/or compatible protecting groups, has allowed the preparation of several Lam-D bioconjugates. All of them show some improved characteristics when compared with the parent lamellarin D. Particularly, **4**, which contains the NLS-peptide, shows a clearly improved cytotoxicity and a colocalization in the nucleus. To the best of our knowledge, **4** is one of the first examples of NLS peptide conjugation with small molecules.

Our results (*9*) indicate that Lam-D derivatives obtained through various chemical modifications may have markedly higher activity than the parent compound in certain tumor cell lines, increasing the selectivity between the tumor cell lines.

ACKNOWLEDGMENT

This study was partially supported by CICYT (Grant BQU 2006-03794 and BQU2005-00315), *Generalitat de Catalunya*, and the Barcelona Science Park. We gratefully acknowledge PharmaMar S.A. for performing the preliminary biological tests, and the Networking Centre on Bioengineering, Biomaterials and

Nanomedicine (CIBER-BBN). This study was partially supported by the Industrial Consortium "NanoFarma" from the Spanish grants of CENIT program. We thank Dr. J. Comas from Flow Cytometry Facility − SCT (UB) for valuable discussions regarding the present work. We also thank Prof. C. Mielke (Heinrich-Heine University, Medical School, Düsseldorf) for generous donation of a sample of GFP−Topo I plasmid.

LITERATURE CITED

(1) Vicent, M. J., and Duncan, R. (2006) Polymer conjugates: nanosized medicines for treating cancer. *Trends Biotechnol. 24*, 39–47.

(2) Torchilin, V. P. (2005) Lipid-core micelles for targeted drug delivery. *Curr. Drug Delivery 2*, 319–327.

(3) Lukyanov, A. N., and Torchilin, V. P. (2004) Micelles from lipid derivatives of water-soluble polymers as delivery systems for poorly soluble drugs. *Adv. Drug Delivery Rev. 56*, 1273–1289.

(4) Greenwald, R. B., Pendri, A., Conover, C. D., Zhao, H., Choe, Y. H., Martínez, A., Shum, K., and Guan, S. (1999) Drug delivery systems employing 1,4- or 1,6-elimination: poly(ethylene glycol) prodrugs of amine-containing compounds. *J. Med. Chem. 42*, 3657–3667.

(5) Nori, A., and Kopecek, J. (2005) Intracellular targeting of polymer-bound drugs for cancer chemotherapy. *Adv. Drug Delivery Rev. 57*, 609–636.

(6) de Koning, M. C., van der Marel, G. A., and Overhand, M. (2003) Synthetic developments towards PNA-peptide conjugates. *Curr. Opin. Chem. Biol. 7*, 734–740.

(7) Yoshikawa, T., Sugita, T., Mukai, Y., Yamanada, N., Nagano, K., Nabeshi, H., Yoshioka, Y., Nakagawa, S., Abe, Y., Kamada, H., Tsunoda, S.-i., and Tsutsumi, Y. (2008) Organelle-targeted delivery of biological macromolecules using the protein transduction domain: potential applications for peptide aptamer delivery into the nucleus. *J. Mol. Biol. 380*, 777–782.

(8) Boulanger, C., Di Giorgio, C., and Vierling, P. (2005) Synthesis of acridine-nuclear localization signal (NLS) conjugates and evaluation of their impact on lipoplex and polyplex-based transfection. *Eur. J. Med. Chem. 40*, 1295–1306.

(9) Pla, D., Francesch, A., Calvo, P., Cuevas, C., Aligué, R., Albericio, F., and Álvarez, M. (2009) Lamellarin D bioconjugates I: synthesis and cellular internalization of PEG-derivatives. *Bioconjugate Chem.* . the previous article in the same issue.

(10) Crespo, L., Sanclimens, G., Pons, M., Giralt, E., Royo, M., and Albericio, F. (2005) Peptide and amide bond-containing dendrimers. *Chem. Rev. 105*, 1663–1682.

(11) Maeda, H., Wu, J., Sawa, T., Matsumura, Y., and Hori, K. (2000) Tumor vascular permeability and the EPR effect in macromolecular therapeutics: a review. *J. Control. Release 65*, 271–284.

(12) Pla, D., Albericio, F., and Álvarez, M. (2008) Recent advances in lamellarin alkaloids: isolation, synthesis and activity. *Anti-Cancer Agents Med. Chem. 8*, 746–760.

(13) Facompré, M., Tardy, C., Bal-Mayeu, C., Colson, P., Pérez, C., Manzanares, I., Cuevas, C., and Bailly, C. (2003) Lamellarin D: a novel potent inhibitor of topoisomerase I. *Cancer Res. 63*, 7392–7399.

(14) Marco, E., Laine, W., Tardy, C., Lansiaux, A., Iwao, M., Ishibashi, F., Bailly, C., and Gago, F. (2005) Molecular determinants of topoisomerase I poisoning by lamellarins: comparison with camptothecin and structure-activity relationships. *J. Med. Chem. 48*, 3796–3807.

(15) Kluza, J., Gallego, M. A., Loyens, A., Beauvillain, J. C., Fernández Sousa-Faro, J. M., Cuevas, C., Marchetti, P., and Bailly, C. (2006) Cancer cell mitochondria are direct proapoptotic targets for the marine antitumor drug lamellarin D. *Cancer Res. 66*, 3177–3187.

(16) Cortés, F., Pastor, N., Mateos, S., and Domínguez, I. (2007) Topoisomerase inhibitors as therapeutic weapons. *Expert Opin. Ther. Patents 17*, 1–12.

(17) Holden, J. A. (2001) DNA topoisomerases as anticancer drug targets: from the laboratory to the clinic. *Curr. Med. Chem.: Anti-Cancer Agents 1*, 1–25.

(18) Dias, N., Vezin, H., Lansiaux, A., and Bailly, C. (2005) Topoisomerase inhibitors of marine origin and their potential use as anticancer agents. *Top. Curr. Chem. 253*, 89–108.

(19) Pommier, Y. (2006) Topoisomerase I inhibitors: camptothecins and beyond. *Nat. Rev. Cancer 6*, 789–802.

(20) Alberts, B., Johnson, A., Lewis, J., Raff, M., Roberts, K., and Walter, P. (2007) *Molecular Biology of the Cell*, Garland Science, London.

(21) Veronese, F. M., and Harris, J. M. (2008) Peptide and protein PEGylation III: advances in chemistry and clinical applications. *Adv. Drug Delivery Rev. 60*, 1–2.

(22) IUPAC nomenclature of Lam-D: 3,11-dihydroxy-2,12-dimethoxy-14-(4-hydroxy-3-methoxyphenyl)-6*H*[1]benzopyrano-[4′,3′:4,5]pyrrolo[2,1-*a*]isoquinoline-6-one.

(23) Skehan, P., Storeng, R., Scudiero, D., Monks, A., McMahon, J., Vistica, D., Waren, J. T., Bokesch, H., Kenney, S., and Boyd, M. R. (1990) New colorimetric cytotoxicity assay for anticancer drug screening. *J. Natl. Cancer Inst. 82*, 1107–1112.

(24) Boyd, M. R., and Paull, K. D. (1995) Some practical considerations and applications of the National Cancer Institute in vitro anticancer drug discovery screen. *Drug Dev. Res. 34*, 91–104.

(25) Mielke, C., Kalfalah, F. M., Christensen, M. O., and Boege, F. (2007) Rapid and prolonged stalling of human DNA topoisomerase I in UVA-irradiated genomic areas. *DNA Repair 6*, 1757–1763.

(26) Cironi, P., Manzanares, I., Albericio, F., and Álvarez, M. (2003) Solid-phase total synthesis of the pentacyclic system lamellarins U and L. *Org. Lett. 5*, 2959–2962.

(27) Bailly, C., Francesch, A., Mateo, C., Jiménez, J. A., Pastor, A., and Cuevas, C. (2004) Pharma Mar, S. A. U., WO 2004/014917 A2, pp 220.

(28) Banwell, M., Flynn, B., and Hockless, D. (1997) Convergent total synthesis of Lamellarin K. *Chem. Commun.* 2259–2260.

(29) The synthesis of **7** is part of a dendrimer project and will be published in due time.

(30) Tulla-Puche, J., Torres, A., Calvo, P., Royo, M., and Albericio, F. (2008) *N*,*N*,*N*′,*N*′-Tetramethylchloroformamidinium hexafluorophosphate (TCFH), a powerful coupling reagent for bioconjugation. *Bioconjugate Chem. 19*, 1968–1971.

BC800504T

End-Functionalized Polymers and Junction-Functionalized Diblock Copolymers Via RAFT Chain Extension with Maleimido Monomers

Scott M. Henry, Anthony J. Convertine, Danielle S. W. Benoit, Allan S. Hoffman, and Patrick S. Stayton*

Department of Bioengineering, University of Washington, Seattle, Washington 98195. Received October 8, 2008; Revised Manuscript Received February 4, 2009

A new strategy is described for functionalizing the ω-terminal end of polymers synthesized by reversible addition−fragmentation chain transfer (RAFT) polymerization that provides spatially controlled bioconjugation sites. Traditional methods for preparing ω-functional polymers require the reduction of the RAFT chain-transfer agent to yield secondary or tertiary thiols of low reactivity or the synthesis of novel chain-transfer agents that contain reactive groups. As an additional strategy, N-substituted maleimido monomers have been used in a modified block polymerization to add a single maleimido unit onto the RAFT polymer with nearly quantitative efficiency. Unique reactive groups contained in the N-substituent are thereby added to the ω-terminal end of the polymer and are subsequently available for conjugation reactions. This technique has been demonstrated using *N*-(2-aminoethyl)maleimide trifluoroacetate to introduce a single primary amine to the ω-terminus of poly(dimethylaminoethyl methacrylate) and poly(*N*-isopropyl acrylamide) and to a specialized block copolymer for siRNA delivery. Evidence for retention of functional RAFT endgroups is provided by synthesis results where chain-extended polyDMAEMA (M_n = 10 600 g/mol, M_w/M_n = 1.14) was used as a macro chain transfer agent for the polymerization of styrene, yielding a diblock polymer of low polydispersity (M_n = 20 300 g/mol, M_w/M_n = 1.11). It is thus also possible to construct diblock copolymers with a bioconjugation site precisely located at the junction between the two blocks. The chain-extended polymers are functionalized with an amine-reactive fluorescent dye or folic acid at conjugation efficiencies of 86 and 94%, respectively. The versatile chain-extension technique described here offers unique opportunities for the synthesis of well-defined polymeric conjugates to molecules of biological and targeting interest.

INTRODUCTION

Controlled radical polymerization (CRP) techniques such as nitroxide-mediated polymerization (NMP) (*1*), atom transfer radical polymerization (ATRP) (*2*), and reversible addition−fragmentation chain transfer polymerization (RAFT) (*3, 4*) offer the ability to produce polymers with predetermined molecular weights, narrow molecular weight distributions, and advanced architectures. For RAFT polymerizations, numerous groups have reported the incorporation of diverse monomers in both organic and aqueous conditions (*5*−*11*). One particularly significant feature of RAFT is that it allows a facile route to prepare telechelic polymers with distinct α and ω functionalities. This feature provides a useful tool for the tailored design of novel polymeric conjugates via coupling to fluorescent dyes, nanoparticles, drugs, peptides, proteins, or targeting moieties (*12*−*17*). In particular, reactive α and ω endgroups offer unique opportunities for the synthesis of well-defined polymeric drug carriers that incorporate both targeting and therapeutic moieties.

Functional endgroups can be prepared using ATRP by modifying the initiator (*18, 19*) or by RAFT through modifications to the chain transfer agent (CTA). The majority of literature reports have focused on RAFT CTAs with functional R groups (*16, 17, 20*−*23*), largely due to the greater stability of the R group following polymerization. Notable examples of RAFT agents with functional Z groups also exist. Liu et al. (*24*) prepared a novel trithiocarbonate CTA containing a pyridyl disulfide group in the Z position that allows for direct coupling to thiol-bearing molecules without postpolymerization modifications. Similarly, Carter et al. prepared a highly branched polymer with imidazole endgroups by employing a Z-functional dithioester (*25*). However, preparation of Z-functionalized RAFT CTAs often requires more difficult synthetic protocols, and many desirable chemical moieties are unsuitable for incorporation into CTA moieties.

RAFT CTAs based on xanthates, dithioesters, dithiocarabamates, and trithiocarbonates can be reduced with primary amines (*26*−*28*) or $NaBH_4$ (*12, 13*) to yield a polymeric thiol endgroup that can be used for conjugation reactions (*29*−*33*). While conjugations to secondary thiols (from styrenic and non-α-substituted monomers) or tertiary thiols (from α-substituted monomers) have been described (*11, 13, 14, 26, 34, 35*), these reactions typically require elevated temperatures, long reaction times, and stoichiometric ratios that can be problematic for many molecules of biological interest due to their expense or instability. A route around this reactivity barrier was described by Scales et al. (*13*), who showed that a secondary thiol could be reacted with a small linker-like molecule for subsequent conjugations. Similarly, York et al. (*34*) obtained 80% conjugation of a fluorescent dye to an α-substituted *N*-(2-hydroxypropyl) methacrylamide block copolymer following reduction of the CTA and subsequent conversion of the tertiary thiol to a primary amine. However, these conversions require reaction conditions that may prove impractical for many polymer compositions. Additional routes to the ω-functionalization of RAFT polymers are needed that are compatible with a wide range of monomers and can be conducted at the time of synthesis under mild conditions.

Our research group has been interested in applications of stimuli-responsive "smart" polymers for therapeutic and diag-

* Corresponding author: Patrick S. Stayton, Ph.D., University of Washington, Department of Bioengineering, Box 355061, Seattle, WA 98195. Tel: (206) 685.8148, Fax: (206) 685.8526, E-mail: stayton@u.washington.edu.

10.1021/bc800426d CCC: $40.75 © 2009 American Chemical Society
Published on Web 05/29/2009

nostic/bioanalytical applications. The therapeutic applications utilize pH-responsive polymers for intracellular delivery of macromolecular biologics such as proteins, peptides, antisense DNA, and small interfering RNA (siRNA) (*36*−*42*). Additionally, we have worked on the development of stimuli-responsive polymers for bioseparations and diagnostic applications (*43*−*45*). These applications would benefit from more efficient chemistries for spatially controlled ω (or Z)-end conjugations, and here, we describe a technique for functionalizing the ω-terminal end of RAFT polymers by chain extension using N-substituted maleimides. Maleimido monomers readily undergo copolymerization with other species but do not efficiently homopolymerize under typical RAFT conditions (*46*−*50*). We show that this property can be exploited in a block polymerization in order to add a single amine-substituted maleimido unit to the end of a RAFT polymer. Because a high percentage of the maleimido-terminated chains are living and a second block can be polymerized from this macro-CTA, the reactive amine can also be positioned precisely at the junction of AA or AB block segments, providing spatial control over the position of a branched bioconjugation site.

EXPERIMENTAL DETAILS

Materials. All reagents were purchased from Sigma-Aldrich and used without further purification unless otherwise noted. Dimethylaminoethyl methacrylate (DMAEMA), butyl methacrylate (BMA), and styrene were purified by vacuum distillation. *N*-Isopropylacrylamide (NIPAM) was recrystallized from hexanes. Propylacrylic acid (PAA) was synthesized as previously published (*51*). Unless noted otherwise, the primary radical source used in all polymerizations was 2,2-azobisisobutyronitrile (AIBN), which was recrystalized from methanol. The trithiocarbonate CTA ethyl cyanovaleric trithiocarbonate (ECT) was synthesized as previously described (*41*) and used as the CTA in all RAFT polymerizations. All polymerizations were conducted under N_2 atmosphere.

RAFT polymerization of pDMAEMA and p(DMAEMA-*b*-DMAEMA/BMA/PAA). Poly(DMAEMA) was obtained by RAFT polymerization using experimental conditions appropriate to target the various molecular weights used in this study. As an example of typical conditions, the $[CTA_o]/[I_o]$ ratio was10:1, the $[CTA_o]/[M_o]$ ratio was 1:150, and the monomer was 50 wt % in *N*,*N*′-dimethylformamide (DMF). The polymerization was conducted at 60 °C for 7 h. The molecular weight and polydispersity were 8100 g/mol and 1.21, respectively. All DMAEMA polymers were isolated by precipitation in an 80/20 v/v pentane/ether mixture, followed by repeated cycles of dissolution in ether and precipitation in pentane. The polymer was dried under vacuum overnight. Molecular weight distributions were determined by gel permeation chromatography (GPC).

The block copolymer p(DMAMEA-*b*-DMAEMA/BMA/PAA) was prepared following previously described protocols (*41*). Briefly, a pDMAEMA macro CTA (M_n = 9000 g/mol, M_w/M_n = 1.30) was employed for the polymerization of the copolymer block using a $[CTA_o]/[I_o]$ ratio of 10:1 and a $[CTA_o]/[M_o]$ ratio of 1:250 in DMF at 40 wt % monomer. The composition of the feed was 40 mol % butylmethacrylate (BMA), 30 mol % propylacrylic acid (PAA), and 30 mol % DMAEMA. 2,2′-Azobis(4-methoxy-2,4-dimethylvaleronitrile) (V70) was the radical source, and the polymerization time was 18 h at 30 °C. The block copolymer was isolated by multiple precipitations in an 80/20 v/v pentane and ether mixture, followed by precipitation in pentane.

RAFT Polymerization of pNIPAM. Poly(NIPAM) was obtained by RAFT polymerization based on previously published conditions (*52*) using a $[CTA_o]/[I_o]$ ratio of 20:1, a $[CTA_o]/[M_o]$ ratio of 1:100, and the monomer was 33 wt % in *p*-dioxane. The polymerization was conducted at 70 °C for 120 min. pNIPAM was isolated by repeated cycles of precipitation into ethyl ether, followed by dissolution in acetone, and dried under vacuum overnight.

Scheme 1. Synthetic Pathway for Maleimido Chain Extension of RAFT Polymers

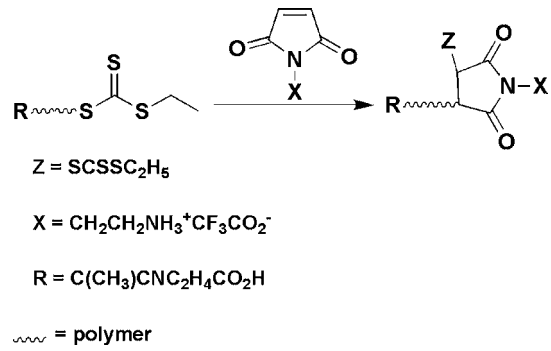

Maleimido Chain Extension. Maleimide chain extension was performed at 60 °C in DMF for 16 h using *N*-(2-aminoethyl)-maleimide trifluoroacetate (AM) as the monomer and poly(DMAEMA), poly(NIPAM), or poly(DMAEMA-*b*-DMAEMA/BMA/PAA) as the macro-CTA (Scheme 1). The polymerizations were conducted with a $[CTA_o]/[I_o]$ ratio of 10:1 and a $[CTA_o]/[M_o]$ ratio of 1:100. The polymerization solution was 60 wt % solvent. As an example of polymerization, 400 mg pDMAEMA (49 μmol) and 1.26 g AM (4.9 mmol) were polymerized with 0.81 mg AIBN (4.9 μmol) in 2.5 g DMF. ^{1}H NMR was used to confirm that the macro-CTAs were free of residual monomer prior to chain extension in order to eliminate the possibility of copolymerization during maleimide chain extension.

Chain-extended pDMAEMA-AM was isolated by six cycles of precipitation in an 80/20 solution of pentane/ether. Between precipitations, the polymer was redissolved in acetone and separated from any insoluble AM by centrifugation and filtration through 0.2 μm syringe filters. Following precipitation, a solution of pDMAEMA-AM was prepared in deionized water (DI) and the polymer was further purified from residual AM monomer using two PD-10 desalting columns (Amersham, Piscataway NJ) in series and lyophilized. Chain-extended pNIPAM-AM was purified from AM by running the reaction mixture through two PD-10 columns following 1:2 dilution in DI, then lyophilized. The extent of AM chain extension was determined using ^{1}H NMR, and the molecular weight distribution was characterized by GPC.

Styrene Polymerization from pDMAEMA-AM. Chain-extended pDMAEMA-AM was used as a macro-CTA for the polymerization of styrene (pDMAEMA-AM-STY) in order to demonstrate retention of functional RAFT chain ends. The $[CTA_o]/[I_o]$ ratio was10:1, the $[CTA_o]/[M_o]$ ratio was 1:250, and the monomer was 50 wt % in DMF. The polymerization was conducted at 60 °C for 24 h, and the polymer was isolated by precipitation in 80/20 v/v pentane/ether as previously described.

Fluorescent Labeling. Amine functionalized pDMAEMA-AM and pDMAEMA-AM-STY were labeled with 1-pyrenebutanoic acid succimidyl ester (PNHS) (Invitrogen). pDMAEMA-AM (75 mg, 10 μmol) was dissolved in 1 mL of anhydrous DMF. Subsequently, diisopropylethylamine (123 mg, 0.96 mmol) was added at 2-fold molar excess relative to the number of DMAEMA residues to ensure removal of the triflate salt from the pDMAEMA-AM primary amine. After 60 min, PNHS (20 mg, 70 μmol) was added to the solution at 7-fold molar excess relative to the number of pDMAEMA-AM chains, and the reaction was allowed to proceed in the dark at room temperature for 18 h under anhydrous conditions. At the end of the reaction

time, free PNHS was precipitated from solution by the addition of 4 mL of DI water and separated by centrifugation. The supernatant was filtered through a 0.2 μm syringe filter, eluted through 2 PD-10 desalting columns, and dried. The sample was then dissolved in 2.5 mL of 50% v/v DI/DMF and eluted through two additional PD-10 columns in series, and frozen and lyophilized. The percent conjugation was determined by GPC using online UV and RI detectors.

pDMAEMA-AM-STY was labeled using a similar procedure, but PNHS was added at 50-fold molar excess to compensate for the increased steric hindrance of the amine caused by the presence of the styrene block. Following labeling, the reaction mixture was added to 50 mL anhydrous ether causing the precipitation of PNHS, which was removed by centrifugation. pDMAEMA-AM-STY was subsequently precipitated from the ether by the addition of 50 vol % pentane and recovered by centrifugation.

To determine the concentration of pyrene associated with pDMAEMA-AM or pDMAEMA-AM-STY, a linear pyrene calibration curve was generated by injecting multiple known concentrations of pyrene on the GPC column and plotting their corresponding UV peak areas at 338 nm. The concentration of pyrene associated with the polymers was subsequently determined by comparison of the polymer conjugate UV peak area ($\lambda = 338$) to the pyrene calibration curve. The UV peak area of the unlabeled polymers was used to account for the contribution of the RAFT CTA to the absorption at 338 nm while maintaining constant RI peak area between the two samples.

Folic Acid Conjugation. Folic acid was activated with dicyclocarbodiimide (DCC) in dry dimethylsulfoxide (DMSO) at a molar ratio of 1:1.1 for 60 min at 4 °C. A solution of pDMAEMA-*b*-DMAEMA/BMA/PAA that had been chain-extended with *N*-(2-aminoethyl)maleimide and TEA (1:1 mol ratio with PAA and AM) in DMSO was added to the activated folate solution (10:1 folate/polymer ratio) and reacted overnight at room temperature. The polymer−folate conjugate was purified by extensive dialysis in water, then lyophilized. The remaining folic acid was separated from the lyophilized conjugate using a series of 5 PD-10 desalting columns until no further reduction in folic acid absorbance ($\lambda = 363$ nm) was observed in the column flow-through. The purified polymer−folate conjugate was dried by lyophilization, and the amount of folate present in the conjugate was determined by UV absorbance relative to a standard curve of free folic acid. No shift in the folate absorbance spectrum was observed as a result of conjugation to the polymer. UV measurements were done in phosphate buffered saline (PBS), pH = 7.4. Concentrations of the polymer−folate conjugate were between 0.1 and 1 mg/mL.

Instrumentation. The polymers in this study were characterized by gel permeation chromatography using three Tosoh TSK-GEL columns (TSK-α3000, α3000, α4000) connected in series to a Viscotek GPCmax VE2001 and Viscotek RI and UV detectors (VE3580 and VE3210, respectively) (Viscotek, Houston, TX). The mobile phase was HPLC-grade DMF containing 0.1 wt % LiBr. Molecular weight distributions were determined relative to a series of poly(methyl methacrylate) standards. Characterization of polymer−folate conjugates was performed on an HP Agilent 8453 UV−vis spectrophotometer. All NMR spectroscopy was done on a Bruker DRX499 system in D_2O.

RESULTS AND DISCUSSION

A single N-substituted maleimido repeat unit can be added to the ω-terminal end of a polymer using RAFT and the common techniques of block polymerization. By varying the identity of the N-substituent, maleimido chain extension provides a method to introduce highly reactive chemical groups at the ω-(Z)-end (Scheme 1). The technique is versatile in that it is compatible with a wide variety of polymers, does not require post-polymerization processing to obtain reactive moieties, and yields functional groups for bioconjugations that are significantly more reactive than the polymeric thiols that can be obtained by CTA reduction. Using the chain extension technique, we have successfully introduced primary amine ω-endgroups to acrylamido and α-substituted methacrylic polymers and at the junction between diblock segments (Figure 1). The utility of the amines has been shown by conjugations to an optical dye and to the targeting moiety folic acid.

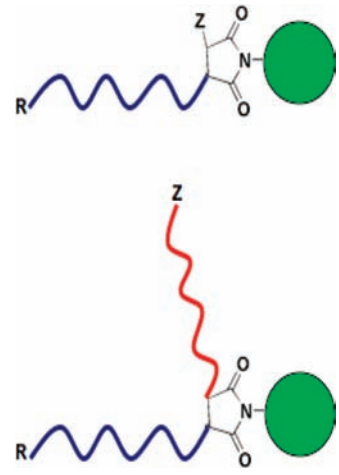

Figure 1. Schematic design of functionalized telechelic RAFT-polymers that provide a convenient route to controlled bioconjugations at the ω(Z)-chain end, or at the branched junction between two block segments. Using the CTA described in the text, the R group is a reactive carboxylate and the Z-group is an unreduced trithiocarbonate or reduced polymeric thiol.

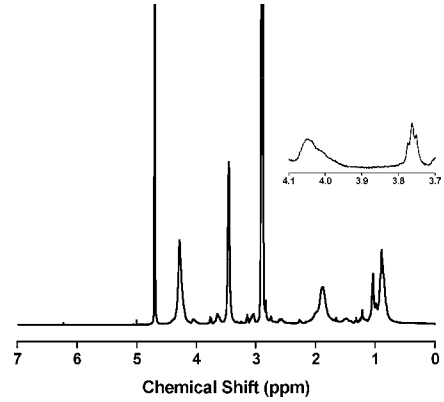

Figure 2. ^{1}H NMR of pDMAEMA after chain extension with *N*-(2-aminoethyl)maleimide trifluoroacetate (AM). The inset shows the triplet at $\delta = 3.77$ that results from the addition of AM to the polymer chain.

Primary amines are highly nucleophilic and have significant synthetic utility in the preparation of polymeric bioconjugates. However, primary amines are commonly used for the reduction of trithiocarbonates and dithiocarbamates, and therefore difficult to incorporate into RAFT polymers or RAFT CTAs. As shown in Scheme 1, we have used the triflate salt of *N*-(2-aminoethyl)maleimide (AM) to introduce primary amine functionality on the ω-end of polymer chains. The triflate salt prevents reduction of the RAFT CTA during chain extension with the maleimide, but does not interfere with subsequent conjugation reactions. The success of this technique can be shown using ^{1}H NMR. Figure 2 shows the spectrum of a chain extended pDMAEMA-AM macro-CTA. The emergence of the triplet at $\delta = 3.77$ corresponding to the ($NC\mathbf{H}_2CH_2$) group in AM and

Table 1. Molecular Weight Distributions, Degree of Chain Extension, and Degree of Conjugation

#	polymer	M_n[a] g/mol	M_w/M_n[a]	% AM extension[b]	% conjugation pyrene[a]	% conjugation folate[c]
P1	pDMAEMA-A	8100	1.26	102	86	--
P2	pDMAEMA-AM-STY	20300	1.11	82	44	--
P3	pNIPAM-AM	20300	1.17	97	--	--
P4	pDMAEMA-b-DMAEMA/BMA/PAA-AM	19500	1.45	--	--	94

[a] Determined by GPC. [b] Determined by ^{1}H NMR. [c] Determined by UV spectroscopy.

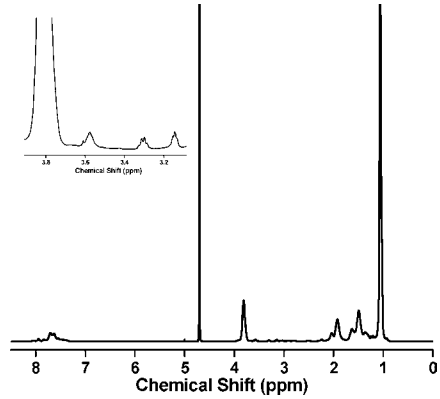

Figure 3. The ^{1}H NMR spectrum of pNIPAM following chain extension with AM. The inset shows the triplet at $\delta = 3.15$ that results from the addition of AM to the polymer chain and the quartet at $\delta = 3.31$ that indicates the presence of intact RAFT Z groups.

the absence of free vinyl peaks at $\delta = 6.8$ shows that AM is incorporated into the pDMAEMA polymer and not present as a contaminating monomer. By comparing the pDMAEMA ($CO_2C\mathbf{H}_2$) peak area at $\delta = 4.1$ to the AM peak area at $\delta = 3.77$, and using the molecular weight of pDMAEMA determined by GPC, the number of AM residues incorporated into each polymer chain is calculated at 1.02 (P1, Table 1). This result clearly shows the addition of a single functional maleimide to the ω-end of the polymer chain.

The chain extension technique is not limited to the preparation of ω-functional methacrylic polymers. Using the thermally responsive polymer poly(*N*-isopropylacrylamide) (pNIPAM), we have shown that acrylamido polymers may be functionalized by maleimido chain extension. Figure 3 shows the ^{1}H NMR spectrum of a chain-extended pNIPAM-AM macro-CTA. The triplet at $\delta = 3.15$ corresponds to the ($CH_2C\mathbf{H}_2NH_2$) group in AM and the spectrum is free of vinyl peaks, indicating incorporation of AM into the pNIPAM polymer. The number of AM residues incorporated into each polymer was determined to be 0.97 (P3, Table 1) by comparing the pNIPAM methine peak area ($NHC\mathbf{H}(CH_3)_2$) at $\delta = 3.81$ to the AM peak area at $\delta = 3.15$ and using the molecular weight of pNIPAM determined by GPC. Moreover, the AM peak area can be compared directly to the ($SC\mathbf{H}_2CH_3$) peak from the Z-group of the CTA at $\delta = 3.31$, indicating that the CTA and AM are present on the polymer in a 1:1 ratio. Calculation of the degree of polymerization based on the pNIPAM methine peak and the CTA peak at $\delta = 3.31$ yields the degree of polymerization expected from GPC measurements, providing further evidence that pNIPAM has been successfully functionalized by a single AM residue and that functional CTA moieties are retained on the polymer chain end. Together with the results of the pDMAEMA chain extension, these results indicate that maleimido chain extension may not be restricted by monomer class and will have synthetic utility with a wide array of commonly used polymers (e.g., (meth)acrylic and (meth)acrylamido).

The chain extension conditions we describe do not result in changes to the molecular weight distribution of the polymer undergoing extension. Figure 4A shows the RI traces for pDMAEMA and pDMAEMA-AM (P1, Table 1) following chain extension. No apparent shift in the peak elution volume results from chain extension, consistent with the addition of a single monomer to the chain end, and no change was observed in the calculated M_n (8100 g/mol) upon chain extension. Moreover, no peak broadening is exhibited in the RI traces, as would be expected if significant polymer−polymer coupling or formation of homomaleimide polymer fragments were to occur ($M_w/M_n = 1.21$ and 1.26 before and after chain extension, respectively). Similarly, no significant changes in molecular weight distribution were observed after chain extension of pNIPAM ($M_n = 8000$ g/mol $M_w/M_n = 1.16$, and $M_n = 8000$ g/mol $M_w/M_n = 1.17$) or the block copolymer pDMAEMA-*b*-DMAEMA/BMA/PAA ($M_n = 19\,400$ g/mol $M_w/M_n = 1.42$, and $M_n = 19\,500$ g/mol $M_w/M_n = 1.45$) (P4, Table 1).

A possible complication of chain extension with a primary amine containing monomer is destruction of the RAFT moiety through aminolysis. If this undesirable reaction were to occur, it would yield polymeric thiols that might result in polymer−polymer coupling by disulfide formation or reaction with maleimide monomers. Although GPC traces provided no evidence of polymer coupling following chain extension, we prepared an additional chain-extended pDMAEMA-AM to serve as a macro-CTA in a subsequent styrene polymerization ($M_n = 10\,600$ g/mol, $M_w/M_n = 1.14$). If destruction of some or all of the RAFT CTA were to occur during chain extension, subsequent block formation using the pDMAEMA-AM macro-CTA would be impossible or would yield polymers with broad or multimodal molecular weight distributions due to the presence of nonfunctional macro-CTA. Figure 4B shows RI traces for the pDMAEMA-AM macro-CTA and for the triblock polymer obtained by block polymerization, pDMAEMA-AM-STY (P2, Table 1). A clear shift in the retention volume of the polymer is observed following polymerization, and the molecular weight distribution of the triblock polymer is characteristically narrow ($M_n = 20\,300$ g/mol and $M_w/M_n = 1.11$). These results strongly suggest that significant aminolysis of the CTA is not occurring. Further evidence in support of this point can be seen by examining the ^{1}H NMR spectrum of pNIPAM-AM, shown in Figure 3.

This spectrum clearly shows the methylene peak from the Z-group of the CTA at $\delta = 3.31$. The ratio of this peak area to the methine peak area in chain-extended pNIPAM-AM is the same as the corresponding ratio in the parent pNIPAM, indicating that no detectable aminolysis of the CTA occurs during chain extension.

The retention of functional RAFT moieties on the polymer following chain extension offers unique synthetic opportunities. The maleimido-terminated chains are living and can be used in subsequent block polymerizations, as illustrated by our polymerization of pDMAEMA-AM-STY. Such polymerizations have the effect of positioning a bioconjugation site precisely at the junction of the AA or AB blocks, whose length and composition can also be readily controlled. Moreover, multiple rounds of block polymerizations could potentially be used to position multiple bioconjugation sites at defined intervals along a polymer backbone of hetero- or homogeneous composition. These materials could be used to prepare therapeutic and diagnostic polymer conjugates with uniquely defined architectures.

To confirm that the amines introduced to the polymers by chain extension were reactive and available, a fluorescent dye was used as a model compound for imaging agent conjugations. Amine-reactive 1-pyrenebutanoic acid succimidyl ester (PNHS) was used

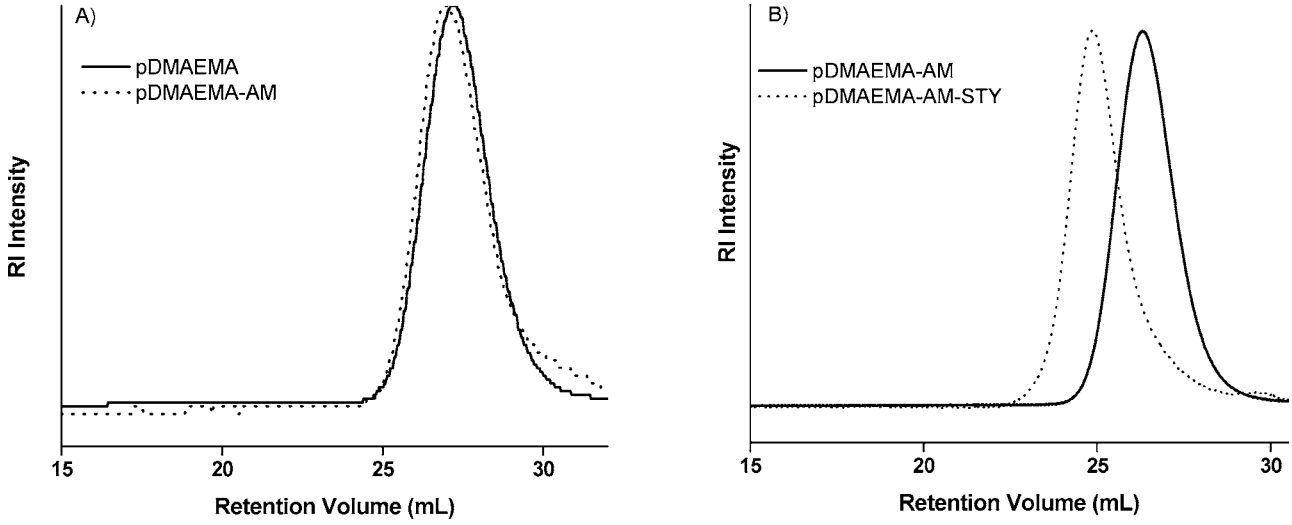

Figure 4. (A) GPC traces showing the molecular weight distribution of pDMAEMA and pDMAEMA-AM following chain extension. (B) GPC traces of a pDMAEMA-AM-STY triblock polymer and the corresponding pDMAEMA-AM macro-CTA.

to label pDMAEMA-AM, and the amount of pyrene conjugated was evaluated by GPC and UV spectroscopy following purification. Figure 5A shows normalized RI and UV traces for pyrene-labeled pDMAEMA-AM. Upon reaction with PNHS, an intense UV signal is observed with polymer elution that is not present in unconjugated pDMAEMA-AM, indicating that the pDMAEMA-AM chains were successfully labeled with pyrene. Figure 5B shows the UV absorbance spectra of pyrene-labeled pDMAEMA-AM and unlabeled pDMAEMA-AM, illustrating the significant increase in absorptivity that occurs upon pyrene addition. The percentage of pDMAEMA-AM chains conjugated to pyrene was determined to be 86.1% (P1, Table 1) by comparing the UV peak area associated with polymer elution to a calibration curve. Similarly, PNHS was also used to label the primary amine located at the maleimido junction of the DMAEMA and STY block segments in pDMAEMA-AM-STY (P2, Table 1). The degree of conjugation to this polymer was 44%, suggesting that the steric effects of the large styrene block reduce the conjugation efficiency.

Recently, our group described the use of the block copolymer pDMAEMA-*b*-DMAEMA/BMA/PAA as a siRNA delivery vehicle (*41*). The positively charged pDMAEMA block functions to condense nucleic acid residues, while the pH-responsive and membrane-disruptive copolymer block mediates intracellular delivery of the complexes following endosomal uptake. Though the block copolymer mediated excellent gene knockdown (up to 80%) (*41*), incorporation of targeting ligands can further enhance knockdown in vitro and facilitate more efficient in vivo delivery (*53, 54*). Folic acid is a commonly used targeting ligand, mediating greater internalization for cells that express or overexpress the folic acid receptor (*55, 56*). As a demonstration of the utility of maleimido chain extension, we conjugated folic acid to the AM chain-extended pDMAEMA-*b*-DMAEMA/BMA/PAA block copolymer. Figure 6A shows the RI and UV GPC traces of the unmodified copolymer, while Figure 6B shows the RI and UV GPC traces of the copolymer−folate conjugate. The unmodified copolymer shows negligible UV absorbance at 363 nm (Figure 6A), while an intense UV signal is associated with polymer elution in the case of the copolymer−folate conjugate (Figure 6B). The degree of folate conjugation to the copolymer was determined by comparison to a calibration curve of free folic acid and found to be 94% (P4, Table 1).

It is important to note that the highly efficient conjugation reactions demonstrated here were conducted for less than 24 h at room temperature and relatively low stoichiometric ratios. These reaction conditions are possible because maleimide chain extension provides a functional group with far greater reactivity than the

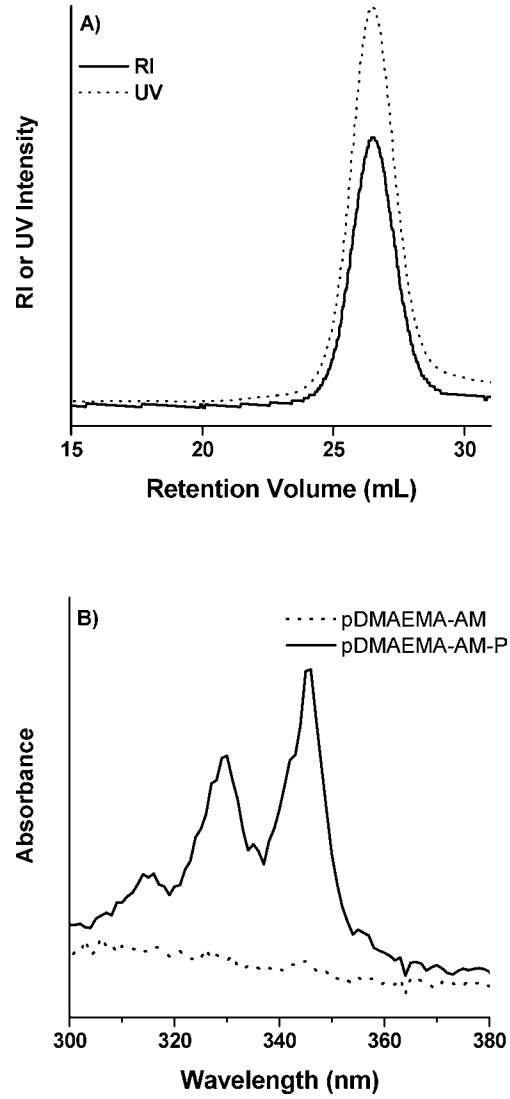

Figure 5. Chain-extended polymers were labeled with an amine-reactive pyrene. (A) RI and UV traces of pDMAEMA-AM-P following pyrene conjugation. (B) Unmodified pDMAEMA-AM shows limited UV absorbance due to the trithiocarbonate moiety on the chain end, while pyrene-labeled pDMAEMA-AM-P exhibits significantly increased absorption.

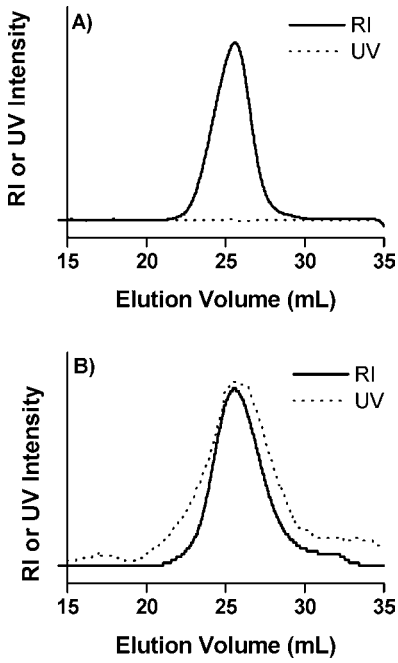

Figure 6. (A) RI and UV traces of pDMAEMA-*b*-DMAEMA/BMA/PAA before conjugation to folic acid. (B) RI and UV traces of pDMAEMA-*b*-DMAEMA/BMA/PAA after the addition of folic acid.

tertiary thiols that can be obtained following reduction of the CTA. For this reason, chain extension is particularly well suited for functionalizing polymers with molecules of biological interest that may be insufficiently stable or prohibitively expensive for use with other ω-functionalization strategies.

CONCLUSION

A facile method to achieve end-functionalization of RAFT polymers with moieties for bioconjugation was demonstrated. Using an N-substituted maleimido monomer, a unique functional group was introduced to the ω-terminal end of RAFT polymers. Specifically, *N*-(2-aminoethyl)maleimide trifluoroacetate (AM) was used to introduce a single primary amine to an α-substituted polymer, dimethylaminoethyl methacrylate (pDMAEMA), *N*-isopropyl acrylamide (pNIPAM) and a block copolymer of DMAEMA, butyl methacrylate (BMA), and propylacrylic acid (PAA), (pDMAEMA-*block*-DMAEMA/BMA/PAA). The primary amine was active, and conjugation efficiencies of 86% to pyrene and 94% to folic acid were readily achieved at room temperature and low stoichiometric ratios. This synthetic approach should provide a versatile method for ω-end functionalization of RAFT polymers, since alternate ω-end functionalities could be readily prepared by altering the identity of the maleimido N-substituent.

ACKNOWLEDGMENT

This work was funded by the National Institutes of Health (R01EB002991). Danielle S.W. Benoit is a Merck Fellow supported by the Damon Runyon Cancer Research Foundation (DRG-1948-07).

LITERATURE CITED

(1) Georges, M. K., Veregin, R. P. N., Kazmaier, P. M., and Hamer, G. K. (1993) Narrow molecular-weight resins by a free-radical polymerization process. *Macromolecules 26*, 2987–2988.

(2) Wang, J. S., and Matyjaszewski, K. (1995) Controlled living radical polymerization - atom-transfer radical polymerization in the presence of transition-metal complexes. *J. Am. Chem. Soc. 117*, 5614–5615.

(3) Maydunne, R. T. A., Rizzardo, E., Chiefari, J., Chang, Y. K., Moad, G., and Thang, S. H. (1999) A more versatile route to block copolymer and other polymers of complex architecture by living radical polymerization: the RAFT process. *Macromolecules 32*, 6977–6980.

(4) Chiefari, J., Chang, Y. K., Ercole, F., Krstina, J., Jeffery, J., Le, T. P. T., Mayadunne, R. T. A., Meijs, G. F., Moad, C. L., Moad, G., Rizzardo, E., and Thang, S. H. (1999) Living free-radical polymerization by reversible addition-fragmentation transfer: the RAFT process. *Macromolecules 31*, 5559–5562.

(5) Convertine, A. J., Ayres, N., Scales, C. W., Lowe, A. B., and McCormick, C. L. (2004) Facile, controlled, room-temperature RAFT polymerization of N-isopropylacrylamide. *Biomacromolecules 5*, 1177–1180.

(6) Moad, G., Rizzardo, E., and Thang, S. H. (2005) Living radical polymerization by the RAFT process. *Aust. J. Chem. 58*, 379–410.

(7) Sumerlin, B. S., Donovan, M. S., Mitsukami, Y., Lowe, A. B., and McCormick, C. L. (2001) Water-soluble polymers. 84. Controlled polymerization in aqueous media of anionic acrylamido monomers via RAFT. *Macromolecules 34*, 6561–6564.

(8) Schilli, C., Lanzendorfer, M. G., and Muller, A. H. E. (2002) Benzyl and cumyl dithiocarbamates as chain transfer agent in the RAFT polymerization of N-isopropylacrylamide. In situ FT-NIR and MALDI-TOF MS investigation. *Macromolecules 35*, 6819–6827.

(9) Vasilieva, Y. A., Thomas, D. B., Scales, C. W., and McCormick, C. L. (2004) Direct controlled polymerization of a cationic methacrylamido monomer in aqueous media via the RAFT p(r)ocess. *Macromolecules 37*, 2728–2737.

(10) Ganachaud, F., Monteiro, M. J., Gilbert, R. G., Dourges, M. A., Thang, S. H., and Rizzardo, E. (2000) Molecular weight characterization of poly(N-isopropylacrylamide) prepared by living free-radical polymerization. *Macromolecules 33*, 6738–6745.

(11) Segui, F., Qiu, X. P., and Winnik, F. M. (2008) An efficient synthesis of telechelic poly(N-isopropylacrylamides) and its application to the preparation of alpha,omega-dicholesteryl and alpha,omega-dipyrenyl polymers. *J. Polym. Sci. Polym. Chem. 46*, 314–326.

(12) Lowe, A. B., Sumerlin, B. S., Donovan, M. S., and McCormick, C. L. (2002) Facile preparation of transition metal nanoparticles stabilized by well-defined (co)polymers synthesized via aqueous reversible addition-fragmentation chain transfer polymerization. *J. Am. Chem. Soc. 124*, 11562–3.

(13) Scales, C. W., Convertine, A. J., and McCormick, C. L. (2006) Fluorescent labeling of RAFT-generated poly(N-isopropylacrylamide) via a facile maleimide-thiol coupling reaction. *Biomacromolecules 7*, 1389–1392.

(14) Kulkarni, S., Schilli, C., Muller, A. H. E., Hoffman, A. S., and Stayton, P. S. (2004) Reversible meso-scale smart polymer-protein particles of controlled sizes. *Bioconjugate Chem 15*, 747–753.

(15) Boyer, C., Bulmus, V., Liu, J. Q., Davis, T. P., Stenzel, M. H., and Barner-Kowollik, C. (2007) Well-defined protein-polymer conjugates via in situ RAFT polymerization. *J. Am. Chem. Soc. 129*, 7145–7154.

(16) De, P., Gondi, S. R., and Sumerlin, B. S. (2008) Folate-conjugated thermoresponsive block copolymers: Highly efficient conjugation and solution self-assembly. *Biomacromolecules 9*, 1064–1070.

(17) Heredia, K. L., Nguyen, T. H., Chang, C., Bulmus, V., Davis, T. P., and Maynard, H. D. (2008) Reversible siRNA-polymer conjugates by RAFT polymerization. *Chem. Commun. 28*, 3245–3247.

(18) Maynard, H. D., Heredia, K. L., Li, R. C., Parra, D. P., and Vazquez-Dorbatt, V. (2007) Thermoresponsive biohybrid materials synthesized by ATRP. *J. Mater. Chem. 17*, 4015–4017.

(19) Venkataraman, S., and Wooley, K. L. (2006) ATRP from an amino acid-based initiator: A facile approach for alpha-functionalized polymers. *Macromolecules 39*, 9661–9664.

(20) Bathfield, M., D'Agosto, F., Spitz, R., Charreyre, M. T., and Delair, T. (2006) Versatile precursors of functional RAFT agents. Application to the synthesis of bio-related end-functionalized polymers. *J. Am. Chem. Soc. 128*, 2546–2547.

(21) Hong, C. Y., and Pan, C. Y. (2006) Direct synthesis of biotinylated stimuli-responsive polymer and diblock copolymer by RAFT polymerization using biotinylated trithiocarbonate as RAFT agent. *Macromolecules 39*, 3517–3524.

(22) Gondi, S. R., Vogt, A. P., and Sumerlin, B. S. (2007) Versatile pathway to functional telechelics via RAFT polymerization and click chemistry. *Macromolecules 40*, 474–481.

(23) Ranjan, R., and Brittain, W. J. (2007) Combination of living radical polymerization and click chemistry for surface modification. *Macromolecules 40*, 6217–6223.

(24) Liu, J., Bulmus, V., Barner-Kowollik, C., Stenzel, M. H., and Davis, T. P. (2007) Direct synthesis of pyridyl disulfide-terminated polymers by RAFT polymerization. *Macromol. Rapid Commun. 28*, 305–314.

(25) Carter, S., Hunt, B., and Rimmer, S. (2005) Highly branched poly(N-isopropylacrylamide)s with imidazole end groups prepared by radical polymerization in the presence of a styryl monomer containing a dithioester group. *Macromolecules 38*, 4595–4603.

(26) Patton, D. L., Mullings, M., Fulghum, T., and Advincula, R. C. (2005) A facile synthesis route to thiol-functionalized alpha,w-telechelic polymers via reversible addition fragmentation chain transfer polymerization. *Macromolecules 38*, 8597–8602.

(27) Deletre, M., and Levesque, G. (1990) Kinetics and mechanism of polythioamidation in solution 0.1. reaction of mono(dithioester)s and bis(dithioester)s with excess amine. *Macromolecules 23*, 4733–4741.

(28) Qiu, X. P., and Winnik, F. M. (2007) Synthesis of alpha-,omega-dimercapto poly(N-isopropylacrylamides) by RAFT polymerization with a hydrophilic difunctional chain transfer agent. *Macromolecules 40*, 872–878.

(29) Roberts, M. J., Bentley, M. D., and Harris, J. M. (2002) Chemistry for peptide and protein PEGylation. *Adv. Drug Delivery Rev. 54*, 459–476.

(30) Toutchkine, A., Nalbant, P., and Hahn, K. M. (2002) Facile synthesis of thiol-reactive Cy3 and Cy5 derivatives with enhanced water solubility. *Bioconjugate Chem. 13*, 387–391.

(31) Dufresne, M. H., Gauthier, M. A., and Leroux, J. C. (2005) Thiol-functionalized polymeric micelles: From molecular recognition to improved mucoadhesion. *Bioconjugate Chem. 16*, 1027–1033.

(32) Wang, L. X., Kristensen, J., and Ruffner, D. E. (1998) Delivery of antisense oligonucleotides using HPMA polymer: Synthesis of a thiol polymer and its conjugation to water-soluble molecules. *Bioconjugate Chem. 9*, 749–757.

(33) Segura, T., and Hubbell, J. A. (2007) Synthesis and in vitro characterization of an ABC triblock copolymer for siRNA delivery. *Bioconjugate Chem. 18*, 736–745.

(34) York, A. W., Scales, C. W., Huang, F. Q., and McCormick, C. L. (2007) Facile synthetic procedure for omega, primary amine functionalization directly in water for subsequent fluorescent labeling and potential bioconjugation of RAFT-synthesized (Co)polymers. *Biomacromolecules 8*, 2337–2341.

(35) Nakayama, M., and Okano, T. (2005) Polymer terminal group effects on properties of thermoresponsive polymeric micelles with controlled outer-shell chain lengths. *Biomacromolecules 6*, 2320–2327.

(36) Henry, S. M., El-Sayed, M. E. H., Pirie, C. M., Hoffman, A. S., and Stayton, P. S. (2006) pH-responsive poly(styrene-alt-maleic anhydride) alkylamide copolymers for intracellular drug delivery. *Biomacromolecules 7*, 2407–2414.

(37) El-Sayed, M. E. H., Hoffman, A. S., and Stayton, P. S. (2005) Rational design of composition and activity correlations for pH-sensitive and glutathione-reactive polymer therapeutics (vol 101, pg 47, 2005). *J. Controlled Release 104*, 415+.

(38) Cheung, C. Y., Stayton, P. S., and Hoffman, A. S. (2005) Poly(propylacrylic acid)-mediated serum stabilization of cationic lipoplexes. *J. Biomater. Sci., Polym. Ed. 16*, 163–179.

(39) Kyriakides, T. R., Cheung, C. Y., Murthy, N., Bornstein, P., Stayton, P. S., and Hoffman, A. S. (2002) pH-sensitive polymers that enhance intracellular drug delivery in vivo. *J. Controlled Release 78*, 295–303.

(40) Johns, R. E., Hoffman, A. S., and Stayton, P. S. (2004) Expression analysis of LPS stimulated THP-1 cells treated with antisense IRAK1 delivered using a pH-sensitive, membrane disruptive polymer. *Mol. Ther. 9*, S242−S242.

(41) Convertine, A. J., Benoit, D. S. W., Duvall, C. L., Hoffman, A. S., and Stayton, P. S. (2008) Novel endosomolytic diblock copolymer for siRNA delivery. *J. Controlled Release*In Press.

(42) Flanary, S., Hoffman, A. S., and Stayton, P. S. (2008) Antigen delivery with poly(propylacrylic acid) conjugation enhances MHC-1 presentation and T-cell activation. *Bioconjugate Chem*In Press.

(43) Narain, R., Gonzales, M., Hoffman, A. S., Stayton, P. S., and Krishnan, K. M. (2007) Synthesis of monodisperse biotinylated p(NIPAAm)-coated iron oxide magnetic nanoparticles and their bioconjugation to streptavidin. *Langmuir 23*, 6299–6304.

(44) Lai, J. J., Hoffman, J. M., Ebara, M., Hoffman, A. S., Estournes, C., Wattiaux, A., and Stayton, P. S. (2007) Dual magnetic-/temperature-responsive nanoparticles for microfluidic separations and assays. *Langmuir 23*, 7385–7391.

(45) Ebara, M., Hoffman, J. M., Stayton, P. S., and Hoffman, A. S. (2007) Surface modification of microfluidic channels by UV-mediated graft polymerization of non-fouling and 'smart' polymers. *Radiat. Phys. Chem. 76*, 1409–1413.

(46) Amou, S., Nishimura, S., Takahashi, A., Hagiwara, T., Hamana, H., and Narita, T. (1999) Synthesis and polymerization of N-(4-tetrahydropyranyloxyphenyl)maleimide. *J. Polym. Sci. Polym. Chem. 37*, 341–347.

(47) Hill, D. T., Shao, L. Y., Pomery, P. J., and Whittaker, A. K. (2001) The radical homopolymerization of N-phenylmaleimide, N-n-hexylmaleimide and N-cyclohexylmaleimide in tetrahydrofuran. *Polymer 42*, 4791–4802.

(48) Zhao, B., Wang, Y., Lu, C., Shen, Q., and Deng, M. (2005) Polymerization of N-phenyl maleimide by lanthanide complexes. *J. Polym. Sci. Polym. Chem. 43*, 3966–3972.

(49) Sandreczki, T. C., and Brown, I. M. (1990) Characterization of the free-radical homopolymerization of N-methylmaleimide. *Macromolecules 23*, 1979–1983.

(50) Caulfield, M. J., and Solomon, D. H. (1999) Studies on polyimides: 2. Formation of high molecular weight poly(N-(hydroxyphenyl) maleimides). *Polymer 40*, 1251–1260.

(51) Ferritto, M., and Tirrell, D. A. (1992) Poly(2-ethylacrylic acid). *Macromol. Synth. 11*, 59–62.

(52) Li, M., De, P., Gondi, S. R., and Sumerlin, B. S. (2008) End group transformations of RAFT-generated polymers with bismaleimides: Functional telechelics and modular block copolymers. *J. Polym. Sci. Polym. Chem. 46*, 5093–5100.

(53) Jeong, J. H., Kim, S. H., Kim, S. W., and Park, T. G. (2005) In vivo tumor targeting of ODN-PEG-folic acid/PEI polyelectrolyte complex micelles. *J. Biomater. Sci., Polym. Ed. 16*, 1409–19.

(54) Song, E., Zhu, P., Lee, S. K., Chowdhury, D., Kussman, S., Dykxhoorn, D. M., Feng, Y., Palliser, D., Weiner, D. B., Shankar, P., Marasco, W. A., and Lieberman, J. (2005) Antibody mediated in vivo delivery of small interfering RNAs via cell-surface receptors. *Nat. Biotechnol. 23*, 709–17.

(55) Hilgenbrink, A. R., and Low, P. S. (2005) Folate receptor-mediated drug targeting: From therapeutics to diagnostics. *J. Pharm. Sci. 94*, 2135–2146.

(56) Bae, K. H., Lee, Y., and Park, T. G. (2007) Oil-encapsulating PEO-PPO-PEO/PEG shell cross-linked nanocapsules for target-specific delivery of paclitaxel. *Biomacromolecules 8*, 650–6.

BC800426D

Monitoring Protein−Polymer Conjugation by a Fluorogenic Cu(I)-Catalyzed Azide−Alkyne 1,3-Dipolar Cycloaddition

A. (Ton) J. Dirks, Jeroen J. L. M. Cornelissen,*,† and Roeland J. M. Nolte

Institute for Molecules and Materials, Radboud University Nijmegen, Toernooiveld 1, 6525 ED, Nijmegen, The Netherlands.
Received October 27, 2008; Revised Manuscript Received March 25, 2009

The Cu(I)-catalyzed azide−alkyne cycloaddition (CuAAC) has recently proven to be a powerful synthetic tool in various fields of chemistry, including protein−polymer conjugation. In this article, we describe a fluorogenic CuAAC, which allows for efficient monitoring of protein−polymer conjugation. We show that profluorescent 3-azido coumarin-terminated polymers can be reacted with an alkyne-functionalized protein to produce a strongly fluorescent triazole-linked conjugate. Upon formation of the product, the evolution of fluorescence can accurately be determined, providing information about the course of the CuAAC. As a proof of concept, we synthesized several 3-azido coumarin terminated poly(ethylene glycol) (PEG) chains and investigated their conjugation with alkyne-functionalized bovine serum albumin (BSA) as a model protein. CuAAC conjugation was shown to be very efficient and proceeded rapidly. Conversion plots were constructed from measuring the fluorescence as function of reaction time. An additional benefit of the fluorogenic CuAAC is the *in situ* labeling of bioconjugates. We envision that the fluorogenic protein−polymer conjugation is not restricted to the reaction system reported in this work, but may also be ideal to screen for optimal reaction conditions of various other systems.

INTRODUCTION

The modification of proteins with synthetic polymers has been demonstrated to be beneficial for applications in medicine and biotechnology (*1*−*5*). A well-known example in this respect is the conjugation of proteins with poly(ethylene glycol) (PEG), termed PEGylation (*6*−*11*). In comparison to native proteins, PEGylated derivatives often exhibit improved biodistribution and pharmacokinetics, reduced immunogenicity, prolonged plasma half-life, and increased solubility (*12, 13*). As a result, several therapeutic protein−PEG conjugates are currently on the market or in clinical development (*10*, *14*). Besides PEGylated proteins, other types of protein−polymer conjugates have also gained much interest. In particular, bioconjugates that comprise stimuli-responsive polymers (e.g., poly(*N*-isopropylacrylamide), pNIPAM) have been widely investigated for their reversible phase transition behavior (*3, 15*−*17*). Somewhat less deeply studied are the conjugates of hydrophobic polymers (e.g., polystyrene; PS) and proteins, which have been shown to act as giant amphiphiles and form bioactive assemblies in water (*18*−*24*).

As protein−polymer conjugates constitute a versatile and interesting class of materials, their synthesis has attracted a lot of attention. Several synthetic routes have now been established, mainly following two approaches: (i) the propagation of a polymer from a protein equipped with initiator moieties (i.e., grafting-from), and (ii) the coupling of an end-functionalized polymer to peripheral amino acid side chains of a protein (i.e., grafting-to) (*25*−*27*). The latter approach is most commonly applied and allows the polymer segment to be presynthesized under conventional, optimized conditions. Obviously, the success of the grafting-to method strongly relies on the selection of an efficient coupling strategy for the joining of bulky building blocks. In the choice of chemistry, it should furthermore be taken into consideration that site-specific conjugation may be required to retain maximum biological activity. Therefore, a frequently used strategy is to couple thiol-reactive polymers to unpaired cysteine residues, which are naturally very scarce (*23, 28, 29*). In fact, many proteins lack free thiol groups, but in those cases, genetic engineering can be used to introduce cysteines residues at specific positions (*30*). Another strategy to create a handle for site-specific conjugation is via the incorporation of non-natural amino acids (*31*). In this way, functional groups such as ketones, azides, and alkynes can be installed, facilitating a bioorthogonal derivatization by oxime ligation (*32*−*36*) or the recently developed Cu(I) catalyzed azide−alkyne 1,3-dipolar cycloaddition (CuAAC) (*37*−*40*). The latter can be considered as a prototypical click reaction (*41*) and has proven to be a powerful synthetic tool in the fields of biohybrid chemistry (*42*−*44*) and materials science (*45, 46*). In terms of protein−polymer conjugation, the CuAAC has successfully been employed in grafting-to approaches to prepare PEGylated enzymes (*47, 48*), glycopolymer−virus particles (*49*), stimuli-responsive bioconjugates (*50*), and giant amphiphiles (*22*).

Protein−polymer conjugation is generally monitored by characterization techniques that discriminate between the size of the starting materials and products, e.g., sodium dodecyl sulfate−polyacrylamide gel electrophoresis (SDS−PAGE) or size exclusion chromatography (SEC). However, we realized that using the CuAAC would also allow for monitoring of the bioconjugation process by a fluorogenic assay. That is, exploiting the fact that profluorescent 3-azido coumarin derivatives become strongly fluorescent upon undergoing a cylcoaddition reaction, as depicted in Figure 1. 3-Azido coumarin derivatives have been developed by Wang and co-workers (*51*) and proved to be very useful to signal for an effective CuAAC with alkynes (*52*−*55*) and cycloaddition with oxanorbornadienes (*56*). Extending on the signaling purposes, it should be possible to determine the progress of coupling 3-azido coumarin-terminated polymers to alkyne-functionalized proteins by simply measuring the increase in fluorescence intensity. In addition, the newly formed bioconjugate would instantly be labeled with

* Corresponding author. Tel: (+31) 24 365 2381. Fax: (+31) 24 365 2929. E-mail: J.J.L.M.Cornelissen@tnw.utwente.nl.

† Present address: Laboratory for Biomolecular Nanotechnology, MESA+ Institute, University of Twente, Enschede, The Netherlands.

10.1021/bc8004667 CCC: $40.75 © 2009 American Chemical Society
Published on Web 05/19/2009

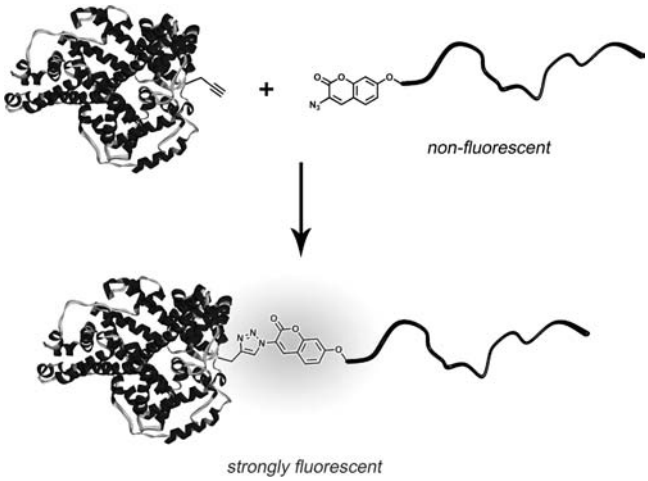

Figure 1. Schematic representation of a fluorogenic Cu(I)-catalyzed azide−alkyne 1,3-dipolar cycloaddition between a protein and a polymer.

a fluorescent probe, which is of great assistance in tracking the materials with established characterization techniques (e.g., SEC and SDS−PAGE). For the reasons described above, we decided to further develop the concept of monitoring protein−polymer conjugation by a fluorogenic CuAAC. Considering the great technological relevance of protein PEGylation, we focused in our proof of concept on the coupling of 3-azido coumarin terminated PEG to an alkyne-functionalized model protein. Bovine serum albumin (BSA) was selected as a model protein because it is readily available and easy to functionalize with a single alkyne group (*22*). In this article, we concentrate on 3-azido coumarin derivatives, but it should be noted that other azide/alkyne-bearing profluorescent probes also may be selected for the same purpose (*57, 58*).

RESULTS AND DISCUSSION

Synthesis of 3-Azido Coumarin Terminated PEG. Nowadays, a range of well-defined PEG derivatives is commercially available. Commonly, these polymers are equipped with hydroxyl end groups, which allow for their functionalization by straightforward modifications. We envisioned that a 3-azido coumarin compound carrying a carboxyl acid group (i.e., compound **3**) would be ideal for coupling to hydroxyl-terminated PEG as well as to other end-functional polymers in future studies. Therefore, acid derivative **3** was synthesized starting from 3-azido-7-hydroxy coumarin (**1**) reported by Wang and co-workers (Scheme 1) (*51*). First, a *tert*-butyl ester was introduced, which could subsequently be deprotected to a carboxylic acid under mild conditions, i.e., treatment with trifluoro acetic acid (TFA). Both reaction steps proceeded smoothly and in good yield. However, a similar route employing a methyl ester was found to be unsuccessful, and no azide-containing coumarin could be recovered after deprotection attempts with 1 M NaOH in THF.

Coumarin **3** was coupled to hydroxyl-terminated PEG (M_n = 2000 and 5000 Da) using 1-ethyl-3-(3′-dimethylaminopropyl) carbodiimide (EDCI) as a coupling reagent. This resulted in end-functional polymers **4** and **5** containing an ester linkage (Scheme 2). Additionally, hydroxyl PEG (M_n = 2000 Da) was used as a starting material for the preparation of amide-linked 3-azido coumarin terminated PEG **8**, which is expected to be more stable under physiological conditions. To this end, the PEG was first reacted with acrylonitrile to give polymer **6**. After reduction of the nitrile to the corresponding amine (**7**), the polymer was coupled to coumarin **3** using EDCI under conditions similar to those employed for the ester derivatives. All 3-azido coumarin terminated polymers were characterized by ^{1}H NMR spectroscopy and SEC. Figure 2 displays the ^{1}H NMR spectra of PEG **4** and **8** (both with M_n = 2000 Da), which clearly show the signals corresponding to the coumarin end groups. It should be noted that for the amide-linked PEG **8**, traces corresponding to ester-linked PEG **4** were observed in the ^{1}H NMR spectrum. This shows that not all chains of PEG **7** were amine terminated, which might be caused by an incomplete Michael addition with acrylonitrile or the occurrence of the reversed reaction. Integration of the α-terminal methoxy signal (*a*) and the protons neighboring the carbonyl (*f* and *h* for **4**/**5** and **8**, respectively) gave a ratio close to 3:2, pointing to quantitative functionalization. For all polymers, the covalent attachment of the coumarin moiety to PEG was confirmed further by SEC using UV detection at λ = 340 nm. The coupled products clearly showed a signal at the expected elution times, while the starting PEG gave no response. As expected, detection by refractive index (RI) afforded comparable results for PEG and the corresponding functionalized derivatives.

Synthesis of Alkyne-Functionalized BSA. To evaluate the concept of monitoring protein−polymer conjugation by a fluorogenic CuAAC, we selected alkyne-functionalized BSA **10** as a model protein. Following up on previous work (*22*), commercially available BSA was coupled to *N*-propargyl maleimide. A CuAAC with 3-azido-7-hydroxy-coumarin (**1**) was successfully conducted to check for functionalization of the protein (see Supporting Information).

Fluorogenic PEGylation via the CuAAC. Before carrying out the PEGylation of BSA, we decided to examine the reactivity of the azido end group of PEG using low molecular weight alkyne **12**. This alkyne derivative was taken as a model for **10**, and was synthesized by reacting *N*-propargyl maleimide with β-mercapto ethanol (Scheme 3). With the help of $CuSO_4$/Na-ascorbate, alkyne **12** was reacted with PEG **4** using THF/water (3:2) as a solvent system. The reaction was accompanied by a clear evolution of fluorescence (when irradiated under a hand-held UV lamp, λ = 366 nm), indicating that the azide moiety was successfully converted into a triazole. Complete conversion of the reaction was confirmed by ^{1}H NMR spectroscopy, which showed a full shift of coumarin H_4 from δ = 7.16 ppm to δ = 8.49 ppm. Furthermore, a distinct signal of the triazole proton was detected at δ = 8.60 ppm. Analysis by matrix-assisted laser desorption/ionization time-of-flight (MALDI-ToF) mass spectrometry showed a single molecular weight distribution (Figure 3) corresponding to the expected mass of a sodium adduct of the clicked polymer **13** (calcd for $[M + Na]^+$ n = 45; 2492.3, found; 2492.1). Consequently, it was confirmed that the coumarin end group is accessible and participates in a fluorgenic CuAAC in aqueous media. The fluorescence properties of the clicked PEG were evaluated in a phosphate buffer (PB), comparable to the conditions of the bioconjugation experiments described below. Figure 4 displays the excitation and emission spectra of the polymer. The emission intensity at λ_{max} = 418 nm was found to depend linearly on the concentration in the range of 16−140 ng/mL. The excitation wavelength of λ = 340 nm was also used for analysis of the reported PEGylation experiments.

In bioconjugation experiments, typically an excess of reagents is used in order to drive the reaction to completion, especially if bulky substrates are to be conjugated. For our fluorogenic PEGylation experiments (Scheme 4), we therefore started off by using 20 equiv of 3-azido coumarin terminated PEG **4** compared to a 10 mg/mL solution of alkyne-functioanlized BSA **10** (0.15 mM) in the presence of 3 mM $CuSO_4$ and 4.5 mM Na-ascorbate. Under these conditions, a significant evolution of fluorescence was evident upon irradiation by a standard UV lamp (λ = 366 nm), within few minutes after the addition of

Scheme 1. Synthesis of an Acid Functionalized 3-Azido Coumarin Derivative 3

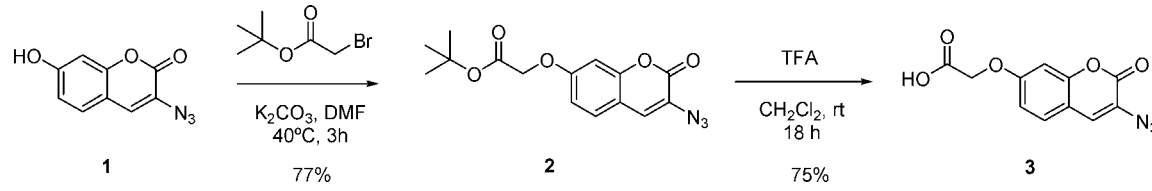

Scheme 2. Preparation of 3-Azido Coumarin Terminated PEG with Ester or Amide Linkage

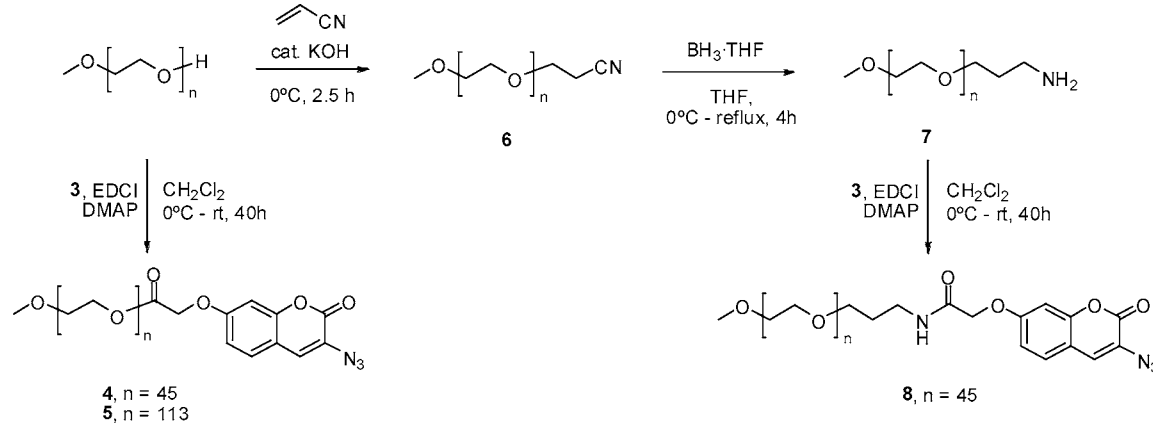

the copper/Na-ascorbate mixture (Figure 5A). A control experiment in which no copper was added hardly showed fluorescence. The fluorescence intensity of the reaction mixture did not seem to increase further after 5 min, and at that point, the fluorescence emission spectrum was measured as depicted in Figure 5B.

The spectrum of the reaction mixture was comparable to that found for PEG **13**. Compared to the model compound PEG **13** (the emission intensity at $\lambda_{max} = 418$ nm was found to depend linearly on the concentration in the range of 16-140 ng/mL); however, the quantified intensity at $\lambda = 418$ nm was found to be approximately three times higher than expected. This implies that either PEG **13** is not a good model for the BSA−PEG conjugate or the number of alkyne moieties in the protein sample was higher than expected. The latter is unlikely because maleimides react ∼1000 times faster with free thiols compared to amines (*28*), and moreover, the excess of *N*-propargyl

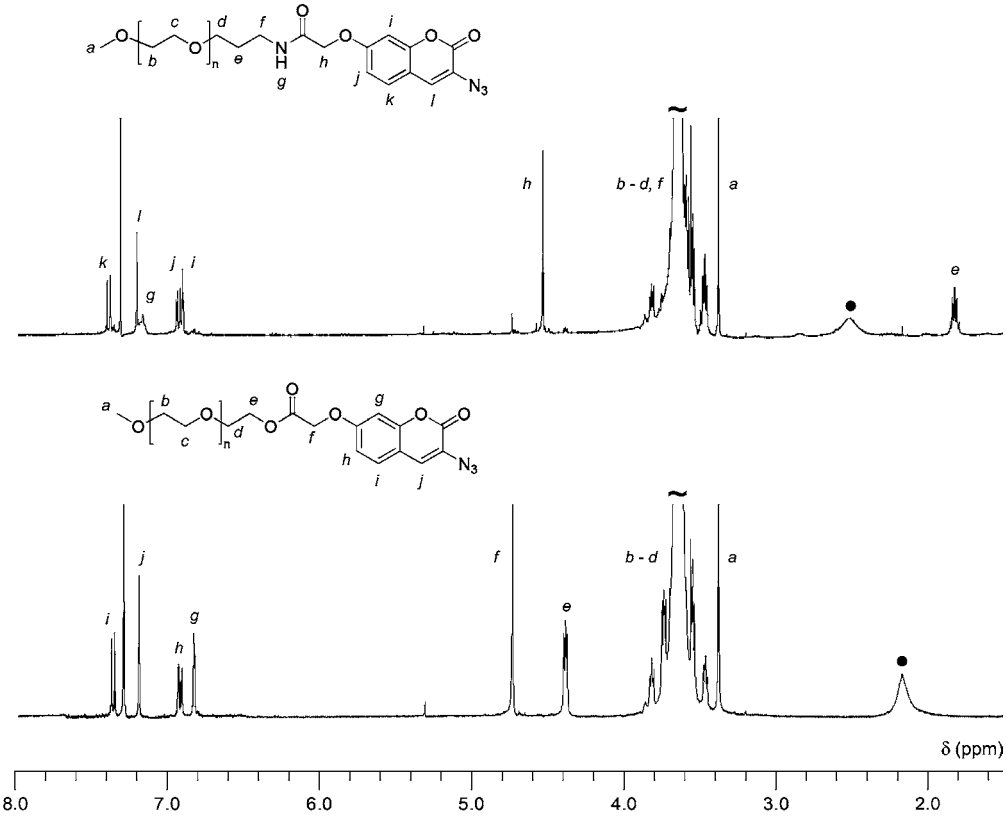

Figure 2. 1H NMR ($CDCl_3$, 400 MHz) spectra of 3-azido coumarin terminated PEG **4** and **8**. The broad signal indicated by ● is assigned to water.

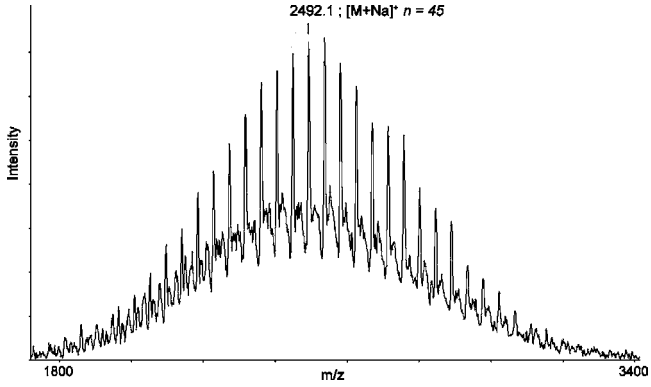

Figure 3. MALDI-ToF mass spectrum of the clicked PEG derivative **13**.

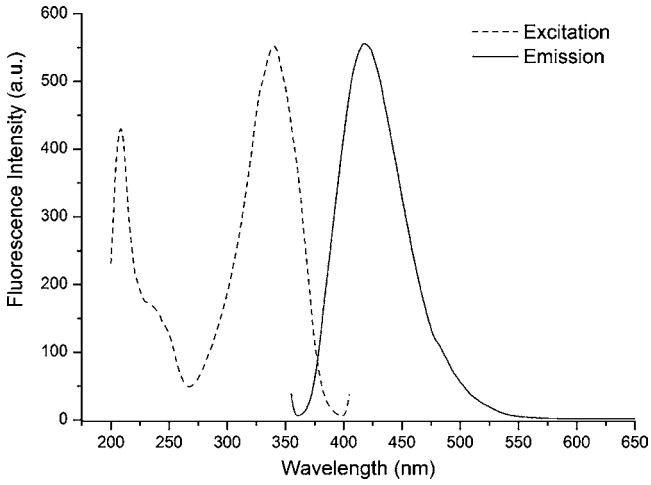

Figure 4. Fluorescence excitation (dashed) and emission (solid) spectra of clicked PEG **13** in PB (50 mM, pH 7.5); $\lambda_{ex.max} = 340$ nm, $\lambda_{em.max} = 418$ nm.

maleimide was removed by size exclusion chromatography (Sephadex G50). Furthermore, aqueous size exclusion does not point to the formation of higher molecular weight polymer−protein conjugates (see below). Another explanation for the difference in fluorescence intensity could be that the protein environment influences the photochemical properties of the coumarin, similar to effects caused by different solvents. Measuring the fluorescence spectra of PEG **13** in different solvents resulted in considerable differences in fluorescence intensity, with toluene giving a 2.3 times lower emission than ethanol or THF and 1.5 times lower than phosphate buffer. The

Scheme 3. Fluorogenic CuAAC at the 3-Azido Coumarin End Group of PEG 4

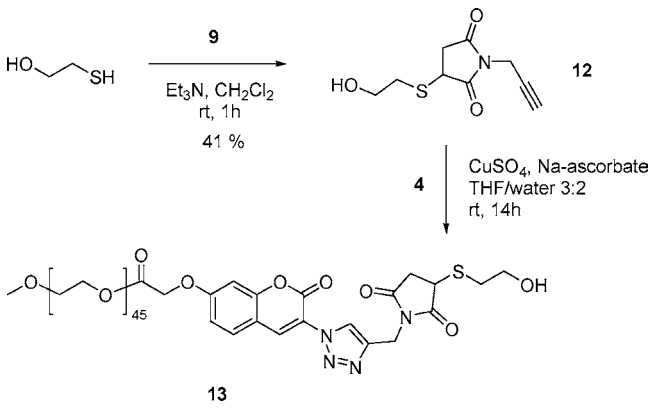

Scheme 4. CuAAC between 3-Azido Coumarin Terminated PEG (4/5/8) and Alkyne-Bearing BSA 10

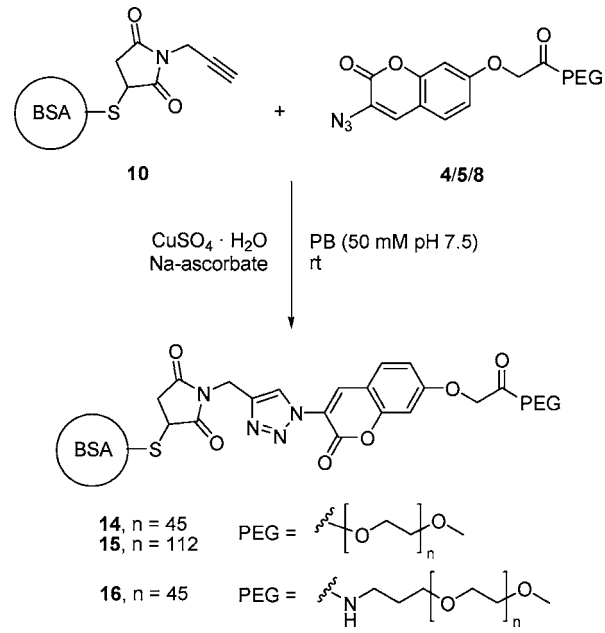

polarity of the environment evidently influences the fluorescence properties of coumarin.

As a consequence, the fluorescence evolving from the protein−polymer conjugation cannot directly be quantified in terms of an absolute conversion. Nevertheless, a relative increase of intensity could be determined, which also provides information about the course of the reaction. The PEGylation reaction was therefore monitored by periodically removing samples from the reaction mixture for spectroscopic analysis. The excess of PEG was lowered to 10 equiv because the initial CuAAC appeared to be extremely fast. Again, a rapid increase in fluorescence intensity (at $\lambda = 418$ nm) was observed, and around 15 min, the measured emission was found not to increase further. Upon addition of an extra amount of catalyst, the fluorescence intensity remained constant, suggesting that the reaction was complete. Plotting the relative fluorescence intensity against time resulted in a curve comparable to a conversion plot (Figure 6). As can be seen from Figure 6, the CuAAC between PEG and BSA is very fast and reaches completion in approximately 15 min. Repeating the reaction with halved concentrations still resulted in a fast conjugation (Figure 6), which seemed to be complete after 40 min. To confirm the covalent attachment of PEG to BSA, the crude mixture at 60 min was subjected to aqueous SEC (Figure 7). This clearly showed the formation of a product with a higher molecular weight than that of starting BSA. Additionally, the newly formed compound showed UV absorbance at both $\lambda = 340$ nm and $\lambda = 280$ nm, whereas starting BSA only shows absorbance at the lower wavelength, confirming the presence of the coumarin moiety. The SEC trace of the conjugate showed some tailing, which may be caused by a residual amount of unreacted BSA; this is inevitable because in commercial batches of BSA, not all thiol groups are available for functionalization (*28*).

Next, the fluorogenic PEGylation of BSA **10** was carried out with PEG **5** and **8**, using the same conditions as discussed above. Plotting the fluorescence emission against reaction time resulted in similar curves (Figure 8), despite the differences in molecular weight between **5** and **8**/**4**. The conjugation product of the higher molecular weight PEG was analyzed by aqueous SEC, and as expected, a peak at higher molecular weight than those of BSA **10** and BSA−PEG **14** was observed. Like conjugate **14**, the peak of **15** showed UV absorbance at both $\lambda = 340$ nm and λ

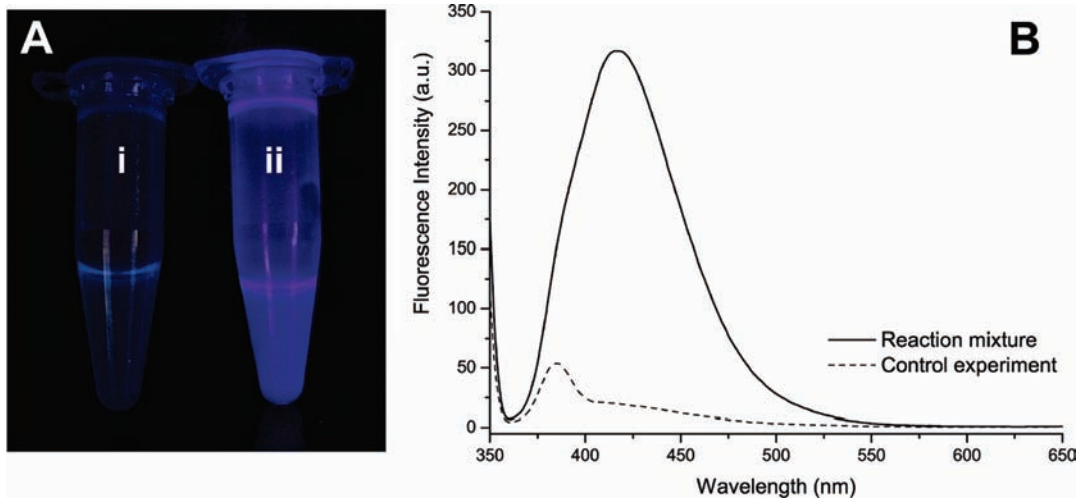

Figure 5. (A) Image taken under UV irradiation (λ = 366 nm) of fluorogenic CuAAC between PEG **4** and BSA **10**; i, control experiment without copper catalyst; ii, conjugation experiment at equal concentration of the other reactants. (B) Fluorescence emission spectrum of the conjugation reaction between **4** and **10** after 5 min (λ_{exc} = 340 nm).

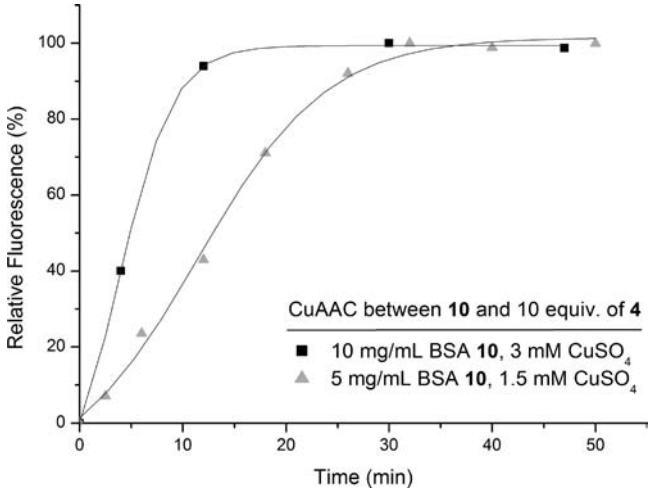

Figure 6. Increase of the fluorescence emission ($\lambda_{em.}$ = 418 nm) during the CuAAC between **4** and **10**, λ_{ex} = 340 nm. Ten equiv of PEG were used. The molar ratio of $CuSO_4$/Na-ascorbate was 1:1.5. Fluoresence is reported relative to the intensity at maximum conversion.

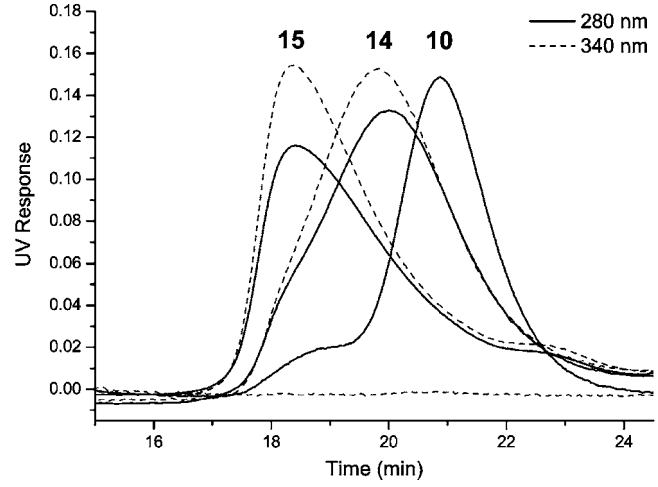

Figure 7. FPLC traces of alkyne-functionalized BSA (**10**) and crude mixtures of BSA−PEG conjugates **14** and **15** after 60 min of reaction time. Phosphate buffer (20 mM, pH 7.5) was used as the eluent in combination with UV detection at λ = 340 nm (dashed lines) and at λ = 280 nm (solid lines).

= 280 nm. The SEC results depicted in Figure 7 demonstrate that the PEGylation had effectively occurred when the fluorescence emission reached a constant level. Accordingly, the fluorescence−time plots (Figures 6 and 8) are considered to be representative for the progression of the bioconjugation reaction.

CONCLUSIONS

A fluorogenic PEGylation reaction via the CuAAC has been described. Several 3-azido coumarin terminated PEG derivatives were synthesized by coupling an acid-functionalized coumarin to a hydroxyl or amine terminus of PEG. The resulting 3-azido coumarin end group was demonstrated to participate in the CuAAC with a low molecular weight alkyne, under clear evolution of fluorescence. Likewise, the polymers were coupled to alkyne-bearing BSA, serving as a model protein. Upon bioconjugation, a clear increase in fluorescence emission was observed. Determination of the fluorescence intensity as a function of reaction time resulted in a conversion plot of the PEGylation process. Completion of the reaction could accurately be determined from the conversion curve and the covalent attachment of PEG to BSA was confirmed by aqueous SEC. Because of the presence of the coumarin moiety, the bioconjugates could easily be traced by SEC.

In summary, the CuAAC of proteins and 3-azido coumarin terminated polymers offers the possibility to monitor the bioconjugation process by a quick fluorogenic assay that is based on the progression of the reaction. This is a procedure that is fast compared to, for example, size exclusion or gel electrophoresis and furthermore allows for a visual check. Although, strictly speaking, the reported procedure at this point does not provide a tool to quantify polymer conjugation, in combination with the highly orthogonal character of the CuAAC it is reasonable to assume that polymers only couple to the acetylene groups on the protein. This is particularly the case when the acetylene groups are incorporated in the aimed protein by residue-specific introduction of noncanonical amino acids (*48*). We believe that the concept is not limited to the PEGylation example used as a proof of principle in this research. In fact, the reported concept may be ideal to screen for optimal reaction conditions in various systems, even in the more laborious coupling of immiscible polymer segments such as in the formation of protein−polymer biohybrid amphiphiles (*18*).

EXPERIMENTAL PROCEDURES

Materials. Unless otherwise stated, all chemicals were obtained from commercial sources and used without further

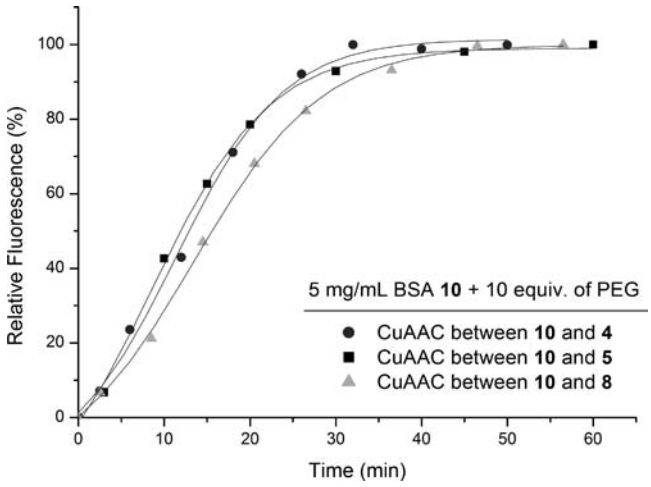

Figure 8. Increase of the fluorescence emission ($\lambda_{em.} = 418$ nm) during the CuAAC between **10** and **4**/**5**/**8**, $\lambda_{em.} = 340$ nm. The concentration of protein and $CuSO_4$ were 5 mg/mL and 1.5 mM, respectively. Ten equiv of PEG were used. The molar ratio of $CuSO_4$/Na-ascorbate was 1:2. Fluoresence is reported relative to the intensity at maximum conversion.

purification. Analytical thin layer chromatography (TLC) was performed on Merck precoated silica gel 60 F254 plates (layer thickness 0.25 mm) with visualization by ultraviolet (UV) irradiation at $\lambda = 254$ nm and/or $\lambda = 366$ nm and/or staining with $KMnO_4$ or Ninhydrin. Purifications by silica gel chromatography were performed using Acros (0.035−0.070 mm, pore diameter ca. 6 nm) silica gel. The water used in the experiments with bovine serum albumin (BSA) was deionized using a Labconco Water Pro PS purification system. THF and Et_2O were distilled under nitrogen from sodium/benzophenone. CH_2Cl_2 was distilled under nitrogen from CaH_2. Styrene was distilled under reduced pressure. Anhydrous DMF was obtained from Biosolve. BSA was obtained from Sigma.

General Instrumentation. NMR spectra were recorded on Bruker DMX300 (300 and 75 MHz for ^1H and ^{13}C, respectively) and Varian Inova 400 (400 MHz) spectrometers. ^1H NMR chemical shifts (δ) are reported in parts per million (ppm) relative to a residual proton peak of the solvent, $\delta = 7.26$ for $CDCl_3$, and $\delta = 2.50$ for DMSO-d_6. Multiplicities are reported as follows: s (singlet), d (doublet), t (triplet), q (quartet), dd (doublet of doublets), dt (doublet of triplets), dq (double quartet), ddd (double, double doublet), ddt (double, double triplet), or m (multiplet). Broad peaks are indicated by the addition of br. Coupling constants are reported as a *J* value in hertz (Hz). The number of protons (*n*) for a given resonance is indicated as *n*H and is based on spectral integration values. ^{13}C NMR chemical shifts (δ) are reported in ppm relative to DMSO-d_6 ($\delta = 39.5$) or $CDCl_3$ ($\delta = 77.0$). IR spectra were recorded on an ATI Matson Genesis Series FTIR spectrometer fitted with an ATR cell. The vibrations (ν) are given in cm^{-1}. Molecular weight distributions were measured with a Shimadzu SEC, equipped with a guard column and a PL gel 5 μm mixed D column (Polymer Laboratories) with differential refractive index (RI) and UV ($\lambda = 254$ nm and $\lambda = 340$ nm) detection using THF as an eluent (1 mL/min at 35 °C). Poly(ethylene glycol) (PEG) standards were used for calibration. Matrix assisted laser desorption/ionization time-of-flight (MALDI-ToF) spectra were measured on a Bruker Biflex III spectrometer, and samples were prepared from THF solutions using indoleacrylic acid (IAA) (20 mg/mL) as a matrix. High resolution mass spectra were recorded on a JEOL AccuToF (ESI) or a MAT900 (EI, CI, and ESI). UV−vis spectra were measured on a Varian Cary 50 spectrophotometer equipped with a RM6 Lauda temperature controller using a 1 cm path-length quartz cuvette. Protein conjugates mixtures were analyzed with a Pharmacia SMART high performance liquid chromatography (HPLC) system, equipped with a Superdex 75 PC 3.2/30 column (optimal separation 3−70 kDa) (Pharmacia) using phosphate buffer (20 mM, pH 7.5) as an eluent (50 μL/min at room temperature) in combination with UV detection ($\lambda = 280$ nm and $\lambda = 340$ nm). Prior to injection, crude reaction mixtures were diluted to a protein concentration of 1.25 mg/mL and filtered over a 0.2 μm nylon filter. Sodium dodecyl sulfate−polyacrylamide gel electrophoresis (SDS−PAGE) was performed using 10% polyacrylamide gels. To denaturate the samples, β-mercapto ethanol was added, and the samples were heated at 95 °C for 10 min. Staining was accomplished using Coomassie blue.

Fluorescence Experiments. Fluorescence measurements were performed on a Perkin-Elmer luminescence spectrometer LS 55 equipped with a RM6 Lauda temperature controller fixed at 23 °C. A 1 cm path-length quartz cuvette was used, and after measurements of protein containing samples, the cuvette was washed thoroughly with deionized water and EtOH. Samples from the bioconjugation experiments were prepared by withdrawing 40 μL of reaction medium followed by dilution in the reaction buffer to a protein concentration of 0.59 μg/mL. The excitation wavelength was set at 340 nm, and the spectra were recorded using excitation and emission slits of 10 nm.

3-Azido-7-hydroxy Coumarin (1). This compound was prepared according to a literature procedure and was obtained as a light brown solid (12% yield). ^1H NMR (DMSO-d_6, 400 MHz): $\delta = 10.53$ (s, 1 H, O*H*), 7.60 (s, 1 H, coumarin H_4), 7.48 (d, $J = 8.5$ Hz, 1 H, coumarin H_5), 6.81 (dd, $J = 8.5$, 2.3 Hz, 1 H, coumarin H_6), 6.76 (d, $J = 2.3$ Hz, 1 H, coumarin H_8). ^{13}C NMR (DMSO, 75 MHz): $\delta = 160.3$, 157.3, 152.7, 129.1, 127.8, 121.1, 113.8, 111.3, 102.0. FT-IR (ATR): 3291, 2115 (νN_3), 1679, 1616, 1303.

3-Azido-7-(*tert*-butylcarboxy methoxy) Coumarin (2). 3-Azido-7-hydroxy-coumarin (803 mg; 3.95 mmol) and K_2CO_3 (580 mg; 4.20 mmol) were suspended in anhydrous DMF (15 mL) under an argon atmosphere and stirred for 10 min at room temperature. The mixture was heated to 40 °C, and *tert*-butyl-2-bromoacetate (584 μL; 3.96 mmol) was added. The mixture was stirred for 3.5 h at 40 °C, after which completion of the reaction was determined by TLC (EtOAc/heptane; 1:1 v/v). After dilution with EtOAc (200 mL), the mixture was washed with water (2 × 150 mL). The aqueous phases were extracted with EtOAc (100 mL), and the combined organic phases were dried over anhydrous Na_2SO_4 and filtered. Upon concentration under reduced pressure, the crude product was obtained as a brown oil. The oil was dissolved in CH_2Cl_2 (10 mL), and this solution was added dropwise to *n*-pentane (400 mL) under stirring, forming a brown precipitate and a yellow solution. After filtration, the precipitation procedure was repeated for the residue. The filtrates were combined and concentrated under reduced pressure, affording the product as a yellowish-brown solid (960 mg, 77%) $R_f = 0.7$ (EtOAc/heptane; 1/1), ^1H NMR (DMSO-d_6, 300 MHz): $\delta = 7.63$ (s, 1H, coumarin H_4), 7.58 (d, $J = 8.6$ Hz, 1H, coumarin H_5), 7.02 (d, $J = 2.4$ Hz, 1H, coumarin H_8), 6.97 (dd, $J = 2.5$, 8.6 Hz, 1H, coumarin H_6), 4.8 (s, 2H, OC*H*$_2$CO$_2$), 1.43 (s, 9H, O^{t}Bu). ^{13}C NMR (DMSO-d_6, 75 MHz): $\delta = 167.3$, 159.7, 157.1, 152.4, 128.8, 127.1, 122.6, 113.2, 101.4, 81.7, 65.3, 27,7. FT-IR (ATR): 2120 (νN_3), 1744, 1722, 1618, 1139.

3-Azido-7-(carboxy methoxy) Coumarin (3). To a solution of 3-azido-7-(*tert*-butylcarboxy methoxy) coumarin (**2**; 700 mg, 2.21 mmol) in CH_2Cl_2 (30 mL) was added trifluoro acetic acid (TFA; 1.5 mL, 20 mmol), and the mixture was stirred at room temperature for 18 h. The reaction was determined to be almost complete by TLC (EtOAC/heptane, 1/1). An extra amount of TFA (1.5 mL, 20 mmol) was added, and the mixture was

allowed to stir for an additional 3 h. The reaction mixture was diluted with CH_2Cl_2 (150 mL) and washed with water (75 mL) and a 10% aqueous solution of citric acid (75 mL). The organic phase was dried over anhydrous Na_2SO_4, filtered, and concentrated *in vacuo*, yielding an brownish-orange solid (434 mg, 75%). ^{1}H NMR (DMSO-d_6, 400 MHz): δ = 13.13 (br s, 1H, COO*H*), 7.64 (s, 1H, coumarin H_4), 7.58 (d, J = 8.6 Hz, 1H, coumarin H_5), 7.03 (d, J = 2.5 Hz, 1H, coumarin H_8), 6.98 (dd, J = 2.5, 8.6 Hz, 1H, coumarin H_6), 4.81 (s, 2H, OC*H*$_2$COOH). ^{13}C NMR (DMSO-d_6, 75 MHz): δ = 169.6, 159.8, 157.1, 152.4, 128.8, 127.2, 122.5, 113.2, 112.9, 101.4, 64.9. FT-IR (ATR): 2152 (νN$_3$), 1748, 1725, 1621, 1245, 1221, 1156. HRMS (ESI-) calcd for $C_{11}H_6N_3O_5$ $(M - H)^-$: 260.03075; found, 260.03172.

Ester-Linked 3-Azido-coumarin Terminated Poly(ethylene glycol). Polymers **4** and **5** were prepared following a similar procedure. Procedure for **4**: To a flame-dried Schlenk vessel were added α-methoxy poly(ethylene glycol) (mPEG, M_n = 2000 g/mol; 259 mg, 0.130 mmol), 3-azido-7-(carboxy methoxy) coumarin (**3**; 51 mg, 0.20 mmol), 4-(dimethylamino)-pyridine (DMAP; 9 mg, 0.07 mmol), and anhydrous CH_2Cl_2 (4 mL) under an argon atmosphere. Next, the mixture was cooled to 0 °C and 1-ethyl-3-(3-dimethylaminopropyl) carbodiimide hydrochloride (EDC·HCl; 38 mg, 0.20 mmol) was added. The mixture was stirred at 0 °C for 1 h followed by 40 h at room temperature. After dilution with CH_2Cl_2 (150 mL), the mixture was washed with a saturated aqueous solution of $NaHCO_3$ (2 × 100 mL) and a saturated aqueous solution of NH_4Cl (100 mL). The organic phase was dried over anhydrous Na_2SO_4, filtered, and concentrated under reduced pressure until approximately 5 mL of the mixture remained. Upon precipitation in Et_2O (450 mL), the product was obtained as a yellow−orange solid (216 mg, 73%). ^{1}H NMR ($CDCl_3$, 400 MHz): δ = 7.35 (d, J = 8.7 Hz, 1H, coumarin H_5), 7.18 (s, 1H, coumarin H_4), 6.92 (dd, J = 2.5, 8.7 Hz, 1H, coumarin H_6), 6.82 (d, J = 2.4 Hz, 1H, coumarin H_8), 4.73 (s, 2H, OC*H*$_2$CO$_2$), 4.41−4.36 (m, 2H, CH$_2$C*H*$_2$OCO), 3.64 (br s, 180H, PEG backbone), 3.38 (s, 3H, OC*H*$_3$). FT-IR (ATR): 2883, 2123 (νN$_3$), 1960, 1725, 1619, 1466, 1341, 1102. SEC (THF): M_n = 1830 g/mol; M_n/M_w = 1.22.

α-Methoxy ω-(2-Cyanoethyl) Poly(ethylene glycol) (6). A solution of α-methoxy poly(ethylene glycol) (mPEG, M_n = 2000 g/mol; 4.0 g, 2.0 mmol) in acrylonitrile (20 mL) was cooled to 0 °C before adding KOH (10 mg, 0.18 mmol). The mixture was stirred at 0 °C for 2.5 h, after which the mixture turned slightly yellow. At this point, the reaction was quenched by the addition of a drop of concentrated HCl. Subsequently, the mixture was concentrated under reduced pressure resulting in an off-white solid (3.94 g, 96%). ^{1}H NMR ($CDCl_3$, 400 MHz): δ = 3.73 (t, J = 6.4 Hz, 2H, overlap with signal at 3.64 ppm, OC*H*$_2$CH$_2$CN), 3.64 (br s, 180H, PEG backbone), 3.38 (s, 3H, OC*H*$_3$), 2.64 (t, J = 6.4 Hz, 2H, OCH$_2$C*H*$_2$CN). FT-IR (ATR): 2883, 2249, 1960, 1466, 1340, 1106.

α-Methoxy ω-(3-Aminopropyl) Poly(ethylene glycol) (7). To a cooled (0 °C) solution of borane−THF complex (5 mL 1 M in THF, 5 mmol) in anhydrous THF (15 mL) was added a solution of α-methoxy ω-(2-cyanoethyl) PEG (**6**; 2.01 g, 0.979 mmol) in anhydrous THF (10 mL) under an argon atmosphere. The mixture was stirred at 0 °C for 30 min, after which it was heated to reflux for 4 h. The mixture was cooled again to 0 °C, and MeOH (5 mL) was added dropwise (resulting in the evolution of hydrogen gas). Next, HCl (0.25 mL) was added slowly, and the mixture was stirred for 1 h, after which it was concentrated under reduced pressure. Trimethyl borate was removed by coevaporation with MeOH (3 × 50 mL). An aqueous solution of NaOH (1 M, 50 mL) was added to the residue, and the resulting mixture was extracted with CH_2Cl_2 (2 × 100 mL). The organic phases were dried over anhydrous Na_2SO_4, filtered, and concentrated *in vacuo*, yielding a white solid (1.94 g, 96%). ^{1}H NMR ($CDCl_3$, 400 MHz): δ = 3.64 (br s, 180H, PEG backbone), 3.55 (m, 2H, overlap with signal at 3.64 ppm, OC*H*$_2$CH$_2$CH$_2$), 3.38 (s, 3H, OC*H*$_3$), 2.80 (t, J = 6.2 Hz, 2 H, CH$_2$C*H*$_2$NH$_2$), 1.73 (m, 2H, OCH$_2$C*H*$_2$CH$_2$). FT-IR (ATR): 2882, 1960, 1466, 1340, 1101.

Amide-Linked 3-Azido Coumarin Terminated Poly(ethylene glycol) (8). To a flame-dried Schlenk vessel were added α-methoxy ω-(3-aminopropyl) poly(ethylene glycol) (**7**; 252 mg, 0.122 mmol), 3-azido-7-(carboxy methoxy) coumarin (**3**; 48 mg, 0.18 mmol), 4-(dimethylamino)-pyridine (DMAP; 38 mg, 0.31 mmol), and anhydrous CH_2Cl_2 (4 mL) under an argon atmosphere. Next, the mixture was cooled to 0 °C and 1-ethyl-3-(3-dimethylaminopropyl) carbodiimide hydrochloride (EDC·HCl; 36 mg, 0.19 mmol) was added. The mixture was stirred at 0 °C for 1 h followed by 40 h at room temperature. After dilution with CH_2Cl_2 (150 mL), the mixture was washed with a saturated aqueous solution of $NaHCO_3$ (2 × 100 mL) and a 10% aqueous solution of citric acid (100 mL). The organic phase was dried over anhydrous Na_2SO_4, filtered, and concentrated under reduced pressure, affording a yellow−orange solid (249 mg, 88%). ^{1}H NMR ($CDCl_3$, 400 MHz): δ = 7.39 (d, J = 8.6 Hz, 1H, coumarin H_5), 7.2 (s, 1H, coumarin H_4), 7.16 (br s, 1H, CH$_2$N*H*CO), 6.93 (dd, J = 2.5, 8.6 Hz, 1H, coumarin H_6), 6.90 (d, J = 2.4 Hz, 1H, coumarin H_8), 4.53 (s, 2H, OC*H*$_2$CONH), 3.64 (br s, 180H, PEG backbone), 3.60−3.53 (m, overlaps with signal at 3.64 ppm), 3.38 (s, 3H, OC*H*$_3$), 1.83 (q, J = 5.9 Hz, 2H, OCH$_2$C*H*$_2$CH$_2$). FT-IR (ATR): 2883, 2125 (νN$_3$), 1964, 1714, 1666, 1619, 1466, 1341. 1104. SEC (THF): M_n = 1830 g/mol; M_n/M_w = 1.24.

***N*-Propargyl Maleimide (9).** Propargylamine (330 μL, 4.84 mmol) was dissolved in a saturated aqueous solution of $NaHCO_3$ (40 mL) and cooled on an ice bath. Then *N*-(methoxy carbonyl) maleimide (751 mg, 4.81 mmol) was added in portions over 20 min under vigorous stirring. The mixture was stirred for 30 min at 0 °C, followed by 45 min at room temperature. After extraction with CH_2Cl_2 (3 × 50 mL), the organic phase was dried over anhydrous Na_2SO_4, filtered, and concentrated *in vacuo*. Purification by silica gel column chromatography (EtOAc/heptane, 1:2) yielded the product as a colorless oil after coevaporation with CH_2Cl_2 and would eventually lead to white crystals (291 mg, 45% yield). R_f = 0.56 (EtOAc/heptane, 1:1 v/v) ^{1}H NMR ($CDCl_3$, 400 MHz): δ = 6.76 (s, 2H, *H*C=C*H*); 4.30 (d, J = 2.5 Hz, 2H, C*H*$_2$C'CH); 2.22 (t, J = 2.5 Hz, 1H, C'C*H*) ^{13}C NMR (75 MHz, $CHCl_3$): δ = 169.2, 134.4, 76.9, 71.5, 26.8. FT-IR (ATR): 3272, 3100, 2972, 2127, 1698, 1430, 1402, 1315, 1348, 1154 cm^{-1}. HRMS (EI+) *m/z* calcd for $C_7H_5NO_2$: 135.0320; found, 135.0324.

3-(2-Hydroxy ethylsulfanyl)-*N*-propargyl-succinimide (18). 2-Mercaptoethanol (25 μL, 0.36 mmol) was added to a solution of *N*-propargyl-maleimide (40 mg, 0.30 mmol) and Et_3N (50 μL, 0.36 mmol) in anhydrous CH_2Cl_2 (2 mL), under an argon atmosphere. The mixture was stirred at room temperature for 1 h. After dilution with CH_2Cl_2 (10 mL), the mixture was washed with 1 M aqueous HCl (2 × 10 mL). The organic phase was dried over anhydrous Na_2SO_4, filtered, and concentrated under reduced pressure, affording the crude product as a colorless oil. Purification by preparative TLC (EtOAc/heptane, 4:1 v/v) yielded the desired compound as a colorless oil (26 mg, 41% yield). R_f = 0.41 (EtOAc/heptane, 4:1 v/v) ^{1}H NMR ($CDCl_3$, 400 MHz): δ = 4.28 (d, J = 2.5 Hz, 2H, C*H*$_2$C'CH), 3.91 (dd, J = 4.1, 9.3 Hz, 1H, CH$_2$C*H*S), 3.92−3.87 (m, 2H, CH$_2$C*H*$_2$OH), 3.22 (dd, J = 9.3, 18.8 Hz, 1H, C*H*$_2$CHS), 3.16 (ddd, J = 4.8, 6.1, 14.4 Hz, 1H, SC*H*$_2$), 2.91 (ddd, J = 4.9, 6.4, 14.4 Hz, 1H, SC*H*$_2$), 2.60 (dd, J = 4.1, 18.8 Hz, 1H, C*H*$_2$CHS) 2.63−2.58 (br m, 1H, O*H*), 2.22 (t, J = 2.5 Hz, 1H,

C'C$\underline{H}$). ^{13}C NMR (75 MHz, $CHCl_3$): δ = 176.2, 173.0, 76.1, 71.8, 61.8, 39.5, 36.3, 35.7, 28.2. FT-IR (ATR): 3421, 3282, 2925, 2850, 2565, 2250, 2127, 1703, 1422, 1392, 1343, 1174, 1060 cm^{-1}. HRMS (ESI+) *m/z* calcd for $C_7H_{11}NO_3SNa$: 236.03544 $(M + Na)^+$; found, 236.03573.

CuAAC between 3-(2-Hydroxy ethylsulfanyl)-*N*-propargyl-succinimide (12) and 3-Azido-coumarin Terminated Poly(ethylene glycol) (4). To a solution of 3-(2-hydroxy ethylsulfanyl)-*N*-propargyl-succinimide (12.5 mg, 58.6 μmol) and 3-azido coumarin terminated PEG **4** (50 mg, 22 μmol) in THF (1.5 mL) was added a mixture of $CuSO_4 \cdot 5H_2O$ (7.0 mg, 28 μmol) and Na-ascorbate (8.3 mg, 42 μmol) in water (1 mL). Upon stirring for 14 h at room temperature, the mixture showed a strong fluorescence when irradiated with UV light (λ = 366 nm). The mixture was diluted with an aqueous solution of ethylenediaminetetraacetic acid (EDTA; 25 mL, 0.065 M) and extracted with CH_2Cl_2 (3 × 25 mL). The combined organic layers were washed with water (25 mL) and dried over anhydrous Na_2SO_4. After filtering and drying *in vacuo*, the crude product was taken up in CH_2Cl_2 (1 mL) and precipitated in Et_2O (15 mL). Upon centrifugation, a yellowish pellet was obtained, which was washed with Et_2O and dried *in vacuo* to yield an off-white to yellowish solid (26 mg, 47% yield). ^{1}H NMR ($CDCl_3$, 400 MHz): δ = 8.60 (s, 1H, triazole H), 8.49 (s, 1H, coumarin H_4), 7.59 (d, J = 8.8 Hz, 1H, coumarin H_5), 7.01 (dd, J = 2.5, 8.7 Hz, 1H, coumarin H_6), 6.89 (d, J = 2.4 Hz, 1H, coumarin H_8), 4.91 (s, 1H, OC$\underline{H}_2$CO$_2$), 4.78 (s, 1H, NC$\underline{H}_2$C=CH), 4.41−4.38 (m, 2H, CH$_2$C$\underline{H}_2$OCO), 3.91 (dd, J = 4.0, 9.3 Hz, 1H, CH$_2$C$\underline{H}$S), 3.89−3.83 (m, 2H, CH$_2$C$\underline{H}_2$OH), 3.65 (br s, PEG backbone), 3.37 (s, 3H, OC$\underline{H}_3$), 3.22 (dd, J = 9.3, 18.8 Hz, 1H, C$\underline{H}_2$CHS), 3.09 (ddd, J = 4.7, 6.1, 14.4 Hz, 1H, SC$\underline{H}_2$), 2.89 (ddd, J = 4.9, 6.4, 14.4 Hz, 1H, SC$\underline{H}_2$), 2.67 (dd, J = 4.0, 18.8 Hz, 1H, C$\underline{H}_2$CHS). MALDI-ToF MS (IAA): calcd for $[M + Na]^+$ n = 45; 2492.3, *m/z* found = 2492.1.

Alkyne-Functionalized Bovine Serum Albumin (10). BSA (66 mg, 1.0 μmol) was placed in a Greiner tube and dissolved in phosphate buffer (PB) (1.5 mL; 50 mM, pH 7.5) by gently mixing for 30 min. Next, a solution of *N*-propargyl maleimide (8 mg, 59 μmol) in THF (0.5 mL) was added, and the mixture was gently mixed on a roller bank for 1.5 h, with exclusion of light. Excess *N*-propargyl maleimide was removed by passing the mixture through a sephadex (G50) column using phosphate buffer (50 mM, pH 7.5) as the eluent. The fractions containing BSA (judged by UV−vis spectroscopy) were combined and stored at 4 °C until further use (typically within a few days). The final concentration was determined by UV−vis spectroscopy using a molar extinction coefficient of 42316 M^{-1} cm^{-1}.

CuAAC of Alkyne-Functionalized BSA (10) and 3-Azido-7-hydroxy-coumarin (1). To an Eppendorf tube was added a solution of alkyne-functionalized BSA **10** (2.1 mg, $3.2 \cdot 10^{-2}$ μmol) in PB (250 μL, 50 mM, pH 7.5) and a solution of 3-azido-7-hydroxy-coumarin (0.18 mg, 0.89 μmol) in THF (54 μL). After the addition of a catalyst mixture (54 μL) containing $CuSO_4 \cdot 5H_2O$ (0.16 mg, 0.63 μmol) and Na-ascorbate (0.19 mg, 0.95 μmol) in PB (50 mM, pH 7.5), the reaction vial was placed on a roller bank for 18 h. The mixture was analyzed by fluorescence spectroscopy and SDS−PAGE without further purification.

Typical Procedure for CuAAC between Alkyne-Functionalized BSA (10) and 3-Azido-coumarin Terminated PEGs. A Greiner tube was loaded with an argon-purged solution of alkyne-functionalized BSA **10** (2.5 mg, $3.8 \cdot 10^{-2}$ μmol) in PB (300 μL, 50 mM, pH 7.5) and a solution of PEG **4** (0.93 mg, 0.41 μmol) in argon-purged PB (100 μL). After the addition of a catalyst mixture (100 μL) containing $CuSO_4 \cdot 5H_2O$ (0.19 mg, 0.76 μmol) and Na-ascorbate (0.29 mg, 1.46 μmol) in argon-purged PB (50 mM, pH 7.5), the reaction mixture was gently shaken, and samples were withdrawn periodically for spectroscopic analysis. Reactions between alkyne-functionalized BSA **10** and PEG **5** or **6** were carried out using a comparable protocol.

ACKNOWLEDGMENT

We thank Eva Sans i Atxer and Eline Mol for their assistance at the initial stage of this research. This work was financially supported by the research school NRSC-Catalysis, the Chemical Council of The Netherlands Organization for Scientific Research (CW-NWO), the European Science Foundation (ESF), and the Royal Netherlands Academy of Arts and Sciences (KNAW).

Supporting Information Available: Fluorogenic conjugation to BSA. This material is available free of charge via the Internet at http://pubs.acs.org.

LITERATURE CITED

(1) Duncan, R. (2003) The dawning era of polymer therapeutics. *Nat. Rev. Drug Discovery 2*, 347–360.
(2) Duncan, R. (2006) Polymer conjugates as anticancer nanomedicines. *Nat. Rev. Cancer 6*, 688–701.
(3) Hoffman, A. S., and Stayton, P. S. (2004) Bioconjugates of smart polymers and proteins: Synthesis and applications. *Macromol. Symp. 207*, 139–151.
(4) Thordarson, P., Le Droumaguet, B., and Velonia, K. (2006) Well-defined protein-polymer conjugates: synthesis and potential applications. *Appl. Microbiol. Biotechnol. 73*, 243–254.
(5) Vandermeulen, G. W. M., and Klok, H.-A. (2004) Peptide/protein hybrid materials: Enhanced control of structure and improved performance through conjugation of biological and synthetic polymers. *Macromol. Biosci. 4*, 383–398.
(6) Abuchowski, A., Vanes, T., Palczuk, N. C., and Davis, F. F. (1977) Alteration of Immunological properties of bovine serum-albumin by covalent attachment of polyethylene-glycol. *J. Biol. Chem. 252*, 3578–3581.
(7) Abuchowski, A., McCoy, J. R., Palczuk, N. C., Vanes, T., and Davis, F. F. (1977) Effect of covalent attachment of polyethylene-glycol on immunogenicity and circulating life of bovine liver catalase. *J. Biol. Chem. 252*, 3582–3586.
(8) Veronese, F. M., and Harris, J. M. (2002) Preface: Introduction and overview of peptide and protein pegylation. *Adv. Drug Delivery Rev. 54*, 453–456.
(9) Roberts, M. J., Bentley, M. D., and Harris, J. M. (2002) Chemistry for peptide and protein PEGylation. *Adv. Drug Delivery Rev. 54*, 459–476.
(10) Pasut, G., and Veronese, F. M. (2007) Polymer-drug conjugation, recent achievements and general strategies. *Prog. Polym. Sci. 32*, 933–961.
(11) Pasut, G., Veronese, F. M. (2006) PEGylation of Proteins As Tailored Chemistry for Optimized Bioconjugates, in *Polymer Therapeutics I: Polymers as Drugs, Conjugates and Gene Delivery Systems*, Vol. 192, pp 95−134, Springer Publishing, New York.
(12) Veronese, F. M. (2001) Peptide and protein PEGylation: a review of problems and solutions. *Biomaterials 22*, 405–417.
(13) Harris, J. M., and Chess, R. B. (2003) Effect of pegylation on pharmaceuticals. *Nat. Rev. Drug Discovery 2*, 214–221.
(14) Veronese, F. M., and Harris, J. M. (2008) Peptide and protein PEGylation III: advances in chemistry and clinical applications. *Adv. Drug Delivery Rev. 60*, 1–2.
(15) Hoffman, A. S., and Stayton, P. S. (2007) Conjugates of stimuli-responsive polymers and proteins. *Prog. Polym. Sci. 32*, 922–932.
(16) Maynard, H. D., Heredia, K. L., Li, R. C., Parra, D. P., and Vazquez-Dorbatt, V. (2007) Thermoresponsive biohybrid materials synthesized by ATRP. *J. Mater. Chem. 17*, 4015–4017.
(17) Heredia, K. L., Bontempo, D., Ly, T., Byers, J. T., Halstenberg, S., and Maynard, H. D. (2005) In situ preparation of protein:

"Smart" polymer conjugates with retention of bioactivity. *J. Am. Chem. Soc. 127*, 16955–16960.
(18) Dirks, A. J., Nolte, R. J. M., and Cornelissen, J. J. L. M. (2008) Protein-polymer hybrid amphiphiles. *Adv. Mater. 20*, 3953–3957.
(19) Reynhout, I. C., Cornelissen, J. J. L. M., and Nolte, R. J. M. (2007) Self-assembled architectures from biohybrid triblock copolymers. *J. Am. Chem. Soc. 129*, 2327–2332.
(20) Le Droumaguet, B., Mantovani, G., Haddleton, D. M., and Velonia, K. (2007) Formation of giant amphiphiles by post-functionalization of hydrophilic protein-polymer conjugates. *J. Mater. Chem. 17*, 1916–1922.
(21) Boerakker, M. J., Botterhuis, N. E., Bomans, P. H. H., Frederik, P. M., Meijer, E. M., Nolte, R. J. M., and Sommerdijk, N. A. J. M. (2006) Aggregation Behavior of giant amphiphiles prepared by cofactor reconstitution. *Chem.−Eur. J. 12*, 6071–6080.
(22) Dirks, A. J., van Berkel, S. S., Hatzakis, N. S., Opsteen, J. A., van Delft, F. L., Cornelissen, J. J. L. M., Rowan, A. E., van Hest, J. C. M., Rutjes, F. P. J. T., and Nolte, R. J. M. (2005) Preparation of biohybrid amphiphiles via the copper catalysed Huisgen [3 + 2] dipolar cycloaddition reaction. *Chem. Commun.* 4172–4174.
(23) Velonia, K., Rowan, A. E., and Nolte, R. J. M. (2002) Lipase polystyrene giant amphiphiles. *J. Am. Chem. Soc. 124*, 4224–4225.
(24) Boerakker, M. J., Hannink, J. M., Bomans, P. H. H., Frederik, P. M., Nolte, R. J. M., Meijer, E. M., and Sommerdijk, N. A. J. M. (2006) Giant amphiphiles by cofactor reconstitution. *Angew. Chem., Int. Ed. 41*, 4239–4241.
(25) Gauthier, M. A., and Klok, H.-A. (2008) Peptide/protein-polymer conjugates: synthetic strategies and design concepts. *Chem. Commun.* 2591–2611.
(26) Heredia, K. L., and Maynard, H. D. (2007) In situ preparation of protein: "Smart" polymer conjugates with retention of bioactivity. *Org. Biomol. Chem. 5*, 45–53.
(27) Nicolas, J., Mantovani, G., and Haddleton, D. M. (2007) Living radical polymerization as a tool for the synthesis of polymer-protein/peptide bioconjugates. *Macromol. Rapid Commun. 28*, 1083–1111.
(28) Mantovani, G., Lecolley, F., Tao, L., Haddleton, D. M., Clerx, J., Cornelissen, J. J. L. M., and Velonia, K. (2005) Design and synthesis of N-maleimido-functionalized hydrophilic polymers via copper-mediated living radical polymerization: A suitable alternative to PEGylation chemistry. *J. Am. Chem. Soc. 127*, 2966–2973.
(29) Bontempo, D., Heredia, K. L., Fish, B. A., and Maynard, H. D. (2004) Cysteine-reactive polymers synthesized by atom transfer radical polymerization for conjugation to proteins. *J. Am. Chem. Soc. 126*, 15372–15373.
(30) Rosendahl, M. S., Doherty, D. H., Smith, D. J., Carlson, S. J., Chlipala, E. A., and Cox, G. N. (2005) A long-acting, highly potent interferon alpha-2 conjugate created using site-specific PEGylation. *Bioconjugate Chem. 16*, 200–207.
(31) Connor, R. E., and Tirrell, D. A. (2007) Non-canonical amino acids in protein polymer design. *Polym. Rev. 47*, 9–28.
(32) Rose, K. (1994) Facile Synthesis of Homogeneous Artificial Proteins. *J. Am. Chem. Soc. 116*, 30–33.
(33) Kochendoerfer, G. G., Chen, S. Y., Mao, F., Cressman, S., Traviglia, S., Shao, H. Y., Hunter, C. L., Low, D. W., Cagle, E. N., Carnevali, M., Gueriguian, V., Keogh, P. J., Porter, H., Stratton, S. M., Wiedeke, M. C., Wilken, J., Tang, J., Levy, J. J., Miranda, L. P., Crnogorac, M. M., Kalbag, S., Botti, P., Schindler-Horvat, J., Savatski, L., Adamson, J. W., Kung, A., Kent, S. B. H., and Bradburne, J. A. (2003) Design and chemical synthesis of a homogeneous polymer-modified erythropoiesis protein. *Science 299*, 884–887.
(34) Schlick, T. L., Ding, Z. B., Kovacs, E. W., and Francis, M. B. (2005) Dual-surface modification of the tobacco mosaic virus. *J. Am. Chem. Soc. 127*, 3718–3723.
(35) Heredia, K. L., Tolstyka, Z. P., and Maynard, H. D. (2007) Aminooxy end-functionalized polymers synthesized by ATRP for chemoselective conjugation to proteins. *Macromolecules 40*, 4772–4779.
(36) Christman, K. L., Broyer, R. M., Tolstyka, Z. P., and Maynard, H. D. (2007) Site-specific protein immobilization through N-terminal oxime linkages. *J. Mater. Chem. 17*, 2021–2027.
(37) Rostovtsev, V. V., Green, L. G., Fokin, V. V., and Sharpless, K. B. (2002) A stepwise Huisgen cycloaddition process: Copper(I)-catalyzed regioselective "ligation" of azides and terminal alkynes. *Angew. Chem., Int. Ed. 41*, 2596–2599.
(38) Tornøe, C. W., Christensen, C., and Meldal, M. (2002) Peptidotriazoles on solid phase: [1,2,3]-triazoles by regiospecific copper(I)-catalyzed 1,3-dipolar cycloadditions of terminal alkynes to azides. *J. Org. Chem. 67*, 3057–3064.
(39) Bock, V. D., Hiemstra, H., and van Maarseveen, J. H. (2005) Cu-I-catalyzed alkyne-azide "click" cycloadditions from a mechanistic and synthetic perspective. *Eur. J. Org. Chem.* 51–68.
(40) Wu, P., and Fokin, V. V. (2007) Catalytic azide-alkyne cycloaddition: Reactivity and applications. *Aldrichimica Acta 40*, 7–17.
(41) Kolb, H. C., Finn, M. G., and Sharpless, K. B. (2001) Click chemistry: Diverse chemical function from a few good reactions. *Angew. Chem., Int. Ed. 40*, 2004–2021.
(42) Kolb, H. C., and Sharpless, K. B. (2003) The growing impact of click chemistry on drug discovery. *Drug Discovery Today 8*, 1128–1137.
(43) Dirks, A. J., Cornelissen, J. J. L. M., van Delft, F. L., van Hest, J. C. M., Nolte, R. J. M., Rowan, A. E., and Rutjes, F. P. J. T. (2007) From (bio)molecules to biohybrid materials with the click chemistry approach. *QSAR Comb. Sci. 26*, 1200–1210.
(44) Breinbauer, R., and Kohn, M. (2003) Azide-alkyne coupling: A powerful reaction for bioconjugate chemistry. *ChemBioChem 4*, 1147–1149.
(45) Binder, W. H., and Sachsenhofer, R. (2007) 'Click' chemistry in polymer and materials science. *Macromol. Rapid Commun. 28*, 15–54.
(46) Lutz, J.-F. (2007) 1,3-dipolar cycloadditions of azides and alkynes: A universal ligation tool in polymer and materials science. *Angew. Chem., Int. Ed. 46*, 1018–1025.
(47) Deiters, A., Cropp, T. A., Summerer, D., Mukherji, M., and Schultz, P. G. (2004) Site-specific PEGylation of proteins containing unnatural amino acids. *Bioorg. Med. Chem. Lett. 14*, 5743–5745.
(48) Schoffelen, S., Lambermon, M. H. L., van Eldijk, M. B., and van Hest, J. C. M. (2008) Site-specific modification of candida antartica lipase B via residue-specific incorporation of a non-canonical amino acid. *Bioconjugate Chem. 19*, 1127–1131.
(49) Sen Gupta, S., Raja, K. S., Kaltgrad, E., Strable, E., and Finn, M. G. (2005) Virus-glycopolymer conjugates by copper(I) catalysis of atom transfer radical polymerization and azide-alkyne cycloaddition. *Chem. Commun.* 4315–4317.
(50) Li, M., De, P., Gondi, S. R., and Summerlin, B. S. (2008) responsive polymer-protein bioconjugates perpared by RAFT polymerization and copper-catalyzed azide-alkyne click chemistry. *Macromol. Rapid Commun. 29*, 1172–1176.
(51) Sivakumar, K., Xie, F., Cash, B. M., Long, S., Barnhill, H. N., and Wang, Q. (2004) A fluorogenic 1,3-dipolar cycloaddition reaction of 3-azidocoumarins and acetylenes. *Org. Lett. 6*, 4603–4606.
(52) O'Reilly, R. K., Joralemon, M. J., Hawker, C. J., and Wooley, K. L. (2006) Fluorogenic 1,3-dipolar cycloaddition within the hydrophobic core of a shell cross-linked nanoparticle. *Chem.−Eur. J. 12*, 6776–6786.
(53) Beatty, K. E., Liu, J. C., Xie, F., Dieterich, D. C., Schuman, E. M., Wang, Q., and Tirrell, D. A. (2006) Fluorescence visualization of newly synthesized proteins in mammalian cells. *Angew. Chem., Int. Ed. 45*, 7364–7367.
(54) Beatty, K. E., Xie, F., Wang, Q., and Tirrell, D. A. (2005) Selective dye-labeling of newly synthesized proteins in bacterial cells. *J. Am. Chem. Soc. 127*, 14150–14151.
(55) Zeng, Q. B., Li, T., Cash, B., Li, S. Q., Xie, F., and Wang, Q. (2007) Chemoselective derivatization of a bionanoparticle by click reaction and ATRP reaction. *Chem. Commun.* 1453–1455.

(56) van Berkel, S. S., Dirks, A. J., Debets, M. F., van Delft, F. L., Cornelissen, J. J. L. M., Nolte, R. J. M., and Rutjes, F P. J. T. (2007) Metal-free triazole formation as a tool for bioconjugation. *ChemBioChem 8*, 1504–1508.

(57) Xie, F., Sivakumar, K., Zeng, Q. B., Bruckman, M. A., Hodges, B., and Wang, Q. (2008) A fluorogenic 'click' reaction of azidoanthracene derivatives. *Tetrahedron 64*, 2906–2914.

(58) Zhou, Z., and Fahrni, C. J. (2004) A fluorogenic probe for the copper(I)-catalyzed azide-alkyne ligation reaction: Modulation of the fluorescence emission via $3(n,\pi^*)$-$^1(\pi, \pi^*)$ inversion. *J. Am. Chem. Soc. 126*, 8862–8863.

BC8004667

Supporting Information:

Monitoring Protein-Polymer Conjugation by a Fluorogenic Cu(I)-Catalyzed Azide-Alkyne 1,3-Dipolar Cycloaddition

A. (Ton) J. Dirks, Jeroen J. L. M. Cornelissen, and Roeland J. M. Nolte*

Institute for Molecules and Materials, Radboud University Nijmegen,

Toernooiveld 1, 6525 ED, Nijmegen, The Netherlands.

Fax (+31) 24 365 2929; Tel: (+31) 24 365 2381

To evaluate the concept of monitoring protein-polymer conjugation by a fluorogenic CuAAC, we selected alkyne-functionalized BSA **10** as a model protein, this protein can readily be prepared by coupling *N*-propargyl maleimide (**9**) to residue CYS34 of commercially available BSA. Previously, *N*-propargyl maleimide was prepared in a two-step procedure, involving the opening of maleic anhydride with propargyl amine followed by a ring closure (*1*). However, an alternative protocol starting from *N*-methoxycarbonyl maleimide (Scheme S1) was later found to rapidly produce the desired maleimide **9** in one clean reaction step. Conjugation of maleimide **9** to BSA was achieved by mixing the reaction partners in phosphate buffer (50 mM, pH 7.5) containing 25 % (v/v) of THF. The resulting alkyne-bearing BSA was purified over a sephadex (G50) column. Subsequently, a CuAAC with 3-azido-7-hydroxy-coumarin (**1**) was conducted to check for a successful functionalization of the protein (Scheme S1). Analysis by fluorescence spectroscopy clearly showed an increase in fluorescence intensity (at $\lambda_{em.}$ = 385 nm, using $\lambda_{ex.}$ = 475 nm) upon the cycloaddition reaction, indicating the presence of the alkyne moiety. Additional analysis by SDS-PAGE showed a fluorescent band at the position of BSA under irradiation with a hand-held UV lamp (λ = 366 nm) (Figure S1). Since a control experiment in which the catalyst was left out did not show a fluorescent band, the results confirm the formation of covalently linked protein-coumarin conjugate **11** *via* the formation of **10**. For the thiol-maleimide coupling to prepare BSA **10**, reduction of the reaction time from 18h, as we previously reported (*2*), to 1.5 h resulted in an equally efficient functionalization reaction.

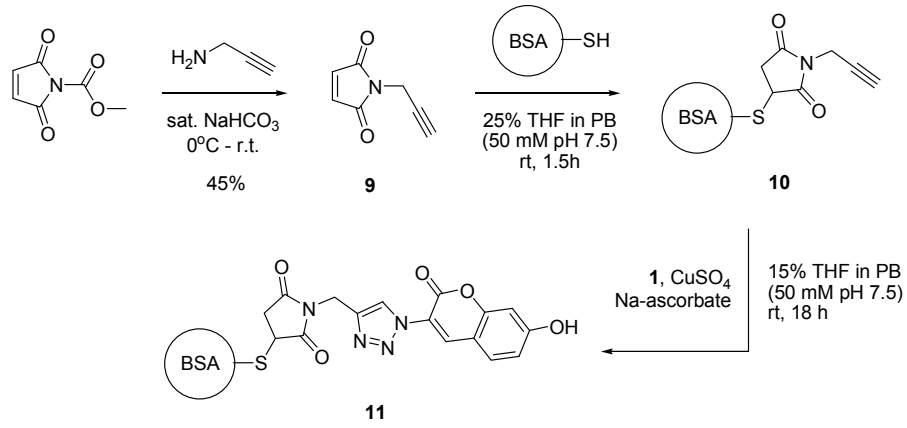

Scheme S1. Synthesis of alkyne-functionalized BSA and subsequent labeling by a CuAAC reaction with 3-azido-7-hydroxy-coumarin (**1**).

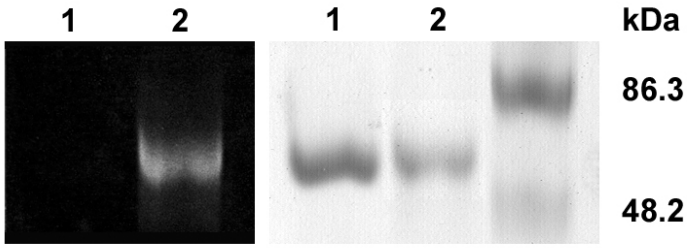

Figure 3. SDS-PAGE (10% running gel) analysis of BSA-coumarin conjugate **11** (lane 2) and a control experiment in which the catalyst was left out (lane 1). The SDS-PAGE gel was first photographed under exposure to UV light (λ = 366 nm) (left image) and subsequently stained with Coomassie Blue (right image).

References:

(1) Karlen, B., Lindeke, B., Lindgren, S., Svensson, K. G., Dahlbom, R., Jenden, D. J., and Giering, J. E. (1970) Acetylene compounds of potential value. XIV. N-(t-aminoalkynyl)-substituted succinimides and maleimides. A class of central anticholinergic agents *J. Med. Chem. 13*, 651-657.

(2) Dirks, A. J., van Berkel, S. S., Hatzakis, N. S., Opsteen, J. A., van Delft, F. L., Cornelissen, J. J. L. M., Rowan, A. E., van Hest, J. C. M., Rutjes, F. P. J. T., and Nolte, R. J. M. (2005) Preparation of biohybrid amphiphiles via the copper catalysed Huisgen [3+2] dipolar cycloaddition reaction. *Chem. Commun.* 4172-4174.

17-[4-(2-[^{18}F]Fluoroethyl)-1*H*-1,2,3-triazol-1-yl]-6-thia-heptadecanoic Acid: A Potential Radiotracer for the Evaluation of Myocardial Fatty Acid Metabolism

Dong Hyun Kim, Yearn Seong Choe,* Joon Young Choi, Yong Choi, Kyung-Han Lee, and Byung-Tae Kim

Department of Nuclear Medicine, Samsung Medical Center, Sungkyunkwan University School of Medicine, 50 Ilwon-dong, Kangnam-ku, Seoul 135-710, Korea. Received October 30, 2008; Revised Manuscript Received May 8, 2009

In this study, we synthesized 17-[4-(2-[^{18}F]fluoroethyl)−1*H*-1,2,3-triazol-1-yl]-6-thia-heptadecanoic acid ([^{18}F]**1**), a PET radiotracer for the evaluation of fatty acid metabolism. [^{18}F]**1** was synthesized in 20−26% decay-corrected radiochemical yields from 17-azido 6-thia-heptadecanoic acid (**9**) and 4-[^{18}F]fluoro-1-butyne using click chemistry. The tissue distribution of [^{18}F]**1** in mice showed high radioactivity accumulation in heart (3.70%ID/g at 1 min, 3.28%ID/g at 10 min, and 3.01%ID/g at 60 min postinjection), a prolonged myocardial elimination half-life (>60 min), and a maximal heart-to-blood uptake ratio at 5 min postinjection (5.55). Pretreatment with etomoxir, a carnitine palmitoyl transferase (CPT) I inhibitor, reduced myocardial radioactivity uptake at 30 min postinjection by 53%, suggesting that [^{18}F]**1** was transported into the mitochondria. Analyses of heart tissue samples showed that most of the radioactivity was present in a tissue pellet (62−63%) after homogenization in $CHCl_3$−CH_3OH followed by extraction with 40% urea and 5% H_2SO_4, which was mostly precipitated with addition of 50% trichloroacetic acid (TCA). These results suggest that [^{18}F]**1** undergoes metabolic trapping via β-oxidation in myocardium and, thus, suggest that it has potential use as a PET radiotracer for the evaluation of myocardial fatty acid metabolism.

INTRODUCTION

Free fatty acids are myocardial energy substrates under aerobic conditions (*1*). In the fasting state, fatty acids undergo β-oxidation, whereas in the nonfasting state, fatty acid oxidation decreases and glucose is utilized as an energy source (*2*−*4*). Therefore, radiolabeled fatty acid analogues can be used to evaluate fatty acid metabolism in myocardium using positron emission tomography (PET) or single photon emission computed tomography (SPECT).

Radioiodinated fatty acid analogues have been previously investigated in this context. 15-(*p*-[^{123}I]Iodophenyl)pentadecanoic acid ([^{123}I]IPPA) was synthesized to overcome some of the drawbacks of [^{123}I]iodoalkyl fatty acid analogues, such as in vivo deiodination and a short myocardial clearance half-time (*5*−*7*). Fatty acid analogues labeled with positron emitting radionuclides have also been developed. 1-[^{11}C]Palmitate was found to show biexponential clearance, composed of rapid washout resulting from β-oxidation and slow washout due to intracellular lipid pool turnover, and ω-[^{11}C]palmitate showed greater heart uptake than 1-[^{11}C]palmitate due to its reduced metabolism in rats (*8*−*10*). To prolong myocardial retention of fatty acid analogues, two different strategies such as methyl group substitution or the insertion of a sulfur atom at a fatty acid chain have been used. As expected, methyl group substitution at C3 of IPPA retarded its myocardial metabolism, and 15-(*p*-[^{123}I]iodophenyl)-3-methylpentadecanoic acid ([^{123}I]BMIPP) and 15-(*p*-[^{123}I]iodophenyl)-3,3-dimethylpentadecanoic acid ([^{123}I]DMIPP) were found to have prolonged myocardial retention as compared with that of [^{123}I]IPPA (*11*). [^{123}I]BMIPP showed more promise than [^{123}I]DMIPP in terms of diagnosing various myocardial disease due to its lower liver uptake (*12*). A similar effect was observed in methyl branched ω-[^{18}F]fluoroheptadecanoic acids at C3 (3-[^{18}F]MFHA) or C5 (5-[^{18}F]MFHA), and these showed higher and prolonged myocardial uptake than unsubstituted ω-[^{18}F]fluoropalmitic acid, except at initial time point (1 min) (*13*). As an alternative strategy, 4- and 6-thiafatty acid analogues were developed and shown to prolong its myocardial retention (*14*−*16*), e.g., 14-[^{18}F]fluoro-6-thia-heptadecanoic acid ([^{18}F]FTHA) was found to have excellent biological properties, e.g., high heart uptake in mice and prolonged myocardial retention (*15*). It has been proposed that [^{18}F]FTHA undergoes β-oxidation and is then metabolically trapped in myocardium. However, none of these metabolites have been identified.

Click chemistry represents triazole formation via the Cu(I)-catalyzed 1,3-cycloaddition of azides and terminal alkynes (*17*) and has been shown to be useful for synthesis of new compounds due to its simple reaction conditions, stereospecificity, wide scope of application, and so forth. Therefore, click chemistry has been used to synthesize various radiotracers, including small organic molecules and peptides (*18*−*23*).

Hence, in the present study, we applied click chemistry to synthesis of 17-[4-(2-[^{18}F]fluoroethyl)-1*H*-1,2,3-triazol-1-yl]-6-thia-heptadecanoic acid ([^{18}F]**1**) and evaluated the fatty acid analogue in mouse heart.

EXPERIMENTAL SECTION

Materials and Methods. Chemicals were obtained from Sigma-Aldrich (St. Louis, MO, USA). ^{1}H NMR spectra were obtained on a Varian Unity Inova 500NB (500 MHz) spectrometer (Palo Alto, CA, USA) at the Cooperative Center for Research Facilities, Sungkyunkwan University (Suwon, Korea). Chemical shifts (δ) are reported as ppm downfield of tetramethylsilane. Electron impact (EI) and fast atom bombardment (FAB) mass spectra were obtained on a JMS-700 Mstation (JEOL Ltd., Tokyo, Japan) at the Korea Basic Science Institute (Seoul, Korea). HPLC was carried out using a Thermo Separa-

* Corresponding author. Yearn Seong Choe, Tel: +82-2-3410-2623, Fax: +82-2-3410-2639, email: ysnm.choe@samsung.com.

10.1021/bc800472a CCC: $40.75 © 2009 American Chemical Society
Published on Web 05/26/2009

tion Products System (Fremont, CA, USA) equipped with a semipreparative column (YMC C18, 5 μ, 10 × 250 mm) or an analytical column (YMC C18, 5 μ, 4.6 × 250 mm). Eluates were simultaneously monitored using a UV (220 nm) detector and a NaI(T1) radioactivity detector. TLC was performed on Merck F_{254} silica plates and analyzed using a Bioscan radio-TLC scanner (Washington, DC, USA). microPET imaging of mice was acquired using an Inveon microPET (Siemens Medical Solutions, Malvern, PA, USA).

[^{18}F]Fluoride was produced by the ^{18}O(p,n)^{18}F reaction using a cyclotron (GE Healthcare PETtrace, Uppsala, Sweden). Radioactivities were measured using a dose calibrator (Biodex Medical Systems, Shirley, NY, USA) and tissue radioactivities using a Wallac automated gamma counter (Boston, MA, USA). All animal experiments were performed in compliance with the requirements of the Samsung Medical Center Laboratory Animal Care, in accord with NIH guidelines.

Synthesis of Methyl 17-Hydroxy-6-thia-heptadecanoate (2). 11-Mercapto-1-undecanol (540 mg, 2.64 mmol) and *N*,*N*-diisopropylethylamine (DIEA; 920 μL, 5.28 mmol) were added to methyl 5-bromovalerate (413 μL, 2.91 mmol) in CH_3CN (5 mL), and the reaction mixture was stirred under N_2 at 85 °C for 18 h. After solvent had been removed in vacuo, the residue was extracted with CH_2Cl_2, washed with water, and dried over anhydrous Na_2SO_4. Flash column chromatography (3:1 hexane/ethyl acetate) gave **2** (597 mg, 71%) as a white solid. ^{1}H NMR ($CDCl_3$, 500 MHz) δ 3.67 (s, 3H), 3.64 (t, 2H, J = 6.5 Hz), 2.53−2.48 (m, 4H), 2.33 (t, 2H, J = 7.0 Hz), 1.76−1.70 (m, 2H), 1.65−1.54 (m, 6H), 1.38−1.24 (m, 14H); MS (EI) *m*/*z* 318 (100), (M^+); HRMS calcd for $C_{17}H_{34}O_3S$ 318.2229, found 318.2230.

Synthesis of Methyl 17-Methanesulfonyloxy-6-thia-heptadecanoate (3). Compound **2** (500 mg, 1.57 mmol) was dissolved in CH_2Cl_2 (7 mL), and to this solution was added triethylamine (438 μL, 3.14 mmol). After stirring for 10 min at room temperature, methanesulfonyl chloride (243 μL, 3.14 mmol) was added dropwise at 0 °C. The reaction mixture was then stirred under N_2 at room temperature for 2 h. After quenching with 1 N HCl, the mixture was extracted with CH_2Cl_2, washed with water, and dried over anhydrous Na_2SO_4. The oily residue so obtained was purified by flash column chromatography (3:1 hexane/ethyl acetate) to give **3** (504 mg, 81%) as a pale yellow solid. ^{1}H NMR ($CDCl_3$, 500 MHz) δ 4.22 (t, 2H, J = 7.0 Hz), 3.67 (s, 3H), 3.00 (s, 3H), 2.53−2.48 (m, 4H), 2.34 (t, 2H, J = 7.0 Hz), 1.78−1.70 (m, 4H), 1.65−1.54 (m, 4H), 1.42−1.28 (m, 14H); MS (EI) *m*/*z* 396 (9.6) (M^+); HRMS calcd for $C_{18}H_{36}O_5S$ 396.2004, found 396.2011.

Synthesis of Methyl 17-Azido-6-thia-heptadecanoate (4). Sodium azide (224 mg, 3.44 mmol) was added to **3** (455 mg, 1.15 mmol) in EtOH (6 mL), and the reaction mixture was stirred at 85 °C for 10 h. After removing solvent in vacuo, the residue was extracted with CH_2Cl_2, washed with water, and dried over anhydrous Na_2SO_4. The oily residue obtained was purified by flash column chromatography (3:1 hexane/ethyl acetate) to give **4** (327 mg, 83%) as a white solid. ^{1}H NMR ($CDCl_3$, 500 MHz) δ 3.67 (s, 3H), 3.25 (t, 2H, J = 7.0 Hz), 2.53−2.48 (m, 4H), 2.33 (t, 2H, J = 7.0 Hz), 1.76−1.70 (m, 2H), 1.65−1.54 (m, 6H), 1.37−1.26 (m, 14H); MS (EI) *m*/*z* 343 (3.1) (M^+); HRMS calcd for $C_{17}H_{33}O_2N_3S$ 343.2293, found 343.2288.

Synthesis of Methyl 17-[4-(2-Hydroxyethyl)-1*H*-1,2,3-triazol-1-yl]-6-thia-heptadecanoate (5). Compound **4** (100 mg, 0.291 mmol) was added to 3-butyn-1-ol (22.1 μL, 0.291 mmol) in a mixture of *tert*-butanol (2 mL) and water (1 mL). To this solution was then added a water solution (1 mL) containing $CuSO_4 \cdot 5H_2O$ (26.8 mg, 0.08 mmol) and sodium ascorbate (40 mg, 0.20 mmol). The reaction mixture was then stirred at room temperature for 1 h, and at the end of reaction, it was extracted with CH_2Cl_2, washed with water, and dried over Na_2SO_4. The crude product obtained was purified by flash column chromatography (30:1 CH_2Cl_2/methanol) to give **5** (96 mg, 80%) as a white solid. ^{1}H NMR ($CDCl_3$, 500 MHz) δ 7.39 (br s, 1H), 4.33 (t, 2H, J = 7.0 Hz), 3.67 (s, 3H), 2.97−2.95 (m, 2H), 2.53−2.48 (m, 4H), 2.33 (t, 2H, J = 7.5 Hz), 1.91−1.88 (m, 4H), 1.76−1.70 (m, 2H), 1.65−1.53 (m, 4H), 1.38−1.26 (m, 14H); MS (EI) *m*/*z* 413 (32.1) (M^+); HRMS calcd for $C_{21}H_{39}O_3N_3S$ 413.2712, found 413.2709.

Synthesis of Methyl 17-[4-(2-Fluoroethyl)-1*H*-1,2,3-triazol-1-yl]-6-thia-heptadecanoate (6). Compound **5** (80 mg, 0.19 mmol) was dissolved in CH_2Cl_2 (5 mL), and diethylaminosulfur trifluoride (DAST; 51.1 μL, 0.39 mmol) was added at −40 °C. After stirring the reaction mixture under N_2 at −40 °C for 2 h, it was warmed up to room temperature, concentrated in vacuo, and purified by flash column chromatography (1:2 hexane/ethyl acetate) to give **6** (41 mg, 52%) as a pale yellow solid. ^{1}H NMR ($CDCl_3$, 500 MHz) δ 7.48−7.46 (m, 1H), 4.72 (dt, 2H, J = 47.0, 6.0 Hz), 4.37−4.34 (m, 2H), 3.67 (s, 3H), 3.18 (dt, 2H, J = 26.0, 6.0 Hz), 2.75−2.64 (m, 2H), 2.55−2.50 (m, 2H), 2.42−2.34 (m, 2H), 1.93−1.91 (m, 2H), 1.87−1.55 (m, 6H), 1.38−1.28 (m, 14H); MS (EI) *m*/*z* 415 (22.2) (M^+); HRMS calcd for $C_{21}H_{38}O_2N_3FS$ 415.2669, found 415.2674.

Synthesis of 17-[4-(2-Fluoroethyl)-1*H*-1,2,3-triazol-1-yl]-6-thia-heptadecanoic Acid (1). Compound **6** (35 mg, 0.084 mmol) was dissolved in ethanol (4 mL) and treated with 0.5 N NaOH (1 mL). After stirring at 80 °C for 2 h, the reaction mixture was cooled, neutralized with 0.1 N HCl in an ice bath, and then extracted with CH_2Cl_2. The organic fraction was dried over anhydrous Na_2SO_4 and purified by flash column chromatography (10:1 CH_2Cl_2/MeOH) to give **1** (15 mg, 44%) as a pale yellow solid. ^{1}H NMR ($CDCl_3$, 500 MHz) δ 7.52 (s, 1H), 4.69 (dt, 2H, J = 47.0, 6.0 Hz), 4.34 (t, 2H, J = 7.5 Hz), 3.12(dt, 2H, J = 26.0, 6.0 Hz), 2.75−2.67 (m, 2H), 2.55−2.50 (m, 2H), 2.39−2.31 (m, 2H), 1.93−1.88 (m, 2H), 1.86−1.54 (m, 6H), 1.39−1.22 (m, 14H); MS (FAB) *m*/*z* 402 (16.3), (M^++H); HRMS calcd for $C_{20}H_{37}O_2N_3FS$ 402.5900, found 402.5891.

Synthesis of 17-Hydroxy-6-thia-heptadecanoic Acid (7). Compound **7** was synthesized as described in the literature (*24*). 11-Mercapto-1-undecanol (800 mg, 3.91 mmol) and KOH (439 mg, 7.83 mmol) in EtOH (8 mL) were added to 5-bromovaleric acid (711.8 mg, 3.91 mmol), and stirred under N_2 at 85 °C for 18 h. At the end of the reaction, the mixture was acidified with 2.5 M H_2SO_4. After removing solvent in vacuo, the residue was extracted with chloroform, washed with water, and dried over anhydrous Na_2SO_4. Flash column chromatography (30:1 CH_2Cl_2/methanol) gave **7** (821 mg, 69%) as a white solid. ^{1}H NMR ($CDCl_3$, 500 MHz) δ 3.65 (t, 2H, J = 6.5 Hz), 2.54−2.49 (m, 4H), 2.50 (t, 2H, J = 7.5 Hz), 2.38 (t, 2H, J = 7.5 Hz), 1.78−1.72 (m, 2H), 1.68−1.51(m, 6H), 1.39−1.28 (m, 14H); MS (FAB) *m*/*z* 305 (100), (M^++H); HRMS calcd for $C_{16}H_{33}O_3S$ 305.2150, found 305.2155.

Synthesis of 17-Methanesulfonyloxy-6-thia-heptadecanoic Acid (8). Compound **8** was prepared using the procedure described for **3**. Flash column chromatography (2:1 hexane/ethyl acetate) gave **8** (350 mg, 63%) as a pale yellow solid. ^{1}H NMR ($CDCl_3$, 500 MHz) δ 4.22 (t, 2H, J = 6.5 Hz), 3.00 (s, 3H), 2.54−2.49 (m, 4H), 2.39 (t, 2H, J = 7.0 Hz), 1.78−1.72 (m, 4H), 1.66−1.57 (m, 4H), 1.40−1.24 (m, 14H); MS (FAB) *m*/*z* 383 (22.0), (M^++H); HRMS calcd for $C_{17}H_{35}O_5S_2$ 383.1926, found 383.1931.

Synthesis of 17-Azido-6-thia-heptadecanoic Acid (9). Compound **9** was prepared using the procedure described for **4**. Flash column chromatography (50:1 CH_2Cl_2/methanol) gave **9** (165 mg, 64%) as a pale yellow solid. ^{1}H NMR ($CDCl_3$, 500 MHz) δ 3.25 (t, 2H, J = 7.0 Hz), 2.54−2.49 (m, 4H), 2.39 (t, 2H, J = 7.0 Hz), 1.77−1.73 (m, 4H), 1.68−1.56 (m, 4H), 1.54−1.27

(m, 14H); MS (FAB) *m*/*z* 330 (55.0), (M^++H); HRMS calcd for $C_{16}H_{32}O_2N_3S$ 330.2215, found 330.2204.

Synthesis of 4-Tosyloxy-1-butyne (10). 3-Butyn-1-ol (175 μL, 2.31 mmol) was dissolved in distilled CH_2Cl_2 (5 mL), and to this solution was added triethylamine (323 μL, 2.31 mmol). After stirring at room temperature for 1 h, the solution was reacted with tosyl chloride (90 mg, 0.45 mmol) for 3 h at 0 °C. The mixture was then extracted with CH_2Cl_2 (30 mL × 3), washed with water, and dried over Na_2SO_4. Flash column chromatography (4:1 hexane/ethyl acetate) gave **10** (374.2 mg, 72%) as a pale yellow oil. ^{1}H NMR ($CDCl_3$, 500 MHz) δ 1.97 (t, 1H, J = 3.0 Hz), 2.46 (s, 3H), 2.54−2.58 (m, 2H), 4.11 (t, 2H, J = 7.5 Hz), 7.35 (d, 2H, J = 8.0 Hz), 7.81 (d, 2H, J = 8.5 Hz); MS (FAB) *m*/*z* 225 (100), ($M + H)^+$; HRMS calcd for $C_{11}H_{13}O_3S$ 225.0586, found 225.0585.

Radiochemical Synthesis of [^{18}F]1. After loading a QMA cartridge with [^{18}F]F^-, radioactivity was eluted using a 1:1 solution of water and CH_3CN (600 μL) containing $K_{2,2,2}$ (13 mg, 0.03 mmol) and K_2CO_3 (3 mg, 0.02 mmol). Solvents were removed under N_2 at 90 °C, and the remaining water was removed by two azeotropic distillations using 100−200 μL aliquots of CH_3CN at 90 °C under a gentle stream of N_2. The resulting K[^{18}F]F was dissolved in CH_3CN (1 mL) and transferred to a vial containing 4-tosyloxy-1-butyne (*23*). This reaction mixture was then stirred at 100 °C for 20 min, while 4-[^{18}F]fluoro-1-butyne was distilled with acetonitrile into the second vial containing the azido precursor **9** (1.1 mg, 5.36 μmol), CuI (3.1 mg, 0.02 mmol), and sodium ascorbate (21 mg, 0.11 mmol) at −50 °C (dry ice in an acetone bath). After completing the distillation, 4-[^{18}F]fluoro-1-butyne was obtained in 43−47% decay-corrected radiochemical yields based on [^{18}F]fluoride ion. The reaction mixture was then warmed to room temperature, and DIEA (14 μL, 0.12 mmol) and water (250 μL) were added. After stirring for 15 min at 90 °C, the resulting mixture was concentrated to remove acetonitrile under N_2 at 50 °C (water bath), diluted with water (500 μL), and then injected onto a HPLC column, which was then eluted with a linear gradient (from 30:70 to 0:100) of water containing acetic acid (2.6%) and methanol over 30 min at a flow rate of 3 mL/min. The desired fraction, which eluted at 20−21 min, was collected, and solvents were removed using a rotary evaporator. Overall, decay-corrected radiochemical yields of [^{18}F]**1** from [^{18}F]fluoride ion were 20−26%. Radiotracer [^{18}F]**1** was then redissolved in ethanol and diluted in saline containing 1% bovine serum albumin (BSA) at 40 °C to give a final solution of 10% ethanol in saline containing 1% BSA. Specific activity was determined by comparing the UV peak area of the desired radiolabeled HPLC peak with those of the standard curve obtained from HPLC analyses of different concentrations of nonradiolabeled compound **1**. This HPLC analysis was performed, as described above using an analytical column at a flow rate of 1 mL/min. An aliquot of [^{18}F]**1** was coinjected with **1** into a HPLC system to confirm its identity.

Tissue Distribution. Institute of Cancer Research (ICR) mice (male, 25−28 g, 4 mice per time point) were fasted for 14 h before injecting [^{18}F]**1** (3.0 MBq/mouse) in 0.2 mL of 10% ethanol−saline containing 1% BSA via a tail vein. Mice were sacrificed by cervical dislocation at 1, 5, 10, 30, and 60 min postinjection. Samples of blood, heart, lung, liver, kidney, and bone were removed, weighed, and counted. Data were expressed as percentages of injected dose per gram of tissue (%ID/g).

In another set of experiments, 14 h fasted ICR mice (male, 25−28 g, 4 mice per time point) were injected intraperitoneally with etomoxir (40 mg/kg) at 2 h prior to a tail-vein injection of [^{18}F]**1** (3.0 MBq/mouse) (*16*). The mice were sacrificed by cervical dislocation at 10 and 30 min postinjection. The remainder of the procedure was the same as that described above.

Metabolite Analysis in Mouse Hearts. ICR mice were injected with [^{18}F]**1** (14.3 MBq) and heart tissue and urine samples were collected at 10 and 30 min postinjection. Separately, a group of mice were injected intraperitoneally with etomoxir (40 mg/kg) at 2 h before a tail-vein injection of radiotracer, and heart tissue and urine samples were collected at 30 min postinjection. Heart tissue samples were homogenized with a 2:1 mixture of $CHCl_3$−CH_3OH (1.25 mL) at 0 °C, and to this homogenate were added 40% urea (0.35 mL) and 5% H_2SO_4 (0.35 mL). This mixture was then vortexed and centrifuged at 3000 *g* for 5 min (*15*). The resulting organic and aqueous fractions, and tissue pellets were then counted. Aqueous fractions and urine samples were analyzed by HPLC using a linear gradient (from 30:70 to 0:100) of water containing acetic acid (2.6%) and methanol over 30 min at a flow rate of 1 mL/min. Organic fractions were then analyzed by TLC using CH_2Cl_2−CH_3OH (15:1) as the developing solvent. An aliquot of the organic fractions were treated with 10 N KOH at 60 °C for 1 h and analyzed by TLC as described above. On the other hand, residual tissue pellet was dissolved in 1 N NaOH at 90 °C for 1 h and treated with 50% TCA, and supernatants and precipitates were counted (*15*).

microPET Imaging of [^{18}F]1 in Normal Mice. ICR mice were fasted for 14 h before injecting [^{18}F]**1** (22.9 MBq), and microPET imaging of two anesthesized mice (28 g) was performed using an Inveon microPET. Dynamic scan of the mice was obtained for 30 min (12 frames × 10 s, 6 frames × 30 s, 5 frames × 60 s, 5 frames × 120 s, and 2 frames × 300 s), and the reconstruction was performed using ordered subset expectation maximization 3D (OSEM3D).

RESULTS

Chemistry. Nonradiolabeled compound **1** was synthesized by the Cu(I)-catalyzed 1,3-cycloaddition of azido precursor **4** and 3-butyn-1-ol, followed by OH group fluorination and methyl ester removal (Scheme 1). The methyl ester at the other end of **5** was found to be necessary for OH group fluorination using DAST to avoid side product formation. The resulting fluoro compound **6** was obtained in higher yield at low temperature (52% at −40 °C vs 11% at 0 °C). Radiotracer [^{18}F]**1** was synthesized as above using click chemistry from the 17-azido-6-thia fatty acid analogue **9** and 4-[^{18}F]fluoro-1-butyne (Scheme 2) and purified by reverse-phase HPLC; although [^{18}F]**1** was purifiable by normal-phase HPLC, the eluted peak was very broad. The radiotracer [^{18}F]**1** obtained using this technique had high radiochemical purity (>99%) and specific activity (55.4 ± 4.2 GBq/μmol), probably because unreacted 4-[^{18}F]fluoro-1-butyne was easily removed due to its low boiling point (45 °C) (*25*). The decay-corrected radiochemical yields of [^{18}F]**1** were 20−26%, and the total synthesis time required, including HPLC purification, was 80−85 min. Radiotracer [^{18}F]**1** was identified by coeluting it with nonradiolabeled compound **1** on HPLC. Use of 4-[^{18}F]fluoro-1-butyne for click chemistry with azide has advantages, such as a little perturbation of biomolecule properties and purification by distillation of 4-[^{18}F]fluoro-1-butyne, although one of the reasons for relatively low yield of [^{18}F]**1** could be derived from incomplete transfer of 4-[^{18}F]fluoro-1-butyne to the second reaction vial, due to its low boiling point.

Tissue Distribution. Since fatty acids are predominantly metabolized in the fasting state, mice were fasted for 14 h prior to experiments. After injecting [^{18}F]**1** into mice, high levels of radioactivity accumulated in blood, heart, lung, liver, and kidneys, and this heart uptake washed out slowly (3.70%ID/g at 1 min, 3.44%ID/g at 5 min, 3.28%ID/g at 10 min, 3.26%ID/g

Scheme 1[a]

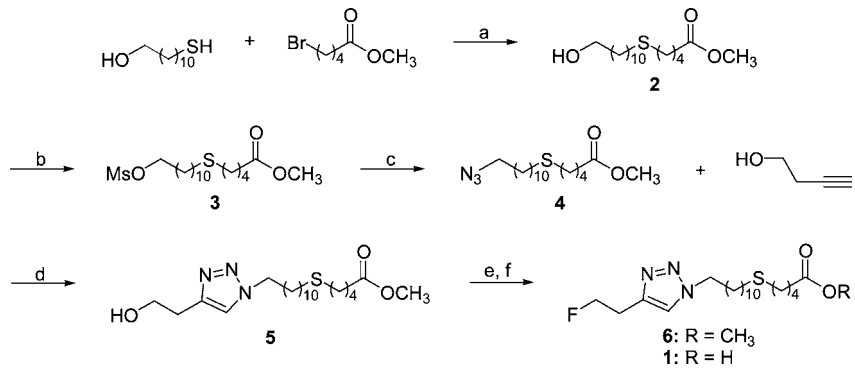

[a] Reaction conditions: (a) DIEA, CH_3CN, 85 °C, 18 h; (b) MsCl, Et_3N, CH_2Cl_2, room temperature, 2 h; (c) NaN_3, EtOH, 85 °C, 10 h; (d) $CuSO_4$, sod. ascorbate, *tert*-butyl alcohol, H_2O, room temperature, 1 h; (e) DAST, CH_2Cl_2, −40 °C, 2 h (f) 0.5 N NaOH, EtOH, 80 °C, 2 h.

Scheme 2[a]

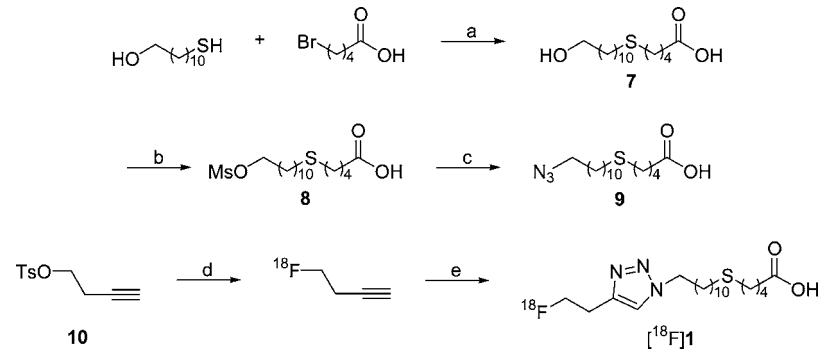

[a] Reaction conditions: (a) KOH, EtOH, 85 °C, 18 h; (b) MsCl, Et_3N, CH_2Cl_2, room temperature, 2 h; (c) NaN_3, EtOH, 85 °C, 10 h; (d) K[^{18}F]F/$K_{2.2.2.}$, CH_3CN, 100 °C, 20 min; (e) **9**, CuI, DIEA, sod. ascorbate, CH_3CN, H_2O, 90 °C, 15 min.

Table 1. Tissue Distributions of [^{18}F]1 in Mice[a]

	%ID/g				
tissue	1 min	5 min	10 min	30 min	60 min
blood	2.17 ± 0.21	0.62 ± 0.04	0.66 ± 0.04	0.66 ± 0.02	0.73 ± 0.05
heart	3.70 ± 0.50	3.44 ± 0.31	3.28 ± 0.05	3.16 ± 0.36	3.01 ± 0.15
lung	3.08 ± 0.10	2.60 ± 0.16	3.41 ± 0.28	3.04 ± 0.10	3.09 ± 0.13
liver	11.81 ± 0.11	12.88 ± 0.69	11.18 ± 0.47	5.32 ± 0.16	4.73 ± 0.25
kidney	8.66 ± 0.41	8.08 ± 0.54	4.68 ± 0.12	3.13 ± 0.20	2.66 ± 0.19
bone	0.68 ± 0.02	0.53 ± 0.03	0.64 ± 0.07	0.77 ± 0.06	1.19 ± 0.09

[a] Values are given as means ± SD of 4 mice.

at 30 min, and 3.01%ID/g at 60 min postinjection) with an elimination half-life of >60 min (Table 1). On the other hand, blood clearance of radioactivity was almost complete within 5 min, and the heart-to-blood uptake ratios of [^{18}F]**1** were 5.55 at 5 min and 4.97 at 10 min postinjection. Constant and low bone uptake suggested that [^{18}F]**1** underwent little metabolic defluorination in vivo (0.53−0.77%ID/g up to 30 min and 1.19%ID/g at 60 min postinjection). Moreover, pretreatment of mice with etomoxir (a CPT I inhibitor) decreased the myocardial uptake of [^{18}F]**1** by 30% and 53% at 10 and 30 min, respectively (Table 2).

Table 2. Tissue Distribution of [^{18}F]1 in Etomoxir-Pretreated Mice[a]

	%ID/g	
tissue	10 min	30 min
blood	0.95 ± 0.24	0.78 ± 0.06
heart	2.31 ± 0.13	1.47 ± 0.08
lung	3.77 ± 0.20	3.40 ± 0.23
liver	12.43 ± 0.64	8.09 ± 0.42
kidney	4.23 ± 0.13	2.30 ± 0.14
bone	0.77 ± 0.14	0.90 ± 0.05

[a] Values are given as means ± SD of 4 mice.

Metabolite Analysis in Mouse Hearts. When heart tissues were homogenized in and extracted with a 2:1 mixture of $CHCl_3$−CH_3OH, 40% urea, and 5% H_2SO_4 (extraction efficiency of 93%), most of the radioactivity in heart tissues was found in tissue pellet (63.4:32.8:3.8 and 62.1:33.4:4.5 (tissue pellet/organic fraction/aqueous fraction) at 10 and 30 min postinjection, respectively) (Table 3). Analysis of aqueous fractions showed a radioactive peak with an HPLC retention time of 19.4−20.1 min, which was identified as [^{18}F]**1** (Figure 1A,C), although most of the radioactivity was not extracted into the aqueous fraction. HPLC analysis of the urine samples also showed the unmetabolized [^{18}F]**1** (Figure 1B,C). TLC analyses of the organic fractions showed that [^{18}F]**1** was being converted into an unidentified nonpolar compound (41:59 and 35:65 at 10 and 30 min postinjection) (Figure 2). The residual tissue pellets were dissolved in 1 N NaOH at 90 °C, which was mostly precipitated with addition of 50% TCA (88%). In addition, the amount to precipitate was reduced to 71% when mice were pretreated with etomoxir at 2 h before [^{18}F]**1** administration.

microPET Imaging of [^{18}F]1 in Normal Mice. Early PET images (first 2 min) of mice injected with [^{18}F]**1** showed high accumulation of the radioactivity in blood pool, which decreased

Table 3. Distribution of Radioactivity in the Heart Homogenates Obtained after Injecting Mice with [^{18}F]1

	% organic fraction	% aqueous fraction	% tissue pellet
10 min	32.8	3.8	63.4
30 min	33.4	4.5	62.1
30 min (etomoxir-pretreated)	54.0	7.2	38.8

rapidly with time. Heart uptake of [^{18}F]**1** was clearly shown during the whole time of the study (30 min after radiotracer injection) (Figure 3), although a high level of radioactivity was also accumulated in liver and kidneys. This result showed high myocardial uptake and prolonged myocardial retention of [^{18}F]**1** in mice.

DISCUSSION

Click chemistry concerns triazole formation via the Cu(I)-catalyzed 1,3-cycloaddition of azides and terminal alkynes and has been found to be useful for synthesizing various triazole-containing compounds (*17*). Furthermore, we synthesized 4-[^{18}F]fluoro-1-butyne, a synthon for click chemistry, and found that the 4-(2-[^{18}F]fluoroethyl)-1*H*-1,2,3-triazolyl group is metabolically stable (*23*). The radiotracer [^{18}F]**1** was prepared from precursor **9** and 4-[^{18}F]fluoro-1-butyne using click chemistry, which did not require carboxylic acid protection (Scheme 2). Because unsubsitituted fatty acid analogues undergo rapid myocardial clearance, a sulfur atom was inserted into the fatty acid chain to stop β-oxidation beyond the sulfur-containing site. The tissue distribution of [^{18}F]**1** showed high uptake by heart tissue (3.44%ID/g at 5 min) and high heart-to-blood uptake ratios in mice. In addition, [^{18}F]**1** underwent little in vivo defluorination, whereas odd-numbered ω-[^{18}F]fluorofatty acid and ω-[^{18}F]fluoro-4-thia-hexadecanoic acid have been shown to suffer from in vivo defluorination in rodents (*16, 26*). In the present study, myocardial retention of [^{18}F]**1** was found to be greater than that of other unsubstituted fatty acid analogues (<10 min), and its elimination half-time could not be determined because it was not reached during this 60 min long study (Table 1). [^{123}I]BMIPP showed prolonged myocardial retention in rats (4.62%ID/g at 5 min, 3.63%ID/g at 30 min, 4.26%ID/g at 60 min, and 2.27%ID/g at 240 min postinjection) with an elimination half-life of ca. 4 h (*11*). 5-Methyl branched ω-[^{18}F]fluorofatty acid (5-[^{18}F]MFHA) had a heart uptake of 3.04%ID/g at 5 min postinjection in rats and an elimination half-life of ca. 30 min (*13*). [^{18}F]FTHA, 6-thiafatty acid analogue, showed high heart uptake of 39.8%ID/g at 5 min postinjection in mice with an elimination half-time of approximately 2 h (*15*).

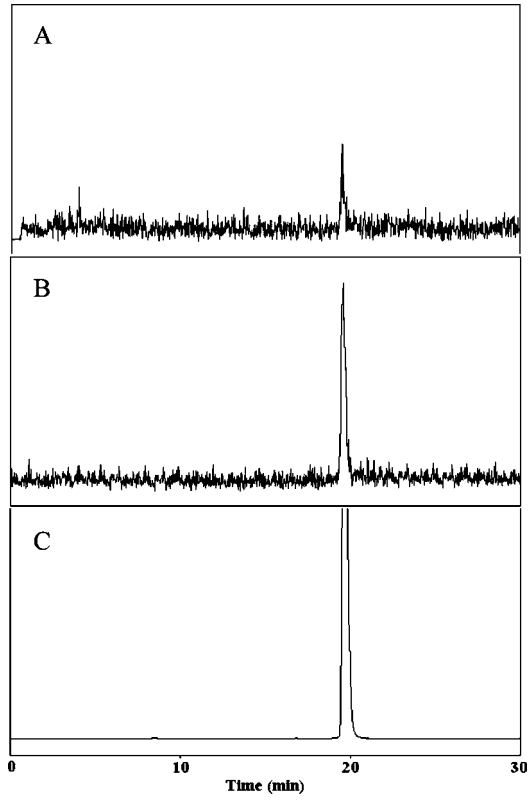

Figure 1. HPLC profiles of a water-soluble heart tissue sample (A) and a urine sample (B) obtained at 10 min after injecting mice with [^{18}F]**1** and HPLC profile of [^{18}F]**1** (C). HPLC analysis was conducted using an analytical column (YMC C18, 5 μ, 4.6 $\times$ 250 mm) and a NaI(T1) radioactivity detector.

CPT I is located in the outer membrane of mitochondria and is responsible for the transportation of long-chain fatty acids into the mitochondria. In the present study, pretreatment of mice with etomoxir (a CPT I inhibitor), prior to injecting radiotracer, was found to reduce myocardial uptake at 30 min postinjection by 53% (Table 2). In the case of [^{18}F]FTHA, 2[5(4-chlorophenyl)pentyl]oxirane-2-carboxylate, POCA (also a CPT I inhibitor) reduced myocardial uptake of radioactivity at 1 and 60 min postinjection by 81% and 87%, respectively (*15*). In addition, the myocardial uptake of 16-[^{18}F]fluoro-4-thia-hexadecanoic acid was also reduced by 81% at 30 min postinjection by etomoxir pretreatment (*16*). Although the extent of myocardial uptake inhibition by CPT I inhibitors is different, these results suggest that the fatty acid analogues are transported into the mitochondria.

It has been proposed that [^{18}F]FTHA undergoes β-oxidation and then is metabolically trapped in myocardium. DeGrado et al. suggested that [^{18}F]FTHA may be metabolized to 12-[^{18}F]fluoro-4-thia-2-pentadecanoyl-CoA and 12-[^{18}F]fluoro-4-thia-3-hydroxy-pentadecanoyl-CoA in the mitochondria (*15*). As shown in the studies by Lau et al., 4-thia-octanoyl-CoA is converted to 4-thia-octenoyl-CoA by acyl-CoA dehydrogenase and accumulates in the mitochondria, in which it is then slowly converted to β-hydroxy-4-thia-octanoyl-CoA by enoyl-CoA hydratase, and then the product splits nonenzymatically into alkyl thiol and malonylsemialdehyde CoA (*27*). As such, 12-[^{18}F]fluoro-4-thia-3-hydroxypentadecanoyl-CoA would be further converted into 8-[^{18}F]fluoroundecane-1-thiol, which has, however, not yet been confirmed (*15*). Therefore, in order to investigate the metabolites of 6-thiafatty acid analogue, metabolites of [^{18}F]**1** were analyzed using mouse heart and urine samples. When the heart tissues were homogenized in a 2:1 mixture of $CHCl_3-CH_3OH$ and subsequently extracted with 40% urea and 5% H_2SO_4, radioactivity was predominantly retained in tissue pellet, and smaller amounts were retained in the organic and the aqueous fractions. We synthesized the proposed β-oxidation metabolite of [^{18}F]**1** (15-[4-(2-[^{18}F]fluoroethyl)-1*H*-1,2,3-triazol-1-yl]-4-thia-pentadecanoic acid) to see whether the metabolite is further used as a substrate for the subsequent β-oxidation steps in the mitochondria. The β-oxidation metabolite, 4-thia-fatty acid analogue, was not detected in either the aqueous or the organic fractions obtained from heart tissues or urine samples (Figures 1 and 2) (HPLC t_R of 15-[4-(2-[^{18}F]fluoroethyl)-1*H*-1,2,3-triazol-1-yl]-4-thia-pentadecanoic acid = 14.2−15.1 min under the same conditions used for metabolite analysis), although a single cycle of β-oxidation was expected to occur, because the sulfur atom was inserted between C5 and C7 of [^{18}F]**1**. This result suggests that the 4-thia-fatty acid analogue could be formed and further used as a substrate for the subsequent β-oxidation steps. In the organic extracts of the heart tissue, [^{18}F]**1** was converted into the more nonpolar radiolabeled metabolite with time (Figure 2). However, our HPLC analysis showed that this nonpolar

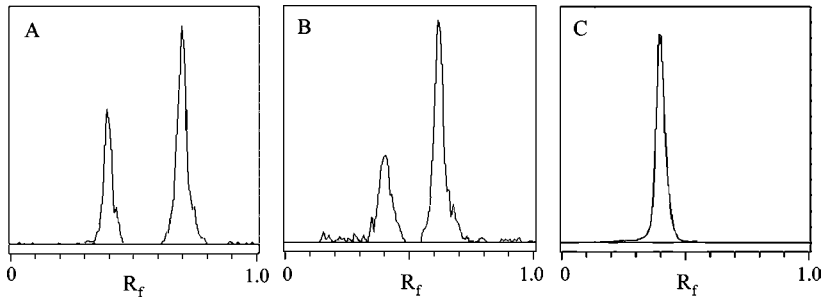

Figure 2. TLC analyses of 10 min (A) and 30 min (B) heart samples extracted with organic solvent after injecting mice with [^{18}F]**1** (R_fs = 0.4 and 0.7) and TLC analysis of [^{18}F]**1** (C) (R_f = 0.4).

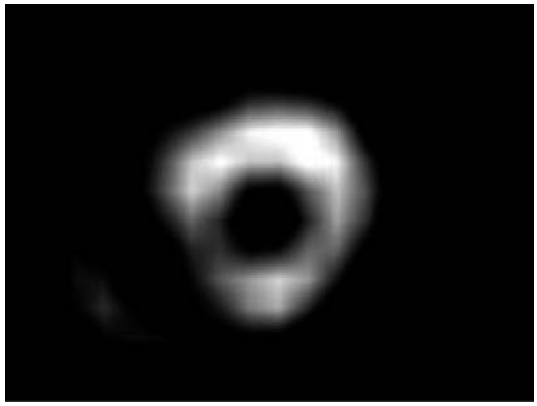

Figure 3. microPET image of midventricular short-axis slice of normal mouse heart acquired 10−20 min postinjection with [^{18}F]**1** (22.9 MBq).

radiolabeled peak did not match with 11-[4-(2-[^{18}F]fluoroethyl)-1*H*-1,2,3-triazol-1-yl]-undecane-1-thiol, which can be obtained from β-oxidation followed by nonenzymatic fragmentation, because the peak was eluted almost 2 min before the nonradiolabeled standard thiol peak by HPLC (t_R = 16.4 min vs 18.1 min; 20:80 aqueous acetic acid (2.6%)/methanol, 1 mL/min) (data not shown). In order to identify the nature of the radiolabeled metabolite, the sulfoxide and sulfone analogues of **1** were synthesized, which were found to be more polar than [^{18}F]**1**, indicating that the radiolabeled metabolite is not the sulfoxide or sulfone analogue of [^{18}F]**1**. Furthermore, this metabolite was not hydrolyzed to [^{18}F]**1** under hot basic conditions (10 N KOH, 60 °C, 1 h), which suggests that it is not the triglyceride form of [^{18}F]**1** (*15*). Therefore, this nonpolar radiolabeled metabolite in the organic fraction remains to be identified. When residual tissue pellets were treated with TCA after dissolution in hot basic solution (1 N NaOH, 90 °C, 1 h), most of the radioactivity precipitated (88%), and the amount of precipitate was reduced to 71% with etomoxir pretreatment (Table 3). This result suggests that most of the radioactivity in the tissue pellet may be derived from protein-bound β-oxidation metabolites or alkyl thiols and that its formation is CPT I dependent. In addition, microPET image of [^{18}F]**1** in mice showed high radioactivity accumulation in heart, liver, and kidneys during the time of study, which is well-correlated with its tissue distribution data (Table 1).

CONCLUSION

Radiotracer [^{18}F]**1** was prepared using click chemistry from azido fatty acid analogue **9** and 4-[^{18}F]fluoro-1-butyne. Tissue distribution studies in mice showed high radioactivity accumulation in heart, high heart-to-blood uptake ratios, and prolonged myocardial retention. Furthermore, our analysis of heart tissue samples suggests that most of the [^{18}F]**1** is metabolically trapped via β-oxidation in myocardium, which indicates that [^{18}F]**1** should be viewed as a potential PET radiotracer for visualizing fatty acid metabolism in myocardium.

ACKNOWLEDGMENT

This research was supported by a grant (CBM33-B3002-01-01-00) from the Center for Biological Modulators of the 21st Century Frontier R&D Program, the Ministry of Science and Technology, Korea.

LITERATURE CITED

(1) Corbett, J. R. (1999) Fatty acids for myocardial imaging. *Sem. Nucl. Med. 29*, 237–258.
(2) Bergmann, S. R., Weinheimer, C. J., Markham, J., and Herrero, P. (1996) Quantitation of myocardial fatty acid metabolism using PET. *J. Nucl. Med. 37*, 1723–1730.
(3) Wisneski, J. A., Gertz, E. W., Neese, R. A., and Mayr, M. (1987) Myocardial metabolism of free fatty acids. *J. Clin. Invest 79*, 359–366, Studies with ^{14}C-labeled substrates in humans.
(4) Nellis, S. H., Liedtke, A. J., and Renstrom, B. (1992) Fatty acid kinetics in aerobic myocardium: characteristics of tracer carbon entry and washout and influence of metabolic demand. *J. Nucl. Med. 33*, 1864–1874.
(5) Freundlieb, C., Höck, A., Vyska, K., Feinendegen, L. E., Machulla, H.-J., and Stöcklin, G. (1980) Myocardial imaging and metabolic studies with [17-^{123}I]iodoheptadecanoic acid. *J. Nucl. Med. 21*, 1043–1050.
(6) Visser, F. C., van Eenige, M. J., Duwel, C. M., and Roos, J. P. (1986) Radioiodinated free fatty acids; can we measure myocardial metabolism? *Eur. J. Nucl. Med. 12*, S20−23.
(7) Machulla, H. J., Dutschka, K., van Beuningen, D., and Chen, T. (1981) Development of 15(p-^{123}I-phenyl-)pentadecanoic acid for in vivo diagnosis of the myocardium. *J. Radioanal. Chem. 65*, 279–286.
(8) Tamaki, N., Morita, K., Kuge, Y., and Tsukamoto, E. (2000) The role of fatty acids in cardiac imaging. *J. Nucl. Med. 41*, 1525–1534.
(9) Lerch, R. A., Bergmann, S. R., Ambos, H. D., Welch, M. J., Ter-Pogossian, M. M., and Sobel, B. E. (1982) Effect of flow-independent reduction of metabolism on regional myocardial clearance of ^{11}C-palmitate. *Circulation 65*, 731–738.
(10) Buckman, B. O., VanBrocklin, H. F., Dence, C. S., Bergmann, S. R., Welch, M. J., and Katzenelenbogen, J. A. (1994) Synthesis and tissue biodistribution of [ω-^{11}C]palmitic acid: a novel PET imaging agent for cardiac fatty acid metabolism. *J. Med. Chem. 37*, 2481–2485.
(11) Goodman, M. M., Kirsch, G., and Knapp, F. F., Jr. (2003) Synthesis of radioiodinated ω-(p-iodophenyl)-substituted methyl-branched long-chain fatty acids. *J. Med. Chem. 27*, 390–397.
(12) Sloof, G. W., Visser, F. C., van Lingen, A., Bax, J. J., Eersels, J., Teule, G. J., and Knapp, F. F., Jr. (1997) Evaluation of heart-to-organ ratios of ^{123}I-BMIPP and the dimethyl-substituted fatty acid analogue in humans. *Nucl. Med. Commun. 18*, 1065–1070.

(13) Takahashi, T., Nishimura, S. I., Ido, T., Ishiwata, K. I., and Iwata, R. (1996) Biological evaluation of 5-methyl-branched-chain ω-[^{18}F]fluorofatty acid: a potential myocardial imaging tracer for positron emission tomography. *Nucl. Med. Biol. 23*, 303–308.

(14) DeGrado, T. R. (1991) Synthesis of 14(*R,S*)-[^{18}F]fluoro-6-thia-heptadecanoic acid (FTHA). *J. Labelled Comp. Radiopharm. 29*, 989–995.

(15) DeGrado, T. R., Coenen, H. H., and Stöcklin, G. (1991) 14(*R, S*)-[^{18}F]Fluoro-6-thia-heptadecanoic acid (FTHA): evaluation in mouse of a new probe of myocardial utilization of long chain fatty acids. *J. Nucl. Med. 32*, 1888–1896.

(16) DeGrado, T. R., Wang, S., Holden, J. E., Nickles, J., Taylor, M., and Stone, C. K. (2000) Synthesis and preliminary evaluation of ^{18}F-labeled 4-thia palmitate as a PET tracer of myocardial fatty acid oxidation. *Nucl. Med. Biol. 27*, 221–231.

(17) Rostovtsev, V. V., Green, L. G., Foskin, V. V., and Sharpless, K. B. (2002) A stepwise Huisgen cycloaddition process: copper(I)-catalyzed regioselective "ligation" of azides and terminal alkynes. *Angew. Chem., Int. Ed. 41*, 2596–2599.

(18) Marik, J., and Sutcliffe, J. L. (2006) Click for PET: rapid preparation of [^{18}F]fluoropeptides using Cu^{I} catalyzed 1,3-dipolar cycloaddition. *Tetrahedron Lett. 47*, 6681–6684.

(19) Li, Z. B., Wu, Z., Chen, K., Chin, F. T., and Chen, X. (2007) Click chemistry for ^{18}F-labeling of RGD peptides and microPET imaging of tumor integrin $\alpha_v\beta_3$ expression. *Bioconjugate Chem. 18*, 1987–1994.

(20) Qu, W., Kung, M. P., Hou, C., Oya, S., and Kung, H. F. (2007) Quick assembly of 1,4-diphenyltriazoles as probes targeting β-amyloid aggregates in Alzheimer's disease. *J. Med. Chem. 50*, 3380–3387.

(21) Hausner, S. H., Marik, J., Gagnon, M. K., and Sutcliffe, J. L. (2008) In vivo positron emission tomography (PET) imaging with an $\alpha_v\beta_6$ specific peptide radiolabeled using ^{18}F-"click" chemistry: evaluation and comparison with the corresponding 4-[^{18}F]fluorobenzoyl- and 2-[^{18}F]fluoropropionyl-peptides. *J. Med. Chem. 51*, 5901–5904.

(22) Tietze, R., Lober, S., Hubner, H., Gmeiner, P., Kuwert, T., and Prante, O. (2008) Discovery of a dopamine D4 selective PET ligand candidate taking advantage of a click chemistry based REM linker. *Bioorg. Med. Chem. Lett. 18*, 983–988.

(23) Kim, D. H., Choe, Y. S., Jung, K. H., Lee, K. H., Choi, J. Y., Choi, Y., and Kim, B. T. (2008) A ^{18}F-labeled glucose analog: synthesis using a click labeling method and in vitro evaluation. *Arch. Pharm. Res. 31*, 587–593.

(24) Jung, C. M., Kraus, W., Leibnitz, P., Pietzsch, H. J., Kropp, J., and Spies, H. (2002) Syntheses and first crystal structures of rhenium complexes derived from ω-functionalized fatty acids as model compounds of technetium tracers for myocardial metabolism imaging. *Eur. J. Inorg. Chem. 2002*, 1219–1225.

(25) Job, B. E., and Sheridan, J. (1962) Propargyl fluoride and its microwave spectrum. *Nature 193*, 677.

(26) Knust, E. J., Kupfernagel, Ch., and Stöcklin, G. (1979) Long-chain F-18 fatty acids for the study of regional metabolism in heart and liver; odd-even effects of metabolism in mice. *J. Nucl. Med. 20*, 1170–1175.

(27) Lau, S.-M., Brantley, R. K., and Thorpe, C. (1989) 4-Thia-*trans*-2-alkenoyl-CoA derivatives: Properties and enzymatic reactions. *Biochemistry 28*, 8255–8262.

BC800472A

^{68}Ga-Labeling of Biotin Analogues and their Characterization

Elisabeth Blom,[†] Bengt Långström,[†,‡,§] and Irina Velikyan*[,†,‡]

Department of Biochemistry and Organic Chemistry, Box 576, Husargatan 3, BMC, S-751 23 Uppsala, Sweden, and Uppsala Applied Science Lab and Uppsala Imanet, GEHC, Box 967, S-751 09 Uppsala, Sweden. Received December 12, 2008; Revised Manuscript Received April 29, 2009

Biotin- and ^{68}Ga-based tracers have been suggested as tools that could be used to monitor the survival of avidin-coated islets of Langerhans isolated from pancreas and used in transplantation, i.e., to liver. Three biotin analogues with various alkyl and poly(ethylene glycol) (PEG) chains coupled to DOTA were synthesized and labeled with ^{68}Ga. The ^{68}Ga labeling was studied at room temperature as well as elevated temperature using either conventional or microwave heating. Radioactivity incorporation reached 95% within 5 and 2 min using the, respectively, conventional and microwave heating modes. The specific activity of the tracers was improved by preconcentration and purification of the generator eluate. The binding of the labeled and nonlabeled conjugates to avidin in solution was compared to the binding of native biotin. All compounds maintained good affinity for avidin, though introducing the linkers and chelator, especially the PEG-groups, somewhat decreased the binding affinity. The extent of binding of the labeled compounds to avidin was 54−91% after 5 min. Blocking experiments were performed confirming the specificity of the binding of biotin analogues to avidin. The stability of the three labeled compounds in human serum was studied. The stability of the biotin analogue **8** (65% within 30 min) and avidin−biotin complex (80% within 120 min) might be sufficient for the monitoring of the islets of Langerhans. The tracers will be evaluated in *in vitro* experiments of avidin-coated islets of Langerhans and in transplantation models *in vivo*.

INTRODUCTION

The transplantation of islets isolated from a donor pancreas into patients with type I diabetes for therapeutic purposes has been studied for decades, with considerable progress. However, obstacles like low graft survival and islet rejection preclude the widespread application of this strategy (*1*). An understanding of the underlying mechanisms and the ability to monitor the procedure *in vivo* would contribute considerably to development of the field. A noninvasive imaging technique like positron emission tomography (PET) may become a useful tool, to evaluate, monitor, and optimize graft survival during islet transplantation (*2*). We have explored a tracer containing ^{68}Ga as the positron emitting radionuclide on biotin analogues as the targeting compounds.

The positron-emitting radionuclide ^{68}Ga ($T_{1/2}$ = 68 min; 89% β^+-emission) is available from a long shelf-life ^{68}Ge/^{68}Ga-generator with 1−2-year shelf life provided by 270 day half-life of the parent ^{68}Ge. The half-life of ^{68}Ga permits ^{68}Ga-based radiopharmaceuticals to be produced and used. The chelator-mediated labeling chemistry is straightforward and site-specific. Biotin (5-[(3*aR*,4*R*,6*aS*)-2-oxohexahydro-1*H*-thieno[3,4-*d*]imidazol-4-yl]pentanoic acid) is a naturally occurring vitamin that is generally found in its protein-bound form. It acts as a carboxyl carrier in four carboxylase enzymes in animals and is important in lipid, glucose, energy, and amino acid metabolism (*3*). Biotin possesses a strong binding affinity to avidin and streptavidin ($K_d \approx 10^{-15}$ M) (*4*). The quarternary structure of avidin ($M_w \approx$ 66 kDa) consists of four noncovalently bound units that combine into the active form (*5*, *6*). Therefore, each avidin unit is capable of binding four biotin molecules (*6*, *7*). This binding property can be exploited to develop a universal tracer that could be used, for example, in the management of various tumor types (*8*) based on pretargeting concept as well as in organ-transplantation medicine. The development of such a tracer would require physiological half-life of the biotin tracer to be prolonged. This feature can be tuned by the introduction of poly(ethylene glycol) (PEG) chains. The PEG polymer is linear, hydrophilic due to the hydrogen bonds to water from the ether oxygens, uncharged and flexible (*9*). It has been investigated for use as a covalent modification of biological macromolecules and surfaces for many pharmaceutical and biotechnology applications (*10, 11*). It is well-known that PEG modifications to therapeutically useful proteins and peptides improve *in vivo* stability, pharmacokinetic, immunogenic, and antigenic properties and show little toxicity (*10, 12, 13*).

The biotin−^{68}Ga-based tracer development and application is exemplified here by the exploration of a tracer that could be used for labeling islets of Langerhans in order to monitor the survival of transplanted avidin-coated islets.

In this study, three biotin counterparts with various alkyl, PEG, and DOTA modifications were synthesized, labeled with ^{68}Ga, and characterized.

EXPERIMENTAL PROCEDURES

Materials. *N*-(5-Aminopentyl)-5-[(3*aR*,4*R*,6*aS*)-2-oxohexahydro-1*H*-thieno[3,4-*d*]imidazol-4-yl]pentanamide, *N*-{2-[2-(2-aminoethoxy)ethoxy]ethyl}-5-[(3*aR*,4*R*,6*aS*)-2-oxohexahydro-1*H*-thieno[3,4-*d*]imidazol-4-yl]pentanamide, and *N*-(2-{2-[2-(2-aminoethoxy)ethoxy]ethoxy}ethyl)-5-[(3*aR*,4*R*,6*aS*)-2-oxohexahydro-1*H*-thieno[3,4-*d*]imidazol-4-yl]pentanamide were obtained from Pierce Biotechnology, Inc. (Rockford, USA) and (+)-biotin was purchased from Alfa Aesar, Chemtronica. 2,2′,2″-(10-{2-[(2,5-Dioxopyrrolidin-1-yl)oxy]-2-oxoethyl}-1,4,7,10-tetraazacyclododecane-1,4,7-triyl)triacetic acid HPF_6·TFA (DOTA-NHS-ester) was purchased from Macrocyclics (Dallas, USA). 2-[4-(2-Hydroxyethyl)piperazin-1-yl]ethane-

* E-mail: Irina.Velikyan@ge.com. Tel: +46-18-180917. Fax: +46-18-180912. Uppsala Imanet, GEHC, Box 967, S-751 09 Uppsala, Sweden.

[†] Department of Biochemistry and Organic Chemistry.

[‡] Uppsala Applied Science Lab.

[§] Uppsala Imanet.

10.1021/bc800538s CCC: $40.75 © 2009 American Chemical Society
Published on Web 05/19/2009

Scheme 1. Outline of Synthesis of Biotin−DOTA Conjugates from the Corresponding Amines[a]

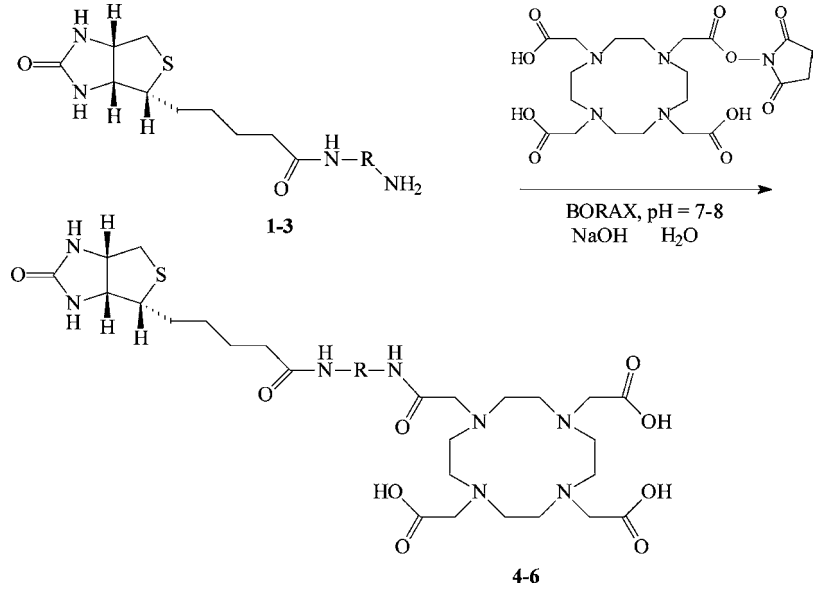

[a] (**1**), (**4**) R = $-(CH_2)_5-$; (**2**), (**5**) R = $-(CH_2)_2-O-(CH_2)_2-O-(CH_2)_2-$; (**3**), (**6**) R = $-(CH_2)_2-O-(CH_2)_2-O-(CH_2)_2-O-(CH_2)_2-$.

Scheme 2. ^{68}Ga-Labeling of Biotin-DOTA Analogues 4−6[a]

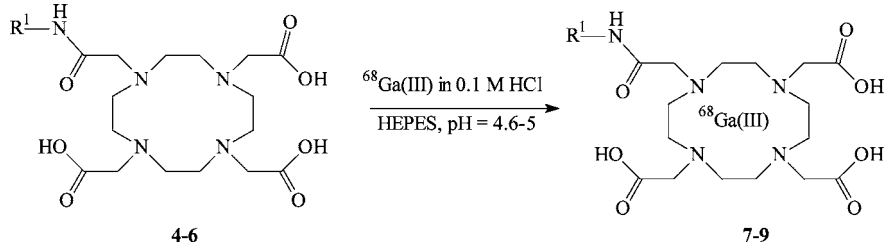

[a] (**4**), (**7**) R1 = biotin−NH−$(CH_2)_5-$; (**5**),(**8**) R1 = biotin−NH−$(CH_2)_2-O-(CH_2)_2-O-(CH_2)_2-$;−(**6**), (**9**) R1 = biotin−NH−$(CH_2)_2-O-(CH_2)_2-O-(CH_2)_2-O-(CH_2)_2-$.

sulfonic acid (HEPES), trifluoroacetic acid (TFA), double-distilled hydrochloric acid (Riedel de Haën), avidin (lyophilized powder, from egg white), sodium tetraborate decahydrate (Borax), and gallium (III) chloride were obtained from Sigma-Aldrich. Sodium dihydrogen phosphate disodium hydrogen phosphate and sodium chloride were obtained from Merck eurolab. The purchased chemicals were used without further purification.

Analytical Methods. HPLC analyses of radiolabeled compounds were performed on a Beckman Nouveau HPLC system equipped with a Beckman 166 variable-wavelength UV detector and a Bioscan β^+-flow detector, using an isocratic elution with water (A) (92%) and acetonitrile (B) (8%), both containing 0.05% TFA, as mobile phase and UV detection at 223 nm. For analytical HPLC, a Grace Vydac C18 Protein and Peptide column (150 × 4.6, 5 μ) was used, with a flow of 1 mL/min. For semipreparative HPLC, a Grace Vydac C18 Protein and Peptide column (150 × 10, 10 μ), 300 Å TP silica, was used on a Gilson HPLC system at a flow of 5 mL/min. Millipore water (18 mΩ) from Purelab Maxima Elga system (Bucks, UK) was used throughout the synthesis. NMR spectra were recorded on a Varian Unity spectrometer at 400 MHz for ^{1}H or 100 MHz for ^{13}C, at 25 °C, in CD_3OD (solvent peak used as reference, ^{1}H 3.31 ppm, ^{13}C 49.00 ppm). LC-MS analysis was performed using a Micromass VG Quattro mass spectrometer with electrospray ionization. The same analytical HPLC column and mobile phases were used at a flow of 0.3 mL/min. The radioactivity was measured in an ion chamber, Veenstra Instrumenten bv, VDC-202.

Microwave Heating. Microwave heating was performed in a SmithCreator monomodal cavity (Biotage AB, Uppsala, Sweden) producing continuous irradiation at 2450 MHz (Biotage AB, Sweden). The temperature, pressure, and microwave power were monitored and controlled. Smith Process Vial microwave vials of 200−1000 μL volume were used.

Preparation of ^{68}Ga. ^{68}Ga ($T_{1/2}$ = 68 min, β^+ = 89%, and EC = 11%) was available from a ^{68}Ge/^{68}Ga generator system (Cyclotron Co., Ltd., Obinsk, Russia) in which ^{68}Ge ($T_{1/2}$ = 270 d) was attached to a column of an inorganic matrix based on titanium dioxide. The initial ^{68}Ge radioactivity loaded onto the generator column was 1850 MBq. The specified shelf-life of the generator was 1−2 years. The ^{68}Ga was eluted with 6 mL of 0.1 M hydrochloric acid.

Preconcentration Procedure (*14*). The ^{68}Ge/^{68}Ga generator was eluted with 6 mL of a 0.1 M HCl (aq) solution. To this eluate solution, 5 mL of 30% HCl was added. The resulting solution was passed through an anion-exchange column (Chromafix 30-PS-HCO_3, Macharey-Nagel (Germany)) at a flow rate of 4 mL/min. Thereafter, the ^{68}Ga ions were eluted with deionized water (4 × 50 μL) at a flow rate of 0.5 mL/min. The final solution was used for labeling reactions.

General Labeling Procedure. HEPES (0.048 g, 0.20 mmol) was dissolved in 200 μL of ^{68}Ga eluate (in 0.1 M HCl (aq)) in a 2 mL Eppendorf tube. Thereafter, an aqueous solution of biotin−DOTA conjugates (**4**−**6**) (1−70 nmol) was added, and the total volume was adjusted to 280 μL by addition of water. The pH was adjusted to 4.6−5 by adding 2 M NaOH (aq) if necessary. The reaction was conducted at room temperature or

Table 1. Retention Times on Analytical HPLC for Compounds 4−9, and log *D* Values

compound	retention time[a] (min)	compound	retention time[a] (min)	log D[b]
4	6.9	**7**	9.4	-1.71 ± 0.07
5	6.1	**8**	7.3	-1.05 ± 0.10
6	9.5	**9**	12.4	-1.50 ± 0.10

[a] Retention time on analytical HPLC column. [b] Partion coefficient for the respective ^{68}Ga-labeled compounds at pH 7.4 between 1-octanol and PBS, experiments performed in triplicate.

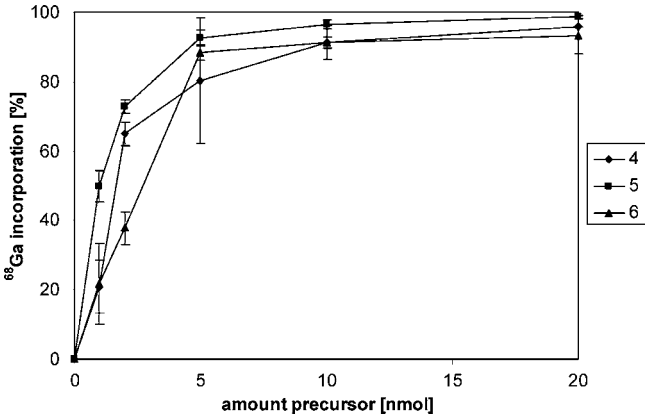

Figure 1. Percent ^{68}Ga(III) incorporation versus amount precursor (compounds **4**−**6**) used in labeling reaction. Heating was performed at 90 ± 5 °C for 5 min, in heating block. The reaction volume was 280 μL. Data are presented as mean ± SD (n = 3).

by using conventional heating at 90 ± 5 °C for 5 min or microwave heating at 90 ± 5 °C for 2 min.

Recovery. The recovery of ^{68}Ga eluate sample on the HPLC system was 88% when an analytical HPLC column was attached and 98% with no column attached. The recovery of a ^{68}Ga-Biotin-DOTA-conjugate sample was 59 ± 4% (n = 2) with column.

Synthesis of ^{69,71}Ga-Reference Compounds. HEPES (0.048 g, 0.20 mmol) was dissolved in 200 μL of ^{68}Ga eluate and the pH was adjusted to 4.6−5 by adding 2 M NaOH (aq). Thereafter, an aqueous solution of the respective precursor **4**−**6** (70 nmol) and $^{69,71}GaCl_3$ (56 mM, 2 μL, 112 nmol) was added. The reaction mixture was heated at 90 °C for 5 min.

ESI-MS: ^{69,71}Ga-**4** *m/z* 784 $[M+H]^+$, 393 $[M+2H]^{2+}$, ^{69,71}Ga-**5** *m/z* 827 $[M+H]^+$, 414 $[M+2H]^{2+}$, ^{69,71}Ga-**6** *m/z* 874 $[M+H]^+$, 438 $[M+2H]^{2+}$.

Lipophilicity. The log D (pH = 7.4) values were determined by the following procedure: a solution of the ^{68}Ga-labeled compounds **7**−**9** (20 μL, 48 μM) was added to a solution of 1-octanol and phosphate buffered saline (PBS) (presaturated with each other), containing 500 μL of each, in a 2 mL Eppendorf tube. After vortexing the obtained solutions, they were centrifuged at 3000 rpm for 10 min. Aliquots (100 μL) were removed from the two phases and the radioactivity was measured in a γ-counter. The experiments were performed in triplicate. The method was published previously (*15*).

Avidin Binding Reactions. Various amounts of biotin, compounds **4**−**6** or ^{69,71}Ga-biotin-**4**−**6** (2−128 nmol) were incubated with a constant amount of avidin (2 nmol) for 5 min at room temperature in water (150 μL total volume). The percentage binding was determined by HPLC analysis monitoring the consumption of avidin. HPLC program: 8% (B) for 12 min, then up to 80% in 10 min for compounds **4** and **5**; 8% (B) for 15 min, then up to 80% in 18 min for compound **6**. The labeled compounds **7**−**9** were incubated with avidin for 5 min at room temperature and analyzed by the same HPLC programs.

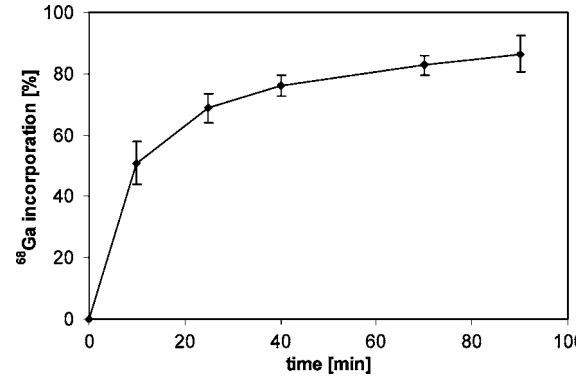

Figure 2. Percent ^{68}Ga(III) incorporation versus reaction time at room temperature, using 10 nmol of compound **5** and a reaction volume of 280 μL. Data are presented as mean ± SD (n = 3).

Blocking Experiment. Avidin (2 nmol) was incubated together with biotin (400 nmol) in water (100 μL) for 10 min. HPLC analysis confirmed the blocking. Thereafter, one of compounds **7**−**9** (8 nmol) was added and incubated together with the blocked avidin for 5 min (total volume 360 μL) before the solution was again analyzed by HPLC. HPLC program: 8% (B) for 12 min, then up to 80% in 10 min for compounds **7** and **8**; 8% (B) for 15 min, then up to 80% in 18 min for compound **9**.

Stability Studies. The stability studies were conducted using modified protocol published elsewhere (*8*). Solutions containing compounds **7**−**9** (10 μL, 0.5 nmol) were incubated for 0, 10, 30, 60, and 120 min at 37 °C together with human serum/saline 1:1 (500 μL). Thereafter, avidin (12 nmol) was added and incubated for 5 min at room temperature. Aliquots (50 μL) were withdrawn, diluted to a total volume of 500 μL with water, subsequently centrifuged in Microcon YM-10 at 14 000 rpm for 30 min, and finally washed with saline (500 μL) and centrifuged again. The fraction of intact ^{68}Ga tracer−avidin complex was determined by radioactivity counts of Microcon filter and vials (γ-counter, in house). In the case of study of the stability of the complex between compound **8** and avidin, compound **8** (8 nmol) was first incubated with avidin (2 nmol) for 5 min at room temperature. Thereafter, diluted serum (500 μL) was added; the mixtures were incubated for 0, 10, 30, 60, and 120 min at 37 °C and analyzed as described previously. The experiments were performed in triplicate.

Chemical Synthesis. *2,2′,2″-[10-(2-Oxo-2-{[5-({5-[(3aR,4R,6aS)-2-oxohexahydro-1H-thieno[3,4-d]imidazol-4-yl]pentanoyl}-amino)pentyl]amino}ethyl)-1,4,7,10-tetraazacyclododecane-1,4,7-triyl]triacetic Acid* (**4**). *N*-(5-Aminopentyl)-5-[(3*aR*,4*R*,6*aS*)-2-oxohexahydro-1*H*-thieno[3,4-*d*]imidazol-4-yl]pentanamide (**1**) (0.015 g, 46 μmol) was dissolved in 250 μL aqueous sodium tetraborate decahydrate (Borax) (0.08 M, pH 9.3). The solution was cooled to 0 °C and 2,2′,2″-(10-{2-[(2,5-dioxopyrrolidin-1-yl)oxy]-2-oxoethyl}-1,4,7,10-tetraazacyclododecane-1,4,7-triyl)triacetic acid HPF_6·TFA (0.057 g, 69 μmol) was added. The pH of the resulting solution was 2. The pH was raised to 7 by adding 200 μL of a 1:1 v/v mixture of 1 M NaOH (aq) and Borax (aq). The reaction mixture was warmed to room temperature and stirred for 24 h. Purification by semipreparative HPLC (6% (B) isocratic) gave the desired product as a colorless oil (0.011 g, 34% yield). ^{1}H NMR (400 MHz, CD_3OD, 25 °C): δ = 4.51 (dd, J = 5.1, 7.9 Hz, 1H), 4.31 (dd, J = 4.6, 7.9 Hz, 1H), 3.98 (m, 4H), 3.83 (m, 12H), 3.25−3.16 (m, 13H), 2.94 (dd, J = 4.9, 12.6 Hz, 1H), 2.73 (d, J = 12.6 Hz, 1H), 2.21 (t, J = 7.2 Hz, 2H), 1.80−1.27 (m, 12H).^{13}C NMR (100 MHz, CD_3OD, 25 °C): δ = 176.0, 165.8, 162.9, 162.0, 63.4, 61.7, 57.0, 54.6, 51.6, 51.1, 50.7, 41.0, 40.5, 40.2, 36.8, 30.1, 29.9,

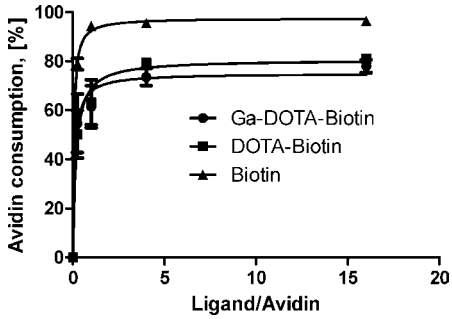

Figure 3. Saturation of the binding of a series of biotin-based counterparts (biotin, compound **5** (DOTA−biotin), and ^{69,71}Ga-labeled **5** (Ga−DOTA−biotin)) to avidin in solution, as determined by HPLC analysis. The incubation was carried out for 5 min at room temperature with varied ligand concentrations resulting in ligand/avidin ratios of 0.25, 1, 4, and 16. Data are presented as mean ± SD (n = 2).

29.7, 29.5, 26.9, 25.2. ESI-MS: *m*/*z* 715 $[M+H]^+$, 358 $[M+2H]^{2+}$. HPLC purity >99%.

*2,2′,2″-(10-{2,13-Dioxo-17-[(3aR,4R,6aS)-2-oxohexahydro-1H-thieno[3,4-d]imidazol-4-yl]-6,9-dioxa-3,12-diazaheptadec-1-yl}-1,4,7,10-tetraazacyclododecane-1,4,7-triyl)triacetic Acid (***5***).* *N*-{2-[2-(2-Aminoethoxy)ethoxy]ethyl}-5-[(3*aR*,4*R*,6*aS*)-2-oxohexahydro-1*H*-thieno[3,4-*d*]imidazol-4-yl]pentanamide (**2**) (0.011 g, 29 μmol) was dissolved in 250 μL aqueous sodium tetraborate decahydrate (Borax) (0.08 M, pH 9.3) or 250 μL aqueous sodium dihydrogen phosphate (*16*) (0.2 M, pH 8.5). The solution was cooled to 0 °C and 2,2′,2″-(10-{2-[(2,5-dioxopyrrolidin-1-yl)oxy]-2-oxoethyl}-1,4,7,10-tetraazacyclododecane-1,4,7-triyl)triacetic acid HPF_6·TFA (0.030 g, 36 μmol) was added. The pH of the resulting solution was 4. The pH was raised to 8 by adding 100 μL of a 1:5 v/v mixture of 1 M NaOH (aq) and Borax (aq). The reaction mixture was warmed to room temperature and stirred for 24 h. Purification by semipreparative HPLC (6% (B) isocratic) gave the desired product as a colorless oil (0.010 g, 47% yield). ^{1}H NMR (400 MHz, CD_3OD, 25 °C): δ = 4.50 (dd, J = 5.0, 8.0 Hz, 1H), 4.31 (dd, J = 4.5, 8.0 Hz, 1H), 3.92 (m, 4H), 3.83 (m, 12H), 3.64−3.62 (m, 4H), 3.60−3.54 (m, 6H), 3.41 (t, J = 5.4 Hz, 2H), 3.39−3.33 (m, 8H), 3.25−3.19 (m, 1H), 2.94 (dd, J = 5.0, 12.8 Hz, 1H), 2.72 (d, J = 12.8 Hz, 1H), 2.23 (t, J = 7.5 Hz, 2H), 1.81−1.54 (m, 4H), 1.50−1.41 (m, 2H). ^{13}C NMR (100 MHz, CD_3OD, 25 °C): δ = 176.3, 166.1, 163.3, 162.5, 71.3, 71.2, 70.6, 70.4, 63.4, 61.7, 57.0, 51.9, 49.8, 41.0, 40.4, 40.3, 36.8, 29.7, 29.5, 26.8. ESI-MS: *m*/*z* 761 $[M+H]^+$, 381 $[M+2H]^{2+}$. HPLC purity >99%.

*2,2′,2″-(10-{2,16-Dioxo-20-[(3aR,4R,6aS)-2-oxohexahydro-1H-thieno[3,4-d]imidazol-4-yl]-6,9,12-trioxa-3,15-diazaicos-1-yl}-1,4,7,10-tetraazacyclododecane-1,4,7-triyl)triacetic Acid (***6***).* *N*-(2-{2-[2-(2-Aminoethoxy)ethoxy]ethoxy}ethyl)-5-[(3*aR*,4*R*,6*aS*)-2-oxohexahydro-1*H*-thieno[3,4-*d*]imidazol-4-yl]pentanamide (**3**) (0.017 g, 40 μmol) was dissolved in 250 μL aqueous sodium tetraborate decahydrate (Borax) (0.08 M, pH 9.3). The solution was cooled to 0 °C and 2,2′,2″-(10-{2-[(2,5-dioxopyrrolidin-1-yl)oxy]-2-oxoethyl}-1,4,7,10-tetraazacyclododecane-1,4,7-triyl)triacetic acid HPF_6·TFA (0.050 g, 60 μmol) was added. The pH of the resulting solution was 2. The pH was raised to 7 by adding 200 μL of a 1:1 v/v mixture of 1 M NaOH (aq) and Borax (aq). The mixture was warmed to room temperature and stirred for 24 h. Purification by semipreparative HPLC (8% (B) isocratic) gave the desired product as a colorless oil (0.012 g, 37% yield). ^{1}H NMR (400 MHz, CD_3OD, 25 °C): δ = 4.50 (dd, J = 4.9, 7.9 Hz, 1H), 4.31 (dd, J = 4.5, 7.9 Hz, 1H), 3.93 (m, 4H), 3.83 (m, 12H), 3.68−3.61 (m, 10H), 3.60−3.53 (m, 4H), 3.41 (t, J = 5.3 Hz, 2H), 3.35−3.30 (m, 8H), 3.25−3.18 (m, 1H), 2.94 (dd, J = 5.0, 12.8 Hz, 1H), 2.72 (d, J = 12.8 Hz, 1H), 2.22 (t, J = 7.4 Hz, 2H), 1.80−1.54 (m, 4H), 1.51−1.40 (m, 2H). ^{13}C NMR (100 MHz, CD_3OD, 25 °C): δ = 176.2, 166.1, 163.0, 162.7, 71.6, 71.5, 71.2, 71.1, 70.5, 70.4, 63.4, 61.7, 57.1, 41.1, 40.4, 40.3, 36.7, 31.6, 29.8, 29.6, 26.9. ESI-MS: *m*/*z* 806 $[M+H]^+$, 404 $[M+2H]^{2+}$. HPLC purity >99%.

RESULTS AND DISCUSSION

Conjugation. The biotin−DOTA (DOTA = 2,2′,2″,2‴-(1,4,7,10-tetraazacyclododecane-1,4,7,10-tetrayl)tetraacetic acid) conjugates **4**−**6** were prepared by reacting the 2,2′,2″-(10-{2-[(2,5-dioxopyrrolidin-1-yl)oxy]-2-oxoethyl}-1,4,7,10-tetraazacyclododecane-1,4,7-triyl)triacetic acid (DOTA-NHS-ester) with the corresponding biotin−amines (**1**−**3**) in water at pH 7−8 using a mixture of sodium tetraborate decahydrate (Borax) and sodium hydroxide as buffer (Scheme 1). The yield of the product after purification by semipreparative HPLC was 34−47%. When the synthesis of compound **5** was attempted at pH 4, using sodium dihydrogen phosphate and no added sodium hydroxide as buffer, the yield was only 7%.

Labeling. The biotin conjugates were labeled with ^{68}Ga(III) cation using a solution in hydrochloric acid of the radiometal eluted from the ^{68}Ge/^{68}Ga generator system and 2-[4-(2-hydroxyethyl)piperazin-1-yl]ethanesulfonic acid (HEPES) as a buffer, as shown in Scheme 2. This buffer is biocompatible and does not need to be removed prior to biological experiments. The labeling reaction was performed at pH 4.6−5.0 at room temperature as well as 90 ± 5 °C, provided by conventional or microwave heating mode (2450 MHz). The radioactivity incorporation of ^{68}Ga(III) could reach 90% within 5 min with conventional heating, and when microwave heating was applied, the reaction time was reduced to 2 min. No major differences in incorporation yield were observed between the two heating modes. When the labeling was performed at room temperature, on the other hand, at least 90 min reaction time was required to reach 90% incorporation. The entire synthesis of the ^{68}Ga-labeled compound under elevated temperature and including subsequent HPLC analysis was accomplished within 30 min. Since the incorporation exceeded 90%, and the solution was buffered with HEPES no further purification was performed. The ^{68}Ga half-life of 68 min in combination with the short synthesis time may allow the use of the resulted tracers for biology experiments during 3−4 h.

Different linkers between the biotin and DOTA moieties of the tracer were used to explore the variability in avidin binding. An alkyl linker was used in compound **7**, and two poly(ethylene glycol) (PEG) linkers of different length were used in compounds **8** and **9**. The retention times for the ^{68}Ga-labeled compounds on the analytical HPLC column increased in the order **8** < **7** < **9**, as shown in Table 1. The "shake-flask" method, with 1-octanol and PBS (pH = 7.4), was used to determine the log D values, which are also shown in Table 1. The order of the determined log D values, **7** < **9** < **8**, was not in agreement with the retention times in HPLC analysis. One could speculate that the two analogues having PEG spacers **8** and **9** would have similar lipophilicites, and also lower compared to the analogue with an alkyl linker **7**, but this was not the case. The size of the molecules can also make contributions.

The incorporation of ^{68}Ga(III) into 1−20 nmol of compounds **4**−**6** by conventional heating at 90 ± 5 °C for 5 min was investigated. The plateau at 95% incorporation was reached at 10 nmol using the described setup, as shown in Figure 1. This amount (10 nmol) was thereafter used in the subsequent labeling reactions. The specific activity when using 10 nmol of compound **5** in labeling reactions was 9 ± 3 GBq/μmol starting from 140 ± 30 MBq (n = 4).

The incorporation kinetics of ^{68}Ga(III) at room temperature was explored using 10 nmol of compound **5** (Figure 2).

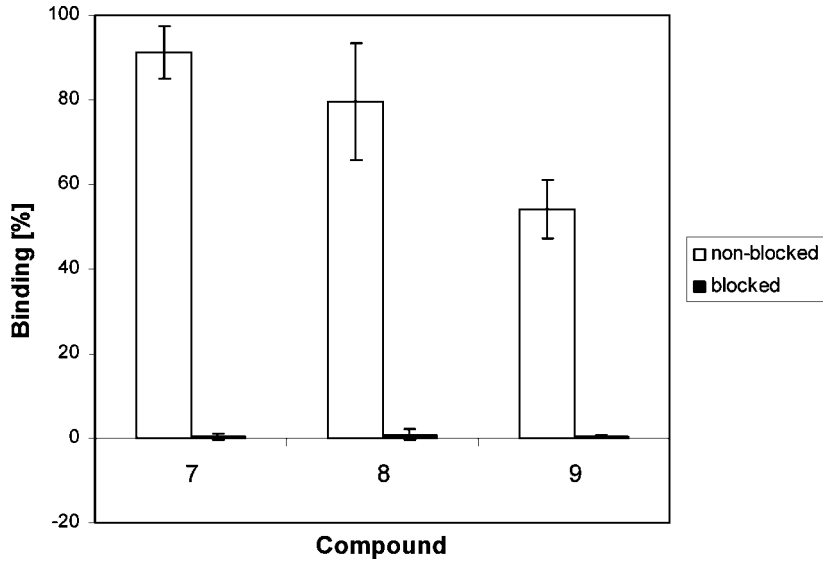

Figure 4. Percent binding of compounds **7**−**9** to avidin, blocked and nonblocked. Data are presented as mean ± SD ($n = 2$).

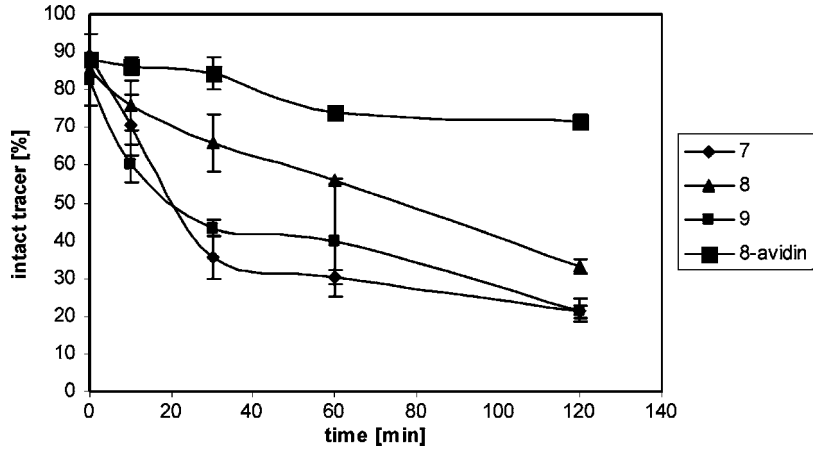

Figure 5. Stability of ^{68}Ga-labeled compounds **7**−**9** and **8**-avidin complex in human serum. Data are presented as mean ± SD ($n = 3$).

Stable gallium isotope (^{69,71}Ga) was introduced to the biotin−DOTA conjugates using an aqueous solution of $GaCl_3$ at 90 ± 5 °C for 5 min and the reaction conditions shown in Scheme 2. The synthesis was conducted under the same conditions using a mixture of ^{68}Ga and ^{69,71}Ga cations. The use of a mixture of radioactive and stable gallium isotopes was twofold: to create a reaction condition identical to the labeling procedure; to make it possible to follow the reaction. The identity of the compounds was confirmed by LC-ESI-MS. The stable gallium-labeled conjugates were added as authentic reference compounds in the LC analysis of labeling reactions in order to identify of the ^{68}Ga-labeled compounds.

The retention times on the analytical HPLC column for **4**−**6** (Table 1) increased when gallium(III) ion coordinated to the conjugate (**7**−**9**), most probably because of the change of the geometry and overall charge of the DOTA chelator upon the complexation.

The ^{68}Ga(III) is eluted from the ^{68}Ge/^{68}Ga generator using 6 mL of a solution of hydrochloric acid. The high volume decreases the radioactivity incorporation and, consequently, specific radioactivity of the product. The reduction of the volume to 200 μL using eluate preconcentration on an anion exchange column (*14*) prior to the labeling experiments improved the specific activity of the products approximately 4-fold.

Binding. The influence of the introduction of alkyl or PEG chains, the DOTA chelator, and radioactive and stable gallium isotopes on the biotin binding capacity was studied. All of the ligands **4**−**9** retained their binding ability to avidin in solution. The results of avidin saturation experiment with the biotin compounds: native biotin, DOTA−biotin (**5**), and Ga−DOTA−biotin (^{69,71}Ga-**5**) are shown in Figure 3. Various amounts of the biotin or its analogues (2−128 nmol) were incubated together with a constant amount of avidin (2 nmol), at room temperature for 5 min. The binding experiments were carried out in both water and HEPES buffer solutions, and the buffer did not affect the binding. The specific binding presented as the avidin consumption on percentage basis was plotted against the ratio of the total molar concentration of added ligands and avidin. The result was analyzed by nonlinear regression using the *GraphPad Prism* software. All the curves reached a maximum value, indicating saturation. Native biotin showed the highest binding, and analogues **4** and **5** reached saturation at approximately 15% below biotin. Compound **6**, with the longer PEG-linker, had the lowest binding, reaching saturation approximately 40% below biotin. In all cases, the binding was somewhat lower when ^{69,71}Ga was inserted into the DOTA chelator, and the molecule became neutral. (Without the gallium ion, the molecule has a −3 charge.) Increasing the incubation time to 40 min did not increase the binding of any of the analogues.

Thus, the modifications of biotin did not deteriorate its avidin-binding ability and the binding of the conjugates might be sufficient to allow their use in labeling avidin-treated islets of Langerhans.

The binding of equimolar amounts of the ^{68}Ga-labeled conjugates and avidin (67 mM each) was studied using HPLC. The biotin analogues **7**−**9** were incubated with avidin at room temperature. Approximately 80−90% of the labeled compounds **7** and **8**, but only 50% of compound **9**, were bound to avidin within 5 min, as shown in Figure 4. The lower binding of compound **9** was also seen in the saturation experiments with avidin (see above). The pegylation, which increases the size of the molecule, especially in the case of compound **9**, led to lower binding. In order to demonstrate that the binding was receptor-specific, a 50-fold excess of native biotin was added to avidin solutions and incubated at room temperature for 10 min, in order to saturate the binding sites of the avidin. Thereafter, an equimolar amount (67 mM) of the labeled compounds **7**−**9** was added and incubated together with the blocked avidin for 5 min. HPLC analysis showed approximately 0.5−1.5% binding of the ^{68}Ga-labeled compounds to the blocked avidin (Figure 4). The binding was therefore site-specific, as it could be precluded by presaturation of avidin with the native ligand, biotin. We were not able to perform these studies at concentration levels corresponding to the K_D of the native biotin−avidin affinity (10^{-15} M) due to the limited sensitivity of the UV and radiodetectors.

The biotin-based tracer could be different from [^{18}F]FDG (*17*, *18*) in terms of binding specificity, accumulation, and longer residence. For example, in porcine islets *in vitro*, [^{18}F]FDG was retained with a half-life of 141.5 min (*17*). The ultimate aim is to provide monitoring and quantification of the transplanted avidin-coated islets of Langerhans.

Stability Studies. The stability in human serum of the three ^{68}Ga-labeled compounds **7**−**9** was studied. The results are presented in Figure 5. After 120 min, approximately 20−30% of the tracers were intact. The stability of the complex between avidin and compound **8** was higher; over 80% of the complex was intact after 120 min. The localization of the avidin target by biotin *in vivo* requires 5−60 min (*19*). Thus, the stability of the analogue **8** (60−75% within 60 min) in combination with the high stability of avidin−biotin complex might be sufficient for the monitoring of the islets of Langerhans within the time frame of the ^{68}Ga half-life.

CONCLUSION

Three ^{68}Ga-labeled biotin−DOTA conjugates with different linkers were synthesized and characterized. The binding of all the analogues to avidin in solution was saturable and specific. All analogues showed binding to avidin in solution. The stability in serum of the biotin analogue **8** (65% within 30 min) and avidin−biotin complex (80% within 120 min) might be sufficient for the monitoring of the islets of Langerhans *in vivo*. The tracers will be evaluated in *in vitro* experiments of avidin-coated islets of Langerhans and in transplantation models *in vivo*.

ACKNOWLEDGMENT

Financial support from The Swedish Science Research Council and Juvenile Diabetes Research Foundation (JDRF) is gratefully acknowledged (EB, BLå). This work was conducted in collaboration with Uppsala Imanet and Uppsala Applied Science Lab, GE Healthcare.

LITERATURE CITED

(1) Shapiro, A. M., Lakey, J. R., Ryan, E. A., Korbutt, G. S., Toth, E., Warnock, G. L., Kneteman, N. M., and Rajotte, R. V. (2000) Islet transplantation in seven patients with type 1 diabetes mellitus using a glucocorticoid-free immunosuppressive regimen. *N. Engl. J. Med. 343*, 230–238.

(2) Paty, B. W., Bonner-Weir, S., Laughlin, M. R., McEwan, A. J., and Shapiro, A. M. (2004) Toward development of imaging modalities for islets after transplantation: insights from the National Institutes of Health Workshop on Beta Cell Imaging. *Transplantation 77*, 1133–1137.

(3) Combs, G. F. J. (1992) *The Vitamins: Fundamental Aspects of Nutrition and Health*, p 336, Academic Press Inc, New York.

(4) Bayer, E. A., and Wilchek, M. (1980) The use of the avidin-biotin complex as a tool in molecular biology. *Methods Biochem. Anal. 26*, 1–45.

(5) DeLange, R. J., and Huang, T.-S. (1971) Egg white avidin. III. Sequence of the 78-residue middle cyanogen bromide peptide. Complete amino acid sequence of the protein subunit. *J. Biol. Chem. 246*, 698–709.

(6) Green, N. M. (1975) Avidin. *Adv. Protein Chem. 29*, 85–133.

(7) Livnah, O., Bayer, E. A., Wilchek, M., and Sussman, J. L. (1993) Three-dimensional structures of avidin and the avidin-biotin complex. *Proc. Natl. Acad. Sci. U.S.A. 90*, 5076–5080.

(8) Sabatino, G., Chinol, M., Paganelli, G., Papi, S., Chelli, M., Leone, G., Papini, A. M., De Luca, A., and Ginanneschi, M. (2003) A new biotin derivative-DOTA conjugate as a candidate for pretargeted diagnosis and therapy of tumors. *J. Med. Chem. 46*, 3170–3173.

(9) Davis, F., Abuchowski, A., Van Es, T., Palczuk, N., Chen, R., Savoca, K., and Wieder, K. (1978) *Enzyme Engl. 4*, 169–173.

(10) Harris, J. M., and Chess, R. B. (2003) Effect of pegylation on pharmaceuticals. *Nat. Rev. Drug Discovery 2*, 214–221.

(11) Harris, J. M., Martin, N. E., and Modi, M. (2001) Pegylation: a novel process for modifying pharmacokinetics. *Clin. Pharmacokinet. 40*, 539–551.

(12) Chen, X., Park, R., Shahinian, A. H., Bading, J. R., and Conti, P. S. (2004) Pharmacokinetics and tumor retention of ^{125}I-labeled RGD peptide are improved by PEGylation. *Nucl. Med. Biol. 31*, 11–19.

(13) Roberts, M. J., Bentley, M. D., and Harris, J. M. (2002) Chemistry for peptide and protein PEGylation. *Adv. Drug. Delivery Rev. 54*, 459–476.

(14) Velikyan, I., Beyer, G. J., and Langstrom, B. (2004) Microwave-supported preparation of (68)Ga bioconjugates with high specific radioactivity. *Bioconjugate Chem. 15*, 554–560.

(15) Antunes, P., Ginj, M., Walter, M. A., Chen, J., Reubi, J. C., and Maecke, H. R. (2007) Influence of different spacers on the biological profile of a DOTA-somatostatin analogue. *Bioconjugate Chem. 18*, 84–92.

(16) Cauchon, N., Langlois, R., Rousseau, J. A., Tessier, G., Cadorette, J., Lecomte, R., Hunting, D. J., Pavan, R. A., Zeisler, S. K., and van Lier, J. E. (2007) PET imaging of apoptosis with (64)Cu-labeled streptavidin following pretargeting of phosphatidylserine with biotinylated annexin-V. *Eur. J. Nucl. Med. Mol. Imaging 34*, 247–258.

(17) Eich, T., Eriksson, O., Sundin, A., Estrada, S., Brandhorst, D., Brandhorst, H., Langstrom, B., Nilsson, B., Korsgren, O., and Lundgren, T. (2007) Positron emission tomography: a real-time tool to quantify early islet engraftment in a preclinical large animal model. *Transplantation 84*, 893–898.

(18) Toso, C., Zaidi, H., Morel, P., Armanet, M., Andres, A., Pernin, N., Baertschiger, R., Slosman, D., Buhler, L. H., Bosco, D., and Berney, T. (2005) Positron-emission tomography imaging of early events after transplantation of islets of Langerhans. *Transplantation 79*, 353–355.

(19) Shoup, T. M., Fischman, A. J., Jaywook, S., Babich, J. W., Strauss, H. W., and Elmaleh, D. R. (1994) Synthesis of fluorine-18-labeled biotin derivatives: biodistribution and infection localization. *J. Nucl. Med. 35*, 1685–1690.

BC800538S

Functional Ubiquitin Conjugates with Lysine-ε-Amino-Specific Linkage by Thioether Ligation of Cysteinyl-Ubiquitin Peptide Building Blocks

Ji Eun Jung,[II,†] Hans-Peter Wollscheid,[II,‡] Andreas Marquardt,[†,‡] Marilena Manea,[†] Martin Scheffner,[‡,§] and Michael Przybylski*[,†,§]

Department of Chemistry, Laboratory of Analytical Chemistry, Department of Biology, Laboratory of Biochemistry, Konstanz Research School Chemical Biology, University of Konstanz, Universitätsstrasse 10, D-78457 Konstanz, Germany. Received December 16, 2008; Revised Manuscript Received April 16, 2009

The modification of ubiquitin to defined oligo-ubiquitinated conjugates has received considerable interest due to the finding that isomeric oligo-ubiquitin conjugates exhibit distinct differences in their biochemical functions, depending on the specific lysine-ε-amino linkage used for conjugate formation. Here, we report the design and development of a thioether linkage-based approach for the synthesis of oligo-ubiquitin conjugates with lysine-specific branching by thioether ligation of a linear ubiquitin peptide containing a C-terminal cysteine residue as the "donor" component, with a corresponding lysine-ε-amino-branched haloacyl-activated ubiquitin "acceptor" peptide. This approach was successfully used for the synthesis of a lysine-63-linked diubiquitin conjugate by ligation of the modified ubiquitin(1−52)-Cys- donor peptide to the N-terminal Arg-54 residue of the branched Lys-63-linked acceptor peptide, ubiquitin$(54-76)_2$. Advantages of the present approach are as follows: (i) the conjugation reaction is performed in solution using suitable preformed donor ubiquitin peptides with a C-terminal Cys residue, and (ii) different corresponding N-chloroacetylated ubiquitin acceptor peptides containing the branched Lys residue are employed, providing broad applicability to the preparation of isomeric oligo-ubiquitin conjugates. The Lys-63-diubiquitin conjugate **7** described here was purified by semipreparative HPLC, and its structure and homogeneity ascertained by HPLC and high-resolution MALDI and electrospray-mass spectrometry. CD spectra and molecular modeling indicate a conformationally stable structure of the conjugate with spatial separation of the ubiquitin parts of the Lys-63 linkage. Moreover, the activity of the thioether-linked diubiquitin conjugate was ascertained by *in vitro* autoubiquitination assay. These results indicate the feasibility of this approach for the preparation of functional oligo-ubiquitin conjugates.

INTRODUCTION

Ubiquitin is an essential eukaryotic protein of 76 amino acids that is highly conserved in all eukaryotes and plays a fundamental role in the control of many biological processes including cell cycle regulation, transcription, DNA repair, and apoptosis (*1*−*4*). Ubiquitin occurs in two general forms within cells, free (monomeric) ubiquitin and ubiquitin molecules that are covalently linked to other proteins. Modification of proteins with ubiquitin, a reaction type termed "ubiquitylation" or "ubiquitination", involves the concerted action of three classes of enzymes, ubiquitin-activating enzymes E1, ubiquitin-conjugating enzymes E2, and ubiquitin ligases E3 (*1*−*4*). In a simplified view, ubiquitinated proteins can be classified into two groups, monoubiquitinated and poly- (or oligo-)ubiquitinated conjugates. In monoubiquitinated proteins, single ubiquitin moieties are attached to one or several lysine residue of the substrate. Polyubiquitinated proteins are modified by so-called ubiquitin chains that consist of several ubiquitin moieties (*5*−*7*). Ubiquitin contains seven lysine residues (K 6, 11, 27, 29, 33, 48, 63), and mass spectrometric analysis of ubiquitinated proteins derived from yeast revealed that each of these lysine residues can be employed for ubiquitin chain formation (*8*). Of particular interest has been the observation that, depending on the specific lysine residue of ubiquitin used for conjugate formation, the corresponding isomeric ubiquitin conjugates exhibit distinct differences in their biochemical functions (*5*−*7*).

The best understood function of ubiquitin chains is as a signal targeting the modified protein to the 26S proteasome for degradation (*1*−*7*). However, it has recently become evident that ubiquitin conjugation may also serve nonproteolytic functions. In fact, the biochemical function of a poly-ubiquitinated protein appears to be critically determined by the specific lysine residue of ubiquitin used for chain formation (*5*−*7*), thus requiring a detailed chemical structure−function evaluation of the respective ubiquitin conjugates. The modification of substrate proteins with K48-linked and, possibly, with K11-linked and K29-linked ubiquitin chains targets these proteins for proteasome-mediated degradation (*5*−*7, 9, 10*). By contrast, K63-linked ubiquitin conjugates have not been found to be substrates for proteasome-mediated degradation but have been suggested to be involved in endocytosis and in other biochemical activities of the modified proteins (*7, 11*−*14*). Beyond the K48-linked ("proteasome flags") and K63-linked ubiquitin chains, the functions of ubiquitin conjugates linked by other lysine residues are presently unclear. NMR studies of K48-linked and K63-linked diubiquitin indicate differences in tertiary structures, which may reflect their different biochemical functions (*15, 16*). This notion (different ubiquitin chains adopt different tertiary structures that, in turn, mediate different functions) is supported by the observation that several proteins have been reported to differentially interact with K48-linked and K63-linked ubiquitin chains (*17*−*21*).

* Corresponding author. Prof. Dr. Michael Przybylski, Department of Chemistry, University of Konstanz. Phone: 0049-7531- 882249, Fax: 0049-7531- 883097. E-mail: Michael.Przybylski@uni-konstanz.de.

[II] Both authors contributed equally to this work.

[†] Department of Chemistry, Laboratory of Analytical Chemistry.

[‡] Department of Biology, Laboratory of Biochemistry.

[§] Konstanz Research School Chemical Biology.

10.1021/bc800539p CCC: $40.75 © 2009 American Chemical Society
Published on Web 05/27/2009

Studies to obtain insight into the biochemical and physiological functions of different ubiquitin chains are hampered by the fact that, besides K48-linked and K63-linked ubiquitin chains, defined chemical or biochemical preparation procedures are not available for isomeric oligo-ubiquitin conjugate formation. Here, we report the design and development of a thioether linkage-based approach for the synthesis of oligo-ubiquitin conjugates with defined lysine-specific linkages. This approach was successfully used for the preparation of K63-linked diubiquitin by ligation of a linear ubiquitin-derived peptide with a C-terminal cysteine as "donor" component with a corresponding K63-branched bis-haloacyl-activated ubiquitin "acceptor" peptide (Figure 1). The K63-branched diubiquitin conjugate prepared was purified and its homogeneity characterized by HPLC, mass spectrometry, and circular dichroism spectroscopy. A corresponding thioether-linked linear ubiquitin conjugate was active in *in vitro* autoubiquitination assays indicating the feasibility of this approach for the preparation of active oligo-ubiquitin conjugates. Thus, the present synthetic pathway should be applicable as a general route for the preparation of oligo-ubiquitin conjugates that can be used (i) to evaluate the biochemical properties of isomeric poly-ubiquitin conjugates and (ii) for the preparation of antibodies that selectively recognize isomeric ubiquitin chains depending on the specific lysine residue of ubiquitin used for chain formation.

EXPERIMENTAL SECTION

Materials. Amino acid derivatives, NovaSyn TGA resins, and benzotriazole-1-yl-oxy-tris-pyrrolidino-phosphonium hexafluorophosphate (PyBOP) were obtained from NovaBiochem (Läufelfingen, Switzerland) and from GL Biochemicals (Shanghai, China). Triisopropylsilane, 4-methylmorpholine (NMM), piperidine, 1,8-diazabicyclo-[*5.4.0*]undec-7-ene (DBU), trifluoroacetic acid (TFA), 1,4-dithiothreitol (DTT), diisopropylcarbodiimide (DIC), and 4-dimethylaminopyridine (DMAP) were obtained from Fluka (Buchs, Switzerland). Dimethyl formamide (DMF) was purchased from Acros Organics (Geel, Belgium). *tert*-Butyl methyl ether, acetonitrile, and other reagents and solvents were obtained from Riedel-deHäen (Seelze, Germany) at analytical grade or highest available purity.

Synthesis of Chloroacetylated Ubiquitin(54−76) Acceptor Peptides 1. The chloroacetylated acceptor peptides, *N*-chloroacetyl ubiquitin(54−76) **1** ((ClAc)-^{54}RTLSDYNIQ**K**ESTLHLVLRLRGG^{76}-OH) and the N^{α}-(N^{ε}-K63)-bis-chloroacetyl-ubiquitin(54−76)$_2$ **2** ((ClAc)-^{54}RTLSDYNIQ**K**ε((ClAc)-^{54}RTLSDYNIQ**K**ESTLHLVLRLRG G^{76}CO-)ESTLHLVLRLRGG^{76}-OH) were synthesized manually by solid-phase peptide synthesis on a NovaSyn TGA resin (0.29 mmol/g coupling capacity) according to the Fmoc strategy. The following side chain protected amino acid derivatives were used: Fmoc-Arg(Pbf[1])-OH, Fmoc-His(Trt)-OH, Fmoc-Ser(*t*Bu)-OH, Fmoc-Glu(O*t*Bu)-OH, Fmoc-Lys(Boc)-OH, Fmoc-Gln(Trt)-OH, Fmoc-Asn(Trt)-OH, Fmoc-Tyr(*t*Bu)-OH, Fmoc-Asp(O*t*Bu)-OH, Fmoc-Thr(*t*Bu)-OH, and Dde-Lys(Fmoc)-OH. The C-terminal G76 residue was preactivated with DIC and attached to the TGA resin in the presence of DMAP. A coupling capacity of 0.19 mmol/g was determined spectrophotometrically at 290 nm. The following synthetic protocol was generally employed for the attachment of the other amino acids: (i) DMF washing for 4 × 1 min; (ii) Fmoc deprotection for 15 min using 2% DBU and 2% piperidine in DMF; (iii) DMF washing for 8 × 1 min; (iv) double coupling using 5 equiv of Fmoc-amino acid/ PyBOP/NMM in DMF for 60 min; (v) DMF washing for 4 × 1 min; (vi) DCM washing for 2 × 1 min. The bromophenol blue test was used to assess the presence of free amines. After completion of the synthesis of ubiquitin(54−76) **1**, the N-terminus of R54 was chloroacetylated using chloroacetic acid-pentachlorophenyl ester in DMF/DCM at 5 mol equiv (*28*). Cleavage of the peptide from the resin was performed for 3 h at 25 °C using a mixture of TFA, triisopropylsilane, and deionized water (90:5:5, v/v/v). The product was then precipitated with cold *tert*-butyl methyl ether, washed three times with diethyl ether, and solubilized in 5% aqueous acetic acid prior to freeze−drying. The crude peptide was purified by reversed-phase HPLC on a preparative C4 column, and the purified peptide characterized by analytical HPLC and mass spectrometry.

The chloroacetylated K63-branched ubiquitin(54−76)$_2$ **2** was synthesized manually on a NovaSyn TGA resin (0.29 mmol/g coupling capacity) described above using the combined Fmoc/*t*Bu protecting chemistry and the analogous side chain protected amino acid derivatives (Figure 2). The C-terminal G76 residue was first preactivated with DIC and attached to the TGA resin as described above, and the subsequent amino acids coupled with incorporation of Dde-K(ε-Fmoc)-OH in position 63. After completion of the linear ubiquitin(63−76), the Fmoc-ε-amino protecting group of K63 was removed by treatment with 2% piperidine/2% DBU in DMF for 20 min and the synthesis of the branching sequence, ubiquitin(63−76) was built up on the free ε-amino group of the K63 residue. After completion of the synthesis of the branched diubiquitin(63−76)$_2$ sequence, the N-terminal Fmoc protecting group of the K63 residue of the branched peptide sequence was removed by treatment with 2% piperidine/2% DBU, and the *N*-α-terminal Dde-protecting group of K63 removed by treatment with 2% hydrazine in DCM for 2 min. The amino acids ubiquitin(54−62) were coupled, and the chloroacetyl group introduced at the N-terminal amino group of both R54 residues by treatment with a 5 mol excess/Arg residue of chloroacetic acid-pentachlorophenyl ester (ClAcOPcp) for 3 h at 25 °C. The final peptide **2** was cleaved from the resin at 25 °C for 3 h using a mixture of TFA, triisopropylsilane, and deionized water (90:5:5, v/v/v). The crude peptide was precipitated with ice-cold *tert*-butyl methyl ether, washed three times with diethyl ether, and solubilized in 5% aqueous acetic acid prior to freeze−drying. The peptide was then redissolved in 0.1% TFA and purified by HPLC on a preparative C4 column; the purified peptide was then characterized by analytical HPLC and FTICR mass spectrometry.

Expression and Isolation of His-Tagged Ubiquitin(1−52)-C 4. A cDNA encoding GSSHHHHHHSSGLVPRGSH-ubiquitin(1−52)-C **4** that consists of an N-terminal His-tag for affinity purification, ubiquitin amino residues 1−52, and a C-terminal cysteine residue was generated by PCR using the primers 5′-GAGATATACATATGCAGATCTTCGTGAAGAC-3′ (forward primer) and 5′-GCGGGATCCTTAACAGTCCTC-GAGCTGCTTACCG (reverse primer). The product was cloned by 5′NdeI and 3′*Bam*HI into the bacterial expression vector pET3a (Novagen) and the ubiquitin peptide **4** expressed in *E. coli* BL21-CodonPlus(DE3)-RIL (Stratagene). For isolation and purification of **4**, cells were lysed in PBS buffer, pH 8.7, with 1% Triton X100 (Sigma) by sonication, and the clarified lysate incubated for 20 min at 75 °C and then cooled on ice for 10 min. Under these conditions, ubiquitin remains in a native-like conformation, while most other proteins in the lysate denature and precipitate. After removal of denatured proteins by centrifugation, DTT was added for removal of possible mixed-disulfide formation at the C-terminal cysteine residue, and the solution was acidified to pH 3. The polypeptide was purified from residual byproducts and detergent by preparative HPLC,

[1]Abbreviations: FTICR-MS, Fourier transform-ion cyclotron resonance mass spectrometry; Pbf, (2,2,4,6,7-Pentamethyldihydro-benzofuran-5-sulfonyl); tBu, *tert*-butyl; OtBu, *tert*-butyl ester; Trt, trityl; Boc, *tert*-butoxycarbonyl; Dde, (1-(4,4-dimethyl-2,6-dioxocyclohex-1-ylidene)ethyl).

and the purified peptide **4** characterized by analytical HPLC and ESI mass spectrometry.

Halide Exchange of Chloroacetylated Ubiquitin(54−76)-Acceptor Peptide and Conjugation of His-Tagged-Ubiquitin(1−52)-C 4. *In situ* halide exchange for the preparation of iodoacetylated ubiquitin-acceptor peptides was performed using chloroacetylated ubiquitin(54−76) (0.3 mg) dissolved in 1 mL of a mixture of 8 M urea, pH 8.7, and 0.1 M Tris buffer, pH 8 (1:1; v/v), and then 1 mL of a saturated solution of KI prepared in 0.1 M Tris buffer was added. After 30 min reaction, a solution of 2 mol equiv of His-tagged ubiquitin(1−52)-C peptide **4** (dissolved in 1 mL of 8 M urea, pH 8.7, and 0.1 M Tris buffer, pH 8 (1:1 v/v)) was added dropwise for 20 min. After 20 h, the conjugation reaction mixture was acidified with TFA to pH 3 and purified by preparative RP-HPLC (Figure 3).

Conjugation of chloroacetylated branched ubiquitin$(54-76)_2$ acceptor peptide **2** ((ClAc)-^{54}RTLSDYNIQKESTLHLVLRL-RGG^{76}-OH)$_2$ (0.3 mg) was performed by dropwise addition of a solution of GSSHHHHHHSSGLVPRGSH-ubiquitin(1−52)-C **4** (0.875 mg) in 500 μL of a 1:10 mixture of 6 M guanidinium hydrochloride and 1 M potassium carbonate. The reaction mixture was stirred for 3 h at 25 °C in a sealed reaction tube, and the ligation reaction was monitored by analytical HPLC (Figure 5). Aliquots of 20−50 μL from the reaction mixtures were isolated and injected into an analytical HPLC; eluted fractions were isolated and analyzed by MALDI and ESI ion trap mass spectrometry. After completion of the reaction, the solution was acidified to pH 3 using 0.1% TFA and subjected to purification by semipreparative HPLC (see below).

High-Performance Liquid Chromatography. Analytical reversed-phase HPLC was performed on a Bio-Rad system (Bio-Rad Laboratories, Richmond, CA) using a Vydac C4 column (250 × 4.6 mm I.D., 5 μm silica, 300 Å pore size) (Hesperia, CA). The samples were dissolved in 200 μL 0.1% TFA (aqueous solution), and peptides were separated using a linear gradient elution (0 min, 0% B; 5 min, 0% B; 105 min, 100% B; 110 min, 100% B; 115 min, 0% B; 120 min, 0% B) with eluent A (0.1% TFA in water) and eluent B (0.1% TFA in acetonitrile−water (80:20 v/v)). The flow rate was 1 mL/min and the peaks were detected at 220 nm wavelength. Preparative HPLC separations of ubiquitin peptides were carried out on a Knauer HPLC system (Knauer, Berlin, Germany) using a preparative Vydac C4 column (250 nm × 10 mm I.D., 10 μm, 300 Å pore size). The same mobile phases and gradient as described above were employed at a flow rate of 10 mL/min.

The purification of diubiquitin conjugate **7** was carried out on a Bio-Rad system (Bio-Rad Laboratories, Richmond, CA) using a semipreparative Nucleosil 300-7 C_8 column (250 nm × 10 mm, 7 μm, 300 Å) (Macherey-Nagel, Düren, Germany) as a stationary phase. Linear gradient elution (0 min, 0% B; 15 min, 35% B; 45 min, 45% B, 65 min, 50% B, 100 min, 100% B; 105 min, 100% B; 110 min, 0% B) with eluent A (0.1% TFA in water) and eluent B (0.1% TFA in acetonitrile−water, (80:20, v/v)) was used at a flow rate of 2 mL/min and the peaks were detected at 220 nm. Purified diubiquitin conjugate **7** was analyzed by analytical RP-HPLC on a Vydac C8 column (250 × 4.6 mm I.D., 5 μm silica, 300 Å pore size) (Hesperia, CA) using the same gradient employed for purification.

Mass Spectrometry. ESI-FTICR mass spectrometry was performed with a Bruker Apex II FTICR mass spectrometer (Bruker Daltonics, Bremen, Germany) equipped with a 7.0 T actively shielded superconducting magnet (Magnex, Oxford, UK), and an APOLLO-II electrospray ionization source (Bruker Daltonics). Nano-ESI-FTICR mass spectrometry was performed with a modified APOLLO electrospray source (Bruker Daltonics) to accommodate a custom-made nanospray system (*35, 43*). A stable spray was obtained by application of a capillary entrance voltage between −880 and −1120 V, while the nanospray needle was grounded. Calibration was performed externally using fragment ions of angiotension I (Bachem, Bubendorf, Switzerland) produced by in-source CID. Acquisition of spectra was performed with the Bruker Daltonics software XMASS and corresponding programs for mass calculation, data calibration, and processing. A 10 μM solution of peptides in 50% methanol/2% aqueous acetic acid (1:1, v/v) was used for sample preparation.

ESI-ion trap mass spectra were recorded on a Bruker Esquire 3000+ ion trap mass spectrometer (Bruker Daltonics, Bremen, Germany) equipped with a direct infusion and ESI-LC-MS source (*33*). In addition, LC-MS experiments were carried out using an Agilent 1100 HPLC with binary pump system and a Zorbox 300SB-C8 column (Agilent, Waldbronn, Germany) with the dimensions as follows: 1.0 × 150 mm, 3.5 μm. *HyStar 3.1* (Bruker Daltonik, Bremen, Germany) control software was used. Samples were introduced by direct infusion with a syringe pump at flow rates 3−5 μL/min, using nitrogen both as nebulizer and as drying gas. The ion source voltages were used as follows: capillary exit −200 V, skimmer 40 V; scanned mass range m/z = 200−3000. For sample preparation, the samples were dissolved in 0.1% formic acid before injection.

MALDI-TOF mass spectrometric analyses were carried out with a Bruker Biflex TOF mass spectrometer (Bruker Daltonics, Bremen, Germany) equipped with a nitrogen UV laser (337 nm), a dual channel plate detector, a 26 sample SCOUT source, a video system, and an XMASS data system for spectra acquisition and instrument control (*42*). A saturated solution of α-cyano-4-hydroxycinnamic acid (HCCA) in acetonitrile/0.1% trifluoroacetic acid in water (2:1, v/v) was used as the matrix. An aliquot of 1 μL of the sample solution and 1 μL of a saturated matrix solution were mixed on the stainless steel MALDI target and allowed to dry. Acquisition of spectra was carried out at an acceleration voltage of 20 kV and a detector voltage of 1.5 kV.

Circular Dichroism Spectroscopy. CD spectra were recorded with a Jasco model J-720 spectropolarimeter at 25 °C in 0.05 cm quartz cells under constant nitrogen flush. The instrument was calibrated with 0.06% (w/v) ammonium-d-camphor-10-sulfonate (Katayama Chemical, Osaka, Japan) in double-distilled water; the sample concentrations were 0.5 μg/μL. The spectra were averages of six scans between 190 and 260 nm, respectively.

Molecular Modeling. The *Hyperchem* 7.01 software was used for the molecular modeling calculations. Geometry optimizations (*in vacuo*) were performed using the Amber99 parameter set for the force field and the Polak-Ribiere algorithm with a rms gradient of 0.1 kcal/(Å*mol).

RESULTS AND DISCUSSION

General Concept for Synthesis of Ubiquitin Conjugates by Thioether Ligation. Due to the well-known problems in solid-phase chemical synthesis of peptides with increasing chain lengths, chemoselective ligation using linear and lysine-branched precursor peptides as building blocks appears appropriate for ubiquitin conjugate synthesis. A number of chemoselective ligation methods have been recently developed and applied in polypeptide synthesis, such as via formation of thioether, oxime, thioester, and hydrazone bonds (*22−27*); and differences in reaction rates and chemical stabilities for several linkages have been determined (*28, 29*). The general approach employed in the present study for the synthesis of specific lysine-linked ubiquitin conjugates by (i) preparation of a linear ubiquitin−"donor" peptide with a C-terminal cysteine and (ii) its conjugation with a corresponding lysine-specific branched bis-haloacyl-ubiquitin "acceptor" peptide by thioether alkylation is shown

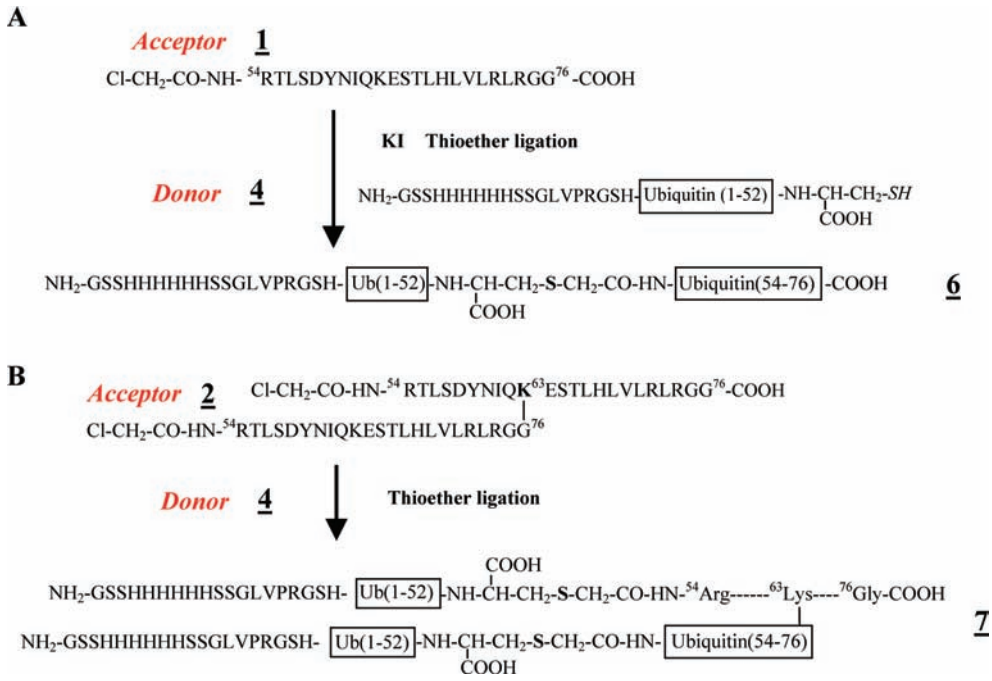

Figure 1. General scheme for the synthesis of oligo-ubiquitin conjugates. (A) Synthesis of linear ubiquitin peptide **6** by thioether ligation of acceptor peptide ubiquitin(54−76) **1** and His-tag-ubiquitin(1−52)-Cys **4**. (B) Thioether ligation of Lys-63-branched acceptor peptide ubiquitin(54−76)$_2$ **2** with ubiquitin donor peptide **4**.

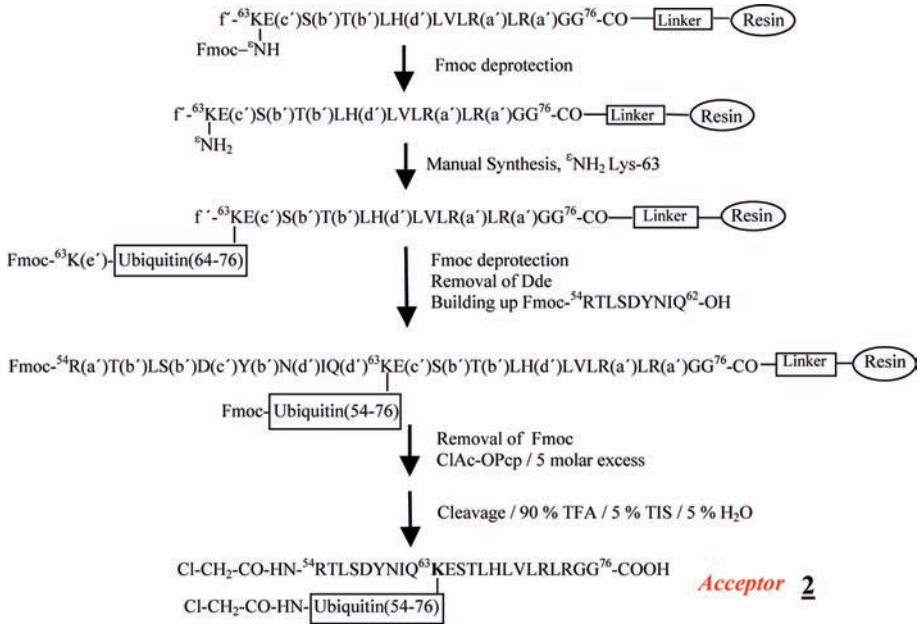

Figure 2. Pathways for the manual synthesis of the branched K63-linked bis-chloroacetylated ubiquitin(54−76)$_2$ acceptor peptide **2**. The protecting groups used are as follows: a′, Pbf, (2,2,4,6,7-pentamethyldihydrobenzofuran-5-sulfonyl); b′, tBu, *tert*-butyl; c′, OtBu, *tert*-butyl ester; d′, Trt, trityl; e′, Boc, *tert*-butoxycarbonyl; f′, Dde, (1-(4,4-Dimethyl-2,6-dioxocyclohex-1-ylidene)ethyl).

in Figure 1. Due to the high chemical and biological stability of thioether bonds and their lack of immunogenicity (*21*, *30*), we decided to use this approach that allows specific ligation between cysteine-thiol and halo-acetylated amino groups for ubiquitin conjugate synthesis.

Synthesis of N-Chloroacetylated Ubiquitin−Acceptor Peptides with Lys-NH$_2^{\varepsilon}$-specific linkage. N-Chloroacetylated ubiquitin peptides comprising the designated Lys-NH$_2^{\varepsilon}$-specific linkage were prepared as "acceptor" components in the first step of the general thioether conjugation approach (Figure 1) by manual synthesis on a NovaSyn TGA resin, using the scheme of insertion of lysine-branching sequences and orthogonal protecting groups shown in Figure 2. The linear N-chloroacetyl−ubiquitin(54−76) **1** containing the N-terminal amino group of Arg54 was prepared using a 5-molar excess of chloroacetic acid pentachlorophenyl ester in DMF/DCM. For isolation and characterization of the N-chloroacetyl-ubiquitin(54−76) **1**, the peptide was cleaved from the resin using a cleavage mixture containing 90% TFA, 5% water and 5% TIS, and the crude product purified by HPLC on a preparative C4 column. The ESI ion trap mass spectrum showed a single homogeneous peptide product with the experimental molecular mass of 2746.02 Da (Table 1; $C_{118}H_{198}N_{37}O_{36}Cl_1$; calculated mass: 2746.52 Da). Further, the N-chloroacetylated peptide **1** was converted into the N-iodoacetylated peptide **3** upon KI treatment,

Table 1. HPLC and Mass Spectrometric Characterization of Ubiquitin Peptides

			MALDI-MS[a]/ESI-ion-trap MS[b]/Nano-ESI-FT-MS[c]		
no.	peptide (code)	yield (%)	calculated [M]	found [M]	HPLC[d,e] R_t (min)
1	ClAc-Ubiquitin(54−76)	94	2746.52	2746.72[a]	17.25[d]
			2746.52	2746.00[b]	
2	$_C$lAc-Ubiquitin(54−76)$_2$	70	5475.02	5473.67[a]	31.49[e]
			5475.02	5474.99[b]	
			5470.89	5470.33[c]	
3	IAc-Ubiquitin(54−76)	70	2837.97	2838.16[a]	17.36[d]
4	GSSHHHHHHSSGLVPRGSH - Ubiquitin(1−52)-Cys	93	7990.94	7990.20[a]	18.58[d]
			7990.94	7991.50[a]	34.19[e]
			7990.94	7990.40[b]	−
			7985.64	7985.69[c]	−
5	GSSHHHHHHSSGLVPRGSH - Ubiquitin(1−52)-Cys dimer	−	15979.86	15976.69[a]	20.32[d]
					38.05[e]
6	Mono-Ubiquitin conjugate	67	10700.99	10699.40[a]	19.47[d]
			10700.99	10699.40[b]	−
			10694.55	10694.99[c]	−
7	Lys63-linked diubiquitin conjugate	14	21383.97	21384.30[a]	41.43[e]
			21383.97	21385.50[b]	−

[a] MALDI-TOF mass spectra were recorded with a Bruker Biflex linear TOF mass spectrometer. [b] Conjugate Lys63-linked diubiquitin was measured by ESI-Ion-Trap-MS. In these cases the deconvoluted molar mass data were calculated from the multicharged peaks. [c] Mono-ubiquitin conjugate was measured by Nano-FT-MS. In these cases the deconvoluted molar mass data were calculated from the multicharged peaks. [d] RP-HPLC column: Vydac C_4, (4.6 × 250 mm, 5 μm silica, 300 Å); eluents: 0.1% TFA in water (A), 0.1% TFA in MeCN-water 80:20 v/v (B); flow rate: 1 mL/min; gradient: 0 min 20% B, 5 min 20% B, 15 min 40% B, 80 min 70% B, 100 min 100% B. [e] RP-HPLC column: Nucleosil 300−7 C_8, (10 × 250 mm, 7 μm silica, 300 Å); eluents: 0.1% TFA in water (A), 0.1% TFA in MeCN-water 80:20 v/v (B); flow rate: 2 mL/min; gradient: 0 min 0% B, 15 min 35% B, 45 min 45% B, 65 min 50% B, 100 min 100% B.

which was used in the thioether ligation with ubiquitin donor peptides (see below).

The designated K63-NH_2^{ε}-branching site was protected with N^{α}-Dde and N^{ε}-Fmoc groups. After completion of the synthesis of the linear ubiquitin(63−76) component and removal of the N^{ε}-Fmoc protecting group, the second branching sequence ubiquitin(63−76) was built up on the K63-ε-amino group using NH_2^{α}-Fmoc-NH_2^{ε}-Boc protection of the branching K63 residue. After completion of the synthesis of the branched diubiquitin(63−76)$_2$ peptide, the N-terminal Dde protecting group of K63 was removed with 2% hydrazine in DCM. The second N^{α}-Fmoc group of K63 was subsequently removed, followed by manual coupling of amino acids (54−62) for both sequences (Figure 2). Following removal of the N-terminal Fmoc protecting groups, the chloroacetyl group was introduced at each N-terminal R54 residue using chloroacetic acid pentachlorophenyl ester. The peptide was cleaved from the resin, and the crude product was purified by HPLC on a preparative C4 column. The purified peptide **2** showed a single homogeneous peak by HPLC at a retention time of 31.49 min and provided molecular ions both by ESI-ion trap and MALDI-TOF mass spectrometry (*31*−*37*) due to a average molecular mass of 5474.99 Da, consistent with the calculated molecular mass of 5475.02 Da ($C_{236}H_{394}N_{74}O_{71}Cl_2$) (Table 1, Figure 5).

Preparation and Characterization of Cysteinyl−Ubiquitin Peptides As Donor Components. A ubiquitin peptide comprising an N-terminal His-tag sequence (GSSHHHHHHSSGLVPRGSH-ubiquitin(1−52)-C) **4** was prepared by bacterial expression as donor component for thioether ligation by replacing the C-terminal G53 with a cysteine residue (cf. Figure 1). Following bacterial expression, isolation, and purification as described in the Experimental Section, the His-tag-G53C mutant ubiquitin peptide **4** was analyzed by HPLC and MALDI-TOF-MS, which provided a singly charged molecular ion corresponding to a molecular mass 7990.94 Da, consistent with the expected molecular mass of the product ($C_{348}H_{558}N_{104}O_{108}S_2$; 7990.20). The HPLC separation of the crude product revealed the presence of an additional peak with a slightly lower retention time (29.2 min) relative to the main component (29.9 min), which was identified by MALDI-TOF-MS as the mixed disulfide of **4** with glutathione (molecular mass 8296.24 Da), present in excess in the biological medium upon isolation (data not shown). Consistent with this finding, HPLC analyses and MALDI-MS characterization of further mutant cysteinyl−ubiquitin peptides prepared with an identical procedure (i.e., ubiquitin-N60C) showed the formation of the mixed GSH-disulfide adducts as major product (data not shown). In order to remove the GSH, the disulfide linkage was reduced with DTT for 1.5 h at 25 °C and the peptide then purified from the residual byproducts and detergent by preparative HPLC (not shown). The structure and homogeneity of the purified ubiquitin peptide **4** was ascertained by ESI-FTICR-MS (*32*, *34*, *37*, *38*), which provided a single homogeneous molecular ion series with the most abundant 10+ charged ion, corresponding to the molecular mass of 7985.64 Da (Table 1). The functional activity of the cysteinyl-containing mutant ubiquitin peptides, G53C, as well as the N60C was ascertained by an auto-ubiquitination assay using two different E3 ligases as described below.

Conjugation of Cysteinyl−Ubiquitin Donor Peptides with K-NH_2^{ε}-Linked Ubiquitin−Acceptor Peptides by Thioether Ligation. The His-tag-ubiquitin donor peptides containing a carboxy-terminal Cys residue were subjected to coupling with the chloroacetylated ubiquitin acceptor peptides via thioether conjugation, as described in the Experimental Section. Due to the relatively low reactivity of the chloroacetylated ubiquitin peptides found in initial experiments, the N-chloroacetyl−acceptor peptide component was activated *in situ* by conversion to the iodoacetyl derivative using a saturated potassium iodide solution in Tris-buffer (pH 8), which increased the reaction rate due to the highly reactive iodoacetyl group (*39*, *40*). The time course of the conjugation reaction was monitored by analytical HPLC on a C4 column, and HPLC fractions were characterized by mass spectrometry, as shown in Figure 3 for the activation and thioether ligation of the His-tag−ubiquitin(1−52)-Cys donor peptide **4** with the N-chloro/iodoacetylated ubiquitin(54−76) acceptor **1** after 6 h. Oxidation of the C-terminal Cys residue and formation of the ubiquitin(1−52)-cystinyl-53 dimer **5** was observed as a significant side reaction competing with the thioether ligation (molecular mass, **5**, 15 979.86 Da; see Figure 3). The monoubiquitin peptide **6** was isolated by preparative

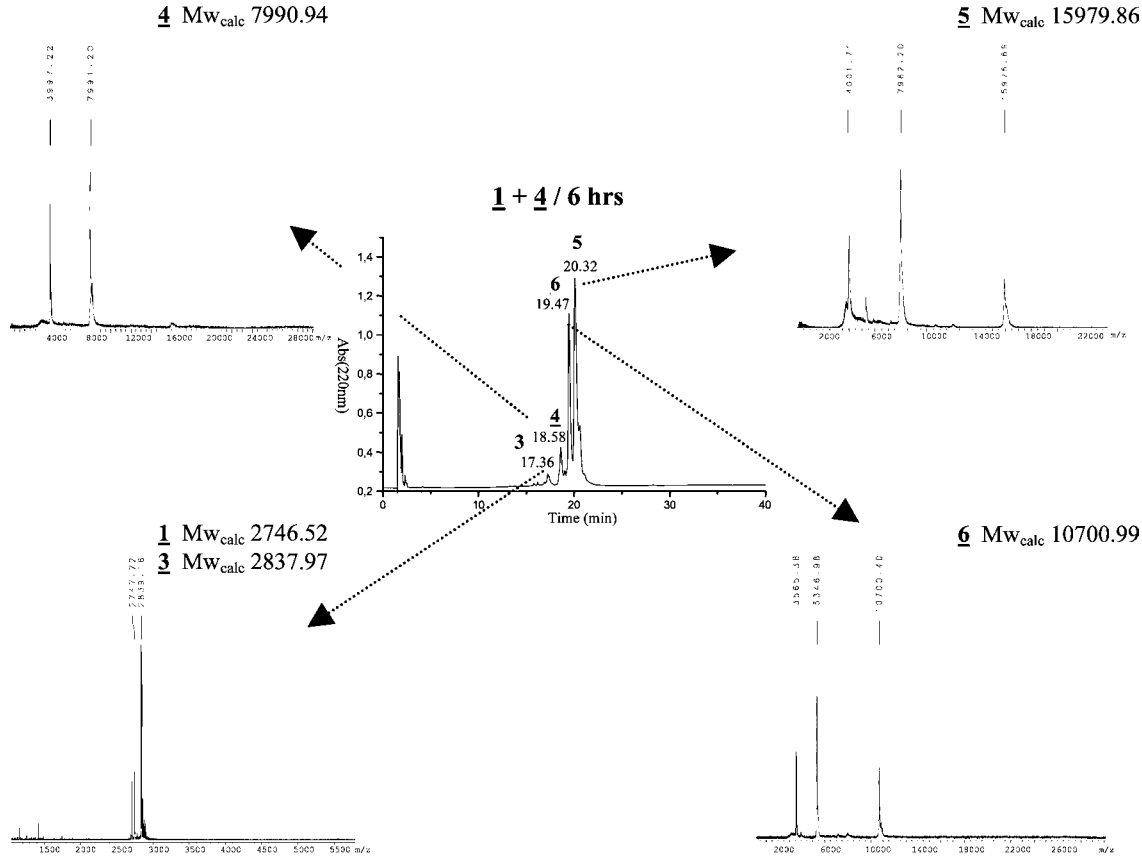

Figure 3. HPLC monitoring and MALDI mass spectrometric characterization of the conjugation of His-tagged ubiquitin(1−52)-Cys donor peptide **4** with N-chloroacetylated ubiquitin(54−76) acceptor peptide **1**, using *in situ* activation to the N-iodoacetyl-ubiquitin(54−76) **3** and thioether ligation. MALDI-mass spectra of the HPLC peaks of residual peptides **1** and **3** are shown on the left, the MALDI spectrum of the cystinyl-dimer oxidation product **5** of the donor peptide is shown on the upper right side.

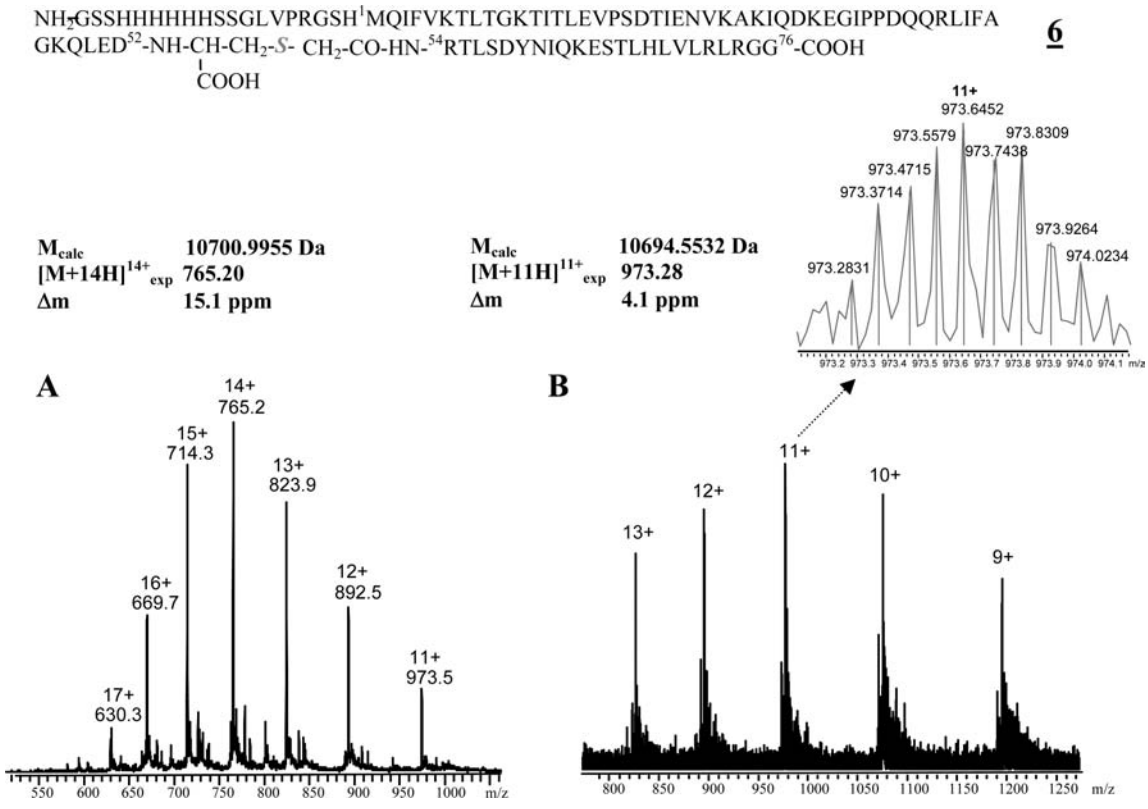

Figure 4. Mass spectrometric characterization of the HPLC-purified monoubiquitin conjugate **6** by thioether ligation of linear His-tagged ubiquitin(1−52)-Cys donor peptide **4** with N-chloroacetylated ubiquitin(54−76) acceptor peptide **1**. (A) ESI-ion trap mass spectrum (average molecular mass). (B) High-resolution Nano-ESI-FTICR mass spectrum (monoisotopic molecular mass).

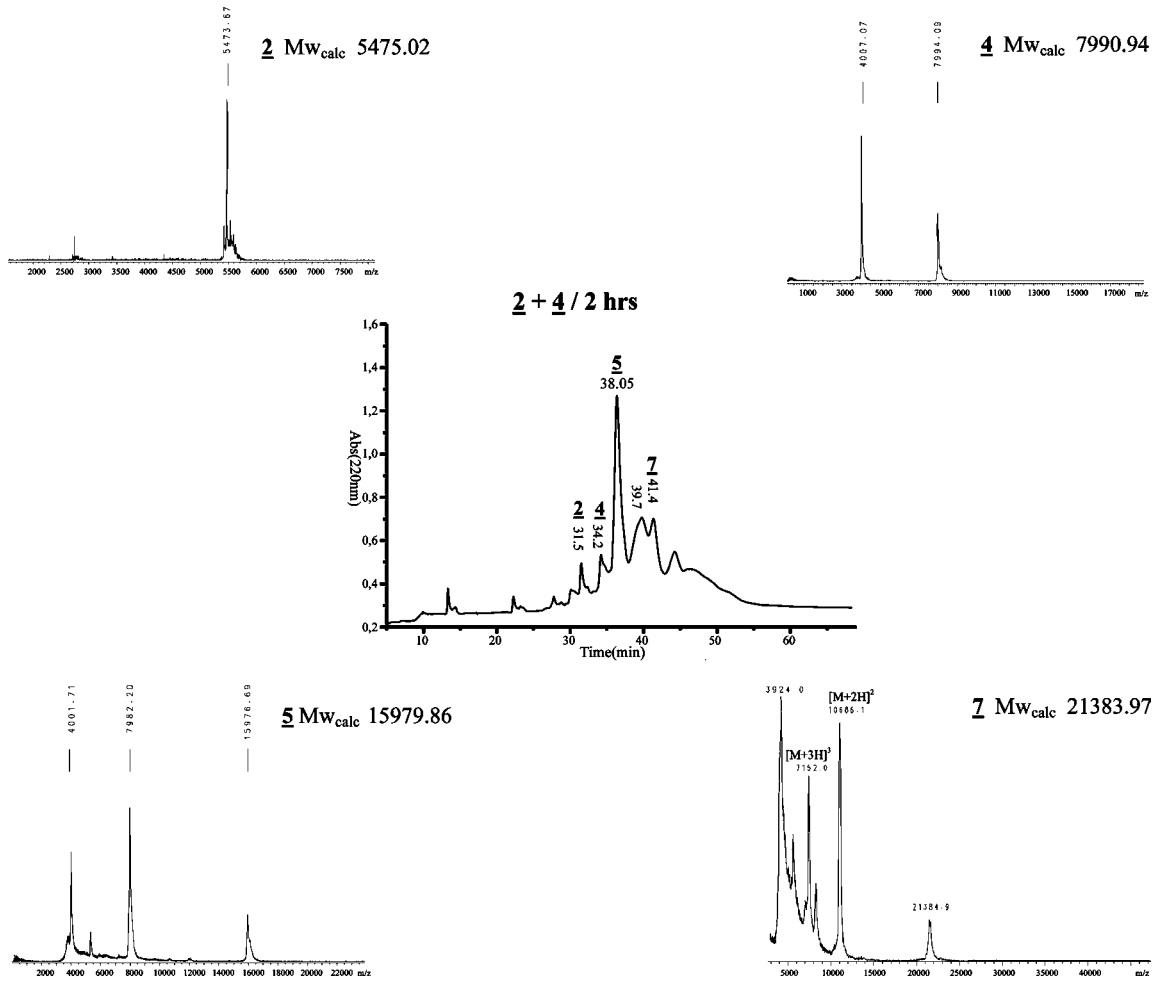

Figure 5. HPLC monitoring and MALDI mass spectrometric characterization of the thioether ligation of His-tagged ubiquitin(1−52)-Cys donor peptide **4** with K63-branched bis-N-chloroacetylated ubiquitin(54−76)$_2$ acceptor peptide **2**, at 2 h reaction time. The MALDI mass spectra of the diubiquitin conjugate **7** and the disulfide dimer **5** are shown on the lower right and left sides, respectively.

HPLC and characterized by mass spectrometry (Figure 4). Both the ESI-ion trap and the high-resolution FT-ICR mass spectra showed the corresponding multiply charged (*37, 38, 41*−*44*), protonated ion series yielding a molecular weight ($C_{466}H_{755}N_{141}O_{144}S_2$; average molecular weight 10 700.99 Da, monoisotopic molecular weight 10 694.55 Da) consistent with the correct sequence of **6**.

Initial studies of the thioether conjugation of the His-tag cysteinyl−ubiquitin donor peptides with the K63-branched ubiquitin(54−76)$_2$ acceptor peptide indicated solubility problems in standard aqueous solution at slightly alkaline pH, in addition to the disulfide oxidation as a side reaction. The chloroacetylated ubiquitin(54−76)$_2$ acceptor component **2** and the mutant ubiquitin(1−52)-C donor peptide **4** were dissolved in a 1:10 (v/v) mixture of 6 M guanidinium hydrochloride and 1 M potassium carbonate as described in the Experimental Section, and the reaction course monitored by analytical HPLC and mass spectrometry (Figure 5). At these conditions, the HPLC profile and MALDI-TOF-MS clearly showed the formation of the diubiquitin conjugate **7** (average molecular weight 21 383.97 Da; found 21 384.30 Da) after 2 h reaction, in addition to the unreacted peptides, chloroacetylated ubiquitin(54−76)$_2$ **2** and His-tag-ubiquitin(1−52)-C **4**, and the disulfide−dimer byproduct **5**. However, purification of the diubiquitin conjugate **7** in homogeneous form was obtained by semipreparative HPLC on a Nucleosil 300−7 C_8 column, as described in the Experimental Section. At the reaction conditions described above, a yield of approximately 29% of conjugate **7** relative to acceptor peptide **2** was obtained after 6 h. The analytical HPLC profile and ESI-ion-trap mass spectrum of the purified diubiquitin conjugate **7** are shown in Figures 6 and 7, respectively; the purity of **7** was estimated to approximately 92%. The deconvolution of the multiply protonated ions in the ESI-ion trap MS (see insert in Figure 7) provided a molecular weight of 21 385.5 Da, consistent with the correct structure ($C_{932}H_{1508}N_{282}O_{287}S_4$; 21 383.97 Da). In addition, the sequence was ascertained by partial ESI-MS/MS of tryptic peptide fragments (data not shown).

A structural model of the diubiquitin conjugate **7**, obtained by molecular modeling using the Hyperchem-7 software, is shown in Figure 9. The Lys-63 linkage is highlighted in the insert, and the thioether bonds used for the conjugation are marked in pink. The overall structure calculated for the conjugate suggests conformational stability with spatial separation of both parts of the Lys-63 branching, in agreement with the CD spectroscopic data (see below).

Conformational Analysis of Thioether-Conjugated Mutant Ubiquitin Peptides by Circular Dichroism Spectroscopy. The monoubiquitin conjugate **6** containing a thioether bond and wild-type bovine ubiquitin (Sigma, Germany) were examined by circular dichroism spectroscopy in water (*45, 46*). Both compounds adopted predominantly helical conformation characterized by two negative bands around 207 and 220 nm (data not shown). No significant differences in the CD spectra of the synthetic, mutant, and wild-type bovine ubiquitin were

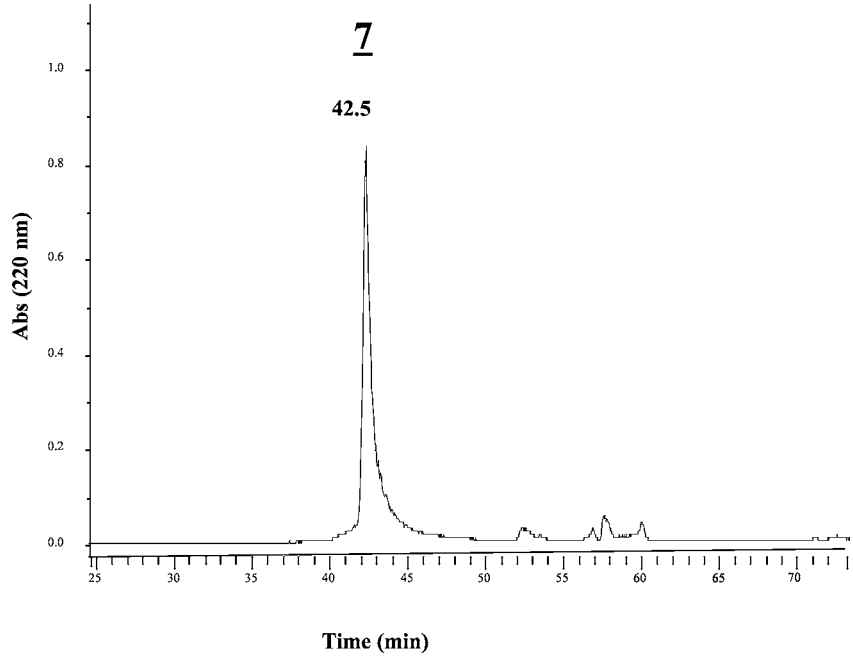

Figure 6. Analytical RP-HPLC profile of purified K63-branched diubiquitin conjugate **7**. Eluents: 0.1% TFA in water (A), 0.1% TFA in MeCN−water 80:20 v/v (B); flow rate, 1 mL/min; gradient, 0 min 0% B, 15 min 35% B, 45 min 45% B, 65 min 50% B, 100 min 100% B.

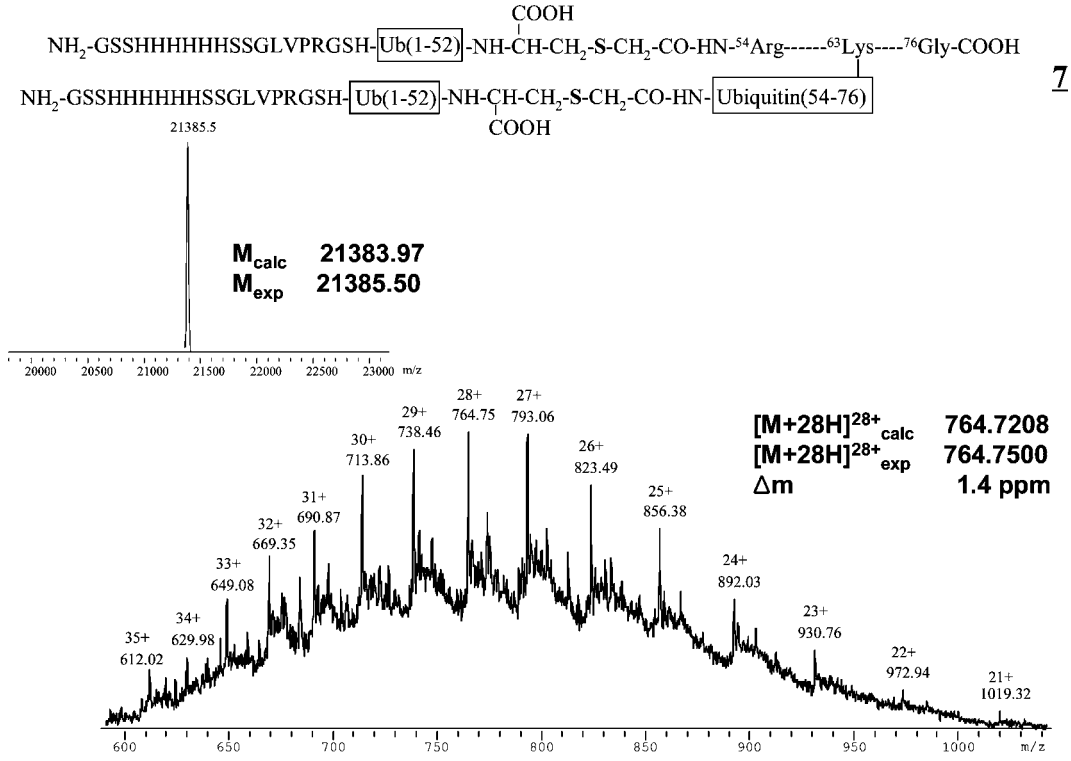

Figure 7. ESI-ion-trap mass spectrum of purified K63-branched diubiquitin conjugate **7**. The insert shows the deconvoluted molecular ion obtained from the series of multiply protonated ions, yielding a molecular weight of 21 385.5 Da.

found, indicating that the presence of a thioether bond in the structure of ubiquitin does not lead to a conformational change.

Functional Characterization of Thioether-Conjugated Mutant Ubiquitin Peptides by *in Vitro* Auto-Ubiquitination. Potential drawbacks of the approach described above are the replacement of G53 of ubiquitin by a cysteine residue and the linkage of C53 to R54 via a thioether bond rather than a peptide bond, as these alterations may result in a ubiquitin mutant that is biochemically inactive (i.e., the mutant cannot be activated and covalently attached by the ubiquitin conjugation system to substrate proteins). To assess the biochemical activity of the mutant cysteinyl−ubiquitin conjugates, the linear monoconjugate **6** of ubiquitin(1−52)-Cys was prepared by ligation with the chloro/iodoacetylated ubiquitin(54−76) peptide (G53C-ubiquitin). The mutant ubiquitin **6** was then analyzed *in vitro* in auto-ubiquitination assays using two different ubiquitin ligases (purified baculovirus-expressed E6AP, data not shown; purified bacterially expressed HectH9, Figure 8) as previously described (*47, 48*).

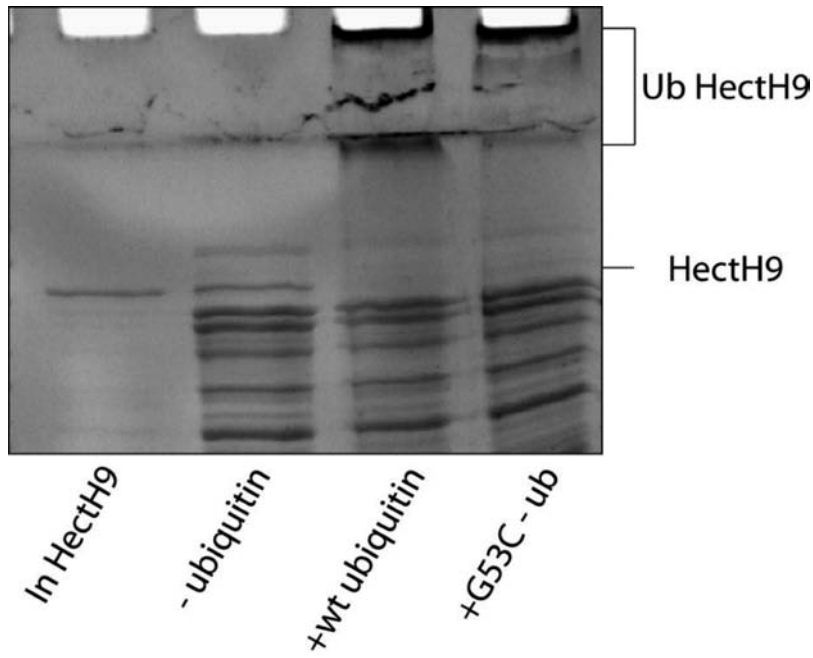

Figure 8. *In vitro* autoubiquitination assay of HectH9 using the mutant monoubiquitin conjugate (G53C-ubiquitin) derived by thioether ligation of His-tagged ubiquitin(1−52)-Cys donor peptide **4** with N-chloroacetylated ubiquitin(54−76) acceptor peptide **1**. The running positions of the nonmodified form of HectH9 (HectH9) and the ubiquitinated forms of HectH9 (Ub HectH9) are indicated. In HectH9, input of bacterially expressed HectH9; − ubiquitin, reaction in the absence of ubiquitin; +wt ubiquitin, reaction in the presence of wild-type ubiquitin; +G53C-ub, reaction in the presence of G53C-ubiquitin.

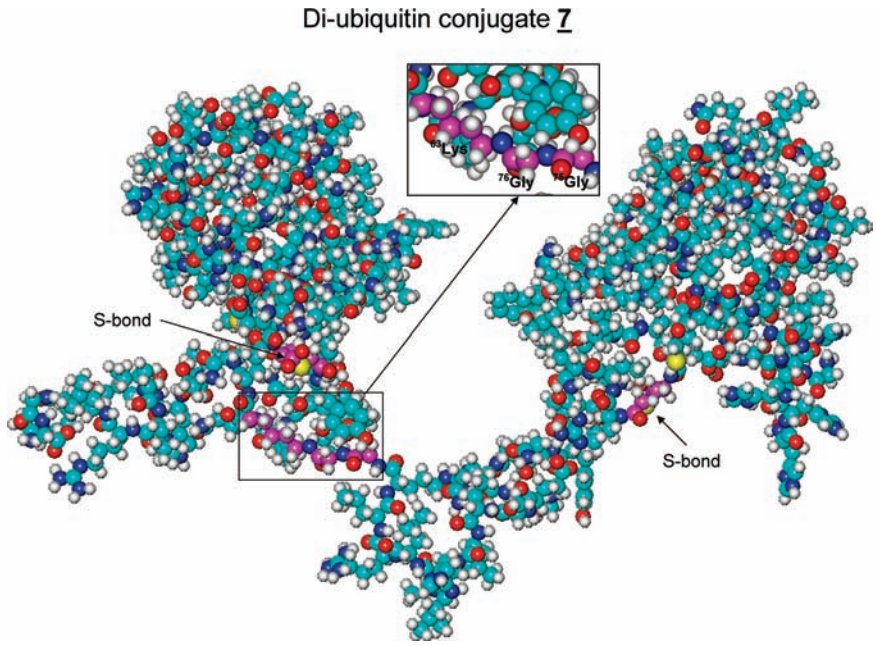

Figure 9. Structure model of the diubiquitin conjugate **7**. The lys-63 linkage is highlighted in the insert; thioether linkages in the conjugate are marked in violet.

As shown in Figure 8, the synthetic cysteinyl−ubiquitin conjugate is used by the ubiquitin conjugation system with an efficiency similar to wild-type ubiquitin, indicating the feasibility of the cystein mutation and thioether ligation approaches in producing biochemically active conjugates.

CONCLUSIONS

In this study, a general approach was developed for the synthesis of oligo−ubiquitin conjugates with defined Lys-ε-amino branching sites. The preparation of specific isomeric Lys-branched conjugates utilizes a chemoselective ligation approach with stable thioether linkages using (i) an activated N-chloroacylated partial ubiquitin acceptor peptide containing the specific Lys-branching residue, prepared by manual synthesis, and (ii) thioether ligation to a ubiquitin peptide donor component that contains a C-terminal Cys residue at the defined conjugation site. In a first example, a K63-branched diubiquitin conjugate was successfully prepared and purified, and the structure of the 21 kDa polypeptide adduct ascertained by ESI mass spectrometry. Although the concomitant oxidation by dimerization at the cysteinyl residues was found as a byproduct, a homogeneous Lys63−diubiquitin conjugate was obtained by HPLC isolation

with a purity of >90% and a yield of approximately 30% at optimized reaction times. The reaction conditions developed here are presently used to the preparation of oligomeric ubiquitin conjugates with amounts suitable to enable (i) their detailed structural characterization by NMR spectroscopy and (ii) the generation of antibodies selectively recognizing ubiquitin chains linked by different lysine residues.

ACKNOWLEDGMENT

This work was supported by grants from the Deutsche Forschungsgemeinschaft (DFG), Bonn, Germany (to M.S. and M.P.). We are grateful to Reinhold Weber for the expert assistance with the high resolution mass spectrometric characterization.

Note Added after ASAP Publication: This paper was published ASAP on May 27, 2009 with an error in the reverse primer in the Experimental Section. The revised version was published on May 29, 2009.

LITERATURE CITED

(1) Pickart, C. M. (2001) Mechanisms underlying ubiquitination. *Annu. Rev. Biochem. 70*, 503–533.
(2) Weissman, A. M. (2001) Themes and variations on ubiquitylation. *Nat. Rev. Mol. Cell. Biol. 2*, 169–178.
(3) Glickman, M. H., and Ciechanover, A. (2002) The ubiquitin-proteasome proteolytic pathway: destruction for the sake of construction. *Physiol. Rev. 82*, 373–428.
(4) Kerscher, O., Felberbaum, R., and Hochstrasser, M. (2006) Modification of proteins by ubiquitin and ubiquitin-like proteins. *Annu. Rev. Cell Dev. Biol. 22*, 159–180.
(5) Pickart, C. M. (2000) Ubiquitin in chains. *Trends Biochem. Sci. 25*, 544–548.
(6) Pickart, C. M., and Fushman, D. (2004) Polyubiquitin chains: polymeric protein signals. *Curr. Opin. Chem. Biol. 8*, 610–616.
(7) Li, W., and Ye, Y. (2008) Polyubiquitin chains: functions, structures, and mechanisms. *Cell. Mol. Life Sci. 65*, 2397–2406.
(8) Peng, J., Schwartz, D., Elias, J. E., Thoreen, C. C., Cheng, D., Marsischky, G., Roelofs, J., Finley, D., and Gygi, S. P. (2003) A proteomics approach to understanding protein ubiquitination. *Nat. Biotechnol. 21*, 921–926.
(9) Thrower, J. S., Hoffman, L., Rechsteiner, M., and Pickart, C. M. (2000) Recognition of the polyubiquitin proteolytic signal. *EMBO J. 19*, 94–102.
(10) Jin, L., Williamson, A., Banerjee, S., Philipp, I., and Rape, M. (2008) Mechanism of ubiquitin-chain formation by the human anaphase-promoting complex. *Cell 133*, 653–665.
(11) Galan, J. M., and Haguenauer-Tsapis, R. (1997) Ubiquitin Lys63 is involved in ubiquitination of a yeast plasma membrane protein. *EMBO J. 16*, 5847–5854.
(12) Spence, J., Gali, R. R., Dittmar, G., Sherman, F., Karin, M., and Finley, D. (2000) Cell cycle-regulated modification of the ribosome by a variant multiubiquitin chain. *Cell 102*, 67–76.
(13) Hoege, C., Pfander, B., Moldovan, G. L., Pyrowolakis, G., and Jentsch, S. (2002) RAD6-dependent DNA repair is linked to modification of PCNA by ubiquitin and SUMO. *Nature 419*, 135–141.
(14) Mukhopadhyay, D., and Riezman, H. (2007) Proteasome-independent functions of ubiquitin in endocytosis and signaling. *Science 315*, 201–205.
(15) Varadan, R., Assfalg, M., Haririnia, A., Raasi, S. i., Pickart, C., and Fushman, D. (2004) Solution conformation of Lys63-linked di-ubiquitin chain provides clues to functional diversity of polyubiquitin signaling. *J. Biol. Chem. 279*, 7055–7063.
(16) Tenno, T., Fujiwara, K., Tochio, H., Iwai, K., Morita, E. H., Hayashi, H., Murata, S., Hiroaki, H., Sato, M., Tanaka, K., and Shirakawa, M. (2004) Structural basis for distinct roles of Lys63- and Lys48-linked polyubiquitin chains. *Genes Cells 9*, 865–875.
(17) Chen, L., Shinde, U., Ortolan, T. G., and Madura, K. (2001) Ubiquitin-associated (UBA) domains in Rad23 bind ubiquitin and promote inhibition of multi-ubiquitin chain assembly. *EMBO Rep. 2*, 933–938.
(18) Wilkinson, C. R., Seeger, M., Hartmann-Petersen, R., Stone, M., Wallace, M., Semple, C., and Gordon, C. (2001) Proteins containing the UBA domain are able to bind to multi-ubiquitin chains. *Nat. Cell Biol. 3*, 939–943.
(19) Raasi, S., and Pickart, C. M. (2003) Rad23 Ubiquitin-associated domains (UBA) inhibit 26 S proteasome-catalyzed proteolysis by sequestering lysine 48-linked polyubiquitin chains. *J. Biol. Chem. 278*, 8951–8959.
(20) Raasi, S., Orlov, I., Fleming, K. G., and Pickart, C. (2004) M. Binding of polyubiquitin chains to ubiquitin-associated (UBA) domains of HHR23A. *J. Mol. Biol. 341*, 1367–1379.
(21) Russell, N. S., and Wilkinson, K. D. (2004) Identification of a novel 29-linked polyubiquitin binding protein, Ufd3, using polyubiquitin chain analogues. *Biochemistry 43*, 4844–4854.
(22) Brunel, F. M., and Dawson, P. E. (2005) Synthesis of constrained helical peptides by thioether ligation: application to analogs of gp41. *Chem. Commun. 20*, 2552–2554.
(23) Mezö, G., Oliveira, E., Krikorian, D., Feijlbrief, M., Jakab, A., Tsikaris, V., Sakarellos, C., Welling-Wester, S., Andreu, D., and Hudecz, F. (2003) Synthesis and comparison of antibody recognition of conjugates containing herpes simplex virus type 1 glycoprotein D epitopeVII1. *Bioconjugate Chem. 14*, 1260–1269.
(24) Manea, M., Mezö, G., Hudecz, F., and Przybylski, M. (2004) Polypeptide conjugates comprising a β-amyloid plaque-specific epitope as new vaccine structures against Alzheimer's disease. *Biopolymers 76*, 503–511.
(25) Mezö, G., Manea, M., Jakab, A., Kapuvári, B., Bösze, S., Schlosser, G., Przybylski, M., and Hudecz., F. (2004) Synthesis and structural characterization of bioactive peptide conjugates using thioether linkage approaches. *J. Pept. Sci. 10*, 701–713.
(26) Sun, Y., Lu, G., and Tam, J. P. (2001) A thioester ligation approach to amphipathic bicyclic peptide library. *Org. Lett. 3* (11), 1681–1684.
(27) Tam, J. P., Yu, Q., and Miao, Z. (1999) Orthogonal ligation strategies for peptide and protein. *Pept. Sci. 51*, 311–322.
(28) Rose, K. (1994) Facile synthesis of homogeneous artificial proteins. *J. Am. Chem. Soc. 116*, 30–33.
(29) Rose, K., Zeng, W., Regamey, P. O., Chernushevich, I. V., Standing, K. G., and Gaertner, H. F. (1996) Natural peptides as building blocks for the synthesis of large protein-like molecules with hydrazone and oxime linkages. *Bioconjugate Chem. 7*, 552–556.
(30) Zeng, W., Ghosh, S., Macris, M., Pagnon, J., and Jackson, D. C. (2001) Assembly of synthetic peptide vaccines by chemoselective ligation of epitopes: influence of different chemical linkages and epitope orientations on biological activity. *Vaccine 19*, 3843–3852.
(31) Bai, Y., Galetskiy, D., Damoc, E., Paschen, C., Liu, Z., Griese, M., Liu, S., and Przybylski, M. (2004) High resolution mass spectrometric alveolar proteomics: Identification of surfactant protein SP-A and SP-D modifications in proteinosis and cystic fibrosis patients. *Proteomics 4*, 2300–2309.
(32) Dyson, P. J., and McIndoe, J. S. (2003) Analysis of organometallic compounds using ion trap mass spectrometry. *Inorg. Chim. Acta 354*, 68–74.
(33) Ingendoh, A., Karas, M., Hillenkamp, F., and Giessmann, U. (1994) Factors affecting the resolution in matrix-assisted laser desorption-ionization mass spectrometry. *Int. J. Mass Spectrom. Ion Processes 131*, 345–354.
(34) Cheng, H. L., and Her, G. R. (2002) Determination of linkages of linear and branched oligosaccharides using closed-ring chromophore labeling and negative ion trap mass spectrometry. *J. Am. Soc. Mass Spectrom. 13*, 1322–1330.
(35) Przybylski, M., and Glocker, M. O. (1996) Electrospray mass spectrometry of biomacromolecular complexes with

noncovalent interactions-new analytical perspectives for supramolecular chemistry and molecular recognition processes. *Angew. Chem. 108*, 879−899; (1996) *Angew. Chem., Int. Ed. Engl. 35*, 06826.

(36) Przybylski, M., Schnaible, V., Kast, J., Bühler, S., Michels, J., Wattenberg, A., Fligge, T. A., Forst, D., Diederichs, K., Zeth, C., Glocker, M. O., and Welte, W. (1998) Approaches to the characterization of tertiary and supramolecular protein structures by combination of protein chemistry and mass spectrometry. In *New Methods for the Study of Biomolecular Complexes* (Ens, W., Standing, K. G., and Chernushevich, I. V., Eds.) pp 17−43, Kluwer Academic Publishers, Amsterdam.

(37) Purves, R. W., and Li, L. (1997) Development and characterization of an electrospray ionization ion trap/linear time-of-flight mass spectrometer. *J. Am. Soc. Mass Spectrom. 8*, 1085–1093.

(38) Hendrickson, C. L., and Emmett, M. R. (1999) Electrospray ionization fourier transform ion cyclotron resorance mass spectrometry. *Annu. Rev. Phys. Chem. 50*, 517–536.

(39) Englebretsen, D. R., Garnham, B., and Alewood, P. F. (2002) A cassette ligation strategy with thioether replacement of three gly-gly peptide bonds: total chemical synthesis of the 101 residue protein early pregnancy factor [$\psi(CH_2S)^{28-29,56-57,76-77}$. *J. Org. Chem. 67*, 5883–5890.

(40) Wilce, J. A., Love, S. G., Richardson, S. J., Alewood, P. F., and Craik, D. J. (2001) Synthesis of an analog of the thyroid hormone-binding protein transthyretin via regioselective chemical ligation. *J. Biol. Chem. 276* (28), 25997–26003.

(41) Bruce, J. E., Smith, V. F., Liu, C., Randall, L. L., and Smith, R. D. (1998) The observation of chaperone-ligand noncovalent complexes with electrospray ionization mass spectrometry. *Protein Sci. 7*, 1180–1185.

(42) Marshall, A. G., Hendrickson, C. L., and Jackson, G. S. (1998) Fourier transform ion cyclotron resorance mass spectrometry: a primer. *Mass Spectrom. Rev. 17*, 1–35.

(43) Damoc, E., Youhnovski, N., Crettaz, D., Tissot, J. D., and Przybylski, M. (2003) High resolution proteome analysis of cryoglobulins using Fourier transform-ion cyclotron resonance mass spectrometry. *Proteomics. 3*, 1425–1433.

(44) Green, M. K., Vestling, M. M., Johnston, M. V., and Larsen, B. S. (1998) Distinguishing small molecular mass differences of proteins by mass spectrometry. *Anal. Biochem. 260*, 204–211.

(45) Greenfield, N., and Fasman, G. D. (1969) Computed circular dichroism spectra for the evaluation of protein conformation. *Biochemistry 8*, 4108–4116.

(46) Ramirez-Alvarado, M., Serrano, L., and Blanco, F. J. (1997) Conformational analysis of peptides corresponding to all the secondary structure elements of protein L Bl domain: Secondary structure propensities are not conserved in proteins with the same fold. *Protein Sci. 6*, 162–174.

(47) Nuber, U., Schwarz, S. E., and Scheffner, M. (1998) The ubiquitin-protein ligase E6-associated protein (E6-AP) serves as its own substrate. *Eur. J. Biochem. 254*, 643–649.

(48) Adhikary, S., Marinoni, F., Hock, A., Hulleman, E., Popov, N., Beier, R., Bernard, S., Quarto, M., Capra, M., Goettig, S., Kogel, U., Scheffner, M., Helin, K., and Eilers, M. (2005) The ubiquitin ligase HectH9 regulates transcriptional activation by myc and is essential for tumor cell proliferation. *Cell 123*, 409–421.

BC800539P

Preparation of Multifunctional Drug Carrier for Tumor-Specific Uptake and Enhanced Intracellular Delivery through the Conjugation of Weak Acid Labile Linker

Caixia Ding, Jingxia Gu, Xiaozhong Qu,* and Zhenzhong Yang*

State Key Laboratory of Polymer Physics and Chemistry, Institute of Chemistry, Chinese Academy of Sciences, Beijing 100190, China. Received December 24, 2008; Revised Manuscript Received April 19, 2009

We demonstrate that multifuctional drug carriers, e.g., polymeric micelles, for tumor-specific uptake and intracellular delivery can be generated from the pH-dependent progressive hydrolysis of a novel benzoic-imine linker in the micelle-forming amphiphilic polymer. The linker, hence the micelle, is stable at physiological pH, partially hydrolyzes at the extracellular pH of the solid tumor, and completely hydrolyzes at the endosomal pH. Meanwhile, the surface property of the micelle converts from neutral to positively charged due to the generation of amino groups from the cleavage of the imine bond at tumor pH. The ionization on the surface facilitates the cellular uptake of the micelles through the electrostatic interaction between the micelle and the cell membrane. Subsequently, at the endosomal pH, with more complete cleavage of the polymer the micellar structure dissociates, and the system becomes very membrane-disruptive, inferring an enhanced intracellular delivery capability via the endosomal pathway.

INTRODUCTION

The ultimate goal of controlled drug delivery is to achieve a desired therapeutic concentration at the targeting site while the drug concentrations at other tissues are kept at safe levels (*1*). An ideal controlled delivery vehicle for antitumor drugs should have long circulation duration, the ability to catch tumor cells, and eventually the ability to efficiently deliver the drug into the cytoplasm (*2, 3*). Therefore, a key issue is to construct multifunctional drug carriers with the ability to tune their interactions with different biological membranes following the change of environmental conditions during the entire delivery procedure (*4*). In addition to the conjugation of various targeting antibodies and ligands (*5*−*8*), surface charge conversion of a drug carrier in response to the change of external pH around 6.8−7.4 would also help to gain smart antitumor drug delivery systems, since the extracellular environment of solid tumors is slightly acidic (pH ∼6.8) compared with the physiological pH (7.4) (*9*−*12*). Recently, a few such multifunctional antitumor drug delivery systems have been reported based on some charge conversion polymers (*4*), such as poly(L-histidine) ($pK_b = 6.5$) (*9*) and poly(sulfonamide) ($pK_a \sim 7.0$) (*10*).

On the other hand, in nanosized delivery systems a protective layer on the surface, usually a PEG corona, is required to prevent nonspecific interaction and stimulation to the immune system during circulation (*13, 14*). However, the PEG corona brings a controversial to hamper the intracellular transport (*14, 15*). In order to enhance the bioavailability of the therapeutic agents, many strategies have focused on the development of intelligent polymeric colloidal systems and liposomes with low-pH triggered membrane disrupting ability (*16*−*19*), because nanosized carriers are mainly taken up by cells via endocytosis and the pH values in endosomes (5.0−6.5) are much lower than the physiological pH (*20*). It is reasonable to insert acid-cleavable linkers in a nanocarrier to induce the destabilization of the carrier in endosome (*21*−*24*), hence the disruption of the endosomal membrane to facilitate the release of incorporated drug into cytoplasm (*16*). So far, acid-labile covalent bonds such as hydrazone (*25*−*28*), acetal (*16, 21, 22, 29*), and orthoester (*30, 31*), which hydrolyze rapidly in the endosomal compartment (pH ∼5), are extensively used to build the intracellular delivery systems. However, unlike the charge conversion polymers, tumor specificity has rarely been gained from the inclusion of these linkers, since the gap between physiological pH (7.4) and the extracellular pH of the tumor (6.8) is so subtle that the degree of the linker cleavage at tumor pH could not cause a significant property change of the carriers (*17*).

Imine bond hydrolyzes under very weak acidic conditions; however, it is scarcely used to construct pH-triggered delivery vehicles, since it is unstable at physiological pH (*32*). However, early studies mainly on Schiff base amphiphiles have shown that $\pi-\pi$ conjugation can significantly improve the stability of imine bond in water (*33, 34*). Thus, the investigation of the pH sensitivity of those structures around physiological pH is interesting and helpful for the design of pH-triggered delivery systems, since the hydrolysis of an imine bond generates an amino group, which could affect the charge property of the system. We have previously studied a benzoic-imine linker and found that it hydrolyzes under very slightly acidic conditions whereas it is stable at neutral and basic pH due to the proper $\pi-\pi$ conjugation extent (*35*). Amphiphilic poly(L-lysine) micelles were PEGylated via the benzoic-imine linker and showed a neutral zeta potential at physiological pH (7.4) but were positively charged under weak acidic conditions. In the present work, another advantage of the benzoic-imine bond was that the hydrolysis level is significantly influenced by the solution pH within a very narrow pH interval (7.4−5.0). In a drug nanocarrier, the pH-dependent hydrolysis of the benzoic-imine bond suggests an internal structural evolution of the carrier, e.g., production of more positively charged groups, with the acidity in body sites such as solid tumors (pH ∼6.8) and endosome (pH ∼5.0−6.5), hence the increase of electrostatic interaction between the carrier and biological membranes. This will probably generate multifunctional nature of the carrier for tumor-

* To whom correspondence should be addressed. Tel.: +86-10-82619206; fax: +86-10-62559373, E-mail address: quxz@iccas.ac.cn; yangzz@icccas.ac.cn.

10.1021/bc800563g CCC: $40.75 © 2009 American Chemical Society
Published on Web 05/27/2009

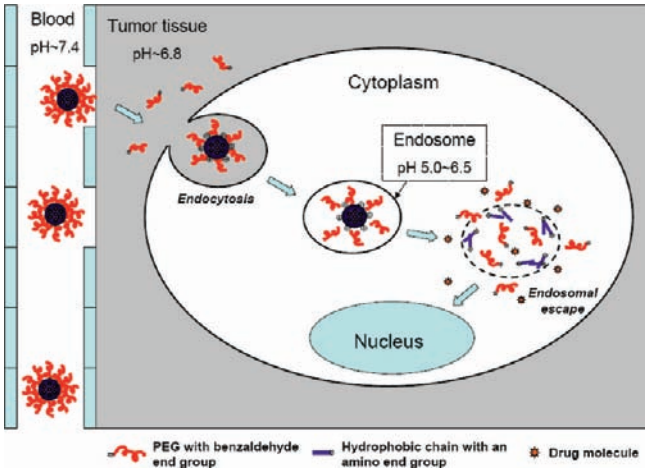

Figure 1. Schematic representation of a multifunctional drug carrier with tumor-targeting capability and intracellular delivery ability originated from the pH-dependent progressive hydrolysis of a chemical bond, e.g., benzoic-imine, in the carrier-forming polymer. The particle has a PEG corona to obtain prolonged circulation in the blood. A suitable particle size would accumulate the carrier in tumor tissue by the "enhanced permeation and retention effect" (EPR). Under the weak acidic condition in a tumor, the particle surface becomes positively charged due to partial hydrolysis of the imine linker, facilitating cellular uptake through adsorptive endocytosis. Subsequently, in the more acidic environment of the endosome, the complete hydrolysis of the imine bond causes the particle to dissociate and destabilize the endosomal membrane to release the therapeutics rapidly into the cytoplasm.

specific uptake and enhanced intracellular delivery even without the inclusion of a biological ligand. The schematic strategy of such a system, i.e., a model polymeric micelle, is shown in Figure 1.

EXPERIMENTAL PROCEDURES

Materials. Methoxy poly(ethylene glycol) (mPEG) (MW = 2k Da), *n*-octadecane amine, dicyclohexyl carbodiimide (DCC), 4-(dimethylamino) pyridine (DMAP), sodium borohydride ($NaBH_4$), pyrene, Triton X-100, doxorubicin (DOX), chloroform-*d* ($CDCl_3$), deuterated water (D_2O), and phosphate buffered saline (PBS) were all purchased from Sigma-Aldrich (St. Louis, US). *p*-Formylbenzoic acid was a generous gift from Beijing Prina Chemical Industry Co., Ltd., China. Solvents and other compounds were obtained form Beijing Chemical Reagents Company, China. All reagents were used as received.

Synthesis of Amphiphilic Polymers (PEG-b-C18 and PEG-C18). Methoxy poly(ethylene glycol) benzaldehyde (PEG-CHO) was synthesized as previously described (*35*). Typically, *p*-formylbenzoic acid (6 g, 10 equiv), DCC (8.2 g, 10 equiv), and DMAP (1.2 g, 2.5 equiv) were added to a solution of mPEG (8 g, 1 equiv) in dichloromethane (DCM) (150 mL). After stirring for 24 h, the solution was filtered. The filtrate was concentrated, dissolved in isopropanol (80 mL), and cooled at 0 °C for 2 h. The resulting crystals were collected by filtration and washed with isopropanol and diethyl ether with 80% yield. ^{1}H NMR ($CDCl_3$): δ 10.12 (s, 1H), 8.23 (d, 2H), 7.95 (d, 2H), 3.65 (m, CH_2 of PEG), 3.32 (s, 3H).

n-Octadecane amine (300 mg, 1 equiv) was dissolved in 10 mL of DMSO. To this solution was added a desired amount of the functionalized PEG (2 g, 0.9 equiv) which was dissolved in 50 mL of DMSO. The mixture was stirred and heated to 40 °C for 4 h before the solvent was evaporated by a rotary evaporator. The rough product was washed with diethyl ether and methanol, and dried under reduced pressure at 40 °C to gain a white powder-like PEG-b-C18 in an 80% yield. ^{1}H NMR ($CDCl_3$): δ 8.34 (d, 1H), 8.10 (d, 2H), 7.80 (d, 2H), 3.66 (m, CH_2 of PEG), 3.40 (s, 3H), 2.06 (m, 2H), 1.63 (m, 2H), 1.28 (m, CH_2 of *n*-octadecane amine), 0.90 (t, 3H).

200 mg of the PEG-b-C18 (1 equiv) was dissolved in 10 mL of ethanol with stirring followed by the addition of 6.5 mg of $NaBH_4$ (2 equiv) to reduce the imine bond to amine. The mixture was stirred overnight, dialyzed against 0.05 M HCl and then water (molecular weight cutoff 2 kDa), and freeze−dried. The resultant white powder was washed with diethyl ether and dried under reduced pressure to gain the non-acid-labile PEG-C18 as a control polymer of the PEG-b-C18 for the property characterizations. The yield was 70%. ^{1}H NMR ($CDCl_3$): δ 8.05 (d, 2H), 7.53 (d, 2H), 4.37 (m, 2H), 3.65 (m, CH_2 of PEG), 3.40 (s, 3H), 2.68 (t, 2H), 1.63 (m, 2H), 1.28 (m, CH_2 of *n*-octadecane amine), 0.90 (t, 3H).

Characterization. ^{1}H NMR analysis was performed on polymer solutions in $CDCl_3$ or in deuterated water (D_2O) at a required pH adjusted by DCl and/or NaOD using a Bruker AMX 600 MHz spectrometer. Infrared spectroscopy (FTIR) of the polymers was recorded using a Bruker Equinox 55 FT-IR spectrometer. Freeze−dried polymer was pressed with KBr under vacuum and scanned from 4000 to 400 cm^{-1} with a resolution of 2 cm^{-1}. To monitor the hydrolysis of the benzoic imine linkage at acidic pH, PEG-b-C18 was dispersed in water at an acidic pH (e.g., 5.0, adjusted by adding 0.1 M HCl), and then aliquots of the dispersion were dropped on KBr, dried, and recorded.

Micelle Formation of the Amphiphilic Polymers. Polymer samples were dispersed in water or PBS buffer with a desired pH by probe sonication using a JY96-II probe sonicator (Zhejiang Xin-Zhi, China) with the output set at 150 W. The solution pH was checked by a Delta 320 pH meter (Mettler-Toledo Instrument Ltd., Switzerland) after sonication.

Dynamic Light Scattering and Zeta Potential Measurement. Particle size measurement was carried out with a Brookhaven Zetaplus analyzer (Brookhaven Instruments Corporation, US), and the zeta potential was measured using a Zetasizer 3000 HS (Malvern Instruments, UK). All samples were passed through a membrane filter (pore size: 450 nm, Millipore) before detection.

Fluorescence Spectrophotometry. Aliquots of pyrene stock solution (1.54×10^{-5} M in acetone, 200 μL) were added to 5 mL volumetric flasks, and acetone was evaporated. Five milliliters of the aqueous polymer solution was then added to the volumetric flasks containing the pyrene residue. The solutions were equilibrated for 4 h at 60 °C. Fluorescence spectra of the polymer solutions were then recorded on a fluorescence spectrometer (Cary Eclipse, Varian, US). The emission spectra were recorded from 350 to 500 nm with an excitation wavelength of 340 nm. The first inflection point of the intensity ratio plot of the third band to the first band (I_3/I_1) against polymer concentration was determined as the critical micelle concentration (cmc).

Drug Loading and Release. Doxorubicin hydrochloride (1−5 mg, 1 equiv) was stirred with TEA (3 equiv) in DMSO for overnight before the solvent was evaporated using a rotary evaporator. An aqueous solution of the polymers (PEG-b-C18 or PEG-C18, 5 mL, 1 mg/mL) was then added, and the mixture was sonicated using a bath sonicator for 20 min. The dispersion was transferred into a dialysis tube (molecular weight cutoff 2 kDa) and dialyzed against water for 24 h at pH = 7.4. The entrapped drug amount was determined by measuring the UV absorbance at 480 nm (UV-1601PC, Shimadzu, Japan). Freeze−dried drug-loaded micelles were dispersed in PBS at different pHs (7.4 and 6.8). Three milliliters of the dispersion was transferred into a dialysis bag (molecular weight cutoff 2 kDa), and the bag was subsequently placed in a 50 mL flask containing 30 mL of PBS adjusted to a required pH. One

milliliter of solution was collected from the flask periodically, and the released drug was determined spectrophotometrically. Volume of the release medium in the flask was kept constant by adding 1 mL of fresh medium after each sampling.

Cell Culture. HepG2 cell, a human hepatocellular liver carcinoma cell line, was purchased from European Collection of Cell Cultures (ECACC), UK, and used for the cell uptake studies. The cells were grown in 75 cm^2 culture flasks as a monolayer using Dulbecco's Modified Eagle Medium (DMEM, Invitrogen, US) supplemented with 10% fetal bovine serum (FBS, Invitrogen, US) at 37 °C in 5% CO_2, 95% humidified atmosphere in an incubator. The cells were subcultured every 48 h and, before testing, were harvested by trypsinization using a 0.05% (w/v) trypsin/0.03% (w/v) EDTA solution.

Confocal Laser Scanning Microscopy Observation. HepG2 cells (2×10^5 cells/well) were cultured onto a plate with six wells; each was placed by a coverslip. They were maintained in DMEM media supplemented with 10% FBS in a humidified atmosphere of 5% CO_2 at 37 °C for 24 h. The medium was then removed, and fresh DMEM was added at a desired pH, adjusted by adding 0.1 M aqueous HCl or NaOH, containing the drug-loaded polymeric micelles (5 wt %) with an equivalent doxorubicin concentration of 10 μg/mL. The cells were incubated for 0.5 to 2 h and were fixed using 4% paraformaldehyde for 30 min at room temperature. The coverslips were then mounted on the glass microscope slide with a drop of 80% glycerol PBS solution. The DOX distribution was observed using a confocal laser scanning microscope (CLSM, Leica TCS-sp2, Germany) at excitation and emission wavelengths of 490 and 590 nm, respectively.

Flow Cytometry. HepG2 cells (2×10^5) were maintained in DMEM supplemented with 10% fetal bovine serum for 24 h at 37 °C in 5% CO_2, 95% humidified atmosphere on a 24-well plate. The medium was then changed by freshly prepared DMEM containing the drug-loaded polymeric micelles with an equivalent doxorubicin concentration of 10 μg/mL at pH 6.8 and 7.4. The cells were incubated for desired time, harvested and washed three times with PBS, and suspended with PBS. Flow cytometry was performed on a FACS calibur (BD Biosciences US).

Hemolysis. Approximately 5 mL of porcine blood was poured into a centrifuge tube. PBS (pH 7.4) was added to 50 mL, and the solution was mixed. The tube was centrifuged (Heraeus Labofuge 400R Centrifuge) at 2500 rpm for 10 min at 4 °C. The erythrocyte pellet was isolated, washed twice with phosphate buffer by resuspending the pellet in PBS (pH 7.4), and centrifuged. The pellet was weighed, and 3 wt % dispersion of the erythrocyte was prepared in PBS. 80 μL of the erythrocyte suspension was pippetted into a 96-microwell plate, followed by adding 80 μL of polymer solution of different concentration in each well. PBS and Triton X-100 (1 vol %) served as the negative and positive control, respectively. The 96-microwell plate was incubated at 37 °C for 1 h and then centrifuged at 2500 rpm for 10 min at 4 °C. The absorbance of the supernatant (100 μL) was measured at 570 nm using a microplate reader (Versamax Tunable Microplate Reader). The results were expressed as percentage hemolysis with the assumption that Triton X-100 causes 100% hemolysis and PBS, 0% hemolysis. The above experiment was repeated at different pHs (6.8, 6.5, and 5.0).

RESULTS AND DISCUSSION

Characterization of Polymer Structure and the pH-Dependent Hydrolysis of PEG-b-C18. The synthesis procedure of the PEG-b-C18 polymer is illustrated in Figure 2. The chemical structure of the polymer was examined using FTIR and ^{1}H NMR in chloroform. In the NMR spectrum,

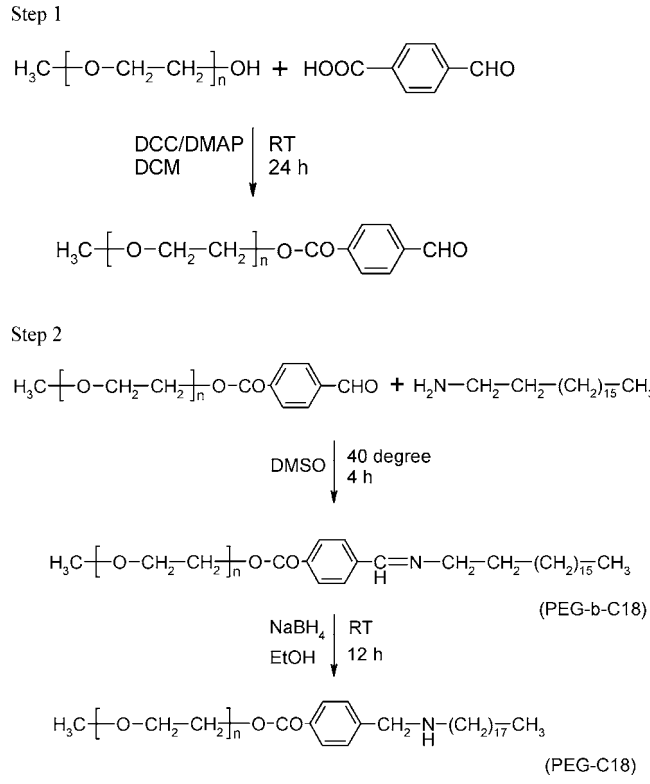

Figure 2. Schematic description of the synthesis of the amphiphilic PEG-b-C18. Further reduction of imine bond in the PEG-b-C18 to amine gets the non-acid-labile PEG-C18.

the aldehyde peak at 9.7 ppm of PEG-CHO was not observed from the purified PEG-b-C18, while the imine proton at 8.1 ppm was clearly seen. The appearance of a specific band at 1648 cm^{-1} in the FTIR spectrum further confirmed the formation of the benzoic imine linkage in the PEG-b-C18 (see Supporting Information) (*35, 36*). The purification of the polymer was also checked by thin layer chromatography (TLC) on a silica plate.

The hydrolysis kinetics as well as the hydrolysis bonding equilibrium of an imine bond is significantly influenced by environmental pH and the substitute groups (*37, 38*). While the imine bond formed from aliphatic amine and aldehyde hydrolyzes in neutral aqueous solution, the imine linkage in a Schiff base amphiphile made from aromatic amine and aldehyde is more stable due to the $\pi-\pi$ conjugation (*32*−*34*). However, for the purpose of pH-triggered drug release, it requires an acid-labile bond in the carrier-building polymer responsive to a subtle pH difference under the physiological conditions, e.g., pH 4.5−7.4 (*39, 40*). Herein, we synthesized the amphiphilic polymer by an aromatic aldehyde (PEG-benzaldehyde) and an aliphatic amine (*n*-octadecane amine) for the formation of a derivate imine linker with proper conjugation extent. The stability and pH-dependent hydrolysis of the benzoic-imine bond in the PEG-b-C18 was monitored using ^{1}H NMR, by dissolving the polymer in aqueous solution at different pHs (see Supporting Information). The aldehyde peak was not detected from the polymer in deuterated water at pH 7.4 for up to 24 h, indicating that the benzoic-imine bond is stable. At a pH of 6.5, the aldehyde peaks appeared where the imine peak still existed, an indication of partial hydrolysis of the polymer. By comparing the integrals of the aldehyde and imine peaks in the NMR spectra, it was shown that the hydrolysis extent of PEG-b-C18 increased with the decrease of solution pH. In addition, the hydrolysis reaction was rapid and reached equilibrium within 10 min, similar to our previous study (*35*). At a more acidic pH, i.e., 5.0, the

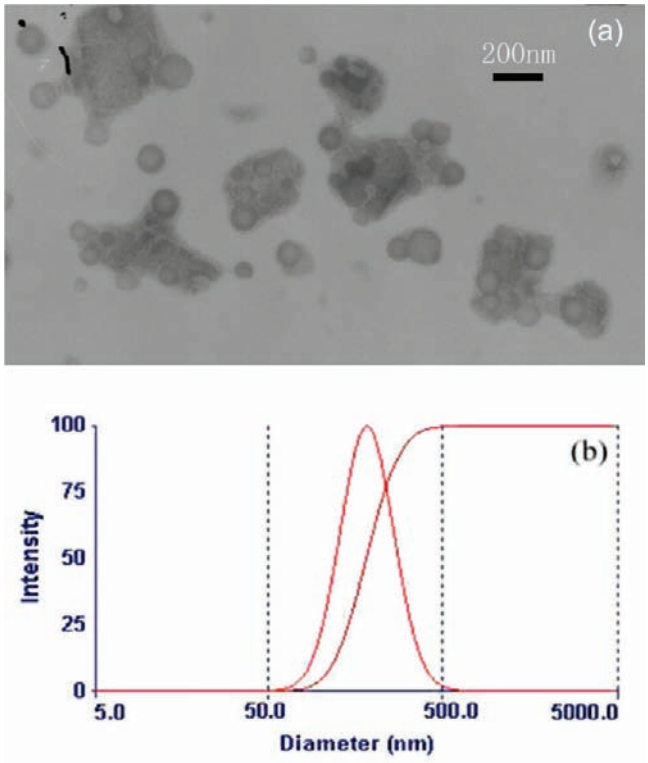

Figure 3. TEM image (a) and DLS diagram (b) of PEG-b-C18 aggregates prepared at pH 7.4.

benzoic imine linker completely hydrolyzed, evidenced by the disappearance of the imine proton peak (8.1 ppm) accompanied by the recovery of the integral of the aldehyde proton at 9.7 ppm in the ^{1}H NMR. FTIR of the PEG-b-C18 dried from a solution at acidic pH (~5.0) further confirmed hydrolysis of the imine linkage by the comparison of the specific band at 1648 cm^{-1} with that of the untreated sample.

Aggregate Formation and pH-Mediated Structural Evolution of PEG-b-C18. Micelles were formed from the PEG-b-C18 in aqueous solution at neutral and basic pH. The cmc was determined as 0.019 mg/mL at pH 7.4 using fluorescence spectrophotometry with pyrene as the probe. The aggregates are spherically shaped in the TEM image (Figure 3a) and have an average size of 181 nm measured by DLS (Figure 3b), implying the formation of a multicore structure through the entanglement of the PEG chains (*41*). The pH dependence of zeta potential and the core polarity of the aggregates, determined by fluorescence emission of pyrene, were plotted in Figure 4. At a pH higher than 7.4, the I_3/I_1 of the PEG-b-C18 micelles is larger than 1 and the zeta potential is nearly zero, because the benzoic imine linker is stable; thus, the micelles contain no charged moiety.

A sharp increase of zeta potential from 0 to 30 mV is observed with the pH decrease from 7.0 to 6.5 for the PEG-b-C18, attributed to the cleavage of PEG chains generating positively charged octadecane amine (pK_a ~11), whereas the zeta potentials of the nondegradable PEG-C18 micelles are nearly constant at different pHs (Figure 4). However, since the I_3/I_1 ratio of pyrene emission remains at a higher value, i.e., 1.15, the micellar structure should be maintained for the PEG-b-C18 at pH 6.5−5.0, while the zeta potential reaches a plateau at 30 mV. The average particle size of the PEG-b-C18 micelle at pH 6.5 is 183 nm (DLS), almost the same as the original 181 nm at pH 7.4. As described above, an acidic pH higher than 5.0 would not cause a complete cleavage of the benzoic-imine bond. It is understandable that the portion of uncleaved PEG-b-C18 molecules prevented

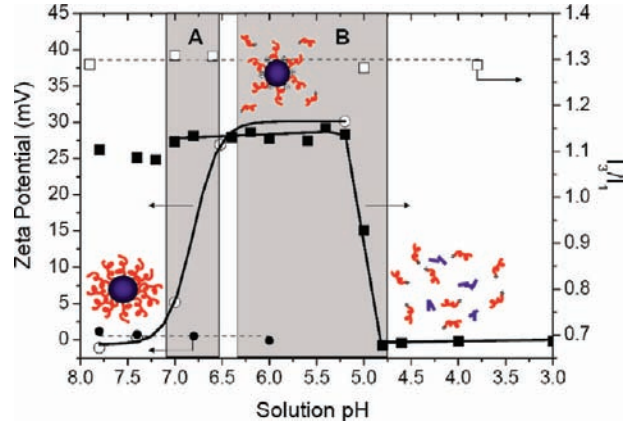

Figure 4. Zeta potential of PEG-b-C18 (○) and PEG-C18 (•) micelles, and I_3/I_1 of pyrene fluorescence emission in PEG-b-C18 (■) and PEG-C18 (□) solution as a function of solution pH. The polymer concentration is fixed at 0.5 mg/mL. pH range A, extracellular pH of solid tumor; B, endosomal pH.

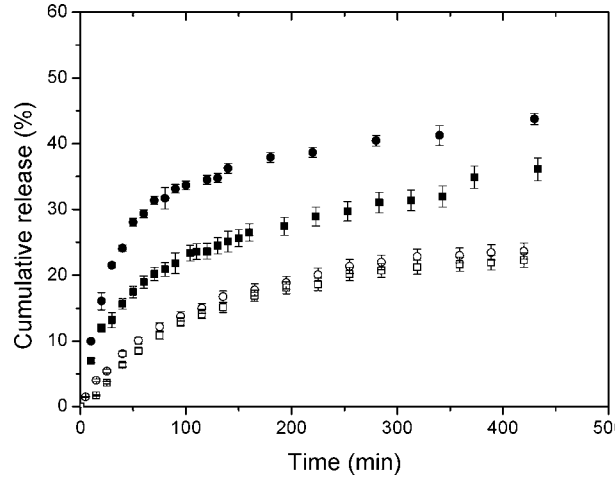

Figure 5. Cumulative release of doxorubicin from the PEG-b-C18 micelles at pH 7.4 (■) and 6.8 (•) and from the PEG-C18 micelles at pH 7.4 (□) and 6.8 (○).

the micellar structure from dissociating, and the residual octadecane amine from the cleaved polymer was solubilized in the core of the micelle with amino groups exposed on the surface leading to a positive zeta potential. The transition pH of the zeta potential is 6.7, defined as the middle value between the two inflections of the curve (Figure 4), lying in the extracellular pH region of solid tumors. The positively charged surface of the PEG-b-C18 micelles will be conducive for cell absorption in the tumor site (*10*).

At a lower pH, i.e., the endosomal pH ~5.0, further cleavage of the PEG-b-C18 will cause dissociation of the micelles. As shown in Figure 4, the I_3/I_1 ratio of the PEG-b-C18 decreases abruptly to a value close to that for water, i.e.. 0.7, an indication of demicellization (*42*). The fluorescence intensity was also reduced significantly at pH 5.0 due to the decrease of the quantum yield and the quenching of fluorescence by the primary amino group of the produced octadecane amine (*43*). Thus, with the environmental pH changing from physiological to tumor and endosomal pHs, the progressive hydrolysis of the benzoic-imine bond in the PEG-b-C18 leads to a surface property change and furthermore a structural change of the aggregates, i.e., from PEG-shielded to positively charged and finally dissociated (Figure 4).

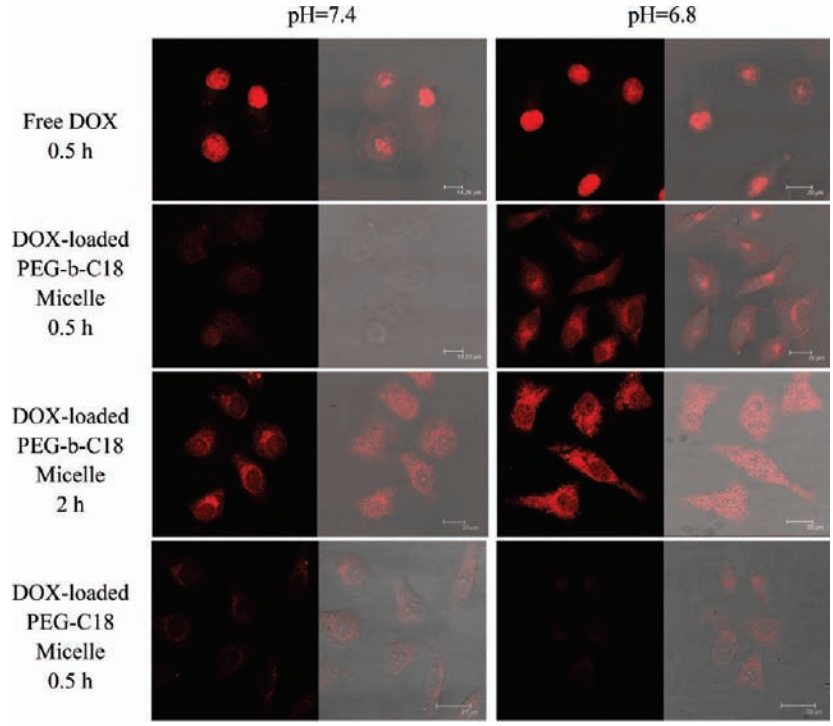

Figure 6. Confocal fluorescence microscopy images (in each column: left, doxorubicin channel; right, overlap of doxorubicin and transmittance channels) of HepG2 cells being treated with free DOX, DOX-loaded PEG-b-C18 micelles, and DOX-loaded PEG-C18 micelles with incubation time of 0.5 and 2 h at pH 7.4 and 6.8.

Drug Loading and in Vitro Release. Doxorubicin was encapsulated in the micelles using the solvent evaporation method. The PEG-b-C18 micelle with a drug loading capacity of 30 wt % has a mean size of 216 nm (DLS), slightly bigger than that of the bare micelle (181 nm). The size increase is attributed to the solubilization of drug within the hydrophobic core. Figure 5 shows the DOX release from the PEG-b-C18 and the PEG-C18 micelles at different pHs. A burst release is observed at early stage of the profiles, which may be explained by the relatively low molecular weight of the polymer especially for the hydrophobic segment, leading to a lower stability of the entrapped drug molecules in the hydrophobic cores (*1*). Nevertheless, by comparison with the PEG-C18 micelles, it could be clearly seen that the release of DOX from the PEG-b-C18 micelles was accelerated by changing the environmental pH from neutral to slightly acidic, i.e., 7.4 to 6.8 (Figure 5). Similar pH dependence on the release of prednisolone, a drug with constant water solubility in the tested pHs, from the PEG-b-C18 micelles was also observed, indicating that the PEG-b-C18 formulations are able to respond to a very subtle change of the environmental pH.

In Vitro Cellular Uptake of DOX-Loaded PEG-b-C18 Micelles at Tumor and Physiological pHs. The intracellular localization of DOX-loaded PEG-b-C18 micelles was investigated using confocal fluorescence microscopy on HepG2 cells (Figure 6). As expected, DOX is mainly distributed in the nuclear region of cells after being treated with free drug solution (*9, 26*). Differently, the fluorescence intensity was detectable in both nucleus and cytoplasm after the cells were incubated with the DOX-loaded PEG-b-C18 micelles. This proves that the internalization mechanism of the PEG-b-C18 micelle is endocytosis (*44*). However, the amount of DOX uptake showed strong pH dependence for the DOX-loaded PEG-b-C18 formulations. Flow cytometry shows that the mean fluorescence intensity is much higher in the cells treated with the drug-loaded PEG-b-C18 micelles at pH 6.8 than that at physiological pH 7.4, whereas it has little difference and stays at a low level after treatment with the noncleavable PEG-C18 formulations at the two pHs (Figure 7). The internalization of noncharged nanoparticles, for example, with a PEGylated surface, normally undergoes a fluid-phase endocytosis mechanism, while positively charged nanoparticles will be taken up by cells through a more efficient adsorptive endocytosis due to the electrostatic interaction between the carrier and the negatively charged cell membrane (*45*). However, both of the processes are nonspecific. In our studied system, the hydrolysis of the benzoic-imine bond in PEG-b-C18 occurs at tumor pH and the micelle surface converts from neutral to positively charged with the micellar structure preserved (Figure 4). Therefore, the adsorptive endocytosis is favored only at the tumor pH (6.8) to the PEG-b-C18 micelles, which would lead to the acceleration of DOX uptake under the tumor condition.

pH-Dependent Membrane Disruption of PEG-b-C18. After being endocytosed, a rapid endosomal escape of the carrier is required for protecting the carried drug from degradation during the lysosome transport. The pH-dependent membrane disruption of the micelle from physiological to endosomal pH was evaluated using porcine erythrocytes as the biological model membrane (*22*, *46*). Under physiological and tumor conditions (pH = 7.4−6.5), hemolysis of the PEG-b-C18 micelle increases slightly with the decrease of pH (Figure 8). This proves again that the positive ionization of the PEG-b-C18 micelle at tumor pH indeed increases the electrostatic interaction between the micelle and the cell membrane. The hemolysis is 22% at pH 7.4 with a polymer concentration of 10 mg/mL, in a reasonable range for intravenous administration, and remains at relatively low levels (<40%) at pH higher than 6.5 possibly due to the existence of residue PEG chains on the micelle surface. With further pH decrease to endosomal pH (5.0), a more complete hydrolysis of the benzoic-imine bond leads to the collapse of the micellar structure of the PEG-b-C18, and the system becomes rather hemolytic. At pH 5.0, hemolysis reaches as high as 60% and 100% for the PEG-b-C18 at

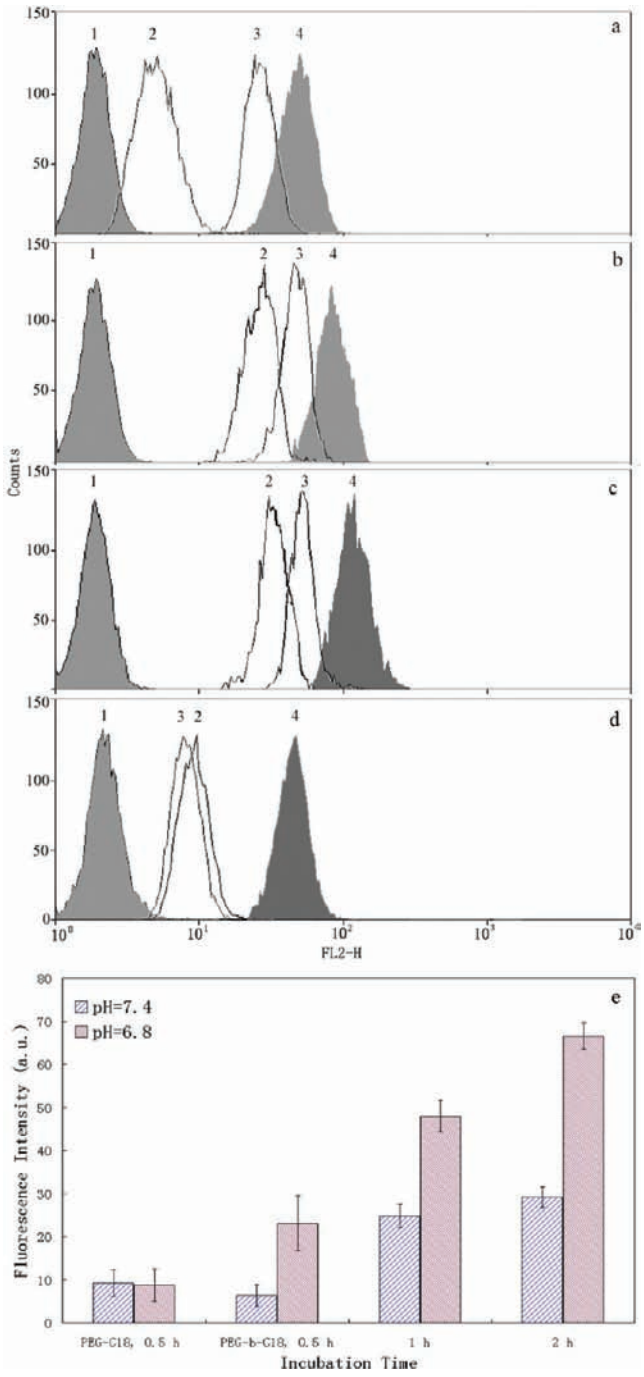

Figure 7. Flow cytometric analysis of HepG2 cells being treated with DOX-loaded PEG-b-C18 for 0.5 h (a), 1 h (b), and 2 h (c), and treated with DOX-loaded PEG-C18 for 0.5 h (d) (1, Medium; 2, DOX-loaded micelles at pH 7.4; 3, DOX-loaded micelles at pH 6.8; 4, free DOX at pH 7.4). (e) Mean fluorescence intensity on HepG2 cells after treatment with DOX-loaded PEG-b-C18 or PEG-C18 micelles at different incubation time and pH measured by flow cytometry.

concentrations of 2.5 mg/mL and 10 mg/mL, respectively (Figure 8), compared to the maximum value of 13% for the nondegradable PEG-C18, inferring the pH-triggered membrane-disrupting ability of the PEG-b-C18 micelle after it was endocytosed, which will help the system to overcome the intracellular barrier and allow the drug to release rapidly into the cytoplasm and then to the nucleus via diffusion. As shown in the CLSM images (Figure 6), DOX is found in the nuclear region only after a short incubation of 0.5 h when treated with the drug-loaded PEG-b-C18 micelles.

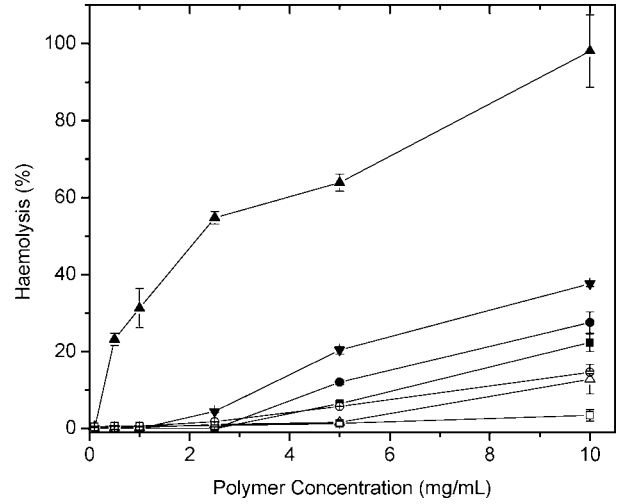

Figure 8. Hemolysis of PEG-b-C18 at pH 7.4 (■), 6.8 (•), 6.5 (▼), 5.0 (▲), and PEG-C18 at pH 7.4 (□), 6.8 (○), and 5.0 (△).

In summary, an amphiphilic polymer PEG-b-C18 was synthesized by conjugating a hydrophilic and a hydrophobic block via a novel pH-responsive benzoic-imine bond. The benzoic-imine linker was stable at physiological pH and cleaves with increasing magnitude following the decrease of pH progressively to tumor and endosomal pHs. Meanwhile, the polymer self-assembled into noncharged micellar aggregates in aqueous solution at physiological pH, which is positively charged on the surface at tumor pH and dissociates at endosomal pH. As a result, the PEG-b-C18 micelle is more easily taken up by cells under tumor condition and has an enhanced membrane disrupting capability in endosomes. The conjugation of benzoic-imine bond will be promising for future design of delivery systems with both tumor-specific uptake and intracellular delivery ability.

ACKNOWLEDGMENT

This work is financially supported by the National Natural Science Foundation of China (50873108, 50733004), State Key Project for Fundamental Research (2003CB716900), and National Center for Nanoscience and Nanotechnology of China. X.Q. is grateful to the Beijing New Star Project on Science and Technology (2006A75).

Supporting Information Available: Supplementary figures. This material is available free of charge via the Internet at http://pubs.acs.org.

LITERATURE CITED

(1) Torchilin, V. P. (2006) Nanocarriers for drug delivery: needs and requirements. in *Nanoparticulates as Drug Carriers*, Imperial College Press.
(2) Nishiyama, N., and Kataoka, K. (2006) Current state, achievements, and future prospects of polymeric micelles as nanocarriers for drug and gene delivery. *Pharmacol. Therapeut. 112*, 630–648.
(3) Park, J. H., Lee, S., Kim, J. H., Park, K., Kim, K., and Kwon, I. C. (2008) Polymeric nanomedicine for cancer therapy. *Prog. Polym. Sci. 33*, 113–137.
(4) Torchilin, V. P. (2006) Multifunctional nanocarriers. *Adv. Drug Delivery Rev. 58*, 1532–1555.
(5) Duncan, R. (2003) The dawning era of polymer therapeutics. *Nat. Rev. Drug. Discovery 2*, 347–360.
(6) Brannon-Peppas, L., and Blanchette, J. O. (2004) Nanoparticle and targeted systems for cancer therapy. *Adv. Drug Delivery Rev. 56*, 1649–1659.

(7) Ruoslahti, E. (2002) Specialization of tumour vasculature. *Nat. Rev. Cancer 2*, 83–90.
(8) Sudimack, J., and Lee, R. J. (2000) Targeted drug delivery via the folate receptor. *Adv. Drug Delivery Rev. 41*, 147–162.
(9) Lee, E. S., Na, K., and Bae, Y. H. (2005) Super pH-sensitive multifunctional polymeric micelle. *Nano Lett. 5*, 325–329.
(10) Sethuraman, V. A., and Bae, Y. H. (2007) TAT peptide-based micelle system for potential active targeting of anti-cancer agents to acidic solid tumors. *J. Controlled Release 118*, 216–224.
(11) Xu, P., Van Kirk, E. A., Zhan, Y., Murdoch, W. J., Radosz, M., and Shen, Y. (2007) Targeted charge-reversal nanoparticles for nuclear drug delivery. *Angew. Chem., Int. Ed. 46*, 4999–5002.
(12) McCormick, L., Seymour, L. C. W., Duncan, R., and Kopecek, J. (1986) Interaction of a cationic N-(2-hydroxypropyl)methacrylamide copolymer with rat visceral yolk sac cultured in vitro and rat liver in vivo. *J. Bioact. Comp. Polym. 1*, 4–19.
(13) Verrecchia, T., Spenlehauer, G., Bazile, D. V., Murrybrelier, A., Archimbaud, Y., and Veillard, M. (1995) Non-stealth (poly(lactic acid/albumin)) and stealth (poly(lactic acid-polyethylene glycol)) nanoparticles as injectable drug carriers. *J. Controlled Release 36*, 49–61.
(14) Ogris, M., Brunner, S., Schuller, S., Kircheis, R., and Wagner, E. (1999) PEGylated DNA/transferrin-PEI complexes: reduced interaction with blood components, extended circulation in blood and potential for systemic gene delivery. *Gene Ther. 6*, 595–605.
(15) Kunath, K., von Harpe, A., Petersen, H., Fischer, D., Voigt, K., Kissel, T., and Bickel, U. (2002) The structure of PEG-modified poly(ethylenimines) influences biodistribution and pharmacokinetics of their complexes with NF-κB decoy in mice. *Pharm. Res. 19*, 810–817.
(16) Murthy, N., Campbell, J., Fausto, N., Hoffman, A. S., and Stayton, P. S. (2003) Design and synthesis of pH-responsive polymeric carriers that target uptake and enhance the intracellular delivery of oligonucleotides. *J. Controlled Release 89*, 365–374.
(17) Lee, Y., Fukushima, S., Bae, Y., Hiki, S., Ishii, T., and Kataoka, K. (2007) A protein nanocarrier from charge-conversion polymer in response to endosomal pH. *J. Am. Chem. Soc. 129*, 5362–5363.
(18) Simoes, S., Nuno Moreira, J., Fonseca, C., Duzgunes, N., and Pedroso de Lima, M. C. (2004) On the formulation of pH-sensitive liposomes with long circulation times. *Adv. Drug Delivery Rev. 56*, 947–965.
(19) Liu, S. Q., Wiradharma, N., Gao, S. J., Tong, Y. W., and Yang, Y. Y. (2007) Bio-functional micelles self-assembled from a folate-conjugated block copolymer for targeted intracellular delivery of anticancer drugs. *Biomaterials 28*, 1423–1433.
(20) Park, J. S., Han, T. H., Lee, K. Y., Han, S. S., Hwang, J. J., Moon, D. H., Kim, S. Y., and Cho, Y. W. (2007) N-acetyl histidine-conjugated glycol chitosan self-assembled nanoparticles for intracytoplasmic delivery of drugs: endocytosis, exocytosis and drug release. *J. Controlled Release 11*, 537–45.
(21) Chan, Y., Bulmus, V., Hadi Zareie, M., Byrne, F. L., Barner, L., and Kavallaris, M. (2006) Acid-cleavable polymeric core-shell particles for delivery of hydrophobic drugs. *J. Controlled Release 115*, 197–207.
(22) Murthy, N., Campbell, J., Fausto, N., Hoffman, A. S., and Stayton, P. S. (2003) Bioinspired pH-responsive polymers for the intracellular delivery of biomolecular drugs. *Bioconjugate Chem. 14*, 412–419.
(23) Akiyama, Y., Nagasaki, Y., and Kataoka, K. (2004) Synthesis of heterotelechelic poly(ethylene glycol) derivatives having α-benzaldehyde and ω-pyridyl disulfide groups by ring opening polymerization of ethylene oxide using 4-(diethoxymethyl)benzyl alkoxide as a novel initiator. *Bioconjugate Chem. 15*, 424–427.
(24) Sawant, R. M., Hurley, J. P., Salmaso, S., Kale, A., Tolcheva, E., Levchenko, T. S., and Torchilin, V. P. (2006) "Smart" drug delivery systems: double-targeted pH-responsive pharmaceutical nanocarriers. *Bioconjugate Chem. 17*, 943–949.
(25) Walker, G. F., Fella, C., Pelisek, J., Fahrmeir, J., Boeckle, S., Ogris, M., and Wagner, E. (2005) Toward synthetic viruses: endosomal pH-triggered deshielding of targeted polyplexes greatly enhances gene transfer in vitro and in vivo. *Mol. Ther. 11*, 418–425.
(26) Bae, Y., Fukushima, S., Harada, A., and Kataoka, K. (2003) Design of environment-sensitive supramolecular assemblies for intracellular drug delivery: polymeric micelles that are responsive to intracellular pH change. *Angew. Chem., Int. Ed. 42*, 4640–4643.
(27) Bae, Y., Nishiyama, N., Fukushima, S., Koyama, H., Yasuhiro, M., and Kataoka, K. (2005) Preparation and biological characterization of polymeric micelle drug carriers with intracellular pH-triggered drug release property: tumor permeability, controlled subcellular drug distribution, and enhanced in vivo antitumor efficacy. *Bioconjugate Chem. 16*, 122–130.
(28) Kale, A., and Torchilin, V. P. (2007) Design, synthesis, and characterization of pH-sensitive PEG-PE conjugates for stimuli-sensitive pharmaceutical nanocarriers: the effect of substitutes at the hydrazone linkage on the ph stability of PEG-PE conjugates. *Bioconjugate Chem. 18*, 363–370.
(29) Murthy, N., Thng, Y. X., Schuck, S., Xu, M. C., and Fréchet, J. M. J. (2002) A novel strategy for encapsulation and release of proteins: hydrogels and microgels with acid-labile acetal cross-linkers. *J. Am. Chem. Soc. 124*, 12398–12399.
(30) Masson, C., Garinot, M., Mignet, N., Wetzer, B., Mailhe, P., Scherman, D., and Bessodes, M. (2004) pH-sensitive PEG lipids containing orthoester linkers: new potential tools for nonviral gene delivery. *J. Controlled Release 99*, 423–434.
(31) Lin, S., Du, F., Wang, Y., Ji, S., Liang, D., Yu, L., and Li, Z. (2008) An acid-labile block copolymer of PDMAEMA and PEG as potential carrier for intelligent gene delivery systems. *Biomacromolecules 9*, 109–115.
(32) Lemieux, G. A., and Bertozzi, C. R. (1998) Chemoselective ligation reactions with proteins, oligosaccharides and cells. *Trends Biotechnol. 16*, 506–511.
(33) Okahata, Y., Ando, R., and Kunitake, T. (1983) Reaction of the azomethine moiety buried in bilayer membranes. *Bull. Chem. Soc. Jpn. 56*, 802–808.
(34) Liang, Y., Wu, L., Tian, Y., Zhang, Z., and Chen, H. (1996) Structure control of synthetic bilayer membranes from single-chain amphiphiles containing the Schiff base segment: I. conformation control and spectral characterization. *J. Colloid Interface Sci. 17*, 8703–713.
(35) Gu, J., Cheng, W. P., Liu, J., Lo, S., Smith, D., Qu, X., and Yang, Z. (2008) pH-triggered reversible "stealth" polycationic micelles. *Biomacromolecules 9*, 255–262.
(36) Kramer, M., Stumbe, J., Turk, H., Krause, S., Komp, A., Delineau, L., Prokhorova, S., Kautz, H., and Haag, R. (2002) pH-responsive molecular nanocarriers based on dendritic core-shell architectures. *Angew. Chem., Int. Ed. 41*, 4252–4256.
(37) Donoso, J., Munioz, F., Garcia Del Vado, A., Echevarria, G., and Garcia Blancot, F. (1986) Study of the hydrolysis and ionization constants of Schiff base from pyridoxal 5′-phosphate and n-hexylamine in partially aqueous solvents. *Biochem. J. 238*, 137–144.
(38) Cordes, E. H., and Jencks, K. P. (1963) The mechanism of hydrolysis of Schiff bases derived from aliphatic amines. *J. Am. Chem. Soc. 85*, 2843–2848.
(39) Ganta, S., Devalapally, H., Shahiwala, A., and Amiji, M. (2008) A review of stimuli-responsive nanocarriers for drug and gene delivery. *J. Controlled Release 126*, 187–204.
(40) Kim, Y. H., Park, J. H., Lee, M., Kim, Y. H., Park, T. G., and Kim, S. W. (2005) Polyethylenimine with acid-labile linkages as a biodegradable gene carrier. *J. Controlled Release 103*, 209–219.
(41) Hsu, Y. H., Chiang, W. H., Chen, C. H., Chern, C. S., and Chiu, H. C. (2005) Thermally responsive interactions between the PEG and PNIPAAm grafts attached to the PAAc backbone and the corresponding structural changes of polymeric micelles in water. *Macromolecules 38*, 9757–9765.

(42) Zhao, C. L., Winnik, M. A., Riess, G., and Croucher, M. D. (1990) Fluorescence probe techniques used to study micelle formation in water-soluble block copolymers. *Langmuir 6*, 514–516.

(43) Bronich, T. K., Solomatin, S. V., Yaroslavov, A. A., Eisenberg, A., Kabanov, V. A., and Kabanov, A. V. (2000) Steric stabilization of negatively charged liposomes by cationic graft copolymer. *Langmuir 16*, 4877–4881.

(44) Yang, S. R., Lee, H. J., and Kim, J.-D. (2006) Histidine-conjugated poly(amino acid) derivatives for the novel endosomolytic delivery carrier of doxorubicin. *J. Controlled Release 114*, 60–68.

(45) Cuchelkar, V., Kopecek, J. (2006) Polymer-drug conjugates, in *Polymers in Drug Delivery*, Taylor & Francis Group, CRC press.

(46) Henry, S. M., El-Sayed, M. E. H., Pirie, C. M., Hoffman, A. S., and Stayton, P. S. (2006) pH-responsive poly(styrene-alt-maleic anhydride) alkylamide copolymers for intracellular drug delivery. *Biomacromolecules 7*, 2407–2414.

BC800563G

Supporting Information

Preparation of multifunctional drug carrier for tumor specific uptake and enhanced intracellular delivery through the conjugation of weak acid labile linker

Caixia Ding, Jingxia Gu, Xiaozhong Qu* and Zhenzhong Yang*

State Key Laboratory of Polymer Physics and Chemistry, Institute of Chemistry, Chinese Academy of Sciences, Beijing 100190, China. (Email: quxz@iccas.ac.cn, yangzz@iccas.ac.cn)

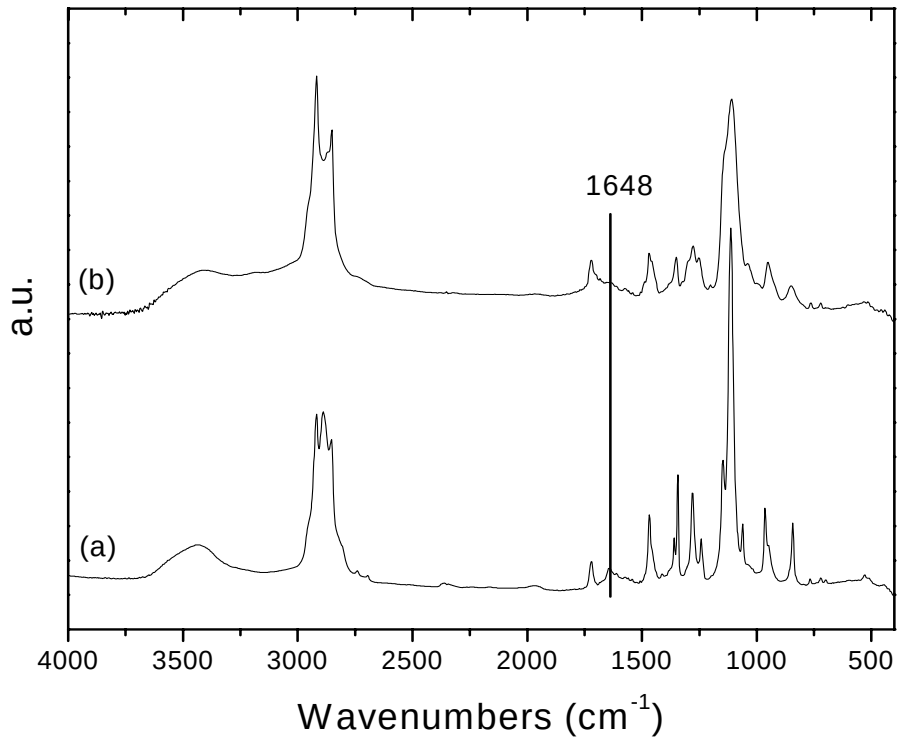

Figure S1 FTIR spectra of PEG-b-C18 (a) and the polymer after treated with an acidic aqueous solution at pH 5.0 (b).

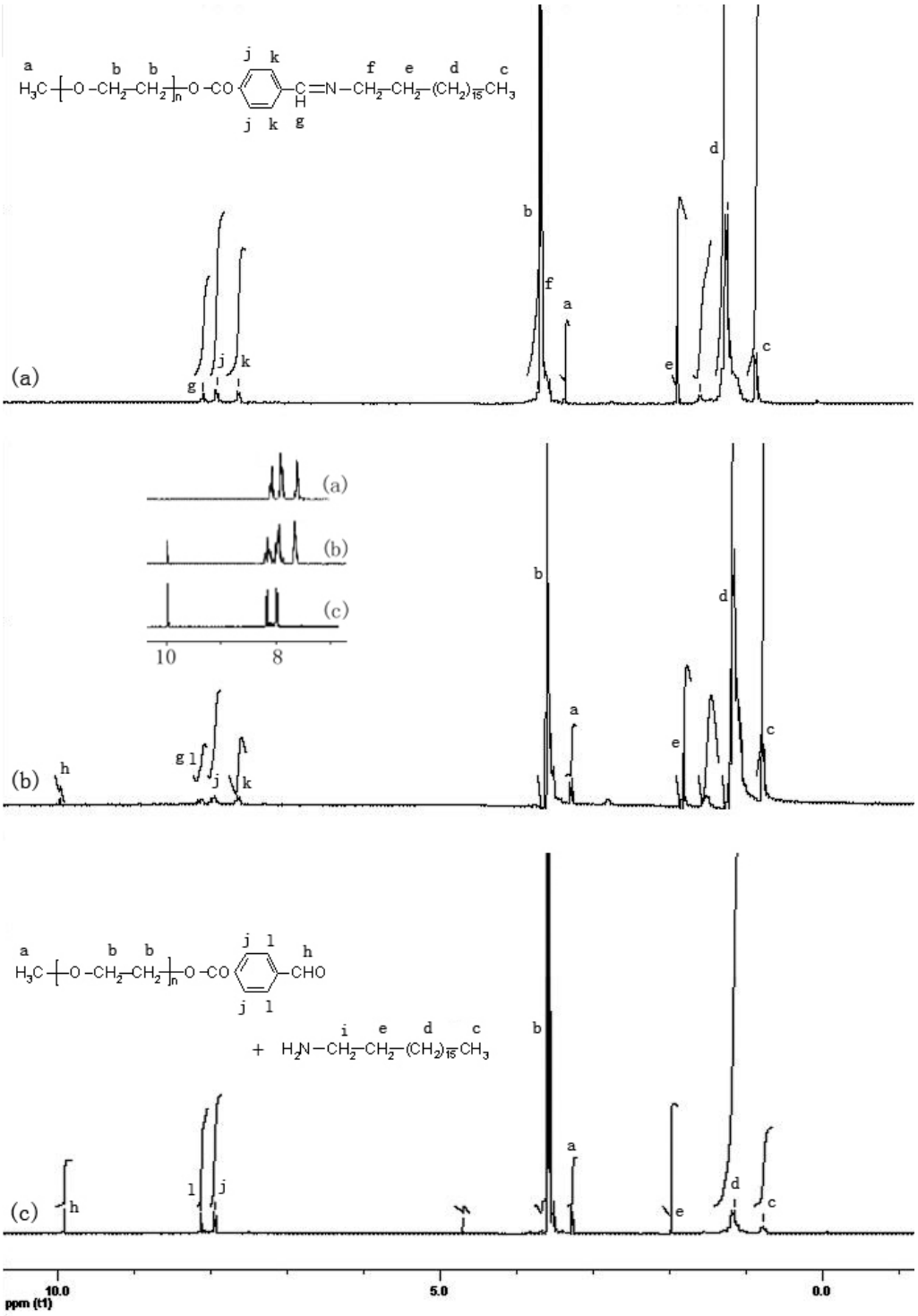

Figure S2 ^{1}H NMR spectra of PEG-b-C18 in deuterated water at pH 7.4 (a), 6.5 (b) and 5.0 (c). The samples were measured after being dissolved in D_2O at the desired pH levels for 30 min.

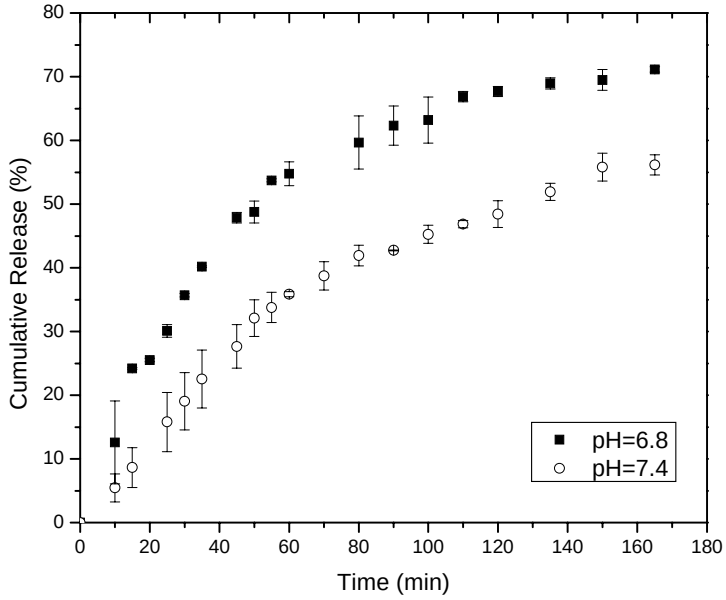

Figure S3 Cumulative release of prednisolone from the PEG-b-C18 micelles at different pHs.

In Vitro and in Vivo Metabolism of Lu-AMBA, a GRP-Receptor Binding Compound, and the Synthesis and Characterization of Its Metabolites

Karen E. Linder,* Edmund Metcalfe, Thangavel Arunachalam, Jianqing Chen, Stephen M. Eaton, Weiwei Feng, Hong Fan, Natarajan Raju, Aldo Cagnolini, Laura E. Lantry, Adrian D. Nunn, and Rolf E. Swenson

Bracco Research USA Inc., 305 College Road East, Princeton, New Jersey 08540. Received January 26, 2009; Revised Manuscript Received April 27, 2009

The metabolism of ^{177}Lu-AMBA (AMBA = DO3A-CH_2CO-G-(4-aminobenzoyl)-QWAVGHLM-NH_2), a radiotherapeutic compound in clinical development that binds to GRP and NMB receptors, was studied in vitro (mouse, rat and human plasma, mouse kidney homogenate) and in vivo (by analysis of mouse and rat plasma and urine following IV injection of ^{177}Lu-AMBA). The primary metabolites were Lu-DO3A-CH_2CO-G-Abz4-R, where R = -Q-OH (A), -QW-OH (B), and -QWAVGH-OH (C). Minor amounts of (D) where R = -QWAVGHLM-OH and (E) -QWAVGHL-OH were also observed. Clearance of ^{177}Lu-AMBA and of radioactivity from mouse and rat blood was rapid in vivo. In mouse and rat urine, only metabolites Lu-A and Lu-B were found—no parent drug was excreted. Unmetalated ligands and ^{nat}Lu and ^{177}Lu complexes for Lu-AMBA metabolites A−E were synthesized, characterized by HPLC and MS, and used to perform in vitro competition and direct binding studies on GRP receptor-positive PC-3 (human prostate) cancer cells. Biodistribution studies with ^{177}Lu-labeled metabolites A−E were performed in PC-3 tumor-bearing mice and the results compared with intact ^{177}Lu-AMBA. IC_{50} values for unmetalated metabolite ligands A−E were >400 nM in PC-3 cells in competition binding studies against ^{177}Lu-AMBA. No direct binding to PC-3 cells was observed with ^{177}Lu-labeled A−C, confirming IC_{50} results. ^{177}Lu-labeled metabolites A−E showed no uptake in GRP-receptor positive tumor or pancreas in PC-3 tumor bearing mice. All metabolites were rapidly excreted via the renal route (~78−87%) within 1 h. These results demonstrate that the tumor uptake observed with ^{177}Lu-AMBA is due to parent drug and not due to any of its identified metabolites.

INTRODUCTION

Bombesin, a 14-amino acid peptide, is an analogue of human gastrin-releasing peptide (GRP) and binds GRP receptors with high affinity and specificity (*1*). ^{177}Lu-AMBA (Figure 1) is a bombesin (7−14) derivative that binds to and is internalized by cells expressing gastrin-releasing peptide (GRP) and Neuromedin B (NMB) receptors (*2, 3*).

GRP receptors are overexpressed in many types of cancers, notably breast, prostate, pancreatic, and lung (*4*−*7*). They are an attractive target for molecular imaging and targeted radiotherapy of cancer, as they are located on the cell membrane and are frequently expressed in high numbers. When an agonist ligand binds to them, the receptor/ligand complex is internalized, thus facilitating either peptide receptor scintigraphy or targeted radiotherapy (*8*−*10*). Many radiolabeled bombesin derivatives have been investigated by different groups, using full-length peptide, bombesin (7−14), or analogues modified to bind to all four receptor subtypes of the bombesin receptor family (*2, 8, 9, 11*−*13*).

Lantry et al. (*2*) have demonstrated that ^{177}Lu-AMBA (AMBA = DO3A-CH_2CO-G-(4-aminobenzoyl)-QWAVGHLM-NH_2) binds with nanomolar affinity to GRP receptors. Preclinical studies demonstrated its therapeutic efficacy in a GRP-R positive PC-3 human prostate tumor-bearing mouse model. ^{177}Lu-AMBA is now in clinical trials for the radiotherapeutic treatment of prostate cancer.

This paper describes the identification of the metabolites of ^{177}Lu-AMBA, their receptor-binding characteristics, and their biodistribution and routes of excretion. The synthesis and characterization of the proposed metabolites and their unmetalated ligands and in vitro and in vivo studies with these authentic standards are also described.

* Communicating author. Karen E. Linder, Bracco Research USA, 305 College Road East, Princeton, NJ 08540, E-mail: karen.linder@bru.bracco.com, Phone: (609) 514-2416, Fax: (609) 514-2446.

EXPERIMENTAL PROCEDURES

Synthesis of AMBA and Metabolite Ligands A, B, C, D, and E. AMBA [(DO3A-CH_2CO-G-(4-aminobenzoyl)-QWAVGHLM-NH_2), DO3A = (1,4,7,10-tetraaza-4,7,10-tris(carboxymethyl)-cyclododecyl)-acetyl] was synthesized using solid-phase peptide synthesis chemistry as described by Lantry et al. (*2*). The Fmoc-protected amino acids used were purchased from Nova-Biochem (San Diego, CA), Advanced ChemTech (Louisville, KY), Chem-Impex International (Wood Dale, Ill), and Multiple Peptide Systems (San Diego, CA). Other chemicals, reagents, and adsorbents were procured from Aldrich Chemical Co. (Milwaukee, WI) and VWR Scientific Products (Bridgeport, NJ).

The peptide chains for unmetalated metabolite ligands A−E (Table 1) were assembled by either of two methods (methods A and B, below) of solid-phase peptide synthesis. For all constructs, the coupling of the glycine to the 4-aminobenzoyl attached resin and the DO3A-acetyl chelating moiety and cleavage from the resin were performed manually as indicated below.

Method A. DIC (4 equiv) was added to a solution of amino acid (4 equiv, 0.25 M in NMP) and HOBT (4 equiv, 0.5 M in NMP). After 5 min, the solution was added to the resin in NMP (15 mL NMP/g of resin). After 4 h of shaking, the resin was filtered and washed 3× with NMP. For the next coupling, the Fmoc group was removed from the resin-bound peptide with 20% piperidine in DMF (15 mL/g resin) with shaking 2× for

10.1021/bc9000189 CCC: $40.75 © 2009 American Chemical Society
Published on Web 05/29/2009

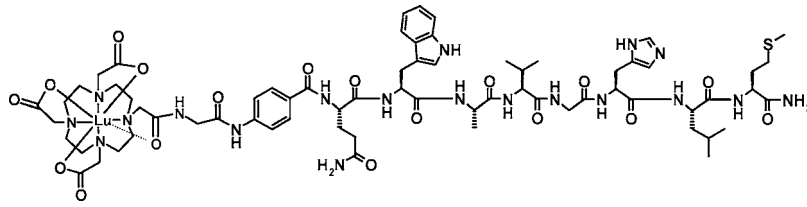

Figure 1. Chemical structure of ^{177}Lu-AMBA showing the proposed coordination of the lutetium chelate.

Table 1. Summary of Ligands Synthesized

ligand (DO3A-CH_2CO-G-Abz4-R) R =	mass spectrum (API-ES)	HPLC system[a]	retention time (purity)
A: -Q-OH	$[M+H]^+$: 709.2	3	2.5 min
	$([M+2H]/2)^{2+}$: 355.1		(100%)
B: -QW-OH	$[M+H]^+$: 895.3	3	4.7 min
	$([M+2H]/2)^{2+}$: 448.2		(100%)
C: -QWAVGH-OH	$[M+H]^+$: 1259.6	3	4.8 min
	$([M+2H]/2)^{2+}$: 630.3		(100%)
D: -QWAVGHLM-OH	$[M+H]^+$: 1503.5	4	5.9 min
	$([M+2H]/2)^{2+}$: 752.3		(>95%)
E: -QWAVGHL-OH	$[M+H]^+$: 1372.6	3	6.1 min
	$([M+2H]/2)^{2+}$: 687.0		(100%)

[a] System 3: XTerra MS C-18 (4.6 × 50 mm, 5 μ particle size): A = H_20 (0.1%TFA), B = ACN (0.1% TFA). Gradient = 0−40% B over 8 min, 3 mL/min. UV detection 220 nm. System 4: Initial condition: 10% B. Gradient = 10−40% B over 10 min.

15 min. The resin was filtered and washed 4× with NMP. The next coupling was repeated as above until the Fmoc-4-aminobenzoic acid had been added to the resin.

Method B. Synthesis of the peptides was carried out using a 0.25 mmol FastMoc protocol on an ABI 433A peptide synthesizer under N_2. In each cycle of this protocol, 1.0 mmol of a dry protected amino acid in a cartridge was dissolved in a solution of 0.9 mmol of HBTU, 2 mmol of DIEA, and 0.9 mmol of HOBT in DMF with additional NMP added. The activated Fmoc-amino acid was transferred directly to the reaction vessel. In the reaction vessel, 0.18 mmol of the C-terminal amino acid on 2-chlorotrityl resin (Novabiochem, resin substitution 0.42 mmol/g) was used. All couplings in this protocol were of 21 min duration. Fmoc deprotection was carried out with 20% piperidine in NMP. The peptide resin was finally washed with NMP for further manual derivatization.

Coupling of Glycine to 4-Aminobenzoic Acid Portion of the Peptide Chain. Fmoc-Gly-OH (10 equiv) was dissolved in NMP (5.0 mL/g) and treated with 10 equiv of HATU. The mixture was stirred under N_2 at 0 °C. DIEA (20 equiv) was directly added to the mixture and stirred for 10 min more before transferring the activated acid to the resin. The coupling was continued for 10 h at RT. The resin was drained of the reactants, and the above coupling procedure was repeated one more time. After draining the resin, it was washed with NMP (3×) and the resin was then taken to the cleavage step.

General Coupling Procedure for DOTA-tri-*t*-Butyl Ester. DOTA-tri-*t*-butyl-OH (8 equiv) was dissolved in NMP (5 mL/g). HBTU (8 equiv) was added and stirred under N_2. DIEA (16 equiv) was added neat to the above mixture and stirred for 10 min at RT before transferring the activated acid to the resin. The total volume of the reaction mixture was adjusted to about 15 mL/g of the resin used. The coupling was continued overnight (20 h). The resin was drained, washed with NMP (3×), and then washed twice with CH_2Cl_2.

Cleavage Procedure. Reagent B (15.0 mL, 88:5:5:2 TFA/water/phenol/TIPS v/v/wt/v) was added to about 1.0 g of the resin, and the vessel was shaken for 4 h at RT. The resin was filtered and then washed twice with TFA (5 mL/g of resin). The filtrates were combined, concentrated to a syrup, triturated with 20 mL of ether/g of the resin used, and centrifuged. The supernatant was decanted, and the process was repeated three times. Crude peptides were purified with a Shimadzu HPLC system using a YMC C-18 or Waters X Terra MS-C18 preparative column. The fractions were analyzed by reversed-phase HPLC and MS; appropriate fractions were combined and lyophilized.

Synthesis of ^{177}Lu and ^{nat}Lu Complexes. All commercial reagents and solvents were of reagent grade or better and used as received. L-(+)-Selenomethionine (Se-Met) was obtained from Sabinsa Corp. Bacteriostatic 0.9% sodium chloride injection (U.S.P.) was purchased from Abbott Laboratories. ASCOR L500 ascorbic acid injection (U.S.P.) [containing 500 mg/mL ascorbic acid and 0.025% (w/v) Na_2EDTA] was obtained from McGuff Pharmaceuticals, Inc. $^{177}LuCl_3$ in 0.05 N HCl was purchased from Missouri University Research Reactor (MURR). Lutetium trichloride·$6H_2O$, 99.9%, was obtained from Alfa Aesar.

^{177}Lu-AMBA. ^{177}Lu-AMBA was prepared and characterized as described by Chen et al. (*14*). For HPLC-purified product, the radiocomplex was separated from free ligand and radioactive and nonradioactive impurities by HPLC (Zorbax Bonus-RP Column, 5 μm, 80 Å pore, 250 mm × 4.6 mm, Agilent). For non-HPLC-purified product, the reaction mixture was diluted to the desired concentration using a 9:1 mixture of Bacteriostatic 0.9% sodium chloride injection USP and ASCOR L500 ascorbic acid injection USP to prevent radiolysis. HPLC-purified product had a specific activity of ∼3−4 Ci/μmol and a radiochemical purity (RCP) of >95%. Non-HPLC-purified product had a specific activity of ∼1.4 Ci/μmol and an RCP of ≥91%.

^{nat}Lu-AMBA and ^{nat}Lu-Labeled Metabolites A−E. $LuCl_3$·$6H_2O$ (14 mg, 0.036 mmol, 1.5 equiv) was added to AMBA (36.5 mg, 0.024 mmol, 1 equiv) dissolved in 5 mL of 0.2 M NaOAc buffer, pH 4.5. The solution was refluxed for 15 min and then cooled to room temperature. The metalated product was purified by HPLC on a Vydac C-18 column (10 × 250 mm) using a gradient of 80% H_2O (0.1% TFA)/20% CH_3CN (0.1% TFA) to 76%/24% in 15 min, a flow rate of 4.5 mL/min and a column temperature of 37 °C. The desired fractions were lyophilized to yield 38 mg (75%) of Lu-AMBA·2TFA·$10H_2O$ as a white solid, based on elemental analysis (C, H, N, S, F, H_2O). Authentic standards of ^{nat}Lu-labeled metabolites ^{nat}Lu-A, -B, -C, -D, and -E were similarly prepared and isolated.

Preparation of ^{177}Lu-Labeled Metabolites A−E for Biodistribution Studies. Ligand C (10 μg in 10 μL of 0.2 M NaOAc, pH 4.8) was mixed with $^{177}LuCl_3$ (5 μL, 2.11 mCi) and 0.2 M

NaOAc pH 4.8 (100 μL). The solution was heated at 100 °C for 10 min, cooled for 2 min in a water bath, and 5 μL of 5% Na_2EDTA solution in water was added. The reaction mixture was purified by HPLC to remove unchelated ligand, and the desired peak was collected into a 9:1 mixture of bacteriostatic saline/Ascor solution containing 0.2% human serum albumin (HSA), evaporated to near dryness, and diluted to 50 μCi/mL for biodistribution studies. ^{177}Lu-labeled metabolites A, B, D, and E were similarly prepared using the appropriate ligand.

Hydrolysis of ^{177}Lu-AMBA in Kidney Homogenate. Kidneys from nude mice were washed in PBS (all operations on ice), minced with scissors in Tris buffer (25 mM Tris, 150 mM NaCl, pH 7.4), and then Dounce-homogenized. The total volume of the homogenate was adjusted to contain 4 mL of Tris buffer for each gram of original tissue and then centrifuged at ~4000 × *g* for 10 min at 4 °C. The supernatant was aliquoted (200 μL) and stored at −80 °C until use. HPLC-purified ^{177}Lu-AMBA (25 μL, 3.50 Ci/μmol, 2.25 μCi, 0.00064 nmol) was incubated at 37 °C in 200 μL of kidney homogenate that was diluted 1:5 in Tris buffer immediately before use. Aliquots were removed and heat-denatured (100 °C, 10 min) at 10, 20, 30, and 60 min. The control was no homogenate, heated at 100 °C for 10 min. All samples were centrifuged at 20 000 × *g* for 6 min at 4 °C, and the supernates were analyzed by HPLC, using radiodetection.

Hydrolysis of ^{nat}Lu-AMBA in Kidney Homogenate. Kidney homogenate (25 μL), Tris buffer (15 μL), and ^{nat}Lu-AMBA (30 μL, 6.9 mg/mL) were incubated at 37 °C. At 0, 30, or 60 min, 23 μL of the mixture was removed, combined with 46 μL of cold methanol on ice, and centrifuged at 4 °C for 10 min at 20 000 × *g* to remove the protein. Preliminary LC/MS analyses were performed on the supernatants using an Agilent 1100 Series LC/MSD and a Waters XTerra C18 column (50 × 4.6 mm, 5 μm pore size) eluted with a gradient of H_2O (0.1% TFA)/ACN (0.1% TFA) at a flow rate of 0.5 mL/min. To confirm the identity of the metabolites, each metabolite peak was isolated from the supernate solution by preparative HPLC on a Vydac C18 column (5 μm, 4.6 × 250 mm) eluted at 1.5 mL/min with a gradient of 0−36% B over 26 min, where A = H_2O (0.1% TFA) and B = ACN (0.085% TFA). The desired peaks were detected at 280 nm. Solvents were evaporated; the samples were redissolved in 1:1 H_2O/ACN and analyzed by direct-injection MS.

In Vitro Metabolism in Mouse, Rat, and Human Plasma. Pooled normal human, rat, and mouse plasma (sodium citrate form) was obtained from Innovative Research, Inc. (Southfield, MI). ^{177}Lu-AMBA was radiolabeled as described above, but bacteriostatic saline and Ascor were omitted to avoid possible interference from EDTA and ascorbic acid. Immediately after labeling, 10 μL (1 mCi) of ^{177}Lu-AMBA was mixed with 0.99 mL of plasma and incubated at 37 °C (n = 4 per time point). At various times, sample solution (200 μL) was mixed with 10 μL of 10 mM DTPA, proteins were precipitated by treatment with 0.1 mL of 50% ice-cold EtOH (containing 5 mg/mL Se-Met) and 0.3 mL of ice-cold ACN, followed by centrifugation for 20 min at 20 000 × *g* at 4 °C. Recovery of radioactivity in the supernates was ~90%; the isolated supernates showed good stability (18 h at RT). These samples were analyzed using HPLC System 1.

HPLC Analysis of in Vitro Plasma Samples (System 1). HPLC analysis of in vitro plasma supernates was performed on a Zorbax Bonus-RP column (4.6 × 250 mm; 5 μm, Agilent) using the gradient in Table 2, where A, H_2O; B, 30 mM $(NH_4)_2SO_4$/0.1% TFA (v/v); C, acetonitrile (ACN); D, methanol (MeOH); flow rate = 1.5 mL/min, with a column temperature of 37 °C.

The amounts of ^{177}Lu-AMBA (% RCP) and metabolites were determined at each time-point from HPLC radiochromatograms.

Table 2

	mobile phases and percentage (%)			
time	A	B	C	D
0−5 min	70	30	0	0
15 min	44	30	13	13
30 min	30	30	20	20
35−40 min	0	30	35	35
45 min	70	30	0	0

A one- or two-compartment open model was used to fit the standard deviation-weighted, mean % RCP data in human, rat, and mouse plasma, using eq 1 [$C = Ae^{-at} + Be^{-bt}$], which was solved using the SAAM II program (*19*−*21*). The Lu-AMBA half-life was then interpolated from the fitted curves.

^{177}Lu-AMBA Metabolism in Normal Mouse and Rats. Animal studies were conducted in accordance with the U.S. Public Health Service Policy on Human Care and Use of Laboratory Animals as well as institutional guidelines. Non-HPLC purified ^{177}Lu-AMBA was diluted to 100 μCi/ 0.1 mL using 9:1 bacteriostatic saline/Ascor solution (RCP = 91%) for studies in mice and 750 μCi/ 0.1 mL (RCP ~94.0%) for studies in rats. ^{177}Lu-AMBA (100 μCi, 0.1 mL) was injected into a lateral tail vein of each of six mice (CD-1 normal males, Charles River Laboratories, ~8 weeks old, 35 g). Two mice each were sacrificed at 2 and 10 min. Urine was collected from the bladders of the sacrificed animals at t = 10 min and pooled. At 30 and 60 min, urine samples were taken from the bladder of one additional mouse each. Blood was taken from the descending aorta following CO_2 asphyxiation and stored on ice. Within 10 min, it was centrifuged at 4 °C for 15 min at 1000 × *g* to remove the cellular fraction, and the plasma fraction was removed and kept on ice. Urine samples were immediately placed on ice and treated in the same fashion as the plasma samples. An accurate aliquot of the plasma or urine was vortexed on ice with an equal volume of 50% EtOH containing 0.1% TFA (v/v), 0.05 mg/mL of Se-Met, and 0.05 mg/mL EDTA; treated with 3 parts of ice-chilled ACN and centrifuged at 4 °C for 15 min at 20 000 × *g*. Extracts were transferred to glass autosampler vials for HPLC analysis.

For studies in normal male CD rats (Charles River Laboratories), 0.1 mL (750 μCi) of ^{177}Lu-AMBA was injected into a lateral tail vein. In the first study, three rats were injected, each ~4 weeks in age and 90 g. In the followup study, a single rat ~6 weeks in age and 150 g was injected in the same manner. Blood was collected from conscious animals restrained in a soft plastic cone from the contralateral tail vein using heparin-rinsed syringes fitted with 21-gauge infusion sets. A separate syringe and infusion set was used for each time point. Urine samples were collected at 30 min and 2 h post injection (n = 1/time point).

HPLC analysis of ^{177}Lu-Labeled Metabolites in Vivo (HPLC System 2). Plasma extracts and urine samples were analyzed by HPLC using an Agilent 1100 series quaternary HPLC equipped with an autosampler and variable wavelength detector. Radioactivity was monitored using a Canberra NaI detector (model 802−2 × 2W) with high-voltage power supply (model 3102D), single channel analyzer (model 2015A), and a linear/logarithmic ratemeter (model 1481LA). Column: Vydac C18 (250 mm × 4.6 mm); column temp 37 ± 1 °C; mobile phase A, H_2O with 0.1% TFA (v/v); mobile phase B, ACN with 0.085% TFA; flow rate, 1.5 mL/min. Gradient: 0% B at 0 min, 20% B at 15 min, 23% B at 27 min, 67% B at 30 min, return to initial conditions at 36 min.

In Vivo Biodistribution of Isolated Metabolites. TAC:Cr:(NCr)-Foxn1^{nu} homozygous 4−5 week old male mice (Taconic Farms Inc.) were xenografted with human prostate cancer PC-3 cells (2 × 10^6). Studies were performed with tumors ranging

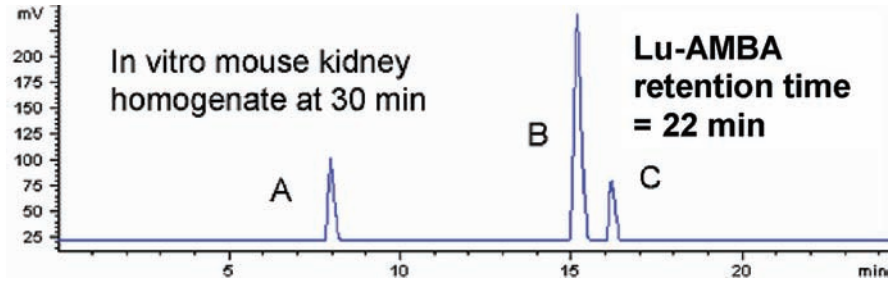

Figure 2. HPLC chromatogram of ^{177}Lu-AMBA (^{177}Lu-DO3A-CH_2CO-QWAVGHLM-NH_2) after 30 min incubation in mouse kidney homogenate at 37 °C. Metabolites A, B, and C are ^{177}Lu-DO3A-CH_2CO-R, where R = -Q-OH, -QW-OH, and -QWAVGH-OH. HPLC System 2 was used for this analysis.

from 125−1800 mm^3. Each subject (n = 4/group) was administered, via i.v. tail vein, a 0.1 mL (5 μCi) dose of HPLC-purified ^{177}Lu-AMBA or ^{177}Lu-labeled metabolite A−E (RCP > 96%, specific activity 1.9−3.54 Ci/μmol). Animals were sacrificed at 1 or 24 h via cervical dislocation, and tissues were harvested, weighed, and assayed for residual radioactivity in a Perkin-Elmer model 1480 Wizard gamma counter.

In Vitro Binding Studies - Cell Culture. Competition and direct binding studies were performed at 4 °C using the human prostate cancer cell line PC-3 (androgen-resistant prostate adenocarcinoma; American type Culture Collection) following procedures described previously (*2*). Plates were used for competition and direct binding studies on day 3 postplating, at which time the cells were confluent. Assays were performed in binding buffer containing protease inhibitors (RPMI-1640 supplemented with 0.2% BSA, 0.5 mM [4-(2-aminoethyl) benzenesulfonyl fluoride] (AEBSF) and Bacitracin (50 mg/500 mL), pH 7.4).

IC_{50} Determination. AMBA or metabolite ligands (A−E) (without added Lutetium) were diluted to concentrations ranging from 1.25× 10^{-9} M to 5× 10^{-7} M in binding buffer. Competition binding studies were performed to determine their inhibitory concentration (IC_{50}) against binding of ^{177}Lu-AMBA. After the addition of the appropriate solutions, plates were incubated for 1 h at 4 °C (n = 3 wells/data point). Incubation was ended by the addition of 200 μL of ice-cold binding buffer. Plates were washed five times, blotted dry, and counted in either an LKB CompuGamma counter or a microplate scintillation counter. Bound cpm (^{177}Lu) was plotted against concentration of metabolites to determine the concentration of the metabolite at 50% inhibition (IC_{50}).

Direct Binding of ^{177}Lu-AMBA Metabolites to PC-3 Cells. HPLC-purified ^{177}Lu-labeled metabolite A, B, or C (75 μL, RCP >98%) was added to triplicate wells at final concentrations of 0−10 μCi/mL in binding buffer. The cells were incubated for 1 h at room temperature. After washing off the unbound radioactivity (0.1% BSA in PBS, pH 7.4), total radioactivity bound to the cells was determined. In a parallel experiment, cells were incubated with various concentrations of ^{177}Lu-labeled metabolites in the presence of their respective unmetalated ligand (2 μM) to determine any nonspecific binding.

RESULTS

In Vitro Metabolism in Liver and Kidney Homogenate. The enzymatic cleavage of ^{177}Lu-AMBA was initially studied in mouse kidney homogenates for up to 60 min, followed by TLC analysis. These studies indicated that ^{177}Lu-AMBA was readily degraded in a time-dependent manner into radioactive products that were more polar than the parent ^{177}Lu-AMBA (data not shown). To identify the hydrolysis/cleavage products, nonradioactive ^{nat}Lu-AMBA or ^{177}Lu-AMBA was incubated with mouse kidney homogenate at 37 °C for 0, 30, and 60 min, and the incubation mixtures analyzed by LC-MS or HPLC. The major products were identified as Lu-DO3A-CH_2CO-G-Abz-Q-OH [m/z 881.3, M+H$^+$], Lu-DO3A-CH_2CO-G-Abz-QW-OH [m/z 1067, M+H$^+$], and Lu-DO3A-CH_2CO-G-Abz4-QWAVGH-OH [m/z 1431, M+H$^+$] based on LC-MS results. The time course for this study (data not shown) suggested that Lu-AMBA was first cleaved to Lu-DO3A-CH_2CO-G-Abz4-R, where R = QWAVGH-OH (Metabolite C), which was in turn further hydrolyzed into smaller metabolites, where R = QW-OH and -Q-OH (Metabolites B and A). After 30 min at 37 °C, ^{177}Lu-AMBA had been completely converted to ^{177}Lu-containing metabolites Lu-A, -B, and -C, as shown in the radiochromatogram in Figure 2.

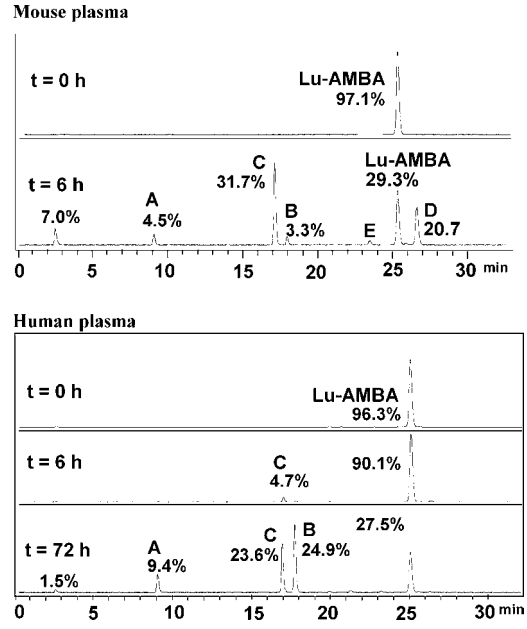

Figure 3. Comparison of the in vitro metabolism of ^{177}Lu-AMBA at 37 °C (retention time = 25 min) in mouse plasma (t = 0 and 6 h) and in human plasma (t = 0, 6, and 72 h). Metabolism is significantly slower in human plasma. The metabolites observed were Lu-DO3A-CH_2CO-G-Abz4-R, where R = Q-OH (A), QW-OH (B), QWAVGH-OH (C), QWAVGHLM-OH (D), and QWAVGHL-OH (E). HPLC System 1 was used for this analysis.

In Vitro Studies in Mouse, Rat and Human Plasma. In contrast to the results obtained with kidney and liver homogenate, the metabolism of ^{177}Lu-AMBA in plasma in vitro was very slow. Figure 3 shows typical radiochromatograms of the time course in these studies in mouse and human plasma. Full data sets for studies in mouse, rat, and human plasma are provided in the Supporting Information (Tables S1−2 and Figures 1−3S).

^{177}Lu-AMBA was metabolized faster in mouse and rat plasma than in human plasma. Radiochemical purity (RCP) data from these studies were used to calculate the half-lives of ^{177}Lu-

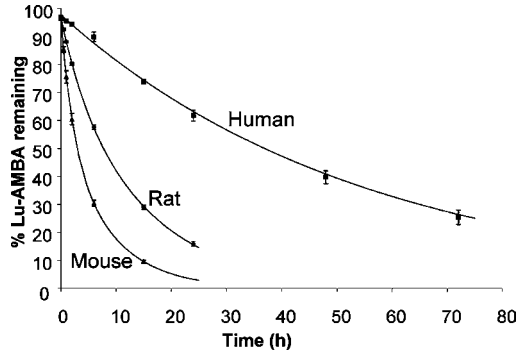

Figure 4. Disappearance of intact ^{177}Lu-AMBA in human, rat, and mouse plasma in vitro. Error bars on experimental data are indicated.

AMBA in human, rat and mouse plasma in vitro. Figure 4 shows the fits to the data. The half-lives of ^{177}Lu-AMBA in human, rat, and mouse plasma in vitro were found to be 38.8 ± 1.3 h, 8.1 ± 3.8 h, and 3.1 ± 0.1 h, respectively.

Nature of Metabolites. Table 3 summarizes the five ^{177}Lu-AMBA metabolites observed in plasma in vitro. Lu-AMBA has a retention time of 25 min in the HPLC system used for analysis of in vitro plasma samples (HPLC System 1). The peaks at t_R =18 min and t_R = 17 min corresponded to the metabolites identified by LC/MS from studies in mouse kidney homogenate: Lu-DO3A-CH_2CO-G-Abz4-QW-OH (B) and Lu-DO3A-CH_2CO-G-Abz4-QWAVGH-OH (C), respectively. The metabolite that elutes after Lu-AMBA (D, t_R = 26 min) coeluted with an authentic standard of Lu-DO3A-CH_2CO-G-Abz4-QWAVGHLM-OH, a compound in which the terminal amide of Lu-AMBA is converted to a carboxylic acid. This metabolite was especially predominant in rat plasma in vitro. The polar metabolite labeled A, t_R= 9 min, coeluted with an authentic standard of Lu-DO3A-CH_2CO-G-Abz4-Q-OH. Minor metabolite E coeluted with an authentic standard of Lu-DO3A-CH_2CO-G-Abz4-QWAVGHL-OH (Lu-AMBA without its terminal methioninamide residue). All assignments were confirmed by coinjection of authentic standards of the proposed metabolites.

Chemical Synthesis of Metabolites. Standards of the unmetalated ligands for Lu-AMBA metabolites A−E were readily synthesized by automated solid-phase peptide synthesis and/or manual methods as described above. HPLC analysis of the peptides showed them all to be >95% pure; the appropriate molecular weight was observed by API-ES mass spectra in all cases (Table 1). Their ^{nat}Lu analogues were prepared by heating excess $LuCl_3 \cdot 6H_2O$ with the appropriate ligand in acetate buffer, followed by HPLC purification and lyophilization. These ^{nat}Lu-metabolite standards showed the appropriate mass spectra and coeluted with their ^{177}Lu analogs, using HPLC Systems 1 and 2 (Table 3).

In Vitro Cell Binding Studies with Synthesized Metabolite Ligands. In vitro competition binding of AMBA metabolites to GRP receptors in PC-3 cells were performed by competing ^{177}Lu-AMBA with increasing concentrations of each of the unmetalated metabolite ligands. The results are shown in Table 4. While AMBA ligand competed with ^{177}Lu-AMBA at 5 nM (IC_{50}), the five metabolite ligands showed little or no competition, with IC_{50} >400−500 nM. Furthermore, direct binding studies performed with the ^{177}Lu-labeled metabolites A, B, and C did not demonstrate any specific binding to PC-3 cells.

In Vivo PK Studies on ^{177}Lu-AMBA - Metabolites in Mouse/Rat Plasma and Urine. The clearance and metabolism of ^{177}Lu-AMBA following injection into male CD-1 mice was studied to determine its pharmacokinetics and the rate at which metabolites formed in vivo. HPLC traces obtained from mouse plasma samples obtained at 2 and 10 min are shown in Figure 5. Fit-functions for ^{177}Lu-AMBA in rats showed an initial clearance phase ($t_{1/2}$ of 0.66 min) and a terminal clearance phase with a $t_{1/2}$ of 8.64 min. Modeling results for the metabolism of Lu-AMBA in rat plasma are shown in Figure 6.

A radiochromatogram of mouse urine at 10 min post-injection is shown in Figure 5. Mouse urine at 60 min and rat urine at 30 min had a similar appearance. No parent ^{177}Lu-AMBA was found in the urine at any time point; only ^{177}Lu-A and ^{177}Lu−B were observed.

In Vivo Biodistribution of Lu-AMBA and Its Metabolites. Biodistribution results for ^{177}Lu-AMBA and its five metabolites at 1 and 24 h are shown in Table 5. The major elimination route for all ^{177}Lu-AMBA metabolites was by renal excretion (78−87%). As reported previously (*2*), ^{177}Lu-AMBA showed high uptake in PC-3 tumors and mouse pancreas, both of which express high numbers of GRP receptors. No significant uptake in tumor or pancreas was noted for any of the ^{177}Lu-AMBA metabolites, confirming the in vitro IC_{50} and direct binding study results.

DISCUSSION

In Vitro Plasma. The metabolites formed from ^{177}Lu-AMBA in mouse, rat, and human plasma in vitro were the same across species, but the relative amounts of the various metabolites formed were different. At intermediate time points in mouse and rat plasma, Lu-labeled metabolites C and D predominated, with only small amounts of Lu-A and -B observed. In contrast, human plasma samples in vitro formed only trace amounts of Lu-labeled D; Metabolites Lu-B and Lu-C were the predominant species observed. Lu-A formed slowly in all cases. In vitro metabolism was slow in all three types of plasma, with observed half-lives of hours (Figure 4).

In vitro metabolism half-lives were significantly slower if performed in plasma containing EDTA as an anticoagulant (data not shown). Inhibition of ^{177}Lu-AMBA metabolism by EDTA strongly suggests that metalloenzymes are responsible for the metabolism of this peptide complex, as EDTA can bind to the metals found in the active site of metalloenzymes, thus inactivating them.

In Vivo Mouse and Rat. In contrast to in vitro results, the metabolism of ^{177}Lu-AMBA in vivo was rapid. Two minutes after IV administration to normal mice, only ∼45% of the radioactivity in the plasma was present as ^{177}Lu-AMBA. The remainder was present as metabolites Lu-A, -B, -C, -D, and -E, the products previously identified from in vitro studies. By 10 min post-injection, 78−87% of the radioactivity in mouse plasma had been converted to these metabolites. Similar results were obtained in the normal rat, although the rate of ^{177}Lu-AMBA metabolism was somewhat slower. By 1 h post-injection, no ^{177}Lu-AMBA was detectable. In both species, metabolites Lu-A, -B, and -C were found in the plasma. Lu-D was also a predominant species in mice, but was much less prominent in samples of rat plasma. Lu-E was found only in trace amounts.

Radioactivity cleared rapidly into the urine in both mouse and rat. For all urine samples analyzed, ∼95−100% of the radioactivity detected was due to metabolites Lu-A and -B. No parent ^{177}Lu-AMBA was excreted into any urine sample.

Nature of the Metabolites. All metabolites identified were due to selective cleavage of the -QWAVGHLM-NH_2 peptide chain responsible for binding to the GRP receptor, including removal of the terminal amide from the methioninamide residue to form metabolite D, loss of methionine to form E, cleavage of the H↑L bond to form C, cleavage of the W↑A bond to form B, and cleavage of the Q↑W bond, forming A. Consistent with the concept of enzymatic control of small bioactive peptides, we note that the metabolites reported here are inactive. Thus, it is clear that attempts to stabilize such

Table 3. Summary of Lu-AMBA Metabolites and Their Sequences[a]

Lu metabolite	Lu-DO3A-CH_2CO-G-Abz4-R R =	MW	mass spectrum	HPLC System 1 t_R (min) (in vitro studies)	HPLC System 2 t_R (min) (in vivo studies)
Parent Lu-AMBA	-QWAVGHLM-NH_2	1674.9	$[M+H]^+$: 1675.3 $[M+2H]^{2+}/2$: 837.9 $[M+Na+H]^{2+}/2$: 848.8	25.2	22.5
Metabolite Lu-A	-Q-OH	880.7	$[M+H]^+$: 881.3 $[M+Na]^+$: 903.4 $[M+2Na]^{2+}/2$: 463.2	9.0	7.9
Metabolite Lu-B	-QW-OH	1066.9	$[M+H]^+$: 1067.5 $[M+Na]^+$: 1089.5 $[M+2Na]^{2+}/2$: 556.2	17.8	14.8
Metabolite Lu-C	-QWAVGH-OH	1431.3	$[M+H]^+$: 1431.4 $[2M+3H]^{3+}/3$: 954.9 $[M+2H]^{2+}/2$: 716.2	17.0	15.6
Metabolite Lu-D	-QWAVGHLM-OH	1675.9	$[M+H]^+$: 1675.4 $[M+2H]^{2+}/2$: 837.8	26.6	23.2
Metabolite Lu-E	-QWAVGHL-OH	1544.4	ND	23	19

[a] ND = not determined; NI = not identified.

Table 4. Competition of Unmetalated Lu-AMBA Metabolite Ligands with ^{177}Lu-AMBA for GRP-R Binding in PC-3 Cells

symbol	metabolite ligands	IC_{50} [nM]
AMBA	DO3A-CH_2CO-G-Abz4-QWAVGHLM-NH_2	5
A	DO3A-CH_2CO-G-Abz4-Q-OH	>500
B	DO3A-CH_2CO-G-Abz4-QW-OH	>500
C	DO3A-CH_2CO-G-Abz4-QWAVGH-OH	>500
D	DO3A-CH_2CO-G-Abz4-QWAVGHLM-OH	>500
E	DO3A-CH_2CO-G-Abz4-QWAVGHL-OH	400

derivatives should focus on stabilization of these bonds. Garoyoa et al. attempted such a strategy in the synthesis of $^{99m}Tc(CO)_3$ derivatives bound to a modified histidyl residue bearing various analogues of -QWAVGHLM-NH_2. Replacement of Leu with the unnatural amino acid cyclohexylalanine (Cha) and/or the replacement of Met with norleucine (Nle) reportedly led to derivatives that had significantly improved stability when incubated in human plasma at 37 °C (*22*). These compounds still showed significant binding to the GRP receptor in vitro, and comparable or improved uptake in GRP receptor-positive pancreas and tumor in PC-3 tumor-bearing mice relative to unstabilized analogues, especially when a suitable spacer was inserted between the targeting group and the *retro*N^{α}-carboxylmethyl histidine residue responsible for coordination to the $Tc(CO)_3$ core. However, for the biodistributions reported, washout of the compounds from such tissues was faster than that observed for ^{177}Lu-AMBA (ref 2 and Table 5), a finding that is not ideal for radiotherapeutic applications. Similarly Höhne et al. (*23*) chose to modify the Leu residue to Statin [(3*S*,4*S*)-4-amino-3-hydroxy-6-methylheptanoic acid], along with N-methylation of the glycyl amide bond for their ^{18}F-labeled derivative 2-(4-(di-*tert*-butylfluorosilyl)phenyl)acetyl-Arg-Ava-Gln-Trp-Ala-Val-NMeGly-His-Sta-Leu-NH_2. This group reported little metabolism of this construct either in vitro or in vivo. However, this agent showed relatively low uptake in GRP-receptor positive pancreas in nude mice (4.67% I.D./g at 1 h), and even lower uptake in PC-3 tumors (0.63% I.D./g), although retention in these tissues over 4 h was good. Thus, the stabilizing effects of the modifications made will need to be balanced by their effects on receptor-binding affinity, internalization, biodistribution, and clearance characteristics.

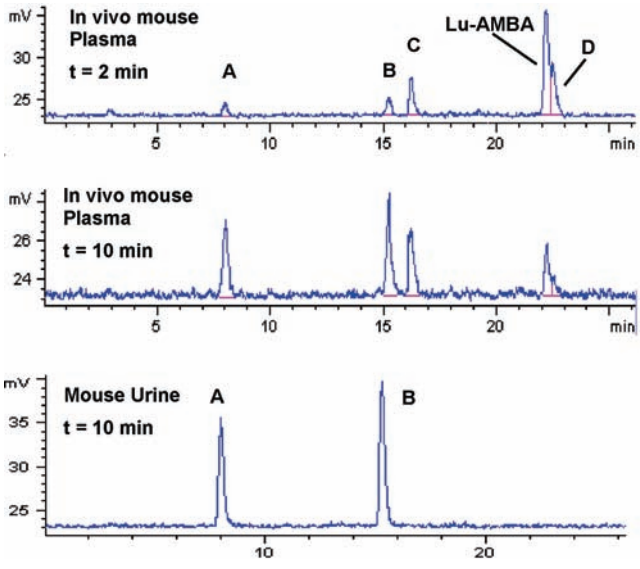

Figure 5. Radiochromatograms of in vivo mouse plasma and urine samples. HPLC System 2 was used for this analysis.

That bombesin and its analogues are readily metabolized has been known for some time. Rapid cleavage is not unexpected, as bombesin-like peptides have potent biological effects, stimulating gastric acid and pancreatic enzyme secretion, gall bladder contraction, modifying gut motility and affecting behavior, food and water intake, and thermoregulation (*1*). Rapid and highly selective proteolytic cleavage of bioactive peptides is common and allows close control over their effects (*15*). Two of the major metabolites observed are consistent with those observed by Shipp et al. (*16*), who studied the hydrolysis of bombesin, GRP, and GRP (14−27) with purified samples of the metalloprotease known as neutral endopeptidase 24.11 (NEP) or neprilysin. They found that cleavage occurred at the Trp-Ala and His-Leu peptide bonds in the conserved 7-amino acid C terminus region of these peptides [i.e., Q/H−W↑AVGH↑LM-NH_2. In Lu-AMBA, such metabolism would give rise to metabolites Lu-B and Lu-C.

Little has been reported on the metabolism of other radiolabeled bombesin derivatives. Zhang et al. (*9*) found that the modified bombesin (6−14) derivative ^{111}In-DTPA-GABA-[D-Tyr^6-QWAV-β-Ala^{11}-H-Thi^{13}Nle^{14} was cleaved in human serum between Ala^{11} and the His residue, followed by metabolism to ^{111}In-DTPA-GABA-D-Tyr-Q-OH and ^{111}In-DTPA. Addition of EDTA slowed the rate of metabolism, suggesting the involvement of a metalloprotease. The enzyme carnosinase was suggested to be the active enzyme responsible for cleavage. The ^{111}In-DTPA-GABA-D-Tyr-Q-OH metabolite is analogous to metabolite Lu-A with Lu-AMBA, but no other similarities were seen. Nock et al. (*17*) reported that the ^{99m}Tc complex of a tetraamime ligand coupled to the bombesin antagonist sequence DPhe^6-QWAVGHL-NHEt showed two polar metabolites in the urine following IV

Table 5. Biodistribution of the Five Known Metabolites of Lu-AMBA in PC-3 Tumor-bearing Tac:Cr:(NCr)-Foxn1 Homozygous Male Nude Mice (1 and 24 h data). 1 h

1 Hour						
	parent	Lu-AMBA metabolites				
organ	^{177}Lu-AMBA	(^{177}Lu-A) $n = 4$	(^{177}Lu−B) $n = 4$	(^{177}Lu−C) $n = 4$	(e ^{177}Lu-D) $n = 4$	(^{177}Lu-E) $n = 4$
tumor (%ID/g)	4.92 ± 1.57	0.35 ± 0.08	0.39 ± 0.08	0.33 ± 0.12	0.62 ± 0.07	0.25 ± 0.16
liver (%ID)	0.26 ± 0.12	0.14 ± 0.05	0.13 ± 0.02	0.12 ± 0.03	0.15 ± 0.04	0.12 ± 0.02
kidney (%ID)	3.93 ± 0.85	0.85 ± 0.33	1.31 ± 1.41	1.27 ± 0.71	1.36 ± 0.72	0.74 ± 0.22
skin (%ID/g)	0.28 ± 0.04	0.27 ± 0.10	0.26 ± 0.11	0.75 ± 1.06	0.34 ± 0.12	0.15 ± 0.02
muscle (%ID/g)	0.07 ± 0.02	0.07 ± 0.04	0.07 ± 0.05	0.07 ± 0.04	0.19 ± 0.24	0.10 ± 0.11
pancreas (%ID)	17.76 ± 1.45	0.08 ± 0.05	0.03 ± 0.00	0.09 ± 0.10	0.26 ± 0.03	0.04 ± 0.02
GI (%ID)	10.93 ± 0.53	1.41 ± 1.77	0.33 ± 0.11	0.25 ± 0.05	0.57 ± 0.27	0.25 ± 0.07
blood (%ID)	0.25 ± 0.05	0.38 ± 0.22	0.29 ± 0.15	0.22 ± 0.11	0.49 ± 0.020	0.21 ± 0.04
blad/urine (%ID)	52.41 ± 6.43	86.76 ± 2.88	78.32 ± 25.01	86.10 ± 6.27	86.45 ± 6.49	86.33 ± 5.06
24 Hour						
	parent	Lu-AMBA metabolites				
organ	^{177}Lu-AMBA	(^{177}Lu-A) $n = 4$	(^{177}Lu−B) $n = 4$	(^{177}Lu−C) $n = 4$	(^{177}Lu-D) $n = 4$	(^{177}Lu-E) $n = 4$
tumor (%ID/g)	3.21 ± 0.51	0.04 ± 0.01	0.06 ± 0.01	0.06 ± 0.01	0.16 ± 0.05	0.07 ± 0.01
liver (%ID)	0.22 ± 0.27	0.04 ± 0.02	0.04 ± 0.00	0.05 ± 0.00	0.05 ± 0.001	0.04 ± 0.01
kidney (%ID)	1.03 ± 0.08	0.23 ± 0.05	0.20 ± 0.04	0.28 ± 0.01	0.30 ± 0.06	0.23 ± 0.04
skin (%ID/g)	0.11 ± 0.04	0.06 ± 0.01	0.07 ± 0.02	0.04 ± 0.01	0.06 ± 0.01	0.07 ± 0.01
muscle (%ID/g)	0.01 ± 0.01	0.01 ± 0.01	0.03 ± 0.01	0.04 ± 0.03	0.02 ± 0.01	0.03 ± 0.01
pancreas (%ID)	13.25 ± 1.03	0.00 ± 0.00	0.00 ± 0.00	0.01 ± 0.00	0.14 ± 0.01	0.01 ± 0.00
GI (%ID)	6.38 ± 0.34	0.04 ± 0.01	0.16 ± 0.10	0.05 ± 0.01	0.14 ± 0.04	0.07 ± 0.01
blood (%ID)	0.01 ± 0.01	0.01 ± 0.01	0.01 ± 0.01	0.00 ± 0.01	0.01 ± 0.01	0.01 ± 0.01

injection, but the nature of these compounds was not determined, except to confirm that the products were not $^{99m}TcO_4^-$.

In summary, Lu-AMBA is a derivative of bombesin and is expected to be metabolized relatively rapidly in vivo. Our in vivo results confirm this expectation. Of the radioactivity remaining in mouse plasma in vivo at 10 min post-injection, an average of 18% was parent ^{177}Lu-AMBA, supporting a plasma half-life of <4 min. Of the radioactivity remaining in rat plasma at 10 min, an average of ∼40% was parent ^{177}Lu-AMBA, supporting a plasma half-life of <8 min in rat. No parent ^{177}Lu-AMBA remained in samples of rat plasma at 60 or 120 min post-injection.

The primary metabolites formed in vivo were ^{177}Lu-labeled A, B, and C. ^{177}Lu-D was also seen in mouse plasma, and to a much lesser extent in the rat plasma. Only minor amounts of E were observed. The only radioactive products observed in mouse and rat urine were metabolites Lu-A and Lu-B.

Neither the metabolite ligands nor their ^{177}Lu-labeled analogues showed any significant binding to GRP-R in PC-3 cells. All metabolite ligands had IC_{50} values >400−500 nM vs unmetabolized ^{177}Lu-AMBA, which was previously demonstrated (*2*) to have a high affinity for the GRP-R (K_d, 1.02 nmol/L).

Biodistributions of the five known metabolites of ^{177}Lu-AMBA, which showed little or no uptake in GRP receptor-positive tissues, confirmed that intact ^{177}Lu-AMBA alone is responsible for the uptake and retention in target and nontarget tissues and that the metabolites were eliminated rapidly via renal excretion. Although it showed rapid in vivo metabolism in these preclinical studies, ^{177}Lu-AMBA showed good radiotherapeutic efficacy in GRP-R(+) PC-3 tumor-bearing nude mice (*2*) and effective targeting of prostate cancer metastases in humans (*18*).

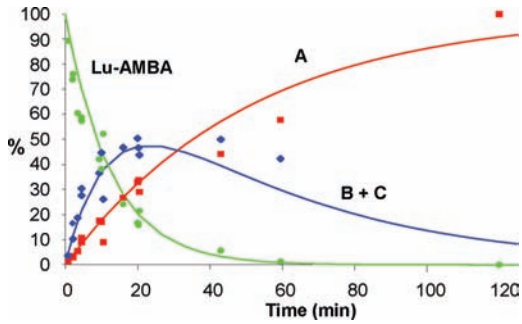

Figure 6. Modeling of Lu-AMBA metabolism in rat plasma (0−120 min) and ingrowth of metabolites.

ACKNOWLEDGMENT

Thanks to Jaclyn Fox, Glen Marszalowicz, and Anthony Pennello for technical assistance in biodistribution studies.

Supporting Information Available: Tables showing the amount of ^{177}Lu-AMBA remaining following in vitro incubation in mouse, rat, and human plasma at 37 °C and the distribution of metabolites in mouse and rat plasma and urine following IV injection of ^{177}Lu-AMBA. Figures showing in vitro metabolism of ^{177}Lu-AMBA in mouse plasma (t = 0, 1, 2, and 6 h), rat plasma (0−24 h), and human plasma (0−72 h0 at 37 °C.This material is available free of charge via the Internet at http://pubs.acs.org.

LITERATURE CITED

(1) Erspamer, V. (1988) Discovery, isolation, and characterization of bombesin-like peptides in "Bombesin-like peptides in health and disease". *Ann. N.Y. Acad. Sci. 547*, 3–9.

(2) Lantry, L. E., Cappelletti, E., Maddalena, M., Stewart-Fox, J., Feng, W., Chen, J., Thomas, R., Eaton, S. M., Bogdan, N. J., Arunachalam, T., Reubi, J. C., Raju, N., Lattuada, L., Linder, K. E., Swenson, R. E., Tweedle, M. F., and Nunn, A. D. (2006) ^{177}Lu-AMBA: Synthesis and characterization of a selective ^{177}Lu-Labeled GRP-R agonist for systemic radiotherapy of prostate cancer. *J. Nucl. Med. 47*, 1144–1152.

(3) Waser, B., Eltschinger, V., Linder, K., Nunn, A., and Reubi, J. C. (2007) Selective in vitro targeting of GRP and NMB receptors in human tumors with the new bombesin tracer [^{177}Lu]-AMBA. *Eur. J. Nucl. Med. Mol. Imaging 34*, 95–100.

(4) Markwalder, R., and Reubi, J. C. (1999) Gastrin-releasing peptide receptors in the human prostate: relation to neoplastic transformation. *Cancer Res. 59*, 1152–1159.

(5) Gugger, M., and Reubi, J. C. (1999) Gastrin-releasing peptide receptors in nonneoplastic and neoplastic human breast. *Am. J. Pathol. 155*, 2067–2076.
(6) Tang, C., Biemond, I., and Lamers, C. B. (1997) Expression of peptide receptors in human endocrine tumours of the pancreas. *Gut 40*, 267–271.
(7) Moody, T. W., Carney, D. N., Cuttitta, F., Quattrocchi, K., and Minna, J. D. (1985) High affinity receptors for bombesin/GRP-like peptides on human small cell lung cancer. *Life Sci. 37*, 105–113.
(8) Smith, C. J., Volkert, W. A., and Hoffman, T. J. (2005) Radiolabeled peptide conjugates for targeting of the bombesin receptor superfamily subtypes. *Nucl. Med. Biol. 32*, 733–740.
(9) Zhang, H., Chen, J., Waldherr, C., Hinni, K., Waser, B., Reubi, J. C., and Maecke, H. R. (2004) Synthesis and evaluation of bombesin derivatives on the basis of pan-bombesin peptides labeled with indium-111, lutetium-177, and yttrium-90 for targeting bombesin receptor-expressing tumors. *Cancer Res. 64*, 6707–6715.
(10) Reubi, J. C., Maecke, H. R., and Krenning, E. P. (2005) Candidates for peptide receptor radiotherapy today and in the future. *J. Nucl. Med. 46* (Suppl 1), 67S–75S.
(11) Varvarigou, A., Bouziotis, P., Zikos, C., Scopinaro, F., and De Vincentis, G. (2004) Gastrin-releasing peptide (GRP) analogues for cancer imaging. *Cancer Biother. Radiopharm. 19*, 219–229.
(12) Maina, T., Nock, B., and Mather, S. (2006) Targeting prostate cancer with radiolabelled bombesins. *Cancer Imaging 6*, 153–157.
(13) Breeman, W. A., de Jong, M., Erion, J. L., Bugaj, J. E., Srinivasan, A., Bernard, B. F., Kwekkeboom, D. J., Visser, T. J., and Krenning, E. P. (2002) Preclinical comparison of ^{111}In-labeled DTPA- or DOTA-bombesin analogs for receptor-targeted scintigraphy and radionuclide therapy. *J. Nucl. Med. 43*, 1650–1656.
(14) Chen, J., Linder, K. E., Cagnolini, A., Metcalfe, E., Raju, N., Tweedle, M. F., and Swenson, R. E. (2008) Synthesis, stabilization and formulation of [^{177}Lu]Lu-AMBA, a systemic radiotherapeutic agent for gastrin releasing peptide receptor positive tumors. *Appl. Radiat. Isot. 66*, 497–505.
(15) Barrett, A. J., Rawlings, N. D., and Woessner, J. F. (2004) Introduction: metallopeptidases and their clan. *Handbook of Proteolytic Enzymes, Volume 1*, 2nd ed., pp. 231−268, Chapter *67*, Elsevier Ltd., London.
(16) Shipp, M. A., Tarr, G. E., Chen, C. Y., Switzer, S. N., Hersh, L. B., Stein, H., Sunday, M. E., and Reinherz, E. L. (1991) CD10/neutral endopeptidase 24.11 hydrolyzes bombesin-like peptides and regulates the growth of small cell carcinomas of the lung. *Proc. Natl. Acad. Sci. U.S.A. 88*, 10662–10666.
(17) Nock, B., Nikolopoulou, A., Chiotellis, E., Loudos, G., Maintas, D., Reubi, J. C., and Maina, T. (2003) [^{99m}Tc]Demobesin 1, a novel potent bombesin analogue for GRP receptor-targeted tumour imaging. *Eur. J. Nuc. Med. Mol. Imaging 30*, 247–258.
(18) Bodei, L., Ferrari, M., Nunn, A., Llull, J.-B., Cremonesi, M., Martano, L., Laurora, G., Scardino, E., Tiberini, S., Bufi, G., Eaton, S., De Cobelli, O., and Paganelli, G. (2007) ^{177}Lu-AMBA bombesin analogue in hormone refractory prostate cancer patients: A phase I escalation study with single-cycle administrations. Annual Congress, European Association of Nuclear Medicine, Oct 13−17, Copenhagen, Denmark (abstract).
(19) *Simulation, Analysis and Modeling Software - SAAM II Program, Version 1.2.1*, 2001, University of Washington, Seattle, WA.
(20) Wagner, J. G. (1979) *Fundamentals of Clinical Pharmacokinetics*, p 83,Drug Intelligence Publications, Hamilton, IL.
(21) Bard, Y. (1974) *Nonlinear Parameter Estimation*, Academic Press, New York.
(22) Garayoa, E. G., Schweinsberg, C., Maes, V., Ruegg, D., Blanc, A., Blauenstein, P., Tourwé, D. A., Beck-Sickinger, A. G., and Schubiger, P. A. (2007) New [^{99m}Tc]bombesin analogues with improved biodistribution for targeting gastrin releasing-peptide receptor-positive tumors. *Q. J. Nucl. Med. Mol. Imaging 51*, 42–50.
(23) Höhne, A., Mu, L., Honer, M., Schubiger, P. A., Ametamey, S. M., Graham, K. T., Stellfeld, T., Borkowski, S., Berndorff, D., Klar, U., Voigtmann, U., Cyr, J. E., Friebe, M., Dinkelborg, L., and Srinivasan, A. (2008) Synthesis, ^{18}F-labeling, and in vitro and in vivo studies of bombesin peptides modified with silicon-based building blocks. *Bioconjugate Chem. 19*, 1871–1879.

BC9000189

Supplementary material for

In vitro and in vivo metabolism of Lu-AMBA, a GRP-receptor binding compound, and the synthesis and characterization of its metabolites

Karen E. Linder, Edmund Metcalfe, Thangavel Arunachalam, Jianqing Chen, Stephen M. Eaton, Weiwei Feng, Hong Fan, Natarajan Raju, Aldo Cagnolini, Laura E. Lantry, Adrian D. Nunn, Rolf E. Swenson

Bracco Research USA Inc., 305 College Road East, Princeton, New Jersey 08540, USA

Table S1: ^{177}Lu-AMBA remaining following in vitro incubation in mouse, rat, and human plasma at 37 ^{o}C (mean ± SD) (n = 4 per time point).

Metabolism of ^{177}Lu-AMBA in Plasma in Vitro (% remaining)			
Time (h)	Mouse plasma	Rat plasma	Human plasma
0	97.0 ± 0.5	97.0 ± 0.5	96.6 ± 0.8
0.5	85.4 ± 1.0	92.5 ± 0.5	nd
1	75.5 ± 2.2	88.1 ± 0.3	95.6 ± 0.4
2	60.4 ± 2.0	80.2 ± 0.5	94.3 ± 0.2
6	30.4 ± 1.1	57.6 ± 0.8	89.8 ± 1.7
15	9.6 ± 0.5	29.0 ± 0.8	73.9 ± 0.8
24	nd	15.9 ± 0.9	61.7 ± 2.0
48	nd	nd	39.7 ± 2.3
72	nd	nd	25.4 ± 2.6

nd= not determined

Table S2. Distribution of metabolites in plasma and urine *in vivo* following IV injection of ^{177}Lu-AMBA.

Sample	**Time (min)**	**Lu-AMBA**	**Metabolites (Relative %)**				
			A	**B**	**C**	**D**	**E**
Mouse Plasma	2	44.6	7.8	12.2	19.7	15.7	<1
		45.9	5.1	7.8	18.3	22.9	<1
	10	13.5	24.7	31.5	23.7	6.6	-
		22.4	18.1	24.5	26.1	9.0	<1
Rat Plasma	2	75.0	3.2	4.2	9.1	2.5	~2
	4.5	58.2	10.0	11.5	17.8	1.3	~2
	9.4	42.1	17.6	16.3	20.3	2.0	-
	20.4	18.1	31.8	25.0	20.5	3.0	-
Mouse urine	10	-	43.1	56.9	-	-	-
	60	-	40.6	59.4	-	-	-
Rat urine	30	-	42.3	57.3	-	-	-
	60	-	63.2	36.8	-	-	-

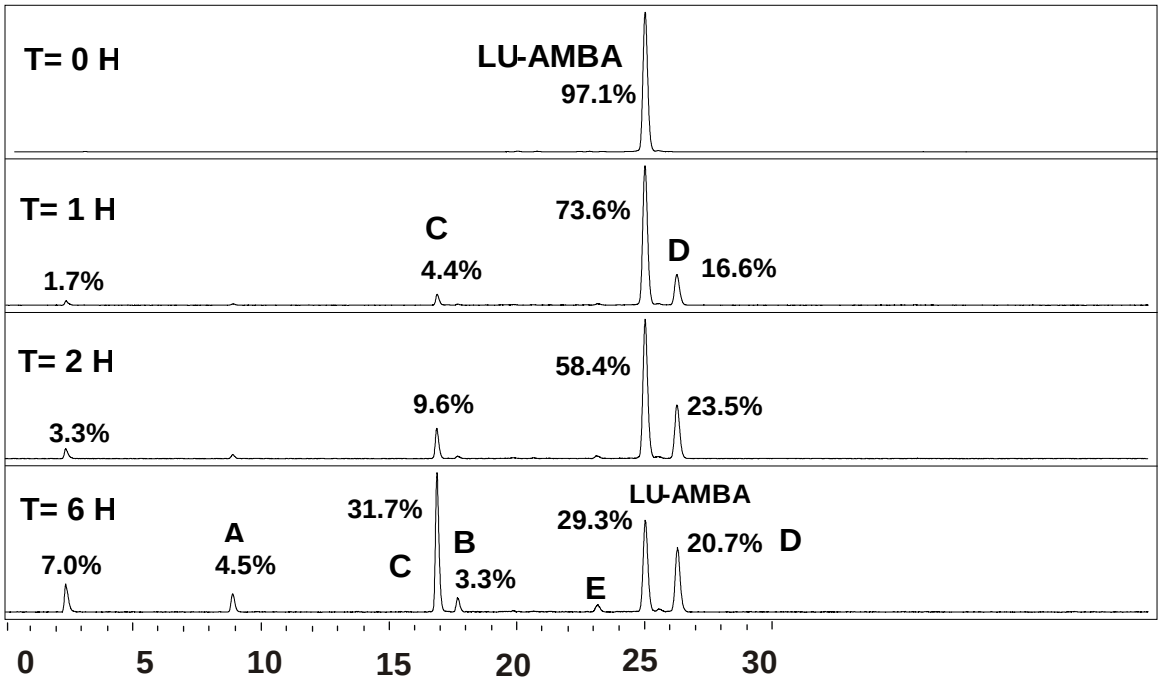

Figure 1S. In vitro metabolism of ^{177}Lu-AMBA at 37 °C (retention time = 25 min) in mouse plasma (t=0, 1, 2, and 6 h). The metabolites observed were Lu-DO3A-CH_2CO-G-Abz4-R, where R= -Q-OH (A), -QW-OH (B), -QWAVGH-OH (C), -QWAVGHLM-OH (D) and -QWAVGHL-OH (E).

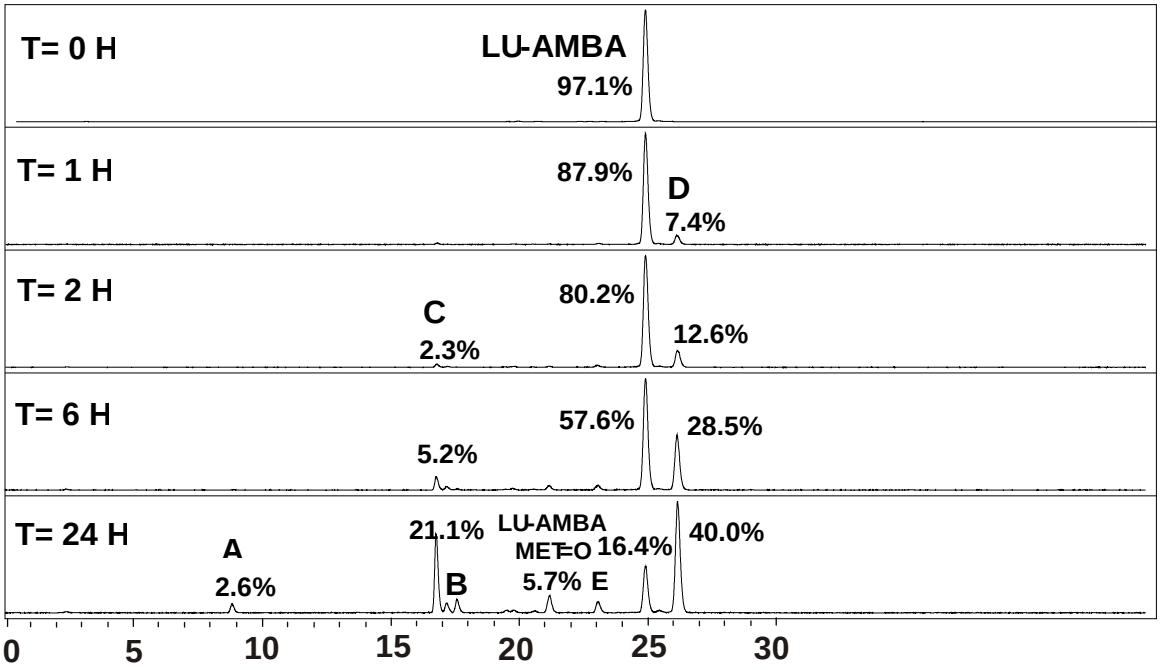

Figure 2S: In vitro metabolism of ^{177}Lu-AMBA (Lu-DO3A-CH_2CO-QWAVGHLM-NH_2) in rat plasma at 37 °C [0 – 24 h]. The metabolites observed were Lu-DO3A-CH_2CO-G-Abz4-R, where R= -Q-OH (A), -QW-OH (B), -QWAVGH-OH (C), -QWAVGHLM-OH (D) and -QWAVGHL-OH (E). Lu-AMBA-Met=O is Lu-AMBA methionine sulfoxide.

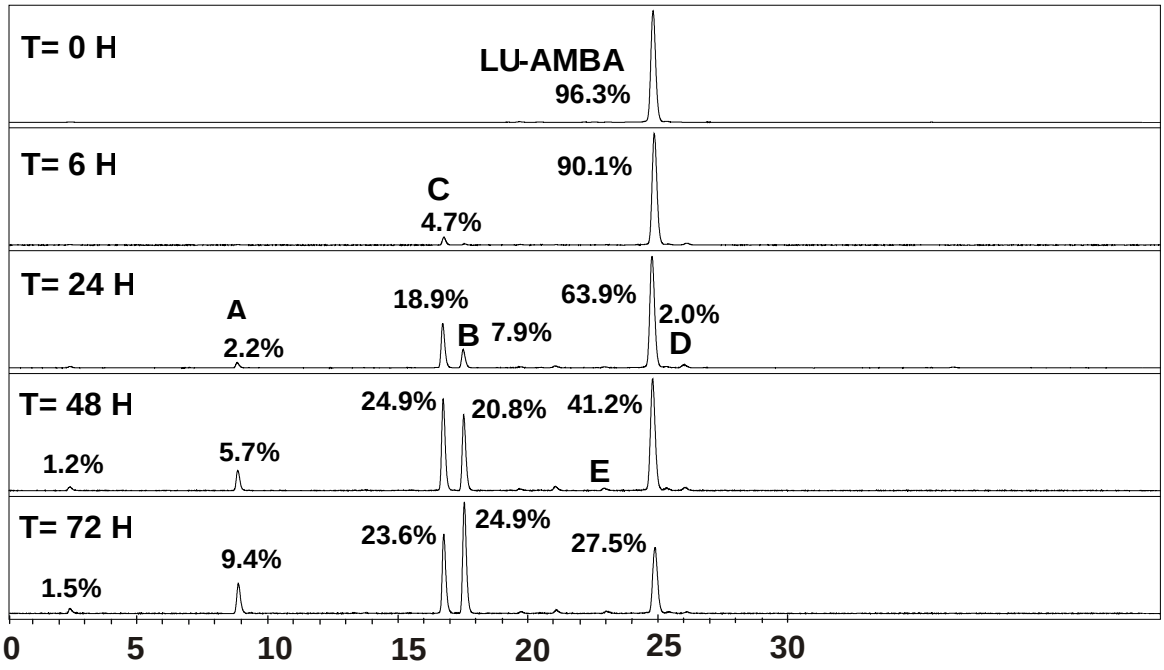

Figure 3S: In vitro metabolism of ^{177}Lu-AMBA [retention time ~25 min] in human plasma at 37 °C [0 – 72 h].

Tailored PEG for rh-G-CSF Analogue Site-Specific Conjugation

Stefano Salmaso, Sara Bersani, Anna Scomparin, Francesca Mastrotto, Rodolfo Scherpfer, Giancarlo Tonon, and Paolo Caliceti*

Department of Pharmaceutical Sciences, University of Padua, Via F. Marzolo, 5, 35131 Padova, Italy, and Bio-Ker, Scientific Park "Polaris", Località Piscinamanna, Pula (Cagliari), Italy. Received January 30, 2009; Revised Manuscript Received April 17, 2009

A new end-tailored monomethoxypoly(ethylene glycol) (PEG) for site-directed protein conjugation was synthesized according to a three-step procedure: (1) linear 20 kDa PEG-NH_2 was conjugated to 12-(Boc-amino)dodecanoic acid; (2) PEG-NHCO$(CH_2)_{11}$-Boc was deprotected by TFA treatment; (3) PEG-NHCO$(CH_2)_{11}$-NH_2 was conjugated to 6-maleimidohexanoic acid to yield PEG-NHCO-$(CH_2)_{11}$-NHCO$(CH_2)_5$-Mal (PEG-C_{18}-Mal). The chemical intermediates as well as the final product were purified by solvent precipitation/extraction and characterized by ^{1}H NMR spectroscopy and colorimetric analysis. The synthesis procedure yielded over 90% activated product [PEG-NHCO-$(CH_2)_{11}$-NHCO$(CH_2)_5$-Mal/PEG-NH_2 molar ratio, %]. Both PEG-C_{18}-Mal and the commercial maleimido activated 20 kDa linear PEG (PEG-Mal) were used for conjugation to ^{17}Cys of recombinant human granulocyte colony stimulating factor (rh-G-CSF). Under denaturing conditions, at pH 7.0, both activated PEGs yielded over 90% protein conjugation. Under native conditions, about 55% and 7% PEGylated protein were obtained with PEG-C_{18}-Mal and PEG-Mal, respectively. Circular dichroism analysis showed that the PEGylation does not induce detectable alteration of the protein secondary structure. On the other hand, the PEGylation conditions were found to affect significantly the protein stability. The derivatives obtained either with the two polymers by unfolding/refolding process or with PEG-Mal under native conditions displayed rapid aggregation with half-life ranging from 30 to 90 min. The derivative obtained with PEG-NHCO-$(CH_2)_{11}$-NHCO$(CH_2)_5$-Mal in the absence of guanidinium chloride displayed remarkably higher stability with aggregation half-life of about 60 h.

INTRODUCTION

The increased demand for more potent and tailored performing biotech drugs has boosted from one side the production of engineered proteins and from the other suitable delivery techniques. PEGylation has become a valuable tool for overcoming poor physicochemical, pharmacokinetic, and immunological properties of many therapeutically useful proteins such as cytokines, hormones, enzymes, antibodies, and other biomodulators (*1*−*3*). Nevertheless, the therapeutic performance of bioconjugates strictly depends upon the polymer features and conjugation strategy: polymer size and shape, extensive or limited modification, site-directed or random conjugation (*3, 4*).

Bioconjugates with well-defined and unique chemical structure are usually difficult to obtain by classical amino-PEGylation protocols. Nevertheless, single site-specific conjugation is essential to endow derivatives with high therapeutic value such as hormones and cytokines, whose activity is dramatically decreased by multipoint/random modification that may hamper the receptor recognition (*5, 6*). In the recent years, few interesting site-specific PEGylation procedures have been indicated to produce mono-PEGylated derivatives. These techniques take advantage of chemical- or enzyme-mediated conjugation to specific amino acids in the protein sequence (*7*−*9*).

A typical example of the advantages of site-directed mono-PEGylation is offered by the recombinant human granulocyte colony stimulating factor (rh-G-CSF), a deglycosylated 19 kDa protein encoded by *Escherichia coli*, which displays its biological activity by controlling the development and proliferation of predominantly neutrophilic granulocyte colony in mammalians. Despite its pharmacological activity, the use of this protein in myelosuppressive chemotherapy and bone marrow transplantation (*10, 11*) is limited by its short half-life in the bloodstream, which requires daily injections with counteract poor patient acceptability and compliance. Furthermore, similarly to many deglycosylated proteins, rh-G-CSF is susceptible to aggregation either in long-term storage or under physiological conditions (*12*). Multiple random PEG attachments were found to enhance the pharmacokinetic properties of this cytokine, but reduced dramatically its biological activity (*8, 13, 14*). On the contrary, the rh-G-CSF conjugate obtained by reductive site-directed attachment of 20 kDaPEG to the terminal α-amino group, which is not directly involved in the receptor recognition, maintains high biological activity and provides for sustained therapeutic levels (*15, 16*).

Cysteine bioconjugation by maleimide, vinyl sulfone, dithiopyridine or iodoacetamide activated PEG represents the most interesting strategy to obtain stable site-directed mono-PEGylated derivatives (*7*). Cys is, in fact, an infrequent amino acid in the protein structure. When natively present, only one Cys residue is usually available for conjugation, as it is engaged in a disulfide bond. Furthermore, Cys can be introduced by site-directed mutagenesis into peptide sequences not directly involved in the biological activity mechanism, thus playing as a unique PEGylation site.

In most proteins, Cys is located inside deep hydrophobic pockets that avoid protein dimerization through disulfide bonding. This Cys inaccessibility prevents the penetration of large hydrated molecules like PEG, making its modification difficult. Protein denaturation under controlled conditions can be successfully used to yield the exposition and modification of hidden amino acids. Nevertheless, the unfolding/refolding process and the access of a hydrophilic macromolecule into a hydrophobic pocket can induce conformational protein alteration, which may

* To whom correspondence should be addressed. Paolo Caliceti, Department of Pharmaceutical Sciences, University of Padua, Via F. Marzolo, 5, 35131 Padova, Italy, e-mail: paolo.caliceti@unipd,it, phone: +39 049 8275695, fax: +39 049 8275366.

10.1021/bc9000432 CCC: $40.75 © 2009 American Chemical Society
Published on Web 05/26/2009

reflect in decreased activity and stability, thus precluding its therapeutic application.

In order to overcome the problems generated by the use of the commercial activated PEG, we prepared a new PEG derivative suitable for modification of low-accessibility amino acids under nondenaturing conditions. Since the use of hydrophobic PEG for modification of amino acids bundled into hydrophobic clefts has not been reported to our knowledge, we investigated this bioconjugation approach using rh-G-CSF as the protein model. A convenient chemical procedure for PEG hydrophobization and activation for Cys conjugation was set up, and rh-G-CSF was modified under different reaction conditions. The effect of the polymer attachment on the protein physicochemical and biological properties was investigated. For comparison, a parallel study was performed by using the commercial PEG-Mal.

MATERIALS AND METHODS

Recombinant human granulocyte colony stimulating factor (rh-G-CSF) (173 AA) was a kind gift of Bio-Ker (Pula, Italy). Linear 20 kDa monoammino-monomethoxy-poly(ethylene glycol) (PEG-NH_2) and linear 20 kDa monomethoxy-poly(ethylene glycol)-maleimide (PEG-Mal) were obtained from Nektar (Huntsville, AL). 12-(Terbutoxycarbonate-amino)dodecanoic acid [Boc-NH-$(CH_2)_{11}$-COOH], dicyclohexylcarbodiimide (DCC), and *N*-hydroxysuccinimide (NHS) were purchased from Fluka Chemika (Buchs, Switzerland). β-Mercaptoethanol was obtained from Merck (Rahway, NJ). Triethylamine (TEA) and trinitrobenzenesulfonic acid (TNBS) were furnished by Aldrich (Milwaukee, WI). 6-Maleimidohexanoic acid, 5,5′-dithiobis(2-nitrobenzoic acid) (DTNB), and all other reagents were supplied by Sigma (St. Louis, MO). Ultrafiltration was carried out using an Amicon system operating with Millipore 10 kDa cutoff membranes (Billerica, MA, USA). ^{1}H NMR analyses were carried out in $CDCl_3$ using a Bruker Spectrospin 300 (Fallanden, Switzerland)). Circular dichroism studies were performed using a J-810 Jasco spectrodichrograph (Tokyo, Japan). Light scattering studies were carried out by a Nicomp 380/ZLS photon correlation spectrometer (Particle Sizing Systems, St. Barbara, CA). The ELISA microplate reader was a Bio-Tek Instrument (Winooski, VT, USA).

Synthesis of PEG-NHCO-$(CH_2)_{11}$-NHCO$(CH_2)_5$-Mal (PEG-C_{18}-Mal). *PEG-NHCO-$(CH_2)_{11}$-NH-Boc.* Linear 20 kDa PEG-NH_2 (500 mg, 25 μmol) was dissolved in 3 mL CH_2Cl_2 solution of dicyclohexylcarbodiimide (DCC) (103 mg, 500 μmol) and Boc-NH-C_{11}-COOH (78.8 mg, 250 μmol). The reaction was maintained overnight under anhydrous conditions and mild stirring at room temperature. Afterward, the mixture was filtered through a sintered filter funnel and added dropwise to 40 mL of ice-cooled diethyl ether. The product was recovered by centrifugation at 5000 rpm, washed three times with diethyl ether, and finally desiccated under reduced pressure.

The product was finally tested for the primary amino group evaluation (*17*).

^{1}H NMR analysis ($CDCl_3$). δ 1.25 [bs, 14H of PEG-NH-CO-$CH_2CH_2(CH_2)_7CH_2CH_2$-NH-Boc]; δ 1.44 (s, 9H, -CH_3 of Boc); δ 2.16 (t, 2H of PEG-NH-CO-CH_2-); δ 3.04 (t, 2H of CH_2-NH-Boc); δ 3.38 (s, 3H of CH_3O-PEG-); δ 3.64 (bs, 1818 H of -CH_2CH_2-O of PEG chain). Other signals, namely, peaks corresponding to PEG-NH-CO-$CH_2CH_2(CH_2)_7CH_2CH_2$-NH-Boc], could not be clearly identified and/or integrated.

PEG-NHCO-$(CH_2)_{11}$-NH_2. PEG-NHCO-$(CH_2)_{11}$-NH-Boc (400 mg, 19.7 μmol) was dissolved in 3 mL of TFA/water mixture (95/5, v/v) and maintained for 1 h at room temperature. The mixture was reduced to half volume under vacuum and poured into 40 mL of ice-cooled diethyl ether. The precipitate was recovered by centrifugation at 5000 rpm, washed three times with diethyl ether, and desiccated under reduced pressure. The product was finally tested for the primary amino group evaluation (*18*).

^{1}H NMR analysis ($CDCl_3$). δ 1.25 [bs, 14H of PEG-NHCO-$CH_2CH_2(CH_2)_7CH_2CH_2$-NH_2]; δ 2.16 [t, 2H of PEG-NH-CO$CH_2CH_2(CH_2)_7CH_2CH_2$-NH_2]; δ 3.04 (t, 2H of CH_2-NH_2); δ 3.38 (s, 3H of CH_3O- of PEG); δ 3.64 (bs, 1818 H of -CH_2CH_2-O of PEG chain).

PEG-NHCO-$(CH_2)_{11}$-NHCO$(CH_2)_5$-Mal (PEG-C_{18}-Mal). PEG-NHCO-$(CH_2)_{11}$-NH_2 (300 mg, 14.8 μmol) was dissolved in 3 mL of CH_2Cl_2 containing 6-maleimidohexanoic acid (31.2 mg, 0.148 mmol) and DCC (61 mg, 0.296 mmol). The reaction mixture was maintained overnight under stirring at room temperature and then filtered. The solution was added dropwise to 30 mL of ice-cooled diethyl ether. The precipitate was recovered by centrifugation at 5000 rpm, washed three times with diethyl ether, and desiccated under vacuum. The final product was tested for the determination of the primary amino groups and the maleimido groups (*19*). The Ellman assay was carried out as follows: 30 μL of 10 mM DTNB solution in 50 mM phosphate buffer pH 8.0 were added to 300 μL of 0.1 M phosphate buffer, 3 M guanidinium HCl, pH 7.0, containing 2 mM of activated PEG preincubated with 2 mM of β-mercaptoethanol. The reaction was maintained at room temperature for 15 min and analyzed at 405 nm by a Bio-Tek Instruments microplate reader.

^{1}H NMR analysis ($CDCl_3$). δ 1.26 [bs, 18H of PEG-NHCO-$CH_2CH_2(CH_2)_7CH_2CH_2$-NHCO-$CH_2(CH_2)_2CH_2CH_2$-Mal]; δ 1.47−1.73 [m, 6H of PEG-NHCO-$CH_2CH_2(CH_2)_7CH_2CH_2$-NHCO-$CH_2(CH_2)_2CH_2CH_2$-Mal]; δ 2.17 [t, 2H PEG-NHCO-$CH_2CH_2(CH_2)_7CH_2CH_2$-NHCO-]; δ 2.35 [t, 2H -NHCO-$CH_2(CH_2)_2CH_2CH_2$-Mal]; δ 3.38 (s, 3H of CH_3O-PEG); δ 3.63 (bs, 1818H of -CH_2CH_2-O of PEG chain); δ 6.68 (s, 2H of -CH=CH- of maleimide).

Light Scattering Analysis. Photon correlation spectroscopy studies were carried out using a Nicomp 380/ZLS instrument with a fixed 90° scattering and external fiber angle. PEG-C_{18}-Mal solutions (0.2−5.0 mg/mL, 0.01−0.25 mM) were prepared by dissolving the polymer solutions in 0.1 M phosphate buffer, pH 7.0, or in 0.1 M phosphate buffer, 3 M guanidinium HCl, pH 7.0. The polymer solutions were filtered with 0.22 μm filters and then analyzed. Analyses were performed also by using 0.2−5.0 mg/mL (0.01−0.25 mM) PEG-C_{18}-Mal solutions in CH_2Cl_2.

rh-G-CSF PEGylation in Guanidinium Chloride. Two milliliter solutions of 4 mg/mL (0.2 mM) of PEG-Mal or PEG-C_{18}-Mal in 0.1 M Tris HCl, 6 M guanidinium chloride, 10 mM EDTA at pH 5.5, 6.0, 7.0, or 8.0 were added to 2 mL solutions of 4 mg/mL (0.2 mM) of rh-G-CSF in 0.1 M Tris HCl, 10 mM EDTA at the same pH. At scheduled times, the native rh-G-CSF and rh-G-CSF-PEG content in the solutions was monitored by RP-HPLC performed by a Jupiter C18 column from Phenomenex (5 μm, 250 × 4.6 mm, 300 Å) thermostatted at 55 °C. The column was eluted with 0.05% TFA in water (eluent A) and 0.05% TFA in acetonitrile (eluent B) in a gradient mode: 0−3 min, 35% eluent B; 3−23 min from 35% to 75% eluent B. The elution flow rate was set at 1 mL/min and UV detector at 280 nm. After 4 h reaction, the samples were purified by gel filtration chromatography using a Sephadex G75 superfine resin eluted with 0.1 M acetate buffer, pH 5.5. The elution fractions were analyzed by UV−vis at 280 nm for protein detection and by iodine test for PEG determination (*20*). The fractions corresponding to the PEGylated rh-G-CSF were collected, pooled, and concentrated by ultrafiltration.

rh-G-CSF PEGylation under Native Conditions. PEG-Mal or PEG-C_{18}-Mal (8 mg, 0.4 μmol) was added to 2 mL solutions of rh-G-CSF (2 mg/mL, 0.1 mM) in 0.1 M TRIS buffer, 10

Scheme 1

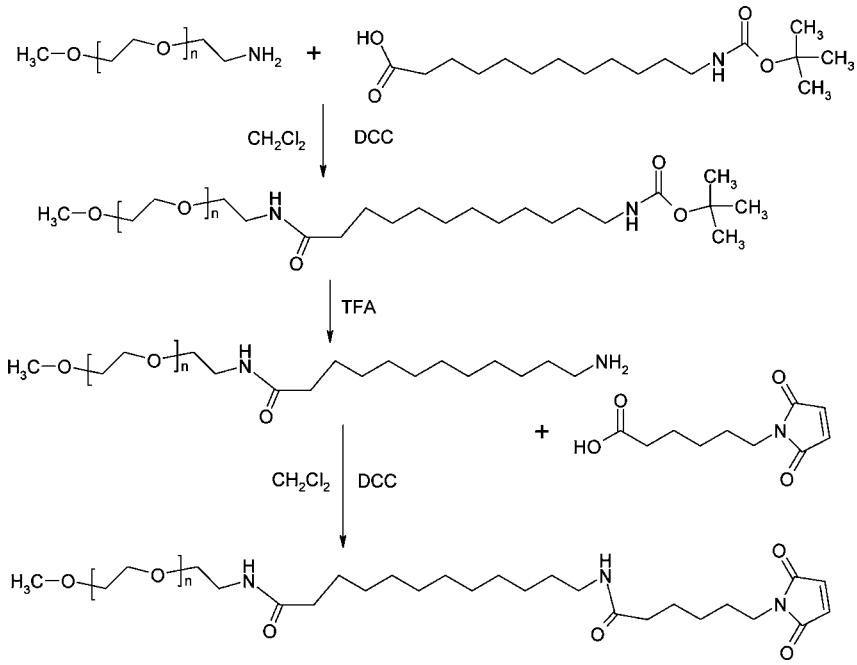

mM EDTA, pH 6.0. The solutions were maintained under gentle upside down mixing at 4 or 25 °C. At scheduled times, aliquot samples were analyzed by RP-HPLC. Once conjugation equilibrium was reached, the rh-G-CSF-PEG derivatives were purified by semipreparative gel filtration as reported above.

Conjugation studies were carried out in the same conditions reported above by ten sequential additions of 100 μL volumes of a 4 mg/mL polymer solution in the same buffer. The samples were analyzed by RP-HPLC.

Structural Studies. Circular dichroism spectra were recorded in the far UV (195−250 nm) using 0.1 mg/mL (5.3 μM) rh-G-CSF solutions or equimolar quantity of PEGylated rh-G-CSF in 20 mM phosphate buffer, 0.15 M NaCl, pH 7.2. The analysis were carried out using a J-810 Jasco spectrodichrograph (Tokyo, Japan).

Stability Study. Native rh-G-CSF or equimolar amounts of PEG conjugated rh-G-CSF solutions (0.33 mg/mL, 0.018 mM) in 0.1 M phosphate buffer, pH 7.2, were incubated at 4, 25, and 37 °C. At scheduled times, the solutions were sampled, centrifuged at 3500 rpm for 3 min, and finally analyzed by gel filtration HPLC using a Zorbax GF-250 analytical column (4 μm, 250 × 4.6 mm) eluted with 63 mM phosphate buffer, 3% isopropanol, pH 7.2. The flow rate was set at 0.3 mL/min and UV detector at 280 nm.

Cell Culture Studies. NFS-60 cells (CLS Cell Line Service, Eppelheim, Germany) were cultured in RPMI 1640 medium supplemented with 5.1 mL L-glutamine (200 mM), 1 mM Na-pyruvate, 10% fetal bovine serum, and 33 IU/ml IL-3 at 37 °C, under humidified atmosphere containing 5% CO_2. The cells were then incubated for 17 h in FBS and IL-3 free medium and seeded in 96-wells tissue culture plates in 100 μL of IL-3 free medium containing 10% FBS at a density of 1×10^4 cells/well. Increasing amounts of rh-G-CSF, Neulasta, or PEG-C_{18}-Mal modified rh-G-GSF ranging from 0 to 10 000 pg/mL in 100 μL volume were serially added to the wells and incubated for 44 h. To the wells were added 20 μL aliquots of WST-1 (Roche 1644807), and the material was further incubated for 4 h and then analyzed by a microplate reader set at 450 and 595 nm. The optical density at 450 nm was subtracted from the value obtained at 595 nm and plotted as function of the cytokine concentration (*21*).

RESULTS

PEG-C_{18}-Mal Synthesis. The three-step chemical procedure used for preparation of PEG-C_{18}-maleimide derivative is depicted in Scheme 1.

In the first step, the linear 20 kDa PEG-NH_2 was reacted with 12-(Boc-amino)dodecanoic acid in the presence of the condensing agent dicyclohexylcarbodiimide (DCC). The excess of 12-(Boc-amino)dodecanoic and DCC used in the reaction was completely removed by extraction in ethyl ether where both reagents are highly soluble. The degree of polymer functionalization, evaluated by the free amino group analysis and ^{1}H NMR, was 98−99% [PEG-NHCO-$(CH_2)_{11}$-NH-Boc/PEG-NH_2 molar ratio, %] and the final product yield was 87−89% (molar yield, %).

In the second step, the Boc group of PEG-NHCO-$(CH_2)_{11}$-NH-Boc was removed using a TFA/water mixture (95/5, v/v), which is typically used in peptide synthesis protocols. After volume reduction, the water content, which was less than 150 μL, did not interfere with the polymer precipitation in 40 mL of diethyl ether. The amino group analysis by the TNBS test showed that the deprotection procedure yielded 97−99% free amino groups [PEG-NHCO-$(CH_2)_{11}$-NH_2/PEG-NHCO-$(CH_2)_{11}$-NH-Boc molar ratio, %]. The ^{1}H NMR spectra did not show the characteristic Boc signal at δ 1.43 confirming that Boc was completely removed by the TFA treatment. The product yield was 80% (molar yield, %).

In the third step, PEG-NHCO-$(CH_2)_{11}$-NH_2 was reacted in the presence of excess of condensing agent DCC. Unreacted 6-maleimidohexanoic acid and DCC were completely removed by extraction in ethyl ether where both reagents are highly soluble. Dicyclohexyl urea produced during condensation reaction was eliminated by filtration.The degree of amino group conjugation [PEG-C_{18}-Mal/PEG-NHCO-$(CH_2)_{11}$-NH_2 molar ratio, %], assessed by the colorimetric TNBS test, was in the range 96−98%. The Ellman assay performed to evaluate the maleimido functions was carried out either in plain phosphate buffer or in buffer containing 3 M guanidinium chloride. In plain

Table 1. rh-G-CSF PEGylation Degree Obtained with PEG-C_{18}-Mal and PEG-Mal in the Presence of 3 M Guanidinium HCl at pH 8.0, 7.2, 6.0, and 5.5

	rh-G-CSF PEGylation degree (%)	
pH	PEG-C_{18}-Mal	PEG-Mal
8.0	50%	55%
7.2	96%	93%
6.0	88%	90%
5.5	75%	70%

buffer, the degree of polymer activation was about 30%, while in the presence of guanidinium chloride, the activation degree was found to be about 96%. The ^{1}H NMR spectra confirmed that the chemical procedure yielded 94−97% polymer activation. The final product yield was about 84% (molar yield, %).

Light scattering analysis demonstrated that, in 0.1 M phosphate buffer, pH 7.0, PEG-C_{18}-Mal can assemble into 30 nm size micelles. In organic solvent or in the presence of guanidinium chloride, the signal corresponding to the micelle disappeared.

pH Effect on rh-G-CSF PEGylation. Under denaturant conditions, PEG-C_{18}-Mal and the PEG-Mal displayed similar reactivity toward rh-G-CSF and the reaction was complete in 30 min. Table 1 shows the conjugation degree obtained after 1 h reaction with the two polymer at different pH values. The maximal polymer reactivity was obtained at pH 7.2 and was fairly unaltered at pH 6.0, while it decreased at higher and lower pH.

rh-G-CSF PEGylation under Nondenaturant Conditions. The rh-G-CSF PEGylation under nondenaturant conditions at pH 6.0 was carried out either at 4 or 21 °C. At 4 °C, the protein modification was very low, as after 200 h, only 5% and 2% of protein was modified with PEG-C_{18}-Mal and PEG-Mal, respectively. At 21 °C, the conjugation reaction was faster than at 4 °C, and it occurred according to first-order kinetics. Figure 1 shows that, after 150 h reaction, about 55% and 7% of rh-G-CSF was modified with PEG-C_{18}-Mal and PEG-Mal, respectively.

Figure 2 shows the bioconjugation kinetics and the native protein disappearance when serial PEG aliquots are added to the protein solution. After 265 h, about 58% and 16% of PEGylated rh-G-CSF were obtained with PEG-C_{18}-Mal (Figure 2A) and PEG-Mal (Figure 2B), respectively. The figures show that the native rh-G-CSF disappearance was more rapid than the bioconjugate formation. After 265 h, the residual native rh-G-CSF was 33% and 22% with PEG-C_{18}-Mal and PEG-Mal, respectively.

Structural Studies. Circular dichroism spectra of native rh-G-CSF and the various bioconjugated derivatives registered in the far-UV are reported in Figure 3. The superimposable spectra indicate that PEGylation does not induce significant alteration of the secondary protein structure.

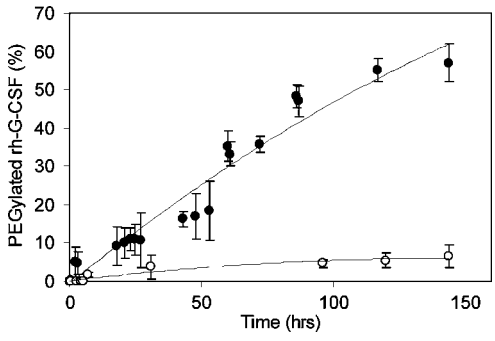

Figure 1. PEGylation profile of rh-G-CSF conjugation with PEG-C_{18}-Mal (•) or PEG-Mal (○). The time point mean values and standard deviation have been calculated on the basis of 5 experiments.

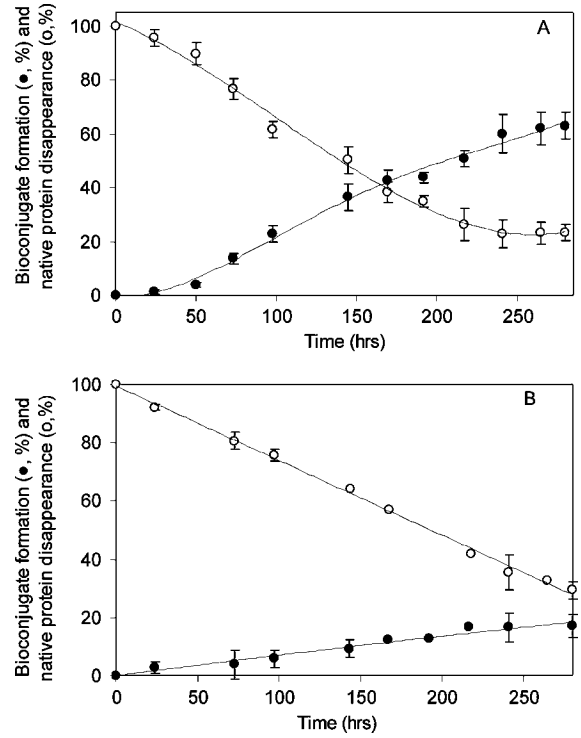

Figure 2. A. Time course PEGylation profile of rh-G-CSF by serial addition of PEG-C_{18}-Mal (A) and PEG-Mal (B). Native rh-G-CSF (○) and PEGylated rh-G-CSF (•). B. The experimental mean values and standard deviation were calculated on the basis of five experiments.

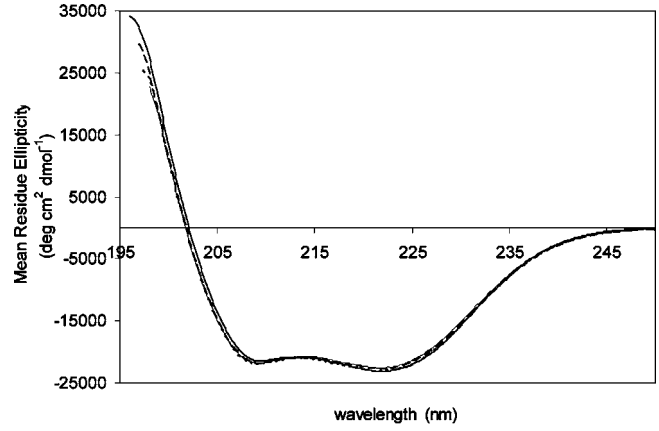

Figure 3. Circular dichroism profile of native rh-G-CSF (—), rh-G-CSF modified with PEG-C_{18} Mal under nondenaturing conditions (- -) or denaturant conditions (------) and rh-G-CSF modified with PEG-C_{18}-Mal under nondenaturing conditions (- -) or denaturant conditions (.....).

Stability Study. Stability studies were performed by incubation of native and PEGylated rh-G-CSF in physiologic medium at 4, 21, and 37 °C. The disappearance of the starting protein due to physical aggregation phenomena was evaluated by gel filtration chromatography. At 4 and 21 °C, all the rh-G-CSF forms displayed a remarkable stability, as neither native nor PEGylated rh-G-CSF underwent significant aggregation throughout 10 days incubation (data not shown).

The aggregation profiles at 37 °C reported in Figure 4 show that all the rh-G-CSF species undergo aggregation according to first-order kinetics. Native rh-G-CSF was the most stable form, as only 3% starting material underwent aggregation in 24 h. The derivatives obtained under denaturing conditions displayed a rapid aggregation with complete disappearance of the bioconjugate in about 6 h. The aggregation half-time was

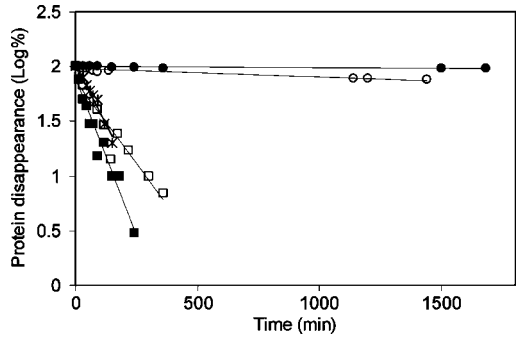

Figure 4. Stability profile of native and PEGylated rh-G-CSF at 37 °C in phosphate buffer pH 7.2: native rh-G-CSF (•, $y = (-8 \times 10^{-5})x + 1.9813$), rh-G-CSF-PEG obtained with PEG-C_{18}-Mal under nondenaturing conditions (○, $y = -(1 \times 10^{-5})x + 1.998$), rh-G-CSF-PEG obtained with PEG-Mal under nondenaturing conditions (*x*, $y = -0.0044x + 2.0247$), rh-G-CSF-PEG obtained with PEG-C_{18}-Mal in the presence of guanidinium chloride (□, $y = -0.0058x + 1.9047$), rh-G-CSF- PEG obtained PEG-Mal in the presence of guanidinium chloride (■, $y = -0.003x + 1.8712$). The time point mean values were calculated on the basis of four experiments.

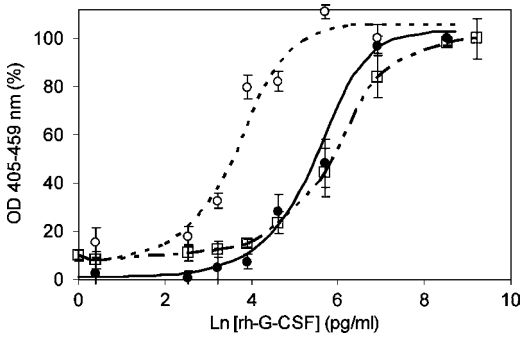

Figure 5. Biological activity of rh-G-CSF (○), Neulasta (•) and rh-G-CSF PEGylated with PEG-C_{18}-Mal under native conditions (□).

30 and 60 min for the derivatives obtained with PEG-Mal and PEG-C_{18}-Mal, respectively. Also, the PEG derivative obtained with PEG-Mal under nondenaturant conditions displayed a rapid aggregation profile. In such a case, the aggregation half-life was about 90 min. On the contrary, the PEGylated rh-G-CSF obtained with PEG-C_{18}-Mal under nondenaturing conditions displayed high stability with an aggregation half-life of about 60 h.

Biological Studies. The biological activity of the rh-G-CSF, rh-G-CSF modified with PEG-C_{18}-Mal under native conditions, and Neulasta was evaluated using NFS-60 cells whose growth responds to this cytokine. The study could not be carried out using the PEGylated rh-G-CSF forms obtained with PEG-Mal or with PEG-C_{18}-Mal under denaturant conditions because of the physical instability of these bioconjugates.

The bioassay profiles reported in Figure 5 show that native rh-G-CSF has higher bioactivity than the PEGylated cytokine, either G-CSF modified with PEG-C_{18}-Mal under native conditions or Neulasta. rh-G-CSF-PEG and Neulasta did not display significant biological activity differences. The EC_{50} values calculated for rh-G-CSF and rh-G-CSF-C_{18}-PEG were found to be about 50 and 250 pM, respectively.

DISCUSSION

Aimed at modifying selectively the ^{17}Cys bundled into a deep hydrophobic pocket of rh-G-CSF (*22*), a new end-hydrophobized maleimido-PEG (PEG-C_{18}-Mal) was designed. Preliminary studies showed that commercial PEGs failed in modifying this low-accessible amino acid under native conditions, probably because of the high hydrodynamic size, flexibility, and bulk energy of the polyoxyethylene chains. On the other hand, the Cys derivatization performed according to an unfolding/refolding procedure in guanidinium chloride solutions was found to induce microstructural protein alterations, which yielded a bioconjugate with poor stability properties.

Linear PEG was used to avoid hindrance problems typical of branched or fork-like polymers that make difficult the modification of amino acids unexposed on the protein surface (*23*). The high molecular weight (20 kDa) was chosen to endow a mono-PEGylated derivative with sustained pharmacokinetic profile. Indeed, several studies demonstrated that the prolonged permanence in the bloodstream of PEGylated proteins depends mainly on a critical polymer mass, which can be achieved either by using multiple polymer attachment or by conjugating high molecular weight PEGs (*24*). Finally, it is worth noting that linear 20 kDa PEG was also successfully used for preparation of the rh-G-CSF-PEG derivative marketed as Neulasta. This derivative, obtained by selective α-amino group conjugation of the terminal amino acid, displays a prolonged permanence in the bloodstream and improved therapeutic performance as compared to the native protein (*25*, *26*).

In order to facilitate the PEG docking to the cysteine residue of rh-G-CSF, the polymer was end-functionalized with a spacer possessing proper length, volume, hydrophobicity, and rigidity. The spacer arm was selected on the basis of the structural properties of the rh-G-CSF analogue, which is a well-structured globular protein presenting antiparallel four-α-helix bundle with a left-handed twist and overall dimensions of 45 Å × 26 Å × 26 Å (*27*).

The length of the diamidoalkyl [-NHCO-$(CH_2)_{11}$-NHCO$(CH_2)_5$-] spacer (26 Å) was calculated as being suitable for reaching the deep protein pocket where the ^{17}Cys residue is hosted. The spacer possesses a smaller volume (350 Å^3) as compared to the oligo-ethylene oxide fragment of similar length (450 Å^3). Furthermore, each ethylene oxide coordinates three water molecules that dramatically increase the hydrodynamic size of the oligomer fragment (*24*). The diamidoalkyl function possesses higher oil/water partitioning coefficient (log $P = 5.2$) and lower polar surface area (PSA = 72) than the oligo-ethylene oxide fragment (log $P = 2.2$, PSA = 96) indicating that the former has more affinity for hydrophobic pockets. Finally, the diamidoalkyl chain possesses higher rigidity than the flexible oligo-ethylene oxide fragment, which should favor the docking into the protein grooves. By virtue of these features, the hydrophobic diamidoalkyl spacer was expected to penetrate into the tightly packed protein structure under physiological conditions without forcing the pocket hosting ^{17}Cys to open up and allowing for the crypted ^{17}Cys residue conjugation via the terminal maleimido group.

As expected, under denaturant conditions, the PEG-C_{18}-Mal and PEG-Mal displayed similar reactivity toward the Cys of the rh-G-CSF analogue. In such a case, in fact, the protein unfolding allows for ^{17}Cys exposure to the bulk (*28*). The differences in the bioconjugation degree obtained at different pH values are due to the dissimilar maleimide stability and to the Cys thiol group nucleophilicty that decreases as the pH decreases. Therefore, the maximal bioconjugation efficiency was obtained at neutral pH where the maleimido hydrolysis and the -SH reactivity are balanced (*29*).

The rh-G-CSF modification under nondenaturing conditions was performed at pH 6.0 to guarantee the maleimido and protein stability over several days. rh-G-CSF was, in fact, demonstrated to display monotonic increase instability as the pH decreases from 7.0 to 4.0 (*12*, *30*). Furthermore, at this pH the conjugation selectivity is maintained, since possible reaction with other nucleophile groups, namely, amino groups of Lys, are minimized.

The rh-G-CSF PEGylation under native conditions was found to depend significantly on both the reaction temperature and the polymer physicochemical properties. At 4 °C, the rh-G-CSF modification was negligible with either PEG-C_{18}-Mal or PEG-Mal. This low reactivity may be ascribed to the low system energy and protein rigidity that may prevent the approach and penetration into the pocket hosting the target ^{17}Cys. As the temperature increased to 21 °C, a higher protein PEGylation degree was obtained with the PEG-C_{18}-Mal as compared to PEG-Mal, indicating that the spacer can easily penetrate into the hydrophobic protein site thus allowing for the Cys bioconjugation. However, the PEGylation was found to proceed slowly probably because of the bulk energy of the PEG chain, which partially hampers the protein interaction. Furthermore, by a kinetic point of view, maleimide inactivation in the reaction medium can compete with polymer conjugation reaction, which requires time for the polymer docking into the hydrophobic cleft.

The serial addition of polymer aliquots to the protein solution resulted in higher PEGylation yield as compared to the one-shot polymer addition, while in the case of PEG-C_{18}-Mal, only negligible differences were observed between the two methods of polymer addition. This result may be explained with the higher PEG-C_{18}-Mal stability in buffer as compared to the PEG-Mal, which undergoes faster inactivation than the former. Light scattering studies demonstrated that PEG-C_{18}-Mal, according to its amphiphilic structure, undergoes assembly forming micelles. Alkyl-terminating PEGs possess, in fact, surfactant properties and, depending on their polymer length and the alkyl structure, may form micelles once dissolved in water (*31*). It is conceivable that the formation of micelle structures, where the maleimide end group of the PEG-C_{18}-Mal is chased into the hydrophobic core of polymeric assemblies, preserves the polymer reactivity toward thiol groups with respect to non-forming micelles PEG-Mal. This hypothesis is supported by the low PEG-C_{18}-Mal reactivity toward the small substrate β-mercaptoethanol observed in plain buffer (only 30%), while in the presence of guanidinium chloride, which disassembled the micelle structure, the polymer was highly reactive (96%).

All the rh-G-CSF-PEG derivatives were found to be fairly stable at 4 and 21 °C, but the stability under physiological conditions (37 °C) was found to depend strictly on the physicochemical properties of the polymer as well as on the bioconjugation conditions. Nevertheless, the protein stability at this temperature is paramount to the pharmaceutical exploitation of the bioconjugate.

Polymer conjugation by the unfolding/refolding process was found to endow derivatives that rapidly aggregate, suggesting that the protein undergoes a misfolding process regardless of the polymer used for the protein PEGylation. Therefore, despite the spectroscopic analysis showing that the native protein structure was substantially recovered after PEGylation and refolding, the process seems to provoke microstructural but relevant conformational alterations, which induce protein aggregation. In particular, subtle tertiary structural changes involving the exposition of hydrophobic amino acids such as Trp have been found to promote cytokine aggregation (*32*). However, the slightly higher stability displayed by the PEG-C_{18}-Mal modified rh-G-CSF seems to indicate that the physicochemical properties of the macromolecule fragment, namely, size, hydrophobicity, and rigidity, directly bound to the Cys has an important role in the protein structure recovery.

The derivative obtained with the PEG-C_{18}-Mal under native conditions was found to be much more stable than the bioconjugate prepared with PEG-Mal. The low stability of the derivative obtained with PEG-Mal was also observed during the bioconjugation reaction where the concentration of the native protein in solution decrease was not balanced by the formation of bioconjugate, which was hampered by aggregation. These results indicate that the penetration of the hydrophobic spacer of PEG-C_{18}-Mal into the protein bundle does not provoke dramatic structural alterations, thus preserving its conformational integrity, which is paramount for the protein stability and activity.

Finally, the biological studies demonstrated that the polymer conjugation slightly decreases the cytokine activity, which is similar to that of Neulasta, probably because of the steric hindrance of the high molecular weight of the polymer. Possibly, the Cys residue is close to the recognition site of the protein; thus, the polymer hampers the receptor/protein interaction. However, similar to what was reported for the PEGylated interferon α 2a and 2b, the biological activity decrease should be largely compensated by the enhanced biopharmaceutical properties of the bioconjugate. Data reported in the literature show, in fact, PEGylated rh-G-CSF to display prolonged permanence in the body upon subcutaneous administration, thus producing a long-lasting therapeutic effect (*26*).

CONCLUSIONS

Nowadays, PEGnology is considered a mature and routine technique for delivering poorly performing proteins. Nevertheless, the demanding requisites for new therapeutically efficient derivatives makes critical a proper design of the PEGylation strategy, which must be tailored according to the protein physicochemical, biopharmaceutical, and therapeutic properties.

PEG tailoring with hydrophobic molecular functions has been found to achieve unexpected conjugation. In particular, shielded seldom amino acids can be selectively conjugated without alteration of the protein conformation, which could result in poor stability and loss of activity of the final product. Therefore, the use of end-hydrophobized polymers can be added to the arsenal of protein PEGylation techniques, which can be properly adopted to produce effective therapeutics.

ACKNOWLEDGMENT

This work has been financially supported by Bio-Ker (Pula, CA, Italy), the Italian Ministry of Research and University (PRIN n. 2006030353) and University of Padua.

LITERATURE CITED

(1) Harris, M. J., and Chess, R. B. (2003) Effect of pegylation on pharmaceuticals. *Nat. Rev. Drug Discovery 2*, 214–221.

(2) Kozlowski, A., and Harris, J. M. (2001) Improvements in protein PEGylation: pegylated interferons for treatment of hepatitis C. *J. Controlled Release 72*, 217–24.

(3) Salmaso, S., Bersani, S., Semenzato, A., and Caliceti, P. (2006) Nanotechnologies in protein delivery. *J. Nanosci. Nanotechnol. 6*, 2736–53.

(4) Mehvar, R. (2000) Modulation of the pharmacokinetics and pharmacodynamics of proteins by polyethylene glycol conjugation. *J. Pharm. Sci. 3*, 125–36.

(5) Bailon, P., and Berthold, W. (1998) Polyethylene glycol-conjugated pharmaceutical proteins. *PSTT 1*, 352–356.

(6) Bowen, S., Tare, N., Inoue, T., Yamasaki, M., Okabe, M., Horii, I., and Eliason, J. F. (1999) Relationship between molecular mass and duration of activity of polyethylene glycol conjugated granulocyte colony-stimulating factor mutein. *Exp. Hematol. 27*, 425–32.

(7) Sato, H. (2002) Enzymatic procedure for site-specific pegylation of proteins. *Adv. Drug Delivery Rev. 54*, 487–504.

(8) Roberts, M. J., Bentley, M. D., and Harris, J. M. (2002) Chemistry for peptide and protein PEGylation. *Adv. Drug Delivery Rev. 54*, 459–476.

(9) Brocchini, S., Godwin, A., Balan, S., Choi, J., Zloh, M., and Shaunak, S. (2008) Disulfide bridge based PEGylation of proteins. *Adv. Drug Delivery Rev. 60*, 3–12.

(10) Anderlini, P., Przepiorka, D., Champlin, R., and Korbling, M. (1996) Biologic and clinical effects of granulocyte colony-stimulating factor in normal individuals. *Blood 88*, 2819–2825.

(11) Welte, K., Gabrilove, J., Bronchud, M. H., Platzer, E., and Morstyn, G. (1996) Filgrastim (r-metHuG-CSF): the first 10 years. *Blood 88*, 1907–1929.

(12) Ricci, M. S., Sarkar, C. A., Fallon, E. M., Lauffenburger, D. A., and Brems, D. N. (2003) pH dependence of structural stability of interleukin-2 and granulocyte colony-stimulating factor. *Protein Sci. 12*, 1030–1038.

(13) Tanaka, H., Satake-Ishikawa, R., Ishikawa, M., Matsuki, S., and Asano, K. (1991) Pharmacokinetics of recombinant human granulocyte colony-stimulating factor conjugated to polyethylene glycol in rats. *Cancer Res. 51*, 3710–3714.

(14) Layton, J. E., Morstyn, G., Fabri, L. J., Reid, G. E., Burgess, A. W., Simpson, R. J., and Nice, E. C. (1991) Identification of a functional domain of human granulocyte colony-stimulating factor using neutralizing monoclonal antibodies. *J. Biol. Chem. 266*, 23815–23823.

(15) Kinstler, O. B., Brems, D. N., Lauren, S. L., Paige, A. G., Hamburger, J. B., and Treuheit, M. J. (1996) Characterization and stability of N-terminally PEGylated rhG-CSF. *Pharm. Res. 13*, 996–1002.

(16) Molineux, G., Kinstler, O., Briddell, B., Hartley, C., McElroy, P., Kerzic, P., Sutherland, W., Stoney, G., Kern, B., Fletcher, F. A., Cohen, A., Korach, E., Ulich, T., McNiece, I., Lockbaum, P., Miller-Messana, M. A., Gardner, S., Hunt, T., and Schwab, G. (1999) A new form of Filgrastim with sustained duration in vivo and enhanced ability to mobilize PBPC in both mice and humans. *Exp. Hematol. 27*, 1724–1734.

(17) Snyder, S. L., and SoBocinsky, P. Z. (1975) An improved 2,4,6-trinitroben-nesulphonic acid method for the determination of amines. *Anal. Biochem. 64*, 284–288.

(18) Habeeb, A. F. S. A. (1966) *Anal. Biochem. 14*, 328–336.

(19) Riddles, P. W., Blakeley, R. L., and Zerner, B. (1979) Ellman's reagent: 5,5′-dithiobis(2-nitrobenzoic acid): a rexamination. *Anal. Biochem. 94*, 75–81.

(20) Sims, G. E. C., and Snape, T. J. (1980) A method for estimation of poly(ethylene glycol) in plasma protein fractions. *Anal. Biochem. 107*, 60–63.

(21) Koike, M., Ishiyama, T., Tomoyasu, S., and Tsuruoka, N. (1995) Spontaneous cytokine overproduction by peripheral blood mononuclear cells from patients with myelodysplastic syndromes and aplastic anemia. *Leukemia Res. 19*, 639–644.

(22) Fujii, I., Nagahara, Y., Yamasaki, M., Yokoo, Y., Itoh, S., and Hirayama, N. (1997) Structure of KW-2228, a tailored human granulocyte colony-stimulating factor with enhanced biological activity and stability. *FEBS Lett. 410*, 131–5.

(23) Veronese, F. M., Monfardini, C., Caliceti, P., Schiavon, O., Scrawen, M. D., and Beer, D. (1996) Improvement of pharmacokinetic, immunological and stability properties of asparaginase by conjugation to linear and branched monomethoxy poly(ethylene glycol). *J. Controlled Release 40*, 199–209.

(24) Caliceti, P., and Veronese, F. M. (2003) Pharmacokinetic and biodistribution properties of poly(ethylene glycol)-protein conjugates. *Adv. Drug Delivery Rev. 55*, 1261–1277.

(25) Molineux, G. (2003) Pegylation: engineering improved biopharmaceuticals for oncology. *Pharmacotherapy 23*, 3S–8S.

(26) Molineux, G. (2004) The design and development of pegfilgrastim (PEG-rmetHuG-CSF, Neulasta). *Curr. Pharm. Des. 10*, 1235–44.

(27) Hill, C. P., Osslund, T. D., and Eisenberg, D. (1993) The structure of granulocyte-colony-stimulating factor and its relationship to other growth factors. *Biochemistry 90*, 5167–5171.

(28) Brems, D. N. (2002) The kinetics of G-CSF folding. *Protein Sci. 11*, 2504–2511.

(29) Tsubery, H., Mironchik, M., Fridkin, M., and Shechter, Y. (2004) Prolonging the action of protein and peptide drugs by a novel approach of reversible polyethylene glycol modification. *J. Biol. Chem. 279*, 38118–38124.

(30) Raso, S. W., Abel, J., Barnes, J. M., Maloney, K. M., Pipes, G., Treuheit, M. J., King, J., and Brems, D. N. (2005) Aggregation of granulocyte-colony stimulating factor in vitro involves a conformationally altered monomeric state. *Protein Sci. 14*, 2246–2257.

(31) Miller, K. E., and Synovec, R. E. (2000) Rapid polymeric surfactant characterization using a novel flow-injection system with dynamic surface tension detection. *Anal. Chim. Acta 412*, 149–160.

(32) Narhi, L. O., Kenney, W. C., and Arakawa, T. (1991) Conformational changes of recombinant human granulocyte-colony stimulating factor induced by pH and guanidine hydrochloride. *J. Protein Chem. 10*, 359–367.

BC9000432

Facile Preparation of a New Gadofullerene-Based Magnetic Resonance Imaging Contrast Agent with High ^{1}H Relaxivity

Chunying Shu,[†] Frank D. Corwin,[‡] Jianfei Zhang,[†] Zhijian Chen,[§] Jonathan E. Reid,[†] Minghao Sun,[‡] Wei Xu,[||] Jae Hyun Sim,[†] Chunru Wang,[||] Panos P. Fatouros,*[,‡] Alan R. Esker,[†] Harry W. Gibson,*[,†] and Harry C. Dorn*[,†]

Chemistry Department, Virginia Polytechnic Institute and State University, Blacksburg, Virginia 24061, Department of Radiology and Department of Neurosurgery, Virginia Commonwealth University, Richmond, Virginia 23298, Institute of Chemistry, Chinese Academy of Sciences, Beijing 100080, China. Received February 2, 2009; Revised Manuscript Received April 10, 2009

A new magnetic resonance imaging (MRI) contrast agent based on the trimetallic nitride templated (TNT) metallofullerene $Gd_3N@C_{80}$ was synthesized by a facile method in high yield. The observed longitudinal and transverse relaxivities r_1 and r_2 for water hydrogens in the presence of the water-soluble gadofullerene **2** $Gd_3N@C_{80}(OH)_{\sim 26}(CH_2CH_2COOM)_{\sim 16}$ (M = Na or H) are 207 and 282 $mM^{-1}\ s^{-1}$ (per C_{80} cage) at 2.4 T, respectively; these values are 50 times larger than those of Gd^{3+} poly(aminocarboxylate) complexes, such as commercial Omniscan and Magnevist. This high ^{1}H relaxivity for this new hydroxylated and carboxylated gadofullerene derivative provides high signal enhancement at significantly lower Gd concentration as demonstrated by *in vitro* and *in vivo* MRI studies. Dynamic light scattering data reveal a unimodal size distribution with an average hydrodynamic radius of ca. 78 nm in pure water (pH = 7), which is significantly different from other hydroxylated or carboxylated fullerene and metallofullerene derivatives reported to date. Agarose gel infusion results indicate that the gadofullerene **2** displayed diffusion properties different from those of commercial Omniscan and those of PEG5000 modified $Gd_3N@C_{80}$. The reactive carboxyl functionality present on this highly efficient contrast agent may also serve as a precursor for biomarker tissue-targeting purposes.

INTRODUCTION

Magnetic resonance imaging (MRI) is a rapidly evolving noninvasive diagnostic tool that provides high-quality anatomical images of soft tissue and, with the application of contrast enhancement agents, clear delineation of tumors and other pathological processes (*1*). Currently used MRI contrast agents are mainly gadolinium poly(aminocarboxylate) chelates with nontargeted biodistribution and limited chelate−site interaction with water, resulting in reduced flexibility. These nonspecific agents accumulate passively throughout the body and are normally excreted intact through the kidneys. In brain imaging, impairment of the blood−brain barrier allows for preferential contrast accumulation in tumor areas and hence for improved lesion delineation if sufficient contrast agent is present. Since the free metal ion is toxic, complexation with a multidentate diethylenetriaminepentaacetic acid (DTPA) ligand (*2, 3*) provides a high safety margin against dissociation of the contrast complex. However, recent reports show that the use of these agents increases the risk of development of a serious medical condition, nephrogenic systemic fibrosis, (NSF) in patients with acute or chronic severe renal insufficiency and patients with renal dysfunction (*4*). Therefore, there is a continuing need for safer gadolinium-based contrast agents with higher sensitivity (relaxivity) and target specificity to increase the ability for molecular/cellular diagnosis (*5*−*8*). To address these issues, efforts have been directed mainly toward the development of alternative contrast materials. For example, Gd-chelated contrast agents with higher relaxivity than Gd-DTPA or Gd-DTPA-BMA, gadobenate dimeglumine (Gd-BOPTA, MultiHance; Bracco Imaging SpA, Milan, Italy) (*9, 10*) have been approved. Though the structure of the gadobenate ion (one extra benzyloxymethyl group) differs slightly from that of the widely used gadopentetate ion, this leads to a slightly higher longitudinal relaxivity for the gadobenate ion (4.39 ± 0.01 vs 3.77 ± 0.01 $mM^{-1}\ s^{-1}$, 0.5 T) (*10*). More importantly, the same gadobenate dimeglumine concentration in serum causes a markedly higher r_1 relaxivity than is observed in water or saline in comparison with other conventional gadopentetate dimeglumine (9.7 vs 4.8 $mM^{-1}\ s^{-1}$) as a result of weak and transient interactions with serum albumin (*10*−*12*). Another important example is gadofosveset (MS-325), which is the first representative member of receptor-induced magnetization enhancement (RIME) contrast agents targeted to the vasculature by exploiting noncovalent binding to the plasma protein of human serum albumin (HSA) (*13*−*15*) and has been approved in the EU. The relaxivity of MS-325 in human plasma is not constant as a function of concentration and decreases from 45 to 30 $mM^{-1}\ s^{-1}$ (20 MHz) from 0.1 to 1 mmol L^{-1}, respectively (*14*), much higher than that of clinically used Gd-DTPA (4.6 $mM^{-1}\ s^{-1}$) (*14*).

Very recently, it has been found that water-soluble gadofullerenes (*16*−*25*) and gadonanotubes (*26*) exhibit much higher relaxivities than commercial Magnevist (gadolinium-diethylenetriaminepentaacetic acid, Gd-DTPA) and Ominiscan (Gd-diethylenetriaminepentaacetate-bismethylamide). Most significantly, the fullerene cage is believed to hinder both chemical attack on the lanthanide ion and the escape of the lanthanide ion, which should effectively suppress the toxicity of naked Gd^{3+} ions. Moreover, the biodistribution can be improved by modifying the cages with biologically active groups that exhibit high and specific affinity for a particular tissue, resulting in accumulation of targeting probes and thus local contrast enhancement (*27, 28*). To date, there are three basic types of Gd-based metallofullerenes reported as potential MRI contrast agents, i.e.,

* Corresponding author e-mail: ppfatouros@vcu.edu; hwgibson@vt.edu; hdorn@vt.edu.

[†] Virginia Polytechnic Institute and State University.

[‡] Department of Radiology, Virginia Commonwealth University.

[§] Department of Neurosurgery, Virginia Commonwealth University.

[||] Chinese Academy of Sciences.

10.1021/bc900051d CCC: $40.75 © 2009 American Chemical Society
Published on Web 05/15/2009

$Gd@C_{82}$ (*16*−*20*, *22*, *27*), $Gd@C_{60}$ (*21*), $Sc_xGd_{3-x}@C_{80}$ ($x = 0$, 1, 2) (*23*, *24*, *29*). Among these materials, $Gd_3N@C_{80}$ potentially exhibits the highest relaxivity in units of mM^{-1} s^{-1} per mM of contrast agent because of the presence of three Gd^{3+} ions/molecule.

Herein, we report that $Gd_3N@C_{80}$ reacts with an acyl peroxide to produce a highly water-soluble derivative, $Gd_3N@C_{80}(OH)_{\sim 26}(CH_2CH_2COOM)_{\sim 16}$ (M = H or Na) in high yield. Since the paramagnetic Gd atoms preclude using standard high-resolution NMR to confirm the structure of these nanomaterials, we have employed $Sc_3N@C_{80}$ as a diamagnetic model and synthesized its analogue, $Sc_3N@C_{80}(OH)_{\sim 33}(CH_2CH_2COOM)_{\sim 19}$, M = Na or H. This acyl peroxide free radical procedure allows for the chemical attachment of a variety of functional groups to the carbon cage through covalent carbon−carbon bonds without destroying the cage. Most importantly, the functionalized $Gd_3N@C_{80}$ exhibited promising properties as an MRI contrast agent, such as significantly high relaxivity, narrow size distribution, and diffusion properties different from Ominiscan in agarose gel, a brain-mimicking material. The *in vivo* experimental results suggest that the long-term stability of this contrast agent around the tumor will be a benefit for long-term diagnostics. On the basis of other examples in the literature (*30*,*31*), these functionalized $Gd_3N@C_{80}$ compounds also could exhibit antioxidative properties.

MATERIALS AND METHODS

$Gd_3N@C_{80}$ was synthesized and purified as reported (*32*, *33*). Succinic acid acyl peroxide (**1**) was synthesized according the literature (*34*).

Fourier transform infrared spectroscopic (FTIR) measurements were performed using a Nicolet magna-IR750 spectrometer. X-ray photoelectron spectroscopy (XPS) measurements were taken with a PHI Quantera SXM scanning photoelectron spectrometer microprobe using Al Kα radiation. The concentration of Gd^{3+} ion in the aqueous solutions was determined by inductively coupled plasma atomic emission spectroscopy (ICP-OES, VARIAN) at 342.247 nm. The relaxation times were measured at three different magnetic field strengths: 0.35 T with a TEACH SPIN PS1-B instrument, 2.4 T with a Bruker/Biospec system, and 9.4 T with a Varian Inova 400 unit. The inversion−recovery method was used to measure T_1 and the Carr-Pucell-Meiboom-Gill method was used for measurement of T_2. The relaxivities (r_1 and r_2 in mM^{-1} s^{-1}) in aqueous solution (pH = 7) and phosphate buffered saline (PBS, pH = 7.4) solution were obtained from linear least-squares determinations of the slopes of relaxation rates ($1/T_1$ and $1/T_2$) vs [Gd_3N] plots. T_1-weighted and T_2-weighted images of gadofullerene solutions were obtained at a 34, 14, and 7 μM of $Gd_3N@C_{80}(OH)_{\sim 26}(CH_2CH_2COOM)_{\sim 16}$ in pure water and PBS solutions, compared with 1.0 and 0.5 mM Omniscan on the 2.4 T MR instrument using a spin−echo pulse sequence with pulse repetition time/echo times T_R/T_E, 700 ms/13 ms and 6000 ms/100 ms, respectively. Dynamic light scattering (DLS) measurements were carried out with a Spectra-Physics HeNe laser producing vertically polarized light of $\lambda_0 = 632.8$ nm and the correlator consisting ca. 288 exponentially spaced channels (ALV/CGS-3 multiple τ correlator) at six different scattering angles (30°, 45°, 60°, 75°, 90°, and 105°). Each sample was filtered with a 0.2 μm cellulose acetate membrane filter. The CONTIN analysis was used to obtain a hydrodynamic radius based on a diffusion coefficient and size distribution. Infusion into 0.6% agarose gel was carried out with solutions of gadofullerene **2** and the commercial agent Omniscan using the convection-enhanced delivery (CED) method.

Scheme 1. Synthesis of Succinic Acid Acyl Peroxide (1) (*34*) and $Gd_3N@C_{80}(OH)_x(CH_2CH_2COOM)_y$ (M = H, Na) (2)

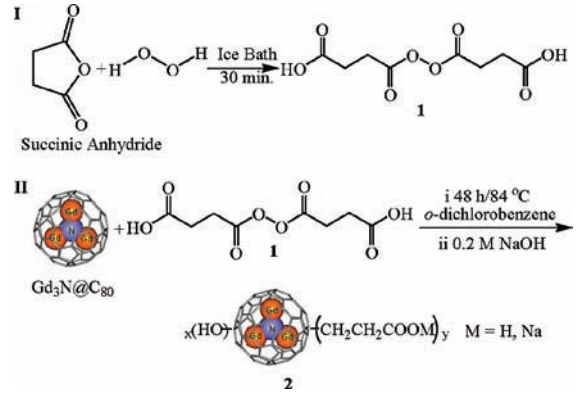

RESULTS AND DISCUSSION

Synthesis of $Gd_3N@C_{80}(OH)_x(CH_2CH_2COOM)_y$ (M = H, Na) (2). For the biomedical application of the fullerenes and endofullerenes, modification of these hydrophobic materials to provide water solubility is essential. Several methods have been reported to modify the precursors of MRI contrast agents, including strong base treatment (*18*), electrophilic reaction or radical reaction (*22*, *24*), and multistep Bingel reaction (*21*, *23*). However, to date, carboxylic acid and amino-functionalized $Gd_3N@C_{80}$ have not been reported, even though these functional groups are of special importance for the tissue-targeting purposes (*23*, *24*). Herein, we report a facile method to modify $Gd_3N@C_{80}$ with carboxylic acid terminal groups (Scheme 1). Briefly, to $Gd_3N@C_{80}$ (4 mg) in 5 mL of *o*-dichlorobenzene was added succinic acid acyl peroxide (**1**) (3.2 mg, 5 equiv). The resultant solution was deaerated with flowing argon and heated at 84 °C for 48 h. In intervals of 12 h, more **1** (3.2 mg, 5 equiv) was added. After the reaction, a brown sludge precipitated from the solution. Then, 8 mL of 0.2 M NaOH aqueous solution was added to extract the water-soluble product. Two layers were obtained; the top layer was deep brown and the bottom layer was colorless (Supporting Information Figure S1a). The top layer was concentrated, and the residue was purified via a Sephadex G-25 (Parmacia) size-exclusion gel column with pure water as eluent to obtain a narrow brown band with pH = 6−7 (Supporting Information Figure S1b). The yield was 95% estimated from the ICP calibration. The solubility of the final product in pure water is ca. 13.2 mg/mL. This fraction were characterized by XPS and FT-IR and studied in detail as an MRI contrast agent.

In a separate experiment, the $Gd_3N@C_{80}(OH)_x(CH_2CH_2COOM)_y$ (M = H, Na) sample **2** was placed in a dialysis membrane (MW cutoff 500 D) and dialyzed for 24 h. The resulting solution outside the membrane was subjected to ICP analysis and Gd^{3+} ion was not detected.

Structural Characterization. The electronic structure of the functionalized gadofullerene **2** was analyzed by measuring the binding energy spectrum for the C_{1s} electrons. The main line of the XPS spectrum (Supporting Information Figure S2a) exhibits a broad and asymmetric line-shape. Gaussian analysis suggests the presence of at least three components (indicated by blue, green, and purple lines, respectively). The intensities of C_{1s} components in **2** were estimated from integration of the peak area under each line to be 66.4%, 20.9%, and 12.7% for the sp^2 nonfunctionalized carbon (C═C) and sp^3 hybridized carbons (C−C and -CH_2−CH_2-), hydroxylated carbon (C−OH), and carboxylate carbon (O═C−O), respectively. Thus, gado-

Table 1. Relaxivities (in units of mM^{-1} s^{-1} per mM of Gadofullerene Molecules) and r_2/r_1 Ratios of 2 in Pure Water and PBS Solutions, at 0.35, 2.4, and 9.4 T, Room Temperature

	0.35 T (15 MHz)			2.4 T (100 MHz)			9.4 T (400 MHz)		
	r_1	r_2	r_2/r_1	r_1	r_2	r_2/r_1	r_1	r_2	r_2/r_1
water	154 ± 7	204 ± 22	1.3 ± 0.2	207 ± 9	282 ± 31	1.8 ± 0.2	76 ± 3	231 ± 25	3.0 ± 0.4
PBS	29 ± 1	37 ± 4	1.3 ± 0.2	35 ± 2	62 ± 7	1.6 ± 0.2	18 ± 1	72 ± 8	4.1 ± 0.5

Table 2. Comparison of Relaxivities (in units of mM^{-1} s^{-1} per mM of Gadolinium Ions)

	relaxivity (r_1/r_2) mM^{-1} s^{-1}		
compound	0.35 T (15 MHz)	2.4 T (100 MHz)	9.4 T (400 MHz)
2	51/68	69/94	25/77
$Gd@C_{82}(OH)_{40}$ (*18*)	67/79 (0.47 T)	81/108 (1.0 T)	31/131 (4.7 T)
$Gd@C_{82}O_2(OH)_{16}[C(PO_3Et_2)]_{10}$ (*27*)	37/42	39/68	20/74
$Gd@C_{82}O_6(OH)_{16}(NHC_2H_4COOH)_8$ (*22*)	16/--	--	--
$Gd@C_{60}(OH)_x$ (*44*)	--	83.2/-- (1.5 T)	--
$Gd@C_{60}[C(COOH)_2]_{10}$ (*44*)	4.6/-- (0.47 T)	24.0/-- (1.5 T)	--
$Sc_2GdN@C_{80}O_m(OH)_n$ (*29*)	--	--	20.7/-- (14.1 T)
$ScGd_2N@C_{80}O_m(OH)_n$			17.6/-- (14.1 T)
$Gd_3N@C_{80}Peg5000(OH)_x$ (*23*)	34/48	48/74	11/49
$Gd_3N@C_{80}R_x$ (*24*)	68/79 (0.47 T)	--	--
$R = N(OH)(CH_2CH_2O)_6CH_3$			
Gd-BOPTA (*45*)	10.9/-- (0.2 T)	7.9/-- (1.5 T)	5.9/-- (3T)
(in human blood plasma)	4.39/5.56 (*9*)[a]		
MS-325 (in human plasma) (*14*)	53.5/-- (0.47 T)	--	--
Gd-DTPA BMA	--	4.1/4.7	--

[a] Under the condition of 0.47 T, pH = 7.4, 39 °C.

fullerene **2** can be designated as $Gd_3N@C_{80}(OH)_{\sim 26}(CH_2CH_2COOM)_{\sim 16}$ (M = Na, H). It was reported that the molecular stability of fullerenols largely depends on the quantity of highly oxygenated carbons, but less on the number of hydroxyl groups (*35*). In compound **2**, there are no highly oxygenated carbons based on the XPS analysis, which may be helpful to stabilize the carbon cage and thus protect the Gd_3N clusters inside from leakage (*36*). Xiao et al. reported the synthesis of [59]fullerenones starting from the fullerene mixed peroxide, $C_{60}(OO\text{-}t\text{-}Bu)_6$ (*37*). They suggested a reaction mechanism of peroxide-mediated stepwise cleavage of fullerene skeletal bonds. However, acyl peroxides, RC(O)OO(O)CR (R = aliphatic, aromatic, or another group), readily decompose to release carbon dioxide and form free radicals R″ upon mild heating (*38*). Yoshida et al. reported a reaction of C_{60} with diacyl peroxides containing perfluoroalkyl groups to yield $C_{60}(R_FOH)$ and $C_{60}(R_FCO_3H)$ (*39*). Succinic acid peroxide, **1**, decomposes to form a $HOOCCH_2CH_2COO^{\cdot}$ radical (*40*), which can subsequently lose CO_2 to yield a 2-carboxyethyl radical and add on the C═C double bonds of metallofullerenes. This method has been successfully applied to the modification of SWNTs (*41*).

The IR spectrum of **2** (Supporting Information Figure S3) displays intense bands at 1576 cm^{-1} and 1402 cm^{-1} (overlap with O—H bending vibration) for the carboxylate ion asymmetrical and symmetrical stretching vibrations, respectively. The C—O stretching absorptions at about 1120 and 1014 cm^{-1}, an intense broad O—H band at ca. 3169 cm^{-1}, and a very strong O—H bending vibration frequency at 1402 cm^{-1} indicated the —C—O—H structure of the compound. The weak peaks at 1649 cm^{-1} and 2893/2826 cm^{-1} are from C═C and C—H vibrations, respectively. It is noteworthy that the antisymmetric Gd—N stretching vibration can be observed at 689 cm^{-1}, a frequency increase of 32 cm^{-1} compared to that of pristine $Gd_3N@C_{80}$, which appears at 657 cm^{-1} (*42*). The higher vibrational energy in **2** reflects a stronger Gd—N bond relative to pristine $Gd_3N@C_{80}$. The broad absorption at 3618 cm^{-1} is from bonded water. These IR absorptions are consistent with the results from XPS analysis.

The UV—vis absorption spectra of **2** and $Gd_3N@C_{80}$ (Supporting Information Figure S4) were measured in water and toluene, respectively. The UV—vis spectra reveal that the $Gd_3N@C_{80}$ derivative **2** has lost most of the characteristic absorbance for $Gd_3N@C_{80}$ that was centered at 706 and 676 nm (*42*, *43*), indicating that the removal of p-orbitals from the π system of the cage by introduction of the hydroxyl and ethylenecarboxyl groups changes the electronic structure.

***In Vitro* MRI Study.** In order to explore the potential of compound **2** as an MRI contrast agent, the proton relaxivities (*1*), r_1 and r_2 values (the paramagnetic longitudinal and transverse relaxation rate enhancement of water protons, respectively, referred to 1 mM concentration), were measured at three different magnetic fields, 0.35, 2.4, and 9.4 T. Generally, the relaxivity, r_i, can be defined by eq 1:

$$\frac{1}{T_{i,\mathrm{obsd}}} = \frac{1}{T_{i,\mathrm{d}}} + \frac{1}{T_{i,\mathrm{para}}} = \frac{1}{T_{i,\mathrm{d}}} + r_i[\mathrm{M}] \quad i = 1, 2 \qquad (1)$$

in which $1/T_1$ and $1/T_2$ are the longitudinal and transverse relaxation rates of the solvent. $1/T_{i,\mathrm{obsd}}$, $1/T_{i,\mathrm{d}}$, and $1/T_{i,\mathrm{para}}$ are the observed relaxation rates in the presence of the paramagnetic species, the values in the absence of the paramagnetic species, and the contribution from the paramagnetic compound, respectively. [M] is the concentration of the paramagnetic species.

As shown in Table 1, the r_1 and r_2 of **2** at 2.4 T (close to clinical used magnetic fields) are 50 and 60 times larger than those of commercial Omniscan (Gd-DTPA BMA, $r_1/r_2 = 4.1/4.7$ mM^{-1} s^{-1} as shown in Table 2) under the same conditions. In contrast, these values decrease greatly in PBS solution, which we ascribe to deaggregation, leading to smaller and faster tumbling complexes and correspondingly lower relaxivities. It can be seen that the r_2/r_1 ratio of the present compound **2** increases as the magnetic field increases. This observation and the high r_2 value strongly suggest that gadofullerene **2** could also be used as a T_2-enhancing MRI contrast agent at higher magnetic fields. Toth and coauthors have reported the first relaxometric studies on $Gd@C_{60}[C(COOH)_2]_{10}$ and $Gd@C_{60}(OH)_x$ and discovered a maximum in the high-field (10—100 MHz) region of their nuclear magnetic resonance dispersion (NMRD) profiles (*36*). They suggest that the relaxivity maxima could arise from an increase in the rotational correlation time, τ_R, of the contrast agent (*46*, *47*). Although a more detailed NMRD profile measurement was not performed in the current study, the maximum at 2.4 T (100 MHz) rather than 0.35 T (15 MHz) and 9.4 T (400 MHz) suggests that the relaxivity maxima may also be due to an increase in the rotational time resulting

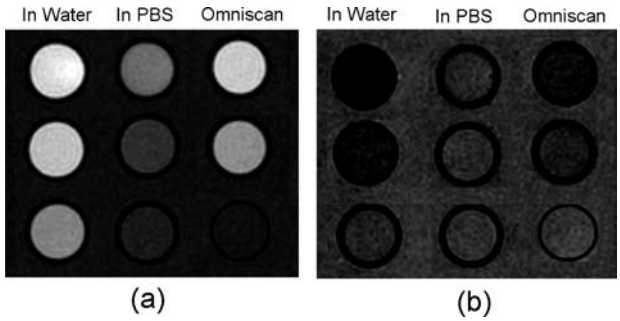

Figure 1. T_1-weighted images with T_R/T_E = 700 ms/13 ms, number of acquisitions (NA) = 4 (a); and T_2-weighted images T_R/T_E = 6000 ms/100 ms, NA = 1 (b); of **2** in pure water and PBS with concentrations of 34, 14, and 7 μM [Gd_3N] from top to bottom, respectively; and Omniscan at [Gd] concentrations of 1.0, 0.5, and 0 mM (pure water) from top to bottom. Matrix: 192 × 192; slice thickness = 2 mm.

from an increase in aggregation of the gadofullerenes in aqueous solution relative to PBS (*vide infra*).

In Table 2, the relaxivities of **2** are compared with those of other gadofullerenes under different conditions as well as the newly approved Gd-based complex in human serum plasma. It should also be noted that another Gd-based carbonaceous nanomaterial, ultrashort (20−80 nm) gadonanotubes, is reported to exhibit very high relaxivities (r_1 = 180, 1.5 T) at pH 6.5 and 37 °C (*26*). The unprecedented relaxivity and corresponding variable-field NMRDs of the latter material are not readily rationalized using classic Solomon-Bloembergen-Morgan (SBM) theory (*46*). Wilson and co-workers suggested that gadonanotubes are likely an example of special properties (magnetic/relaxivity) arising from the nanoscalar confinement of Gd^{3+} ion clusters within their carbon capsule sheaths (*26*). At clinically used field strengths (1.0−3 T), polyhydroxylated Gd@C_{82} (*18*) and Gd@C_{60} (*44*) exhibit higher relaxivities due to the larger aggregates and fast exchange with water via OH groups. The Gd_3N@C_{80} derivatives are the second member of agents with high relaxivities, but the C_{80} cage can entrap three gadolinium ions and concentrate them safely, thus providing substantially higher relaxivities (r_1/r_2 from 69/94 per Gd and 207/282 per cage). The new compound **2** together with reported Gd_3N@$C_{80}R_x$ (R = N(OH)$(CH_2CH_2O)_6CH_3$) (*24*) exhibits higher relaxivity than Gd_3N@C_{80}[Peg5000$(OH)_x$] (*23*). Additionally, compound **2** with carboxylic groups may provide a unique platform for coupling with molecular targeting moieties. Under similar conditions, Gd-BOPTA and MS-325 exhibit great advantages in human plasma relative to the routinely used Gd-DTPA-BMA, but their relaxivities are still significantly lower than those of gadofullerenes.

To confirm the large MRI signal enhancement of **2** at lower Gd concentration over that required for the commercial contrast agent Omniscan, T_1- and T_2-weighted MR images of Gd_3N@$C_{80}$$(OH)_{\sim 26}$$(CH_2CH_2COOM)_{\sim 16}$ solutions at concentrations of 34, 14, and 7 μM [Gd_3N] and Omniscan at concentrations of 1.0 and 0.5 mmol Gd/L were generated using a spin−echo pulse sequence. A strong MRI signal enhancement was observed for **2** at 14 μM, whereas Omniscan exhibits similar contrast at a concentration of 0.5 mM (over 2 magnitudes higher concentration), confirming that the MRI signal-enhancing efficiency of gadofullerene **2** is indeed much higher than that of Omniscan (Figure 1) and gadofullerene **2** is also a good T_2-enhancing contrast agent (Figure 1b). These MRI data are in conformity with the high r_1 and r_2 values reported in Table 1.

So far, several types of functionalized MRI contrast agents based on classical metallofullerenes Gd@C_{2n} ($2n$ = 60, 82) and TNT metallofullerene Gd_3N@C_{80} have been reported, such as the polyhydroxylated (*16−18, 20, 29*) and the carboxylated Gd@C_{2n} ($2n$ = 60, 82) (*21, 22*), sulfonated (*48*), and phosphated

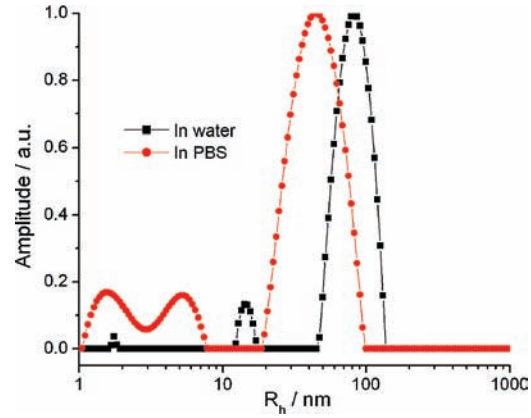

Figure 2. Intensity-weighted (intensity percent) size distribution profiles of **2** in pure water, pH = 7.0, (black line) and PBS, pH = 7.4, (red dash) at 90° scattering angle. Temperature = 25 °C.

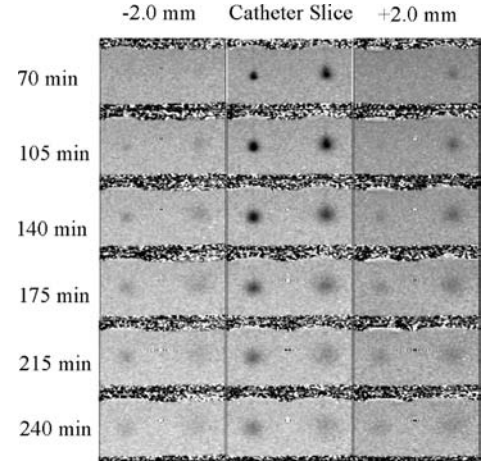

Figure 3. T_1 computed map images of bilaterial infusion into 0.6% agarose gel of 0.005 mM Gd_3N@$C_{80}$$(OH)_{\sim 26}$$(CH_2CH_2COOM)_{\sim 16}$ (left side of each image) and 0.25 mM Omniscan (right side of each image). Displayed times are in minutes post-beginning of infusion. Infusion was applied for 120 min at 0.2 μL/min on both ports. At each time point, three contiguous slices are shown with infusion carried out in the middle slice.

(*27*) Gd@C_{82}, the PEGylated hydroxylated Gd_3N@C_{80} (*23*) and Gd_3N@$C_{80}R_x$ (R = N(OH)$(CH_2CH_2O)_6CH_3$) (*24*). Polyhydroxylated metallofullerenes with high reticuloendothelial system (RES) uptake exhibited much higher relaxivity than the sulfonated and carboxylated systems, which exhibit a favorable non-RES distribution. Although water molecules are not directly coordinated to the encapsulated metal ion, these gadofullerene-based MRI contrast agents exhibit much higher relaxivities than the Gd chelates. The mechanisms ascribed to these high relaxivities include (a) the presence of three Gd^{3+} ions within the cage; the charge transfer between the Gd_3N cluster and the C_{80} cage leads to a very stable nanoparticle and the ferromagnetic coupling gives rise to a large magnetic moment, 21 μB (*49, 50*); (b) a large number of hydroxyl groups attached to the carbon cage, which facilitate exchange of protons with surrounding water protons; this exchange transmits the paramagnetic relaxation to the bulk water; (c) a longer rotational correlation time τ_R (the order of nanoseconds) as a result of aggregation; and (d) the presence of a pool of water molecules that are trapped within the aggregates are relaxed by the gadofullerenes and exchange rapidly with the bulk water molecules (*51*). This is in contrast to the conventional Gd-DTPA complex, which has a single water molecule bound in the first coordination sphere of the metal ion and the entire complex tumbles very rapidly ($\tau_R \sim$ 58 ps) (*1*).

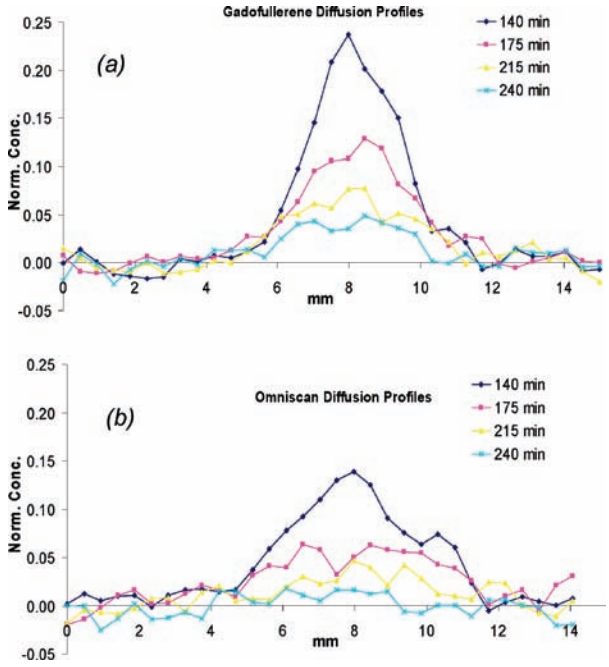

Figure 4. Concentration profiles normalized to the infused concentrations through the gadofullerene infusate (a) and Omniscan infusate (b) at different time points.

Notably, the hydrodynamic diameter distribution of as-synthesized $Gd_3N@C_{80}(OH)_{\sim 26}(CH_2CH_2COOM)_{\sim 16}$ in water is unimodal. This is significantly different from the results found for $Gd@C_{60}(OH)_x$ and $Gd@C_{60}[C(COOH)_2]_{10}$ (*52*), but is similar to that of our formerly synthesized $Gd@C_{82}O_6(OH)_{16}$-$(NHCH_2CH_2COOH)_8$ (*53*). In the PBS medium, the relatively larger aggregates were reduced in size by the intercalation of phosphate, since the $H_2PO_4^-$ and HPO_4^{2-} ions can break up intermolecular H-bonding (*44*); the resulting smaller size aggregate distribution relative to that in pure water leads to faster tumbling entities and correspondingly lower ^1H relaxivity. This interpretation is consistent with the multimodal distributions in PBS (Figure 2), which indicate a dynamic aggregation/deaggregation process. The downward shift of the intensity-weighted size distribution in PBS solution (Figure 2) led to a marked decrease of proton relaxivities (r_1/r_2 = 35/62 mM^{-1} s^{-1} at 2.4 T) relative to those in pure water (r_1/r_2 = 207/282 mM^{-1} s^{-1}), indicating that the aggregation size in this range is not large enough to increase the rotational time of entities to the nanosecond range. Recently, Fatouros et al. (*23*) reported an MRI contrast agent based on a trimetallic nitride templated metallofullerene (TNT EMF), $Gd_3N@C_{80}$, which was PEGylated and hydroxylated. This compound also exhibited extremely high relaxivities due to the advantages described above. However, the small size distribution (less than 10 nm) of $Gd_3N@C_{80}[Peg5000(OH)_x]$ leads to a lower relaxivity compared to compound **2** (48 mM^{-1} s^{-1} vs 69 mM^{-1} s^{-1} at 2.4 T), which exhibits an average hydrodynamic diameter of ca. 78 nm (Figure 2). Notably, $Gd_3N@C_{80}R_x$ (R = $N(OH)(CH_2CH_2O)_6CH_3$) was found to have small particle size of 10−15 nm but high relaxivity (68 mM^{-1} s^{-1} at 0.47 T**)** (*24*). These $Gd_3N@C_{80}$-based derivatives may lead to different tissue uptake (*21*) due to the different aggregating behaviors.

Agarose Gel Infusion Experiment. In order to understand the distribution of the new gadofullerene compound **2** upon direct infusion by convection-enhanced delivery (CED) into the extracellular space of the brain, agarose gel (0.6%) was used as a surrogate for *in vivo* brain tissues. With the CED method, a bilateral infusion of 0.005 mM gadofullerene **2** and 0.25 mM Ominscan was administered into the agarose gel phantom. The infusion was applied for 120 min at 0.2 μL/min. To obtain comparable T_1-weighted images, the concentration values of the infusates (0.005 mM of gadofullerene and 0.25 mM of Gd-DTPA-BMA, respectively) were adjusted using our measured r_1 values (ratio = 207/4.1 = 50).

Figure 3 displays successive T_1 computed maps of $Gd_3N@C_{80}(OH)_{\sim 26}(CH_2CH_2COOM)_{\sim 16}$ and Omniscan in the agarose gel. The displayed times are in minutes after the start of infusion. The T_1 maps shown demonstrate different diffusion patterns. That is, the gadofullerene **2** bolus is more compact, diffuses more slowly, and lingers longer—see the higher residual at 240 min vs the Omniscan. To investigate the diffusion of the new compound quantitatively, we have converted these T_1 maps into concentration maps by means of eq $1/T_1 = 1/T_{10} + r_1[M]$. Concentration profiles normalized to the infused concentrations through the two infusates at different time points are shown in Figure 4. The slower diffusion of the gadofullerene

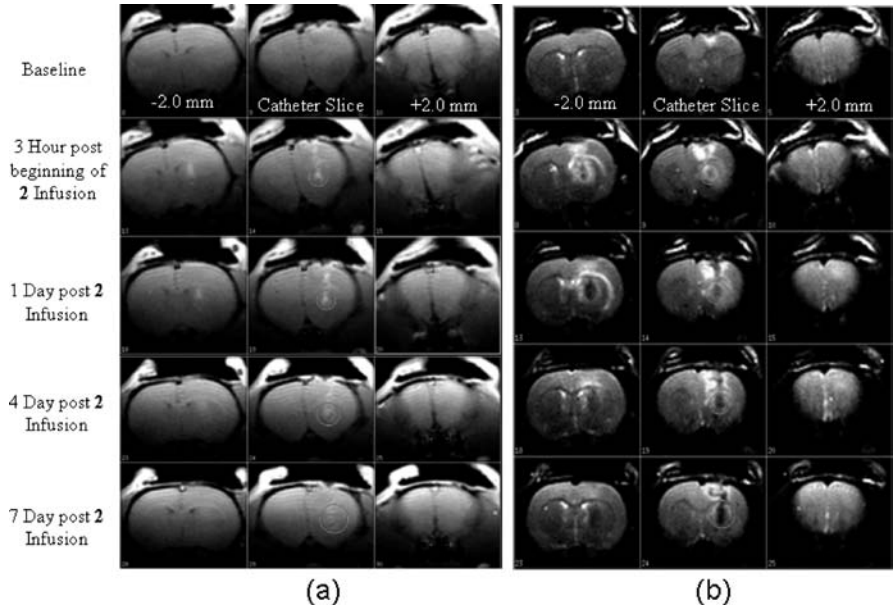

Figure 5. T_1 weighted images (T_R/T_E = 700 ms/10 ms) (a) and T_2 weighted images (T_R/T_E = 6000 ms/100 ms) (b) of direct infusion into T9 tumor-bearing rat brain of 0.0475 mM $Gd_3N@C_{80}(OH)_{\sim 26}(CH_2CH_2COO_m)_{\sim 16}$ (**2**). Infusion was applied for 120 min at 0.2 μL/min.

is consistent with the dependence of the width of the diffusion profile on diffusion coefficient D and time of diffusion t: full-width at half-maximum (fwhm) $\propto (D \cdot t)^{1/2}$ assuming an approximate Gaussian profile. From the Stokes−Einstein equation and the known particle radii, the diffusion coefficient for the gadofullerene **2** is 40−50 times smaller than Omniscan; hence, the gadofullerene **2** diffusion time is 40−50 times longer. Our present study further qualified the diffusion time of compound **2** relative to formerly reported $Gd_3N@C_{80}$[Peg5000$(OH)_x$] (*23*), which may have a shorter diffusion time due to the small size distribution.

***In Vivo* Infusion Experiment.** To further document and quantitate the diffusion profile of the infused gadofullerene *in vivo*, we have used a Fischer 344 female rat as an animal model of an experimental brain glioma tumor: 5×10^4 T9 glioblastoma cells were directly deposited into the brain parenchyma through a guide cannula. Before direct infusion of $Gd_3N@C_{80}(OH)_{\sim 26}(CH_2CH_2COO_m)_{\sim 16}$ (**2**) into T9 tumor-bearing rat brain on day 13 post cell implantation, a baseline image of the anesthetized animal was acquired for comparison. Then, direct infusion of 0.0475 mM $Gd_3N@C_{80}(OH)_{26}(CH_2CH_2COO_m)_{16}$ (**2**) into the brain at the nascent tumor site was applied for 120 min at 0.2 μL/min using a slow, low-pressure process. The anesthetized animal was imaged in a 2.4 T/40 cm MR Bruker/Biospec system at days 13, 14, 17, and 20 post cell implantation (or at 3 h, 1 d, 4 d, and 7d post **2** infusions). Seven days after the injection, an established tumor was clearly identifiable at the implantation site.

Figure 5 shows T_1 weighted images (T_R/T_E = 700 ms/10 ms) and T_2 weighted images (T_R/T_E = 6000 ms/100 ms). From these successive images, we can see clearly that the new contrast agent provides contrast enhancement (red circles) at very low concentration (0.0475 mM, 24 μL). Notice that a larger tumor bolus can be imaged clearly even after 7 days post-injection, indicating that a prolonged stay of this contrast agent in the tumor can work as a long-term diagnostic agent.

CONCLUSION

In conclusion, a new gadofullerene-based MRI contrast was synthesized by a facile method in high yield. This new MRI contrast agent exhibited equivalent contrast enhancement at dosage levels 1/50 of that of the commercial MRI contrast agent, Omniscan. DLS results displayed a particle size shift from 78 nm in pure water to 44 nm in PBS solutions. Agarose gel infusion experiments revealed different diffusion properties of gadofullerene **2** from clinically used Omniscan. The functional carboxyl terminal groups, -COOH, may enable the conjugation of biomarkers for future tissue-targeting studies. The *in vivo* experimental results demonstrate that this new contrast agent can provide high contrast enhancement at very low concentration and work as long-term diagnostic agent due to its slow diffusion behavior relative to Omniscan.

ACKNOWLEDGMENT

P.P.F., H.W.G., and H.C.D. are grateful for support of this work by the National Science Foundation [DMR-0507083] and the National Institutes of Health [1R01-CA119371].

Supporting Information Available: Experimental details; graphic illustration of extraction and isolation of $Gd_3N@C_{80}(OH)_x(CH_2CH_2COOM)_y$, M = Na or H; C_{1s} XPS spectra of $Gd_3N@C_{80}(OH)_x(CH_2CH_2COOM)_y$ and $Sc_3N@C_{80}(OH)_x(CH_2CH_2COOM)_y$; ^{13}C NMR of $Sc_3N@C_{80}(OH)_{\sim 26}(CH_2CH_2COOM)_{\sim 16}$ (M = Na or H); FTIR and UV−vis spectra of $Gd_3N@C_{80}(OH)_x(CH_2CH_2COOM)_y$. This material is available free of charge via the Internet at http://pubs.acs.org.

LITERATURE CITED

(1) Caravan, P., Ellision, J. J., McMurry, T. J., and Lauffer, R. B. (1999) Gadolinium(III) chelates as MRI contrast agents: structure, dynamics, and applications. *Chem. Rev. 99*, 2293–2352.

(2) Franano, F. N., Edwards, W. B., Welch, M. J., Brechbiel, M. W., Gansow, O. A., and Duncan, J. R. (1995) Biodistribution and metabolism of targeted and nontargeted protein-chelated-gadolinium complexes-Evidence for gadolinium dissociation in vitro and in vivo. *Magn. Reson. Imaging 13*, 201–214.

(3) Rebizak, R., Schaefer, M., and Dellacherie, E. (1998) Polymeric conjugates of Gd^{3+}-diethylenetriaminepentaacetic acid and dextran. 2. Influence of spacer arm length and conjugate molecular mass on the paramagnetic properties and some biological parameters. *Bioconjugate Chem. 9*, 94–99.

(4) Gadolinium-Based Contrast Agents for Magnetic Resonance Imaging (MRI): marketed as Magnevist, MultiHance, Omniscan, OptiMARK, ProHance; http://www.fda.gov/medwatch/safety/2007/safety07.htm#Gadolinium.

(5) Sosnovik, D. E., and Weissleder, R. (2007) Emerging concepts in molecular MRI. *Curr. Opin. Biotechnol. 18*, 4–10.

(6) Anderson, S. A., Lee, K. K., and Frank, J. A. (2006) Gadolinium-fullerenol as a paramagnetic contrast agent for cellular imaging. *Invest. Radiol. 41*, 332–338.

(7) Sitharaman, B., Tran, L. A., Pham, Q. P., Bolskar, R. D., Muthupillai, R., Flamm, S. D., Mikos, A. G., and Wilson, L. J. (2007) Gadofullerenes as nanoscale magnetic labels for cellular MRI. *Contr. Media Mol. Imag, 2*, 139–146.

(8) Hartman, K. B., Wilson, L. J., and Rosenblum, M. G. (2008) Detecting and treating cancer with nanotechnology. *Mol. Diagn. Ther. 12*, 1–14.

(9) Uggeri, F., Aime, S., Anelli, P. L., Botta, M., Brocchetta, M., Dehaen, C., Ermondi, G., Grandi, M., and Paoli, P. (1995) Novel contrast agents for magnetic resonance imaging. Synthesis and characterization of the ligand BOPTA and its Ln(III) complexes (Ln = Gd, La, Lu). X-ray structure of disodium (*TPS*-9−145337286-C-S)-[4-carboxyl-5,8,11-tri(carboxymethyl)-1-phenyl-2-oxa-5,8,11-triazatridecan-13-oato(5-)]gadolinate(2-) in a mixture with its enantiomer. *Inorg. Chem. 34*, 633–642.

(10) Cavagna, F. M., Maggioni, F., Castelli, P. M., Dapra, M., Imperatori, L. G., Lorusso, V., and Jenkins, B. G. (1997) Gadolinium chelates with weak binding to serum proteins - A new class of high-efficiency, general purpose contrast agents for magnetic resonance imaging. *Invest. Radiol. 32*, 780–796.

(11) Pintaske, J., Martirosian, P., Graf, H., Erb, G., Lodemann, K. P., Claussen, C. D., and Schick, F. (2006) Relaxivity of gadopentetate dimeglumine (Magnevist), gadobutrol (Gadovist), and gadobenate dimeglumine (MultiHance) in human blood plasma at 0.2, 1.5, and 3 T. *Invest. Radiol. 41*, 213–221.

(12) Giesel, F. L., von Tengg-Kobligk, H., Wilkinson, I. D., Siegler, P., von der Lieth, C. W., Frank, M., Lodemann, K. P., and Essig, M. (2006) Influence of human serum albumin on longitudinal and transverse relaxation rates (R1 and R2) of magnetic resonance contrast agents. *Invest. Radiol. 41*, 222–228.

(13) Parmelee, D. J., Walovitch, R. C., Ouellet, H. S., and Lauffer, R. B. (1997) Preclinical evaluation of the pharmacokinetics, biodistribution, and elimination of MS-325, a blood pool agent for magnetic resonance imaging. *Invest. Radiol. 32*, 741–747.

(14) Lauffer, R. B., Parmelee, D. J., Dunham, S. U., Ouellet, H. S., Dolan, R. P., Witte, S., McMurry, T. J., and Walovitch, R. C. (1998) MS-325: Albumin-targeted contrast agent for MR angiography. *Radiology 207*, 529–538.

(15) Caravan, P., Cloutier, N. J., Greenfield, M. T., McDermid, S. A., Dunham, S. U., Bulte, J. W. M., Amedio, J. C., Looby, R. J., Supkowski, R. M., Horrocks, W. D., McMurry, T. J., and Lauffer, R. B. (2002) The interaction of MS-325 with human serum albumin and its effect on proton relaxation rates. *J. Am. Chem. Soc. 124*, 3152–3162.

(16) Zhang, S. R., Sun, D. Y., Li, X. Y., Pei, F. K., and Liu, S. Y. (1997) Synthesis and solvent enhanced relaxation property of

water-soluble endohedral metallofullerenols. *Fullerene Sci. Technol. 5*, 1635–1643.
(17) Wilson, L. J. (1999) Medical application of fullerenes and metallofullerenes. *Electrochem. Soc. Interface* (Winter), 24–28.
(18) Mikawa, M., Kato, H., Okumura, M., Narazaki, M., Kanazawa, Y., Miwa, N., and Shinohara, H. (2001) Paramagnetic water-soluble metallofullerenes having the highest relaxivity for MRI contrast agents. *Bioconjugate Chem. 12*, 510–514.
(19) Okumura, M., Mikawa, M., Yokawa, T., Kanazawa, Y., Kato, H., and Shinohara, H. (2002) Evaluation of water-soluble metallofullerenes as MRI contrast agents. *Academ. Radiol. 9*, S495–S497.
(20) Kato, H., Kanazawa, Y., Okumura, M., Taninaka, A., Yokawa, T., and Shinohara, H. (2003) Lanthanoid endohedral metallofullerenols for MRI contrast agents. *J. Am. Chem. Soc. 125*, 4391–4397.
(21) Bolskar, R. D., Benedetto, A. F., Husebo, L. O., Price, R. E., Jackson, E. F., Wallace, S., Wilson, L. J., and Alford, J. M. (2003) First soluble M@C_{60} derivatives provide enhanced access to metallofullerenes and permit in vivo evaluation of Gd@C_{60}[$C(COOH)_2$]$_{10}$ as a MRI contrast agent. *J. Am. Chem. Soc. 125*, 5471–5478.
(22) Shu, C. Y., Gan, L. H., Wang, C. R., Pei, X. L., and Han, H. B. (2006) Synthesis and characterization of a new water-soluble endohedral metallofullerene for MRI contrast agents. *Carbon 44*, 496–500.
(23) Fatouros, P. P., Corwin, F. D., Chen, Z. J., Broaddus, W. C., Tatum, J. L., Kettenmann, B., Ge, Z., Gibson, H. W., Russ, J. L., Leonard, A. P., Duchamp, J. C., and Dorn, H. C. (2006) In vitro and in vivo imaging studies of a new endohedral metallofullerene nanoparticle. *Radiology 240*, 756–764.
(24) MacFarland, D. K., Walker, K. L., Lenk, R. P., Wilson, S. R., Kumar, K., Kepley, C. L., and Garbow, J. R. (2008) Hydrochalarones: a novel endohedral metallofullerene platform for enhancing magnetic resonance imaging contrast. *J. Med. Chem. 51*, 3681–3683.
(25) Dunsch, L., and Yang, S. (2007) Metal nitride cluster fullerenes: Their current state and future prospects. *Small 3*, 1298–1320.
(26) Hartman, K. B., Laus, S., Bolskar, R. D., Muthupillai, R., Helm, L., Toth, E., Merbach, A. E., and Wilson, L. J. (2008) Gadonanotubes as ultrasensitive pH-smart probes for magnetic resonance imaging. *Nano Lett. 8*, 415–419.
(27) Shu, C. Y., Wang, C. R., Zhang, J. F., Gibson, H. W., Dorn, H. C., Corwin, F. D., Fatouros, P. P., and Dennis, T. J. S. (2008) Organophosphonate functionalized Gd@C_{82} as a magnetic resonance imaging contrast agent. *Chem. Mater. 20*, 2106–2109.
(28) Shu, C. Y., Ma, X. Y., Zhang, J. F., Corwin, F. D., Sim, J. H., Zhang, E. Y., Dorn, H. C., Gibson, H. W., Fatouros, P. P., Wang, C. R., and Fang, X. H. (2008) Conjugation of a water-soluble gadolinium endohedral fulleride with an antibody as a magnetic resonance imaging contrast agent. *Bioconjugate Chem. 19*, 651–655.
(29) Zhang, E. Y., Shu, C. Y., Feng, L., and Wang, C. R. (2007) Preparation and characterization of two new water-soluble endohedral metallofullerenes as magnetic resonance imaging contrast agents. *J. Phys. Chem. B 111*, 14223–14226.
(30) Chen, C. Y., Xing, G. M., Wang, J. X., Zhao, Y. L., Li, B., Tang, J., Jia, G., Wang, T. C., Sun, J., Xing, L., Yuan, H., Gao, Y. X., Meng, H., Chen, Z., Zhao, F., Chai, Z. F., and Fang, X. H. (2005) Multi hydroxylated [Gd@$C_{82}(OH)_{22}$]$_n$ nanoparticles: Antineoplastic activity of high efficiency and low toxicity. *Nano Lett. 5*, 2050–2057.
(31) Wang, J. X., Chen, C. Y., Li, B., Yu, H. W., Zhao, Y. L., Sun, J., Li, Y. F., Xing, G. M., Yuan, H., Tang, J., Chen, Z., Meng, H., Gao, Y. X., Ye, C., Chai, Z. F., Zhu, C. F., Ma, B. C., Fang, X. H., and Wan, L. J. (2006) Antioxidative function and biodistribution of [Gd@$C_{82}(OH)_{22}$]$_n$ nanoparticles in tumor-bearing mice. *Biochem. Pharmacol. 71*, 872–881.
(32) Stevenson, S., Rice, G., Glass, T., Harich, K., Cromer, F., Jordan, M. R., Craft, J., Hadju, E., Bible, R., Olmstead, M. M., Maitra, K., Fisher, A. J., Balch, A. L., and Dorn, H. C. (1999) Small-bandgap endohedral metallofullerenes in high yield and purity. *Nature 401*, 55–57.
(33) Ge, Z. X., Duchamp, J. C., Cai, T., Gibson, H. W., and Dorn, H. C. (2005) Purification of endohedral trimetallic nitride fullerenes in a single, facile step. *J. Am. Chem. Soc. 127*, 16292–16298.
(34) Clover, A. M., and Houghton, A. C. (1904) Action of hydrogen peroxide on anhydrides and the formation of organic acid, peroxides, and peracids. *Am. Chem. J. 32*, 43–68.
(35) Xing, G. M., Zhang, J., Zhao, Y. L., Tang, J., Zhang, B., Gao, X. F., Yuan, H., Qu, L., Cao, W. B., Chai, Z. F., Ibrahim, K., and Su, R. (2004) Influences of structural properties on stability of fullerenols. *J. Phys. Chem. B 108*, 11473–11479.
(36) Toth, E., Bolskar, R. D., Borel, A., Gonzalez, G., Helm, L., Merbach, A. E., Sitharaman, B., and Wilson, L. J. (2005) Water-soluble gadofullerenes: Toward high-relaxivity, pH-responsive MRI contrast agents. *J. Am. Chem. Soc. 127*, 799–805.
(37) Xiao, Z., Yao, J. Y., Yang, D. Z., Wang, F. D., Huang, S. H., Gan, L. B., Jia, Z. S., Jiang, Z. P., Yang, X. B., Zheng, B., Yuan, G., Zhang, S. W., and Wang, Z. M. (2007) Synthesis of [59]fullerenones through peroxide-mediated stepwise cleavage of fullerene skeleton bonds and x-ray structures of their water-encapsulated open-cage complexes. *J. Am. Chem. Soc. 129*, 16149–16162.
(38) *Organic Peroxides* (Swern, D., Ed.) (1971) Wiley-Interscience, New York.
(39) Yoshida, M., Morinaga, Y., Iyoda, M., Kikuchi, K., Ikemoto, I., and Achiba, Y. (1993) Reaction of C_{60} with diacyl peroxides containing perfluoroalkyl groups. The first example of electron transfer reaction via C_{60}^+ in solution. *Tetrahedron Lett. 34*, 7629–7632.
(40) Fieser, L. F., and Turner, R. B. (1947) Naphthoquinone acids and ketols. *J. Am. Chem. Soc. 69*, 2338–2341.
(41) Peng, H. Q., Alemany, L. B., Margrave, J. L., and Khabashesku, V. N. (2003) Sidewall carboxylic acid functionalization of single-walled carbon nanotubes. *J. Am. Chem. Soc. 125*, 15174–15182.
(42) Krause, M., and Dunsch, L. (2005) Gadolinium nitride Gd_3N in carbon cages: The influence of cluster size and bond strength. *Angew. Chem., Int. Ed. 44*, 1557–1560.
(43) Yang, S. F., Kalbac, M., Popov, A., and Dunsch, L. (2006) Gadolinium-based mixed metal nitride clusterfullerenes $Gd_xSc_{3-x}N@C_{80}$ ($x = 1, 2$). *ChemPhysChem 7*, 1990–1995.
(44) Laus, S., Sitharaman, B., Toth, V., Bolskar, R. D., Helm, L., Asokan, S., Wong, M. S., Wilson, L. J., and Merbach, A. E. (2005) Destroying gadofullerene aggregates by salt addition in aqueous solution of Gd@$C_{60}(OH)_x$ and Gd@C_{60}[$C(COOH)_2$]$_{10}$. *J. Am. Chem. Soc. 127*, 9368–9369.
(45) Schneider, G., Altmeyer, K., Kirchin, M. A., Seidel, R., Grazioli, L., Morana, G., and Saini, S. (2007) Evaluation of a novel time-efficient protocol for gadobenate dimeglumine (Gd-BOPTA)-enhanced liver magnetic resonance imaging. *Invest. Radiol. 42*, 105–115.
(46) Toth, E., and Merbach, A. E. (2001) In *The Chemistry of Contrast Agents in Medical Magnetic Resonance Imaging*, Wiley, Chichester.
(47) Sharp, R. R. (2003) Paramagnetic NMR. *Nucl. Magn. Reson.* 473–519.
(48) Lu, X., Xu, J. X., Shi, Z. J., Sun, B. Y., Gu, Z. N., Liu, H. D., and Han, H. B. (2004) Studies on the relaxivities of novel MRI contrast agents two water-soluble derivatives of Gd@C_{82}. *Chem. J. Chin. Univ.-Chin. 25*, 697–700.
(49) Qian, M. C., and Khanna, S. N. (2007) An *ab* initio investigation on the endohedral metallofullerene $Gd_3N@C_{80}$, *J. Appl. Phys.* 101, 09E105 (1−3).
(50) Qian, M. C., Ong, S. V., Khanna, S. N., and Knickelbein, M. B. (2007) Magnetic endohedral metallofullerenes with floppy interiors. *Phys. Rev. B 75*, 104424. 1−6.

(51) Laus, S., Sitharaman, B., Toth, E., Bolskar, R. D., Helm, L., Wilson, L. J., and Merbach, A. E. (2007) Understanding paramagnetic relaxation phenomena for water-soluble gadofullerenes. *J. Phys. Chem. C 111*, 5633–5639.

(52) Sitharaman, B., Bolskar, R. D., Rusakova, I., and Wilson, L. J. (2004) $Gd@C_{60}[C(COOH)_2]_{10}$ and $Gd@C_{60}(OH)_x$: Nanoscale aggregation studies of two metallofullerene MRI contrast agents in aqueous solution. *Nano Lett. 4*, 2373–2378.

(53) Shu, C. Y., Zhang, E. Y., Xiang, J. F., Zhu, C. F., Wang, C. R., Pei, X. L., and Han, H. B. (2006) Aggregation studies of the water-soluble gadofullerene magnetic resonance imaging contrast agent: $[Gd@C_{82}O_6(OH)_{16}(NHCH_2CH_2COOH)_8]_x$. *J. Phys. Chem. B 110*, 15597–15601.

BC900051D

Supporting Information

Facile Preparation of a New Gadofullerene-Based Magnetic Resonance Imaging Contrast Agent with High ^{1}H Relaxivity

Chunying Shu,[†] Frank D. Corwin,[‡] Jianfei Zhang,[†] Zhijian Chen,[#] Jonathan E. Reid,[†] Minghao Sun,[‡] Wei Xu,[§] Jae Hyun Sim,[†] Chunru Wang,[§] Panos P. Fatouros,*[,‡] Alan R. Esker,[†] Harry W. Gibson*[,†] and Harry C. Dorn*[,†]

[†]Chemistry Department, Virginia Polytechnic Institute and State University, Blacksburg, VA 24061
[‡]Department of Radiology, Virginia Commonwealth University, Richmond, VA 23298
[#]Department of Neurosurgery, Virginia Commonwealth University, Richmond, VA 23298
[§]Institute of Chemistry, Chinese Academy of Sciences, Beijing, China 100080

E-mail: ppfatouros@vcu.edu; hwgibson@vt.edu; hdorn@vt.edu

TABLE OF CONTENTS

Experimental Details.

Figure S1. Graphic illustration of the extraction and isolation of $Gd_3N@C_{80}(OH)_x(CH_2CH_2COOM)_y$, M = Na or H

Figure S2. C_{1s} XPS spectra of $Gd_3N@C_{80}(OH)_x(CH_2CH_2COOM)_y$, **2**, (a); and $Sc_3N@C_{80}(OH)_x(CH_2CH_2COOM)_y$ (b). M = H or Na. The curve-fitting analysis reveals at least three different types of carbon atoms centered at binding energies of 284.8, 286.2 and 288.2 eV, respectively.

Figure S3. ^{13}C NMR (125 MHz) of $Sc_3N@C_{80}(OH)_{33}(CH_2CH_2COOM)_{19}$, M=Na or H in D_2O.

Figure S4. FTIR spectrum of $Gd_3N@C_{80}(OH)_x(CH_2CH_2COOM)_y$ in KBr pellet.

Figure S5. UV-visible spectral comparison between $Gd_3N@C_{80}$ in toluene (red line) and **2** in water (black line).

Experimental Details

Succinic acid acyl peroxide (1): Succinic anhydride (4 g) as a fine powder was added to 10 mL of ice cold hydrogen peroxide (8 %) and stirred for 30 min until all of the powder dissolved and a white gel-like solution formed (**Scheme 1-I**). The solution was filtered with a 0.45 μm pore size PTFE membrane filter (PALL); the solid was washed with a small amount of water and air-dried for 10 min. The white peroxide product, mp 106° [lit.(*1*) mp 105-107°] was transferred to a glass vial and vacuum-dried at room temperature for 24 h. Approximately 2.4 g of peroxide **1** was obtained using this one-step procedure reported by Clover et al.(*1*). ^{1}H NMR (500 MHz, acetone-d_6): 2.71 ppm (m); ^{13}C NMR (125 MHz, acetone-d_6): 24.84, 28.03, 168.54, 172.44 ppm.

$Gd_3N@C_{80}(OH)_x(CH_2CH_2COOM)_y$ (M = H, Na) (2): To $Gd_3N@C_{80}$ (4 mg) in 5 mL of *o*-dichlorobenzene was added succinic acid acyl peroxide (**1**) (3.2 mg, 5 eq). The resultant solution was deaerated with flowing argon and heated at 84 °C for 48 h. In intervals of 12 h, more **1** (3.2 mg, 5 eq) was added. After the reaction, a brown sludge precipitated from the solution. Then 8 mL of 0.2 M NaOH aqueous solution were added to extract the water soluble product. Two layers were obtained; the top layer was deep brown and the bottom layer was colorless (Figure S1a). The top layer was concentrated and the residue was purified via a Sephadex G-25 (Parmacia) size-exclusion gel column with pure water as eluent to obtain a narrow brown band with pH = 6~7 (Figure S1b). The yield was 95 % estimated from the ICP calibration. The solubility of the final product in pure water is ca. 13.2 mg/mL. This fraction was characterized by XPS, FT-IR and studied in detail as an MRI contrast agent.

In a separate experiment, the $Gd_3N@C_{80}(OH)_x(CH_2CH_2COOM)_y$ (M = H, Na) sample **2**, was placed in a dialysis membrane (MW cutoff 500 D) and dialyzed for 24 hours. The resulting solution outside the membrane was subjected to ICP analysis and no Gd ion was detected.

$Sc_3N@C_{80}(OH)_x(CH_2CH_2COOM)_y$ (M = H, Na): To $Sc_3N@C_{80}$ (4 mg) in 5 mL of *o*-dichlorobenzene was added succinic acid acyl peroxide (**1**) (4.2 mg, 5 eq). The resultant solution was deaerated with flowing argon and heated at 84 °C for 48 h. In intervals of 12 h, more **1** (4.2 mg, 5 eq) was added. After the reaction, a brown sludge precipitated from the solution. Then 8 mL of 0.2 M NaOH aqueous solution were added to extract the water soluble product. Two layers were obtained; the top layer was deep brown and the bottom layer was colorless. The top layer was concentrated and the residue was purified via a Sephadex G-25 (Parmacia) size-exclusion gel column with pure water as eluent to obtain a narrow brown band with pH = 6~7. This fraction was characterized by XPS, FT-IR together with ^{1}H NMR and ^{13}C NMR. ^{1}H NMR (500 MHz, D_2O): 2.4 ppm (br.); ^{13}C NMR (125 MHz, D_2O/ acetone-d_6): 180 (*C*OOM), 160~120 (C=C), 60~85 (*C*OH), 20~40 ppm (CH_2CH_2).

In a separate experiment, the $Sc_3N@C_{80}(OH)_x(CH_2CH_2COOM)_y$ (M = H, Na) was placed in a dialysis membrane (MW cutoff 500 D) and dialyzed for 24 hours. The resulting solution outside the membrane was subjected to ICP analysis and no Sc ion

(1) Clover, A. M., and Houghton, A. C. (1904) Action of hydrogen peroxide on anhydrides and the formation of organic acid, peroxides, and peracids. *Am. Chem. J. 32*, 43-68.

was detected.

Agarose gel (0.6 %)(*2*): A mixture of agarose powder and 1X TBE (89 mmol/L of tris(hydroxymethyl)aminomethane (Tris, T), 89 mmol/L of boric acid (B) and 2 mmol/L of ethylenediaminetetraacetic acid (E), pH of 8.4) was heated until all the powder had dissolved, and then boiled for 5 min. After it had cooled to 50 ^{o}C, the resulting solution (20 mL) was poured into a thin-wall container mounted with a guide cannula serving as the guidance path for the infusion cannula. The agarose gel solidified as it cooled to room temperature.

---

(2) Fatouros, P. P., Corwin, F. D., Chen, Z. J., Broaddus, W. C., Tatum, J. L., Kettenmann, B., Ge, Z., Gibson, H. W., Russ, J. L., Leonard, A. P., Duchamp, J. C., and Dorn, H. C. (2006) In vitro and in vivo imaging studies of a new endohedral metallofullerene nanoparticle. *Radiology 240*, 756-764.

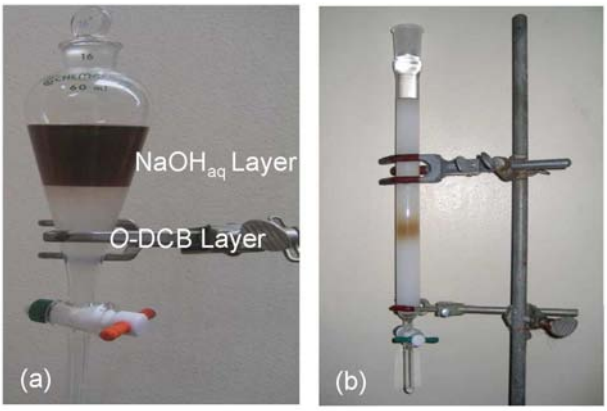

Figure S1. Graphic illustration of the extraction and isolation of $Gd_3N@C_{80}(OH)_x(CH_2CH_2COOM)_y$, M = Na or H.

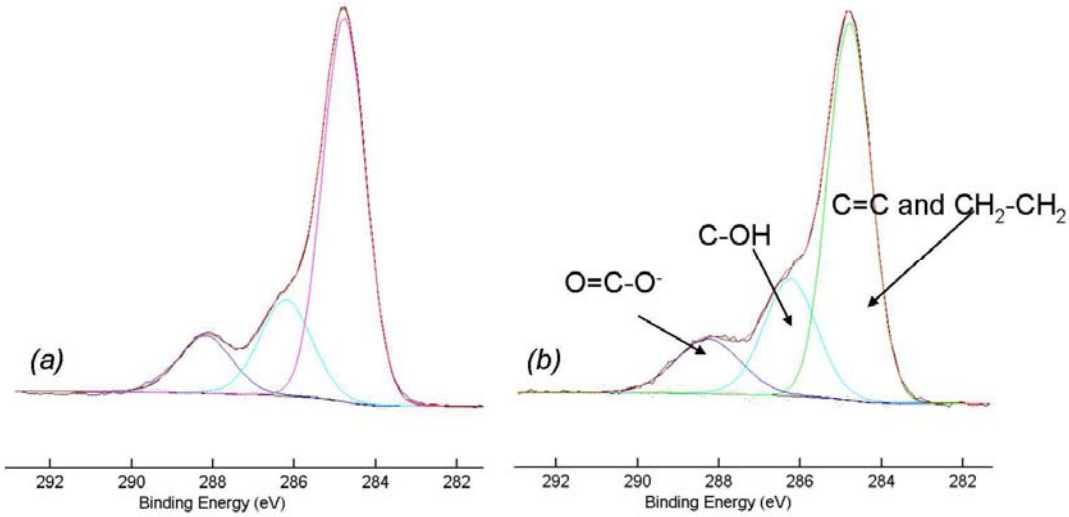

Figure S2. C_{1s} XPS spectrum of $Gd_3N@C_{80}(OH)_x(CH_2CH_2COOM)_y$, **2**, (a); and $Sc_3N@C_{80}(OH)_x(CH_2CH_2COOM)_y$ (b). M = H or Na. The curve-fitting analysis reveals at least three different types of carbon atoms centered at binding energies of 284.8, 286.2 and 288.2 eV, respectively.

The electronic structure of the functionalized gadofullerene **2** was analyzed by measuring the binding energy spectrum for the C_{1s} electrons. The main line of the XPS spectrum (**Figure S2a**) exhibits a broad and asymmetric line-shape. Gaussian analysis suggests the presence of at least three components (indicated by blue, green and purple lines, respectively). The C_{1s} binding energies observed for nonfunctionalized sp^2 carbons and some sp^3 hybridized carbons (C–C and $–CH_2–CH_2–$) are centered at 284.8

eV. Those for hydroxylated (C–OH) and carboxylate (O=C–O) carbons are centered at 286.2 and 288.2 eV, respectively. The intensities of C_{1s} components in **2** were estimated from integration of the peak area under each line. The relative intensities for the sp^2 nonfunctionalized carbon (C=C) and sp^3 hybridized carbons (C–C and $–CH_2–CH_2–$), hydroxylated carbon (C–OH), and carboxylate carbon (O=C–O) are 66.4, 20.9 and 12.7%, respectively. Thus, gadofullerene **2** can be designated as $Gd_3N@C_{80}(OH)_{\sim 26}(CH_2CH_2COOM)_{\sim 16}$ (M = Na, H). As for the water-soluble derivative of $Sc_3N@C_{80}$ (**Figure S2b**), three fitting peaks for C_{1s} were found at 284.8 (61.8%), 286.2 eV (24.3%) and 288.3 eV (13.9%). Therefore, its molecular formula is proposed as $Sc_3N@C_{80}(OH)_{33}(CH_2CH_2COOM)_{19}$, M = Na or H.

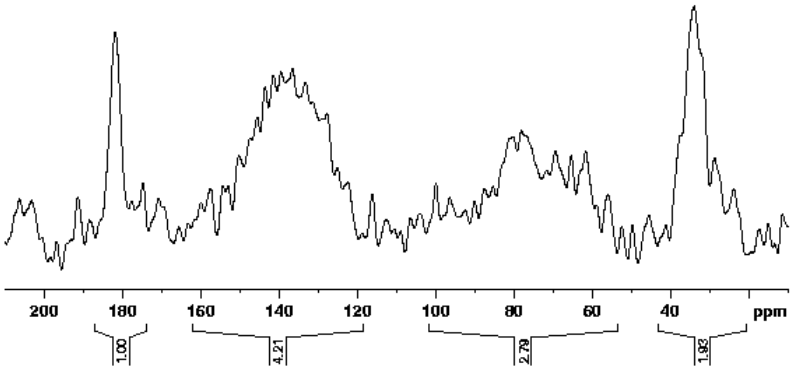

Figure S3. ^{13}C NMR (125 MHz) of $Sc_3N@C_{80}(OH)_{33}(CH_2CH_2COOM)_{19}$, M=Na or H in D_2O/ acetone-d_6.

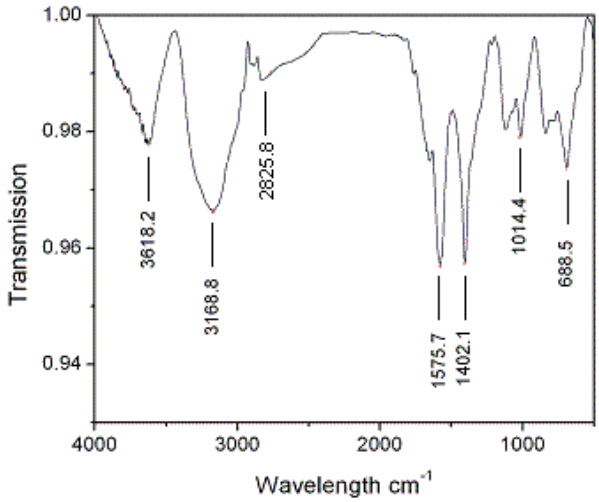

Figure S4. FTIR spectrum of **2** in a KBr pellet.

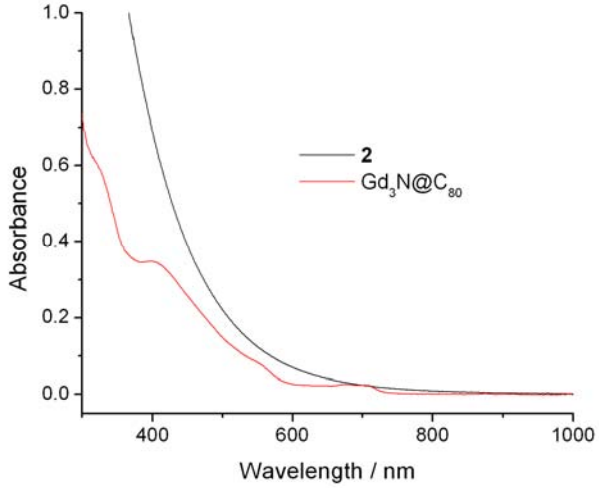

Figure S5. UV-visible spectral comparison between $Gd_3N@C_{80}$ in toluene (red line) and **2** in water (black line).

Synthesis and Immunological Characterization of Toll-Like Receptor 7 Agonistic Conjugates

Michael Chan,[†] Tomoko Hayashi,*[,†] Crystal S. Kuy,[†] Christine S. Gray,[†] Christina C. N. Wu,[†] Maripat Corr,[‡] Wolfgang Wrasidlo,[†] Howard B. Cottam,[†] and Dennis A. Carson[†]

Moores Cancer Center and Department of Medicine, University of California, San Diego. Received February 3, 2009; Revised Manuscript Received March 30, 2009

Activation of toll-like receptors (TLRs) on cells of the innate immune system initiates, amplifies, and directs the antigen-specific acquired immune response. Ligands that stimulate TLRs, therefore, represent potential immune adjuvants. In this study, a potent TLR7 agonist was conjugated to phospholipids, poly(ethylene glycol) (PEG), or phospholipid-PEG via a versatile benzoic acid functional group. Compared to the unmodified TLR7 agonist, each conjugate displayed a distinctive immunological profile in vitro and in vivo. In mouse macrophages and human peripheral blood mononuclear cells, the phospholipid TLR7 agonist conjugate was at least 100-fold more potent than the free TLR7 ligands, while the potency of PEG−phospholipid conjugate was similar to that of the unmodified TLR7 agonist. When administered systemically in mice, the phospholipid and phospholipid−PEG TLR7 conjugates induced prolonged increases in the levels of proinflammatory cytokines in serum, compared to the unmodified TLR7 activator. When the conjugates were used as adjuvants during vaccination, only the phospholipid TLR7 agonist conjugates induced both Th1 and Th2 antigen-specific immune responses. These data show that the immunostimulatory activity of a TLR7 ligand can be amplified and focused by conjugation, thus broadening the potential therapeutic application of these agents.

INTRODUCTION

Toll-like receptors (TLRs) are pattern recognition molecules present on diverse cell types that recognize common ligands in microbes such as bacteria, viruses, and fungi (*1*). Various TLRs interact with lipoprotein (TLR2), double-stranded RNA (TLR3), lipopolysaccharide (LPS, TLR4), flagellin (TLR5), single-stranded RNA (TLR7/8), and unmethylated CpG DNA (TLR9). All TLRs, except TLR3, signal through the myeloid differentiation primary response gene 88 (MyD88) adapter protein, resulting in the activation of NF-κB and the cytokine genes that it regulates (*2*).

The active form of TLR7 is located mainly in the endosomal compartment of innate immune cells, including dendritic cells, mast cells, and B lymphocytes (*3, 4*). The natural ligand for TLR7 was identified as guanine and uridine-rich single-stranded RNA (*5*). In addition, several low molecular weight activators of TLR7 have been discovered, including imidazoquinolines, and purine-like molecules (*3, 6, 7*). Among the latter, 9-benzyl-8-hydroxy-2-(2-methoxyethoxy) adenine (SM360320; designated here as **SM**) has been shown to be a potent and specific TLR7 agonist (*8*). In a previous study, we synthesized a derivative of SM-designated UC1V150, in which the aldehyde functional group on the benzyl moiety enabled coupling the agonist to different auxiliary chemical entities through a bifunctional linker molecule containing a hydrazine and *N*-hydroxysuccinimide activated ester function (*9*). Conjugation to mouse serum albumin (MSA) increased potency by 10- to 100-fold and improved in vivo pharmacodynamics, compared with the free drug (**9**). Moreover, the conjugate (MSA-UC1 V150) could be delivered effectively to the respiratory system by intranasal or intratracheal administration, without inducing a systemic cytokine syndrome. Drug delivery by the intranasal route was effective in reducing mortality in mouse models of bacterial and viral infection (*9*).

An important aspect of TLR biology is the connection between receptor localization, cell activation, and cytokine production. TLR7 and TLR9 are only active when proteolytically processed and loaded into endosomes (*10–12*). The conjugation of various chemical entities to phospholipids is known to facilitate endocytosis. Therefore, we hypothesized that conjugation of a TLR7 activator to a phospholipid would enhance innate immune activation. The conjugation of drugs to poly(ethylene glycol) can promote their circulation time in the blood and potentially increase solubility in water (*13*). It was therefore of interest to determine if conjugation of a TLR7 agonist to PEG could alter its in vivo pharmacodynamics.

EXPERIMENTAL PROCEDURES

Materials. 1,2-Dioleoyl-*sn*-glycero-3-phosphoethanolamine (DOPE) was purchased from Avanti Polar Lipids (Alabaster, AL). All other reagents were purchased as at least reagent grade from Sigma-Aldrich (St. Louis, MO) without further purification. Solvents were purchased from Fischer Scientific (Pittsburgh, PA) and were either used as purchased or redistilled with an appropriate drying agent. Ovalbumin (OVA, grade V) was purchased from Sigma-Aldrich.

Endotoxin levels in the reagents and conjugates for experiments of immunological activities were measured using the QCL1000 end point chromogenic Limulus Amoebocyte Lysate (LAL) assay purchased from BioWhittaker (Walkerville, MD). Reagents that contained less than 1 pg endotoxin per μg protein or drug were used throughout the experiments. Since DOPE gave false positive results in the chromogenic endotoxin assay, bone marrow derived macrophages (BMDM) from lipopolysaccharide unresponsive mutant mice (C3H/HeJ) were used to test

* Corresponding author: Tomoko Hayashi, University of California San Diego, Moores Cancer Center, 3855 Health Science Drive, La Jolla CA 92093-0820; phone 858-822-0253, FAX 858-534-5399, thayashi@ucsd.edu.

[†] Moores Cancer Center.

[‡] Department of Medicine.

10.1021/bc900054q CCC: $40.75 © 2009 American Chemical Society
Published on Web 05/15/2009

contamination by endotoxin (Supporting Information Figure 1). The levels of cytokine production by bone marrow derived mononuclear cells from C3H/HeJ mice were similar to the levels in cells derived from the wild-type C3H/HeOuJ strain, indicating that endotoxin contamination was negligible (Supporting Information Figure 1).

All conjugates were stored at −80 C° as dry powders. The conjugates were dissolved in DMSO at 100 mM and further diluted before immunological assays.

Instrumentation. Analytical TLC was performed using precoated TLC silica gel 60 F_{254} aluminum sheets purchased from EMD (Gibbstown, NJ) and visualized using UV light. Flash chromatography was carried out on EMD silica gel 60 (40−63 μm) using the specified solvent system. Chromatography and mass spectra (ESI) for compounds without phospholipids were recorded on a 1100 LC/MSD (Agilent Technologies, Inc., Santa Clara, CA) with a Supelco Discovery HS C18 column (Sigma-Aldrich) with purity above 98% by percent area. Mass spectra (ESI) of phospholipid-containing compounds were recorded on a Finnigan LCQDECA (Thermo Fisher Scientific Inc., Waltham, MA). ^{1}H NMR spectra were obtained on a Varian Mercury Plus 400 (Varian, Inc., Palo Alto, CA). The chemical shifts are expressed in parts per million (ppm) using suitable deuterated NMR solvents in reference to TMS at 0 ppm. UV absorbance for solubility experiments were measured using a NanoDrop ND-1000 spectrophotometer (Wilmington, DE).

4-{[6-Amino-2-(2-methoxyethoxy)-8-oxo-7*H*-purin-9(8*H*)-yl]methyl}benzoic Acid (5). To 4-{[6-amino-8-methoxy-2-(2-methoxyethoxy)-9*H*-purin-9-yl]methyl}benzonitrile (**1**) (0.10 g, 0.28 mmol) was added 1:1 ethanol/10M NaOH (20 mL) and refluxed for 8 h. The reaction mixture was allowed to cool and acidified to pH 2 with conc HCl. The aqueous solution was extracted with dichloromethane (DCM) (3 × 20 mL), dried over $MgSO_4$, and evaporated in vitro to yield a mixture of the 8-oxo-9-benzoic acid (**5**), 8-methoxy-9-benzoic acid, and 8-oxo-9-ethyl benzoate. Once dried, the products were dissolved in CH_3CN (25 mL) and NaI (0.14 g, 0.96 mmol) was added. To this solution was added chlorotrimethylsilane (12 μL, 0.96 mmol) dropwise with stirring. The reaction mixture was heated at 40 °C for 4 h, then cooled, filtered, and washed with water (20 mL) and then diethyl ether (20 mL) to obtain a white solid in 85% yield. ^{1}H NMR (400 MHz, DMSO-d_6) δ (ppm): 10.33 (s, 1H), 7.89 (d, J = 8 Hz, 2H), 7.37 (d, J = 8 Hz, 2H), 6.65 (s, 2H), 4.92 (s, 2H), 4.24 (t, J = 4 Hz, 2H), 3.56 (t, J = 4 Hz, 2H), 3.25 (s, 3H). Retention time (Rt) on HPLC = 14.3 min. ESI-MS (positive ion mode): calculated for $C_{16}H_{17}N_5O_5$ m/z [M+1] 360.34; found 360.24.

2-(4-{[6-Amino-2-(2-methoxyethoxy)-8-oxo-7*H*-purin-9(8*H*)-yl]methyl}benzamido)ethyl 2,3-Bis(oleoyloxy)propyl Phosphate (6). To a solution of compound **5** (0.022 g, 0.06 mmol) in anhydrous *N*,*N*-dimethylmethanamide (DMF) (1 mL) was added *O*-(7-azabenzotriazol-1-yl)-*N*,*N*,*N*′,*N*′-tetramethyluronium hexafluorophosphate (HATU) (0.026 g, 0.067 mmol) and anhydrous triethylamine (TEA) (17.0 μL, 0.12 mmol). A solution of 1,2-dioleoyl-*sn*-glycero-3-phosphoethanolamine (0.05 g, 0.067 mmol) in anhydrous 1:1 DCM/DMF (1 mL) was prepared and slowly added to the reaction mixture. The reaction mixture was stirred at room temperature until completion and then evaporated in vitro. The product was purified by flash chromatography using 15% methanol (MeOH) in DCM to give 0.038 g of white solid in 58% yield. ^{1}H NMR (400 MHz, DMSO-d_6) δ (ppm): 9.7 (s, 1H), 7.87 (d, J = 8.3 Hz, 2H), 7.32 (d, J = 8.3 Hz, 2H), 6.61 (s, 2H), 5.30 (m, 4H), 5.05 (m, 1H), 4.88 (s, 2H), 4.26 (m, 4H), 4.06 (m, 1H), 3.77 (m, 4H), 3.57 (m, 2H), 3.35 (m, 2H), 3.26 (s, 3H), 2.23 (m, 4H), 1.95 (m, 8H), 1.46 (m, 4H), 1.22 (m, 40H), 0.83 (m, 6H). ESI-MS (negative ion mode): calculated for $C_{57}H_{92}N_6O_{12}P$ m/z [M−1] 1083.35; found 1083.75. HR-ESI-FT-MS (positive ion mode): calculated for $C_{57}H_{92}N_6O_{12}PNa$ m/z [M+Na+1] 1107.6481; found 1107.6477.

4-{[6-Amino-8-hydroxy-2-(2-methoxyethoxy)-9*H*-purin-9-yl]-methyl}-*N*-(32-azido-3,6,9,12,15,18,21,24,27,30-decaoxadotriacontyl)benzamide (7). To a solution of compound **5** (0.100 g, 0.278 mmol) in anhydrous DMF (5 mL) was added HATU (0.117 g, 0.306 mmol) and anhydrous TEA (77.014 μL, 0.556 mmol). A solution of *O*-(2-aminoethyl)-*O*′-(2-azidoethyl)nonaethylene glycol (0.150 g, 0.306 mmol) in anhydrous DMF (1 mL) was prepared and slowly added to the reaction mixture. The reaction mixture was stirred at room temperature until completion and then evaporated in vitro. The product was purified by flash chromatography using 5% MeOH in DCM to give 0.224 g of an opaque oil in 93% yield. Rt = 12 min. ^{1}H NMR (400 MHz, DMSO-d_6) δ (ppm): 10.01 (s, 1H), 8.45 (t, J = 5.6 Hz, 1H), 7.78 (d, J = 8.3 Hz, 2H), 7.35 (d, J = 8.3 Hz, 2H), 6.49 (s, 2H), 4.90 (s, 2H), 4.25 (t, J = 4 Hz, 2H), 3.57 (m, 4H), 3.5 (m, 36H), 3.4 (M, 6H), 3.26 (s, 3H). ESI-MS (positive ion mode): calculated for $C_{38}H_{61}N_9O_{14}$ m/z [M+1] 868.94; found 868.59.

3-{1-[1-(4-{[6-Amino-8-hydroxy-2-(2-methoxyethoxy)-9*H*-purin-9-yl]methyl}phenyl)-1-oxo-5,8,11,14,17,20,23,26,29,32-decaoxa-2-azatetratriacontan-34-yl]-1*H*-1,2,3-triazol-4-yl}propanoic Acid (8). Compound **7** (0.218 g, 0.251 mmol) and 4-pentynoic acid (0.074 g, 0.753 mmol) was dissolved in 1:1 *t*-butanol/H_2O (3 mL). Sodium ascorbate (0.02 g, 100 mmol) and $Cu(OAc)_2$ (0.009 g,50 mmol) in 1:1 *t*-butanol/H_2O (1 mL) was slowly added to the reaction mixture and stirred at room temperature until compound **7** was fully reacted by TLC. The product was extracted with DCM (10 mL) and H_2O (10 mL), and the organic layer was dried over $MgSO_4$ to give 0.230 g of an opaque oil in 95% yield. Rt = 11.5 min. ^{1}H NMR (400 MHz, DMSO-d_6) δ (ppm): 13.48 (s, 1H), 7.76 (d, J = 8.29 Hz, 2H), 7.75 (s, 1H), 7.23 (d, J = 8.29, 2H), 4.88 (s, 2H), 4.41 (t, J = 5.12 Hz, 2H), 4.23 (t, J = 4 Hz, 2H), 3.74 (t, J = 5.12 Hz, 2H), 3.57 (t, J = 4 Hz, 2H), 3.51 (m, 8H), 3.42 (m, 36H), 3.26 (s, 3H), 2.79 (t, J = 7.56 Hz, 2H), 2.24 (t, J = 7.56 Hz, 2H). ESI-MS (positive ion mode): calculated for $C_{43}H_{67}N_9O_{16}$ m/z [M+1] 966.04; found 966.67.

2-(3-{1-[1-(4-{[6-Amino-8-hydroxy-2-(2-methoxyethoxy)-9*H*-purin-9-yl]methyl}phenyl)-1-oxo-5,8,11,14,17,20,23,26,29,32-decaoxa-2-azatetratriacontan-34-yl]-1*H*-1,2,3triazole-4-yl}propanamido)ethyl 2,3-Bis(oleoyloxy)propyl Phosphate (9). To a solution of compound **8** (96 mg, 0.1 mmol) and HATU (42 mg, 0.11 mmol) in anhydrous DMF (1 mL) was added anhydrous TEA (2.7 uL, 0.2 mmol). A solution of DOPE (81.4 mg, 0.11 mmol) in 1:1 DCM/DMF (1 mL) was added dropwise to the reaction mixture and stirred at room temperature until completion. Upon completion, the product was isolated by evaporation in vitro followed by flash chromatography using 15% MeOH in DCM to give 155 mg of opaque oil in 92% yield. ^{1}H NMR (400 MHz, DMSO-d_6) δ (ppm): 8.5 (s, 2H), 8.39 (s, 1H), 7.79 (m, 3H), 7.33 (d, J = 6.23 Hz, 2H), 6.91 (s, 2H), 5.31 (m, 4H), 5.05 (m, 1H), 4.89 (s, 2H), 4.46 (m, 2H), 4.23 (m, 4H), 4.08 (t, J = 8 Hz, 2 H), 3.76 (m, 4H), 3.63 (t, J = 8 Hz, 2H), 3.56 (t, J = 8 Hz, 2H), 3.48 (m, 36H), 3.26 (m, 5H), 3.17 (m, 2H), 2.82 (t, J = 8 Hz, 2H), 2.39 (t, J = 8 Hz, 2H), 2.24 (m, 4H), 1.96 (m, 8H), 1.48 (m, 4H), 1.23 (m, 40H), 0.84 (m, 6H). ESI-MS (positive ion mode): calculated for $C_{84}H_{142}N_{10}O_{23}P$ m/z [M+1] 1691.05; found 1692.82.

Mice. 6−8 week old female C57BL/6 mice were purchased from Charles River Laboratories (San Diego, CA). C3H/HeJ and C3H/HeOuJ mice were purchased from The Jackson Laboratories (Bar Harbor, ME). TLR7 deficient mice were a gift from Dr. S. Akira, (Osaka University, Osaka, Japan) and were backcrossed ten generations onto the C57BL/6 background. Animals were bred and maintained at UCSD in rooms at 22 ±

0.5 °C on a 12/12 h light−dark cycle from 7 a.m. to 7 p.m. All procedures and protocols were approved by the Institutional Animal Care and Use Committee.

In Vitro Measurements of Cytokine Induction. The RAW264.7 (mouse leukemic monocyte macrophage cell line) was obtained from the ATCC (Rockville, MD) and cultured in DMEM (Irvine Scientific, Irvine, CA) supplemented with 10% heat-inactivated fetal bovine serum, 2 mM L-glutamine, and 100 U/mL penicillin/100 μg/mL streptomycin. BMDM were prepared from C57BL/6, TLR7 deficient, C3H/HeJ, and C3H/HeOuJ mice as described (*9*). The cells (1×10^6/mL) were incubated with the conjugates for 18 h at 37 °C, 5% CO_2, and culture supernatants were collected. The levels of cytokines (IL-6, IL-12, or TNFα) in the supernatants were determined by ELISA (BD Biosciences Pharmingen, La Jolla, CA) (*12*). Minimum detection levels of these cytokines were 15 pg/mL, respectively.

Human blood peripheral mononuclear cells (PBMC) were isolated from human buffy coats obtained from The San Diego Blood Bank (San Diego, CA) as described previously (*11*). PBMC (1×10^6/mL) were incubated with various compounds for 18 h at 37 °C, 5% CO_2, and culture supernatants were collected. The levels of cytokines (IL-6, TNFα, or IFNα1) in the supernatants were determined by Luminex bead assays (Invitrogen, Carlesbad, CA) due to the relatively small sample volume. The minimum detection levels of IL-6, TNFα, and IFNα1 were 6 pg/mL, 10 pg/mL, and 15 pg/mL, respectively.

In Vivo Experimental Procedures. For in vivo pharmacokinetic experiments, 6 to 8 week old C57BL/6 mice were intravenously injected with the TLR7 agonist and its conjugates (40 nmol **4a** or 200 nmol **SM**, **6**, **8**, or **9** per mouse as described in the figure legends). The solubility was measured in 10% DMSO in saline at room temperature for 30 min at a maximum theoretical concentration of 1 mM. The aqueous concentrations of compounds **SM**, **6**, **8**, and **9** were measured by UV absorption, and the concentration was derived by comparison to standard curves with four calibration concentrations in DMSO (Supporting Information Table 1). The solutions were homogeneous, and no precipitates were noted prior to i.v. administration. Blood samples were collected 2, 4, 6, 24, or 48 h after the injections. Sera were separated and kept at −20 °C until use. The levels of cytokines in the sera were measured by Luminex bead microassay due to the small sample volume. The minimum detection levels of IL-6 and TNFα were 5 pg/mL and 10 pg/mL, respectively.

For the adjuvanticity experiments, mice were subcutaneously immunized with 20 μg ovalbumin (OVA) with 10 nmol of TLR7 equivalent dose per mouse in various TLR7 conjugates on days 0 and 7. A TLR9 activating immunostimulatory oligonucleotide sequence (ISS-ODN, 1018) was used as a positive control for a Th1 inducing adjuvant (*10*). Sera were collected on days 0, 7, 14, 21, 28, 42, and 56. Mice immunized with saline or OVA mixed with vehicle served as controls. Mice were sacrificed on day 56, and the spleens were harvested. Approximately 2.5×10^6/mL spleen cells were aliquoted into round-bottom tissue culture microtiter plates in triplicate in a total volume of 200 μL RPMI 1640 complete medium [RPMI1640 (Irvine Scientific, Irvine, CA) supplemented with 10% heat-inactivated FCS, 2 mM L-glutamine, and 100 U/mL penicillin/100 μg/mL streptomycin] and restimulated with either 100 μg/mL OVA or medium alone. Cultures were then incubated at 37 °C, 5% CO_2, and supernatants harvested after 72 h. The levels of IFNγ in the culture supernatants were measured by ELISA (BD Bioscience PharMingen) as per the manufacturer's instructions (*14*). The average total spleen cell numbers in each group were calculated and compared to the control group to monitor spleen cell proliferation.

Anti-OVA antibodies of the IgG subclasses, IgGl and IgG2a, were measured by ELISA, as described (*12*). Each ELISA plate contained a titration of a previously quantitated serum to generate a standard curve. The titer of this standard was calculated as the highest dilution of serum that gave an absorbance reading that was double the background. The various sera samples were tested at a 1:100 dilution. The results are expressed in units per mL, calculated based on the units/mL of the standard serum, and represent the mean ± SEM of five animals in each group.

In some experiments, the site of injection was examined 24 h after immunization for signs of inflammation or local reaction. Mice were observed for locomotor activity to assess a "sickness" response to immunization and then weighed weekly.

Histological Examination. In the adjuvanticity experiments, the spleens, lungs, livers, hearts, and kidneys were collected on day 56. The organs were fixed in 10% buffered formalin (Fisher Scientific) and embedded in paraffin. Sections 5 μm thick were stained with hematoxylin and eosin (H&E) and evaluated under the microscope.

Statistical Analysis. A software package (*Prism 4.0*, GraphPad, San Diego CA) was used for statistical analyses including regression analyses. Data were plotted and fitted by nonlinear regression assuming a Gaussian distribution with uniform standard deviations between groups. The statistical differences were analyzed by two-way ANOVA with Bonferroni's post hoc, Dunnett's post hoc, or Student's *t* test. A value of $P < 0.05$ was considered statistically significant.

RESULTS

Chemical Synthesis. The synthesis of compound **4** from compound **1** yielded a consistent conjugation ratio of 5:1 UC1 V150 to MSA protein (*9*). Basic hydrolysis of the 9-benzylnitrile of compound **1** (*8*) provided a versatile benzoic acid functional group (*5*) in 85% yield and allowed for the assembly of conjugates **6**, **8**, and **9** (Scheme 1). The benzoic acid was coupled with DOPE by activation with HATU in the presence of TEA in anhydrous DMF to give compound **6** in 58% yield. Due to the difficulty in dissolution of compound **6** in suitable solvents for testing, a PEG spacer was coupled to provide improved solubility. A readily available amine/azide bifunctional PEG was coupled to the benzoic acid by activation with HATU in the presence of TEA in anhydrous DMF to give compound **7** in 93% yield. The formation of a 1,2,3-triazole through a copper(I)-catalyzed azide−alkyne cycloaddition with 4-pentynoic acid gave compound **8** in 95% yield. Finally, compound **9** was prepared by HATU activated amide formation with DOPE and compound **8** (92% yield).

Cytokine Induction by a Phospholipid-Conjugated TLR7 Agonist. The in vitro potency of the phospholipids TLR agonist conjugate (**6**), PEG-TLR7 agonist conjugate (**8**), PEG-phospholipid (**9**) conjugate, and the MSA-TLR7 agonist conjugate were compared using the murine macrophage cell line, RAW264, and primary bone marrow derived macrophages (BMDM) (Figure 1A,B). The respective cells were stimulated for 18 h with serially diluted TLR7 agonist conjugates, and the levels of cytokines released in the media were measured by ELISA and compared to the unconjugated TLR7 agonist (**SM**).

As previously shown, the MSA-TLR7 agonist conjugate (**4a**) was approximately 100-fold more potent as a cytokine inducer compared to the unconjugated agonist. In the same system, the phospholipid-TLR7 conjugate was 10-fold more potent, when normalized to the molar level of the pharmacophore ($P < 0.0001$ compared to unconjugated TLR7 agonist in RAW cells and BMDM). Although the PEG-TLR7 agonist conjugates (**8**) showed less potency compared to the unconjugated TLR7 agonist (**SM**) ($P < 0.001$ in RAW cells), the hybrid phospho-

Scheme 1. Synthesis of the Phospholipid- (6), PEG- (8), Phospholipid-PEG (9) TLR7 Conjugates[a]

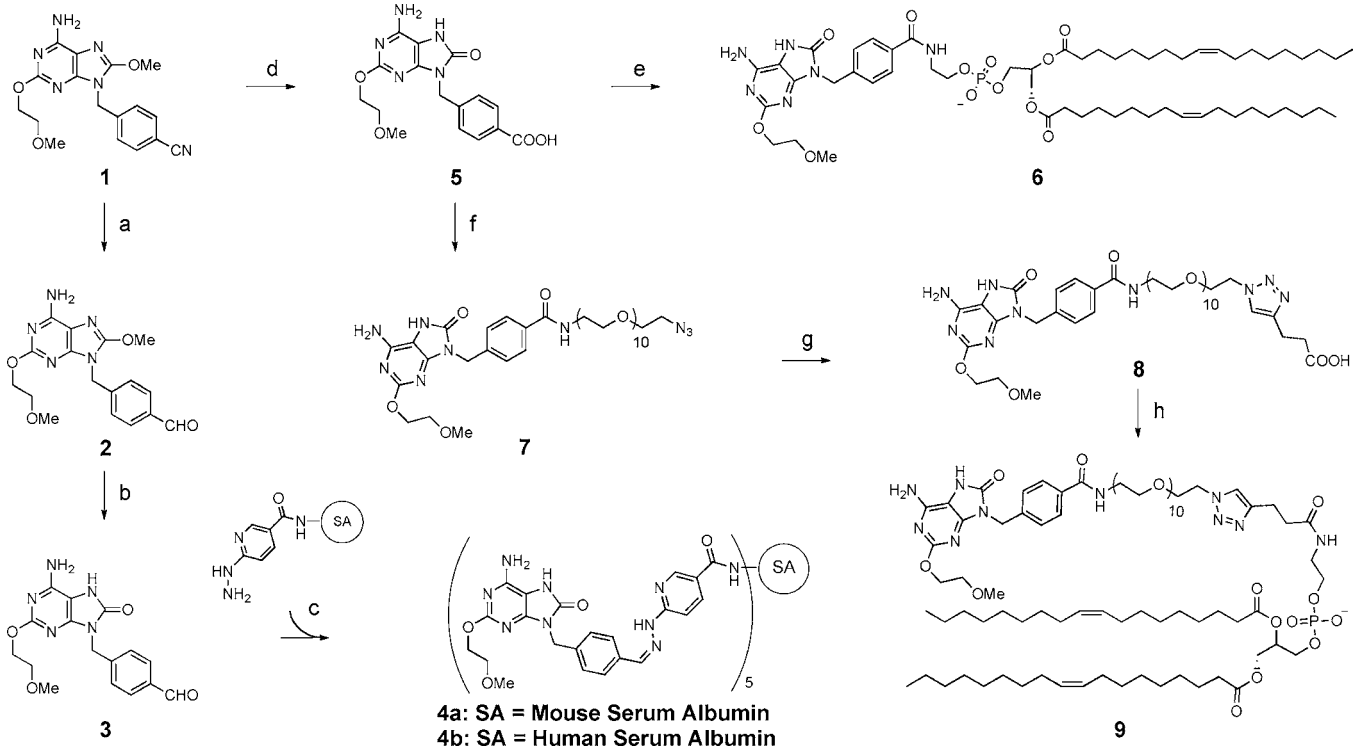

[a] (a) Lithium *N*,*N*′-methylethylenediaminoaluminum hydrides THF, 0° C; (b) NaI, chlorotrimethylsilane, CH_3CN, r.t; (c) PBS, r.t.; (d) NaOH: EtOH 1:1, reflux; (e) DOPE, HATU, triethylamine,DMF/DCM 1:1, r.t.; (f) *O*-(2-Aminoethyl)-*O*$_2$-(2-azidoethyl)nonaethylene glycol, HATU, triethylamine, DMF, r.t.; (g) 4-pentyonic acid, sodium ascorbate, $Cu(OAc)_2$, t-BuOH/H_2O/THF 2:2:1, r.t; (h) DOPE, HATU, triethylamine, DMF/DCM 1:1, r.t.

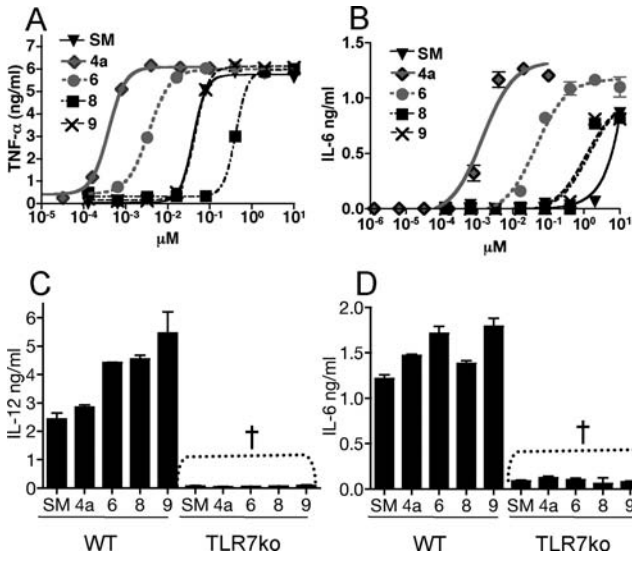

Figure 1. In vitro immunological characterization of TLR7 conjugates in murine macrophages. 1×10^6/mL RAW 264.7 cells (A), or 0.5×10^6/mL BMDM derived from wild-type (B−D) or TLR7 deficient mice (C,D) were incubated with serially diluted TLR7 conjugates for 18 h. Serial dilutions of **SM** (triangle), **6** (gray circle), **8** (solid square), and **9** (ex) were prepared (steps of 1:5) starting from 10 μM. **4a** (gray rhombus) was serially diluted (steps of 1:5), starting from 0.1 μM. The levels of TNFα, IL-6, and IL-12 in the culture supernatants were measured by ELISA. Data are mean ± SEM of triplicates and are representatives of three independent experiments. $P < 0.001$ by two-way ANOVA with Bonferroni post hoc test in comparison between **SM** and **6**. * denotes $P < 0.01$ by Student's *t* test compared to the corresponding data of wild-type macrophages.

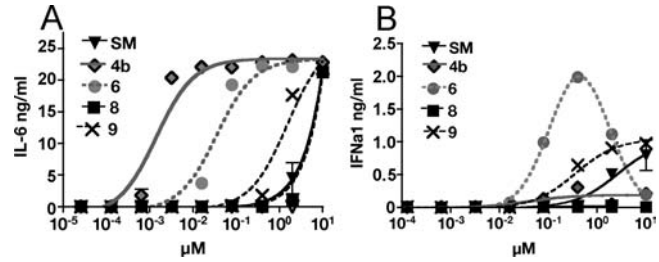

Figure 2. In vitro immunological characterization of TLR7 conjugates in human PBMC. 2×10^6/mL human PBMC were incubated with serially diluted TLR7 conjugates for 18 h. Serial dilutions of SM (triangle), 6 (gray circle), 8 (solid square), and 9 (ex) were prepared (steps of 1:5) starting from 10 μM. **4a** (gray rhombus) was serially diluted (steps of 1:5), starting from 0.1 μM. The levels of IL-6 (A) and IFNα1 (B) in the culture supernatants were determined by Luminex assay in duplicate. Data are means ± SEM and are representative of three independent experiments. The order of potency is **4b** > **6** > **9** > **SM** = **8** ($P < 0.0005$ by two-way ANOVA test for compounds **4b**, **6**, **9**, and **SM**; $P = 0.2$ by two-way ANOVA test for compound **8**).

lipid-PEG-TLR7 agonist was as potent as the unconjugated drug (**SM**). Equivalent concentrations of MSA, phospholipid, or PEG, processed without TLR7 conjugation, induced minimal or no cytokine levels in RAW264.7 cells and BMDM, respectively (data not shown).

To confirm that the conjugated forms of the TLR7 agonist stimulated exclusively via TLR7 activation, BMDM derived from TLR7 deficient mice were analyzed (Figure 1C,D). Compounds **4a**, **6**, **8**, **9**, and **SM** induced little or no IL-12 and IL-6 production in the TLR7 deficient cells, whereas these conjugates were active in wild-type BMDM. To assess the immunological effects of the conjugates in human cells, PBMC from three separate donors were treated with the different agents, and the levels of IL-6 and IFNα1 released into the supernatants were determined (Figure 2A,B). Human serum albumin (HSA) conjugated to the TLR7 agonist (**4b**) was used instead of MSA-

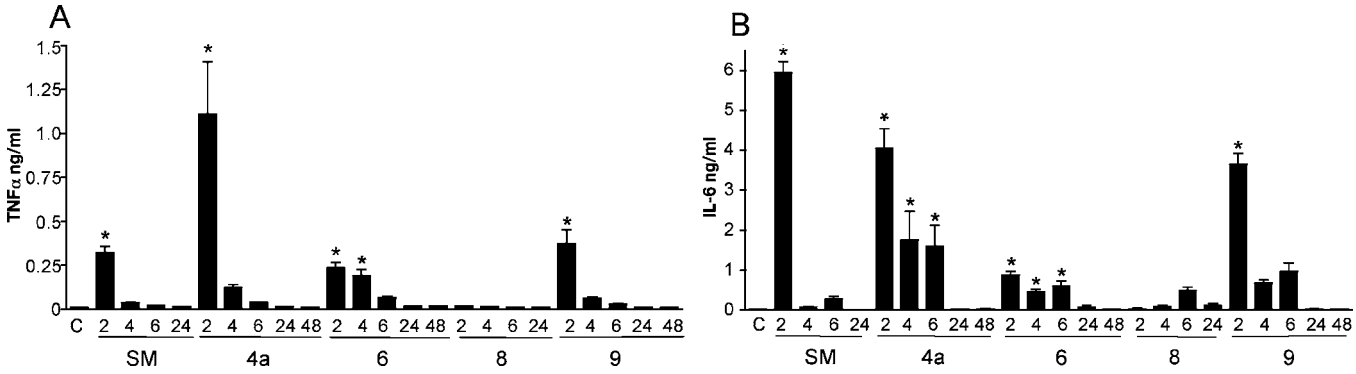

Figure 3. Kinetics of proinflammatory cytokine induction by TLR7 conjugates in vivo. C57BL/6 mice ($n = 5$ per group) were intravenously injected TLR7 conjugates (**SM**, 200 nmol; **4a**, 40 nmol; **6**, 200 nmol; **8**, 200 nmol; **9**, 200 nmol). Serum samples were collected 2, 4, 6, 24, and 48 h after injection. The levels of TNFα (A) and IL-6 (B) were measured by Luminex assay. Data are means ± SEM of five mice and are representative of two independent experiments. (C) Control naïve mice. * denotes $p < 0.05$ compared to the naïve mice by one-way ANOVA tests with Bonferroni post hoc testing.

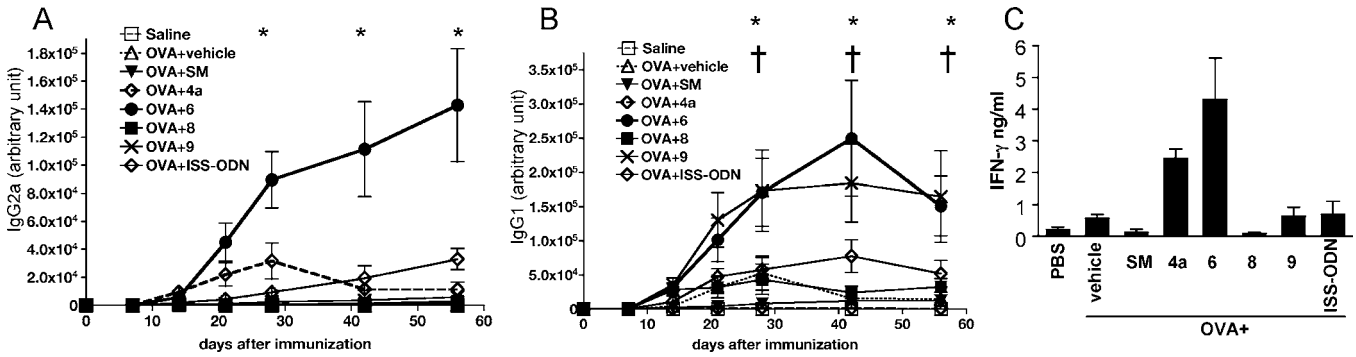

Figure 4. Adjuvanticity of TLR7 conjugates in vivo. Groups of C57BL/6 ($n = 5$ per group) were subcutaneously immunized with 20 μg OVA mixed with TLR7 conjugates (10 nmol TLR7 equivalent dose per mouse) on days 0 and 7. Sera were collected days 0, 7, 14, 21, 28, 42, and 56. OVA specific IgG1 and IgG2a were measured by ELISA (A and B). On day 56, mice were sacrificed, and splenocytes were cultured with OVA (100 μg/mL) in RPMI1640 for 3 d. IFNγ level in the supernatant was measured by ELISA (C). Data are means ± SEM of 5 mice/group and are representative of 3 independent experiments. * and † denote $P < 0.05$ and $P < 0.01$ by one-way ANOVA with Dunnett's post hoc comparison to the mice immunized with OVA mixed with vehicle, respectively.

conjugates (**4a**) for this experiment, to avoid any effects of anti-MSA antibodies. The order of potency of the conjugates was similar in human PBMC and mouse BMDM (**4b** > **6** > **9** > **SM** = **8**) (Figure 2A). Compound **4b** induced minimal levels of IFNα1 in all of the human PBMC samples tested (Figure 2B).

In Vivo Kinetics of Induction of Pro-Inflammatory Cytokines by TLR Agonist Conjugates. To compare the in vivo immunological properties of the different TLR7 agonist conjugates, C57BL/6 mice were injected intravenously with the agents, and cytokine levels in sera were assayed at various time intervals (Figure 3A,B). On the basis of the results of a previous study (*9*), compound **4a** was used at a lower concentration (40 nmol per animal) than compounds **SM**, **6**, **8**, and **9** (200 nmol per animal). The maximum induction of TNFα and IL-6 was observed 2 h after injection with all the TLR7 conjugates (Figure 3A,B). Although the levels of the cytokines induced by the unconjugated TLR7 agonist (**SM**) declined rapidly after 2 h, cytokine induction by compounds **4a**, **6**, and **9** was sustained for up to 6 h. Compound **8** induced only a low level of IL-6, and undetectable TNFα, 6 h after injection (Figure 3B). Sera from control mice that received saline, MSA, or DOPE revealed little or no detectable cytokine levels (data not shown).

Phospholipid-TLR7 Agonist Conjugates Promote Rapid and Long-Lasting Humoral Immune Responses. The adjuvanticity of the different conjugates was assessed by the levels and isotypes of antigen-specific IgG induced after immunization of mice with ovalbumin (OVA) and drug (*15*), as well as by antigen-induced synthesis of interferon γ (IFNγ). Groups of C57BL/6 ($n = 5$ animals per group) were subcutaneously injected with OVA mixed with the various TLR7 conjugates. A TLR9 activating immunostimulatory oligonucleotide sequence (ISS-ODN, 1018) is known to stimulate Th1 immune response and was used as a positive control for a Th1 inducing adjuvant (*10*). The kinetics of OVA-specific serum IgG1 and G2a on days 0, 7, 14, 21, 28, 42, and 56 were monitored by immunoassay (Figure 4A,B). Induction of IgG was observed as early as 14 days in mice immunized with OVA and compound **4a** or compound **6** (Figure 4A). The anti-OVA IgG2a levels increased thereafter in mice immunized with OVA and compound **6**, while the levels in mice immunized with OVA and compound **4a** mixture declined progressively. The spleen cells of mice immunized with OVA combined with compound **4a** or **6** displayed enhanced OVA-specific IFNγ secretion, compared to mice immunized with OVA alone or OVA and a TLR9 agonist (Figure 4C).

Adverse Effects. We previously reported that 150 nmol of the TLR7 agonist **SM** induced anorexia and weight loss in mice after intranasal administration (*16*). We, therefore, monitored both body weights and local skin inflammation in mice immunized with the phospholipid-TLR7 agonist conjugate. At the dose of TLR7 agonist that was an effective adjuvant (10 nmol per mouse), no weight loss or behavioral changes were noted. Chronic administration of TLR7 agonists can also stimulate hematopoietic cell proliferation, leading to spleen and lymph node hyperplasia (*17*). However, there were no significant differences in the numbers of splenocytes or myeloid cells between mice immunized with OVA alone, compared to TLR7 agonist conjugates and the saline control mice (Figure 5A).

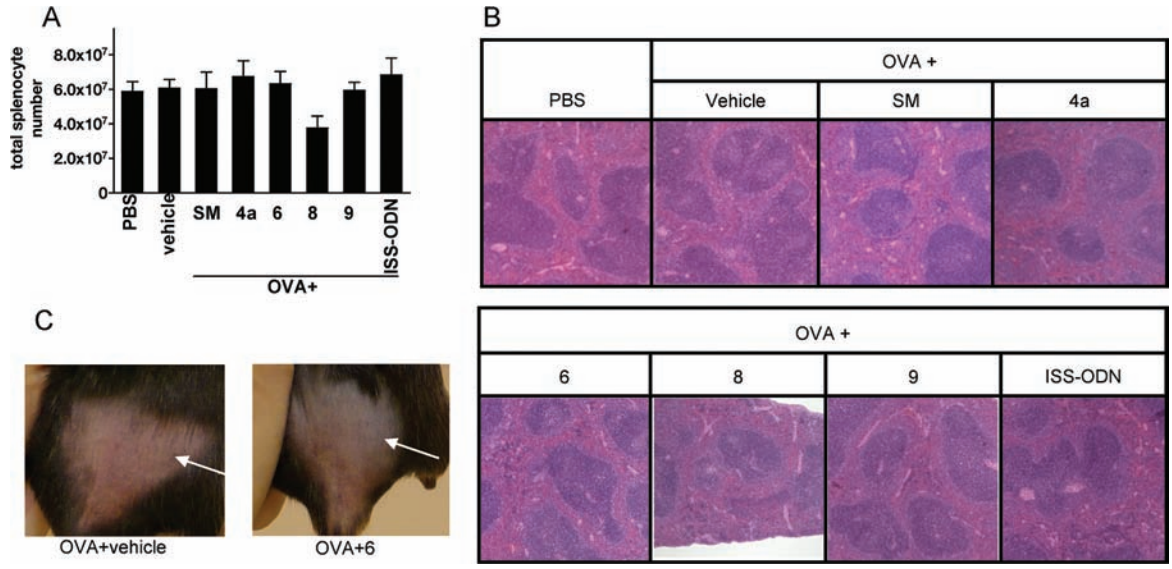

Figure 5. Evaluation of possible adverse effects of TLR7 conjugates. C57BL/6 mice were immunized with OVA 20 μg with TLR7 conjugate. On day 56, mice were sacrificed, and the number of total splenocytes was determined (A). The spleens were collected and submitted for histological examination ($\times$100) (B). The skin at injection sites was inspected 24 h after injection (C). There was no significant difference in the splenocyte number between the mice immunized with OVA plus TLR7 conjugates and the mice immunized with OVA alone (A). Histological examination of the spleens from mice immunized with OVA mixed with TLR7 conjugates did not show any disruption of the white pulps or increased cellularity in red pulp (B). The skin at injection sites did not have visible redness (C).

Histological examination of spleens from mice immunized with OVA plus TLR7 agonist conjugate showed no structural disruption of the white pulp and no increased cellularity in the red pulp (Figure 5B). Moreover, no significant differences were observed in the histological appearance of the liver, lung, heart, and kidney samples collected from each group (data not shown). There was also no significant erythema or warmth at the sites of injection (Figure 5C).

DISCUSSION

TLR7 agonists are not active unless delivered to endosomal vesicles where the active receptor resides (*18*). Previous experiments showed that the conjugation of a TLR7 agonist to serum albumin greatly increased potency, compared to the unconjugated drug (**9**). Presumably, the modified albumin quickly interacted with scavenger receptors on macrophages and dendritic cells, followed by endocytosis. However, modified proteins are not generally suitable for adjuvants, as they are difficult to standardize, store, and administer, and may be immunogenic. Therefore, we conjugated a TLR7 agonist to phospholipids (**6**), which are widely used to deliver drugs to cells. The phospholipid-TLR7 conjugated was 10-fold more potent as a cytokine inducer in mouse and human cells, compared to the unconjugated TLR7 agonist. More importantly, the phospholipid conjugate was a rapidly acting and potent adjuvant for vaccination. It induced antibody responses by 14 days after primary immunization and stimulated both antibody production and antigen specific interferon production. In contrast, the conjugation of the same TLR7 agonist to PEG (**8**) reduced its potency in vitro, unless a phospholipid moiety was included in the conjugated molecule (**9**). Experiments using TLR7 deficient mouse cells confirmed that all the conjugates used in this study stimulated immune responses exclusively through TLR7.

One would normally expect that the same TLR7 activating pharmacophore, conjugated to different delivery molecules, would induce comparable patterns of cytokine synthesis. However, this was clearly not the case. The TLR7 agonist albumin conjugates (**4b**) induced high levels of IL-6 in human blood leukocytes but very low levels of type I interferons. In contrast, the TLR7 agonist phospholipid conjugate (**6**) induced abundant IL-6 and type I interferon. In humans and mice, the major source of type 1 interferon is plasmacytoid dendritic cells (pDC) (*19*), while other dendritic cells, mast cells, and B lymphocytes can produce IL-6. Furthermore, it is mainly TLRs in early, newly formed endosomes that are linked to type I interferon synthesis (*20*). Interaction of a TLR agonist and its receptor in the early endosome triggers the interferon induction pathway, whereas interaction in the late endosome induces cytokines dependent on the NF-κB pathway, such as TNFα and IL-6 (*20*). The results emphasize the complexity of TLR7 signal transduction, which may be regulated by target cell type, endosomal localization, and receptor occupancy time. The conjugation of a TLR7 pharmacophore to different accessory molecules could affect all these parameters. In particular, the TLR7 phospholipid conjugate could promote uptake by plasmacytoid dendritic cells or enhance intracellular persistence of the ligand in early endosomal vesicles.

It is well-established that the antibody class and subtype induced by vaccination can be influenced by the type of coadministered adjuvant (*21*). In mice, IgG2 production is a surrogate marker for activation of Th1-type cells, which also promote delayed hypersensitivity responses. In contrast, Th2-type cells preferentially enhance IgG1 synthesis and do not foster delayed hypersensitivity. However, both antibody and T-cell mediated delayed hypersensitivity responses are optimally needed to control many infections. The TLR7 agonist conjugated to albumin or phospholipid caused rapid elevation of IgG2a antibodies. However, levels of IgG2a in the mice receiving the albumin conjugate (**4a**) declined by three weeks after the last immunization, while the mice immunized with the phospholipid conjugates sustained and even increased antigen-specific IgG2a levels without further boosting. One possible explanation for the divergent effects is that the phospholipid conjugate acted as a depo, delivering the TLR7 activating pharmacophore over a more prolonged period.

The unconjugated TLR7 active SM molecule is very poorly soluble in aqueous solutions. Conjugation to poly(ethylene glycol) (PEG) improved its solubility but decreased its ability to induce cytokines (Figure 3). However, a hybrid conjugate

containing both PEG and a phospholipid retained cytokine inducing activity. Vaccination with the hybrid conjugate as adjuvant induced a significant Th2 immune response but a minimal Th1 response.

Imiquimod, a specific but relatively weak TLR7 agonist, is currently approved for treatment of skin disorders such as viral warts and superficial basal cell carcinomas (*22*, *23*). The TLR7 phospholipid conjugate described here is approximately 1000-fold more potent as a cytokine inducer. Although the hybrid conjugate containing both phospholipids and PEG was somewhat less potent, its water solubility renders it useful for systemic administration. In contrast, the phospholipid conjugate may be preferable for local administration, where persistent stimulation of in situ immune cells is desirable. The phospholipid moiety may also facilitate drug penetration through the epidermal barrier. Thus, the conjugation of a TLR7 agonist to phospholipid or PEG moieties is a promising strategy to expand the clinical uses of these agents for infectious, malignant, or atopic diseases.

ACKNOWLEDGMENT

We are grateful to Rommel Tawatao and Tetsuko Fukuda for their technical assistance. This work is supported in part by grant U01 AI077989-01 and Telormedix (TH, Bioggio Switzerland).

Supporting Information Available: Figure S1. Evaluation of endotoxin contamination using LPS unresponsive mutant and wild type macrophages. Table S1. Solubililty of the compounds used in vivo were measured by UV absorbance. This material is available free of charge via the Internet at http://pubs.acs.org.

LITERATURE CITED

(1) Takeda, K., and Akira, S. (2005) Toll-like receptors in innate immunity. *Int. Immunol. 17*, 1–14.

(2) Akira, S., and Takeda, K. (2004) Toll-like receptor signalling. *Nat. Rev. Immunol. 4*, 499–511.

(3) Hemmi, H., Kaisho, T., Takeuchi, O., Sato, S., Sanjo, H., Hoshino, K., Horiuchi, T., Tomizawa, H., Takeda, K., and Akira, S. (2002) Small anti-viral compounds activate immune cells via the TLR7 MyD88-dependent signaling pathway. *Nat. Immunol. 3*, 196–200.

(4) Akira, S. (2006) TLR signaling. *Curr. Top. Microbiol. Immunol. 311*, 1–16.

(5) Diebold, S. S., Kaisho, T., Hemmi, H., Akira, S., and Reis e Sousa, C. (2004) Innate antiviral responses by means of TLR7-mediated recognition of single-stranded RNA. *Science 303*, 1529–31.

(6) Lee, J., Chuang, T. H., Redecke, V., She, L., Pitha, P. M., Carson, D. A., Raz, E., and Cottam, H. B. (2003) Molecular basis for the immunostimulatory activity of guanine nucleoside analogs: activation of Toll-like receptor 7. *Proc. Natl. Acad. Sci. U.S.A. 100*, 6646–51.

(7) Lee, J., Mo, J. H., Katakura, K., Alkalay, I., Rucker, A. N., Liu, Y. T., Lee, H. K., Shen, C., Cojocaru, G., Shenouda, S., Kagnoff, M., Eckmann, L., Ben-Neriah, Y., and Raz, E. (2006) Maintenance of colonic homeostasis by distinctive apical TLR9 signalling in intestinal epithelial cells. *Nat. Cell Biol. 8*, 1327–36.

(8) Kurimoto, A., Ogino, T., Ichii, S., Isobe, Y., Tobe, M., Ogita, H., Takaku, H., Sajiki, H., Hirota, K., and Kawakami, H. (2004) Synthesis and evaluation of 2-substituted 8-hydroxyadenines as potent interferon inducers with improved oral bioavailabilities. *Bioorg. Med. Chem. 12*, 1091–9.

(9) Wu, C. C., Hayashi, T., Takabayashi, K., Sabet, M., Smee, D. F., Guiney, D. D., Cottam, H. B., and Carson, D. A. (2007) Immunotherapeutic activity of a conjugate of a Toll-like receptor 7 ligand. *Proc. Natl. Acad. Sci. U.S.A. 104*, 3990–5.

(10) Roman, M., Martin-Orozco, E., Goodman, J. S., Nguyen, M. D., Sato, Y., Ronaghy, A., Kornbluth, R. S., Richman, D. D., Carson, D. A., and Raz, E. (1997) Immunostimulatory DNA sequences function as T helper-1-promoting adjuvants [see comments]. *Nat. Med. 3*, 849–54.

(11) Hayashi, T., Rao, S. P., Takabayashi, K., Van Uden, J. H., Kornbluth, R. S., Baird, S. M., Taylor, M. W., Carson, D. A., Catanzaro, A., and Raz, E. (2001) Enhancement of innate immunity against *Mycobacterium avium* infection by immunostimulatory DNA is mediated by indoleamine 2,3-dioxygenase. *Infect. Immunol. 69*, 6156–64.

(12) Cho, H. J., Takabayashi, K., Cheng, P. M., Nguyen, M. D., Corr, M., Tuck, S., and Raz, E. (2000) Immunostimulatory DNA-based vaccines induce cytotoxic lymphocyte activity by a T-helper cell-independent mechanism. *Nat. Biotechnol. 18*, 509–14.

(13) Veronese, F. M., and Mero, A. (2008) The impact of PEGylation on biological therapies. *BioDrugs 22*, 315–29.

(14) Kobayashi, H., Horner, A. A., Martin-Orozco, E., and Raz, E. (2000) Pre-priming: a novel approach to DNA-based vaccination and immunomodulation. *Springer Semin. Immunopathol. 22*, 85–96.

(15) Mosmann, T. R., and Coffman, R. L. (1989) TH1 and TH2 cells: different patterns of lymphokine secretion lead to different functional properties. *Annu. Rev. Immunol. 7*, 145–73.

(16) Hayashi, T., Cottam, H. B., Chan, M., Jin, G., Tawatao, R. I., Crain, B., Ronacher, L., Messer, K., Carson, D. A., and Corr, M. (2008) Mast cell-dependent anorexia and hypothermia induced by mucosal activation of Toll-like receptor 7. *Am. J. Physiol. Regul. Integr. Comp. Physiol. 295*, R123–32.

(17) Baenziger, S.; Heikenwalder, M.; Johansen, P.; Schlaepfer, E.; Hofer, U.; Miller, R. C.; Diemand, S.; Honda, K.; Kundig, T. M.; Aguzzi, A.; Speck, R. F. (2008) Triggering TLR7 in mice induces immune activation and lymphoid system disruption, resembling HIV-mediated pathology. *Blood 113*, 377–32.

(18) Lee, J., Wu, C. C., Lee, K. J., Chuang, T. H., Katakura, K., Liu, Y. T., Chan, M., Tawatao, R., Chung, M., Shen, C., Cottam, H. B., Lai, M. M., Raz, E., and Carson, D. A. (2006) Activation of anti-hepatitis C virus responses via Toll-like receptor 7. *Proc. Natl. Acad. Sci. U.S.A. 103*, 1828–33.

(19) Rothenfusser, S., Tuma, E., Endres, S., and Hartmann, G. (2002) Plasmacytoid dendritic cells: the key to CpG. *Hum. Immunol. 63*, 1111–9.

(20) Kagan, J. C., Su, T., Horng, T., Chow, A., Akira, S., and Medzhitov, R. (2008) TRAM couples endocytosis of Toll-like receptor 4 to the induction of interferon-beta. *Nat. Immunol. 9*, 361–8.

(21) Kenney, J. S., Hughes, B. W., Masada, M. P., and Allison, A. C. (1989) Influence of adjuvants on the quantity, affinity, isotype and epitope specificity of murine antibodies. *J. Immunol. Methods 121*, 157–66.

(22) Purdon, C. H., Azzi, C. G., Zhang, J., Smith, E. W., and Maibach, H. I. (2004) Penetration enhancement of transdermal delivery--current permutations and limitations. *Crit. Rev. Ther. Drug Carrier Syst. 21*, 97–132.

(23) Chang, Y. C., Madkan, V., Cook-Norris, R., Sra, K., and Tyring, S. (2005) Current and potential uses of imiquimod. *South Med. J. 98*, 914–20.

BC900054Q

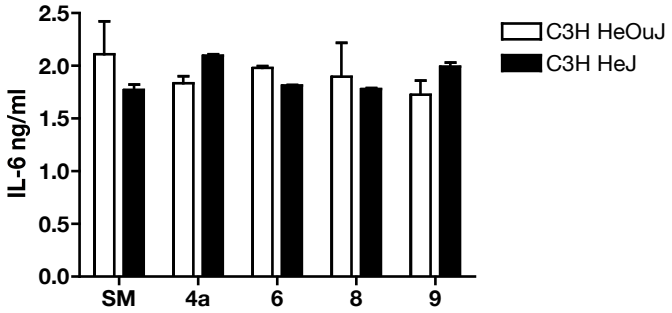

Supplementary Figure 1. Evaluation of endotoxin contamination using LPS unresponsive mutant and wild type macrophages.

0.5×10^6/ml BMDM derived from C3H/HeJ (LPS unresponsive mutant) or C3H/HeOuJ(wild type) were incubated with TLR7 conjugates (10 μM SM, 0.1 μM 4a, 10 μM 6, 10 μM 8 or 10 μM 9) for 18 hours. The levels of IL-6 or IL-12 in the culture supernatants were measured by ELISA. Each TLR7 conjugates induced similar levels of IL-6 both in TLR4 mutant and wild type mice, indicating LPS contamination of these conjugates is minimum.

Supplementary Table 1.
Solubility in Vehicle

Compound	Solubility[a] (mM)
SM	0.051
6	0.049
8	0.964
9	0.157

[a] Solubility was measured in 10% DMSO in saline at room temperature with a maximum theoretical concentration of 1mM. Concentration was measured by UV absorbance.

Targeting of Epidermal Growth Factor Receptor (EGFR)-Expressing Tumor Cells with Sterically Stabilized Affibody Liposomes (SAL)

Julia Beuttler,[†] Miriam Rothdiener,[†] Dafne Müller,[†] Fredrik Y. Frejd,[‡] and Roland E. Kontermann*[,†]

Institut für Zellbiologie und Immunologie, Universität Stuttgart, Allmandring 31, 70569 Stuttgart, Germany, Affibody AB, P.O. Box 20137, SE-161 02 Bromma, Sweden, and Unit of Biomedical Radiations Sciences, Rudbeck Laboratory, Uppsala University, SE-751 85 Uppsala, Sweden. Received February 9, 2009; Revised Manuscript Received April 16, 2009

Affibody molecules are small and stable antigen-binding molecules derived from the B domain of protein A. We applied a bivalent, high-affinity epidermal growth factor receptor (EGFR)-specific affibody molecule for the generation of targeted PEGylated liposomes. These sterically stabilized affibody liposomes (SAL) were produced by chemical coupling of the cysteine-modified affibody molecule to maleimide-PEG_{2000}-DSPE and subsequent insertion into PEGylated liposomes. These SAL showed strong and selective binding to EGFR-expressing tumor cell lines. Binding was dependent on the amount of inserted affibody molecule−lipid conjugates and could be blocked by soluble EGF. Approximately 30% of binding activity was still retained after 6 days of incubation in human plasma at 37 °C. Binding of SAL to cells led to efficient internalization of the liposomes. Using mitoxantrone-loaded liposomes, we observed for SAL, compared to untargeted liposomes, an enhanced cytotoxicity toward EGFR-expressing cells. In summary, we show that SAL can be easily prepared from affibody molecules and thus may be suitable for the development of carrier systems for targeted delivery of drugs.

INTRODUCTION

The epidermal growth factor receptor (EGFR) is a transmembrane glycoprotein and a member of the erbB receptor tyrosine kinase family. Dysregulation of EGFR signaling has been shown to contribute to malignant transformation (*1*). Elevated levels of EGFR are found on different types of solid tumors, e.g., breast, ovarian, lung, head and neck, prostate, and colorectal cancers, and have been proposed as prognostic marker for disease progression and survival (*2*). Consequently, strategies targeting EGFR have been developed as treatment option, including monoclonal antibodies, small molecule inhibitors of EGFR signal transduction, and antibody-based immunoconjugates, e.g., immunotoxins (*3*). Some of these reagents have already been approved for therapy, such as monoclonal antibodies (cetuximab, panitumumab) and small molecule inhibitors (gefitinib, erlotinib) (*4*).

Antibodies recognizing EGFR have also been applied for the targeting of drug-loaded liposomes. Liposomes are small, vesicular carrier systems consisting of one or more lipid bilayers composed of natural or synthetic lipids, e.g., phospholipids and cholesterol (*5*). Encapsulation of drugs into the liposomal interior or the lipid bilayer alters the drug pharmacokinetics, e.g., protects the drug from rapid elimination and degradation, and has been shown to improve efficacy and safety (*6*). Half-life of liposomal drugs can be drastically improved by incorporating polymers such as poly(ethylene glycol) into the lipid bilayer, thus sterically stabilizing the liposomes. Coupling of antibodies to the surface results in immunoliposomes allowing for an active targeting to tumor cells and receptor-mediated internalization (*7*−*9*). In order to avoid Fc-mediated uptake of immunoliposomes by phagocytic cells, recent applications focused on the use of antibody fragments (Fab′) and recombinant formats (e.g., scFv)[1](for review, see 10). Both, anti-EGFR Fab′ and scFv molecules have been employed for the preparation of anti-EGFR immunoliposomes (*11*−*13*). Selective binding and internalization into EGFR-overexpressing tumor cells as well as selective cytotoxicity of drug-loaded anti-EGFR immunoliposomes has been demonstrated in vitro in these studies. Superiority of immunoliposomal delivery of various drugs, e.g., doxorubicin, epirubicin, and vinorelbine, over free drug and nontargeted liposomal formulations was confirmed in xenograft tumor models (*12*).

Obviously, the antigen-binding moiety of an antibody is sufficient and advantageous to confer target specificity of immunoliposomes. Recently, various antibody mimetics based on nonimmunoglobulin scaffolds have been proposed as an alternative for antibodies (*14*). Several of these antibody mimetics have been developed into high-affinity antigen binders. For example, affibody molecules are small molecules (7 kDa) based on a 58 amino acid residue three-helix bundle domain from staphylococcal protein A (*15*−*17*). Anti-EGFR affibody molecules were selected from a phage display library and further affinity matured into molecules with low nanomolar affinity (*18,19*). One of these anti-EGFR affibody molecules, $(Z_{EGFR:955})_2$, was shown to be efficiently internalized into EGFR-overexpressing A431 squamous carcinoma cells similar to monoclonal antibody cetuximab (*20*).

Here, we applied a bivalent anti-EGFR affibody molecule for the generation of targeted liposomes. This was achieved by chemical coupling of the cysteine-modified affibody molecule to maleimide-PEG_{2000}-DSPE and subsequent insertion into sterically stabilized liposomes. The resulting sterically stabilized

* Corresponding author. Prof. Roland E. Kontermann, Institut für Zellbiologie and Immunologie, Universität Stuttgart, Allmandring 31, 70569 Stuttgart, Germany. Tel. +49 711 685-66989. Fax. +49 711 685-67484. roland.kontermann@izi.uni-stuttgart.de.

[†] Universität Stuttgart.

[‡] Affibody AB and Uppsala University.

[1]Abbreviations: EPC, egg phosphatidylcholine; Chol, cholesterol; DOPC, dioleoyl-phosphatidylcholine; Mal-PEG_{2000}-DSPE, 1,2-distearoyl-*sn*-glycero-3-phosphoethanolamine-*N*-[maleimide(polyethylene glycol)2000]; mPEG_{2000}-DSPE, 1,2-distearoyl-*sn*-glycero-3-phosphoethanolamine-*N*-[methoxy(poly(ethylene glycol))-2000]; MTO, mitoxantrone; SAL, sterically stabilized affibody liposomes; SL, sterically stabilized liposomes; scFv, single-chain fragment variable.

10.1021/bc900061v CCC: $40.75 © 2009 American Chemical Society
Published on Web 05/12/2009

affibody liposomes (SAL) showed strong and selective binding to various EGFR-expressing tumor cell lines and subsequent internalization. Furthermore, compared to untargeted drug-loaded liposomes, targeting led to a selective increase in cytotoxicity of mitoxantrone-loaded SAL toward EGFR-expressing tumor cell lines. These findings demonstrate that affibody molecules are useful molecules for the generation of targeted nanocarrier systems suitable for delivery of drugs and other agents, e.g., for diagnostic purposes.

MATERIALS AND METHODS

Materials. Phospholipids were purchased from Avanti Polar Lipids (Alabaster, USA) and cholesterol from Calbiochem (Gibbstown, USA). DiI and mitoxantrone were purchased from Sigma-Aldrich (Taufkirchen, Germany). Human plasma (stabilized with citrate-phosphate-dextrose solution (CPD)) was kindly provided by the blood donation center of the Katharinenhospital (Stuttgart, Germany). A PE-labeled anti-EGFR monoclonal antibody (clone EGFR.1) was purchased from BD Pharmingen (San Jose, USA). A431, MDA-MB-468, MDA-MB-231, SKBR3, and MCF-7 were grown in RPMI, 10% FCS, 2 mM glutamine. Colo205, LS174T, and HEK293 were grown in RPMI, 5% FCS, 2 mM glutamine.

Expression and Purification of $(Z_{EGFR:1907})_2$-cys. The non his-tagged dimeric EGFR-binding affibody molecule $(Z_{EGFR:1907})_2$-cys was expressed in *Escherichia coli* BL21(DE3) cells as previously described (*21*). Pelleted bacterial cells harboring $(Z_{EGFR:1907})_2$-cys were suspended in 20 mM Tris-HCl pH 7.1 and heat-treated at 85 °C for 3 min to disrupt the cells and release the intracellular content. The lysate was clarified by centrifugation followed by filtration and loaded on 25 mL Q Sepharose FF (GE Healthcare), previously equilibrated with 20 mM Tris−HCl pH 7.1. After wash with 20 mM Tris−HCl pH 7.1, bound protein was eluted with a linear gradient 0−0.5 M NaCl in 20 mM Tris−HCl pH 7.1. Fractions containing $(Z_{EGFR:1907})_2$-cys were pooled and pH was adjusted to 8.0 by addition of 1 M Tris−HCl pH 8.0 to a final concentration of 50 mM. The C-terminal cysteine was reduced by addition of DTT to 20 mM, followed by incubation at 40 °C for 3 min. After reduction, acetonitrile (ACN) was added to a final concentration of 5% and reduced $(Z_{EGFR:1907})_2$-cys was loaded on 1 mL Resource 15 RPC columns (GE Healthcare), previously equilibrated with RPC A-buffer (0.1% TFA, 5% ACN, 95% water). After wash with RPC A-buffer, bound proteins were eluted with a linear gradient 0−40% RPC B-buffer (0.1% TFA, 80% ACN, 20% water). Fractions containing pure $(Z_{EGFR:1907})_2$-cys were identified by SDS-PAGE analysis and pooled. The buffer was exchanged to 10 mM ammonium hydrogen carbonate pH 8.0 using a PD-10 desalting column (GE Healthcare). Finally, $(Z_{EGFR:1907})_2$-cys was lyophilized and stored at 4 °C until use. Determination of the concentration of $(Z_{EGFR:1907})_2$-cys solutions was performed by measuring the absorbance at 280 nm. The purity of $(Z_{EGFR:1907})_2$-cys was assessed in SDS-PAGE analysis using approximately 10 μg $(Z_{EGFR:1907})_2$-cys. The identity was verified with LC/MS-analyses using an Agilent 1100 LC/MSD system, equipped with API-ESI and single quadruple mass analyzator.

Determination of Protein Melting Point. The melting point of the affibody molecule was determined with the ZetaSizer Nano ZS (Malvern, Herrenberg, Germany). 50 μg of purified affibody molecule was diluted in PBS to a total volume of 500 μL and sterile filtered into a quartz cuvette. Dynamic laser light scattering intensity was measured while the temperature was increased in 1 °C intervals from 30 to 70 °C with 2 min equilibration for each temperature step. The melting point was defined as the temperature at which the light scattering intensity and size dramatically increased.

Size Exclusion Chromatography. HPLC size exclusion chromatography of the affibody molecule was performed on a BioSep-Sec-S3000 column (Phenomenex, Torrance, CA). Mobil phase was PBS, 1 M NaCl, with a flow rate of 0.5 mL/min. The following standard molecules were employed: thyroglobulin, apoferritin, β-amylase, bovine serum albumin, carbonic anhydrase, cytochrome c, and aprotinin.

Generation of Sterically Stabilized Affibody Liposomes (SAL). Affibody liposomes were generated by postinsertion of affibody molecule-conjugated micelles into preformed PEG-liposomes as described previously for the generation of scFv immunoliposomes (*22*). In brief, liposomes composed of EPC/Chol/$mPEG_{2000}$-DSPE at a molar ratio of 6.5:3:0.5 were prepared by the film hydration−extrusion method. For binding studies, 0.3 mol % DiI was included. The lipid film was hydrated with 1 mL 10 mM Hepes buffer pH 6.7 with a final lipid concentration of 10 μmol lipid per ml buffer. The resulting multilamellar vesicle dispersion was extruded 21 times through 50 nm polycarbonate membranes using a LiposoFast extruder (Avestin, Ottawa, Canada). Mal-PEG_{2000}-DSPE micelles were prepared dissolving dried lipid in ddH_2O at 65 °C to a final concentration of 10 mg/mL. Purified affibody molecules were reduced in 2 mM tris(2-carboxyethyl)phosphine (TCEP) for 2 h at room temperature followed by removal of TCEP by dialysis against oxygen-free 10 mM Na_2HPO_4/NaH_2PO_4 buffer, 0.2 mM EDTA, 30 mM NaCl (pH 6.7) overnight at 4 °C. Micellar lipid and reduced affibody molecule were mixed at a molar ratio of 4.67:1 and incubated at room temperature for 30 min. The coupling reaction was quenched with 1 mM L-cysteine, 0.02 mM EDTA, pH 5.5. Coupling efficiency was determined by SDS-PAGE analysis and quantification of Coomassie-stained bands of free and lipid-conjugated affibody molecule. The affibody molecule-coupled micelles were inserted into preformed PEGylated liposomes by incubation at 55 °C for 30 min (0.02 mol % to 2 mol % micellar lipid in respect to liposomal lipid). Unbound affibody molecules were removed by gel-filtration using a Sepharose CL4B column (Amersham, Braunschweig, Germany). Liposome size (ζ-average) and ζ-potential were measured using a ZetaSizer Nano ZS (Malvern, Herrenberg).

Generation of Drug-Loaded Affibody Liposomes. Mitoxantrone-loaded liposomes were produced by remote loading (*23*). Sterically stabilized liposomes (SL) composed of DOPC, Chol, and $mPEG_{2000}$-DSPE (45:50:5) were prepared as described above (final conc. 100 μmol lipid/mL) using 300 mM citrate buffer (pH 4) for rehydration. After extrusion, liposomes were neutralized by adding 200 μL 0.5 M Na_2HPO_4 and 49 μ 2 N NaOH to 200 μL liposomes, adjusting the pH to 7.5. Liposomes were then preheated to 55 °C in a water bath for 5 min, and 120 μL mitoxantrone (10 mg/mL in water) was added resulting in a drug/lipid ratio of 0.12. After further incubation for 10 min at 55 °C and 20 min at room temperature, affibody molecules coupled to Mal-PEG_{2000}-DSPE micelles were inserted as described above using 0.6 mol % micellar lipid in respect to liposomal lipid. Drug-loaded affibody liposomes were separated from free drug and uninserted micelles by gel filtration on a sepharose CL4B column. Encapsulated drug was quantified measuring absorption at 590 nm after lysis of liposomes with 2% Triton-X 100. Encapsulation efficiency was between 99−100%.

Flow Cytometry. Cells were detached from cell culture dishes using 0.05% trypsin, 0.02% EDTA (GIBCO). Approximately 200 000 cells were incubated with DiI-labeled affibody liposomes (10 nmol lipid) in PBS containing 2% FBS, 0.02% sodium azide (PBA) for 1 h at 4 °C in the dark. After washing cells three times with PBA buffer (4 °C), cells were resuspended in 500 μL PBA buffer and analyzed by flow cytometry (Cytomics FC 500, Beckmann-Coulter). Binding of

PE-labeled anti-EGFR antibody was determined by incubating detached cells with antibody (diluted 1:20) in PBA buffer for 1 h at 4 °C. Cells were then washed three times with PBA as described and analyzed for binding by flow cytometry. Data were evaluated with *WinMDI 2.9*.

In Vitro Plasma Stability. To analyze plasma stability, SAL were preincubated in the presence of 50% human plasma for up to 6 days at 37 °C in a total volume of 60 μL. Subsequently, binding of SALs to cells was analyzed by flow cytometry as described above.

Internalization Studies. A431 cells were seeded onto collagen-coated coverslips (100 000 cells/well) and allowed to adhere overnight. Cells were then incubated with DiI-labeled SAL (50 nmol lipid) for 1 h at 37 °C, washed, and incubated for additional 8 h. Coverslips were washed twice with PBS, fixed with 4% PFA for 20 min at room temperature, and washed again twice with PBS. Cells were then counter-stained with Alexa-488-labeled cetuximab (0.8 μg/mL) and fixed again with 4% PFA. Nuclei were stained by subsequent incubation of cells with DAPI (1 μg/mL) for 20 min at RT. Coverslips were mounted with Moviol and analyzed by fluorescence microscopy (Zeiss Cell Observer) and confocal fluorescence microscopy (Leica TCS SP 2). Alternatively, A431 cells were grown in a 12 well plate (200 000 cells/well). The next day, DiI-labeled anti-EGFR SAL were added (50 nmol lipid) and incubated for up to 8 h. Cells were washed twice with 1 mL ice-cold PBS or 50 mM glycine, 150 mM NaCl, pH 2.7, respectively. Cells were washed again with PBS, trypsinized, and analyzed by flow cytometry as described above.

In Vitro Cytotoxicity Assay. Cells were grown in 96 well plates (15 000 cells/well) for 24 h, and varying amounts of free drug or drug-loaded liposomes were added. After incubation for 20 h, wells were washed 3 times with ice-cold PBS, and viable cells were determined using an MTT ([3-(4,5-dimethylthiazol-2-yl)-2,5-diphenyltetrazolium bromide]) assay. In brief, microtiter plates were incubated with 50 μL/well RPMI + 10% FCS and 5 μL/well MTT (5 mg/mL) for 2 h at 37 °C. Then, the cells were lysed by adding 45 μL/well 10% SDS, 50% *N*,*N*-dimethylformamide, pH 4.7, overnight by shaking at room temperature. Absorbance was measured at 570 and 660 nm. For analysis, the 660 nm values were subtracted as unspecific background from the 570 nm values.

RESULTS

Anti-EGFR affibody ($Z_{EGFR:1907}$)$_2$-cys. SDS-PAGE analysis of purified ($Z_{EGFR:1907}$)$_2$-cys revealed a single band of 14 kDa under reducing conditions and a major band (approximately 96%) corresponding to dimeric molecules (25 kDa) under nonreducing conditions (Figure 1a). The presence of dimeric molecules was confirmed by size exclusion chromatography (SEC) (Figure 1c). Here, ($Z_{EGFR:1907}$)$_2$-cys eluted at a major peak corresponding to a molecular mass of 28 kDa. A melting point of 46 °C was determined for ($Z_{EGFR:1907}$)$_2$-cys by dynamic light scattering analysis (Figure 1b).

Sterically Stabilized Anti-EGFR Affibody Liposomes. Anti-EGFR sterically stabilized affibody liposomes (SAL) were produced by coupling reduced ($Z_{EGFR:1907}$)$_2$-cys to Mal-PEG$_{2000}$-DSPE micelles and subsequent insertion into preformed PE-Gylated liposomes using 2 mol % micellar lipid in relation to liposomal lipid. Efficiency of coupling of ($Z_{EGFR:1907}$)$_2$-cys to Mal-PEG$_{2000}$-DSPE micelles was determined to be 53 ± 5% (n = 5). Postinsertion was performed at 55 °C for 30 min. Although the melting point of ($Z_{EGFR:1907}$)$_2$-cys is only 46 °C, the resulting SAL showed binding to a panel of EGFR-expressing tumor cell lines (Figure 2). For most cell lines analyzed, binding strength correlated with expression of EGFR as determined by flow cytometry analysis with an anti-EGFR monoclonal antibody.

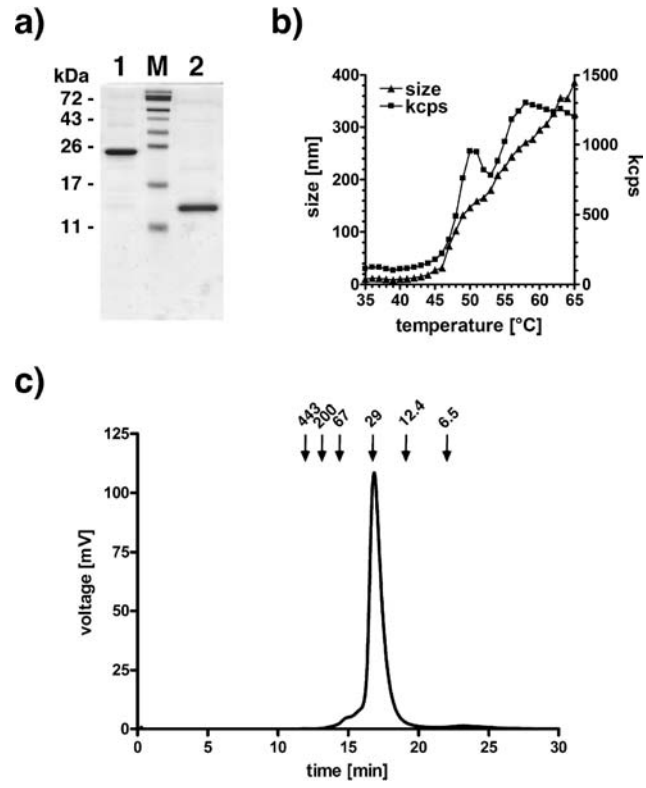

Figure 1. (a) SDS-PAGE analysis of purified affibody ($Z_{EGFR:1907}$)$_2$-cys. Affibody (5 μg/lane) was separated on a 20% SDS-polyacrylamide gel under nonreducing (1) and reducing (2) conditions, respectively, and stained with Coomassie blue. (b) Determination of protein melting point by dynamic light scattering (kcps, kilocounts per second). (c) Size exclusion chromatography of purified affibody ($Z_{EGFR:1907}$)$_2$-cys.

Exceptions were cell lines MDA-MB-231 and Colo 205, which expressed moderate to low levels of EGFR but did not bind anti-EGFR SAL. Binding was strongest with human squamous carcinoma cell line A431. Binding to this cell line was analyzed in more detail using anti-EGFR SAL produced by postinsertion of 0.02 to 2 mol % affibody molecule-coupled micellar lipid, corresponding to approximately 2 to 200 pmol affibody molecule/μmol lipid. All liposomes had a size in the range 90−97 nm and a slightly negative ζ potential (Table 1). Flow cytometry showed that binding to A431 cells increases with increasing concentrations of lipid and affibody molecule density, i.e., inserted micellar lipid (Figure 3a). At the highest lipid concentration (100 nmol lipid/assay), we observed a reduction in binding for SAL prepared by insertion of 0.6 and 2 mol % micellar lipid, which was most pronounced for SAL with 2 mol % micellar lipid. Binding of anti-EGFR SAL (10 nmol lipid, 2 mol % inserted micellar lipid) to A431 was blocked by excess amounts (10 μg/mL) of soluble ($Z_{EGFR:1907}$)$_2$-cys as well as soluble EGF (EGF$_{m1}$) (*24*) but not by an irrelevant affibody molecule, (Z_{Taq})$_2$-cys (Figure 3b). Furthermore, SAL produced from (Z_{Taq})$_2$-cys directed against Taq polymerase did not show any binding to A431 (Figure 3c).

Stability and Internalization of anti-EGFR SAL. In order to determine stability of SAL under physiological conditions, anti-EGFR SAL (2 mol % inserted micellar lipid) were incubated with human plasma at 37 °C for up to 6 days and subsequently analyzed for cell binding by flow cytometry. Approximately 70% of the initial binding activity of the anti-EGFR-SAL was retained after 1 day of incubation, which gradually decreased to a value of approximately 30% after 6 days (Figure 4). Anti-EGFR SAL were efficiently internalized as shown by flow cytometry analysis. A431 were incubated for up to 8 h at 37 °C with DiI-labeled anti-EGFR SAL and then

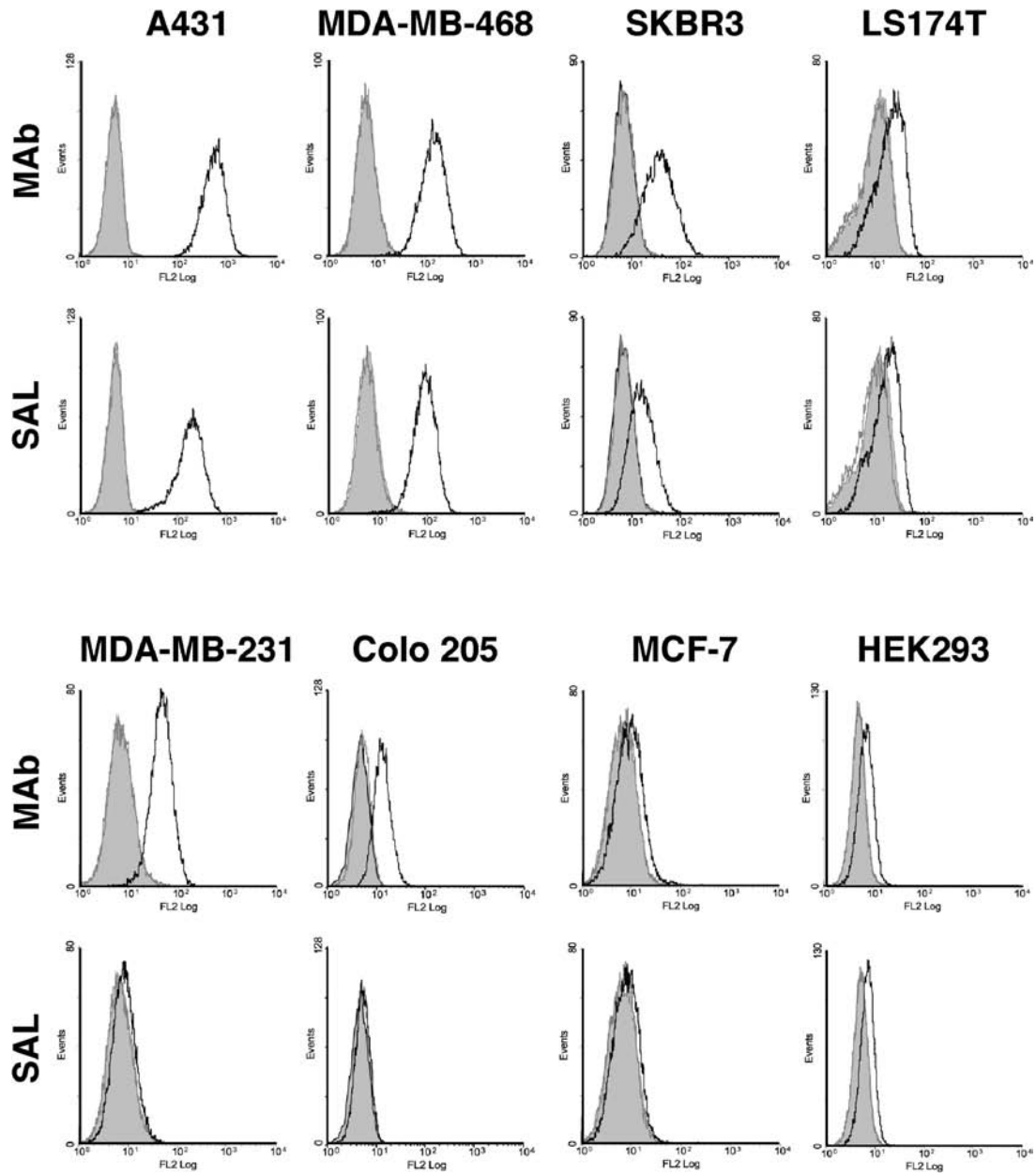

Figure 2. Binding of SAL to EGFR-expressing cells. Flow cytometry analysis of binding of PE-labeled anti-EGFR monoclonal antibody (mAb) or sterically stabilized anti-EGFR affibody liposomes (SAL) to various cell lines (A431, MDA-MB-468, SKBR3, LS174T, MDA-MB-231, Colo 205, MCF-7, HEK293). 200 000 cells were incubated with 10 nmol lipid or 10 μg/mL anti-EGFR mAb, respectively, (gray, cells alone; bold line, cells incubated with antibody or SAL).

Table 1. Characterization of anti-EGFR SAL

inserted micelles (mol %)	affibody molecule	size (nm)	polydispersity index	ζ-potential (mV)
2.0	−	99.6 ± 0.6	0.20	−0.57
2.0	+	93.9 ± 1.5	0.08	−0.04
0.6	+	96.9 ± 1.3	0.14	−0.90
0.2	+	92.9 ± 0.6	0.10	−2.24
0.06	+	95.1 ± 0.8	0.09	−0.46
0.02	+	90.2 ± 0.4	0.07	0.12

washed with PBS (pH 7.4) or acidic glycine buffer (pH 2.7). An increase of fluorescence was observed over time (Figure 5). Fluorescence of cells washed with acidic buffer, which removes liposomes bound to the cell membrane (*25*), was weaker than that measured for cells washed with PBS but also increased over time to approximately 90% of fluorescence of PBS-washed cells after 8 h indicating that the majority of SALs was internalized. Internalization was further shown by conventional and confocal fluorescence microscopy of A431 cells incubated for 9 h with DiI-labeled anti-EGFR SAL (Figure 6a,d). A431 incubated with SAL at 4 °C showed only binding to the cell surface (Figure 6b). Furthermore, no binding and internalization was observed for nontargeted SL included as negative control (Figure 6c).

In Vitro Cytotoxicity. In order to analyze the effects of affibody-mediated delivery of liposomal drugs, we prepared mitoxantrone (MTO)-loaded SL (MTO-SL) and SAL (MTO-SAL). Because SAL prepared by insertion of 2 mol % micellar lipid show a strong reduction of binding at very high lipid concentrations, we used SAL prepared by the insertion of 0.6 mol % affibody molecule-coupled micelles for cytotoxicity assays. The size of the drug-loaded liposomes was 116 ± 5 nm for MTO-SL and 110 ± 1 nm for MTO-SAL (n = 9). MTO-SL and anti-EGFR MTO-SAL were tested for cytotoxicity on A431, MDA-MB-468, and MCF-7, the latter included as negative cell line (see Figure 2). In these experiments, cells were incubated with drug for 20 h and the viability of remaining cells

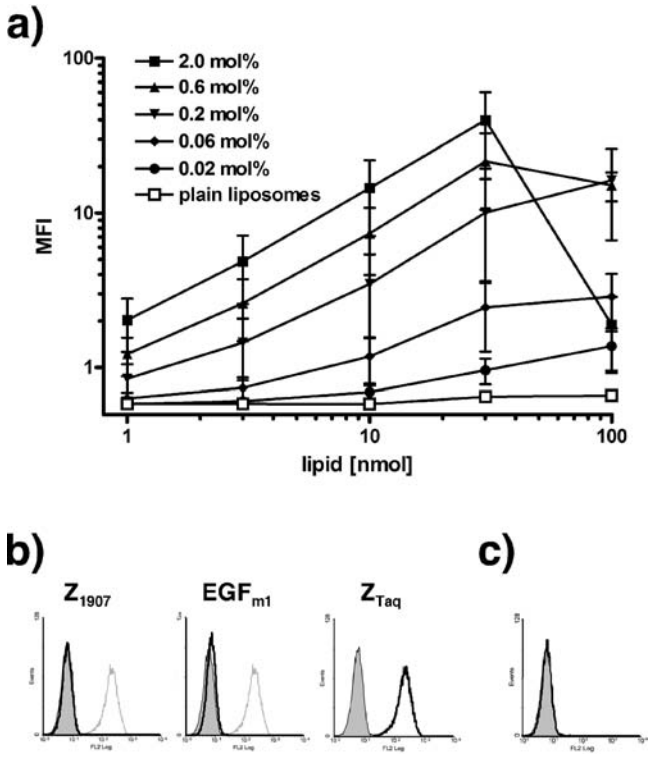

Figure 3. (a) Binding to A431 cells of anti-EGFR SAL generated by insertion of different micellar-conjugated affibody $(Z_{EGFR:\ 1907})_2$-cys (2 to 0.02 mol %) at varying lipid concentrations (1 to 100 nmol lipid per 200 000 cells). Plain liposomes (incubated with cysteine to block the maleimide group) were included as negative control. Shown is the mean fluorescence intensity (MFI) of cells incubated with liposomes and analyzed by flow cytometry ($n = 2$). (b) Blocking of binding of anti-EGFR SAL to A431 cells by soluble affibody $(Z_{EGFR:1907})_2$-cys or a EGF variant (EGFm1) but not with an irrelevant affibody (Z_{Taq}) (gray, cells alone; gray thin line, cells incubated with anti-EGFR SAL; bold line, cells incubated with anti-EGFR SAL + soluble proteins as indicated. (c) Flow cytometry analysis of SAL generated from control affibody Z_{Taq} tested for binding to A431 cells at 10 nmol lipid/200 000 cells (gray, cells alone; bold line, cells incubated with SAL).

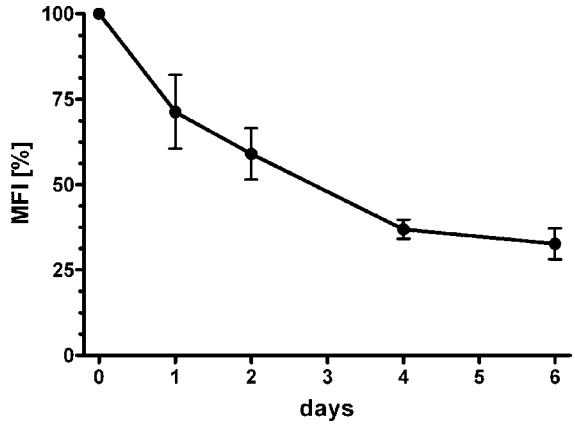

Figure 4. Stability of anti-EGFR SAL. Anti-EGFR SAL were incubated with human plasma at 37 °C for up to 6 days and subsequently analyzed for binding to A431 cells. Shown is the mean fluorescence intensity (% of untreated SAL) of cells incubated with liposomes ($n = 3$).

was determined by MTT assay. All 3 cell lines were sensitive for MTO with IC_{50} values between 1.3−18 μM (Figure 7; Table 2). MTO-loaded liposomes (MTO-SL) showed a reduced cytotoxicity demonstrating the protective properties of encapsulation of drug into PEGylated liposomes. Compared to MTO-SL, an increased cytotoxicity of MTO-SAL was observed for the two EGFR-expressing cell lines (A431, MDA-MB-468),

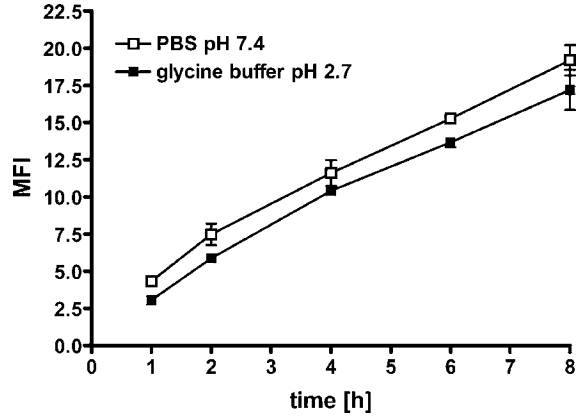

Figure 5. Internalization of anti-EGFR SAL. A431 cells were incubated with anti-EGFR SAL for up to 8 h at 37 °C, washed either with PBS or with glycine buffer (pH 2.7), respectively, and subsequently analyzed by flow cytometry ($n = 3$).

while no differences were found for the EGFR-negative cell line (MCF-7) (Figure 7, Table 2). Anti-EGFR SAL not loaded with drug showed no growth inhibition on MDA-MB-468 cells and only little cytotoxicity on A431 cells up to a concentration of 33 μmol lipid/mL (corresponding to the highest lipid concentration used for the MTO-loaded SAL) (Figure 8a). Furthermore, soluble $(Z_{EGFR:1907})_2$-cys did not inhibit growth of MDA-MB-468 cells and was only slightly inhibitory on A431 cells up to a concentration of 6.7 μg/mL (Figure 8b).

DISCUSSION

We applied a bivalent affibody molecule directed against EGFR and possessing a free cysteine residue at the C-terminus, $(Z_{EGFR:1907})_2$-cys for the generation of targeted liposomes. The resulting affibody liposomes (SAL), which were sterically stabilized by incorporating mPEG into the lipid bilayer, showed selective and strong binding to a variety of EGFR-expressing tumor cell lines. Thus, coupling of the affibody molecule to Mal-PEG_{2000}-DSPE and insertion into PEGylated liposomes does not interfere with antigen-binding activity. This is comparable to recent findings for an anti-HER2 affibody molecule, which was used for the production of targeted nanoparticle-affibody molecule bioconjugates composed of poly(D,L-lactic acid), PEG, and Mal-PEG (*26*). These nanoparticles also showed selective binding to HER2-expressing cell lines and efficient internalization. In another study, HER2-specific affibody molecule-conjugated thermosensitive liposomes, composed of DPPC, Mal-PEG_{2000}-DSPE, and PEG_{2000}-DSPE, were produced, however, no binding data were reported (*27*). Binding of anti-EGFR SAL to A431 was efficiently blocked by soluble $(Z_{EGFR:1907})_2$ as well as EGF. This is in accordance with recent binding studies of the low-affinity precursor of $Z_{EGFR:1907}$, $(Z_{EGFR:955})_2$, where binding of the affibody molecule was blocked by EGF and anti-EGFR mAb cetuximab (*20*). We also observed efficient internalization of anti-EGFR SAL into A431 cells, which gradually increased over time. Internalization of a bivalent, ^{125}I-labeled anti-EGFR affibody molecule ($(Z_{EGFR:955})_2$) was recently shown to reach a maximum after 8 h, similar to that of cetuximab, while internalization of EGF occurred more rapidly with a maximum reached already after 2 h (20). Thus, anti-EGFR SAL behave similarly to free affibody molecule in terms of internalization.

Applying dynamic light scattering, a melting point of approximately 46 °C was determined for purified $(Z_{EGFR:1907})_2$. Interestingly, the affibody molecule retained its antigen-binding activity after the postinsertion step, which was performed for 30 min at 55 °C. This indicates that the affibody molecule is

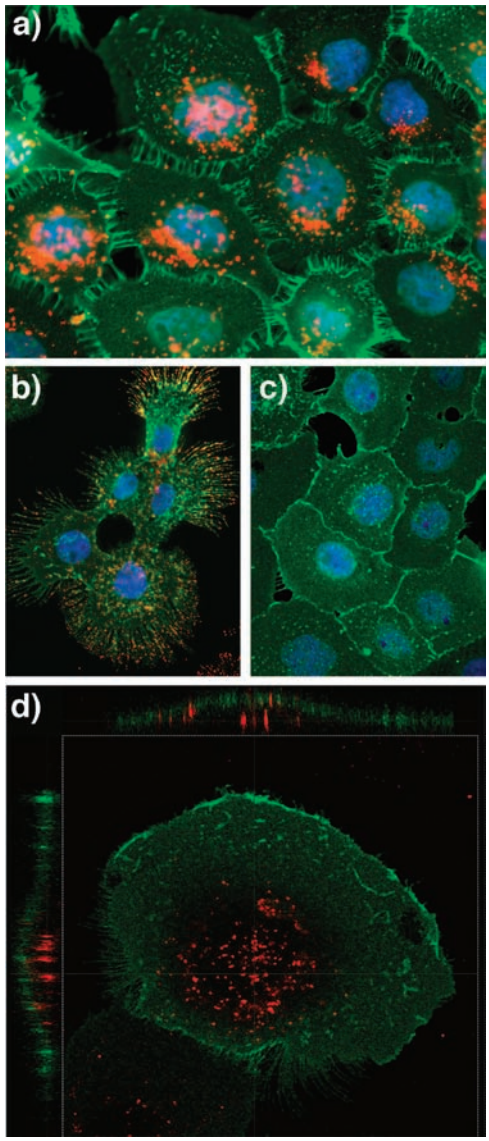

Figure 6. Internalization of anti-EGFR SAL. (a) Fluorescence microscopy of A431 cells incubated with anti-EGFR SAL (red) for 9 h at 37 °C. (b) Fluorescence microscopy of A431 cells incubated with anti-EGFR SAL (red) for 1 h at 4 °C. (c) Fluorescence microscopy of A431 cells incubated with control SL (red) for 9 h at 37 °C. (d) Confocal fluorescence microscopy of a representative A431 cell as shown in (a) including sections through the *z* axes. In all images, fixed cells were counterstained with Alexa-488-labeled cetuximab (green) to visualize the cell membrane. Nuclei in (a−c) are stained with DAPI (blue).

capable of refolding into its native configuration after the postinsertion. The capacity to refold after denaturation is a general feature observed for affibody molecules (*28, 29*). In this regard, affibody molecules behave differently from antibody molecules. For example, scFv molecules with a similar melting point did not survive the postinsertion step performed at 50 °C or higher temperatures, thus were not capable of refolding into active molecules (unpublished personal data). Compared to antibodies, affibody molecules possess several further advantages for the generation of targeted liposomes and other nanocarriers. First, they do not require any disulfide bonds to assemble into stable and active molecules. Hence, a single cysteine residue can be easily introduced and used for site-directed and defined conjugation, e.g., the formation of stable thioether bonds, without interfering with domain assembly and stability. Second, affibody molecules have been shown to possess similar selectivity and picomolar to low nanomolar affinities as antibodies (*19, 30*) but lack the Fc-mediated

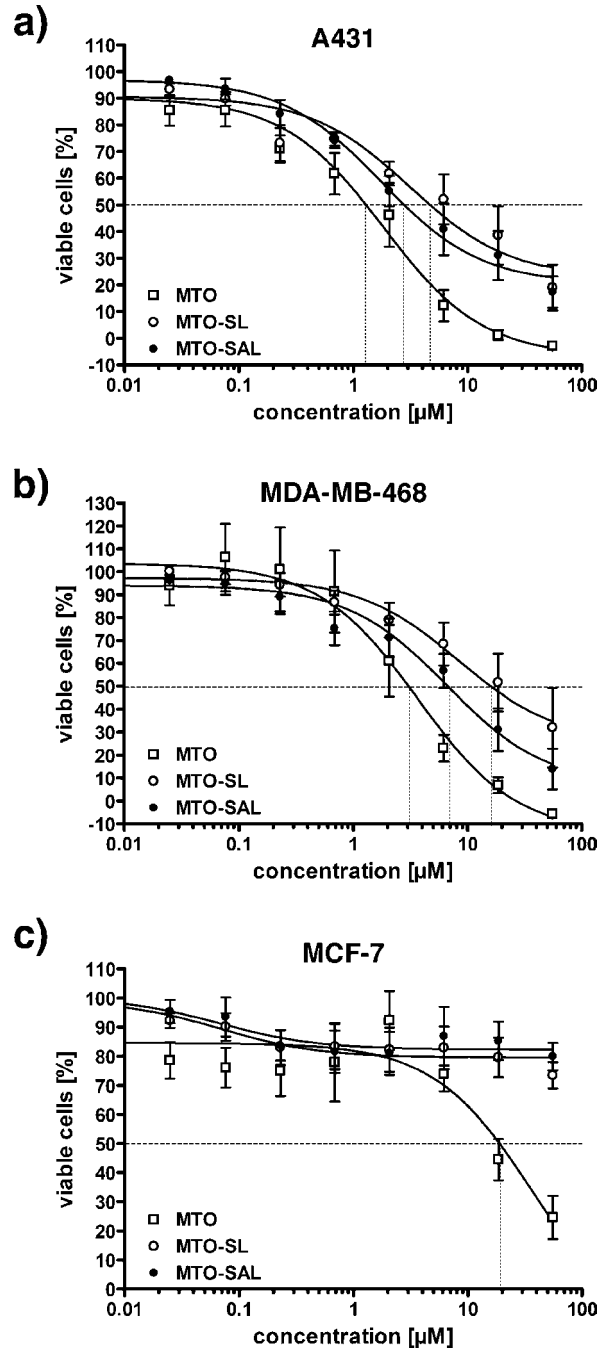

Figure 7. Cytotoxicity. (a) A431 ($n = 6$), (b) MDA-MB-468 ($n = 6$), and (c) MCF-7 ($n = 6$) were incubated with free mitoxantrone (MTO), mitoxantrone-loaded liposomes (MTO-SL), or mitoxantrone-loaded anti-EGFR SAL (MTO-SAL) for 20 h, and cell viability was determined by MTT assay.

Table 2. IC_{50} Values of Mitoxantrone and Mitoxantrone-Loaded Liposomes (in μM)

cell line	free MTO	MTO-SL	MTO-SAL
A431	1.3	4.7	2.8
MDA-MB-468	3	16	6.8
MCF-7	18	>100	>100

activities, which have been shown to be involved in rapid clearance of immunoliposomes produced from whole antibodies. Finally, they can be produced at large quantities in bacteria without the need for periplasmic secretion as required for recombinant antibody molecules.

Using mitoxantrone-loaded anti-EGFR SAL, we showed that binding to EGFR-expressing cells translates into increased

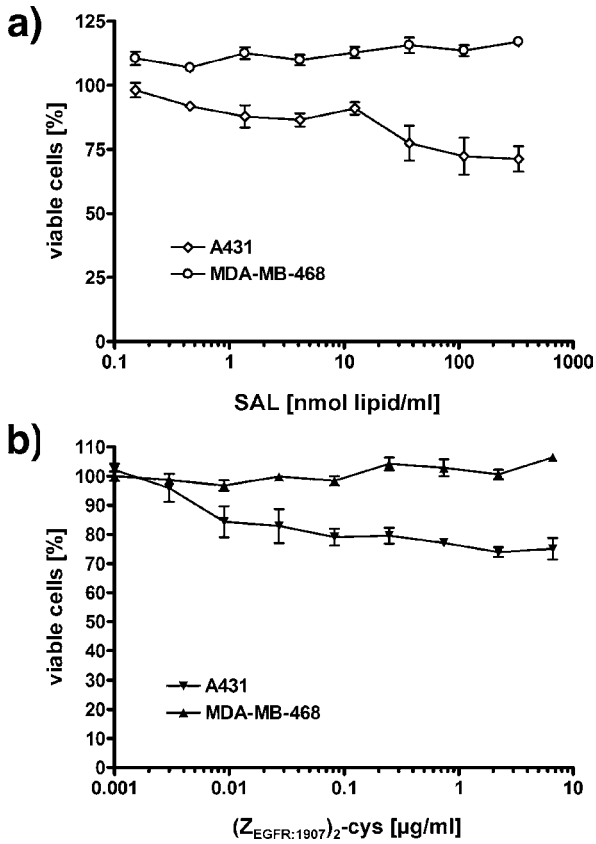

Figure 8. Effects of SAL and soluble affibody molecules on cell growth. MDA-MB-468 and A431 were incubated for 20 h with increasing concentrations of anti-EGFR SAL (a) or soluble affibody molecule (ZEGFR: 1907)$_2$-cys (b) and viable cells were determined by MTT assay.

cytotoxicity compared to drug-loaded SL. Anti-EGFR SAL not loaded with drug were nontoxic, indicating that cytotoxicity was not mediated by the affibody molecule displayed on the liposome surface. The MTO-SAL formulation used in this study did not reach the cytotoxicity of the free drug. This is in accordance with studies for anti-EGFR immunoliposomal formulations of doxorubicin, which also reported IC_{50} values between those of free drug and nontargeted liposomes (*13*). These findings indicate that there is room for improvement, e.g., by increasing stability and thus reducing nonspecific cytotoxicity probably mediated by drug leakage. Furthermore, intracellular drug release from internalized liposomes is a subject for further improvement, e.g., by the incorporation of pH-dependent release mechanisms or by increasing fluidity of lipid bilayer through incorporation of short-chain phospholipids (*31*−*33*). In vivo efficacy of targeted liposomal drug formulations might also be influenced by other factors (*34*). For instance, the kind of drug can determine efficacy, as shown for anti-CD19 immunoliposomes loaded with doxorubicin and vincristine, respectively (*35*). Finally, the affibody molecule itself might influence efficacy of SAL. For example, affibody molecules with strong internalization capacity should result in increased intracellular delivery of the liposomal drug, as shown for anti-ErbB2 scFv immunoliposomes (*36*−*39*).

In summary, we have established a method to produce targeted liposomes from cysteine-modified affibody molecules as ligands. This method should be broadly applicable to the generation of affibody liposomes and other carrier systems for targeted delivery of drugs or other reagents.

ACKNOWLEDGMENT

The authors would like to thank doctors Per Jonasson and Nina Bandmann (Affibody AB, Stockholm, Schweden), for valuable assistance with purification of $(Z_{EGFR:1907})_2$-cys, and Dr. Thomas Mürdter (Dr. Margarete Fischer-Bosch Institut für Klinische Pharmakologie, Stuttgart, Germany) for providing Alexa-488-labeled cetuximab.

LITERATURE CITED

(1) Mendeson, J., and Baselga, J. (2006) Epidermal growth factor receptor targeting in cancer. *Semin. Oncol. 33*, 369–385.

(2) Nicholson, R. I., Gee, J. M. W., and Harper, M. E. (2001) EGFR and cancer prognosis. *Eur. J. Cancer 37*, S9−S15.

(3) Mamot, C., and Rochlitz, C. (2006) Targeting the epidermal growth factor receptor (EGFR) - a new therapeutic option in oncology? *Swiss Med. Wkly. 136*, 4–12.

(4) Rocha-Lima, C. M., Soares, H. P., Raez, L. E., and Singal, R. (2007) EGFR targeting of solid tumors. *Cancer Control 14*, 295–304.

(5) Samad, A., Sultana, Y., and Aqil, M. (2007) Liposomal drug delivery systems: an update review. *Curr. Drug Delivery 4*, 297–305.

(6) Drummond, D. C., Meyer, O., Hong, K., Kirpotin, D. B., and Papahadjopoulos, D. (1999) Optimizing liposomes for delivery of chemotherapeutic agents to solid tumors. *Pharmacol. Rev. 51*, 691–743.

(7) Park, J. W., Benz, C. C., and Martin, F. J. (2004) Future directions of liposome- and immunoliposome-based cancer therapeutics. *Semin. Oncol. 31* (1), 196–205.

(8) Sapra, P., Tyagi, P., and Allen, T. A. (2005) Ligand-targeted liposomes for cancer treatment. *Curr. Drug Delivery 2*, 369–381.

(9) Sofou, S., and Sgouros, G. (2008) Antibody-targeted liposomes in cancer therapy and imaging. *Expert Opin. Drug Delivery 5*, 189–204.

(10) Kontermann, R. E. (2006) Immunoliposomes for cancer therapy. *Curr. Opin. Mol. Ther. 8*, 39–45.

(11) Mamot, C., Drummond, D. C., Greiser, U., Hong, K., Kirpotin, D. B., Marks, J. D., and Park, J. W. (2003) Epidermal growth factor receptor (EGFR)-targeted immunoliposomes mediate specific and efficient drug delivery to EGFR- and EGFRvIII-overexpressing tumor cells. *Cancer Res. 63*, 3154–3161.

(12) Mamot, C., Drummond, D. C., Noble, C. O., Kallab, V., Guo, Z., Hong, K., Kirpotin, D. B., and Park, J. W. (2005) Epidermal growth factor receptor-targeted immunoliposomes significantly enhance the efficacy of multiple anticancer drugs in vivo. *Cancer Res. 65*, 11631–11638.

(13) Mamot, C., Ritschard, R., Küng, W., Park, J. W., Herrmann, R., and Rochlitz, C. F. (2006) EGFR-targeted immunoliposomes derived from the monoclonal antibody EMD72000 mediate specific and efficient drug delivery to a variety of colorectal cancer cells. *J. Drug Targeting 14*, 215–223.

(14) Holliger, P., and Hudson, P. J. (2005) Engineered antibody fragments and the rise of single domains. *Nat. Biotechnol. 23*, 1126–1136.

(15) Tolmachev, V., Orlova, A., Nilsson, F. Y., Feldwisch, J., Wennborg, A., and Abrahmsén, L. (2007) Affibody molecules: potential for in vivo imaging of molecular targets for cancer therapy. *Exp. Opin. Biol. Ther. 7* 555–568.

(16) Nilsson, F. Y., and Tolmachev, V. (2007) Affibody molecules: new protein domains for molecular imaging and targeted tumor therapy. *Curr. Opin. Drug Discovery Dev. 10*, 167–175.

(17) Nygren, P. Å. (2008) Alternative binding proteins: affibody binding proteins developed from a small three-helix bundle scaffold. *FEBS J. 275*, 2668–2676.

(18) Friedman, M., Nordberg, E., Hoidén-Guthenberg, I., Brismar, H., Adams, G. P., Nilsson, F. Y., Carlsson, J., and Ståhl, S. (2007)

Phage display selection of affibody molecules with specific binding to the extracellular domain of the epidermal growth factor receptor. *Protein Eng. Des. Sel. 20*, 189–199.
(19) Friedman, M., Orlova, A., Johansson, E., Eriksson, T. L. J., Höidén-Guthenberg, I., Tolmachev, V., Nilsson, F. Y., and Ståhl, S. (2008) Directed evolution to low nanomolar affinity of a tumor-targeting epidermal growth factor receptor 1-binding affibody molecule. *J. Mol. Biol. 376*, 1388–1402.
(20) Nordberg, E., Friedman, M., Göstring, L., Adams, G. P., Brismar, H., Nilsson, F. Y., Ståhl, S., Glimelius, B., and Carlsson, J. (2007) Cellular studies of binding, internalization and retention of a radiolabeled EGFR-binding affibody molecule. *Nucl. Med. Biol. 34*, 609–618.
(21) Tolmachev, V., Friedman, M., Sandström, M., Eriksson, T. L. J., Rosik, D., Hodik, M., Ståhl, S., Frejd, F. Y., and Orlova, A. (2009) Affibody molecules for epidermal growth factor receptor targeting in vivo: aspects of dimerization and labeling chemistry. *J. Nucl. Med. 50*, 274–283.
(22) Messerschmidt, S. K. E., Kolbe, A., Müller, D., Knoll, M., Pleiss, J., and Kontermann, R. E. (2008) Novel single-chain Fv' formats for the generation of immunoliposomes by site-directed coupling. *Bioconjugate Chem. 19*, 362–369.
(23) Lim, H. J., Masin, D., Mctintosh, N. L., Madden, T. D., and Bally, M. B. (2000) Role of drug release and liposome-mediated drug delivery in govering the therapeutic activity of liposomal mitoxantrone used to treat human A431 and LS180 solid tumors. *J. Pharmacol. Exp. Ther. 292*, 337–345.
(24) Bach, M., Hölig, P., Schlosser, E., Völkel, T., Graser, A., Müller, R., and Kontermann, R. E. (2003) Isolation from phage display libraries of lysine-deficient human epidermal growth factor variants for directional coupling as targeting ligands. *Protein Eng. 16*, 1107–1113.
(25) Lee, R. J., and Low, P. S. (1994) Delivery of liposomes into cultured KB cells via folate receptor-mediated endocytosis. *J. Biol. Chem. 269*, 3198–3204.
(26) Alexis, F., Basto, P., Levy-Nissenbaum, E., Radovic-Moreno, A. F., Zhang, L., Pridgen, E., Wang, A. Z., Marein, S. L., Westerhof, L., Molnar, L. K., and Farokhzad, O. C. (2008) HER-2-targeted nanoparticle-affibody conjugates for cancer therapy. *ChemMedChem 3*, 1839–1843.
(27) Puri, A., Kramer-Marek, G., Campbell-Massa, R., Yavlovich, A., Tele, S. C., Lee, S.-B., Clogston, J. D., Patri, A. K., Blumenthal, R., and Capala, J. (2008) HER-2-specific affibody-conjugated thermosensitive liposomes (Affisomes) for improved delivery of anticancer agents. *J. Liposome Res. 18*, 293–307.
(28) Orlova, A., Feldwisch, J., Abrahmsén, L., and Tolmachev, V. (2007) Update: affibody molecules for molecular imaging and therapy for cancer. *Cancer Biother. Radiopharm. 22*, 573–584.
(29) Arora, P., Oas, T. G., and Myers, J. K. (2004) Fast and faster: a desgined variant of the B-domain of protein A folds in 3 μsec. *Protein Sci. 13*, 847–853.
(30) Orlova, A., Magnusson, M., Eriksson, T. L., Nilsson, M., Larsson, B., Hoidén-Guthenberg, I., Widstörm, C., Carlsson, J., Tolmachev, V., Stahl, S., and Nilsson, F. Y. (2006) Tumor imaging using a picomolar affinity HER2 binding affibody molecule. *Cancer Res. 66*, 4339–4348.
(31) Simões, S., Moreira, J. N., Fonseca, C., Düzgunes, N., and Pedroso de Lima, M. (2004) On the formulation of pH-sensitive liposomes with long circulation times. *Adv. Drug Delivery Rev. 56*, 947–965.
(32) Ishida, T., Okada, Y., Kobayashi, T., and Kiwada, H. (2006) Development of pH-sensitive liposomes that efficiently retain encapsulated doxorubicin (DXR) in blood. *Int. J. Pharmaceut. 309*, 94–100.
(33) Kawano, K., Onose, E., Hattori, Y., and Maitani, Y. (2008) Higher liposomal membrane fluidity enhances the in vitro antitumor activity of folate-targeted liposomal mitoxantrone. *Mol. Pharm. 6*, 98–104.
(34) Sapra, P., and Allen, T. M. (2003) Ligand-targeted liposomal anticancer drugs. *Prog. Lipid Res. 42*, 439–462.
(35) Sapra, P., Moase, E. H., Ma, J., and Allen, T. M. (2004) Improved therapeutic responses in a xenograft model of human B lymphoma (Namalwa) for liposomal vincristine versus liposomal doxorubicin targeted via anti-CD19 IgG2a or Fab' fragments. *Clin. Cancer Res. 10*, 1100–1111.
(36) Nielson, U. B., Kirpotin, D. B., Pickering, E. M., Hong, K., Park, J. W., Shalaby, M. R., Shao, Y., Benz, C. C., and Marks, J. D. (2002) Therapeutic efficacy of anti-ErbB2 immunoliposomes targeted by a phage antibody selected for cellular endocytosis. *Biochim. Biphys. Acta 1591*, 109–118.
(37) Park, J. W., Kirpotin, D. B., Hong, K., Shalaby, R., Shao, Y., Nielson, U. B., Marks, J. D., Papahadopoulos, D., and Benz, C. C. (2001) Tumor targeting using anti-her2 immunoliposomes. *J. Controlled Release 74*, 95–113.
(38) Drummond, D. C., Shao, Y., Shalaby, M. R., Nielson, U. B., Marks, J. D., Benz, C. C., and Park, J. W. (2006) Antibody targeting of long-circulating lipidic nanoparticles does not increase tumor localization but does increase internalization in animal models. *Cancer Res. 66*, 6732–6740.
(39) Shmeeda, H., Tzemach, D., Mak, L., and Gabizon, A. (2009) Her2-targeted pegylated liposomal doxorubicin: retention of target-specific binding and cytotoxicity after in vivo passage. *J. Controlled Release* [Online early access] DOI: 10.1016/j.jconrel.2009.02.002.

BC900061V

Radiolabeling of Biodegradable Polymeric Microspheres with $[^{99m}Tc(CO)_3]^+$ and *in Vivo* Biodistribution Evaluation using MicroSPECT/CT Imaging

Katayoun Saatchi and Urs O. Häfeli*

Faculty of Pharmaceutical Sciences, University of British Columbia, 2146 East Mall, Vancouver, BC V6T 1Z3, Canada.
Received February 11, 2009; Revised Manuscript Received April 22, 2009

Poly(L-lactide) (PLA) microspheres tailored with a tridentate chelating group were radiolabeled with $[^{99m}Tc(H_2O)_3(CO)_3]^+$ and optimized for labeling efficiency and stability. Various ligand−polymer blend compositions with commercial PLA (from 2% to 100%) were evaluated. Labeling efficiencies over 95% were achieved in a 5 min reaction using 100% of the ligand−polymer or within 15 min using a 5% ligand−polymer blend. The addition of 1.5% of PEGylated copolymer to the blend did not affect the labeling efficiency of these particles but changed their *in vivo* behavior. MicroSPECT/CT imaging showed significant uptake of non-PEGylated microspheres by the murine lung, while only the liver and spleen took up PEGylated microspheres. Such ^{99m}Tc radiolabeled biodegradable microspheres will be useful diagnostic imaging agents for visualization of the functioning reticuloendothelial system (RES). Similarly, other sizes of the same microspheres will allow imaging of lung perfusion, bone marrow, lymph and inflammation scintigraphy, and radioembolization therapy.

INTRODUCTION

In nuclear medicine, particles of various sizes are radiolabeled to diagnose different conditions (*1*). The particle-bound radioactivity is made visible by imaging, typically with a single photon emission computed tomography (SPECT) instrument. Examples of such particle-based imaging include lung perfusion imaging with ^{99m}Tc-labeled macroaggregated albumin (MAA) particles sized between 10−90 μm (*2, 3*) liver and spleen function imaging with ^{99m}Tc-sulfur colloid sized 0.1−1 μm (*4, 5*) or with ^{99m}Tc-albumin colloid sized 0.4−2 μm (*6, 7*), both of which are taken up by the reticulo-endothelial system (RES); and bone marrow, inflammation, and lymph scintigraphy which uses even smaller, less than 0.08 μm, ^{99m}Tc-albumin colloid (*8, 9*).

A major drawback of these imaging methods is that the main material used to prepare the diagnostic radiopharmaceuticals is albumin, a human protein with all the inherent risks (e.g., hepatitis C, HIV) associated with blood products. To eliminate these risks and their associated liability, several manufacturers have taken albumin-based products (e.g., Technescan, Microlite, and Isojex) off the market.

Particulate radiopharmaceuticals used in nuclear medicine, including the nonalbumin ones (Table 1), are associated with a second disadvantage. Specifically, their wide size distribution results in an uptake by other than the target tissue or organ. As a result, higher background activities are seen in these areas, leading to the deterioration of the imaging signal and resulting in the need for higher injection activities in order to obtain statistically sound images from the imaging region. The high background makes it thus impossible to minimize the injected activity and, therefore, the radiation dose received by the patient.

To circumvent the problems associated with particulate albumin radiopharmaceuticals, we sought to develop a replacement particle of narrowly controlled size. Such particles would form the basis of a radiolabeling kit for the preparation of radioactive microspheres for both diagnostic and therapeutic applications. A successful radiolabeling kit must, in addition to containing nontoxic biodegradable microparticles of narrow size distribution, show excellent labeling efficiency and stability. Diagnostic applications of such radiopharmaceuticals in nuclear medicine include lung perfusion imaging, imaging of the reticuloendothelial system (RES) and of bone marrow, as well as inflammation and deep vein thrombosis imaging (Table 1). Therapeutic applications of such radiopharmaceuticals in radiation oncology include the radioembolization of liver tumors, uterine fibroids, meningiomas and arteriovenous malformations, and the local treatment of leftover and recurring disease (Table 1).

We have previously developed biodegradable microspheres (made of FDA-approved polylactide or polylactide-*co*-glycolide) that can be made in different sizes (*10, 11*) with relatively narrow size distributions. We have also synthesized tailored polymers to accommodate metal coordination using a simple one-pot synthesis of biodegradable tailored polylactide with a built-in tridentate ligand to coordinate selected metal ions, "polymers with a grip" (*12*) (Figure 1). To follow up on both of these studies, and to investigate a potential replacement product for the discontinued albumin-based particles (e.g., Microlite, Table 1), this work describes the radiolabeling of these custom polymers or a blend thereof with commercially available polymers in the shape of microspheres (0.5−1.5 μm) with $[^{99m}Tc(CO)_3]^+$ (Figure 1). The labeling conditions were also investigated and optimized for microspheres containing additional poly(ethylene glycol) (PEG) groups and then compared for their biological distribution in mice.

EXPERIMENTAL PROCEDURES

Materials. Poly(L-lactide) (PLA) with a molecular weight (MW) of 2 kDa was purchased from Boehringer Ingelheim (Resomer L104; Ingelheim, Germany). Poly(vinyl alcohol) (PVA) with a MW of 13−23 kDa and 98% hydrolyzed was obtained from Aldrich. All other chemicals were purchased from Sigma/Aldrich and used as received. The PEGylated copolymer $MePEG_{17}$-b-PCL_{10} was kindly provided by the Burt lab in the Faculty of Pharmaceutical Sciences at The University of British Columbia (*13*). Double-distilled water was used in all experiments.

* Corresponding author. Urs Hafeli, Faculty of Pharmaceutical Sciences, University of British Columbia, 2146 East Mall, Vancouver, BC V6T 1Z3, Canada; e-mail: uhafeli@interchange.ubc.ca; Tel. (604) 822-7133; Fax (604) 822-3035.

10.1021/bc900066j CCC: $40.75 © 2009 American Chemical Society
Published on Web 06/03/2009

Table 1. Particle-Based Radiopharmaceuticals for Imaging and Therapy

radiopharmaceutical	particle size	application	labeling	availability	ref
^{99m}Tc-MAA	10−90 μm (90%), all <150 μm	lung perfusion imaging, detection of deep vein thrombosis in lower extremities	10 min @ RT[a]; >90%	Draximage, Pharmalucence	2, 3
^{99m}Tc-albumin colloid	0.4−2 μm	RES (liver, spleen) imaging	2 min @ RT; ∼100%	Microlite, Du Pont discontinued	6, 7
^{99m}Tc-albumin colloid	<0.08 μm, mean 0.03 μm	bone marrow imaging (15% of colloid ends up there), inflammation scintigraphy, lymphoscintigraphy	5−10 min@ RT; ∼100%	Nanocoll, Du Pont discontinued	8, 9
^{99m}Tc-sulfur colloid	0.1−1 μm (mean 0.3 μm)	liver and spleen imaging, bone marrow (2−5% ends up there) and lymph imaging, GI blood loss studies, gastric emptying studies (egg sandwich)	5−10 min @ boiling; >99%	Pharmalucence	4, 5
^{99m}Tc-antimony sulfur colloid	mean 0.01 μm	lymphoscintigraphy	30 min @ boiling; ∼100%	-	5, 30
^{32}P-chromic phosphate colloid	2 μm	treatment of peritoneal or pleural effusions caused by metastatic disease, interstitial injection	ready for injection	Phosphocol P32, Covidien	31−33
^{90}Y glass microspheres*	25−35 μm	radioembolization of liver tumors	neutron activation; 100%	Therasphere, MDS Nordion	34
^{90}Y resin microspheres*	25−35 μm	radioembolization of liver tumors	neutron activation; 100%	SIR-Spheres, SIRTEX	35

[a] RT = room temperature.

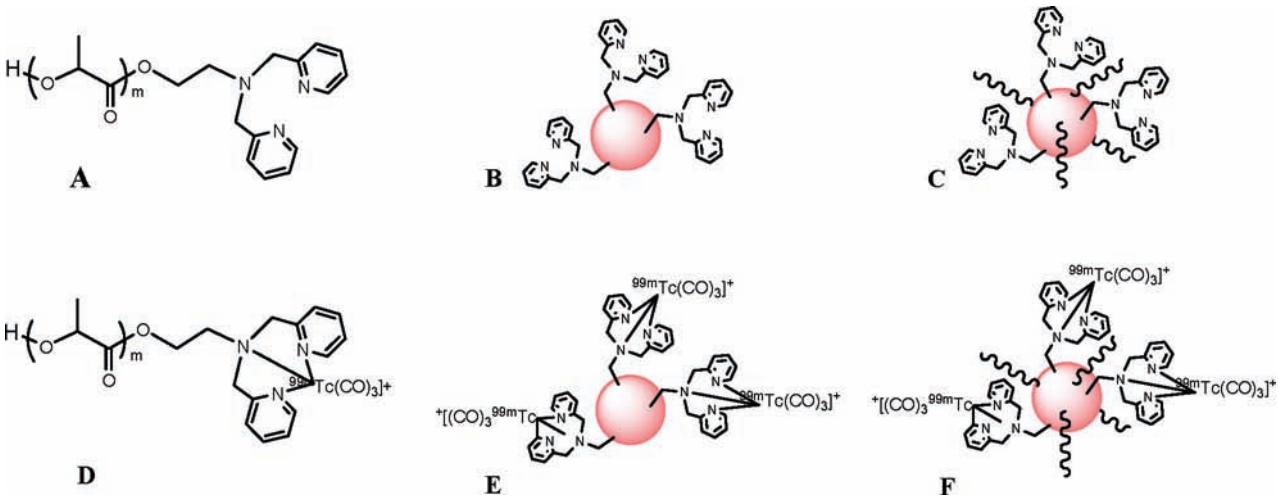

Figure 1. (A) Structure of "chelomer"; (B) cartoon of a microsphere with ligands on the surface; (C) PEGylated blend chelomer (wiggly line, PEG); D,E,F) Matching coordinated/radiolabeled chelomer and microspheres.

The radioisotope used herein,^{99m}Tc, is present in almost all particle-based radiopharmaceuticals including Technescan and Microlite and is currently the most used imaging agent in nuclear medicine due to its ideal physical properties ($t_{1/2}$ = 6 h, E = 140 keV, 89% abundance), suitable dosimetry (low radiation dose) and high specific activity. It is generator produced (^{99}Mo/^{99m}Tc) and available at a reasonable cost. The most recent labeling precursor to yield ^{99m}Tc radiopharmaceuticals is the $[^{99m}Tc(CO)_3(H_2O)_3]^+$ complex cation (*14, 15*). This complex is suitable for coordination to a wide variety of ligands, because it has a robust [*fac*-$Tc(CO)_3]^+$ core, a small size, and is kinetically inert and thermodynamically stable. Its three potential binding sites are readily available for coordination, since the aqua ligands are labile and easily replaced (*16*−*18*). We prepared the $[^{99m}Tc(H_2O)_3(CO)_3]^+$ precursor from Isolink kits generously provided by Mallinckrodt (now Covidien, St. Louis, MO).

Thin layer chromatography (TLC) was performed on black TEC-Control strips (Cat# 150−005; Biodex, Shirley, NY, USA) using saline as the mobile phase. The radioactive TLCs were made visible using a phosphor imager (Cyclone storage phosphor imager with 20 × 25 cm^2 phosphor screen, Perkin-Elmer, Waltham, MA, USA) and analyzed using OptiQuest software. Microspheres were separated by centrifugation using an Eppendorf Centrifuge 5415 C at 6000 rpm (6611 g). A polytron (PT 10/35; Kinematica, Lucerne, Switzerland) was used for homogenization during microsphere preparation. Scanning electron microscopy (SEM) was performed on a Hitachi S-3000N (acceleration voltage 20.0 KV, SE mode, 15.0 mm working distance). The particles were sputtered with a 10 nm layer of Au/Pd (60:40) prior to imaging. Activity measurements were carried out using a Packard Cobra II gamma counter (Perkin-Elmer).

Chelomer Preparation. The ligand-polymer, nick-named "*Chelomer*" in our laboratories (***Chel***ating P**o**ly***mer*) (Figure 1A), was prepared by ring-opening polymerization of L-lactide as previously reported (*12*). Briefly, L-lactide was polymerized

using bis(2-(aminomethyl)pyridine)ethanol for the initiator and tin(octoate) as the catalyst at 125 °C for 3.5 h. The product was completely characterized before use by ^{1}H NMR, ^{13}C NMR, MALDI-TOF MS, and FTIR (*12*).

Microsphere Preparation. All microspheres were made using a double emulsion solvent evaporation technique (*19*). Briefly, the polymer(s) were dissolved in 4 mL of CH_2Cl_2. The first emulsion (w/o) was prepared by homogenization (27 000 rpm) of 400 μL H_2O in the polymer CH_2Cl_2 solution for 2.5 min in an ice bath. PVA (1% w/v, 15 mL) was added to this mixture and homogenized for another 2.5 min to make the second emulsion (w/o/w). This mixture was quickly poured into a stirred 1% solution of PVA (85 mL) at 2000 rpm for 5 min. Stirring continued for 2.5 h, after which the mixing speed was reduced to 500 rpm, and the suspension was stirred long enough for the foam to settle. The microspheres were washed several times in water by serial centrifugation at 5000 rpm (2683 g) and then resuspended in 1 mL water and stored at 4 °C. Since the microsphere preparation is just a physical transformation, no characterization was carried out to determine the nature of particles. However, the size and shape of the particles were measured using scanning electron microscopy.

Functionalized Microspheres. The chelomer and various blends (wt % mixture of the chelomer with commercial PLA) of chelomer with PLA were used to produce chelating microspheres. The 2% chelomer microspheres were, for example, made by dissolving 4 mg chelomer and 196 mg of PLA in 4 mL CH_2Cl_2. Additional microspheres containing 5%, 10%, 25%, and 100% chelomer were also produced, while 0% chelomer (= 100% PLA) microspheres were used as controls in all studies. Pegylated microspheres were made by blending (a) 5% chelomer, 1.5% $MePEG_{17}$-*b*-PCL_{10} with 93.5% PLA; and (b) 10% chelomer, 3% $MePEG_{17}$-*b*-PCL_{10} with 87% PLA.

Radiolabeling. The precursor complex $[^{99m}Tc(H_2O)_3(CO)_3]^+$ was prepared by injecting a saline solution of $Na[^{99m}TcO_4]$ (740−1850 MBq), diluted to 1 mL total volume with water, into the Isolink vial and heating for 25 min in boiling water. After cooling, the vial was vented and 0.2 mL HCl (0.1 M) added to neutralize the solution (pH = 7). The volume was adjusted to 2 mL with water. A >94% yield for the reaction was confirmed by TLC of the reaction mixture in saline, in agreement with the information provided by Covidien.

After addition of the desired activity A_T (9−260 MBq) to a 2 mg suspension of microspheres (total combined volume $V_T \leq 300$ μL), the mixture was heated to 75 °C, shaken at 1000 rpm for varying times (2 min to 2 h), and cooled to room temperature. At each time point, the suspension was centrifuged for 15 min at 6611 *g* and a known volume V_S (50 μL) of supernatant removed and its activity A_S measured. The labeling efficiency was then calculated with time-corrected activities as

$$\text{labeling efficiency}(\%) = \frac{A_S \times V_T}{V_S \times A_T} \times 100 \qquad (1)$$

Each experiment was performed with a minimum of 3 and up to 6 replicates. Microspheres made from commercial PLA were used as controls in all studies. Variables affecting labeling (heating time, heating temperature, chelomer fraction) were optimized to achieve maximum labeling efficiency at minimum heating time.

Cysteine Challenge. After radiolabeling, a 1 mM cysteine solution in PBS was added to the labeled microspheres to a total of 1 mL. The samples were shaken at 1000 rpm and 37 °C for 1 h, centrifuged, and the activity in 300 μL supernatant aliquots measured. Dissociation of $[^{99m}Tc(CO)_3]^+$ was measured by TLC. The remaining cysteine solution (700 μL) was shaken for an additional 23 h and another 300 μL supernatant aliquot analyzed. After the 48 h time point, the last aliquot was sampled, the radioactivity of all aliquots analyzed in a gamma counter, and the percentage of microsphere-bound activity calculated.

Biodistribution. To investigate if the microspheres were appropriate for RES imaging, the biodistribution of the 5% blended microspheres, with and without 1.5% of the PEGylated block copolymer, was determined using microSPECT/CT imaging on an X-SPECT instrument (Gamma Medica, Northridge, CA; now Siemens) at McMaster University's Centre for Preclinical and Translational Imaging in Hamilton, Ontario. Microspheres were labeled as explained above immediately prior to the imaging studies at the Nuclear Medicine Department's Radiopharmacy. Groups of four female PyVMT transgenic mice with mammary tumors and four female C57BL/6 mice with subcutaneous neck tumors grown from a primary cell line at passage six of PyVMT mouse tumors were injected intravenously into the tail vein with 18.5 MBq of the non-PEGylated microspheres and with 18.5 MBq of the ^{99m}Tc-tricarbonyl precursor, respectively. These mice were predestined to be sacrificed, so rather than healthy mice, they were used to give us the additional benefit of investigating tumor uptake for the precursor ^{99m}Tc-tricarbonyl complex and confirming no particle uptake in the tumor. Later, an additional group of four female C57BL/six mice without tumors received 18.5 MBq of the ^{99m}Tc-labeled PEGylated microspheres. At 2, 4, and 6 h after injection, a SPECT scan (32 projections for initially 18 s and at the later two time points 46 s) was performed under isoflurane anesthesia in the supine position, followed by a CT scan (512 projections), after which the animals were sacrificed and the organs removed, weighed, and their activity determined using a Packard Cobra II auto gamma-counter. Results were expressed as the percentage of the injected dose per organ and per gram of tissue (%ID/g), and the tumor-to-blood ratios calculated from the %ID/g values. The biodistribution of the precursor complex $[^{99m}Tc(H_2O)_3(CO)_3]^+$ was investigated and compared to that of the microspheres as a control.

RESULTS AND DISCUSSION

Biodegradable polymers for the delivery of radiation have been seriously under-investigated in nuclear medicine. Such polymers if designed properly are suitable tools for many different diagnostic or therapeutic applications. Depending on the polymer's physical shape, for example, in the form of microspheres and nanospheres, and the radioisotope used, these compounds can replace currently used products such as macroaggregated albumin particles, nonbiodegradable sulfur colloids, or even TheraSphere and SIR-Spheres (Table 1). In a different physical shape, for example, in the form of films, disks, and wafers, such a radiolabeled polymer could be used to deliver local radiation, in a similar way as the Gliadel wafers deliver an anticancer drug for the prevention of recurring disease.

Our goal in this work was to create a simple microsphere radiolabeling kit suitable for various *in vivo* applications. For this purpose, we prepared particles in the 0.5−2 μm size range that would be appropriate for RES imaging and could therefore replace the discontinued albumin colloids (Microlite). Our microspheres (Figure 1B and 2A) were made from the chelomer, or a blend of chelomer and a nonchelating commercial polymer, using a double emulsion, solvent extraction/evaporation procedure (*20*). In this water-in-oil-in-water (w/o/w) process, water-soluble or water-dispersible components are dissolved or dispersed in an aqueous solution, which is then emulsified in an organic solvent containing the chelomer. The primary water-in-oil emulsion (w/o) is then dispersed in a second aqueous phase, containing a suitable emulsifier, and forms a double emulsion (w/o/w). Solid microspheres are collected following the complete removal of the volatile organic solvent by

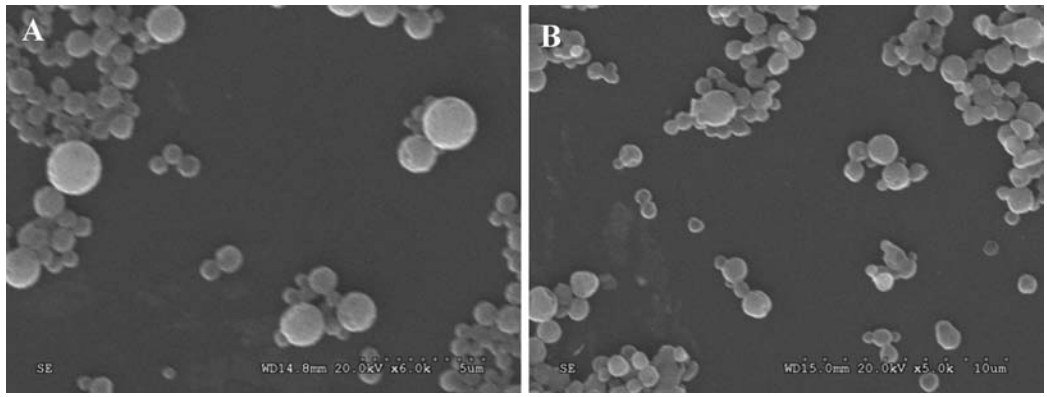

Figure 2. SEM pictures of the 10% blend PEGylated microspheres (A) before (scale bar 5 μm) and (B) after (scale bar 10 μm) radiolabeling.

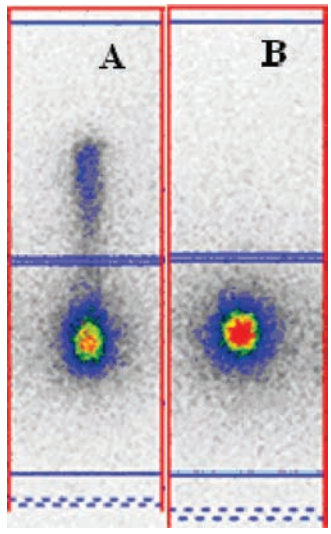

Figure 3. Developed TLCs of labeled microspheres made from (A) commercially available polymer (control) and (B) 100% chelomer. Saline was used as the mobile phase.

extraction into the surrounding water phase and evaporation. The first (inner) emulsion allows drug loading, and the second solidifies the particles. In the present studies, no drug was loaded into the microspheres. Instead, the microspheres consisted of a PLA core with the ligand bis(picolylamine) at the outer surface having the capability to bind metals. This technique of making microspheres does not involve chemical or physicochemical changes to the polymeric material; it is just a physical transformation of shape from a solid powder to microspheres.

Radiolabeling was readily achieved with the 100% chelomer microspheres. These microspheres suspended in the $[^{99m}Tc(H_2O)_3(CO)_3]^+$ solution and heated to 75 °C for 30 min took up 94.8 ± 1.5% of the radioactivity compared to 79.9 ± 7.4% for the control microspheres. The reaction conditions, especially heating at 75 °C, did not affect the physical appearance of the microspheres (Figure 2B). This is important for *in vivo* applications, as any changes in size and shape affect microsphere biodistribution (*21*).

Figure 3 compares the TLC of the chelomer-containing microspheres to that of control microspheres. Chelomer microsphere activity was found exclusively at $R_f = 0$, whereas an additional spot was observed for the control microspheres. The R_f of the additional spot was similar to that of $[^{99m}Tc(H_2O)_3(CO)_3]^+$, indicating random release. The labeling efficiency of the control polymer varied from sample to sample, as a result of nonspecific weak binding of $[^{99m}Tc(CO)_3]^+$ to the particles.

Once the initial radiochemical stability was confirmed, the labeling conditions were optimized in terms of chelomer fraction, heating time, and temperature. Table 2 shows the labeling efficiency for various blend compositions of microspheres reacted for varying times with $[^{99m}Tc(H_2O)_3(CO)_3]^+$. For all polymer blends containing more than 5% of the chelomer, the average labeling efficiency was about 95%, whereas the labeling efficiency for the 2% blend and the control (100% commercial PLA) were only slightly higher than 80%. Although low, the labeling efficiency for the 2% chelomer microspheres was consistent, while the results for the control (0% chelomer) varied wildly. This is depicted in Figure 4 by plotting the labeling efficiency of chelomer blends vs heating times for a subset of these experiments. Blended polymers containing 100% (A), 25% (B), or 10% (C) of the chelomer showed excellent labeling efficiency and high stability in the cysteine challenge. The control microspheres, 0% (D), however, were labeled less efficiently and could not withstand the cysteine challenge, as most of the radioactivity was released within 24 h.

For additional reaction times of 2, 5, and 120 min, only the 100% and 0% blends were examined. The 100% chelomer microspheres showed 86.8 ± 9.4%, 96.7 ± 0.5%, and 96.8 ± 3.1% radiolabeling efficiency, respectively, while the control microspheres took up only 62.3 ± 11.5%, 75.8 ± 11.8%, and 65.1 ± 6.1%. This indicates that a minimum reaction time of 5 min is needed to achieve labeling efficiencies suitable for clinical applications.

The thermodynamic stability of the radiolabeled complex for *in vivo* applications is generally evaluated by cysteine or histidine challenges, where the radioactive metal complex is placed in a concentrated solution of the competitive *in vivo* ligands cysteine or histidine (*22*). We performed a cysteine challenge after each labeling experiment. After 30 min of radiolabeling (Table 2), the cysteine challenge to microspheres consisting of 100% chelomer resulted in microsphere-bound activity of 89.3 ± 1.9% and 81.2 ± 2.2% at the 1 and 24 h time points, respectively. For the 0% chelomer microspheres (controls), only 37.9 ± 2.3% and 1.9 ± 3.6% of the activity remained microsphere-bound at the 1 and 24 h time points, respectively. This confirmed the stability of the complexation of $[^{99m}Tc(CO)_3]^+$ to the chelomer's bis(picolylamine) binding site after 24 h. Overall, for microspheres consisting of a more than 5% chelomer blend, stability after 15 to 60 min reaction time was approximately 95% activity as determined by the cysteine challenge. An average of 90% activity remained after 24 h of cysteine competition for the same groups.

To evaluate how much activity could be loaded onto the microspheres, the 5%, 10% and 25% chelomer blends were radiolabeled with increasing amounts of $[Tc(CO)_3]^+$ (74, 128, and 260 MBq). For all activities, the 10% blend chelomer had ≥93% labeling efficiency (Figure 5), with good cysteine

Table 2. Labeling Efficiency and Stability Results Measured at 37 °C for Microspheres Made from Polymer Blends with Different Amounts of Chelomer

		labeling efficiency (%)		cysteine challenge 1 h (%)		cysteine challenge 24 h (%)	
labeling time (min)	chelomer amount (%)	average	± S.D.	average	± S.D.	average	± S.D.
15	0	81.6	6.6	55.0	14.7	21.9	24.5
	2	82.9	1.6	62.2	0.2	42.5	0.4
	5	97.4	0.2	95.4	0.2	93.0	0.2
	10	96.6	1.4	93.5	2.5	89.7	3.4
	25	94.2	0.6	89.2	1.1	83.8	1.2
	100	94.3	0.5	89.1	0.3	81.0	0.3
30	0	80.0	7.4	53.4	17.1	44.5	25.2
	2	84.4	1.2	69.5	2.3	54.7	4.1
	5	96.5	0.2	94.3	0.2	91.7	0.1
	10	96.0	1.6	92.5	3.0	88.3	4.0
	25	93.9	0.3	88.6	0.6	82.3	0.9
	100	94.8	1.5	89.3	1.9	81.2	2.2
60	0	79.0	7.5	52.4	13.4	30.7	18.6
	2	88.1	0.9	78.1	0.7	67.2	1.2
	5	95.5	0.3	92.6	0.4	89.1	0.8
	10	94.6	1.3	90.4	2.6	85.4	3.7
	25	91.9	0.6	85.2	1.2	77.4	1.4
	100	92.0	0.6	84.7	1.0	74.9	1.4

Table 3. Organ/Blood Ratio of non-PEGylated and PEGylated ^{99m}Tc-Radiolabeled Microspheres and the ^{99m}Tc-Tricarbonyl Precursor at the 6 h Time Point ($n = 4$)

	Non-PEGylated ^{99m}Tc-microspheres		PEGylated ^{99m}Tc microspheres		$[^{99m}Tc(H_2O)_3(CO)_3]^+$	
organ	average	± S.D.	average	± S.D.	average	± S.D.
blood	1.00	0.00	1.00	0.00	1.00	0.00
heart	3.80	1.03	0.51	0.09	0.30	0.07
tumor	0.36	0.10	-	-	0.28	0.23
liver	17.10	1.00	29.47	3.99	1.06	0.16
kidneys	2.82	0.05	3.74	0.45	1.42	0.33
lungs	74.86	43.56	4.50	2.69	0.68	0.40
small intestine	0.75	0.10	0.59	0.05	0.34	0.04
brain	0.74	0.12	0.03	0.00	0.03	0.01
bladder	1.09	0.52	0.94	0.49	0.30	1.29
muscle	0.18	0.09	0.09	0.02	0.04	0.01
spleen	14.24	5.64	15.11	10.41	0.26	0.00
stomach	-	-	0.26	0.39	0.18	0.03

challenge results at 1 and 24 h. The 5% and 25% chelomer blends were only labeled with 74 and 128 MBq of activity and had 98% and 93% labeling efficiency, respectively.

We also evaluated the temperature of the radiolabeling reaction. As expected, lowering the radiolabeling temperature to less than 75 °C decreased thermal energy and led to increased reaction time or decreased labeling efficiency. For example, heating microspheres with 100% chelomer to 50 °C for 30 min resulted in a labeling efficiency of 50%. Since the biodegradable microspheres are sensitive to heat, we determined that 75 °C was the upper temperature limit to achieve labeling without affecting the polymer matrix integrity. Further shortening of the overall radiolabeling procedure would be possible only by speeding up the radiolabeling of the precursor $[Tc(H_2O)_3(CO)_3]^+$ using microwave heating (*23*).

The biodistribution of the 10% chelomer microspheres radiolabeled with 18.5 MBq of ^{99m}Tc (labeling efficiency 94%) (Figure 1E) was then investigated in mice after tail vein injection using microSPECT/CT imaging (Figure 6B) and organ activity analysis at the end of the experiment (Figure 7). Most microspheres accumulated in the liver, with additional substantial uptake in the lungs. The high lung uptake was unexpected since the microspheres sized between 1 and 2 μm (Figure 2A) were not large enough to clog the lung capillaries of between 5 and 7 μm. Two factors could be potential contributors to this uptake: the charge of the complex cation on the particle surface or *in vivo* agglomeration of the particles and accumulation in the lung capillaries. Upon checking, no *in vitro* aggregation of the radiolabeled microspheres was observed microscopically. No other organs received significant amounts of microspheres, and the tumors virtually excluded them.

As mentioned earlier, our experimental design did not include tumor-bearing mice initially, but since there were tumor-mice available destined to be sacrificed, we chose to use them for two main reasons. First, from literature data, it is well-known that microspheres are in general captured by the RES in the liver and spleen (*24*). Micrometer-sized particles are not expected to be taken up by a tumor—for that, they would have to be smaller than about 200 nm, which would increase their blood circulation time and make it possible for the particles to nonspecifically accumulate in newly grown tumors' leaky vasculature by the enhanced permeation and retention (EPR) effect (*25*). Using tumor-bearing animals would confirm this expectation. The second reason for using the available mice with tumors was that there is no published report about the biodistribution of the ^{99m}Tc-tricarbonyl precursor in the literature. Investigating this in mice with tumors might add more information to the reader than by doing it in normal mice. However, since there was no indication of tumor uptake with the microspheres, the later biodistribution study with the PEGylated microspheres was performed in mice without tumors.

To further investigate the significant lung uptake of the microspheres, we decided to make microspheres with additional PEGylated polymers incorporated into the surface (Figure 1C). PEGylation has been shown to enhance surface hydrophilicity of microspheres and to prevent agglomeration and clumping, not only *in vitro*, but also *in vivo* (*26*). To prepare PEGylated microspheres, 1.5% of a PEGylated polymer was simply added to the polymer blend during the preparation of the microspheres. The good labeling efficiency seen in non-PEGylated microspheres was maintained, as 2 mg of the PEGylated microspheres radiolabeled with 40 MBq of $[Tc(CO)_3]^+$ achieved a 97.8 ±

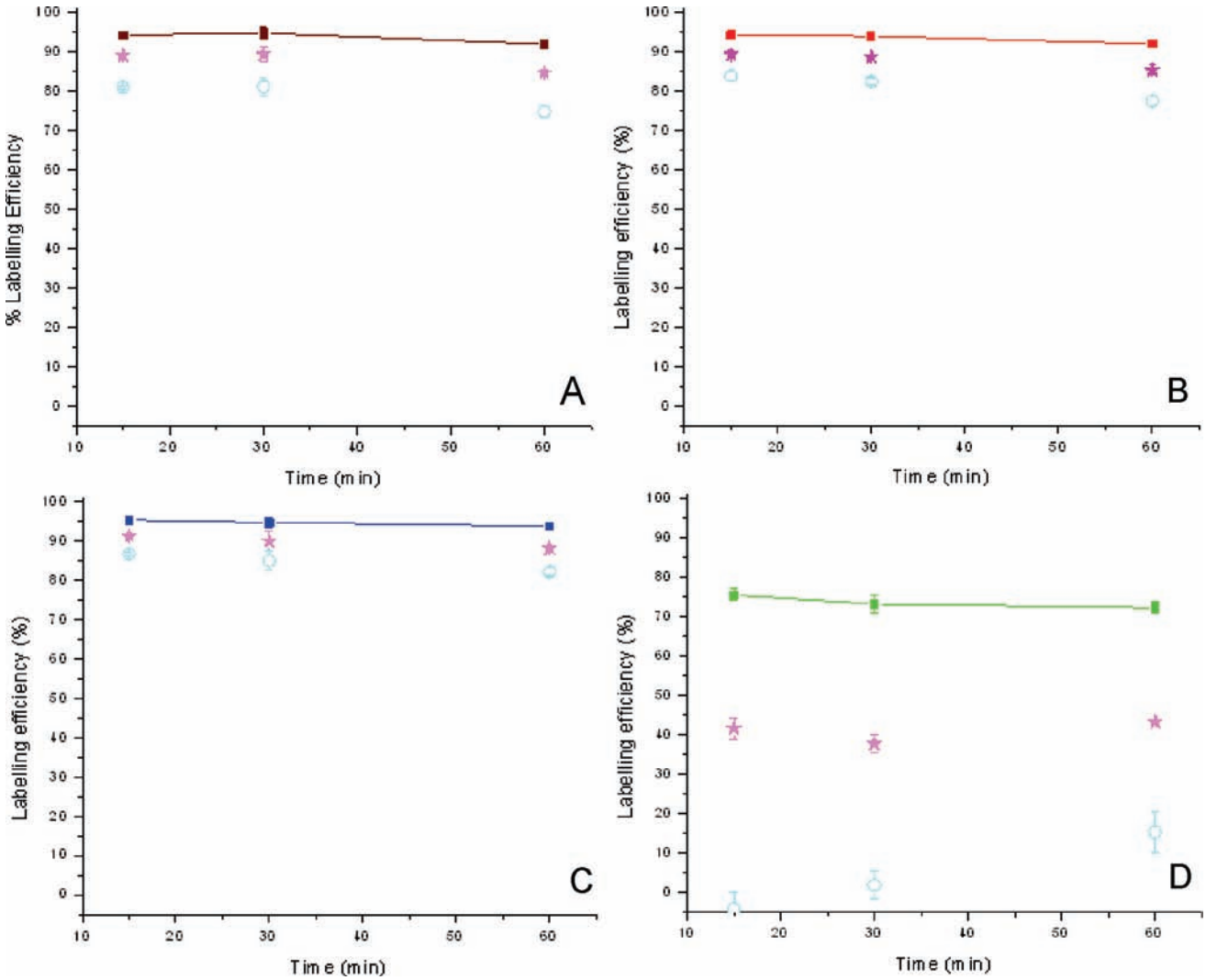

Figure 4. Plots of labeling efficiency vs initial reaction time along with the stability testing against cysteine for (A) 100%, (B) 25%, (C) 10%, and (D) 0%. Cysteine challenge results are given at 1 h (stars) and 24 h (hollow circles). For all experiments, 2 mg of microspheres were radiolabeled with 9.5 MBq (250 μCi) of $[Tc(CO)_3]^+$.

0.4% labeling efficiency. The radiochemical stability of these microspheres was as good as that of non-PEGylated microspheres: the cysteine challenge showed that 97% and 93% of the activity were still microsphere-bound after 1 and 24 h, respectively.

The biodistribution of PEGylated 10% chelomer microspheres radiolabeled with 18.5 MBq of ^{99m}Tc (Figure 1F) was also investigated in mice after tail vein injection. As seen by microSPECT/CT imaging (Figure 6C), almost all lung uptake could be avoided by using PEGylated microspheres. The charge on the microspheres was, therefore, not responsible for the lung uptake of microspheres observed previously. Uptake of the PEGylated microspheres by the liver increased, and all other organs received proportionally less of the radioactive microspheres (Figure 7).

To be able to evaluate the *in vivo* stability of the $[^{99m}Tc(CO)_3]^+$ complexation to the chelomer, an additional group of 4 animals received the same activity of the precursor complex $[^{99m}Tc(CO)_3(H_2O)_3]^+$ so that the biodistribution of the complex could be compared to that of the radiolabeled microspheres (Figure 6A). After 6 h, approximately one-third of the injected charged tricarbonyl compound was still found in the animals, mainly circulating in the blood. The heart with the highest blood concentration was, thus, highly visible in the SPECT scan. While a large part of the precursor complex $[^{99m}Tc(CO)_3(H_2O)_3]^+$ was

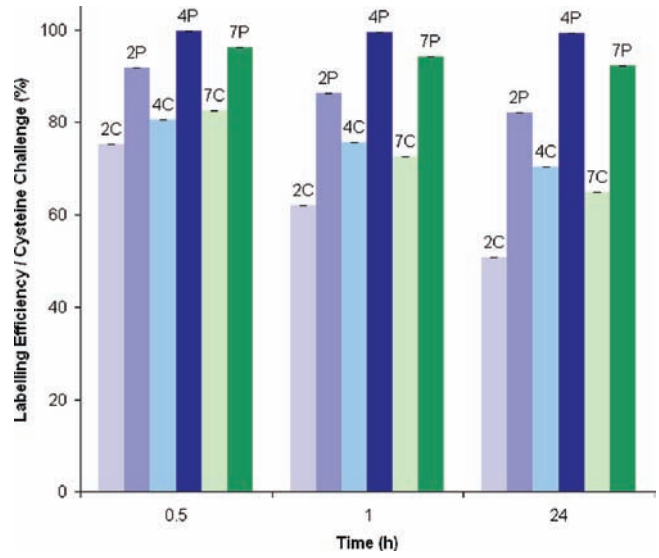

Figure 5. Graph showing labeling efficiency by increasing initial labeling activity from 74 MB (2 mCi) to 260 MBq (7 mCi) for 10% chelomer (P) vs control (C) microspheres. The first time point at 0.5 h is the labeling efficiency, while the 1 and 24 h time point are results of the cysteine challenge.

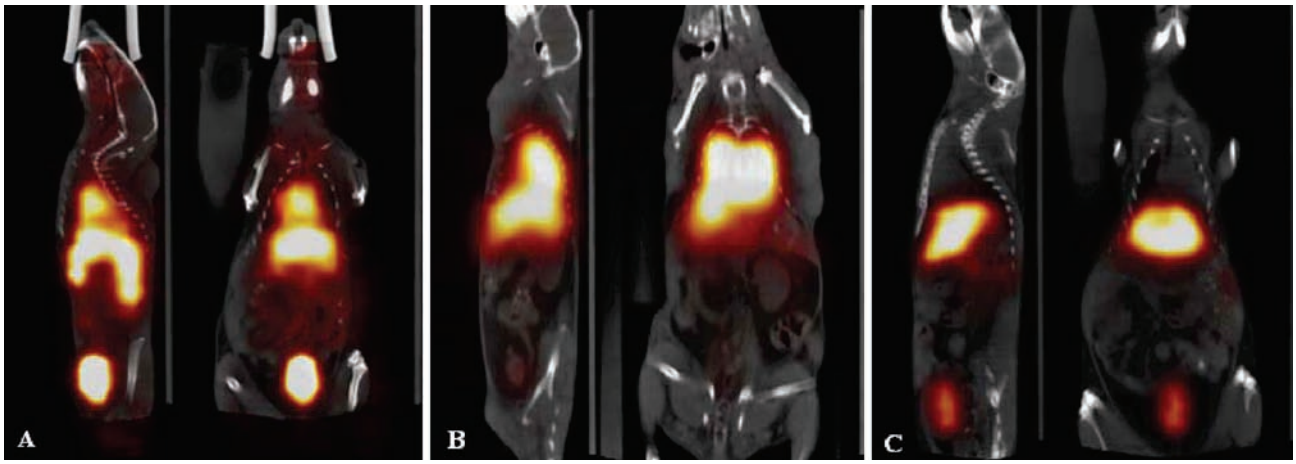

Figure 6. Sagittal (left) and coronal (right) microSPECT/CT images of (A) $[^{99m}Tc(H_2O)_3(CO)_3]^+$, (B) non-PEGylated microspheres, and (C) PEGylated microspheres 6 h after tail vein injection.

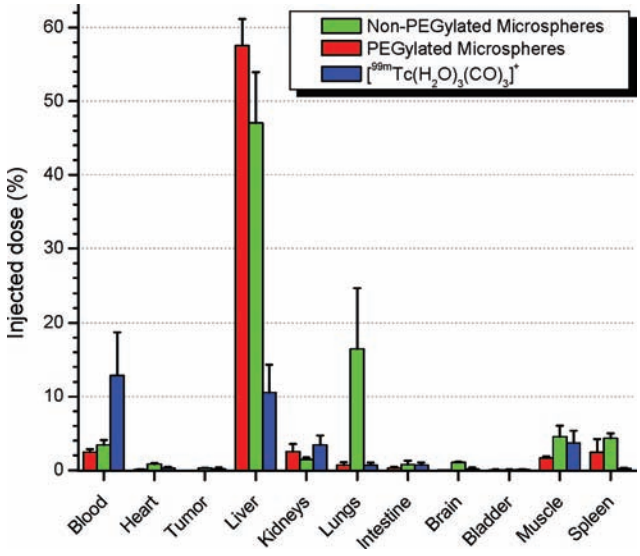

Figure 7. Biodistribution of non-PEGylated and PEGylated ^{99m}Tc-radiolabeled microspheres and the ^{99m}Tc-tricarbonyl precursor at the 6 h time point ($n = 4$).

excreted through the urine, some may have rapidly exchanged its three labile water molecules and ended up in coordination with potential donors from serum proteins, for example, transferrin, to coordinate the $[^{99m}Tc(CO)_3]^+$ core. Since transferrin is excreted and/or stored in the liver, the 11% of the activity found in the liver at the 6 h time point could further implicate transferrin as a carrier protein for $[^{99m}Tc(CO)_3]^+$.

The transferrin proteins are the most prominent metal binding proteins in the body fluids (*27*). Although it is the Fe^{3+} ion that is normally found in the active site of transferrin, this protein also has a high affinity for many other metal ions (*27*, *28*). Transferrin's metal binding depends mainly on its structural organization. Both the C and the N lobes in the transferrins contain the same four donor atoms to bind various metal ions, two phenolic O from two tyrosines, an N from the histidine imidazole, and a carboxylate O from aspartic acid. It has been reported that accommodating metal ions depends on the conformation of both the apoprotein (metal-free protein) as well as the metal bound protein. Transferrin conformation changes from the initial open state to the closed state after metal binding. It is likely that the protein can accommodate $[^{99m}Tc(CO)_3]^+$ binding in the open state, since it acts as a potential tetra dentate ligand able to readily fill the three vacant positions around ^{99m}Tc. However, whether this binding puts much stress on the structure and hinders the conformational change (from open to closed), due to the size of $[^{99m}Tc(CO)_3]^+$, requires a thorough investigation. If transferrin's binding site cannot properly close, then the metal ion might be removed easily.

Biodistribution analysis at the 6 h time point via the organ/blood ratios (Table 3) confirmed that both PEGylated and non-PEGylated microspheres were mainly taken up by the monophagocytic system in the liver and spleen, and to a very similar extent. The only difference between the two types of microspheres was the 20-fold higher accumulation of the more hydrophobic, non-PEGylated microspheres in the lungs. While the reason for this lung accumulation is not known, the charge of the metal complex can be excluded as the cause, since both PEGylated and non-PEGylated microspheres had the same ligand moiety and generated similar complex cations. Agglomeration is more likely related to hydrophobic interactions with blood proteins, which can, for the most part, be prevented by PEGylation of the microspheres. Changes in the poly(ethylene glycol) chain length or in the total amount used (currently only 1.5%) might further reduce agglomeration in the lungs. The kidney to blood ratio of $[^{99m}Tc(CO)_3]^+$ after 6 h confirmed that the urinary system was its main path of excretion. The initially expected uptake of the positively charged $[Tc(CO)_3(H_2O)_3]^+$ in the heart, similar to that seen in the also positively charged radiopharmaceuticals sestamibi and tetrofosmin (*29*), was not confirmed (Table 3)—the $[^{99m}Tc(CO)_3(H_2O)_3]^+$ compound is likely not sufficiently lipophilic. The low heart to blood ratio of 0.30 suggests that the highly visible heart during SPECT imaging at the 6 h time point was due to the large volume of radioactive blood in the heart and not due to local binding of the radioactive compound to the myocardium.

Unfortunately, colloidal albumin kits in the same size range as our particles are no longer available, making direct comparison of our labeling and biodistribution results difficult. We have, however, compared our findings to those by Scheffel et al., who described the preparation of human serum albumin (HSA) microspheres with an average size of 0.6 μm (*24*). The values for the percentage of injected dose per organ measured after 4.25 h were similar to our findings measured after 6 h (Figure 7). For example, the blood activity was 0.9% vs 2.5%; the liver uptake was 73.2% vs 57.6%; the spleen uptake was 1.0% vs 2.5%, and finally the lung uptake was 0.3% vs 0.7%, accordingly (Scheffel et al. vs our data for the PEGylated microspheres). Differences might have mainly to do with the different size distribution and/or time point of analysis.

In conclusion, chelomer-formulated microspheres are promising candidates for imaging, as they exhibit excellent radiolabeling efficiency and radiochemical stability. The PEGylated microspheres showed no agglomeration, a key factor for *in vivo* utilization of these particles. Therefore, the PEGylated chelomer microspheres are excellent tools for RES imaging. Other potential applications with the same microspheres of larger size (around 10 μm) include lung perfusion imaging. And even larger, around 40 μm, the biodegradable microspheres could be radiolabeled with the β-emitter ^{188}Re and used for the therapeutic radioembolization of liver tumors. The easy and complete kit-based labeling and the fact that the particles do not agglomerate will allow for reliable and repeatable imaging, and potentially even therapy. Furthermore, all biohazards connected with the handling of blood products are eliminated with these nontoxic, biocompatible, and biodegradable microspheres.

ACKNOWLEDGMENT

We thank Dr. Troy Farncombe, Chantal Saab, and Rod Rhem at McMaster's Centre for Preclinical and Translational Imaging in Hamilton, Ontario, Canada, for excellent imaging support. We also thank Scott McNaughton, radiopharmacist at McMaster's University Health Centre, for providing ^{99m}Tc and space for the radiolabeling, and Dr. Don Lyster, at Vancouver General Hospital, Vancouver, British Columbia, Canada for many discussions. We appreciate support for this research from a Natural Sciences and Engineering Research Council of Canada (NSERC) grant.

LITERATURE CITED

(1) Saha, G. B. (2004) *Fundamentals of nuclear pharmacy*, 5th ed., Springer, New York.

(2) Rhodes, B. A., Zolle, I., Buchanan, J. W., and Wagner, H. N. (1969) Radioactive albumin microspheres for studies of the pulmonary circulation. *Radiology 92*, 1453–1460.

(3) Davis, M. A. (1975) Particulate radiopharmaceuticals for pulmonary studies, in *Radiopharmaceuticals* (Subramaniam, B., Rhodes, B., Cooper, D. R., Sodd, V. J., Eds.) pp 267−281, Society of Nuclear Medicine, Reston, VA.

(4) Sty, J. R., and Conway, J. J. (1985) The spleen: development and functional evaluation. *Semin. Nucl. Med. 15*, 276–298.

(5) Desai, A. G., and Thakur, M. L. (1985) Radiopharmaceuticals for spleen and bone marrow studies. *Semin. Nucl. Med. 15*, 229–38.

(6) Toki, H., Hersh, E. M., Murphy, S., Glenn, H., Haynie, T. P., and White, R. A. (1981) Use of mini-microaggregated albumin to study reticuloendothelial system (RES) function in *C. parvum*-treated animals. *Int. J. Immunopharmacol. 3*, 147–52.

(7) Bolognesi, M., Merkel, C., and Gatta, A. (1987) The use of human albumin microspheres tagged with ^{99m}Tc in the evaluation of the removal capacity of the reticuloendothelial system. *Eur. J. Nucl. Med. 13*, 254–257.

(8) Mirzaei, S., Knoll, P., Hoffmann, B., Kreuzer, W., and Kohn, H. (2001) Optimized mammary lymphoscintigraphy using larger colloid particles. *J. Nucl. Med. 42*, 826.

(9) Fowler, J. C., Solanki, C. K., Barber, R. W., Ballinger, J. R., and Peters, A. M. (2007) Dual-isotope lymphoscintigraphy using albumin nanocolloid differentially labeled with ^{111}In and ^{99m}Tc. *Acta Oncol. 46*, 105–110.

(10) Zhao, H., Saatchi, K., and Häfeli, U. O. (2009) Preparation of biodegradable magnetic microspheres with poly(lactic acid) coated magnetite. *J. Magn. Magn. Mater. 321*, 1356–1363.

(11) Schneider, T., Zhao, H., Jackson, J. K., Chapman, G. H., Dykes, J., and Häfeli, U. O. (2008) Use of hydrodynamic flow focusing for the generation of biodegradable camptothecin-loaded polymer microspheres. *J. Pharm. Sci. 97*, 4943–4954.

(12) Saatchi, K., and Häfeli, U. O. (2007) One-pot syntheses, coordination and characterization of application-specific biodegradable ligand-polymers. *Dalton Trans. 39*, 4439–4445.

(13) Zastre, J., Jackson, J., Bajwa, M., Liggins, R., Iqbal, F., and Burt, H. (2002) Enhanced cellular accumulation of a P-glycoprotein substrate, rhodamine-123, by Caco-2 cells using low molecular weight methoxypolyethylene glycol-block-polycaprolactone diblock copolymers. *Eur. J. Pharm. Biopharm. 54*, 299–309.

(14) Egli, A., Alberto, R., Tannahill, L., et al. (1999) Organometallic Tc-99m-aquaion labels peptide to an unprecedented high specific activity. *J. Nucl. Med. 40*, 1913–1917.

(15) Alberto, R., Ortner, K., Wheatley, N., Schibli, R., and Schubiger, P. A. (2001) Synthesis and properties of boranocarbonate: a convenient in situ CO source for the aqueous preparation of $[^{99m}Tc(OH_2)_3(CO)_3]^+$. *J. Am. Chem. Soc. 123*, 3135–3136.

(16) Amann, A., Decristoforo, C., Ott, I., et al. (2001) Surfactant protein B labeled with $[Tc\text{-}99m(CO)_3(H_2O)_3]^+$ retains biological activity in vitro. *Nucl. Med. Biol. 28*, 243–250.

(17) Petrig, J., Schibli, R., Dumas, C., Alberto, R., and Schubiger, P. A. (2001) Derivatization of glucose and 2-deoxyglucose for transition metal complexation: substitution reactions with organometallic 99mTc and Re precursors and fundamental NMR investigations. *Chemistry 7*, 1868–73.

(18) Waibel, R., Treichler, H., Schaefer, N. G., et al. (2008) New derivatives of vitamin B12 show preferential targeting of tumors. *Cancer Res. 68*, 2904–11.

(19) Zhao, H., Gagnon, J., Häfeli, U. O. (2007) Process and formulation variables in the preparation of injectable and biodegradable magnetic microspheres. *Biomagn. Res. Technol. 5:2*.

(20) Cleland, J. L. (1998) Solvent evaporation processes for the production of controlled release biodegradable microsphere formulations for therapeutics and vaccines. *Biotechnol. Prog. 14*, 102–107.

(21) Arshady, R., Monshipouri, M. (2001) Targeted delivery of microparticulate carriers: particle size controlled targeting, in *Microspheres, Microcapsules & Liposomes: Medical & Biotechnology Applications*, (Arshady, R., Ed.) pp 410−414, Vol MML2, Kentus, London.

(22) Hnatowich, D. J., Virzi, F., Fogarasi, M., Rusckowski, M., and Winnard, P. (1994) Can a cysteine challenge assay predict the in vivo behavior of ^{99m}Tc-labeled antibodies? *Nucl. Med. Biol. 21*, 1035–44.

(23) Causey, P. W., Besanger, T. R., Schaffer, P., and Valliant, J. F. (2008) Expedient multi-step synthesis of organometallic complexes of Tc and Re in high effective specific activity. A new platform for the production of molecular imaging and therapy agents. *Inorg. Chem. 47*, 8213–21.

(24) Scheffel, U., Rhodes, B. A., Natarajan, T. K., and Wagner, H. N. (1972) Albumin microspheres for study of the reticuloendothelial system. *J. Nucl. Med. 13*, 498–503.

(25) Tanaka, T., Shiramoto, S., Miyashita, M., Fujishima, Y., and Kaneo, Y. (2004) Tumor targeting based on the effect of enhanced permeability and retention (EPR) and the mechanism of receptor-mediated endocytosis (RME). *Int. J. Pharm. 277*, 39–61.

(26) Wattendorf, U., and Merkle, H. P. (2008) PEGylation as a tool for the biomedical engineering of surface modified microparticles. *J. Pharm. Sci. 97*, 4655–69.

(27) Baker, H. M., Baker, C. J., Smith, C. A., and Baker, E. N. (2000) Metal substitution in transferrins: specific binding of cerium(IV) revealed by the crystal structure of cerium-substituted human lactoferrin. *J. Biol. Inorg. Chem. 5*, 692–8.

(28) Sun, H., Li, H., and Sadler, P. J. (1999) Transferrin as a metal ion mediator. *Chem. Rev. 99*, 2817–42.

(29) Schaefer, W. M., Moka, D., Brockmann, H. A., Schomaecker, K., and Schicha, H. (2002) ^{201}Tl, ^{99m}Tc-MIBI, ^{99m}Tc-tetrofosmin and ^{99m}Tc-furifosmin: relative retention and clearance kinetics in retrogradely perfused guinea pig hearts. *Nucl. Med. Biol. 29*, 243–54.

(30) Tsopelas, C. (2001) Particle size analysis of ^{99m}Tc-labeled and unlabeled antimony trisulfide and rhenium sulfide colloids intended for lymphoscintigraphic application. *J. Nucl. Med. 42*, 460–466.

(31) Harbert, J. C. (1996) Radiocolloid therapy of cystic brain tumors, in *Nuclear medicine: Diagnosis and therapy* (Harbert, J. C., Eckelman, W. C., and Neumann, R. D., Eds.) pp 1083−1091, Thieme Medical Publishers, New York.

(32) Nolan, T. R., Grady, E. D., Crumbley, A. J., Larose, J. H., and Cheek, W. V. (1975) Internal hepatic radiotherapy: I. Organ distribution of colloid Cr-(P-32)PO4 injected into a peripheral vein, the portal vein, or the arterial supply of the gastrointestinal tract in the rat. *Am. J. Roentg. Rad. Ther. Nucl. Med. 124*, 590–595.

(33) Anghileri, L. J. (1968) Studies on colloidal chromic phosphate: an improved method of preparation and in situ precipitation by injection of papain. *Int. J. Appl. Radiat. Isot. 19*, 415–20.

(34) Salem, R., and Hunter, R. D. (2006) Yttrium-90 microspheres for the treatment of hepatocellular carcinoma: a review. *Int. J. Radiat. Oncol. Biol. Phys. 66*, S83−S88.

(35) Kennedy, A., Nag, S., Salem, R., et al. (2007) Recommendations for radioembolization of hepatic malignancies using yttrium-90 microsphere brachytherapy: a consensus panel report from the radioembolization brachytherapy oncology consortium. *Int. J. Radiat. Oncol. Biol. Phys. 68*, 13–23.

BC900066J

Rapid Synthesis of DNA-Functionalized Gold Nanoparticles in Salt Solution Using Mononucleotide-Mediated Conjugation

Wenting Zhao,[†] Li Lin,[†] and I-Ming Hsing*[,†,‡]

Bioengineering Graduate Program and Department of Chemical and Biomolecular Engineering, The Hong Kong University of Science and Technology, Clear Water Bay, Kowloon, Hong Kong SAR. Received February 20, 2009; Revised Manuscript Received April 8, 2009

DNA functionalized gold-nanoparticles (Au-nps) have been broadly used as labeling reagents in the development of molecular diagnostics as well as building blocks in nanotechnology. Conventional methods for the synthesis of DNA functionalized Au-nps require long incubation, typically overnight, and delicate control of the ionic strength to compensate for the charge repulsion between the nanoparticles surface and the DNA strands, which generally affect the stability of the nanoparticles and the DNA loading density. In this study, we present a novel mononucleotide-mediated conjugation approach to synthesize DNA-functionalized Au-nps within 4 h in a high ionic strength environment. Au-nps covered with a thermally tunable stabilization layer through mononucleotide adsorption were shown to readily conjugate with thiol-DNAs in 0.1 M NaCl solution upon heating. Monitoring this mononucleotide-mediated conjugation reaction through dynamic light scattering and UV−vis spectroscopy demonstrated the formation of stable DNA/Au-nps conjugates. The resulting conjugates, as characterized by fluorescence spectroscopy, are loaded by ∼80 strands per particle, comparable to the DNA loading density of current approaches. The general applicability of this approach was further verified in a nanoparticle-bound DNA hybridization test. Our results show that mononucleotide-mediated thermal conjugation is an attractive alternative that allows temperature-controlled and salt-enhanced functionalization of gold nanoparticles with DNAs in just a few hours.

INTRODUCTION

DNA-functionalized gold nanoparticles (Au-nps) play an important role in biosensing and nanobiotechnology. A synergistic combination of the sequence-specific hybridization-based molecular recognition of DNA molecules and the size-dependent chemical, physical, and plasmonic properties of Au-nps has enabled DNA/Au-nps conjugates to find many critical applications in molecular diagnostics (*1–5*), nanofabrication (*6–9*), molecular nanoelectronics (*10–12*), cell imaging (*13*), and gene regulation (*14*). The use of DNA-functionalized gold nanoparticles is still in its infancy, and many more interesting approaches are expected. One of the key essentials to fully developing their application potentials is the fast and reproducible synthesis of stable DNA/Au-nps conjugates.

On the basis of the chemistry of thiol self-assembly on gold, a widely accepted protocol to immobilize specific DNAs onto Au-nps surfaces was developed by Mirkin and co-workers (*15*). In their approach, a 2 day incubation process was needed to directly link thiol-terminated oligonucleotides to citrate-stabilized Au-nps (referred to as direct conjugation approach). Specifically, salt was added after an initial overnight incubation to neutralize the charge repulsion, and then, a 40 h aging step was performed to achieve a high DNA loading density, which is critical for the stabilization of the conjugates. Improvement on the direct conjugation approach was later reported by Brust and co-workers, who applied vacuum centrifugation instead of a long aging step to speed up the formation of stable conjugates, and the conjugation process was completed in ∼20 h (*16*). They suggested that the vacuum centrifugation step was essential to ensure a gradual and simultaneous rise of solution DNA concentration and ionic strength with a concomitant increase of DNA loading density on particles. Other than the direct conjugation method, Alivisatos and co-workers reported a strategy to minimize the salt effect on the particle stability by the complexation of Au-nps with bis(*p*-sulfonatophenyl)phenylphosphine dehydrate dipotassium salt (BSPP) prior to the immobilization of thiol-DNA molecules (referred to as BSPP coating approach) (*17, 18*). With BSPP protection, the salt-dependent aggregation of Au-nps was controlled and the conjugation process could be done in ∼12 h. However, this process is suitable for the synthesis of mono or low DNA conjugated Au-nps, but not intended for preparing DNA/Au-nps conjugates with a high DNA loading density.

In this study, we report a new conjugation method enabling a rapid immobilization of high-density DNAs on stable Au-nps in a salt environment, which to our knowledge has never been reported in the literature. The essence of our strategy relies on the fast and reversible binding of mononucleotides to Au-nps surfaces. This binding was used to quickly stabilize Au-nps in salt solution by forming a mononucleotide layer on particle surface, and the adsorption/desorption of this layer is also thermally tunable (*19*). As shown in Scheme 1, our conjugation process starts with a reversible adsorption of mononucleotides on the Au-nps for nanoparticle stabilization in salt solutions, followed by a temperature-facilitated ligand-exchange reaction between the incoming thiol-DNA and the protecting mononucleotides on Au-nps surface. Our experimental characterization data will show that the synthesis of DNA/Au-nps conjugates by our method could be achieved within several hours and the resulting conjugates have similar or better characteristic attributes (DNA loading density and stability) in comparison with those synthesized by conventional methods. The ability to modify Au-nps with specific DNAs in an efficient

* Corresponding author. I-Ming Hsing, E-mail: kehsing@ust.hk, Telephone: (852) 2358-7131, Fax: (852) 3106-4857.

[†] Bioengineering Graduate Program.

[‡] Department of Chemical and Biomolecular Engineering.

10.1021/bc900080p CCC: $40.75 © 2009 American Chemical Society
Published on Web 05/08/2009

Scheme 1. Mononucleotide-Mediated Conjugation of Thiol-DNA to Gold Nanoparticles

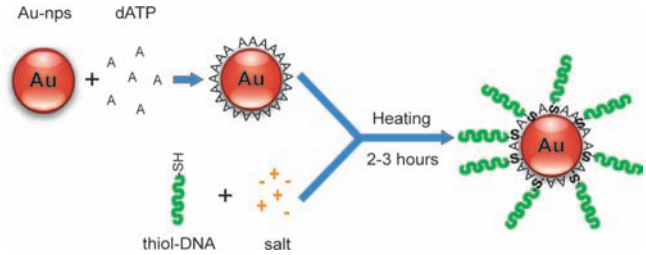

and controlled manner opens up opportunities in molecular diagnostics and bionanotechnology.

EXPERIMENTAL PROCEDURES

Materials. Thirteen nanometer Au-nps were prepared by reduction of tetrachloroaurate as reported previously (*20, 21*), while 20 nm Au-nps, hydrogen tetrachloroaurate trihydrate ($HAuCl_4 \cdot 3H_2O$), sodium citrate, and poly(L-lysine) were purchased from Sigma. dATP (10 mM) was purchased from Invitrogen, and oligonucleotides were synthesized by Integrated DNA Technologies. Other salts were provided by USB Corporation. The water used in all experiments was purified with NANOpure Diamond TOC Analytical Ultrapure Water System (Barnstead, U.S.A.) and autoclaved by ES-215/ES-315 Autoclaves (Tomy, Japan) prior to use.

Conjugation of DNA/Au-nps. The procedure for mononucleotide-mediated conjugation of DNA/Au-nps is illustrated in Scheme 1. Citrate-stabilized Au-nps were first incubated with dATP in a molar ratio (dATP/Au-nps) of 1000 for 15 min. The mixture was then brought to 10 mM sodium phosphate buffer (pH 8.0) and 0.1 M NaCl. After brief vortexing, thiol-DNA (thiol-T30, 5′-TTT TTT TTT TTT TTT TTT TTT TTT TTT TTT TTT-C3-thiol-3′, 500 μM) was introduced in a molar ratio (thiol-DNA to Au-nps) of 500, followed by heating (Eppendorf Mastercycler personal thermal cycler) at a constant temperature for 3 h. Except for the temperature effect study, all the heating steps were conducted at 60 °C. Afterward, the particles were washed three times in 10 mM sodium phosphate buffer (pH 8.0) with 0.1 M NaCl through centrifugation (13 200 rpm, 20 min) to remove excess reagents. Finally, the resulting conjugates were resuspended in 100 μL sodium phosphate buffer (10 mM, pH 8.0) with NaCl (0.3 M). For the direct conjugation and BSPP coating approaches, the procedure is the same as previously reported (*15, 17, 18*).

Hybridization of Au-nps Linked DNAs. Hybridization test was performed using DNA/Au-nps conjugates of different sizes and labeled with DNAs of complementary sequences. Specifically, two conjugates were prepared using the mononucleotide-mediated approach: Au-nps of 13 and 20 nm functionalized with respective cDNA sequences (thiol-T30, 5′-TTT TTT TTT TTT TTT TTT TTT TTT TTT TTT TTT-C3-thiol-3′, to Au-nps of 20 nm (**thiol-T30/Au20**) and thiol-A30, 5′-AAA AAA AAA AAA AAA AAA AAA AAA AAA AAA AAA-C3-thiol-3′, to Au-nps of 13 nm (**thiol-A30/Au13**)). Two conjugates were mixed overnight at a molar ratio of 1:10 (thiol-T30/Au20:thiol-A30/Au13) in 10 mM sodium phosphate buffer with 0.3 M NaCl (pH 8.0). In the negative control, the thiol-A30 was substituted with a nonthiol-DNA (nonthiol-A24, 5′-AAA AAA AAA AAA AAA AAA AAA AAA-3′, forming nonthiol-A24/Au13). The resulting solutions of hybrids were imaged with TEM.

UV−vis Spectroscopy. A 1 mL cuvette (Bragg and Co.) was used, and all spectra were obtained through Ultrospec 4300 pro UV−vis spectrophotometer (Amersham Biosciences).

Dynamic Light Scattering (DLS). Measurements were performed using a ZetaPlus (Brookhaven Instruments Corporation). Incident light was provided by a 35 mW solid state laser (660 nm). Scattered light was collected at a fixed angle of 90°. All samples were filtered through a 0.22 μm acetate membrane filter prior to measure. Five runs were performed per sample with 30 s per run.

Fluorescence-Based Quantification of the DNA Loading Density on Au-nps. Centrifugation pellets of 300 μL Cy3-A20-thiol/Au13 conjugates were incubated overnight with 50 μL mercaptoethanol (ME) (12 mM in 0.3 M PBS). The solution containing displaced Cy3-A20-thiol was separated from the Au-nps by centrifugation. The fluorescence signal of each sample was measured using Applied Biosystems 7300 real-time PCR system. Standard curves were prepared to convert the fluorescence reading to molar concentration.

Transmission Electron Microscopy (TEM). Specimens were prepared by deposition of a drop of colloidal solutions on 0.01% poly(L-lysine) pretreated carbon-nonporous film supported by copper grid (SPI Supplies Inc., 400 mesh). All the samples were examined in a JEM 2010 transmission electron microscope (JEOL) operated at 200 kV. Images were taken by GATAN MSC 794 CCD Camera and analyzed with *GATAN Digital Microscopy* software.

RESULTS

Scheme 1 illustrates our strategy for the synthesis of DNA/Au-nps conjugates. As shown, the process involves the protection of Au-nps from salt-induced aggregation by the mononucleotide adsorption and the thermally enhanced ligand exchange reaction between the surface-bound mononucleotides and the incoming DNA molecules. Deoxyadenosine triphosphate (dATP) was chosen among the four different mononucleotides, as in our previous study dATP-covered Au-nps were found to have a higher salt tolerance than the Au-nps protected by other mononucleotides (*19*). A detailed working procedure for conjugate synthesis is described in the Experimental Procedures. Critical characterization results of this conjugation approach are delineated in the following paragraphs.

Conjugate Stability. It would be useful to understand the stability of the synthesized DNA/Au-nps conjugates, since the conjugates might also be vulnerable to the irreversible salt-induced aggregation at high temperature and high ionic strength as the mononucleotide-coated Au-nps do. From the measurement of surface plasmon resonance (SPR) using UV−vis spectroscopy, it is clear in Figure 1 that our DNA/Au-nps conjugates (thiol-T30/Au13) are stable at a salt solution (0.1 M NaCl) and exhibit a characteristic adsorption peak at 520 nm before and after the heat treatment at 80 °C. On the other hand, dATP-covered Au-nps without thiol-DNA attachments were found to suffer aggregation with an obvious color change from red to blue and a significant shift of the adsorptive peak to a higher wavelength (e.g., 650 nm), which is consistent with the previous report (*19*). The conjugate stability of the 20 nm Au-nps was also evaluated using UV−vis spectroscopy. Similar stability results (see Supporting Information) were observed. It is believed that the enhanced stability of the DNA/Au-nps conjugate comes from the ligand replacement of the initial dATP protection layer by thiol-DNA linkage, that stabilizes the conjugate even at high ionic strength and at elevated temperature. Other than a few-nanometer red shift caused by the newly formed thiol-DNA/Au linkage, the conjugate shows a similar SPR peak to that of the citrate Au-nps without salt.

Effective Diameter of DNA/Au-nps Conjugates. In addition to assessing the dispersion of Au-nps, effectiveness of the dATP-mediated conjugation method could also be reflected by measuring the "effective diameter" of DNA and nanoparticle conjugates using the dynamic light scattering (DLS) technique. The effective diameter of the DNA/Au-nps conjugates should

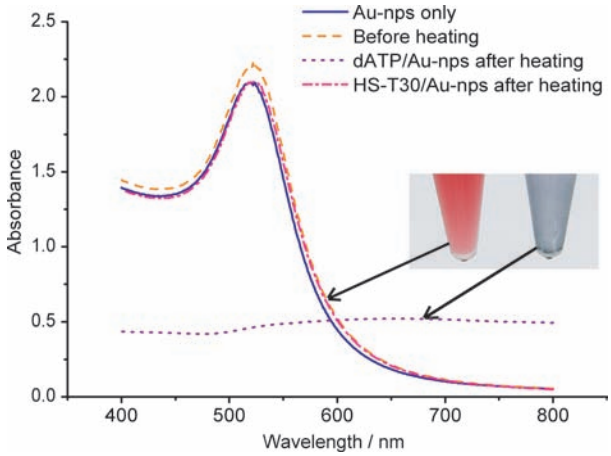

Figure 1. UV−vis spectra of the solution mixture in the mononucleotide-mediated conjugation approach. Solid line (blue), Au-nps (13 nm) serving as control without dATP and salt; dashed line (yellow), thiol-T30 and dATP protected Au-nps (thiol-T30/Au13) with 0.1 M NaCl before heat treatment; dotted line (purple), dATP protected Au-nps with 0.1 M NaCl after 3 h heat treatment at 80 °C; dash−dotted line (pink), thiol-T30 and dATP protected Au-nps (thiol-T30/Au13) with 0.1 M NaCl after 3 h heat treatment at 80 °C. The inset image shows the observed colors of the dATP protected Au-nps (right, blue) and the mixture of thiol-T30 and dATP protected Au-nps (left, red) after the heat treatment.

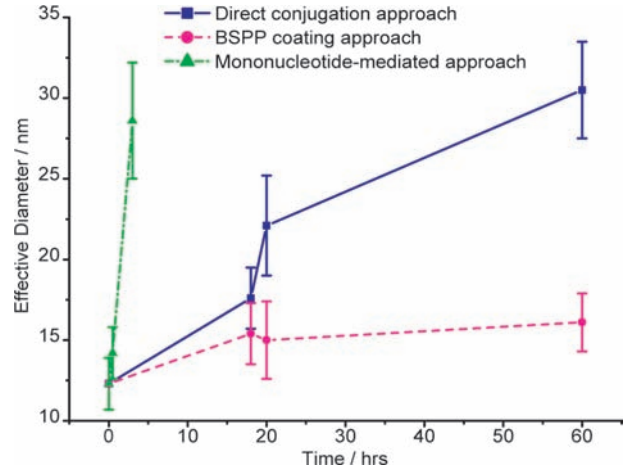

Figure 2. Effective diameter of thiol-DNA/Au-nps conjugate during the time course of conjugate synthesis. Solid line (blue) with square mark (■), direct conjugation approach; dashed line (pink) with circle mark (•), BSPP coating approach; dash−dotted line (green) with triangle mark (▲), mononucleotide-mediated approach. The starting size of bare Au-nps is 13 nm, and the error bars represent standard deviation for five independent measurements.

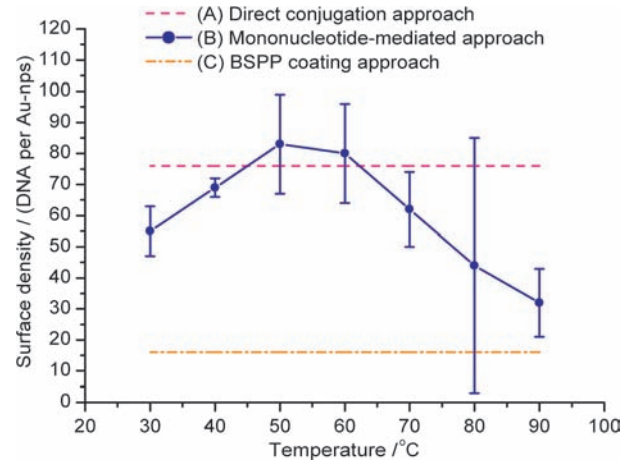

Figure 3. Temperature effect on DNA surface loading density. (A) dashed line (pink), direct conjugation approach; (B) solid line (blue) with circle mark (•), mononucleotide-mediated approach; (C) dash−dotted line (yellow), BSPP coating approach. The error bars represent standard deviation for three independent fluorescence measurements.

be significantly larger than that of the bare gold particles. Although the salt concentration might have influence on the effective diameter through its impact on the DNA inter/intrastrand repulsion, the overall size of the conjugate is dominated by the surface loading density of thiol DNAs on Au-nps (*22*). The higher the density, the larger is the size. In Figure 2,[1] the effective diameters of our conjugates during the time course of conjugate synthesis was benchmarked with the ones synthesized by the conventional direct conjugation and BSPP-based methods. The effective diameter of the conjugates by the BSPP coating method was found to be the smallest among the three methods, and there is no significant size change of the conjugate during the synthesis. The limited size growth could be due to the low salt concentration and the hindered diffusion of DNAs during the synthesis. The conjugates prepared by our approach and the direct conjugation show very significant size increase (from 13 nm to ∼30 nm). However, the direct conjugation approach requires a much higher synthesis time, while the mononucleotide-mediated approach achieves a similar effective diameter in just 3 h.

Temperature Effect on the Mononucleotide-Mediated Conjugation. The effect of temperature on the mononucleotide-mediated conjugation process was evaluated using fluorescence techniques (*23*), by which the surface density of DNA per particle could be measured as a function of the conjugation temperature. As shown in Figure 3, the DNA loading densities on DNA/Au-nps synthesized by the three different approaches are compared. Straight lines (Figure 3A,C) were used here to represent the DNA surface density achieved by the conventional isothermal methods (direct conjugation approach and BSPP coating approach, respectively) for the convenience in comparison with the values achieved by mononucleotide-based approach under different temperatures. Our approach shows an increase of DNA density per particle (up to 80 oligo strands per particle) with temperature rising from 30 to 60 °C, and the density drops at higher temperatures, which indicates that the DNA loading on Au-nps could be optimized at an elevated temperature of ∼50 °C (Figure 3B).

Validation of Hybridization by DNA/Au-np Conjugates. As the molecular orientation of immobilized DNAs may greatly affect the sensitivity in many hybridization-based biosensing applications (*3, 24*), hybridization experiments were therefore conducted to verify the functionality of immobilized DNAs. As shown by the TEM micrographs (Figure 4B), star-shaped aggregates were observed for the DNA/Au-nps conjugates with complementary thiol-DNA sequences (thiol-A30/Au13 and thiol-T30/Au20). However, in the negative control experiments, the hybridization between the thiol-T30/Au-20 conjugate and the 13 nm Au-with nonthiol-DNAs (nonthiol-A24/Au13) was not successful, and thus, no aggregates were found in Figure 4A. Misorientation of the nonthiol-DNA or the nonspecific

[1]The data were taken in the following operating time points: the first data point was taken at 0 h for the citrate-coated Au-nps for all the three methods. In the direct conjugation, the data points (A) at overnight incubation of thiol-DNA and Au-nps (18 h), salt concentration adjusting to 0.1 M NaCl (20 h) and after 40 h aging step (60 h) were taken. In BSPP method, the data points (B) at the formation of BSPP coating layer (18 h) and thiol-DNA incubation (20 and 60 h) were taken. In the mononucleotide-mediated approach, the data points (C) at the introduction of dATP and salts (0.5 h) and after thermal treatment (3 h) were taken.

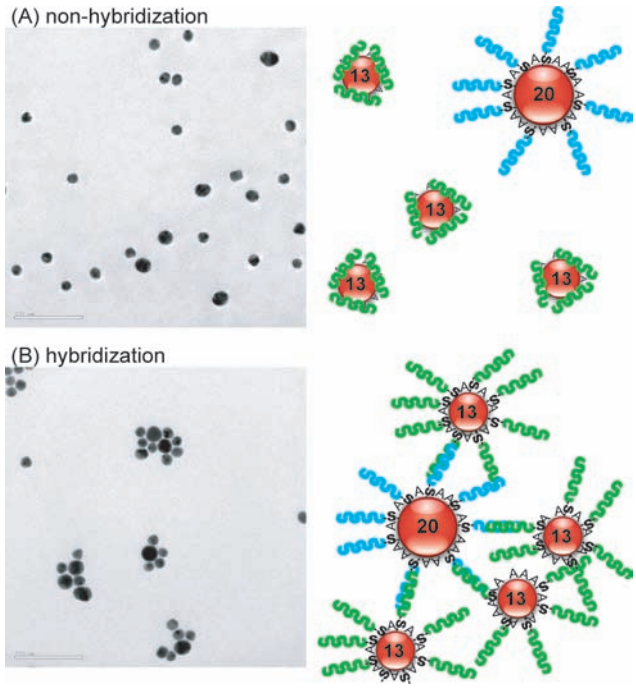

Figure 4. TEM images of DNA/Au-nps conjugates after hybridization. (A) thiol-T30/Au20 conjugates with nonthiol A24/Au13 particles; (B) thiol-T30/Au20 conjugates with thiol-A30/Au13 conjugates. All the conjugates were synthesized through mononucleotide-mediated conjugation approach. (Scale bar: 100 nm.) Schematic representations of scenarios (A) and (B) are placed next to the TEM micrographs.

adsorption of DNA on Au-nps could result in hybridization failure, as demonstrated in the negative control group. DNA/Au-nps conjugates synthesized by the dATP-mediated approach retain DNA functionality and possess rich DNA strands per particle for hybridization-based medical diagnostic and biosensing applications.

DISCUSSION

In the direct conjugation approach, careful control of the salt concentration is needed. Diffusion of thiol-linked DNA to citrate-covered Au-nps would require salt ions to reduce the repulsive force between the negatively charged incoming DNA molecules and the negatively charged citrate-capping on Au-nps surface. However, too much salt could cause an irreversible aggregation of nanoparticles. Therefore, gradual addition of salts and long incubation are generally required in the direct conjugation approach in order to balance the need for DNA conjugation without causing particle aggregation. To address the long-standing issue related to salt tolerance, our approach utilizes the adsorbed mononucleotides as a mediating layer on Au-nps to perform the conjugation of thiol-DNA to citrate Au-nps in salt solutions. The conjugates prepared by our approach and the direct conjugation show very significant size increase (from 13 nm to ~30 nm). However, the direct conjugation approach requires a much higher synthesis time, while the mononucleotide-mediated approach achieves a similar effective diameter in just 3 h. The mediating component dATP plays an important role in shortening the synthesis time. Without the need for overnight incubation and a long aging step, the salt concentration in our approach can be adjusted to a higher value prior to the introduction of thiol-DNA, as the dATP-covered Au-nps could resist a much higher salt concentration without the salt-induced aggregation than that of the citrate-based counterpart. The controlled salt concentration and the temperature-monitored removal of mononucleotide from Au-nps facilitate the ligand exchange reaction between the incoming thiol-DNA and the outgoing dATP.

Temperature plays an important role in the mononucleotide-mediated conjugation. Although the removal rate of dATP is larger at higher temperatures (i.e., >60 °C), the re-exposed Au-np surfaces without dATP protection would suffer salt-induced aggregation and the bond of Au-thiol DNA might not survive at high-temperature (*25*). The increased loading density of thiol-DNA on Au-nps due to the high dATP removal rate could be compromised by the unstable Au-thiol bonding at higher temperatures, which could result in the temperature dependence described earlier. In comparison with the DNA loading densities per Au-np particle in the direct conjugation method (~76 oligo strands) and in the BSPP method (~16 oligo strands) measured using the same procedure, we believe that the dATP-mediated approach, which demonstrates a loading density of 80 oligo strand, offers a synthesis strategy for rapid DNA/Au-nps conjugation with comparable quality of the established methods. In the direct conjugation method, other researchers reported loading density of ~70 strands per 15 nm particle for a oligo DNA sample with poly dA spacer and 100 ± 30 DNA per 15 nm Au-np with the vacuum evaporation enhancement (*16*, *23*, *26*). Their results are consistent with ours (~76 per 13 nm Au-np) for the direct conjugation approach. By balancing dATP displacement at a specific temperature and ion strength, stable DNA/Au-nps conjugates could be made within 4 h, which is much shorter than the conventional approaches. Moreover, dATP, a monomer unit of nucleic acids, shares similar nonthiol functional groups in DNA, and thus, dATP residues on Au-nps help to reduce the nonspecific DNA binding to the particle through the nonthiol entities. The reduction of nonspecific binding by dATPs contributes to the right molecular orientation of the immobilized DNAs for hybridization.

Our study has demonstrated that a novel mononucleotide-mediated conjugation approach enables the rapid DNA functionalization of Au-nps with DNA surface coverage comparable to that obtained by the direct conjugation method. The stable conjugates with about 80 DNA strands per particle can be formed in salt solution (0.1 M NaCl) at 60 °C without special equipment required, and the resulting conjugates are able to hybridize. We envision that this mononucleotide-mediated method will offer an attractive alternative for the preparation of DNA/Au-nps conjugates, and similar methodology can be readily applicable for the synthesis of nanoparticle conjugates with various biomolecules (e.g., DNA and peptides). The ability to modify Au-nps with biomolecules in a rapid and controlled manner would provide more opportunities in nanobiotechnology.

ACKNOWLEDGMENT

The authors thank the funding support from the Research Grants Council of the Hong Kong Special Administrative Region Government (Project No.: HKUST 601305) and a University research grant (Project No: RPC07/08.EG21). Laboratory facilities provided by the Bioengineering Laboratory and Materials Characterization & Preparation Facility of HKUST are also acknowledged.

Supporting Information Available: UV−vis spectra for the stability evaluation of 20 nm Au-nps during the mononucleotide-mediated conjugation process. This material is available free of charge via the Internet at http://pubs.acs.org.

LITERATURE CITED

(1) Xu, X. Y., Han, M. S., and Mirkin, C. A. (2007) A gold-nanoparticle-based real-time colorimetric screening method for endonuclease activity and inhibition. *Angew. Chem., Int. Ed. 46*, 3468–3470.

(2) Lee, J. S., Han, M. S., and Mirkin, C. A. (2007) Colorimetric detection of mercuric ion (Hg2+) in aqueous media using DNA-

functionalized gold nanoparticles. *Angew. Chem., Int. Ed. 46*, 4093–4096.
(3) Nam, J. M., Thaxton, C. S., and Mirkin, C. A. (2003) Nanoparticle-based bio-bar codes for the ultrasensitive detection of proteins. *Science 301*, 1884–1886.
(4) Park, S. J., Taton, T. A., and Mirkin, C. A. (2002) Array-based electrical detection of DNA with nanoparticle probes. *Science 295*, 1503–1506.
(5) Elghanian, R., Storhoff, J. J., Mucic, R. C., Letsinger, R. L., and Mirkin, C. A. (1997) Selective colorimetric detection of polynucleotides based on the distance-dependent optical properties of gold nanoparticles. *Science 277*, 1078–1081.
(6) Alivisatos, A. P., Johnsson, K. P., Peng, X. G., Wilson, T. E., Loweth, C. J., Bruchez, M. P., and Schultz, P. G. (1996) Organization of 'nanocrystal molecules' using DNA. *Nature 382*, 609–611.
(7) Mirkin, C. A., Letsinger, R. L., Mucic, R. C., and Storhoff, J. J. (1996) A DNA-based method for rationally assembling nanoparticles into macroscopic materials. *Nature 382*, 607–609.
(8) Park, S. Y., Lytton-Jean, A. K. R., Lee, B., Weigand, S., Schatz, G. C., and Mirkin, C. A. (2008) DNA-programmable nanoparticle crystallization. *Nature 451*, 553–556.
(9) Nykypanchuk, D., Maye, M. M., van der Lelie, D., and Gang, O. (2008) DNA-guided crystallization of colloidal nanoparticles. *Nature 451*, 549–552.
(10) Cohen, H., Nogues, C., Naaman, R., and Porath, D. (2005) Direct measurement of electrical transport through single DNA molecules of complex sequence. *Proc. Natl. Acad. Sci. U.S.A. 102*, 11589–11593.
(11) Cohen, H., Nogues, C., Ullien, D., Daube, S., Naaman, R., and Porath, D. (2006) Electrical characterization of self-assembled single- and double-stranded DNA monolayers using conductive AFM. *Faraday Discuss. 131*, 367–376.
(12) Ullien, D., Cohen, H., and Porath, D. (2007) The effect of the number of parallel DNA molecules on electric charge transport through 'standing DNA'. *Nanotechnology 18*, 424015.
(13) Seferos, D. S., Giljohann, D. A., Hill, H. D., Prigodich, A. E., and Mirkin, C. A. (2007) Nano-flares: Probes for transfection and mRNA detection in living cells. *J. Am. Chem. Soc. 129*, 15477–15479.
(14) Rosi, N. L., Giljohann, D. A., Thaxton, C. S., Lytton-Jean, A. K. R., Han, M. S., and Mirkin, C. A. (2006) Oligonucleotide-modified gold nanoparticles for intracellular gene regulation. *Science 312*, 1027–1030.
(15) Storhoff, J. J., Elghanian, R., Mucic, R. C., Mirkin, C. A., and Letsinger, R. L. (1998) One-pot colorimetric differentiation of polynucleotides with single base imperfections using gold nanoparticle probes. *J. Am. Chem. Soc. 120*, 1959–1964.
(16) Kanaras, A. G., Wang, Z. X., Bates, A. D., Cosstick, R., and Brust, M. (2003) Towards multistep nanostructure synthesis: Programmed enzymatic self-assembly of DNA/gold systems. *Angew. Chem., Int. Ed. 42*, 191–194.
(17) Loweth, C. J., Caldwell, W. B., Peng, X. G., Alivisatos, A. P., and Schultz, P. G. (1999) DNA-based assembly of gold nanocrystals. *Angew. Chem., Int. Ed. 38*, 1808–1812.
(18) Claridge, S. A., Goh, S. L., Frechet, J. M. J., Williams, S. C., Micheel, C. M., and Alivisatos, A. P. (2005) Directed assembly of discrete gold nanoparticle groupings using branched DNA scaffolds. *Chem. Mater. 17*, 1628–1635.
(19) Zhao, W. T., Lee, T. M. H., Leung, S. S. Y., and Hsing, I. M. (2007) Tunable stabilization of gold nanoparticles in aqueous solutions by mononucleotides. *Langmuir 23*, 7143–7147.
(20) Turkevich, J., Stevenson, P. S., and Hillier, J. (1951) A study of the nucleation and growth processes in the synthesis of colloidal gold. *Discuss. Faraday Soc. 11*, 55–75.
(21) Frens, G. (1973) Controlled nucleation for the regulation of the particle size in monodisperse gold suspensions. *Nat. Phys. Sci. 241*, 20–22.
(22) Parak, W. J., Pellegrino, T., Micheel, C. M., Gerion, D., Williams, S. C., and Alivisatos, A. P. (2003) Conformation of oligonucleotides attached to gold nanocrystals probed by gel electrophoresis. *Nano Lett. 3*, 33–36.
(23) Demers, L. M., Mirkin, C. A., Mucic, R. C., Reynolds, R. A., Letsinger, R. L., Elghanian, R., and Viswanadham, G. (2000) A fluorescence-based method for determining the surface coverage and hybridization efficiency of thiol-capped oligonucleotides bound to gold thin films and nanoparticles. *Anal. Chem. 72*, 5535–5541.
(24) Oh, B. K., Nam, J. M., Lee, S. W., and Mirkin, C. A. (2006) A fluorophore-based bio-barcode amplification assay for proteins. *Small 2*, 103–108.
(25) Li, Z., Jin, R. C., Mirkin, C. A., and Letsinger, R. L. (2002) Multiple thiol-anchor capped DNA-gold nanoparticle conjugates. *Nucleic Acids Res. 30*, 1558–1562.
(26) Hurst, S. J., Lytton-Jean, A. K. R., and Mirkin, C. A. (2006) Maximizing DNA loading on a range of gold nanoparticle sizes. *Anal. Chem. 78*, 8313–8318.

BC900080P

Supporting Information for

Journal: Bioconjugate Chemistry

Manuscript ID: bc-2009-00080p

Title: "Rapid Synthesis of DNA-functionalized Gold Nanoparticles in Salt Solution Using Mononucleotide-Mediated Conjugation"

Author(s): *Wenting Zhao*[†], *Li Lin*[†] *and I-Ming Hsing*[†‡*]

Address: Bioengineering Graduate Program[†] and Department of Chemical and Biomolecular Engineering[‡], the Hong Kong University of Science and Technology, Clear Water Bay, Kowloon, Hong Kong SAR

*** Corresponding author:** I-Ming Hsing, E-mail: kehsing@ust.hk, Telephone: (852) 2358-7131, Fax: (852) 3106-4857.

Supporting Information

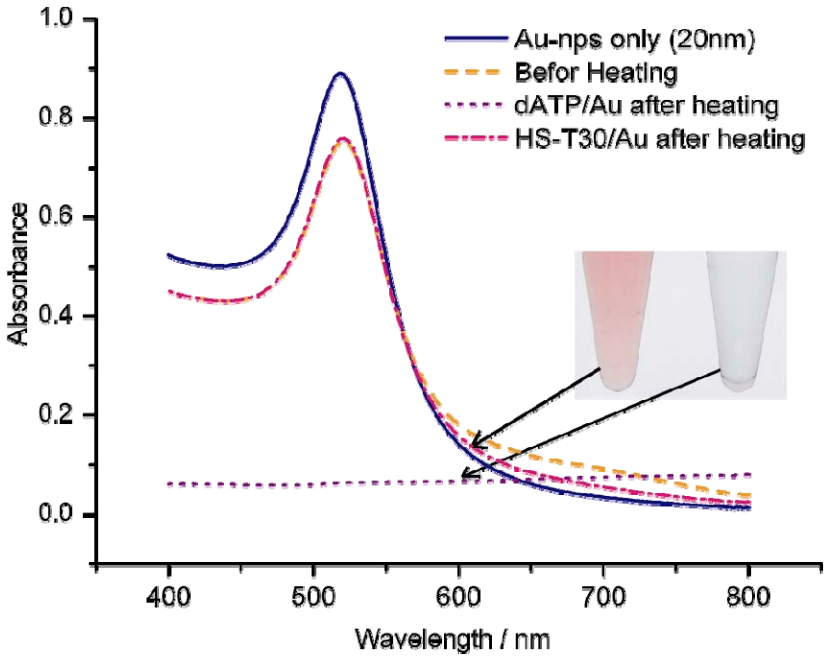

Figure S1. UV-vis spectra for the stability evaluation of 20 nm Au-nps in mononucleotide-mediated conjugation process. Solid line (blue), Au-nps (20 nm) serving as control without dATP and salt; dashed line (orange), thiol-T30 and dATP protected Au-nps (thiol-T30/Au20) with 0.1 M NaCl before heat treatment; dotted line (purple) dATP protected Au-nps with 0.1 M NaCl after 3 h heat treatment at 55 °C; dash-dotted line (pink), thiol-T30 and dATP protected Au-nps (thiol-T30/Au20) with 0.1 M NaCl after 3 h heat treatment at 55 °C. The inset image shows the observed colors of the dATP protected Au-nps (right, blue) and the mixture of thiol-T30 and dATP protected Au-nps (left, red) after the heat treatment.

Optical Antisense Tumor Targeting in Vivo with an Improved Fluorescent DNA Duplex Probe

Minmin Liang,[†] Xinrong Liu,[†] Dengfeng Cheng,[†] Kayoko Nakamura,[‡] Yi Wang,[†] Shuping Dou,[†] Guozheng Liu,[†] Mary Rusckowski,[†] and Donald J. Hnatowich*,[†]

Department of Radiology, University of Massachusetts Medical School, Worcester, Massachusetts, and Department of Radiology, Keio University School of Medicine, Tokyo, Japan. Received March 2, 2009; Revised Manuscript Received May 13, 2009

Fluorescent conjugated DNA oligonucleotides for antisense targeting of mRNA has the potential of improving tumor/normal tissue ratios over that achievable by nuclear antisense imaging. By conjugating the Cy5.5 emitter to the 3′ equivalent end of a 25 mer phosphorothioate (PS) antisense major DNA and hybridizing with a shorter 18 mer phosphodiester (PO) complementary minor DNA (cDNA) with the Black Hole inhibitor BHQ3 on its 5′ end (i.e., PS DNA25-Cy5.5/PO cDNA18-BHQ3), we previously achieved antisense optical imaging in mice as a proof of this concept. In a process of optimization, we have now evaluated the stability of a small series of duplexes with variable-length minor strands. From these results, a new study anti-mdr1 antisense duplex was selected with a 10 mer minor strand (i.e., PS DNA25-Cy5.5/PO cDNA10-BHQ3). The new study duplex shows stability in serum environments at 37 °C and provides a dramatically enhanced fluorescence in KB-G2 (pgp++) cells when compared with KB-31 (pgp±) as evidence of antisense dissociation at its mdr1 mRNA target. The duplex was also administered to KB-G2 tumor bearing mice, and when compared to the duplex used previously, the fluorescence from the tumor thigh was more obvious and the tumor-to-background fluorescence ratio was improved. In conclusion, by a process designed to optimize the duplex for optical antisense tumor targeting, the fluorescence signal was improved both in cells and in tumored mice.

INTRODUCTION

Oligomers such as DNA for antisense imaging of mRNA are potentially powerful candidates for detection of endogenous gene expression in vivo (*1*−*5*). In conventional imaging of mRNA expression in vivo, antisense oligonucleotides are usually radiolabeled with gamma ray emitting radionuclides. However, our experience and that of other laboratories suggest that achieving adequate tumor/normal radioactivity ratios by antisense nuclear imaging is often problematic (*6*). As an alternative to nuclear imaging, optical imaging has the potential to improve tumor/normal tissue ratio by modulating the detectable signal in the target through the judicious use of fluorescence resonance energy transfer (FRET) (*7*−*11*). We have been developing an approach to optical antisense imaging that in principle should provide fluorescence images in tumored subjects by an antisense mechanism that are free of background fluorescence (*12*). In this method, linear fluorophor-conjugated oligomer duplexes are arranged to inhibit fluorescence and to dissociate only in the presence of their target mRNA. Thus, the fluorescence signal should in principle be inhibited everywhere except in the target cell. The approach is illustrated in Scheme 1.

Recently, we reported on our first optical DNA duplex consisting of a Cy5.5 conjugated 25 mer phosphorothioate (PS) DNA hybridized to a BHQ3 conjugated complementary 18 mer phosphodiester (PO) cDNA for optical antisense imaging (i.e., PS DNA25-Cy5.5/PO cDNA18-BHQ3) (*12*). Although fluorescence in the tumor was clearly evident, this duplex also provided a fluorescence background making obvious the need for duplex optimization. In a process of optimization, we now report that five DNA duplexes differing in the length of the complementary minor strand were compared for stability using a simple thiazole orange (TO) fluorescence assay (*13*). On the basis of the screening results, the shortest minor strand (10 mer) was selected and, after hybridization to the 25 mer PS antisense major strand, was studied in cells and in tumored animals in comparison to that of the 18 mer major strand used previously.

Scheme 1. Schematic Diagram Illustrating the Principle of Antisense Optical Imaging

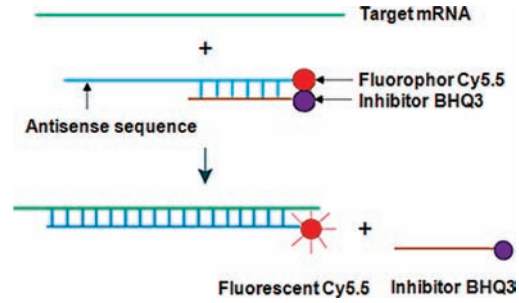

MATERIALS AND METHODS

As in our earlier investigation, all duplexes used the 25 mer anti-mdr1 uniform PS antisense (5′-AAG-ATC-CAT-CCC-GAC-CTC-GCG-CTC-C-3′) major strand (*14*−*16*), either native or conjugated with the Cy5.5 fluorophor on the 3′ end attached via a three carbon linker. The native duplexes were formed by hybridization with a complementary uniform native PO minor strand with one of five chain lengths. The study conjugated duplexes were formed by hybridization of the same major strand with either a 10 or 18 mer PO minor strand conjugated with a Black Hole Quencher 3 (BHQ3) quencher on the 5′ end attached via a two carbon linker. Controls for the two study conjugated duplexes were identical except that the two fluorophors were reversed:

* Corresponding author. Donald J. Hnatowich, E-mail: Donald.Hnatowich@umassmed.edu. Tel: 508-856-4256. Fax: 508-856-4572.

[†] University of Massachusetts Medical School.

[‡] Keio University School of Medicine.

10.1021/bc9000933 CCC: $40.75 © 2009 American Chemical Society
Published on Web 06/03/2009

Native Duplexes.
PS-DNA25/PO-cDNA25
PS-DNA25/PO-cDNA22
PS-DNA25/PO-cDNA18
PS-DNA25/PO-cDNA14
PS-DNA25/PO-cDNA10

Conjugated Study and Control Duplexes.
PS-DNA25-Cy5.5/PO-cDNA10-BHQ3 (study duplex)
PS-DNA25-BHQ3/PO-cDNA10-Cy5.5 (control)
PS-DNA25-Cy5.5/PO-cDNA18-BHQ3 (comparison duplex)
PS-DNA25-BHQ3/PO-cDNA18-Cy5.5 (control)

The native DNAs (Integrated DNA Technologies, Coralville, IA) and the conjugated DNAs (Biosearch Technologies, Novato, CA) were purchased HPLC purified. The TO dye was obtained from Sigma-Aldrich (St Louis, MO) and was used as received. The KB-G2 (pgp++) and KB-31 (pgp±) human epidermoid carcinoma cell lines were a gift from Isamu Sugawara (Research Institute of Tuberculosis, Tokyo, Japan) and were cultured overnight at 37 °C, 5% CO_2, in Dulbecco's modified Eagle's medium (DMEM, Invitrogen, Carlsbad, CA, USA) containing 10% fetal bovine serum (FBS). The cells were incubated with DNAs in 1% FBS/DMEM medium.

Measurement of Native Duplexes. The five native duplexes were screened for stability in serum using a simple TO assay developed in this laboratory (*13*). Each duplex was added to a 96 well microplate at 100 μL per well and incubated at 500 nM in 70% normal mouse serum (Jackson Immuno Research Laboratories, Inc., West Grove, PA) at 37 °C for different times before the addition of the indicator TO at 6 μM. Fluorescence intensities were measured at room temperature on a Fluorescence Microplate Reader (Safire, Tecan Group Ltd.). In this case, 504 nm was used for excitation and 527 nm for detection of TO fluorescence. The TO concentration that was just sufficient to saturate the duplexes was determined by trial and error to be 6 μM. In the screening assay, decreased fluorescence was an indication of TO release and therefore of duplex instability due to dissociation and/or degradation.

Measurement of Conjugated Duplexes in Solution. Both the 10 mer and 18 mer conjugated study duplexes were prepared at different molar ratios by mixing the 10 or 18 mer cDNA with the DNA25-Cy5.5 at a molar ratio of 1:1, 2:1, 3:1, 5:1, 8:1, and 10:1 in wells of a 96 well microplate before the fluorescence was measured on the Microplate Reader. In this case, 685 nm was used for excitation and 706 nm for detection of Cy5.5 fluorescence. The DNA25-Cy5.5 concentration was 50 nM in all cases to provide a convenient fluorescence intensity.

The stability in serum of the DNA25-Cy5.5/cDNA10-BHQ3 duplex was measured by adding 100 μL of each duplex solution in a 96 well plate in quadruplicate to a final duplex concentration of 50 nM in 70% normal mouse serum (Jackson Immuno Research Laboratories, Inc., West Grove, PA) and incubated at 37 °C for up to 25 h. As control, the singlet DNA25-Cy5.5 was added to serum at the identical molar concentration in the identical manner. The fluorescence intensity was measured at each time point on the Microplate Reader.

Measurement of Conjugated Duplexes in Cells. The cell studies were performed in KB-G2 and KB-31 cells in quadruplicate in 96 well plates seeded at 10 000 cells per well and incubated with 10% FBS/DMEM culture medium overnight. In one experiment, both study and control duplexes were incubated in KB-G2 cells in 1% FBS/DMEM medium at 50, 100, 300, and 500 nM for 3 h at 37 °C. In another experiment, all four conjugated duplexes were incubated with both KB-G2 and KB-31 cells in 1% FBS/DMEM medium at 500 nM for 3 h at 37 °C. In all cases, the cells were washed twice with 1% FBS/DMEM culture medium and twice with PBS. To improve the reproducibility of the measurement, the cells were lysed before measuring the fluorescence. The lysis buffer (150 mM PBS, pH 7.2, 1% Triton X-100) was added at 100 μL per well, and the cells were incubated for 1 h at 37 °C. The fluorescence intensity of each lysis solution was measured on the Microplate Reader.

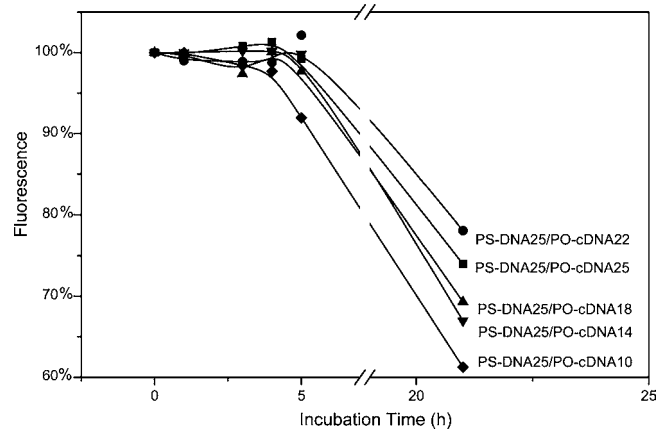

Figure 1. Percent fluorescence change for five duplexes in 70% serum at 37 °C as a function of incubation time. In each case, the fluorescence at time zero was set as 100%.

Animal Studies. All animal studies were performed with the approval of the UMMS Institutional Animal Care and Use Committee. Male nude mice (NIH Swiss, Taconic Farms, Germantown, NY) at 7 weeks of age were each injected subcutaneously in the left thigh with 100 μL suspension containing 10^6 KB-G2 cells with greater than 95% viability. Mice were used for imaging studies when tumors were about 0.7 cm in any dimension and after having been on a chlorophyll-free diet (AIN-93G Purified Diet, Harlan Teklad, Madison, WI) for 5 days prior to imaging. Mice bearing KB-G2 tumor were administered 3 nmol of DNA25-Cy5.5/cDNA10-BHQ3 duplex in 100 μL of PBS via a tail vein. In vivo fluorescence imaging was performed on an IVIS 100 small animal imaging system (Xenogen, Alameda, CA) using a Cy5.5 filter set. During imaging, the animals were lightly anesthetized with 1.5% isoflurane in 2 L/min oxygen. Fluorescence images were acquired at 20 min, 2 h, 7 h, and 23 h after injection using a 0.5 s exposure time (f/stop 4). Image presentation and quantification were performed using *Living Image 2.5* software (Xenogen). Ellipsoid regions of interest (ROI) of equal area were drawn on the tumor and on the contralateral muscle in the normal thigh.

RESULTS

Measurement of Native Duplexes. The five native DNA duplexes, each with the same 25 mer major strand but different length of minor strand, were incubated at 37 °C in 70% normal mouse serum at 500 nM for different times before the addition of the TO indicator. The fluorescence was measured immediately after TO addition with shaking. Instability of the DNA duplex will result in a decreased fluorescence signal as denaturation of the duplex will reduce TO intercalation. Figure 1 presents the change of fluorescence intensity as a function of the incubation time in 37 °C serum and shows in all cases no change in fluorescence for at least 5 h of incubation. Thus, all duplexes appear to be stable in serum for a period sufficiently long for tumor targeting in vivo. Because of the similar stabilities, the duplex with the shortest minor strand (i.e., PS-DNA25/PO-cDNA10) was selected for further study on the assumption that it would exhibit the least stability in the presence of its mRNA target. The duplex of our earlier investigation (i.e., PS-DNA25/PO-cDNA18) was used for comparison.

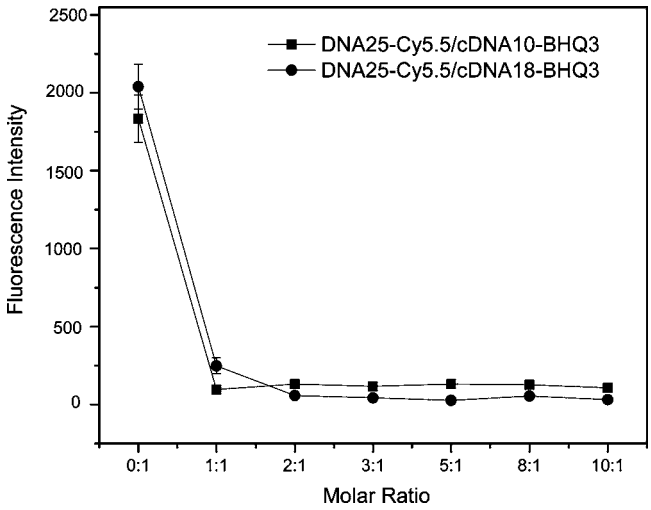

Figure 2. Fluorescence intensity of DNA25-Cy5.5 in PBS solution alone and after hybridized with increasing molar ratios of cDNA10-BHQ3 or cDNA18-BHQ3. Error bars represent standard deviations for three replicates and are too small to be visible on most data points.

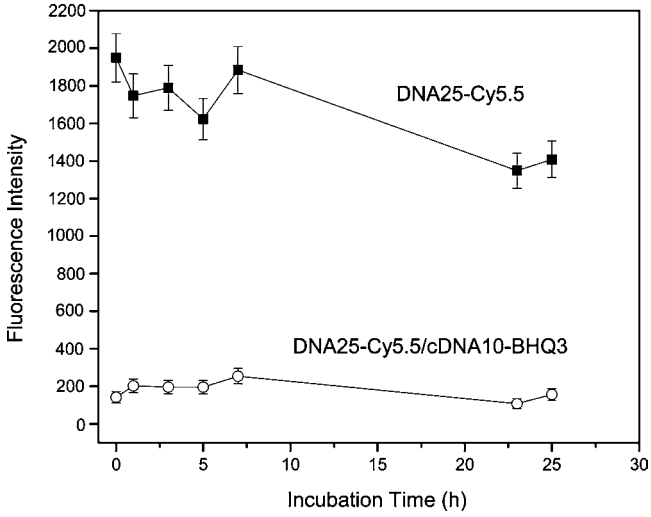

Figure 3. Fluorescence intensity showing stability of DNA25-Cy5.5/cDNA10-BHQ3 duplex compared to the DNA25-Cy5.5 single strand in 70% normal mouse serum at 37 °C over 25 h. Error bars represent standard deviations for three replicates.

Measurement of Conjugated Duplexes in Solution. Figure 2 presents the fluorescence intensity of DNA-Cy5.5 when different molar ratios of cDNA10-BHQ3 or cDNA18-BHQ3 were added. The results show that about 90% of the fluorescence signal of Cy5.5 is quenched when hybridized with either cDNA at a 1:1 molar ratio.

As mentioned above, the duplex with the shortest minor strand (i.e., PS-DNA25/PO-cDNA10) was selected as the study duplex on the assumption that it would exhibit the least stability in the presence of its mRNA target. The stability of this conjugated duplex was therefore evaluated over 25 h, again at 100 nM in 70% normal mouse serum at 37 °C, and the results compared to that of the singlet DNA25-Cy5.5. As shown in Figure 3, the study duplex did not show a substantial change in fluorescence over 25 h, suggesting duplex stability over this period.

Measurement of Conjugated Duplexes in Cells. The KB-G2 cells were incubated with the study anti mdr1 mRNA antisense DNA25-Cy5.5/cDNA10-BHQ3 duplex and its control duplex in which the fluorophors were reversed. For comparison, the antisense DNA25-Cy5.5/cDNA18-BHQ3 duplex of our previous investigation (*12*) was also studied as a comparison

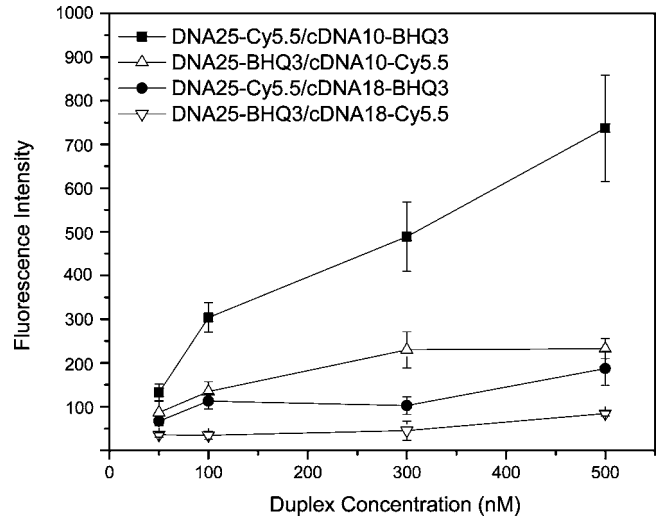

Figure 4. Cellular fluorescence of KB-G2 cells after incubation for 3 h with the 10 mer anti-mdr1 study duplex (DNA25-Cy5.5/cDNA10-BHQ3), its 10 mer control duplex with fluorophors reversed (DNA25-BHQ3/cDNA10-Cy5.5) and the 18 mer comparison duplex and its control at four concentrations. Error bars represent standard deviations for four replicates.

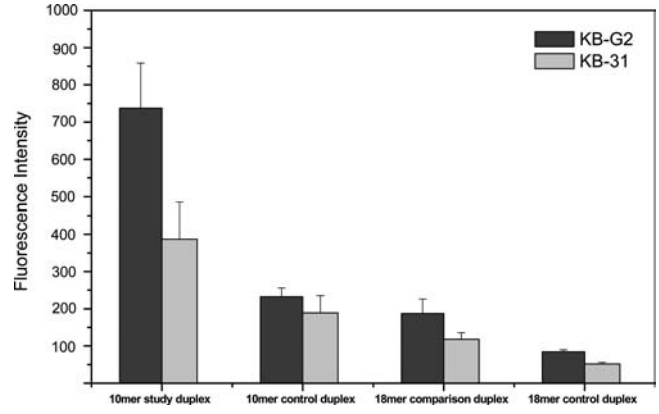

Figure 5. Cellular fluorescence of KB-G2 and KB-31 cells after incubation for 3 h with the 10 mer anti-mdr1 study duplex (DNA25-Cy5.5/cDNA10-BHQ3), its 10 mer control duplex with fluorophors reversed (DNA25-BHQ3/cDNA10-Cy5.5), and the corresponding 18 mer comparison duplex and its control duplex at 500 nM. (Error bars represent standard deviations for four replicates.)

duplex along with its similar control. Incubations were for 3 h at 37 °C at concentrations between 50 nM and 500 nM. Figure 4 presents the cellular fluorescence intensity vs duplex concentration and shows that the fluorescence signal of the cells is in all cases significantly higher ($p < 0.05$) when incubated with the 10 mer study or 18 mer comparison duplex compared to their respective control duplexes that differ only in reversed fluorophors. However, the fluorescence of cells incubated with the 10 mer study duplex is about 4-fold higher than cells incubated with the 18 mer comparison duplex as evidence of the decreased stability of the 10 mer compared to the 18 mer duplex, most probably due to antisense targeting.

If the higher fluorescence of KB-G2 cells incubated with the study compared to the 18 mer comparison duplex was due to antisense dissociation as is likely, then the fluorescence should be reduced in KB-31 cells because of its limited mdr1 expression. Figure 5 presents the results of incubating both the KB-G2 and KB-31 cells with the same four duplexes as above at 500 nM. No significant differences in fluorescence were observed between the two cell lines when incubated with either the 10 mer or 18 mer control duplexes presumably because the

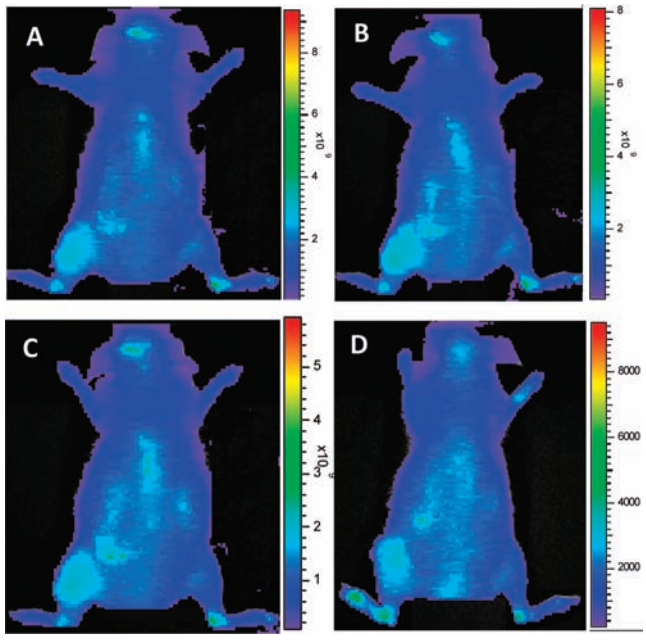

Figure 6. Whole-body dorsal fluorescence images of one mouse bearing a KB-G2 tumor in the left thigh at (A) 20 min; (B) 2 h; (C) 7 h; and (D) 23 h postinjection of 3 nmol study duplex (DNA25-Cy5.5/cDNA10-BHQ3).

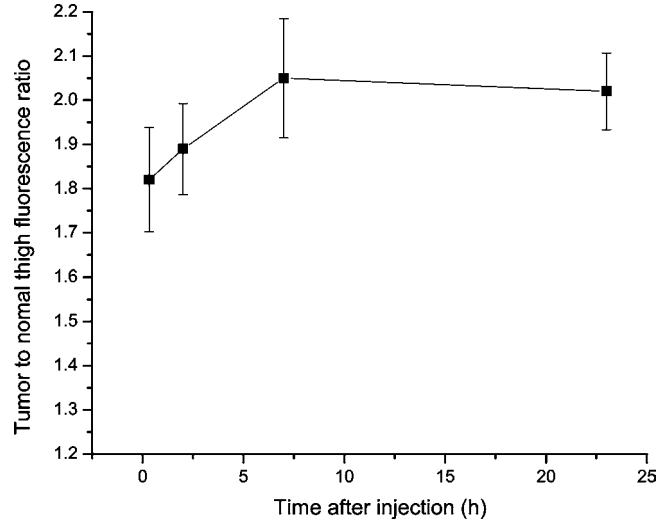

Figure 7. Average tumor-to-normal thigh fluorescence ratios vs time after injection of the study duplex. Error bars represent standard deviations for three animals. Fluorescence quantitation was accomplished using *Living Image 2.5* software (Xenogen).

Cy5.5 fluorophor is, in these cases, on the minor strand of each duplex that are either not dissociated (presumably in KB-31 cells) or are dissociated and released from the cell if binding does occur (presumably in KB-G2 cells). In both cases, the results would be the same: an absence of fluorescence. By contrast, the fluorescence of KB-G2 cells was statistically higher ($p < 0.05$) compared to the KB-31 cells when incubated with either the study 10 mer or 18 mer comparison duplex presumably because of the limited expression of the mRNA targets in KB-31. However, compared to the 18 mer duplex, the shorter 10 mer study duplex produces a much stronger fluorescence signal.

Animal Study. Three nude mice each bearing KB-G2 tumors in the left thigh received an injection of 3 nmol DNA25-Cy5.5/cDNA10-BHQ3 study duplex and were imaged at different times over 2 days. Images of one mouse obtained without contrast manipulation are shown in Figure 6. Tumor fluorescence is evident at all times. The fluorescence intensity ratios at four postinjection time points were calculated for the three animals, and the averages are shown in Figure 7. A positive tumor/normal thigh ratio was achieved as early as 20 min postinjection and was followed by a constant increase until a maximum at 2.05 was reached at 7 h postinjection and was constant thereafter.

Compared to the images obtained earlier in the same mouse tumor model following administration of the comparison DNA25-Cy5.5/cDNA18-BHQ3 duplex (*12*), the study DNA25-Cy5.5/cDNA10-BHQ3 duplex of this investigation provided images with a more intense fluorescence in the tumor thigh and an averaged tumor-to-background ratio superior to the 1.6 ratio observed by us previously (*12*). The most likely explanation for the improved results is increased instability of the duplex with the shorter minor strand in the presence of the target mRNA.

DISCUSSION

Optical imaging is a rapidly developing biomedical technology that enables the investigation of biological/molecular events in both cell culture and small live animals and is already practical in the clinic for imaging surface cancers and those accessible by endoscopy. However, self-absorption of the optical signal can seriously complicate optical imaging even when employing near-infrared fluorescence (NIRF) imaging probes with fluorescence emission in the near-infrared where tissue hemoglobin and water, the major absorbers of visible and infrared light, respectively, have their lowest absorption coefficients (*17*−*19*). While self-absorption of γ rays in connection with nuclear imaging is much more limited, nuclear imaging, unlike optical imaging, does not offer the possibility of modulating the signal at its target site. Through the judicious use of fluorescence resonance energy transfer (FRET), optical imaging has the potential to improve the tumor/normal tissue ratio and thus become an attractive alternative to nuclear imaging (*20*−*23*).

Previously, we reported on a successful optical antisense imaging study using a Cy5.5 conjugated 25 mer antisense PS−DNA hybridized to a BHQ3 conjugated complementary 18 mer PO−DNA showing fluorescence only upon dissociation (*12*). The duplex was designed to resist dissociation except by an antisense mechanism in the presence of its target mRNA in tumor. Although there was obvious tumor fluorescence obtained with this duplex, there was also a background in normal tissue and therefore a less than optimal tumor/nontarget ratio. The low tumor/nontarget ratio was attributed to a combination of excessive duplex stability in the presence of the mRNA target and excessive duplex instability in circulation and in tissues and led to the conclusion that optimization was required. In this investigation, optimization was focused on varying the DNA chain length rather than changing the backbone of the phosphorothioate and phosphdiester DNAs to that of second generation oligomer analogues such as phosphodiamidate morpholinos. While keeping the antisense major strand at 25 mer, the complementary sense minor strand was varied from 25 to 10 mer and the stabilities of the duplexes measured in 37 °C serum by the TO assay. Complementary chain lengths of less than 10 mer were not considered due to concerns of low duplex binding specificity and low stability (*24*, *25*). The results, shown in Figure 1, demonstrate that all five native duplexes were sufficiently stable by this assay in serum, and therefore, the shortest 10 mer chain length was selected for further investigation.

The results presented in Figures 4 and 5 both provide evidence of antisense targeting for both the 10 and 18 mer study duplexes. In the first instance, a significantly higher fluorescence was observed in the mdr1 expressing KB-G2 cells for the study

duplexes compared to the control duplexes with fluorophors reversed, a result that would not be expected by nonspecific accumulation. In the case of the control duplexes, presumably after dissociation, the Cy5.5 PO cDNA is rapidly degraded and the fluorophor cleared from the cell. In the second instance, the fluorescence intensity of the mdr1 expressing KB-G2 cells was significantly higher than that of the control low level mdr1 expressing KB-31 cells especially in the case of the 10 mer study duplex, again providing evidence of antisense targeting.

Furthermore, the shorter DNA25-Cy5.5/cDNA10-BHQ3 study duplex provided a much higher fluorescence in cells compared to the 18 mer DNA25-Cy5.5/cDNA18-BHQ3 comparison duplex, presumably due to a lower stability toward dissociation of the study duplex in the presence of its target mRNA. Finally, the whole-body fluorescence images in KB-G2 tumor bearing mice, one of which is presented in Figure 6, show obvious fluorescence in tumor at all time points, and an improvement in the average tumor/background fluorescence ratio of 2.05 for this duplex compared to an average value of 1.6 obtained previously in the same mouse model with the comparison duplex (*12*).

Taken together, the work presented here provides further evidence that optical antisense imaging with fluorescent duplexes is possible and our results have been improved by the process described herein designed to optimize duplex stabilities for this application. However, it is noteworthy that there is still some unexpected fluorescence background in animals administered the optimized duplex. Obviously, the Cy5.5 in these animals is not quenched completely by the BHQ3 inhibitor, indicating that the duplex has partly dissociated in some nontarget tissues such as liver due to instability of the fluorophors and/or duplex instability to nucleases therein. A better understanding of the properties of these duplex probes in vivo will be required to further optimize this approach.

ACKNOWLEDGMENT

We thank Dr. Isamu Sugawara (Research Institute of Tuberculosis, Tokyo, Japan) for providing the KB-G2 and KB-31 cell lines for this investigation. This investigation was funded by the NIH (CA-12959).

LITERATURE CITED

(1) Lewis, M. R., and Jia, F. (2003) Antisense imaging: and miles to go before we sleep? *J. Cell. Biochem. 90*, 464–472.

(2) Rosi, N. L., Giljohann, D. A., Thaxton, C. S., Lytton-Jean, A. K. R., Han, M. S., and Mirkin, C. A. (2006) Oligonucleotide-modified gold nanoparticles for intracellular gene regulation. *Science 312*, 1027–1030.

(3) Hnatowich, D. J., and Nakamura, K. (2004) Antisense targeting in cell culture with radiolabeled DNAs-a brief review of recent progress. *Ann. Nucl. Med. 18*, 363–368.

(4) Hnatowich, D. J., and Nakamura, K. (2006) The influence of chemical structure of DNA and other oligomer radiopharmaceuticals on tumor delivery. *Curr. Opin. Mol. Ther. 8*, 136–143.

(5) Dewanjee, M. K., Ghafouripour, A. K., Kapadvanjwala, M., Dewanjee, S., Seafini, A. N., Lopez, D. M., and Sfakianakis, G. N. (1994) Noninvasive imaging of *c-myc* oncogene messenger RNA with Indium-111-antisense probes in a mammary tumor-bearing mouse model. *J. Nucl. Med. 35*, 1054–1061.

(6) Nakamura, K., Fan, C., Liu, G., Gupta, S., He, J., Dou, S., Kubo, A., Rusckowski, M., and Hnatowich, D. J. (2004) Evidence of antisense tumor targeting in mice. *Bioconjugate Chem. 15*, 1475–1480.

(7) Becker, A., Hessenius, C., Licha, K., Ebert, B., Sukowski, U., Semmler, W., Wiedenmann, B., and Grotzinger, C. (2001) Receptor-targeted optical imaging of tumors with near-infrared fluorescent ligands. *Nat. Biotechnol. 19*, 327–331.

(8) Weissleder, R., Tung, C. H., Mahmood, U., and Bogdanov, A. (1999) In vivo imaging of tumors with protease-activated near-infrared fluorescent probes. *Nat. Biotechnol. 17*, 375–378.

(9) Ogawa, M., Kosaka, N., Choyke, P. L., and Kobayashi, H. (2009) In vivo molecular imaging of cancer with a quenching near-Infrared fluorescent probe using conjugates of monoclonal antibodies and indocyanine green. *Cancer Res. 69*, 1268–1272.

(10) Ogawa, M., Kosaka, N., and Choyke, P. L. (2009) Tumor-specific detection of an optically targeted antibody combined with a quencher-conjugated neutravidin "quencher-chaser": a dual "quench and chase" strategy to improve target to nontarget ratios for molecular imaging of cancer. *Bioconjugate Chem. 20*, 147–154.

(11) Silverman, A. P., and Kool, E. T. (2005) Quenched probes for highly specific detection of cellular RNAs. *Trends Biotechnol. 23*, 225–230.

(12) Liu, X., Wang, Y., Nakamura, K., Liu, G., Dou, S., Kubo, A., Rusckowski, M., and Hnatowich, D. J. (2007) Optical antisense imaging of tumor with fluorescent DNA duplexes. *Bioconjugate Chem. 18*, 1905–1911.

(13) Liang, M., Liu, X., Nakamura, K., Chen, X., Cheng, D., Liu, G., Dou, S., Wang, Y., Rusckowski, M., Hnatowich, D. J. (2009) A convenient thiazole orange fluorescence assay for the evaluation of DNA duplex hybridization stability. *Mol. Imaging Biol.* In Press.

(14) Nakamura, K., Wang, Y., Liu, X., Kubo, A., and Hnatowich, D. J. (2007) Cell culture and xenograft-bearing animal studies of radiolabeled antisense DNA carrier nanoparticles with streptavidin as a linker. *J. Nucl. Med. 48*, 1845–1852.

(15) Nakamura, K., Kubo, A., and Hnatowich, D. J. (2005) Antisense targeting of P-glycoprotein expression in tissue culture. *J. Nucl. Med. 46*, 509–513.

(16) Liu, X., Nakamura, K., Wang, Y., Zhang, S., He, J., Liu, G., Dou, S., Kubo, A., Rusckowski, M., and Hnatowich, D. J. (2006) Improved delivery in cell culture of radiolabeled antisense DNAs by duplex formation. *Mol. Imaging Biol. 8*, 278–283.

(17) Cheng, Z., Levi, J., Xiong, Z., Gheysens, O., Keren, S., Chen, X., and Gambhir, S. S. (2006) Near-infrared fluorescent deoxyglucose analogue for tumor optical imaging in cell culture and living mice. *Bioconjugate Chem. 17*, 662–669.

(18) Ntziachristos, V., Bremer, C., and Weissleder, R. (2003) Fluorescence imaging with near-infrared light: new technological advances that enable in vivo molecular imaging. *Eur. Radiol. 13*, 195–208.

(19) Kaijzel, E. L., van der Pluijm, G, and Lowik, C. W. G. M. (2007) Whole-body optical imaging in animal models to assess cancer development and progression. *Clin. Cancer Res. 13*, 3490–3497.

(20) Jares-Erijman, E., and Jovin, T. (2003) FRET imaging. *Nat. Biotechnol. 21*, 1387–1395.

(21) Kim, S., Lim, Y. T., Soltesz, E. G., Grand, De A. M., Lee, J., Nakayama, A., Parker, J. A., Mihaljevic, T., Laurence, R. G., Dor, D. M., Cohn, L. H., Bawendi, M. G., and Frangioni, J. V. (2004) Near-infrared fluorescent type II quantum dots for sentinel lymph node mapping. *Nat. Biotechnol. 22*, 93–97.

(22) Gao, X., Cui, Y., Levenson, R. M., Chung, L. W. K., and Nie, S. (2004) In vivo cancer targeting and imaging with semiconductor quantum dots. *Nat. Biotechnol. 22*, 969–976.

(23) Montet, X., Ntziachristos, V., Grimm, J., and Weissleder, R. (2005) Tomographic fluorescence mapping of tumor targets. *Cancer Res. 65*, 6330–6336.

(24) Sugimoto, N., Nakano, S., Katoh, M., Matsumura, A., Nakamuta, H., Ohmichi, T., Yoneyama, M., and Sasaki, M. (1995) Thermodynamic parameters to predict stability of RNA/DNA hybrid duplexes. *Biochemistry 34*, 11211–11216.

(25) Wetmur, J. G. (1991) DNA probes: applications of the principles of nucleic acid hybridization. *Crit. Rev. Biochem. Mol. Biol. 26*, 227–259.

BC9000933

Site Specific Conjugation of Fluoroprobes to the Remodeled Fc N-Glycans of Monoclonal Antibodies Using Mutant Glycosyltransferases: Application for Cell Surface Antigen Detection

Elizabeth Boeggeman,[†,‡,§] Boopathy Ramakrishnan,[†,‡,§] Marta Pasek,[†] Maria Manzoni,[†] Anu Puri,[‡] Kristin H. Loomis,[‡] Timothy J. Waybright,[‡,||] and Pradman K. Qasba*[,†]

Structural Glycobiology Section, CCR-Nanobiology Program, Membrane Structure and Function Section, CCR-Nanobiology Program, Basic Research Program, SAIC-Frederick, Inc., and Laboratory of Proteomics and Analytical Technologies, SAIC-Frederick, Inc. Received March 6, 2009; Revised Manuscript Received April 15, 2009

The Fc N-glycan chains of four therapeutic monoclonal antibodies (mAbs), namely, Avastin, Rituxan, Remicade, and Herceptin, released by PNGase F, show by MALDI analysis that these biantennary N-glycans are a mixture of G0, G1, and G2 glycoforms. The G0 glycoform has no galactose on the terminal GlcNAc residues, and the G1 and G2 glycoforms have one or two terminal galactose residues, respectively, while no N-glycan with terminal sialic acid residue is observed. We show here that under native conditions we can convert the N-glycans of these mAbs to a homogeneous population of G0 glycoform using β1,4 galactosidase from *Streptococcus pneumoniae*. The G0 glycoforms of mAbs can be galactosylated with a modified galactose having a chemical handle at the C2 position, such as ketone or azide, using a mutant β1,4-galactosyltransferase (β1,4Gal-T1-Y289L). The addition of the modified galactose at a specific glycan residue of a mAb permits the coupling of a biomolecule that carries an orthogonal reactive group. The linking of a biotinylated or a fluorescent dye carrying derivatives selectively occurs with the modified galactose, C2-keto-Gal, at the heavy chain of these mAbs, without altering their antigen binding activities, as shown by indirect enzyme linked immunosorbent assay (ELISA) and fluorescence activated cell sorting (FACS) methods. Our results demonstrate that the linking of cargo molecules to mAbs via glycans could prove to be an invaluable tool for potential drug targeting by immunotherapeutic methods.

INTRODUCTION

Monoclonal antibodies are increasingly becoming important therapeutic agents to target drugs to the tissue in need of treatment, leaving the normal tissue unharmed (*1*). They are commonly used in combination with chemotherapeutic agents for cancer treatment (*2*). The concept of making of antibody−drug conjugates (ADC) by which the antibody is used as a vehicle to deliver a cargo molecule to the tumor cell is gaining immense interest (*3*−*5*). Generally, the ADCs are antibodies conjugated to cytotoxic substances, such as drugs, toxins, and radioisotopes. The conjugated antibody recognizes and binds to cell surface antigen(s). At this point, the cargo molecules must be internalized into the target cells and released from the antibodies for activation of the drug.

All licensed therapeutic antibodies are of the IgG class; these are complex glycoproteins with two main functions, including a multivalent antigen binding through the Fab variable domains and effector functions through the Fc constant domain. IgG molecules are N-glycosylated in the CH_2 domain of the Fc fragment at the conserved Asn 297. In human IgG1, which is the main subtype used for therapeutics, the majority of the Fc glycans are complex biantennary structures with variable galactosylation: 0, 1, or 2 terminal galactoses corresponding to G0, G1, and G2 glycoforms, respectively, and <10−14% are sialylated (*6*, *7*). Only 15−20% of human IgG1 are also glycosylated in the Fab region of the molecule (*7*, *8*). Recent in vitro studies have established the importance of the Fc glycosylation profile of the IgG molecule on its effector functions: complement-dependent, cell-mediated cytotoxicity (CDC) and antibody-dependent, cell-mediated cytotoxicity (ADCC), such that removal of terminal galactose from the IgG can reduce the CDC but not affect ADCC activity (*9*). However, the use of rat hybridoma YB2/0 cells has permitted the production of mAbs that lack fucose in the conserved core oligosaccharide increasing the ADCC activity of the IgG, allowing the antibody to be effective at lower doses (*10*). Thus, glycosylation of recombinant monoclonal antibodies has been the focus of attention of the pharmaceutical industry to produce a homogeneous human-type glycosylation product, irrespective of the system/means by which the antibodies are produced.

After years of work to produce successful monoclonal antibodies as targeted drug therapeutics, researchers have developed 6 unconjugated and 3 antibody−drug conjugates that are currently approved for cancer treatment (*11*). Generally, the labeling of antibodies with the cargo molecules involves chemical methods which are difficult to control because the chemical reactions occur at tyrosine, lysine, aspartic, and glutamic acid residues that are distributed randomly on the surface of the protein. The result is the production of proteins with compromised activities (*12*). In order to maintain the biological activity of the protein and to optimize the production of homogeneous proteins, several methods have been developed for site-specific modification of the carriers. In the monoclonal antibodies, this site should be selected such that it is away from the antigen binding site. The oligosaccharide moieties of

* Corresponding author. Structural Glycobiology Section, CCR-Nanobiology Program, NCI-Frederick, Building 469, Room 221, Frederick, Maryland 21702. E-mail: qasba@helix.nih.gov. Phone: (301) 846-1934. Fax: (301) 846-7149.

† Structural Glycobiology Section, CCR-Nanobiology Program.

‡ Membrane Structure and Function Section, CCR-Nanobiology Program.

§ Basic Research Program, SAIC-Frederick, Inc.

|| Laboratory of Proteomics and Analytical Technologies, SAIC-Frederick, Inc.

10.1021/bc900103p CCC: $40.75 © 2009 American Chemical Society
Published on Web 05/08/2009

immunoglobulins are not involved in the process of antigen binding and are N-linked to Asn297 on the heavy chain in the Fc domain of the immunoglobulin far from the antigen binding site. The conjugation of monoclonal antibodies to the cargo molecules via the oligosaccharides has been carried out by chemical or enzymatic methods, resulting in the formation of aldehydes (*13, 14*). Generally, the chemistry used for the modification of the sugar moieties present on glycoproteins such as the immunoglobulin's is mild periodate oxidation of sialic acid residues, resulting in the generation of aldehyde groups, which can then be used for coupling (*15, 16*). However, less than 10−14% of mAbs are sialylated (*6, 7*). An alternative method for the generation of aldehyde groups on the oligosaccharide moieties of glycoproteins is the use of enzymes (*16−18*). However, the maximum number of aldehyde groups is dictated by the structure/linkage of the sugar; thus, the heterogeneous nature of the sugar moieties on the monoclonal antibodies can result in poor conjugation.

Recently, new chemoenzymatic methods for conjugation have been developed for site-specific conjugation (*19−21*). We have shown the utility of the galactosyltransferase mutant to transfer a sugar residue with a chemically reactive functional group (e.g., C2-keto-Gal or GalNAz) from their UDP derivatives to the N-acetylglucosamine residue of glycoproteins or glycopeptides (*20, 21*). Using this method, we have shown that the N-glycan moiety of the IgG molecule can be used as the substrate for the transfer of C2-keto-Gal sugar by the mutant β1,4Gal-T1-Y289L (*20*). After the transfer of the modified sugar residue, the chemical handle is used for selective conjugation with a biomolecule that has an orthogonal reactive group, such as an aminooxy linked to biotin (*19−21*).

Here, we show that one can take advantage of the unique heterogeneous oligosaccharide linked at Asn297 in the mAbs that can be made homogeneous by a simple enzymatic procedure and obtain a population of mAbs having a set of glycans of the G0 glycoform that are subsequently fully galactosylated to a G2 glycoform, with the modified C2-keto-Gal as monitored by MALDI-TOF analysis of the PNGase F-treated samples. The transferred C2-keto-Gal is coupled to an aminooxy-biotin, which was previously detected by chemiluminescence techniques (*20, 22*) and here by MALDI-TOF analysis of the N-glycans. Using ELISA methodology, we show that the coupling of aminooxy-biotin to C2-keto-Gal does not compromise the antigen (Ag) binding site. Furthermore, Herceptin with C2-keto-Gal modified N-glycans coupled to Alexa Fluor 488 C_5-aminooxyacetamide binds to HER2-receptor-expressing cells, as shown by FACS methodology. Therefore, our conjugation technology presents a viable method to quantify the cargo molecules to be used for detection and targeting therapies.

EXPERIMENTAL PROCEDURES

REAGENTS. Rituxan (Rituximab) and Remicade (Infliximab) are recombinant chimeric monoclonal antibodies (mAbs), and Avastin (Bevacizumab) and Herceptin (Trastuzumab) are recombinant humanized mAbs (Genentech, Inc., South San Francisco, CA), purchased via the NIH pharmacy (Bethesda, MD). FITC-conjugated goat antihuman IgG (whole molecule) was from Sigma-Aldrich (St. Louis, MO). Alexa Fluor 488 C_5-aminooxyacetamide, bis (triethylammonium) salt (Alexa Fluor 488 hydroxylamine) was from Invitrogen (Eugene, OR). Recombinant β1,4-galactosidase from *Streptococcus pneumoniae* was from Calbiochem (San Diego, CA). Peptide *N*-glycoside F (PNGase F) was from New England Biolabs (Ipswich, MA). Microcon Ultracel YM-50 centrifugation devices came from Millipore Corporation, (Bedford, MA). Protein A-Sepharose 4B conjugate was from Invitrogen (Eugene, OR). 2,5-Dihydrobenzoic acid (DHB) came from Sigma-Aldrich (St. Louis, MO). Micro biospin chromatography columns P-30 were from Bio-Rad (Hercules, CA). Recombinant human vascular endothelial growth factor (VEGF) was from Thermo Scientific and *p*-nitrophenyl phosphate from Sigma-Aldrich (St. Louis, MO). UDP-C2-keto-Gal was synthesized as described previously (*19*).

β 1,4 Galactosyltransferase Expression in *E. coli* and in Vitro Folding of Inclusion Bodies. The enzymes β1,4Gal-T1[1] and β1,4Gal-T1-Y289L used in this study have been previously described (*23, 24*). Inclusion bodies were purified from the bacterial pellet as described earlier (*23, 24*). The in vitro folding of the enzymes was carried out in a way similar to that of β1,4Gal-T1 (*23*), with a few modifications. Typically, 100 mg of sulfonated protein were folded for 48 h in 1 L of folding solution that contained oxido-shuffling reagents and 550 mM arginine-HCL (*23*). The presence of arginine in the folding solution enhances the folding efficiency of β1,4Gal-T1-Y289L.

Degalactosylation of Monoclonal Antibodies. Avastin, Rituxan, Remicade, or Herceptin were washed with 50 mM sodium phosphate pH 6.0, using a Microcon Ultracel YM-50 centrifugation device. The samples at 8 mg mL^{-1} were incubated with 100 mU of recombinant *Streptococcus pneumoniae* β1,4-galactosidase for 24 h at 37 °C. Removal of terminal galactose residues was confirmed by analysis of the N-glycans released after PNGAse F treatment by MALDI TOF spectrometry. Approximately 3 μg of mAbs was incubated in the presence or absence of PNGase F (2500 units), 16 h at 37 °C in 10 μL of G7 buffer. Samples were then purified on microspin charcoal columns (Harvard Apparatus, MA). Samples were eluted with 30% acetonitrile and analyzed by mass spectrometry. Degalactosylated monoclonal antibodies were then purified by protein A affinity chromatography.

Protein A Affinity Chromatography of mAbs. Degalactosylated samples were diluted 1:1 with 1 × PBS, pH 7.4 (binding buffer), and then added to the protein A columns (Invitrogen). The columns were washed several times with binding buffer and the mAbs were eluted with 100 mM glycine-HCL, pH 2.7. The eluted mAbs were neutralized with 1 M Tris−HCl buffer pH 8.0, concentrated, and washed with 1 × PBS, pH 7.4, using the Microcon Ultracel YM-50 centrifugation device. Protein amounts were determined using the Bio-Rad protein assay kit based on the method of Bradford (BIO-RAD), and the purity of all mAbs further verified by SDS-PAGE electrophoresis.

Transfer of C-2 keto Galactose from Its UDP-Derivative to Free GlcNAc Residues on mAbs using the Mutant β1,4Gal-T1-Y289L and Biotinylation of the mAbs. Monoclonal antibodies (12 μg) were incubated with 2 mM UDP-C2 keto-Gal and 12 μg of the mutant β1,4Gal-T1-Y289L in a 25 μL final incubation mixture containing 10 mM $MnCl_2$ and 25 mM Tris−HCl (pH 8.0). Reactions were incubated at 30 °C for 12 h. The ketone-labeled proteins were subsequently diluted to 30 μL in a mixture containing 50 mM NaOAc (pH 3.9) and 3 mM *N*-aminooxy-methylcarbonylhydrazino-D-biotin (AOB), purchased from Dojindo Laboratories. The biotinylation reactions were incubated with gentle shaking for 12−16 h at 25

[1]Abbreviations: β1,4-Gal-T1, β1,4-galactosyltransferase; ELISA, enzyme linked immunosorbent assay; FACS, fluorescence activated cell sorting; PNGase F, peptide N-glycosidase F; DHB, 2,5-dihydrobenzoic acid; DMA, *N*,*N*-dimethylaniline; Gal, galactose; GlcNAc, *N*-acetylglucosamine; *N*-acetyl-azido-galactosamine (Gal-2-NHCO-CH_2-N_3), GalNAz; UDP-Gal, uridine 5′-diphosphogalactose; UDP-2-keto-Gal, Uridine 5′-diphospho-2-acetonyl-2-deoxy-galactose; UDP-GalNAc, uridine 5′-diphospho-*N*-acetylgalactosamine; UDP-GalNAz, uridine 5′-diphospho-*N*-acetyl-azido-galactosamine; MALDI, matrix-assisted laser desorption ionization; MS, mass spectra; AOB, *N*-aminooxy-methylcarbonylhydrazino-D-biotin; HRP, horseradish peroxidase; FBS, fetal bovine serum; BSA, bovine serum albumin; PBS, phosphate buffer saline.

°C. A portion of the sample was treated with PNGase F for the MALDI-TOF analysis of the glycan chain, and a portion was boiled in Tris-Glycine-SDS sample buffer containing β-mercaptoethanol and analyzed by Western blot analysis as described (*19*−*21*).

SDS-PAGE Analysis of mAbs and Western Blotting of IgGs. The SDS-PAGE analyses of native or biotinylated mAbs, respectively, before and after PNGase F treatment, were performed in 14% Tris−glycine gels (Invitrogen). For Western blotting analysis, the proteins from the gels were then transferred by electrophoresis to nitrocellulose paper (0.45 μm pore size) for 2 h at 25 V and biotinylated protein bands identified as described previously (*20*).

Fluorescent Labeling of Herceptin. Fluorescent labeling reactions were carried out by treating 10 μg of C2-keto-Gal labeled Herceptin with 400 μM of Alexa Fluor 488 C_5-aminooxyacetamide in 27 μL containing 166 mM NaOAc (pH 4.9). The reactions were incubated for 2−6 h at 37 °C. The unreacted fluorescent dye was removed by purification on micro biospin chromatography columns P-30 from Bio-Rad (Hercules, CA), as per manufacturer's directions. Purified samples were separated by SDS-PAGE and fluorescence was detected using a multi view FMBIO II scanner (Hitachi).

Indirect ELISA. The binding activity of Avastin to recombinant human vascular endothelial growth factor (VEGF) was determined in a solid-phase binding assay using soluble Avastin and coated VEGF. Binding of antibodies was then detected by a specific secondary antibody in an enzyme-linked immunosorbent assay. Briefly, flat-bottom 96-well microtiter plates (Costar 3690, Corning Inc., NY) were coated with the appropriate amounts of VEGF overnight at 4 °C and were washed three times with phosphate buffer saline (PBS) pH 7.4 containing 0.05% Tween-20 and 0.1% sodium azide. The plates were blocked with 3% bovine serum albumin (BSA) in PBS with 0.05% Tween-20 for 1 h at room temperature. A serial dilution of native or modified Avastin was added to the VEGF-coated plate and incubated for 1 h at room temperature. The detection antibody conjugate (antihuman-Fc-phosphatase) (Thermo Scientific) was then applied for 1 h at room temperature. The detection of alkaline phosphatase was performed with *p*-nitrophenyl phosphate (Sigma). Samples were measured at 405 nm with a plate reader.

Matrix-Assisted Laser Desorption/Ionization Mass Spectrometry. Typically 1−2 μL of sample was mixed with an equal volume of 2,5-dihydrobenzoic acid (DHB) matrix solution prepared by dissolving 100 mg of DHB (Sigma Chemicals) in 1 mL of a 1:1 solution of water and acetonitrile. In some instances, a matrix solution of a mixture of DHB/DMA (*N*,*N*-dimethylaniline) was used, which was prepared by adding 30 μL of distilled DMA to the DHB matrix (*25*). Mixtures were spotted onto a stainless steel plate after mixing the samples and matrix solutions (1 μL each). The samples were dried by evaporation at room temperature. A hybrid triple-quad time-of-flight (QqTOF) mass spectrometer (QSTAR XL, Applied Biosystems, Inc., Framingham, MA) was configured for matrix-assisted laser desorption/ionization (MALDI). Mass spectrometry (MS) data was obtained using a laser intensity = 21 000 μj, pulse rate = 20 Hz, collision gas (CAD) = 3 (high purity argon, Airgas, Inc., Frederick, MD), focusing potential (FP) = 35 V, declustering potential (DP) = 0 V, declustering potential 2 (DP2) = 20 V, and ion energy (IE1) = 0.8 V. All samples were analyzed in the positive mode with a 3 min accumulation time over an *m*/*z* range of 150−3000 amu.

Cell Surface Immunostaining of HER2 Receptor by FACS Analysis. To determine if the modifications in Herceptin influenced its ability to bind to the cellular HER2 receptor, we used either indirect immunostaining (when using modified Herceptin) or direct immunostaining of cells when using Alexa-conjugated-Herceptin. HER2 receptor expressing human breast adenocarcinoma cells (SKBR-3) and HER2 receptor negative human breast adenocarcinoma cells (MDA-MB-468) were purchased from the American type Culture Collection (ATCC, Manassas, VA). The cells were cultured in DMEM/F12 medium supplemented with 10% (v/v) heat-inactivated fetal bovine serum (FBS) and penicillin/streptomycin as antibiotics at 37 °C in a humidified atmosphere containing 5% CO_2. Other culture reagents were bought from Invitrogen (Carlsbad, CA). For immunostaining experiments, cells were harvested using a PBS-based, enzyme-free cell dissociation buffer, and suspended to a concentration of 10^7 cells per mL in PBS containing 5% FBS. The cells were further incubated for 15 min at room temperature, centrifuged and washed twice with cold PBS supplemented with 0.1% BSA (PBS−BSA), and resuspended in PBS−FBS at a concentration of 10^7 per mL. For incubation with antibodies, 100 μL cell suspension (containing 10^6 cells) were placed in 1.5 mL Eppendorf tubes. Native Herceptin, modified Herceptin, or Alexa-conjugated Herceptin (4 μg each) was added to individual samples, and incubations were continued for 1 h at 4 °C in the dark with constant shaking. At the end of incubations, samples were washed twice with cold PBS−BSA, and resuspended in 100 μL PBS−FBS. The samples incubated with Alexa-conjugated Heceptin were analyzed by FACS. The cells incubated with native Herceptin or modified Herceptin were incubated with a 1:32 dilution of FITC-conjugated goat antihuman IgG for 1 h at 4 °C in the dark with constant shaking. Cells were washed twice with PBS−BSA, and resuspended in PBS−BSA (1 mL per sample). Control samples were incubated without any primary antibody, with only the FITC-conjugated goat antihuman IgG. Cells were analyzed using a FACS Calibur flow cytometer (Becton Dickinson, San Jose, CA). Each sample was analyzed for 10 000 counts of viable cells, and all samples were run at least in duplicate.

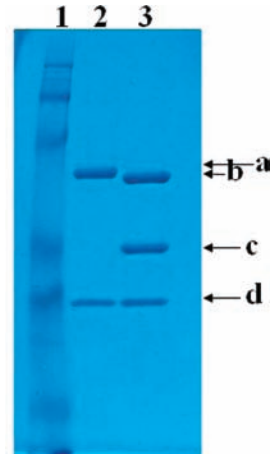

Figure 1. SDS-PAGE analysis of monoclonal antibody before and after PNGase F treatment. (1) Kaleidoscope prestained standards; (2) the native IgG; (3) IgG after treatment with PNGase F. Arrows show from top to bottom: (a) heavy chain of native IgG, (b) deglycosylated heavy chain of IgG, (c) PNGase F used for deglycosylation, and (d) light chain of IgG.

RESULTS

Glycoforms of Therapeutic Monoclonal Antibodies; MS Analysis of Native and β-galactosidase-treated IgGs. The human IgGs are N-glycosylated in the CH_2 domain of the Fc fragment and only ∼15−20% are also glycosylated in the Fab domain (*7*, *8*). SDS-PAGE analysis of mAbs, Avastin, Rituxan, Remicade, and Herceptin, before and after the PNGase F treatment, shows the mobility difference only in the heavy chain

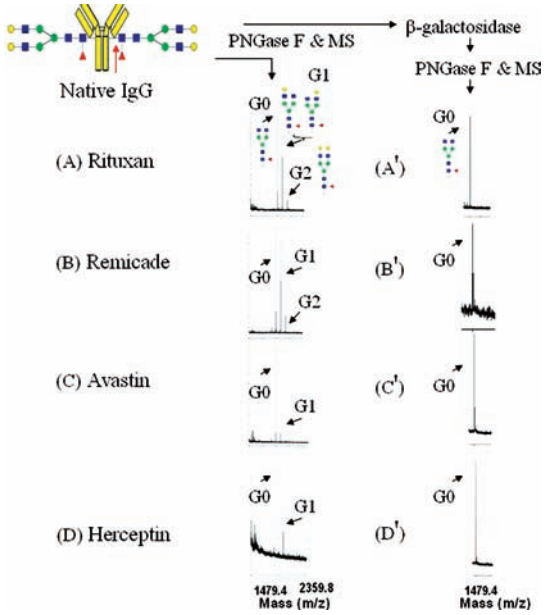

Figure 2. Glycoforms of therapeutic monoclonal antibodies; MS analysis of N-glycans after β-galactosidase treatment of IgG's. (A−D) MALDI-TOF MS analysis of N-glycans released by PNGase F treatment (red arrow shows the cleavage site) of native Rituxan (A), Remicade (B), Avastin (C), and Herceptin (D). G0 glycoform with a peak at 1485.6 *m/z*, the G1 glycoform with a peak at 1647.6 *m/z*, and G2 glycoform with a peak at 1809.6 *m/z*. mAbs were treated with β-galactosidase to obtain a homogeneous G0 glycoform population (A′−D′) MALDI-TOF analysis of N-glycans released by PNGase F treatment of β-galactosidase treated Rituxan (A′), Remicade (B′), Avastin (C′), and Herceptin (D′), respectively. Only the G0 glycoform with a peak at 1485.6 *m/z* is seen after treatment. Major peaks are annotated with the carbohydrate structure shown in the symbols for monosaccharides, according to the nomenclature adopted by the consortium for functional glycomics: GlcNAc (blue squares), mannose (green spheres), galactose (yellow spheres), and fucose (red triangles). The symbols were drawn using the GlycoWorkbench program found in the Eurocarb database http://www. Eurocarb.org/.

protein band, and not in the light chain, indicating that the oligosaccharide chain is released only from the IgG heavy chain, and not from the light chain (Figure 1).

The degree of heterogeneity of the oligosaccharides in the native mAbs was determined by carrying out the MALDI-TOF analysis of the oligosaccharide released after PNGase F treatment of mAbs. MS analysis of oligosaccharides released after PNGase F treatment of native forms of Rituxan and Remicade show that they carry oligosaccharides of G0, G1, and G2 glycoforms (Figure 2A,B), corresponding to 0, 1, and 2 galactose residues, respectively, while Avastin and Herceptin have only G0 and G1 glycoforms (Figure 2C,D). None had sialylated structures as observed with some mAbs (*6*). To selectively remodel the oligosaccharide of the monoclonal antibodies at Asn 297 in the Fc domain and to obtain a homogeneous population of glycoforms, the IgGs were degalactosylated by β1,4-galactosidase from *S. pneumoniae* for 24 h. After galactosidase treatment, the degree to which the mAbs glycans were degalactosylated was confirmed by MALDI-TOF analysis of the N-glycans after PNGase F treatment. 24 h incubation of 8 mg/mL^{-1} of mAbs with 100 mU units of galactosidase in 50 μL incubation mixture completely converts the IgG in G0 glycoform (Figure 2A′−D′).

Reglycosylation of G0 Glycoform of mAbs Using Either UDP-Gal or UDP-GalNAc as Sugar Donors. The mutant β1,4Gal-T1-Y289L enzyme, in contrast to the wild-type enzyme β1,4Gal-T1, exhibits both β1,4Gal transferase and β1,4GalNAc transferase activities (*24*). Using chemoenzymatic methods, it was shown that the mutant enzyme can transfer the C2-keto-Gal from its UDP-derivative to the GlcNAc residue on the N-glycan chain of an asialo-agalacto IgG molecule (*20*). In the present studies, we investigated the transfer of UDP-sugars to the protein A purified G0 glycoform of Herceptin by the wild-type and a mutant β1,4-galactosyltransferse. Figure 3 shows the MALDI-TOF profile of the oligosaccharide after the transfer of galactose by the wild-type β1,4Gal-T1 (Figure 3A) and the transfer of N-acetylgalactosamine (Figure 3B) by the mutant enzyme β1,4Gal-T1-Y289L to the free GlcNAc residues on the G0 glycoforms of Herceptin (Figure 2D′). Nearly 100% galactosylation of both arms of the N-glycan of the IgG-G0 glycoform

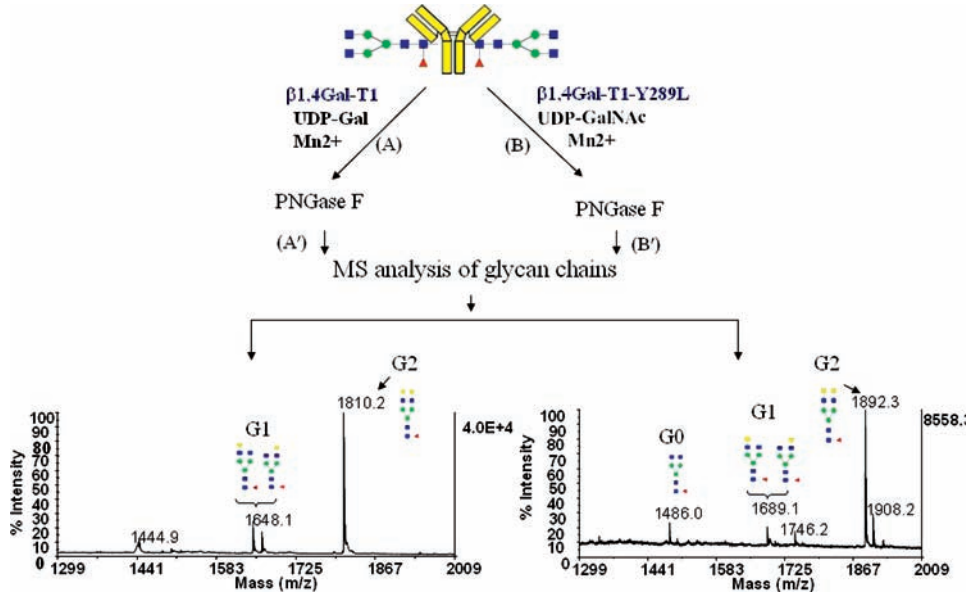

Figure 3. Reglycosylation of β-galactosidase treated mAbs using natural UDP-sugar donors. To the degalactosylated G0 glycoform of the IgG, (A) galactose moiety was transferred from UDP-Galactose using the wild-type enzyme β1,4Gal-T1 or (B) GalNAc moiety was transferred from UDP-GalNAc using the mutant β1,4Gal-T1-Y289L. After overnight incubation, mixtures were treated with PNGase F prior to MS analysis. (A′) After galactose transfer, ions at 1648.1 *m/z* and 1810.2 are assigned to G1 and G2 glycoforms, respectively, and (B′) after GalNAc transfer, ions at 1486.0 *m/z*, 1689.1 *m/z*, and 1892.3 *m/z* are assigned to G0, G1, and G2 glycoforms, respectively.

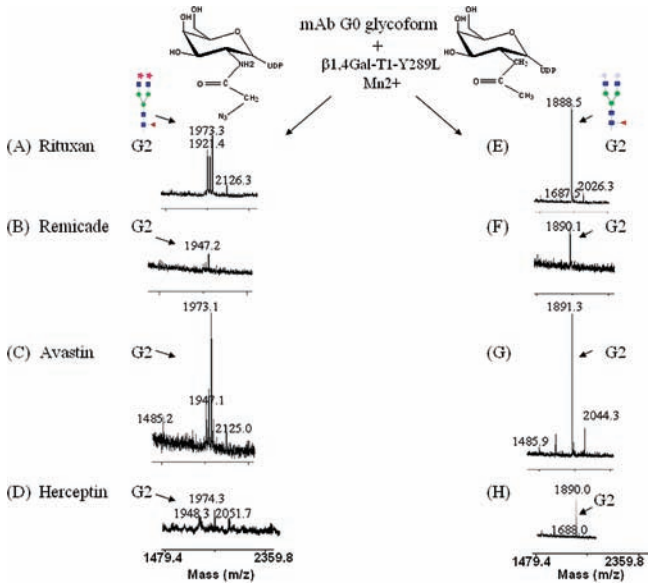

Figure 4. Reglycosylation of G0 glycoform using C-2 modified sugar donors: The mutant enzyme β1,4Gal-T1-Y289L was used to transfer the C-2 modified sugars from their respective UDP-sugar nucleotides to the degalactosylated mAbs; UDP-2-keto-Gal (right panel) and UDP-2-azido-Gal (left panel). MALDI mass analysis after treatment of N-glycans with a mixture of sialydase and β-galactosidase (not shown), gave the same G0 glycoform profile, upon PNGase F treatment, as did the β-galactosidase treatment alone. The transfer of the modified sugar nucleotide was analyzed by mass spectrometry of the modified N-glycans released after PNGase F treatment. β-Galactosidase treated mAbs having a G0 glycoform are fully galactosylated to the G2 glycoform after transfer of GalNaz moiety to the terminal GlcNAc residues showing a peak of 1973 *m/z* (left panel A, C, and D). The G2 glycoform peak at 1947 *m/z* in (B) is due to partial fragmentation of the azido group that can take place during mass spectrometry analysis. The peak at 2126 *m/z* corresponds to the matrix DHB adduct. Right panel (E−H) shows the transfer of C2-keto-Gal moiety to the terminal GlcNAc residues in the G0 glycoform (middle panel). A peak at ~1891 *m/z* corresponds to the G2 glycoform and peaks at 2026 *m/z* and 2044 *m/z* correspond to the DHB adduct. GalNAz (pink stars) and C2-keto-Gal (purple circles).

(Figure 2D′) was observed when 80 pmol of IgG (12 μg) were incubated at 30 °C for 12 h with 120 pmol of β1,4Gal-T1 enzyme (4 μg) at 1.5 mM concentration of the sugar donor substrate UDP-Gal (Figure 3A′). A peak occurred at *m/z* 1810.2, corresponding to the G2 form, and a very small peak at *m/z* 1648.1, corresponding to the G1 form where galactosylation is on either the 1,3 or 1,6 arm of the N-glycan. The transfer of GalNAc (Figure 3B′) by the mutant enzyme β1,4Gal-T1-Y289L to both arms of the G0 glycoform (Figure 2 D′) is observed as a main peak at *m/z* 1892.3 corresponding to the G2 glycoform of the mAb. Minor peaks at *m/z* 1486 and 1689 correspond to the G0 and G1 glycoforms, respectively. Under the conditions described here, the transfer of galactose and of GalNAc to both GlcNAc residues on each arm of the N-linked structure is observed.

Transfer of C2-keto-Gal to the Free GlcNAc Residues on the N-Glycan Chains of mAbs by the Mutant Enzyme β1,4Gal-T1-Y289L. In a previous study, we showed that the transfer of C2-keto-Gal to the N-linked oligosaccharides of the IgG by the mutant β1,4Gal-T1-Y289L (*20*) can be detected by the chemoenzymatic method. In this study, we followed the transfer of C2-keto-Gal to mAbs by the MALDI-TOF of the PNGase F-released oligosaccharides. There is nearly full conversion of 80 pmol of the G0 form of IgG (12 μg) to the G2 form with either C2-GalNAz (Figure 4A−D) or C2-keto-Gal (Figure 4E−G) using 2 mM concentration of sugar donor substrate UDP-C2-GalNAz or UDP-2-keto-Gal, respectively, with ~360 pmol of β1,4Gal-T1-Y289L mutant enzyme (12 μg) in a 25 μL incubation mixture. The appearance of a major peak at *m/z* 1973.5 after the transfer of C2-GalNAz (Figure 4A−D), and at *m/z* 1890.0 after the transfer of C2-keto-Gal (Figure 4E−G), shows that the transfer occurs under these conditions on both arms of the G0 glycoform.

Biotinylation of the Glycosylated IgG. The transfer of C2-keto-Gal has been followed by coupling the biotinylated aminooxy biotin to the ketone group at the C2 position of the galactose (Figure 5A) and detected by a sensitive chemiluminescence assay (*19*−*21*). MALDI-TOF analysis of the oligosaccharides released after PNGase F treatment of the C2-keto-galactosylated mAbs showed a major peak at *m/z* 2519, corresponding to the G2 glycoform of the antibodies (Figure 5B) having 4 molecules of C2-keto-Gal transferred per IgG molecule. The conjugated proteins were also analyzed by SDS-PAGE, followed by Western blotting and detection by the streptavidin-HRP technique, as previously described (*19*−*21*). The lack of chemiluminescence band in the Western blot analysis after PNGase F treatment of the mAbs (Figure 5C) supports the conclusion that the biotinylated aminooxy ligand is linked only to the C2-keto-Gal modified N-glycan chain of the IgG heavy chain.

Comparing the Binding of Native and Modified Avastin to VEGF by the ELISA Method. We used an indirect ELISA method described previously (*26*) to analyze the binding of native and modified Avastin to VEFG immobilized on a microtiter plate surface. Remodeling of the Fc N-glycans of Avastin did not change the binding to VEGF, when compared to the binding of the native mAb (Figure 6).

Herceptin Labeling with Alexa Fluor 488 C_5−Aminooxyacetamide. Since C2-keto galactosylated mAbs could be successfully coupled to aminooxy containing ligands (Figure 5B,C) without affecting the antigen binding, as observed by the ELISA method (Figure 6), we linked the C2-keto-Gal modified Herceptin (Figure 4H) to the Alexa Fluor 488 C_5-aminooxyacetamide and analyzed the protein by fluorescence imaging of the SDS-PAGE (Figure 7A), and subsequent staining of the gel with Coomassie blue (Figure 7B). Results from the fluorescence imaging indicate that there is a selective labeling of the heavy chain of the mAb, and this signal is almost lost following PNGase F treatment of the fluorescent-tagged antibody, which removes the N-linked sugars in the Fc domain of the IgG (Figure 7A). No fluorescence was detected at other protein bands seen after Coomassie blue staining of the SDS-PAGE gel (Figure 7B). Conjugation of Alexa Fluor 488 to enzyme-modified Herceptin was further confirmed using a spectrofluorometer (model FluoroMax 3, HORIBA Jobin Yvon Inc., NJ) to measure fluorescence at Ex/Em 494/518 nm (not shown).

Effect of Herceptin Modification(s) on its Binding to HER2 Receptor. To evaluate the effect of carbohydrate modifications in Herceptin on its biological activity, we examined its binding to HER2 receptor using a human breast adenocarcinoma cancer cell line (SKBR-3) that overexpresses this receptor. MDA-MB-468 cells, that do not express the HER2 receptor, were used as controls. The immunostaining with Alexa Fluor 488 C_5-aminooxyacetamide-conjugated Herceptin or modified Herceptin was performed as described in the Methods section. The results are presented in Figures 8 and 9, respectively.

Alexa-conjugated Herceptin showed binding only to SKBR-3 cells (receptor expressing) (Figure 8B). In contrast, under identical conditions, we did not observe any binding above background for MDA-MB-468 cells (receptor negative) (Figure 8A). Therefore, the conjugation of Alexa Fluor 488 and

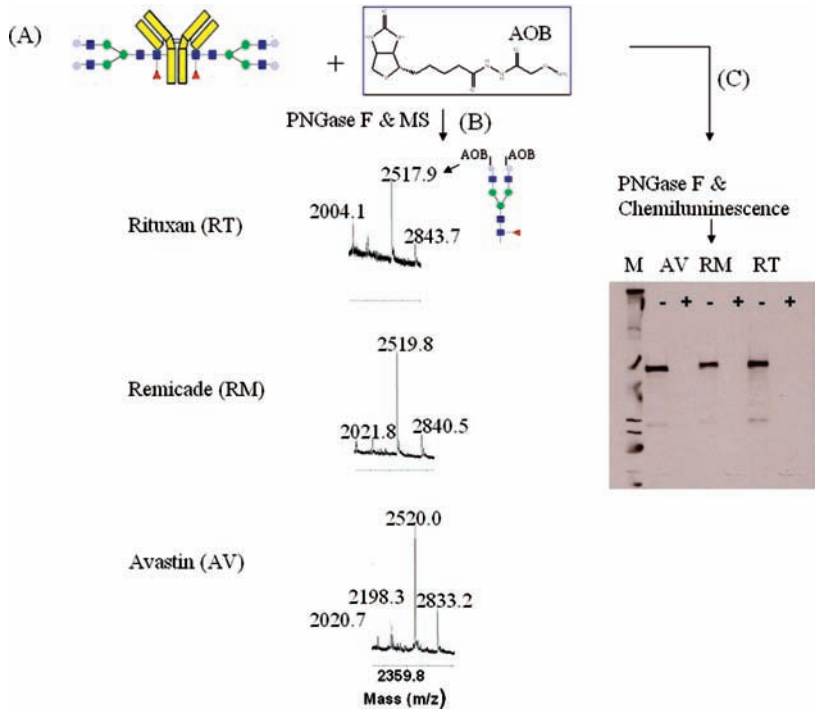

Figure 5. Detection by chemiluminescence technique of the transfer of the C2-keto-Gal to free GlcNAc residues on the N-glycan chains of mAbs. (A) The C2-keto-Gal has been transferred to the free GlcNAc residues in the N-linked carbohydrate of IgG. (B) Detection of the transferred C2-keto-Gal is accomplished by linking to aminooxy biotin followed by PNGase F treatment and MS analysis of the N-glycans. The peaks at 2517.9 *m*/*z*, 2519.8 *m*/*z*, and 2520.0 *m*/*z* correspond to AOB being transferred to both arms of N-glycans carrying C2-keto-Gal in Rituxan (RT), Remicade (RM), and Avatin (AV), respectively. The peaks at 2843.7 *m*/*z*, 2840.5 *m*/*z*, and 2833.2 *m*/*z* correspond to AOB transferred to the sugars at the reducing end. (C) The linked AOB-C2-keto-Gal of AV, RM, and RT is also detected on Western blots by chemiluminescence. In contrast to the samples that were not treated with PNGase F (−), the samples treated with PNGase F (+) showed no chemiluminescence. C2-keto-Gal (purple circles).

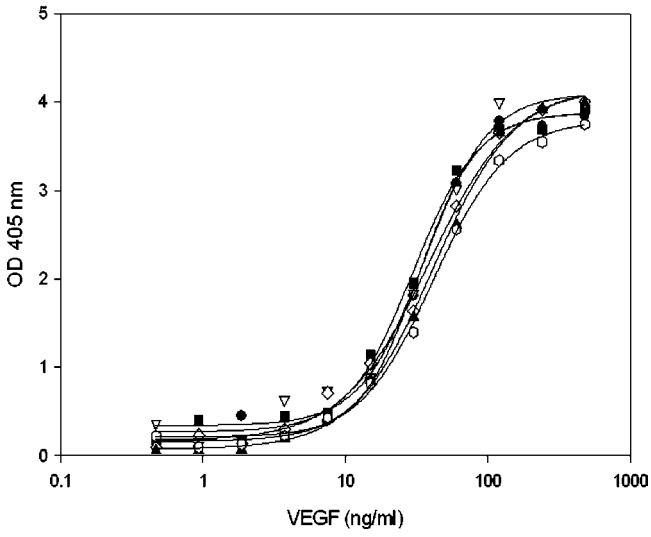

Figure 6. VEGF ELISA comparing the binding of modified Avastin. Avastin, native or modified, was bound to VEGF immobilized on a microtiter plate surface, and was detected with an antihuman Fc antibody conjugated to alkaline phosphatase. The transfer of various substrates by the mutant β1,4Gal-T1-Y289L, namely, GalNAc and C2-keto-Gal to Avastin did not perturb the binding to VEGF. Aminooxy biotin is also linked to the modified C2-keto-Gal without perturbing the Fab domain. (●) Avastin native. (▽) Degalactosylated Avastin. (□) Degalactosylated Avastin+ GalNAc. (◇) Degalactosylated Avastin+ no UDP-GalNAc+β1,4Gal-T1-Y289L. (□) Degalactosylated Avastin+ C2-keto-Gal. (⬡) Degalactosylated Avastin+ C2-keto-Gal +AOB.

Herceptin did not have any effect on its receptor-binding activity, suggesting that these conjugates may serve as suitable tools for imaging.

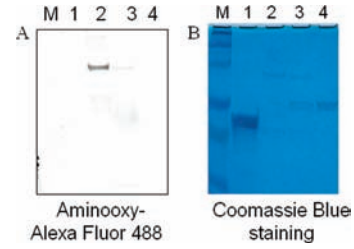

Figure 7. Herceptin labeling with Alexa Fluor 488 C_5-aminooxy acetamide. C2-keto-Gal modified Herceptin was conjugated with Alexa Fluor 488 C_5-aminooxyacetamide and analyzed by SDS-PAGE (see Materials and Methods). (A) Fluorescence imaging of the SDS-PAGE. (B) The gel was subsequently stained with Coomassie blue. (M) Kaleidoscope standard, (1) β1,4Gal-T1-Y289L, (2) C2-keto-Gal modified Herceptin conjugated to Alexa Fluor 488 C_5-aminooxy acetamide, (3) C2-keto-Gal modified Herceptin conjugated to Alexa Fluor 488 C_5-aminooxyacetamide digested with PNGase F, and (4) PNGase F.

Next, we examined the effect of carbohydrate modifications in Herceptin, other than Alexa Fluor 488, on the binding to the HER2 receptor expressing cells. We performed cell sorting experiments using indirect immunostaining (using the FITC-conjugated goat antihuman IgG, see Methods). The results are presented in Figure 9. SKBR-3 (receptor positive) cells bound to native and to modified Herceptin conjugates with similar efficiency (Figure 9 F−H). In contrast, FITC-conjugated goat antihuman IgG alone did not show any significant binding above background (Figure 9 E). Our data also show that MDA-MB-468 cells (receptor negative) did not bind to Herceptin (or modified Herceptin) above background (Figure 9A−D). Therefore, carbohydrate modifications and/or subsequent conjugation

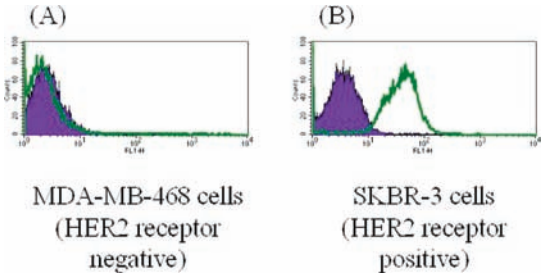

Figure 8. Binding of Alexa Fluor 488 conjugated Herceptin to HER2-receptor expressing cells. Herceptin was enzymatically modified with C2-keto-Gal and conjugated with Alexa Fluor 488 C_5-aminooxyacetamide. Alexa-conjugated Herceptin (4 μg) was incubated with 10^6 cells/100 μL PBS−FBS for 60 min at 4 °C while shaking in the dark. The cells were washed twice with PBS−BSA and resuspended in 1 mL PBS−BSA. Samples were analyzed by FACS (see Materials and Methods). (A) MDA-MB-468 control cells and (B) SKBR-3 cells. The purple area indicates the background value. The empty area defines the fluorescence of Herceptin conjugated Alexa Fluor 488 C_5-aminooxyacetamide (green line).

via the introduced functional groups do not alter their receptor binding activity.

DISCUSSION

The mAbs are used as powerful therapeutic agents for the treatment of various diseases. They can be used "naked" with their inherent effector functions or as targeting vehicles. Here, we used an enzymatic method (*19*−*21*) for the production of the conjugated targeting vehicle of mAbs that has the advantage (I) of being site-specific and accessible for conjugation; (II) the cargo does not interfere with or modify the Fab domain; (III) the conjugation of a cargo molecule to a mAb makes it possible to direct the cargo to the desired site; (IV) mAb conjugated with fluoroprobes via glycan chains are suitable probes for imaging and clinical applications.

We have previously shown that the mutant enzyme β1,4Gal-T1-Y289L can transfer GalNAc and galactose from its UDP-derivatives to GlcNAc residues present at the nonreducing end of proteins (*24*). We have also shown that this mutant can transfer modified sugars such as 2-keto-Gal from their UDP derivatives for detection of O-GlcNAc modifications in proteins (*19*) or detection of free GlcNAc residues at the nonreducing end of the N-glycans of proteins (*20*). Our findings led us to propose that two glycoproteins having modified sugars with unique chemical handles could be conjugated via linkers having orthogonal chemical reactive groups, allowing the design of novel mAb-drug conjugates and imaging agents (*27*).

The present study extends our previous work by showing: (1) Fc N-glycans of native therapeutic antibodies are highly heterogeneous; (2) it is possible to modify the therapeutic monoclonal antibodies from a heterogeneous to a homogeneous glycoform population; (3) the modification at the N-linked oligosaccharide occurs in a site-specific manner without compromising the antigen binding site; and (4) we have been able to produce mAb-fluoroprobes conjugates for imaging applications.

The glycosylation profile of recombinant mAbs has been well-characterized and is known to be highly heterogeneous with respect to core fucosylation, terminal sialylation, and galactosylation (*28*). The difference between the observed glycoform types depends on the enzymes/host cell type, substrates, and culture conditions utilized for their production. The MALDI-TOF analysis of PNGase F-released oligosaccharides of the mAbs used in our study concur with the published data (*28*). These N-glycans are core-fucosylated with differences in the terminal sugars having a mixture of G0, G1, and G2 glycoforms. None of the mAb used here had terminal sialic acids. Previously, we showed that the C2-keto-Gal from its UDP derivative was transferred by β1,4-Gal-T1-Y289L to free GlcNAc residues on the N-linked glycan chains of a heterogeneous population of IgG molecules (*20*). An important issue in this study was the transfer of the modified sugar to each available GlcNAc present in a homogeneous mAb glycoform population. In order to obtain a population of mAb having a single G0 glycoform with 2 mol of GlcNAc available for transfer to each IgG heavy chain, we tested galactosidases from various sources to remove the

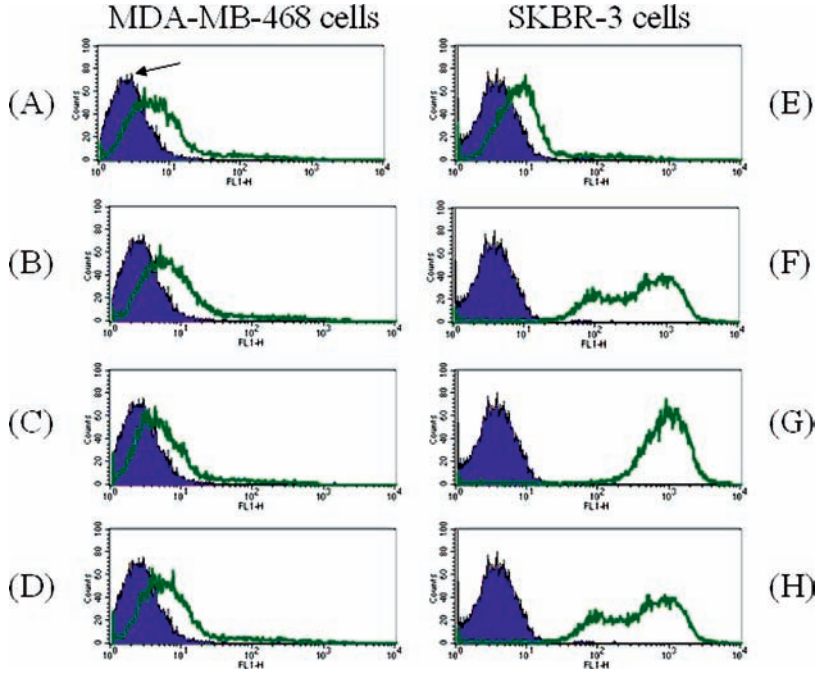

Figure 9. Effect of carbohydrate modification of Herceptin on its binding to HER2-receptor expressing cells. Herceptin was subjected to various enzyme treatments (see Materials and Methods). Native and modified Herceptin molecules were incubated with MDA-MB-468 cells or SKBR-3, followed by incubation with FITC-conjugated goat antihuman IgG. The samples were analyzed by FACS (see Methods section). (A,E) secondary antibody alone; (B,F) Herceptin untreated; (C,G) Herceptin treated with β-galactosidase; (D,H) Herceptin treated with β-galactosidase + C2-keto-Gal. The arrow indicates background fluorescence of cells in the absence of antibodies.

nonreducing end galactose residues in the G1 and G2 glycoforms. Only after using β1,4 galactosidase from *Streptococcus pneumoniae* (*9*), we were able to show, by MALDI-TOF analysis of the PNGase F-released carbohydrates, a single-type G0 glycoform. The β1,4 galactosidase from other sources did not yield 100% fully degalactosylated glycoforms. Having demonstrated the production of a single glycoform, the G0 form, by enzymatic degalactosylation, we explored the transfer of the modified sugar and the coupling of the ketone handle to aminooxy-biotin, which was then detected by MALDI-TOF analysis of N-glycan chains or by chemiluminescence (*20*), or coupling to aminooxi Alexa Fluor 488, which was detected by a fluorescence technique after SDS-PAGE and FACS analysis. Both chemiluminescence and fluorescence analysis showed that the method of coupling described here is highly specific; almost all the chemiluminescence and fluorescence from the antibody conjugates were associated with binding to the heavy chain. Thus, the cargo is linked in a site-directed manner and only occurs where the sugar binds in the Fc domain of the IgG.

This study also shows that the linking of the target agent, either biotin or Alexa Fluor 488, to the mAb via the N-linked carbohydrates does not modify the antibody affinity for the antigen. One important goal in using this conjugation method is to generate a delivering agent: an antibody−cargo conjugate that will not interfere in its binding to the target cells. The results from ELISA assays using native mAb showed no detectable loss of antigen (Ag) binding activity. Moreover, all antibodies described in this study, obtained either by removal or by addition of sugars, when conjugated via glycan chains, did not show a loss of Ag binding activity. The Ag binding activity of the Fc-N-glycan modified antibodies was comparable to the results obtained with the native mAb. Also, the results obtained by FACS are consistent with the ELISA assay in that the binding of mAb conjugate to HER-2-expressing cells was not affected by the modification.

In conclusion, the present study describes an enzymatic method for conjugation of monoclonal antibodies at a unique site, away from the Ag binding domain. This method using modified sugars for conjugation provides a specific labeling with 4 molecules of fluorescent dyes if the IgG molecule has free GlcNAc residues available on the Fc N-glycan chains. To our knowledge, this is the first report on the site-specific conjugation of fluoroprobes to the N-linked glycans of intact mAb using an enzymatic method. Other laboratories have reports on the use of molecular imaging probes using mAbs; however, they use chemical conjugation methods, which lead to random labeling (*29, 30*). Thus, this conjugated fluoroprobe may be used as a probe for imaging and clinical applications.

ACKNOWLEDGMENT

We thank Dr. Natalia Mercer for critical reading of the manuscript and Dr. Linda Hsieh-Wilson, CalTech, for helping Dr. Maria Manzoni during the synthesis of UDP-C2-keto-Gal. We also thank Dr. John T. Simpson, Protein Chemistry Laboratory, NCI-Frederick, for helping with mass spectrometric analysis. This project has been funded in part with Federal funds from the National Cancer Institute, National Institutes of Health, under contract no. N01-CO-12400. The content of this publication does not necessarily reflect the view or policies of the Department of Health and Human Services, nor does mention of trade names, commercial products, or organizations imply endorsement by the U.S. Government. This research was supported [in part] by the Intramural Research Program, Center for Cancer Research, National Cancer Institute, NIH.

LITERATURE CITED

(1) Brumlik, M. J., Daniel, B. J., Waehler, R., Curiel, D. T., Giles, F. J., and Curiel, T. J. (2008) Trends in immunoconjugate and ligand receptor-based targeting development for cancer therapy. *Expert Opin. Drug Deliv. 5*, 87–103.

(2) Ross, J. S., Schenkein, D. P., Pietrusko, R., Rolfe, M., Linette, G. P., Stec, J., Stagliano, N. E., Ginsburg, G. S., Symmans, W. F., Pusztai, L., and Hortobagyi, G. N. (2004) Targeted therapies for cancer. *Am. J. Clin. Pathol. 122*, 598–609.

(3) Hamann, P. R. (2005) Monoclonal antibody-drug conjugates. *Expert Opin. Thera. Patents 15*, 1087–1103.

(4) Carter, P. J., and Senter, P. D. (2008) Antibody-drug conjugates for cancer therapy. *Cancer J. 14*, 154–169.

(5) Trail, P. A., King, H. D., and Dubowchik, G. M. (2003) Monoclonal antibody drug immunoconjugates for targeted treatment of cancer. *Cancer Immunol. Immunother. 52*, 328–337.

(6) Arnold, J. N., Dwek, R. A., Rudd, P. M., and Sim, R. B. (2006) Mannan binding lectin and its interaction with immunoglobulins in health and in disease. *Immunol. Lett. 106*, 103–110.

(7) Jefferis, R. (2005) Glycosylation of recombinant antibody therapeutics. *Biotechnol. Prog. 21*, 11–16.

(8) Holland, M., Yagi, H., Takahashi, N., Kato, K., Savage, C. O., Goodall, D. M., and Jefferis, R. (2006) Differential glycosylation of polyclonal IgG, IgG-Fc and IgG-Fab isolated from the sera of patients with ANCA-associated systemic vasculitis. *Biochim. Biophys. Acta 1760*, 669–677.

(9) Hodoniczky, J., Zheng, Y. Z., and James, D. C. (2005) Control of recombinant monoclonal antibody effector functions by Fc N-glycan remodeling in vitro. *Biotechnol. Prog. 6*, 1644–1652.

(10) Shinkawa, T., Nakamura, K., Yamane, N., Shoji-Hosaka, E., Kanda, Y., Sakurada, M., Uchida, K., Anazawa, H., Satoh, M., Yamasaki, M., Hanai, N., and Shitara, K. (2003) The absence of fucose but not the presence of galactose or bisecting *N*-acetylglucosamine of human IgG1 complex-type oligosaccharides shows the critical role of enhancing antibody-dependent cellular cytotoxicity. *J. Biol. Chem. 278*, 3466–3473.

(11) Sharkey, R. M., and Goldenberg, D. M. (2008) Use of antibodies and immunoconjugates for the therapy of more accessible cancers. *Adv. Drug Delivery Rev. 60*, 1407–1420.

(12) Byrne, J. D., Betancourt, T., and Brannon-Peppas, L. (2008) Active targeting schemes for nanoparticle systems in cancer therapeutics. *Adv. Drug Delivery Rev. 60*, 1615–1626.

(13) Garnett, M. C. (2001) Targeted drug conjugates: principles and progress. *Adv. Drug Delivery Rev. 53*, 171–216.

(14) O'Shannessy, D. J., and Quarles, R. H. (1971) Labeling of the oligosaccharide moieties of immunoglobulins. *J. Immunol. Methods 99*, 153–161.

(15) Van Lenten, L., and Ashwell, G. (1971) Studies on the chemical and enzymatic modifications of glycoproteins. A general method for the tritiation of sialic-acid containing glycoprotein. *J. Biol. Chem. 246*, 1889–1894.

(16) Chua, M., Fan, S., and Karush, F. (1984) Attachment of immunoglobulin to liposomal membrane via protein carbohydrate. *Biochim. Biophys. Acta 800*, 291–300.

(17) Morell, A. G., Van den Hamer, C. J., Scheinberg, I. H., and Ashwell, G. (1966) Physical and chemical studies on ceruloplasmin. IV. Preparation of radioactive, sialic acid-free ceruloplasmin labeled with tritium on terminal D-galactose residues. *J. Biol. Chem. 241*, 3745–3749.

(18) Wilchek, M., and Bayer, E. A. (1984) The avidin-biotin complex in immunology. *Immunol. Today 5*, 39–43.

(19) Khidekel, N., Arndt, S., Lamarre-Vincent, N., Lippert, A., Poulin-Kerstien, K. G., Ramakrishnan, B., Qasba, P. K., and Hsieh-Wilson, L. C. (2003) A chemoenzymatic approach toward the rapid and sensitive detection of *O*-GlcNAc posttranslational modifications. *J. Am. Chem. Soc. 125*, 16162–16163.

(20) Boeggeman, E., Ramakrishnan, B., Kilgore, C., Khidekel, N., Hsieh-Wilson, L. C., Simpson, J. T., and Qasba, P. K. (2007)

Direct identification of nonreducing GlcNAc residues on N-glycans of glycoproteins using a novel chemoenzymatic method. *Bioconjugate Chem. 18*, 806–814.
(21) Ramakrishnan, B., Boeggeman, E., and Qasba, P. K. (2007) Novel method for in vitro O-glycosylation of proteins: application for bioconjugation. *Bioconjugate Chem. 18*, 1912–1918.
(22) Qasba, P. K., Boeggeman, E., and Ramakrishnan, B. (2008) Site-specific linking of biomolecules via glycan residues using glycosyltransferases. *Biotechnol. Prog. 24*, 520–526.
(23) Boeggeman, E., Ramakrishnan, B., and Qasba, P. K. (2003) The *N*-terminal stem region of bovine and human ∃1,4-galactosyltransferase I increases the in vitro folding efficiency of their catalytic domain from inclusion bodies. *Prot. Expres. Purif. 30*, 219–220.
(24) Ramakrishnan, B., and Qasba, P. K. (2002) Structure-based design of beta-1,4-galactosyltransferase-I (beta 4Gal-T1) with equally efficient N-Acetylgalactosaminyltransferase activity: point mutation broadens beta 4Gal-T1 donor specificity. *J. Biol. Chem. 277*, 20833–20839.
(25) Snovida, S. I., and Perreault, H. (2007) A 2,5-dihydroxybenzoic acid/N, N-dimethylaniline matrix for the analysis of oligosaccharides by matrix-assisted laser desorption/ionization mass spectrometry. *Rapid Commun. Mass Spectrom. 21* (24), 3711–3715.
(26) Bock, F., Onderka, J., Dietrich, T., Bachmann, B., Kruse, F. E., Paschke, M., Zahn, G., and Cursiefen, C. (2007) Bevacizumab as a potent inhibitor of inflammatory corneal angiogenesis and lymphangiogenesis. *Invest. Ophthalmol. Vis. Sci. 48*, 2545–2552.
(27) Ramakrishnan, B., Boeggeman, E., and Qasba, P. K. (2008) Applications of glycosyltransferases in the site-specific conjugation of biomolecules and the development of a targeted drug delivery system and contrast agents for MRI. *Expert Opin. Drug Delivery 5*, 149–153.
(28) Raju, T. S., Briggs, J. B., Borge, S. M., and Jones, A. J. (2000) Species-specific variation in glycosylation of IgG: evidence for the species-specific sialylation and branch-specific galactosylation and importance for engineering recombinant glycoprotein therapeutics. *Glycobiology 10*, 477–486.
(29) Hama, Y., Urano, Y., Koyama, Y., Choyke, P. L., and Kobayashi, H. (2007) Activatable fluorescent molecular imaging of peritoneal metastases following pretargeting with a biotinylated monoclonal antibody. *Cancer Res. 67*, 3809–3817.
(30) Koyama, Y., Barrett, T., Hama, Y., Ravizzini, G., Choyke, P. L., and Kobayashi, H. (2007) In vivo molecular imaging to diagnose and subtype tumors through receptor-targeted optically labeled monoclonal antibodies. *Neoplasia 9*, 1021–1029.

BC900103P

Violet ZnSe/ZnS as an Alternative to Green CdSe/ZnS in Nanocrystal−Fluorescent Protein FRET Systems

Vitor R. Hering,*[,†] Tanize E. S. Faulin,[‡] Eduardo R. Triboni,[†] Silvio D. Rodriguez,[§] Delia L. Bernik,[§] Robert I. Schumacher,[†] Victor P. Mammana,[||] Adelaide Faljoni-Alario,[⊥] Dulcineia S. P. Abdalla,[‡] Gary Gibson,[#] and Mário J. Politi[†]

Department of Biochemistry, Chemistry Institute, University of São Paulo, São Paulo, SP 05513-970, Brazil, Faculty of Pharmaceutical Sciences, University of São Paulo, São Paulo, SP 05508-900, Brazil, Faculty of Exact and Natural Sciences, University of Buenos Aires, Buenos Aires, BA 1428EGA, Argentina, Renato Archer Information Technology Center, Campinas, SP 13069-901, Brazil, Natural and, Human Sciences Center, Federal University of ABC, Santo André, SP 09210-170, Brazil, and Hewlett-Packard Laboratories, Palo Alto, California 94304. Received March 10, 2009; Revised Manuscript Received April 27, 2009

Fluorescent proteins from the green fluorescent protein family strongly interact with CdSe/ZnS and ZnSe/ZnS nanocrystals at neutral pH. Green emitting CdSe/ZnS nanocrystals and red emitting fluorescent protein dTomato constitute a 72% efficiency FRET system with the largest alteration of the overall photoluminescence profile, following complex formation, observed so far. The substitution of ZnSe/ZnS for CdSe/ZnS nanocrystals as energy donors enabled the use of a green fluorescent protein, GFP5, as energy acceptor. Violet emitting ZnSe/ZnS nanocrystals and green GFP5 constitute a system with 43% FRET efficiency and an unusually strong sensitized emission. ZnSe/ZnS-GFP5 provides a cadmium-free, high-contrast FRET system that covers only the high-energy part of the visible spectrum, leaving room for simultaneous use of the yellow and red color channels. Anisotropic fluorescence measurements confirmed the depolarization of GFP5 sensitized emission.

INTRODUCTION

Semiconductor nanocrystals and fluorescent proteins can be assembled in fluorescence (or Förster) energy transfer (FRET) systems. Both nanocrystals and fluorescent proteins present outstanding properties as biological probes (*1*), and their coupled use provides a research tool of promising potential.

Semiconductor nanocrystals have large absorption cross sections, high photoluminescence (PL) quantum yields (QY), size-tunable PL spectra, exceptional photochemical stability (*2, 3*), and good dispersibility in biological fluids (*3*−*7*). The green fluorescent protein (GFP) family is composed of a group of homologous, colored, compact proteins that spontaneously generate their own fluorophore (*8*−*10*). They have been extensively used as gene-based probes in molecular and cell biology (*11*). The diversity of emission and absorption profiles of these elements provide a variety of possible donor−acceptor FRET pairs.

The nanocrystal−fluorescent protein FRET pairs commonly used to date are composed of green emitting CdSe/ZnS nanocrystals and yellow or red emitting fluorescent proteins (*12*−*15*). Such systems have been used to create three chromophore FRET systems (*13*) and to research cell penetration and nanoparticle mediated drug delivery (*14*).

In the present work, we extend the available nanocrystal−fluorescent protein FRET pairs by substituting the previously used red emitting protein HcRed1 (quantum yield 5% (*12*)) with the high quantum yield dTomato (quantum yield 69% (*16*)) and by introducing ZnSe/ZnS as a cadmium-free, blue-shifted nanocrystal donor substitute for CdSe/ZnS. The CdSe/ZnS−dTomato system exhibits highly efficient FRET with larger overall PL alteration under complex formation than nanocrystal−fluorescent protein pairs used previously (*12*−*15*). ZnSe/ZnS nanocrystals are advantageous not only because they are free of toxic cadmium (*17*), but also because their emission peak is blue-shifted to 400 nm, leaving all color channels from blue to red available for other probes. The ZnSe/ZnS−GFP5 system presents particularly attractive characteristics such as unusually intense sensitized emission and excellent contrast due to the large separation, 100 nm, between donor and acceptor PL peaks.

EXPERIMENTAL PROCEDURES

Nanocrystals. Mercaptoundecanoic acid (MUA) coated CdSe/ZnS nanocrystals were purchased from NN Laboratories. The emission spectrum of these CdSe/ZnS nanocrystals is provided in Figure 1. Mercaptopropionic acid (MPA) coated ZnSe/ZnS nanocrystals were synthesized in accordance with a protocol derived from ref 18. MPA was added to 60 mL of Milli-Q water containing 1 mM zinc perchlorate, to a final concentration of 2.4 mM. The pH of the solution was raised to 10.5 by the addition of sodium hydroxide. The solution was then stirred and put under a nitrogen flux for 10 min. In parallel, 9.6 mg of selenium powder and 10 mg of sodium borohydride were mixed in a 15 mL Falcon flask. To this mixture 2 mL of Milli-Q water was added, and the solution was sonicated for 5 min, keeping the Falcon's cap loose to let the evolving gas escape. 0.5 mL of this solution was injected in the zinc perchlorate solution and stirred. Thirty milliliters of the resulting solution were collected and poured inside a 50 mL total volume Teflon-lined autoclave. The Teflon set was then placed inside an oven at 70 °C for 24 h. 0.85 mL of the autoclaved solution was collected and placed inside a 1 mL quartz cuvette. 4.4 μL of MPA were diluted in 1 mL of Milli-Q water containing 0.1 mM sodium hydroxide, and 0.15 mL of this solution was also

* Corresponding author. E-mail: vrhering@uol.com.br. Phone number: 55 11 8335 5536.
[†] Chemistry Institute, University of São Paulo.
[‡] Faculty of Pharmaceutical Sciences, University of São Paulo.
[§] University of Buenos Aires.
[||] Renato Archer Information Technology Center.
[⊥] Federal University of ABC.
[#] Hewlett-Packard Laboratories.

10.1021/bc9001085 CCC: $40.75 © 2009 American Chemical Society
Published on Web 05/27/2009

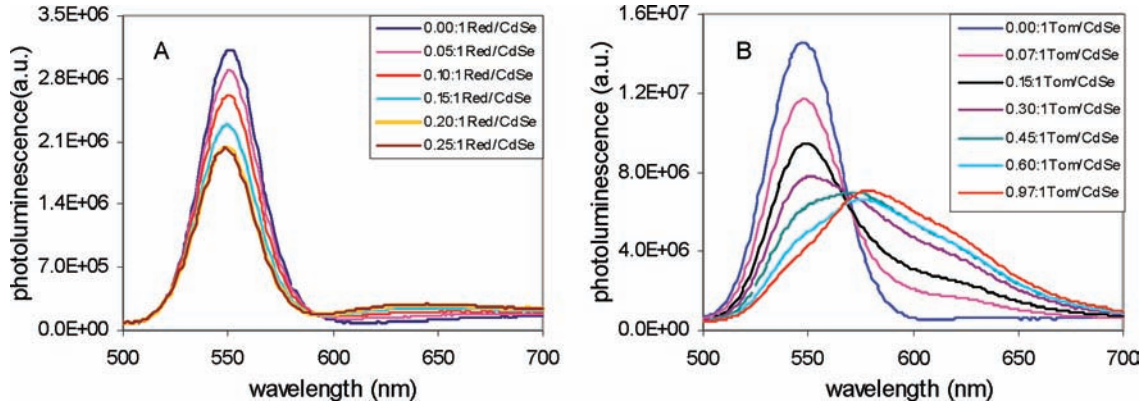

Figure 1. (A) Evolution of the photoluminescence spectra of CdSe/ZnS nanocrystals in CdSe/ZnS-HcRed1 ("Red") assemblies versus increasing HcRed1 to CdSe/ZnS molar ratio. (B) Evolution of the photoluminescence spectra of CdSe/ZnS nanocrystals in CdSe/ZnS−dTomato assemblies versus increasing dTomato to CdSe/ZnS molar ratio.

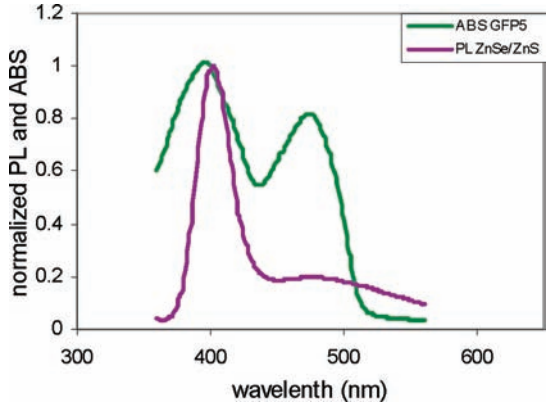

Figure 2. Normalized photoluminescence (PL) spectrum of ZnSe/ZnS nanocrystals and absorption (ABS) spectrum of GFP5 solutions.

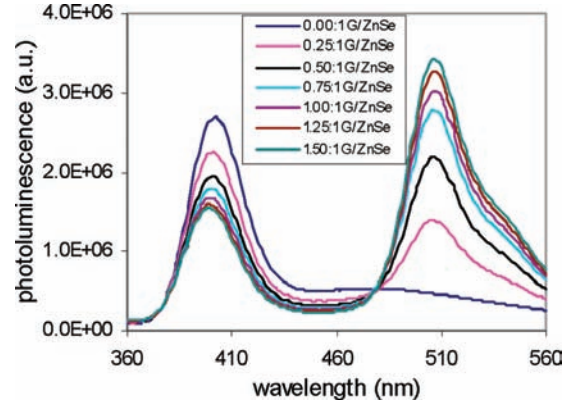

Figure 3. Evolution of the photoluminescence spectra of ZnSe/ZnS-GFP5 assemblies versus increasing GFP5 (G) to ZnSe/ZnS molar ratio. Excitation at 310 nm, pH 7.4.

added to the quartz cuvette. The cuvette was then capped and placed 20 cm from a commercial 27 W UV light (emission peak at 370 nm) inside an oven held at 60 °C, where it was kept for 4 h. Absorption and emission spectra of the ZnSe/ZnS nanocrystals are shown in Figures 2 and 5. The approximate concentration, 2.7 nM, and diameter, 3 nm, of the nanocrystals were inferred in accordance to *refs* 19 *and* 20. The quantum yield of the colloidal solution, 50%, was estimated by comparison with quinine in aqueous 0.5 M sulfuric acid (quantum yield: 54.5% (*21*)).

Fluorescent Proteins. HcRed1 on plasmid pHcRed1 was purchased from Clontech. Plasmid pHcRed1 was used without modifications. HcRed1 does not encode a hexa-histidine sequence. dTomato was generously provided by R. Y. Tsien (University of California at San Diego) on plasmid pRSET-B dTomato. pRSET-B (Invitrogen) encodes a hexa-histidine sequence at the N-terminus of the dTomato coding sequence. pRSET-B dTomato plasmid was used without modification. GFP5 was generously provided by J. Haseloff (University of Cambridge) on plasmid pBIN m-GFP5-ER. The gene encoding GFP5 was excised by digestion with *Eco*RI and *Sac*I and ligated in the same sites at the multiple cloning site of the pET-28a (+) (Novagen). pET-28a (+) also encodes a hexa-histidine sequence at the N-terminus of the GFP5 coding sequence. Each plasmid was respectively introduced into BL21(DE3) *E. coli* cells (Invitrogen) and expression induced with 0.16 mM isopropyl-β-D-thiogalactopyranoside (IPTG, Sigma) for 20 h at 30 °C, before harvesting the cells by centrifugation. His-tagged proteins were purified from soluble cell lysates using Ni-NTA Resin (Qiagen) eluted with 500 mM imidazole and dialyzed. The absorption spectrum of GFP5 is shown in Figure 2. Figure 3 shows the emission spectrum of the ZnSe/ZnS-GFP5 system as a function of the GFP5 (G) to ZnSe/ZnS molar ratio.

Nanocrystal−Fluorescent Protein Conjugates. To assemble CdSe/ZnS-HcRed1 and CdSe-dTomato, the proteins at the appropriate molar ratios were added to 33 nM of CdSe/ZnS (capped with MUA) in 5 mM phosphate, 5 mM NaCl, pH 6 at room temperature. To assemble ZnSe/ZnS-GFP5, GFP5 at the appropriate molar ratios was added to 120 nM of ZnSe/ZnS (capped with MPA) in phosphate buffered saline (137 mM NaCl, 10 mM phosphate, 2.7 mM KCl, pH 7.4, PBS) at room temperature. Conjugates were characterized through the quenching of the nanocrystals' fluorescence and enhancement of the proteins' fluorescence, which was monitored by measuring the steady-state fluorescence using a SPEX Fluorolog 1691 (Spex industries) spectrophotometer equipped with a 450 W Xenon lamp. The SPEX software MCORRECT.SPT was used to correct the responsivity of the spectrophotometer. Polarizers were introduced into the SPEX to measure the polarization anisotropy (r). Anisotropy was calculated using the equation:

$$r = \frac{VV - gVH}{VV + 2gVH}$$

Vertically polarized excitation of the donor was used in combination with capture of both horizontal (*VH*) and vertical (*VV*) polarizations. The factor g corrects for polarization bias in the instrument (*22*, *23*). g was calculated using the equation

$$g = \frac{HV}{HH}$$

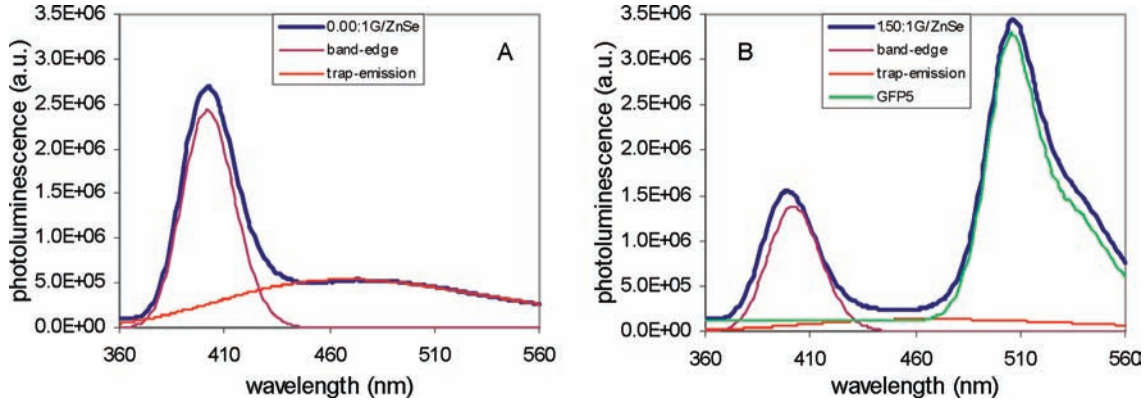

Figure 4. (A) Deconvolution of the ZnSe/ZnS nanocrystals photoluminescence spectrum with two Gaussians corresponding to band-edge and trap emission. (B) Deconvolution of the ZnSe/ZnS−GFP assembly photoluminescence spectrum at GFP5 (G) saturation.

In this case, horizontally polarized excitation of the donor was used in combination with capture of both vertical (*HV*) and horizontal (*HH*) polarizations.

RESULTS AND DISCUSSION

We have previously reported the occurrence of FRET from green emitting CdSe/ZnS nanocrystals to the red emitting protein HcRed1 (*12*), as shown in Figure 1A. At that time it was pointed out that the low quantum yield of HcRed1, 5%, was the reason for the weak intensity of the sensitized emission. We have now replaced HcRed1 with the red emitting protein dTomato (*16*), which has a quantum yield of 69%, and a substantial increase of the sensitized emission intensity was observed, as shown in Figure 1B.

In both cases, the titration was conducted at pH 6. The FRET efficiency for the pair CdSe/ZnS−dTomato, calculated by using the relative fluorescence intensity of the donor, in the absence and presence of acceptor is 72% (*22*). The strong overall fluorescence transition undergone by the CdSe/ZnS−dTomato system during complex formation makes it an excellent tool for FRET-based characterization.

Bulk CdSe exhibits band gap emission centered at 713 nm. Due to quantum confinement, it is possible to tune the emission of CdSe nanocrystals over the visible spectrum by controlling their diameter. However, blue emitting CdSe nanocrystals require very small diameters, which renders them unstable and restricts their commercial availability (*20*). This limitation is the primary reason there are no reports of CdSe nanocrystals as FRET donors in the blue spectral region. To overcome this limitation, we have substituted CdSe nanocrystals. Bulk ZnSe emits at 459 nm, and there are a large number of references reporting aqueous synthesis of efficient ZnSe/ZnS nanocrystals (*18*, *20*, *24*). We decided to synthesize ZnSe/ZnS nanocrystals at our lab, which demanded a considerable effort in refining the available protocols and adapting them to the lab conditions. At pH 10.5, immediately after synthesis, our nanocrystals presented a quantum yield of 50%, with emission centered at 400 nm. The quantum yield slowly decreases with time and was 25% one month after synthesis. Such a decrease in quantum yield is possibly related to the long-term dynamics undergone by the MPA ligand at the nanocrystal surface (*25*). ZnSe/ZnS nanocrystals are promising candidates for FRET donors at the shorter wavelength end of the visible spectrum. Moreover, the violet emission of these nanocrystals overlaps well with the GFP5 absorption spectrum, as can be seen in Figure 2. GFP5 is a mutant form of GFP especially designed to be expressed in *E. coli* (*26*).

Unlike the MUA coated CdSe/ZnS nanocrystals, the lab synthesized ZnSe/ZnS nanocrystals were coated with MPA. MPA, however, confers poor protection for pH changes. At a pH below 7, the ZnSe/ZnS nanocrystals barely fluoresce. Consequently, assays with ZnSe/ZnS were made in PBS buffer at pH 7.4, whereas assays made with CdSe/ZnS nanocrystals had been conducted at pH 6. At pH 7.4, the ZnSe/ZnS nanocrystals present a quantum yield of 15%, which is substantially smaller than the quantum yield of 50% at pH 10.5 but is still satisfactory for FRET characterization, as can be seen in Figure 3. Actually, there is a tradeoff between lowering the pH to increase the electrostatic attraction among nanocrystals and fluorescent proteins (*12*) and augmenting the pH to increase the nanocrystal fluorescence quantum yield. As a compromise, we decided to conduct the assays at an intermediate pH value, 7.4.

The calculated FRET efficiency using the relative fluorescence intensity of the donor, in the absence and presence of acceptor, is 43% (*22*). Despite the lower FRET efficiency when compared to the CdSe/ZnS−dTomato pair, the high intensity of the sensitized emission is an outstanding characteristic of the new system. GFP5 has an elevated quantum yield, 77% (*26*, *27*), and the nanocrystals, at pH 7.4, have a quantum yield of only 15%. Probably, some of the nanocrystal energy is being rapidly transferred to the GFP5 before it is emitted or nonradiatively recombined, causing the substantial enhancement of the GFP5 emission (*28*). Bidentate anchors like dihydrolipoic acid (DHLA) confer superior stability for the nanocrystals than single sulfur molecules like MPA, improving their quantum yield at neutral pH (*13*, *14*). Tests are being conducted to verify the effect of DHLA on the energy transfer among ZnSe/ZnS and GFP5. Preliminary results show that the addition of 5 mM DHLA, after the UV processing, immediately increases the nanocrystal emission intensity as well as has a positive effect on retaining the nanocrystal quantum yield at neutral pH. Studies concerning the long-term stability and dilution effects over the nanocrystal quantum yield at neutral pH are being conducted.

The ZnSe/ZnS nanocrystal emission spectrum has two components, one related to the band-edge emission, centered at 402 nm, and the other related to the trap emission, centered at 468 nm (*18*), which can be represented by two Gaussians, as shown in Figure 4A. In Figure 4B, the two Gaussians, together with a curve corresponding to pure GFP5, are used to deconvolute the emission spectrum of a ZnSe/ZnS−GFP5 assembly at a saturating concentration of GFP5. Analyzing Figure 4B, two considerations were made. First, the nanocrystals suffer a blue shift of 3 nm when put into close proximity to GFP5, which is characteristic of an environment change at the nanocrystal surface (*15*). Second, comparing the deconvolution curves for the emission spectra of ZnSe/

ZnS alone and for the assembly ZnSe/ZnS−GFP5 it comes out that the deconvolution factor for the trap emission was more strongly reduced, 75%, than the deconvolution factor for the band-edge emission, which was reduced by only 43%, possibly because the ratio of the Förster exchange rate from the traps to the GFP5 is proportionally larger than the Förster exchange rate from the band-edge states to the GFP5. In spite of the possible high trap emission Förster exchange rate, we intend to improve the postprocessing protocol for the ZnSe/ZnS nanocrystals to further reduce the trap emission. As can be seen in Figure 4B, the trap emission causes a signal contamination in the GFP5 emission spectrum, and its elimination would override any spectral overlapping, further improving the resolution of this FRET system.

The ZnSe/ZnS−GFP5 constitutes a sensitive and well-resolved, cadmium-free nanocrystal−fluorescent protein FRET system. Moreover, due to its low wavelength position in the visible spectrum, this system is particularly suitable for extension to a multifluorophore FRET system. For example, GFP5 emits at 506 nm, and a ternary FRET system having yellow fluorescent protein as the second energy acceptor can be envisioned. Such a system would include FRET among fluorescent proteins along with nanocrystal donors. Multifluorophore FRET systems are useful for the elucidation of multicomponent molecular assemblies, characteristic of highly coordinated biological supramolecular interactions (*13*).

The enhanced fluorescence emission of GFP5 was also characterized by polarization fluorimetry to confirm the FRET. The direct emission of fluorescent proteins is highly polarized, while the depolarization of its fluorescence is observed only in the presence of energy transfer (*22*, *23*). This characteristic provides the means to detect the FRET with great accuracy in high-throughput screening assays (*23*). In Figure 5, it is possible to verify that the anisotropy of GFP5 complexed with the ZnSe/ZnS tends to zero when the absorption of the nanocrystals becomes strong, i.e., when the emission of GFP5 is mainly due to energy transfer. The anisotropy of GFP5 alone, on the other hand, is essentially wavelength independent.

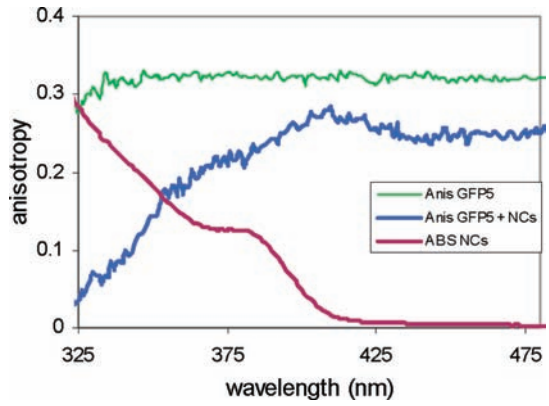

Figure 5. Steady-state anisotropy was calculated from fluorescence excitation spectra with emission set at 506 nm for solutions containing GFP5 alone and GFP5 complexed with ZnSe/ZnS nanocrystals. The absorbance spectrum of the nanocrystals is also depicted.

ACKNOWLEDGMENT

The authors thank Dr. Jim Haseloff for providing the gene coding for GFP5 and Dr. R. Y. Tsien for providing the gene coding for dTomato. The authors wish to express their gratitude to the Brazilian funding agencies CNQP, FAPESP, CAPES, and CONICET being also thankful for the support from the Biochemistry Department of the Chemistry Institute of the University of São Paulo, Brazil.

LITERATURE CITED

(1) Giepmans, B. N. G., Adams, S. R., Ellisman, M. H., and Tsien, R. Y. (2006) The fluorescent toolbox for assessing protein location and function. *Science 312*, 217–224.

(2) Wagnier, R., Baranov, A. V., Maslov, V. G., Stsiapura, V., Artemyev, M., Pluot, M., Sukhanova, A., and Nabiev, I. (2004) Energy transfer in aqueous solutions of oppositely charged CdSe/ZnS Core/Shell quantum dots and in quantum dot-nanogold assemblies. *Nano Lett. 4*, 451–457.

(3) Dabbousi, B. O., Rodriguez-Viejo, J., Mikulec, F. V., Heine, J. R., Mattoussi, H., Ober, R., Jensen, K. F., and Bawendi, M. G. (1997) (CdSe)ZnS Core-Shell quantum dots: synthesis and characterization of a size series of highly luminescent nanocrystallites. *J. Phys. Chem. B 101*, 9463–9475.

(4) Ma, J., Chen, J., Guo, J., Wang, C. C., Yang, W. L., Xu, L., and Wang, P. N. (2006) Photostability of thiol-capped CdTe quantum dots in living cells: the effect of photo-oxidation. *Nanotechnology 17*, 2083–2089.

(5) Sukhanova, A., Devy, J., Venteo, L., Kaplan, H., Artemyev, M., Oleinikov, V., Klinov, D., Pluot, M., Cohen, J. H. M., and Nabiev, I. (2004) Biocompatible fluorescent nanocrystals for immunolabeling of membrane proteins and cells. *Anal. Biochem. 324*, 60–67.

(6) Wenhua, L., Haiyan, X., Zhixiong, X., Zhexue, L., Jianhong, O., Xiangdong, C., and Ping, S. (2004) Exploring the mechanism of competence development in Escherichia coli using quantum dots as fluorescent probes. *J. Biochem. Biophys. Methods 58*, 59–66.

(7) Dubertret, B., Skourides, P., Norris, D. J., Noireaux, V., Brivanlou, A. H., and Libchaber, A. (2002) In vivo imaging of quantum dots encapsulated in phospholipid micelles. *Science 298*, 1759–1762.

(8) Wachter, R. M. (2006) The family of GFP-like proteins: structure, function, photophysics and biosensor applications. Introduction and perspective. *Photochem. Photobiol. 82*, 339–344.

(9) Ormo, M., Cubitt, A. B., Kallio, K., Gross, L. A., Tsien, R. Y., and Remington, S. J. (1996) Crystal structure of the Aequorea victoria green fluorescent protein. *Science 273*, 1392–1395.

(10) Yang, F., Moss, L. G., and Phillips, G. N. (1996) The molecular structure of green fluorescent protein. *Nat. Biotechnol. 14*, 1246–1251.

(11) Tsien, R. Y. (1998) The green fluorescent protein. *Annu. Rev. Biochem. 67*, 509–544.

(12) Hering, V. R., Gibson, G., Schumacher, R. I., Faljoni-Alario, A., and Politi, M. J. (2007) Energy transfer between CdSe/ZnS core/shell quantum dots and fluorescent proteins. *Bioconjugate Chem. 18*, 1705–1708.

(13) Lu, H., Schps, O., Woggon, U., and Niemeyer, C. M. (2008) Self-assembled donor comprising quantum dots and fluorescent proteins for long-range fluorescence resonance energy transfer. *J. Am. Chem. Soc. 130*, 4815–4827.

(14) Medintz, I. L., Pons, T., Delehanty, J. B., Susumo, K., Brunel, F. M., Dawson, P. E., and Mattoussi, H. (2008) Intracellular delivery of quantum dot-protein cargos mediated by cell penetrated peptides. *Bioconjugate Chem. 19*, 1785–1795.

(15) Geissbuehler, I., Hovius, R., Martinez, K. L., Adrian, M., Thampi, K. R., and Vogel, H. (2005) Lipid-coated nanocrystals as multifunctionalized luminescent scaffolds for supramolecular biological assemblies. *Angew. Chem., Int. Ed. 44*, 1388–1392.

(16) Shaner, N. C., Steinbach, P. A., and Tsien, R. Y. (2005) A guide to choosing fluorescent proteins. *Nat. Meth. 2*, 905–909.

(17) Pradhan, N., Goorskey, D., Thessing, J., and Peng, X. (2005) An alternative of CdSe nanocrystal emitters: pure and tunable impurity emissions in ZnSe nanocrystals. *J. Am. Chem. Soc. 127*, 17586–17587.

(18) Lan, G. Y., Lin, Y. W., Huang, Y. F., and Chang, H. T. (2007) Photo-assisted synthesis of highly fluorescent ZnSe(S) quantum dots in aqueous solution. *J. Mater. Chem. 17*, 2661–2666.

(19) Shim, M., and Guyot, S. (1999) Permanent dipole moment and charges in colloidal semiconductor quantum dots. *J. Chem. Phys. 11*, 6955–6964.

(20) Reiss, P. (2007) ZnSe based colloidal nanocrystals: synthesis, shape control, core/shell, alloy and doped systems. *New J. Chem. 31*, 1843–1852.

(21) Wrighton, M. S., Ginley, D. S., and Morse, D. L. (1974) Technique for the determination of absolute emission quantum yields of powdered samples. *J. Phys. Chem. 78*, 2229–2232.

(22) Lakowicz, J. R. (2006) *Principles of Fluorescence Spectroscopy*, 3rd ed., Springer, Berlin.

(23) Rizzo, M. A., and Piston, D. W. (2004) High-contrast imaging of fluorescent protein FRET by fluorescence polarization microscopy. *Biophys. J.: Biophys Lett.* L14–L16.

(24) Li, C. L., Nishikawa, K., Ando, M., Enomoto, H., and Murase, N. (2007) Highly luminescent water-soluble ZnSe nanocrystals and their incorporation in a glass matrix. *Colloids Surf., A 294*, 33–39.

(25) Wang, C. L., Zhang, H., Zhang, J., Lv, N., Li, M., Sun, H., and Yang, B. (2008) Ligand dynamics of aqueous CdTe nanocrystals at room temperature. *J. Phys. Chem. C 112*, 6330–6336.

(26) Siemering, K. R., Golbik, R., Sever, R., and Haseloff, J. (1996) Mutations that suppress the thermosensitivity of green fluorescent protein. *Curr. Biol. 6*, 1653–1663.

(27) Heim, R., and Tsien, R. Y. (1996) Engineering green fluorescent protein for improved brightness, longer wavelengths and fluorescence energy transfer. *Curr. Biol. 6*, 178–182.

(28) Clapp, A. R., Medintz, I. L., Mauro, J. M., Fisher, B. R., Bawendi, M. G., and Mattoussi, H. (2004) Fluorescence resonance energy transfer between quantum dot donors and dye-labeled protein acceptors. *J. Am. Chem. Soc. 126*, 301–310.

BC9001085

Design, Synthesis, and Biological Evaluation of Antibody−Drug Conjugates Comprised of Potent Camptothecin Analogues

Patrick J. Burke,*[,†] Peter D. Senter,[†] David W. Meyer,[†] Jamie B. Miyamoto,[†] Martha Anderson,[†] Brian E. Toki,[†] Govindarajan Manikumar,[‡] Mansukh C. Wani,[‡] David J. Kroll,[§] and Scott C. Jeffrey[†]

Seattle Genetics, Inc., 21823 30th Drive SE, Bothell, Washington 98021, Research Triangle Institute, Natural Products Laboratory, Research Triangle Park, North Carolina 27709, and North Carolina Central University, Pharmaceutical Sciences, BRITE, Durham, North Carolina 27707. Received March 12, 2009; Revised Manuscript Received April 10, 2009

Antibody−drug conjugates (ADCs) were prepared with potent camptothecin analogues attached to monoclonal antibodies (mAbs) via dipeptide or glucuronide-based linkers. Aniline-containing camptothecin analogues were employed to provide a site of linker attachment via carbamate bonds that would be stable in circulation. The camptothecin analogues, 7-butyl-10-amino-camptothecin and 7-butyl-9-amino-10,11-methylenedioxy-camptothecin, are generally 10−1000 times more potent than camptothecin. Dipeptide and glucuronide drug linkers were employed containing self-immolative spacers that release drug following lysosomal degradation upon ADC internalization into antigen-positive cell lines. The camptothecin drug linkers were conjugated to three antibodies: chimeric BR96, chimeric AC10, and humanized 1F6, which bind to the Lewis-Y antigen on carcinomas, CD30 on hematologic malignancies, and CD70 present on hematologic malignancies and renal cell carcinoma, respectively. ADCs bearing the potent camptothecin analogue, 7-butyl-9-amino-10,11-methylenedioxy-camptothecin, were highly potent and immunologically specific on a panel of cancer cell lines in vitro, and efficacious at well-tolerated doses in a renal cell carcinoma xenograft model.

INTRODUCTION

In an attempt to enhance activity and mitigate toxicity of cancer chemotherapy, there has been a great deal of interest in the use of monoclonal antibodies (mAbs) for the targeted delivery of cytotoxic agents to cancer cells (*1*−*3*). The principle behind this approach is that, by covalent attachment of a cytotoxic drug to a mAb that binds selectively to a tumor-specific antigen, the activity of the drug could be enhanced through high intratumoral concentrations while sparing normal, nontarget tissue from indiscriminant damage. Early-generation ADCs[1] have demonstrated that several parameters are important for efficient targeted cell kill, such as drug potency, drug linker stability, efficient on-target drug release, mAb immunogenicity, and normal tissue expression of the tumor antigen (*1*−*3*). More recently, significant progress in ADC design has led to the clinical advancement of two new immunoconjugates: SGN-35 for CD30-positive hematologic malignancies (*3*−*5*) and trastuzumab-DM1 for HER2-positive metastatic breast cancer (*6, 7*). In phase I clinical trials both ADCs induced tumor regressions at well-tolerated doses (*6, 8*−*10*), providing further validation of the use of ADCs as an emerging treatment modality.

We are interested in all classes of drugs that may be suitable for empowering mAbs. Early immunoconjugates used clinically approved cytotoxic agents due to their availability and known toxicological properties. This approach is exemplified by BR96-doxorubicin ADC targeted to the Lewis-Y antigen present on human carcinomas. Doxorubicin was attached to the mAb via an acid-sensitive hydrazone linker, and free drug was released upon ADC internalization into acidic lysosomes (*11*). In vivo efficacy was observed in tumor-bearing mice, albeit at elevated (>100 mg ADC/kg) dose levels. Clinical trials revealed low levels of activity in patients with Lewis-Y positive carcinomas (*11*−*13*). The limitations associated with this ADC included drug linker instability, antigen expression on normal tissues, and low drug potency. It has been proposed that optimized ADCs must address these issues to achieve maximal therapeutic efficacy (*1, 2*).

As part of our search for new chemotypes suitable for use in ADCs, we sought to evaluate conjugates consisting of potent camptothecin (CPT) analogues. Camptothecin (**1**) is a natural product that exerts cytotoxic activity through the inhibition of topoisomerase I, leading to cell death (*14*). As a consequence of its broad-spectrum antitumor activity and cytotoxic mechanism, there has been a substantial effort toward the development of clinical camptothecin analogues. To date, two water-soluble analogues have received FDA approval: topotecan and irinotecan. Topotecan is used primarily in the treatment of advanced ovarian cancer and non-small cell lung cancer and was recently approved for cervical cancer (*15*). Irinotecan is a prodrug that is converted into SN-38, a more potent CPT analogue, under the action of carboxylesterases (*16*) and is used primarily in the treatment of colorectal cancer (*15*). Clinical studies with irinotecan, topotecan, and other camptothecin analogues in development indicate that optimal efficacy is achieved with dosing regimens that provide for prolonged exposure to low levels of camptothecin (*17*). This suggests that camptothecin, or potent CPT analogues, may be ideally suited for mAb targeting, as antibodies often have extended circulation half-lives, ranging from many days to weeks (*1, 3*).

* To whom correspondence should be addressed. Phone: 425-527-4766; Fax: 425-527-4109; email: pburke@seagen.com.

† Seattle Genetics, Inc.

‡ Research Triangle Institute.

§ North Carolina Central University.

[1]Abbreviations: ADC, antibody-drug conjugate; AUC, area under the curve; CPT, camptothecin; DIPEA, *N*,*N*-diisopropylethylamine; DMF, dimethylformamide; DMSO, dimethyl sulfoxide; DOX, doxorubicin; ES, electrospray; IC_{50}, concentration that inhibits 50% cell growth; mAb, monoclonal antibody; mc-val-cit, maleimidocaproyl-valine-citrulline; NHS, *N*-hydroxysuccinimide; PABA, *para*-aminobenzyl alcohol; PBS, phosphate-buffered saline; SCID, severe combined immunodeficient; THF, tetrahydrofuran.

10.1021/bc9001097 CCC: $40.75 © 2009 American Chemical Society
Published on Web 05/26/2009

An ADC of CPT has already been described (*18*). It was found that BR96-CPT had a similar level of potency as BR96-DOX (*18, 19*). In addition, the CPT-containing ADC was relatively unstable, due to the use of a labile carbonate linker (*18*). Other camptothecin ADCs bearing SN-38 were more potent, but were also composed of labile linkers (*20*). On the basis of our previous work with optimized auristatin-containing ADCs (*4*), we felt that it was necessary to use camptothecin analogues with much higher potency than CPT, and to incorporate linkers that provide high serum stability.

Camptothecins have been subjected to extensive structure−activity relationship studies (*21*), which indicate that 7-position alkyl substituents and a methylenedioxy group spanning the 10 and 11 positions confer enhanced biochemical and cellular potency (*22, 23*). The selected camptothecin analogues, 7-butyl-10-amino-CPT (**2**) and the des-amino precursor (**12**) to 7-butyl-9-amino-10,11-methylenedioxy-CPT (**3**), are substantially more potent (1−3 logs) than camptothecin (*22, 24, 25*). These molecules are ideally suited for ADC application, not only because of their potencies, but also because they (**2** and **3**) contain functional groups that allow for stable mAb attachment. We now report the design, synthesis, and biological evaluation of ADCs comprising highly potent camptothecin analogues. This investigation resulted in CPT ADCs that were well-defined, potent, and immunologically specific in vitro and displayed good in vivo efficacy at well-tolerated doses.

EXPERIMENTAL PROCEDURES

General Methods and Materials. All commercially available anhydrous solvents were used without further purification and were stored under a nitrogen atmosphere. NMR spectral data were collected on a Varian Mercury 400 MHz spectrometer. Chemical shifts (δ) were reported in ppm and referenced off the deuterium solvent signal. Coupling constants (*J*) are reported in hertz. Mass spectral data were obtained on a ZMD Micromass mass spectrometer interfaced to an HP Agilent 1100 HPLC instrument configured for LC-MS analysis. 7-Butyl-10-amino-camptothecin (**2**) and 7-butyl-10,11-methylenedioxy-camptothecin (**12**) were prepared via Friedlander condensation as previously described (*23*).

Analytical HPLC was performed on two different HPLC systems. Data collected by "gradient A" were obtained on an HP Agilent 1100 HPLC equipped with a C12 Phenomenex Synergi 2.0 × 150 mm, 4 μm, 80 Å reverse-phase column. The acidic eluent consisted of a linear gradient of acetonitrile from 5% to 95% in 0.1% aqueous formic acid over 10 min, followed by isocratic 95% acetonitrile for 5 min (flow rate = 0.4 mL/min). Data collected by "gradient B" were obtained on a Waters 2690 HPLC interfaced with a Waters 996 PDA and Millenium[32] software. Samples were eluted over a C12 Phenomenex Synergi 2.0 × 150 mm, 4 μm, 80 Å reverse-phase column. The neutral eluent consisted of a linear gradient of acetonitrile from 10% to 90% in 5 mM ammonium phosphate pH 7 over 10 min, followed by isocratic 90% acetonitrile for 5 min (flow rate = 1.0 mL/min).

Preparative HPLC was carried out on a Varian ProStar 210 solvent delivery system configured with a Varian ProStar 330 PDA detector. Products were purified over a C12 Phenomenex Synergi 10.0 × 250 mm, 4 μm, 80 Å reverse-phase column eluting with 0.05% TFA in water (solvent A) and 0.05% TFA in acetonitrile (solvent B). Purification Method A consisted of the following gradient of solvent A to solvent B: 90:10 from 0 to 5 min; 90:10 to 40:60 from 5 to 45 min; 40:60 to 10:90 from 45 to 50 min; followed by isocratic 10:90 for 5 min. The flow rate was 4.6 mL/min with monitoring at 254 nm. Purification Method B consisted of the following gradient of solvent A to

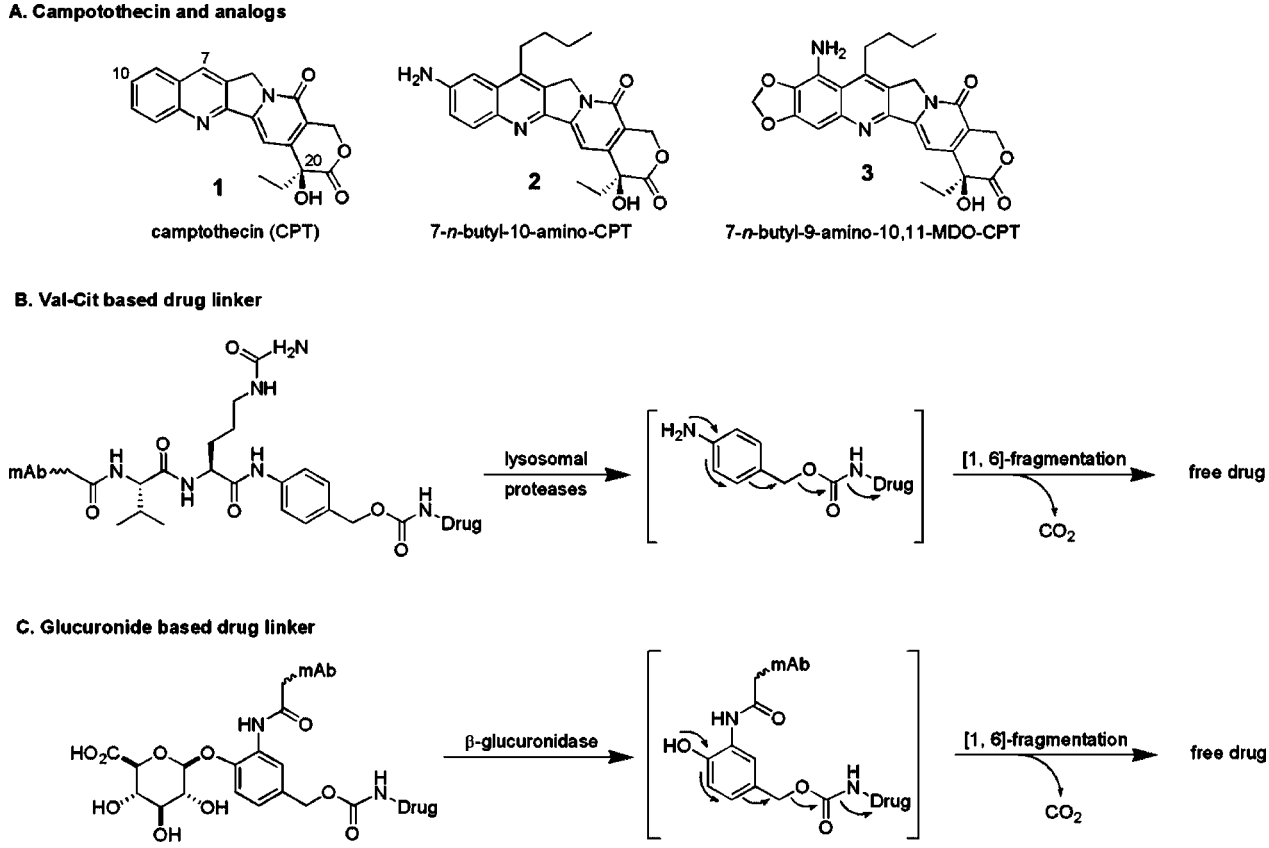

Figure 1. Structures and mechanism of release of active CPT drugs; (A) camptothecin and potent analogues prepared via Friedlander condensation; (B) val-cit dipeptide based drug linker; (C) glucuronide based drug linker.

solvent B: isocratic 90:10 from 0 to 5 min; 90:10 to 60:40 from 5 to 45 min; 60:40 to 10:90 from 45 to 50 min; followed by isocratic 10:90 for 5 min. The flow rate was 4.6 mL/min with monitoring at 254 nm.

Analytical thin layer chromatography was performed on silica gel 60 F_{254} aluminum sheets (EMD Chemicals, Gibbstown, NJ). Whatman 60 Å 230−400 mesh silica gel was used for flash chromatographic purification. Radial chromatography was performed on a Chromatotron instrument (Harris Research, Palo Alto, CA).

7-Butyl-9-amino-10,11-methylenedioxy-camptothecin (3). To a stirred solution of 7-butyl-10,11-methylenedioxy-camptothecin (**12**, 50 mg, 112 μmol) was added 2 mL of concentrated sulfuric acid. The reaction was cooled to 0 °C and sodium nitrate (14 mg, 166 μmol) was added. The reaction was warmed to room temperature and stirred for 30 min, at which time LC/MS revealed complete conversion to product. The reaction was then poured into ice-water and extracted with methylene chloride. The combined extracts were washed with water and concentrated under reduced pressure to provide the nitrated material (54 mg, 98%). UV λ_{max}: 225, 305, and 385 nm. LC-MS: *m/z* (ES^+) found 494.14 $(M+H)^+$, *m/z* (ES^-) found 492.10 $(M-H)^-$. The material was carried forward without further characterization. A stirred solution of the nitrated material (54 mg, 110 μmol) in ethanol was warmed to facilitate dissolution, and then the reaction vessel was purged with nitrogen. At room temperature, 10% palladium on carbon (100 mg) was added, and the reaction mixture was exposed to a hydrogen atmosphere. After 30 min, LC-MS indicated conversion to product. The reaction was filtered through a plug of Celite that was subsequently washed with 300 mL methanol. The filtrate was concentrated under reduced pressure and purified by radial chromatography on a 1 mm plate eluted with a CH_2Cl_2/MeOH mixture (97:3 to 95:5 CH_2Cl_2/MeOH) to provide **3** (29 mg, 57%). ^1H NMR ($CDCl_3$) δ (ppm): 1.02 (m, 6H), 1.57 (m, 3H, under HOD), 1.82 (m, 2H), 1.87 (m, 3H), 3.35 (m, 3H), 3.73 (m, 1H), 5.21 (s, 1H), 5.22 (s, 1H), 5.51 (AB, $J = 16.4$ Hz, 2H), 6.17 (d, $J = 2.0$ Hz, 2H). UV λ_{max} 229, 280, 335, and 381 nm. Analytical HPLC: gradient A, t_R = 12.56 min, $AUC_{255} = 97.9\%$; gradient B, $t_R = 8.35$ min, $AUC_{255} = 97.5\%$. LC-MS: *m/z* (ES^+) found 464.00 $(M+H)^+$, *m/z* (ES^-) found 461.97 $(M-H)^-$.

4-((*S*)-2-((*S*)-2-(6-(2,5-Dioxo-2*H*-pyrrol-1(5*H*)-yl)hexanamido)-3-methylbutanamido)-5-ureidopentanamido)benzyl-(7-butyl-10-aminocamptothecin)carbamate (4). An oven-dried flask was charged with a solution of **2** (10 mg, 23.8 μmol) in 0.5 mL anhydrous CH_2Cl_2. The solution was stirred at room temperature under nitrogen, and 0.4 mL of a 20% phosgene solution in toluene was added. The resultant brown suspension was stirred for 18 h at room temperature. The solution was then evaporated to dryness with a stream of nitrogen gas and further concentrated by rotary evaporation. To the residue obtained was added maleimidocaproyl-valine-citrulline-*para*-aminobenzyl alcohol (**13**, 20.5 mg, 35.7 μmol) (henceforth called mcVal-Cit-PABA (*26*)) dissolved in 0.5 mL anhydrous DMF. The solution was then heated to 45 °C under nitrogen. LC/MS revealed the formation of a product corresponding to the desired molecular weight. The reaction was diluted with 1.5 mL of DMSO and desired product isolated by preparative HPLC (Method A) to give **4** (3.6 mg, 15%). ^1H NMR (DMSO-d_6) δ (ppm): 0.87 (m, 9H), 0.97 (t, $J = 7.6$ Hz, 3H), 1.19 (m, 2H), 1.48 (m, 8H), 1.70 (m, 4H), 1.85 (m, 4H), 2.15 (m, 4H), 3.10 (m, 5H), 4.19 (m, 1H), 4.38 (m, 1H), 5.17 (s, 2H), 5.29 (s, 2H), 5.43 (s, 2H), 5.98 (m, 1H), 7.00 (s, 2H), 7.28 (s, 1H), 7.41 (d, $J = 8.6$ Hz, 2H), 7.65 (d, $J = 8.0$ Hz, 2H), 7.81 (d, $J = 9.2$ Hz, 1H), 7.90 (m, 1H), 8.10 (d, $J = 9.0$ Hz, 2H), 8.43 (s, 2H), 10.03 (s, 1H), 10.27 (s, 1H). UV λ_{max}: 225, 267, and 385 nm. Analytical HPLC: gradient A, $t_R = 12.38$ min, $AUC_{255} = 98.5\%$; gradient B, t_R = 7.81 min, $AUC_{255} = 93.9\%$. LC-MS: *m/z* (ES^+) found 1018.33 $(M+H)^+$, *m/z* (ES^-) found 1017.06 $(M-H)^-$.

4-((*S*)-2-((*S*)-2-(6-(2,5-Dioxo-2*H*-pyrrol-1(5*H*)-yl)hexanamido)-3-methylbutanamido)-5-ureidopentanamido)benzyl-(7-butyl-9-amino-10,11-methylendioxycamptothecin)carbamate (5). Drug linker **5** was prepared from CPT **3** (24 mg, 51.8 μmol) in an analogous reaction to that described for **4**. The crude reaction material was purified by flash chromatography on silica gel eluted with MeOH in CH_2Cl_2 (98:2 to 95:5 to 90:10 CH_2Cl_2/MeOH) to yield **5** (11.2 mg, 20%). ^1H NMR (DMF-d_7) δ (ppm): 0.96 (m, 9H), 1.28 (m, 3H), 1.56 (m, 8H), 2.00 (m, 3H), 2.16 (m, 1H), 2.29 (m, 2H), 3.08 (q, $J = 6.2$ Hz, 1H), 3.26 (m, 3 H), 3.46 (t, $J = 6.8$ Hz, 2H), 4.36 (t, $J = 7.6$ Hz, 1H), 4.63 (bt, 1H), 5.20 (s, 2H), 5.31 (s, 2H), 5.51 (s, 2H), 5.66 (m, 1H), 6.27 (bt, 1H), 6.37 (s, 1H), 6.49 (s, 1H), 7.02 (s, 2H), 7.37 (s, 1H), 7.45 (d, $J = 8.0$ Hz, 1H), 7.55 (s, 1H), 7.84 (d, $J = 8.0$ Hz, 1H), 7.90 (d, $J = 8.4$ Hz, 1H), 8.16 (d, $J = 7.6$ Hz, 1H), 9.37 (s, 1H), 10.11 (s, 1H). UV λ_{max}: 227, 253, and 383 nm. Analytical HPLC: gradient A, $t_R = 12.11$ min, $AUC_{255} = 96.2\%$; gradient B, $t_R = 7.41$ min, $AUC_{255} = 94.9\%$. LC-MS: *m/z* (ES^+) found 1062.45 $(M+H)^+$, *m/z* (ES^-) found 1060.29 $(M-H)^-$.

(2*S*,3*S*,4*S*,5*R*,6*S*)-Methyl 6-(2-(3-(((9*H*-fluoren-9-yl)methoxy)-carbonylamino)propanamido)-4-(((7-butyl-10-aminocamptothecin)carbamoyloxy)methyl)phenoxy)-3,4,5-triacetoxy-tetrahydro-2*H*-pyran-2-carboxylate (6). A flame-dried flask was charged with the known (*27*) protected glucuronide linker fragment (**14**, 28.5 mg, 38.1 μmol) dissolved in 1.5 mL anhydrous CH_2Cl_2. Anhydrous pyridine (37 μL, 457 μmol) was added, and the solution was cooled to −78 °C under a nitrogen atmosphere. Diphosgene (5.5 μL, 46 μmol) was added; the light yellow, limpid solution was stirred for 3 h at −78 °C. A solution of **2** (16.0 mg, 38.1 μmol) in 1.5 mL anhydrous THF was then added, and the reaction was warmed to 0 °C over 1 h. Analytical HPLC at 1 h revealed the formation of product. The reaction was poured into 50 mL EtOAc, and the organic phase was washed with 20 mL water, then 20 mL brine. The organic layer was dried over Na_2SO_4, filtered, and concentrated. The residue so obtained was purified by flash chromatography on silica gel eluted with a CH_2Cl_2/MeOH mixture (98:2 to 97:3 CH_2Cl_2/MeOH) to provide **6** (28.8 mg, 64%). ^1H NMR ($CDCl_3$) δ (ppm) 0.95 (t, $J = 7.6$ Hz, 3H), 0.99 (t, $J = 7.2$ Hz, 3H), 1.46 (m, 3H), 1.66 (m, 3H), 1.86 (m, 3H), 2.03 (s, 3H), 2.05 (s, 6H), 2.73 (m, 2H), 3.05 (q, $J = 8.0$ Hz, 1H), 3.57 (m, 2H), 3.72 (s, 3H), 4.12 (t, $J = 7.2$ Hz, 1H), 4.31 (m, 4H), 5.15 (m, 7H), 5.42 (m, 1H), 5.59 (m, 1H), 5.76 (bt, 1H), 6.95 (d, $J = 8.4$ Hz, 1H), 7.04 (d, $J = 8.0$ Hz, 1H), 7.21 (m, 1H), 7.22 (s, 1H), 7.32 (t, $J = 7.2$ Hz, 2H), 7.52 (d, $J = 7.2$ Hz, 2H), 7.59 (d, $J = 8.4$ Hz, 1H), 7.68 (m, 3H), 8.06 (m, 2H), 8.29 (s, 1H), 8.41 (s, 1H). UV λ_{max}: 267 and 385 nm. LC-MS: *m/z* (ES^+) found 1194.84 $(M+H)^+$, *m/z* (ES^-) found 1192.57 $(M-H)^-$.

(2*S*,3*S*,4*S*,5*R*,6*S*)-Methyl 6-(2-(3-(((9*H*-fluoren-9-yl)methoxy)-carbonylamino)propanamido)-4-(((7-butyl-9-amino-10,11-methylendioxycamptothecin)carbamoyloxy)methyl)phenoxy)-3,4,5-triacetoxy-tetrahydro-2*H*-pyran-2-carboxylate (7). A flame-dried flask was charged with **3** (10 mg, 21 μmol) dissolved in 0.5 mL anhydrous CH_2Cl_2. The solution was stirred at room temperature under nitrogen, and 0.4 mL of a 20% phosgene solution in toluene was added. The reaction was stirred for 18 h at room temperature; a small aliquot of the reaction was quenched with methanol, and the methyl carbamate (indicating formation of the isocyanate) was detected by LC-MS. The solution was then evaporated to dryness with a stream of nitrogen gas and further concentrated by rotary evaporation. To the residue obtained was added the known (*27*) protected glucuronide linker fragment (**14**, 30 mg, 40 μmol) dissolved in 0.2 mL anhydrous DMF. The reaction was stirred at room

temperature for 2 h, after which time LC-MS revealed conversion to product. The reaction was then concentrated, redissolved in minimal CH_2Cl_2, and purified by radial chromatography eluting CH_2Cl_2/MeOH (97:3 to 95:5 CH_2Cl_2/MeOH) to give **7** (10 mg, 38%). ^{1}H NMR ($CDCl_3$) δ (ppm): 0.88 (m, 3H), 1.00 (t, J = 7.6 Hz, 3H), 1.26 (s, 2H), 1.42 (m, 3H), 1.87 (m, 2H), 2.06 (s, 9H), 2.74 (m, 2H), 2.99 (bs, 1H), 3.18 (bs, 1H), 3.61 (m, 2H), 3.74 (s, 3H), 4.19 (q, J = 6.8 Hz, 2H), 4.39 (q, J = 10 Hz, 2H), 5.16 (m, 9H), 5.43 (q, J = 8.8 Hz, 1H), 5.65 (d, J = 16.4 Hz, 1H), 5.85 (s, 1H), 6.17 (s, 3H), 6.96 (m, 3H), 7.22 (s, 1H), 7.32 (t, J = 6.8 Hz, 2H), 7.45 (s, 1H), 7.59 (m, 3H), 7.67 (d, J = 7.2 Hz, 2H), 8.14 (s, 1H), 8.47 (s, 1H). UV λ_{max}: 229, 263, and 383 nm. LC-MS: *m/z* (ES^+) found 1237.95 $(M+H)^+$, *m/z* (ES^-) found 1236.85 $(M-H)^-$.

(2*S*,3*S*,4*S*,5*R*,6*S*)-6-(2-(3-Aminopropanamido)-4-(((7-butyl-10-aminocamptothecin)carbamoyloxy)methyl)phenoxy)-3,4,5-trihydroxy-tetrahydro-2*H*-pyran-2-carboxylic Acid (8). A flask charged with **6** (24.0 mg, 20.1 μmol) dissolved in a solvent mixture of 2.5 mL MeOH, 3.0 mL THF, and 2.5 mL water, was cooled to 0 °C. To the stirred solution was added LiOH monohydrate (8.6 mg, 212 μmol) and the reaction was warmed to room temperature. After 3 h, LC-MS revealed complete conversion to product. Glacial acetic acid (12.7 μL, 222 μmol) was added, and the reaction was evaporated to dryness. Purification of residue by preparative HPLC using Method B gave **8** (12.7 mg, 67%). ^{1}H NMR (CD_3OD) δ (ppm) 0.96 (t, J = 7.6 Hz, 3H), 0.99 (t, J = 7.2 Hz, 3H), 1.49 (q, J = 7.2 Hz, 2H), 1.65 (m, 2H), 1.89 (m, 2H), 2.62 (s, 1H), 2.86 (t, J = 6.0 Hz, 2H), 2.95 (bt, 2H), 3.53 (m, 3H), 3.93 (m, 1H), 4.84 (d, J = 7.6 Hz, 1H), 4.91 (s, 2H), 5.11 (s, 2H), 5.34 (AB, J = 16.0 Hz, 2H), 7.20 (m, 2H), 7.40 (s, 1H), 7.60 (m, 1H), 7.82 (d, J = 8.8 Hz, 1H), 8.12 (s, 1H), 8.22 (s, 1H), 9.63 (s, 1H). UV λ_{max}: 227, 267, 385 nm. LC-MS: *m/z* (ES^+) found 832.20 $(M+H)^+$, *m/z* (ES^-) found 830.27 $(M-H)^-$.

(2*S*,3*S*,4*S*,5*R*,6*S*)-6-(2-(3-Aminopropanamido)-4-(((7-butyl-9-amino-10,11-methylendioxycamptothecin)carbamoyloxy)methyl)phenoxy)-3,4,5-trihydroxy-tetrahydro-2*H*-pyran-2-carboxylic Acid (9). Drug linker **9** was prepared from **7** (25.0 mg, 25.2 μmol) in the same manner as that described for **8**. The reaction gave **9** (17.6 mg, 92%). UV λ_{max}: 223 and 383 nm. LC-MS: *m/z* (ES^+) found 875.94 $(M+H)^+$, *m/z* (ES^-) found 873.95 $(M-H)^-$. The material was carried forward without further characterization.

(2*S*,3*S*,4*S*,5*R*,6*S*)-6-(2-(3-(6-(2,5-Dioxo-2*H*-pyrrol-1-(5*H*)-yl)hexanamido)propanamido)-4-(((7-butyl-10-aminocamptothecin)carbamoyloxy)methyl)phenoxy)-3,4,5-trihydroxy-tetrahydro-2*H*-pyran-2-carboxylic Acid (10). To a solution of **8** (23.0 mg, 27.6 μmol) dissolved in 1.5 mL anhydrous DMF was added maleimidocaproyl NHS ester (12.8 mg, 41.4 μmol), followed by DIPEA (14.4 μL, 82.8 μmol). The reaction was stirred at room temperature under nitrogen for 4 h, at which time LC-MS revealed conversion to product. The crude reaction was diluted in DMSO and purified by preparative HPLC (Method A) to give **10** (20.5 mg, 72%). ^{1}H NMR (DMF-d_7) δ (ppm): 0.99 (m, 6H), 1.26 (p, J = 8.4 Hz, 2H), 1.57 (m, 6H), 1.81 (p, J = 7.2 Hz, 2H), 2.01 (m, 2H), 2.16 (t, J = 7.2 Hz, 2H), 2.68 (t, J = 6.8 Hz, 2H), 3.21 (t, J = 8.0 Hz, 2H), 3.57 (m, 10H), 4.10 (d, J = 9.6 Hz, 2H), 5.03 (m, 1H), 5.23 (s, 2H), 5.36 (s, 2H), 5.52 (d, J = 2.4 Hz, 2H), 6.52 (bs, 1H), 7.01 (s, 2H), 7.19 (dd, J = 8.4, 2.0 Hz, 1H), 7.27 (d, J = 8.4 Hz, 1H), 7.43 (s, 1H), 7.94 (t, J = 5.6 Hz, 1H), 8.09 (dd, J = 9.2, 2.0 Hz, 1H), 8.18 (d, J = 9.2 Hz, 1H), 8.48 (s, 1H), 8.57 (s, 1H), 9.36 (s, 1H), 10.37 (s, 1H). UV λ_{max}: 267 and 385 nm. Analytical HPLC: gradient A, t_R = 11.93 min, AUC_{255} = 94.7%; gradient B, t_R = 5.76 min, AUC_{255} = 97.1%. LC-MS: *m/z* (ES^+) found 1025.40 $(M+H)^+$, *m/z* (ES^-) found 1023.29 $(M-H)^-$.

(2*S*,3*S*,4*S*,5*R*,6*S*)-6-(2-(3-(6-(2,5-Dioxo-2*H*-pyrrol-1-(5*H*)-yl)hexanamido)propanamido)-4-(((7-butyl-9-amino-10,11-methylendioxycamptothecin)carbamoyloxy)methyl)phenoxy)-3,4,5-trihydroxy-tetrahydro-2*H*-pyran-2-carboxylic Acid (11). Drug linker **11** was prepared from **9** (16.3 mg, 18.6 μmol) in the same manner as that described for **10**. The reaction gave **11** (12.9 mg, 65%). ^{1}H NMR (DMF-d_7) δ (ppm): 0.93 (t, J = 7.2 Hz, 3H), 0.99 (t, J = 8.0 Hz, 3H), 1.27 (m, 2H), 1.56 (m, 8H), 1.70 (m, 2H), 1.98 (m, 2H), 2.17 (t, J = 7.6 Hz, 2H), 2.69 (m, 2H), 3.52 (m, 10H), 4.10 (d, J = 9.2 Hz, 2H), 5.03 (d, J = 6.4 Hz, 2H), 5.19 (s, 2H), 5.30 (s, 2H), 5.51 (d, J = 2.8 Hz, 2H), 6.37 (m, 3H), 7.02 (d, J = 3.6 Hz, 2H), 7.18 (d, J = 8.4 Hz, 1H), 7.28 (d, J = 8.4 Hz, 1H), 7.37 (s, 1H), 7.55 (s, 1H), 8.50 (s, 1H), 9.36 (s, 1H), 9.43 (s, 1H). UV λ_{max}: 223 and 383 nm. Analytical HPLC: gradient A, t_R = 11.70 min, AUC_{255} = 97.2%; gradient B, t_R = 5.47 min, AUC_{255} = 97.7%. LC-MS: *m/z* (ES^+) found 1069.44 $(M+H)^+$, *m/z* (ES^-) found 1067.37 $(M-H)^-$.

Antibody−Drug Conjugate Preparation. The immunoconjugates were prepared as previously described (*4*, *28*). Briefly, the mAbs (4−5 mg/mL) in PBS containing 50 mM sodium borate at pH 7.4 were reduced with tris(carboxyethyl)phosphine hydrochloride at 37 °C. The progress of the reaction, which reduces interchain disulfides, was monitored by reaction with 5,5′-dithiobis(2-nitrobenzoic acid) and allowed to proceed until the desired level of thiols/mAb was achieved. The reduced antibody was then cooled to 0 °C and alkylated with 1.5 equiv of maleimide drug linker per antibody thiol. After 1 h, the reaction was quenched by the addition of 5 equiv of *N*-acetyl cysteine (NAC). Quenched drug linker was removed by gel filtration over a PD-10 column. The ADC was then sterile-filtered through a 0.22 μm syringe filter. Protein concentration and drug loading were determined by spectral analysis at 280 and 375 nm, respectively, with correction for the contribution of drug absorbance at 280 nm. Size-exclusion chromatography was used to determine the extent of antibody aggregation, and RP-HPLC confirmed the absence of remaining NAC-quenched drug linker.

ADC Binding Assay. Karpas 299 cells were treated with serial dilutions of cAC10 or cAC10-**10** in PBS. cBR96-**10** was also included as a nonbinding control. After 30 min on ice, the cells were washed and resuspended in 4 °C PBS. Secondary goat antibody-FITC was added to detect bound mAb or ADC. The cells were then washed, fixed with paraformaldehyde, and analyzed by flow cytometry.

Stability Assay. The stability of cBR96-**10** was assessed by incubation in citrated CD-1 mouse plasma. cBR96-**10** was incubated at 37 °C in plasma over the course of two weeks. Aliquots were withdrawn as a function of time and protein precipitated through the addition of 5 volumes ice-cold methanol containing 0.1% formic acid and spiked with a camptothecin reference standard. The protein was then removed by centrifugation for 5 min at 16 100 *g*; the supernatant was collected and analyzed by LC-MS (ES^+ mode) using gradient A for the detection of counts at *m/z* 420.2 $(M+H)^+$ at a retention time of 11.78 min, corresponding to free drug **2**. A standard calibration curve spanning the range 1−100% drug release was employed to convert the *m/z* 420.2 AUC at 11.78 min to a concentration value.

In Vitro Growth Inhibition. The cytotoxic activity of the immunoconjugates was assessed using a resazurin (Sigma, St. Louis, MO, USA) reduction assay (*4*). Karpas 299 (2000 cells/well), H3396 (2000 cells/well), L540cy (7000 cells/well), and Caki-1 (1000 cells/well) cells cultured in log-phase growth were seeded for 24 h in 96-well plates containing 150 μL RPMI 1640 supplemented with 20% FBS. Serial dilutions of ADC in cell culture media were prepared at 4× working concentration; 50 μL of each dilution was added to the 96-well plates. Following

Scheme 1

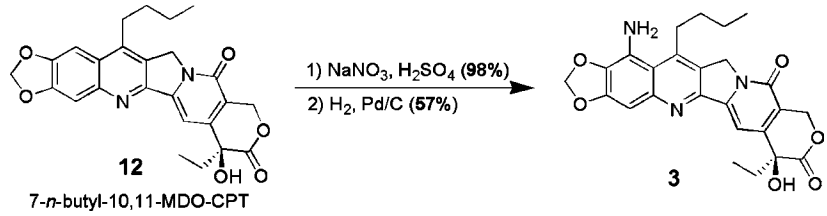

addition of ADC, the cells were incubated with test articles for 4 or 8 d at 37 °C. Resazurin was then added to each well to achieve a 50 μM final concentration, and the plates were incubated for an additional 4 h at 37 °C. The plates were then read for the extent of dye reduction on a Fusion HT plate reader (Packard Instruments, Meridien, CT, USA) with excitation and emission wavelengths of 530 and 590 nm, respectively. The IC_{50} value, determined in triplicate, is defined here as the concentration that results in a 50% reduction in cell growth relative to untreated controls.

In Vivo Therapy Experiments. All experiments were conducted in concordance with the Animal Care and Use Committee in a facility fully accredited by the Association for Assessment and Accreditation of Laboratory Animal Care. In vivo tolerability was first assessed to ensure that the conjugates were tolerated at clinically relevant doses. BALB/c mice were treated with escalating doses of ADC formulated in PBS with 0.01% Tween 20. Mice were monitored for weight loss following drug treatment; those that experienced 20% weight loss or other signs of morbidity were euthanized.

The efficacy experiment was conducted in a renal cell carcinoma xenograft model. Caki-1 tumor fragments were implanted into the right flank of Nude mice. Mice were randomized to study groups ($n = 5$) on day nine with each group averaging around 100 mm^3 tumor volume. The ADC or controls were dosed ip according to a q4dx4 schedule. Tumor volume as a function of time was determined using the formula ($L \times W^2$)/2. Animals were euthanized when tumor volumes reached 1000 mm^3. Mice showing durable regressions were terminated on day 96 post-implant.

RESULTS

Drug Linker Design. There are two significant challenges associated with designing an immunoconjugate with camptothecin: lack of a suitable functional group for conjugation, and hydrophobicity, which can cause antibody aggregation. The first obstacle requires designing a drug linker that combines a high level of stability in circulation with rapid drug release upon internalization into targeted cells. The only readily accessible functional group in camptothecin is the C20 tertiary hydroxyl. The use of ester or carbonate linkages to assemble conjugates with aliphatic alcohols is common (*18, 20, 29*−*31*). However, as cited earlier, this can be a liability, as mouse plasma contains high levels of esterase activity and readily cleaves ester and carbonate functional groups (*32*).

To address drug linker stability, we envisioned employing a carbamate bond to an amine-containing camptothecin such as 7-butyl-10-amino-CPT (**2**) shown in Figure 1. Carbamate bonds typically provide superior stability relative to ester and carbonate bonds with respect to hydrolysis (*33*). Alternatively, we installed an amine into the known (*23, 24*) analogue 7-butyl-10,11-methylenedioxy-CPT (**12**, Scheme 1). In both cases, the presence of the amine provided for the use of a cathepsin B-cleavable valine-citrulline-PABA dipeptide linker (val-cit) system (Figure 1B). The val-cit dipeptide linker system is designed to achieve circulation stability and rapid lysosomal drug release upon internalization into the targeted cancer cells (*4, 34*).

A second obstacle associated with this class is manifest in the hydrophobic nature of these compounds. Camptothecins possess a rigid, extended aromatic ring system that confers limited aqueous solubility and can induce significant antibody aggregation. To address this issue, hydrophilic glucuronide-based CPT drug linkers (Figure 1C) were pursued in addition to dipeptide drug linkers. The glucuronide linker system is characterized by its ability to provide monomeric ADCs with a high degree of circulation stability and rapid drug release in the presence of endogenous β-glucuronidase at the target site (*27*).

Drug Linker Synthesis. The syntheses of CPT analogues **2** and **12** were achieved by the well-precedented Friedlander condensation route (*23, 25*). Regioselective nitration and subsequent hydrogenation of **12** provided the 9-amino analogue **3** in 56% overall yield, as shown in Scheme 1. The protease-cleavable dipeptide drug linkers were prepared in two synthetic steps (Scheme 2). Camptothecins **2** and **3** were treated with phosgene to convert their respective amines to isocyanates in situ. The isocyanates were subsequently trapped by benzyl alcohol linker **13** (*26*) (mcVal-Cit-PABA), forming the carbamate linkages in drug linkers **4** and **5**, respectively.

The glucuronide drug linkers were prepared according to the synthetic sequence in Scheme 3. The synthesis commenced by converting the protected glucuronide benzyl alcohol **14** (*27*) to the chloroformate with diphosgene, which was then trapped in situ with camptothecin **2** to provide intermediate **6**. The more sterically hindered amine in **3** was converted to the isocyanate with phosgene and trapped with glucuronide benzyl alcohol **14**. Exhaustive saponification and simultaneous Fmoc-deprotection of **6** and **7** yielded free amines **8** and **9**, respectively. The synthetic sequence was then completed via the coupling of amines **8** and **9** with the NHS ester of maleimidocaproic acid

Scheme 2

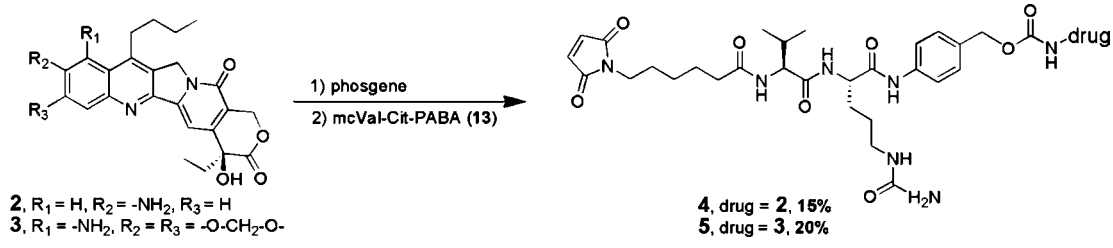

Scheme 3

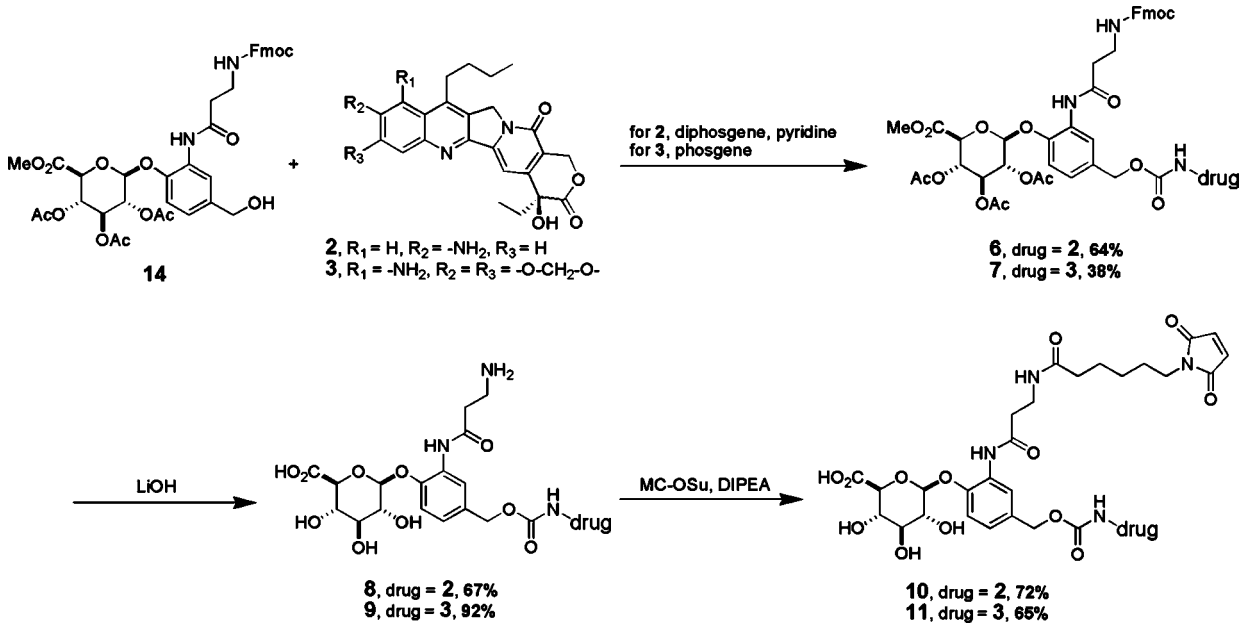

(MC-OSu), providing drug linkers **10** and **11**, respectively, in moderate overall yield.

Preparation of Antibody−Drug Conjugates. Conjugates comprising antibodies cBR96, cAC10, and h1F6 and drug linkers **4**, **5**, **10**, and **11** were prepared following standard protocols (*4, 28*). Reduced interchain disulfides were alkylated with drug linker, forming Michael adducts between the mAb cysteines and drug linker maleimide. Upon completion of the conjugation reaction, excess drug linker was quenched with *N*-acetylcysteine and removed by gel filtration, which was confirmed by HPLC. Drug loading was assessed by chromatographic analysis and UV absorption of the ADCs with correction for the contribution of the camptothecin chromophore at 280 nm.

The extent of ADC aggregation was determined by size-exclusion chromatography. Glucuronide drug linkers **10** and **11** provided ADCs with 4 drugs or 8 drugs per antibody with minimal (<5%) aggregation (Tables 1 and 2). The dipeptide drug linkers **4** and **5** led to antibody aggregation to a greater extent than the more hydrophilic glucuronide drug linkers. ADCs loaded with 4 drugs per antibody contained 4−16% aggregate. ADCs comprising **4** or **5** loaded with 8 drugs/mAb gave much higher levels of aggregation. For example, cAC10 loaded with drug linker **4** was >80% aggregated (Table 1). Highly aggregated (>20%) ADCs were excluded from the biological evaluation.

ADC Binding. As previously shown (*4*), alkylation of interchain disulfides typically has negligible effect on ADC antigen binding activity. To ensure that this was the case with the camptothecins, cAC10-**10** (7 drug/mAb) was assayed for binding affinity relative to unconjugated mAb with CD30+ Karpas 299 cells. The results, shown in Figure 2, indicate that conjugation did not significantly impact the antigen binding. Antigen-negative cBR96 displayed no appreciable binding.

Drug Linker Stability. Val-Cit-PAB and glucuronide carbamate drug linkers have been previously shown to be highly stable toward hydrolysis in various matrices, including plasma (*4,28*). To corroborate these observations with the camptothecin series, cBR96-**10** (7 drug/mAb) was incubated in mouse plasma, and the appearance of free drug was assessed by a calibrated LC/MS assay. After 14 d at 37 °C, the free drug (**2**) signal was below the limit of detection of the assay, which is <1% of the theoretical maximum drug release. This suggests that the carbamate linkage is stable to hydrolysis in mouse plasma. Control experiments established efficient recovery of free drug from the matrix.

In Vitro Biological Evaluation. The activities of ADCs containing 7-butyl-10-amino-CPT (**2**) incorporated via dipeptide (**4**) or glucuronide (**10**) drug linker were assessed on Karpas 299 (CD30+) ALCL and H3396 (LeY+) breast carcinoma cell lines following 4 or 8 d treatment (Table 1). ADCs comprising dipeptide drug linker **4** displayed negligible activity following a 4 d treatment (data not shown). When the treatment time was extended to 8 d, modest immunologically specific activity was observed. ADCs bearing glucuronide drug linker **10** were weakly

Table 1. Cytotoxic Activities of ADCs Containing 2

					IC_{50} values (nM)	
cytotoxic agent	treatment time (d)	antigen	drug/mAb ratio	percent aggregate	Karpas 299[a] (CD30+, LeY−)	H3396[a] (CD30−, LeY+)
cAC10−**4**		CD30	8	>80	nt	nt
cBR96−**4**		LeY	8	>80	nt	nt
cAC10−**4**	8	CD30	3.7	9	26	no effect
cBR96−**4**	8	LeY	4.2	16	110	13
cAC10−**10**	4	CD30	7	<5	160	>500[b]
cBR96−**10**	4	LeY	7	<5	>500[b]	22
cAC10−**10**	8	CD30	7	<5	1.8	460
cBR96−**10**	8	LeY	7	<5	170	21
1	4	–	–	–	9.7	7.4
2	4	–	–	–	1.0	0.9

[a] Cells were treated with test articles for 4 or 8 d, and cell viability was determined by resazurin conversion. The IC_{50} values represent the concentrations (nM) of the drug component of the ADC. [b] IC_{50} values are greater than the highest concentration tested.

Table 2. Cytotoxic Activities of ADCs Containing 3 Following 4 d Treatment

				IC_{50} (nM)		
cytotoxic agent	antigen	drug/mAb ratio	percent aggregate	Karpas 299[a] (CD30+, CD70−)	L540cy[a] (CD30+, CD70−)	Caki-1[a] (CD 30−, CD70+)
cAC10−**5**	CD30	3.8	8	4.4	0.32	>150[b]
h1F6−**5**	CD70	4.2	4	>190[b]	no effect	6.2
cAC10−**11**	CD30	4.4	3	0.91	0.23	>210[b]
h1F6−**11**	CD70	4.5	1	>220[b]	190	1.5
cAC10−**11**	CD30	8	2	0.89	0.41	510
h1F6−**11**	CD70	8	1	650	280	3.3
1	–	–	–	9.7	7.4	7.0
3	–	–	–	0.06	0.03	0.05

[a] Cells were treated with test articles for 4 d, and cell viability was determined by resazurin conversion. The IC_{50} values represent the concentrations (nM) of the drug component of the ADC. [b] IC_{50} values are greater than the highest concentration tested.

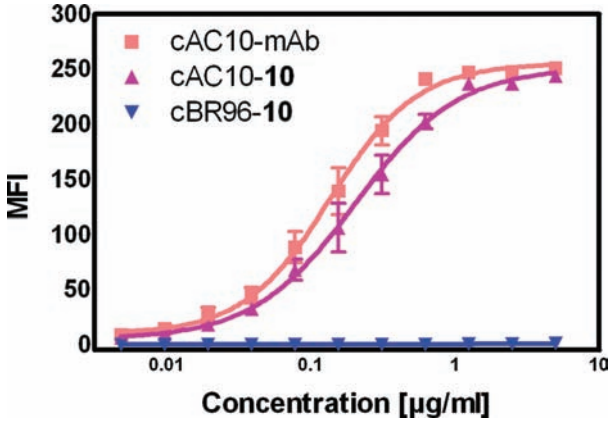

Figure 2. FACS analysis of antigen binding of glucuronide drug linker cAC10-**10** relative to cAC10 mAb and nonbinding cBR96-**10** on CD30+ Karpas 299 cells.

active, albeit more potent than mAb−**4** conjugates, over the course of a 4 d drug treatment with IC_{50} values of 160 nM and 22 nM on Karpas 299 and H3396, respectively. When drug treatment was extended to 8 d, cAC10−**10** displayed a substantial increase in potency on Karpas 299. An analogous increase in potency on H3396 cells was not observed. The activities of conjugates comprising h1F6 or cAC10 and **5** and **11** were tested on Karpas 299, L540cy (Hodgkin lymphoma), and Caki-1 (renal cell carcinoma) following a 4 d treatment (Table 2). The conjugates were immunologically specific and highly potent on the three cell lines, with IC_{50} values ranging from 0.23 to 4.4 nM across the panel.

In Vivo Biological Evaluation. In light of the superior in vitro potency of ADCs armed with camptothecin analogue **3** relative to **2**, in vivo evaluation focused on ADCs bearing drug linkers **5** and **11**. ADCs were initially evaluated for mouse tolerability prior to efficacy experiments. BALB/c mice were injected once ip with cAC10−**5** (4 drug/mAb) or cAC10−**11** (4 drug/mAb) and evaluated for weight loss and morbidity. Both the glucuronide (cAC10−**11**) and the val-cit dipeptide (cAC10−**5**) conjugates were well-tolerated at 50 mg/kg. At 100 mg/kg, cAC10−**5** resulted in moderate weight loss (5−10%) and cAC10−**11** was toxic. From these results, the maximum tolerated doses (MTD) for cAC10−**5** and cAC10−**11** are approximately 100 mg/kg and 50 mg/kg, respectively.

An efficacy experiment with immunoconjugates h1F6−**5** and h1F6−**11** was carried out in the Caki-1 renal cell carcinoma model. Nude mice bearing Caki-1 tumors were treated four times every 4 d (q4d × 4) with ADCs once the average tumor size was approximately 100 mm^3 (Figure 3). At 3 mg/kg, the val-cit immunoconjugate (h1F6−**5**) had no effect on tumor growth. In contrast, the glucuronide conjugate (h1F6−**11**) induced substantial tumor growth delay. At 10 mg/kg, the glucuronide conjugate again

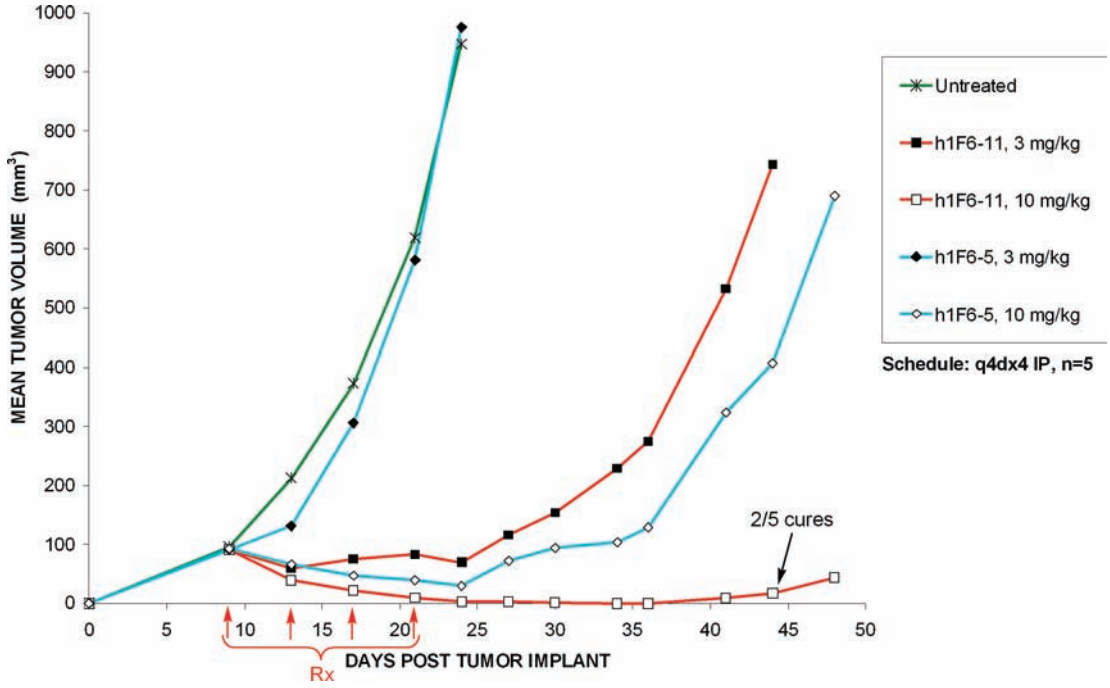

Figure 3. In vivo efficacy of camptothecin ADCs in a Caki-1 renal cell carcinoma xenograft model; all ADCs contain 4 dr/mAb.

outperformed the val-cit conjugate. Mice treated with h1F6−**5** achieved 5/5 partial regressions, while mice treated with h1F6−**11** had 5/5 complete regressions with 2/5 mice cured.

DISCUSSION

Early work on ADCs established drug potency as an important parameter contributing to the conjugate activity. The camptothecin analogues employed here are substantially more potent than CPT or related clinical analogues, irinotecan and topotecan. Among the two CPT analogues evaluated, the more potent analogue (**3**) provided significantly more potent ADCs (Tables 1 and 2). ADCs bearing **3** provided in vitro potencies 20- to 400-fold greater than CPT ADCs (*18*). More recently, ADCs bearing SN-38 were reported to be active at the single-digit nM level (*20*). Specificity controls were not included, however, and it is possible that nonspecific drug release from the carbonate or ester drug linker significantly contributed to the observed conjugate potency. The ADCs bearing **3** led to high levels of immunologically specific cell kill at subsaturating doses (Table 2). Immunological specificity implies that the linker is stable since the cells were continuously exposed to the ADCs for 96 h. The binding ADCs were less potent than the respective free drugs (Tables 1 and 2). It is possible that free drug accumulation via passive cellular uptake over the course of the 96 h treatment exceeds the intracellular drug concentration achieved through antigen-mediated delivery. This has been previously observed with other ADCs (*5*, *35*, *36*).

Camptothecins are an especially compelling drug class for ADCs because they can be produced synthetically, modified to give analogues with high potency, and have been shown to possess pronounced clinical activity. However, aqueous insolubility presents a significant challenge in utilizing the CPT drug class. Clinical camptothecins, irinotecan and topotecan, were designed to overcome this by inclusion of solubilizing amine groups (*15*). From the standpoint of ADC development, upon conjugation, CPT hydrophobicity can lead to significant mAb aggregation. The glucuronide linker system is ideal in addressing this issue. The glucuronide drug linkers consistently provided monomeric ADCs when loaded at 4 and 8 drug/mAb, whereas the dipeptide drug linkers tended to provide ADCs with a greater degree of aggregation (Tables 1 and 2). This is consistent with our previous work with hydrophobic minor groove binders (*37*).

We have described the preparation and biological evaluation of ADCs empowered with camptothecin analogues that were selected on the basis of the presence of an amine functional group and enhanced cellular potency. The amine functional group was deemed important because it facilitated the use of carbamate-based linkers such as the val-cit dipeptide and the glucuronide linker systems. On the basis of these results, immunoconjugates comprising the more potent analogue (**3**) linked via val-cit dipeptide or glucuronide drug linker systems are well-suited for further development.

LITERATURE CITED

(1) Carter, P. J., and Senter, P. D. (2008) Antibody-drug conjugates for cancer therapy. *Cancer J. 14*, 154–169.

(2) Chari, R. V. J. (2008) Targeted cancer therapy: conferring specificity to cytotoxic drugs. *Acc. Chem. Res. 41*, 98–107.

(3) Wu, A. M., and Senter, P. D. (2005) Arming antibodies: prospects and challenges for immunoconjugates. *Nat. Biotechnol. 23*, 1137–1146.

(4) Doronina, S. D., Toki, B. E., Torgov, M. Y., Mendelsohn, B. A., Cerveny, C. G., Chace, D. F., DeBlanc, R. L., Gearing, R. P., Bovee, T. D., Siegall, C. B., Francisco, J. A., Wahl, A. F., Meyer, D. L., and Senter, P. D. (2003) Development of potent monoclonal antibody auristatin conjugates for cancer therapy. *Nat. Biotechnol. 21*, 778–784.

(5) Francisco, J. A., Cerveny, C. G., Meyer, D. L., Mixan, B. J., Klussman, K., Chace, D. F., Rejniak, S. X., Gordon, K. A., DeBlanc, R. L., Toki, B. E., Law, C.-L., Doronina, S. D., Siegall, C. B., Senter, P. D., and Wahl, A. F. (2003) cAC10-vcMMAE, an anti-CD30-monomethyl auristatin E conjugate with potent and selective antitumor activity. *Blood 102*, 1458–1465.

(6) Beeram, M., Krop, I. E., Modi, S., Tolcher, A. W., Rabbee, N., Girish, S., Tibbitts, J., Holden, S. N., Lutzker, S. G., and Burris, H. A. (2007) A phase I study of trastuzumab-MCC-DM1 (T-DM1), a first-in-class HER2 antibody-drug conjugate (ADC), in patients (pts) with HER2+ metastatic breast cancer (BC). *J. Clin. Oncol.* 25 Abstract 1042.

(7) Phillips, G. D. L., Li, G., Dugger, D. L., Crocker, L. M., Parsons, K. L., Mai, E., Blattler, W. A., Lambert, J. M., Chari, R. V. J., Lutz, R. J., Wong, W. L. T., Jacobson, F. S., Koeppen, H., Schwall, R. H., Kenkare-Mitra, S. R., Spencer, S. D., and Sliwkowski, M. X. (2008) Targeting HER2-positive breast cancer with trastuzumab-DM1, an antibody-drug conjugate. *Cancer Res. 68*, 9280–9290.

(8) Krop, I. E., Beeram, M., Modi, S., Rabbee, N., Girish, S., Tibbitts, J., Holden, S. N., Lutzker, S. G., and Burris, H. A. 30th Annual San Antonio Breast Cancer Symposium, 2007, Abstract 310.

(9) Younes, A., Forero-Torres, A., Bartlett, N. L., Leonard, J. P., Lynch, C., Kennedy, D. A., and Sievers, E. L. American Society of Hematology National Meeting, 2008a, Abstract 1006.

(10) Younes, A., Forero-Torres, A., Bartlett, N. L., Leonard, J. P., Rege, B., Kennedy, D. A., Lorenz, J. M., and Sievers, E. L. American Society of Clinical Oncology, 2008b, Abstract 8526.

(11) Trail, P. A., Willner, D., Lasch, S. J., Henderson, A. J., Hofstead, S., Casazza, A. M., Firestone, R. A., Helllstrom, I., and Hellstrom, K. E. (1993) Cure of xenografted human carcinomas by BR96-doxorubicin immunoconjugates. *Science 261*, 212–215.

(12) Saleh, M. N., Sugarman, S., Murray, J., Ostroff, J. B., Healey, D., Jones, D., Daniel, C. R., LeBherz, D., Brewer, H., Onetto, N., and LaBuglio, A. F. (2000) Phase I trial of the anti-Lewis Y drug immunoconjugate BR96-doxorubicin in patients with Lewis Y-expressing epithelial tumors. *J. Clin. Oncol. 18*, 2282–2292.

(13) Tolcher, A. W., Sugarman, S., Gelman, K. A., Cohen, R., Saleh, M., Isaacs, C., Young, L., Healey, D., Onetto, N., and Slichenmyer, W. (1999) Randomized phase II study of BR96-doxorubicin conjugate in patients with metastatic breast cancer. *J. Clin. Oncol. 17*, 478–484.

(14) Pommier, Y. (2006) Topoisomerase I inhibitors: camptothecins and beyond. *Nat. Rev. Cancer 6*, 789–802.

(15) Garcia-Carbonero, R., and Supko, J. G. (2002) Current perspectives on the clinical experience, pharmacology, and continued development of the camptothecins. *Clin. Cancer Res. 8*, 641–661.

(16) Satoh, T., Hosokawa, M., Atsumi, R., Suzuki, W., Hakusui, H., and Nagai, E. (1994) Metabolic activation of CPT-11, 7-ethyl-10-[4-(1-piperidino)-1-piperidino]carbonyloxycamptothecin, a novel antitumor agent, by carboxylesterase. *Biol. Pharm. Bull. 17*, 662–664.

(17) Gerrits, C. J. H., de Jonge, M. J. A., Schellens, J. H. M., Stoter, G., and Verweij, J. (1997) Topoisomerase I inhibitors: the relevance of prolonged exposure for present clinical development. *Br. J. Cancer 76*, 952–962.

(18) Walker, M. A., Dubowchik, G. M., Hofstead, S. J., Trail, P. A., and Firestone, R. A. (2002) Synthesis of an immunoconjugate of camptothecin. *Bioorg. Med. Chem. Lett. 12*, 217–219.

(19) Willner, D., Trail, P. A., Hofstead, S. J., King, H. D., Lasch, S. J., Braslawsky, G. R., Greenfield, R. S., Kaneko, T., and Firestone, R. A. (1993) (6-Maleimidocaproyl)hydrazone of doxorubicin - A new derivative for the preparation of immunoconjugates of doxorubicin. *Bioconjugate Chem. 4*, 521–527.

(20) Moon, S. J., Govindan, S. V., Cardillo, T. M., D'Souza, C. A., Hansen, H. J., and Goldenberg, D. M. (2008) Antibody conjugates of 7-ethyl-10-hydroxycamptothecin (SN-38) for targeted cancer chemotherapy. *J. Med. Chem. 51*, 6916–6926.

(21) Thomas, C. J., Rahier, N. J., and Hecht, S. M. (2004) Camptothecin: current perspectives. *Bioorg. Med. Chem. 12*, 1585–1604.

(22) Adams, D. J., Webba da Silva, M., Flowers, J. L., Kohlhagen, G., Pommier, Y., Colvin, O. M., Manikumar, G., and Wani, M. C. (2006) Camptothecin analogs with enhanced activity against human breast cancer cells. I. Correlation of potency with lipophilicity and persistence in the cleavage complex. *Cancer Chemother. Pharmacol. 57*, 135–144.

(23) Wani, M. C., Manikumar, G., Wall, M. E., and Wall, M. A. (2004) (US PTO, Ed.), US 2004/0266803 A1, Research Triangle Institute, USA.

(24) Vladu, B., Woynarowski, J. M., Manikumar, G., Wani, M. C., Wall, M. A., Von Hoff, D. D., and Wadkins, R. M. (2000) 7- and 10-substituted camptothecins: dependence of topoisomerase I-DNA cleavable complex formation and stability on the 7- and 10-substituents. *Mol. Pharmacol. 57*, 243–251.

(25) Wall, M. A., Wani, M. C., Nicholas, A. W., Manikumar, G., Tele, C., Moore, L., Truesdale, A., Leitner, P., and Besterman, J. M. (1993) Plant antitumor agents. 30. Synthesis and structure activity of novel camptothecin analogs. *J. Med. Chem. 36*, 2689–2700.

(26) Dubowchik, G. M., Firestone, R. A., Padilla, L., Willner, D., Hofstead, S. J., Mosure, K., Knipe, J. O., Lasch, S. J., and Trail, P. A. (2002) Cathepsin B-labile dipeptide linkers for lysosomal release of doxorubicin from internalizing immunoconjugates: model studies of enzymatic drug release and antigen-specific in vitro anticancer activity. *Bioconjugate Chem. 13*, 855–869.

(27) Jeffrey, S. C., Andreyka, J. B., Bernhardt, S. X., Kissler, K. M., Kline, T., Lenox, J. S., Moser, R. F., Nguyen, M. T., Okeley, N. M., Stone, I. J., Zhang, X., and Senter, P. D. (2006) Development and properties of beta-glucuronide linkers for monoclonal antibody-drug conjugates. *Bioconjugate Chem. 17*, 831–840.

(28) Jeffrey, S. C., Torgov, M. Y., Andreyka, J. B., Boddington, L., Cerveny, C. G., Denny, W. A., Gordon, K. A., Gustin, D., Haugen, J., Kline, T., Nguyen, M. T., and Senter, P. D. (2005) Design, synthesis, and in vitro evaluation of dipeptide-based antibody minor groove binder conjugates. *J. Med. Chem. 48*, 1344–1358.

(29) de Groot, F. H. M., Busscher, G. F., Aben, R. W. M., and Scheeren, H. W. (2002) Novel 20-carbonate linked prodrugs of camptothecin and 9-aminocamptothecin designed for activation by tumour-associated plasmin. *Bioorg. Med. Chem. Lett. 12*, 2371–2376.

(30) de Groot, F. H. M., Loos, W. J., Koekkoek, R., van Berkom, L. W. A., Busscher, G. F., Seelen, A. E., Albrecht, C., de Bruijn, P., and Scheeren, H. W. (2001) Elongated multiple electronic cascade and cyclization spacer systems in activatible anticancer prodrugs for enhanced drug release. *J. Org. Chem. 66*, 8815–8830.

(31) Lerchen, H. G., Baumgarten, J., von dem Bruch, K., Lehmann, T. E., Sperzel, M., Kempka, G., and Fiebig, H. H. (2001) Design and optimization of 20-O-linked camptothecin glycoconjugates as anticancer agents. *J. Med. Chem. 44*, 4186–4195.

(32) Liederer, B. M., and Borchardt, R. T. (2006) Enzymes involved in the bioconversion of ester-based prodrugs. *J. Pharm. Sci. 95*, 1177–1195.

(33) Huang, T. L., Szekacs, A., Uematsu, T., Kuwano, E., Parkinson, A., and Hammock, B. D. (1993) Hydrolysis of carbonates, thiocarbonates, carbamates, and carboxylic esters of alpha-naphthol, beta-naphthol, and para-nitrophenol by human, rat, and mouse liver carboxylesterases. *Pharm. Res. 10*, 639–648.

(34) Dubowchik, G. M., and Firestone, R. A. (1998) Cathepsin B-sensitive dipeptide prodrugs. 1. A model study of structural requirements for efficient release of doxorubicin. *Bioorg. Med. Chem. Lett. 8*, 3341–3346.

(35) Jeffrey, S. C., Nguyen, M. T., Andreyka, J. B., Meyer, D. L., Doronina, S. D., and Senter, P. D. (2006) Dipeptide-based highly potent doxorubicin antibody conjugates. *Bioorg. Med. Chem. Lett. 16*, 358–362.

(36) Tassone, P., Gozzini, A., Goldmacher, V., Shammas, M. A., Whiteman, K. R., Carrasco, D. R., Li, C., Allam, C. K., Venuta, S., Anderson, K. C., and Munshi, N. C. (2004) In vitro and in vivo activity of the maytansinoid immunoconjugate huN901-N2′-deacetyl-N2′-(3-mercapto-1-oxopropyl)-maytansine against CD56+ multiple myeloma cells. *Cancer Res. 64*, 4629–4636.

(37) Jeffrey, S. C., Nguyen, M. T., Moser, R. F., Meyer, D. L., Miyamoto, J. B., and Senter, P. D. (2007) Minor groove binder antibody conjugates employing a water soluble beta-glucuronide linker. *Bioorg. Med. Chem. Lett. 17*, 2278–2280.

BC9001097

Multimodal Nanoagents for the Detection of Intravascular Thrombi

Jason R. McCarthy,*,† Purvish Patel,†,‡ Ion Botnaru,‡ Pouneh Haghayeghi,† Ralph Weissleder,† and Farouc A. Jaffer*,†,‡

Center for Molecular Imaging Research, Harvard Medical School and Massachusetts General Hospital, 149 13th Street, Room 5406, Charlestown, Massachusetts 02129, and Cardiovascular Research Center, Cardiology Division, Harvard Medical School and Massachusetts General Hospital, 185 Cambridge St Room 3206, Boston Massachusetts 02114. Received March 14, 2009; Revised Manuscript Received April 30, 2009

Thrombosis underlies numerous life-threatening cardiovascular syndromes. Development of thrombosis-specific molecular imaging agents to detect and monitor thrombogenesis and fibrinolysis in vivo could improve the diagnosis, risk stratification, and treatment of thrombosis syndromes. To this end, we have synthesized efficient multimodal nanoagents targeted to two different constituents of thrombi, namely, fibrin and activated factor XIII. These agents are targeted via the conjugation of peptide-targeting ligands to the surface of fluorescently labeled magnetic nanoparticles. As demonstrated by in vitro and in vivo studies, both nanoagents possess high affinities for thrombi, and enable mutimodal fluorescence and magnetic resonance imaging.

INTRODUCTION

Thrombosis is characterized by the accumulation of platelets and fibrin induced by the activation of coagulation factors. Thrombosis underlies several life-threatening cardiovascular syndromes including myocardial infarction, stroke, and pulmonary embolism, leading causes of mortality in the developed world (*1*). It is thus important to localize and characterize thrombi in vivo, in order to determine treatment options and their resultant efficacy.

Several conventional and molecular imaging strategies have been developed in order to visualize thrombus formation (*2*). Platelets, which adhere to the damaged vessel wall, have been fluorescently or radioactively labeled in order to visualize their accumulation (*3*−*5*). Alternately, agents targeted to specific molecules within the thrombus have been investigated (*3, 4, 6*−*9*). We have previously reported on the synthesis of a peptide-based fluorescent imaging agent targeted to activated factor XIII (FXIIIa) (*9*). FXIIIa is responsible for the cross-linking of fibrin α- and γ-chains, increasing fibrinolytic resistance, and is a hallmark of biologically acute thrombi, as its activity diminishes over time. This peptide agent is covalently cross-linked into clots actively undergoing thrombogenesis by FXIIIa, thereby exhibiting a time-dependent increase in the fluorescence signal and as such may be utilized to distinguish acute from subacute thrombi in vivo.

Another thrombosis-targeting strategy utilizes the noncovalent binding of a fibrin-avid peptide to thrombi. The tripeptide Gly-Pro-Arg comprises the N-terminal sequence of the α-chain of fibrin, and can inhibit fibrin and thrombin clotting (*10*). Subsequent iterations have identified the peptide Gly-Pro-Arg-Pro-Pro (GPRPP) as a highly avid fibrin-binding agent possessing increased resistance to proteolysis (*8, 11*). This pentapeptide has previously been used to scintigraphically image pulmonary emboli in swine by the addition of a C-terminal radionuclide binding sequence, Gly-(D)-Ala-Gly-Gly (GAGG), and labeling with ^{99m}Tc. However, few fibrin-targeted molecular imaging agents are available for high-resolution in vivo optical/near-infrared fluorescence (NIRF) imaging, a modality that offers utility in noninvasive imaging (*12*), intravital microscopy (*2*), as well as high-resolution intravascular molecular imaging catheters compatible with human coronary arteries (*13*).

Table 1. Thrombus-Targeted Imaging Agents

agent	targeting sequence	target	fluorophore
CLIO-Cy7	n/a	n/a	Cy7
CLIO-GPRPP	GP**R**PPGGSKGC-NH2	fibrin	Cy7
CLIO-GPSPP	GP**S**PPGGSKGC-NH2	fibrin control	Cy7
CLIO-VT680	n/a	n/a	VT680
CLIO-FXIII	GN**Q**EQVSPLTLLKC-NH2	FXIIIa	VT680
CLIO-CXIII	GN**A**EQVSPLTLLKC-NH2	FXIIIa control	VT680

Herein, we discuss the synthesis and characterization of two multimodal thrombus-targeted nanoagents exhibiting either covalent or noncovalent binding to thrombi. Functionalization of fluorescently labeled cross-linked iron oxide (CLIO) nanoparticles with targeting peptides for fibrin or FXIIIa yields thrombus-targeted agents detectable by both magnetic resonance (MR) and optical imaging modalities (Table 1). These agents utilize two spectrally distinct fluorescence channels, which allows for the simultaneous monitoring of thrombus formation, the determination of biological thrombus age, and the efficacy of thrombolytic therapies.

EXPERIMENTAL PROCEDURES

General. All solvents and reagents used were of reagent grade or better and were used as received. Cross-linked iron oxide nanoparticles (CLIO) were synthesized as described previously and obtained from the Center for Molecular Imaging Research Chemistry Core (*14, 15*). All peptides were synthesized by the Peptide Synthesis/Protein Sequencing Core at the Massachusetts General Hospital using conventional Fmoc synthesis strategies on Rink amide resin. The peptides (0.1 mmol scale) were received on Rink amide resin with the N-terminus *t*-butoxucarbonyl (Boc)-protected. High performance liquid chromatography (HPLC) was performed on a Varian ProStar HPLC. Gradients were run with buffer A (H_2O/0.1% trifluoroacetic acid (TFA)) and buffer B (acetonitrile/10% buffer A). For analytical HPLC, a Varian C-18 reversed-phase column was used with

* To whom correspondence should be addressed. Tel: 617-726-5788. Fax: 617-726-5708. E-mail: jason_mccarthy@hms.harvard.edu (J.R.M.); fjaffer@mgh.harvard.edu (F.A.J.).

† Center for Molecular Imaging Research.

‡ Cardiovascular Research Center.

10.1021/bc9001163 CCC: $40.75 © 2009 American Chemical Society
Published on Web 05/20/2009

dimensions of 250 mm × 4.6 mm. For semipreparative HPLC, a Varian C-18 reversed-phase column was used with dimensions of 250 mm × 21.2 mm. UV−vis spectra were recorded on a Cary 50 spectrophotometer and fluorescence emission spectra on a Cary Eclipse spectrofluorometer. Electrospray ionization (ESI) mass spectra were recorded on a Waters Micromass ZQ mass spectrometer in the solvents indicated. Near-infrared fluorophores in the far-red (VT680, 660 nm excitation and 735 nm emission) or near-infrared channel (Cy7, 762 nm excitation and 800 nm emission) were employed for agent synthesis to enable translatable near-infrared fluorescence imaging. Fluorescence reflectance imaging was accomplished on either a Siemens BonSAI or Olympus OV100 system. To augment spin dephasing-induced MRI signal changes from iron oxide nanoparticles, T_2*-weighted MR imaging was conducted on a 4.7 T Bruker Pharmascan.

Peptide Cleavage and Purification. The peptide resin was swelled in *N*,*N*-dimethylformamide (DMF) for 15 min and filtered. The peptide was then cleaved from the resin and deprotected by reaction with TFA/triisopropylsilane/water (95:2.5:2.5, 5 mL) for 3 h. The resin was filtered, and the peptide contained in the supernatant was precipitated by the addition of excess methyl *tert*-butyl ether (MTBE). The precipitate was recovered following centrifugation and washed twice more with MTBE. The resulting crude peptide was purified by HPLC.

GNQEQVSPLTLLKC Peptide for Factor XIII (FXIII) Targeting. The peptide was purified by HPLC (gradient, 80% buffer A to 20% buffer A over 30 min; retention time (*rt*) = 12.8 min). ESI+ MS (30 V, H_2O/0.1% TFA) *m*/*z* = 1715.0 (MH^+).

GNAEQVSPLTLLKC Peptide Control (CXIII). The above FXIII peptide underwent a single amino acid substitution (Q → A) to generate a control peptide with weak binding by FXIII (*9*). The CXIII peptide was purified by HPLC (gradient, 80% buffer A to 20% buffer A over 30 min; *rt* = 13.3 min). ESI+ MS (30 V, H_2O/0.1% TFA) *m*/*z* = 1658.1 (MH^+).

GPRPPGGSKGC Peptide for Fibrin Targeting (GPRPP). The peptide was purified by HPLC (gradient, 100% buffer A to 60% buffer A over 30 min; *rt* = 10.1 min). ESI+ MS (30 V, H_2O/0.1% TFA) *m*/*z* = 941.8 (MH^+).

GPSPPGGSKGC Peptide Control Peptide (GPSPP). The control peptide with minimal binding to fibrin was purified by HPLC (gradient, 100% buffer A to 60% buffer A over 30 min; *rt* = 11.1 min). ESI+ MS (30 V, H_2O/0.1% TFA) *m*/*z* = 1011.8 (MH^+).

CLIO-VT680. To CLIO (20 mg) in PBS (2.37 mL) was added the succinimidyl ester of VivoTag 680 (1 mg, VisEn Medical) dissolved in 400 μL of dimethylsulfoxide (DMSO). The reaction was allowed to proceed for 16 h, at which time it was purified by filtration through Sephadex G-25 to yield 3 dyes per CLIO, as determined spectrophotometrically.

CLIO-Cy7. To CLIO (20 mg) in PBS (2.37 mL) was added the succinimidyl ester of Cy7 (1 mg, GE Healthcare) dissolved in 400 μL of dimethylsulfoxide (DMSO). The reaction was allowed to proceed for 16 h, at which time it was purified by filtration through Sephadex G-25 to yield 2 dyes per CLIO, as determined spectrophotometrically.

FXIII-CLIO-VT680 (CLIO-FXIII). To CLIO-VT680 (5 mg) in PBS (602 μL) was added succinimidyl iodoacetate (SIA, 5 mg) dissolved in DMSO (100 μL) The reaction proceeded for 4 h, at which time it was purified by filtration through Sephadex G-25. To the resulting particle was added the **FXIII** peptide (5 mg) dissolved in DMSO (200 μL). The reaction was allowed to proceed for 16 h, at which time it was purified by filtration through Sephadex G-25. This procedure typically conjugates 10−12 peptides per particle, as described previously (*16*).

CXIII-CLIO-VT680 (CLIO-CXIII). CLIO-CXIII was synthesized as described above for **CLIO-FXIII** using the **CXIII** peptide.

GPRPPGGSKGC-CLIO-Cy7 (CLIO-GPRPP). To CLIO-Cy7 (5 mg) in PBS (531 μL) was added succinimidyl iodoacetate (SIA, 5 mg) dissolved in DMSO (100 μL) The reaction proceeded for 3 h, at which time it was purified by filtration through Sephadex G-25. To the resulting particle was added the **GPRPP** peptide (5 mg) dissolved in DMSO (200 μL). The reaction was allowed to proceed for 16 h, at which time it was purified by filtration through Sephadex G-25. This procedure typically conjugates 10−12 peptides per particle, as described previously (*16*).

GPSPPGGSKGC-CLIO-Cy7 (*CLIO-GPSPP*). CLIO-GPSPP was synthesized as described above for **CLIO-GPRPP** using the **GPSPP** peptide.

In Vitro Clot Binding. Clots were created from fresh frozen plasma (FFP) in 96 well plates. Each well received 180 μL of FFP, 10 μL of 0.4 M $CaCl_2$, and 10 μL of thrombin (0.1 U/μL PBS). The plate was incubated at 37 °C for 90 min to form plasma clots. Thereafter, 6 μg of various nanoparticle preparations (∼2 mg Fe/mL) was added to respective wells and then incubated at 37 °C for an additional 30 min. The clots were then washed twice with PBS and centrifuged at 500 rpm for 10 min. They were then washed twice more with PBS and imaged by fluorescence reflectance imaging on the BonSAI system in the Cy7 or VT680 channels (exposure times from 1−10 s).

For magnetic resonance (MR) imaging, representative clots from the above FRI experiment were embedded in 2% agar and imaged using a T_2*-weighted pulse sequence with the following imaging parameters: multislice 2D fast low angle shot (FLASH) sequence, repetition time (*TR*) 500 ms, echo time (*TE*) 8 ms, flip angle 30°, matrix 128 × 128, in-plane resolution 0.3 × 0.3 mm, slice thickness 0.8 mm, and 8 averages. Following MR imaging, the gel was imaged on the OV100 system for correlation of fluorescence and magnetic resonance images.

In Vivo Thrombosis Binding. Animal studies were approved by the Hospital Subcommittee of Research Animal Care. In vivo thrombi were induced by ferric chloride ($FeCl_3$) injury to the jugular vein (*6*, *9*). Mice were anesthetized using an intraperiotenal (IP) ketamine (50 mg/mL, 330 μL), xylazine (100 mg/mL, 50 μL), and sterile saline (380 μL) mixture. Each mouse received a 60 μL IP induction dose of the resulting mixture, followed by 30−50 μL IP hourly for continued anesthesia. A paramedian neck incision was then made exposing approximately 1 cm of the jugular vein. $FeCl_3$ was locally applied to the jugular vein using a 2 mm × 1 mm strip of Whatman No. 1 filter paper soaked in 10% $FeCl_3$ in distilled water. The filter paper was applied to the anterior surface of the vein for 5 min. Thereafter, the filter paper was removed, and the injured vessel was irrigated with sterile saline. At 30 min after injury, a respective thrombus-targeted agent (CLIO-GPRPP, CLIO-FXIII) or control agent (CLIO-GPSPP, CLIO-CXIII) was injected i.v. via a tail vein catheter. All agents were injected at 7.5 mg Fe/kg mouse (200 μL total volume). Thrombus binding by imaging agents was determined by ex vivo fluorescence reflectance imaging (FRI) of the resected thrombosed and contralateral control jugular veins. At 30 min after injection of the agent, the mice were sacrificed by cervical dislocation and perfused with 20 mL saline. The jugular vein containing the thrombus and contralateral control jugular vein were then excised and imaged in the Cy7 (fibrin) or VT680 (FXIII) channel on an OV100 FRI system.

Image Analysis. Image analyses were performed with ImageJ 1.37v software (NIH) using manual region-of-interest tracing. Signal-to-background ratios (SBRs) were determined using the formula SBR = mean thrombus signal/mean background signal.

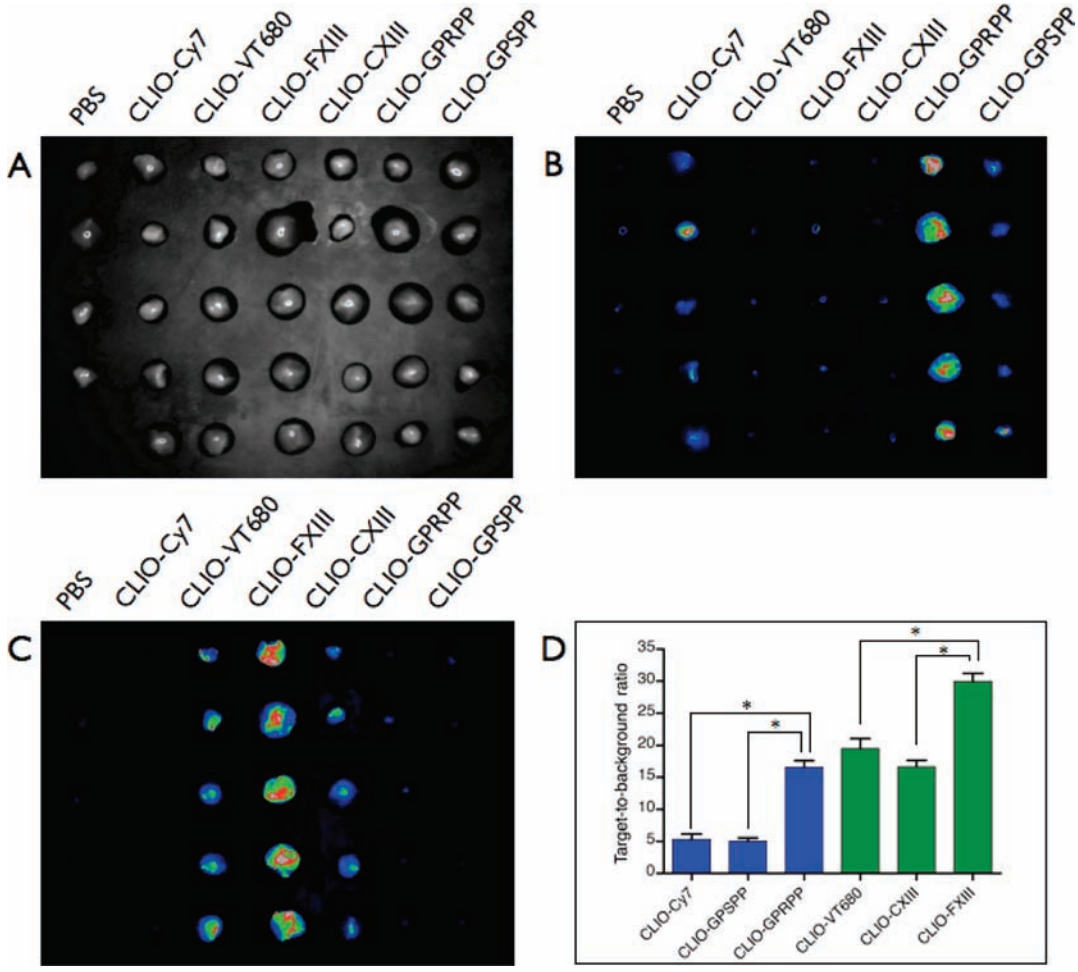

Figure 1. Fluorescence reflectance imaging of in vitro binding of agents to FFP clots (A, bright field image) as imaged in the (B) Cy7 and (C) VT680 channels. (D) The target-to-background ratios of the targeted agents were significantly greater than those of the control agents. All differences were statistically significant (*$P < 0.0001$).

For in vitro FRI studies, background was defined as the fluorescence signal from the clots incubated with PBS. For ex vivo FRI studies, background was defined as the nonthrombosed contralateral jugular vein. The statistical significance of the results was calculated using either a one way ANOVA or unpaired *t*-test, depending upon the number of groups in the comparison.

RESULTS AND DISCUSSION

Thrombus-Targeted Probe Synthesis. The fibrin-avid pentapeptide Gly-Pro-Arg-Pro-Pro was synthesized with the addition of the C-terminal sequence Gly-Gly-Ser-Lys-Gly-Cys (GGSKGC), in order to impart functionality on the peptide. GGSKGC has been used with peptides derived from phage screening libraries and contains an amine for modification via amide bond formation as well as a free thiol for conjugation via disulfide or thioester bonds. The peptide, Gly-Pro-Arg-Pro-Pro-Gly-Gly-Ser-Lys-Gly-Cys (**GPRPP** peptide) was synthesized by typical Fmoc methods, with Boc-protection at the N-terminus. This allows for the glycine to remain unmodified after cleavage from the resin, preventing a possible loss of binding affinity due to steric interference. Similar to the fibrin-targeting peptide, an analogous control peptide with scant FXIII avidity was synthesized with one amino acid replaced (*9*). The sequence Gly-Pro-Ser-Pro was previously shown to have minimal fibrin binding (*10*) and thus served as a suitable control peptide. This peptide sequence was initially identified in defective human fibrinogen (fibrinogen Detroit) (*17*). The peptide, Gly-Pro-Ser-Pro-Pro-Gly-Gly-Ser-Lys-Gly-Cys (**GPSPP** peptide), was synthesized as described above for the **GPRPP** peptide.

The fibrin-targeted nanoparticulate agents (**GPRPP-CLIO** and **GPSPP-CLIO**) were synthesized by modification of cross-linked iron oxide (CLIO) nanoparticles with the respective peptides. CLIO consists of a 5 nm iron oxide core surrounded by a dextran coating that has been cross-linked with epichlorohydrin and aminated (*14*). Initially, the particles were appended with Cy7 by reaction of the amines with the succinimidyl ester of the dye to yield 2 fluorophores per particle, as determined spectrophotometrically. The resulting magnetofluorescent particle was then reacted with succinimidyl iodoacetate (SIA) in order to impart reactivity toward sulfhydryl groups and subsequently reacted with the C-terminal cysteine of the peptide. Often, peptides are modified with a chromophore, such as fluorescein (FITC), prior to conjugation to the particle, in order to calculate the number of peptides per particle. In this case, this is not possible as the ultimate utility of these particles is the monitoring of clot formation in vivo, and the FITC channel is often necessary for fluorescence angiography during multichannel intravital microscopy. As the procedure for the conjugation of the peptide to the particle is well established, it is assumed that there are approximately 10 peptides per nanoparticle (*16*).

The nanoagent targeted to FXIIIa and its corresponding control (CXIII) were synthesized using the peptide sequences previously reported (*9, 18*). The N-terminus of α_2-antiplasmin,

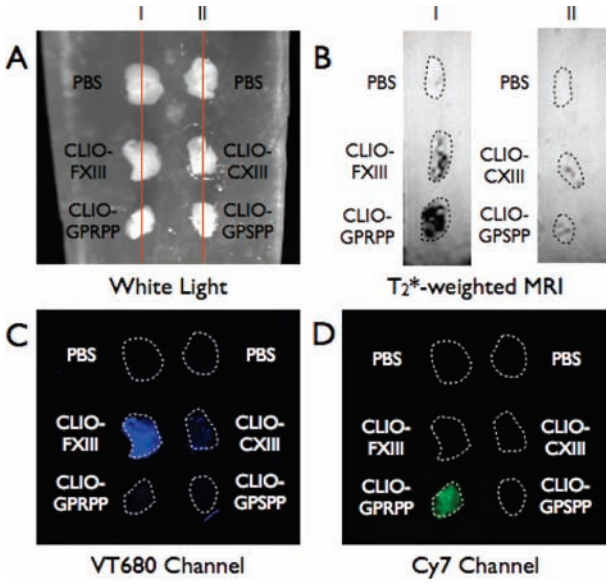

Figure 2. FRI and MRI imaging of FFP clots embedded in 2% agar. (A) White light image of FFP clots. Lines depict where sagittal view of clots was acquired in MRI. (B) T_2*-weighted MR image of FFP clots depicting strong T_2 decreases in clots incubated with CLIO-FXIII and CLIO-GPRPP. (I) and (II) correlate with lines (I) and (II) of the white light image. (C) FRI image of the gel in the VT680 channel demonstrating the binding of CLIO-FXIII to the FFP clot. (D) FRI image of the gel in the Cy7 channel demonstrating the binding of CLIO-GPRPP to the FFP clot.

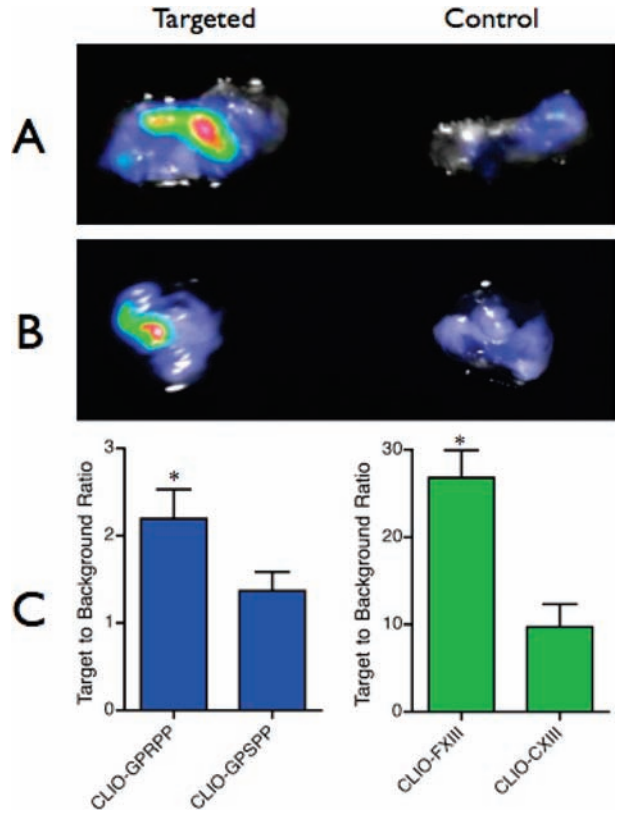

Figure 3. In vivo targeting of acute thrombi. Representative ex vivo FRI composite images of fibrin-targeted (A) and FXIII-targeted (B) nanoagents, and their respective control agents. The fluorescence images of the fibrin-targeted agent were acquired in the Cy7 channel and the FXIII-targeted agent in the VT680 channel. (C) Ex vivo FRI signal-to-background ratios for all agents studied (*$P < 0.05$).

N_{13}QEQVSPLTLLK$_{24}$, is specifically cross-linked into thrombi by the transglutaminase FXIIIa via a covalent bond between the glutamine 14 residue and the ε-amino group of a lysine residing within fibrin. In order to facilitate use as an imaging agent, this sequence was modified at its N-terminus with a glycine and at its C-terminus with a tryptophan spacer and a cysteine, to allow for conjugation to a particle. The control peptide sequence was identical to the FXIII peptide with the exception of an alanine replacement of glutamine 14. This modification results in negligible binding of the peptide to FXIII (*9*, *18*).

Analogous to the fibrin-targeted nanoparticle synthesis, the FXIII and CXIII peptides were conjugated to CLIO via the C-terminal cysteine after modification of the particle surface with SIA. The main difference between the nanoplatforms utilized for FXIIIa and fibrin is the wavelength of the fluorescent dye. For CLIO-FXIII, we chose to utilize VT680-labeled CLIO, as this will allow for simultaneous in vivo imaging of the accumulation of the two agents as the excitation and emission wavelengths of Cy7 and VT680 are spectrally distinct, which enables simultaneous fluorescence imaging of FXIII and fibrin via multichannel fluorescence imaging approaches. Specifically, these agents can be utilized to localize thrombi via the fibrin-targeted nanoparticle and determine thrombus age and lysis potential via the FXIII-targeted agent.

In Vitro Clot Binding. The targeting ability of the synthesized agents was tested with fresh frozen plasma (FFP) clots. Clots were formed in 96-well plates by the addition of $CaCl_2$ and thrombin to FFP, followed by incubation for 90 min. The agents were then incubated with the clots for an additional 30 min and were washed and centrifuged to remove the unbound agent.

Fibrin. The plate was initially imaged by FRI in the Cy7 channel. Clots incubated with the fibrin-targeted imaging agent (**CLIO-GPRPP**) demonstrated considerably greater NIRF signal than clots incubated with control agents **CLIO-GPSPP** and **CLIO-Cy7** (Figure 1B). The signal-to-background ratio (SBR) of **CLIO-GPRPP** clots (16.6 $\pm$ 1.7) was more than 3-fold the SBR of control **CLIO-GPSPP** (5.0 $\pm$ 1.2) and **CLIO-Cy7** (5.3 $\pm$ 0.8).

FXIIIa. When imaged in the VT680 channel, clots incubated with the FXIIIa-targeted imaging agent (**CLIO-FXIII**) demonstrated considerably greater NIRF signal than clots incubated with control agents **CLIO-CXIII** and **CLIO-VT680** (Figure 1C). The SBR of **CLIO-FXIII** clots (30 $\pm$ 2.8) was more than 1.5-fold higher than the SBR of control **CLIO-CXIII** (16.6 $\pm$ 2.3) and **CLIO-VT680** (19.5 $\pm$ 3.4). This high level of control agent background suggests an intrinsic avidity of VT680-bearing CLIO for thrombi, given the much lower SBRs obtained for **CLIO-Cy7** incubated clots.

MRI. The multimodal capabilities of the nanoagents was next tested by MRI. Representative FFP clots from the above experiments were embedded within 2% agar (Figure 2A) and then underwent T_2*-weighted MR imaging at 4.7 T. Consistent with the well-known MRI signal effects of iron oxide nanoparticles, clots binding targeted CLIO agents (**CLIO-GPRPPP** and **CLIO-FXIII**) demonstrated strong MRI signal loss on T2*-weighted images resulting in high thrombus-to-agar contrast-to-noise ratios (CNR) of 50.4 and 30.6, respectively (Figure 2B). In contrast, clots incubated with the control agents (**CLIO-CXIII** and **CLIO-GPSPP**) demonstrated negligible signal changes resulting in low CNR values (8.6 and -1.2, respectively) (Figure 2B). FRI of the agar clot phantom after MRI confirmed increased deposition of the targeted FXIII nanoparticle in the VT680 channel (Figure 2C) and targeted fibrin nanoparticles in the Cy7 channel (Figure 2D), further illustrating the multimodal nature of the agents.

In Vivo Thrombosis Binding. The targeting ability of the nanoagents was tested in vivo in an $FeCl_3$-induced thrombosis

model in wild-type C57Bl6 mice. Application of 10% $FeCl_3$ laden filter paper directly to the jugular vein for 5 min induced thrombus formation. After 30 min, mice were injected intravenously with targeted or control agents, followed by a 30 min circulation time. The thombosed jugular vein and contralateral normal jugular vein were resected and imaged by FRI. As is evident in Figure 3, the fibrin and FXIII-targeted agents preferentially accumulated within thrombi and generated higher SBR ratios as compared to those of their respective control agents. **CLIO-GPRPP** displayed a 1.6-fold greater SBR than the control particle, **CLIO-GPSPP** (SBR $= 2.19 \pm 0.33$ vs 1.37 ± 0.21, respectively), while the SBR for **CLIO-FXIII** was 2.7-fold greater than that of **CLIO-CXIII** (SBR $= 26.8 \pm 3.2$ vs 9.7 ± 2.6, respectively). The differences in the magnitude of the SBRs can be attributed to the sensitivity of the instrument in the distinct fluorescent channels. The longest wavelength channel, Cy7, is much less sensitive than the VT680 channel due to fewer photons being transmitted by the OV100 broadband light source. Longer acquisition times are thus required for image formation, which concomitantly produces greater background signals.

CONCLUSIONS

In this work, we demonstrate the synthesis of two novel multimodal nanoagents targeted to key molecules in thrombi, namely, fibrin and FXIIIa. In vitro clot studies demonstrated strong binding of the agents, which is detectable by near-infrared fluorescence and magnetic resonance imaging. In vivo thrombosis studies in mice further demonstrated that these nanoagents readily accumulated within vascular thrombi preferentially over analogously synthesized control agents. Further in vivo studies will utilize these agents to image the biological expression of fibrin and factor XIII in acute and subacute thrombi, to examine the role of fibrin and FXIIIa in predicting fibrinolysis and stent thrombosis.

ACKNOWLEDGMENT

This work was supported by NIH grants U24-CA092782 (to R.W.) and U01-HL080731 (to J.R.M., F.A.J., and R.W.), American Heart Association Scientist Development Grant (to F.A.J.), Howard Hughes Medical Institute Career Development Award (to F.A.J.), and NIH grants U54-CA119349 (to R.W.) and U54-CA126515 (to R.W.). We thank Dr. Ashok Khatri for synthesizing the peptide, Dr. Matthias Nahrendorf and Gregory Wojtkiewicz, MS for assistance with MRI, and Zach Mueller for assistance with FRI.

Supporting Information Available: HPLC traces of all peptides synthesized and ex vivo FRI images acquired during this study. This material is available free of charge via the Internet at http://pubs.acs.org.

LITERATURE CITED

(1) Murray, C. J., and Lopez, A. D. (1997) Alternative projections of mortality and disability by cause 1990−2020: Global Burden of Disease Study. *Lancet. 9064*, 1498–1504.
(2) Jaffer, F. A., Libby, P., and Weissleder, R. (2007) Molecular imaging of cardiovascular disease. *Circulation 9*, 1052–1061.
(3) Flaumenhaft, R., Tanaka, E., Graham, G. J., De Grand, A. M., Laurence, R. G., Hoshino, K., Hajjar, R. J., and Frangioni, J. V. (2007) Localization and quantification of platelet-rich thrombi in large blood vessels with near-infrared fluorescence imaging. *Circulation 1*, 84–93.
(4) Massberg, S., Enders, G., Matos, F. C., Tomic, L. I., Leiderer, R., Eisenmenger, S., Messmer, K., and Krombach, F. (1999) Fibrinogen deposition at the postischemic vessel wall promotes platelet adhesion during ischemia-reperfusion in vivo. *Blood 11*, 3829–3838.
(5) Sim, D. S., Merrill-Skoloff, G., Furie, B. C., Furie, B., and Flaumenhaft, R. (2004) Initial accumulation of platelets during arterial thrombus formation in vivo is inhibited by elevation of basal cAMP levels. *Blood 6*, 2127–2134.
(6) Jaffer, F. A., Tung, C. H., Gerszten, R. E., and Weissleder, R. (2002) In vivo imaging of thrombin activity in experimental thrombi with thrombin-sensitive near-infrared molecular probe. *Arterioscler., Thromb., Vasc. Biol. 11*, 1929–1935.
(7) Falati, S., Gross, P., Merrill-Skoloff, G., Furie, B. C., and Furie, B. (2002) Real-time in vivo imaging of platelets, tissue factor and fibrin during arterial thrombus formation in the mouse. *Nat. Med. 10*, 1175–1181.
(8) Thakur, M. L., Pallela, V. R., Consigny, P. M., Rao, P. S., Vessileva-Belnikolovska, D., and Shi, R. (2000) Imaging vascular thrombosis with 99mTc-labeled fibrin alpha-chain peptide. *J. Nucl. Med. 1*, 161–168.
(9) Jaffer, F. A., Tung, C. H., Wykrzykowska, J. J., Ho, N. H., Houng, A. K., Reed, G. L., and Weissleder, R. (2004) Molecular imaging of factor XIIIa activity in thrombosis using a novel, near-infrared fluorescent contrast agent that covalently links to thrombi. *Circulation 2*, 170–176.
(10) Laudano, A. P., and Doolittle, R. F. (1978) Synthetic peptide derivatives that bind to fibrinogen and prevent the polymerization of fibrin monomers. *Proc. Natl. Acad. Sci. U.S.A. 7*, 3085–3089.
(11) Aruva, M. R., Daviau, J., Sharma, S. S., and Thakur, M. L. (2006) Imaging thromboembolism with fibrin-avid 99mTc-peptide: evaluation in swine. *J. Nucl. Med. 1*, 155–162.
(12) Ntziachristos, V., Tung, C.-H., Bremer, C., and Weissleder, R. (2002) Fluorescence molecular tomography resolves protease activity in vivo. *Nat. Med. 8*, 757–761.
(13) Jaffer, F. A., Vinegoni, C., John, M. C., Aikawa, E., Gold, H. K., Finn, A. V., Ntziachristos, V., Libby, P., and Weissleder, R. (2008) Real-time catheter molecular sensing of inflammation in proteolytically active atherosclerosis. *Circulation 18*, 1802–1809.
(14) Josephson, L., Tung, C. H., Moore, A., and Weissleder, R. (1999) High-efficiency intracellular magnetic labeling with novel superparamagnetic-Tat peptide conjugates. *Bioconjugate Chem. 2*, 186–191.
(15) Perez, J. M., O'Loughin, T., Simeone, F. J., Weissleder, R., and Josephson, L. (2002) DNA-based magnetic nanoparticle assembly acts as a magnetic relaxation nanoswitch allowing screening of DNA-cleaving agents. *J. Am. Chem. Soc. 12*, 2856–2857.
(16) Wunderbaldinger, P., Josephson, L., and Weissleder, R. (2002) Tat peptide directs enhanced clearance and hepatic permeability of magnetic nanoparticles. *Bioconjugate Chem. 2*, 264–268.
(17) Blomback, M., Blomback, B., Mammen, E. F., and Prasad, A. S. (1968) Fibrinogen Detroit--a molecular defect in the N-terminal disulphide knot of human fibrinogen? *Nature 5137*, 134–137.
(18) Tung, C. H., Ho, N. H., Zeng, Q., Tang, Y., Jaffer, F. A., Reed, G. L., and Weissleder, R. (2003) Novel Factor XIII Probes for Blood Coagulation Imaging. *ChemBioChem 9*, 897–899.

BC9001163

Supplementary Material to:

Multimodal Nanoagents for the Detection of Intravascular Thrombi

Jason R. McCarthy,[1] Purvish Patel,[1,2] Ion Botnaru,[2] Pouneh Haghayeghi,[1] Ralph Weissleder,[1] and Farouc A Jaffer[1,2]*

1. Center for Molecular Imaging Research, Harvard Medical School and Massachusetts General Hospital, 149 13th St., Rm 5406, Charlestown, MA 02129, USA

2. Cardiovascular Research Center, Cardiology Division, Harvard Medical School and Massachusetts General Hospital, 185 Cambridge St Room 3206, Boston MA 02114

Analytical HPLC traces of synthesized peptides:

GPRPPGGSKGC (GPRPP).

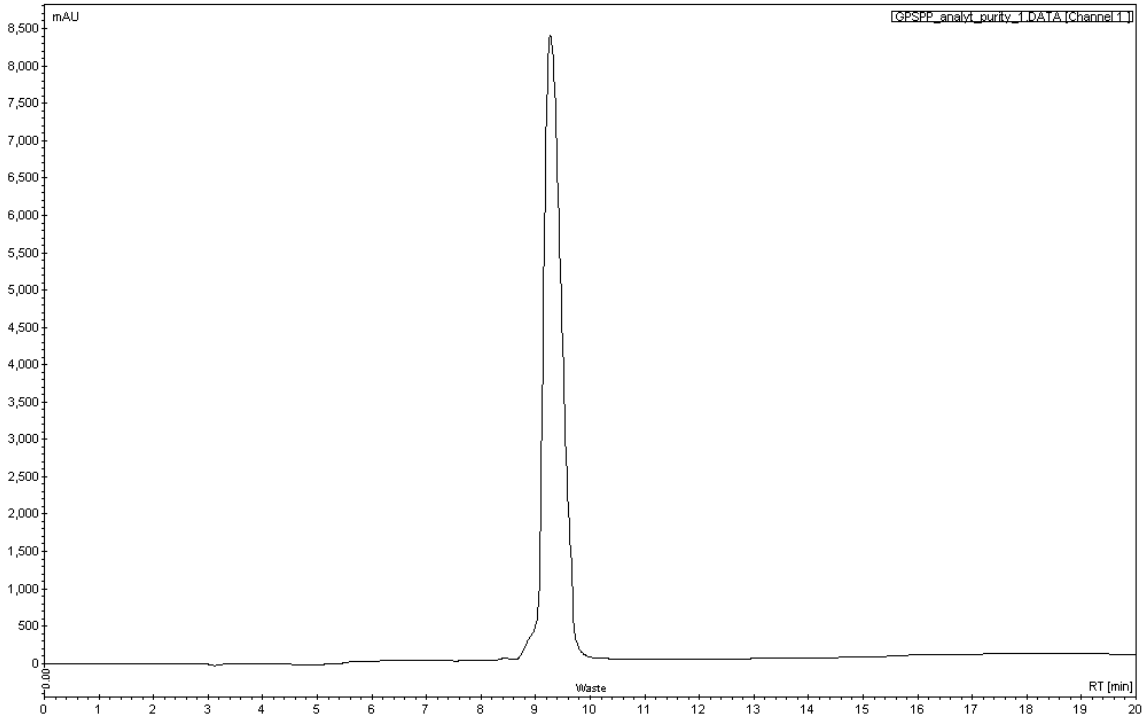

GPSPPGGSKGC (GPSPP).

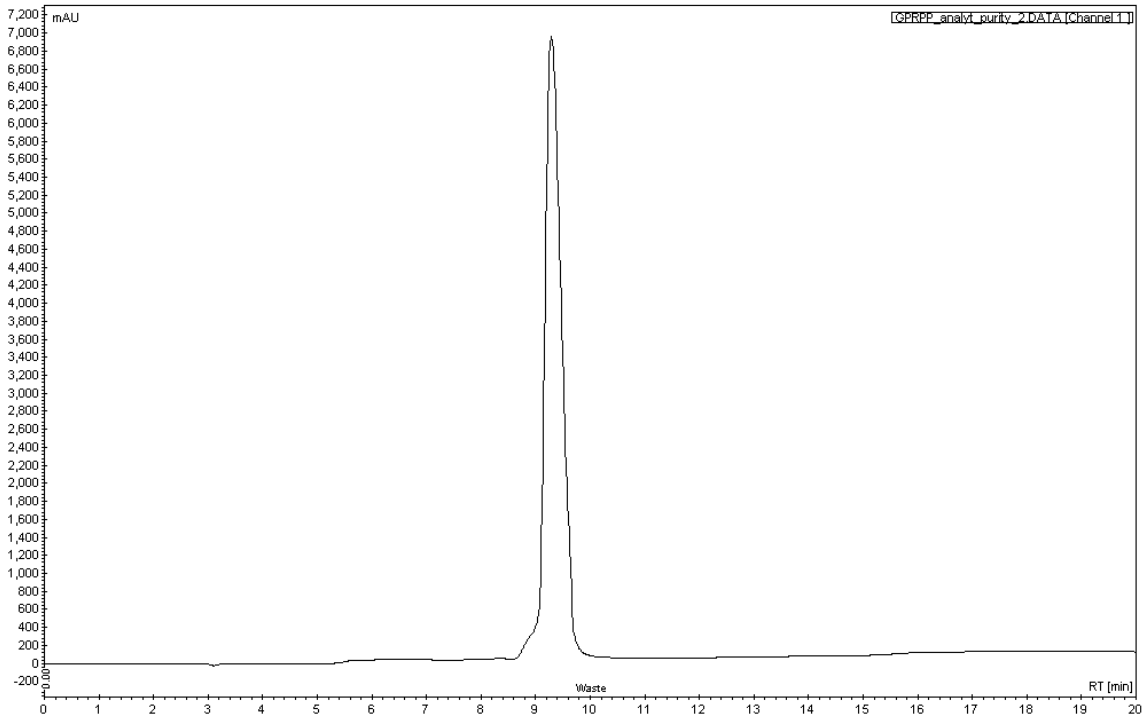

GNQEQVSPLTLLKC (FXIII).

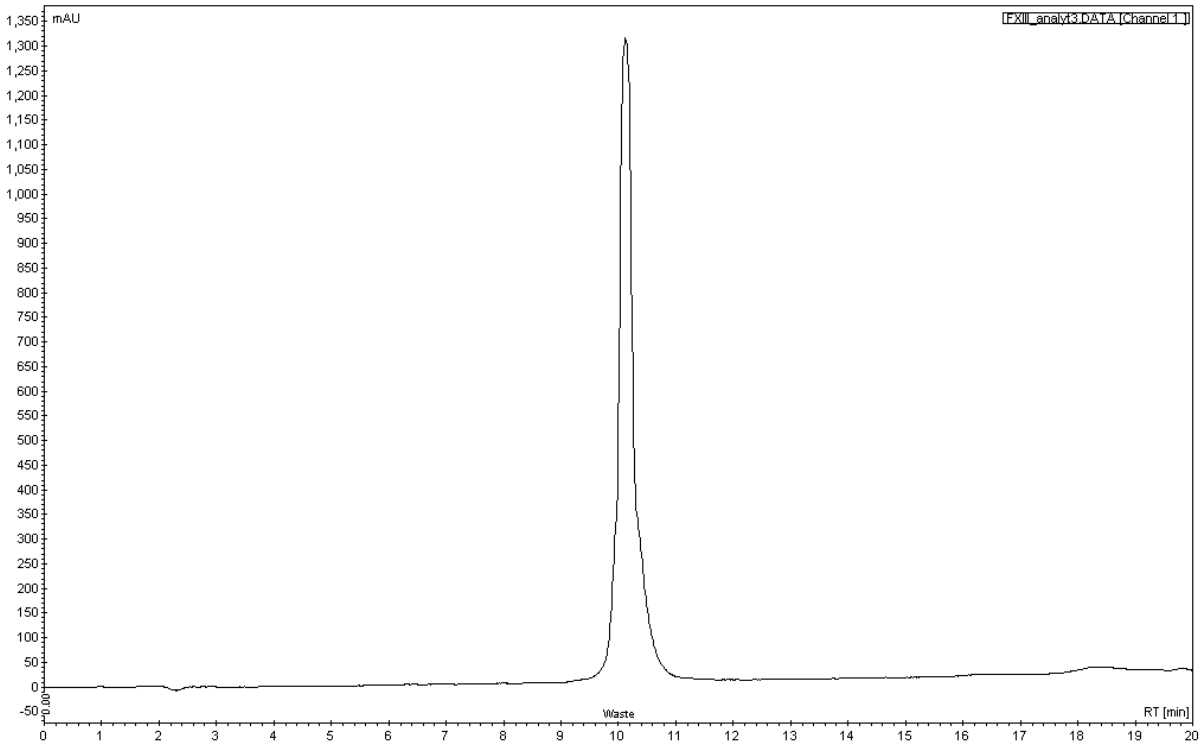

GNAEQVSPLTLLKC (CXIII).

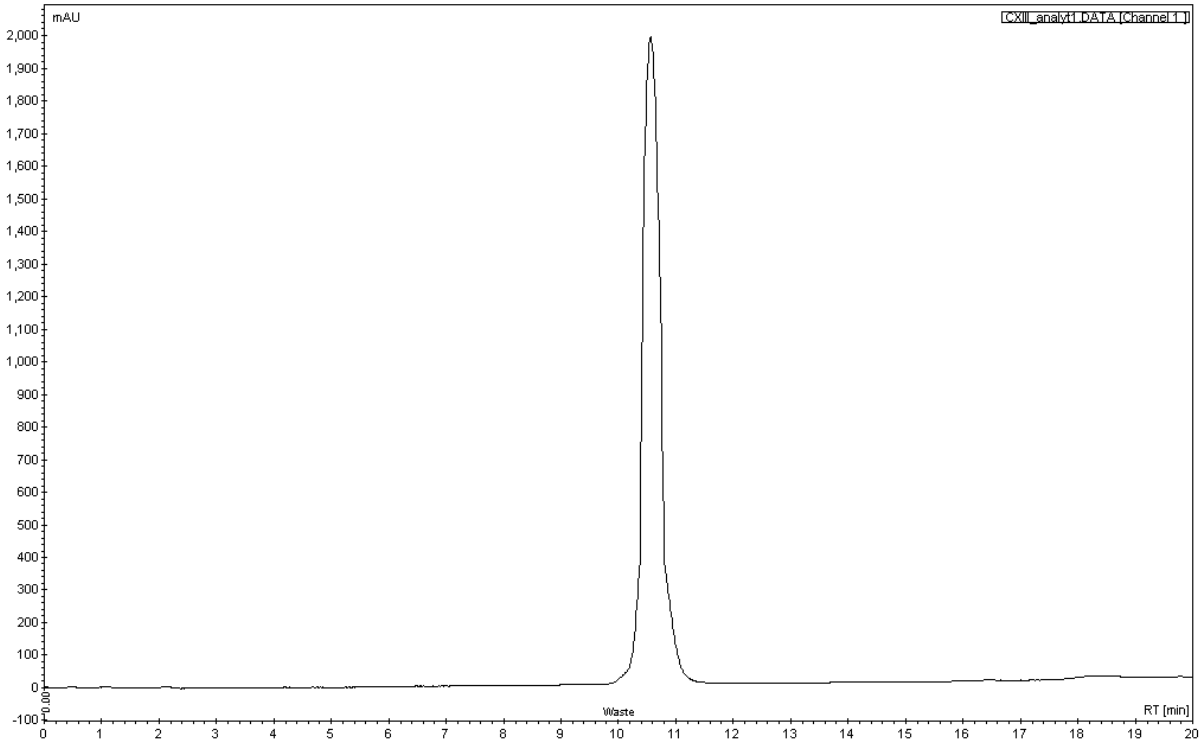

Full merged images of ex vivo thrombi.

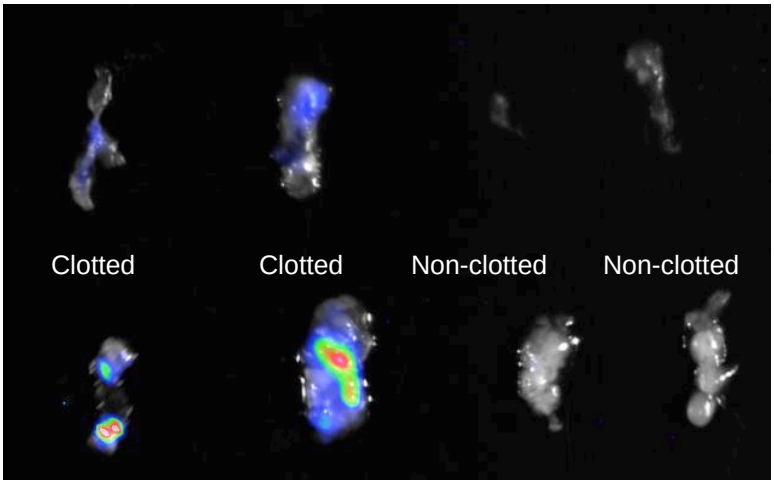

CLIO-GPSPP

CLIO-GPRPP

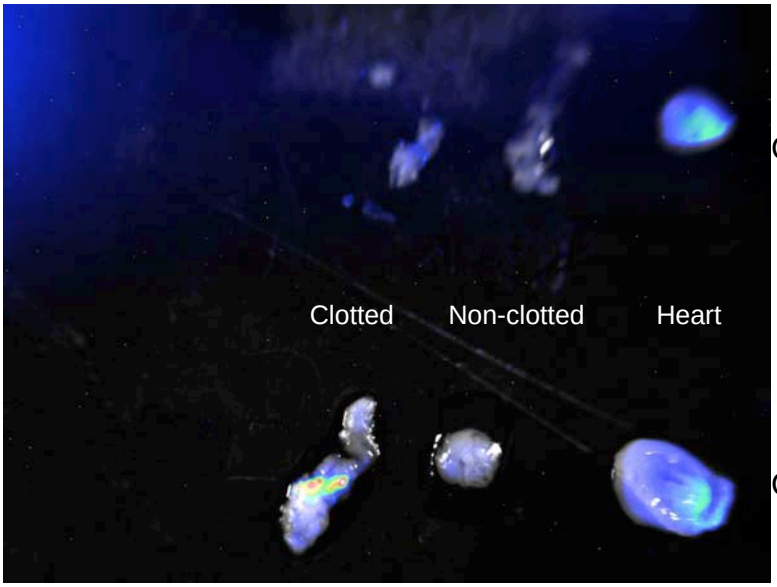

CLIO-GPSPP

CLIO-GPRPP

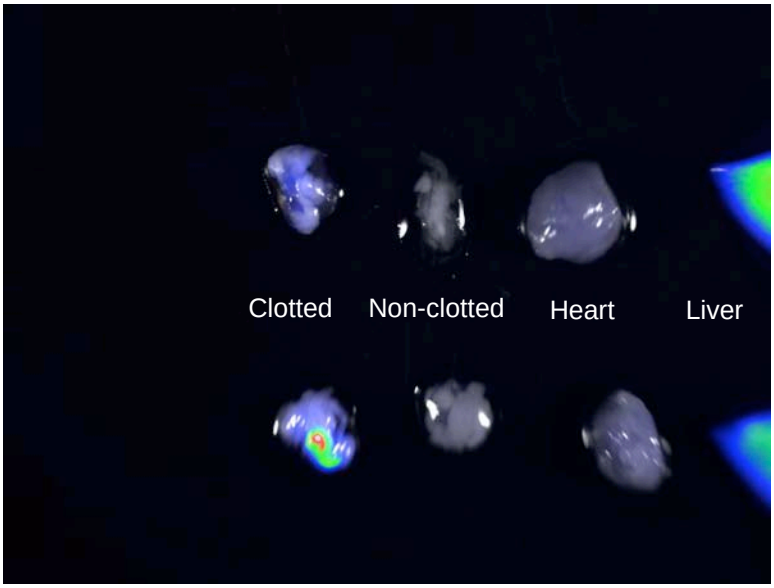

CLIO-CXIII

CLIO-FXIII

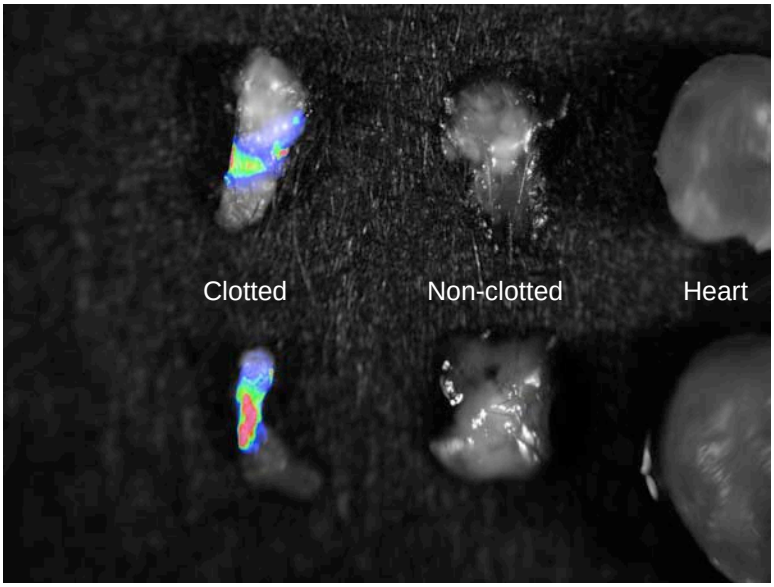

CLIO-CXIII

CLIO-FXIII

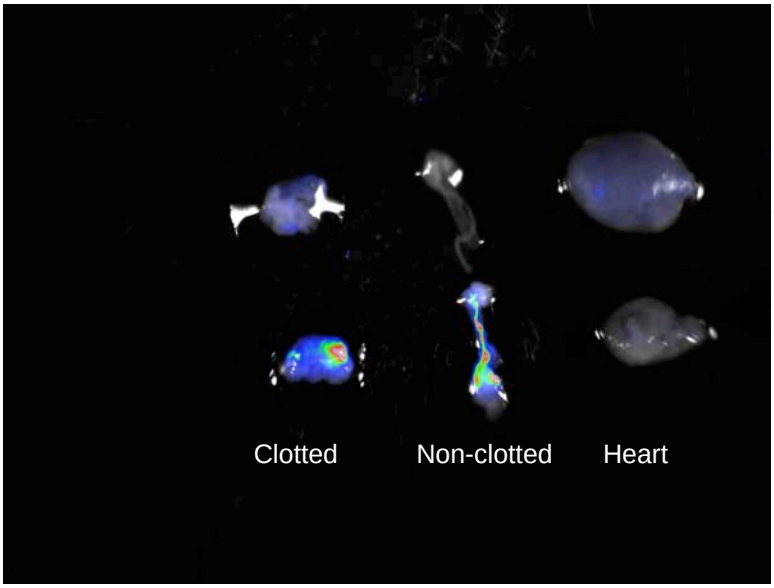
CLIO-CXIII
CLIO-FXIII
Clotted
Non-clotted
Heart

Hybridization-Sensitive Fluorescent Probe for Long-Term Monitoring of Intracellular RNA

Takeshi Kubota, Shuji Ikeda, Hiroyuki Yanagisawa, Mizue Yuki, and Akimitsu Okamoto*

Advanced Science Institute, RIKEN (The Institute of Physical and Chemical Research), Wako, Saitama 351-1098, Japan.
Received March 18, 2009; Revised Manuscript Received April 8, 2009

Nuclease-resistant hybridization probes for long-term intracellular RNA imaging were synthesized. Newly designed probes with a 2′-*O*-MeRNA structure showed high resistance against nucleases, which is in contrast to the low resistance of DNA probes. These modified probes retained the function on the on−off switching of fluorescence emission in sensitive response to RNA recognition, based on the mechanism of interdye excitonic interaction, and functioned effectively for the long-term monitoring of RNA-stained living cells.

INTRODUCTION

Recent developments of techniques for visualizing compounds, organs, and processes in the living cell have paved the way for advanced studies of cell function. The visualization of intracellular RNA is, however, still immature, compared to the analysis of live cells using proteins fused with fluorescent proteins. It is mainly the fluorescence-labeled nucleic acid probes that are used for the visualization of RNA (*1*−*5*). Conventional probes always emit fluorescence when excitation light is shone on probe-containing RNA samples. Therefore, fluorescence from probes that do not take part in labeling of the target RNA causes strong background fluorescence. Furthermore, the DNA backbone of probes is readily digested by intracellular nucleases in a short time, and thus conventional probes, even well-known molecular beacon DNA probes (*6, 7*), are not suitable for long-term RNA monitoring in a living cell.

We recently developed a doubly thiazole orange-labeled probe to achieve high fluorescence intensity for a hybrid with the target DNA or RNA, and effective quenching for a single-strand state of the probe (*8*−*10*). Emission from the probe was controlled by interdye excitonic interaction. The clear change in fluorescence intensity depending on hybridization is useful for visible RNA analysis (*10*). However, this probe has a 2′-deoxyribose backbone and will therefore be unstable under conditions where nucleases are present. The usefulness of the probe may be limited to in vitro or short-term experiments in cells before degradation by cellular nucleases. For the long-term observation of target RNA in living cells, a new type of the probe structure is required that is not degraded by nucleases and maintains the hybridization-sensitive on−off fluorescence switching function.

Here, we report on the novel design of an RNA detection probe that is tolerant to exposure to intracellular nucleases. A sugar-modified structure (2′-*O*-MeRNA) was adopted for a new exciton-controlled probe. The probe showed high resistance against nucleases and maintained a high on−off performance as a hybridization-sensitive fluorescent probe.

EXPERIMENTAL PROCEDURES

Probe Synthesis. Probes were synthesized by a conventional phosphoramidite method. The diamino-modified nucleoside phosphoramidite was synthesized as described in our previous paper (*8*). The synthesized oligomer was cleaved from the support with 28% aqueous ammonia and deprotected at 55 °C for 8 h. After removal of ammonia from the solution under reduced pressure, the unlabeled oligomer was purified by reversed-phase HPLC on a 5-ODS-H column (10 mm × 150 mm, elution with a solvent mixture of 0.1 M triethylammonium acetate (TEAA), pH 7.0, linear gradient over 30 min from 5% to 37.5% acetonitrile at a flow rate of 3.0 mL/min).

Table 1. Sequences of Synthetic Probes and the Complementary RNA Used in This Study

probes	sequences (5′→3′)[a]
Probe$_{dna}$1	CGCAATXTAACGC
Probe$_{omr}$1[b]	CGCAAUXUAACGC
RNA1	GCGUUAAAUUGCG
Probe$_{dna}$2	ATCCACTCTCTCXTTCCA
Probe$_{omr}$2[b]	AUCCACUCUCUCXUUCCA
RNA2	UGGAAAGAGAGAGUGGAU
Probe$_{dna}$3	CCTCXCCTTGTTCCTGCC
Probe$_{omr}$3[b]	CCUCXCCUUGUUCCUGCC
RNA3	GGCAGGAACAAGGAGAGG
Probe$_{dna}$4	CAAATCCXCTCAACCTCT
Probe$_{omr}$4[b]	CAAAUCCXCUCAACCUCU
RNA4	AGAGGUUGAGAGGAUUUG
Probe$_{dna}$5	TTTTTTXTTTTTT
Probe$_{omr}$5[b]	UUUUUUXUUUUUU
RNA5	AAAAAAAAAAAAA

[a] X denotes a doubly thiazole orange-labeled deoxyuridine as shown in Figure 1. [b] Probes have 2′-*O*-methylribose backbones, except X that has a 2′-deoxyribose.

A solution of the succinimidyl ester of dye (50 equiv to an active amino group of the synthesized oligomer) in DMF was added to a solution of deprotected oligomer in 100 mM sodium carbonate buffer (pH 9.0) and incubated at 25 °C for 16 h. The reaction mixture was diluted with ethanol. After centrifuging at 4 °C for 20 min, the supernatant was removed. The residue was dissolved in a small volume of water, and then, the solution was passed through a 0.45 μm filter. The product was purified by reversed-phase HPLC on a 5-ODS-H column (10 mm × 150 mm, elution with a solvent mixture of 0.1 M TEAA, pH 7.0, linear gradient over 30 min from 5% to 37.5% acetonitrile at a flow rate of 3.0 mL/min). The synthesized probes are listed in Table 1. They were identified by MALDI-TOF mass spectrometry. (Here, the molecular weight of the counteranions of dyes is not included in the value of M, and X denotes a doubly thiazole orange-labeled deoxynucleotide.): **Probe$_{dna}$1**, calcd for $C_{180}H_{217}N_{56}O_{78}P_{12}S_2$ 4848.8 $[M - H]^+$, found, 4846.5;

* To whom correspondence may be addressed. Phone: (+81) 48-467-9238. Fax: (+81) 48-467-9205. E-mail: aki-okamoto@riken.jp.

10.1021/bc900120a CCC: $40.75 © 2009 American Chemical Society
Published on Web 05/14/2009

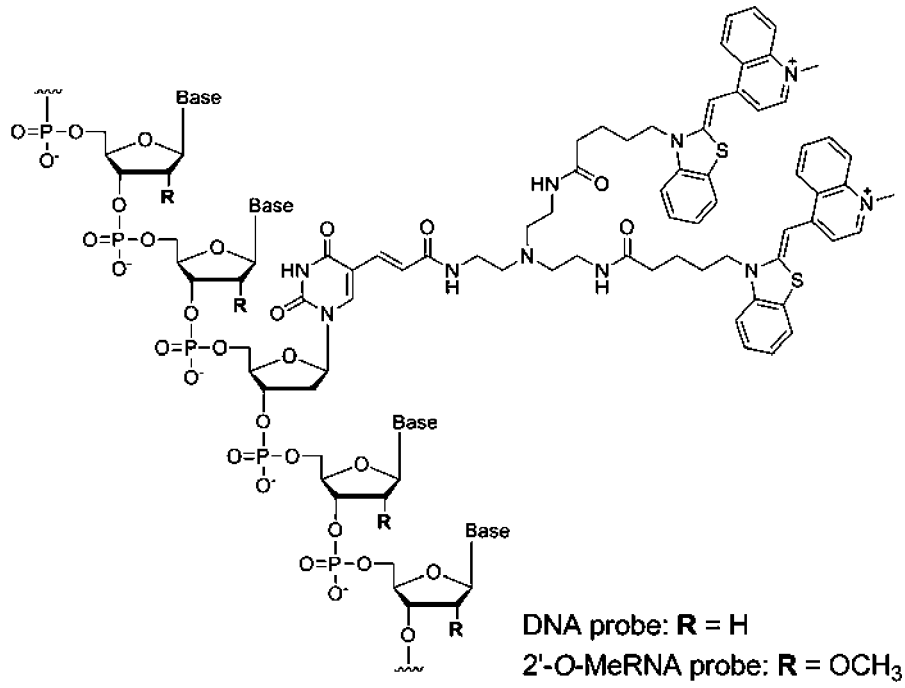

Figure 1. Structure of the hybridization probe controlled by excitonic interaction between thiazole orange dyes.

Probe$_{omr}$1, calcd for $C_{190}H_{237}N_{56}O_{90}P_{12}S_2$ 5181.1 $[M - H]^+$, found, 5180.4; **Probe$_{dna}$2**, calcd for $C_{226}H_{281}N_{61}O_{113}P_{17}S_2$ 6250.7 $[M - H]^+$, found, 6248.3; **Probe$_{omr}$2**, calcd for $C_{237}H_{303}N_{61}O_{130}P_{17}S_2$ 6677.0 $[M - H]^+$, found, 6678.8; **Probe$_{dna}$3**, calcd for $C_{225}H_{281}N_{59}O_{116}P_{17}S_2$ 6258.7 $[M - H]^+$, found, 6257.7; **Probe$_{omr}$3**, calcd for $C_{236}H_{303}N_{59}O_{133}P_{17}S_2$ 6684.9 $[M - H]^+$, found, 6686.0; **Probe$_{dna}$4**, calcd for $C_{226}H_{279}N_{67}O_{109}P_{17}S_2$ 6268.7 $[M - H]^+$, found, 6269.7; **Probe$_{omr}$4**, calcd for $C_{239}H_{305}N_{67}O_{126}P_{17}S_2$ 6723.0 $[M - H]^+$, found, 6725.4; **Probe$_{dna}$5**, calcd for $C_{184}H_{228}N_{34}O_{92}P_{12}S_2$ 4822.8 $[M - H]^+$, found, 4820.7; **Probe$_{omr}$5**, calcd for $C_{184}H_{228}N_{34}O_{104}P_{12}S_2$ 5014.8 $[M - H]^+$, found, 5011.6.

Melting Temperature. All melting temperature (T_m) values of probe−RNA duplexes (1 μM, final duplex concentration) were recorded in a HEPES-buffered solution (120 mM KCl, 5 mM NaCl, 25 mM HEPES, pH 7.2). Absorbance vs temperature profiles were measured at 260 nm. The absorbance of the samples at 260 nm was monitored from 10 to 90 °C at a heating rate of 0.5 °C/min. First derivatives were calculated from these profiles to determine the T_m values.

Absorption and Fluorescence Data. Absorption and fluorescence spectra of the probes (1.0 μM single-stranded or duplex concentration) were measured in a HEPES-buffered solution (120 mM KCl, 5 mM NaCl, 25 mM HEPES, pH 7.2), using a quartz cuvette with a 1 cm path length. The excitation and emission bandwidths were 1.5 nm. The fluorescence quantum yield (Φ) was determined using 9,10-diphenylanthracene as a reference, with a known value of $\Phi = 0.95$ in ethanol. The quantum yield was calculated using the following equation.

$$\Phi_{(S)}/\Phi_{(R)} = [A_{(S)}/A_{(R)}] \times [(Abs)_{(R)}/(Abs)_{(S)}] \times [n_{(S)}^2/n_{(R)}^2] \quad (1)$$

Here, $\Phi_{(S)}$ and $\Phi_{(R)}$ are the fluorescence quantum yields of the sample and the reference, respectively. The terms $A_{(S)}$ and $A_{(R)}$ are the areas under the fluorescence spectra of the sample and the reference, respectively; $(Abs)_{(S)}$ and $(Abs)_{(R)}$ are the optical densities of the sample and the reference solution at the wavelength of excitation, respectively; and $n_{(S)}$ and $n_{(R)}$ are the values of the refractive index for the solvents used for the sample ($n_{(S)} = 1.333$) and the reference ($n_{(R)} = 1.383$).

Cell Culture. Dulbecco's modified Eagle's medium (DMEM) and fetal bovine serum (FBS) were purchased from GIBCO. HeLa cells were cultured at 37 °C in DMEM containing 10% heat-inactivated FBS, 25 U/mL penicillin, and 25 mg/mL streptomycin, under a humidified atmosphere with 5% CO_2. For experimental use, cells (passage numbers 5−9) were cultured in glass-based dishes. Prior to microscope observation, the culture medium was washed and exchanged to phenol red free DMEM.

Transfection and Cell Imaging. A probe solution in water (50 μM, 2 μL) was introduced using 2 μL of lipofectamine 2000 (Invitrogen). After incubation for 1 h in a solution of lipofectamine 2000 and probe, cells were washed twice with PBS and observed in phenol red free DMEM. Cells were maintained under culturing conditions using an incubation system during the observation. Images were acquired with a motorized inverted microscope (Axio Observer Z1; Zeiss) equipped with a 20× objective and a filter set (ex 500/24−25, dm 520, em 542/25−27). Acquired images were analyzed and processed with *AxioVision 4.2*.

Digestion of Probe by Nucleases. Nuclease sensitivity was analyzed with single-stranded probes (200 pmol). Digestion of the probes with an exonuclease (Exonuclease I, Takara, 1.5 U) was performed at 37 °C in 67 mM glycine−KOH (pH 9.5, 50 μL), 6.7 mM $MgCl_2$, 1 mM dithiothreitol. Digestion of the probes with an endonuclease (S1 nuclease, Takara, 0.5 U) was performed at 37 °C in 50 μL buffer of 30 mM NaOAc (pH 4.6), 280 mM NaCl, 1 mM $ZnSO_4$. After the digestion treatment, the mixture was diluted with 500 μL ice-cold water and analyzed immediately by reversed-phase HPLC on a 5-ODS-H column (10 mm × 150 mm, elution with a solvent mixture of 0.1 M TEAA, pH 7.0, with a linear gradient over 24 min from 5% to 35% acetonitrile, at a flow rate of 3.0 mL/min). Probes were detected at 480 nm, and the quantities determined from the absorption peak areas. For the fluorescent spectra of single-stranded and hybridized probes, the reaction samples were used after 10 times dilution with HEPES buffer.

Digestion of RNA by RNaseH. A solution containing a probe and the complementary RNA (0.1 μM each) in 1600 μL HEPES buffer containing 5 mM magnesium chloride was prepared. The

Table 2. Photophysical Properties of Hybridization-Sensitive Probes

probes	T_m[a] ($\Delta T_{m(natural)}$[b])/°C	λ_{max} (ε)/nm	λ_{em} (λ_{ex})/nm	Φ_f	I_{hybrid}/I_{probe}[c]
Probe$_{dna}$1		478 (128220)	537 (518)	0.04	
		504 (57700)			
Probe$_{dna}$1/RNA1	54 (+8)	509 (119060)	530 (514)	0.37	20
Probe$_{omr}$1		480 (106400)	550 (514)	0.17	
		507 (80400)			
Probe$_{omr}$1/RNA1	60 (+14)	512 (130400)	532 (516)	0.44	7
Probe$_{dna}$2		485 (69300)	537 (515)	0.07	
		507 (83900)			
Probe$_{dna}$2/RNA2	71 (+5)	508 (99800)	529 (512)	0.43	9
Probe$_{omr}$2		476 (110700)	534 (514)	0.01	
		505 (52200)			
Probe$_{omr}$2/RNA2	81 (+16)	512 (108400)	532 (516)	0.37	121
Probe$_{dna}$3		480 (77100)	534 (517)	0.09	
		510 (67200)			
Probe$_{dna}$3/RNA3	73 (+2)	510 (90700)	533 (514)	0.36	6
Probe$_{omr}$3		477 (101700)	534 (516)	0.03	
		504 (48800)			
Probe$_{omr}$3/RNA3	77 (+6)	511 (91600)	534 (515)	0.36	25
Probe$_{dna}$4		480 (98600)	534 (514)	0.03	
		509 (67100)			
Probe$_{dna}$4/RNA4	65 (+4)	511 (114000)	530 (516)	0.41	30
Probe$_{omr}$4		477 (106800)	536 (514)	0.03	
		507 (58300)			
Probe$_{omr}$4/RNA4	67 (+6)	511 (99600)	535 (517)	0.41	26
Probe$_{dna}$5		477 (86000)	535 (517)	0.01	
		505 (43900)			
Probe$_{dna}$5/RNA5	49 (+13)	509 (87200)	532 (514)	0.51	145
Probe$_{omr}$5		477 (99300)	536 (517)	0.01	
		504 (41600)			
Probe$_{omr}$5/RNA5	40 (+4)	509 (85300)	534 (514)	0.37	209

[a] All T_m values of probe−RNA duplexes (1 μM) were taken in a HEPES-buffered solution (120 mM KCl, 5 mM NaCl, 25 mM HEPES, pH 7.2). [b] Values given by subtraction of the T_m of the natural DNA/RNA duplex with the same sequence from the T_m of the probe−RNA duplex. [c] Ratio of the fluorescence intensities of hybrid and nonhybrid (probe only) at the wavelength of the fluorescence maximum of hybrids.

time course data were recorded at 25 °C for 1 h, with and without 4 U RNaseH.

RESULTS AND DISCUSSION

Design and Synthesis. We designed a new hybridization-sensitive probe, which has both a 2′-*O*-methylribose backbone and a doubly fluorescence-labeled deoxyuridine unit (Figure 1). A modified nucleic acid containing 2′-*O*-methyl-RNA (2′-*O*-MeRNA) is known to bind more tightly to complementary RNA sequences than analogous DNA oligomers, and it has improved resistance to degradation by nucleases (*11, 12*). Four nucleoside phosphoramidites for 2′-*O*-MeRNA synthesis and a phosphoramidite of the 2′-deoxyuridine derivative with two amino linkers at C5 were used for probe synthesis using a conventional DNA synthesis method (*8*). Double fluorescence labeling was carried out by mixing the diamino-modified oligomer with the thiazole orange derivative with a carboxy-activated alkyl linker. Synthesized DNA and 2′-*O*-MeRNA probes are listed in Table 1.

Duplex Stability and Photophysics. 2′-*O*-MeRNA is known to exhibit higher affinity for RNA targets than the corresponding DNA, resulting in higher T_m values (*13, 14*). The T_m values of the hybrids of our new 2′-*O*-MeRNA probes with the complementary RNA (1 μM) were initially measured in a HEPES buffer solution (pH 7.2). The absorbance of the hybrids was monitored at 260 nm from 10 to 90 °C, and from these profiles, the first derivatives were calculated to determine the value of T_m. The hybrid of the 2′-*O*-MeRNA probe with the complementary RNA strand was thermally stable (Table 2). For example, a 2′-*O*-MeRNA probe, **Probe$_{omr}$1**, exhibited a 6 °C higher T_m value when bound to an RNA target **RNA1** than a DNA probe, **Probe$_{dna}$1**. Other 2′-*O*-MeRNA probes also showed similarly higher T_m values, except in the case of the polypyrimidine/polypurine hybrid, **Probe$_{omr}$5/RNA5**. The T_m values of probe−RNA hybrids were 4−16 °C higher compared with those

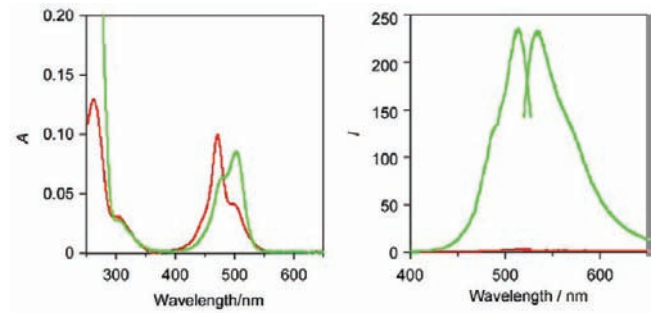

Figure 2. Absorption, and excitation and fluorescence spectra of a 2′-*O*-MeRNA probe. Absorption spectra of **Probe$_{omr}$5** (1 μM) are shown in the left panel and the excitation and fluorescence spectra (1 μM) are shown in the right panel. The spectra for single strand (ss, red) and hybrid with 1 equiv of **RNA5** (ds, green) were measured in 5 mM NaCl, 120 mM KCl, and 25 mM HEPES (pH 7.2)−KOH at 25 °C. Excitation spectra for ss and ds were measured for emission at 536 and 534 nm, respectively. The samples, ss and ds, for emission spectra were excited at 517 and 514 nm, respectively.

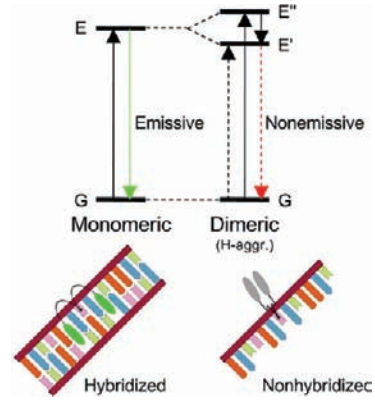

Figure 3. Schematic representation of the energy levels of the single- and double-stranded states of the hybridization probe controlled by excitonic interaction between thiazole orange dyes.

of the corresponding natural DNA/RNA duplexes, suggesting that two cationic probe dyes effectively bind to duplexes formed with the target sequence (*8*).

We next measured the absorption, excitation, and emission spectra of 2′-*O*-MeRNA probes before and after hybridization with the complementary RNA strands. Absorption spectra of the 2′-*O*-MeRNA probes exhibited the hybridization-dependent shift of absorption maximum. For example, the absorption band of **Probe$_{omr}$5** appeared at shorter wavelength (477 nm) more strongly when probes were in a single-stranded state, whereas an absorption band at longer wavelength (509 nm) became predominant when the probe was hybridized with the complementary RNA strand (Figure 2, left).

The shift of absorption maxima observed in the single-strand state can be explained in terms of the exciton coupling theory (*15*), in which the excited state of the dye H-aggregate (*16*−*18*) splits into two energy levels (Figure 3). On the basis of this theory, the transition to the upper excitonic state is allowed for the H-aggregates, which rapidly deactivate to the lower excitonic state. However, emission from the lower energy level is forbidden. On the other hand, hybridization with the complementary strand will result in dissociation of dye aggregates. The aggregate dissociation at the hybrid state was indicated by a shift of the absorption maximum to longer wavelength. Disruption of the excitonic interaction in the aggregate gave strong emission from the hybrid (Figure 2, right). The emission spectra of the 2′-*O*-MeRNA probes hybridized with the target RNA strands were observed at approximately 530 nm as a single broad

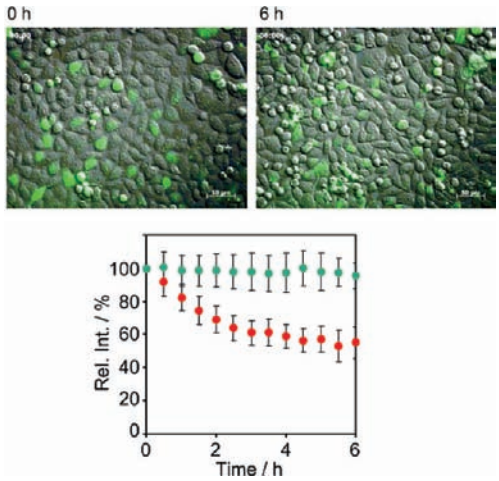

Figure 4. Differential interference contrast and fluorescence images of probe-transfected HeLa cells. The sample was excited through a 500/24−25 band-pass filter, and the fluorescence was collected through a 542 ± 25 nm band-pass filter. Bar: 50 μm. Above: an example of the transfection of 2′-*O*-MeRNA probe **Probe$_{omr}$5** to HeLa cells (0 and 6 h after 1 h incubation and washing processes). Below: plots of the average of fluorescence intensities (mean ± SD) observed for several transfected cells (**Probe$_{dna}$5** (red), $n = 10$; **Probe$_{omr}$5** (green), $n = 7$).

band. The strong emission of the hybrid of the 2′-*O*-MeRNA probe and RNA was at similar level to that of DNA probes. In contrast, the emission intensity of the probes before hybridization was much weaker. The excitation spectra displayed a single broad peak at approximately 510 nm, regardless of their structural states. This wavelength is in good agreement with the absorption band at the longer wavelength, indicating that the absorption participating in the fluorescence emission is only the band corresponding to the state released from excitonic interaction.

The on−off switching of 2′-*O*-MeRNA probes by hybridization with the complementary RNA is adequately effective to detect the complementary RNA. It is especially the fluorescence intensity ratio of the hybrid and nonhybrid of **Probe$_{omr}$2** and **Probe$_{omr}$3** that increased drastically, because of effective quenching in the nonhybrid state (Table 2). The sequence dependence of the fluorescence intensity ratio of the hybrid and nonhybrid did not deviate from the "self-dimer avoidance" rule for effective design of hybridization-sensitive fluorescent probes described in our previous paper (*9*). The modification of the sugar moiety from a hydrogen atom to a methoxy group did not inhibit fluorescence control by the excitonic interaction of thiazole orange dyes in a probe.

Fluorescence in Long-Term Cell Observation. Having established that the 2′-*O*-MeRNA probe is an effective RNA detection probe, the fluorescence behavior of the probe in living cells was investigated next. The probes capable of binding to the polyA tail of mRNA, **Probe$_{dna}$5** and **Probe$_{omr}$5**, were transfected to HeLa cells using one of the common transfection reagents, lipofectamine 2000. After incubation for 1 h, the cells were washed twice with PBS buffer. In this incubation, approximately 37% of cells in the observation field emitted fluorescence at about 542 nm, which was observed mainly in nuclei. The retention of the fluorescence intensity was determined using the average of the total intensity of fluorescence from several cells (**Probe$_{dna}$5**, $n = 10$; **Probe$_{omr}$5**, $n = 7$) (Figure 4). The fluorescence from cells where the 2′-*O*-MeRNA probe **Probe$_{omr}$5** was incorporated almost retained the initial intensity over 6 h observation, whereas the fluorescence of cells labeled with DNA probe **Probe$_{dna}$5** gradually decreased to about 50% of the initial intensity within 6 h. **Probe$_{omr}$5**-transfected cells

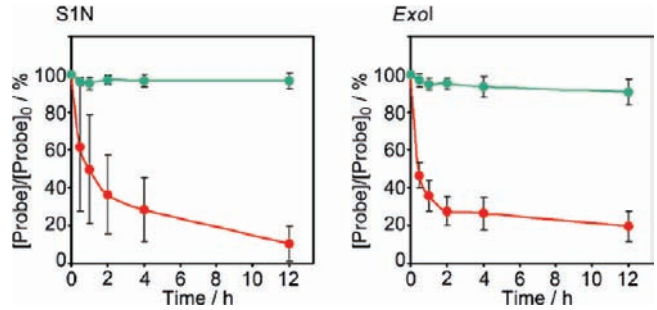

Figure 5. Probe degradation by nuclease digestion. The results of HPLC signal analysis after treatment with S1 nuclease are shown in the left panel, and the results after exonuclease I treatment are shown in the right panel. The average data for five DNA probes **Probe$_{dna}$1−5** (red) and five 2′-*O*-MeRNA probes **Probe$_{omr}$1−5** (green) are plotted (mean ± SD, $n = 5$).

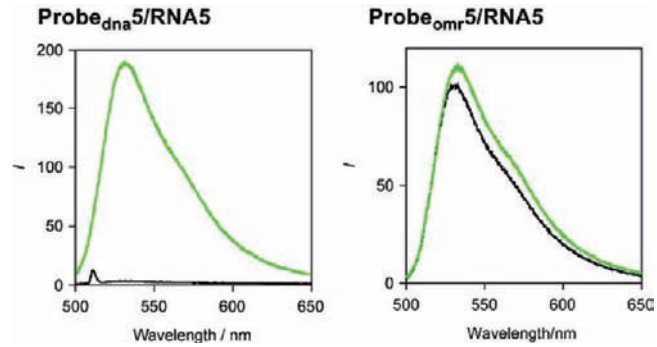

Figure 6. Fluorescence spectra of the mixture of the S1N-digested probe and the complementary RNA. The spectra for the mixture of DNA probe **Probe$_{dna}$5** and **RNA5** (0.5 μM) are shown in the left panel, and the spectra for the mixture of 2′-*O*-MeRNA probe **Probe$_{omr}$5** and **RNA5** (0.5 μM) are shown in the right panel. These spectra were measured in 5 mM NaCl, 120 mM KCl, and 25 mM HEPES (pH 7.2)−KOH at 25 °C. The mixture of the nondigested probe and RNA (green) and the mixture of the S1N-digested probe and RNA (black). The samples were excited at 514 nm.

emitted strong fluorescence, even after 24 h monitoring under culturing conditions.

Nuclease Resistance. It has been shown that the stability of the 2′-*O*-MeRNA probe fluorescence is much higher in the cell compared with the low stability of the DNA probe fluorescence. This may be because of the high nuclease resistance of the 2′-*O*-MeRNA probe. The 2′-*O*-MeRNA structure is known to have many advantages over DNA probes for detecting RNA targets, including increased stability of the hybrid with RNA and higher resistance against nucleases (*19*). These advantages may render 2′-*O*-MeRNA probes superior to DNA probes for use in assays that detectthe target RNA in a cell. In order to investigate the nuclease resistance ability of probes, both 2′-*O*-MeRNA and

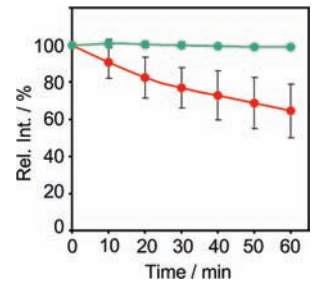

Figure 7. RNA degradation by RNaseH. The probe fluorescence at 530 nm was monitored on the excitation at 514 nm. The average data for five DNA probes **Probe$_{dna}$1−5** (red) and five 2′-*O*-MeRNA probes **Probe$_{omr}$1−5** (green) are plotted (mean ± SD, $n = 5$).

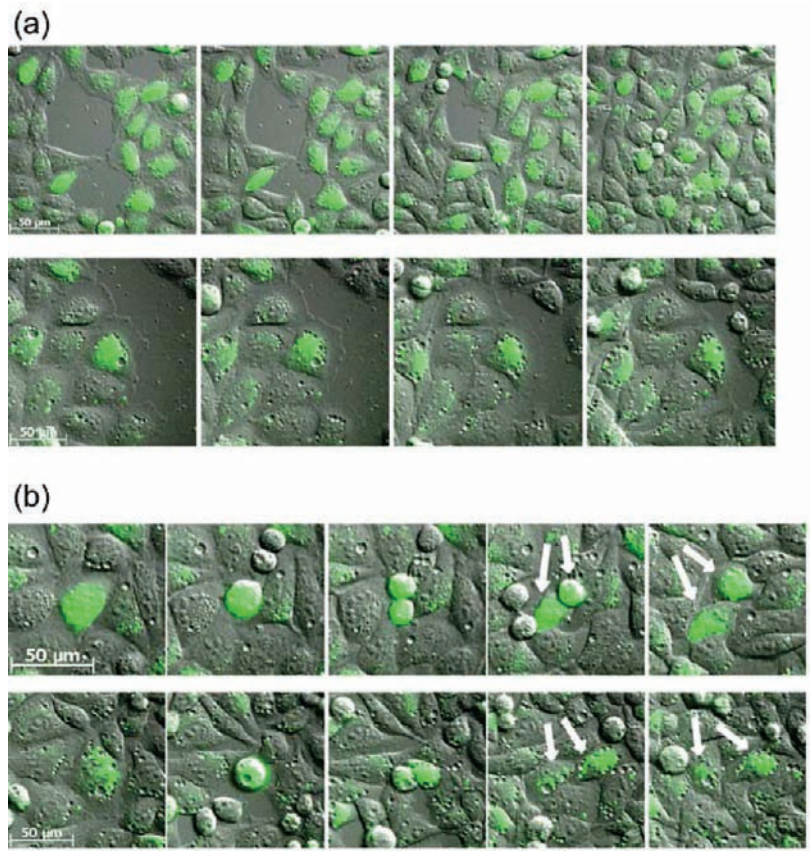

Figure 8. Differential interference contrast and fluorescence images of **Probe$_{omr}$5**-transfected HeLa cells. The sample was excited through a 500/24−25 band-pass filter, and the fluorescence was collected through a 542 ± 25 nm band-pass filter. Bar: 50 μm. (a) Two examples of cell migration: from left, initial state, and 2, 4, and 6 h later. (b) Two examples of cell division: from left, initial state, and 1, 1.5, 2.5, and 4 h later. Divided cells are indicated by white arrows.

DNA probes were treated with an endonuclease and an exonuclease, and then the decrease in the HPLC peak area of undigested probe was analyzed. S1 nuclease (S1N) is an endonuclease that catalyzes the specific degradation of single-stranded DNA or RNA to 5′-mononucleotides (*20*, *21*). Degradation curves were drawn by plotting the quantity of undigested probe as the function of the incubation time with S1N (Figure 5, left). S1N (500 mU) degraded about 90% of DNA probes (200 pmol) within 12 h, whereas about 95% of 2′-*O*-MeRNA probes (200 pmol) were still undigested after 12 h incubation. 2′-*O*-MeRNA probes showed high resistance against not only an endonuclease, but also an exonuclease (Figure 5, right). Exonuclease I (*Exo*I) is 3′→5′ exonuclease specific for a single-stranded polynucleotide, and it results in the production of 5′-mononucleotides (*22*, *23*). Digestion of the DNA probes proceeded rapidly, and only 20% of the DNA probes were undigested after 12 h. On the other hand, digestion of 2′-*O*-MeRNA probes was suppressed.

Probe degradation caused a significant decrease in fluorescence intensity in a solution containing the target RNA. Digestion of a DNA probe by S1N resulted in loss of fluorescence intensity because of a decrease in the binding ability to RNA (Figure 6). In contrast, 2′-*O*-MeRNA probes retained fluorescence in the presence of RNA, even after 12 h S1N treatment, suggesting that the probes maintain the function of RNA detection in this nuclease condition.

Inhibition of RNA Degradation. DNA probes are exposed to attack by nucleases even after hybridization with RNA. As a typical example, ribonuclease H (RNaseH) is known to catalyze the specific degradation of the RNA strand binding to DNA (*24*). Damage of the probe-hybridizing RNA by RNaseH may spoil the original function of RNA as well as reduce the probe fluorescence. In order to investigate the influence of RNaseH on the maintenance of RNA and the fluorescence intensity of a probe for a probe-RNA hybrid, RNaseH (4 U) was added to a solution containing the probe and the complementary RNA, and the fluorescence of the mixture was measured after 1 h. The hybrids of DNA probes and RNA strands showed a gradual fluorescent decrease to about 65% within 1 h (Figure 7). No decrease in fluorescence intensity of the hybrids was observed in the absence of RNaseH, and probes were not degraded by RNaseH. Therefore, the fluorescent decrease was attributed to RNA damage by RNaseH and dissociation of probes from damaged RNA. In contrast, when 2′-*O*-MeRNA probes were used, a significant decrease of fluorescence was not observed, even in the presence of RNaseH. 2′-*O*-MeRNA probes prevented RNaseH from degrading RNA in the hybrid.

Live Cell Imaging. The high resistance of 2′-*O*-MeRNA probes against nucleases makes long-term live cell RNA imaging possible. The probe showed no severe cytotoxicity, by appropriately selecting the sequence that does not obstruct the RNA activity. Cell life events, for example, migration and division of **Probe$_{omr}$5**-transfected cells, were also observed in a long-term monitoring and were similar to those observed for normal cells (Figure 8). During cell migration and division, the probe fluorescence was detected mainly from nuclei, and translocation of fluorescence to the cytoplasm region was also observed. In cell division, the fluorescence in the mother cell was evenly distributed to two daughter cells. In addition, stronger fluorescence was observed for the cell at the mitotic phase compared with the fluorescence at the interphase, sug-

gesting that a huge amount of mRNA expresses and works during cell division.

CONCLUSION

In conclusion, we have reported on nuclease-resistant probes for long-term intracellular RNA imaging. The 2′-*O*-MeRNA probes that we synthesized showed high resistance against nucleases, in contrast to the low resistance of DNA probes. Furthermore, this modified probe retained the function on the on−off switching of fluorescence emission in sensitive response to RNA recognition, based on interdye excitonic interaction. The long-term monitoring of the migration and division of RNA-stained living cells was attained using this highly functional fluorescent probe. Our probe settled the issue of probe damage by nucleases, and now, we anticipate that it will be a practical tool for effective monitoring of the spatiotemporal characteristics of RNAs in living cells.

LITERATURE CITED

(1) Paillasson, S., van de Corput, M., Dirks, R. W., Tanke, H. J., Robert-Nicoud, M., and Ronot, X. (1997) In situ hybridization in living cells: Detection of RNA molecules. *Exp. Cell Res. 231*, 226–233.

(2) Pernthaler, J., Glockner, F. O., Schonhuber, W., and Amann, R. (2001) Fluorescence in situ hybridization (FISH) with rRNA-targeted oligonucleotide probes. *Methods Microbiol. 30*, 207–226.

(3) Asseline, U. (2006) Development and applications of fluorescent oligonucleotides. *Curr. Org. Chem. 10*, 491–518.

(4) Marti, A. A., Jockusch, S., Stevens, N., Ju, J., and Turro, N. J. (2007) Fluorescent hybridization probes for sensitive and selective DNA and RNA detection. *Acc. Chem. Res. 40*, 402–409.

(5) Rodriguez, A. J., Condeelis, J., Singer, R. H., and Dictenberg, J. B. (2007) Imaging mRNA movement from transcription sites to translation sites. *Semin. Cell Dev. Biol. 18*, 202–208.

(6) Tyagi, S., and Kramer, F. R. (1996) Molecular beacons: Probes that fluoresce upon hybridization. *Nat. Biotechnol. 14*, 303–308.

(7) Hopkins, J. F., and Woodson, S. A. (2005) Molecular beacons as probes of RNA unfolding under native conditions. *Nucleic Acids Res. 33*, 5763–5770.

(8) Ikeda, S., and Okamoto, A. (2008) Hybridization-sensitive on-off DNA probe: Application of the exciton coupling effect to effective fluorescence quenching. *Chem. Asian J. 3*, 958–968.

(9) Ikeda, S., Kubota, T., Kino, K., and Okamoto, A. (2008) Sequence dependence of fluorescence emission and quenching of doubly thiazole orange-labeled DNA: Effective design of a hybridization-sensitive probe. *Bioconjugate Chem. 19*, 1719–1725.

(10) Kubota, T., Ikeda, S., and Okamoto, A. (2009) Doubly thiazole orange-labeled DNA for live cell RNA imaging. *Bull. Chem. Soc. Jpn. 82*, 110–117.

(11) Inoue, H., Hayase, Y., Imura, A., Iwai, S., Miura, K., and Ohtsuka, E. (1987) Synthesis and hybridization studies on two complementary nona(2′-*O*-methyl)ribonucleotides. *Nucleic Acids Res. 15*, 6131–6149.

(12) Majlessi, M., Nelson, N. C., and Becker, M. M. (1998) Advantages of 2′-*O*-methyl oligoribonucleotide probes for detecting RNA targets. *Nucleic Acids Res. 26*, 2224–2229.

(13) Freier, S. M., and Altmann, K. H. (1997) The ups and downs of nucleic acid duplex stability: structure-stability studies on chemically-modified DNA:RNA duplexes. *Nucleic Acids Res. 25*, 4429–4443.

(14) Lesnik, E. A., and Freier, S. M. (1998) What affects the effect of 2′-alkoxy modifications? 1. Stabilization effect of 2′-methoxy substitutions in uniformly modified DNA oligonucleotides. *Biochemistry 37*, 6991–6997.

(15) Kasha, M. (1963) Energy transfer mechanisms and molecular exciton model for molecular aggregates. *Radiat. Res. 20*, 55–70.

(16) Khairutdinov, R. F., and Serpone, N. (1997) Photophysics of cyanine dyes: Subnanosecond relaxation dynamics in monomers, dimers, and H- and J-aggregates in solution. *J. Phys. Chem. B 101*, 2602–2610.

(17) Sagawa, T., Tobata, H., and Ihara, H. (2004) Exciton interactions in cyanine dye-hyaluronic acid (HA) complex: reversible and biphasic molecular switching of chromophores induced by random coil-to-double-helix phase transition of HA. *Chem. Commun.* 2–4.

(18) Fürstenberg, A., Julliard, M. D., Deligeorgiev, T. G., Gadjev, N. I., Vasilev, A. A., and Vauthey, E. (2006) Ultrafast excited-state dynamics of DNA fluorescent intercalators: New insight into the fluorescence enhancement mechanism. *J. Am. Chem. Soc. 128*, 7661–7669.

(19) Cramer, H., and Pfleiderer, W. (2000) Nucleotides LXIV[1]: Synthesis, hybridization and enzymatic degradation studies of 2′-*O*-methyl-oligoribonucleotides and 2′-*O*-methyl/deoxy gapmers. *Nucleosides Nucleotides Nucleic Acids 19*, 1765–1777.

(20) Ando, T. (1966) A nuclease specific for heat-denatured DNA isolated from a product of *Aspergillus oryzae*. *Biochim. Biophys. Acta 114*, 158–168.

(21) Wiegand, R. C., Godson, G. N., and Radding, C. M. (1975) Specificity of S1 nuclease from *Aspergillus oryzae*. *J. Biol. Chem. 250*, 8848–8855.

(22) Lehman, I. R., and Nussbaum, A. L. (1964) The deoxyribonucleases of *Escherichia coli*. V. On the specificity of exonuclease I (phosphodiesterase). *J. Biol. Chem. 239*, 2628–2636.

(23) Kusher, S. R., Nagaishi, H., Templin, A., and Clark, A. J. (1971) Genetic recombination in *Escherichia coli*: The role of Exonuclease I. *Proc. Natl. Acad. Sci. U.S.A. 68*, 824–827.

(24) Berkower, I., Leis, J., and Hurwitz, J. (1973) Isolation and characterization of an endonuclease from *Escherichia coli* specific for ribonucleic acid in ribonucleic acid·deoxyribonucleic acid hybrid structures. *J. Biol. Chem. 248*, 5914–5921.

BC900120A

Development of a Novel Nonviral Gene Silencing System That Is Effective Both in Vitro and in Vivo by Using a Star-Shaped Block Copolymer (Star Vector)

Taisuke Mori,*[,†] Ayaka Ishikawa,[‡,▽] Yasushi Nemoto,[‡,§] Nobuaki Kambe,[▽] Michiie Sakamoto,[‡] and Yasuhide Nakayama*[,‡]

Department of Pathology, School of Medicine, Keio University, Sinjuku-ku, Tokyo, 160-8582, Japan, Department of Bioengineering, Advanced Medical Engineering Center, National Cardiovascular Center Research Institute, Osaka, 565-8565, Japan, Department of Applied Chemistry, Graduate School of Engineering, Osaka University, Osaka, 565-0871, Japan, and Chemical Products Development Department, Bridgestone Company. Received March 26, 2009; Revised Manuscript Received April 30, 2009

The objective of our study was to develop a novel nonviral gene silencing system using small interfering RNA (siRNA) or short hairpin RNA (shRNA) complexes using star vector (SV), which is a star-shaped, four-branched, cationic−nonionic-blocked copolymer, as the water-soluble delivery system. This vector was previously designed as a carrier for high-efficiency gene delivery of plasmid DNA. The lamin gene was used as the target for developing siRNAs. SV was shown to condense and interact with siRNAs to yield SV/siRNA polyion complexes with a diameter of ca. 90 nm and having considerable stability. By using these complexes, siRNA was successfully delivered to almost all human hepatocellular carcinoma cells used in this study, and both siRNAs and shRNAs could produce significant gene silencing in these cells without affecting cell viability. The silencing efficacy of these complexes was similar to that of commercially available high-efficiency siRNA transfection reagent (Darmafect-4). After injecting SV/siRNA complexes into mice, effective gene silencing was also observed in vivo in the liver and lung, suggesting that the SV/siRNA complexes were stable under in vivo conditions, and their transfection efficiency was retained after intravenous administration. Thus, SV was a potential carrier for siRNA and shRNA delivery in both in vitro and in vivo conditions; this finding suggests that it may offer a new clinical therapeutic approach in gene therapy.

INTRODUCTION

Gene therapy is an attractive new approach for the treatment of inherited disorders (*1, 2*). However, current gene therapy techniques have not yielded successful results in clinical trials. Generally, there are two kinds of gene delivery systems—viral and nonviral. Viral vectors such as retrovirus, lentivirus, and adenovirus have been proven to be efficient means for gene delivery (*3*−*5*); however, the possibility of negative outcomes resulting from viral transformations cannot be completely ruled out (*6*). On the other hand, various types of nonviral vectors have been reported recently. These vectors are attracting considerable attention, since they are easier to handle and induce weaker immune responses (*7*−*9*).

Recently, in order to improve the efficiency of gene transfection, we designed a novel nonviral vector, namely, star vector (SV), which is a star-shaped and cation-based polymer (*10, 11*), or its cross-linked complexes (*12*). These vectors have been shown to be effective in inducing gene expression from plasmid DNA (pDNA). In addition, in combination with ligands such as C45D18 peptide, which promotes nuclear trafficking (*13*), or an integrin-binding RGD peptide (*14*), DNA could be selectively delivered to macrophages or endothelial cells, respectively.

RNA interfering (RNAi) is the process by which double-stranded RNA (dsRNA) directs the sequence-specific degradation of complementary mRNA (*15*−*18*). RNAi is an effective method for gene-function analysis as well as a powerful therapeutic agent for silencing pathogenic gene products associated with diseases, including cancer, viral infections, and autoimmune disorders. Small interfering RNAs (siRNAs) can be directly introduced into cells in the form of synthetic siRNAs or short hairpin RNAs (shRNAs) (*19*). RNA polymerase III-driven expression cassettes can be used for the constitutive expression of shRNA molecules. Although both viral and nonviral vectors can be used to deliver siRNA into cells, viral vectors are not sufficiently capable of delivering siRNA-expressing constructs such as shRNA. Commercially available cationic lipids such as oligofectamine can effectively deliver siRNAs into cells (*20*); however, such cationic lipids are highly toxic and hence cannot be effectively used for systemic delivery of siRNAs in vivo.

In this study, the possibility of using SVs as carriers for RNA delivery was evaluated both in vitro and in vivo. One of the most effective pDNA carriers among the various SVs (*11*), i.e., a four-branched diblock copolymer containing an inner domain of cationic poly(*N*,*N*-dimethylaminopropylacrylamide) chains (chain length, ca. 50 kDa) and an outer domain of nonionic poly(*N*,*N*-dimethylacrylamide) chains (chain length, ca. 33 kDa), was selected as an RNA carrier in this study. The in vitro gene

* To whom correspondence should be addressed. Yasuhide Nakayama, Department of Bioengineering, Advanced Medical Engineering Center, National Cardiovascular Center Research Institute, Osaka, 565-8565, Japan. Tel: +81-6-6833-5004 (ex. 2624). Fax: +81-6-6872-8090. E-mail: nakayama@ri.ncvc.go.jp. Taisuke Mori, Department of Pathology, School of Medicine, Keio University, 35 Shinnano-machi, Sinjuku-ku, Tokyo, 160-8582, Japan. Tel: +81-3-5363-3764. Fax: +81-3-3353-3290. E-mail: taisuke@sc.itc.keio.ac.jp.

† Keio University.

‡ National Cardiovascular Center Research Institute.

§ Bridgestone Company.

▽ Graduate School of Engineering, Osaka University.

10.1021/bc9001294 CCC: $40.75 © 2009 American Chemical Society
Published on Web 05/20/2009

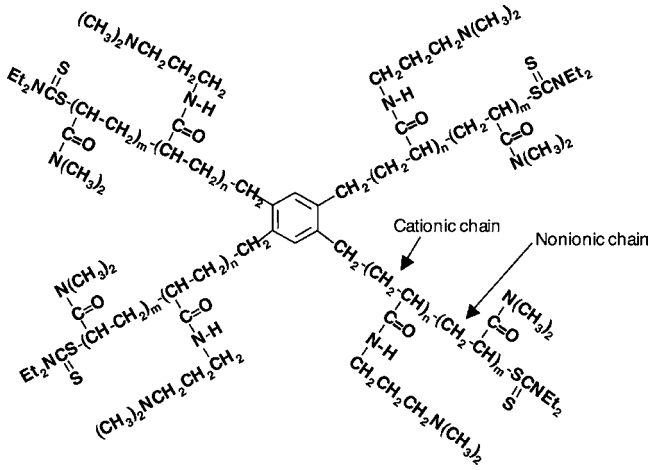

Figure 1. Chemical structure of star vector (SV) containing an inner domain of cationic polymer chains (chain length: ca. 50 kDa) and an outer domain of nonionic polymer chains (chain length: ca. 33 kDa).

silencing efficacy of SV/siRNA or SV/shRNA complexes was evaluated using human hepatocellular carcinoma cell line. In addition, the in vivo gene silencing efficacy was evaluated by injecting SV/siRNA complexes in mice and investigating their effects in the liver and lung. The possibility of using SV/RNA complexes as therapeutic agents has also been discussed.

EXPERIMENTAL PROCEDURES

Materials. *N,N*-Dimethylacrylamide was purchased from Wako Pure Chemical Ind., Ltd. (Osaka, Japan) and 3-(*N,N*-dimethylamino)propyl acrylamide from Tokyo Kasei Kogyo Co., Ltd. (Tokyo, Japan). Other chemical reagents were commercially obtained from Wako. Monomers were distilled under reduced pressure before use in order to remove the stabilizer, and if required, other reagents were also purified before use.

Preparation of SV. SV—poly(3-(*N,N*-dimethylamino)propyl acrylamide)-*block*-poly(*N,N*-dimethylacrylamide), four-branched block copolymer—was synthesized by iniferter-based photoliving radical polymerization of 1,2,4,5-tetrakis(*N,N*-diethyldithiocarbamylmethyl)benzene, which was used as a four-functional iniferter, with 3-(*N,N*-dimethylamino)propyl acrylamide and *N,N*-dimethylacrylamide, which were used as cationic and nonionic monomers, respectively, in accordance with our previously reported method (*11*).

Briefly, 1,2,4,5-tetrakis(*N,N*-diethyldithiocarbamylmethyl)-benzene (72 mg, 0.1 mmol) and 3-(*N,N*-dimethylamino)propyl acrylamide (3.43 g, 22.0 mmol) were dissolved in 20 mL of methanol and irradiated using a 200 W high-pressure mercury lamp (1 mW/cm^2 at 250 nm; SPOT CURE, USHIO, Tokyo, Japan) for 30 min under bubbling with N_2 gas (99.9999%) at room temperature. The reaction mixture was purified by precipitating it in a large amount of ether. Reprecipitation was carried out using methanol ether to yield a four-branched cationic polymer (conv. 40%). The molecular weight was M_n 50 kDa, as determined by gel permeation chromatography (GPC). ^{1}H NMR (300 MHz, D_2O, ppm) δ: 1.7−1.5 (-C$\underline{H}_2$-CH- and -CH$_2$-C$\underline{H}_2$-CH$_2$-), 2.0−1.8 (-C$\underline{H}$-CO), 2.2−2.1 (-N-C$\underline{H}_3$), 2.4−2.2 (-C$\underline{H}_2$-N(CH$_3$)$_2$), 3.2−3.0 (-NH-C$\underline{H}_2$-), 7.8−7.4 (-NH).

The resultant four-branched cationic polymer (M_n 50 kDa, 125 mg, 2.5 μmol) and *N,N*-dimethylacrylamide (2.97 g, 30 mmol) were dissolved in 20 mL of methanol solution and irradiated for 30 min under the above-mentioned conditions. After reprecipitation in a methanol-ether system, the four-branched block copolymer, namely, star vector (SV), was obtained (conv. 19%). The total molecular weight was 83 kDa, as determined by ^{1}H NMR. ^{1}H NMR (300 MHz, D_2O, ppm) δ: 1.0−1.7 (-C$\underline{H}_2$CH- and -CH$_2$C$\underline{H}_2$CH$_2$-), 1.9 (-CH$_2$C$\underline{H}$- of PDMAPAAm), 2.1 (-N(C$\underline{H}_3$)$_2$ of PDMAPAAm), 2.3 (-C$\underline{H}_2$N-(CH$_3$)$_2$), 2.4−2.7 (-CH$_2$C$\underline{H}$- of PDMAAm), 2.8−2.9 (-N(C$\underline{H}_3$)$_2$ of PDMAAm), 3.0 (-CONHC$\underline{H}_2$-).

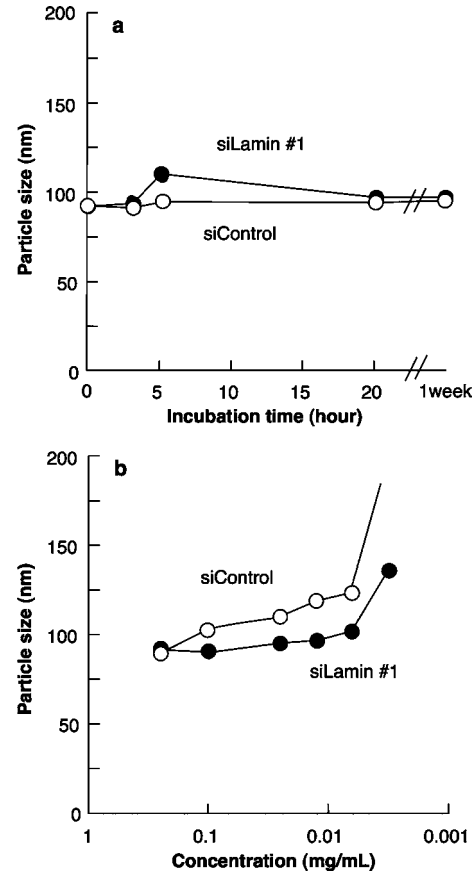

Figure 2. Changes in mean diameter of SV/siRNA complexes in aqueous solutions at 37 °C depending on incubation time (a) and after dilution in biological saline (b). The SV/siRNA complexes were prepared by mixing SV (20 μg/50 μL) and siLamin #1 or siControl (5 μg/50 μL) at an N/P ratio of 5.

Biophysical Characterization of SV/siRNA Complexes. The SVs were dissolved in biological saline. An aliquot of the saline solution containing SV (20 μg/50 μL) was added to the saline solution containing siRNA (5 μg/50 μL) to obtain SV/siRNA complexes with the N/P ratio of 5. The mean diameters of the complexes were measured by the dynamic light scattering (DLS) method using an ELS-8000 system (Otuska Electronics Co., Osaka, Japan) equipped with a 10-mW He−Ne laser. The concentration-dependent colloidal stability of SV/siRNA complexes was studied by the DLS method at 37 °C.

Real-Time Quantitative RT-PCR Analysis. Real-time quantitative-polymerase chain reaction (qRT-PCR) analysis was performed as described previously (*21*). The primer sets used were as follows: for human lamin A/C, 5′-GCCTACCG-CAAGCTCTTGGA-3′ (forward) and 5′-CTAGTGCGTGCGT-GCTGTGA-3′ (reverse); and for mouse lamin A/C, 5′-TTCCC-ACCGAAGTTCACCCTAA-3′ (forward) and 5′-ATGGTCA-GTGAGCGCACCAG-3′ (reverse). In order to standardize the amount of RNA, the expression level of glyceradehyde-3-phosphate dehydrogenase (GAPDH) in each sample was quantified by using the following primer sets: for human GAPDH, 5′-GAAGGTGAAGGTCGGAGTC-3′ (forward) and 5-CCCG-AATCACATTCTCCAAGAA-3′ (reverse); and for mouse GAPDH, 5′-AAATGGTGAAGGTCGGTGTG-3′ (forward) and 5′-

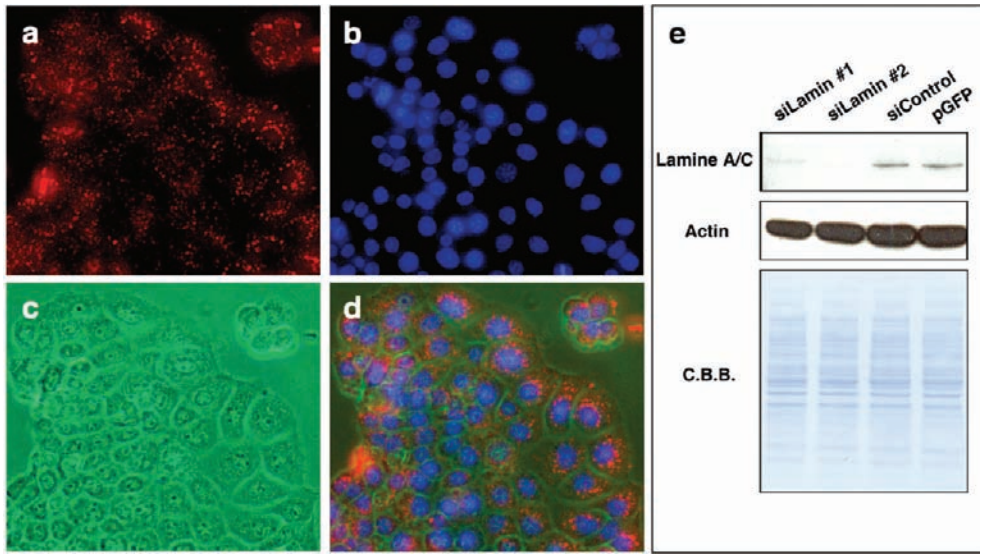

Figure 3. (a) Fluorescence microscopic image of Cy3-labeled siLamin #1 in human hepatocellular carcinoma cells delivered by SV/siRNA complexes, (b) after diaminophenylindole (DAPI) staining, (c) phase-contrast microscopic image, and (d) all three images merged into one. (e) Immunoblotting of Lamin A/C after treatment of human hepatocellular carcinoma cells with SV/siRNA or SV/pGFP complexes. Actin expression levels and coomassie brilliant blue (CBB) staining were used as loading controls.

TGAAGGGGTCGTTGATGG-3′ (reverse). All PCR reactions were performed using a SYBR RT-PCR kit (Takara Bio, Tokyo, Japan).

Western Blot Analysis. Western blot analysis of the Lamin A/C (sc-7292) and actin (using a mouse monoclonal Ab: 1:1000 dilution; Santa Cruz Biotechnology Inc., CA, USA) from human hepatocellular carcinoma cell lines (PLC/PRF/5: Alexander) was performed, as described previously (*22*).

RNA Interference (siRNA Duplexes). All purified and pre-annealed siRNA molecules were obtained from Dharmacon Research, Inc. (Lafayette, CO). siGL2 Lamin A/C siRNA (human/mouse/rat) (Cy3-labeled siLamin A/C #1: sense, 5′-GGUGGUGACGACGAUCUGGGCUdTdT-3′; antisense, 5′-AGCCCAGAUCGUCACCACCdTdT-3′), siGL2 Lamin A/C siRNA human (Cy3-labeled siLamin A/C #2: sense, 5′-ACCAGGUGGAGCAGUAUAAdTdT-3′; antisense, 5′-UUAUACUGCUCCACCUGGUdTdT-3′), and siControl nontargeting siRNA #1 (siControl: sense, 5′-UAGCGACUAAACACAUCAAUU-3′; antisense, 5′-UUGAUGUGUUUAGUCGCUAUU-3′) are unmodified siRNA duplexes bioinformatically designed to minimize the potential for targeting any known human or mouse genes.

Vector Construction. shRNA expression vector, pDEST-CL-SI-MSCVpuro (previously designated as pSI-CMSCVpuroDEST), and the entry vector, pENTR-H1R-stuffer, were constructed in accordance with the previous report (*23*).

In Vitro Transfection. Human hepatocellular carcinoma (PLC/PRF/5: Alexander) cells were seeded into 6-well plates (5×10^4 to 1×10^5 cells per well) 2 days prior to transfection and grown in RPMI-1640 (Sigma, St. Louis, MO) medium supplemented with 10% fetal bovine serum (FBS) and antibiotics. SV/RNA or SV/DNA complexes were prepared by mixing an aliquot of phosphate buffered saline (PBS) containing SV (10 μg for RNA and 4 μg for DNA) with an aliquot of PBS containing siRNA or shRNA (2.5 μg/well) and plasmid green fluorescent protein (pGFP) DNA (pmaxGFP, Amaxa Inc., MD) (1 μg /well) at a N/P ratio of 5. The resultant complexes were maintained at room temperature for 30 min. On the other hand, complexes of siRNA (2.5 μg/well) and Dharmafect-4 (TR; Dharmacon Research, Inc., Lafayette, CO, USA) (TR/siRNA complexes) were prepared according to the manufacturer's instructions. All the complexes were applied to each well in a total volume of 2 mL. The transfection medium (Opti-MEM, Invitrogen, Carlsbad, CA) was replaced with the complete medium after 4 h.

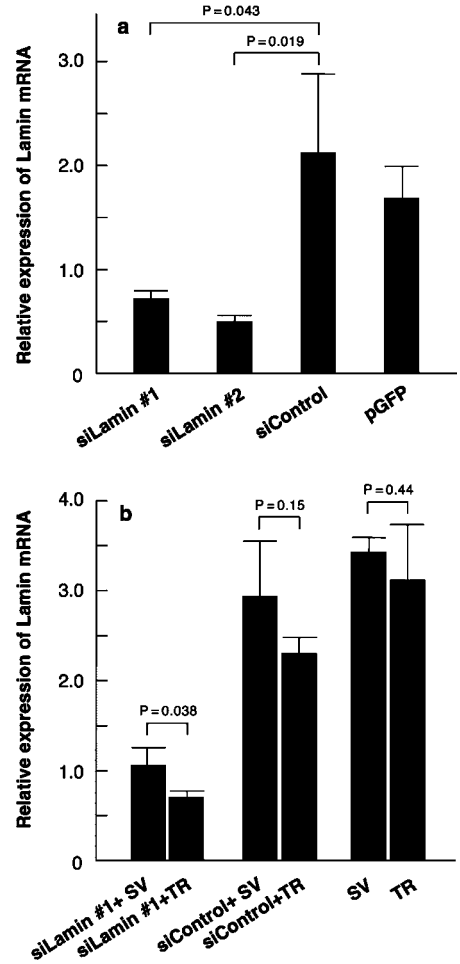

Figure 4. In vitro lamin mRNA silencing efficiency of SV/siRNA complexes in human hepatocellular carcinoma cells, as analyzed by quantitative RT-PCR. (a) Comparison between siLamin #1 and siLamin #2. (b) Comparison between SV and TR (Darmafect-4) using siLamin #1.

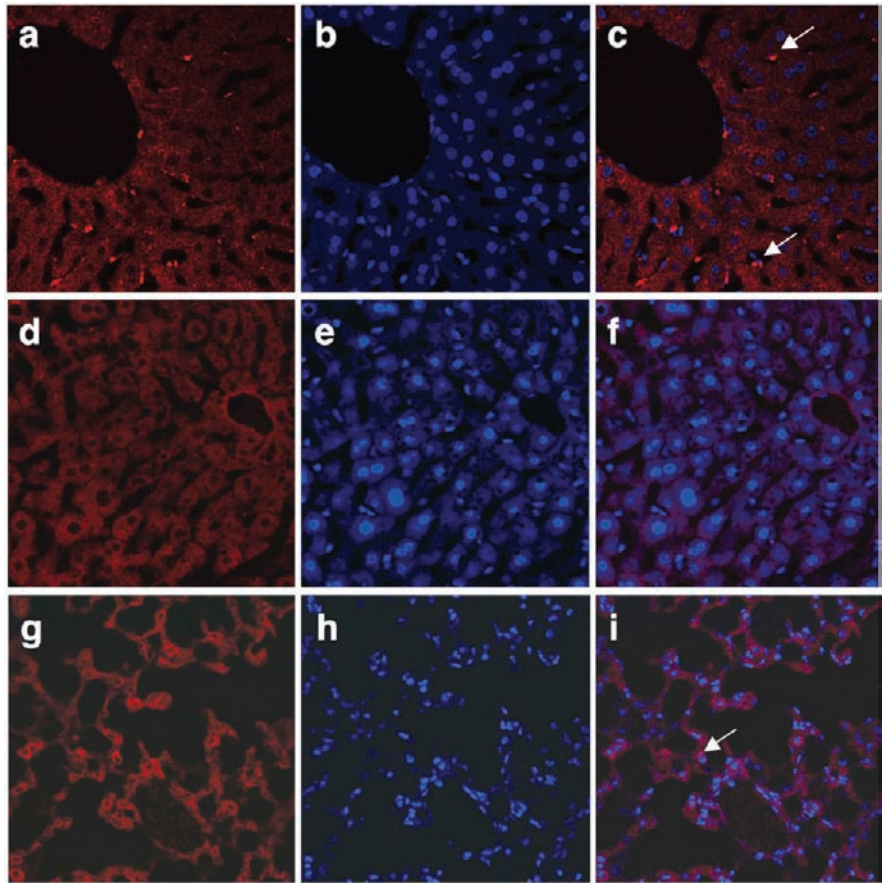

Figure 5. Images of mice liver and lung tissues transfected with SV/siRNA complexes observed under confocal microscope. Cy3-labeled siRNA detected in the mouse tissues (a−c, Cy3-labeled siLamin-injected liver specimen; d−f, nonlabeled siControl-injected liver specimen; g−i, Cy3-labeled siLamin-injected lung specimen). Cy3 labeling (a,d,g), DAPI staining (b,e,h), and merged image (c,f,i). Cy3-labeled siLamins were detected in the liver and lung tissues (white arrows in c and i).

In Vivo Transfection (Tail-Vein Injection of SV/siRNA Complexes). Male CH3/HeN mice (7−9-week old) weighing about 20 g were used ($n = 8$). Using the animal protocols that were approved by the institutional Animal Care and Use Committee of Keio University School of Medicine (approval #060042), 200 μL of SV/siRNA complex was injected into each mouse via the tail vein over a period of 5 s (10 μg siRNA per 20 g mouse). The N/P ratio was set at 5. Mice were euthanized 48 h after the injection, and the livers and lungs were dissected and rapidly frozen for subsequent mRNA and protein analysis. For immunofluorescence study, dissected specimens were fixed in 4% paraformaldehyde (PFA) and analyzed under a confocal laser-scanning microscope (LSM 510; Carl Zeiss, Oberkochen, Germany) after staining with 4,6-diamidino-2-phenylindole (DAPI) (Wako) at 1:1000 dilution.

Statistical Analysis. Data are expressed as mean ± standard error (SE). The relative mRNA expression levels were compared using unpaired *t*-test, and all statistical analyses were performed using *Statcel* software (OSM, Tokyo, Japan).

RESULTS

Formation of SV/siRNA Complexes and Their Stability. The chemical structure of the SV used in this study was four-branched, blocked copolymer, with an inner domain of cationic chains (chain length, ca. 50 kDa) and an outer domain of nonionic chains (chain length, ca. 33 kDa), as shown in Figure 1. When the saline solution of SV was mixed with the saline solution of siRNA at the N/P ratio of 5, highly scattered intensity was observed in the DLS analysis for both lamin and control siRNAs, indicating the formation of SV/siRNA complexes. These complexes were considered polyion complexes that were formed by nonspecific electrostatic interactions between the cationic SVs and anionic RNAs.

The effective diameters of the resultant SV/siRNA complexes of both lamin and control RNAs were found to be approximately 90 nm, as revealed by DLS analysis, and their size remained smaller even 1 week after complex formation (Figure 2A). There was a small change in the size of the complexes after an approximately 40-fold dilution with PBS (Figure 2B). SV-based complexes of both the RNAs clearly showed good colloidal stability.

SV/siRNA-Mediated Lamin Knockdown in Vitro. Induction efficiency in vitro, which was mediated by SV/siRNA, was evaluated by monitoring Cy3-labeled siRNA. In order to eliminate serum effects, the human hepatocellular carcinoma cells were cultured in serum-free media, and the media was changed every 4 h after transfection with SV/siRNA complexes to avoid nonspecific interaction. Fluorescence microscopic examination revealed Cy3 labeling in almost all cells (Figure 3a−d). In other words, SV was able to deliver siRNA to almost all cells.

The gene silencing efficiency of the SV/siRNA complex was evaluated as follows. First, two different alignments of siRNA against lamin (siLamin #1 for human/mouse/rat and siLamin #2 for human) were designed; these were used as positive controls. A nontargeting control siRNA (siControl) or a green fluorescent protein (GFP)-expression vector (pGFP) was used as a negative control. After 24 h of transfection with SV/siRNA complexes, lamin mRNA expression levels in the human hepatocellular carcinoma cells were evaluated. The results of

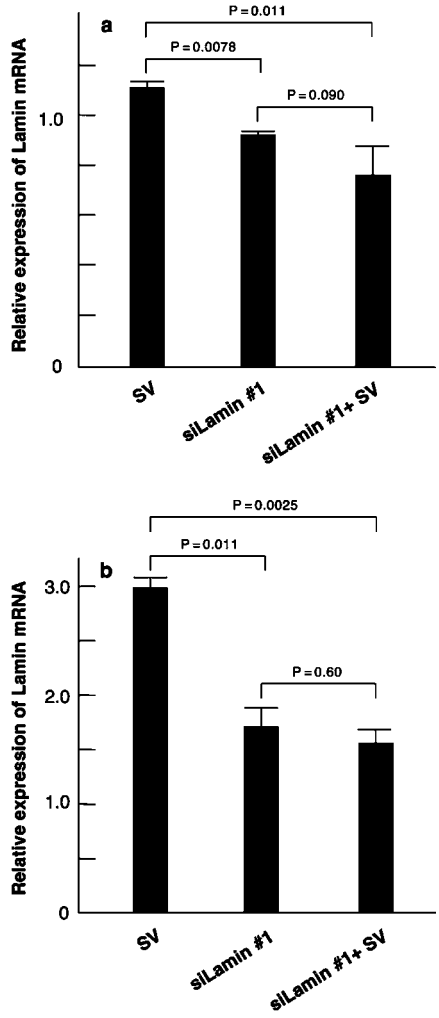

Figure 6. In vivo lamin mRNA silencing efficiency of SV/siRNA complexes in mice liver or lung tissue, as analyzed by quantitative RT-PCR. SV/siRNA was transfected by tail vain injection. Comparison of siLamin before and after the SV/siLamin #1 complex formation in the liver (a) or the lung (b).

qRT-PCR indicated that the lamin mRNA expression levels were significantly reduced in the cells transfected with siLamin #1 and #2 compared to those in the cells transfected with the control siRNA (siLamin #1 vs siControl, $P = 0.043$; siLamin #2 vs siControl, $P = 0.019$) (Figure 4a). A significant decrease in the levels of lamin protein was also observed in the cells transfected with siLamin #1 and #2 compared with those transfected with the controls (Figure 3e).

The transduction efficiency of SV was compared with a commercially available high-efficiency siRNA transfection reagent (TR; Darmafect-4). Both SV and TR could effectively down-regulate lamin expression mRNA levels (mean relative expression levels: SV/siLamin #1 vs TR/siLamin #1, 1.06 vs 0.71, $P = 0.038$; SV/siCont vs TR/siCont. = 2.93 vs 2.29, $P = 0.145$; SV vs TR = 3.40 vs 3.09, $P = 0.44$) (Figure 4b).

SV/siRNA-Mediated Gene Silencing in Vivo. The in vivo gene silencing efficiency of SV/siRNA complex was assessed by using Cy3-labeled siLamin #1 or Cy3-labeled siControl. Cy3-labeled SV/siLamin #1 or SV/siControl complexes were injected into each mouse via the tail vein. Mice were euthanized 48 h after injection, and the liver or lung was dissected for subsequent analysis.

Cy3-labeled siRNAs were detected in all the liver and lung specimens, as observed under the confocal laser-scanning microscope (Figure 5). In addition, Cy3-labeled siRNAs were observed in the kidney/renal tubules (data not shown). This confirms that the siRNAs were effectively delivered into the liver and lung by using SV. The silencing efficacy of SV (without siLamin), naked-siLamin (without SV), and SV/siLamin complex were quantitatively analyzed in the liver and lung specimens by measuring the lamin mRNA levels. Lamin expression levels were efficiently down-regulated after transfection with both siLamin groups with or without SV in both the tissues (mean relative lamin mRNA levels in the liver, SV vs siLamin (naked) vs siLamin/SV = 1.11 vs 0.92 vs 0.76; mean relative lamin mRNA levels in the lung, SV vs siLamin (naked) vs siLamin/SV = 3.00 vs 1.71 vs 1.54). There was no statistical difference between the transfection efficiency of SV and of naked siLamin ($n = 3$; $P > 0.05$) (Figure 6).

SV/shRNA-Mediated Lamin Knockdown in Vitro. The possibility of SV-induced gene silencing using shRNAs (plasmid DNA) was also evaluated. Confocal laser scanning microscopy showed that shRNA was delivered to almost all carcinoma cells treated with SV/shRNA complexes, including about 30% of cells showing strong shRNA induction (Figure 7). In the preliminal experiment, the lamin gene expression level was strongly down-regulated by SV/shRNA complexes (Figure 8). Although statistical analysis was not performed for the lack of experimental number, the inhibition efficacy of SV/shRNA complex was almost similar to that of TR/shRNA complex (mean relative lamin levels, SV/shLamin vs SV/shCont. = 1.17 vs 2.40; TR/shLamin vs TR/shCont. = 0.82 vs 2.02).

DISCUSSION

We showed that SV promotes siRNA- or shRNA-mediated gene silencing in vitro in human hepatocellular carcinoma cells and also in vivo in mice liver or lung. SV is a synthetic cation-based polymer that was previously developed as a carrier for DNA delivery. The gene transfection efficiency of SV was 10-fold higher than that of polyethyleneimine (PEI), which is one of the best vectors popularly used for gene transfer. Recently, several types of SVs were bioinformatically designed to enhance gene transfection efficacy or develop novel transfection methods. Among the various types of SV, the four-branched poly(*N*,*N*-dimethylaminopropylacrylamide)-*block*-poly(*N*,*N*-dimethyacrylamide) that was used in this study is the standard structure; this SV is one of the most effective gene delivery vectors.

SV could be used to form siRNA/SV complexes merely by mixing siRNA and SV in aqueous media even though the molecular weight of RNA is smaller than that of DNA. Since in our previous study a minimum N/P ratio of 5 was required for stable complex formation between SV and DNA, the N/P ratio was fixed at 5; cellular toxicity was minimal at this N/P ratio. The complex may be formed by electrostatic interactions between cationic SV and anionic RNAs in a manner similar to the complex formation between DNA complexes and SV. SV is easy to handle, does not require specific conditions for complex formation with RNAs, and is considerably water-soluble; hence, no organic solvent was required for preparing its aqueous solution. Thus, solvent-based toxicity was avoided. The complexes had a small particle size and were stable in saline for at least up to 1 week and even after dilution up to approximately 40-fold (Figure 2); this feature is of great advantage for use in animal studies. Almost all cationic polymers can conjugate with anionic RNAs to prepare polymer/RNA polyion complexes immediately after mixing by electrostatic affinity. However, the complexes are gradually aggregated with an increase in incubation time to grow micrometer size by similar electrostatic affinity. Therefore, in general, it was reported that gene silencing efficacy was low in large particles due to difficulty internalizing polyion complexes into the cells, which is one of key steps in polyion-complex-mediated gene

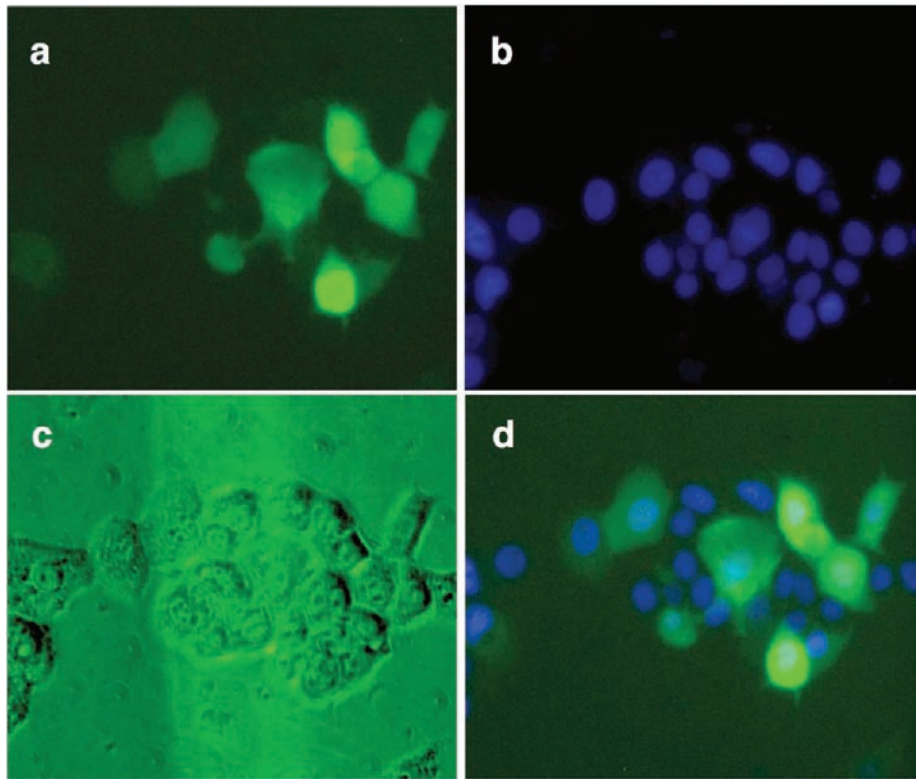

Figure 7. Fluorescence microscopic image of GFP expression in human hepatocellular carcinoma cells after transfection with plasmid DNA using SV/shRNA complexes. (a) GFP, (b) DAPI, (c) phase-contrast microscope image, and (d) all three images merged into one.

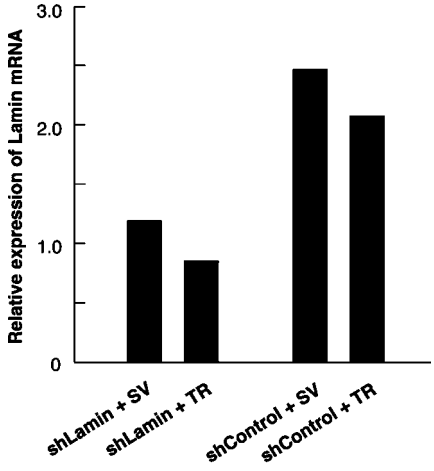

Figure 8. In vitro lamin mRNA silencing efficacy of SV/shRNA complexes in human hepatocellular carcinoma cells, as analyzed by quantitative RT-PCR. Comparison of transfection efficacy of SV/shRNA complexes with TR (Darmafect-4)-shRNA complexes.

silencing. On the other hand, in SV with a combination of cationic and nonionic chains the aggregation of the complexes was prevented by nonionic chains, which might exist at the outermost surfaces of the complexes. In addition, complexes formed from RNA and cationic homopolymer may be generally more rigid than those from RNA and SV, because nonionic chains in SV can function as a buffer layer between RNA and polymer. Therefore, it is considered that the only cationic polymer-based polyion complexes may not dissociate easily. That is, this may prevent RNA release from the complexes, which is also one of key steps in gene silencing. For these two reasons, SV is considered to have higher gene silencing efficiency.

RNAi is an effective tool for gene silencing and can be used as a potential therapeutic agent against many diseases, including cancer (*16*). RNAi effector molecules can be directly introduced into cells as synthetic siRNAs or indirectly as shRNAs. Although in vitro transfection methods using commercially available cationic lipids such as oligofectamine can deliver siRNA into cells with high efficiency, they are highly toxic, and hence, their usage in in vivo systemic delivery systems is generally avoided. In addition, previous reports showed that the delivery of siRNA into subcutaneous tumors for gene silencing was possible by using the tail vein approach (*23, 24*). However, the concentration of siRNA used in the above-mentioned study was 5-fold higher (50 μg/20 g body weight in mice) than that used in our study, and this result may have included artifacts or drug (siRNA and/or reagents) side effects. Thus, it is not feasible to use this approach in clinical interventions. In fact, we observed that 2 of the 9 mice died within 24 h after in vivo oligofectamin transfection.

The transfection efficiency of SV was similar to that obtained using cationic lipids as vectors such as TR (Dramafect-4) that are commonly used for siRNA-mediated gene silencing (Figures 3 and 4). We selected the lamin gene as the target for siRNA-mediated gene silencing. The lamin siRNA was established for siRNA positive correlation of fluorescence with transfection efficiency and target gene silencing. Moreover, Lamin A/C is abundantly expressed in most of the human, mouse, and rat cells, and knockdown of the mRNA corresponding to lamin does not affect cell viability. In order to investigate the accuracy of the siRNAs, two different conformations of siRNAs with varying sequences, i.e., siLamin #1 designed to target human, mouse, and rat lamin and siLamin #2 designed to target only human lamin, were used. Both siRNAs showed similar high-performance gene silencing in the in vitro study (Figure 4). In addition, our in vitro study also demonstrated that SV could be a beneficial tool for gene silencing using shRNA as a plasmid DNA vector (Figure 8). In the in vivo study, we chose to examine effects on the liver, which is one of the reticuloendothelial organs that can trap foreign particles entering through

the veins, and we observed that the SV/siRNA complexes were effective even at low doses. After the tail vein injection, the complexes flowed through the venous return and were trapped by the reticuloendothelial system of the liver. We hypothesized that the complexes were initially trapped in the interstitial region and some of them were phagocytosed by the Kupffer cells, following which they entered the surrounding cells. The lamin mRNA expression level in the entire liver was less than 10% after injection of the complexes compared with the expression levels of the control livers. These results suggest that gene silencing was effective not only in the Kupffer cells but also in other liver cells such as the hepatocytes, endothelial cells, and all liver architectonic cells. In addition, there was no incidence of sudden death in the treated mice caused by embolism resulting from the injected materials.

Our results demonstrate that SV can be a promising tool for gene therapy against cancer, although we did not investigate the effectiveness of the complexes against in vivo tumors. Therefore, further studies need to be performed in the future to elucidate this new approach. Most of the cervical cancers are associated with HPV-16 infection, which results in the expression of *E6* and *E7* genes encoded by the viral genome. The expression of these oncogenes is imperative for tumor development and the maintenance of malignancy. Recently, Yoshinouchi et al. reported that siRNA-mediated gene silencing suppressed the expression of *E6* and *E7* genes in HPV-16-positive cancer cells and had a remarkable effect on reducing tumor size (*26*). Thus, these genes are ideal targets for cancer gene therapy. Other candidate genes that may be targeted are *LMP-1* (Epstein−Barr (EB) virus genome) (*27*−*29*) and retinoblastoma gene (*Rb*) (*30*). At present, we are investigating two different approaches for targeting genes. The first approach is by the inhibition of inducer genes involved in early-stage carcinogenesis, and the second is by the inhibition of transmembrane receptors such as multidrug resistance receptor (MDR). Furthermore, we would also be evaluating whether gene transfection using SV could cause organ-specific injury (i.e., in the heart, brain, liver, and kidney) due to drug accumulation.

In conclusion, we have developed a novel nonviral gene silencing system based on our previously developed polymeric four-branched, cationic-blocked star vector (SV), which can efficiently deliver both siRNAs and shRNAs in vitro and in vivo. These results suggest that SV can be a potential nonviral vector and also offer a new clinical therapeutic approach for the treatment and management of disease.

ACKNOWLEDGMENT

We would like to express our sincere thanks to Shinji Saito (Bridgestone Corp., Yokohama, Japan) for support throughout the work, M. Fujiwara, M. Morioka, and M. Konno for providing expert technical assistance. This work was supported in part by a Keio University Grant-in-Aid for Encouragement of Young Medical Scientists, special grant for Keio Health Counseling, and Grant-in-Aid for Young Scientists (B), The Ministry of Education, Culture, Sports, Science and Technology (MEXT) to TM.

LITERATURE CITED

(1) Novina, C. D., Murray, M. F., Dykxhoorn, D. M., Beresford, P. J., Riess, J., Lee, S. K., Collman, R. G., Lieberman, J., Shankar, P., and Sharp, P. A. (2002) siRNA-directed inhibition of HIV-1 infection. *Nat. Med. 8*, 681–686.

(2) Sakurai, K., Iizuka, S., Shen, J. S., Meng, X. L., Mori, T., Umezawa, A., Ohashi, T., and Eto, Y. (2004) Brain transplantation of genetically modified bone marrow stromal cells corrects CNS pathology and cognitive function in MPS VII mice. *Gene Ther. 11*, 1475–1481.

(3) Mori, T., Kiyono, T., Imabayashi, H., Takeda, Y., Tsuchiya, K., Miyoshi, S., Makino, H., Matsumoto, K., Saito, H., Ogawa, S., Sakamoto, M., Hata, J., and Umezawa, A. (2005) Combination of hTERT and bmi-1, E6, or E7 induces prolongation of the life span of bone marrow stromal cells from an elderly donor without affecting their neurogenic potential. *Mol. Cell. Biol. 25*, 5183–5195.

(4) Rubinson, D. A., Dillon, C. P., Kwiatkowski, A. V., Sievers, C., Yang, L., Kopinja, J., Rooney, D. L., Zhang, M., Ihrig, M. M., McManus, M. T., Gertler, F. B., Scott, M. L., and Van Parijs, L. (2003) A lentivirus-based system to functionally silence genes in primary mammalian cells, stem cells and transgenic mice by RNA interference. *Nat. Genet. 33*, 401–406.

(5) Peng, D., Qian, C., Sun, Y., Barajas, M. A., and Prieto, J. (2000) Transduction of hepatocellular carcinoma (HCC) using recombinant adeno-associated virus (rAAV): in vitro and in vivo effects of genotoxic agents. *J. Hepatol. 32*, 975–985.

(6) Ohbayashi, F., Balamotis, M. A., Kishimoto, A., Aizawa, E., Diaz, A., Hasty, P., Graham, F. L., Caskey, C. T., and Mitani, K. (2005) Correction of chromosomal mutation and random integration in embryonic stem cells with helper-dependent adenoviral vectors. *Proc. Natl. Acad. Sci. U.S.A. 102*, 13628–13633.

(7) Demeneix, B., Hassani, Z., and Behr, J. P. (2004) Towards multifunctional synthetic vectors. *Curr. Gene Ther. 4*, 445–455.

(8) Fumoto, S., Kawakami, S., Ito, Y., Shigeta, K., Yamashita, F., and Hashida, M. (2004) Enhanced hepatocyte-selective in vivo gene expression by stabilized galactosylated liposome/plasmid DNA complex using sodium chloride for complex formation. *Mol. Ther. 10*, 719–729.

(9) Li, S. D., and Huang, L. (2006) Gene therapy progress and prospects: non-viral gene therapy by systemic delivery. *Gene Ther. 13*, 1313–1319.

(10) Nakayama, Y., Masuda, T., Nagaishi, M., Hayashi, M., Ohira, M., and Harada-Shiba, M. (2005) High performance gene delivery polymeric vector: nano-structured cationic star polymers (star vectors). *Curr. Drug Delivery 2*, 53–57.

(11) Nakayama, Y., Kakei, C., Ishikawa, A., Zhou, Y. M., Nemoto, Y., and Uchida, K. (2007) Synthesis and in vitro evaluation of novel star-shaped block copolymers (blocked star vectors) for efficient gene delivery. *Bioconjugate Chem. 18*, 2037–2044.

(12) Nemoto, Y., Zhou, Y. M., Tatsumi, E., and Nakayama, Y. (2008) Photoinduced cross-linking of star vector for improvement of gene transfer efficiency. *Bioconjugate Chem. 19*, 2513–2519.

(13) Mizoguchi, I., Ooe, Y., Hoshino, S., Shimura, M., Kasahara, T., Kano, S., Ohta, T., Takaku, F., Nakayama, Y., and Ishizaka, Y. (2005) Improved gene expression in resting macrophages using an oligopeptide derived from Vpr of human immunodeficiency virus type-1. *Biochem. Biophys. Res. Commun. 338*, 1499–1506.

(14) Ishikawa, A., Zhou, Y. M., Kambe, N., and Nakayama, Y. (2008) Enhancement of star vector-based gene delivery to endothelial cells by addition of RGD-peptide. *Bioconjugate Chem. 19*, 558–561.

(15) Tuschl, T. (2002) Expanding small RNA interference. *Nat. Biotechnol. 20*, 446–448.

(16) Elbashir, S. M., Harborth, J., Lendeckel, W., Yalcin, A., Weber, K., and Tuschl, T. (2001) Duplexes of 21-nucleotide RNAs mediate RNA interference in cultured mammalian cells. *Nature 411*, 494–498.

(17) Dorsett, Y., and Tuschl, T. (2004) siRNAs: applications in functional genomics and potential as therapeutics. *Nat. Rev. Drug Discovery 3*, 318–329.

(18) Scherer, L. J., and Rossi, J. J. (2003) Approaches for the sequence-specific knockdown of mRNA. *Nat. Biotechnol. 21*, 1457–1465.

(19) Barton, G. M., and Medzhitov, R. (2002) Retroviral delivery of small interfering RNA into primary cells. *Proc. Natl. Acad. Sci. U.S.A. 99*, 14943–14945.

(20) Bertrand, J. R., Pottier, M., Vekris, A., Opolon, P., Maksimenko, A., and Malvy, C. (2002) Comparison of antisense

oligonucleotides and siRNAs in cell culture and in vivo. *Biochem. Biophys. Res. Commun. 296*, 1000–1004.

(21) Shibata, R., Mori, T., Du, W., Chuma, M., Gotoh, M., Shimazu, M., Ueda, M., Hirohashi, S., and Sakamoto, M. (2006) Overexpression of cyclase-associated protein 2 in multistage hepatocarcinogenesis. *Clin. Cancer Res. 12*, 5363–5368.

(22) Haga, K., Ohno, S., Yugawa, T., Narisawa-Saito, M., Fujita, M., Sakamoto, M., Galloway, D. A., and Kiyono, T. (2007) Efficient immortalization of primary human cells by p16INK4a-specific short hairpin RNA or Bmi-1, combined with introduction of hTERT. *Cancer Sci. 98*, 147–154.

(23) Bartlett, D. W., and Davis, M. E. (2006) Insights into the kinetics of siRNA-mediated gene silencing from live-cell and live-animal bioluminescent imaging. *Nucleic Acids Res. 34*, 322–333.

(24) Layzer, J. M., McCaffrey, A. P., Tanner, A. K., Huang, Z., Kay, M. A., and Sullenger, B. A. (2004) In vivo activity of nuclease-resistant siRNAs. *RNA 10*, 766–771.

(25) Zhou, Y. M., Ishikawa, A., Okahashi, R., Uchida, K., Nemoto, Y., Nakayama, M., and Nakayama, Y. (2007) Deposition transfection technology using a DNA complex with a thermo-responsive cationic star polymer. *J. Controlled Release 123*, 239–246.

(26) Yoshinouchi, M., Yamada, T., Kizaki, M., Fen, J., Koseki, T., Ikeda, Y., Nishihara, T., and Yamato, K. (2003) In vitro and in vivo growth suppression of human papillomavirus 16-positive cervical cancer cells by E6 siRNA. *Mol. Ther. 8*, 762–768.

(27) Murray, P. G., and Young, L. S. (2001) Epstein-Barr virus infection: basis of malignancy and potential for therapy. *Expert Rev. Mol. Med. 3*, 1–20.

(28) Lopes, V., Young, L. S., and Murray, P. G. (2003) Epstein-Barr virus-associated cancers: aetiology and treatment. *Herpes 10*, 78–82.

(29) Awaya, N., Adachi, A., Mori, T., Kamata, H., Nakahara, J., Yokoyama, K., Yamada, Y., Kizaki, M., Sakamoto, M., Ikeda, Y., and Okamoto, S. (2006) Fulminant Epstein-Barr virus (EBV)-associated T-cell lymphoproliferative disorder with hemophagocytosis following autologous peripheral blood stem cell transplantation for relapsed angioimmunoblastic T-cell lymphoma. *Leuk. Res. 30*, 1059–1062.

(30) Weinberg, R. A. (1995) The retinoblastoma protein and cell cycle control. *Cell 81*, 323–330.

BC9001294

Integrin $\alpha_v\beta_3$ Targeted Gene Delivery Using RGD Peptidomimetic Conjugates with Copolymers of PEGylated Poly(ethylene imine)

Olivia M. Merkel,[†] Oliver Germershaus,[†] Carol K. Wada,[‡] Peter J. Tarcha,[‡] Thomas Merdan,[‡] and Thomas Kissel*[,†]

Department of Pharmaceutics and Biopharmacy, Philipps-Universität Marburg, Ketzerbach 63, 35032 Marburg, Germany, and Abbott Laboratories Incorporated, 200 Abbott Park Road, Abbot Park, Illinois 60064. Received April 14, 2009; Revised Manuscript Received May 12, 2009

This study describes the synthesis and characterization of five conjugates of poly(ethylene glycol) modified polyethylenimine (PEG-PEIs) coupled in two different synthesis routes to a nonpeptidic pentacyclic RDG-mimetic for integrin receptor-targeted gene delivery. Synthesis of this panel of different conjugates allowed for systematic analysis of structure−activity relationships. Conjugates were therefore characterized regarding molecular composition, DNA condensation, size, and zeta potential of self-assembled polyplexes. In vitro characterization included investigation of blood compatibility, binding affinity to receptor-positive and receptor-negative cells measured by flow cytometry, cellular uptake quantified by scintillation counting, and efficiency and specificity of transfection assayed by reporter gene expression. In a first synthetic approach, low molecular weight PEI (LMW-PEI) was PEGylated using a heterobifunctional PEG linker and coupling of the RGD-mimetic was achieved at the distal end of PEG chains. In a second synthesis route, the RGD-mimetic was directly coupled to AB-block-copolymers of PEI (25 kDa) and PEG (30 kDa). Interactions of RGD-PEG-LMW-PEI conjugates with DNA were strongly impaired, whereas PEG-PEI-RGD conjugates were more promising candidates due to their physicochemical properties and higher receptor specificity. The binding, uptake, and transfection efficiency in receptor-positive cells was strongly increased upon conjugation of the RGD-mimetic to AB-block-copolymers of PEG-PEI and depended on the degree of peptide substitution. The conjugates of PEG-PEI AB-block-copolymers with low ligand density of the RGD-mimetic appear to be promising candidates for in vivo cancer gene therapy.

INTRODUCTION

The integrin receptor $\alpha_v\beta_3$ is a known marker of angiogenic vascular tissue (*1*). The so-called vitronectin receptor represents a highly interesting therapeutic target because of its role in a wide range of pathologies which have been reviewed elsewhere, e.g., angiogenesis (*2*). Vitronectin, fibronectin and fibrinogen, contains the tripeptide motif Arg-Gly-Asp, abbreviated as RGD, which is recognized by integrin receptors. Extensive neovascularization in tumors makes integrin receptor $\alpha_v\beta_3$ a promising target for cancer gene therapy. Targeted delivery of pDNA (*3*−*5*) and siRNA (*6*) condensed by poly(ethylene imine)-*graft*-poly(ethylene glycol) (PEG-PEI) copolymers bearing cyclic RGD peptides was reported earlier in the context of cancer gene therapy. In fact, the N-alkylated cyclic pentapeptide c(-RGD-f[NMe]V-) is currently being tested in phase II clinical trials under the name "Cilengitide" as an angiogenesis inhibitor in glioblastoma multiforme (*7*). Because of metabolic instability of peptides and bioavailability reasons, nonpeptidic small molecule RGD-mimetics were developed, such as β-amino acid-based azacarba analogues with increased lipophilicity (*8*), hydantoin scaffolds (*9*), aminobenzoyl and isonipecotyl groups as arginine mimetic, and C-terminal tryptophan to maintain ionic and hydrophobic interaction (*10*) or attachment of aliphatic carbamate linkers (*11*). Another class of substances which is similar to the one used in our study was described by Ishikawa et al. (*12*), suggesting that a cyclic guanidine at the N-terminus generates suitable adhesion, receptor inhibition, and water solubility. None of the RGD-mimetics mentioned above have so far been used for targeted gene delivery.

In this study, we used as a targeting ligand thiol and maleimide derivatives of a pentaycyclic peptidomimetic substance of a class of 1-α-*Z*-2,3-diaminopropionic acid substituted 4-amino-1*H*-pyrimidin-2-ones previously reported to exhibit high affinities to the vitronectin receptor in the nanomolar range (*13*). This ligand was coupled to different derivatives of PEI using two different synthetic approaches to generate five different bioconjugates for targeted gene delivery based on a novel RGD-mimetic. The position and ligand density were varied to identify the most suitable synthetic strategy and composition of the conjugates.

MATERIALS AND METHODS

Materials. PEI 25 kDa (Polymin, 25 kDa) was a gift from BASF (Ludwigshafen, Germany); low molecular weight poly(ethylene imine) (LMW-PEI) with a low degree of branching (*14*) and the block copolymer poly(ethylene glycol)-poly(ethylene imine) (PEI25k-PEG30k) (*15*) were synthesized as described earlier.

RGD-mimetics (RGD-M) were obtained as maleimide derivative ($C_{34}H_{36}N_8O_7$, M_w 668.70 g/mol) or as sulfhydryl derivative ($C_{30}H_{35}N_7O_5S$, M_w 605.71 g/mol) from Abbott Laboratories (Abbott Park, IL, USA) as shown in Figure 1. Orthopyridyl-disulfide poly(ethylene glycol)-succinimidyl propionic acid (NHS-PEG2 kDa-OPSS) was purchased from Nektar Therapeutics (San Carlos, CA, USA), the luciferase encoding plasmid pCMV-Luc from The Plasmid Factory (Bielefeld, Germany), Luciferase Assay Reagent (LAR) and Cell Culture

* Corresponding author. Prof. Thomas Kissel, Department of Pharmaceutics and Biopharmacy, Ketzerbach 63, 35032 Marburg, Tel: +49 6421 28 25881, Fax: +49 6421 28 27016, E-mail: kissel@staff.uni-marburg.de.

[†] Philipps-Universität Marburg.

[‡] Abbott Laboratories Incorporated.

10.1021/bc9001695 CCC: $40.75 © 2009 American Chemical Society
Published on Web 05/28/2009

A

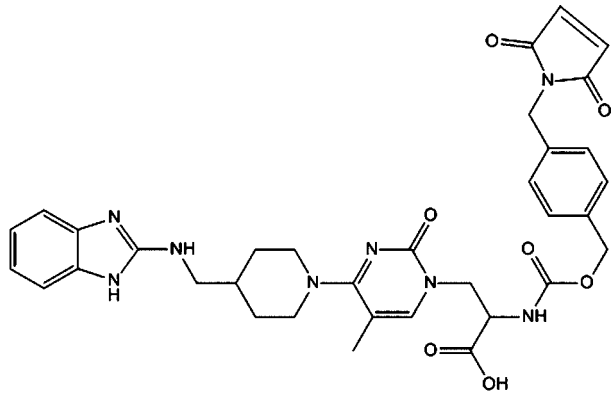

Chemical Formula: $C_{34}H_{36}N_8O_7$
Exact Mass: 668.27
Molecular Weight: 668.7
m/z: 668.27 (100.0%), 669.27 (40.0%), 670.28 (6.8%), 670.27 (2.5%), 671.28 (1.3%)
Elemental Analysis: C, 61.07; H, 5.43; N, 16.76; O, 16.75

B

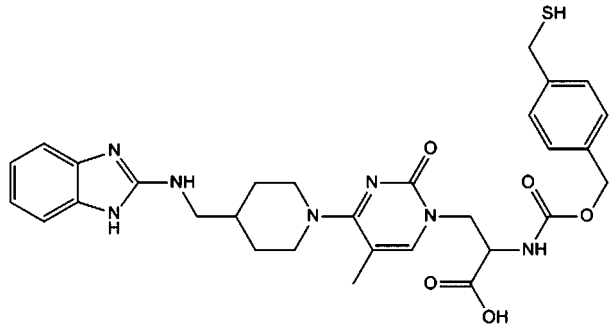

Chemical Formula: $C_{30}H_{35}N_7O_5S$
Exact Mass: 605,24
Molecular Weight: 605,71
m/z: 605,24 (100,0%), 606,25 (33,0%), 607,25 (6,3%), 607,24 (5,7%), 606,24 (3,4%), 608,24 (1,5%), 608,25 (1,0%)
Elemental Analysis: C, 59.49; H, 5.82; N, 16.19; O, 13.21; S, 5.29

Figure 1. (A) Maleimide and (B) thiol derivatives of the 1-α-*Z*-2,3-diaminopropionic acid substituted 4-amino-1*H*-pyrimidin-2-one RGD-mimetic with a 2-aminobenzimidazole moiety connected to the piperidine ring via one methylene group, which was used for coupling via PEG-linker (A) or direct coupling (B).

Lysis Reagent (CCLR) were bought from Promega (Mannheim, Germany), ion exchange columns SP Sepharose HP from Amersham Pharmacia Biotech (Freiburg, Germany), and centricon YM-30 from Millipore (Millipore, Schwalbach, Germany). Fluorescein-5-isothiocyanate (FITC), dithiothreitol (DTT), and 2,4,6-trinitrobenzenesulfonic acid (TNBS) were purchased from Sigma-Aldrich Laborchemikalien GmbH (Seelze, Germany); dimethylacetamide (DMAc) and all other chemicals were used of analytical grade.

Conjugate Synthesis. Conjugates were synthesized using two different approaches. Either (i) prePEGylated PEI (PEI25k-PEG30k), synthesized as described previously (*15*), was coupled directly with a maleimide-derivative of the RGD-M, or (ii) LMW-PEI (PEI 5 kDa) was PEGylated with a 2 kDa SPA-PEG2k-OPSS linker which was activated with DTT before coupling to a thiol derivative of the RGD-M. For the first synthetic approach (i), shown in Figure 2, 23.3 mg PEG-PEI, corresponding to 10 mg PEI (0.4 μmol), was diluted to 500 μL in either double distilled water (conjugate 10−1) or HEPES buffered saline (HBS, 20 mM HEPES, 150 mM NaCl, pH 7.5) (conjugates 10−2 and 5−2) in a 1.5 mL Eppendorf cup. RGD-M was dissolved in dimethylacetamide (DMAc) and amounts of 2.67 mg (4.0 μmol) (conjugates 10−1 and 10−2) or 1.33 mg (2.0 μmol) (conjugate 5−2) were added to the polymer solution, vortexed for 30 s and incubated under constant shaking on a sample shaker TH 15 (Edmund Bühler, Hechingen, Germany) at room temperature for 24 h. After incubation, purification was accomplished by ultrafiltration using centricon YM-30 spin columns.

The second synthetic approach (ii; Figure 3) involved coupling of a PEG linker to LMW-PEI. For this step, 5 mg LMW-PEI (1 μmol) was dissolved in HEPES buffered saline, pH 7.5, and reacted for 8 h with either 11.5 mg (5 μmol) (conjugate I) or 23 mg (10 μmol) (conjugate II) PEG linker, which had been dissolved in 200 μL absolute ethanol. Purification of the conjugates was achieved by modified ion exchange chromatography on an ÄKTA FPLC system equipped with 2 SP Sepharose HP cation exchange columns (ÄKTA Prime, Amersham Pharmacia Biotech, Freiburg, Germany) as previously described (*16*, *17*). The intermediate products, namely, the PEGylated PEI precursors, which were eluted with a high ionic strength buffer (3 M NaCl, 20 mM HEPES) from the ion exchange column, were desalted using centricon YM-3 spin columns as recommended by the manufacturer. They were characterized regarding their PEI concentration by copper complexation (*18*, *19*) and regarding their coupling degree by a pyridon-2-thion release assay (*20*). For this assay and for activation of the PEG-linker, PEG-PEIs were treated with a 10-fold molar excess of DTT for 4 h at room temperature. Pyridon-2-thion release was measured spectrophotometrically at 343 nm, and the activated PEG-PEIs were purified using centricon YM-3 spin columns

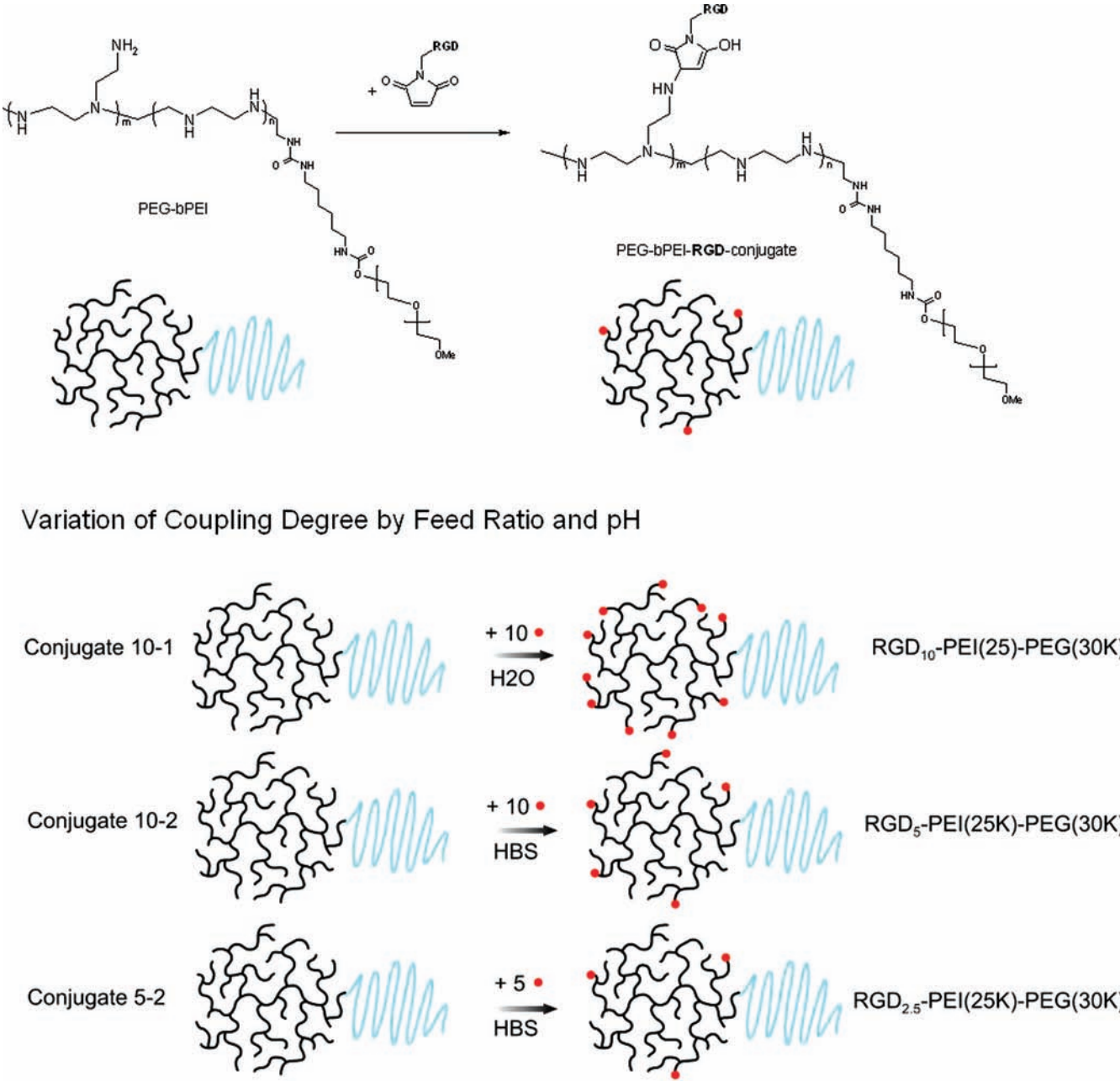

Figure 2. Synthesis of PEG-bPEI-RGD conjugates via direct coupling. Feeds of different excesses of RGD-Mimetic and synthesis at different pH values yielded three conjugates (Conjugate 10−1, 10−2, and 5−2) schematically illustrated below the synthesis scheme.

in the presence of 10 mM EDTA to avoid metal-catalyzed sulfhydryl oxidation (*21*). The activated, purified, and characterized precursors were mixed with a 3-fold (Conjugate I) or 10-fold (Conjugate II) molar excess of a sulfhydryl derivative of the RGD-M dissolved in DMAc and were coupled by formation of disulfide bonds. After another ultrafiltration step, coupling degree of all conjugates was determined spectrophotometrically at 297 nm, the wavelength that had shown maximal absorption in a wavescan of RGD-M. Measured absorption was compensated with the blank value of the noncoupled precursor.

Fluorescent Labeling of Polymers and Conjugates. Polymers were labeled as previously reported (*22*). Briefly, 20 mg polymer was dissolved in 2 mL 0.1 M sodium bicarbonate buffer, pH 9.0, and mixed with 1 mg FITC in 200 mL DMSO, stirred in the dark for 3 h at room temperature, and purified by ultrafiltration using centricon YM-10 spin columns with a MWCO of 10 kDa. The concentration of the purified sample was determined at 405 nm after formation of a picrate with 2,4,6-trinitrobenzenesulfonic acid (TNBS) in an assay previously described (*23*). The absorbance of the fluorescent dye was found not to interfere with the results from the TNBS assay.

FITC-labeled conjugates were obtained by labeling the presynthesized conjugates as described above. Since the targeting ligand, namely, the RGD-M, does not contain primary amines, we presumed that postlabeling would not negatively affect the conjugates, whereas prelabeling could interfere with the coupling steps of either RGD-Mal or the PEG-linker.

Radioactive Labeling of Conjugate 5−2. Similar to the fluorescent labeling, conjugate 5−2 was dissolved in 1 mL 0.1 M sodium bicarbonate buffer, pH 9.0, at a concentration of 10 mg/mL, mixed with p-SCN-Bn-DTPA (Macrocyclics, Dallas, TX, USA) in DMSO at a final concentration of 1 mg/mL and reacted for 1 h at room temperature. The reaction was stopped by addition of 0.1 M citrate buffer, pH 5.0, before the reaction

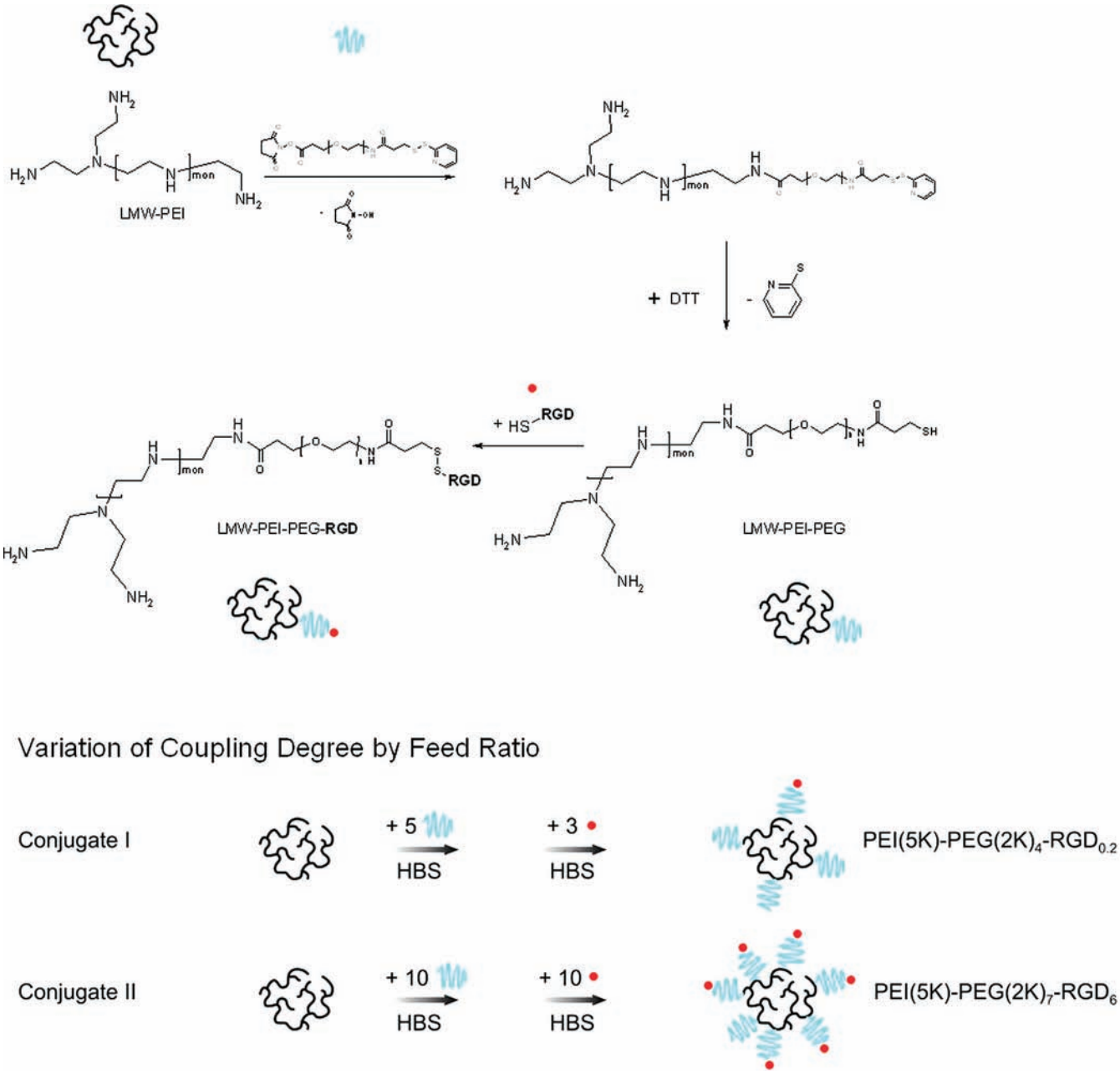

Figure 3. Synthesis of LMW-PEI-PEG-RGD conjugates via heterobifunctional PEG. Feeds of different excesses of RGD-Mimetic and PEG linker yielded two different conjugates (Conjugates I and II) schematically illustrated below the synthesis scheme.

mixture was purified by ultrafiltration using centricon YM-10 spin columns with a MWCO of 10 kDa. The concentration of the purified sample was determined at 405 nm using the TNBS-assay (*23*).

An amount of 100 μg of DTPA coupled polymer or conjugate was diluted in 0.1 M acetate buffer, pH 4.5, and mixed with 10 MBq $^{111}InCl_3$ for 30 min at room temperature, followed by size exclusion chromatography using a PD-10 Sephadex G25 prepacked column from Amersham Pharmacia Biotech (Freiburg, Germany).

Polyplex Formation. Polyplexes were formed by mixing equal volumes (25 μL each) of pDNA and polymer or conjugate diluted in 150 mM NaCl solution to obtain the desired nitrogen to DNA phosphate ratio (N/P ratio). Briefly, the appropriate amount of polymer was added to a pDNA dilution (0.04 μg/μL) to yield a final concentration of 0.02 μg DNA per μL, vortexed for 10 s, and incubated for equilibration for 10 min.

Dynamic Light Scattering (DLS) and Laser Doppler Anemometry (LDA). For measurements of hydrodynamic diameters, polyplexes were prepared as described above. 50 μL of the polyplex solution was pipetted into a disposable cuvette (UVette, Eppendorf, Wesseling-Berzdorf, Germany) and measured in the "General Purpose" mode, which best fits the correlation function of sizes measured with polyplexes. Attenuator and position were optimized by the device. Subsequently, polyplex solutions were diluted with 5% glucose solution to 800 μL and pipetted into a folded capillary cell (Malvern Instruments, Herrenberg, Germany) for zeta potential measurement. Measurements were performed in replicates of five using a Zetasizer Nano ZS (Malvern Instruments, Herrenberg, Germany) equipped with a 4 mW He−Ne laser at a wavelength of 633 nm at 25 °C. Scattered light was detected at a 173° backward scattering angle. The viscosity and refractive index of water at 25 °C was used for data analysis with the Dispersion

Technology Software 5.00 (Malvern Instruments, Herrenberg, Germany). The accuracy of the instrument was validated using reference polymer particles (Nanosphere Size Standards of 50, 100, and 200 nm, Duke Scientific Corp., Palo Alto, CA, USA) and with Zeta Potential Transfer Standard (Malvern Instruments, Herrenberg, Germany).

Ethidium Bromide Quenching Assay. To investigate if condensation efficiency of the polymers used for conjugate synthesis would be influenced by coupling of PEG or the targeting ligand, 4 μg of herring testes DNA (Sigma-Aldrich Chemie GmbH, Schnelldorf, Germany) were complexed with polymers or conjugates at different N/P ratios. After incubation for 20 min at room temperature, 20 μL of a 0.1 mg/mL ethidium bromide solution (Carl Roth GmbH, Karlsruhe, Germany) was added and the samples incubated briefly in the dark after intensive mixing. Intercalation-caused fluorescence was quantified using a fluorescence plate reader (LS 50 B, Perkin-Elmer, Rodgau-Jügesheim, Germany) at 518 nm excitation and 605 nm emission wavelengths. Experiments were performed in triplicate; results are given as mean relative fluorescence intensity values where intercalation of free DNA represents 100% fluorescence and nonintercalating ethidium bromide in buffer represents 0% remaining fluorescence.

Hemolytic Activity. Surface activity leading to hemolysis was quantified after treating human erythrocytes with polyplexes made of polymers or conjugates. Therefore, erythrocytes were isolated from fresh citrated blood from healthy volunteers by centrifugation, washed with PBS buffer, and diluted to 5×10^8 cells/mL. Polyplexes of 0.1 μg pDNA per mL were prepared at N/P 5, and 50 μL aliquots of polyplex solutions, 1% Triton-X 100 (100% lysis), or 150 mM NaCl (0% lysis) were mixed with 50 μL erythrocyte suspension. After incubation for 30 min at 37 °C, samples were centrifuged at 400 *g*. Hemolysis of replicates of three was measured spectrophotometrically in supernatants at 541 nm and is given as mean percentage of the released hemoglobin normalized to total hemolysis induced by 1% Triton-X 100.

Cell Culture. MeWo (human malignant skin melanoma; ATCC: HTB-65) and A549 (human non-small-cell lung carcinoma; ATCC: CCL-185) cells were purchased from ATCC (Teddington, UK) and maintained in DMEM (PAA Laboratories, Cölbe, Germany) supplemented with 10% fetal calf serum (Cytogen, Sinn, Germany) in humidified atmosphere with 5% CO_2 at 37 °C.

Immunofluorescence Staining of Integrin $\alpha_v\beta_3$ Receptors on the Cell Surface. MeWo and A549 cells were seeded with 60 000 cells per well on 24 well plates (Nunc, Wiesbaden, Germany). After incubation for 24 h, cells were washed with Earle's Balanced Salt Solution (EBSS, Hyclone, Thermo Fisher, Schwerte, Germany) and incubated with either 3% bovine serum albumin in phosphate buffered saline (PBS/BSA) only (blank cells and secondary antibody only cells) or with integrin $\alpha_v\beta_3$ antibody ([BV3] (ab7166), Abcam, Cambridge, MA, USA) at a concentration of 1 μg/mL in PBS/BSA for 1 h in the dark. Cells were washed three times with ice cold PBS before all wells except for blanks were treated with a 1:100 dilution of a FITC-labeled goat polyclonal to mouse IgG H&L (ab6785, Abcam, Cambridge, MA, USA) antibody in PBS/BSA for 30 min in the dark. Afterward, cells were washed three times with ice-cold PBS before they were trypsinized with 100 μL trypsin/EDTA (PAA Laboratories, Cölbe, Germany) and fixed with 200 μL of a 1:1 mixture of FACSFlow (BD Biosciences, San Jose, CA) and 4% paraformaldehyde in PBS. Cell suspensions were stored refrigerated in the dark until analysis by flow cytometry. All experiments were performed with replicates of three.

Binding Assay. MeWo and A549 cells were seeded with 60 000 cells per well in 24 well plates (Nunc, Wiesbaden, Germany). After incubation for 24 h, medium was aspirated and cells were supplied with cold serum-containing medium before they were transfected with polyplexes containing 1 μg DNA per well and FITC-labeled polymer or conjugate at N/P 5. Triplicates of cells were incubated with the polyplexes for 15 min at 4 °C before they were washed three times with PBS, trypsinized, and fixed with a 1:1 mixture of FACSFlow (BD Biosciences, San Jose, CA) and 4% paraformaldehyde in PBS. Cell suspensions were stored refrigerated in the dark until analysis by flow cytometry.

Flow Cytometry. Suspensions of fixed cells were measured on a FACScan (BD Biosciences, San Jose, CA) with excitation at 488 nm and the emission filter set to a 530/30 bandpass. Cells were gated, 10,000 viable cells were evaluated in each experiment, and results are given as the mean of 3 independent measurements. Data acquisition and analysis was performed using CellQuest Pro (BD Biosciences, San Jose, CA) and FCS Express V3.00 (DeNovo Software, Thornhill, Canada). Results were statistically analyzed using one-way ANOVA with Bonferroni posthoc test.

Quantification of Uptake. MeWo and A549 cells were seeded with 60 000 cells per well in 24 well plates (Nunc, Wiesbaden, Germany). After incubation for 24 h, triplicates of cells were treated with polyplexes prepared of various amounts of pCMV-Luc and radiolabeled conjugate 5−2 at N/P 5. Cells were incubated for 4 h before they were treated as described by Haigler et al. (*24*) to make sure only internalized activity was measured. Briefly, the cells were first treated with 0.5 mL acetic acid (0.2 M NaAc containing 0.5 M NaCl, pH 2.5) for 6 min at 4 °C followed by a quick washing with an additional amount of 0.5 mL acetic acid to remove any remaining membrane-bound activity. The cell-associated activity, which was extracted by treating the cells with 0.5 mL 1 M NaOH for 80 min at 37 °C, was considered to be internalized. The extracts in 0.5 mL NaOH were collected, and the wells were then washed with an additional 0.5 mL NaOH. Before analysis in the gamma counter, the samples were adjusted to neutral pH by adding drops of 3 M HCl.

In Vitro Cell Transfection. MeWo and A549 cells were seeded with 30 000 cells per well in 24 well plates (Nunc, Wiesbaden, Germany). After incubation for 24 h, cells were treated with polyplexes prepared of the "gold standard" PEI 25 kDa, LMW-PEI, PEG-PEI, or the various conjugates at N/P 5. After 4 h of incubation, medium was changed and cells were incubated for another 44 h before they were washed with PBS and lysed with cell culture lysis reagent (CCLR, Promega, Mannheim, Germany). Lysates of triplicates were assayed for luciferase expression with a commercial luciferase assay reagent (LAR, Promega, Mannheim, Germany) on a luminescence plate reader LUMIstar OPTIMA (BMG Labtech, Offenburg, Germany).

Competitive Inhibition of in Vitro Cell Transfection. For competitive inhibition of cell transfection, MeWo and A549 cells were seeded with 30 000 cells per well in 24 well plates (Nunc, Wiesbaden, Germany). After incubation for 24 h, cells were pretreated with increasing amounts increasing from 0.05 to 1.5 nmol per mL of the free targeting ligand for 15 min at 37 °C. Polyplexes prepared of PEG-PEI or conjugate 5−2 at N/P 5 were added into the RGD-M containing medium. Replicates of 3 were incubated for 4 h before medium was changed and thereafter treated as described above.

RESULTS AND DISCUSSION

Synthetic Outcome. RGD-peptides were reported to be good targeting ligands for tumor endothelium using nonviral lipoplexes (*25, 26*) or polyplexes containing siRNA (*6, 27, 28*) and pDNA (*4, 5*) or protein delivery systems bearing antisense

Table 1. Molecular Composition of Polymers and Conjugates, and Size and Zeta Potential of Their Complexes with pDNA

	PEI 25k	PEG-PEI	Con 5−2	Con 10−2	Con 10−1	LMW-PEI	Con I	Con II
PEI M_w [kDa]	25	25	25	25	25	5	5	5
PEG M_w [kDa]	-	1*30	1*30	1*30	1*30	-	4*2	7*2
RGD [mol/mol]	-	-	2.5	5	10	-	0.2	6
coupled	-	-	directly	directly	directly	-	via PEG	via PEG
size [nm]	90.1 ± 10.1	162 ± 5.34	387 ± 101	271 ± 6.3	92.1 ± 3.23	116 ± 2.07	677 ± 211	597 ± 111
zeta [mV]	28.2 ± 2.16	10.9 ± 1.21	2.79 ± 0.35	9.33 ± 1.03	4.88 ± 0.72	20.2 ± 1.02	−27.9 ± 1.08	−32.5 ± 6.05

oligonucleotides (*29*). Integrin targeting is an approach adopted from nature: several pathogenic organisms, such as adenoviruses (*30*), use the integrin receptor to promote their cellular internalization. While RGD-PEG-PEI has successfully been reported to efficiently deliver nucleic acids into tumors (*6*), cRGD bearing micelles did not show enhanced uptake but modulated intracellular trafficking (*4*). RGD-mimetics, on the other hand, have, to our knowledge, so far only been used as therapeutic agents, e.g., as angiogenesis inhibitors (*31*), inhibitors of monocyte-derived macrophages (*32*), enhancers of osseointegration (*33*), and imaging tracers for atheriosclerotic plaques (*34*), and they were were recently described as ligands for 5-FU (*35*) or TNFα carrying liposomes (*36*). In this study, we describe for the first time synthesis of five RGD-M conjugates of different molecular composition in two different coupling approaches (compare Figures 2 and 3) for nonviral gene delivery by coupling of a 1-α-*Z*-2,3-diaminopropionic acid substituted 4-amino-1*H*-pyrimidin-2-one. This small molecule (*13*) exhibits nanomolar affinity to the vitronectin receptor (IC50 = 1.3 nM) as determined by ELISA and therefore binds more strongly than the physiologic ligand vitronectin (IC50 = 6 nM (*37*)) and is comparable to the cyclic pentapeptide Cilengitide (IC50 = 0.86 nM (*38*)) which is being studied in clinical trials. The advantages of this targeting ligand compared to peptides are its metabolic stability and low molecular weight. Two types of conjugates were synthesized consisting either of AB-block-copolymers of PEI (25 kDa) and PEG (30 kDa) directly coupled with RGD-M ligands attached to PEI amines (Figure 2) or of a low molecular weight PEI core, which was PEGylated using a heterobifunctional PEG linker that was decorated with RGD-M molecules at the distal end of the PEG chains (Figure 3), similar to (*6*, *28*). Coupling of PEG to LMW-PEI in HBS buffer, pH 7.5, yielded coupling degrees of 70−80% of the feed, as shown in Figure 3. Coupling of RGD-M to activated PEG depended not only on the excess of RGD-M, but also on the amount of PEG-linker present. Synthesis of Conjugate I, for which a 5-fold molar excess of PEG over PEI and 3-fold molar excess of RGD-M over PEI was used, resulted in a conjugate that can be described as LMW-PEI-$(PEG2k)_4$-$RGD_{0.2}$ (final yield of LMW-PEI: 10.0%), whereas Conjugate II, for which the feed contained a 10-fold molar excess of PEG linker and a 10-fold molar excess of RGD-M over PEI, yielded the conjugate LMW-PEI-$(PEG2k)_7$-RGD_6 (final yield of LMW-PEI: 5.8%). Coupling of RGD-mimetic-maleimide turned out to be strongly influenced by pH. PEG-PEI dissolved in double-distilled water produced a pH of 10, where most of the amines in PEI are deprotonated and available for addition to RGD-mimetic-maleimide. Mixing the two components yielded quantitative reaction, whereas only 50% of the feed reacted with PEG-PEI in HEPES buffered saline adjusted to pH 7.5. Thus, Conjugate 10−1, where a 10-fold molar excess of RGD-M over PEI was added to PEG-PEI in water, reacted to a compound which can be described as PEG30k-PEI25k-RGD_{10} (final yield of PEG-PEI: 86.0%). Conjugates 10−2 and 5−2, where 10- and 5-fold excesses of RGD-M, respectively, were added to PEG-PEI in HBS, resulted in PEG30k-PEI25k-RGD_5 (final yield of PEG-PEI: 84.0%) and PEG30k-PEI25k-$RGD_{2.5}$ (final yield of PEG-PEI: 88.0%). While LMW-PEI-PEG-RGD conjugates were purified in several steps by ion exchange chromatography and buffer was additionally exchanged by ultrafiltration, PEG-PEI-RGD conjugates were only ultrafiltered and revealed much higher yields. All conjugates and their syntheses are depicted schematically in Figures 2 and 3 and Table 1.

Hydrodynamic Diameter and Zeta Potential. Both PEI and PEGylated PEIs are known to efficiently form polyplexes with p-DNA (*39*); hence, we measured hydrodynamic diameters of self-assembled complexes containing plasmid DNA and conjugates and compared their sizes to polyplexes prepared with the polymers that had been used for synthesis. It was reported earlier that PEI 25 kDa formed smaller particles than LMW-PEI at low N/P ratios (*40*), which is in good agreement with our findings (compare Figure 4). Interestingly, conjugation of RGD-M to PEG-PEI influenced size of particles in different ways. In theory, conjugation shifts the ratio of primary/secondary/tertiary amines and thus the protonation profile. Additionally, the targeting ligand itself can be protonated and influence interaction with polyanions. Therefore, its spatial orientation is most relevant. In our case, Conjugate 10−1, bearing 10 molecules RGD-M, formed particles that are smaller (92.1 ± 3.23 nm) than unmodified PEG-PEI (162 ± 5.34 nm). Conjugate 5−2, on the other hand, which bears the smallest amount of RGD-M molecules, formed larger complexes (387 ± 101 nm) than PEG-PEI, and Conjugate 10−2 (271 ± 6.3 nm), bearing twice as many RGD-M molecules as Conjugate 5−2 and half as many as Conjugate 10−1, still formed bigger complexes than PEG-PEI but smaller ones than the conjugate bearing the least targeting ligands. Obviously, the targeting moiety affected complex formation, which resulted in the smallest complexes formed by the conjugate bearing the highest density of RGD-M. Surprisingly, conjugates of lower coupling degree formed significantly larger particles. This can be explained by spatial orientation of the targeting ligands, which do not seem to be involved in complex formation if coupled in low density but may be oriented toward the surface of the complexes yielding nonspherical particles which can only be measured via hydrodynamic diameters by dynamic light scattering. Conjugates I and II, on the other hand, both exhibited a

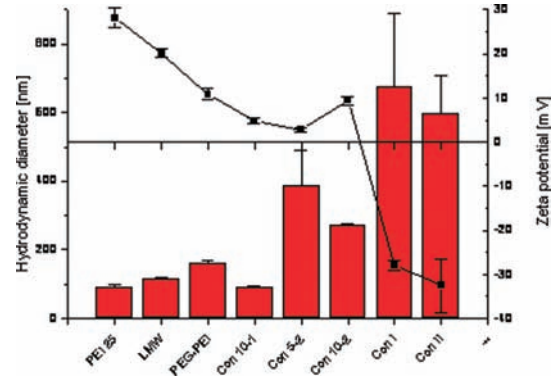

Figure 4. Size (bars) and zeta potential (squares) of pDNA complexes formed with polymers and conjugates at N/P 5 were significantly affected by conjugation. Conjugates I and II synthesized by PEGylation of LMW-PEI were not able to condense DNA into small particles, also shown by the negative zeta potential, whereas sizes of directly coupled PEG-PEI-RGD conjugates decrease with increasing ligand density and exhibit only slight differences in surface charge.

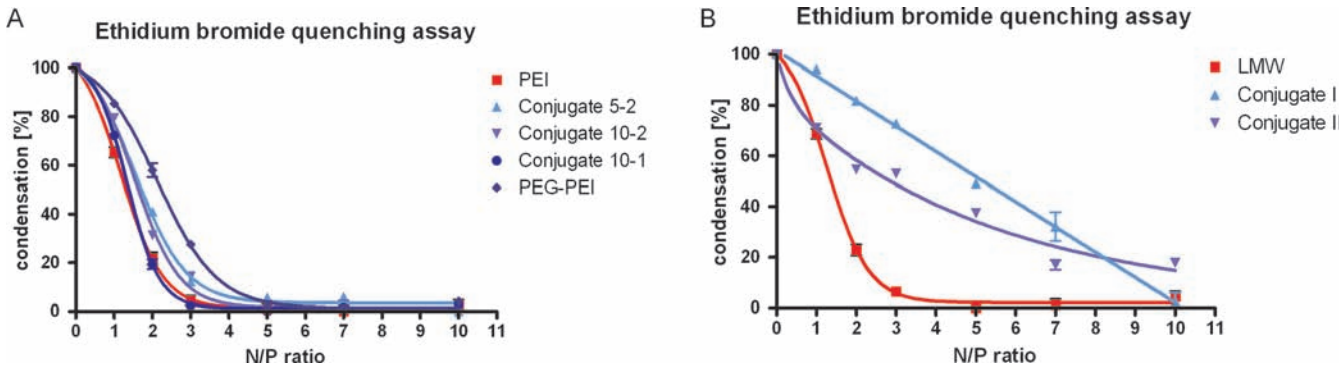

Figure 5. Quenching of intercalation caused ethidium bromide fluorescence upon condensation of DNA with (A) PEI 25k, PEG-PEI, or PEG-PEI conjugates and (B) LMW-PEI or LMW-PEI-PEG conjugates. Increase of ligand density increased condensation of DNA. While only minor differences were observed among PEG-PEI and its conjugates, condensation of LMW-PEI was strongly influenced upon conjugation.

strong hindrance in nanoplex formation compared to LWM-PEI. The LMW-PEI used in our study was less branched than PEI 25 kDa, and coupling of PEG decreased electrostatic interaction of LMW-PEI with negatively charged DNA both by a shift of the ratio of primary/secondary/tertiary amines and by modification of a small (5 kDa) ionic polymer with a relatively large (2 kDa) nonionic polymer, yielding a small portion of PEI in the overall copolymer conjugates, in fact, less than 50%. The increased number of targeting ligands in Conjugate II seemed to decrease the size of the polyplexes, which is a indication of interaction between the targeting ligand and DNA. However, differences in size between Conjugates I (677 ± 211 nm) and II (597 ± 111 nm) were not significant. In a previously published paper, it was reported that branched PEI 25k even after coupling of 40 molecules PEG and RGD peptide still formed small particles of about 200 nm at N/P ratio >1 (*28*). Therefore, we hypothesized that LMW-PEI, which in addition to its shorter chain length contains a lower branching degree, is not suitable for DNA condensation after PEGylation. It is known that particles <200 nm in size are taken up by most cell lines and that larger particles sediment faster, thereby enhancing transfection efficiency under in vitro conditions (*41*). Polyplexes showing aggregation, on the other hand, are not suitable for systemic administration. Aggregation tendency, of course, has to be evaluated in the context of surface charge. Therefore, zeta potentials of the various complexes were measured by LDA, as shown in Figure 4. Polyplexes formed with PEI25k revealed the highest surface charge, which can easily be understood as a function of the high number of protonable amines. LMW-PEI polyplexes, which have a lower branching degree (*14*) and therefore a smaller number of primary amines, exhibited a decreased zeta potential, followed by PEG-PEI polyplexes, where the positive surface charge is believed to be shielded by nonionic PEG (*42*, *43*). Polyplexes prepared with RGD-PEG-PEI conjugates showed slightly lower surface charges compared to PEG-PEI. This could be explained by the coupling of the targeting ligands, which most probably are attached to secondary amines, which exhibit a high electron density but lower steric hindrance than tertiary amines. By coupling, secondary amines are turned into tertiary ones, which are less prone to protonation than secondary amines, decreasing the protonation of the conjugate compared to the polymer. Additionally, it is possible that the targeting ligand, if oriented toward the surface of the polyplex, may shield the positive surface charges of the polyplexes as described for transferrin-PEI polyplexes (*44*), PEG-PEI conjugates with anti-OA3 Fab′ (*45*), and PEG-PEI conjugates with trastuzumab (*46*). LMW-PEI-PEG conjugates, on the other hand, formed polyplexes with net negative surface charge, which was probably caused by insufficient condensation of DNA. As already seen in size measurements, PEGylation of LMW-PEI impaired condensation

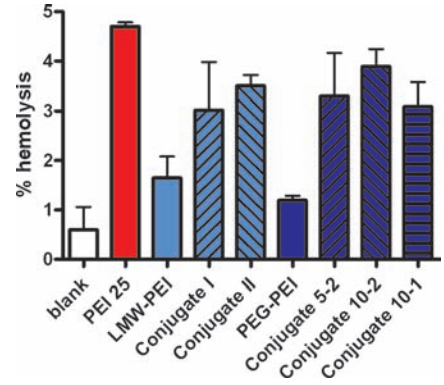

Figure 6. Percentage of hemolytic activity of pDNA complexes formed with PEI 25k, LMW-PEI, LMWPEI-PEG conjugates, PEG-PEI, or PEG-PEI conjugates compared to total hemolysis caused by 1% Triton X. Both LMW-PEI and PEG-PEI caused fewer hemolytic effects than PEI 25 kDa, while their conjugates displayed lower biocompatibility but still less hemolysis than PEI 25 kDa.

of DNA. In the case of LMW-PEI conjugates, a relatively small polymer (5 kDa) was substantially modified with several comparably large PEG chains (2 kDa). Although the targeting moiety is a small molecule, the assumption that conjugation can influence complex formation (*47*) explained the differences in sizes between LMW-PEI conjugate complexes and LMW-PEI complexes.

Condensation of DNA. A means to quantify condensation and protection of DNA inside the core of polyplexes is detection of intercalation-caused fluorescence of double strands that are available for reaction with ethidium bromide. DNA condensation efficiency of the different polymers and conjugates at different N/P ratios was therefore measured in ethidium bromide quenching assays. PEG-PEI conjugates (see Figure 5A) showed an obvious trend: Unmodified PEI25k incorporated and protected DNA best, showing full condensation at N/P 3, whereas PEG-PEI reached full condensation at N/P > 5. By increasing the amount of RGD-M molecules per PEG-PEI, condensation efficiency was gradually increased, and Conjugate 10−1 showed similar values to PEI25k. This was in line with the trends observed in dynamic light scattering, where Conjugate 10−1 formed polyplexes as small as PEI25k. Better condensation and higher stability of PEG-PEI conjugate complexes compared to their unmodified counterpart were previously described for trastuzumab-coupled PEG-PEI conjugates (*46*). LMW-PEI-PEG conjugates (Figure 5B) yielded condensation properties much different from those of LMW-PEI. The latter exhibited condensation efficiency almost as good as PEI 25k with complete condensation above N/P of 5. Conjugate I, on the other hand, did not show sigmoidal dose−response condensation efficiency but a linear trend, which proves impairment of the usual

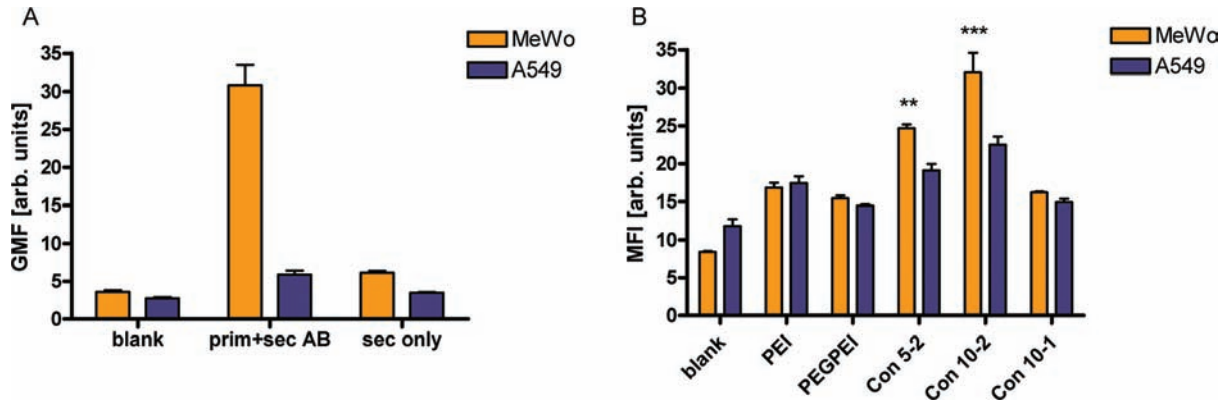

Figure 7. (A) Flow cytometric analysis of relative expression of integrin $\alpha_v\beta_3$ in A549 and MeWo cells compared to blank cells and cells treated with the fluorescently labeled secondary antibody only. MeWo cells known to express a noticeable amount of integrin receptors proved significantly stronger binding of the primary antibody. (B) Flow cytometric binding analysis of fluorescently labeled polymer and conjugate complexes to the surface of A549 and MeWo cells. Conjugate 10−2 with a medium ligand density shows the strongest differences concerning binding to receptor positive and receptor negative cells. Cells treated with Conjugate 10−1 were macroscopically observed to be detached from the plate.

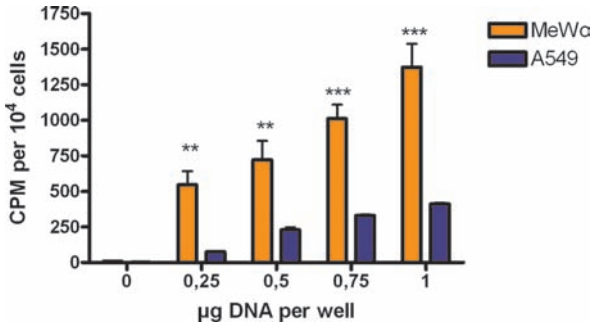

Figure 8. Radioactive internalization analysis of radiolabeled conjugate 5−2 complexes into A549 and MeWo cells at different concentrations. Up to 1 mg DNA per mL, increasing uptake of radiolabeled polyplex is maintained with increasing concentration.

condensation behavior of DNA by PEI. As already seen in size and zeta potential measurements, DNA seemed to be loosely bound to the conjugates at N/P 5 and was not well-condensed into small polyplexes. Interestingly, at N/P = 10, full condensation was reached, and it can be hypothesized that the small amount of targeting ligand in this conjugate gained importance only at higher N/P ratios. Conjugate II exhibited another profile, which was attributed to the higher graft density of RGD-M. At low N/P ratios, Conjugate II showed better condensation than Conjugate I, but full condensation was not reached at N/P of 10. This assay of course only mirrors in vitro condensation. Complex stability in the presence of serum is currently being addressed in our present study, and in vivo stability will eventually be the subject of an in vivo study if biocompatibility of the conjugates proves suitable.

Biocompatibility. Nonspecific interaction of polyplexes with cell surfaces is known for polycations such as PEI, PPI, PLL, or PAMAM and can provoke nano hole formation caused toxicity (*48*). PEGylation of polycations is an effective shielding approach to decrease interaction with blood components (*15*). Since all of the conjugates showed nearly neutral or even negative zeta potentials, a strong decrease of nonspecific interactions was expected. In order to investigate blood compatibility of the conjugates, red blood cells were treated with polyplexes composed of DNA and polymers or conjugates and analyzed for hemolysis (see Figure 6). Polyplexes prepared with PEI25k caused the strongest hemolytic effects; LMW-PEI and PEG-PEI polyplexes showed significantly (*** $p < 0.001$) decreased hemolytic activity. Interestingly, conjugation with the targeting ligand increased hemolysis: Conjugate II, despite its negative surface charge, caused significantly (* $p < 0.05$) higher hemolysis than LMW-PEI, and Conjugates 10−1 (* $p < 0.05$), 10−2 (** $p < 0.01$), and 5−2 (*** $p < 0.001$) showed stronger hemolysis than PEG-PEI. This could be an indication of surface activity or different spatial orientation of the targeting ligand depending on the coupling degree. RGD sequences do not only interact with integrin $\alpha_v\beta_3$ (*49*). Since erythrocytes do not carry integrins but rather an integrin-associated protein (IAP) CD47 (*50*), nonspecific interactions in this assay could lead to cross reactivity of the conjugates with CD47. Agglutination of the red blood was strongly observed in cells treated with unmodified PEI25k and slightly in LMW-PEI treated cells. PEG-PEI and conjugates did not cause agglutination despite the slightly higher hemolytic effects of the conjugates (data not shown). In order to test the conjugates in an in vivo study, minimal hemolysis and cross-linking of cells is a prerequisite. Further toxicity assays will show whether the conjugates we synthesized are safe enough to be applied intravenously in a tumor model. Other options could be intratumoral injections or local administration.

Expression of Integrin Receptor. To test specific bioactivity of the conjugates in $\alpha_v\beta_3$ integrin overexpressing cells compared to cells that do not show overexpression of this receptor, expression status of MeWo human melanoma and A549 carcinomic human alveolar basal epithelial cells, two cell lines previously used for integrin targeted gene delivery (*51*), was quantified after immunostaining by flow cytometry (Figure 7A). A549 cells treated with primary and secondary antibody did not show significantly stronger fluorescence than after treatment with secondary antibody only, proving that fluorescence was only caused by nonspecific binding of the secondary antibody. MeWo cells, on the other hand, showed clear overexpression of CD51/CD61. A549 cells were therefore considered receptor-negative, whereas MeWo cells were considered receptor-positive.

Cell Binding of Polyplexes. Binding of fluorescently labeled polyplexes to the receptor expressing or nonexpressing cell surface of MeWo or A549 cells, respectively, was tested at 4 °C, where energy-dependent processes such as receptor-mediated endocytosis are deactivated. Flow cytometric analysis proved that only Conjugates 10−2 and 5−2 with substitution degrees of 5 and 2.5 RGD-M per molecule displayed differences concerning binding to receptor-positive or receptor-negative cells (Figure 7B). Conjugate 10−1, on the other hand, which bears the highest number of RGD-M molecules, did not show significantly higher binding to MeWo compared to A549 cells. Due to higher stability of the complex, possibly at least parts of the targeting ligand in Conjugate 10−1 are involved in complex formation and are therefore either oriented toward the inside of the complex or hidden by DNA with which they interact. Therefore, Conjugate 10−1 forms the smallest particles, condenses DNA as well as PEI25k, and does not bind to MeWo

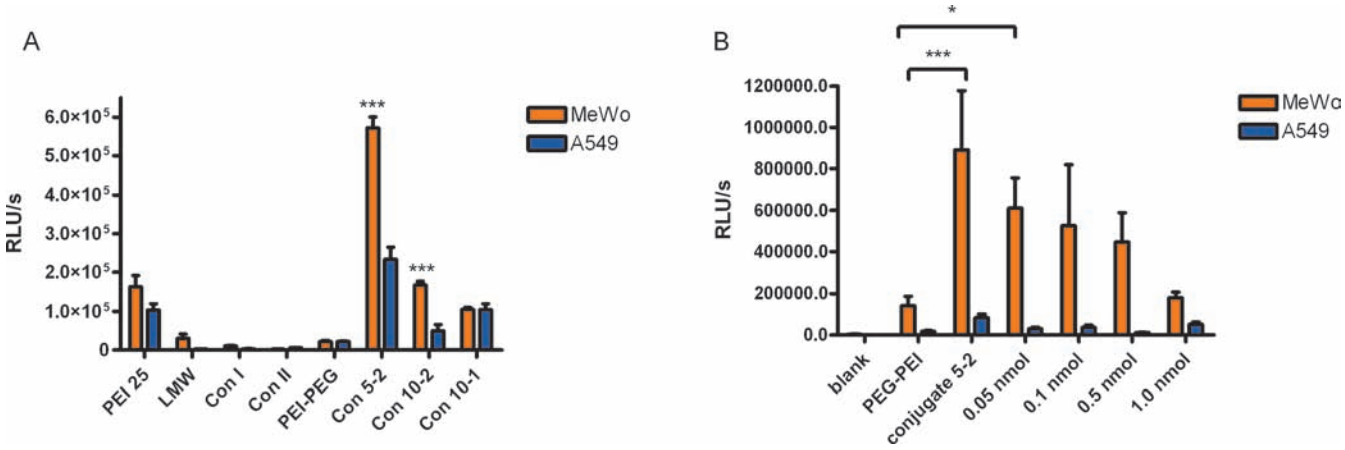

Figure 9. (A) Transfection efficiency of polymer and conjugate complexes in A549 and MeWo cells. Conjugate 5−2 with the lowest ligand density revealed the highest transgene expression. (B) Competitive inhibition of transfection efficiency of conjugate complexes in A549 and MeWo cells. At a concentration of 0.1 nmol/mL of free targeting ligand or higher, transfection efficiency of Conjugate 5−2 could be comparatively inhibited to values significantly higher than that of PEG-PEI.

cells specifically more strongly than to A549 cells. Concerning substitution degree, linker chemistry, and their correlation to specificity, there are contrary reports in literature. While Garg et al. (*35*) reported increasing specific uptake with increasing amounts of targeting ligand in a range of coupling degree below 8−10 mol %, they also described lipoplex destabilization above that degree. This amount is still much below the coupling degree of all the conjugates in our study, and it is possible that polyplexes could as well be destabilized at high coupling degrees. It must also be kept in mind that the RGD-M used for conjugate synthesis is a receptor antagonist. Vitronectin-receptor antagonists are known to cause detachment of cells. The high amount of RGD-M present in Conjugate 10−1 therefore detached cells effectively interacting with Conjugate 10−1, which could be observed macroscopically. The detached cells were aspirated in one of the washing steps leading to low fluorescence values measured by flow cytometry. It was reported earlier that integrin dimerization, cluster formation, and activation of downstream effects depend on ligand density and affinity (*52*). This could explain that conjugates bearing a higher ligand density have a stronger inhibitory effect on cell attachment than those with lower ligand density.

Transfection Efficacy. To investigate whether the strong interaction of the conjugates with MeWo cells was only a concentration-dependent surface effect of the targeting ligand, uptake, which was assumed to be receptor-mediated endocytosis due to a previous report (*53*), was studied in a radioactive assay. Here, surface-bound material could be removed and distinct information about internalization could be obtained. In order to test for concentration-dependent effects, MeWo and A549 cells were treated with increasing concentrations of Conjugate 5−2/DNA polyplexes, which had caused strong nonspecific effects in the hemolysis assay, which could be interpreted as an indication of a surface effect. However, scintillation counting of cell lysates confirmed cell specificity of uptake at each concentration as shown in Figure 8. Up to 1 μg of DNA per well, an increasing abundance of RGD-M leads to increasing uptake of polyplexes without any sign of cell detachment.

Finally, transgene expression after transfection of receptor-positive and receptor-negative cells with polymer and conjugate complexes was measured. PEI 25k, the "gold standard" in polymeric nonviral gene delivery, was used for comparison in each experiment (compare Figure 9A). LMW-PEI and PEG-PEI complexes exhibited lower transfection efficiency compared to PEI25 kDa, due to decreased nonspecific cell interaction. LMW-PEI-PEG conjugates were even inferior to LMW-PEI concerning transfection efficiency, which can be explained by insufficient condensation and protection of DNA inside the complex. In a previous study, it was shown that attaching the targeting ligand to PEI via PEG spacer achieved higher transfection efficiency than direct coupling (*46*), but in this panel of conjugates, PEGylated LMW-PEI conjugates did not exhibit desirable qualities. By PEGylation of LWM-PEI, the interaction between polycation and polyanion was obviously impaired, shown by poor condensation and large polyplex sizes. In another report, conjugation of an RGD peptide to PEI via PEG was inefficient, whereas coupling via SPDP-mediated efficient and specific transfection efficiency (*51*) is in accordance with our results. Directly coupled Conjugate 10−1 yielded higher transfection efficiency than PEG-PEI but no specific differences between the cell lines. This comparably low transfection efficacy of Conjugate 10−1 can again be explained by cell detachment, which falsified the results. Conjugate 5−2, on the other hand, showed 28-fold higher transgene expression in MeWo cells than PEG-PEI and highly significantly (*** $p < 0.001$) stronger expression than in A549. The low ligand density in this conjugate obviously did not cause any inhibitory effects on cell attachment. Conjugate 10−2 achieved very good and specific (** $p < 0.01$) transfection efficiency in MeWo as well, which was comparable to that of the PEI 25 kDa but might be decreased compared to Conjugate 5−2 due to cell detachment. The fact that some of the conjugates also showed better transfection efficiency in A549 cells compared to nontargeted PEG-PEI can be explained by a constitutive expression of integrin receptor on almost all cells which was shown to be much lower in A549 than in MeWo cells but not fully absent (Figure 7A).

Specificity of Transfection Efficacy. To ascertain receptor specificity of transfection efficiency, which had also yielded higher values for conjugates in A549 cells, uptake of conjugate complexes was competitively inhibited by free ligand. Eventually, transfection efficiency was measured and compared to that of nontargeted PEG-PEI complexes, as shown in Figure 9B. Conjugate 5−2 complexes again caused significantly higher (*** $p < 0.001$) transfection efficiency in MeWo than PEG-PEI complexes, but transgene expression was decreased by increasing amounts of free ligand. At 0.1 nmol inhibitor per mL and higher concentrations, transfection efficiency in MeWo cells was not significantly different from that of PEG-PEI complexes. Interestingly, Conjugate 5−2 complexes also again caused slightly higher transgene expression in A549 cells than PEG-PEI complexes, and this increase was reversed in A549 cells, too, in the presence of free targeting ligand. Since A549 cells do express a low number of integrin receptors, this result is not

very surprising. Conjugate 5−2 was exemplarily investigated in this assay, as it has shown the highest transfection efficacy in the absence of competing free RGD-M. Since we were able to prove the specificity of its receptor-mediated delivery of pDNA, we hypothesize that this uptake route is also true in case of the other conjugates.

CONCLUSIONS

In conclusion, with our panel of differently synthesized conjugates, we have been able to investigate structure−function relationships. The high-affinity small molecule we used for integrin receptor targeting proved to be a suitable coupling reagent for in vitro gene delivery systems. Depending on the coupling route, more and less effective conjugates were obtained. Obviously, LMW-PEI lost its ability to condense DNA into small particles and to protect it upon coupling of substantial amounts of PEG. The RGD-M-coupled LMW-PEI-PEG conjugates therefore did not perform well in vitro and did not generate high transgene expression. The PEG-PEI conjugates, where the targeting ligand was coupled to the PEI domain of a diblock-like copolymer, on the other hand, seemed to be very promising compounds. PEG-PEI was not strongly affected concerning DNA condensation upon conjugation, which is shown by ethidium bromide quenching and size measurements of the polyplexes. The coupling degree of the targeting moiety had an impact on sizes, zeta potentials, and complexation of DNA but even more strongly influenced bioactivity. Whereas Conjugate 10−1 lacked specific interaction with MeWo cells, Conjugates 10−2 and 5−2 exhibited significantly higher binding and transgene expression in integrin receptor overexpressing cells, which could be inhibited by free targeting ligand. In these conjugates, DNA was tightly bound, but targeting ligands were obviously easily accessible for interaction with cell surface receptors. Considering the biologic effect of the RGD-M, conjugates with a rather low coupling degree revealed the best results in vitro, with transfection efficacy inversely correlating with coupling degree. In this study, we were able to identify Conjugates 10−2 and especially 5−2 as promising candidates for in vivo cancer gene therapy.

ACKNOWLEDGMENT

We are grateful to Dr. Cornelia Brendel (FACS laboratory, Department of Hematology, Oncology and Immunology, University Hospital Marburg) and Prof. Dr. Thomas Behr (Nuclear Medicine Department, University Hospital Marburg) for the generous use of equipment and facilities and to Eva Mohr (Department of Pharmaceutics and Biopharmacy, Philipps-Universität Marburg) for excellent technical support.

LITERATURE CITED

(1) Brooks, P. C., Clark, R. A., and Cheresh, D. A. (1994) Requirement of vascular integrin alpha v beta 3 for angiogenesis. *Science 264*, 569–71.

(2) Hodivala-Dilke, K. (2008) alphavbeta3 integrin and angiogenesis: a moody integrin in a changing environment. *Curr. Opin. Cell Biol. 20*, 514–9.

(3) Kim, W. J., Yockman, J. W., Jeong, J. H., Christensen, L. V., Lee, M., Kim, Y. H., and Kim, S. W. (2006) Anti-angiogenic inhibition of tumor growth by systemic delivery of PEI-g-PEG-RGD/pCMV-sFlt-1 complexes in tumor-bearing mice. *J. Controlled Release 114*, 381–8.

(4) Oba, M., Aoyagi, K., Miyata, K., Matsumoto, Y., Itakav, K., Nishiyama, N., Yamasaki, Y., Koyama, H., Kataoka, K. (2008) Polyplex micelles with cyclic RGD peptide ligands and disulfide cross-links directing to the enhanced transfection via controlled intracellular trafficking. *Mol Pharm*.

(5) Oba, M., Fukushima, S., Kanayama, N., Aoyagi, K., Nishiyama, N., Koyama, H., and Kataoka, K. (2007) Cyclic RGD peptide-conjugated polyplex micelles as a targetable gene delivery system directed to cells possessing alphavbeta3 and alphavbeta5 integrins. *Bioconjugate Chem. 18*, 1415–23.

(6) Schiffelers, R. M., Ansari, A., Xu, J., Zhou, Q., Tang, Q., Storm, G., Molema, G., Lu, P. Y., Scaria, P. V., and Woodle, M. C. (2004) Cancer siRNA therapy by tumor selective delivery with ligand-targeted sterically stabilized nanoparticle. *Nucleic Acids Res. 32*, e149.

(7) Reardon, D. A., Fink, K. L., Mikkelsen, T., Cloughesy, T. F., O'Neill, A., Plotkin, S., Glantz, M., Ravin, P., Raizer, J. J., Rich, K. M., Schiff, D., Shapiro, W. R., Burdette-Radoux, S., Dropcho, E. J., Wittemer, S. M., Nippgen, J., Picard, M., and Nabors, L. B. (2008) Randomized phase II study of cilengitide, an integrin-targeting arginine-glycine-aspartic acid peptide, in recurrent glioblastoma multiforme. *J. Clin. Oncol. 26*, 5610–7.

(8) Peyman, A., Wehner, V., Knolle, J., Stilz, H. U., Breipohl, G., Scheunemann, K. H., Carniato, D., Ruxer, J. M., Gourvest, J. F., Gadek, T. R., and Bodary, S. (2000) RGD mimetics containing a central hydantoin scaffold: alpkha(v)beta3 vs alpha(IIb)beta3 selectivity requirements. *Bioorg. Med. Chem. Lett. 10*, 179–82.

(9) Sulyok, G. A., Gibson, C., Goodman, S. L., Holzemann, G., Wiesner, M., and Kessler, H. (2001) Solid-phase synthesis of a nonpeptide RGD mimetic library: new selective alphavbeta3 integrin antagonists. *J. Med. Chem. 44*, 1938–50.

(10) Pollina, E. (1996) Design and Ssynthesis of RGD mimetics as potent inhibitors of platelet aggregation. *J. Undergrad. Sci 3*, 119–126.

(11) Burnett, C. A., Xie, J., Quijano, J., Shen, Z., Hunter, F., Bur, M., Li, K. C., and Danthi, S. N. (2005) Synthesis, in vitro, and in vivo characterization of an integrin alpha(v)beta(3)-targeted molecular probe for optical imaging of tumor. *Bioorg. Med. Chem. 13*, 3763–71.

(12) Ishikawa, M., Kubota, D., Yamamoto, M., Kuroda, C., Iguchi, M., Koyanagi, A., Murakami, S., and Ajito, K. (2006) Tricyclic pharmacophore-based molecules as novel integrin alpha(v)beta3 antagonists. Part 2: synthesis of potent alpha(v)beta3/alpha(IIb-)beta3 dual antagonists. *Bioorg. Med. Chem. 14*, 2109–30.

(13) Zechel, C., Backfisch, G., Delzer, J., Geneste, H., Graef, C., Hornberger, W., Kling, A., Lange, U. E., Lauterbach, A., Seitz, W., and Subkowski, T. (2003) Highly potent and selective alphaVbeta3-receptor antagonists: solid-phase synthesis and SAR of 1-substituted 4-amino-1H-pyrimidin-2-ones. *Bioorg. Med. Chem. Lett. 13*, 165–9.

(14) Fischer, D., Bieber, T., Li, Y., Elsasser, H. P., and Kissel, T. (1999) A novel non-viral vector for DNA delivery based on low molecular weight, branched polyethylenimine: effect of molecular weight on transfection efficiency and cytotoxicity. *Pharm. Res. 16*, 1273–9.

(15) Petersen, H., Fechner, P. M., Fischer, D., and Kissel, T. (2002) Synthesis, characterization, and biocompatibility of polyethylenimine-graft-poly(ethylene glycol) block copolymers. *Macromolecules 35*, 6867–6874.

(16) Kircheis, R., Kichler, A., Wallner, G., Kursa, M., Ogris, M., Felzmann, T., Buchberger, M., and Wagner, E. (1997) Coupling of cell-binding ligands to polyethylenimine for targeted gene delivery. *Gene Ther. 4*, 409–18.

(17) Germershaus, O., Merdan, T., Bakowsky, U., Behe, M., and Kissel, T. (2006) Trastuzumab-polyethylenimine-polyethylene glycol conjugates for targeting Her2-expressing tumors. *Bioconjugate Chem. 17*, 1190–9.

(18) von Harpe, A. (2000) in *Department Pharmaceutics and Biopharmacy*, Philipps-Universität, Marburg.

(19) Ungaro, F., De Rosa, G., Miro, A., and Quaglia, F. (2003) Spectrophotometric determination of polyethylenimine in the presence of an oligonucleotide for the characterization of controlled release formulations. *J. Pharm. Biomed. Anal. 31*, 143–9.

(20) Carlsson, J., Drevin, H., and Axen, R. (1978) Protein thiolation and reversible protein-protein conjugation. N-Succinimidyl 3-(2-

pyridyldithio)propionate, a new heterobifunctional reagent. *Biochem. J. 173*, 723–37.
(21) Hermanson, G. T. (1996) *Bioconjugate Techniques*, Academic Press, San Diego.
(22) Merdan, T., Kunath, K., Fischer, D., Kopecek, J., and Kissel, T. (2002) Intracellular processing of poly(ethylene imine)/ribozyme complexes can be observed in living cells by using confocal laser scanning microscopy and inhibitor experiments. *Pharm. Res. 19*, 140–6.
(23) Snyder, S. L., and Sobocinski, P. Z. (1975) An improved 2,4,6-trinitrobenzenesulfonic acid method for the determination of amines. *Anal. Biochem. 64*, 284–8.
(24) Haigler, H. T., Maxfield, F. R., Willingham, M. C., and Pastan, I. (1980) Dansylcadaverine inhibits internalization of 125I-epidermal growth factor in BALB 3T3 cells. *J. Biol. Chem. 255*, 1239–41.
(25) Temming, K., Schiffelers, R. M., Molema, G., and Kok, R. J. (2005) RGD-based strategies for selective delivery of therapeutics and imaging agents to the tumour vasculature. *Drug Resist. Updates 8*, 381–402.
(26) Zuhorn, I. S., Kalicharan, D., Robillard, G. T., and Hoekstra, D. (2007) Adhesion receptors mediate efficient non-viral gene delivery. *Mol. Ther. 15*, 946–53.
(27) Schiffelers, R. M., Mixson, A. J., Ansari, A. M., Fens, M. H., Tang, Q., Zhou, Q., Xu, J., Molema, G., Lu, P. Y., Scaria, P. V., Storm, G., and Woodle, M. C. (2005) Transporting silence: design of carriers for siRNA to angiogenic endothelium. *J. Controlled Release 109*, 5–14.
(28) Schiffelers, R. M., and Storm, G. (2006) ICS-283: a system for targeted intravenous delivery of siRNA. *Expert Opin. Drug Delivery 3*, 445–54.
(29) Kang, H., Alam, M. R., Dixit, V., Fisher, M. , Juliano, R. L. (2008) Cellular delivery and biological activity of antisense oligonucleotides conjugated to a targeted protein carrier. *Bioconjugate Chem.*
(30) Bai, M., Campisi, L., and Freimuth, P. (1994) Vitronectin receptor antibodies inhibit infection of HeLa and A549 cells by adenovirus type 12 but not by adenovirus type 2. *J. Virol. 68*, 5925–32.
(31) Kerr, J. S., Wexler, R. S., Mousa, S. A., Robinson, C. S., Wexler, E. J., Mohamed, S., Voss, M. E., Devenny, J. J., Czerniak, P. M., Gudzelak, A., Jr., and Slee, A. M. (1999) Novel small molecule alpha v integrin antagonists: comparative anticancer efficacy with known angiogenesis inhibitors. *Anticancer Res. 19*, 959–68.
(32) Ballana, E., Pauls, E., Senserrich, J., Clotet, B., Perron-Sierra, F., Tucker, G. C., and Este, J. A. (2008) Cell adhesion through alphaV-containing integrins is required for efficient HIV-1 infection in macrophages. *Blood*.
(33) Petrie, T. A., Reyes, C. D., Burns, K. L., and Garcia, A. J. (2008) Simple application of fibronectin-mimetic coating enhances osseointegration of titanium implants. *J. Cell Mol. Med*.
(34) Burtea, C., Laurent, S., Murariu, O., Rattat, D., Toubeau, G., Verbruggen, A., Vansthertem, D., Vander Elst, L., and Muller, R. N. (2008) Molecular imaging of alpha v beta3 integrin expression in atherosclerotic plaques with a mimetic of RGD peptide grafted to Gd-DTPA. *Cardiovasc. Res. 78*, 148–57.
(35) Garg, A.; Tisdale, A. W.; Haidari, E.; Kokkoli, E. Targeting colon cancer cells using PEGylated liposomes modified with a fibronectin-mimetic peptide. *Int. J. Pharm.* In Press.
(36) Demirgoz, D., Garg, A., and Kokkoli, E. (2008) PR_b-Targeted PEGylated liposomes for prostate cancer therapy. *Langmuir*.
(37) Orlando, R. A., and Cheresh, D. A. (1991) Arginine-glycine-aspartic acid binding leading to molecular stabilization between integrin alpha v beta 3 and its ligand. *J. Biol. Chem. 266*, 19543–50.
(38) Mitjans, F., Meyer, T., Fittschen, C., Goodman, S., Jonczyk, A., Marshall, J. F., Reyes, G., and Piulats, J. (2000) In vivo therapy of malignant melanoma by means of antagonists of alphav integrins. *Int. J. Cancer 87*, 716–23.
(39) Petersen, H., Fechner, P. M., Martin, A. L., Kunath, K., Stolnik, S., Roberts, C. J., Fischer, D., Davies, M. C., and Kissel, T. (2002) Polyethylenimine-graft-poly(ethylene glycol) copolymers: influence of copolymer block structure on DNA complexation and biological activities as gene delivery system. *Bioconjugate Chem. 13*, 845–54.
(40) Kunath, K., von Harpe, A., Fischer, D., Petersen, H., Bickel, U., Voigt, K., and Kissel, T. (2003) Low-molecular-weight polyethylenimine as a non-viral vector for DNA delivery: comparison of physicochemical properties, transfection efficiency and in vivo distribution with high-molecular-weight polyethylenimine. *J. Controlled Release 89*, 113–25.
(41) Mahato, R. I., Rolland, A., and Tomlinson, E. (1997) Cationic lipid-based gene delivery systems: pharmaceutical perspectives. *Pharm. Res. 14*, 853–9.
(42) Lucas, B., Remaut, K., Sanders, N. N., Braeckmans, K., De Smedt, S. C., and Demeester, J. (2005) Studying the intracellular dissociation of polymer-oligonucleotide complexes by dual color fluorescence fluctuation spectroscopy and confocal imaging. *Biochemistry 44*, 9905–12.
(43) Mao, S., Neu, M., Germershaus, O., Merkel, O., Sitterberg, J., Bakowsky, U., and Kissel, T. (2006) Influence of polyethylene glycol chain length on the physicochemical and biological properties of poly(ethylene imine)-graft-poly(ethylene glycol) block copolymer/SiRNA polyplexes. *Bioconjugate Chem. 17*, 1209–18.
(44) Ogris, M., Brunner, S., Schuller, S., Kircheis, R., and Wagner, E. (1999) PEGylated DNA/transferrin-PEI complexes: reduced interaction with blood components, extended circulation in blood and potential for systemic gene delivery. *Gene Ther. 6*, 595–605.
(45) Merdan, T., Callahan, J., Petersen, H., Kunath, K., Bakowsky, U., Kopeckova, P., Kissel, T., and Kopecek, J. (2003) Pegylated polyethylenimine-Fab' antibody fragment conjugates for targeted gene delivery to human ovarian carcinoma cells. *Bioconjugate Chem 14*, 989–96.
(46) Germershaus, O., Neu, M., Behe, M., and Kissel, T. (2008) HER2 targeted polyplexes: the effect of polyplex composition and conjugation chemistry on in vitro and in vivo characteristics. *Bioconjugate Chem. 19*, 244–53.
(47) Ogris, M., Steinlein, P., Carotta, S., Brunner, S., and Wagner, E. (2001) DNA/polyethylenimine transfection particles: influence of ligands, polymer size, and PEGylation on internalization and gene expression. *AAPS PharmSci 3*, E21.
(48) Hong, S., Leroueil, P. R., Janus, E. K., Peters, J. L., Kober, M. M., Islam, M. T., Orr, B. G., Baker, J. R., Jr., and Banaszak Holl, M. M. (2006) Interaction of polycationic polymers with supported lipid bilayers and cells: nanoscale hole formation and enhanced membrane permeability. *Bioconjugate Chem. 17*, 728–34.
(49) Takagi, J. (2004) Structural basis for ligand recognition by RGD (Arg-Gly-Asp)-dependent integrins. *Biochem. Soc. Trans. 32*, 403–6.
(50) Brown, E., Hooper, L., Ho, T., and Gresham, H. (1990) Integrin-associated protein: a 50-kD plasma membrane antigen physically and functionally associated with integrins. *J. Cell Biol. 111*, 2785–94.
(51) Kunath, K., Merdan, T., Hegener, O., Haberlein, H., and Kissel, T. (2003) Integrin targeting using RGD-PEI conjugates for in vitro gene transfer. *J. Gene Med. 5*, 588–99.
(52) Boontheekul, T., Kong, H. J., Hsiong, S. X., Huang, Y. C., Mahadevan, L., Vandenburgh, H., and Mooney, D. J. (2008) Quantifying the relation between bond number and myoblast proliferation. *Faraday Discuss. 139*, 53−70; discussion105−28, 41920.
(53) Schraa, A. J., Kok, R. J., Berendsen, A. D., Moorlag, H. E., Bos, E. J., Meijer, D. K., de Leij, L. F., and Molema, G. (2002) Endothelial cells internalize and degrade RGD-modified proteins developed for tumor vasculature targeting. *J. Controlled Release 83*, 241–51.

BC9001695

JULY 2009
Volume 20, Number 7

© *Copyright 2009 by the American Chemical Society*

Bioconjugate Chemistry

REVIEWS

Nonnatural Amino Acids for Site-Specific Protein Conjugation

Albert J. de Graaf,[†] Marlous Kooijman,[†] Wim E. Hennink, and Enrico Mastrobattista*

Department of Pharmaceutics, Utrecht Institute for Pharmaceutical Sciences (UIPS), Faculty of Science, Utrecht University, P.O. Box 80.082, 3508 TB Utrecht, The Netherlands. Received July 12, 2008; Revised Manuscript Received November 17, 2008

Over the years, several chemical reactions have been developed that enable the covalent conjugation of synthetic molecules to natural proteins. The resulting bioconjugates have become important tools in the study of natural proteins. Furthermore, they form a new class of protein-based pharmaceuticals and biomaterials. However, classical bioconjugation reactions to natural amino acids suffer from poor site-specificity. To overcome this problem, a variety of uniquely reactive non-natural amino acids have recently been designed. These can be incorporated into proteins by specifically engineered bacterial strains. Such reactive non-natural amino acids create new possibilities for bio-orthogonal conjugation to proteins. This review first gives an overview of the various methods for site-specific introduction of non-natural amino acids into proteins. Both semisynthetic and entirely recombinant methods are addressed. Then, a detailed description is given of the reactive non-natural amino acids that have already been recombinantly introduced into proteins. The bio-orthogonal reactions that can be used for conjugation to these reactive non-natural amino acids are also discussed. These include the alkyne/azide 'click' reaction, carbonyl condensations, Michael-type additions, and Mizoroki-Heck substitutions.

INTRODUCTION

Proteins are responsible for the majority of functional attributes of all living organisms. They act as building blocks of the cell structure and as catalysts in the metabolism of cells. Furthermore, signal transduction within and between cells, as well as cell morphology and stability, are dependent on a large number of proteins. Many of these functions are dependent on post-translational modifications (e.g., glycosylation or lipidation) at specific sites of the proteins involved.

Scientists have long been inspired by the mechanisms of nature to couple different molecules to proteins and have explored them in order to synthesize (nonnatural) protein bioconjugates. As a result of this research, different chemoselective conjugation methods have been developed in the last decades. These chemoselective conjugation methods have proven to be very useful, e.g., to attach probes or drugs to proteins. Another application is the attachment of hydrophilic polymers (e.g., poly(ethylene glycol) (PEG)) to therapeutic proteins. PEGylation reduces the immunogenicity and antibody recognition of therapeutic proteins. This leads to increased stability and body residence time. PEGylation has also improved the targeting and tissue penetration of protein pharmaceuticals (*1*−*5*).

Furthermore, fusion proteins and proteins with new functionalities have been developed using bioconjugation reactions (*2*−*8*). Finally, chemoselective conjugation reactions are useful tools for the design of new biomaterials (*9*−*12*).

A drawback of the conventional chemoselective bioconjugation reactions is the heterogeneity of the product that is

* Corresponding author. Tel.: +31 302539392; fax: +31 302517839. E-mail address: E.Mastrobattista@uu.nl.
[†] These authors contributed equally to this work.

10.1021/bc800294a CCC: $40.75 © 2009 American Chemical Society
Published on Web 02/03/2009

Table 1. Reactive Natural Amino Acid Side Chains

Amino acid	Side chain	pKa
Aspartic acid		3.7-4.0
Glutamic acid	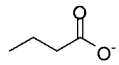	4.2-4.5
Histidine	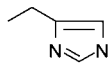	6.7-7.1
Lysine	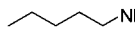	9.3-9.5
Arginine	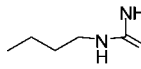	>12
Tyrosine	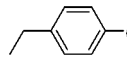	9.7-10.1
Cysteine		8.8-9.1
Methionine	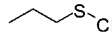	
Tryptophan	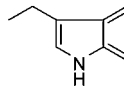	
C-terminus		2.1-2.4
N-terminus		7.6-8.0

formed. This is due to the fact that more than one residue of the targeted amino acid species may be present in a protein. To overcome this limitation, orthogonally reactive nonnatural amino acids can be introduced into proteins. Various methods to incorporate nonnatural amino acids into proteins are outlined below. Being able to attach molecules only to the introduced nonnatural amino acid, without derivatizing the natural amino acids in the protein, one can achieve exact control over the site and number of conjugations to a protein. In this way, highly defined products can be obtained. In principle, such bio-orthogonal conjugation reactions can be carried out in the presence of other proteins that contain only natural amino acids.

This review analyzes the potential of bio-orthogonal conjugation reactions to proteins containing nonnatural amino acids. First, the most common techniques for incorporation of nonnatural amino acids into proteins are discussed. Then, an overview is given of chemically reactive nonnatural amino acids that have been introduced into proteins, together with a discussion of the reactions that can be used for conjugation to these amino acids.

CONJUGATION TO NATURAL AMINO ACIDS

Most bioconjugation reactions make use of the reactivities of natural amino acids. Though not the scope of this review, a short account of these reactions is given here to clarify the need for nonnatural amino acids with bio-orthogonal reactivities.

There are nine canonical amino acids that may in principle be derivatized at their side chains, since these amino acids possess functional groups (Table 1).

Nucleophile-to-electrophile attacks are the most common protein conjugation reactions. The strongest nucleophile present in natural proteins is the cysteine thiol group. However, this amino acid is relatively rare, and when it is present in a protein, it is often involved in the catalytic center or in disulfide bridges. Cysteine residues are therefore not always optimal as sites for conjugation reactions. Consequently, the main targets of protein conjugation are the ε-lysil amino groups (together with the N-terminal (α-) amino group). The natural occurrence of lysine residues in mammalian proteins is around 6% (*13*). Therefore, site-specificity can be difficult to achieve. When there are no lysine residues available, or lysine residues form part of the active site of a protein, conjugation to carboxylic acid groups can be considered. However, it is then difficult to avoid cross-linking with the amino groups of the protein itself (*1*).

In nature, the range of functions of proteins is extended by posttranslational modifications of amino acid residues. Other functional groups, peptides, or proteins can be attached and structural changes can be made. Even the very chemical nature of an amino acid residue can be changed (*14*). The enzymes that naturally induce such posttranslational modifications can be used for bioconjugation as well. Transglutaminase can, for example, be used for polyamination (*15*); farnesyltransferase and geranylgeranyltransferase can be used for prenylation (*16, 17*); and *N*-myristoyltransferase can be used for myristoylation (*18, 19*). Once again, the limitation of these reactions is that the essential amino acid residues must be available and the modification of an amino acid residue should not induce loss of structural integrity and functionality.

In general, due to the abundance of amino acids containing functional side groups within proteins, site-specific conjugation reactions to canonical amino acids are often difficult to achieve. Conjugations at undesired sites within the protein may induce loss of structural integrity and functionality.

TRANSLATIONAL INCORPORATION OF NONNATURAL AMINO ACIDS

With the recent developments in synthetic biology, it has become possible to engineer bacteria and yeast in such a way that they can incorporate nonnatural amino acids with selective reactivities into proteins. With this technique, the possibilities for site-specific conjugation to functionally active proteins can be substantially increased. Several methods that currently exist for the translational incorporation of nonnatural amino acids are discussed here.

Use of Auxotrophic Strains. The simplest and oldest method for incorporation of nonnatural amino acids into recombinantly produced proteins makes use of *Escherichia coli* strains that are auxotrophic for a certain amino acid. This means they are unable to synthesize it and therefore dependent on uptake from the growth medium. In the growth medium, this particular amino acid can be replaced by a structurally similar nonnatural analogue. The bacteria then build in this analogue. For this substitution method, the gene encoding the protein of interest has to be under tight inducible control. The bacteria can then first be grown in normal medium, followed by washing and transfer to medium containing the nonnatural analogue instead of the natural amino acid. After allowing the bacteria some time to deplete their intracellular stocks of the natural amino acid, production of the target protein is induced. Virtually, all copies of the target protein will then contain the nonnatural amino acid.

Incorporation efficiency can be greatly enhanced by overexpressing the relevant aminoacyl tRNA transferase and by somewhat relaxing the substrate specificity of its synthetase and proofreading active sites (*20*−*23*).

Codons for leucine (*24*), isoleucine (*25*), phenylalanine (*26*), tryptophan (*27, 28*), proline (*29*), and especially methionine (*20, 30*−*35*) have been reassigned in order to incorporate nonnatural amino acids using this method. Methionine is a frequently used amino acid for this technique, since it is one of the least common natural amino acids. Global replacement of methionine by nonnatural amino acids can therefore be expected

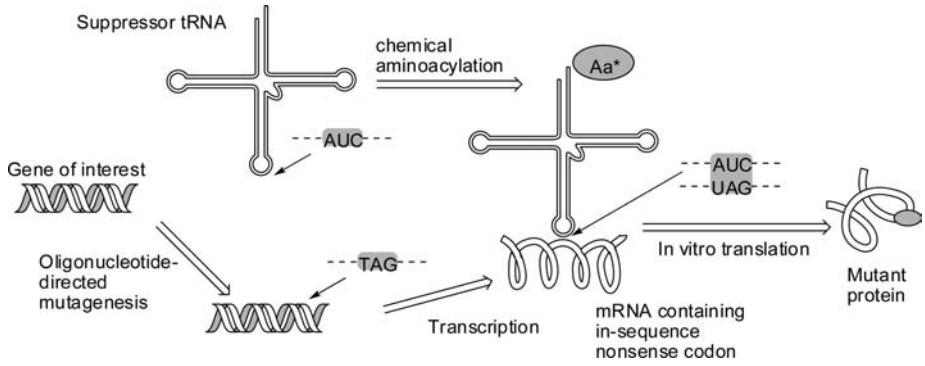

Figure 1. tRNA suppressing the amber codon.

to have less impact on protein structure and function than substitution of other amino acids. Furthermore, due to its hydrophobicity methionine is usually not located at the surface of natural proteins. This makes it possible to introduce, e.g., an alkyne or azide methionine analogue in a unique and well-defined place on the outside of a protein, accessible for subsequent modification by the azide/alkyne 'click' reaction.

Obviously, the major drawback of the substitution technique is that it leads to incorporation of the nonnatural amino acid at *every* site where the substituted amino acid is encoded. This may impair the protein's structure and function. Furthermore, incorporation in the cell's own proteins may lead to toxic effects. Finally, it is not possible to incorporate both the nonnatural amino acid and the substituted natural amino acid.

Stop Codon Suppressor tRNAs. To overcome the above-mentioned problems, Noren et al. (1989) developed a different method to translationally incorporate nonnatural amino acids into proteins. They used a tRNA that specifically recognizes one of the three stop codons. By chemically aminoacylating this tRNA and injecting it into *Xenopus* oocytes, a nonnatural 21st amino acid could be incorporated into proteins in response to the stop codon (*36*) (Figure 1).

tRNAs that efficiently recognize the amber (UAG) stop codon occur naturally in yeast. Such amber-suppressor tRNAs prevent release factor I (RF-I) from binding to the UAG codon. Therefore, the ribosome will continue elongating the protein. Because the ribosome does not proofread amino acids during translation, the cell does not recognize this "error" in the protein and therefore does not destroy it (*37*). By aminoacylating such a suppressor tRNA with a desired nonnatural amino acid (e.g., through chemical aminoacylation), it becomes possible to site-specifically incorporate a 21st amino acid in response to the amber codon (*36*−*39*).

The main advantage of the termination readthrough mechanism is that nonnatural amino acids are only incorporated at the amber codon and therefore can be incorporated *in addition to* the 20 standard amino acids. Due to this characteristic, amber suppression has become a popular tool for incorporation of nonnatural amino acids (*40*). Since the elongation factor and peptidyltransferase show relatively broad substrate specificity, site-specific insertion of any desired amino acid may in principle be achieved (*36*).

To achieve high product yield and homogeneity, the suppressor tRNA must efficiently insert the amino acid in response to the UAG codon. Furthermore, it must be neither acylated nor deacylated by any of the naturally occurring aminoacyl-tRNA synthetases (AARS) of the host organism (*36, 37*).

Orthogonal Aminoacyl-tRNA Synthetases. A major drawback of the above-mentioned approach is that tRNAs are too large to be taken up by the host cell after chemical aminoacylation. Therefore, they have to be microinjected (*41, 42*). This limits the applicability of this technique to large cells such as

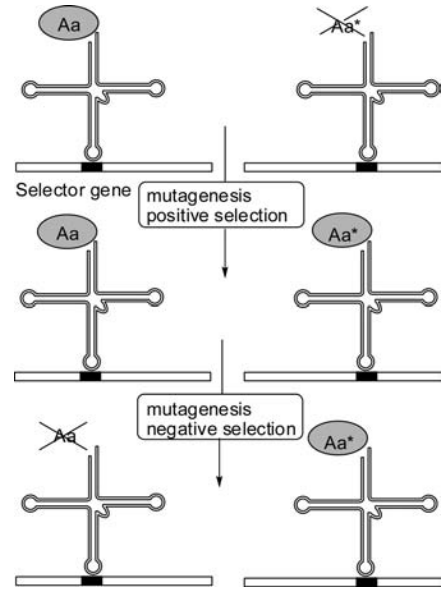

Figure 2. Strategy to select for an orthogonal AARS pair. (A) The starting AARS charges the suppressor tRNA with a natural amino acid Aa but not with the nonnatural amino acid Aa*. An amber codon (UAG) is inserted into a gene that codes for a selectable marker such as antibiotic resistance, GFP, or the Gal4 repressor. (B) A positive selection yields AARS* variants that incorporate both the natural and nonnatural amino acids. (C) Negative screening or selection yields an AARS** variant that rejects the natural amino acid.

Xenopus oocytes (*43, 44*). A variant to this approach is in vitro protein translation in cell free extracts (*45, 46*). However, these two methods are only applicable on a very small scale. To overcome this problem, the host cell can be genetically engineered to produce the suppressor tRNA and a corresponding AARS itself (*47*). This AARS/tRNA pair has to be orthogonal to the host AARS/tRNA pairs. This means that the introduced tRNA should function efficiently in protein translation but should not be a substrate for any of the host AARS. Furthermore, the introduced AARS should not aminoacylate any of the endogenous host tRNAs (*37, 40*). There are two methods to develop an orthogonal AARS/tRNA pair: it can be borrowed from unrelated organisms (*48*), or it can be designed (*37, 49*). Figure 2 illustrates the general selection method to develop orthogonal AARS/tRNA pairs (*37*).

When using orthogonal AARS/tRNA pairs, the nonnatural amino acid has to be available in the cytoplasm of the host. Therefore, the nonnatural amino acid has to be designed such that it can be passively or actively transported into the host cell. It is even possible to genetically modify *E. coli*, giving it the capability of biosynthesizing a nonnatural amino acid itself (*50*).

Although successful, incorporating nonnatural amino acids by tRNA suppression of nonsense codons is somewhat limited

by its low efficiency. The efficiency of the incorporation of one nonnatural amino acid per protein by amber suppression is dependent on the host organism, but on average, an efficiency of 20−30% (defined as the ratio of full-length protein to truncated protein) can be achieved. The low efficiency is a result of two factors. First, the acylation of suppressor tRNAs is sometimes a problem. Second, RF-1 will always compete with the suppressor tRNA for the stop codon (*37, 38, 40, 51*). If the number of amber codons in a gene increases, the efficiency decreases multiplicatively (*51*). Consequently, multiple incorporations of nonnatural amino acids by using more than one amber codon are not feasible. Combining the suppression of another stop codon with amber codon supression is not feasible either, since the suppression efficiency of the other stop codons (UAA and UGA) is even smaller (*52*). Apart from these limitations, it has also been observed that charged amino acids are incorporated less efficiently than hydrophobic ones. D- and β-amino acids are not compatible with stop codon suppression (*53*).

Apart from bacteria, mammalian cells are also used for the production of certain proteins. Whether the method of stop codon suppression can ever be exploited for the introduction of nonnatural amino acids in these systems is uncertain, because the occurrence of the amber termination codon is higher in mammals then in *E. coli.* In human genes, for example, 23% of stop codons is UAG. It is therefore likely that amber suppression will be toxic, since essential proteins are not terminated correctly. The use of the other termination codons seems even less promising because their occurrence is even higher (UAA, 30%; UGA, 47%) (*51, 54*).

An exciting recent variation to stop codon reassignment is the reassignment of degenerate *sense* codons. Kwon et al. (2003) demonstrated the feasibility of this approach by breaking the degeneracy of the phenylalanine codons UUU and UUC. The anticodon sequence of $tRNA^{Phe}$ is AAG, but this tRNA also binds to the UUU codon by "wobbling". Kwon et al. introduced a heterologous tRNA having the anticodon AAA into an *E. coli* host. At the same time, they introduced an AARS that specifically loaded this tRNA with 2-naphtylalanine. By doing so, they were able to reach an incorporation efficiency of 80% for 2-naphtylalanine in response to UUU, while all UUC was still translated as phenylalanine (*55*).

Another recent addition to the technique of stop codon suppression is the development of an orthogonal ribosome−mRNA pair (*51, 56*). In this technique, the mRNA encoding for the protein of interest is given a modified Shine−Dalgarno (SD) sequence. The SD sequence is the part of the mRNA that initiates binding to the ribosome. The modified SD sequence is not recognized by natural ribosomes. The used expression strain is therefore given two sets of ribosomes: one that only recognizes normal SD sequences and one that only recognizes the modified SD sequence. In this way, the production of the cell's own proteins is separated from the production of the desired protein containing the nonnatural amino acid. Furthermore, the mutant ribosome has an adjusted structure that rejects RF-1 (Figure 3). The use of such an orthogonal ribosome−mRNA pair therefore increases the suppression efficiency. Using this technique, a readthrough efficiency of 60% has been achieved (*51*).

Expanding Size of Codons. The number of different amino acids that can be incorporated into one protein is ultimately limited by the fact that natural codons consist of only three bases. The discovery of frameshift suppressor tRNAs, together with the ability of ribosomes to handle a wide variety of codon/anticodon pairs, has made it possible to create new codons by expanding the size of codons from triplets to quadruplets or even quintets (*52, 57, 58*). This method was pioneered by

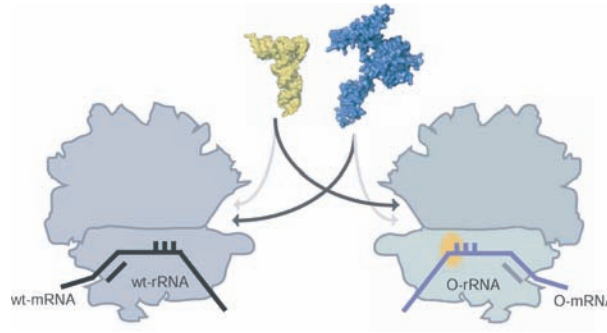

Figure 3. Orthogonal ribosome−tRNA pairs. The natural ribosome (left) and the orthogonal ribosome (right) translate wild-type (black) and orthogonal (purple) mRNAs, respectively. RF-1 (blue) cannot compete efficiently for UAG codons in the modified A-site (orange) of the orthogonal ribosome. Therefore, the orthogonal ribosome efficiently accepts the suppressor tRNA (yellow). Translation of the cell's own mRNAs is unaffected because the orthogonal ribosome does not read mRNAs with a normal SD sequence, but the natural ribosome is unaltered. Reprinted by permission from Macmillan Publishers Ltd.: *Nature Biotechnology* 25(7) p771, copyright 2007.

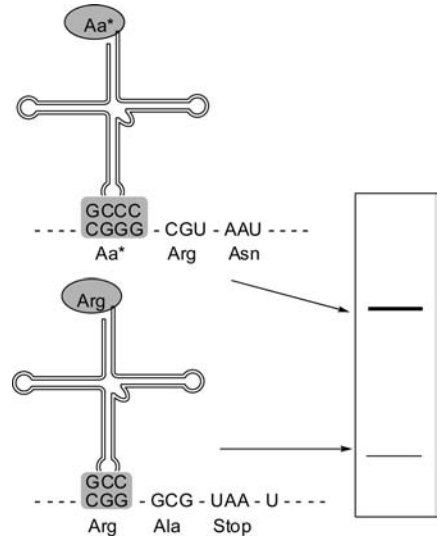

Figure 4. Principle of the four-base codon strategy. The target protein (right, upper band) can easily be separated by gel electrophoresis from the byproduct resulting from insertion of a natural amino acid (lower band).

Hohsaka and Sisido (2000) (*57*). It has created the possibility to develop additional codons and thereby has made incorporation of several different nonnatural amino acids at a time possible (*59*).

Figure 4 illustrates the basic principle of this frameshift suppressor tRNA strategy. The gene containing the quadruplet or the quintet is generated by PCR (*57*). During this process, an extra nucleotide is inserted at a specific place to create the quadruplet codon. In the case of a quintet, two nucleotides are inserted. Besides the modified DNA, the relevant orthogonal tRNA as well as a corresponding AARS are required for this method. When the frameshift suppressor tRNA successfully reads the concerning quadruplet/quintet, a frameshift will take place as planned and the protein will be completed to a full-length protein containing the nonnatural amino acid. However, if the concerning sequence is read by a naturally occurring tRNA, the planned frameshift does not occur. The reading frame is then shifted backward by one or two bases, which results in truncation of the protein at the next occurring stop codon (*52, 57*).

Many four-base codons have been examined in *E. coli*. Hohsaka et al. (2001) found that five quadruplet codon/anticodon

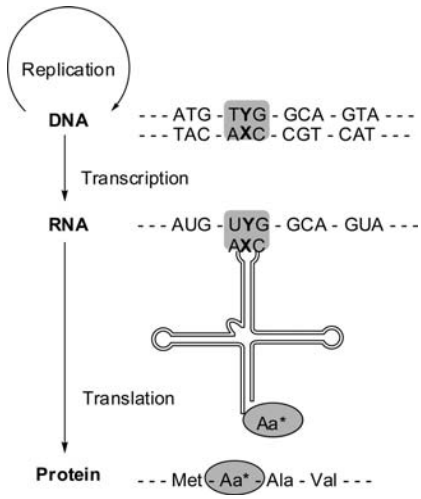

Figure 5. The expansion of the genetic alphabet with a nonnatural base pair X and Y.

Scheme 1. General Concept of Orthogonal Peptide Ligation[a]

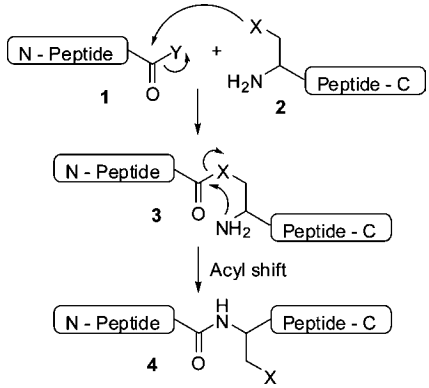

[a] X and Y represent a good nucleophile and a good leaving group, respectively. For example, in native chemical ligation X = SH and Y = SR.

pairs (AGGU, CGGU, CCCU, CUCU, and GGGU) are orthogonal and very efficient (e.g., GGGU has an efficiency of 80% with respect to the wild-type protein) (*58*). Several different quadruplets can in principle be used to incorporate more than one nonnatural amino acid into one protein. Hohsaka and Sisido (2000) also examined the quintet codons $CGGN_1N_2$. The suppression efficiency was comparable for all the different quintets and was estimated at 16% for the incorporation of nitrophenylalanine in cell-free extracts. This is comparable to the efficiency of the amber suppression method with the same nonnatural amino acid (*57*). Other amino acid analogues that have been introduced using this technique are homoglycine (*59*) and 2-hydroxy-3-(4-hydroxyphenyl)propionic acid, which introduces a hydrolyzable ester bond instead of an amide bond into the protein backbone (*60*).

Efforts have been undertaken to use frameshift suppression in vivo, but these have not been very successful until now (*37, 59*).

Nonnatural Base Pairs. A challenging method to expand the genetic code is to develop nonnatural base pairs. Creating a new base pair that is orthogonal to the naturally occurring base pairs generates great opportunities. With an additional base pair, the genetic code can be expanded from 64 coding triplets to 216 coding triplets. The basic principle behind this approach is illustrated in Figure 5.

Switzer et al. developed the first new base pair and thereby a 65th codon in 1989 (*61*). They incorporated the base pair

Scheme 2. Native Chemical Ligation with Homocysteine

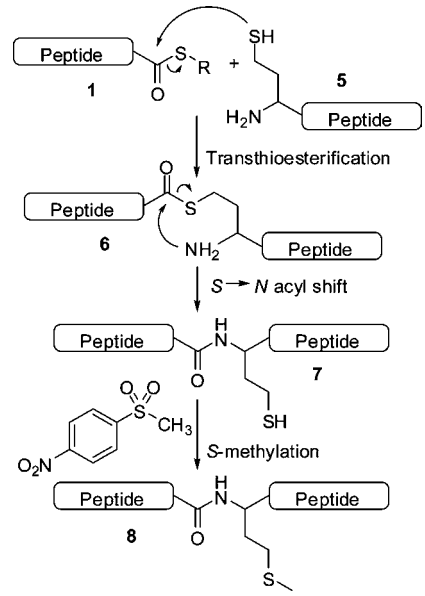

Scheme 3. Chemical Ligation Using Removable Auxiliaries

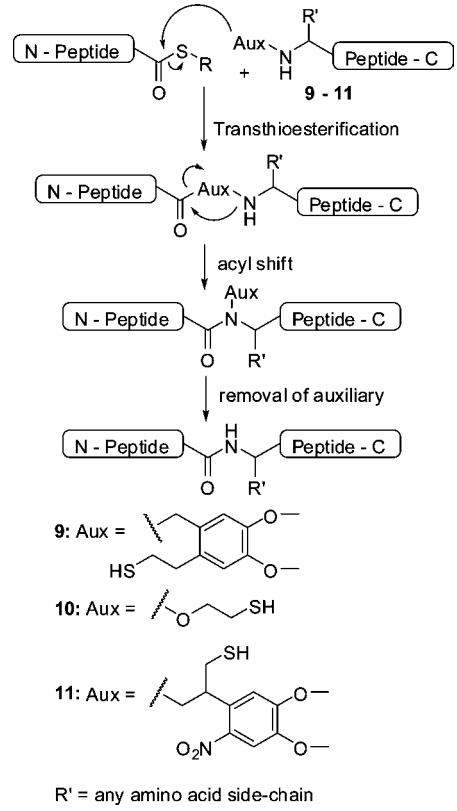

isoC and isoG into DNA and managed to transcribe the DNA containing these nonnatural bases into mRNA, which in turn was successfully translated with the help of a synthetic tRNA into a protein containing a nonnatural amino acid. This approach seemed very promising, but the main problem was that the DNA containing the nonnatural base pairs had a limited stability (*62*). Apart from the stability of the DNA, the success of a nonnatural nucleotide base pair is dependent on many other factors. The base pair must be completely orthogonal to the other nucleotide bases, but they must couple to each other with high affinity and high fidelity. In addition, the artificial base pair must be accepted and recognized by

Scheme 4. Intein-Mediated Production of a C-Terminal Thioester

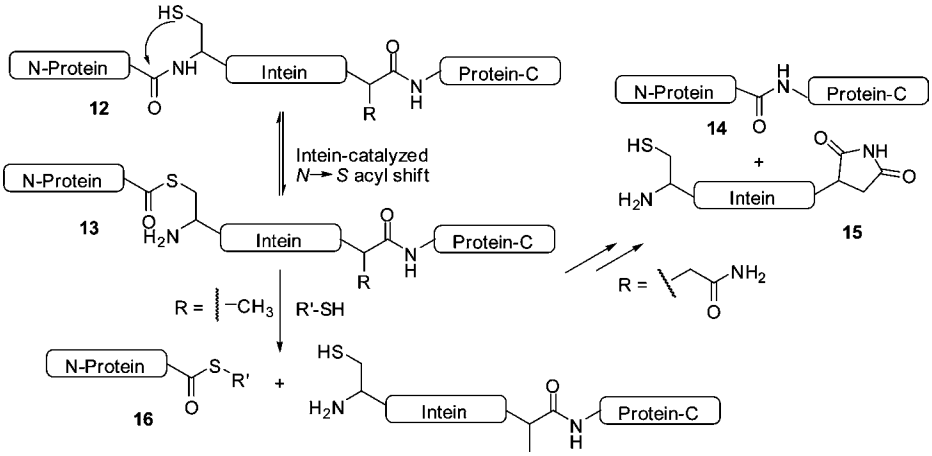

Scheme 5. Staudinger Ligation

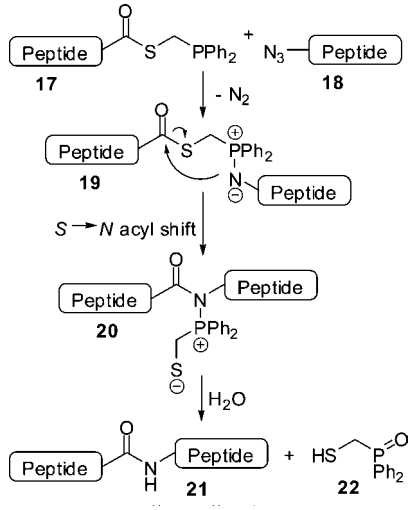

Scheme 6. A Selection of 'Click' Reactions

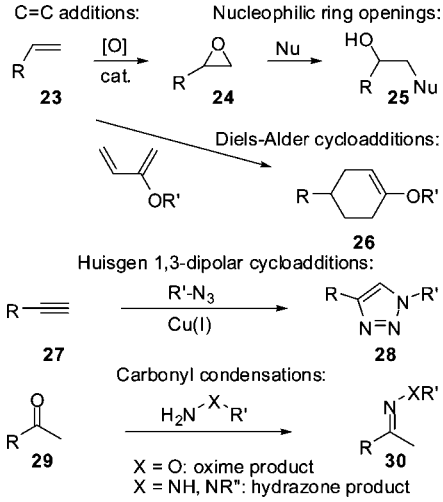

the DNA polymerase and RNA polymerase to make replication and transcription possible (*52, 63, 64*). Despite the fact that it is not easy to satisfy these requirements, Ohtsuki et al. (*65*), Hirao et al. (*66, 67*), and the group of Romesberg (*63, 64*) succeeded to develop several nonnatural nucleotide base pairs which are promising candidates for expanding the genetic code. However, the orthogonality, fidelity, and DNA synthesis efficiency of these nonnatural base pairs is still insufficient for practical application.

SEMISYNTHETIC INCORPORATION OF NONNATURAL AMINO ACIDS

Through the progression in solid-phase peptide synthesis (SPPS) methodology, the synthesis of peptides and small proteins has become routine. With SPPS, it is easy to incorporate all sorts of nonnatural amino acids into peptides. However, the solid-phase methodology has some drawbacks. These include accumulation of side products arising from incomplete deprotection or coupling reactions, the difficulty of synthesizing highly hydrophobic peptides, and nonnative folding of the products. Therefore, the method is limited to the synthesis of polypeptides not larger than 50 amino acid residues. In contrast, the average length of a natural protein is about 250 amino acid residues.

To circumvent these size limitations of the solid-phase methodology, several semisynthetic approaches have been developed to incorporate nonnatural amino acids (*68*). The principal strategy encompasses synthesizing the desired protein in two parts. The part that contains the nonnatural amino acid(s) is synthesized by SPPS. The rest of the target protein is produced by recombinant techniques. The two fragments are then modified at their termini with mutually reactive, bio-orthogonal groups. Finally, the two fragments are linked to each other to yield a full-length semisynthetic protein containing one or more nonnatural amino acids (*69*). Schnolzer and Kent (1992) were among the first to prove this powerful concept through the chemoselective synthesis of a human immunodeficiency virus 1 (HIV-1) protease analogue having a modified backbone. They used this analogue for the study of backbone involvement in inhibitor binding (*70, 71*).

A variety of chemoselective protein ligation reactions have been developed (*70*). Some of these reactions generate a nonnatural structure at the ligation site. Examples include the thioester and thioether ligations (*72*−*75*) and the imine/pseudoproline ligation (discussed below). In addition to these, there are now a number of ligation reactions available that generate a native peptide bond. Generally, these consist of a two-step sequence (Scheme 1). The first step is a chemoselective capture between an electrophile at the C-terminus of peptide **1** and a nucleophile at the N-terminus of peptide **2**. The type of bond that is formed depends on the nucleophile and electrophile used in the capture reaction. If the formed bond is an ester or a thioester, a spontaneous intramolecular acyl shift will occur (through the five-membered intermediate **3**) to form an amide bond in the product **4** (*69, 76*).

Native Chemical Ligation. The native chemical ligation approach of Dawson et al. (1994) was the first approach that

Table 2. Applications of 'Click' Reactions

reaction	examples	examples of applications	restrictions
cycloaddition reactions	Huisgen 1,3-dipolar cycloaddition (*95*)	-glyco-polycycles and macrocycles	-glycosylation efficiency
		-glycopeptides	-stereo- and regio-control
	Diels−Alder reaction (*96*)	-polyketides -alkaloids	-product inhibition if a catalyst is used
nucleophilic ring-opening reactions	aziridine reactions (*97*)	-Dopamine antagonist AS-8112[23]	-harsh conditions for subsequent N-deprotection
		-(*R*)-1-(benzofuran-2-yl)-2-propylaminopentane	
	aziridinium ion reactions (*97*)	-Ecopipam -antitumor agent R-116010	
carbonyl condensation r eactions	oxime ligation (*98, 99*)	-aminooxy-peptides	-*N*-overacylation
		-neoglycolipid probes	- stability at low pH
	hydrazone ligation (*100, 101*)	-lipopeptides -*R*-melanocyte-stimulating hormone	
addition to carbon−carbon multiple bonds	Michael additions (*102*)	-reaction between cysteine and PEG-maleimide	-all nucleophiles in a protein may react to some extent
	epoxidation addition (*103*)	-polyether polyols	-side reactions of H_2O_2 with cysteine and methionine

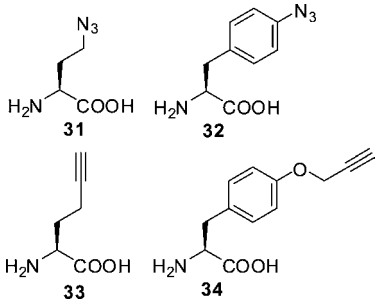

Figure 6. Nonnatural amino acids having azide and alkyne functionalities.

did not cause a nonnatural structure at the ligation site (*77*). The principle behind this method is that each peptide fragment has a unique, mutually reactive functionality which enables a chemoselective reaction. Because of this chemoselectivity, the ligation can take place with unprotected peptide fragments in aqueous solution. In the native chemical ligation approach, the peptide **2** bears an N-terminal cysteine and the peptide **1** bears a C-terminal thioester. There are several solid-phase methods and recombinant strategies based on protein splicing to synthesize a C-terminal thioester (*77, 78*). The first step of the ligation is a chemoselective transthioesterification reaction involving the thiol group of the N-terminal cysteine of peptide **2** and the C-terminal thioester moiety of peptide **1**. The intermediate product **3** then undergoes a rapid intramolecular S→N acyl shift, which results in an amide bond at the ligation site in the final product **4** (*68*).

This reaction is applicable to peptides with all (non-) canonical amino acid residues, as long as one of the peptides bears a thioester at the C-terminus and the other peptide has an N-terminal cysteine residue. The nature of the thioester leaving group and the pH both influence the rate and the efficiency of the reaction (*68*). The most important limitation of this method is that a cysteine residue always results at the ligation site. In a semisynthetic approach, the location of cysteines in the desired product therefore dictates the length of the recombinantly and synthetically produced parts. Since the occurrence of cysteine is only 1.7%, this can lead to impractically long sequences that have to be produced by SPPS.

Several alternative methods have been developed to overcome this problem (*79*). For example, Tam and Yu (1998) devised a route that leads to a methionine at the ligation site (*80*). This approach is illustrated in Scheme 3. Instead of a cysteine, the peptide **5** has an N-terminal homocysteine residue. The start of the reaction is the same as for the native chemical ligation, but the intermediate product **6** is different: the intramolecular S→N acyl shift occurs through a six-membered ring instead of a five-membered ring. After the ligation reaction, the homocysteine residue can be converted to a methionine by methylation. Comparable ligation reactions can be executed with selenocysteine and the imidazole side chain of histidine (*68*). Another versatile method to overcome the requirement of an N-terminal cysteine residue is to mimic the characteristics of the cysteine residue through the use of a removable auxiliary. Several types of auxiliaries have been developed. These are shown in Scheme 3. Several researchers have replaced the N-terminal cysteine residue by 2-mercaptobenzylamine **9** (*68, 81*). Canne et al. (1996) used oxyethanethiol **10** (*82*) and Kawakami and Aimoto (2003) used the photoremovable *o*-nitrobenzyl scaffold **11** to substitute the N-terminal cysteine residue (*83*). The principle behind this method is that, by mimicking the characteristics of the cysteine residue, it is possible to ligate the peptides by native chemical ligation regardless of the kind of amino acid residue at the N-terminus of peptides **9**−**11**. The reaction is the same except that there is one additional step at the end to remove the N-terminal substitute (*83*). A significant limitation of all

Scheme 7. Imine Ligation of N-Terminal Cys-, Ser-, and Thr-Containing Peptides to Form Pseudoprolines through Thiazolidine and Oxazolidine Ring Formation

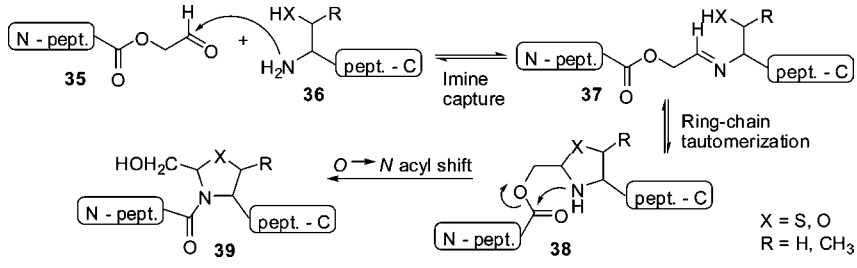

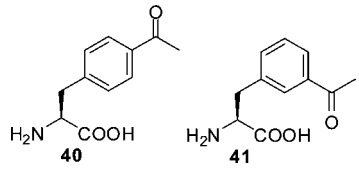

Figure 7. Nonnatural amino acids having carbonyl functionalities.

Scheme 8. Possible Bioconjugation Reactions to the Diketone-Containing Nonnatural Amino Acid 42

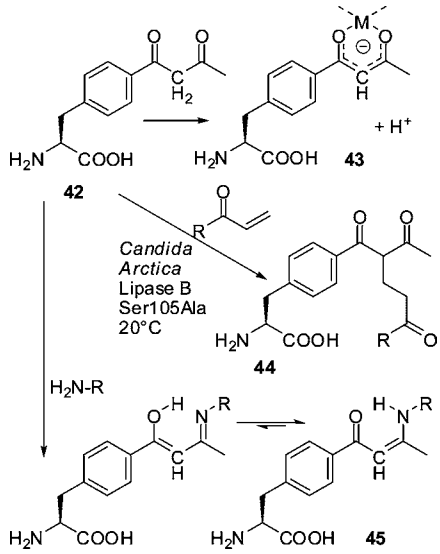

auxiliaries is, however, that they are currently only applicable to synthetic C-terminal peptides (*84*).

Use of recombinantly produced protein fragments in (native) chemical ligation reactions requires that they possess either an N-terminal cysteine residue or a C-terminal thioester. The latter has become possible due to the expressed protein ligation method developed by Muir and co-workers. They used intein-mediated posttranscriptional protein splicing (Scheme 4). This is a naturally occurring process whereby a protein **12** undergoes an intramolecular rearrangement resulting in the extrusion of an internal sequence (intein **15**) and the joining of the lateral sequences (exteins) to form the protein **14**. This reaction is autocatalyzed by the intein domain. An intermediate product of the reaction is thioester **13**. By mutating the site between the intein and the C-terminal protein from arginine to alanine, the splicing reaction can be stopped halfway. Addition of a thiol then results in the natural protein **16** having a C-terminal thioester (*78, 85, 86*). This product can subsequently be used for native chemical ligation (*87*).

Staudinger Ligation. The groups of Raines and Bertozzi independently developed an elegant method to overcome the limitation of the original native chemical ligation method (*88, 89*). Their approach is based on the Staudinger reaction (*90*). Scheme 5 illustrates the ligation of two peptides by this modified Staudinger reaction. The C-terminus of peptide **17** needs to bear a phophinothioester group, and the second peptide **18** needs to bear an N-terminal azide group.

Like in the classical Staudinger reaction, the first step is the reaction between the C-terminal phophinothioester **17** and the N-terminal azide **18** to form the intermediate iminophosphorane **19**. **19** then undergoes an intramolecular S→N acyl shift leading to the amidophosphonium salt **20**. Through hydrolysis, this salt is converted to the amide product **21** and the phosphine **22**.

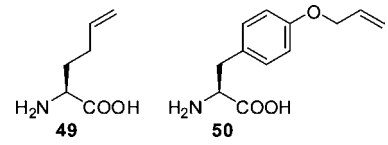

Figure 8. Nonnatural amino acids having vinyl functionalities.

Scheme 9. Conversion of Selenium-Containing Nonnatural Amino Acids into Dehydroalanine

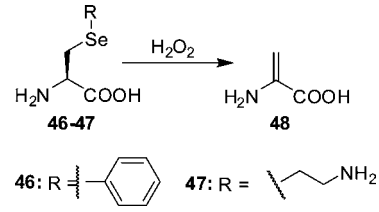

The disadvantages of this method are that the peptide chains must be fully protected because of the high reactivity of the intermediate aza-ylide and that diphenyl phosphine oxide traces always remain in the product (*68, 91*). To overcome the latter disadvantage, a "traceless" Staudinger ligation has also been developed (*89, 91*).

In biochemistry, these reactions are particularly valuable because the azide function is (i) virtually absent in biological macromolecules, (ii) exhibits a high intrinsic reactivity with a very limited number of reactants, and (iii) can be easily introduced in peptides or proteins using either organic chemistry or recombinant techniques (*91*).

BIO-ORTHOGONAL CONJUGATION TO NONNATURAL AMINO ACIDS

Several classes of nonnatural amino acids have been successfully incorporated into proteins by the methods described above. The following section describes the nonnatural amino acids that have bio-orthogonal reactivities which can be used in bioconjugation reactions. Most of these nonnatural amino acids have been incorporated using either the substitution method or the termination readthrough method (*92*).

'Click' Chemistry. Many of the bioconjugation reactions that are discussed below can be referred to as 'click' reactions. In a narrow sense, this term is often used specifically for the Huisgen 1,3-dipolar cycloaddition (discussed below). However, the term is used here in its original, much broader sense. 'Click' chemistry is a synthetic approach inspired by the simplicity and efficiency of the chemistry of nature (*91*). Nature prefers building its products from simple building blocks linked by carbon-heteroatom bonds rather than carbon−carbon bonds (*93, 94*). The Sharpless group has identified a set of reactions that they termed 'click' reactions. These reactions mimic nature in "[being] modular, wide in scope, give very high yields, generate only inoffensive byproducts that can be removed by nonchromatographic methods, and [being] stereo-specific (but not necessarily enantioselective)" (*94*). Furthermore, the process should have simple reaction conditions, have readily available starting materials and reagents, and require no or easily removable solvents. The term 'click' reaction refers to the high rate and high selectivity of these reactions (*94*). Examples of such reactions are given in Scheme 6 and Table 2.

Alkyne and Azide Functionalities. The most frequently applied 'click' reaction is the Huisgen 1,3-dipolar cycloaddition reaction of alkynes and azides catalyzed by copper(I) (*93*). The general principle of this reaction is outlined in Scheme 6 (**27** to **28**). This is a straightforward reaction which can be performed

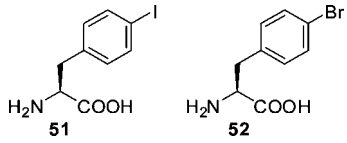

Figure 9. Nonnatural amino acids having aryl halide functionalities.

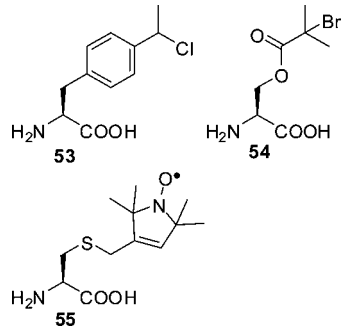

Figure 10. Nonnatural amino acids having ATRP initiator functionalities (**53** and **54**) and nitroxide chain transfer capability (**55**).

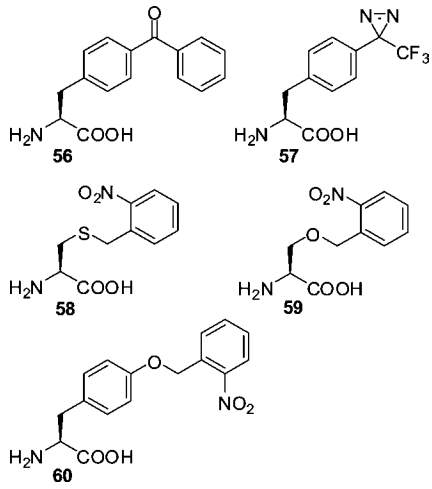

Figure 11. Nonnatural amino acids carrying photoreactive groups.

at room or body temperature and in a variety of solvents. Furthermore, the reaction is compatible with several other functional groups (*91*).

As a result of the popularity of the azide/alkyne 'click' reaction, many attempts have been undertaken to incorporate nonnatural amino acids containing azide or alkyne functionalities into proteins. The nonnatural amino acids azidohomoalanine **31** and homopropargylglycine **33** have been designed to closely mimic the natural amino acid methionine. Indeed, they have been shown to be effectively introduced into proteins by methionine auxotrophic bacterial strains. Strable et al. (2008) proved this concept by first incorporating **31** or **33** into hepatitis B virus by reassigning the methionine sense codon. Subsequently, the azide or alkyne containing virus particles were successfully labeled using alkyne or azide functionalized fluorescein, rhodamine, biotin, or gadolinium-tetraazacyclododecanetetraacetic acid (Gd-DOTA) (*104*). 'Click' reactions to incorporated nonnatural amino acids **31** and **33** have also been successfully used to PEGylate proteins (*105*), glycosylate proteins (*106, 107*), label proteins with fluorophore tags (*108, 109*), and cross-link several proteins into supramolecular structures (*33, 104*). Even live *E. coli* cells have been biotinylated at their outer membrane proteins using this method (*110*).

The aromatic amino acids *p*-azidophenylalanine **32** and *p*-propargyloxyphenylalanine **34** have been incorporated site-

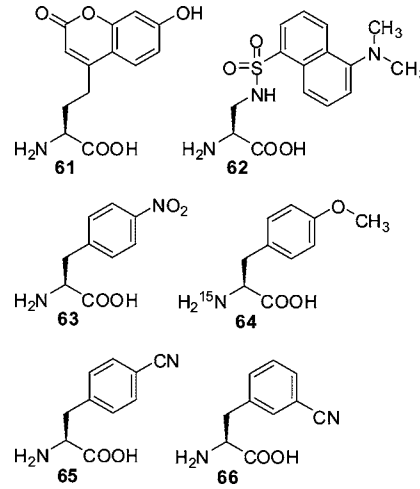

Figure 12. Nonnatural amino acids carrying biophysical probes.

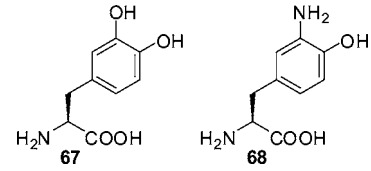

Figure 13. Redox-active nonnatural amino acids.

specifically into proteins by reassigning the UAG stop codon. In *Saccharomyces cerevisiae*, this has been achieved by introducing an *E. coli* mutant tyrosyl-tRNA synthetase (*111*) and in *E. coli* by using a mutant *Methanococcus jannaschii* tyrosyl-tRNA synthetase (*112*). By means of the azide/alkyne 'click' reaction, **34** has been used to site-specifically functionalize cytochrome c3 with the electron donor azidoviologen (*113*). **32** has been used for site-specific PEGylation of proteins by reaction with alkyne-functionalized PEG segments (*114*).

Apart from azide/alkyne 'click' chemistry, bio-orthogonal conjugation to peptides can also be achieved using Staudinger ligation at azide-containing nonnatural amino acids such as **31** and **32** (*115, 116*). Another interesting application of **31** is its ability to be cleaved by a phosphine or dithiol. This reaction yields a reactive C-terminal homoserine lactone in a fashion similar to cyanogen bromide cleavage but under very mild conditions (*117*).

Keto/aldehyde Functionalities. Another class of 'click' reactions that are gaining interest are certain nucleophilic additions to carbonyl groups. Carbonyl groups do not occur in natural proteins. They have a slightly acidic α-hydrogen due to keto−enol tautomerization and are easily attacked by nucleophiles (Scheme 6: **29**−**30**). If carbonyl groups are introduced into recombinant proteins, some imine formation with the ε-amino groups of lysine residues will therefore occur. However, this reaction is reversible and at physiological pH the equilibrium lies toward the free carbonyl and amine (*118*).

Hydrazides, alkoxyamines, and semicarbazides react rapidly and quantitatively with carbonyl groups to form hydrazones, oximes, and semicarbazones, respectively (*119*−*121*). These reaction products are stable under physiological conditions. An additional advantage of these reactions is that they occur in only slightly acidic aqueous medium and require no auxiliaries or catalysts.

The oxime ligation method involves an imine capture between an ester, an aldehyde, or a ketone **29** and an aminooxy nucleophile, yielding the oxime **30** (*122, 123*). The hydrazone ligation method is one of the oldest ligation methods and is

comparable with the oxime ligation method. However, a hydrazide rather than an aminooxy is used for the ligation, and therefore, a hydrazone bond is formed in the product **30** (*124*). No side chain protection is needed for these ligation methods, because on one hand aminooxy and hydrazide groups are more nucleophilic than natural amino acid side chains, and on the other hand the carbonyl groups are more electrophilic than natural side chains.

Another useful carbonyl reaction is imine ligation (Scheme 7), which produces a proline-like structure at the ligation site. This reaction can be used for conjugation to a nucleophilic N-terminal amino acid **36**. The carbonyl group of the conjugating agent **35** is attacked by the nucleophilic N-terminal amino acid **36**, forming the imine **37**. **37** subsequently undergoes a rapid ring−chain tautomerization, which results in the heterocycle **38**. This intermediate product facilitates an acyl transfer, forming a proline-like imidic bond in the product **39**. This reaction is well-represented by ligation methods using cysteine, threonine, tryptophan, histidine, or asparagine as N-terminal nucleophiles, yielding a variety of mono-, bi-, and tricyclic side chains at the ligation site (*76*). The ring−chain tautomerization in the formation of the heterocyclic ring **38** affords the specificity of the imine ligation (*122*). The central feature of imine capture is that the reaction is driven by the weakly basic N-terminus of **36**, which induces the formation of a heterocyclic ring. Given that imine ligation is performed under slightly acidic aqueous conditions, lysine and arginine side chains will be protonated and are therefore not reactive (*122*).

Although the ketones and aldehydes that are required for these reactions do not occur in natural proteins, they can be introduced into proteins by sodium periodate oxidation of an N-terminal threonine or serine, respectively. Serine-derived aldehydes have been used to attach a hydrazide-functionalized biotin tag and aminooxy-functionalized PEG chain to the N-terminus of proteins (*119, 125*). Furthermore, they have been used to couple two peptide or protein segments by hydrazone or oxime linkages (*120, 121, 126, 127*).

The method of sodium periodate oxidation is, however, hampered by the fact that it is only applicable to the N-terminus of a protein. Therefore, several groups have developed carbonyl-containing nonnatural amino acids. The nonnatural amino acids *p*-acetylphenylalanine **40** and *m*-acetylphenylalanine **41** have been introduced site-specifically into recombinantly produced proteins by the amber suppression method (*129*−*133*). In addition, **40** has also been introduced using a phenylalanine auxotrophic bacterial strain (*128*). The resulting proteins were successfully reacted in vitro and in vivo with biotin hydrazide (*128*−*130*) or fluorescein hydrazide (*129*−*131*). In addition, **40** has also been coupled to aminooxy-functionalized biotin (*132*). Another published application of **40** involves recombinant incorporation followed by reaction with aminooxy-functionalized saccharides. In this way, proteins have been site-specifically glycosylated (*133*).

The β-diketone analogue **42** has also been genetically incorporated into proteins using stop codon suppression. Subsequently, it was labeled with aminooxy-functionalized biotin and Alexa Fluor 488 (*127*). Furthermore, **42** is expected to have a number of other reactivities (Scheme 8). For example, the hydrogen atoms between the two keto groups are relatively acidic. The deprotonated **43** may therefore be able to chelate metal ions. **42** is also expected to react enzymatically with α,β-unsaturated carbonyl compounds in a carbon−carbon bond forming Michael reaction yielding **44** (*127, 134*). Finally, **42** can form the enamine adduct **45** by reacting with a primary amine. **45** is stable at physiological pH due to a six-membered intramolecular hydrogen bridge (*127, 135*).

Alkenes. A fourth functional group that is very common to synthetic organic and polymer chemistry but rare in natural proteins is the carbon−carbon double bond. The simplest amino acid containing an alkene functionality is dehydroalanine **48**, which occurs sometimes as a posttranslational modification of cysteine (*136*). This amino acid has not been introduced directly into recombinant proteins. Instead, its precursors phenylselenocysteine **46** and selenalysine **47** have been used. For the incorporation of **46**, the amber suppression strategy was used (*138*). **47** was substituted for lysine in a cell-free translation system (*137*). Upon mild oxidative elimination, these two nonnatural amino acids yield **48**, which has been reacted in a Michael addition reaction with various thiol reagents (*137, 138*).

Two alkene-containing amino acids that have been directly incorporated into proteins are homoallylglycine **49** (*34*) and *O*-allyltyrosine **50** (*139*). **49** was incorporated by a methionine auxotrophic strain. In another experiment, it was used for cyclization of peptides by ruthenium-catalyzed alkene metathesis (*140*). **50** was incorporated by stop codon suppression. Bioconjugation reactions involving **50** have not yet been described to our knowledge. However, it can be expected to have the same reactivity as the other alkene-containing amino acids.

***p*-Halophenylalanines.** Using a palladium catalyst in aqueous environment, aryl halides can undergo a Mizoroki−Heck substitution reaction with alkenes or alkynes. This has been exploited by the incorporation of *p*-iodophenylalanine **51** into proteins in a cell-free translation system, followed by reaction with vinylated biotin (*141*). *p*-Bromophenylalanine **52** has been incorporated into recombinant proteins by both the stop codon suppression method and the substitution method, using a phenylalanine auxotrophic *E. coli* strain (*22, 142*). However, a subsequent coupling to an alkene or alkyne has, to our knowledge, not yet been described for this amino acid.

Radical Polymerization Initiators and Chain Transfer Agents. One particularly challenging field of bioconjugation chemistry is the chemical synthesis of polymers starting from a protein as macroinitiator or macro-chain-transfer agent (the so-called "grafting from" approach) (*143*). The ribosomal incorporation of nonnatural amino acids that can give proteins these functionalities would give this field of research a considerable impulse.

Recent progress in this direction is the successful use of *p*-(1-chloroethyl)phenylalanine **53** and *O*-(2-bromoisubutyryl)serine **54** as ATRP initiators. However, these have at present only been incorporated into solid-phase synthesized peptides (*144*). The depicted stable radical containing cysteine derivative **55** has been incorporated into proteins by stop codon suppression in *E. coli* and *Xenopus* oocytes (*145, 146*). In these experiments, it was used as a spin label. However, **55** might also be used as a chain transfer agent in nitroxide-mediated controlled radical polymerization.

Other Functional Nonnatural Amino Acids. Apart from the above-mentioned chemically reactive amino acids, many amino acids with other functionalities have been site-specifically introduced into proteins. This makes it possible to incorporate a certain functionality directly into the protein of interest, without having to perform a bioconjugation reaction after protein production. So, whereas some nonnatural amino acids expand the possibilities for bioconjugation, others even make bioconjugation superfluous. To illustrate this vast potential of nonnatural amino acids, a short overview of the functionalities that have been incorporated is given here.

Amino acids carrying photoreactive groups such as *p*-benzoylphenylalanine **56** and *p*-(3-trifluoromethyl-3*H*-diazirin-3-yl)-phenylalanine **57**, but also *p*-azidophenylalanine **32**,

can be used as probes of protein interactions, protein structure, and protein dynamics in vitro and in vivo. They can therefore be useful in identifying receptors for ligands (*147*−*155*). Other types of photoreactive amino acids are the photocaged cysteine, serine, and tyrosine analogues **58**, **59**, and **60**. Substituted nitrobenzyl groups block the side-chain hydroxy or thiol groups of these amino acids. These protective groups can be cleaved off by irradiation with 365 nm light in vitro or in vivo, making it possible to "switch proteins on" by illumination (*156*, *157*).

The fluorescent probes **61** and **62** (*158*, *159*), the distance probe **63** (a tryptophan autofluorescence quencher) (*160*), the site-selective ^{15}N NMR probe **64** (*161*), and the infrared probes **65** and **66** (*162*) are all examples of recombinantly incorporated nonnatural amino acids carrying biophysical probes. These functional groups can visualize protein conformational changes, localization, protein dynamics, local environment, and intermolecular interactions. The amino acids **51** and **52** also belong to this class, as their heavy halogen atoms induce single-wavelength anomalous diffraction (*163*).

Electron transfers are involved in a large number of biological processes such as enzyme catalysis and the primary charge separation processes in photosynthesis. To aid in studying these phenomena, the redox-active nonnatural amino acids dihydroxyphenylalanine **67** and 3-aminol-tyrosine **68** have been site-specifically incorporated into proteins (*38*, *39*, *164*). Both can be used to probe and manipulate electron-transfer processes in proteins because they can undergo a two-electron oxidation.

CONCLUSION AND FUTURE PROSPECTS

The research areas of bioconjugation to proteins and incorporation of nonnatural amino acids into proteins are both growing at a fast pace. This is driven by the need for innovative ways of probing protein structure and interactions and the rapid increase in the number of potential therapeutic proteins.

The field of recombinant introduction of nonnatural amino acids is relatively new. The possibilities in this field are actively being expanded at present. In the near future, this may lead to the incorporation of metal-chelating amino acids, amino acids carrying electron-transfer mediators, near-infrared probes, and long-chain alkanes, as well as amino acids with altered backbones (e.g., β-amino acids). It might eventually become possible to create biopolymers with ester rather than amide linkages in the backbone or even generate multicellular organisms that contain nonnatural amino acids (*92*). In addition, research into bioconjugation to nonnatural amino acids is currently emerging.

As shown in this review, several reactive nonnatural amino acids have already been incorporated into proteins. A significant number of conjugation reactions to these amino acids have been described. These include the alkyne/azide 'click' reaction, carbonyl condensations, Michael-type additions, and Mizoroki−Heck substitutions. More examples can be expected in the near future. Further elaboration of this field will lead to the creation of powerful strategies to synthesize complex nonnatural proteins by combining methods to incorporate nonnatural amino acids with bio-orthogonal conjugation methods.

We anticipate that this as-yet relatively unexplored field of bioconjugation holds a great potential and will fast-forward developments in the design of, e.g., therapeutic protein derivatives and semisynthetic biomaterials.

LITERATURE CITED

(1) Veronese, F. M., and Morpurgo, M. (1999) Bioconjugation in pharmaceutical chemistry. *Il Farmaco. 54*, 497–516.
(2) Monfardini, C., and Veronese, F. M. (1998) Stabilization of substances in circulation. *Bioconjugate Chem. 9*, 418–450.
(3) Nucci, M. L., Shorr, R., and Abuchowski, A. (1991) The therapeutic value of poly(ethylene glycol)-modified proteins. *Adv. Drug Delivery Rev. 6*, 133–151.
(4) Maeda, H. (1991) SMANCS and polymer-conjugated macromolecular drugs: Advantages in cancer chemotherapy. *Adv. Drug Delivery Rev. 6*, 181–202.
(5) Sehon, A. H. (1991) Suppression of antibody responses by conjugates of antigens and monomethoxypoly(ethylene glycol). *Adv. Drug Delivery Rev. 6*, 203–217.
(6) Yeo, D. S., Srinivasan, R., Chen, G. Y., and Yao, S. Q. (2004) Expanded utility of the native chemical ligation reaction. *Chemistry 10*, 4664–72.
(7) Gaertner, H. F., Offord, R. E., Cotton, R., Timms, D., Camble, R., and Rose, K. (1994) Chemo-enzymic backbone engineering of proteins. site-specific incorporation of synthetic peptides that mimic the 64−74 disulfide loop of granulocyte colony-stimulating factor. *J. Biol. Chem. 269*, 7224–30.
(8) Kratz, F. Albumin as a drug carrier: Design of prodrugs, drug conjugates and nanoparticles. *J. Controlled Release*, In press, corrected proof.
(9) Wang, C., Stewart, R. J., and Kopecek, J. (1999) Hybrid hydrogels assembled from synthetic polymers and coiled-coil protein domains. *Nature 397*, 417–20.
(10) Yang, J., Xu, C., Kopeckova, P., and Kopecek, J. (2006) Hybrid hydrogels self-assembled from HPMA copolymers containing peptide grafts. *Macromol. Biosci. 6*, 201–9.
(11) Hentschel, J., tenCate, M. G. J., and Borner, H. G. (2007) Peptide-guided organization of peptide-polymer conjugates: Expanding the approach from oligo- to polymers. *Macromolecules 40*, 9224–9232.
(12) Wu, K., Yang, J., Konák, C., Kopecková, P., and Kopecek, J. (2008) Novel synthesis of HPMA copolymers containing peptide grafts and their self-assembly into hybrid hydrogels. *Macromol. Chem. Phys. 209*, 467–475.
(13) Wu, G., Ott, T. L., Knabe, D. A., and Bazer, F. W. (1999) Amino acid composition of the fetal pig. *J. Nutr. 129*, 1031–1038.
(14) Mann, M., and Jensen, O. N. (2003) Proteomic analysis of post-translational modifications. *Nat. Biotechnol. 21*, 255–261.
(15) Lentini, A., Abbruzzese, A., Caraglia, M., Marra, M., and Beninati, S. (2004) Protein-polyamine conjugation by transglutaminase in cancer cell differentiation: Review article. *Amino Acids 26*, 331–337.
(16) Basso, A. D., Kirschmeier, P., and Bishop, W. R. (2006) Thematic review series: Lipid posttranslational modifications. farnesyl transferase inhibitors. *J. Lipid Res. 47*, 15–31.
(17) Casey, P. J., and Seabra, M. C. (1996) Protein prenyltransferases. *J. Biol. Chem. 271*, 5289–5292.
(18) Farazi, T. A., Waksman, G., and Gordon, J. I. (2001) The biology and enzymology of protein N-myristoylation. *J. Biol. Chem. 276*, 39501–39504.
(19) Raju, R. V. S., Datla, R. S. S., Moyana, T. N., Kakkar, R., Carlsen, S. A., and Sharma, R. K. (2000) N-myristoyltransferase. *Mol. Cell. Biochem. 204*, 135–155.
(20) Kiick, K. L., Weberskirch, R., and Tirrell, D. A. (2001) Identification of an expanded set of translationally active methionine analogues in *Escherichia coli*. *FEBS Lett. 502*, 25–30.
(21) Ibba, M., and Hennecke, H. (1995) Relaxing the substrate specificity of an aminoacyl-tRNA synthetase allows in vitro and in vivo synthesis of proteins containing unnatural amino acids. *FEBS Lett. 364*, 272–275.
(22) Sharma, N., Furter, R., Kast, P., and Tirrell, D. A. (2000) Efficient introduction of aryl bromide functionality into proteins in vivo. *FEBS Lett. 467*, 37–40.
(23) Tang, Y., and Tirrell, D. A. (2002) Attenuation of the editing activity of the escherichia coli leucyl-tRNA synthetase allows incorporation of novel amino acids into proteins in vivo. *Biochemistry 41*, 10635–10645.

(24) Tang, Y., and Tirrell, D. A. (2001) Biosynthesis of a highly stable coiled-coil protein containing hexafluoroleucine in an engineered bacterial host. *J. Am. Chem. Soc. 123*, 11089–11090.

(25) Wang, Q., Chan, T. R., Hilgraf, R., Fokin, V. V., Sharpless, K. B., and Finn, M. G. (2003) Bioconjugation by copper(I)-catalyzed azide-alkyne [3 + 2] cycloaddition. *J. Am. Chem. Soc. 125*, 3192–3193.

(26) Yoshikawa, E., Fournier, M. J., Mason, T. L., and Tirrell, D. A. (1994) Genetically engineered fluoropolymers. synthesis of repetitive polypeptides containing p-fluorophenylalanine residues. *Macromolecules 27*, 5471–5475.

(27) Budisa, N., Alefelder, S., Bae, J. H., Golbik, R., Minks, C., Huber, R., and Moroder, L. (2001) Proteins with β-(thienopyrrolyl)alanines as alternative chromophores and pharmaceutically active amino acids. *Protein Sci. 10*, 1281–1292.

(28) Bae, J. H., Alefelder, S., Kaiser, J. T., Friedrich, R., Moroder, L., Huber, R., and Budisa, N. (2001) Incorporation of β-selenolo[3,2-*b*]pyrrolyl-alanine into proteins for phase determination in protein X-ray crystallography. *J. Mol. Biol. 309*, 925–936.

(29) Renner, C., Alefelder, S., Bae, J. H., Budisa, N., Huber, R., and Moroder, L. (2001) Fluoroprolines as tools for protein design and dngineering13. *Angew. Chem., Int. Ed. 40*, 923–925.

(30) Kiick, K. L., and Tirrell, D. A. (2000) Protein engineering by in vivo incorporation of nonnatural amino acids: Control of incorporation of methionine analogues by methionyl-tRNA synthetase. *Tetrahedron 56*, 9487–9493.

(31) Kiick, K. L., Saxon, E., Tirrell, D. A., and Bertozzi, C. R. (2002) Incorporation of azides into recombinant proteins for chemoselective modification by the Staudinger ligation. *Proc. Natl. Acad. Sci. U.S.A. 99*, 19–24.

(32) Link, A. J., and Tirrell, D. A. (2003) Cell surface labeling of escherichia coli via copper(I)-catalyzed [3 + 2] cycloaddition. *J. Am. Chem. Soc. 125*, 11164–11165.

(33) Link, A. J., Vink, M. K. S., and Tirrell, D. A. (2004) Presentation and detection of azide functionality in bacterial cell surface proteins. *J. Am. Chem. Soc. 126*, 10598–10602.

(34) van Hest, J. C. M., and Tirrell, D. A. (1998) Efficient introduction of alkene functionality into proteins in vivo. *FEBS Lett. 428*, 68–70.

(35) Kiick, K. L., van Hest, J. C. M., and Tirrell, D. A. (2000) Expanding the scope of protein biosynthesis by altering the methionyl-tRNA synthetase activity of a bacterial expression Host13. *Angew. Chem., Int. Ed. 39*, 2148–2152.

(36) Noren, C. J., Anthony-Cahill, S. J., Griffith, M. C., and Schultz, P. G. (1989) A general method for site-specific incorporation of unnatural amino acids into proteins. *Science 244*, 182–188.

(37) Hendrickson, T. L., De Crécy-Lagard, V., and Schimmel, P. (2004) Incorporation of nonnatural amino acids into proteins. *Annu. Rev. Biochem. 73*, 147–176.

(38) Hohsaka, T., and Sisido, M. (2002) Incorporation of non-natural amino acids into proteins. *Curr. Opin. Chem. Biol. 6*, 809–815.

(39) Hecht, S. M., Alford, B. L., Kuroda, Y., and Kitano, S. (1978) "Chemical aminoacylation" of tRNA's. *J. Biol. Chem. 253*, 4517–4520.

(40) Wiltschi, B., and Budisa, N. (2007) Natural history and experimental evolution of the genetic code. *Appl. Microbiol. Biotechnol. 74*, 739–753.

(41) Wang, L., and Schultz, P. G. (2002) Expanding the genetic code. *Chem. Commun. (Cambridge)* (1), 1–11.

(42) Rodriguez, E. A., Lester, H. A., and Dougherty, D. A. (2007) Improved amber and opal suppressor tRNAs for incorporation of unnatural amino acids in vivo. part 2: Evaluating suppression efficiency. *RNA 13*, 1715–1722.

(43) Nowak, M. W., Kearney, P. C., Sampson, J. R., Saks, M. E., Labarca, C. G., Silverman, S. K., Zhong, W., Thorson, J., Abelson, J. N., and Davidson, N. (1995) Nicotinic receptor binding site probed with unnatural amino acid incorporation in intact cells. *Science 268*, 439–442.

(44) Turcatti, G., Nemeth, K., Edgerton, M. D., Meseth, U., Talabot, F., Peitsch, M., Knowles, J., Vogel, H., and Chollet, A. (1996) Probing the structure and function of the tachykinin neurokinin-2 receptor through biosynthetic incorporation of fluorescent amino acids at specific sites. *J. Biol. Chem. 271*, 19991–19998.

(45) Kiga, D., Sakamoto, K., Kodama, K., Kigawa, T., Matsuda, T., Yabuki, T., Shirouzu, M., Harada, Y., Nakayama, H., Takio, K., Hasegawa, Y., Endo, Y., Hirao, I., and Yokoyama, S. (2002) An engineered *Escherichia coli* tyrosyl-tRNA synthetase for site-specific incorporation of an unnatural amino acid into proteins in eukaryotic translation and its application in a wheat germ cell-free system. *Proc. Natl. Acad. Sci. U.S.A. 99*, 9715–9720.

(46) Swartz, J. R., Jewett, M. C., and Woodrow, K. A. (2004) Cell-free protein synthesis with prokaryotic combined transcription-translation. *Methods Mol. Biol. 267*, 169–182.

(47) Xie, J., and Schultz, P. G. (2005) Adding amino acids to the genetic repertoire. *Curr. Opin. Chem. Biol. 9*, 548–554.

(48) Wang, L., and Schultz, P. G. (2001) A general approach for the generation of orthogonal tRNAs. *Chem. Biol. 8*, 883–890.

(49) Sakamoto, K., Hayashi, A., Sakamoto, A., Kiga, D., Nakayama, H., Soma, A., Kobayashi, T., Kitabatake, M., Takio, K., Saito, K., Shirouzu, M., Hirao, I., and Yokoyama, S. (2002) Site-specific incorporation of an unnatural amino acid into proteins in mammalian cells. *Nucleic Acids Res. 30*, 4692–4699.

(50) Mehl, R. A., Anderson, J. C., Santoro, S. W., Wang, L., Martin, A. B., King, D. S., Horn, D. M., and Schultz, P. G. (2003) Generation of a bacterium with a 21 amino acid genetic code. *J. Am. Chem. Soc. 125*, 935–939.

(51) Wang, K., Neumann, H., Peak-Chew, S. Y., and Chin, J. W. (2007) Evolved orthogonal ribosomes enhance the efficiency of synthetic genetic code expansion. *Nat. Biotechnol. 25*, 770–777.

(52) Sisido, M., and Hohsaka, T. (2001) Introduction of specialty functions by the position-specific incorporation of nonnatural amino acids into proteins through four-base codon/anticodon pairs. *Appl. Microbiol. Biotechnol. 57*, 274–281.

(53) Dougherty, D. A. (2000) Unnatural amino acids as probes of protein structure and function. *Curr. Opin. Chem. Biol. 4*, 645–652.

(54) Liu, W., Brock, A., Chen, S., Chen, S., and Schultz, P. G. (2007) Genetic incorporation of unnatural amino acids into proteins in mammalian cells. *Nat. Methods 4*, 239–244.

(55) Kwon, I., Kirshenbaum, K., and Tirrell, D. A. (2003) Breaking the degeneracy of the genetic code. *J. Am. Chem. Soc. 125*, 7512–7513.

(56) Rackham, O., and Chin, J. W. (2005) A network of orthogonal ribosome x mRNA pairs. *Nat. Chem. Biol. 1*, 159–166.

(57) Hohsaka, T., and Sisido, M. (2000) Incorporation of nonnatural amino acids into proteins by using five-base codon-anticodon pairs. *Nucleic Acids Symp. Ser. 44*, 99–100.

(58) Hohsaka, T., Ashizuka, Y., Taira, H., Murakami, H., and Sisido, M. (2001) Incorporation of nonnatural amino acids into proteins by using various four-base codons in an escherichia coli in vitro translation system. *Biochemistry 40*, 11060–11064.

(59) Rodriguez, E. A., Lester, H. A., and Dougherty, D. A. (2006) In vivo incorporation of multiple unnatural amino acids through nonsense and frameshift suppression. *Proc. Natl. Acad. Sci. U.S.A. 103*, 8650–8655.

(60) Taki, M., Hohsaka, T., and Sisido, M. (2001) Site-specific cleavage of a protein via introducing a hydroxy acid derivative in the main chain by using four-base codon/anticodon pairs. *Nucleic Acids Symp. Ser. 1*, 227–228.

(61) Switzer, C., Moroney, S. E., and Benner, S. A. (1989) Enzymatic incorporation of a new base pair into DNA and RNA. *J. Am. Chem. Soc. 111*, 8322–8323.

(62) Bain, J. D., Switzer, C., Chamberlin, R., and Bennert, S. A. (1992) Ribosome-mediated incorporation of a non-standard amino acid into a peptide through expansion of the genetic code. *Nature 356*, 537–539.

(63) Matsuda, S., Fillo, J. D., Henry, A. A., Rai, P., Wilkens, S. J., Dwyer, T. J., Geierstanger, B. H., Wemmer, D. E., Schultz, P. G.,

Spraggon, G., and Romesberg, F. E. (2007) Efforts toward expansion of the genetic alphabet: Structure and replication of unnatural base pairs. *J. Am. Chem. Soc. 129*, 10466–10473.
(64) Leconte, A. M., Hwang, G. T., Matsuda, S., Capek, P., Hari, Y., and Romesberg, F. E. (2008) Discovery, characterization, and optimization of an unnatural base pair for expansion of the genetic alphabet. *J. Am. Chem. Soc. 130*, 2336–2343.
(65) Ohtsuki, T., Kimoto, M., Ishikawa, M., Mitsui, T. O., Hirao, I., and Yokoyama, S. (2001) Unnatural base pairs for specific transcription. *Proc. Natl. Acad. Sci. U.S.A. 98*, 4922–4925.
(66) Hirao, I., Kimoto, M., Mitsui, T., Fujiwara, T., Kawai, R., Sato, A., Harada, Y., and Yokoyama, S. (2006) An unnatural base pair system for in vitro replication and transcription. *Nucleic Acids Symp. Ser. 50*, 33–34.
(67) Hirao, I. (2006) Unnatural base pair systems for DNA/RNA-based biotechnology. *Curr. Opin. Chem. Biol. 10*, 622–627.
(68) Kimmerlin, T., and Seebach, D. (2005) '100 years of peptide synthesis': Ligation methods for peptide and protein synthesis with applications to β-peptide assemblies*. *J. Pept. Res. 65*, 229–260.
(69) Han, S., and Viola, R. E. (2004) Splicing of unnatural amino acids into proteins: A peptide model study. *Protein Pept. Lett. 11*, 107–114.
(70) Lemieux, G. A., and Bertozzi, C. R. (1998) Chemoselective ligation reactions with proteins, oligosaccharides and cells. *Trends Biotechnol. 16*, 506–513.
(71) Schnolzer, M., and Kent, S. B. H. (1992) Constructing proteins by dovetailing unprotected synthetic peptides: Backbone-engineered HIV protease. *Science 256*, 221–225.
(72) Rademann, J. (2004) Organic protein chemistry: Drug discovery through the chemical modification of proteins. *Angew. Chem., Int. Ed. 43*, 4554–4556.
(73) Borgia, J. A., and Fields, G. B. (2000) Chemical synthesis of proteins. *Trends Biotechnol. 18*, 243–251.
(74) Englebretsen, D. R., Choma, C. T., and Robillard, G. T. (1998) Synthesis of a designed transmembrane protein by thioether ligation of solubilised segments: Nα-haloacetylated peptides survived resin cleavage using TFA with EDT as scavenger. *Tetrahedron Lett. 39*, 4929–4932.
(75) Brunel, F. M., and Dawson, P. E. (2005) Synthesis of constrained helical peptides by thioether ligation: Application to analogs of gp41. *Chem.Commun. (Cambridge) 20*, 2552–2554.
(76) Tam, J. P., Xu, J., and Eom, K. D. (2001) Methods and strategies of peptide ligation. *Pept. Sci. 60*, 194–205.
(77) Dawson, P. E., Muir, T. W., Clark-Lewis, I., and Kent, S. B. H. (1994) Synthesis of proteins by native chemical ligation. *Science 266*, 776–779.
(78) Severinov, K., and Muir, T. W. (1998) Expressed protein ligation, a novel method for studying protein-protein interactions in transcription. *J. Biol. Chem. 273*, 16205–16209.
(79) Nilsson, B. L., Soellner, M. B., and Raines, R. T. (2005) Chemical synthesis of proteins. *Annu. Rev. Biophys. Biomol. Struct. 34*, 91–118.
(80) Tam, J. P., and Yu, Q. (1998) Methionine ligation strategy in the biomimetic synthesis of parathyroid hormones. *Biopolymers 46*, 319–327.
(81) Offer, J., and Dawson, P. E. (2000) Nα−2-mercaptobenzylamine-assisted chemical ligation. *Org. Lett. 2*, 23–26.
(82) Canne, L. E., Bark, S. J., and Kent, S. B. H. (1996) Extending the applicability of native chemical ligation. *J. Am. Chem. Soc. 118*, 5891–5896.
(83) Kawakami, T., and Aimoto, S. (2003) A photoremovable ligation auxiliary for use in polypeptide synthesis. *Tetrahedron Lett. 44*, 6059–6061.
(84) Macmillan, D. (2006) Evolving strategies for protein synthesis converge on native chemical ligation. *Angew. Chem., Int. Ed. 45*, 7668–7672.
(85) Muir, T. W., Sondhi, D., and Cole, P. A. (1998) Expressed protein ligation: A general method for protein engineering. *Proc. Natl. Acad. Sci. U.S.A. 95*, 6705–6710.
(86) Muir, T. W. (2003) Semisynthesis of proteins by expressed protein ligation. *Annu. Rev. Biochem. 72*, 249–289.
(87) Buskas, T., Ingale, S., and Boons, G. J. (2006) Glycopeptides as versatile tools for glycobiology. *Glycobiology 16*, 113R–136.
(88) Nilsson, B. L., Kiessling, L. L., and Raines, R. T. (2000) Staudinger ligation: A peptide from a thioester and azide. *Org. Lett. 2*, 1939–1941.
(89) Saxon, E., Armstrong, J. I., and Bertozzi, C. R. (2000) A "traceless" staudinger ligation for the chemoselective synthesis of amide bonds. *Org. Lett. 2*, 2141–2143.
(90) Staudinger, H., and Meyer, J. (1919) New organic compounds of phosphorus. III. phosphinemethylene derivatives and phosphinimines. *Helv. Chim. Acta 2*, 635–646.
(91) Lutz, J. F., and Borner, H. G. (2008) Modern trends in polymer bioconjugates design. *Prog. Polym. Sci. 33*, 1–39.
(92) Xie, J., and Schultz, P. G. (2006) A chemical toolkit for proteins - an expanded genetic code. *Nat. Rev. Mol. Cell Biol. 7*, 775–782.
(93) Moses, J. E., and Moorhouse, A. D. (2007) The growing applications of click chemistry. *Chem. Soc. Rev. 36*, 1249–1262.
(94) Kolb, H. C., Finn, M. G., and Sharpless, K. F. (2001) Click chemistry: Diverse chemical function from a few good reactions. *Angew. Chem., Int. Ed. 40*, 2004–2021.
(95) Dedola, S., Nepogodiev, S. A., and Field, R. A. (2007) Recent applications of the CuI-catalysed huisgen azide-alkyne 1,3-dipolar cycloaddition reaction in carbohydrate chemistry. *Org. Biomol. Chem. 5*, 1006–1017.
(96) Stocking, E. M., and Williams, R. M. (2003) Chemistry and biology of biosynthetic diels-alder reactions. *Angew. Chem., Int. Ed. 42*, 3078–3115.
(97) Dahanukar, V., and Zavialov, L. (2002) Aziridines and aziridinium ions in the practical synthesis of pharmaceutical intermediates - A perspective. *Curr. Opin. Drug Discov. Devel. 5*, 918–927.
(98) Foillard, S., Rasmussen, M. O., Razkin, J., Boturyn, D., and Dumy, P. (2008) 1-ethoxyethylidene, a new group for the stepwise SPPS of aminooxyacetic acid containing peptides. *J. Org. Chem. 73*, 983–991.
(99) Liu, Y., Feizi, T., Campanero-Rhodes, M. A., Childs, R. A., Zhang, Y., Mulloy, B., Evans, P. G., Osborn, H. M. I., Otto, D., Crocker, P. R., and Chai, W. (2007) Neoglycolipid probes prepared via oxime ligation for microarray analysis of oligosaccharide-protein interactions. *Chem. Biol. 14*, 847–859.
(100) Dubs, P., Bourel-Bonnet, L., Subra, G., Blanpain, A., Melnyk, O., Pinel, A. M., Gras-masse, H., and Martinez, J. (2007) Parallel synthesis of a lipopeptide library by hydrazone-based chemical ligation. *J. Comb. Chem. 9*, 973–981.
(101) Gras-Masse, H. (2001) Chemoselective ligation and antigen vectorization. *Biologicals 29*, 183–188.
(102) Mather, B. D., Viswanathan, K., Miller, K. M., and Long, T. E. (2006) Michael addition reactions in macromolecular design for emerging technologies. *Prog. Polym. Sci. 31*, 487–531.
(103) Metzger, J., and Bornscheuer, U. (2006) Lipids as renewable resources: Current state of chemical and biotechnological conversion and diversification. *Appl. Microbiol. Biotechnol. 71*, 13–22.
(104) Strable, E., Prasuhn, D. E., Udit, A. K., Brown, S., Link, A. J., Ngo, J. T., Lander, G., Quispe, J., Potter, C. S., Carragher, B., Tirrell, D. A., and Finn, M. G. (2008) Unnatural amino acid incorporation into virus-like particles. *Bioconjugate Chem. 19*, 866–875.
(105) Cazalis, C. S., Haller, C. A., Sease-Cargo, L., and Chaikof, E. L. (2004) C-terminal site-specific PEGylation of a truncated thrombomodulin mutant with retention of full bioactivity. *Bioconjugate Chem. 15*, 1005–1009.
(106) van Kasteren, S. I., Kramer, H. B., Gamblin, D. P., and Davis, B. G. (2007) Site-selective glycosylation of proteins: Creating synthetic glycoproteins. *Nat. Protoc. 2*, 3185–3194.
(107) van Kasteren, S. I., Kramer, H. B., Jensen, H. H., Campbell, S. J., Kirkpatrick, J., Oldham, N. J., Anthony, D. C., and Davis, B. G. (2007) Expanding the diversity of chemical protein

modification allows post-translational mimicry. *Nature 446*, 1105–1109.
(108) Beatty, K. E., Liu, J. C., Xie, F., Dieterich, D. C., Schuman, E. M., Wang, Q., and Tirrell, D. A. (2006) Fluorescence visualization of newly synthesized proteins in mammalian cells. *Angew. Chem., Int. Ed. 45*, 7364–7367.
(109) Beatty, K. E., Xie, F., Wang, Q., and Tirrell, D. A. (2005) Selective dye-labeling of newly synthesized proteins in bacterial cells. *J. Am. Chem. Soc. 127*, 14150–14151.
(110) Link, A. J., and Tirrell, D. A. (2003) Cell surface labeling of *Escherichia coli* via copper(I)-catalyzed [3 + 2] cycloaddition. *J. Am. Chem. Soc. 125*, 11164–11165.
(111) Deiters, A., Cropp, T. A., Mukherji, M., Chin, J. W., Anderson, J. C., and Schultz, P. G. (2003) Adding amino acids with novel reactivity to the genetic code of *Saccharomyces cerevisiae*. *J. Am. Chem. Soc. 125*, 11782–11783.
(112) Deiters, A., and Schultz, P. G. (2005) In vivo incorporation of an alkyne into proteins in *Escherichia coli*. *Bioorg. Med. Chem. Lett. 15*, 1521–1524.
(113) Iida, S., Asakura, N., Tabata, K., Okura, I., and Kamachi, T. (2006) Incorporation of unnatural amino acids into cytochrome c3 and specific viologen binding to the unnatural amino acid. *ChemBioChem 7*, 1853–1855.
(114) Deiters, A., Cropp, T. A., Summerer, D., Mukherji, M., and Schultz, P. G. (2004) Site-specific PEGylation of proteins containing unnatural amino acids. *Bioorg. Med. Chem. Lett. 14*, 5743–5745.
(115) Kiick, K. L., Saxon, E., Tirrell, D. A., and Bertozzi, C. R. (2002) Incorporation of azides into recombinant proteins for chemoselective modification by the Staudinger ligation. *Proc. Natl. Acad. Sci. U.S.A. 99*, 19–24.
(116) Tsao, M., Tian, F., and Schultz, P. G. (2005) Selective Staudinger modification of proteins containing p-azidophenylalanine. *ChemBioChem 6*, 2147–2149.
(117) Back, J. W., David, O., Kramer, G., Masson, G., Kasper, P. T., de Koning, L. J., de Jong, L., van Maarseveen, J. H., and de Koster, C. G. (2005) Mild and chemoselective peptide-bond cleavage of peptides and proteins at azido homoalanine. *Angew. Chem., Int. Ed. 44*, 7946–7950.
(118) Godoy-Alcántar, C., Yatsimirsky, A. K., and Lehn, J. (2005) Structure-stability correlations for imine formation in aqueous solution. *J. Phys. Org. Chem. 18*, 979–985.
(119) Geoghegan, K. F., and Stroh, J. G. (1992) Site-directed conjugation of nonpeptide groups to peptides and proteins via periodate oxidation of a 2-amino alcohol. application to modification at N-terminal serine. *Bioconjugate Chem. 3*, 138–46.
(120) Shao, J., and Tam, J. P. (1995) Unprotected peptides as building blocks for the synthesis of peptide dendrimers with oxime, hydrazone, and thiazolidine linkages. *J. Am. Chem. Soc. 117*, 3893–3899.
(121) Rose, K. (1994) Facile synthesis of homogeneous artificial proteins. *J. Am. Chem. Soc. 116*, 30–33.
(122) Tam, J. P., Yu, Q., and Miao, Z. (1999) Orthogonal ligation strategies for peptide and protein. *Pept. Sci. 51*, 311–332.
(123) Löwik, D., Ayres, L., Smeenk, J., and Van Hest, J. (2006) Synthesis of bio-inspired hybrid polymers using peptide synthesis and protein engineering. *Adv. Polym. Sci. 202*, 19–52.
(124) Köhn, M., and Breinbauer, R. (2004) The staudinger ligation - A gift to chemical biology. *Angew. Chem., Intl. Ed. 43*, 3106–3116.
(125) Gaertner, H. F., and Offord, R. E. (1996) Site-specific attachment of functionalized poly(ethylene glycol) to the amino terminus of proteins. *Bioconjugate Chem. 7*, 38–44.
(126) Canne, L. E., Ferre- D'Amare, A. R., Burley, S. K., and Kent, S. B. H. (1995) Total chemical synthesis of a unique transcription factor-related protein: CMyc-max. *J. Am. Chem. Soc. 117*, 2998–3007.
(127) Zeng, H., Xie, J., and Schultz, P. G. (2006) Genetic introduction of a diketone-containing amino acid into proteins. *Bioorg. Med. Chem. Lett. 16*, 5356–5359.
(128) Datta, D., Wang, P., Carrico, I. S., Mayo, S. L., and Tirrell, D. A. (2002) A designed phenylalanyl-tRNA synthetase variant allows efficient in vivo incorporation of aryl ketone functionality into proteins. *J. Am. Chem. Soc. 124*, 5652–5653.
(129) Wang, L., Zhang, Z., Brock, A., and Schultz, P. G. (2003) Addition of the keto functional group to the genetic code of *Escherichia coli*. *Proc. Natl. Acad. Sci. U.S.A. 100*, 56–61.
(130) Zhang, Z., Smith, B. A. C., Wang, L., Brock, A., Cho, C., and Schultz, P. G. (2003) A new strategy for the site-specific modification of proteins in vivo. *Biochemistry 42*, 6735–6746.
(131) Ye, S., Koehrer, C., Huber, T., Kazmi, M., Sachdev, P., Yan, E. C. Y., Bhagat, A., RajBhandary, U. L., and Sakmar, T. P. (2008) Site-specific incorporation of keto amino acids into functional G protein-coupled receptors using unnatural amino acid mutagenesis. *J. Biol. Chem. 283*, 1525–1533.
(132) Taki, M., Tokuda, Y., Ohtsuki, T., and Sisido, M. (2006) Design of carrier tRNAs and selection of four-base codons for efficient incorporation of various nonnatural amino acids into proteins in spodoptera frugiperda 21 (Sf21) insect cell-free translation system. *The Society for Biotechnology, Japan 102*, 511–517.
(133) Liu, H., Wang, L., Brock, A., Wong, C., and Schultz, P. G. (2003) A method for the generation of glycoprotein mimetics. *J. Am. Chem. Soc. 125*, 1702–1703.
(134) Svedendahl, M., Hult, K., and Berglund, P. (2005) Fast carbon-carbon bond formation by a promiscuous lipase. *J. Am. Chem. Soc. 127*, 17988–17989.
(135) Barbas, C. F., 3rd, Heine, A., Zhong, G., Hoffmann, T., Gramatikova, S., Bjornestedt, R., List, B., Anderson, J., Stura, E. A., Wilson, I. A., and Lerner, R. A. (1997) Immune versus natural selection: Antibody aldolases with enzymic rates but broader scope. *Science 278*, 2085–2092.
(136) Bar-Or, R., Rael, L. T., and Bar-Or, D. (2008) Dehydroalanine derived from cysteine is a common post-translational modification in human serum albumin. *Rapid Commun. Mass Spectrom. 22*, 711–716.
(137) Seebeck, F. P., and Szostak, J. W. (2006) Ribosomal synthesis of dehydroalanine-containing peptides. *J. Am. Chem. Soc. 128*, 7150–7151.
(138) Wang, J., Schiller, S. M., and Schultz, P. G. (2007) A biosynthetic route to dehydroalanine-containing proteins. *Angew. Chem., Int. Ed. 46*, 6849–6851.
(139) Zhang, Z., Wang, L., Brock, A., and Schultz, P. G. (2002) The selective incorporation of alkenes into proteins in *Escherichia coli*. *Angew. Chem., Int. Ed. 41*, 2840–2842.
(140) Clark, T. D., and Ghadiri, M. R. (1995) Supramolecular design by covalent capture. design of a peptide cylinder via hydrogen-bond-promoted intermolecular olefin metathesis. *J. Am. Chem. Soc. 117*, 12364–12365.
(141) Kodama, K., Fukuzawa, S., Nakayama, H., Kigawa, T., Sakamoto, K., Yabuki, T., Matsuda, N., Shirouzu, M., Takio, K., Tachibana, K., and Yokoyama, S. (2006) Regioselective carbon-carbon bond formation in proteins with palladium catalysis; new protein chemistry by organometallic chemistry. *ChemBioChem 7*, 134–139.
(142) Kwon, I., Wang, P., and Tirrell, D. A. (2006) Design of a bacterial host for site-specific incorporation of p-bromophenylalanine into recombinant proteins. *J. Am. Chem. Soc. 128*, 11778–11783.
(143) Bontempo, D., and Maynard, H. D. (2005) Streptavidin as a macroinitiator for polymerization: In situ protein-polymer conjugate formation. *J. Am. Chem. Soc. 127*, 6508–9.
(144) Broyer, R. M., Quaker, G. M., and Maynard, H. D. (2007) Designed amino acid ATRP initiators for the synthesis of biohybrid materials. *J. Am. Chem. Soc. 130*, 1041–1047.
(145) Cornish, V. W., Benson, D. R., Altenbach, C. A., Hideg, K., Hubbell, W. L., and Schultz, P. G. (1994) Site-specific incorporation of biophysical probes into proteins. *Proc. Natl. Acad. Sci. U.S.A. 91*, 2910–2914.

(146) Shafer, A. M., Kalai, T., Liu, S. Q. B., Hideg, K., and Voss, J. C. (2004) Site-specific insertion of spin-labeled L-amino acids in *Xenopus* oocytes. *Biochemistry 43*, 8470–8482.
(147) Chin, J. W., Cropp, T. A., Anderson, J. C., Mukherji, M., Zhang, Z., and Schultz, P. G. (2003) An expanded eukaryotic genetic code. *Science 301*, 964–967.
(148) Chin, J. W., Santoro, S. W., Martin, A. B., King, D. S., Wang, L., and Schultz, P. G. (2002) Addition of p-azido-L-phenylalanine to the genetic code of *Escherichia coli*. *J. Am. Chem. Soc. 124*, 9026–9027.
(149) Farrell, I. S., Toroney, R., Hazen, J. L., Mehl, R. A., and Chin, J. W. (2005) Photo-cross-linking interacting proteins with a genetically encoded benzophenone. *Nat. Methods 2*, 377–384.
(150) Chin, J. W., Martin, A. B., King, D. S., Wang, L., and Schultz, P. G. (2002) Addition of a photocrosslinking amino acid to the genetic code of *Escherichia coli*. *Proc. Natl. Acad. Sci. U.S.A. 99*, 11020–11024.
(151) Chin, J. W., and Schultz, P. G. (2002) In vivo photocrosslinking with unnatural amino acid mutagenesis. *ChemBioChem 3*, 1135–1137.
(152) Kauer, J. C., Erickson-Viitanen, S., Wolfe, H. R., Jr., and and DeGrado, W. F. (1986) p-Benzoyl-L-phenylalanine, a new photoreactive amino acid. photolabeling of calmodulin with a synthetic calmodulin-binding peptide. *J. Biol. Chem. 261*, 10695–10700.
(153) Schlieker, C., Weibezahn, J., Patzelt, H., Tessarz, P., Strub, C., Zeth, K., Erbse, A., Schneider-Mergener, J., Chin, J. W., Schultz, P. G., Bukau, B., and Mogk, A. (2004) Substrate recognition by the AAA+ chaperone ClpB. *Nat. Struct. Mol. Biol. 11*, 607–615.
(154) Weibezahn, J., Tessarz, P., Schlieker, C., Zahn, R., Maglica, Z., Lee, S., Zentgraf, H., Weber-Ban, E. U., Dougan, D. A., Tsai, F. T., Mogk, A., and Bukau, B. (2004) Thermotolerance requires refolding of aggregated proteins by substrate translocation through the central pore of ClpB. *Cell. 119*, 653–665.
(155) Hino, N., Okazaki, Y., Kobayashi, T., Hayashi, A., Sakamoto, K., and Yokoyama, S. (2005) Protein photo-cross-linking in mammalian cells by site-specific incorporation of a photoreactive amino acid. *Nat. Methods 2*, 201–206.
(156) Wu, N., Deiters, A., Cropp, T. A., King, D., and Schultz, P. G. (2004) A genetically encoded photocaged amino acid. *J. Am. Chem. Soc. 126*, 14306–14307.
(157) Deiters, A., Groff, D., Ryu, Y., Xie, J., and Schultz, P. G. (2006) A genetically encoded photocaged tyrosine. *Angew. Chem., Int. Ed. 45*, 2728–2731.
(158) Wang, J., Xie, J., and Schultz, P. G. (2006) A genetically encoded fluorescent amino acid. *J. Am. Chem. Soc. 128*, 8738–8739.
(159) Summerer, D., Chen, S., Wu, N., Deiters, A., Chin, J. W., and Schultz, P. G. (2006) A genetically encoded fluorescent amino acid. *Proc. Natl. Acad. Sci. U.S.A. 103*, 9785–9789.
(160) Tsao, M. L., Summerer, D., Ryu, Y., and Schultz, P. G. (2006) The genetic incorporation of a distance probe into proteins in *Escherichia coli*. *J. Am. Chem. Soc. 128*, 4572–4573.
(161) Deiters, A., Geierstanger, B. H., and Schultz, P. G. (2005) Site-specific in vivo labeling of proteins for NMR studies. *ChemBioChem 6*, 55–58.
(162) Suydam, I. T., and Boxer, S. G. (2003) Vibrational stark effects calibrate the sensitivity of vibrational probes for electric fields in proteins. *Biochemistry 42*, 12050–12055.
(163) Xie, J., Wang, L., Wu, N., Brock, A., Spraggon, G., and Schultz, P. G. (2004) The site-specific incorporation of p-iodo-L-phenylalanine into proteins for structure determination. *Nat. Biotechnol. 22*, 1297–1301.
(164) Alfonta, L., Zhang, Z., Uryu, S., Loo, J. A., and Schultz, P. G. (2003) Site-specific incorporation of a redox-active amino acid into proteins. *J. Am. Chem. Soc. 125*, 14662–14663.

BC800294A

COMMUNICATIONS

Fluorescence Emission and Polarization for Analyzing Binding of Ruthenium Metalloglycocluster to Lectin and Tetanus Toxin C-Fragment

Tomoko Okada,* Taro Makino, and Norihiko Minoura

Graduate School of Bionics, Tokyo University of Technology, Katakura, Hachioji, Tokyo 192-0982, Japan. Received March 6, 2009; Revised Manuscript Received May 15, 2009

We have designed and synthesized ruthenium complexes bearing clustered galactose Ru(bpy-2Gal)$_3$ and glucose Ru(bpy-2Glc)$_3$. Changes in fluorescence emission (FE) and fluorescence polarization (FP) of the metalloglycoclusters were measured by adding each lectin (*peanut agglutinin* (PNA), *Ricinus communis agglutinin 120* (RCA), *concanavalin A* (ConA), or *wheat germ agglutinin* (WGA)) or tetanus toxin c-fragment (TCF). Following the addition of PNA and ConA, the FE spectra of Ru(bpy-2Gal)$_3$ and Ru(bpy-2Glc)$_3$ showed new emission peaks, respectively. In addition, Ru(bpy-2Gal)$_3$ and Ru(bpy-2Glc)$_3$ exclusively increased the FP values by addition of PNA and ConA. Since other combinations of the metalloglycoclusters and lectin caused little change, specific bindings of galactose to PNA and glucose to ConA were confirmed by the FE and FP measurement. From the FP analyses, the dissociation constants (K_d) of Ru(bpy-2Gal)$_3$ to PNA and Ru(bpy-2Glc)$_3$ to ConA were calculated to be ca. 6.1×10^{-6} M and 1.8×10^{-5} M. Furthermore, the FP analyses proved specific binding of Ru(bpy-2Gal)$_3$ to TCF.

Carbohydrates are well-known to play important roles in biological processes. Specific binding between carbohydrate and protein (lectin) can induce serious infections from virus and pathogenic toxins (*1*). Therefore, development of a useful method is desirable to investigate the affinity property of the carbohydrate. Fluorescence polarization (FP) analysis is an effective method to evaluate a binding event of a small carbohydrate molecule and large protein (*2*). Since the FP analysis requires a fluorescent-labeled carbohydrate probe, this study aimed to apply a fluorescent metalloglycocluster as a probe molecule. A metalloglycocluster, a group of a glycocluster containing a metal center, is an especially attractive carbohydrate probe, since the metal center gives characteristic photochemical and electrochemical properties that can be utilized as an indicator. Moreover, the clustered carbohydrate around the metal center would enhance the binding constant of generally weak interaction between carbohydrate and protein. Recently, many researchers reported the enhanced binding constant achieved by clustering the carbohydrate, such as dendrimers modified with carbohydrates at their branches, organic polymers possessing carbohydrate branches at each monomer unit, and ruthenium metalloglycoclusters (*3*−*6*). Since the ruthenium metalloglycocluster possesses characteristic fluorescence emission (FE) property, both the FE and FP analyses are applicable for the affinity evaluation. In this study, we propose the utility of FE and FP analyses using a ruthenium metalloglycocluster for evaluating the affinity property between carbohydrate and lectins.

We designed metalloglycoclusters, Ru(bpy-2Gal)$_3$ and Ru(bpy-2Glc)$_3$, as carbohydrate probes (Figure 1). Ru(bpy-2Gal)$_3$ and Ru(bpy-2Glc)$_3$ have a ruthenium metal center coordinated by three bpy-2Gal and bpy-2Glc. Since the ruthenium(II) complex adopts octahedral geometry, six galactoses or glucoses are clustered around the metal center. These designed metalloglycoclusters were synthesized by chemical synthetic procedures. For the affinity evaluation, both ruthenium complexes were used without isolation of diastereomers (Λ- and Δ-forms).

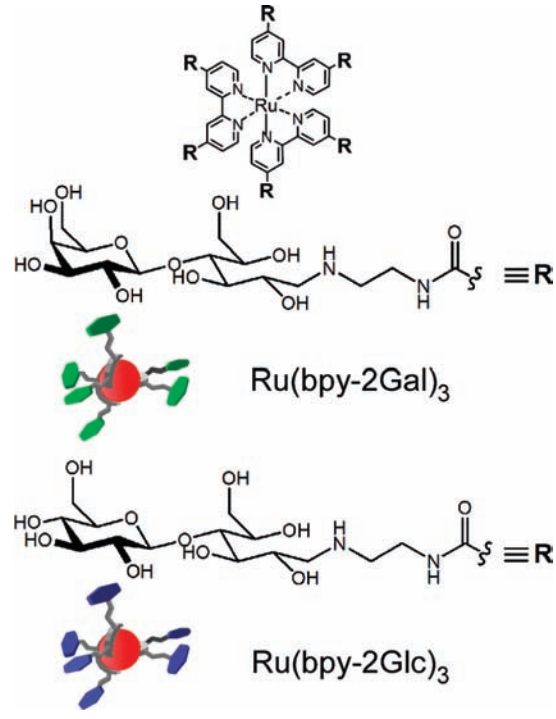

Figure 1. Schematic representation of the metalloglycoclusters Ru(bpy-2Gal)$_3$ and Ru(bpy-2Glc)$_3$.

* tomoko@bs.teu.ac.jp.

10.1021/bc900101u CCC: $40.75 © 2009 American Chemical Society
Published on Web 06/19/2009

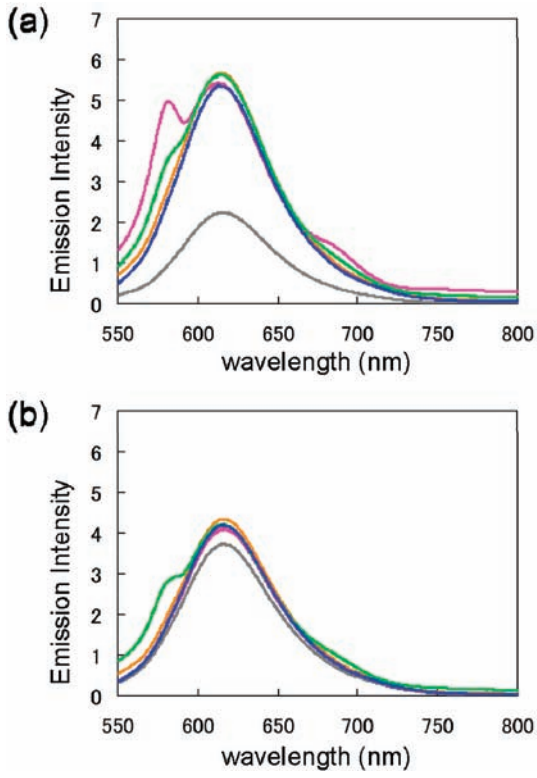

Figure 2. Fluorescence emission spectra of the metalloglycoclusters (20 μM), (a) Ru(bpy-2Gal)$_3$ and (b) Ru(bpy-2Glc)$_3$, with lectin (5 μM) (PNA (pink), RCA (orange), ConA (green), and WGA (blue)) or without lectin (gray). Excitation wavelength was 468 nm.

To examine the binding properties of Ru(bpy-2Gal)$_3$ and Ru(bpy-2Glc)$_3$, fluorescence emission spectra were measured for each probe before and after the addition of each lectin (PNA, RCA, ConA, and WGA). Figure 2a shows the emission spectra of Ru(bpy-2Gal)$_3$ with or without each lectin. Addition of PNA caused the most drastic change to the spectral shape compared with the other lectins (RCA, ConA, and WGA). In particular, a new emission peak appeared at ca. 580 nm, and this new peak disappeared following addition of galactose to the solution. The emission spectral change suggests that Ru(bpy-2Gal)$_3$ specifically binds to PNA, and the local environment of Ru(bpy-2Gal)$_3$ becomes more hydrophobic compared with when the Ru(bpy-2Gal)$_3$ presents alone in PBS (*7*). This assumption is supported by the emission spectrum of Ru(bpy-2Gal)$_3$ in ethanol that is a more hydrophobic solvent than PBS. Following the addition of ethanol to the PBS solution of Ru(bpy-2Gal)$_3$, a new emission peak was observed at 580 nm. Therefore, the new emission peak observed for Ru(bpy-2Gal)$_3$ with PNA is evidence that Ru(bpy-2Gal)$_3$ specifically binds to the hydrophobic binding pocket of PNA. A similar spectral change was observed for Ru(bpy-2Glc)$_3$ with ConA. Since the appearance of the new emission peak was not observed with other lectins (PNA, RCA, and WGA), the FE analysis confirms that Ru(bpy-2Glc)$_3$ specifically binds to ConA. These FE measurements confirmed that galactose and glucose bind specifically to PNA and ConA, respectively. Such a drastic change in emission spectra is unusual during the course of the binding event between the ruthenium metalloglycocluster and lectin.

The affinity evaluation method using the FE spectrum depends on the hydrophobicity of lectin. In contrast, the FP analysis allows direct investigation of the molecular motion (namely, molecular size) in the absence of contributions derived from the environmental conditions that the metalloglycoclusters experience. Therefore, the FP measurement was performed to confirm the affinity property of the metalloglycocluster to lectin.

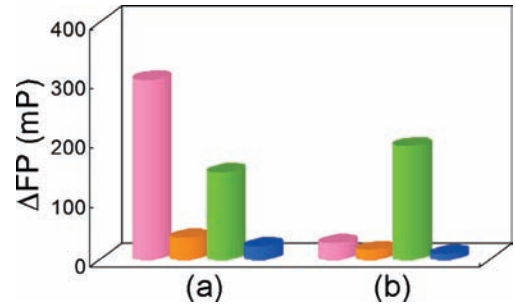

Figure 3. Changes in fluorescence polarization of the metalloglycoclusters (20 μM), (a) Ru(bpy-2Gal)$_3$ and (b) Ru(bpy-2Glc)$_3$, following addition of lectins (5 μM) (PNA (pink), RCA (orange), ConA (green), and WGA (blue)). Excitation wavelength was 468 nm, and polarization values were used at 580 nm.

Figure 3 shows the increased FP values when PNA, RCA, ConA, or WGA was added to each metalloglycocluster. Unlike the other lectins, FP value of Ru(bpy-2Gal)$_3$ increased the most by the addition of PNA. In contrast, Ru(bpy-2Glc)$_3$ showed the greatest increment when ConA was added to the solution. These drastic increments in FP values confirm that Ru(bpy-2Gal)$_3$ and Ru(bpy-2Glc)$_3$ specifically bind to PNA and ConA, respectively. Besides, electrostatic interaction between the divalent metalloglycoclusters and lectin is negligible because the emission spectrum of Ru(bpy)$_3$ showed no changes following addition of each lectin. Therefore, the FE and FP analyses determined specific bindings of galactose to PNA and glucose to ConA, which are consistent with the previous reports showing high affinity of galactose to PNA and glucose to ConA. Changes in the FE and FP of Ru(bpy-2Gal)$_3$ were unexpectedly negligible, suggesting poor affinity of Ru(bpy-2Gal)$_3$ to RCA, despite the previous paper reports high affinity of galactose-bearing metalloglycocluster to RCA (*3*). Surface plasmon resonance analysis also proved that the RCA used in this study showed high affinity to galactose (4-aminophenyl-galactopyranoside) immobilized on a gold surface. Therefore, the low affinity is assumed to have a structural cause of the metalloglycocluster examined in this study, and molecular dynamics calculations are now underway to assess the possible reason.

By varying the concentrations of PNA and ConA, FP values were collected to examine the detailed binding properties of Ru(bpy-2Gal)$_3$ to PNA and Ru(bpy-2Glc)$_3$ to ConA (Figure 4). The horizontal axis represents the concentration of the binding sites from each lectin, which possesses four independent binding sites for every lectin molecule. Ru(bpy-2Gal)$_3$ showed a greater change in polarization than Ru(bpy-2Glc)$_3$ signifying higher affinity of PNA to galactose than glucose. The FP value for Ru(bpy-2Gal)$_3$ increased as the PNA increased and then plateaued. Nonlinear least-squares fitting determines the dissociation constant (K_d) of Ru(bpy-2Gal)$_3$ and PNA as 6.1×10^{-6} M. In a similar manner, Figure 4b shows higher affinity of ConA to glucose than galactose, and the K_d value was estimated to be 1.8×10^{-5} M. These dissociation constants prove that the affinity of clustered galactose and glucose is higher than that of nonclustered galactose and glucose ($K_d \approx 10^{-3}$ to 10^{-4} M) (*1*). To confirm the clustering effect on the lectin binding event, K_d of a metalloglycocluster having two galactose residues, Ru(bpy)$_2$(bpy-2Gal), was examined following the similar FP analysis with Ru(bpy-2Gal)$_3$ (*8*). The K_d of Ru(bpy)$_2$(bpy-2Gal) to PNA was estimated to be more than 10^{-4} M. Since highly clustered Ru(bpy-2Gal)$_3$ showed lower K_d than Ru(bpy)$_2$(bpy-2Gal), the clustered galactose of Ru(bpy-2Gal)$_3$ was confirmed to raise its affinity to PNA.

On the basis of the elucidated FP properties, affinity of the metalloglycoclusters (2 μM), Ru(bpy-2Gal)$_3$ and Ru(bpy-2Glc)$_3$, was examined using 0.05 μM of tetanus toxin c-fragment (TCF).

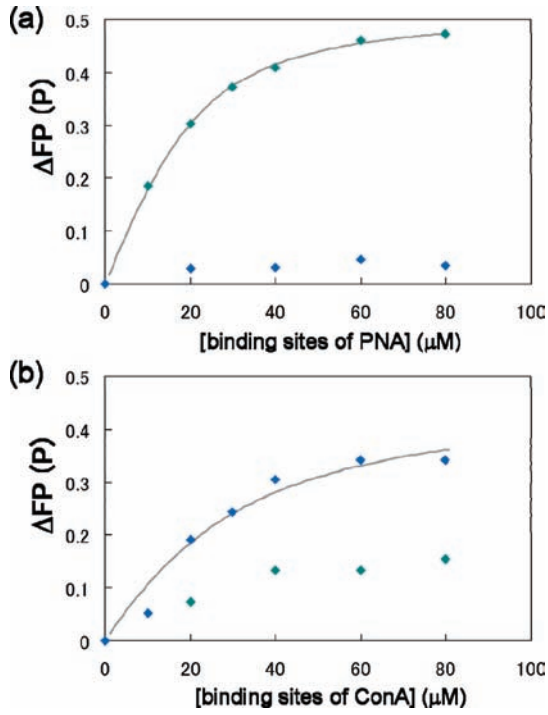

Figure 4. Changes in fluorescence polarization of metalloglycoclusters (20 μM), Ru(bpy-2Gal)$_3$ (green) or Ru(bpy-2Glc)$_3$ (blue), following addition of (a) PNA and (b) ConA. Excitation wavelength was 468 nm and polarization values were used at 580 nm. The gray line represents a fitted curve obtained from nonlinear least-squares fitting.

The TCF reportedly has affinity for galactose (*9, 10*). Following the addition of TCF, Ru(bpy-2Gal)$_3$ increased the polarization value by 47 mP; however, Ru(bpy-2Glc)$_3$ increased only by 7 mP. Because of the distinctive increment of the FP value for Ru(bpy-2Gal)$_3$, specific binding of galactose to TCF was confirmed.

In summary, the FE and FP analyses showed that the synthesized novel metalloglycoclusters, Ru(bpy-2Gal)$_3$ and Ru(bpy-2Glc)$_3$, bind specifically to PNA and ConA, respectively. The results in this report proved that the combination of FE and FP analyses would empower evaluation of affinity properties between carbohydrate and lectins. Ru(bpy-2Gal)$_3$ and Ru(bpy-2Glc)$_3$ with the clustered galactose and glucose were confirmed to raise affinity to the lectin. Moreover, specific binding of Ru(bpy-2Gal)$_3$ to TCF was proven by the FP analysis. These results ensure that the FP analysis using the ruthenium metalloglycocluster is useful for evaluating interactions between carbohydrates and toxins.

Supporting Information Available: Experimental details. This material is available free of charge via the Internet at http://pubs.acs.org.

LITERATURE CITED

(1) Bertozzi, C., and Kiessling, L. (2001) Chemical glycobiology. *Science 291*, 2357–2364.
(2) Jelinek, R., and Kolusheva, S. (2004) Carbohydrate biosensors. *Chem. Rev. 104*, 5987–6015.
(3) Hasegawa, T., Yonemura, T., Matsuura, K., and Kobayashi, K. (2003) Artificial metalloglycoclusters: Compact saccharide shell to induce high lectin affinity as well as strong luminescence. *Bioconjugate Chem. 14*, 728–737.
(4) Kikkeri, R., García-Rubio, I., and Seeberger, P.-H. (2009) Ru(II)-carbohydrate dendrimers as photoinduced electron transfer lectin biosensors. *Chem. Commun. 125*, 235–237.
(5) Gottschaldt, M., and Schubert, U. (2009) Prospects of metal complexes peripherally substituted with sugars in biomedicinal applications. *Chem.—Eur. J. 15*, 1548–1557.
(6) Sakai, S., Shigemasa, Y., and Sasaki, T. (1999) Iron(II)-assisted assembly of trivalent GalNAc clusters and their interactions with GalNAc-specific lectins. *Bull. Chem. Soc. Jpn. 72*, 1313–1319.
(7) See Figure S3 in Supporting Information.
(8) Identification of Ru(bpy)$_2$(bpy-2Gal) is in Supporting Information.
(9) Emsley, P., Fotinou, C., Black, I., Fairweather, N., Charles, I., Watts, C., Hewitt, E., and Isaacs, N. (2000) The structures of the tetanus toxin c-fragment with carbohydrate subunit complexes provide insight into ganglioside binding. *J. Biol. Chem. 275*, 8889–8894.
(10) Singh, A., Harrison, S., and Schoeniger, J. (2000) Gangliosides as receptors for biological toxins: Development of sensitive fluoroimmunoassays using ganglioside-bearing liposomes. *Anal. Chem. 72*, 6019–6024.

BC900101U

Supporting Information

Syntheses and identification of metalloglycoclusters.

Metalloglycoclusters, $Ru(bpy\text{-}2Gal)_3$ and $Ru(bpy\text{-}2Glc)_3$, were synthesized by following the scheme S1.

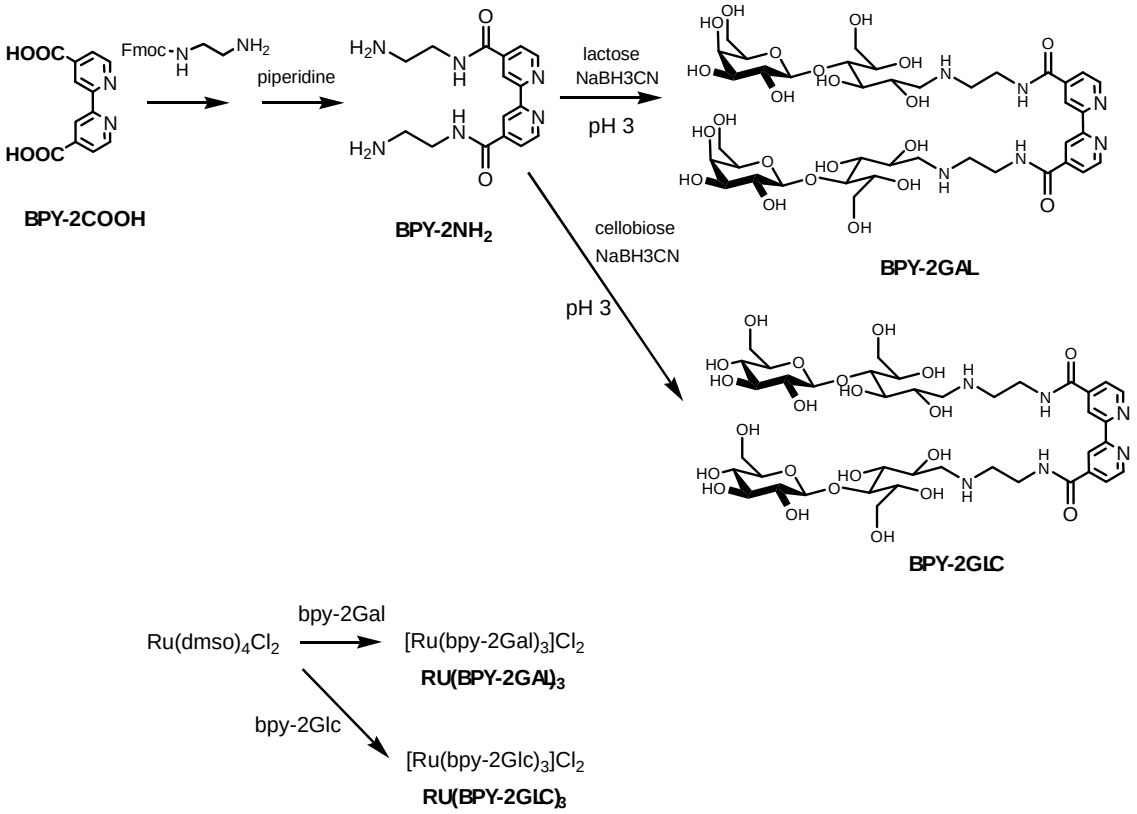

Scheme S1 Synthetic scheme of the metalloglycoclusters.

Materials. All chemical reagents were purchased from the chemical companies and used without further purification. Ruthenium(III) chloride, 2, 2'-bipyridine-4, 4'-dicarboxylic acid (bpy-2COOH), lactose and cellobiose were obtained from Sigma-Aldrich. Tetanus toxin c-fragment was purchased from Funakoshi and used without further purification. Reversed phase column chromatography (RP-HPLC) was performed on LC-8A and SPD-M10A (Shimadzu). The purified products were identified by electrospray ionization (ESI) time-of-flight (TOF) mass spectrometry performed on a JMS-T100LC (JEOL) and matrix-assisted laser desorption ionization (MALDI) TOF mass Ultraflex III (Bruker). ^{1}H and ^{13}C NMR spectra were recorded on a FT-NMR (Bruker).

bpy-2NH$_2$. Bpy-2COOH (100 mg, 4.1×10^{-4} mol) was added to 10 mL of thionyl chloride and the mixture was

refluxed for 6 h. After the mixture turned into yellow solution, the solution was evaporated. The yellow solid was dissolved to the mixture of THF (10 mL) and CH_2Cl_2 (10 mL). Fmoc-NH-$(CH_2)_2$-NH_2 (325 mg, 10.2×10^{-4} mol) dissolved in THF (5 mL), CH_2Cl_2 (5 mL), and DIEA (2 mL) was added in dropwise to the yellow solutioin and kept overnight. After quenching the reaction by adding methanol, piperidine (9 mL) was added to the crude product dissolved in methanol and stirred at rt for 12 h. The crude product was purified by a silica-gel column chromatography to give colorless solid (67% in yield). ^{1}H NMR (400 MHz, CD_3OD) δ 8.90 (d, *J* = 5.1 Hz, 2H; C*H(bpy)*), 8.69 (s, 2H; C*H(bpy)*), 7.93 (d, *J* = 5.0 Hz, 2H; C*H(bpy))* 3.70 (t, *J* = 6.1 Hz, 4H; CH_2 *(linker moiety)*), 3.14 (t, *J* = 6.8 Hz, 4H; CH_2); ^{13}C NMR (100 MHz, CD_3OD) δ 167.6, 156.5, 155.8 ,150.3, 149.6, 143.0, 122.1, 121.2, 119.5, 44.5, 39.7, 39.5; ESI-MS *m/z* (M = $C_{16}H_{20}N_6O_2$) 329.1 $[M + H]^+$ (calcd: 329.2), 351.1 $[M + Na]^+$ (calcd: 351.2).

bpy-2Gal. Bpy-2NH_2 (80 mg, 2.4×10^{-4} mol) was dissolved in H_2O (10 mL), then β-lactose (1.66 g, 4.9×10^{-5} mol) and DMAC (10 mL) were added to the solution. The solution was stirred in a water bath at 315 K and acetic acid (2 mL) was added to keep acidity of the solution. Sodium cyanoborohydrate (0.772 g, 0.123 mol) was added to the solution and the mixture was stirred until the MS signal for bpy-2NH_2 disappeared. The crude product was purified by a RP-HPLC with CAPCELL PAK C18 MGII column (4.6 mm × 250 mm) (Shiseido) (11% in yield). ^{1}H NMR (400 MHz, D_2O) δ 8.84 (br, 2H; *CH(bpy)*), 8.45 (br, 2H; *CH(bpy)*), 7.85 (br, 2H; *CH(bpy)*), 4.20 – 3.50 (m, 38H; *CH_2 and CH of carbohydrate and linker moieties*); ^{13}C NMR (100 MHz, D_2O) δ 169.1 169.0 158.6 150.4 142.7 122.1 119.9 102.9 102.8 79.0 78.8 78.3 75.4 75.3 72.4 71.0 70.9 70.8 70.6 70.1 68.7 68.6 67.7 66.4 66.3 66.1 61.9 61.8 61.3 61.2 61.1 49.8 47.3; ESI-MS *m/z* (M = $C_{40}H_{64}N_6O_{22}$) 981.3 $[M + H]^+$ (calcd: 981.4), 491.1 $[M + 2H]^{2+}$ (calcd: 491.2).

bpy-2Glc. Using bpy-NH_2 (41 mg, 1.3×10^{-4} mol), β-cellobiose (171 mg, 4.9×10^{-4} mol), and sodium cyanoborohydrate (316 mg, 5.0×10^{-3} mol), bpy-2Gal was synthesized by the same procedure with bpy-2Gal described above (13% in yield). ^{1}H NMR (400 MHz, CD_3OD) δ 8.76 (br, 1H; C*H(bpy)*), 8.38 (br, 1H; C*H(bpy)*), 7.78 (br, 1H; C*H(bpy))* 3.90 – 3.20 (m, 19H; *CH_2 and CH of carbohydrate and linker moieties*); ^{13}C NMR (100 MHz, CD_3OD) δ 168.9, 155.5, 150.3 ,142.6, 122.1, 119.9, 102.3, 78.7, 76.0, 75.4, 73.2, 70.9, 70.6, 69.5, 67.7, 61.9, 60.6, 49.9, 47.3, 36.7; ESI-MS *m/z* (M = $C_{40}H_{64}N_6O_{22}$) 981.3 $[M + H]^+$ (calcd: 981.4), 491.1 $[M + 2H]^{2+}$ (calcd: 491.2).

Ru(bpy-2Gal)$_3$. $[Ru(dmso)_4Cl_2]$ (0.8 mg, 1.7×10^{-6} mol) and 3 equiv. of bpy-2Gal (5.0 mg, 5.0×10^{-6} mol)

were dissolved in H_2O (0.4 mL), then the reaction mixture was refluxed for 13 hours to give a dark red solution. After removing the solvent, the crude product was purified by a RP-HPLC with CAPCELL PAK C18 MGII column (4.6 mm × 250 mm) (Shiseido) with acetonitrile/H_2O (0.1% HCl) to give the titled compound as dark orange solid (quantitative). The compound was used for the binding analysis without purification of diastereomers (Λ- and Δ- forms). ^{1}H NMR (400 MHz, D_2O) δ 8.97 (br, 6H; *CH(bpy)*), 7.92 (br, 6H; *CH(bpy)*), 7.74 (br, 6H; *CH(bpy)*), 4.00 – 3.16 (m, 114H; *CH_2 and CH of carbohydrate and linker moieties*). MALDI-MS *m/z* (M = $C_{120}H_{192}N_{18}O_{66}Ru$) 3042.1 $[M - H]^+$ (calcd: 3042.1).

Ru(bpy-2Glc)$_3$. Using $[Ru(dmso)_4Cl_2]$ (0.8 mg, 1.7×10^{-6} mol) and 3 equiv. of bpy-2Glc (5.0 mg, 5.0×10^{-6} mol), Ru(bpy-2Glc)$_3$ was synthesized by the same procedure with Ru(bpy-2Gal)$_3$ (80% in yield). The compound was used for the binding analysis without purification of diastereomers (Λ- and Δ- forms). ^{1}H NMR (400 MHz, D_2O) δ 9.02 (br, 6H; *CH(bpy)*), 7.93 (br, 6H; *CH(bpy)*), 7.73 (br, 6H; *CH(bpy)*), 4.10 – 3.10 (m, 114H; *CH_2 and CH of carbohydrate and linker moieties*). MALDI-MS *m/z* (M = $C_{120}H_{192}N_{18}O_{66}Ru$) 3042.5 $[M - H]^+$ (calcd: 3042.1).

Ru(bpy)$_2$(bpy-2Gal). Bipyridine (165 mg, 9.6×10^{-4} mol, 2 equiv) and $RuCl_3$ (100 mg, 4.8×10^{-4} mol) were mixed in 5 mL of 1M HCl. The mixture was kept for 1 week, then the precipitation was collected by a suction filtration. The collected dark green solid, Ru(bpy)$_2$Cl$_2$, (5 mg, 1.0×10^{-5} mol) was suspended in 5 mL of H_2O. After adding bpy-2Gal (10 mg, 1.0×10^{-5} mol) and LiCl (3 mg, 7.3×10^{-5} mol), the reaction mixture was refluxed for 20 h. Solution was removed by evaporation to give a crude product. The residue was chromatographed (RP-HPLC) through CAPCELL PAK C18 MGII column (4.6 mm × 250 mm) (Shiseido) with acetonitrile/H_2O (0.1% HCl) as eluent to obtain the titled compound. ^{1}H NMR (400 MHz, D_2O) δ 8.91 (s, 1H; *CH(bpy)*), 8.71 (d, 2H; *CH(bpy)*), 8.15 (m, 3H; *CH(bpy)*), 7.72 (m, 2H; *CH(bpy)*), 7.66 (br, 1H; *CH(bpy)*), 7.35 (t, 2H; *CH(bpy)*), 3.95 - 3.28 (m, 19H; *CH_2 and CH of carbohydrate and linker moieties*); ESI-MS *m/z* (M = $C_{60}H_{80}N_{10}O_{22}Ru$) 697.2 $[M]^{2+}$ (calcd: 697.2).

UV-vis and ^{1}H NMR titration of metal ions to confirm formation of ML$_3$ (M = Fe^{II}, L = bpy-2Gal or bpy-2Glc) complex.

(UV-vis titration) $FeCl_2$ was added to an aqueous solution of bpy-2Gal (1.0×10^{-3} mol/L). At every molar ratio (Fe:bpy-2Gal), UV-vis absorption spectrum was recorded using a quartz cell (path length: 10 mm). Fig. S1 summarizes the absorption spectra. and absorption coefficients following addition of Fe^{II} ions. Since the intensity

change plateued when the molar ratio of Fe:bpy-2Gal reached 1:3, the UV-vis titration experiment supports quantitative formation of ML_3 complex in the examined condition.

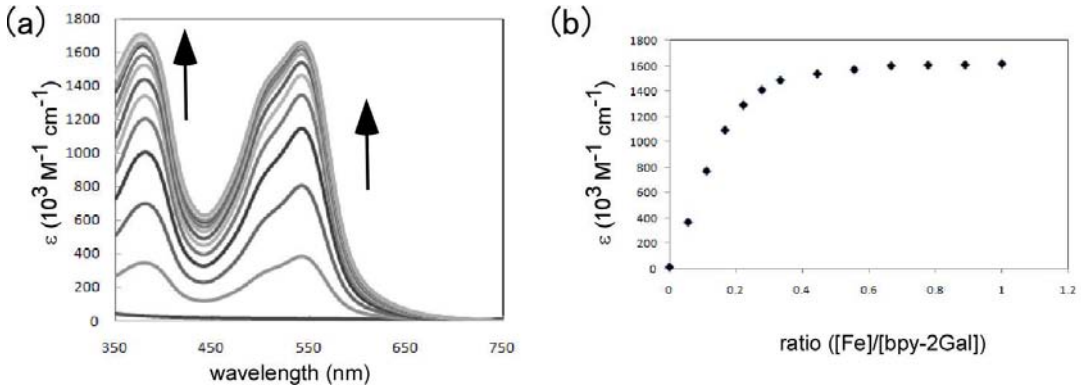

Fig. S1 (a) absorption spectra of bpy-2Gal with Fe^{II} (0 – 1.0×10^{-3} mol/L) and (b) absorption coefficient at 550 nm plotted against the molar ratio (Fe:bpy-2Gal).

(^{1}H NMR titratio) To a solution of bpy-2Gal (1.0×10^{-4} mol/L) in D_2O (0.4 mL), $FeCl_2$ in D_2O was added in stepwise. By addition of $FeCl_2$, a new set of the signals appeared and signals of free ligand decreased. When molar ratio (Fe:bpy-2Gal) reached 1:3, the signals of free ligand disappeared. This titration result supports that bpy-2Gal forms thermodynamically stable ML_3 complex in aqueous solution.

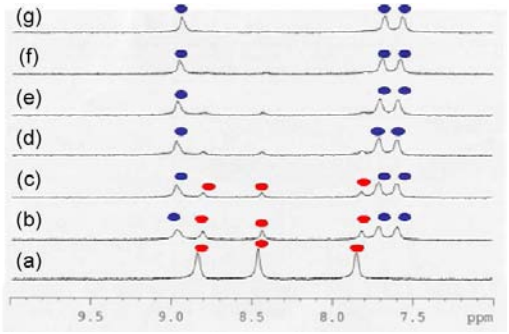

Fig. S2 ^{1}H NMR spectra of bpy-2Gal with Fe^{II} at molar ratio (Fe:bpy-2Gal) (a) 0:3, (b) 1/3:3, (c) 2/3:3, (d) 1:3, (e) 4/3:3, (f) 5/3:3, and (g) 2:3. Red and blue circles represent free bpy-2Gal and $[Fe(bpy\text{-}2Gal)_3]^{2+}$, respectively.

Fluorescence emission intensity and polarization measurements. Emission intensity and fluorescence polarization was recorded on a fluorescence spectrophotometer (HITACHI, F-7000) equipped with an auto-polarization-measurement-system. All spectra of the metalloglycoclusters were measured using 20 μM of the metalloglycocluster with or without 5 μM of lectin in PBS buffer at 298 K. For analyzing binding properties including a dissociation constant, the concentration of the metalloglycocluster was 20 μM and that of PNA or

ConA was varied from 0 – 20 μM. Excitation wavelength was at 468 nm for $Ru(bpy\text{-}2Gal)_3$ and $Ru(bpy\text{-}2Glc)_3$, and at 450 nm for $Ru(bpy)_3$.

Fluorescence polarization (P) was calculated by the equation, $P = (I_{\parallel} - I_{\perp} \times G)/ (I_{\parallel} + I_{\perp} \times G)$, where I is the fluorescence intensity using the polarizer at 0° for excitation ($I_{\parallel}$ and $I_{\perp}$ were observed using the emission polarization filter at 0° and 90°, respectively). The correction factor G was determined by the following equation, $G = i_{\parallel} / i_{\perp}$, where i is the fluorescence intensity using at 90° for excitation ($i_{\parallel}$ and $i_{\perp}$ were observed using the emission polarization filter at 0° and 90°, respectively). For each sample, G factors were defined by measuring $i_{\parallel}$ and $i_{\perp}$ at individual wavelength.

Emission spectral change caused by addition of ethanol.

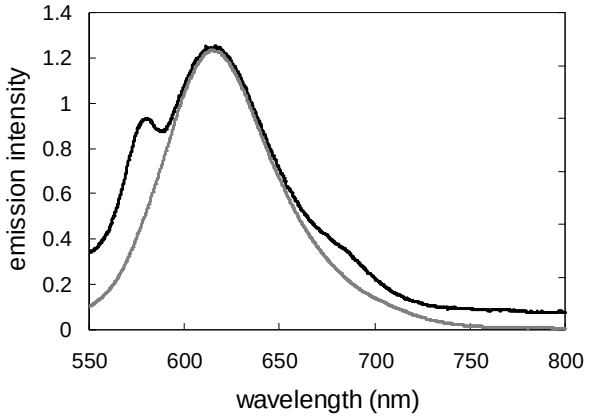

Fig. S3 Emission spectra of 20 μM Ru(bpy-2Gal)$_3$ in PBS (gray) and in PBS with 50% ethanol (black) (λ_{ex}: 468 nm, T: 298 K).

Calculation of the dissociation constant

Dissociation constants (K_d) between PNA and Ru(bpy-2Gal)$_3$, or ConA and Ru(bpy-2Glc)$_3$ were determined with non-linear least squares fitting. Using the fluorescence polarization value, the data was fitted to the following equation, $P/P_{max} = [(K_d + [probe]_{toatal} + [lectin]_{total}) - \{(K_d + [probe]_{total} + [lectin]_{total})^2 - 4[probe]_{total}[lectin]_{total}\}] / 2[probe]_{total}$, where P is the polarization value, P_{max} is the maximum polarization value, $[probe]_{total}$ is the total concentration of Ru(bpy-2Gal)$_3$ or Ru(bpy-2Glc)$_3$, and $[lectin]_{total}$ is the total concentration of PNA or ConA. The simulation results were summarized in Table S1.

Table S1 Results of Non-Linear Squares Fitting using Polarization Value

	P_{max}	K_d (M)	Correlation
Ru(bpy-2Gal)$_3$	0.52	6.1×10^{-6}	0.9996
Ru(bpy-2Glc)$_3$	0.46	1.8×10^{-5}	0.9824

Affinity Evaluation of Tetanus Toxin c-Fragment.

Fluorescence polarization values were recorded on a fluorescence spectrophotometer (HITACHI, F-7000) equipped with an auto-polarization-measurement-system. The metalloglycoclusters, $Ru(bpy\text{-}2Gal)_3$ and $Ru(bpy\text{-}2Glc)_3$, were measured using 2 μM of the PBS solution. Polarization values of the metalloglycocluster with or without 0.05 μM tetanus toxin c-fragment were collected in PBS buffer at 298 K. Excitation wavelength was at 468 nm for $Ru(bpy\text{-}2Gal)_3$ and $Ru(bpy\text{-}2Glc)_3$.

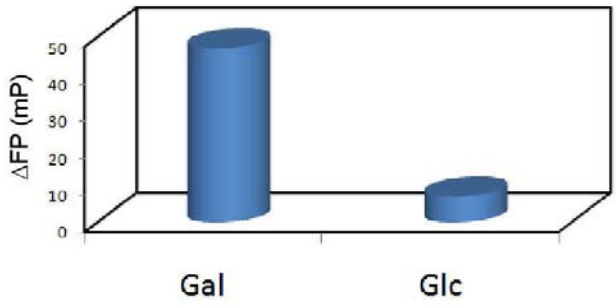

Fig. S4 Changes in fluorescence polarization values of 2 μM $Ru(bpy\text{-}2Gal)_3$ or $Ru(bpy\text{-}2Glc)_3$ in PBS (λ_{ex}: 468 nm, T: 298 K) when 0.05 μM tetanus toxin c-fragment was added.

ARTICLES

In Vivo Imaging of Mesenchymal−Epithelial Transition Factor (c-Met) Expression using an Optical Imaging System

Eun-Mi Kim, Eun-Hye Park, Su-Jin Cheong, Chang-Moon Lee, Hwan-Jeong Jeong,* Dong Wook Kim, Seok Tae Lim, and Myung-Hee Sohn

Department of Nuclear Medicine, Research Institute of Clinical Medicine, Cyclotron Research Center, Chonbuk National University Medical School and Hospital, Jeonju, Jeonbuk, Republic of Korea. Received January 6, 2009; Revised Manuscript Received May 12, 2009

Mesenchymal−epithelial transition factor (c-Met) is a receptor tyrosine kinase that has been shown to be overexpressed and mutated in a variety of malignancies, such as glioma. We have recently found that an ^{125}I-radiolabeled Gly-Gly-Gly (GGG)- or 8-aminooctanoic acid (AOC)-containing c-Met binding peptide (cMBP) specifically targets c-Met receptor *in vivo* and *in vitro*. In this report, cyanine dye 5.5 (Cy5.5)-conjugated GGG- or AOC-containing cMBPs were evaluated in human cancer cell xenografts in order to investigate the possibility of c-Met receptor targeting using an optical imaging system. The receptor binding affinity of Cy5.5-conjugated peptides was tested in 96-well plates coated with a c-Met/Fc chimeric protein. Optical imaging studies were performed in U87MG and Ramos bearing athymic mice. The binding affinities of Cy5.5-conjugated GGG- or AOC-containing cMBPs were determined to be 0.318 and 0.342 μM, respectively. Confocal images show that Cy5.5-conjugated peptides bound mainly to the cell surface and that peptide binding was clearly inhibited by free cMBP. Subcutaneous U87MG tumors were clearly visualized with each of the two fluorescent probes. Of the two, cMBP-AOC−Cy5.5 displayed higher tumor uptake and tumor-to-normal tissue ratios at 10 min to 24 h postinjection in the U87MG tumor model. For the *in vivo* blocking study, cMBP-AOC−Cy5.5 (4 nmol) was co-injected with cold cMBP (0.13 μmol) into the U87MG xenograft mice. Image-based tumoral uptake decreased up to approximately 35%. These results suggest that Cy5.5-conjugated cMBP could potentially be used to detect c-Met-positive cancers *in vivo*. However, additional modifications to this optical imaging agent are needed to further improve its efficacy.

INTRODUCTION

As new disease-specific imaging targets (e.g., cell surface receptors) are being identified, demand for targeted imaging agents is increasing. Peptides are receiving much attention for *in vivo* cancer detection because excellent tissue-specific uptake can be achieved (*1*). Mesenchymal−epithelial transition factor (c-Met) is expressed by most carcinomas, and its elevated expression relative to normal tissue has been detected in a number of cancers including lung, breast, colorectal, prostate, pancreatic, head and neck, gastric, hepatocellular, ovarian, renal, glioma, melanoma, and a number of sarcomas (*2*−*5*). Receptor tyrosine kinases are important therapeutic targets for antineoplastic molecularly targeted therapies. In this respect, the c-Met receptor appears to be a good candidate for detection of cancer. Recently, Kim et al. have reported that an epitope-mimicking peptide, NH_2-Lys^1-Ser^2-Leu^3-Ser^4-Arg^5-His^6-Asp^7-His^8-Ile^9-His^{10}-His^{11}-His^{12}-Ac (c-Met binding peptide, cMBP), from a phage display of a combinatorial peptide library, binds to c-Met and inhibits the HGF−c-Met interaction (*6*).

Emerging optical imaging techniques have recently proven to be powerful tools for *in vivo* molecular imaging of specific target structures. Although poor light penetration through tissues makes their utilization in humans difficult, these techniques have been successfully applied in preclinical small animal research (*7*−*9*). Near-infrared (NIR) fluorescence imaging, which uses neither ionizing radiation nor radioactive materials, is emerging as a complement to nuclear imaging methods. A relatively low-cost, safe, and easy-to-use NIR fluorescence imaging system has proven to be a powerful tool for noninvasive imaging of diseases in preclinical models such as rodents (*10*). The NIR fluorescent dye cyanine dye 5.5 (Cy5.5) has proven to be a promising *in vivo* agent. It has an absorbance maximum at 675 nm and emission maximum at 694 nm and can be detected *in vivo* at subnanomole quantities and at depths sufficient for experimental and clinical imaging (*11*−*13*).

We have reported recently that an ^{125}I-radiolabeled cMBP targets c-Met receptor both *in vitro* and *in vivo* (*14*). We were therefore interested in exploring the possibility that tumor-specific optical images could be obtained using optical dye conjugated cMBP. In this study, we report on the targeting of c-Met receptor in human cancer cell xenografted mice using Cy5.5-conjugated cMBPs containing 8-aminooctanoic acid (AOC) or Gly-Gly-Gly (GGG) linkers.

* To whom correspondence should be addressed. Mailing address: Department of Nuclear Medicine, Chonbuk National University Medical School, 634-18 Geumam-2 dong, Duckjin-gu, Jeonju, Jeonbuk 561-712, Republic of Korea Tel: 82-63-250-2171. Fax: 82-63-255-1172. E-mail: jayjeong@chonbuk.ac.kr.

10.1021/bc8005539 CCC: $40.75 © 2009 American Chemical Society
Published on Web 06/17/2009

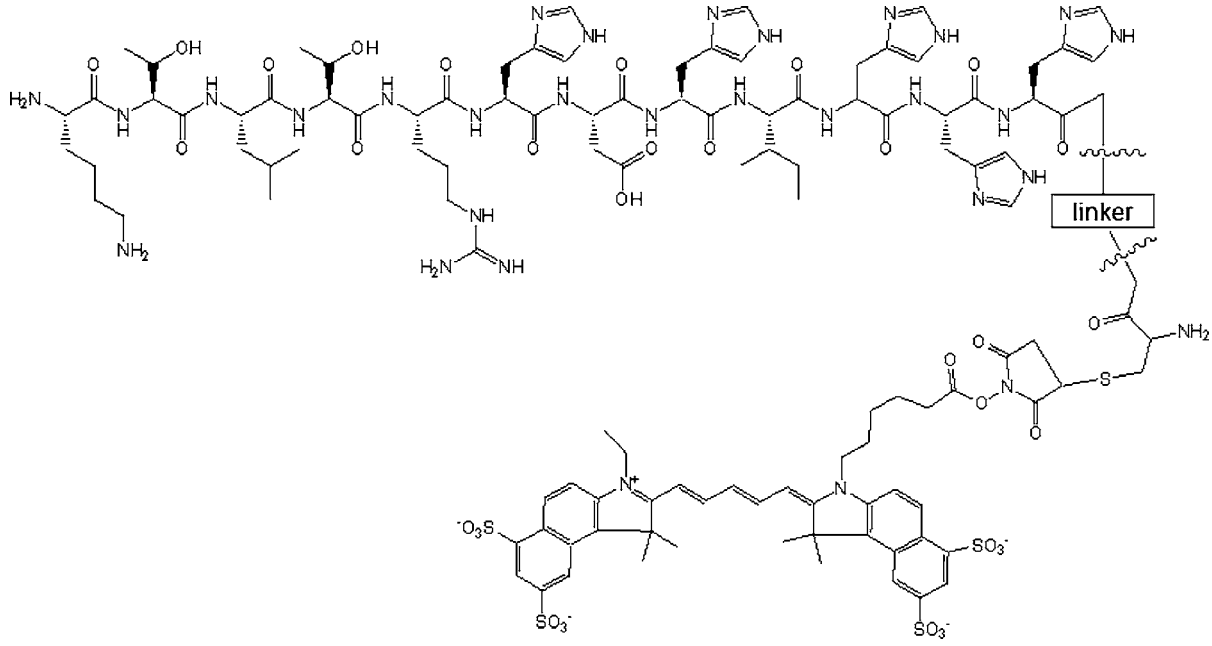

Figure 1. Chemical structure of the cMBP-X−Cy5.5 conjugates. Linker (X) indicates 8-aminooctanoic acid (AOC) or Gly-Gly-Gly (GGG).

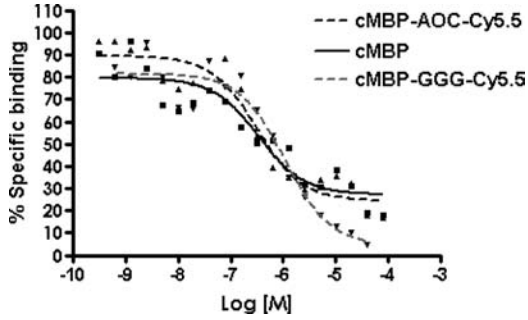

Figure 2. Competitive c-Met receptor assay for cMBP-GGG−Cy5.5, cMBP-AOC−Cy5.5, and cMBP tested with the c-Met/Fc chimeric protein. All experiments were done in duplicate. The IC_{50} values for cMBP-GGG−Cy5.5, cMBP-AOC−Cy5.5, and cMBP were determined to be 318 nM, 342 nM, and 1.5 μM, respectively.

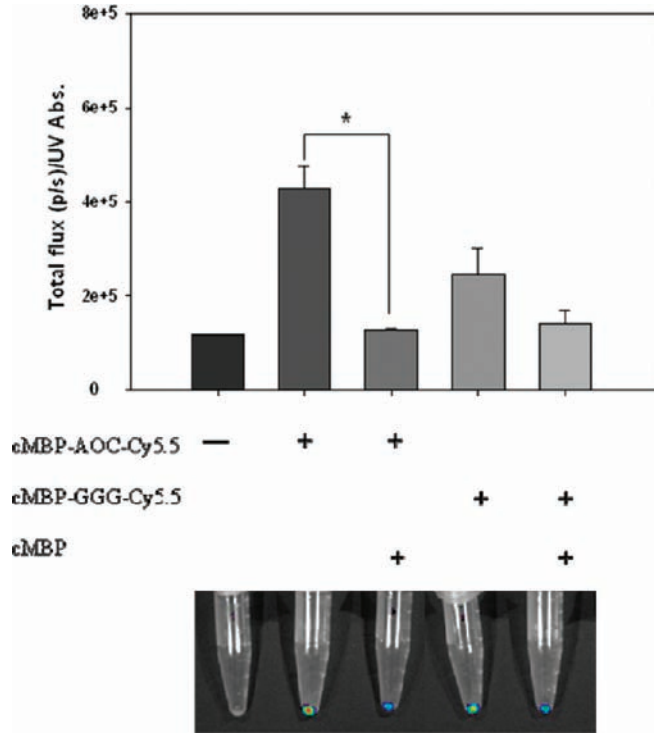

Figure 3. Cellular uptake of cMBP-GGG−Cy5.5 or cMBP-AOC−Cy5.5 in U87MG cells. Cells were incubated with cMBP-AOC−Cy5.5 or cMBP-GGG−Cy5.5 (2 nmol), and cMBP was used as inhibitor (86 nmol). The representative fluorescence images were acquired using an optical imaging system. The data are presented as the mean ± SD (* indicates $P < 0.05$).

EXPERIMENTAL PROCEDURES

Reagents and Chemicals. $Na^{125}I$ was obtained from Perkin-Elmer Life Science, Inc. (Boston, MA). cMBP, cMBP-GGG-SC, and cMBP-AOC-C were synthesized by Peptron using standard Fmoc chemistry (Seoul, Korea). The purity of all samples was over 90%. Cy5.5−maleimide was purchased from GE healthcare (Uppsala, Sweden).

Synthesis and Characterization of cMBP-X−Cy5.5. c-Met binding peptides, cMBP-GGG-SC (1 mg, 0.53 μmol, MW = 1863) and cMBP-AOC-C (1 mg, 0.57 μmol, MW = 1747), dissolved in phosphate-buffered saline (PBS, pH 7.2, EDTA 5 mM) were mixed with Cy5.5−maleimide (0.618 μg, 0.59 μmol, MW = 1152) in the dark at room temperature for 6 h. The final product was lyophilized and dried. Purification of the crude product was carried out on a MWCO 2000 dialysis cassette (Pierce, Rockford, IL). The molecular mass was determined by matrix-assisted laser desorption/ionization time-of-flight mass spectrometry (MALDI-TOF-MS) (KBSI, Jeonju, Korea). The analytic reversed-phase high-performance liquid chromatography (RP-HPLC) method was performed with a spectra system SCM100 degasser, a P4000 pump, and an UV/vis 3000 detector (Thermo Scientific, Waltham, MA). The absorbance was monitored at 218 nm and a Hypersil gold column (250 mm × 4.6 mm, Thermo Scientific) was used. ChromQuest 4.2 software was used to record chromatograms. The flow was 1 mL/min, with the mobile phase varying from 97% solvent A (0.1% trifluoroacetic acid in water) and 3% solvent B (0.1% trifluoroacetic acid in acetonitrile; 0−4 min) to 40% solvent B for 10 min, 50% solvent B for 15 min, 40% solvent B for 10 min, and 90% solvent B for 25 min. The final products, cMBP-GGG-

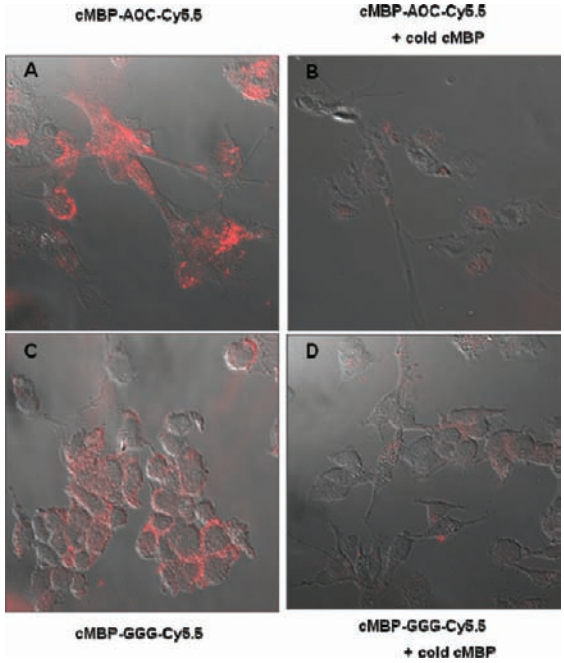

Figure 4. NIR fluorescence images of U87MG cells were obtained after incubation for 1 h in the presence of cMBP-AOC−Cy5.5 or cMBP-GGG−Cy5.5 (2 nmol) with (B, D) or without (A, C) a blocking dose of cMBP peptide (86 nmol). Cellular uptake was blocked by cold peptide. Blocking images demonstrate the high c-Met receptor specificity of Cy5.5-conjugated cMBPs.

SC−Cy5.5 and cMBP-AOC-C−Cy5.5 are referred to as cMBP-GGG−Cy5.5 and cMBP-AOC−Cy5.5, respectively. The absorption and fluorescence emission characteristics of Cy5.5-conjugated cMBP peptides were measured in H_2O using a UV−vis spectrophotometer (HP8453, Hewlett-Packard, Palo Alto, CA).

Determination of log *P*. Approximately 370 kBq of ^{125}I-cMBP-GGG−Cy5.5 and ^{125}I-cMBP-AOC−Cy5.5 in 500 μL of PBS (pH 7.4) was added to 500 μL of octanol in a microcentrifuge tube. The mixture was vigorously vortexed for 1 min at room temperature. The two phases were separated by centrifugation at 12 500 rpm, and 200 μL aliquots of both layers were counted using a γ-counter (Packard, Meriden, CT). The experiment was carried out five times. The value was expressed as mean ± SD.

Cell Lines. Human glioblastoma cell line U87MG (c-Met receptor positive), nasopharyngeal carcinoma cell line KB (c-Met receptor positive), and B-lymphoma cell line Ramos (c-Met receptor negative) (*15*) were obtained from the Korean cell line bank (Seoul, South Korea) and maintained at 37 °C in a humidified atmosphere containing 5% CO_2 in RPMI-1640 medium with 10% fetal bovine serum (GIBCO, Carlsbad, CA).

***In Vitro* Binding Assay and Cellular Uptake.** cMet/Fc chimeric protein was purchased from R&D Systems (Minneapolis, MN) and dissolved in coating buffer (carbonate buffer, pH 9.75). The cMet/Fc chimeric protein was coated onto 96-well plates (16 h, 4 °C), and plates were blocked with blocking buffer (Pierce, Rockford, IL). After washing with washing buffer (PBS, 0.1% Tween 20), ^{125}I-cMBP was added to the 96-well plates with serially diluted peptides cMBP, cMBP-AOC−Cy5.5, or cMBP-GGG−Cy5.5 at concentrations ranging from 0.04 nM to 150 μM. The plates were then incubated for 2 h at 37 °C and washed and dried before 0.1 mL of 2 N NaOH was added to each well to facilitate cell lysis. Lysates were collected and counted on a γ-counter. The 50% inhibitory concentration (IC_{50}) value for the displacement binding was calculated by nonlinear regression analysis (sigmoidal dose response equation) using the GraphPad Prism 4.0 computer-fitting program (Graph-Pad Software, San Diego, CA). All the experiments were done in duplicate.

For *in vitro* studies, 5×10^5 U87MG cells were seeded into 6 cm dishes. The next day, media was replaced with serum-free media. Cells were incubated with cMBP-AOC−Cy5.5 or cMBP-GGG−Cy5.5 (2 nmol) for 1 h. For blocking studies, cells were cotreated with cMBP-AOC−Cy5.5 or cMBP-GGG−Cy5.5 and nonfluorescent cMBP peptide (86 nmol). After incubation, the cells were detached with trypsin and collected. Cell fluorescence was acquired using an IVIS system (f-stop = 1, binning = 8, field of view = 12.8, exposure time = 1 s; Caliper Lifescience, Hopkinton, MA). Protein amounts were determined by a BCA assay (Pierce, Rockford, IL).

Confocal Microscopy. For laser confocal microscopy, U87MG and KB cells were grown on a 12-mm microscope cover glass (Marlenfeld GmbH, Germany) and incubated at 37 °C in the presence of cMBP-AOC−Cy5.5 or cMBP-GGG−Cy5.5 (2 nmol) for 1 h. For blocking studies, cells were cotreated with cMBP-AOC−Cy5.5 or cMBP-GGG−Cy5.5 and nonfluorescent cMBP peptide (86 nmol). Cells were washed in ice-cold PBS and examined with a HFT405/488/543/633 dichroic beam splitter, with simultaneous 488-nm excitation, 505−530 nm emission for autofluorescence, 633-nm excitation, and ChS1 636−754 nm emission for Cy5.5 and both lasers for (nonconfocal) bright-field transmitted light (LSM 510META, Carl Zeiss, Germany).

Tumor Xenografts. All animal experiments were performed in compliance with the Institutional Animal Care and Use Committee for animal treatment of Chonbuk National University. Female athymic nude mice (4-wk, *nu*/*nu*) were obtained from Orient-Bio (Seoul, Korea). Mice were anesthetized by subcutaneous injection with a mixture of ketamine (50 mg/kg) and xylazine (10 mg/kg). After sedation, glioblastoma (U87MG) and lymphoma (Ramos) tumors were established by subcutaneous injection in the right flank with 5×10^6 tumor cells mixed in Matrigel. When the tumors reached 0.7 or 1 cm in length, the tumor-bearing mice were subjected to *in vivo* imaging studies.

***In Vivo* Optical Imaging.** *In vivo* fluorescence imaging was performed with an IVIS spectrum small-animal *in vivo* imaging system (Caliper Lifescience, Hopkinton, MA), that has both bioluminescence and fluorescence capabilities. U87MG xenograft mice were given injections of cMBP-GGG−Cy5.5 or cMBP-AOC−Cy5.5 (4 nmol) via their tail vein and were anesthetized with 1.5−2% isoflurane before being placed in the camera bed positioned laterally and imaged at various time points postinjection while remaining sedated (f-stop = 2, binning = 8, field of view = 12.8, exposure time = 1 s, sample depth = 1.5 cm). Ramos xenograft mice were given injections of cMBP-AOC−Cy5.5 (4 nmol). For *in vivo* blocking studies, U87MG xenograft mice received an injection of a mixed sample of cMBP-AOC−Cy5.5 (4 nmol) and cold cMBP (0.13 μmol). Images were acquired at various time points after injection. After 2 h, the tumor and major tissue and organs were dissected, and the fluorescence image was obtained (f-stop = 2, binning = 8, field of view = 12.8, exposure time = 1 s, sample depth = 1.5 cm). Excitation filters were 640, 604, and 570 nm, and the emission filter was 700 nm. After three images were acquired, background subtraction was performed using Living Image software (Caliper Lifescience, Hopkinton, MA).

RNA Extraction and Reverse Transcriptase Polymerase Chain Reaction (RT-PCR). Total RNA from cells and tumor tissue was extracted using Trizol reagent according to the manufacturer's instructions (Invitrogen, Carlsbad, CA) and quantified based on the measured absorbance at 260 and 280

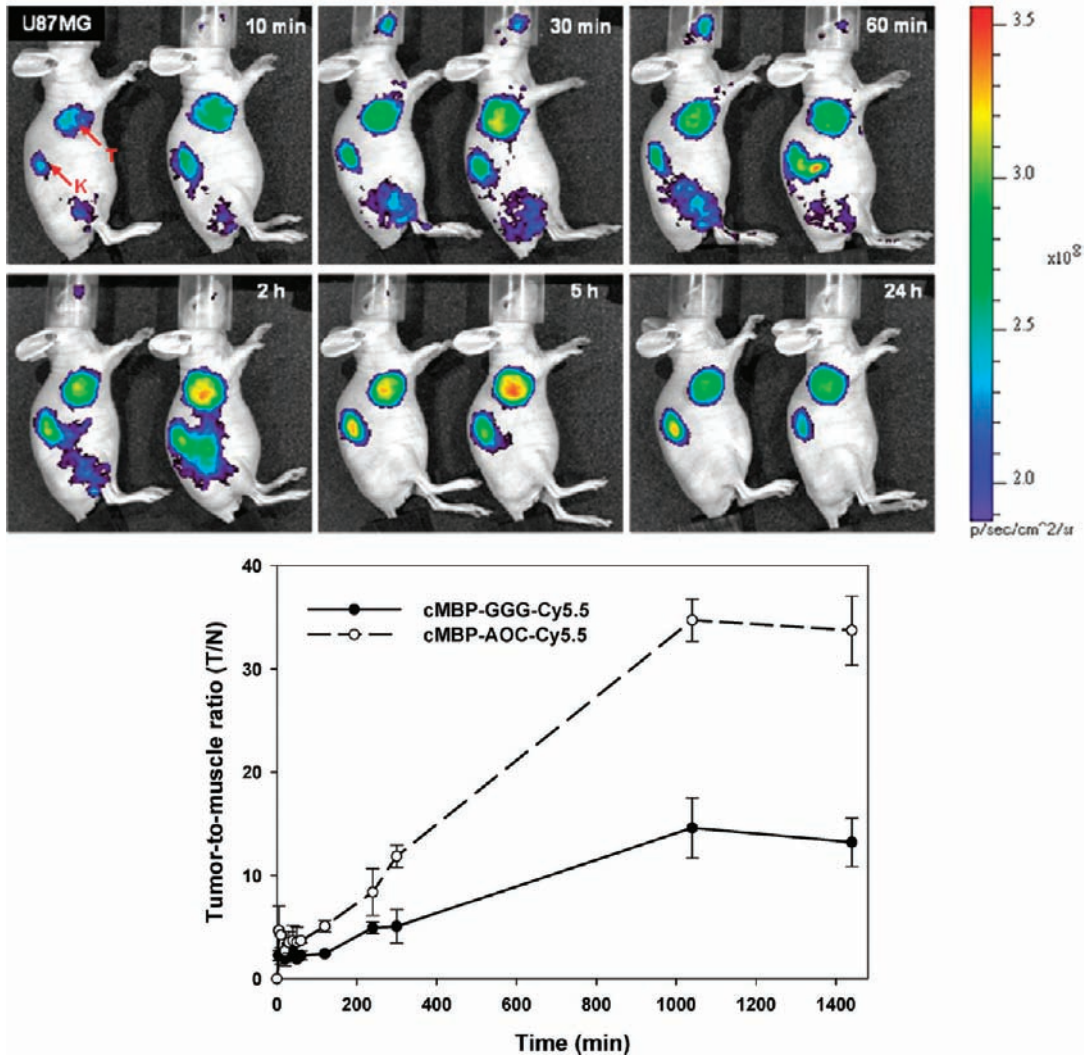

Figure 5. *In vivo* fluorescence imaging of athymic nude mice bearing U87MG xenografts after iv injection of 4 nmol of cMBP-GGG−Cy5.5 (left) or cMBP-AOC−Cy5.5 (right). Red arrows indicate the tumor (T) or kidney (K). All NIR fluorescence images were acquired with a 1-s exposure time at 10 min, 30 min, 60 min, 2 h, 5 h, and 24 h, and background fluorescence was subtracted. Fluorescence signal from Cy5.5 was pseudocolored red. The tumor-to-muscle (T/M) ratio as a function of time postadministration of cMBP-GGG−Cy5.5 (●) or cMBP-AOC−Cy5.5 (○) is shown in the bottom panel.

nm. RT-PCR procedures for c-Met were performed as described previously by Kim et al. (*14*).

Data Processing and Statistics. All data are given as mean ± SD. Statistical analysis was performed using one-way analysis of variance (ANOVA). Statistical significance was assigned for P values <0.05. For determining tumor contrast, mean fluorescence intensities (average radiance, p/(s·cm^2·sr)) of the tumor area, normal muscle area, and kidney were calculated by the region-of-interest (ROI) function of Living Image software.

RESULTS

Synthesis and Characterization of cMBP-X−Cy5.5. The synthesis of cMBP-X−Cy5.5, where X stands for linker, was achieved through conjugation of Cy5.5−maleimide with the thiol group of the cysteine residue of the cMBP-GGG-SC or cMBP-AOC-C peptides. The chemical structures of cMBP-X−Cy5.5 are shown in Figure 1. The final products were purified by dialysis. The purity of Cy5.5-conjugated peptides was over 90% by analytical RP-HPLC. The yield of Cy5.5-labeled peptides were typically over 65%. The retention times on analytical RP-HPLC for cMBP-GGG−Cy5.5 and cMBP-AOC−Cy5.5 were 9.40 and 9.91 min, respectively. The purified Cy5.5 conjugates were characterized by MALDI-TOF-MS: GGG-containing cMBP-X−Cy5.5, m/z = 2989 for $[M + H]^+$ (calculated MW = 2990); AOC-containing cMBP-X−Cy5.5: m/z = 2874 for $[M + H]^+$ (calculated MW = 2876). The absorption and fluorescence emission characteristics of Cy5.5-labeled cMBP peptide conjugates were identical to those of free Cy5.5; the spectra were measured in H_2O using a UV−vis spectrophotometer (Figure S1, Supporting Information). The octanol−water partition coefficient (log P) for cMBP-GGG−Cy5.5 and cMBP-AOC−Cy5.5 was −1.028 ± 0.08 and −1.109 ± 0.06.

***In Vitro* Binding Assay and Cellular Uptake.** The receptor binding affinity assay for Cy5.5-conjugated cMBPs for c-Met receptor was carried out using a cMet/Fc chimeric recombinant protein. We compared the receptor binding affinity of the two probes by performing competitive displacement studies with ^{125}I-cMBP as the radioligand (Figure 2). The IC_{50} values for cMBP, cMBP-GGG−Cy5.5, and cMBP-AOC−Cy5.5 were 1.5 μM, 318 nM, and 342 nM, respectively. The binding affinity of the Cy5.5-conjugated cMBPs was in the nanomolar range and lower than nonconjugated cMBPs. The IC_{50} values using U87MG cells

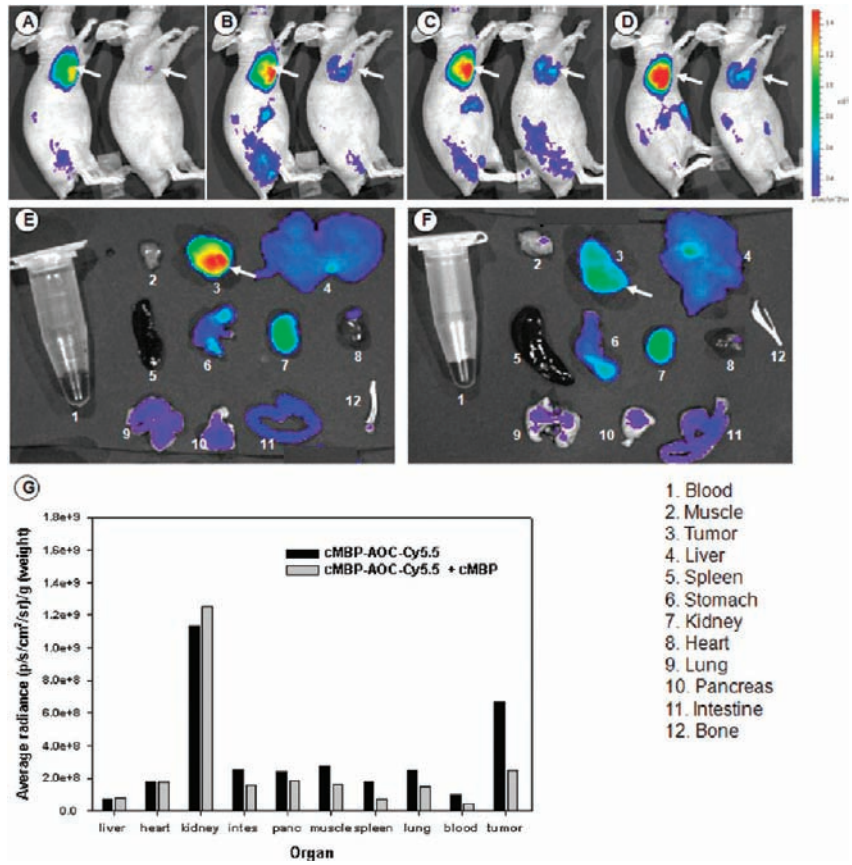

Figure 6. Blocking images in U87MG tumor-bearing nude mice: 10 min (A), 30 min (B), 60 min (C), 120 min (D). The left image shows the result after injection of cMBP-AOC−Cy5.5 (2 nmol), and the right image shows the result after co-injection of cMBP-AOC−Cy5.5 (4 nmol) and cMBP (0.13 μmol). After acquisition, *ex vivo* images also were acquired. Representative images of dissected organs of a cMBP-AOC−Cy5.5-injected mouse (E) and a mouse cotreated with inhibitor (F) are shown. The tumors are indicated with white arrows. Tumoral uptake of cMBP-AOC−Cy5.5 was clearly inhibited by free cMBP peptide. Flux (p/(s·cm^2·sr)) was divided by the weight of organ (G) (intes = intestine, panc = pancreas).

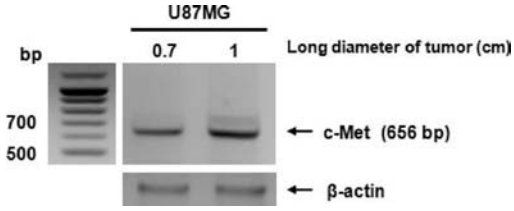

Figure 7. Expression of the c-Met receptor in U87MG tumor tissue was determined by RT-PCR. Fragments of the 656 bp transcript were detected to confirm the expression of c-Met mRNA in U87MG tumor tissue. β-actin was used as an internal loading control. The c-Met-to-actin ratio was 0.74 in the 0.7 cm tumor and 1.24 in the 1 cm tumor ($n = 3$).

of cMBP-GGG-SC, and cMBP-AOC-C were 65 and 85.3 nM, respectively. These values were previously reported elsewhere (*14*).

The cellular uptake is shown in Figure 3. cMBP-AOC−Cy5.5 exhibited a higher total flux/UV absorbance ratio than cMBP-GGG−Cy5.5 in U87MG cells. cMBP-AOC−Cy5.5 was significantly inhibited by nonfluorescent cMBP. cMBP-GGG−Cy5.5 uptake by U87MG cells was not significantly inhibited by cMBP.

Confocal Microscopy. To determine the c-Met receptor specificity and cellular binding of the Cy5.5-conjugated cMBPs, the peptides were incubated with U87MG, and images were taken with a confocal microscope (Figure 4). Cy5.5-conjugated cMBPs were further analyzed in the presence of a blocking dose of free cMBP peptide. cMBP-GGG−Cy5.5 or cMBP-AOC−Cy5.5 bound mainly to the cell surface of U87MG cells (A, C). More cMBP-AOC−Cy5.5 was bound than cMBP-GGG−Cy5.5. This pattern was similar in KB cells and is also correlated with cellular uptake images of Figure 3. The bound peptides on the cell surface were inhibited by cotreatment with peptides (B, D). KB cells also showed specific binding to the cell surface (Figure S2, Supporting Information).

***In Vivo* Optical Imaging.** In U87MG tumor models, cMBP-AOC−Cy5.5 showed a higher tumor-to-muscle ratio than cMBP-GGG−Cy5.5. The tumor-to-kidney (T/N) and tumor-to-muscle (T/M) ratio was calculated and is shown in Figure 5. Receptor specificities of the probes were validated by a blocking experiment. A U87MG tumor xenograft mouse was injected with cMBP-AOC−Cy5.5, and another was injected with a mixture of cMBP-AOC−Cy5.5 and free peptide. As shown in Figure 6, tumoral uptake *in vivo* was clearly inhibited by free peptide. To further characterize the distribution of cMBP-AOC−Cy5.5 in U87MG *in vivo*, the tumor-bearing mice were sacrificed after noninvasive imaging at 2 h. Tumor fluorescence intensity (p/(s·cm^2·sr·g)) was successfully reduced from 6.62×10^8 to 2.4×10^8 (Figures 6E−G). On the other hand, cMBP-AOC−Cy5.5 was not accumulated in the tumor site in the Ramos tumor model (Figure S3, Supporting Information).

RNA Extraction and RT-PCR. The expression of c-Met mRNA in U87MG and Ramos cells was compared (Figure S4, Supporting Information). The expression of c-Met mRNA in Ramos cells was very weak compared with that of U87MG cells. To confirm the expression of c-Met mRNA in U87MG tumor tissue, total RNA was isolated and analyzed. As shown in Figure 7B, c-Met mRNA was expressed in U87MG tumor tissue, as

depicted by the c-Met/actin ratio, which was higher in large size tumors. The ratio correlated well with tumor uptake *in vivo*.

DISCUSSION

Since Met was discovered as an oncogene two decades ago (*16*), the HGF/c-Met signaling pathway has come into the spotlight as a promising therapeutic target for inhibiting tumor growth. Activation or upregulation of c-Met is a negative prognostic indicator in patients with various carcinomas, multiple myeloma, or glioma (*17*−*21*). For these reasons, several strategies to block the activation of Met are under development, such as the use of Met/HGF inhibitors, tyrosine kinase inhibitors, or monoclonal antibodies, and some of these compounds have already been used in clinical trials (*22*−*27*). Together with development of therapeutic agents, noninvasive biomarkers suitable for monitoring and predicting therapeutic response are needed. Recently, other groups showed ^{89}Zr-labeled c-Met antibody for PET imaging (*28*) and gadolinium-labeled c-Met antibody for MRI imaging (*29*). However, optical imaging has not been studied, and in this study, we studied the possibility of the c-Met receptor target using an optical imaging agent.

We reported previously that ^{125}I-radiolabeled cMBP bound specifically to U87MG cells and tumors. This peptide showed unacceptably rapid elimination from the body, so modification was needed to improve its pharmacokinetics. We hypothesized that the introduction of hydrophobic amino acids or aliphatic carbon chain linkers would help reduce radioactive accumulation in the kidney and rapid elimination. GGG or AOC linker was added to the cMBP peptide. This study showed that the GGG linker containing peptide had a higher tumor-to-muscle ratio than the peptide with the AOC linker. Thus, changes in the linker can have a profound effect on tumor uptake (*14*).

On the basis of these results, we also studied whether Cy5.5-conjugated cMBPs can target the c-Met receptor *in vitro* and *in vivo*. The present study demonstrated that the NIR dye Cy5.5-conjugated cMBPs are able to target c-Met receptor *in vitro* and *in vivo* specifically. The molecular mass of Cy5.5 is 1152 g/mol. After conjugation to the peptides, the molecular mass of the product is approximately 3000 g/mol. This is large enough to be separated from free Cy5.5 by the dialysis method. We purified the peptides by dialysis and used RP-HPLC to check the purity of Cy5.5-conjugated cMBPs. RP chromatograms show a single species with retention times of 9.4 min for GGG and 9.91 min for AOC. Free Cy5.5 and unbound peptides were removed effectively by dialysis. Both Cy5.5 conjugates showed similar binding affinity. The IC_{50} of cMBP-GGG−Cy5.5 and cMBP-AOC−Cy5.5 was 318 and 342 nM, respectively, which is higher than the value for nonconjugated native cMBP peptides (cMBP-GGG-SC = 65 nM; cMBP-AOC-C = 85.3 nM). Although the binding affinities were similar, their pharmacokinetic properties were influenced by the linker. The RP-HPLC retention times reflect the inherent hydrophilic/hydrophobic nature of the two conjugates and correlate well with the *in vivo* distribution.

To demonstrate the c-Met specificity and subcellular localization of cMBP-GGG−Cy5.5 and cMBP-AOC−Cy5.5, the peptides were incubated with U87MG cells, and images were taken with a fluorescent confocal microscope. cMBP-GGG−Cy5.5 and cMBP-AOC−Cy5.5 bound predominantly to the cell surface (Figure 4A,C) and were assumed not to be taken up by receptor-mediated endocytosis, despite their large size. These results correlate well with our previous result that ^{125}I-radiolabeled cMBP did not show cellular internalization (*14*). Binding of the peptides was clearly inhibited by free cMBP peptides (86 nmol) (Figure 4B,D). To test whether the cell surface binding phenomenon was general, *in vitro* cellular uptake was also tested in KB nasopharyngeal epidermal carcinoma cell line. This cell line showed c-Met expression like U87MG cells, and similar to U87MG cells, cMBP-GGG−Cy5.5 and cMBP-AOC−Cy5.5 bound specifically to the KB cell surface (Figure S2, Supporting Information).

To acquire NIR fluorescence images, 640, 604, and 570 nm excitation filters and a 700 nm emission filter were used. Even without the optic dye, the mouse body shows autofluorescence. For this reason, 604 and 570 nm excitation filters were used to remove background signal. After three images were acquired, the background subtraction was performed using Living Image software. The background autofluorescence signal was effectively removed to obtain clearer images. NIR fluorescence images in tumor xenograft mice with cMBP-GGG−Cy5.5 or cMBP-AOC−Cy5.5 show apparent tumor uptake. cMBP-AOC−Cy5.5 showed higher tumor uptake than cMBP-GGG−Cy5.5 in U87MG xenograft mice. As shown in Figure 5, the tumor-to-muscle ratio difference of the two Cy5.5-conjugated peptides become more obvious over time (33.71 ± 3.34 for GGG and 13.21 ± 2.33 for AOC, at 24 h). cMBP-GGG−Cy5.5 showed higher kidney uptake than cMBP-AOC−Cy5.5. Both showed fast elimination via the bladder. In a previous study, ^{125}I-radiolabeled cMBP-GGG-SC showed higher tumor uptake than cMBP-AOC-C. However, the tumoral uptake pattern changed after Cy5.5 conjugation. Also ^{125}I-radiolabeled cMBPs showed high pancreatic uptake, but Cy5.5 conjugates did not show this. The differences in tumor and pancreatic retention might be accounted for by factors relating to differences in the size or properties of Cy5.5. Lower pancreas uptake might be caused by Cy5.5 hydrolysis from the peptides but in the case of ^{125}I-radiolabeled cMBPs, the radiolabel taken up by the pancreas was ^{125}I-radiolabeled histidine or histidine as a free amino acids (*14*). Since the octanol−water partition coefficients of the cMBP-GGG-SC and cMBP-AOC−Cy5.5 were similar, the greater tumor uptake of the cMBP-AOC−Cy5.5 could be attributable to the fact that this conjugate showed increased interaction with tumor cells (Figure 5). Tumor uptake was specific, because the signal decreased upon administration of the blocking agent to 2 h as seen in *ex vivo* images with reduced tumor signal. However, there was also a reduction in signal accumulation in noncancerous organs, such as the intestine, pancreas, lungs, liver, muscle, and spleen. The blockage in these organs suggests that the uptake of cMBPs is at least partially c-Met receptor mediated. c-Met receptors are widely expressed in a variety of tissues, and their expression is normally confined to cells of epithelial and mesenchymal origin (*30*, *31*). The glioma uptake of cMBP-AOC−Cy5.5 is significantly higher than its lymphoma tumor uptake. Tumor-to-muscle ratio in lymphoma mice was 1.05, 0.56, 0.51, and 0.21 at 10, 30, 60 min and 2 h, respectively. This is consistent with the result that the U87MG glioma cells have a higher level of c-Met receptor expression than Ramos lymphoma cells (Figures S3 and S4, Supporting Information).

In conclusion, we evaluated the Cy5.5-conjugated c-Met receptor binding peptide analogues with amino acid or aliphatic carbon chain linkers and found that the addition of a lipophilic carbon linker improved their *in vitro* and *in vivo* characteristics. However, additional modifications to the linkers are needed to further improve these optical imaging agents.

ACKNOWLEDGMENT

This work was supported by grants from the Nuclear Research & Development Program of the Korea Science and Engineering Foundation (KOSEF) (Grants M20702000003-08N0200-00310 and M20701005301-07B0100-30110) and National R&D Program for Cancer Control, Ministry of Health, Welfare and Family affairs, Republic of Korea (Grant 0620220).

Supporting Information Available: UV−vis spectra of cMBP-AOC−Cy5.5 and cMBP-GGG−Cy5.5, confocal images of KB cells, NIR fluorescence images of Ramos xenograft mice, and the expression c-Met mRNA in Ramos cells and U87MG cells. This material is available free of charge via the Internet at http://pubs.acs.org.

LITERATURE CITED

(1) Okarvi, S. M. (2004) Peptide-based radiopharmaceuticals: Future tools for diagnostic imaging of cancers and other diseases. *Med. Res. Rev. 24*, 357–397.

(2) Christensen, J. G., Burrows, J., and Salgia, R. (2005) c-Met as a target for human cancer and characterization of inhibitors for therapeutic intervention. *Cancer Lett. 225*, 1–26.

(3) Birchmeier, C., Birchmeier, W., Gherardi, E., and Vande Woude, G. F. (2003) Met, metastasis, motility and more. *Nat. Rev. Mol. Cell Biol. 4*, 915–925.

(4) Maulik, G., Shrikhande, A., Kijima, T., Ma, P. C., Morrison, P. T., and Salgia, R. (2002) Role of the hepatocyte growth factor receptor, c-Met, in oncogenesis and potential for therapeutic inhibition. *Cytokine Growth Factor Rev. 13*, 41–59.

(5) Yang, Y., Wislez, M., Fujimoto, N., Prudkin, L., Izzo, J. G., Uno, F., Ji, L., Hanna, A. E., Langley, R. R., Liu, D., Johnson, F. M., Wistuba, I., and Kurie, J. M. (2008) A selective small molecule inhibitor of c-Met, PHA-665752, reverses lung premalignancy induced by mutant K-ras. *Mol. Cancer Ther. 7*, 952–960.

(6) Kim, K., Hur, Y., Ryu, E. K., Rhim, J. H., Choi, C. Y., Baek, C. M., Lee, J. H., and Chung, J. (2007) A neutralizable epitope is induced on HGF upon its interaction with its receptor cMet. *Biochem. Biophy. Res. Commun. 354*, 115–121.

(7) Hsu, A. R., Hou, L. C., Veeravagu, A., Greve, J. M., Vogel, H., Tse, V., and Chen, X. (2004) *In vivo* near-infrared fluorescence imaging of integrin $\alpha v\beta 3$ in brain tumor xenografts. *Cancer Res. 64*, 8009–8014.

(8) Levi, J., Cheng, Z., Gheysens, O., Patel, M., Chan, C. T., Wang, Y., Namavari, M., and Gambhir, S. S. (2007) Fluorescent fructose derivatives for imaging breast cancer cells. *Bioconjugate Chem. 18*, 628–634.

(9) Kim, S., Lim, Y. T., Soltesz, E. G., De Grand, A. M., Lee, J., Nakayama, A., Parker, J. A., Mihaljevic, T., Laurence, R. G., Dor, D. M., Cohn, L. H., Bawendi, M. G., and Frangioni, J. V. (2004) Near infrared fluorescent type II quantum dots for sentinel lymph node mapping. *Nat. Biotechnol. 22*, 93–97.

(10) Cheng, Z., Wu, Y., Xiong, Z., Gambhir, S. S., and Chen, X. (2005) Near-infrared fluorescent RGD peptides for optical imaging of integrin $\alpha_v\beta_3$ expression in living mice. *Bioconjugate Chem. 16*, 1433–1441.

(11) Ke, S., Wen, X., Gurfinkel, M., Charnsangavej, C., Wallace, S., Sevick-Muraca, E. M., and Li, C. (2003) Near-infrared optical imaging of epidermal growth factor receptor in breast cancer xenografts. *Cancer Res. 63*, 78707875.

(12) Ntziachristos, V., Tung, C.-H., Bremer, C., and Weissleder, R. (2002) Fluorescence molecular tomography resolves protease activity *in vivo*. *Nat. Med. 8*, 757–760.

(13) Weissleder, R., Tung, C. H., Mahmood, U., and Bogdanov, A., Jr. (1999) In vivo imaging of tumors with protease-activated near-infrared fluorescent probes. *Nat. Biotechnol. 17*, 375–378.

(14) Kim, E. M., Park, E. H., Cheong, S. J., Lee, C. M., Kim, D., Jeong H. J., Lim, S., Sohn, M. H., Kim, K., Chung, J. (2009) Characterization, biodistribution, and small-animal SPECT of I-125 labeled cMBP in mice bearing c-Met receptor tyrosine kinase-positive tumor xenografts. *Nucl. Med. Biol.*, in press.

(15) Weimar, I. S., Weijer, K., van den Berk, P. C., Muller, E. J., Miranda, N., Bakker, A. Q., Heemskerk, M. H., Hekman, A., de Gast, G. C., and Gerritsen, W. R. (1999) HGF/SF and its receptor c-MET play a minor role in the dissemination of human B-lymphoma cells in SCID mice. *Br. J. Cancer 81*, 43–53.

(16) Cooper, C. S., Park, M., Blair, D. G., Tainsky, M. A., Huebner, K., Croce, C. M., and Vande Woude, G. F. (1984) Molecular cloning of a new transforming gene from a chemically transformed human cell line. *Nature 311*, 29–33.

(17) Miller, C. T., Lin, L., Casper, A. M., Lim, J., Thomas, D. G., Orringer, M. B., Chang, A. C., Chambers, A. F., Giordano, T. J., Glover, T. W., and Beer, D. G. (2006) Genomic amplification of MET with boundaries within fragile site FRA7G and upregulation of MET pathways in esophageal adenocarcinoma. *Oncogene 25*, 409–418.

(18) Stellrecht, C. M., Phillip, C. J., Cervantes-Gomez, F., and Gandhi, V. (2007) Multiple myeloma cell killing by depletion of the MET receptor tyrosine kinase. *Cancer Res. 67*, 9913–9920.

(19) Garcia, S., Dales, J. P., Charafe-Jauffret, E., Carpentier-Meunier, S., Andrac-Meyer, L., Jacquemier, J., Andonian, C., Lavaut, M. N., Allasia, C., Bonnier, P., and Charpin, C. (2007) Overexpression of c-Met and of the transducers PI3K, FAK and JAK in breast carcinomas correlates with shorter survival and neoangiogenesis. *Int. J. Oncol. 31*, 49–58.

(20) Puri, N., Ahmed, S., Janamanchi, V., Tretiakova, M., Zumba, O., Krausz, T., Jagadeeswaran, R., and Salgia, R. (2007) c-Met is a potentially new therapeutic target for treatment of human melanoma. *Clin. Cancer Res. 13*, 2246–2253.

(21) You, W. K., and McDonald, D. M. (2008) The hepatocyte growth factor/c-Met signaling pathway as a therapeutic target to inhibit angiogenesis. *J. Biochem. Mol. Biol. 41*, 833–839.

(22) Migliore, C., and Giordano, S. (2008) Molecular cancer therapy: Can our expectation be MET? *Eur. J. Cancer 44*, 641–651.

(23) Date, K., Matsumoto, K., Shimura, H., Tanaka, M., and Nakamura, T. (1997) HGF/NK4 is a specific antagonist for pleiotrophic actions of hepatocyte growth factor. *FEBS Lett. 420*, 1–6.

(24) Burgess, T., Coxon, A., Meyer, S., Sun, J., Rex, K., Tsuruda, T., Chen, Q., Ho, S. Y., Li, L., Kaufman, S., McDorman, K., Cattley, R. C., Sun, J., Elliott, G., Zhang, K., Feng, X., Jia, X. C., Green, L., Radinsky, R., and Kendall, R. (2006) Fully human monoclonal antibodies to hepatocyte growth factor with therapeutic potential against hepatocyte growth factor/c-Met-dependent human tumors. *Cancer Res. 66*, 1721–1729.

(25) Kim, K. J., Wang, L., Su, Y. C., Gillespie, G. Y., Salhotra, A., Lal, B., and Laterra, J. (2006) Systemic anti-hepatocyte growth factor monoclonal antibody therapy induces the regression of intracranial glioma xenografts. *Clin. Cancer Res. 12*, 1292–1298.

(26) Berthou, S., Aebersold, D. M., Schmidt, L. S., Stroka, D., Heigl, C., Streit, B., Stalder, D., Gruber, G., Liang, C., Howlett, A. R., Candinas, D., Greiner, R. H., Lipson, K. E., and Zimmer, Y. (2004) The Met kinase inhibitor SU11274 exhibits a selective inhibition pattern toward different receptor mutated variants. *Oncogene 23*, 5387–5393.

(27) Ma, P. C., Schaefer, E., Christensen, J. G., and Salgia, R. (2005) A selective small molecule c-MET Inhibitor, PHA665752, cooperates with rapamycin. *Clin. Cancer Res. 11*, 2312–2319.

(28) Perk, L. R., Stigter-van, Walsum, M., Visser, G. W., Kloet, R. W., Vosjan, M. J., Leemans, C. R., Giaccone, G., Albano, R., Comoglio, P. M., and van Dongen, G. A. (2008) Quantitative PET imaging of Met-expressing human cancer xenografts with 89Zr-labelled monoclonal antibody DN30. *Eur. J. Nucl. Med. Mol. Imaging 35*, 1857–1867.

(29) Towner, R. A., Smith, N., Doblas, S., Tesiram, Y., Garteiser, P., Saunders, D., Cranford, R., Silasi-Mansat, R., Herlea, O., Ivanciu, L., Wu, D., and Lupu, F. (2008) *In vivo* detection of c-Met expression in a rat C6 glioma model. *J. Cell. Mol. Med. 12*, 174186.

(30) Di Renzo, M. F., Narsimhan, R. P., Olivero, M., Bretti, S., Giordano, S., Medico, E., Gaglia, P., Zara, P., and Cormoglio, P. M. (1991) Expression of the Met/HGF receptor in normal and neoplastic human tissues. *Oncogene 6*, 1997–2003.

(31) Sonnenberg, E., Meyer, D., Weidner, K. M., and Birchmeier, C. (1993) Scatter factor/hepatocyte growth factor and its receptor, the c-met tyrosine kinase, can mediate a signal exchange between mesenchyme and epithelia during mouse development. *J. Cell Biol. 123*, 223–235.

BC8005539

Supplementary Materials for the Manuscript Entitled

"*In vivo* Imaging of c-Met Expression using Optical Imaging System"

Eun-Mi Kim, Eun-Hye Park, Su-Jin Cheong, Chang-Moon Lee, Hwan-Jeong Jeong*, Dong Wook Kim, Seok Tae Lim, Myung-Hee Sohn

by

Department of Nuclear Medicine, Research Institute of Clinical Medicine, Cyclotron Research Center, Chonbuk National University Medical School and Hospital, Jeonju, Jeonbuk, Republic of Korea.

Running title: NIR fluorescence imaging of c-Met receptor

*To whom correspondence should be addressed

Department of Nuclear Medicine

Chonbuk National University Medical School,

634-18, Geumam-2 dong, Duckjin-gu, Jeonju,

Jeonbuk, Republic of Korea 561-712

TEL : 82-63-250-2171

FAX : 82-63-255-1172

E-mail : jayjeong@chonbuk.ac.kr

Contents of Supporting Information

Figure S1. UV-VIS spectra.

Figure S2. NIR fluorescence images of KB cells were obtained after incubation for 1 h in the presence of cMBP-GGG-Cy5.5, or cMBP-AOC-Cy5.5 (2 nmol) with (B, D) or without (A, C) blocking dose of cMBP peptide (86 nmol). Cellular uptake was clearly blocked by cold peptide. Blocking images demonstrate high c-Met receptor specificity of Cy5.5 conjugated cMBPs. Upper images show the fluorescence image and lower images show the merge image.

Figure S3. *In vivo* fluorescence imaging of athymic nude mice bearing Ramos xenografts after *i.v.* injection of 4 nmol cMBP-AOC-Cy5.5. Red arrows indicate the tumor (T), kidney (K) and bladder (B). All NIR fluorescence images were acquired with a 1-sec exposure time at 10, 30, 60 min, and 2 h.

Figure S4. Expression of c-Met mRNA in U87MG and Ramos cells as determined by RT-PCR. The 656 bp fragments were detected and confirmed the expression of c-Met mRNA in U87MG and Ramos cells. β-actin was used as an internal loading control.

Figure S1. UV-VIS spectra.

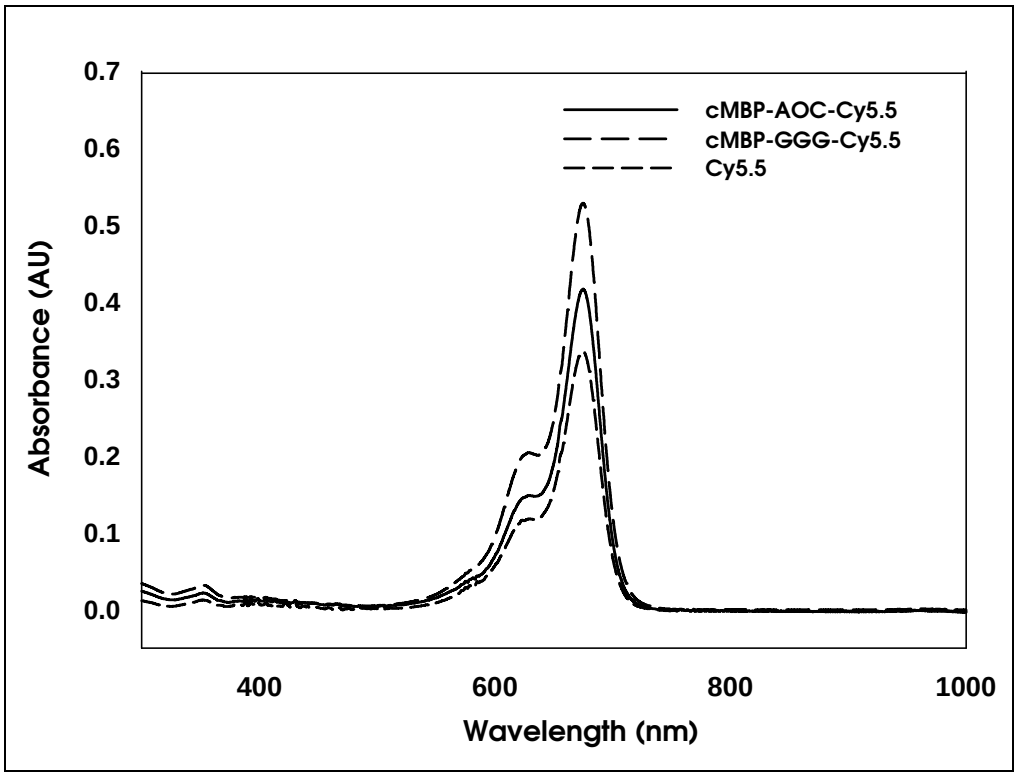

Figure S2. NIR fluorescence images of KB cells were obtained after incubation for 1 h in the presence of cMBP-GGG-Cy5.5, or cMBP-AOC-Cy5.5 (2 nmol) with (B, D) or without (A, C) blocking dose of cMBP peptide (86 nmol). Cellular uptake was clearly blocked by cold peptide. Blocking images demonstrate high c-Met receptor specificity of Cy5.5 conjugated cMBPs.

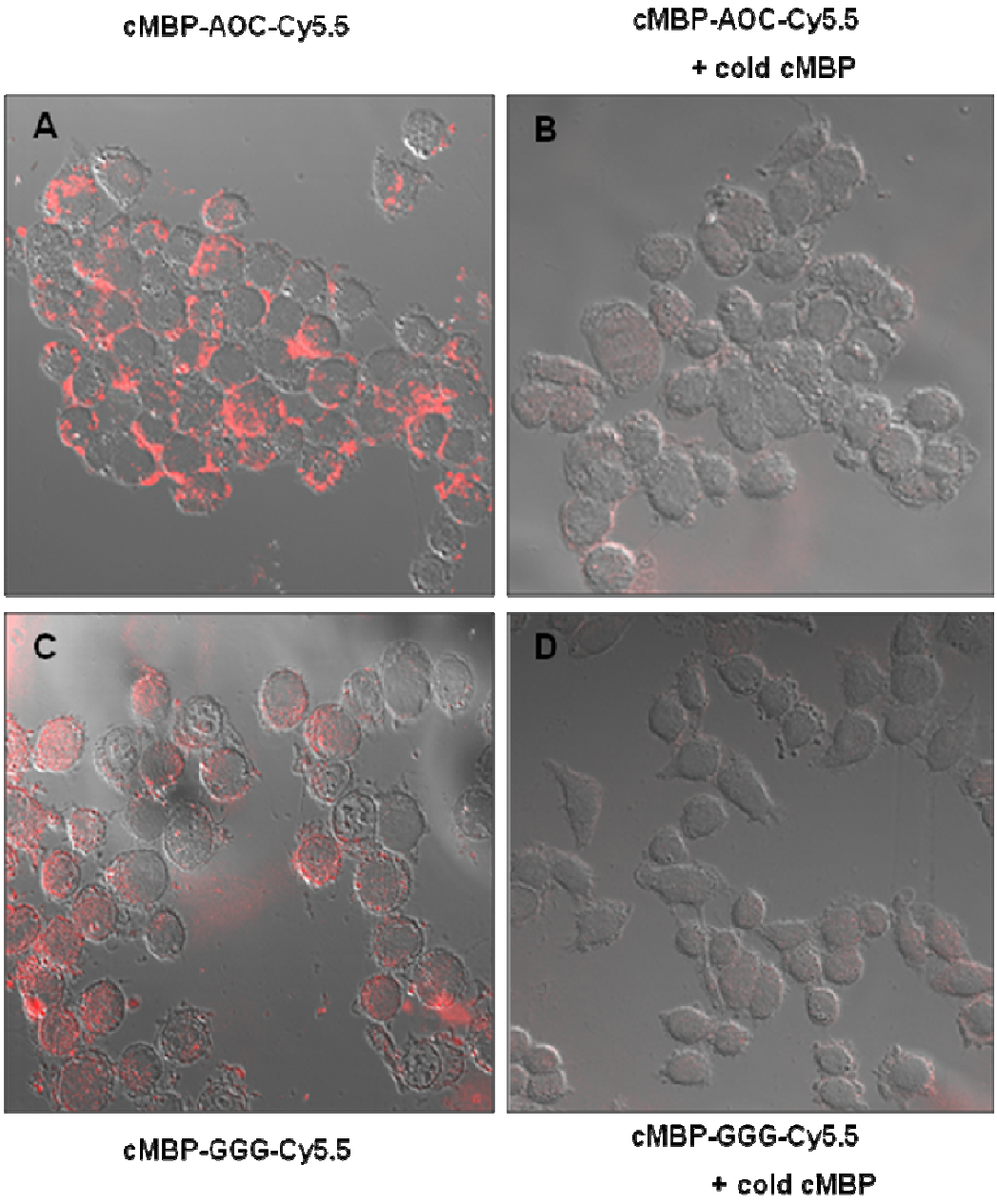

Figure S3. *In vivo* fluorescence imaging of athymic nude mice bearing Ramos xenografts after *i.v.* injection of 4 nmol cMBP-AOC-Cy5.5. Red arrows indicate the tumor (T), kidney (K) and bladder (B). All NIR fluorescence images were acquired with a 1-sec exposure time at 10, 30, 60 min, and 2 h.

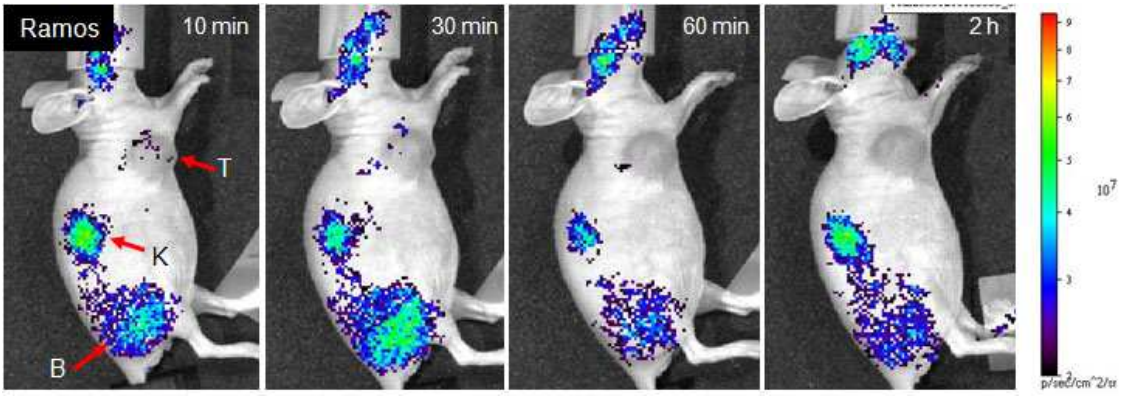

Figure S4. Expression of c-Met mRNA in U87MG and Ramos cells as determined by RT-PCR. The 656 bp fragments were detected and confirmed the expression of c-Met mRNA in U87MG and Ramos cells. β-actin was used as an internal loading control.

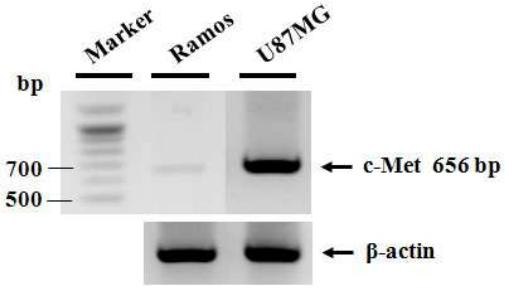

Synthesis and Studies on Cell-Penetrating Peptides

Jean-Remi Bertrand,[†] Claude Malvy,[†] Tiphanie Auguste,[†] Gábor K. Tóth,[‡] Orsolya Kiss-Ivánkovits,[‡] Eszter Illyés,[§] Miklós Hollósi,[§] Sándor Bottka,[||] and Ilona Laczkó*[,||]

Institute Gustave Roussy, CNRS UMR 8121, University Paris 11, Villejuif, France, Institute of Medical Chemistry, University of Szeged, Szeged, Hungary, Department of Organic Chemistry, Institute of Chemistry, Eötvös Lóránd University, Budapest, Hungary, and Institute of Plant Biology, Institute of Biophysics, Biological Research Center, Szeged, Hungary. Received January 7, 2009; Revised Manuscript Received May 13, 2009

The ability of different synthetic cell penetrating peptides, as Antennapedia (wild and Phe^6 mutated penetratins), flock house virus, and integrin peptides to form complexes with a 25mer antisense oligonucleotide was compared and their conformation was determined by circular dichroism spectroscopy. The efficiency for oligonucleotide delivery into cells was measured using peptides labeled with a coumarin derivative showing blue fluorescence and the fluorescein-labeled antisense oligonucleotide showing green fluorescence. Fluorescence due to the excitation energy transfer confirmed the interaction of the antisense oligonucleotide and cell-penetrating peptides. The most efficient oligonucleotide delivery was found for penetratins. Comparison of the two types of penetratins shows that the wild-type penetratin proved to be more efficient than mutated penetratin. The paper also emphasizes that the attachment of a fluorescent label may have an effect on the conformation and flexibility of cell-penetrating peptides that must be taken into consideration when evaluating biological experiments.

INTRODUCTION

Genomic rearrangements leading to intragenic gene fusion are found in particular types of hematopoietic malignancies and sarcomas. These chimeric genes frequently encode aberrant transcription factors, which are responsible for cellular transformation and in consequence for oncogenesis. The Ewing sarcoma (EWS) family of tumors (ESFT) belongs to this type of translocation-induced cancers (*1*). The EWS-Fli1 protein is an aberrant transcription factor that has been shown by different authors to regulate various genes. In a recent study, it was shown that, when EWS-Fli1 is specifically inhibited by a short interfering RNA (siRNA) in Ewing A673 cells, 80 genes were found up- and down-regulated, respectively, at least 2-fold (*2*). Because chromosome rearrangement occurs in the cancerous cell, the nucleic acid sequence of the junction is present only in the mRNA of tumor cells. It is, therefore, an extremely attractive target for selective therapy of Ewing sarcoma. To our knowledge, no attempts have been made to target the fusion gene at the DNA level, but antisense strategies allow for inhibition of EWS-Fli1 at the mRNA level after splicing. For this purpose, two strategies are useful: siRNA and antisense oligonucleotides (AS-ODNs).

The short interfering RNAs (siRNAs) are double-stranded oligoribonucleotides with a full duplex of 19 bases, and a 2−3-base overhang at the 3′ termini (*3*, *4*). They induce the sequence-specific cleavage of mRNA in the cytoplasm by directing the RNA-induced silencing cleavage complex (RISC) to the complementary sequence on the target RNA. It is a very powerful strategy to inhibit gene expression at the RNA level, and it represents many fields of application for fundamental research. The use of siRNAs as therapeutics is in development, but some recent results show dramatic toxicity on animal models. This will require a modification of their administration ways (*5*, *6*).

Antisense oligonucleotides are short, synthetic strands of DNA (or analogues) that are complementary, or antisense, to a target sequence (DNA or RNA) designed to halt a biological event, such as transcription, translation, or splicing. The mechanism of action of antisense oligonucleotides is enzymatic cleavage of the RNA strand by RNase H (*7*).

Cellular penetration is one of the main challenges to be solved for both strategies to improve their efficiency. Cationic lipids are generally used for cell application, but because of their liver capture and potential toxicity, they are limited to *in vitro* studies. Cell-penetrating virus derivative peptides have been described as molecules able to facilitate the nonendocytic membrane passage of compounds associated to them (*8*−*10*). Nevertheless, depending on the protein origin some cell penetrating peptides (CPPs) use the endocytotic pathways (*8*). The complex formation of antisense oligonucleotides with CPPs may be accomplished either by covalent coupling or by electrostatic interaction.

This paper reports the synthesis and circular dichroism (CD) studies on cell-penetrating peptides as well as epifluorescence microscopic investigation of peptide-mediated delivery of the 5′-fluorescein labeled 25mer EWS-Fli1 antisense oligonucleotide into cells. Antennapedia peptides (wild-type and Trp^6 → Phe^6 mutant penetratins) (*11*, *12*), integrin sequences (*13*), and flock-house virus peptides (*14*) (Table 1) were chosen to probe the cell-penetrating efficiency of CPPs. The peptides were prepared with free N-terminus and in N-terminal fluorescent-labeled form. The 4-(7-hydroxycoumaryl)-acetyl (Hca) group served as fluorescent label (*15*). The direct interactions of the different CPPs with living cells have also been studied. Finally, their ability to deliver the fluorescein labeled AS-ODN into the cells was also measured.

MATERIALS AND METHODS

Materials. Diisopropylcarbodiimide (DIC), 1,8-diazabicyclo[5.4.0]undec-7-ene (DBU), *N*,*N*′-diisopropylethylamine

* Corresponding author. Ilona Laczkó, H-6726 Szeged, Temesvári krt. 62. Phone: +36-62-599608; Fax: +36-62-433133; E-mail: laczko@brc.hu.

[†] CNRS UMR 8121.

[‡] University of Szeged.

[§] Eötvös Lóránd University.

[||] Biological Research Center.

10.1021/bc900005j CCC: $40.75 © 2009 American Chemical Society
Published on Web 06/25/2009

Table 1. Amino Acid Sequence, ESI-MS, and RP-HPLC Characterization of the Synthesized Peptides[a]

peptides	numbering	MW calcd	MW [MH^+] found	RP-HPLC R_t
	Penetratins			
H-RQIKI**W**FQNRRMKWKK-NH_2	**1**	2244.3	2245.7	24.2[b]
Hca-RQIKI**W**FQNRRMKWKK-NH_2	**1a**	2446.3	2447.2	19.5
H-RQIKI**F**FQNRRMKWKK-NH_2	**2**	2206.3	2206.8	23.1[b]
Hca-RQIKI**F**FQNRRMKWKK-NH_2	**2a**	2408.3	2408.6	18.5[c]
	Integrin Peptides			
H-SRYDDSVPRYHAVRIRKEEREIKDEK-NH_2	**3**	3272.7	3273.6	14.9[d]
Hca-SRYDDSVPRYHAVRIRKEEREIKDEK-NH_2	**3a**	3476.6	3477.0	18.9[d]
H-LEAEKERRKSGLSS-NH_2	**4**	1587.9	1588.8	18.3[b]
Hca-LEAEKERRKSGLSS-NH_2	**4a**	1789.1	1789.9	22.4[c]
	FHV Peptides			
H-ASMWERVKSIIKSSLAAASNI-NH_2	**5**	2261.2	2261.8	26.0[c]
Hca-ASMWERVKSIIKSSLAAASNI-NH_2	**5a**	2462.2	2463.6	27.5[c]
H-IGVAASGISGLSALFEGFGF-NH_2	**6**	1898.3	1899.3	28.8[c]
Hca-IGVAASGISGLSALFEGFGF-NH2	**6a**	2101.0	2101.4	32.0[c]

[a] Eluent A: 0.08% TFA/H_2O; B: 0.064% TFA/MeCN-H_2O (95:5, v/v), flow rate: 1 mL/min. [b] Gradient 5−50% B in 25 min. [c] Gradient 15−70% B in 30 min. [d] Gradient 5−60% B in 25 min.

(DIEA), hydrogen fluoride (HF), 1-hydroxybenztriazole (HOBt), and trifluoroacetic acid (TFA) were obtained from Fluka. Trifluoroethanol (TFE, Uvasol, Merck, for spectroscopy) was used for CD measurements. Acetonitrile (MeCN), dichloromethane (DCM), and dimethylformamide (DMF) are from Reanal (Budapest, Hungary). Boc-amino acid derivatives and 4-methyl benzhydrylamine resin were from Bachem (Bubendorf, Switzerland). 4-(7-Hydroxycoumaryl)acetic acid (Hca) was prepared by the method of Baker et al. (*15*). Dulbecco's modified Eagle's medium (DMEM), newborn calf serum, and penicillin−streptomycin solution were purchased from Gibco. Trizol was purchased from Invitrogen and RNasin from Promega.

Oligonucleotide. The 5′-fluorescein labeled 25mer EWS-Fli1 AS-ODN is targeted toward the junction sequence between EWS and Fli1 genes as described by Tanaka et al. (*16*) and corresponds to the nucleotides 832−856. EWS-Fli1 AS-ODN inhibits proliferation of human Ewing's sarcoma and primitive neuroectodermal tumor cells (*16*−*18*). To protect it from nuclease degradation, all phosphate groups were changed into phosphorothioate. The AS-ODN sequence 5′-GACTGAGTCATAAGAAGGGTTCTGC-3′ was provided by Eurogentec (Belgium), HPLC-purified and mass spectrometry controlled. A control phosphorothioate sequence (Ct-ODN) was used for the PCR studies with the following sequence: 5′-GCAGAACCCTTCTTATGACTCAGTC-3′

The EWS-Fli1 AS-ODN, without fluorescein label, was synthesized with an Expedite 8909 synthesizer (Applied Biosystems, USA), using solid-supported standard β-cyanoethyl phosphoramidite chemistry at a nominal scale of 1 μmol. Purification was performed by HPLC on a Kromasil 100-C18 250 × 10 mm ID column, using a MeCN 0.1 M triethylammonium acetate (pH 7.0) mixture as eluent. This results in the triethylammonium salt of ODN.

Peptide Synthesis. Peptides (Table 1) were synthesized by manual solid-phase methodology, using Boc/Bzl strategy (*19*) and 4-methyl benzhydrylamine resin (0.7 mmol/g). All amino acids were coupled as Boc-derivatives. The amino acid side chain protection was the following: Boc-Asn(Xan)-OH, Boc-Asp(OcHex)-OH, Boc-Arg(Tos)-OH, Boc-Gln(Xan)-OH, Boc-Glu(OcHex)-OH, Boc-His(Tos)-OH, Boc-Lys-(2ClZ)-OH, Boc-Ser(Bzl)-OH, Boc-Trp(For)-OH [xan (xanthyl), cHex (cyclohexyl), Tos (tosyl), 2ClZ (2-Cl-benzyloxycarbonyl), Bzl (benzyl), For (formyl)]. The Hca coupling was performed by using the DIC/HOBt method (3 equiv of each) (*20*). The coupling efficacy was monitored by the ninhydrin (*21*) assay. Boc-groups were removed by 35% TFA in DCM. Neutralization together with the removal of the formyl-group of Trp was carried out with DBU/piperidine before the final cleavage from the resin with HF containing *p*-cresol as scavenger at 0 °C for 1.5 h. The crude products were analyzed and purified by reverse-phase HPLC as described below.

High-Performance Liquid Chromatography. Analytical RP-HPLC (Jasco, Japan) was performed using an Alltech Alltima C18 WP column (250 × 5 mm) with 5 μm particle size and 300 Å pore size. Depending on peptide composition (Table 1), a linear gradient elution was developed from 5−50% eluent B in 25 min, 15−70% eluent B in 30 min, or 5−60% B in 35 min; eluent A is 0.08% TFA in water and eluent B is 0.064% TFA in acetonitrile−water (95−5%). Detection was performed at 220 and 280 nm. Experiments were carried out at a flow rate of 1 mL/min, at ambient temperature. Samples were applied at 0.1 mg/0.1 mL concentration in eluent A. Purification of peptides was achieved on an Alltech Alltima C18 WP column (250 × 25 mm) with 5 μm particle size and 300 Å pore size using gradient elution with the same eluents, 10 mL/min flow rate, and 20 mg/mL sample concentration. Homogeneity of the pure peptides was confirmed by analytical RP-HPLC.

Electrospray Ionization Mass Spectrometry (ESI-MS). The identification of the peptides was achieved by mass spectrometry (*20*). Electrospray ionization mass spectrometry was performed with a Bruker Daltonics Esquire 3000 Plus (Bremen, Germany) mass spectrometer, operating in continuous sample injection at 4 μL/min flow rate. Samples were dissolved in 50% acetonitrile−water mixture. Mass spectra were recorded in positive mode in the *m*/*z* 200−1500 range. R_f values of purified peptides, calculated, and found masses are listed in Table 1.

Circular Dichroism Spectroscopic Studies. CD spectra were recorded on a Jasco J-810 dichrograph (calibrated with ammonium *d*-10-camphor sulfonate) at room temperature using a 0.02 cm cell for measurements when TFE/water was used as solvent. All measurements are the average of four scans, and the resolution was 0.2 nm. The concentration of the peptides ranged from 0.5 to 1 mM depending on the absorption. The conformational change of penetratins **1** and **2** and the FHV peptide **5** was also monitored in the presence of 5 mM aqueous anionic micelles [L-α-lysophosphatidylcholine (LPC) to L-α-lysophosphatidylserine (LPS) molar ratio (r_M) was 9]. The concentration of the peptides was in this case 40 μM, and a 0.1 cm cell was used.

The CD spectra of AS-ODN and peptide-(AS-ODN) complexes were recorded in the range 250−320 nm in a 0.1 cm cell. The AS-ODN concentration in the samples was in each case 20 μM, and the peptide concentration varied in the interval

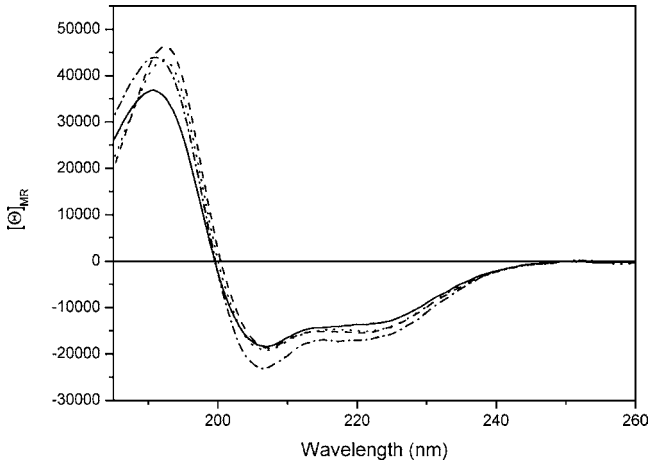

Figure 1. Far-UV CD spectrum of penetratins **1** (—), **1a** (-•-•-), **2** (---), and **2a** (•••) in TFE:water, 9:1 (v/v).

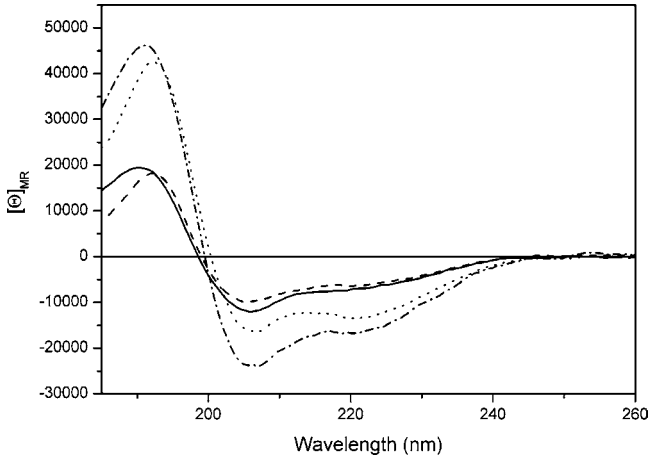

Figure 2. Far-UV CD spectrum of penetratins **1** (—), **1a** (-•-•-), **2** (---), and **2a** (•••) TFE/water, 1:1 (v/v).

20−200 μM. Prior to scanning, the AS-ODN was incubated with the peptides for 1 h. The CD spectra were expressed as mean residue ellipticity $[\Theta]_{MR}$ and were given in units of deg cm^2 $dmol^{-1}$, using a mean residue weight of 114 for the peptides and 306 for the ODN.

Including the free N-terminus, the wild-type (**1**) and mutant penetratin (**2**) comprise eight basic groups but no acidic ones. The Hca-labeled peptides **1a** and **2a** comprise one less basic side-chain group. With this taken into account, the penetratin peptides **1** and **2** bind eight, **1a** and **2a** seven, trifluoroacetic acid molecules that significantly increase their molecular mass. Quantitative amino acid analysis of the penetratin peptides resulted in peptide contents which agreed with the decreased values calculated from the molecular mass of peptide−TFA salts. In the case of peptides **3**−**6**, the TFA content was calculated for the net positive charge (number of basic residues minus number of acidic residues). The $[\Theta]_{MR}$ values were calculated for the increased molecular mass.

AS-ODN Delivery to Cells. NIH/3T3 cells stably transformed by EWS-Flil oncogene (NIH/3T3-EF) were grown in DMEM medium supplemented by 10% heat-inactivated newborn calf serum and penicillin−streptomycin solution. The cells were seeded into 6-well plate at 2×10^5 cell in 1 mL of medium and grown at 37 °C with 5% CO_2 in a moist atmosphere before treatment. Twenty-four hours later, the medium was discarded and replaced by 900 μL of new one. Fluorescein-labeled AS-ODN (0.5 nmol) was incubated for 10 min in 100 μL of 100 mM NaCl, 10 mM Hepes buffer, pH 7.2 containing 17 nmol of

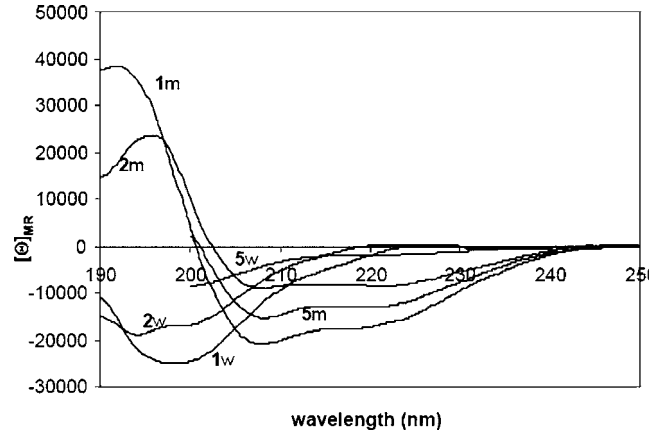

Figure 3. Far-UV CD spectrum of peptides **1**, **2**, and **5** in water (curves 1w, 2w, 5w) and in the presence of 5 mM aqueous anionic micelles (LPC/LPS, $r_M = 9$) (curves 1m, 2m, 5m). Peptide concentration was 40 μM.

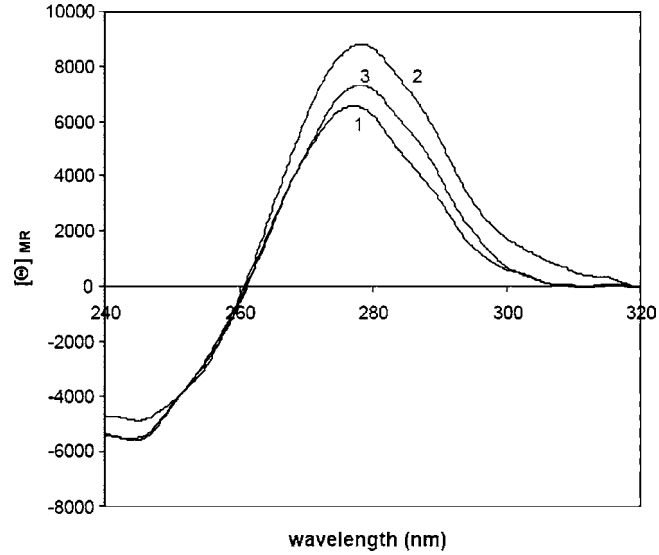

Figure 4. Near-UV CD spectrum of AS-ODN (curve 1), associates of (AS-ODN)-wild-type penetratin (curve 2), and (AS-ODN) mutant penetratin (curve 3) in water. Peptide/ODN, $r_M = 2.5$.

peptide **1a** or **2a**, 15 nmol of peptide **3a**, 30 nmol of peptide **4a**, and 40 nmol of peptide **5a** or **6a** (arbitrary value because these latter peptides do not contain any cationic amino acid) to obtain a charge ratio (r_{CH}) of 5 (positive charges of peptide vs the negative charges of ODN). The charge ratio of 5 has been selected from previous studies (*22*, *23*). The complexes were then added to the cells and incubated for 3 h. The cells were washed two times with a PBS solution, treated with a 4% formaldehyde solution in PBS for 20 min, washed two times with PBS, and observed under epifluorescence microscopy (*24*) (Axiovert 100, Zeiss) with a CCD camera. The same cell treatments were performed with the Hca-peptides alone at 50 μM or the fluorescent AS-ODN alone at 500 nM final concentrations. Fluorescence was observed using an emission multiwavelength filter (460/10, 530/25, 625/50 nm, maximum/band-pass). For the detection of the Hca blue light and the fluorescein green light emission, excitation filters of 365/12 and 494/17 were used, respectively.

Determination of EWS-Fli1 Expression by RT-PCR. The NIH/3T3-EF cells were grown in 6 well plates and seeded one day before the treatment with (AS-ODN)−peptide complexes at 3×10^5 cells/mL in DMEM containing 10% newborn calf serum, 100 U/mL streptomycin, and 100 μg/mL penicillin. After

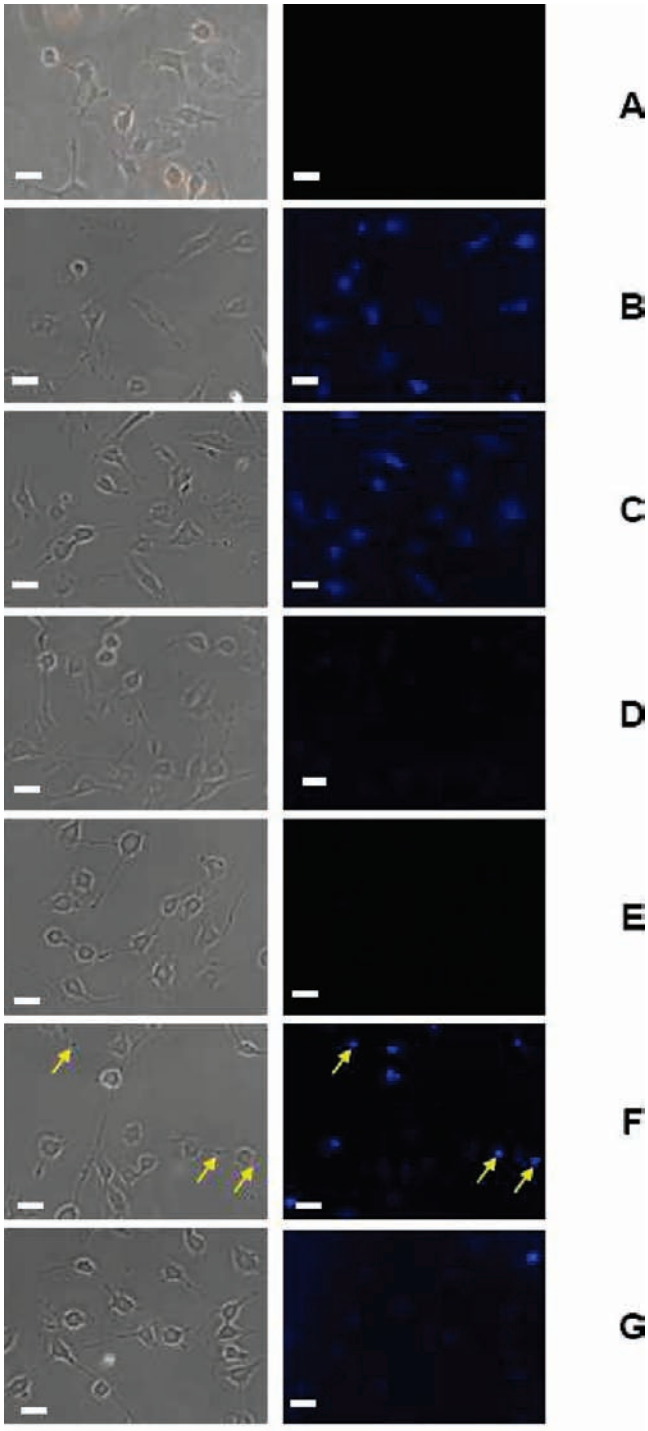

Figure 5. Interaction of peptides with cells. NIH/3T3 cells, incubated for 3 h alone (A) or with 50 μM wild-type penetratin **1a** (B); mutated penetratin **2a** (C); integrin peptide **3a** (D); integrin peptide **4a** (E); FHV peptide **5a** (F); and FHV peptide **6a** (G). The cells were observed with white light (left panel) or excitating Hca at 365 nm (right panel) to detect the different Hca-labeled peptides. Scale bar is 20 μm.

24 h treatment, the cells were washed with PBS buffer (Gibco) and then lysed with 800 μL Trizol, 130 μL of chloroform/isoamylalcohol (49:1, v/v). After centrifugation at 13 000 rpm for 15 min, 350 μL of the aqueous phase was precipitated with an aquivalent volume of isopropanol. Total RNA were then collected by centrifugation at 13 000 rpm for 15 min, washed two times with 75% ethanol solution, and air-dried. The RNA pellet was solved in 10 μL water containing 0.5 U/μL of RNasin, and the solution concentration was determined by absorption spectroscopy. The cDNA was produced on 1 μg of total RNA after hybridization with 2 μL of random primer 50 μg/mL (Promega) in 14.5 μL final volume by heating the solution for 5 min at 65 °C. The cDNA synthesis is performed for 1 h at 42 °C after addition of 4 μL of 5× more concentrated buffer (Biolabs), 0.5 μL 20 mM dNTP, 0.5 μL RNasin 40 U/μL, and 0.5 μL Mo-MuLV reverse transcriptase (Biolabs) 200 U/μL. PCR reaction was performed on 2 μL of cDNA prepared as described above, 5 μL of 10-fold concentrated buffer (Biolabs), 0.5 μL 20 mM dNTP, 0.5 μL of each primer 50 μg/mL, and 0.5 μL of Taq DNA polymerase 5 U/μL (Biolabs). Primer sequences are EWS-Fli1 forward 5′-AGC-AGT-TAC-TCT-CAG-CAG-AAC-AAC-3′ and reverse 5′-CCA-GGA-TCT-GAT-ACG-GAT-CTG-GCT-G-3′. G3PDH was used as the housekeeping gene, and the sequence of the corresponding primers is forward 5′-CAT-TGT-CAT-ACC-AGG-AAA-TC-3′. Amplification conditions were as follows: (i) fusion 94 °C (30 s), (ii) hybridization 56 or 63 °C (30 s) for EWS-Fli1 or G3PDH, respectively, and (iii) elongation 72 °C (50 s). The amplified fragments were detected on 2% agarose gel electrophoresis in TAE buffer and ethidium bromide staining with a CCD camera and corresponding gel analysis system (Ingenius, Syngene).

RESULTS AND DISCUSSION

Circular Dichroism Spectroscopy. The conformational preferences and the effect of fluorescent labeling upon conformation of peptides were probed by CD spectroscopy. The spectra were taken in TFE/water 9:1 (v/v), TFE/water 1:1 (v/v) mixtures, and water. (The wild-type penetratin peptide **1** is not soluble in neat TFE.) TFE is a helix promoting solvent; it is frequently used to mimic cell membranes or their vicinity (*25*). Figure 1 shows the effect of N-terminally coupled Hca-group on the conformation of wild-type (**1**) and mutant (**2**) penetratin in TFE/water, 9:1. The spectrum of **1** is characteristic of peptides featuring high helix content. The phenylalanine-containing mutant peptide **2** also shows a typical helix-type CD spectrum in the same solvent mixture, but the intensity of the positive band at 192.5 nm is higher than that of **1** at 190.5 nm, while the negative bands are less intense. The flock-house virus (FHV) sequence **5** shows a CD spectrum reflecting lower helicity (spectra not shown). As reference, the CD spectra of two integrin sequences **3** and **4** were also measured in TFE. The band amplitudes in the spectrum of the longer sequence **3** are larger as a sign of higher helicity of the 26-mer peptide (spectra not shown).

It is an intriguing question whether or not the attachment of the fluorescent label 4-(7-hydroxycoumaryl)-acetyl (Hca) group has an effect upon the conformation of the peptide. In the far-UV spectrum of 4-(7-hydroxycoumaryl)-acetic acid (Hca-OH), two bands appear at 198 nm ($A = 3.28 \times 10^4$) and 217.5 nm ($A = 1.24 \times 10^4$). Thus, the Hca-group is expected to have a CD spectral effect in the far-UV region if the conformational movement of the N-terminus of the peptide is restricted. As shown in Figure 1, the Hca-group increases the intensity of both the negative and positive bands of wild-type penetratin (**1a**), but it does not have a significant effect upon the spectrum of the mutant penetratin (**2a**). The Hca-group has an effect only on the negative bands in the CD spectrum of the FHV peptide [λ_{nm} ($[\Theta]_{MR}$) values in TFE/water (9:1) for **5**, 218 (−13 240), 207 (−15 200), 190 (26 500), and **5a**, 221 (−11 200), 207 (−12 700), 190.5 (26 200)].

On the basis of the higher band intensities of the exciton couplet in the region of $\pi-\pi^*$ transition, the mutant penetratin **2** shows a more expressed tendency to adopt a helical structure than the wild-type peptide **1**. The attachment of the Hca-group stabilizes the helical conformation of **1** likely through $\pi-\pi$ interaction between the indole ring of tryptophan and the hydroxycoumaryl group at the N-terminus. They are located in

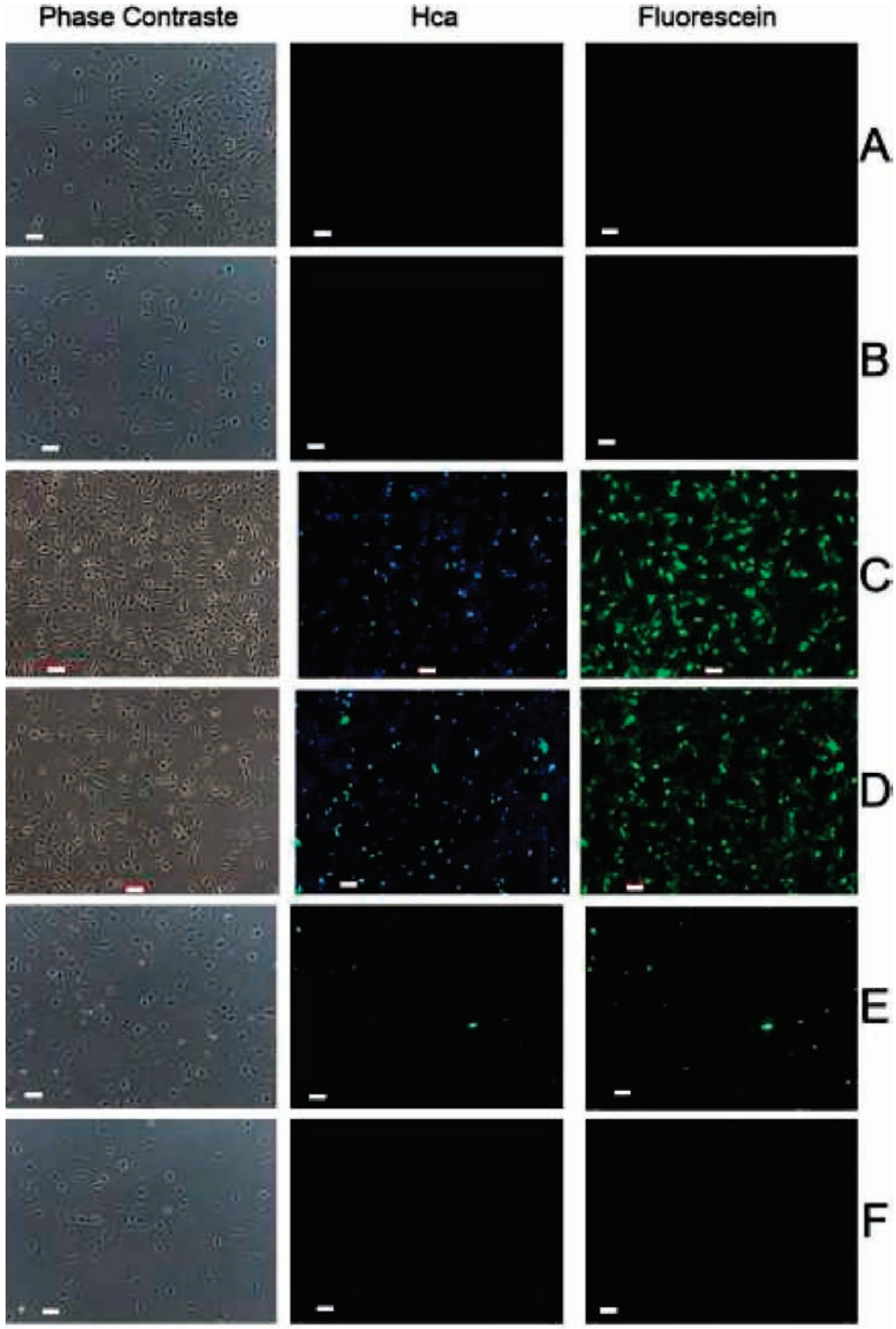

Figure 6. Oligonucleotide interactions with NIH/3T3 cells transformed by EWS-Flil ncogene. Cells incubated for 3 h alone (A); or with 500 nM fluorescein labeled AS-ODN (B); the same labeled AS-ODN complexes to wild-type penetratin **1a** (C); mutated penetratin **2a** (D); FHV peptide **5a** (E); and FHV peptide **6a** (F). The cells were observed with white light (left panel) or exciting Hca at 365 nm (middle panel) and fluorescein at 494 nm (right panel) to detect the interaction between cells and AS-ODN. Fluorescence emission was observed using a three band-pass filter on color camera as described in Materials and Methods. Scale bar is 20 μm.

sterically close position on the same side of the helix cylinder. The phenyl group of phenylalanine in **2** cannot effectively interact with the coumarin ring.

The relative stability of the helices of **1**, **1a**, **2**, and **2a** was probed by measuring their CD spectra in TFE/water 1:1 (v/v). The helical structure of the Hca-penetratins **1a** and **2a** is more resistant to the effect of aqueous environment than that of **1** or **2** (Figure 2). In water, **1**, **2**, and **5** show CD spectra reflecting dominantly unordered conformation (Figure 3). More interestingly, CD spectra in Figure 3 demonstrate that peptides **1**, **2**, and **5** are prompted to adopt α-helical conformation in aqueous solution in the presence of anionic micelles (LPC/LPS, r_M = 9). The induced helicity is more expressed for the wild-type **1** than for the mutant penetratin **2** (Figure 3).

On the basis of CD studies reported earlier, the wild-type penetratin **1** and the FHV peptide **5** interact with an 18-mer AS-ODN in water and in the presence of anionic micelles (*26*). The 25-mer AS-ODN used in this study was found to form complexes with both **1** and **2** (Figure 4). However, the spectral change in the near UV region, characteristic of ODN, is more

pronounced in the presence of **1** than **2** at peptide to ODN molar ratio $r_M = 2.5$. (Above these ratios, the solutions become opaque as a sign of aggregate formation that obscures the measurements of CD.)

Interaction of Hca-Peptides with Cells. NIH/3T3 EWS-Fli1 cells treated by the Hca-peptides were observed under epifluorescence microscopy taking advantage of the blue emission of Hca under UV excitation (365 nm). No fluorescence was observed for untreated cells (Figure 5A) Both the wild-type (**1a**) and mutated (**2a**) penetratin peptides were found to interact strongly with the cells (Figure 5B,C) with a cytoplasmic and nuclear localization. The mutant peptide **2** was earlier described as an inefficient cell-penetrating peptide (*24*). The association of these positively charged peptides to the cells is probably due to electrostatic interaction with the negatively charged cell membrane. Although confocal microscopy could not be used for the detection of Hca fluorescence because of the lack of laser with an emission band corresponding to Hca, the blue fluorescence observed at the nucleus position indicated that the peptides did enter the cell. If the peptides were localized on the cytoplasmic membrane, a pericellular flourescence would have been observed.

The fusogenic region of FHV (**5a**) interacts weakly with the cells with a cytoplasmic localization (Figure 5F). The intense fluorescence spots observed in this case correspond to peptide aggregates located on the external side of membranes as indicated by the yellow arrows on the left panel (bright field) and right panel (fluorescence) slides. The RNA binding peptide sequence (**6a**) of FHV has a low solubility and forms aggregates, which interact unspecifically with dead cells (Figure 5G). The Hca−integrin peptides (**3a** and **4a**) do not interact efficiently with the cells in our experimental conditions (Figure 5D,E).

Peptide-Mediated Delivery of AS-ODN into Cells. To determine the ability of the peptides to facilitate the AS-ODN penetration, cells were incubated for 3 h with fluorescein-labeled AS-ODN (500 nM) alone or in the presence of different peptides ($r_{CH} = 5$; see Materials and Methods). After incubation of AS-ODN with peptides **1a**, **2a**, or **5a**, we observed that the solutions became opalescent, probably due to formation of complexes between the AS-ODN and peptides. No green fluorescence was observed under epifluorescence microscopy of untreated NIH/3T3 cells expressing EWS-Flil oncogene (Figure 6A). After cell treatment with 500 nM AS-ODN for 3 h, a fraction of cells displayed a weak fluorescence (Figure 6B).

The Antennapedia derivative peptides can both make the AS-ODN penetrate into the cells (Figure 6C,D) independently of the mutation. The AS-ODN has mainly a cytoplasmic localization. The higher intensity of the fluorescein emission in Figure 6C compared to Figure 6D indicated that **1a** peptide is much more efficient for AS-ODN delivery than **2a**. This is consistent with an earlier finding where the wild-type penetratin was 2× more efficient for ODN delivery than the Phe^6 mutant penetratin (*25*). The blue fluorescence corresponding to the peptide **1a** and **2a** was still detected on cells after the complex was formed between peptide and AS-ODN. Nevertheless, the fluorescence intensity was much higher compared to that when the cells were treated only with the peptides (compare Figure 5B to Figure 6C and Figure 5C to Figure 6D) suggesting a cooperation between peptides and ODN for interaction with cells.

It can be seen in Figure 6C,D that all the cells present green and blue fluorescence indicating that peptides **1a** and **2a** are very efficient in interaction with the cells and in AS-ODN transfer. Observation of the cells with higher magnification (Figure 7) confirms these results.

Surprisingly, when the slides were illuminated using a filter of 365 nm for exciting Hca we observed green dots in the medium and in the cell membrane level (Figures 6C,D and Figure 7). (This is possible because the emission filter possesses three band passes: blue, green, and red). It is known that if the fluorescence emission spectrum of a donor molecule and the absorption spectrum of an acceptor molecule overlap excitation energy transfer occurs. The intensity of this transfer is inversely proportional to the square of distance between the donor and the acceptor molecules. The wavelength maximum of the emission spectrum of Hca is 460 nm (*20*), and that of the excitation spectrum of fluorescein is 494 nm; hence upon formation of complex between the AS-ODN and the peptide, an increased emission of the fluorescein at 530 nm was observed illuminating the slides at the excitation wavelength (365 nm) of Hca (Figure 6C,D and Figure 7). These complexes are mainly localized on the bottom of the plate (Figure 7, yellow arrow) or on the cell membrane (Figure 7, white arrow). The amount of complex localized on the membrane is higher for peptide **1a** than for **2a**. This means that membrane localization for peptide **1a** is not only of statistical origin. Figure 7 shows that no fluorescence transfer occurs in the cell-bound complex [under Hca fluorescence condition (excitation at 365 nm), the cells are blue]. This result indicates that after interaction with the cell membrane the complexes are dissociated, that is, AS-ODNs and the peptides are located at a large distance that excludes fluorescence transfer. The dissociation is probably favorable for the antisense activity of AS-ODNs.

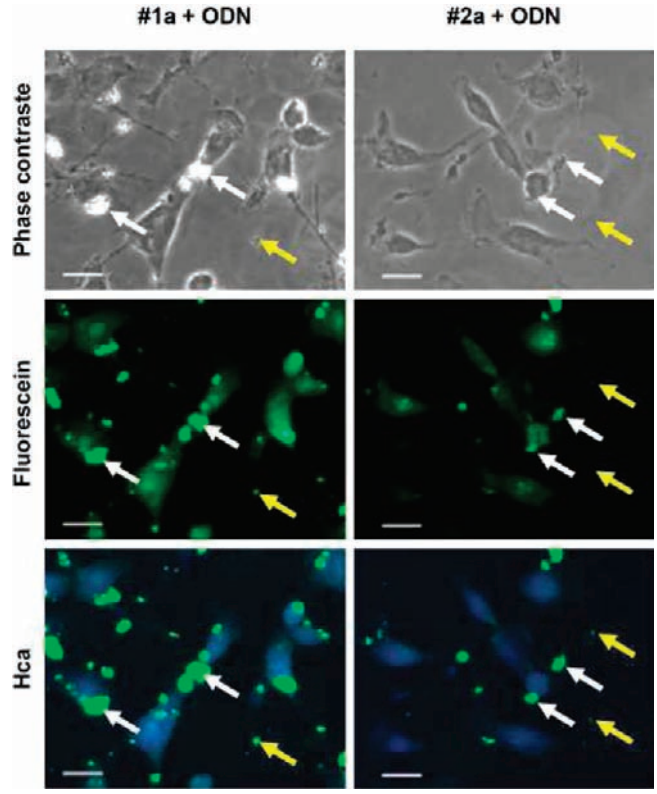

Figure 7. Oligonucleotide interactions with NIH/3T3 cells transformed by EWS-Fli1 oncogene. The cells were incubated for 3 h with 500 nM fluorescein labeled (AS-ODN)-wild-type penetratin **1a** or (AS-ODN)-mutated penetratin **2a** complexes. The cells were observed with white light (top panel) or exciting the fluorescein at 494 nm (middle panel) and Hca at 365 nm (bottom panel) to detect the interaction between cells and AS-ODN. Fluorescence emission was observed using a three band-pass filter on color camera as described in Materials and Methods. Arrows indicate the position of the (AS-ODN)-peptide aggregates: white arrows show aggregates localized on the bottom of the plate; yellow arrows show aggregates localized on cell membrane. Scale bar is 20 μM.

Integrin peptides **3** and **4** are not able to cause efficient penetration of the AS-ODN into cells (results not shown). The

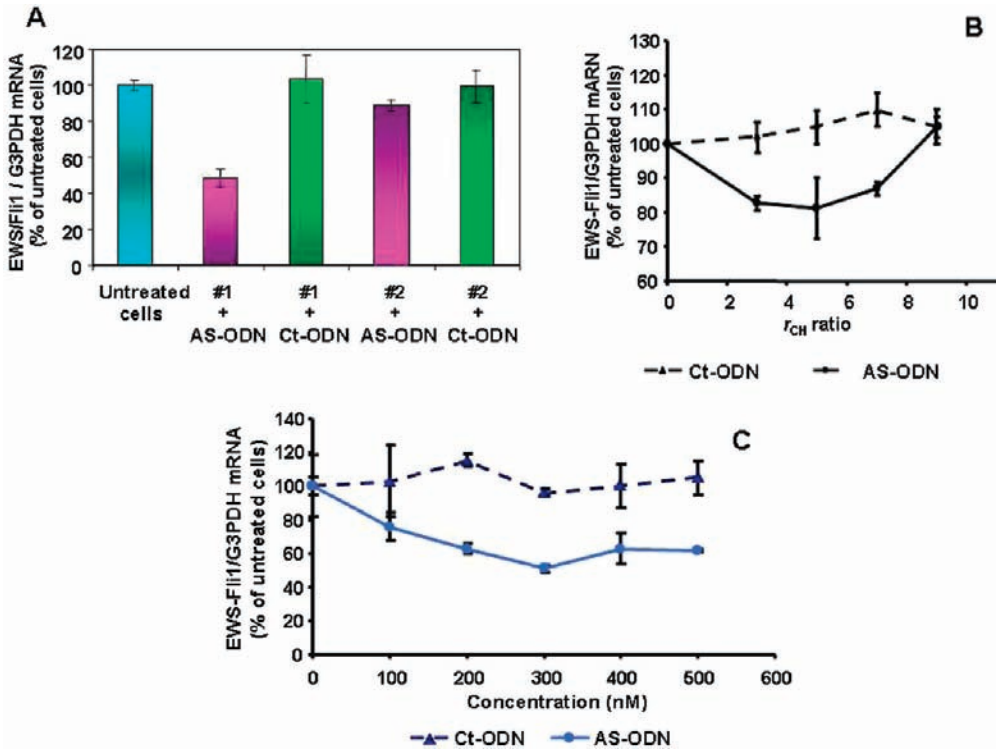

Figure 8. Inhibition of EWS-Fli1 mRNA expression in NIH/3T3-EF cells by antisense ODN (As-ODN) or control sequence (Ct-ODN). (A) The ODN is vectorized by wild-type (**1**) or mutated (**2**) penetratins. Measurement was performed by RT-PCR. ODN concentration was 500 nM and $r_{CH} = 5$. (B) Influence of the r_{CH} ratio on AS-ODN penetration into cell by wild-type penetratin **1**. The cells were treated for 24 h with 200 nM ODN and peptide **1** with r_{CH} varying from 0 to 9. (C) Dose effect of ODN vectorized by wild-type peptide **1** at $r_{CH} = 5$ on EWS-Fli1 expression in cell after 24 h treatment. Gene expression is determined by RT-PCR.

AS-ODN fluorescence intensity is the same that observed for AS-ODN alone and may be attributed to a nonspecific ODN interaction with cell membranes.

The FHV derived peptide **5a** corresponding to the fusogenic part of the protein causes a weak penetration of the AS-ODN into cells (Figure 6E). Fluorescence transfer is observed in aggregates close to the cells (similarly to that found with **1a** and **2a**) indicating the formation of complexes between AS-ODN and peptide **5a** (Figure 6E). The peptide **6**, bearing no positive charges, does not form a complex with the AS-ODN (Figure 6F).

According to CD studies (Figure 1), the attachment of the Hca-group increases the helicity of the wild-type penetratin, while the Hca-group weakly decreases the helicity of the mutant peptide. Anionic micelles induce helicity in the case of both **1** and **2** peptides, which is a more expressed for **1** than **2** (Figure 3). On the basis of CD studies, the wild-type penetratin **1** has a more flexible conformation than the mutant **2**, which is likely more favorable for ODN binding and cell penetration.

Inhibition of EWS-Fli1 Expression by AS-ODN Vectorized by Antennapedia Derivative Peptides. The ability of wild-type and mutated Antennapedia peptides to vectorize efficiently AS-ODN into cells was studied by the measurement of targeted oncogene expression. After cell treatment, total RNA is extracted, and EWS-Fli1 mRNA expression is measured by RT-PCR. It can be seen in Figure 8 that wild-type penetratin is able to inhibit EWS-Fli1 expression only if associated to the AS-ODN. In the same condition, control ODN has no effect. These results indicate that the lower transfection efficiency of mutated penetratin is correlated with the loss of gene inhibition. It has been proposed that association of penetratin peptides to the cell membrane is due to electrostatic interactions. The conformational change of penetratin upon $Trp^6 \rightarrow Phe^6$ mutation must be responsible for the decrease of cell penetration. Indeed, it has been described that the $Gln^8 \rightarrow Pro^8$ change presents a similar effect confirming the key role of this domain for the cell penetration (*27*).

The efficiency of transfection of nucleic acids by noncovalently linked CPP is largely dependent on the ratio of charges (r_{CH}) between the two components. The inhibition of EWS-Fli1 expression determined by PCR was performed for different ODN to CPP charge ratio ($r_{CH} = 0-9$) using the wild-type Antennapedia peptide **1**. Figure 8B shows that maximum inhibition was obtained for r_{CH} ratio of 5 confirming the results obtained previously (*22*, *23*). Dose-dependent treatment (Figure 8C) of the cells shows a maximum inhibition at 300 nM in As-ODN associated to peptide **1**. Under the same conditions, the Ct-ODN displays no inhibition, confirming the specificity of the treatment. For higher concentrations, the efficiency of inhibition was not increased, probably because aggregate formation between the ODN and the peptide might take place. This is unfavorable for ODN delivery and may be associated with a toxic effect.

SUMMARY

Antennapedia peptides were previously described as efficient agents for the delivery of oligonucleotides either by covalent linking or through ionic interaction (*28*, *29*). The action has been attributed to a conformational change of the molecule when interacting with the membrane. The introduction of a mutation inside this peptide was found to result in a dramatic decrease in oligonucleotide delivery. Surprisingly, in our hands both the wild-type and mutated peptides interact strongly with cells (Figure 5). The CD spectra of the wild (**1**) and mutated (**2**) penetratins in TFE solution show that the helicity of the mutated peptide is higher than that of the wild-type, while the Hca-labeled penetratins show similar CD spectra (as a sign of comparable helix content) and interaction with cells (Figure 6). It is likely that the increased helicity of the membrane-bound

wild-type Hca-penetratin (**1a**) explains its improved ability to cross the cell membrane. It should be emphasized here that the attachment of a fluorescent label may have an effect on the conformation and the flexibility of cell-penetrating peptides that must be taken into consideration when evaluating biological experiments.

ACKNOWLEDGMENT

This work was supported by the following grants: CNRS exchange convention with Hungary; European STREP Prothets devoted to Ewing Sarcoma to J.-R.B. and C.M.; NI 68466 to M.H.; RET108/2004 to I.L.

LITERATURE CITED

(1) Maksimenko, A., and Malvy, C. (2005) Oncogene-targeted antisense oligonucleotides for the treatment of Ewing sarcoma. *Expert Opin. Ther. Targets 9*, 825–830.

(2) Prieur, F., Tirode, P., Cohen, O., and Dellatre, O. (2004) EWS/Fli-1 silencing and gene profiling of Ewing cells reveal downstream oncogenic pathways and a crucial role for repression of insulin-like growth factor binding protein 3. *Mol. Cell. Biol. 24*, 7275–7283.

(3) Elbashir, S. M., Harborth, J., Lendeckel, W., Yalcin, A., Weber, K., and Tuschl, T. (2001) Duplexes of 21-nucleotide RNAs mediate RNA interference in cultured mammalian cells. *Nature 411*, 494–498.

(4) Elbashir, S. M., Lendeckel, W., and Tuschl, T. (2001) RNA interference is mediated by 21-and 22-nucleotide RNAs. *Genes Dev. 15*, 188–200.

(5) Couzin, J. (2006) Molecular biology - RNAi safety comes under scrutiny. *Science 312*, 1121–1124.

(6) Frantz, S. (2006) Safety concerns raised over RNA interference. *Nat. Rev. Drug Discovery 5*, 528–529.

(7) Crooke, S. T. (2004) Progress in antisense technology. *Annu. Rev. Med. 55*, 61–95.

(8) Fischer, P. M. (2007) Cellular uptake mechanisms and potential therapeutic utility of peptidic cell delivery vectors: Progress 2001−2006. *Med. Res. Rev. 27*, 755–795.

(9) Pujals, S., Fernandez-Carneado, J., Lopez-Iglesias, C., Kogan, M. J., and Giralt, E. (2006) Mechanistic aspects of CPP-mediated intracellular drug delivery: Relevance of CPP self-assembly. *Biochim. Biophys. Acta 1758*, 264–279.

(10) Patel, L. N., Zaro, J. L., and Shen, W. C. (2004) Cell penetrating peptides: intracellular pathways and pharmaceutical perspectives. *Pharm. Res. 24*, 1977–1992.

(11) Derossi, D., Joliot, A., Chassaing, G., and Prochiantz, A. (1994) The third helix of the Antennapedia homeodomain translocates through biological membranes. *J. Biol. Chem. 269*, 10444–10450.

(12) Lindgren, M., Hällbrink, M., Prochiantz, A., and Langel, Ü. (2000) Cell-penetrating peptides. *Trends Pharmacol. Sci. 21*, 99–103.

(13) Tamura, R. N., Rozzo, C., Starr, L., Chambers, J., Reichardt, L. F., Cooper, H. M., and Quaranta, V. (1990) Epithelial integrin alpha-6beta-4 - complete primary structure of alpha-6 and variant forms of beta-4. *J. Cell Biol. 111*, 1593–1604.

(14) Bong, D. T., Janshoff, A., Steinem, C., and Ghadiri, R. M. (2000) Membrane partitioning of the cleavage peptide in flock house virus. *Biophys. J. 78*, 839–845.

(15) Baker, W., Haksar, C. N., and McOmie, J. F. N. (1950) Fluorescent reagents. Acyl chlorides and acyl hydrazides. *J. Chem. Soc.* 170–174.

(16) Tanaka, K., Iwakuma, T., Harimaya, K., Sato, H., and Iwamoto, Y. (1997) EWS-Fli1 antisense oligodeoxynucleotide inhibits proliferation of Human Ewing's sarcoma and primitive neuroectodermal tumor cells. *J. Clin. Invest. 99*, 239–247.

(17) Lambert, G., Bertrand, J.-R., Fattal, E., Subra, E. F., Pinto-Alphandary, H., Malvy, C., Auclair, C., and Couvreur, P. (2000) EWS Fli-1 antisense nanocapsules inhibits Ewing sarcoma-related tumor in mice. *Biochem. Biophys. Res. Commun. 279*, 401–406.

(18) Toub, N., Bertrand, J.-R., Malvy, C., Fattal, E., and Couvreur, P. (2006) Antisense oligonucleotide nanocapsules efficiently inhibit EWS-Fli1 expression in a Ewing's sarcoma model. *Oligonucleotides 16*, 158–168.

(19) Stewart, J. M., and Young, J. D. (1984) *Solid Phase Peptide Synthesis*, Pierce Chemical Company, Rockford, IL.

(20) Kele, P., Illyés, E., Mezõ, G., Dóda, M., Mák, M., Kaposi, D. A., and Sebestyén, F. (1999) Fluorescent derivatives of bovine neurotensin 8−13 fragment. *Lett. Pept. Sci. 6*, 225–238.

(21) Kaiser, E., Colescott, R. L., Bossinger, C. D., and Cook, P. I. (1970) Color test for detection of free terminal amino groups in solid-phase synthesis of peptides. *Anal. Biochem. 34*, 595–598.

(22) Toth, J., Böszörményi, I., Majer, Zs., Laczkó, I., Malvy, C., Hollósi, M., and Bertrand, J.-R. (2002) A two step model aimed at delivering antisense oligonucleotides in targeted cells. *Biochem. Biophys. Res. Commun. 293*, 18–22.

(23) Laczkó, I., Váró, Gy., Bottka, S., Bálint, Z., Illyés, E., Vass, E., Bertrand, J.-R., Malvy, C., and Hollósi, M. (2006) N-terminal acylation of the SV40 nuclear localization signal peptide enhances its oligonucleotide binding and membrane translocation efficiencies. *Arch. Biochem. Biophys. 454*, 146–154.

(24) Dom, G., Shaw-Jackson, C., Matis, C., Bouffioux, O., Picard, J. J., Prochiantz, A., Mingeot-Leclercq, M. P., Brasseur, R., and Rezsohazy, R. (2003) Cellular uptake of Antennapedia Penetratin peptides is a two-step process in which phase transfer precedes a tryptophan-dependent translocation. *Nucleic Acid Res. 31*, 556–561.

(25) Jackson, M. and, and Mantsch, H. H. (1992) Halogenated alcohols as solvents for proteins: FTIR spectroscopic studies. *Biochim. Biophys. Acta 1118*, 139–143.

(26) Laczkó, I., Bottka, S., Tóth, G. K., Malvy, C., Bertrand, J.-R., and Hollósi, M. (2004) Interaction of fusogenic peptides with an antisense oligonucleotide in solution and in the presence of micelles: conformational studies. *Biochem. Biophys. Res. Commun. 313*, 356–361.

(27) Lindgren, M., Gallet, X., Soomets, U., Hallbrink, M., Brakenhielm, E., Pooga, M., Brasseur, R., and Langel, U. (2000) Translocation properties of novel cell penetrating transportan and penetratin analogues. *Bioconjugate Chem. 11*, 619–626.

(28) Mäe, M., and Langel, Ü. (2006) Cell-penetrating peptides as vectors for peptide, protein and oligonucleotide delivery. *Curr. Opin. Pharmacol. 6*, 509–514.

(29) Veldhoen, S., Laufer, S. D., Trampe, A., and Restle, T. 2006: Cellular delivery of small interfering RNA by a non-covalently attached cell-penetrating peptide: quantitative analysis of uptake and biological effect. *Nucleic Acids Res. 34*, 6561–6573.

BC900005J

Identification of Glycosylated Sites in *Rapana* Hemocyanin by Mass Spectrometry and Gene Sequence, and Their Antiviral Effect

Pavlina Dolashka-Angelova,*[,†] Bernhard Lieb,[‡] Ludmila Velkova,[†] Nina Heilen,[§] Koen Sandra,[||] Lubomira Nikolaeva-Glomb,[⊥] Aleksander Dolashki,[#] Angel S. Galabov,[⊥] Jozef Van Beeumen,[||] Stefan Stevanovic,[§] Wolfgang Voelter,[#] and Bart Devreese[||]

Institute of Organic Chemistry with Centre of Phytochemistry, Bulgarian Academy of Sciences, 9 G. Bonchev St., Sofia 1113, Bulgaria, Institute of Zoology, University of Mainz, Müllerweg 6, Mainz 55099, Germany, Department of Immunology, Institute for Cell Biology, University of Tübingen, Auf der Morgenstelle 15, D-72076 Tübingen, Germany, Laboratory of Protein Biochemistry and Biomolecular Engineering, Ghent University, KL Ledeganckstraat 35, 9000 Ghent, Belgium, The Stephan Angeloff Institute of Microbiology, Bulgarian Academy of Sciences, 26 G. Bonchev St., Sofia 1113, Bulgaria, and Institute of Biochemistry, University of Tübingen, Hoppe-Seyler-Strasse 4, D-72076 Tübingen, Germany. Received January 28, 2009; Revised Manuscript Received May 6, 2009

Molluscan hemocyanins (Hcs) have recently received particular interest due to their significant immunostimulatory properties. This is mainly related to their high carbohydrate content and specific monosaccharide composition. We have now analyzed the oligosaccharides and the carbohydrate linkage sites of the *Rapana venosa* hemocyanin (RvH) using different approaches. We analyzed a number of glycopeptides by LC/ESI-MS/MS and identified the sugar chains and peptide sequences of 12 glycopeptides. Additionally, the potential carbohydrate linkage sites of 2 functional units, RvH-b and RvH-c, were determined by gene sequence analysis. Only RvH-c shows a potential N-glycosylation site. During this study, we discovered a highly conserved linker-intron, separating the coding exons of RVH-b and RvH-c. Following reports on antiviral properties from arthropod hemocyanin, we conducted a preliminary study of the antiviral activity of RvH and the functional units RvH-b and RvH-c. We show that the glycosylated FU RvH-c has antiviral properties against the respiratory syncytial virus (RSV), whereas native RvH and the nonglycosylated FU RvH-b have not. This is the first report of the fact that also molluscan hemocyanin functional units possess antiviral activity.

INTRODUCTION

Hemocyanins (Hcs) are large, oligomeric blue copper-containing glycoproteins that play a role as dioxygen carriers in the hemolymph of most molluscs and several arthropods (*1*−*4*). Despite their common function as dioxygen binding proteins, arthropod and molluscan hemocyanins evolved independently (*3*). The organization and size of molluscan and arthropodan Hc molecules differ significantly in size and oligosaccharide moieties (*5*−*7*).

Carbohydrate structures of hemocyanins from *Helix pomatia* and *Sepia officinalis* and keyhole limpet hemocyanin (KLH) have been identified using different methods (*8*, *9*). Thirteen potential N-glycosylation sites were identified in the gene sequence analysis of one subunit of *Haliotis tuberculata* hemocyanin (HtH1) (*10*) and seven in Nautilus hemocyanin FUs (*11*). Seven potential N-glycosylation sites are present in *Octopus dofleini* hemocyanin (Od) (*12*). A single N-linkage site and three O-linkage sites were found in the arthropod *Carcinus aestuarii* hemocyanin (CaH) (*13*, *14*). Although it is generally accepted that the oligosaccharide constituents of Hc are of prime significance for their antigenicity and biomedical properties, knowledge on the carbohydrate structures of these glycoproteins is still incomplete.

In this work, we focus on the structure and properties of *Rapana venosa* hemocyanin, isolated from the Black Sea. Eight functional units (FUs) with molecular mass of 45−50 kDa, namely, from RvH-a to RvH-h, have been isolated from both structural subunits RvH1 and RvH2 (*5*, *7*, *15*), but the oligosaccharide moieties of only a few of them have been reported (*16*−*19*).

Recently, it was shown that KLH also possesses potential antitumor activity, and this effect was ascribed to the presence of the disaccharide epitope Gal (β1−3)GalNAc, because it is cross-reactive with an equivalent surface epitope of superficial bladder tumor cells (*20*). The KLH dependent cumulative humoral and cellular immune response is expressed as a cytolytic reduction of tumor growth. Further analyses of KLH1 and KLH2 confirmed the multiepitopic potential of these molecules (*21*).

Hcs from other gastropods were considered to be possible substitutes for KLH as immunostimulants. It was found that marine *Haliotis tuberculata* (HtH) (*21*), Chilean gastropod, *Concholepas concholepas* (CcH) (*22*), and *Rapana venosa* (RvH) (*23*, *24*) Hcs have significant antitumor activity against mouse bladder carcinoma cells. The occurrence of xylose in *Helix pomatia* Hc (HpH) is considered to be highly immunogenic in mammalian species (*8*, *25*).

Subsequently, it was found that the arthropodan *Penaeus monodon* hemocyanin has antiviral activity against the spot syndrome virus (WSSV) and Singapore grouper iridovirus (SGIV) (*26*), although the antiviral mechanism is still unclear. The antiviral effect of molluscan Hcs has not been studied yet.

* Corresponding author. Assoc. Prof. Dr. P. Dolashka-Angelova, Institute of Organic Chemistry with Centre of Phytochemistry, Bulgarian Academy of Sciences, str. G. Bonchev 9, 1113 Sofia. Tel.: 35929606163, Fax: 35928700225, E-mail: pda54@yahoo.com.

† Institute of Organic Chemistry, Bulgarian Academy of Sciences.

‡ University of Mainz.

§ Institute for Cell Biology, University of Tübingen.

|| Ghent University.

⊥ The Stephan Angeloff Institute of Microbiology, Bulgarian Academy of Sciences.

Institute of Biochemistry, University of Tübingen.

10.1021/bc900034k CCC: $40.75 © 2009 American Chemical Society
Published on Web 06/08/2009

Since the biological effects of hemocyanins on immunostimulatory properties are attributed to their high carbohydrate content and specific monosaccharide composition, we hypothesized that antiviral effects might have a similar origin. We therefore characterized several glycopeptides from *R. venosa* hemocyanin by LC/ESI-MS/MS and investigated their antiviral effects.

MATERIALS AND METHODS

Materials. *Rapana venosa* Hc was isolated from marine snails living in the Black Sea as described before (*4*). Two structural subunits RvH1 and RvH2 were separated on a Resource Q column using an FPLC system. Two functional units RvH2-b and RvH2-c were isolated from structural subunit RvH2 as described by Dolashka et al. (*7, 15*). All other (bio)chemicals, unless noted, were purchased from Sigma-Aldrich.

RNA Extraction and RT-PCR. RNA was extracted using the RNeasy extraction-Kit (Qiagen) according to the manufacturer's instructions using 200 mg of foot tissue. RT-PCR was performed using 1 μg of RNA, Transcriptor reverse transcriptase (Roche), and a degenerated hemocyanin specific oligonucleotide (*27*). PCR was performed using 5 μL of the RT assay. Each PCR was supplied with 1 μM primer, 200 μM dNTP, 3 mM $MgCl_2$, 5 μL of 10× PCR buffer, and 2.5 units of recombinant Taq polymerase (Invitrogen, Germany). Samples were denatured for 2 min at 94 °C, followed by 35 amplification cycles (10 s at 94 °C, 30 s at 55 °C, 2 min at 72 °C) and final extension for 10 min at 72 °C.

Gel Electrophoresis, DNA Purification, and Sequencing Reactions. PCR products were separated by electrophoresis in a 0.8% agarose gel (1× TBE buffer) and extracted using the Peqlab gel extraction kit (Peqlab, Germany). The isolated fragments were either sequenced directly or after being cloned using the StrataClone PCR Cloning Kit (Startagene, USA). Sequencing reactions were performed with the Taq DyeTerminator system (Perkin-Elmer) using standard primers and electrophoretically analyzed by Genterprise (Germany).

Bioinformatics. Alignments were created by *ClustalX* V1.81 (*28*) and optimized manually using *Genedoc* (*29*). Database searches and further analyses were performed using sequence analysis tools [e.g., *Blastn* and *Blastx* (*30*) available at the NCBI (www.ncbi.nlm.nih.gov). 3D models were created using the Swiss PDB viewer (*31*), and phylogenetic analyses were carried out using *Mega* 3.1 (*32*).

Mass Spectrometric Analysis of Glycopeptides by Nanoelectrospray MS/MS. Four milligrams of RvH1 and RvH2 were digested with trypsin, and the glycopeptides were isolated as described by Dolashka-Angelova et al. (*16*). HPLC fractions, detected at a wavelength of $\lambda = 206$ nm, were collected, lyophilized, and analyzed for carbohydrates with orcinol/H_2SO_4 on silica gel plates (*18*). Glycopeptides containing fractions were analyzed by nanoelectrospray ionization (ESI) mass spectrometry (MS) on a hybrid quadrupole orthogonal acceleration time-of-flight tandem mass spectrometer (Q-TOF; Micromass, Manchester, United Kingdom) as described (*33*). Alternatively, glycopeptides were sequenced on a Q-Trap LC/MS/MS system (Applied Biosystems/MDS Sciex, Concord, ON, Canada) equipped with a nanospray ion source (Protana, Odense, Denmark) as described by Sandra et al. (*19*).

Antiviral Effects of the Glycosylated and Nonglycosylated Functional Units. The *in vitro* hemocyanin antiviral effects on the replication of poliovirus type 1 (LSc-2ab), coxsackievirus B1 (CV−B1), and respiratory syncytial virus (RSV) were studied using native RvH and its glycosylated (RvH-c) and nonglycosylated (RvH-b) functional units at a concentration of 1000 μg/mL in 15 mM phosphate buffer, pH 7.1. Polio virus type 1 (LSc-2ab) and CV−B1 were grown in FL cells and RSV was grown in Hep-2 cell cultures. The cultures were grown in a growth medium of DMEM (Gibco BRL, USA), containing 5% fetal calf serum, supplemented with antibiotics (penicillin 100 IU/mL, streptomycin 100 μg/mL, and gentamycin 50 μg/mL) and 20 mM HEPES buffer (Gibko BRL, USA) in a humidified atmosphere at 37 °C and 5% CO_2. Cells were routinely subcultured twice a week. Viruses were replicated on monolayer cells in a maintenance medium of DMEM, supplemented with 0.5% fetal calf serum, 20 mM HEPES buffer, and antibiotics.

Cytotoxicity Test. For cytotoxicity tests, Hep-2 cells were seeded in flat-bottomed 96-well plates by adding 0.2 mL per well of the cell suspension, containing $(1.5-2) \times 10^5$ cells/mL. After formation of a cell monolayer, growth medium was discarded and 0.2 mL containing 0.5 μg serial dilution concentrations of the tested substances, diluted in a maintenance medium, were added, followed by further incubation of cells in a humidified atmosphere at 37 °C and 5% CO_2 and monitoring the microscopic cytotoxic effect after 24 and 48 h. The highest concentration showing no cytotoxic effect was recorded at 48 h post-inoculation and was considered as the maximum of tolerated nontoxic concentration (MTC).

Antiviral Test. The cytopathic effect (CPE) inhibition test was used to measure the antiviral effect of the compounds against the replication of polio virus type 1 (LSc-2ab), CV−B1, and RSV. Briefly, monolayer cells in 96-well plates were inoculated with 0.1 mL virus suspension containing 100 or 10 $CCID_{50}$. After virus adsorption for 1 h at room temperature for polio virus type 1 (LSc-2ab) and CV−B1, and for 2 h at 37 °C and 5% CO_2 for RSV, excessive virus suspension was discarded, and cells were inoculated with 0.2 mL of maintenance medium containing 1 mg/mL RvH-c or RvH-b. Cells were incubated (Hera Cell, 150, Hereaus, Germany) in a humidified atmosphere at 37 °C and 5% CO_2. Virus-induced CPE was scored daily by inverted light microscopy (Olympus CK40, Japan) at 125× and 400× magnification on a 0−4 basis (4 representing total cell destruction and 0 the intact cell monolayer) until the appearance of its maximum in the untreated virus control wells (with no compound in the maintenance medium). This was on the 48th hour for polio virus type and CV−B1 and on the 120th hour for RSV. Virus-induced CPE in treated and nontreated virus control wells was compared, and the percent of CPE inhibition was calculated.

Virucidal Test. The quantitative suspension test was used to detect the virucidal effect of the compounds. Equal volumes of undiluted virus suspension and each of the compounds at their highest initial concentrations were mixed and kept for 1 h at room temperature. The residual infectious virus was determined in monolayer cells by inoculating 0.1 mL of serial 10-fold dilutions of the virus suspension samples, followed by 1 or 2 h adsorption at 37 °C and 5% CO_2. Then, excessive virus was discarded, and cells were inoculated with 0.2 mL of maintenance medium and further incubated at 37 °C and 5% CO_2. The virus CPE was scored daily until its maximum in the virus control wells.

RESULTS AND DISCUSSION

KLH has already been in use for several years as an immunotherapeutic agent in the treatment of bladder carcinoma and other cancer types (*34*). The relevance of specific glycosylation patterns as a differentiating factor for immunostimulatory properties has already been raised in studies on the hemocyanin isoforms KLH1 and KLH2 of *Megathura crenulata* (*20, 21*). Molluscan hemocyanin genes contain several potential N-glycosylation sites, and some of those have been already effectively demonstrated to be glycosylated using a series of analytical strategies (*8, 13*). For a functional unit of *Octopus dofleini* hemocyanin OdH-g, this has been confirmed by X-ray

Table 1. Amino Acid Sequence and Carbohydrate Structure of Glycopeptides Isolated from RvH and Analyzed Using Different Techniques[a]

	glycopeptides	glycans	*m/z*
		ESI-MS	
1	[QK]AEN**L**TTTR	Fuc $Man_3GlcNAc_2Hex_3$	1036 $[M+2H]^{2+}$
2	AEN**L**TTTR	Fuc $Man_3GlcNAc_2Hex_3$	972 $[M+2H]^{2+}$
3	HHGHV[···K···**N**···]R	Fuc $Man_3GlcNAc_2Hex_3$	1396 $[M+2H]^{2+}$
4	FSGEVDGH**N**TSR	$Man_3GlcNAc_2$	1099 $[M+2H]^{2+}$
5	YE[IL]HAV**N**GST[IL]AA[IL]	$Hex_2Man_3GlcNAc_2$	1338 $[M+2H]^{2+}$
6	YE[IL]HAV**N**GST[IL]AA[IL]	$Hex_3Man_3GlcNAc_2$	1419 $[M+2H]^{2+}$
		Q trap-LC/MS/MS	
7	MGQYG**NL**S**T**NNTR	Hex $Man_3HexNAc_2$	837.97$[M+2H]^{3+}$
8	SV**N**GTLLGSQILGKPY	Fuc $Man_3GlcNAc_2$	
	SV**N**GTLLGSQILGK	$Man_3GlcNAc_2$	
9	FSGEVDGH**N**TSR	$Man_3GlcNAc_2$	1099 $[M+2H]^{2+}$
10	AEN**I**TTTR	Fuc $Man_3GlcNAc_2$	972 $[M+2H]^{2+}$
11	FA**N**ATSIDGPNA	SO_4 $MeHexAMeHexNAc_2Man_3GlcNAc_2$	2786 $[M+H]^+$
12	EMLTL**N**GTNLA	$MeHex_2AHexNAc_2Man_3GlcNAc_2$	2846 $[M+H]^+$
13	IHSYSGSYI**N**ASLLHGPSII	$MeManMan_2GlcNAc_2$	2848 $[M+H]^+$

[a] The exact order of the residues between brackets could not be established, and X represents unknown amino acids.

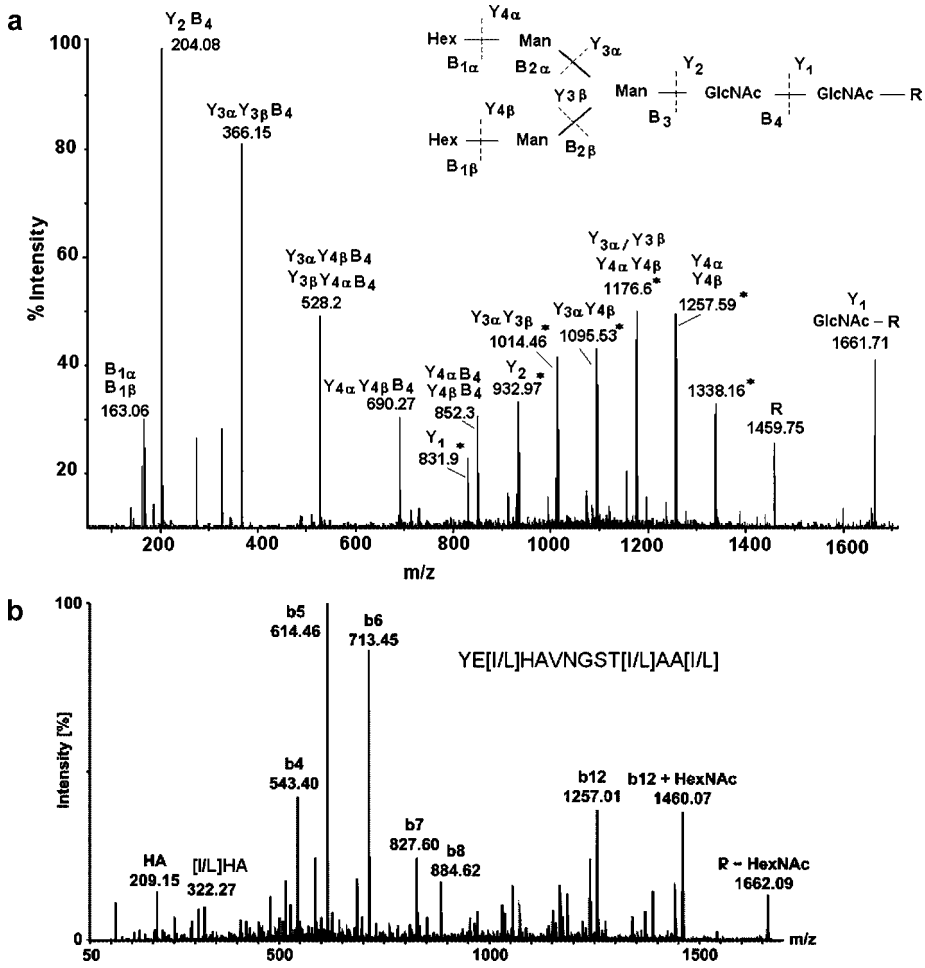

Figure 1. Fragment spectra of the glycopeptide G1 with determined *m/z* 1338.16 $[M+2H]^{2+}$. (a) MS/MS analysis of the sugar moiety, using a collision energy of 37 eV. Annotation of sugar fragments. The insert shows the complete carbohydrate structure and the cleavage points leading to the respective fragments. * corresponds to the doubly charged ions. (b) Pseudo-MS/MS/MS experiment (in-source and collision-induced fragmentation) of the peptide moiety (YEXHAVN*GSTXAAX) still carrying one HexNAc (*m/z* 1662.09, $[M-H]^+$), using a cone voltage of 95 V and a collision energy of 80 eV. R corresponds to the peptide.

crystallography (*35*). Previous analyses of the oligosaccharide moiety of RvH revealed a small set of carbohydrate structures (*16*−*19*). We extended this study here implementing advanced separation and mass spectrometric techniques to analyze the binding sites and the carbohydrate heterogeneity of the structural subunits RvH1 and RvH2.

We used two approaches to analyze the glycosylation sites in *Rapana venosa* hemocyanin. The first approach included the isolation of glycopeptides from structural subunits RvH1 and RvH2, and analysis of their amino acid sequences and structures of the linked oligosaccharides by mass spectrometry. Thirteen glycopeptides, given in Table 1 (No 1−13), were identified using ESI-MS and Q-Trap-LC/MS/MS. Some of them were previously characterized by capillary electrophoresis (*19*) or HPLC/electrospray ionization mass spectrometry (*17*, *18*). The second approach involved identification of the linkage sites by gene sequencing.

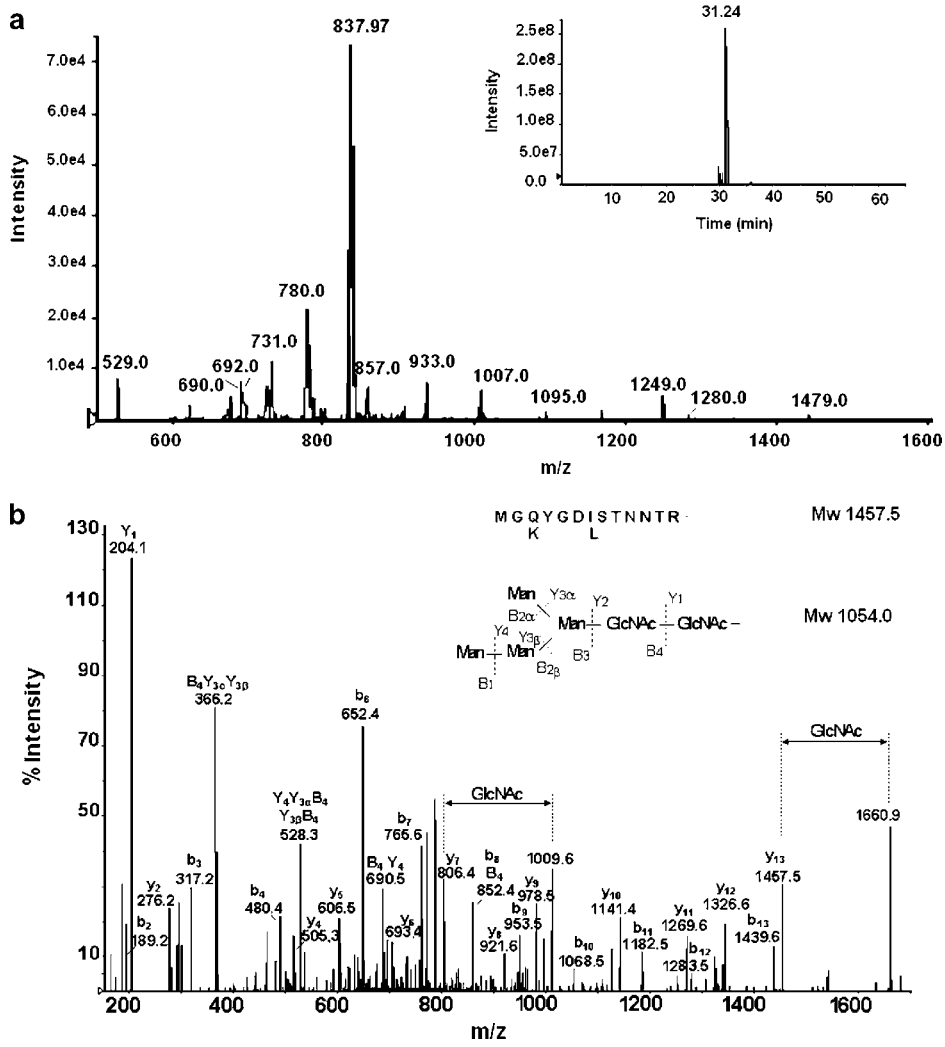

Figure 2. Precursor (a) scan of the ion at time 31.24 min of the chromatographic separation (insert) and enhanced product ion (EPI) scan of the ion (b) at *m*/*z* 837.97.

Glycopeptides were isolated after overnight digestion of the structural subunits RvH1 and RvH2 with trypsin, and the resulting peptides were subjected to reversed phase separation using a Nucleosil 7 C_{18} column. Fractions testing positive in the orcinol test were lyophilized and studied by mass spectrometry.

Characterization of Glycopeptides Using HPLC Fractions Analyzed by Flow Injection Analysis on a Q-TOF ESI-MS. Six glycopeptides were characterized in detail by analyzing the corresponding HPLC fraction by ESI-MS/MS. As an example, we outline here the result of a peptide (Table 1, No 5) that appeared as a doubly protonated molecule of *m*/*z* 1338.16 $[M+2H]^{2+}$ in the MS spectrum (not shown). The MS/MS spectra obtained from this glycopeptide are displayed in Figure 1. Figure 1A shows the MS/MS spectrum after collisional induced dissiocation. The fragment ion at *m*/*z* 1661.71 corresponds to the peptide (designated R-, *m*/*z* 1459.75), which is N-glycosylated, with a single residual GlcNAc residue. The spectrum is further dominated by glycan fragments, which correspond to a classical mannose type of oligosaccharide, consisting of two N-acetylhexosamines (HexNAc) monomers as well as five hexose (Hex) residues. In a pseudo-MS (*3*) experiment, the sugar side chain was removed by in-source fragmentation, and the peptide with one remaining HexNAc residue was further fragmented in the hexapole collision cell. This allowed the sequence analysis of the peptide and the determination of the site to which the sugar chain was attached (Figure 1B). The amino acid sequence of the peptide was revealed to be YEXHAV**N*GS**TXAAX. The glycosylation site N* was identified as part of the typical N-glycosylation motif N-aa-S/T, where aa can be any amino acid except Proline. X represents a leucine or isoleucine residue, which could not be distinguished by the applied MS methods. Five additional glycopeptides (Table 1, peptides 1−6) were characterized in the same way.

Characterization of Glycopeptides Using Q-Trap LC/MS/MS System. The Q-Trap system with its capabilities to perform typical triple quadrupole scans was additionally used for this purpose. Glycopeptides, selectively detected in a proteolytic mixture by the appearance of collisionally induced marker oxonium ions such as *m*/*z* 163 (Hex^+), 204 ($HexNAc^+$), or 366 ($HexHexNAc^+$), were sequenced.

The insert of Figure 2a shows the LC/MS/MS total ion current (TIC) chromatogram of the precursor ion scan (monitoring *m*/*z* 204) of the HPLC fraction at time 31.24 min. The enhanced resolution scan (not shown) showed that the glycopeptide with mass 2511.91 eluting at this moment was triply charged at *m*/*z* 837.97 $[M+3H]^{3+}$. The precursor ion scan at time 31.24 min is presented in Figure 2a. The spectrum is dominated by glycan fragmentation corresponding to the Domon/Costello nomenclature. However, peptide fragmentation (Roepstorff/Biemann cleavages) became more dominant when the collision energy was increased, allowing one to deduce the peptide sequence MGQYGD(I/L)ST*N*NTR from the series of y- and b-ions (Figure 2b). The ion b_{13} (*m*/*z* 1439.6) or y13 (*m*/*z* 1457.5) corresponds to the peptide, which contains two potential linkage

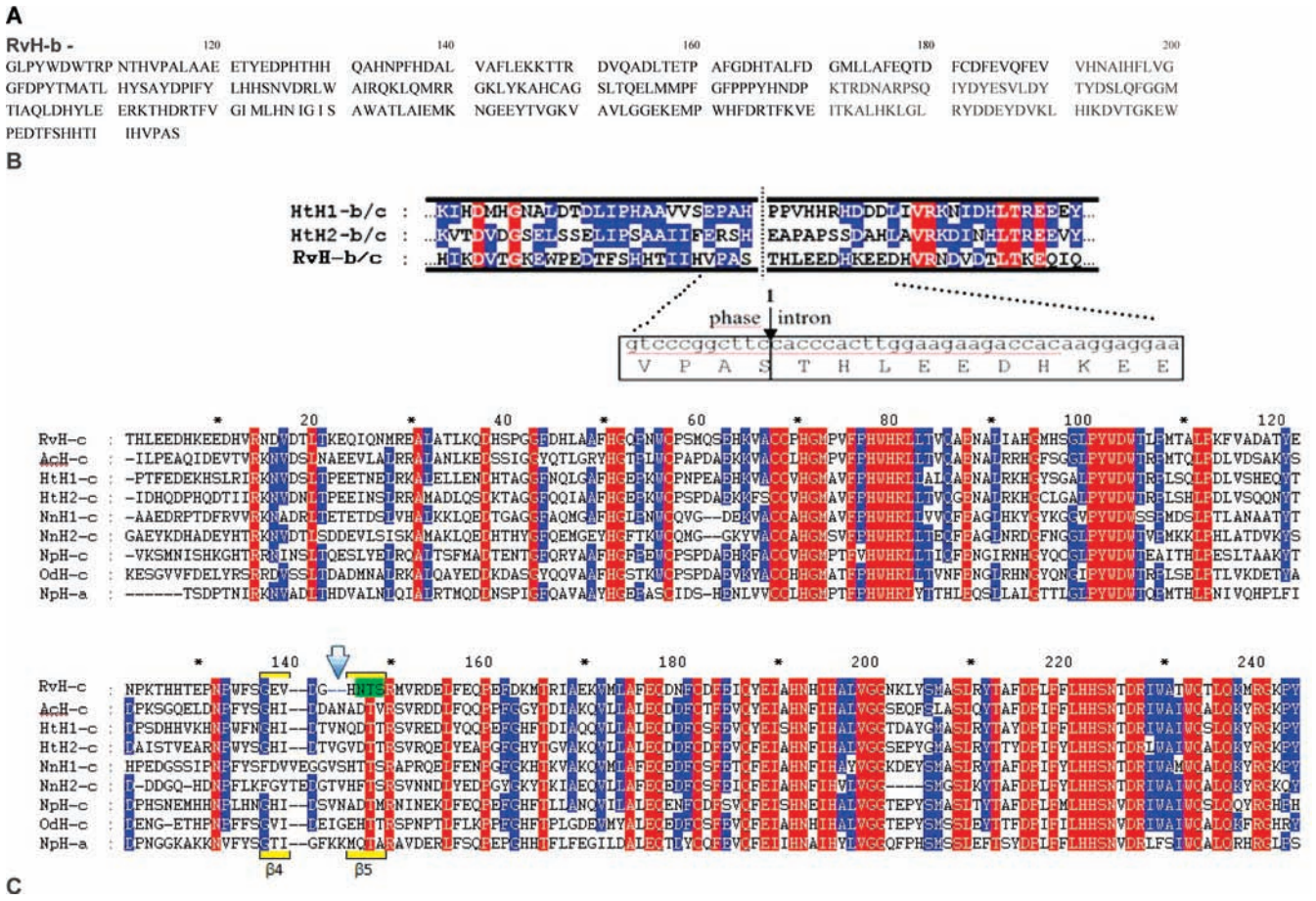

Figure 3. (A) Partially primary structure of functional unit RvH-b, of RvH as predicted from its cDNA sequence. (B-insert) A multiple sequence alignment of the linker intron identified in RvH-c in comparison to *Haliotis tuberculata* (two isoforms: HtH1-b/c, HtH2- b/c). (B) A multiple sequence alignment of the RvH-c with other FUs-c (the N-glycosylated site in RvH-c in green, other such sites are underlined. Residues in red and blue are conserved, or nearly conserved, respectively). Abbreviations of species: RvH, *Rapana venosa* Hc, AcH, *Aplysia californica* Hc, HtH, *Haliotis tuberculata* Hc. The secondary structural elements β4 and β5 are those occurring in the 3D structure of *Octopus dofleini* Hc (*35*).

sites -D(L/I)S- and -NNT-. Normally, D(L/I)S is not expected to be a linkage site, but, just in the unlikely event that deglycosylation of a glycan linked asparagine occurred during sample preparation, we thoroughly investigated this option. The ion y7 at *m/z* 806.4 corresponds to the C-terminal fragment of the peptide -(I/L)STNNTR, and the ion at *m/z* 1009.6 represents the same fragment still containing one GlcNAc moiety. This suggests that only the linkage site -NNT- is glycosylated, most likely via a high mannose-like structure. The ion at *m/z* 1660.9 corresponds to the intact peptide, represented as ion y13 (*m/z* 1457.5), which is N-glycosylated with a single GlcNAc residue. The glycan structure of this peptide could be revealed by this MS/MS spectrum, which displayed the typical ions (represented as Y and B) at *m/z* 204.1 (GlcNAc), *m/z* 366.2 (HexGlcNAc), *m/z* 528.3 ($Hex_2GlcNAc$), 690.5 ($Hex_3GlcNAc$), and 852.4 ($Hex_4GlcNAc$) (Figure 2B). Combining all data, the carbohydrate structure of 1054.0 Da ($Hex_2Man_3GlcNAc_2$) could be suggested.

Additional carbohydrate structures were analyzed in the same way and authentic binding sites could be revealed. The results are summarized in Table 1.

Identification of the Gene Sequence of Two RvH Functional Units. To better frame these results, we sequenced the cDNA of two FUs from RvH. To obtain the complete coding sequence for *R. venosa* hemocyanin (RvH) subunits, we performed RT-PCR using degenerated primers derived from the copper binding site A of *H. tuberculata* hemocyanin (*36*). The obtained fragments were cloned, sequenced, and identified by Blast analysis. We were able to determine the sequence of one hemocyanin coding fragment of 1668 bp in length coding for 556 amino acids, which in fact consisted of two subfragments. Since single functional units (FU) of hemocyanins can be assigned to their orthologs by multiple sequence alignment (*27*), we assume these two fragments partially code for of FU-b (Figure 3A) and FU-c (Figure 3B). The fragment of RvH-b comprises 316 amino acids lacking the first ca. 100 amino acids referring to the complete FU-b of known hemocyanins (*10, 27, 36*). The fragment of the FU-c comprises 240 amino acids, lacking ca. 200 residues of the C-terminus of complete FU-c. However, we can identify 14 amino acids to be part of a conserved phase 1 linker-intron, which exactly corresponds to both the intron phase and the position of the linker introns of functional unit b or c from the first structural subunit of *H. tuberculatos* (HtH1-b/c) and functional unit b or c from the second structural subunit of *H. tuberculatos* (HtH2-b/c) (Figure 3B-insert). The partitioning of the complete fragment into two separate FUs was done according to the known gene structures of *H. tuberculatos*, *O. dofleini*, and *N. pompilius* hemocyanins (*10*−*12, 36*) (Figure 3A,B).

Concerning the intron in the gene region of RvH-bc, we should mention that two types of introns were recognized in each gene of *Haliotis tuberculata* hemocyanin and *Octopus dofleini* hemocyanin: (i) introns positioned within the linker coding region between two functional units, referred to as "linker introns", and (ii) introns within a functional unit exon, consequently termed "internal introns". All hemocyanin linker introns identified so far are strictly phase 1 introns. According to these findings, the intron we observed in RvH is such a linker intron.

A

	HtH1-b	HtH2-b	RvH-b	HtH1-c	HtH2-c	RvH-c
HtH1-b	100	66	52	45	45	46
HtH2-b	66	100	51	42	44	47
RvH-b	52	51	100	43	44	53
HtH1-c	45	42	43	100	69	60
HtH2-c	45	44	44	69	100	57
RvH-c	46	47	53	60	57	100

B

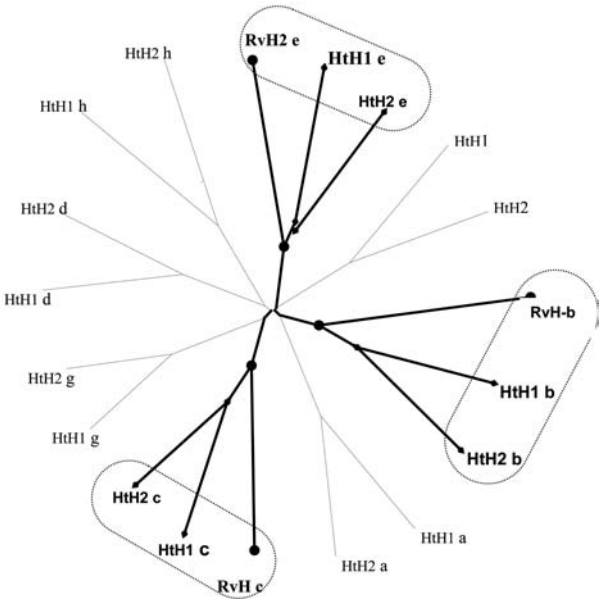

Figure 4. (A) Matrix of percentage identity between known hemocyanin sequences of FUs from *Rapana venosa* and *Haliotis tuberculata*. (B) A radial phylogenetic tree with of molluscan hemocyanin functional units sequences from three FUs from *Rapana venosa* (RvH-a,c,e) and *Haliotis tuberculata* (two isoforms: HtH1, HtH2).

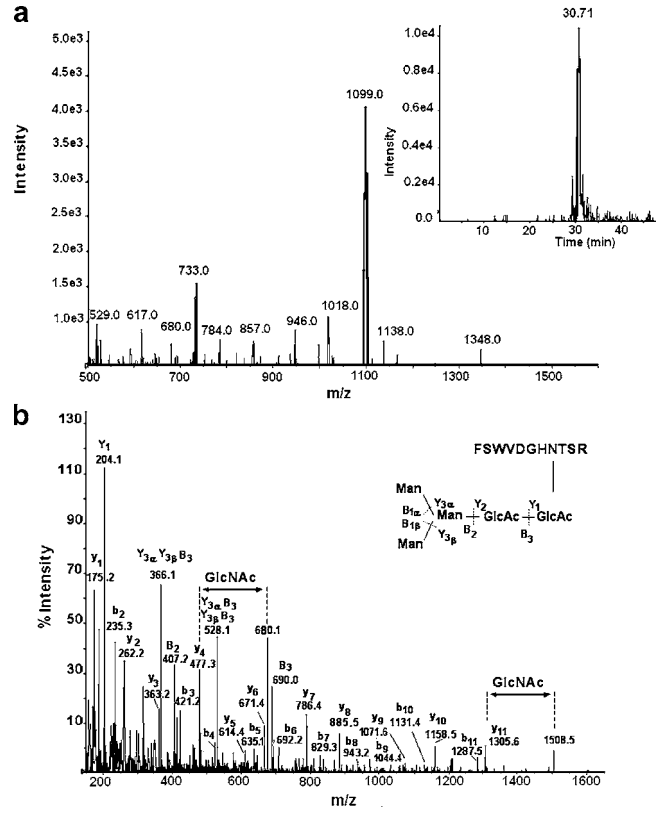

Figure 5. Precursor ion scan (A) at time 30.71 min of the chromatographic separation (insert) and enhanced product ion (EPI) scan of the ion (B) at *m*/*z* 1099.

In addition to the assignment of the orthologous FUs, the multiple sequence alignment of the separated FUs shows that RvH-b shares an identity of 52% and 51% with the vetigastropod hemocyanin isoforms HtH1-b and HtH2-b of *Haliotis tuberculata*, respectively, whereas the corresponding FU-c shares an identity of 57% and 60% with HtH1-c and HtH2-c, respectively (Figure 4A). This clearly suggests a closer relationship of RvH to HtH, which was also suggested by biochemical studies based on immunological assays. Due to the similar identity relationships of HtH1 and HtH2, the closer relationship of RvH and HtH2 cannot be seen in the molecular tree (Figure 4B). Moreover, they do not differ notably from any typical hemocyanin primary structure (Figure 4B) (*27*). No significant similarity to known N-terminal sequence data of isolated RvH1-b/c or RvH2-b/c subunits could be detected (*16*).

Comparisons of RvH-c and the deduced complete primary structures of other molluscan FUs-c shown in Figure 3C (only partial alignments are shown), reveal that only four of the nine c-FUs of *Rapana venosa* (RvH-c), *H. tuberculatos* (HtH2-c), *O. dofleini* (OdH-c), and *N. pompilius* (NpH-c) contain putative N-linkage sites.

Localization of the Carbohydrate Linkage Sites from the Gene Sequence. No carbohydrate linkage site was identified within the 316 amino acids of RvH-b. The finding that the orcinol/H_2SO_4 glycosylation test was negative for FU-b (data not shown) is thus corroborated by the gene sequence data and suggests that the N-terminal region of 100 residues contains no N-glycosylation site. Both isoforms of HtH-b contain at least one potential N-glycosylation site, which cannot be detected within the C-terminal 316 residues of RvH-b.

The finding that RvH-c does react with the reagent likewise corresponds to the gene sequence data, which reveal the presence of a glycosylation site at position 143. This NTS site is unique compared to the other sequences given in Figure 3C and matches perfectly well with the site identified the glycopeptide of mass 1099 $[M+2H]^{2+}$ by mass spectrometry (Table 1, peptides 4 and 9).

Several mass spectral results revealed that the carbohydrate structure $Man_3GlcNAc_2$ is branched to the RvH-c peptide FS**GE**VDGH*N*TSR. The precursor ion scan (monitoring *m*/*z* 204) at time 30.71 min during chromatography, the enhanced resolution (ER) scan of the most dominant ion (973), and the MS/MS spectrum of that ion are presented in Figure 5. It was determined that the glycopeptide has a 2× charge. By subtracting the peptide masses from the molecular ion 1099.19 $[M+2H]^{2+}$ ($[1099.19.2 \times 2] - 1 = 2197.38$), the glycan structure could be derived. The $Man_3GlcNAc_2$ glycan appears to occupy the -**N**TS- glycosylation site. This was confirmed by further investigation of the MS/MS spectrum. The ions at *m*/*z* 680.1 and 1508.5 correspond to the ion y4 (-**N**TSR-) and y11 (peptide), attached with one GlcNAc. The ion y11 at *m*/*z* 1305.6 corresponds to the peptide without the glycan. The *m*/*z* values for y8 and y9 differs by the mass of one tryptophan residue, and the peptide sequence FSWVDGHNTSR was determined. However, it differs by the gene sequence, because mass spectrometric fragmenting around a Gly residue often results in very small peaks and because a glycine-glutamic acid dipeptide is isobaric to a single tryptophan. Therefore, we now conclude that the gene sequence is likely to be correct.

The position, determined by model building, shows that the carbohydrate chain is exposed at the surface of the functional unit (Figure 6), at a similar position within the well-characterized structure of cephalopod *Octopus dofleini* (OdH) hemocyanin (*35*). In addition, it might be essential for establishing or maintaining any contact with other FUs and might contribute to the overall stability of the oligomeric hemocyanin; this remains to be determined.

Figure 6. Presumed 3D structure of FU RvH-c, based on the strongly homologous structure of *Octopus dofleini* Hc (35) and position of carbohydrate structure attached to the polypeptide chain.

Table 2. Testing for Antiviral Activity against the Replication in Vitro of RSV

		CPE score on a 0−4 basis (mean of four wells)			
compounds	concentration (μg/mL)	100 $CCID_{50}$/well	CPE inhibition %	10 $CCID_{50}$/well	CPE inhibition %
RvH	1000	3.5	0	1.5	0
	0	3.5	-	1.5	-
RvH-b	1000	3.5	0	1.5	0
	0	3.5	-	1.5	-
RvH-c	1000	1	71.4	0	100
	0	3.5	-	1.5	-

Antiviral Effect of RvH. Molluscan hemocyanins possess certain inhibitory properties against bacteria, but, so far, it was not shown to have any antiviral potential. We demonstrate here, for the first time, the inhibitory effect of molluscan hemocyanin RvH against viruses. We investigated whether this inhibition effect is linked to the presence of carbohydrate chains in RvH. To study the antiviral effect of RvH-oligosaccharides, polio virus type 1 (LSc-2ab), coxsackie virus B1 (CV−B1), and respiratory syncytial virus (RSV) were treated with native RvH and with nonglycosylated and glycosylated functional units RvH-b and RvH-c (0.45 and 2.0 mg/mL). Cytotoxicity, virucidal, and antiviral effects of glycosylated RvH-c and nonglycosylated FUs RvH-b were studied in FL or HEp-2 monolayer cells depending on the virus tested.

The compounds were nontoxic to monolayer cells even at the highest initial levels of concentration. Monolayer cells, treated with the highest given concentrations of the tested substances, remained completely intact, and no visible changes were detected by inverted light microscopy 24 and 48 h after treatment. Cytotoxicity control was carried out in parallel with the CPE inhibition test. Cells in this case were monitored for signs of toxicity until 120 h p.i. No toxicity was recorded either.

Virucidal and Antiviral Tests. The virucidal quantitative suspension test did not show any virucidal effect against polio virus type 1 (LSc-2ab), CV−B1, and RSV. The cytopathic effect (CPE) inhibition test was used to measure the antiviral effect of hemocyanin against the replication of poliovirus type 1 (LSc-2ab), CV−B1, and RSV. The results showed no antiviral effects of native RvH and of both FUs against polio virus type 1 (LSc-2ab) and CV−B1 (data not shown). However, the results presented in Table 2 show that the glycosylated FU RvH-c possesses some antiviral effect against the replication of RSV, at both viral doses tested. When the effect was tested against the lower virus dose of 10 $CCID_{50}$, the antiviral activity reached even 100% inhibition of the virus-induced cytopathic effect. Although not so strongly expressed, the antiviral effect is evident also at higher virus doses of 100 $CCID_{50}$ (which is the standard virus dose used in the CPE inhibition test), exceeding the 50% inhibition of the virus CPE.

In contrast, non-glycosylated FU RvH-b does not reveal any antiviral activity against the replication of RSV. The compounds also do not show antiviral effect against the replication of poliovirus type 1 (LSc-2ab) and CV−B1.

In conclusion, CPE-inhibition tests of the native RvH and both FUs against the replication of polio virus type 1 (LSc-2ab), CV−B1, and RSV revealed that there is no inhibitory effect on these viruses for native RvH and for non-glycosylated FU-b. However, the glycosylated FU RvH-c does show antiviral effect in the case of RSV replicated in HEp-2 cells. In order to understand the mechanism of this effect, further investigations are under way.

ACKNOWLEDGMENT

This work was supported by a research grant by the Ministry of Sciences and Education through the grant: DAAD-17/2007 (VU-L-310/07) and TK01/496, DFG (Deutsche Forschungsgemeinschaft) (Germany), Fund for Scientific Research-Flanders (FWO-Vlaanderen) through project VS.011.06N and CNR (Italy). Assoc. Prof. P. Dolashka-Angelova also thanks DAAD for granting a scholarship.

LITERATURE CITED

(1) Paoli, M., Giomi, F., Hellmann, N., Jaenicke, E., Decker, H., Di Muro, P., and Beltramini, M. (2007) The molecular heterogeneity of hemocyanin: Structural and functional properties of the 4 × 6-meric protein of *Upogebia pusilla* (Crustacea). *Gene 398*, 177–182.

(2) Van Holde, K. E., Miller, K. I., and Decker, H. (2001) Hemocyanins and invertebrate evolution. *J. Biol. Chem. 276*, 15563–15566.

(3) Burmester, T. (2001) Molecular evolution of the arthropod hemocyanin superfamily. *Mol. Biol. Evol. 18*, 184–195.

(4) Dolashka-Angelova, P., Schwarz, H., Dolashki, A., Stevanovic, S., Fecker, M., Saeed, M., and Voelter, W. (2003) Oligomeric stability of *Rapana venosa* hemocyanin (RvH) and its structural subunits. *Biochim. Biophys. Acta 1646*, 77–85.

(5) Dolashka, P., Genov, N., Pervanova, K., Voelter, W., Geiger, M., and Stoeva, S. (1996) Rapana thomasiana grosse (gastropoda) haemocyanin: spectroscopic studies of the structure in solution and the conformational stability of the native protein and its structural subunits. *Biochem. J. 315*, 139–144.

(6) Giomi, F., and Beltramini, M. (2007) The molecular heterogeneity of hemocyanin: Its role to the adaptive plasticity of Crustacea. *Gene 398*, 192–201.

(7) Dolashka-Angelova, P., Stevanovic, S., Dolashki, A., Devreese, B., Tzvetkova, B., Voelter, W., Van Beeumen, J., and Salvato, B. (2007) A challenging insight on the structural unit 1 of molluscan *Rapana venosa* hemocyanin. *Arch. Biochem. Biophys. 459*, 50–58.

(8) Gielens, C., De Geest, N., Compernolle, F., and Preaux, G. (2004) Glycosylation sites of hemocyanins of *Helix pomatia* and *Sepia officinalis*. *Micron 35*, 99–100.

(9) Wuhrer, M., Robijn, M. L. M., Koeleman, C. A. M., Balog, C. I. A., Geyer, R., Deelder, A. M., and Hokke, C. H. (2004) A novel Gal(β1−4)Gal(β1−4)Fuc(α1−6)-core modification attached to the proximal N-acetylglucosamine of keyhole limpet hemocyanin (KLH) N-glycans. *Biochem. J. 378*, 625–632.
(10) Lieb, B., Altenhein, B., and Markl, J. (2000) The sequence of a gastropod hemocyanin (HtH1 from *Haliotis tuberculata*). *J. Biol. Chem. 25*, 5675–81.
(11) Bergmann, S., Lieb, B., Ruth, P., and Markl, J. (2006) The hemocyanin from a living fossil, the cephalopod Nautilus pompilius: protein structure, gene organization, and evolution. *J. Mol. Evol. 62*, 3362–74.
(12) Miller, K. I., Cuff, M. E., Lang, W. F., Varga-Weisz, P., Field, K. G., and van Holde, K. E. (1998) Sequence of the *Octopus dofleini* hemocyanin subunit: structural and evolutionary implications. *J. Mol. Biol. 278*, 827–842.
(13) Dolashka-Angelova, P., Beltramini, M., Dolashki, A., Salvato, B., and Voelter, W. (2001) Carbohydrate composition of *Carcinus aestuarii* hemocanin. *Arch. Biochem. Biophys. 389*, 153–158.
(14) Dolashka-Angelova, P., Dolashki, A., Savvides, S. N., Hristova, R., Van Beeumen, J., Voelter, W., Devreese, B., Weser, U., Di Muro, P., Salvato, B., and Stevanovic, S. (2005) Structure of hemocyanin subunit CaeSS2 of the crustacean mediterranean crab *Carcinus aestuarii*. *J. Biochemistry 138*, 303–312.
(15) Stoeva, S., Dolashka, P., Pervanova, K., Genov, N., and Voelter, W. (1997) Multidomain structure of the *Rapana thomasiana* (Gastropod) hemocyanin structural subunit RHSS1. *Comp. Biochem. Physiol. 118 B*, 927–934.
(16) Dolashka-Angelova, P., Beck, A., Dolashki, A., Stevanovic, S., Beltramini, M., Salvato, B., Hristova, R., Velkova, L., and Voelter, W. (2004) Carbohydrate moieties of molluscan *Rapana venosa* hemocyanin. *Micron 35*, 101–104.
(17) Dolashka-Angelova, P., Beck, A., Dolashki, A., Beltramini, M., Stevanovic, S., Salvato, B., and Veolter, W. (2003) Characterization of the carbohydrate moieties of the functional unit RvH1-a of *Rapana venosa* haemocyanin using HPLC/electrospray ionization MS and glycosidase digestion. *Biochem. J. 374*, 185–192.
(18) Beck, A., Hillen, N., Dolashki, A., Stevanovic, S., Salvato, B., Voelter, W., and Dolashka-Angelova, P. (2007) Oligosaccharide structure of a functional unit RvH1-b of Rapana venosa hemocyanin using HPLC/electrospray ionization mass spectrometry. *Biochimie 89*, 938–949.
(19) Sandra, K., Dolashka-Angelova, P., Devreese, B., and Van Beeumen, J. (2007) Novel methodologies in glyco-analysis reveal new insights in *Rapana venosa* hemocyanin N-glycosylation. *Glycobiology 17*, 141–56.
(20) Wirguin, I., Suturkova Milosevic, L., Briani, C., and Latov, N. (1995) Keyhole limpet hemocyanin contains Gal(β1−3)-GalNAc determinants that are cross-reactive with the T antigen. *Cancer Immunol. 40*, 307–310.
(21) Markl, J., Lieb, B., Gebauer, W., Altenhein, B., Meissner, U., and Harris, R. (2001) Marine tumor vaccine carriers: structure of the molluscan hemocyanins KLH and HtH. *J. Cancer Res. Clin. Oncol. 127* (2), R3–R9.
(22) (a) Moltedo, B., Faunes, F., Haussmann, D., De Ioannes, P., De Ioannes, A. E., Puente, J., and Becker, M. I. (2006) Immunotherapeutic effect of Concholepas hemocyanin in the murine bladder cancer model: evidence for conserved antitumor properties among hemocyanins. *J Urol. 176*, 2690–2695.
(23) Toshkova, R., Velkova, L., Voelther, W., and Dolashka-Angelova, P. (2006) Protective effect of *Rapana venosa* hemocyanin (RvH) on survivability of hamsters with transplanted myeloid graffi tumours. *C. R. Acad. Bulg. Sci. 59*, 977–982.
(24) Toshkova, R., Ivanova, E., Nastke, M., Stevanovic, S., Velkova, L., Voelter, W., and Dolashka-Angelova, P. (2006) Hemocyanins as immunostimulators. *Global J. Mol. Sci. 1*, 22–32.
(25) Van Kuik, J. A., Sijbesma, R. P., Kamerling, J. P., Vliegenthart, J. F. G., and Wood, E. J. (1987) Primary structure determination of seven novel N-linked carbohydrate chains derived from hemocyanin of Lymnaea stagnalis. 3-O-Methyl-D-galactose and N-acetyl-D-galactosamine as constituents of xylose-containing N-linked oligosaccharides in an animal glycoprotein. *Eur. J. Biochem. 169*, 399–411.
(26) Zhang, X., Huang, C., and Qin, Q. (2004) Antiviral properties of hemocyanin isolated from shrimp Penaeus monodon. *Antiviral Res. 61*, 93–99.
(27) Lieb, B., Altenhein, B., Markl, J., Boisguérin, V., Gebauer, W., and Markl, J. (2004) cDNA sequence, protein structure, and evolution of the single hemocyanin from Aplysia californica, an opisthobranch gastropod. *J. Mol. Evol. 59*, 536–45.
(28) Topham, R., Tesh, S., Westcott, A., Cole, G., Mercatante, D., Kaufman, G., and Bonaventura, C. (1999) Disulfide bond reduction: A powerful, chemical probe for the study of structure-function relationships in the hemocyanins. *Arch. Biochem. Biophys. 369*, 261–266.
(29) Nicholas, K. B., and Nicholas, H. B., Jr. (1997)GeneDoc: analysis and. visualization of genetic variation. http://www.psc.edu/biomed/genedoc/.
(30) Bairoch, A., and Apweiler, R. (1999) The SWISS-PROT protein sequence data bank and its supplement TrEMBL. *Nucleic Acids Res. 27*, 49–54.
(31) Guex, N., and Peitsch, M. C. (1997) SWISS-MODEL and the Swiss-PdbViewer: An environment for comparative protein modeling. *Electrophoresis 18*, 2714–2723.
(32) Tamura, T., and Akutsu, T. (2007) Subcellular location prediction of proteins using support vector machines with alignment of block sequences utilizing amino acid composition. *BMC Bioinformatics 8*, 466.
(33) Carr, S. A., Huddleston, M. J., and Bean, M. F. (1993) Selective identification and differentiation of N- and O-linked oligosaccharides in glycoproteins by liquid chromatography-mass spectrometry. *Protein Sci. 2*, 183–196.
(34) Lamm, L. D., Petegolli, I. J., and Riggs, R. D. (2000) Keyhole limpet Hemocyanin immunoterapia del cancero alla vescica: laboratorio e studi clinici. *Eur. Urol. 37*, 41–44.
(35) Cuff, M. E., Miller, K. I., van Holde, K. E., and Hendrickson, W. A. (1998) Crystal structure of a functional unit from Octopus hemocyanin. *J. Mol. Biol. 278*, 855–870.
(36) Altenhein, B., Markl, J., and Lieb, B. (2002) Gene structure and hemocyanin isoform HtH2 from the mollusc *Haliotis tuberculata* indicate early and late intron hot spots. *Gene 301*, 53–60.

BC900034K

Versatile Conjugation of Octreotide to Dendrimers by Cycloaddition ("Click") Chemistry to Yield High-Affinity Multivalent Cyclic Peptide Dendrimers

Cheng-Bin Yim,[†,‡] Otto C. Boerman,[‡] Monique de Visser,[§] Marion de Jong,[§] Annemarie C. Dechesne,[†] Dirk T. S. Rijkers,[†] and Rob M. J. Liskamp*[,†]

Medicinal Chemistry and Chemical Biology, Utrecht Institute for Pharmaceutical Sciences, Department of Pharmaceutical Sciences, Faculty of Science, Utrecht University, Sorbonnelaan 16, 3584 CA Utrecht, The Netherlands, Department of Nuclear Medicine, Radboud University Nijmegen Medical Centre, Geert Grooteplein 10, 6525 GA Nijmegen, The Netherlands, and Department of Nuclear Medicine, Erasmus Medical Center Rotterdam, Dr. Molewaterplein 40, 3015 GD Rotterdam, The Netherlands. Received February 5, 2009; Revised Manuscript Received May 13, 2009

The somatostatin analogue Tyr[3]-octreotide, which has a high binding affinity for the SSTR2 receptor (somatostatin receptor subtype 2) expressed on tumor cells, is used clinically for the diagnosis and treatment of a variety of neuroendocrine tumors and gastrointestinal disorders. There is growing interest in the development of multivalent peptide systems, because they may have enhanced binding affinity compared to monovalent analogues. In this report, we describe the design and synthesis of a series of Tyr[3]-octreotide-containing monomeric, dimeric, and tetrameric dendrimeric conjugates. These multivalent dendrimeric cyclic peptides were obtained using Cu(I)-catalyzed 1,3-dipolar cycloaddition between peptidyl azides and dendrimeric alkynes. Their affinities for the SSTR2 receptor were determined by a competitive binding assay on rat brain sections.

INTRODUCTION

Somatostatin is a cyclic peptide hormone, which circulates in the blood in two biologically active forms: somatostatin-14 and its N-terminally extended form somatostatin-28, consisting of 14 and 28 amino acids, respectively (*1*−*3*). Both hormones exert different biological effects in the gastrointestinal system and in the nervous system. These effects are mediated by high-affinity G protein-coupled somatostatin receptors (SSTRs) and include modulation of hormone release and neurotransmitter release and inhibition of cell proliferation (*4*, *5*). Five different SSTR subtypes have been identified and characterized (SSTR1−5) (*6*). As some of these receptors are overexpressed in several human tumors, especially neuroendocrine tumors and their metastases, there is growing interest in the development of potent analogues to target these receptors. The octapeptide analogues octreotide and octreotate, having high binding affinity for SSTR2-receptor-expressing tumor cells, are used clinically for the diagnosis and treatment of a variety of neuroendocrine tumors and gastrointestinal disorders (*7*−*11*).

Much research has focused on the development of multivalent dendrimeric molecules, because they show interesting properties for enhancing the overall binding affinity compared to monovalent ligands (*12*−*16*). Several research groups have prepared multimers of cyclic Arg-Gly-Asp (RGD) peptides and evaluated their binding characteristics toward the $\alpha_v\beta_3$ integrin receptor (*17*−*19*). Our studies have shown that tumor uptake of a tetrameric RGD dendrimer was significantly higher compared to that of the monomeric and dimeric analogues, presumably due to enhanced statistical rebinding (*20*, *21*). These findings have inspired us to prepare dendrimeric multivalent octreotide-based molecules. On the basis of our experience with previously developed dendrimeric conjugates (*22*−*26*), these octreotide-based dendrimers may have enhanced binding affinity for the SSTR2 receptor. The aim of this study was to synthesize multivalent peptide dendrimers of octreotide, and to compare their in vitro binding characteristics with monovalent congeners.

Especially challenging is the efficient conjugation of these biologically active peptides to the dendrimer. A fast coupling reaction with high efficiency and chemoselectivity is desirable to allow the conjugation of unprotected peptides to dendrimers to obtain well-defined multivalent peptide dendrimers with preservation of receptor binding affinity. Several methodologies have been investigated, and the Huisgen 1,3-dipolar cycloaddition (*27*) of an azide and an alkyne forming a triazole linkage is particularly suitable for chemoselective bioconjugation reactions. The copper-catalyzed variant (*28*, *29*), which regiospecifically gives 1,4-disubstituted 1,2,3-triazoles has led to many applications ranging from therapeutics to macromolecules (*30*−*35*). We recently showed that unprotected peptides could be efficiently attached to an alkyne-derivatized version of our earlier developed dendrimers (*36*−*39*) using the 1,3-dipolar cycloaddition reaction (*21*, *40*). Thus, in this report we describe the synthesis of multivalent dendrimeric octreotide peptides from dendrimeric alkynes and azido peptides. To evaluate the effect of multivalency, the SSTR2 receptor binding characteristics of the corresponding monovalent, divalent, and tetravalent octreotide peptide dendrimers were studied in comparison to octreotide.

EXPERIMENTAL PROCEDURES

Materials and Instruments. Unless stated otherwise, chemicals were obtained from commercial sources and used without purification. Peptide-grade solvents were purchased from Bio-

* To whom correspondence should be addressed. Rob M. J. Liskamp, Medicinal Chemistry and Chemical Biology, Utrecht Institute for Pharmaceutical Sciences, Department of Pharmaceutical Sciences, Faculty of Science, Utrecht University, PO Box 80082, 3508 TB Utrecht, The Netherlands. Phone: +31 30 253 7396. Fax: +31 30 253 6655. E-mail: r.m.j.liskamp@uu.nl.

[†] Utrecht University.

[‡] Radboud University Nijmegen Medical Centre.

[§] Erasmus Medical Center Rotterdam.

10.1021/bc900052n CCC: $40.75 © 2009 American Chemical Society
Published on Web 06/18/2009

solve and used directly except for dimethylformamide (DMF), *N*-methylpyrrolidone (NMP), and dichloromethane (DCM), which were dried on 4 Å molecular sieves prior to (solid phase) synthesis. 2-Chlorotrityl chloride resin was purchased from Tianjin Nankai Hecheng Science & Technology Company Ltd. and N^{α}-fluorenylmethyloxycarbonyl (Fmoc) amino acids were purchased from Advanced ChemTech, Alexis, or Novabiochem. Solid-phase synthesis was carried out in plastic syringes with PE frit (20 μm) obtained from Applied Separations Inc. Analytical HPLC runs were carried out on a Shimadzu HPLC system, and preparative HPLC runs were performed on a Kratos HPLC workstation. Analytical HPLC runs were performed on an Alltech Alltima C8 column (250 × 4.6 mm, pore size 90 Å, particle size 5 μm) at a flow rate of 1.0 mL/min using a linear gradient of buffer B (0−100% in 20 min) in buffer A (buffer A: 0.1% trifluoroacetic acid (TFA) in CH_3CN/H_2O 5:95 v/v, buffer B: 0.1% TFA in CH_3CN/H_2O 95:5 v/v). Preparative HPLC runs were performed on an Alltech Adsorbosphere XL C8 column (250 × 22 mm, pore size 90 Å, particle size 10 μm), and semipreparative HPLC runs were performed on an Alltech Adsorbosphere XL C18 column (250 × 10 mm, pore size 90 Å, particle size: 10 μm) at a flow rate of 12.0 mL/min (semipreparative HPLC: 4.8 mL/min) using a linear gradient of buffer B (0−100% in 120 min) in buffer A (buffer A: 0.1% TFA in CH_3CN/H_2O 5:95 v/v, buffer B: 0.1% TFA in CH_3CN/H_2O 95:5 v/v). Electrospray ionization (ESI) mass spectrometry was measured on a Shimadzu QP8000 single quadruple benchtop mass spectrometer operating in a positive ionization mode. MALDI-TOF analysis was performed on a Kratos Axima CFR apparatus with human ACTH(18−39) (monoisotopic $[M+H]^+$ 2465.198), bovine insulin oxidized B chain (monoisotopic $[M+H]^+$ 3494.651), or bovine insulin (monoisotopic $[M+H]^+$ 5730.609) as external references and α-cyano-4-hydroxycinnamic acid as matrix. ^{1}H NMR spectra were recorded on a Varian G-300 (300 MHz) spectrometer, and chemical shifts are given in ppm (δ) relative to TMS. ^{13}C NMR spectra were recorded on a Varian G-300 (75.5 MHz) spectrometer, and chemical shifts are given in ppm (δ) relative to $CDCl_3$ (77.0 ppm). The ^{13}C NMR spectra were recorded using the attached proton test (APT) sequence. Solid-phase synthesis was monitored with the Kaiser (*41, 42*) or the bromophenol blue (BPB) test (*43*). Where needed, the resin loading was determined by measuring the UV absorbance of the piperidine−dibenzofulvene adduct (λ_{max} 300 nm) (*44*) using a Thermo Electron Corporation UV/vis spectrophotometer. Solution-phase reactions were monitored by thin layer chromatography (TLC), and R_f values were determined on Merck precoated silica gel 60 F-254 (0.25 mm) plates. Spots were visualized with UV light or ninhydrin or by staining with chlorine/*N*,*N*,*N*′,*N*′-tetramethyl-4,4′-diaminodiphenylmethane (TDM) (*45*). The syntheses of compounds **1** and **2** are given in the Supporting Information. The syntheses of dendrimers **5**−**10** have been described previously (*21, 40*).

Chemistry. *N_3-Ahx-D-Phe-Cys-Tyr-D-Trp-Lys-Thr-Cys-Threol (3).* The 2-chlorotrityl chloride resin (909 mg, 1.00 mmol) was treated with $SOCl_2$/DCM (1:1 v/v; 2 × 10 mL, 10 min) to convert it completely into the chloride form prior loading of the first amino acid derivative. To remove any residual $SOCl_2$, the resin was extensively washed with DCM (6 × 10 mL, 10 min). Then, Fmoc-Thr(^{t}Bu)Ψ[CH_2OH] **2** (1.53 g, 4.00 mmol) was dissolved in DCM (10 mL), and to this solution *N*,*N*-diisopropylethylamine (DIPEA) (1.42 mL, 8.00 mmol) followed by the 2-chlorotrityl chloride resin were added and the obtained slurry was gently swirled for 2 h at room temperature. The resin was subsequently washed with DCM/CH_3OH/DIPEA (17:2:1 v/v/v; 3 × 10 mL, 10 min) to quench any remaining reactive 2-chlorotrityl chloride, followed by a washing step with DCM (3 × 10 mL, 2 min), DMF (3 × 10 mL, 2 min), and DCM (3 × 10 mL, 2 min). The loading of the resin, as calculated from an Fmoc determination, was 60% (0.66 mmol/g). The linear peptide sequence was synthesized according to Fmoc/^{t}Bu solid-phase peptide synthesis protocols (*32*). In a typical 2-(1*H*-benzotriazole-1-yl)-1,1,3,3-tetramethyluronium hexafluoro phosphate (HBTU)/*N*-hydroxybenzotriazole (HOBt)-coupling procedure, the resin was treated for 3 h with a 4-fold excess of a selected amino acid. After coupling of the N-terminal Fmoc-D-Phe-OH, a portion of the resin (0.60 g, 0.23 mmol) was treated with 20% piperidine/NMP (3 × 5 mL, 10 min) to remove the N-terminal Fmoc group, followed by washing with NMP and DCM. The 6-azido-hexanoic acid **1** (0.15 mg, 0.94 mmol) was dissolved in NMP (4 mL) in the presence of HBTU and HOBt (0.35 mg and 0.14 mg, respectively, 0.94 mmol, 1 equiv), and to this solution DIPEA (0.31 mL, 1.88 mmol, 2 equiv) followed by the peptide resin were added and the obtained slurry was gently swirled for 16 h at room temperature. The resin was subsequently washed (NMP, DCM), dried, suspended in TFA/H_2O/triisopropylsilane (TIS) (95:2.5:2.5 v/v/v; 10 mL) and stirred for 4 h to cleave the peptide alcohol from the resin and to remove the side chain protecting groups. The crude peptide was isolated by precipitation with cold (−20 °C) methyl *tert*-butyl ether (MTBE)/hexane (1:1 v/v). After centrifugation, the pellet was dissolved in CH_3CN/H_2O (1:1 v/v), lyophilized and subsequently purified by HPLC (C8), and fractions collected at 46% buffer B (44% CH_3CN). The linear peptide **3** was obtained in 29% (78 mg) yield. R_t: 20.17 min (C8). ESI-MS: m/z = 1176.30 $[M+H]^+$, 1198.25 $[M+Na]^+$, ($C_{55}H_{77}N_{13}O_{12}S_2$: M = 1175.53).

N_3-Ahx-D-Phe-cyclo(Cys-Tyr-D-Trp-Lys-Thr-Cys)-Threol (4). Compound **4** was obtained by dimethylsulfoxide (DMSO)-mediated oxidation of **3**, according to a procedure of Tam *et al.* (*47*). Peptide **3** (44 mg, 37.4 μmol) was dissolved in aqueous 2.5% acetic acid (50 mL), and the pH was adjusted to 6.0 with aqueous ammonia (25%). To this solution, DMSO (12 mL) was added. After stirring overnight at room temperature, the solution was partially concentrated in vacuo and the remaining DMSO was evaporated. The residue was dissolved in CH_3CN/H_2O, filtered, and purified by HPLC (C8), and fractions of pure peptide were collected at 44% buffer B (42% CH_3CN). The cyclic peptide **4** was obtained in 79% (35 mg) yield. R_t: 20.05 min (C8). ESI-MS: m/z = 1174.00 $[M+H]^+$, 1196.10 $[M+Na]^+$, ($C_{55}H_{75}N_{13}O_{12}S_2$: M = 1173.51).

Monovalent Tyr^3-Octreotide Peptide Conjugate (11). The synthesis of **11** was performed using activated copper-in-charcoal (Cu/C) as the catalyst (*48, 49*). Alkyne **5** (0.5 mg, 2.9 μmol) and azide **4** (3.7 mg, 3.2 μmol, 1.1 equiv) were dissolved in DMF (200 μL). To this solution, Cu/C (10 mg, excess) and triethylamine (TEA) (5 μL) were added. The mixture was allowed to react under microwave conditions (100 °C) for 5−10 min. The cycloaddition reaction was monitored by HPLC. A yellow-brownish solution was formed during the reaction. Following microwave irradiation, the mixture was filtered over Hyflo and concentrated in vacuo. The residue was dissolved in CH_3CN/H_2O (1:1 v/v), lyophilized, and purified by semipreparative HPLC (C18). Yield: 1.8 mg (46%). R_t: 20.48 min (C8). ESI-MS: m/z = 1364.30 $[M+H]^+$, 1386.65 $[M+Na]^+$. MALDI-TOF: 1364.693 $[M+H]^+$, 1386.749 $[M+Na]^+$ ($C_{66}H_{85}N_{13}O_{15}S_2$: M = 1363.573).

Divalent Tyr^3-Octreotide Peptide Dendrimer (12). Alkyne **6** (0.7 mg, 2.8 μmol) and azide **4** (6.9 mg, 5.9 μmol, 2.1 equiv) were dissolved in degassed DMF (200 μL). To this solution CuOAc (0.8 mg, 6.5 μmol, 2.2 equiv) was added, and the mixture was allowed to react under microwave conditions (100 °C) for 20 min. Following microwave irradiation, the obtained yellow mixture was concentrated in vacuo, and the residue was

dissolved in CH_3CN/H_2O (1:1 v/v) and lyophilized. After purification by semipreparative HPLC (C18), compound **12** was obtained in 42% yield (3.1 mg). R_t: 27.33 min (C18). ESI-MS: m/z = 1296.90 $[M+2H]^{2+}$. MALDI-TOF: m/z = 2593.995 $[M+H]_{ave}^{+}$, 2616.045 $[M+Na]_{ave}^{+}$, 2632.121 $[M+K]_{ave}^{+}$, ($C_{124}H_{162}N_{26}O_{28}S_4$: M_{ave} = 2593.074).

*Tetravalent Tyr³-Octreotide Peptide Dendrimer (**13**).* Analogous to the preparation of **12**, alkyne **7** (0.7 mg, 1.0 μmol), azide **4** (5.3 mg, 4.5 μmol, 4.5 equiv), and CuOAc (0.5 mg, 4.1 μmol, 4.1 equiv) were used in DMF (200 μL) as the solvent. After purification by semipreparative HPLC (C18), compound **13** was obtained in 24% yield (1.5 mg). R_t: 29.17 min (C18). MALDI-TOF: m/z = 5375.938 $[M+H]_{ave}^{+}$, 5397.834 $[M+Na]_{ave}^{+}$, 5414.927 $[M+K]_{ave}^{+}$, ($C_{258}H_{334}N_{54}O_{58}S_8$: M_{ave} = 5376.349).

*Monovalent 1,4,7,10-Tetraazacyclododecane-1,4,7,10-tetraacetic acid (DOTA)-Conjugated Tyr³-Octreotide Construct (**14**).* Synthesis of **14** was performed using a combination of $CuSO_4$ and copper powder as the catalyst (*50*). Alkyne **8** (4.2 mg, 5.4 μmol, 1.1 equiv) and azide **4** (5.5 mg, 4.7 μmol, 1.0 equiv) were dissolved in DMF/H_2O (1:1 v/v; 0.2 mL). To this solution, aqueous 0.1 M $CuSO_4$ (50 μL, 5.0 μmol, 1.1 equiv) and copper powder (5 mg) were added, and the mixture was stirred for 18 h at room temperature. Then, the copper powder was removed by filtration, the solvent was evaporated under reduced pressure, and the residue was taken up in CH_3CN/H_2O (1:1 v/v; 2 mL) and lyophilized. The crude product was purified by semipreparative HPLC (C8, 5→95% CH_3CN in 90 min) to yield *tert*-butyl-protected **14** (lyophilized: 8.0 mg, 87%). The *tert*-butyl esters of the DOTA moiety were cleaved by treatment with $TFA/TIS/H_2O$ (95:2.5:2.5 v/v/v; 2 mL) for 3 h. The solvent was removed under reduced pressure, and the residue was dissolved in CH_3CN/H_2O (1:1 v/v; 2 mL) and lyophilized. After semipreparative HPLC (C8, 5→95% CH_3CN in 90 min) and subsequent lyophilization, **14** (3.4 mg, 1.9 μmol) was isolated in overall yield of 40%. R_t: 18.10 min (C8). MALDI-TOF: m/z = 1780.234 $[M+H]_{ave}^{+}$, 1801.672 $[M+Na]_{ave}^{+}$, 1843.146 $[M+Cu]_{ave}^{+}$, ($C_{83}H_{115}N_{19}O_{21}S_2$: M_{ave} = 1779.05).

*Divalent DOTA-Conjugated Tyr³-Octreotide Dendrimer (**15**).* Alkyne **9** (2.2 mg, 2.7 μmol, 1.0 equiv), azide **4** (6.8 mg, 5.8 μmol, 2.1 equiv), aqueous 0.1 M $CuSO_4$ (55 μL, 5.5 μmol, 2.0 equiv), and copper powder (5 mg) were added to DMF/H_2O (1:1 v/v; 0.2 mL), and the mixture was stirred for 18 h at room temperature. The workup, TFA treatment, and isolation of **15** were similar to that described for **14**. After semipreparative HPLC and subsequent lyophilization, **15** (0.9 mg, 0.3 μmol) was isolated in an overall yield of 12%. R_t: 18.48 min (C8). MALDI-TOF: m/z = 3008.674 $[M+H]_{ave}^{+}$, 3070.520 $[M+Cu]_{ave}^{+}$, ($C_{141}H_{192}N_{32}O_{34}S_4$: M_{ave} = 3007.49).

*Tetravalent DOTA-Conjugated Tyr³-Octreotide Dendrimer (**16**).* Alkyne **10** (1.8 mg, 1.5 μmol, 1.0 equiv), azide **4** (7.6 mg, 6.5 μmol, 4.3 equiv), aqueous 0.1 M $CuSO_4$ (58 μL, 5.8 μmol, 3.9 equiv), and copper powder (10 mg) were added to DMF/H_2O (1:1 v/v; 0.2 mL), and the mixture was stirred for 18 h at room temperature. The workup, TFA treatment, and isolation of **16** were similar to that described for **14**. After semipreparative HPLC and subsequent lyophilization, **16** (0.9 mg, 0.16 μmol) was isolated in overall yield of 11%. R_t: 18.93 min (C8). MALDI-TOF: m/z = 5790.326 $[M+H]_{ave}^{+}$, 5851.068 $[M+Cu]_{ave}^{+}$, ($C_{275}H_{364}N_{60}O_{64}S_8$: M_{ave} = 5790.72).

Receptor Autoradiography. The receptor binding affinity of the peptide dendrimers was determined in a competitive binding assay on rat brain cryostat sections (10 μm) using methods previously described with minor modifications (*51*). The sections were incubated for 1 h at room temperature with 0.1 nM [^{111}In-DOTA^0,Tyr^3]octreotate (135 MBq/nmol) in 167 mM tris(hydroxymethyl)aminoethane (Tris) (pH 7.6), supplemented with 5 mM $MgCl_2$, 1% bovine serum albumin (BSA), and 40 μg/mL bacitracin. To generate the competitive inhibition curves, the sections were incubated in the presence of an increasing amount (10^{-10} to 10^{-5} M) of the nonradioactive dendrimeric octreotide constructs. After incubation, the sections were washed two times for 5 min each in 167 mM Tris (pH 7.6), 5 mM $MgCl_2$, 0.25% BSA, (4 °C), 5 min in 167 mM Tris (pH 7.6), 5 mM $MgCl_2$ (4 °C), and finally rinsed in Milli-Q water (4 °C). The sections were then dried and exposed to phosphor imaging screens (Perkin-Elmer) for 48 h. The imaging screens were read using a Cyclone Storage Phosphor System (Packard), and the autoradiograms were quantified using Optiquant Software (Packard). Fitting of IC_{50} curves and calculation of IC_{50} values were performed with *GraphPad Prism 4.02* (GraphPad Software Inc.).

RESULTS AND DISCUSSION

Syntheses of Cyclic Tyr³-Octreotide Azides and Dendrimeric Alkynes. Azido octreotide **4** was prepared on the solid phase via Fmoc/^{t}Bu chemistry protocols (*46*), as depicted in Scheme 1. To enable click chemistry, an N-terminal azide functionality was introduced via 6-azidohexanoic acid **1**, which was prepared from 6-bromohexanoic acid (*52*). The preparation of octreotide required a C-terminal threoninol derivative. For this purpose, Fmoc-protected threonine was reduced to its corresponding alcohol **2** (*53*). Following coupling of the protected threoninol, peptide **3** was prepared on the solid phase, and 6-azidohexanoic acid **1** was coupled to the N-terminal D-phenylalanine before cleavage from the resin. After cleavage and concomitant removal of the side chain protection groups, the unprotected peptide **3** was obtained in an isolated yield of 29%. Despite the fact that the azide is susceptible to reduction in the presence of free thiols as are present in cysteine-2 and cysteine-7, the synthesis and subsequent ring closure by a DMSO-mediated disulfide formation of the peptide proceeded without noticeable side reactions and the azide remained stable throughout this procedure. Thus, linear peptide **3** was oxidized to the cyclic disulfide **4** by treatment with DMSO (*47*). After HPLC purification, the cyclic azido octreotide **4** was obtained in an overall yield of 23%.

Several studies have reported on the convergent synthesis of amino acid based dendrimers with peripheral propargyl groups to enable a 1,3-dipolar cycloaddition ("click") reaction with peptide derived azides (*21, 40*). A similar methodology was used here to prepare alkyne-derivatized dendrimers **5**−**7** and their corresponding DOTA-conjugated derivatives **8**−**10** (Figure 1) as a scaffold for the multimerization of octreotide.

Conjugation of Octreotide to Dendrimers by the Click Cycloaddition Reaction Procedure. After obtaining azide-functionalized octreotide **4** and alkynes **5**−**10**, the stage was set for the preparation of dendrimeric peptide systems using chemoselective "click" chemistry, as shown in Scheme 2. To prove the concept, the first experiments were conducted with alkynes **5**−**7** according to the literature procedure for microwave-assisted cycloaddition chemistry. Azide **4** was reacted with acetylene **5** in the presence of $CuSO_4$/Na-ascorbate in DMF/H_2O (9:1 v/v) for 5−15 min under microwave irradiation. Since the R_f values of the starting material and product were comparable on TLC, HPLC analysis was used to monitor the progress of the click cycloaddition reaction. After 5 min at 100 °C, the monovalent cycloaddition conjugate **11** was formed. Different sources of copper catalyst, including CuOAc and activated copper-in-charcoal (Cu/C) (*48*, *49*), were used for comparison to find the best procedure and to assess the versatility of this approach. Microwave-assisted cycloaddition with any of the three Cu(I)-sources afforded monovalent cycloadducts in yields ranging from 40% to 70%, with Cu/C giving the highest yield. However, the use of CuOAc showed

Scheme 1. Synthesis of the Cyclic *N*-ω-Azido Hexanoyl Octreotide Peptide 4

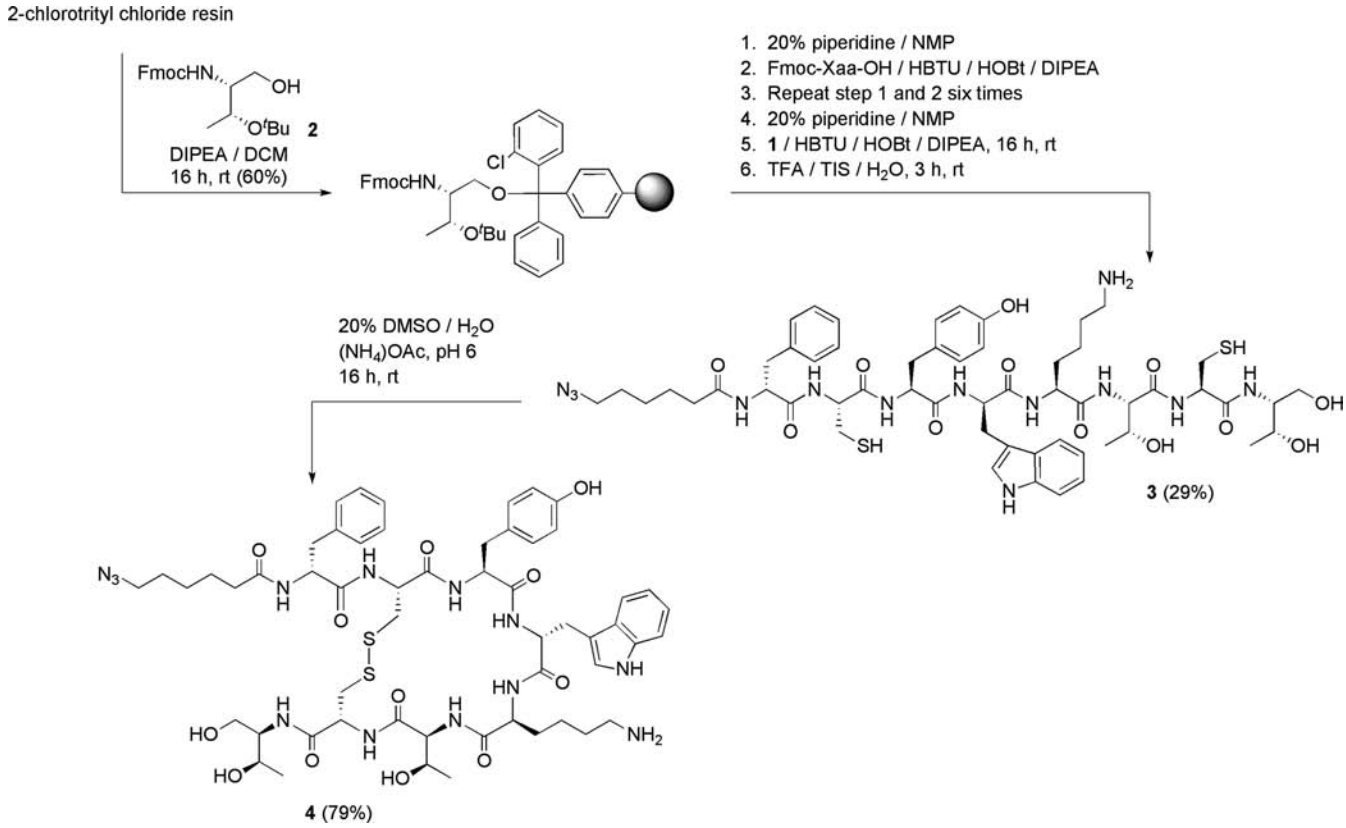

improved results in attaching peptidyl azide **4** to the divalent alkyne **6** giving divalent octreotide conjugate **12**. Therefore, CuOAc was chosen as the catalyst for the subsequent click conjugation reaction with the tetravalent dendrimeric alkyne **7**. Considerable amount of side products were observed during the reactions toward divalent and especially tetravalent peptide dendrimers, and LC-MS analyses showed most of these to be incomplete cycloadducts. These incomplete conjugates hampered purification by HPLC and resulted into a low isolated yield of the desired product. The formation of **11** and **13** was complete after 5 to 10 min microwave irradiation at 100 °C, whereas the reaction time for **12** had to be extended to 20 min.

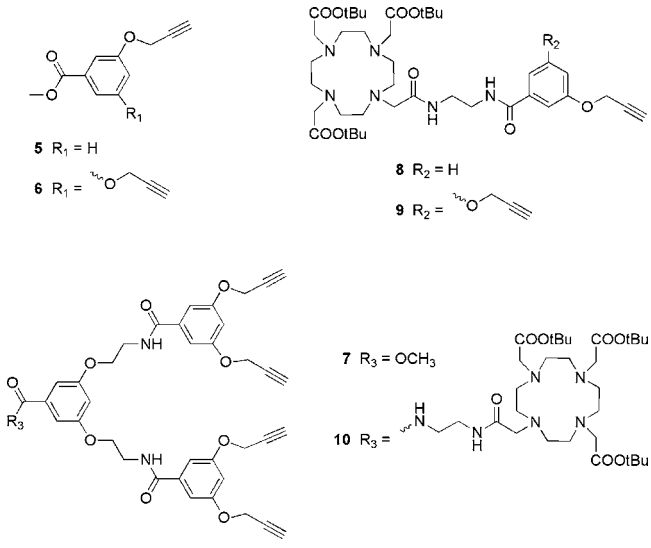

Figure 1. Structures of the mono-, di-, and tetravalent dendrimeric alkynes **5**, **6**, and **7**, and their corresponding DOTA conjugates **8**, **9**, and **10**.

It turned out that using an equimolar amount of CuOAc gave the best result for all cycloaddition reactions. When using more equivalents of copper catalyst, increasing amounts of impurities were detected by HPLC. The identity of the cycloadducts **11**−**13** was confirmed by MALDI-TOF and the spectrum of cyclic octreotide tetramer **13** is shown in Figure 2 as a representative example.

Scheme 3 shows the synthetic route toward DOTA-conjugated octreotide dendrimers **14**, **15**, and **16**. In contrast to the synthesis of conjugated peptide dendrimers **11**−**13**, the DOTA moiety of dendrimers **8**−**10** required a different copper catalyst, since none of the above-mentioned Cu(I)-sources resulted in the desired products. Fortunately, using a combination of $CuSO_4$ and copper powder as described by Kessler and co-workers (*50*) gave the desired conjugates in acceptable yields. Figure 3 shows the analytical HPLC trace of azido octreotide **4** and alkyne **8** (A) and the resulting DOTA-conjugated ^{t}Bu-protected precursor of **14** after the click reaction (B), respectively. Conjugate **14** was obtained in 40% yield after purification. The isolated yields for dimer **15** and tetramer **16** were 12% and 11%, respectively. These relative low values were mainly due to the presence of incomplete coupling products and concomitantly difficult purification to obtain the pure compound.

Since a relatively high amount of copper had to be used during the synthesis of **14**, **15**, and **16**, Cu-DOTA complexes were formed in addition to the desired copper-free products, as was inferred from the mass spectra. To remove residual copper from the DOTA moieties, the product was treated with Na_2S as described in the literature (*50*). This treatment, however, reduced the disulfide bridges in octreotide, which had to be restored by a reoxidation step in aqueous DMSO. Figure 4 shows the mass spectrum of conjugate **14** with no indication of Cu-DOTA complexes. However, mass analysis of either dimer **15** or tetramer **16** still clearly showed copper-bound adducts

Scheme 2. Synthesis of Mono-, Di-, and Tetravalent Octreotide Dendrimeric Constructs 11, 12, and 13

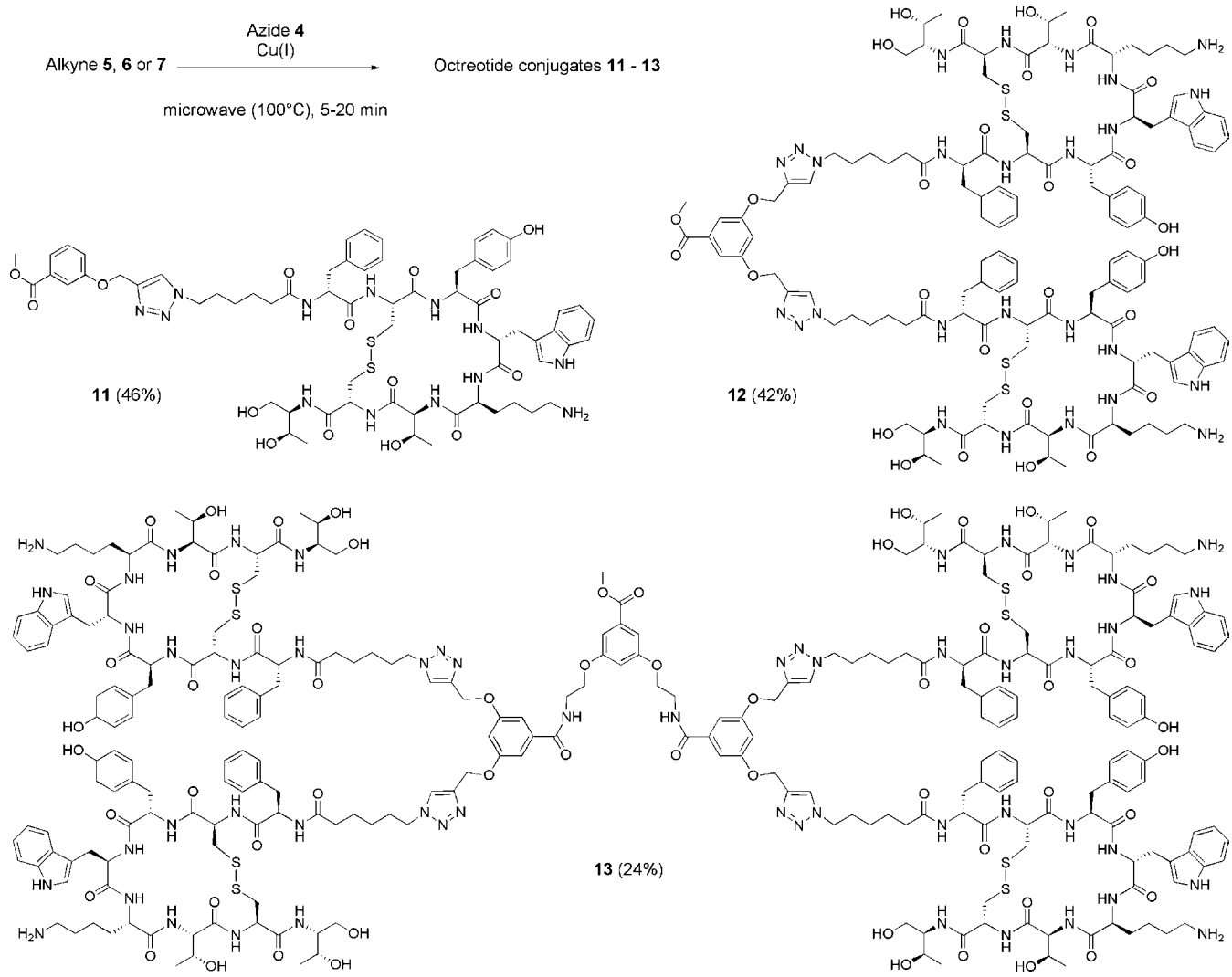

after Na_2S treatment (Supporting Information Figures SI 8,9, respectively).

To avoid copper contamination of the desired end-product, since it is cytotoxic toward mammalian cells and also hampers efficient loading of the DOTA moiety with radioactive metals, approaches toward metal-free azide−alkyne cycloadditions are particularly relevant (*54*). In a recent paper by Rutjes and co-workers (*55*), it was shown that a copper-free tandem 1,3-dipolar cycloaddition retro-Diels−Alder ligation enabled the efficient synthesis of ^{111}In-labeled cyclic RGD−DTPA conjugates. Alternative copper-free "click" approaches to obtain DOTA-conjugated multimeric octreotide dendrimers are currently under investigation in our laboratory.

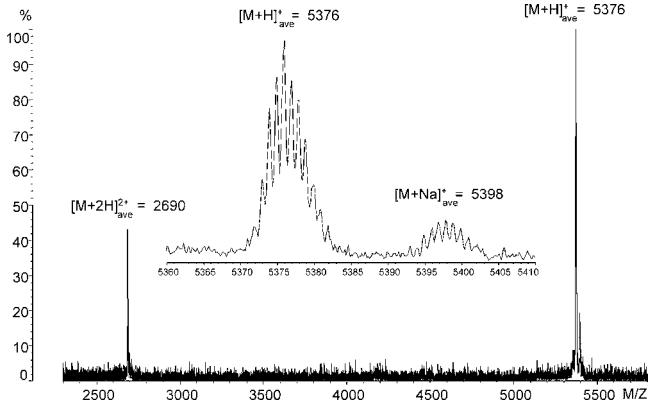

Figure 2. MALDI-TOF spectrum of tetravalent cyclic octreotide dendrimer **13**.

Receptor Binding Assay. Binding affinities toward the somatostatin receptor of the mono-, di-, and tetravalent DOTA conjugates of octreotide **14**, **15**, and **16**, respectively, were determined by a competitive binding assay on rat SSTR2-positive brain cryostat sections, using [^{111}In-DOTA^0,Tyr^3]octreotate as a radiotracer. Figure 5 represents a typical example of an autoradiogram, in which [^{111}In-DOTA^0,Tyr^3]octreotate was displaced by tetravalent octreotide dendrimer **13** (first and second column) and azido octreotide **4** (third and fourth column) in a concentration range from 10^{-10} to 10^{-5} M (from top to bottom) in two independent experiments. The autoradiograms were quantified, and the IC_{50} values were calculated from fitted sigmoidal displacement curves as shown in Figure 6 and summarized in Table 1. On the basis of these data, it became clear that the IC_{50} values of conjugate **14**, dimer **15**, and tetramer **16** were all within the low nanomolar range. However, no significant increase in receptor affinity for the tetramer **16** compared to either dimer **15** or conjugate **14** could be measured. A possible explanation for the absence of the multivalency effect may be found in the nonoptimized spacer-arm length either between the DOTA chelator and the dendrimeric core or between the dendrimer core and the peptide. However, it is known from our earlier work that elongating the spacer-arm length, between the dendrimer core and the carbohydrate moiety of a

Scheme 3. Synthesis of Mono-, Di-, and Tetravalent DOTA-Conjugated Octreotide Dendrimeric Constructs 14, 15, and 16

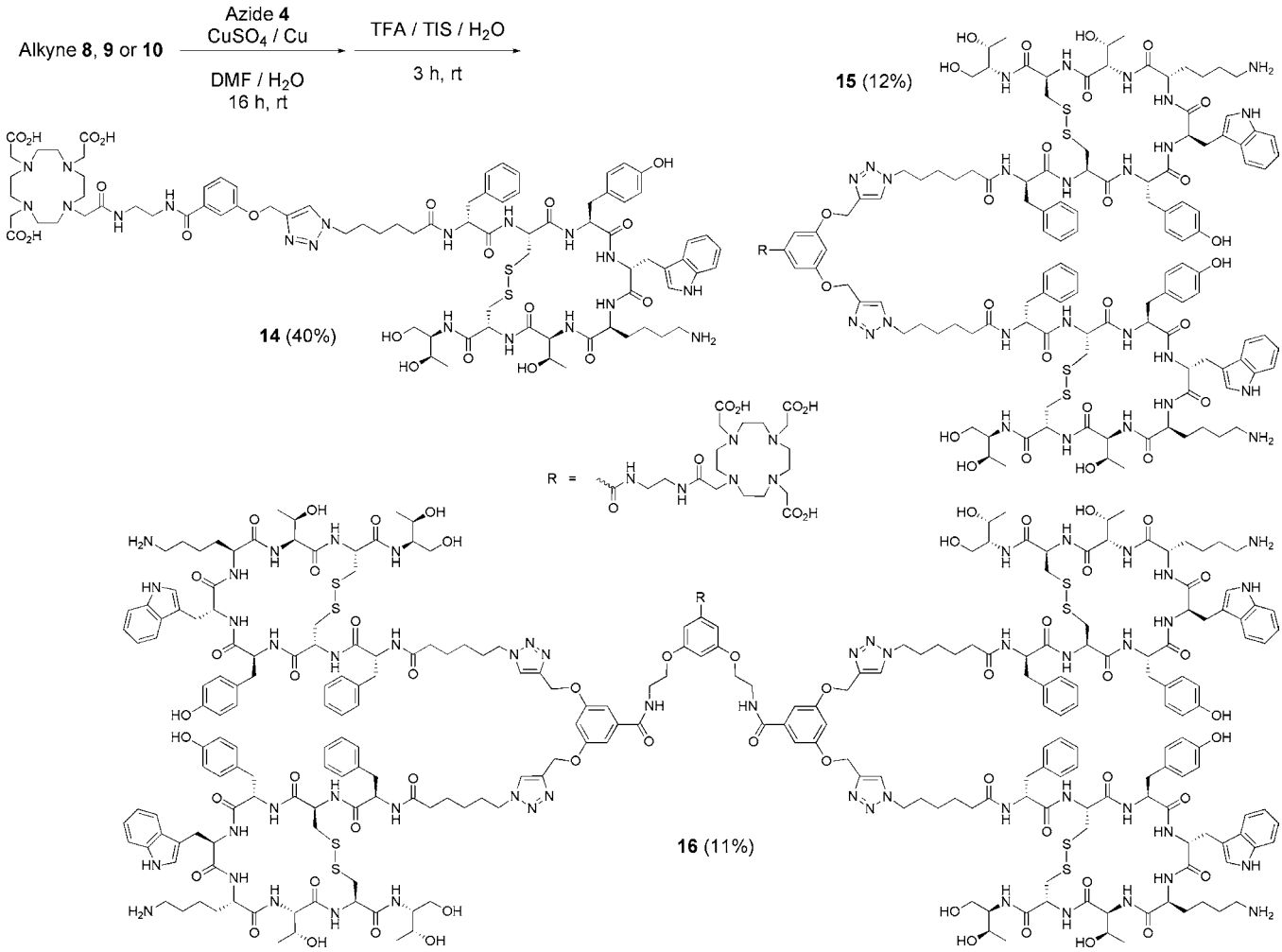

divalent galabiose derivative, resulted in a 2-fold increase in IC_{50} value for the inhibition of *Streptococcus suis* bacteria (*23*), compared to the analogue without a spacer. Therefore, the present dendrimeric systems of the octreotide cyclic peptide may not be ideal for augmenting receptor binding. Furthermore, the importance of the linker or other solubilizing moieties connected directly to the dendrimer scaffold was also apparent from similar binding experiments using conjugates **11**−**13** without the DOTA-moiety (Supporting Information Table SI 1 and Figure SI 10). The resulting IC_{50} values found for conjugate **11** and dimer **12** were higher than those for their corresponding DOTA conjugates **14** and **15**; probably, a poor aqueous solubility of tetramer **13** prevented even the calculation of a reliable IC_{50} value. Incorporating the DOTA moiety, which contains three hydrophilic carboxylic acid func-

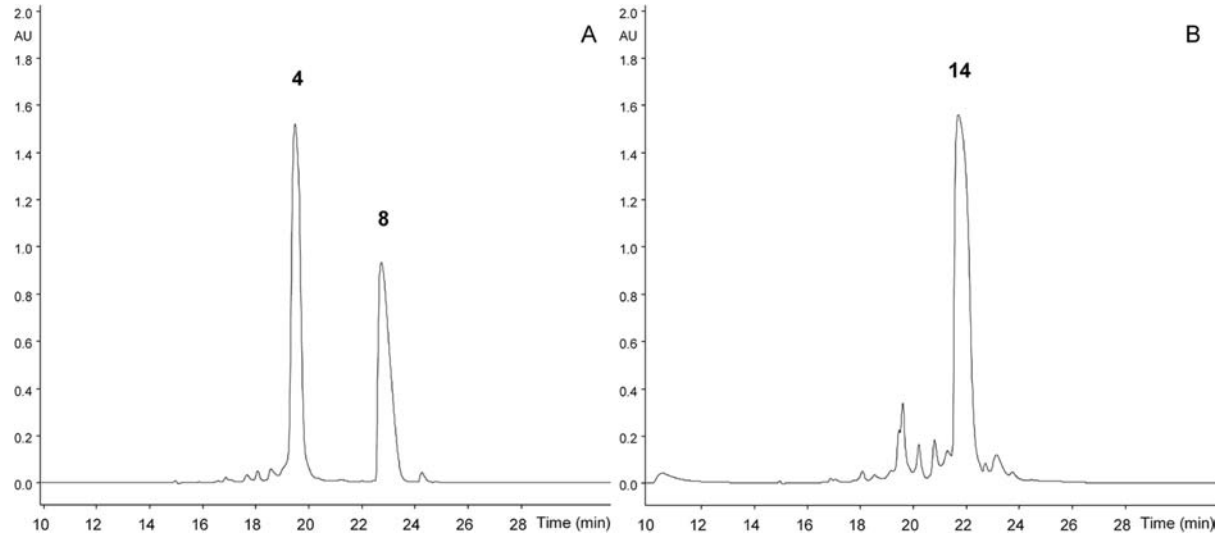

Figure 3. (A) Analytical C8 HPLC trace (UV 220 nm) of peptidyl azide **4** (R_t: 19.6 min) and alkyne **8** (R_t: 22.9 min). (B) Analytical C8 HPLC trace (UV 220 nm) of crude ^{t}Bu-protected precursor of **14** (R_t: 21.8 min) obtained after the click reaction.

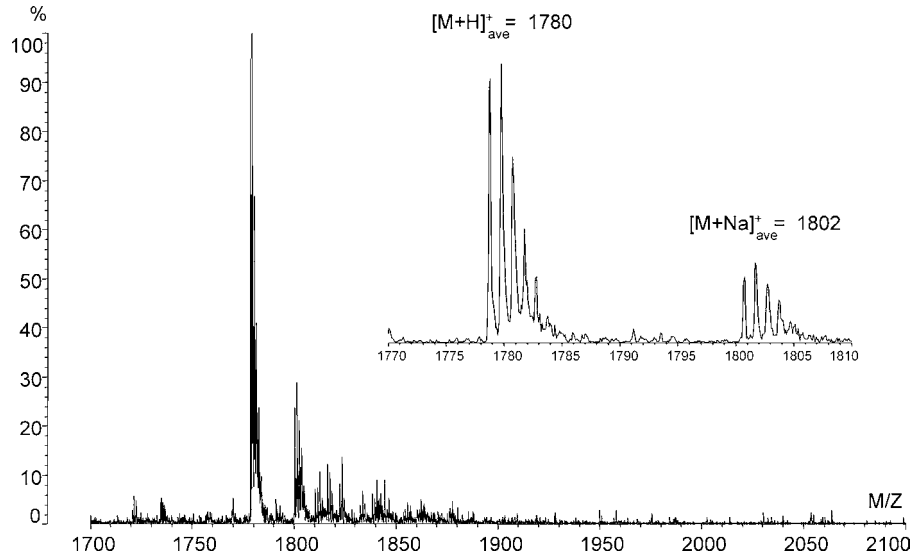

Figure 4. MALDI-TOF spectrum of monovalent DOTA-conjugated cyclic octreotide construct **14**.

Figure 5. Autoradiograms of tetravalent octreotide peptide dendrimer **13** (first two columns) and azido octreotide **4** (last two columns). Concentrations used (from top to bottom): 10 μM, 1 μM, 100 nM, 50 nM, 10 nM, 5 nM, 1 nM, 0.5 nM, and 0.1 nM, respectively.

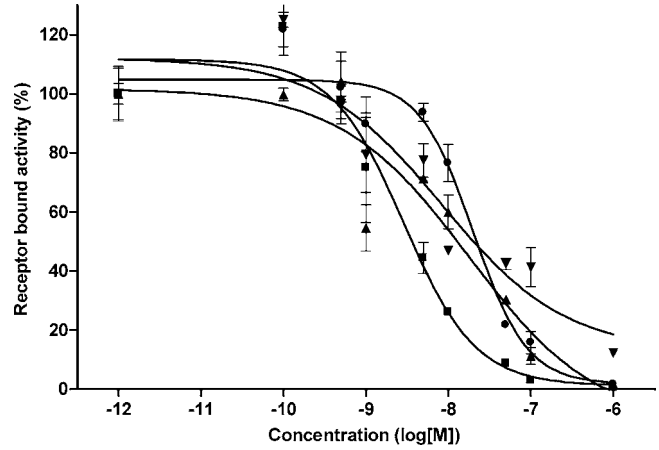

Figure 6. Competitive binding assay of mono-, di-, and tetravalent DOTA-conjugated systems of octreotide **14** (■), **15** (▲), and **16** (▼) displacing [^{111}In-DOTA^0,Tyr^3]octreotate in rat SSTR2-positive brain sections (n = 2 for each data point). [DOTA^0,Tyr^3]-conjugated octreotide **17** (•) was used as reference compound. The error bars indicate the range of the 95% confidence interval.

Table 1. IC_{50} Values for Competitive Binding Assay of Mono-, Di-, and Tetravalent DOTA-Conjugated Systems of Octreotide Displacing [^{111}In-DOTA^0,Tyr^3]octreotate in Rat SSTR2-Positive Brain Sections (n = 2 for each data point)

competing ligand	IC_{50} (nM)	95% CI (nM)
DOTA-conjugate **14**	2.86	1.51−5.41
DOTA-dimer **15**	17.6	2.61−119
DOTA-tetramer **16**	8.34	1.55−44.7
DOTA-octreotide **17**	20.0	10.8−37.1

tionalities, improved the overall solubility, and an IC_{50} value for tetramer **16** could be determined.

CONCLUSIONS

We have reported on the versatile conjugation of octreotide to dendrimers by the Cu(I)-catalyzed 1,3-dipolar cycloaddition ("click") reaction leading to the successful synthesis of multivalent octreotide-based dendrimers, either in the absence or in the presence of the strong metal chelating DOTA moiety. This conjugation method represents a chemoselective approach for the preparation of these dendrimeric peptides from *unprotected cyclic* peptidyl azides and dendrimeric alkynes. We have tested the hypothesis regarding whether functionalization of our DOTA-conjugated dendrimeric alkynes **8**−**10** with octreotide **4** will augment the binding affinity between receptor and multivalent ligand. Competitive binding assays showed no significant increase in receptor affinity for the DOTA-conjugated tetramer **16** or dimer **15** compared to

the monomer **14**. The role of the spacer between the scaffold and the cyclic peptide could play a major role in improving binding affinity of the dimeric and tetrameric conjugates, and this aspect is currently under investigation. Furthermore, to ensure an efficient radiolabeling, alternative copper-free "click" approaches to obtain DOTA-conjugated multimeric octreotide dendrimers are currently being developed in our laboratory.

Supporting Information Available: Synthesis of 6-azidohexanoic acid **1**, Fmoc-Thr(^{t}Bu)[CH_2OH] **2**, DOTA-conjugated Tyr^3-octreotide **17**, characterization of linear Tyr^3-octreotide **3**, cyclic Tyr^3-octreotide **4**, HPLC, ESI-MS, and receptor binding analysis of octreotide conjugates **11**−**13**, and HPLC and MALDI-TOF analysis of DOTA-conjugated octreotide compounds **14**−**16**. This material is available free of charge via the Internet at http://pubs.acs.org.

LITERATURE CITED

(1) Brazeau, P., Vale, W., Burgus, R., Ling, N., Butcher, M., Rivier, J., and Guillemin, R. (1973) Hypothalamic polypeptide that inhibits the secretion of immunoreactive pituitary growth hormone. *Science 179*, 77–9.

(2) Reichlin, S. (1983) Somatostatin. *N. Engl. J. Med. 309*, 1495–501.

(3) Reichlin, S. (1983) Somatostatin (Second of two parts). *N. Engl. J. Med. 309*, 1556–63.

(4) de Herder, W. W., Hofland, L. J., van der Lely, A. J., and Lamberts, S. W. J. (2003) Somatostatin receptors in gastroenteropancreatic neuroendocrine tumours. *Endocr. Relat. Cancer 10*, 451–8.

(5) Lamberts, S. W. J., Krenning, E. P., and Reubi, J.-C. (1991) The role of somatostatin and its analogs in the diagnosis and treatment of tumors. *Endocr. Rev. 12*, 450–82.

(6) Patel, Y. C. (1999) Somatostatin and its receptor family. *Front. Neuroendocrinol. 20*, 157–98.

(7) de Jong, M., Kwekkeboom, D. J., Valkema, R., and Krenning, E. P. (2003) Radiolabelled peptides for tumour therapy: current status and future directions. *Eur. J. Nucl. Med. Mol. Imaging 30*, 463–9.

(8) van Eijck, C. H. J. (2005) Treatment of advanced endocrine gastroenteropancreatic tumours using radiolabelled somatostatin analogues. *Br. J. Surg. 92*, 1333–4.

(9) Kaltsas, G. A., Papadogias, D., Makras, P., and Grossman, A. B. (2005) Treatment of advanced neuroendocrine tumours with radiolabelled somatostatin analogues. *Endocr. Relat. Cancer 12*, 683–99.

(10) Kwekkeboom, D. J., Mueller-Brand, J., Paganelli, G., Anthony, L. B., Pauwels, S., Kvols, L. K., O'Dorisio, T. M., Valkema, R., Bodei, L., Chinol, M., Mäcke, H. R., and Krenning, E. P. (2005) Overview of results of peptide receptor radionuclide therapy with 3 radiolabeled somatostatin analogs. *J. Nucl. Med. 46*, 62S–6S.

(11) Forrer, F., Valkema, R., Kwekkeboom, D. J., de Jong, M., and Krenning, E. P. (2007) Peptide receptor radionuclide therapy. *Best Pract. Res. Clin. Endocrinol. Metabol. 21*, 111–29.

(12) Varki, A. (1993) Biological roles of oligosaccharides: all of the theories are correct. *Glycobiology 3*, 97–130.

(13) Mammen, M., Choi, S.-K., and Whitesides, G. M. (1998) Polyvalent interactions in biological systems: implications for design and use of multivalent ligands and inhibitors. *Angew. Chem., Int. Ed. 37*, 2754–94.

(14) Newkome, G. R., Moorefield, C. N., and Vögtle, F. (2001) *Dendrimers and dendrons: concept, synthesis, applications*, Wiley, New York.

(15) Lee, C. C., MacKay, J. A., Fréchet, J. M. J., and Szoka, F. C. (2005) Designing dendrimers for biological applications. *Nat. Biotechnol. 23*, 1517–26.

(16) Wester, H.-J., and Kessler, H. (2005) Molecular targeting with peptides or peptide-polymer conjugates: Just a question of size. *J. Nucl. Med. 46*, 1940–5.

(17) Thumshirn, G., Hersel, U., Goodman, S. L., and Kessler, H. (2003) Multimeric cyclic RGD peptides as potential tools for tumor targeting: solid-phase peptide synthesis and chemoselective oxime ligation. *Chem.—Eur. J. 9*, 2717–25.

(18) Janssen, M., Frielink, C., Dijkgraaf, I., Oyen, W. J. G., Edwards, D. S., Liu, S., Rajopaghye, M., Massuger, L., Corstens, F. H. M., and Boerman, O. C. (2004) Improved tumor targeting of radiolabeled RGD peptides using rapid dose fractionation. *Cancer Biother. Radiopharm. 19*, 399–404.

(19) Wu, Y., Zhang, X., Xiong, Z., Cheng, Z., Fisher, D. R., Liu, S., Gambhir, S. S., and Chen, X. (2005) microPET imaging of glioma integrin $\alpha_v\beta_3$ expression using ^{64}Cu-labeled tetrameric RGD peptide. *J. Nucl. Med. 46*, 1707–18.

(20) Dijkgraaf, I., Kruijtzer, J. A. W., Liu, S., Soede, A. C., Oyen, W. J. G., Corstens, F. H. M., Liskamp, R. M. J., and Boerman, O. C. (2007) Improved targeting of the $\alpha_v\beta_3$ integrin by multimerisation of RGD peptides. *Eur. J. Nucl. Med. Mol. Imaging 34*, 267–73.

(21) Dijkgraaf, I., Rijnders, A. Y., Soede, A., Dechesne, A. C., van Esse, G. W., Brouwer, A. J., Corstens, F. H. M., Boerman, O. C., Rijkers, D. T. S., and Liskamp, R. M. J. (2007) Synthesis of DOTA-conjugated multivalent cyclic-RGD peptide dendrimers via 1,3-dipolar cycloaddition and their biological evaluation: implications for tumor targeting and tumor imaging purposes. *Org. Biomol. Chem. 5*, 935–44.

(22) Autar, R., Khan, A. S., Schad, M., Hacker, J., Liskamp, R. M. J., and Pieters, R. J. (2003) Adhesion inhibition of F1C-fimbriated *Escherichia coli* and *Pseudomonas aeruginosa* PAK and PAO by multivalent carbohydrate ligands. *ChemBioChem 4*, 1317–25.

(23) Joosten, J. A. F., Loimaranta, V., Appeldoorn, C. C. M., Haataja, S., Ait El Maate, F., Liskamp, R. M. J., Finne, J., and Pieters, R. J. (2004) Inhibition of *Streptococcus suis* adhesion by dendritic galabiose compounds at low nanomolar concentration. *J. Med. Chem. 47*, 6499–508.

(24) Arosio, D., Vrasidas, I., Valentini, P., Liskamp, R. M. J., Pieters, R. J., and Bernardi, A. (2004) Synthesis and cholera toxin binding properties of multivalent GM1 mimics. *Org. Biomol. Chem. 2*, 2113–24.

(25) André, S., Pieters, R. J., Vrasidas, I., Kaltner, H., Kuwabara, I., Liu, F.-T., Liskamp, R. M. J., and Gabius, H.-J. (2001) Wedge-like glycodendrimers as inhibitors of binding of mammalian galectins to glycoproteins, lactose maxiclusters, and cell surface glycoconjugates. *ChemBioChem 2*, 822–30.

(26) Joosten, J. A. F., Tholen, N. T. H., Ait El Maate, F., Brouwer, A. J., van Esse, G. W., Rijkers, D. T. S., Liskamp, R. M. J., and Pieters, R. J. (2005) High-yielding microwave-assisted synthesis of triazole-linked glycodendrimers by copper-catalyzed [3 + 2] cycloaddition. *Eur. J. Org. Chem. 2005*, 3182–5.

(27) Huisgen, R. (1984) 1,3-Dipolar cycloadditions - introduction, survey, mechanism. *1,3-Dipolar cycloaddition chemistry* (Padwa, A., Ed.) pp 1−176, Vol *1*, Wiley, New York.

(28) Tornøe, C. W., Christensen, C., and Meldal, M. (2002) Peptidotriazoles on solid phase: [1,2,3]-triazoles by regiospecific copper(I)-catalyzed 1,3-dipolar cycloadditions of terminal alkynes to azides. *J. Org. Chem. 67*, 3057–64.

(29) Rostovtsev, V. V., Green, L. G., Fokin, V. V., and Sharpless, K. B. (2002) A stepwise Huisgen cycloaddition process: copper(I)-catalyzed regioselective "ligation" of azides and terminal alkynes. *Angew. Chem., Int. Ed. 41*, 2596–9.

(30) Kolb, H. C., Finn, M. G., and Sharpless, K. B. (2001) Click chemistry: diverse chemical function from a few good reactions. *Angew. Chem., Int. Ed. 40*, 2004–21.

(31) Bock, V. D., Hiemstra, H., and van Maarseveen, J. H. (2006) Cu^I-catalyzed alkyne-azide "click" cycloadditions from a mechanistic and synthetic perspective. *Eur. J. Org. Chem.* 51–68.

(32) Moses, J. E., and Moorhouse, A. D. (2007) The growing applications of click chemistry. *Chem. Soc. Rev. 36*, 1249–62.

(33) Fournier, D., Hoogenboom, R., and Schubert, U. S. (2007) Clicking polymers: a straightforward approach to novel macromolecular architectures. *Chem. Soc. Rev. 36*, 1369–80.
(34) Lutz, J.-F., and Zarafshani, Z. (2008) Efficient construction of therapeutics, bioconjugates, biomaterials and bioactive surfaces using azide-alkyne "click" chemistry. *Adv. Drug Delivery Rev. 60*, 958–70.
(35) Meldal, M., and Tornøe, C. W. (2008) Cu-catalyzed azide-alkyne cycloaddition. *Chem. Rev. 108*, 2952–3015.
(36) Mulders, S. J. E., Brouwer, A. J., van der Meer, P. G. J., and Liskamp, R. M. J. (1997) Synthesis of a novel amino acid based dendrimer. *Tetrahedron Lett. 38*, 631–4.
(37) Mulders, S. J. E., Brouwer, A. J., and Liskamp, R. M. J. (1997) Molecular diversity of novel amino acid based dendrimers. *Tetrahedron Lett. 38*, 3085–8.
(38) Brouwer, A. J., Mulders, S. J. E., and Liskamp, R. M. J. (2001) Convergent synthesis and diversity of amino acid based dendrimers. *Eur. J. Org. Chem.* 1903–15.
(39) Brouwer, A. J., Mulders, S. J. E., and Liskamp, R. M. J. (2005) Synthesis of novel dendrimeric systems containing NLO ligands. *Eur. J. Org. Chem.* 487–95.
(40) Rijkers, D. T. S., van Esse, G. W., Merkx, R., Brouwer, A. J., Jacobs, H. J. F., Pieters, R. J., and Liskamp, R. M. J. (2005) Efficient microwave-assisted synthesis of multivalent dendrimeric peptides using cycloaddition reaction (click) chemistry. *Chem. Commun.* 4581–3.
(41) Kaiser, E., Colescott, R. L., Bossinger, C. D., and Cook, P. I. (1970) Color test for detection of free terminal amino groups in the solid-phase synthesis of peptides. *Anal. Biochem. 34*, 595–598.
(42) Sarin, V. K., Kent, S. B. H., Tam, J. P., and Merrifield, R. B. (1981) Quantitative monitoring of solid-phase peptide synthesis by the ninhydrin reaction. *Anal. Biochem. 117*, 147–157.
(43) Krchnák, V., Vágner, J., Safár, P., and Lebl, M. (1988) Noninvasive continuous monitoring of solid-phase peptide synthesis by acid-base indicator. *Collect. Czech. Chem. Commun. 53*, 2542–8.
(44) Meienhofer, J., Waki, M., Heimer, E. P., Lambros, T. J., Makofske, R. C., and Chang, C.-D. (1979) Solid phase synthesis without repetitive acidolysis. Preparation of leucyl-alanyl-glycyl-valine using 9-fluorenylmethyloxycarbonylamino acids. *Int. J. Pept. Protein Res. 13*, 35–42.
(45) Arx, E. von, Faupel, M., and Brugger, M. (1976) Das 4,4′-tetramethyldiamino-diphenylmethan reagens (TDM): Eine modifikation der Chlor-o-tolidin Farbereaktion für die Dünnschicht-chromatographie. *J. Chromatogr. 120*, 224–8.
(46) Fields, G. B., and Noble, R. L. (1990) Solid phase peptide synthesis utilizing 9-fluorenylmethoxycarbonyl amino acids. *Int. J. Pept. Protein Res. 35*, 161–214.
(47) Tam, J. P., Wu, C.-R., Liu, W., and Zhang, J.-W. (1991) Disulfide bond formation in peptides by dimethyl sulfoxide - scope and applications. *J. Am. Chem. Soc. 113*, 6657–62.
(48) Lipshutz, B. H., Frieman, B. A., and Tomaso, A. E., Jr. (2006) Copper-in-charcoal (Cu/C): heterogeneous, copper-catalyzed asymmetric hydrosilylations. *Angew. Chem., Int. Ed. 45*, 1259–64.
(49) Lipshutz, B. H., and Taft, B. R. (2006) Heterogeneous copper-in-charcoal-catalyzed click chemistry. *Angew. Chem., Int. Ed. 45*, 8235–8.
(50) Knör, S., Modlinger, A., Poethko, T., Schottelius, M., Wester, H.-J., and Kessler, H. (2007) Synthesis of novel 1,4,7,10-tetraazacyclodecane-1,4,7,10-tetraacetic acid (DOTA) derivatives for chemoselective attachment to unprotected polyfunctionalized compounds. *Chem.—Eur. J. 13*, 6082–90.
(51) Reubi, J. C., Kvols, L. K., Waser, B., Nagorney, D. M., Heitz, P. U., Charboneau, J. W., Reading, C. C., and Moertel, C. (1990) Detection of somatostatin receptors in surgical and percutaneous needle biopsy samples of carcinoids and Islet cell carcinomas. *Cancer Res. 50*, 5969–77.
(52) Grandjean, C., Boutonnier, A., Guerreiro, C., Fournier, J.-M., and Mulard, L. A. (2005) On the preparation of carbohydrate-protein conjugates using the traceless Staudinger ligation. *J. Org. Chem. 70*, 7123–32.
(53) Rodriguez, M., Llinares, M., Doulut, S., Heitz, A., and Martinez, J. (1991) A facile synthesis of chiral N-protected beta-amino alcohols. *Tetrahedron Lett. 32*, 923–6.
(54) Lutz, J.-F. (2008) Copper-free azide-alkyne cycloadditions: new insights and perspectives. *Angew. Chem., Int. Ed. 47*, 2182–4.
(55) van Berkel, S. S., Dirks, T. J., Meeuwissen, S. A., Pingen, D. L. L., Boerman, O. C., Laverman, P., van Delft, F. L., Cornelissen, J. J. L. M., and Rutjes, F. P. J. T. (2008) Application of metal-free triazole formation in the synthesis of cyclic RGD-DTPA conjugates. *ChemBioChem 9*, 1805–15.

BC900052N

SUPPORTING INFORMATION

Versatile Conjugation of Octreotide to Dendrimers by Cycloaddition ("Click") Chemistry to Yield High Affinity Multivalent Cyclic Peptide Dendrimers

Cheng-Bin Yim,[†,‡] Otto C. Boerman,[‡] Monique de Visser,[§] Marion de Jong,[§] Annemarie C. Dechesne,[†] Dirk T. S. Rijkers[†], and Rob M. J. Liskamp[†]

[†]Medicinal Chemistry & Chemical Biology, Utrecht Institute for Pharmaceutical Sciences, Department of Pharmaceutical Sciences, Faculty of Science, Utrecht University, Sorbonnelaan 16, 3584 CA Utrecht, the Netherlands.
[‡]Department of Nuclear Medicine, Radboud University Nijmegen Medical Centre, Geert Grooteplein 10, 6525 GA Nijmegen, the Netherlands.
[§]Department of Nuclear Medicine, Erasmus Medical Center Rotterdam, Dr. Molewaterplein 40, 3015 GD Rotterdam, the Netherlands.

[*]To whom correspondence should be addressed. Rob M. J. Liskamp, Medicinal Chemistry and Chemical Biology, Utrecht Institute for Pharmaceutical Sciences, Department of Pharmaceutical Sciences, Faculty of Science, Utrecht University, PO Box 80082, 3508 TB Utrecht, the Netherlands. Phone: +31 30 253 7396. Fax: +31 30 253 6655. E-mail: r.m.j.liskamp@uu.nl.

Table of contents

Synthesis of 6-azidohexanoic acid (**1**)	S2	
Synthesis of Fmoc-Thr(tBu)Ψ[CH_2OH] (**2**)	S2	
Synthesis of DOTA-D-Phe-*cyclo*(Cys-Tyr-D-Trp-Lys-Thr-Cys)-Threol (**17**)	S2	
ESI-MS analysis of N_3-Ahx-D-Phe-Cys-Tyr-D-Trp-Lys-Thr-Cys-Threol (**3**)	S3	Fig. SI 1
HPLC and ESI-MS analysis of N_3-Ahx-d-Phe-*cyclo*(Cys-Tyr-D-Trp-Lys-Thr-Cys)-Threol (**4**)	S4	Fig. SI 2AB
HPLC and ESI-MS analysis of DOTA-D-Phe-*cyclo*(Cys-Tyr-D-Trp-Lys-Thr-Cys)-Threol (**17**)	S5	Fig. SI 3AB
HPLC and MALDI-TOF analysis of monovalent octreotide peptide construct (**11**)	S6	Fig. SI 4AB
HPLC and MALDI-TOF analysis of divalent octreotide peptide dendrimer (**12**)	S7-8	Fig. SI 5ABC
HPLC and MALDI-TOF analysis of tetravalent octreotide peptide dendrimer (**13**)	S9	Fig. SI 6AB
HPLC and MALDI-TOF analysis of DOTA-conjugated monovalent octreotide construct (**14**)	S10	Fig. SI 7AB
HPLC and MALDI-TOF analysis of DOTA-conjugated divalent octreotide dendrimer (**15**)	S11	Fig. SI 8AB
HPLC and MALDI-TOF analysis of DOTA-conjugated tetravalent octreotide dendrimer (**16**)	S12	Fig. SI 9AB
Receptor binding affinity of compounds **11** – **13**	S13	Fig. SI 10
Receptor binding affinity of compounds **11** – **13**	S13	Table SI 1

Synthesis

6-Azidohexanoic acid (1): To a stirred solution of 6-bromohexanoic acid (3.9 g, 20 mmol) in DMF (10 mL) NaN_3 (2.6 g, 40 mmol) was added. The mixture was stirred for 3 h at 85°C. The reaction mixture was diluted with DCM and the obtained solution was washed with 0.1 N aqueous HCl. The organic layer was dried (Na_2SO_4) and concentrated under reduced pressure. Compound **1** was obtained as a colorless oil in 89% yield (2.8 g) and used without further purification. ^{1}H-NMR (300 MHz, $CDCl_3$) δ: 1.44 (m, 2H, γCH_2), 1.65 (m, 4H, $\beta CH_2/\delta CH_2$), 2.38 (m, 2H, αCH_2), 3.28 (m, 2H, εCH_2), 11.5 (broad s, 1H, OH); ^{13}C-NMR (75.5 MHz, $CDCl_3$) δ: 24.3, 26.3, 28.7, 34.0, 51.3, 179.7.

Fmoc-Thr(^{t}Bu)Ψ[CH_2OH] (2): To a cold (−15°C) and stirred solution of Fmoc-Thr(^{t}Bu)-OH (2.0 g, 5.0 mmol) in 1,2-dimethoxyethane (5.0 mL), N-methyl morpholine (0.56 mL, 5.0 mmol) followed by isobutyl chloroformate (0.68 mL, 5.0 mmol) were added. The reaction mixture was stirred overnight under an N_2 atmosphere. The precipitated hydrochloride was removed by filtration over a Hyflo® plug. To the cooled filtrate a solution of $NaBH_4$ (0.50 g, 13 mmol) in H_2O (5 mL) was added as a single portion, followed by the addition of H_2O (200 mL). The reaction mixture was concentrated in vacuo and the residue was redissolved in DCM (100 mL), and this solution was washed with H_2O (100 mL), 1N $KHSO_4$ (100 mL) and brine (100 mL). The organic layer was dried (Na_2SO_4) and concentrated to dryness. The residue was purified by column chromatography (eluens: EtOAc/hexane 1:1 v/v) and **2** was obtained as a clear oil in 94% yield (1.8 g). R_f(EtOAc/hexane 1:1 v/v): 0.32; ^{1}H-NMR (300 MHz, $CDCl_3$) δ: 1.17 (d, 3H, CH_3), 1.22 (s, 9H, $(CH_3)_3$), 2.69 (broad s, 1H, OH), 3.65 (broad m, 3H, NH-C*H*/C*H*$_2$OH), 3.95 (broad d, 1H, C*H*-CH_3), 4.23 (m, 1H, Fmoc CH), 4.42 (broad m, 2H, Fmoc CH_2), 5.23 (broad d, 1H, urethane NH), 7.30-7.78 (m, 8H, arom Fmoc); ^{13}C-NMR (75.5 MHz, $CDCl_3$) δ: 20.3, 28.9, 47.5, 57.4, 63.8, 67.0, 67.3, 74.5, 120.2, 125.3, 127.3, 127.9, 141.6, 144.2, 157.2.

DOTA-D-Phe-*cyclo*(Cys-Tyr-D-Trp-Lys-Thr-Cys)-Threol (17): Resin-bound Fmoc-protected octreotide (60 mg, 0.39 mmol/g, 23 µmol) was treated with 20% piperidine/NMP and subsequently washed with NMP and DCM. DOTA$(OtBu)_3$ (40 mg, 70 µmol, 3.0 equiv) was dissolved in NMP (2 mL) with equivalent amounts of HBTU and HOBt (27 mg and 11 mg, respectively) and DIPEA (24 µL, 140 µmol, 6.0 equiv) was added; this mixture was transferred to the resin-bound peptide and the obtained slurry was gently swirled for 16 h at room temperature. Subsequently, the resin was washed (NMP, DCM), dried and mixed with TFA/TIS/H_2O (10 mL, 95:2.5:2.5 v/v/v) and stirred for 3 h at room temperature. The crude peptide was isolated by precipitation with cold (-20 °C) MTBE/hexane (1:1 v/v). After centrifugation, the pellet was dissolved in CH_3CN/H_2O (1:1 v/v), lyophilized and purified by HPLC (C8). The linear peptide was obtained in 72% yield (24 mg). R_t = 20.45 min (C18); ESI-MS: *m/z* = 1424.19 $[M+H]^+$, 1446.02 $[M+Na]^+$, ($C_{65}H_{94}N_{14}O_{18}S_2$: *M* = 1423.65). The linear peptide (24 mg, 17 µmol) was dissolved in H_2O (26 mL, 2% acetic acid). The pH was adjusted to 6.0 with a 1.0 M ammonium acetate solution. To this solution, DMSO (9 mL) was added. After stirring overnight at room temperature, the solution was partially concentrated in vacuo and the remaining DMSO was evaporated with a rotational vacuum concentrator (Christ, Alpha-RVC). The lyophilized residue was dissolved in CH_3CN/H_2O, filtrated and loaded into a preparative C8 HPLC column. The cyclic peptide was obtained in 10% yield (2.4 mg). R_t: 19.43 min (C18); ESI-MS: *m/z* = 1421.45 $[M+H]^+$, ($C_{65}H_{92}N_{14}O_{18}S_2$: *M* = 1421.64).

N_3-Ahx-D-Phe-Cys-Tyr-D-Trp-Lys-Thr-Cys-Threol (3)

Figure SI 1. The ESI-MS spectrum of linear peptide **3**; ESI-MS: *m/z* = 1176.30 $[M+H]^+$, 119.25 $[M+Na]^+$, ($C_{55}H_{77}N_{13}O_{12}S_2$: *M* = 1175.53).

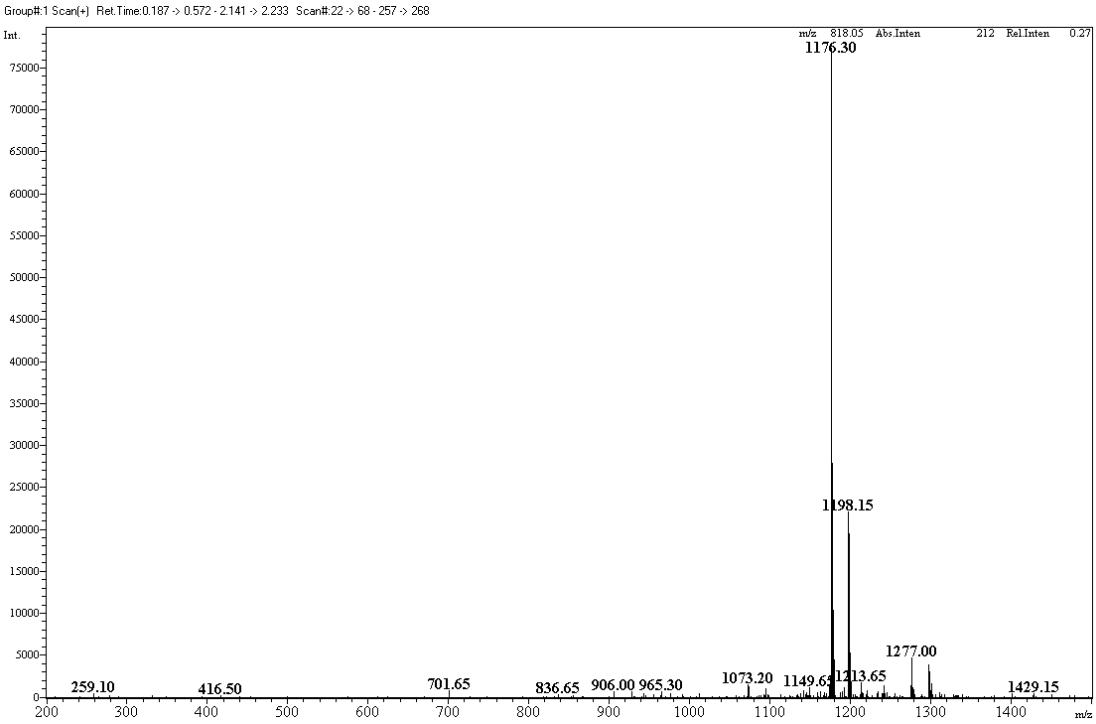

N_3-Ahx-D-Phe-*cyclo*(Cys-Tyr-D-Trp-Lys-Thr-Cys)-Threol (4)

Figure SI 2. (A) A baseline corrected HPLC trace of cyclic azido-functionalized octreotide **4** (R_t: 15.78 min (C8)). A linear gradient from 30% to 70% buffer B in 20 min was applied to give a better resolution with linear azido-functionalized octreotide **3** (R_t: 16.62 min (C8)). **(B)** ESI-MS: *m/z* = 1174.00 $[M+H]^+$, 1196.10 $[M+Na]^+$, ($C_{55}H_{75}N_{13}O_{12}S_2$: M = 1173.51).

(A)

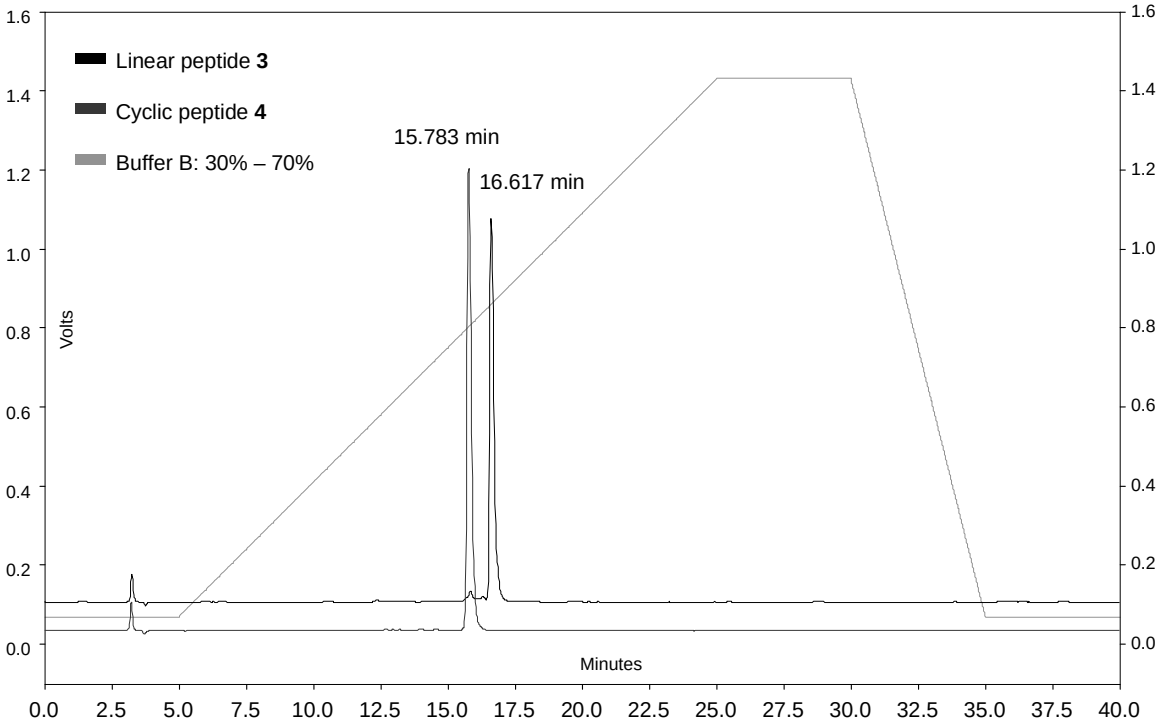

(B)

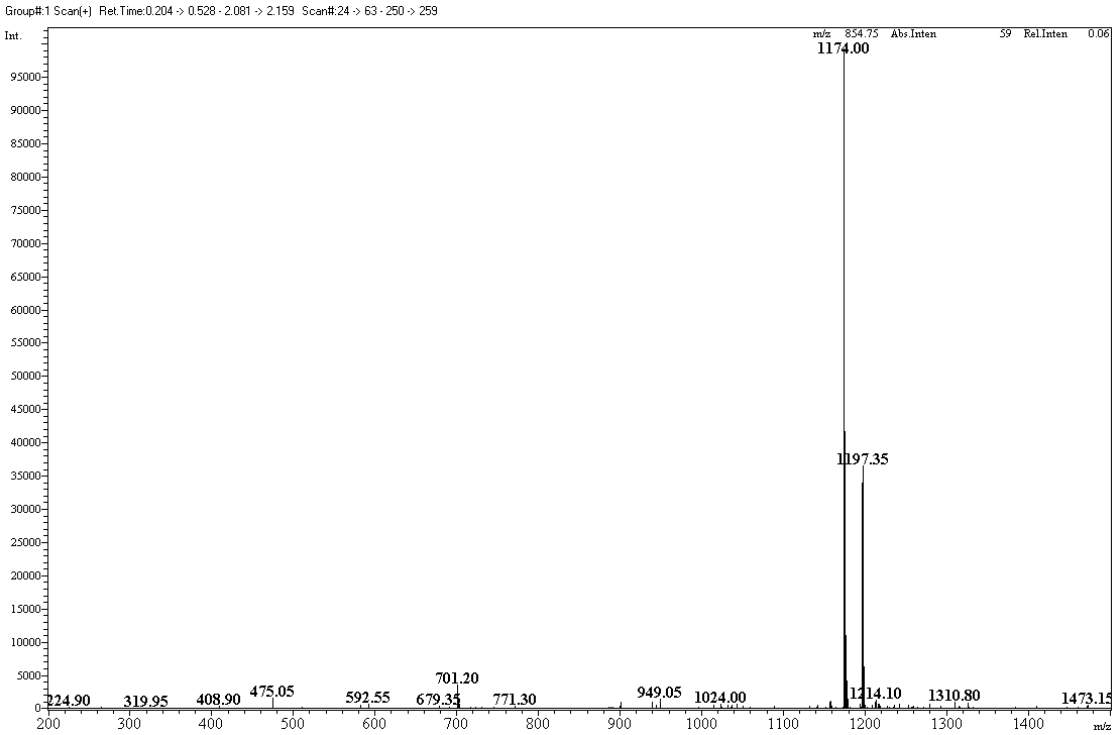

DOTA-D-Phe-*cyclo*(Cys-Tyr-D-Trp-Lys-Thr-Cys)-Threol (17)

Figure SI 3. (A) A baseline corrected HPLC trace (R_t: 19.43 min (C18)). **(B)** ESI-MS: *m/z* = 1421.45 $[M+H]^+$, ($C_{65}H_{92}N_{14}O_{18}S_2$: *M* = 1421.64).

(A)

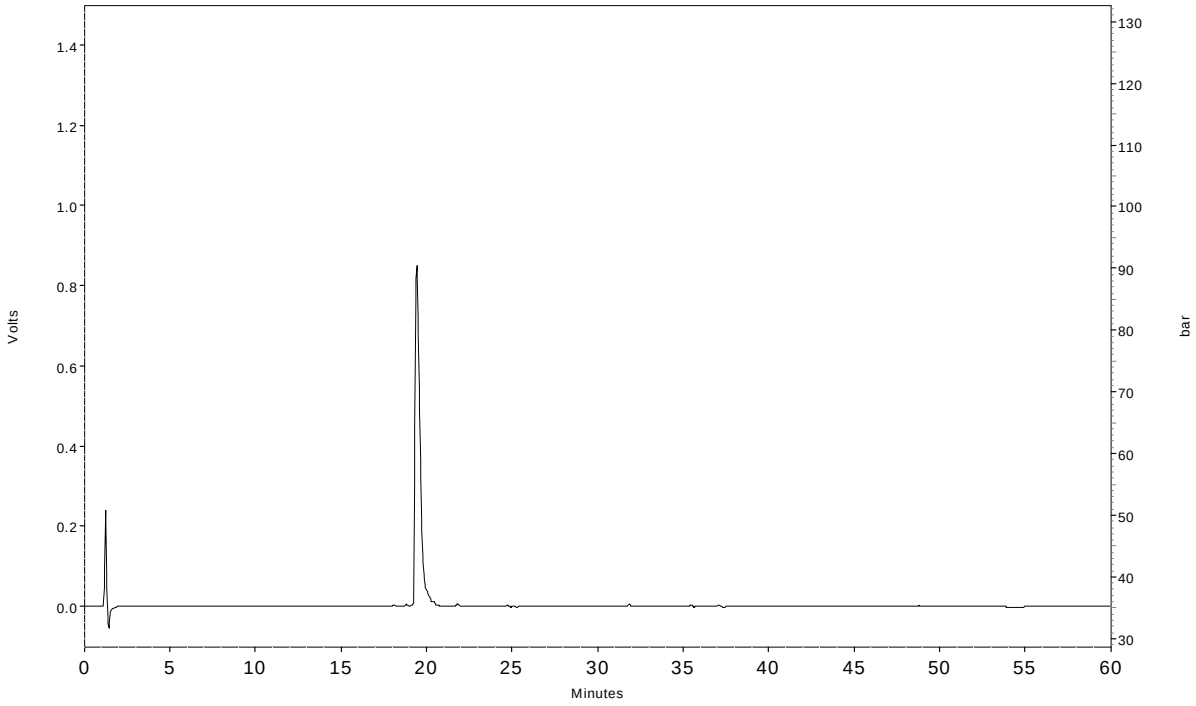

(B)

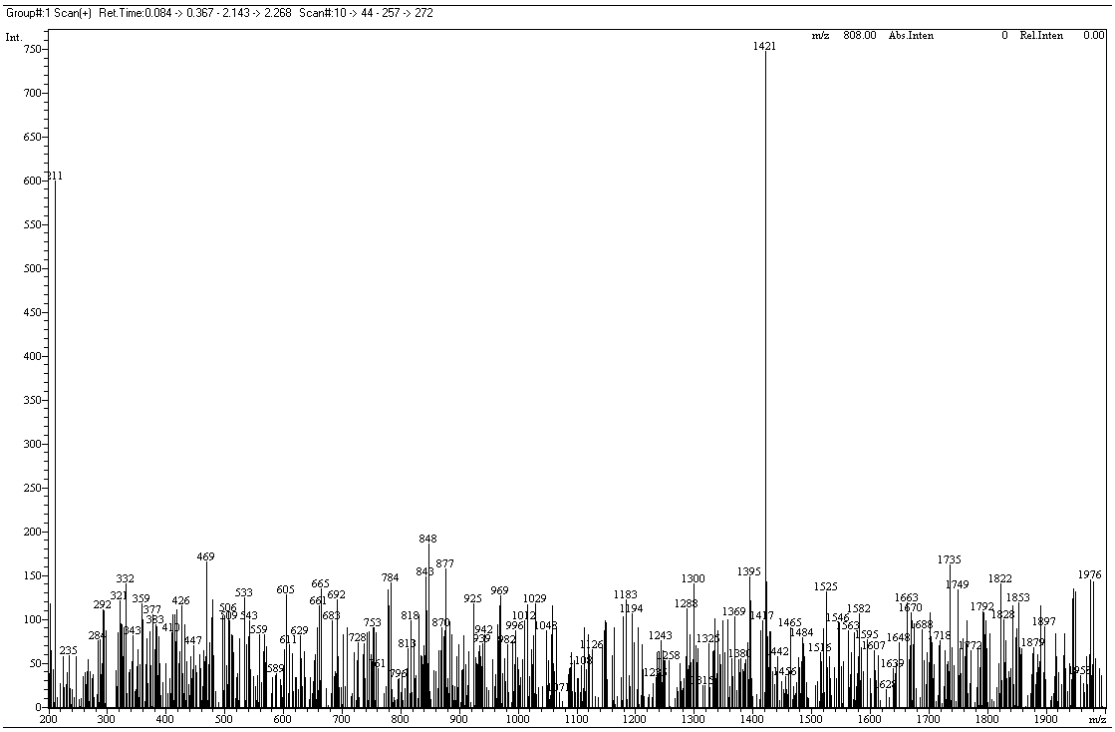

Octreotide peptide construct (11)

Figure SI 4. (A) A baseline corrected HPLC trace (R_t: 20.48 min (C8)). **(B)** MALDI-TOF: *m/z* = 1364.693 $[M+H]^+$, 1386.749 $[M+Na]^+$ ($C_{66}H_{85}N_{13}O_{15}S_2$: *M* = 1363.573).

(A)

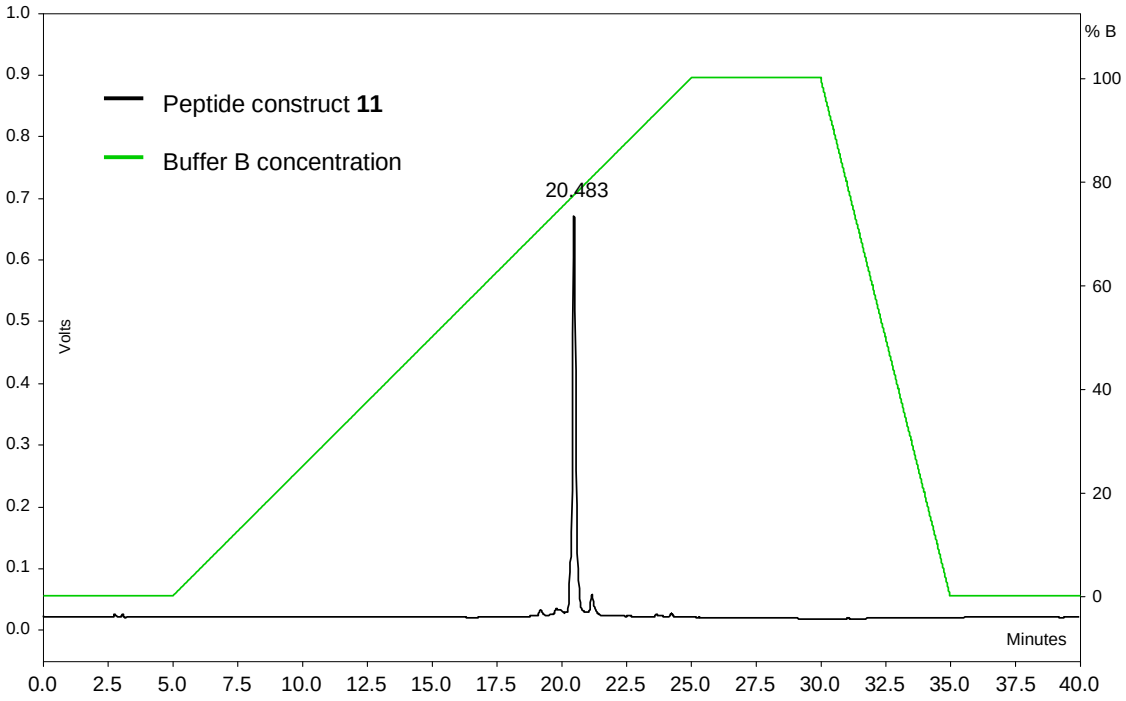

(B)

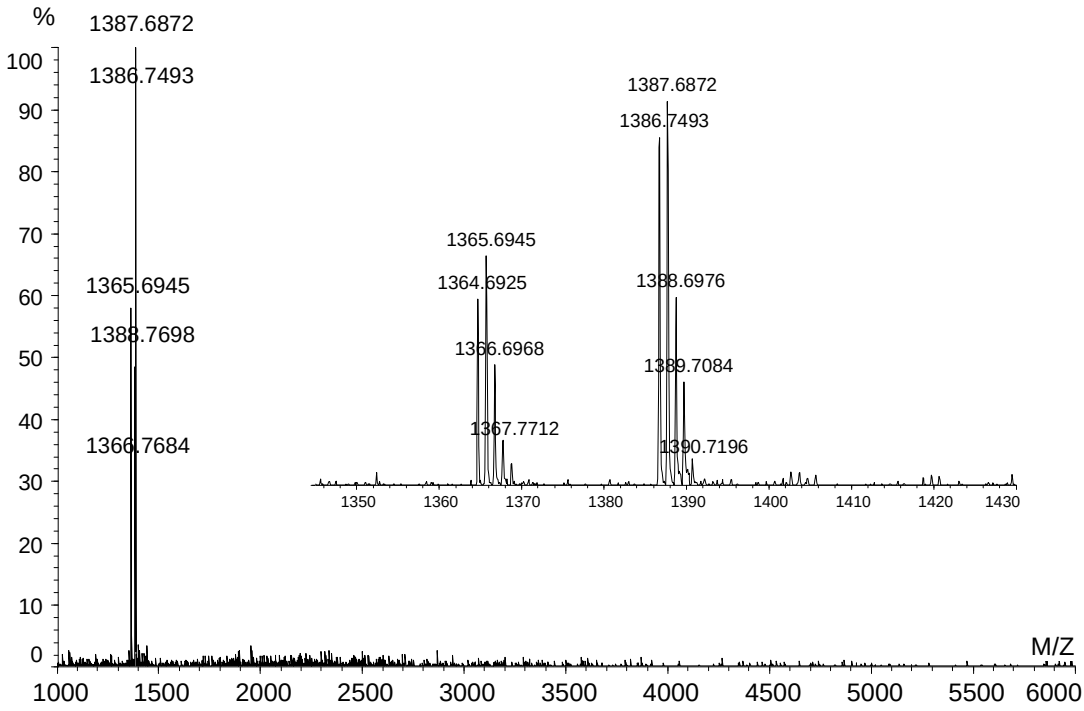

Divalent octreotide peptide dendrimer (12)

Figure SI 5. (A) A baseline corrected HPLC trace (R_t: 27.33 min (C18)). **(B)** MALDI-TOF: *m/z* = 2593.995 $[M+H]_{ave}^{+}$, 2616.045 $[M+Na]_{ave}^{+}$, 2632.121 $[M+K]_{ave}^{+}$, ($C_{124}H_{162}N_{26}O_{28}S_4$: M_{ave} = 2593.074). **(C)** Detail of the MALDI-TOF spectrum.

(A)

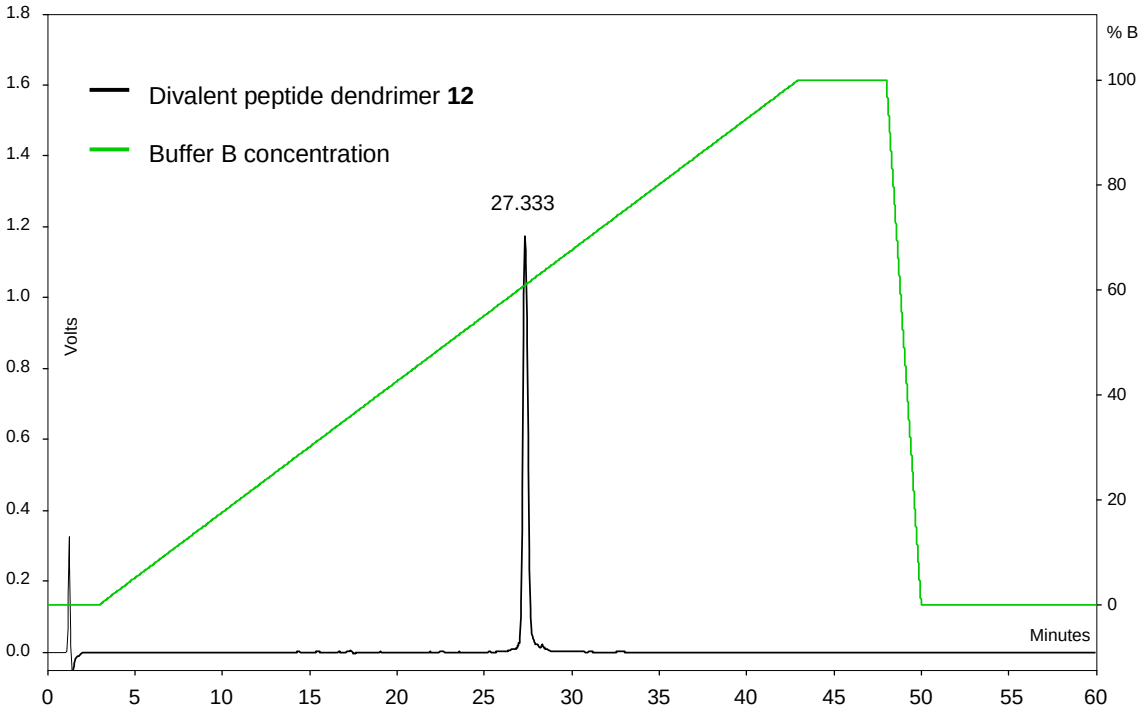

(B)

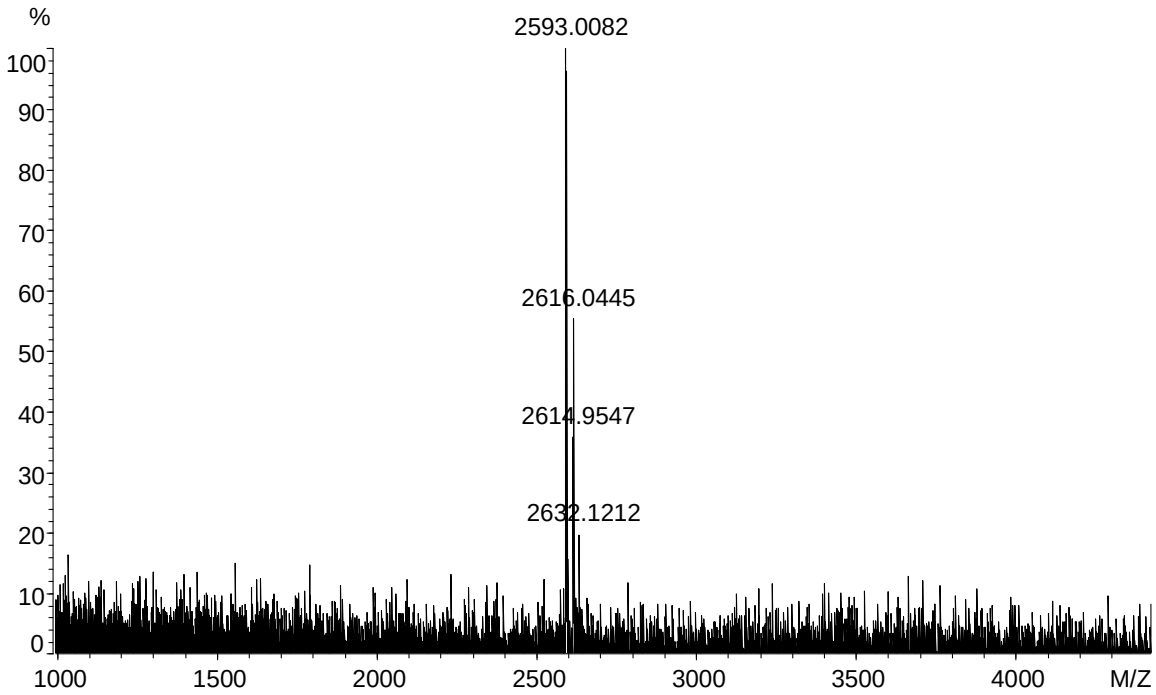

(C)

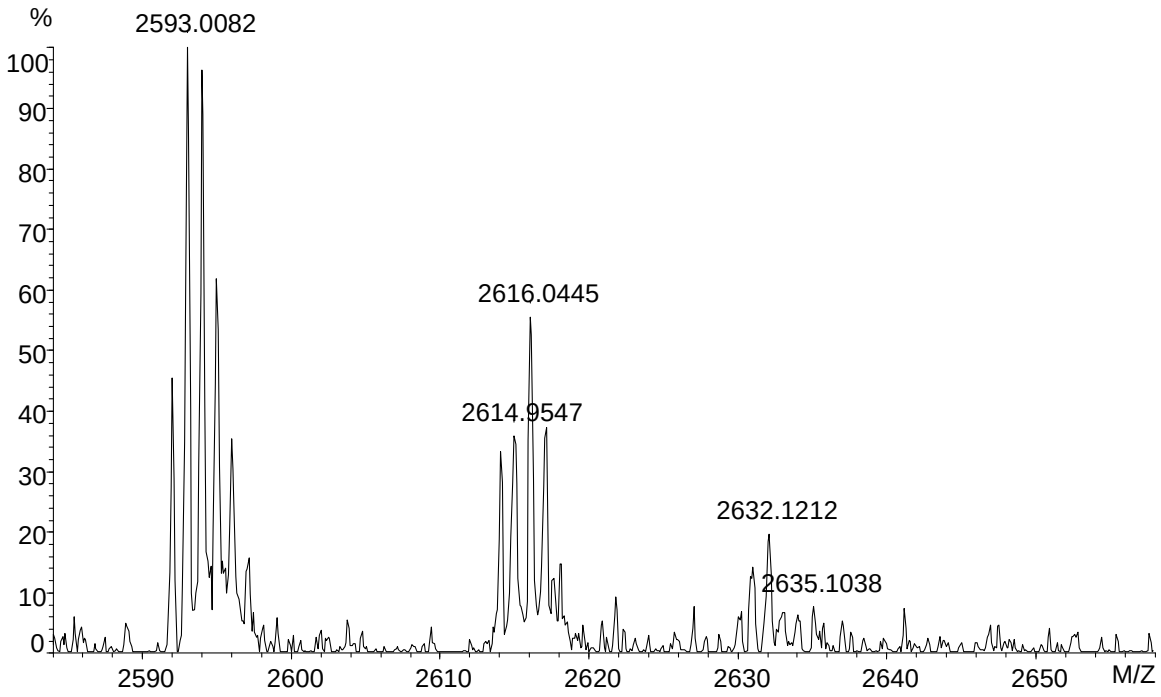
%
2593.0082
2616.0445
2614.9547
2632.1212
2635.1038
100
90
80
70
60
50
40
30
20
10
0
2590
2600
2610
2620
2630
2640
2650
M/Z

Tetravalent octreotide peptide dendrimer (13)

Figure SI 6. (A) A baseline corrected HPLC trace (R_t: 29.17 min (C18)). **(B)** MALDI-TOF: *m/z* = 5375.938 $[M+H]_{ave}^{+}$, 5397.834 $[M+Na]_{ave}^{+}$, 5414.927 $[M+K]_{ave}^{+}$, ($C_{258}H_{334}N_{54}O_{58}S_8$: M_{ave} = 5376.349).

(A)

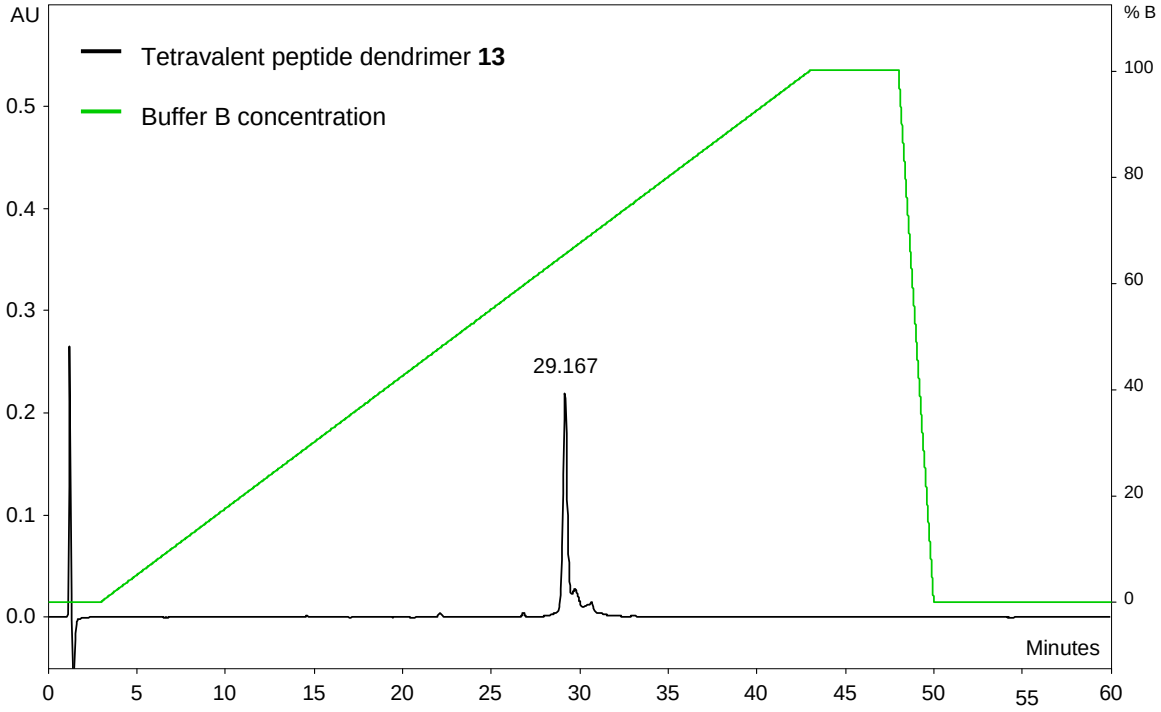

(B)

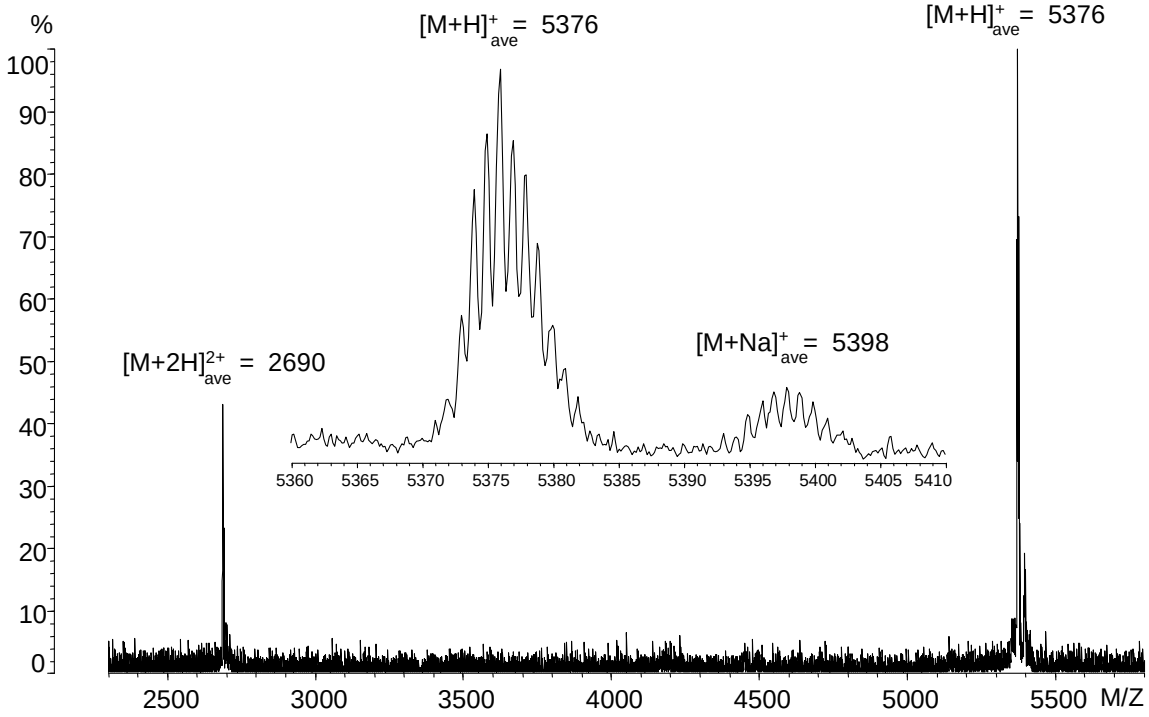

DOTA-conjugated octreotide peptide construct (14)

Figure SI 7. (A) A baseline corrected HPLC trace (R_t = 18.07 min (C8 Alltima)). **(B)** MALDI-TOF: *m/z* = 1780.234 $[M+H]_{ave}^{+}$, 1801.672 $[M+Na]_{ave}^{+}$ 1843.146 $[M+Cu]_{ave}^{+}$, ($C_{83}H_{115}N_{19}O_{21}S_2$: M_{ave} = 1779.05).

(A)

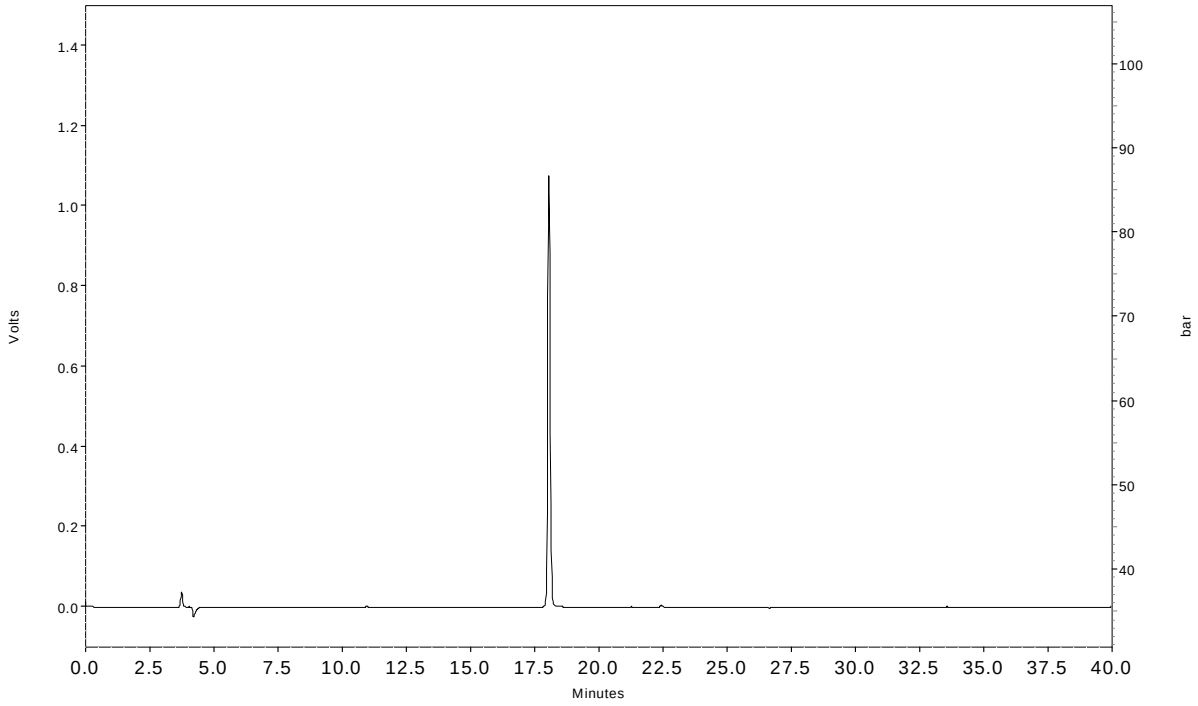

(B)

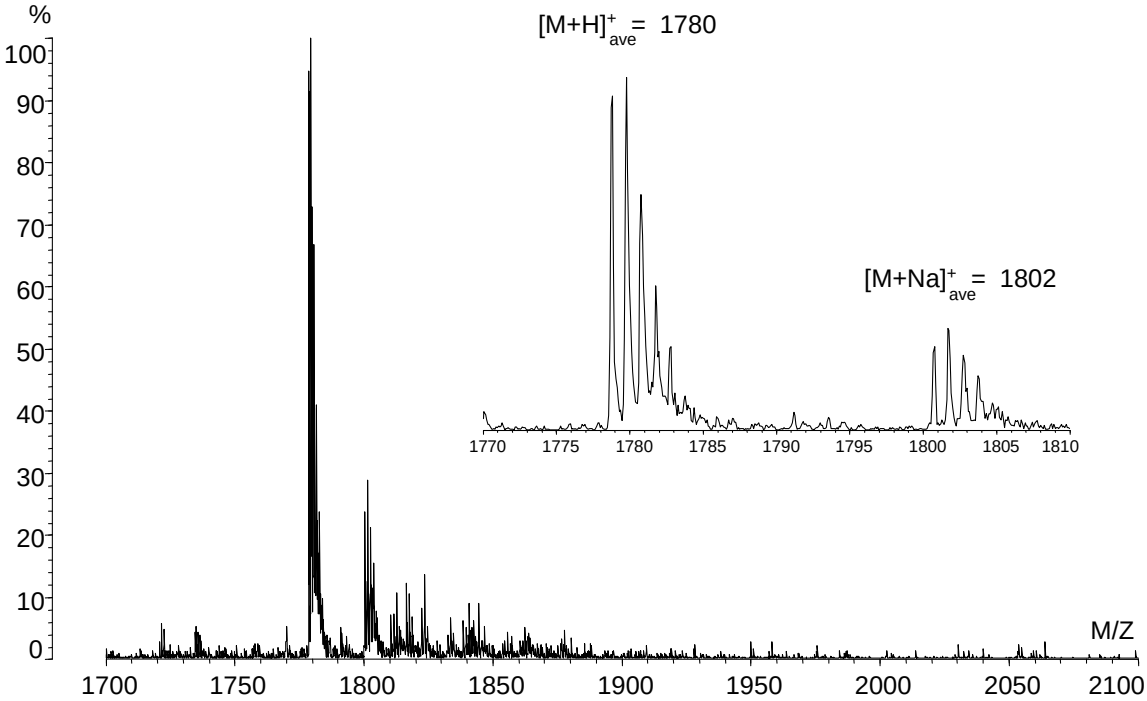

Divalent DOTA-conjugated octreotide dendrimer (15)

Figure SI 8. (A) A baseline corrected HPLC trace (R_t = 18.68 min (C8 Alltima)). **(B)** MALDI-TOF: *m/z* = 3008.674 $[M+H]_{ave}^{+}$, 3070.520 $[M+Cu]_{ave}^{+}$, ($C_{141}H_{192}N_{32}O_{34}S_4$: M_{ave} = 3007.49).

(A)

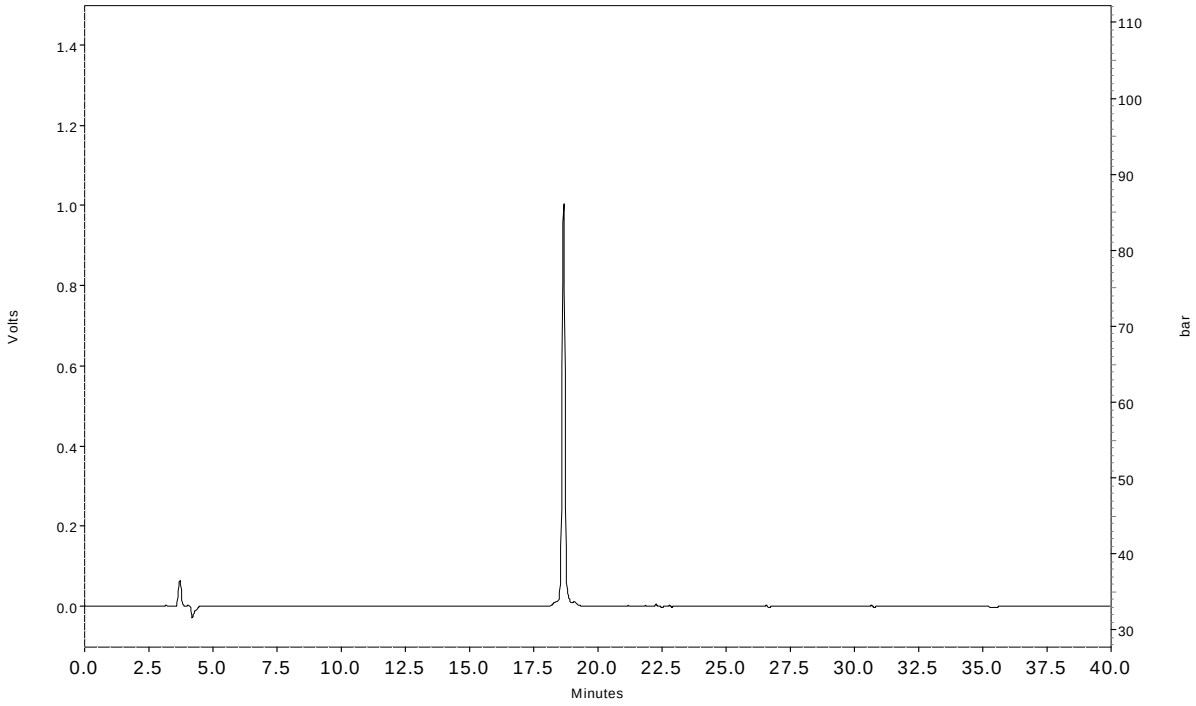

(B)

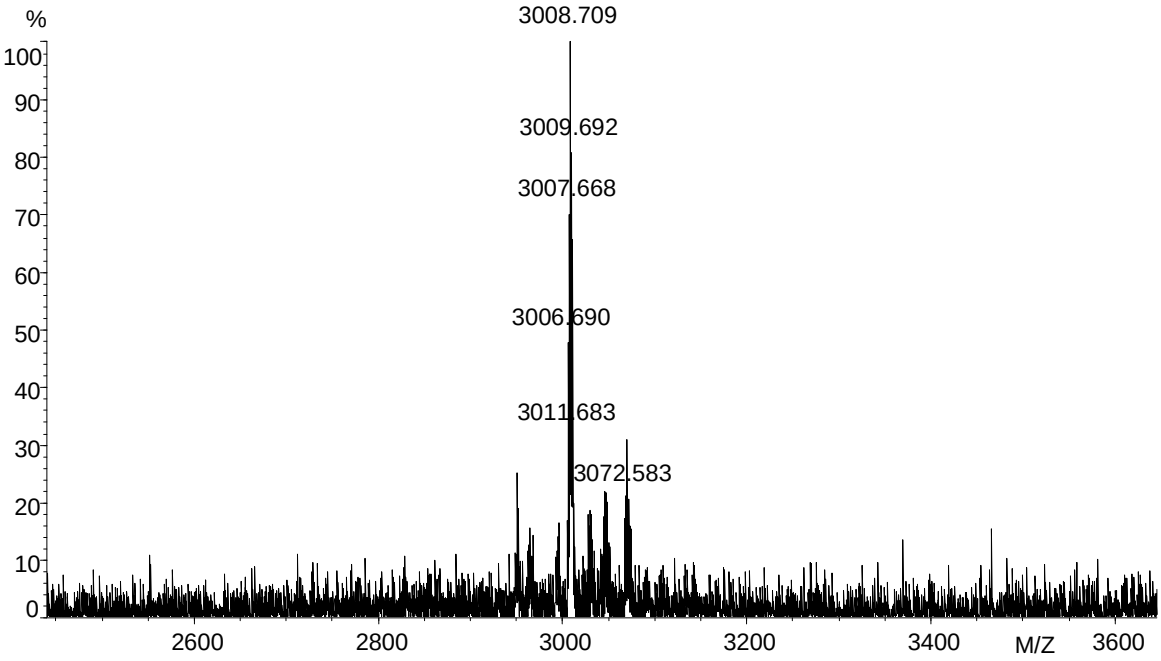

Tetravalent DOTA-conjugated octreotide dendrimer (16)

Figure SI 9. (A) A baseline corrected HPLC trace (R_t = 18.93 min (C8 Alltima)). **(B)** MALDI-TOF: *m/z* = 5790.326 $[M+H]_{ave}^{+}$, 5851.068 $[M+Cu]_{ave}^{+}$, ($C_{275}H_{364}N_{60}O_{64}S_8$: M_{ave} = 5790.72).

(A)

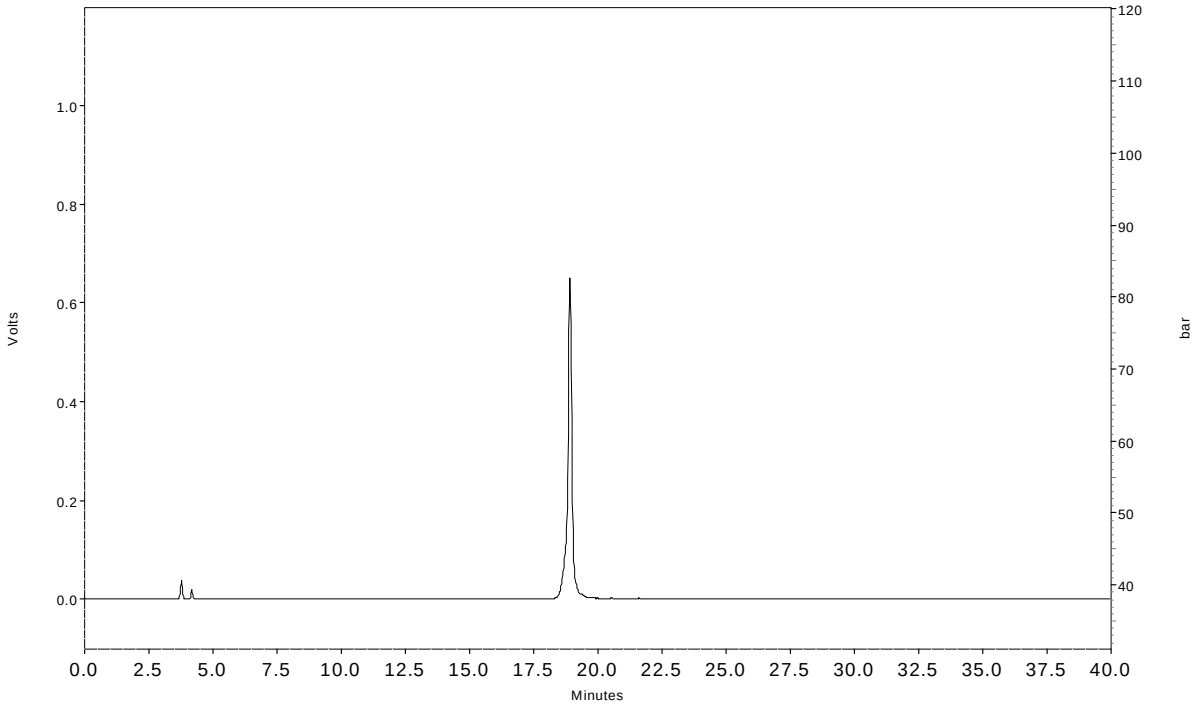

(B)

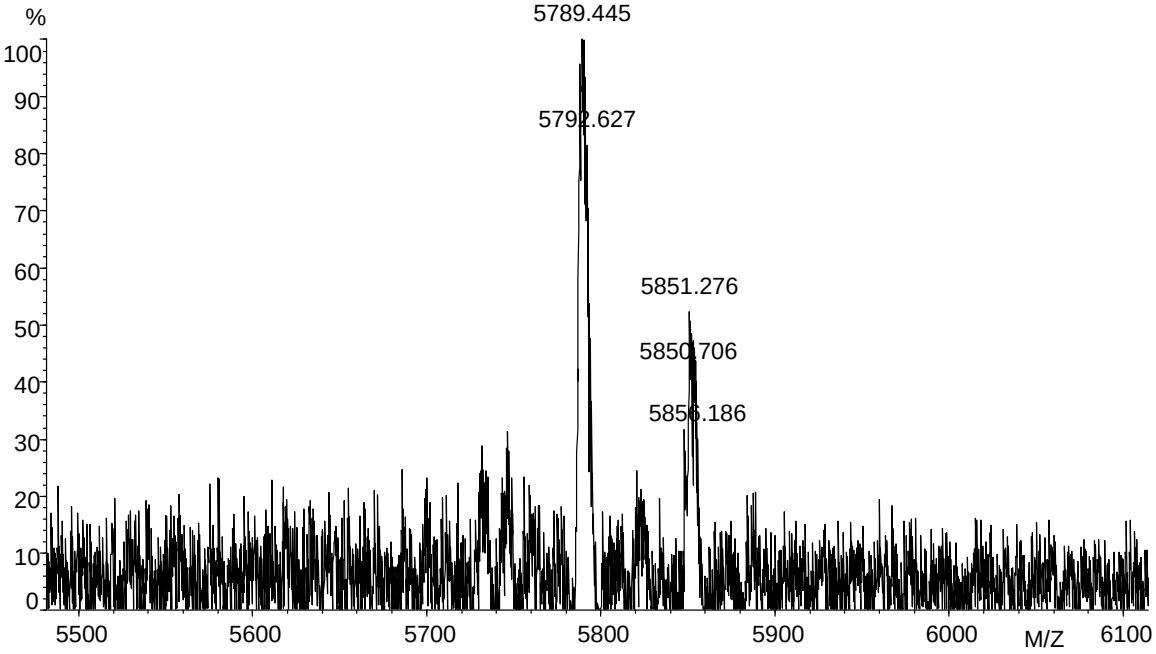

Receptor binding studies for conjugates 11 – 13

Figure SI 10 and Table SI 1 represent the results of the competitive binding assay of mono-, di- and tetravalent systems of octreotide **11** (■), **12** (▲) and **13** (▼) in their potency to displace receptor-bound [^{111}In-DOTA^{0},Tyr^{3}]octreotate in rat SSTR2-positive brain sections (n = 2 for each data point). Compounds **4** (♦) and **17** (●) are control compounds.

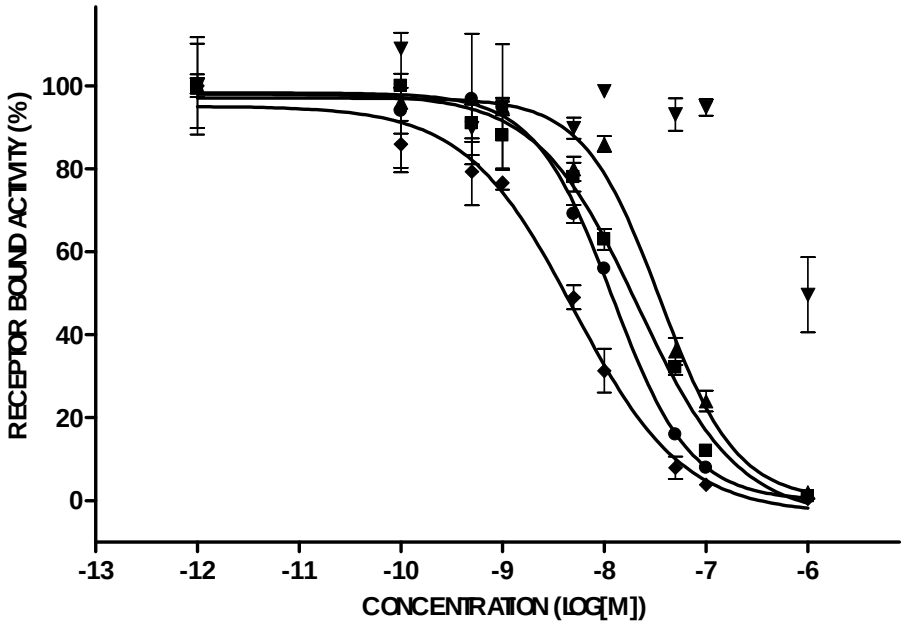

Figure SI 10.

Table SI 1.

Competing ligand	IC_{50} (nM)	95% CI (nM)
Conjugate **11**	21.3	14.2-31.9
Divalent **12**	35.3	19.5-63.7
Tetravalent **13**	n. d.[a]	n. d.[a]
Azido-octreotide **4**	5.03	3.24-7.79
DOTA-octreotide **17**	12.0	7.5-19.1

[a] Not determined: poor aqueous solubility prevented the calculation of reliable IC50 value.

Release of Liposomal Contents by Cell-Secreted Matrix Metalloproteinase-9

Jayati Banerjee,[†] Andrea J. Hanson,[†] Bhushan Gadam,[†] Adekunle I. Elegbede,[†] Shakila Tobwala,[‡] Bratati Ganguly,[‡] Anil V. Wagh,[†] Wallace W. Muhonen,[§] Benedict Law,[†] John B. Shabb,[§] D. K. Srivastava,[‡] and Sanku Mallik*[,†]

Department of Pharmaceutical Sciences, Department of Chemistry, Biochemistry and Molecular Biology, North Dakota State University, Fargo, North Dakota 58108, and Department of Biochemistry and Molecular Biology, School of Medicine and Health Sciences, University of North Dakota, Grand Forks, North Dakota 58202. Received February 11, 2009; Revised Manuscript Received June 1, 2009

Liposomes have been widely used as a drug delivery vehicle, and currently, more than 10 liposomal formulations are approved by the Food and Drug Administration for clinical use. However, upon targeting, the release of the liposome-encapsulated contents is usually slow. We have recently demonstrated that contents from appropriately formulated liposomes can be rapidly released by the cancer-associated enzyme matrix metalloproteinase-9 (MMP-9). Herein, we report our detailed studies to optimize the liposomal formulations. By properly selecting the lipopeptide, the major lipid component, and their relative amounts, we demonstrate that the contents are rapidly released in the presence of cancer-associated levels of recombinant human MMP-9. We observed that the degree of lipid mismatch between the lipopepides and the major lipid component profoundly affects the release profiles from the liposomes. By utilizing the optimized liposomal formulations, we also demonstrate that cancer cells (HT-29) which secrete low levels of MMP-9 failed to release a significant amount of the liposomal contents. Metastatic cancer cells (MCF7) secreting high levels of the enzyme rapidly release the encapsulated contents from the liposomes.

INTRODUCTION

Liposomes are lipid bilayers encapsulating an aqueous core (*1, 2*). Due to the ease of preparation in a size-controlled manner and biocompatibility, they are widely used as lipid-based nanoparticles for drug delivery (*3, 4*). Hydrophilic molecules are encapsulated in the aqueous interior of the liposomes, and hydrophobic molecules partition into the lipid bilayers (*5, 6*). Incorporation of poly(ethylene glycol) (PEG) containing lipids reduces opsonization and renders the liposomes long-circulating in the bloodstream (*7, 8*). After intravenous administration, long-circulating liposomes passively accumulate in the tumor tissues due to the enhanced permeation and retention effect (*9*). For active targeting, antibodies (*10*), peptides (*11*), and small molecules (*12*) have been conjugated to the surface of the liposomes.

The side effects of anticancer drugs are considerably reduced by encapsulating them in the liposomes (*13*). There are currently about 10 liposomal drug formulations approved by the U.S. Food and Drug Administration (FDA) for human use (*14*). Numerous clinical trials are currently in progress using liposome-encapsulated anticancer drugs (*15*). However, upon targeting, the release of the encapsulated drugs is usually very slow (*16*). An attractive solution to this problem is to formulate liposomes with appropriate lipids such that the contents are released in response to an external trigger. Temperature (*17*), pH (*18*), light (including near-infrared (*19*)), ultrasound (*20*), metal ions (*21*), and enzymes (*22, 23*) have been used as triggers. We have recently demonstrated the release of liposomal contents by the cancer-associated enzyme matrix metalloproteinase-9 (MMP-9) (*24, 25*).

Matrix metalloproteinases (MMPs) are a family of 23 Zn^{2+} and Ca^{2+} dependent extracellular enzymes responsible for the degradation and remodeling of the extracellular matrix (*26, 27*). The expression level and activation of these enzymes are regulated at multiple levels (*28*). Increased expression of MMPs is associated with many diseases, including various types of cancers (*29, 30*). MMP-9 is involved in the progression and metastasis of many cancers (*31, 32*).

Herein, we report our detailed mechanistic and optimization studies on the triggered release of liposomal contents by MMP-9. We have prepared triple helical peptide substrates for MMP-9 and conjugated them with fatty acids to synthesize the corresponding lipopeptides. Liposomes incorporating these lipopeptides released the encapsulated contents in response to cancer-associated levels of recombinant MMP-9. We optimized the system by systematically varying the triple helicity of the lipopeptides, its amount, and the structure of the major lipid component of the liposomes. We observed that the content release is dependent on the degree of mismatch between the fatty acids of the lipopeptides and the major lipid of the liposomes. Using the optimized formulation, we demonstrate that the liposomal contents are released by MMP-9 secreted from the breast adenocarcinoma cells, MCF7. The colorectal adenocarcinoma cells HT29 do not secrete high levels of MMP-9 and failed to release significant amounts of the encapsulated contents from the liposomes.

MATERIALS AND METHODS

Synthesis of the Lipopeptides. The lipopeptides were synthesized by employing a microwave-assisted peptide synthesizer (Liberty, CEM corporation, Matthews, NC) using standard Fmoc-protected amino acids (0.1 mmol scale). The commercially available Fmoc-Gly-CLEAR acid resin was used

* Corresponding author. Tel: 701-231-7888; Fax: 701-231-8333; E-mail: Sanku.Mallik@ndsu.edu.

[†] Department of Pharmaceutical Sciences, North Dakota State University.

[‡] Department of Chemistry, Biochemistry and Molecular Biology, North Dakota State University.

[§] University of North Dakota.

10.1021/bc9000646 CCC: $40.75 © 2009 American Chemical Society
Published on Web 06/24/2009

as the solid support. The reactions were carried out in a 30 mL reaction vessel housed within the microwave chamber (CEM Discover) of the peptide synthesizer. A mixture of HOBT/HBTU in 5-fold excess was used as the coupling reagent. Each coupling step (with the exception of Arg) was performed at 50 °C under 20 W microwave power for 5 min. The coupling of amino acid Arg was done twice at 25 °C for 25 min without the use of microwave. The N-terminal fatty acid was also subjected to double coupling. The activator base used was 5 equiv of diisopropylethylamine dissolved in *N*-methylpyrrolidone. The Fmoc deprotection was accomplished with 5% (by weight) of piperazine in DMF. Cleavage from the solid support was performed inside the microwave chamber for 35 min using a cocktail of TFA-tri-isopropylsilane and water (95%/2.5%/2.5%). The crude peptides were precipitated as white solids with ice-cold ether, centrifuged, and purified by a semipreparatory RP-HPLC. The monoisotopic masses of purified peptides were determined with an Applied Biosystems/MDS SCIEX 4800 MALDI ToF/ToF analyzer.

Conditions for Analytical HPLC. The analytical HPLC was performed with Vydac analytical diphenyl column (RP219TP5415) with a linear gradient of 0−70% acetonitrile in water as eluant, with each solvent containing 0.1% TFA. The flow rate was maintained at 1.5 mL/min for 25 min. The UV detection wavelength was kept at 214 nm.

Conditions for Semipreparatory HPLC. Vydac diphenyl (RP219TP510) RP HPLC column was used. A linear gradient of 0−70% acetonitrile in water was maintained for 60 min at flow rate 8 mL/min. Each solvent contained 0.1% TFA. The purification was monitored at a detector wavelength of 235 nm.

Liposome Formation. Stock solutions of lipopeptides were prepared by weighing appropriate amounts of the lipopeptide and then dissolving in 5:1 chloroform/methanol to a final concentration of 1 mg/mL. Stock solutions of phospholipids were prepared in chloroform to obtain a final concentration of 2 mg/mL. The lipopeptide and the phospholipid were mixed in appropriate volumes in a 10 mL round-bottom flask. A thin lipid film was obtained by evaporating this mixture in a rotary evaporator at 40 °C. The thin film was kept under high vacuum overnight to remove any residual organic solvents. The dry lipid film was hydrated with 1.5 mL buffer containing 6-carboxyfluorescein at 60 °C for 1−2 h. The hydrated solution was stored for 3−4 h to ensure complete hydration and to allow for proper folding of the lipopeptides into triple helices. In the next step, the large multilamellar vesicles were broken into unilamellar vesicles of appropriate sizes by probe sonication in a heating block for 1 h at 56 °C. After sonication, the liposome solution was centrifuged to remove any suspended metal particles from the probe tip and extruded through a 100 nm polycarbonate filter (Avanti Polar lipids, AL). The unencapsulated carboxyfluorescein was removed from the liposomes by gel filtration through a Sephadex G-100 column. The Sephadex G-100 was hydrated for 24 h at 60 °C and equilibrated with 5 times the volume of the assay buffer before loading of the liposomes. The osmolarity of this eluant buffer was made equal to the osmolarity of the carboxyfluorescein solution used for hydration by adding appropriate amount of NaCl. This ensured minimum background leakage of carboxyfluorescein due to osmotic shock during the actual leakage experiment.

For CD experiments, the thin film prepared in a similar manner as discussed above was hydrated with 1 mL of 5 mM phosphate buffer (pH 8.0) at 60 °C for 1 h. The liposomes after 2 h were subjected to probe sonication for 30 min. The CD spectra were recorded at 25 °C immediately after the probe sonication.

Buffer Solutions. The buffer used in making carboxyfluorescein solution was 25 mM HEPES (pH = 8.0) containing 100 mM carboxyfluorescein, 10 mM $CaCl_2$, 10 μM $ZnCl_2$, and 100 mM NaCl. The buffer used for column equilibration, elution of liposomes from the column, and release experiment consisted of 25 mM HEPES (pH 8.0) with 10 mM $CaCl_2$, 10 μM $ZnCl_2$, and 100−150 mM NaCl. The buffer prepared for the liposome CD experiments was 5 mM phosphate buffer at pH 8.0.

Circular Dichromism Spectroscopy. CD spectra were recorded in a Jasco J815 CD spectrometer using 1 mm path length quartz cuvette. For temperature-dependent CD spectra, the concentration of the lipopeptides used was 1 mg/mL in aqueous solution. The solutions were stored for 12 h at 4 °C before recording the spectra. For each sample, the equilibration time was set for 15 min at each temperature. For each temperature, an average of 3 scans were recorded at a scan speed of 50 nm/min. The response time set was 0.25 s. The melting temperature was obtained by plotting the CD intensity maxima at 225 nm vs temperature. For the liposome CD spectra, the average of 50 scans was recorded with a scan speed of 100 nm/min.

Release Studies. The kinetics of carboxyfluorescence release from the liposomes was monitored by recording the intensity of fluorescence emission at 518 nm using a spectrophotometer (Spectrmax, Molecular Devices) with an excitation wavelength at 480 nm. Each experiment was conducted in triplicate wells on a 96 standard opaque fluorescent well plate. The final reading taken was the average reading from 3 wells. For experiments involving recombinant human MMP-9, the activity of the enzyme was tested with a commercially available fluorogenic substrate prior to the experiment to ensure that the enzyme is fully active. The fluorescence emission was recorded at 20 s interval for 1 h. After 1 h, the liposomes were ruptured using optimized concentration of Triton-X to allow complete leakage of the dye. The fluorescence emission corresponding to this leakage was taken as the maximum emission possible in calculating the percentage release. The percentage release was calculated using a formula reported previously (*25*).

Growth and Maintenance of Cells. All cells were obtained from American type Culture Collection (Manassas, VA, USA). MCF7 (human breast adenocarcinoma) and HT-29 (human colorectal adenocarcinoma) cell lines were cultured in Eagle's Minimum Essential medium and McCoy's 5a medium, respectively, at 37 °C in humidified atmosphere containing 5% CO_2. All media were supplemented with 5% penicillin and streptomycin solution and 10% fetal bovine serum. When the cells achieved 70% of confluency, the old culture media were replaced with fresh culture media without phenol red. The cells were further incubated for 24 h, collected, and centrifuged. The supernatants were collected for further experiments. For cell-based liposomal release experiments, 50 μL of cell media was added to a total volume of 200 μL in each well, and the intensity of emission spectra of carboxyfluorescein at 518 nm ($\lambda_{ex} = 480$ nm) was monitored as discussed in the recombinant MMP-9 release studies.

RESULTS AND DISCUSSION

Synthesis of Lipopeptides. The natural substrate for the MMP-9 is gelatin (*33*). Gelatin and collagen-mimetic triple-helical peptides have been used as models to study substrate selectivity of the MMPs (*34*), as scaffolds and functional biomaterials for tissue engineering (*35*), and as targeting moieties for liposomes (*36*). Structurally, the collagen-mimetic peptides contain repeat units of the amino acid triad Gly-Pro-Hyp (GPO). For these studies, we prepared homotrimeric collagen-mimetic peptides containing the cleavage site for MMP-9 employing a microwave-assisted, solid-phase peptide synthesizer (*37*). The peptides have the general structure of $CH_3(CH_2)_{16}$CONH-GPQGIAGQR$(GPO)_n$GG-COOH, where the

Table 1. Synthesized Lipopeptides, Their Calculated and Observed Molecular Masses, the Calculated Rpn Values at 5 °C, and the Melting Temperatures (T_m)

no.	name	*n*	calcd. M^+	obsd. M^+	Rpn	T_m (°C)
1	**GPO3**	3	2065.06	2066.07	0.08	43
2	**GPO4**	4	2332.24	2332.27	0.11	56
3	**GPO5**	5	2600.37	2599.40	0.13	64

MMP-9 cleavage site is the peptide bond connecting Gly and Ile. In order to vary the triple helicity, the number of GPO repeat units in the peptides (i.e., *n*) were systematically varied (Table 1). We employed the microwave-assisted peptide synthesizer to conjugate the fatty acids to the peptides.

In order to determine the structural resemblance of the synthesized lipopeptides with collagen (and gelatin), we recorded the CD spectra in aqueous solution (1 mg/mL). In CD spectra, the presence of a positive peak at 225 nm and a large negative peak at 195−200 nm confirmed the triple helical structure of the lipopeptides (Figure 1A 38). The calculated Rpn values (*38*) at 5 °C and the melting temperatures (T_m) of the lipopeptides are also shown in Table 1. Since the Rpn value for natural collagen is 0.13 (*38*), we concluded that the lipopeptides adopt triple helical conformation, similar to collagen in aqueous solution. The lipopeptides **GPO3** and **GPO4** showed triple helical conformation in 5 mM phosphate buffer (pH = 8.0). However, the lack of sufficient solubility of the lipopeptides **GPO5** in this buffer prevented us from recording and comparing the spectra for all the lipopeptides at pH = 8.0.

Subsequently, we prepared liposomes containing 30 mol % of the synthesized lipopeptides in 25 mM phosphate buffer, pH = 8.0. The major lipid component of the liposomes was varied among POPC (1-palmitoyl-2-oleoyl-*sn*-glycero-3-phosphocholine), DOPC (1,2-dioleoyl-*sn*-glycero-3-phosphocholine), and DSPC (1,2-distearoyl-*sn*-glycero-3-phosphocholine), and the CD spectra were recorded. Highest triple helicities for the liposome-incorporated lipopeptides were observed in the POPC liposomes (Figure 1B, red trace), possibly reflecting the mismatch between the fatty acids of the lipopeptides and POPC and the resultant demixing of the major lipid and the lipopeptides. When we incubated these liposomes with 3.0 μM recombinant MMP-9 for 30 min, the triple helicity of the liposome-incorporated lipopeptides was reduced substantially (Figure 1B, blue trace) indicating that the cleavage of the surface-exposed peptide substrates by the enzyme decreases the triple helicity of the lipopeptides.

As an independent measure of the triple helicity of the liposome-incorporated lipopeptides, we synthesized a pyrene-containing analogue of **GPO4** (**PyGPO4**, Scheme 1, synthetic details are included in Supporting Information). The CD spectrum of this lipopeptide in aqueous solution showed a positive peak at 225 nm and a large negative peak at 198 nm, indicating the formation of triple helix (T_m = 36 °C, Supporting Information). Subsequently, we recorded the fluorescence emission spectra (λ_{ex} = 340 nm) of POPC liposomes incorporating 30 mol % of **PyGPO4** in 25 mM HEPES buffer (pH = 8.0). The presence of a strong excimer peak in the emission spectrum (471 nm) indicated the proximity of the pyrene groups in the hydrophobic fatty acids of the lipopeptides (Figure 2, blue trace). Upon incubation of the liposomes with 3 μM MMP-9 for 15 min, we observed that the pyrene excimer emission peak decreased and the monomer emission peaks increased in intensity (Figure 2, red trace). These results indicate that the lipopeptide **PyGPO4** is demixed in the lipid bilayer of the liposomes. Hydrolysis of the peptides by MMP-9 leads to the reorganization of the lipids with increased separation between the pyrene groups.

Next, we proceeded to determine the optimal liposomal formulation for the release methodology. We varied the amounts, the triple helicity of the lipopeptides, and the major lipid component of the liposomes. First, the amount of lipopeptide in the liposomes (30 mol % of **GPO3**) and the concentration of MMP-9 (2.3 μM) were kept constant, and the major lipid component was varied (DOPC, POPC, and DSPC). The rates of release of encapsulated carboxyfluorescein from these liposomal formulations were monitored (λ_{ex} = 480 nm, λ_{em} = 518 nm; Figure 3). When DOPC was the major lipid, we observed complete release of the encapsulated dye within 30 min (Figure 3A). However, these liposomes released about 25% of the contents during the same time in the absence of any enzyme (Figure 3A). For the POPC liposomes, 90% of the encapsulated dye was released by MMP-9 in 30 min (Figure 3B). We were pleased to note that, for these liposomes, no dye released in the absence of MMP-9 (Figure 3B). When DSPC was the major lipid, no significant dye release from the liposomes was observed either in the presence and or in the absence of MMP-9 (data now shown). As discussed before, incorporation of the lipopeptides in the liposomes results in lipid demixing. The degree of this demixing depends on the mismatch between the hydrophobic fatty acid moieties of the lipopeptides and the major lipid component of the liposomes. For the synthesized lipopeptides, the saturated stearoyl moiety does not mix well with the unsaturated oleoyl groups of the lipids POPC and DOPC in the liposomes. However, when DSPC is the major component, the lipopeptides are well-mixed within the lipid bilayer of the liposomes.

Previously, we have observed that the dye release profiles for liposomes incorporating 30 mol % of the lipopeptide **GPO4** were single exponential in nature (*25*). The dye release profiles shown in Figure 3 can be fitted best with a biexponential rate equation: F (release) = $F_0 - (A_1 \times e^{-k1t} + A_2 \times e^{-k2t})$ to obtain the rate constants k_1 and k_2 for the dye release and the amplitudes A_1 and A_2. The calculated rate constants for the dye release from the DOPC and POPC liposomes are shown in Table 2. For the POPC liposomes, both rate constants were faster compared to those for the DOPC liposomes (Table 2). When we prepared liposomes incorporating 30 mol % of the lipopeptide **GPO5** with POPC as the major lipid, encapsulating a sufficient concentration of carboxyfluorescein was found to be very difficult. It should be noted that the triple helices are formed on the outside as well as in the inside of the liposomes. The increased molecular volume of the lipopeptide of **GPO5** possibly hinders the efficient encapsulation of carboxyfluorescein inside the liposomes. When we decreased the amount of **GPO5** to 20 mol % in the POPC liposomes, the dye was encapsulated efficiently. However, the release from these liposomes was inefficient (<40%, Supporting Information) in the presence of 2.3 μM MMP-9. The stability of the triple helices increases with the number of GPO repeat units (Table 1 (*44*)). Increased thermal stability of the triple helices leads to decreased cleavage rates by the MMPs (*44*).

On the basis of these results, we selected POPC as the major lipid component of the liposomes. Our next objective was to determine the amount of lipopeptide needed in the liposomes for optimal release of encapsulated carboxyfluorescein. We have previously observed that 30 mol % of lipopeptide **GPO4** in POPC liposomes exhibited a high amount of contents release (>95%) in the presence of MMP-9 and low amount of background release (<10%) in the absence of the enzyme (*25*). When 30 mol % of the lipopeptide **GPO3** was incorporated in POPC liposomes, 90% of the encapsulated carboxyfluorescein was released in 30 min in the presence of 2.3 μM MMP-9 (Figure 3B). No release of the dye from the liposomes was observed in the absence of the enzyme (Figure 3B). When we reduced the amount of **GPO3** to 20 mol % in the POPC liposomes, 80% of the contents were released in the presence

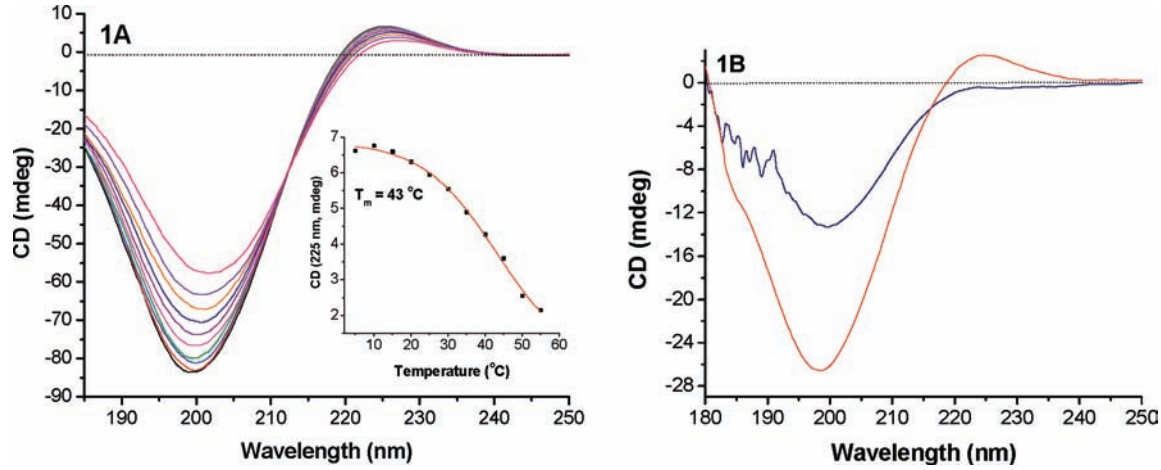

Figure 1. The temperature-dependent CD spectra (5−55 °C) of the lipopeptide **GPO3** in aqueous solution (A) and in POPC liposomes prepared in 5 mM phosphate buffer, pH = 8.0 (B, red trace) are shown. The presence of the positive peak at 225 nm and the large negative peak at 198 nm indicates triple helical structure of this lipopeptide in aqueous solution as well as in liposomes. The inset of (A) shows the melting curve for **GPO3** monitored at 225 nm. When the liposomes were incubated with 2.3 μM recombinant MMP-9 for 30 min, the triple helicity of the liposome-incorporated **GPO3** decreased substantially (B, blue trace). To improve the signal-to-noise ratio, the spectra shown for the liposome-incorporated **GPO3** are the averages of 50 scans. For the last spectrum, the CD spectrum of MMP-9 was subtracted.

Scheme 1. Synthesis of the Lipopeptide PyGPO4

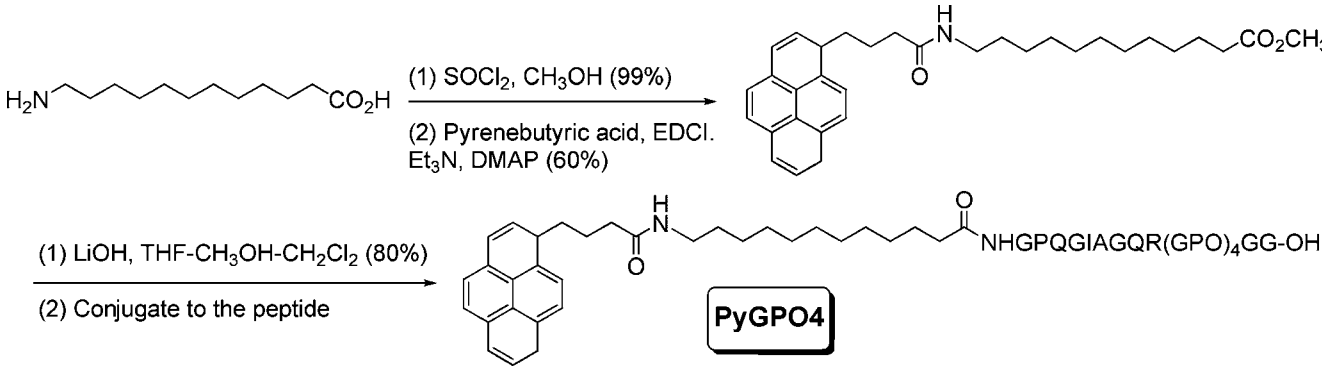

of 2.3 μM MMP-9 (Figure 4, blue squares). For these liposomes, we observed that 10% of the encapsulated dye was released in the absence of any enzyme (Figure 4, red squares). If the liposomes contained 10 mol % of the lipopeptide **GPO3**, only 38% of the contents were released by MMP-9 (2.3 μM) in 1 h (Figure 4, green circles) with a background release of 10% in the absence of the enzyme (Figure 4, magenta circles). Increasing the amount to **GPO3** to 40 mol % in the liposomes led to a drastic reduction of the release efficiency (<10%, data not shown) in the presence of 2.3 μM of MMP-9. We do not have an explanation for this observation yet. However, this is not due to insufficient peptide cleavage due to shortage of MMP-9, as addition of more enzyme did not improve the release efficiency. Variation of the amount of **GPO5** in the POPC liposomes did not improve the efficiency of the contents release in the presence of the enzyme (Supporting Information).

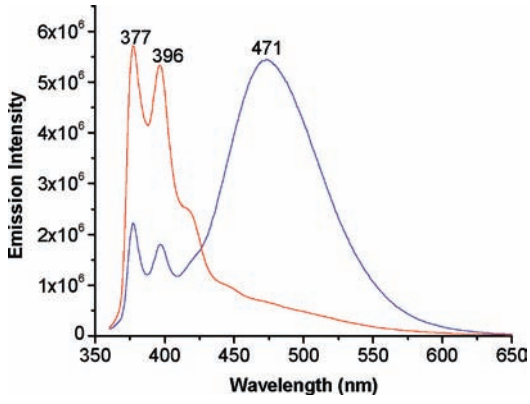

Figure 2. Emission spectra of POPC liposomes incorporating 30 mol % of the lipopeptide **PyGPO4** (blue trace) in 25 mM HEPES buffer, pH = 8.0, containing 100 mM NaCl, 10 mM $CaCl_2$, and 10 μM $ZnCl_2$. The presence of the intense emission at 471 nm indicated the pyrene excimer formation with the lipid bilayer of the liposomes. The emission spectrum of the liposomes after incubation with 2.3 μM MMP-9 for 15 min is shown with the red trace.

Interestingly, these release data also exhibited biexponential rate profiles. The release of the liposomal contents involves several intermediate steps: binding of the enzyme to the exposed peptides, hydrolysis of the peptides, creation of lipid "defects" and lipid reorganization, release of encapsulated carboxyfluorescein, and repairing of the "defects" created in the lipid bilayer. Fitting the observed release data by a biexponential rate equation is clearly an oversimplification of the complex set of steps involved in the triggered release process. Notably, when we decreased the amount of the lipopeptide **GPO3** in the liposomes, the magnitudes of the rate constants for the release remained nearly the same, but the amplitude of the faster rate process progressively increased and the amplitude for the slower step decreased (Table 3). It is possible that the faster of the two steps is the repair of the "defects" created in the lipid bilayer as MMP-9 hydrolyzes the exposed peptides. With less lipopeptide incorporated in the liposomes, it is expected that lower amount of "defects" are created in the bilayers, and hence, they are

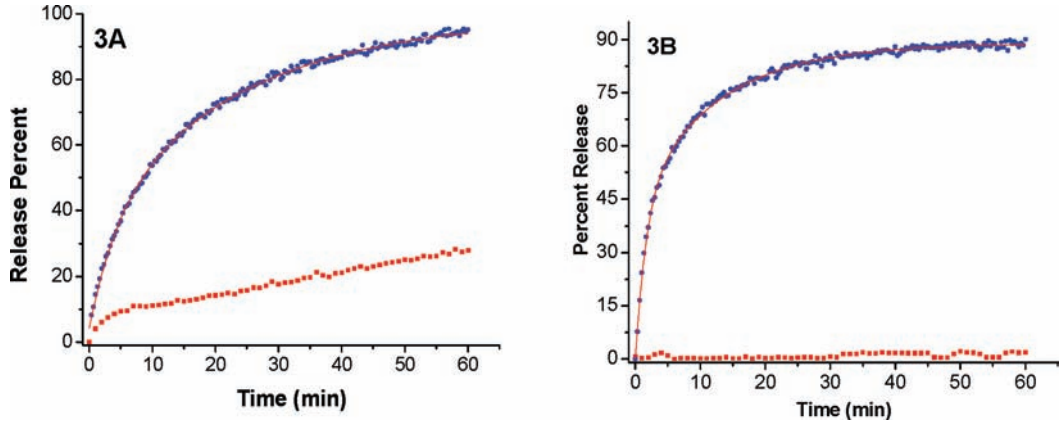

Figure 3. The release profiles for encapsulated carboxyfluorescein (λ_{ex} = 480 nm; λ_{em} = 518 nm) for the liposomes incorporating 30 mol % of the lipopeptide **GPO3** in the presence and absence of MMP-9 in 25 mM HEPES buffer, pH = 8.0 containing 100 mM NaCl, 10 mM $CaCl_2$, and 10 μM $ZnCl_2$. For DOPC liposomes (A), complete dye release was observed (blue circles) in the presence of 2.3 μM MMP-9, and about 25% release was observed in the absence of the enzyme (red squares). For POPC liposomes (B), 90% of the encapsulated dye was released with 2.3 μM MMP-9 (blue circles); in the absence of the enzyme, no dye release was detected (red squares). The lines through the release profiles are the fitted curves using a biexponential rate equation.

Table 2. Calculated Rate Constants (k_1, k_2) and Amplitudes for the Release of Encapsulated Carboxyfluorescein from DOPC and POPC Liposomes Containing 30 mol % of GPO3 in the Presence of 2.3 μM MMP-9 (errors: 3−6%)

major lipid	k_1 (s^{-1})	amplitude (%)	k_2 (s^{-1})	amplitude (%)
DOPC	7.0×10^{-4}	67	3.8×10^{-3}	33
POPC	1.3×10^{-3}	51	9.9×10^{-3}	49

Table 3. Calculated Rate Constants (k_1, k_2) and Amplitudes for the Release of Encapsulated Carboxyfluorescein from POPC Liposomes Containing Varying Amounts of the Lipopeptide GPO3 in the Presence of 2.3 μM MMP-9 (errors: 3−6%)

amount of GPO3 (mol %)	k_1 (s^{-1})	amplitude (%)	k_2 ($^{-1}$)	amplitude (%)
30	1.3×10^{-3}	51	9.9×10^{-3}	49
20	1.7×10^{-3}	37	11.1×10^{-3}	63
10	1.9×10^{-3}	18	11.8×10^{-3}	72

repaired quickly. On the basis of these observations, we selected 30 mol % as the optimal amount of lipopeptide in our liposomal formulations.

After optimizing the major lipid component and the amount of lipopeptides in the liposomes, we turned our attention to the response of the release methodology to MMP-9 concentration. It is reported that, in normal tissues, the concentration of the active form of MMP-9 is about 10 nM (*39*). However, for lung cancer patients, the concentration of this enzyme in the bronchial lavage fluid can be as high as 200 nM (*40*). We have previously observed that, for the POPC liposomes containing 30 mol % of the lipopeptide **GPO4**, the rates and the amounts of content release progressively decreased with decreasing concentrations of MMP-9 (*25*). While 2.3 μM MMP-9 completely released the contents within 30 min, 50% of the encapsulated dye release was observed in 1 h in the presence of 200 nM enzyme (*25*). In order to determine if such a desirable property exists for the POPC liposomes containing 30 mol % of the lipopeptide **GPO3**, we added varying concentrations of recombinant human MMP-9 to these liposomes and monitored the release of encapsulated carboxyfluorescein (Figure 5A).

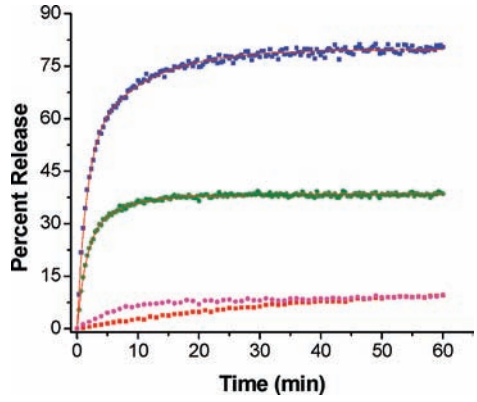

Figure 4. Release profiles for liposome-encapsulated carboxyfluorescein (λ_{ex} = 480 nm; λ_{em} = 518 nm) in the presence and absence of 2.3 μM MMP-9 in 25 mM HEPES buffer, pH = 8.0, containing 100 mM NaCl, 10 mM $CaCl_2$, and 10 μM $ZnCl_2$ for POPC liposomes incorporating 20 mol % (blue squares) and 10 mol % of lipopeptide **GPO3** (green circles). The background releases of the dye in the absence of the enzyme are also shown (red squares, 20 mol % **GPO3**; magenta circles, 10 mol % **GPO3**). The lines through the release profiles are the fitted curved using a biexponential rate equation.

When the concentration of the enzyme was decreased from 2.3 μM to 1.2 μM, we observed a significant reduction in the amount of dye release from the liposomes (Figure 5A). In the presence of 900 nM of MMP-9, only 15% of the encapsulated dye was released. The difference in release profiles between the lipopeptides **GPO4** and **GPO3** may be related to their triple helicity. The Rpn value for **GPO4** is 0.11, while that for **GPO3** is 0.08 (Table 1). Thus, lesser fractions of the lipopeptide **GPO3** exist in triple helical conformation compared to **GPO4**. Upon peptide hydrolysis by MMP-9, the structural perturbation within the lipid bilayer of the liposomes will be more pronounced in the case of the lipopeptide **GPO4** compared to **GPO3**. The liposomes did not release any significant amount of the encapsulated dye in the presence of other MMPs, which cannot hydrolyze triple helical peptides (e.g., MMP-7 and -10; Figure 5B) or in the presence of trypsin (data not shown). Taking into consideration all of these results, we decided to proceed to the cell-based studies employing liposomal formulation incorporating 30 mol % of the lipopepide **GPO3** or **GPO4** with POPC as the major lipid component.

After optimizing the liposomal formulations for contents release triggered by recombinant human MMP-9, we proceeded to determine the release property in the presence of cell-secreted enzyme. We noted, a priori, that our recombinant MMP-9 contains the catalytic and fibronectin domains, but the cell-secreted enzyme has the additional hemopexin domain (*41*). For the cell-based studies, the metastatic breast adenocarcinoma cells MCF7 was selected, as this cell line is known to secrete high amounts of MMP-9 and -2 in the extracellular matrix (*42*). The

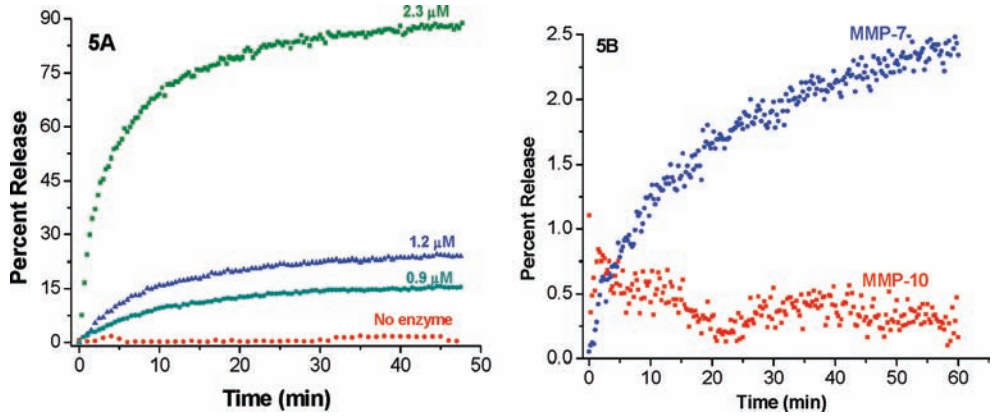

Figure 5. The release profiles for POPC liposome-encapsulated carboxyfluorescein ($\lambda_{ex} = 480$ nm; $\lambda_{em} = 518$ nm) containing 30 mol % of lipopeptide **GPO3** in the presence 2.3 μM (green squares), 1.2 μM (blue triangles), and 900 nM (cyan circles) of MMP-9 in 25 mM HEPES buffer, pH = 8.0, (A) containing 100 mM NaCl, 10 mM $CaCl_2$, and 10 μM $ZnCl_2$. The background release in the absence of any MMP-9 is shown in red circles (A). Part B shows the release of the encapsulated dye from these liposomes in the presence of 2.3 μM MMP-7 (blue circles) and 2.3 μM MMP-10 (red squares) under the same conditions.

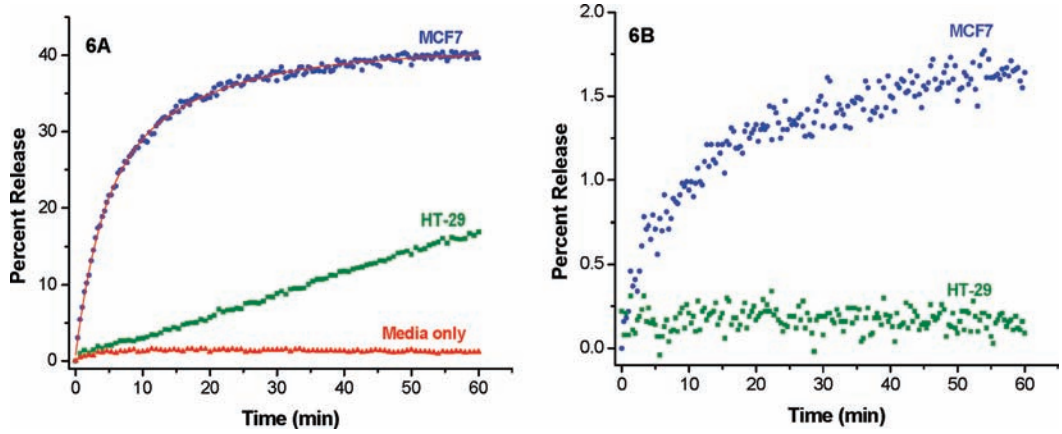

Figure 6. The release profiles for POPC liposome-encapsulated carboxyfluorescein ($\lambda_{ex} = 480$ nm; $\lambda_{em} = 518$ nm) containing 30 mol % of lipopeptide **GPO4** in the presence of cell-secreted MMP-9 in 25 mM HEPES buffer, pH = 8.0, containing 100 mM NaCl, 10 mM $CaCl_2$, and 10 μM $ZnCl_2$ (A). The conditioned media from MCF7 cells released 40% of the encapsulated dye (blue circles) in 30 min; the conditioned media from the HT-29 cells released less than 10% of the contents in 30 min (green squares), and the culture media did not release any contents from the liposomes (red triangles). The line through the blue circles represents the fitted curve using the biexponential rate equation. The liposomes containing 30 mol % of lipopeptide **GPO3** failed to release significant amount of the encapsulated dye under identical experimental conditions with conditioned media from MCF7 (B, blue circles) and HT-29 (B, green squares).

human colorectal adenocarcinoma cells HT-29 were used as the control, since these cells do not secrete high levels of MMP-9 and -2 in the extracellular matrix (*43*). All cells were obtained and cultured following the protocols from American type Culture Collection (Manassas, VA, USA). When the cells achieved 70% of confluency, the old culture medium was replaced with fresh culture medium without phenol red. The cells were further incubated for 24 h, collected, and centrifuged. The supernatants were collected for the release experiments from the liposomes.

For the POPC liposomes containing 30 mol % of the lipopeptide **GPO4**, the conditioned media collected from the cultured MCF7 cells rapidly released 40% of the encapsulated dye within 30 min (Figure 6A). The release data can be fitted with a biexponential rate equation, with $k_1 = 1.0 \times 10^{-3}$ s^{-1} (44% amplitude) and $k_2 = 2.5 \times 10^{-3}$ s^{-1} (56% amplitude). These liposomes in the presence of the conditioned media collected from the HT-29 cells showed a very different profile (linear), slowly releasing less that 10% of the contents in 30 min. The cell culture media (for both cells) did not release any liposome-encapsulated dye during the same period of time (Figure 6A). However, liposomes incorporating 30 mol % lipopeptide **GPO3** failed to release any encapsulated contents in the presence of conditioned media from the MCF7 or the HT-29 cells (Figure 6B).

The concentrations of active MMP-9 and -2 were estimated to be 150 nM in the conditioned media from the MCF7 cells and 25−30 nM for the conditioned media from the HT-29 cells (by employing a fluorogenic MMP-9 activity assay kit from Biomol International). Previously, we observed that POPC liposomes with 30 mol % of lipopeptide **GPO4** released 50% of the encapsulated contents in the presence of 200 nM recombinant, two-domain MMP-9 (*25*). Since the additional hemopexin domain present in the cell-secreted MMP-9 does not participate in unwinding or catalysis of small triple helical peptide substrates (*44*), the results obtained with the recombinant MMP-9 corroborate the results with cell-secreted MMP-9. The substrate selectivities for MMP-9 and -2 are very similar (*34*), and it is expected that the MMP-2 present in the conditioned media will also hydrolyze the triple-helical peptides on the liposome surface and contribute to the release of the encapsulated dye.

The release profile in Figure 6A in the presence of the conditioned media from the MCF7 cells showed an initial linear phase followed by a slowly decreasing phase. The first step in the enzymatic release of the dye from the liposomes is the cleavage of the lipopeptide **GPO4** by the cell-secreted MMP-2 and -9. We estimated the concentration of **GPO4** on the outer lipid layer of the liposomes to be about 100 nM and the

concentration of MMP-2 and -9 in the conditioned media to be about 150 nM. Initially, the lipopeptides are rapidly cleaved by MMP-2 and -9 in the conditioned media, leading to the rapid release of the encapsulated carboxyfluorescein. As the concentration of **GPO4** decreases, the rate of cleavage of this substrate by MMP-2 and -9 is reduced, leading to the slow release of the liposomal contents. On the other hand, the concentration of MMP-2 and -9 in the conditioned media from the HT-29 cells is about 30 nM. Since the concentrations of **GPO4** in the liposomes are higher compared to the MMP concentration, the substrate cleavage by the enzymes proceeds slowly. This is reflected in the slow linear release of the liposome-encapsulated dye in the presence of the conditioned media from the HT-29 cells (Figure 6A).

CONCLUSION

We have demonstrated that, by optimizing the structure and the amount of the lipopeptide substrate and the major lipid component, liposomal contents can be rapidly released in the presence of the extracellular pathogenic enzyme MMP-9. The amount of contents released depends on the mismatch between the fatty acid moieties of the lipopeptide and the major lipid of the liposomal formulations. By utilizing the optimized liposomal formulations, we also demonstrated that, while cancer cells (HT-29) which secrete low levels of MMP-9 failed to release significant amounts of the liposomal contents, metastatic cancer cells (MCF7) secreting high amounts of the enzyme rapidly released the encapsulated contents from the liposomes. We are currently optimizing the liposomal formulations by incorporating 10 mol % of a poly(ethylene glycol)-containing lipid to impart a long-circulating property to the liposomes. These studies and release studies using a mouse model of metastatic breast adenocarcinoma will be reported in the future.

ACKNOWLEDGMENT

This research was supported by the NIH grants 1R01 CA113746, 1 R01 CA 132034 and NSF DMR-0705767 to S.M. and D.K.S. J.S. thanks the support of the proteomics core facility by NIH Grant P20 RR016741 from the INBRE Program of the NCRR.

Supporting Information Available: . Synthetic details for the synthesis of the pyrene containing fatty acid, liposomal release studies with the lipopeptide **GPO5**. This material is available free of charge via the Internet at http://pubs.acs.org.

LITERATURE CITED

(1) Jesorka, A., and Orwar, O. (2008) Liposomes: technologies and analytical applications. *Annu. Rev. Anal. Chem. 1*, 801–832.
(2) Bangham, A. D., Standish, M. M., and Watkens, J. C. (1965) Diffusion of univalent ions across lamellae of swollen phospholipids. *J. Mol. Biol. 13*, 238–252.
(3) Torchilin, V. P. (2005) Recent advances with liposomes as pharmaceutical carriers. *Nat. Rev. Drug Discovery 4*, 145–160.
(4) Samad, A., Sultana, Y., and Aqil, M. (2007) Liposomal drug delivery systems: an update review. *Curr. Drug Delivery 4*, 297–305.
(5) Torchilin, V. P. (2007) Targeted pharmaceutical nanocarriers for cancer therapy and imaging. *AAPS J. 9*, 128–147.
(6) Gomez-Hens, A., and Fernandez-Romero, J. (2005) The role of liposomes in analytical processes. *Trends Anal. Chem. 24*, 9–19.
(7) Allen, T M., Hansen, C., and Rutledge, J. (1989) Liposomes with prolonged circulation times: factors affecting uptake by reticuloendothelial and other tissues. *Biochim. Biophys. Acta. 981*, 27–35.
(8) O' Shaughnessy, J. A. (2003) Pegylated liposomal doxorubicin in the treatment of breast cancer. *Clin. Breast Cancer 4*, 318–328.
(9) Peer, D., Karp, J. M., Hong, S., Farokhzad, O. C., Margalit, R., and Langer, R. (2007) Nanocarriers as an emerging platform for cancer therapy. *Nat. Nanotechnol. 2*, 751–760.
(10) ElBayoumi, T. A., and Torchilin, V. P. (2009) Tumor-specific anti-nucleosome antibody improves therapeutic efficacy of doxorubicin-loaded long-circulating liposomes against primary and metastatic tumor in mice. *Mol. Pharmaceutics 6*, 246–254.
(11) Garg, A., Tisdale, A. W., Haidari, E., and Kokkoli, E. (2009) Targeting colon cancer cells using PEGylated liposomes modified with a fibronectin-mimetic peptide. *Int. J. Pharm. 366*, 201–210.
(12) Kawano, K., Onose, E., Hattori, Y., and Maitani, Y. (2009) Higher liposomal membrane fluidity enhances the in vitro antitumor activity of folate - targeted liposomal mitoxantrone. *Mol. Pharmaceutics 6*, 98–104.
(13) Boman, N. L., Bally, M. B., Cullis, P. R., Mayer, L. D., and Webb, M. S. (1995) Encapsulation of vincristine in liposomes reduces toxicity and improves antitumor efficacy. *J. Liposome Res. 5*, 523–541.
(14) For a list of FDA-approved liposomal drugs to treat cancer, see http://www.icare.org/fda.htm (accessed Feb 9, 2009).
(15) There are currently 357 clinical trials in progress on the use of liposomes to treat various diseases, including cancer (http://www.clinicaltrials.gov; accessed Feb 9, 2009).
(16) Chandra, B., Mallik, S., and Srivastava, D. K. (2005) Design of photocleavable lipids and their application in liposomal "uncorking". *J. Chem. Soc., Chem. Commun.* 3021–3023.
(17) Dromi, S., Frenkel, V., Luk, A., Traughber, B., Angstadt, M., Bur, M., Poff, J., Xie, J., Libutti, S. K., Li, K. C. P., and Wood, B. J. (2007) Pulsed-high intensity focused ultrasound and low temperature-sensitive liposomes for enhanced targeted drug delivery and antitumor effect. *J. Clin. Cancer Res. 13*, 2722–2727.
(18) Sawant, R. M., Hurley, J. P., Salmaso, S., Kale, A., Tolcheva, E., Levchenko, T. S., and Torchilin, V. P. (2006) "SMART" drug delivery systems: double-targeted pH-responsive pharmaceutical nanocarriers. *Bioconjugate Chem. 17*, 943–949.
(19) Wu, G., Mikhailovsky, A., Khant, H. A., Fu, C., Chiu, W., and Zasadzinski, J. A. (2008) Remotely triggered liposome release by near-infrared light absorption via hollow gold nanoshells. *J. Am. Chem. Soc. 130*, 8175–8177.
(20) Huang, S.-L., and MacDonald, R. C. (2004) Acoustically active liposomes for drug encapsulation and ultrasound - triggered release. *Biochim. Biophys. Acta 1665*, 134–141.
(21) Davis, S. C., and Szoka, F. C. (1998) Cholesterol phosphate derivatives: synthesis and incorporation into a phosphatase and calcium-sensitive triggered release liposome. *Bioconjugate Chem 9*, 783–792.
(22) Foged, C., Nielsen, H. M., and Frokjaer, S. (2007) Phospholipase A2 sensitive liposomes for delivery of small interfering RNA (siRNA). *J. Liposome Res. 17*, 191–196.
(23) Romberg, B., Flesch, F. M., Hennink, W. E., and Storm, G. (2008) Enzyme-induced shedding of a poly (amino acid)-coating triggers contents release from dioleoyl phosphatidylethanolamine liposomes. *Int. J. Pharm. 355*, 108–113.
(24) Sarkar, N., Banerjee, J., Hanson, A. J., Elegbede, A. I., Rosendahl, T., Krueger, A. B., Banerjee, A. L., Tobwala, S., Wang, R., Lu, X., Mallik, S., and Srivastava, D. K. (2008) Matrix Metalloproteinase-assisted triggered release of liposomal contents. *Bioconjugate Chem. 19*, 57–64.
(25) Elegbede, A. I., Banerjee, J., Hanson, A. J., Tobwala, S., Ganguli, B., Wang, R., Lu, X., Srivastava, D. K., and Mallik, S. (2008) Mechanistic studies of the triggered release of liposomal contents by matrix metalloproteinase-9. *J. Am. Chem. Soc. 130*, 10633–10642.
(26) Nagase, H., Woessner, J., and Frederick, Jr. (1999) Matrix metalloproteinases. *J. Biol. Chem. 274*, 21491–21494.

(27) Abraham, D., Ponticos, M., and Nagase, H. (2005) Connective tissue remodeling: cross-talk between endothelins and matrix metalloproteinases. *Curr. Vasc. Pharmacol. 3*, 369–379.

(28) McCawley, L. J., and Matrisian, L. M. (2000) Matrix metalloproteinases: multifunctional contributors to tumor progression. *Mol. Med. Today 6*, 149–156.

(29) Murphy, G., and Nagase, H. (2008) Progress in matrix metalloproteinase research. *Mol. Aspects Med. 29*, 290−308.

(30) Curran, S., and Murray, G. I. (2000) Matrix metalloproteinases. Molecular aspects of their roles in tumor invasion and metastasis. *Eur. J. Cancer 36*, 1621–1630.

(31) Tai, K. Y., Shieh, Y. S., Lee, C. S., Shiah, S. G., and Wu, C. W. (2008) Axl promotes cell invasion by inducing MMP - 9 activity through activation of NF-κ B and Brg-1. *Oncogene 27*, 4044–4055.

(32) Owen, J. L., Torroella-Kouri, M., and Iragavarapu-Charyulu, V. (2008) Molecular events involved in the increased expression of matrix metalloproteinase-9 by T lymphocytes of mammary tumor-bearing mice. *Int. J. Mol. Med. 21*, 125–134.

(33) Cauwe, B., Martens, E., Van den Steen, P. E., Proost, P., Van Aelst, I., Blockmans, D., and Opdenakker, G. (2008) Adenylyl cyclase-associated protein-1/CAP1 as a biological target substrate of gelatinase B/MMP-9. *Exp. Cell Res. 314*, 2739–2749.

(34) Lauer-Fields, J. L., Sritharan, T., Stack, M. S., Nagase, H., and Fields, G. B. (2003) Selective hydrolysis of triple-helical substrates by matrix metalloproteinase-2 and -9. *J. Biol. Chem. 278*, 18140–18145.

(35) Cejas, M. A., Kinney, W. A., Chen, C., Vinter, J. G., Jr., Balss, K. M., Maryanoff, C. A., Schmidt, U., Breslav, M., Mahan, A., Lacy, E., and Maryanoff, B. E. (2008) Thrombogenic collagen-mimetic peptides: self-assembly of triple helix-based fibrils driven by hydrophobic interactions. *Proc. Natl. Acad. Sci. U.S.A. 105*, 8513–8518.

(36) Sarkar, N. R, Rosendahl, T., Krueger, A. B., Banerjee, A. L., Benton, K., Mallik, S., and Srivastava, D. K. (2005) "Uncorking" of liposomes by matrix metalloproteinase-9. *J. Chem. Soc., Chem. Commun.* 999–1001.

(37) Sabatino, G., and Papini, A. M. (2008) Advances in automatic, manual and microwave-assisted solid-phase peptide synthesis. *Curr. Opin. Drug Discovery Dev. 11*, 762–770.

(38) Feng, Y., Melacini, G., Taulane, J. P., and Goodman, M. (1996) Acetyl-terminated and template-assembled collagen-based polypeptides composed of Gly-Pro-Hyp sequences. 1. Synthesis and conformational analysis by circular dichroism, ultraviolet absorbance, and optical rotation. *J. Am. Chem. Soc. 118*, 10351–10358.

(39) Iizasa, T., Fujisawa, T., Suzuki, M., Motohashi, S.-I., Yasufuku, K., Yasukawa, T., Baba, M., and Shiba, M. (1999) Elevated levels of circulating plasma matrix metalloproteinase 9 in non-small cell lung cancer patients. *Clin. Cancer Res. 5*, 149–153.

(40) Turpeenniemi-Hujanen, T. (2005) Gelatinases (MMP-2 and -9) and their natural inhibitors as prognostic indicators in solid cancers. *Biochimie 87*, 287–297.

(41) Ezhilarasan, R., Jadhav, U., Mohanam, I., Rao, J. S., Gujrati, M., and Mohanam, S. (2009) The hemopexin domain of MMP-9 inhibits angiogenesis and retards the growth of intracranial glioblastoma xenograft in nude mice. *Int. J. Cancer 124*, 306–315.

(42) Cortes-Reynosa, P., Robledo, T., Macias-Silva, M., Wu, S. V., and Salazar, E. P. (2008) Src kinase regulates metalloproteinase-9 secretion induced by type IV collagen in MCF-7 human breast cancer cells. *Matr. Biol. 27*, 220–231.

(43) Svetlana, A. T., Moriggl, R., Corvinus, F. M., Wiederanders, B., Schutz, A., Kovacic, B., and Friedrich, K. (2007) Signal transducer and activator of transcription 3 activation promotes invasive growth of colon carcinomas through matrix metalloproteinase induction. *Neoplasia 9*, 279–291.

(44) Minond, D., Lauer-Fields, J. L., Cudic, M., Overall, C. M., Pei, D., Brew, K., Visse, R., Nagase, H., and Fields, G. B. (2006) The roles of substrate thermal stability and the P2 and P1' subsite identity on matrix metalloproteinase triple-helical peptidase activity and collagen specificity. *J. Biol. Chem. 281*, 28302–38313.

BC9000646

Supporting Information

Release of Liposome Contents by Cell-Secreted Matrix Metalloproteinase-9

Jayati Banerjee,[†] Andrea J. Hanson,[†] Bhushan Gadam,[†] Adekunle I. Elegbede,[†] Shakila Tobwala,[‡] Bratati Ganguly,[‡] Anil Wagh,[†] Wallace W. Muhonen,[§] Benedict Law,[†] John B. Shabb,[§] D. K. Srivastava[‡] and Sanku Mallik*[†]

[†]Department of Pharmaceutical Sciences and [‡]Department of Chemistry, Biochemistry and Molecular Biology, North Dakota State University, Fargo, North Dakota 58108 and [§]Department of Biochemistry and Molecular Biology, School of Medicine and Health Sciences, University of North Dakota, Grand Forks, North Dakota 58202.

Synthetic details for PyGPO4:

Reagents were purchased from Alfa Aesar or TCI America. EDCI.HCl was purchased from ChemPep, Inc. All organic solvents used were distilled. Melting points were determined using a micro melting point apparatus. ^{1}H and ^{13}C NMR spectra were recorded on 300 or 400 MHz spectrometer. NMR spectra was recorded either using $CDCl_3$ or DMSO-d_6 as solvents with TMS as the internal standard. TLC was performed with Adsorbil plus IP, 20 x 20 cm plate, 250 μm (Altech Associates, Inc). TLC plates were visualized under UV light or in an iodine chamber. Flash column chromatography was carried out with Merck Silica gel 60.

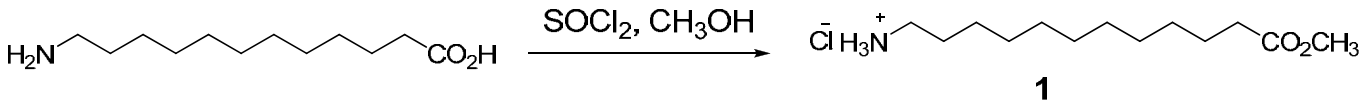

1

Compound 1: To a suspension of 12-aminolauric acid (5.0 g, 23.2 mmol, 1 equiv) in methanol (50 mL) under nitrogen, thionyl chloride (2.7 mL, 1.6 equiv) was added at 0 ^{o}C. The reaction mixture was stirred under a nitrogen atmosphere at room temperature for 2 h and then heated to reflux for 2 h. After cooling the reaction to room temperature, the organic solvents were evaporated in a rotary evaporator giving a white solid. The white solid was dried under vacuum and used for the next step without further purification. Yield: 5.30 g (99%), mp: 157-160 ^{o}C; ^{1}H NMR ($CDCl_3$, 400 MHz): δ ppm 1.22-1.44 (m, 14H) 1.55-1.66 (m, 2H) 1.76 (quin, J = 7.5 Hz, 2H) 2.30 (t, J = 7.5 Hz, 2H) 2.98 (t, J = 7.7 Hz, 2H) 3.67 (s, 3H) 8.31 (br, s, 3H).

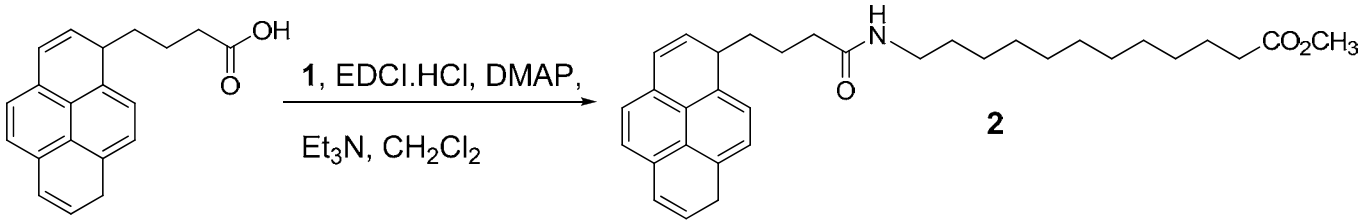

2

Compound 2: To a suspension of pyrenebutyric acid (2.0 g, 6.93 mmol) in CH_2Cl_2 (180 mL) under nitorgen triethylamine (1.32 mL, 9.47 mmol) was added. The resultant mixture was stirred for 5 min, cooled to 0 ^{o}C and compound **1** (1.446 g, 6.30 mmol), 4-(N,N-dimethylamino)pyridine (DMAP; 0.924 g, 7.56 mmol) and EDCI.HCl (1.450 g, 7.56 mmol) were added sequentially. The reaction mixture was stirred at room temperature under nitrogen overnight. The reaction was quenched with water and the organic layer was washed with 1 N HCl, 1 N NaOH and brine respectively. The organic layer was then

dried over $MgSO_4$ and the solvent was removed under reduced pressure. The crude product was purified by silica gel flash chromatography (eluant: 1:1 ethylacetate in hexane, R_f = 0.3) to obtain the pure product as yellowish brown solid. Yield: 2.08 g (60%), mp: 95-97 ^oC; ^1H NMR ($CDCl_3$, 300 MHz): δ ppm 1.24 (br, s, 14H) 1.45 (br, s, 2H) 1.51-1.67 (m, 3H) 2.13-2.33 (m, 6H) 3.17-3.29 (m, 2H) 3.40 (t, J = 7.0 Hz, 2H) 3.66 (s, 3H) 5.34 (br, s, 1H) 7.87 (d, J = 7.7 Hz, 1H) 7.95-8.06 (m, 3H) 8.08-8.20 (m, 4H) 8.31 (d, J = 9.3 Hz, 1H). ^{13}C NMR (DMSO-d_6, 100 MHz): δ ppm 25.05, 27.07, 28.31, 29.07, 29.28, 29.40, 29.50, 29.55, 29.63, 29.82, 32.94, 33.89, 35.76, 39.06, 51.81 124.14, 124.83, 125.43, 125.61, 126.80, 127.18, 127.89, 128.10, 128.85, 129.96, 129.99, 131.11, 131.56, 137.24, 172.31, 174.00.

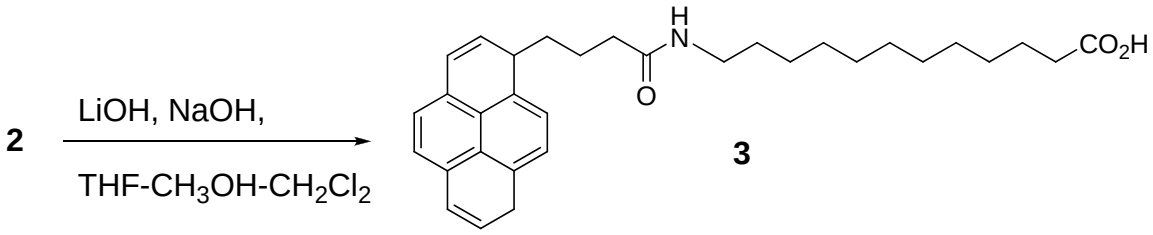

Compound 3: The ester **2** (1.264 g, 2.52 mmol) was hydrolyzed with LiOH (1.057 g, 25.1 mmol) in MeOH-THF-CH_2Cl_2 (20-10-5 mL). A few drops of 1 N NaOH was also added. The reaction mixture was stirred overnight when a white residue formed. On acidification with 2 N HCl, the white solid dissolved. After evaporation of the solvents, the white solid obtained was washed with water, filtered and lyophilized. Yield: 1.162 g (94%), mp: 129-132 ^oC; ^1H NMR (DMSO-d_6, 300 MHz) δ ppm 1.19 (m, 14H) 1.33-1.48 (m, 4H) 2.02 (d, J = 6.8 Hz, 2H) 2.14 (t, J = 7.0 Hz, 2H) 2.22 (d, J = 6.4 Hz, 2H) 3.06 (d, J = 6.0 Hz, 2H) 3.21-3.32 (m, 2H) 7.83 (br, s, 1H) 7.94 (d, J = 7.7 Hz, 1H) 8.07 (d, J = 7.7 Hz, 1H) 8.14 (s, 2H) 8.19-8.31 (m, 4H) 8.38 (d, J = 9.3 Hz, 1H). ^{13}C NMR (DMSO-d_6, 100 MHz): δ ppm 24.43, 26.39, 27.61, 28.49, 28.68, 28.72, 28.86, 28.90, 28.96, 29.14, 32.24, 33.62, 35.05, 38.38, 38.89, 123.45,124.22, 124.75, 124.89, 126.10, 126.46, 127.16, 127.42, 127.46, 128.13, 129.28, 130.40, 130.87, 136.55, 171.61, 174.45.

Synthesis of pyrene conjuagted lipo-peptide PyGPO4:

The synthesized pyrene conjugated fatty acid (compound **3**) was used in 5 fold excess for coupling with the N-terminus of the peptide under microwave condition, following the same protocol as discussed in the experimental procedure. The purification procedure was the same as described for **GPO4** in the manuscript and characterized by MALDI-ToF mass spectrum. M^+ calculated: 2535.43; observed: 2534.54.

Liposome preparation using PyGPO4:

A stock solution of the lipo-peptide was prepared by dissolving the compound in methanol:chloroform (1:5) mixture to give a final concentration of 1 mg/mL. A lipid thin film was prepared by adding 1.4 mL of this stock solution to 250 μL of POPC solution in $CHCl_3$ and rotary evaporating the organic solvents at 40 ^{0}C. The thin film was dried overnight in vacuum. The dry lipid film was next hydrated with 25 mM HEPES buffer (pH = 8.0) containing 100 mM NaCl, 10 mM $CaCl_2$ and 10 μM $ZnCl_2$ by slow rotation at 60 ^{0}C for 1 h. After storing at 4 ^{0}C for 3 h, the hydrated solution was sonicated by probe sonicator for 1 h followed by 11 cycles of extrusion through a 100 nm polycarbonate membrane. The liposomes were diluted 20 times before recording the fluorescent spectra.

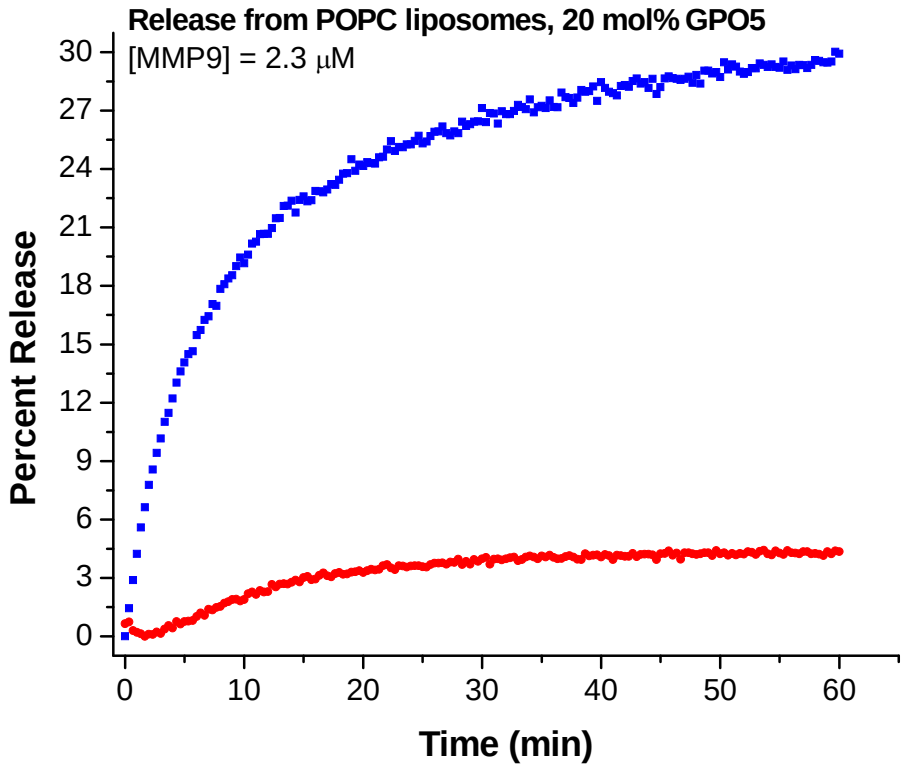

Figure S1. The carboxyfluorescein release profiles from POPC liposome containing 20 mol% of the lipopeptide **GPO5** (λ_{ex} = 480 nm; λ_{em} = 518 nm) in the presence and absence of 2.3 μM MMP-9 in 25 mM HEPES buffer, pH = 8.0 containing 100 mM NaCl, 10 mM $CaCl_2$ and 10 mM $ZnCl_2$. The enzyme released 30% of the dye in 1 h (blue squares). In the absence of MMP-9, <5% of the dye was released in 1 h (red circles).

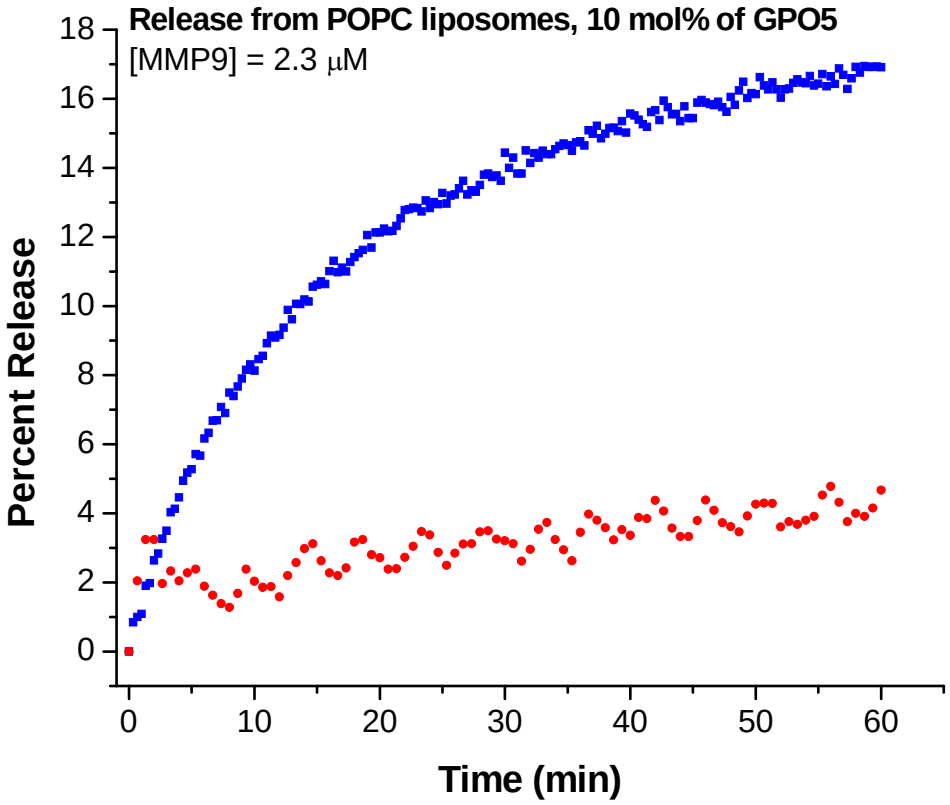

Figure S2. The carboxyfluorescein release profiles from POPC liposome containing 10 mol% of the lipopeptide **GPO5** (λ_{ex} = 480 nm; λ_{em} = 518 nm) in the presence and absence of 2.3 μM MMP-9 in 25 mM HEPES buffer, pH = 8.0 containing 100 mM NaCl, 10 mM $CaCl_2$ and 10 mM $ZnCl_2$. The enzyme released 18% of the dye in 1 h (blue squares). In the absence of MMP-9, <5% of the dye was released in 1 h (red circles).

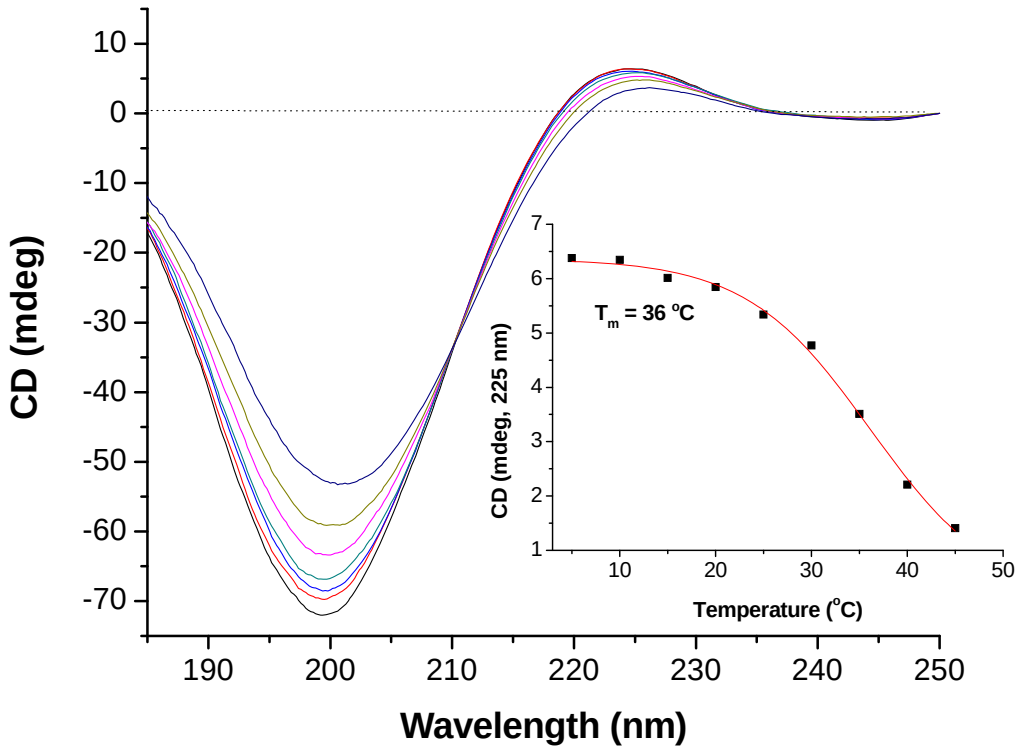

Figure S4. The temperature dependent CD spectra (5 – 45 °C) of the lipopeptide **PyGPO4** in aqueous solution. The presence of the positive peak at 225 nm and the large negative peak at 198 nm indicate triple helical structure of this lipopeptide in aqueous solution. The inset shows the melting curve for **GPO5** monitored at 225 nm. The melting temperature was calculated to be 36 °C.

Radiosynthesis of New [^{90}Y]-DOTA-Based Maleimide Reagents Suitable for the Prelabeling of Thiol-Bearing L-Oligonucleotides and Peptides

Joern Schlesinger,[†] Cindy Fischer,[†] Inge Koezle,[†] Stefan Vonhoff,[‡] Sven Klussmann,[‡] Ralf Bergmann,[†] Hans-Jurgen Pietzsch,*[,†] and Joerg Steinbach[†]

Institute of Radiopharmacy, Forschungszentrum Dresden-Rossendorf, Germany, and NOXXON Pharma AG, Berlin, Germany.
Received March 4, 2009; Revised Manuscript Received June 8, 2009

We describe the radiosynthesis of two new [^{90}Y]-DOTA-based maleimide reagents, suitable for the mild radiolabeling of L-RNAs and peptides modified with thiol-bearing linkers. The synthesis procedure of both maleimide-bearing ^{90}Y complexes, [{(2*S*)-2-[4-(2,5-dioxo-2,5-dihydro-1*H*-pyrrol-1-yl)benzyl]-1,4,7,10-tetraazacyclododecane-1,4,7,10-tetrayl}tetraacetato][^{90}Y]yttrate(1-)([^{90}Y]**3**) and [{(2*S*)-2-(4-{[4-(2,5-dioxo-2,5-dihydro-1*H*-pyrrol-1-yl)butanoyl]amino}benzyl)-1,4,7,10-tetraaza-cyclododecane-1,4,7,10-tetrayl]tetraacetato}[^{90}Y]yttrate(1-)([^{90}Y]**4**), was optimized in terms of an easy purification method via solid-phase extraction (SPE). Application as well as reactivity of both maleimide reagents were initially evaluated by the prelabeling of glutathione (GSH) and a thiol-modified 12mer L-RNA as model substances. In comparison to the *N*-aryl maleimide-bearing complex [^{90}Y]**3**, *N*-alkyl maleimide-bearing complex [^{90}Y]**4** showed an increased hydrolytic stability at pH ≥ 7. A slightly higher reactivity was found for [^{90}Y]**3** by prelabeling of 0.1 and 1 μg glutathione, respectively, in phosphate buffer (pH 7.2) at room temperature. In terms of very high radiochemical yields, the direct radiolabeling of DOTA−L-RNA conjugate with [^{90}Y]YCl_3 proved to be more suitable than the prelabeling of the thiol-modified 12mer L-RNA derivative with [^{90}Y]**4**.

INTRODUCTION

Radioisotopes of yttrium and the lanthanides are increasingly becoming an important component of several medical applications, e.g., for molecular imaging and targeted radionuclide therapy of cancer diseases (*1*, *2*). The trivalent radiometals are routinely conjugated to targeting molecules via the bifunctional chelator (BFC)[1]approach. A frequently utilized chelator for these radiometals is (1,4,7,10-tetraazacyclododecane-1,4,7,10-tetrayl)tetraacetic acid (DOTA). DOTA is known to form thermodynamically stable complexes with lanthanides and yttrium isotopes, and the corresponding radiometal complexes exhibit in many cases high kinetic inertness *in vivo* (*3*). However, the slow complexation rates of trivalent radiometals with DOTA necessitate elevated temperatures (up to 80 °C) to achieve sufficient radiochemical yields (RCYs) (*4*). This may be a drawback, especially for the radiolabeling of thermally sensitive molecules, such as biopharmaceuticals (e.g., DOTA-modified antibodies or antibody fragments). On this account, previous works already focused on optimization of radiolabeling conditions to achieve high RCY without compromising the biological activity (*5*, *6*).

A promising alternative to the "direct" radiolabeling of DOTA-(bio)conjugates ("postlabeling") is the use of so-called "prelabeling" agents. Such a reagent is constituted of the radiometal complex and a reactive coupling moiety, e.g., a bromoacetyl or isothiocyanato group. In such a way, primary amine groups of thermally sensitive molecules can be radiolabeled under mild conditions (≤37 °C) by reaction with the prelabeling agent. However, until now only a few radiometal-DOTA-based prelabeling agents were described (see Figure 1) (*7*−*11*). Another attractive coupling moiety of such a prelabeling agent could be the maleimide group. Maleimide reagents readily react with thiols (e.g., from cysteine residues of proteins or peptides) under physiological conditions (37 °C, pH 7.4) to form thioether bonds (*12*).

In this work, we present the synthesis of two novel [^{90}Y]-DOTA-based maleimide reagents (see Figure 2), suitable for a mild radiolabeling of a peptide or a thiol-modified L-RNA. An L-RNA is a mirror-image oligonucleotide constructed of L-configured riboses and characterized by an extraordinarily high stability against enzymatic degradation (*13*). By using ^{90}Y-labeled L-RNAs as molecular probes, we pursue a strategy for an improved radioimmunotherapy of cancer using pretargeting methods (*14*, *15*). However, the *in vivo* application of the ^{90}Y-labeled L-RNA requires a high effective specific activity (ESA), to prevent unlabeled L-RNA molecules from saturating the complementary L-oligonucleotide strands, which are present in the target tissue. Thus, both prelabeling and postlabeling of an L-RNA have been performed, to compare the two approaches with respect to the achievable RCYs and ESAs. The purpose of this work was to enhance RCY and ESA for ^{90}Y-labeled L-RNAs, by using prelabeling methods. Therefore, application as well as reactivity of both maleimide reagents were initially evaluated by the labeling of glutathione (GSH) as a model substance.

EXPERIMENTAL PROCEDURES

Materials. L-RNA [sequence: 5′-(1-hydroxy-7,8-dithia-tetradecyl) UGACUGACUGAC-3′, MW 4124] was synthesized at NOXXON Pharma AG (Germany). Synthesis of the DOTA-modified 12mer L-RNA **10** was described elsewhere (*16*). Glutathione (reduced) was from Fluka (Germany). (*S*)-2-(4-

* Author to whom correspondence should be addressed. H.-J. Pietzsch, Institute of Radiopharmacy, Forschungszentrum Dresden-Rossendorf, PF 51 01 19, 01314 Dresden, Germany. (h.j.pietzsch@fzd.de).

[†] Forschungszentrum Dresden-Rossendorf.

[‡] NOXXON Pharma AG.

[1]Abbreviations: BFC, bifunctional chelator; DIBD, (2*S*)-2-(4-{[4-(2,5-dioxo-2,5-dihydro-1*H*-pyrrol-1-yl)butanoyl]amino}benzyl)-DOTA; DID, (2*S*)-2-[4-(2,5-dioxo-2,5-dihydro-1*H*-pyrrol-1-yl)benzyl)-DOTA; DOTA, (1,4,7,10-tetraazacyclododecane-1,4,7,10-tetrayl)tetraacetic acid; DTPA, diethylene triamine pentaacetic acid; EDTA, ethylene diamine tetraacetic acid; ESA, effective specific activity; GMBS, *N*-(γ-maleimidobutyryloxy)succinimide ester; GSH, glutathione; RCP, radiochemical purity; RCY, radiochemical yield; SAP, square antiprism; TBE, Tris/Borate/EDTA; TEAA, triethylammonium acetate; TSAP, twisted square antiprism.

10.1021/bc900095k CCC: $40.75 © 2009 American Chemical Society
Published on Web 06/25/2009

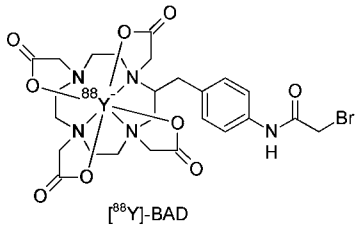

[88Y]-BAD

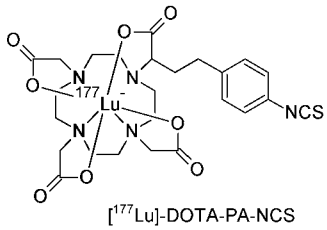

[177Lu]-DOTA-PA-NCS

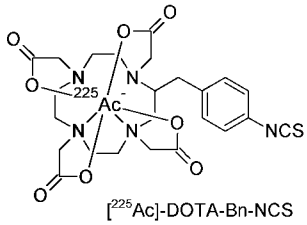

[225Ac]-DOTA-Bn-NCS

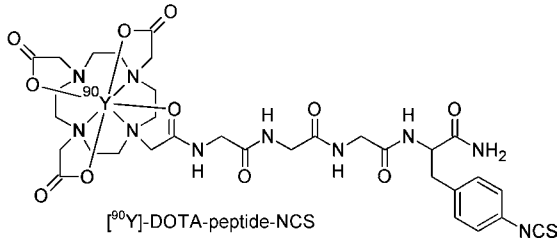

[90Y]-DOTA-peptide-NCS

Figure 1. Chemical structures of previously described prelabeling agents based on radiometal-DOTA complexes: [88Y]-DOTA-(4-bromoacetamidobenzyl) ([88Y]-BAD) (*7*), [177Lu]-1,4,7,10-tetraaza-*N*-(1-carboxy-3-(4-isothiocyanotophenyl)propyl)-*N′*,*N″*,*N‴*-tris(acetic acid)cyclododecane ([177Lu]-DOTA-PA-NCS) (*8*), [225Ac]-DOTA-(2-(4-isothiocyanatobenzyl)) ([225Ac]-DOTA-Bn-NCS) (*9*), [90Y]-DOTA-Gly_3-L-(4-isothiocyanato)-phenylalanine amide ([90Y]-DOTA-peptide-NCS) (*10, 11*).

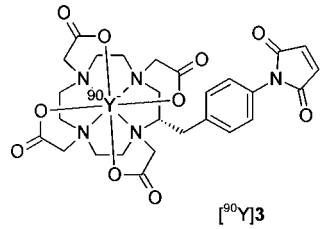

[90Y]**3**

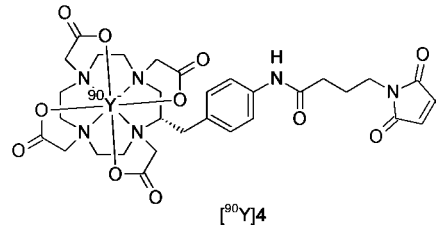

[90Y]**4**

Figure 2. Chemical structures of the new [90Y]-DOTA-based maleimide reagents [90Y]**3** and [90Y]**4**.

Aminobenzyl)-1,4,7,10-tetraazacyclododecane-*N*,*N′*,*N″*,*N‴*-tetraacetic acid (**1**) was purchased from Macrocyclics (Dallas, TX, USA). The radionuclide 90Y was purchased as [90Y]YCl_3 in 0.04 M HCl (500 μL) from QSA Global GmbH (Germany) or Polatom (Poland). Measurements of 90Y were done in the 90Y channel of a dose calibrator ISOMED 2000 (Nuklear-Medizintechnik Dresden GmbH, Germany) by measuring the *bremsstrahlung*. Reactions and incubations were performed in 1.5 mL DNA low-binding tubes (Eppendorf, Germany) using a Thermomixer Comfort (Eppendorf, Germany). For evaporation of small sample volumes, a Concentrator 5301 (Eppendorf, Germany) was used. Lyophilization was carried out using an Alpha 2-4 LSC (Christ, Germany). L-RNA concentrations were determined via measurement of the UV absorbance at 260 nm using an Eppendorf (Germany) BIOPhotometer. Measurements of the pH value in small volumes were performed using the pH-sensor Biotrode (Metrohm, Germany).

Chromatographic Purification and Analysis. HPLC analyses were performed with a WellChrom 2700 system (Knauer, Germany), coupled with the radioactivity detector VA-S-968 (Robotron, Germany). HPLC purifications were also performed with a WellChrom K-2201 system. The HPLC columns were as follows: (A) Aqua C_{18} column (Phenomenex, USA) 250 × 4.6 mm i.d., 5 μm, (B) Aqua C_{18} column (Phenomenex, USA) 250 × 10 mm i.d., 5 μm, and (C) XTerra MS C_{18} column (Waters, USA) 3.0 × 50 mm i.d., 2.5 μm. System A(I): flow 1 mL/min, UV 235 nm, 50 mM triethylammonium acetate buffer (TEAA) containing 7% CH_3CN (a) and 50% CH_3CN (b), gradient (a): 0 min 100%, 10 min 80%, 15 min 60%, 20 min 0%. System A(II): flow 1 mL/min, UV 240 or 260 nm, 50 mM NH_4OAc buffer (pH 7.0) containing 5% CH_3CN (a) and 50% CH_3CN (b), gradient (a): 0 min 100%, 30 min 80%, 35 min 60%, 38 min 0%. System A(III): flow 1 mL/min, UV 240 nm, 0−25 min 50 mM TEAA (pH 7.0) containing 7% CH_3CN. System B(I): flow 4 mL/min, UV 240 nm, 50 mM TEAA containing 7% CH_3CN (a) and 50% CH_3CN (b), gradient (a): 0 min 100%, 10 min 90%, 15 min 60%, 20−25 min 0%. System B(II): flow 4 mL/min, UV 240 nm, 50 mM TEAA containing 7% CH_3CN (a) and 50% CH_3CN (b), gradient (*a*): 0−20 min 100%, 40−55 min 0%. System C(I): flow 0.35 mL/min, UV 260 nm, 50 mM TEAA containing 7% CH_3CN (a) and 50% CH_3CN (b), gradient (a): 0 min 100%, 10 min 90%, 15 min 60%, 22 min 0%.

TLC was performed on precoated RP18 plates (Merck, Germany) with System I (50 mM TEAA containing 20% CH_3CN) and System II (MeOH/10% NH_4OAc (9:1 v/v)). The dried TLC plates were exposed to phosphor imaging plates for 10 min and scanned with a Fujix BAS 5000 (Fujifilm Europe, Germany). Radiochemical yields (RCYs) of the reactions and radiochemical purity (RCP) of the compounds were calculated from the activity area of the product peak related to the total activity area using AIDA software (Raytest, Germany). Non-radioactive compounds were visualized under UV-light at 254 nm.

Solid-phase extractions (SPE) were performed on SepPak Plus C_{18} and SepPak QMA Acell Plus cartridges (Waters, USA). Elution profiles of **1**, Y**2**, Y**3**, and Y**4** and the corresponding hydrolysis products Y**12** and Y**13** were initially monitored at 254 nm on the cartridges using an ÄKTAprime plus system (GE Healthcare, Germany). UV-chromatograms were evaluated with PrimeView software (GE Healthcare, Germany).

Gel Electrophoresis. PAGE was performed with vertical electrophoresis unit TV200YK (Biostep, Germany) running native 20% polyacrylamide gels at 10 mA and 10 °C in 1× TBE running buffer. A 10 bp DNA ladder (Fermentas, USA) was applied as a molecular weight standard. After electrophoresis, gels were exposed to phosphor imaging plates for 2−4 min. The plates were scanned and the RCYs of the conjugations and RCP of the radiolabeled L-RNA derivatives were calculated as

described above using AIDA software (Raytest, Germany). Subsequently, the gel was stained using ethidium bromide, and the DNA ladder was visualized under UV-light and photographed (Gene Flash, Syngene, UK).

Mass Spectrometry. Mass spectra were recorded on a Quattro Ultima ESI-MS (Micromass, UK) and on a Daltonics Autoflex II TOF/TOF50 (Bruker). The MALDI-TOF matrix, 3-hydroxypicolinic acid, was purchased from Aldrich. The L-RNA probes were desalted for MALDI-TOF measurements using C_{18} purification tips (ZipTip, Millipore, USA) as described elsewhere (*17*).

Chemistry. Synthesis, purification, and characterization of the $\Delta(\delta\delta\delta\delta)$ (twisted square antiprism, TSAP) and $\Lambda(\delta\delta\delta\delta)$ (square antiprism, SAP) isomers of [(2*S*)-2-(4-aminobenzyl)-1,4,7,10-tetraazacyclododecane-1,4,7,10-tetrayl]tetraacetato}-yttrate(1-) (Y**2**) were described in-depth elsewhere (*13*). Following experimental procedures for synthesis of the TSAP and SAP isomers of Y**3**, Y**4**, Y**6**, Y**7**, and Y**9**, respectively, based on the corresponding TSAP and SAP isomers of Y**2**.

*Preparation of [{(2S)-2-[4-(2,5-Dioxo-2,5-dihydro-1H-pyrrol-1-yl)benzyl]-1,4,7,10-tetraazacyclo-dodecane-1,4,7,10-tetrayl}tetra-acetato]yttrate(1-) (Y***3***).* The synthesis of Y**3** was adapted and optimized from ref 18. Briefly, *N*-methoxycarbonylmaleimide (15 mg, 96 μmol) was dissolved in 150 μL 1,4-dioxane and added to a solution of Y**2** (3.1 mg, 5.2 μmol) in 300 μL H_2O and 150 μL saturated $NaHCO_3$. The reaction mixture (pH 9.3) was incubated at 25 °C for a maximum reaction time of 15 min. The mixture was diluted with (250 μL) 1 M HCl to adjust pH 2. Subsequently, the mixture was fractionized by HPLC. HPLC fractions containing Y**3** were concentrated by evaporation and lyophilized to obtain 2.9 mg (4.3 μmol) of Y**3** as a white powder. ESI-MS: Y**3** (TSAP and SAP isomer) *m*/*z*: 674 $[M]^-$. HPLC: A(I): R_T(Y**3** TSAP) 17.1 min, R_T(Y**3** SAP) 17.3 min. B(I): R_T(Y**3** TSAP) 17.4 min, R_T(Y**3** SAP) 17.6 min. TLC: (I): R_f(Y**3**) 0.3, (II) R_f(Y**3**) 0.6.

*Preparation of [{(2S)-2-(4-{[4-(2,5-Dioxo-2,5-dihydro-1H-pyrrol-1-yl)butanoyl]amino}benzyl)-1,4,7,10-tetraazacyclododecane-1,4,7,10-tetrayl]tetraacetato}yttrate(1-) (Y***4***).* *N*-(γ-Maleimidobutyryloxy)succinimide ester (GMBS, 7.8 mg, 27.8 μmol) was dissolved in 250 μL DMSO and added to a solution of Y**2** (2.6 mg, 4.4 μmol) in (750 μL) 67 mM sodium phosphate buffer (pH 7.2). The reaction mixture (pH 7.9) was incubated at 25 °C for 30 min. Subsequently, the mixture was fractionized by HPLC. HPLC fractions containing Y**4** were concentrated by evaporation and lyophilized to obtain 3.0 mg (4.0 μmol) of Y**4** as a white powder. ESI-MS: Y**4** (TSAP and SAP isomer) *m*/*z*: 761 $[M]^-$. HPLC: A(II): R_T(Y**4** TSAP) 33.5 min, R_T(Y**4** SAP) 35.8 min. B(II): R_T(Y**4** TSAP) 31.4 min, R_T(Y**4** SAP) 31.6 min. TLC: (I): R_f(Y**4**) 0.3, (II) R_f(Y**4**) 0.7.

*Preparation of Y-DID-GSH (Y***6***).* The lyophilized compound Y**3** (1.1 mg, 1.6 μmol) and GSH **5** (2.7 mg, 8.8 μmol) were dissolved in (600 μL) 67 mM sodium phosphate buffer (pH 6.8). The reaction mixture (pH 5.1) was incubated at 25 °C for 25 min. Subsequently, the product Y**6** was fractionized by HPLC and lyophilized to obtain 1.4 mg (1.5 μmol) of Y**6**. ESI-MS: Y**6** (TSAP and SAP isomer) *m*/*z*: 981 $[M]^-$. HPLC: A(I): R_T(Y**6** TSAP) 7.1 min, R_T(Y**6** SAP) 9.0 min. TLC: (II) R_f(Y**6**) 0.1.

*Preparation of Y-DIBD-GSH (Y***7***).* The lyophilized compound Y**4** (1.0 mg, 1.3 μmol) and GSH **5** (3.0 mg, 9.8 μmol) were dissolved in (600 μL) 67 mM sodium phosphate buffer (pH 7.2). The reaction mixture (pH 6.6) was incubated at 25 °C for 25 min. Subsequently, the product Y**7** was fractionized by HPLC and lyophilized to obtain 1.4 mg (1.3 μmol) of Y**7**. ESI-MS: Y**7** (TSAP and SAP isomer) *m*/*z*: 1066 $[M]^-$. HPLC: A(II): R_T(Y**7** TSAP) 27.9 min, R_T(Y**7** SAP) 28.3 min. TLC: (II) R_f(Y**7**) 0.1.

Conjugation of L-RNA 8 with Y4. The thiol-modified L-RNA was protected as a disulfide (5′-(1-hydroxy-7,8-dithia-tetradecyl) UGACUGACUGAC-3′). The protecting group was initially removed by treatment with dithiotreitol (DTT). Briefly, L-RNA (5 mg, 1.2 μmol) and DTT (9.3 mg, 60 μmol) were dissolved in (1.76 mL) 67 mM sodium phosphate buffer (pH 8.0) and incubated for 60 min at 25 °C. Subsequently, 5′-thiolhexyl L-RNA **7** was purified via size exclusion chromatography (SEC) using an ÄKTAprime plus system (GE Healthcare, Germany) with a Superdex 75 HR 10/30 column (GE Healthcare, Germany) and 67 mM sodium phosphate buffer (pH 7.0, saturated with nitrogen) as mobile phase at a flow rate of 30 mL/h. SEC-fractions containing **8** were lyophilized and stored at −24 °C. The identity of the 5′-thiolhexyl L-RNA **7** was verified by mass spectrometry.

The lyophilized compound Y**4** (0.12 mg, 160 nmol) and L-RNA **8** (0.24 mg, 60 nmol) were dissolved in (250 μL) 67 mM sodium phosphate buffer (pH 7.0). The reaction mixture (pH 6.6) was incubated for 25 min at 25 °C under argon atmosphere. Subsequently, the product Y**9** was fractionized by HPLC and lyophilized to obtain 0.27 mg (57 nmol) of Y**9**. Maldi-TOF: **8** *m*/*z* 3991 $[M + H]^+$, Y**9** (TSAP and SAP isomer) *m*/*z* 4751 $[M + H]^+$. SEC: V_R(**8**) 12.4 mL. HPLC: A(II): R_T(**8**) 25.4 min, R_T(Y**9** TSAP) 28.5 min, R_T(Y**9** SAP) 29.1 min.

Determination of Hydrolytic Stability of Y3 and Y4. First, the corresponding hydrolysis products [(2*Z*)-4-oxo-4-{[4-({(2*S*)-1,4,7,10-tetrakis[(carboxymethyl]-1,4,7,10-tetraazacyclododecan-2-yl}methyl)phenyl]amino}but-2-enoato(4-)]yttrate(1-) (Y**12**) and [(2*Z*)-4-oxo-4-[(4-oxo-4-{[4-({(2*S*)-1,4,7,10-tetrakis[(carboxymethyl]-1,4,7,10-tetraazacyclododecan-2-yl}methyl)phenyl]amino}butyl)amino]but-2-enoato(4-)]yttrate(1-) (Y**13**) of the maleimides Y**3** and Y**4** were synthesized. Briefly, Y**3** and Y**4** were hydrolyzed after their synthesis by the addition of NaOH to the reaction mixtures (pH 9.0). The corresponding maleamic acid derivatives Y**12** and Y**13** were separated via HPLC and analyzed by ESI-MS. To determine the hydrolytic stability of Y**3** and Y**4** depending on time, Y**3** (1 mg, 1.5 μmol) and Y**4** (1 mg, 1.3 μmol) were separately dissolved in (500 μL) 67 mM sodium phosphate buffer (pH 7.0) and incubated at 25 °C for 96 h. Aliquots were sampled after 0, 1, 2, 3, 4, 5, 23, 48, and 96 h, and the samples were analyzed via HPLC. The experiments were repeated three times.

HPLC fractions, containing separately Y**3** and Y**4** in a mixture of 50 mM TEAA/CH_3CN (4:1 v/v, pH 6.25), were adjusted with acetic acid and triethylamine to pH 6.0, 6.6, 7.1, 7.5, 7.8, 8.0, and 8.4, respectively. All mixtures were incubated at 25 °C for 30 min and analyzed via HPLC. ESI-MS: Y**12** (TSAP and SAP isomer) *m*/*z* 694 $[M + 2H]^+$, Y**13** (TSAP and SAP isomer) *m*/*z* 779 $[M + 2H]^+$. HPLC: A(I): R_T(Y**12** TSAP) 10.5 min, R_T(Y**12** SAP) 11.6 min. A(II): R_T(Y**13** TSAP) 12.1 min, R_T(Y**13** SAP) 14.4 min.

Radiochemistry. *Preparation of [(2S)-2-(4-Aminobenzyl)-1,4,7,10-tetraazacyclododecane-1,4,7,10-tetrayl]tetra-acetato}[*^{90}*Y]-yttrate(1-) ([*^{90}*Y]***2***).* Chelator **1** (100 μg, 0.15 μmol) in (500 μL) 0.6 M NaOAc buffer (pH 6.8) was added to 80 μL [^{90}Y]YCl_3 (13 MBq) in 0.04 M HCl. The mixture (pH 6.5) was incubated at 95 °C for 20 min. A solution of DTPA (15 μL, 0.45 μmol) was added, and the reaction mixture was incubated at 40 °C for 10 min to complex unreacted [^{90}Y]Y^{3+}. The radiometal complex [^{90}Y]**2** was separated from [^{90}Y]Y-DTPA and **1** using a SepPak Plus C_{18} cartridge (Waters, USA). After elution of **1** and [^{90}Y]Y-DTPA with (10 mL) 67 mM sodium phosphate buffer (pH 7.0), [^{90}Y]**2** was selectively eluted: (a) with 2 mL CH_3CN/H_2O (4:1 v/v) and evaporated to dryness under a stream of nitrogen at 95 °C for 40 min, or (b) fractionized with (2 mL) 67 mM sodium phosphate buffer/CH_3CN (1:1 v/v, pH 8.1). The product [^{90}Y]**2** was found to be >99% radiochemically pure.

Scheme 1. Complexation of $[^{90}Y]Y^{3+}$ with Chelator 1 and Subsequent Synthesis of the Maleimide Reagent [90Y]3 by Reaction of the SPE-Purified Complex [90Y]2 with *N*-Methoxycarbonylmaleimide

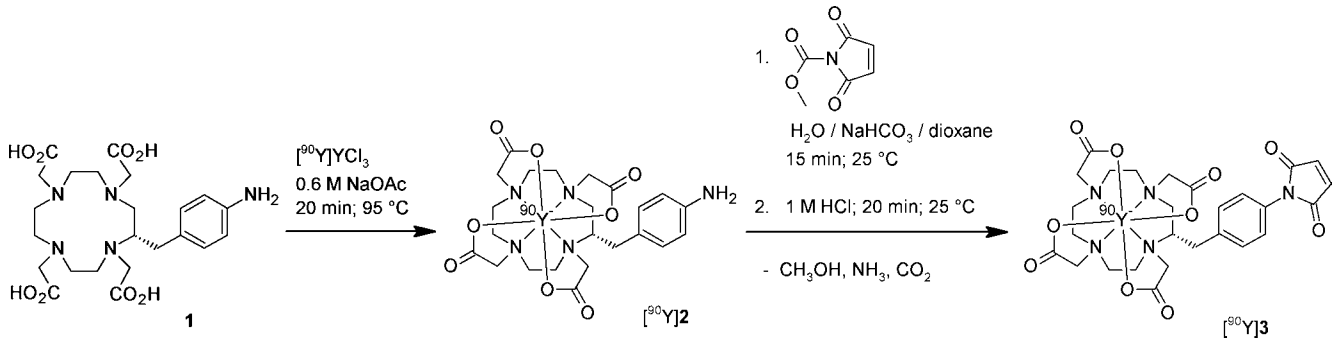

Scheme 2. Synthesis of the Maleimide Reagent [90Y]4 by Reaction of [90Y]2 with GMBS

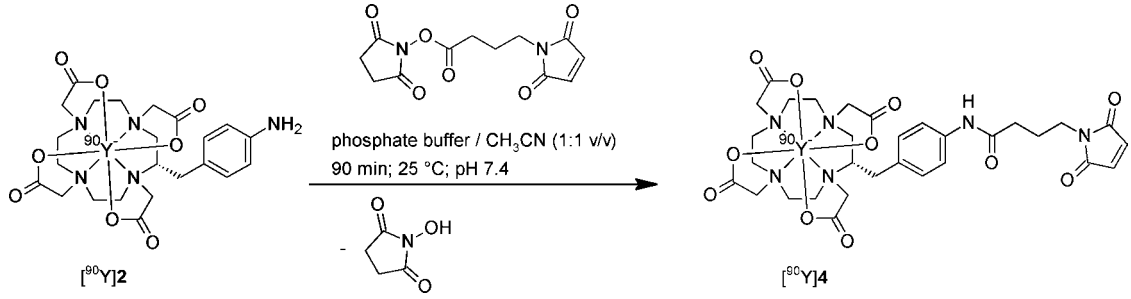

HPLC: A(III): R_T([90Y]**2** TSAP) 9.1 min, R_T([90Y]**2** SAP) 13.3 min. TLC: (I): R_f([90Y]**2**) 0.5, (I) R_f([90Y]**2**) 0.7.

*Preparation of [{(2S)-2-[4-(2,5-Dioxo-2,5-dihydro-1H-pyrrol-1-yl)benzyl]-1,4,7,10-tetraazacyclo-dodecane-1,4,7,10-tetrayl}tetraacetato][90Y]yttrate(1-) ([90Y]**3**).* The residue of the SPE-purified (scheme a) radiometal complex [90Y]**2** (9.5 MBq) was redissolved in 100 μL H_2O and 50 μL saturated $NaHCO_3$. *N*-Methoxycarbonylmaleimide (5 mg, 32 μmol) was solved in 50 μL 1,4-dioxane and added to the solution of [90Y]**2**. The reaction mixture (pH 9.1) was incubated at 25 °C for 15 min. The mixture was carefully diluted with 1 M HCl (70 μL) to adjust pH < 3, and the tube was left open at room temperature for 20 min. Subsequently, the mixture was diluted with (20 mL) 50 mM NH_4OAc solution (pH 6.0) and applied onto a SepPak Plus C_{18} cartridge. The cartridge was washed with (10 mL) 50 mM NH_4OAc solution (pH 6.0) and (2 mL) 50 mM NH_4OAc/CH_3CN (9:1 v/v, pH 6.5). The final product [90Y]**3** was selectively eluted with (2 mL) 0.1 M NH_4OAc/CH_3CN (1:1 v/v, pH 6.5) and [90Y]**3** was found to be >95% radiochemically pure. HPLC: A(I): R_T([90Y]**3**) 17.4 min. TLC: (I): R_f([90Y]**3**) 0.3, (II) R_f([90Y]**3**) 0.6.

*Preparation of {[(2S)-2-(4-{[4-(2,5-Dioxo-2,5-dihydro-1H-pyrrol-1-yl)butanoyl]amino}benzyl)-1,4,7,10-tetraazacyclododecane-1,4,7,10-tetrayl]tetraacetato}[90Y]yttrate(1-) ([90Y]**4**).* The SPE eluate, which contained the radiometal complex [90Y]**2** (33.4 MBq) in (0.6 mL) 67 mM sodium phosphate buffer/CH_3CN (1:1 v/v, pH 8.1), was added to GMBS (3 mg, 10.7 μmol). The reaction mixture (pH 7.4) was incubated at 25 °C for 90 min. Subsequently, the mixture was diluted with 20 mL H_2O and applied onto a SepPak QMA cartridge. The cartridge was washed with 10 mL H_2O, and the final product [90Y]**4** was directly eluted on a SepPak Plus C_{18} cartridge with (6 mL) 0.5 M NaCl/CH_3CN (95:5 v/v, pH 3.5). The SepPak Plus C_{18} cartridge was washed with (4 mL) 50 mM NH_4OAc/CH_3CN (9:1 v/v, pH 6.8), and compound [90Y]**4** was selectively eluted with 2 mL H_2O/CH_3CN (4:1 v/v). The product [90Y]**4** was found to be >98% radiochemically pure. HPLC: A(II): R_T([90Y]**4** TSAP) 34.5 min, R_T([90Y]**4** SAP) 36.3 min. TLC: (I): R_f([90Y]**4**) 0.3, (II) R_f([90Y]**4**) 0.7.

Conjugation of Glutathione (GSH) 5 with [90Y]3 and [90Y]4. Dilution series with 1000, 100, 10, 1, and 0.1 μg GSH **5** (corresponding to 3300, 330, 33, 3.3, and 0.33 nmol **5**) in (1 mL) 67 mM sodium phosphate buffer (pH 7.2) were prepared. Both maleimide reagents, [90Y]**3** (0.2 MBq in (150 μL) 0.1 M NH_4OAc/CH_3CN (1:1 v/v, pH 6.5)) and [90Y]**4** (0.2 MBq in 150 μL H_2O/CH_3CN (4:1 v/v, pH 7.0)), were separately added to each solution of **5**. The reaction mixtures were incubated under argon atmosphere at 25 °C for 2 h. For determination of the RCYs, aliquots of the reaction mixtures with the corresponding products [90Y]Y-DID-GSH [90Y]**6** and [90Y]Y-DIBD-GSH [90Y]**7**, respectively, were analyzed after 5, 15, 30, 60, and 120 min by TLC. TLC: (II): R_f([90Y]**6**) 0.1, R_f([90Y]**7**) 0.1.

Conjugation of L-RNA 8 with [90Y]4 via Prelabeling. Dilution series with 400, 200, 100, 40, 20, 8, 2, and 0.4 μg L-RNA **8** (corresponding to 100, 50, 25, 10, 5, 2, 0.5, and 0.1 nmol **8**) in (100 μL) 67 mM sodium phosphate buffer (pH 7.0) were prepared. The maleimide reagent [90Y]**4** (0.5 MBq in 65 μL H_2O/CH_3CN (4:1 v/v, pH 7.0)) was added to each solution of **8**. The reaction mixtures were incubated under argon atmosphere at 25 °C for 2 h. For determination of the RCYs, aliquots of the reaction mixtures with the corresponding product [90Y]Y-DIBD-L-RNA [90Y]**9** were sampled (after 60 and 120 min), evaporated (Concentrator 5314, Eppendorf, Germany), and analyzed via PAGE and HPLC. HPLC: A(II): R_T([90Y]**8** TSAP) 28.6 min, R_T([90Y]**8** SAP) 29.2 min. PAGE: see Supporting Information Figures S3 and S4.

Preparation of the 90Y-Labeled L-RNA [90Y]11 via Postlabeling. Dilution series with 440, 220, 110, 44, 22, 4, 2, and 0.4 μg DOTA−L-RNA **10** (corresponding to 100, 50, 25, 10, 5, 2, 0.5, and 0.1 nmol **10**) in 250 μL NH_4OAc buffer (0.5 M, pH 7.0) were prepared. [90Y]YCl_3 (8 μL, 2.4 MBq) in 0.04 M HCl was added to each solution of **10**. After incubation of the reaction mixtures at 90 °C for 20 min, DTPA (10 μL, 30 mM in 0.5 M NH_4OAc) was added, and the reaction mixtures were kept at room temperature for 10 min to complex unreacted $[^{90}Y]Y^{3+}$ as [90Y]Y-DTPA complex. Aliquots of the reaction mixtures were analyzed via PAGE and HPLC to determine the

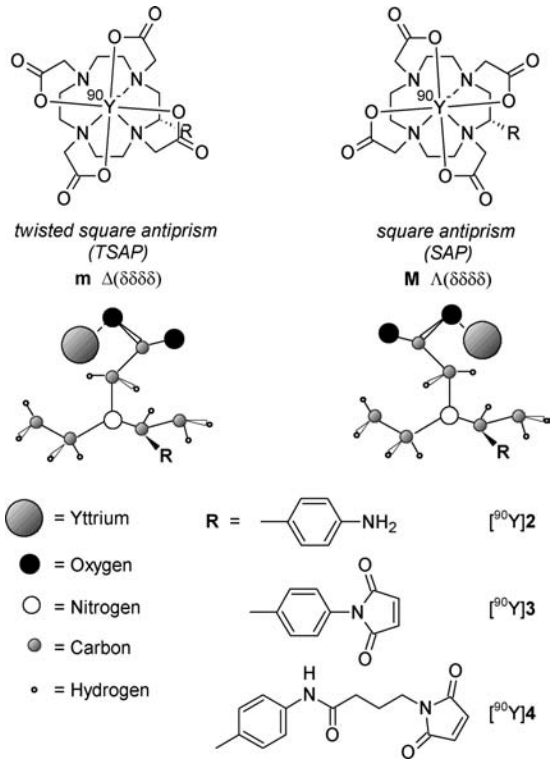

Figure 3. Isomers of the differently substituted [^{90}Y]-DOTA complexes [^{90}Y]**2**, [^{90}Y]**3**, and [^{90}Y]**4** are represented schematically. Only the geometry around the N-CH_2-COO group next to the (*S*)-configured carbon atom is given.

RCYs in dependence of the amount of **10**. HPLC: C(I): R_T([^{90}Y]**11**) 15.3 min. PAGE: see Supporting Information Figure S5.

RESULTS AND DISCUSSION

Synthesis of [^{90}Y]3 and [^{90}Y]4. A straightforward method to synthesize both [^{90}Y]-DOTA-based maleimide reagents [^{90}Y]**3** and [^{90}Y]**4** is to initially complex [^{90}Y]Y^{3+} with chelator **1** and subsequently transform the purified complex [^{90}Y]**2** into the corresponding maleimides, by using activating agents (see Schemes 1 and 2). As previously shown, [^{90}Y]**2** exists as two conformers, adopting the Δ($\delta\delta\delta\delta$) (twisted square antiprism, TSAP) and Λ($\delta\delta\delta\delta$) (square antiprism, SAP) configurations (see Figure 3) (*13*). On this account, two further conformers of [^{90}Y]**3** and [^{90}Y]**4**, respectively, derived from both isomers of [^{90}Y]**1**. Having shown that the differences in the helicity of the carboxylate side arms (Λ or Δ) does not affect the biodistribution of the corresponding radiolabeled L-RNA (*13*), both isomers of [^{90}Y]**2** were used for all radiosyntheses in this work without separation.

*Synthesis and SPE-Purification of [^{90}Y]***2.** The synthesis of [^{90}Y]**2** was performed in an analogous manner as previously described (*13*). By adding DTPA to the solution, unreacted [^{90}Y]Y^{3+} was finally complexed as [^{90}Y]Y-DTPA. Solid-phase extraction (SPE) was used to purify the radiometal complex [^{90}Y]**2** from the excess chelator **1** and [^{90}Y]Y-DTPA complex. In this process, the negatively charged complex [^{90}Y]**1** was retarded on a SepPak Plus C_{18} cartridge applying an aqueous solution of the ion pair reagents TEAA, NH_4OAc, and NaOAc, respectively, whereas **1** and [^{90}Y]Y-DTPA were eluted with these eluents. This observation indicates that triethylammonium, ammonium, and Na^+-cations provide a comparable interaction of [^{90}Y]**2** with the reversed-phase material by masking the negative charge of [^{90}Y]**2**. Furthermore, no differences were observed for these cations in the performance of separation of [^{90}Y]**2** from the side products **1** and [^{90}Y]Y-DTPA. For the synthesis of [^{90}Y]**3**, the radiometal complex [^{90}Y]**2** was selectively eluted from the cartridge with a mixture of CH_3CN and H_2O (4:1 v/v) and evaporated to dryness. To minimize expenditure of time, [^{90}Y]**2** was alternatively eluted with 67 mM sodium phosphate buffer/CH_3CN (1:1 v/v, pH 8.1) and used without any further processing for the radiosynthesis of [^{90}Y]**4**.

*Synthesis of [^{90}Y]***3.** To synthesize [^{90}Y]**3**, the primary amine group of [^{90}Y]**2** reacted with *N*-methoxycarbonylmaleimide (see Scheme 1). This reaction is a comparably mild method for the transformation of amine groups into maleimides. As recently shown with *N*-methoxycarbonylmaleimide (*18*), radiochemical yields (RCYs) greater 90% were already achieved at room temperature after 10 min for a ^{18}F-labeled maleimide reagent. On the basis of this work (*18*), we adapted and optimized these reaction conditions for synthesis of [^{90}Y]**3**. The residue of the SPE-purified radiometal complex [^{90}Y]**2** was redissolved in $NaHCO_3$ solution. After adding *N*-methoxycarbonylmaleimide, the mixture was incubated at room temperature and pH 9.1 for a maximum reaction time of 15 min. In a second step, the pH was lowered from 9.1 to ~2 by addition of 1 M HCl.

*SPE Purification of [^{90}Y]***3.** An efficient purification of [^{90}Y]**3** in regard to short purification time and high RCYs was performed with solid-phase extraction (SPE). For that purpose, elution profiles of **1**, Y**2**, Y**3**, the corresponding hydrolysis product Y**12**, and *N*-methoxycarbonylmaleimide were initially analyzed on a SepPak Plus C_{18} cartridge. On the basis of the elution characteristics of these nonradiolabeled compounds, the following procedure was conducted to purify [^{90}Y]**3** with only

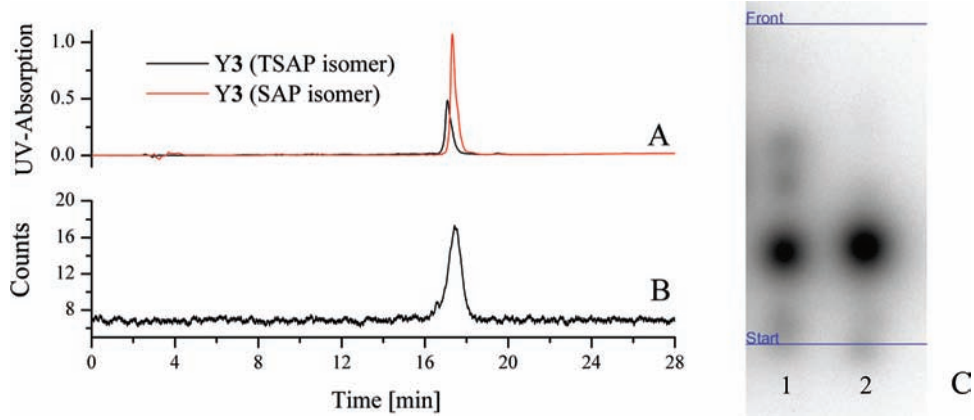

Figure 4. Radio-HPLC and radio-TLC chromatograms of the maleimide reagent [^{90}Y]**3**. (A) Overlay of HPLC profiles of the TSAP and SAP isomer of Y**3** as references. (B) SPE-purified [^{90}Y]**3**. The TSAP and SAP isomer of [^{90}Y]**3** could not be separated under the used HPLC conditions. (C) Radio-TLC analysis of the reaction mixture containing [^{90}Y]**3** (1) and the SPE-purified [^{90}Y]**3** (2) with TLC system **I**.

Table 1. Time-Dependent Radiochemical Yields (RCYs) of [90Y]4 (RCYs Were Determined via Radio-TLC Analysis)

reaction time [min]	15	30	45	60	75	90
RCY [%]	30	38	46	58	62	66

one SepPak Plus C_{18} cartridge: (A) First, the concentration of dioxane was reduced from 25% in the reaction mixture to 0.5% by adding 20 mL NH_4OAc solution. Higher dioxane concentrations would lead to an elution of [90Y]**3**. (B) Subsequently, the cartridge was washed with a solution of 10 mL 50 mM NH_4OAc (pH 6.0) and a mixture of (2 mL) 50 mM NH_4OAc and CH_3CN (9:1 v/v, pH 6.5), to elute both unreacted *N*-methoxycarbonylmaleimide and the hydrolyzed species [90Y]**12** from the cartridge. (C) Finally, compound [90Y]**2** was selectively eluted with a mixture of (2 mL) 0.1 M NH_4OAc and CH_3CN (1:1 v/v, pH 6.5). A pH value of ≤6.5 in the final elution mixture proved to be important for preventing hydrolysis of the maleimide [90Y]**3**. The obtained maleimide reagent [90Y]**3** was used for the prelabeling of GSH **5** without any further processing. Hence, in a typical experiment starting with the complexation of 11 MBq [90Y]YCl_3 with **1**, 3.7 MBq of [90Y]**3** was obtained with a radiochemical purity of >95% within 145 min (Figure 4).

*Synthesis of [90Y]***4.** The transformation of the primary amine [90Y]**2** into a maleimide group can also be conducted with heterobifunctional reagents, e.g., *N*-(γ-maleimidobutyryloxy)-succinimide ester (GMBS). At pH 7.0−7.5, GMBS readily reacts with both primary amines via the chemically reactive succinimidyl group and thiols via the maleimide group. The nucleophilic substitution of the primary amine [90Y]**2**, by reaction with the activated carbonyl carbon in GMBS, leads to the formation of [90Y]**4** (see Scheme 2).

To synthesize [90Y]**4**, SPE-purified [90Y]**2** (33.4 MBq) in 0.6 mL sodium phosphate/CH_3CN (1:1 v/v) was added directly to GMBS. Subsequently, the solution was vigorously mixed at room temperature. The pH value of the reaction mixture (pH 7.4) remained constant over the reaction time of 90 min. The kinetics of the reaction was monitored by radio-TLC analysis. The time-dependent RCYs of the maleimide formation are shown in Table 1. Compound [90Y]**4** was obtained with the maximum RCY of 66% after 90 min. In a competing side reaction, GMBS was hydrolyzed to the corresponding byproduct *N*-hydroxysuccinimide and 4-maleimidobutyric acid, as confirmed by HPLC. Thus, reaction times longer than 90 min would not lead to higher RCYs.

*SPE Purification of [90Y]***4.** Separation of *N*-hydroxysuccinimide, 4-maleimidobutyric acid and the unreacted complex [90Y]**2** from the maleimide reagent [90Y]**4** was performed via SPE. For that purpose, elution profiles of these compounds on different cartridges were initially analyzed. On the basis of their elution characteristics, the following procedure was conducted to purify [90Y]**4** efficiently with an anion-exchanger (SepPak QMA Acell Plus) and a C_{18}-cartridge (SepPak Plus C_{18}): (A) Prior to loading the reaction mixture onto the anion-exchanger the concentration of phosphate ions was reduced from 67 to 6 mM by adding 20 mL H_2O, thus preventing an elution of [90Y]**4** during the loading step. (B) The anion-exchanger was washed with 10 mL H_2O to elute unreacted GMBS. (C) The maleimide reagent [90Y]**4** was eluted directly onto the C_{18}-cartridge with a mixture of (6 mL) 0.5 M NaCl and CH_3CN (95:5 v/v). (D) Subsequently, the C_{18}-cartridge was washed with (4 mL) 50 mM NH_4OAc/CH_3CN (9:1 v/v), to elute all byproduct from the cartridge. Under these conditions, almost 70% of the product [90Y]**4** remained on the C_{18}-cartridge. (E) Finally, compound [90Y]**4** was selectively eluted with 2 mL H_2O/CH_3CN (1:1 v/v, pH 7.0) from the cartridge. Hence, in a typical experiment starting with the complexation of 39 MBq [90Y]YCl_3 with **1**, 8 MBq of [90Y]**4** was obtained with a radiochemical purity of >98% within 170 min (Figure 5).

Scheme 3. Maleamic Acid Derivatives [90Y]12 and [90Y]13 Derived from the Basic Hydrolysis of the Maleimide Reagents [90Y]3 and [90Y]4

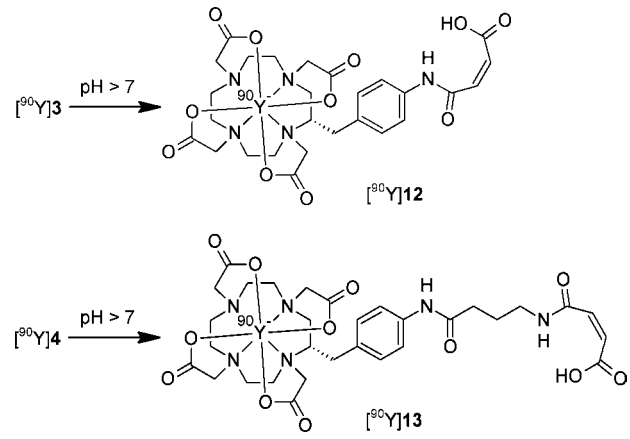

Hydrolytic Stability of [90Y]3 and [90Y]4. During the preparation process, the maleimide reagents [90Y]**3** and [90Y]**4** hydrolyzed at pH values greater than 7.0 into the corresponding nonreactive maleamic acids [90Y]**12** and [90Y]**13** (Scheme 3) (*12*, *19*). Differences were found in the hydrolytic stability of the *N*-aryl maleimide [90Y]**3** and the *N*-alkyl maleimide [90Y]**4**. By examining heterobifunctional linkers, Kitagawa et al. observed a higher hydrolytic stability of *N*-alkyl against *N*-aryl maleimides in aqueous solutions at pH 8.0 (*20*). Thus, only 8−12% hydrolysis products were found for *N*-alkyl

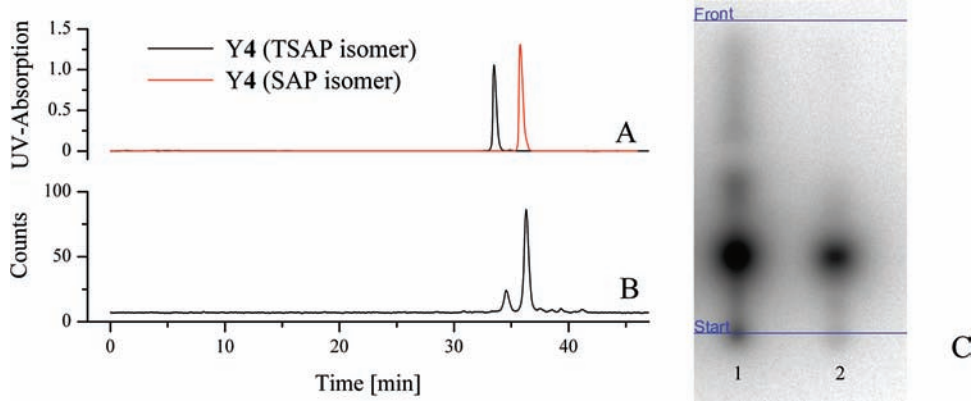

Figure 5. Radio-HPLC and radio-TLC chromatograms of the maleimide reagent [90Y]**4**. (A) Overlay of HPLC profiles of the TSAP and SAP isomer of Y**4** as references. (B) SPE-purified [90Y]**4**. (C) Radio-TLC analysis of the reaction mixture containing [90Y]**4** (1) and the SPE-purified [90Y]**4** (2) with TLC system I.

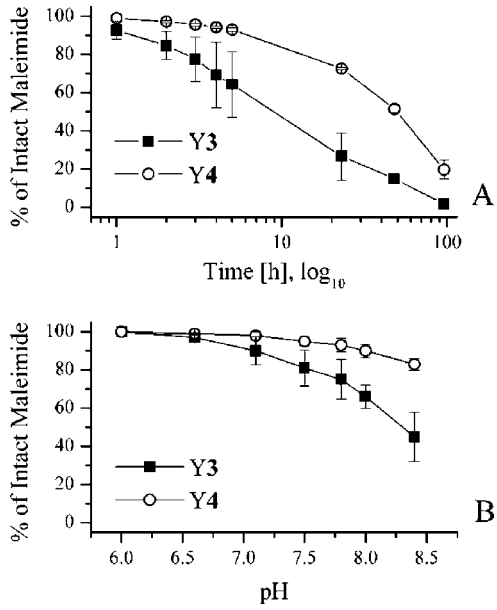

Figure 6. Hydrolytic stability of the maleimides Y**3** and Y**4**: (A) as a function of time at pH 7.0, (B) as a function of pH value for 30 min ($n = 3$).

maleimides, whereas 41−69% of the *N*-aryl maleimides were hydrolyzed under the same conditions (after 30 min at 30 °C). The highest stability was observed for all maleimides in weak acid solutions at pH 6.0.

To verify the hydrolytic stability of the maleimide reagents [^{90}Y]**3** and [^{90}Y]**4**, hydrolysis rates of the nonradioactive maleimides Y**3** and Y**4** were analyzed as a function of time and pH (see Figure 6). In agreement with the previous observations of Kitagawa et al. (*20*), *N*-alkyl maleimide Y**4** showed increased stability at pH 7.0 over a period of 96 h, in comparison to *N*-aryl maleimide Y**3**. Hydrolysis ratios of 73% for Y**3**, but only of 27% for Y**4** were estimated after 23 h incubation time. As expected, Y**4** was more stable than Y**3** at higher pH values (7.8−8.4). Therefore, a careful control of reaction time and pH seems to be important for the synthesis of [^{90}Y]**3**, since the formation of [^{90}Y]**3** competes with the base-catalyzed ring-opening of the maleimide group in the first reaction step (see Scheme 1). HPLC analyses also confirmed that 10% of the corresponding maleamic acid derivative Y**12** was already formed 20 min after addition of *N*-methoxycarbonylmaleimide to the nonradioactive precursor Y**2** (data not shown). Therefore, in order to get higher RCYs a reaction time of 15 min and pH 9 should not be exceeded in the first reaction step.

Prelabeling of GSH as Model Peptide with [^{90}Y]3 and [^{90}Y]4. To evaluate the application and reactivity of both maleimide reagents [^{90}Y]**3** and [^{90}Y]**4**, the prelabeling approach was initially tested with GSH **5** as a model substance. The conjugations of both maleimide reagents [^{90}Y]**3** and [^{90}Y]**4** to **5** were conducted with different amounts of **5** in 1 mL of phosphate buffer (pH 7.2) at room temperature (see Scheme 4). The kinetics of these reactions was monitored via radio-TLC analysis. Time-dependent RCYs of both prelabeling reactions are summarized in Table 2. For [^{90}Y]**6** and [^{90}Y]**7**, RCYs greater than 85% were reached already after 5 min reaction time in batches with 10 to 1000 μg **5**. Slight differences in the obtained RCYs were only observed for both maleimide reagents at amounts of 0.1 and 1 μg **5**. At these low amounts of **5**, higher RCYs were achieved for maleimide reagent [^{90}Y]**3** than for [^{90}Y]**4**. This points to a slightly higher reactivity of [^{90}Y]**3** compared to [^{90}Y]**4**. In contrast, the higher hydrolytic stability of [^{90}Y]**4** showed no influence on the RCYs. In summary, higher RCYs were obtained for both conjugations with increasing amounts of **5** and longer reaction times. Similar results were found for the radiolabeling of GSH **5** with both [^{90}Y]-DOTA-based maleimide reagents [^{90}Y]**3** and [^{90}Y]**4** as already known for a [^{18}F]-based maleimide (*21*).

^{90}Y-Labeling of an L-RNA via the Pre- and Postlabeling Approach. For the evaluation of achievable RCYs and ESAs both pre- and postlabeling were performed with a 12mer L-RNA as model substance. Due to its higher hydrolytic stability, only [^{90}Y]**4** was used for the prelabeling of the 12mer L-RNA **8**. On

Scheme 4. Conjugation of Glutathione (GSH) 5 with [^{90}Y]3 and [^{90}Y]4, Respectively

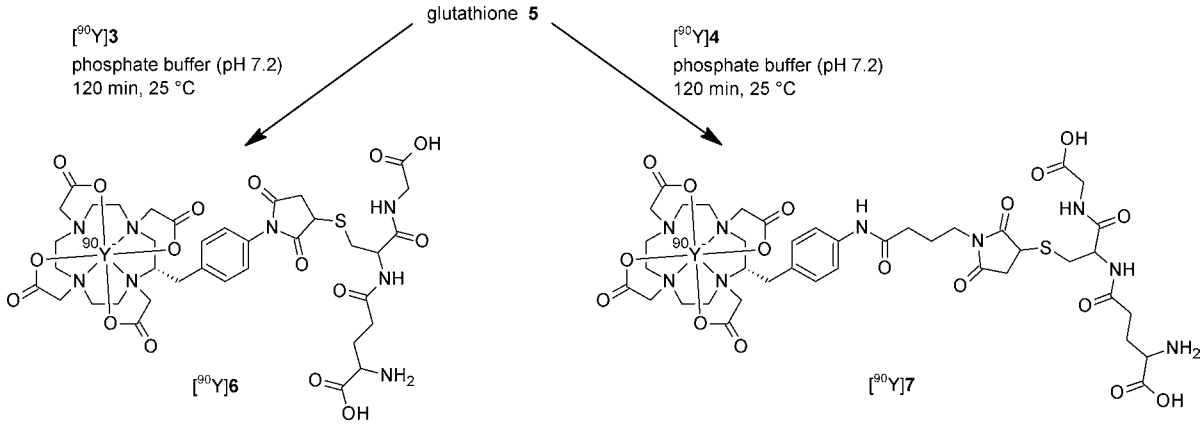

Table 2. RCYs (%) of Conjugates [^{90}Y]6 and [^{90}Y]7 as a Function of the Time and Amount of 5 (Presented as Data ± SD, RCYs Were Determined via Radio-TLC Analysis ($n = 3$ ([^{90}Y]6), $n = 4$ ([^{90}Y]7))

	5 min		10 min		30 min		60 min		120 min	
GSH [μg]	[^{90}Y]**6**	[^{90}Y]**7**	[^{90}Y]**6**	[^{90}Y]**7**	[^{90}Y]**6**	[^{90}Y]**7**	[^{90}Y]**6**	[^{90}Y]**7**	[^{90}Y]**6**	[^{90}Y]**7**
0.1	20 (2.6)	14 (3.5)	29 (5.0)	20 (3.4)	35 (8.5)	25 (1.9)	37 (9.6)	30 (5.3)	39 (11.9)	34 (9.0)
1	74 (9.2)	44 (4.9)	85 (4.5)	65 (9.2)	88 (3.1)	76 (9.6)	89 (1.5)	82 (7.0)	89 (1.5)	84 (4.9)
10	86 (4.0)	87 (5.9)	88 (2.5)	88 (4.7)	89 (2.1)	88 (4.2)	90 (2.0)	88 (4.2)	90 (2.0)	89 (3.9)
100	87 (4.6)	88 (4.7)	88 (2.5)	89 (4.6)	89 (1.7)	90 (4.4)	90 (2.0)	90 (3.9)	91 (2.3)	90 (4.2)
1000	89 (1.5)	90 (5.0)	91 (2.3)	91 (4.5)	91 (2.3)	91 (4.7)	91 (2.3)	92 (3.7)	91 (2.3)	92 (3.7)

Scheme 5. ^{90}Y-Labeling of L-RNA via the Pre- and Postlabeling Approach[a]

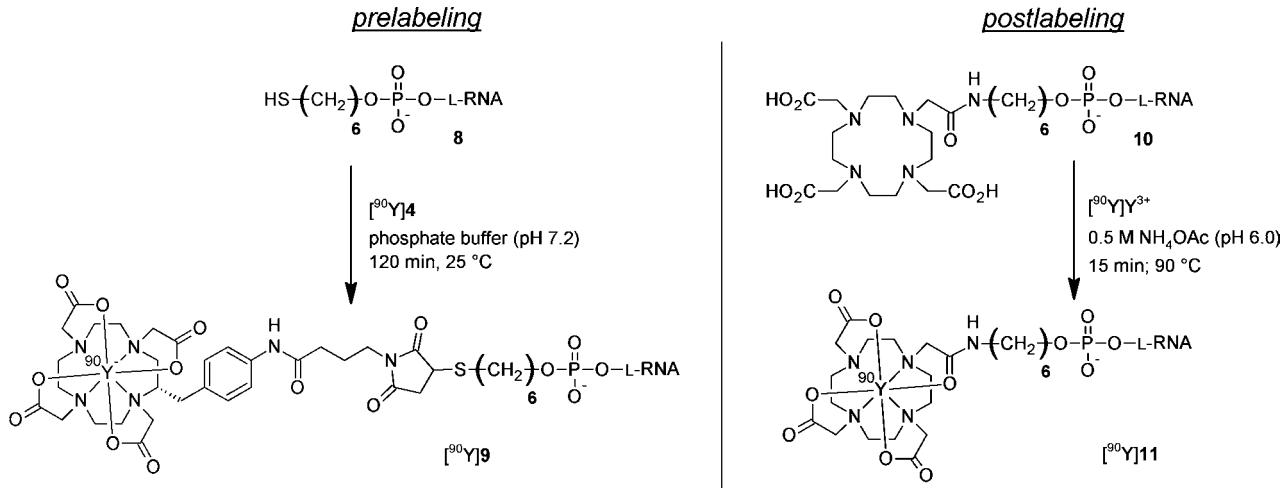

[a] Prelabeling approach: Compound [^{90}Y]**9** was formed by reaction of L-RNA **8** with [^{90}Y]**4** under mild conditions. Postlabeling approach: [^{90}Y]Y^{3+} labeling of DOTA−L-RNA **10** results in formation of [^{90}Y]**11**.

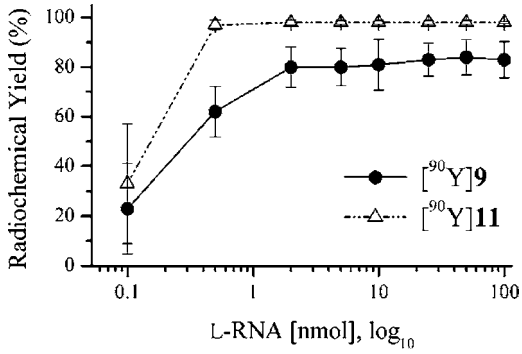

Figure 7. RCYs (%) of [^{90}Y]**9** and [^{90}Y]**11** as a function of the amount of L-RNA derivatives **8** and **10**. The results were obtained by PAGE analysis (n = 4 ([^{90}Y]**9**), n = 3 ([^{90}Y]**11**)).

this account, the prelabeling of **8** with [^{90}Y]**4** was compared with the direct radiolabeling of DOTA-L-RNA **10** with [^{90}Y]YCl_3.

Prelabeling of a Thiol-Modified L-RNA **8** *with [^{90}Y]***4.** The 12mer L-RNA was derivatized with a 5′-hexyl disulfid group, and after removal the protective group, the free thiol group of **8** was used to attach the maleimide reagent [^{90}Y]**4**. The conjugation was performed at room temperature in 0.1 mL phosphate buffer at pH 7.2 (Scheme 5). The dependence of the RCY of the prelabeling reaction on the amount of **8** was estimated in range 0.1−100 nmol of **8**. The progress of the reaction was monitored by gel electrophoresis after 2 h reaction time (Supporting Information Figure S3B). The difference in the retention factor values of [^{90}Y]**4** (R_F 0.39; 0.70) and the product [^{90}Y]**9** (R_F 0.61) allowed a quantitative analysis of the reaction (Supporting Information Figure S4). The obtained RCYs of the conjugation, as a function of the amount of **8**, is shown in Figure 7.

Postlabeling of DOTA−L-RNA **10** *with [^{90}Y]YCl_3.* The ^{90}Y-labeling of DOTA−L-RNA **10** was performed in an analogous manner to that previously described (*16*). The dependence of the RCY of the postlabeling reaction on the amount of **10** was monitored in the range 0.1−100 nmol of **10** and estimated by gel electrophoresis (Supporting Information Figure S5B). Before analyzing the reaction aliquots, unreacted [^{90}Y]Y^{3+} was first complexed as [^{90}Y]Y-DTPA by adding DTPA to the solution. The RCYs of the complexation, obtained from PAGE analyses, are graphically shown in Figure 7.

Comparison of Both Radiolabeling Methods. In the range 0.1−100 nmol of L-RNA, higher RCYs of ^{90}Y-labeling were

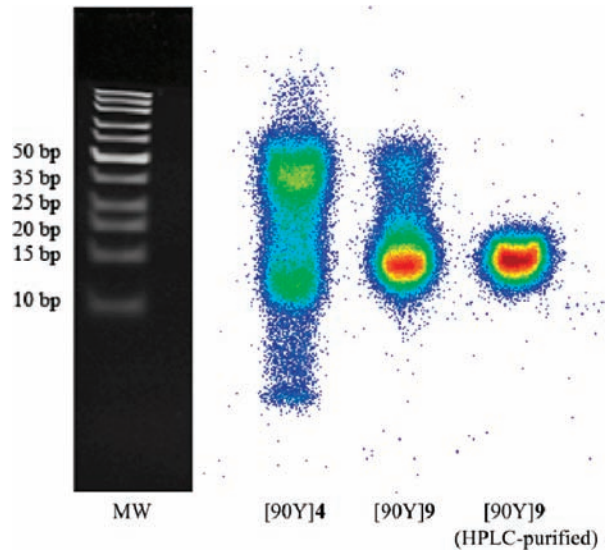

Figure 8. Image fusion of the autoradiogram of the exposed 20% polyacrylamide gel and the photographed 10 bp DNA ladder (MW) after staining with ethidium bromide. Applied samples in the lanes: maleimide reagent [^{90}Y]**4**, ^{90}Y-labeled L-RNA [^{90}Y]**9** before (aliquot of the crude reaction mixture) and after HPLC separation.

obtained by the postlabeling approach. Using 2.4 MBq [^{90}Y]Y^{3+}, RCYs higher than 97% were already achieved with 0.5 nmol **10**. A higher effective specific activity (ESA) of up to 4 GBq/μmol [^{90}Y]**11** was obtained with the postlabeling approach. Furthermore, an additional HPLC separation of [^{90}Y]**11** (R_T 15.3 min) from excess **10** (R_T 16.8 min) would theoretically enhance the ESA to 29 GBq/μmol (Supporting Information Figure S2, HPLC system C(I)).

In contrast, prelabeling experiments with 0.5 MBq [^{90}Y]**4** gave lower RCYs of ^{90}Y-labeling in the range 0.1−100 nmol L-RNA. The maximum RCY of 84% was obtained at 50 nmol **8**. In comparison to 35% and 97% RCY for postlabeling at 0.1 and 0.5 nmol of L-RNA **10**, respectively, 23% and 62% RCY was calculated for prelabeling at the same amounts of L-RNA **8**. HPLC separation of [^{90}Y]**9** resulted in an ESA of 0.7 GBq/μmol [^{90}Y]**9** and a radiochemical purity of 99%, as determined by HPLC and PAGE analysis (Figure 8). The ESA calculated for the HPLC purified [^{90}Y]**9**, was approximately six times lower than the 4 GBq/μmol found for [^{90}Y]**11**. HPLC analysis showed

a ratio of both isomers of [^{90}Y]**9** of 1:5 (TSAP/SAP) after HPLC separation (Supporting Information Figure S1C).

CONCLUSIONS

The purpose of the present work was to investigate the applicability of two new [^{90}Y]-DOTA-based maleimide reagents, the *N*-aryl maleimide [^{90}Y]**3** and *N*-alkyl maleimide [^{90}Y]**4**, for the prelabeling approach. On this account, we were able to radiolabel GSH and a 12mer L-RNA as model substances using these new prelabeling agents. Both maleimide reagents showed a high potential for that purpose. However, concerning high RCYs, the direct labeling of DOTA−L-RNA with [^{90}Y]YCl_3 proved to be more efficient than the prelabeling of the thiol-modified 12mer L-RNA derivative with [^{90}Y]**4** at low activity levels. With regard to ^{90}Y-labelings of thermally sensitive molecules, such as biopharmaceuticals, prelabeling could have more advantages than the direct radiolabeling, due to the milder labeling conditions. To enhance both RCY of the prelabeling approach and ESA of the corresponding ^{90}Y-labeled molecules, further optimizations of the SPE-separation process of both maleimide reagents [^{90}Y]**3** and [^{90}Y]**4** seem to be necessary.

ACKNOWLEDGMENT

This work was supported by the EU-FP6 integrated project BioCare contract no. 505785.

Supporting Information Available: HPLC chromatograms, gel electrophoresism, and autoradiography data of the ^{90}Y-labeled L-RNAs [^{90}Y]**9** and [^{90}Y]**11**. This material is available free of charge via the Internet at http://pubs.acs.org.

LITERATURE CITED

(1) Cremonesi, M., Ferrari, M., Bodei, L., Tosi, G., and Paganelli, G. (2006) Dosimetry in peptide radionuclide receptor therapy: a review. *J. Nucl. Med. 47*, 1467–1475.

(2) Rosch, F. (2007) Radiolanthanides in endoradiotherapy: an overview. *Radiochim. Acta 95*, 303–311.

(3) Harrison, A., Walker, C. A., Parker, D., Jankowski, K. J., Cox, J. P., Craig, A. S., Sansom, J. M., Beeley, N. R., Boyce, R. A., Chaplin, L., et al. (1991) The in vivo release of 90Y from cyclic and acyclic ligand-antibody conjugates. *Int. J. Rad. Appl. Instrum. B 18*, 469–476.

(4) Breeman, W. A., de Jong, M., Visser, T. J., Erion, J. L., and Krenning, E. P. (2003) Optimising conditions for radiolabelling of DOTA-peptides with ^{90}Y, ^{111}In, and ^{177}Lu at high specific activities. *Eur. J. Nucl. Med. Mol. Imaging 30*, 917–920.

(5) Lewis, M. R., Raubitschek, A., and Shively, J. E. (1994) A facile, water-soluble method for modification of proteins with DOTA. Use of elevated temperature and optimized pH to achieve high specific activity and high chelate stability in radiolabeled immunoconjugates. *Bioconjugate Chem. 5*, 565–576.

(6) Kukis, D. L., DeNardo, S. J., DeNardo, G. L., O'Donnell, R. T., and Meares, C. F. (1998) Optimized conditions for chelation of yttrium-90-DOTA immunoconjugates. *J. Nucl. Med. 39*, 2105–2110.

(7) Deshpande, S. V., DeNardo, S. J., Kukis, D. L., Moi, M. K., McCall, M. J., DeNardo, G. L., and Meares, C. F. (1990) Yttrium-90-labeled monoclonal antibody for therapy: labeling by a new macrocyclic bifunctional chelating agent. *J. Nucl. Med. 31*, 473–479.

(8) Schlom, J., Siler, K., Milenic, D. E., Eggensperger, D., Colcher, D., Miller, L. S., Houchens, D., Cheng, R., Kaplan, D., and Goeckeler, W. (1991) Monoclonal antibody-based therapy of a human tumor xenograft with a ^{177}lutetium-labeled immunoconjugate. *Cancer Res. 51*, 2889–2896.

(9) McDevitt, M. R., Ma, D., Simon, J., Frank, R. K., and Scheinberg, D. A. (2002) Design and synthesis of ^{225}Ac radioimmunopharmaceuticals. *Appl. Radiat. Isot. 57*, 841–847.

(10) DeNardo, S. J., Zhong, G. R., Salako, Q., Li, M., DeNardo, G. L., and Meares, C. F. (1995) Pharmacokinetics of chimeric L6 conjugated to indium-111- and yttrium-90-DOTA-peptide in tumor-bearing mice. *J. Nucl. Med. 36*, 829–836.

(11) Li, M., Meares, C. F., Salako, Q., Kukis, D. L., Zhong, G. R., Miers, L., and DeNardo, S. J. (1995) Prelabeling of chimeric monoclonal antibody L6 with ^{90}yttrium- and ^{111}indium-1,4,7,10-tetraazacyclododecane-N, N', N", N‴-tetraacetic acid (DOTA) chelates for radioimmunodiagnosis and therapy. *Cancer Res. 55*, 5726s–5728s.

(12) Hermanson, G. T. (2008) Bioconjugate chemistry: The chemistry of reactive groups, *Bioconjugate Techniques*, pp 183−184, Chapter 2, Academic Press, San Diego.

(13) Schlesinger, J., Koezle, I., Bergmann, R., Tamburini, S., Bolzati, C., Tisato, F., Noll, B., Klussmann, S., Vonhoff, S., Wuest, F., Pietzsch, H. J., and Steinbach, J. (2008) An ^{86}Y-labeled mirror-image oligonucleotide: Influence of Y-DOTA isomers on the biodistribution in rats. *Bioconjugate Chem. 19*, 928–939.

(14) Bos, E. S., Kuijpers, W. H., Meesters-Winters, M., Pham, D. T., de Haan, A. S., van Doornmalen, A. M., Kaspersen, F. M., van Boeckel, C. A., and Gougeon-Bertrand, F. (1994) In vitro evaluation of DNA-DNA hybridization as a two-step approach in radioimmunotherapy of cancer. *Cancer Res. 54*, 3479–3486.

(15) Liu, G., Dou, S., Pretorius, P. H., Liu, X., Rusckowski, M., and Hnatowich, D. J. (2008) Pretargeting CWR22 prostate tumor in mice with MORF-B72.3 antibody and radiolabeled cMORF. *Eur. J. Nucl. Med. Mol. Imaging 35*, 272–280.

(16) Schlesinger, J., Bergmann, R., Klussmann, S., and Wuest, F. (2006) Synthesis and radiopharmacological characterisation of ^{86}Y- and ^{68}Ga-labelled L-RNA oligonucleotides as molecular probes for positron emission tomography (PET). *Lett. Drug Des. Discovery 3*, 330–335.

(17) Ragas, J. A., Simmons, T. A., and Limbach, P. A. (2000) A comparative study on methods of optimal sample preparation for the analysis of oligonucleotides by matrix-assisted laser desorption/ionization mass spectrometry. *Analyst 125*, 575–581.

(18) de Bruin, B., Kuhnast, B., Hinnen, F., Yaouancq, L., Amessou, M., Johannes, L., Samson, A., Boisgard, R., Tavitian, B., and Dolle, F. (2005) 1-[3-(2-[^{18}F]fluoropyridin-3-yloxy)propyl]pyrrole-2,5-dione: design, synthesis, and radiosynthesis of a new [^{18}F]fluoropyridine-based maleimide reagent for the labeling of peptides and proteins. *Bioconjugate Chem. 16*, 406–420.

(19) Lewis, M. R., and Shively, J. E. (1998) Maleimidocysteineamido-DOTA derivatives: new reagents for radiometal chelate conjugation to antibody sulfhydryl groups undergo pH-dependent cleavage reactions. *Bioconjugate Chem. 9*, 72–86.

(20) Kitagawa, T., Shimozono, T., Aikawa, T., Yoshida, T., and Nishimura, H. (1981) Preparation and characterization of heterobifunctional cross-linking reagents for protein modifications. *Chem. Pharm. Bull. 29*, 1130–1135.

(21) Berndt, M., Pietzsch, J., and Wuest, F. (2007) Labeling of low-density lipoproteins using the ^{18}F-labeled thiol-reactive N-[6-(4-[^{18}F]fluorobenzylidene)aminooxyhexyl]maleimide. *Nucl. Med. Biol. 34*, 5–15.

BC900095K

SUPPORTING INFORMATION

Radiosynthesis of new [^{90}Y]-DOTA-Based Maleimide Reagents suitable for the Prelabeling of thiol-bearing L-Oligonucleotides and Peptides

Joern Schlesinger,[†] Cindy Fischer,[†] Inge Koezle,[†] Stefan Vonhoff,[‡] Sven Klussmann,[‡] Ralf Bergmann,[†] Hans-Jurgen Pietzsch,*[,†] and Joerg Steinbach[†]

[†]Institute of Radiopharmacy, Forschungszentrum Dresden-Rossendorf, Germany

[‡]NOXXON Pharma AG, Berlin, Germany

---

*Author to whom correspondence should be adressed:

H.-J. Pietzsch, Institute of Radiopharmacy, Forschungszentrum Dresden-Rossendorf,

PF 51 01 19, 01314 Dresden, Germany. (h.j.pietzsch@fzd.de).

HPLC Analyses

*HPLC Analysis of the ^{90}Y-labeled L-RNA [^{90}Y]**9**.*

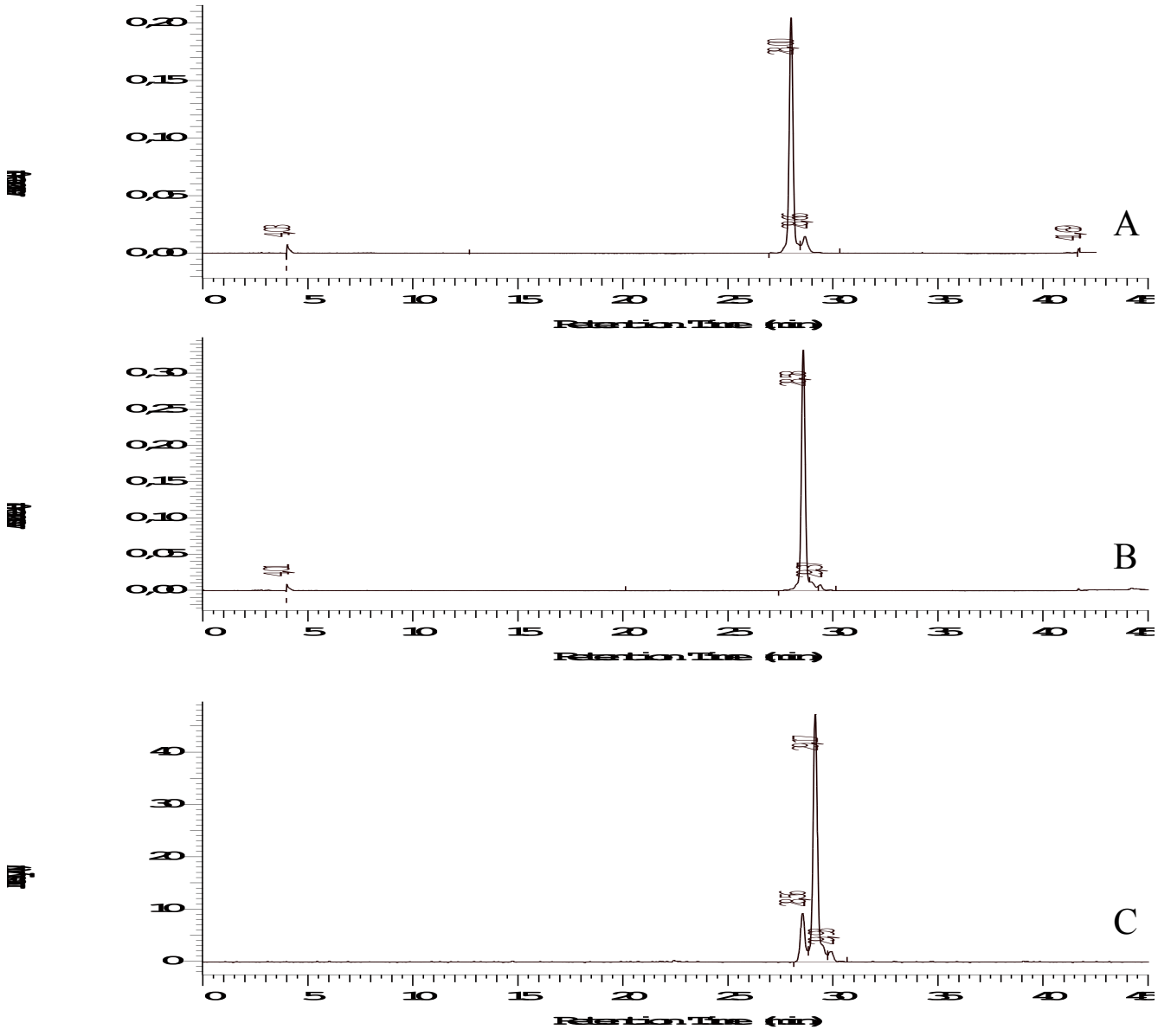

Figure S1. HPLC profiles of the L-RNA Y**9** and ^{90}Y-labeled L-RNA [^{90}Y]**9**. A: UV-profile of Y**9** (TSAP isomer, R_T 28.0 min), B: UV-profile of Y**9** (SAP isomer, R_T 28.6 min) as references. C: Analysis of the HPLC purified [^{90}Y]**9** gave a ratio of 1:5 of the TSAP isomers (R_T 28.6 min) and SAP isomer (R_T 29.2 min) in the radiometric profile.

*HPLC Analysis of the ^{90}Y-labeled L-RNA [^{90}Y]**11**.*

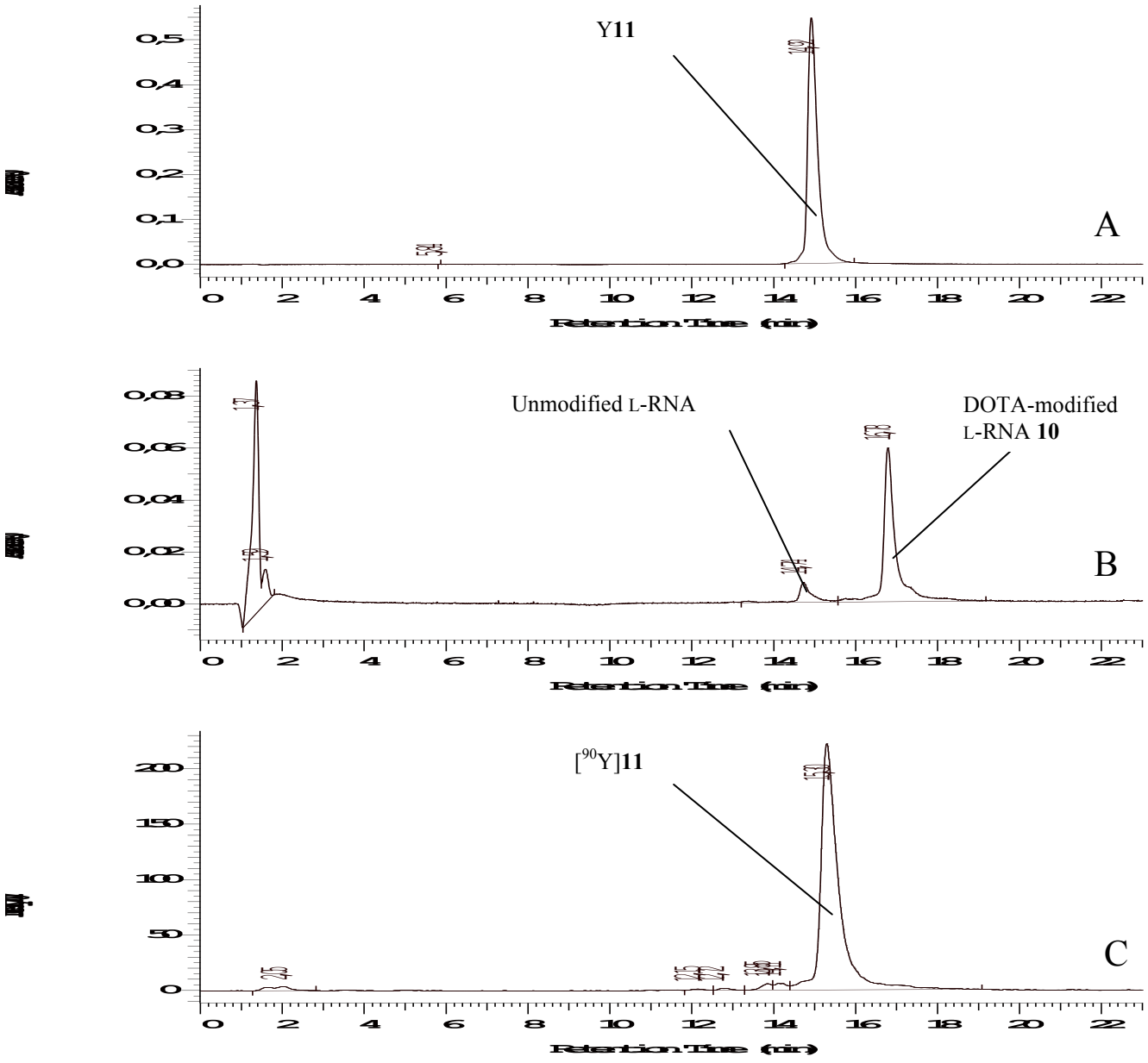

Figure S2. HPLC analysis of the ^{90}Y-labeled L-RNA [^{90}Y]**11**. A: UV-profile of Y-DOTA-L-RNA Y**11** as reference. B: UV-profile and C: radiometric profile of the crude reaction mixture of [^{90}Y]**11** (0.5 nmol batch).

Gel Electrophoresis and Autoradiography.

*PAGE Analysis of the ^{90}Y-labeled L-RNA [^{90}Y]**9**.*

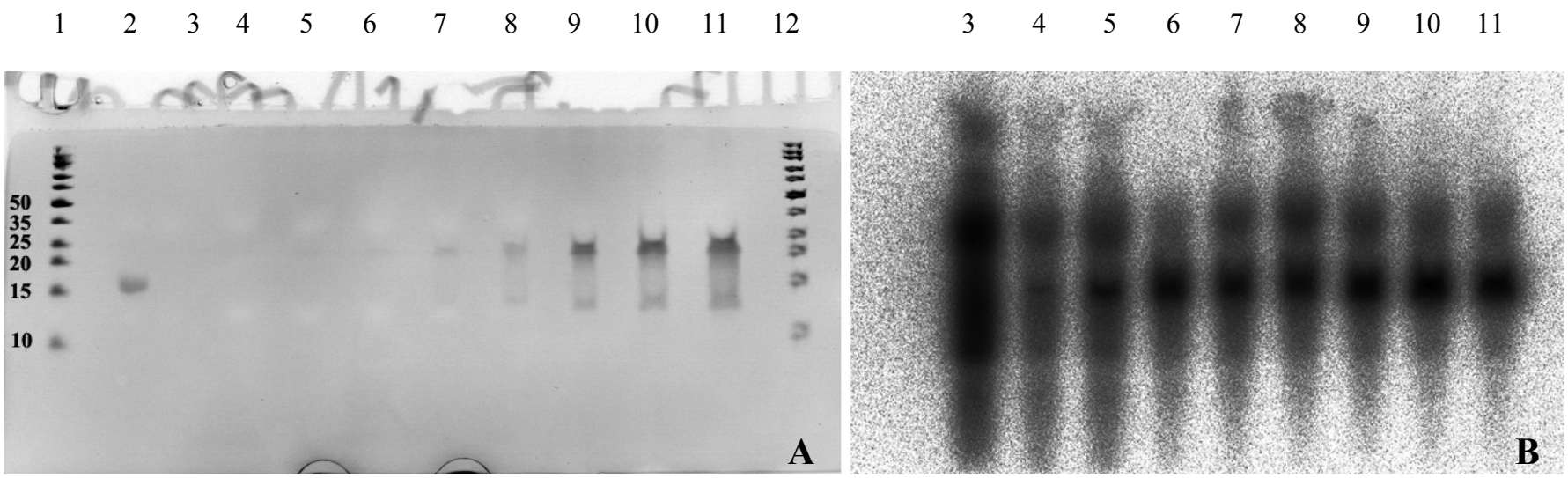

Figure S3. PAGE analysis of the formation of [^{90}Y]**9** after two hours as a function of the amount of L-RNA **8** (native 20% polyacrylamide gel). A: UV-image of the gel (negative image) after staining with ethidium bromide. B: Autoradiogram of the gel. Applied reaction aliquots in the lanes with the specification of the amount of L-RNA **8** in the batches (from right): (1, 12) molecular weight marker (10 bp); (2) Y**9** as reference; (3) [^{90}Y]**4** as reference; (4) 0.1 nmol; (5) 0.5 nmol; (6) 2 nmol; (7) 5 nmol; (8) 10 nmol; (9) 25 nmol; (10) 50 nmol; (11) 100 nmol.

*Estimation of Retention Factor Values of [^{90}Y]**4** and the ^{90}Y-labeled L-RNA [^{90}Y]**9**.*

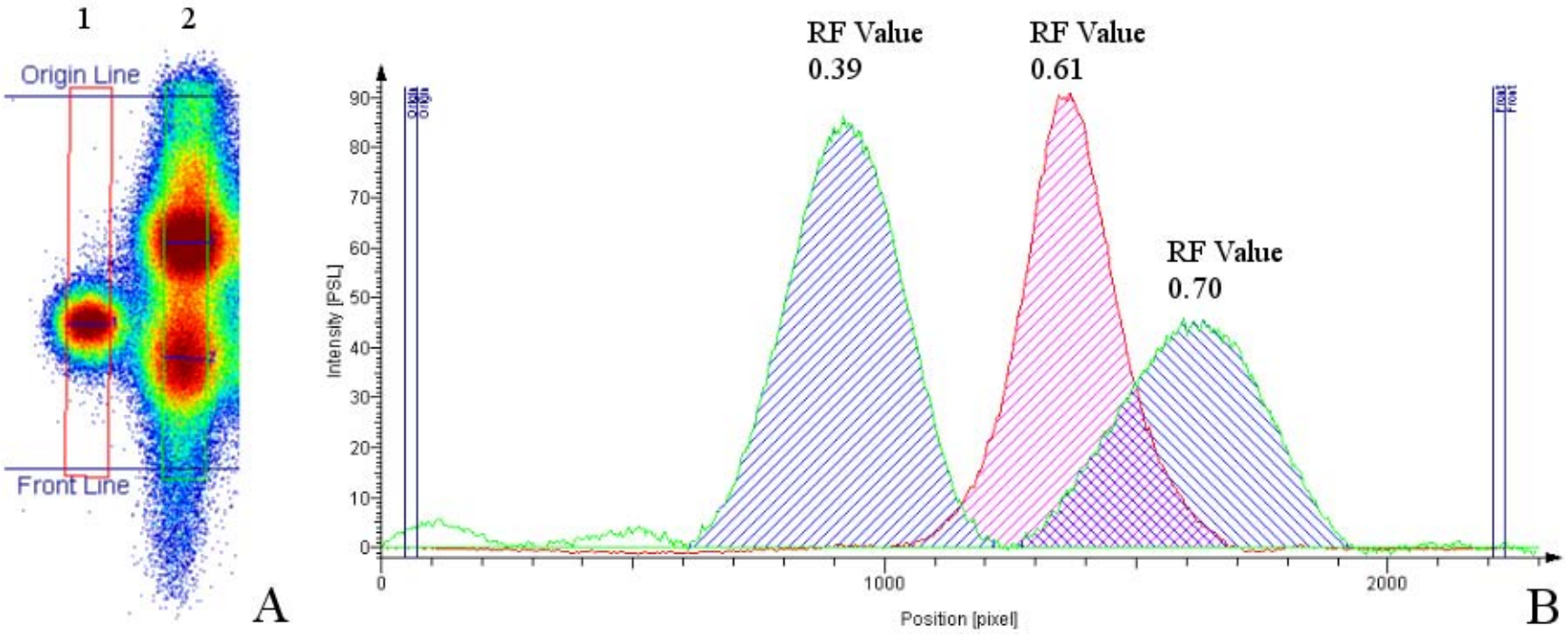

Figure S4. A: Evaluation of an autoradiogram of an exposed 20% polyacrylamide gel. Applied samples in the lanes: (1) HPLC purified [^{90}Y]**9**; (2) [^{90}Y]**4**. B: Overlay of the corresponding profiles of [^{90}Y]**9** (red profile) and [^{90}Y]**4** (blue profile).

*PAGE Analysis of the ^{90}Y-labeled L-RNA [^{90}Y]**11**.*

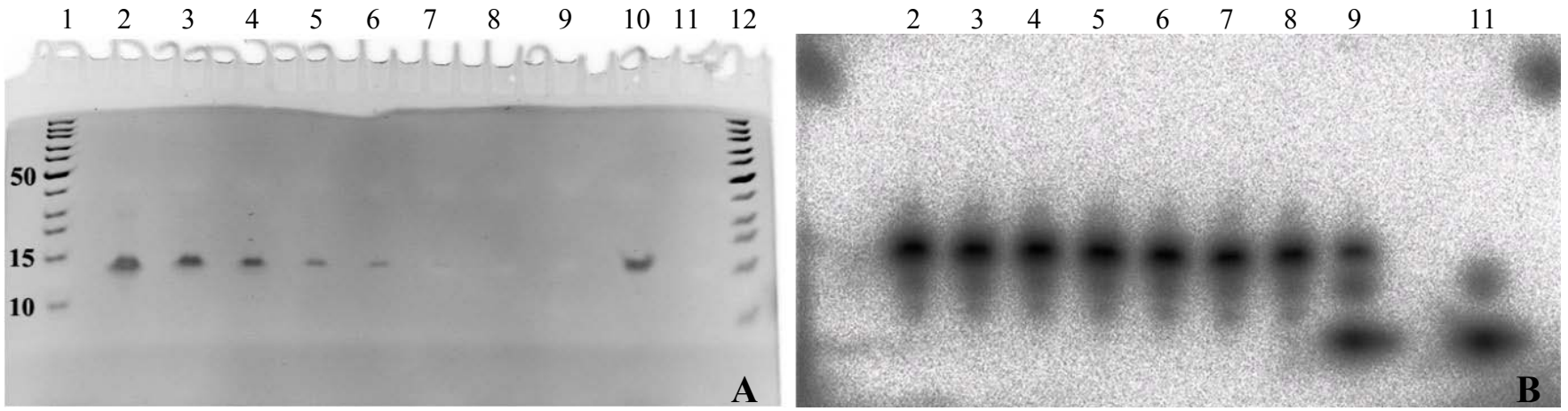

Figure S5. PAGE analysis of the formation of [^{90}Y]**11** after two hours as a function of the amount of L-RNA **10** (native 20% polyacrylamide gel). A: UV-image of the gel (negative image) after staining with ethidium bromide. B: Autoradiogram of the gel. Applied reaction aliquots in the lanes with the specification of the amount of **10** in the batches (from right): (1, 12) molecular weight marker (10 bp); (2) 100 nmol; (3) 50 nmol; (4) 25 nmol; (5) 10 nmol; (6) 5 nmol; (7) 2 nmol; (8) 0.5 nmol; (9) 0.1 nmol; (10) Y**11** as reference; (11) [^{90}Y]Y-DTPA as reference.

Photoinitiated Coupling of Unmodified Monosaccharides to Iron Oxide Nanoparticles for Sensing Proteins and Bacteria

Li-Hong Liu,[†] Hervé Dietsch,[‡] Peter Schurtenberger,[‡] and Mingdi Yan*[,†]

Department of Chemistry, Portland State University, P.O. Box 751, Portland, Oregon 97207-0751, and Adolphe Merkle Institute and Fribourg Center for Nanomaterials, University of Fribourg, Route de l'ancienne Papeterie CP 209, CH-1723 Marly 1, Switzerland. Received March 12, 2009; Revised Manuscript Received May 13, 2009

We report a versatile approach for the immobilization of unmodified monosaccharides onto iron oxide nanoparticles. Covalent coupling of the carbohydrate onto iron oxide nanoparticle surfaces was accomplished by the CH insertion reaction of photochemically activated phosphate-functionalized perfluorophenylazides (PFPAs), and the resulting glyconanoparticles were characterized by IR, TGA, and TEM. The surface-bound D-mannose showed the recognition ability toward *Concanavalin A* and *Escherichia coli* strain ORN178 that possesses mannose-specific receptor sites. Owing to the simplicity and versatility of the technique, together with the magnetic property of iron oxide nanoparticles, the methodology developed in this study serves as a general approach for the preparation of magnetic glyconanoparticles to be used in clinical diagnosis, sensing, and decontamination.

INTRODUCTION

Naturally occurring carbohydrates and glycoconjugates (glycoproteins, glycolipids) present at the surface of nearly every cell in the living system are known to play crucial roles in biological events as recognition sites between cells and factors. They can trigger various phenomena such as cell growth, inflammatory responses, or viral infections. Surface-exposed carbohydrate moieties that are characteristic of a given microbe may serve as key biomarkers for pathogen and toxin identification, diagnosis, and vaccine development. Carbohydrates as a detection platform have recently emerged and have demonstrated tremendous potential to achieve superior sensitivity and selectivity (*1*−*4*). Compared to antibodies used in immunoassays that are often fragile and unstable, carbohydrates are stable entities. Carbohydrate-based assays have the potential to be an alternative benchmark detection technology for a wide range of biomolecules including proteins, bacteria, pathogens, and toxins (*5*).

A key technology requirement in receptor/ligand-based sensing and detection is the surface conjugation chemistry leading to efficient and effective coupling of ligands to solid substrates (*6*). The performance of the device, the detection sensitivity, and the dynamic range are largely governed by the ligand to be immobilized, the nature of the coupling chemistry, the ligand density, and the presentation. There is a great demand for effective conjugation chemistry that is general, versatile, and can accommodate ligand diversity and give stable interfaces, yet is simple and reproducible. Reported strategies for the covalent immobilization of carbohydrates on surfaces mostly rely on conventional coupling chemistry, such as amines with ester (*7, 8*) thiols with maleimides (*9, 10*), and azide with alkynes (*11, 12*), which requires sometimes laborious synthesis of carbohydrates having a specific functional group or tether. Coupling chemistry that does not require chemical derivatization of carbohydrates is appealing. There are a few methods reported in literature. One approach uses hydrazide-modified gold substrates, where the hydrazide reacts with the terminal aldehyde group of the carbohydrates (*13, 14*). A similar approach employs amine-functionalized surfaces, and the coupling with carbohydrates takes place by reductive amination to yield an amine conjugate (*15, 16*). In both cases, reducing sugars are necessary, and for monosaccharides, the coupled products often become acyclic and lose their binding affinity. Photochemically initiated immobilization and patterning of biological molecules has been explored (*17*), although few reports have focused on carbohydrates (*18, 19*).

We have developed a photochemically initiated coupling chemistry that employs functionalized perfluorophenyl azides (PFPAs) to attach molecules and materials to solid substrate surfaces (*20*−*22*). Upon light activation, the azide moiety converts to a highly reactive nitrene that, notably, inserts into CH and NH bonds, creating highly robust covalent linkages. We have successfully employed PFPAs in surface modification, targeting polymeric materials that lack reactive functional groups for surface coupling (*23, 24*). Carbohydrates, being complex in structure and challenging to chemically derivatize, are another class of compounds that are well-suited for the PFPA photocoupling chemistry. The design of our approach is to prepare PFPA-functionalized iron oxide nanoparticles that can be subsequently used to covalently couple, in principle, any carbohydrate structures by way of the insertion reactions of photochemically activated nitrene species.

Iron oxide nanoparticles are attractive due to their inherent magnetic properties that make them useful for magnetic resonance imaging, magnetic field-assisted transport, as well as sensing and separation (*25*−*27*). In addition, iron oxide nanoparticles are nonporous, which avoid delay due to diffusion, and thus the equilibrium is reached rapidly and fast response can be achieved. A number of methods have been reported for functionalizing iron oxide nanoparticles with organic compounds (*28, 29*) such as silanes (*30, 31*) and phosphoric acids (*32*−*38*). Silanes form robust siloxane bonds with surface −OH groups; the drawback is the self-condensation reaction leading to multilayer formation or deposition of aggregates on the substrate surface. Phosphates, on the other hand, do not undergo self-condensation reactions. These agents couple with surface −OH groups creating the stable Fe−O−P structure (*28, 32*).

* To whom correspondence should be addressed. Phone: 503-725-5756, E-mail: yanm@pdx.edu.

[†] Portland State University.

[‡] University of Fribourg.

10.1021/bc900110x CCC: $40.75 © 2009 American Chemical Society
Published on Web 06/17/2009

Here, we report the synthesis of phosphate-functionalized PFPAs and their uses for the covalent immobilization of monosaccharides on iron oxide nanoparticles. The recognition ability of the surface-bound ligands are tested using *Concanavalin A* (*Con A*), an oligomannose-binding lectin, and *Escherichia coli* (*E. coli*) strain ORN178 that possesses mannose-specific receptor sites (*39*). *Con A* and *E. coli* also serve as the model systems allowing us to test the ability of these carbohydrate-functionalized iron oxide nanoparticles for sensing and detecting proteins and bacteria.

EXPERIMENTAL SECTION

Materials and Instrumentation. Chemicals and solvents were purchased from TCI, Sigma-Aldrich, ACROS, or Fisher Scientific. Methylene chloride was distilled from calcium hydride. Triethylamine was distilled before use. All other solvents and commercial grade reagents were used without further purification. Milli-Q water having a resistivity of 18.2 $mW \cdot cm^{-1}$ was used for the synthesis of spindle-type hematite particles. ^1H NMR and ^{13}C NMR spectra were recorded in $CDCl_3$ on a Bruker AMX-400 MHz spectrometer. Chemical shifts were reported in parts per million (ppm) relative to TMS and referenced to the residual solvent. Elemental analysis was performed by Quantitative Technologies Inc. (Whitehouse, NJ). Infrared spectra were obtained on a Perkin-Elmer 2000 series FT-IR spectrometer. TEM images were obtained on a JEOL 100C transmission electron microscope. Photolysis was carried out at the ambient temperature with a 450 W medium pressure Hg lamp (Hanovia). The lamp reached its full power after a 2 min warmup to an intensity of 5.0 mW/cm^2, as measured by a model UVX radiometer and UVX-36 sensor (Upland, CA). A 280 nm optical filter was used during irradiation. Thermogravimetric analysis (TGA) was performed on a Perkin-Elmer TGA7 Analyzer. Samples were combusted in nitrogen flow at a heating rate of 10 °C/min from 50 to 900 °C.

2-(2′-(2″-(4-Azidoethoxy)ethoxy)ethanol (3). 2-(2′-(2″-Chloroethoxy)ethoxy)ethanol (0.5 g, 2.97 mmol), NaI (0.09 g, 0.6 mmol), and NaN_3 (2.0 g, 30 mmol) were dissolved in water (10 mL), and the solution was stirred at 50 °C for 48 h. The reaction mixture was then filtered, and the aqueous phase was extracted with ethyl acetate (4 × 10 mL). The organic extracts were collected and evaporated to give **3** as a light yellow liquid (0.4 g, 77%). ^1H NMR (400 MHz, $CDCl_3$, δ): 3.72 (t, 2H, J = 5.0 Hz), 3.68 (m, 6H), 3.60 (t, 2H, J = 5.0 Hz), 3.40 (t, 2H, J = 5.0 Hz), 3.19 (br, 1H). ^{13}C NMR (100 MHz, $CDCl_3$, δ): 72.63, 70.59, 70.34, 69.98, 61.56, 50.61.

2-(2′-(2″-Aminoethoxy)ethoxy)ethanol (4). 2-(2′-(2″-(4-Azidoethoxy)ethoxy)ethanol (**3**) (400 mg, 2.4 mmol) was dissolved in dry THF (10 mL), and the solution was cooled to 0 °C. Triphenyl phosphine (600 mg, 2.4 mmol) was added, and the reaction mixture was stirred at room temperature for 10 h. Water (0.12 mL, 6.7 mmol) was added, and the mixture was stirred for another 5 h. The reaction mixture was diluted with water and washed with toluene (3 × 10 mL). The aqueous layers were collected and evaporated to give **4** as a colorless liquid (240 mg, 70% crude). This compound was used directly in the next step without further purification.

4-Azido-2,3,5,6-tetrafluoro-*N*-(2-(2′-(2″-hydroxyethoxy)-ethoxy)ethyl)benzamide (5). Dry CH_2Cl_2 (10 mL) was added to a mixture of *N*-succinimidyl 4-azidotetrafluorobenzoate (*40*) (400 mg, 1.2 mmol) and 2-(2′-(2″-aminoethoxy)ethoxy)ethanol (**4**) (180 mg, 1.2 mmol) via syringe, and the mixture was purged with argon for 30 min and stirred at room temperature for 6 h. Water (10 mL) was added, and the mixture was extracted by $CHCl_3$ (3 × 10 mL). The organic layers were combined, dried over anhydrous Na_2SO_4, and evaporated in vacuo. The residual was purified by column chromatography (10/4/0.5, ethylacetate/hexanes/methanol) to give **5** as a white waxy solid (180 mg, 41%).^1H NMR (400 MHz, $CDCl_3$, δ): 7.04 (1H), 3.65 (m, 10H), 3.55 (t, 2H, J = 5.0 Hz), 2.69 (br, 1H). ^{13}C NMR (100 MHz, $CDCl_3$, δ): 157.93, 145.28, 142.78, 141.74, 139.08, 121.60, 111.85, 72.47, 70.28, 70.23, 69.47, 61.51, 39.99. Anal. Calcd. for $C_{13}H_{14}F_4N_4O_4$: C 42.63; H 3.85; N 15.30. Found: C 42.43; H 3.87; N 15.27.

2-(2′-(2″-(4-Azido-2,3,5,6-tetrafluorobenzamido)ethoxy)-ethoxy)ethyl Dihydrogen Phosphate (1). 4-Azido-2,3,5,6-tetrafluoro-*N*-(2-(2′-(2″-hydroxyethoxy)ethoxy)ethyl) benzamide (**5**) (180 mg, 0.49 mol) was dissolved in dry CH_2Cl_2, and the solution was purged with argon. Anhydrous triethylamine (0.1 mL, 0.7 mmol) was added, and the mixture was cooled to 0 °C with an ice bath before $POCl_3$ (0.06 mL, 0.7 mmol) was added dropwise. The reaction mixture was allowed to warm to room temperature and stirred for another 6 h. Water (10 mL) was added, and the mixture was stirred for 1 h. The reaction mixture was extracted with $CHCl_3$ (3 × 10 mL). The organic layers were collected, dried over anhydrous Na_2SO_4, and evaporated to give **1** as a light yellow, highly viscous clear liquid (120 mg, 55%). ^1H NMR (400 MHz, $CDCl_3$, δ): 6.94 (br, 1H), 4.44 (m, 2H), 3.80 (m, 2H), 3.67 (m, 8H). ^{13}C NMR (100 MHz, $CDCl_3$, δ): 157.94, 145.30, 142.80, 141.76, 139.09, 121.63, 111.82, 71.03, 70.77, 70.32, 69.43, 68.97, 40.01. Anal. Calcd. for $C_{13}H_{15}F_4N_4O_7P$: C 34.99; H 3.39; N 12.56. Found: C 34.72; H 3.18; N 12.23.

4-Azido-2,3,5,6-tetrafluoro-*N*-(8-hydroxyoctyl)benzamide (6). *N*-Succinimidyl 4-azidotetrafluoro benzoate (200 mg, 0.6 mmol) and 8-aminooctan-1-ol (90 mg, 0.6 mmol) were added to dry CH_2Cl_2 (10 mL), and the solution was purged with argon for 30 min and stirred at room temperature for 6 h. Water (10 mL) was then added, and the mixture was extracted with $CHCl_3$ (3 × 10 mL). The organic layers were combined, dried over anhydrous Na_2SO_4, and evaporated in vacuo. The residual was purified by column chromatography (10/4/0.5, ethylacetate/hexanes/methanol) to give **6** as a white power (110 mg, 50%). ^1H NMR (400 MHz, $CDCl_3$, δ): 5.96 (s, 1H), 3.64 (t, 2H, J = 7.0 Hz), 3.45 (q, 2H, J = 7.0 Hz), 1.59 (m, 4H), 1.35 (m, 8H). ^{13}C NMR (100 MHz, $CDCl_3$, δ): 157.59, 145.34, 142.79, 141.63, 139.15, 121.82, 111.61, 62.99, 40.33, 32.70, 29.27, 29.23, 29.10, 26.65, 25.61. Anal. Calcd. for $C_{15}H_{18}F_4N_4O_2$: C 49.72; H 5.01; N 15.46. Found: C 49.63; H 5.18; N 15.47.

8-(4-Azido-2,3,5,6-tetrafluorobenzamido)octyl Dihydrogen Phosphate (2). 4-Azido-2,3,5,6- tetrafluoro-*N*-(8-hydroxyoctyl)benzamide (**6**) (250 mg, 0.69 mmol) was dissolved in dry THF (10 mL), and the solution was purged with argon. Anhydrous triethylamine (0.13 mL, 0.9 mmol) was added, and the mixture was cooled to 0 °C with an ice bath before $POCl_3$ (0.08 mL, 0.9 mmol) was added dropwise. The reaction mixture was allowed to warm to room temperature and stirred for another 6 h. Water (10 mL) was added, and the mixture was stirred for another 1 h. The reaction mixture was extracted with $CHCl_3$ (3 × 10 mL). The organic layers were collected, dried over anhydrous Na_2SO_4, and was evaporated to give **2** as a light amber viscous liquid (140 mg, 45%). ^1H NMR (400 MHz, $CDCl_3$, δ): 7.01 (s, 1H), 4.33 (m, 2H), 3.39 (q, 2H, J = 7.0 Hz), 1.81 (m, 2H), 1.59 (t, 2H, J = 7.0 Hz), 1.36 (m, 8H). ^{13}C NMR (100 MHz, $CDCl_3$, δ): 158.05, 145.13, 142.63, 141.69, 139.04, 121.61, 111.73, 72.57, 40.31, 29.42, 29.04, 28.91, 28.76, 26.54, 25.11.

Preparation of Spindle-Type Hematite α-Fe_2O_3. The nanoparticles were synthesized following a slightly modified literature procedure (*41*). In a typical reaction, $Fe(ClO_4)_3 \cdot 6H_2O$ (11.56 g), NaH_2PO_4 (162 mg), and urea (1.50 g) are solubilized into 250 mL of Milli-Q water at room temperature. The obtained solution was sonicated for 2 h, transferred to a preheated oven at 100 °C for 24 h, and then cooled down to room temperature.

Scheme 1. Functionalization of Hematite Nanoparticles with 1 Followed by Coupling of D-Mannose and Subsequent Binding with *Con A*

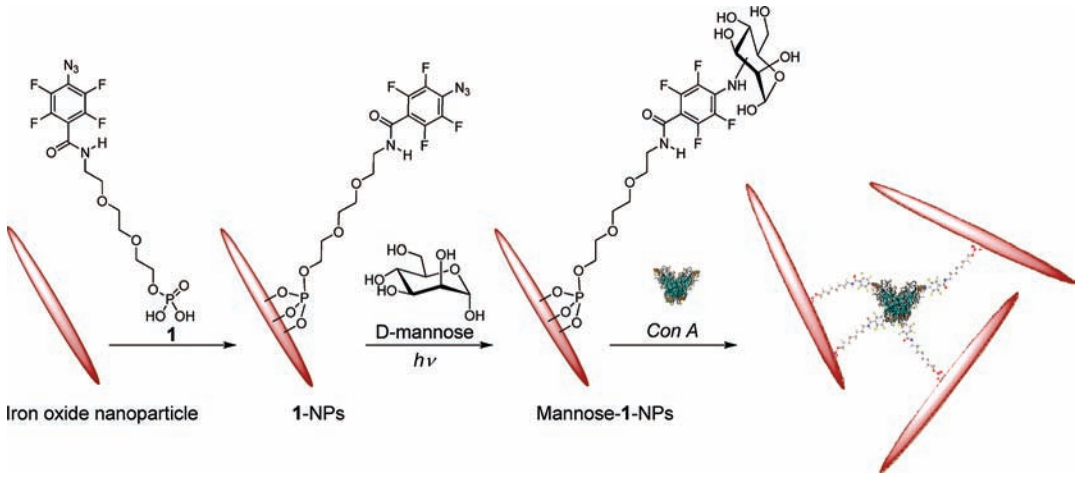

After settling, half of the supernatant was removed and the rest of the mixture was centrifuged. The solid was cleaned 5 times at 10 000 rpm for 20 min each with Milli-Q water. The obtained brick red hematite nanoparticles were stored in Milli-Q water.

Preparation of Magnetite Fe_3O_4 Nanoparticles. Magnetite Fe_3O_4 nanoparticles were prepared by the coprecipitation method (*4*, *42*). The Fe^{3+} solution (1 M) was prepared by dissolving ferric chloride hexahydrate ($FeCl_3 \cdot 6H_2O$) in 2 M HCl, and the Fe^{2+} solution (1 M) was prepared by dissolving ferrous sulfate heptahydrate ($FeSO_4 \cdot 7H_2O$) in 2 M HCl. The two solutions, 100 mL of Fe^{3+} and 50 mL of Fe^{2+}, were mixed in a degassed flask. NH_4OH (30%) was added dropwise until the solution pH reached 11. The mixture was stirred vigorously for 30 min at room temperature. The resulting black precipitates were isolated by applying a permanent external magnet and washed 3 times with Milli-Q water. The mixture was then centrifuged, and the solid washed copiously with ethanol to give magnetite Fe_3O_4 nanoparticles.

Preparation of PFPA-Functionalized Iron Oxide Nanoparticles. Hematite (α-Fe_2O_3) and supraparamagnetic (Fe_3O_4) nanoparticles were functionalized with PFPA using the following procedure (*33*). PFPA **1** or **2** and nanoparticles (1:1 w/w, 50 mg each) were mixed in $CHCl_3$ (15 mL), and the mixture was sonicated for 30 min until the particles were well-dispersed. Excess **1** or **2** was removed by copiously washing the nanoparticles with ethanol and centrifuging. Functionalized hematite nanoparticles were labeled as **1**-NP and **2**-NP, respectively, and functionalized Fe_3O_4 nanoparticles were labeled as **1**-Fe_3O_4-NPs.

Coupling Carbohydrates to PFPA-Functionalized Nanoparticles. PFPA-functionalized nanoparticles (5 mg) and the carbohydrate solution (50 μL, 1 mg/mL) were added to water/ethanol (1.5 mL), and UV irradiated for 30 min with a medium pressure Hg lamp with a 280 nm long-path optical filter. The irradiation time of 30 min was determined by FTIR when the azide antisymmetric stretch at 2126 cm^{-1} completely disappeared. The resulting nanoparticles were washed 5 times with water and 3 times with ethanol, and stored in ethanol for further uses.

Binding of Con A to Carbohydrate-Functionalized Nanoparticles. Mannose-functionalized hematite nanoparticles (mannose-**1**-NPs) was incubated with a solution of pH 7.4 PBS buffer containing 0.1% Tween 20 and 3% BSA (w/v) for 30 min and washed with pH 7.4 PBS buffer containing 0.1% Tween 20 for 20 min. The nanoparticles (500 μg/mL) were then incubated with a solution of *Con A* (15 mg/mL) in pH 7.4 PBS containing 0.01% Tween 20 for 6 h at room temperature. The resulting nanopartilces were washed thoroughly with the buffer solution followed by five times with Milli-Q water.

Binding of Mannose-1-NPs to *E. coli* K-12 Strains ORN178 and ORN208. *E. coli* ORN178 and ORN208 were grown in the Luria-Bertain Broth medium at 37 °C to an optical density of 0.9 at 600 nm (approximately 10^9 cells per mL) and precipitated by centrifugation at 3000 rpm for 4 min (*43*). After centrifuging-suspending twice with pH 7.4 PBS buffer, the bacteria (500 μL) was mixed with 500 μL mannose-functionalized nanoparticles (500 μg/mL), and the mixture was gently shaken at room temperature for 1 h.

Transmission Electron Microscopy (TEM). Samples of *E. coli* ORN178 and ORN208 treated with mannose-**1**-NPs were placed onto a 200 mesh carbon-coated copper grids, and the suspension was allowed to settle for 1 min, and the excess liquid was removed by a filter paper. A drop of 1% phosphotungstic acid was used to negatively stain the samples for 1 min before they were examined by TEM.

RESULTS AND DISCUSSION

The design of our approach is to prepare PFPA-functionalized iron oxide nanoparticles which can then be used to covalently couple carbohydrates by way of the CH insertion reaction of photochemically activated PFPA (Scheme 1). Phosphate-functionalized PFPA photocoupling agents **1** and **2** were synthesized, where **1** contains ethylene oxide units which are polar and hydrophilic, whereas **2** has methylene units, which are nonpolar and hydrophobic. The ethylene oxide linkage has the additional property of being protein resistant; thus, it has been widely used to create biocompatible and antifouling surfaces (*44*, *45*). Compounds **1** and **2** are prepared following the synthetic sequence shown in Scheme 2.

Spindle-type hematite α-Fe_2O_3 nanoparticles were synthesized by precipitating iron(III) perchlorate in the presence of urea and sodium dihydrogen phosphate, following a modified method by Ocaña (*41*). We found that, by adjusting experimental parameters such as the type of iron salt, the concentration, and the ionic strength of the solution, the size, morphology, and surface functionality of hematite nanoparticles can be controlled (*46*). Nanoparticles of ~250 nm and ~40 nm in equatorial diameters along the *x* and *y* axes, and ~40 nm in the polar diameter along the *z* axis, were synthesized and used in the present study. These particles were functionalized with **1** or **2** following a slightly modified literature method (*33*). In the experiment, nanoparticles were sonicated in the solution of **1** or **2** in $CHCl_3$ for 30 min followed by copious washing to remove the excess coupling

Scheme 2. Synthesis of Photocoupling Agents 1 and 2

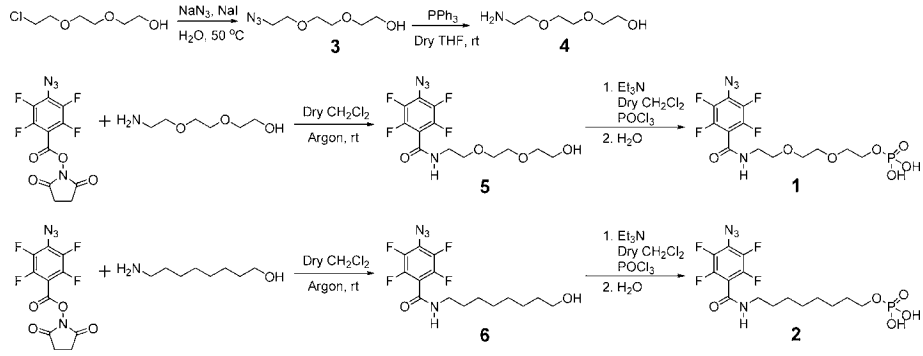

agent. The IR spectra of the resulting nanoparticles showed the azide ($-N_3$) antisymmetrical stretch at 2126 cm^{-1}, amide stretch at 1653 cm^{-1}, and P−O−C and P−O−Fe stretches from 1270 to 990 cm^{-1} (*47*), indicating that the nanoparticles have been successfully functionalized with the PFPA-phosphate coupling agent (Figure 1). Control studies were conducted with compounds **5** and **6** that are precursors of **1** and **2** and do not possess the phosphate group. The experiments were carried out following the same preparation procedure for **1**-NPs and **2**-NPs. The IR spectra of the resulting nanoparticles did not show the characeristic azide ($-N_3$) antisymmetrical stretch at 2126 cm^{-1} (Figure S3, Supporting Information), demonstrating that the phosphate group in **1** and **2** is responsible for the attachment of these coupling agents to the nanoparticles.

The successful surface functionalization of the nanoparticles was further supported by a solvent dispersion study. Nanoparticles functionalized with **1** or **2** (**1**-NPs, **2**-NPs) were mixed and sonicated in different solvents of water, ethanol, and acetonitrile. As shown in Figure 2, **1**-NPs dispersed well in water and ethanol but precipitated in acetonitrile. **2**-NPs, however, showed the opposite behavior; the particles precipitated in water and ethanol but dispersed well in acetonitrile. The ethylene oxide linkage in **1** is capable of forming hydrogen bonds with protic solvents of water and ethanol, thus improving the miscibility of the resulting nanoparticles in these media (*48*, *49*). Acetonitrile, lacking the hydrogen bonding ability, is more compatible with the hydrophobic alkyl linkage in **2**. Therefore, depending on the nature of the ligands to be attached, the corresponding coupling agent can be selected, for example, **1** for aqueous-soluble molecules and **2** for organic solvent-soluble compounds. For carbohydrates that are highly polar and water soluble, **1** was used as the coupling agent, and **1**-NPs were used throughout the study.

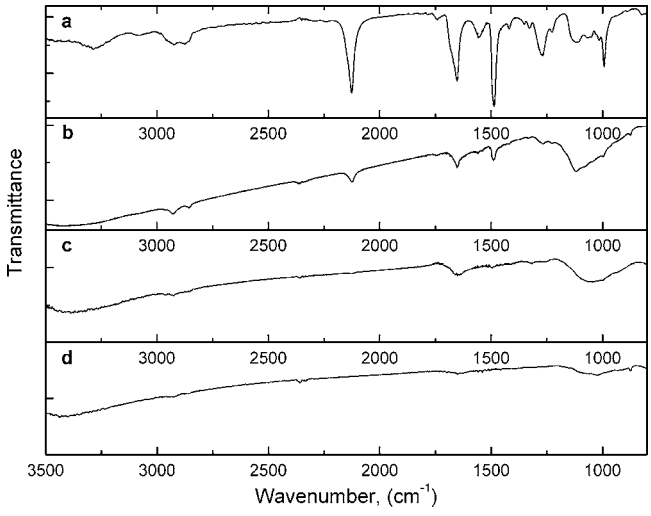

Figure 1. FTIR spectra of (a) PFPA-phosphate ligand **1**; (b) hematite nanoparticles functionalized with **1**; (c) nanoparticles coupled with D-mannose; (d) unfunctionalized hematite nanoparticles.

Subsequent coupling of carbohydrates to **1**-NPs were carried out using D-mannose. Monosaccharides are the smallest carbohydrate structures and the most challenging for this coupling chemistry. The probability of the CH insertion reaction increases as the size of the carbohydrate structure or the number of CH bonds increases. Additionally, monosaccharides are the lowest-affinity ligands, therefore lacking the multivalency effect that can occur in their oligosaccharide counterparts (*50*). Thus, if these monosaccharide ligands can be successfully coupled to NPs, and the resulting conjugated ligands retain their recognition abilities, the methodology developed can be readily applied to other large and more complicated carbohydrate structures. The coupling reaction was carried out by irradiating a mixture of **1**-NPs and the monosaccharide in water/ethanol for 30 min while stirring. The $-N_3$ absorption at 2126 cm^{-1} disappeared in the IR spectrum of the resulting nanoparticles (Figure 1c) indicating that the azide was activated. The surface property of the NPs changed after the monosaccharide coupling. While the as-prepared hematite NPs tend to agglomerate (Figure 3a), NPs coated with D-mannose were well-separated (Figure 3b). In addition, the D-mannose-coated NPs were readily dispersed in water to give a homogeneous dispersion.

The amount of carbohydrate ligands bound to the nanoparticles was determined by the thermogravimetric analysis (TGA). TGA measures the mass loss of the organic materials as they decompose upon heating. When TGA was conducted on **1**-NPs and mannose-**1**-NPs, the percentage mass changes relative to the weight of the hematite NPs were small and within the experimental error of the instrument. To overcome this problem, smaller iron oxide nanoparticles were prepared to increase the percentage of the organic mass relative to that of the nanoparticles. Spherical superparamagnetic Fe_3O_4 nanoparticles of ∼10 nm in diameter were synthesized by the coprecipatation method according to the literature procedure (*4*, *42*). The particles were functionalized with **1**, and the subsequent D-mannose coupling was carried out following the same protocol described above for the hematite NPs. Figure 4 shows the weight loss of each sample as a function of heating temperature. The unfunctionalized NPs showed a decrease in mass up to ∼400 °C, probably due to the presence of volatile residuals trapped inside the nanoparticles. Compared to the unfunctionalized NPs, nanoparticles functionalized with **1** showed a 3.3% weight loss at 600 °C accounting for the mass of the coupling agent. After D-mannose was attached to the nanoparticles, weight loss of

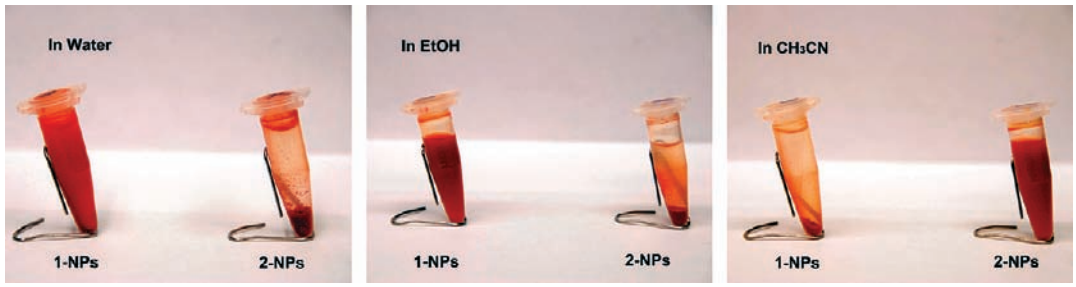

Figure 2. Functionalized nanoparticles **1**-NPs and **2**-NPs in water, ethanol, and acetonitrile (~3.3 mg/mL). Samples were sonicated for 30 min and allowed to settle for over 2 h.

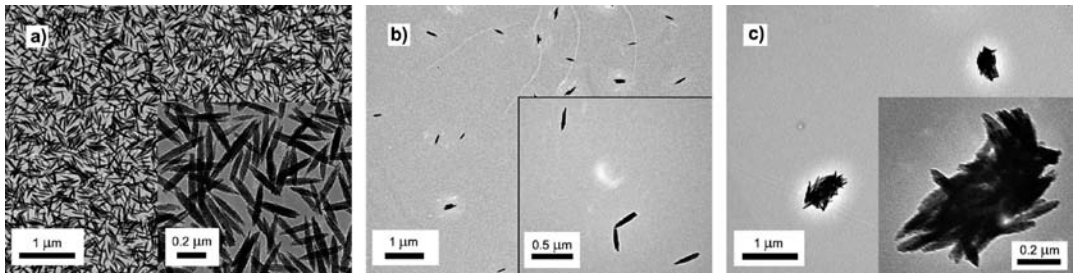

Figure 3. TEM images of (a) hematite nanoparticles, (b) mannose-**1**-NPs (500 μg/mL), and (c) subsequent treatment with *Con A*.

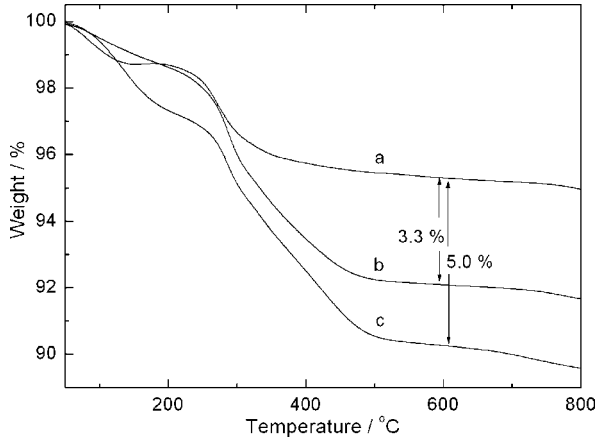

Figure 4. TGA curves of (a) Fe_3O_4 nanoparticles; (b) **1**-Fe_3O_4-NPs; (c) mannose-**1**-Fe_3O_4-NPs.

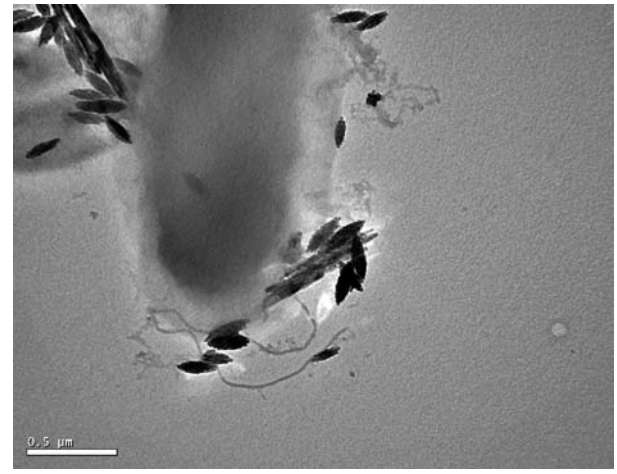

Figure 5. TEM images of *E. coli* ORN178 strain after treating with mannose-functionalized hematite nanoparticles.

5.0% at 600 °C was observed. This corresponds to the combined mass of D-mannose and the coupling agent **1**.

On the basis of these results, the number of organic molecules on each nanoparticle (N) can be calculated from eq 1

$$N = \frac{\frac{4}{3}\pi r^3 \rho w}{\mathrm{MW}} N_\mathrm{A} \qquad (1)$$

where w is the percentage of the weight loss (%), r is the radius of the Fe_3O_4 nanoparticles (averaged 5 nm by TEM), N_A is the Avogadro number, ρ is the density of Fe_3O_4 (5.1 g/cm^3 or 5.1 $\times$ 10^{-21} g/nm^3), and MW is the formula weight of the organic molecule after attaching to the nanoparticle (446 g/mol for **1** and 626 g/mol for mannose-**1** linked to nanoparticle surface). Therefore, weight losses of 3.3% and 5.0% correspond to 119 PFPA-phosphate ligands **1** and 128 mannose-**1** on one nanoparticle surface, respectively. This result means that there are roughly the same number of the coupling agent and the coupled D-mannose on the nanoparticles, indicating that the carbohydrate coupling reaction is fairly efficient.

The mannose-functionalized hematite NPs were subsequently evaluated to test if the conjugated D-mannose retains its recognition ability. *Con A*, a plant lectin that specifically binds mannopyranoside and glucopyranosides (*39*, *50*, *51*), was chosen for this study. Above pH 7, *Con A* exists as a tetramer with each face having two binding sites for the carbohydrate ligand. When mannose-**1**-NPs were treated with *Con A*, they assembled into bundled clusters (Figure 3c). Note that the mannose-**1**-NPs were well-dispersed before binding with *Con A* (Figures 3b). The aggregation can be explained by considering *Con A* as an equivalent of a tetrafunctional cross-linking agent, which upon interacting with D-mannose on NPs, brings together the nanoparticles forming a cross-linked network structure (*52*).

The recognition ability of D-mannose tethered to the hematite NPs was further evaluated in a bacteria binding study. Two *E. coli* strains, ORN178 and ORN208, were selected (*53*). ORN 178 has a mannose specific binding domain, i.e., the FimH lectin on type 1 pili, whereas ORN 208 is deficient of mannose-binding FimH protein (*53*−*57*). After the mannose-**1**-NPs were incubated with ORN 178, spindle nanoparticles were observed attaching themselves at the lateral ends and along the pili of the bacteria (Figure 5) (*53*, *54*, *58*). The strong binding between the nanoparticles

and the pili of ORN178 can be attributed to the multivalent interactions between the surface-confined mannose with the FimH lectin domain on type 1 pili. On the contrary, nanoparticles were absent on the *E. coli* ORN208 strain confirming the FimH-specific binding of the mannose ligands.

CONCLUSIONS

In summary, phosphate-containing PFPA coupling agents were synthesized and applied to functionalize iron oxide nanoparticles. Monosaccharides were successfully coupled to PFPA-functionalized nanoparticles by the photochemically induced CH insertion reaction of PFPA, which does not require chemical derivatization of the carbohydrate structures. The immobilized carbohydrates retained their recognition abilities, as demonstrated by the strong affinity with their corresponding carbohydrate-binding proteins and bacteria. The method developed can be readily applied to other carbohydrate structures including oligosaccharides, polysaccharides, and glycoconjugates. This general coupling chemistry, together with the magnetic properties of iron oxide nanoparticles, offer an attractive platform for rapid qualitative clinical diagnosis, decontamination of biological threats, and biomedical applications.

ACKNOWLEDGMENT

The authors thank the financial support from NIH (R01GM-080295-01 and R15GM066279-02), and ONAMI ARL Center. We gratefully acknowledge financial support from the Adolphe Merkle Foundation and the Swiss National Science Foundation. We thank Professor Paul E. Orndorff (North Carolina State University) for providing *E. coli* ORN178 and ORN208 strain, Professor Ken Stedman and Mr. Jim Laidler for discussions and assistance with *E. coli* experiment, Mr. Xin Wang for TEM images.

Supporting Information Available: ^{1}H NMR spectra of **1** and **2**, and FTIR of control experiments. This material is available free of charge via the Internet at http://pubs.acs.org.

LITERATURE CITED

(1) Paulson, J. C., Blixt, O., and Collins, B. E. (2006) Sweet spots in functional glycomics. *Nat. Chem. Biol. 2*, 238–248.

(2) Stevens, J., Blixt, O., Paulson, J. C., and Wilson, I. A. (2006) Glycan microarray technologies: tools to survey host specificity of influenza viruses. *Nat. Rev. Microbiol. 4*, 857–864.

(3) Wang, H. F., Gu, L. R., Lin, Y., Lu, F. S., Meziani, M. J., Luo, P. G. J., Wang, W., Cao, L., and Sun, Y. P. (2006) Unique aggregation of anthrax (*Bacillus anthracis*) spores by sugar-coated single-walled carbon nanotubes. *J. Am. Chem. Soc. 128*, 13364–13365.

(4) El-Boubbou, K., Gruden, C., and Huang, X. (2007) Magnetic glyco-nanoparticles: A unique tool for rapid pathogen detection, decontamination, and strain differentiation. *J. Am. Chem. Soc. 129*, 13392–13393.

(5) Ngundi, M. M., Kulagina, N. V., Anderson, G. P., and Taitt, C. R. (2006) Nonantibody-based recognition: alternative molecules for detection of pathogens. *Exp. Rev. Proteomics 3*, 511–524.

(6) Laurent, N., Voglmeir, J., and Flitsch, S. L. (2008) Glycoarrays - tools for determining protein-carbohydrate interactions and glycoenzyme specificity. *Chem. Commun.* 4400–4412.

(7) Liang, P. H., Wang, S. K., and Wong, C. H. (2007) Quantitative analysis of carbohydrate-protein interactions using glycan microarrays: Determination of surface and solution dissociation constants. *J. Am. Chem. Soc. 129*, 11177–11184.

(8) Disney, M. D., and Seeberger, P. H. (2004) The use of carbohydrate microarrays to study carbohydrate-cell interactions and to detect pathogens. *Chem. Biol. 11*, 1701–1707.

(9) Park, S., Lee, M. R., Pyo, S. J., and Shin, I. (2004) Carbohydrate chips for studying high-throughput carbohydrate-protein interactions. *J. Am. Chem. Soc. 126*, 4812–4819.

(10) Brun, M. A., Disney, M. D., and Seeberger, P. H. (2006) Miniaturization of microwave-assisted carbohydrate functionalization to create oligosaccharide microarrays. *ChemBioChem 7*, 421–424.

(11) Michel, O., and Ravoo, B. J. (2008) Carbohydrate microarrays by microcontact "click" chemistry. *Langmuir 24*, 12116–12118.

(12) Bryan, M. C., Fazio, F., Lee, H. K., Huang, C. Y., Chang, A., Best, M. D., Calarese, D. A., Blixt, C., Paulson, J. C., Burton, D., Wilson, I. A., and Wong, C. H. (2004) Covalent display of oligosaccharide arrays in microtiter plates. *J. Am. Chem. Soc. 126*, 8640–8641.

(13) Lee, M., and Shin, I. (2005) Facile preparation of carbohydrate microarrays by site-specific, covalent immobilization of unmodified carbohydrates on hydrazide-coated glass slides. *Org. Lett. 7*, 4269–4272.

(14) Zhi, Z. L., Powell, A. K., and Turnbull, J. E. (2006) Fabrication of carbohydrate microarrays on gold surfaces: Direct attachment of nonderivatized oligosaccharides to hydrazide-modified self-assembled monolayers. *Anal. Chem. 78*, 4786–4793.

(15) Xia, B. Y., Kawar, Z. S., Ju, T. Z., Alvarez, R. A., Sachdev, G. P., and Cummings, R. D. (2005) Versatile fluorescent derivatization of glycans for glycomic analysis. *Nat. Methods 2*, 845–850.

(16) Seo, J. H., Adachi, K., Lee, B. K., Kang, D. G., Kim, Y. K., Kim, K. R., Lee, H. Y., Kawai, T., and Cha, H. J. (2007) Facile and rapid direct gold surface immobilization with controlled orientation for carbohydrates. *Bioconjugate Chem. 18*, 2197–2201.

(17) Ito, Y. (2006) Photoimmobilization for microarrays. *Biotechnol. Prog.* 924–932.

(18) Carroll, G. T., Wang, D. N., Turro, N. J., and Koberstein, J. T. (2008) Photons to illuminate the universe of sugar diversity through bioarrays. *Glycoconjugate J. 25*, 5–10.

(19) Carroll, G. T., Wang, D. N., Turro, N. J., and Koberstein, J. T. (2006) Photochemical micropatterning of carbohydrates on a surface. *Langmuir 22*, 2899–2905.

(20) Yan, M. (2007) Photochemically initiated single polymer immobilization. *Chem. Eur. J. 13*, 4138–4144.

(21) Pei, Y. X., Yu, H., Pei, Z. C., Theurer, M., Ammer, C., Andre, S., Gabius, H. J., Yan, M., and Ramstrom, O. (2007) Photoderivatized polymer thin films at quartz crystal microbalance surfaces: Sensors for carbohydrate-protein interactions. *Anal. Chem. 79*, 6897–6902.

(22) Pei, Z. C., Yu, H., Theurer, M., Walden, A., Nilsson, P., Yan, M., and Ramstrom, O. (2007) Photogenerated carbohydrate microarrays. *ChemBioChem 8*, 166–168.

(23) Liu, L., Engelhard, M. H., and Yan, M. (2006) Surface and interface control on photochemically initiated immobilization. *J. Am. Chem. Soc. 128*, 14067–14072.

(24) Liu, L., and Yan, M. (2006) A general approach to the covalent immobilization of single polymers. *Angew. Chem., Int. Ed. 45*, 6207–6210.

(25) Lu, A. H., Salabas, E. L., and Schuth, F. (2007) Magnetic nanoparticles: Synthesis, protection, functionalization, and application. *Angew. Chem., Int. Ed. 46*, 1222–1244.

(26) Laurent, S., Forge, D., Port, M., Roch, A., Robic, C., Elst, L. V., and Muller, R. N. (2008) Magnetic iron oxide nanoparticles: Synthesis, stabilization, vectorization, physicochemical characterizations, and biological applications. *Chem. Rev. 108*, 2064–2110.

(27) Gupta, A. K., and Gupta, M. (2005) Synthesis and surface engineering of iron oxide nanoparticles for biomedical applications. *Biomaterials 26*, 3995–4021.

(28) Neouze, M. A., and Schubert, U. (2008) Surface modification and functionalization of metal and metal oxide nanoparticles by organic ligands. *Monatsh. Chem. 139*, 183–195.
(29) Latham, A. H., and Williams, M. E. (2008) Controlling transport and chemical functionality of magnetic nanoparticles. *Acc. Chem. Res. 41*, 411–420.
(30) Veiseh, O., Sun, C., Gunn, J., Kohler, N., Gabikian, P., Lee, D., Bhattarai, N., Ellenbogen, R., Sze, R., Hallahan, A., Olson, J., and Zhang, M. Q. (2005) Optical and MRI multifunctional nanoprobe for targeting gliomas. *Nano Lett. 5*, 1003–1008.
(31) De Palma, R., Peeters, S., Van Bael, M. J., Van den Rul, H., Bonroy, K., Laureyn, W., Mullens, J., Borghs, G., and Maes, G. (2007) Silane ligand exchange to make hydrophobic superparamagnetic nanoparticles water-dispersible. *Chem. Mater. 19*, 1821–1831.
(32) Mutin, P. H., Guerrero, G., and Vioux, A. (2005) Hybrid materials from organophosphorus coupling molecules. *J. Mater. Chem. 15*, 3761–3768.
(33) White, M. A., Johnson, J. A., Koberstein, J. T., and Turro, N. J. (2006) Toward the syntheses of universal ligands for metal oxide surfaces: Controlling surface functionality through click chemistry. *J. Am. Chem. Soc. 128*, 11356–11357.
(34) Bin Na, H., Lee, I. S., Seo, H., Il Park, Y., Lee, J. H., Kim, S. W., and Hyeon, T. (2007) Versatile PEG-derivatized phosphine oxide ligands for water-dispersible metal oxide nanocrystals. *Chem. Commun.* 5167–5169.
(35) Matsuno, R., Yamamoto, K., Otsuka, H., and Takahara, A. (2004) Polystyrene- and poly(3-vinylpyridine)-grafted magnetite nanoparticles prepared through surface-initiated nitroxide-mediated radical polymerization. *Macromolecules 37*, 2203–2209.
(36) Georgelin, T., Moreau, B., Bar, N., Villemin, D., Cabuil, V., and Horner, O. (2008) Functionalization of gamma-Fe_2O_3 nanoparticles through the grafting of an organophosphorous ligand. *Sens. Actuators, B 134*, 451–454.
(37) Yee, C., Kataby, G., Ulman, A., Prozorov, T., White, H., King, A., Rafailovich, M., Sokolov, J., and Gedanken, A. (1999) Self-assembled monolayers of alkanesulfonic and -phosphonic acids on amorphous iron oxide nanoparticles. *Langmuir 15*, 7111–7115.
(38) Griep-Raming, N., Karger, M., and Menzel, H. (2004) Using benzophenone-functionalized phosphonic acid to attach thin polymer films to titanium surfaces. *Langmuir 20*, 11811–11814.
(39) Lis, H., and Sharon, N. (1998) Lectins: Carbohydrate-specific proteins that mediate cellular recognition. *Chem. Rev. 98*, 637–674.
(40) Keana, J. F. W., and Cai, S. X. (1990) New reagents for photoaffinity-labeling - synthesis and photolysis of functionalized perfluorophenyl azides. *J. Org. Chem. 55*, 3640–3647.
(41) Ocana, M., Morales, M. P., and Serna, C. J. (1999) Homogeneous precipitation of uniform alpha-Fe_2O_3 particles from iron salts solutions in the presence of urea. *J. Colloid Interface Sci. 212*, 317–323.
(42) Cheng, F. Y., Su, C. H., Yang, Y. S., Yeh, C. S., Tsai, C. Y., Wu, C. L., Wu, M. T., and Shieh, D. B. (2005) Characterization of aqueous dispersions of Fe_3O_4 nanoparticles and their biomedical applications. *Biomaterials 26*, 729–738.
(43) Sezonov, G., Joseleau-Petit, D., and D'Ari, R. (2007) *Escherichia coli* physiology in Luria-Bertani broth. *J. Bacteriol. 189*, 8746–8749.
(44) Harris, J. M. (1992) in *Poly(Ethylene Glycol) Chemistry* Plenum, New York.
(45) Harder, P., Grunze, M., Dahint, R., Whitesides, G. M., and Laibinis, P. E. (1998) Molecular conformation in oligo(ethylene glycol)-terminated self-assembled monolayers on gold and silver surfaces determines their ability to resist protein adsorption. *J. Phys. Chem. B 102*, 426–436.
(46) Dietsch, H., Malik, V., Reufer, M., Dagallier, C., Shalkevich, A., Saric, M., Gibaud, T., Cardinaux, F., Scheffold, F., Stradner, A., and Schurtenberger, P. (2008) Soft nanotechnology - from colloid physics to nanostructured functional materials. *Chimia 62*, 805–814.
(47) Daou, T. J., Begin-Colin, S., Greneche, J. M., Thomas, F., Derory, A., Bernhardt, P., Legare, P., and Pourroy, G. (2007) Phosphate adsorption properties of magnetite-based nanoparticles. *Chem. Mater. 19*, 4494–4505.
(48) Zolk, M., Eisert, F., Pipper, J., Herrwerth, S., Eck, W., Buck, M., and Grunze, M. (2000) Solvation of oligo(ethylene glycol)-terminated self-assembled monolayers studied by vibrational sum frequency spectroscopy. *Langmuir 16*, 5849–5852.
(49) Wang, R. L. C., Kreuzer, H. J., and Grunze, M. (2000) The interaction of oligo(ethylene oxide) with water: a quantum mechanical study. *Phys. Chem. Chem. Phys. 2*, 3613–3622.
(50) Dam, T. K., and Brewer, C. F. (2002) Thermodynamic studies of lectin-carbohydrate interactions by isothermal titration calorimetry. *Chem. Rev. 102*, 387–429.
(51) Bouckaert, J., Loris, R., Poortmans, F., and Wyns, L. (1995) Crystallographic structure of metal-free concanavalin A at 2.5 angstrom resolution. *Proteins: Struct., Funct., Bioinf. 23*, 510–524.
(52) Gupta, D., Bhattacharyya, L., Fant, J., Macaluso, F., Sabesan, S., and Brewer, C. F. (1994) Observation of unique cross-linked lattices between multiantennary carbohydrates and soybean lectin - presence of pseudo-2-fold axes of symmetry in complex type carbohydrates. *Biochemistry 33*, 7495–7504.
(53) Lin, C. C., Yeh, Y. C., Yang, C. Y., Chen, C. L., Chen, G. F., Chen, C. C., and Wu, Y. C. (2002) Selective binding of mannose-encapsulated gold nanoparticles to type 1 pili in *Escherichia coli*. *J. Am. Chem. Soc. 124*, 3508–3509.
(54) Krogfelt, K. A., Bergmans, H., and Klemm, P. (1990) Direct evidence that the fimh protein is the mannose-specific adhesin of *Escherichia coli* type-1 fimbriae. *Infect. Immun. 58*, 1995–1998.
(55) Choudhury, D., Thompson, A., Stojanoff, V., Langermann, S., Pinkner, J., Hultgren, S. J., and Knight, S. D. (1999) X-ray structure of the FimC-FimH chaperone-adhesin complex from uropathogenic *Escherichia coli*. *Science 285*, 1061–1066.
(56) Harris, S. L., Spears, P. A., Havell, E. A., Hamrick, T. S., Horton, J. R., and Orndorff, P. E. (2001) Characterization of *Escherichia coli* type 1 pilus mutants with altered binding specificities. *J. Bacteriol. 183*, 4099–4102.
(57) Tchesnokova, V., Aprikian, P., Yakovenko, O., Larock, C., Kidd, B., Vogel, V., Thomas, W., and Sokurenko, E. (2008) Integrin-like allosteric properties of the catch bond-forming FimH adhesin of *Escherichia coli*. *J. Biol. Chem. 283*, 7823–7833.
(58) Ryu, J. H., Lee, E., Lim, Y. B., and Lee, M. (2007) Carbohydrate-coated supramolecular structures: Transformation of nanofibers into spherical micelles triggered by guest encapsulation. *J. Am. Chem. Soc. 129*, 4808–4814.

BC900110X

Supporting Information

Photoinitiated Coupling of Unmodified Monosaccharides to Iron Oxide Nanoparticles for Sensing Proteins and Bacteria

Li-Hong Liu,[†] Hervé Dietsch,[‡] Peter Schurtenberger,[‡] and Mingdi Yan*,[†]

† Department of Chemistry, Portland State University, P.O. Box 751, Portland, Oregon 97207-0751

‡ Adolphe Merkle Institute and Fribourg Center for Nanomaterials, University of Fribourg, Route de l'ancienne Papeterie CP 209, CH-1723 Marly 1, Switzerland

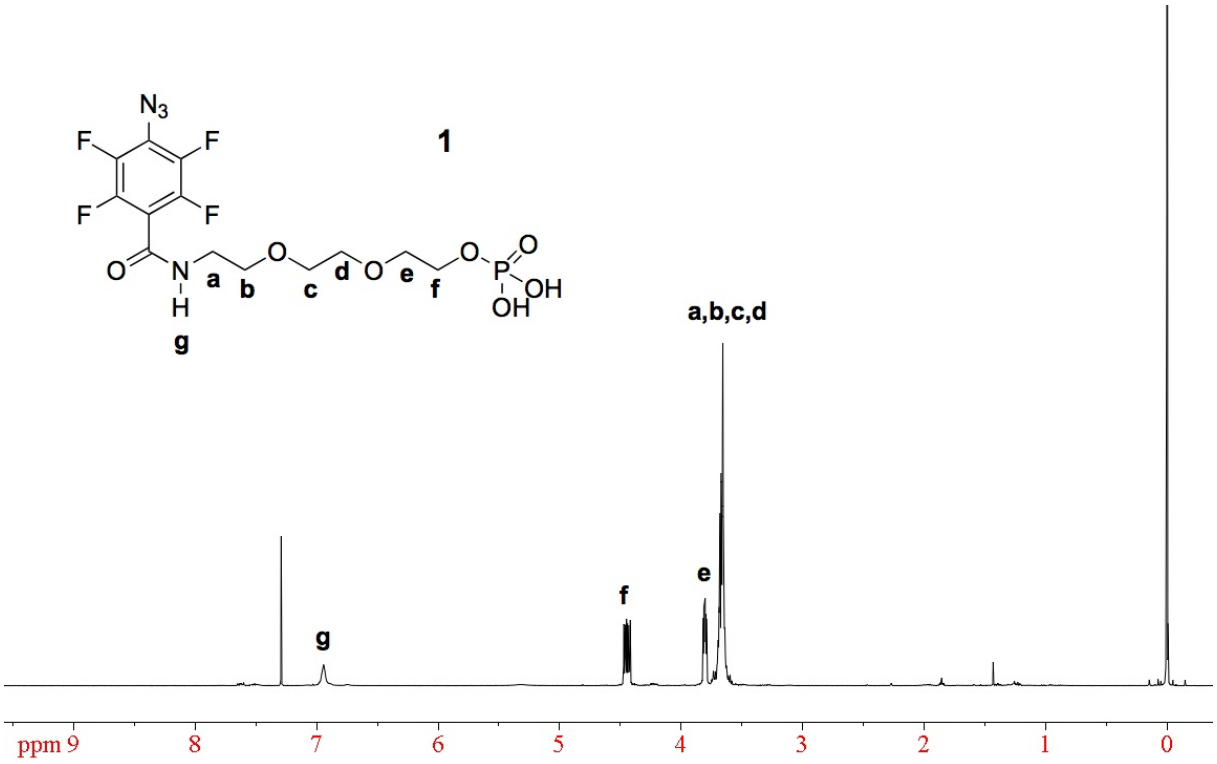

Figure S1. The proton NMR spectrum of **1**. ^{1}H NMR (400 MHz, $CDCl_3$, δ): 6.94 (br, 1H, N*H*), 4.44 (m, 2H, CH_2), 3.80 (m, 2H, CH_2), 3.67 (m, 8H, CH_2).

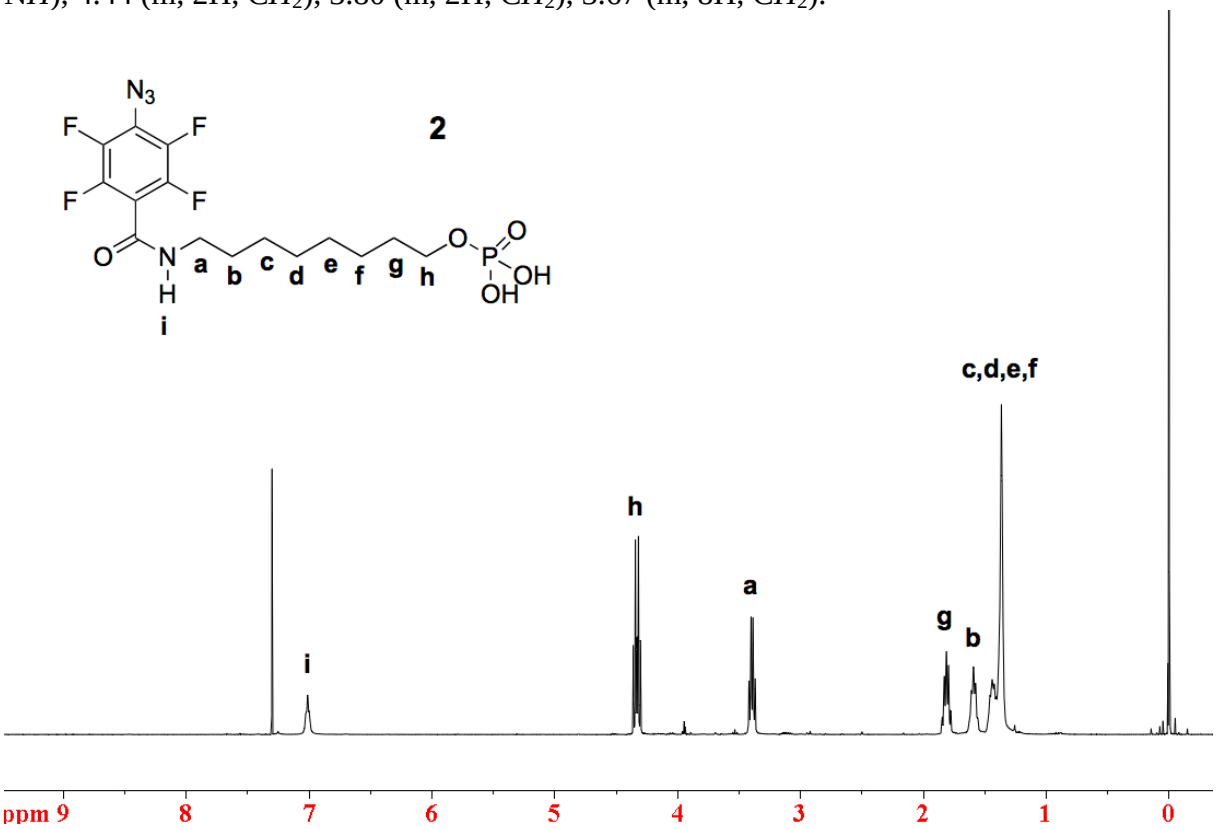

Figure S2. The proton NMR spectrum of **2**. ^{1}H NMR (400 MHz, $CDCl_3$, δ): 7.01 (s, 1H, N*H*), 4.33 (m, 2H, CH_2), 3.39 (q, 2H, *J* = 7.0 Hz, CH_2), 1.81 (m, 2H, CH_2), 1.59 (t, 2H, *J* = 7.0 Hz, CH_2), 1.36 (m, 8H, CH_2).

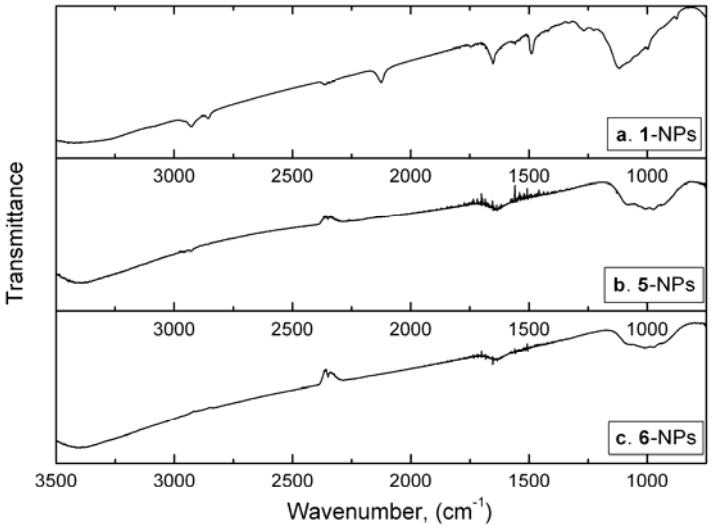

Figure S3. FTIR spectra of PFPA-phosphate ligand **1**-functionalized hematite nanoparticles (a), hematite nanoparticles after treating with compound **5** (b) and **6** (c).

PEGylation Promotes Hemoglobin Tetramer Dissociation

Dario Caccia,[†,‡] Luca Ronda,[†,||] Raffaella Frassi,[‡] Michele Perrella,[‡] Elena Del Favero,[§] Stefano Bruno,[||] Barbara Pioselli,[||] Stefania Abbruzzetti,[⊥] Cristiano Viappiani,[⊥] and Andrea Mozzarelli*[,||,#]

Dipartimento di Scienze e Tecnologie Biomediche, Dipartimento di Chimica, Biochimica e Biotecnologie per la Medicina, Università degli Studi di Milano, and LITA (Laboratorio Interdisciplinare di Tecnologie Avanzate), 20090 Segrate, Milano, Italy, and Dipartimento di Biochimica e Biologia Molecolare, Dipartimento di Fisica, Università di Parma, and NEST CNR-INFM, Istituto Nazionale di Biostrutture e Biosistemi, 43100 Parma, Italy. Received March 26, 2009; Revised Manuscript Received May 19, 2009

Hemoglobin conjugated with poly(ethylene glycol) (PEG) acts as an oxygen carrier free in plasma, substituting red blood cells in supplementing oxygen in hypo-oxygenation pathologies. Given the complexity of oxygen delivery controls, subtle structural and functional differences in PEGylated hemoglobins might be associated with distinct physiological responses and, potentially, adverse effects. We have compared hemoglobin PEGylated under anaerobic conditions, called PEG-Hb^{deoxy}, with hemoglobin PEGylated under aerobic conditions, called PEG-Hb^{oxy}, a product that mimics Hemospan, produced by Sangart, Inc. SDS PAGE and MALDI-TOF analyses demonstrated that PEG conjugation yields products characterized by a broad distribution of PEG/hemoglobin ratios. The elution profiles in size-exclusion chromatography indicate that both products exhibit a more homogeneous distribution of molecular weight/hydrodynamic volume under deoxy conditions and at higher concentrations. PEG-Hb^{oxy} shows high oxygen affinity, low modulation of allosteric effectors, almost no cooperativity, a fast and monophasic CO binding, and a limited dependence of functional properties on concentration, whereas PEG-Hb^{deoxy} exhibits oxygen binding curves that significantly depend on protein concentration, and a slow CO binding, similar to native hemoglobin. PEGylated CO-hemoglobins, probed by flash photolysis, exhibited a lower amplitude for the geminate rebinding phase with respect to native hemoglobin and a negligible T state bimolecular CO rebinding phase. These findings are explained by an increased dissociation of PEGylated hemoglobins into dimers and perturbed T and R states with decreased quaternary transition rates. These features are more pronounced for PEG-Hb^{oxy} than PEG-Hb^{deoxy}. The detected heterogeneity might be a source of adverse effects when PEGylated Hbs are used as blood substitutes.

Hemoglobin-based oxygen carriers (HBOC)[1] (*1*−*4*) are potential therapeutic agents for clinical needs that cannot be fullfilled by blood transfusions, such as (i) acute hemorrhages associated with accidents or weapon wounds in location far from hospitals, (ii) immunoreactivity against all red blood cell determinants, (iii) oxygen supply to patients that do not accept blood transfusions for religious dictates, (iv) oxygenation of ischemic tissues where red blood cells cannot diffuse (*5, 6*), and (v) increase in oxygen concentration in solid tumors for the improvement of radiation therapy (*7, 8*). Moreover, HBOCs can be used for (i) partial substitution of normal transfusion to save blood units during orthopedic surgeries, (ii) reduction of the exposure of preterm infants to adult red cells, potentially causing severe chronic pathologies (*9*), and (iii) safe supply of an oxygen supplier in world countries where blood units from healthy donors are limited. The absence of cross-matching, the room temperature storage, the more than one year shelf life, and the possibility of tuning hemoglobin (Hb) oxygen affinity depending on clinical requirements are other advantages for HBOCs with respect to red blood cell transfusions. Several products have been developed based on approaches aimed at increasing the molecular size of Hb via either subunit cross-linking (*10*−*14*) or conjugation with poly(ethylene glycol) (PEG) (*15*−*18*) to avoid vessel extravasation and renal ultrafiltration. Only a few of these products, manufactured by companies, have progressed and been evaluated in phase II and III trials (*12, 19*−*22*). So far, no products have been approved by the FDA. Moreover, a meta-analysis of the recent clinical trials has evidenced that, to some extent, all products cause medium to severe adverse effects, such as death, myocardial infarction, and pancreatitis (*23*), strongly questioning their safe use. However, companies have expressed concerns on the validity of the meta-analysis (*24, 25*).

It should be fully appreciated that HBOC is a peculiar drug because the amount of product that is injected into the plasma is on the order of grams in comparison to milligrams or micrograms for most other drugs. Thus, even a small amount

* Corresponding author. Andrea Mozzarelli, Dipartimento di Biochimica e Biologia Molecolare, Università di Parma, Viale G.P. Usberti 23/A, 43100 Parma, Italy. Fax 39-0521-905151. E-mail: andrea.mozzarelli@unipr.it.

† These two authors contributed equally to the work.

‡ Dipartimento di Scienze e Tecnologie Biomediche, Università degli Studi di Milano.

§ Dipartimento di Chimica, Biochimica e Biotecnologie per la Medicina, Università degli Studi di Milano.

|| Dipartimento di Biochimica e Biologia Molecolare, Università di Parma.

⊥ Dipartimento di Fisica, Università di Parma, and NEST CNR-INFM.

Istituto Nazionale di Biostrutture e Biosistemi.

[1] Abbreviations: ACN, acetonitrile; $C_{12}E_8$, octaethylene glycol monododecyl ether; DLS, dynamic light scattering; 2,3-BPG, 2,3-diphophoglycerate; Hb, hemoglobin; HBOC, hemoglobin-based oxygen carrier; IHP, inositol hexaphosphate; IMT, 2-iminothiolane; MAL-PEG, maleimidoethyl poly(ethylene glycol); MS, mass spectroscopy; M_r, relative molecular mass; *n*, Hill's cooperativity coefficient; NEM, *N*-ethylmaleimide; NES-Hb, hemoglobin thiolated and treated with NEM under anaerobic conditions; ODC, oxygen dissociation curve; PEG, poly(ethylene glycol); PEG-BSA, PEGylated bovine serum albumin; PEG-Hb, PEGylated hemoglobin, PEG-Hb^{deoxy} and PEG-Hb^{oxy}, hemoglobin thiolated and PEGylated under anaerobic and aerobic conditions, respectively; SLS, static light scattering; TFA, trifluoro acetic acid.

10.1021/bc900130f CCC: $40.75 © 2009 American Chemical Society
Published on Web 06/17/2009

Table 1. Biochemical Characterization of Hb Derivatives[a]

species	reaction cycles	total SH	free SH	conjugation (NEM or MAL-PEG)
HbA	–	–	2.3	–
NEM-Hb	2 cycles IMT+NEM	7.7	2.3	5.3 (NEM)
PEG-Hb^{deoxy}	1 cycle IMT+MAL-PEG	9.0	2.3	6.7 (MAL-PEG)
PEG-Hb^{oxy}	1 cycle IMT+MAL-PEG	6.9	1.0	5.9 (MAL-PEG)
PEG-BSA	1 cycle IMT+MAL-PEG	5.9	0.2	5.7 (MAL-PEG)

[a] IMT-modified amino groups before (total SH) and after reaction with NEM or MAL-PEG (free SH) as determined on a tetramer basis by thiol titration with the method of Ampulsky et al. (*39*) The number of residues conjugated with NEM or MAL-PEG was equal to the difference between total SH and free SH. The titre of Cysβ93 of native Hb yielded by the method was 2.3.

of byproduct and heterogeneity generated by the chemical procedures or slight deviation of the functional properties from the physiological needs might be responsible for some of the observed adverse effects. However, so far, no investigation has been carried out to link structural and functional properties of products with the observed adverse effects. One of these products, MP4, trade name Hemospan, is obtained via the conjugation of Hb with an average of 6−7 PEG 5000 (M_r) chains under oxygenated conditions in a two-step procedure: first, oxyHb is thiolated by treatment with iminothiolane (IMT), and then, thiols react with the PEG-maleimido derivative MAL-PEG (*16, 26*). Hemospan has completed phase III clinical trials to test its capacity for prevention and treatment of hypotension during orthopedic surgery (*22, 25, 27*). Hemospan exhibits high oxygen affinity and low cooperativity, which makes it more similar to Hb dimers than to the physiological tetrameric oxygen carrier. These features might have originated from the interference of PEG molecules with Hb amino groups of the organic phosphate binding pocket and the sulfhydryl groups of Cysβ93 (*28*−*31*), which are involved in NO binding (*16, 32, 33*). Recently, it was also demonstrated that PEGylated Hb exhibits an increase in the nitrite reductase activity (*31*).

With the aim of protection from PEGylation function-associated groups, PEGylation of Hb was carried out under anaerobic conditions, in the presence of IHP and Cl^- (*34*). This PEGylated Hb exhibits lower oxygen affinities than Hemospan and normal or moderately reduced response to 2,3-BPG, and retains about 50% of the cooperativity of native Hb (*34, 35*). Otherwise, in transfused rats, retention time, renal filtration, and pressure effects of Hb, PEGylated under anaerobic conditions with seven PEG and seven propionyl groups, called Euro PEG-Hb, were found to be similar to those observed for Hb PEGylated under aerobic conditions (*35*). The altered oxygen affinity and cooperativity of the PEGylated products might not be due solely to lysines modifications. It is known that interface mutants or chemically modified Hbs characterized by an increased oxygen affinity and reduced cooperativity exhibit perturbed tetramer−dimer equilibria, favoring the latter species (*36, 37*). This might also be the effect of PEGylation on Hb.

In the perspective of the use of PEGylated Hb products as a blood substitute and in light of the recently observed adverse effects (*25*), we have carried out a detailed comparison of the structural and functional properties between a product prepared using the procedure reported for Hemospan (*16, 26*), that we named PEG-Hb^{oxy}, that is conjugated with six PEG molecules under aerobic conditions, and Hb, similarly modified with an average of six PEG molecules, under anaerobic conditions, that we named PEG-Hb^{deoxy}. We have studied the molecular weight distribution, physicochemical properties, oxygen binding curves, and time courses of CO binding as a function of protein concentrations, in the absence and presence of allosteric effectors. Results were correlated with elution profiles in size exclusion chromatography under deoxygenated and oxygenated conditions. Our studies suggest that PEG-Hb^{oxy} more than PEG-Hb^{deoxy} exhibits altered tetramer−dimer equilibria, due to slower association rates of the PEGylated dimers as compared with native Hb, thus accounting for most of the observed distinct functional properties. This conclusion is in keeping with a very recent study carried out on Hb PEGylated at both Valα1 and Valβ1 (*38*).

EXPERIMENTAL PROCEDURES

Materials. IMT, IHP, NEM, molecular weight markers, BSA, and MALDI calibration kit were purchased from Sigma Aldrich. Reagents and equipment for SDS-PAGE were from Biorad Laboratories Inc. Ultrafiltration membranes and kits were from Sartorius Stedim and Millipore. MAL-PEG (molecular mass 5.6 kDa) was from Nektar Molecule Engineering (Nektar Therapeutics).

Protein Modification. Conjugated Hbs were prepared by treating HbA in 50 mM Na-phosphate, 100 mM NaCl, 0.5 mM EDTA, pH 7 at 20 °C, with an excess of IMT and MAL-PEG, or NEM, under anaerobic conditions in the presence of IHP, as previously described (*34*) to produce PEG-Hb^{deoxy}. The amount of IMT and the reaction time were adjusted to achieve the desired degree of thiolation and, thus, the number of conjugated PEG molecules. Concentrated and deoxygenated lysine and cysteine solutions were added to stop IMT and MAL-PEG reactions, respectively. PEG-Hb^{deoxy} was then equilibrated with 100 mM NaCl by seven ultrafiltration cycles, under aerobic conditions, at 5 °C, using a 30 kDa cutoff Amicon membrane. The solution was concentrated to one-third of the initial volume before redilution with NaCl solution. The number of conjugated PEG chains was estimated by treating deoxy Hb with IMT under the same conditions without the addition of MAL-PEG. The thiol titer determined by a biochemical method (*39*), corrected for the titer determined after treatment with MAL-PEG, or NEM, yielded the number of conjugated PEG/tetramer, or NEM/tetramer (*34*). PEG-Hb^{oxy} was prepared as described by Vandegriff et al. (*16*). Hb, PEG-Hb^{deoxy}, and PEG-Hb^{oxy} were stored in liquid nitrogen. The ferric Hb content was <2%. Hb concentration is expressed on a heme basis. BSA (68 kDa, 59 lysines) was PEGylated under aerobic conditions by the same procedure described for PEG-Hb^{deoxy} to obtain a protein conjugated with an average number of 6 PEG/molecule. Since the BSA sample was contaminated by 5% IgG immunoglobulin, the product was also contaminated by PEGylated IgG, which showed up in size exclusion chromatography as an inflection of the leading edge of the elution profile of PEG-BSA. The characteristics of the various preparations are summarized in Table 1.

SDS-PAGE and Protein Extraction. SDS-PAGE was carried out according to Laemli (*40*) using acrylamide and piperazine diacrylylamide as the cross-linker. Gels were stained with BioSafe G-250 Coomassie Brilliant Blue compatible with MS analysis and scanned using Quantity One software. Protein bands were excised from the gels and destained with a 40/10 (v/v) mixture of methanol/acetic acid. The proteins were recovered by passive elution at 37 °C using the SDS-PAGE running buffer and concentrated by Vivaspin 2 (Sartorius) centrifugal concentrators, which facilitates SDS removal.

Mass Spectrometry. A layer of sinapinic acid in acetone was spotted onto the sample well before adding 1 μL protein aliquotes diluted with matrix solution containing 30 mg/mL sinapinic acid in 50/50 (v/v) ACN/0.1% TFA. MALDI TOF mass spectra were obtained using a MALDI-LR mass spectrometer (Waters Italia) operated in negative linear mode. External calibration was carried out in the 7−70 kDa mass range using protein standards from the ProteoMass Peptide and Protein MALDI-MS Calibration kit: apomyoglobin (equine) ($M+H^+$: 16 952.27), aldolase ($M+H^+$: 39 212.28), albumin ($M+H^+$: 66 430.09) and High Mass Post Acceleration Linear detector to increase the sensitivity for the PEGylated molecules.

Static and Dynamic Light Scattering. Laser light scattering was carried out with a goniometer (BI-200SM Brookhaven Instrument Corporation) equipped with a BI9K Digital correlator and a solid-state 676 nm light source. Independent SLS and DLS measurements were carried out at 20 °C, under aerobic conditions, on Hb, PEG-Hb^{deoxy}, and PEG-Hb^{deoxy} in a solution containing 50 mM Na-phosphate, 100 mM NaCl, 0.5 mM EDTA, 0.5 mM NaCN, pH 7, at 40−280 μM concentration range. The hydrodynamic radii were determined by Cumulant and Fourier Transform analysis of the intensity correlation function measured by DLS (*41*). Independent SLS measurements provided information about the average molecular weight and concentration of macromolecules after absolute intensity calibration with a 0.02 mg/mL $C_{12}E_8$ solution (*42*).

Size Exclusion Chromatography. Chromatography was carried out in 50 mM Na-phosphate, 100 mM NaCl, 0.5 mM EDTA, pH 7, with an AKTA Prime instrument and a HiLoad Superdex 200 column (≈120 mL bed volume, 600 kDa mass exclusion limit), thermostatted at 20 °C, at flow rate of 1.5 mL/min (Amersham Pharmacia Biotech). The retention time was 40−70 min using 0.5 mL samples of PEGylated Hb. To carry out anaerobic chromatography, the buffer reservoir was kept under nitrogen and 1 mM Na-dithionite was added to the buffer. Samples were loaded after deoxygenation by nitrogen tonometry and addition of Na-dithionite. The eluate from Hb chromatographic analysis was monitored at 436 nm to avoid dithionite interference, whereas the flowthrough of BSA chromatographic analysis was monitored at 280 nm. Chromatograms were normalized to absorbance values versus molecular mass derived from standard proteins calibration.

To determine the tetramer−dimer equilibrium constant of oxy Hb and oxy NES-Hb, a HiLoad Sephacryl S-200 column was used (bed volume ≈79 mL, matrix volume ≈3 mL, according to the manufacturer specifications, and void volume ≈38 mL, as determined by Blue Dextran, 250 kDa mass exclusion limit). Solute saturation was achieved by loading 15 mL samples. The column was run at 0.5 mL/min flow rate at 20 °C. A solute in rapid tetramer−dimer equilibrium, as Hb, loaded on such a column under solute saturating conditions, shows an elution profile characterized by a plateau region between a leading and a trailing edge. The solute elution volume at the inflection point of the leading edge, V, is related to the fraction of dissociated tetramers, α, through eq 1 (*43*):

$$V = V_0 + [\sigma_T + \alpha(\sigma_D - \sigma_T)]V_i \quad (1)$$

where V_0 is the void volume, V_i the internal matrix volume, provided by the manufacturer, and σ_T and σ_D are parameters that characterize the matrix interactions with tetramers and dimers, respectively. These parameters were obtained using enough high and low Hb concentrations to justify the assumption that the protein was in tetrameric and dimeric form, respectively. The gradient of the elution profile was analyzed to precisely determine the elution volume at the inflection point of the leading edge. The dissociation constant is related to α through eq 2:

$$K_d = \alpha^2 C/(1 - \alpha) \quad (2)$$

where C is the solute plateau concentration. Under deoxy conditions, the method could not be used since both normal and NES-Hb require dilution much beyond the limit of concentration detection of the technique and the tetramer−dimer equilibration is not rapid relative to the time scale of the chromatographic run.

Oxygen Affinity Measurements. Oxygen dissociation curves (ODCs) as a function of protein concentration were carried out at 15 °C in a solution containing the enzymatic metHb reducing system (*44*), at pH 7.0, using a novel homemade apparatus (*45*). The gas mixture generated by Environics 200 and 4000 (Environics, Inc.) flows in a thermostatted humidifier and then in the sample chamber consisting of a 2 mm optical path cuvette fused to a 25 mL open-top threaded reservoir with fittings for inlet and outlet gas lines. The chamber is thermostatted in a shaking bath. The sample compartment of a CARY 400 spectrophotometer (Varian, Inc.) is also thermostatted. Fractional oxygen saturations and oxidized hemes were determined by fitting the observed spectra to a linear combination of reference spectra (*46*, *47*). ODCs of PEG-Hb^{deoxy}, in the absence of allosteric effectors, at different protein concentrations, were globally fitted using eq 3, assuming two independent species ***a*** and ***b***, characterized by p50$_a$ and Hill coefficient n_a, and p50$_b$ and Hill coefficient n_b, respectively, varying only the relative fraction of species ***a***, f_a, as a function of concentration:

$$Y = f_a \frac{pO_2^{na}}{pO_2^{na} + p50_a^{na}} + (1 - f_a) \frac{pO_2^{nb}}{pO_2^{nb} + p50_b^{nb}} \quad (3)$$

ODCs in the presence of the allosteric effectors Cl^- and CO_2 were fitted with eq 1, constraining p50$_a$ and n_a to be equal to those calculated in the absence of allosteric effectors. It was assumed that functional properties of species ***a*** are unaffected by effectors because this species corresponds to Hb dimers, whereas functional properties of species ***b*** are affected because this species corresponds to Hb tetramers (see Results). ODCs of PEG-Hb^{oxy} and Hb were fitted to a single species characterized by p50 and Hill coefficient n.

CO Binding Kinetics. CO binding to HbA, PEG-Hb^{deoxy}, and PEG-Hb^{oxy} was followed by stopped-flow apparatus (SX.18 MV, Applied Photophysics) at a single wavelength (435 nm). Two millimolar Na-dithionite was added to deoxygenated protein and ligand solutions to completely remove oxygen. Depending on Hb concentration, a path length of 0.2 or 1 cm was used.

Flash photolysis experiments were performed with a setup described elsewhere (*48*, *49*), following the absorbance change at 436 nm. Photolysis yields for all species were evaluated and found to be similar. The rebinding kinetic traces were first converted to fraction of deoxy-protein as a function of time. The lifetime distribution associated with the observed CO rebinding kinetics was evaluated using the program MemExp (version 3.0) (*50*). The program MemExp uses a maximum entropy method (MEM) and either nonlinear least-squares (NLS) or maximum likelihood (ML) fitting to analyze a general time-dependent signal in terms of distributed and discrete lifetimes. A distribution of effective log-lifetimes, $g(\log(\tau))$, was extracted from the data without restriction to any functional form, as previously described (*51*−*53*).

Stopped-flow and flash photolysis experiments were carried out in a solution containing 1 atm CO, 100 mM Hepes, 1 mM EDTA, pH 7.0, at 15 °C.

RESULTS

Analysis of PEGylated Hbs by SDS-PAGE and Mass Spectrometry. A previous mass spectrometry (MS) study of Hb PEGylated under anaerobic conditions showed that 5 lysines

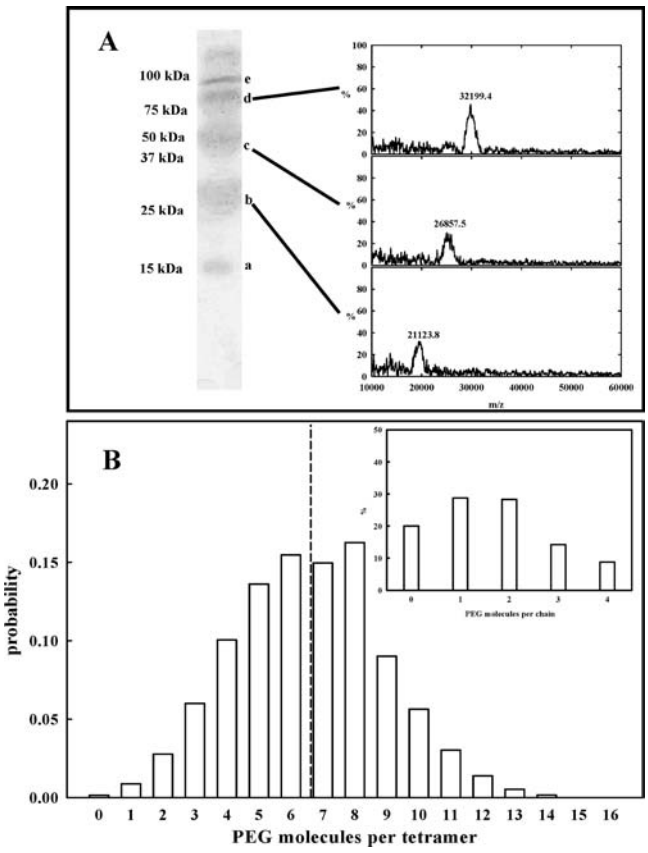

Figure 1. PEG-Hb^{deoxy} heterogeneity. (A) SDS-PAGE and molecular weight determination by MALDI-TOF of PEGylated Hb products. PEG-Hb^{deoxy} was separated by SDS-PAGE (left panel). The molecular weight of species ***a*** was 16 kDa, according to molecular weight markers (not shown). The *m*/*z* values of the species extracted from bands b, c, and d and analyzed by MALDI-TOF MS (right panel) were 21123, 26857, 32199, respectively, indicating the addition of 1, 2, and 3 5.6 kDa PEG molecules. (B) Distribution of unmodified and PEGylated species in a sample of PEG-Hb^{deoxy} calculated from the relative amounts of the various chains determined in Figure 1A. Relative proportions of unmodified and PEGylated chains, as determined by the analysis of the intensities of the stained bands of the SDS-PAGE separations, are reported in Figure 1B, inset.

per subunit were modified by IMT at a significantly higher rate than three additional lysines, both on the α and β chains (*34*). The reactivity differences between these 5 reactive lysines do not allow the preparation of a homogeneous product. Only 6−7 residues per tetramer are PEGylated, showing a significant population of unmodified chains that suppressed the ionization of PEGylated chains in MALDI-TOF MS, thus yielding only a qualitative information on the presence of non-PEGylated Hb chains (*34*). To obtain a quantitative estimate of the proportion of unmodified vs PEGylated tetramers, PEG-Hb^{deoxy} was characterized by SDS-PAGE, which was proven effective in separating nonconjugated and conjugated Hb chains (Figure 1A, left panel). A similar study has recently been carried out for Hemospan (*26*). Since the species in band a runs as HbA chains (data not shown), it was assumed that this species corresponds to the unmodified globin chains. Bands b, c, d, and e migrate with an apparent molecular weight of approximately 25, 45, 75, and 90 kDa, respectively, as calculated using protein molecular weight standards. The species extracted from the bands were individually characterized by MALDI-TOF MS, as shown in Figure 1A, right panel. Bands b, c, and d were assigned to globin chains conjugated with one, two, and three 5.6 kDa PEG molecules, respectively. The protein recovery from the low-intensity band e was not sufficient to collect reliable data in MALDI TOF analysis. However, it is reasonable to assume that this component is conjugated with four PEG molecules per globin chain. The tetramer distribution as a function of the number of conjugated PEG molecules (Figure 1B) was calculated using the densitometric analysis of the stained protein bands (Figure 1B, inset). It displays a wide distribution, spanning from unmodified to 12 PEG molecules per tetramer. The weighted mean is 6.6 PEG molecules/tetramer, in good agreement with the biochemical estimation (see Experimental Procedures, Table 1). Such a distribution indicates that, under these conditions, a wide variety of PEGylated Hb species is present and the probability to find either unmodified or highly PEGylated tetramers (>12−13 PEG molecules) is negligible. Furthermore, samples of PEG-Hb^{oxy} and PEG-Hb^{deoxy} were analyzed by native gel electrophoresis (data not shown). The densitometric profiles indicate that both PEG-Hb^{oxy} and PEG-Hb^{deoxy} are heterogeneous products (see also ref 26).

Analysis of PEGylated Hbs by Static and Dynamic Light Scattering. Solutions containing HbA, PEG-Hb^{oxy}, and PEG-Hb^{deoxy}, at a concentration of 40−280 μM, were characterized by static light scattering (SLS) and dynamic light scattering (DLS) measurements. The observed weight average molecular masses were 68 ± 5, 105 ± 2, and 99 ± 1 kDa, respectively. The average number of PEG chains per tetramer, 6.6 (PEG-Hb^{deoxy}) and 5.6 (PEG-Hb^{oxy}), calculated from these mass values agreed with the values obtained by the biochemical characterization and mass spectroscopy measurements (Table 1). The average hydrodynamic diameters of HbA, PEG-Hb^{deoxy}, and PEG-Hb^{oxy} were 59, 105, and 104 Å, respectively, within 5% error. Using the static and dynamic measurements, it was calculated that Hb hydrodynamic radius agreed with the dimension of a globular particle with 66 kDa molecular mass. In the case of PEG-Hb^{deoxy} and PEG-Hb^{oxy}, PEGylation brought about a significant increase in hydrodynamic radius with respect to the increase in the molecular mass, suggesting a Hb core surrounded by a 15−20 Å thick shell of highly hydrated flexible PEG monomers.

Analysis of PEGylated Hbs by Size Exclusion Chromatography. Column chromatography of oxy Hb and oxy NES-Hb, at 20 °C in 50 mM phosphate, 100 mM NaCl, 0.5 mM EDTA, 0.1 mM NaCN, pH 7, under aerobic conditions and protein column saturation, yielded single plateau regions at all protein concentrations in the 4−4000 μM range. The averaged dimer/tetramer $K_{d(oxy)}$ values were 0.26 ± 0.08 and 0.42 ± 0.07 μM, respectively, comparable to published values of 0.48−1.9 μM for liganded human Hbs under similar conditions (*36, 37*). Under anaerobic conditions, the dimer/tetramer $K_{d(deoxy)}$ values of deoxy NES-Hb could not be obtained by this approach due to the extremely low value of the equilibrium dissociation constant, as already known for Hb (*54*).

The chromatography of PEG-Hb^{deoxy} and PEG-Hb^{oxy}, under aerobic conditions, failed to yield a single plateau because of either the heterogeneity of the PEGylated proteins or the slow equilibration of the species during chromatography. To clarify this issue, we carried out size exclusion chromatography using nonsaturating column conditions. Oxy Hb at all concentrations was eluted as a single, nearly symmetrical peak, which shifted from 65 ± 3 kDa at 800 μM to lower values upon dilution due to the increased fraction of dimers in rapid equilibrium with tetramers (data not shown). Deoxy Hb was eluted as a single, 65 kDa symmetrical peak at all concentrations (data not shown). Chromatography of PEG-BSA (Figure 2A, inset) showed a single main peak with an inflection in the leading edge due to the presence of PEGylated IgG immunoglobulin. This clearly indicates that under the conditions of the chromatography the molecular sieve could not resolve species differing in the number of conjugated PEG chains. However, a shift in the apparent molecular weight from 540 ± 25 to 640 ± 25 kDa occurred

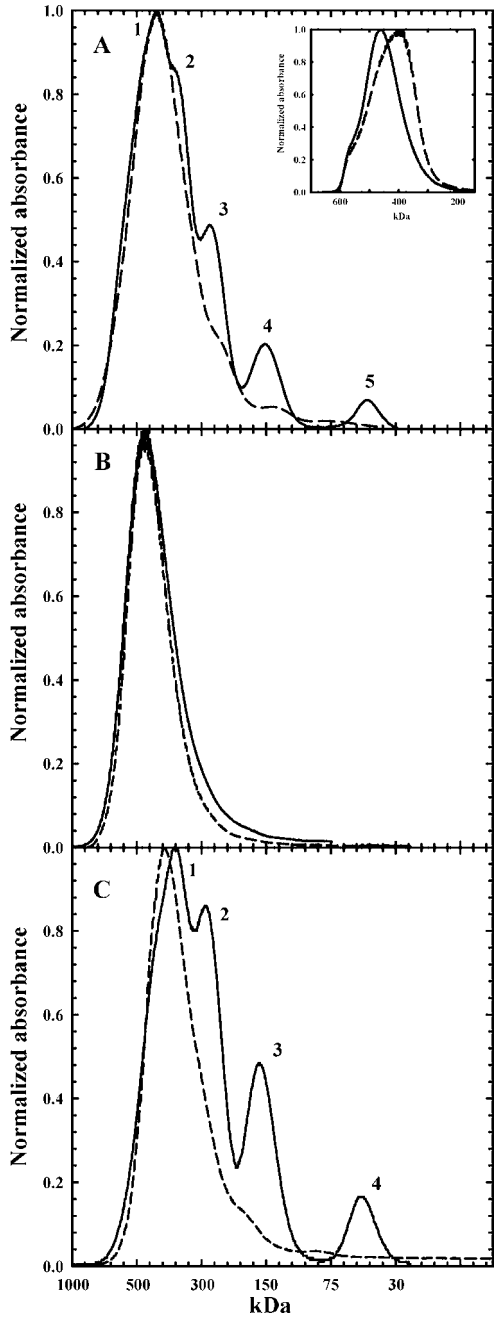

Figure 2. Size exclusion chromatography. A HiLoad Superdex 200 column (about 120 mL bed volume) was equilibrated at 20 °C with 50 mM Na-phosphate, 100 mM NaCl, 0.5 mM Na-EDTA, 0.1 mM NaCN, pH 7. Samples (0.5 mL) were eluted at a 1.5 mL/min flow rate. The elution volumes in the abscissa were transformed into molecular weight units (kDa) by column calibration using known standards. Absorbance values on the ordinate were normalized to the highest value. (A) (dash line) 800 and (solid line) 8 μM oxy PEG-Hb^{deoxy}. The species eluted in peaks 1−5 were not identified. The apparent molecular weight of peak 1 is 460 kDa. Inset: 800 μM (solid line) and 8 μM (dash line) PEG-BSA. The apparent molecular weights are 540 and 640 kDa, respectively. The inflection of the leading edge indicates the presence of PEGylated IgG, which contaminated the native BSA sample (5%). (B) 8 μM deoxy PEG-Hb^{deoxy} in the presence of 1 mM Na-dithionite. (dash line), sample prepared by dilution of a deoxygenated 800 μM solution. (solid line), sample prepared by Na-dithionite addition to a 8 μM oxygenated solution. The apparent molecular weight of the peak is 500 kDa. (C) 8 μM PEG-Hb^{oxy} under aerobic (solid line) and anaerobic (dash line) conditions. The species in peaks 1−4 were not identified. The apparent molecular weight of peak 1 is 380 kDa. The 8 μM deoxy PEG-Hb^{oxy} sample was obtained by the addition of Na-dithionite to a 8 μM oxygenated sample before loading. The apparent molecular weight of the peak is 430 kDa.

upon dilution (Figure 2A, inset), due to non-ideality of the solute−matrix interactions. The non-ideality effect was also observed using Hb at high concentrations where dissociation into dimers is not significant (data not shown). At 800 μM concentration, oxy PEG-Hb^{deoxy} was eluted as a main species with an apparent molecular weight of 460 ± 25 kDa, more than four times the value calculated on the basis of the average PEG/tetramer number (Figure 2A). A trailing edge, however, indicated the presence of small amounts of other components. At 2 μM concentration, four additional unidentified components, partially or completely resolved, were observed (Figure 2A). The formation of low relative molecular mass (M_r) components upon dilution was reversible, since a 8 μM sample of oxy PEG-Hb^{deoxy} reconcentrated to 800 μM was eluted as the original undiluted 800 μM sample (data not shown). PEG-Hb^{deoxy} chromatography under anaerobic conditions, at all concentrations, yielded a single peak with an apparent molecular weight of 500 kDa. However, the slight trailing observed with diluted samples depended on the modality of sample dilution. When a 800 μM oxygenated sample was deoxygenated before dilution to 8 μM, trailing was minimal (Figure 2B). If dilution to 8 μM was carried out under aerobic conditions followed by rapid deoxygenation with Na-dithionite, trailing was more pronounced (Figure 2B). Under aerobic conditions and at 8 μM concentration (Figure 2C), PEG-Hb^{oxy} showed at least a five-component elution pattern with the main component, **1** (Figure 2C), shifted to an apparently lower molecular weight (380 kDa) than component **1** in the PEG-Hb^{deoxy} elution pattern, Figure 2A, and a significant increase in the relative proportions of partially or completely resolved species as compared with PEG-Hb^{deoxy} under the same conditions (Figure 2C). Under anaerobic conditions and when rapid deoxygenation of 8 μM oxy PEG-Hb^{oxy} was carried out by Na-dithionite addition (Figure 2C), the apparent M_r of the main peak was 430 kDa and the presence of incompletely reassociated species was more evident than in the case of PEG-Hb^{deoxy} (Figure 2B).

Oxygen Binding Curves of PEG-Hb^{deoxy} and PEG-Hb^{oxy} as a Function of Protein Concentration, in the Absence and Presence of Allosteric Effectors. ODCs were carried for PEG-Hb^{deoxy} at protein concentrations between 11 and 550 μM, for PEG-Hb^{oxy} at 219 μM and for HbA at 13 and 193 μM in a solution containing 100 mM Hepes, 1 mM EDTA, pH 7, at 15 °C (Figure 3). The apparent oxygen affinity for PEG-Hb^{deoxy} was found to increase as protein concentration decreased. ODCs were globally fitted to two components, ***a*** with $p50_a = 0.80 \pm 0.12$ Torr and $n_a = 1.33 \pm 0.09$ and ***b*** with $p50_b = 3.18 \pm 0.08$ Torr and $n_b = 2.54 \pm 0.19$. The fraction of species ***a***, f_a, decreases with increasing Hb concentration, remaining constant above 200 μM (Figure 3, inset). The dependence of f_a on Hb concentration was fitted to a binding isotherm with a dissociation constant K_d of 21.5 ± 2.3 μM.

ODCs for HbA (Figure 3) do not exhibit variation as a function of protein concentration and were fitted to an equation for a single oxygen binding species with a p50 of 2.65 ± 0.02 Torr and Hill *n* of 2.39 ± 0.05, values very close to those exhibited by species ***b***. ODC for PEG-Hb^{oxy} (Figure 3) was well fitted to a single species with p50 of 0.66 ± 0.03 Torr and Hill *n* of 1.36 ± 0.03, values very close to those exhibited by species ***a***. However, when ODCs were measured for PEG-Hb^{oxy} fractions separated by native PAGE (data not shown), p50 values were found to even 2-fold different between them.

PEGylated Hbs obtained under anaerobic conditions exhibited nearly normal oxygen affinity modulation by 2,3-BPG, due to the organic phosphate binding pocket protection by IHP during the chemical modification and a Bohr effect reduced by 20−25% (*34*). However, more relevant in view of the use of PEG-Hbs as HBOC are the effects of CO_2 and Cl^-, which are allosteric

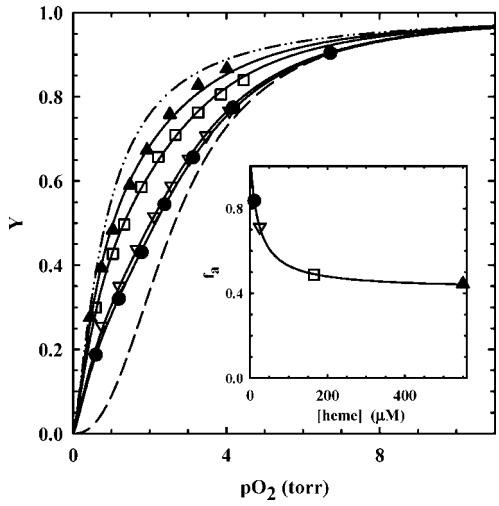

Figure 3. Concentration dependence of oxygen binding to PEG-Hb^{deoxy}, PEG-Hb^{oxy}, and Hb. ODCs at 11 (closed up-triangles), 25 (open squares), 165 (open down-triangles), and 550 μM (closed circles) concentrations of PEG-Hb^{deoxy} were determined in 100 mM Hepes, 1 mM EDTA, pH 7, at 15 °C. ODCs were determined under the same conditions for 193 μM HbA (dash line) and 219 μM PEG-Hb^{oxy}. (dash-dot-dot line). ODCs for PEG-Hb^{deoxy} were globally fitted (solid lines) assuming different fractions of component **a** ($p50_a = 0.80$ Torr and $n_a = 1.33$) and **b** ($p50_b = 3.18$ Torr, $n_b = 2.54$). HbA and PEG-Hb^{oxy} were fitted to a single species with p50 of 2.61 ± 0.05 Torr and Hill n of 2.36 ± 0.06 and p50 of 0.85 ± 0.02 Torr and Hill n of 1.34 ± 0.04, respectively. Inset: dependence of the fraction of component **a** on concentration. The dependence was fitted to a binding isotherm with an apparent tetramer−dimer equilibrium constant $K_d = 21.5 \pm 2.3$ μM.

effectors present in the plasma. The comparison of p50 and Hill n values for Hb, NES-Hb, PEG-Hb^{deoxy}, and PEG-Hb^{oxy}, in the absence and presence of physiological concentrations of CO_2 and saturating concentration of Cl^- (Table 2), shows a decrease in oxygen affinity brought about by the allosteric ligands on both PEGylated Hbs, although to an extent that is less than on HbA.

CO Binding Kinetics to HbA, PEG-Hb^{deoxy}, and PEG-Hb^{oxy}. Binding kinetics of CO to HbA is characterized by an autocatalytic behavior due to the shift of the quaternary T to R state equilibrium as a function of ligand saturation (*55, 56*). The observed log rate constants, expressed as M^{-1} s^{-1} of 0.5 atm CO binding to Hb, determined by stopped-flow measurements (Figure 4), were 5.034 ± 0.001 and 5.776 ± 0.008 at 107 μM HbA, and only slightly higher (5.101 ± 0.002 and 5.782 ± 0.009) at 3.5 μM HbA, in good agreement with previously determined values (*57*). The kinetics of CO binding to 96 and 14 μM PEG-Hb^{oxy} (Figure 4) were monophasic with a log rate constant of ~5.3, independent of protein concentration. The CO binding kinetics to 88 and 6.6 μM PEG-Hb^{deoxy} (Figure 4) were nearly monophasic with log rate constants of 5.073 ± 0.001 and 5.120 ± 0.001, respectively.

The kinetic trace of CO rebinding to HbA after laser flash photolysis (Figure 5A) originates from three distinct processes: a nanosecond geminate rebinding of CO still present in the heme pocket of R state molecules that have not yet relaxed to the T state, a microsecond bimolecular rebinding of CO from the solvent to R state molecules, and a millisecond bimolecular rebinding of CO from solvent to tetramers that have switched to the T quaternary state (*58, 59*). The kinetics is more complex due to the overlapping tertiary and quaternary conformational changes triggered by the ligation state (*59*). The associated lifetime distribution (Figure 5B) exhibits three bands centered at 90 ns, 200 μs, and 6 ms, in good agreement with previously reported data (*59, 60*).

CO rebinding to PEG-Hb^{deoxy} and PEG-Hb^{oxy}, in the absence of IHP, exhibits a lower geminate rebinding amplitude than HbA and an almost negligible T state bimolecular rebinding (Figure 5A). The associated lifetime distributions (Figure 5B) show two major bands centered at ≈ 90 ns and ≈ 200 μs, corresponding to geminate and bimolecular rebinding, respectively. A barely detectable band appears at 10 ms. The amplitude of the band associated with geminate recombination is lower for PEGylated Hbs than in HbA and becomes broader in the case of PEG-Hb^{oxy}. The band centered around 200 μs displays only minimal differences among samples, suggesting that the rate for CO rebinding to R is similar for all samples.

The presence of the allosteric effector IHP leads to a slight decrease in the amplitude of the geminate phase for both PEG-Hb^{deoxy} and PEG-Hb^{oxy} and a concomitant onset of millisecond T state bimolecular rebinding. The comparison of the rebinding kinetics in the absence and presence of IHP for PEG-Hb^{oxy} (Figure 6A) and the corresponding lifetime distributions (Figure 6B) indicates that, in the presence of IHP, the nanosecond and microsecond bands appear to be slightly shifted toward longer times, with the geminate phase becoming a bit smaller, and a clearly distinguishable additional band at ≈ 9 ms. These effects demonstrate for PEG-Hb^{oxy} and, similarly, for PEG-Hb^{deoxy} (data not shown) that the allosteric effectors bias the distribution of molecules toward states with T-like reactivity.

CO rebinding kinetics were measured for 13 and 98 μM PEG-Hb^{deoxy} (Figure 7A). When PEG-Hb^{deoxy} concentration is increased, an additional kinetic phase appears in the millisecond range. Accordingly, three distinct peaks are present in the MEM lifetime distribution (Figure 7B), corresponding to geminate rebinding (100 and 130 ns, at 13 and 98 μM, respectively) and to bimolecular rebinding to R-like structures (230 and 250 μs, at 13 and 98 μM, respectively) and to T-like structures (12 ms at 98 μM; at 13 μM this band is barely detectable and has a maximum at 7 ms). It is worthwhile to notice that the bands become broader when the protein concentration is increased. Analogous results were obtained for PEG-Hb^{oxy} (data not shown).

Variation of the amplitude of the geminate phase and the concomitant increased amplitude of the slow second-order rebinding in the presence of allosteric effectors (Figure 6), increasing protein concentration (Figure 7), and increasing photolysis level (data not shown) indicate that an R to T quaternary conformational change is occurring upon photolysis also for PEG-Hb^{deoxy} and PEG-Hb^{oxy}. However, when compared to rebinding to HbA, the bimolecular rebinding to T-like structures measured for PEG-Hb^{deoxy} and PEG-Hb^{oxy} exhibits a lower amplitude, suggesting that the bias toward a T-like structure is much lower for these products than for HbA due to a higher concentration of the liganded dimers and a slow kinetics of dimer to tetramer association in the unliganded state.

DISCUSSION

PEG-Hb Heterogeneity. The PEGylation procedure yields topologically heterogeneous products because the similar accessibility of the lysine residues (5−7 per Hb chain) reacting with IMT does not allow an absolute selectivity (*34*). In addition, these modifiable sites are not fully saturated by PEG conjugation because the usual HBOC preparation adds only 6−8 PEG per Hb tetramer, which leaves a small fraction of unmodified chains. The MALDI MS analyses carried out on the chains isolated by SDS-PAGE allowed a reliable quantitative determination of unmodified and differently PEGylated chains distribution. The PEG moiety distribution for PEG-Hb^{deoxy} indicates that the bulk of this product (65−70%) consists of tetramers conjugated with a number of PEG chains centered at the value of 6.6 ± 1. Procedures have been developed for the direct coupling to Hb

Table 2. Effects of CO_2 and Cl^- on Oxygen Affinity[a]

species	stripped p50$_b$ (Torr)	n_b	CO_2 p50$_b$(Torr)	n_b	Cl^- p50$_b$(Torr)	n_b
HbA[b]	2.61 ± 0.05	2.36 ± 0.06	4.09 ± 0.02	2.70 ± 0.04	5.15 ± 0.01	3.08 ± 0.02
NEM-Hb	2.23 ± 0.03	2.35 ± 0.04	3.16 ± 0.05	2.28 ± 0.06	4.14 ± 0.05	2.60 ± 0.06
PEG-Hb^{deoxy}	3.18 ± 0.08	2.54 ± 0.19	3.71 ± 0.03	2.21 ± 0.03	3.66 ± 0.05	2.23 ± 0.06
PEG-Hb^{oxy}[b]	0.85 ± 0.02	1.34 ± 0.04	1.23 ± 0.03	1.33 ± 0.06	1.38 ± 0.04	1.44 ± 0.06

[a] p50$_b$ of HbA, NEM-Hb, PEG-Hb^{deoxy}, and PEG-Hb^{oxy}, in the absence and presence of physiological concentrations of CO_2 and saturating concentration of Cl^- (200 mM), in a solution containing 100 mM Hepes, 1 mM EDTA, at 15°C, pH 7.0. The sample concentration is 110−200 μM. [b] For HbA and PEG-Hb^{oxy}, p50 and n were obtained by fitting ODCs to a single species.

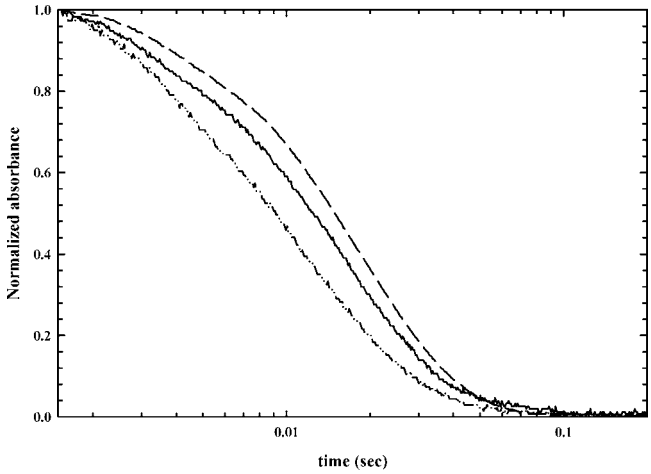

Figure 4. CO binding kinetics to PEG-Hb^{deoxy}, PEG-Hb^{oxy}, and Hb, in the absence of allosteric effectors. Normalized absorbance changes at 435 nm followed upon rapid mixing of deoxy 14 μM PEG-Hb^{oxy} (dash-dot-dot line), 6.6 μM PEG-Hb^{deoxy} (solid line), and 3.5 μM HbA (dash line) in a solution containing 100 mM Hepes, 1 mM EDTA, pH 7, 0.5 atm CO at 15 °C.

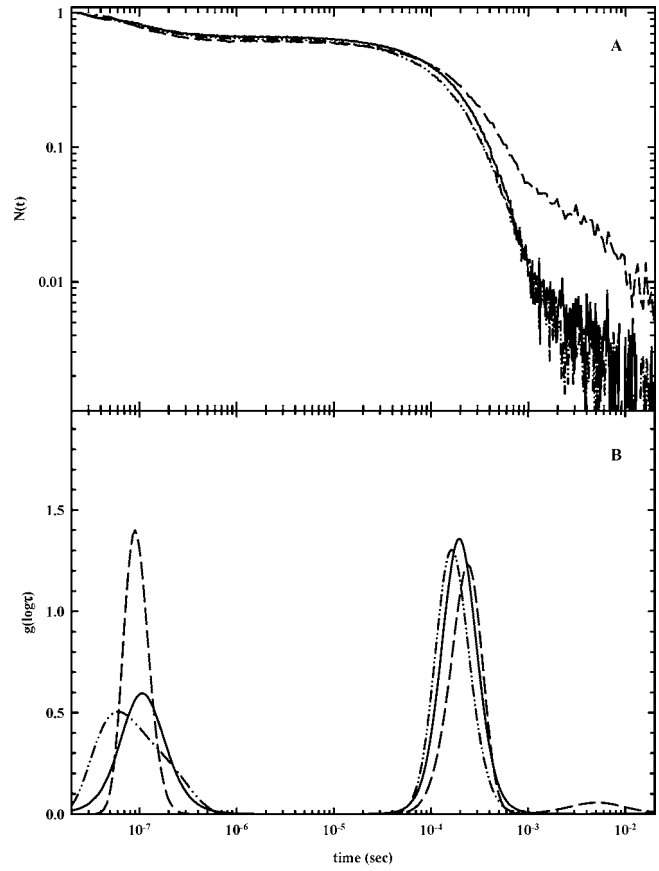

Figure 5. Ligand rebinding kinetics to HbA, PEG-Hb^{deoxy}, and PEG-Hb^{oxy}, after photodissociation of the CO complex. (A) Kinetic progress curves for the fraction of deoxyhemes vs time are reported for HbA (dashed line), PEG-Hb^{deoxy} (solid) and PEG-Hb^{oxy} (dash-dot-dot line) in a solution containing 100 mM Hepes, 1 mM EDTA, pH 7.0, 1 atm CO, at 15 °C, 105 μM HbA, 110 μM PEG-Hb^{deoxy} and 107 μM PEG-Hb^{oxy}. (B) Lifetime distributions associated with the kinetics shown in panel A, calculated using MEM analysis.

of functionalized PEG (*61*, *62*). It cannot be excluded that bound bulky PEG molecules steer the attachment of other PEG molecules leading to products less heterogeneous than those obtained in the two-step PEGylation procedure. However, the issue of molecular weight heterogeneity may also concern these products because of the large number of potential attachment sites, 42 lysines and 4 α-amino groups, with respect to the much lower number, 6−8, of bound PEGs. Thus, it seems unavoidable that PEGylated Hb is a heterogeneous product. This relatively wide species heterogeneity leads to different physicochemical and physiological properties that should be taken into account when in vivo experiments are analyzed and might be responsible for some of the observed adverse effects (*23*).

PEGylated Hb Tetramer Stability. Native Hb undergoes a reversible tetramer−dimer equilibrium as depicted by eq 4:

$$(\alpha\beta)(\alpha\beta) \underset{k_{ass}}{\overset{k_{diss}}{\rightleftharpoons}} 2(\alpha\beta) \qquad (4)$$

where $(\alpha\beta)(\alpha\beta)$ represents the tetrameric form and $(\alpha\beta)$ the dimeric form of the protein.

The rate of dissociation, k_{diss}, is ligation-dependent with $k_{diss(deoxy)} \ll k_{diss(oxy)}$, whereas the rate of association, k_{ass}, is ligation-independent (*37*). The reactions in eq 4 have several important implications for evaluation of the in vitro and in vivo properties of PEGylated Hbs: (i) the exchange of dimers among species differing in the number and distribution of conjugated PEG-Hb yields hybrid species. This phenomenon could contribute in vitro to smoothing out the molecular weight heterogeneity of the species and their properties in solution, such as oxygen affinity, allosteric effects, redox potential; (ii) in the circulation, at the interface with tissues, selective permeation of some species may occur leading to a change in the bulk properties of the PEGylated species confined in the plasma; (iii) the order of magnitude of the equilibrium constants for the dissociation of deoxy Hb and oxy Hb are 10^{-11} and 10^{-6} M, respectively. Most Hb mutants with increased oxygen affinity and decreased cooperativity show an increase in $k_{diss(deoxy)}$, although a few cases are known in which an increase in $k_{diss(oxy)}$ has also been observed (*36*, *37*). Since the tetramer−dimer equilibrium is an oxygen-linked property, it could be involved in the cooperativity reduction of PEGylated Hbs, mimicking mutant species. A direct study of the reactions in eq 4 by various methods, such as haptoglobin binding (*63*) and hybridization techniques (*64*, *65*) was not feasible due to the interference of conjugated PEG.

The equilibrium gel permeation study of NES-Hb showed that the product exhibits the same $K_{diss(oxy)}$ as normal Hb. The $K_{diss(deoxy)}$ value could not be measured because the product was not significantly dissociated under the most dilute conditions, as known for normal Hb. The various PEGylated species in the polydisperse solution of PEG-BSA were not resolved by size

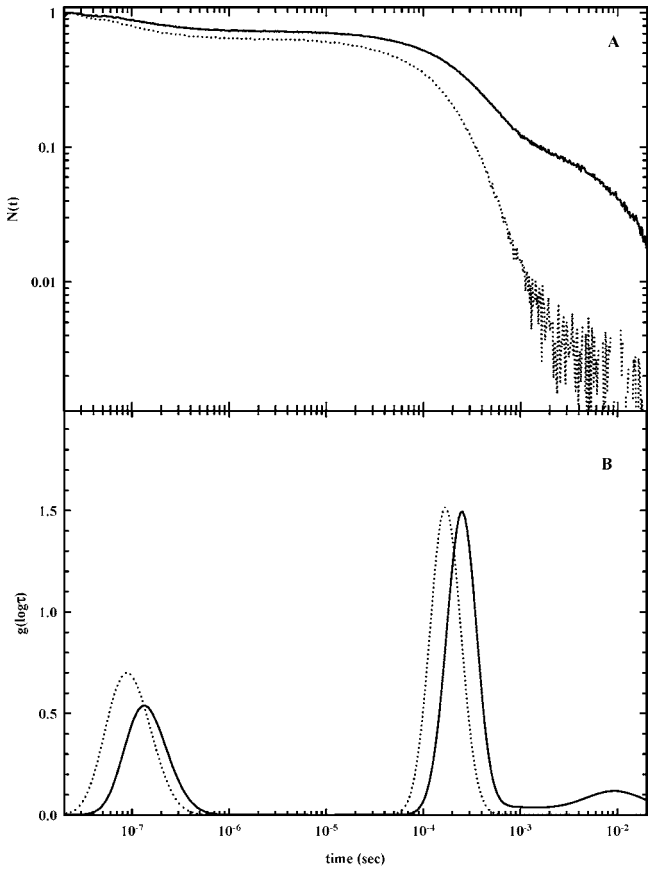

Figure 6. Effect of IHP on PEG-Hb^{oxy} CO rebinding kinetics. (A) CO rebinding kinetics in 100 mM Hepes, 1 mM EDTA, pH 7.0, 1 atm CO, 15 °C, to PEG-Hb^{ox} in the absence (dotted line) and presence (solid line) of 10 mM IHP, at 107 and 100 μM PEG-Hb^{oxy}, respectively. (B) Lifetime distributions associated with the kinetic traces shown in A, calculated using MEM analysis.

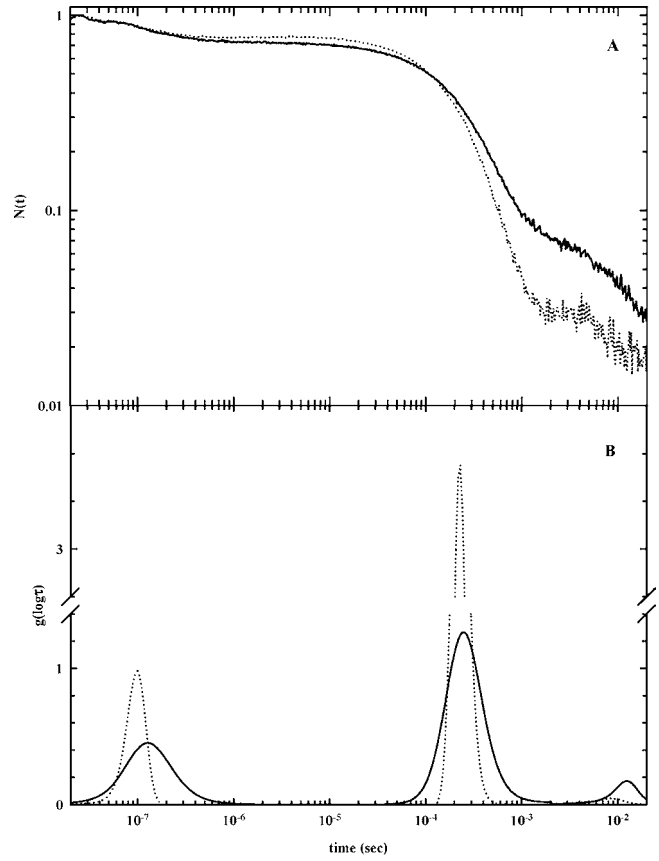

Figure 7. Effect of protein concentration on PEG-Hb^{deoxy} CO rebinding kinetic. (A) CO rebinding kinetics to PEG-Hb^{deoxy} at 13 μM (dotted line) and 98 μM (solid line), 10 mM IHP, 100 mM Hepes, 1 mM EDTA, pH 7.0, 1 atm CO, 15 °C. (B) Lifetime distributions associated with the kinetic traces, shown in A, calculated using MEM analysis.

exclusion chromatography both at high and low product concentration, at which trailing was completely absent. On the contrary, PEG-Hb^{deoxy} under aerobic conditions was resolved into a multiplicity of components upon similar dilution, in agreement with the electrophoretic pattern under native conditions (data not shown). Some of these components had apparent molecular weights consistent with monomeric PEGylated species. Since the phenomenon was completely reversible, the most plausible interpretation is that oxy PEG-Hb^{deoxy} dissociates rapidly into dimers as normal oxy HbA does, but the PEGylated subunits reassociate at a low rate compared with the time scale of the chromatography, in contrast with oxy HbA behavior. This interpretation is consistent with the observation that the slight residual trailing under deoxy conditions was minimal when the sample was obtained by dilution of a deoxygenated solution in which the low molecular weight species had not been given enough time to form (Figure 2B, dashed line). When deoxygenation was carried out rapidly by the addition of dithionite to the diluted oxygenated solution, trailing was more significant because some of the low molecular weight species had not been given enough time to reassociate (Figure 2B, solid line). Two possible explanations for this behavior are the slower translational/rotational coefficient of the PEGylated dimeric species, as suggested by the DLS measurements in dilute solution, also reported by other authors (*32, 66*), and steric interference by PEG in the mechanism of subunit reassociation. The PEG-Hb^{deoxy} chromatography under anaerobic conditions did not show a multiplicity of components. The slight trailing observed at high concentration was not significantly increased upon dilution. This can be attributed to the very slow rate of dissociation of the various PEGylated tetramers as compared with the elution rate.

The size exclusion chromatography studies indicate that under aerobic conditions PEG-Hb^{oxy} was more markedly dissociated into dimers than PEG-Hb^{deoxy} and, under anaerobic conditions, a more pronounced trailing was observed if deoxygenation was achieved by dithionite addition to dilute oxy PEG-Hb^{oxy} (Figure 2C). Fully in keeping with this finding, functional properties of PEG-Hb^{oxy} were found to be less affected by dilution than PEG-Hb^{deoxy} (see below). Therefore, PEGylation carried out under aerobic conditions favors the modification of sites crucial for function and tetramer assembly, likely leading to a very large population of dimeric species. These sites are less severely modified in the anaerobic procedure for PEG-Hb^{deoxy} preparation.

Oxygen Binding Affinity and CO Binding Rate, in the Absence and Presence of Allosteric Effectors. The concentration dependence of the oxygen affinity of PEG-Hb^{deoxy} (Figure 3) and the corresponding analysis (Figure 3, inset) indicates that at least two species are in equilibrium in solution. On the basis of the p50s, Hill coefficients, and responses to allosteric effectors, the more straightforward interpretation is that one species corresponds to PEG-Hb tetramers, characterized by functional properties close to native HbA and the other corresponds to PEG-Hb dimers because its amount increases on dilution. It is interesting to note that the latter species exhibits functional properties very similar to PEG-Hb^{oxy}, that as demonstrated by native electrophoresis and ODC is likely to be composed of heterogeneous highly reactive dimeric species. An alternative interpretation is that the high oxygen affinity species is associated to a perturbed R state tetramer in which the

quaternary transition is either prevented or dramatically slowed down by PEGylation. Such an interpretation is consistent with the hypothesis suggested by Svergun et al. (*33*) that PEG chains may interfere with the T/R transition by binding at the dimer interface, thereby reducing cooperativity. However, the ODC dependence on concentration favors the former interpretation.

PEG-Hb^{deoxy} more than PEG-Hb^{oxy} responds to the physiological concentrations of CO_2 and Cl^- by reducing the oxygen affinity, although not to the same extent as native HbA (Table 2). This can be explained since one of the binding sites common to both ligands involves the α-amino groups of the α chains. PEGylation of Lysα7 likely interferes with the salt bridge formed by Valα1 and removes part of the oxygen-linked CO_2, Cl^-, and Bohr effects involving this site (*34, 67*). However, the protection of the 2,3-BPG binding pocket during PEGylation for PEG-Hb^{deoxy}, but not PEG-Hb^{oxy}, allows CO_2 modulation through binding in the deoxy structure to the amino groups of Val1β, the major site of CO_2 binding (*68*), and Cl^- modulation through binding to Lysβ82 (*69*). These data support the notion that PEGylation of deoxy Hb exhibits a less dramatic impact on protein functional properties.

The comparison of CO binding and rebinding kinetics of PEG-Hb^{deoxy}, PEG-Hb^{oxy}, and HbA, at high and low concentration, in the absence and presence of IHP, allows further identification of functional differences, associated with distinct species. First, it is interesting to note that CO binding to deoxy PEG-Hb^{deoxy} and PEG-Hb^{oxy} is monophasic, lacks the autocatalytic process typical of native Hb, and is concentration-independent over about a 10-fold range of concentrations (10−100 μM). In particular, the observed rate constant for PEG-Hb^{deoxy} exhibits the same value of the rate associated with the slow phase of HbA, whereas the rate constant for CO binding to PEG-Hb^{oxy} is higher but still lower than the rate of the fast phase observed for HbA. These findings suggest that (i) deoxy PEG-Hb^{deoxy} is predominantly present as T state tetramers converting to the R state slower than CO binding, and (ii) deoxy PEG-Hb^{oxy} is present as a mixture of perturbed dimers and T state tetramers, in keeping with the chromatographic measurements, that slowly are converted to the R state. A more detailed analysis is hampered by the fast rate of reaction, leading to the loss of a significant portion of the kinetic traces. Nevertheless, these data provide complementary information with respect to the more robust results generated from flash photolysis experiments. It was found that CO rebinding to both PEGylated samples, in the absence of IHP, did not show significant bimolecular rebinding to T state. This can be explained by either PEGylation reducing the rate of the R to T quaternary transition or the liganded PEGylated Hbs being predominantly present as dimers that, upon deligation, form T state tetramers on a time scale slower than CO rebinding. The reduced amplitude of the geminate rebinding indicates a faster escape to solvent, as observed in myoglobin. The appearance of milliseconds bimolecular rebinding in the presence of IHP, at higher concentrations or higher pulse energy, clearly signals an increased accumulation of T state tetramers. However, their amount is much lower than in native Hb due to a slow quaternary R to T transition and/or dimer association upon deligation.

In a recent paper, CO binding kinetics was measured for Hemospan (*70*), observing a CO rebinding lacking the geminate phase. This discrepancy with respect to our laser flash photolysis data is most probably due to the instrumental setup used in the previous work that did not allow detection of submicrosecond processes.

Overall, results indicate that PEG-Hb^{oxy} is predominantly in a highly reactive state, characterized by high oxygen affinity and a high rate of CO binding. Ligand binding triggers the formation of dimers faster than the quaternary T to R transition. The same picture holds for PEG-Hb^{deoxy}, assuming that the PEG-Hb^{deoxy} tetrameric T state is more stable than PEG-Hb^{oxy} and the T to R quaternary transition efficiently competes with tetramer dissociation. Thus, under physiological conditions, PEG-Hb^{oxy} and PEG-Hb^{deoxy}, in spite of containing the same average number of PEG molecules, are expected to deliver different amounts of oxygen, react with NO and nitrite with different rates, and trigger different regulatory signals because they exhibit distinct functional and structural properties.

CONCLUSIONS

PEGylation affects Hb in distinct ways: (i) perturbation of the T and R states (*31*), (ii) perturbation of the quaternary transitions (*33*), and (iii) influence on the tetramer−dimer equilibrium (*38*). Although animal studies carried out using PEG-Hb^{deoxy} and other similar products showed only moderately adverse pressure and renal filtration effects in the short period (2−3 h), the long-term effects of the stability upon dilution of the various PEGylated tetramers and dimers should be considered with regard to both the physicochemical and physiological properties of the bulk product in the circulation. The observed anomalous equilibrium of the PEGylated tetramers and product heterogeneity should also be considered in the evaluation of the extravasation and renal filtration behavior of these HBOCs. In view of the reported adverse effects of most HBOCs (*23*), it is mandatory to tightly link functional and structural HBOC properties with biochemical and physiological parameters, including proteomic analyses, associated to organ damages, oxidative stress, and inflammatory signals. This is our long-term ongoing challenge.

ACKNOWLEDGMENT

This work was supported by grant COFIN (programmi di ricerca cofinanziati) 2003 from the MiUR (Ministero dell'Istruzione, dell'Università e della Ricerca Scientifica) to M.P., a grant (LSHB-CT-2004-505023) from the European Union Sixth Framework STREP (Specific Targeted Research Project) to M.P. and A.M. and a grant from Fondazione Cariparma to A.M. We are grateful to the Interdepartmental Measurement Center (CIM), University of Parma, for the use of MALDI-TOF.

LITERATURE CITED

(1) Campanini, B., Bruno, S., Raboni, S., and Mozzarelli, A. (2003) Oxygen Delivery by Allosteric Effectors of Hemoglobin, Blood Substitutes, and Plasma Expanders, in *Cardiovascular Agents and Endocrines* (Abraham, D. J., Ed.) pp 385−442, John Wiley and Sons, Inc., New York.
(2) Winslow, R. M. (2006) *Blood Substitutes*, Elsevier, Amsterdam.
(3) Chang, T. M. S. (1997) *Blood Substitutes - Principles, Methods, Products & Clinical Trials*, Karger, S., Publisher Inc., Basel.
(4) Mozzarelli, A. (2008) Hemoglobin-based oxygen carriers as blood substitutes. *Biochim. Biophys. Acta 1784*, 1363–1364.
(5) Morisaki, H., and Sibbald, W. J. (2004) Tissue oxygen delivery and the microcirculation. *Crit. Care Clin. 20*, 213–223.
(6) Sakai, H., and Tsuchida, E. (2006) Performances of PEG-modified hemoglobin-vesicles as artificial oxygen carriers in microcirculation. *Clin. Hemorheol. Microcirc. 34*, 335–40.
(7) Linberg, R., Conover, C. D., Shum, K. L., and Shorr, R. G. (1998) Increased tissue oxygenation and enhanced radiation sensitivity of solid tumors in rodents following polyethylene glycol conjugated bovine hemoglobin administration. *In Vivo 12*, 167–73.
(8) Teicher, B. A., Holden, S. A., Ara, G., Herman, T. S., Hopkins, R. E., and Menon, K. (1992) Effect of a bovine hemoglobin preparation (SBHS) on the response of two murine solid tumors to radiation therapy or chemotherapeutic alkylating agents. *Biomater. Artif. Cells Immobil. Biotechnol. 20*, 657–60.

(9) Dani, C., Martelli, E., Bertini, G., Pezzati, M., Rossetti, M., Buonocore, G., Paffetti, P., and Rubaltelli, F. F. (2004) Effect of blood transfusions on oxidative stress in preterm infants. *Arch. Dis. Child Fetal Neonatal. Ed. 89*, F408–11.

(10) Chatterjee, R., Welty, E. V., Walder, R. Y., Pruitt, S. L., Rogers, P. H., Arnone, A., and Walder, J. A. (1986) Isolation and characterization of a new hemoglobin derivative cross-linked between the alpha chains (lysine 99 alpha 1–lysine 99 alpha 2). *J. Biol. Chem. 261*, 9929–37.

(11) Vandegriff, K. D., Medina, F., Marini, M. A., and Winslow, R. M. (1989) Equilibrium oxygen binding to human hemoglobin cross-linked between the alpha chains by bis(3,5-dibromosalicyl) fumarate. *J. Biol. Chem. 264*, 17824–33.

(12) Cheng, D. C., Mazer, C. D., Martineau, R., Ralph-Edwards, A., Karski, J., Robblee, J., Finegan, B., Hall, R. I., Latimer, R., and Vuylsteke, A. (2004) A phase II dose-response study of hemoglobin raffimer (Hemolink) in elective coronary artery bypass surgery. *J. Thorac. Cardiovasc. Surg. 127*, 79–86.

(13) Hughes, G. S., Jr., Antal, E. J., Locker, P. K., Francom, S. F., Adams, W. J., and Jacobs, E. E., Jr. (1996) Physiology and pharmacokinetics of a novel hemoglobin-based oxygen carrier in humans. *Crit. Care Med. 24*, 756–64.

(14) Sehgal, L. R., Gould, S. A., Rosen, A. L., Sehgal, H. L., and Moss, G. S. (1984) Polymerized pyridoxylated hemoglobin: a red cell substitute with normal oxygen capacity. *Surgery 95*, 433–8.

(15) Iwashita, Y., Yabuki, A., Yamaji, K., Iwasaki, K., Okami, T., Hirata, C., and Kosaka, K. (1988) A new resuscitation fluid "stabilized hemoglobin" preparation and characteristics. *Biomater. Artif. Cells Artif. Organs 16*, 271–80.

(16) Vandegriff, K. D., Malavalli, A., Wooldridge, J., Lohman, J., and Winslow, R. M. (2003) MP4, a new nonvasoactive PEG-Hb conjugate. *Transfusion 43*, 509–516.

(17) Conover, C. D., Malatesta, P., Lejeune, L., Chang, C. L., and Shorr, R. G. (1996) The effects of hemodilution with polyethylene glycol bovine hemoglobin (PEG-Hb) in a conscious porcine model. *J. Invest. Med. 44*, 238–46.

(18) Nho, K., Linberg, R., Johnson, M., Gilbert, C., and Shorr, R. (1994) PEG-hemoglobin: an efficient oxygen-delivery system in the rat exchange transfusion and hypovolemic shock models. *Artif. Cells Blood Substit. Immobil. Biotechnol. 22*, 795–803.

(19) Jahr, J. S., Moallempour, M., and Lim, J. C. (2008) HBOC-201, hemoglobin glutamer-250 (bovine), Hemopure(R) (Biopure Corporation). *Exp. Opin. Biol. Ther. 8*, 1425–1433.

(20) Smani, Y. (2008) Hemospan: a hemoglobin-based oxygen carrier for potential use as a blood substitute and for the potential treatment of critical limb ischemia. *Curr. Opin. Invest. Drugs 9*, 1009–19.

(21) Levy, J. H., Goodnough, L. T., Greilich, P. E., Parr, G. V., Stewart, R. W., Gratz, I., Wahr, J., Williams, J., Comunale, M. E., Doblar, D., Silvay, G., Cohen, M., Jahr, J. S., and Vlahakes, G. J. (2002) Polymerized bovine hemoglobin solution as a replacement for allogeneic red blood cell transfusion after cardiac surgery: results of a randomized, double-blind trial. *J. Thorac. Cardiovasc. Surg. 124*, 35–42.

(22) Olofsson, C., Ahl, T., Johansson, T., Larsson, S., Nellgard, P., Ponzer, S., Fagrell, B., Przybelski, R., Keipert, P., Winslow, N., and Winslow, R. M. (2006) A multicenter clinical study of the safety and activity of maleimide-polyethylene glycol-modified Hemoglobin (Hemospan) in patients undergoing major orthopedic surgery. *Anesthesiology 105*, 1153–63.

(23) Natanson, C., Kern, S. J., Lurie, P., Banks, S. M., and Wolfe, S. M. (2008) Cell-free hemoglobin-based blood substitutes and risk of myocardial infarction and death: a meta-analysis. *J. Am. Med. Assoc. 299*, 2304–12.

(24) Greenburg, A. G., Pitman, A., Pearce, B., and Kim, H. W. (2008) Clinical contextualization and the assessment of adverse events in HBOC trials. *Artif. Cells Blood Substit. Immobil. Biotechnol. 36*, 477–486.

(25) Young, M. A., Lohman, J., Malavalli, A., Vandegriff, K. D., Winslow, R. M. (2009) Hemospan improves outcome in a model of perioperative hemodilution and blood loss in the rat: comparison with hydroxyethyl starch. *J. Cardiothorac. Vasc. Anesth. 23*, 339–347.

(26) Vandegriff, K. D., Malavalli, A., Mkrtchyan, G. M., Spann, S. N., Baker, D. A., and Winslow, R. M. (2008) Sites of modification of hemospan, a poly(ethylene glycol)-modified human hemoglobin for use as an oxygen therapeutic. *Bioconjugate Chem. 19*, 2163–2170.

(27) Olofsson, C., Nygards, E. B., Ponzer, S., Fagrell, B., Przybelski, R., Keipert, P. E., Winslow, N., and Winslow, R. M. (2008) A randomized, single-blind, increasing dose safety trial of an oxygen-carrying plasma expander (Hemospan) administered to orthopaedic surgery patients with spinal anaesthesia. *Transfus. Med. 18*, 28–39.

(28) Jia, L., Bonaventura, C., Bonaventura, J., and Stamler, J. S. (1996) S-nitrosohaemoglobin: a dynamic activity of blood involved in vascular control. *Nature 380*, 221–6.

(29) Pawloski, J. R., Hess, D. T., and Stamler, J. S. (2001) Export by red blood cells of nitric oxide bioactivity. *Nature 409*, 622–6.

(30) Stamler, J. S., Jia, L., Eu, J. P., McMahon, T. J., Demchenko, I. T., Bonaventura, J., Gernert, K., and Piantadosi, C. A. (1997) Blood flow regulation by S-nitrosohemoglobin in the physiological oxygen gradient. *Science 276*, 2034–7.

(31) Lui, F. E., Dong, P., and Kluger, R. (2008) Polyethylene glycol conjugation enhances the nitrite reductase activity of native and cross-linked hemoglobin. *Biochemistry 47*, 10773–80.

(32) Manjula, B. N., Tsai, A., Upadhya, R., Perumalsamy, K., Smith, P. K., Malavalli, A., Vandegriff, K., Winslow, R. M., Intaglietta, M., Prabhakaran, M., Friedman, J. M., and Acharya, A. S. (2003) Site-specific PEGylation of hemoglobin at Cys-93(beta): correlation between the colligative properties of the PEGylated protein and the length of the conjugated PEG chain. *Bioconjugate Chem. 14*, 464–72.

(33) Svergun, D. I., Ekstrom, F., Vandegriff, K. D., Malavalli, A., Baker, D. A., Nilsson, C., and Winslow, R. M. (2008) Solution structure of poly(ethylene) glycol-conjugated hemoglobin revealed by small-angle X-ray scattering: implications for a new oxygen therapeutic. *Biophys. J. 94*, 173–81.

(34) Iafelice, R., Cristoni, S., Caccia, D., Russo, R., Rossi-Bernardi, L., Lowe, K. C., and Perrella, M. (2007) Identification of the sites of deoxyhaemoglobin PEGylation. *Biochem. J. 403*, 189–196.

(35) Portoro, I., Kocsis, L., Herman, P., Caccia, D., Perrella, M., Ronda, L., Bruno, S., Bettati, S., Micalella, C., Mozzarelli, A., Varga, A., Vas, M., Lowe, K. C., and Eke, A. (2008) Towards a novel haemoglobin-based oxygen carrier: Euro-PEG-Hb, physico-chemical properties, vasoactivity and renal filtration. *Biochim. Biophys. Acta 1784*, 1402–1409.

(36) LiCata, V. J., Speros, P. C., Rovida, E., and Ackers, G. K. (1990) Direct and indirect pathways of functional coupling in human hemoglobin are revealed by quantitative low-temperature isoelectric focusing of mutant hybrids. *Biochemistry 29*, 9771–83.

(37) Turner, G. J., Galacteros, F., Doyle, M. L., Hedlund, B., Pettigrew, D. W., Turner, B. W., Smith, F. R., Moo-Penn, W., Rucknagel, D. L., and Ackers, G. K. (1992) Mutagenic dissection of hemoglobin cooperativity: effects of amino acid alteration on subunit assembly of oxy and deoxy tetramers. *Proteins 14*, 333–50.

(38) Hu, T., Li, D., Manjula, B. N., Brenowitz, M., Prabhakaran, M., and Acharya, S. A. (2009) PEGylation of Val-1(alpha) destabilizes the tetrameric structure of hemoglobin. *Biochemistry 48*, 608–16.

(39) Ampulski, R. S., Ayers, V. E., and Morell, S. A. (1969) Determination of the reactive sulfhydryl groups in heme proteins with 4,4′-dipyridinedisulfide. *Anal. Biochem. 32*, 163–9.

(40) Laemmli, U. K. (1970) Cleavage of structural proteins during the assembly of the head of bacteriophage T4. *Nature 227*, 680–5.

(41) Cantu, L., Corti, M., Lago, P., Musolino, M. (1991) In *Photon Correlation Spectroscopy: Multicomponent Systems* (Kenneth, S. S., Ed.) pp 144−159, SPIE, Los Angeles.

(42) Degiorgio, V., Corti, M., and Minero, C. (1984) Laser light scattering in micellar solutions. *Il Nuovo Cimento D 3*, 44–61.

(43) Winzor, D. J., and Scheraga, H. A. (1963) Studies of chemically reacting systems on Sephadex. I. Chromatographic demonstration of the Gilbert theory. *Biochemistry 2*, 1263–1267.

(44) Hayashi, A., Suzuki, T., and Shin, M. (1973) An enzymic reduction system for metmyoglobin and methemoglobin, and its application to functional studies of oxygen carriers. *Biochim. Biophys. Acta 310*, 309–16.

(45) Ronda, L., Bruno, S., Faggiano, S., Bettati, S., and Mozzarelli, A. (2008) Oxygen binding to heme proteins in solution, encapsulated in silica gels, and in the crystalline state. *Methods Enzymol. 437*, 311–28.

(46) Bettati, S., and Mozzarelli, A. (1997) T state hemoglobin binds oxygen noncooperatively with allosteric effects of protons, inositol hexaphosphate, and chloride. *J. Biol. Chem. 272*, 32050–32055.

(47) Rivetti, C., Mozzarelli, A., Rossi, G. L., Henry, E. R., and Eaton, W. A. (1993) Oxygen binding by single crystals of hemoglobin. *Biochemistry 32*, 2888–2906.

(48) Abbruzzetti, S., Bruno, S., Faggiano, S., Ronda, L., Grandi, E., Mozzarelli, A., and Viappiani, C. (2008) Characterization of ligand migration mechanisms inside hemoglobins from the analysis of geminate rebinding kinetics. *Methods Enzymol. 437*, 329–45.

(49) Abbruzzetti, S., Bruno, S., Faggiano, S., Grandi, E., Mozzarelli, A., and Viappiani, C. (2006) Time-resolved methods in Biophysics. 2. Monitoring haem proteins at work with nanosecond laser flash photolysis. *Photochem. Photobiol. Sci. 5*, 1109–20.

(50) Steinbach, P. J. (1996) Two-dimensional distributions of activation enthalpy and entropy from kinetics by the maximum entropy method. *Biophys. J. 70*, 1521–8.

(51) Sottini, S., Abbruzzetti, S., Spyrakis, F., Bettati, S., Ronda, L., Mozzarelli, A., and Viappiani, C. (2005) Geminate rebinding in R-state hemoglobin: kinetic and computational evidence for multiple hydrophobic pockets. *J. Am. Chem. Soc. 127*, 17427–17432.

(52) Abbruzzetti, S., Giuffrida, S., Sottini, S., Viappiani, C., and Cordone, L. (2005) Light-induced protein-matrix uncoupling and protein relaxation in dry samples of trehalose-coated MbCO at room temperature. *Cell Biochem. Biophys. 43*, 431–7.

(53) Sottini, S., Abbruzzetti, S., Viappiani, C., Ronda, L., and Mozzarelli, A. (2005) Determination of microscopic rate constants for CO binding and migration in myoglobin encapsulated in silica gels. *J. Phys. Chem. B 109*, 19523–8.

(54) Antonini, E. , Brunori, M. (1971) *Hemoglobin and Myoglobin in Their Reactions with Ligands*, Amsterdam.

(55) MacQuarrie, R., and Gibson, Q. H. (1972) Ligand binding and release of an analogue of 2,3-bisphosphoglycerate from human hemoglobin. *J. Biol. Chem. 247*, 5686–5694.

(56) Reisberg, P. I., and Olson, J. S. (1980) Kinetic and cooperative mechanisms of ligand binding to hemoglobin. *J. Biol. Chem. 255*, 4159–4169.

(57) Noble, R. W., Kwiatkowski, L. D., Hui, H. L., Bruno, S., Bettati, S., and Mozzarelli, A. (2002) Correlation of protein functional properties in the crystal and in solution: The case study of T-state hemoglobin. *Protein Sci. 11*, 1845–1849.

(58) Hofrichter, J., Sommer, J. H., Henry, E. R., and Eaton, W. A. (1983) Nanosecond absorption spectroscopy of hemoglobin: elementary processes in kinetic cooperativity. *Proc. Natl. Acad. Sci. U.S.A. 80*, 2235–9.

(59) Henry, E. R., Jones, C. M., Hofrichter, J., and Eaton, W. A. (1997) Can a two-state MWC allosteric model explain hemoglobin kinetics? *Biochemistry 36*, 6511–28.

(60) Goldbeck, R. A., Paquette, S. J., Bjorling, S. C., and Kliger, D. S. (1996) Allosteric intermediates in hemoglobin. 2. Kinetic modeling of HbCO photolysis. *Biochemistry 35*, 8628–39.

(61) Hu, T., Manjula, B. N., Li, D., Brenowitz, M., and Acharya, S. A. (2007) Influence of intramolecular cross-links on the molecular, structural and functional properties of PEGylated haemoglobin. *Biochem. J. 402*, 143–51.

(62) Hu, T., Prabhakaran, M., Acharya, S. A., and Manjula, B. N. (2005) Influence of the chemistry of conjugation of poly(ethylene glycol) to Hb on the oxygen-binding and solution properties of the PEG-Hb conjugate. *Biochem. J. 392*, 555–64.

(63) Thomas, J. O., and Edelstein, S. J. (1972) Observation of the dissociation of unliganded hemoglobin. *J. Biol. Chem. 247*, 7870–4.

(64) Bunn, H. F., and McDonough, M. (1974) Asymmetrical hemoglobin hybrids. An approach to the study of subunit interactions. *Biochemistry 13*, 988–93.

(65) Perrella, M., Samaja, M., and Rossi-Bernardi, L. (1979) Hybrid formation for liganded hemoglobins A and C at subzero temperatures. *J. Biol. Chem. 254*, 8748–50.

(66) Li, D., Manjula, B. N., and Acharya, A. S. (2006) Extension arm facilitated PEGylation of hemoglobin: correlation of the properties with the extent of PEGylation. *Protein J. 25*, 263–74.

(67) Perutz, M. F. (1970) Stereochemistry of cooperative effects in haemoglobin. *Nature 228*, 726–39.

(68) Perrella, M., Kilmartin, J. V., Fogg, J., and Rossi-Bernardi, L. (1975) Identification of the high and low affinity CO2-binding sites of human haemoglobin. *Nature 256*, 759–61.

(69) Nigen, A. M., Manning, J. M., and Alben, J. O. (1980) Oxygen-linked binding sites for inorganic anions to hemoglobin. *J. Biol. Chem. 255*, 5525–9.

(70) Vandegriff, K. D., Young, M. A., Lohman, J., Bellelli, A., Samaja, M., Malavalli, A., and Winslow, R. M. (2008) CO-MP4, a polyethylene glycol-conjugated haemoglobin derivative and carbon monoxide carrier that reduces myocardial infarct size in rats. *Br. J. Pharmacol. 154*, 1649–1661.

BC900130F

In Vivo Stable Tumor-Specific Painting in Various Colors Using Dehalogenase-Based Protein-Tag Fluorescent Ligands

Nobuyuki Kosaka,[†] Mikako Ogawa,[†] Peter L. Choyke,[†] Natasha Karassina,[‡] Cesear Corona,[‡] Mark McDougall,[‡] David T. Lynch,[§] Clifford C. Hoyt,[§] Richard M. Levenson,[§] Georgyi V. Los,*[,‡] and Hisataka Kobayashi*[,†]

Molecular Imaging Program, Center for Cancer Research, National Cancer Institute, NIH, Bldg. 10, Room 1B40, MSC 1088, 10 Center Drive, Bethesda, Maryland 20892-1088, Promega Corporation, 2800 Woods Hollow Road, Madison, Wisconsin 53711, and Cambridge Research and Instrumentation, 35B Cabot Road, Woburn, Massachusetts 01801. Received March 27, 2009; Revised Manuscript Received April 27, 2009

In vivo fluorescence cancer imaging is an important tool in understanding tumor growth and therapeutic monitoring and can be performed either with endogenously produced fluorescent proteins or with exogenously introduced fluorescent probes bound to targeting molecules. However, endogenous fluorescence proteins cannot be altered after transfection, thus requiring rederivation of cell lines for each desired color, while exogenously targeted fluorescence probes are limited by the heterogeneous expression of naturally occurring cellular targets. In this study, we adapted the dehalogenase-based protein-Tag (HaloTag) system to *in vivo* cancer imaging, by introducing highly expressed HaloTag receptors (HaloTagR) in cancer cells coupled with a range of externally injected fluorophore-conjugated dehalogenase-reactive reactive linkers. Tumor nodules arising from a single transfected cell line were stably labeled with fluorescence varying in emission spectra from green to near-infrared. After establishing and validating a SHIN3 cell line stably transfected with HaloTagR (HaloTagR-SHIN3), *in vivo* spectral fluorescence imaging studies were performed in live animals using a peritoneal dissemination model. The tumor nodules arising from HaloTagR-SHIN3 could be successfully labeled by four different fluorophore-conjugated HaloTag-ligands each emitting light at different wavelengths. These fluorophores could be alternated on serial imaging sessions permitting assessment of interval growth. Fluorescence was retained in histological specimens after fixation. Thus, this tagging system proves versatile both for *in vivo* and *in vitro* imaging without requiring modification of the underlying cell line. Thus, this strategy can overcome some of the limitations associated with the use of endogenous fluorescent proteins and exogenous targeted optical agents in current use.

INTRODUCTION

In vivo fluorescence imaging is performed either with endogenously produced fluorescent proteins (e.g., GFP, RFP) (*1*, *2*) or with exogenously introduced organic or inorganic fluorescent probes (e.g., fluorescein, rhodamine, cyanine) bound to targeting ligands (*3*). Each method has its advantages and disadvantages. Endogenous fluorescent proteins emit strong signals with minimal photobleaching and are consistently produced in stably transfected cells (*2*, *4*). The choice of the encoded fluorescent protein depends on the task to be accomplished and includes considerations such as the depth of the target tissue (due to limited light penetration at lower wavelengths), the tissue-specific spectral characteristics of autofluorescence or other competing fluorescent compounds, and the desired brightness of the fluorescence. However, once a particular fluorescent protein has been selected, the fluorescent properties of the transfected cells cannot be changed; instead, another stable transfection and cloning must be performed. This is not only time-consuming, but may also alter the biologic characteristics of the cell line in ways that introduce new variables into experiments so that each new clone must be extensively validated against prior clones. In contrast, exogenous fluorescent probes utilize a wide range of colors, from blue to near-infrared. These injectable fluorescent probes must be conjugated to targeting moieties to improve their specificity, but are limited to naturally occurring cellular targets that are often heterogeneously expressed in tumors and may be in low abundance compared to background signals.

An alternative approach is to use a gene reporter in which nonfluorescent markers (enzymes, receptors, antigens, etc.) are introduced into cells but are later "tagged" with an exogenous fluorescent ligand unique to that reporter. Such "tag" reporter systems (e.g., Flag-Tag, Snap-Tag, Clip-Tag, or Halo-Tag), have been widely used to label target molecules in cells *in vitro* (*5*, *6*). By introducing highly expressed "Tag" receptors into the target cells, the target to background (TBR) can be markedly improved. This approach increases the flexibility of fluorescence imaging, since many different fluorophores, exhibiting a broad range of emission wavelengths, can be conjugated to the tag-ligand. Therefore, "Tag" methods have the potential to overcome some of the disadvantages of both endogenous fluorescent proteins and exogenous fluorescent probes in *in vivo* fluorescence cancer imaging.

The dehalogenase-based protein-Tag (HaloTag) system is a protein labeling method that uses an enzymatic reaction to covalently tether organic probes directly to a specially designed reporting protein expressed on the membrane surface of live cells (*6*, *7*). This receptor protein is a modified haloalkane dehalogenase that covalently binds to a ligand containing a chloride-terminated reactive linker (HaloTag ligand; HaloTagL).

* Requests for reprints to Hisataka Kobayashi, Molecular Imaging Program, Center for Cancer Research, National Cancer Institute, NIH, Building 10, Room 1B40, MSC1088, Bethesda, MD 20892-1088. Phone: 301-451-4220. Fax: 301-402-3191. E-mail: kobayash@mail.nih.gov. Georgyi V. Los, Promega Corporation, 2800 Woods Hollow Rd. Madison, WI 53711. Phone: 608-298-4657. FAX: 608-298-4818. E-mail: georgyi.los@promega.com.

[†] National Cancer Institute.

[‡] Promega Corporation.

[§] Cambridge Research Incorporated.

10.1021/bc9001344 CCC: $40.75 © 2009 American Chemical Society
Published on Web 06/10/2009

By genetically fusing this modified haloalkane dehalogenase (HaloTag receptor; HaloTagR) protein with a target protein, the HaloTagL can provide spatial information about target fusion-proteins in live cells. Although the HaloTag system has been employed extensively *in vitro*, it could also be used as an *in vivo* imaging reporter by coupling it with an externally injected fluorescent tag, thus overcoming the disadvantages of both endogenous and exogenous fluorescence. For instance, this would allow conjugation of the tag to a variety of organic fluorophores ranging in emission wavelength from blue to near-infrared, which would create a highly flexible *in vivo* research imaging system that does not require constant modification of the underlying cell lines. Here, we demonstrate the capability of the HaloTag system for multicolor *in vivo* cancer imaging using an established human cell line stably transfected with HaloTagR (HaloTagR-SHIN3) (*8*).

EXPERIMENTAL PROCEDURES

Plasmid Preparation of HaloTag Receptor Protein. The vector encoding β1-Integrin-HaloTag 7 fusion protein (β1Int-HaloTag) was designed according to the protocol described previously (*9*). Briefly, the human β1-Integrin sequence was synthesized (Blue Heron Biotech, Bothell, WA) with a signal peptide (amino acids 1−20), a truncated extracellular domain (amino acids 190−217, 722−730), a transmembrane domain (amino acids 731−756), and a truncated cytoplasmic domain (amino acids 757−762). The HaloTag 7 gene was cloned downstream of the signal peptide and upstream of the extracellular domain. The fusion construct was confirmed by restriction digest analysis and sequencing. DNA was purified using endotoxin free Maxiprep kit (Qiagen, Valencia, CA).

HaloTag Ligands. The HaloTagL-TMR and HaloTagL-Alexa488 are commercially available and were provided by Promega Corporation (Madison, WI). The HaloTagL-Dy633 and HaloTagL-IR800 were synthesized by Promega Inc. The structures of all four ligands are shown in Figure 1, and the synthesis methods for HaloTagL-Dy633 and HaloTagL-IR800 are as follows:

A. HaloTagL-Dy633. To a stirring solution of Dy633 succinimidyl ester (10 mg, 0.012 mmol) (Dyomics GmbH, Jena, Germany) in 1 mL anhydrous DMF (stored over molecular sieves) was added 18-chloro-3,6,9,12-tetraoxaoctadecan-1-amine hydrochloride as a 0.5 M solution in DMF (34 μL, 0.017 mmol) followed by diisopropylethylamine (5 μL, 0.024 mmol). The reaction mixture was allowed to stir for 12 h in the dark, diluted with 1 mL of acetonitrile, and subjected to preparative HPLC purification, giving the product (8.98 mg, 74%) as a dark solid.

MS: *m*/*z* for $C_{51}H_{76}ClN_3O_{12}S_2^+$: 1021 (100%), 1022 (50.8%). Found: 1021.0.

B. HaloTagL-IR800. To a stirring solution of IRDye 800CW succinimidyl ester (5 mg, 0.0043 mmol) (LI-COR Bioscience, Lincoln, NE) in 750 μL anhydrous DMF (stored over molecular sieves) was added 18-chloro-3,6,9,12-tetraoxaoctadecan-1-amine hydrochloride as a 0.5 M solution in DMF (34 μL, 0.017 mmol) followed by a catalytic amount of K_2CO_3. The reaction mixture was allowed to stir for 12 h in the dark, diluted with 1 mL of acetonitrile, and subjected to preparative HPLC purification, giving the product (5 mg, 86%) as a dark solid.

MS: *m*/*z* for $C_{60}H_{83}ClN_3O_{18}S_4^+$: 1296 (100%), 1298 (50.8%). Found: 1298.

Cell Culture. An established ovarian cancer cell line SHIN3 (8) was employed for this study. The cell lines were grown in RPMI 1640 medium (Invitrogen Corporation, Carlsbad, CA) containing 10% fetal bovine serum (FBS) (Invitrogen Inc.), 0.03% L-glutamine at 37 °C, 100 units/mL penicillin, and 100 μg/mL streptomycin in 5% CO_2.

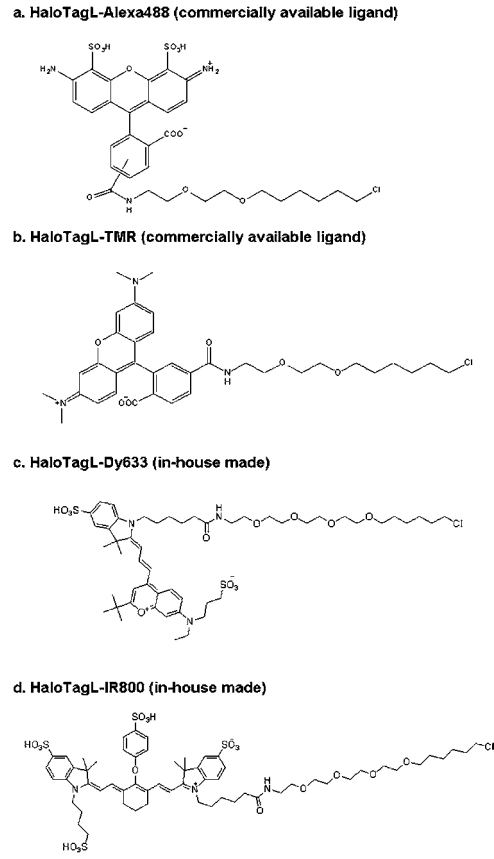

Figure 1. Chemical structures of HaloTag ligands. Chemical structures of all four HaloTagLs, which we used in this study, are shown.

Transfection of HaloTag Receptor Protein to the SHIN3 Cells. The HaloTagR plasmid described above was transfected into SHIN3 cells simultaneously with a neomycin-resistant plasmid (Promega) using the cationic liposome method. Three micrograms of HaloTagR plasmid and 1 μg of neomycin-resistant plasmid were mixed well with 20 μL of cationic liposome solution (DNA fectin, Life Technologies, Rockville, USA) and incubated for 30 min at room temperature. The plasmid-cationic liposome mixture was added to 1×10^5 SHIN3 cells plated in a 25 cm^2 cell culture flask and incubated for 6 h at 37 °C in 5% CO_2 before being placed back into the regular media and kept overnight. The next day, the initial selection of cells was achieved with 1.5 mg/mL neomycin in the regular culture media and colonies were allowed to grow over 2 weeks. HaloTagR-positive colonies were selected by staining with HaloTagL-TMR and spread in culture dishes. This cloning process was repeated twice to derive a stable SHIN3-HaloTagR positive cell line.

Mammalian Cells Culturing, Labeling and Imaging. HaloTagR-SHIN3 cells were maintained in RPMI1640 media supplemented with Hepes, MEM NEAA, Glutamine, and 10% FBS (Invitrogen) at 37 °C and 5% carbon dioxide. For imaging experiments, cells were plated on an 8-well Lab-Tech II chamber cover glass (Thermo Fisher Scientific, Rochester, NY), labeled with HaloTagL, and imaged directly or fixed, permeabilized, and then processed for immunocytochemistry using HaloTag polyclonal Ab (Promega) and Alexa Fluor 594 goat antirabbit IgG Ab (Invitrogen) or Alexa Fluor 488 goat antirabbit IgG Ab (Invitrogen) prior to imaging. All procedures were performed according to the manufacturer's protocol. All imaging was performed sequentially using an Olympus FV500 confocal microscope (Olympus America, Inc., Melville, NY) equipped with appropriate filter sets.

Detection of Halo-Tag Protein by SDS-PAGE. HaloTagR-SHIN3 cells were labeled with either HaloTagL-Alexa488 or HaloTagL-TMR or both ligands. The cells were lysed, and proteins were resolved by SDS-PAGE according to the manufacturer's protocol (Promega). Gels were analyzed on a fluorescence imager Typhoon 9400 (GE Healthcare, Pisctaway, NJ) using appropriate filters for each fluorophore. Quantitation of bands was performed using ImageQuant software (GE Healthcare).

Tumor Model. All procedures were approved by the National Cancer Institute Animal Care and Use Committee. The intraperitoneal tumor implants were established by intraperitoneal injection of 2×10^6 cells suspended in 200 μL of PBS in female nude mice (National Cancer Institute Animal Production Facility, Frederick, MD). Experiments with tumor-bearing mice were performed at 14 days for the parent SHIN3 mouse model and 21 days for the HaloTagR-SHIN3 mouse model.

Spectral Fluorescence Imaging Study. *Comparison Study of Parent-SHIN3 and HaloTagR-SHIN3 Bearing Mice.* After establishing peritoneal tumor implants with either the parent-SHIN3 or HaloTagR-SHIN3 cell lines ($n = 5$, each group), 20 nmol of HaloTagL-TMR diluted in 300 μL PBS with 0.4% bovine serum albumin (Sigma Chemical, St. Louis, MO) were injected into the peritoneal cavities of each mouse 24 h prior to imaging. Mice were sacrificed with carbon dioxide, and the abdominal cavities were exposed. Spectral fluorescence images were obtained using the Maestro In-Vivo imaging system (Cambridge Research and Instrumentation, Woburn, MA). Five sets of side-by-side whole abdominal cavity images of animals harboring tumors from the parent-SHIN3 or HaloTagR-SHIN3 cell lines, as well as images of all tumor nodules, were obtained. The brief setting of imaging parameters was described in the Supporting Information.

Comparison Study of Injected Amounts of HaloTag Ligands. Either 10 nmol or 100 nmol of HaloTagL-Alexa488 or HaloTagL-TMR diluted in 300-μL PBS with 0.4% bovine serum albumin (Sigma Chemical) was injected into the peritoneal cavities of each mouse 24 h prior to imaging. Mice were sacrificed with carbon dioxide, and the abdominal cavities were exposed. Spectral fluorescence images were obtained using the Maestro In-Vivo imaging system (CRi). Three sets of side-by-side whole abdominal cavity images of animals harboring tumors, as well as images of tumor nodules, were obtained. The brief setting of imaging parameters were described in the Supporting Information.

Multicolor in Vivo Spectral Fluorescence Imaging. HaloTagL-Alexa488, -TMR, -Dy633, and -IR800 ligands were used for this study. 60 nmol of each ligand diluted in 300-μL PBS with 0.4% bovine serum albumin was injected into the peritoneal cavities of mice with intraperitoneal dissemination of HaloTagR-SHIN3 24 h prior to imaging. Mice were anesthetized with subcutaneously administered 10% pentobarbital sodium (Nembutal; Abbott Laboratories, Abbott Park, IL), followed by *in vivo* spectral fluorescence imaging using the Maestro In-Vivo imaging system. Since the most efficient filter settings varied depending on the characteristics of the fluorophore, a multiexcitation acquisition (*10*) was employed. The imaging parameters are described in the Supporting Information. After obtaining *in vivo* spectral fluorescence images in live mice, all mice were sacrificed with carbon dioxide, and their abdominal cavities were exposed and imaged with the same acquisition settings. Finally, all spectral fluorescence images were unmixed to distinguish autofluorescence from the four different fluorophores using commercial software (*Maestro* software, CRi). This experiment was performed twice with similar results.

Serial in Vivo Spectral Fluorescence Imaging Study. Sixty nanomoles of either HaloTagL-TMR or HaloTagL-IR800 diluted in 300 μL PBS with 0.4% bovine serum albumin was injected into the peritoneal cavities of mice bearing intraperitoneal HaloTagR-SHIN3 tumors. HaloTagL-IR800 was initially injected into the animal, and imaging was performed at 24 and 48 h. After the 48 h image, the same amount of HaloTagL-TMR was administered, and imaging was obtained at 72 and 96 h after initial injection. The order of administration of the two fluorophores was also reversed in another group of two mice. For each imaging session, mice were anesthetized with Isoflurane (IsoFlu; Abbott Laboratories, Abbott Park, IL) and then imaged using the Maestro In-Vivo imaging system. Two single excitation spectral fluorescence images were acquired for each mouse with either green filter settings or near-infrared filter settings. Other settings of the image acquisition were held constant. The spectral fluorescence images consisting of autofluorescence spectra and either TMR or IR800 spectra were obtained and then unmixed, based on their spectral patterns using commercial software (*Maestro* software, CRi). All mice were subsequently sacrificed with carbon dioxide. This experiment was repeated twice.

In Vivo Real-Time Fluorescence Endoscopy. After establishing peritoneal tumor implants with HaloTagR-SHIN3 cell lines, 60 nmol of either HaloTagL-Alexa488 or -TMR diluted in 300-μL PBS with 0.4% bovine serum albumin was injected into the peritoneal cavities 24 h prior to imaging ($n = 3$, each group). *In vivo* fluorescence endoscopy was performed with clinical endoscopic system (EVIS Ecera II CLV-180, Olympus Corporation, Tokyo, Japan) equipped with an in-house developed fluorescence imaging system. A blue filter setting (excitation filter, 465 to 500 nm; emission filter, 516 to 556 nm band-pass) for HaloTagL-Alexa488 and a green filter setting (531 to 556 nm, 570 to 625 nm band-pass) for HaloTagL-TMR were employed for single-excitation acquisition.

Tissue Processing. *Embedding Tissue.* Formalin-fixed tissues were washed in water to remove formalin, then immersed in multiple baths of progressively less concentrated ethanol from 100% to 70%, followed by HistoClear Xylene (Fisher Scientific, Pittsburgh, PA) and then hot molten paraffin wax. Embedded tissue blocks were then cut into very thin (0.5−1 μm) sections using a microtome, and slices were placed on glass slides (*11, 12*).

Dewaxing and Antigen Retrieval. Paraffin sections were dewaxed by immersion in the following solutions, each for 3 min at RT: 3 times in HistoClear xylene, 2 times in 100% ethanol, once in 95% ethanol, and then once in 70% ethanol. Antigen retrieval was done by incubating slides in warm (94−96 °C) 0.01 M citrate buffer pH = 6.0 for 30 min, followed by cooling step at RT (*11*−*13*).

Immunolabeling. All incubation steps were done in a humidified chamber at RT with gentle rocking. Slides were first incubated in a blocking buffer, PBS +60 min; primary Ab to HaloTag (2 μg/mL, Promega Inc.) were applied for overnight incubation at +4 °C and finally Alexa Fluor 594 goat antirabbit IgG Ab (Invitrogen Inc.) or Alexa Fluor 488 goat antirabbit IgG Ab (Invitrogen Inc.) for 60 min. After washing three times in PBS for 5 min, slides were mounted in Vectashield (Vector Laboratories, Burlingame, CA) and stored at 4 °C. All tissue fluorescence and confocal imaging was done using an Olympus BX61 fluorescence and an FV500 confocal microscope (Olympus America Inc.) in sequential mode equipped with appropriate filter sets.

RESULTS

HaloTagR Stably Expresses in SHIN3 Cells Transfected with HaloTagR Protein Gene (HaloTagR-SHIN3) *in Vitro.* SHIN3 cells were transfected with the HaloTagR protein gene fused to β1-integrin-encoding gene, creating a unique cell membrane marker (*9*); cloning was performed using HaloTagL-

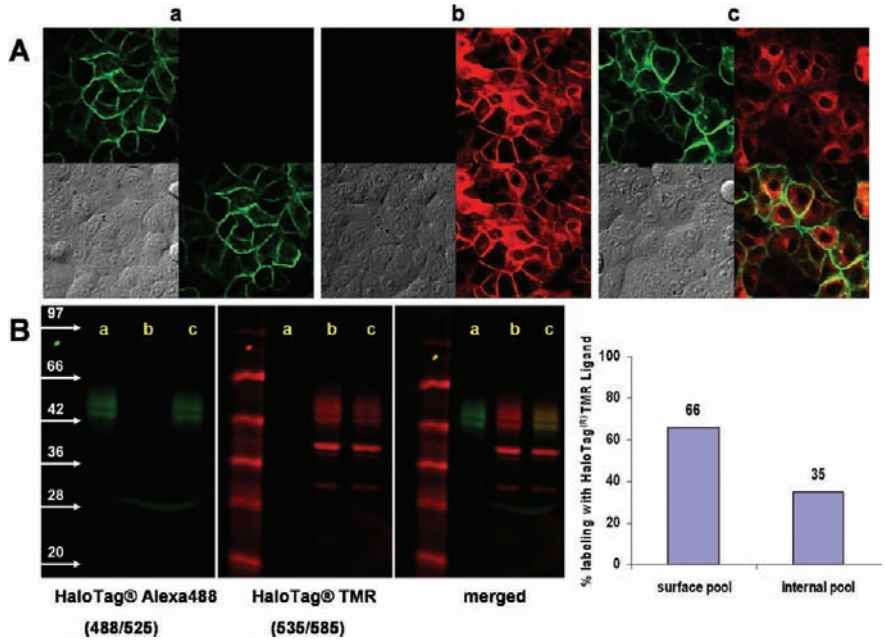

Figure 2. (A) Confocal images of the SHIN3 cells stably expressing HaloTagR (HaloTagR-SHIN3). HaloTagR-SHIN3 cells were labeled with HaloTagL-Alexa488 at 5 μM for 15 min (a) or HaloTagL-TMR at 1 μM for 15 min (b) or pulsed HaloTagL-Alexa488/chased HaloTagL-TMR (c). Images were collected sequentially with appropriate filter sets. Fluorescence images of HaloTagL-Alexa488 (upper left), HaloTag-TMR (upper right), merged image of HaloTag-Alexa488 and TMR (lower right), and DIC images (lower left). (B) SDS-PAGE analysis of the fluorescently labeled β1Int-HaloTag fusion protein stably expressed in the SIHN3 cells. The HaloTagR-SHIN3 cells were labeled as described above. The cells were lysed, cell proteins were resolved on SDS-PAGE, and analyzed on a fluorescence imager Typhoon 9400 using appropriate filter settings. HaloTagL-Alexa488 is cell impermeant and binds only to the surface exposed (glycosylated) HaloTagRS. The HaloTagL-TMR is cell permeant, and binds to the surface exposed (glycosylated) pool and to the intracellular (glycosylated and non-glycosylated) pool of the HaloTagRs. Fluorescence of the protein bands was quantified using ImageQuant software.

TMR to select a colony of cells that stably expressed the HaloTagR on the cell surface and endoplasmic vesicles without interfering with cellular proliferation or tumorigenesis. After establishing the HaloTagR-SHIN3 cell line, the HaloTagR expression was validated by confocal microscopy (Figure 2A), SDS-PAGE (Figure 2B), and immunohistochemical analysis (Supporting Information Figure 1). After validation of HaloTagR-SHIN3, tumor-bearing mice underwent *in vivo* spectral fluorescence imaging.

HaloTagL Specifically Binds to Tumor Nodules Arising from HaloTagR-SHIN3 *in Vivo.* To validate the HaloTag system *in vivo*, spectral fluorescence imaging was performed on HaloTagR-SHIN3 and nontransfected parental SHIN3 tumors after intraperitoneal injection in mice. The SHIN3 tumor model replicates the peritoneal metastases commonly seen in human ovarian cancers. After tumors were established, HaloTagL-TMR was injected intraperitoneally to label the transfected cells. SHIN 3 tumors composed of cells expressing the HaloTagR (HaloTagR-SHIN3) were identified *in vivo* by unmixing the TMR spectrum from background signal. Nontransfected SHIN3 tumors demonstrated no focal fluorescence (Figure 3). These results suggest that the HaloTagL-TMR binds to the HaloTagR-expressing SHIN3 tumors *in vivo* while unbound HaloTagL is cleared from the body within a day.

Larger Amount of HaloTagL Shows Brighter and More Homogeneous HaloTagR-SHIN3 Tumor Staining *in Vivo.* In order to evaluate the dose effect to the HaloTagL to the tumor *in vivo*, a comparative imaging study was performed using HaloTagR-SHIN3 tumor-bearing mice injected with 10 nmol or 100 nmol of either HaloTagL-Alexa488 or HaloTagL-TMR ligands. Tumors in mice, which received 100 nmol HaloTag, showed brighter staining with both fluorophores. These results suggested that an insufficient dose of HaloTagL did not saturate the HaloTagR expressing in the HaloTagR-SHIN3 tumor.

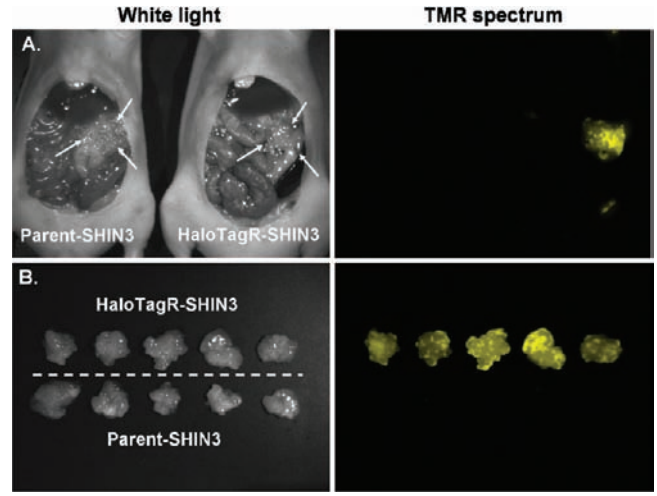

Figure 3. Comparative spectral fluorescence imaging study demonstrated specific binding of HaloTagL to SHIN3 stably expressing stm-HaloTag 7 (HaloTagR-SHIN3) tumor growing in mice. The side-by-side comparative spectral fluorescence images of the representative pair (A) and all excised tumor nodules (B) are shown here. Both mice received the same amount of HaloTagL-TMR ligand 24 h prior to imaging. On the white light images, the same-sized tumors can be identified in both mice (arrows). The unmixed spectral fluorescence images show that HaloTagR-SHIN3 tumor is depicted by the specific wavelength light that corresponded to TMR spectrum with very low background signal, while parent SHIN3 tumor does not. These results support the concept that the HaloTagL specifically binds to HaloTagR expressing SHIN3 tumor.

Tumor Nodules Arising from HaloTagR-SHIN3 Can Be Depicted by Various Fluorophore-Conjugated HaloTagLs *in Vivo.* To demonstrate the ability of this system to accommodate multiple colors, *in vivo* multicolor spectral fluorescence imaging

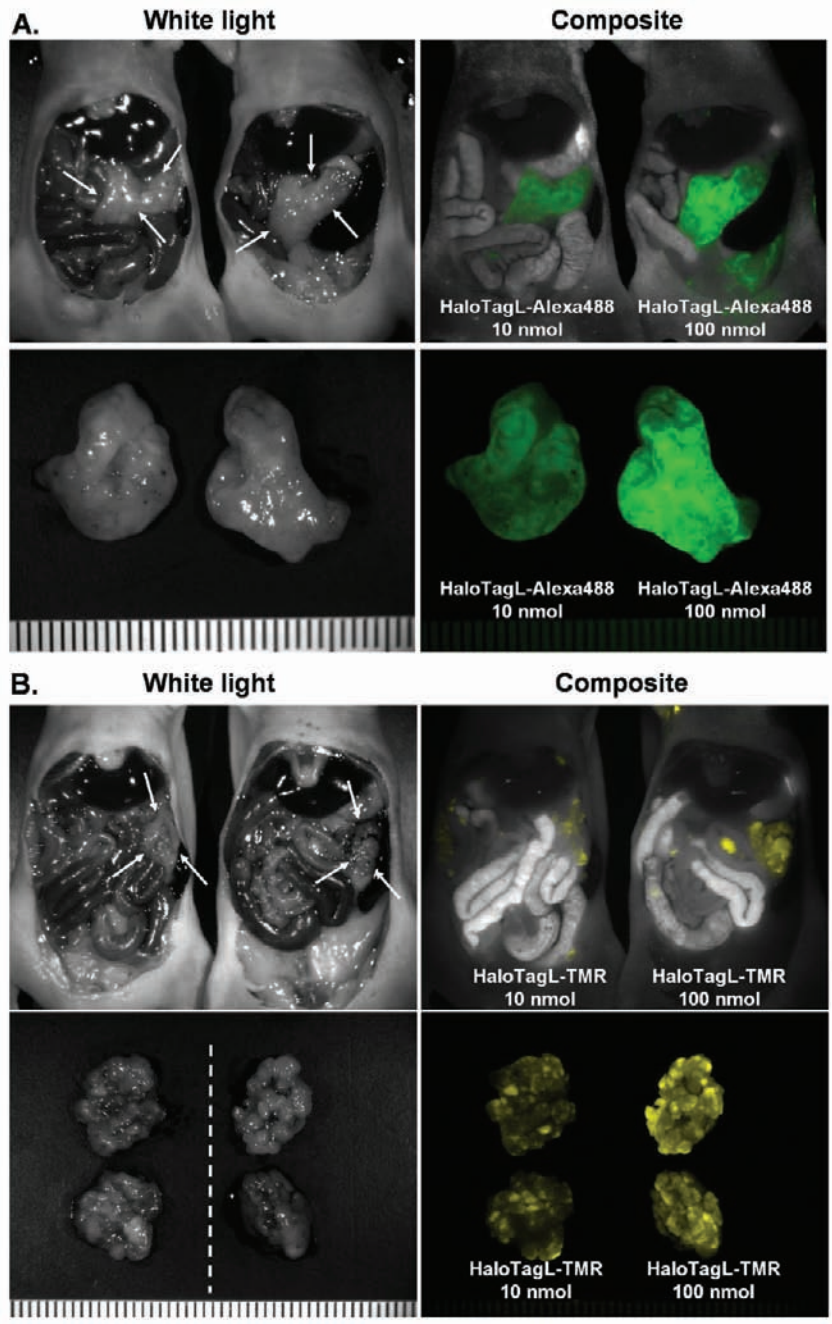

Figure 4. Comparison of injected amounts of HaloTag ligands. A comparative imaging study was performed using HaloTagR-SHIN3 tumor-bearing mice injected with 10 nmol or 100 nmol of either HaloTagL-Alexa488 (A) or HaloTagL-TMR (B) ligands. Tumors in mice, which received 100 nmol HaloTagL-TMR, show brighter and more homogeneous staining with both fluorophores.

was performed after the injection of fluorescent HaloTagLs labeled with several different fluorophores (Alexa488, TMR, Dy633, and IR800) ranging in emission wavelength from green to near-infrared in different tumor-bearing mice. In mice with peritoneal metastases arising from the HaloTagR-SHIN3 cell line, different-colored HaloTagLs resulted in multicolored depiction of the tumors arising from the same transfected cell line (Figure 5A).

Fluorescence Signals Can Be Switched on Alternate Imaging Sessions. The serial *in vivo* spectral fluorescence images showed that the tumor nodules were detected for at least 96 h in the anesthetized live mice after the single administration of either ligand (Figure 5B). Moreover, when two different (e.g., yellow and NIR) fluorophores were used alternately on serial imaging sessions, it was possible to label the interval tumor growth occurring between each imaging session using different colors (Figure 5B). However, the light intensity arising from each ligand-conjugate gradually weakened during the course of observation, probably due to metabolism and photobleaching.

***In Vivo* Real-Time Endoscopy of the HaloTagR-SHIN3 Tumor Labeled by Either HaloTagL-Alexa488 or HaloTagL-TMR.** *In vivo* real-time endoscopy showed that peritoneal tumor implants, which originated from the same HaloTagR-SHIN3 cell lines, emitted different fluorescence signals from preinjected HaloTag-ligands 24 h before imaging (Supporting Information videos, HaloTagL-Alexa488(A) and HaloTagL-TMR(B)). Both real-time endoscopic images specifically depicted small peritoneal implants of HaloTagR-SHIN3 tumors.

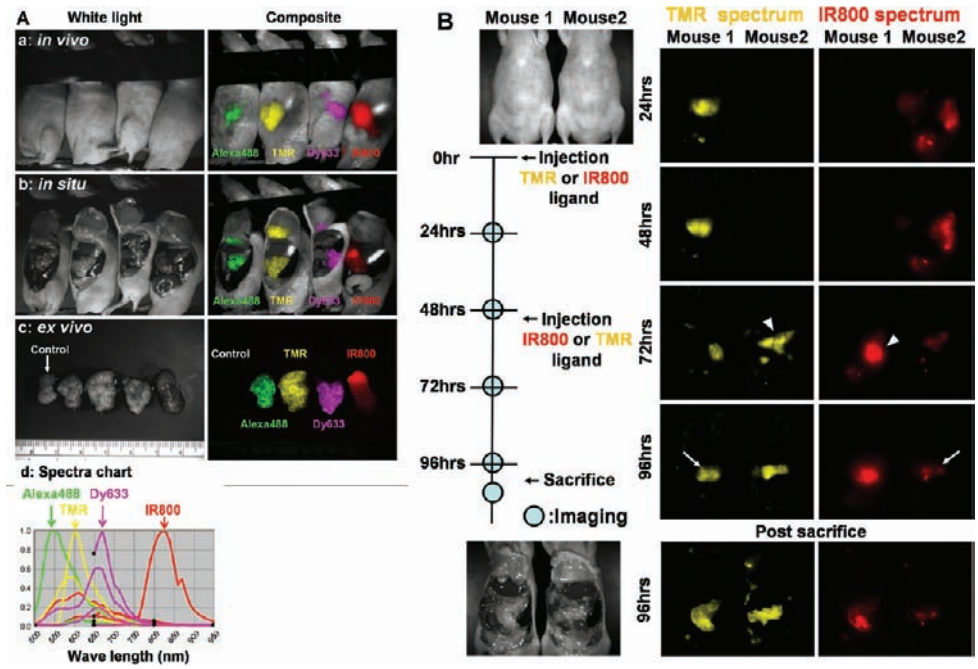

Figure 5. (A) Multiple-colored *in vivo* spectral fluorescence imaging. Unmixed multiple-colored spectral fluorescence images of live, anesthetized mice (a), the exposed abdominal cavities (b), and the excised tumor nodules (c) are shown. All mice were injected i.p. with the HaloTagR-SHIN3 cell line. Twenty-four hours prior to imaging, the mice received HaloTagLs labeled with different fluorophores (left to right: HaloTagL-Alexa488, -TMR, -Dy633, and -IR800 ligands). The tumor nodules are depicted at different wavelengths corresponding to the emission spectra of the fluorophores conjugated to the HaloTagLs. The spectral pattern of each fluorophore (d) is shown. Note that tumors removed from a HaloTagR-SHIN3 mouse, which did not receive ligand, were included as a control (arrow). (B) Serial "pulse-chase" *in vivo* spectral fluorescence imaging. Imaging sessions took place at 24, 48, 72, and 96 h after injection of either HaloTagL-TMR or HaloTagL-IR800. After the images were acquired at 48 h, the same amounts of HaloTagL-TMR were given to the mice in same fashion, and vice versa. The unmixed spectral fluorescence images show that the tumor nodules are detected for at least 96 h in the anesthetized live mice after the single administration of either ligand (arrows). Furthermore, additional colors can be added (arrow heads) and simultaneously spectrally resolved. However, the light intensity arising from each ligand-conjugate gradually weakened during the course of observation, probably due to metabolism and photobleaching.

Histological Validation of HaloTag Receptor Expression in the HaroTagR-SHIN3 Tumor. Formalin-fixed paraffin-embedded tumor tissue specimens, which were obtained from mice shown in Figure 5, were imaged without any additional staining on an Olympus BX61 fluorescence microscope with the appropriate filter sets (Figure 6A). Immunohistochemistry of β1Int-HaloTag fusion protein expressed in HaloTagR-SHIN3 cells, in the same formalin-fixed paraffin-embedded mouse tumor tissue used above, confirmed HaloTagR expression in the HaloTagR-SHIN3 tumor (Figure 6B).

DISCUSSION

The wide range of fluorophores available to bind to the HaloTagL enables the selection of the optimal color to meet the requirements of a particular experiment such as avoiding overlap with the spectrum of an administered drug, avoiding autofluorescence, or adapting to available imaging equipment, without creating new, genetically modified cell lines (*14*). Furthermore, an appropriate near-infrared (NIR) probe may be selected for visualizing deep tumors due to the better tissue penetration and low background signal in the NIR (Figure 5; also see Supporting Information Figure 3), whereas a green fluorophore, with higher quantum efficiency, may be preferred for surface imaging applications such as endoscopy (Supporting Information Videos). Thus, using HaloTagR-transfected tumor cell lines, the tumor can be "painted" with any color as needed without changing the underlying tumor model.

A desirable feature of this system is that the colors could be successfully switched or added on serial *in vivo* imaging sessions. This feature has also been described for injectable target probes including labeled monoclonal antibodies and other receptor ligands, which target naturally occurring receptor proteins. By alternating colors, interval growth can be measured. However, such targeting agents require stably and homogenously expressing endogenous targets on tumor cells as well as sufficient affinity to their respective target antigens. In contrast, the HaloTag system artificially induces sufficient numbers of cell targets by translating the HaloTagR enzyme receptor in the majority of transfected cells, enabling highly specific, stable covalent binding to the tag-ligand which, in turn, can be labeled with a broad range of fluorophores conjugated to HaloTagL.

There are several limitations to this method. First, while HaloTagR was highly expressed in the majority of cells, some tumors were inhomogeneously labeled (Figure 6A) mainly due to inhomogeneous intratumoral distribution of HaloTagL and partly due to variable expression of the HaloTagR protein. The former is overcome by increasing the dose of HaloTagL. When the dose of HaloTagL was increased up to 100 nmol (a 10-fold increase), the brightness of the tumors became more homogeneous compared to the initial dose of 10 nmol (Figure 4). Additionally, deeper tumors were not labeled as effectively as superficial tumors, although HaloTagR expression detected by immunohistochemistry was relatively homogeneous compared with the *in vivo* distribution of HaloTagLs (Figure 6B; also see Supporting Information Figure 2). Since the HaloTagL can bind strongly and quickly to HaloTagR, tumor cells on the surface of tumor implants were more likely to be detected than tumor cells located deeper to the surface (Figure 6A). The brightness of tumors or cells using the HaloTag system was dependent on

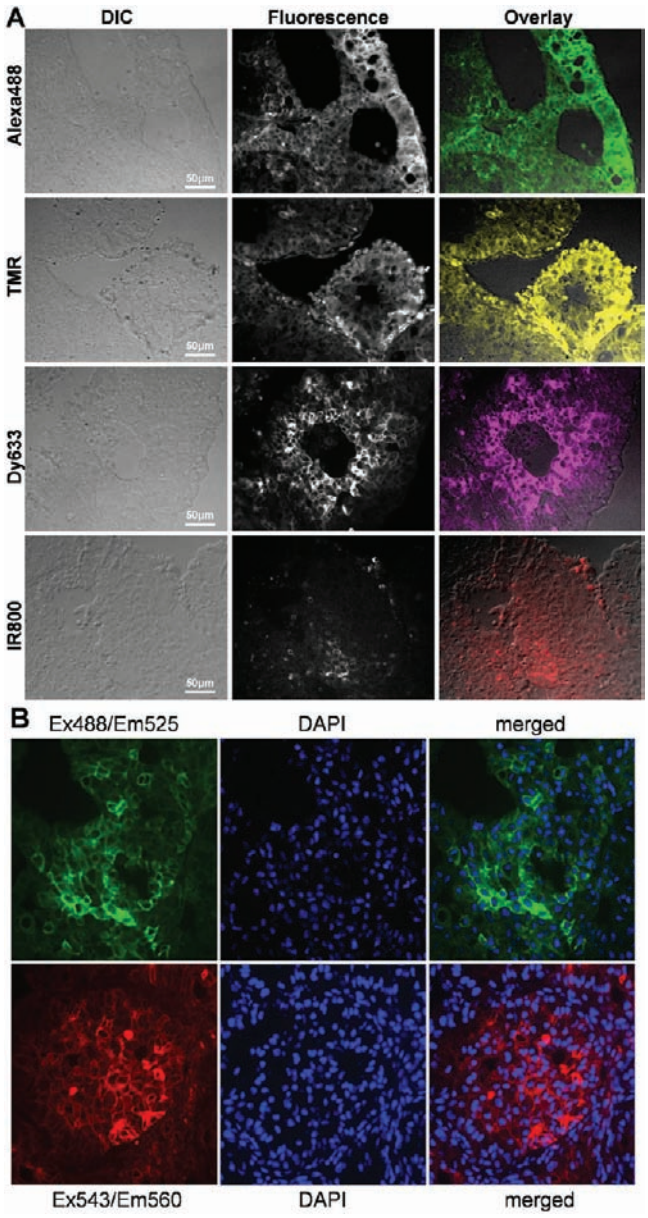

Figure 6. Histological validation of HaloTag receptor expression in the HaroTagR-SHIN3 tumor. (A) Formalin-fixed paraffin-embedded tumor tissue specimens were imaged on an Olympus BX61 fluorescence microscope with the appropriate filter sets for HaloTagL-Alexa488, HaloTagL-TMR, HaloTagL-Dy633, or HaloTagL-IR800. (B) Formalin-fixed paraffin-embedded tumor tissue was processed for immunohistochemistry and probed with anti-HaloTag Ab. Fluorescent signal (secondary Ab) indicates expression of the β1Int-HaloTag fusion protein expressed in the cells forming the HaloTagR-SHIN3 tumor. DAPI stains cell nuclei (blue).

the number of transcripts expressing HaloTagR per cell and the dose of HaloTagL injected into the mouse; however, in our hands the brightness of a green fluorescent HaloTagL was greater than that of a comparable GFP construct both *in vitro* and *in vivo*. Finally, during acquisition of serial *in vivo* images, the intensity of fluorescence gradually diminished especially with the IR800 ligand, possibly due to catabolism or photobleaching (Figure 5B). Therefore, to assess longitudinal tumor growth with this method, multiple injections of ligands with proper timing of the imaging, a use-mode analogous to that of bioluminescence imaging, will be required. In this experiment, despite its shorter emission wavelength, TMR-ligand showed comparable brightness to IR800-ligand probably because TMR-ligand could bind to both membrane and cytoplasmic receptors, while IR800-ligand bound only to the membrane receptors. However, we were still able to validate persistent HaloTagR expression over time in tumor cells by detecting retained fluorescence signal in histological specimens even after fixation (Figure 6). It is possible that *in vivo* imaging of intracellular fusion protein targets could be performed as well by using appropriate permeable ligands such as HaloTagL-TMR as shown in Figure 2B.

In conclusion, we demonstrate the ability of the HaloTag reporter system to successfully perform *in vivo* cancer imaging, and we verify that numerous fluorophores spanning a broad spectrum of emission wavelengths can be used with the same transfected cell line. Thus, the HaloTag reporter system can be used in practically every step of cancer imaging studies including *in vitro* cell-sorting or cloning, *in vitro* validation and quantification of receptor expression, *in vivo* longitudinal animal imaging, and *ex vivo* histological analysis. Furthermore, the system is flexible, because virtually any kind of tumor can be transfected with the HaloTagR protein and imaged with virtually any fluorophore that can be conjugated to HaloTagL. This strategy can overcome some of the limitations associated with the use of endogenous fluorescent proteins or exogenous targeted optical agents, and could become a valuable research approach for *in vivo* cancer imaging in animals.

ACKNOWLEDGMENT

N. Ko. and M. O. equally contributed to this work. We gratefully acknowledge Chad Zimprich and Shana Svendsen for the cloning of β1Int-HaloTag7 and initial characterization of the β1Int-HaloTag 7 fusion protein. This work was supported by the Intramural Research Program of the National Institutes of Health, National Cancer Institute, Center for Cancer Research.

Supporting Information Available: Supplementary videos: *In vivo* real-time endoscopic videos of the HaloTagR-SHIN3 tumor labeled by either HaloTagL-Alexa488 (A) or HaloTagL-TMR (B): These endoscopic videos show that peritoneal tumor implants, which originated from the same HaloTagR-SHIN3 cell lines, emit different fluorescence signals from preinjected HaloTag-ligands (HaloTagL-Alexa488 (A) and HaloTagL-TMR (B)) 24 h before imaging. Both real-time endoscopic images specifically depict small peritoneal implant of HaloTagR-SHIN3 tumors. Left: image without emission filter, right: fluorescence image through an appropriate emission filter. First half: white light image, Second half: excitation light image specific for Alexa488 (A) and TMR (B). Setting of imaging parameter, and additional *in vitro* and histological data are also available. This material is available free of charge via the Internet at http://pubs.acs.org.

LITERATURE CITED

(1) Hoffman, R. M. (2005) Advantages of multi-color fluorescent proteins for whole-body and in vivo cellular imaging. *J. Biomed. Opt. 10*, 41202.

(2) Hoffman, R. M. (2005) The multiple uses of fluorescent proteins to visualize cancer in vivo. *Nat. Rev. Cancer 5*, 796–806.

(3) Weissleder, R., and Pittet, M. J. (2008) Imaging in the era of molecular oncology. *Nature 452*, 580–589.

(4) Kogure, T., Karasawa, S., Araki, T., Saito, K., Kinjo, M., and Miyawaki, A. (2006) A fluorescent variant of a protein from the stony coral Montipora facilitates dual-color single-laser fluorescence cross-correlation spectroscopy. *Nat. Biotechnol. 24*, 577–581.

(5) Gautier, A., Juillerat, A., Heinis, C., Correa, I. R., Jr., Kindermann, M., Beaufils, F., and Johnsson, K. (2008) An engineered protein tag for multiprotein labeling in living cells. *Chem. Biol. 15*, 128–136.

(6) Los, G. V., Encell, L. P., McDougall, M. G., Hartzell, D. D., Karassina, N., Zimprich, C., Wood, M. G., Learish, R., Ohana, R. F., Urh, M., Simpson, D., Mendez, J., Zimmerman, K., Otto, P., Vidugiris, G., Zhu, J., Darzins, A., Klaubert, D. H., Bulleit, R. F., and Wood, K. V. (2008) HaloTag: a novel protein labeling technology for cell imaging and protein analysis. *ACS Chem. Biol. 3*, 373–382.

(7) Los, G. V., and Wood, K. (2007) The HaloTag: a novel technology for cell imaging and protein analysis. *Methods Mol. Biol. 356*, 195–208.

(8) Imai, S., Kiyozuka, Y., Maeda, H., Noda, T., and Hosick, H. L. (1990) Establishment and characterization of a human ovarian serous cystadenocarcinoma cell line that produces the tumor markers CA-125 and tissue polypeptide antigen. *Oncology 47*, 177–184.

(9) Svendsen, S., Zimprich, C., McDougall, M. G., Klaubert, D. H., and Los, G. V. (2008) Spatial separation and bidirectional trafficking of proteins using a multi-functional reporter. *BMC Cell Biol 9*, 17.

(10) Koyama, Y., Barrett, T., Hama, Y., Ravizzini, G., Choyke, P. L., and Kobayashi, H. (2007) In vivo molecular imaging to diagnose and subtype tumors through receptor-targeted optically labeled monoclonal antibodies. *Neoplasia 9*, 1021–1029.

(11) Key, M. (2006) *Immunohistochemical Staining Methods*, Dako, Carpenteria, CA.

(12) Robertson, D., Savage, K., Reis-Filho, J. S., and Isacke, C. M. (2008) Multiple immunofluorescence labelling of formalin-fixed paraffin-embedded (FFPE) tissue. *BMC Cell Biol. 9*, 13.

(13) Viegas, M. S., Martins, T. C., Seco, F., and do Carmo, A. (2007) An improved and cost-effective methodology for the reduction of autofluorescence in direct immunofluorescence studies on formalin-fixed paraffin-embedded tissues. *Eur. J. Histochem. 51*, 59–66.

(14) Verkhusha, V. V., and Lukyanov, K. A. (2004) The molecular properties and applications of Anthozoa fluorescent proteins and chromoproteins. *Nat. Biotechnol. 22*, 289–296.

BC9001344

Supporting information

In Vivo Stable Tumor-Specific Painting in Various Colors Using Dehalogenase-Based Protein-Tag Fluorescent Ligands

Nobuyuki Kosaka[1], Mikako Ogawa[1], Peter L. Choyke[1], Natasha Karassina[2], Caesar Corona[2], Mark McDougall[2], David Lynch[3], Clifford Hoyt[3], Richard Levenson[3], Georgyi V. Los[2]* and Hisataka Kobayashi[1]*

1. Molecular Imaging Program, Center for Cancer Research, National Cancer Institute, NIH, Bldg. 10, Room 1B40, MSC 1088, 10 Center Dr., Bethesda, MD 20892-1088.
2. Promega Corporation, 2800 Woods Hollow Rd. Madison, WI 53711.
3. Cambridge Research Incorporation, 35B Cabot Road, Woburn, MA 01801

Imaging parameters

Spectral Fluorescence imaging study

Comparison study of parent-SHIN3 and HaloTagR-SHIN3 bearing mice:

Comparison study of injected amounts of Halotag ligands:

Spectral fluorescence images were obtained using the Maestro In-Vivo imaging system (CRi, Inc., Woburn, MA) with a blue-filter settings (excitation filter: 445 to 490 nm, emission filter: 515 nm long pass) or green-filter setting (excitation filter: 503 to 555 nm, emission filter: 580 nm long pass). The tunable filter was automatically stepped in 10 nm increments from 550 to 800 nm while the camera captured images at each wavelength interval. The spectral fluorescence images consisting of autofluorescence, Alexa488 and TMR spectra were obtained and then unmixed, based on their spectral patterns using commercial software (Maestro software, CRi).

Multi-color in vivo spectral fluorescence imaging:

Multi-excitation spectral fluorescence images were obtained using the Maestro In-Vivo imaging system (CRi, Inc.). Blue filter settings, green-filter settings, yellow-filter settings (575 to 605 nm, 645 nm long pass), and near-infrared-filter settings (710 to 760 nm, 800nm long pass) were employed for multi-excitation acquisition. The tunable filter in the Maestro camera was automatically stepped in 10 nm increments from 550 to 800 nm for blue and green filter settings, 650-950 nm for the yellow and near infrared filter settings while the camera captured images at each wavelength interval.

Supplemental figures

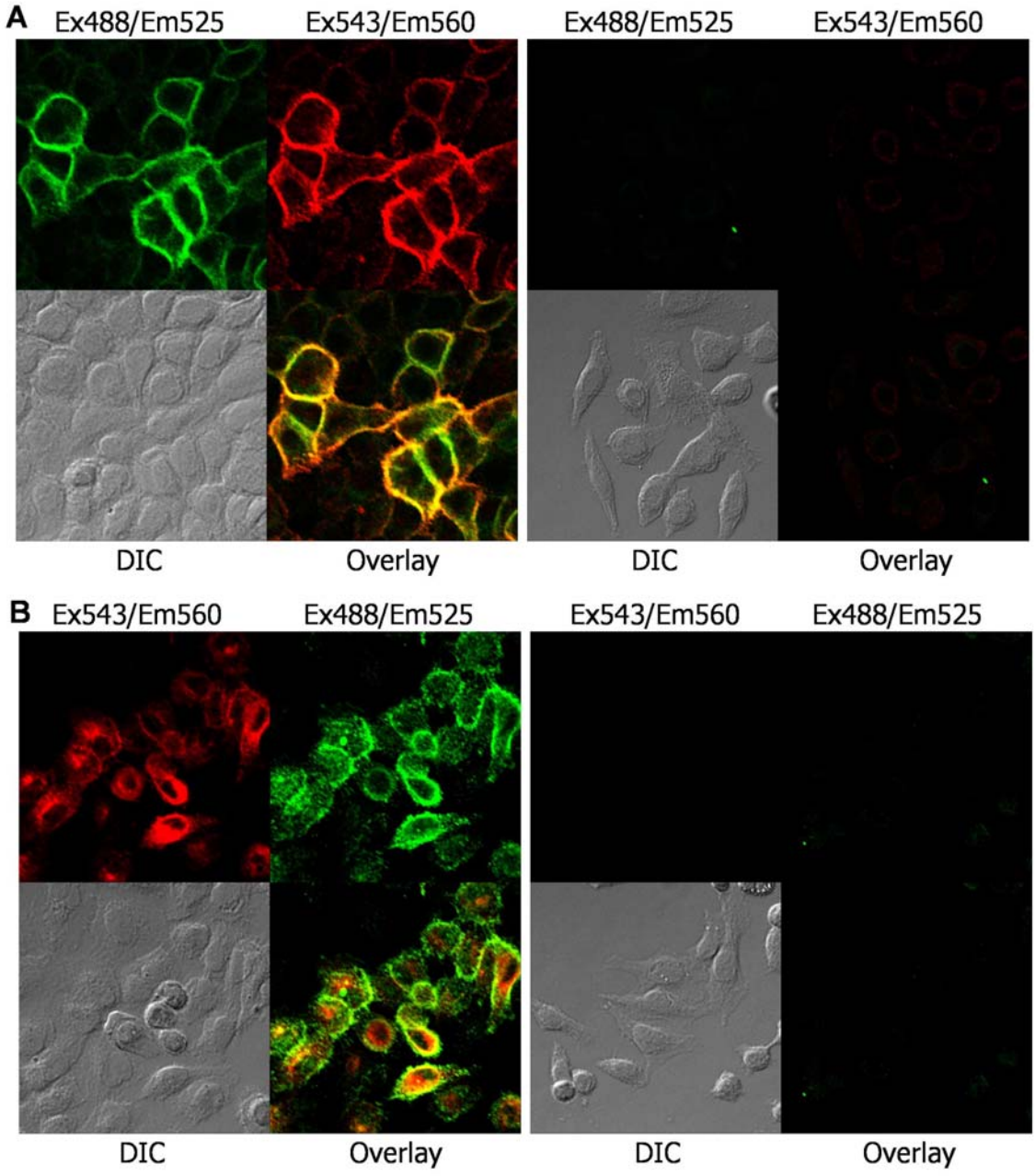

Supplementary Figure 1 Multiplexing live-cell labeling with immunocytochemistry in fixed SHIN3 cells stably expressing stm-HaloTag® 7. SHIN3 cells stably expressing (left panel) or non-expressing (right panel) stm-HaloTag 7 labeled with HaloTagL-Alexa488 (A) or HaloTagL-TMR Ligand (B), fixed with permiabilization and processed for ICC using HaloTag® antibody followed by Alexa Fluor® 594 goat anti-rabbit IgG antibody (Invitrogen). Both HaloTagLs are well co-localized with HaloTagRs, which are detected with HaloTagR antibody.

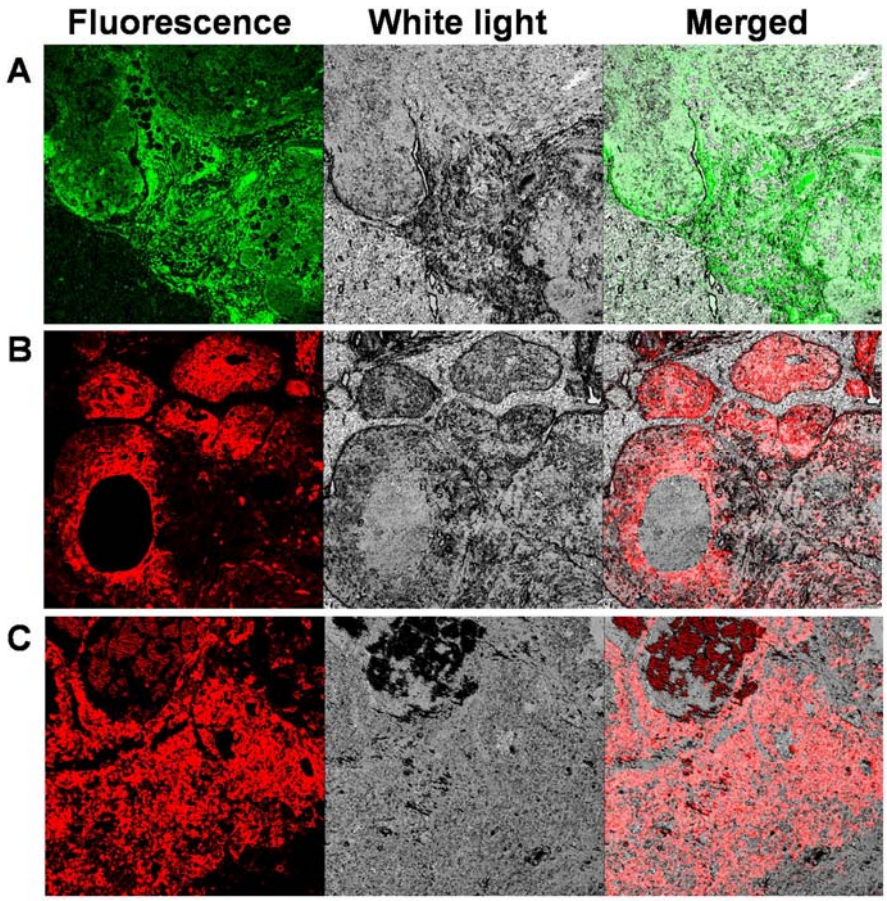

Supplementary Figure 2; Confocal microscopic validation of HaloTagR expression in the HaloTagR-SHIN3 tumor. Formalin-fixed paraffin-embedded of mouse tumor tissue specimens were imaged on Olympus FV500 confocal microscope with the appropriate filter sets for HaloTagL-Alexa488 (A) or HaloTagL-TMR (B) or HaloTagL-Dy633 (C). Since our Olympus FV500 confocal microscope did not have an appropriate filter set for IR800, images taken with HaloTagL-IR800 could not show the signal from the ligand because of low sensitivity.

A. HaloTag-Cy5.5

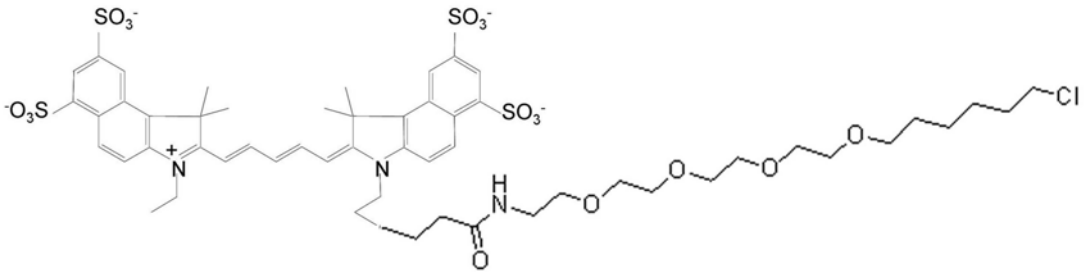

B.

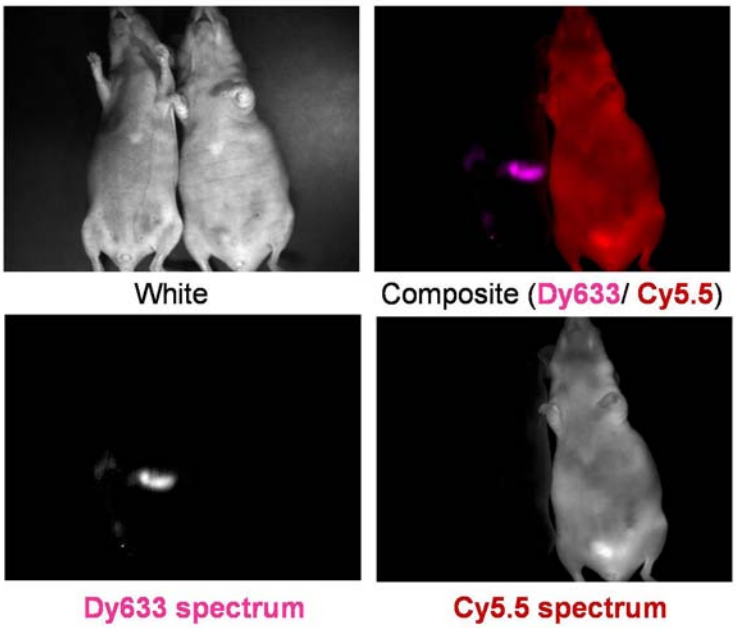

Supplementary Figure 3; HaloTagL-Cy5.5 demonstrates high non-specific binding, thus reducing the target-to-background. We also synthesized Cy5.5 (GE Healthcare) based HaloTagL (A). However, the pharmacokinetics of HaloTagL-Cy5.5 were quite different from other HaloTagLs (B). HaloTagL-Cy5.5 (right mouse) showed much higher background signal than any other ligand, used in this study, and did not depict the HaloTagR-SHIN3 tumor even 24 hours after i.p. injection. We show side-by-side comparison with HaloTagL-Dy633 (left mouse), which clearly depicted the HaloTagR-SHIN3 tumor with low background.

PARACEST Properties of a Dinuclear Neodymium(III) Complex Bound to DNA or Carbonate

Kido Nwe, Christopher M. Andolina, Ching-Hui Huang, and Janet R. Morrow*

Department of Chemistry, University at Buffalo, State University of New York, Buffalo, New York 14260. Received April 2, 2009; Revised Manuscript Received June 6, 2009

A dinuclear Nd(III) macrocyclic complex of **1** (1,4-bis[1-(4,7,10-tris(carbamoylmethyl)-1,4,7,10-tetraazacyclododecane]-*p*-xylene) and mononuclear complexes of 1,4,7-tris-1,4,7,10-tetraazacyclododecane, **2**, and 1,4,7-tris[(*N*-*N*-diethyl)carbamoylmethyl]-1,4,7,10-tetraazacyclododecane, **3**, are prepared. Complexes of **1** and **2** give rise to a PARACEST (paramagnetic chemical exchange saturation transfer) peak from exchangeable amide protons that resonate approximately 12 ppm downfield from the bulk water proton resonance. The dinuclear Nd(III) complex is promising as a PARACEST contrast agent for MRI applications, because it has an optimal pH of 7.5 and the rate constant for amide proton exchange (2700 s^{-1}) is nearly as large as it can be within slow exchange conditions with bulk water. Dinuclear Ln_2(**1**) complexes (Ln(III) = Nd(III), Eu(III)) bind tightly to anionic ligands including carbonate, diethyl phosphate, and DNA. The CEST amide peak of Nd_2(**1**) is enhanced by certain DNA sequences that contain hairpin loops, but decreases in the presence of diethyl phosphate or carbonate. Direct excitation luminescence studies of Eu_2(**1**) show that double-stranded and hairpin-loop DNA sequences displace one water ligand on each Eu(III) center. DNA displaces carbonate ion despite the low dissociation constant for the Eu_2(**1**) carbonate complex (K_d = 15 μM). Enhancement of the CEST effect of a lanthanide complex by binding to DNA is a promising step toward the preparation of PARACEST agents containing DNA scaffolds.

INTRODUCTION

CEST (chemical exchange saturation transfer) agents are a promising new class of MRI contrast agent. Contrast is produced by applying a presaturation pulse at the resonance frequency of NH or OH protons of an amino acid, sugar, nucleotide, or other metabolite. Transfer of the proton magnetization to the bulk water through chemical exchange results in the reduction of the bulk water signal (*1*). The chemical shifts of the diamagnetic NH or OH protons are only 2−5 ppm different than that of bulk water, which makes it difficult to avoid direct saturation of the bulk water (*2*−*5*). This limitation is overcome by forming complexes with lanthanide ions. Paramagnetic lanthanide CEST agents (PARACEST agents) possess mobile protons such as OH, NH of chelating amide or alcohol ligands or water ligands with resonance frequencies that are often more than 20 ppm away from that of bulk water (*6*−*8*).

For CEST agents, the maximum reduction of the bulk water signal is reached when the magnetization of the nuclei of exchangeable protons are completely saturated and the bulk water protons are not directly irradiated by the presaturation pulse that excites the exchangeable protons (*8*). This condition is met when the presaturation pulse power is optimized and the chemical shift difference between exchangeable protons and bulk water protons ($\Delta\omega$) is large enough so that direct irradiation of the bulk water resonance is negligible. Under these conditions, the saturation transfer percent (ST%) is expressed as shown in eq 1 where I is the signal intensity of the bulk water protons taken immediately after pulse is applied to the exchangeable (mobile) protons of CEST agent, I_0 the initial intensity of bulk water protons in the absence of saturation, k_{ex} is the exchange rate constant, n is the number of saturated protons per CEST molecule, C is the concentration of the CEST agent, and T_1 is the longitudinal relaxation time of bulk water protons (*6*).

$$\mathrm{ST\%} = \left(1 - \frac{I}{I_0}\right)100 = \frac{k_{ex}[C]n}{\frac{111.2}{T_1} + k_{ex}[C]n} \times 100 \qquad (1)$$

An important goal in the development of PARACEST contrast agents is to decrease the concentration of agent required. One option is to increase the number of exchangeable protons (n in eq 1). This has been accomplished through studies on macromolecules with multiple exchangeable groups such as a dendrimers (*9, 10*), albumin (*11*), poly-U (*12*), or peptides (*13*) as CEST agents. Sherry's studies on Yb(III) complexes with pendant amide groups featured eight amide protons in two sets of four equivalent protons (*14*). To further increase the number of exchangeable protons, we linked two macrocyclic complexes together to produce dinuclear Ln(III) complexes with twelve amide protons (Chart 1). A potential drawback in this design is that the amide protons in these complexes are chemically inequivalent. For Ln(**2**), all amide protons for the commonly observed capped square antiprism diastereomer are inequivalent. The presence of an additional diastereomer such as a capped twisted square antiprism would give rise to second set of resonances. For Ln_2(**1**), there are two such Ln(III) centers. In practice, however, the chemical shift of the amide resonances may be sufficiently similar to produce overlapping resonances that increase the efficiency of the CEST agent.

In addition to their large number of exchangeable protons, dinuclear Ln(III) complexes have unique binding properties for small molecules. Such specific binding events may lead to new MRI responsive agents that report on the concentration of metabolites or macromolecules (*15*−*17*). For example, dinuclear complexes of Eu(III) bind more strongly to phosphate esters than do their mononuclear analogues (*18*). Dinuclear Ln(III) complexes of macrocycles related to **1** bind to compounds containing carboxylates (*19*). An anion of primary importance for the application of these dinuclear Ln(III) complexes as PARACEST agents that has not been quantitatively studied is

* Janet R. Morrow, jmorrow@buffalo.edu, phone: 716-645-6800-2152, fax: 716-645-6963.

10.1021/bc900146z CCC: $40.75 © 2009 American Chemical Society
Published on Web 06/25/2009

Chart 1

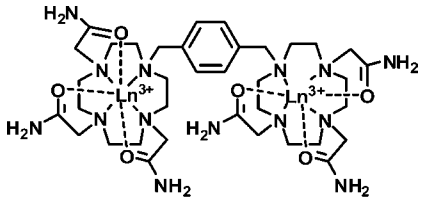

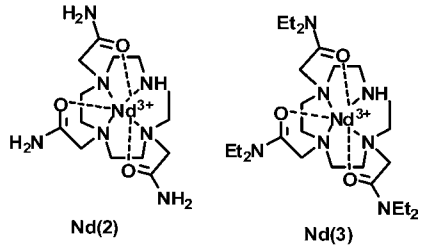

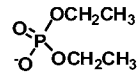

carbonate. Carbonate is present in millimolar concentrations in most tissues in the body and many lanthanide complexes bind carbonate strongly (*20*, *21*). Thus, the influence of carbonate complexes on the CEST properties of these lanthanide complexes is of interest.

Macromolecule binding to Ln(III) complexes modulates their CEST properties by changing the rate of proton exchange and the chemical shift of the mobile protons. This has been demonstrated for Ln(III) complexes of proteins including albumin and ferritin (*11*, *22*). A further example includes a supramolecular Tm(III) complex of poly(L-arginine) that gives rise to an intense CEST effect (*6*). By contrast, the effect of nucleic acid binding to Ln(III) complexes that are PARACEST agents has not yet been reported despite interest in using contrast agents to monitor DNA delivery for gene therapy (*9*, *12*, *23*, *24*) and to use DNA as a scaffold for attaching multiple Ln(III) contrast agents (*25*).

Here, we report on a Nd(III) dinuclear complex that functions as a PARACEST agent through exchange of amide protons. Comparisons are made to two mononuclear complexes. The most efficient CEST agent of these complexes, Nd_2(**1**), binds DNA and certain DNA sequences to give an increased CEST effect. DNA and carbonate binding are further characterized by direct excitation lanthanide luminescence spectroscopy studies of the Eu_2(**1**) analogue.

EXPERIMENTAL SECTION

Materials. $Ln(CF_3SO_3)_3$ salts were purchased from Aldrich. Synthetic DNAs were purchased from Integrated DNA Technologies (IDT) in desalted form and the different oligonucleotides were annealed by heating to 90 °C for 10 min and allowed to cool to room temperature overnight. 1,4-Bis[1-(4,7,10-tris(carbamoylmethyl)-1,4,7,10-tetraazacyclododecane]-*p*-xylene (**1**) was prepared as described previously (*18*). Syntheses of 1,4,7-tris(carbamoylmethyl)-1,4,7,10-tetrazacyclododecane (**2**) and 1,4,7-tris[(*N*-*N*-diethyl)carbamoylmethyl]-1,4,7,10-tetraazacyclododecane (**3**) have been reported elsewhere (*18*). Milli-Q purified water was boiled and bubbled with nitrogen gas for 1 h prior to use in CEST experiments or in luminescence measurements to minimize carbonate concentrations.

Instrumentation. An Orion research digital ionalyzer, model 510, equipped with a temperature compensation probe was used for all pH measurements. All ^1H and ^{13}C NMR were recorded on a Varian Gemini-300, Varian Inova-400, or Inova-500 spectrometer. A Beckman Coulter DU 800 UV−vis spectrophotometer equipped with a high-performance Peltier temperature controller was utilized for all thermal melting experiments. Data were fit by using the *Meltwin 3.5* program. The melting temperatures for HP1 and HP2 (Chart 1) were independent of concentration over the range 40−200 μM DNA, consistent with a hairpin-loop structure. Values of T_m for HP1, HP2, and GGCCGGCC (50 μM) were 60, 63, and 60 °C, respectively, at pH 7.0 with 20 mM HEPES, 50 mM $NaNO_3$. Addition of 1 equiv of Nd_2(**1**) increased the T_m of all sequences by 2−3 °C.

Ln(III) Complexes. The Nd(III) complex was prepared by heating $Nd(CF_3SO_3)_3$ and the macrocyclic ligand (**1**) to reflux in dry methanol for 8 h. In a typical preparation, 0.200 g (0.253 mmol) of ligand and 0.301 g (0.507 mmol) of $Nd(CF_3SO_3)_3$ were heated to reflux in 20 mL of dry methanol for 8 h. The solvent was reduced to 1 mL, and chloroform was slowly added until a precipitate formed at the bottom of the flask. The precipitation was repeated one more time. The supernatant was decanted, and the solid was dried under vacuum to give a white solid. Yield 90%. ^{13}C NMR (300 MHz, D_2O): δ = 19.3, 30.8, 32.5, 34.5, 44.8, 51.8, 60.2, 130.0, 131.8, 175.3. Anal. Cald for $C_{42}H_{64}N_{14}O_{24}F_{18}S_6Nd$: C 23.89, H 2.96, 8.87. Found C 23.78, H 2.88, N 8.75. The synthesis of Eu(III) complex of ligand **1** has been reported elsewhere (*18*). This procedure was modified to reduce the concentration of the carbonate complex. The complex was formed in an aqueous solution by incubation of 1.00 mM ligand **1**, 2.00 mM $Eu(CF_3SO_3)_3$, and 20.0 mM HEPES (pH 7.0) over a period of an hour. Complex formation was verified by Eu(III) luminescence spectroscopy and by ESI-MS spectroscopy. In a few experiments, 25 mM $Pb(NO_3)_2$ was added to the Eu_2(**1**) solution to precipitate adventitious carbonate as $Pb(CO_3)$. To remove the excess Pb(II), 25 mM NaCl followed by 25 mM NaOH (carbonate-free) was added to bring the solution to neutral pH. The solution was vortexed for 30 s and spun in a refrigerated Savant μ-SpeedFuge SFR 13K centrifuge for 60 min at an RFC of 13,000 *g*. The supernatant was removed from the white pellet. Nd(III) complexes of ligands **2** and **3** were prepared by heating $Nd(CF_3SO_3)_3$ and the macrocyclic ligands to reflux in dry methanol for 8 h. The solvent was then reduced to 1 mL and chloroform was slowly added until a precipitate formed at the bottom of the flask. Nd(**2**) Yield 90%. ESI *m*/*e*: 783, 784, 785, 786, 787, 789, 790 ([Nd(**2**)]$(CF_3SO_3)_3$ − $(CF_3SO_3^-)$). ^{13}C NMR (300 MHz, D_2O): δ = 22.1, 23.3, 28.5, 38.3, 40.8, 62.0, 152.5, 176.8. Anal. Cald for $C_{17}H_{29}N_7O_{12}F_9S_3Nd$: C 21.99, H 3.30, 10.22. Found C 21.94, H 3.21, N 10.38. Nd(**3**); Yield 90%. ESI *m*/*e*: 951, 952, 953, 954, 955, 957, 959 ([Nd(**3**)]$(CF_3SO_3)_3$ − $(CF_3SO_3^-)$). ^{13}C NMR (300 MHz, D_2O): δ = 13.5, 14.0, 38.5, 42.0, 43.1, 44.8, 47.5, 48.2, 49.2, 50.5, 160.8, 172.6. Anal. Cald for $C_{29}H_{52}N_7O_{12}F_9S_3Nd$: C 27.55, H 4.18, N 7.41. Found C 27.62, H 4.16, N 7.28.

NMR Measurements. All experiments were carried out on a Varian Inova 500 MHz spectrometer operating at 11.75 T. The saturation transfer experiments were carried out at 298 K by irradiating the sample at 1 ppm incremental steps. The presaturation pulse power was 1000 Hz except where noted. The sample contains 10 mM HEPES buffer (pH 6.5−8.0) and 50 mM $NaNO_3$. An insert coaxial NMR tube was utilized, and the volume of the sample was 100 μL. CEST spectra were measured by recording the bulk water signal intensity as a function of presaturation frequency (in ppm). Studies were conducted using a presaturation pulse irradiation over the range of 20 to −20 ppm with a fixed irradiation time of 3s. CEST

spectra were obtained by plotting the intensity ratio of bulk water signal in the absence of presaturating RF pulse (I_0) and presence of RF irradiation (I) against the frequency of the RF pulse (in ppm). Supporting Information Figure S1 shows CEST spectra as a function of irradiation (saturation) time. The spectra show only minor differences, and the CEST effects are also nearly identical at approximately around 12 ppm where proton exchange occurs. This is an indication that the efficiency of saturation transfer (ST) reaches a steady-state value, and also that the exchange between amide NH and bulk water protons reaches equilibrium with 3 s of irradiation time (*6, 26*), the value used for all CEST data acquisition here.

The longitudinal relaxation time (T_1) of bulk water protons was measured by inversion recovery method. This was done by applying a 180° pulse to invert the magnetization of the bulk water protons followed by a 90° pulse prior to acquisition. Upon completion of the acquisition, Varian Inova software was used to calculate the T_1 value based on the experimental data. Triplicate measurements of T_1 on different samples and different days gave values that were reproducible to ±40%.

Luminescence Spectroscopy. Eu(III) excitation spectra and excited-state lifetimes were obtained using a Spectra-Physics Quanta Ray PRO-270-10 *Q*-switched Nd:YAG pump laser (10 Hz, 60 mJ/pulse) and a MOPO-SL for all luminescence measurements (*27*). The $^7F_0 \rightarrow {}^5D_0$ transition of the Eu(III) ion was scanned between 578 and 581 nm, while the $^5D_0 \rightarrow {}^7F_2$ emission band was monitored at 614 nm using a band-pass filter. Excitation spectra were fit by using the program Peak Fit 4.12 (Jandel). Time-resolved luminescence measurements were collected by using a digital Tektronix TDS 3034B oscilloscope. Five data sets per wavelength were fit to a single exponential decay by using Graphpad *Prism 4* (Graphpad Prism Software, Inc.) and averaged. The number of bound waters, *q*, was estimated by using eq 2 (*28, 29*) where *A* is specific to Eu(III) (1.2 ms), and k_{H2O} and k_{D2O} are the rate constants for luminescence decay in H_2O and D_2O, respectively. The $k_{HNC=O}$ term is for quenching by amides 0.075 ms^{-1}, δ is the number of amide NH groups in the innersphere and α is the total outersphere quenching 0.25 ms^{-1}.

$$q = A(k_{H2O} - k_{D2O} - \delta k_{NHC=O} - \alpha) \qquad (2)$$

DNA binding curves were fit to eq 3 for a simple solution system that involves noncompetitive tight binding of metal complex to multiple binding sites on DNA (*30*). Here, I_0 and I are the luminescence intensity in the absence and presence of nucleic acid, R_b is the luminescence intensity of the bound complex, M is concentration of the complex, K_d is the dissociation constant, n is the number of bases per binding sites, A is the nucleic acid concentration, x is equal to the concentration of DNA times the number of bases in the sequence. The solution includes 25 μM complex, 20 mM HEPES buffered at pH 7.0, 50 mM $NaNO_3$, and 5−50 μM nucleic acid.

$$(I - I_0) = 0.5\left(\frac{R_b}{n}\right)\left\{\frac{n}{K_d} + nM + Ax - \sqrt{\left(\frac{n}{K_d} + nM + Ax\right)^2 - 4nMAx}\right\} \qquad (3)$$

For simple substrates with 1:1 binding stoichiometry, data were fit to eq 4. I_0 and I are the luminescence intensities in the absence and presence of nucleic acid, I_{max} is the maximum luminescence intensity, M is the concentration of Eu_2(**1**), L is the sodium bicarbonate concentration, and K_d is the dissociation constant. The solution includes 20 μM complex, 20 mM HEPES buffer, 50 mM $NaNO_3$, and 20−300 μM concentrations of sodium bicarbonate. This is a method to determine equilibrium binding constant using a nonlinear least-squares fit of the experimental data (*31*).

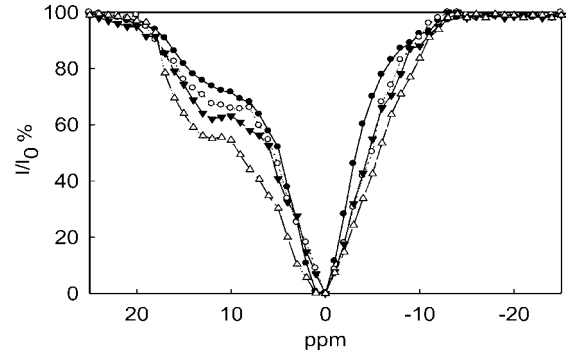

Figure 1. CEST spectra of 5.0 mM (●), 10 mM (○), 15 mM (▼) and 20 mM (△) Nd_2(**1**) at pH 7.0, 10 mM HEPES, 50 mM $NaNO_3$, 25 °C.

$$(I - I_0) = (I_{max})\frac{(M + L + K_d) - \sqrt{(K_d + M + L)^2 - (4 \times M \times L)}}{2 \times L} \qquad (4)$$

RESULTS

CEST Spectra. The CEST spectrum of Nd_2(**1**) is shown in Figure 1. The vertical axis shows the percent reduction of the intensity of the bulk water peak upon irradiation with a presaturation pulse in 1 ppm steps over the range 25 to −25 ppm with the bulk water resonance set at 0 ppm. There is a broad shoulder observed at approximately 12 ppm downfield from the bulk water proton resonance that we attribute to the protons of the NH groups. This assignment was supported by a CEST study of a Nd(III) derivative that lacks NH groups (see below). The only other exchangeable protons are from water ligands, and these are expected to exchange too rapidly to observe a CEST signal. Attempts to assign the NH amide proton resonances by ^1H NMR studies of Nd_2(**1**) in H_2O failed (Supporting Information Figure S2), even at lowered temperatures (5 °C) where slower exchange rate constants may facilitate the observation of these resonances. The absence of a proton resonance in the chemical shift range of the CEST shoulder is attributed to broadening of the NH protons by exchange with water. As discussed below, the rate constants for NH proton exchange are fast in comparison to those of other lanthanide amide complexes, and the observed rate constant suggests that the Nd(III) complex is at the limit of the NMR spectroscopy slow exchange regime.

The CEST spectrum of the Nd_2(**1**) complex was further investigated as a function of concentration and pH (Figures 1 and 2). The CEST enhancement upon increasing pH in the 6.5−7.5 interval is consistent with previously observed enhancements due to base catalysis of the exchange of the amide protons (*32*). A decrease in the CEST enhancement at the 12 ppm shoulder concomitant with a shift of the CEST peak toward the bulk water peak (Supporting Information Figure S3) suggests that exchange becomes even more rapid at pH 8.0, leading to the loss of the CEST peak as the NH peak begins to merge with the bulk water peak at high pH values. The concentration dependence of the CEST spectrum of Nd_2(**1**) is shown in Figure 1.

Figure 3 shows that the dinuclear Nd_2(**1**) complex has a stronger CEST amide NH peak than the mononuclear Nd(**2**) complex at equivalent concentrations. This is presumably due to the larger number of exchangeable amide NH protons in Nd_2(**1**) compared to Nd(**2**), although as noted above, both complexes have several sets of chemically distinct NH protons.

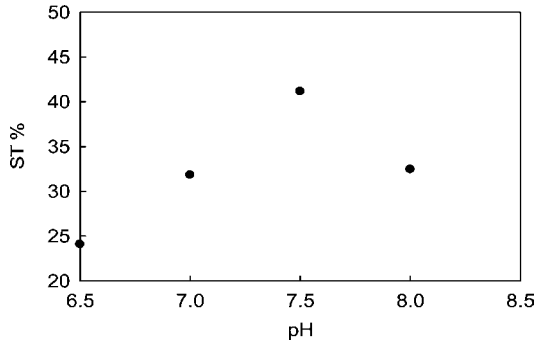

Figure 2. The pH dependence of saturation transfer (ST) efficiency of Nd_2(**1**) at 25 °C, 10 mM buffer, 50 mM $NaNO_3$.

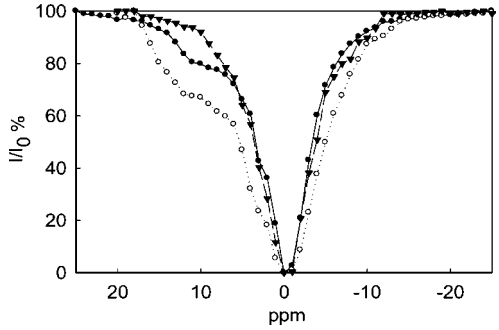

Figure 3. CEST spectra of 5.0 mM Nd_2(**1**) (○), 5.0 mM Nd(**2**)(●) and 5.0 mM Nd(**3**)(▼), B_1 = 1,200 Hz, at pH 7.0, 10 mM HEPES, 50 mM $NaNO_3$, 25 °C.

For comparison, Figure 3 shows a CEST spectrum of the Nd(III) complex of **3**, a ligand lacking NH groups. Nd(**3**) has no discernible CEST peak and only shows a peak for direct irradiation of bulk water. This suggests that the CEST effects centered around 11 ppm for Nd(**2**) and 12 ppm for Nd_2(**1**) are for amide NH protons. Nd(III) macrocyclic complexes with peptide pendant groups have NH CEST peaks with similar chemical shifts (*33*).

By contrast, the Eu_2(**1**) complex has no observable CEST peaks under these conditions (Supporting Information Figure S4). This result is similar to previously reported mononuclear Eu(III) complex analogues that have a barely discernible NH CEST shoulder because their amide NH resonance is very close to the bulk water resonance (*33, 34*).

To estimate the rate constant for NH proton exchange, a concentration study for the saturation transfer of Nd_2(**1**) ranging 5−20 mM was carried out. The plot of the saturation transfer (ST, eq 1) efficiency as a function of concentration is shown in Figure 4. The data are fit to eq 1 to give an exchange rate constant of k_{ex} of 2700 s^{-1} for a measured longitudinal relaxation time (T_1) of bulk water protons of 0.18 s.

Our interest in the design of lanthanide(III) DNA conjugates as MRI contrast agents led us to study the interaction of Nd_2(**1**) with phosphate esters and DNA to determine whether certain DNA structural elements might support or even enhance the CEST effect (Figure 6, Chart 2). Addition of diethyl phosphate (DEP) led to a slight decrease in the CEST peak attributed to the NH group (Supporting Information Figure S5). By contrast, certain structured DNA sequences modestly increased the CEST shoulder at 12 ppm. The hairpin DNA (HP1) was the most efficient (Chart 2) with a 15% enhancement of CEST over the complex alone upon addition of 0.50 mM DNA (Figure 5). Mutation of the closing base pair gives a DNA sequence that enhances the CEST spectrum to a smaller extent at 5%. This suggests that the CEST efficiency is dependent on structural differences in the DNA that are dictated by the closing base

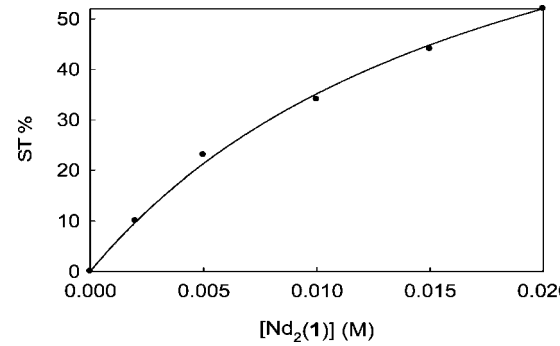

Figure 4. Saturation transfer (ST) effect as a function of Nd_2(**1**) concentration with 50 mM $NaNO_3$ at pH 7.0 and 25 °C. The data were fit to eq 1 to obtain a k_{ex} of 2.7 × 10^3 s^{-1}.

Chart 2

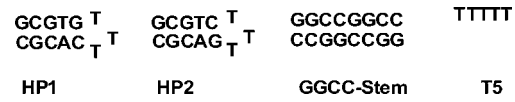

pair. In comparison, neither the self-complementary oligonucleotide GGCCGGCC nor single-stranded T5 measurably affects the CEST spectrum under similar conditions (data not shown).

The effect of carbonate on the CEST spectrum of Nd_2(**1**) was examined. Addition of an equivalent of carbonate to the dinuclear complex at pH 7.4 gave a decrease in the amide CEST peak (Supporting Information Figure S6), consistent with suppression of the NH amide CEST effect for the carbonate complex. Addition of $Pb(NO_3)_2$ to a solution of Nd_2(**1**) to sequester carbonate had little effect on the CEST spectrum. This result suggests that freshly prepared and degassed solutions of Nd_2(**1**) do not contain carbonate complexes in appreciable quantities. Interaction of Ln_2(**1**) with carbonate and DNA was studied quantitatively by using luminescence spectroscopy for the Eu(III) analogue (see below).

Luminescence Spectroscopy. Direct excitation luminescence spectroscopy of the Eu_2(**1**) complex was studied to probe interactions with phosphate esters, DNA and carbonate. The $^7F_0 \rightarrow {}^5D_0$ transition for Eu(III) is between two nondegenerate levels and thus useful for determining the number of species in solution. The $^7F_0 \rightarrow {}^5D_0$ excitation spectrum of Eu_2(**1**) is shown in Figure 6. As shown previously (*18*), the major peak at 579.82 nm is attributed to the dinuclear complex with four bound water ligands (Eu_2(**1**)$(H_2O)_4$), and the red-shifted shoulder and peak at 580.22 and 580.53 nm are attributed to a carbonate complex that forms in water at neutral pH upon exposure of the complex to the atmosphere or upon addition of carbonate ion in buffered solutions. For selected studies, the concentration of carbonate complex was reduced to obtain a solution with predominantly (Eu_2(**1**)$(H_2O)_4$). This was accomplished by treating the Eu_2(**1**)

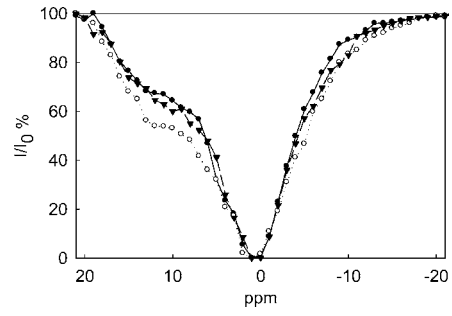

Figure 5. CEST spectra of Nd_2(**1**) 5.0 mM (●) titrated with 0.20 mM (▼) and 0.50 mM (○) HP1 at pH 7.0, 10 mM HEPES, 50 mM $NaNO_3$, 25 °C.

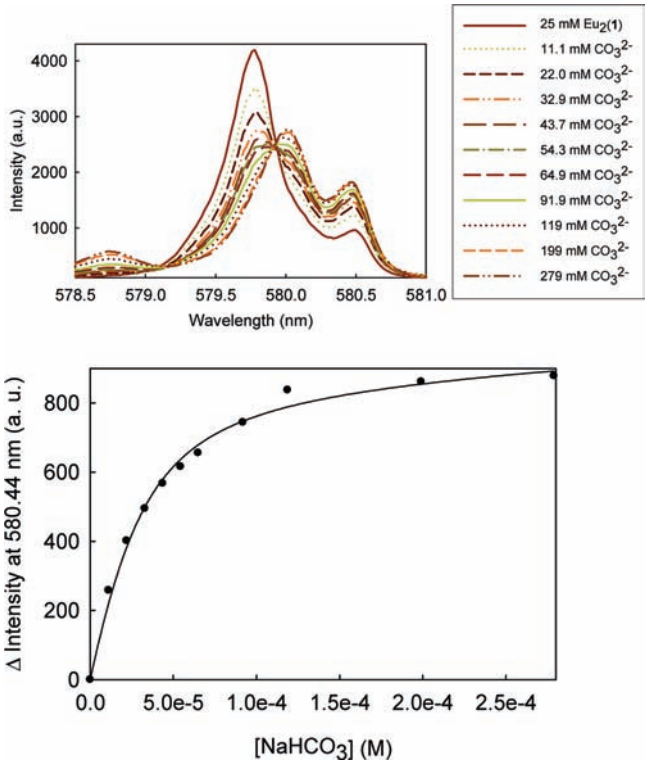

Figure 6. The effect of carbonate on the $^7F_0 \rightarrow {}^5D_0$ excitation band of Eu_2(**1**) for solutions containing 25 μM Eu_2(**1**), 20 mM HEPES, pH 7.0, 50 mM $NaNO_3$ (top). Data are fit to eq 4 with a K_d of 15 uM (bottom).

Table 1. Luminescence Lifetimes of Eu_2(1) upon Binding of DNA or Carbonate[a]

anion	wavelength (nm)	H_2O μs	D_2O μs	anion (μM)	q [b]
HP1	579.64	537	1700	50	0.96
HP2	579.70	512	1630	50	0.93
GGCC	579.70	490	1600	50	1.1
CO_3^{2-}	580.45	608	1330	20	0.50
CO_3^{2-}	580.20	587	1360	20	0.59

[a] Solutions contained 50 mM $NaNO_3$, 20 mM HEPES, pH 7.0, with 25 μM Eu_2(**1**). [b] The number of bound water molecules, q, was calculated by using eq 2. Standard deviations in lifetime values are typically ≤7% in H_2O and ≤3% in D_2O (*27*).

complex with $Pb(NO_3)_2$ to form insoluble $Pb(CO_3)$ followed by precipitation of any remaining Pb(II) with chloride ion.

Addition of carbonate to solutions containing Eu_2(**1**) gives rise to two pronounced excitation peaks at 580.20 and 580.45 nm (Figure 6). These two peaks are attributed to two different isomers, both of which have bound carbonate and have low q values of 0.5 to 0.6 (Table 1). The small peak at 578.74 nm that grows in with increasing carbonate concentration is assigned as the free Eu(III) ion (*27*). A plot of the luminescence intensity as a function of bicarbonate gives a binding isotherm with a K_d of 15 μM by fitting the data to eq 4.

Titration of Eu_2(**1**) with HP1 DNA gives a decrease in the major excitation peak to give a new peak that is slightly blue-shifted (579.69 nm). A plot of the change in luminescence intensity as a function of DNA gives a binding constant of 2.5 μM and $n = 8.2$ (number of bases in binding site) by fitting the data to eq 3 (Figure 7). HP2 DNA and the self-complementary GGCCGGCC DNA give similar excitation peaks and binding curves with dissociation constants of 4.2 μM ($n = 12$) and 28 μM ($n = 6.9$), respectively (Supporting Information Figures S7, S8). By contrast, T5 has only a small effect on luminescence intensity (Supporting Information Figure S9), and a plot of this change in intensity with DNA concentration suggests that

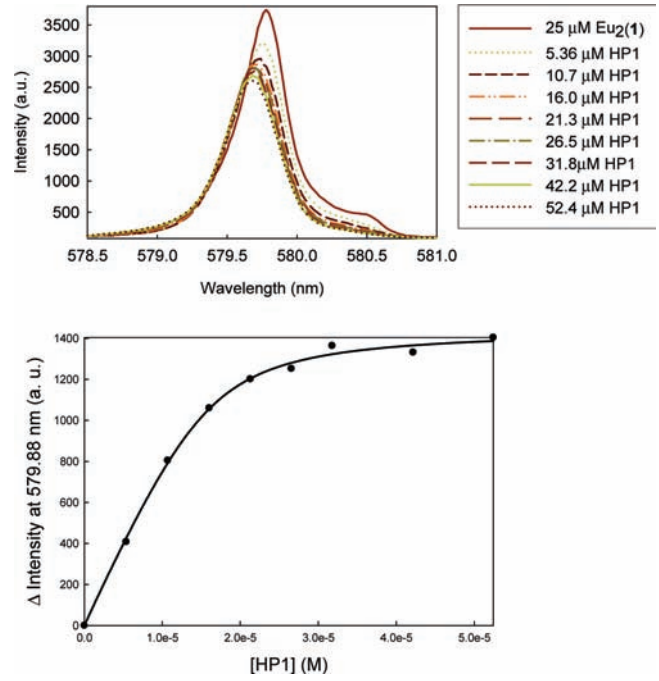

Figure 7. $^7F_0 \rightarrow {}^5D_0$ excitation spectra ($^5D_0 \rightarrow {}^7F_2$ emission) of solutions of 25 μM Eu_2(**1**) titrated with HP1 DNA at pH 7.0, 20 mM HEPES, 50 mM $NaNO_3$ (top). Data are fit to eq 3 with a K_d of 2.5 μM and n of 8.2 (bottom).

binding is weak under conditions of the titration. Luminescence lifetime studies show that there is a reduction in the number of bound waters on each Eu(III) center of the aqua complex (excitation at 579.82 nm) upon DNA binding to hairpin or double-stranded DNA (Table 1). In addition, excitation luminescence studies of the Eu_2(**1**) carbonate complex treated with DNA (Supporting Information Figure S10) show that the carbonate ligand is displaced by DNA.

DISCUSSION

Nd_2(**1**) shows a more pronounced CEST effect than the mononuclear complex Nd(**2**) under the conditions studied here, corresponding to the larger number of mobile amide protons for the dinuclear complex at equal concentrations of complex. In addition, the relatively large exchange rate constant for Nd_2(**1**) amide protons (2700 s^{-1}) contributes favorably to the efficiency of CEST. By comparison, mononuclear Nd(III) complexes have NH proton exchange rate constants that range from 125 s^{-1} to 826 s^{-1} (*14, 32*). The rate constant for Nd_2(**1**) is nearly as large as it can be (6500 s^{-1}) before slow exchange conditions no longer hold $\Delta\omega \cdot \tau \geq 1$. Notably, peaks in the CEST spectrum are observed for mobile protons that approach or even exceed this limit whose resonances are consequently broadened into the baseline (*16*).

The solution chemistry of Ln_2(**1**) complexes is dominated by carbonate complex formation. Indeed, isolation of a carbonate-free complex of Eu_2(**1**) is difficult in aqueous solution without the addition of a carbonate sequestering agent. Eu_2(**1**) binds carbonate more strongly than related monomeric complexes (*18*). This is consistent with the propensity of the dinuclear complex to bind tightly to anions including phosphate esters, carbonate, and sulfonates (*18*). An increased affinity for anions is attributed in part to the aromatic linker which leads to increased Lewis acidity of the Ln(III) centers as well as the possible interaction of anions with both Ln(III) centers. The two distinct excitation peaks for the carbonate complex are attributed to two isomers. One possibility is that the two isomers have similar numbers of bound waters, based on their nearly identical q numbers

derived from luminescence lifetimes. However, the nonintegral q number for the isomers (0.5 and 0.6) suggests an alternate explanation. The two carbonate complex isomers that give rise to two distinct excitation peaks may actually differ by the number of bound water molecules (q values of approximately 1 and 0) but are in rapid exchange on the luminescence emission time scale to give an apparent q that is the average of the two complexes (*35*). This case would be similar to the hydration isomers observed for Eu(EDTA)$(H_2O)_x$ ($x = 2$ or 3) (*27, 36*) that give rise to two excitation peaks but a single luminescence lifetime. For the complexes here, an equilibrium between a bidentate carbonate complex with $q = 0$ (*37*) and a monodentate carbonate complex with a $q = 1$ would be involved. The relatively large difference in the excitation peak frequencies is consistent with this alternative. Also supportive of this assignment is that other carbonate complexes we have reported to date, including both dinuclear and mononuclear Eu(III) complexes of septadentate macrocycles, have two peaks at similar frequencies to those observed here (*18*). These similarities suggest that the isomers do not involve interactions that are specific to dinuclear complexes such as bridging carbonate.

Excitation luminescence studies of complexes related to Eu_2(**1**) show that DEP coordinates to dinuclear Eu(III) complexes with a binding constant of 0.43 mM (*18*). Luminescence lifetime studies are consistent with displacement of one water molecule at each Eu(III) center upon DEP binding (*38*). Assuming a similar binding constant between Nd_2(**1**) and DEP, DEP should be fully bound in the CEST experiment shown in Supporting Information Figure S5. Binding of DEP results in a 10% decrease of the amide CEST peak of the Nd(III) complex. The origin of this decrease may involve a change in the rate constants for amide proton exchange upon binding of DEP mediated by a change in the Lewis acidity of the metal ion center upon complexation of DEP. Alternately, there may be a change in the chemical shift dispersion of the different amide protons for the Nd(III) complex of DEP so that the CEST peak shape is changed. A similar decrease in the CEST amide peak is observed for carbonate binding to Nd_2(**1**). Thus, complexation of either of these two simple anionic ligands leads to a decrease in the CEST amide peak of Nd_2(**1**).

The preparation of biopolymers, polymers, and nanoparticles conjugated to multiple copies of CEST agents is of interest in order to increase the number of CEST agents at a targeted tissue (*15, 39*−*41*). For Ln(III) PARACEST agents, the close proximity of a biopolymer may give rise to changes in the CEST peaks attributed to the influence of the biopolymer environment on the complex (*22*). Thus, it is important to choose an environment that supports or enhances the CEST effect. Typically, interactions of Ln(III) PARACEST agents with other molecules lead to changes in the rate constants for the mobile protons, and this may either enhance or decrease the CEST effect (*16, 17*). In some cases, Ln(III) complexes form supramolecular complexes that induce hyperfine shifting of multiple macromolecular protons to enhance the CEST effect (*6*). In addition to proteins, DNA is of interest for conjugation of lanthanide MRI contrast agents (*24, 25*). Our work here shows that Eu_2(**1**) and Nd_2(**1**) complexes interact strongly with DNA and both binding strength and CEST effect modulation are dependent on DNA secondary structure.

Titration of the Eu_2(**1**) complex with HP1, HP2, and the GGCC stem leads to a decrease in luminescence intensity to form a new complex with a single bound water for each Eu(III) center ($q = 1$, Table 1). Fitting of the data to a binding isotherm for DNA sequences with multiple binding sites shows that all three DNA sequences bind tightly to Eu_2(**1**) with binding constants that are in the micromolar range. The large binding site sizes for the hairpins ($n = 8$−11) are most consistent with a complex involving one to two Eu_2(**1**) bound to DNA. For the GGCC stem, data are most consistent with that of two Eu_2(**1**) binding sites. In any case, these data suggest that, under the conditions of the CEST experiments which contain higher concentrations of Nd(III) complex and DNA, all DNA is bound to the lanthanide complex. Only single-stranded T5 binds weakly to the dinuclear complex, demonstrating that double helical DNA is required for tight binding. The tight binding constants of the hairpin loops and double-stranded DNA led us to initially anticipate that these DNA sequences would have similar effects on the CEST spectrum of Nd_2(**1**).

Modulation of the CEST spectrum is, however, DNA sequence dependent. The CEST peak of Nd_2(**1**) increases upon addition of the hairpin DNA sequences but not with addition of the GGCC stem or T5. At this juncture, it is not known which protons in the Nd_2(**1**) bound DNA complex give rise to the CEST peak. It is likely that, given the large number of amide protons of the Nd(III) complex and the presence of this complex in excess over DNA, the CEST peak results from a favorable increase in the amide proton exchange rate by interaction of the complex with DNA. In addition, it is noteworthy that nucleic acids such as poly-U act as CEST agents through both amide NH and alcohol protons. However, the exchangeable DNA amide protons would have to be hyperfine-shifted by the Nd(III) complex (*12*) to produce the observed CEST peak in our studies. Our data suggest that there is a specific interaction of the Nd_2(**1**) complex with the hairpin loop of HP1 that enhances the CEST peak at 12 ppm. This is supported by the lack of an effect of the GGCC-stem sequence on the CEST spectrum despite strong binding of this DNA to the Ln(III) complex. Even more remarkable is the fact that a change in the hairpin closing base pair (CG to GC) affects the Nd_2(**1**)-DNA complex CEST intensity, although both hairpins bind nearly equally as strongly. Given the important role of the closing base pair on DNA hairpin loop structure (*42*), these data suggest that loop structure is important in the association of the complex. The limited number of DNA secondary structures studied here prevents us from formulating rules for effective enhancement of Ln(III) CEST agents. Our data suggest, however, that secondary structures such as hairpin loops that have been shown to bind lanthanide ions such as the thymidine triloop studied here (*43*) give rise to increased CEST effects. Speculation on the mode of Ln(III) complex DNA interactions is premature, but it is noteworthy that a simple phosphate diester decreases the CEST effect. DNA of a particular sequence and structure gives rise to the modestly enhanced CEST spectrum of the Nd_2(**1**)-DNA complex.

CONCLUSIONS

The presence of a large number of exchangeable amide protons in combination with a relatively rapid amide proton exchange rate in the Nd_2(**1**) complex suggests that further development of dinuclear complexes as PARACEST agents is warranted. Binding of carbonate to complexes of Ln_2(**1**) will influence the solution and PARACEST properties of these complexes in biological systems where carbonate concentrations are high. Interestingly, the carbonate acts as a masking agent that is readily displaced by anionic ligands such as DNA that bind even more strongly than carbonate. This work shows that DNA complexes of PARACEST agents are promising for the design of new nanosized biocompatible systems that use DNA as a carrier or as a scaffold. The position of lanthanide ion complex conjugation to DNA and the secondary structure of the DNA conjugate, however, require further study to optimize the CEST effect. This will require the study of different DNA sequences toward a better understanding of the basis for the modulation of the PARACEST effect by macromolecule binding.

ACKNOWLEDGMENT

We thank the National Institutes of Health for support of this work (EB-04609) and the National Science Foundation for a major instrumentation award (CHE-0321058) to build the MOPO laser system.

Supporting Information Available: CEST spectra and Eu(III) excitation luminescence titrations with DNA with binding curves. This material is available free of charge via the Internet at http://pubs.acs.org.

LITERATURE CITED

(1) Ward, K. M., Aletras, A. H., and Balaban, R. S. (2000) A new class of contrast agents for MRI based on proton chemical exchange dependent saturation transfer (CEST). *J. Magn. Reson. 143*, 79–87.

(2) Zhou, J., Payen, J.-F., Wilson, D. A., Traystman, R. J., and van Zijl, P. C. M. (2003) Using the amide proton signals of intracellular proteins and peptides to detect pH effects in MRI. *Nat. Med. 9*, 1085–1090.

(3) Guivel-Scharen, V., Sinnwell, T., Wolff, S. D., and Balaban, R. S. (1998) Detection of proton chemical exchange between metabolites and water in biological tissues. *J. Magn. Reson. 133*, 36–45.

(4) Sun, P. Z., Zhou, J., Sun, W., Huang, J., and van Zijl, P. C. M. (2005) Suppression of lipid artifacts in amide proton transfer imaging. *Mag. Res. Med. 54*, 222–225.

(5) Zhou, J., and van Zijl, P. C. M. (2006) Chemical exchange saturation transfer imaging and spectroscopy. *Prog. NMR Spectrosc. 48*, 109–136.

(6) Aime, S., Castelli, D. D., and Terreno, E. (2002) Novel pH-reporter MRI contrast agents. *Angew. Chem., Int. Ed. 41*, 4334–4336.

(7) Zhang, S., Winter, P., Wu, K., and Sherry, A. D. (2001) A novel europium(III)-based MRI contrast agent. *J. Am. Chem. Soc. 123*, 1517–1518.

(8) Zhang, S., Merritt, M., Woessner, D. E., Lenkinski, R. E., and Sherry, A. D. (2003) PARACEST agents: modulating MRI contrast via water proton exchange. *Acc. Chem. Res. 36*, 783–790.

(9) Goffeney, N., Bulte, J. W. M., Duyn, J., Bryant, L. H., and van Zijl, P. C. M. (2001) Sensitive NMR detection of cationic-polymer-based gene delivery systems using saturation transfer via proton exchange. *J. Am. Chem. Soc. 123*, 8628–8629.

(10) Pikkemaat, J. A., Wegh, R. T., Lamerichs, R., van de Molengraaf, R. A., Langereis, S., Burdinski, D., Raymond, A. Y. F., Janssen, H. M., de Waal, B. F. M., Willard, N. P., Meijer, E. W., and Grüll, H. (2007) Dendritic PARACEST contrast agents for magnetic resonance imaging. *Contr. Media Mol. Imaging 2*, 229–239.

(11) Ali, M. M., Woods, M., Suh, E. H., Kovacs, Z., Tircso, G., Zhao, P., Kodibagkar, V. D., and Sherry, A. D. (2007) Albumin-binding PARACEST agents. *J. Biol. Inorg. Chem. 12*, 855–865.

(12) Snoussi, K., Bulte, J. W. M., Guéron, M., and van Zijl, P. C. M. (2003) Sensitive CEST agents based on nucleic acid imino proton exchange: detection of poly(rU) and of a dendrimer-poly(rU) model for nucleic acid delivery and pharmacology. *Magn. Reson. Med. 49*, 998–1005.

(13) Yoo, B., and Pagel, M. D. (2007) Peptidyl molecular imaging contrast agents using a new solid-phase peptide synthesis approach. *Bioconjugate Chem. 18*, 903–911.

(14) Zhang, S., Michaudet, L., Burgess, S., and Sherry, A. D. (2002) The amide protons of an ytterbium(III) dota tetraamide complex act as efficient antennae for transfer of magnetization to bulk water. *Angew. Chem., Int. Ed 41*, 1919–1921.

(15) Yoo, B., and Pagel, M. D. (2008) An overview of responsive MRI contrast agents for molecular imaging. *Front. Biosci. 13*, 1733–1752.

(16) Huang, C.-H., and Morrow, J. R. (2009) A PARACEST agent responsive to inner- and outer-sphere phosphate ester interactions for MRI applications. *J. Am. Chem. Soc. 131*, 4206–4207.

(17) Aime, S., Delli Castelli, D., Fedeli, F., and Terreno, E. (2002) A paramagnetic MRI-CEST agent responsive to lactate concentration. *J. Am. Chem. Soc. 124*, 9364–9365.

(18) Nwe, K., Andolina, C., and Morrow, J. R. (2008) Tethered dinuclear Eu(III) catalysts for the cleavage of RNA. *J. Am. Chem. Soc. 130*, 14861–14871.

(19) Harte, A. J., Jensen, P., Plush, S. E., Kruger, P. E., and Gunnlaugsson, T. (2006) A dinuclear lanthanide complex for the recognition of bis(carboxylates): formation of terbium(III) luminescent self-assembly ternary complexes in aqueous solution. *Inorg. Chem. 45*, 9465–9474.

(20) Dickins, R. S., Gunnlaugsson, T., Parker, D., and Peacock, R. D. (1998) Reversible anion binding in aqueous solution at a cationic heptacoordinate lanthanide center: selective bicarbonate sensing by time-delayed luminescence. *Chem. Commun.* 1643–1644.

(21) Murray, B. S., New, E. J., Pal, R., and Parker, D. (2008) Critical evaluation of five emissive europium(iii) complexes as optical probes: correlation of cytotoxicity, anion and protein affinity with complex structure, stability and intracellular localisation profile. *Org. Biomol. Chem. 6*, 2085–2094.

(22) Vasalatiy, O., Zhao, P., Zhang, S., Aime, S., and Sherry, A. D. (2006) Catalytic effects of apoferritin interior surface residues on water proton exchange in lanthanide complexes. *Contr. Media Mol. Imaging 1*, 10–14.

(23) Himmelreich, U., Aime, S., Hieronymus, T., Justicia, C., Uggeri, F., Zenke, M., and Hoehn, M. (2006) A responsive MRI contrast agent to monitor functional cell status. *NeuroImage 32*, 1142–1149.

(24) Crich Simonetta, G., Lanzardo, S., Barge, A., Esposito, G., Tei, L., Forni, G., and Aime, S. (2005) Visualization through magnetic resonance imaging of DNA internalized following "in vivo" electroporation. *Mol. Imaging 4*, 7–17.

(25) Cai, J., Shapiro, E. M., and Hamilton, A. D. (2009) Self-assembling DNA quadruplex conjugated to MRI contrast agents. *Bioconjugate Chem. 20*, 205–208.

(26) McMahon, M. T., Zhou, J., Gilad, A. A., Bulte, J. W. M., and van Zijl, P. C. M. (2007) Physical mechanism and applications of CEST contrast agents. *Mol. Cell. MRI* 85–100.

(27) Andolina, C. M., Holthoff, W. G., Page, P. M., Mathews, R. A., Morrow, J. R., and Bright, F. V. (2009) Spectroscopic system for direct lanthanide photoluminescence spectroscopy with nanomolar detection limits. *Appl. Spectrosc. 63*, 483–493.

(28) Supkowski, R. M., and Horrocks, W. D. (2002) On the determination of the number of water molecules, q, coordinated to europium(III) ions in solution from luminescence decay lifetimes. *Inorg. Chim. Acta 340*, 44–48.

(29) Beeby, A., Clarkson, I. M., Dickins, R. S., Faulkner, S., Parker, D., Royle, L., de Sousa, A. S., Williams, J. A. G., and Woods, M. (1999) Non-radiative deactivation of the excited states of europium, terbium and ytterbium complexes by proximate energy-matched OH, NH and CH oscillators: an improved luminescence method for establishing solution hydration states. *J. Chem. Soc., Perkin Trans. 2*, 493–504.

(30) Stootman, F. H., Fisher, D. M., Rodger, A., and Aldrich-Wright, J. R. (2006) Improved curve fitting procedures to determine equilibrium binding constants. *Analyst 131*, 1145–1151.

(31) Ye, Y., Lee, H.-W., Yang, W., Shealy, S., and Yang, J. J. (2005) Probing site-specific calmodulin calcium and lanthanide affinity by grafting. *J. Am. Chem. Soc. 127*, 3743–3750.

(32) Terreno, E., Castelli, D. D., Cravotto, G., Milone, L., and Aime, S. (2004) Ln(III)-DOTAMGly complexes: a versatile series to assess the determinants of the efficacy of paramagnetic chemical exchange saturation transfer agents for magnetic resonance imaging applications. *Invest. Radiol. 39*, 235–243.

(33) Wojciechowski, F., Suchy, M., Li, A. X., Azab, H. A., Bartha, R., and Hudson, R. H. E. (2007) A robust and convergent synthesis of dipeptide-DOTAM conjugates as chelators for

lanthanide ions: new PARACEST MRI agents. *Bioconjugate Chem. 18*, 1625–1636.

(34) Woods, M., Woessner, D. E., Zhao, P., Pasha, A., Yang, M.-Y., Huang, C.-H., Vasalitiy, O., Morrow, J. R., and Sherry, A. D. (2006) Europium(III) macrocyclic complexes with alcohol pendant groups as chemical exchange saturation transfer agents. *J. Am. Chem. Soc. 128*, 10155–10162.

(35) Bruno, J., Herr, B. R., and Horrocks, W. D., Jr. (1993) Laser-induced luminescence studies of europium hexaazamacrocycle Eu(HAM) $^{3+}$. An evaluation of complex stability and the use of the gadolinium analog as a relaxation agent in yttrium-89 NMR. *Inorg. Chem. 32*, 756–762.

(36) Graeppi, N., Powell, D. H., Laurenczy, G., Zekany, L., and Merbach, A. E. (1995) Coordination equilibria and water exchange kinetics of lanthanide(III) propylenediaminetetraacetates and other magnetic resonance imaging related complexes. *Inorg. Chim. Acta 235*, 311–326.

(37) Dickins, R. S., Aime, S., Batsanov, A. S., Beeby, A., Botta, M., Bruce, J. I., Howard, J. A. K., Love, C. S., Parker, D., Peacock, R. D., and Puschmann, H. (2002) Structural, luminescence, and NMR studies of the reversible binding of acetate, lactate, citrate, and selected amino acids to chiral diaqua ytterbium, gadolinium, and europium complexes. *J. Am. Chem. Soc. 124*, 12697–12705.

(38) Nwe, K., Richard, J. P., and Morrow, J. R. (2007) Direct excitation luminescence spectroscopy of Eu(III) complexes of 1,4,7-tris(carbamoylmehtyl)-1,4,7,10-tetraazacyclododecane derivatives and kinetic studies of their catalytic cleavage of an RNA analog. *Dalton Trans.* 5171–5178.

(39) Liu, G., Li, Y., and Pagel, M. D. (2007) Design and characterization of new irreversible responsive PARACEST MRI contrast agent that detects nitric oxide. *Magn. Reson. Med. 58*, 1249–1256.

(40) Trokowski, R., Zhang, S., and Sherry, A. D. (2004) Cyclen-based phenylboronate ligands and their Eu^{3+} complexes for sensing glucose by MRI. *Bioconjugate Chem. 15*, 1431–1440.

(41) Zhang, S., Trokowski, R., and Sherry, A. D. (2003) A paramagnetic CEST agent for imaging glucose by MRI. *J. Am. Chem. Soc. 125*, 15288–15289.

(42) Moody, E. M., and Bevilacqua, P. C. (2003) Folding of a stable DNA motif involves a highly cooperative network of interactions. *J. Am. Chem. Soc. 125*, 16285–16293.

(43) Mathews, R. A. (2008) Cleavage of an RNA analog by mononuclear Zn(II) macrocyclic complexes and metal ion and metallodrug interactions with deoxyribonucleic acids, Ph.D. Thesis, University at Buffalo, State University of New York.

BC900146Z

Supplementary Material for:

PARACEST Properties of a Dinuclear Neodymium (III) Complex Bound to DNA or Carbonate

Kido Nwe, Christopher M. Andolina, Ching-Hui Huang and Janet R. Morrow*

Department of Chemistry, University at Buffalo, State University of New York, Buffalo, NY 14260

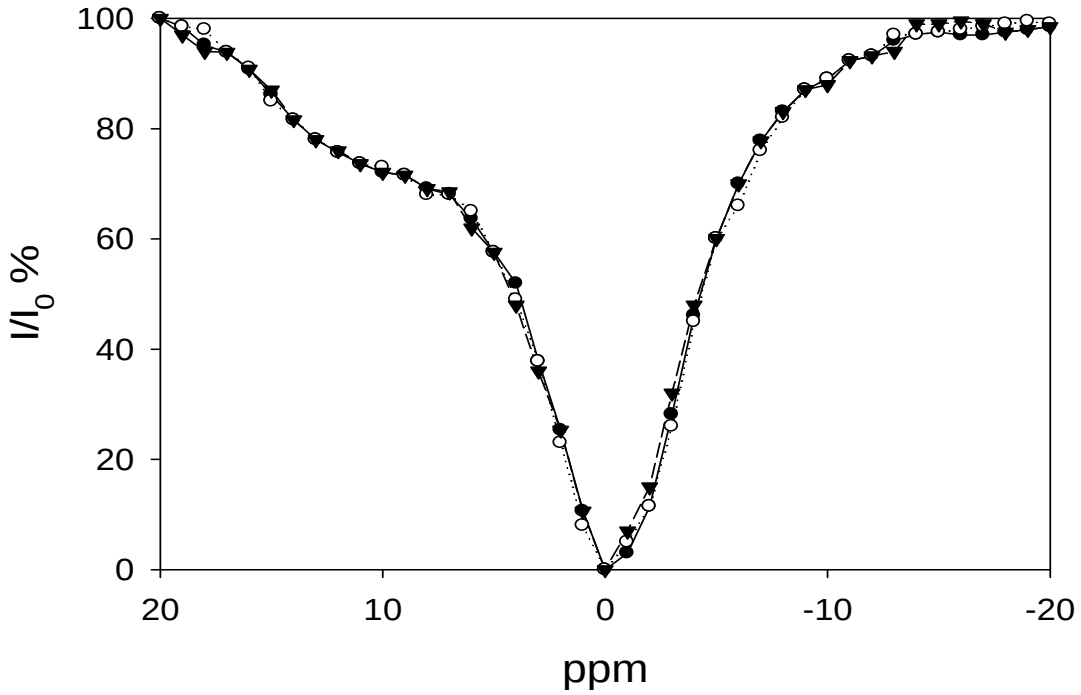

Figure S1. CEST spectra of Nd_2(**1**) (5.0 mM complex, 10 mM HEPES, 50 mM $NaNO_3$) as a function of irradiation time (●) 3s (○), (Δ) 5s and (▼) 7s. B_1 = 1,000 Hz, T = 25°C

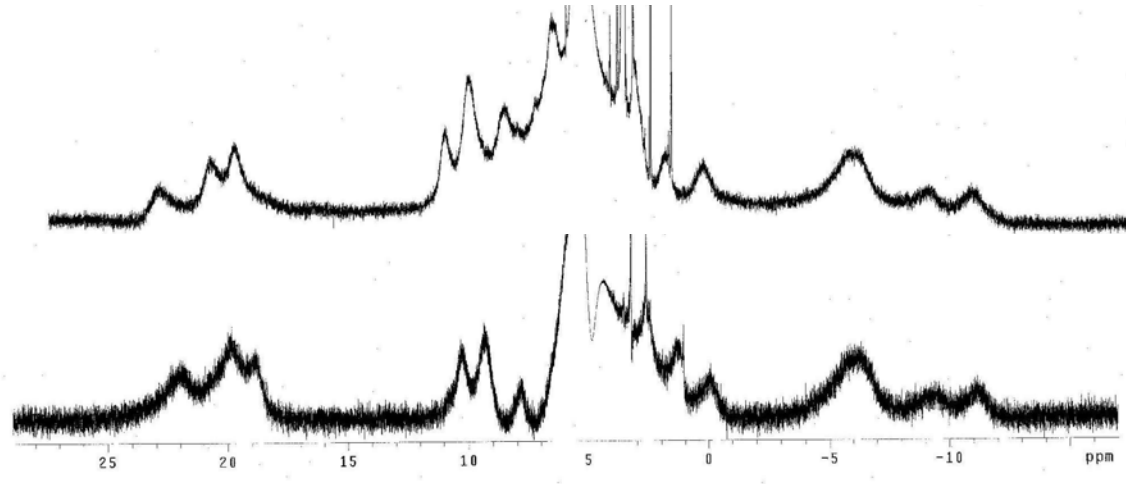

Figure S2. ^{1}H NMR spectra of 5 mM Nd_2(**1**) in H_2O (top) and D_2O (bottom) pH 7.4 (pD 7.0), 10 mM HEPES and 25ºC. Note the lack of a proton resonance corresponding to the CEST peak for the amide protons at 16-17 ppm.

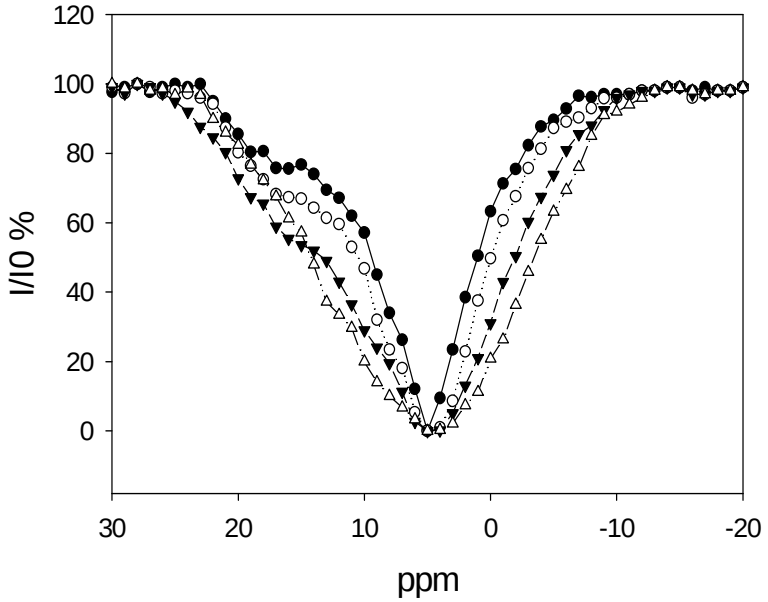

Figure S3. Top: CEST spectra of Nd_2(**11**) (5.0 mM complex, 10 mM hepes, 50 mM $NaNO_3$) at pH 6.5 (●), 7.0 (○), 7.5 (▼) and 8.0 (△). B_1 = 1,500 Hz, T = 25°C. shift water to zero

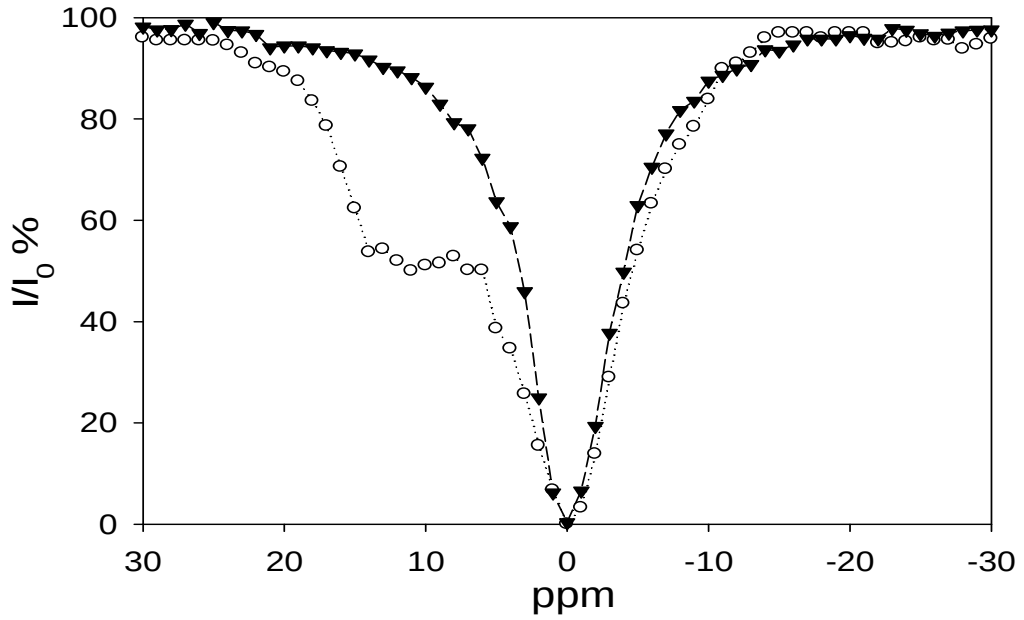

Figure S4. CEST spectra of 10 mM Nd_2(**1**) (○), and 10 mM of Eu_2(**1**)(◄) at pH 7.0, 10 mM Hepes buffer, 50 mM $NaNO_3$, 25 °C, B_1 = 1,500 Hz.

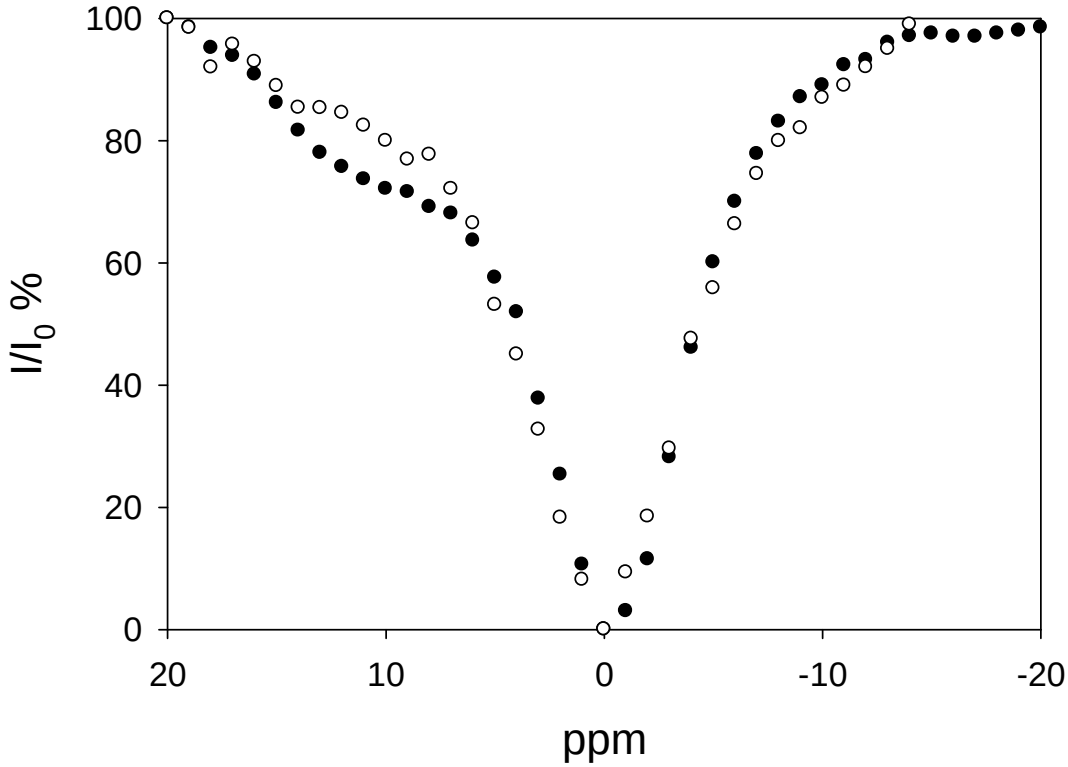

Figure S5. CEST spectra of Nd_2(**1**) 5.0 mM (●) titrated with 0 mM **DEP** (●), 5.0 mM DEP (○) at pH 7.0, 10 mM HEPES, 50 mM $NaNO_3$, 25 °C.

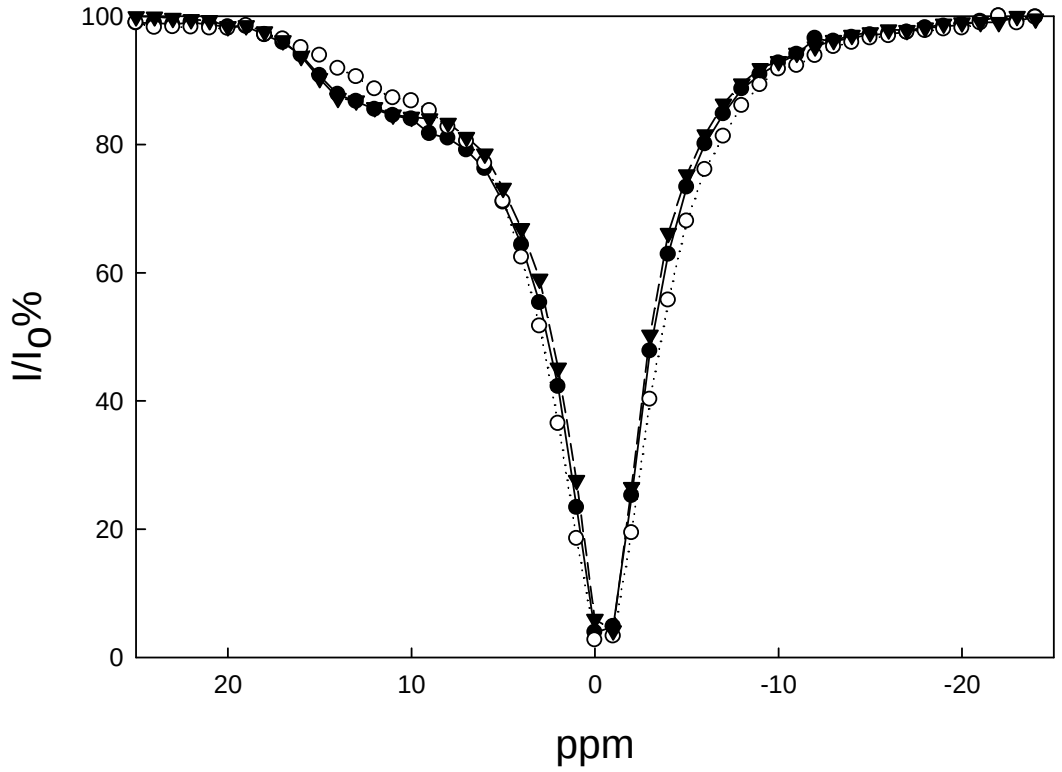

Figure S6. The CEST effect of Nd_2(1) is decreased upon addition of carbonate. CEST spectra of Nd_2(**1**) (5.0 mM complex, 10 mM HEPES, 50 mM $NaNO_3$) (●), addition of 5mM $NaHCO_3$ (○), carbonate removed by treatment with $Pb(NO_3)_2$ (▼), T = 25°C.

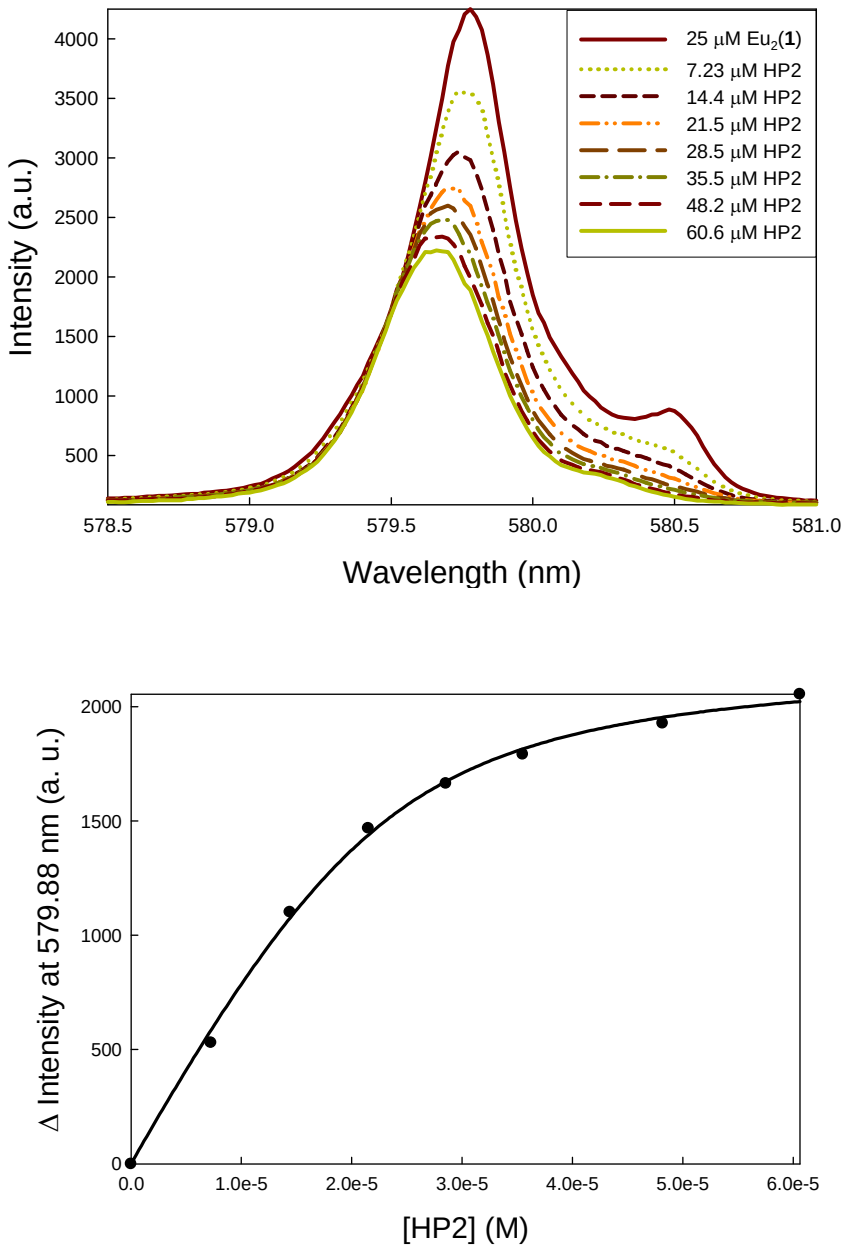

Figure S7. $^7F_0 \rightarrow {}^5D_0$ excitation spectra ($^5D_0 \rightarrow {}^7F_2$ emission) of solutions of 25 μM Eu_2(**1**) (●) titrated with **HP2** DNA at pH = 7.0, 20 mM HEPES, 50 mM $NaNO_3$. Binding isotherm is fit to eq. 3 with a K_d of 4.2 μM (n=12).

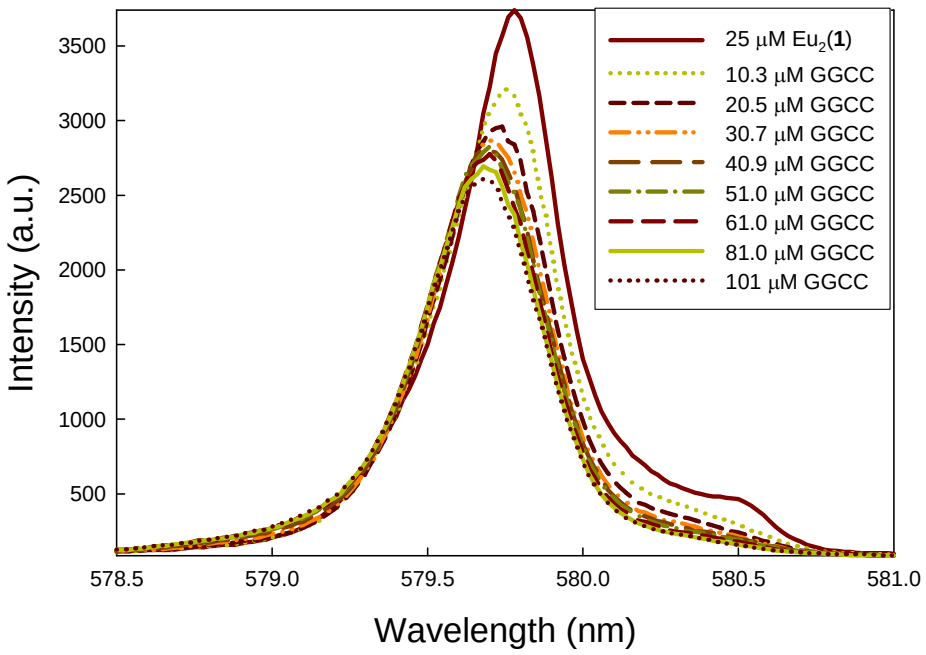

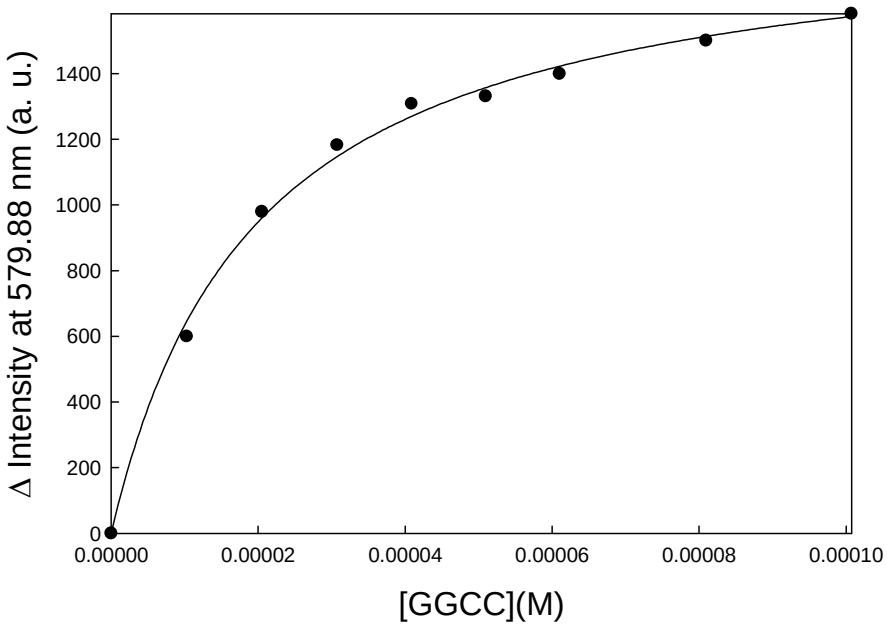

Figure S8. $^7F_0 \rightarrow {}^5D_0$ excitation spectra ($^5D_0 \rightarrow {}^7F_2$ emission) of solutions of 25 μM Eu_2(**1**) (●) titrated with double stranded **GGCCGGCC** DNA at pH = 7.0, 20 mM HEPES, 50 mM $NaNO_3$. Binding isotherm is fit to eq. 3 with K_d of 28 μM (n=6.9).

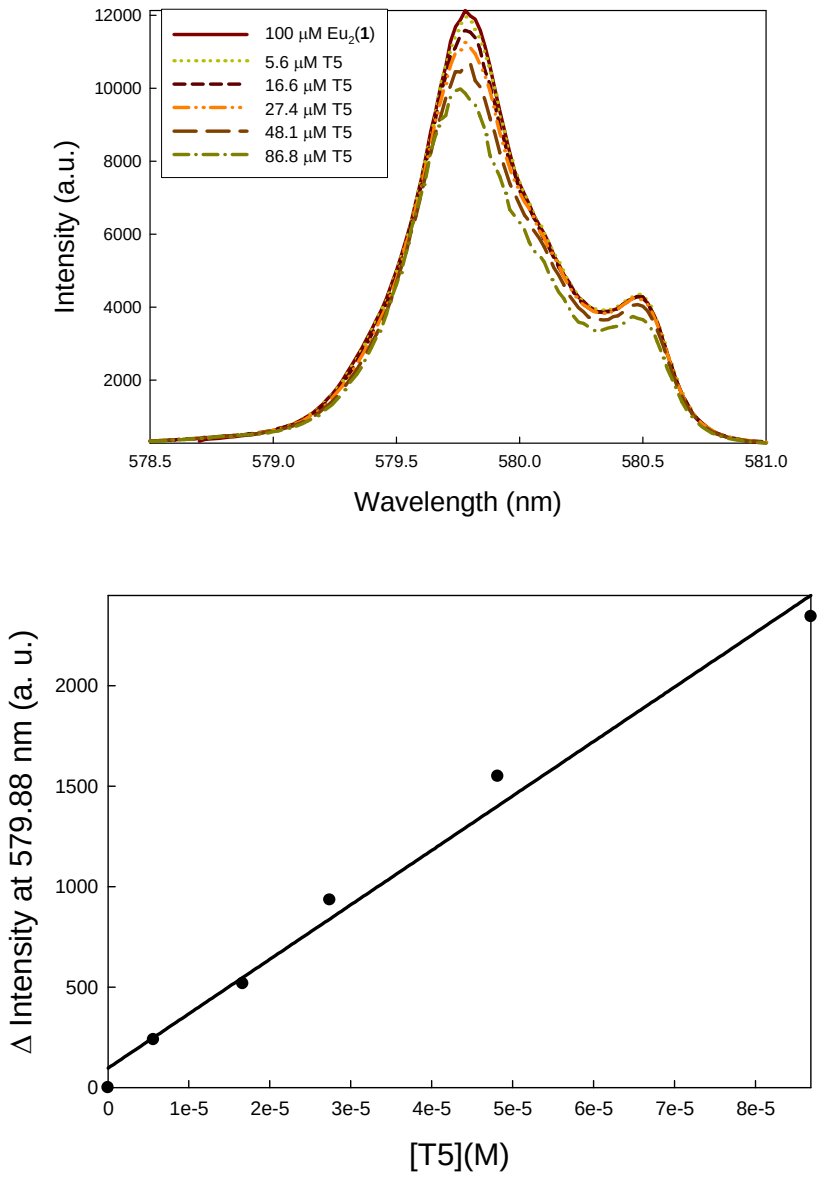

Figure S9. $^7F_0 \rightarrow {}^5D_0$ excitation spectra ($^5D_0 \rightarrow {}^7F_2$ emission) of solutions of 100 μM Eu_2(**1**) titrated with **HP1** DNA at pH = 7.0, 20 mM HEPES, 50 mM $NaNO_3$. Binding isotherm is fit a linear equation.

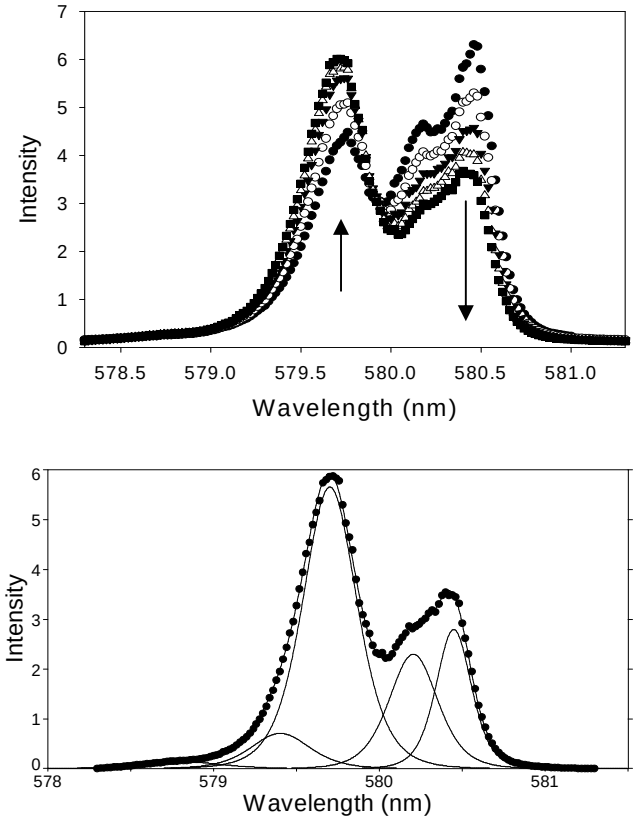

Figure S10. $^7F_0 \rightarrow {}^5D_0$ excitation spectra ($^5D_0 \rightarrow {}^7F_2$ emission) of solutions of 20 μM Eu_2(**1**) carbonate complex (●) titrated with 2 μM (○), 4 μM (▼), 6 μM (Δ) and 8 μM (■) **HP1** DNA at pH = 7.0, 20 mM HEPES, 50 mM $NaNO_3$. b) Deconvoluted $^7F_0 \rightarrow {}^5D_0$ excitation spectra of Eu_2(**1**) (20 μM) in the presence of 8 μM of **HP1** DNA. Peaks centered at 580.20 and 580.45 nm are attributed to carbonate complex. The peak that grows in at 578.82 nm is the Eu_2(**1**) complex with **HP1**.

Multiple Site-Specific *in Vitro* Labeling of Single-Chain Antibody

Boopathy Ramakrishnan,[†,||] Elizabeth Boeggeman,[†,||] Maria Manzoni,[†] Zhongyu Zhu,[‡,||] Kristin Loomis,[§] Anu Puri,[§] Dimiter S. Dimitrov,[‡] and Pradman K. Qasba*[,†]

Structural Glycobiology Section, Protein Interaction Group, Membrane Structure and Function Section, and Basic Research Program, SAIC-Frederick, Inc., Center for Cancer Research Nanobiology Program, Center for Cancer Research; NCI-Frederick, Frederick, Maryland 21702. Received April 3, 2009; Revised Manuscript Received May 11, 2009

For multiple site-specific conjugations of bioactive molecules to a single-chain antibody (scFv) molecule, we have constructed a human anti HER2 receptor, scFv, with a C-terminal fusion polypeptide containing 1, 3, or 17 threonine (Thr) residues. The C-terminal extended fusion polypeptides of these recombinant scFv fusion proteins are used as the acceptor substrate for human polypeptide-α-N-acetylgalactosaminyltransferase II (h-ppGalNAc-T2) that transfers either GalNAc or 2-keto-Gal, a modified galactose with a chemical handle, from their respective UDP-sugars to the side-chain hydroxyl group of the Thr residue(s). The recombinant scFv fusion proteins are expressed in *E. coli* as inclusion bodies and *in vitro* refolded and glycosylated with h-ppGalNAc-T2. Upon protease cleavage, the MALDI-TOF spectra of the glycosylated C-terminal fusion polypeptides showed that the glycosylated scFv fusion protein with a single Thr residue is fully glycosylated with a single 2-keto-Gal, whereas the glycosylated scFv fusion protein with 3 and 17 Thr residues is found as an equal mixture of 2−3 and 5−8 2-keto-Gal glycosylated fusion proteins, respectively. These fusion scFv proteins with the modified galactose are then conjugated with a fluorescence probe, Alexa488, that carries an orthogonal reactive group. The fluorescence labeled scFv proteins bind specifically to a human breast cancer cell line (SK-BR-3) that overexpresses the HER2 receptor, indicating that the *in vitro* folded scFv fusion proteins are biologically active and the presence of conjugated multiple Alexa488 probes in their C-terminal end does not interfere with their binding to the antigen.

INTRODUCTION

Conjugation of monoclonal antibodies with bioactive molecules such as toxins, drugs, and radioisotopes is an emerging strategy in the treatment and diagnosis of cancer (*1*−*5*). Not only is the conjugation of a multiple number of bioactive molecules to a single antibody molecule desired, but also, site-specific conjugation of these molecules is important. The former enhances the sensitivity of detection and better treatment of cancer, while the latter enables the production of a homogeneous antibody−drug complex that ensures the full activity of both the antibody and the bioactive molecule in an antibody−drug conjugate. Multiple site-specific conjugation has been achieved by engineering the target protein, either by the introduction of free Cys residues (*6*, *7*) or by introducing genetically encoded aldehydes at either terminal end of the protein or by site-directed introduction of azido/alkynyl-tagged methionine analogues into proteins (*8*−*10*). However, protein with free Cys residue(s) needs special handling to prevent its free Cys residues from undergoing undesired oxidation while in the process of introducing the methionine analogue all the methionine residues in the protein are modified. Not many site-specific conjugation methods offer multiple site conjugations.

We have developed a unique, site-specific conjugation method using the mutant galactosyltransferase enzymes, where we first enzymatically transfer 2-acetonyl-2-deoxy-galactose (2-keto-Gal) sugar with a unique chemical handle to a specific sugar moiety, βGlcNAc or βGal1-4GlcNAc, present at the nonreducing end of the glycan of the glycoprotein; then, the chemical handle present in the modified sugar is used for site-specific conjugation with biologically important molecules having a corresponding orthogonal chemical group (*11*−*14*). Using this method, we have recently shown that the biantenary *N*-glycans of a therapeutic IgG molecule have been used as the substrate for the mutant Y298L-Gal-T1 enzyme to transfer 2-keto-Gal sugar and further conjugated with bioactive molecules such as biotin to both arms of the biantenary *N*-glycans, thus producing the native IgG molecule with four biotin molecules site-specifically conjugated (*12*, *14*). However, this method requires the presence of a specific sugar moiety of a glycan chain in the glycoprotein and cannot be used for nonglycosylated proteins, such as single-chain antibodies or bacterial toxins expressed in *E. coli.*

For proteins that lack glycosylation motifs, we have recently developed a method using the human polypeptide-α-*N*-acetylgalactosaminyltransferase II enzyme (h-ppGalNAc-T2), which transfers *N*-acetylgalactosamine sugar (GalNAc) from UDP-GalNAc to Thr/Ser residues on an acceptor polypeptide that is at least 11 amino acids long (*15*, *16*). In this method, we have engineered the acceptor polypeptide substrate of the h-ppGalNAc-T2 with one Thr residue as a fusion peptide at the C-terminus of a bacterial glutathione-*S*-transferase (GST), which is not normally glycosylated. We used this fusion polypeptide moiety as an acceptor substrate for the h-ppGalNAc-T2 to transfer modified Gal with chemical handle such as 2-keto-Gal or GalNAz, thus enabling us to site-specifically conjugate bioactive molecules with a corresponding orthogonal chemical group (*15*). Using this method, in the present study we demonstrate that an anti human HER2 receptor single-chain antibody (anti HER2 scFv) with a fusion peptide containing more than one Thr residue at its C-terminal end can be successfully glycosylated with 2-keto-Gal and then conjugated

* Corresponding author. Structural Glycobiology Section, CCRNP, CCR, NCI-Frederick, Building 469, Room 221, Frederick, Maryland 21702; e-mail: qasba@helix.nih.gov. Phone: (301) 846-1934; Fax: (301) 846-7149.

[†] Structural Glycobiology Section.

[‡] Protein Interaction Group.

[§] Membrane Structure and Function Section.

[||] Basic Research Program.

10.1021/bc900149r CCC: $40.75 © 2009 American Chemical Society
Published on Web 06/09/2009

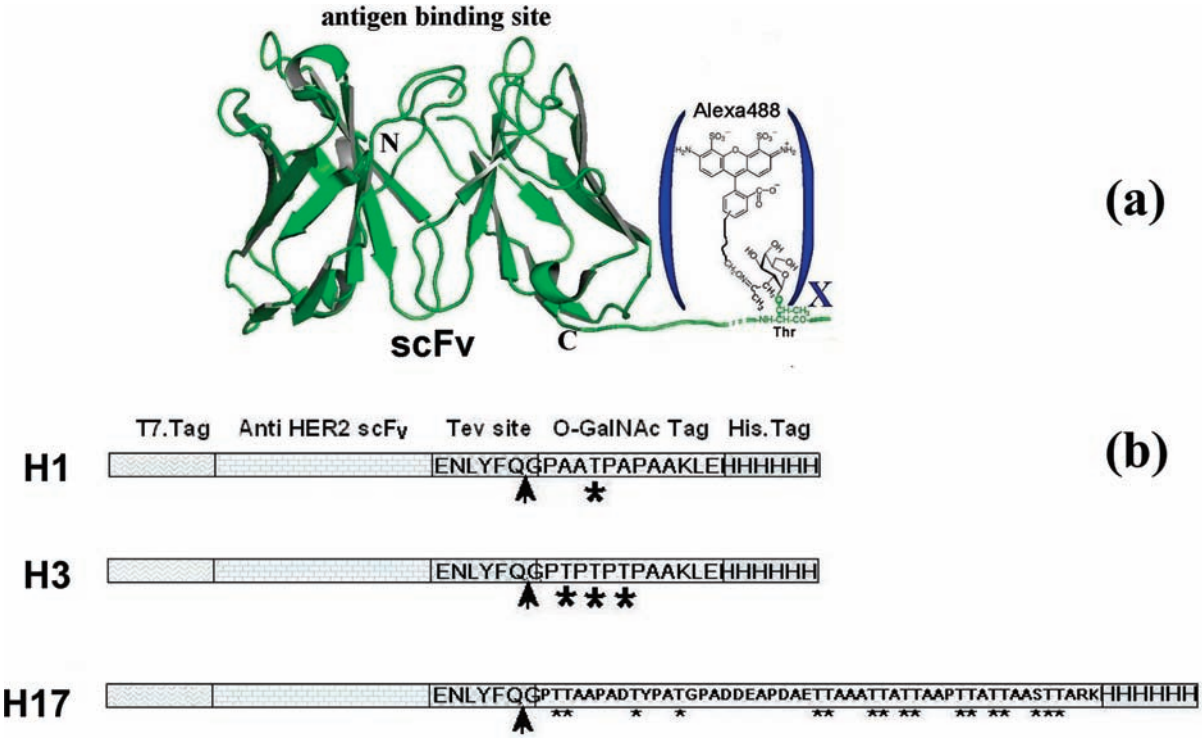

Figure 1. (a) Schematic molecular structure of the Alexa488-conjugated scFv fusion protein. In the present study a single-chain antibody against human HER2 receptor (anti HER2 scFv) with *x* number of Alexa488 molecules conjugated through the modified sugar is named H*x*. The anti HER2 scFv protein has been designed to have specific 1 to 17 O-glycosylation sites. (b) Schematic diagram of the design of anti HER2 scFv proteins with multiple glycosylation sites. The antihuman HER2 receptor single-chain antibody (anti HER2 scFv) expressed in *E. coli* contains a N-terminal T7-tag, a C-terminal Tev protease-cleavable O-glycosylation tag, and an His tag. The proteins with 1, 3, and 17 Thr residues in their O-glycosylation tags (shown as stars at their bottom) are named H1, H3, and H17, respectively. The Tev protease cleavage site is indicated by an arrow. In the presence of Mn^{2+}, the polypeptide-α-*N*-acetylgalactosaminyltransferase II (h-ppGalNAc-T2) enzyme transfers GalNAc or 2-keto-Gal sugar from their UDP derivatives to the side-chain hydroxyl group of the Thr residue present in the O-glycosylation tag.

with Alexa488, a fluorescence probe. Furthermore, our cell surface immunostaining analysis of HER2-receptor expressing SK-BR-3 cells (by fluorescent-activated cell sorting [FACS]) shows that antibody binding to the HER2 receptor is not affected by the one or more Alexa488 molecules present at the C-terminal end of these scFv molecules.

EXPERIMENTAL PROCEDURES

Anti HER2 Single-Chain Antibody Gene Construction and Expression in *E. coli.* The antihuman HER2 scFv gene was constructed from a fully human Fab isolated from a large native phage display Fab library, using HER2 ectodomain as a target (Zhu, Z., and Dmitrov, D., unpublished data). For the construction of H1 and H3 scFv proteins, the anti HER2 scFv gene was repeatedly amplified with the 5-primer, 3-primer-1, and 3-primer2, which introduces a 17-amino-acid peptide as a C-terminal extension following a Tev protease cleavage site. A final PCR amplification with either 3-H(1) or 3-H(3) primer results in a product with a C-terminal O-glycosylation tag without a stop codon, having *Eco*RI and Xho I restriction enzyme sites at their 5′ and 3′ termini, respectively. This construction uses the stop codon at the 3′ terminal in the vector after the His-tag.

5-primer: GCC CCG *GAA TTC* GGG CGC GGC GAA GTG CAG CTG GTG CAG TCT GGA GCA GAG GTG AAA AAG.

3-Primer 1: GCC TTG GAA GTA AAG GTT TTC TAG GAC GGT GAC CTT GGT CCC AGA TCC GAA GAC AGC AAT.

3-Primer 2: TTT AGC TGC CGG TGC GGG AGT AGC TGC AGC GCC TTG GAA GTA AAG GTT TTC.

3-H1 Primer: GTG GTG GTG *CTC GAG* TTT AGC TGC CGG TGC GGG ACT AGC TGC AGG GCC.

3-H3 Primer: GTG GTG GTG *CTC GAG* TTT AGC TGC CGG TGT GGG AGT AGG TGT AGG GCC.

The PCR-amplified product was digested with *Eco*RI and Xho I restriction enzymes and ligated with the pET23a vector digested with the same enzymes. The ligated vector was transfected into XL2 supercompetent cells. The ampicillin-resistant clones were screened for the presence of the anti HER2 scFv gene in their plasmid DNA between their *Eco*RI and Xho I restriction sites. The N-terminal T7-tag, which enhances the protein expression in *E. coli* and the C-terminal His × 6 tag, followed by a stop codon, comes from the pET23a vector DNA. For the construction and expression of H17 scFv protein, the cDNA for the scFv protein was first cloned into the pET23a vector between the *Eco*RI and Hind III restricted enzyme sites without the stop codon. This cloning was followed by inserting between the Hind III and Xho I site a cDNA sequence coding for a Tev protease cleavage site and the 50 amino-acid-long polypeptide of the O-glycosylation region of the human small breast epithial mucin protein (BC111421) (*17*) without the stop codon. This construction uses the stop codon at the 3′ terminal in the vector after the His-tag, similar to H1 and H3 scFv gene constructs. The positive clones were sequenced and transfected into Rosetta (DE3) LysS competence cells for expression of the protein.

In Vitro* Folding of Inclusion Bodies of Anti-HER2 scFv Protein from *E. coli. The Rosetta (DE3) LysS cells containing the anti HER2 scFv cDNA sequence in the pET23a vector were grown to an optical density of 0.7−0.8 and then induced with IPTG. The inclusion bodies were purified from the bacterial pellet as described earlier (*18*). From 1 L of bacterial culture, 60 to 70 mg of protein were obtained as inclusion bodies. The *in vitro* folding of anti HER2 scFv was

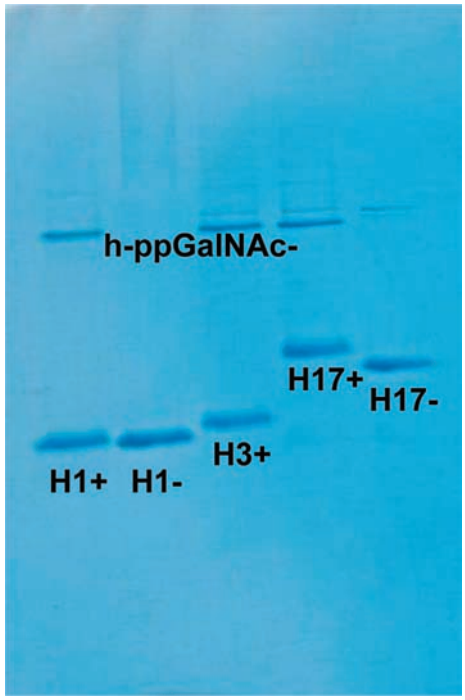

Figure 2. SDS-PAGE gel analysis of the unglysoylated (H1- and H17-) and 2-keto-Gal glycosylated (H1+, H3+, and H17+) proteins: The unglycosylated H1 and H17 proteins are labeled as H1- and H17-, respectively, while the 2-keto-Gal glycosylated H1, H3, and H17 are labeled as H1+, H3+, and H17+, respectively. The h-ppGalNAc-T2 in the glycosylation mixture is also labeled. MALDI-TOF analysis of the H1+, H3+, and H17+ anti HER2 scFv proteins show that these proteins carry 2-keto-Gal (see below). The large difference in the mobility between unglycosylated and glycosylated H17 protein is due to glycosylation, however the microhetrogenity in its glycosylation is not observed (see below). Similarly the mobility difference between the H1 unglycosylated protein and the H1+ and H3+ glycosylated protein may be due to their glycosylation.

carried out in a way similar to that of β4Gal-T1 (*18*). Typically, 100 mg of sulfonated protein was folded for 48 h in 1 L of folding solution that contains oxido-shuffling agents and 500 mM arginine HCl. After refolding the protein, the folding solution was extensively dialyzed against water. During dialysis, the misfolded protein precipitated out, while the folded protein remained soluble. The soluble protein was concentrated to a concentration of 1 mg/mL on an Amicon stirred cell, using a YM-10 membrane, and further purified on a Ni-column. There was no significant loss of protein observed during concentration or during Ni-column purification steps, as estimated by measuring the protein concentration using the Bradford method (BioRad). Nearly 20 mg of folded anti HER2 scFv protein was obtained from 1 L of folding solution. The C-terminal glycosylation peptide tag was released from a 5 μg protein by Tev protease cleavage and analyzed by mass spectrometry.

Glycosylation and Alexa488 Conjugation of Anti HER2 scFv. The cloning, expression, and refolding of the h-ppGalNAc-T2 enzyme has been previously published (*15*). UDP-GalNAc was purchased from Sigma chemicals while the UDP-2-keto-Gal was synthesized in-house. Forty micrograms of anti HER2 scFv fusion protein—H1, H3, or H17—were incubated overnight at room temperature 20 °C with 20 μg of h-ppGalNAc-T2 in the presence of 25 mM Tris-HCl (pH 8.0), 10 mM $MnCl_2$, and 0.5 mM UDP-sugar (UDP-GalNAc, or UDP-2-keto-Gal,) in a total volume of 100 μL (Figure 2). The amount of h-ppGalNAc-T2 enzyme used in these experiments to fully glycosylate the fusion peptide using UDP-GalNAc as the donor substrate was first determined in separate experiments. To remove the entire reaction buffer, the glycosylated anti HER2 scFv protein was precipitated with 40% ammonium sulfate and desalted three times by repeated dilution to 500 μL with water and concentrated each time to 40 μL using microcon centrifuge filters with 10K molecular weight cutoff. The salt-free glycosylated anti HER2 scFv protein was reconstituted in 40 μL water, and an aliquot (2 μL) was cut with Tev protease and analyzed by mass spectrometry (MALDI-TOF).

The entire 40 μg of the desalted 2-keto-Gal glycosylated anti HER2 ScFv protein was conjugated in 60 μL with 75 mM sodium acetate buffer (pH 5.0) and 8 μL *N*-aminoxymethylcarbonylhydrazino-Alexa488 (1 mg/mL in DMSO). Nearly 1000-fold excess of Alexa-488 molecules, more than the manufacturer (Invitrogen) suggested amount, was used in this conjugation reaction. The reaction was carried out in the dark, overnight, at room temperature. The conjugated protein was precipitated with 40% ammonium sulfate, redissolved in water to a 1 μg/μL concentration and used for cell binding. The presence of Alexa488 was confirmed by visualizing as little as 10 ng of protein in SDS-PAGE. The mass spectroscopic analyses were carried out in the Protein Chemistry Laboratory, NCI-Frederick, Frederick, MD.

Cell Binding Assays. The human cancer cell lines SK-BR-3 (HER2 receptor-positive) and MDA-MB-468 (HER2 receptor-negative) were used to test receptor binding activity of the scFv fusion proteins. HER2 receptor expressing human breast adenocarcinoma cells (SKBR-3) and HER2 receptor negative human breast adenocarcinoma cells (MDA-MB-468) were purchased from the American type Culture Collection (ATCC, Manassas, VA). The cells were cultured in McCoy's 5A medium supplemented with 10% (v/v) heat-inactivated fetal bovine serum (FBS) and penicillin/streptomycin as antibiotics at 37 °C in a humidified atmosphere containing 5% CO_2. Other culture reagents were bought from Invitrogen (Carlsbad, CA). In a typical experiment, cells were suspended in enzyme-free cell dissociation buffer (Invitrogen Corp, Carlsbad, CA) and pelleted. The cells were resuspended in phosphate buffer saline (PBS) supplemented with 5% fetal calf serum (PBS-FCS) at a concentration of 10^7 cells per mL. The samples were incubated at room temperature for 15 min to block nonspecific binding sites. The cells were washed twice with cold PBS with 1% bovine serum albumin (PBS-BSA), resuspended in PBS-FCS (10^7 cells /ml), and aliquoted in 0.1 mL samples. Various amounts (0.2, 0.5, and 1 μg) of Alexa-conjugated scFv were added to the cells, and incubations were continued for 45 min on a rotator at 4 °C in the dark. The cells were washed twice with cold PBS-BSA, suspended in PBS-BSA, and analyzed using a FACS caliber flow cytometer (Becton Dickinson, San Jose, CA), analyzing 10 000 events per sample. Herceptin was used as a positive control in these experiments to confirm HER2 expression on SK-BR-3 cells (HER2-positive) and MDA-MB-468 cells (HER2 receptor-negative).

RESULTS AND DISCUSSION

We have previously developed a novel site-specific glycoconjugation of glutathion-S-transferase, by engineering a C-terminal fusion peptide containing one Thr residue that can be glycosylated by h-ppGalNAc-T2 with a modified sugar having a chemical handle (*15*). This site-specific glycan moiety can then be conjugated with bioactive molecules carrying an orthogonal chemical group. Here, we have extended this strategy to engineer, not just one glycosylation site at its C-terminal end, but multiple sites on an antihuman HER2 receptor single-chain antibody (anti HER2 scFv) (Figure 1a). The anti HER2 scFv fusion protein is designed to have a N-terminal T7-tag, which enhances its protein expression in *E. coli* and at the C-terminal end a Tev protease cleavage site, an O-glycosylation peptide followed by a His × 6 tag (Figure 1b). For the present study,

three forms of anti HER2 scFv proteins have been constructed: the H1, H3, and H17, with C-terminal extensions having 1, 3, and 17 Thr residues in their O-glycosylation tag, respectively (Figure 1b). The two C-terminal extension peptides, H1 and H3, were designed based on the preferred acceptor peptide sequence for h-ppGalNAc-T2 enzyme, as described earlier (*15, 16*).

Expression of the Anti Her2 scFv Proteins in *E. coli* and Their *in Vitro* Folding. Although many scFv proteins have been expressed as soluble active proteins in *E. coli*, the anti HER2 scFv proteins, H1, H3, and H17, mostly formed inclusion bodies; and only less than 100 μg of soluble active protein could be obtained from 1 L of bacterial culture. Previously in our laboratory, we have used the *in vitro S*-sulfonation and refolding method to produce large quantities of active β-1,4-galactosyltransferase (β4Gal-T1) enzyme from inclusion bodies (*18*). Using the same method, a large quantity of a soluble form of anti HER2 scFv proteins H1, H3, and H17, with C-terminal extension, has been obtained. The scFv fusion protein has four Cys residues and has two disulfide bonds. The *in vitro* folded protein, nonreduced and reduced with β-mercaptanol, shows in SDS-PAGE a significant mobility difference between the protein bands confirming the presence of disulfide bond(s) in the soluble protein. The yield of the *in vitro* folded protein for H1, H3, and H17 proteins corresponds to 10, 10, and 2.5 mg per liter of bacterial culture. Thus, it seems that the presence of the 17 amino acid C-terminal tag does not interfere with the folding of scFv molecules. Nevertheless, the 50 amino-acid-long tag significantly reduces the folding efficiency. All the refolded proteins can be concentrated to at least 10 to 15 mg/mL concentrations, without any precipitation.

Glycosylation of H1, H3, and H17 anti-HER2 scFv Proteins. As a first step, the H1, H3, and H17 scFv fusion proteins were glycosylated overnight with h-ppGalNAc-T2, using UDP-GalNAc as the donor sugar substrate. The C-terminal fusion polypeptide from these proteins was released by Tev protease digestion and analyzed by mass spectrometry (MALDI-TOF) (Figure 3). The MS analysis of the glycosylated peptide tags from H1 and H3 proteins showed that they carry 1 and 3 GalNAc sugars, respectively (Figure 3a,b), suggesting that the H1 protein has been fully and homogenously glycosylated while the H3 proteins is mostly glycosyled with three GalNAc sugars. However, the polypeptide released from H17 scFv protein by Tev protease was glycosylated with a maximum of 11 sugars instead of 17 sugars (Figure 3c). The catalytic reaction using UDP-α-2-keto-Gal as donor substrate was carried out under the same conditions as the one used for UDP-GalNAc. After the glycosylation, a small amount of the glycoprotein was subjected to the Tev digestion, and the released C-terminal fusion glycopeptides was analyzed by MALDI-TOF analysis. The glycopeptide from the H1 protein was found fully glycosylated with a single 2-keto-Gal sugar, whereas the glycopeptide from H3 and H17 was found to be a mixture of peptides with 2 to 3 and 5 to 8 2-keto-Gal sugars, respectively (Figure 3d,e,f). These results show that all the Thr residues present in the O-glycosylation tag of the H3 and H17 scFv proteins are not homogenously glycosylated by the h-ppGalNAc-T2, particularly with the modified sugar.

In humans, the h-ppGalNAc-T2 enzyme exists as a family of 17 enzymes, namely, ppGalNAc-T1 to ppGalNAc-T17 (*19*). It is well-known that h-ppGalNAc-T2 efficiently glycosylates nonconsecutive Thr residues, while ppGalNAc-T10 uses glycopeptide as the substrate and efficiently glycosylates the consecutive Thr residues if either one is glycosylated (*16, 20*). The O-glycosylation tag of the H17 fusion protein has 10 nonconsecutive Thr residues. Thus, it is not surprising to observe that its tag is glycosylated by h-ppGalNAc-T2 with only 11 GalNAc sugars, and to fully glycosylate this tag, it may be essential to use the ppGalNAc-T10 enzyme, in addition to h-ppGalNAc-T2. Even though the 2-keto moiety in the 2-keto-Gal resembles the N-acetyl moiety in GalNAc, due to its conformational flexibility, the 2-keto-Gal sugar may not be as preferred a donor sugar substrate as is GalNAc by the h-ppGalNAc-T2 enzyme; therefore, the catalytic efficiency of h-ppGalNAc-T2 is expected to be slightly poorer for the 2-keto-Gal transfer than for GalNAc.

Preparation of Alexa488-Anti-Her2ScFv Conjugates and Their Binding to HER2-Receptor-Expressing Cells. To demonstrate a site-specific conjugation, the H1, H3, and H17 scFv proteins with 2-keto-Gal sugars were conjugated with a fluorescence probe, Alexa488, with an orthogonal chemical group, the aminoxy group. The Alexa488-conjugated H1, H3, and H17 scFv proteins can be detected on an SDS-PAGE by their fluorescence emission, even at nanogram amounts (Figure 4a). Interestingly, the H3 and H17 scFv proteins that carry more than one Alexa488 molecule are observed as sharp protein bands in the SDS-PAGE. This is in contrast to limited but random conjugated proteins, where the conjugated proteins are often observed as a smeared broad band in SDS-PAGE. For example, the streptavidin-Alexa488 conjugate protein from Invitrogen is observed as a broad band in SDS-PAGE (Figure 4b). Thus, observation of a sharp protein band on the gel indicates conjugation of the fluoroprobes to unique site(s) on the protein molecules. The observation that the fluorescence emission from H17 protein was not significantly enhanced, compared to the H1 scFv protein, may be due to self-quenching of conjugated Alexa488 molecules. It is known that multiple fluorescence probes conjugated to protein molecules show self-quenching. It is interesting to observe that even though the H3 and H17 protein-Alexa488 conjugates are heterogeneous, arising from their glycosylation with 2-keto-Gal, the protein bands in the SDP-PAGE gel remain sharp. Although the actual number of Alexa-488 molecules that are conjugated to the 2-Keto-galactosylated scFv molecules could not be determined by conventional MALDI-TOF analysis, in our previous studies it was shown that when, instead of Alexa488, biotin molecule was used for conjugation under similar reaction condition, all the 2-keto-Gal sugar molecules were completely biotinylated as determined by MALDI-TOF analysis (*14, 15*). Since we have used nearly 1000-fold excess of Alexa488 molecules in the conjugation reaction, all the 2-keto-Gal sugar molecules are expected to be conjugated with Alexa488 molecules.

Cell-binding assay by FACS methodology analysis shows that Alexa488-conjugated scFv fusion proteins H1, H3, and H17 bind specifically to cells that express HER2 receptors on the cell surface (Figure 5). We did not observe any binding of these modified scFv molecules above background levels when MDA-MB-468 cells (HER2 receptor-negative) were used (Figure 5b). In these experiments, FACS spectra using various amount of scFv fusion proteins ranging from 200 ng to 2.5 μg showed no significant difference, suggesting that even a nanogram quantity of the H1, H3, or H17 protein was sufficient for the detection of HER2 receptor. Although there is enhanced fluorescence emission (FL1-H) with H3 and H17, compared to H1, it is not linearly proportional to the number of additional fluorescence probes conjugated to these proteins (Figure 5a, insert table). This kind of observation for the multiple conjugations of protein probes to proteins is known due to the internal quenching. However, our technology is likely to yield similar conjugates with multiple numbers of MRI image contrast agents (on a single protein molecule), since there is no quenching effect in MRI. The present results suggest that the *in vitro* folded scFv is biologically active and the incorporation of the sugar and the Alexa488 moieties at the C-terminal end had no or little effect on their affinity for the HER2 receptor, thus demonstrating that

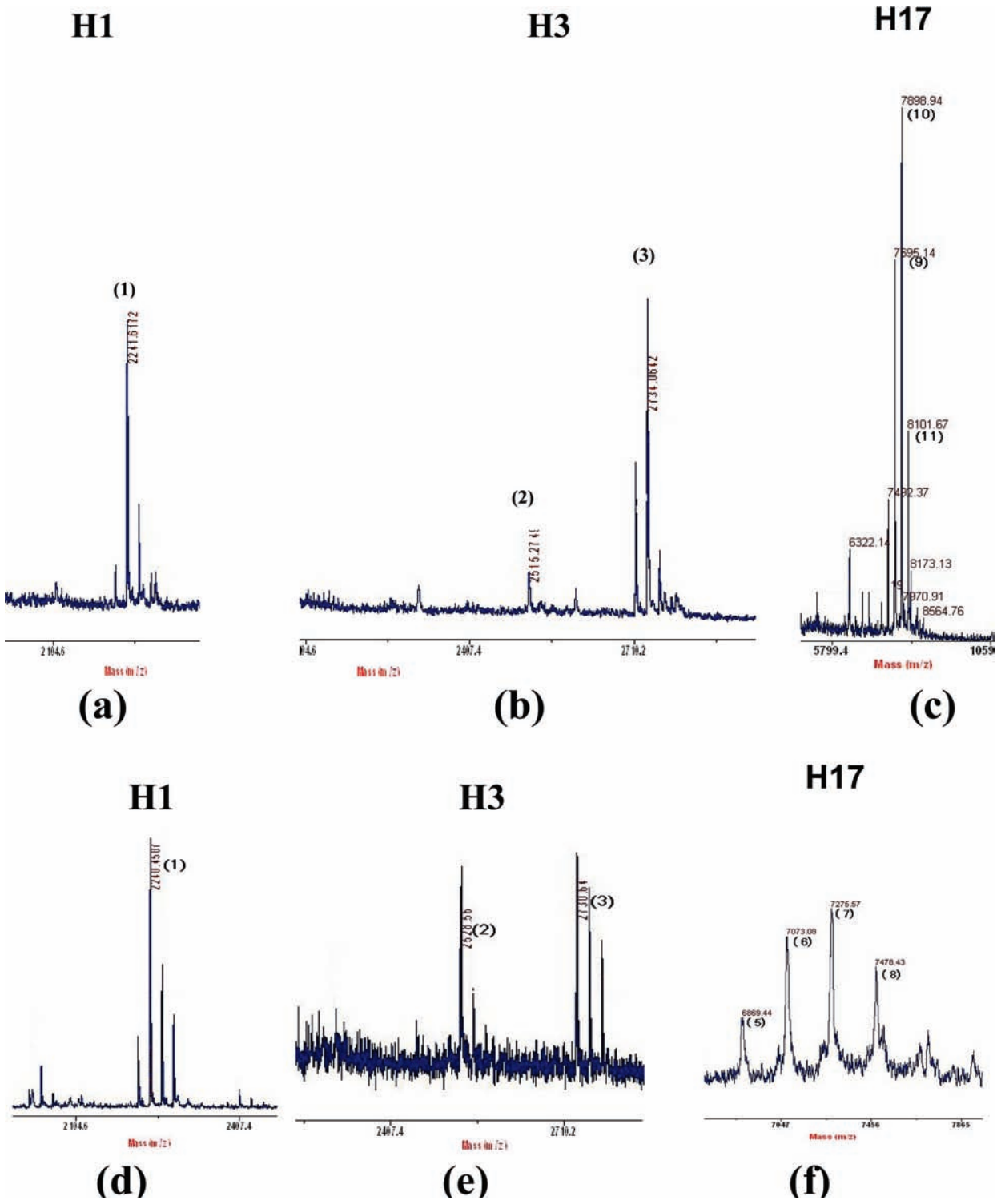

Figure 3. The mass spectrum (MALDI-TOF) of the Tev protease cleaved glycosylated polypeptides with GalNAc (a,b,c) and 2-keto-Gal (d,e,f) from H1, H3, and H17 anti HER2 scFv fusion proteins, respectively. The number of sugar molecules present in the peptide is shown in the parentheses next to the mass value of the corresponding peptide peak. The H1 protein is fully glycosylated with GalNAc sugar (a) while a small trace amount of unglycosylated peptide is observed when 2-keto-Gal was used (d). Although all three Thr residues in the fusion peptide from H3 have been mostly glycosylated with GalNAc, a small trace amount of mono- and diglycosylated forms are observed (b). However, under the same glycosylation condition, a mixture of fusion peptides with two and three 2-keto-Gal has been observed (e) for the H3 protein. Similarly, the H17 fusion protein is glycosylated to a maximum of 11 Thr residues with GalNAc sugar (c), compared to eight with 2-keto-Gal (f).

even a large fusion protein with many conjugated fluorescence probes does not affect the affinity of the scFv to its antigen.

CONCLUSION

Our current method offers a unique possibility not only for site-specific conjugation but also for multiple site conjugations of bioactive molecules at the C-terminal end of the scFv molecule through modified sugars. The proteolysis of the fusion peptide is an important factor for *in vivo* studies. The presence of glycosylation is known to hinder the proteolysis of peptides, and furthermore, the modified sugars are conjugated with bulky bioactive molecules; thus, their susceptibility to proteolysis is

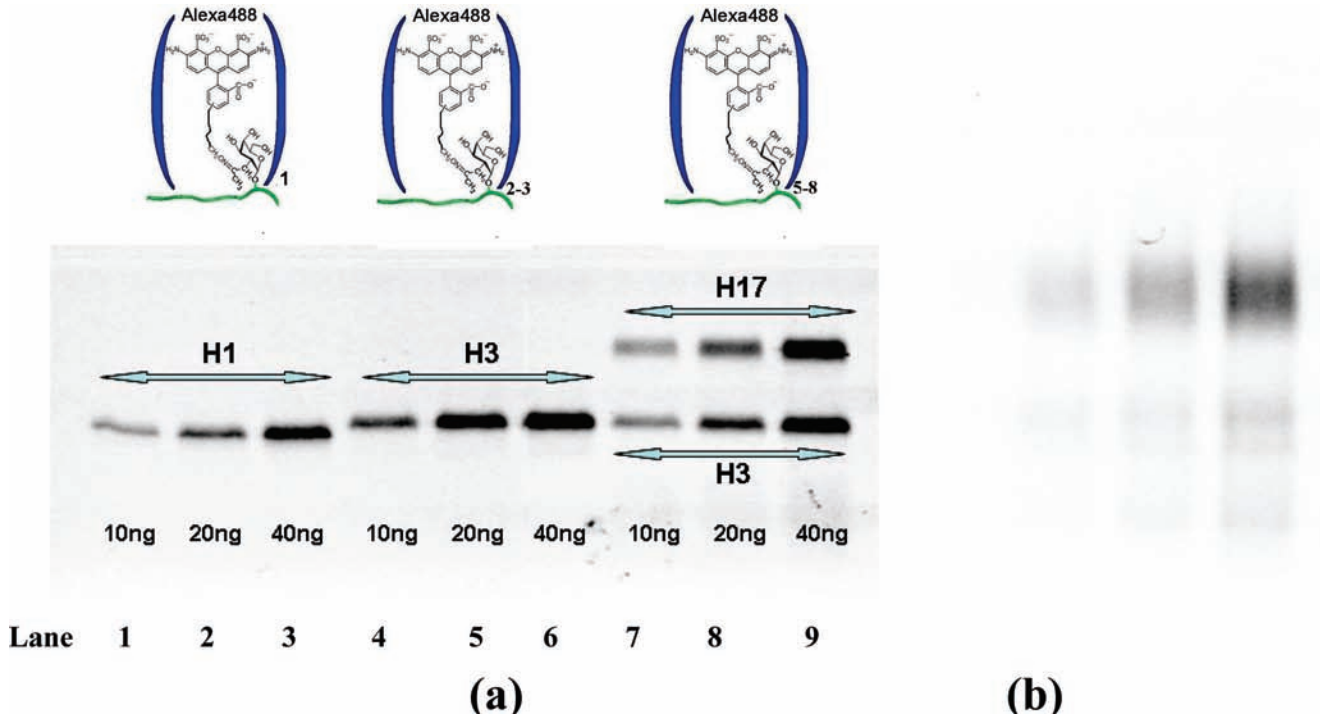

Figure 4. (a) Fluorescence emission of the Alexa488 conjugated H1, H3, and H17 anti HER2 scFv fusion proteins from the nonreduced SDS-PAGE. Lanes 1−3, 3−5, and 7−9 show each 10 ng, 20 ng, and 40 ng of H1, H3, and a mixture of H3 and H17 proteins, respectively. The H17 protein has 5 to 8 conjugated molecules of Alexa488. The fluorescence emission image of the SDS-PAGE gel was scanned using Hitachi FMBIO II fluorescence imaging system. Even 10 ng fusion proteins can be very well detected, and the protein bands are sharp. (b) Fluorescence emission from various amounts of streptavidin-Alexa488 conjugate on nonreduced SDS-PAGE. The protein conjugate from Invitrogen was prepared by a random but limited conjugation method.

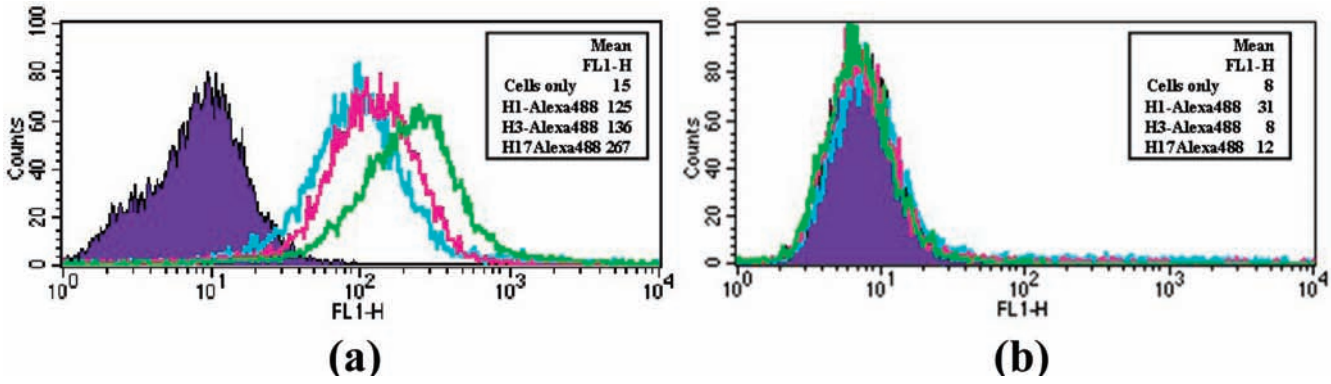

Figure 5. (a) FACS analysis on the binding of Alexa488 conjugated H1, H3, and H17 fusion proteins to SKBR3 cells. 200 ng of the each conjugated protein was used in the assay. (b) Binding of H1, H3, and H17 proteins did not occur with MDAMB-468 cells, since these cells do not express HER2 receptors. The insert table lists the mean FL1-H value for cells without and with bound antibody conjugates. Although the H17 conjugates have nearly seven more fluorescence probes, compared to H1, due to self-quenching there was no linear increase in the fluorescence emission.

expected to be much more limited compared to that of nonglycosylated fusion peptide. Similarly immunogenicity due to the fusion peptide and the modified sugars may be concern. However, it is possible that the fusion peptide may not be well exposed to the environment due to the presence of bulky conjugated bioactive molecules that may reduce the *in vivo* immunogenic effect. Such concerns are associated with most conjugated molecules that are being used or planned for use in *in vivo* studies.

Previously, scFv protein with large protein-like green fluorescence protein fused at its C-terminal end has been found to bind to the antigen without compromising its affinity (*21*). Also, a large mucin protein like, muc6, has been expressed as a soluble protein in *E. coli* and has been *in vitro* glycosylated with more than 50 sugars with GalNAc, using ppGalNAc-T1 (*22*). Therefore, using our present site-specific and multiple site conjugating method, scFv proteins with a C-terminal muc6 fusion protein can be glycosylated with modified sugars and conjugated with bioactive molecules. Such complexes are expected to carry not just a few but several tens of bioactive molecules conjugated to scFv molecules. The methodology described here can generate site-specific and multiple site-conjugated antibody-bioactive molecules that are in great need for the development of targeted MRI image contrast agents and a targeted drug delivery system.

ACKNOWLEDGMENT

We thank Dr. John T. Simpson, Protein Chemistry Laboratory, NCI-Frederick, for the mass spectroscopic analysis of the samples. This project has been funded in part with Federal funds from the National Cancer Institute, National Institutes of Health, under contract no. N01-CO-12400. The content of this publication does not necessarily reflect the view or policies of the

Department of Health and Human Services, nor does mention of trade names, commercial products, or organizations imply endorsement by the U.S. Government. This research was supported [in part] by the Intramural Research Program of the NIH, National Cancer Institute, Center for Cancer Research.

LITERATURE CITED

(1) Carter, P. J., and Senter, P. D. (2008) Antibody-drug conjugates for cancer therapy. *Cancer J. 14*, 154–69.

(2) Deonarain, M. P. (2008) Recombinant antibodies for cancer therapy. *Expert Opin. Biol. Ther. 8*, 1123–41.

(3) Wu, A. M., and Senter, P. D. (2005) Arming antibodies: prospects and challenges for immunoconjugates. *Nat. Biotechnol. 23*, 1137–46.

(4) Schrama, D., Reisfeld, R. A., and Becker, J. C. (2006) Antibody targeted drugs as cancer therapeutics. *Nat. Rev. Drug Discovery 5*, 147–59.

(5) Lambert, J. M. (2005) Drug-conjugated monoclonal antibodies for the treatment of cancer. *Curr. Opin. Pharmacol. 5*, 543–9.

(6) Stimmel, J. B., Merrill, B. M., Kuyper, L. F., Moxham, C. P., and Hutchins, J. T. (2000) Site-specific conjugation of serine → cysteine variant monoclonal antibodies. *J. Biol. Chem. 275*, 30445–50.

(7) Albrecht, H., Burke, P. A., Natarajan, A., Xiong, C. Y., and Kalicinsky, M. (2004) Production of soluble ScFvs with C-terminal-free thiol for site-specific conjugation or stable dimeric ScFvs on demand. *Bioconjugate Chem. 15*, 16–26.

(8) Carrico, I. S., Carlson, B. L., and Bertozzi, C. R. (2007) Introducing genetically encoded aldehydes into proteins. *Nat. Chem. Biol. 3*, 321–2.

(9) Kiick, K. L., Saxon, E., Tirrell, D. A., and Bertozzi, C. R. (2002) Incorporation of azides into recombinant proteins for chemo-selective modification by the Staudinger ligation. *Proc. Natl. Acad. Sci. U.S.A. 99*, 19–24.

(10) Davis, B. G., Lloyd, R. C., and Bryan Jones, J. (1998) Controlled site-selective glycosylation of proteins by a combined site-directed mutagenesis and chemical modification approach. *J. Org. Chem. 63*, 9614–5.

(11) Ramakrishnan, B., and Qasba, P. K. (2002) Structure-based design of beta 1,4-galactosyltransferase I (beta 4Gal-T1) with equally efficient N-acetylgalactosaminyltransferase activity: point mutation broadens beta 4Gal-T1 donor specificity. *J. Biol. Chem. 277*, 20833–9.

(12) Boeggeman, E., Ramakrishnan, B., Kilgore, C., Khidekel, N., Hsieh-Wilson, L. C., Simpson, J. T., and Qasba, P. K. (2007) Direct identification of nonreducing GlcNAc residues on N-glycans of glycoproteins using a novel chemoenzymatic method. *Bioconjugate Chem. 18*, 806–14.

(13) Pasek, M., Ramakrishnan, B., Boeggeman, E., Manzoni, M., Waybright, T. J., and Qasba, P. K. (2009) Bioconjugation and detection of lactosamine moiety using alpha1,3-Galactosyltransferase mutants that transfer C2-modified galactose with a chemical handle. *Bioconjugate Chem. 20*, 609–18.

(14) Qasba, P. K., Boeggeman, E., and Ramakrishnan, B. (2008) Site-specific linking of biomolecules via glycan residues using glycosyltransferases. *Biotechnol. Prog. 24*, 520–6.

(15) Ramakrishnan, B., Boeggeman, E., and Qasba, P. K. (2007) Novel method for in vitro O-glycosylation of proteins: application for bioconjugation. *Bioconjugate Chem. 18*, 1912–8.

(16) Gerken, T. A., Raman, J., Fritz, T. A., and Jamison, O. (2006) Identification of common and unique peptide substrate preferences for the UDP-GalNAc:polypeptide alpha-N-acetylgalactosaminyltransferases T1 and T2 derived from oriented random peptide substrates. *J. Biol. Chem. 281*, 32403–32416.

(17) Hubé, F., Mutawe, M., Leygue, E., and Myal, Y. (2004) Human small breast epithelial mucin: the promise of a new breast tumor biomarker. *DNA Cell Biol. 23*, 842–9.

(18) Boeggeman, E. E., Ramakrishnan, B., and Qasba, P. K. (2003) The N-terminal stem region of bovine and human beta1,4-galactosyltransferase I increases the in vitro folding efficiency of their catalytic domain from inclusion bodies. *Protein Expr. Purif. 30*, 219–29.

(19) Ten Hagen, K. G., Fritz, T. A., and Tabak, L. A. (2003) All in the family: the UDP-GalNAc:polypeptide N-acetylgalactosaminyltransferases. *Glycobiology 13*, 1R–16R.

(20) Kubota, T., Shiba, T., Sugioka, S., Furukawa, S., Sawaki, H., Kato, R., Wakatsuki, S., and Narimatsu, H. (2006) Structural basis of carbohydrate transfer activity by human UDP-GalNAc: polypeptide alpha-N-acetylgalactosaminyltransferase (pp-GalNAc-T10). *J. Mol. Biol. 359*, 708–27.

(21) Peipp, M., Saul, D., Barbin, K., Bruenke, J., Zunino, S. J., Niederweis, M., and Fey, G. H. (2004) Efficient eukaryotic expression of fluorescent scFv fusion proteins directed against CD antigens for FACS applications. *J. Immunol. Methods 285*, 265–80.

(22) Freire, T., Lo-Man, R., Piller, F., Piller, V., Leclerc, C., and Bay, S. (2006) Enzymatic large-scale synthesis of MUC6-Tn glycoconjugates for antitumor vaccination. *Glycobiology 16*, 390–401.

BC900149R

Use of a Temporary "Solubilizing" Peptide Tag for the Fmoc Solid-Phase Synthesis of Human Insulin Glargine via Use of Regioselective Disulfide Bond Formation

Mohammed Akhter Hossain,[†] Alessia Belgi,[†,‡] Feng Lin,[†] Suode Zhang,[†] Fazel Shabanpoor,[†,§] Linda Chan,[†] Chris Belyea,[⊥] Hue-Trung Truong,[⊥] Amy R. Blair,[||] Sof Andrikopoulos,[||] Geoffrey W. Tregear,[†,‡] and John D. Wade*[,†,§]

Howard Florey Institute, Department of Biochemistry and Molecular Biology, School of Chemistry, Department of Medicine (AH/NH), The University of Melbourne, Victoria 3010, Australia, and Metabolic Pharmaceuticals Ltd, 2/320 Lorimer Street, Port Melbourne, Victoria 3207, Australia. Received April 20, 2009; Revised Manuscript Received May 20, 2009

Solid-phase peptide synthesis has been refined to a stage where efficient preparation of long and complex peptides is now achievable. However, the postsynthesis handling of poorly soluble peptides often remains a significant hindrance to their purification and further use. Several synthetic schemes have been developed for the preparation of such peptides containing modifications to aid their solubility. However, these require the use of complex chemistry or yield non-native sequences. We describe a simple approach based on the use of penta-lysine "tags" that are linked to the C-terminus of the peptide of interest via a base-labile linker. After ready purification of the now freely solubilized peptide, the "tag" is removed by simple, brief base treatment giving the native sequence in much higher overall yield. The applicability of the method was demonstrated by the novel preparation of insulin glargine via solid-phase synthesis of each of the two chains—including the notoriously poorly soluble A-chain—followed by their combination in solution via regioselective disulfide bond formation. At the conclusion of the chain combination, the solubilizing peptide tag was removed from the A-chain to provide synthetic human glargine in nearly 10% overall yield. This approach should facilitate the development of new insulin analogues as well as be widely applicable to the improved purification and acquisition of otherwise poorly soluble synthetic peptides.

INTRODUCTION

Solid-phase peptide synthesis (SPPS) has continued to mature and develop to the stage where it is now possible to almost routinely prepare peptides of up to 50 residues. Many of the long-standing problems associated with the methodology, including aspartimide formation, premature loss of peptide from the solid support, incomplete amino acid acylation, and N^{α}-deprotection, have been largely, if not wholly, overcome (*1*). However, the often-vexing issue of postsynthesis handling and purification of poorly soluble synthetic peptides remains generally unresolved. Methods for the solubilization of such peptides include the use of strong solvents such as the toxic hexafluoroisopropanol (HFIP), dimethylformamide (DMF), dimethylsulfoxide (DMSO), and trifluoroethanol (TFE), or strong acids including trifluoroacetic acid (TFA), or chaotropes including urea and guanidinium hydrochloride (*2*−*4*). However, such solutions do not allow convenient purification by, for example, RP-HPLC nor their chemical characterization including by mass spectrometry. The result is that such peptides are obtained in very poor overall yield, if at all.

Alternative approaches to improving the solubility of synthetic peptides have involved temporary chemical modification of the peptide itself. Sheppard and his colleagues showed that peptide backbone secondary amide protection afforded by the *N*-(2-hydroxy-4-methoxy)benzyl (Hmb) group can significantly inhibit intrachain association during solid-phase synthesis that can contribute to failed assembly (*5*). Furthermore, at the completion of synthesis, Hmb *O*-acetylation yields a TFA-stable acetyl-Hmb backbone-protected peptide which, following release from the solid support, possesses significantly enhanced solubility. After conventional purification, the acetyl-Hmb group can be deacetylated by treatment with dilute hydrazine to provide the target peptide. Penta-acetyl-Hmb amyloid-β 1−43 was shown to possess remarkable solubility of greater than 137 mg/mL in 0.1% TFA/acetonitrile compared to the virtually insoluble native peptide (*6*). Similar results were observed for penta-acetyl-Hmb amyloid-β 1−40 (*7*). However, use of Hmb backbone protection as a means for increased solubility has not been popular presumably due to the high cost of the special Fmoc−amino acid derivatives required for the introduction of the Hmb group together with the need for a convenient amino acid sequence for their optimum placement. More recently, the use of *O*-acyl isoacylpeptides has been demonstrated to be a highly effective tool for the synthesis of difficult sequence-containing peptides (*8*−*10*). These consist of a Boc-protected serine or threonine derivative in which the β-hydroxyl group is acylated by an Fmoc−amino acid. Importantly, the resulting depsipeptides obtained directly from the TFA cleavage reaction are often remarkably more soluble than the native target sequence. Following their purification and use, the desired native peptide can be obtained following rearrangement of the isoacyl peptide in neutral to slightly basic buffer. The disadvantages of this approach are the high costs of the isoacyl dipeptide derivatives for use in solid-phase synthesis, the need for convenient serine and/or threonine placements within the target peptide, and the

* Corresponding author. Professor John D. Wade, Howard Florey Institute, University of Melbourne, Victoria 3010, Australia. Ph: +61 3 8344 7285. Fax: +61 3 9348 1707. E-mail: john.wade@florey.edu.au.

[†] Howard Florey Institute, The University of Melbourne.

[‡] Department of Biochemistry and Molecular Biology, The University of Melbourne.

[§] School of Chemistry, The University of Melbourne.

[||] Department of Medicine (AH/NH), The University of Melbourne.

[⊥] Metabolic Pharmaceuticals Ltd.

10.1021/bc900181a CCC: $40.75 © 2009 American Chemical Society
Published on Web 06/24/2009

avoidance of neutral to basic buffers for the purification of the isoacylpeptide intermediate.

Polycationic peptides have long been known to enhance the solubility of peptides and proteins (*11*). Consequently, one of the first attempts to exploit this to address the problem of poor synthetic peptide solubility was undertaken by Englebretsen and his colleagues who used Boc-SPPS to attach a solubilizing poly-(Gly-Arg)-Gly peptide via a base-labile glycolamide linker to the C-terminus of the poorly soluble dodecaalanine (*12*). Following purification of the soluble conjugate, the solubilizing peptide was removed by treatment with mild aqueous base. A urethane linker has also been developed for temporary attachment of solubilizing peptides to the N-terminus of poorly solubilizing peptides via Boc-SPPS (*13*). Again, liberation of the target peptide was achieved following mild aqueous base treatment. Use of both these methods is restricted to Boc-SPPS due to the lability of the linkers to the base employed for N^{α}-deprotection in Fmoc-SPPS. However, this limitation could be avoided by use of an ester linkage based on 4-hydroxymethyl benzoic acid. This enabled tethering of $Gly(Arg\text{-}Gly\text{-}Gly)_3$ as a solubilizing tail peptide to the C-terminus of the target peptide and is stable to the conditions of Fmoc-SPPS. Release of the tail was achieved by brief treatment with aqueous sodium hydroxide (*14*). The favorable solubilizing propensity of polycationic peptides was also demonstrated by the recent work of Aimoto and his colleagues who employed penta-Arg to solubilize one of two segments of the membrane opioid receptor-like 1 for their successful native chemical ligation (*15*). A similar approach was also successfully adapted by Kent for the native chemical ligation of integral membrane proteins (*16*, *17*).

A recent detailed study of the solubilizing propensity of one, three, and five Lys or Arg residues on a low-solubility model protein, BPTI-22 (a BPTI variant containing 22 Ala residues), showed that pronounced solubilization was afforded by five Lys or Arg (more so with six Arg) residues and that the effect was greater if the polycationic peptides were at the C-terminus rather than the N-terminus of the target protein (*18*). Given that lysine derivatives are significantly cheaper and generally less difficult to polyacylate in SPPS compared to arginine derivatives, we sought to exploit this finding in a refinement of Englebretsen's 4-hydroxymethyl benzoic acid linkage procedure as a simpler yet effective means of preparing postsynthesis solubilized peptides via Fmoc-SPPS. This was achieved by utility of efficient solid-phase synthesis protocols together with a base-labile linker that allowed temporary tethering of a pentalysine cationic peptide to the C-terminus of an otherwise poorly soluble peptide. On completion of the purification of the tagged peptide, the linker was cleaved to liberate the native sequence. This was illustrated by the first solid-phase synthesis of human insulin glargine, which possesses a poorly soluble A-chain that has long been problematic for the preparation and study of this essential glucose regulatory hormone.

EXPERIMENTAL PROCEDURES

Materials. 9-Fluorenylmethoxycarbonyl (Fmoc) protected L-α-amino acids and 1-[bis(dimethylamino)methylene]-1*H*-benzotriazolium hexafluorophosphate 3-oxide (HBTU) were purchased from GL Biochem (Shanghai, China). (DMF), piperidine, and (TFA) were obtained from Auspep (Melbourne, Australia). Fmoc-Gly-PAC-PEG-PS, Fmoc-L-Arg(Pmc)-PAC-PEG-PS, and PAL-PEG-PS resins with substitution of ca. 0.20 mmol/g were purchased from Applied Biosystems Inc. (Melbourne, Australia). Methanol, diethyl ether, and dichloromethane were from Merck (Melbourne, Australia), 3,6-Dioxa-1,8-octanedithiol (DODT), triisopropylsilane (TIPS), diisopropylethylamine (DIPEA), and trifluoromethanesulfonic acid (TFMSA) were purchased from Sigma-Aldrich (Sydney, Australia), and 2,2′-dipyridyl disulfide (DPDS) from Fluka (Switzerland). Acetonitrile was obtained from BDH Laboratory Supplies, (Poole, UK). All other reagents were from Sigma-Aldrich (Sydney, Australia). Recombinant derived human glargine (Lantus) was obtained from Sanofi-Aventis (Sydney, Australia).

Methods. *Peptide Synthesis.* All non-solubilizing tagged peptides were solid-phase synthesized as C-terminal acids on PAC-PEG-PS resin. Peptides C-terminally linked to a solubilizing tag were assembled on PAL-PEG-PS such that the polycationic tag itself possessed a C-terminal amide. SPPS employed Fmoc chemistry on one of the following instruments: CEM Liberty microwave peptide synthesizer (Ai Scientific, Queensland, Australia), PerSeptive Biosystems Pioneer continuous-flow peptide synthesizer (Framingham, MA, USA), or Protein Technologies Tribute batchwise peptide synthesizer (Tucson, AZ, USA). The side chain protecting groups of trifunctional amino acids were TFA-labile, except for acetamidomethyl (Acm)-protected cysteines in insulin glargine positions A20 and B19, and *tert*-butyl (tBu)-protected cysteine in position A7. All peptides were synthesized on a 0.1 mmol scale using instrument default protocols with either a 4- or 5-fold molar excess of Fmoc-protected amino acids (0.4 or 0.5 mmol) that were activated by using 4- or 5-fold excess of HBTU in the presence of DIPEA (0.8 or 1.0 mmol). N^{α}-Fmoc protecting groups were removed by treating the resin-attached peptide with piperidine (20% v/v) in DMF. Using the microwave synthesizer, the coupling and deprotection were carried out at 75 °C using 25 W microwave power for 5 min and 60 W microwave power for 3 min, respectively. For the conventional continuous flow (Pioneer) or batch (Tribute) synthesizer, the coupling and deprotection were carried out for 30 and 10 min, respectively.

Preparation of Resin-Bound Base Labile Handle-Linked Solubilizing Tagged Peptide. Fmoc-PAL-PEG-PS (0.1 mmol) was N^{α}-deprotected and then carried through five cycles of acylation with Fmoc-Lys(Boc)-OH and N^{α}-deprotection as described above. The base-labile linker, 4-hydroxymethylbenzoic acid (5 equiv), was attached via a 1 h acylation using 5 equiv of HBTU and DIPEA. The C-terminal residue (in the case of human insulin glargine, Gly) was attached to the resin-bound linker via a double 1 h acylation with the Fmoc−amino acid symmetrical anhydride (5 equiv) in the presence of 0.1 equiv of catalyst, DMAP.

Peptide−Resin Cleavage. On completion of solid-phase synthesis, the peptide (including each of the A- and B-chains of human insulin glargine) was cleaved from the solid support by treatment with (TFA) containing (DODT)/anisole/(TIPS) (94%/1.5%/2.5%/2%, 20 mL) for 90 min. The cleaved product was precipitated in ice-cold diethyl ether and centrifuged at 3000 rpm for 3 min. The pellet was washed by resuspending it in ice-cold diethyl ether and centrifuging it again. This washing process was repeated at least three times.

General Procedure for the Cleavage of the Solubilizing Tag from Target Peptide. To the purified synthetic solubilizing tag-linked peptide (0.25 mmol) was added 1 mL of ice-cold 0.1 N NaOH. The whole was stirred for 2−5 min after which the pH was made acidic by the addition of 0.1% aq TFA. The solution was then applied directly onto an RP-HPLC column for purification as described below.

Synthesis of Human Insulin Glargine. Insulin Glargine A-Chain-Lys_5 Intramolecular Disulfide Bond Formation. The crude [Cys6,11 (S-thiol), Cys7 (tBu), Cys20 (Acm)] A-chain linked to Lys_5 via the base-labile linker (104.6 mg, 32.4 μmol) was dissolved in 100 mL of deionized H_2O. To this was added 10 mL of 4 mM (DPDS) in MeOH, and the stirred reaction progress was monitored by analytical RP-HPLC analysis, which confirmed that the reaction was completed in 20 min at RT. For the purification, the solution was loaded onto a preparative

RP-HPLC column in four lots via the instrument's C-line and purified and freeze−dried to give 27.2 mg of pure, Cys6-Cys11 intramolecularly disulfide-bonded [Cys7 (tBu), Cys20 (Acm)] A-chain C-terminally linked to Lys_5 (8.4 μmol, 25.9%). MALDI-TOF MS showed a single species with *m*/*z* 3227.88 [$(M+H)^+$] (theory: 3226.61).

Insulin Glargine A-Chain-Lys_5 Conversion of Cys7 (tBu) to Cys7 (Pyr). The purified monodisulfide [Cys7 (tBu), Cys20 (Acm)] A-chain (27.0 mg, 8.4 μmol) and 2-DPDS (11.2 mg, 50.8 μmol) were dissolved in 0.6 mL TFA and anisole (9:1 v/v). The solution was chilled on ice before 0.6 mL of (TFMSA)/TFA (1:4 v/v) was added. The reaction was allowed to continue for 1 h at 0 °C before the peptide was collected by diethyl ether precipitation followed by centrifugation, and purified on a preparative RP-HPLC column. The freeze−dried purified product weighed 15.3 mg (4.7 μmol, 55.7%) and was identified as [Cys7(Pyr), Cys20(Acm)] A-chain by MALDI-TOF MS (*m*/*z* 3282.98 [$(M+H)^+$], theory 3280.61).

Combination of Insulin Glargine A-Chain-Lys_5 with Insulin Glargine B-Chain. The [Cys7(Pyr), Cys20(Acm)] A-chain-Lys_5 peptide (10.9 mg, 3.3 μmol) was dissolved in 3 mL of 6 M GnHCl, 0.1 M Gly/NaOH buffer (pH 8.5). The [Cys7(S-thiol), Cys19(Acm)] B-chain (12.7 mg, 3.2 μmol) was dissolved in deionized water (3 mL) and added slowly to the A-chain solution. The reaction was monitored by analytical RP-HPLC analysis and was found to be complete after 30 min at RT as shown by the absence of the starting products and emergence of a new one. The reaction was stopped by the addition of neat TFA, and the product was purified by preparative RP-HPLC and freeze−dried to give 17.7 mg (2.5 μmol, 78.1% relative to B-chain) of [Cys20A(Acm)/Cys19B(Acm)]-A-(Lys_5)-B. MALDI-TOF MS (*m*/*z* 7001.45 [$(M+Na)^+$], calcd. 7002.61.61).

Insulin Glargine with A-Chain C-Terminal Lys_5. The A-(Lys_5)-B peptide [Cys20A(Acm)/Cys19B(Acm)] (13.2 mg, 1.89 μmol) was dissolved in 7 mL of solvent mixture (6.3 mL glacial acetic acid, 0.7 mL of 60 mM HCl). 8.4 mL of 20 mM iodine/acetic acid was then added to the solution. The reaction was monitored by analytical RP-HPLC. After 30 min, the reaction was stopped by precipitation of the peptide following direct addition of ice-cold diethyl ether (*19*). The solubilizing tag-linked insulin glargine was purified by preparative RP-HPLC and freeze−dried to give 2.3 mg (0.34 μmol, 17.9%) (Figure 5A). The peptide was identified by MALDI-TOF MS as a single species (*m*/*z* 6840.01 [$(M+H)^+$], calcd. 6837.96).

Glargine. A-(Lys_5)-B insulin glargine (1.7 mg, 0.25 μmol) was treated with 0.1 N NaOH as described elsewhere in the Methods section. After purification by preparative RP-HPLC and freeze−drying, 0.9 mg (0.15 μmol, 60.0%) of insulin glargine was obtained. The overall yield was 8.5% relative to the B-chain. The peptide was identified by MALDI-TOF MS as a single species (*m*/*z* 6063.92 [$(M+H)^+$], calcd. 6064.12), and the purity was further confirmed by analytical RP-HPLC (Figure 5B).

Peptide Characterization. Matrix-assisted laser desorption ionization time-of-flight mass spectrometry (MALDI-TOF MS) was carried out on a Bruker Ultraflex II instrument (Bruker Daltonics, Bremen, Germany) and used to characterize the peptides at each intermediate step using sinapinic acid (α-cyano-4-hydroxycinnamic acid) or 2,5-dihydroxybenzoic acid (Bruker Daltonics, Germany) as matrix depending upon the molecular size of the peptide. The matrices were made up of 70% acetonitrile containing 0.1% TFA. The peptide content was determined using vapor-phase acid hydrolysis in 6 M HCl containing 2% phenol at 110 °C for 24 h. The individual amino acids were converted to stable, fluorescent derivatives using Waters AccQ.Tag kit (Waters, Sydney, Australia). The derivatized amino acids were separated using a Shim-Pak XR-ODS (3 × 75 mm, 2.2 μm) column on Shimadzu RP-HPLC system (Shimadzu, Victoria, Australia).

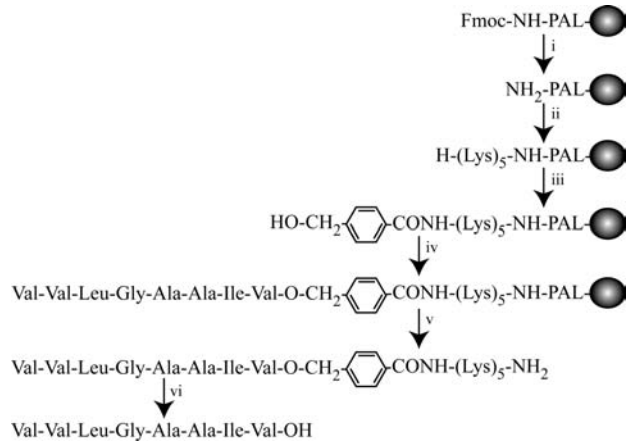

Figure 1. Scheme for the solid-phase synthesis of poorly soluble peptides via a C-terminal-linked penta-Lys "solubilizing tag". (i) 20% piperidine/DMF. (ii) Five successive Fmoc-Lys(Boc)-OH acylations and N^{α}-deprotections. (iii) Acylation with 4-hydroxymethylbenzoic acid. (iv) Double DMAP-mediated 1 h coupling of symmetrical anhydride of C-terminal residue of target sequence followed by solid-phase peptide synthesis. (v) Cleavage of solubilizing tagged peptide from solid support with 95% TFA. (vi) Release of solubilizing tag from target peptide by 2 min treatment with aqueous 0.1 N NaOH. Abbreviation: PAL, 5-(aminomethyl-3,5-dimethoxyphenoxy)valeryl.

Insulin Tolerance Test. Insulin tolerance tests were performed as previously described (*20*). Briefly, fed 8−10-week-old male C57BL/6J mice were anesthetized with sodium pentobarbitone (100 $mg.kg^{-1}$) and injected intraperitoneally with 1 unit of Lantus or synthetic insulin glargine per kg body weight. Blood samples were taken from the tail vein, and glucose concentration was measured using a glucometer (Precision Q.I.D., MediSense, MA, USA).

RESULTS AND DISCUSSION

The concept of use of suitably linked polycationic amino acid tags for temporary solubilization of synthetic peptides was originally developed and exploited by Englebretsen (*14*). His choice of solubilizing peptide tag, poly-(Gly-Arg)-Gly, which was temporarily attached to the C-terminus of the target peptide via a 4-hydroxymethylbenzoic acid linker, is more complex than required. The results of the studies of Kato and colleagues showed that pronounced solubilization could be afforded by attachment of just five consecutive lysine residues at the C-terminus of the peptide of interest (*18*). Thus, we sought to simplify and refine Englebretsen's protocol by the use of a penta-Lys tail and assessed its capacity to solubilize the octapeptide, NH_2-V-V-L-G-A-A-I-V-OH, as outlined in Figure 1. The latter peptide alone is virtually insoluble in water and other aqueous buffers. In contrast, the synthetic C-terminally penta-Lys-linked peptide was freely soluble (results not shown). Removal of the solubilizing tag by 2 min treatment with 0.1 N NaOH resulted in an insoluble mixture (results not shown). Following this proof of concept, the method was then applied to the chemical synthesis of human insulin glargine.

The chemical synthesis of insulin was first achieved by the Shanghai Insulin Research group in 1965 using solution synthesis methods for the assembly of each of the two chains followed by their combination in solution (*21*). This monumental achievement took ten years to complete and required enormous manpower. In contrast, the advent of Merrifield's solid-phase technique enabled the synthesis of the bovine hormone to be completed in a matter of weeks (*22*). However, it was evident from the very early stages of studies on insulin chains that the

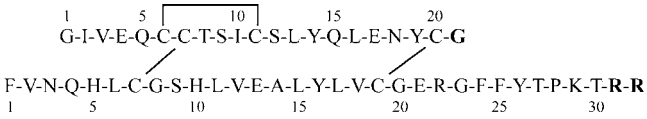

Figure 2. Primary structure of human insulin glargine. The key differences between insulin and glargine are highlighted in bold and are the replacement of A-chain C-terminal Asn with Gly and the addition of two Arg residues to the C-terminus of the B-chain.

A-chain possessed physicochemical properties that hampered both its chemical synthesis and subsequent handling (*23*−*25*). It was thus necessary to convert the S-reduced form of the A-chain into its S-sulfonate in order to improve its solubility and subsequent handling and purification. Despite much effort, no useful alternative to S-sulfonated A-chain and its analogues has been developed, which, in turn, has been a major hindrance to the rational and facile chemical preparation of insulin and its analogues for detailed structure−function relationship analysis and the development of newer generation therapeutics for the treatment of diabetes. Particularly restrictive has been the inability of the conventional chain combination approach to yield insulin analogues with truncated or secondary structure-modified chains which hinder the combination and folding pathway. Nevertheless, there have been some impressive analogue achievements via this synthetic methodology, which have, in turn, significantly contributed to insulin structure−function relationship studies (*26*−*29*). However, the continuing difficulties associated with the need for S-sulfonated chains. together with the generally very low yields of chain-combined products (rarely better than *ca*. 1% overall), have led to the authors of a recent review to state that "a high-yield synthetic route to preparation of insulin analogues remains a high priority yet is seemingly overlooked by the peptide community" (*30*).

Numerous analogues of insulin have been prepared over the past three decades for use in diabetic therapy (*31*). One of the most important of these is human insulin glargine (*32*), which was developed by Sanofi-Aventis and launched in the clinic in 2001 under the trade name of Lantus. It is one of two long-acting (basal) insulins (the other is Levemir; Novo-Nordisk) and is characterized by a substitution of Gly in place of Asn at the C-terminus of the A-chain and an addition of two Arg residues to the C-terminus of the B-chain (Figure 2). These modifications cause a change in the isoelectric point (from pH 5.4 to 6.7), which makes it less soluble at physiological pH than insulin itself. Insulin glargine precipitates in the subcutaneous tissue following injection with the result that its uptake is delayed leading to an extension of duration of activity. In isoglycaemic clamp studies and following subcutaneous injection, insulin glargine plateaus at a concentration 2−3 times lower than human insulin within 6−8 h, remains essentially unchanged for 24 h and is unaffected by the site of injection (*33*). In contrast, insulin peaks within 3−6 h and returns to baseline within 16 h (*34*). Insulin glargine remains one of the most important therapies for type I diabetes today. It is produced by recombinant DNA methods via a single-chain analogue which, upon enzymatic treatment, yields the native two-chain structure. Given that a crucial goal of continued insulin development is the preparation of new generation analogues with improved pharmacokinetic and physiological properties and that insulin glargine is a valuable lead peptide for such study, there is an urgent need for its ready chemical synthesis. In the past decade, our laboratory has developed efficient solid-phase synthesis protocols which, combined with regioselective disulfide bond formation (*35*), have allowed the acquisition of several insulin-like peptides including mouse relaxin and insulin-like peptide 3 in very good overall yields (*36*−*39*). Importantly, such methods of forced and sequential disulfide bond formation have allowed

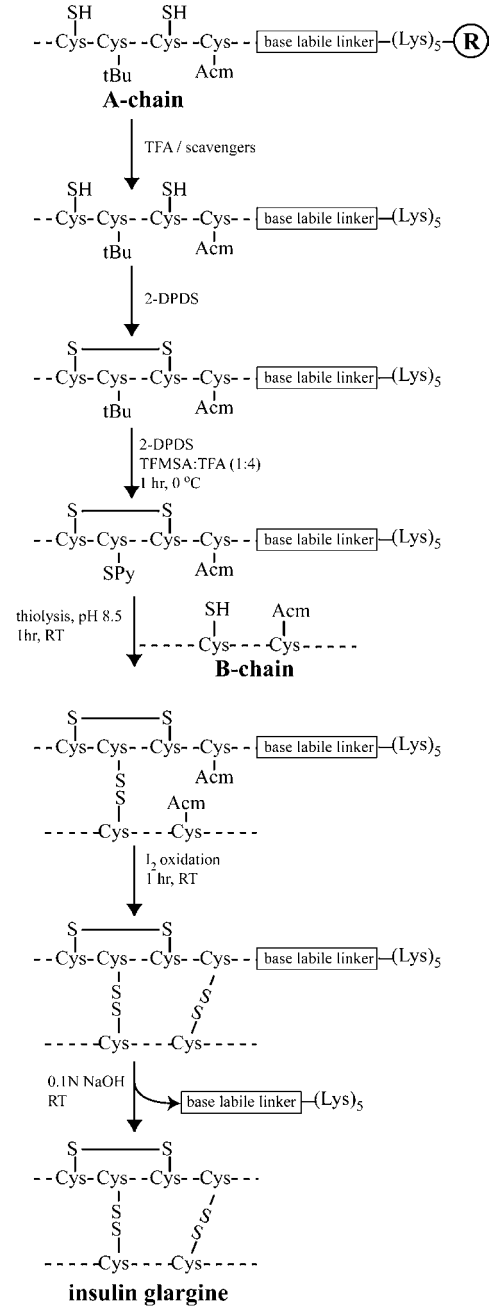

Figure 3. Scheme for the solid-phase synthesis of human glargine via regioselective disulfide bond formation and solubilizing peptide tagged A-chain.

numerous analogues of these peptides to be successfully prepared, which would otherwise not be possible via the conventional chain combination approach. However, application of these methods to the preparation of either human insulin or human insulin glargine did not afford usefully improved yields due to the very poor solubility of the intermediate A-chain peptide, which resulted in little combination with the B-chain (unpublished observations). Consequently, we undertook to assemble insulin glargine via a combination of use of a temporary solubilizing tag on the A-chain and our established regioselective disulfide bond formation protocol (Figure 3).

Solid-phase synthesis of both the nontagged and tagged A-chains as well as B-chain of insulin glargine was achieved without difficulty regardless of the instrumentation or default synthetic protocol employed. The crude selectively S-protected peptides were each of good purity as determined by analytical RP-HPLC and MALDI-TOF MS. Of interest was the curious

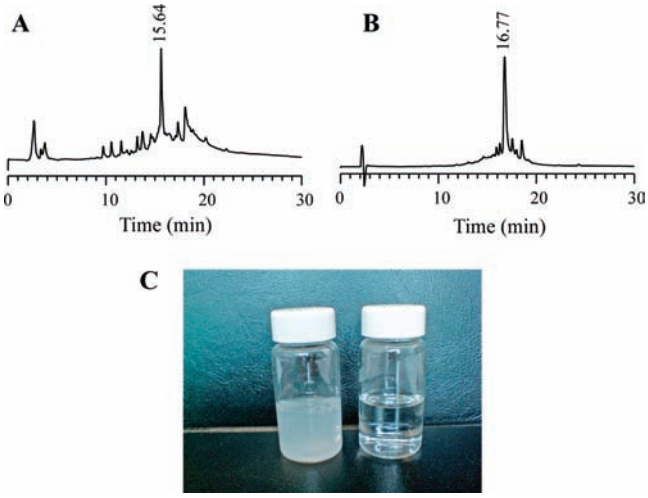

Figure 4. RP-HPLC of crude synthetic human insulin glargine A-chain without (A) and with (B) a C-terminal penta-Lys solubilizing tail. Conditions: Vydac C4 column (4.6 × 250 mm, pore size 300 Å, particle size 5 μ); Buffer A, 0.1% aq. TFA; Buffer B, 0.1% TFA in CH3CN. Gradient = 10−90% B over 30 min. (C) Comparison of relative solubility of the crude synthetic human insulin glargine A-chain without (left) and with (right) a C-terminal penta-Lys solubilizing tail. Peptides added to deionized and distilled water at a concentration of 1.0 mg/mL.

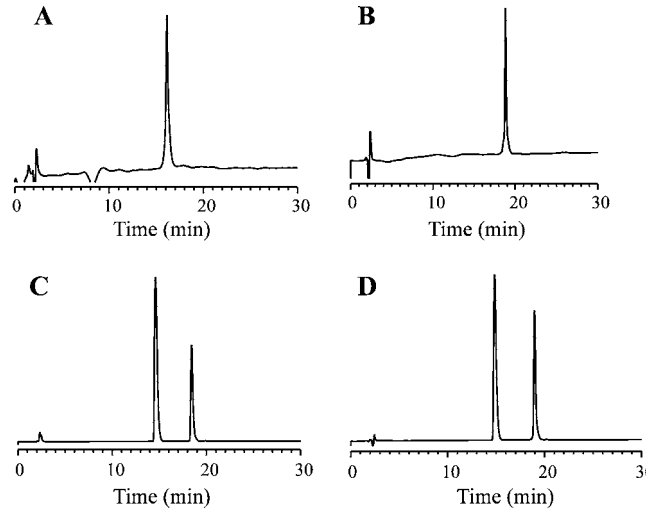

Figure 5. RP-HPLC of (A) synthetic human insulin glargine with solubilizing tail attached to the C-terminus of the A-chain. (B) Synthetic human glargine after removal of solubilizing tail. (C) Commercial Lantus (peak at 14.8 min corresponds to *m*-cresol preservative present in the solution). (D) Coinjection of Lantus and synthetic human insulin glargine. Conditions: Vydac C18 column (4.6 × 250 mm, pore size 300 Å, particle size 5 μ); Buffer A, 0.1% aq. TFA; Buffer B, 0.1% TFA in CH_3CN. Gradient = 20−50% B over 30 min.

observation that the far more hydrophilic tagged A-chain analogue eluted a little later on the RP-HPLC column compared to the nontagged peptide (Figure 4A,B). However, the latter peptide was very poorly soluble, making both its characterization and purification very difficult. Yields of the intramolecular disulfide bonded intermediate were so poor as to deter further effort and subsequent combination with the corresponding B-chain. In contrast, the same peptide containing a C-terminal linked penta-Lys was completely soluble in all aqueous buffers including water alone (Figure 4C) allowing its ready characterization and purification in good yield by RP-HPLC.

The intramolecular disulfide bond within the A-chain was formed by DPDS-mediated oxidation of the free thiol groups of the Cys6 and Cys11 residues (*40*). The Cys7 side chain protecting group (tBu) was then converted to an S-pyridinyl group by reaction of the peptide with DPDS in the presence of TFMSA after which the resulting intermediate was combined with the insulin glargine B-chain. The free thiol group of Cys7 within the B-chain led to thiolysis of the S-pyridinyl group of the A-chain and subsequent formation of the first intermolecular disulfide bond. Following purification by RP-HPLC, the resulting double-disulfide two-chain peptide containing two S-Acm groups on CysA20 and CysB19 was then treated with iodine in hydrochloric acid and acetic acid to generate the second, and final, intermolecular disulfide bond (Figure 5A). The penta-Lys tag was removed from the C-terminal of the insulin glargine by brief base treatment. Following a final RP-HPLC purification step, overall yield of insulin glargine was 8.5% relative to crude starting B-chain, which is satisfactory given the multiple steps involved in its preparation. This compares favorably with the reported yields of other synthetic insulin-like peptides and their analogues with a range of ca. 5−15% (*36*−*39*). Yields of chemically prepared insulin via random chain combination are rarely better than 1%. A solid-phase synthesis of human insulin by an alternative regioselective disulfide bond formation approach but without the aid of a solubilizing tail and involving one fewer step from the initial combination of the two chains resulted in a yield of ca. 1% (*41*).

The synthetic insulin glargine was shown to be highly purified as assessed by analytical RP-HPLC (Figure 5B) and

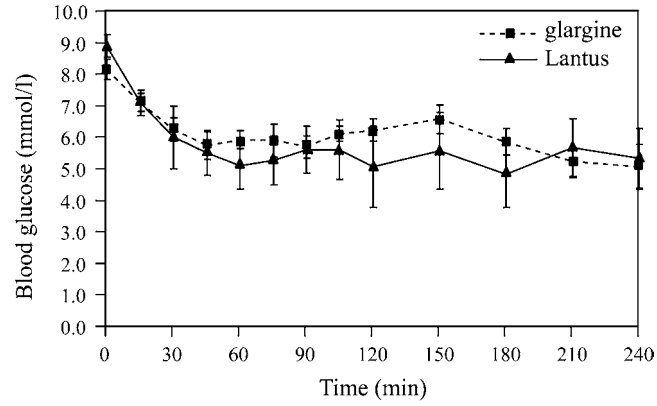

Figure 6. Biological activity of synthetic human insulin glargine in the insulin tolerance test. Synthetic or commercially obtained (Lantus) insulin glargine was injected in 8−10-week-old male C57BL/6 mice at 1 unit/kg body weght and blood glucose levels determined over 240 min. Results are presented as mean ± SEM (n = 4).

MALDI-TOF MS (found MH+ 6063.92; calc. MH+ 6064.12). Coinjection of the peptide with commercially obtained Lantus (which contains *m*-cresol as preservative; see Figure 5C) on RP-HPLC resulted in the two peptides coeluting (Figure 5D). The biological activity of both synthetic and commercial insulin glargine was also assessed using the insulin tolerance test. The synthetic insulin glargine was as effective in reducing glycemia over a 4 h period in mice as the commercially available insulin glargine (Lantus), suggesting equivalent bioactivity (Figure 6).

In conclusion, a simple modification of SPPS methodology has been exploited to enable the preparation of poorly soluble peptides in a form that enables their improved handling and purification. It employs a polylysine solubilizing "tag" temporarily linked to the insoluble peptide via a base-labile handle. Our experience thus far suggests that five Lys residues are adequate for significant solubilization enhancement, although the method readily allows additional Lys residues to be used if necessary. One potential limitation of this approach is that the

base-mediated cleavage step may cause aspartimide formation in sensitive sequences, but this will remain to be investigated. Application of this approach resulted in the acquisition of insulin glargine in nearly 10% overall yield as a consequence of much improved handling of the intractable A-chain. Access to analogues of insulin glargine with potentially improved pharmacological properties should thus be greatly and readily facilitated. Preloaded resins bearing poly-Lys and functionalized linkers may afford an attractive and effective addition to the current armory of methods for handling poorly solubilized synthetic peptides. More broadly, we believe that this simple bioconjugate approach should be more widely employed for the preparation of poorly soluble peptides.

ACKNOWLEDGMENT

This work was partially funded by the National Health and Medical Research Council of Australia Project grants #350284 and 50995 to JDW.

LITERATURE CITED

(1) Kates, S. A., and Albericio, F., Eds. (2000) *Solid-phase synthesis. A practical guide*, Marcel Dekker, Inc., New York.
(2) Narita, M., Honda, S., Umeyama, H., and Obana, S. (1988) The solubility of peptide intermediates in organic solvents. Solubilizing potential of hexafluoro-2-propanol. *Bull. Chem. Soc. Jpn. 61*, 281–284.
(3) Grant, G. A., Ed. (1992) *Synthetic peptides: A user's guide*. W. H. Freeman and Co., New York.
(4) Lateef, S. S., Gupta, S., Jayathilaka, L. P., Krisnanchettiar, S., Huang, J.-S., and Lee, B.-S. (2007) An improved protocol for coupling synthetic peptides to carrier proteins for antibody production using DMF to solubilize peptides. *J. Biomol. Tech. 18*, 173–176.
(5) Johnson, T., Quibell, M., and Sheppard, R. C. (1995) N,O-bisFmoc derivatives of N-(2-hydroxy-4-methoxybenzyl)-amino acid derivatives: useful intermediates in peptide synthesis. *J. Pept. Sci. 1*, 11–25.
(6) Quibell, M., Turnell, W. G., and Johnson, T. (1994) Preparation and purification of β-amyloid (1−43) via soluble, amide backbone protected intermediates. *J. Org. Chem. 59*, 1745–1750.
(7) Clippingdale, A. B., Macris, M., Wade, J. D., and Barrow, C. J. (1998) Synthesis and secondary structural studies of penta(acetyl-Hmb) Aβ (1−40). *J. Pept. Res. 53*, 665–672.
(8) Mutter, M., Chandravarkar, A., Boyat, C., Lopez, J., Dos Santos, S., Mandal, B., Mimna, R., Murat, K., Patiny, L., Saucède, L., and Tuchscherer, G. (2004) Switch peptides in statu nascendi: induction of conformational transitions relevant to degenerative diseases. *Angew. Chem., Int. Ed. 43*, 4172–4178.
(9) Sohma, Y., and Kiso, Y. (2006) "Click peptides" - chemical biology-oriented synthesis of Alzheimer's disease-related amyloid beta peptide (abeta) analogues based on the "O-acyl isopeptide method". *ChemBioChem 7*, 1549–1557.
(10) Sohma, Y., Yoshiya, T., Taniguchi, A., Kimura, T., Hayashi, Y., and Kiso, Y. (2007) Development of O-acyl isopeptide method. *Biopolymers 88*, 253–262.
(11) Smith, J. C., Derbyshire, R. B., Cook., E., Dunthorne, L., Viney, J., Brewer, S. J., Sassenfeld, H. M., and Bell, L. D. (1984) Chemical synthesis and cloning of poly(arginine)-coding gene fragment designed to aid polypeptide purification. *Gene 32*, 321–327.
(12) Englebretson, D. R., and Alewood, P. F. (1996) Boc SPPS of two hydrophobic peptides using a "solubilizing tail" strategy: dodecaalanine and chemotactic protein 1042−55. *Tetrahedron Lett. 37*, 8431–8434.
(13) Englebretsen, D. R., and Robilliard, G. T. (1999) An N-terminal method for peptide solubilization. *Tetrahedron Lett. 55*, 6623–6634.
(14) Choma, C. T., Robillard, G. T., and Englebretsen, D. R. (1998) Synthesis of hydrophobic peptides: An Fmoc "solubilizing tail" method. *Tetrahedron Lett. 39*, 2417–2420.
(15) Sato, T., Saito, Y., and Aimoto, S. (2005) Synthesis of the C-terminal region of opioid receptor like 1 in an SDS micelle by the native chemical ligation: effect of thiol additive and SDS concentration on ligation efficiency. *J. Pept. Sci. 11*, 410–416.
(16) Johnson, E. C. B., and Kent, S. B. H. (2007) Towards the total chemical synthesis of integral membrane proteins: a general method for the synthesis of hydrophobic peptide-$^{\alpha}$thioester building blocks. *Tetrahedron Lett. 48*, 1795–1799.
(17) Johnson, E. C., Malito, E., Shen, Y., Rich, D., Tang, W. J., and Kent, S. B. (2007) Modular total chemical synthesis of of a human immunodeficiency virus type I protease. *J. Am. Chem. Soc. 129*, 11480–11490.
(18) Kato, A., Maki, K., Ebina, T., Kuwajima, K., Soda, K. And., and Kuroda, Y. (2006) Mutational analysis of protein solubility enhancement using short peptide tags. *Biopolymers 85*, 12–18.
(19) Zhang, S., Lin, F., Hossain, M. A., Shabanpoor, F., Tregear, G. W., and Wade, J. D. (2008) Simultaneous post-cysteine S-acetomidomethyl (Acm) group removal quenching of iodine and isolation of peptide by one-step ether precipitation. *Int. J. Pept. Res. Ther. 14*, 301–305.
(20) Lamont, B. J., Visinoni, S., Fam, B. C., Kebede, M., Weinrich, B., Papapostolou, S., Massinet, H., Proietto, J., Favaloro, J., and Andrikopoulos, S. (2006) Expression of human fructose-1,6-bisphosphatase in the liver of transgenic mice results in increased glycerol gluconeogenesis. *Endocrinology 147*, 2764–2772.
(21) Kung, Y. T., Du, Y. C., Huang, C. C., and Ke, L. T. (1965) Total synthesis of crystalline bovine insulin. *Sci. Sin. 14*, 1710–1716.
(22) Marglin, A., and Merrifield, R. B. (1966) The synthesis of bovine insulin by the solid phase method. *J. Am. Chem. Soc. 88*, 5051–5052.
(23) Jiang, J. Q., Du, Y. C., and Tsou, C. L. (1963) Further increase in the activity regenerated in the resynthesis of insulin from its glycyl and phenylalanyl chains. *Sci. Sin. 12*, 452–454.
(24) Mayer, J. P., Brooke, G. S. DiMarchi, R. D. (1990) Chemical synthesis of the A-chain of human insulin. Peptides. Chemistry, Structure and Biology. *Proceedings of the 11th American Peptide Symposium* (Rivier, J. E. Marshall, G. R., Eds.) pp 1061−1062, ESCOM, Leiden, The Netherlands.
(25) Zakhariev, S. G., Guarnaccia, C., Gattner, H.-G., Pongor, S. And Brandeburg, D. (1995) Solid phase synthesis of insulin A-chain and analogues via Fmoc-strategy. Peptides 1994. *Proceedings of the 23rd European Peptide Symposium.* (Maia, H. L. S., Ed.) pp 297−298, ESCOM, Leiden, The Netherlands.
(26) Hua, Q. X., Hu, S. Q., Frank, B. H., Jia, W., Chu, Y. C., Wang, S. H., Burke, G. T., Katsoyannis, P. G., and Weiss, M. A. (1996) Mapping the functional surface of insulin by design: structure and function of a novel A-chain analogue. *J. Mol. Biol. 264*, 390–403.
(27) Huang, Y. D., Yang, S. Z., Feng, Y. M., and Niu, C. I. (1999) An insulin analogue with γ-amino butyric acid substitution for A13Leu-A14Tyr. *J. Pept, Res. 54*, 18–22.
(28) Weiss, M. A., Hua, Q. X., Jia, W., Nakagawa, S. H., Chu, Y. C., Hu, S. Q., and Katsoyannis, P. G. (2001) Activities of monomeric insulin analogues at position A8 are uncorrelated with their thermodynamic stabilities. *J. Biol. Chem. 276*, 40018–40024.
(29) Wan, Z., Xu, B., Huang, K., Chu, Y. C., Li, B., Nakagawa, S. H., Qu, Y., Hu, S. Q., Katsoyannis, P. G., and Weiss, M. A. (2004) Enhancing the activity of insulin at the receptor interface: crystal structure and photo-crosslinking of A8 analogues. *Biochemistry 43*, 16119–161133.
(30) Mayer, J. P., Zhang, F., and DiMarchi, R. D. (2007) Insulin structure and function. *Biopolymers (Pept. Sci.) 88*, 687–713.
(31) Sheldon, B., Russell-Jones, D., and Wright, J. (2009) Insulin analogues: an example of applied medical science. *Diabetes Obes. Metab. 11*, 5–19.

(32) Bolli, G. B., DiMarchi, R. D., Park, G. D., Pramming, S. And., and Koivisto, V. A. (1999) Insulin analogues and their potential in the management of diabetes mellitus. *Diabetologia 42*, 1151–1167.

(33) Owens, D. R., Coates, P. A., Luzio, S. D., Tinbergen, J. P., and Kurzhals, R. (2000) Phamacokinetics of 125I-labelled insulin glargine (HOE901) in healthy men - comparison with NPH insulin and the influence of different subcutaneous injection sites. *Diabetes Care 23*, 813–819.

(34) Lepore, M., Pampanelli, S., Fanelli, C., Porcellati, F., Bartocci, L., Di Vincenzo, A., Cordoni, C., Costa, E., Brunetti, P., and Bolli, G. B. (2000) Pharmacokinetics and pharmacodynamics of the long-acting human insulinanalog glargine, NPH insulin, and ultralente human insulin injected subcutaneously, and continuous subcutaneous infusion of insulin lispro. *Diabetes 49*, 2142–2148.

(35) Bathgate, R. A. D., Lin, F., Hanson, N. F., Otvos, Jr. L., Guidolin, A., Giannakis, C., Bastiras, S., Layfield, S., Ferraro, T., Ma, S., Zhao, C., Gundlach, A. L., Samuel, C. S., Tregear, G. W., and Wade, J. D. (2006) Relaxin-3: Improved synthesis strategy and demonstration of its high-affinity interaction with the relaxin receptor LGR7 both in vitro and in vivo. *Biochemistry 45*, 1043–1053.

(36) Rosengren, K. J., Zhang, S., Lin, F., Daly, N. L., Scott, D. J., Hughes, R. A., Bathgate, R. A. D., Craik, D. J., and Wade, J. D. n/a Solution structure and characterization of the receptor binding surface of insulin-like peptide 3. *J. Biol. Chem. 281*, 28287−28295.

(37) Samuel, C. J., Lin, F., Zhao, C., Layfield, S. L., Hossain, M. A., Zhang, S., Giannakis, E., Bathgate, R. A., Tregear, G. W., and Wade, J. D. (2007) Improved chemical synthesis and demonstration of relaxin receptor binding activity and biological activity of mouse relaxin. *Biochemistry 46*, 5374–5381.

(38) Hossain, M. A., Bathgate, R. A., Kong, C., Shabanpoor, F., Zhang, S., Haugaard-Jönsson, L. M., Rosengren, K. J., Tregear, G. W., and Wade, J. D. (2008) Synthesis, conformation and receptor binding activity of human insulin-like peptide 5 (INSL5). *ChemBioChem 9*, 1816–1822.

(39) Shabanpoor, F., Hughes, R. A., Bathgate, R. A. D., Zhang, S., Scanlon, D. B., Lin, F., Hossain, M. A., Separovic, F., and Wade, J. D. (2008) Solid-phase synthesis of europium-labelled human INSL3 as a novel probe for the study of ligand-receptor interactions. *Bioconjugate Chem. 19*, 1456–1463.

(40) Maruyama, K., Nagasawa, H., and Suzuki, A. (1999) 2,2′-Bispyridyl disulfide rapidly induces intramolecular disulfide bonds in peptides. *Peptides 20*, 881–884.

(41) Akaji, K., Fujino, K., Tatsumi, T., and Kiso, Y. (1993) Total synthesis of human insulin by regioselective disulfide formation using the silyl chloride-sulfoxide method. *J. Am. Chem. Soc. 115*, 11384–11392.

BC900181A

TECHNICAL NOTES

Silver-Catalyzed azaGly Ligation. Application to the Synthesis of Azapeptides and of Lipid−Peptide Conjugates

Nathalie Ollivier, Soizic Besret, Annick Blanpain, and Oleg Melnyk*

UMR 8161 CNRS/Université de Lille 1 et 2, Institut Pasteur de Lille, IFR 142 Institut de Biologie de Lille, 1 rue du Pr Calmette, 59021 Lille Cedex, France. Received January 16, 2009; Revised Manuscript Received May 27, 2009

Glycine is a amino acid frequently found in peptides. Substitution of a glycine residue by an azaglycine allows the modulation of peptide conformation, bioactivity, or stability. Azapeptides are usually prepared using solid-phase synthetic procedures. We show here that azaGly peptides can be assembled chemoselectively and without racemization using unprotected peptide fragments by silver-catalyzed reaction of C-terminal peptide hydrazides with N-terminal phenylthiocarbonyl peptides. The reaction was performed in a *t*BuOH/water mixture and the control of apparent pH permitted the clean formation of the azaGly bond in the presence of lysine residues. We show also that this novel ligation method, called azaGly ligation, can be used for the assembly of lipopeptides. For this, lipid hydrazides were reacted with a phenylthiocarbonyl peptide in the presence of silver ions. This ligation method allows incorporation of acid-sensitive lipid moieties that are incompatible with standard solid-phase peptide synthesis procedures, and more generally should be of interest for the modification of peptides by sensitive acyl moieties.

INTRODUCTION

Azapeptides are peptide analogues in which the α-CH moiety of one or more amino acid residues in the peptide chain is replaced by a nitrogen atom (*1*, *2*). This modification has been shown to induce a β-turn geometry due to electronic repulsion between the adjacent nitrogen lone pairs and/or to the formation of intramolecular hydrogen bonds (*3*−*6*). The better stability of azapeptides in biological medium relative to native peptides may be due to the induction of a bent shape by aza-amino acid residue and to the increased chemical stability of urea-type bonds compared to amide bonds. Aza-amino acids can thus be used to improve the stability and bioavailability of peptide drugs (*7*) and also for the design of prodrugs (*8*). Aza-amino acid modification has been exploited also for the design of protease inhibitors (*9*). The inhibition of Ser or Cys proteases is mainly due to the slower hydrolysis of the acyl-enzyme complex by water relative to the native peptide (*9*−*12*).

Gly is a common amino acid in peptides and proteins. Glycine is the most flexible among the 20 coded amino acids due to the absence of a side chain on the α-carbon. Several reports have highlighted the interest of replacing Gly by azaGly (Agly) to improve the stability and/or potency of bioactive peptides. Recently, peptide Z-Arg-Leu-Arg-Agly-Ile-Val-OMe has been described as the strongest ($K(i)$ = 480 pM) and the most selective inhibitor of cathepsin B to date (*11*).

The synthesis of Agly peptides is usually performed using solid-phase methods. One strategy relies on the use of N-protected hydrazine and a peptidyl resin modified on the N-terminus by an isocyanate or active carbamate (*13*). Lubell et al. have recently improved the solid-phase synthesis of azapeptides by coupling N-Boc-aza-dipeptides (*14*) or phosgene-activated N′-alkyl fluoren-9-ylmethyl carbazates (*15*) to the growing peptide chain. More recently, the same group described the preparation of Agly peptides on the solid phase using diphenyl hydrazone protection (*16*).

Scheme 1. Strategies Used for the Chemoselective Assembly of Agly-Peptides

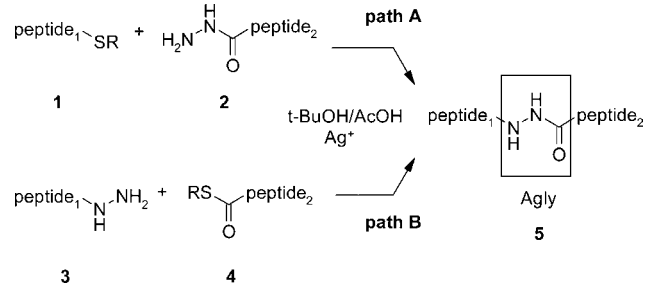

We show in the first part of this article that Agly peptides can be synthesized using a convergent approach by ligating chemoselectively unprotected peptide fragments in solution (Scheme 1). Two strategies have been explored: the reaction between hydrazinocarbonyl peptides and C-terminal peptide thioesters (Scheme 1, path A) or the reaction between C-terminal peptide hydrazides and phenylthiocarbonyl peptides (Scheme 1, path B). Both reactions required the presence of silver ions to activate the alkyl or arylthiocarbonyl groups. In the second part, the utility of azaGly ligation for the synthesis of lipopeptides was examined. For this, a phenylthiocarbonyl peptide was reacted with a series of lipid hydrazides derived from cholesterol or C18 unsaturated fatty acids in the presence of silver ions. Lipopeptides featuring an azaGly residue between the lipid moiety and the peptide chain were isolated successfully.

* E-mail: oleg.melnyk@ibl.fr.

10.1021/bc9000195 CCC: $40.75 © 2009 American Chemical Society
Published on Web 06/12/2009

EXPERIMENTAL PROCEDURES

Synthesis of Thioester Peptides 1a and 1b. The experimental procedure for the synthesis of the thioesters was described in detail elsewhere (*17*). MALDI-TOF (α-cyano-4-hydroxycinnaminic acid, monoisotopic): calcd for **1a** $C_{52}H_{88}N_{14}O_{15}S_2$ $[M+H]^+$ 1213.6, found 1213.6; calcd for **1b** $C_{53}H_{90}N_{14}O_{15}S_2$ $[M+H]^+$ 1227.6, found 1227.2.

Synthesis of Hydrazinocarbonyl Peptides 2b,c, Typical Experimental Procedure for 2b. Peptide elongation: Peptide elongation was performed on NovaSyn TGR resin (0.38 g, 0.095 mmol, 0.25 mmol/g) using standard Fmoc/*tert*-butyl chemistry on a Pioneer synthesizer (Applied Biosystems) using TBTU/HOBt/DIEA activation in DMF. A capping step was performed after each coupling with Ac_2O/DIEA. At the end of the synthesis, the Fmoc protecting group of the last amino acid was removed using 20% piperidine in DMF. The resin was washed with DMF (4 × 2 min).

Preparation of reagent 7 and coupling to the peptidyl resin: *tert*-Butyl carbazate (125.5 mg, 0.95 mmol) and carbonyldiimidazole (154 mg, 0.95 mmol) were dissolved in dry DMF (4.7 mL) under argon atmosphere. The reaction was complete after 1 h at rt as shown by TLC analysis. This solution was added to the resin and the suspension was agitated at rt for 1 h 30 min. The resin was then washed with DMF (3 × 2 min), CH_2Cl_2 (5 × 2 min), and Et_2O (2 × 2 min) and dried in vacuo.

Deprotection and cleavage: The resin was suspended in TFA/TIS/anisole: 95/2.5/2.5 by vol. (9.5 mL) over a period of 1 h at rt. The peptide was precipitated in Et_2O/pentane 1/1 by vol (95 mL), solubilized in triethylamine acetate buffer (TEAA) (200 mM, pH 6.5, 4 mL), and lyophilized to give 139.9 mg of crude hydrazinocarbonyl peptide **2b**. The crude product was purified by RP-HPLC (C18 hyperprep column, rt, detection at 230 nm, eluent A 10 mM triethylamine acetic acid aqueous buffer (TEAA, pH 6.5), eluent B *i*-PrOH/water 2/3 by vol containing 10 mM TEAA, 0−15% B in 15 min then 15−100% B in 283 min, flow rate 3 mL/min) to give 63.3 mg (54% yield) of peptide **2b**. MALDI-TOF (α-cyano-4-hydroxycinnaminic acid, monoisotopic): calcd for $C_{47}H_{80}N_{16}O_{13}$ $[M+H]^+$ 1077.6, found 1077.1.

Similarly, peptide **2c** was prepared starting from NovaSyn TGR resin (0.36 g, 0.09 mmol, 0.25 mmol/g). Reaction with **7** was performed overnight to give 69.7 mg (66% yield) of peptide **2c** after RP-HPLC purification (see above). MALDI-TOF (α-cyano-4-hydroxycinnaminic acid, monoisotopic): calcd for $C_{45}H_{77}N_{15}O_{12}$ $[M+H]^+$ 1020.6, found 1020.3.

Synthesis of Hydrazide Peptides 3b,c, Typical Experimental Procedure for 3b. *Coupling of Fmoc-Gly-OH.* Fmoc-Gly-OH (594.6 mg) was solubilized under argon in dry CH_2Cl_2 (7 mL) and anhydrous DMF (700 μL). Diisopropylcarbodiimide (156.6 μL) was added in one portion. The reaction mixture was stirred on ice for 20 min. CH_2Cl_2 was then evaporated. The residue was dissolved in DMF (3 mL) and added on Novasyn TG HMBA resin (869.6 mg, 0.2 mmol, 0.23 mmol/g) swelled in DMF. 4-*N*,*N*-Dimethylaminopyridine (2.44 mg) dissolved in DMF (500 μL) was added to the suspension which was agitated 1 h at rt. The resin was washed with DMF (4 × 2 min) and CH_2Cl_2 (4 × 2 min).

Peptide Elongation. Peptide elongation was performed using standard Fmoc/*tert*-butyl chemistry on a Pioneer synthesizer (Applied Biosystems) using TBTU/HOBt/DIEA activation in DMF. A capping step was performed after each coupling with Ac_2O/DIEA. At the end of the synthesis, the Fmoc protecting group of the last amino acid was removed using 20% piperidine in DMF. The resin was acetylated, washed with CH_2Cl_2 (3 × 2 min) and Et_2O (3 × 2 min), and dried in vacuo.

Deprotection. The dry resin was suspended during 1 h in TFA/H_2O/EDT: 95/2.5/2.5 by vol (20 mL) at rt. The resin was filtered and washed with neat TFA, CH_2Cl_2 (5 × 2 min), DIEA 10% in CH_2Cl_2 (5 × 2 min), and DMF (5 × 2 min).

Hydrazinolysis. The resin was suspended in hydrazine hydrate 5% in DMF (20 mL). After 1 h, the resin was filtered and washed with DMF (2 × 2 min). The combined filtrates were concentrated in vacuo. The peptide was precipitated in Et_2O/heptane 1/1 by vol and purified by RP-HPLC (C3 zorbax column, rt, detection at 230 nm, buffer A 100% water containing 0.05% TFA, buffer B CH_3CN/water 4/1 by vol containing 0.05% TFA, isocratic 0% B, flow rate 6 mL/min) to give 94 mg (31.4% yield) of hydrazide peptide **3b**. MALDI-TOF (α-cyano-4-hydroxycinnaminic acid, monoisotopic): calcd for $C_{57}H_{89}N_{17}O_{16}$ $[M+H]^+$ 1268.7, found 1268.5.

3c was obtained similarly: 8.5 mg (6% yield) of pure hydrazide peptide **3c**. MALDI-TOF (α-cyano-4-hydroxycinnaminic acid, monoisotopic): calcd for $C_{58}H_{91}N_{17}O_{16}$ $[M+H]^+$ 1282.7, found 1283.1.

Synthesis of Phenylthiocarbonyl Peptide 4a. *Peptide Elongation.* Peptide elongation was performed on NovaSyn TGR resin (1.304 g, 0.23 mmol/g) using standard Fmoc/*tert*-butyl chemistry on a Pioneer synthesizer (Applied Biosystems) using TBTU/HOBt/DIEA activation in DMF. A capping step was performed after each coupling with Ac_2O/DIEA. At the end of the synthesis, the Fmoc protecting group of the last amino acid was removed using 20% piperidine in DMF. The resin was washed with DMF (3 × 2 min) and anhydrous THF (8 × 2 min).

Phenylthiocarbonyl Functionalization. The resin was suspended in anhydrous THF (12 mL) under argon. Anhydrous Et_3N (154 μL) and phenylthiochloroformate (173 μL) were added to the resin, which was agitated at rt during 1 h 30 min. The resin was washed with anhydrous THF (3 × 2 min), CH_2Cl_2 (2 × 2 min), and Et_2O (2 × 2 min) and dried in vacuo.

Deprotection and cleavage: The dry resin was suspended for 1 h in TFA/H_2O/thioanisole 96.5/2.5/1 by vol (30 mL) at rt. The resin was filtered, and the filtrate was precipitated in Et_2O/pentane 1/1 by vol (300 mL). The crude peptide was purified by RP-HPLC (C18 hyperprep column, rt, detection at 230 nm, buffer A 100% water containing 0.05% TFA, buffer B CH_3CN/water 4/1 by vol containing 0.05% TFA, 0−35% B in 30 min, flow rate 3 mL/min) to give 192.6 mg (55% yield) of peptide **4a**. MALDI-TOF (α-cyano-4-hydroxycinnaminic acid, monoisotopic): calcd for $C_{53}H_{82}N_{14}O_{13}S_1$ $[M+H]^+$ 1155.6, found 1155.6.

Synthesis of azaGly Peptides. Solvent A is *tert*-BuOH/water 4/1 by vol containing acetic acid (40 mM final concentration). Solvent B is *tert*-BuOH/100 mM pH = 3.9 acetate buffer 4/1 by vol.

Synthesis of Azaglycine Peptide 5a. Dowex 1 × 4 Cl^- resin (12.81 g, Fluka, 100−200 Mesh, 3.5 mequiv/g) was washed with water (150 mL), MeOH (50 mL), 2.24 M sodium acetate (3 × 200 mL, 3 × 15 min), and finally with water (10 × 100 mL) until the pH of the filtrate was 5−6.

Semicarbazide hydrochloride (51.7 mg) dissolved in water (50 mL) was added to the resin. After 1 h, the resin was filtered and washed with water. The filtrates were combined and lyophilized to give 50 mg of semicarbazide **2a** as the hydrochloride salt.

Semicarbazide **2a** (4.4 mg) was dissolved in solvent B (774 μL) and added to thioester peptide **1a** (22 mg). $AgNO_3$ (5.3 mg) was dissolved in solvent B (400 μL) and added to the above reaction mixture. The reaction was stirred 26 h at rt. The mixture was diluted with water (7 mL) and purified by RP-HPLC (C18 Nucleosil column, rt, detection at 230 nm, buffer A 100% water containing 0.05% TFA, buffer B CH_3CN/water 4/1 by vol containing 0.05% TFA, 0−20% B in 20 min, then 20−70% B in 151 min, flow rate 3 mL/min) to give 9 mg (46% yield) of pure peptide **5a**. MALDI-TOF (α-cyano-4-hydroxy-

cinnaminic acid, monoisotopic): calcd for $C_{47}H_{79}N_{15}O_{13}$ $[M+H]^+$ 1062.6, found 1062.7. ^1H NMR (H_2O/D_2O, 300 MHz): selected NMR data $\delta = 8.65$ (d, 1H, $J = 7.5$ Hz, αNH His[7]), $\delta = 8.47$ (t, 1H, $J = 5.7$ Hz, αNH Gly[8]), $\delta = 8.39$ (d, 1H, $J = 5.7$ Hz, αNH Ala[9]), $\delta = 8.31-8.23$ (m, 4H, αNH Lys[3], Leu[2], Glu[4], Ile[1]), $\delta = 8.12$ (d, 1H, $J = 6.9$ Hz, αNH Val[6]).

Synthesis of Azaglycine Peptides 5b,c, Typical Experimental Procedure for 5b. Camphorsulfonic acid (1.24 mg) was dissolved in solvent A (52 μL). This solution was added to hydrazinocarbonyl peptide **2b** (6.7 mg). This solution was then mixed with thioester peptide **1b** (5.2 mg) dissolved in solvent A (52 μL). $AgNO_3$ dissolved in solvent A (253.3 μL, 4.8 mg/mL) was then added to the reaction mixture, which was stirred 25 h at 18 °C. NaCl (10 mM in water, 714 μL) was added to quench silver ions. The reaction mixture was filtered and purified by RP-HPLC (C18 Nucleosil column, rt, detection at 215 nm, buffer A 100% water containing 0.05% TFA, buffer B CH_3CN/water 4/1 by vol containing 0.05% TFA, 0−15% B in 15 min, then 15−100% B in 283 min, flow rate 3 mL/min) to give 2.5 mg (28% yield) of pure Agly peptide **5b**. MALDI-TOF (α-cyano-4-hydroxycinnaminic acid, monoisotopic): calcd for $C_{93}H_{154}N_{28}O_{25}$ $[M+H]^+$ 2064.2, found 2063.9.

5c was obtained similarly: 2.7 mg (34% yield) of pure Agly peptide **5c**. MALDI-TOF (α-cyano-4-hydroxycinnaminic acid, monoisotopic): calcd for $C_{91}H_{151}N_{27}O_{24}$ $[M+H]^+$ 2007.1, found 2006.9.

Synthesis of Agly Peptide 5d. Acetic hydrazide **3a** (3.25 mg) was dissolved in solvent A (200 μL) and added to phenylthiocarbonyl peptide **4a** (23.3 mg). $AgNO_3$ (5.74 mg) was dissolved in solvent A (200 μL) and added to the reaction mixture. The reaction was stirred 23 h at rt. NaCl (10 mM, 3.4 mL) was added to quench silver ions. The reaction mixture was filtered and purified by RP-HPLC (C18 Nucleosil column, rt, detection at 215 nm, buffer A 100% water containing 0.05% TFA, buffer B CH_3CN/water 4/1 by vol containing 0.05% TFA, 0−10% B in 10 min, then 10−30% B in 30 min, flow rate 6 mL/min) to give 9.7 mg (43% yield) of peptide **5d**. MALDI-TOF (α-cyano-4-hydroxycinnaminic acid, monoisotopic): calcd for $C_{49}H_{82}N_{16}O_{14}$ $[M+H]^+$ 1119.6, found 1119.3.

Synthesis of Agly Peptides 5e,f, Typical Experimental Procedure for 5e. Phenylthiocarbonyl peptide **4a** (10.20 mg) and hydrazide peptide **3b** (21.93 mg) were dissolved in solvent A (200 μL for each peptide) and mixed. $AgNO_3$ (2.54 mg) was dissolved in solvent A (323 μL) and was added to the reaction mixture. The reaction was stirred 27 h at 18 °C. NaCl (10 mM, 1.45 mL) was added to quench silver ions. The reaction mixture was filtered and purified by RP-HPLC (C18 Nucleosil column, rt, detection at 215 nm, buffer A 100% water containing 0.05% TFA, buffer B CH_3CN/water 4/1 by vol containing 0.05% TFA, 0−15% B in 15 min, then 15−35% B in 100 min, flow rate 3 mL/min) to give 9.6 mg (48% yield) of azaglycine peptide **5e**. MALDI-TOF (α-cyano-4-hydroxycinnaminic acid, monoisotopic): calcd for $C_{104}H_{165}N_{31}O_{29}$ $[M+H]^+$ 2313.2, found 2313.1.

5f was obtained similarly: 3 mg (41% yield) of pure phenyl azaglycine peptide **5f**. MALDI-TOF (2,5-dihydroxy-benzoic acid, monoisotopic): calcd for $C_{105}H_{167}N_{31}O_{29}$ $[M+H]^+$ 2327.3, found 2327.3.

Synthesis of Lipopeptides. Solvent C is *tert*-BuOH/water/CH_2Cl_2 80/15/5 by vol acetic acid (40 mM final concentration).

Lipopeptide 9a. Cholesterol derivative **8a** (13.6 mg, 30.8 μmol, 4 equiv) was dissolved in solvent C and added to phenylthiocarbonyl peptide **4a** (10.62 mg, 7.68 μmol, 10 mM, 1 equiv). $AgNO_3$ (2.61 mg, 15.36 μmol, 2 equiv) was dissolved in the same solvent, and this solution was added to the reaction mixture. The reaction was stirred at 18 °C for 24 h and monitored by RP-HPLC on a C3 Zorbax column (0−100% B in 30 min, 1 mL/min, 50 °C, detection at 215 nm). The product was purified on a C3 Zorbax column (0−30% B in 10 min, then 30−70% B in 30 min, 6 mL/min, 70 °C, detection at 215 nm) and lyophilized to give 5.1 mg (39%) of lipopeptide **9a** as a white powder.

RP-HPLC purity (C3 Zorbax, 50 °C, detection at 215 nm) >99%, MALDI-TOF (α-cyano-4-hydroxycinnaminic acid, monoisotopic): calcd for $C_{75}H_{124}N_{16}O_{15}$ $[M+H]^+$ 1489.95, found 1490.0, CZE purity citrate buffer (15 min, 15 kV) >99%.

Lipopeptide 9b. Oleyl hydrazide **8b** (9.06 mg, 29.4 μmol, 4 equiv) was dissolved in solvent C and added to phenylthiocarbonyl peptide **4a** (10.17 mg, 7.35 μmol, 10 mM, 1 equiv). $AgNO_3$ (2.54 mg, 14.7 μmol, 2 equiv) was dissolved in the same solvent, and this solution was added to the reaction mixture. The reaction was stirred at 18 °C for 18 h and monitored by RP-HPLC on a C3 Zorbax column (0−100% B in 30 min, 1 mL/min, 50 °C, detection at 215 nm). The product was purified on a C3 Zorbax column (0−30% B in 10 min, then 30−70% B in 30 min, 6 mL/min, 70 °C, detection at 215 nm) and lyophilized to give 4.1 mg (36%) of lipopeptide **9b** as a white powder.

RP-HPLC purity (C3 Zorbax, 50 °C, detection at 215 nm) >99%, MALDI-TOF (α-cyano-4-hydroxycinnaminic acid, monoisotopic): calcd for $C_{65}H_{112}N_{16}O_{14}$ $[M+H]^+$ 1341.86, found 1341.9, CZE purity citrate buffer (15 min, 15 kV) >99%.

Lipopeptide 9c. Linoleyl hydrazide **8c** (9.2 mg, 31.2 μmol, 4 equiv) was dissolved in solvent C and added to phenylthiocarbonyl peptide **4a** (10.78 mg, 7.8 μmol, 10 mM, 1 equiv). $AgNO_3$ (2.65 mg, 15.6 μmol, 2 equiv) was dissolved in the same solvent, and this solution was added to the reaction mixture. The reaction was stirred at 18 °C for 18 h and monitored by RP-HPLC on a C3 Zorbax column (0−100% B in 30 min, 1 mL/min, 50 °C, detection at 215 nm). The product was purified on a C3 Zorbax column (0−30% B in 10 min, then 30−70% B in 30 min, 6 mL/min, 70 °C, detection at 215 nm) to give 4.02 mg (33%) of lipopeptide **9c** as a white powder.

RP-HPLC purity (C3 Zorbax, 50 °C, detection at 215 nm) >99%, MALDI-TOF (α-cyano-4-hydroxycinnaminic acid, monoisotopic): calcd for $C_{65}H_{110}N_{16}O_{14}$ $[M+H]^+$ 1339.84, found 1340.00, CZE purity citrate buffer (15 min, 15 kV) >99%.

RESULTS AND DISCUSSION

The formation of peptide bonds by reaction of α-amino groups with silver ion activated thioacids or thioesters has been studied in detail in the past (*18*−*20*). Thus far, segment couplings were performed essentially with partially protected peptide fragments to avoid competing reactions ε-amino groups of Lys residues (*19*, *20*). In addition, peptide thioesters with a C-terminal Gly residue were the most frequently used ones for segment coupling, because silver ion activation of the thioester usually results in the partial racemization of the C-terminal residue. More recently, Tam et al. reported the synthesis of cyclic peptides using unprotected precursors and silver-activated thioesters for macrocyclization (*21*). The ratio of α/ε-lactamization was highly dependent on the N-terminal amino acid and partial racemization of C-terminal amino acid was also observed.

We hypothesized that the sulfur atom of peptides **1** or **4** and hydrazino group of peptides **2** or **3** (Scheme 1) might simultaneously complex a silver ion. Silver ion was expected to favor Agly bond formation by placing the reactive ends of the peptide fragments in close proximity and by activating the thiocarbonyl moiety. Interestingly, the pK_as of acetylhydrazine and semicarbazide are 3.24 and 3.65, respectively. The reaction could be thus envisaged below pH 5, the threshold pH above which the ε-amino groups of Lys residues usually compete in such reactions (*22*), opening the possibility of forming the Agly bond starting from unprotected peptide precursors. Because silver ion complex formation is known to be favored in apolar solvents,

Table 1. Synthesis of Agly-Peptides by Ligating Peptide Thioesters with Hydrazinocarbonyl Peptides (Path A)[a]

entry	Peptide-SR R = $(CH_2)_nNHSO_2(CH_2)_3CONH_2$	H_2NNHCO-peptide	Agly peptide	yield[b] (rac.)[c]
1	**1a** Ac-ILKEPVHGA-SR, $n = 2$	**2a** $H_2NNHCO-NH_2$	**5a** Ac-ILKEPVHGAazaG-NH_2	46
2	**1b** Ac-ILKEPVHGA-SR, $n = 3$	**2b** H_2NNHCO-GILKEPVHGA-NH_2	**5b** Ac-ILKEPVHGAazaGGILKEPVHGA-NH_2	28 (30)
3	**1b** Ac-ILKEPVHGA-SR, $n = 3$	**2c** H_2NNHCO-ILKEPVHGA-NH_2	**5c** Ac-ILKEPVHGAazaGILKEPVHGA-NH_2	34 (39)

[a] Conditions: Peptide **1** (**1a** 13 mM, **1b** 10 mM), peptide **2** (**2a** 2 equiv, **2b**,**c** 1.5 equiv), and $AgNO_3$ (2 equiv) in tBuOH/water 4/1 by vol containing 40 mM of AcOH (18 °C, 23−27 h). **2b**,**c** were purified by RP-HPLC using a water/acetonitrile gradient buffered at pH 6.5 with triethylamonium acetate. 1.5 equiv of camphorsulfonic acid was added with peptide **2b**,**c** to avoid the increase in pH due to the basicity of peptides **2**. [b] Isolated yield (%) after RP-HPLC purification. [c] Percent of racemization of Ala residue in bold is indicated in parentheses.

Scheme 2. Synthesis of Hydrazinocarbonyl Peptides 2 and of Phenylthiocarbonyl Peptides 4

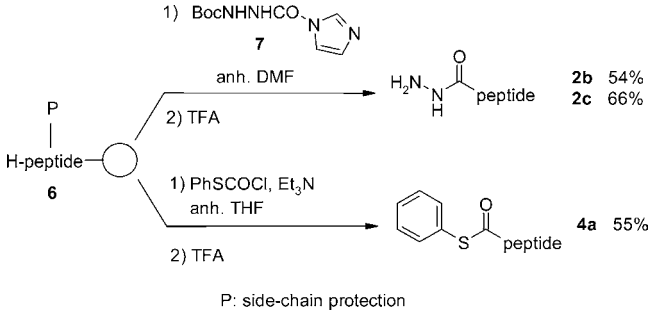

we examined the interest of *t*BuOH/water mixture for the reaction, since this solvent has been already used for the solubilization of large unprotected peptide fragments (*22*, *23*).

Peptides used in this study feature a Lys residue within their sequence to document the chemoselectivity of the reaction. Thioesters **1** (Table 1) were prepared using the Kenner sulfonamide linker and a solid-phase N,S-acyl shift as described elsewhere (*17*). The synthesis of peptides **2**, i.e., peptides modified at the N-terminus by an Agly residue, was not described to the best of our knowledge (Scheme 2). Usually, once introduced, the Agly residue is acylated on the solid phase before deprotection and cleavage from the resin to give an azapeptide with an internal Agly residue. The synthesis of **2b**,**c** was performed by coupling Boc-Agly imidazole **7** to the peptidyl resin assembled using Fmoc/*t*-Bu strategy (Scheme 2). Hydrazinocarbonyl peptides **2b**,**c** were found to be stable during TFA deprotection and cleavage. Complete hydrolysis of hydrazinoacetyl moiety occurred, however, within minutes during RP-HPLC purification at pH 2 in a water/acetonitrile gradient containing TFA. Alternately, increasing the pH of the eluent from 2 to 6.5 by switching to triethylamonium acetate buffer permitted successful isolation of the target peptides **2b**,**c**. These peptides were stored at −20 °C and were found to be stable for months.

In a first approach, the reaction between thioester **1a** and semicarbazide **2a** (acetate salt) in AcONa pH 3.9/*t*BuOH 1/4 was examined (Table 1, entry 1). The reaction proceeded efficiently and chemoselectively to yield Agly peptide with 46% yield. Hydrolysis of thioester **1a** was negligible. No reaction occurred with semicarbazide hydrochloride, showing the importance of free silver ions for the ligation to proceed. This encouraging result led us to examine the reaction between thioester **1b** and hydrazinocarbonyl peptide **2b**. In this case, similar experimental conditions led to poor results (16% RP-HPLC yield) due to lack of selectivity and significant peptide thioester hydrolysis.

The lower nucleophilicity of the hydrazinocarbonyl moiety of peptide **2b** relative to semicarbazide **2a**, due to the electron withdrawing effect of the peptide chain, might explain this result. Lowering the apparent pH (pH_{app}) of the acetate buffer/*t*BuOH mixture was envisioned as a way to improve the selectivity of the reaction and to minimize thioester hydrolysis. In this context, the influence of *t*BuOH on pH_{app} was examined. The pH_{app} of

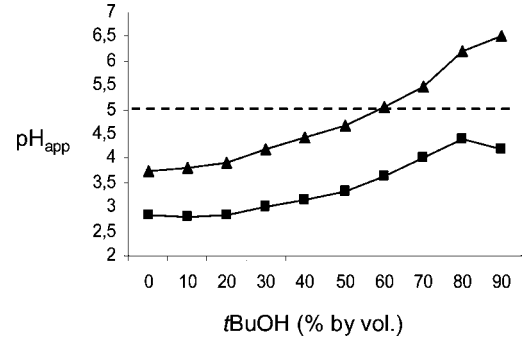

Figure 1. Effect of *t*BuOH on pH_{app} at 18 °C (triangles, 40 mM sodium acetate buffer pH 3.7; squares, 40 mM acetic acid). The horizontal dotted line represents the threshold above which the selectivity of the ligation is affected by the nucleophilicity of ε-amino groups of Lys residues.

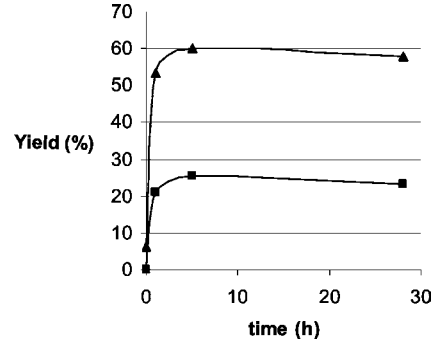

Figure 2. Ligation between peptide hydrazide **3c** and phenylthiocarbonyl peptide **4a** (see Table 2 for experimental conditions). RP-HPLC yield for the ligation product **5f** (triangles) or peptide H-GILKEPVHGA-NH_2 (squares) arising from the hydrolysis of **4a**. RP-HPLC of the crude reaction mixture can be found in Supporting Information.

acetate buffer increases by addition of an organic solvent (*24*, *25*). The impact of the drift of pH_{app} induced by the organic solvent on the selectivity of the silver ion-assisted peptide bond formation has not been discussed in the literature. Figure 1 shows indeed that addition of *t*BuOH up to 80% by vol to a pH 3.7 AcONa buffer results in an increase of pH_{app} of ∼2.5 pH units. Consequently, pH_{app} is ∼1.2 pH units above pH 5, the threshold of selectivity. Obviously such a large increase in pH_{app} might be responsible for the loss of selectivity and thioester hydrolysis observed in the preliminary experiment above.

Alternately, the pH_{app} of a 40 mM acetic acid solution in the presence of *t*BuOH remains below the threshold pH of 5 even for the highest *t*BuOH concentrations tested. This solvent mixture was thus selected for the rest of the study. In addition, 1.5 equiv of camphorsulfonic acid was added with peptide **2b**,**c** to avoid the increase in pH due to the basicity of peptides **2**. Ligation between **1b** and **2b** or **2c** using these optimized experimental conditions proceeded efficiently to give Agly peptides **5b** or **5c** with 28−34% yield after purification. The major side reaction was peptide thioester hydrolysis (15% by RP-HPLC). Peptide **5b** was trypsinized and analyzed by MALDI-TOF spectrometry. Three fragments were detected as

Table 2. Synthesis of Agly-Peptides by Ligating Peptide Hydrazides with Phenylthiocarbonyl Peptides (Path B)[a]

entry	Peptide-$NHNH_2$	PhSCO-peptide	Agly peptide	yield[b] (rac.)[c]
1	**3a** Ac-$NHNH_2$	**4a** PhSCO-GILKEPVHGA-NH_2	**5d** Ac-azaGGILKEPVHGA-NH_2	43
2	**3b** Ac-FSLKEPAVHQG-$NHNH_2$	**4a** PhSCO-GILKEPVHGA-NH_2	**5e** Ac-FSLKEPAVHQGazaGGILKEPVHGA-NH_2	48
3	**3c** Ac-FSLKEPAVHQA-$NHNH_2$	**4a** PhSCO-GILKEPVHGA-NH_2	**5f** Ac-FSLKEPAVHQAazaGGILKEPVHGA-NH_2	41 (0)

[a] Conditions: **3a**−**c** (2 equiv), peptide **4a** (10 mM), and $AgNO_3$ (2 equiv) in tBuOH/water 4/1 by vol containing 40 mM of AcOH (18 °C, 23−27 h). [b] Isolated yield (%) after RP-HPLC purification. [c] Percent of racemization of Ala residue in bold is indicated in parentheses.

Scheme 3. Synthesis of Lipopeptides Using Agly Ligation between Lipid Hydrazides 8a−c and Phenylthiocarbonyl Peptide 4a

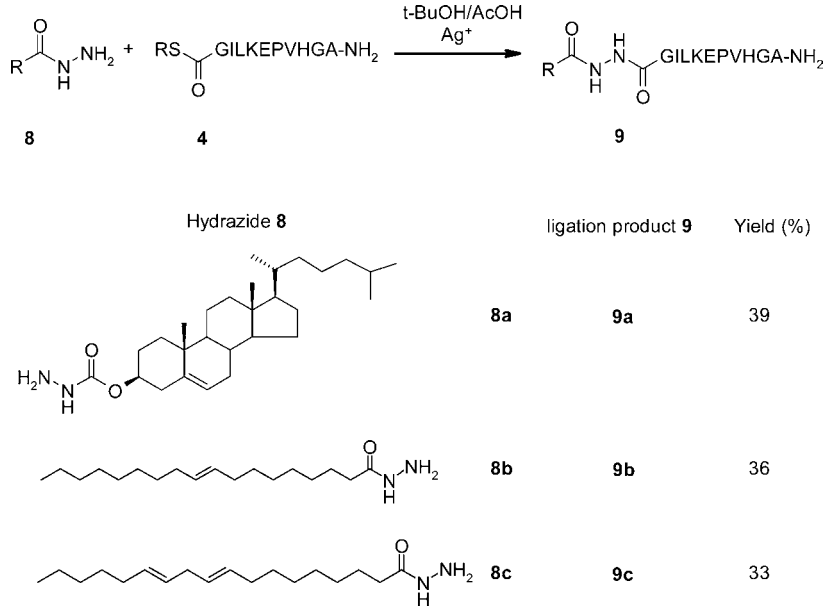

expected. Their sequence was confirmed by postsource decay analysis. GC-MS amino acid analysis of peptides **5b** and **5c** after hydrolysis in 6 N DCl in D_2O showed, however, 30% and 39% of racemization, respectively, for the Ala residue originally at the C-terminus of thioester fragment **1b** (*26*). The extent of racemization using path A (Scheme 1) led us to explore path B as an alternative strategy.

Phenylthiocarbonyl peptide **4a** was prepared as shown in Scheme 2 by reacting commercially available phenylthiochloroformate with the corresponding peptidyl resin assembled using the Fmoc/*t*Bu strategy (*27*). C-terminal peptide hydrazides **3** were synthesized by hydrazinolysis of a deprotected peptide assembled on an HMBA resin (*28*). This method gives access to peptide hydrazides without racemization of the C-terminal amino acid.

In a preliminary experiment, peptide **4a** was reacted with acetylhydrazide **3a** using again 40 mM acetic acid in *t*BuOH/water: 4/1 by vol. as the solvent mixture. Reaction proceeded cleanly to give Agly peptide **5d** with 43% yield. No reaction or degradation occurred in the absence of silver ions, showing as for path A the importance of silver ions for the ligation to proceed. Ligation between peptide hydrazide **3b** and phenylthiocarbonyl peptide **4a** was performed likewise. Because peptide hydrazides were purified using a pH 2 water/acetonitrile gradient, no increase in pH due to peptides **3** was observed, and consequently, addition of camphorsulfonic acid was not required. These experimental conditions led to the chemoselective formation Agly peptide **5e** (48% yield). Likewise, ligation between peptide hydrazides **3c** and **4a** gave Agly peptide **5f** with 41% yield. The unique side reaction observed was the hydrolysis of phenylthiocarbonyl peptide which amounted to 22% (see Supporting Information for RP-HPLC of the crude reaction mixture). Degradation of phenylthiocarbonyl peptide **4a** into the corresponding hydantoin was not observed. Figure 2 shows the time course of the reaction, which was almost complete after 1 h. GC-MS amino acid analysis of **5f** after hydrolysis in 6 N DCl in D_2O confirmed as expected the absence of racemization for Ala residue present originally at the C-terminus of peptide hydrazide **3c**. Finally, all the Agly peptides synthesized in this study were trypsinized and analyzed by MALDI-TOF spectrometry. All the observed fragments were consistent with the proposed structures (see Supporting Information).

AzaGly ligation between a peptide hydrazide and a phenylthiocarbonyl peptide has been shown to be an efficient method for assembling azaGly peptides starting from unprotected peptide fragments. Because a large diversity of hydrazides are commercially available or can be synthesized easily starting from carboxylic acids, azaGly ligation was also envisioned as an interesting method for the modification of peptides by various acyl moieties. The method is particularly useful for incorporating sensitive acyl moieties that cannot survive the experimental conditions used during the solid-phase peptide synthesis. To illustrate the usefulness of azaGly ligation for the synthesis of such conjugates, we have examined the assembly of lipopeptides by reacting phenylthiocarbonyl peptide **4a** with a series of lipid hydrazides derived from cholesterol (**8a**) or C18 unsaturated fatty acids (**8b**,**c**) (Scheme 3). Hydrazides **8a**−**c** feature one or two carbon−carbon double bonds within their structure, which are not compatible with the acid treatment used for deprotecting the peptide chain after the solid-phase peptide elongation step (*22*, *23*, *29*).

Experimental conditions used for the synthesis of Agly peptides were modified to allow the solubilization of the lipid hydrazides. Addition of only 5% by vol of methylene chloride to the *t*BuOH/water solvent mixture permitted the solubilization of both the lipid hydrazides and of the phenylthiocarbonyl peptide **4a**. Ligation proceeded successfully in the presence of silver ions as above. Lipopeptides **9a**−**c** were isolated with a 33−39% yield following RP-HPLC purification. This modest

yield is understandable given the scale of synthesis, the low solubility of lipopeptides in aqueous media, and the known difficulty to purify lipopeptides by RP-HPLC.

CONCLUSIONS

Two strategies were explored for the chemoselective assembly of Agly peptides. The first one, based on the silver ion-assisted reaction between C-terminal peptide thioesters and hydrazinocarbonyl peptides, resulted in the significant racemization of the C-terminal amino acid from the thioester fragment. The second one, based on the silver ion-assisted coupling of C-terminal peptide hydrazides with N-terminal phenylthiocarbonyl peptides, gave better yields and no racemization. The reaction was performed in a *t*BuOH/water mixture, and the control of apparent pH permitted the chemoselective formation of the azaGly bond in the presence of lysine residues. They show also that azaGly ligation can be used for the assembly of lipopeptides, by reacting lipid hydrazides with phenylthiocarbonyl peptides in the presence of silver ions. This ligation method allows incorporation of acid-sensitive lipid moieties that are incompatible with standard solid-phase peptide synthesis procedures.

ACKNOWLEDGMENT

We gratefully acknowledge financial support from CNRS, Université de Lille 1 and 2, Institut Pasteur de Lille, Région Nord Pas de Calais, the European Community, and from Cancéropôle Nord-Ouest. We thank Hervé Drobecq for MALDI-TOF mass spectra and Gérard Montagne for NMR experiments. This research was performed using the Chemistry Systems Biology platform (http://csb.ibl.fr).

Supporting Information Available: Characterization data for all compounds. This material is available free of charge via the Internet at http://pubs.acs.org.

LITERATURE CITED

(1) Gante, J. (1966) Peptide and azapeptide synthesis by means of a new N-activated amino acid derivative. *Chem. Ber. 99*, 1576–9.
(2) Gante, J. (1989) *Synthesis* 405–413.
(3) Lee, H. J., Park, H. M., and Lee, K. B. (2007) The beta-turn scaffold of tripeptide containing an azaphenylalanine residue. *Biophys. Chem. 125*, 117–26.
(4) Didierjean, C., Del Duca, V., Benedetti, E., Aubry, A., Zouikri, M., Marraud, M., and Boussard, G. (1997) X-ray structures of aza-proline-containing peptides. *J. Pept. Res. 50*, 451–7.
(5) Zouikri, M., Vicherat, A., Aubry, A., Marraud, M., and Boussard, G. (1998) Azaproline as a beta-turn-inducer residue opposed to proline. *J. Pept. Res. 52*, 19–26.
(6) Jean, F., Melnyk, O., and Tartar, A. (1995) One-pot synthesis of dissymmetrical 4,6-disubstituted dibenzofurans. *Tetrahedron Lett. 36*, 7657–7660.
(7) Dutta, A. S., Furr, B. J. A., Giles, M. B., and Morley, J. S. (2008) Synthesis and biological activity of alpha-azapeptides: alpha-aza-analogs of luteinizing hormone releasing hormone. *Clin. Endocrinol. 5*, s291−s298.
(8) Wipf, P., Li, W., Adeyeye, C. M., Rusnak, J. M., and Lazo, J. S. (1996) Synthesis of chemoreversible prodrugs of ara-C with variable time-release profiles. Biological evaluation of their apoptotic activity. *Bioorg. Med. Chem. 4*, 1585–1596.
(9) Din, H., Gray, C. J., Ireson, J. C., and McDonald, R. (1991) Inhibition of trypsin by t-butyloxycarbonyl-alpha-aza-(4-aminophenyl)alanine phenyl ester. *J. Chem. Technol. Biotechnol. 50*, 181–9.
(10) Wieczerzak, E., Jankowska, E., Rodziewicz-Motowidlo, S., Gieldon, A., Lagiewka, J., Grzonka, Z., Abrahamson, M., Grubb, A., and Bromme, D. (2005) Novel azapeptide inhibitors of cathepsins B and K. Structural background to increased specificity for cathepsin B. *J. Pept. Res. 66* (1), 1–11.
(11) Wieczerzak, E., Rodziewicz-Motowidlo, S., Jankowska, E., Gieldon, A., and Ciarkowski, J. (2007) An enormously active and selective azapeptide inhibitor of cathepsin B. *J. Pept. Sci. 13*, 536–43.
(12) Wieczerzak, E., Drabik, P., Lankiewicz, L., Oldziej, S., Grzonka, Z., Abrahamson, M., Grubb, A., and Bromme, D. (2002) Azapeptides structurally based upon inhibitory sites of cystatins as potent and selective inhibitors of cysteine proteases. *J. Med. Chem. 45*, 4202–11.
(13) Liley, M., and Johnson, T. (2000) Solid phase synthesis of azapeptides utilising reversible amide bond protection to prevent hydantoin formation. *Tetrahedron Lett. 41*, 3983–3985.
(14) Melendez, R. E., and Lubell, W. D. (2004) Aza-amino acid scan for rapid identification of secondary structure based on the application of N-Boc-aza(1)-dipeptides in peptide synthesis. *J. Am. Chem. Soc. 126*, 6759–64.
(15) Boeglin, D., and Lubell, W. D. (2005) Aza-amino acid scanning of secondary structure suited for solid-phase peptide synthesis with fmoc chemistry and aza-amino acids with heteroatomic side chains. *J. Comb. Chem. 7*, 864–78.
(16) Bourguet, C. B., Sabatino, D., and Lubell, W. D. (2008) Benzophenone semicarbazone protection strategy for synthesis of aza-glycine containing aza-peptides. *Biopolymers*.
(17) Ollivier, N., Behr, J. B., El-Mahdi, O., Blanpain, A., and Melnyk, O. (2005) Fmoc solid-phase synthesis of peptide thioesters using an intramolecular *N, S*-acyl shift. *Org. Lett. 7*, 2647–50.
(18) Blake, J. (1981) Peptide segment coupling in aqueous medium: silver ion activation of the thiolcarboxyl group. *Int. J. Pept. Protein Res. 17*, 273–4.
(19) Hojo, H., and Aimoto, S. (1991) Polypeptide synthesis using the S-alkyl thioester of a partially protected peptide segment. Synthesis of the DNA-binding domain of c-Myb protein (142−193)-NH2. *Bull. Chem. Soc. Jpn. 64*, 111–117.
(20) Aimoto, S. (1999) Polypeptide synthesis by the thioester method. *Biopolymers 51*, 247–65.
(21) Zhang, L., and Tam, J. P. (1997) Lactone and lactam library synthesis by silver ion-assisted orthogonal cyclization of unprotected peptides. *J. Am. Chem. Soc. 121*, 3311–3320.
(22) Bonnet, D., Ollivier, N., Gras-Masse, H., and Melnyk, O. (2001) Chemoselective acylation of fully deprotected hydrazino acetyl peptides. Application to the synthesis of lipopetides. *J. Org. Chem. 66*, 443–9.
(23) Bonnet, D., Rommens, C., Gras-Masse, H., and Melnyk, O. (2000) Chemoselective acylation of hydrazinopeptides: a novel and mild method for the derivatization of peptides with sensitive fatty acids. *Tetrahedron Lett. 41*, 45–48.
(24) Mukerjee, P., and Ostrow, J. D. (1998) Effects of added dimethylsulfoxide on pK[alpha] values of uncharged organic acids and pH values of aqueous buffers. *Tetrahedron Lett. 39*, 423–426.
(25) Homandberg, G. A., Mattis, J. A., and Laskowski, M., Jr. (1978) Synthesis of peptide bonds by proteinases Addition of organic cosolvents shifts peptide bond equilibria toward synthesis. *Biochemistry 17*, 5220–7.
(26) Amelung, W., and Brodowski, S. (2002) In vitro quantification of hydrolysis-induced racemization of amino acid enantiomers in environmental samples using deuterium labeling and electron-impact ionization mass spectrometry. *Anal. Chem. 74*, 3239–46.
(27) Besret, S., Ollivier, N., Blanpain, A., and Melnyk, O. (2008) Thiocarbamate-linked peptides by chemoselective peptide ligation. *J. Pept. Sci. 14*, 1244–50.
(28) Mellor, S. L., Wellings, D. A., Fehrentz, J.-A., Paris, M., Martinez, J., Ede, N. J., Bray, A. M., Evans, D. J., and Bloomberg, G. B. (2000) *Synthesis of modified peptides in Fmoc*

solid phase peptide synthesis: a practical approach (Chan, W. C. and White, P. D., Eds.) pp 147−148, Oxford University Press, Oxford.

(29) Bourel-Bonnet, L., Bonnet, D., Malingue, F., Gras-Masse, H., and Melnyk, O. (2003) Simultaneous lipidation of a characterized peptide mixture by chemoselective ligation. *Bioconjugate Chem 14*, 494–9.

BC9000195

Silver-catalyzed azaGly ligation. Application to the synthesis of azapeptides and of lipid-peptide conjugates

Nathalie Ollivier, Soizic Besret, Annick Blanpain and Oleg Melnyk
UMR 8161-CNRS-Université de Lille 1 et 2, Institut Pasteur de Lille, IFR 142, 1 rue du Pr Calmette, 59021 Lille, France

Supporting Information

Table of Contents

Analytical data for thioester peptide 1a **S-3**
RP-HPLC S-3
MALDI-TOF S-4
CZE S-5

Analytical data for thioester peptide 1b **S-7**
RP-HPLC S-7
MALDI-TOF S-8
CZE S-9

Analytical data for hydrazinocarbonyl peptide 2b **S-11**
RP-HPLC S-11
MALDI-TOF S-12
CZE S-13

Analytical data for hydrazinocarbonyl peptide 2c **S-15**
RP-HPLC S-15
MALDI-TOF S-16
CZE S-17

Analytical data for Agly-peptide 5a **S-19**
RP-HPLC S-19
MALDI-TOF S-21
CZE S-22
^{1}H NMR S-24
HSQC S-27
HMBC S-29
TOCSY S-33
Trypsic digestion spectra S-37

Analytical data for Agly-peptide 5b **S-38**
RP-HPLC S-38
MALDI-TOF S-39

CZE S-40
Trypsic digestion spectra S-42

Analytical data for Agly-peptide 5c **S-43**
RP-HPLC S-43
MALDI-TOF S-44
CZE S-45
Trypsic digestion spectra S-47

Analytical data for hydrazide peptide 3b **S-48**
RP-HPLC S-48
MALDI-TOF S-49
CZE S-50

Analytical data for hydrazide peptide 3c **S-52**
RP-HPLC S-52
MALDI-TOF S-53
CZE S-54

Analytical data for phenylthiocarbonyl peptide 4a **S-56**
RP-HPLC S-56
MALDI-TOF S-57
CZE S-58

Analytical data for Agly-peptide 5d **S-60**
RP-HPLC S-60
MALDI-TOF S-61
CZE S-62
Trypsic digestion spectra S-64

Analytical data for Agly-peptide 5e **S-65**
RP-HPLC S-65
MALDI-TOF S-66
CZE S-67
Trypsic digestion spectra S-69

Analytical data for Agly-peptide 5f **S-70**
RP-HPLC of the crude reaction mixture S-70
RP-HPLC S-71
MALDI-TOF S-72
CZE S-73
Trypsic digestion spectra S-75

Analytical data for lipopeptide 9a **S-76**
RP-HPLC S-76
MALDI-TOF S-77
CZE S-78

Analytical data for lipopeptide 9b **S-79**
RP-HPLC S-79

MALDI-TOF S-80
CZE S-81

Analytical data for lipopeptide 9c **S-82**
RP-HPLC S-82
MALDI-TOF S-83
CZE S-84

Analytical data for thioester peptide **1a**

- RP-HPLC, C18 nucleosil column, 1mL/min, λ=215 nm, 0-100% B in 60 min, 30°C

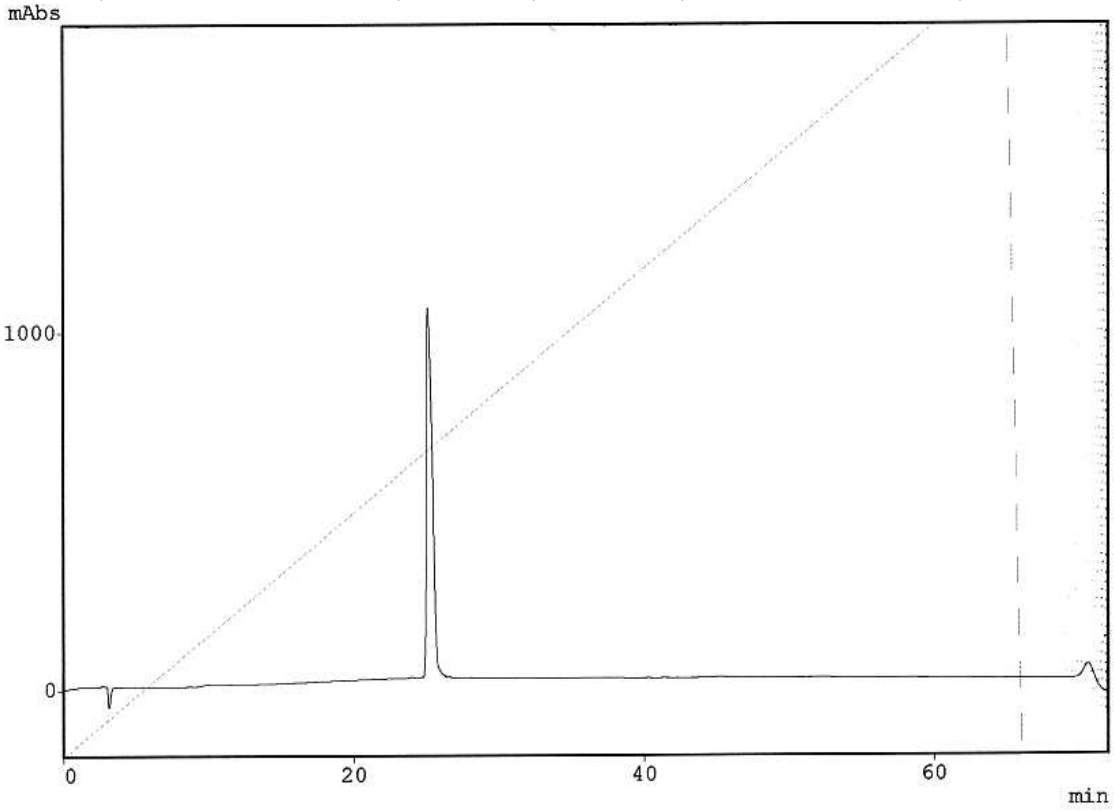

*** Peak Report ***

TIME	AREA	HEIGHT	CONC	PKNO
25.106	29296741	1031607	99.9514	1
26.584	14256	1622	0.0486	2
	29310996	1033229	100.0000	

- MALDI-TOF α-cyano-4-hydroxy-cinnaminic acid matrix

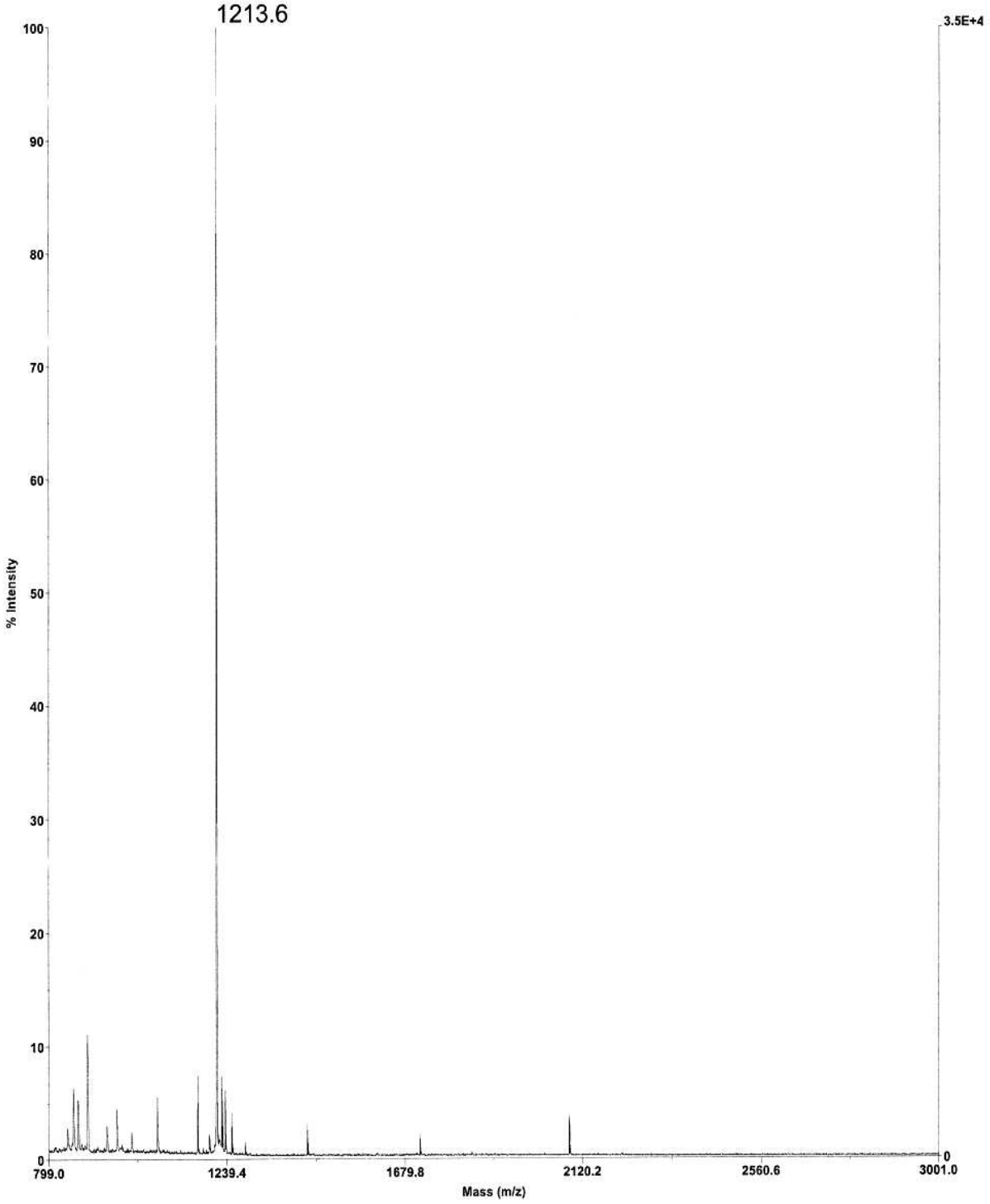

- CZE pH=3 sodium citrate buffer

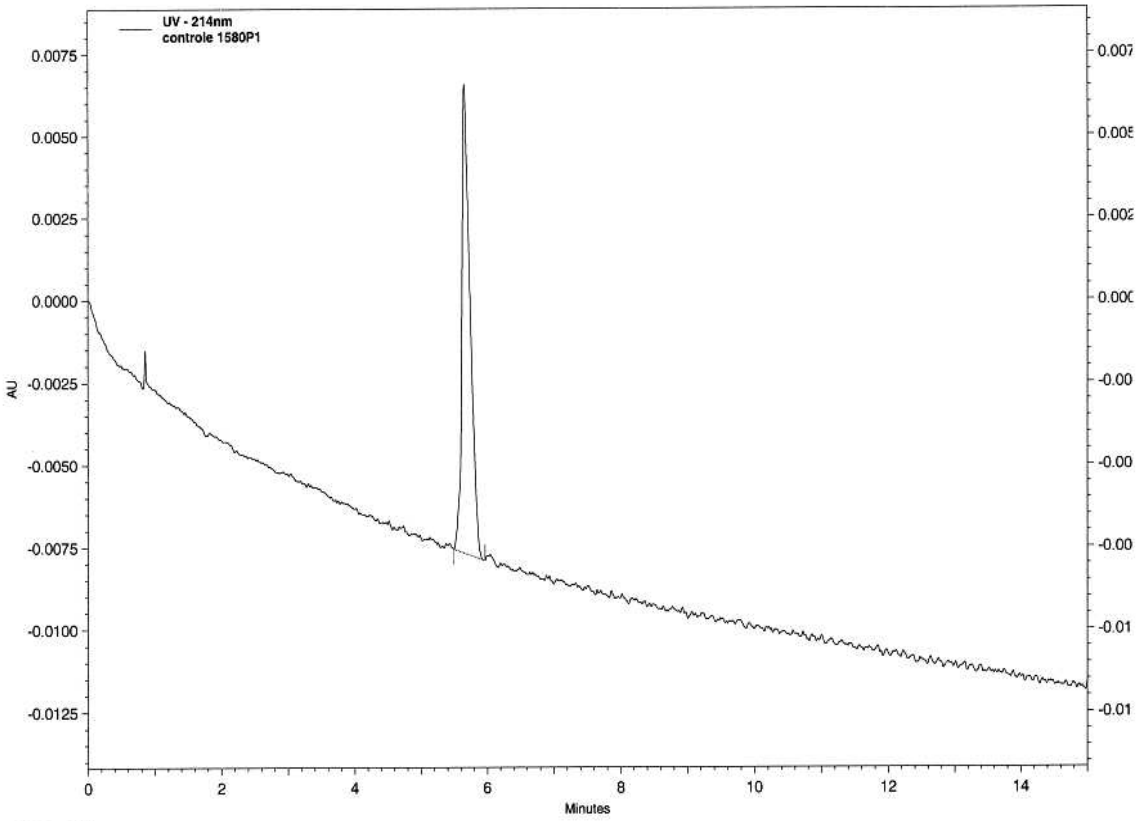

UV - 214nm
Results

Time	Area	Area %	Corrected Area	Corrected Area Percent
5.646	123575	100.00	7296	100.00
Totals	123575	100.00	7296	100.00

- CZE pH=4.5 sodium acetate buffer

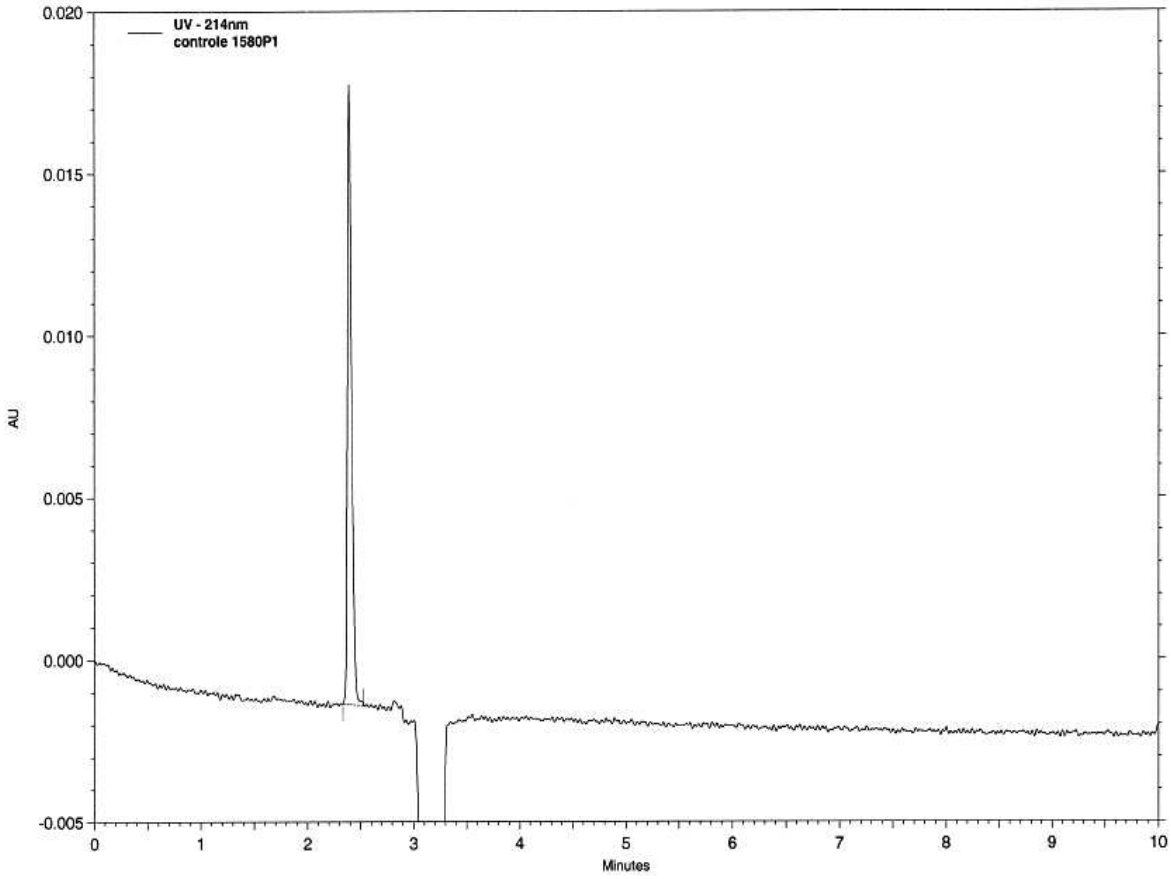

UV - 214nm
Results

Time	Area	Area %	Corrected Area	Corrected Area Percent
2.392	53206	100.00		
Totals	53206	100.00		

Analytical data for thioester peptide **1b**

- RP-HPLC, C18 nucleosil column, 1mL/min, λ=215 nm, 0-100% B in 30 min, 30°C

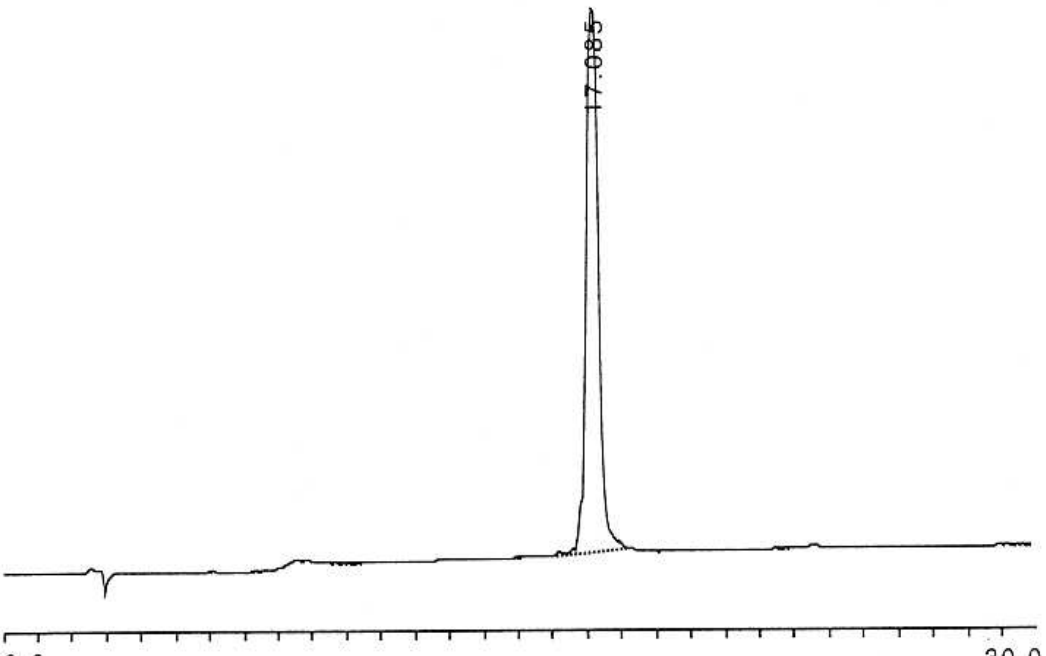

Analysis: Channel A

Peak No.	Time	Type	Height(μV)	Area(μV-sec)	Area%
	16.185	N1	1019	8918	0.223
1	17.085	N2	190987	3975885	99.776
Total Area				3984803	99.999

- MALDI-TOF α-cyano-4-hydroxy-cinnaminic acid matrix

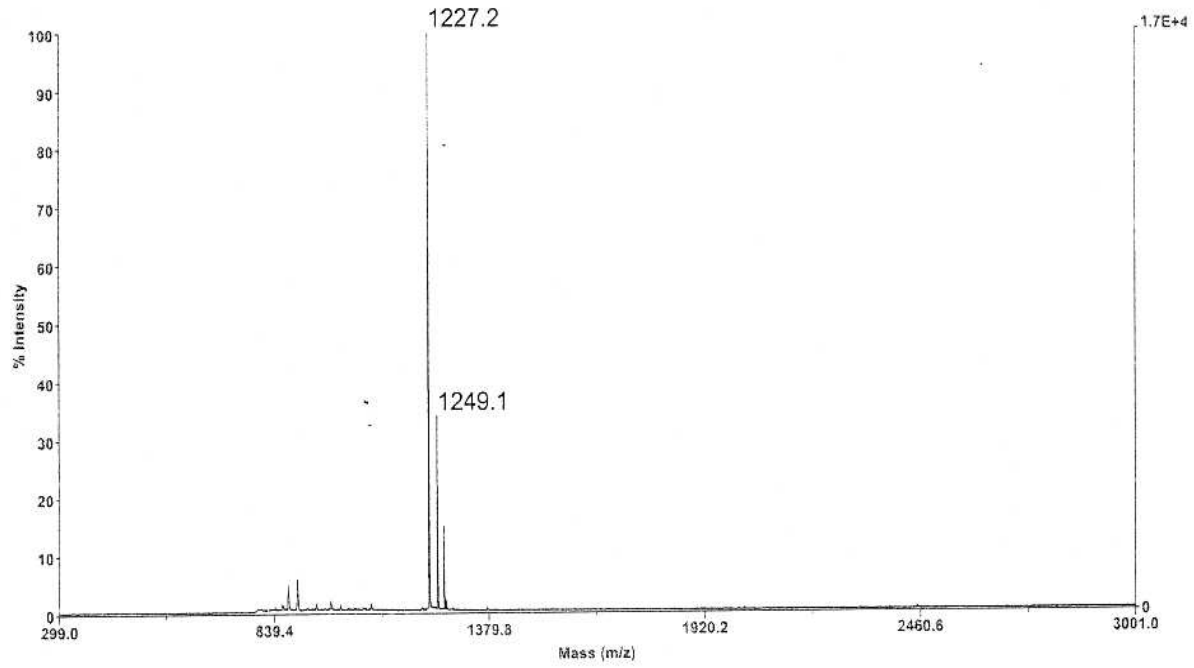

- CZE pH=3 sodium citrate buffer

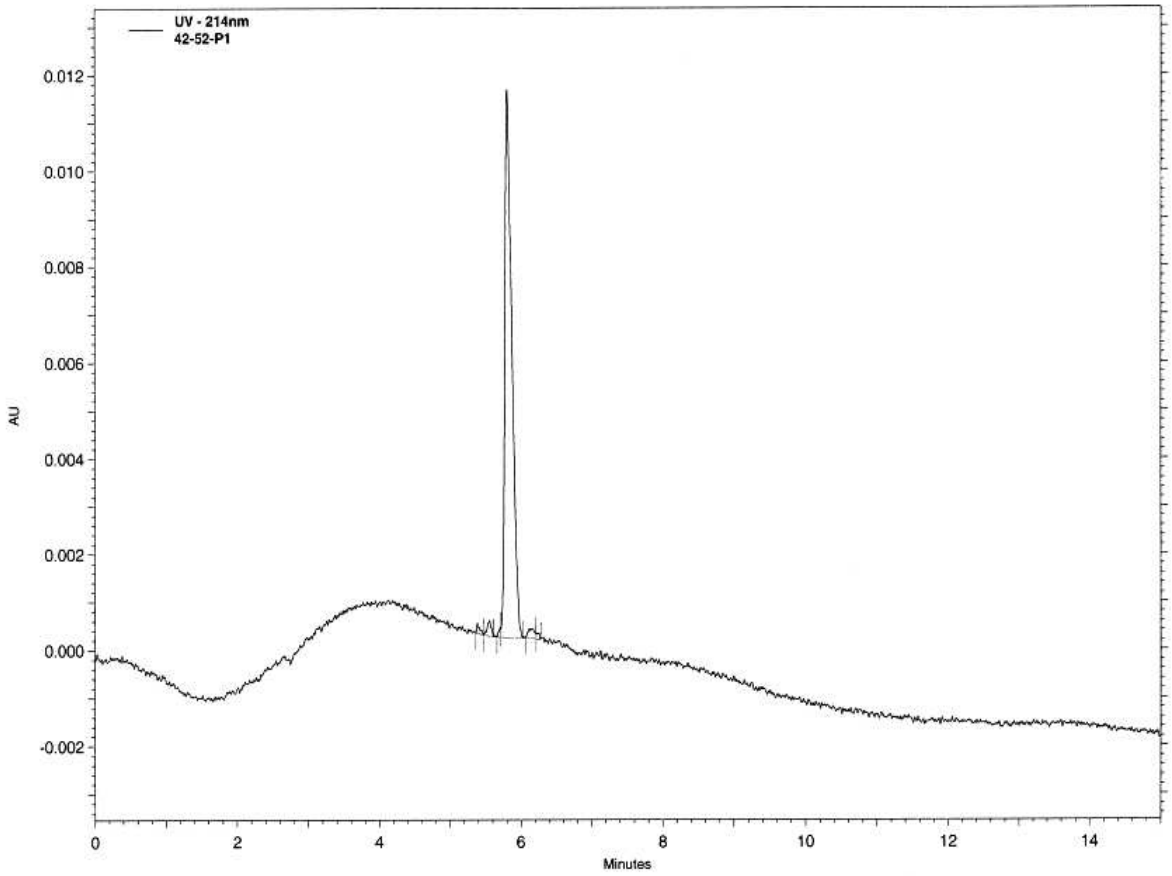

UV - 214nm
Results

Time	Area	Area %	Corrected Area	Corrected Area Percent
5.388	635	0.78		
5.558	1237	1.51		
5.704	408	0.50		
5.796	77971	95.24		
6.117	1233	1.51		
6.229	382	0.47		
Totals	81 866	100		

- CZE pH=4.5 sodium acetate buffer

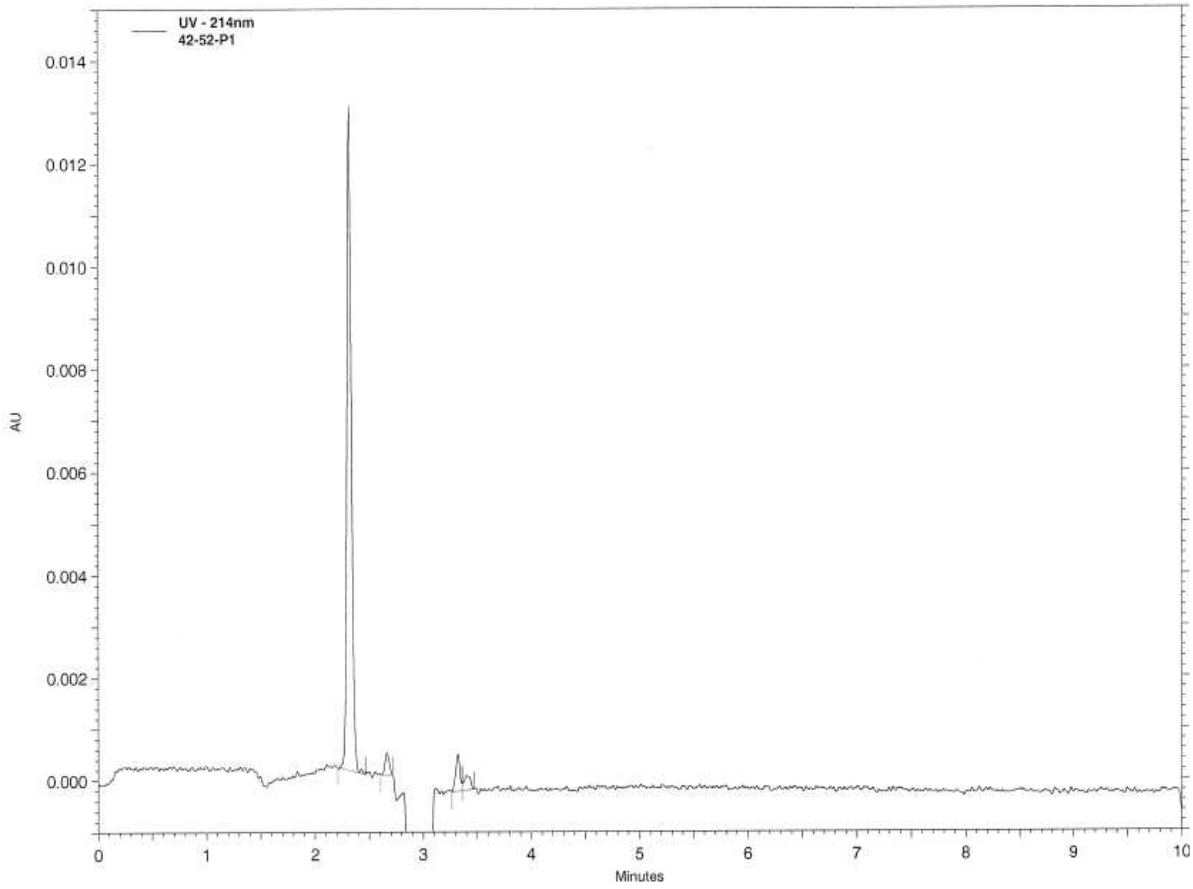

UV - 214nm
Results

Time	Area	Area %	Corrected Area	Corrected Area Percent
2.313	37819	89.97		
2.663	1095	2.60		
3.321	1932	4.60		
3.400	1191	2.83		
Totals	42037	100.00		

Analytical data for hydrazinocarbonyl peptide **2b**

- RP-HPLC, C18 deltapak column, 1mL/min, λ=215 nm, 0-100% B in 60 min, 25°C

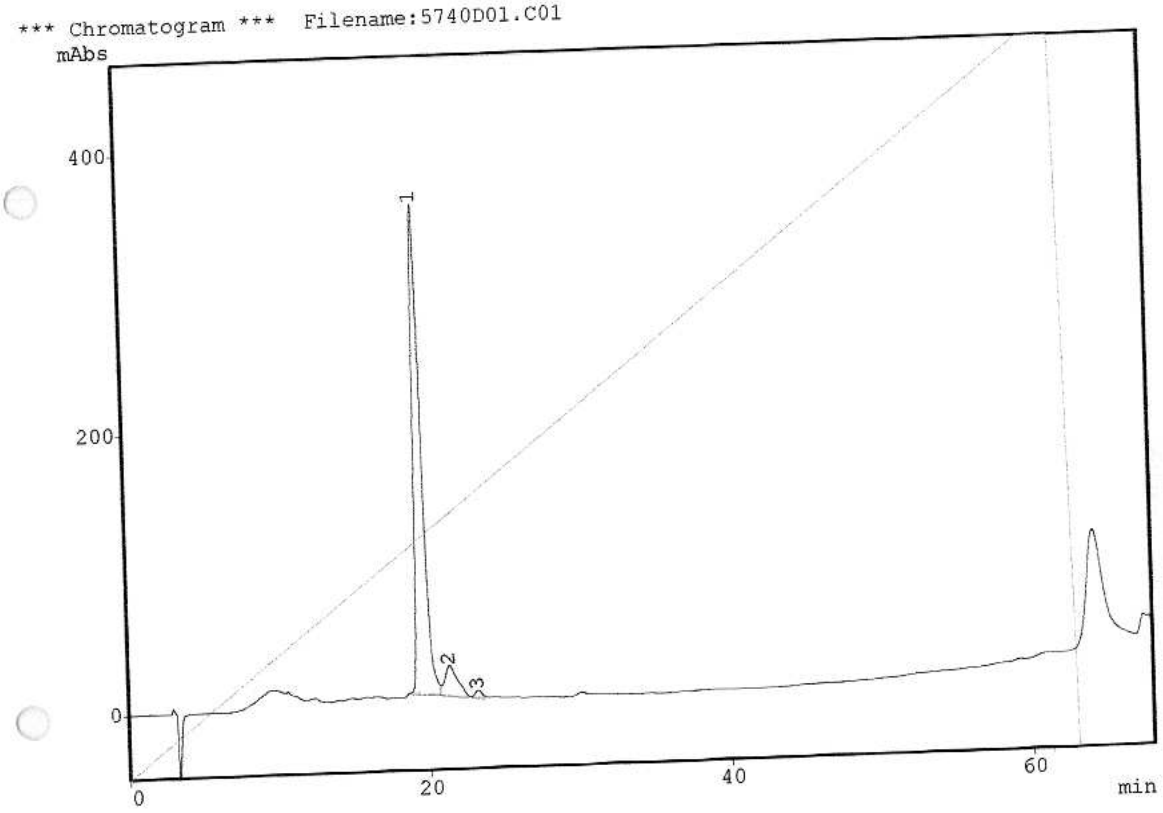

*** Peak Report ***

PKNO	TIME	AREA	HEIGHT	CONC
1	19.512	12706023	350003	90.4239
2	21.332	1209412	21127	8.6069
3	23.197	136179	4777	0.9691
		14051614	375907	100.0000

- MALDI-TOF α-cyano-4-hydroxy-cinnaminic acid matrix

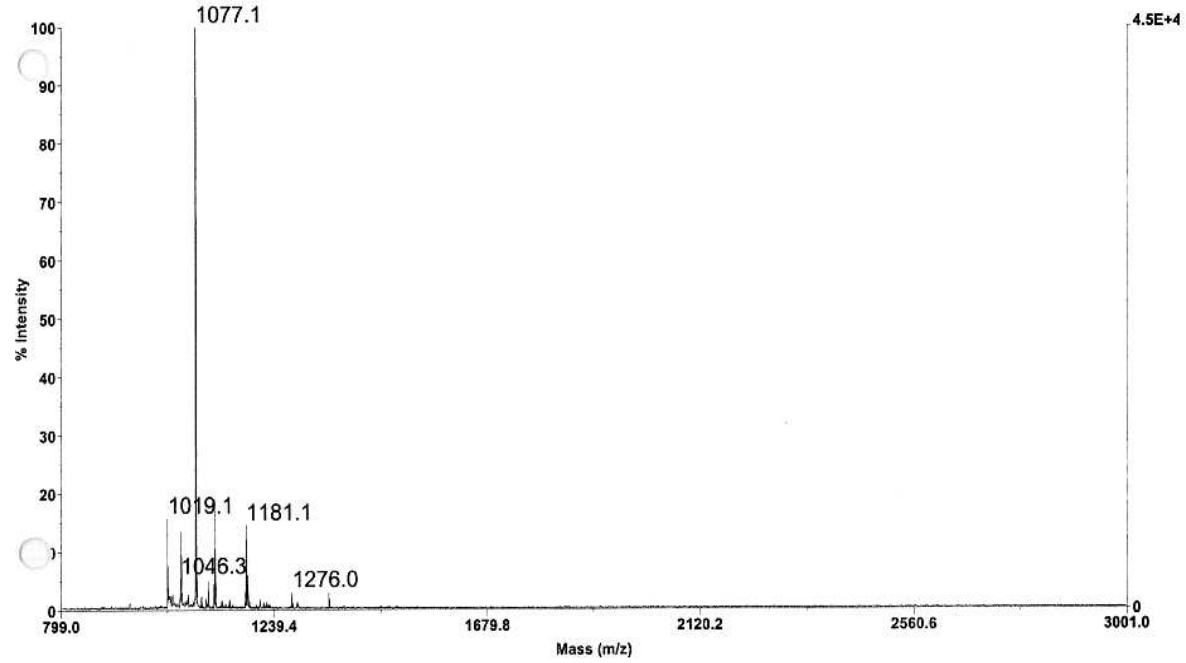

- CZE pH=3 sodium citrate buffer

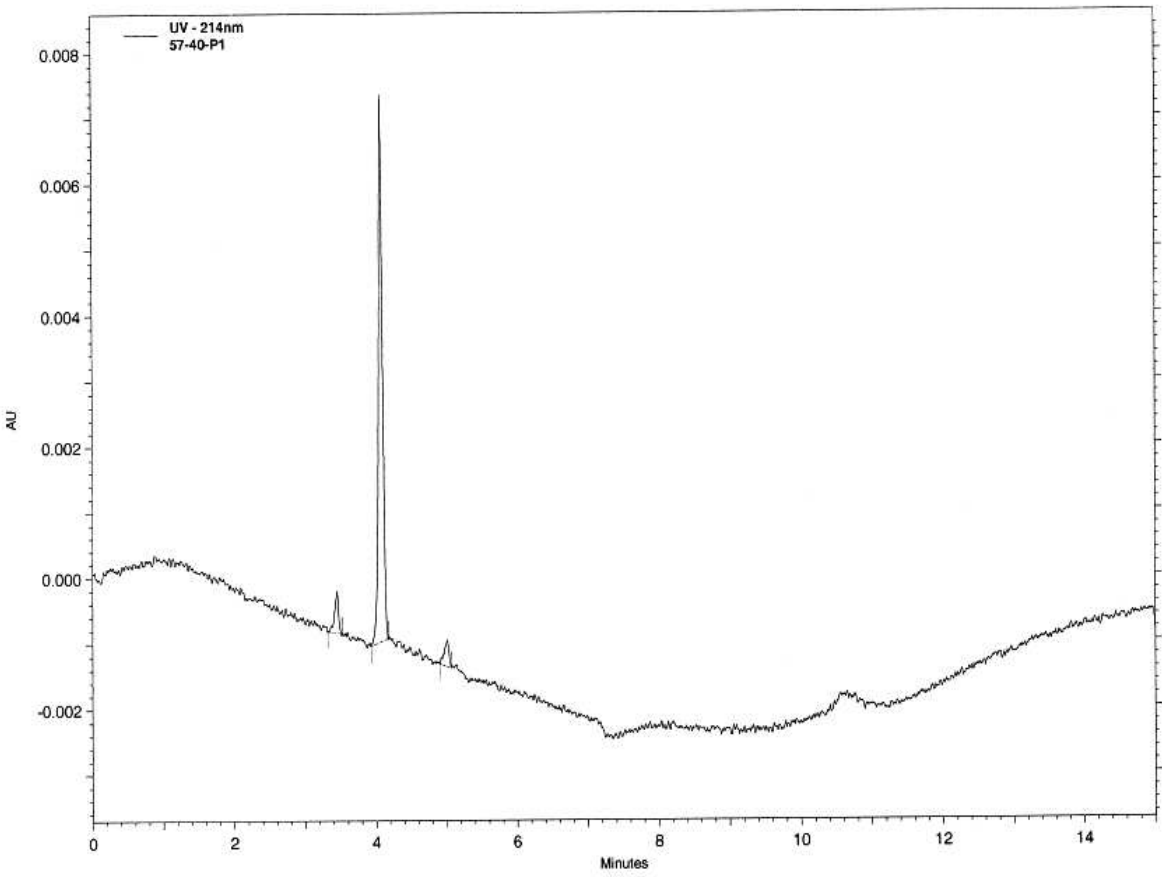

UV - 214nm
Results

Time	Area	Area %	Corrected Area	Corrected Area Percent
3.450	2346	6.15		
4.071	33958	88.95		
5.004	1873	4.91		
Totals	38177	100.00		

- CZE pH=4.5 sodium acetate buffer

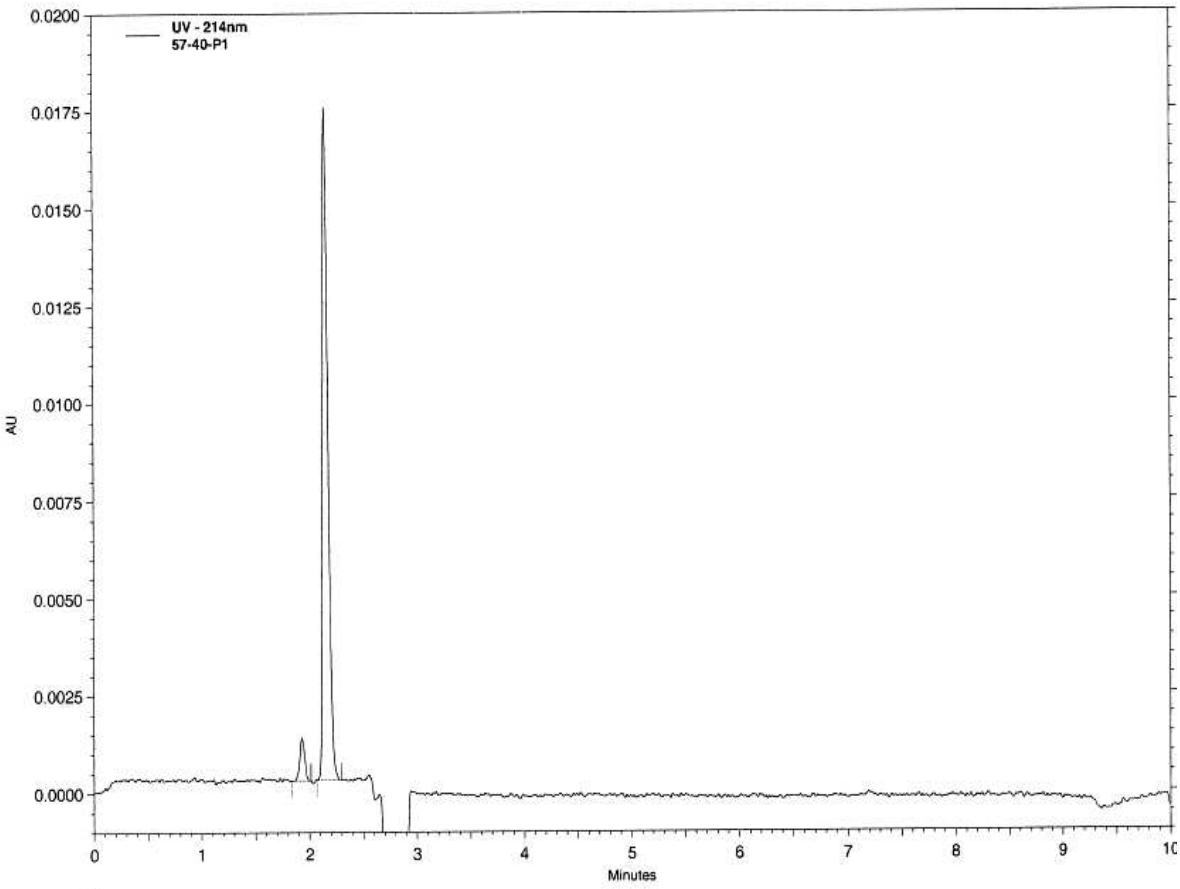

UV - 214nm
Results

Time	Area	Area %	Corrected Area	Corrected Area Percent
1.929	3372	5.40		
2.150	59049	94.60		
Totals	62421	100.00		

Analytical data for hydrazinocarbonyl peptide **2c**

- RP-HPLC, C18 deltapak column, 1mL/min, λ=215 nm, 0-100% B in 60 min, 25°C

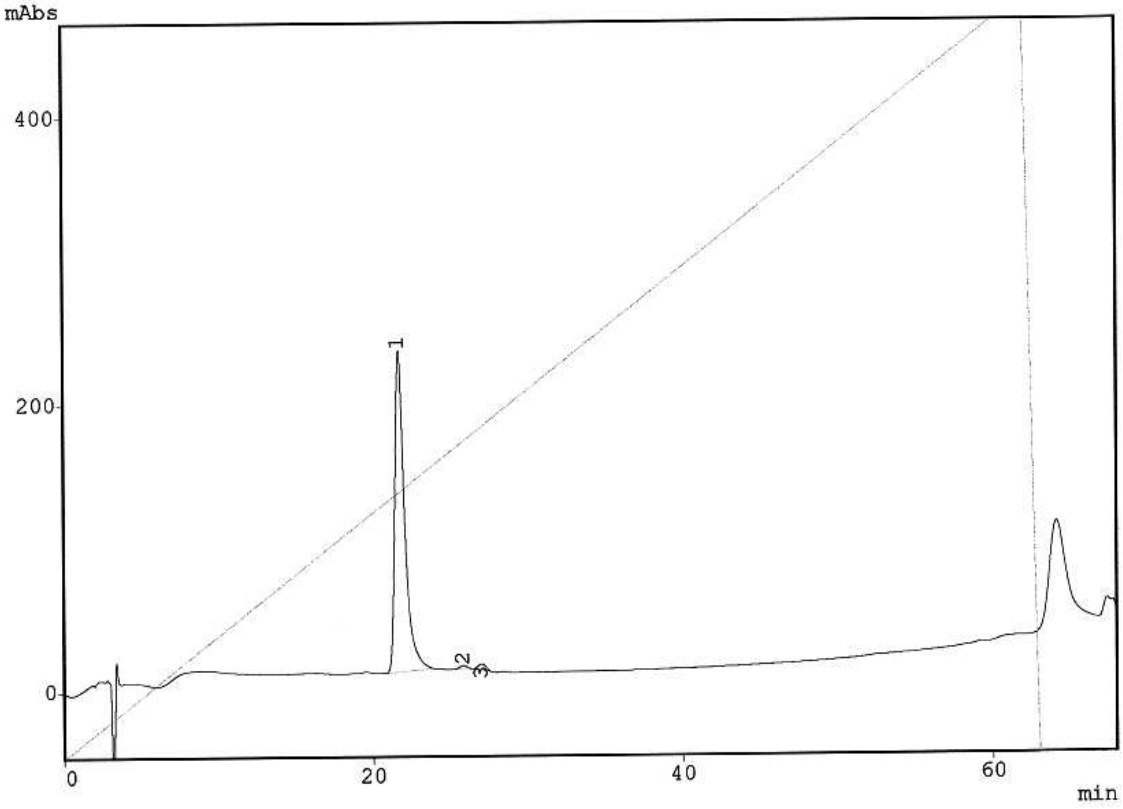

*** Peak Report ***

PKNO	TIME	AREA	HEIGHT	CONC
1	21.662	9823431	223675	98.1338
2	25.807	53945	1914	0.5389
3	26.977	132863	3930	1.3273
		10010239	229519	100.0000

- MALDI-TOF α-cyano-4-hydroxy-cinnaminic acid matrix

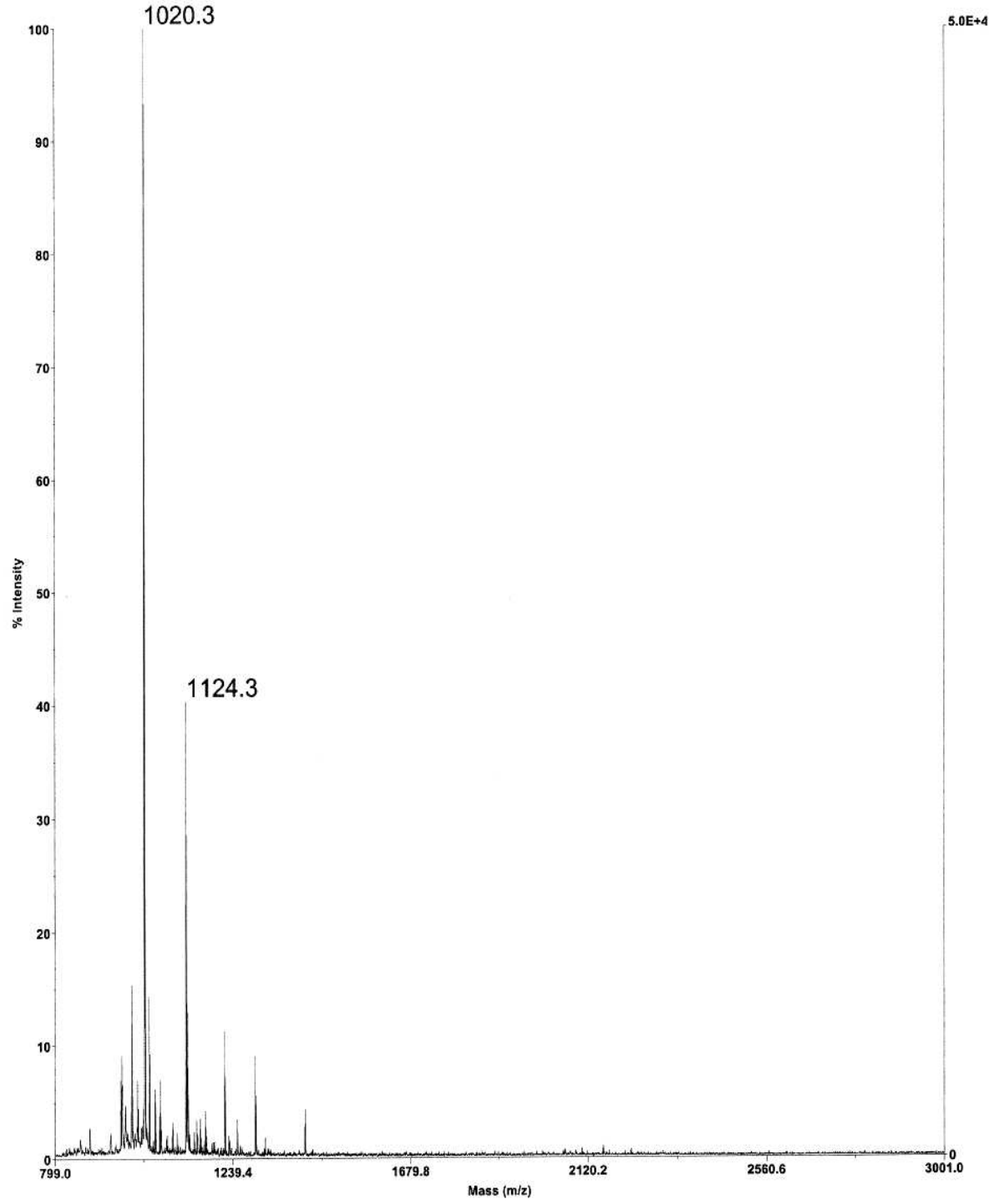

- CZE pH=3 sodium citrate buffer

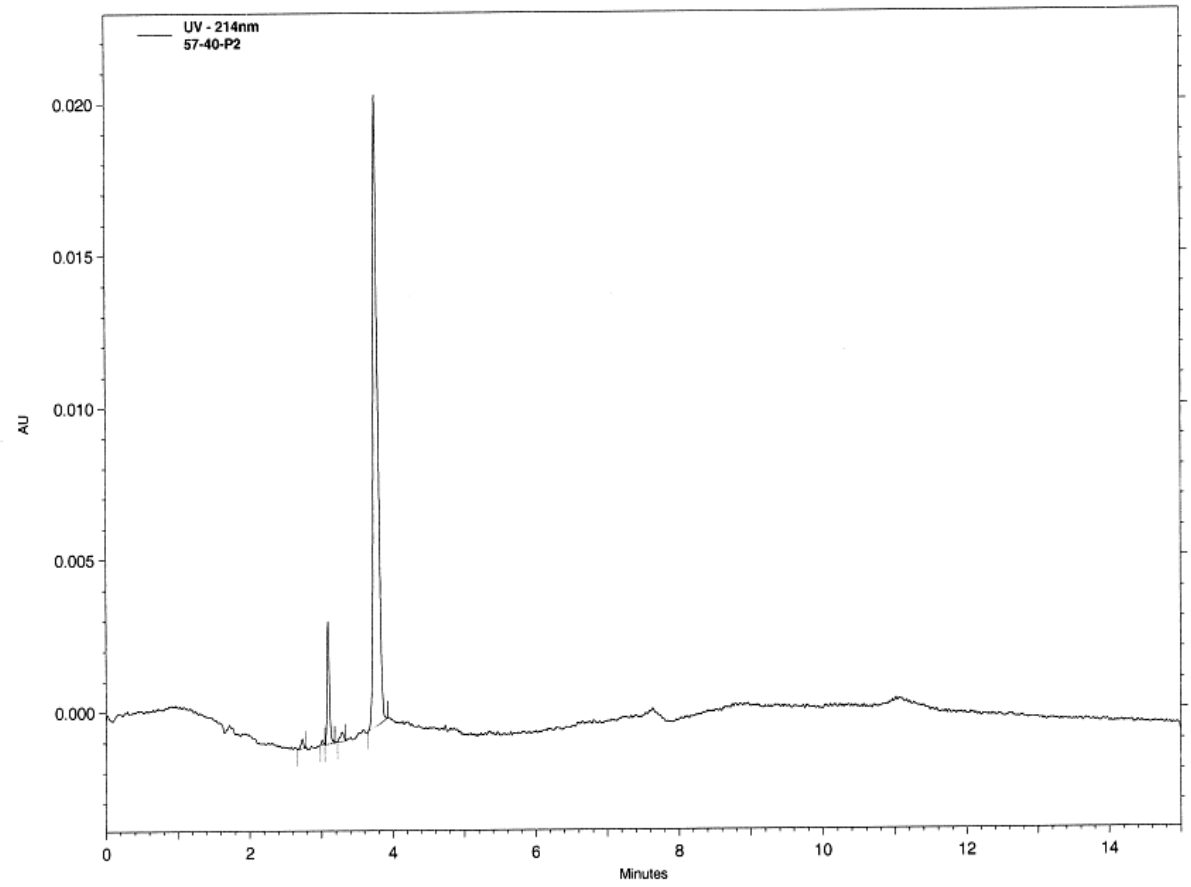

UV - 214nm
Results

Time	Area	Area %	Corrected Area	Corrected Area Percent
2.733	678	0.66		
3.013	326	0.32		
3.092	9653	9.39		
3.288	1095	1.06		
3.758	91074	88.57		
Totals	102826	100.00		

- CZE pH=4.5 sodium acetate buffer

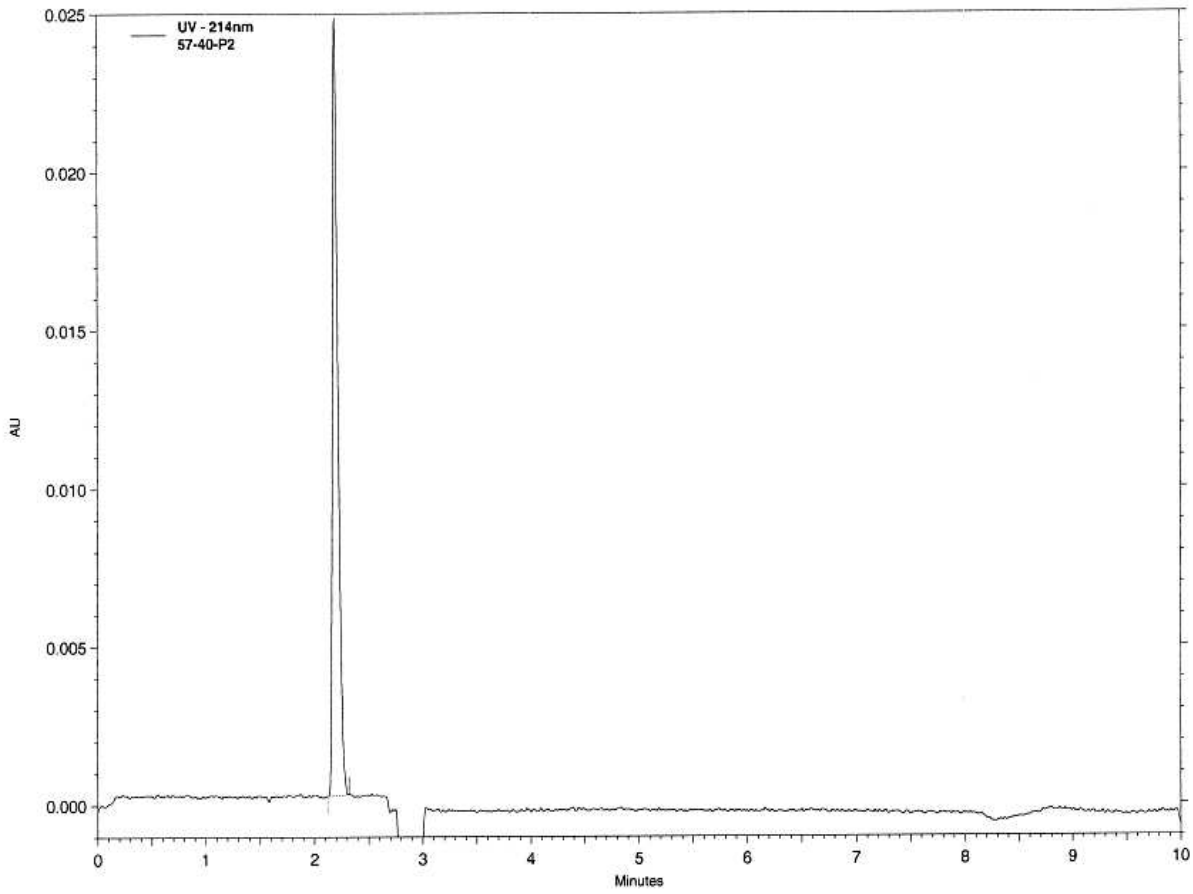

UV - 214nm
Results

Time	Area	Area %	Corrected Area	Corrected Area Percent
2.188	86247	100.00		
Totals	86247	100.00		

Analytical data for Agly-peptide **5a**

- RP-HPLC, C18 nucleosil column, 1mL/min, λ=215 nm, 0-100% B in 60 min, 50°C

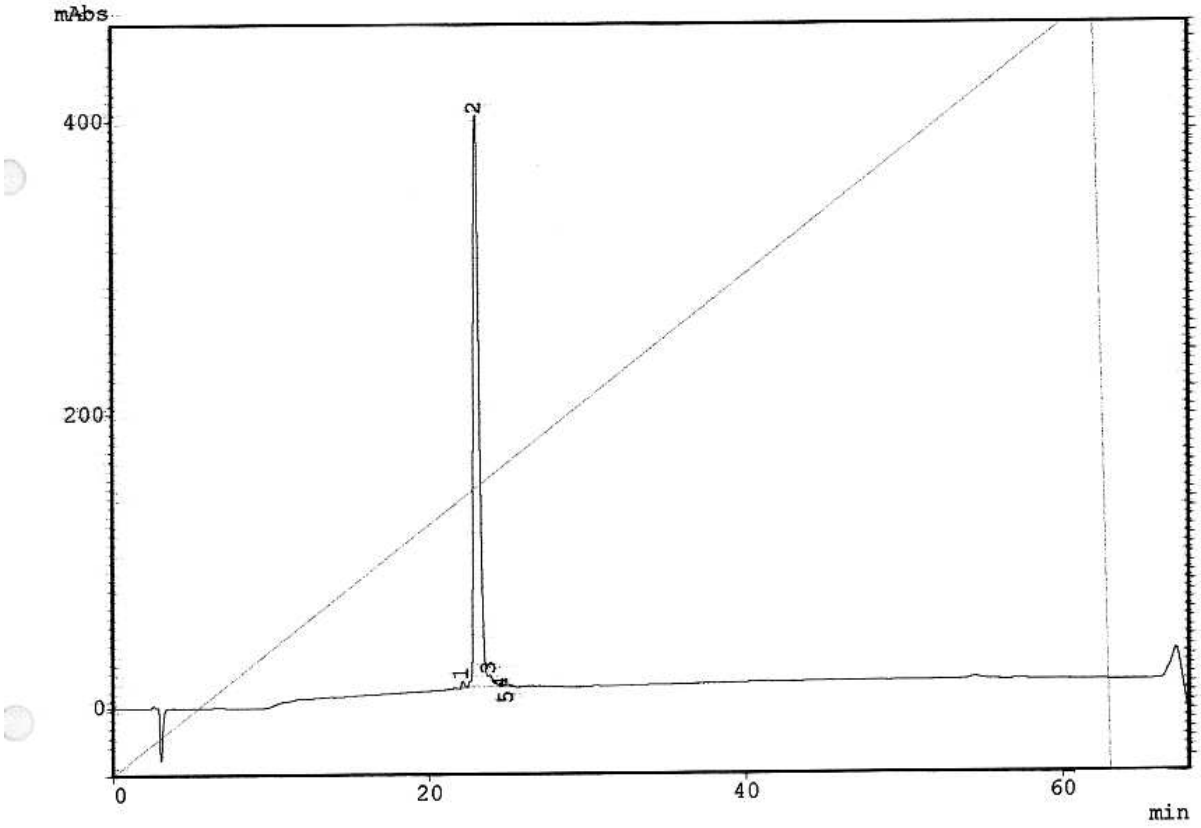

*** Peak Report ***

PKNO	TIME	AREA	HEIGHT	CONC
1	22.082	51616	4504	0.5059
2	22.954	10092150	389766	98.9082
3	23.802	17347	1552	0.1700
4	24.511	17897	1527	0.1754
5	24.890	24541	1250	0.2405
		10203550	398598	100.0000

- RP-HPLC, C4 column, 1mL/min, λ=215 nm, 0-100% B in 60 min, 50°C

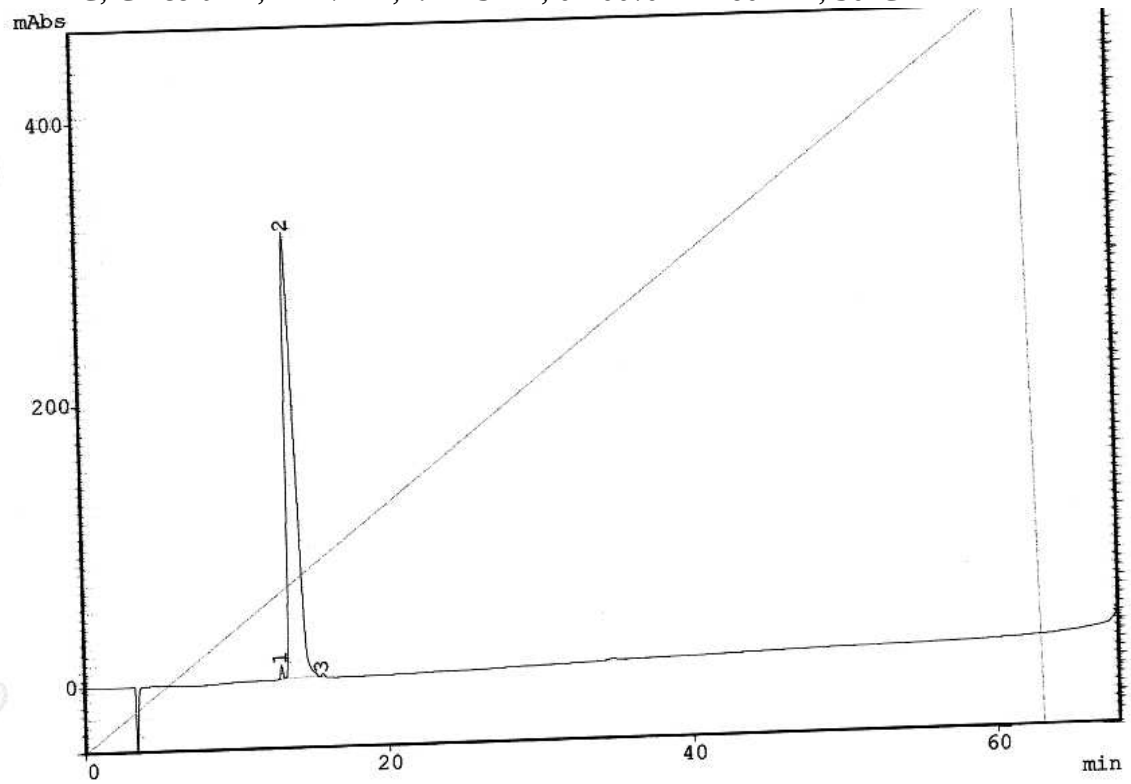

*** Peak Report ***

PKNO	TIME	AREA	HEIGHT	CONC
1	12.954	97290	9721	0.7660
2	13.617	12576283	315850	99.0177
3	15.682	27469	2397	0.2163
		12701042	327968	100.0000

- MALDI-TOF α-cyano-4-hydroxy-cinnaminic acid matrix

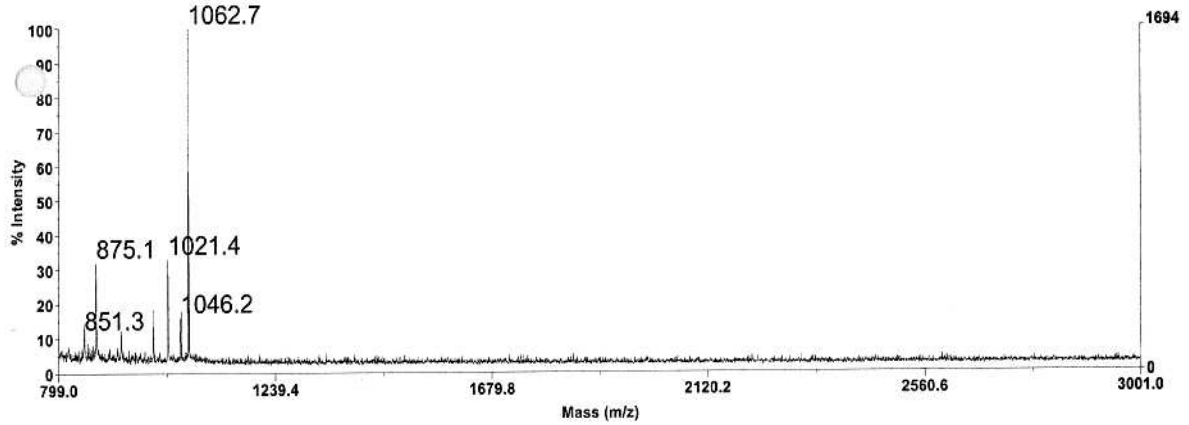

- CZE pH=3 sodium citrate buffer

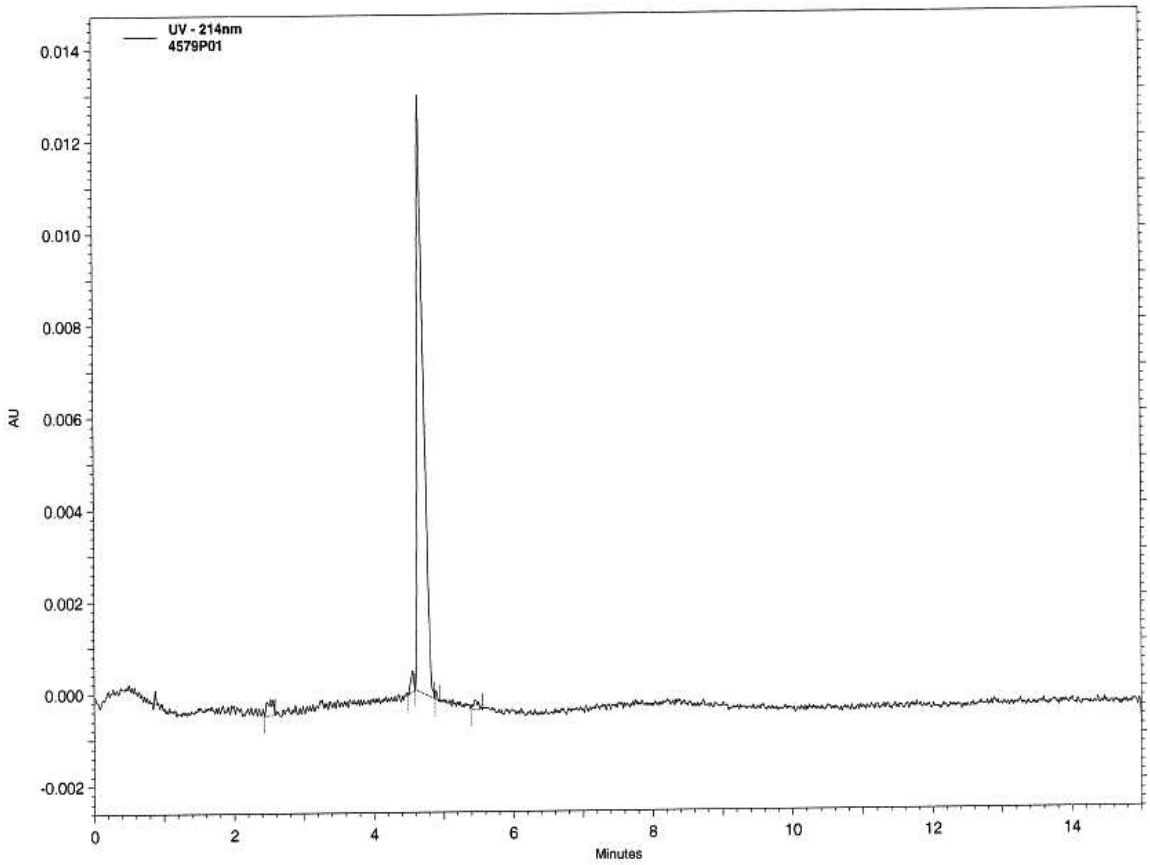

UV - 214nm
Results

Time	Area	Area %	Corrected Area	Corrected Area Percent
2.525	2059	2.36	272	4.28
4.558	1360	1.56	99	1.57
4.662	82498	94.53	5898	92.82
4.896	309	0.35	21	0.33
5.450	1042	1.19	64	1.00
Totals	87268	100.00	6354	100.00

- CZE pH=4.5 sodium acetate buffer

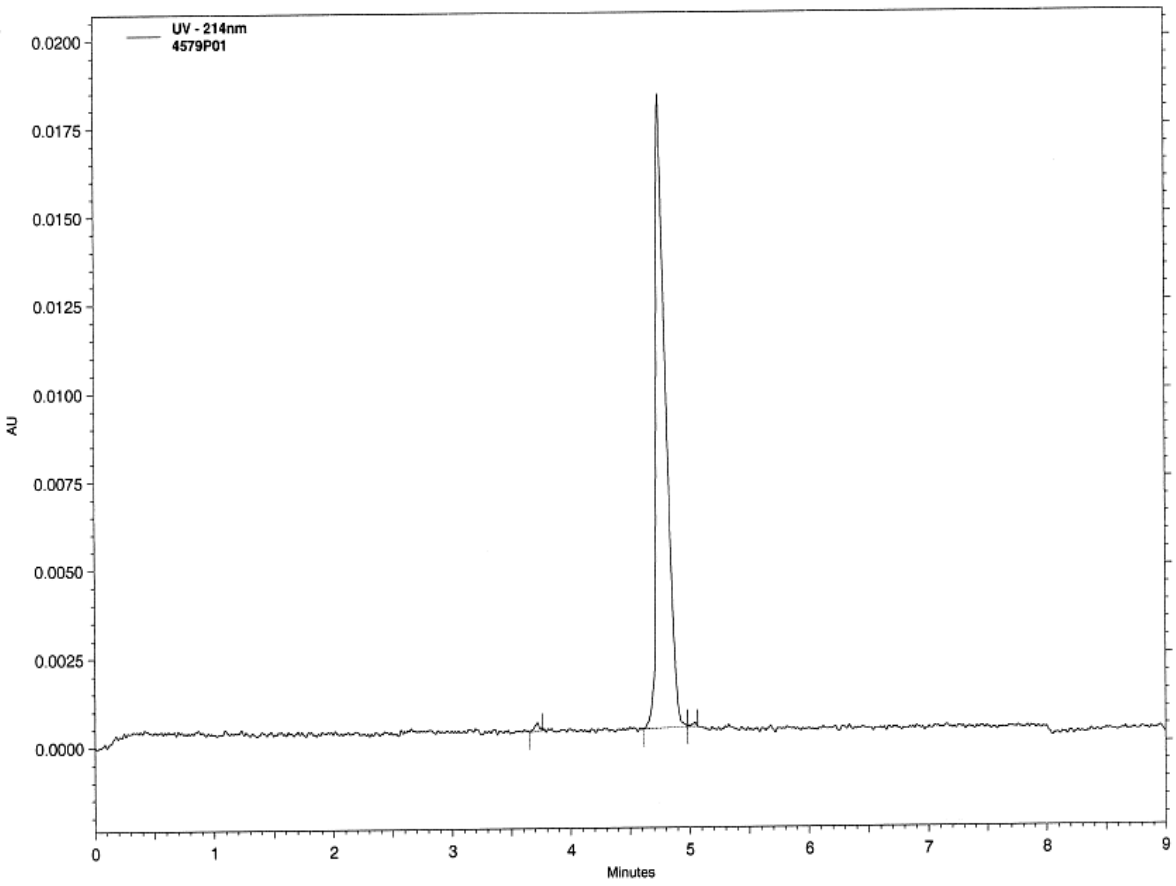

UV - 214nm
Results

Time	Area	Area %	Corrected Area	Corrected Area Percent
3.721	661	0.63	59	0.80
4.746	103905	99.08	7298	98.93
5.046	303	0.29	20	0.27
Totals	104869	100.00	7377	100.00

- NMR ^{1}H, $H2O/D_2O$, 300 MHz

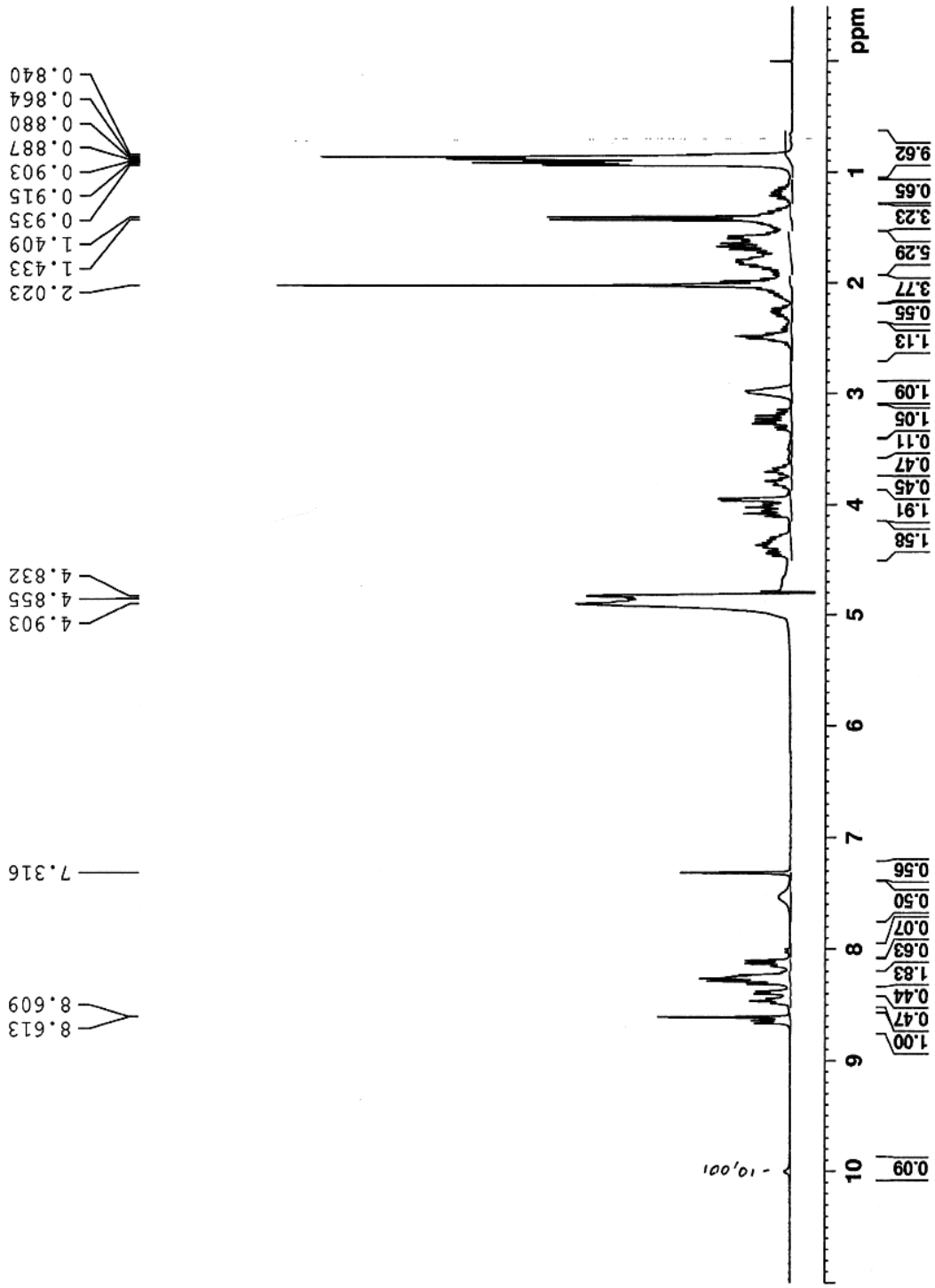

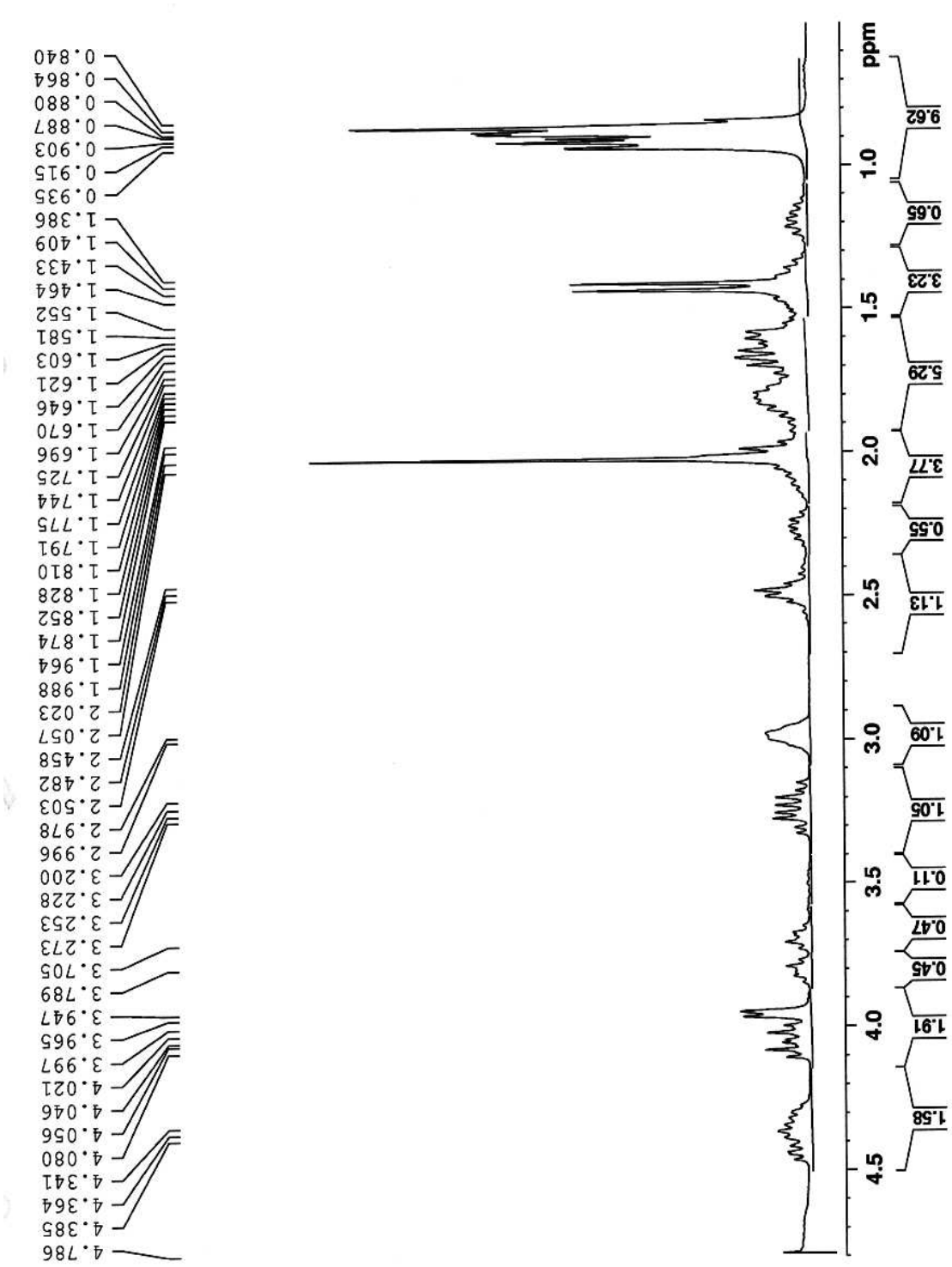
0.840
0.864
0.880
0.887
0.903
0.915
0.935
1.386
1.409
1.433
1.464
1.552
1.581
1.603
1.621
1.646
1.670
1.696
1.725
1.744
1.775
1.791
1.810
1.828
1.852
1.874
1.964
1.988
2.023
2.057
2.458
2.482
2.503
2.978
2.996
3.200
3.228
3.253
3.273
3.705
3.789
3.947
3.965
3.997
4.021
4.046
4.056
4.080
4.341
4.364
4.385
4.786
ppm
1.0
1.5
2.0
2.5
3.0
3.5
4.0
4.5
9.62
0.65
3.23
5.29
3.77
0.55
1.13
1.09
1.05
0.11
0.47
0.45
1.91
1.58

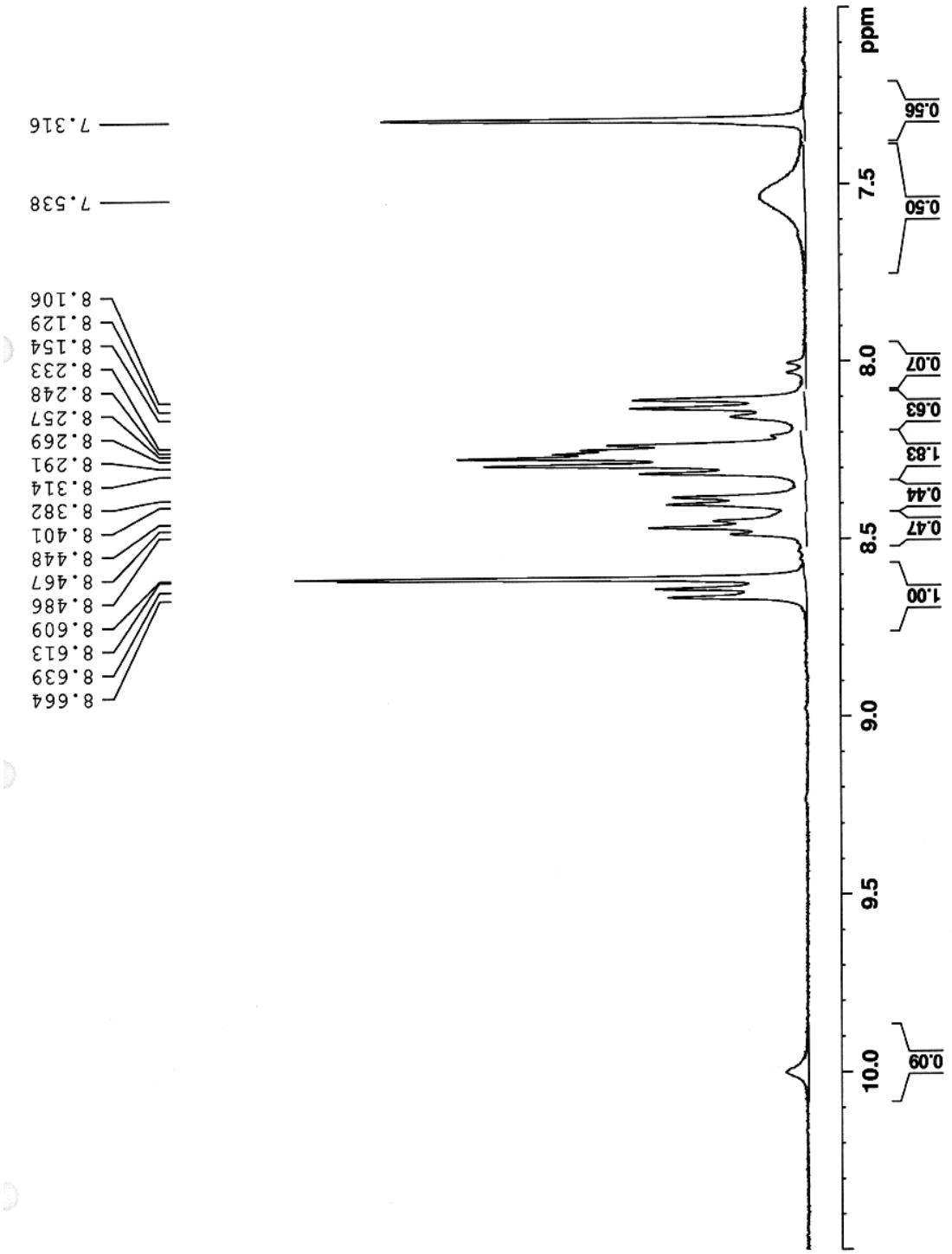
ppm
10.0
9.5
9.0
8.5
8.0
7.5
0.09
1.00
0.47
0.44
1.83
0.63
0.07
0.50
0.56
8.664
8.639
8.613
8.609
8.486
8.467
8.448
8.401
8.382
8.314
8.291
8.269
8.257
8.248
8.233
8.154
8.129
8.106
7.538
7.316

- NMR HSQC, H2O/D_2O, 300 MHz

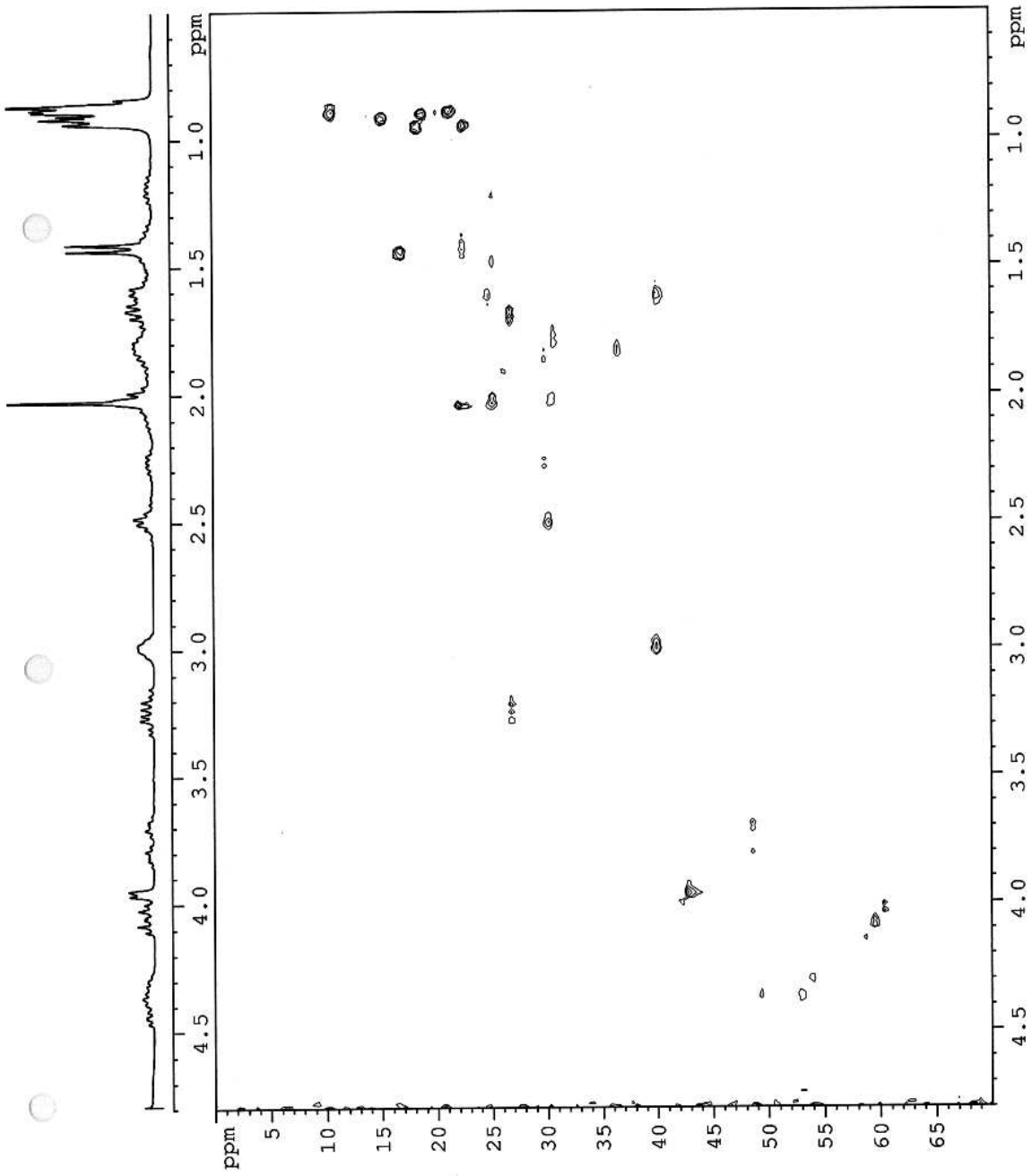

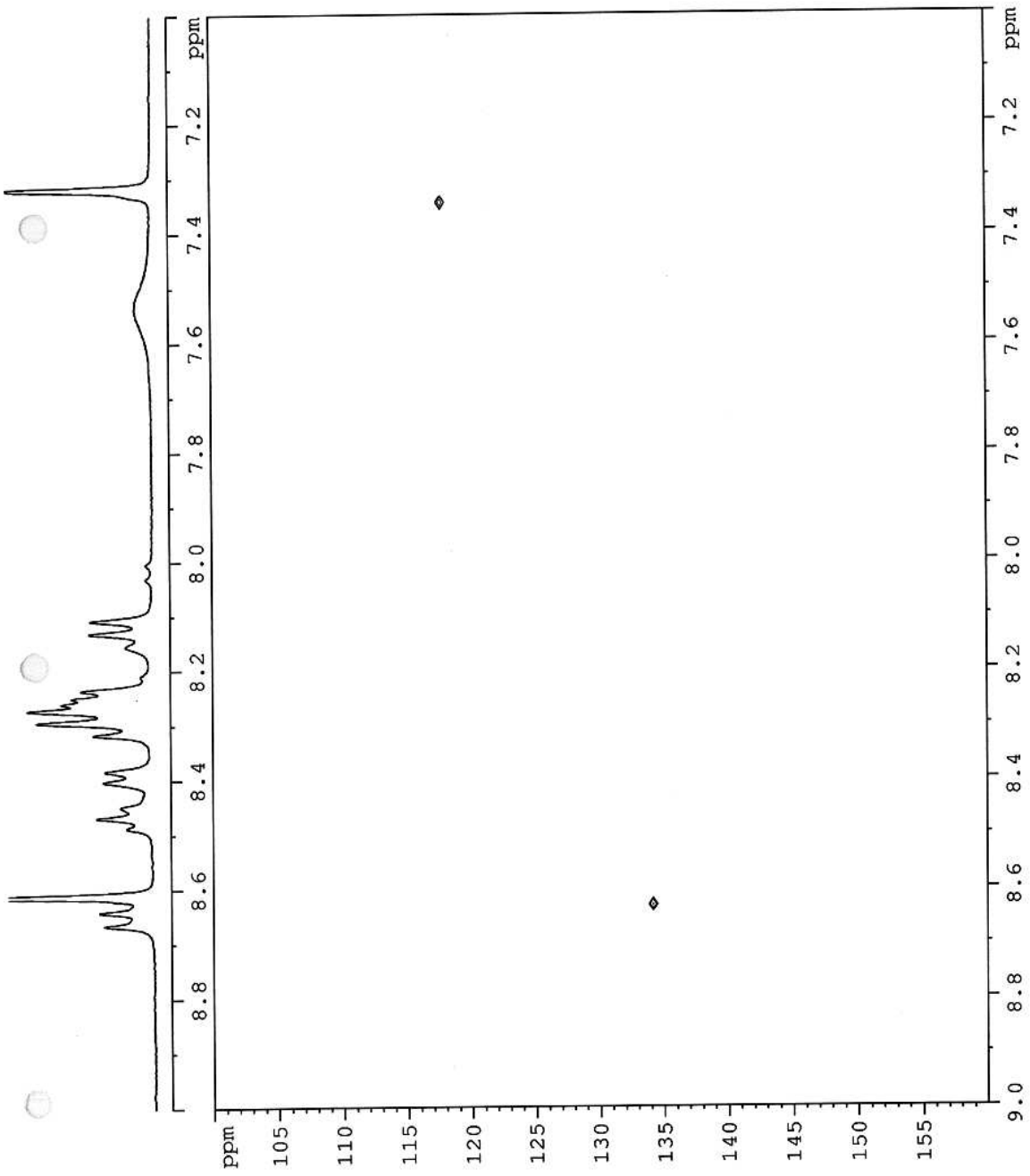
ppm
8.8
8.6
8.4
8.2
8.0
7.8
7.6
7.4
7.2
ppm
105
110
115
120
125
130
135
140
145
150
155
9.0
8.8
8.6
8.4
8.2
8.0
7.8
7.6
7.4
7.2
ppm

- NMR HMBC, $H2O/D_2O$, 300 MHz

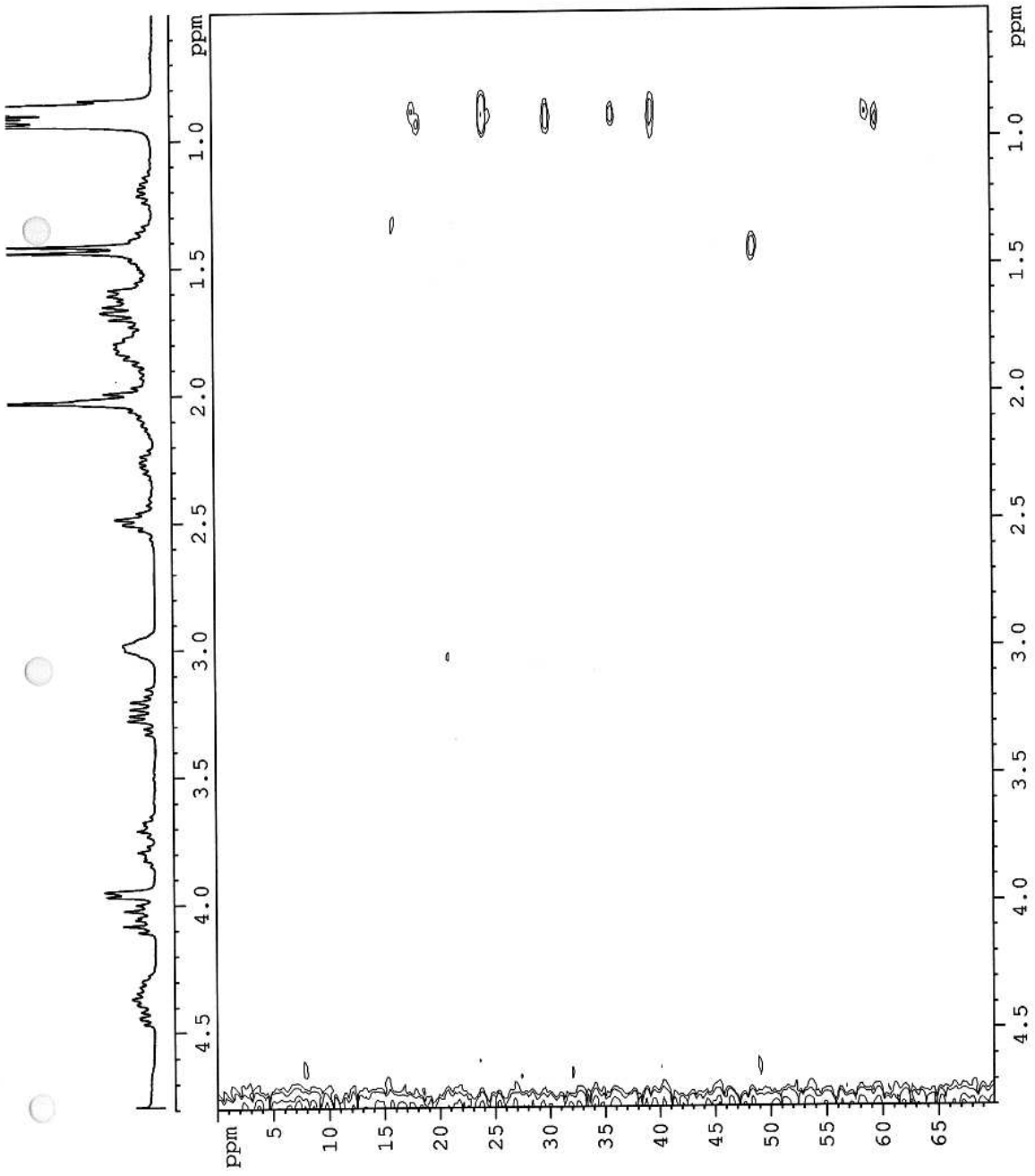

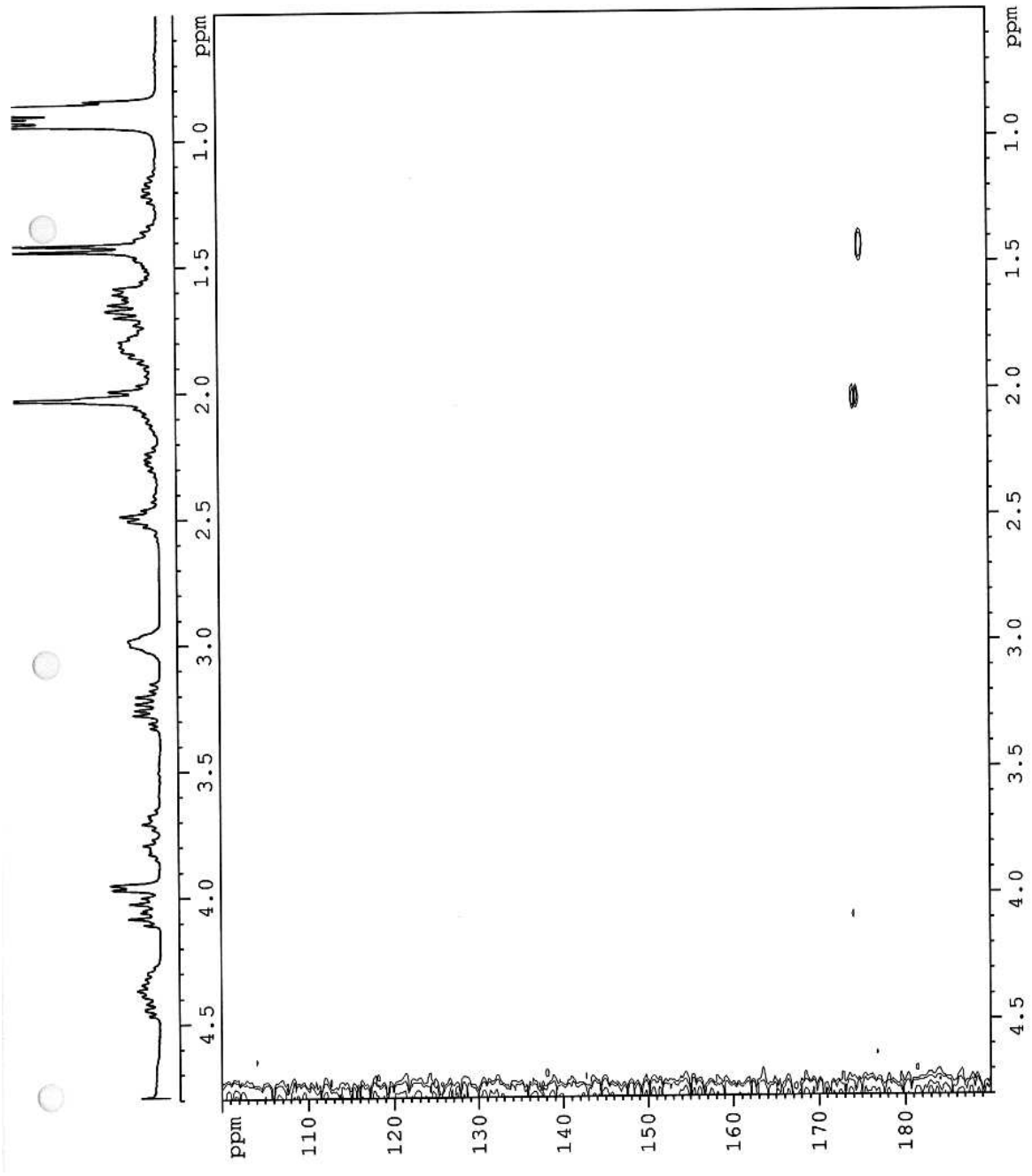
ppm
4.5
4.0
3.5
3.0
2.5
2.0
1.5
1.0
ppm
110
120
130
140
150
160
170
180

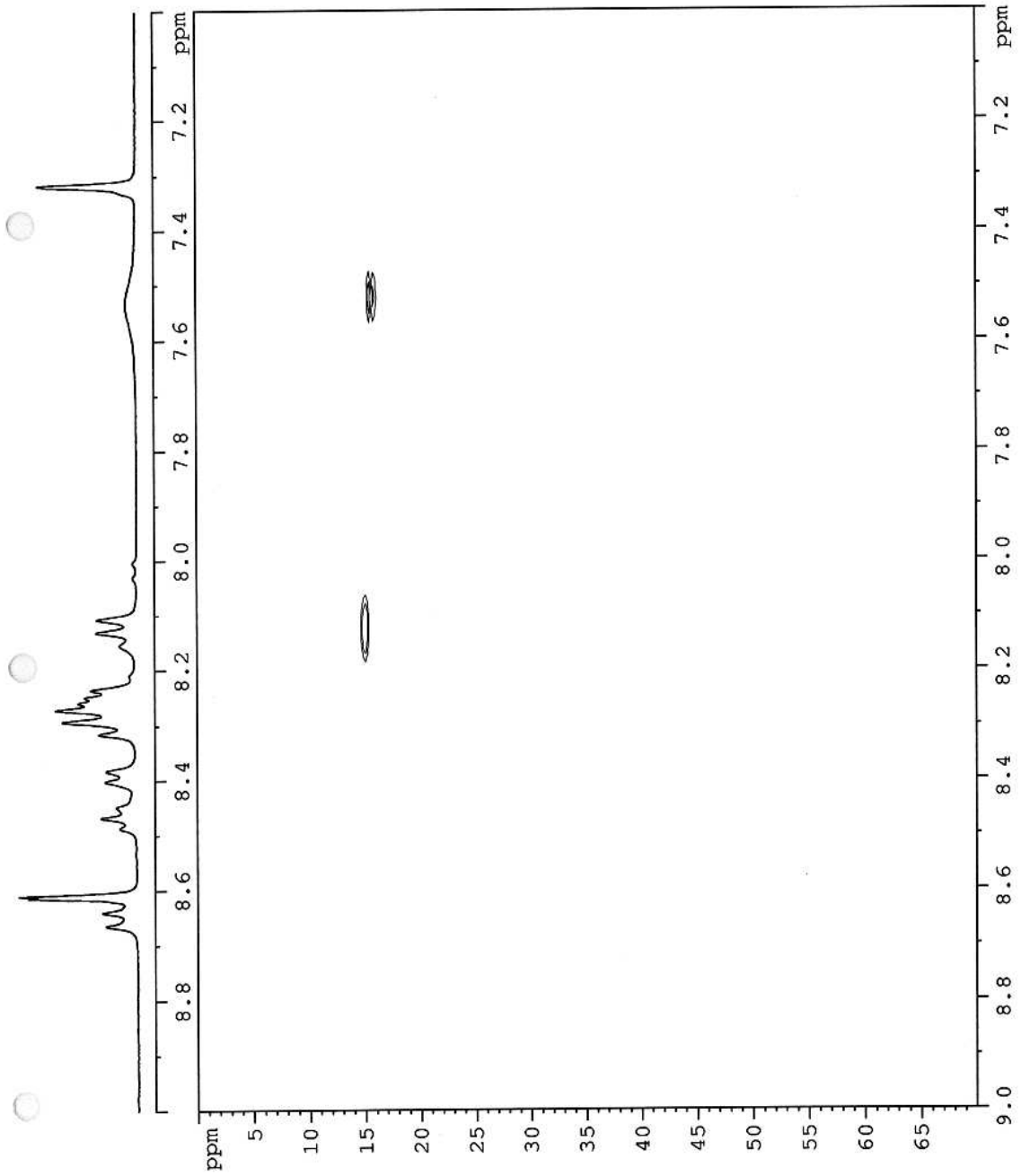
ppm
8.8
8.6
8.4
8.2
8.0
7.8
7.6
7.4
7.2
ppm
ppm
5
10
15
20
25
30
35
40
45
50
55
60
65
9.0
8.8
8.6
8.4
8.2
8.0
7.8
7.6
7.4
7.2
ppm

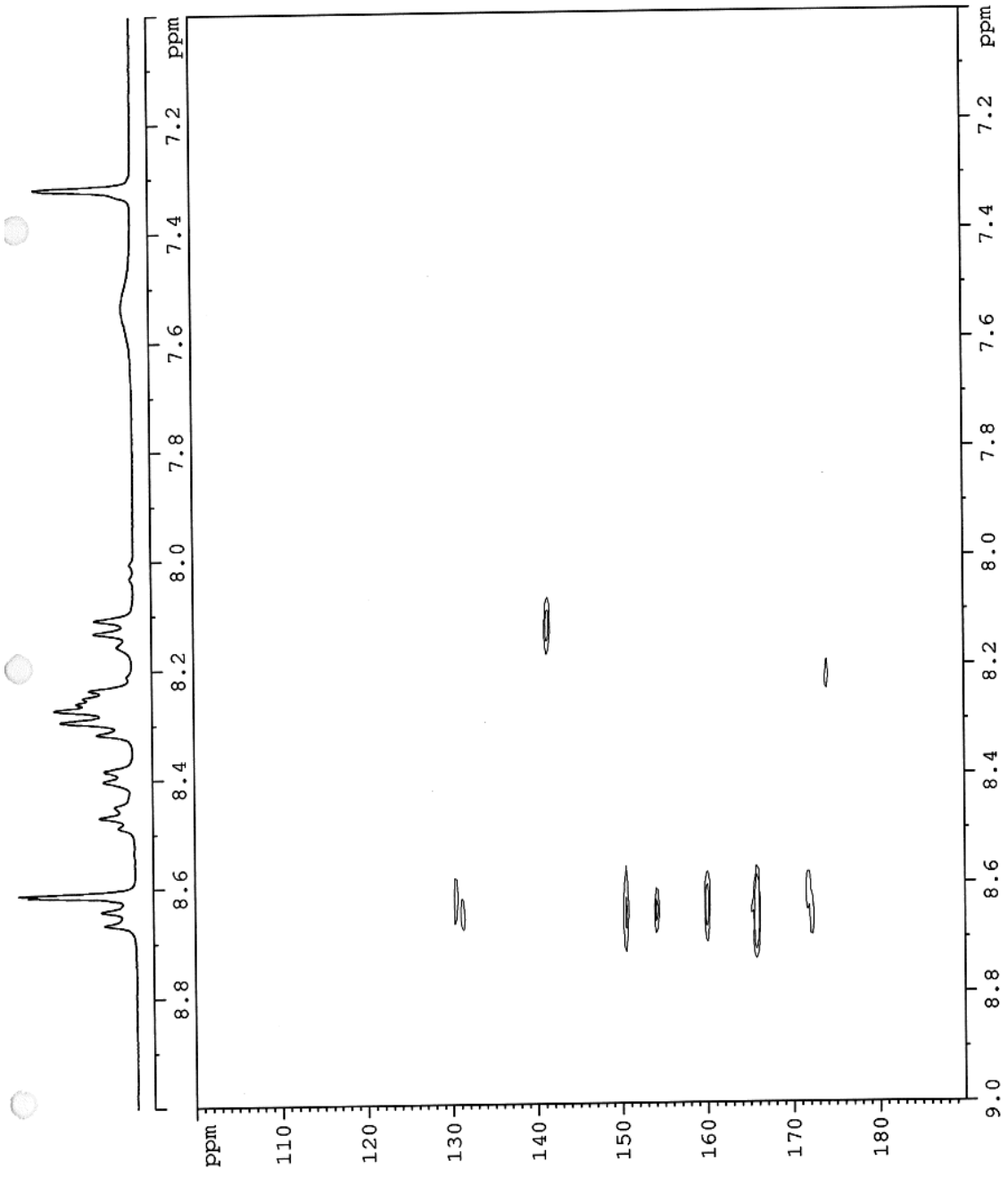
ppm
8.8
8.6
8.4
8.2
8.0
7.8
7.6
7.4
7.2
ppm
ppm
110
120
130
140
150
160
170
180
9.0
8.8
8.6
8.4
8.2
8.0
7.8
7.6
7.4
7.2
ppm

- NMR TOCSY, $H2O/D_2O$, 300 MHz

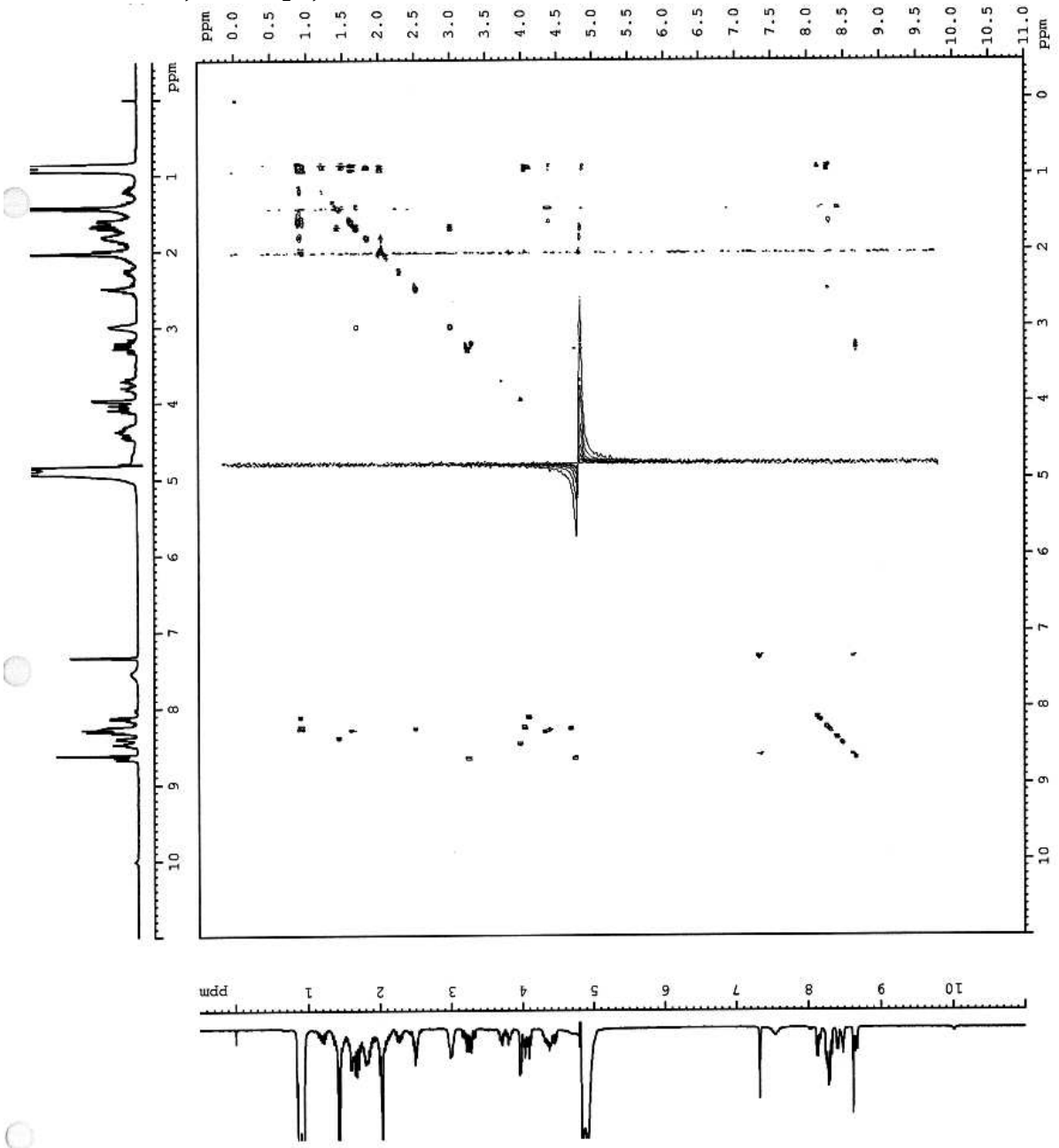

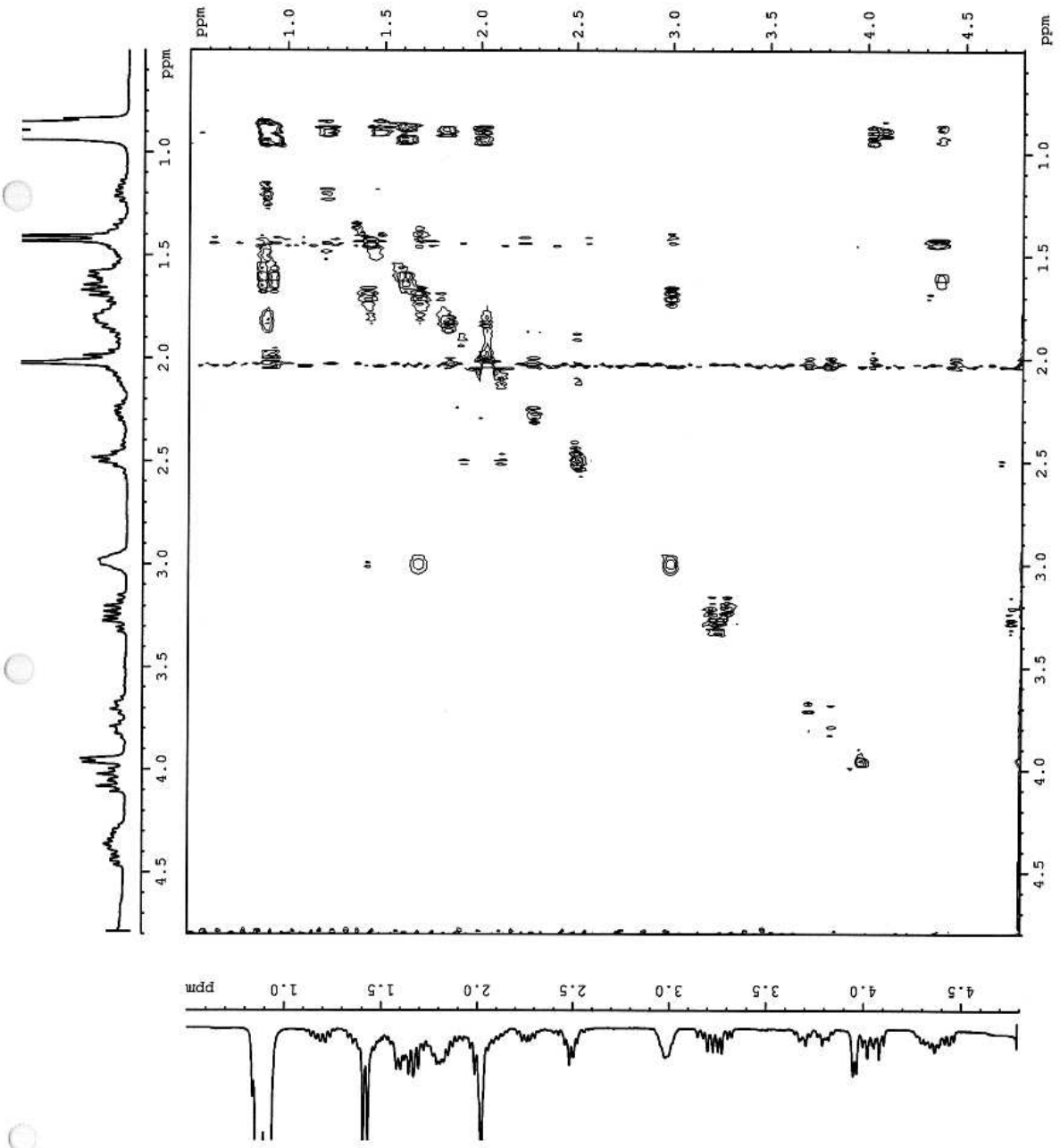
ppm
1.0
1.5
2.0
2.5
3.0
3.5
4.0
4.5

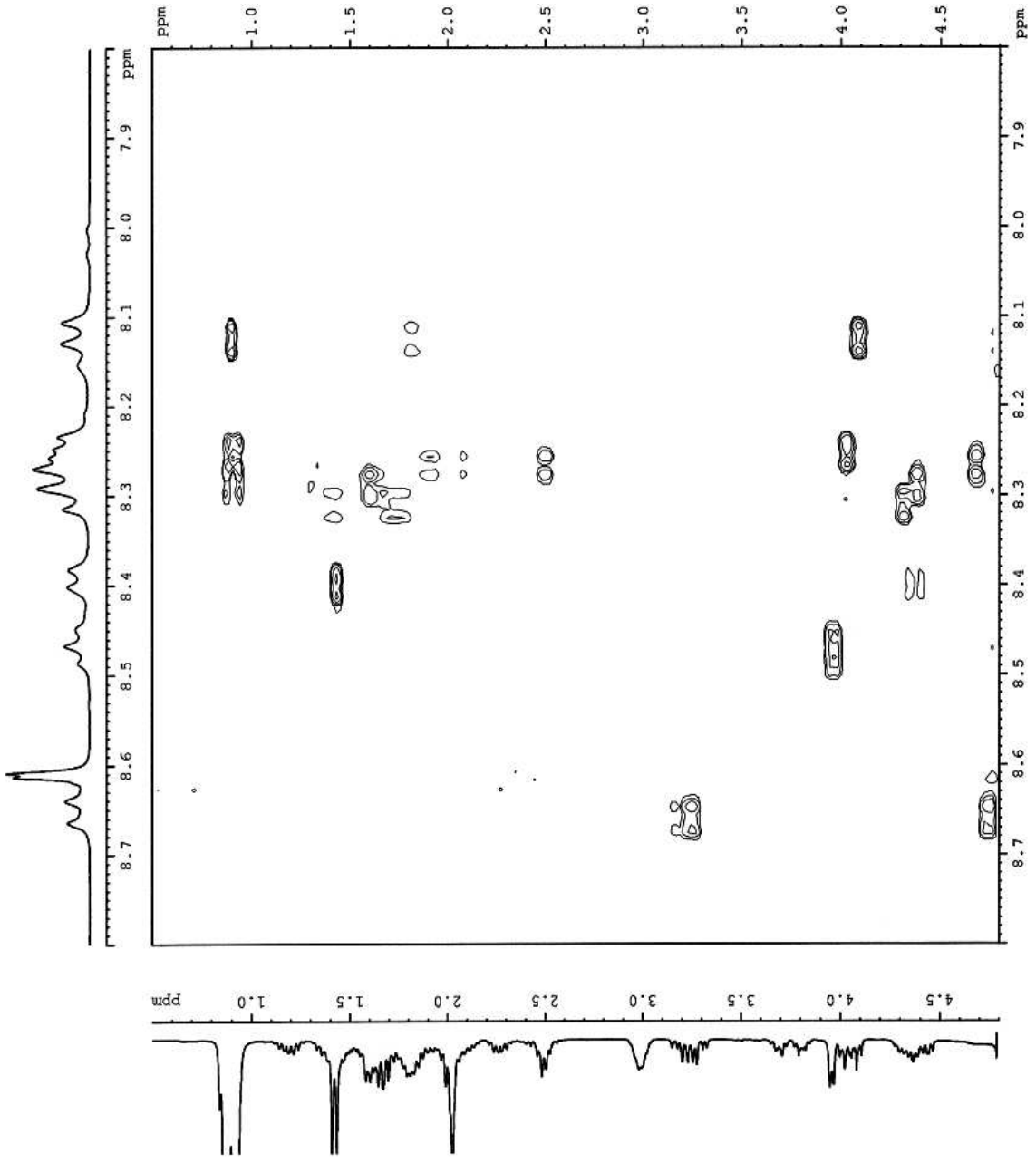
ppm
1.0
1.5
2.0
2.5
3.0
3.5
4.0
4.5
7.9
8.0
8.1
8.2
8.3
8.4
8.5
8.6
8.7

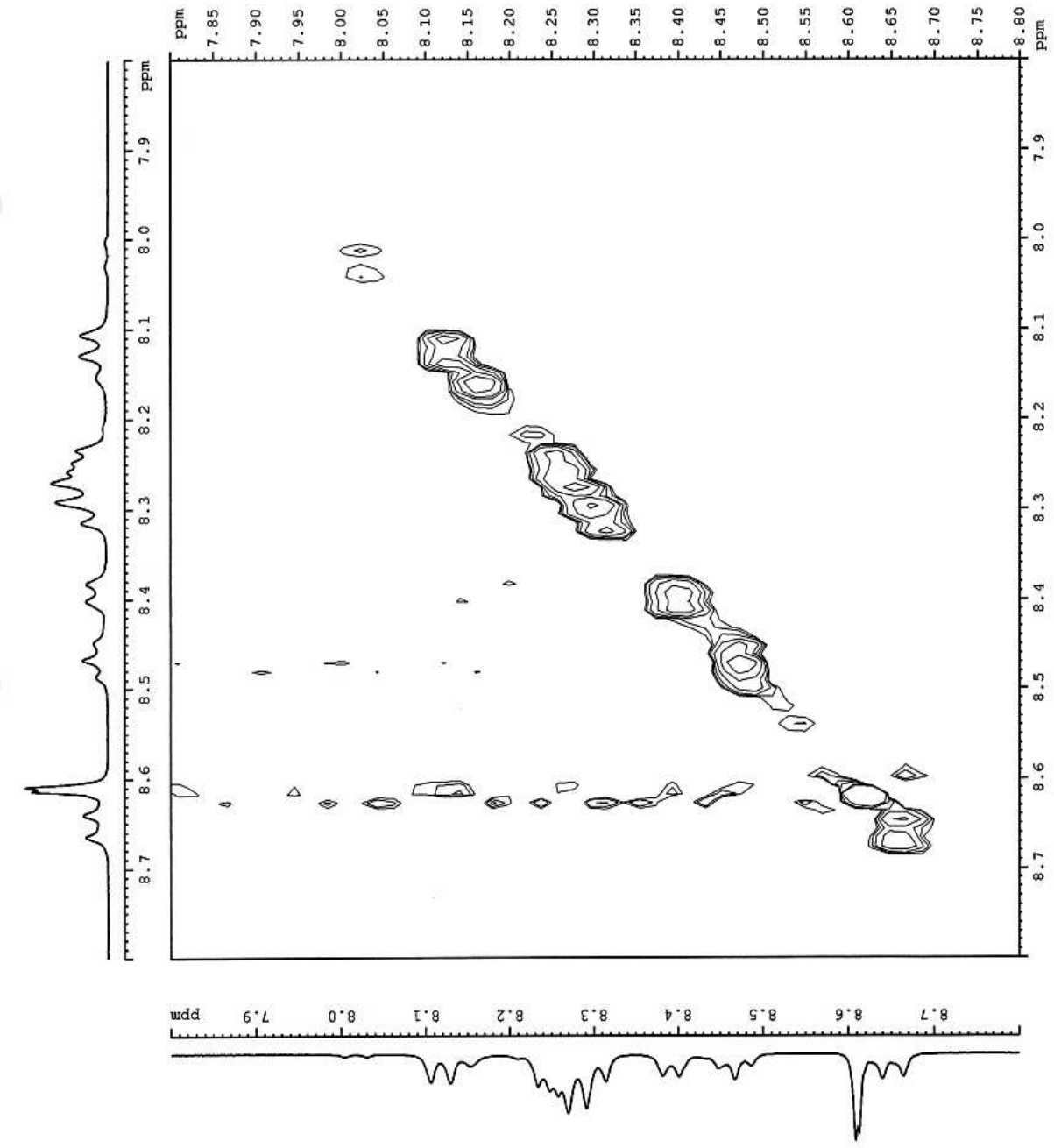
ppm
7.85
7.90
7.95
8.00
8.05
8.10
8.15
8.20
8.25
8.30
8.35
8.40
8.45
8.50
8.55
8.60
8.65
8.70
8.75
8.80
7.9
8.0
8.1
8.2
8.3
8.4
8.5
8.6
8.7
8.7
8.6
8.5
8.4
8.3
8.2
8.1
8.0
7.9
ppm

Trypsic digestion spectra

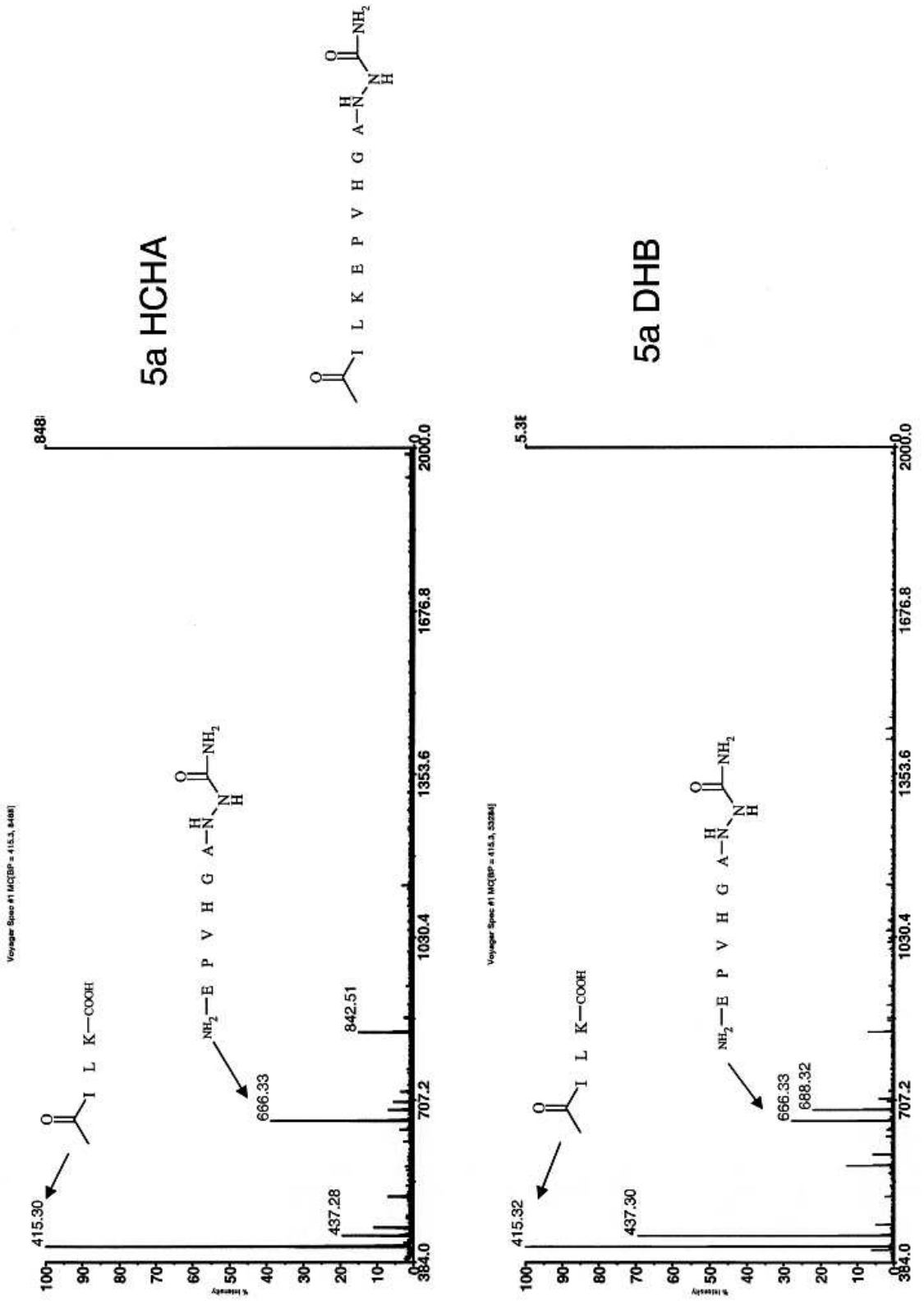

Analytical data for Agly-peptide **5b**

- RP-HPLC, C18 Xbridge BEH column, 1mL/min, λ=215 nm, 0-100% B in 60 min, 30°C

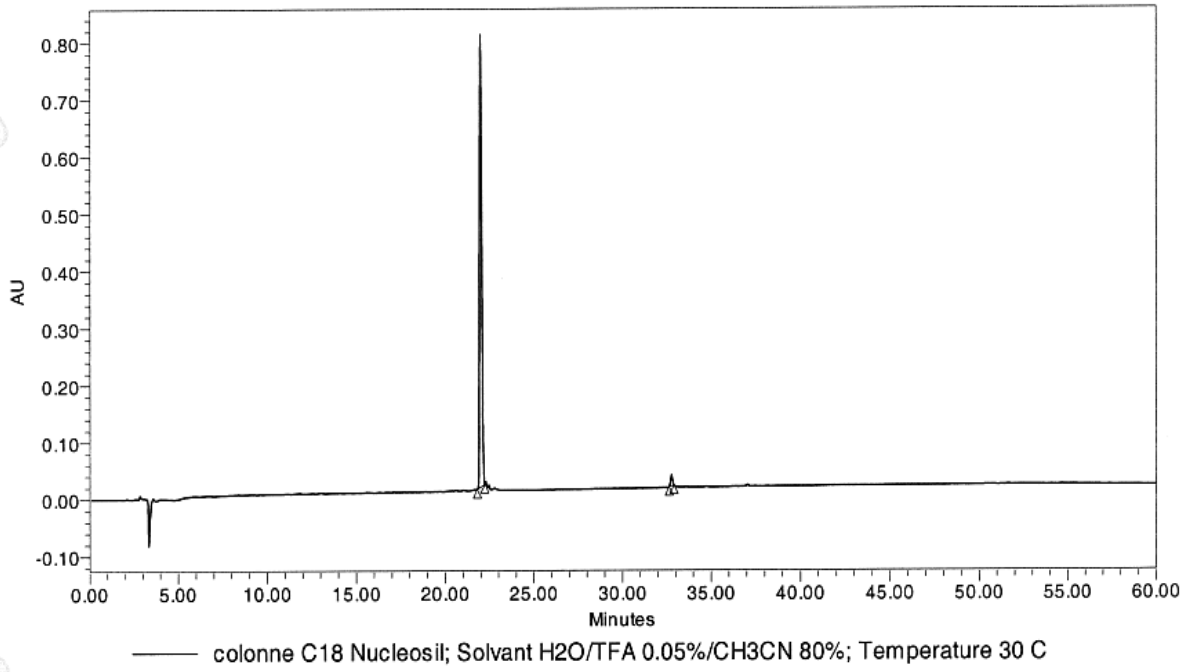

	RT	Area	% Area	Height
1	21.987	6249268	97.82	796849
2	32.768	139209	2.18	19232

- MALDI-TOF α-cyano-4-hydroxy-cinnaminic acid matrix

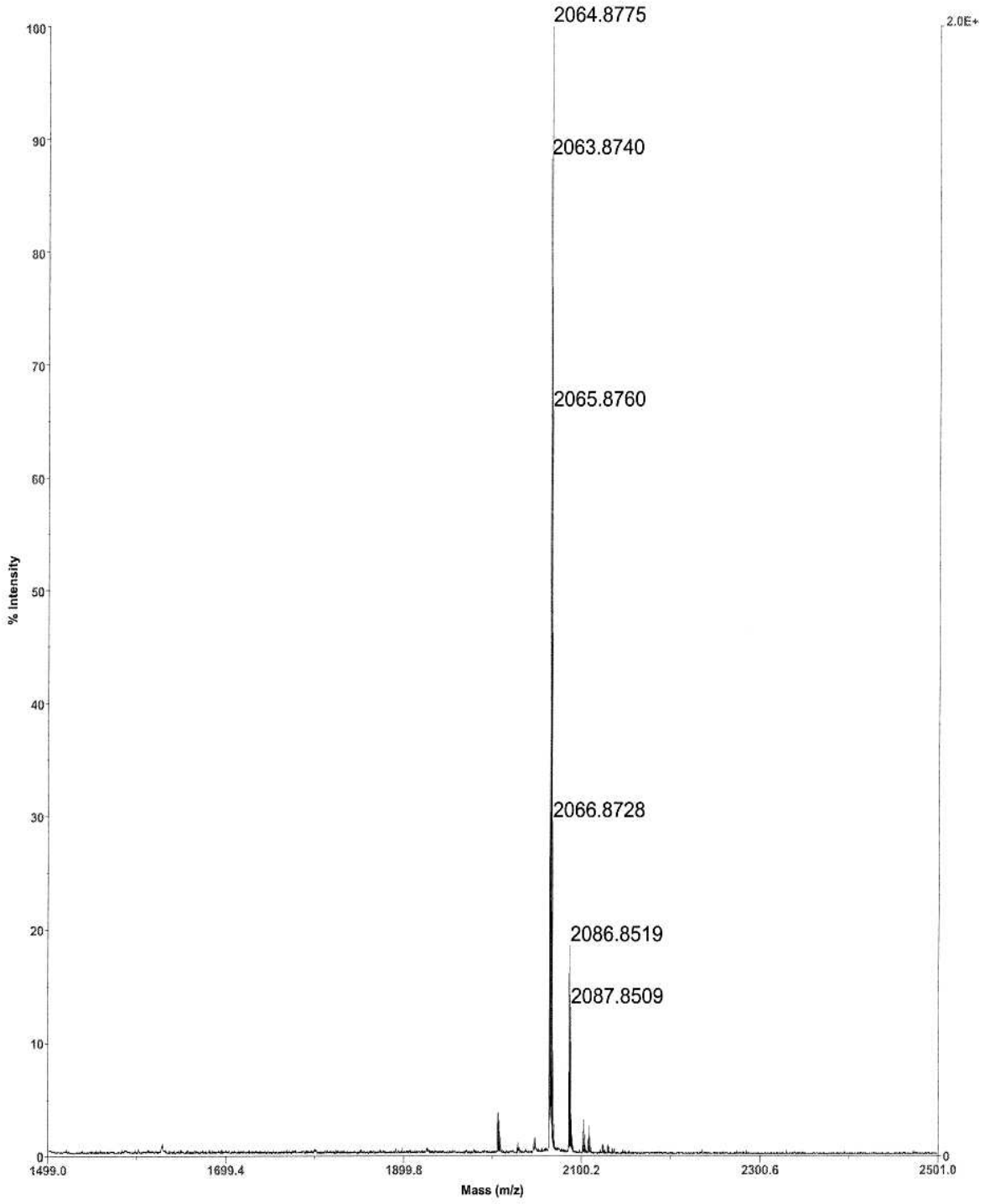

- CZE pH=3 sodium citrate buffer

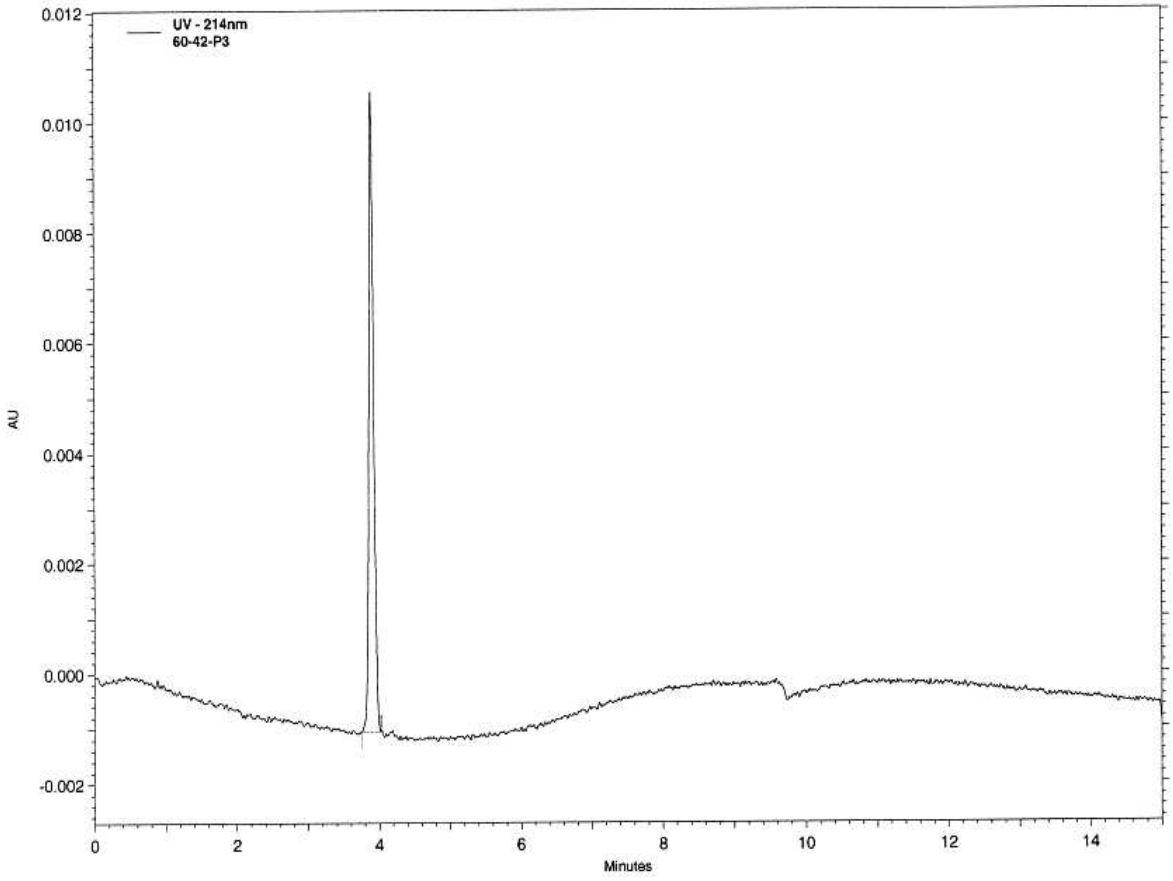

UV - 214nm
Results

Time	Area	Area %	Corrected Area	Corrected Area Percent
3.888	53967	100.00		
Totals	53967	100.00		

- CZE pH=4.5 sodium acetate buffer

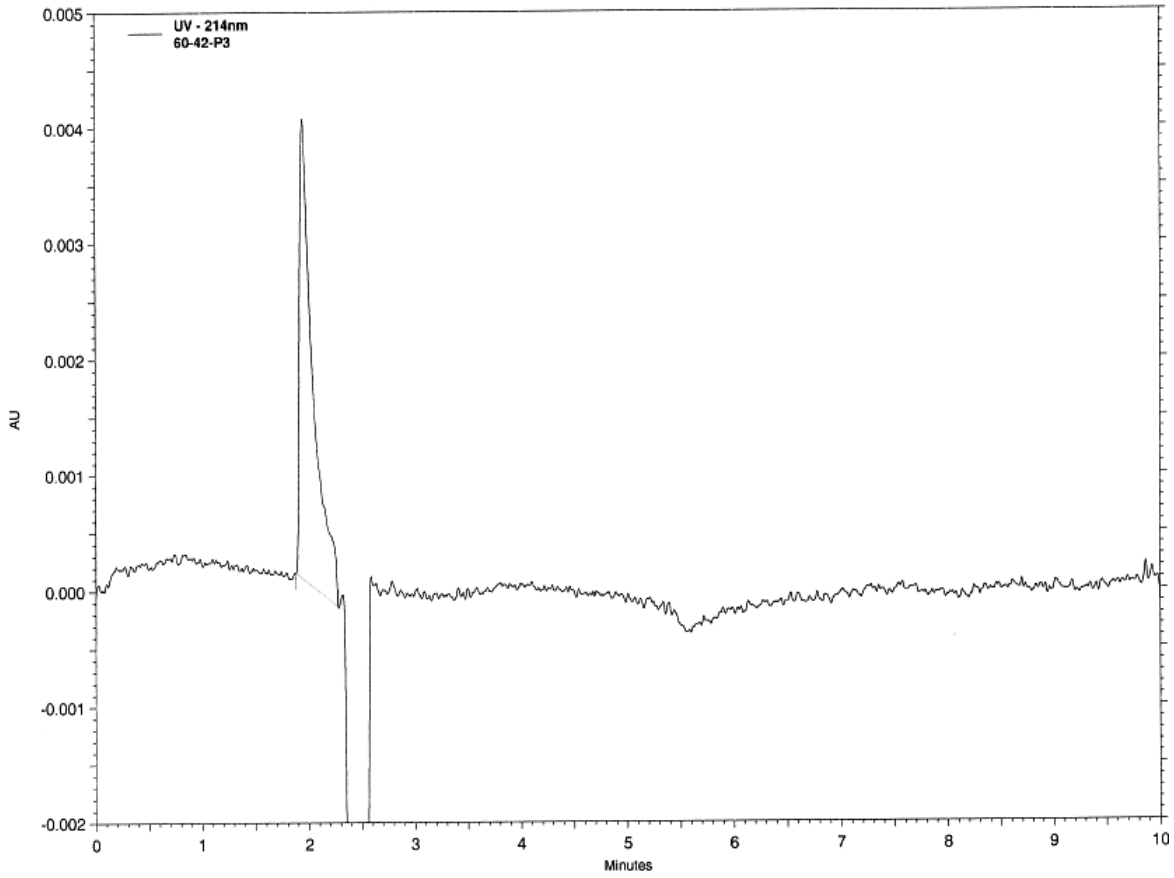

UV - 214nm
Results

Time	Area	Area %	Corrected Area	Corrected Area Percent
1.946	34698	100.00		
Totals	34698	100.00		

Trypsic digestion spectra

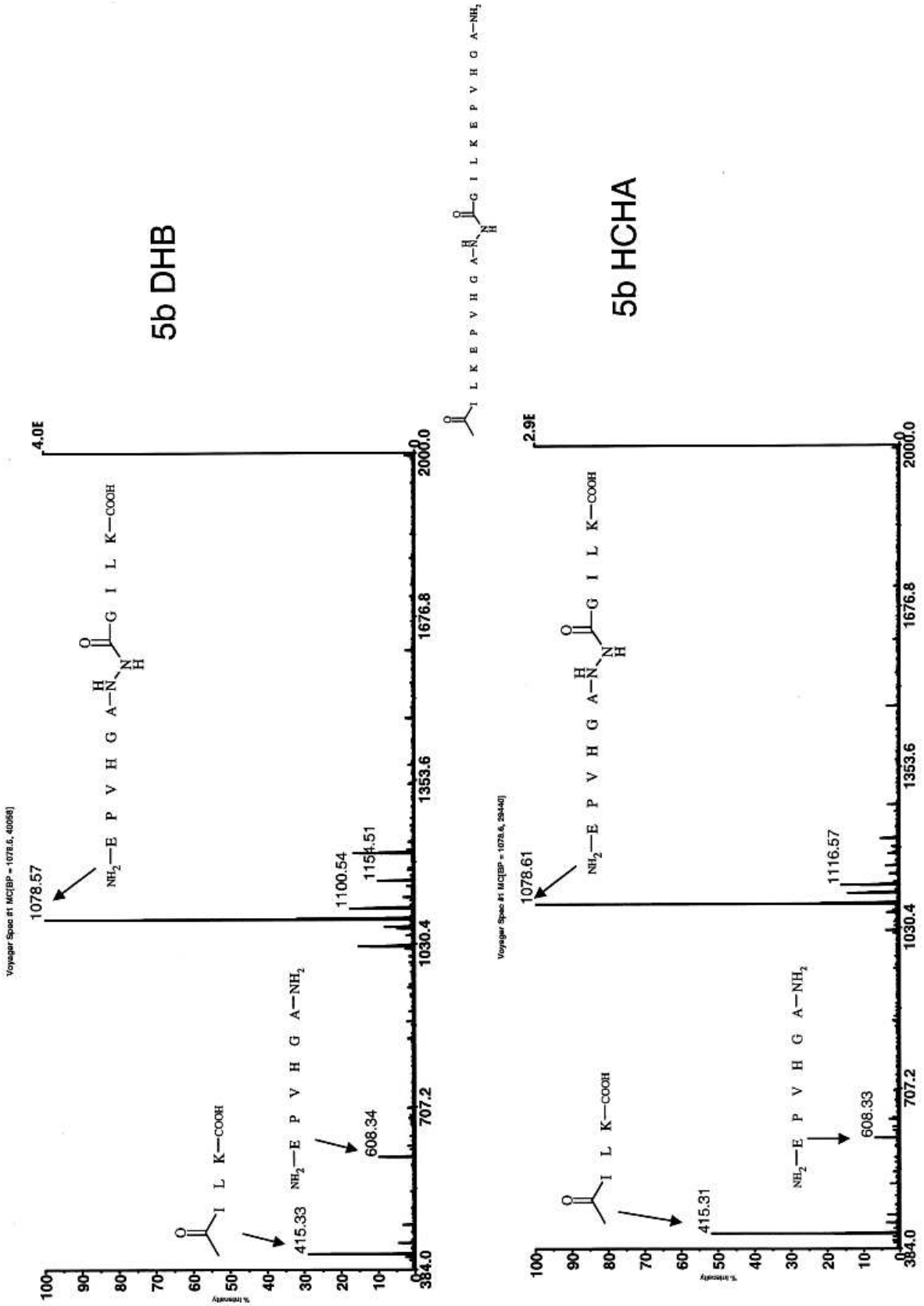

Analytical data for Agly-peptide **5c**

- RP-HPLC, C18 Xbridge BEH column, 1mL/min, λ=215 nm, 0-100% B in 60 min, 30°C

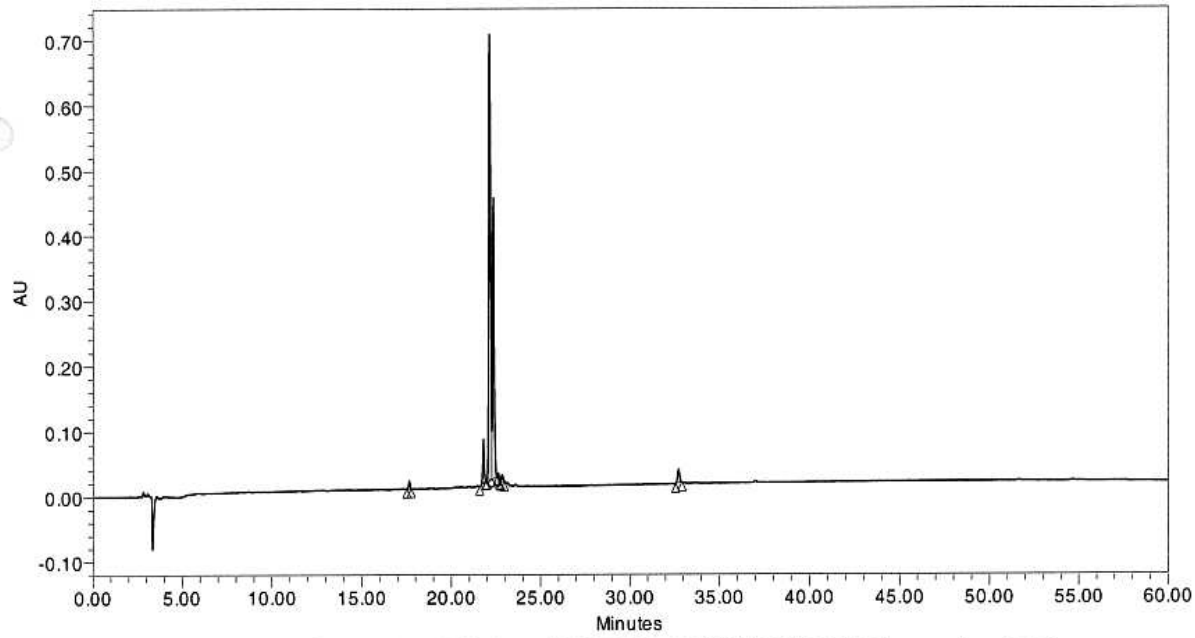

	RT	Area	% Area	Height
1	17.654	62518	0.78	12487
2	21.800	372250	4.61	66303
3	22.137	4560668	56.54	683898
4	22.350	2815533	34.90	429704
5	22.626	29813	0.37	7303
6	22.852	65057	0.81	10839
7	32.733	160472	1.99	20509

- MALDI-TOF α-cyano-4-hydroxy-cinnaminic acid matrix

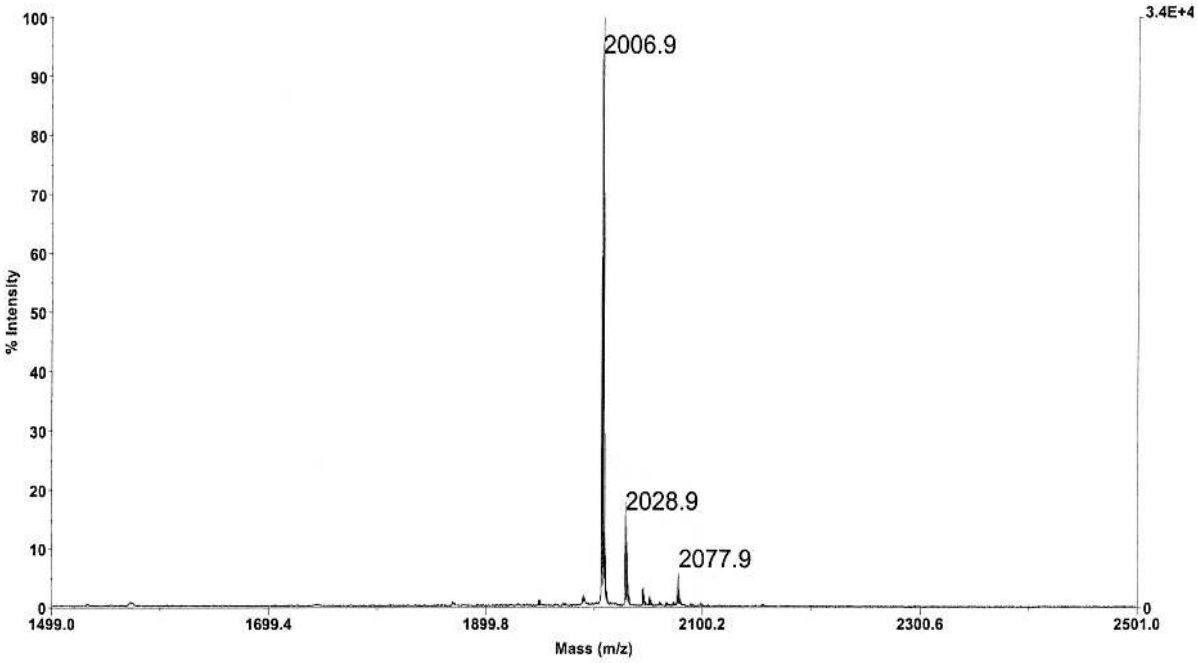

- CZE pH=3 sodium citrate buffer

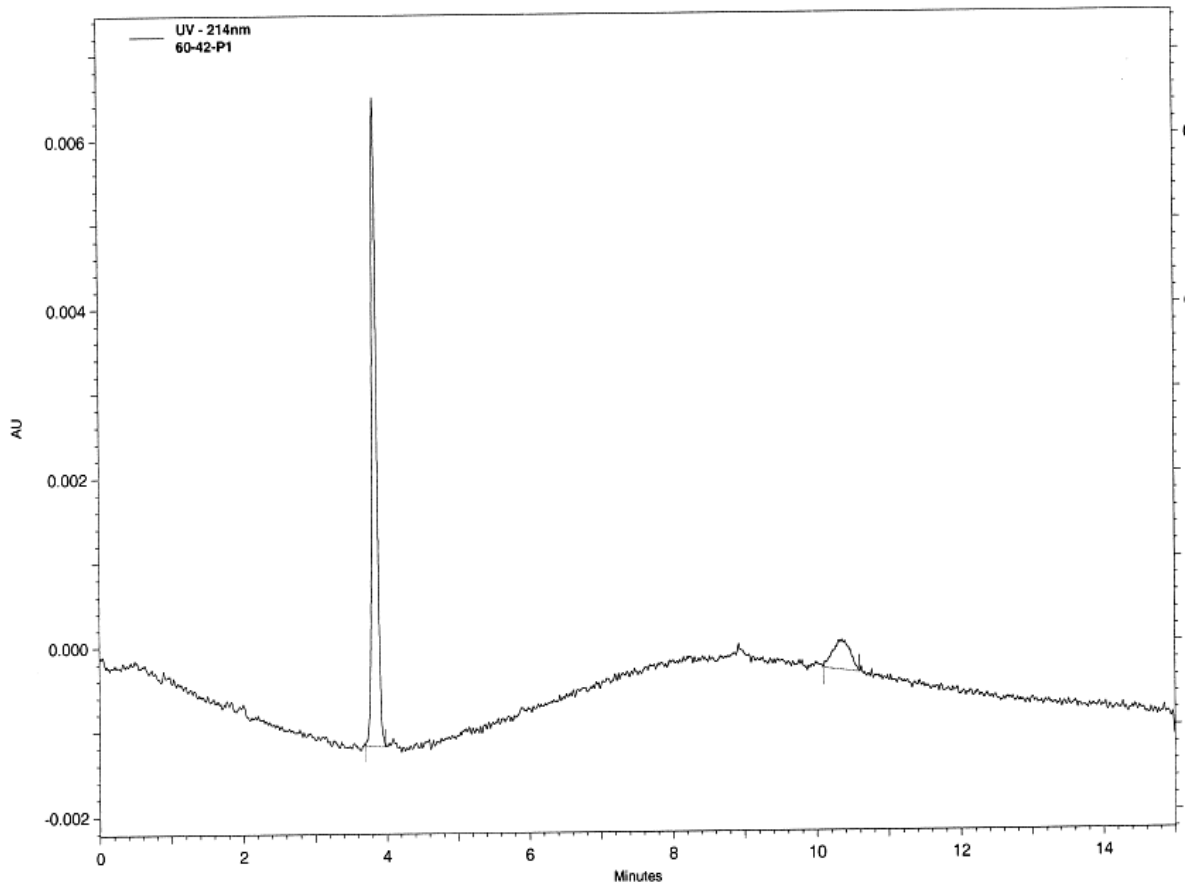

UV - 214nm
Results

Time	Area	Area %	Corrected Area	Corrected Area Percent
3.842	36121	85.82		
10.363	5969	14.18		
Totals	42090	100.00		

- CZE pH=4.5 sodium acetate buffer

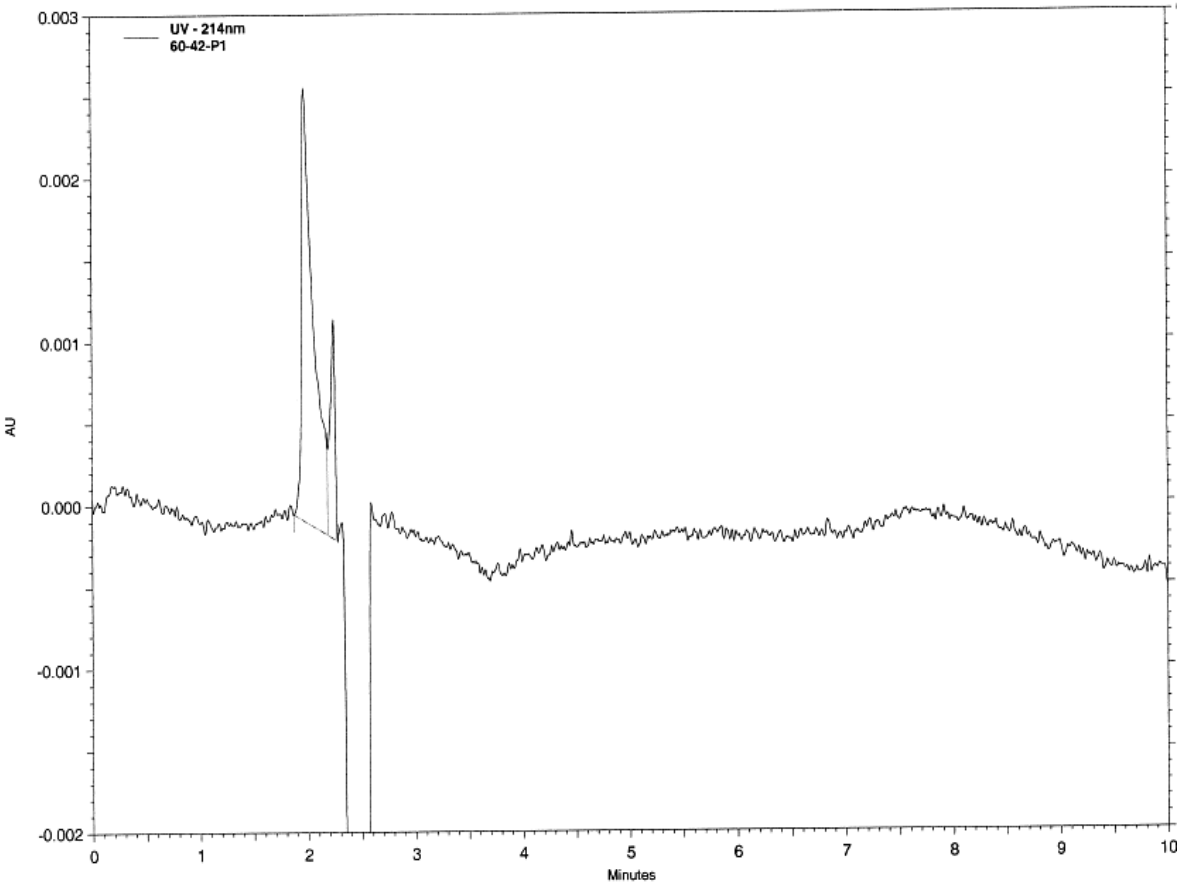

UV - 214nm
Results

Time	Area	Area %	Corrected Area	Corrected Area Percent
1.979	20156	82.77		
2.246	4195	17.23		
Totals	24351	100.00		

Trypsic digestion spectra

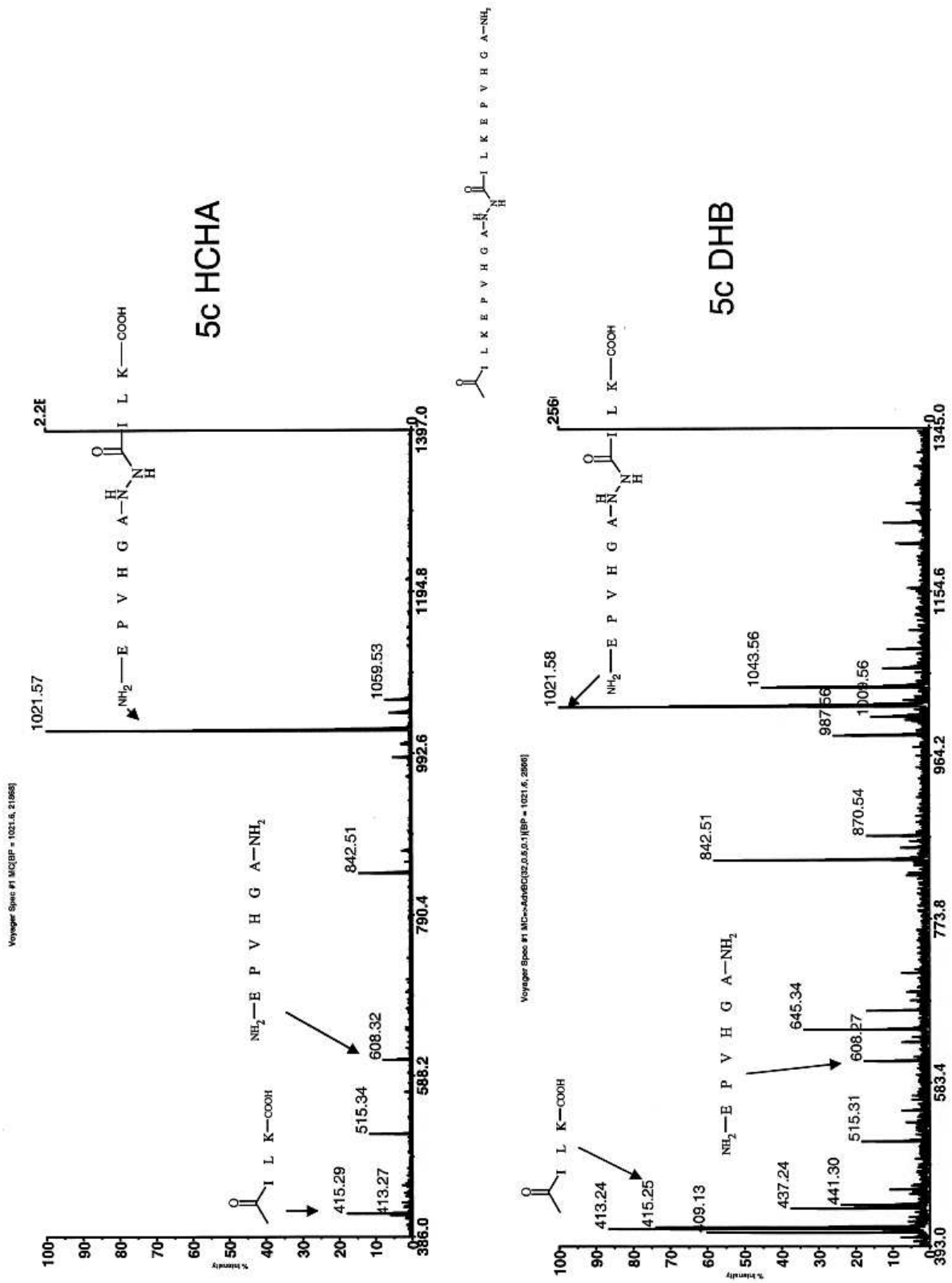

Analytical data for hydrazide peptide **3b**

- RP-HPLC, C3 zorbax column, 1mL/min, λ=215 nm, 0-100% B in 30 min, 30°C

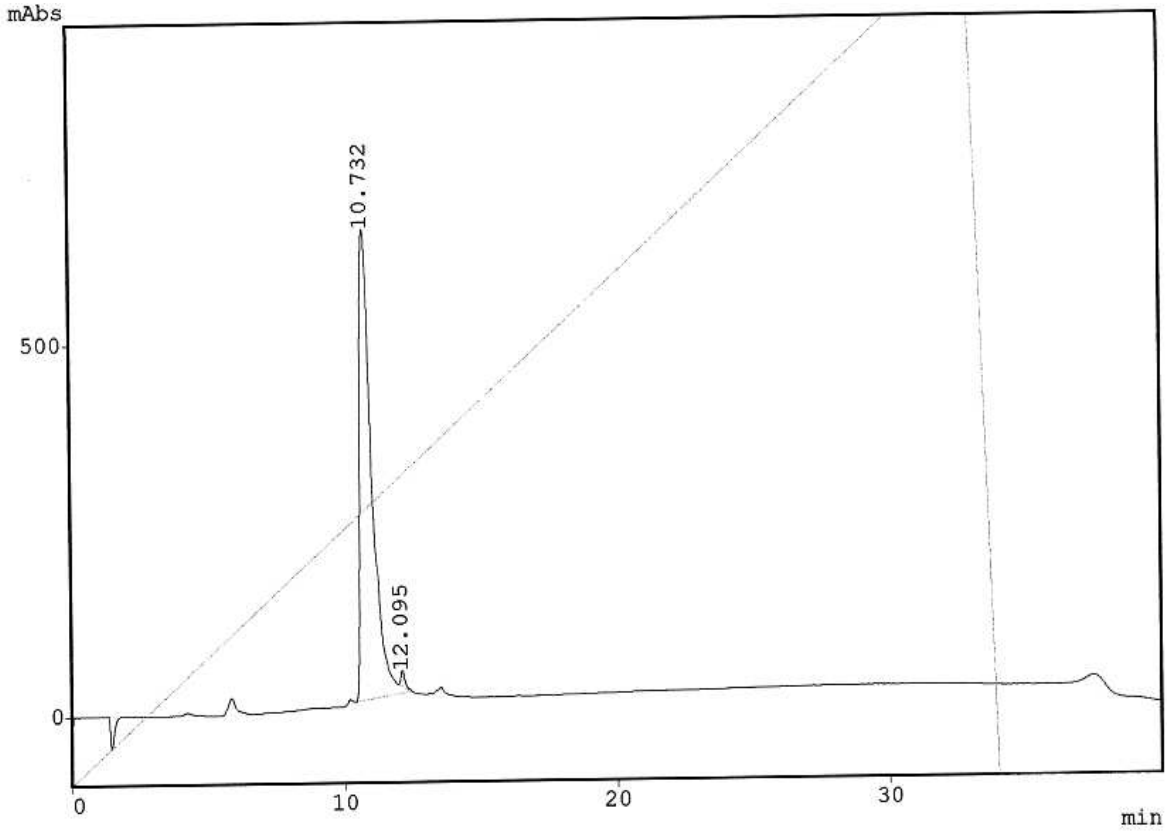

*** Peak Report ***

PKNO	TIME	AREA	HEIGHT	CONC
1	10.732	19356508	633310	99.0102
2	12.095	193502	21036	0.9898
		19550009	654346	100.0000

- MALDI-TOF 2,5-dihydroxy-benzoic acid matrix

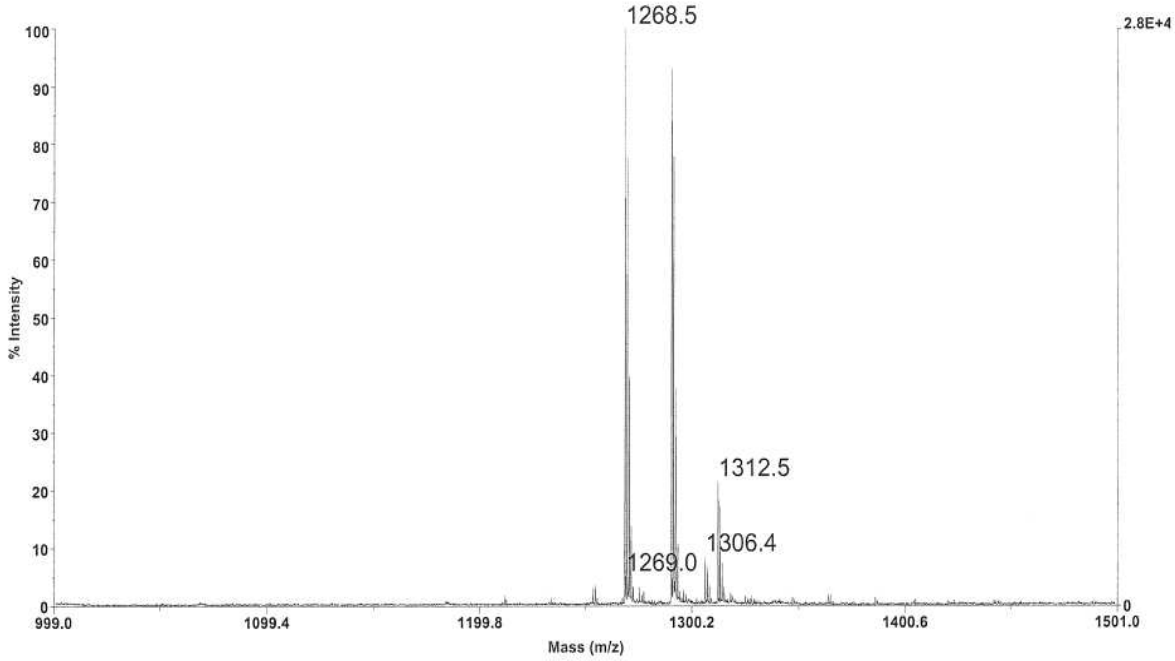

Voyager Spec #1[BP = 1268.5, 28020]

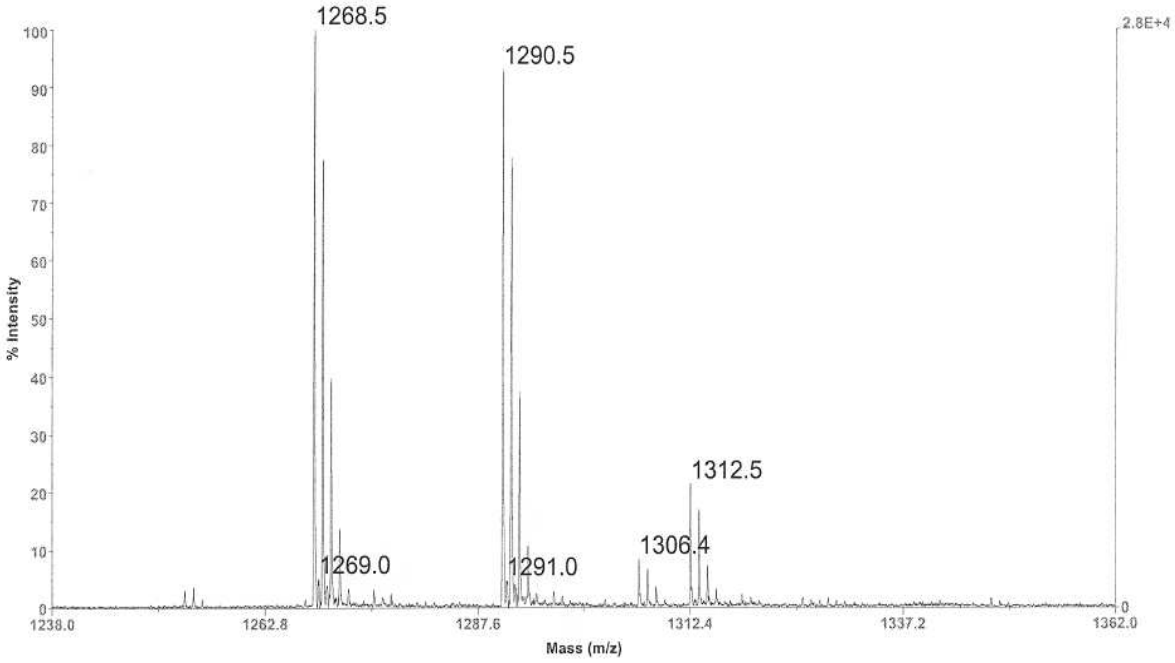

- CZE pH=3 sodium citrate buffer

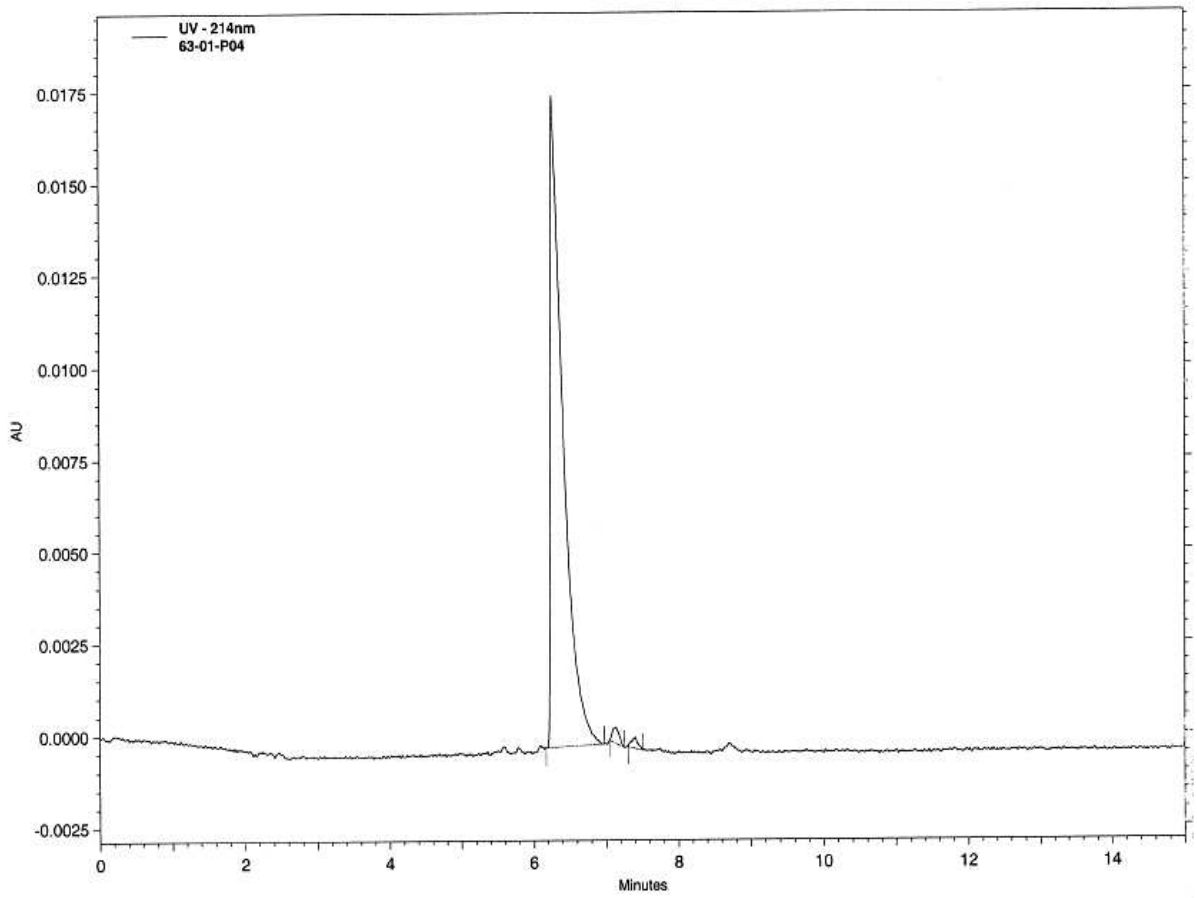

UV - 214nm
Results

Time	Area	Area %	Corrected Area	Corrected Area Percent
6.263	217969	97.93		
7.133	2724	1.22		
7.408	1877	0.84		
Totals	222570	100.00		

- CZE pH=4.5 sodium acetate buffer

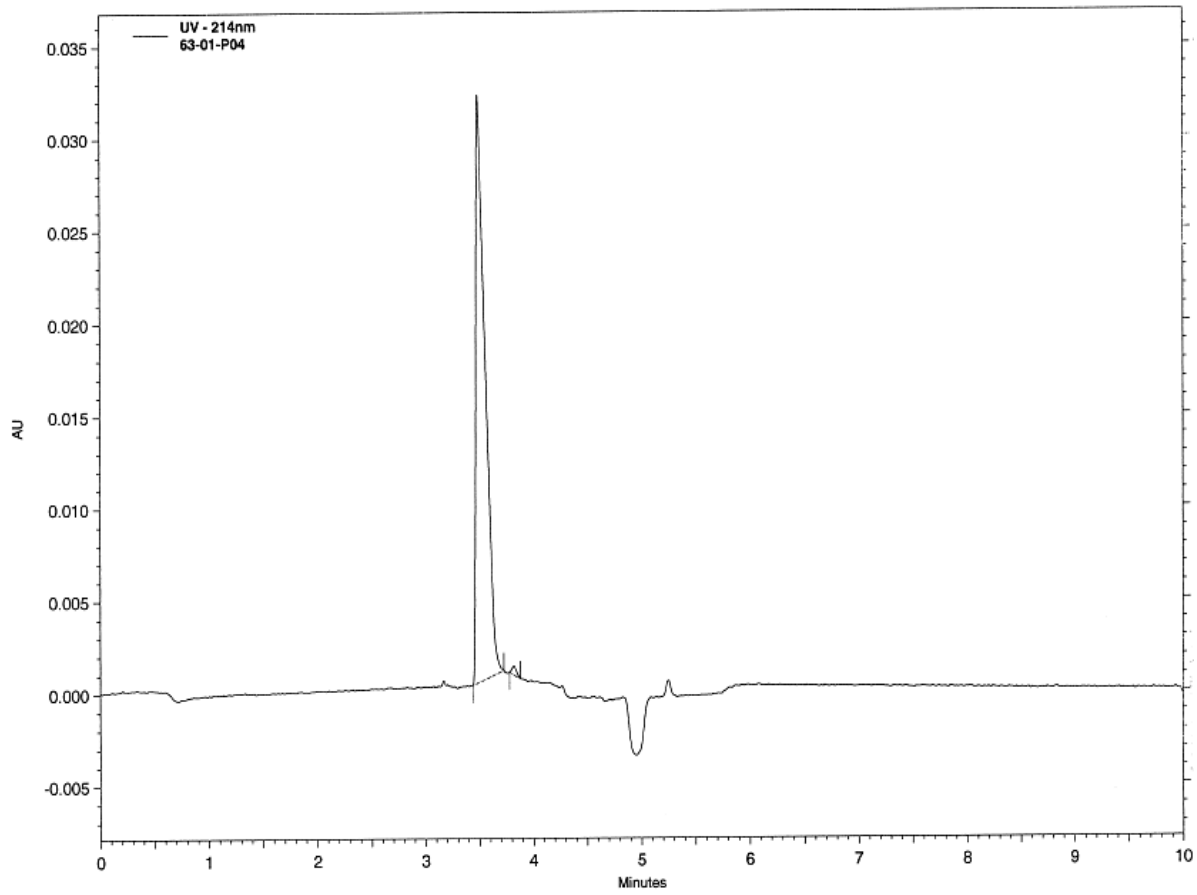

UV - 214nm
Results

Time	Area	Area %	Corrected Area	Corrected Area Percent
3.487	191254	99.24		
3.821	1474	0.76		
Totals	192728	100.00		

Analytical data for hydrazide peptide **3c**

- RP-HPLC, C3 Zorbax column, 1mL/min, λ=215 nm, 0-100% B in 60 min, 30°C

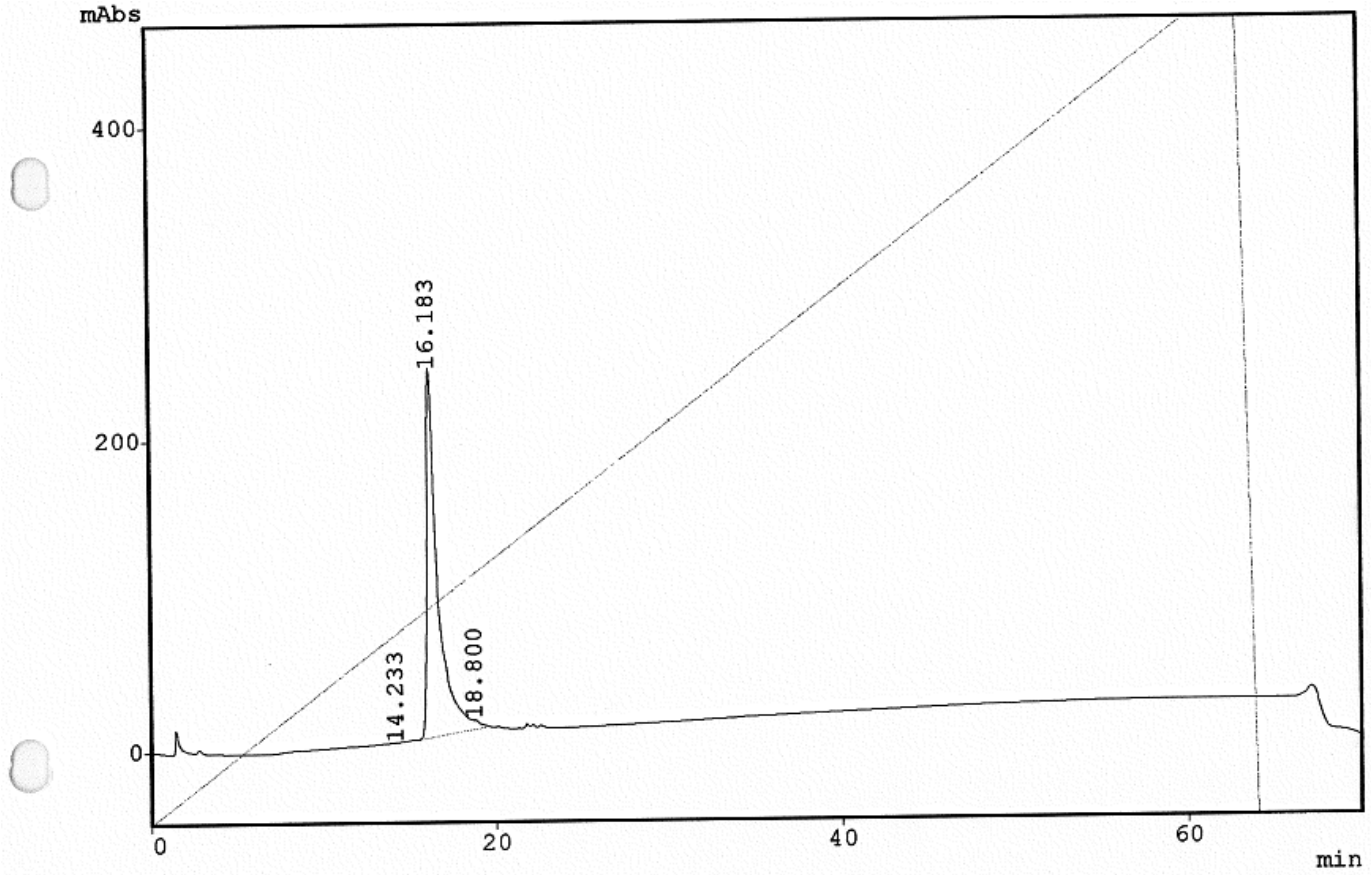

*** Peak Report ***

PKNO	TIME	AREA	HEIGHT	CONC
1	14.233	2758	239	0.0260
2	16.183	10592904	236474	99.8641
3	18.800	11654	1284	0.1099
		10607316	237996	100.0000

- MALDI-TOF 2,5-dihydroxy-benzoic acid matrix

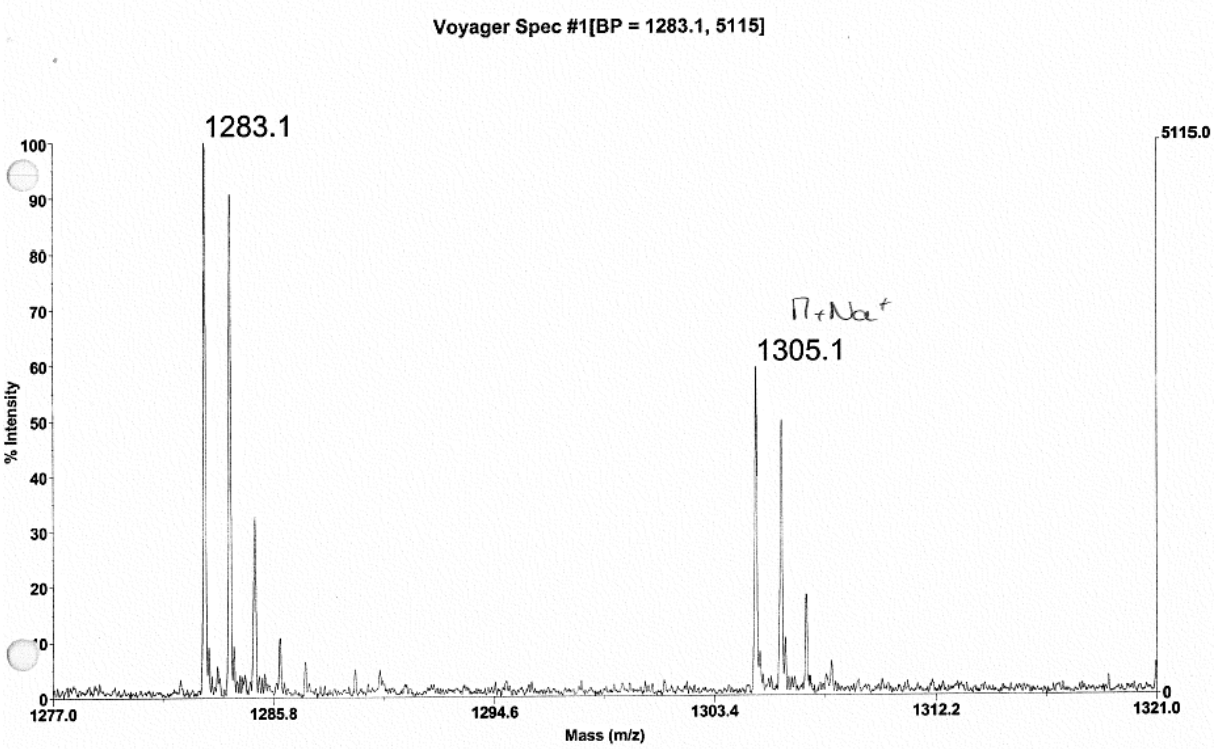

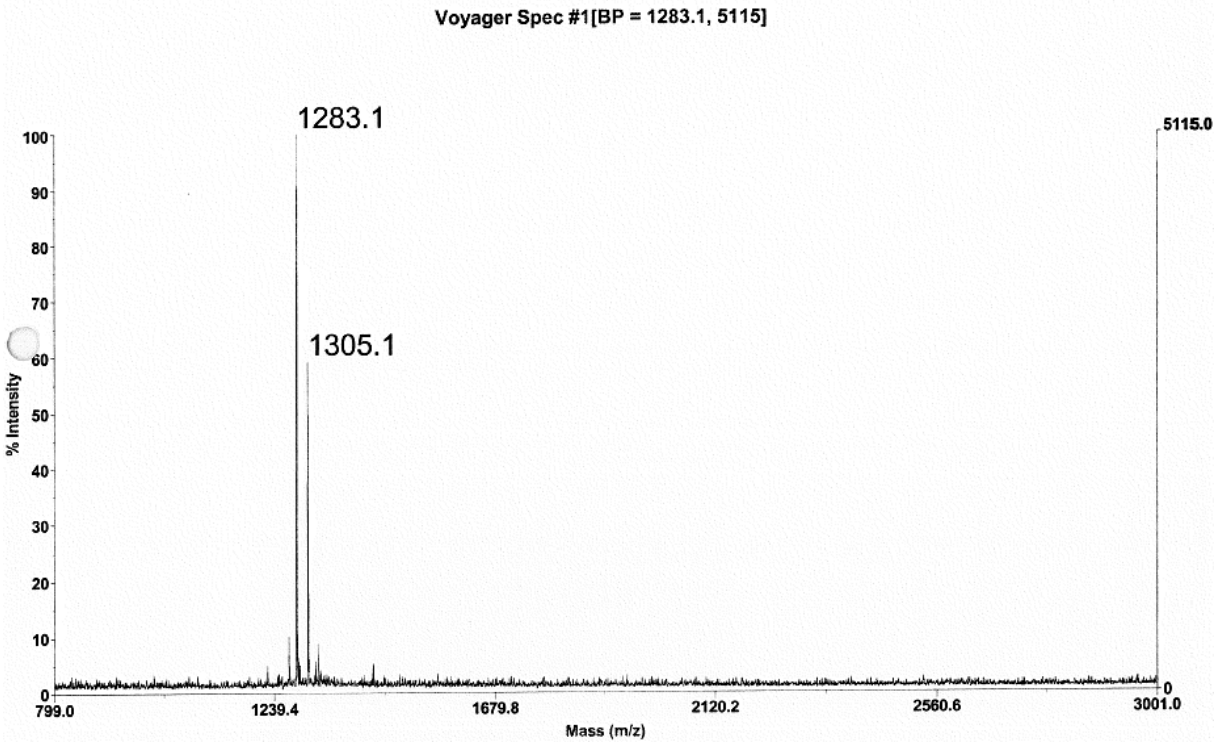

- CZE pH=3 sodium citrate buffer

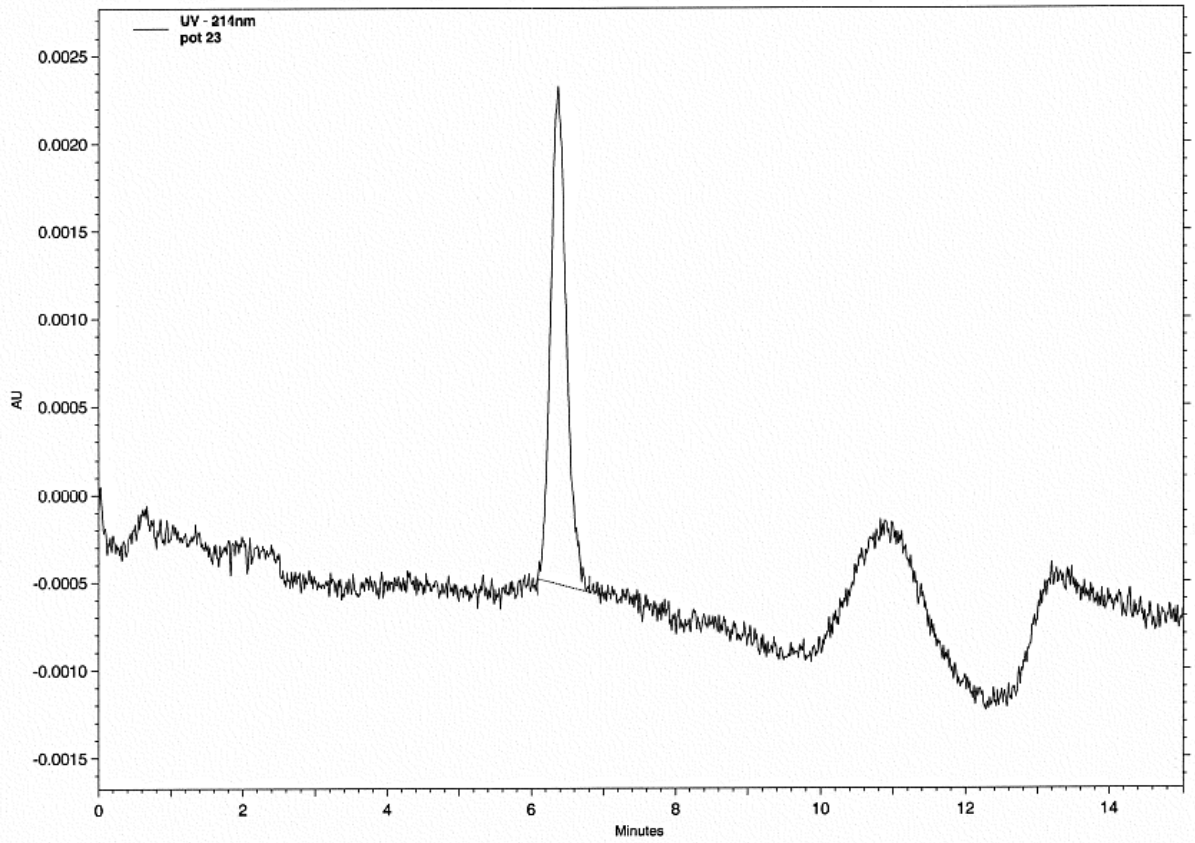

UV - 214nm
Results

Time	Area	Area %	Corrected Area	Corrected Area Percent
6.367	43191	100.00		
Totals	43191	100.00		

- CZE pH=4.5 sodium acetate buffer

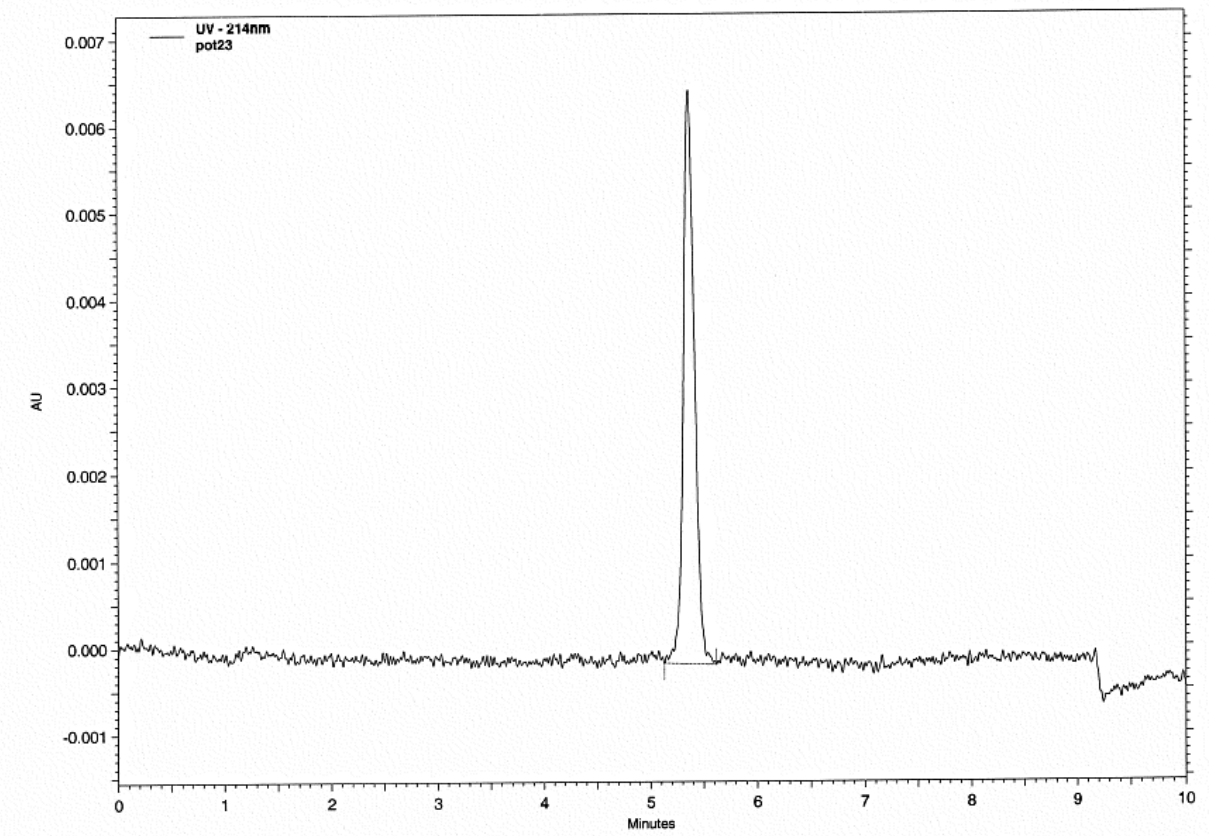

UV - 214nm
Results

Time	Area	Area %	Corrected Area	Corrected Area Percent
5.362	48044	100.00		
Totals	48044	100.00		

Analytical data for phenylthiocarbonyl peptide **4a**

- RP-HPLC, C18 Nucleosil column, 1mL/min, λ=215 nm, 0-100% B in 60 min, 30°C

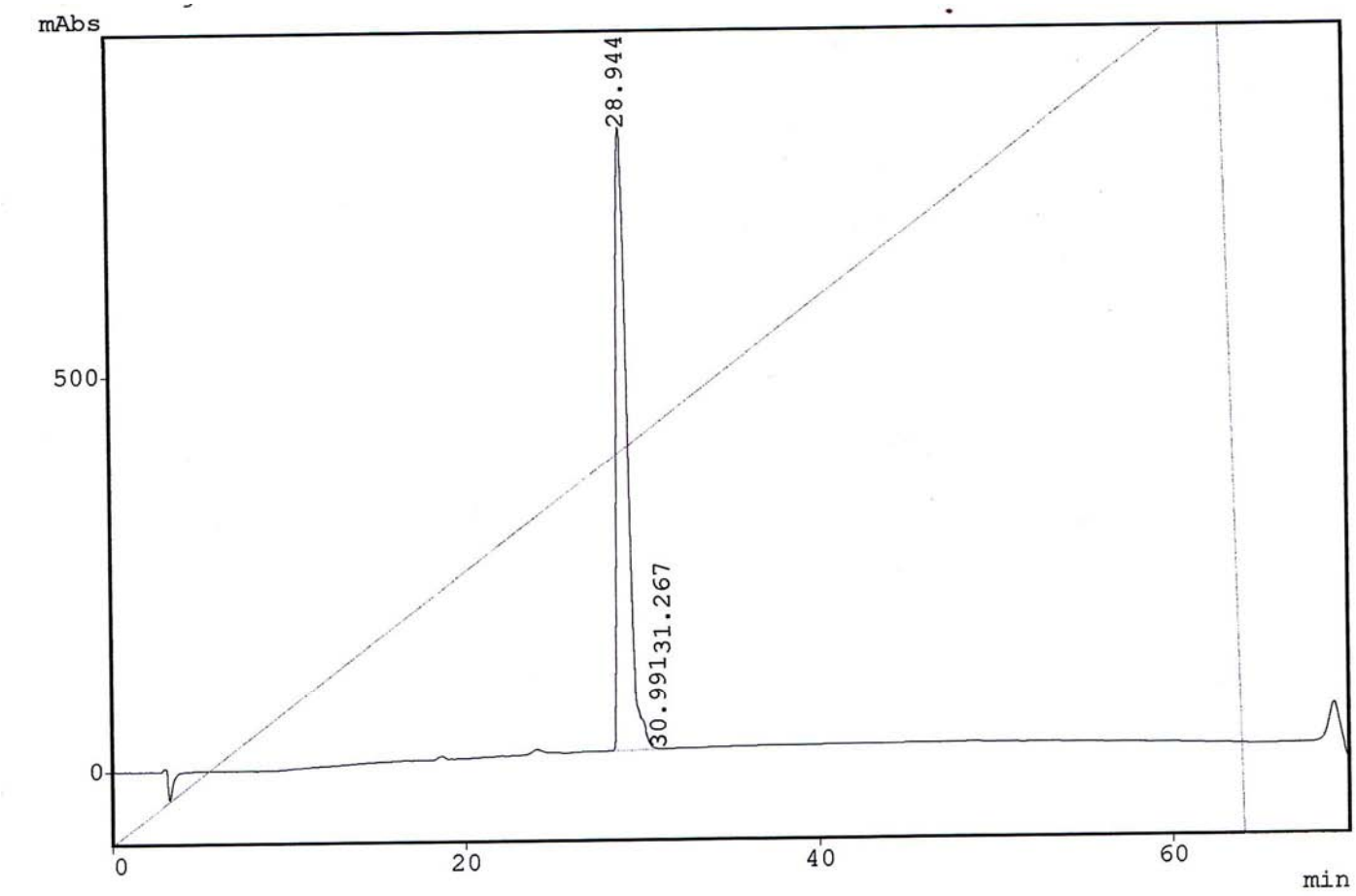

*** Peak Report ***

PKNO	TIME	AREA	HEIGHT	CONC
1	28.944	33139601	788250	99.9928
2	30.991	1205	117	0.0036
3	31.267	1189	110	0.0036
		33141995	788478	100.0000

- MALDI-TOF α-cyano-4-hydroxy-cinnaminic acid matrix

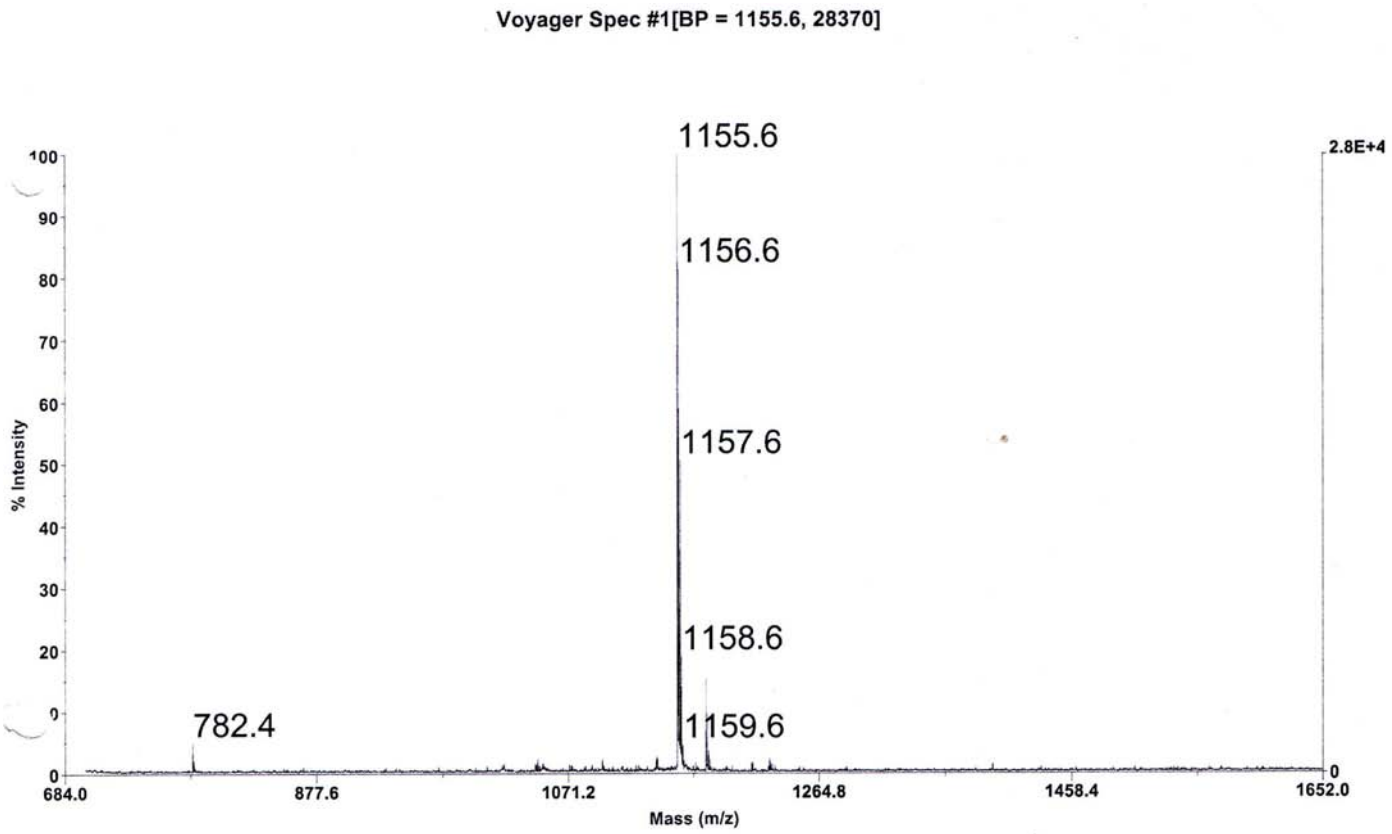

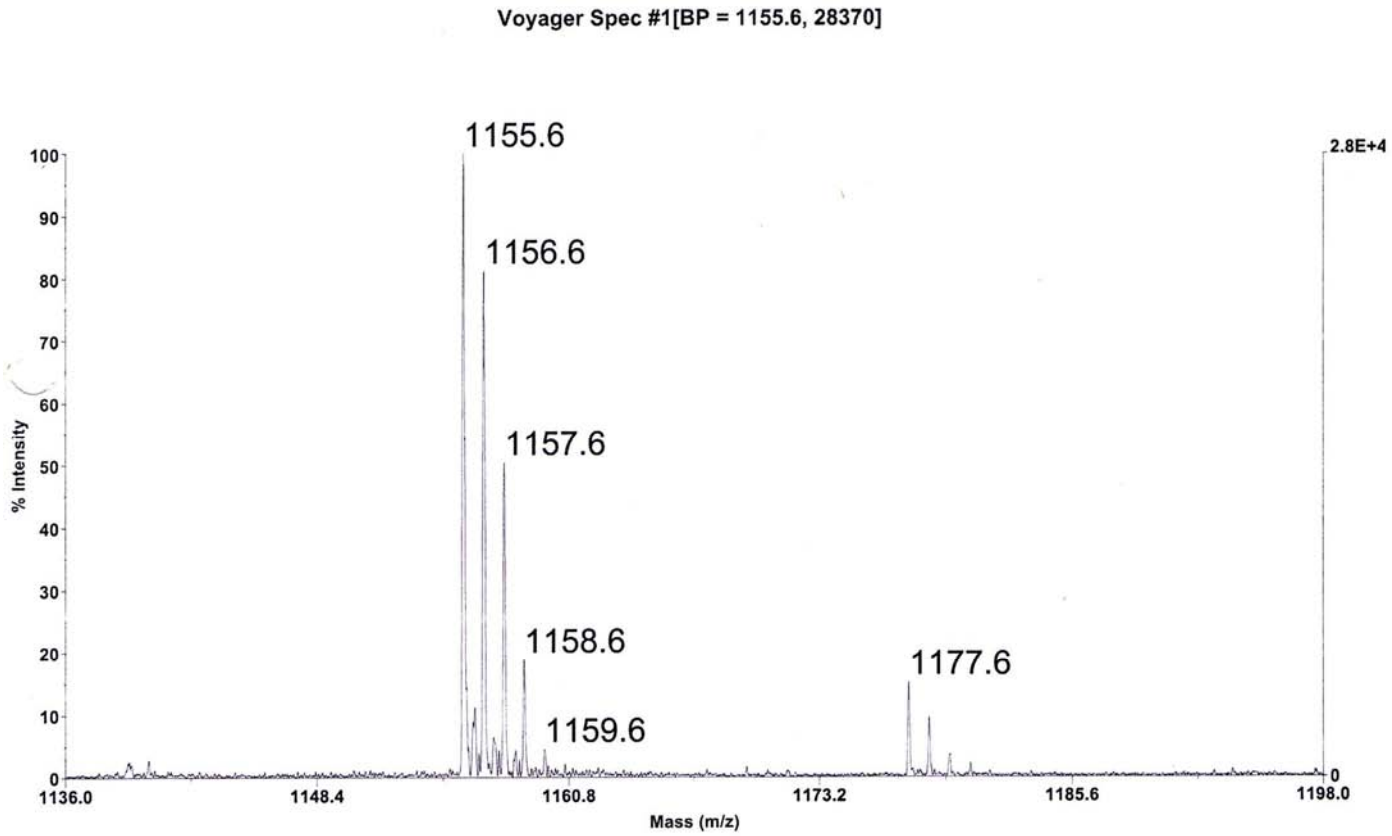

- CZE pH=3 sodium citrate buffer

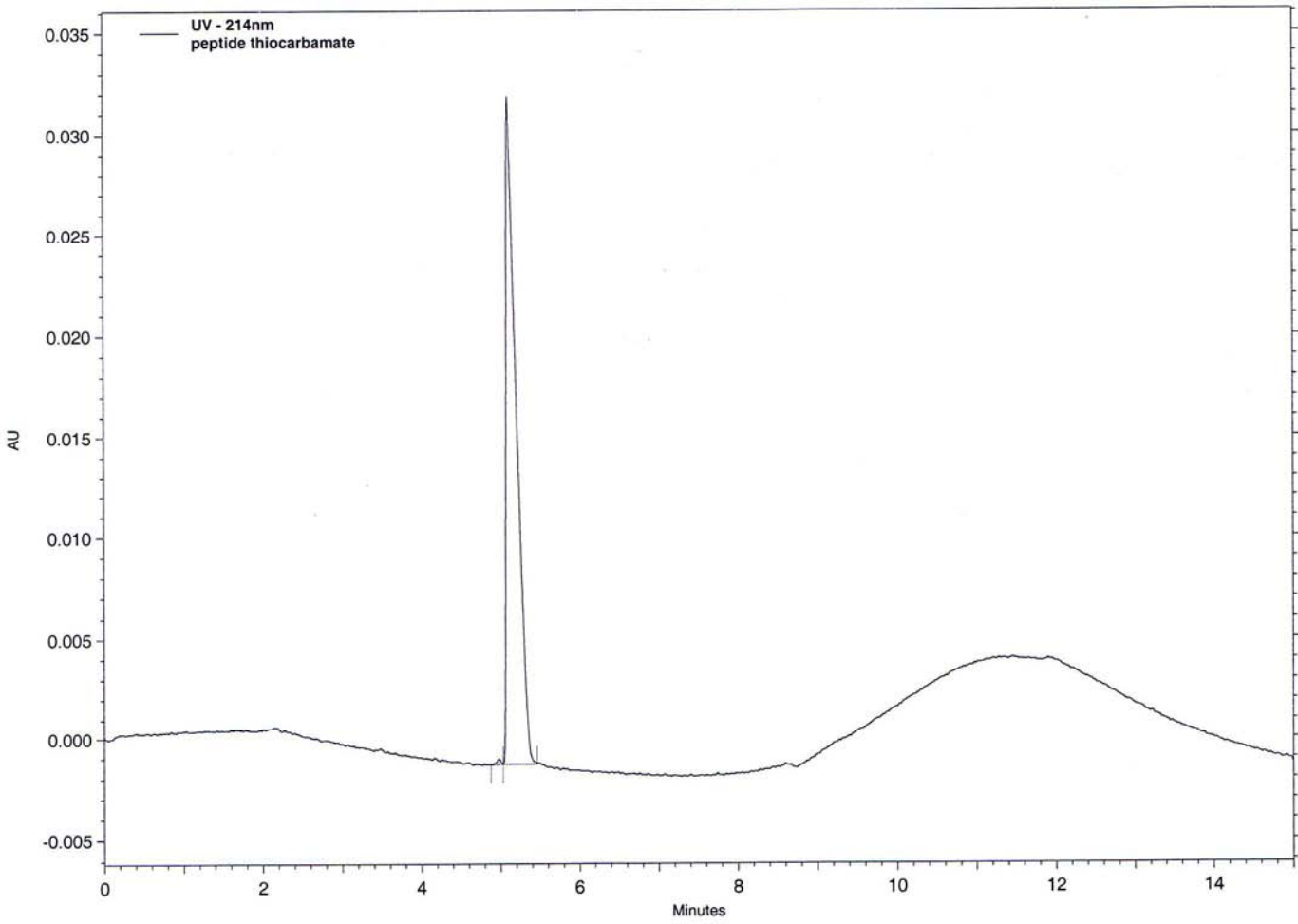

UV - 214nm
Results

Time	Area	Area %	Corrected Area	Corrected Area Percent
4.975	1034	0.35		
5.100	296062	99.65		
Totals	297096	100.00		

- CZE pH=4.5 sodium acetate buffer

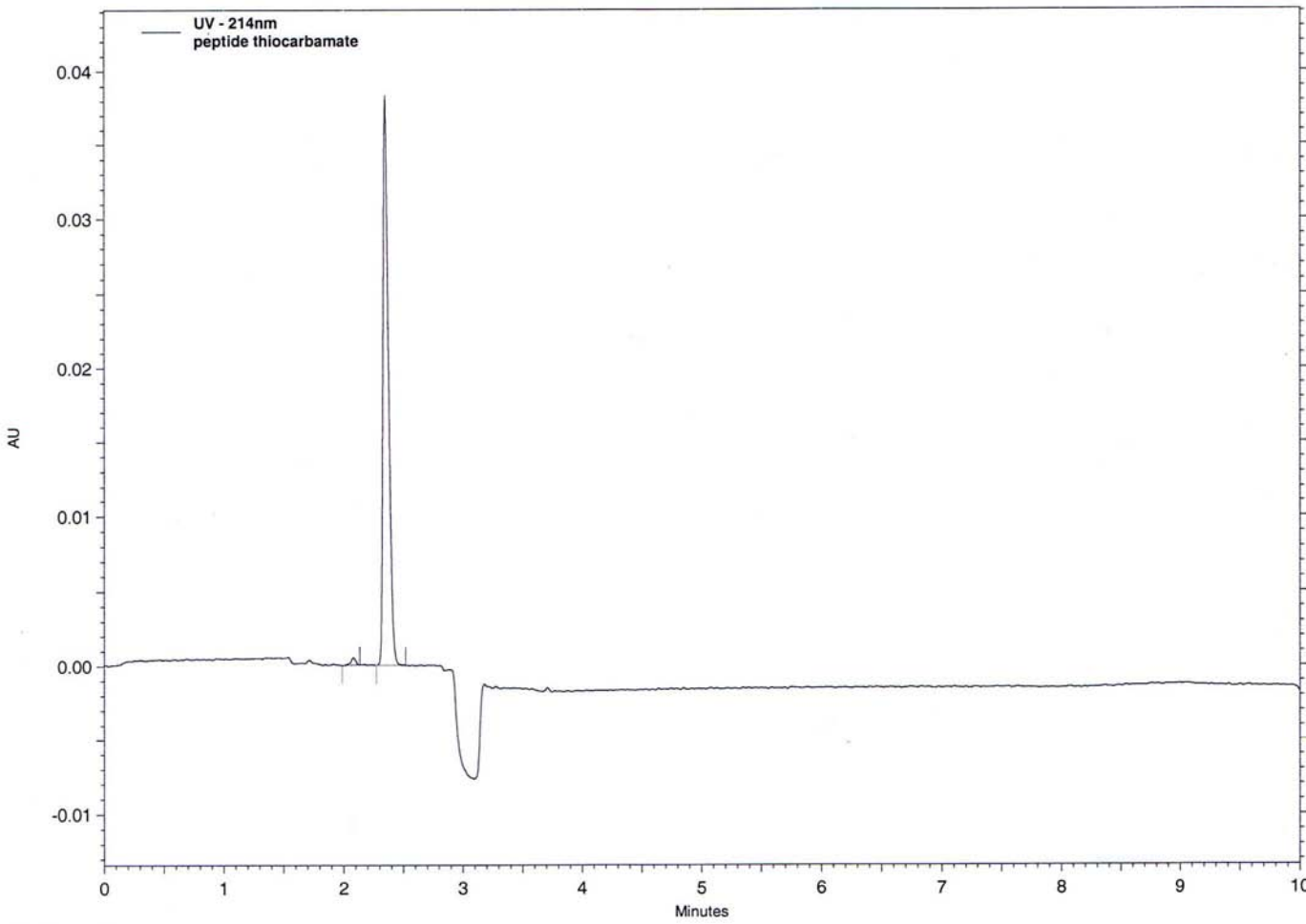

UV - 214nm
Results

Time	Area	Area %	Corrected Area	Corrected Area Percent
2.083	1461	1.19		
2.346	120860	98.81		
Totals	122321	100.00		

Analytical data for Agly-peptide **5d**

- RP-HPLC, C18 Nucleosil column, 1mL/min, λ=215 nm, 0-100% B in 30 min, 30°C

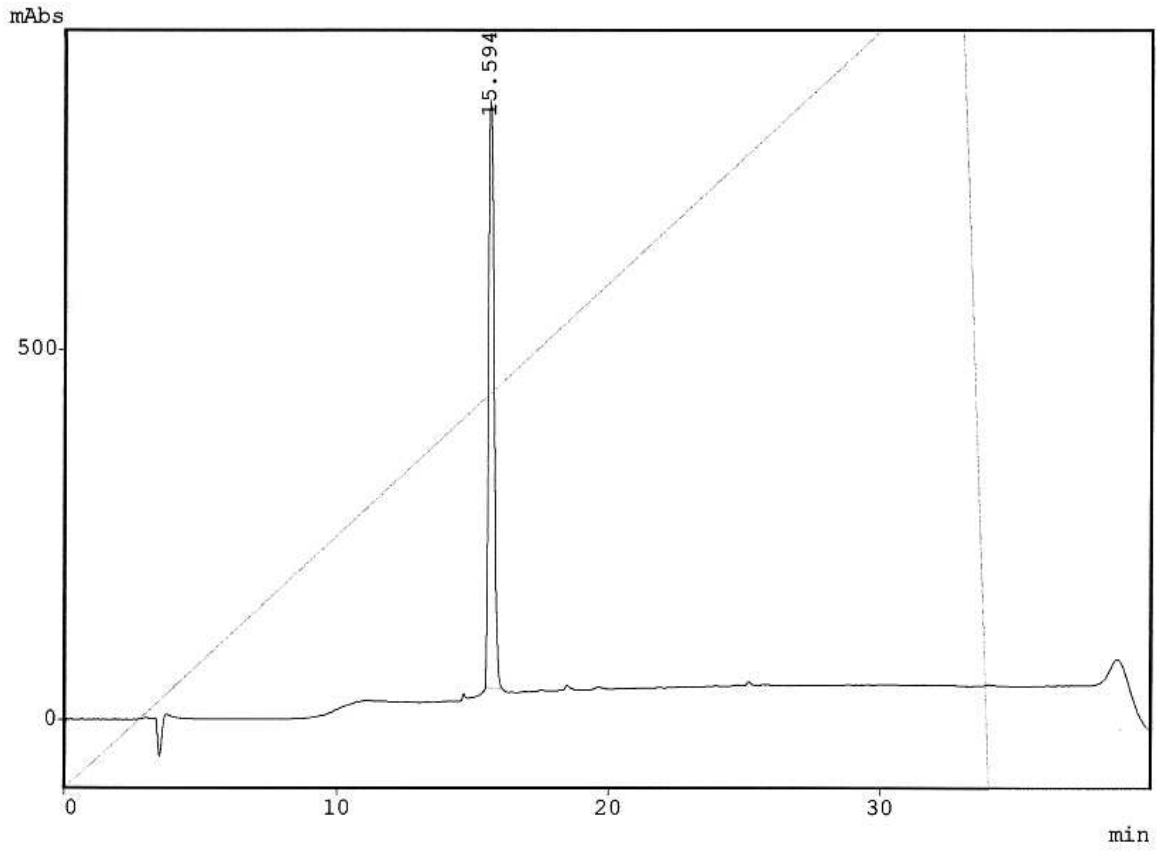

*** Peak Report ***

PKNO	TIME	AREA	HEIGHT	CONC
1	15.594	11355620	792911	100.0000
		11355620	792911	100.0000

- MALDI-TOF α-cyano-4-hydroxy-cinnaminic acid matrix

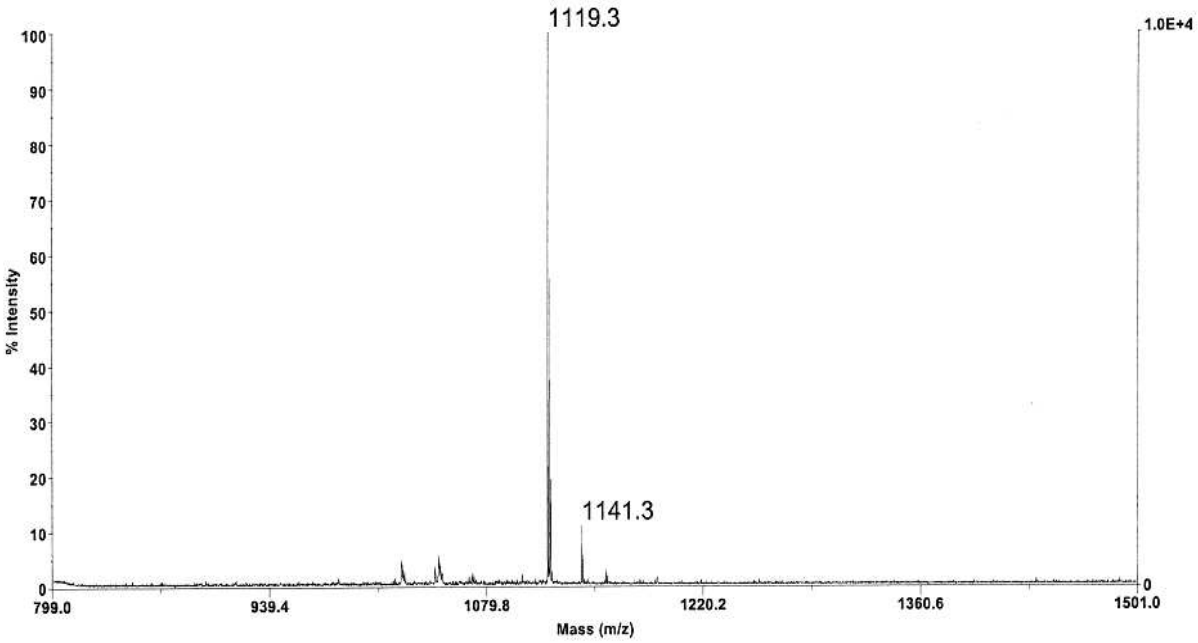

- CZE pH=3 sodium citrate buffer

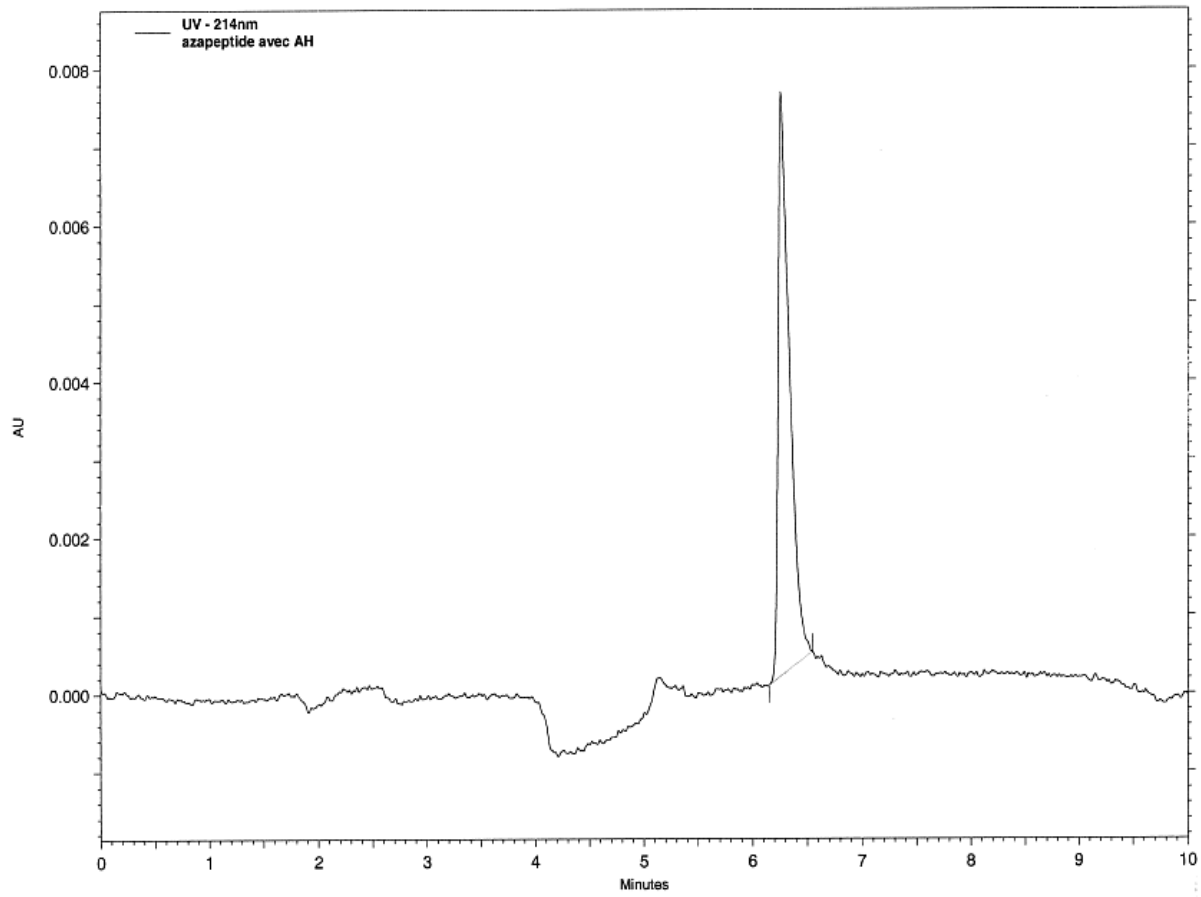

UV - 214nm
Results

Time	Area	Area %	Corrected Area	Corrected Area Percent
6.254	53961	100.00		
Totals	53961	100.00		

- CZE pH=4.5 sodium acetate buffer

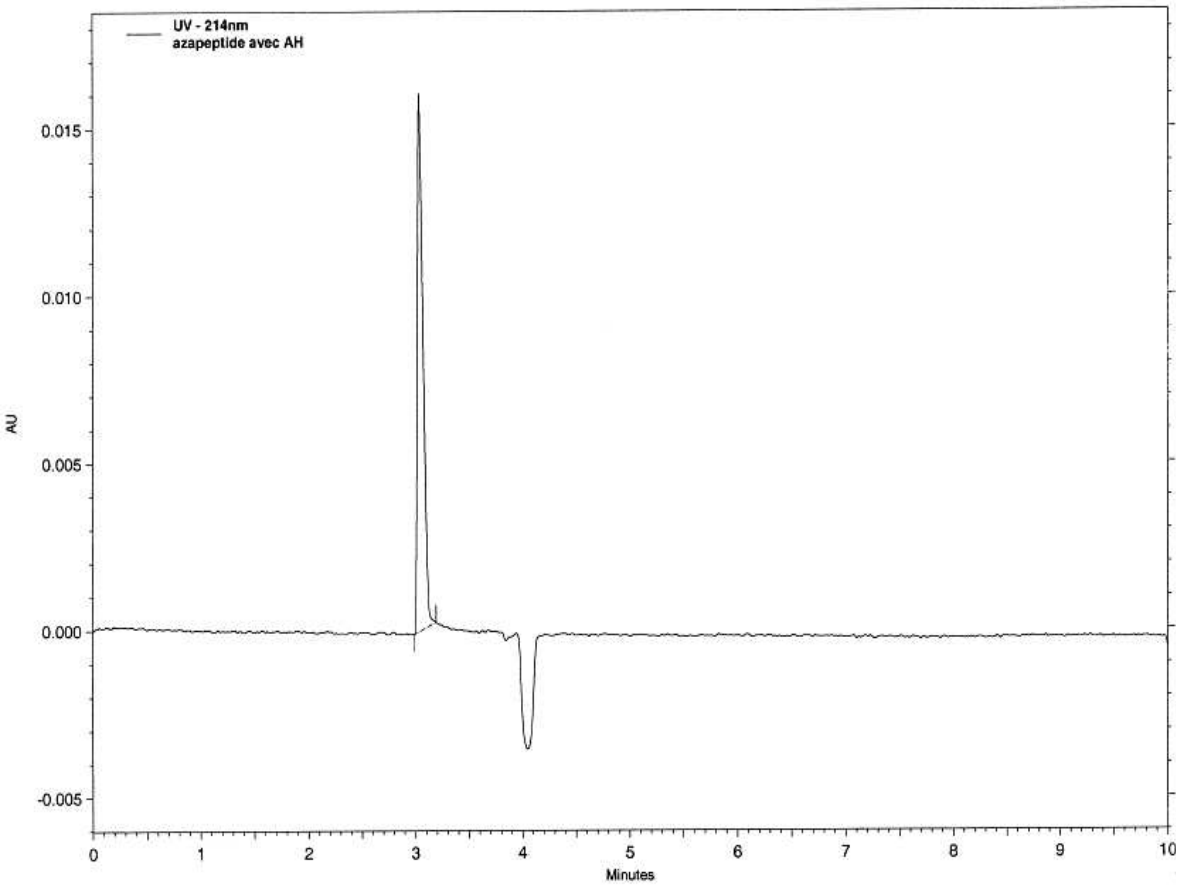

UV - 214nm
Results

Time	Area	Area %	Corrected Area	Corrected Area Percent
3.033	57815	100.00		
Totals	57815	100.00		

Trypsic digestion spectra

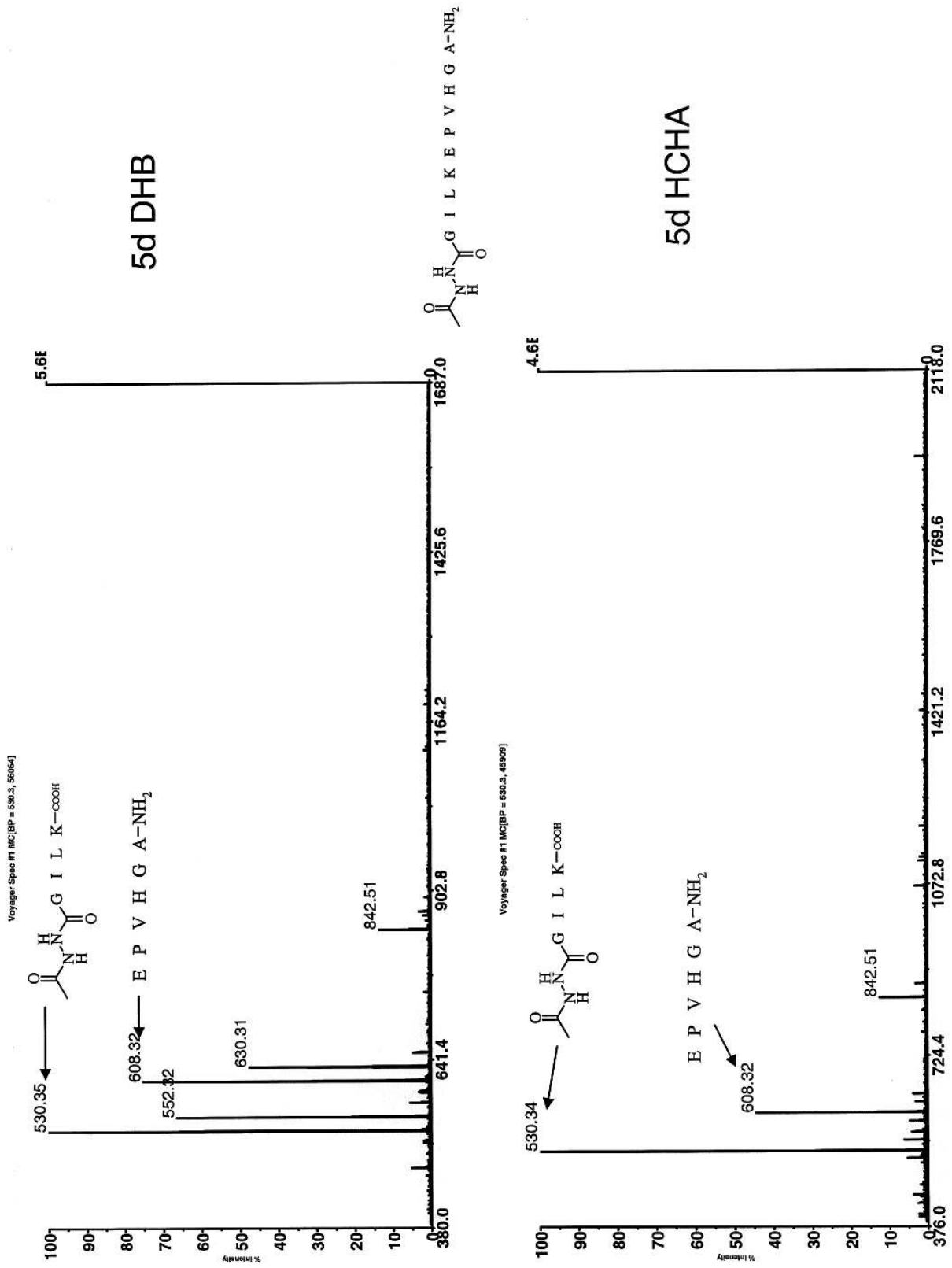

Analytical data for Agly-peptide **5e**

- RP-HPLC, C18 Nucleosil column, 1mL/min, λ=215 nm, 0-100% B in 60 min, 30°C

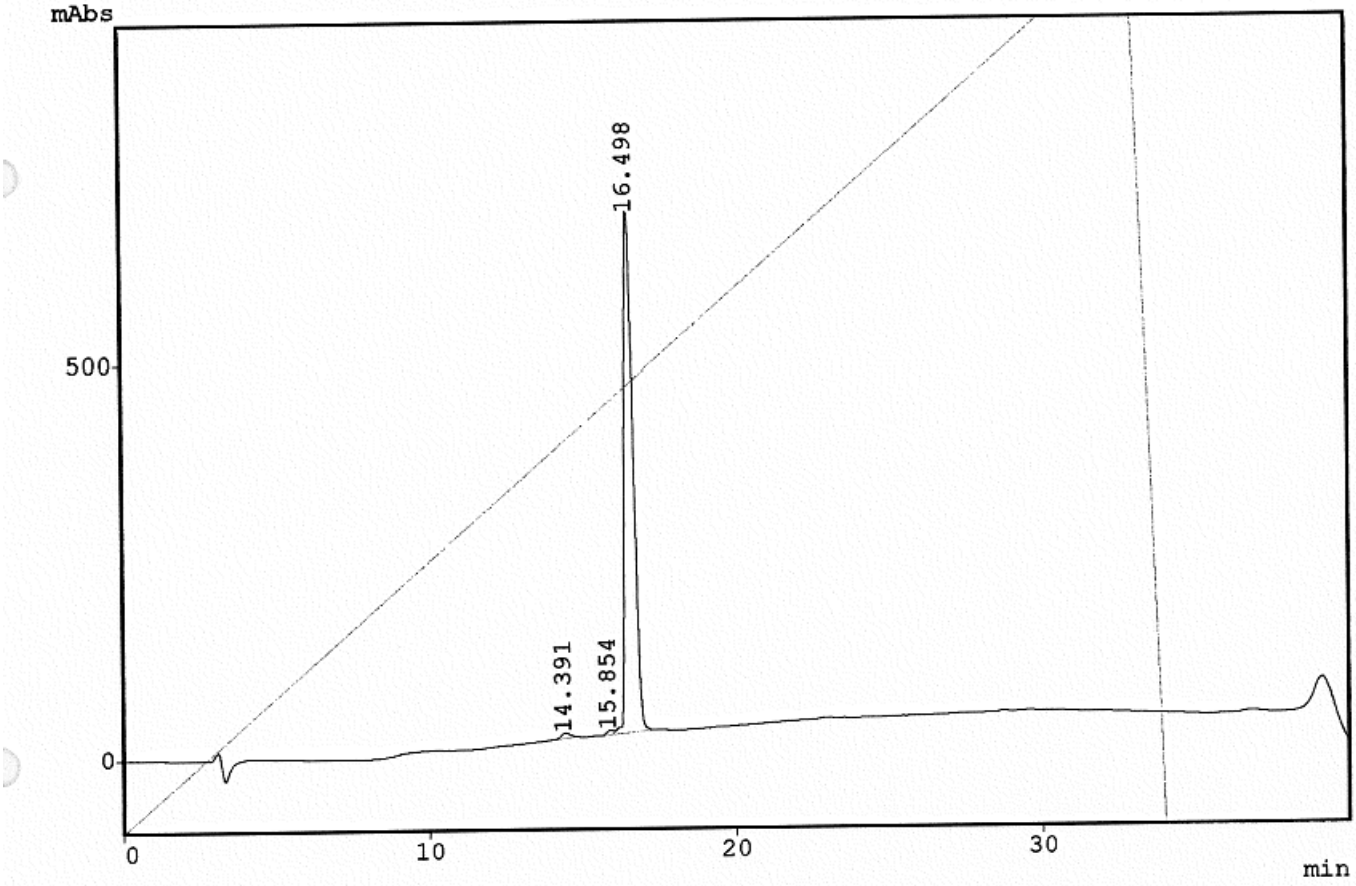

*** Peak Report ***

PKNO	TIME	AREA	HEIGHT	CONC
1	14.391	146546	7023	1.0941
2	15.854	84615	5737	0.6317
3	16.498	13163487	659429	98.2742
		13394647	672189	100.0000

- MALDI-TOF α-cyano-4-hydroxy-cinnaminic acid matrix

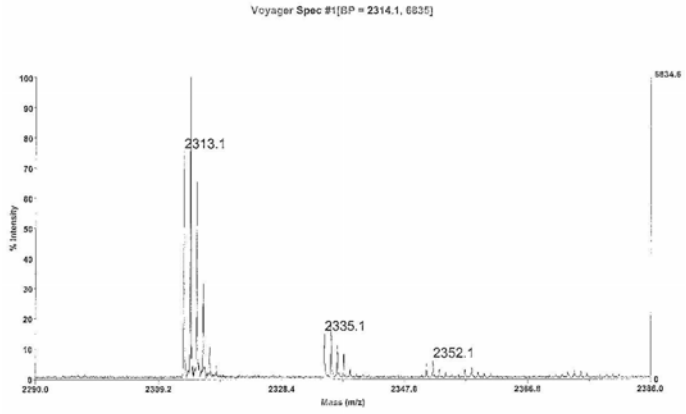

Laser Intensity = 1804

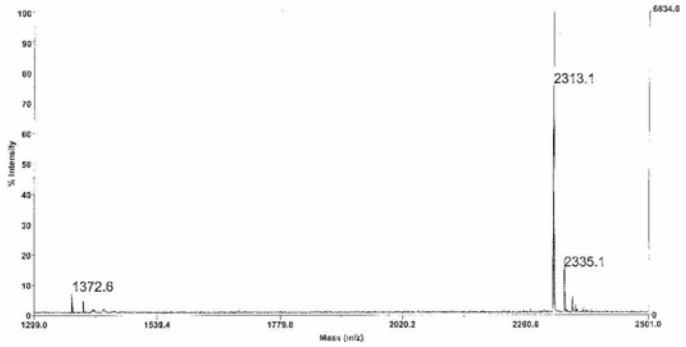

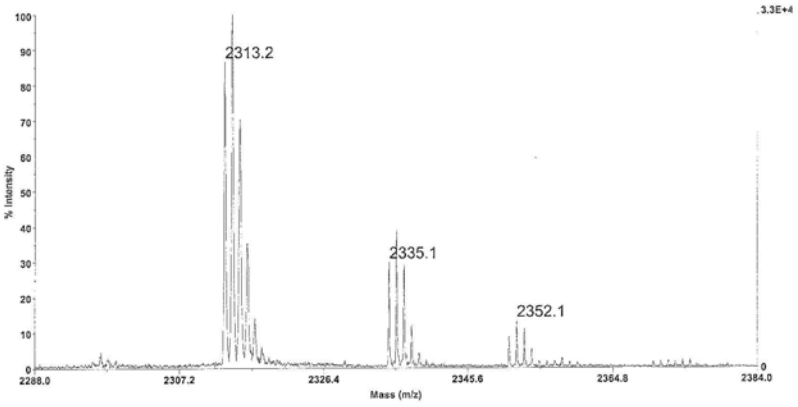

Laser Intensity = 2004

Voyager Spec #1[BP = 2314.2, 33488]

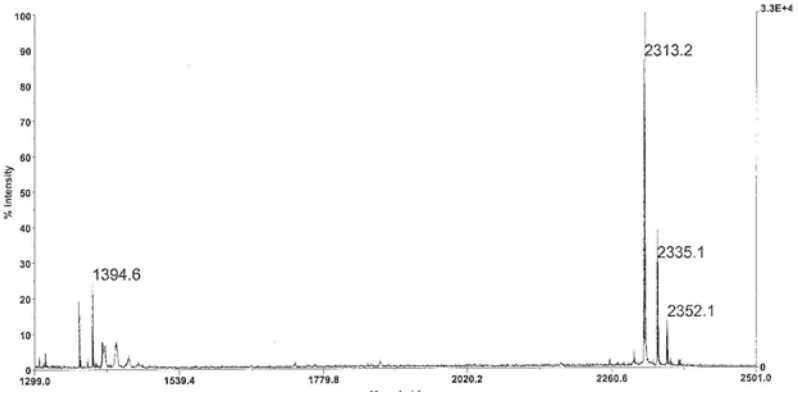

- CZE pH=3 sodium citrate buffer

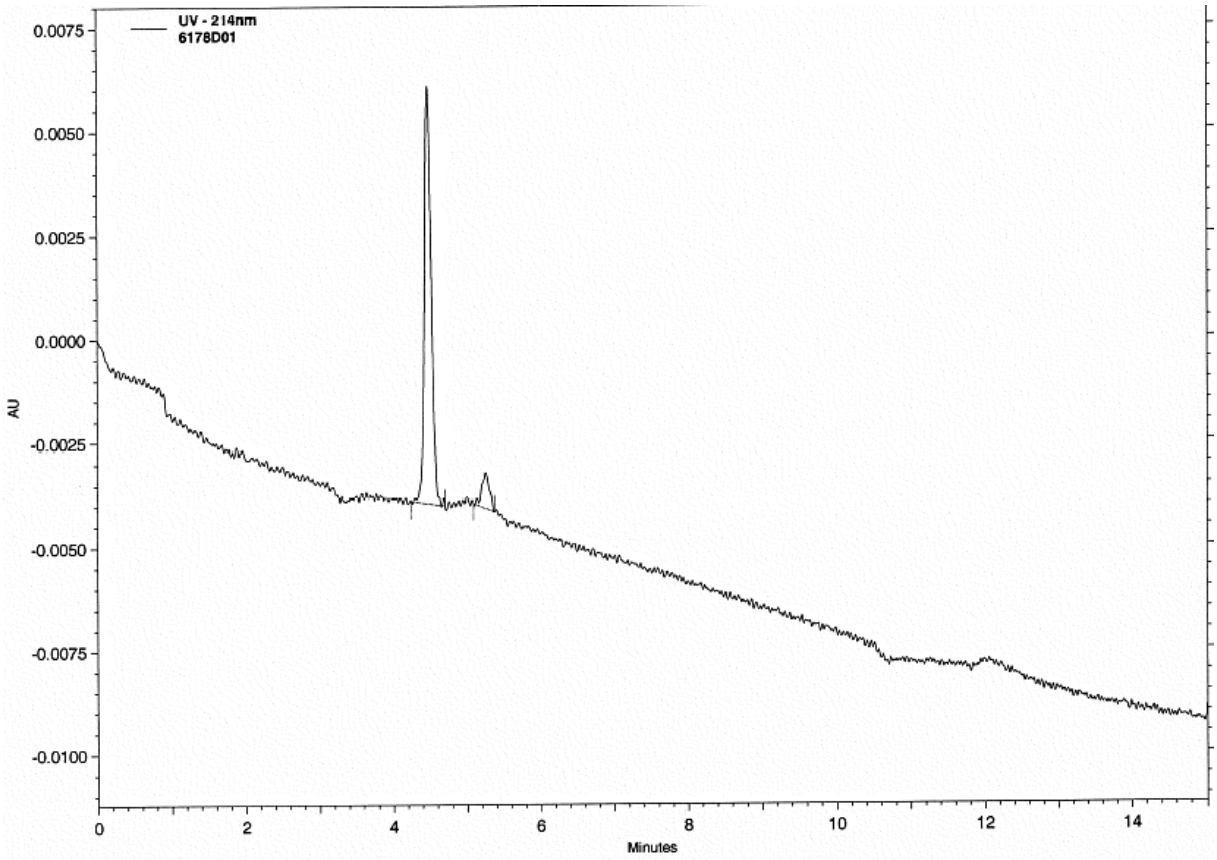

UV - 214nm
Results

Time	Area	Area %	Corrected Area	Corrected Area Percent
4.475	64524	91.45		
5.258	6036	8.55		
Totals	70560	100.00		

- CZE pH=4.5 sodium acetate buffer

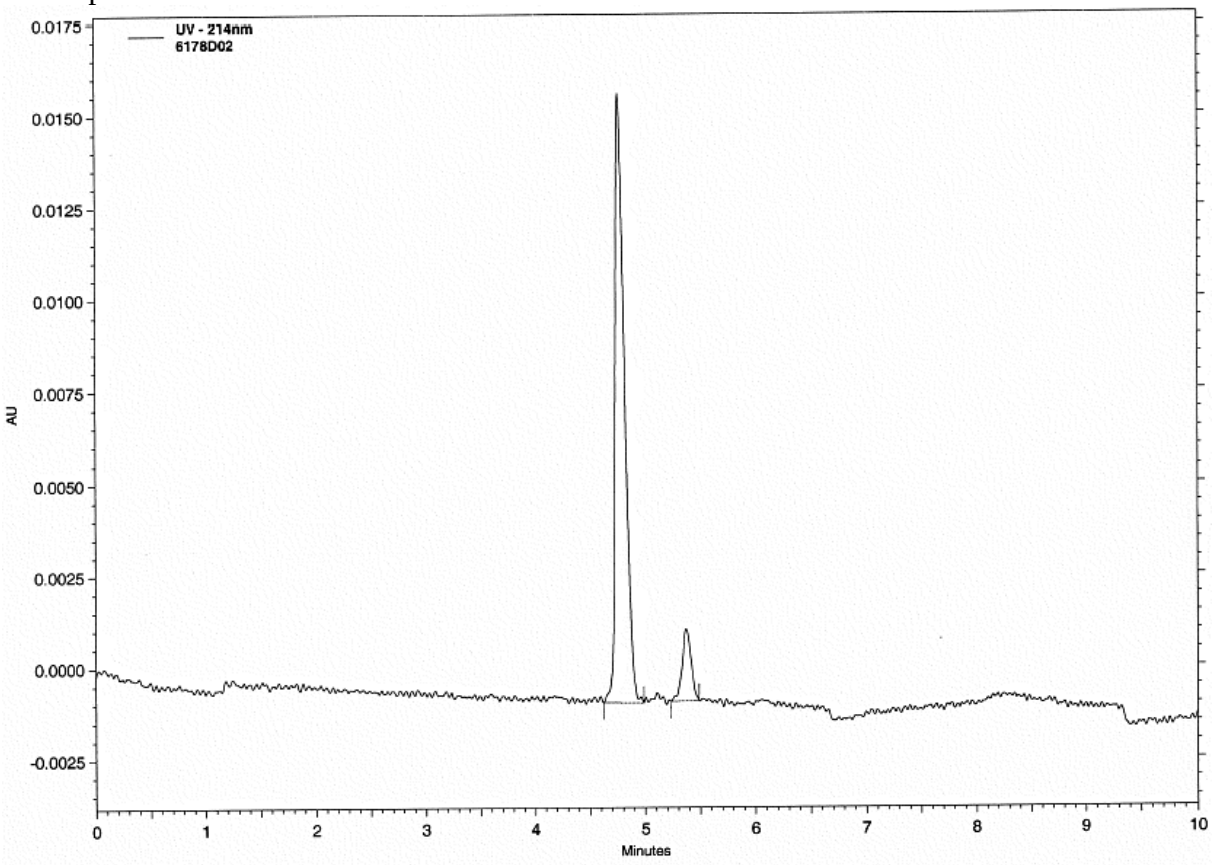

UV - 214nm
Results

Time	Area	Area %	Corrected Area	Corrected Area Percent
4.758	97004	89.65		
5.371	11199	10.35		
Totals	108203	100.00		

Trypsic digestion spectra

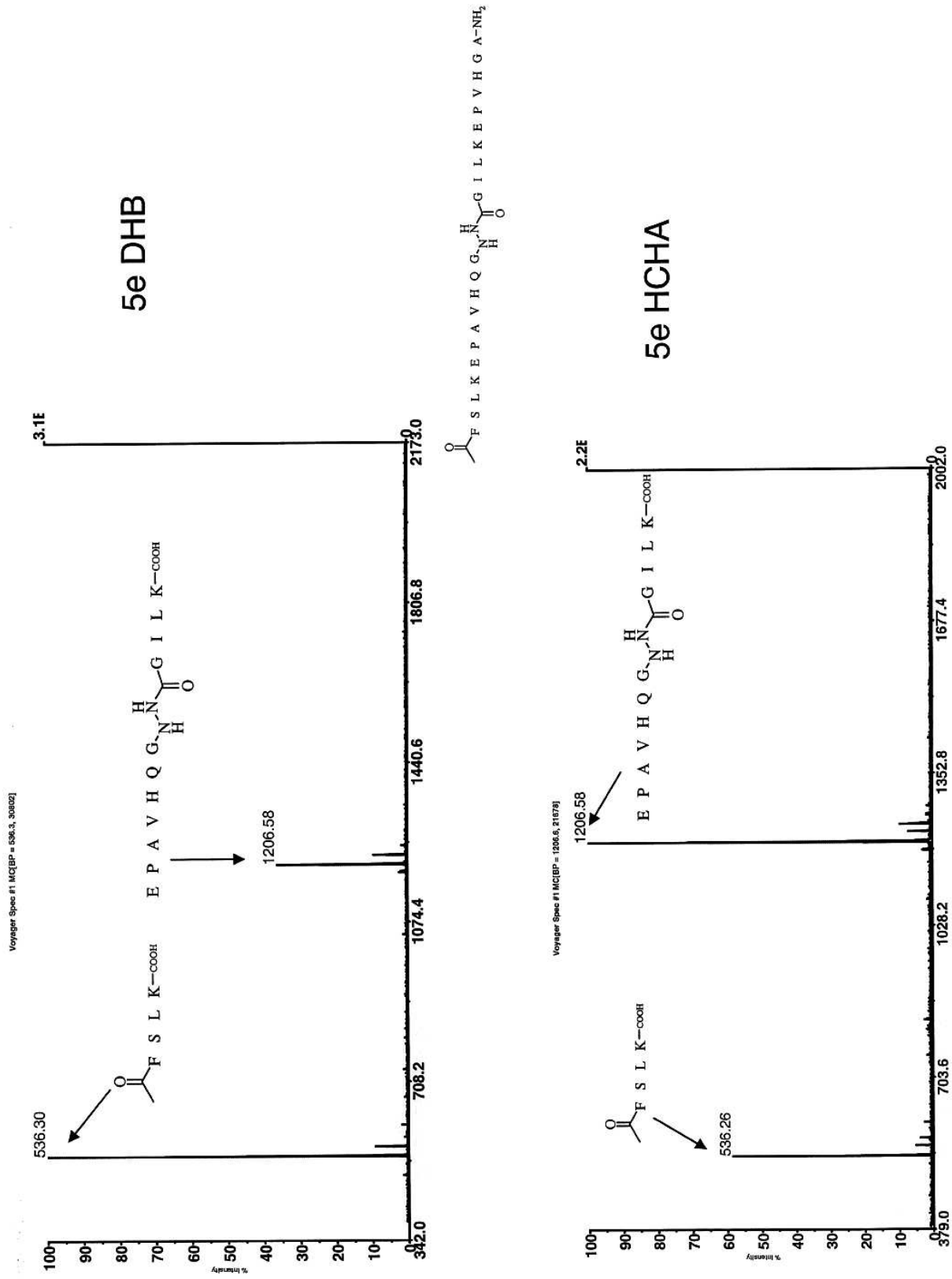

Analytical data for Agly-peptide **5f**

-RP-HPLC profile of crude reaction mixture between hydrazide peptide **3c** and phenylthiocarbonyl peptide **4a**, at t=24h.
C18 Nucleosil column, 1mL/min, λ=215 nm, 0-100% B in 30 min, 30°C

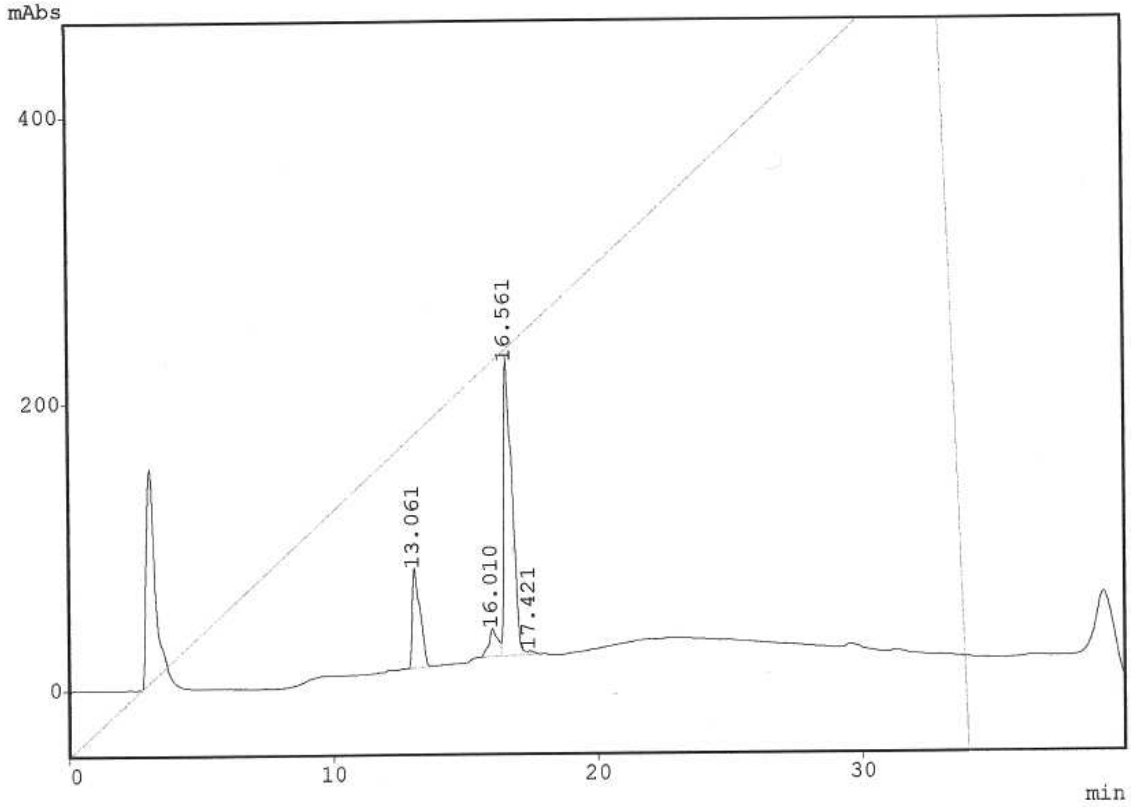

*** Peak Report ***

PKNO	TIME	AREA	HEIGHT	CONC
1	13.061	1427250	70259	22.4456
2	16.010	475803	19591	7.4827
3	16.561	4442295	208786	69.8617
4	17.421	13351	873	0.2100
		6358698	299509	100.0000

- RP-HPLC, C18 Nucleosil column, 1mL/min, λ=215 nm, 0-100% B in 60 min, 30°C

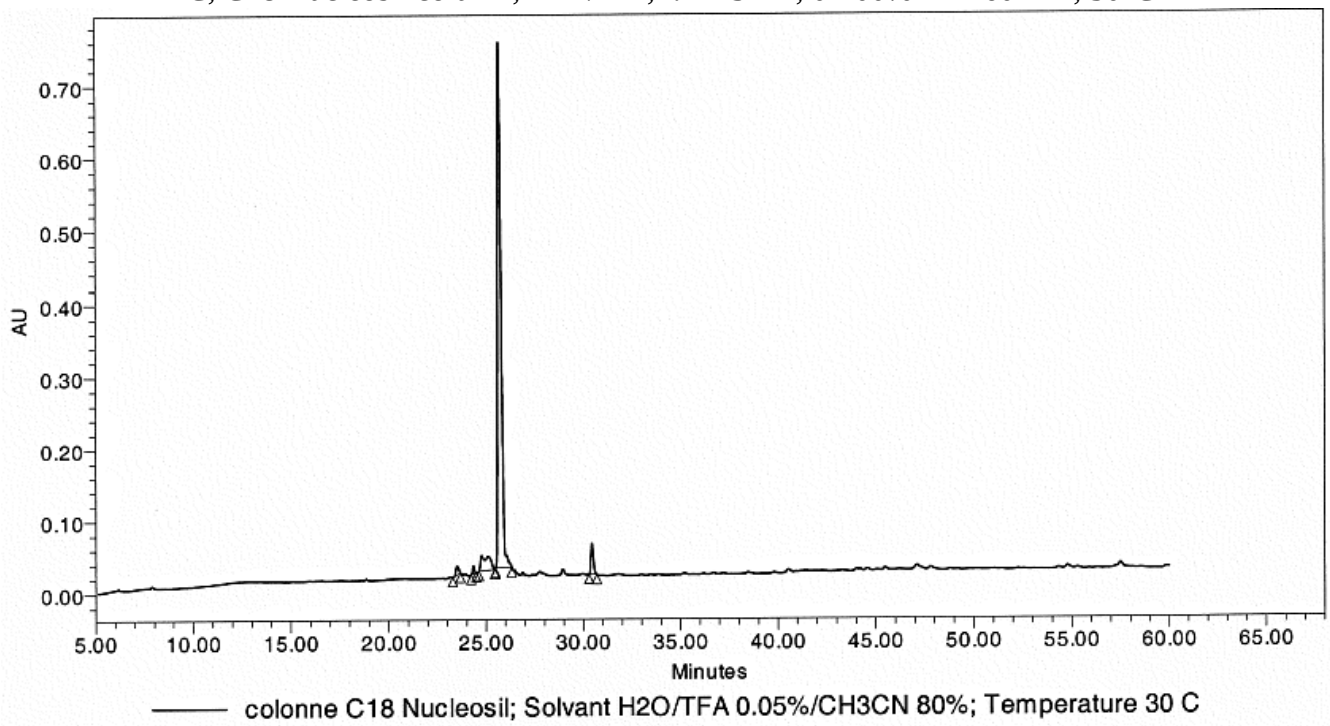

	RT	Area	% Area	Height
1	23.506	119146	1.18	12069
2	24.342	78220	0.77	11414
3	24.771	645072	6.38	21452
4	25.670	8891506	87.94	725625
5	30.442	376605	3.72	43098

- MALDI-TOF 2,5-dihydroxy-benzoic acid matrix

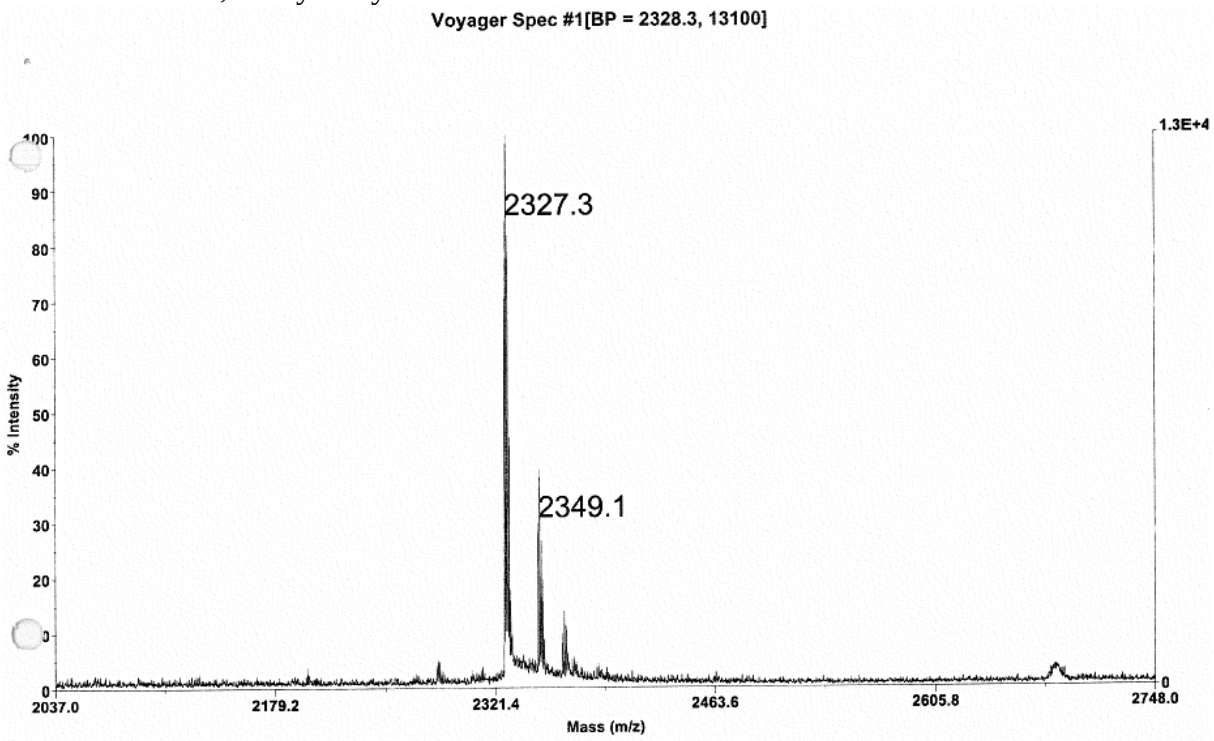

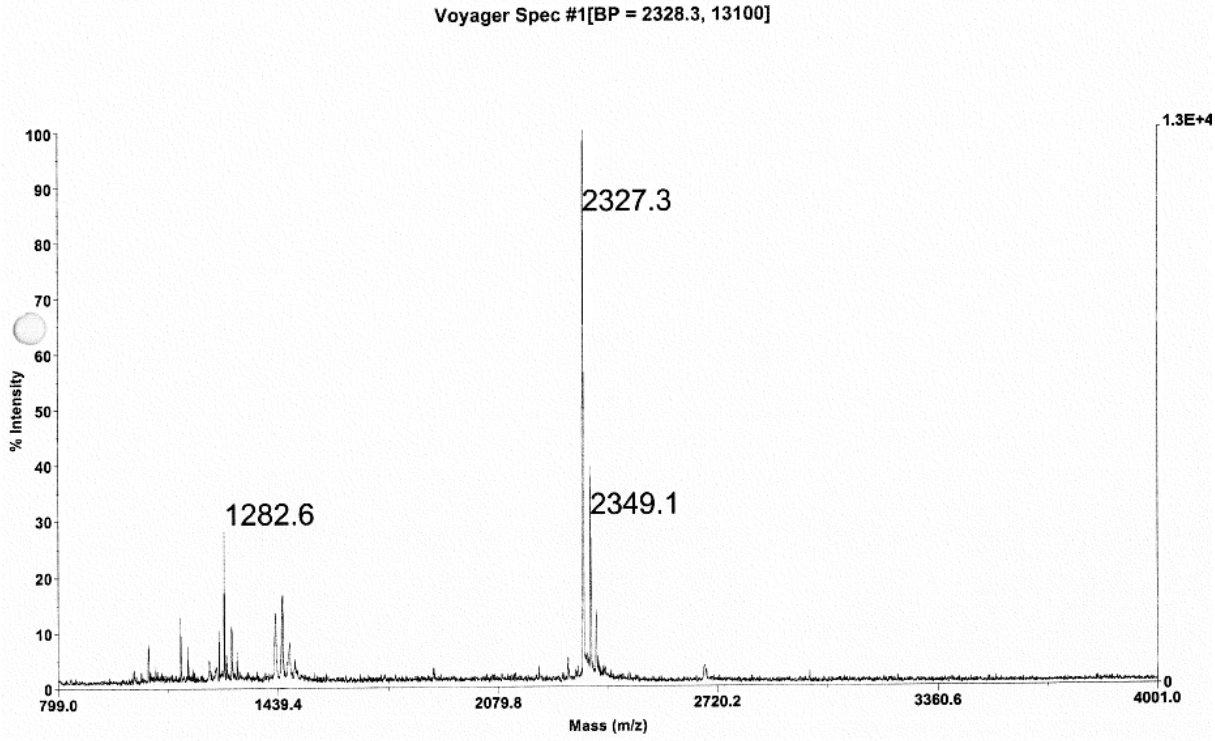

- CZE pH=3 sodium citrate buffer

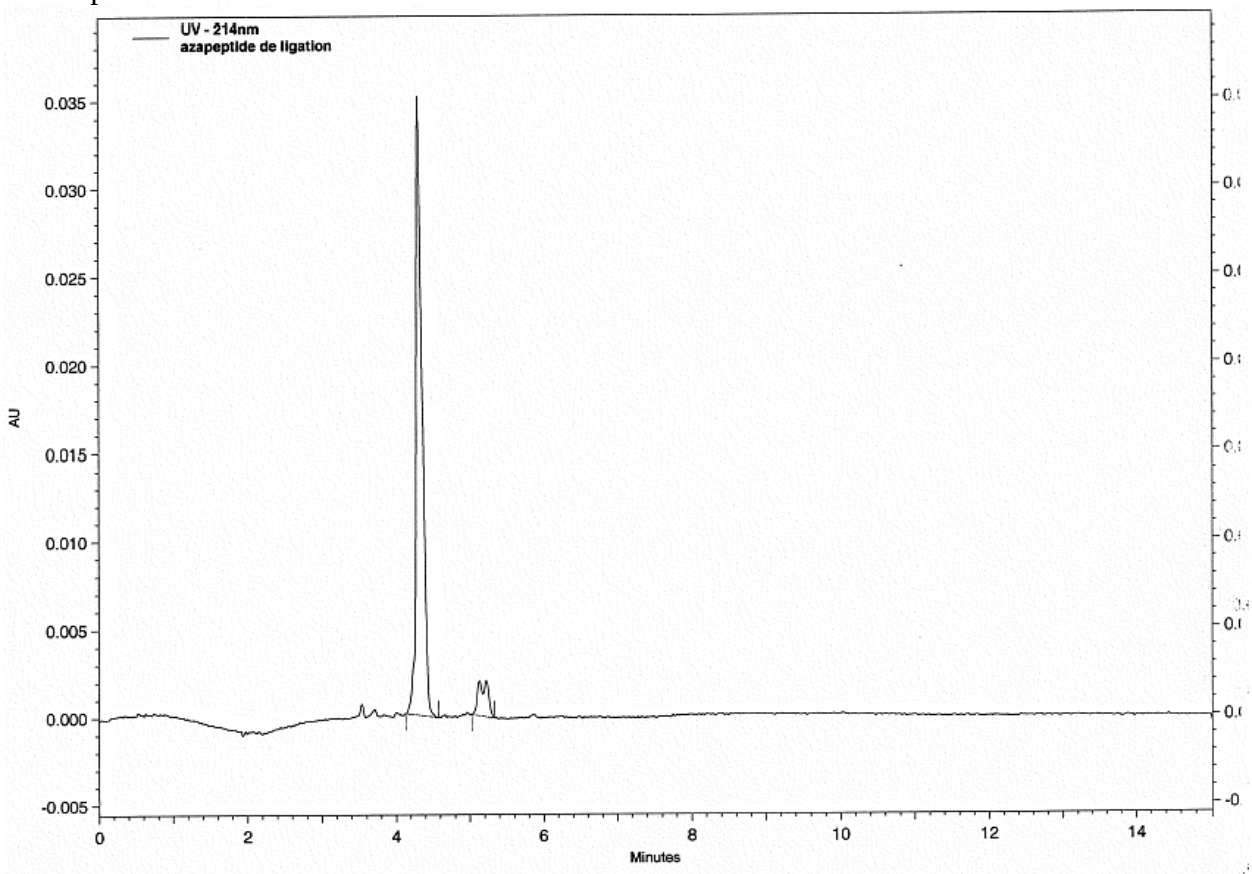

UV - 214nm
Results

Time	Area	Area %	Corrected Area	Corrected Area Percent
4.296	206722	91.60	16041	92.99
5.221	18953	8.40	1210	7.01
Totals	225675	100.00	17251	100.00

- CZE pH=4.5 sodium acetate buffer

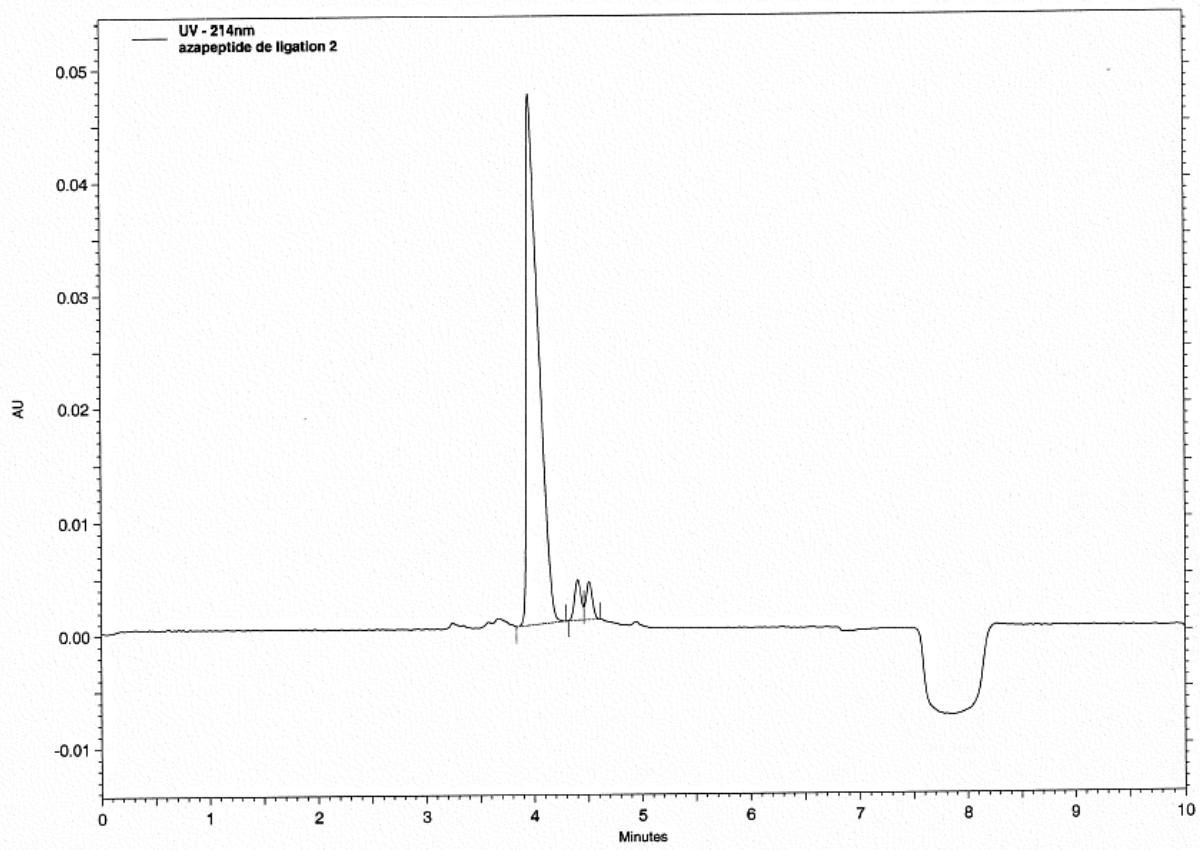

UV - 214nm
Results

Time	Area	Area %	Corrected Area	Corrected Area Percent
3.962	365298	92.75		
4.404	14859	3.77		
4.508	13700	3.48		
Totals	393857	100.00		

Trypsic digestion spectra

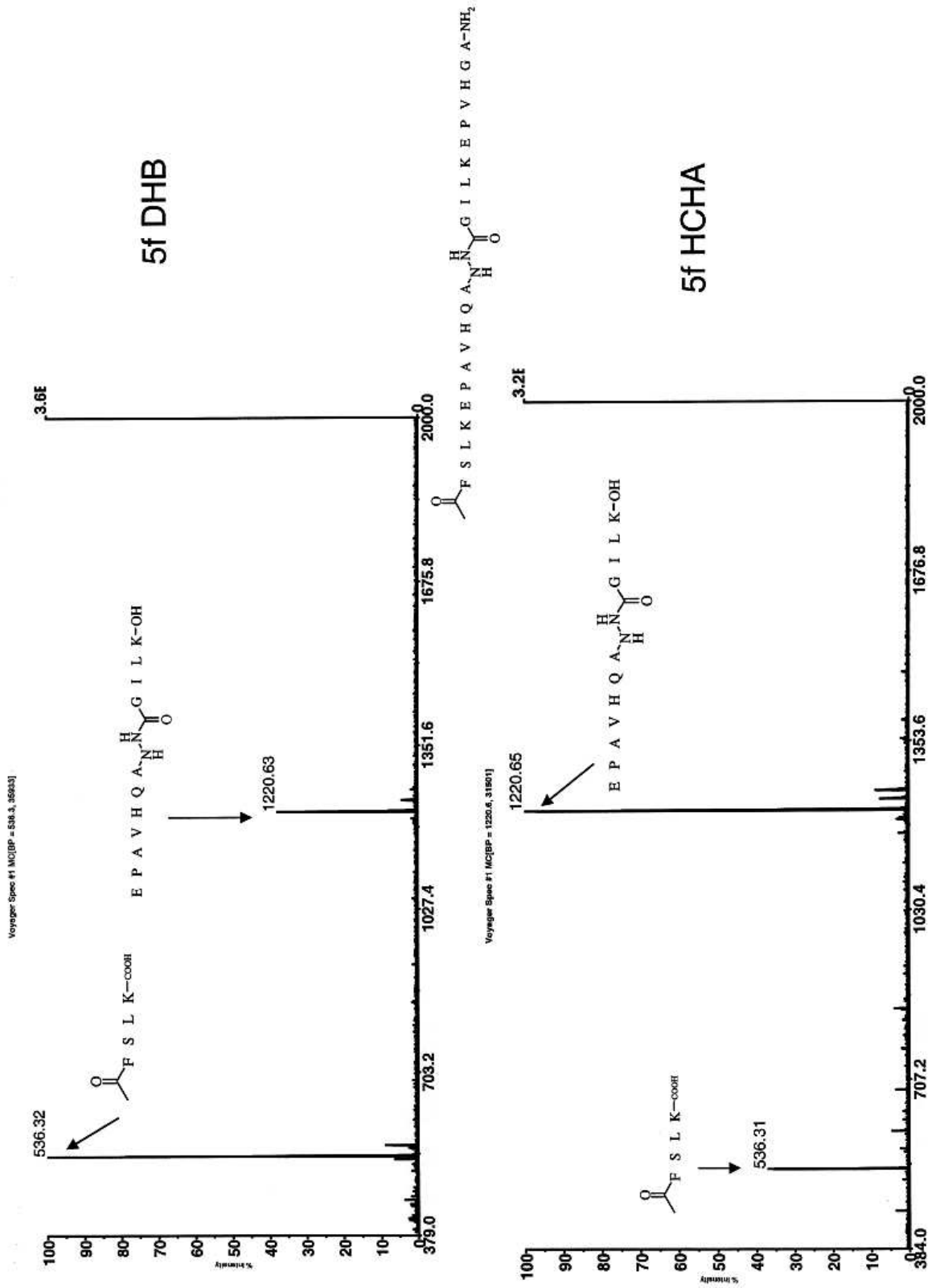

Analytical data for lipopeptide **9a**

- RP-HPLC, C3 Zorbax column, 1mL/min, λ=215 nm, 0-100% B in 30 min, 50°C

SAMPLE INFORMATION

Sample Name:	8591P01	Date Acquired:	3/23/2009 1:34:38 PM
Sample Type:	Unknown	Acq. Method Set:	30 min sb
Vial:	20	Date Processed:	3/23/2009 2:33:34 PM
Injection #:	1	Processing Method:	Default
Injection Volume:	50.00 ul	Channel Name:	Wvln Ch1
Run Time:	38.0 Minutes	Proc. Chnl. Descr.:	PDA 215.0 nm
Sample Set Name:	lipopeptides C3	Acquired By:	System

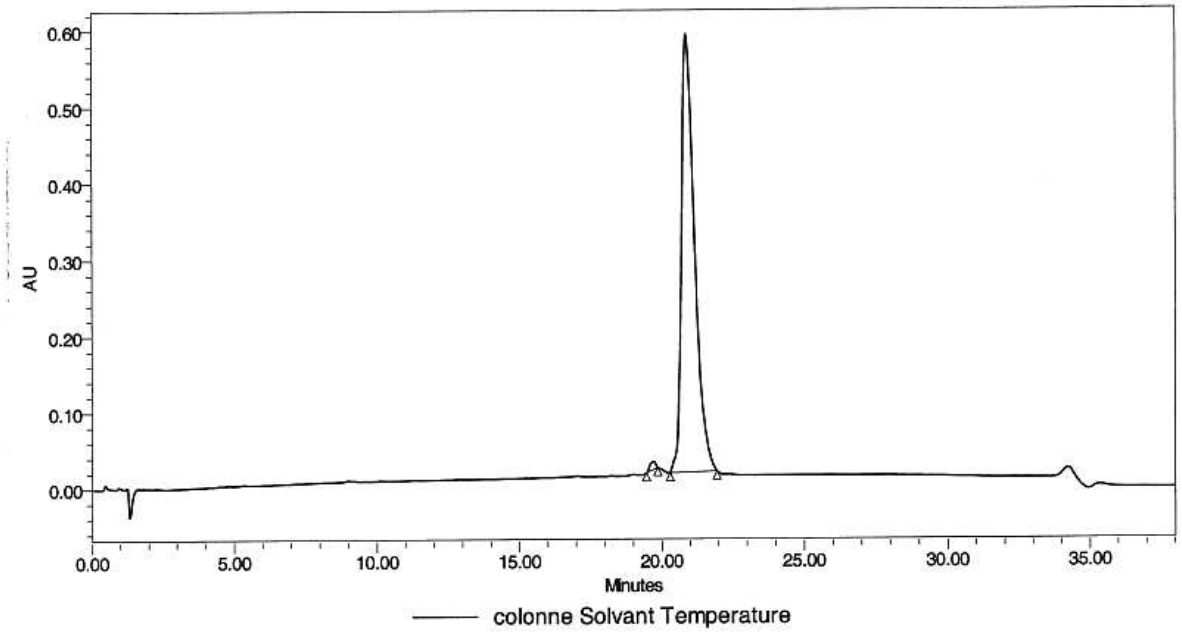

	RT	Area	% Area	Height
1	19.715	154273	0.83	10766
2	20.869	18359331	99.17	573831

- MALDI-TOF α-cyano-4-hydroxy-cinnaminic acid matrix

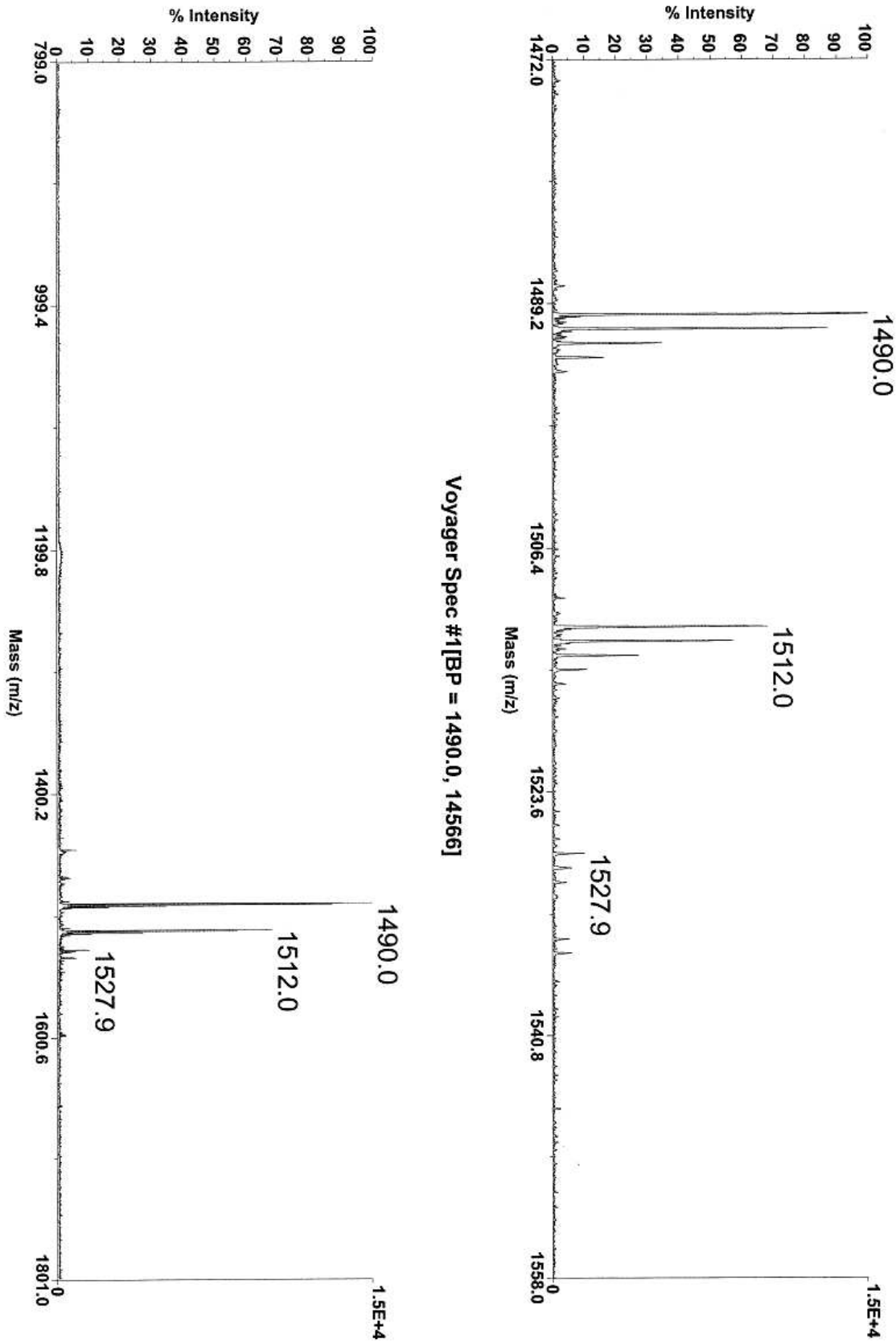

- CZE pH=3 sodium citrate buffer

Data File: D:\32Karat\Projects\Labo\Data\8597D07
Sample ID : 8591P01
Method: D:\32Karat\Projects\Labo\Method\hervé\15 min (15 Kv)citrate 36 vials.met
Acquired: 3/24/2009 2:04:26 PM
Printed: 3/24/2009 2:29:43 PM

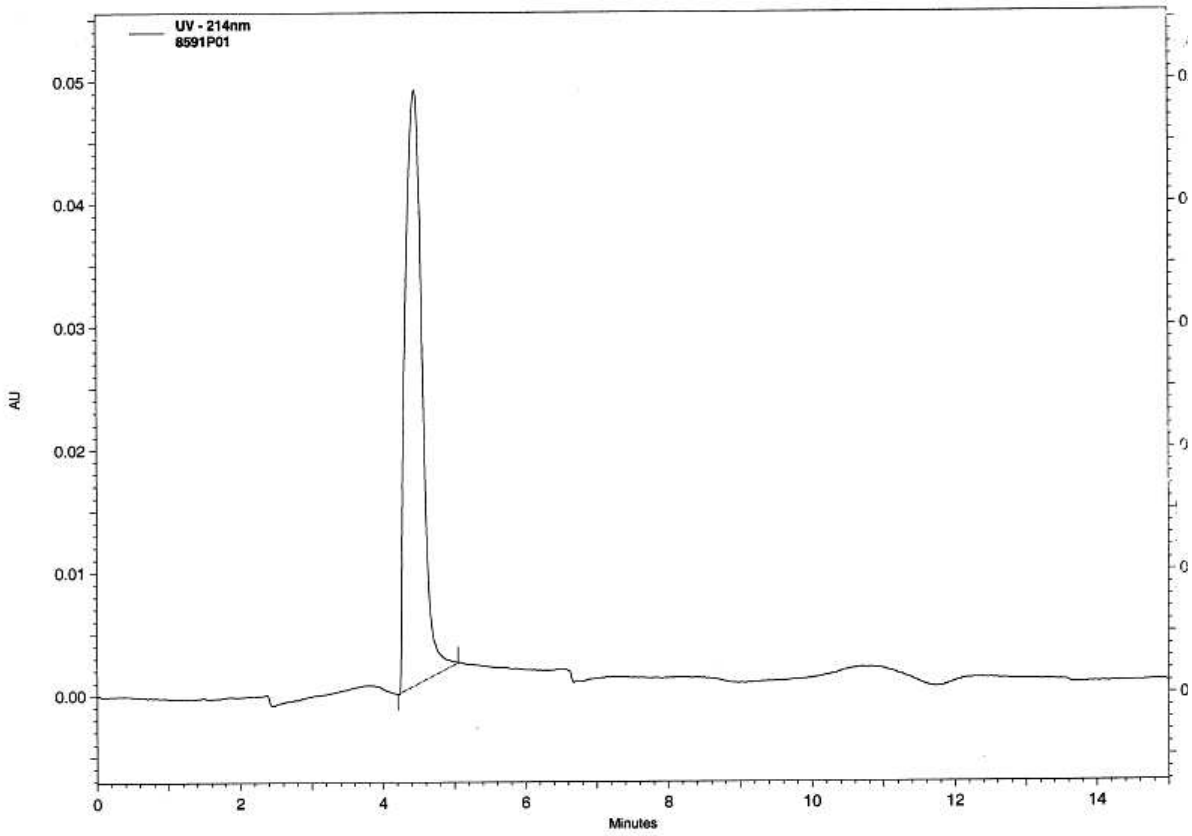

UV - 214nm
Results

Time	Area	Area %	Corrected Area	Corrected Area Percent
4.450	792202	100.00		
Totals	792202	100.00		

Analytical data for lipopeptide **9b**

- RP-HPLC, C3 Zorbax column, 1mL/min, λ=215 nm, 0-100% B in 30 min, 50°C

SAMPLE INFORMATION

Sample Name:	8594P01	Date Acquired:	3/23/2009 2:13:55 PM
Sample Type:	Unknown	Acq. Method Set:	30 min sb
Vial:	21	Date Processed:	3/23/2009 3:10:11 PM
Injection #:	1	Processing Method:	Default
Injection Volume:	50.00 ul	Channel Name:	Wvln Ch1
Run Time:	38.0 Minutes	Proc. Chnl. Descr.:	PDA 215.0 nm
Sample Set Name:	lipopeptides C3	Acquired By:	System

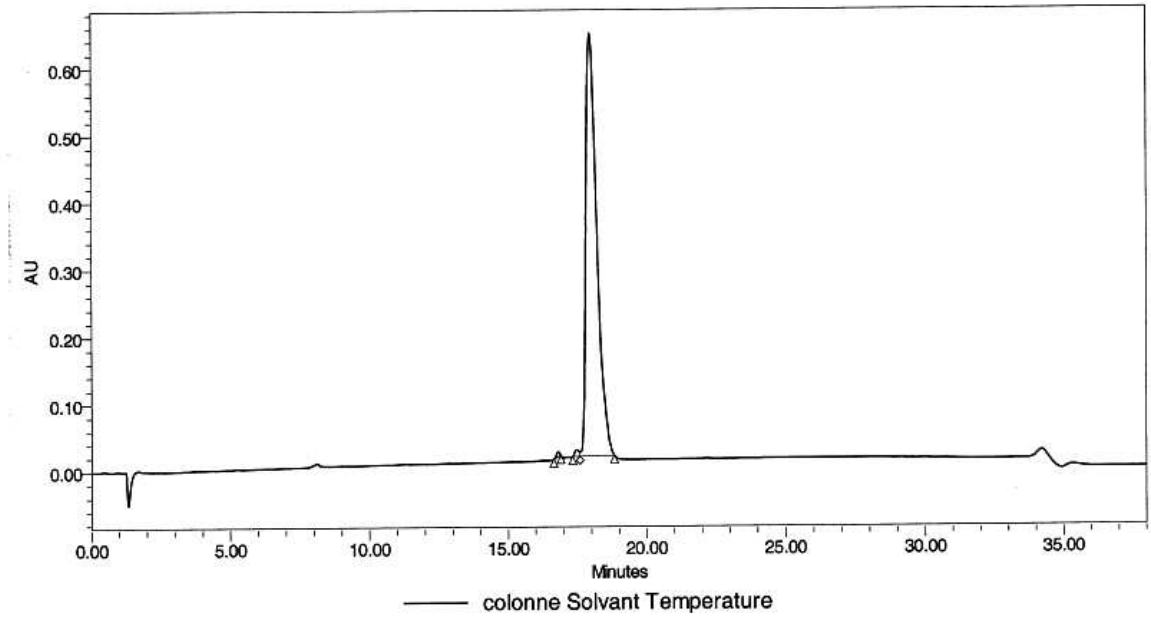

	RT	Area	% Area	Height
1	16.817	62126	0.36	7091
2	17.481	112399	0.65	10284
3	17.971	17164631	98.99	629154

- MALDI-TOF α-cyano-4-hydroxy-cinnaminic acid matrix

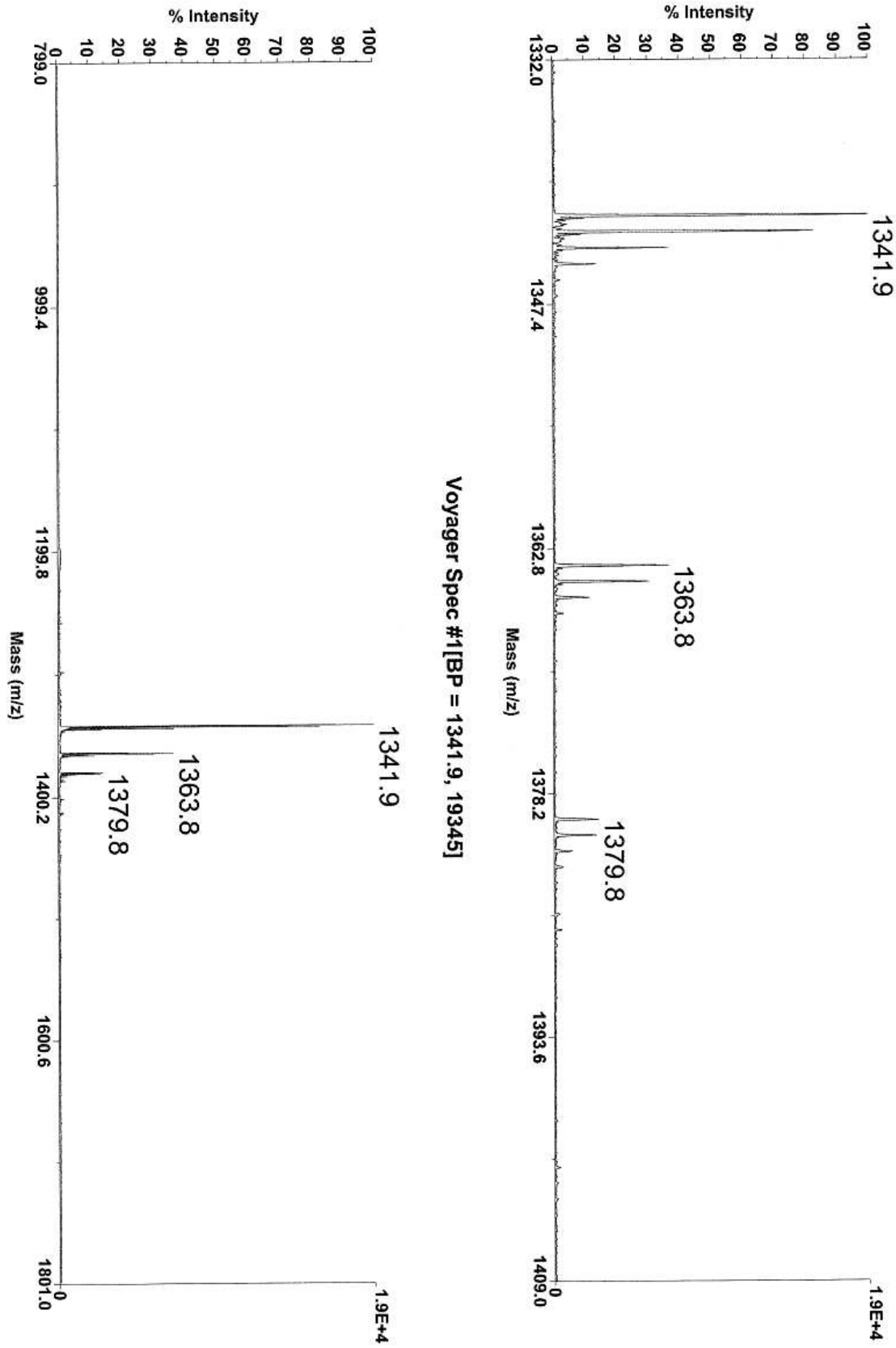

- CZE pH=3 sodium citrate buffer

Area % Report

Data File: D:\32Karat\Projects\Labo\Data\8597D04
Sample ID : 8594P01
Method: D:\32Karat\Projects\Labo\Method\hervé\15 min (15 Kv)citrate 36 vials.met
Acquired: 3/24/2009 12:34:00 PM
Printed: 3/24/2009 2:29:12 PM

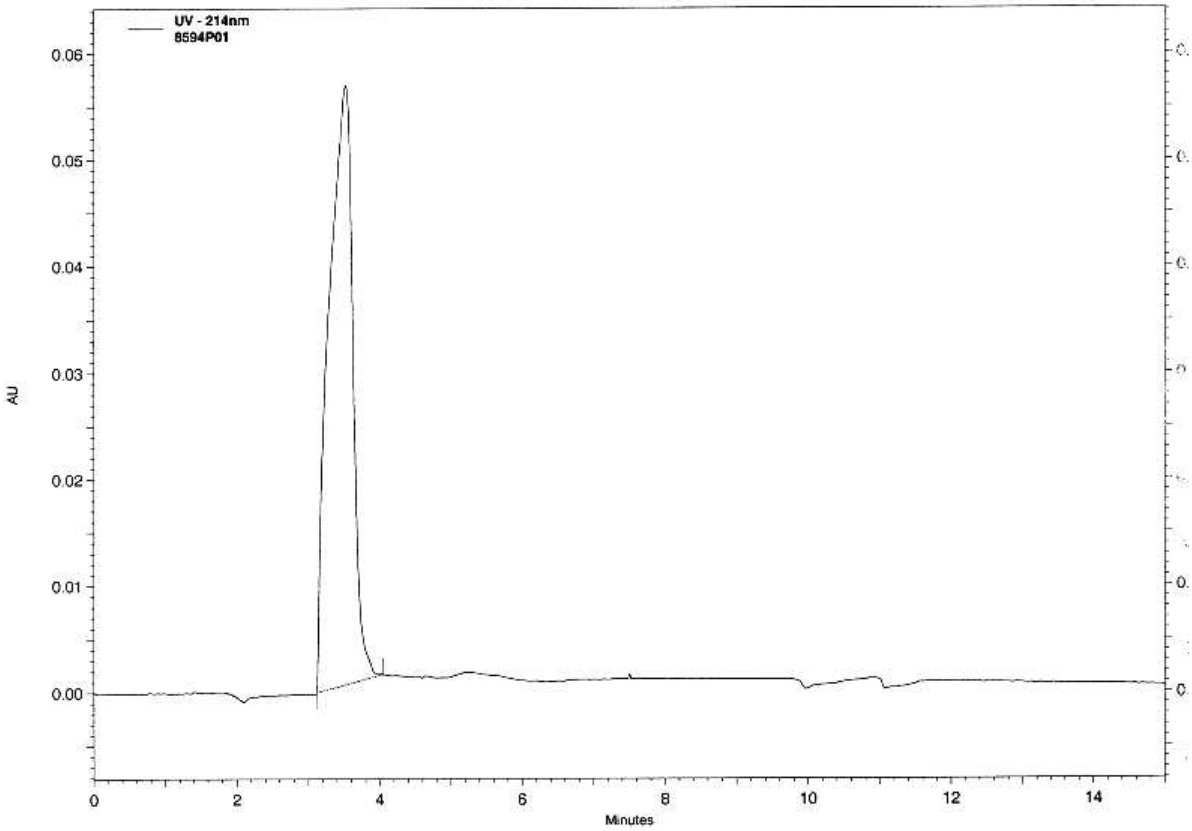

UV - 214nm
Results

Time	Area	Area %	Corrected Area	Corrected Area Percent
3.517	1316807	100.00		
Totals	1316807	100.00		

Analytical data for lipopeptide **9c**

- RP-HPLC, C3 Zorbax column, 1mL/min, λ=215 nm, 0-100% B in 30 min, 50°C

SAMPLE INFORMATION

Sample Name:	8595P01	Date Acquired:	3/25/2009 9:20:16 AM
Sample Type:	Unknown	Acq. Method Set:	30 min sb
Vial:	30	Date Processed:	3/25/2009 10:22:47 AM
Injection #:	1	Processing Method:	Default
Injection Volume:	50.00 ul	Channel Name:	Wvln Ch1
Run Time:	38.0 Minutes	Proc. Chnl. Descr.:	PDA 215.0 nm
Sample Set Name:	lipopeptide 4	Acquired By:	System

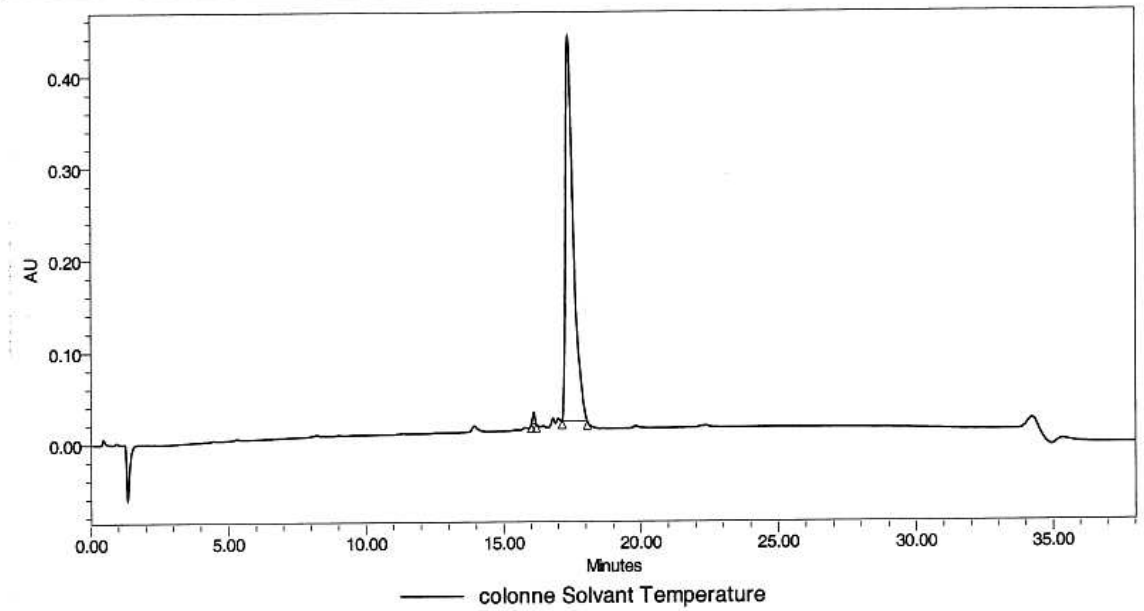

	RT	Area	% Area	Height
1	16.107	76032	0.91	13009
2	17.385	8257799	99.09	419551

- MALDI-TOF α-cyano-4-hydroxy-cinnaminic acid matrix

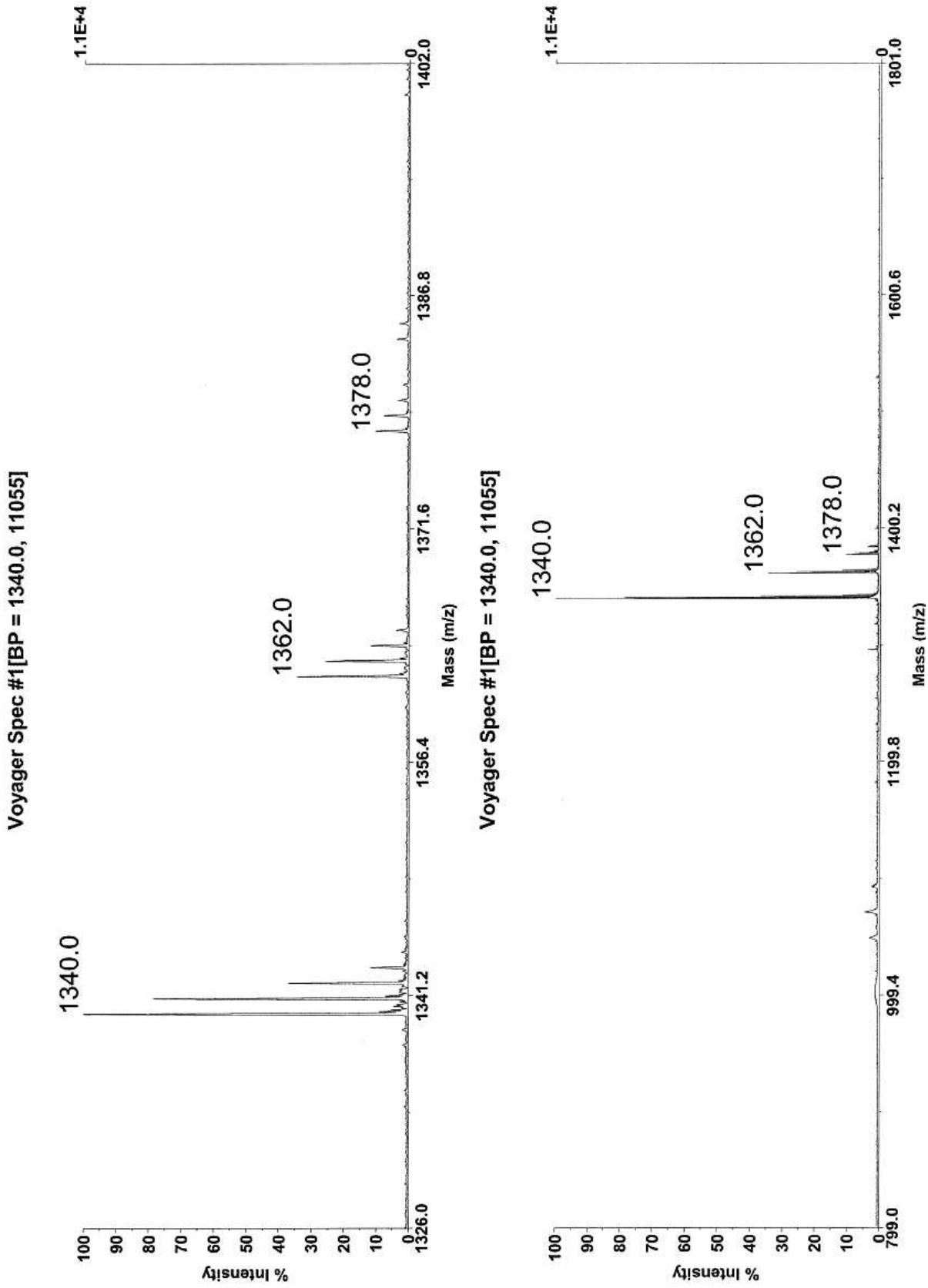

- CZE pH=3 sodium citrate buffer

Area % Report

Data File: D:\32Karat\Projects\Labo\Data\8599D04
Sample ID : 8595P01
Method: D:\32Karat\Projects\Labo\Method\hervé\15 min (15 Kv)citrate 36 vials.met
Acquired: 3/25/2009 10:00:24 AM
Printed: 3/25/2009 10:39:04 AM

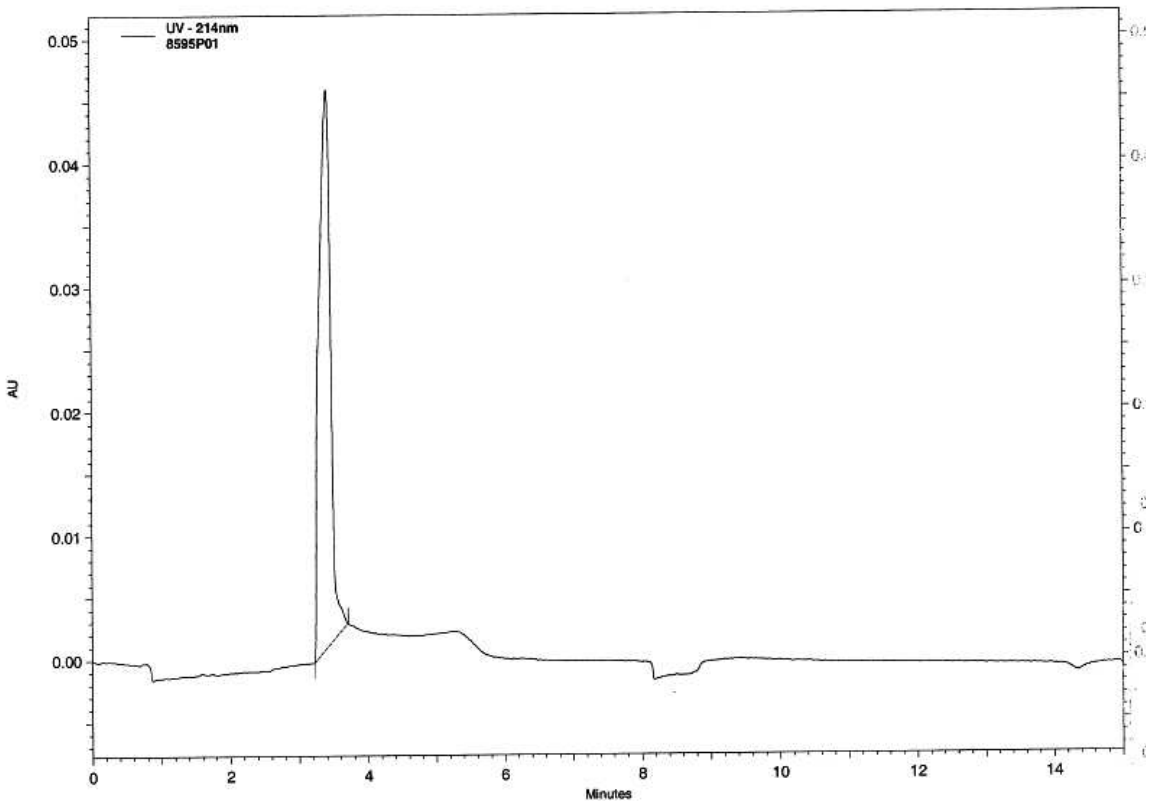

UV - 214nm
Results

Time	Area	Area %	Corrected Area	Corrected Area Percent
3.425	518290	100.00		
Totals	518290	100.00		

Synthesis of a Labeled RGD−Lipid, Its Incorporation into Liposomal Nanoparticles, and Their Trafficking in Cultured Endothelial Cells

Sonya Cressman,* Ian Dobson, Justin B. Lee, Yuen Yi C. Tam, and Pieter R. Cullis

Department of Biochemistry and Molecular Biology, University of British Columbia, Life Sciences Centre, 2350 Health Sciences Mall, Vancouver, Canada V6T 1Z3. Received January 29, 2009; Revised Manuscript Received May 25, 2009

The use of targeting ligands to enhance the delivery of liposomal nanoparticles (LNs) has moved slowly toward clinical application. This relative lack of clinical progression is further complicated by the existence of conflicting *in vivo* results in the literature. In this work, we describe new formulations of LNs that are targeted with an arginine-glycine-aspartic acid-containing peptide, cRGDfK, conjugated to the lipid distearoyl phosphatidylethanolamine (DSPE). These formulations may be able to circumvent some of the challenges encountered during the development of targeted-LNs. Of the constructs studied, a fluorescently labeled peptide−lipid conjugate was incorporated into LNs with high yield and accuracy. It is shown that the resulting targeted-LNs bind to human umbilical vein endothelial cells (HUVECs) with increasing avidity as the amount of peptide displayed on the LN surface increases. We specifically demonstrate the ability of targeted-LNs loaded with doxorubicin and incubated with HUVECs to deliver the drug to the cytosol. The cell does not internalize nontargeted LNs, supporting the notion that the RGD motif is associated with internalization of the targeted LN.

INTRODUCTION

In order for liposomal nanoparticles (LNs) to reach cancer cells, they must survive for prolonged amounts of time in the circulatory system (*1*). The addition of a targeting ligand to the surface of an LN is thought to increase the accumulation of the LN by increasing its affinity for a specific target on the surface of diseased cells. Vascular targeting, as opposed to targeting tumor cells themselves, offers the additional advantage of being a relatively general therapy for the treatment of solid tumors, given that all tumors require neovasculature in order to survive (*2*). Cells that make up the tumor vasculature (mainly endothelial cells) are also ideal anticancer targets, as they are not expected to generate drug-resistant variants. The methods described here utilize an arginine-glycine-aspartic acid (RGD) peptide to aid in targeting LNs to endothelial cells containing the molecular target, the $\alpha_v\beta_3$ integrins.

RGD-conjugated drugs have been investigated for their ability to bind to the $\alpha_v\beta_3$ integrins for over fifteen years (*3*). In the late 1990s, medicinal chemists pinpointed a highly selective RGD peptide, which is now an antiangiogenesis drug candidate in phase II clinical trials (*4, 5*). Since the early 2000s, RGD-targeted drugs (*6*), imaging agents (*7*−*9*), antibodies (*10*), and LNs (*11*−*13*) have used cyclic RGD-containing peptides to guide cargo to the tumor-associated vasculature *in vivo*. The timely rate of clinical progression of RGD peptides without cargo and well-defined RGD-imaging agents indicates that RGD-based drugs may be promising new therapies of the future (*9, 14*). RGD-targeted LNs, on the other hand, do not show a sufficient rate of clinical progression.

Targeted-LNs, in general, have held the interest of pharmaceutical innovators since the 1980s (*15*−*17*). RGD-targeted LNs are the most structurally simplified of the known targeting ligands. Despite the relative simplicity of using short peptides as targeting ligands, studies on RGD-LNs tend not to describe the physical and chemical properties of the final product (*11*−*13*). The current theories of the *in vivo* behavior of RGD-LNs are also divergent. While some reports indicate that RGD-LNs share similar *in vivo* circulation lifetimes to nontargeted LNs (*11, 12*), others report the accelerated clearance of RGD-LNs (*13*).

Perhaps the greatest accomplishment toward clinical advancement of targeted-LNs is the first report on the preclinical manufacture of a protein−polymer−lipid micelle, which focuses solely on characterization (*18, 19*). For clinical progression, targeted-LN drug candidates will be required to demonstrate compliance with the regulatory codes of good manufacturing practice. We propose that, in order to move RGD-LN technology toward the clinic, a step backward is necessary to understand what is happening in targeted-LN formulation.

This study focuses on the construction of well-defined RGD-LNs. The RGD-lipid construct with the best formulation properties was purified and qualitatively assessed. A fluorescent label, methoxycoumarin (MCA), was used to track the amount of the purified RGD-lipid construct that is incorporated into an RGD-LN by one of two published methods: either the postinsertion method (*20*) or by classic liposome formulation methods (*21*). Our results also describe the optimal mole fraction of RGD-lipid that enables high target binding and drug delivery via defined RGD-LNs to the cytosol of $\alpha_v\beta_3$-expressing cells.

EXPERIMENTAL PROCEDURES

Materials and Reagents. Unless specified, all reagents were of reagent-grade quality or better. Reversed-phase HPLC (RP-HPLC) was performed using gradients of aqueous acetonitrile containing 0.1% trifluoroacetic acid (TFA) (aqACN) applied to C18 columns. Analytical gradients were run using a 150 mm × 4.6 mm column with a flow rate of 1 mL per minute. Peptides were purified on a preparative scale with a 250 mm × 22 mm column and a flow rate of 10 mL per minute.

Peptide Synthesis. Dimethylformamide (DMF) was the main solvent used for peptide synthesis, unless otherwise specified. The linear sequence D(t-Bu)fK(Z)R(Pbf)G (The RGD-containing peptide) was synthesized by FMOC-based solid-phase peptide synthesis as described previously (*22*). Briefly, peptides were assembled on 0.5 mmol of 2-chlorotrityl resin using 1.3 mol equiv (to carboxylic acid) of the following activating agents:

* E-mail: scressman@bccrc.ca. Lab Phone: (604)-822-4955. Office Phone: (604)-822-6263. Fax: (604)-822-4843.

10.1021/bc900041f CCC: $40.75 © 2009 American Chemical Society
Published on Web 06/17/2009

O-benzotriazole-*N*,*N*,*N*′,*N*′-tetramethyl-uronium hexafluorophosphate (HBTU) and *N*-hydroxybenzotriazole (HOBT). Peptides were activated *in situ* with triethylamine (TEA), then coupled to the resin for at least 1 h. FMOC removal steps were performed upon each amino acid addition by soaking the resin in a solution of 20% piperidine in DMF for 5 min and repeated once. Between each step, the resin was washed with a constant flow of DMF for at least 1 min. Linear peptides were cleaved in 0.1% TFA in dichloromethane (DCM) with 2.5% triisopropyl silane (TIS) and H_2O (v/v). The crude peptide was analyzed by RP-HPLC with a linear gradient of 30−90% aqACN over 30 min (retention time = 16.3 min) and by electrospray mass spectrometry (ESI-MS).

Lyophilized linear peptides were cyclized at 0.5 mM in DMF using benzotriazol-1-yl-oxytripyrrolidiniophosphonium hexafluorophosphate (PyBop) and HOBT to produce cR(Pbf)GD(t-Bu)fK(Z). Cyclization yields were typically greater than 95% and occurred within 30 min, as indicated by RP-HPLC, with a retention time of 19.5 min on the same gradient as the linear peptide and a difference of −18 in the observed molecular weight by ESI-MS. ^{1}H NMR NOE assignments for all α-amide bonds confirmed a head-to-tail cyclic compound.

The benzyl group on the lysine side chain was removed by hydrogenation using a palladium/carbon catalyst. The amine-functionalized peptide, cR(Pbf)GD(t-Bu)K (100 mM in DMF), was modified with 10 mol equiv of succinic anhydride to produce cR(Pbf)GD(t-Bu)fK(succ). The reaction mixture was purified with an RP-HPLC gradient of 10−60% aqACN over 1 h. A 95% pure product eluting after 40 min was characterized both by ESI-MS (MW = 1011.47 ± 1) and by analytical RP-HPLC using a 30−90% aqACN gradient, a product of >95% purity was obtained, with a retention time of 12.1 min.

cR(Pbf)GD(t-Bu)fK-PEG$_2$-K(MCA)-PEG$_2$-COOH Synthesis. Four strategies to synthesize RGD-lipids were investigated (see Supporting Information for a summary of these approaches). We focus on the RGD-lipid construct, which displayed the best characteristics for producing a targeted LN. The synthesis of this chosen construct is described herein.

The spacer−peptide conjugate was assembled as follows: 0.112 mmol 2-chlorotrityl resin was loaded with 2.5 mol equiv of *O*-(*N*-Fmoc-3-aminopropyl)-*O*′-(*N*-diglycoyl-3-aminopropyl)-di(ethylene glycol) (Fmoc-NH-PEG$_2$-COOH) over the course of 3 h, under nitrogen gas with gentle stirring. FMOC was removed by soaking the resin in a solution of 20% piperidine in DMF for 5 min, and repeated once. Ninhydrin assays were used to monitor the success of solid-phase synthesis reactions. 2.5 mol equiv of Fmoc-Lys-(MCA)-OH were then coupled to the free amine using 1.2 mol equiv to carboxylic acid of HOBT, HBTU, and TEA for 1 h, then subsequently, 5 mol equiv of the second Fmoc-NH-PEG$_2$-COOH unit was incorporated over 3 h using 1.2 mol equiv to carboxylic acid of PyBop, HOBT, and TEA. Trial cleavages (performed in a solution of 0.1% TFA in DCM, 2.5% H_2O, 2.5% TIS (v/v)) proved to be more reliable than ninhydrin assays for monitoring the success of each coupling reaction from this point on, presumably due to the shielding effect of PEG. The product (after step d of Figure 1) was retained for 21 min by an analytical RP-HPLC gradient 0−85% aqACN over 30 min. Successful Fmoc removal resulted in a shift in retention time to 14.5 min, using the same gradient. 1.2 mol equiv (to amine) of the cyclic peptide, cR(Pbf)GD(t-Bu)fK(succ), was coupled overnight to the spacer under nitrogen gas using 1.2 mol equiv of PyBop and HOBT and TEA to acid. The product cR(Pbf)GD(t-Bu)fK-PEG$_2$-K(MCA)-PEG$_2$-COOH was purified directly by preparative RP-HPLC (0−85% aqACN) eluting after 40 min.

The dry yield of the peptide−spacer construct was 80 mg. The product was clearly resolved by TLC (chloroform ($CHCl_3$)/methanol (MeOH), 8.8/2.2), R_f = 0.18, and purified to >95% purity as indicated by analytical RP-HPLC (0−85% aqACN). The correct product was validated by ESI-MS.

Synthesis of cRGDfK-PEG$_2$-K(MCA)-PEG$_2$-DSPE. The peptide−spacer construct was conjugated with the lipid anchor, DSPE in a solution. The purified and lyophilized peptide−PEG constructs were dissolved in 2 mL DCM and activated with 5 mol equiv of *N*-hydroxysuccinimide and diisopropylcarbodiimide. The active ester formed within 30 min, and 3.5 mol equiv to acid of distearylphosphatidyl ethanolamine (DSPE) was dissolved in 1 mL $CHCl_3$ at 60 °C. The activated ester was then added to the lipid with 1.2 mol equiv (to ester) of TEA. The reaction occurred within 1 h at 60 °C, and the resulting product was purified on 100 g of silica gel, mobile phase MeOH/$CHCl_3$. The product, cR(Pbf)GD(t-Bu)fK-PEG$_2$-K(MCA)-PEG$_2$-DSPE, eluted between 30−50% methanol in $CHCl_3$ and was identified by TLC ($CHCl_3$/MeOH 8.8/2.2, R_f = 0.74).

The compound was concentrated and redissolved in 95% aqueous TFA to deprotect the arginine and aspartic acid side chains. The product formed within 2 h. TFA was removed by gentle evaporation under a stream of nitrogen, precipitated into ice-cold diethyl ether, centrifuged, rinsed with diethyl ether, and centrifuged again. A yield of 40.8 mg of cRGDfK-SUCC-PEG$_2$(MCA)-PEG$_2$-DSPE (herein, referred to as the RGD-lipid) resulted. The ESI-MS MW for RGD-lipid was 2415.5 ± 1 (predicted MW = 2414.89). Purity of RGD-lipid was confirmed by TLC detected with iodine and UV (MeOH/EtOH/H_2O/TEA (6/3/1/1) R_f = 0.25. Excitation (325 nm) and emission (389 nm) spectra were collected for the construct between 280 and 500 nm using a fluorometer.

Formation of Liposomal Nanoparticles. Dry lipids were dissolved in warm $CHCl_3$ at 60 °C. The solvent was removed under a stream of nitrogen gas to form a thin film, and residual solvent was removed by lyophilization. For empty vesicles, the thin film was hydrated in 100 mM HEPES buffer containing 144 mM NaCl, pH 7.5 (HBS), warmed to 60 °C. The resulting multilamellar vesicles were extruded through two polycarbonate filters with a 100 nm pore size. The vesicles were extruded ten times using an extruder, to form unilamellar LNs.

The mean diameter of the LNs was characterized by dynamic light scattering (DLS) using a Nicomp 370 particle sizer for size distribution analysis. LNs were further characterized by a phosphate assay using the method of Fiske and Subbarow, and by fluorescence emission at 590 nm, upon excitation at 530 nm. RGD-lipids were then incorporated into LNs by one of two methods, either the "post-insertion method" or the "formulation method".

Post-Insertion Method of Incorporating cRGDfK-PEG$_2$-K(MCA)-PEG$_2$-DSPE into Preformed LNs. The post-insertion method of incorporating a ligand-conjugated lipid into preformed LNs has been described previously (*20*). Our LNs were composed of the following lipids: 54 mol % distearylphosphatidylcholine (DSPC)/45 mol % cholesterol (Chol)/0.5 mol % Rhodamine-labeled phosphatidylethanolamine (Rhod:PE). After LNs were prepared as described in the above section, the required amount of RGD-lipid needed to make 1 mol % (RGD-lipid) was prepared as a micelle solution in HBS, at 65 °C. The LNs and RGD-lipid micelles were coincubated together at 65 °C for 2 h. The mixture was purified on a 40 mL Sephadex G50 column. Incorporation of the RGD-lipid into the LN was measured by MCA emission at 389 nm, following excitation at 325 nm in HBS containing 1% Tween 20 and compared against a standard curve made with known amounts of the RGD-lipid.

Formulation Method of Incorporating RGD-Lipids Into LNs. Empty RGD-LNs were also made using the "formulation method". We chose this method to manufacture RGD-LNs for studies on the drug retention characteristics of the LNs and for

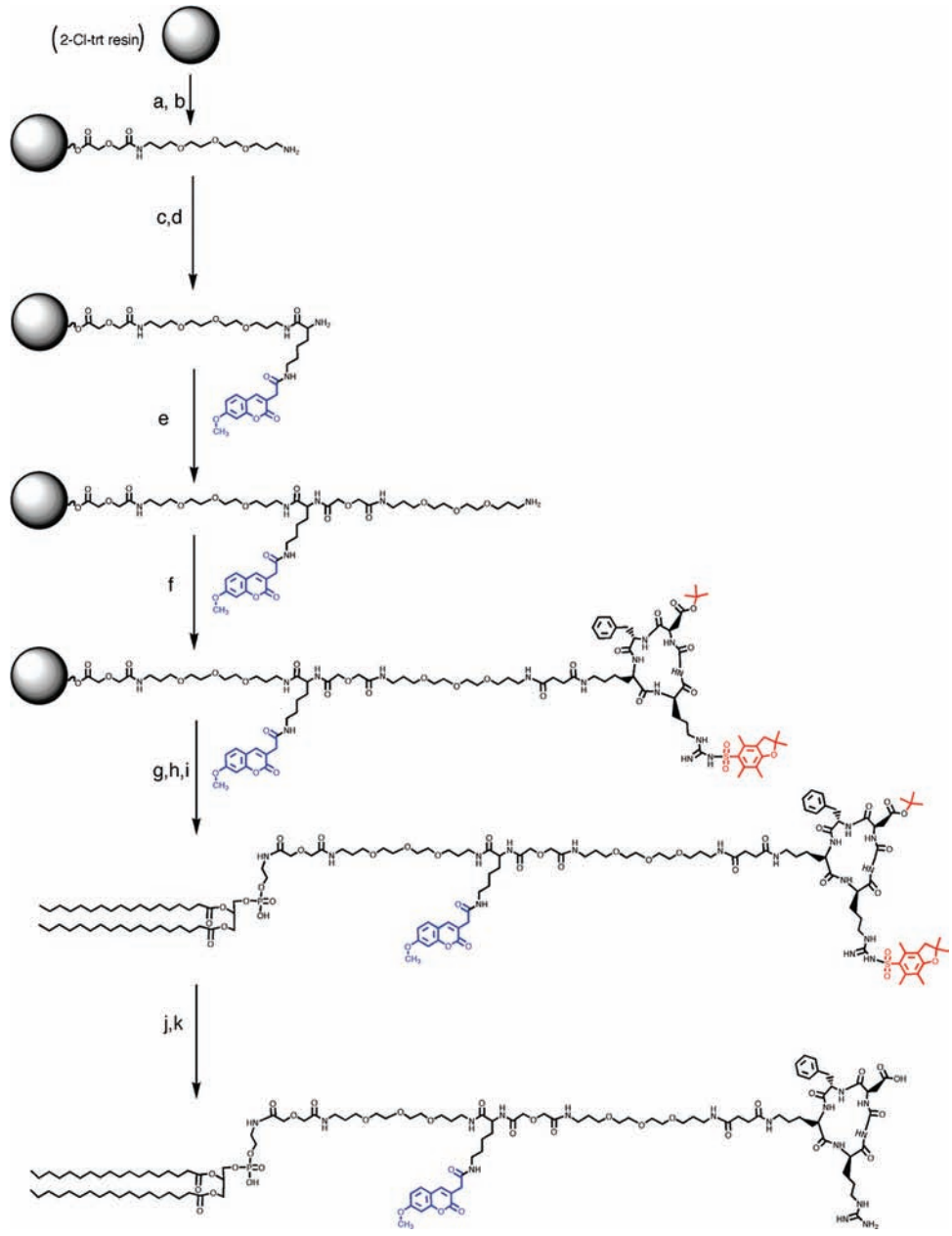

Figure 1. Synthesis of cRGDfK-PEG_2-K(MCA)-PEG_2-DSPE. (a) FMOC-PEG_2-OH, 3 h; (b) 20% piperidine in DMF; (c) Fmoc-Lys(MCA)-OH, HBTU/HOBT; (D) 20% piperidine in DMF; (e) FMOC-PEG_2-OH, PyBop/HOBT, 6 h; (f) cR(Pbf)GD(tBu)fK-succinic acid, PyBop/HOBT, 12 h; (g) 0.1% TFA, 1% TIS, 3.9% H_2O, 95% DCM; (h) RP-HPLC; (i) DSPE, PyBOP/HOBT, $CHCl_3$, 60 °C; (j) silica gel chromatography; (k) 95% TFA, 5% DCM, silica gel chromatography.

all cell-based assays. We varied the amount of RGD per LN by increasing the mol % of the RGD-lipid added before the LNs were formed. The series of RGD-LNs containing different amounts of RGD were formulated as follows: 0.5 mol % RGD-LN was made by incorporating: 54 mol % distearylphosphatidylcholine (DSPC)/45 mol % cholesterol (Chol)/0.5 mol % Rhodamine-labeled phosphatidylethanolamine (Rhod:PE)/0.5 mol % RGD-lipid (i.e., 54:45:0.5:0.5 mol:mol), 1 mol % RGD-LN (53.5:45:0.5:1) mol:mol), 2.5 mol % (52:45:0.5:2.5 mol:mol), and 5 mol % (49.5:45:0.5:5 mol:mol). Nontargeted LNs were formulated as (54.5:45:0.5:0 mol:mol). For drug retention and biological assays on intracellular delivery, 0.5 mol % RGD-LNs were used.

The amount of surface-exposed RGD-lipid per liposome was estimated under the assumption that one LN contains approximately 148 641 lipids (based on the average diameter of the particle being 116 nm, and the average surface area of a lipid headgroup as 0.5 nm^2). For this diameter, the proportion of those lipids residing in the outer leaflet is approximately 57% of the total lipid composition.

Comparison of the Post-Isertion and Formulation Methods for RGD-LN Formation. The postinsertion and formulation methods were compared with regard to their ability to incorporate RGD-lipid into LNs. In order to quantify the amount of the RGD-lipid that was incorporated into the LN by either method, the fluorescence emission and excitation spectra were obtained for the RGD-lipid (Figure 2). The amount of the targeting ligand that was incorporated by either the post-insertion or the formulation method was subsequently measured by fluorometry. Fluorometric measurements were conducted in the presence of 1% Tween 20 in order to disrupt the LN structure. A linear increase in the fluorescence signal corresponded to increasing amounts of RGD-LNs;therefore, a standard curve was established from known amounts of the RGD-lipid in the presence of nontargeted LNs. The amount of RGD-lipid present

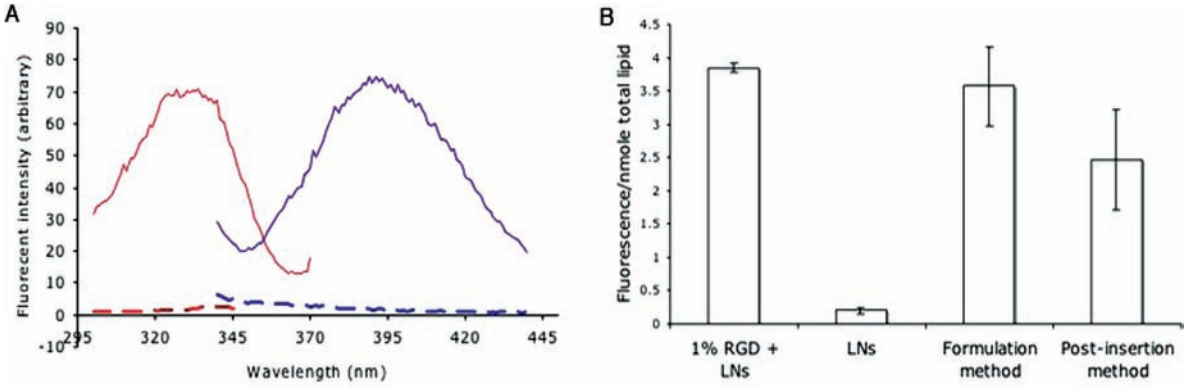

Figure 2. () Excitation (red) and emission (blue) spectra obtained for RGD-LNs with the RGD-lipid embedded in the bilayer. The spectrum for nontargeted LNs is shown by dashed lines. () Fluorescence measurements of the relative amounts of the RGD-lipid in RGD-LNs made by either the formulation method or the postinsertion method. The starting concentrationsof RGD-lipid (1 mol % of the total lipid concentration) plus nontargeted LNs represents the maximum possible RGD-lipid incorporation that was used before the RGD-lipid was incorporated into an LN.

in LNs made by the two different techniques was calculated as shown in Figure 2B.

HPTS Loading. In order to track intracellular delivery of LN contents, the pH-sensitive probe, 8-hydroxypyrene-1,3,6-trisulfonic acid (HPTS),was loaded into nontargeted LN and 0.5% RGD-LN (i.e., HPTS/N (55:45:0:0 mol:mol) and HPTS/GD-LN (54.5:45:0:0.5 mol:mol)). LNs were hydrated in 10 mL of HBS containing 40 mM HPTS, extruded,and dialyzed three times for 12 h against 4 L HBS. The resulting HPTS-LNs were characterized by DLS, phosphorus content,and HPTS fluorescence emission at 450 nm following excitation at 395 nm. The contribution from the MCA group of the RGD-lipid was examined and found to be negligible at this wavelength of detection.

Doxorubicin Loading ito the Interior of LNs. Doxorubicin was loaded into preformed nontargeted LNs and 0.5% RGD-LNs using the ammonium sulfate method described previously (*23*). Briefly, LN lipids were dried to a thin film,then hydrated in 10 mL of 300 mM ammonium sulfate, extruded,and dialyzed twice over 12 h against 150 mM NaCl. Phosphate assays were conducted to determine the amount of doxorubicin required to achieve a drug-to-lipid ratio of 0.2 (mol:mol). The appropriate amount of doxorubicin was dissolved in 1 mL of 150 mM NaCl, and the appropriate volume was delivered to each solution of LNs. Doxorubicin and LNs were coincubated at 55 °C for 1 h to load the drug, and then the free drug was removed by size exclusion chromatography, with a 40 mL Sephadex G50 column, equilibrated in 150 mM NaCl. Doxorubicin-encapsulated LNs (Dox:LNs) eluted within the first 10 mL fraction, and free doxorubicin eluted over the following 15 mL fractions. The size of the resulting particles was estimated by dynamic light scattering and assayed for phosphate content. The amount of encapsulated material was determined by RP-HPLC, using a standard curve made from the integrated peak area of doxorubicin's 280 nm UV absorbance. Free doxorubicin elutes on a 0−85% aqACN gradient at 15.8 min.

Doxorubicin Leakage Assay. The amount of doxorubicin that was retained in the LNs was measured over 24 h by the following doxorubicin leakage assay. Doxorubicin-loaded 0.5% RGD-LN and nontargeted LN (i.e., Dox:RGD-LN and Dox:LN), corresponding to an assay-confirmed concentration of 0.25 mM free doxorubicin, were incubated with 30% (v/v) FBS, total volume 1.5 mL, at 37 °C over 24 h. During this time, 100 μL was removed in duplicate at 0 min, 30 min, 1 h, 2 h, 5 h, and 24 h time points. The sample was applied to a spin column composed of 750 μL Sephadex G50 and centrifuged at 100 rpm for 1 min. One milliliter of 10% Triton X-100 (v/v) in 150 mM NaCl was added to the eluent in order to release the LN-entrapped doxorubicin. Doxorubicin content was subsequently assayed using the fluorescence emission of doxorubicin at 590 nm when compared to a standard curve made from free doxorubicin in 10% Triton X-100, 150 mM NaCl.

Cell Culture and LN Binding Assays. HUVEC cells, media, and supplements were obtained from Cascade Biologics (Portland, OR). M21 and M21L melanoma cell lines were obtained from Dr. D. Cheresh and were maintained in Dulbecco's Modified Eagle Medium supplemented with 10% fetal bovine serum (FBS). Rhodamine-labeled LNs varying in their RGD content (i.e., containing between 0 and 5 mol % of the targeting lipid) were added to cells to construct binding isotherms (Figure 3). LNs were adjusted to have equivalent phosphate content by dilution with HBS, then added to cells at concentrations between 0 and 4 mM (total lipid content). The final volume was adjusted to 500 μL with 5% FBS in PBS (PBS/FBS). Cells were incubated with LNs for 1 h at either 4 or 37 °C. After incubation, unbound LNs were removed with 5 mL of PBS/FBS, followed by centrifugation at 1100 rpm for 5 min, repeated twice. Unfixed cells were kept on ice and immediately analyzed by flow cytometry using a BD LSR II flow cytometer equipped with an air-cooled argon laser. Light scattering and fluorescence channels were set to a logarithmic scale and 10 000 events were collected per sample. Data were analyzed using *Flow Joe* (version 4.5.9, Stanford, CA). Electronic gates were established using unstained live cells based on their ability to exclude the uptake of propidium iodide. The mean fluorescence intensity was plotted versus the concentration of LN. Statistical analyses were conducted using *GraphPad Instat*, version 3.0. A Tukey-Kramer multiple comparisons test was used, with n values of 3, representing triplicate data points. P values greater than 0.05 were considered insignificant.

Cellular HPTS Uptake. HPTS:LNs and HPTS:RGD-LNs were added to cells and incubated at 37 °C for 0, 5, 15, 30, and 90 min time points. The cells were rinsed and assayed for cell-associated HPTS fluorescence by flow cytometry. At neutral pH, HPTS fluoresces at 519 nm when excited by light at 488 nm. Acidification of the vesicles (pH ~6.5−7) was monitored by detecting fluorescence emission at 455 nm following excitation at 405 nm. The background binding shown by nontargeted HPTS-containing LNs was low, and this measurement was subtracted from the fluorescence signals produced by RGD-LNs.

Doxorubicin Uptake into Cells as Determined by Flow Cytometry. 80 μM of doxorubicin (either encapsulated within the LN or as the free drug) was added to each aliquot of M21, M21L or HUVEC cells. The mixture was incubated for 90 min

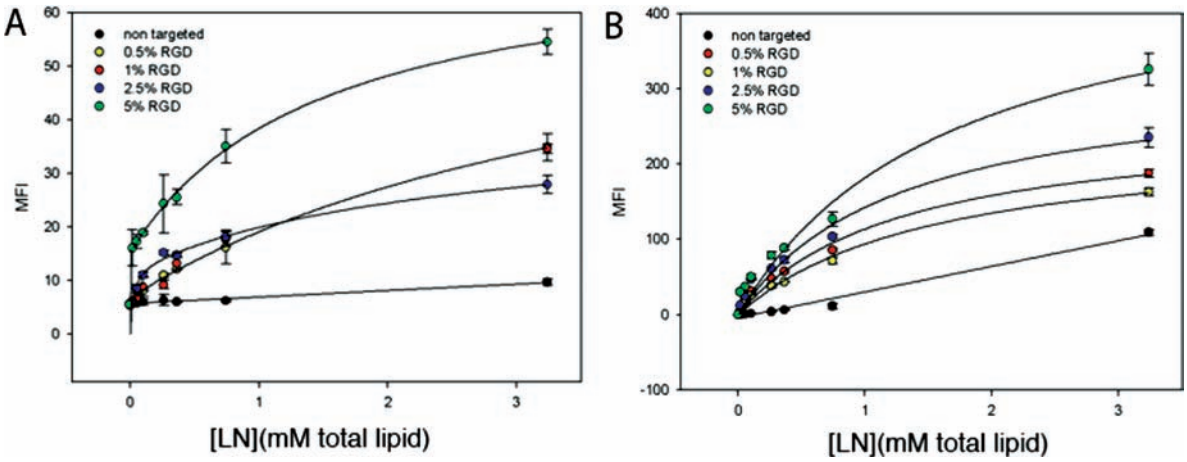

Figure 3. (A) Saturation curves describing the binding of LN to HUVEC following a 1 h incubation at 4 °C (endocytosis is prohibited at low temperatures). The LNs contain between 0 and 5 mol % RGD-lipid. (B) The same binding experiment conducted at endocytosis permissive temperatures (37 °C).

at 37 °C, then assayed for cell-associated doxorubicin fluorescence by flow cytometry as described in the above section.

LN Uptake into Cells as Observed by Fluorescence Microscopy. HUVEC cells were grown to confluence on four chambered glass slides (BD, Franklin Lakes, NJ). Cells were rinsed three times with PBS/FBS. 0.265 mM of doxorubicin was added for a final volume of 125 μL. For HPTS uptake, 1.36 mM (total lipid concentration) was added with a final volume of 200 μL. LNs or free drug were added to the cells; the mixture was incubated at 37 °C for 30 min, rinsed twice with PBS/FBS, and the cells were then fixed with 3.5% paraformaldehyde in PBS for 15 min and rinsed once again with PBS/FBS. Immediately before imaging, chambers were removed and slides were prepared using Vectashield mounting media (Vector Laboratories, Burlingame, USA) containing the blue nuclear stain, 4′,6-diamidino-2-phenylindole (DAPI). Images were captured using a Zeiss Axiovert 200 fluorescence microscope equipped with a Retiga 200R camera. Those acquired under a bright field used a 0.3 s exposure time and in the fluorescence field were acquired using three fluorescence filters with the following exposure times: red 3.5 s, green 5.5 s, DAPI 0.5 s.

RESULTS

Synthesis of Targeting Lipids. We synthesized the RGD-lipid, cRGDfK-SUCC-PEG$_2$(MCA)-PEG$_2$-DSPE using a straightforward solid-phase synthesis procedure, as shown in Figure 1. The final product had a purity of greater than 95% and an overall yield of 42% (or 40.8 mg using our synthesis scale). The peptide showed excellent analytical characteristics due to the presence of the methylcoumarin (MCA) fluorescent label. The MCA fluorophore also facilitated subsequent purification steps, owing to the ability to detect the compound. In our experience, PEG-lipid constructs without a fluorescent label have proven difficult to synthesize and purify (see Supporting Information). The MCA fluorophore was found to be essential once the targeting lipid was incorporated into an LN, as the exact mole percentage of RGD-lipid in LN could then be calculated.

Incorporation of the Targeting Lipid into LNs. The amount of RGD-lipid that was incorporated into RGD-LNs made via the postinsertion method was slightly reduced ($p < 0.05$), when compared to the amount of RGD-lipid that was initially added to the LN (Figure 2). The reason that the RGD-lipid did not fully integrate into the LN bilayer may be due to the adherence of the RGD-lipid micelles to glassware and the relatively small scale of our experiments. No significant decrease in the amount of RGD-lipid was detected for RGD-LNs made by the formulation method ($p > 0.05$). Because the formulation method was more straightforward and had good incorporation yields, it was the method of choice in subsequent experiments.

Table 1. Characterization of RGD-LNs

LN formulation	number of RGD molecules at LN surface[a]	size (nm)	HUVEC binding K_d (nM)[b,c]
nontargeted	0	102.4 ± 27.3	n/a
0.5% RGD	423	102.2 ± 32.0	2.59 ± 0.58
1% RGD	846	94.2 ± 20.7	1.98 ± 0.35
2.5% RGD	2113	128.9 ± 68.0	0.38 ± 0.07
5% RGD	4226	117.4 ± 66.0	0.59 ± 0.02

[a] This value was estimated using the assumptions that 100% of the RGD-lipid was incorporated into the LN and that 57% of the total RGD-lipid resides on the outer leaflet of the LN lipid bilayer. [b] Error is expressed as ± the standard error of the estimate from the nonlinear regression curve for binding. [c] The K_d value is expressed as the concentration of RGD-LN required to achieve half saturation of HUVEC cells and is derived from the data presented in Figure 3.

RGD-LN Characterization. The RGD-lipid was readily incorporated into LNs by the formulation method. When combined with other lipids such as DSPC, cholesterol, and a fluorescently labeled PE (Rhodamine-PE), LNs exhibiting a regular Gaussian size distribution with an average diameter of approximately 100 nm could be formed using up to 5 mol % of the RGD-lipid without obvious signs of aggregation. As summarized in Table 1, the LN particle size increased slightly, with an increase in the standard deviation (an indicator of LN aggregation) when 2.5 or 5 mol % of the RGD-lipid were included in the formulation. The apparent binding constants (expressed as K_d values) shown in Table 1 were calculated from the specific binding at 4 °C (data presented in Figure 3).

RGD-LN Binding Affinities. The apparent K_d values presented in Figure 3 decrease as the proportion of RGD-lipid is increased to 2.5 mol %. It can also be observed from the data in Figure 3A that the B_{max} values observed for the 5 mol % RGD-LNs is higher than the other formulations by 1.7-fold, which could be due to some limited aggregation of the RGD-LNs at these high contents of RGD-lipid. It is important to note that the K_d value observed in Table 1 accounts for a sum of several possible cellular processes and has been simplified here to describe the overall binding of RGD-LNs to live HUVEC cells.

Drug Retention in RGD-Targeted LNs. In some cases, it has been shown that when targeting ligands are incorporated into LNs, the permeability of the LN membrane to the drug

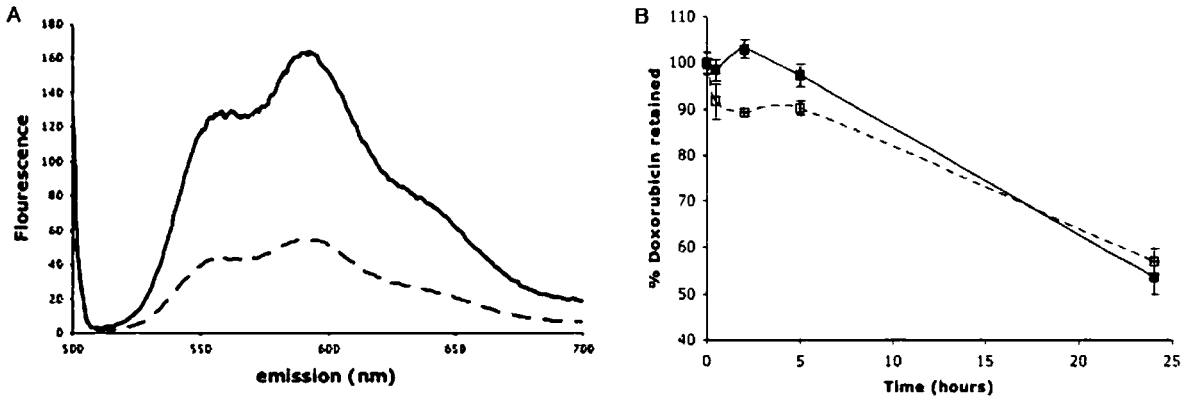

Figure 4. Doxorubicin retention in RGD-LNs versus nontargeted LNs. (A) Emission spectrum (following excitation at 490 nm) of 1.5 μg of doxorubicin dissolved in water (dashed line) or 10% Triton X-100 (solid line). (B) Release of doxorubicin from RGD-LNs made via the formulation method (solid line) and nontargeted LNs (dashed line) in a 10% FBS solution. Error is given as $\pm$ the standard deviation of three data points from the average doxorubicin emission (590 nm) determined in the presence of 10% Triton X-100.

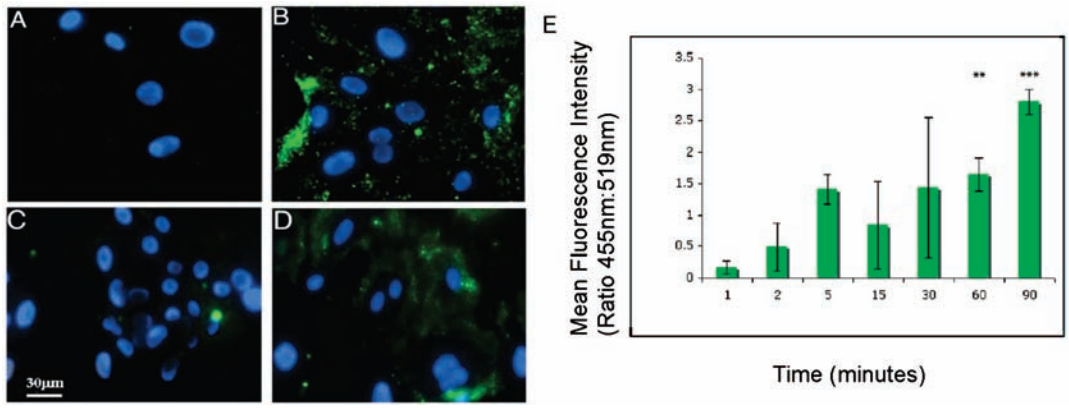

Figure 5. RGD-LNs are internalized and acidified by HUVEC. Panels A−D show fluorescence microscopy images demonstrating LN-associated HPTS uptake by HUVEC, while panel E reflects data obtained by flow cytometry which shows that the LN experiences an increasingly acidic environment as reflected by a progressive shift in the HPTS fluorescence toward fluorescence at 455 nm. LNs loaded with HPTS were coincubated with HUVEC cells at 37 °C. (A) Nontargeted LNs, 10 min incubation; (B) 1% RGD-targeted LNs, 10 min incubation. Panels C and D show HPTS:LNs that were internalized after a 40 min incubation; (C) shows the uptake of HPTS-loaded nontargeted LNs and (D) shows the 40 min uptake of 1% HPTS:RGD-LNs.

may also increase (*24*) (*25*). For this reason, the release of a commonly used anticancer drug, doxorubicin, from LN containing RGD-lipid was investigated.

Doxorubicin was loaded into LN and RGD-LN (containing 1 mol % RGD-lipid, and made by the formulation method) and the LNs were incubated in an aqueous buffer containing blood serum, over 24 h. At specified times, aliquots were withdrawn, free drug removed with a spin column, and the amount of doxorubicin remaining in the LN (upon release with Triton X-100) was assayed (Figure 4A). Little difference could be observed between the release of doxorubicin from RGD-LNs or nontargeted LNs (Figure 4B) indicating that the RGD-lipid did not significantly ($p > 0.05$) enhance the permeability of the LN membrane to doxorubicin over a 24 h period. It should be noted that the loss of nearly 30% of the LN's loaded material over 24 h is somewhat higher than that from the commercial LN formulations of doxorubicin. We attribute the relatively high loss of doxorubicin from the interior of the vesicles to the presence of serum proteins, lack of PEG coating, and incubation at physiological temperatures.

Cellular Uptake and Processing of RGD-LNs. The internalization and subsequent acidification of an RGD-LN within the cell was tracked with the pH-sensitive, membrane-impermeable probe HPTS. When HPTS is acidified, the emission spectrum shifts to shorter wavelengths. HPTS was loaded into LNs as indicated in Experimental Procedures. The LNs were then added to HUVECs and subjected to fluorescence microscopy. Green fluorescence in punctate cytoplasmic vesicles could be observed within 10 min in cells incubated with RGD-LNs, but not in cells incubated with nontargeted LNs (Figure 5A,B). The fluorescent signal detected after a 40 min incubation (Figure 5D) is noticeably more diffuse, suggesting that the fluorophore escapes the endosome at some time between 10 and 40 min following association of the RGD-LN with the HUVEC.

Figure 5E supports the notion that acidification is a function of incubation time. The fluorescence properties of HPTS were investigated with flow cytometry, using the indication of a neutral pH environment (fluorescence emission at 519 nm following excitation at 495 nm) or an acidic environment (emission at 455 nm following excitation at 405 nm). These results indicate that internalization of the particle commenced as early as 5 min. A significant increase in the relative 455 nm fluorescence was observed after 60 min suggesting that the contents within the particle are processed in a manner that coincides with endosomal maturation.

In Vitro Drug Delivery by RGD-LNs. Fluorescence microscope images comparing the delivery of doxorubicin by LNs versus the free drug are presented in Figure 6. Free, unencapsulated doxorubicin has a high affinity for the cell nucleus and rapidly permeates the plasma membrane. Thus, the fluorescence signal for free doxorubicin almost entirely colocalizes with the nuclear stain, DAPI (Figure 6A). Conversely, 1 mol % RGD-LNs deliver doxorubicin to cytoplasmic compartments (Figure 6B). Doxorubicin delivered by nontargeted LNs shows minimal

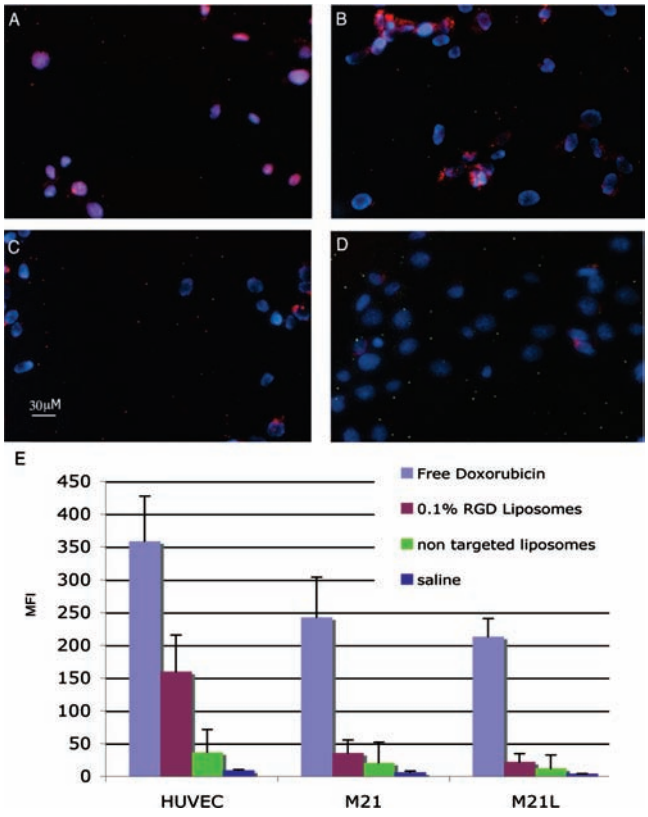

Figure 6. Cellular uptake of doxorubicin as a free drug, encapsulated in nontargeted LNs or in RGD-LNs. Panels A−D: Doxorubicin uptake by HUVEC cells as monitored by fluorescence microscopy following a 30 min incubation at 37 °C with the same amount of doxorubicin (0.265 mM) delivered to cells as (A) free drug, (B) 1% RGD-LN, (C) nontargeted LN, or (D) saline background control. (E) Doxorubicin uptake (as measured by flow cytometry) by three cell lines with different levels of $\alpha_v\beta_3$ expressed on their surface, HUVEC, M21, or M21L. 0.08 mM of doxorubicin was added to cells as either free, RGD-LN, or nontargeted LN formulations and incubated for 1 h at 37 °C prior to analysis.

background staining with uptake levels similar to the saline control (Figure 6C,D).

The ability of RGD-LNs to deliver doxorubicin to $\alpha_v\beta_3$-expressing cells is supported by the flow cytometry experiments shown in Figure 6E. HUVECs express approximately 263 000 $\alpha_v\beta_3$ integrins per cell, whereas M21 and M21L melanoma cells express approximately 56 700 and 1400 integrins per cell, respectively (*22*). RGD-LNs deliver more doxorubicin to HUVECs than nontargeted LN ($p < 0.05$) and appear to deliver modestly higher amounts to M21 cells over the nontargeted LNs; however, this increase is not statistically significant ($p > 0.05$). In contrast, M21L cells that express a relatively low amount of the receptor do not show enhanced uptake of doxorubicin-containing RGD-LNs.

DISCUSSION

This study describes well-defined RGD-lipid formulations that can target anticancer drugs to endothelial cells. Much of our ability to define the RGD-LNs used in this study is attributable to the inclusion of a defined-length, PEG-based spacer. We found that using this spacer improved upon the handling properties of the compound and facilitated analysis by ESI-MS, enabling a defined mass to confirm the identity of the compound. On several occasions, the shielding effect of PEG units was problematic toward the synthesis and purification of the construct. This was particularly important for confirmation of successful couplings while the construct was on a solid phase. In such case, robust qualitative methods (ESI-MS) were required to confirm couplings. The same concern may be raised toward the analysis of a successful purification when the construct was cleaved from the resin.

It is important to note that the PEG−lipid conjugate used in this study differs from commonly used PEG polymers, which are an average molecular weight of PEG repeats. The approximate bond length of the spacer is 75.7 Å. This estimate does not consider the bending and rotation of the spacer in aqueous solutions, which could be more accurately assessed using SPR-based techniques. Such techniques describe the extension of PEG-spacers in water. Using this methodology, it has been shown that PEG_{2000} spacers (commonly used in the manufacture of long-circulating LNs) extend approximately 200 Å from the surface of a lipid bilayer (*26*).

The ability to accurately characterize RGD-LNs is also partly attributable to the use of a fluorescent label within the RGD-lipid architecture. This was found to be essential for the accurate purification and chromatographic identification of the final product. The use of an identifying species such as a fluorescent label may lead to future preclinical targets, which may visualize and treat tumors at the same time. Indeed, RGD-conjugates to deliver imaging agents are quickly progressing through clinical trials (*27*).

Of the different methods employed to produce RGD-LNs, the formulation method was found to be the most straightforward and most effective. In our case, the post-insertion method resulted in incomplete transfer of a lipid particle between the RGD-lipid micelle and the preformed LN. It is generally thought that the post-insertion method of integrating a targeted lipid into the LN bilayer favors the orientation of the targeting lipid toward the outside layer of the LN bilayer (*28*).

A third method exists that is heavily used in the published literature on targeted LNs. This method entails reacting a targeted ligand with a functionalized group on the LN outer surface. Removal of unreacted or nonproduct species from the LN is impossible under these conditions. Furthermore, the measure of the amount of targeting ligand that ends up on the LN surface is generally unknown when using this approach.

Using defined RGD-LNs, we were able to synthesize a series of LNs that were composed of varying densities of the RGD−lipid. When the RGD-LNs were added to HUVECs, we found that an overall decrease in the observed K_d values correlated with an increase in the amount of RGD per LN. This may suggest that the improved binding of the LN can be attributed to the increased RGD valency of the LN. These findings are consistent with results published by Montet and colleagues, who found improved binding for multivalent presentations of their RGD-nanoparticles compared to their monovalent versions (*29*). In our study, we found a modest increase in K_d when the RGD−lipid is incorporated at 5 mol % versus 2.5 mol %. This small increase suggests that the optimal mole percentage of RGD−lipid per LN is within this range. It may also be possible that, after a certain concentration, there is lateral segregation of the RGD−lipid into larger aggregates. The data collected here appear to indicate that a more complex physical association is favored when RGD−lipids are incorporated at higher ratios (i.e., 2.5 and 5 mol % RGD-LNs appeared to have larger variation in particle size) to the other LN lipids. A manuscript which specifically focuses on RGD/HUVEC binding has recently been published by our group (*22*).

The major emphasis of this study is on the synthesis of a pure RGD−lipid and RGD-subsequent formulation into an RGD-LN. Our RGD−lipid is unique since it can be quantitatively formulated into LNs at the time of manufacture. The inclusion of the MCA molecule facilitated this and did not appear to affect the targeting function of the RGD−lipid. We

believe that providing good quantitative analytical data for the RGD-LN is important for *in vitro* analyses as shown in this study and will also be crucial for future *in vivo* characterization.

ACKNOWLEDGMENT

We thank Dr. David Cheresh for the melanoma cell lines, Dr. Mark Okon for NMR expertise, and Dr. Scott Covey for assistance with microscopy. Sonya Cressman is supported by funds from the National Science and Research Council. Pieter Cullis's lab is supported by grants from the Canadian Institute for Health Research and Tekmira Pharmaceuticals Inc.

Supporting Information Available: The synthesis and formulation properties of three other RGD-lipids. This material is available free of charge via the Internet at http://pubs.acs.org.

LITERATURE CITED

(1) Allen, T. M., and Chonn, A. (1987) Large unilamellar liposomes with low uptake into the reticuloendothelial system. *FEBS Lett. 223*, 42–6.

(2) Folkman, J. (1990) What is the evidence that tumors are angiogenesis dependent? *J. Natl. Cancer Inst. 82*, 4–6.

(3) Brooks, P. C., Clark, R. A., and Cheresh, D. A. (1994) Requirement of vascular integrin alpha v beta 3 for angiogenesis. *Science 264*, 569–71.

(4) Dechantsreiter, M. A., Planker, E., Matha, B., Lohof, E., Holzemann, G., Jonczyk, A., Goodman, S. L., and Kessler, H. (1999) N-Methylated cyclic RGD peptides as highly active and selective alpha(V)beta(3) integrin antagonists. *J. Med. Chem. 42*, 3033–40.

(5) Haubner, R., Gratias, R., Diefenbach, B., Goodman, S. L., Jonczyk, A., and Kessler, H. (1996) Structural and functional aspects of RGD-containing cyclic pentapeptides as highly potent and selective integrin avB3 antagonists. *J. Am. Chem. Soc. 118*, 7461–7472.

(6) Kim, J. W., and Lee, H. S. (2004) Tumor targeting by doxorubicin-RGD-4C peptide conjugate in an orthotopic mouse hepatoma model. *Int. J. Mol. Med. 14*, 529–35.

(7) Chen, X., Hou, Y., Tohme, M., Park, R., Khankaldyyan, V., Gonzales-Gomez, I., Bading, J. R., Laug, W. E., and Conti, P. S. (2004) Pegylated Arg-Gly-Asp peptide: 64Cu labeling and PET imaging of brain tumor alphavbeta3-integrin expression. *J. Nucl. Med. 45*, 1776–83.

(8) Xiong, X. B., Huang, Y., Lu, W. L., Zhang, X., Zhang, H., Nagai, T., and Zhang, Q. (2005) Intracellular delivery of doxorubicin with RGD-modified sterically stabilized liposomes for an improved antitumor efficacy: in vitro and in vivo. *J. Pharm. Sci. 94*, 1782–93.

(9) Wang, L., Shi, J., Kim, Y. S., Zhai, S., Jia, B., Zhao, H., Liu, Z., Wang, F., Chen, X., Liu, S. (2008) Improving tumor-targeting capability and pharmacokinetics of (99m)Tc-labeled cyclic RGD dimers with PEG(4) linkers. *Mol. Pharm*.

(10) Schraa, A. J., Kok, R. J., Moorlag, H. E., Bos, E. J., Proost, J. H., Meijer, D. K., de Leij, L. F., and Molema, G. (2002) Targeting of RGD-modified proteins to tumor vasculature: a pharmacokinetic and cellular distribution study. *Int. J. Cancer 102*, 469–75.

(11) Dubey, P. K., Mishra, V., Jain, S., Mahor, S., and Vyas, S. P. (2004) Liposomes modified with cyclic RGD peptide for tumor targeting. *J. Drug Targeting 12*, 257–64.

(12) Xiong, X. B., Huang, Y., Lu, W. L., Zhang, X., Zhang, H., Nagai, T., and Zhang, Q. (2005) Intracellular delivery of doxorubicin with RGD-modified sterically stabilized liposomes for an improved antitumor efficacy: in vitro and in vivo. *J. Pharm. Sci. 94*, 1782–93.

(13) Holig, P., Bach, M., Volkel, T., Nahde, T., Hoffmann, S., Muller, R., and Kontermann, R. E. (2004) Novel RGD lipopeptides for the targeting of liposomes to integrin-expressing endothelial and melanoma cells. *Protein Eng. Des. Sel. 17*, 433–41.

(14) Nabors, L. B., Mikkelsen, T., Rosenfeld, S. S., Hochberg, F., Akella, N. S., Fisher, J. D., Cloud, G. A., Zhang, Y., Carson, K., Wittemer, S. M., Colevas, A. D., and Grossman, S. A. (2007) Phase I and correlative biology study of cilengitide in patients with recurrent malignant glioma. *J. Clin. Oncol. 25*, 1651–7.

(15) Torchilin, V. (1985) Liposomes as targetable drug carriers. *Crit. Rev. Ther. Drug Carrier Syst. 2*, 65–115.

(16) Jansons, V. K., and Mallett, P. L. (1981) Targeted liposomes: a method for preparation and analysis. *Anal. Biochem. 111*, 54–9.

(17) Heath, T. D., Montgomery, J. A., Piper, J. R., and Papahadjopoulos, D. (1983) Antibody-targeted liposomes: increase in specific toxicity of methotrexate-gamma-aspartate. *Proc. Natl. Acad. Sci. U.S.A. 80*, 1377–81.

(18) Nellis, D. F., Ekstrom, D. L., Kirpotin, D. B., Zhu, J., Andersson, R., Broadt, T. L., Ouellette, T. F., Perkins, S. C., Roach, J. M., Drummond, D. C., Hong, K., Marks, J. D., Park, J. W., and Giardina, S. L. (2005) Preclinical manufacture of an anti-HER2 scFv-PEG-DSPE, liposome-inserting conjugate. 1. Gram-scale production and purification. *Biotechnol. Prog. 21*, 205–20.

(19) Nellis, D. F., Giardina, S. L., Janini, G. M., Shenoy, S. R., Marks, J. D., Tsai, R., Drummond, D. C., Hong, K., Park, J. W., Ouellette, T. F., Perkins, S. C., and Kirpotin, D. B. (2005) Preclinical manufacture of anti-HER2 liposome-inserting, scFv-PEG-lipid conjugate. 2. Conjugate micelle identity, purity, stability, and potency analysis. *Biotechnol. Prog. 21*, 221–32.

(20) Allen, T. M., Sapra, P., and Moase, E. (2002) Use of the post-insertion method for the formation of ligand-coupled liposomes. *Cell Mol. Biol. Lett. 7*, 217–9.

(21) Olson, F., Hunt, C. A., Szoka, F. C., Vail, W. J., and Papahadjopoulos, D. (1979) Preparation of liposomes of defined size distribution by extrusion through polycarbonate membranes. *Biochim. Biophys. Acta 557*, 9–23.

(22) Cressman, S., Sun, Y., Maxwell, E. J., Fang, N., Chen, D. D. Y., Cullis, P. (2009) Binding and uptake of RGD-containing ligands to cellular $\alpha v\beta 3$. *Int. J. Pept. Res. Ther. 15*.

(23) Haran, G., Cohen, R., Bar, L. K., and Barenholz, Y. (1993) Transmembrane ammonium sulfate gradient in liposomes produce efficient and stable entrapment of amphipathic weak bases. *Biochim. Biophys. Acta 1151*, 201–15.

(24) Ishida, T., Iden, D. L., and Allen, T. M. (1999) A combinatorial approach to producing sterically stabilized (Stealth) immunoliposomal drugs. *FEBS Lett. 460*, 129–33.

(25) Nallamothu, R., Wood, G. C., Kiani, M. F., Moore, B. M., Horton, F. P., and Thoma, L. A. (2006) A targeted liposome delivery system for combretastatin A4: formulation optimization through drug loading and in vitro release studies. *PDA J. Pharm. Sci. Technol. 60*, 144–55.

(26) Jeppesen, C., Wong, J. Y., Kuhl, T. L., Israelachvili, J. N., Mullah, N., Zalipsky, S., and Marques, C. M. (2001) Impact of polymer tether length on multiple ligand-receptor bond formation. *Sciences 293*, 465–8.

(27) Iagaru, A., Chen, X., and Gambhir, S. S. (2007) Molecular imaging can accelerate anti-angiogenic drug development and testing. *Nat. Clin. Pract. Oncol. 4*, 556–7.

(28) Lammers, T., Hennink, W. E., and Storm, G. (2008) Tumour-targeted nanomedicines: principles and practice. *Br. J. Cancer 99*, 392–7.

(29) Montet, X., Funovics, M., Montet-Abou, K., Weissleder, R., and Josephson, L. (2006) Multivalent effects of RGD peptides obtained by nanoparticle display. *J. Med. Chem. 49*, 6087–93.

BC900041F

SUPPORTING INFORMATION

Towards Clinical Progression of Targeted Liposomal Nanoparticles

Sonya Cressman*, Ian Dobson, Justin B. Lee, Yuen Yi C. Tam,

Pieter R. Cullis

Contents:

Figure S.1. RGD-lipids

Table S. 1. Summary of RGD-lipids synthesized

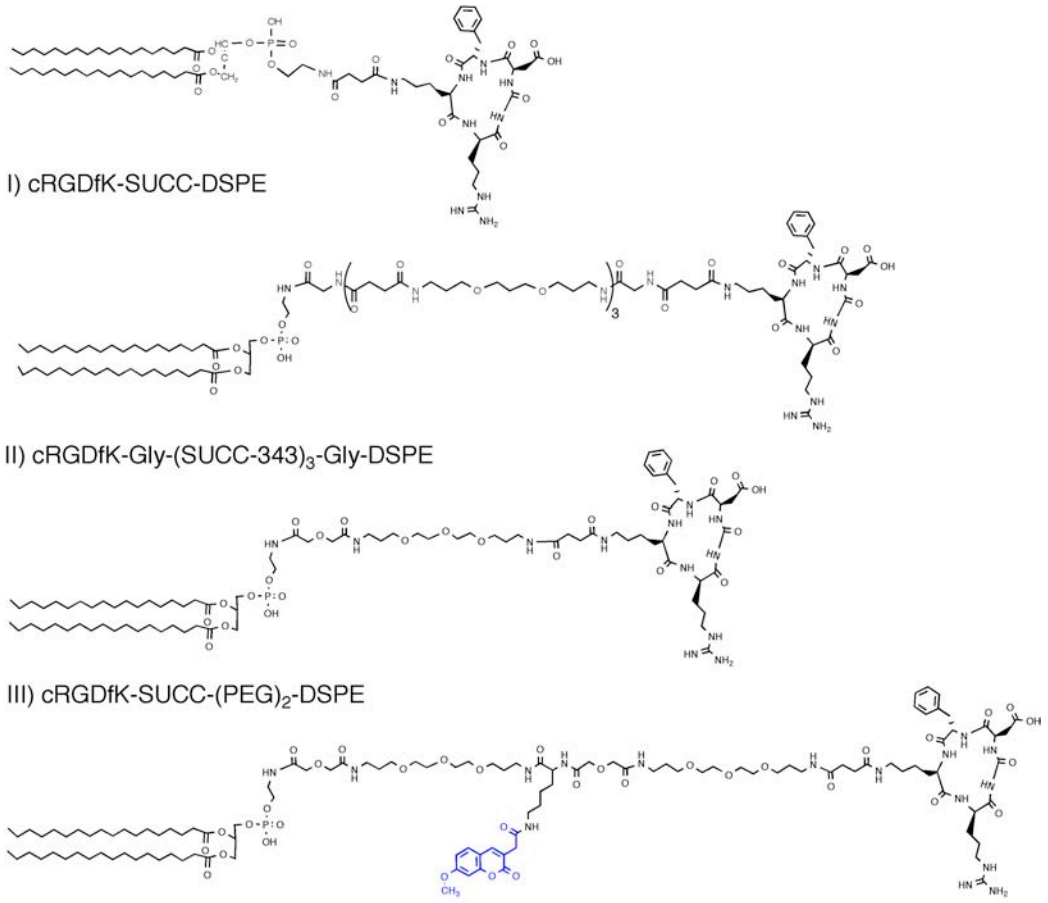

Figure S.1. Compounds I-IV were synthesized for assessment as LN targeting agents. Compound IV was chosen for further studies, since the fluorescent labeling molecule enabled accurate quantitation and the presence of the PEG spacer reduced aggregation effects noted for compound 1.

Table S.1 Summary of RGD-lipids synthesized

Compound	Synthesis	Length of spacer(Å)†	Purity	Yield*	Conclusion
I	Facile, cost effective	12.0	>85% (TLC)	~10mg (14 %)	Poor characterization Induces LN aggregation
II	Difficult	97.5	<50% (TLC)	<1 %	Difficult to analyze Low yield
III	Facile, cost effective	43.0	> 85% (ESI-MS)	27mg (22%)	Excellent synthesis Difficult to analyze
IV	Facile	75.7	>95% (TLC, ESI-MS)	40.8mg (42%)	Lead candidate for LN formulation

†total bond length from phosphate to ε-amine of cRGDfK
*calculated from peptide+spacer to the lipid coupling

A New Approach in the Preparation of Dendrimer-Based Bifunctional Diethylenetriaminepentaacetic Acid MR Contrast Agent Derivatives

Kido Nwe,[†] Heng Xu,[†] Celeste Aida S. Regino,[‡] Marcelino Bernardo,[‡,§] Lilia Ileva,[§] Lisa Riffle,[§] Karen J. Wong,[‡] and Martin W. Brechbiel*[,†]

Radioimmune and Inorganic Chemistry Section, Radiation Oncology Branch, and Molecular Imaging Program, National Cancer Institute, 10 Center Drive, Bethesda, Maryland 20892, and Research Technology Program, SAIC-Frederick, Inc., NCI-Frederick, Frederick, Maryland 21702. Received February 4, 2009; Revised Manuscript Received June 7, 2009

In this paper, we report a new method to prepare and characterize a contrast agent based on a fourth-generation (G4) polyamidoamine (PAMAM) dendrimer conjugated to the gadolinium complex of the bifunctional diethylenetriamine pentaacetic acid derivative (1B4M-DTPA). The method involves preforming the metal−ligand chelate in alcohol prior to conjugation to the dendrimer. The dendrimer-based agent was purified by a Sephadex G-25 column and characterized by elemental analysis. The analysis and SE-HPLC data gave a chelate to dendrimer ratio of 30:1 suggesting conjugation at approximately every other amine terminal on the dendrimer. Molar relaxivity of the agent measured at pH 7.4 displayed a higher value than that of the analogous G4 dendrimer based agent prepared by the postmetal incorporation method ($r_1 = 26.9$ vs 13.9 mM^{-1} s^{-1} at 3 T and 22 °C). This is hypothesized to be due to the higher hydrophobicity of this conjugate and the lack of available charged carboxylate groups from noncomplexed free ligands that might coordinate to the metal and thus also reduce water exchange sites. Additionally, the distribution populations of compounds that result from the postmetal incorporation route are eliminated from the current product simplifying characterization as quality control issues pertaining to the production of such agents for clinical use as MR contrast agents. In vivo imaging in mice showed a reasonably fast clearance ($t_{1/2} = 24$ min) suggesting a viable agent for use in clinical application.

INTRODUCTION

The quest for the development of a more efficient contrast agent for magnetic resonance imaging (MRI) is an ongoing process. Although clinically used low molecular weight paramagnetic chelates, such as Gd(III)-diethylenediaminepentaacetic acid (GdDTPA) (Magnevist) and Gd(III)-*N*,*N*′,*N*″,*N*‴-tetracarboxymethyl-1,4,7,10-tetraazacyclododecane (Gd-DOTA) (*1, 2*), are thermodynamically stable within the context of their usage, they suffer from rapid clearance from vascular circulation and renal excretion.

Dendrimer-based macromolecular MR contrast agents in which numerous chelated gadolinium ions (Gd(III)) are covalently attached to a multivalent dendritic architecture are a promising class of diagnostic agents for medical imaging applications (*3*−*6*). There are also growing applications of dendrimers in preparation of macromolecules for radioimmunotherapy (*7*−*9*). Due to their macromolecular size and weight, dendrimer-based MR agents feature higher molar relaxivities along with longer retention and circulation times as compared to the clinically approved Magnevist (Gd(III)-DTPA), thereby resulting in greatly enhanced sensitivity and operational window (*10*). Extensive efforts have been expanded on the preparation and evaluation of these agents in our laboratory along with several other research groups worldwide to study their *in vivo* properties and to eventually reach the goal of producing viable imaging agents that might be translated into clinical use (*4, 11*−*14*). Preclinical results have been promising in animal studies and by virtue of choosing generation size, core elements, and other exterior modifications dendrimer-based MR agents have been successfully employed for the imaging blood pool (*14*), specific organs such as kidney (*4, 5*) and liver, lymphatics (*6*), and tumor vasculature (*12, 13*) in mice with acceptable clearance rates.

The typical procedure for preparation of these agents usually involves three key steps. The first step is conjugation of an isothiocyanate or *N*-hydroxysuccinimidyl active ester form of either 2-(4-isothiocyanatobenzyl)-6-methyl-diethylenetriaminepentaacetic acid (1B4M-DTPA) or 1,4,7,10-tetraazacyclododecane-1,4,7,10-tetraacetic acid (DOTA) derivatives to the multiple periphery functional groups (e.g., $-NH_2$) of various types of polyamino-terminated dendrimers in either aqueous or organic solution. The second step has been complexation of paramagnetic metal Gd(III) ions with the conjugated DTPA or DOTA chelates attached on the dendrimers. The final and highly important step has been the purification of the product to completely remove "free" Gd(III) ions usually by an extensive dialysis technique using appropriate filtration membranes (*3, 5, 6, 10, 15*).

Unlike small molecules, macromolecular agents are usually difficult to define with accurate and precise chemical structures and to characterize their purities by traditional means. This limitation generates real challenges to establishing quality control for reproducible preparation of agents. For instance, even when the same protocol is followed for preparation of these macromolecular dendrimer-based agents, it is exceedingly difficult to ensure that both the same number of conjugated chelates and the same number of Gd(III) ions for each batch will be achieved. This is particularly so when considering that there are potentially hundreds of reactive sites in higher-

* Correspondence to Martin W. Brechbiel, Ph.D., Radioimmune & Inorganic Chemistry Section, Radiation Oncology Branch, NCI, NIH, Building 10, Room 1B40, 10 Center Drive, Bethesda, MD 20892-1088; Fax: (301) 402-1923; E-mail: martinwb@mail.nih.gov.

[†] Radioimmune and Inorganic Chemistry Section, Radiation Oncology Branch, National Cancer Institute.

[‡] Molecular Imaging Program, National Cancer Institute.

[§] Research Technology Program, SAIC-Frederick, Inc.

10.1021/bc900057z This article not subject to U.S. Copyright. Published 2009 by the American Chemical Society
Published on Web 06/25/2009

generation dendrimers, e.g., a generation 8 PAMAM dendrimer potentially has 1024 terminal primary amines (*16*, *17*). One has to be aware that these products are also effectively a distribution of chelate conjugate products that has been carried forward into another distribution of Gd(III) complexes and that while characterization reports numbers of chelates and Gd(III) those numbers represent average numbers. For clinical use, however, these agents need to have a narrow molecular weight range and the same chemical composition to ensure reproducible expected *in vivo* behavior. The Gd(III) metal content in these dendrimer-based MR contrast agents is a critical factor not only to the level of contrast efficacy, but also to the biological properties (e.g., PD/PK). In our prior synthetic approaches, and to the best of our knowledge of all others, the Gd(III) metal incorporation has always been performed as the last step, following conjugation of bifunctional chelating agents to the dendrimer. In general, by combustion analysis data, this sequence generally results in ~80% of the bifunctional chelating agents being complexed with Gd(III) ions, while the remaining ~20% of those chelates remain vacant of Gd(III) (*18*, *19*).

These 20% "open" chelates possess a significant number of carboxyl groups, which may impact overall hydrophilicity and charge of the agents at the physiological conditions. Accurate determination of what role these vacant or "open" chelates play is an extremely difficult task to perform. Additionally, concerns pertaining to chelation of exogenous biologically relevant metal ions *in vivo* impacting toxicity may be valid when taking into account absolute molar injected amounts versus clearance rates. Lastly, as noted above, these products are actually complex mixtures of products, and elimination of some aspect of that character should strengthen the potential of their clinical translation. With that impetus in hand, we felt it necessary to explore a means to simplify the process while arriving at a more defined product by limiting these variables as much as possible.

With this note, we report a refined synthetic procedure for the preparation of dendrimer-based MR contrast agents, wherein (1B4M-DTPA) is first used to sequester Gd(III) and thereafter the resulting metal complexes are covalently attached to the terminal $-NH_2$ groups in a PAMAM G4 dendrimer. Such an approach allows creation of a simplified standard procedure making small molecule Gd(III) complexes thereby eliminating a manipulation step in preparation of the macromolecular dendrimer molecules while also ensuring full saturation of all of the conjugated chelates with Gd(III) to simultaneously eliminate an entire array of product distribution mixture. The PAMAM generation 4 dendrimer (G4D) with amine surface groups ($-NH_2$) is a convenient building block or core for the conjugation of metal chelates, and the G4D Gd(III) chelate conjugate is known to have moderate blood circulation time and relatively fast excretion via the kidney (*18*).

In order to validate the agent, the molar relaxivity of the generation 4 1B4M-DTPA Gd(III) conjugate (G4-(1B4M-Gd)$_{30}$(CS)) was determined for comparison to the analogous generation 4 dendrimer-based agent, G4-(1B4M)$_{60}$[Gd$_{42}$](CS), prepared in our laboratory using the previously established published synthesis route (*18*). Additionally, sets of mice (n = 2) were imaged with both G4-(1B4M-Gd) $_{30}$(CS) or G4-(1B4M)$_{60}$[Gd$_{42}$](CS) to establish what impact, if any, elimination of the vacant chelators on the exterior of the dendrimer product has on the quality of MR imaging.

EXPERIMENTAL SECTION

Materials and Methods. PAMAM dendrimer generation 4 (G4 dendrimer) with an ethylenediamine core in MeOH (10% w/v) was obtained from Dendritech. Gadolinium nitrate pentahydrate ($Gd(NO_3)_3 \cdot 5H_2O$) was purchased from Aldrich (St. Louis, MO). G4-(1B4M)$_{60}$[Gd$_{42}$](CS) prepared and purified as previously reported was employed in these studies (*18*). Phosphate buffered saline (1× PBS) at pH 7.4 was obtained from Digene (Gaithersburg, MD). Size exclusion HPLC (SE-HPLC) was performed using a Beckman System Gold (Fullerton, CA) equipped with model 126 solvent delivery module and a model 168 UV detector (λ 254 and 280 nm) controlled by 32 Karat software. Size exclusion chromatography was performed on a TSK-gel G2000SW 6 μm, 7.8 mm × 300 mm (Tosoh Bioscience, Montgomeryville, PA), with a TSK-gel 10 μm guard column (Tosoh Bioscience, Montgomeryville, PA) using phosphate buffered saline (1× PBS) solution as the eluent at 0.5 mL/min and 1.0 mL/min, respectively. Reverse-phase HPLC was performed by using a Beckman System Gold HPLC equipped with 165 UV−vis detector with peak detection at 254 and 280 nm and a C_{18} Varian microsorb-mv column (250 × 4.6 mm; 5 um). A gradient system composed of a pH 9.0 buffer (50 mM triethylamine/acetic acid) and methanol (25 min linear gradient from 0% to 100% methanol) with a flow rate of 1 mL/min was employed. All water used was purified using a Hydro Ultrapure Water Purification system (Rockville, MD). The Sephadex G-25 resin was purchased from Pharmacia (Sweden). The resin was pretreated with 1× PBS and loaded to a Pharmacia Biotech column 2.6 × 39.7 cm (Uppsala, Sweden). Elemental analyses were performed by Galbraith Laboratories, Inc. (Knoxville, TN) using combustion analysis method for C, H, and N and inductively coupled plasma-atomic emission spectroscopy (ICP-OES) method for determining the S and Gd. The Bio-Rad's gel filtration standard used to compare the molecular weight of the dendrimer conjugate was purchased from Bio-Rad (Hercules, CA).

Syntheses. *2-(4-Nitrobenzyl)-6-methyl-diethylenetriaminepentaacetic acid·5HCl.* The HCl salt of the bifunctional ligand, 2-(4-nitrobenzyl)-6-methyl-diethylenetriaminepentaacetic acid, **1B4M** from this point on, was prepared as previously described with a brief modification (*20*). Briefly, the pentaester form of the ligand (8.1 g, 9.8 mmol) was treated with HCl (g) saturated 1,4-dioxane (600 mL), and the mixture was stirred for 18 h. The product was precipitated with ethyl ether (400 mL), filtered, and dried to afford a whitish solid (4.8 g, 90%). (See the reference for NMR data.) ESI *m*/*e*: 543 (M+1). Calcd for $C_{22}H_{30}N_4O_{12} \cdot 5HCl$: C, 36.44; H, 4.83; N, 7.72. Found: C, 36.57; H, 5.05; N, 7.89.

*2-(4-Nitrobenzyl)-6-methyl-diethylenetriaminepentaacetic Acid Gadolinium Complex (p-NO$_2$-1B4M-[Gd] (**1**).* 1B4M·5HCl ligand (0.50 g, 0.69 mmol) and $Gd(NO_3)_3 \cdot 5H_2O$ (0.31 g, 0.72 mmol) in 20 mL MeOH were refluxed for 6 h. The solvent was reduced to 1.5 mL, and CH_2Cl_2 was added until a precipitate formed. The supernatant was decanted and the solid was dried. The precipitation process was repeated one more time to yield a pale yellow solid (0.65 g, 80%). ESI *m*/*e*: 700 (M+1). Reverse-phase HPLC t_R = 13.77 min. Calcd for $C_{22}H_{30}N_4O_{12}Gd \cdot 3NO_3 \cdot 5HCl \cdot 2CH_3OH$: C, 25.33; H, 3.78; N, 8.62. Found: C, 25.21; H, 3.67; N, 8.67.

*2-(4-Aminobenzyl)-6-methyl-diethylenetriaminepentaacetic Acid Gadolinium Complex (p-NH$_2$-1B4M-[Gd] (**2**).* A solution of compound **1** (0.50 g, 0.42 mmol) and 10% Pd/C (0.10 g) in H_2O (10 mL) was placed in a Parr hydrogenator at 15 psi. The reaction was allowed to go until the consumption of H_2 gas was completed (~3 h), which was confirmed by HPLC. The mixture was filtered on a glass frit through a pad of Celite (Celite 535 Coarse; Fluka) and washed with H_2O (20 mL). The solvent was evaporated under high vacuum to afford amine **2** (0.41 g, 87%) as a yellowish solid. ESI *m*/*e*: 670 (M+1). Reverse-phase HPLC t_R = 11.32 min. Calcd for $C_{22}H_{32}N_4O_{10}Gd \cdot 3NO_3 \cdot 5HCl$: C, 25.44; H, 3.57; N, 9.44. Found: C, 25.32; H, 3.59; N, 9.57.

*2-(4-Isothiocyanatobenzyl)-6-methyl-diethylenetriaminepentaacetic Acid Gadolinium Complex (SCN-1B4M-[Gd] (**3**)).* A solution

of 0.5 mL of thiophosgene in CH_2Cl_2 (3 mL) was added dropwise into a solution of **2** (1.0 g, 0.96 mmol) in H_2O (5 mL). The mixture was continued to stir for 1 h. The aqueous was separated and washed with CH_2Cl_2 (5 mL) and dried to afford compound **3** as a yellow solid (0.81 g, 75%). ESI *m*/*e*: 712 (M+1). Reverse-phase HPLC t_R = 19.17 min. Calcd for $C_{23}H_{30}-N_4SO_{10}Gd\cdot 3NO_3\cdot 5HCl\cdot 2H_2O$: C, 24.69; H, 3.67; N, 8.77. Found: C, 24.61; H, 3.65; N, 8.78.

Conjugation of G4 with **3** *- (G4-(1B4M-Gd)$_{30}$(CS)).* G4 PAMAM dendrimer (1.34 g, 0.0145 mmol; 15.35% w/w) in a 500 mL round-bottom flask was dried under vacuum to remove MeOH. The flask was charged with 350 mL 1× conjugation buffer with EDTA (0.48 M $NaHCO_3$ + 0.02 M Na_2CO_3 + 1.5 M NaCl + 0.005 M EDTA) (pH ~ 8.5) (250 mL). Compound **3** (1.51 g, 1.85 mmol) was added in portions while the pH was adjusted to 8.5 with 1 M NaOH. The mixture was stirred at room temperature for 5 d and 35 °C for 1 d. The solution was cooled to room temperature and filtered. The solvent was reduced under high vacuum to ~30 mL at room temperature. The dendrimer chelate was purified by a Sephadex G-25 column eluted with water (pH 7.5; the pH was adjusted with NaOH). The first band was collected and lyophilized to yield the conjugate as a yellow spongy solid (65% based on dendrimer). SE-HPLC t_R = 14.0. Calcd for $C_{622}H_{1250}N_{250}O_{125}\cdot 30(C_{23}H_{30}N_4SO_{10}Gd)\cdot 49Na\cdot 50H_2O$ [G4-(1B4M-Gd)$_{30}$(CS)$Na_{49}(H_2O)_{50}$]: 41.01 (C), 5.87 (H), 13.51 (N), 2.50 (S), 12.29(Gd). Found: 40.77, 5.94, 13.79, 2.49, 12.03.

Molar Relaxivity Measurements. The molar relaxivity of G4-(1B4M)$_{60}$[Gd_{42}](CS) was measured as reported elsewhere (*18*). Stock solutions of the G4 dendrimer agents, G4-(1B4M-Gd)$_{30}$ (5.0 Mm in Gd), were diluted to concentrations of 0.1, 0.25, 0.50, 0.75, and 1.0 mM in 1× PBS (300 μL). Solutions of Gd(III)-DTPA (Magnevist) at 0.25, 0.50, 0.75, 1.0, 1.25, 1.5, and 2.0 mM were prepared in 1× PBS (300 μL) and used as a reference standard. Relaxivity measurements were obtained at ~22 °C using a 3-T clinical scanner (Signa Excite, GE Medical System, Waukesha, WI) equipped with a rectangular single-loop receiver coil (84 × 126 × 6 mm^3). A series of single-slice 2D inversion recovery (IR) fast spin−echo images of all the solutions were acquired at the same time with a TE around 9 ms and using different inversion recovery times (TI = 50, 100, 350, 750, 1250, 2500, and 5000 ms) followed by a single-slice 8-echo SE image (TE = 9 ms). The R_1 values for each dilution were determined by fitting ROI intensity values from variable IR images using Igor Pro (http://www.wavemetrics.com). R_2 values were measured from ROI values from T_2 maps, which were calculated from the multiecho images in *ImageJ* (http://rsb.info.nih.gov/ij) using the MRI analysis plug-in (http://rsb.info.nih.gov/ij/plugins/mri-analysis.html). The molar relaxivities, r_1 and r_2, were obtained from the slope of $1/T_1$ or $1/T_2$ vs [Gd(III)] plots determined from region of interest measurements.

***In Vivo* Magnetic Resonance Imaging (MRI).** Mice were imaged two at a time to increase throughput using a 3T clinical scanner (Achieva, Philips Healthcare, Best, Holland) equipped with a dual mouse coil comprising two parallel receive-only coils (saddle-shaped Helmholtz coils, 38 mm in diameter × 70 mm in length) connected to independent receiver channels and spaced 43 mm apart. Each mouse was placed in a physical restraint while a catheter line (30 gauge needle on a 0.010 in i.d. × 6 in long Tygon tubing) filled with 1× PBS was inserted into the tail vein, anesthetized using gas mixtures of 3% isoflurane in O_2, and then carefully placed in a mouse bed equipped with a nose cone, respiratory pad, and fiber optic temperature sensor for physiology monitoring. The mice were positioned in the dual mouse coil which was heated with air to maintain the mice at 34 °C. The anesthesia gas was adjusted between 1.5% and 2.5% isoflurane to maintain a respiration rate of ~30 bpm during the acquisition of all images. After acquiring a triplanar gradient echo survey, a coronal-view T_1-weighted 3D-fast spoiled gradient echo image with a low flip angle (repetition time of 14 ms, echo time of 2.4 ms, flip angle of 8°, field of view of 80 mm, matrix size of 512 × 512 pixels, 40 slices, slice thickness of 0.6 mm and 1 average; scan time of 2.3 min) was acquired, followed by a dynamic series using a higher flip angle of 24° repeated every 2.5 min for 1 h. The contrast agent was injected (50 μL of 12 mM Gd(III) in 1× PBS pushed with 50 μL of 1× PBS) after the first dynamic image at a rate of 150 μL/min using a syringe pump (BS-9000-8, Braintree Scientific, Braintree, MA). Blood clearance rates were determined from ROI intensity measurements of the jugular vein in the low flip angle image and high flip angle dynamic images using *ImageJ*. The intensity values during the dynamic scans were then converted to gadolinium concentration, and the resulting [Gd] time curves were fitted to a single exponential function using an Igor Pro (Wavemetrics) macro.

RESULTS AND DISCUSSION

The preparative scheme leading to the formation of the title conjugate G4-(1B4M-Gd)$_{30}$(CS) is shown in Figure 1. The Gd(III) complex **1** was prepared by treatment of the ligand 1B4M with $Gd(NO_3)_3\cdot 5H_2O$ in methanol. Complex **1** could also be prepared by incubation of the ligand with $Gd(NO_3)_3\cdot 5H_2O$ in H_2O with the pH maintained at 5.5, but preparation of the Gd(III) complex in methanol was chosen as a more convenient route, especially for ligands that have limited solubility in water. Previous studies showed that complexes formed in methanol were stable (*21*, *22*). ESI-MS spectrum of the predominant ion for the three complexes showed the presence of carboxylate arm protons. This is in line with the ESI-MS data reported for the commercially available products such as $Gd(DTPA)^{-2}$ and $Gd(DOTA)^{-1}$ (*23*). Other authors have also reported ESI-MS data of lanthanide complexes with numbers of carboxylate protons ranging from 1 to 3 (*24*−*26*). This observation might be due to the nature of the initial electrostatic interaction, instead of covalent bonding, between the cationic metal ion and the anionic carboxylate ion, however having protonated complexes is not unreasonable. Additionally, the complex was isolated as the HCl salt as the starting ligand was in the HCl form also with nitrate as the counterion for the metal ion. Nitrate is known to be a better counterion for lanthanide ions than chloride (*27*−*29*). Lastly, for all the complexes the amount of the free metal ion determined by the UV/vis spectroscopic method was 0.002% (0.2 μM/10 mM) of the total (*30*). Indeed, if one examines the synthesis of the DTPA[Gd(III)] complex directly from DTPA and Gd_2O_3, this route produces a diprotonated complex that requires the addition of 2 equiv of base to make this complex physiologically acceptable (*31*).

For the purpose of comparison, the Gd(III) complex was formed in methanol by refluxing the ligand and the metal salt in the presence of 7 equiv of a solid base (NaOH) for 18 h. The Gd(III) complex was also formed under aqueous condition as previously reported (*26*). The ESI-MS data of both complexes indicated the presence of the complex with two fewer protons (697). However, these two latter complexes were also less stable than that formed in methanol alone. As soon as thiophosgene in CH_2Cl_2 was added to form complex **3** (for the third step), an insoluble precipitate formed when using the Gd(III) complexes formed by the latter means. This result was not observed for the complex formed in methanol without base. The reason for that behavior may reside with those carboxylic acid protons or the fact that the complex is protonated. Once deprotonated by base, the complex becomes vulnerable to attack by acidic

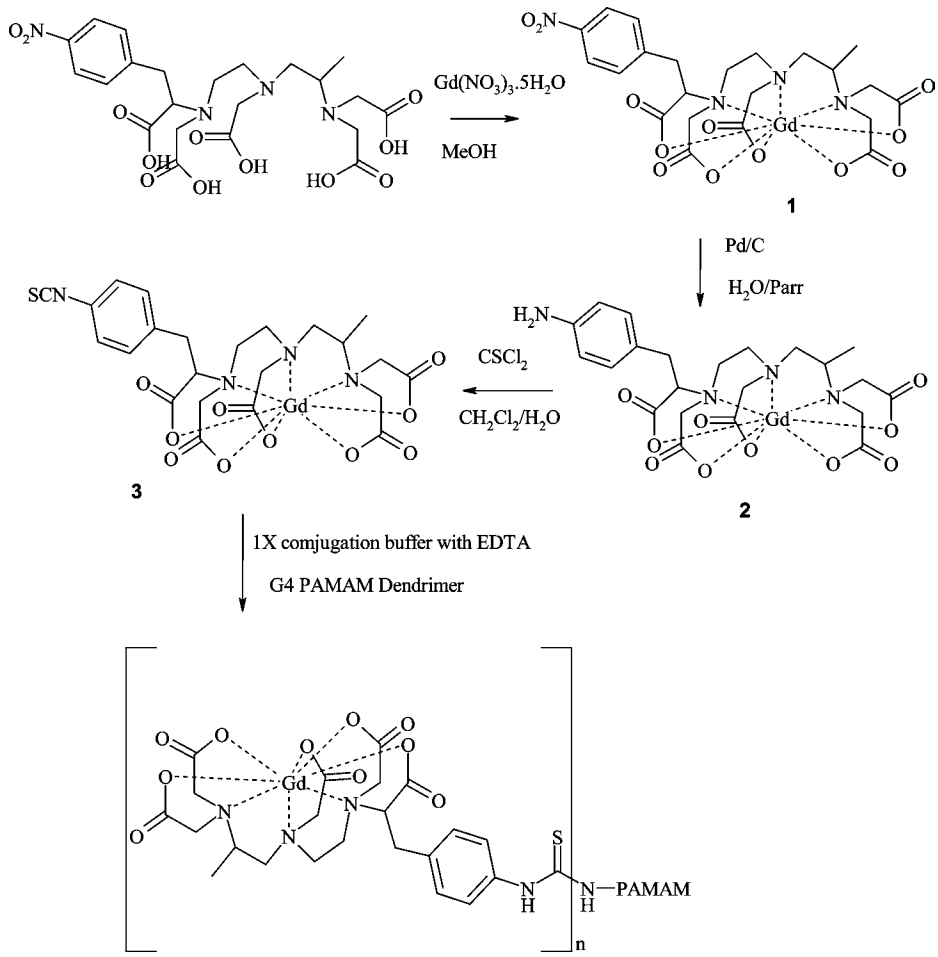

Figure 1. Synthetic scheme of the G4-(1B4M-Gd)$_{30}$(CS).

protons generated by the thiophosgene reaction that could perturb the M−O coordination and cause the metal to dissociate; a protonated complex eliminates this problem. It is also worth noting that the reaction with thiophosgene brought the pH of the solution down to ∼2. For that very reason, we chose to form the complex in methanol without a base. A full and thorough comparative study of the fundamental coordination chemistry of these three complexes will be reported in due course.

The reduction of the nitro group to amine was done using a Parr hydrogenator at 15 psi within a short period of time (∼3 h). The ESI-MS and combustion analysis data did not indicate any sign of the cleavage of the nitrobenzyl group (over-reduction product) or any dissociation of the metal ion from the ligand cavity. For preparation of complex **3**, a mixture of thiophosgene in dichloromethane was added dropwise, and the reaction was allowed to stir for 1 h thereafter, which was sufficient to complete the reaction. This also limits the exposure of the metal complex to low pH (1−2) over an extended period of time, which might induce the dissociation of the Gd(III) from the complex.

The conjugation reaction was done in 1× conjugation buffer (see Experimental Section) with EDTA at pH of 8.5. EDTA was used to sequester the free metal ion (Gd^{3+}), in case it dissociates from the chelate, which is rarely the case under this experimental condition. The dendrimer-based conjugate was purified by a Sephadex G-25 column. This method proved to be more efficient as compared to the exhaustive and time-consuming transverse-flow filtration (TFF) method (*18*). No reasonable MALDI-TOF could be obtained due to extreme broadening of the peak. However, we utilized SE-HPLC to determine the approximate molecular weight of the dendrimer conjugate by comparing with the Bio-Rad gel filtration standard combined with the elemental analysis data. On the basis of the analysis data and the SE-HPLC results, the formula of [G4-(1B4M-Gd)$_{30}$Na$_{49}$(H$_2$O)$_{50}$] was obtained.

To the best of our knowledge, the number of chelates conjugated to dendrimer is sensitive to the method used to append them to the dendrimer. The method used in a previous report to prepare the G4-(1B4M-Gd)$_X$(CS) conjugate, which is under aqueous condition, managed to occupy all of the available sites yielding G4-(1B4M-Gd)$_{64}$(CS)) (*32*). However, a later report, where the conjugation reaction was also done in aqueous condition, but with different buffer, yielded a lower number of chelates (G4-(1B4M$_{60}$-Gd$_{42}$)(CS) (*18*). An even lower number conjugated was achieved when the conjugation reaction was done in methanol followed by the metal chelation under aqueous condition (G4-(1B4M$_{57}$-Gd$_{41}$)(CS)) (*18*). It is worth noting that all these preparations focused on inserting the metal ion (Gd^{3+}) in the final step. In this report, we have inserted the metal ion early on to simplify the solution chemistry and the distribution of the species of the products.

We noticed in these studies that it was not possible to achieve the number of chelates higher than the reported value even in an extended period of time or higher temperature (ca. 45 °C) or even when using large excesses of the Gd(III) complex. On the basis of the number of chelates that we obtained, G4-(1B4M-Gd)$_{30}$(CS)), we hypothesized that the chelate with the metal ion in it may be less soluble and the intermetal or protonated complex interactions might limit the numbers of complexes adjacent to one another, or an equilibrium reaction with the solvent water limits the actual concentration of reactive isothio-

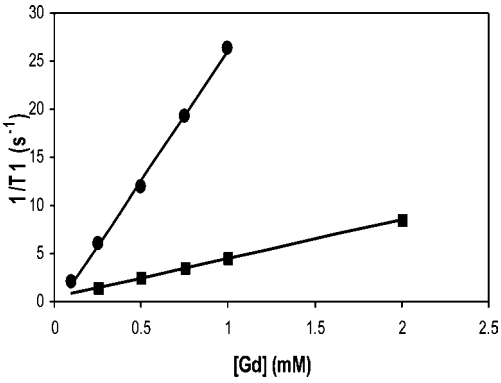

Figure 2. Molar relaxivity plots of G4-(1B4M-Gd)$_{30}$(CS) (•; 26.9 mM^{-1} s^{-1}) and magnevist (■; 4.2 mM^{-1} s^{-1}).

Table 1. Comparison of Results Between G4-(1B4M-Gd)$_{30}$(CS) (A) and G4-(1B4M)$_{60}$[Gd$_{42}$] (CS) (B)

agent	G4:chelate	r_1[a] (mM^{-1} s^{-1})	r_2[a] (mM^{-1}s^{-1})	half life[b] (min)	rate of clearance[c] (min^{-1})
A	1:30	26.9 ± 1.2	56.1 ± 1.4	24.4 ± 4.74	0.029 ± 0.0047
B	1:42	13.9 ± 1.6	33.6 ± 3.1	72.7 ± 17.31	0.010 ± 0.0026

[a] Molar relaxivity values obtained from phantom measurements. [b] Blood clearance half-life as measured from R_1 map of the jugular vein in dynamic MR angiographic images. [c] Blood clearance rates. Reported numbers are the average values and errors are reported as standard deviations.

cyanate species present. It is known that the isothiocyanide slowly reacts with water. Nevertheless, the relaxivity of this conjugate prepared by the reported means here is higher than any of the above-mentioned, which is one of the most important factors to be a viable agent. This is clear evidence that higher number of chelates, greater numbers of Gd(III), and thus higher molecular weight does not always translate to higher relaxivity.

Figure 2 shows a plot of inverse longitudinal relaxation time ($1/T_1$) versus gadolinium concentration for G4-(1B4M-Gd)$_{30}$(CS) conjugate (0.1−1 mM) and magnevist (0.25−2 mM). Although G4-(1B4M)$_{60}$[Gd$_{42}$](CS) has a higher dendrimer to metal chelate ratio (1:42), the molar relaxivity of the G4-(1B4M-Gd)$_{30}$(CS) conjugate reported here is almost twice the value reported for the G4-(1B4M)$_{60}$[Gd$_{42}$](CS) (13.9 vs 26.9 mM^{-1} s^{-1}) (Table 1) (*3*, *18*). There are three factors that might have contributed to this higher value. First, the conjugate prepared here does not have any free uncomplexed chelate (chelate without Gd) population of dendrimer conjugation products unlike the former method, G4-(1B4M)$_{60}$[Gd$_{42}$](CS) (Figure 3). This condition eliminates the possibility of a negatively charged carboxylate group from an unoccupied adjacent DTPA to coordinate to the metal ion and thus delete the availability of the water binding site. A reduced number of water-exchangeable sites results in lower relaxivity. A reduced water exchange site through anion binding has been well documented with protein binding (*33*), human serum albumin (*25*), carbonate (*34*), and phosphate (*35*) anions. Second, the conjugate prepared here is more hydrophobic than the G4-(1B4M)$_{60}$[Gd$_{42}$](CS), attributable to the lack of charged noncomplexed chelates. Hydrophobic interaction slows down the tumbling time (τ_R), which results in increasing relaxivity. The rotational correlation time (τ_R) is one of the key parameters contributing to the efficacy of the agent. Such a phenomenon has been reported by Wiener (*11*), Kellar (*36*), and Caravan (*37*). Third, the impact of steric hindrance needs to be taken into consideration, which also contributes to the availability of second sphere water molecules. Because the agent here is not fully saturated, that is, not all the available amino sites (64) are occupied, or lack free noncomplex chelating agents that could either replace

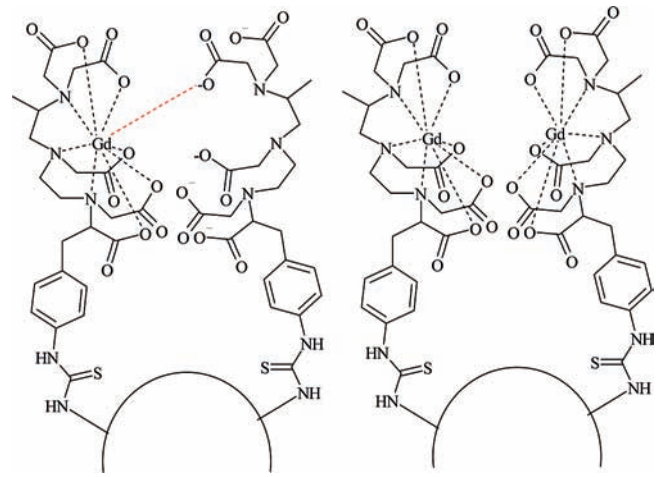

Figure 3. A representation of dendrimers with (left) and without (right) free noncomplexed chelate.

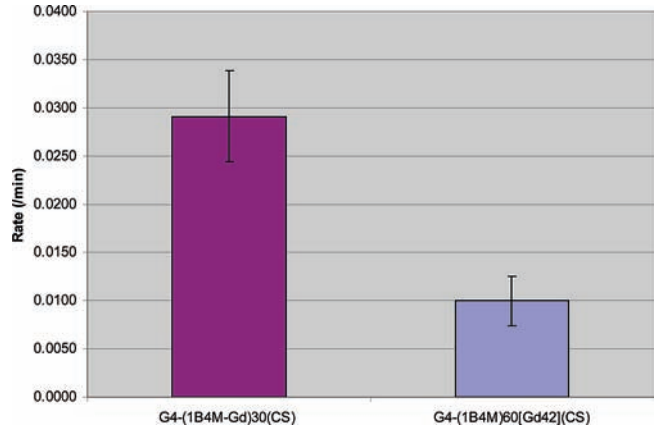

Figure 4. Average blood clearance rates measured at the jugular vein of G4-(1B4M-Gd)$_{30}$(CS) and G4-(1B4M)$_{60}$[Gd$_{42}$](CS).

water binding site or hinder the path of exchanging water molecules, more second-sphere water molecules may be readily available for exchange (*38*). This also helps to explain why previously prepared dendrimer conjugates with high chelate numbers, which are also then more sterically hindered, also have low relaxivity. This is additional evidence that greater numbers of chelates and thus also higher molecular weight may not automatically translate to higher relaxivity.

Table 1 also compares the half-life and rates of clearance between G4(1B4M-DTPA[Gd])$_{30}$(CS) and G4-(1B4M)$_{60}$[Gd$_{42}$]-(CS). The clearance data were fit to a single exponential decay (Figure 4). The rate of clearance of G4-(1B4M)$_{60}$[Gd$_{42}$] (CS) is 2.9 times lower than G4-(1B4M-Gd)$_{30}$(CS). We hypothesize that the agent was cleared mainly through kidneys. The data also indicate that there was a higher tissue uptake for G4-(1B4M-Gd)$_{30}$(CS) that can be useful as a targeting agent. Overall, G4-(1B4M-Gd)$_{30}$(CS) has a faster rate of clearance and a shorter half-life, which is expected for a more positively charged hydrophobic agent. One might be tempted to think that G4-(1B4M-Gd)$_{30}$(CS) is behaving like a small molecule based on the data presented, but the SE-HPLC data clearly indicates that the two agents have about the same size under the same conditions (t_R = 13.2 vs 14.0). This indicates that the charge is the contributing factor in high relaxivity and fast clearance.

Dynamic contrast-enhanced MR images shown in Figure 5 illustrate differences in circulation properties between G4-(1B4M-Gd)$_{30}$(CS) and G4-(1B4M)$_{60}$[Gd$_{42}$](CS). We found that the signal intensity in the kidney increased gradually 10 min after injection due to the high blood flow through this area and

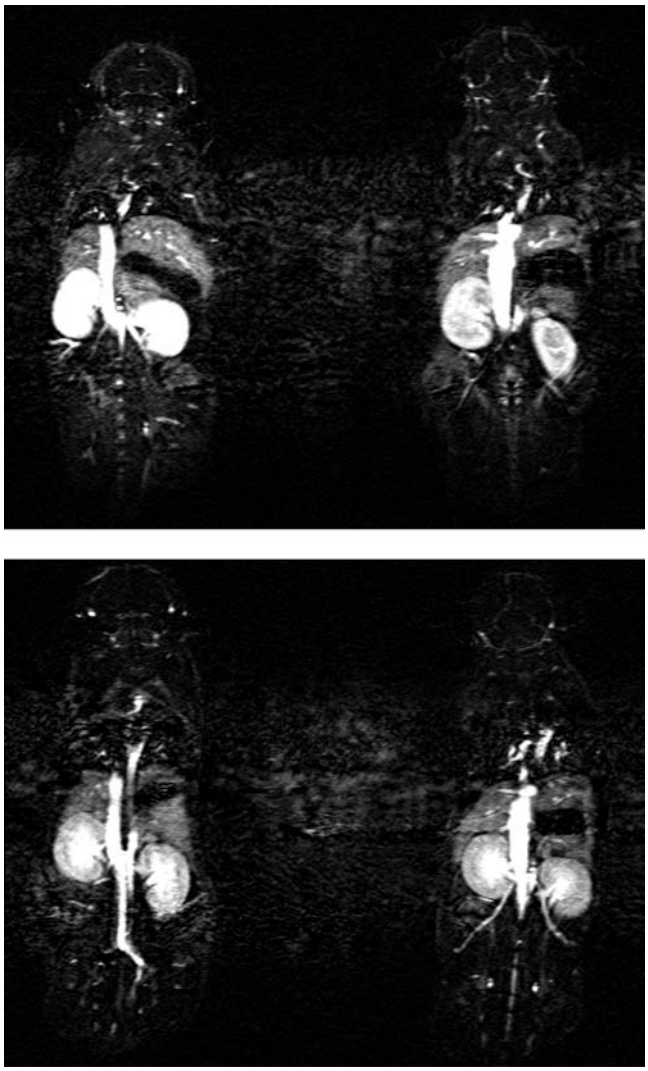

Figure 5. Whole-body 3D-micro-MR images of mice injected with 0.03 mmol/kg of G4-(1B4M-Gd)$_{30}$(CS) (above) and G4-(1B4M)$_{60}$[Gd$_{42}$](CS) (below). Both images were acquired at 30 min postinjection.

fast clearance of the agent. It is also observed that after 40 min postinjection images have no observable signal indicating the total clearance of the agent from the body. The signal intensity is low in kidneys for G4-(1B4M)$_{60}$[Gd$_{42}$](CS) when compared at the same acquisition time. This is expected due to the slow clearance (Table 1) and possible lower tissue uptake.

In conclusion, we herein report an improved synthesis to prepare PAMAM G4 dendrimer-based MR contrast agents, which features full saturation of all of the conjugated chelates with Gd(III) by using preformed Gd(III) complexes as reagents. This better defined chemistry provides less complex products compared to our established published syntheses, which routinely had formed the chelating agent dendrimer conjugate first, followed by addition of Gd(III). We believe that this new chemistry will strengthen the potential of translating these dendrimer-based MR agents into clinical trials by simplifying characterization as quality control issues pertaining to the production of such agents for clinical use as MR contrast agents.

ACKNOWLEDGMENT

This research was supported by the Intramural Research Program of the NIH, National Cancer Institute, Center for Cancer Research.

LITERATURE CITED

(1) Caravan, P., Ellison, J. J., McMurry, T. J., and Lauffer, R. B. (1999) Gadolinium(III) chelates as MRI contrast agents: structure, dynamics, and applications. *Chem. Rev. 99*, 2293–2352.

(2) Lauffer, R. B. (1987) Paramagnetic metal complexes as water proton relaxation agents for NMR imaging: theory and design. *Chem. Rev. 87*, 901–927.

(3) Xu, H., Regino, C. A. S., Koyama, Y., Hama, Y., Gunn, A. J., Bernardo, M., Kobayashi, H., Choyke, P. L., and Brechbiel, M. W. (2007) Preparation and preliminary evaluation of a biotin-targeted, lectin-targeted dendrimer-based probe for dual-modality magnetic resonance and fluorescence imaging. *Bioconjugate Chem. 18*, 1474–1482.

(4) Dear, J. W., Kobayashi, H., Jo, S.-K., Holly, M. K., Xuzhen, H., Yuen, P. S. T., Brechbiel, M. W., and Star, R. A. (2005) Dendrimer-enhanced MRI as a diagnostic and prognostic biomarker of sepsis-induced acute renal failure in aged mice. *Kidney Int. 67*, 2159–2167.

(5) Kobayashi, H., Jo, S.-K., Kawamoto, S., Yasuda, H., Hu, X., Knopp, M. V., Brechbiel, M. W., Choyke, P. L., and Star, R. A. (2004) Polyamine dendrimer-based MRI contrast agents for functional kidney imaging to diagnose acute renal failure. *J. Magn. Reson. Imaging 20*, 512–518.

(6) Kobayashi, H., Kawamoto, S., Choyke, P. L., Sato, N., Knopp, M. V., Star, R. A., Waldmann, T. A., Tagaya, Y., and Brechbiel, M. W. (2003) Comparison of dendrimer-based macromolecular contrast agents for dynamic micro-magnetic resonance lymphangiography. *Magn. Reson. Med. 50*, 758–766.

(7) WÄngler, C., Moldenhauer, G., Eisenhut, M., Haberkorn, U., and Mier, W. (2008) Antibody−dendrimer conjugates: the number, not the size of the dendrimers, determines the immunoreactivity. *Bioconjugate Chem. 19*, 813–820.

(8) Kobayashi, H., Sato, N., Saga, T., Nakamoto, Y., Ishimori, T., Toyama, S., Togashi, K., Konishi, J., and Brechbiel, M. W. (2000) Monoclonal antibody-dendrimer conjugates enable radiolabeling of antibody with markedly high specific activity with minimal loss of immunoreactivity. *Eur. J. Nucl. Med. 27*, 1334.

(9) Wu, C., Brechbiel, M. W., Kozak, R. W., and Gansow, O. A. (1994) Metal-chelate-dendrimer-antibody constructs for use in radioimmunotherapy and imaging. *Bioorg. Med. Chem. Lett. 4*, 449–454.

(10) Lebduskova, P., Sour, A., Helm, L., Toth, E., Kotek, J., Lukes, I., and Merbach, A. E. (2006) Phosphinic derivative of DTPA conjugated to a G5 PAMAM dendrimer: an ^{17}O and ^{1}H relaxation study of its Gd(III) complex. *Dalton Trans.* 3399–3406.

(11) Wang, S. J., Brechbiel, M. W., and Weiner, E. C. (2003) *Invest. Radiol. 38*, 662–668.

(12) Zhu, W., Okollie, B., Bhujwalla, Z. M., and Artemov, D. (2008) PAMAM dendrimer-based contrast agents for MR imaging of Her-2/<I > neu</I> receptors by a three-step pretargeting approach. *Magn. Reson. Med. 59*, 679–685.

(13) Kobayashi, H., Kawamoto, S., Saga, T., Sato, N., Hiraga, A., Konishi, J., Togashi, K., and Brechbiel, M. W. (2001) Micro-MR angiography of normal and intratumoral vessels in mice using dedicated intravascular MR contrast agents with high generation of polyamidoamine dendrimer core: Reference to pharmacokinetic properties of dendrimer-based MR contrast agents. *J. Magn. Reson. Imaging 14*, 705–713.

(14) Wiener, E., Brechbiel, M. W., Brothers, H., Magin, R. L., Gansow, O. A., Tomalia, D. A., and Lauterbur, P. C. (1994) Dendrimer-based metal chelates: A new class of magnetic resonance imaging contrast agents. *Magn. Reson. Med. 31*, 1–8.

(15) Laus, S., Sour, A., Ruloff, R., Tóth, E., and Merbach, A. E. (2005) Rotational dynamics account for pH-dependent relaxivities of PAMAM dendrimeric, Gd-based potential MRI contrast agents. *Chem.−Eur. J. 11*, 3064–3076.

(16) Yang, H., and Kao, W. J. (2006) Dendrimers for pharmaceutical and biomedical applications. *J. Biomater. Sci., Polym. Ed. 17*, 3–19.

(17) Diallo, M. S., Balogh, L., Shafagati, A., Johnson, J. H., Goddard, W. A., and Tomalia, D. A. (1999) Poly(amidoamine) dendrimers: a new class of high capacity chelating agents for Cu(II) ions. *Environ. Sci. Technol. 33*, 820–824.

(18) Xu, H., Regino, C. A. S., Bernardo, M., Koyama, Y., Kobayashi, H., Choyke, P. L., and Brechbiel, M. W. (2007) Toward improved syntheses of dendrimer-based magnetic resonance imaging contrast agents: new bifunctional diethylenetriaminepentaacetic acid ligands and nonaqueous conjugation chemistry. *J. Med. Chem. 50*, 3185–3193.

(19) Ali, M. M., Woods, M., Caravan, P., Opina, A. C. L., Spiller, M., Fettinger, J. C., and Sherry, A. D. (2008) Synthesis and relaxometric studies of a dendrimer-based pH-responsive MRI contrast agent. *Chem.—Eur. J. 14*, 7250–7258.

(20) Brechbiel, M. W., Beitzel, P. M., and Gansow, O. A. (1997) Purification of p-nitrobenzyl C-functionalized diethylenetriamine pentaacetic acids for clinical applications using anion-exchange chromatography. *J. Chromatogr., A 771*, 63–69.

(21) Nwe, K., Andolina, C. M., and Morrow, J. R. (2008) Tethered dinuclear europium(III) macrocyclic catalysts for the cleavage of RNA. *J. Am. Chem. Soc.*

(22) Nwe, K., Richard, J. P., and Morrow, J. R. (2007) Direct excitation luminescence spectroscopy of Eu(III) complexes of 1,4,7-tris(carbamoylmethyl)-1,4,7,10-tetraazacyclododecane derivatives and kinetic studies of their catalytic cleavage of an RNA analog. *Dalton Trans.* 5171–5178.

(23) KuÌnemeyer, J., Terborg, L., Nowak, S., Scheffer, A., Telgmann, L., Tokmak, F., GuÌnsel, A., WiezsmuÌller, G., Reichelt, S., and Karst, U. (2008) Speciation analysis of gadolinium-based MRI contrast agents in blood plasma by hydrophilic interaction chromatography/electrospray mass spectrometry. *Anal. Chem. 80*, 8163–8170.

(24) Chang, C. A., Francesconi, L. C., Malley, M. F., Kumar, K., Gougoutas, J. Z., Tweedle, M. F., Lee, D. W., and Wilson, L. J. (1993) Synthesis, characterization, and crystal structures of M(DO3A) (M = iron, gadolinium) and Na[M(DOTA)] (M = Fe, yttrium, Gd). *Inorg. Chem. 32*, 3501–3508.

(25) Hamblin, J., Abboyi, N., and Lowe, M. P. (2005) A binaphthyl-containing Eu(III) complex and its interaction with human serum albumin: a luminescence study. *Chem. Commun.* 657–659.

(26) Woods, M., Aime, S., Botta, M., Howard, J. A. K., Moloney, J. M., Navet, M., Parker, D., Port, M., and Rousseaux, O. (2000) Correlation of water exchange rate with isomeric composition in diastereoisomeric gadolinium complexes of tetra(carboxyethyl)dota and related macrocyclic ligands. *J. Am. Chem. Soc. 122*, 9781–9792.

(27) Khopkar, P. K., and Narayanankutty, P. (1971) Effect of ionic media on the stability constants of chloride, nitrate and thiocyanate complexes of americium(III) and europium(III). *J. Inorg. Nuc. Chem. 33*, 495–502.

(28) Bansal, B. M. L., Patil, S. K., and Sharma, H. D. (1964) Chloride, nitrate and sulphate complexes of europium (III) and americium (III). *J. Inorg. Nucl. Chem. 26*, 993–1000.

(29) Ikeda, A., Itoh, K., Suzuki, T., Aida, M., Fujii, Y., Mitsugashira, T., Hara, M., and Ozawa, M. (2006) Effect of counteranions on the adsorption of trivalent actinides and lanthanides on tertiary pyridine resin in alcoholic chloride and nitrate solutions. *J. Alloys Compd. 408−412*, 1052–1055.

(30) Barge, A., Cravotto, G., Gianolio, E., and Fedeli, F. (2006) How to determine free Gd and free ligand in solution of Gd chelates. A technical note. *Contrast Med. Mol. Imaging 1*, 184–188.

(31) Weinmann, H. J., Brasch, R. C., Press, W. R., and Wesbey, G. E. (1984) Characteristics of gadolinium-DTPA complex: a potential NMR contrast agent. *Am. J. Roentgenol. 142*, 619–624.

(32) Kobayashi, H., Kawamoto, S., Saga, T., Sato, N., Hiraga, A., Ishimori, T., Akita, Y., Mamede, M. H., Konishi, J., Togashi, K., and Brechbiel, M. W. (2001) Novel liver macromolecular MR contrast agent with a polypropylenimine diaminobutyl dendrimer core: Comparison to the vascular MR contrast agent with the polyamidoamine dendrimer core. *Magn. Res. Med. 46*, 795–802.

(33) Aime, S., Gianolio, E., Terreno, E., Giovenzana, G. B., Pagliarin, R., Sisti, M., Palmisano, G., Botta, M., Lowe, M. P., and Parker, D. (2000) Ternary Gd(III)L-HSA adducts: evidence for the replacement of inner-sphere water molecules by coordinating groups of the protein. Implications for the design of contrast agents for MRI. *J. Biol. Inorg. Chem. 5*, 488–497.

(34) Messeri, D., Lowe, M. P., Parker, D., and Botta, M. (2001) A stable, high relaxivity, diaqua gadolinium complex that suppresses anion and protein binding. *Chem. Commun.* 2742–2743.

(35) Nonat, A., Fries, P. H., Pécaut, J., and Mazzanti, M. (2007) Structure, stability, dynamics, high-field relaxivity and ternary-complex formation of a new tris(aquo) gadolinium complex. *Chem.—Eur. J. 13*, 8489–8506.

(36) Kellar, K. E., Henrichs, P. M., Hollister, R., Koenig, S. H., Eck, J., and Wei, D. (1997) High relaxivity linear Gd(DTPA)-polymer conjugates: The role of hydrophobic interactions. *Magn. Reson. Med. 38*, 712–716.

(37) Zech, S. G., Eldredge, H. B., Lowe, M. P., and Caravan, P. (2007) Protein binding to lanthanide(III) complexes can reduce the water exchange rate at the lanthanide. *Inorg. Chem. 46*, 3576–3584.

(38) Avedano, S., Tei, L., Lombardi, A., Giovenzana, G. B., Aime, S., Longo, D., and Botta, M. (2007) Maximizing the relaxivity of HSA-bound gadolinium complexes by simultaneous optimization of rotation and water exchange. *Chem. Commun.* 4726–4728.

BC900057Z

Bioconjugate Chemistry

AUGUST 2009
Volume 20, Number 8

© Copyright 2009 by the American Chemical Society

REVIEWS

Artificial Oxygen Carriers, Hemoglobin Vesicles and Albumin−Hemes, Based on Bioconjugate Chemistry

Eishun Tsuchida,*[,†] Keitaro Sou,[†] Akito Nakagawa,[†] Hiromi Sakai,[†] Teruyuki Komatsu,[†,‡] and Koichi Kobayashi[§]

Research Institute for Science and Engineering, Waseda University, Tokyo 169-8555, Japan, PRESTO, Japan Science and Technology Agency (JST), and Department of General Thoracic Surgery, School of Medicine, Keio University, Tokyo 160-8582, Japan. Received October 10, 2008; Revised Manuscript Received December 10, 2008

Hemoglobin (Hb, Mw: 64 500) and albumin (Mw: 66 500) are major protein components in our circulatory system. On the basis of bioconjugate chemistry of these proteins, we have synthesized artificial O_2 carriers of two types, which will be useful as transfusion alternatives in clinical situations. Along with sufficient O_2 transporting capability, they show no pathogen, no blood type antigen, biocompatibility, stability, capability for long-term storage, and prompt degradation in vivo. Herein, we present the latest results from our research on these artificial O_2 carriers, Hb-vesicles (HbV) and albumin−hemes. (i) HbV is a cellular type Hb-based O_2 carrier. Phospholipid vesicles (liposomes, 250 nm diameter) encapsulate highly purified and concentrated human Hb (35 g/dL) to mimic the red blood cell (RBC) structure and eliminate side effects of molecular Hb such as vasoconstriction. The particle surface is modified with PEG-conjugated phospholipids, thereby improving blood compatibility and dispersion stability. Manipulation of physicochemical parameters of HbV, such as O_2 binding affinity and suspension rheology, supports the use of HbV for versatile medical applications. (ii) Human serum albumin (HSA) incorporates synthetic Fe^{2+}porphyrin (FeP) to yield unique albumin-based O_2 carriers. Changing the chemical structure of incorporated FeP controls O_2 binding parameters. In fact, PEG-modified HSA-FeP showed good blood compatibility and O_2 transport in vivo. Furthermore, the genetically engineered heme pocket in HSA can confer O_2 binding ability to the incorporated natural Fe^{2+}protoporphyrin IX (heme). The O_2 binding affinity of the recombinant HSA (rHSA)-heme is adjusted to a similar value to that of RBC through optimization of the amino acid residues around the coordinated O_2.

1. INTRODUCTION

Transfusion of donor blood is currently an indispensable routine procedure in modern medical treatments because the risk of transmission of viral illness has became extremely low. Nevertheless, this level of safety has been achieved at great cost and hepatitis virus or unknown pathogens cannot be excluded completely, even by the nucleic acid amplification test (NAT) system. Furthermore, the transfusion of donor blood necessitates cross matching and compatibility tests to avoid a hemolytic reaction in the recipient, and the donated red blood cells (RBCs) must be refrigerated at 4 °C (up to 3 weeks in Japan). These requirements limit the availability of blood transfusion in disaster or emergency situations.

* To whom correspondence should be addressed. Eishun Tsuchida, Ph.D. Phone: +81-3-5286-3120. Fax: +81-3-3205-4740. E-mail: eishun@waseda.jp.
[†] Waseda University.
[‡] JST.
[§] Keio University.

10.1021/bc800431d CCC: $40.75 © 2009 American Chemical Society
Published on Web 02/10/2009

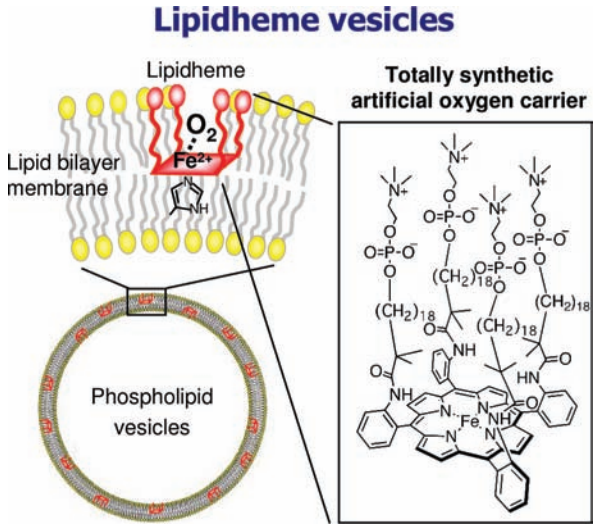

Figure 1. Lipidheme phospholipid vesicles as a totally synthetic artificial O_2 carrier (*7*).

During the past several decades, various artificial O_2 carriers have been synthesized and studied for as RBC substitutes by many scientists in the fields of organic chemistry, inorganic chemistry, biochemistry, and polymer chemistry. These O_2 carriers are classified as perfluorocarbon-based materials, synthetic Fe^{2+}porphyrin-based materials, and Hb-based materials. In this review, we highlight recent developments of our research related to RBC substitutes of the latter two types.

Actually, Hb consists of four polypeptide chains (globin proteins), each of which has an Fe^{2+}protoporphyrin IX (heme) as a prosthetic group. The globin chain forms a compact globular conformation; the heme group is incorporated into the hydrophobic pocket with an axial coordination of histidine (*1*). On exposure of the Hb solution to O_2, the heme forms a stable O_2 adduct complex. However, if the heme is eliminated from the globin wrapping, the heme complex is oxidized immediately and irreversibly to its Fe^{3+} state by proton-driven oxidation or μ-oxo dimer formation (*2*). In the 1970s and 1980s, much research was directed to mimic the O_2 carrier by synthesizing substituted porphyrin derivatives. In aprotic solvents, the proton-driven oxidation is excluded completely. Therefore, the remaining problem is how to suppress irreversible oxidation via dimerization. One successful approach was steric modification of porphyrin. Some superstructured Fe^{2+}porphyrins were prepared using an elegant organic synthesis technique (*2*−*4*). In particular, Collman reported that the tetrakis(α,α,α,α-*o*-pivalamido)phenylporphinatoiron complex with 1-methylimidazole can reversibly bind O_2 in benzene at room temperature (*5, 6*). Nevertheless, these synthetic porphyrins were all oxidized irreversibly in aqueous media.

To create a hydrophobic environment in water, it is possible to use a bilayer membrane of a phospholipid vesicle instead of globin protein. In 1983, we synthesized an amphiphilic Fe^{2+}porphyrin having four alkylphosphocholine groups (lipidheme), which is efficiently embedded into the bilayer of the phospholipid vesicle to yield a homogeneous hybrid. This lipidheme/phospholipid vesicle can bind and release O_2 under physiological conditions (Figure 1) (*7*−*9*). The 10 mM lipidheme/phospholipid vesicle solution dissolves 29 mL O_2/dL compared to 27 mL/dL of human blood. Subsequent to that finding, we synthesized over 60 lipidheme molecules. A new lipidheme having four dialkyl-*sn*-glycerophosphocholine groups is self-organized in water to form self-assembled porphyrin bilayer vesicles without phospholipid (*10*). Furthermore, in 1995, we found that synthetic Fe^{2+} porphyrin bearing a covalently linked proximal base (FeP**1**) is incorporated into human serum albumin (HSA) and the obtained HSA-FeP**1** hybrid coordinates O_2 in aqueous medium (*11*).

In 1985, we began the study of Hb-based O_2 carriers using purified human Hb aiming at the beneficial utilization of outdated RBC to support the present blood donation−transfusion system. This project has been supported for a long time by Japanese Red Cross Society and Ministry of Health and Welfare, Japan. On the basis of a fundamental concept that the cellular structure of RBC is necessary for O_2 transport in the bloodstream, we designed the phospholipid vesicle encapsulating Hb: the so-called Hb-vesicle. It has to be emphasized that the Hb-vesicle comprises a concentrated Hb solution and four kinds of natural and synthetic lipids that assemble to form a hierarchical corpuscle structure (molecular assembly) through the well-regulated secondary interactions, such as hydrophobic and electrostatic interactions. To date, chemically modified Hb of several types have been developed as RBC substitutes or O_2 therapeutic reagents. Herein, we review the latest developments of our research into Hb-vesicles and albumin−hemes.

2. HEMOGLOBIN VESICLES THAT MIMIC THE RBC CELLULAR STRUCTURE

2.1. Physiological Importance of Cellular Structure of RBC for Encapsulated Hb Design. Historically, stroma-free Hb isolated from RBCs were tested as a principal material for carrying O_2. However, the plasma retention time of stroma-free Hb is particularly short (half-life of 0.5−1.5 h) because of the dissociation of the Hb tetramer ($\alpha_2\beta_2$; Mw, 64 500; 6.5 nm diameter) into dimers ($2\alpha\beta$), which are subsequently filtered by the kidney (*12*). Cell-free Hb-based O_2 carriers have been developed to overcome the problems of stroma-free Hb through chemical modification, "bioconjugation", of Hb molecules (Figure 2). They include intramolecularly cross-linked Hb (DCLHb) to prevent dimerization, recombinant cross-linked Hb produced by *E. coli*, polymerized Hb using glutaraldehyde or other cross-linkers, and polymer-conjugated Hb such as PEG-conjugated Hb and polysaccharide-conjugated Hb (*13*−*21*). During the long history of the development of cell-free Hb-based O_2 carriers (HBOCs), the many side effects of stroma-free Hb and chemically modified Hbs have been well-documented: renal toxicity; entrapment of gaseous messenger molecules (NO and CO) inducing vasoconstriction, hypertension, reduced blood flow, and reduced tissue oxygenation at microcirculatory levels (*22*−*25*); neurological disturbances; malfunction of esophageal motor function (*18*); myocardial lesions (*26, 27*); and death (*28*). These side effects of Hb molecules underscore the importance of the large dimension of HBOCs or the RBC cellular structure. Retrospective and recent observations have indicated the main justifications for Hb encapsulation in RBCs: (i) a decreased high colloidal osmotic pressure (*15*); (ii) prevention of the removal of Hb from blood circulation; (iii) prevention of direct contact of toxic Hb molecules and the endothelial lining (*29*); (iv) retardation of reactions with endogenous NO and CO (*24, 25, 30, 31*) (Figure 3); (v) preservation of the chemical environment in cells, such as the concentration of phosphates (2,3-DPG, ATP, etc.) and other electrolytes; (vi) RBCs are the major component that renders blood as non-Newtonian and viscous, which is necessary to pressurize the peripheral artery for homogeneous blood distribution and for maintenance of blood circulation (*32*); (vii) the RBC cellular structure retards O_2-release in comparison to acellular Hb solutions (*33, 34*), thereby retaining O_2 to peripheral tissues where O_2 is required. For those reasons, the optimal structure of Hb-based O_2 carriers might be to mimic the RBC cellular structure.

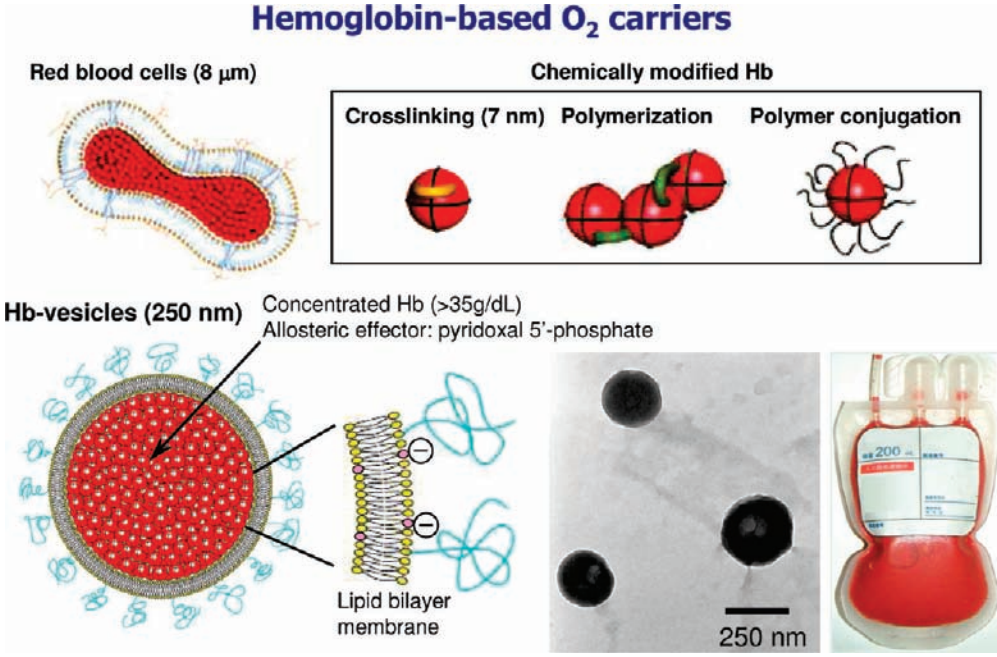

Figure 2. Schematic representation of a series of Hb-based O_2 carriers. Cross-linked Hb, polymerized Hb, and polymer-conjugated Hb are based on the chemical modification of Hb molecules (chemically modified Hbs). In the case of Hb-vesicles, a purified and concentrated Hb solution (35 g/dL) is encapsulated in phospholipid vesicles and the surface is modified using PEG chains. The particle size is well-regulated at 250 nm.

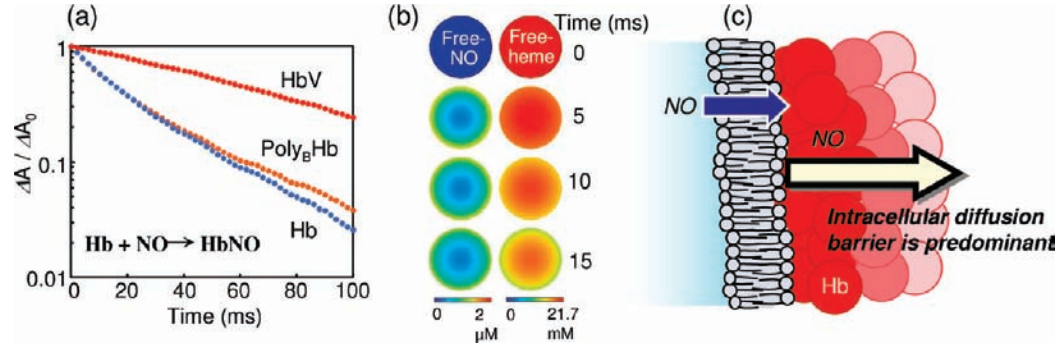

Figure 3. Encapsulation of Hb in vesicles retards NO binding. (a) Time courses of NO binding with HbV, human Hb with PLP (Hb/PLP = 1:2.5 by mol), and polymerized bovine Hb (Poly$_B$Hb) observed by stopped-flow rapid scan spectrophotometry. The level of reaction was plotted on a semilogarithmic graph as a ratio of absorption at 430 nm (ΔA) at time t, to the initial absorption (ΔA_0) at time 0. NO-bubbled PBS ([NO] = 3.8 μM) and deoxygenated-Hb-containing solutions in PBS ([heme] = 3.0 μM) were mixed (*31*). (b) Schematic two-dimensional representation of the simulated time courses of distributions of unbound free NO and unbound free heme in one HbV (250 nm). Both free NO and unbound hemes are distributed heterogeneously. The concentration changes gradually from the surface to the core, indicating formation of the intracellular diffusion barrier (*30*). (c) The phospholipid bilayer membrane cannot have any barrier function to gas diffusion. The determinant factor of retardation of NO-binding should be the intracellular diffusion barrier, which was induced by (i) intrinsically larger binding rate constant of NO to a heme in an Hb molecule, (ii) numerous hemes as sites of gas entrapment at a higher Hb concentration, (iii) a slowed gas diffusion in the intracellular viscous Hb solution, and (iv) a longer gas diffusion distance in a larger capsule.

In 1957, Chang performed the pioneering work of Hb encapsulation to mimic the cellular structure of RBCs (*35*); microcapsules (5 μm) were prepared using nylon, collodion, and other materials. Toyoda in 1965 (*36*) and the Kambara−Kimoto group in 1968 (*37*) also investigated encapsulation of Hbs with gelatin, gum arabic, silicone, and so forth. Nevertheless, results emphasized the extreme difficulty of regulating the particle size to be appropriate for blood flow in the capillaries and to obtain sufficient biocompatibility. After Bangham and Horne reported in 1964 (*38*) that phospholipids assemble to form vesicles in an aqueous medium and encapsulated water-soluble materials in their inner aqueous interior (*39*), it seemed reasonable to use such vesicles for Hb encapsulation. Djordjevich and Miller in 1977 (*40*) prepared liposome-encapsulated Hb (LEH) composed of phospholipids, cholesterol, fatty acids, and so forth. The US Naval Research Laboratories and collaborators demonstrated remarkable progress in the use of LEH (*41*−*43*). Terumo Corp. (Tokyo) developed different LEH, so-called Neo Red Cells (*44*, *45*) (Table 1).

However, some intrinsic issues of encapsulated Hbs remained, which were related mainly to the nature of molecular assembly and particle dispersion. What we call Hb-vesicles (HbV), with their high-efficiency production processes and improved properties, were established by our group based on technologies of molecular assembly in concert with precise analyses of their pharmacological and physiological aspects (*46*−*48*) (Tables 2 and 3). We use stable carbonylhemoglobin (HbCO) for purification with pasteurization at 60 °C for 10 h. The purity of the obtained Hb solution is extremely high (*49*, *50*). Use of the stable and purified HbCO enables concentration of the Hb solution to more than 40 g/dL using ultrafiltration and easy handling of Hb encapsulation using the extrusion method,

Table 1. List of Representative Liposome-Encapsulated Hbs (LEH) Extensively Studied Aiming at Industrialization and Other Potential Encapsulated Hbs Using Biodegradable Polymers

product name	group	characteristics	current status
Hb vesicles (HbV)	Waseda Univ. and Keio Univ.	1. Pasteurization of HbCO at 60 °C for virus inactivation 2. Lipid composition to improve blood compatibility 3. PEG modification and deoxygenation for 2 yr storage 4. [Hb] = 10 g/dL	preclinical
Neo Red Cells (NRC)	Terumo Corp.	1. Inositol hexaphosphate to regulate P_{50} (= 40−50 Torr) 2. Lipids: HSPC/cholesterol/fatty acid/PEG-lipid 3. Storage in a refrigerator for 6 months 4. [Hb] = 6 g/dL	preclinical
artificial red cells (ARC)	NOF Corp. and Waseda Univ.	1. Polymerized lipids (DODPC) for stabilization 2. Storage in powdered or frozen state 3. Difficulty in degradation in RES	suspended
liposome-encapsulated Hb (LEH)	US Naval Research Laboratory	1. Freeze-dried powder with trehalose 2. Low Hb encapsulation efficiency 3. Thrombocytopenia, complement activation	suspended
synthetic erythrocytes	Rush-Presbyterian-St. Luke's Medical Center, Univ. Illinois	1. The first attempt of LEH	suspended
Hb-loaded particles (HbP)	East China Univ. of Science and Technology	1. Hb encapsulation by poly(ε-caprolactone) (PCL) and poly(ε-caprolactone-ethylene glycol) (PCL-PEG) 2. Double emulsion and solvent diffusion/evaporation method 3. Biodegradable	basic study
polymersome-encapsulated Hb (PEH)	The Ohio State Univ.	1. Self-assembly of amphiphilic diblock copolymers composed of poly(ethylene oxide) (PEO), poly(caprolactone) (PCL), and poly(lactide) (PLA) 2. Biodegradable and biocompatible	basic study

Table 2. Physicochemical Characteristics of Hb Vesicles

parameter	
particle diameter	250−280 nm
P_{50} (O_2)[a]	25−28 Torr
[Hb]	10 g/dL
[heme]	6.2 mM
[metHb]	<3%
[HbCO]	<2%
suspending medium	physiologic saline solution (0.9% NaCl)
colloid osmotic pressure	0 Torr
intracellular Hb concentration	ca. 35 g/dL
lipid composition	DPPC/cholesterol/DHSG/DSPE-PEG_{5000}
ζ potential[b]	−18.7 mV
weight ratio of Hb to lipids	1.6−1.9 (w/w)
viscosity[c]	3.8 cP
lamellarity	nearly 1
stability for storage at room temperature	>2 years, purged with N_2
circulation half-life	35 h (rats)

[a] Measured with a Hemox Analyzer (pH 7.4, 37 °C). [b] Measured with a Zeta-Sizer Nano ZS ([NaCl] = 20 mM, pH 7.4). [c] Measured with Anton Parr Rheometer M301 (268 s^{-1}, 25 °C).

Table 3. Characteristics of Hb-Vesicles As a Transfusion Alternative

1. Human derived Hb solution is purified rigorously by pasteurization and ultrafiltration. The blood type antigens and pathogens are eliminated for utmost safety.
2. Encapsulation of concentrated Hb solution (>35 g/dL), like RBCs.
3. Small particle size (250 nm) for homogeneous distribution in the plasma phase of circulating blood.
4. Shielding of the side effects of molecular Hbs by the lipid membrane.
5. PEG modification for dispersion stability for long-term storage and in the bloodstream.
6. Surface properties of HbV (PEG, negative charge, etc.) for blood compatibility.
7. Prompt degradation and excretion of the components after entrapment in RES.
8. Sufficient oxygen transporting capacity ([Hb] = 10 g/dL, *cf*, [Hb] of blood = 12−15 g/dL).
9. Physicochemical properties are easily adjustable because of the nature of the "molecular assembly".

without causing Hb denaturation. It has been confirmed that HbV encapsulates nearly 35 g/dL within a thin bilayer membrane. In final processing, CO of HbCO in HbV is photodissociated by irradiation of visible light under an O_2 atmosphere, and it converts to HbO_2 (*51*).

In fact, Hb autoxidizes to form metHb and loses its O_2-binding ability during storage and during blood circulation (*52*−*56*). For that reason, metHb formation must be prevented. A method exists to preserve deoxygenated Hbs in a liquid state from using intrinsic characteristics of Hb: the Hb oxidation rate in a solution is dependent on the O_2 partial pressure; moreover, deoxyHb is not autoxidized at ambient temperatures (*56*). In the case of HbV, not only the encapsulated Hb but also the capsular structure (liposome) must be physically stabilized to prevent irreversible intervesicular aggregation, fusion, and leakage of the encapsulated Hb.

In addition to HbV, new encapsulated Hbs without liposomes have emerged with the use of recent advanced nanotechnologies, such as polymersome (*57*) and PEG-poly(ε-caprolactone) copolymer nanoparticles (*58*). In vivo evaluation of O_2-carrying capacities of these new materials is anticipated. Encapsulation of Hb can reduce the toxicity of cell-free Hbs. However, numerous hurdles must be surmounted to realize encapsulated Hbs because of the components of the capsules themselves and their structural complexity as a molecular assembly. It is also important to consider the larger dosage requirement of encapsulated Hb for blood substitution than those of conventional drug delivery systems, which require no large dosage.

2.2. Structural Stabilization and Destabilization using Polymerization or PEG Conjugation. Liposomes, as molecular assemblies, have generally been characterized as structurally unstable. The US Naval Research Laboratory tested the addition of cryoprotectants and lyoprotectants such as trehalose to LEH for its preservation as a powder without causing hemolysis after rehydration (*59*, *60*). In addition, many researchers have developed stabilization methods for liposomes that use polymer chains (*61*−*64*). Polymerization of phospholipids that contain two dienoyl groups (1,2-dioctadecadienoyl-*sn*-glycero-3-phosphatidylcholine; DODPC) was studied extensively by our group. For example, gamma-ray irradiation induces radiolysis of water molecules and generates OH radicals that initiate intermolecular polymerization of dienoyl groups in DODPC. This method produces remarkably stable liposomes, resembling rubber balls, which are resistant to freeze−thawing, freeze−drying, and rehydration (*65*, *66*). Actually, the polymerized liposomes were so stable that they were not degraded easily in the macrophages,

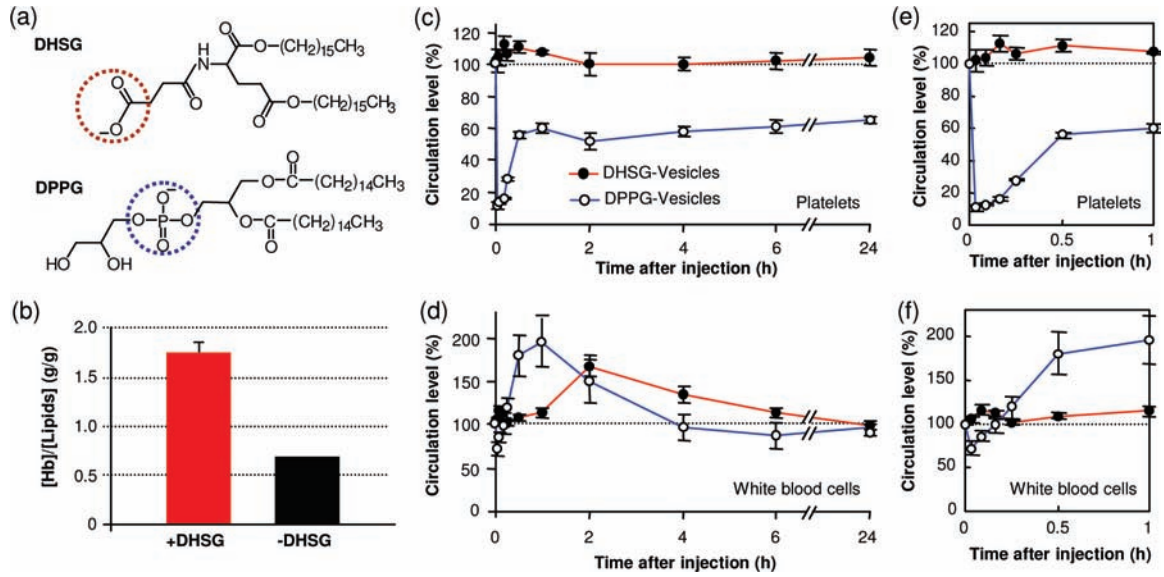

Figure 4. Effect of negatively charged vesicles on encapsulation capability and blood compatibility of HbV. (a) Chemical structures of negatively charged lipids, 1,5-*O*-dihexadecyl-*N*-succinyl-L-glutamate (DHSG) and 1,2-dipalmitoyl-*sn*-glycelo-phosphatidylglycerol (DPPG). (b) Effect of DHSG on encapsulation efficiency of Hb (35 g/dL). (c−f) Circulation levels of platelets (c) and white blood cells (d) after intravenous infusion of vesicles containing 9 mol % DHSG (DHSG-vesicles) or 9 mol % DPPG (DPPG-vesicles) in rats (lipids; 280 mg/kg body weight). The right side graphs show the initial fluctuations in platelets (e) and white blood cells (f).

even 30 days after injection (*67*). It became widely believed that polymerized lipids are inappropriate for intravenous injection because of the difficulty in excretion. Subsequently, it was clarified that selection of appropriate lipids (phospholipid/cholesterol/negatively charged lipid/PEG-conjugated phospholipid) and that their composition is important to enhance the stability of nonpolymerized liposomes (*45, 68*). Surface modification of liposomes with PEG-conjugated lipids is sufficient for dispersion stability (*69*). In fact, in comparison to RBCs, HbV is highly resistant to hypotonic shock, freeze−thawing, and enzymatic attack by phospholipase A_2 (*70*).

We investigated the possibility of long-term preservation of HbV during storage for two years through a combination of deoxygenation and PEG modification (*71*). As little as 0.3 mol % PEG-conjugated lipid stabilizes the dispersion state and prevents aggregation and fusion for two years through steric hindrance (*71*−*73*). The original metHb content (ca. 3%) before preservation decreased gradually to less than 1% after 1 month because of the presence of a reductant, such as homocysteine, inside the vesicles that consumed the residual O_2 and gradually reduced the trace amount of metHb. The rate of metHb formation was strongly dependent on the O_2 partial pressure: a lack of increase in the metHb formation was observed because of the intrinsic stability of the deoxygenated Hb. In fact, the metHb content did not increase for two years. These results suggest the possibility that the HbV suspension can be stored at room temperature for at least two years, which would enable stockpiling of HbV for any emergency.

2.3. Vesicular Surface Modification with PEG and Negative Charges for Blood Compatibility. Liposome is not a solute: it is a particle in a suspension. The particle surface might be recognized, leading to interaction with blood components including complements. The so-called *injection reaction*, or pseudoallergy, results from complement activation, giving rise to anaphylatoxins, which trigger various hypersensitivity reactions. This reaction is observed sometimes not only with liposomal products (*74*), but also with fat emulsions (*75*), and a perfluorocarbon emulsion (*76*). Therefore, examination of blood compatibility of encapsulated Hbs is important for clinical use. Transient thrombocytopenia and pulmonary hypertension in relation to complement activation is an extremely important hematologic effect observed in rodent models after infusion of LEH (containing DPPG: 1,2-dipalmitoyl-*sn*-glycero-3-phosphatidylglycerol) developed by the US Naval Research Laboratory (*77, 78*) and other products. In our group, exchange transfusion of prototype HbV (containing DPPG, no PEG modification) in anesthetized rats engendered transient thrombocytopenia and slight hypertension (*79*). Similar effects were also observed for administration of negatively charged liposomes (*80, 81*). The transient reduction in platelet counts caused by complement-bound liposomes was also associated with sequestration of platelets in the lung and liver. Such nonphysiological platelet activation probably engenders initiation and modulation of inflammatory responses because platelets contain several potent proinflammatory substances. A negatively charged lipid is required for encapsulating a large amount of Hb using a minimum amount of lipids (*46*−*48*). Therefore, we had to overcome the problem of conventional negatively charged vesicles to achieve blood compatibility. In the present formation of HbV, we use a negatively charged lipid (DHSG: 1,5-*O*-dihexadecyl-*N*-succinyl-L-glutamate) and confirmed the considerable improvement of Hb encapsulation efficiency (Figure 4a,b**)**. It must be emphasized that the present vesicle formulation for HbV apparently does not induce thrombocytopenia or complement activation in animal experiments (Figure 4c−f) (*82, 83*), probably because the present HbV contains PEG-modification and a different type of negatively charged lipid (DHSG), not DPPG or a fatty acid.

Ikeda and his co-workers (*83*−*86*) thoroughly examined blood compatibility of HbV to human blood in vitro. The present PEG-modified HbV containing DHSG did not affect the extrinsic or intrinsic coagulation activities of human plasma, although HbV containing DPPG and no PEG modification tended to shorten the intrinsic coagulation time. The kallikrein-kinin cascade of the plasma was activated slightly by the prototype DPPG-HbV, but not by the present PEG-DHSG-HbV. The exposure of human platelets to high concentrations of the present HbV (up to 40%) in vitro did not cause platelet activation and did not adversely affect the formation and secretion of prothrombotic substances or proinflammatory substances that are triggered by platelet agonists. These results imply that HbV, at concentrations of up to 40%, has aberrant interactions with neither unstimulated

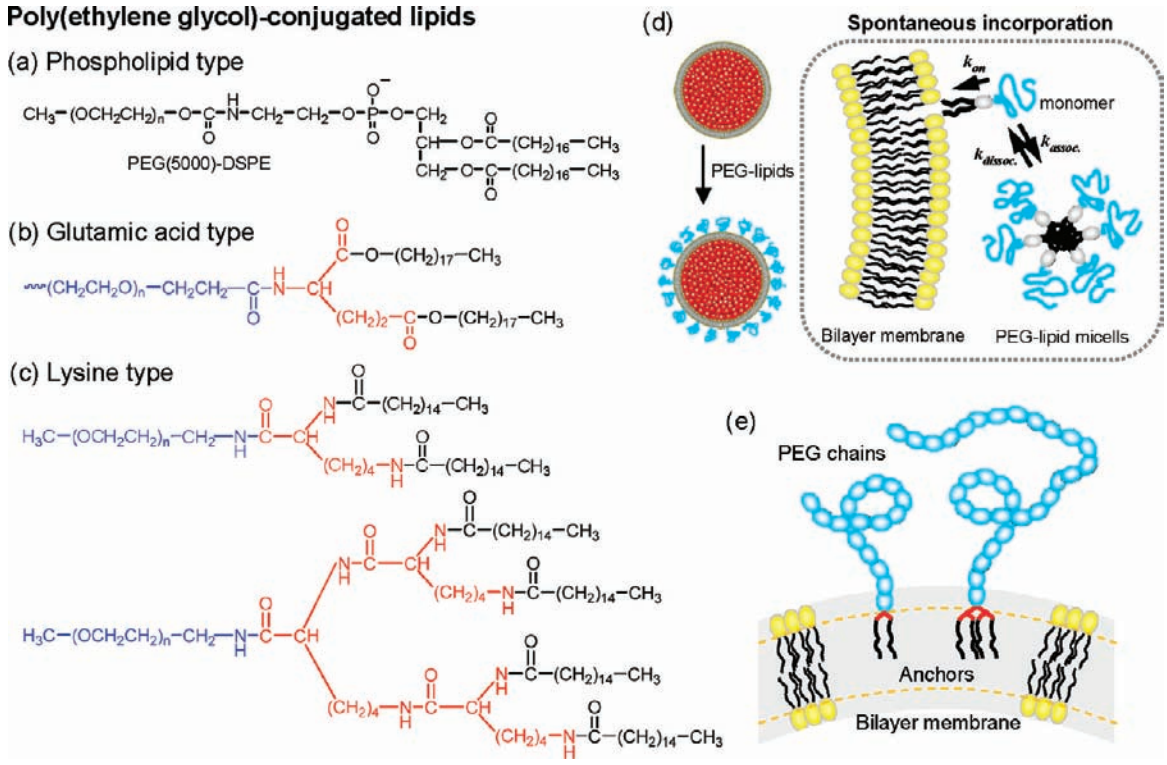

Figure 5. Surface modification of HbV with PEG chains. (a−c) Chemical structures of PEG-conjugated lipids. (a) PEG(5000)-DSPE is commercially available and widely used for surface modification of lipid vesicles. (b) Glutamic acid-type and (c) lysine-type PEG-conjugated lipids were reported previously (*87, 88*). (d) PEG-modification of the HbV using the spontaneous incorporation of a PEG-lipid into the bilayer membrane (*72*). (e) Immobilization of the large water-soluble polymers on the bilayer membranes (*87, 89*).

nor agonist-induced platelets. It can be concluded that the present PEG-DHSG-HbV has higher blood compatibility.

For surface modification of HbV with PEG chains, several PEG-conjugated lipids having amino acid backbone have been synthesized, as presented in Figure 5b,c (*87, 88*). For other applications, these PEG-conjugated lipids are available to modify the surfaces of not only HbV but also lipid vesicles. Because the PEG-lipids having a large hydrophilic group form thermodynamically unstable self-assemblies, called micelles (*73*), they easily dissociate to monomers and spontaneously incorporate only to the outer surface of preformed HbV, as illustrated in Figure 5d (*45, 72*). Using this method, the required amount of PEG-conjugated lipid can be reduced by half or less because only the outer surface of HbV requires PEG chains. In addition, the PEG chains extending from the inner surface are expected to reduce the interior volume for encapsulation because of their exclusion volume effect. Therefore, modification only to the outer surface is important to encapsulate large amounts of Hb in lipid vesicles. To immobilize the hydrophilic macromolecules stably, such as PEG chains and proteins on lipid vesicles, a large hydrophobic anchor having a tetraacyl structure has been synthesized (Figure 5c,e). It has been confirmed that this hydrophobic anchor can stably immobilize PEG chains of high molecular weight (Mw 12 500) or water-soluble proteins (*87, 89*). These surface modification technologies and lipid chemistry have been applied to the development of other functional biomaterials (*87*−*93*).

2.4. Circulation Time, Biodistribution, and Metabolism. The dosage of blood substitutes is expected to be considerably larger than those of other drugs, while their circulation time is considerably shorter than that of RBCs. Therefore, their biodistribution, metabolism, excretion, and side effects must be characterized in detail, especially in relation to the reticuloendothelial system (RES, alternatively, the mononuclear phagocytic system, MPS). Normally, free Hb released from RBCs is bound rapidly to haptoglobin and is consequently removed from circulation by hepatocytes. However, when the Hb concentration is greater than the haptoglobin binding capacity, unbound Hb is filtered through the kidney, where it is actively absorbed. Hemoglobinuria and eventual renal failure occur when the kidney reabsorption capacity is exceeded. The encapsulation of Hb in vesicles completely suppresses renal excretion. However, HbV in the bloodstream is ultimately captured by phagocytes in the RES in much the same manner as senescent RBCs are, as confirmed by radioisotope ^{99m}Tc-labeled HbV injection (*42, 94*). The circulation half-life is dose-dependent: for the dosage of 14 mL/kg body weight, the circulation half-life was 34.8 h in rats and 62.6 h in rabbits (Figure 6a). The HbV are finally distributed mainly in the liver, spleen, and bone marrow (Figure 6b). The species-dependent circulation time is inferred to be dependent upon the species-specific weight balance of phagocyte organs, particularly the liver, spleen, and bone marrow, against body weight (*94*). The circulation half-life in the case of the human body can be estimated as about 2−3 days at the same dosage.

It is generally accepted that the liposome clearance by RES at a small dosage is accelerated by opsonization (absorption of plasma proteins such as antibodies and complements on the liposomal surface). In fact, PEG-modification prevents opsonization for prolonged circulation times (*95*). However, considering a condition in which the dosage of HbV is extremely high and requires a considerable amount of opsonins, and in which HbV does not induce complementary activation (*82, 83*), then opsonin-dependent phagocytosis would not be a major component in the case of HbV with a large dosage. Actually, opsonin-independent phagocytosis, a direct recognition by macrophages, has been clarified in some studies (*96, 97*).

Analysis of the spleen by transmission electron microscopy (TEM) 1 day after infusion of HbV revealed the presence of HbV particles in the phagosomes of macrophages (*98*) (Figure

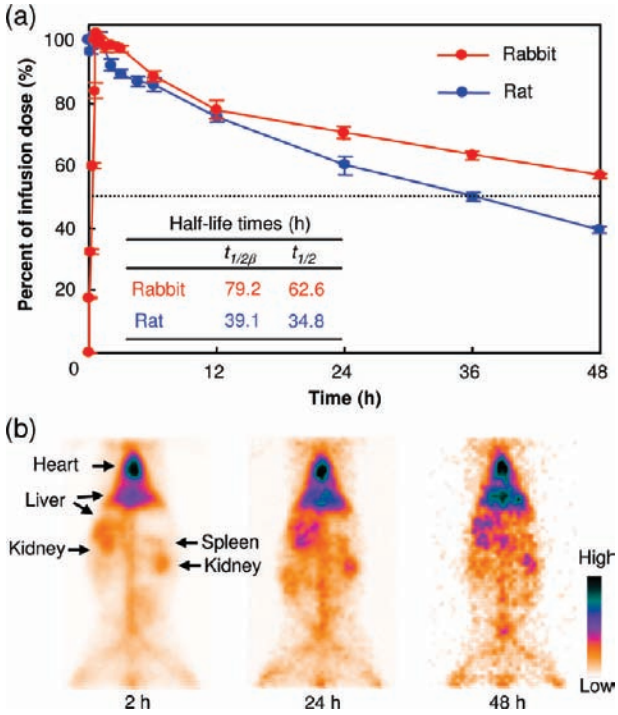

Figure 6. Circulation kinetics and organ distribution of HbV labeled with technetium-99m after top-loading intravenous infusion (14 mL/kg) in rats and rabbits (*94*). (a) Elimination profiles of HbV from blood. (b) Static gamma camera images of a rabbit acquired at 2, 24, and 48 h after HbV infusion.

7). However, after 7 days, the HbV structure cannot be observed. We confirmed transient splenomegaly with no irreversible damage to the organs and complete metabolism within a week. The phagocytic activity transiently, but not completely, decreased 1 day after injection, and it turned to increasing at 3 days. The influence on the defense function and its mechanism has been carefully examined in the ongoing research. Immunochemical staining with a polyclonal anti-human Hb antibody was used as the marker of Hb in the HbV. Results clarified that HbV had almost disappeared in both the spleen and liver after 7 days.

Bilirubin and iron are believed to be released during metabolism of Hb, but our animal experiments of topload infusion, daily repeated infusions, and 40% blood exchange showed that neither of those products increased in the plasma within 14 days (*99*−*101*). Bilirubin would normally be excreted in the bile as a normal pathway; no obstruction or stasis of the bile is expected to occur in the biliary tree. Berlin blue staining revealed considerable deposition of hemosiderin in the liver and spleen, even after 14 days. Moderate splenomegaly and hemosiderin deposition were also confirmed in the spleen after injection of stored RBCs, partly because of the accumulation and degradation of stored RBCs with lowered membrane deformability and shortened circulation half-life (*101*).

As for membrane components of Hb-vesicles, the plasma cholesterol level elevated transiently 3 days after injection: cholesterol was released from macrophages after degradation of HbV in phagosomes (*99, 101*). It was recently clarified using ^{3}H-cholesterol that cholesterol of HbV is released from macrophages to blood; it is ultimately excreted in feces. The PEG chain is widely used for surface modification of liposomal products. The chemical cross-linker succinic acid ester of PEG-conjugated phospholipid is susceptible to hydrolysis to release PEG chains during metabolism. Actually, immunohistochemistry using an anti-methoxy-PEG antibody clarified that PEG had disappeared from the liver and spleen in one week (*102*). The

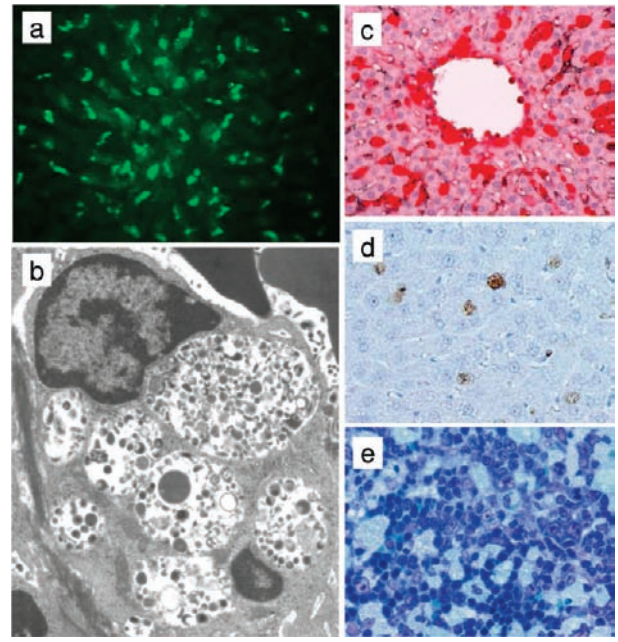

Figure 7. Histopathological examination of livers and spleens of rodents after injection of HbV. (a) Hamster liver 1 h after injection of fluorescence-labeled HbV, observed by a confocal laser scanning microscopy. The strong fluorescence indicates that HbV particles accumulate in Kupffer cells. (b) TEM of rat spleen macrophage 1 day after injection of HbV. The small black dots are HbV particles in phagosomes. The particles disappeared within a week (data not shown) (*98*). (c) Rat liver 1 day after injection of HbV. It was immunohistochemically stained with anti-human Hb antibody. The red parts indicate the presence of human Hb in HbV. It disappeared within a week (data not shown) (*98*). (d) Rat liver 7 day after injection of HbV. It was immunochemically stained with anti-methoxy-PEG antibody. The brown parts indicate the presence of PEG derived from PEG-lipid of HbV during the degradation. Fourteen days after injection, PEG was not detectable (data not shown) (*102*). (e) Rat spleen 3 days after 40% exchange transfusion with HbV. It was stained with Giemsa method. A large amount of blue cells, erythroblasts, are seen, indicating the enhanced hematopoiesis for the complete recovery of hematocrit within one week, while HbV are degraded in RES (*101*).

released PEG chains, which are known as inert macromolecules, are expected to be excreted in urine through the kidneys (*103*).

To determine the physiological capacity of RES for degradation of HbV, we tested massive intravenous doses by daily repeated infusion of 10 mL/kg body weight/day into Wistar rats for 14 days. The cumulative dosage was 140 mL/kg body weight (Hb and lipids, 20 689 mg/kg body weight). The total volume was equal to 2.5 times the total blood volume (56 mL/kg body weight) (*100*). Although splenohepatomegaly was considerable, all rats tolerated the infusions; their body weight increased during the succeeding 14 days until their intended sacrifice. The phagocyted HbV had disappeared, though the considerable hemosiderin deposition was confirmed in the spleen, liver, kidney, adrenal grand, and bone marrow. We were unable to define a lethal dose of HbV in this experiment.

The profile of liposome clearance is species-dependent. More precise data are necessary to extrapolate the phenomena observed in animal experiments to humans. However, these results imply that the metabolism of HbV and excretion are within the physiological capacity that has been well-characterized for the metabolism of senescent RBCs and conventional liposomal products.

2.5. Regulation of O_2 Transporting Capability (MetHb Reduction, $P_{50}(O_2)$). Actually, Hb encapsulation provides a unique opportunity to add new functions to particles by coencapsulation or embedding of functional molecules (*52*−*56, 104*−*106*). MetHb formation of HbV during the

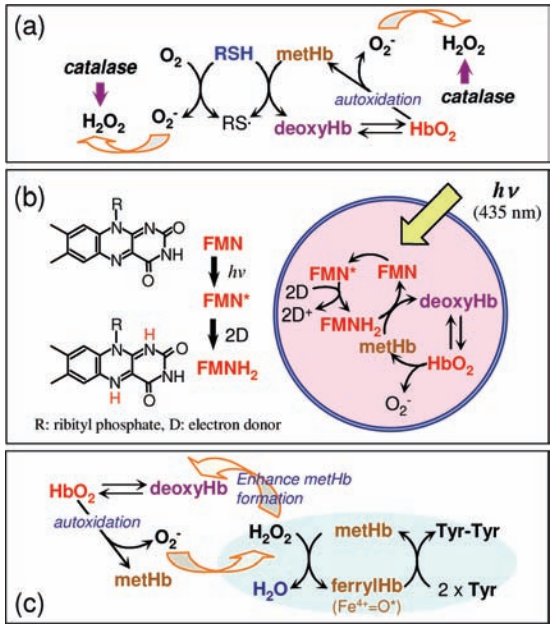

Figure 8. Artificial metHb reduction systems in HbV. (a) Coencapsulation of thiols (RSH), such as glutathione and homocyteine, reduces metHb. However, thiols react with O_2 to generate O_2^- and H_2O_2. A more reactive thiol such as cysteine shows extremely rapid reaction with O_2 and adversely facilitates metHb formation. Coencapsulation of catalase effectively eliminates H_2O_2 and prevent such reactions (*52, 53, 56*). (b) Photoreduction system by coencapsulation of flavin monomucleotide (FMN) and an electron donor such as EDTA and methionine. Visible light irradiation (435 nm) primarily converts FMN to the photoexcited triplet FMN*, and this reacts with two electron donors (D) to generate $FMNH_2$. MetHb is rapidly reduced once $FMNH_2$ is produced (*54*). (c) During autoxidation of Hb and in blood circulation, H_2O_2 is a potent metHb enhancer. A combination of L-tyrosine (Tyr) and metHb effectively eliminates H_2O_2 and prolongs the functional lifetime of HbV (*55*).

preservation is completely prevented simply by deoxygenation. However, autoxidation of HbO_2 is initiated once HbV is administered into the bloodstream because the entire metHb enzymatic system is eliminated during the Hb purification for the utmost safety from infection. An artificial metHb reducing system is required to prolong the O_2-carrying capacity of HbV. We have tested coencapsulation of reductants to directly reduce metHb and a photoreduction system using a photosensitizer such as flavin mononucleotide (FMN). A more practical method is to create an artificial enzymatic system using L-tyrosine (Tyr) and metHb that eliminates H_2O_2 as does catalase (Figure 8).

Without a chemical modification of Hb, O_2 binding affinity (expressed as $P_{50}(O_2)$, O_2 tension at which Hb is half-saturated with O_2) of HbV can be regulated by coencapsulation of an allosteric effector (*105, 106*) (Figure 9a). The $P_{50}(O_2)$ of purified Hb in a saline solution (in the presence of Cl^-) is about 14 Torr; Hb strongly binds O_2 and does not release O_2 at 40 Torr (partial pressure of mixed venous blood). Historically, it has been regarded that the O_2 affinity is expected to be regulated similarly to that of RBC, namely, about 25−30 Torr, using an allosteric effector or by a direct chemical modification of the Hb molecules. This enables sufficient O_2 unloading during blood microcirculation, as evaluated by the arterio-venous difference in the levels of O_2 saturation in accordance with an O_2 equilibrium curve. Pyridoxal 5′-phosphate (PLP) is coencapsulated in HbV as an allosteric effector to regulate $P_{50}(O_2)$ (*105, 106*). The main binding site of PLP is the N-terminal of the α-chain and β-chain and β-82 Lysine within the β-cleft, which is part of the binding site of the natural allosteric effector, 2,3-diphosphoglyceric acid (2,3-DPG). The bound PLP retards the dissociation of the ionic linkage between the β-chains of Hb during conversion of deoxy to oxyHb in the same manner as 2,3-DPG does. Therefore, the O_2 affinity of Hb decreases in the presence of PLP. The $P_{50}(O_2)$ of HbV can be regulated to 8−150 Torr by coencapsulating the appropriate amount of PLP or inositol hexaphosphate as an allosteric effector. Equimolar PLP to Hb (PLP/Hb = 1/1 by mol) was coencapsulated, and $P_{50}(O_2)$ was regulated to 18 Torr. Furthermore, $P_{50}(O_2)$ was regulated to 32 Torr when the molar ratio PLP/Hb was 3/1. The O_2 affinities of HbV can be regulated easily without changing other physical parameters, whereas in the case of the other modified Hb solutions, their chemical structures determine their O_2 binding affinities. Consequently, regulation is difficult. The present HbV contains PLP at PLP/Hb = 2.5 by mol; the resulting $P_{50}(O_2)$ is about 25−28 Torr, which shows sufficient O_2 transporting capacity as a transfusion alternative. Actually, HbV has been shown to provide O_2-transport capacity that is both sufficient and comparable to that of RBCs in experiments related to extreme blood exchange (*68, 69, 79, 105, 107, 108*) and fluid resuscitation from hemorrhagic shock (*102, 109−112*) (Figure 10). A recent experiment of HbV as a priming solution for cardiopulmonary bypass (CPB) in a rat model showed that HbV protects neurocognitive function by transporting O_2 to brain tissue even when the hematocrit is reduced markedly (*113*).

The appropriate O_2 binding affinities for O_2 carriers have not yet been decided completely. However, the easy regulation of the O_2 binding affinity might be useful to meet the requirement of clinical indications such as oxygenation of ischemic tissues. The $P_{50}(O_2)$ of HbV without PLP and Cl^- is 8−9 Torr. This formulation is effective for targeted O_2 delivery to anoxic tissues caused by reduced blood flow (*107, 114, 115*).

2.6. Rheological Properties and Their Physiological Implications for Tissue Oxygenation. The extremely high concentration of the HbV suspension ([Hb] = 10 g/dL; [lipids] = 6 g/dL, volume fraction, ca. 40 vol %) imparts an O_2 carrying capacity that is comparable to that of blood. The HbV suspension does not possess a colloid osmotic pressure (COP), because one HbV particle (ca. 250 nm diameter) contains about 30 000 Hb molecules. In fact, HbV acts as a particle, not as a solute. Therefore, HbV must be suspended in or coinjected with an aqueous solution of a plasma substitutes. This requirement is identical to that for emulsified perfluorocarbon, which does not possess COP (*116, 117*); it contrasts to characteristics of other Hb-based O_2 carriers, intramolecular cross-linked Hbs, polymerized Hbs, and polymer-conjugated Hbs, which all possess very high COP as protein solutions (*15, 118*) (Figure 9b).

Animal tests of HbV suspended in plasma-derived HSA or rHSA showed an O_2 transporting capacity that is comparable to that of blood (*110, 113*). We reported previously that HbV suspended in plasma-derived HSA or rHSA was almost Newtonian: no aggregation was detected microscopically (*68, 69*). In Japan, rHSA was very recently approved for clinical use, in May 2008 (*119*), but various plasma substitutes are used worldwide, such as hydroxylethyl starch (HES), dextran (DEX), and modified fluid gelatin (MFG). The selection among these plasma substitutes is best determined not only according to their safety and efficacy, but also according to their associated price, experience of clinicians, and customs of respective countries. Water-soluble polymers generally interact with particles such as polystyrene beads, liposomes, and RBCs to induce aggregation or flocculation (*120, 121*). For that reason, it is important to determine the compatibility of HbV with these plasma substitutes. With that background, we studied rheological properties of HbV suspended in these plasma substitute solutions using a complex rheometer and a microchannel array (*122*). The rheological property of an Hb-based O_2 carrier is important

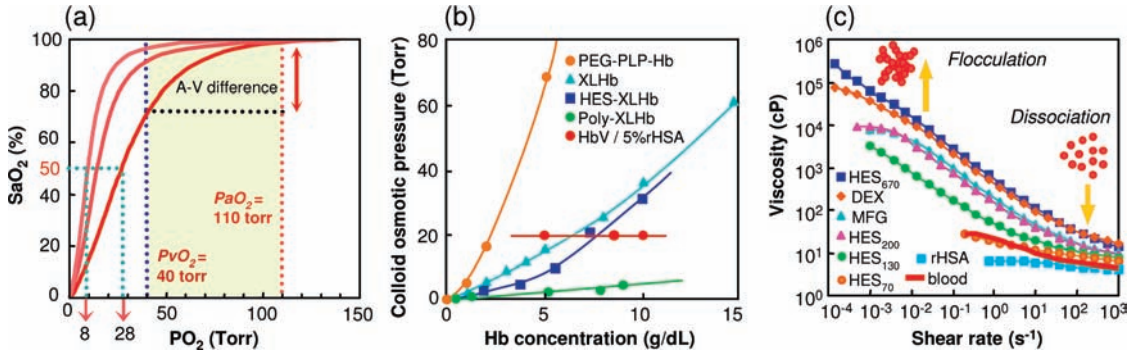

Figure 9. Regulation of physicochemical properties of HbV for versatile applications. (a) Oxygen dissociation curves of HbVs. Oxygen affinity (P_{50}, partial pressure of oxygen at which Hb is half-saturated with oxygen) is regulated by coencapsulation of PLP (*105, 106*). (b) Colloid osmotic pressure (COP) of chemically modified Hb solutions increase with the Hb concentration (*15*). In contrast, HbV particles have no oncotic effect. The figure shows 20 Torr when HbV is suspended in 5% rHSA. XLHb, intramolecularly cross-linked Hb. (c) Rheological properties of HbV suspended in various plasma substitute solutions (*122*). [Hb] = 10 g/dL, 25 °C.

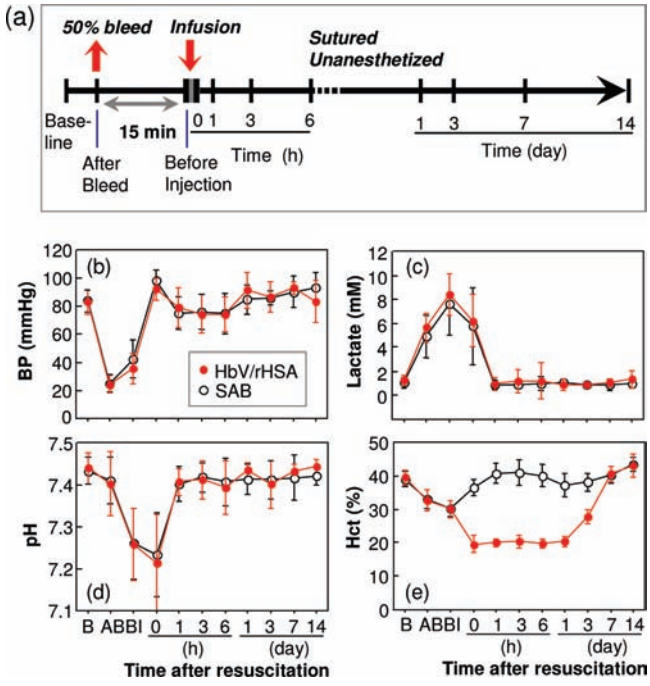

Figure 10. (a) Scheme depicting the experimental protocol of hemorrhagic shock and resuscitation (*102*). Shock was induced by withdrawing 50% of circulating blood volume from Wistar rats. After 15 min, they were resuscitated with either HbV suspended in recombinant human serum albumin (HbV/rHSA) or shed autologous blood (SAB), (b) blood pressure, (c) lactate, (d) pH, and (e) hematocrit (Hct). Mean ± SD. B, Baseline; AB, after bleeding; BI, before injection (B-6 h, n = 24; 1−14 days, n = 5).

because the infusion amount is expected to be considerably large, which might affect the blood viscosity and hemodynamics.

The HbV suspended in rHSA was nearly Newtonian (Figure 9c). Its viscosity was similar to that of blood, and the mixtures with RBCs at various mixing ratios showed viscosities of 3−4 cP. Other polymers, HES, DEX, and MFG, induced flocculation of HbV, possibly by depletion interaction, and rendered the suspensions as non-Newtonian with the *shear-thinning* profile (*122*). These HbV suspensions showed high viscosity and a high storage modulus (G') because of the presence of flocculated HbV. On the other hand, HbV suspended in rHSA exhibited a very low G'. The viscosities of HbV suspended in DEX, MFG, and high-molecular-weight HES solutions responded quickly to rapid step changes of shear rates of 0.1−100 s^{-1} and a return to 0.1 s^{-1}, indicating that flocculation formation is both rapid

Table 4. Publications of Preclinical Studies Aiming at Applications of Hb-Vesicles for a Transfusion Alternative and for Oxygen Therapeutics

indication	ref
1. Resuscitative fluid for hemorrhagic shock	102, 109−112
2. Hemodilution	68, 69, 79, 101, 105, 107, 108
3. Priming fluid for extracorporeal membrane oxygenator (ECMO) for cardiopulmonary bypass	113
4. Perfusate for resected organs (transplantation)	24, 129
5. Oxygenation of ischemic brain (stroke)	130
6. Oxygenation of ischemic skin flap (plastic surgery)	115, 127, 128
7. Tumor oxygenation for sensitization to irradiation	131
8. CO carrier for cytoprotection at reperfusion	132

and reversible. Microscopically, the flow pattern of the flocculated HbV perfused through microchannels (4.5 μm deep, 7 μm wide, 20 cmH_2O applied pressure) showed no plugging. Furthermore, the time required for passage was directly related to the viscosity.

It has been regarded that lower blood viscosity after hemodilution is effective for tissue perfusion. However, microcirculatory observation shows that, in some cases, lower "plasma viscosity" decreases shear stress on the vascular wall, causing vasoconstriction and reducing the functional capillary density (*123*). Therefore, an appropriate viscosity might exist, which maintains the normal tissue perfusion level. The large molecular dimension of HbV can result in a transfusion fluid with high viscosity. A large molecular dimension is also effective to reduce vascular permeability and to minimize the reaction with NO and CO as vasorelaxation factors (*24, 25, 30, 31*) (see Figure 3). These new concepts suggest reconsideration of the design of artificial O_2 carriers (*124*). Actually, new products are appearing, although they are in the preclinical stage, not only HbV but also zero-link polymerized Hb (*125*) and others with larger molecular dimensions and higher O_2 affinities (*126*). Erni et al. clarified that HbV with a high O_2 binding affinity (low $P_{50}(O_2)$, such as 8−15 Torr) and high viscosity (such as 11 cP) suspended in a high-molecular-weight HES solution was effective for oxygenation of an ischemic skin flap (*115, 127, 128*). That study showed that HbV retains O_2 in the upper arterioles, then perfuses through collateral arteries and delivers O_2 to the targeted ischemic tissues, a concept of targeted O_2 delivery by an Hb-based O_2 carrier (*114*). A high O_2 binding affinity (low $P_{50}(O_2)$) would also be effective to improve the O_2 saturation of Hb in pulmonary capillaries when exposed to a hypoxic atmo-

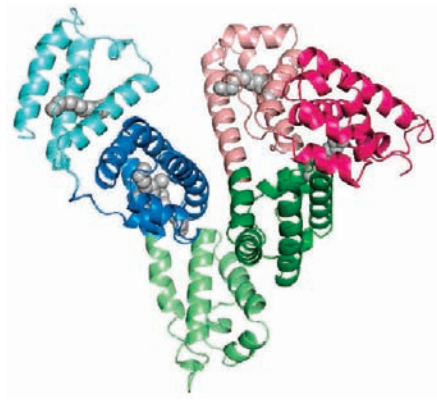

Figure 11. Crystal structure of HSA with myristate (PDB ID: 1BJ5) from ref (*136*).

sphere or with an impaired lung function. Some plasma substitutes cause flocculation of HbV and hyperviscosity. However, reports show that hyperviscosity would not necessarily be deteriorative and might be, in some cases, advantageous in the body (*32*). HbV provides a unique opportunity to manipulate the suspension rheology, $P_{50}(O_2)$, and other physicochemical properties, not only as a transfusion alternative, but also for other clinical applications such as oxygenation of ischemic tissues and ex vivo perfusion systems (*129*−*132*) (Table 4).

3. ALBUMIN-HEMES AS O_2 CARRYING PLASMA PROTEINS

3.1. HSA Incorporating Synthetic Fe^{2+} Porphyrin (HSA-FeP). HSA (Mw: 66 500) has a remarkable ability to bind a wide variety of exogenous compounds in the human circulatory system (*133*). This carrier protein comprises 3 homologue helical domains (I−III) with 9 loops formed by 17 disulfide linkages; each domain contains 2 subdomains (A and B) (Figure 11) (*134*−*137*). It is known that many common drugs such as warfarin, diazepam, and ibuprofen bind to one of the two primary sites (site 1 in subdomain IIA, site 2 in subdomain IIIA) (*138*). In fact, HSA helps to solubilize these compounds to achieve high concentration in the bloodstream; otherwise, they would easily aggregate and be poorly distributed.

In 1995, we found that tetrakis(*o*-pivalamido)phenylporphinatoiron bearing a covalently linked proximal imidazole (FeP**1**, Figure 12) was incorporated into HSA, yielding a red HSA-FeP**1** hybrid (*11*). This synthetic hemoprotein can reversibly bind and release O_2 under physiological conditions (pH 7.4, 37 °C) in much the same way as Hb. The HSA host adsorbs a maximal eight FeP**1** molecules. Their stepwise binding constants (K_1−K_8) range from 1.2×10^6 to 1.2×10^4 (M^{-1}) (Table 3) (*139, 140*). Solution properties of the HSA-FeP**1** solution ([rHSA] = 5 wt %, FeP/HSA=1−8, mol/mol) are almost identical to those of HSA itself: the specific gravity, 1.013; viscosity, 1.1 cP; and COP, 20 Torr. Circular dichroism (CD) spectroscopy and isoelectric focusing measurement revealed that the second-order structure and surface charge distribution of HSA were unaltered after binding of FeP**1**. The obtained solution showed a long shelf-life of over two years at room temperature (*141*). Furthermore, HSA-FeP**1** has no effect on the morphology of blood cell components (*142*) and does not engender immunological reaction and platelet activation (*143*). Upon addition of O_2 gas through this solution, the visible absorption spectrum immediately changed to that of the O_2 adduct complex. After exposure to CO gas, a stable carbonyl complex of HSA-FeP**1** was formed (*139, 140*). The coordination structure of FeP**1** and spin-state of the central ferrous ion was characterized by IR, resonance Raman, and magnetic circular dichroism (MCD) spectroscopy (*139, 140, 144*). The carbonyl HSA-FeP**1** moved to the NO adduct complex after bubbling NO gas (*145*). Subsequent ESR spectroscopy revealed that FeP**1** in albumin formed a six-coordinate nitrosyl complex. The proximal imidazole moiety does not dissociate from the central ferrous ion when NO binds to the trans side (*146*).

The $P_{50}(O_2)$ value of HSA-FeP**1** is always constant (33 Torr, 37 °C) independent of the binding number of FeP**1** (eq 1, Table 5)

$$\text{HSA-FeP} + \text{L} \underset{k_{off}(\text{L})}{\overset{k_{on}(\text{L})}{\rightleftarrows}} \text{HSA-FeP(L)} \quad [\text{L}: \text{O}_2 \text{ or CO}]$$

$$K(\text{L}) = [P_{50}(\text{L})]^{-1} = k_{on}(\text{L})/k_{off}(\text{L}) \quad (1)$$

The O_2 binding equilibrium curve shows no cooperativity. However, the O_2 transporting efficiency between the lungs [$P(O_2)$: ca. 110 Torr] and muscle tissue [$P(O_2)$: ca. 40 Torr] is 22%, which is identical to that for RBC.

The O_2 association and dissociation rate constants [$k_{on}(O_2)$ and $k_{off}(O_2)$] can be measured using laser flash photolysis (*147, 148*). Interestingly, the rebinding process of O_2 to HSA-FeP**1** included two phases (fast and slow phase), perhaps because of the different environment around each FeP**1** in the protein (*149*). The $P_{50}(O_2)$ value can be controlled by tuning the chemical structure of FeP**1**. We have synthesized quantities of Fe(II)porphyrins (Figure 12) and evaluated the O_2 binding parameters of their HSA-FeP hybrids (Table 6).

Actually, FeP**2** has a bulky 1-methylcyclohexanamide group on the porphyrin ring plane (*150*). The O_2 binding affinity of HSA-FeP**2** [$P_{50}(O_2)$: 35 Torr] was almost identical to that of HSA-FeP**1**. However, the stability of the oxygenated complex increased to 4.5 times its usual value [half-life $\tau_{1/2}(O_2)$, 9 h; pH 7.3; 37 °C] (*150*).

In general, the basicity and structure of the proximal base greatly influences the O_2 binding property of Fe^{2+}porphyrin. Both FeP**3** and FeP**4**, similar analogues having an His ligand, showed high O_2 binding affinities [$P_{50}(O_2)$: 3 Torr] (Figure 13, Table 6). Kinetically, substitution of the 2-methylimidazole to His reduces the O_2 dissociation rate constant (*150*). Although one might think that high O_2 binding affinity is not useful as a blood substitute, it can be efficient for oxygenation of hypoxic regions in tumors. Furthermore, the HSA-FeP**4** showed long $\tau_{1/2}(O_2)$ of 25 h (37 °C), which is 13-fold longer than that of HSA-FeP**1**.

Another HSA-FeP**5**, in which the active porphyrin has 3-methyl-L-hisitidine as a proximal base, exhibits an extraordinarily high O_2 binding affinity [$P_{50}(O_2)$: 1 Torr] that approaches those of relaxed-state Hb and Mb (*151*). It is remarkable that replacement of the 3-methyl-L-histidine moiety by 1-methyl-L-histidine isomer (HSA-FeP**6**) reduced O_2 binding affinity to 1/35th of its former level. The low O_2 affinity of FeP**6** is predominantly reflected by the high $k_{off}(O_2)$ value. The axial Fe−N(1-methyl-L-histidine) coordination might be restrained by steric interaction between the 4-methylene group of the His ring and the porphyrin plane (*151*).

The proximal histidyl side chain can be introduced easily into the β-pyrrolic position of the porphyrin via an acyl bond in two steps, FeP**7** (*152*). Although an electron-withdrawing acyl group is bound at the porphyrin periphery, the O_2 binding affinity of HSA-FeP**7** is slightly higher than that of HSA-FeP**4**. The rigid His-Gly(carboxy)butanoyl spacer of FeP**7** probably produces a favorable geometry to fix the imidazole onto the central Fe^{2+} of the porphyrin.

Double-sided porphyrins (FeP**8**, FeP**9**, and FeP**10**) were also incorporated into HSA (*153*). We expected that steric encumbrances on both sides of the porphyrin enable the HSA-FePs to form a stable O_2 adduct complex. Actually, the $\tau_{1/2}(O_2)$ of HSA-

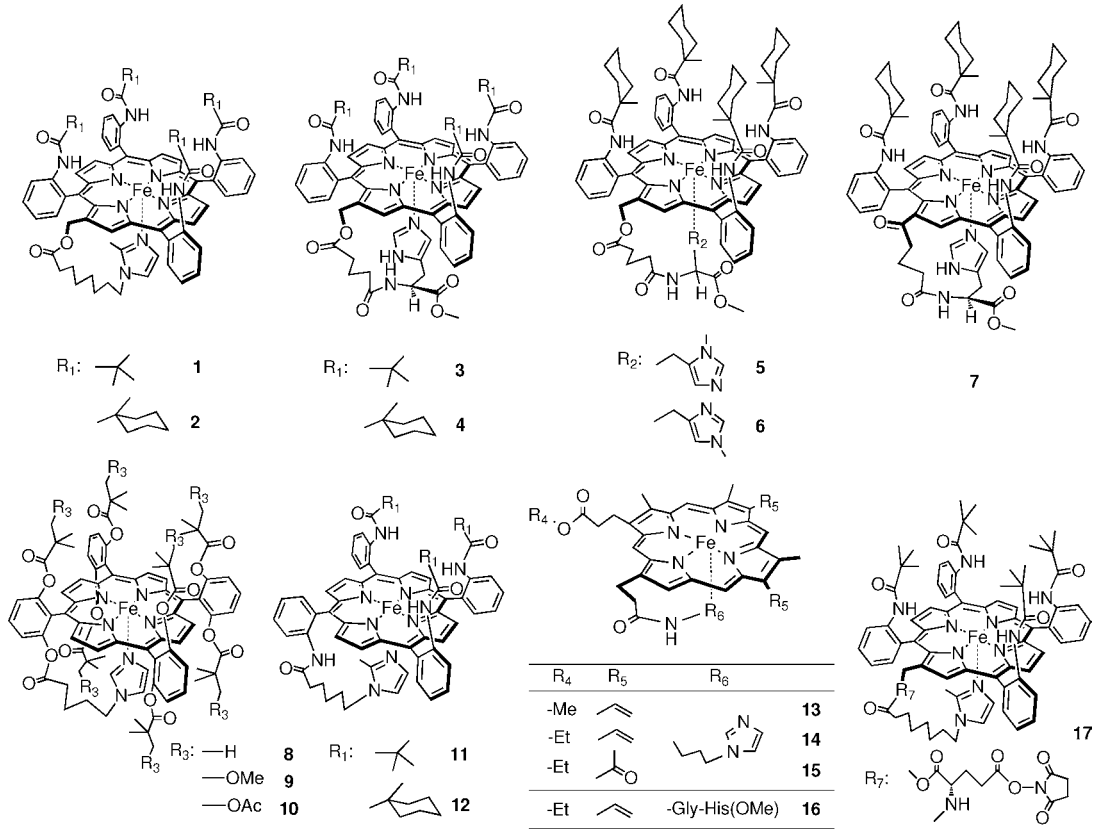

Figure 12. Structure of FePs in HSA-FePs.

Table 5. Solution Properties and Characteristics of HSA-FeP1

binding number of FeP**1** (*n*)	1−8
binding constant of FeP**1**	$1.2 \times 10^6 - 1.2 \times 10^4$ M^{-1}
M_w	(66.5 + 1.3*n*) kDa
*p*I	4.8
viscosity[a,b]	1.1 cP
COP[a,b,c]	20 Torr
shelf life[a,d]	>2 years

[a] In phosphate buffered solution (pH 7.3), [HSA]: 5 g/dL. [b] At 37 °C. [c] A membrane filter with a cutoff (M_w, 30×10^3) was used. [d] At 25 °C.

FeP**8** was 5 h, which is 2.5-fold longer than that of HSA-FeP**1**. In addition, HSA-FeP**8** showed high stability against hydrogen peroxide. The HSA incorporating double-sided porphyrins would be useful for the synthetic analogue of the oxidation enzyme.

Tailed porphyrins having an α,α,α,*β*-conformer, FeP**11** and FeP**12**, were synthesized easily via four steps from atropisomers of tetrakis(*o*-aminophenyl)porphyrin relative to eight steps of FeP**1** (*154*). Although HSA-FeP**12** binds O_2 reversibly, HSA-FeP**11** was quickly oxidized by O_2. We concluded that the 1-methylcyclohexanamide groups are necessary for the tailed porphyrin to form an O_2 adduct complex under physiological conditions.

Investigations have also revealed that heme [Fe^{2+}protoporphyrin IX; protoheme] derivatives having a proximal base at the propionate side chain (FeP**13**−FeP**16**) were incorporated into HSA (*155, 156*). The oxidation process of HSA-FeP**13**(O_2) to the inactive ferric state obeyed first-order kinetics, suggesting that the *μ*-oxo dimer formation was prevented by the immobilization of FeP**13** into albumin. In fact, HSA-FeP**15** showed lower O_2 binding affinity [high $P_{50}(O_2)$] than the others did. The acetyl groups at the 3,8-positions of FeP**15** decrease the electron density of the porphyrin macrocycle, thereby reducing the O_2 binding affinity. Actually, HSA-FeP**16**, in which the His-Gly tail coordinates to the Fe^{2+} center, showed the most stable O_2 adduct complexes [$\tau_{1/2}(O_2)$, 90 min; pH 7.3; 25 °C] of any of these heme compounds.

3.2. Surface-Modified HSA-FeP with PEG. A remaining defect of HSA-FeP is that the active Fe^{2+} porphyrin sites dissociate slowly from HSA when infused into animals because FeP is bound noncovalently to albumin. One possible solution is to bind the FeP molecule covalently to the protein. We have synthesized FeP**17** having a succinimide side chain; it can react with the Lys amino group of HSA (*157*). The O_2 binding property of HSA-FeP**17** is almost identical to that of HSA-FeP**1**.

Another approach is surface modification with PEG. Actually, PEG decollations of proteins and liposomes are well-known to enhance their plasma half-life, thermostability, nonimmunogenicity, and solubility in organic solvents (*158*−*163*). We surmised that surface modification of HSA-FeP**2** by PEG might help to prolong the circulation lifetime of FeP**2** and retain its O_2 transporting ability in vivo for a long period. Consequently, HSA-FeP**2** (FeP**2**/HSA = 4/1, mol/mol) was modified with maleimide-PEG, and the solution properties, O_2 binding behavior, and circulatory persistence of the PEG-modified HSA-FeP**2** [PEG(HSA-FeP**2**)] were examined (*164*). A thiolation reagent, iminothiolane, first reacted with the Lys amino groups of HSA to create active thiols that bind to α-maleimide-*ω*-methoxy PEG (Figure 14a). Mass spectroscopy measurements and quantification of the mercapro group of PEG(HSA-FeP**2**) revealed the conjugation of six PEG chains on the HSA-FeP**2** surface. The initial FeP**2**/HSA ratio 4/1 (mol/mol) was unchanged after the PEG binding. The adjustment of viscosity is important to design an artificial O_2 carrier. Maintenance of viscosity is necessary to preserve shear stress on the vascular wall that prevents loss of the functional capillary density (*123, 165*). The viscosity and COP of PEG(HSA-FeP**2**) were modulated to some degree by changing the molecular weight of PEG [M_w: 2×10^3 (PEG_{M2}) and 5×10^3 (PEG_{M5})] (Figure 14b). In fact, PEG_{M2}(HSA-FeP**2**) showed almost identical values of viscosity

Table 6. O_2 Binding Properties of HSA-FePs in Phosphate Buffered Solution (pH 7.3, 25 °C)

	$k_{on}(O_2)$ (μM^{-1} s^{-1})		$k_{off}(O_2)$ (ms^{-1})			
FeP	fast	slow	fast	slow	$P_{50}(O_2)$[a] (Torr)	refs
1	34	9.5	0.75	0.20	13 (33)	139, 149, 150
2	46	7.3	0.98	0.16	13 (35)	150
3	36	6.1	0.059	0.010	1 (3)	150
4	54	8.8	0.089	0.014	1 (3)	150
5	54	6.8	0.02	0.0024	0.2 (1)	151
6	54	8.1	0.62	0.093	7 (22)	151
7	34	4.5	0.045	0.0059	0.8 (2)	152
8	11	1.5	0.50	0.069	28	153
9	11	2.0	0.41	0.076	23	153
10	8.9	2.3	0.34	0.088	23	153
12	29	4.4	1.10	0.16	22 (45)	154
13	–	–	–	–	0.1	155, 156
14	–	–	–	–	0.1	155, 156
15	–	–	–	–	0.4	156
16	–	–	–	–	0.1	155, 156
17	28	–	0.33	–	9 (27)	157

[a] At 37 °C in parentheses.

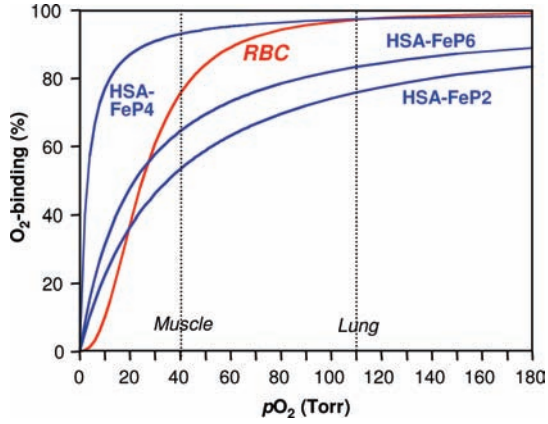

Figure 13. O_2 binding equilibrium curve of HSA-FePs under physiological conditions (pH 7.3, 37 °C).

and COP to those of the nonmodified HSA-FeP**2**. In contrast, PEG_{M5}(HSA-FeP**2**) showed a higher viscosity and more pronounced hyperoncotic property relative to those of HSA-FeP**2**. Nevertheless, PEG_{M5} conjugate may be useful as an efficient plasma expander (*118, 166*).

Under physiological conditions, PEG_{Mn}(HSA-FeP**2**) binds and releases O_2. The $P_{50}(O_2)$ values were almost identical to those of the original HSA-FeP**2**, indicating that the O_2 binding equilibrium was not influenced by the presence of the PEG chains (Figure 14b). Surface modification by PEG delays proton-driven oxidation of the O_2 adduct complex, giving HSA-FeP**2** the $\tau_{1/2}(O_2)$ of 12 h, which is almost equal to that of a natural hemoprotein, Mb [$\tau_{1/2}(O_2)$, 12 h; pH 7, 35 °C] (*167*). The conjugated PEG might change the local proton concentration of the HSA interior compared to the outer aqueous solution.

The circulation persistence of FeP**2** in the bloodstream was measured after administration of PEG_{Mn}(HSA-FeP**2**) to anesthetized rats (*164*). The PEG_{Mn}(HSA-FeP**2**) solution (20% volume of the circulatory blood) was injected intravenously into rats from the tail vein. The concentration decays of PEG_{Mn}(HSA-FeP**2**) in the blood showed single exponentials with half-life [$\tau_{1/2}$(FeP**2**)] of 13−16 h (Figure 14c). These values are considerably longer than those of the corresponding nonmodified HSA-FeP**1** (*168*). Surface modification of HSA-FeP**2** by PEG prevented the rapid clearance of the incorporated FeP**2**. On the basis of these findings, we can conclude that surface modification of HSA-FeP**2** by PEG comprehensively improved its O_2 transporting ability.

We then proceeded to evaluate physiological responses to an exchange transfusion with PEG_{M2}(HSA-FeP**2**) in an acute anemia rat model (*169*) (Figure 15). The animals were first placed in a 65 vol % hemodilution with 5 g/dL HSA. They subsequently underwent a 30 vol % blood replacement with the PEG_{M2}(HSA-FeP**2**) solution. As negative and positive control groups, a 5 g/dL HSA solution (HSA group) and washed RBC suspension (RBC group) were infused, respectively, to similarly operated rats in hemorrhage. The isovolemic 65% hemodilution with HSA reduced the Hb concentration, thereby decreasing the O_2 supply to the tissue. Consequently, the mean arterial pressure (MAP), renal cortical O_2 partial pressure [$PtO_2(R)$], and O_2 partial pressure of muscle tissue [$PtO_2(M)$] were decreased. During hemorrhagic shock by 30% bleeding, significant decreases in the MAP, venous O_2 pressure (PvO_2), $PtO_2(R)$, and $PtO_2(M)$ were observed by the loss of the circulation blood volume. The heart rate (HR) and respiration rate were also decreased. In contrast, arterial O_2 pressure (PaO_2) increased to about 160% of the basal value (b.v.). The arterial CO_2 pressure ($PaCO_2$) decreased to about 62% of the b.v.; the pH increased to 7.55.

The injection of the sample solutions increased the blood volume and improved the circulatory flow. Lactate was washed out from the tissues and into the circulatory system, which decreased the pH to the initial level of 7.43 in all groups. The administration of HSA restored no parameters: death occurred within 41 min. In contrast, the infusion of PEG_{M2}(HSA-FeP**2**) or RBC kept all the rats alive until the end of measurements. After injection of PEG_{M2}(HSA-FeP**2**), the animals showed marked and rapid recovery in MAP, HR, PaO_2, PvO_2, $PaCO_2$, and pH, resembling that shown in the RBC group. These results demonstrate the O_2 transporting capability of the PEG_{M2}(HSA-FeP**2**) solution as a resuscitative fluid. We observed that albumin-based oxygen carrier does not induce hypertensive action, because of its low permeability through the vascular endothelium in comparison with that of Hb molecules. The heart rate responses after the injection were also negligibly small. Visualization of the intestinal microcirculatory changes clearly revealed the widths of the venule and arteriole to be fairly constant (*170*).

Reversible oxygenation of PEG_{M2}(HSA-FeP**2**) was observed even in the solid state (*171*). The aqueous solution of PEG_{M2}(HSA-FeP**2**(CO)) complex was spread on the glass plate and dried overnight at room temperature, producing a red transparent solid membrane (Figure 16a). In contrast, HSA-FeP**2** without PEG decollation yielded a brittle membrane with many cracks. Scanning electron microscopy (SEM) observations of the PEG_{M2}(HSA-FeP**2**) membrane showed a uniform thickness of 15 μm and a smooth surface (Figure 16b). The $\tau_{1/2}(O_2)$ was 40 h, which is three times longer than the value in water. The

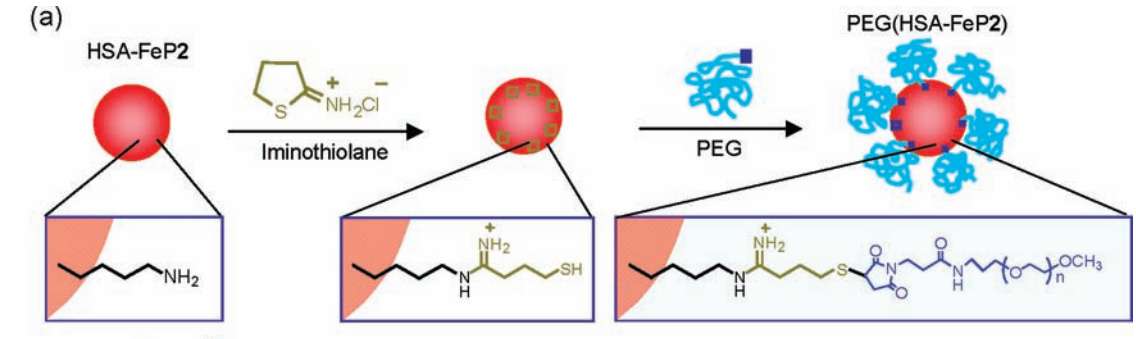

(b)

Solution and O_2 binding properties of PEG_{Mn}(HSA–FeP**2**)[a]

Samples	M_w of PEG	Viscosity (cP)	COP (Torr)	P_{50} (Torr)
PEG_{M2}(HSA–FeP**2**)	2 × 10³	1.14	27	32
PEG_{M5}(HSA–FeP**2**)	5 × 10³	2.34	65	31
HSA–FeP**2**	-	1.05	21	35

a) In phosphate buffered solution ([HSA]: 5g/dL, PEG_{Mn}/HSA–FeP**2**= 6, mol/mol) in average, pH 7.3, 37°C.

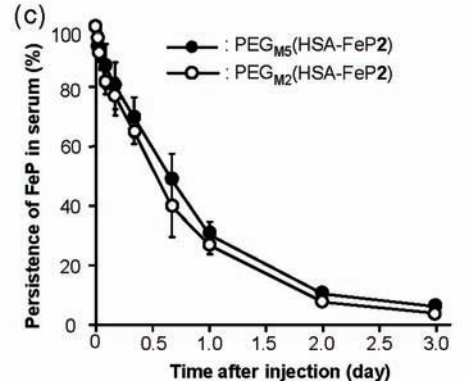

Figure 14. Surface modification of HSA-FeP with poly(ethylene glycol). (a) Synthetic scheme of PEG_{Mn}(HSA-FeP**2**). (b) Solution and O_2 binding properties. (c) Persistence of FeP**2** in serum after administration of PEG_{Mn}(HSA-FeP**2**) into Wistar rats. Each value represents the mean ± SD of four rats.

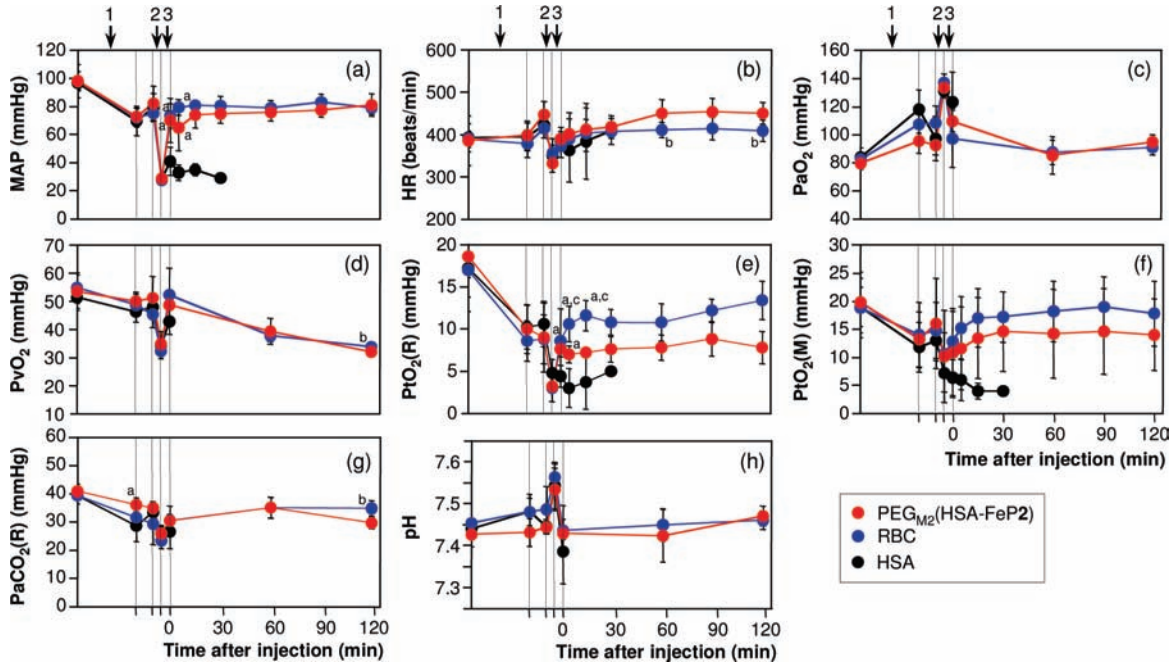

Figure 15. Effect of PEG_{M2}(HSA-FeP**2**) solutions on (a) MAP, (b) HR, (c) PaO_2, (d) PvO_2 (e) PtO_2(R), (f) PtO_2(M), (g) $PaCO_2$, and (h) pH in anesthetized rats subjected to hemodilution and hemorrhage. Each value represents the mean ± SD of five rats [red, PEG_{M2}(HSA-FeP**2**) group; blue, washed RBC group; and black, HSA group]. Arrows (1), (2), and (3), respectively, indicate the periods of 65% hemodilution, 30% bleeding, and sample infusion. [a]$p < 0.05$ versus HSA group (Tukey-Kramer test), [b]$p < 0.05$ versus PEG_{M2}(HSA-Fe**2**) group (unpaired *t*-test), and [c]$p < 0.05$ versus PEG_{M2}(HSA-FeP**2**) group (Tukey-Kramer test).

O_2 binding affinity was about a half that of the monomeric PEG_{M2}(HSA-FeP**2**).

We subsequently added hyaluronic acid (HA) as a supporting polymer to the protein solution and prepared the solid membrane on a poly(styrene) dish. Actually, HA is known as a glycosaminoglycan component of connective tissues, hyaline bodies, and extracellular matrix (*172*). Water evaporation of the PEG_{M2}(HSA-FeP**2**)/HA mixture ([HSA]: 2.5 wt % and [HA]: 0.2 wt %) produced a uniform red solid membrane that was easily peeled from the dish, yielding a free-standing homogeneous thin film of the PEG(HSA-FeP**2**)/HA hybrid (Figure 16c,d).

The PEG_{M2}(HSA-FeP**2**) solution is useful as a valuable O_2-carrying plasma. Membranes of PEG_{M2}(HSA-FeP**2**) with micrometer thickness can serve as a RBC substitute that can be preserved anywhere and reproduced as a saline solution at any time.

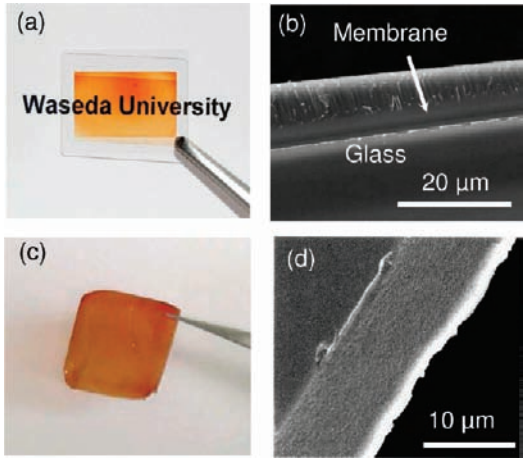

Figure 16. The solid membrane of PEG_{M2}(HSA-FeP). (a) Photograph of the membrane on the glass, (b) SEM of the membrane section, (c) photograph of the flexible film peeled from the poly(styrene) dish, and (d) SEM of the isolated film.

3.3. Recombinant HSA-Heme (rHSA-Heme) Prepared Using Site-Directed Mutagenesis. Hemin [Fe^{3+}protoporphyrin IX] released from metHb during enucleation of RBC or through hemolysis is captured by HSA with a high binding constant ($K \approx 10^8\ M^{-1}$) (*173*). Crystallographic studies have revealed that hemin is bound within a narrow D-shaped hydrophobic cavity in subdomain IB with axial coordination of Tyr-161 to the central ferric ion and electrostatic interactions between the porphyrin propionates and a triad of basic amino acid residues (Arg-114, His-146, and Lys-190) (Figure 17) (*174, 175*). In terms of the general hydrophobicity of this α-helical heme pocket, the subdomain IB of HSA potentially has similar features to the heme binding site of Hb or Mb. However, when one reduces HSA-hemin to obtain the ferrous complex, it is autoxidized rapidly by O_2, even at low temperature (~0 °C), because HSA lacks the proximal His, which, in Hb and Mb, enables the prosthetic heme group to bind O_2. Knowledge of the detailed architecture of the heme binding site in HSA enables us to design mutagenesis experiments to construct a tailor-made heme pocket for stable O_2 binding. Therefore, we used site-directed mutagenesis to introduce an His into the heme binding site that was expected to provide axial coordination to the central Fe^{2+} atom of the heme and thereby promote O_2 binding.

Results of our modeling experiments suggested that a favorable position for the axial imidazole insertion would be Ile-142 (Figure 17). The N_ϵ(His)-Fe distances were estimated as 2.31 Å for H142 (compared to 2.18 Å for Mb). We therefore designed and produced two single mutants I142H and a double mutant I142H/Y161L (HL) (*176*).

In the UV−vis absorption spectrum of rHSA(HL)-hemin, the ligand-to-metal charge transfer band at 625 nm was weakened because of the Y161L mutation. The MCD spectrum of rHSA(HL)-hemin showed a similar S-shaped pattern in the Soret band region resembling that of ferric Mb (*177, 178*). These results suggest that rHSA(HL)-hemin is in a predominantly ferric high-spin complex having a water molecule as the sixth ligand. The rHSA-hemin was easily reduced to the ferrous complex by adding a small molar excess of aqueous sodium dithionite under an Ar atmosphere (Figure 18). A single broad absorption band (λ_{max}: 559 nm) in the visible absorption spectrum and the MCD spectrum of rHSA(HL)-heme indicated the formation of a five-N-coordinate high-spin complex (*176, 177, 179*). The heme therefore appears to be accommodated in the mutated heme pocket with an axial coordination involving His-142. Upon exposure of rHSA(HL)-heme solution to O_2, the UV−vis absorption changed immediately to that of the O_2 adduct complex (Figure 18). It formed a carbonyl complex under a CO atmosphere. The single mutant rHSA(I142H)-heme, which retains Y161, was unable to bind O_2. The polar phenolate residue at the top of the porphyrin plane is likely to accelerate the proton-driven oxidation of the Fe^{2+} center. The replacement of Tyr-161 in rHSA(I142H)-heme by Leu enhanced stabilization of the O_2 adduct complex.

To evaluate the kinetics of O_2 and CO bindings to rHSA-hemes, laser flash photolysis experiments were carried out (Tables 7 and 8). It is noteworthy that the absorbance decay accompanying the CO recombination to rHSA(HL)-heme was composed of double-exponential profiles, which is normally not observed in Mb (the faster phase is defined as species I; the slower phase is defined as species II). The ratio of the amplitude of the species I and the species II was approximately 3:2. On the other hand, the rebinding of O_2 to rHSA(HL)-heme followed a simple monophasic decay. Numerous investigations of synthetic model hemes have helped to reveal the relation between the structure around the hemes and their O_2 and CO binding abilities (*4, 147, 148*). A bending strain in the proximal base coordination to the central Fe^{2+} atom, the "proximal-side steric (proximal pull) effect", is known to be capable of both increasing the dissociation rate for CO and decreasing the association rate. Simultaneously, it increases the O_2 dissociation rate without greatly altering the O_2 association kinetics. Consequently, one possible explanation for the existence of the two phases is that two different geometries of the axial His (His-142) coordination to the central ferrous ion of the heme might exist, each one accounting for a component of the biphasic kinetics of CO rebinding.

3.4. Modulation of O_2 Binding Property of rHSA-(mutant)−Heme. To control the O_2 binding affinity of rHSA-heme, we designed and produced diverse rHSA(mutant)−hemes in which bulky hydrophobic or hydrophilic amino acids were introduced around the O_2 binding site (Tyr-161, Leu-182, Leu-185, and Arg-186) (Figure 17). More recently, the beneficial effect of low-dose CO on the microcirculation by a hemoglobin-based artificial oxygen carrier has been discussed (*132, 182*). Control of the CO binding affinity of rHSA−heme is also tempting.

A. Substitution of Tyr-161 with Leu or Phe. The first, Tyr-161, was substituted to noncoordinating and hydrophobic amino acids (Leu or Phe). The O_2 and CO binding properties of rHSA(HL)−heme and rHSA(I142H/Y161F)−heme [rHSA(HF)−heme] showed that the presence of a Phe rather than a Leu at position 161 results in 6-fold and 4-fold increases in the O_2 binding affinity for species I and II, respectively (Table 7). This enhancement is mainly attributable to an increase in the O_2 association rate constant. The same trend was observed for CO binding [3-fold increase in k_{on}(CO)] (Table 8). The substitution of Leu-161 (102 $Å^3$) by Phe-161 (137 $Å^3$) (*183*) replaces an isopropyl group with a rigid benzyl group within the heme pocket. In rHSA(HL), the small side chain of Leu-161 might enable free rotation of the side chain of neighboring Leu-185, thereby reducing the volume on the distal side of the porphyrin plane (Figure 19a,b). On the other hand, the bulkier aromatic side chain of Phe-161 might prevent rotation of the isopropyl group of Leu-185 and thereby provide greater room of the distal pocket; this effect might provide easier access to the heme Fe^{2+} atom and account for the increased association rates for O_2 and CO.

B. Substitution of Leu-185 with Polar Amino Acid. Leu-185 was substituted with a more hydrophilic amino acid (Asn, Gln, or His), which was expected to interact with the coordinated O_2 by hydrogen bond and to stabilize the O_2 adduct complex similarly to Hb and Mb. In rHSA(mutant)−hemes in which Gln or His was introduced into Leu-185, they formed ferrous six-coordinated low-spin complexes under an Ar atmosphere. That

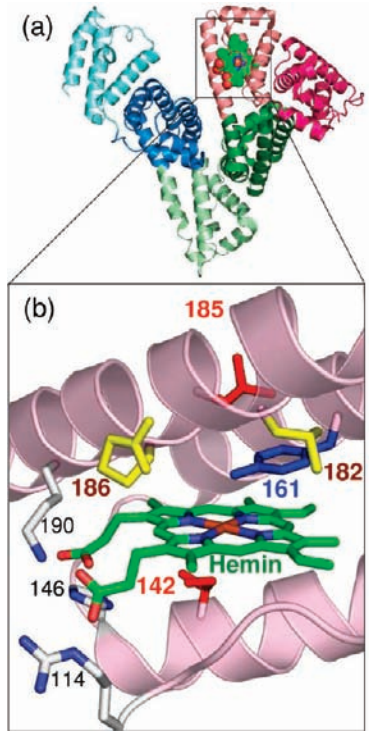

rHSA–heme	Position				
	142	161	182	185	186
Wild type	Ile	Tyr	Leu	Leu	Arg
I142H	***His***	Tyr	Leu	Leu	Arg
I142H/Y161L (HL)	***His***	***Leu***	Leu	Leu	Arg
I142H/Y161F (HF)	***His***	***Phe***	Leu	Leu	Arg
HL/L185N	***His***	***Leu***	Leu	***Asn***	Arg
HF/L185N	***His***	***Phe***	Leu	***Asn***	Arg
HL/L185Q	***His***	***Leu***	Leu	***Gln***	Arg
HF/L185Q	***His***	***Phe***	Leu	***Gln***	Arg
HF/L185H	***His***	***Phe***	Leu	***His***	Arg
HL/R186L	***His***	***Leu***	Leu	Leu	***Leu***
HL/R186F	***His***	***Leu***	Leu	Leu	***Phe***

Figure 17. (a) Crystal structure of HSA-hemin complex (1O9X) from ref 174. Hemin is shown in a space-filling representation. (b) Heme pocket structure in subdomain IB and positions of amino acids where site-specific mutations were introduced. Abbreviations of rHSA(mutant)s are shown in the table.

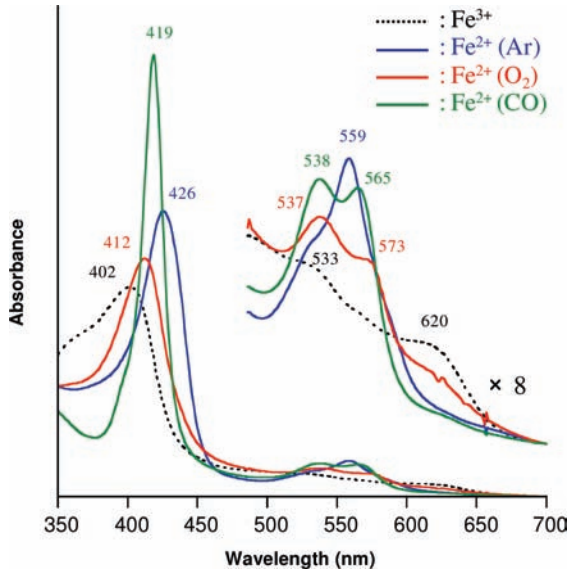

Figure 18. UV−vis absorption spectral changes of rHSA(HL)-heme in potassium phosphate buffered solution (pH 7.0).

result suggests that the introduced amino acid coordinates to the heme iron as a sixth ligand under an Ar atmosphere. Upon exposure of the solutions to O_2, they were oxidized. Bis-histidyl hemochromes are known to be oxidized by O_2 rapidly via an outer sphere mechanism (*184*−*186*). On the other hand, rHSA(HL/L185N)−heme and rHSA(HF/L185N)−heme in which Asn was introduced at Leu-185 formed ferrous five-coordinated high-spin complexes under an Ar atmosphere. They formed O_2 adduct complexes under O_2 atmosphere. The introduced Asn is estimated to be too far to coordinate to the heme.

Marked differences were apparent in a comparison of the O_2 and CO binding parameters for rHSA(HL)−heme and rHSA(HL/L185N)−heme. First, the presence of Asn rather than Leu at

Table 7. O_2 Binding Parameters of rHSA(Mutant)-Heme Complexes in Phosphate Buffered Solution (pH 7.0) at 22 °C

hemoproteins	$k_{on}(O_2)$ ($\mu M^{-1}s^{-1}$)	$k_{off}(O_2)$ ($m\ s^{-1}$) I	$k_{off}(O_2)$ ($m\ s^{-1}$) II	$P_{50}(O_2)$ (Torr) I	$P_{50}(O_2)$ (Torr) II
rHSA(HL)-heme	7.5	0.22	1.70	18	134
rHSA(HF)-heme	20	0.10	0.99	3	31
rHSA(HL/L185N)-heme	14	0.02	0.29	1	14
rHSA(HF/L185N)-heme	26	0.10	1.03	2	24
rHSA(HL/R186L)-heme	25	0.41	8.59	10	209
rHSA(HL/R186F)-heme	21	0.29	7.01	9	203
Mb[a]	14	0.012		0.51	
RBC[b]				8	

[a] Sperm whale myoglobin in 0.1 M potassium phosphate buffer (pH 7.0, 20 °C); ref 180. [b] Human red cell suspension in isotonic buffer (pH 7.4, 20 °C); ref 181.

Table 8. CO Binding Parameters of rHSA(Mutant)-Heme Complexes in Phosphate Buffered Solution (pH 7.0) at 22 °C

hemoproteins	$k_{on}(CO)$ ($\mu M^{-1}\ s^{-1}$) I	$k_{on}(CO)$ ($\mu M^{-1}\ s^{-1}$) II	$k_{off}(CO)$ (s^{-1}) I	$k_{off}(CO)$ (s^{-1}) II	$P_{50}(CO)$ (Torr) I	$P_{50}(CO)$ (Torr) II
rHSA(HL)-heme	2.0	0.27	0.013	0.079	0.0053	0.240
rHSA(HF)-heme	6.8	0.72	0.009	0.061	0.0011	0.068
rHSA(HL/L185N)-heme	6.8	1.60	0.008	0.039	0.0010	0.020
rHSA(HF/L185N)-heme	7.7	1.09	0.008	0.043	0.0008	0.032
rHSA(HL/R186L)-heme	5.0	0.57	0.011	0.165	0.0018	0.234
rHSA(HL/R186F)-heme	7.9	1.12	0.010	0.148	0.0010	0.107
Mb[a]	0.51		0.019		0.03	

[a] Sperm whale myoglobin in 0.1 M potassium phosphate buffer (pH 7.0, 20 °C); ref 180.

position 185 caused 2-fold and 3−6-fold increases, respectively, in the $k_{on}(O_2)$ and $k_{on}(CO)$ values. The Asn might partly rotate upward, which provides somewhat greater space of the distal pocket. Second, Asn-185 induced 18-fold and 10-fold increases in the O_2 binding affinity for species I and II, because the $k_{off}(O_2)$

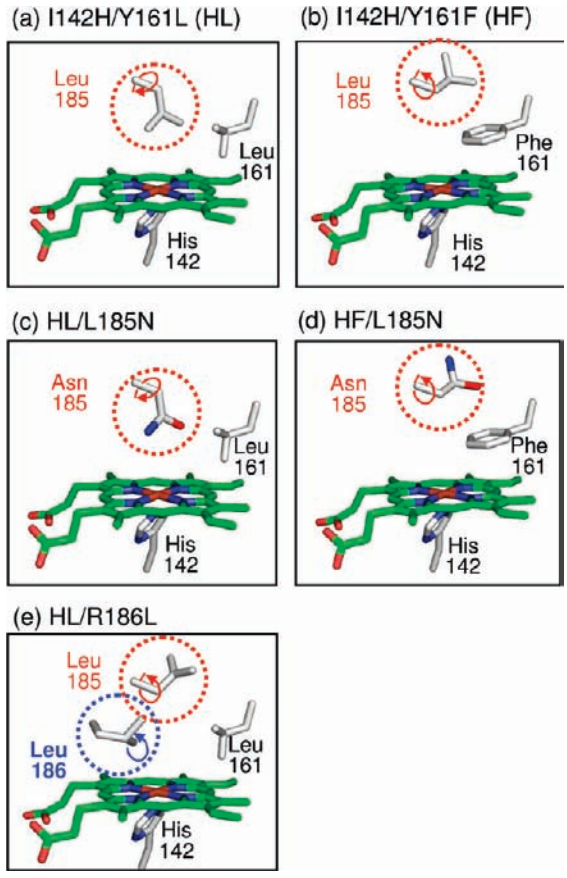

Figure 19. The proposed configuration of Leu-185 in (a) rHSA(HL)−heme and (b) rHSA(HF)−heme, Asn-185 in (c) rHSA(HL/L185N)−heme and (d) rHSA(HF/L185N)−heme, and Leu-186 in (e) rHSA(HL/R186L)–heme.

values were 1/6−1/11 of their former values. This corresponds to a free energy difference of −1.8 kcal mol^{-1} at 22 °C. The magnitude of the effect seems to be reasonable considering that, in HbO_2 and MbO_2, the distal His-64 stabilizes the coordinated O_2 by −0.6 to −1.4 kcal mol^{-1} because of the hydrogen bond (*187*). In contrast, The O_2 and CO binding parameters for rHSA(HF)−heme and rHSA(HF/L185N)−heme showed no significant differences. The bulky benzyl side chain of Phe-161 can prevent rotation of the polar amide group of Asn-185 and thereby decrease the effect of polarity and size on O_2 and CO binding parameters (Figure 19c,d) (*188*).

C. Substitution of Arg-186 with Leu or Phe. For administration into the human circulatory system, it would be better if the affinity were similar to the human RBC [$P_{50}(O_2)$: 8 Torr, 25 °C]. It is expected that providing a certain degree of hydrophobicity into the distal side of the heme by insertion of a nonpolar residue would reduce the O_2 binding affinity of the rHSA−heme complex. The most suitable position for that introduction might be at Arg-186, which is the entrance of the heme pocket and which is rather close to the central Fe(II) ion. Therefore, rHSA(HL/R186L)−hemin and rHSA(HL/R186F)−hemin were prepared. The O_2 dissociation rate constants of rHSA(HL/R186L)−heme and rHSA(HL/R186F)−heme were 3−4-fold higher than that of rHSA(HF)−heme, which reduced the O_2 binding affinities [larger $P_{50}(O_2)$]. This reduction might be attributable to the increased hydrophobicity in the distal pocket. The O_2 binding affinities of rHSA(HL/R186L)−heme [$P_{50}(O_2)$: 10 Torr] and rHSA(HL/R186F)−heme [$P_{50}(O_2)$: 9 Torr] have become equivalent to those of human RBC. The important structural factor in these mutants is Y161L, which enables the rotation of the isopropyl group of Leu-185 above the O_2 coordination site. Unexpectedly, the $k_{on}(O_2)$ and $k_{on}(CO)$ values of rHSA(HL/R186L)−heme and rHSA(HL/R186F)−heme were 3-fold and 3−4-fold higher than those of rHSA(HL)−heme and in the same range as that of rHSA(HF)−heme. In fact, Leu-161 is small, but the hydrophobic Leu-186 or Phe-186 might be integrated into the heme pocket from the entrance and might push up the neighboring Leu-185 residue (Figure 19e) (*188*).

We have engineered mutant rHSA−heme complexes that can bind O_2. Principal modifications to the heme pocket that are necessary to confer reversible O_2 binding are (i) replacement of Tyr-161 by hydrophobic amino acid (Leu or Phe), and (ii) introduction of His as a proximal base at position Ile-142. Furthermore, (iii) modification of the distal amino acid has a considerable effect on the modulation of O_2 and CO binding affinities.

4. CONCLUSIONS

The structures of our artificial O_2 carriers differ greatly from those of sophisticated RBCs. However, clear advantages of simplified artificial O_2 carriers are readily apparent: the absence of blood-type antigens and infectious viruses, stability for long-term storage at room temperature for any emergency, all of which overwhelm the functionality of RBCs. The shorter half-life of artificial O_2 carriers in the bloodstream (ca. 3 days) limits their use, but they are applicable as a transfusion alternative for shorter periods of use. Easy manipulation of physicochemical properties such as $P_{50}(O_2)$ and viscosity supports their possible development of tailor-made O_2 carriers to suit various clinical indications. The achievements of ongoing research described above give us confidence in advancing the further development with the expectation of its eventual realization.

ACKNOWLEDGMENT

The authors gratefully acknowledge Prof. H. Nishide, Prof. S. Takeoka (Waseda Univ.), Prof. R. Yozu, Prof. M. Suematsu, Dr. H. Horinouchi, Dr. M. Watanabe, Dr. E. Ikeda, Dr. Y. Izumi, Dr. M. Yamamoto, Dr. T. Ikeda (Keio Univ.), Dr. H. Ikeda, Dr. H. Azuma, Dr. M. Fujiwara, Dr. H. Abe (Hokkaido Red Cross Blood Center), Dr. M. Takaori (East Takarazuka Satoh Hospital), Prof. M. Otagiri (Kumamoto Univ.), Prof. M. Intaglietta (Univ. of California, San Diego), Prof. W. T. Phillips (Univ. of Texas, San Antonio), Prof. D. Erni (Inselspital Hospital, Univ. of Berne), Prof. M. Okamoto (Weill Med. College, Cornell Univ.), Prof. S. Curry (Imperial College London) and their active colleagues for meaningful discussions and contributions to this research. This work was partly supported by Health Sciences Research Grants (Research on Regulatory Science) from the Ministry of Health, Labour and Welfare, Japan, and Grant-in-Aid for Scientific Research from JSPS. The authors are the holders of patents related to the production and utilization of HbV and albumin−hemes.

LITERATURE CITED

(1) Perutz, M. F. (1970) Stereochemistry of cooperative effects in haemoglobin. *Nature 228*, 726–739.
(2) Jones, R. D., Summerville, A., and Basolo, F. (1979) Synthetic oxygen carriers related to biological systems. *Chem. Rev. 79*, 139–179.
(3) Collman, J. P. (1977) Synthetic model for the oxygen-binding hemoproteins. *Acc. Chem. Res. 10*, 265–272.
(4) Momenteau, M., and Reed, C. (1994) Synthetic heme dioxygen complexes. *Chem. Rev. 94*, 659–698.
(5) Collman, J. P., Gagne, R. R., Halbert, T. R., Marchon, J.-C., and Reed, C. A. (1973) Reversible oxygen adduct formation in ferrous complexes derived from "picket fence" porphyrins. A model for oxymyoglobin. *J. Am. Chem. Soc. 73*, 7868–7870.

(6) Collman, J. P., Gagne, R. R., Reed, C. A., Halbert, T. R., Lang, G., and Robinson, W. T. (1975) "Picket fence porphyrins." Synthetic models for oxygen binding hemoproteins. *J. Am. Chem. Soc. 97*, 1427–1439.
(7) Matsushita, Y., Hasegawa, E., Eshima, K., and Tsuchida, E. (1983) Synthesis of amphiphilic porphinatoiron complexes having phosphocholine groups. *Chem. Lett. 1983*, 1387–1389.
(8) Tsuchida, E. (1985) Liposome-embedded iron-porphyrins as an artificial oxygen carrier. *Ann. N.Y. Acad. Sci. 446*, 429–442.
(9) Tsuchida, E., and Nishide, H. (1986) Hemoglobin model - artificial oxygen carrier composed of porphinatoiron complexes. *Top. Curr. Chem. 1132*, 63–99.
(10) Komatsu, T., Moritake, M., Nakagawa, A., and Tsuchida, E. (2002) Self-organized lipid-porphyrin bilayer membranes in vesicular form: nanostructure, photophysical properties and dioxygen coordination. *Chem. Eur. J. 8*, 5469–5480.
(11) Komatsu, T., Ando, K., Kawai, N., Nishide, H., and Tsuchida, E. (1995) O_2-transport albumin - a new hybrid hemoprotein incorporating tetraphenylporphinatoiron(II). *Chem. Lett.* 813–814.
(12) Savitsky, J. P., Doczi, J., Black, J., and Arnold, J. D. (1978) A clinical safety trial of stroma-free hemoglobin. *Clin. Pharm. Ther. 23*, 73–80.
(13) Greenwald, R. B., Pendri, A., Martinez, A., Gilbert, C., and Bradley, P. (1996) PEG thiazolidine-2-thione, a novel reagent for facile protein modification: conjugation of bovine hemoglobin. *Bioconjugate Chem. 7*, 638–641.
(14) Kluger, R., and Li, X. (1997) Efficient chemical introduction of a disulfide cross-link and conjugation site into human hemoglobin at β-lysine-82 utilizing a bifunctional aminoacyl phosphate. *Bioconjugate Chem. 8*, 921–926.
(15) Sakai, H., Yuasa, M., Onuma, H., Takeoka, S., and Tsuchida, E. (2000) Synthesis and physicochemical characterization of a series of hemoglobin-based oxygen carriers: objective comparison between cellular and acellular types. *Bioconjugate Chem. 11*, 56–64.
(16) Hai, T. T., Pereira, D. E., Nelson, D. J., Catarello, J., and Srnak, A. (2000) Surface modification of diaspirin cross-linked hemoglobin (DCLHb) with chondroitin-4-sulfate derivatives. Part 1. *Bioconjugate Chem. 11*, 705–713.
(17) Manjula, B. N., Tsai, A., Upadhya, R., Perumalsamy, K., Smith, P. K., Malavalli, A., Vandegriff, K., Winslow, R. M., Intaglietta, M., Prabhakaran, M., Friedman, J. M., and Acharya, A. S. (2003) Site-specific PEGylation of hemoglobin at Cys-93(β): correlation between the colligative properties of the PEGylated protein and the length of the conjugated PEG chain. *Bioconjugate Chem. 14*, 464–472.
(18) Murray, J. A., Ledlow, A., Launspach, J., Evans, D., Loveday, M., and Conklin, J. L. (1995) The effects of recombinant human hemoglobin on esophageal motor function in humans. *Gastroenterology 109*1241–1248.
(19) Chatterjee, R., Welty, E. V., Walder, R. Y., Pruitt, S. L., Rogers, S. L., Arnone, A., and Walder, J. A. (1986) Isolation and characterization of a new hemoglobin derivative cross-linked between the a chains (lysine $99\alpha_1 \gg$ lysine $99\alpha_2$). *J. Biol. Chem. 261*, 9929–9937.
(20) Iwashita, Y. (1991) Pyridoxalated hemoglobin-polyoxyethylene conjugate (PHP) as an O_2 carrier. *Artif. Organs Today 1*, 89–114.
(21) Riess, J. G. (2001) Oxygen carriers ("blood substitutes") - raison d'etre, chemistry, and some physiology. *Chem. Rev. 101*, 2797–2920.
(22) de Figueiredo, L. F., Mathru, M., Solanki, D., Macdonald, V. W., Hess, J., and Kramer, G. C. (1997) Pulmonary hypertension and systemic vasoconstriction might offset the benefits of acellular hemoglobin blood substitutes. *J. Trauma 42*, 847–854.
(23) Tsai, A. G., Kerger, H., and Intaglietta, M. (1995) Microcirculatory consequences of blood substitution with $\alpha\alpha$-hemoglobin. In *Blood Substitutes: Physiological Basis of Efficacy* (Winslow, R. M., Vandegriff, K., Intaglietta, M., Eds.) pp155−174, Birkhauser, Boston.
(24) Goda, N., Suzuki, K., Naito, M., Takeoka, S., Tsuchida, E., Ishimura, Y., Tamatani, T., and Suematsu, M. (1998) Distribution of heme oxygenase isoforms in rat liver. Topographic basis for carbon monoxide-mediated microvascular relaxation. *J. Clin. Invest. 101*, 604–612.
(25) Sakai, H., Hara, H., Yuasa, M., Tsai, A. G., Takeoka, S., Tsuchida, E., and Intaglietta, M. (2000) Molecular dimensions of Hb-based O_2 carriers determine constriction of resistance arteries and hypertension. *Am. J. Physiol. Heart Circ. Physiol. 279*, H908−H915.
(26) Burhop, K., Gordon, D., and Estep, T. (2004) Review of hemoglobin-induced myocardial lesions. *Artif. Cells Blood Substit. Immobil. Biotechnol. 32*, 353–374.
(27) Neragi-Miandoab, S., and Vlahakes, G. J. (2006) Elevated troponin I level with hemoglobin based oxygen carrying solutions (HBOCs) as a priming solution despite improved left ventricular function. *Interact. Cardiovasc. Thorac. Surg. 5*, 135–138.
(28) Natanson, C., Kern, S. J., Lurie, P., Banks, S. M., and Wolfe, S. M. (2008) Cell-free hemoglobin-based blood substitutes and risk of myocardial infarction and death: a meta-analysis. *JAMA 299*, 2304–2312.
(29) Balla, J., Jacob, H. S., Balla, G., Nath, K., Eaton, J. W., and Vercellotti, G. M. (1993) Endothelial-cell heme uptake from heme proteins: induction of sensitization and desensitization to oxidant damage. *Proc. Natl. Acad. Sci. U.S.A. 90*, 9285–9289.
(30) Sakai, H., Sato, A., Masuda, K., Takeoka, S., and Tsuchida, E. (2008) Encapsulation of concentrated hemoglobin solution in phospholipid vesicles retards the reaction with NO, but not CO, by intracellular diffusion barrier. *J. Biol. Chem. 283*, 1508–1517.
(31) Sakai, H., Sato, A., Sobolewski, P., Takeoka, S., Frangos, J. A., Kobayashi, K., Intaglietta, M., and Tsuchida, E. (2008) NO and CO binding profiles of hemoglobin vesicles as artificial oxygen carriers. *Biochim. Biophys. Acta 1784*, 1441−1447.
(32) Martini, J., Cabrales, P., Tsai, A. G., and Intaglietta, M. (2006) Mechanotransduction and the homeostatic significance of maintaining blood viscosity in hypotension, hypertension and haemorrhage. *J. Intern. Med. 259*, 364–372.
(33) Sakai, H., Suzuki, Y., Kinoshita, M., Takeoka, S., Maeda, N., and Tsuchida, E. (2003) O_2 release from Hb vesicles evaluated using an artificial, narrow O_2-permeable tube: comparison with RBCs and acellular Hbs. *Am. J. Physiol. Heart Circ. Physiol. 285*, H2543−H2555.
(34) Vandegriff, K. D., and Olson, J. S. (1984) The kinetics of O_2 release by human red blood cells in the presence of external sodium dithionite. *J. Biol. Chem. 259*, 12609–12618.
(35) Chang, T. M. S. (2005) Therapeutic applications of polymeric artificial cells. *Nat. Rev. Drug Discov. 4*, 221–235.
(36) Toyoda, T. (1965) Artificial blood. *Kagaku 35*, 7–13 (in Japanese).
(37) Kimoto, S., Hori, M., Toyoda, T., and Sekiguchi, W. (1968) Artificial red cells. *Gekachiryou (Surgical Therapy) 19*, 324–332 (in Japanese).
(38) Bangham, A. D., and Horne, R. W. (1964) Negative staining of phospholipids and their structure modification by surface-active agents as observed in the electron microscope. *J. Mol. Biol. 8*, 660–668.
(39) Bangham, A. D., Standish, M. M., and Watkins, J. C. (1965) Diffusion of univalent ions across the lamellae of swollen phospholipids. *J. Mol. Biol. 13*, 238–252.
(40) Djordjevich, L., and Miller, I. F. (1977) Lipid encapsulated hemoglobin as a synthetic erythrocyte. *Fed. Proc. 36*, 567–571.
(41) Farmer, M. C., Rudolph, A. S., Vandegriff, K. D., Hayre, M. D., Bayne, S. A., and Johnson, S. A. (1988) Liposome-encapsulated hemoglobin: oxygen binding properties and respiratory function. *Biomater. Artif. Cells Artif. Organs 16*, 289–299.
(42) Rudolph, A. S., Klipper, R. W., Goins, B., and Phillips, W. T. (1991) In vivo biodistribution of a radiolabeled blood substitute: ^{99m}Tc-labeled liposome-encapsulated hemoglobin in an anesthetized rabbit. *Proc. Natl. Acad. Sci. U.S.A. 88*, 10976–10980.

(43) Phillips, W. T., Klipper, R. W., Awasthi, V. D., Rudolph, A. S., Cliff, R., Kwasiborski, V., and Goins, B. A. (1999) Polyethylene glycol-modified liposome-encapsulated hemoglobin: a long circulating red cell substitute. *J. Pharmacol. Exp. Ther. 288*, 665–670.

(44) Usuba, A., Osuka, F., Kimura, T., Sato, R., Ogata, Y., Gotoh, H., Kimura, T., and Fukui, H. (1998) Effect of liposome-encapsulated hemoglobin, neo red cells, on hemorrhagic shock. *Surg. Today 28*, 1027–1035.

(45) Yoshioka, H. (1991) Surface modification of haemoglobin-containing liposomes with polyethylene glycol prevents liposome aggregation in blood plasma. *Biomaterials 12*, 861–864.

(46) Sakai, H., Hamada, K., Takeoka, S., Nishide, H., and Tsuchida, E. (1996) Physical properties of hemoglobin vesicles as red cell substitutes. *Biotechnol. Prog. 12*, 119–125.

(47) Takeoka, S., Ohgushi, T., Terase, K., Ohmori, T., and Tsuchida, E. (1996) Layer-controlled hemoglobin vesicles by interaction of hemoglobin with a phospholipid assembly. *Langmuir 12*, 1755–1759.

(48) Sou, K., Naito, Y., Endo, T., Takeoka, S., and Tsuchida, E. (2003) Effective encapsulation of proteins into size-controlled phospholipid vesicles using freeze-thawing and extrusion. *Biotechnol. Prog. 19*, 1547–1552.

(49) Sakai, H., Takeoka, S., Yokohama, H., Seino, Y., Nishide, H., and Tsuchida, E. (1993) Purification of concentrated Hb using organic solvent and heat treatment. *Protein Expression Purif. 4*, 563–569.

(50) Abe, H., Ikebuchi, K., Hirayama, J., Fujihara, M., Takeoka, S., Sakai, H., Tsuchida, E., and Ikeda, H. (2001) Virus inactivation in hemoglobin solution by heat treatment. *Artif. Cells Blood Substit. Immobil. Biotechnol. 29*, 381–388.

(51) Chung, J., Hamada, K., Sakai, H., Takeoka, S., and Tsuchida, E. (1995) Ligand-exchange reaction of carbonylhemoglobin to oxyhemoglobin in a hemoglobin liquid membrane. *Nippon Kagaku Kaishi 2*, 123–127 (in Japanese).

(52) Takeoka, S., Sakai, H., Kose, T., Mano, Y., Seino, Y., Nishide, H., and Tsuchida, E. (1997) Methemoglobin formation in hemoglobin vesicles and reduction by encapsulated thiols. *Bioconjugate Chem. 8*, 539–544.

(53) Teramura, Y., Kanazawa, H., Sakai, H., Takeoka, S., and Tsuchida, E. (2003) Prolonged oxygen-carrying ability of hemoglobin vesicles by coencapsulation of catalase *in vivo*. *Bioconjugate Chem. 14*, 1171–1176.

(54) Sakai, H., Masada, Y., Onuma, H., Takeoka, S., and Tsuchida, E. (2004) Reduction of methemoglobin via electron transfer from photoreduced flavin: restoration of O_2-binding of concentrated hemoglobin solution coencapsulated in phospholipid vesicles. *Bioconjugate Chem. 15*, 1037–1045.

(55) Atoji, T., Aihara, M., Sakai, H., Tsuchida, E., and Takeoka, S. (2006) Hemoglobin vesicles containing methemoglobin and L-tyrosine to suppress methemoglobin formation *in vitro* and *in vivo*. *Bioconjugate Chem. 17*, 1241–1245.

(56) Sakai, H., Takeoka, S., Seino, Y., and Tsuchida, E. (1994) Suppression of methemoglobin formation by glutathione in a concentrated hemoglobin solution and in a Hb-vesicle. *Bull. Chem. Soc. Jpn. 67*, 1120–1125.

(57) Rameez, S., Alosta, H., and Palmer, A. F. (2008) Biocompatible and biodegradable polymersome encapsulated hemoglobin: a potential oxygen carrier. *Bioconjugate Chem. 19*, 1025–1032.

(58) Zhao, J., Liu, C. S., Yuan, Y., Tao, X. Y., Shan, X. Q., Sheng, Y., and Wu, F. (2007) Preparation of hemoglobin-loaded nanosized particles with porous structure as oxygen carriers. *Biomaterials 28*, 1414–1422.

(59) Rudolph, A. S. (1988) The freeze-dried preservation of liposome encapsulated hemoglobin: a potential blood substitute. *Cryobiology 25*, 277–284.

(60) Rabinovici, R., Rudolph, A. S., Vernick, J., and Feuerstein, G. (1994) Lyophilized liposome encapsulated hemoglobin: evaluation of hemodynamic, biochemical, and hematologic responses. *Crit. Care Med. 22*, 480–485.

(61) Ringsdorf, H., Schlarb, B., and Venzmer, J. (1988) Molecular architecture and function of polymeric oriented systems - models for the study of organization, surface recognition, and dynamics of biomembranes. *Angew. Chem., Int. Ed. 27*, 113–158.

(62) Kato, A., Arakawa, M., and Kondo, T. (1984) Preparation and stability of liposome-type artificial red blood cells stabilized with carboxymethylchitin. *J. Microencapsul. 1*, 105–112.

(63) Mobed, M., Nishiya, T., and Chang, T. M. (1992) Preparation of carboxymethylchitin-incorporated submicron bilayer-lipid membrane artificial cells (liposomes) encapsulating hemoglobin. *Biomater. Artif. Cells Immobil. Biotechnol. 20*, 365–368.

(64) Li, S., Nickels, J., and Palmer, A. F. (2005) Liposome-encapsulated actin-hemoglobin (LEAcHb) artificial blood substitutes. *Biomaterials 26*, 3759–3769.

(65) Tsuchida, E., Hasegawa, E., Kimura, N., Hatashita, M., and Makino, C. (1992) Polymerization of unsaturated phospholipids as large unilamellar liposomes at low temperature. *Macromolecules 25*, 2007–212.

(66) Sakai, H., Takeoka, S., Yokohama, H., Nishide, H., and Tsuchida, E. (1992) Encapsulation of Hb into unsaturated lipid vesicles and gamma-ray polymerization. *Polym. Adv. Technol. 3*, 389–394.

(67) Akama, K., Awai, K., Yano, Y., Tokuyama, S., and Nakano, Y. (2000) In vitro and in vivo stability of polymerized mixed liposomes composed of 2,4-octadecadienoyl groups of phospholipids. *Polym. Adv. Technol 11*, 280–287.

(68) Sakai, H., Takeoka, S., Park, S. I., Kose, T., Nishide, H., Izumi, Y., Yoshizu, A., Kobayashi, K., and Tsuchida, E. (1997) Surface-modification of hemoglobin vesicles with poly(ethylene glycol) and effects on aggregation, viscosity, and blood flow during 90%-exchange transfusion in anesthetized rats. *Bioconjugate Chem. 8*, 23–30.

(69) Sakai, H., Tsai, A. G., Kerger, H., Park, S. I., Takeoka, S., Nishide, H., Tsuchida, E., and Intaglietta, M. (1998) Subcutaneous microvascular responses to hemodilution with red cell substitutes consisting of polyethylene glycol-modified vesicles encapsulating hemoglobin. *J. Biomed. Mater. Res. 40*, 66–78.

(70) Sakai, H., Okamoto, M.,; Ikeda E., Horinouchi H., Kobayashi K., and Tsuchida, E. (2008) Histopathological changes of rat brain after direct injection of hemoglobin vesicles (oxygen carriers) and neurological impact in an intracerebral hemorrhage model. *J. Biomed. Mater. Res., Part A* (in press).

(71) Sakai, H., Tomiyama, K., Sou, K., Takeoka, S., and Tsuchida, E. (2000) Poly(ethylene glycol)-conjugation and deoxygenation enable long-term preservation of hemoglobin vesicles as oxygen carriers in a liquid state. *Bioconjugate Chem. 11*, 425–432.

(72) Sou, K., Endo, T., Takeoka, S., and Tsuchida, E. (2000) Poly(ethylene glycol)-modification of the phospholipid vesicles by using the spontaneous incorporation of poly(ethylene glycol)-lipid into the vesicles. *Bioconjugate Chem. 11*, 372–379.

(73) Sato, T., Sakai, H., Sou, K., Buchner, R., and Tsuchida, E. (2007) Poly(ethylene glycol)-conjugated phospholipids in aqueous micellar solutions: hydration, static structure, and interparticle interactions. *J. Phys. Chem. B 111*, 1393–1401.

(74) Szebeni, J. (2005) Complement activation-related pseudoallergy: a new class of drug-induced acute immune toxicity. *Toxicology 216*, 106–121.

(75) Van de Velde, M., Wouters, P. F., Rolf, N., Van Aken, H., and Vandermeersch, E. (1998) Comparative hemodynamic effects of three different parenterally administered lipid emulsions in conscious dogs. *Crit. Care Med. 26*, 132–137.

(76) Vercellotti, G. M., Hammerschmidt, D. E., Craddock, P. R., and Jacob, H. S. (1982) Activation of plasma complement by perfluorocarbon artificial blood: probable mechanism of adverse pulmonary reactions in treated patients and rationale for corticosteroids prophylaxis. *Blood 59*, 1299–1304.

(77) Phillips, W. T., Klipper, R., Fresne, D., Rudolph, A. S., Javors, M., and Goins, B. (1997) Platelet reactivity with liposome-encapsulated hemoglobin in the rat. *Exp. Hematol. 25*, 1347–1356.

(78) Szebeni, J., Fontana, J. L., Wassef, N. M., Mongan, P. D., Morse, D. S., Dobbins, D. E., Stahl, G. L., Bunger, R., and Alving, C. R. (1999) Hemodynamic changes induced by liposomes and liposome-encapsulated hemoglobin in pigs: a model for pseudoallergic cardiopulmonary reactions to liposomes. Role of complement and inhibition by soluble CR1 and anti-C5a antibody. *Circulation 99*, 2302–2309.

(79) Izumi, Y., Sakai, H., Kose, T., Hamada, K., Takeoka, S., Yoshizu, A., Horinouchi, H., Kato, R., Nishide, H., Tsuchida, E., and Kobayashi, K. (1997) Evaluation of the capabilities of a hemoglobin vesicle as an artificial oxygen carrier in a rat exchange transfusion model. *ASAIO J. 43*, 289–297.

(80) Loughrey, H. C., Bally, M. B., Reinish, L. W., and Cullis, P. R. (1990) The binding of phosphatidylglycerol liposomes to rat platelets is mediated by complement. *Thromb. Haemost. 64*, 172–176.

(81) Chonn, A., Cullis, P. R., and Devine, D. V. (1991) The role of surface charge in the activation of the classical and alternative pathways of complement by liposomes. *J. Immunol. 146*, 4234–4241.

(82) Sou, K., and Tsuchida, E. (2008) Electrostatic interactions and complement activation on the surface of phospholipid vesicle containing acidic lipids: effect of the structure of acidic groups. *Biochim. Biophys. Acta - Biomembr. 1778*, 1035–1041.

(83) Abe, H., Azuma, H., Yamaguchi, M., Fujihara, M., Ikeda, H., Sakai, H., Takeoka, S., and Tsuchida, E. (2007) Effects of hemoglobin vesicles, a liposomal artificial oxygen carrier, on hematological responses, complement and anaphylactic reactions in rats. *Artif. Cells Blood Substit. Biotechnol. 35*, 157–172.

(84) Abe, H., Fujihara, M., Azuma, H., Ikeda, H., Ikebuchi, K., Takeoka, S., Tsuchida, E., and Harashima, H. (2006) Interaction of hemoglobin vesicles, a cellular-type artificial oxygen carrier, with human plasma: effects on coagulation, kallikrein-kinin, and complement systems. *Artif. Cells Blood Substit. Immobil. Biotechnol. 34*, 1–10.

(85) Wakamoto, S., Fujihara, M., Abe, H., Yamaguchi, M., Azuma, H., Ikeda, H., Takeoka, S., and Tsuchida, E. (2005) Effects of hemoglobin vesicles on resting and agonist-stimulated human platelets *in vitro*. *Artif. Cells Blood Substit. Immobil. Biotechnol. 33*, 101–111.

(86) Wakamoto, S., Fujihara, M., Abe, H., Sakai, H., Takeoka, S., Tsuchida, E., Ikeda, H., and Ikebuchi, K. (2001) Effects of poly(ethyleneglycol)-modified hemoglobin vesicles on agonist-induced platelet aggregation and RANTES release *in vitro*. *Artif. Cells Blood Substit. Immobil. Biotechnol. 29*, 191–201.

(87) Takeoka, S., Mori, K., Ohkawa, H., Sou, K., and Tsuchida, E. (2000) Synthesis and assembly of poly(ethylene glycol)-lipids with mono-, di-, and tetraacyl chains and a poly(ethylene glycol) chain of various molecular weights. *J. Am. Chem. Soc. 122*, 7927–7935.

(88) Okamura, Y., Maekawa, I., Teramura, Y., Maruyama, H., Handa, M., Ikeda, Y., and Takeoka, S. (2005) Hemostatic effects of phospholipid vesicles carrying fibrinogen gamma chain dodecapeptide *in vitro* and *in vivo*. *Bioconjugate Chem. 16*, 1589–1596.

(89) Ohkawa, H., Teramura, Y., Takeoka, S., and Tsuchida, E. (2000) Synthesis of multiacyl poly(ethylene glycol) for the conjugation of cytochrome c to phospholipid vesicle. *Bioconjugate Chem. 11*, 815–821.

(90) Sou, K., Goins, B., Takeoka, S., Tsuchida, E., and Phillips, W. T. (2007) Selective uptake of surface-modified phospholipid vesicles by bone marrow macrophages *in vivo*. *Biomaterials 28*, 2655–2666.

(91) Teramura, Y., and Iwata, H. (2008) Islets surface modification prevents blood-mediated inflammatory responses. *Bioconjugate Chem. 19*, 1389–1395.

(92) Obata, Y., Suzuki, D., and Takeoka, S. (2008) Evaluation of cationic assemblies constructed with amino acid based lipids for plasmid DNA delivery. *Bioconjugate Chem. 19*, 1055–1063.

(93) Sou, K., Inenaga, S., Takeoka, S., and Tsuchida, E. (2008) Loading of curcumin into macrophages using lipid-based nanoparticles. *Int. J. Pharm. 352*, 287–293.

(94) Sou, K., Klipper, R., Goins, B., Tsuchida, E., and Phillips, W. T. (2005) Circulation kinetics and organ distribution of Hb vesicles developed as a red blood cell substitute. *J. Pharmacol. Exp. Ther. 312*, 702–709.

(95) Bradley, A. J., Devine, D. V., Ansell, S. M., Janzen, J., and Brooks, D. E. (1998) Inhibition of liposome-induced complement activation by incorporated poly(ethylene glycol)-lipids. *Arch. Biochem. Biophys. 357*, 185–194.

(96) Hu, Q., and Liu, D. (1996) Co-existence of serum-dependent and serum-independent mechanisms for liposome clearance and involvement of non-Kupffer cells in liposome uptake by mouse liver. *Biochim. Biophys. Acta 1284*, 153–161.

(97) Shibuya-Fujiwara, N., Hirayama, F., Ogata, Y., Ikeda, H., and Ikebuchi, K. (2001) Phagocytosis *in vitro* of polyethylene glycol-modified liposome-encapsulated hemoglobin by human peripheral blood monocytes plus macrophages through scavenger receptors. *Life Sci. 70*, 291–300.

(98) Sakai, H., Horinouchi, H., Tomiyama, K., Ikeda, E., Takeoka, S., Kobayashi, K., and Tsuchida, E. (2001) Hemoglobin-vesicles as oxygen carriers: influence on phagocytic activity and histopathological changes in reticuloendothelial system. *Am. J. Pathol. 159*, 1079–1088.

(99) Sakai, H., Horinouchi, H., Masada, Y., Takeoka, S., Kobayashi, K., and Tsuchida, E. (2004) Metabolism of hemoglobin-vesicles (artificial oxygen carriers) and their influence on organ functions in a rat model. *Biomaterials 25*, 4317–4325.

(100) Sakai, H., Masada, Y., Horinouchi, H., Ikeda, E., Sou, K., Takeoka, S., Suematsu, M., Takaori, M., Kobayashi, K., and Tsuchida, E. (2004) Physiologic capacity of reticuloendothelial system for degradation of hemoglobin-vesicles (artificial oxygen carriers) after massive intravenous doses by daily repeated infusions for 14 days. *J. Pharmacol. Exp. Ther. 311*, 874–884.

(101) Sakai, H., Horinouchi, H., Yamamoto, M., Ikeda, E., Takeoka, S., Takaori, M., Tsuchida, E., and Kobayashi, K. (2006) Acute 40% exchange-transfusion with hemoglobin-vesicles (HbV) suspended in recombinant human serum albumin solution: degradation of HbV and erythropoiesis in a rat spleen for 2 weeks. *Transfusion 46*, 339–347.

(102) Sakai, H., Seishi, Y., Obata, Y., Takeoka, S., Horinouichi, H., Tsuchida, E., and Kobayashi, K. (2009) Fluid resuscitation with artificial oxygen carriers in hemorrhaged rats: Profiles of hemoglobin-vesicle degradation and hematopoiesis for 14 days, *Shock 31*, 192−200.

(103) Yamaoka, T., Tabata, Y., and Ikada, Y. (1994) Distribution and tissue uptake of poly(ethylene glycol) with different molecular weights after intravenous administration to mice. *J. Pharm. Sci. 83*, 601–606.

(104) Ohki, N., Kimura, T., and Ogata, Y. (1998) The reduction of methemoglobin in Neo Red Cell. *Artif. Cells Blood Substit. Immobil. Biotechnol. 26*, 477–485.

(105) Sakai, H., Tsai, A. G., Rohlfs, R. J., Hara, H., Takeoka, S., Tsuchida, E., and Intaglietta, M. (1999) Microvascular responses to hemodilution with Hb vesicles as red cell substitutes: Influences of O_2 affinity. *Am. J. Physiol. Heart Circ. Physiol. 276*, H553−H562.

(106) Wang, L., Morizawa, K., Tokuyama, S., Satoh, T., and Tsuchida, E. (1992) Modulation of oxygen-carrying capacity of artificial red cells (ARC). *Polym. Adv. Technol. 4*, 8–11.

(107) Cabrales, P., Sakai, H., Tsai, A. G., Takeoka, S., Tsuchida, E., and Intaglietta, M. (2005) Oxygen transport by low and normal oxygen affinity hemoglobin vesicles in extreme hemodilution. *Am. J. Physiol. Heart Circ. Physiol. 288*, H1885−H1892.

(108) Izumi, Y., Sakai, H., Hamada, K., Takeoka, S., Yamahata, T., Kato, R., Nishide, H., Tsuchida, E., and Kobayashi, K. (1996) Physiologic responses to exchange transfusion with hemoglobin vesicles as an artificial oxygen carrier in anesthetized rats: changes in mean arterial pressure and renal cortical oxygen tension. *Crit. Care Med. 24*, 1869–1873.

(109) Sakai, H., Takeoka, S., Wettstein, R., Tsai, A. G., Intaglietta, M., and Tsuchida, E. (2002) Systemic and Microvascular responses to the hemorrhagic shock and resuscitation with Hb vesicles. *Am. J. Physiol. Heart Circ. Physiol. 283*, H1191−H1199.

(110) Sakai, H., Masada, Y., Horinouchi, H., Yamamoto, M., Ikeda, E., Takeoka, S., Kobayashi, K., and Tsuchida, E. (2004) Hemoglobin vesicles suspended in recombinant human serum albumin for resuscitation from hemorrhagic shock in anesthetized rats. *Crit. Care Med. 32*, 539–545.

(111) Yoshizu, A., Izumi, Y., Park, S. I., Sakai, H., Takeoka, S., Horinouchi, H., Ikeda, E., Tsuchida, E., and Kobayashi, K. (2004) Hemorrhagic shock resuscitation with an artificial oxygen carrier hemoglobin vesicle (HbV) maintains intestinal perfusion and suppresses the increase in plasma necrosis factor alpha (TNFα). *ASAIO J. 50*, 458–463.

(112) Terajima, K., Tsueshita, T., Sakamoto, A., and Ogawa, R. (2006) Fluid resuscitation with hemoglobin vesicles in a rabbit model of acute hemorrhagic shock. *Shock 25*, 184–189.

(113) Yamazaki, M., Aeba, R., Yozu, R., and Kobayashi, K. (2006) Use of hemoglobin vesicles during cardiopulmonary bypass priming prevents neurocognitive decline in rats. *Circulation 114* (1 Suppl), I220−I225.

(114) Tsai, A. G., Vandegriff, K. D., Intaglietta, M., and Winslow, R. M. (2003) Targeted O_2 delivery by low-P_{50} hemoglobin: a new basis for O_2 therapeutics. *Am. J. Physiol. Heart Circ. Physiol. 285*, H1411−H1419.

(115) Plock, J. A., Tromp, A. E., Contaldo, C., Spanholtz, T., Sinovcic, D., Sakai, H., Tsuchida, E., Leunig, M., Banic, A., and Erni, D. (2007) Hemoglobin vesicles reduce hypoxia-related inflammation in critically ischemic hamster flap tissue. *Crit. Care Med. 35*, 899–905.

(116) Nolte, D., Pickelmann, S., Lang, M., Keipert, P., and Messmer, K. (2000) Compatibility of different colloid plasma expanders with perflubron emulsion: an intravital microscopic study in the hamster. *Anesthesiology 93*, 1261–1270.

(117) Jouan-Hureaux, V., Audonnet-Blaise, S., Lacatusu, D., Krafft, M. P., Dewachter, P., Cauchois, G., Stoltz, J. F., Longrois, D., and Menu, P. (2006) Effects of a new perfluorocarbon emulsion on human plasma and whole-blood viscosity in the presence of albumin, hydroxyethyl starch, or modified fluid gelatin: an in vitro rheologic approach. *Transfusion 46*, 1892–1898.

(118) Vandegriff, K. D., McCarthy, M., Rohlfs, R. J., and Winslow, R. M. (1997) Colloid osmotic properties of modified hemoglobins: chemically cross-linked versus polyethylene glycol surface-conjugated. *Biophys. Chem. 69*, 23–30.

(119) Kobayashi, K. (2006) Summary of recombinant human serum albumin development. *Biologicals 34*, 55–59.

(120) Meyuhas, D., Nir, S., and Lichtenberg, D. (1996) Aggregation of phospholipid vesicles by water-soluble polymers. *Biophys. J. 71*, 2602–2612.

(121) Neu, B., and Meiselman, H. J. (2002) Depletion-mediated red blood cell aggregation in polymer solutions. *Biophys. J. 83*, 2482–2490.

(122) Sakai, H., Sato, A., Takeoka, S., and Tsuchida, E. (2007) Rheological property of hemoglobin vesicles (artificial oxygen carriers) suspended in a series of plasma substitute aqueous solutions. *Langmuir 23*, 8121–8128.

(123) Tsai, A. G., Friesenecker, B., McCarthy, M., Sakai, H., and Intaglietta, M. (1998) Plasma viscosity regulates capillary perfusion during extreme hemodilution in hamster skinfold model. *Am. J. Physiol. Heart Circ. Physiol. 275*, H2170−H2180.

(124) Intaglietta, M., Cabrales, P., and Tsai, A. G. (2006) Microvascular perspective of oxygen-carrying and -noncarrying blood substitutes. *Annu. Rev. Biomed. Eng. 8*, 289–321.

(125) Rebel, A., Ulatowski, J. A., Kwansa, H., Bucci, E., and Koehler, R. C. (2003) Cerebrovascular response to decreased hematocrit: effect of cell-free hemoglobin, plasma viscosity, and CO_2. *Am. J. Physiol. Heart Circ. Physiol. 285*, H1600−H1608.

(126) Dimino, M. L., and Palmer, A. F. (2007) High O_2 affinity hemoglobin-based oxygen carriers synthesized via polymerization of hemoglobin with ring-opened 2-chloroethyl-β-D-fructopyranoside and 1-o-octyl-β-D-glucopyranoside. *Biotechnol. Bioeng. 97*, 462–472.

(127) Plock, J. A., Contaldo, C., Sakai, H., Tsuchida, E., Leunig, M., Banic, A., Menger, M. D., and Erni, D. (2005) Is the Hb in Hb vesicles infused for isovolemic hemodilution necessary to improve oxygenation in critically ischemic hamster skin? *Am. J. Physiol. Heart Circ. Physiol. 289*, H2624−H2631.

(128) Contaldo, C., Plock, J., Sakai, H., Takeoka, S., Tsuchida, E., Leunig, M., Banic, A., and Erni, D. (2005) New generation of hemoglobin-based oxygen carriers evaluated for oxygenation of critically ischemic hamster flap tissue. *Crit. Care Med. 33*, 806–812.

(129) Verdu, E. F., Bercik, P., Huang, X. X., Lu, J., Al-Mutawaly, N., Sakai, H., Tompkins, T. A., Croitoru, K., Tsuchida, E., Perdue, M., and Collins, S. M. (2008) The role of luminal factors in the recovery of gastric function and behavioral changes after chronic *Helicobacter pylori* infection. *Am. J. Physiol. Gastrointest. Liver Physiol. 295*, G664−G670.

(130) Komatsu, H., Furuya, T., Sato, N., Ohta, K., Matsuura, A., Ohmura, T., Takagi, S., Matsuura, M., Yamashita, M., Itoda, M., Itoh, J., Horinouchi, H., and Kobayashi, K. (2007) Effect of hemoglobin vesicle, a cellular-type artificial oxygen carrier, on middle cerebral artery occlusion- and arachidonic acid-induced stroke models in rats. *Neurosci. Lett. 421*, 121–125.

(131) Yamamoto, M., Izumi, Y., Horinouchi, H., Teramura, Y., Sakai, H., Kohno, M., Watanabe, M., Kawamura, M., Adachi, T., Ikeda, E., Takeoka, S., Tsuchida, E., Kobayashi, K. (2009) Systemic administration of hemoglobin vesicle elevates tumor tissue oxygen tension and modifies tumor response to irradiation. *J. Surg. Res*. doi:10.1016/j.jss. 2007 12 770.

(132) Sakai, H., Horinouchi, H., Tsuchida, E., Kobayashi, K. (2008) Hemoglobin-vesicles and red blood cells as carriers of carbon monoxide prior to oxygen for resuscitation after hemorrhagic shock in a rat model. *Shock*. doi:10 1097/SHK.0b013e318189017a.

(133) Peters, T. (1996) *All about Albumin*: Biochemistry, Genetics and Medical Applications, Academic Press, San Diego.

(134) He, X. M., and Carter, D. C. (1992) Atomic structure and chemistry of human serum albumin. *Nature 358*, 209–215.

(135) Carter, D. C., and Ho, J. X. (1994) Structure of serum albumin. *Adv. Protein Chem. 45*, 153–203.

(136) Curry, S., Madelkow, H., Brick, P., and Franks, N. P. (1998) Crystal structure of human serum albumin complexed with fatty acid reveals an asymmetric distribution of binding sites. *Nat. Struct. Biol. 5*, 827–835.

(137) Bhattacharya, A. A., Grune, T., and Curry, S. (2000) Crystal structures of human serum albumin complexed with monounsaturated and polyunsaturated fatty acids. *J. Mol. Biol. 303*, 721–732.

(138) Ghuman, J., Zunszain, P. A., Petitpas, I., Bhattacharya, A. A., Otagiri, M., and Curry, S. (2007) Structural basis of the drug-binding specificity of humans serum albumin. *J. Mol. Biol. 353*, 38–52.

(139) Tsuchida, E., Komatsu, T., Matsukawa, Y., Hamamatsu, K., and Wu, J. (1999) Human serum albumin incorporating tetrakis(o-pivalamido)phenyl porphinatoiron(II) derivative as a totally synthetic O_2-carrying hemoprotein. *Bioconjugate Chem. 10*, 797–802.

(140) Komatsu, T., Hamamatsu, K., Wu, J., and Tsuchida, E. (1999) Physicochemical properties and O_2-coordination structure of human serum albumin incorporating tetrakis-(o-pivalamido) phenylporphyrinatoiron(II) derivatives. *Bioconjugate Chem. 10*, 82–86.

(141) Tsuchida, E., Komatsu, T., Yanagimoto, T., and Sakai, H. (2003) Preservation stability and *in vivo* administration of albumin-heme hybrid solution as an entirely synthetic O_2-carrier. *Polym. Adv. Technol. 13*, 848–850.

(142) Huang, Y., Komatsu, T., Nakagawa, A., Tsuchida, E., and Kobayashi, S. (2003) Compatibility *in vitro* of albumin-heme

(O_2 carrier) with blood cell components. *J. Biomed. Mater. Res. 66A*, 292–297.
(143) Komatsu, T., Huang, Y., Wakamoto, S., Abe, H., Fujihara, M., Azuma, H., Ikeda, H., Yamamoto, H., Horinouchi, H., and Kobayashi, K. (2007) Influence of O_2-carrying plasma hemoprotein "albumin-heme" on complement system and platelet activation *in vitro* and physiological responses to exchange transfusion. *J. Biomed. Mater. Res. 81A*, 821–826.
(144) Tsuchida, E., Nakagawa, A., and Komatsu, T. (2003) Coordination structure of active site in synthetic hemoprotein (albumin-heme) with dioxygen and carbon monoxide. *Macromol. Symp. 195*, 275–280.
(145) Komatsu, T., Matsukawa, Y., and Tsuchida, E. (2000) Nitrosyl iron(II) complex of *meso*-tetrakis(α,α,α,α-o-pivalamidophenyl)porphyrin with a covalently linked 2-methylimidazolylalkyl group. *Chem. Lett.* 1060–1061.
(146) Komatsu, T., Matsukawa, Y., and Tsuchida, E. (2001) Reaction of nitric oxide with synthetic hemoprotein, human serum albumin incorporating tetraphenylporphinatoiron(II) derivatives. *Bioconjugate Chem. 12*, 71–75.
(147) Collman, J. P., Brauman, J. I., Iverson, B. L., Sessler, J. L., Morris, R. M., and Gibson, Q. H. (1983) O_2 and CO binding to iron(II) porphyrins: A comparison of the "picket fence" and "pocket" porphyrins. *J. Am. Chem. Soc. 105*, 3052–3064.
(148) Traylor, T. G., Tsuchiya, S., Campbell, D., Mitchell, M., Stynes, D., and Koga, N. (1985) Anthracene-heme cyclophanes. Sterice in CO, O_2 and RNC binding. *J. Am. Chem. Soc. 107*, 604–614.
(149) Komatsu, T., Matsukawa, Y., and Tsuchida, E. (2000) Kinetics of CO and O_2 binding to human serum albumin-heme hybrid. *Bioconjugate Chem. 11*, 772–776.
(150) Komatsu, T., Matsukawa, Y., and Tsuchida, E. (2002) Effect of heme structure on O_2-binding properties of human serum albumin-heme hybrids: intramolecular histidine coordination provides a stable O_2-adduct complex. *Bioconjugate Chem 13*, 397–402.
(151) Nakagawa, A., Komatsu, T., Iizuka, M., and Tsuchida, E. (2008) O_2 binding to human serum albumin incorporating iron porphyrin with a covalently linked methyl-L-histidine isomer. *Bioconjugate Chem. 19*, 581–584.
(152) Nakagawa, A., Komatsu, T., and Tsuchida, E. (2007) meso-Tetrakis(α,α,α,α-o-amidophenyl) porphinatoiron(II) bearing a proximal histidyl group at the β-pyrrolic position via an acyl bond: synthesis and O_2 coordination in aqueous media. *Chem. Lett. 36*, 640–641.
(153) Komatsu, T., Okada, T., Moritake, M., and Tsuchida, E. (2001) O_2-binding properties of double-sided porphinatoiron(II)s with polar substituents and their human serum albumin hybrids. *Bull. Chem. Soc. Jpn. 74*, 1695–1702.
(154) Nakagawa, A., Komatsu, T., Iizuka, M., and Tsuchida, E. (2006) Human serum albumin hybrid incorporating tailed porphyrinatoiron(II) in the α,α,α,β-conformer as an O_2-binding site. *Bioconjugate Chem. 17*, 146–151.
(155) Nakagawa, A., Komatsu, T., Ohmichi, N., and Tsuchida, E. (2003) Synthetic dioxygen-carrying hemoprotein. human serum albumin including iron(II) complex of protoporphyrin IX with an axially coordinated histidylglycyl-propionate. *Chem. Lett. 32*, 504–505.
(156) Nakagawa, A., Komatsu, T., Ohmichi, N., and Tsuchida, E. (2004) Synthesis of protoheme IX derivatives with a covalently linked proximal base and their human serum albumin hybrids as artificial hemoprotein. *Org. Biomol. Chem. 2*, 3108–3112.
(157) Wang, R.-M., Komatsu, T., Nakagawa, A., and Tsuchida, E. (2005) Human serum albumin bearing covalently attached iron(II) porphyrins as O_2-coordination sites. *Bioconjugate Chem. 16*, 23–26.
(158) Harris, J. M. (1992) *Poly(ethylene glycol) Chemistry: Biotechnical and Biomedical Applications* (Harris, J. M., Ed.) Plenum Press, New York.
(159) Veronese, F. M., and Harris, J. M. (2002) Introduction and overview of peptide and protein PEGylation. *Adv. Drug Delivery Rev. 54*, 453–456.
(160) Roberts, M. J., Bentley, M. D., and Harris, J. M. (2002) Chemistry for peptide and protein PEGylation. *Adv. Drug Delivery Rev. 54*, 459–476.
(161) Veronese, F. M. (2001) Peptide and protein PEGylation: a review of problems and solutions. *Biomaterials 22*, 405–417.
(162) Nucci, M. L., Shorr, R., and Abuchowski, A. (1991) The therapeutic value of poly(ethylene glycol) modified proteins. *Adv. Drug Delivery Rev. 6*, 133–151.
(163) Kawahara, N. Y., and Ohno, H. (1997) Induced thermostability of poly(ethylene oxide)-modified hemoglobin in glycols. *Bioconjugate Chem. 8*, 643–648.
(164) Huang, Y., Komatsu, T., Wang, R.-M., Nakagawa, A., and Tsuchida, E. (2006) Poly(ethylene glycol)-conjugated human serum albumin including iron porphyrins: surface modification improves the O_2-transporting ability. *Bioconjugate Chem. 17*, 393–398.
(165) Cabrales P., Tsai, A. G., Intaglietta, M. (2004) Microvascular pressure and functional capillary density in extreme hemodilution with low- and high-viscosity dextran and a low-viscosity Hb-based O_2 carrier. *Am. J. Physiol. Heart Circ. Physiol. 287*, H363−H373.
(166) Martini, J., Cabrales, P., K, A., Acharya, S. A., Intaglietta, M., Tsai, A. G. (2008) Survival time in severe hemorrhagic shock after perioperative hemodilution is longer with PEG-conjugated human serum albumin than HES 130/0.4: a microvasucular perspective. *Crit. Care 12*, R54.
(167) Sugawara, Y., and Shikama, K. (1980) Autoxidation of native oxymyoglobin. *Eur. J. Biochem. 110*, 241–246.
(168) Tsuchida, E., Komatsu, T., Hamamatsu, K., Matsukawa, Y., Tajima, A., Yoshizu, A., Izumi, Y., and Kobayashi, K. (2000) Exchange transfusion with albumin-heme as an artificial O_2-infusion into anesthetized rats: physiological responses, O_2-delivery, and reduction of the oxidized hemin sites by red blood cells. *Bioconjugate Chem. 11*, 46–50.
(169) Huang, Y., Komatsu, T., Yamamoto, H., Horinouchi, H., Kobayashi, K., and Tsuchida, E. (2006) PEGylated albumin-heme as an oxygen-carrying plasma expander: exchange transfusion into acute anemia rat model. *Biomaterials 27*, 4477–4483.
(170) Tsuchida, E., Komatsu, T., Matsukawa, Y., Nakagawa, A., Sakai, H., Kobayashi, K., and Suematsu, M. (2003) Human serum albumin incorporating synthetic heme: red blood cell substitute without hypertension by nitric oxide scavenging. *J. Biomed. Mater. Res. 64A*, 257–261.
(171) Nakagawa, A., Komatsu, T., Huang, H., Lu, G., and Tsuchida, E. (2007) O_2-binding albumin thin films: solid membranes of poly(ethylene glycol)-conjugated human serum albumin incorporating iron porphyrin. *Bioconjugate Chem. 18*, 1673–1677.
(172) Goa, K. L., and Benfield, P. (1994) Hyaluronic-acid - a review of its pharmacology and use as a surgical and in ophthalmology, and its therapeutic potential in joint disease and wound-healing. *Drugs 47*, 536–566.
(173) Adams, P. A., and Berman, M. C. (1980) Kinetics and mechanism of the interaction between human serum albumin and monomeric haemin. *Biochem. J. 191*, 95–102.
(174) Zunszain, P. A., Ghuman, J., Komatsu, T., Tsuchida, E., and Curry, S. (2003) Crystal structural analysis of human serum albumin complexed with hemin and fatty acid. *BMC Struct. Biol. 3*, 6.
(175) Wardell, M., Wang, Z., Ho, J. X., Robert, J., Ruker, F., Ruble, J., and Carter, D. C. (2002) The atomic structure of human methemalbumin at 1.9 Å. *Biochem. Biophys. Res. Commun. 291*, 813–819.
(176) Komatsu, T., Ohmichi, N., Zunszain, P. A., Curry, S., and Tsuchida, E. (2004) Dioxygenation of human serum albumin having a prosthetic-heme group in a tailor-made heme pocket. *J. Am. Chem. Soc. 126*, 14304–14305.
(177) Komatsu, T., Ohmichi, N., Nakagawa, A., Zunszain, P. A., Curry, S., and Tsuchida, E. (2005) O_2 and CO binding properties of artificial hemoproteins formed by complexing iron protoporphyrin IX with human serum albumin mutants. *J. Am. Chem. Soc. 127*, 15933–15942.
(178) Vickery, L., Nozawa, T., and Sauer, K. (1976) Magnetic circular dichroism studies of myoglobin complexes. Correlation

with-heme spin state and axial ligation. *J. Am. Chem. Soc. 98*, 343–350.
(179) Antonini, E., and Brunori, M. *Hemoglobin and Myoglobin in Their Reactions with Ligands*, p 18, North-Holland Publishers, Amsterdam.
(180) Rohlfs, R., Mathews, A. J., Carver, T. E., Olson, J. S., Springer, B. A., Egeberg, K. D., and Sligar, S. G. (1990) The effects of amino acid substitution at position E7 (residue 64) on the kinetics of ligand binding to sperm whale myoglobin. *J. Biol. Chem. 265*, 3168–3176.
(181) Imai, K., Morimoto, H., Kotani, M., Watari, H., Hirata, W., and Kuroda, M. (1970) Studies of the function of abnormal hemoglobins I. An improved method for automatic measurement of the oxygen equilibrium curve of hemoglobin. *Biochim. Biphys. Acta 200*, 189–197.
(182) Vandegriff, K. D., Young, M. A., Lohman, J., Bellelli, A., Samaja, M., Malavalli, A., and Winslow, R. M. (2008) CO-MP4, a polyethylene glycol-conjugated haemoglobin derivative and carbon monoxide carrier that reduces myocardial infarct size in rats. *Br. J. Pharmacol. 154*, 1649–1561.
(183) Creighton, T. E. (1992) *Proteins: Structures and Molecular Properties*, p 242, W. H. Freeman and Co., New York.
(184) Chu, M. M. L., Castro, C. E., and Hathaway, G. M. (1978) Oxidation of low-spin iron(II) porphyrins by molecular oxygen. An outer sphere mechanism. *Biochemistry 17*, 481–486.
(185) Tsuchida, E., Nishide, H., Sato, Y., and Kaneda, M. (1982) The preparation of protoheme mono-N-[5-(2-methyl-1-imidazolyl)pentyl]amide and its oxygenation. *Bull. Chem. Soc. Jpn. 55*, 1890–1895.
(186) Uno, T., Sakamoto, R., and Tomisugi, Y. (2003) Inversion of axial coordination in myoglobin to create a "proximal" ligand binding pocket. *Biochemistry 42*, 10191–10199.
(187) Springer, B. A., Sligar, S. G., Olson, J. S., and Philips, G. N. (1994) Mechanisms of a ligand recognition in myoglobin. *Chem. Rev. 94*, 699–714.
(188) Komatsu, T., Nakagawa, A., Zunszain, P. A., Curry, S., and Tsuchida, E. (2007) Genetic engineering of the heme pocket in human serum albumin: modulation of O_2 binding of iron protoporphyrin IX by variation of distal amino acids. *J. Am. Chem. Soc. 129*, 11286–11295.

BC800431D

COMMUNICATIONS

Byproduct with Altered Fluorescent Properties Is Formed during Standard Deprotection Step of Hexachlorofluorescein Labeled Oligonucleotides

A. N Chuvilin,*[,†] M. V. Serebryakova,[†] I. P Smirnov,[†,‡] and G. E. Pozmogova[†,§]

Research Institute of Physical-Chemical Medicine, Moscow, Belozerskii Institute of Physico-Chemical Biology, Moscow State University, Moscow, and Bioengineering Center, Russian Academy of Science, Moscow, Russian Federation. Received February 17, 2009; Revised Manuscript Received June 25, 2009

HEX-labeled oligonucleotides obtained via typical synthetic protocols may contain more than 15% of material with altered spectral characteristics. We discovered hexachlorofluorescein residue transformation unknown earlier for standard DNA ammonolysis step. HEX residue reacts with ammonium hydroxide yielding acridine derivative, which has differed UV−VIS and fluorescent properties compared to HEX. Therefore, for critical bioassays where sensitivity and/or fluorescent signal differentiation (e.g., in quantitative or multiplexed assays) are essential, the careful RP-HPLC purification step is required.

INTRODUCTION

Fluorescently labeled oligonucleotides are now routinely used in molecular biology and medical diagnostics (*1, 2*). Most common methods of such oligomer synthesis assume the introduction of a label during the chain elongation process. In this case, a fluorophore undergoes all deblocking procedures and may be modified. For example, ammonolysis leads to partial conversion of the thiourea fragment of the FITC-label to urea and/or guanidine fragments (*3*).

It is a generally accepted opinion that carefully synthesized RT-PCR probes are not needed in additional purification (*4*). HEX (hexachlorofluorescein), being one of the popular red fluorescent dyes, is widely used in PCR-based assays, including multiplexed RT-PCRs (*5*). We have performed more than 200 HPLC separations of various HEX-labeled oligonucleotides obtained after automated synthesis and purified by PAGE, ion exchange chromatography, or RP cartridges. These oligonucleotides had >95% purity by gel electrophoresis analysis. In all of them, we found the presence of more than 15% full-size oligomers with altered fluorescent and UV−VIS spectral properties. For typical HPLC profiles and separation conditions, please see the Supporting Information. In the case of RT-PCR, the presence of such byproduct may lead to a decline in the sensitivity of RT-PCR assays and may have an impact on quantitation (*6*). Moreover, the fluorescent signal of these byproducts may interfere with signals from other labels, such as fluorescein, leading to a false positive response. Therefore, it is very important to understand the nature of this phenomenon.

RESULTS AND DISCUSSION

As a model object for investigation of the chemical mechanism of HEX-labeled oligonucleotide transmutation, we chose the simplest target oligonucleotide, 5′-HEX-T_{10}. The HPLC profile of the 5′-HEX-T_{10} postammonolysis mixture exhibited two main peaks (Figure 1A), labeled **1** and **2**. Fraction **1** demonstrated spectral properties expected for HEX-derivatives, while **2** had hypochromic shifts both in VIS (42 nm) (Figure 1B) and in fluorescent emission spectra (18 nm) (Figure 1C). Because of a significant shift of the emission maximum, this byproduct interferes with the working range of FITC and FAM labels. This can lead to false positive detection errors of multiplexed fluorescent-based assays.

The ratio of **1**/**2** peak intensities depends on ammonolysis conditions and, as shown on the Figure 1A, varies from 20% to 60% total oligonucleotide content. The yield of compound **1** is reduced with prolongation of time and/or elevation of ammonolysis temperature (see Figure 1A). The highest yields of oligonucleotide **1** were obtained with 25% ammonia either at room temperature/24 h or at 50 °C/5 h. More gentle deblocking conditions enhanced **1**/**2** ratio, but decreased overall yield of oligonucleotide **1** possibly because of incomplete removal of pivalic protection groups from 3,6-positions of the fluorophore.

Repeating ammonolysis of HPLC purified HEX-T_{10} (**1**) led to the appearance of the same compound **2** on the HPLC profile (data not shown). It is noteworthy that the alkaline treatment (1 M NaOH) in the same conditions did not cause such transformations (data not shown). It means that the presence of ammonium hydroxide is essential for change of the HEX label.

We were not able to detect the difference in molecular masses of oligonucleotides **1** and **2** within the mass accuracy of the MALDI TOF linear mode (±1 Da). To obtain better isotopic resolution, the synthesis of low-molecular-weight HEX−isopropylphosphate was undertaken.

* Andrey N. Chuvilin. 119992. Russian Federation, Moscow, Malaya Pirogovskaya str., 1a. Tel.: 7(499)246-4570, fax: 7(499)246-4501, e-mail: achuvilin@yandex.ru.

† Research Institute of Physical-Chemical Medicine.

‡ Moscow State University.

§ Bioengineering Center.

10.1021/bc900076e CCC: $40.75 © 2009 American Chemical Society
Published on Web 07/14/2009

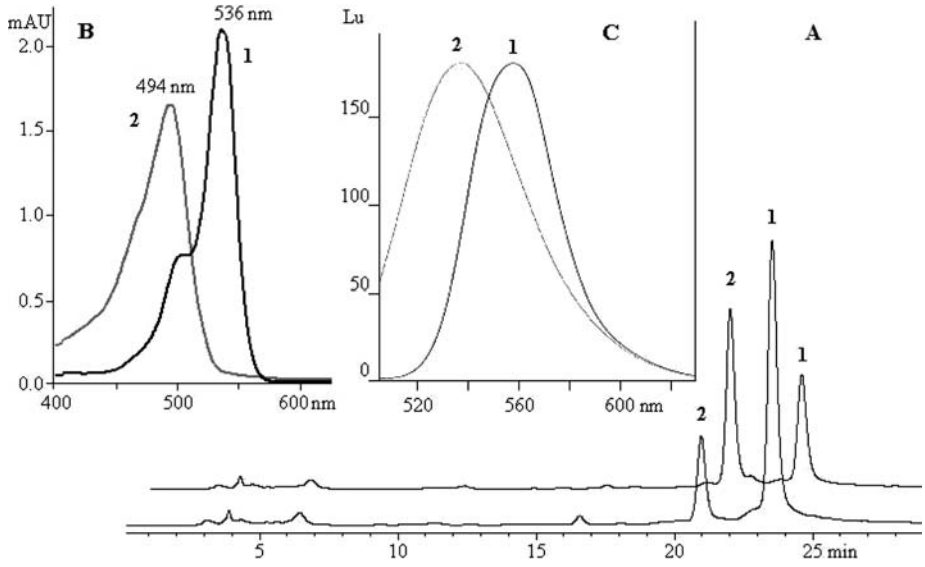

Figure 1. Transformation of 5′-HEX-T_{10} oligonucleotide. A. HPLC profiles of 5′-HEX-T_{10} isolation after ammonolysis at 50 °C/5 h (bottom curve) and at 50 °C/24 h (top curve). Column Diasorb C16T, 0.4 × 25 cm (Elsica, RF). Gradient of acetonitrile (10−20%/35 min) in 0.1 M ammonium acetate, flow 0.8 mL/min, temperature 35 °C. UV detector, λ 260 nm. B. VIS spectra of HEX-T_{10} **1** and of its acridine analogue **2** in 0.1 M NH_4OAc buffer, pH 6.7, normalized to adsorption maximum at 260 nm (UV areas are very similar, not shown). C. Fluorescence emission spectra of HEX-T_{10} **1** and of its acridine analogue **2** in the same buffer, λ_{ex} 480 nm.

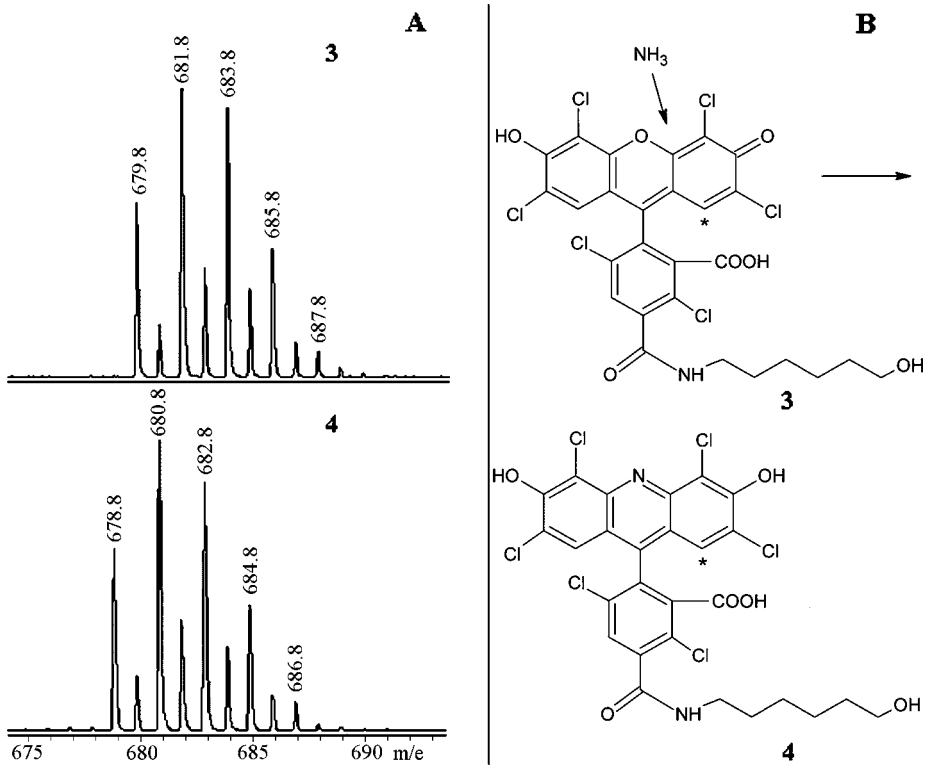

Figure 2. MALDI mass spectra (A) and the structures (B) of model fluorone **3** and acridine **4** derivatives. The arrow marks the interquartile point of ammonia nucleophilic attack. Asterisks mark locations of one of the protons that differed in ^{1}H NMR spectra of **3** and **4**.

Intermediate HEX−cyanoethylisopropylphosphite obtained by condensation of HEX-amidite (Glen Research, USA) with dry isopropyl alcohol in the presence of tetrazole was converted with standard iodine−water−pyridine oxidizer to corresponding phosphotriester, which without isolation was treated with 25% ammonia−tetrahydrofuran (9:1). Since phosphotriester had low solubility in this mixture, ammonolysis time was increased up to 66 h/60 °C. Under these conditions, significant hydrolysis of the phosphoester bonds occurred. HPLC profile of the resulting reaction mixture contained mainly two aromatic nonphosphorylated products, **3** and **4** (Figure 2A) in 7.5:1 integral ratio, according to adsorption at 260 nm. This pair of **3** and **4** had the same differences in fluorescent and VIS spectra as the pair of **1** and **2** (Figure 1B,C).

Mass spectra of compounds containing six chlorine atoms have very specific isotope signal distribution due to the natural abundance of ^{35}Cl and ^{36}Cl. The mass spectrum of **3** exhibits the same shape of the isotopic envelope as theoretically simulated (program *IsoPro* v 3.0 (*7*)) spectrum for 2,4,5,7,2′,5′-hexachloro-4′-(6″-hydroxyhexylaminocarbonyl)-fluorescein (simulation not shown). All signals observed in the mass spectrum (reflectron mode) of **4** were shifted by −1 Da in comparison

with corresponding isotopic signals of compound **3**, while the isotopic distribution remained the same (Figure 2A). These data prove that there are the same number of chlorine atoms in molecules **3** and **4**, and that there is a possibility of single oxygen atom substitution by NH group.

^{1}H NMR spectra of **3** and **4** were practically identical, including the aliphatic proton field (1−3 ppm, 12H) and the peak of the aromatic proton at the phenyl C3′ (7.63 ppm, 1H). The most important similarity is that the signals of both H atoms at C1 and C8 (Figure 2B) in both heterocycles **3** and **4** are singlets (6.96 ppm, 2H, for HEX (**3**), and 6.87 ppm, 2H, for **4**), which suggests preservation of the symmetry of the heterocycle after reaction with ammonia. There exists the sole possibility of symmetric incorporation of ammonia into the fluorone structure, the substitution of heterocyclic O10 with the NH group. Therefore, compound **4** is the acridine derivative—2,4,5,7-tetrachloro-3,6-dihydroxy-9-(2′,5′-dichloro-4′-[6″-hydroxyhexyl-aminocarbonyl]-6′-carboxyphenyl)acridine (see Figure 2B).

We observed a similar reaction of water ammonia with tetrabromo- (eosine) and tribromofluorescein (data not shown) and did not see it for the dibromo derivatives of fluorescein. In agreement with these data, all attempts at long-term ammonolysis (60 °C/6 days) of oligonucleotides labeled with nonhalogenated fluorescein (FAM-label) or with TET-label (containing dichloroxanthene group) also failed to lead to the noticeable formation of acridine structures (like **2** and **4**).

We speculate that the presence of more than two halogen atoms in the xanthene cycle of fluorones at o- and p-positions to carbon atoms near bridge atom O10 significantly facilitates ammonia nucleophilic attack leading to substitution of O10 by NH and formation of acridine structure (see Figure 2B; the most stable tautomer is shown). This effect makes possible the conversion of hexachlorofluoresceins into acridine derivatives (**2**, **4**) and explains the stability of the twice- or non-halogenated xanthene cycle of fluorone residues at the same mild conditions of ammonolysis.

The reaction of fluorone transformation to acridines under very stringent conditions was described a very long time ago, in 1899. Fluorescein ammonium salt in a dry ammonia stream has been converted to 3,6-diaminoacridine derivative at 180−200 °C in 5 days (*8*). However, at lower temperature (110 °C) dry ammonia did not change tetrachloroeosine (*9*). In turn, we did not detect 3,6-hydroxyl substitution with water ammonia at temperatures up to 70 °C.

Here, for the first time we report partial transformation of hexachlorofluorescein derivatives under mild ammonolysis conditions applied in obtaining oligonucleotides.

CONCLUSIONS

There is a possibility of conversion of halogenated fluorone labels of oligonucleotides into their acridine derivatives in mild ammonolysis conditions, which may be useful for future bioconjugate transformations.

During the standard ammonolysis step of hexachlorofluorescein- (HEX-) labeled oligonucleotides, this label undergoes substantial transformation into corresponding acridine derivative.

Post synthetic HPLC purification of HEX-labeled oligonucleotides is essential for demanding applications, where sensitivity and/or fluorescent signal differentiation (e.g., in quantitative and multiplexed assays) are critical and the possibility of false positive response must be minimized.

Supporting Information Available: Additional information as described in the text. This material is available free of charge via the Internet at http://pubs.acs.org.

LITERATURE CITED

(1) Li, Y., Zhou, X., and Ye, D. (2008) Molecular beacons: an optimal multifunctional biological probe. *Biochem. Biophys. Res. Commun. 373*, 457–461.

(2) Marras, S. A., Tyagi, S., and Kramer, F. R. (2006) Real-time assays with molecular beacons and other fluorescent nucleic acid hybridization probes. *Clin. Chim. Acta 363*, 48–60.

(3) Dubey, I., Pratviel, G., and Meunier, B. (1998) Modification of the thiourea linkage of a fluorescein-oligonucleotide conjugate to a guanidinium motif during ammonia deprotection. *Bioconjugate Chem. 9*, 627–632.

(4) Yeung, A. T., Holloway, B. P., Adams, P. S., and Shipley, G. L. (2004) Evaluation of dual-labeled fluorescent DNA probe purity versus performance in real-time PCR. *Biotechniques 36*, 266–270, 272, 274−276.

(5) Probert, W. S., Schrader, K. N., Khuong, N. Y., Bystrom, S. L., and Graves, M. H. (2004) Real-time multiplex PCR assay for detection of *Brucella* spp., *B. abortus*, and *B. melitensis*. *J. Clin. Microbiol. 42*, 1290–1293.

(6) Tatarinova, O. N., Lukyanova, T. N., Zaitseva, M. A., Vereemeev, K. Y., Karpov, V. A., Chuvilin, A. N., Petrunin, D. D., and Pozmogova, G. E. (2008) Significance of methods for purification of oligodeoxyribonucleotide probes for the efficiency of gene diagnosis by real-time PCR. *Bull. Exp. Biol. Med. 145*, 312–316.

(7) Software program *IsoPro* v 3.0; www.members.aol.com/msmssoft.

(8) Meyer, R., and Gross, R. (1899) Zur Kenntniss der Benzoflavine. *Chem. Ber. 32*, 2352–2371.

(9) Orndorff, W. R., and Hitch, E. F. (1914) Tetrachlorofluorescein and some of its derivatives. *J. Am. Chem. Soc. 48*, 680–725.

BC900076E

The examples of HPLC purification of HEX-labeled oligonucleotides.

BHQ2 is "Black Hole 2", a popular quencher of fluorescence.

HPLC were performed in gradient of acetonitrile (MeCN) in 0.1 M water ammonium acetate, pH 6.7, on thermostated columns:

A - Diasorb C16T, 10 mkm, 4*250 mm (Elsica, Russia).

B - Nucleosil 300 C18, 5 mkm, 4.6*250 mm (Teknokroma, Spain).

Peaks I correspond to target oligonucleotide HEX-derivatives, peaks II are acridine ones. We note that example 3 demonsrates not perfect HPLC profile. However, for all often used HEX-oligonucleotides we have found optimal HPLC conditions.

Table of HPLC conditions for HEX-labeled oligonucleotides.

Sam-ple	Bulk content	Column	Flow rate, ml/min	Tempe-rature, ^oC	MeCN gradient	Scale of synthesis, mkmol
1	HEX-$A_{13}C_3G_{11}T_{10}$-BHQ2	A	0.8	35	10-26%/40 min	0.1
2	HEX-$A_6C_8G_2T_6$-BHQ2	A	0.8	50	16.5-35%/35 min	0.1
3	HEX-$A_5C_8G_2T_6$-BHQ2	A	0.8	40	13.5-33%/40 min	0.1
4	HEX-$A_9C_9T_1$	B	0.9	40	9-20%/40 min	0.1
5	HEX-$A_7C_{10}G_{14}T_6$-BHQ2	B	0.9	40	12-22%/40 min	0.2
6	HEX-$A_9C_{11}G_{14}T_6$-BHQ2	B	0.85	40	12.5-24%/40 min	0.15
7	HEX-$A_7C_{10}G_{14}T_5$-BHQ2	B	0.9	40	12-22.5%/40 min	0.15
8	HEX-$A_{10}C_{13}G_{10}T_8$-BHQ2	B	0.9	40	12.5-21%/40min,	0.15
9	HEX-$A_3C_7G_7T_6$-BHQ2	B	0.85	40	12-24%/40 min	0.1

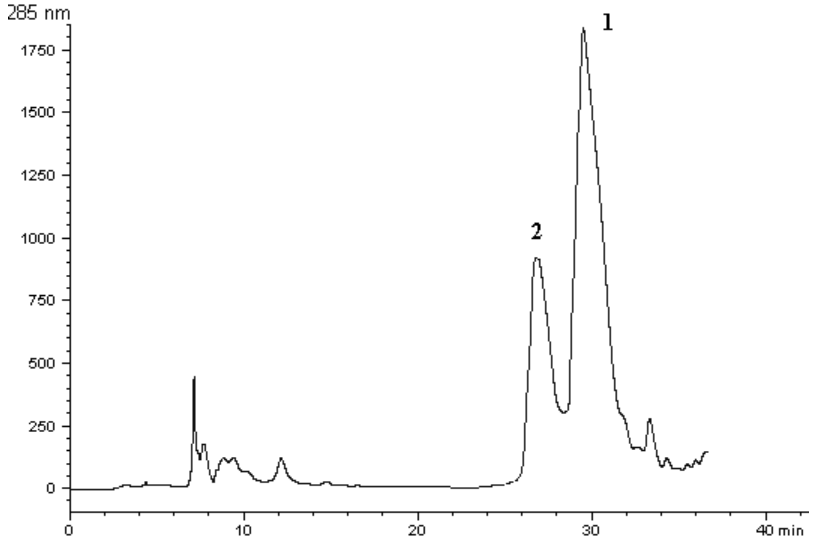

1. HEX-37mer-BHQ2

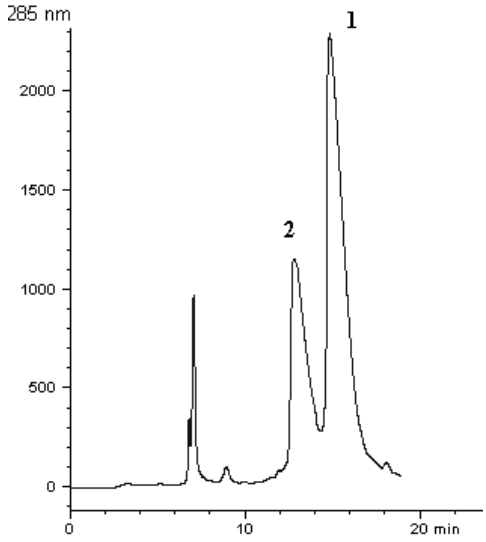

2. HEX-22mer-BHQ2

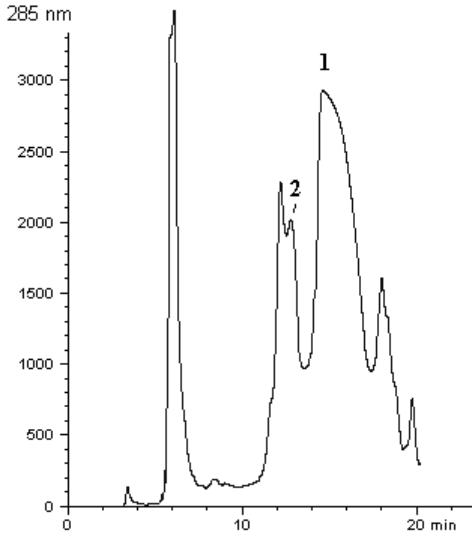

3. HEX-21mer-BHQ2

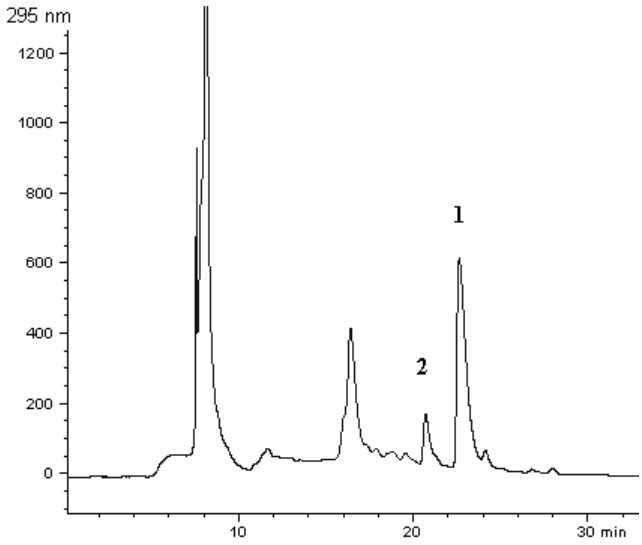

4. HEX-19mer

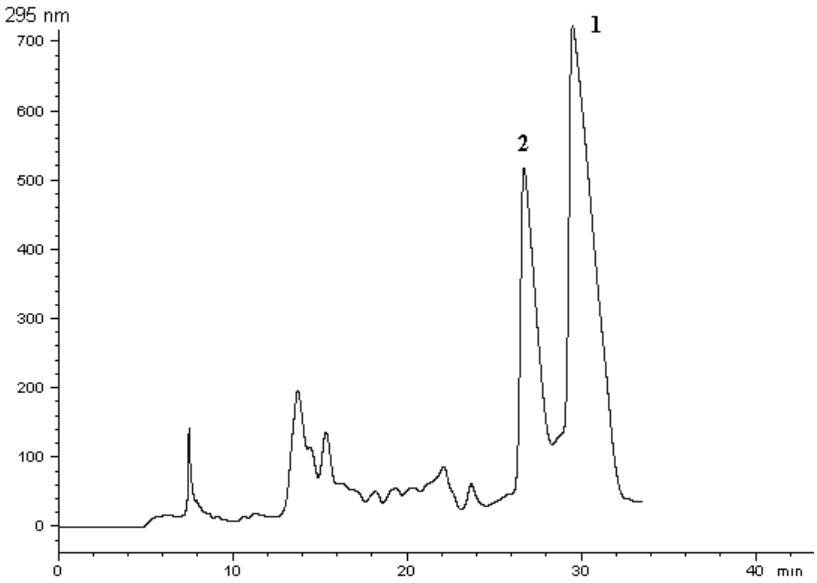

5. HEX-37mer-BHQ2

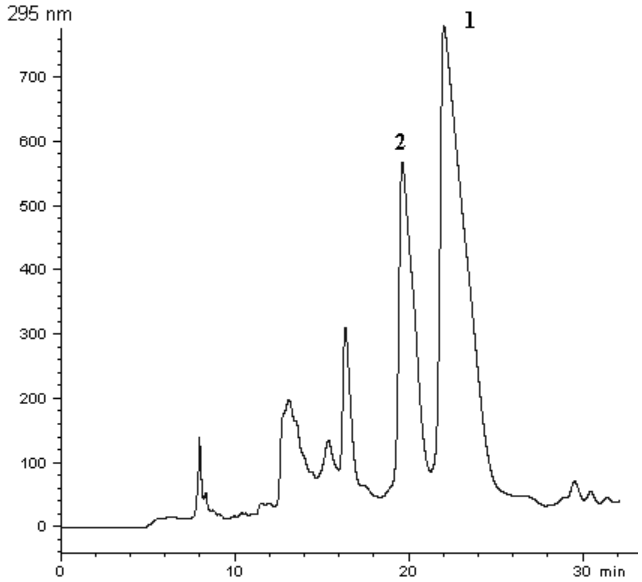

6. HEX-40mer-BHQ2

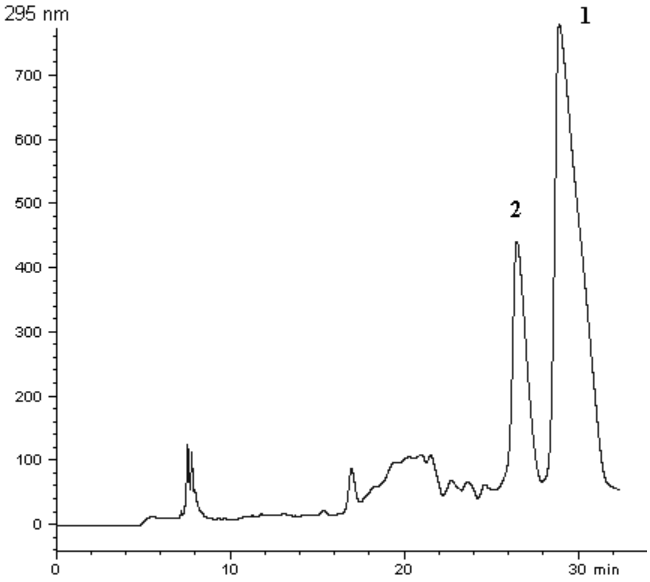

7. HEX-36mer-BHQ2

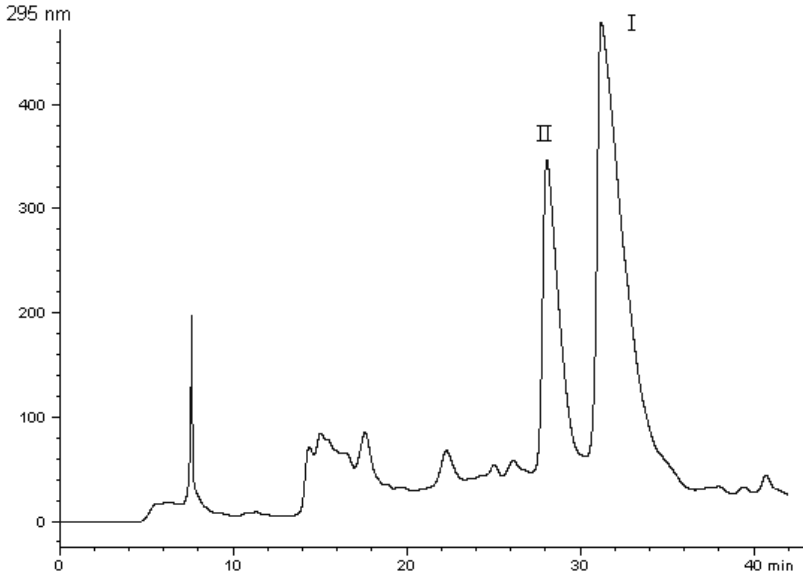

8. HEX-41mer-BHQ2

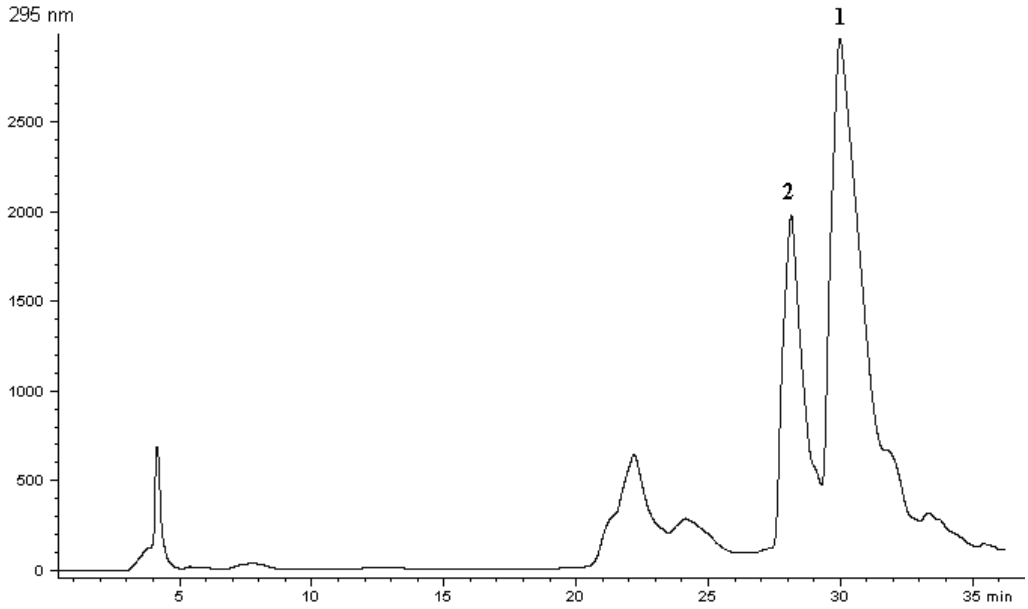

9. HEX-23mer-BHQ2

ARTICLES

Plate Capture Assay of Fluorescent Oligonucleotide Duplex Reporter−Transcription Factor Complexes

Surong Zhang[†] and Alexei Bogdanov, Jr.*[,†,‡]

Laboratory of Molecular Imaging Probes, Department of Radiology, and Department of Cell Biology, University of Massachusetts Medical School, 55 Lake Avenue North, Worcester, Massachusetts 01655. Received March 30, 2009; Revised Manuscript Received June 16, 2009

We previously developed prototype oligodeoxyribonucleotide (ODN) duplex fluorescence energy transfer (FRET) reporters for optical sensing of NF-κB transcription factor. We report here a plate-binding assay designed for optimizing the above reporters. Nitrilotriacetate-bearing plates were prepared by using sequential (1) aminosilylation; (2) carboxylation; (3) coupling of *N*α,*N*α-bis(carboxymethyl)-L-lysine or, alternatively, by replacing steps 1 and 2 by treating the glass with 3-(triethoxysilyl)propylsuccinic anhydride. FRET reporters were obtained by covalent linking of Cy5.5 (fluorescence donor) and IRdye800CW (fluorescence acceptor) to complementary ODN strands encoding a high-affinity p50 binding site. Recombinant 6 × His tagged NF-κB p50 was used for immobilizing the protein on glass plates via linked NTA-Ni(II) groups. Imaging and quantification of the fluorescence intensity in the wells was performed in two channels (700 and 800 nm) using a near-infrared scanning device with microscopic resolution. The fluorescence intensity of the ODN duplex reporter was detectible in the plates at the concentration of 5 pM. NF-κB p50-ODN reporter interaction was studied by measuring the ratio of 700 nm (donor) to 800 nm (acceptor) fluorescence intensities. Using the plate assay, we were able to measure p50-mediated interference with FRET at low density of plate binding.

INTRODUCTION

We previously developed probes for optical sensing of NF-κB p50 protein-oligodeoxyribonucleotide (ODN) duplex interactions (*1, 2*). The sensors were based on the effect of fluorescence resonance energy transfer between fluorescence donor (Cy5.5 carbocyanine dye) and acceptor (e.g., IRdye800CW), which were covalently linked to complementary strands encoding a high-affinity transcription factor binding site. We determined that if the donor and acceptor dyes were separated by 8 base pairs the radiative FRET efficiency exceeded 75%. Since the efficiency of FRET between a pair of near-infrared dyes is sensitive to protein binding to ODN duplex-encoded sequence, the reporters can be potentially used for direct sensing protein−DNA interactions (*1, 2*). We initially measured the changes of donor and acceptor fluorescence by using a single-cuvette spectrofluorometer. This testing approach provided high spectral accuracy and precision in determining normalized fluorescence intensity ratios. However, measurements performed in the presence of non-stoichiometric ratios of oligonucleotide probe/transcription factor could also be affected by the excess of free ODN duplex reporter. In addition, the setup lacked multiplexing capabilities and had a low throughput. By using a microtiter assay format, one can potentially achieve high throughputs and better accuracy, since the protein−probe complex can be isolated from the nonbound fluorescence probes by using binding of transcription factor to the plate surface. For isolating such reporter complexes, it is desirable to immobilize them on the microplates using noncovalent, affinity-based strategies (*3*). There are several alternative strategies for achieving the above goal. The alternatives include the use of specific antibodies against transcription factor epitopes (*4, 5*), as well as against fusion peptide tags introduced in the sequence of recombinant transcription factor proteins (*6*). We chose to study ODN duplex reporter-p50 protein complex separation conditions using NTA-Ni(II)-mediated affinity binding of the p50s fusion hexahistidine residue (6 × His) tag (*7*), since commercially available purified transcription factors are usually available as affinity-tagged proteins. We anticipated a potentially high density of 6 × His-tag binding sites that can be covalently linked to the glass surface, in contrast to a less dense coating with antibodies that are prone to activity loss during the storage. Glass has low autofluorescence in red and near-infrared spectral ranges and can be easily modified with sylilation agents affording further chemical modification. We hypothesized that the high efficacy of ODN duplex reporter-p50 protein complex retrieval from the solution could potentially translate into more accurate fluorescence readouts.

Therefore, we compared glass microplate modification protocols and tested the obtained plates for immobilizing NF-κB p50 and for detecting the interactions between NF-κB p50 and ODN duplex.

MATERIALS AND METHODS

Materials. 3-(Triethoxysilyl)propylsuccinic anhydride (TPSA) was purchased from Gelest Inc. (Morrisville PA). 3-Aminopropyltriethoxylsilane (APTS), *N*-(3-dimethylaminopropyl)-*N*′-

* Author to whom correspondence should be addressed. E-mail: Alexei.Bogdanov@umassmed.edu, S2-804, Laboratory of Molecular Imaging Probes, Department of Radiology, University of Massachusetts Medical School, 55 Lake Ave North, Worcester MA 01655, Tel. 508-856-5571, FAX 508-856-1860.

[†] Laboratory of Molecular Imaging Probes.

[‡] Department of Cell Biology.

10.1021/bc900137y CCC: $40.75 © 2009 American Chemical Society
Published on Web 07/02/2009

ethylcarbodiimide hydrochloride (EDC), *N*-hydroxysulfosuccinimide (sulfo-NHS), ethylenediamine, 2,4,6-trinitrobenzenesulfonic acid (TNBS), and glycine were purchased from Sigma-Aldrich (St. Louis, MO). Tris (2-carboxyethyl)phosphine (TCEP) was obtained from Pierce (Rockford, IL). *N*α,*N*α-bis(carboxymethyl)-L-lysine hydrate (BCML) was purchased from Fluka (Switzerland). Triethylammonium acetate solution (2 M, TEAA), pH 7.0, was purchased from Glen Research (Sterling VA); Cy5.5 maleimide was from GE Healthcare (Piscataway NJ); IRDye 800CW NHS ester was from Li-COR (Lincoln NE). 96-well glass-bottom microplates were purchased from Thermo Fisher Scientific (Hudson, NH).

Oligodeoxyribonucleotide (ODN) Synthesis and Modification. The synthesis, purification, and characterization of the ODNs used in this study were performed as in ref 8. The capped 3′-dithiolinker was introduced by using commercially available CPG derivatives (Glen Research). The conjugation of the donor fluorochrome (Cy5.5 mono maleimide) was achieved after reducing hydroxyethyl dithiopropyl linker on the 3′-end of the oligonucleotide 5′-AGCTATGAGGGACTTTCCG-Y-3′ (ODN1) with DTT. The conjugation of *N*-hydroxysuccinimide ester of IRDye 800CW acceptor fluorochrome was performed by using an internucleoside amino linker positioned between thymidine and cytosine in complementary 5′-CGGAAAGT*CCCTCAT-AGCT-3′ (ODN2), designated by an asterisk. The latter was introduced by using a thymidine phosphoramidite synthon (5′-*O*-DMTr-thymidine-3′-*O*-(2-(2-(2-trifluoroacetamidoethoxy)-ethoxy)ethyl)-*N*,*N*-diisopropylphosphoramidite) with a protected primary amino group linked via a triethylene glycol linker to phosphorus. The separation of donor and acceptor fluorochromes by 8 base pairs resulted in measured radiative FRET efficiency exceeding 75%.

Spectral Measurements. All UV spectral measurements were performed at room temperature unless otherwise stated by using Cary 50 spectrophotometer (Varian). All fluorescence spectral measurements were carried out at room temperature unless otherwise noted in quartz microcuvettes using Cary Eclipse fluorescence spectrophotometer (Varian).

Preparation of ODN Duplexes. Oligodeoxynucleotide (ODN) duplexes were prepared by mixing equimolar amounts of the corresponding ODNs dissolved in 25 mM Hepes, 1 mM $MgCl_2$, 50 mM NaCl, pH 7.4. The duplex mixtures were heated between 90 and 95 °C for 5 min to dissociate any intrastrand secondary structures and allowed to cool at room temperature to attain equilibrium. Each duplex formation was confirmed by measuring UV and fluorescence spectra. Two duplexes were used in this study: (1) FRET duplex: Cy5.5−ODN1/800CW-ODN2; (2) 800 nm fluorescent control duplex: ODN1/800CW−ODN2.

Plate Surface Treatment. For glass surface activation, the following sequence of washes was used: (1) 1 M NaOH, 10 min; (2) water, 5 min; (3) 1 M HCl, 1 h; (3) water, 5 min; (4) H_2SO_4/H_2O (1/1, v/v), 5 min. The plate was then washed in water followed by anhydrous ethanol and dried in a vacuum oven at RT for 1−2 h.

Two-Step Method of NTA Linking to the Glass Surface (Figure 1A). 5% 3-(Triethoxysilyl) propylsuccinic anhydride (TPSA) in anhydrous DMSO was added to the plate and reacted for 1 h followed by washing with DMSO three times; 0.025 mL of 0.2 M *N*α,*N*α-bis(carboxymethyl)-L-lysine (BCML) in 0.2 M Na_2CO_3 (pH 9) and 0.075 mL DMSO were added to each well and incubated for 3 h, followed by washings with water.

Multistep Method of NTA Linking (Figure 1B). Amino sylilation was performed by adding an APTS/DMSO (5/95, v/v) mixture to the plate and incubating for 1 h (*9, 10*). The sylilated plate was then washed three times with DMSO. Plate carboxylation was performed by mixing 0.03 mL 0.1 M succinic anhydride in DMSO with 0.27 mL, 0.2 M $NaHCO_3$, in the wells of the plate, incubated at room temperature for 1−2 h and washed with water three times. Fifty microliters of water was added to each well and the plate was put on ice. To each well, a mixture of 50 mM EDC/20 mM sulfo-NHS in water was added, followed by incubating for 5 min. Then, 0.05 mL of 0.1 M BCML/0.2 M $NaHCO_3$ solution was added. The mixture was incubated with mixing at room temperature for 2 h. The plate was washed three times with water.

Amino Group Titration. For determining amino groups on the glass surface, 0.1 mL of 0.1 M sodium tetraborate pH 9.0, 0.05 mL 0.1% Ipegal, and 0.1 mL 10 mM TNBS were added to the wells. The plate was incubated 1 h at RT, and the absorbance was measured on a SpectraMax M5 microplate reader (Molecular Devices). To test carboxylate-modified plates, ethylenediamine was used for reacting with EDC-activated carboxyl groups in the presence of sulfo-NHS. TNBS/tetraborate/igepal solution was then added to each well. Unmodified plate wells were used as blank controls, and amino group terminated plate wells were used as positive controls. Carboxyl group terminated plate well was used as a negative control.

Ni(II) Chelation. 0.1 mL of 0.1 mM $NiCl_2$/10 mM sodium acetate (pH 5.0) was added to each well, and the plate was incubated at room temperature for 1 h. The plate was washed with 0.05% Tween-20 and then 50 mM Tris HCl, 500 mM NaCl, pH 7.5.

NF-κB p50 Direct Labeling by Fluorochromes and Plate Binding Assay. NF-κB p50 (2 μg in 0.05 mL of 0.1 M $NaHCO_3$, 0.1% Tween-20, pH 8.5) was incubated in the presence of 5-fold molar excess of IRDye800CW-NHS at room temperature for 1 h. The mixture was separated on Micro Bio-Spin P-30 columns (Bio-Rad) equilibrated with plate binding buffer (PPB: 10 mM Tris, 100 mM KCl, 2 mM $MgCl_2$, 0.1 mg/mL tRNA, 10% glycerol, 5 mM TCEP, pH 7.5). The labeled NF-κB p50−800CW protein conjugate was added to the plate in the binding buffer and incubated at room temperature for 1 h. The negative control sample was prepared as above but in the absence of NF-κB p50. The plate was washed with washing buffer (WB: 10 mM Tris HCl, 500 mM NaCl, 0.05% Tween-20, pH 7.5) three times followed by fluorescence readout as described below.

NF-κB p50 Binding Assay. ODN duplex−p50 complex solution in 0.05 mL PPB was prepared by adding 0.4 pmol ODN duplex and 2.4 pmol NF-κB p50 incubated at room temperature for 30 min before being loaded to the plate. The plate was incubated at room temperature for 1 h followed by three washes with WB.

mAb-Coated Plate. According to the manufacturer's instructions, affinity-purified rabbit polyclonal antibody (NFκB p105/p50, Abcam Inc., Cambridge, MA) was adsorbed on a surface of polystyrene 96-well plate at 1 μg/well in 0.01 M carbonate buffer; the plate was washed with PBS-T (0.05% Tween 20) and blocked with BSA. Complexes of ODN and p50 were incubated in the plate for 1 h at room temperature, and fluorescence was determined by using the Odyssey system as described below.

Electrophoretic Mobility Shift Assays (EMSAs). EMSAs were performed using a reaction mixture containing 18 nM ODN duplexes incubated 30 min RT in a volume of 0.01 mL NF-κB p50 solution in PPB. Samples were loaded and run on 10% TBE Ready Gels (Bio-Rad Laboratories, Hercules CA) using 0.5 × TBE buffer. The gels were imaged and digitized using Odyssey Infrared Imaging system (LI-COR Biosciences, Lincoln, NE).

Fluorescence Measurements Using Odyssey Infrared Imaging System. The instrument utilizes simultaneous solid diode excitation of fluorescence at 685 and 785 nm and measures emitted light by using a dichroic mirror transmitting above 810

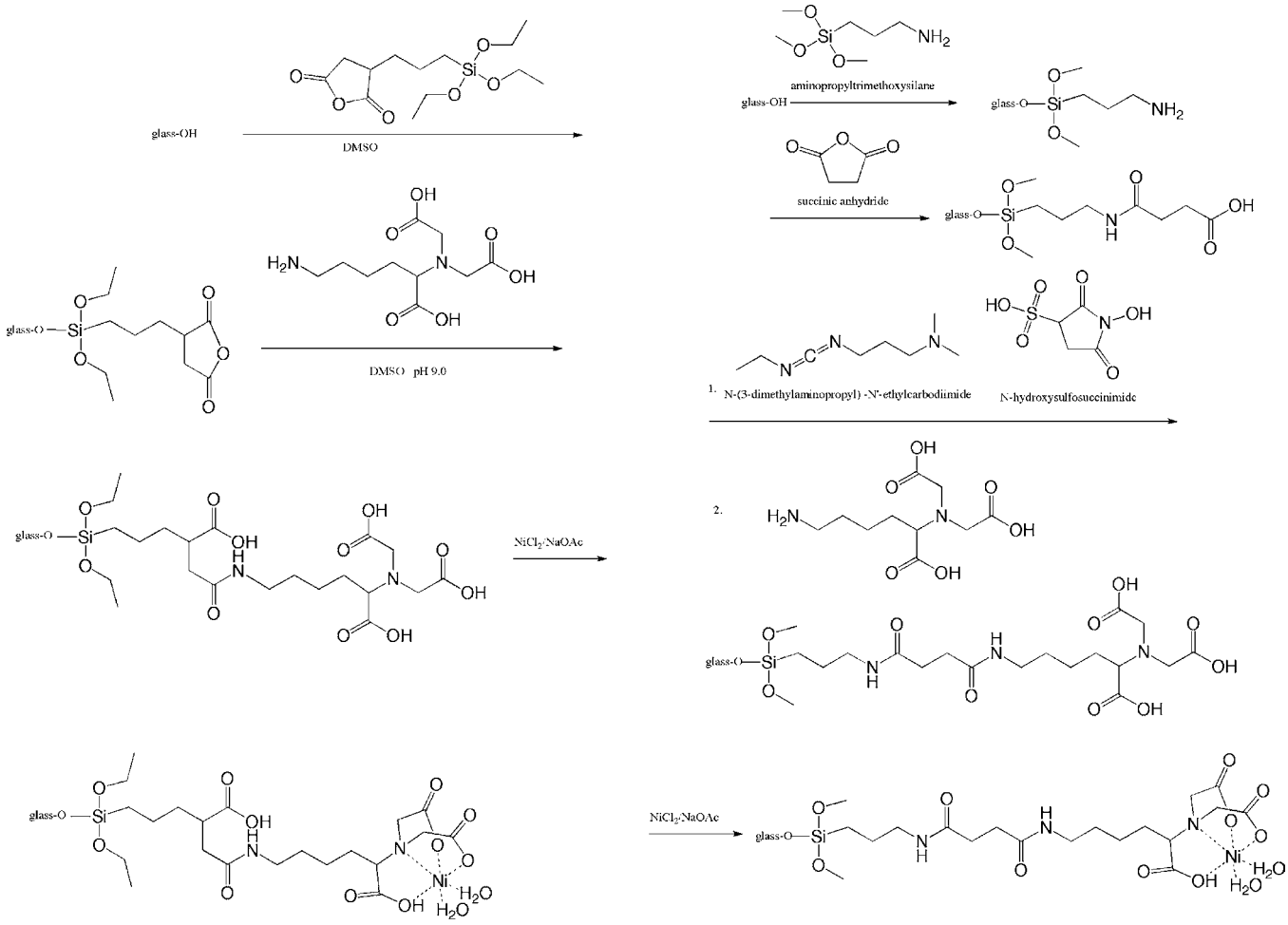

Figure 1. Scheme of NTA-Ni(II) glass plate surface activation. (A) a two-step method including glass surface activation using silylation with 3-(triethoxysilyl) propylsuccinic anhydride (TPSA) followed by coupling of N_α,N_α-bis(carboxymethyl)-L-lysine hydrate (BCML); (B) a multistep synthesis requiring aminosilylation using 3-aminopropyltriethoxylsilane (APTS) with subsequent acylation with succinic anhydride and coupling of BCML in the presence of water-soluble carbodiimide and sulfosuccinimide.

nm ("800 channel" fluorescence band) and reflecting below 750 nm ("700 channel"fluorescence band). Fluorescence signals were processed to filter scattered and stray light. The obtained images (16 bit TIFF) were analyzed, colorized, and fused using *ImageJ 1.38* (NIH).

The standard for measurements in 800 channels was prepared by loading the plate with different concentrations of 800 channel control duplex. FRET duplex was also measured to calculate FRET efficiency.

Statistical Analysis. All experiments were performed in triplicate. Values were expressed as the mean ± the standard deviation (SD) and compared using double-tailed unpaired *t* test with Welch's correction (Prism 4.0, GraphPad).

RESULTS AND DISCUSSION

Preparation and Testing of NTA Glass Plates. We initially compared two strategies of carboxyl group linking to the surface of the glass plates: (1) silylation with 3-(triethoxysilyl) propylsuccinic anhydride and reacting the obtained anhydride group with *N*α,*N*α-bis(carboxymethyl)-L-lysine (Figure 1A); (2) a multistep synthesis requiring aminosilylation using 3-aminopropyltriethoxylsilane (APTS), reacting the glass-linked amino groups with succinic anhydride, and, finally, activating the coupled carboxyls by using water-soluble carbodiimide before adding BCML (Figure 1B). To determine the amounts of amino groups and carboxyl groups on the surface of the plates, we used TNBS as amino group test reagent and measured absorbance of the mixture at 420 nm (*11*).

We used ethylene diamine coupling to either anhydride (first two-step method, Figure 1A) or to EDC/Sulfo-NHS activated carboxyls (Figure 2B) for comparing the efficacy of plate surface modification. By reacting anhydride residues with diamine and treating the conjugated amino groups with TNBS, we showed that at least 60 nmol of reactive carboxyl groups were linked to the surface of each well of a 96-well plate as a result of sylilation with TPSA. In contrast, the multistep approach resulted in 2× less amino groups linked to each well. The multistep conjugation strategy has potential advantages allowing conjugation via longer linker between the glass and chelating group and the absence of additional carboxyl groups in the linker moiety that can potentially weakly bind Ni^{2+} cations. However, the advantage of the first method was in simplicity due to a two-step activation and the higher number of reactive groups linked to the glass. Since the first strategy resulted in 2× more reactive carboxyl groups/well, we used the two-step glass modification approach in the further experiments.

To obtain glass-immobilized quadridentate NTA-Ni(II) chelate and to reduce nonspecific binding, the plate was first blocked with BSA followed by nickel chelation with glass-conjugated NTA groups. To test whether the obtained NTA-Ni(II) plate has 6 × His-tag binding affinity, we labeled NF-κB p50 directly with IRDye800CW fluorochrome and compared binding of labeled protein with the free dye (Figure 2A). No free IRDye800CW binding to the plate was detected, whereas the 800CW-labeled NF-κB p50 showed binding that was directly proportional to the added protein concentration. As shown in

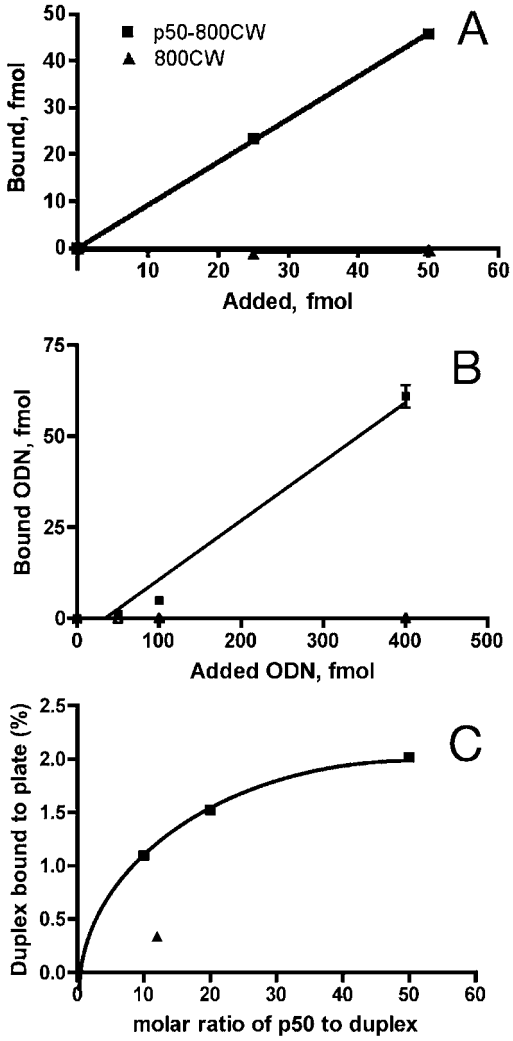

Figure 2. Testing NTA-Ni(II) plate in binding assays. (A) p50 binding to NTA-Ni(II) plate. NF-κB p50 labeled with IRDye800CW (squares), IRDye800CW dye alone (triangles); (B) ODN1/800CW-ODN2 binding to NTA-Ni(II) plate either in the presence of p50 (squares) or in the absence of p50 (diamonds); (C) efficacy of p50−duplex binding to the NTA-Ni(II) plate (squares) at various p50−duplex molar ratios or to anti-p50 antibody-coated plate (triangle) at p50−duplex molar ratio of 12:1.

Figure 2A, in the range below 50 fmol (less than 1 nM p50 added) 90−95% 800CW-p50 was bound to the NTA-Ni plate.

NTA-Ni(II) Plate Binding Assay for Detecting ODN Reporter-p50 Interactions. We tested two types of p50-binding ODN duplexes: a reporter duplex Cy5.5−ODN1/800CW-ODN2 carrying a pair of FRET fluorochromes (Cy5.5, donor and 800CW, acceptor) on complementary strands, as well as non-FRET duplex ODN1/800CW-ODN2 as a standard. According to the results of EMSA, both duplex probes (i.e., reporter and control) were efficiently binding p50 (not shown). ODN duplex ODN1/800CW-ODN2 was initially chosen for testing the binding of ODN duplex probes in the NTA-Ni(II) plate binding assay, since fluorescent signal at 800 nm has a very high signal/background ratio (Figure 2B). ODN1/800CW-ODN2 duplex was first incubated with human recombinant His × 6-tagged p50 at various duplex/p50 molar ratios and then added to the wells of NTA-Ni(II) plates. The measured bound fluorescence values showed that approximately 1−2% of added duplex-p50 complex was bound to the NTA-Ni plate (Figure 2C, squares). Alternatively, ODN duplex−p50 complex (1:12 molar ratio) was captured on the plates using affinity-purified antibody. In contrast to the NTA-Ni(II) strategy, only 0.34% of added duplexes was bound to the plate surface reflecting random immobilization of antibody molecules on the plate and, consequently, a potentially lower density of p50 binding centers (Figure 2C, triangles).

Fluorescence measurements in glass plates demonstrated high sensitivity to the presence of ODN reporter. The limit of FRET ODN duplex reporter detection in solution was 5 pM when fluorescence was measured at 800 nm. To perform testing of ODN duplex probes in the developed NTA-Ni(II) plate binding assay, ODN duplexes (2.4 pmol, 8 nM) were first incubated with human recombinant p50 at the molar ratio of 1:12 at room temperature for 30 min. To test the specificity of p50−ODN duplex recovery from the solution, we added 0−8 nM ODN duplex to the NTA-Ni(II) plate, either in the presence or in the absence of p50 protein. After a 1 h incubation period followed by washings, we measured the fluorescence intensity associated with the plate using a two-channel imaging system (Figure 3A). For quantification of both free and bound duplex, the fluorescence intensity was measured in the 800 nm channel was excited at 785 nm, i.e., the fluorescence intensities of non-FRET duplex ODN1/800CW-ODN2 and FRET duplex Cy5.5−ODN1/800CW-ODN2 measured at 800 nm were treated as unaffected by FRET and plotted on the same scale (Figure 3B). Fluorescence intensities of both Cy5.5 and 800CW fluorochromes measured in the wells after adding FRET ODN duplex−p50 complex showed duplex concentration-dependent increase (Figure 3A,B), whereas free FRET ODN duplex showed no concentration-dependent association with the plate surface (see Figure 3A, upper row). To determine whether FRET efficiency in ODN duplex reporter complex was changing as a result of p50 binding, we performed measurements of fluorescence at 700 nm (donor fluorochrome) to 800 nm (acceptor fluorochrome) and calculated the resultant emission light intensity ratios. Measurements of fluorescence intensity at 800 nm enabled calculation of the duplex amount bound to the plate. By comparing ratiometric measurements performed in the case of free Cy5.5−ODN1/800CW-ODN2 duplex and Cy5.5−ODN1/800CW-ODN2-p50 complex bound to NTA-Ni(II) plate, we showed that in the low range of bound duplex amounts (less than 20 fmol/well) FRET ODN duplex reporter−p50 complex had higher Cy5.5/800CW ratio values than the free duplex (Figure 3C). The above result indicates that p50 partially interferes with the intraduplex FRET effect normally present in p50-free duplex reporter. However, at higher amounts of the duplex bound to the well (>60 fmol/well) we observed a loss of measurable ratiometric difference between duplex reporter−p50 complex bound to the plate and free duplex reporter alone (Figure 3C). This effect can be explained by Cy5.5 fluorochrome partial self-quenching at high local concentrations next to the plate surface (nonemitting FRET).

Therefore, we performed optimization steps for preparing NTA-Ni(II) linked glass plate and used the obtained plates for separating free ODN duplexes from a complex formed between the His × 6-tagged NF-κB p50 protein and fluorescent ODN duplex. This approach enabled reliable ratiometric measurements of FRET effects in ODN reporters bound to the plate surface. The alternative approaches would require coating of the plate with antitranscription factor antibodies or linking the duplexes to the surface as described in refs 5, 12. The antibody-coated plate showed a lower efficacy than the NTA-Ni(II) strategy. The use of covalent conjugation of fluorochrome-linked duplexes to the plate with the subsequent analysis of fluorescence changes after incubating with recombinant NF-κB proteins can be used as a potential alternative. The advantage is that the use of His-tagged proteins, which have a lower DNA-binding affinity (*13*), is not required. However, the latter strategy requires the use of additional linking of reporter ODNs to the glass, for

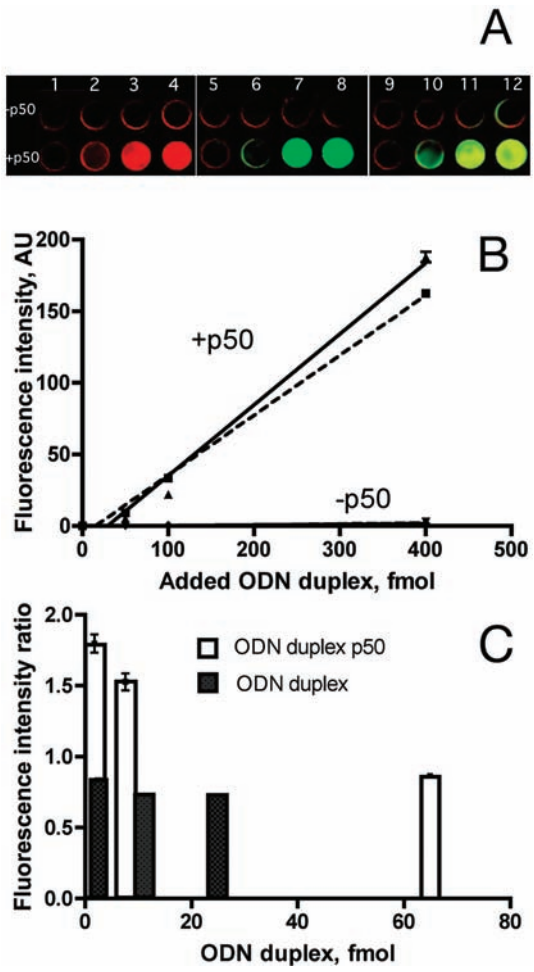

Figure 3. NTA-Ni(II) plate binding of two-fluorochrome labeled FRET reporter duplexes. (A) Dual channel fluorescence imaging of NTA-Ni(II) plate. The upper row, binding of FRET duplex Cy5.5-ODN1/800CW-ODN2 to the plate surface in the absence of p50; the lower row, binding of the FRET duplex to the plate after a complex formation with p50. Lanes 1−8 duplex amounts: lanes 1,5 − control, 0 fmol; lanes 2,6 − 100 fmol; lanes 3,7 − 200 fmol; lanes 4,8 − 400 fmol. Lanes 9−12 show an overlay of images acquired at 700 nm (red) and 800 nm (green). (B) ODN duplex reporters Cy5.5-ODN1/800CW-ODN2 binding to the NTA-Ni(II) plate in the absence or in the presence of p50 protein. Triangles (solid line), fluorescence intensity at 800 nm; squares (hatched line), fluorescence intensity at 700 nm. Results presented as mean ± SD ($n = 3$). (C) Ratiometric measurements (700 channel/800 channel fluorescence intensities) performed using NTA-Ni(II) plate bound Cy5.5-ODN1/800CW-ODN2 ODN duplex reporters in the absence (open bars, free duplex in solution) or in the presence of p50 protein (closed bars, p50-duplex complex bound to the plate).

example, via 3′- or 5′-dithio linkers (*14*), creating potential sterical hindrances for transcriptional factor binding. The assay proposed in our work was specifically designed to capture preformed transcription factor−duplex complexes and allowed selective measurement of FRET in the fraction of protein−ODN duplex complexes. The developed method will be used for optimizing duplex ODN reporter design for potential detection of functional NF-κB components in vitro and in vivo.

ACKNOWLEDGMENT

This work was supported in part by NIH R33 CA134385 technology development grant to A.B. We are grateful to Drs. Valeri Metelev (Department of Chemistry Moscow State University, Moscow, Russia) and David Tabatadze (Antisense Unit, Cancer Center, Massachusetts General Hospital, Charlestown, MA) for oligodeoxynucleotide synthesis and purification.

LITERATURE CITED

(1) Zhang, S., Metelev, V., Tabatadze, D., Zamecnik, P., Bogdanov, A., Jr. (2008) Near-infrared fluorescent oligodeoxyribonucleotide reporters for sensing NF-κB DNA interactions in vitro. *Oligonucleotides.*

(2) Zhang, S., Metelev, V., Tabatadze, D., Zamecnik, P. C., and Bogdanov, A., Jr. (2008) Fluorescence resonance energy transfer in near-infrared fluorescent oligonucleotide probes for detecting protein-DNA interactions. *Proc. Natl. Acad. Sci. U.S.A. 105,* 4156–61.

(3) Paborsky, L. R., Dunn, K. E., Gibbs, C. S., and Dougherty, J. P. (1996) A nickel chelate microtiter plate assay for six histidine-containing proteins. *Anal. Biochem. 234,* 60–5.

(4) Li, J. L., Chen, H., Li, M., Hua, D., Lu, Z., and Wang, J. (2007) An optimized assay for transcription factor NF-κB with dsDNA-coupled microplate. *Colloids Surf., B 55,* 31–7.

(5) Shen, Z., Peedikayil, J., Olson, G. K., Siebert, P. D., and Fang, Y. (2002) Multiple transcription factor profiling by enzyme-linked immunoassay. *Biotechniques 32,* 1168, 1170−2, 1174.

(6) Oehme, F., Jonghaus, W., Narouz-Ott, L., Huetter, J., and Flamme, I. (2004) A nonradioactive 96-well plate assay for the detection of hypoxia-inducible factor prolyl hydroxylase activity. *Anal. Biochem. 330,* 74–80.

(7) Hochuli, E., Dobeli, H., and Schacher, A. (1987) New metal chelate adsorbent selective for proteins and peptides containing neighbouring histidine residues. *J. Chromatogr. 411,* 177–84.

(8) Tabatadze, D., Zamecnik, P., Yanachkov, I., Wright, G., Pierson, K., Zhang, S., Bogdanov, A., Jr., and Metelev, V. (2008) A novel thymidine phosphoramidite synthon for incorporation of internucleoside phosphate linkers during automated oligodeoxynucleotide synthesis. *Nucleosides Nucleotides Nucleic Acids 27,* 157–72.

(9) Masuko, M. (2003) Hybridization of an immobilized PNA probe with its complementary oligodeoxyribonucleotide on the surface of silica glass. *Nucleic Acids Res. Suppl.* 145–6.

(10) Adessi, C., Matton, G., Ayala, G., Turcatti, G., Mermod, J. J., Mayer, P., and Kawashima, E. (2000) Solid phase DNA amplification: characterisation of primer attachment and amplification mechanisms. *Nucleic Acids Res. 34,* 322–33, 28, E87.

(11) Snyder, S. L., and Sobocinski, P. Z. (1975) An improved 2,4,6-trinitrobenzenesulfonic acid method for the determination of amines. *Anal. Biochem. 64,* 284–8.

(12) Wang, J., Li, M. L., Hua, D., and Chen, Q. (2006) Exonuclease-mediated ELISA-like assay for detecting DNA-binding activity of transcription factors: measurement of activated NF-κB. *Biotechniques 41,* 79–88, 90.

(13) Buning, H., Gartner, U., von Schack, D., Baeuerle, P. A., and Zorbas, H. (1996) The histidine tail of recombinant DNA binding proteins may influence the quality of interaction with DNA. *Anal. Biochem. 234,* 227–30.

(14) Metelev, V., Weissleder, R., and Bogdanov, A., Jr. (2004) Synthesis and properties of fluorescent NF-kappa B-recognizing hairpin oligodeoxyribonucleotide decoys. *Bioconjugate Chem 15,* 1481–7.

BC900137Y

Comb-Shaped Copolymers Composed of Hydroxypropyl Cellulose Backbones and Cationic Poly((2-dimethyl amino)ethyl methacrylate) Side Chains for Gene Delivery

F. J. Xu,*,† Y. Ping,‡ J. Ma,§ G. P. Tang,|| W. T. Yang,*,† J. Li,‡ E. T. Kang,⊥ and K. G. Neoh⊥

State Key Laboratory of Chemical Resource Engineering, College of Materials Science & Engineering, Beijing University of Chemical Technology, Beijing 100029, China, Division of Bioengineering, National University of Singapore, 7 Engineering Drive 1, 117574 Singapore, State Key Laboratory of Molecular Oncology, Cancer Institute & Hospital, Chinese Academy of Medical Sciences, Beijing 100021, China, Institute of Chemical Biology and Pharmaceutical Chemistry, Zhejiang University, Hangzhou, 310028, People's Republic of China, and Department of Chemical and Biomolecular Engineering, National University of Singapore, Kent Ridge, 119260 Singapore. Received January 30, 2009; Revised Manuscript Received July 10, 2009

Cationic polymers have been of interest and importance as nonviral gene delivery carriers. Herein, well-defined comb-shaped cationic copolymers (HPDs) composed of long biocompatible hydroxypropyl cellulose (or HPC) backbones and short poly((2-dimethyl amino)ethyl methacrylate) (or P(DMAEMA)) side chains were prepared as gene vectors via atom transfer radical polymerization (ATRP) from the bromoisobutyryl-terminated HPC biopolymers. The P(DMAEMA) side chains of HPDs can be further partially quaternized to produce the quaternary ammonium HPDs (QHPDs). HPDs and QHPDs were assessed in vitro for nonviral gene delivery. HPDs exhibit much lower cytotoxicity and better gene transfection yield than high-molecular-weight P(DMAEMA) homopolymers. QHPDs exhibit a stronger ability to complex pDNA, due to increased surface cationic charges. Thus, the approach to well-defined comb-shaped cationic copolymers provides a versatile means for tailoring the functional structure of nonviral gene vectors to meet the requirements of strong DNA-condensing ability and high transfection capability.

INTRODUCTION

Gene therapy shows much promise in tackling various genetic diseases and cancers, viral infection, and cardiovascular disorders (*1*−*3*). Successful gene therapy depends on the design of gene delivery vectors with low cytotoxicity and high transfection efficiency (*4, 5*). In comparison with viral vectors and cationic lipids, cationic polymers have been receiving considerable attention as the major type of nonviral gene delivery vectors, because of their low host immunogenicity, high flexibility, and easy preparation (*6, 7*). Polycations can spontaneously condense negatively charged DNA by electrostatic interaction into compact nanocomplexes and reduce the electrostatic repulsion between DNA and cell surfaces. Polycationic vectors can also protect plasmid DNA from enzymatic degradation by nucleases and facilitate cellular transfection. A great number of polycations, including polyethylenimine (PEI) (*8*), poly((2-dimethyl amino)ethyl methacrylate) (*6, 9, 10*), poly(L-lysine) (*11*), polyamidoamine (*12*), and polysaccharide-based cationic carriers (*5, 13*), have been reported to deliver nucleic acids. Among these cationic polymers, PEI with a molecular weight of 25 kDa is considered the gold standard for polymeric nonviral gene delivery due to its high transfection efficiency (*7*). However, most of them suffer from either low gene transfection efficiency or significant toxicity.

Natural polysaccharides are very suitable candidates for gene delivery, because they are renewable, nontoxic, biodegradable, and excellent biocompatible materials. Hydroxypropyl cellulose (HPC) is a derivative of natural polysaccharide cellulose with both water and organic solubility, where some of the hydroxyl groups of cellulose have been hydroxypropylated to form propylene oxide groups (*14*−*17*). HPC materials have been approved by the United States Food and Drug Administration (FDA) and widely used in food and drug formulations (*15, 18, 19*). Comb-shaped cationic copolymers have been of interest and importance as nonviral gene carriers (*4, 20*−*22*). The reactive hydroxyl groups on HPC can be used as initiation sites for forming side chains to produce the comb-like copolymers via living radical polymerizations (*16, 23*). In the present work, well-defined comb-shaped cationic copolymers (HPDs) of long, biocompatible HPC backbones and short poly((2-dimethyl amino)ethyl methacrylate) (P(DMAEMA)) side chains are prepared via atom transfer radical polymerization (ATRP) (*24*) from the bromoisobutyryl-terminated HPC (HPC-Br) backbones (Scheme 1). The P(DMAEMA) side chains can be further partially quaternized to produce the quaternary ammonium HPDs (QHPDs). HPDs and QHPDs can condense plasmid DNA (pDNA) into complex nanoparticles of 150 to 200 nm in size at nitrogen/phosphate (N/P) ratios of 5 or higher. In comparison with the long P(DMAEMA) homopolymer, HPDs show much lower cytotoxicity and higher gene transfection efficiency. QHPDs exhibit a stronger ability to complex pDNA, due to increased surface cationic charges. The novel HPDs and QHPDs may have potential application as nonviral gene vectors for future gene therapy.

EXPERIMENTAL PROCEDURES

Materials. Hydroxypropyl cellulose powder (HPC, Sigma-Aldrich cat #435007: M_n = 10 000 g/mol and M_w = 80 000

* To whom correspondence should be addressed. E-mail: xufj@mail.buct.edu.cn (Xu FJ), yangwt@mail.buct.edu.cn (Yang WT).
† Beijing University of Chemical Technology.
‡ Division of Bioengineering, National University of Singapore.
§ Chinese Academy of Medical Sciences.
|| Zhejiang University.
⊥ Department of Chemical and Biomolecular Engineering, National University of Singapore.

10.1021/bc900044h CCC: $40.75 © 2009 American Chemical Society
Published on Web 07/31/2009

Scheme 1. Schematic Diagram Illustrating the Preparation Processes of Cationic Comb-Shaped Copolymers Composed of HPC Backbones and Short Partially Quaternized P(DMAEMA) Side Chains

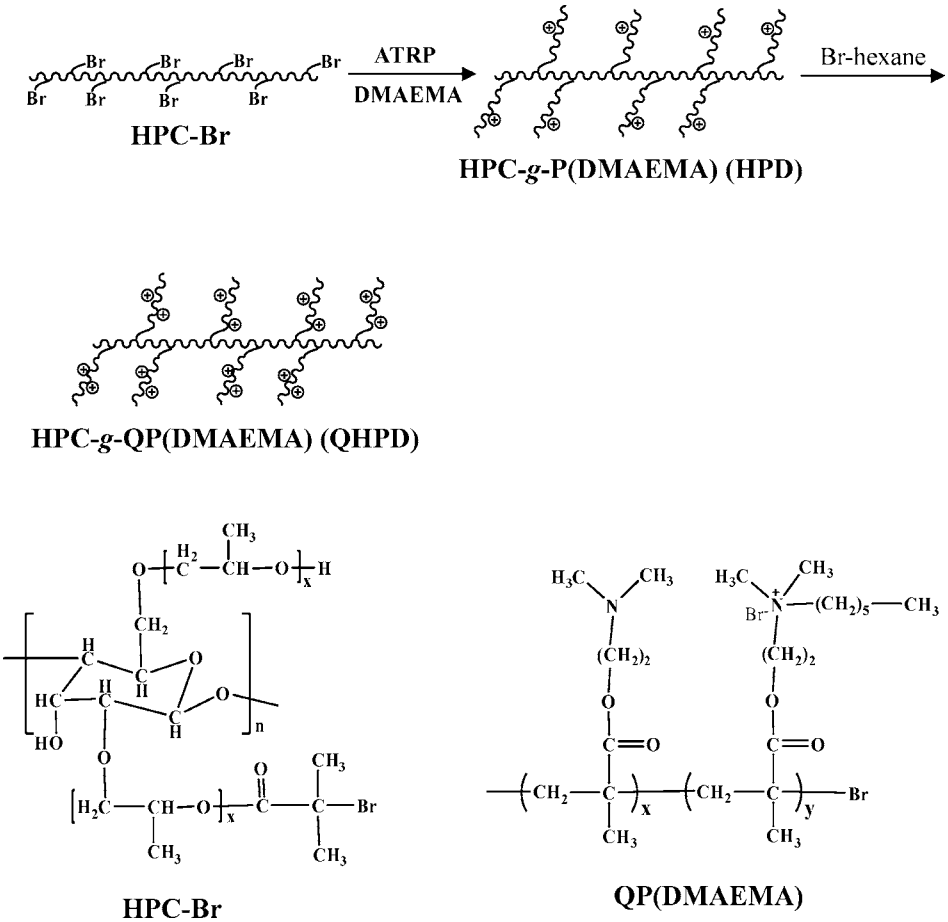

g/mol; from gel permeation chromatography (GPC) with THF as mobile phase: M_n = 28 015 g/mol and M_w = 64 655 g/mol; molar substitution of propylene oxide groups (MS) of about 3 per glucose unit *16, 17*), branched polyethylenimine (PEI, M_w ~25 000 Da), 1,4,7,10,10,-hexamethyl triethylenetetramine (HMTETA, 99%), copper(I) bromide (CuBr, 99%), 2-bromoisobutyryl bromide (BIBB, 98%), and (2-dimethylamino)ethyl methacrylate (DMAEMA, >98%) were obtained from Sigma-Aldrich Chemical Co., St. Louis, MO. DMAEMA was used after removal of the inhibitors in a ready-to-use disposable inhibitor-removal column (Sigma-Aldrich). 3-(4,5-Dimethylthiazol-2yl)-2,5-diphenyl tetrazolium bromide (MTT), penicillin, and streptomycin were purchased from Sigma Chemical Co., St. Louis, MO. HEK293 cell lines were purchased from the American type Culture Collection (ATCC, Rockville, MD). The control P(DMAEMA) homopolymer with about 180 repeat units of DMAEMA was prepared via ATRP, using the reported ethylene glycol di-2-bromoisobutyrate as the initiator (*24*).

Synthesis of Comb-Shaped Cationic Copolymers via ATRP. The starting bromoisobutyryl-terminated HPC (HPC-Br) was synthesized following the procedures. About 2.0 g of HPC was dissolved completely in 100 mL of anhydrous methylene chloride with stirring and then kept in an ice bath. About 0.3 mL of BIBB in 5 mL of methylene chloride was added dropwise into the flask through an equalizing funnel for a period of 10 min at 0 °C. After this addition, the flask was sealed. The reaction was allowed to proceed at room temperature for another 5 h to produce the HPC-Br macroinitiator. The final reaction mixture was precipitated with 1000 mL of diethyl ether. The crude polymer was purified by reprecipitation thrice in diethyl ether. Finally, the HPC-Br for the subsequent ATRP was dried under reduced pressure.

The HPC-*g*-P(DMAEMA) comb-like polymers (HPDs, Scheme 1) were synthesized using a molar feed ratio (DMAEMA (about 1 mL))/(CuBr)/(HMTETA) of 60:1:1.2 at room temperature in 8 mL of isopropanol/water (20/1, v/v) containing 0.2 g of HPC-Br. The reaction was performed in a 25 mL flask equipped with a magnetic stirrer and under the typical conditions for ATRP (*24*). DMAEMA, HPC-Br, and HMTETA were introduced into the flask containing 8 mL of isopropanol/water (20/1, v/v). After HPC-Br had dissolved completely, the reaction mixture was degassed by bubbling argon for 30 min. Then, CuBr was added into the mixture under an argon atmosphere. The reaction mixture was purged with argon for another 10 min. The flask was then sealed with a rubber stopper under an argon atmosphere. The polymerization was allowed to proceed under continuous stirring at room temperature for 2 to 8 h. The reaction was stopped by diluting with THF. The catalyst complex was removed by passing the blue dilute polymer solution through a short aluminum oxide column. A colorless solution was obtained. After removal of THF in a rotary evaporator, the HPDs were precipitated in excess *n*-hexane. The crude polymer was purified by reprecipitation twice in hexane to remove the reactant residues, prior to being dried under reduced pressure. The HPD1 (from ATRP time of 2 h) and HPD2 (from ATRP time of 8 h) yields are about 0.4 and 0.72 g, respectively. The HPC-*g*-QP(DMAEMA) (QHPDs) with partially quaternized P(DMAEMA) side chains were prepared at 50 °C for 24 h in 5 mL of THF containing 0.4 g of HPD2 and 200 or 400 μL of 1-bromohexane. The QHPDs were precipitated in excess *n*-hexane and dried under reduced pressure.

Polymer Characterization. The molecular weights of polymers were determined by gel permeation chromatography (GPC), chemical composition by X-ray photoelectron spectroscopy (XPS), and chemical structure by nuclear magnetic resonance (NMR) spectroscopy. GPC measurements were performed on a Waters GPC system equipped with Waters Styragel columns, a Waters-2487 dual wavelength (λ) UV detector, and a Waters-2414 refractive index detector. THF containing 2 vol % triethylamine was used as the eluent at a low flow rate of 1.0 mL/min. Monodispersed polystyrene standards were used to generate the calibration curve. The XPS measurements were performed on a Kratos AXIS HSi spectrometer equipped with a monochromatized Al Kα X-ray source (1486.6 eV photons), using the same procedures as those described earlier (*24*).^{1}H NMR spectra were measured by accumulation of 1000 scans at a relaxation time of 2 s on a Bruker ARX 300 MHz spectrometer, using $CDCl_3$ or D_2O as the solvent.

Characterization of Polymer/Plasmid DNA Complexes. The plasmid (encoding *Renilla* luciferase) used in this work was pRL-CMV (Promega Co., Cergy Pontoise, France), which was cloned originally from the marine organism *Renilla reniformis*. The plasmid DNA (pDNA) was amplified in *Escherichia coli* and purified according to the supplier's protocol (Qiagen GmbH, Hilden, Germany). The purity and concentration of the purified DNA were determined by absorption at 260 and 280 nm and by agarose gel electrophoresis (*9*). The purified pDNA was resuspended in tris-EDTA (TE) buffer and kept in aliquots of 0.5 mg/mL in concentration. All polymer stock solutions were prepared at a nitrogen concentration of 10 mM in distilled water. Solutions were filtered via sterile membranes (0.2 μm) of average pore size and stored at 4 °C. Comb-like polymers to DNA ratios are expressed as molar ratios of nitrogen (N) in the HPDs and QHPDs to phosphate (P) in DNA (or as N/P ratios). The average mass weight of 325 per phosphate group of DNA was assumed (*8*). All polymer/pDNA complexes were formed by mixing equal volumes of polymer and pDNA solutions to achieve the desired N/P ratio. Each mixture was vortexed and incubated for 30 min at room temperature.

Each cationic polymer was examined for its ability to bind pDNA through agarose gel electrophoresis using the similar procedures as those described earlier (*9*). The polymer/pDNA complexes at various N/P ratios were investigated. Gel electrophoresis was carried out in TAE running buffer (40 mM Tris-acetate, 1 mM EDTA) with a voltage of 110 V for 30 min in a Sub-Cell system (Bio-Rad Lab, Hercules, CA). DNA bands were visualized and photographed by a UV transilluminator and BioDco-It imaging system (UVP Inc., Upland, CA). The particle sizes and zeta potentials of the polymer/pDNA complexes were measured using a Zetasizer Nano ZS (Malvern Instruments, Southborough, MA) and procedures similar to those described earlier (*9*). The polymer/pDNA complexes were also observed with a field-emission scanning electron microscope equipped with a scanning transmission electron microscopy (STEM) detector (JEOL JSM-6700F) and procedures similar to those described earlier (*9*). The complexes were visualized by transmitted electrons (STEM-in-SEM mode) at a low voltage of 15 kV, in comparison to about 200 kV for the conventional TEM. Such low voltage can minimize damage to the polymer/pDNA complex and allow visualization of the complex in the TEM mode at high spatial resolution.

Cell Viability and in Vitro Transfection Assay. The cytotoxicity of the comb-like polymers was evaluated using the MTT assay in HEK293 cell lines. They were cultured in Dulbecco's modified eagle medium (DMEM), supplemented with 10% heat-inactivated fetal bovine serum (FBS), 100 units/mL of penicillin, and 100 μg/mL of streptomycin at 37 °C, under 5% CO_2 and 95% relative humidity atmosphere. The cells were seeded in a 96-well microtiter plate at a density of 10^4 cells/well and incubated in 100 μL of DMEM/well for 24 h. The culture media were replaced with fresh culture media containing serial dilutions of polymers, and the cells were incubated for 24 h. Then, 10 μL of sterile-filtered MTT stock solution in PBS (5 mg/mL) was added to each well, reaching a final MTT concentration of 0.5 mg/mL. After 5 h, the unreacted dye was removed by aspiration. The produced formazan crystals were dissolved in DMSO (100 μL/well). The absorbance was measured using a microplate reader (Spectra Plus, Tecan, Zurich, Switzerland) at a wavelength of 570 nm. The cell viability (%) relative to control cells cultured in media without polymers was calculated from $(A)_{test}/(A)_{control} \times 100\%$, where $(A)_{test}$ and $(A)_{control}$ are the absorbance values of the wells (with the polymers) and control wells (without the polymers), respectively. For each sample, the final absorbance was the average of those measured from six wells in parallel.

Transfection assays were performed using plasmid pRL-CMV as the reporter gene in HEK293 cell lines. In brief, the cells were seeded in 24-well plates at a density of 5×10^4 cells in the 500 μL of medium/well and incubated for 24 h. The comb-shaped polymer/pDNA complexes (20 μL/well containing 1.0 μg of pDNA) at various N/P ratios from 7 to 22 were prepared by adding the polymer into the DNA solutions, followed by vortexing and incubation for 30 min at room temperature. At the time of transfection, the medium in each well was replaced with 300 μL of serum-free medium or fresh normal medium (supplemented with 10% FBS). The complexes were added into the transfection medium and incubated with the cells for 4 h under standard incubator conditions. Then, the medium was replaced with 500 μL of the fresh normal medium (supplemented with 10% FBS). The cells were further incubated for an additional 20 h under the same conditions, resulting in a total transfection time of 24 h. The cultured cells were washed with PBS twice and lysed in 100 μL of the cell culture lysis reagent (Promega Co., Cergy Pontoise, France) using the similar procedures as those described earlier (*9*). Luciferase gene expression was quantified using a commercial kit (Promega Co., Cergy Pontoise, France) and a luminometer (Berthold Lumat LB 9507, Berthold Technologies GmbH. KG, Bad Wildbad, Germany). Protein concentration in the cell samples was analyzed using a bicinchoninic acid assay (Biorad Lab, Hercules, CA). Gene expression results were expressed as relative light units (RLUs) per milligram of cell protein lysate (RLU/mg protein).

Statistical Analysis. All experiments were repeated at least three times. The data were collected in triplicate and expressed as mean $\pm$ standard deviation. Error bars represent the standard deviation. The statistical assay was performed using *t*-test, and the differences were considered statistically significant with $p < 0.05$.

RESULTS AND DISCUSSION

Synthesis and Characterization of Comb-Shaped Cationic Copolymers Composed of HPC Backbones and P(DMAEMA) Side Chains. The preparation of functional polymers is usually carried out in organic solvent. Because of its unique characterisitcs of both water and organic solubility, HPC is an ideal substrate for developing novel polysaccharide biopolymer-based cationic carriers. The molecular weight (M_n) of the HPC used in this work from gel permeation chromatography (GPC) is about 2.80×10^4 g/mol, and its corresponding polydispersity index (PDI) is about 2.3. The C 1s core-level X-ray photoelectron spectrum (XPS) (Figure 1a) of the pristine HPC can be curve-fitted by three peak components with binding energies (BEs) at about 284.6, 286.2, and 287.6 eV, attributable to the

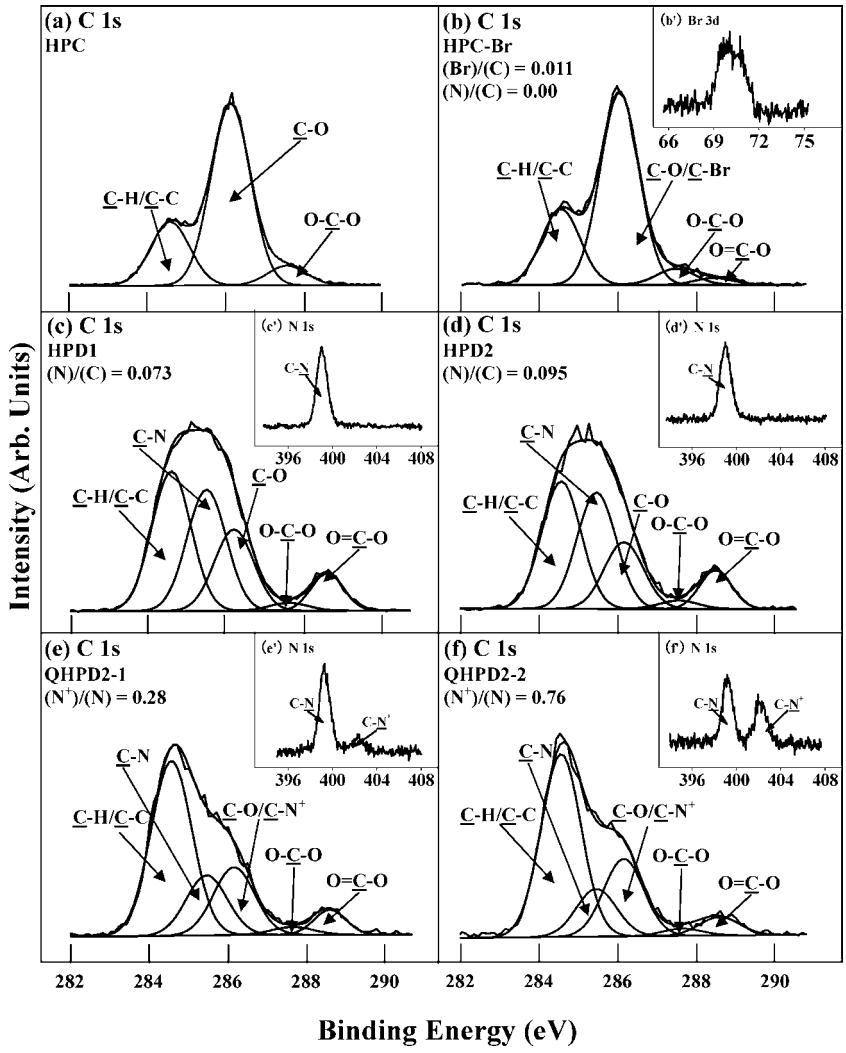

Figure 1. XPS C 1s core-level spectra of (a) HPC, (b) HPC-Br, (c) HPD1, (d) HPD2, (e) QHPD2−1, and (f) QHPD2−2, Br 3d core-level spectrum of (b′) HPC-Br, and N 1s core-level spectra of (c′) HPD1, (d′) HPD2, (e′) QHPD2−1, and (f′) QHPD2−2.

C-H/C-C, C-O, and O-C-O species, respectively (*9*, *24*). From the (C-O)/(O-C-O) ratio of 11, the average number of propylene oxide groups ($-OCH_2CH(OH)CH_3$) per anhydroglucose unit of HPC is about 3, consistent with that (2.9) determined using ^{1}H NMR (*16*, *17*).

In order to prepare comb-shaped copolymers using HPC as a backbone via ATRP, it is essential to introduce alkyl halide into HPC. In this work, the bromoisobutyryl-terminated HPC (HPC-Br) was prepared via the reaction of hydroxyl groups of HPC with 2-bromoisobutyryl bromide (BIBB) (Scheme 1). When ATRP is carried out from a multifunctional backbone with a high local concentration of initiation sites, the radical−radical coupling of the propagating chains will occur and result in a gel. In order to avoid potential gelation and introduce some flexibility onto the comb-like cationic copolymers, the starting HPC-Br with moderate initiation sites is desired for preparing well-defined comb-shaped copolymers. The C 1s core-level XPS spectrum (Figure 1b) of HPC-Br can be curve-fitted by four peak components with BEs at about 284.6, 286.2, 287.6, and 288.4 eV, attributable to the C-H/C-C, C-O/C-Br, O-C-O, and O=C-O species, respectively (*9*, *24*). The new O-C=O peak component is associated with the bromide-capped ester groups of HPC-Br. The corresponding Br 3d core-level spectrum is shown in Figure 1b′. From the (Br)/(C) ratio of 0.011 (determined from the sensitivity factor-corrected Br 3d and C 1s core-level spectral area ratio), it was calculated that about six glucose units of HPC-Br possess one ATRP initiation site. The chemical structure of HPC-Br is also characterized by ^{1}H NMR spectroscopy (Figure 2a). The chemical shift at $\delta = 1.12$ ppm is attributable to the methyl protons of propylene oxide groups (***a***, CH_3). The chemical shift at $\delta = 1.92$ ppm is associated with the methyl protons (***b***, C(Br)-CH_3) of the 2-bromoisobutyryl groups (*24*). The broad chemical shifts in the wide region 2.9−4.3 ppm are mainly associated with the inner methylidyne and methylene protons (***c***, ***c′***, CH and CH_2) on glucose units and propylene oxide groups. From the area ratio of peak ***a*** and peak ***b***, the initiator density of HPC-Br is that every 6.8 glucose units possess one initiation site, fairly consistent with that determined by XPS.

Well-defined comb-shaped copolymers (HPDs) of HPC and P(DMAEMA), or HPC-*g*-P(DMAEMA), were subsequently synthesized via ATRP of DMAEMA from HPC-Br (Scheme 1). The HPDs with different lengths of P(DMAEMA) side chains can be synthesized by varying the ATRP time. Table 1 summarizes the GPC results of HPD1 (from 2 h of ATRP) and HPD2 (from 8 h of ATRP). With the increase in reaction time from 2 to 8 h, the M_n of HPD from GPC using linear polystyrene standards increases from 5.42×10^4 to 8.86×10^4 g/mol, and the total number of DMAEMA repeat units per side chain increases accordingly from 13 to 30. These values are lower than those determined by XPS and ^{1}H NMR (Table 1), probably due to the differences in hydrodynamic volumes between comb-like and linear polymers. In addition, the PDIs of HPDs are comparable to that of the pristine HPC, indicating that the ATRP

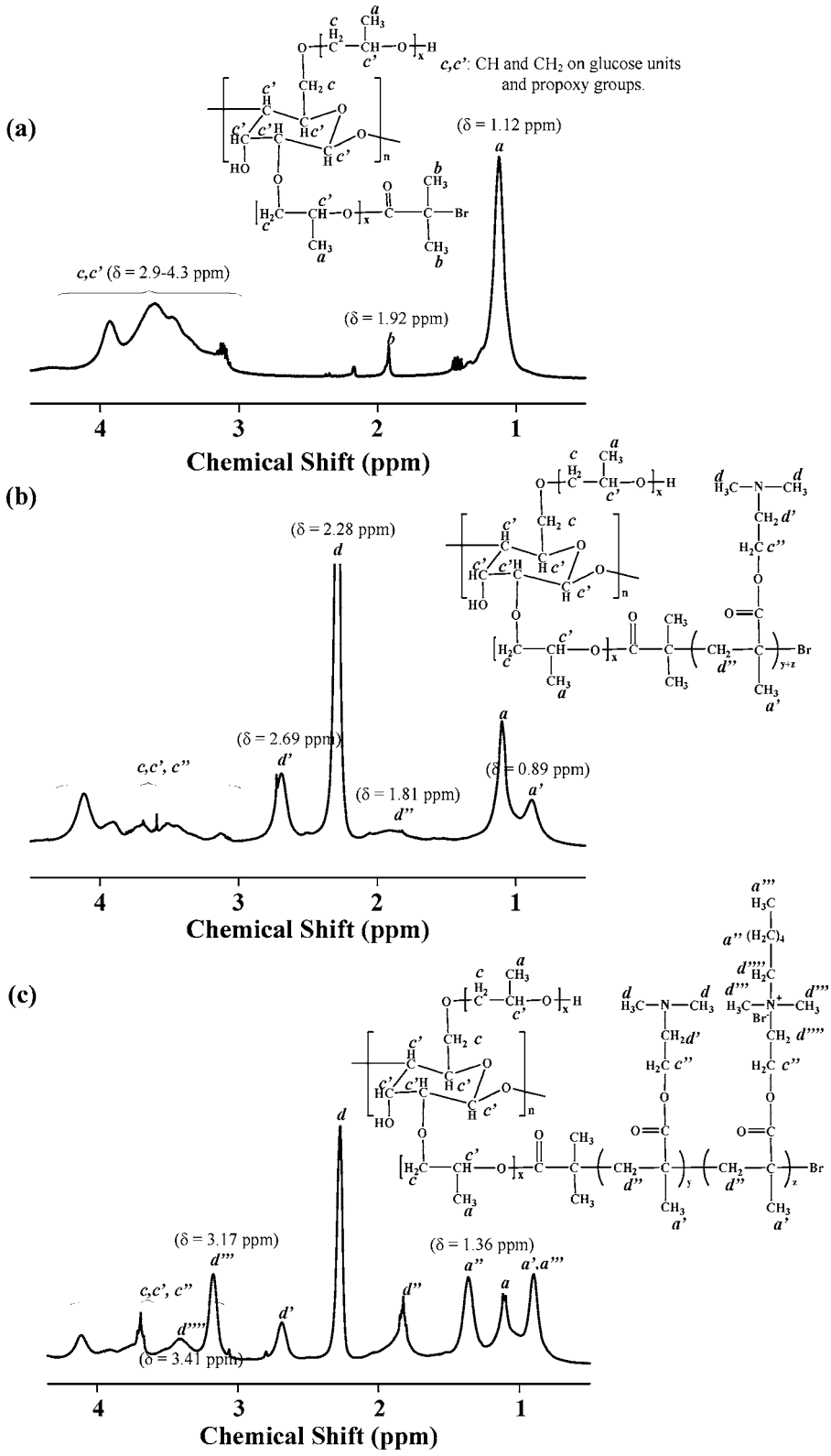

Figure 2. 300 MHz ^{1}H NMR spectra of the (a) HPC-Br, (b) HPD2, and (c) QHPD2−1 polymers.

of DMAEMA is well-controlled. In order to increase the surface cationic charges, the P(DMAEMA) side chains of HPD can be partially quaternized to produce the HPC-*g*-QP(DMAEMA) (QHPD) with quaternary ammonium groups. In this work, the QHPD2−1 and QHPD2−2 with different quaternization contents were prepared by using HPD2 and 1-bromohexane (Scheme 1 and Table 1).

The C 1s core-level spectra of HPD1 and HPD2 (Figure 1c and d) can be curve-fitted into five peak components with BEs of about 284.6, 285.5, 286.2, 287.6, and 288.4 eV, attributable to the C-H/C-C, C-N, C-O, O-C-O, and O=C-O species, respectively. The C-N peak is associated with the P(DMAEMA) side chains. In comparison with the C 1s core-level spectrum (Figure 1b) of HPC-Br, the increase (and decrease) in intensities of the C-N (and C-O) species with ATRP time is consistent with the increase in P(DMAEMA) contents. The corresponding N 1s core-level spectra of HPD1 and HPD2 are shown in Figure 1c′ and d′, respectively. From the (N)/(C) ratios determined by

Table 1. Characterization of the Comb-Shaped Cationic Polymers

sample	reaction time (h)	M_n (g/mol)[c]	PDI[c]	(N)/(C)[d]	$(N^+)/(N)+(N^+)$[d]	DMAEMA repeat units (per side chain)		
HPC	–	2.80×10^4	2.3	–	–		–	
HPC-*g*-P(DMAEMA)1 or HPD1[a]	2	5.42×10^4	2.2	0.073	–	13[e]	16[f]	15[g]
HPC-*g*-P(DMAEMA)2 or HPD2[a]	8	8.86×10^4	1.8	0.095	–	30[e]	35[f]	37[g]
HPC-*g*-QP(DMAEMA)2−1 or QHPD2−1[b]	24	–	–	–	0.22		–	
HPC-*g*-QP(DMAEMA)2−2 or QHPD2−2[b]	24	–	–	–	0.43		–	

[a] Synthesized using a molar feed ratio (DMAEMA (1 mL)):(CuBr):(HMTETA) of 60:1:1:1.2 at room temperature in 8 mL of isopropanol/water (20/1, v/v) containing 0.2 g of HPC-Br. The calculated molecular format of glucose units of HPC is $C_{15}H_{28}O_8$, and about six glucose units of HPC-Br possess one initiation site. [b] Synthesized at 50 °C in 5 mL of THF containing 0.4 g of HPD2 and 200 (for QHPD2−1) or 400 μL (for QHPD2−2) of 1-bromohexane. [c] Determined from GPC results. PDI = Weight average molecular weight/Number average molecular weight, or M_w/M_n. [d] Determined from XPS. [e] Determined from M_n and the molecular weights of DMAEMA (157 g/mol). [f] Determined from (N)/(C) ratio, where $(N)/(C) \approx n_{(DMAEMA)}/((6 \times 15 + 4) + 8n_{(DMAEMA)})$. [g] Determined from the ^{1}H NMR spectroscopy data.

XPS, the P(DMAEMA) contents of HPDs can be calculated (Table 1). After quaternization, the C 1s core-level spectra of QHPD2−1 and QHPD2−2 (Figure 1e and f) can be curve-fitted into five peak components with BEs at about 284.6, 285.5, 286.2, 287.6, and 288.4 eV, attributable to the C-H/C-C, C-N, C-O/C-N^+, O-C-O, and O=C-O species, respectively (*25*). In comparison with the C 1s core-level spectrum (Figure 1d) of the starting HPD2, the increase in intensities of the C-H/C−C and C-O/C-N^+ species of QHPD2−1 and QHPD2−2 indicates that the P(DMAEMA) side chains have been successfully quaternized by 1-bromhexane. In comparison with the monopeak component of the N 1s core-level spectrum (Figure 1d′) of HPD2, the N 1s core-level spectra (Figure 1e′ and f′) of QHPD2−1 and QHPD2−2 can be curve-fitted into two peak components with BEs at about 399 and 402 eV, attributable to the amino (C-N) and positively charged nitrogen (C-N^+) species, respectively (*25*). The quaternization extent of P(DMAEMA) side chains can be expressed as the $(N^+)/((N) + (N^+))$ ratio (determined from the corresponding N^+ peak component and total nitrogen spectral area ratio). The average $(N^+)/((N) + (N^+))$ ratios for QHPD2−1 and QHPD2−2 are about 0.22 and 0.43, respectively (Table 1), indicating that about 1 out of every 4.5 (for QHPD2−1) or 2.3 (for QHPD2−2) DMAEMA repeat units had been quaternized.

Figure 2b and c shows the respective ^{1}H NMR spectra of HPD2 and QHPD2−1 in D_2O. The typical chemical shifts at about 0.89, 1.81, 2.28, and 2.69 ppm are mainly attributable to the (***a′***) C-CH_3 methyl, (***d″***) C-CH_2 methylene, (***d***) N-CH_3 methyl, and (***d′***) N-CH_2 methylene protons of the P(DMAEMA) side chains, respectively. The chemical shift associated with the methylene protons adjacent to the oxygen moieties of the ester linkages (***c″***, CH_2−O−C=O) overlapped completely with glucose peaks of HPC. The signal intensities associated with the HPC backbone (***a***, ***c***, ***c″***) have decreased substantially. From the area ratio of peaks ***d***, ***d′***, ***d″*** and peaks ***a***, ***a′***, the P(DMAEMA) contents of HPDs can be calculated, and the results are comparable to those obtained from XPS (Table 1). After quaternization, the new signals at about 3.17 and 3.41 ppm are attributable to the (***d‴***) N^+-CH_3 methyl and (***d⁗***) N^+-CH_2 methylene protons of the quaternized P(DMAEMA) side chains, respectively (*26*). The chemical shift at about 1.36 ppm corresponds to the methylene protons of hexane (***a″***, CH_2-C). Due to the serious overlaps in the characteristic shifts of the components, it is very difficult to quantify the P(DMAEMA) and QP(DMAEMA) segments by ^{1}H NMR.

Polymer/Plasmid DNA Complexes. For cellular transfection, DNA has to be first condensed by cationic polymers into polymer/plasmid nanoparticles suitable for cellular entry. Thus, the DNA condensation capability is a prerequisite for polymeric gene vectors. In this work, the ability of the comb-shaped cationic copolymers to condense plasmid DNA (pDNA) into particulate structures was confirmed by agarose gel electrophoresis, particle size, and zeta potential measurements, as well as STEM imaging. Figure 3 shows the gel retardation results

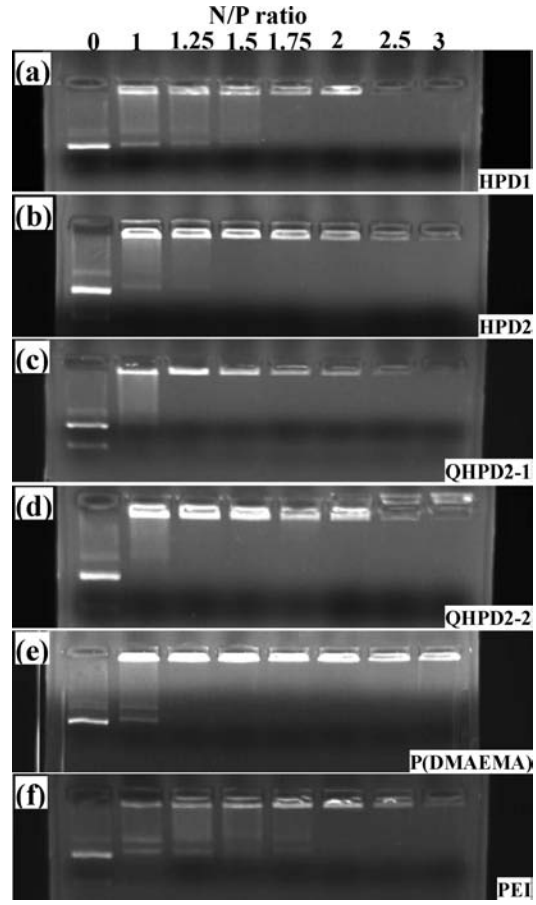

Figure 3. Electrophoretic mobility of plasmid DNA (pDNA) in the complexes of the cationic polymers ((a) HPD1, (b) HPD2, (c) QHPD2−1, (d) QHPD2−1, (e) P(DMAEMA), and (f) PEI at various N/P ratios.

of the cationic comb copolymer (HPD1, HPD2, QHPD2−1, and QHPD2−2)/pDNA complexes with increasing nitrogen (N)/phosphate (P) (or N/P) ratios, in comparison with those of the P(DMAEMA) homepolymer (with about 180 DMAEMA repeat units)/pDNA and branched PEI (25 kDa)/pDNA complexes. HPD1 and HPD2 can compact pDNA effectively at N/P ratios of 1.75 and 1.5, respectively, due to the increasing density of amino groups in the comb-like copolymers (Table 1). The migration of pDNA was completely retarded by QHPD2−1 or QHPD2−2 at an N/P ratio of 1.25, indicating that the increased surface cationic charges from quaternization could enhance the condensation capability of the comb copolymers. The control P(DMAEMA) and PEI could inhibit the migration of pDNA at N/P ratios of 1.25 and 2.0, respectively, indicating that the prepared comb copolymers have good condensation capability.

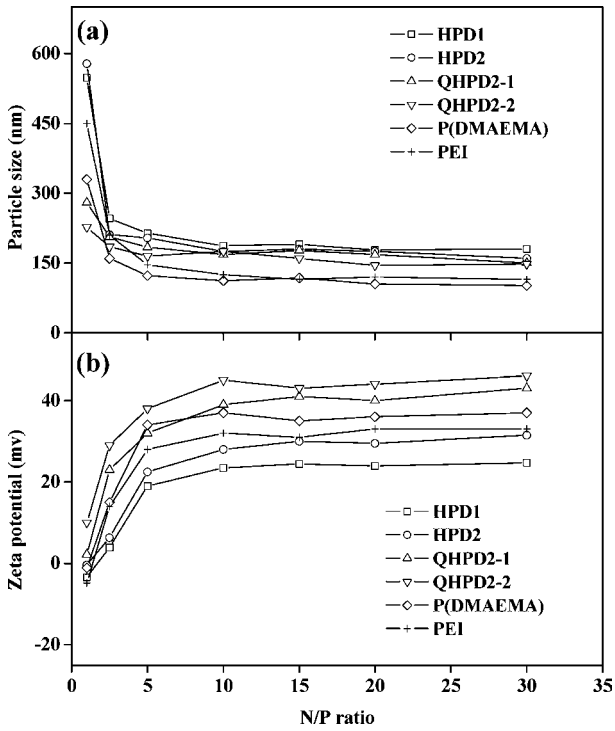

Figure 4. Particle size (a) and zeta potential (b) of the complexes between the cationic polymers (HPD1, HPD2, QHPD2−1, QHPD2−2, P(DMAEMA), and PEI) and pDNA at various N/P ratios.

The (a) particle size and (b) zeta potential of the cationic polymer (HPD1, HPD2, QHPD2−1, and QHPD2−2)/pDNA complexes are compared to those of the P(DMAEMA)/pDNA and PEI/pDNA complexes at various N/P ratios in Figure 4. All the cationic comb copolymers can efficiently compact pDNA into nanoparticles. Generally, the hydrodynamic sizes of the complexes decrease with increasing N/P ratios. After reaching the N/P ratio of 5, all the comb copolymers can condense pDNA into nanoparticles of 150 to 200 nm diameter. The polymer/pDNA complex within this size range can readily undergo endocytosis (*27*). Zeta potential is an indicator of surface charges on the polymer/pDNA naoparticles. A positively charged surface allows electrostatic interaction with negatively charged cell surfaces and facilitates cellular uptake. For the pDNA complexes of HPD1, HPD2, QHPD2−1, QHPD2−2, P(DMAEMA), and PEI, the net surface charge increases dramatically as the N/P ratio increases from 1 to 5, and stabilizes at N/P ratios of 10 and above (Figure 4b). After reaching the N/P ratio of 10, the zeta potentials of the pDNA complexes of all the cationic polymers are strongly positive. Due to the increasing quaternization of the P(DMAEMA) side chains, the pDNA complexes of HPD2, QHPD2−1, and QHPD2−2 show increasing surface cationic charges, indicating that they will produce increasing affinity for anionic cell surfaces. On the other hand, the excess cationic polymers probably do not exert any significant effect on the particle size and zeta potential of the complexes (Figure 4). In addition, the observed N/P ratios for completely retarding the migration of pDNA in the agarose gel electrophoresis (Figure 3) represented the starting points where the polymer/pDNA complexes become positively charged. At such N/P ratios, pDNA cannot be packed tightly. With increasing N/P ratios, the hydrodynamic sizes (or net surface charges) of the complexes decrease (or increase) and stabilize at higher N/P ratios (Figure 4). Therefore, the results from electrophoresis are consistent with those from Figure 4.

Figure 5 shows the representative STEM images of the (a) HPD2/pDNA (at a N/P ratio of 1), (b) HPD2/pDNA (at a N/P ratio of 15), and (c) QHPD2−1/pDNA (at a N/P ratio of 15) complexes. The FESEM equipped with a STEM detector allows the visualization of polymer complexes in the TEM mode at a low voltage of 15 kV to avoid destruction of the polymer/pDNA complex. The images clearly reveal the morphological difference between the polymer/pDNA complexes at different N/P ratios. For the HPD2/pDNA complex at a ratio of 1, loose aggregates (>400 nm), supercoiled pDNA, and compact nanoparticles (<10 nm) are observed at the same time, indicating that pDNA has been partially condensed. At the N/P of 15, pDNA can be packed tightly and condensed completely. The compacted complexes of pDNA with HPD2 and QHPD2−1 exist in the form of spherical nanoparticles (<200 nm in size). No obvious difference was observed among the spherical nanoparticles.

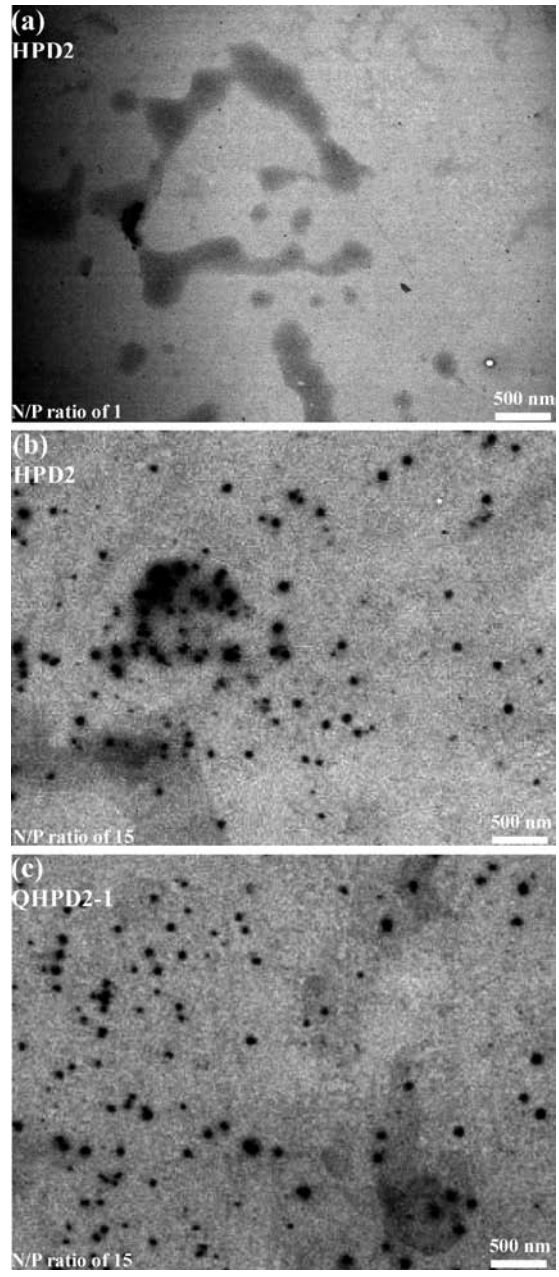

Figure 5. STEM images of the (a) HPD2/pDNA (at a ratio of 1), (b) HPD2/pDNA (at a ratio of 15), and (c) QHPD2−1/pDNA (at a ratio of 15) complexes.

Cytotoxicity of Comb-Shaped Cationic Copolymers. Cytotoxicity is one of the most important factors to be considered in selecting polymeric gene carriers. Figure 6 shows the in vitro MTT assay results of cytotoxicity of HPD1,

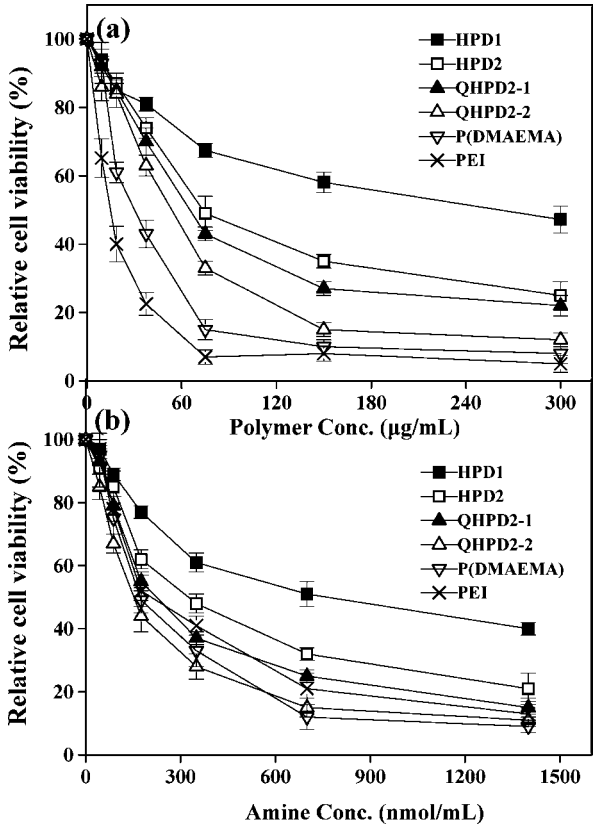

Figure 6. Cell viability assay in HEK293 cells with various concentrations of HPD1, HPD2, QHPD2−1, QHPD2−2, P(DMAEMA), and PEI (a, polymer concentration; b, amine concentration). Cell viability was determined by the MTT assay and expressed as a percentage of the control cell culture. Error bars represent the standard deviation of six measurements.

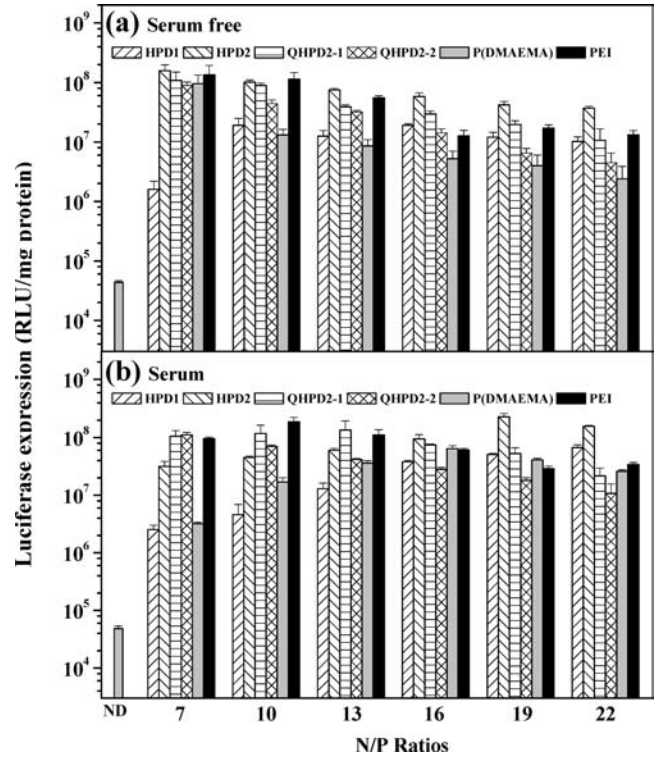

Figure 7. In vitro gene transfection efficiency of the cationic polymers (HPD1, HPD2, QHPD2−1, QHPD2−2, P(DMAEMA), and PEI)/pDNA complexes in comparison with that of naked DNA (ND) at various N/P ratios in HEK293 cells in the absence (a) and presence (b) of serum. Error bars represent the standard deviation of three measurements.

HPD2, QHPD2−1, QHPD2−2, P(DMAEMA), and PEI in HEK293 cells with the vairous polymer (a) and amine (b) concentraions. All of the cationic polymers exhibit a dose-dependent cytotoxicity effect. The slopes of the dose-dependent cytotoxicity curves for P(DMAEMA) are much steeper than those for the HPDs copolymers. The concentrations of amino groups, as well as molecular structure (*27*), are always considered to be important factors affecting cytotoxicity. The introduction of the biocompatible HPC backbones not only results in a lower relative concentration of amino groups, but has also imparted biocompatible characteristics to the cationic carriers. It was also well-known that the cytotoxicity of polycations increases with the molecular weight (*27*). Because of its longer P(DMAMEA) side chains, HPD2 exhibited higher cytotoxicity than HPD1. Both the high-molecular-weight HPD1 and HPD2 produced lower cytotoxicity than P(DMAEMA) homopolymer. The averaged number (about 11 for HPD1 and 34 for HPD2, Table 1) of DMAEMA repeat units per side chain of HPDs is much lower than that (about 180) of the control P(DMAEMA) homopolymer. Therefore, it was indicated that the molecular structure of the high-molecular-weight comb copolymers composed of long biocompatible HPC backbones and low-molecular-weight P(DMAEMA) side chains cannot produce high cytotoxicity. In addition, HPD2, QHPD2−1, and QHPD2−2 exhibit increasing toxicity, indicating that the introduced quaternary ammonium groups can increase the cytotoxicity (*28*), although the quaternization of the P(DMAEMA) side chains could enhance the surface cationic charges and DNA-condensing ability. The above results are also supported by the calculated median inhibitory concentration (IC_{50}). IC_{50} is defined as the polymer concentration of a gene carrier at which the relative cell viability decreases to 50% (*27*). The IC_{50} values of P(DMAEMA) and PEI are about 30 and 24 μg/mL, respectively, in comparison with those of HPD1 (245 μg/mL), HPD2 (70 μg/mL), QHPD2−1 (61 μg/mL), and QHPD2−2 (45 μg/mL).

Gene Transfection Mediated by Comb-Shaped Cationic Copolymers. The in vitro gene transfection efficiency of the cationic polymers/pDNA complexes was assessed using luciferase as a gene reporter in HEK293 cells. Figure 7 shows the gene transfection efficiency of HPD1, HPD2, QHPD2−1, and QHPD2−2 in comparison with those of P(DMAEMA) and PEI at N/P ratio from 7 to 22 in the absence (a) and presence (b) of serum. In the present work, the optimal N/P ratios in the serum (or serum-free) case for HPD1, HPD2, QHPD2−1, and QHPD2−2, and P(DMAEMA) are 22 (or 16), 19 (or 7), 10 (or 7), 7 (or 7), and 16 (or 7), respectively. HPD2, QHPD2−1, and QHPD2−2 exhibit decreasing optimal N/P ratio in the presence of serum, indicating that that the introduced quaternary ammonium groups can increase the DNA-binding ability. The optimal N/P ratio for the control PEI is about 10 at both cases. The transfection efficiency generally increases at lower N/P ratios and then decreases with the increase in N/P ratio. At lower N/P ratios, pDNA cannot be condensed efficiently by the polymers, and the resultant loose polymer/pDNA complex cannot enter the cell easily. At higher polymer/plasmid ratios, the transfection formulation also contains free polymer, besides the compact and positively charged polymer/pDNA complexes. For example, when the N/P ratio was increased to 22, the percentage of free PEI in the PEI/pDNA formulation was at least 55% (=(22 − 10)/22 × 100%) based on the optimal N/P ratio of 10. Due to the presence of an increasing amount of free cationic polymers with the increase in N/P ratios, the increasing cytotoxicity decreases the cell viabilities and results in a reduction in the transfection efficiency. In particular, the

transfection efficiencies mediated by QHPD2−2, P(DMAEMA) and PEI decreases dramatically with the increase in N/P ratios, due to the high cytotoxicity of the three polymers.

As shown in Figure 7, the transfection efficiency mediated by HPD1 is lower than that mediated by HPD2 at various N/P ratios. This observation indicates that the transfection efficiency for HPDs is dependent on the side lengths of P(DMAEMA). The long P(DMAEMA) side chains can increase the binding ability and complex stability, probably leading to a much higher transfection efficiency. It is worth noting that the transfection efficiency mediated by HPD2 is higher than that mediated by the control P(DMAEMA) homopolymer. The averaged number of DMAEMA repeat units per side chain of HPD2 is about 34, much lower than that (about 180) of the P(DMAEMA) homopolymer, indicating that the high-molecular-weight comb copolymers composed of long biocompatible HPC backbones and low-molecular-weight P(DMAEMA) side chains can enhance gene transfection efficiency. One possible reason is that such unique architectures could enhance the interaction of the cationic P(DMAEMA) with pDNA or cellular membranes.

Due to increased surface cationic charges, QHPD2−1 and QHPD2−2 were expected to strongly complex pDNA and result in a higher transfection yield than HPD2. However, at the optimal N/P ratios of HPD2, QHPD2−1, and QHPD2−2, the maximum transfection efficiency follows the order QHPD2−2 < QHPD2−1 < HPD2. This observation indicates that quaternary ammonium groups could not further enhance the transfection efficiency, probably due to the increased cytotoxicity (*28*) and decreased buffering capacity of polymer/DNA complexes. After cellular entry, the polymer/plasmid complexes are transported into the lysosome. The cationic polymers should retain substantial buffering capacity over a wide range of pHs, not only to protect the DNA from degradation inside the lysosome, but it is thought to also lead to lysosomal swelling and rupture via protonization. The latter process in turn provides an escape mechanism for DNA particles into the cytoplasm (*29*, *30*). The released pDNA is subsequently transported into the nucleus for gene expression. The QHPDs with quaternization groups may possess the lower buffering capacity inside the lysosome, which prevents the subsequent release of pDNA from the strongly condensed complexes.

CONCLUSIONS

Well-defined comb-shaped copolymers (HPDs) consisting of long biocompatible HPC backbones and short cationic P(DMAEMA) side chains were prepared via ATRP from the bromoisobutyryl-terminated HPC biopolymers. The P(DMAEMA) side chains can be further partially quaternized to produce the QHPDs with quaternary ammonium groups. At N/P ratios of 5 or higher, HPDs and QHPDs as gene carriers can effectively bind pDNA to form nanoparticle complexes of 150 to 200 nm in size. In comparison with long P(DMAEMA) homopolymers, HPDs exhibit much lower cytotoxicity and better gene transfection efficiency. QHPDs show stronger ability to complex pDNA than HPDs. Thus, structural tailoring of functional comb-shaped cationic copolymers provides a unique and versatile means for designing novel gene carriers.

LITERATURE CITED

(1) Anderson, W. F. (1998) Human gene therapy. *Nature 392*, 25–30.

(2) Wagner, E., and Kloecker, J. (2006) Gene delivery using polymer therapeutics. *Adv. Polym. Sci. 192*, 135–173.

(3) Hunt, K. K., and Vorburger, S. A. (2002) Gene therapy: hurdles and hopes for cancer treatment. *Science 297*, 415–416.

(4) De Smedt, S. C., Demeesterm, J., and Hennink, W. E. (2000) Cationic polymer based gene delivery systems. *Pharm. Res. 17*, 113–126.

(5) Yudovin-Farber, I., and Domb, A. J. (2007) Cationic polysaccharides for gene delivery. *Mater. Sci. Eng., C 27*, 595−598.

(6) Jiang, X., Lok, M. C., and Hennink, W. E. (2007) Degradable-brushed pHEMA-pDMAEMA synthesized via ATRP and click chemistry for gene delivery. *Bioconjugate Chem. 18*, 2077–2084.

(7) Yang, C., Li, H., Goh, S. H., and Li, J. (2007) Cationic star polymers consisting of α-cyclodextrin core and oligoethylenimine arms as nonviral gene delivery vectors. *Biomaterials 28*, 3245–3254.

(8) Bisht, H. S., Manickam, D. S., You, Y., and Oupicky, D. (2006) Temperature-controlled properties of DNA complexes with poly(ethylenimine)-*graft*- poly(*N*-isopropylacrylamide). *Biomacromolecules 7*, 1169–1178.

(9) Xu, F. J., Li, H. Z., Li, J., Zhang, Z. X., Kang, E. T., and Neoh, K. G. (2008) Pentablock copolymers of poly(ethylene glycol), poly((2-dimethyl amino)ethyl methacrylate) and poly(2-hydroxyethyl methacrylate) from consecutive atom transfer radical polymerizations for non-viral gene delivery. *Biomaterials 29*, 3023–3033.

(10) Agarwal, A., Unfer, R., and Mallapragada, S. K. (2005) Novel cationic pentablock copolymers as non-viral vectors for gene therapy. *J. Controlled Release 103*, 245–258.

(11) Dimitrova, M., Arntz, Y., Lavalle, P., Meyer, F., Wolf, M., Schuster, C., Haïkel, Y., Voegel, J. C., and Ogier, J. (2007) Adenoviral gene delivery from multilayered polyelectrolyte architectures. *Adv. Funct. Mater. 17*, 233–245.

(12) Kukowska-Latallo, J. F., Bielinska, A. U., Johnson, J., Spindler, R., Tomalia, D. A., and Baker, J. R., Jr. (1996) Efficient transfer of genetic material into mammalian cells using starburst polyamidoamine dendrimers. *Proc. Natl. Acad. Sci. U.S.A. 93*, 4897–4902.

(13) Thanou, M., Florea, B. I., Geldof, M., Junginger, H. E., and Borchard, G. (2002) Quaternized chitosan oligomers as novel gene delivery vectors in epithelial cell lines. *Biomaterials 23*, 153–159.

(14) Marsano, E., Bianchi, E., and Sciutto, L. (2003) Microporous thermally sensitive hydrogels based on hydroxypropyl cellulose crosslinked with poly-ethyleneglicol diglycidyl ether. *Polymer 44*, 6835–6841.

(15) Gao, J., Haidar, G. H., Lu, X., and Hu, Z. (2001) Self-association of hydroxypropylcellulose in water. *Macromolecules 34*, 2242–2247.

(16) Östmark, E., Harrisson, S., Wooley, K. L., and Malmström, E. E. (2007) Comb polymers prepared by ATRP from hydroxypropyl cellulose. *Biomacromolecules 8*, 1138–1148.

(17) Östmark, E., Lindqvist, J., Nyström, D., and Malmström, E. (2007) Dendronized hydroxypropyl cellulose: synthesis and characterization of biobased nanoobjects. *Biomacromolecules 8*, 3815–3822.

(18) Harsh, D. C., and Gehrke, S. H. (1991) Controlling the swelling characteristics of temperature-sensitive cellulose ether hydrogels. *J. Controlled Release 17*, 175–186.

(19) Stamatialis, D. F., Rolevink, H. H. M., Gironès, M., Nymeijer, D. C., and Koopsm, G. H. (2004) In Vitro evaluation of a hydroxypropyl cellulose gel system for transdermal delivery of timolol. *Curr. Drug Delivery 1*, 313–319.

(20) Benns, J. M., Choi, J. S., Mahato, R. I., Park, J. S., and Kim, S. W. (2000) pH-sensitive cationic polymer gene delivery vehicle: N-Ac-poly(L-histidine)-graft-poly(L-lysine) comb shaped polymer. *Bioconjugate Chem. 11*, 637–645.

(21) Choi, S. W., Yamayoshi, A., Hirai, M., Yamano, T., Takagi, M., Sato, A., Kano, A., Shimamoto, A., and Maruyama, A. (2007) Cationic comb-type copolymers having high density of PEG graft chains for gene carriers. *Macromol. Symp. 249/250*, 312–316.

(22) Asayama, S., Maruyama, A., Cho, C. S., and Akaike, T. (2007) Design of comb-type polyamine copolymers for a novel pH-sensitive DNA carrier. *Bioconjugate Chem. 8*, 833–838.

(23) Stenzel, M. H., Davis, T. P., and Fane, A. G. (2003) Honeycomb structured porous films prepared from carbohydrate based polymers synthesized *via* the RAFT process. *J. Mater. Chem. 13*, 2090–2097.

(24) Xu, F. J., Kang, E. T., and Neoh, K. G. (2006) pH- and temperature-responsive hydrogels from crosslinked triblock copolymers prepared via consecutive atom transfer radical polymerizations. *Biomaterials 27*, 2787–2796.

(25) Cheng, Z., Zhu, X., Shi, Z. L., Neoh, K. G., and Kang, E. T. (2005) Polymer microspheres with permanent antibacterial surface from surface-initiated atom transfer radical polymerization. *Ind. Eng. Chem. Res. 44*, 7098–7104.

(26) Ma, Y., Tang, Y., Billingham, N. C., Armes, S. P., Lewis, A. L., Lloyd, A. W., and Salvage, J. P. (2003) Well-defined biocompatible block copolymers via atom transfer radical polymerization of 2-methacryloyloxyethyl phosphorylcholine in protic media. *Macromolecules 36*, 3475–3484.

(27) Wetering, P. V. D., Moret, E. E., Nieuwenbroek, N. M. E., Steenbergen, M. J. V., and Hennink, W. E. (1999) Structure-activity relationship of water-soluble cationic methacrylate/methacrylmide polymers for nonviral gene delivery. *Bioconjugate Chem. 10*, 589–597.

(28) Yudovin-Farber, I., Yanay, C., Azzam, T., Linial, M., and Domb, A. J. (2005) Quaternary ammonium polysaccharides for gene delivery. *Bioconjugate Chem. 16*, 1196–1203.

(29) Tang, M. X., and Szoka, F. C. (1997) The influence of polymer structure on the interactions of cationic polymers with DNA and morphology of the resulting complexes. *Gene Ther. 4*, 823–832.

(30) Ferrari, S., Moro, E., Pettenazzo, A., Behr, J. P., Zacchello, F., and Scarpa, M. (1997) ExGen 500 is an efficient vector for gene delivery to lung epithelial cells in vitro and in vivo. *Gene Ther. 4*, 1100–1106.

BC900044H

Carbodiimide EDC Induces Cross-Links That Stabilize RNase A C-Dimer against Dissociation: EDC Adducts Can Affect Protein Net Charge, Conformation, and Activity

Jorge P. López-Alonso,[†] Fernando Diez-García,[†] Josep Font,[§] Marc Ribó,[§] Maria Vilanova,[§] J. Martin Scholtz,[||] Carlos González,[†] Francesca Vottariello,[‡] Giovanni Gotte,[‡] Massimo Libonati,[‡] and Douglas V. Laurents*,[†]

Instituto de Química Física "Rocasolano" (C.S.I.C.), Serrano 119, E-28006, Madrid, Spain, Dipartimento di Scienze Morfologico-Biomediche, Sezione di Chimica Biologica, Facoltà di Medicina e Chirurgia, Università di Verona, Strada Le Grazie 8, I-37134, Verona, Italy, Laboratori d'Enginyeria de Proteïnes, Departament de Biología, Facultad de Ciències, Universitat de Girona, Campus Montilivi, 17071 Girona, Spain, and Department of Medical Biochemistry, Texas A&M University School of Medicine, College Station, Texas 77478. Received September 16, 2008; Revised Manuscript Received June 17, 2009

RNase A self-associates under certain conditions to form a series of domain-swapped oligomers. These oligomers show high catalytic activity against double-stranded RNA and striking antitumor actions that are lacking in the monomer. However, the dissociation of these metastable oligomers limits their therapeutic potential. Here, a widely used conjugating agent, 1-ethyl-3-(3-dimethylaminoisopropyl) carbodiimide (EDC), has been used to induce the formation of amide bonds between carboxylate and amine groups of different subunits of the RNase A C-dimer. A cross-linked C-dimer which does not dissociate was isolated and was found have augmented enzymatic activity toward double-stranded RNA relative to the unmodified C-dimer. Characterization using chromatography, electrophoresis, mass spectrometry, and NMR spectroscopy revealed that the EDC-treated C-dimer retains its structure and contains one to three novel amide bonds. Moreover, both the EDC-treated C-dimer and EDC-treated RNase A monomer were found to carry an increased number of positive charges (about 6 ± 2 charges per subunit). These additional positive charges are presumably due to adduct formation with EDC, which neutralizes a negatively charged carboxylate group and couples it to a positively charged tertiary amine. The increased net positive charge endowed by EDC adducts likely contributes to the heightened cleavage of double-stranded RNA of the EDC-treated monomer and EDC-treated C-dimer. Further evidence for EDC adduct formation is provided by the reaction of EDC with a dipeptide Ac-Asp-Ala-NH_2 monitored by NMR spectroscopy and mass spectrometry. To determine if EDC adduct formation with proteins is common and how this affects protein net charge, conformation, and activity, four well-characterized proteins, ribonuclease Sa, hen lysozyme, carbonic anhydrase, and hemoglobin, were incubated with EDC and the products were characterized. EDC formed adducts with all these proteins, as judged by mass spectrometry and electrophoresis. Moreover, all suffered conformational changes ranging from slight structural modifications in the case of lysozyme, to denaturation for hemoglobin as measured by NMR spectroscopy and enzyme assays. We conclude that EDC adduct formation with proteins can affect their net charge, conformation, and enzymatic activity.

INTRODUCTION

Bovine pancreatic ribonuclease A (RNase A) is a 124-residue monomeric enzyme that catalyzes the breakdown of single-stranded RNA with specificity for pyrimidines at the 3′-side of the cleavage site. RNase A forms oligomers by a three-dimensional domain swapping mechanism (*1*). Dimers can be formed when two monomers swap their N-terminal α-helices (*2*) or their C-terminal *β*-strands (*3*). These dimers are called the N-dimer and C-dimer, respectively. Higher oligomers form by combinations of N-terminal or C-terminal swapping or both (*4*−*7*). This oligomerization can be induced by lyophilization from 40% glacial acetic acid (*1*) or incubation at elevated temperature at high concentration in water (*8*) or in alcohol/water solution (*9*).

The oligomerization of RNase A has been shown to endow the protein with a marked increased catalytic activity against double-stranded poly(A)·poly(U) or double-stranded viral RNA (dsRNA) (*10*) and, even more remarkably, a potent and selective toxicity *in vivo* against human tumors (*11*). The activity on dsRNA and the cytotoxicity of RNase A oligomers increases with their size (*12*). All RNase oligomers formed are metastable and dissociate over time into monomers. The dissociation of the larger oligomers into smaller ones is markedly faster than the disassociation of the dimers into monomers. The lifetime of the dimers can be as long as months in optimal conditions, namely, 4 °C, pH 7, in phosphate buffer. However, their lifetime is considerably lower at physiological temperatures. RNase S, the product of the mild digestion of RNase A into two fragments which remain associated by noncovalent interactions, forms a 3D domain-swapped C-dimer (*13*). By conjugation of the small fragment with DNA or PNA, it is possible to form semisynthetic RNase S monomers and C-dimers with modulated activities (*14*). However, the study and application of semisynthetic RNase S dimers is impeded by their rather strong tendency to dissociate. Therefore, the addition of cross-links to stabilize RNase A or RNase S oligomers could maintain their novel activity and increase their *in vivo* antitumor activity.

In this paper, we have selected 1-ethyl-3-(3-dimethylaminoisopropyl) carbodiimide (EDC), which induces the formation

* To whom correspondence should be addressed: dlaurents@iqfr.csic.es.
[†] C.S.I.C.
[‡] Università di Verona.
[§] Universitat de Girona.
[||] Texas A&M University School of Medicine.

10.1021/bc9001486 CCC: $40.75 © 2009 American Chemical Society
Published on Web 07/16/2009

of isopeptide bonds between nearby amine and carboxylate groups, as a suitable cross-linking reagent for RNase oligomers. We have identified suitable conditions for obtaining cross-linked RNase A C-dimers. Using these conditions, we have produced and purified cross-linked RNase A C-dimers and determined their enzymatic activities against ssRNA and dsRNA. We also isolated and characterized RNase A monomers carrying EDC adducts which result from a side reaction. The EDC adducts endow RNase A monomers with an increased positive charge and an augmented ribonucleolytic activity on dsRNA.

EDC is a popular reagent for cross-linking two proteins or for activation of carboxylate groups for reaction with other molecules containing amines. The formation of carbodiimide adducts to proteins is well-documented in the literature up until 1995 (*15*−*18*), but the effects of these adducts on protein conformation and function is relatively unexplored. Therefore, a second objective of this work has been to determine how EDC adducts affect protein stucture and activity. To this end, we studied the reaction of EDC with the dipeptide Ac-Asp-Ala-NH_2, and we reacted four well-characterized proteins: ribonuclease Sa (RNase Sa), hen egg white lysozyme, carbonic anhydrase, and hemoglobin with EDC. Using modern biophysical techniques, we show that EDC forms adducts with all four proteins and affects their net charge, conformation, and enzymatic activities to varying degrees.

EXPERIMENTAL PROCEDURES

Materials. Bovine pancreatic ribonuclease A (RNase A) was obtained from Sigma and further purified by cation-exchange chromatography as described previously (*4*). Ribonuclease Sa was expressed in *E. coli* and purified as previously described (*19*). An Asp-Ala dipeptide with the N- and C-termini blocked by acetyl and amide groups, respectively, was purchased from GenScript Corp. It is over 97% pure, and its identity was confirmed by mass spectrometry and NMR spectroscopy. The best grades of hen egg white lysozyme, bovine carbonic anhydrase II, and human hemoglobin were obtained from Sigma and were used without further purification. Yeast single-stranded RNA, synthetic double-stranded poly(A)·poly(U), and 4-methylumbelliforyl D-D-*N*,*N*′,*N*″-triacetylchitotrioside were purchased from Sigma. Sodium dihydrogen phosphate and sodium hydrogen phosphate were obtained from Merck and MES was from Sigma. Sodium azide (99%) was from Panreac. Double-distilled water was deionized using a Milli-Q system. Glacial acetic acid (99.9%) was from Quimipur. 1-Ethyl-3-(3-dimethylaminoisopropyl)carbodiimide (EDC) and *N*-hydroxysulfosuccinimide (sulfo-NHS) were purchased from Pierce.

Structure Analysis and pK_a Prediction. The atomic structures of the RNase A C-dimer (pdb: 1f0v) (*3*) and N-dimer (pdb: 1a2w) (*2*) were examined using the program *Mage* (v 6.30) to measure distances between amine groups and carboxylate groups. The program *MolMol* was used to calculate the percent solvent-accessible surface of carboxylate oxygen atoms in the RNase A C-dimer (*20*). pK_a values in the RNase A C-dimer were predicted using the empirical approach implemented in the program *Propka* (*21*).

Oligomer Formation. RNase A oligomers were obtained by incubation in 40% glacial acetic acid/60% water for 1 h, followed by lyophilization (*1*), and purified as previously described (*4*). Briefly, lyophilized samples were dissolved in sodium phosphate buffer (0.065 M, pH 6.70) containing 0.02% sodium azide, and the C-dimer of RNase A was isolated by cation exchange chromatography with a Source 15S HR 16/10 column using a gradient of 0.09−0.20 M sodium phosphate, pH 6.7, which also contained 0.02% sodium azide. The flow rate was 1.2 mL per min. All chromatography procedures were preformed at room temperature. After isolation, the C-dimer was concentrated using Centriplus concentrators with an M_r cutoff of 3 kDa or 10 kDa.

EDC Reaction. A series of trial reactions were performed at various concentrations of EDC (6 to 180 mM), RNase A (0.2 to 0.7 mg/mL), NaCl (0 to 0.5 M), and different pH values (4.0 to 7.0) with a 2 h reaction time at room temperature. The yield of cross-linked C-dimer was determined by integrating the dimer and monomer peaks after heating the sample to dissociate non-cross-linked C-dimer. Using the paper printout of the chromatogram, integration was performed manually by cutting out the peaks corresponding to cross-linked C-dimer and monomer and weighing them on a high-precision balance. The most satisfactory yields of cross-linked C-dimer were obtained using a concentration of C-dimer of 0.5 mg/mL, in 100 mM MES at pH 5.0 with 68 mM EDC. These same conditions and reactant concentrations were used for the reaction of EDC with RNase Sa, hen lysozyme, carbonic anhydrase, and hemoglobin. Some RNase A reaction trials included 5 mM sulfo-NHS. EDC (∼100 mM) reactions with the dipeptide Ac-Asp-Ala-NH_2 (8 mM) in 20 mM MES buffer were carried out at 25 °C and pH 5.5−5.8 and monitored by NMR spectroscopy and mass spectrometry.

Product Isolation and Characterization. Superdex 75 gel filtration columns, equilibrated with 0.2 M sodium phosphate buffer at pH 6.7 was used at room temperature at a flow rate of 0.5 mL/min to purify and characterize the RNase A reaction products. Further purification and characterization of the product species was performed using cation exchange chromatography using a Mono S column. After reaction with EDC, RNase Sa, hen lysozyme, carbonic anhydrase, and hemoglobin were desalted using a PD-10 column (GE Healthcare) and concentrated using Centricon concentrators with a M_r cutoff of 10 kDa.

Gel Electrophoresis. Denaturing SDS polyacrylamide gel electrophoresis (PAGE) was used for analysis (*22*).Ten percent polyacrylamide gels containing SDS were run at 20 mA for 90 min at room temperature. Cathodic PAGE under nondenaturing conditions was performed according to ref 23 with the slight modification of using β-alanine/acetic acid buffer at pH 4.0 as described previously (*6*). The 12.5% polyacrylamide gels were run at 20 mA for 100−120 min at 4 °C. For both types of gels, fixing and staining were performed with 12.5% trichloroacetic acid and 0.1% Coomassie brilliant blue. Densitometry and molecular weight estimations were performed using the *GeneTools* computer program (v 3.06) from SynGene/SynOptics Ltd., Cambridge, England.

Mass Spectrometry. Matrix-assisted laser desorption ionization time-of-flight (MALDI-TOF) mass spectra were registered with an Applied Biosystems Voyager System 6214 mass spectrometer as previously described (*24*).

Peptide Mapping using Proteolysis and HPLC/Electrospray Mass Spectrometry. The position of the EDC modified carboxylate groups in RNase A was characterized by proteolysis with subtilisin and trypsin. First, RNase A or EDC modified RNase A was cleaved with subtilisin. The amount of subtilisin added was 1/100th (w/w) that of RNase A. The solution is then incubated at room temperature at pH 8.0 in 25 mM ammonium acetate buffer. This buffer was chosen because it is one of the least interferring salts for mass spectrometry. Small amounts of KOH were added over the course of 3−$3^1/_2$ h to maintain the pH close to 8.0. The reaction was performed at room temperature. After this time, the pH of the solution was reduced to <3 and maintained there for 10 min. This treatment serves to irreversibly denature subtilisin so that it does not make secondary cleavages in RNase S in the presence of trypsin (*25*). Next, the pH of the solution was increased once again to pH 8.0 using KOH and trypsin (1:100 wt/wt relative to RNase A) is added. After incubating the solution for 3 h at RT, the solution

was flash-frozen in liquid nitrogen and maintained at −20 °C until analysis.

Alternatively, pepsin was used to cleave EDC modified RNase A. First, the pH of the protein was lowered to 1.6 with 0.1 M HCl and pepsin (1/100th wt/wt relative to RNase A) was added (*26*). After allowing the reaction to proceed for 30 min at room temperature, the pH of the sample was increased to pH 5 to inactivate pepsin and the samples were flash-frozen in liquid nitrogen and stored at −20 °C until analysis.

For peptide mapping analysis, tandem high-pressure liquid chromatography−electrospray ionization mass spectrometry (HPLC-ESI-MS) experiments were performed using a Finnigan Surveyor pump with quaternary gradient system coupled in-line to a Finnigan LCQ Deca ion trap mass spectrometer using an ESI interface. Sample injections (7 μL) were carried out by a Finnigan Surveyor autosampler. All instruments were from Thermo Fisher Scientific (San José, CA, USA).

The samples were diluted 2:3 with water, and their separation performed at 25 °C on a HyPurity C18(100 mm × 2.1 mm, 3 μm resin beads) column (Thermo Fisher Scientific) at a flow rate of 100 μL min^{-1}. A gradient of two eluents was used: eluent A consisted in 0.05% (v/v) of formic acid (analytical grade, Merck, Darmstadt, Germany) in water (Milli-Q water, Millipore, Bedford, USA), and eluent B in acetonitrile (LC-MS Chromasolv grade, Riedel-de Haën, Seelz, Germany) containing 0.05% formic acid (v/v). The elution program was applied as follows: at the start, 7% B; after 5 min, the percentage of B was linearly increased to 60% in 30 min; 60−95% B linear from 35 to 35 min; 95% B isocratic from 35 to 55 min; ramped to original composition in 1 min; and then equilibrated for 10 min.

The mass spectrometer spray voltage was set at 4.5 kV, the capillary temperature was 200 °C, nitrogen (99.5% purity) was used as the sheath (0.6 L min^{-1}) and the auxiliary (6 L min^{-1}) gas, and helium (99.9990% purity) was employed as the collision gas. The LC-MS system, data acquisition, and processing were managed by *Xcalibur* software (1.2 version, Thermo Fisher Scientific).

NMR Spectroscopy. The reaction of monomeric RNase A with EDC at 25 °C was followed by NMR spectroscopy using a Bruker AV 600 NMR spectrometer with an active shielded *z*-gradient coil and equipped with a cryoprobe for increased sensitivity. The reaction conditions were essentially the same as those indicated previously, except the protein sample used was more concentrated (8 mg/mL) and was recombinant RNase A uniformly labeled with ^{13}C and ^{15}N (*27*). 1D ^{1}H and 2D ^{1}H−^{13}C and ^{1}H−^{15}N HSQC spectra (*28*) were recorded on ^{13}C^{15}N-RNase A samples in 100 mM MES at pH 5.0 or 7.0 dissolved in 90/10 H_2O/D_2O. The ^{1}H−^{15}N HSQC spectra were ^{13}C decoupled. The pH of the MES buffer was altered by varying the relative concentration of the MES acid and sodium MES. The addition of EDC to MES buffer was found to have a negligible effect on the pH. 1D ^{1}H, 1D ^{13}C, and 2D ^{1}H COSY (*29*), NOESY (*30*), ^{1}H−^{13}C HSQC, and 2D ^{1}H−^{15}N HSQC spectra were recorded on EDC, Ac-Asp-Ala-NH_2, and MES solutions individually and mixed to obtain the assignments of EDC and hydrolyzed EDC, the dipeptide and MES, and to follow the reaction of EDC and the dipeptide. 1D ^{1}H NMR spectra on RNase Sa, hen lysozyme, carbonic anhydrase, and hemoglobin were recorded before and after reaction with EDC at 25 °C in 1 to 5 mM sodium phosphate buffer, pH 6.6 in 90/10 H_2O/D_2O. All NMR samples also contained 50 μM sodium-4,4-dimethyl-4-silapentane-1-sulfonate (DSS) as the internal chemical shift reference.

Enzyme Kinetics. The enzymatic activities of Ribonuclease A monomers and dimers, and Ribonuclease Sa and these species modified by EDC were measured against single-stranded yeast RNA (ssRNA) using the assay of Kunitz (*31*) and against double-stranded poly (A)·poly(U) as previously described (*32*). All assays were repeated at least twice, and the uncertainty of these activity values is typically about ±7% and ±15%, against ssRNA and dsRNA, respectively (*4*).

Table 1. Neighboring Amine and Carboxylate Groups in RNase A Swapped Dimers

dimer Species	amine	carboxylate	distance (Å)[a]	INTER- or intra-molecular
C-dimer	Lys 66	Asp 121	3.7	INTERmolecular
C-dimer	Lys 7	Glu 2	5.7	intramolecular
C-dimer	Lys 37	Asp 38	5.4	intramolecular
C-dimer	Lys 104	Asp 83	4.8	intramolecular
C-dimer	Lys 1	Glu 2	11.7	intramolecular
C-dimer	Lys 98	Asp 83	11.7	intramolecular
N-dimer	Lys 66	Asp 121	5.3	intramolecular
N-dimer	Lys 7	Glu 2	8.0	intramolecular
N-dimer	Lys 91	Glu 86	9.5	intramolecular
N-dimer	Lys 104	Asp 83	4.5	intramolecular
N-dimer	Lys 98	Asp 83	7.9	intramolecular

[a] The distance between the Lys ε N atom and the nearest O atom of the carboxylate group.

Carbonic anhydrase activity was assayed using the electrometric method of Wilbur and Anderson (*33*), which monitors the decrease in pH occurring when an alkaline solution of Tris buffer is mixed with water saturated with CO_2. The drop in pH is more rapid when the enzyme catalyzes the conversion of $CO_2 + H_2O$ to carbonic acid. Some modifications in the procedure were implemented. First, a 1.5 mL Eppendorf tube cooled over ice was used instead of a special reaction vessel. Second, rather than mixing the Tris and CO_2 saturated water solutions with syringes, 0.7 mL of 50 mM Tris buffer (pH 9.1), with or without enzyme, was equilibrated over ice, and at time zero, 0.7 mL of ice cold CO_2 saturated water was added and mixed with a pipet. The pH of the resulting solution was recorded every 10 s for 3 min. Third, to determine the activity, a linear function was fit to the decrease in pH vs time between pH 8.5 and 8.0 (controls without enzyme) or pH 8.5 and 7.0 (experiments with enzyme). The activity was calculated using the following equation:

$$\text{activity} = \frac{\Delta\text{pH}/\Delta\text{time(enzyme)} - \Delta\text{pH}/\Delta\text{time(average of controls)}}{\text{concentration of carbonic anhydrase in mg/mL}} \quad (1)$$

Lysozyme activity was measured using the assay of Yang and Hamaguchi (*34*), which is based on the conversion of 4-methylumbelliforyl D-D-*N*,*N*′,*N*″-triacetylchitotrioside into a fluorescent product when it is hydrolyzed. Reactions were performed at 42 °C in a buffer solution composed of 93 mM KCl and 7 mM potassium acetate/acetic acid, pH = 5.0. The substrate concentration was 300 μM and the protein concentration was 0.60 μM for both lysozyme and EDC-modified lysozyme. The apparent activity was measured as the slope of the increase in fluorescence (λ_{ex} = 360 nm, λ_{em} = 450 nm) measured using a Jobin Yvon Fluormax 4 spectrofluorimeter at 25 °C. The assay was repeated twice.

RESULTS

Properties of Possible Target Carboxylate and Amine Groups. We examined the atomic structures of the C-dimer and N-dimer of RNase A to determine if they contain amine and carboxylate groups, which are close enough to form an isopeptide bond (Table 1, Figure 1). Several amine and carboxylate groups are within 10 Å of each other, but almost all are found within the same subunit and therefore would lead to the formation of an intramolecular cross-link. Such a bond

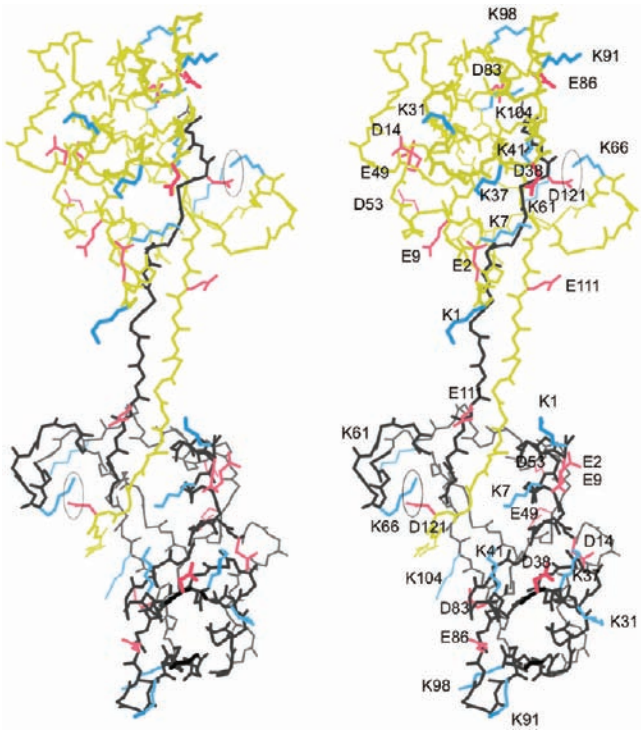

Figure 1. Cross-eyed stereo view of the structure of the RNase A C-dimer (Liu et al. 2001, pdb file 1F0V). The main chains of the two monomers are colored in dark gray and gold. Lysine side chains are shown in blue, while Asp and Glu side chains are colored red. For clarity, all other side chains have been deleted. An ellipse is drawn around the side chains of Lys 66 and Asp 121.

would not be expected to stabilize the metastable dimers against dissociation. However, Lys 66 from one subunit and Asp 121 from the other in the C-dimer are close enough together to form an isopeptide bond, which could stabilize the C-dimer against dissociation.

In order to react with cross-linking agents, carboxylate groups should be solvent-exposed. The percent solvent accessible surface areas are listed in Table 2. It can be seen that Asp 121 is one of the most solvent-exposed groups. Carboxylate groups must be in the charged carboxylate form instead of the neutral carboxylic acid form in order to react with most cross-linking agents. The experimental pK_a values of the carboxylate groups in monomeric RNase A (*35*) are also given in Table 2, along with predicted pK_a values for the same groups in the C-dimer. Asp 121 has a pK_a of about 3.0 in both the monomer and the C-dimer; therefore, about 99% of this residue should be in the charged form at pH 5, the optimal pH for the EDC cross-linking reaction (see below). Asp carboxylate groups typically have a pK_a of 4.0. Asp 121 has a lower pK_a value because the charged carboxylate form is stabilized by electrostatic interactions with Lys 66 and His 119, as inferred by their proximity and detected by the PROPKA program. These interactions might be expected to hinder the reaction of Asp 121 with cross-linking agents. Glu 2, Asp 14, Asp 38, and Asp 83 also have lower than normal pK_a values in the RNase A monomer and C-dimer. These suppressed pK_a values are due to hydrogen bonding and salt bridge formation with Arg 10, Tyr 25, Tyr 92, and Tyr 97, respectively (*36, 37*). These interactions and the lower surface exposure of Glu 2, Asp 14, Asp 38, and Asp 83 can be expected to impede the reaction of their carboxylate groups with cross-linking agents.

Selection of EDC as a Suitable Cross-Linking Reagent. We sought a cross-linking reagent to stabilize RNase A and RNase S domain-swapped oligomers. The ideal reagent would introduce a short, specific cross-link without inactivation or loss of the positive charge density on RNase A. A high net positive charge is crucial for the special biological acitivies of RNase A oligomers. Diethylpyrocarbonate was excluded from consideration, as it aggregates and inactivates RNase A (*38*). Stable cross-linked oligomers have been previously prepared using diimido esters (*39*). These reagents react with Lys amine groups and reduce the net positive charge on the protein and introduce a relatively long cross-link. This leads to a somewhat lower dsRNase activity for these covalent oligomers relative to their swapped counterparts. However, an extraordinary increase in dsRNase activity (*40*) and *in vivo* antitumoral activity (*24*) is obtained by cross-linking these covalent dimers to polyspermine. Two cross-linking reactions, divinylsulfone and 1,5-difluoro-2,4-dinitrobenzene, have been used successfully to covalently cross-link RNase A domain swapped oligomers (*6*). However, these reagents react with catalytic residues at the active site and produce a complete loss of activity. Many other cross-linking agents, i.e., UV light, tetranitromethane, formaldehyde, and so forth, are known (*41*) but also have undesirable properties.

Recently, Hefford and co-workers have discovered and characterized an RNase A dimer formed by heating the lyophilized protein *in vacuo*, which induces the formation of a isopeptide bond between Glu 9 and Lys 66 (*42*). Characterization of this dimer revealed a novel, nonswapped quaternary structure that is resistant to dissociation and ribonuclease inhibitor binding. Its dsRNase activity, although double that of monomeric RNase A, is lower than that of RNase A C-dimer. These results suggest that the formation of an isopeptide bond could be a useful approach for cross-linking RNase A swapped oligomers.

The water-soluble reagent 1-ethyl-3-(3-dimethylaminoisopropyl)carbodiimide (EDC) is capable of promoting the formation isopeptide bonds between the amine group of lysine and the carboxylate group of Glu or Asp in proteins in aqueous solution (*43*). Since EDC introduces no spacer, it is likely to favor the formation of isopeptide bonds between carboxylates and lysines, which are already nearby in the protein structure. The reaction removes both a negatively charged group and a positively charged one and thus does not alter the net charge on the protein. The mechanism of cross-linking with EDC involves formation of an adduct—an O-acylisourea derivate—between the EDC and the carboxylate group of Glu or Asp followed by a nucleophilic substitution with an amine group, most often the ε-NH_2 of lysine (Figure 2). In the absence of amine groups, the active O-acylisourea undergoes rapid hydrolysis regenerating the original carboxylate. A side reaction

Table 2. Properties of Carboxylate Groups in the RNase A C-dimer

carboxylate	% SASA[a]	pK_a monomer[b]	pK_a C dimer[c]	interacting groups	relative reactivity[d]
Glu 2	30	2.8	2.7	Arg 10	n. r. d.
Glu 9	64	4.0	4.6		+ + +
Asp 14	12	<2.0	−0.1	Tyr 25	n. r. d.
Asp 38	69	3.1[e]	4.2	Tyr 92	+
Glu 49	49	4.7	3.7		+ + + +
Asp 53	61	3.9	3.4		+ + + + +
Asp 83	37	3.5	4.2	Tyr 97	n. r. d.
Glu 86	34	4.1	4.1		+ + +
Glu 111	87	3.5	4.6		+ +
Asp 121	84	3.1	2.8	Lys 66 His 119	n. r. d.
Val 124 (C-terminus)	100	2.4	2.8		n. r. d.

[a] solvent accessible surface area. [b] From ref 35. [c] Calculated using the *PropKa* program. [d] Toward 1-cyclohexyl-3-(2-morpholinoethyl)carbodiimide metho-*p*-toluenesulfonate at pH 4.5 (*15*). n. r. d., no reactivity detected. The number of "+" correlates with the relative reactivity. [e] M. Rico, personal communication; the value given in the original publication is 3.5.

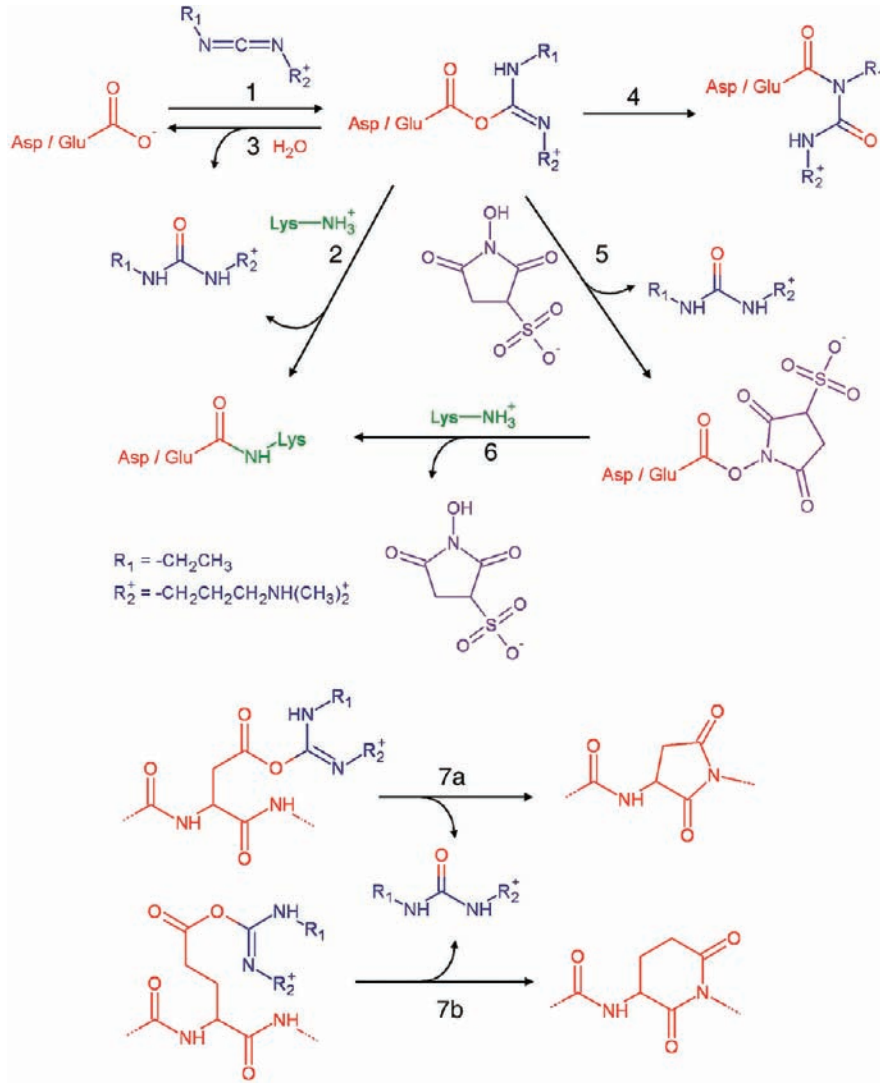

Figure 2. The reactions of EDC with carboxylates: **1**. The carboxylate oxygen (red) attacks the electrophillic carbon of EDC (blue). **2**. The resulting *O*-acylisourea intermediate can react with a nearby Lys amine group (green) to form an amide bond. Note that the formation of the peptide bond eliminates both a positive and a negative charge, so the net charge change is zero. The O-acylisourea, being highly reactive, can readily hydrolyze (**3**) or rearrange to form a relatively stable N-acylisourea (**4**); this side reaction removes a negatively charged carboxylate group and adds a positively charged adduct. The O-acylisourea intermediate can react with added sulfo-NHS (violet) to yield another intermediate (**5**), which has been reported to hydrolyze much more slowly and lead to higher yields of the desired peptide bond (**6**). Finally, another possible side reaction involves the attack of the amide nitrogen of the consecutive residue leading to the formation a cyclic imide with a 5 (Asp: **7a**) or 6 (Glu: **7b**) membered ring and the loss of a negative charge.

which rearranges the O-acylisourea intermediate to produce a more stable N-acylisourea has been observed (*15*, *16*) especially at high EDC concentrations (*18*). The hydrolysis or rearrangement of the O-acylisourea intermediate has been reported to be minimized by the addition of sulfo-NHS (*17*). The same authors found that the addition of sulfo-NHS leads to an increased formation of the desired isopeptide bond.

Reaction of the RNase A C-Dimer with EDC. We found that the most favorable conditions were pH 5.0 in 100 mM MES buffer with no NaCl, 10.6 mg/mL of EDC (68 mM EDC), and 0.5 mg/mL protein. Moreover, no substantial improvement of the yield of a heat stable C_D was obtained by adding sulfo-NHS to the reaction mixture.

Isolation and Characterization of Reaction Products Using Chromatography. A slight shift in elution volume from a gel filtration column of C_D was found after the reaction (Figure 3). The obtained products were heated at 55 °C for 30 min, which is sufficient to fully dissociate un-cross-linked C_D into monomers. A new peak was found at 14 mL and a small one remained at 12.5 mL; their relative peak areas were 93.5% and 6.5%, respectively. On the basis of the elution volumes of unmodified RNase A monomer and C-dimer, these new peaks were designated as EDC-modified monomer (M_{EDC}) and EDC-modified dimer ($C_{D\cdot EDC}$).

We attempted to isolate the products using cationic exchange chromatography, but they elute later, i.e., at higher phosphate concentrations, and did not show enough resolution to achieve their purification. As will be shown below, the M_{EDC} and $C_{D\cdot EDC}$ products contain EDC adducts, which endows them with increased positive charge. Incomplete resolution of cationized RNase species by ion exchange chromatography has been observed previously by Yamada and co-workers (*44*) and Libonati and co-workers (*24*). Considering that cationic exchange chromatography has sufficient resolution to separate RNase species that differ by just a single charge (*45*), the overlapping of the different EDC species is likely due to differences not only in the number of charges but also in the position of the modified carboxylate groups. As the N-acylisourea linkage of the EDC adduct has been reported to be labile to mild alkaline conditions (*15*, *18*), we dialyzed samples

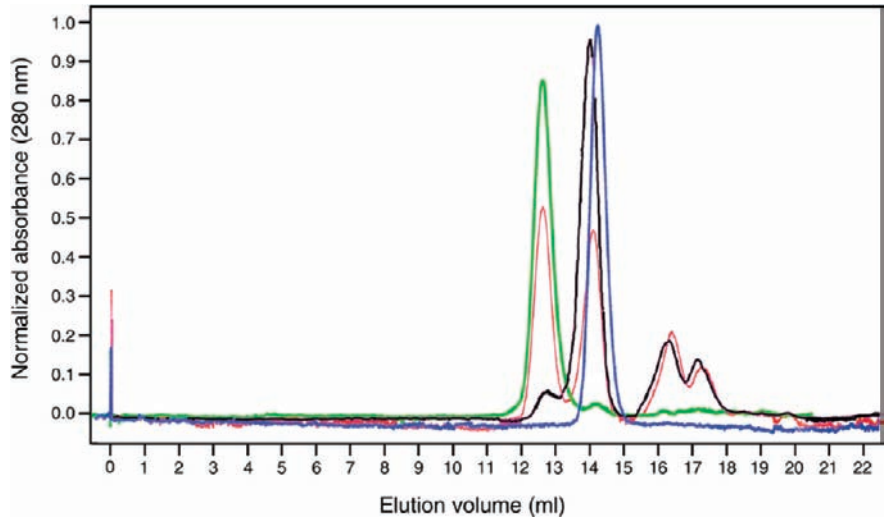

Figure 3. Chromatographic purification and analysis of RNase A EDC reaction products. Gel filtration chromatograms of monomer of RNase A (blue), C-dimer (green), and products of the reaction of RNase A C-dimer with EDC before (red) and after heating (black).

of M_{EDC} overnight against sodium borate buffer at pH 9.00. However, we observed no substantial change in the ion-exchange chromatogram before and after alkaline treatment.

Electrophoretic Characterization of EDC Modified RNase A Monomer and C-Dimer. The M_{EDC} and $C_{D\cdot EDC}$ fractions isolated from gel filtration chromatography were characterized by gel electrophoresis (Figure 4). When subjected to SDS-PAGE, which chiefly separates species according to their size, $C_{D\cdot EDC}$ produced an intense band flanked by two faint bands (Figure 4a). On the basis of the mobility of the molecular weight standards, the two faint bands were estimated to have molecular weights of 43 kDa and 13.5 kDa, which are in fair agreement with the values expected for an RNase A trimer (41 kDa) and monomer (13.7 kDa), respectively. The intense band has an estimated MW is 31 kDa; this is rather close to the value calculated for an RNase A dimer (27.4 kDa). On the basis of the relative intensity of the bands, about 80% of the sample is dimeric, 20% is monomeric, and only a trace (~0.5%) is trimeric. On the basis of these results, we tentatively conclude that $C_{D\cdot EDC}$ is a dimer and contains an intersubunit cross-link, since SDS normally dissociates noncovalent C-dimer into monomers. Turning to the M_{EDC} fraction, it produced a faint band whose mobility corresponds to dimeric RNase A, two faint bands intermediate between dimer and monomer, an intense band with a MW (14.1 kDa) corresponding to monomer, and a broad, fast-moving band corresponding to smaller molecules whose identity is unknown.

Both the M_{EDC} and $C_{D\cdot EDC}$ fractions were also subjected to nondenaturating cathodic PAGE (Figure 4b). In these gels, both the size and the charge of the species affect their mobility, with smaller and more positively charged molecules moving the quickest. Interestingly, $C_{D\cdot EDC}$ was found to migrate faster than unmodified RNase A C-dimer or monomer. As the $C_{D\cdot EDC}$ is a dimer, as tentatively concluded in the preceding paragraph, its faster mobility indicates that it has an increased positive charge. This higher positive charge could result from the side reaction of EDC with carboxylate groups, which removes a negative charge and results in the formation of a positively charged adduct (Figure 2). The broadness of the main $C_{D\cdot EDC}$ band suggests some heterogeneity in the number and position of the new positive charges. The M_{EDC} sample produced a series of fast-moving and overlapping bands (Figure 4b, right-most lane). These bands are assignable to monomeric RNase A species with increased positive charge.

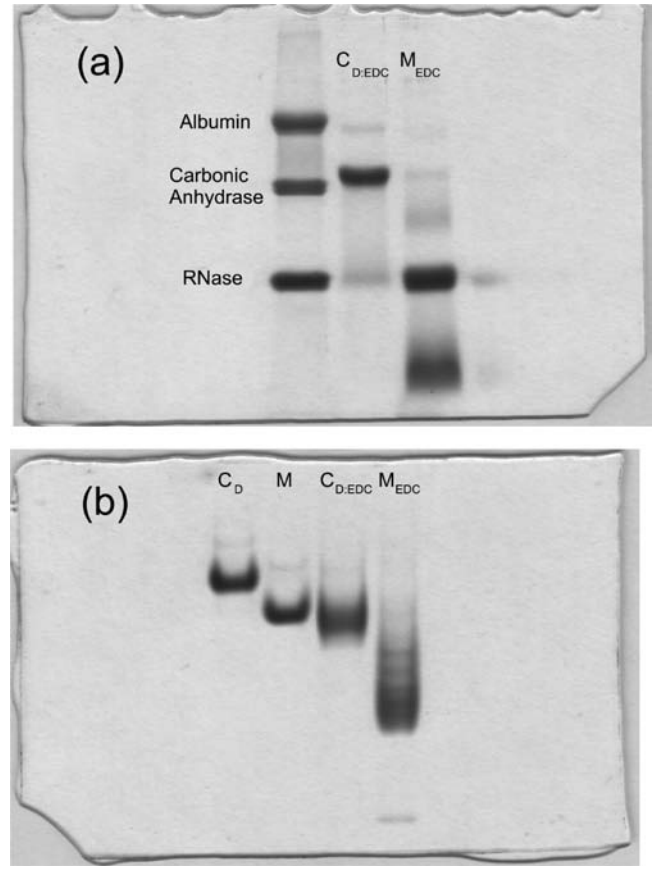

Figure 4. Denaturing and nondenaturing polyacrylamide gel electrophoresis of the products of RNase A C-dimer with EDC. (a) SDS-PAGE: In the first lane, RNase A monomer (14 kDa), carbonic anhydrase (29 kDa), and albumin (45 kDa); in the second lane, $C_{D\cdot EDC}$; and in the third one, M_{EDC}. (b) Cathodic PAGE: From left to right, RNase A C-dimer, RNase A monomer, $C_{D\cdot EDC}$, and M_{EDC}.

Mass Spectra of RNase A Monomer and C-Dimer Modified by EDC. The results of gel electrophoresis indicate that M_{EDC} and $C_{D\cdot EDC}$ contain additional positive charges. If these additional positive charges were due to formation of an N-acylisourea adduct with EDC (Figure 2), then the resulting increase in the molecular weight, 155 Da per EDC adduct, should be detectable by mass spectrometry. The more intense peaks observed have masses expected for monomeric RNase

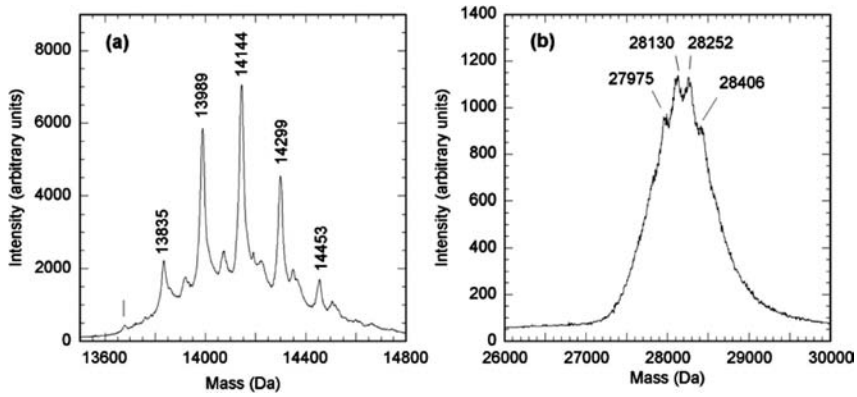

Figure 5. MALDI-TOF mass spectra of (a) M_{EDC} and (b) $C_{D\cdot EDC}$. The minor peaks present in panel (a) and the broadness of the underlying peak in panel (b) could be due to the formation of fragmented EDC adducts and the loss of a water molecule due to cyclization of the polypeptide chain. The dash in (a) marks a tiny peak corresponding to the expected mass (13 679 Da) of monomeric RNase A.

Table 3. Masses Expected and Observed for C-Dimer upon Coupling to EDC and Due to Water Loss[a]

# EDC adducts	−0 H_2O	−1 H_2O	−2 H_2O	−3 H_2O	−4 H_2O
1	27524	27506	27488	27470	27452
2	27680	27662	27644	27626	27608
3	**27836**	*27818*	**27800**	**27782**	27764
4	**27992**	*27974*	**27956**	**27938**	**27920**
5	**28148**	*28130*	**28112**	**28094**	**28076**
6	**28304**	**28286**	**28268**	*28250*	**28232**
7	28460	**28442**	**28424**	*28406*	**28388**
8	28616	28597	28579	28561	28543

[a] Masses in italics are observed as discrete peaks in the mass spectrum. Species with masses in boldface could also be present but have a population that is too low or too overlapped with other peaks to be observed individually. Masses in plain text do not appear to be present.

A (13 679 Da) plus one (13 835 Da), two (13 989), three (14 144), four (14 299), and five (14 453 Da) EDC adducts (Figure 5a). No significant change in the number of EDC adducts occurred after overnight incubation in sodium borate buffer, pH 9, as detected by mass spectroscopy (data not shown).

Regarding the mass spectrum of $C_{D\cdot EDC}$ shown in Figure 5b, a series of peaks whose masses correspond to the molecular weights of RNase A dimers with approximately three to seven EDC adducts and having shed one to three water molecules are observed (Table 3). The broadness of these peaks is likely due to the lower resolution of this instrument at higher masses, the possible presence of fragmented EDC adducts (see the description of the reaction of EDC with $AcAspAlaNH_2$ below). and the contribution of isotopes such as ^{13}C. Whereas unmodified C-dimers dissociate into monomers when subjected to MALDI-TOF mass spectroscopy, the observation of peaks with masses expected for RNase A dimers indicates that $C_{D\cdot EDC}$ is a bona fide dimer whose monomers are coupled by one or more covalent bonds. The loss of water molecules is a hallmark of the formation of isopeptide bonds between carboxylate and amine groups (Figure 2). This suggests that isopeptide bonds are the covalent bonds linking the monomers of $C_{D\cdot EDC}$. The species composing $C_{D\cdot EDC}$ could contain up to two additional isopeptide bonds. These are likely to be formed by second pair of Lys 66 and Asp 121 in the other monomers or intramolecular amine and carboxylate groups, which are close together in the same monomer (Table 1). However, water loss is also expected from the formation of intramolecular imide bonds (Figure 2). Therefore, the species of $C_{D\cdot EDC}$ that have lost two or three water molecules might contain one or two intramolecular imide bonds in addition to the amide bond which links the two subunits.

Reaction of EDC with RNase A Observed by NMR Spectroscopy. We used NMR spectroscopy to determine whether or not EDC modifies the three-dimensional structure

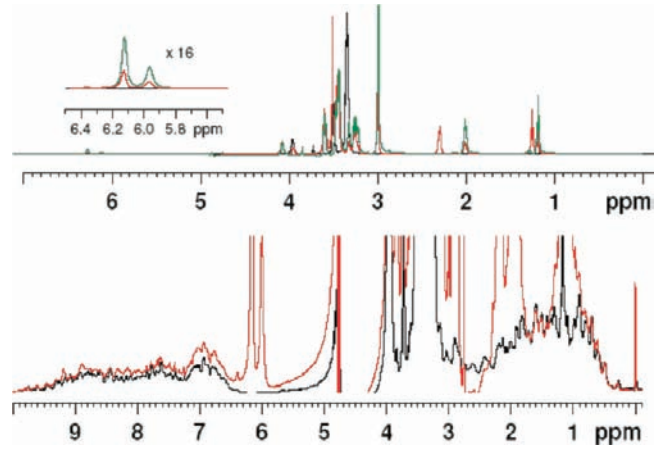

Figure 6. NMR spectra of RNase A, EDC, and EDC modified RNase A. $^{13}C,^{15}N$ labeled RNase A (0.6 mM) at 25 °C in 100 mM MES buffer before (black) and after (red) addition and incubation with EDC. Top panel 1D ^1H spectra. The green spectrum was recorded after 3 h incubation and shows new peaks arising from hydrolyzed EDC. Bottom panel: A 128× view of the 1D ^1H spectra from the top panel revealing the ^1H resonances of RNase A.

of RNase A. The 1D ^1H, 2D $^1H-^{15}N$ HSQC, and $^1H-^{13}C$ HSQC spectra obtained here on RNase A in 100 mM MES buffer at pH 5.0 or 7.0 are very similar to those previously recorded and assigned for RNase A in mildly acidic solutions (*46, 47*) (Figure 6, Supporting Information Figure 1). These spectra indicate that the protein is folded in the native conformation. Upon addition of dry EDC powder to the NMR sample, new resonances corresponding to EDC hydrogens and carbons appear in the 1D ^1H and 2D $^1H-^{13}C$ HSQC spectra. Changes in 1D ^1H signals of EDC over time indicate that it hydrolyzes with a half-life of about 310 min at pH 5 (with no RNase A present) and 90 min at pH 7 (with RNase A present), respectively. Addition of EDC produced a general weakening of the RNase A NMR resonances. This is due to a well-known decreased NMR pulse efficiency at higher ionic strengths. Some new signals near 8.35−7.85 ppm (^1H) and 126−128 ppm (^{15}N) appear in the $^1H-^{15}N$ HSQC spectrum of RNase A after EDC addition. The similarity of these signals' chemical shifts to those appearing in the $^1H-^{15}N$ of $Ac\text{-}Asp\text{-}Ala\text{-}NH_2$ in the presence of EDC suggests that they could result from the reaction of EDC with carboxylate groups near the amide hydrogens. No evidence for protein fragment formation is detected, and no change is observed in the signal arising from the amide group of Lys 66. Essentially, no changes are observed in the ^1H (Figure 6) or ^{13}C (Supporting Information Figure 1) signals of RNase A. Since the magnetic environment of each nucleus is exquisitely sensitive to its local conformation,

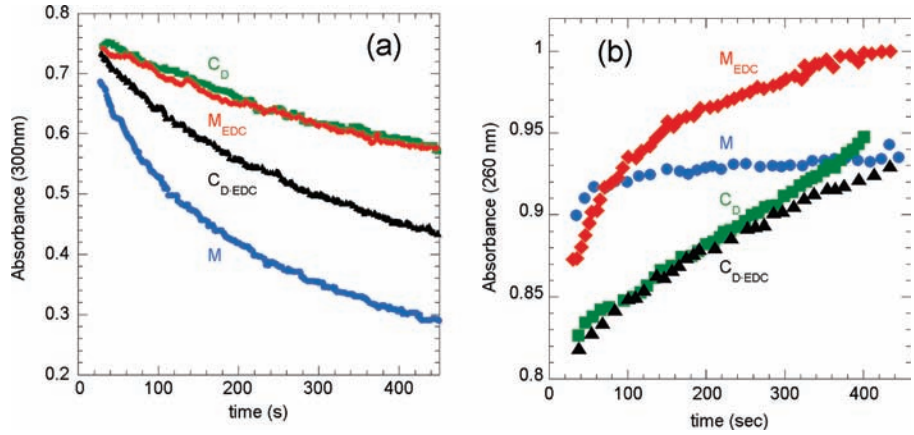

Figure 7. Activity of the products of RNase A C-dimer with EDC against RNA: Activity of RNase A monomer (blue circles), RNase A C-dimer (green squares), M_{EDC} (red diamonds), and $C_{D\cdot EDC}$ (black triangles) against yeast single-stranded RNA (a) and double-stranded poly(A)·poly(U) RNA (b). The protein concentrations were 0.5 μg/mL for all species in the ssRNA assay. Against dsRNA, the concentrations were 12 μg/mL for the RNase A monomer, 6 μg/mL for C_D and M_{EDC}, and 1 μg/mL for $C_{D\cdot EDC}$.

the general absence of change indicates that the conformation of RNase A is not perturbed by reaction with EDC beyond minor alterations near the adduct site.

Ribonucleolytic Activities. We measured the activity of RNase A species against ssRNA and dsRNA (Figure 7a). The activities against single-stranded RNA in Kunitz units normalized to 100 for the RNase A monomer were 100 ± 15 for RNase A monomer, 31 ± 5 for RNase A C-dimer, 47 ± 7 for M_{EDC}, and 37 ± 6 for $C_{D\cdot EDC}$. Relative enzymatic activities against double-stranded poly(A)·poly(U) (Figure 7b) were 1 ± 0.15 for RNase A monomer, 12 ± 2 for RNase A C-dimer, 78 ± 20 for M_{EDC}, and 85 ± 20 for $C_{D\cdot EDC}$.

EDC Reactions with the Dipeptide Ac-Asp-Ala-NH_2. Despite its common use in cross-linking proteins or attaching proteins to substrates for surface plasmon resonance measurements (*48*), the formation of EDC adducts to proteins has not been examined by NMR spectroscopy or mass spectrometry. To better characterize the formation of EDC adducts and other EDC side reactions with proteins, we have studied the reaction of EDC with the dipeptide Ac-Asp-Ala-NH_2, as a simple model for a carboxylate group in a protein. The ^{1}H, ^{13}C, ^{15}N NMR chemical shift assignments of EDC, hydrolyzed EDC, Ac-Asp-Ala-NH_2, and MES were obtained by analysis of 1D and 2D NMR spectra and are reported in Supporting Information Figure 2. Incubation of this dipeptide with excess EDC under reaction conditions similar to those used for proteins (pH 5, 25 °C), namely, 7.72 mM Ac-Asp-Ala-NH_2 in 20 mM MES buffer (pH 6.2) containing 10% D_2O and 50 μM DSS as the chemical shift reference (total volume = 505 μL).

At time = 0, 10.29 mg of EDC (corresponding to a final concentration of about 106 mM) was added to the solution of dipeptide and MES, and the mixture was placed in a 5 mm NMR tube. Over the course of time, the NMR resonances corresponding to the unmodified amide groups of the dipeptide decreased. In the case of the C-terminal $-NH_2$ moiety of the dipeptide, there is a concominant disappearance of the original peaks and an increase of new resonances (Figure 8). For the NH group of Asp, a small peak at 8.71 ppm builds up slowly with time. Essentially all of the original Ala NH peak is gone after 250 min of reaction, and in its place, there is only a series of very small peaks HN with spin systems assignable to Ala in the chemical shift range 8.44−8.25 ppm (Figure 8a,b) and 126 ppm ^{15}N (data not shown). Important spectral changes are also observed in the 1D ^{13}C spectra recorded as a function of time (Supporting Information Figure 3). These spectral changes cannot be accounted for by differences in the chemical shifts of the dipeptide or EDC due to changes in the pH (Supporting Information Figure 4). Therefore, they constitute clear evidence that the dipeptide has indeed reacted with EDC.

Following NMR spectroscopy, the dipeptide/EDC sample was flash-frozen in liquid nitrogen until analysis by HPLC−ESI−MS. A peak whose *m*/*z* value corresponds to the value expected for the dipeptide−EDC adduct is the major peak in this spectrum when recorded in the positive mode (Figure 8c). Also detected are peaks assignable to the cyclized dipeptide, which would result from reaction 7a shown in Figure 1, and to dipeptide adducted to fragments of EDC. The structure of these putative adduct fragments is shown in Supporting Information Figure 5. In agreement with the NMR spectroscopic results, the amount of unreacted dipeptide observed by mass spectrometry is small.

Characterization of EDC Adduct Sites in RNase A. The position of the carboxylate groups in RNase A modified by EDC was characterized by peptide mapping. The results, some representative details of which are shown in Supporting Information Figure 6, strongly suggest that Glu 2, Glu 9, Asp 14, Asp 83, Glu 86, Asp 121, and the C-terminal carboxylate are not modified or are modified in a minority of molecules, whereas Asp 38, Glu 49, Asp 53, and Glu 111 are modified in a relatively large fraction of molecules. These findings are consistent with the observation that Glu 49, Asp 53, and Glu 111 are relatively solvent-exposed and do not interact with other groups in RNase A (Table 2). Except for Glu 9, these results are also in good agreement with the previous results obtained upon reaction of RNase A with different water-soluble carbodiimides under somewhat different conditions (*15*).

How General is EDC Adduct Formation with Protein and What Are Its Effects? We incubated EDC with four well-characterized proteins, namely, RNase Sa, hen lysozyme, carbonic anhydrase, and hemoglobin, under the same reaction conditions as those used to form M_{EDC} and $C_{D\cdot EDC}$ to test for the formation of EDC adducts and to characterize their effects on protein structure and activity. The samples of these proteins, before and after reaction with EDC, were subjected to nondenaturing cathodic PAGE and mass spectrometry to gauge the formation of adducts. Moreover, the proteins and their EDC modified forms were characterized by 1D ^{1}H NMR spectroscopy and enzyme assays to estimate the effect of EDC adducts on their overall structure and activity. The results of all these experiments are summarized in Table 4.

Native cationic gel electrophoresis can provide qualitative data on the extent of protein−EDC adduct formation, since the migration of the protein in the gel increases with its positive charge (Figure 9). Although native RNase Sa is negatively charged and does not enter the gel, EDC treatment of this

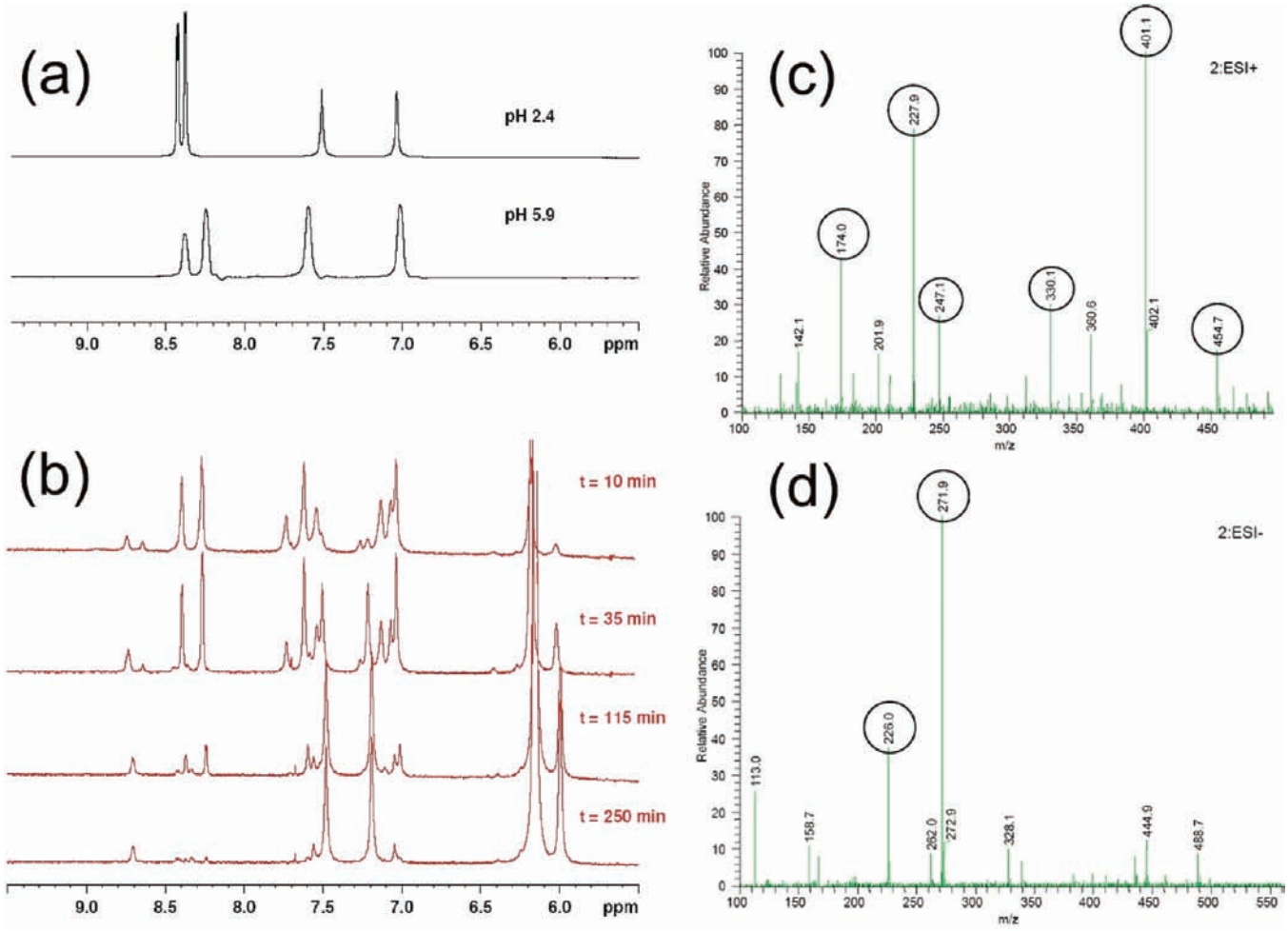

Figure 8. Reaction of the dipeptide Ac-Asp-Ala-NH_2 with EDC. (a) The amide region of the 1D ^{1}H NMR spectrum of the dipeptide at 8 mM concentration at two different pHs and 25 °C. (b) A series of 1D ^{1}H spectra at different times following the addition of 100 mM EDC (final concentration) to the same dipeptide solution. The peaks at 6.00 and 6.15 ppm belong to the amide groups of hydrolyzed EDC. (c) Electrospray mass spectrometry (+ mode) of this sample. The species corresponding to the circled peaks are (*m*/*z* in Da, from left to right) 174.0, EDC + H^+; 227.9, cyclized dipeptide + H^+; 247.1, unreacted dipeptide + H^+; 330.1, dipeptide adducted to a large fragment of EDC + H^+; 401.1, dipeptide adducted to EDC + H^+. 454.7 (cyclized dipeptide)$_2^+$. (d) Electrospray mass spectrometry (− mode) of the same sample. The species corresponding to the circled peaks are 226.0, (cyclized dipeptide − H^+)$^-$; 271.9 (dipeptide adducted to a small fragment of EDC − H^+)$^-$.

Table 4. EDC Adduct Formation by RNase Sa, Lysozyme, Carbonic Anhydrase, and Hemoglobin

protein	native cationic gel electrophoresis	mass spectra[a]	1D ^{1}H NMR	enzyme activity[b]
RNase Sa	no bands	10 570 Da, 10 571 Da	folded	100
RNase Sa·EDC	broad smear with bands at RF = 0.30, 0.49, 0.57, and 0.66	11 195−11 662 Da, 3−7, **5**	folded, but some loss of fine dispersion	40
lysozyme	1 band, RF = 0.76	14 324 Da, 14 293 Da	folded	100
lysozyme·EDC	broad bond, RF = 0.80−0.89	14 451−14 911 Da,1−4, **2**	folded, with only minor changes	50−100
carbonic anhydrase	series of bands, RF = 0.07, 0.13, 0.21, and 0.29	29 121 Da, 29 025 Da	folded	100
carbonic anhydrase·EDC	broad smear with bands, RF = 0.28, 0.37, 0.54, and 0.58	29 100−30 800 Da, 0−12, **6**	substantially unfolded	33
hemoglobin	broad band, RF = 0.39 and 0.47	α 15 261 Da, 15 128 Da β 1 6 111 Da, 15 869 Da	folded	not measured
hemoglobin·EDC	series of broad bands with RF = 0.38, 0.45, 0.54, 0.59, and 0.72	α 15 100−15 400 Da, 0−2, **1** β 16 025−16 400 Da, 1−4, **2**	thoroughly unfolded	

[a] Native: MW calculated from the sequence is given, followed by the MW of the chief peak in the mass spectrum. EDC modified: the approximate MWs of species or range of MWs after EDC treatment is given, followed on the next line by the estimated range of the approximate number of EDC adducts attached per protein molecule. Finally, the most common number of EDC adducts is written in **bold**. [b] In % activity relative to the activity of the unmodified protein.

enzyme produced about four different positively charged species. Gel electrophoresis reveals that lysozyme is also modified by EDC treatment, but to a lesser extent than RNase Sa or carbonic anhydrase. The two bands observed for native hemoglobin could arise from the α and β subunits; EDC treatment endows them with a greater positive charge as inferred from their increased migration in the gel.

Mass spectrometry (Table 4, Figure 10) revealed higher masses for all four proteins after EDC treatment. On the basis of the molecular weight differences of the chief peaks before

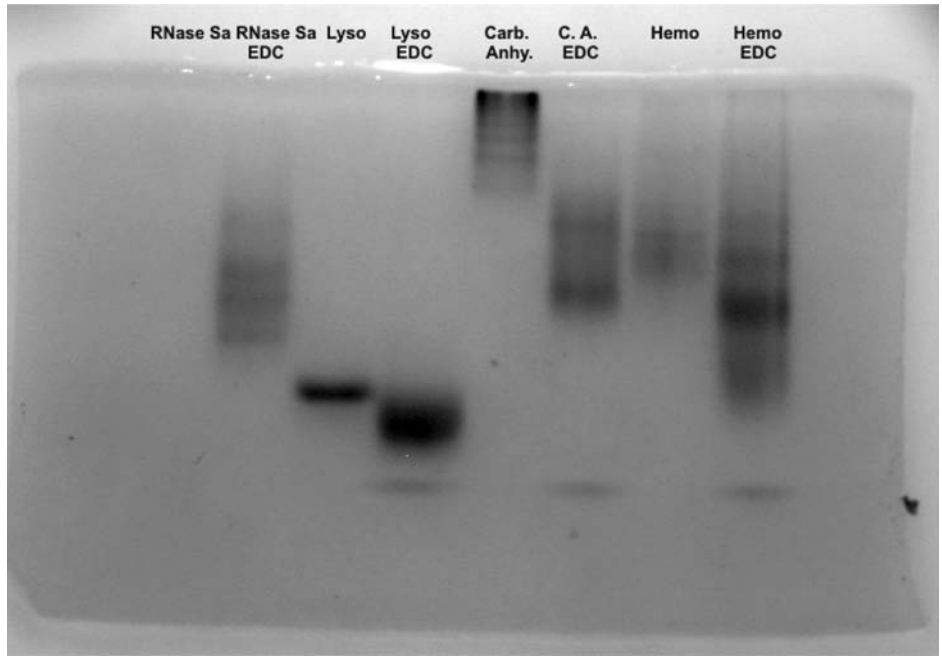

Figure 9. Nondenaturing cationic gel electrophoresis of RNase Sa, lysozyme, carbonic anhydrase, and hemoglobin before and after EDC treatment.

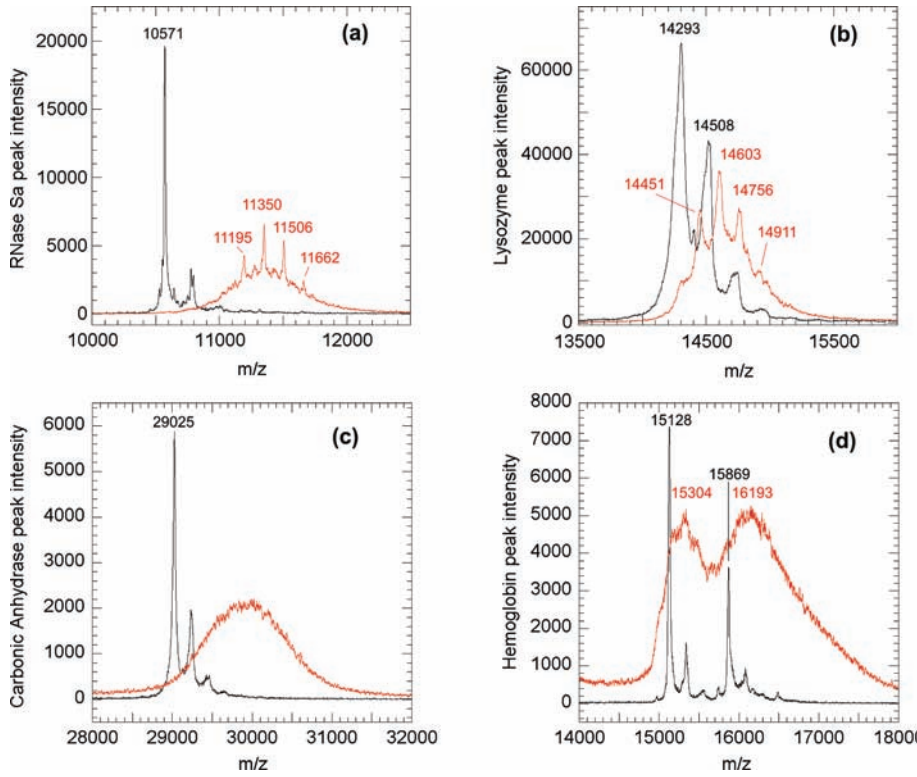

Figure 10. Mass spectra of (a) RNase Sa, (b) lysozyme, (c) carbonic anhydrase, and (d) hemoglobin before (black curves) and after (red) EDC treatment. The increase in the broadness of the peaks after reaction with EDC could result from the formation of EDC adducts, or fragmented EDC adducts, or the loss of a water molecule due to cyclization of the polypeptide chain or combinations of these changes.

and after reaction with EDC, we could estimate that RNase Sa acquired, on average, approximately 5 EDC adducts. This is, in general greater than the number of EDC adducts attached to lysozyme (whose mean value is roughly 2) or the hemoglobin α and β subunits (typically about 1 or 2). Carbonic anhydrase was extensively modified by EDC and acquired, on average, roughly 6 EDC adducts.

1D ^{1}H NMR spectroscopy is commonly used qualitatively to judge if a protein is folded, completely denatured, or in the molten globule state (*49, 50*). The good chemical shift dispersion observed for RNase Sa, lysozyme, carbonic anhydrase, and hemoglobin in their respective 1D ^{1}H NMR spectra reveals that they are in the native, folded conformation (Figure 11) (*51*) (*52*). After EDC treatment, the NMR spectrum of RNase Sa loses some fine dispersion, which can be interpreted as a partial loss of native structure. In contrast, the NMR spectrum of EDC treated lysozyme shows only minor differences as relative to untreated protein. The substantial loss of signal dispersion and

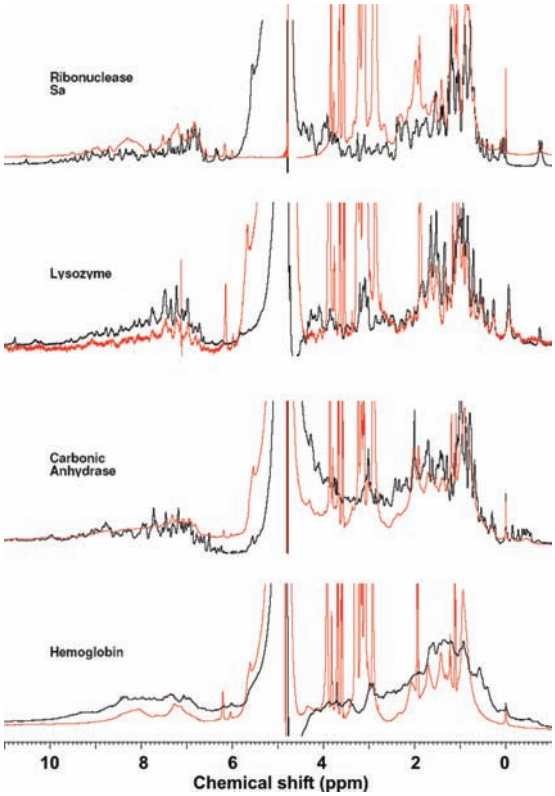

Figure 11. 1D ^{1}H NMR spectra of RNase Sa, hen lysozyme, carbonic anhydrase, and hemoglobin in 1−5 mM sodium phosphate pH 6.6 before (black curves) and after (red curves) EDC modification.

the appearance of a broad NMR peak near 0.90 ppm, which is assignable to unfolded methyl hydrogens, indicates that carbonic anhydrase suffers significant denaturation upon EDC treatment (*52*). Similar, but more drastic spectral changes indicating thorough denaturation are seen for EDC-treated hemoglobin.

Using the Kunitz assay, we found that EDC treatment causes RNase Sa to lose about 60% of the activity of the unmodified protein toward yeast ssRNA (Figure 12a). Neither RNase Sa nor EDC treated RNase Sa showed any detectable activity against double-stranded poly(A)·poly(U); this result is consistent with this enzyme's strict specificity for G. The enzymatic assay for lysozyme and EDC-modified lysozyme indicates that the latter retains most of the enzymatic activity of the former (Figure 12b). The results of the assays of carbonic anhydrase show that EDC treatment reduces the protein's activity by two-thirds (Figure 12c). The mean enzymatic activities were found to be 225 ± 36 for carbonic anhydrase and 72 ± 3 for EDC-modified carbonic anhydrase where the uncertainty given is the standard deviation (1σ).

DISCUSSION

RNase A oligomers, including the C-dimer, show increased ribonucleolytic activity against double-stranded RNAs and potent *in vivo* antitumor activities. These activities are lost as the oligomers slowly disassociate into monomers. In this paper, we have used EDC, a carbodiimide, to cross-link the subunits of the C-dimer. The resulting C-dimer, called $C_{D\cdot EDC}$, is not dissociated by procedures such as heating, SDS PAGE, or MALDI-TOF mass spectroscopy, which do dissociate the unmodified C-dimer. EDC and other carbodiimides induce the formation of amide bonds (also called isopeptide bonds) between nearby carboxylate and amine groups (Figure 2). Although solid evidence is lacking, we infer that Lys 66 and Asp 121 are presumably the residues which form the cross-linking amide

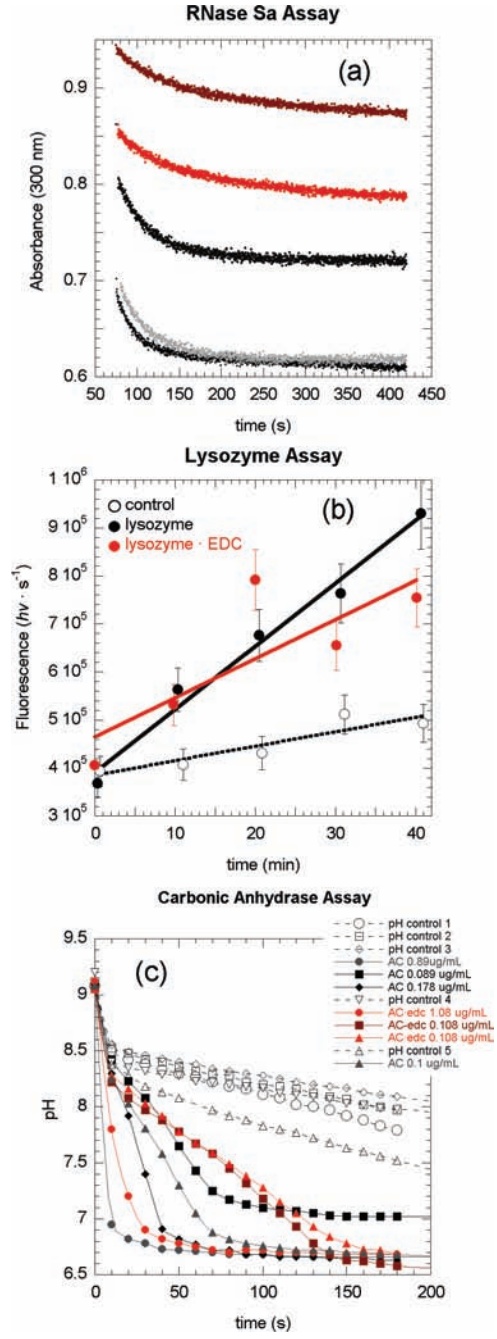

Figure 12. Enzymatic assays of RNase Sa, lysozyme, and carbonic anhydrase and these proteins treated by EDC. (a) Some representative RNase assays against yeast ssRNA are shown. Black curves: RNase Sa 4.4 μg/mL. Red curves: EDC modified RNase Sa 4.9 μg/mL. Curves are offset along the *y*-axis for ease of comparison. (b) Lysozyme assay using 300 μM 4-methylumbelliforyl D-D-*N*,*N*′,*N*″-triacetylchitotrioside and 600 nM lysozyme (solid points), or EDC-modified lysozyme (red solid points). (c) Carbonic anhydrase assays. Open symbols, control experiments; filled symbols, carbonic anhydrase; red-filled circles, EDC-modifed carbonic anhydrase.

bond in $C_{D\cdot EDC}$, since they bear the only amine and carboxylate groups that are in close proximity in the C-dimer structure (Table 1, Figure 1). The yield of the cross-linked C-dimer is rather low (6.5%). This appears to be consistent with the low reactivity of Asp 121 with EDC as detected by peptide mapping as well as the results of Riehm and Scheraga who found this residue to be relatively unreactive toward a water-soluble carbodiimide (*15*).

EDC Forms Adducts with Ribonuclease A. The relatively high concentration of EDC needed to induce C-dimer cross-

linking leads to adduct formation in which EDC is stably linked to a carboxylate group by an N-acylisourea bond (Figure 1). Using MALDI-TOF mass spectrometry, RNase A monomers treated with EDC, called M_{EDC}, were found to carry approximately one to five EDC adducts per molecule, and $C_{D\cdot EDC}$ molecules were observed to bear, in round numbers, three to seven EDC adducts. These mass spectroscopy results and the heterogeneity detected by cation exchange chromatography and nondenaturing cathodic PAGE indicate that M_{EDC} and $C_{D\cdot EDC}$ are rich mixtures of species carrying EDC adducts which vary both in number and in position (*15*) with Asp 38, Glu 49, Asp 53, and Glu 111 being the most heavily modified as gauged by peptide mapping.

Activity of M_{EDC} and $C_{D\cdot EDC}$ against Yeast Single-Stranded RNA. The ribonucleolytic activity against single-stranded RNA decreases somewhat when RNase A is conjugated with EDC. There are three plausible explanations for this loss of activity. First, it is possible that the increased positive charge on the protein surface compromises the conformational stability and thereby decreases the amount of protein present in the native, catalytically active state. However, it has been reported that the substitution of multiple solvent-exposed carboxylate groups by Lys or neutral side chains had modest effects on the conformation stability of T4 Lysozyme (*53*) or RNase Sa (*54*) and on the pKas of their remaining ionizable groups. Moreover, peptides composed chiefly of Ala, Ile, and Lys can form well-folded highly stable four-helix bundle proteins despite the high net charge (+12) conferred by the Lys (*55*). Furthermore, it is striking that RNase 3 (also called eosinophil cationic protein), the mostly positively charged member of the RNase A family, is also the member that has the highest conformational stability (*56*). Finally, NMR spectroscopy shows that the native conformation of RNase A is hardly affected by reaction with EDC. All this evidence points to the conclusion that the low single-strand ribonucleolytic activity of the M_{EDC}, other cationized RNases, and RNase A oligomers is not due to a loss of conformational integrity provoked by electrostatic repulsion. Second, chemical modification of Lys 66 and Asp 121 could affect the activity, since the former participates in RNA binding (*57*) and the latter enhances the activity of the catalytic residue His 119 (*58*). While Lys 66 and Asp 121 are moderately well conserved in the sequences of human ribonucleases (*59*), nevertheless genetic selection experiments have shown that neither is essential for structure or activity in RNase A (*60*). A third possible cause of the loss of activity is that the additional positive charges lead to unproductive binding of RNA to the surface of RNase A away from the active site or retards product release after hydrolysis. This possible explaination has been put forward previously to account for the lower single-strand ribonucleolytic activity of the RNase A oligomers, including the C-dimer (*61*). Lower single-strand ribonucleolytic activity was previously observed for RNase species cationized by chemical coupling (*24*, *44*, *62*).

Reactivity of M_{EDC} and $C_{D\cdot EDC}$ against dsRNA. The increased net positive charge bestowed by the EDC adducts endows both M_{EDC} and $C_{D\cdot EDC}$ with augmented ribonucleolytic activity against the double-stranded poly(A)·poly(U). Increased dsRNase activity, cytotoxicity, and antitumor actions have been observed previously for RNase A species or homologues which carry higher positive charge density, including RNase A oligomers (*32*), variants (*63*−*65*), other cationized RNase A monomers (*40*, *44*, *62*, *66*), cationized RNase A dimers (*24*), BS-RNase (*10*, *67*), and human RNase 1 (*68*). The increase in these activities has been attributed to an improved ability to stabilize transient single-strand regions in double-stranded RNAs (*32*). On the basis of these previous results, we propose that M_{EDC} and $C_{D\cdot EDC}$ might have heightened cytotoxic and/or antitumor activity. An increased positive charge density can promote the intracellular delivery of RNases (*69*, *70*) and augment their capacity to cleave intracellular tRNAs, rRNAs, which are rich in double-stranded regions, and the poly(A) tail of mRNAs, which adopts a double helix (*71*). Raines and co-workers have, however, recently pointed out that an increased positive charge density achieved by site-directed mutagenesis also increases the binding of ribonucleases to the cytoplasmic ribonuclease inhibitor (*70*), and this binding decreases the RNase activity and cytotoxicity. On the other hand, Yamada and co-workers found that the binding of cRI to a series of RNase A species which were cationized by the EDC-mediated coupling of carboxylate groups to ethylenediamine actually *decreased* as the net positive charge of the species increased, an observation which led them to propose that the reduced cytotoxicity of the most cationic RNase A species is due to an increased rate of protein degradation (*44*). Among the carboxylate group carrying residues which are more heavily modified by EDC, Asp 38 and Glu 111 make contact with the cRI (*70*, *72*). It is possible that cRI binding decreases and cytotoxicity increases when these groups were modified by ethylenediamine, thus accounting for the observations of Raines, Yamada, and their co-workers. In support of this possible explanation, the mutation of Asp 38 (*73*) and Glu 111 (*74*) has been shown to reduce cRI binding.

Reaction of EDC with Ac-Asp-Ala-NH_2. The reaction of EDC with a carboxylate containing dipeptide has been monitored for the first time by NMR spectroscopy and mass spectrometry. The reaction produces four detectable dipeptide species, which are putatively the dipeptide−EDC adduct, two species with the dipeptide being adducted to a large or small part of EDC, and the cyclized dipeptide. By mass spectrometry, the dipeptide−EDC adduct seems to be the most populated species. Cyclization reactions due to Asn deamidation are disfavored in folded RNase A (*75*) or its glycosylated form RNase B (*45*) due to the rigidity of the polypeptide chain. This suggests that the cyclization reaction observed here in the dipeptide could be less favored in the context of a folded protein. All of these reactions will remove a negative charge from the modified carboxylate group, and two of them will endow it with a new positive charge.

EDC Adduct Formation in General Alters Protein Net Charge, Conformation, and Activity. Unlike RNase A, RNase Sa is a microbial enzyme endowed with an excess of negative charges. The substitution of five surface carboxylate groups of RNase Sa by Lys causes only very modest effects on the protein's conformational stability and enzymatic activity toward poly(I) (*76*) but confers cytotoxicity (*77*). The modest loss of fine tertiary structure and hydrolytic activity toward ssRNA observed here could arise from the EDC modification of some RNase Sa molecules at Glu 54, which is a catalytic residue, or at Asp 33, Asp 84, or Asp 93, which make important contributions to the conformational stability (*54*).

The neligible to low loss of lysozyme activity upon EDC treatment suggests that the catalytic carboxylate groups, Glu 35 and Asp 52, are not substantially modified by EDC. Previous modifications experiments identified Glu 35 and Asp 52 as being the least reactive carboxylates toward carbodiimide (*78*), whereas Asp 102 is the most reactive (*79*). Although Asp 102 forms part of the first two (A,B) of the six substrate subsites in lysozyme, it would not expected to contribute to binding to the shorter three-residue sugar substrate used in our assay.

Regarding hemoglobin, Acharya and Seetharam (*80*) found using tryptic peptide mapping that EDC readily modifies Glu 22 and Glu 43 of the β chain of human S-hemoglobin. These researchers performed their reaction at conditions similar to ours except they used a slightly higher pH (6.0) and a lower EDC concentration (20 mM). Both bovine carbonic anhydrase II (*81*)

and human hemoglobin (*82*) are known to adopt molten globule or other denatured conformations at pH ≤ 5. It is possible that carboxylate groups that are buried and protected against EDC modification at neutral pH become exposed and react with EDC at pH 5.0 in these partly denatured states. The modification of normally buried carboxylate groups could prevent refolding at pH 6.6 and account for the extensive and severe denaturation observed for these proteins by NMR.

CONCLUSION

The RNase A C-dimer has augmented enzymatic, cytotoxic, and antitumoral activities as compared to the RNase A monomer, but loses these properties upon dissociation. Here, the carbodiimide EDC has been used to induce the formation of isopeptide bonds in the RNase A C-dimer which prevent it from dissociating. This cross-linked C-dimer retains the native protein conformation and shows activity against dsRNA that is even higher than that of the unreacted C-dimer. This further increase in activity is due to the formation of positively charged EDC adducts on the protein surface. Asp 38, Glu 49, Asp 53, and Glu 111 appear to have the carboxylate groups most susceptible to EDC modification. Both the stability against dissociation and the increased positive charge density are likely to be advantageous features for the development of RNase A based therapeutics. EDC is widely used for cross-linking proteins or for activating carboxylate groups for reaction with amines. By using a model dipeptide, EDC adduct formation and peptide cyclization are substantiated for the first time by NMR spectroscopy and mass spectrometry. In this work, these adducts have been found to affect the net charge, conformation, and enzymatic activity of four well-characterized proteins. This side reaction and its consequences should be considered when EDC is used to couple proteins to each other or to substrates for surface plasmon resonance measurements.

ACKNOWLEDGMENT

We thank Dr. Luis Simón for helpful discussion and Prof. Marta Bruix for critically reading the manuscript. We owe our grateful thanks to Dr. David Pantoja and Dr. Plácido Galindo Iranzo for expert technical assistance with NMR spectroscopy and mass spectrometry, respectively. We are especially grateful to D. Alberto Ogbechie Condés for his contribution to the experiments on RNase Sa, Lysozyme, Carbonic Anhydrase and Hemoglobin, and to Prof. C. Nick Pace for his generous gift of RNase Sa. This work was supported by grants CTQ2007-68014-C02-02 and BFU2006-15543-CO2-02 from the Spanish Ministry of Education and Science and ex-60% GOTTE06 from the Italian "M.I.U.R." and the University of Verona. JPLA gratefully acknowledges a fellowship from the Consejería de Educación de la Comunidad de Madrid y el Fondo Social Europeo.

Supporting Information Available: Supporting graphs showing: (1) $^{1}H-^{15}N$ HSQC and $^{1}H-^{13}C$ HSQC spectra of RNase A and EDC·modified $^{13}C,^{15}N$ RNase A. (2) NMR chemical shift assignments for EDC, MES, and the dipeptide Ac-Asp-Ala-NH_2. (3) 1D ^{13}C spectra of the dipeptide Ac-Asp-Ala-NH_2, EDC alone and during their reaction. (4) Comparison of the chemical shifts in Ac-Asp-Ala-NH_2 alone and upon incubation with EDC. (5) Putative structures of the dipeptide−EDC fragment adducts detected by electrospray mass spectrometry. (6) Representative peptide mapping results. This material is available free of charge via the Internet at http://pubs.acs.org.

Note Added after ASAP Publication: This manuscript was published on July 16, 2009 with erroneous references to Figures 1 and 2. The revised version was published on July 24, 2009.

LITERATURE CITED

(1) Crestfield, A. M., Stein, W. H., and Moore, S. (1962) On the agregation of bovine pancreatic ribonuclease. *Arch. Biochem. Biophys. 1 (Suppl.)* 217–222.

(2) Liu, Y., Hart, P. J., Schlunegger, M. P., and Eisenberg, D. (1998) The crystal structure of a 3D domain-swapped dimer of RNase A at 2.1 Å resolution. *Proc. Natl. Acad. Sci. U.S.A. 95*, 3437–3442.

(3) Liu, Y., Gotte, G., Libonati, M., and Eisenberg, D. (2001) A domain-swapped RNase A dimer with implications for amyloid formation. *Nat. Struct. Biol. 8*, 211–214.

(4) Gotte, G., Bertoldi, M., and Libonati, M. (1999) Structural versatility of bovine ribonuclease A. Distinct conformers of trimeric and tetrameric aggregates of the enzyme. *Eur. J. Biochem. 265*, 680–687.

(5) Gotte, G., Laurents, D. V., and Libonati, M. (2006) Three-dimensional domain-swapped oligomers of ribonuclease A: identification of a fifth tetramer, pentamers and hexamers, and detection of trace heptameric, octameric and nonameric species. *Biochim. Biophys. Acta 1764*, 44–54.

(6) Gotte, G., and Libonati, M. (2004) Oligomerization of ribonuclease A: two novel three-dimensional domain-swapped tetramers. *J. Biol. Chem. 279*, 36670–36679.

(7) Cozza, G., Moro, S., and Gotte, G. (2008) Elucidation of the ribonuclease A aggregation process mediated by 3D domain swapping: a computational approach reveals possible new multimeric structures. *Biopolymers 89*, 26–39.

(8) Park, C., and Raines, R. T. (2000) Dimer formation by a "monomeric" protein. *Protein Sci. 9*, 2026–2033.

(9) Gotte, G., Vottariello, F., and Libonati, M. (2003) Thermal aggregation of ribonuclease A. A contribution to the understanding of the role of 3D domain swapping in protein aggregation. *J. Biol. Chem. 278*, 10763–10769.

(10) Libonati, M., and Floridi, A. (1969) Breakdown of double-stranded RNA by bull semen ribonuclease. *Eur. J. Biochem. 8*, 81–87.

(11) Matousek, J., Gotte, G., Pouckova, P., Soucek, J., Slavik, T., Vottariello, F., and Libonati, M. (2003) Antitumor and other biological actions of oligomers of ribonuclease A. *J. Biol. Chem. 278*, 23817–23822.

(12) Libonati, M., Bertoldi, M., and Sorrentino, S. (1996) The activity on double-stranded RNA of aggregates of ribonuclease A higher than dimers increases as a function of the size of the aggregates. *Biochem. J. 318*, 287–290.

(13) López-Alonso, J. P., Bruix, M., Font, J., Ribó, M., Vilanova, M., Rico, M., Gotte, G., Libonati, M., González, C., and Laurents, D. V. (2006) Formation, structure and dissociation of the RNase S 3D domain-swapped dimer. *J. Biol. Chem. 281*, 9400–9406.

(14) Pulido, D., López-Alonso, J. P., Marchán, V, González, C., Grandas, A., and Laurents, D. V. (2008) Preparation of ribonuclease S domain-swapped dimers conjugated with DNA and PNA: Modulating the activity of Ribonucleases. *Bioconjugate Chem. 19*, 263–270.

(15) Riehm, J. P., and Scheraga, H. A. (1966) Structural studies of ribonuclease. XXI. The reaction between ribonuclease and a water-soluble carbodiimide. *Biochemistry 5*, 99–115.

(16) Timkovick, R. (1977) Detection of the stable addition of carbodiimide to proteins. *Anal. Biochem. 79*, 135–143.

(17) Staros, J. V., Wright, R. W., and Swingle, D. M. (1986) Enhancement by N-hydroxysulfosuccinimide of water-soluble carbodiimide-mediated coupling reactions. *Anal. Biochem. 156*, 220–222.

(18) Nakajima, N., and Ikada, Y. (1995) Mechanism of amide formation by carbodiimide for bioconjugation in aqueous media. *Bioconjugate Chem. 6*, 123–130.

(19) Hebert, E. J., Grimsley, G. R., Hartley, R. W., Horn, G., Schell, D., Garcia, S., Both, V., Sevcik, J., and Pace, C. N. (1997) Purification of ribonucleases Sa, Sa2 and Sa3 after expression in Escherichia coli. *Protein Express. Purif. 11*, 162–168.

(20) Koradi, R., Billeter, M., and Wüthrich, K. (1996) MOLMOL: a program for display and analysis of macromolecular structures. *J. Mol. Graphics 14*, 51–55.

(21) Li, H., Robertson, A. D., and Jensen, J. H. (2005) Very fast empirical prediction and rationalization of protein pKa values. *Proteins 61*, 704–721.

(22) Laemmli, U. K. (1970) Cleavage of structural proteins during the assembly of the head of bacteriophage T4. *Nature 227*, 680–685.

(23) Goldenberg, D. P. (1989) In *Protein Structure. A practical approach* (Creighton, T. E., Ed.) pp 225−250, Oxford University Press, IRL Press, Oxford, UK.

(24) Poucková, P., Morbio, M., Vottariello, F., Laurents, D. V., Matousek, J., Soucek, J., Gotte, G., Donadelli, M., Costanzo, C., and, and Libonati, M. (2007) Cytotoxicity of polyspermine-ribonuclease A and polyspermine-dimeric ribonuclease A. *Bioconjugate Chem. 18*, 1946–1955.

(25) Richards, F. M., and Vithayathil, P. J. (1959) The preparation of subtilisin-modified ribonuclease and separation of the peptide and protein components. *J. Biol. Chem. 234*, 1469–1465.

(26) Huang, W. Y., and Tang, J. (1969) On the specificity of human gastricsin and pepsin. *J. Biol. Chem. 244*, 1085–1091.

(27) Ribó, M., Benito, A., Canals, A., Nogués, M. V., Cuchillo, C. M., and Vilanova, M. (2001) Purification of engineered human pancreatic ribonuclease. *Methods Enzymol. 341*, 221–234.

(28) Bodenhausen, G., and Ruben, D. J. (1980) Natural abundance nitrogen-15 NMR by enhanced heteronuclear spectroscopy. *Chem. Phys. Lett. 69*, 185–189.

(29) Aue, W. P., Bartholdi, E., and Ernst, R. R. (1976) Two-dimensional spectroscopy. Application to nuclear magnetic resonance. *J. Chem. Phys. 64*, 2229–2246.

(30) Kumar, A., Ernst, R. R., and Wüthrich, K. (1980) A two dimensional nuclear Overhauser enhancement (2D NOE) experiment for the elucidation of complete proton-proton cross-relaxation network in biological macromolecules. *Biochem. Biophys. Res. Commun. 95*, 1–6.

(31) Kunitz, M. (1946) A spectrophotometric method for the measurement of ribonuclease activity. *J. Biol. Chem. 164*, 563–568.

(32) Libonati, M., and Sorrentino, S. (2001) Degradation of double-stranded RNA by mammalian pancreatic-type ribonucleases. *Methods Enzymol. 341*, 234–248.

(33) Wilbur, K. M., and Anderson, N. G. (1948) Electrometric and Colormetric determination of carbonic anhydrase. *J. Biol. Chem. 176*, 147–154.

(34) Yang, Y., and Hamaguchi, K. (1980) Hydrolysis of 4-methylumbelliteryl N-acetyl-chitotrioside catalyzed by hen and turkey lysozymes. *J. Biochem. 87*, 1003–1014.

(35) Rico, M., Santoro, J., González, C., Bruix, M., and Neira, J. L. (1990) In *Structure, Mechanism and Function of Ribonucleases. Proceedings of the 2nd International Meeting* (Cuchillo, C. M., de Llorens, R., Nogués, M. V., and Parés, X., Eds.) Universitat Autònoma de Barcelona, Sant Feliu de Guíxols, Girona, Spain.

(36) Rico, M., Gallego, E., Santoro, J., Bermejo, F. J., Nieto, J. L., and Herranz, J. (1984) On the fundamental role of the Glu 2-... Arg 10+ salt bridge in the folding of isolated ribonuclease A S-peptide. *Biochem. Biophys. Res. Commun. 123*, 757–763.

(37) Juminaga, D., Wedemeyer, W. J., Garduño-Júarez, R., McDonald, M. A., and Scheraga, H. A. (1997) Tyrosyl interactions in the folding and unfolding of bovine pancreatic ribonuclease A: a study of tyrosine-to-phenylalanine mutants. *Biochemistry 36*, 10131–10145.

(38) Wolf, B., Lesnaw, J. A., and Reichmann, M. E. (1970) A mechanism of the irreversible inactivation of bovine pancreatic ribonuclease by diethylpyrocarbonate. A general reaction of diethylpyrocarbonate with proteins. *Eur. J. Biochem. 13*, 519–525.

(39) Gotte, G., Testolin, L., Costanzo, C., Sorrentino, S., Armato, U., and Libonati, M. (1997) Cross-linked trimers of bovine ribonuclease A: activity on double-stranded RNA and antitumor action. *FEBS Lett. 415*, 308–312.

(40) Wang, D., and Moore, S. (1977) Polyspermine-Ribonuclease prepared by cross-linkage with dimethyl suberimidate. *Biochemistry 16*, 2937–2942.

(41) Kunkel, G. R., Mehrabian, M., and Martinson, H. G. (1981) Contact-site cross-linking agents. *Mol. Cell. Biochem. 34*, 3–13.

(42) Simons, B. L., Kaplan, H., Fournier, S. M., Cyr, T., and Hefford, M. A. (2007) A novel cross-linked RNase A dimer with enhanced enzymatic properties. *Proteins: Struct. Funct. Bioinformatics 66*, 183–195.

(43) Sheehan, J. C., and Hlavka, J. J. (1957) The cross-linking of gelatin using a water-soluble carbodiimide. *J. Am. Chem. Soc. 79*, 4528–4529.

(44) Futami, J., Nukui, E., Maeda, T., Kosaka, M., Tada, H., Seno, M., and Yamada, H. (2002) Optimal modification for the highest cytotoxicity of cationized ribonuclease. *Biochem. J. 132*, 223–228.

(45) Gotte, G., Libonati, M., and Laurents, D. V. (2003) Glycosylation and specific deamidation of ribonuclease B affect the formation of 3D domain-swapped oligomers. *J. Biol. Chem. 278*, 46241–46251.

(46) Rico, M., Bruix, M., Santoro, J., González, C., Neira, J. M., Nieto, J. M., and Herranz, J. (1989) Sequential 1H-NMR assignment and solution structure of bovine pancreatic ribonuclease A. *Eur. J. Biochem. 183*, 623–638.

(47) Shimotakahara, S., Rios, C. B., Laity, J. H., Zimmerman, D. E., Scheraga, H. A., and Montelione, G. T. (1997) NMR structural analysis of an analog of an intermediate formed in the rate-determining step of one pathway in the oxidative folding of bovine pancreatic ribonuclease A: automated analysis of 1H, 13C, and 15N resonance assignments for wild-type and [C65S, C72S] mutant forms. *Biochemistry 36*, 6915–6929.

(48) Johnsson, D., Löfås, S., and Lindquist, G. (1991) Immobilization of protein to a carboxymethyldextran - modified gold surface for biospecific interaction analysis in surface plasmon resonance. *Anal. Biochem. 198*, 268–271.

(49) Campbell, I. D., Dobson, C. M., and Williams, R. J. (1985) The study of conformational states of proteins by nuclear magnetic resonance. *Biochem. J. 231*, 1–10.

(50) Dyson, H. J., and Wright, P. E. (1998) Equilibrium NMR studies of unfolded and partially folded proteins. *Nat. Struct. Biol. NMR Suppl.* 499–503.

(51) Laurents, D. V., Pérez-Cañadillas, J. M., Santoro, J., Rico, M., Schell, D., Pace, C. N., and Bruix, M. (2001) Solution structure and dynamics of ribonuclease Sa. *Proteins: Struct., Funct., Genet. 44*, 200–211.

(52) Wüthrich, K. (1986) *NMR of Proteins and Nucleic Acids*, Wiley, New York.

(53) Sun, D. P., Söderlind, E., Baase, W. A., Wozniak, J. A., Sauer, U., and Matthews, B. W. (1991) Cumulative site-directed charge-change replacements in bacteriophage T4 lysozyme suggest that long-range electrostatic interactions contribute little to protein stability. *J. Mol. Biol. 221*, 837–878.

(54) Laurents, D. V., Huyghues-Despointes, B. M., Bruix, M., Thurlkill, R. L., Schell, D., Newsom, S., Grimsley, G. R., Shaw, K. L., Trevino, S., Rico, M., Briggs, J. M., Antosiewicz, J. M., Scholtz, J. M., and Pace, C. N. (2003) Charge-charge interactions are key determinants of the pK values of ionizable groups in ribonuclease Sa (pI = 3.5) and a basic variant (pI = 10.2). *J. Mol. Biol. 325*, 1077–1092.

(55) López de la Osa, J., Bateman, D. A., Ho, S., González, C., Chakrabartty, A., and Laurents, D. V. (2007) Getting specificity from simplicity in putative proteins from the prebiotic Earth. *Proc. Natl. Acad. Sci. U.S.A. 104*, 14941–14946.

(56) Maeda, T., Mahara, K., Kitazoe, M., Futami, J., Takidani, A., Kosaka, M., Tada, H., Seno, M., and Yamada, H. (2002) RNase 3 (ECP) is an extraordinarily stable protein among human pancreatic type RNases. *J. Biochem. 132*, 737–742.

(57) Moussaoui, M., Guasch, A., Boix, E., Cuchillo, C. M., and Nogués, M. V. (1996) The role of non-catalytic binding subsites in the endonuclease activity of bovine pancreatic ribonuclease A. *J. Biol. Chem. 271*, 4687–4692.

(58) Stern, M. S., and Doscher, M. S. (1984) Aspartic acid-121 functions at the active site of bovine pancreatic ribonuclease. *FEBS Lett. 171*, 253–256.

(59) Cho, S., Beintema, J. J., and Zhang, J. (2005) The ribonuclease A superfamily of mammals and birds: Identifying new members and tracing evolutionary histories. *Genomics 85*, 208–220.

(60) Smith, B. D., and Raines, R. T. (2006) Genetic selection for critical residues in ribonucleases. *J. Mol. Biol. 362*, 459–478.

(61) Libonati, M., and Gotte, G. (2004) Aggregation of bovine ribonuclease A: Structural and functional features of its oligomers. *Biochem. J. 380*, 311–327.

(62) Futami, J., Kitazoe, M., Maeda, T., Nukui, E., Sakaguchi, M., Kosaka, J., Miyazaki, M., Kosaka, M., Tada, H., Seno, M., Sasaki, J., Huh, N.-H., Namba, M., and Yamada, H. (2005) Intracellular delivery of proteins into mammalian living cells by polyethylenimine-cationization. *J. Biosci. Bioeng. 99*, 95–103.

(63) Di Donato, A., Cafaro, V., and D'Alessio, G. (1994) Ribonuclease A can be transformed into a dimeric ribonuclease with antitumor activity. *J. Biol. Chem. 269*, 17394–17396.

(64) Cafaro, V., Bracale, A., Di Maro, A., Sorrentino, S., D'Alessio, G., and Di Donato, A. (1998) New muteins of RNase A with enhanced antitumor action. *FEBS Lett. 437*, 149–152.

(65) Piccoli, R., Di Gaetano, S., De Lorenzo, C., Grauso, M., Monaco, C., Spalletti-Cernia, D., Laccetti, P., Cinátl, J., Matousek, J., and D'Alessio, G. (1999) A dimeric mutant of human pancreatic ribonuclease with selective cytotoxicity toward malignant cells. *Proc. Natl. Acad. Sci. U.S.A. 96*, 7768–7773.

(66) Futami, J., Maeda, T., Kitazoe, M., Nukui, E., Tada, H., Seno, M., Kosaka, M., and Yamada, H. (2001) Preparation of potent cytotoxic ribonucleases by cationization: enhanced cellular uptake and decreased interaction with ribonuclease inhibitor by chemical modification of carboxyl groups. *Biochemistry 40*, 7518–7524.

(67) Sica, F., Di Fiore, A., Merlino, A., and Mazzarella, L. (2004) Structure and stability of the non-covalent swapped dimer of bovine seminal ribonuclease. *J. Biol. Chem. 279*, 36753–36760.

(68) Sorrentino, S., and Libonati, M. (1994) Human pancreatic-type and nonpancreatic-type ribonucleases: a direct side-by-side comparison of their catalytic properties. *Arch. Biochem. Biophys. 312*, 340–348.

(69) Fuchs, S. M., and Raines, R. T. (2006) Internalization of cationic peptides. *Cell. Mol. Life Sci. 63*, 1819–1822.

(70) Johnson, R. J., Chao, T. Y., Lavis, L. D., and Raines, R. T. (2007) Cytotoxic ribonucleases: the dichotomy of Coulombic forces. *Biochemistry 46*, 10308–10316.

(71) Rich, A., Davies, D. R., Crick, F. H., and Watson, J. D. (1961) The molecular structure of polyadenylic acid. *J. Mol. Biol. 3*, 71–86.

(72) Kobe, B., and Deisenhofer, J. (1996) Mechanism of ribonuclease inhibition by ribonuclease inhibitor protein based on the crystal structure of its complex with ribonuclease A. *J. Mol. Biol. 264*, 1028–1043.

(73) Rutkoski, T. J., Kurten, E. L., Mitchell, J. C., and Raines, R. T. (2005) Disruption of shape-complementarity markers to create cytotoxic variants of ribonuclease A. *J. Mol. Biol. 354*, 41–54.

(74) Gaur, D., Swaminathan, S., and Batra, J. K. (2001) Interaction of human pancreatic ribonuclease with human ribonuclease inhibitor. Generation of inhibitor-resistant cytotoxic variants. *J. Biol. Chem. 276*, 24978–24984.

(75) Di Donato, A., Ciardiello, M. A., de Nigris, M., Piccoli, R., Mazzarella, L., and D'Alessio, G. (1993) Selective deamidation of ribonuclease A. Isolation and characterization of the resulting isoaspartyl and aspartyl derivatives. *J. Biol. Chem. 268*, 4745–4751.

(76) Shaw, K. L., Grimsley, G. R., Yakovlev, G. I., Makarov, A. A., and Pace, C. N. (2001) The effect of net charge on the solubility, activity and stability of ribonuclease Sa. *Protein Sci. 10*, 1206–1215.

(77) Ilinskaya, O. N., Dreyer, F., Mitkevich, V. A., Shaw, K. L., Pace, C. N., and Makarov, A. A. (2002) Changing the net charge from negative to positive makes ribonuclease Sa cytotoxic. *Protein Sci. 10*, 2522–2525.

(78) Lin, T. Y., and Koshland, D. E. (1969) Carboxyl group modification and the activity of lysozyme. *J. Biol. Chem. 244*, 505–508.

(79) Yamada, H., Imoto, T., Fujiti, K., Okazaki, K., and Motomura, M. (1981) Selective modification of aspartic acid-101 in lysozyme by carbodiimide reaction. *Biochemisty 20*, 4836–4842.

(80) Acharya, A. S., and Seetharam, R. (1985) Reactivity of Glu-22(beta) of hemoglobin S for amidation with glucosamine. *Biochemistry 24*, 4885–4890.

(81) Semisotnov, G. V., Rodionova, N. A., Razgulyaev, O. I., Uversky, V. N., Gripas, A. F., and Gilmanshin, R. I. (1991) Study of the molten globule intermediate state in protein folding by a hydrophobic fluorescent probe. *Biopolymers 31*, 119–128.

(82) Steinhardt, J., and Hiremath, C. B. (1967) A comparison of the resistance of human and horse ferrihemoglobin to acid denaturation. *J. Biol. Chem. 242*, 1294–1301.

BC9001486

Supporting Information for

"The Carbodiimide EDC Induces Crosslinks that Stabilize the RNase A C-Dimer Against Dissociation: EDC Adducts Can Affect Protein Net Charge, Conformation and Activity.

by

Jorge P. López-Alonso, Fernando Díez, Josep Font, Marc Ribó, María Vilanova, J. Martin Scholtz, Carlos González, Francesca Vottariello, Giovanni Gotte, Massimo Libonati & Douglas V. Laurents

List of Contents:

Supporting Figure 1: ^{1}H-^{15}N HSQC and ^{1}H-^{13}C HSQC Spectra of RNase A and EDC·modified ^{13}C,^{15}N RNase A.

Supporting Figure 2: NMR Chemical Shift Assignments for EDC, MES and the dipeptide Ac-Asp-Ala-NH_2.

Supporting Figure 3: 1D ^{13}C Spectra of the Dipeptide Ac-Asp-Ala-NH_2, EDC Alone and During their Reaction.

Supporting Figure 4: Comparison of the Chemical Shifts in Ac-Asp-Ala-NH_2 Alone and Upon Incubation with EDC.

Supporting Figure 5: Putative Structure of the Dipeptide – EDC Fragment Adducts Detected by Electrospray Mass Spectrometry

Supporting Figure 6. Representative Peptide Mapping Results

Supporting Figure 1: A: ^{1}H-^{15}N HSQC Spectra of RNase A (black) and EDC·modified ^{13}C,^{15}N RNase A (red). Some representative resonances in RNase A (based on the assignments from Shimotakahara *et al.* (1997) *Biochemistry 36:* 6915-6929 are labeled. A dotted circle is drawn around new signals appear after EDC treatment which could be due to amide groups near EDC modified carboxylate groups.

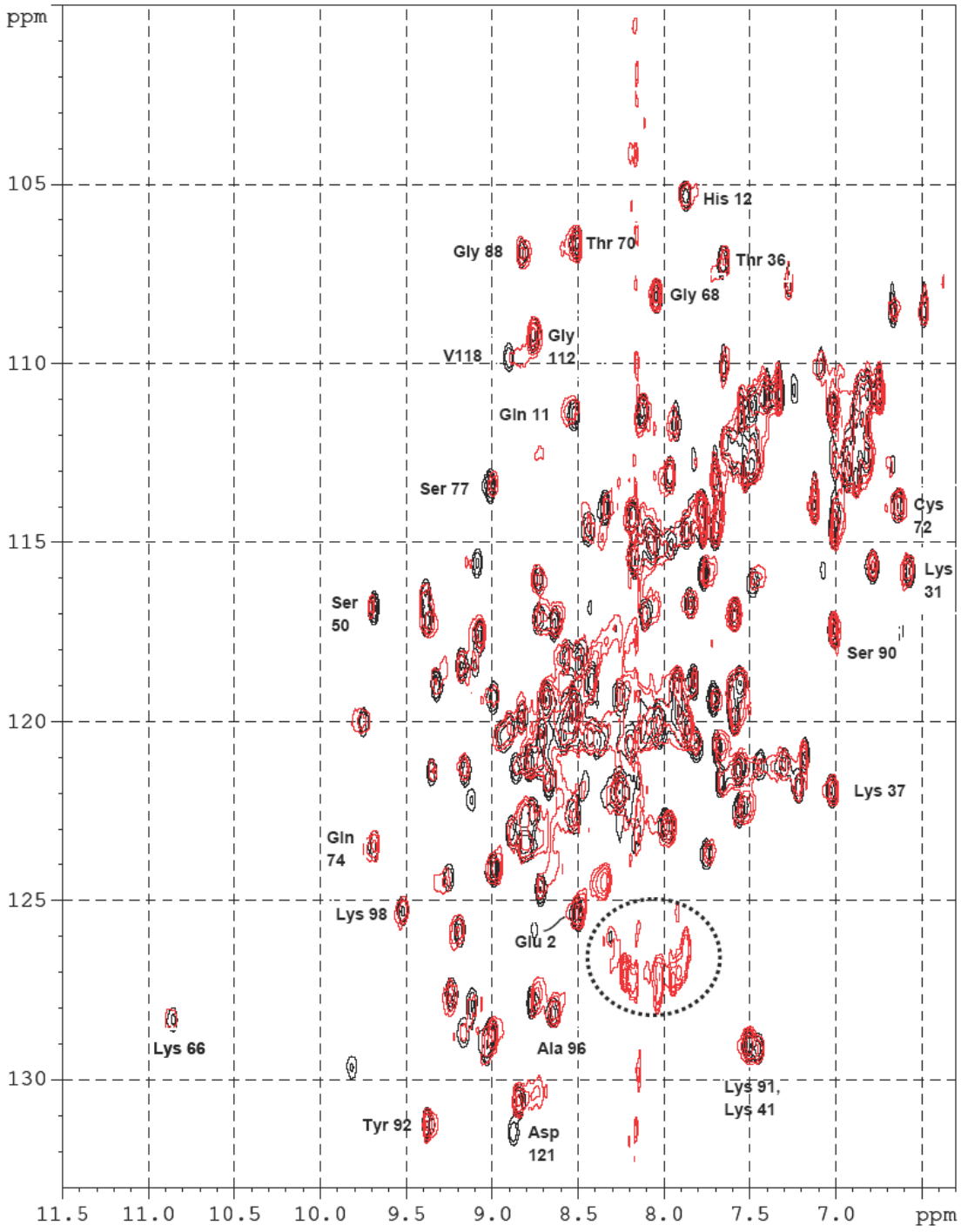

Supporting Figure 1B: ^{1}H-^{13}C HSQC Spectra of RNase A (black) and EDC·modified ^{13}C,^{15}N labeled RNase A (red). Ovals are drawn around signals arising from EDC or hydrolyzed EDC and squares surround resonances coming from MES buffer.

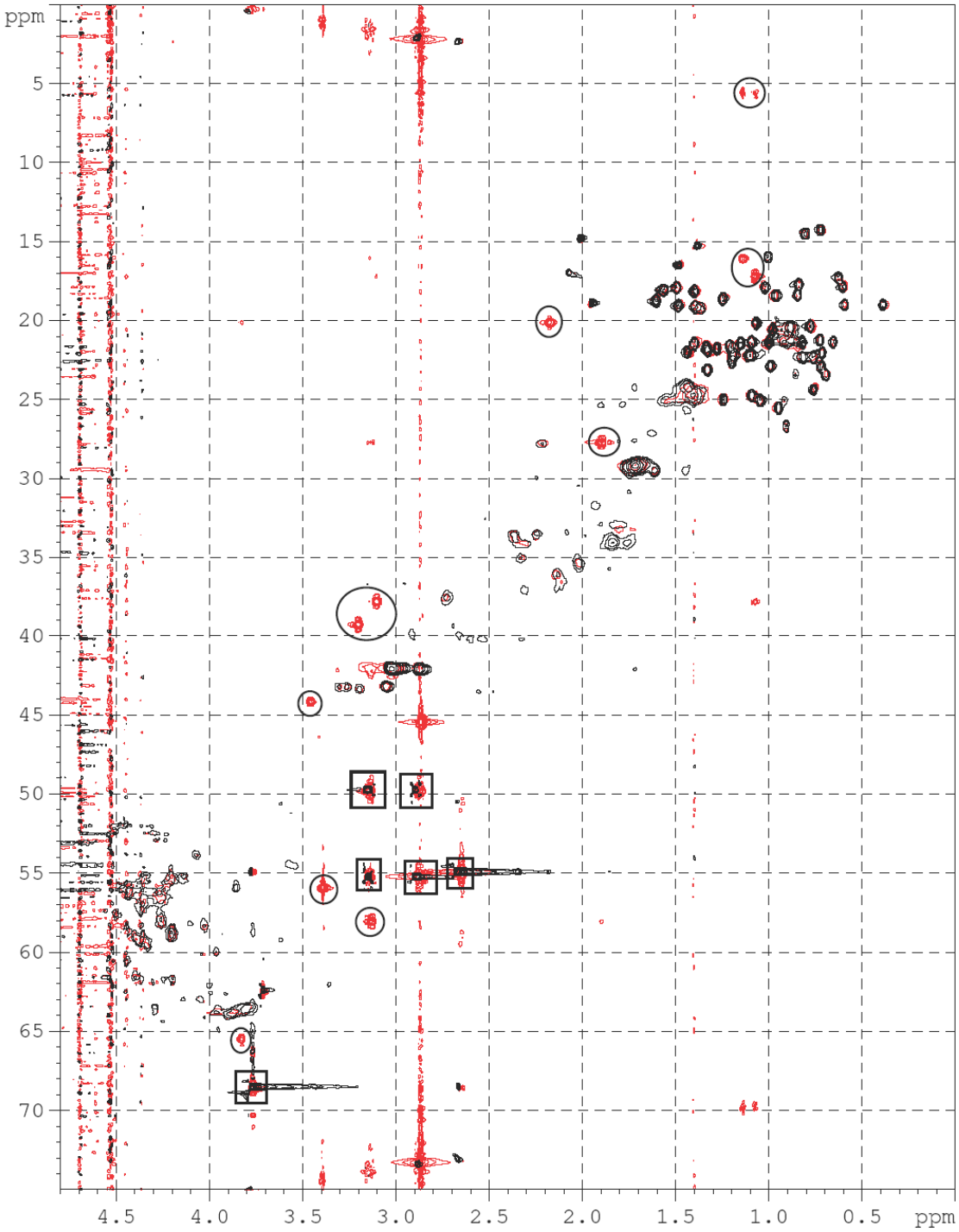

Supporting Figure 2:

NMR assignments of EDC, Ac-Asp-Ala-NH_2 and MES

EDC: (200mM, pH 4.7, 25ºC)

CH_3-CH_2-N=C=N-CH_2-CH_2-CH_2-NH^+-(-CH_3)$_2$

δ(ppm) ^{1}H	1.13	3.14			3.46	2.18	3.84		3.40
^{13}C	**16.1**	**42.4**		**150.0**	**44.2**	**20.1**	**65.5**		**55.9**

Hydrolyzed EDC:

CH_3-CH_2-NH-C(=O)-NH-CH_2-CH_2-CH_2-NH^+-(-CH_3)$_2$

δ(ppm) ^{1}H	1.07	3.11	5.99	6.15	3.19	1.89	3.14		2.88
^{13}C	**17.2**	**37.8**		**163.5**	**39.2**	**27.8**	**58.1**		**45.5**
^{15}N			122.4	129.6					

Ac-Asp-Ala-NH_2: 36 mM, pH 4.78, 25 ºC

180.1 COO^-

41.5 CH_2 2.68, 2.58 **19.4** CH_3 1.40

CH_3-CO-NH-CH-CO-NH-CH-CO-NH_2

δ(ppm) ^{1}H	2.03		8.26	4.54		8.37	4.28		7.59, 7.02
^{13}C	**24.7**	**180.8**		**54.6**	**176.5**		**52.4**	**177.2**	
^{15}N			125.5			126.4			106.15

Supporting Figure 2 Cont.

MES 100 mM 25 ºC

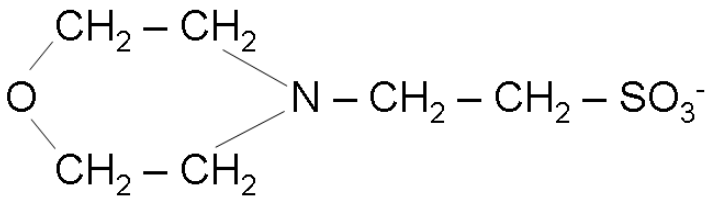

δ (ppm) ^{1}H	3.80	2.81	3.19	3.01	pH 6.4
^{13}C	**68.9**	**55.5**	**50.0**	**55.9**	
δ(ppm) ^{1}H	3.96	3.35	3.36	3.51	pH 5.1
^{13}C	**66.7**	**54.8**	**47.6**	**55.2**	

The assignments of these two methylene groups could be swapped. Literature values of the $^{13}CH_2$ α and β to an $-SO_3$ group {F. Freeman & C. N. Angeletakis, Org. Mag. Res. (1983) 31(2) 86-93} and of methyl morpholine (Aldrich Spectral Viewer) suggest that the assignments shown are the most probable.

EDC or EDC fragment

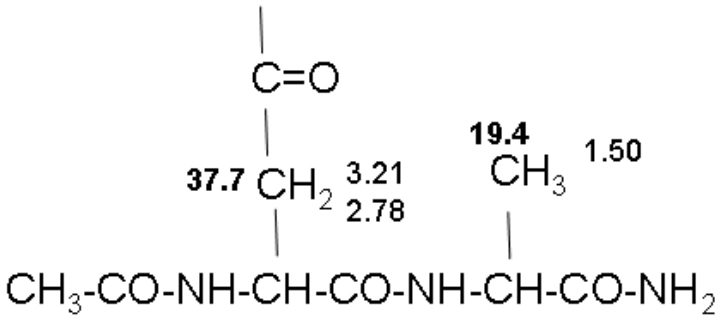

δ(ppm) ^{1}H	**2.03**	**8.70 4.52**	**8.33 4.90**	**7.48, 7.19**	
^{13}C	**24.2**	**52.0**	**52.5**		
^{15}N		120.7	125.2	106.7	

(^{13}CO at 180.4, 179.8, 177.4, 176.8, could not be assigned to individual nuclei)

Supporting Figure 3. 1D ^{13}C Spectra of the Dipeptide Ac-Asp-Ala-NH_2, EDC alone and during their reaction.

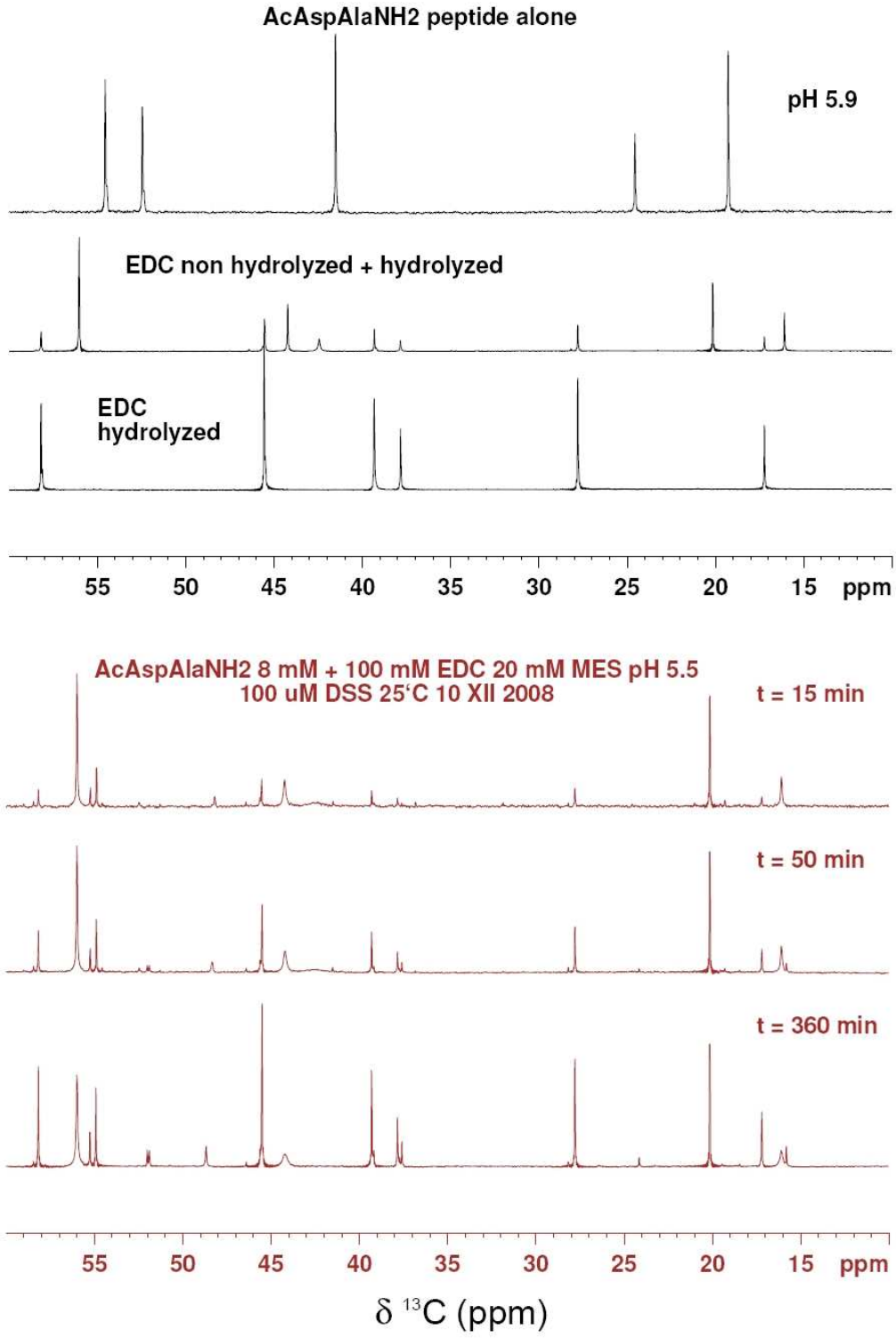

Supporting Figure 4: Comparison of the Chemical Shifts in Ac-Asp-Ala-NH_2 alone and upon incubation with EDC.

In each graph, the chemical shifts of the unmodified dipeptide is shown in open symbols and the chemical shifts of the dipeptide in the EDC reaction mixture is shown in closed symbols. The curve shows the fit of the Henderson-Hasselbach equation to the data. This comparison shows that whereas the chemical shifts of the dipeptide do depend on pH, this pH variation can not account for the new resonances appearing upon incubation with EDC. We therefore conclude that the dipeptide does indeed react with EDC.

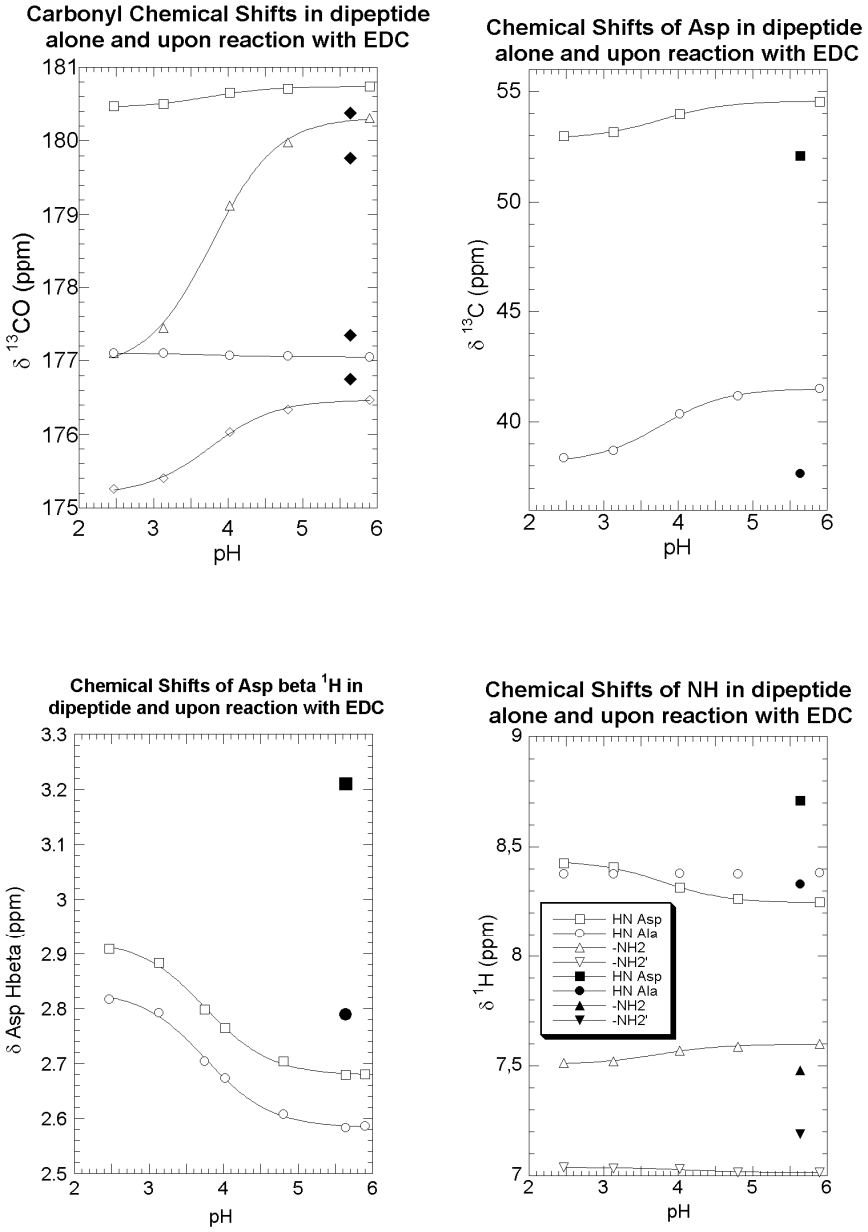

Supporting Figure 5

Putative Structure of the Dipeptide – EDC Fragment Adducts Detected by Electrospray Mass Spectrometry

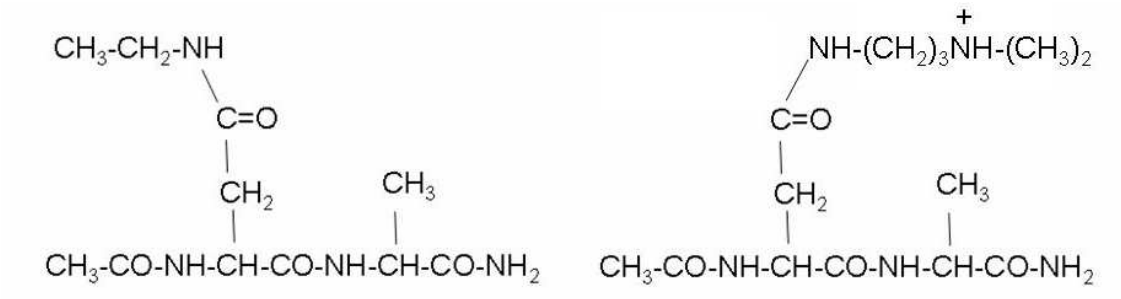

Adduction to a small EDC fragment Adduction to a large EDC fragment

Supporting Figure 6. Representative Peptide Mapping Results

A. HPLC chromatogram of unmodified RNase A digested by subtilisin and trypsin :

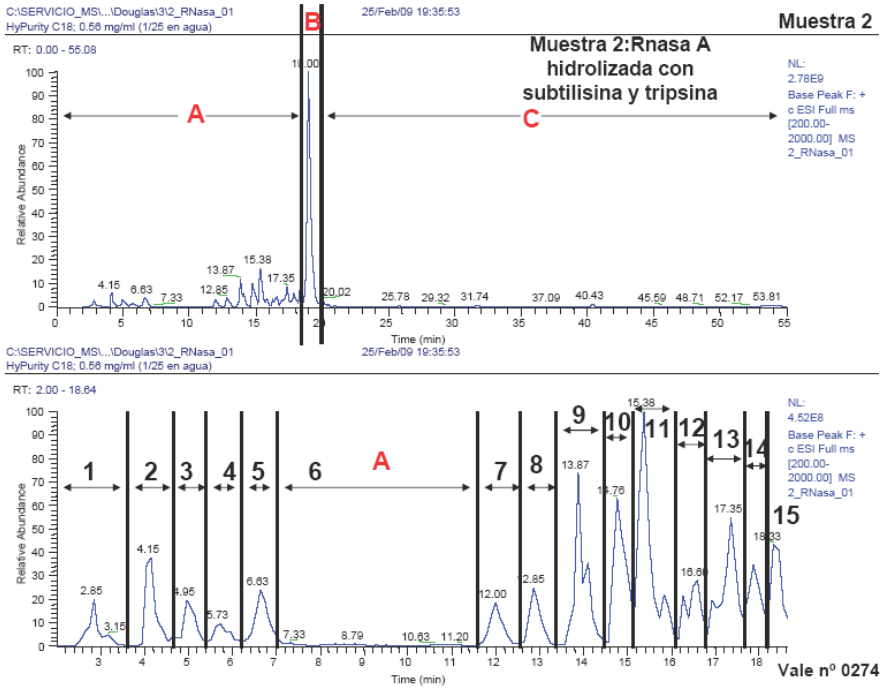

B. HPLC chromatogram of RNase A modified by EDC and digested by subtilisin and trypsin:

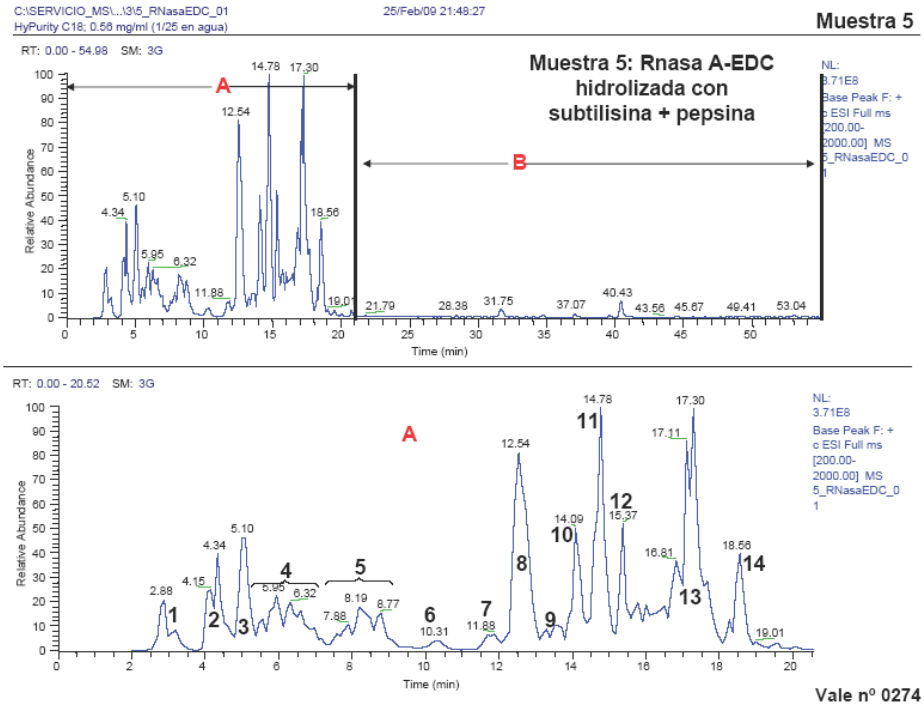

C. Observe that peaks A3 (top panel) and 3 (bottom panel) elute in similar positions in both chromatograms. The mass spectra of these peaks:

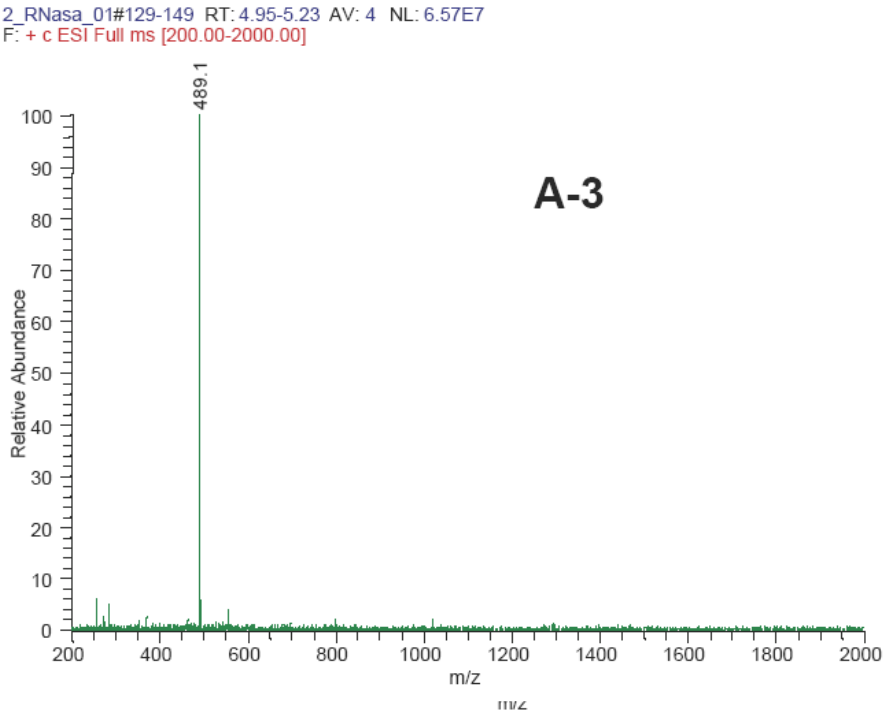

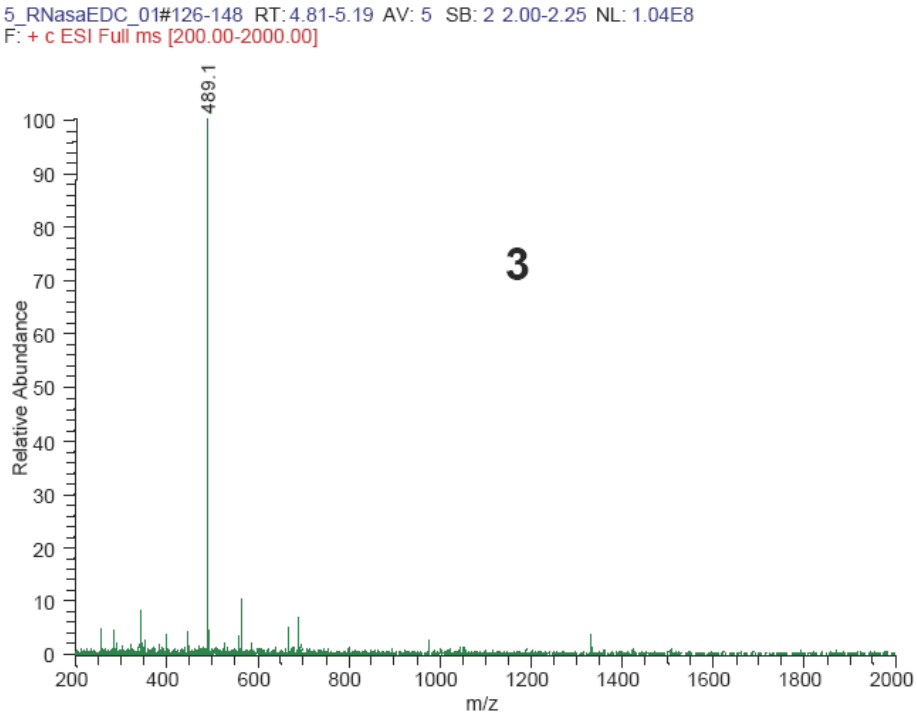

reveal identical peaks corresponding to Fragment II + K^+. Since Fragment II contains Glu 9, these data are good evidence that Glu 9 is not modified or that it is modified in a minority of RNase molecules treated with EDC.

D. Observe that the peak "B" eluting after 18 minutes in the top panel is missing in the bottom panel. The mass spectrum of this peak:

B

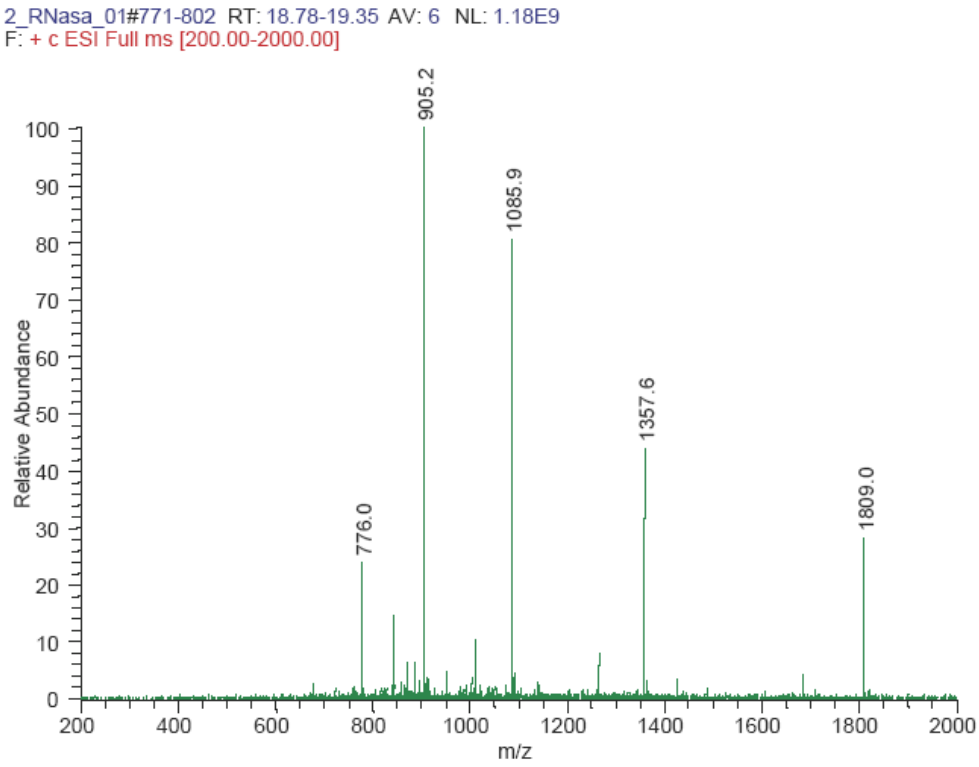

reveals peaks corresponding to fragment XIII + IX (5425.2 Da) with the peaks 1809, 1357.6, 1085.9 and 905.2 carrying 3, 4, 5 and 6 positive charges (H+), respectively. The fact that fragments XIII + IX are not separated is not unexpected as the bond between Lys 41 and Pro 42 is known to be only slowly cleaved by trypsin.

The absence of this peak in the chromatogram of RNaseA · EDC cleaved by trypsin suggests that one or more of the carboxylates in this portion of the protein have been modified by EDC. These carboxylates are Glu 49, Asp 53, Glu 111, Asp 121 and Val 124

E. Regarding the chromatograms of RNase A (top panel) and RNase A · EDC (bottom panel) hydrolyzed by pepsin:

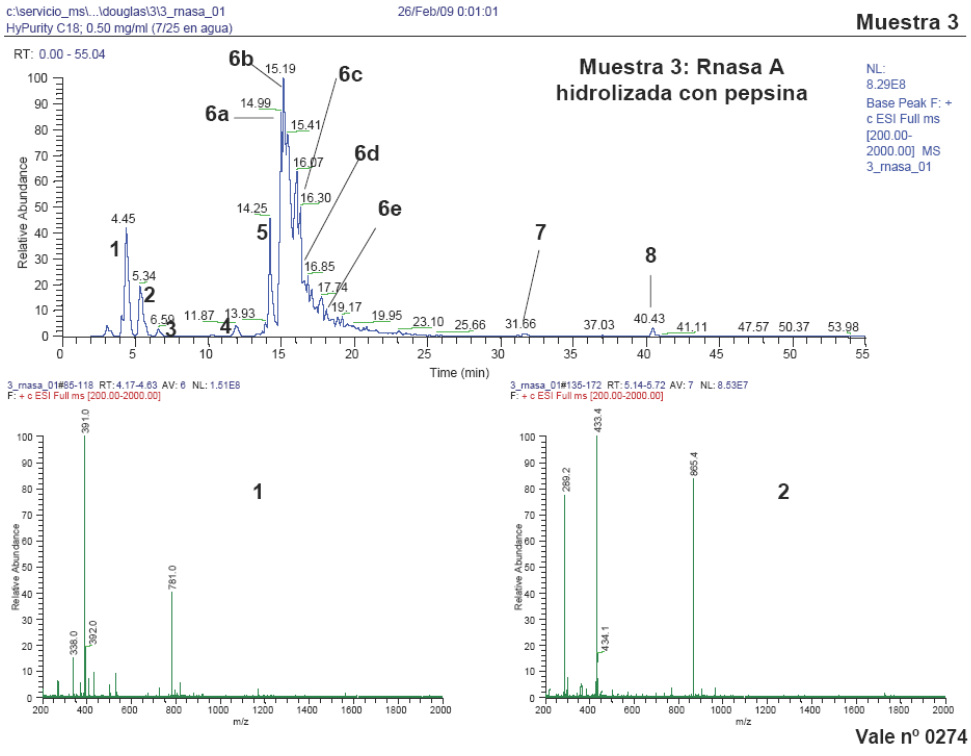

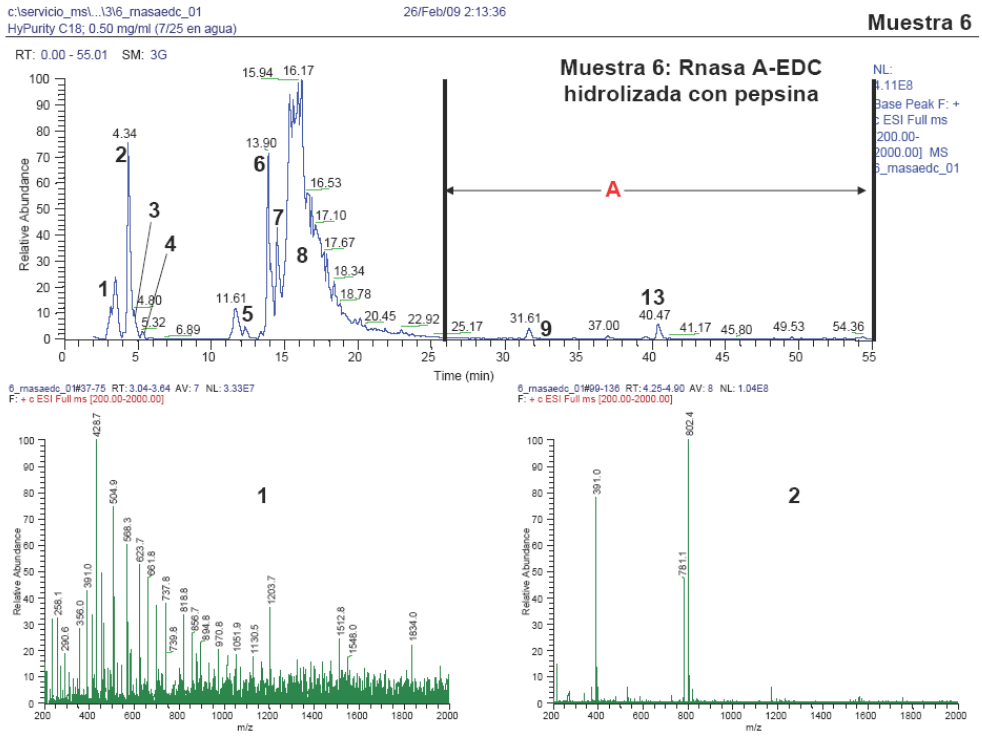

One can see that peak 1 in the chromatogram of RNase A cleaved by pepsin corresponds in elution time to peak 2 in the chromatogram of RNase A · EDC cleaved by pepsin and that both have a peak whose mass corresponds to the C-terminal tetrapeptide Asp121-Ala122-Ser123-Val-124. Therefore, we can conclude that Asp 121 and Val 124 are not modified or that they are modified in a minority of RNase molecules treated with EDC.

On the basis of the other data and a similar way of reasoning, we have reached the following conclusions:

Not modified or modified in a minority of RNase A molecules treated with EDC	Modified in many if not a majority of RNase A molecules treated with EDC
Glu 2	Asp 38
Glu 9	Glu 49
Asp 14	Asp 53
Asp 83	Glu 111
Glu 86	
Asp 121	
Val 124 (C-terminal carboxylate)	

Cys-diabody Quantum Dot Conjugates (ImmunoQdots) for Cancer Marker Detection

Bhaswati Barat,[†] Shannon J. Sirk,[†] Katelyn E. McCabe,[†] Jianqing Li,[‡] Eric J. Lepin,[†] Roland Remenyi,[§] Ai Leen Koh,[§] Tove Olafsen,[†] Sanjiv S. Gambhir,[||] Shimon Weiss,[‡] and Anna M. Wu*[,†]

Crump Institute for Molecular Imaging, Department of Molecular and Medical Pharmacology, David Geffen School of Medicine at UCLA, 570 Westwood Plaza, Los Angeles, California 90095, Department of Chemistry and Biochemistry, University of California, 607 Charles E. Young Drive East, Los Angeles, California 90095, Materials Science and Engineering Department, Stanford University, Stanford, California 94305, and Molecular Imaging Program at Stanford (MIPS), Department of Radiology and Department of Bioengineering, Stanford University, 300 Pasteur Drive, Stanford, California 94305. Received October 1, 2008; Revised Manuscript Received June 12, 2009

The present work demonstrates the use of small bivalent engineered antibody fragments, cys-diabodies, for biological modification of nanoscale particles such as quantum dots (Qdots) for detection of target antigens. Novel bioconjugated quantum dots known as immunoQdots (iQdots) were developed by thiol-specific oriented coupling of tumor specific cys-diabodies, at a position away from the antigen binding site to amino PEG CdSe/ZnS Qdots. Initially, amino PEG Qdot 655 were coupled with reduced anti-HER2 cys-diabody by amine-sulfhydryl-reactive linker [*N*-ε-maleimidocaproyloxy] succinimide ester (EMCS) to produce anti-HER2 iQdot 655. Spectral characterization of the conjugate revealed that the spectrum was symmetrical and essentially identical to unconjugated Qdot. Specific receptor binding activity of anti-HER2 iQdot 655 was confirmed by flow cytometry on HER2 positive and negative cells. Immunofluorescence results showed homogeneous surface labeling of the cell membrane with Qdot 655 conjugate. In addition, cys-diabodies specific for HER2, as well as prostate stem cell antigen (PSCA), were conjugated successfully with amino PEG Qdot 800. All of these iQdots retain the photoluminescence properties of the unconjugated Qdot 800 as well as the antigen binding specificity of the cys-diabody as demonstrated by flow cytometry. Simultaneous detection of two tumor antigens on LNCaP/PSCA prostate cancer cells (which express PSCA and HER2) in culture was possible using two iQdots, anti-HER2 iQdot 655 and anti-PSCA iQdot 800. Thus, these iQdots are potentially useful as optical probes for sensitive, multiplexed detection of surface markers on tumor cells. The present thiol-specific conjugation method demonstrates a general approach for site-specific oriented coupling of cys-diabodies to a wide variety of nanoparticles without disturbing the antigen binding site and maintaining small size compared to intact antibody.

INTRODUCTION

In recent years, optical imaging has emerged as a sensitive detection method for diagnostic and therapeutic purposes. Quantum dots (Qdots), nanometer-scale semiconductor materials, represent an important class of fluorescent probe for biomolecular and cellular imaging (*1*). Qdots are promising as optical probes because they exhibit high quantum yields, are resistant to photobleaching, have narrow and size-tunable emission wavelengths, and have broad excitation spectra. These unique optical properties of Qdots make them appealing as *in vivo* and *in vitro* fluorophores in a variety of biological investigations. Furthermore, since the emission wavelength is readily tuned by controlling the size of the Qdots, they can be synthesized to emit different colors, allowing multiplex imaging, which is increasingly important in the analysis of complex biological systems (*2*). The use of Qdots as optical probes was originally pioneered by Alivisatos and Weiss and by Nie, in 1998. In the investigations of Alivisatos et al., two different-sized CdSe-CdS core−shell nanocrystals enclosed in a silica shell were prepared for fluorescent imaging of mouse fibroblast cells (*3*). Nie et al. investigated receptor mediated endocytosis of transferrin receptor in cultured HeLa cells using CdSe-ZnS Qdots coupled with transferrin (*4*). By chemically conjugating antibodies and peptides to their surface, quantum dots can specifically target cellular ligands of interest. Biocompatible Qdots have thus been applied for labeling cells (fixed and live) and tissues (*5*−*7*), long-term cell trafficking (*8*), multicolor cell imaging (*9*), tumor cell extravasation tracking (*10, 11*), fluorescence resonance energy transfer (FRET)-based sensing (*12*), bioluminescence resonance energy transfer (BRET)-based imaging (*13*), and sentinel lymph-node mapping (*14*). In addition, semiconductor Qdots have been shown to be suitable for real-time *in vivo* imaging and Qdots surface-modified with poly(ethylene glycol) (PEG) were reported to be biocompatible for *in vivo* cancer targeting and imaging (*15*−*17*).

Antibodies can be engineered into a wide variety of formats that retain binding specificity with target antigen and exhibit optimal properties such as rapid targeting and controlled blood clearance for *in vitro* or *in vivo* applications (*18, 19*). Intact monoclonal antibodies are large (150 kDa) protein molecules. For coupling to Qdots, smaller antibody fragments would be preferable to intact IgGs (Figure 1A); otherwise, the overall size of the antibody−Qdot conjugate becomes quite large. Smaller antibody fragments have been shown to be superior in their

* Author to whom correspondence should be addressed. Anna M. Wu, Crump Institute for Molecular Imaging, Department of Molecular and Medical Pharmacology, David Geffen School of Medicine at UCLA, 570 Westwood Plaza, CNSI 4335, Los Angeles, CA 90095, USA. Tel: 310 794 5088; Fax: 310 206 8975; E-mail: awu@mednet.ucla.edu.

[†] David Geffen School of Medicine at UCLA.

[‡] Department of Chemistry and Biochemistry, University of California.

[§] Materials Science and Engineering Department, Stanford University.

[||] Molecular Imaging Program at Stanford.

10.1021/bc800421f CCC: $40.75 © 2009 American Chemical Society
Published on Web 07/31/2009

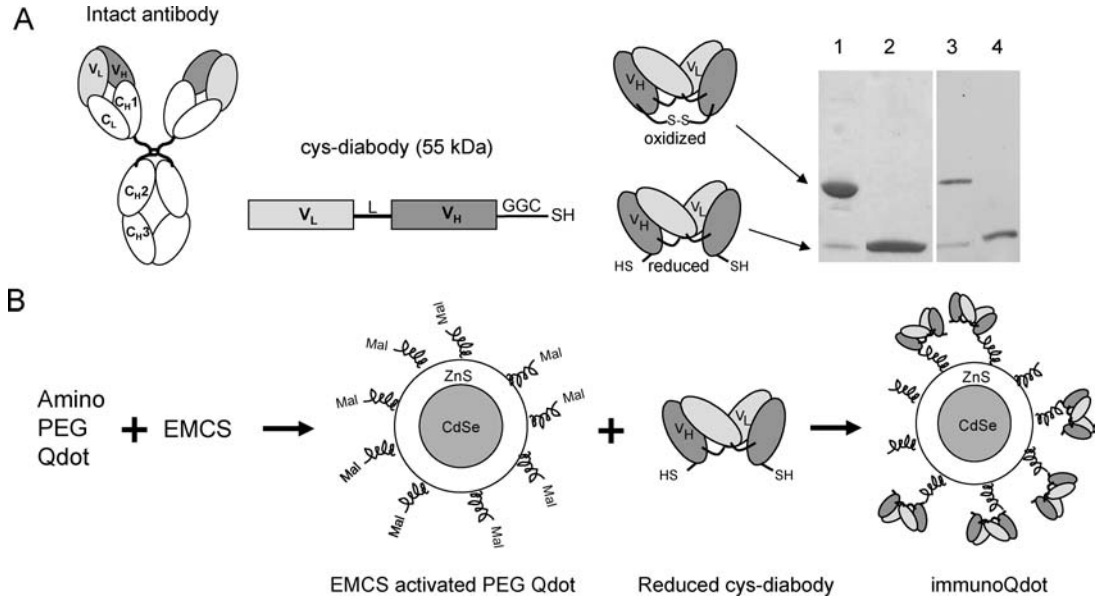

Figure 1. (A) Schematic drawing of an intact antibody showing variable light (V_L) and heavy (V_H) chain regions and constant (C) regions. Cys-diabody was formed by connecting V_L and V_H domains with either 5 or 6 amino acid linker (L) and GGC added to the C-termini for cysteine modification. DNA construct and oxidized and reduced forms of protein are shown. SDS-PAGE of two cys-diabodies: lanes 1 and 2, oxidized and reduced forms of anti-HER2 cys-diabody; 3 and 4, oxidized and reduced forms of anti-PSCA cys-diabody. Nonreduced samples migrate at expected size for covalent dimer (50 kDa), and reduced samples migrate at expected size for monomeric scFv (25 kDa). (B) Schematic illustration of the process of conjugating amino PEG Qdot with cys-diabody. EMCS: [*N*-ε-Maleimidocaproyloxy] succinimide ester. Mal: maleimide group.

ability to extravasate and penetrate solid tumors *in vivo*, when compared with intact antibodies (*20*). Genetically fusing the variable light (V_L) and heavy (V_H) chain domains of a parental antibody through a peptide linker results in the production of a single-chain variable fragments (scFv, 27 kDa), at about 1/6 the size of native antibody, with the same specificity as that of parental intact antibody. Shortening the peptide linker results in formation of noncovalent dimers of scFvs, called diabodies (Db, 55 kDa) which retain full antigen binding activity and specificity in smaller formats (*21*). Our lab has previously demonstrated that radiolabeled diabodies against cell surface cancer antigens efficiently target tumors *in vivo* by microPET (*22, 23*). Their small size (5 × 7 nm) makes these engineered antibody fragments specifically appropriate for conjugation to nanoscale particles.

Conjugation by random chemical modification may be risky for small antibody fragments, due to the possibility of inadvertently disrupting the binding site. Site-specific conjugation is more likely to preserve the binding activity of an antibody. X-ray crystallographic structure of the anti-CEA T84.66 diabody shows that the C-termini of the diabody subunits are almost 70 Å apart and on an alternate face from the antigen-combining site (*24*). Introduction of cysteine residues at the C-termini of scFv fragment has been considered as an approach to allow site-specific, thiol-reactive coupling at a site away from the antigen binding site to a wide variety of agents (Figure 1A) (*25*−*28*). Previous work from our laboratory demonstrated site-specific conjugation and radiolabeling of an anti-CEA diabody with C-terminal cysteine (cys-diabody) for rapid tumor targeting and imaging in CEA-positive xenograft bearing mouse by microPET (*26*).

Numerous studies indicate that the avidity effect of having more than one binding site improves the targeting and retention of antibodies and immunoconjugates. For eventual *in vivo* delivery, an antibody-nanoparticle conjugate needs to be small but also bivalent. Use of a bivalent cys-diabody as the targeting moiety ensures that (at least) two binding sites are attached to the particle, and optimization should allow production of 1:1 conjugates. In contrast, in order to achieve bivalency using monovalent scFv fragments, titration and optimization will be more challenging and yields probably lower, since a broad distribution of conjugation ratios, including monovalent complexes, will be obtained.

The present study demonstrates oriented site-specific coupling of bivalent cys-diabodies specific for well-characterized cancer cell surface antigens, HER2 and prostate stem cell antigen (PSCA) to fluorescent semiconductor amino PEG Qdots using thiol chemistry. Cys-diabody conjugated Qdots are termed immunoQdots (iQdots). Initial biophysical and functional characterization was performed with anti-HER2 iQdot 655. This iQdot demonstrated dual functionality: retention of HER2 antigen binding specificity as well as fluorescence signal of Qdot. Using two iQdots, anti-HER2 iQdot 655 and anti-PSCA iQdot 800, simultaneous detection of two antigens, HER2 and PSCA, on LNCaP/PSCA cells can be possible by *in vitro* optical imaging. This study allows a general approach for biological modification of a variety of nanoscale particles with small bivalent engineered antibody fragments in an oriented fashion without affecting the antigen binding site and maintaining the overall small size compared to intact antibody.

EXPERIMENTAL PROCEDURES

Design, Expression and Purification of Cys-diabodies. The anti-HER2 cys-diabody was constructed from trastuzumab (Herceptin; Genentech, San Francisco, CA) human variable regions using an existing single-chain variable fragment (scFv) gene construct as template (*29*). Affinity matured recombinant scFv fragment, derived from humanized anti-PSCA antibody (hu1G8 mAb) (*30*) was used as a template for anti-PSCA cys-diabody (Lepin, E. unpublished data). Overlap-extension PCR and site-directed mutagenesis (QuickChange XL, Stratagene, La Jolla, CA) were used to generate both of the cys-diabody constructs with the following orientation: V_L-linker-V_H-C-terminal cysteine modification (GGC) (*28*). 5-Amino acid linker, SGGGG, and 6-amino acid linker, SGGGGS, are the linkers used to construct anti-HER2 and anti-PSCA cys-diabodies, respectively. The final PCR product of anti-HER2 cys-diabody was cloned in the pEE12 mammalian expression vector (Lonza

Biologics, Slough, UK) (*28*) containing a mammalian leader sequence for secretion. The anti-PSCA cys diabody was cloned into pSyn1 plasmid for bacterial expression (gift of Dr. James D. Marks, University of California, San Francisco) (*31*).

For expression of anti-HER2 cys-diabody, 2.5×10^6 NS0 cells (*32*) were transfected by electroporation with 10 μg linearized plasmid DNA and selected in glutamine-deficient media as described (*25*). Anti-HER2 cys-diabody expression was screened by Coomassie stained SDS-PAGE precast 4−20% gels (Bio-Rad, Hercules, CA), under reducing and nonreducing conditions. The highest-expressing clones were expanded into triple flasks (Nunclon, Rochester, NY).

For bacterial expression of the anti-PSCA cys-diabody, *Escherichia coli* BL21 cells transformed with the pSyn1 expression vector were grown in Luria-Bertani broth (LB) to an OD_{600} of 0.7, induced with a final concentration of 1 mM IPTG, and grown for 4 h at 37 °C. Periplasmic extracts were prepared using Peripreps Periplasting Kits (Epicenter, Madison, WI).

Both of the cys-diabodies, anti-HER2 and anti-PSCA, were purified by immobilized protein L chromatography according to the manufacturer's instructions (Pierce, Rockford, IL). The final concentration of the purified proteins was determined by $A_{280\ nm}$ using an extinction coefficient $\varepsilon = 1.4$. Purified proteins were analyzed by SDS-PAGE under reducing and nonreducing conditions. Cys-diabodies were also subjected to gel filtration chromatography on a Superdex 75 HR 10/30 column (GE Healthcare, Piscataway, NJ). Final protein yields were 3.0 mg/L of mammalian culture supernatant for anti-HER2 cys-diabody and 0.2 mg/L of bacterial culture supernatant for anti-PSCA cys-diabody.

Coupling of Qdots to Tumor-Specific Cys-diabodies. Cys-diabodies were covalently conjugated to Qdot 655 and Qdot 800 amino (PEG) quantum dots (Invitrogen, Carlsbad, CA). Briefly, Qdots were activated with the heterobifunctional cross-linker[*N*-ε-maleimidocaproyloxy] succinimide ester (EMCS) (Pierce) for 30 min at room temperature in 50 mM borate buffer (pH 7.4), yielding a maleimide-modified particle. In each reaction, 60 μg of cys-diabodies were simultaneously reduced by incubating in 20 mM DTT in PBS at room temperature for 30 min. Excess EMCS and DTT were removed using Bio-Spin 6 (Bio-Rad) desalting columns. Mock conjugation controls were also treated under the same conditions, with no cys-diabody added. Then, activated Qdots were incubated with reduced antibody fragment at room temperature for 1 h in 50 mM borate buffer (pH 7.4). The molar ratio of antibody fragment to Qdot was 22:1. The reaction was quenched by adding 34 μg of *N*-ethyl maleimide (NEM, 10 mg/mL in DMSO, Pierce) per mg of antibody fragment. The uncoupled free cys-diabody and excess NEM were removed by three washes using a 100 KDa ultrafiltration unit, Amicon Ultra-4 (Millipore Corp., Bedford, MA). The final iQdot complex was stored in 10 mM borate buffer at 4 °C.

Cell Lines. NS0 mouse myeloma cells (*32*) and human breast cancer cell lines MCF7 (American type Culture Collection [ATCC], Manassas, VA; #HTB-22) transfected with HER2 (MCF7/HER2 (*33*)) were maintained as described (*29*). Human prostate cancer cell lines LNCaP (American type Culture Collection (ATCC; #CRL-1740) transfected with PSCA (LNCaP/PSCA (*34*)) and human B-cell lymphoma cell line SKW 6.4 (ATCC; #TIB-215) transfected with PSCA (SKW6.4/PSCA) (a generous gift of Dr. Robert Reiter, UCLA) were maintained as described (*35*). SK-OV-3, the human ovarian carcinoma cell line (ATCC; #HTB-77) was maintained in McCoy's 5A medium (Mediatech, Inc., Herndon, VA) supplemented with 10% FBS, and Jurkat helper T cell lines (ATCC # TIB-152) were maintained as recommended by ATCC.

Photoluminescence Spectra. The emissions of unconjugated and conjugated Qdot 655 were determined using a QuantaMaster QM-6 steady state spectrofluorometer (Photon Technology International, Inc., Birmingham, NJ) with a 75 W xenon lamp and a 928R PMT. All NIR emission spectra were recorded on a CCD-array based SPM-002 spectrometer (Photon Control Inc., British Columbia, Canada) with a 532 nm diode pumped laser as pumping source.

Flow Cytometry. MCF7/HER2 cells were incubated with either anti-HER2 iQdot 655 or anti-HER2 iQdot 800 for 1 h at 4 °C in PBS containing 1% FBS. LNCaP/PSCA cells were incubated with anti-PSCA iQdot 800 using the same conditions. Approximately 0.83 pmol of Qdots were used in flow cytometry experiments. The cells were then washed with PBS containing 1% FBS. Antibody fragments binding to tumor cells were quantified by FACSCalibur flow cytometer (Becton Dickinson, UK), and data were analyzed using Cell Quest software (Becton Dickinson). FL3 (λ_{em}: 670 nm long pass) and FL5 (λ_{em}: 740 nm long pass) filters were used for Qdot 655 and Qdot 800, respectively.

For competitive cell binding assays, experiments were performed in triplicate on MCF7/HER2 cells by the addition of a fixed concentration of anti-HER2 iQdot 655 (10 nM) and increasing concentrations of anti-HER2 antibody fragment, minibody (*29*) (0.1−1000 nM) as competitor. Binding of anti-HER2 iQdot 655 on cells was examined by flow cytometry. Result was normalized to the signal obtained in the absence of competitor.

Confocal Microscopy. MCF7/HER2 cells were plated on poly(L-lysine)-coated glass coverslips (BD Biosciences, San Jose, CA) in 12-well plates in DMEM medium containing 5% FBS for 24 h. The next day, cells were incubated with mock conjugated Qdot 655 and anti-HER2 iQdot 655 in PBS/1% FBS on ice for 1 h. Approximately 1.7 pmol of Qdots were used in confocal microscopy experiments. Cells were fixed with 3.7% paraformaldehyde at 4 °C for 30 min. Cell nuclei were counterstained with DAPI. Coverslips were mounted on glass slides and observed using a Zeiss LSM510 META confocal imaging system (excitation: argon laser 488 nm) (Carl Zeiss Inc., Thornwood, NY) equipped with a 100× oil immersion objective lens.

Fluorescence Imaging of Qdot Labeled Cells. LNCaP/PSCA cells were incubated with two different iQdots, anti-HER2 iQdot 655 and anti-PSCA iQdot 800 in microfuge tubes. For control experiment, cells were incubated with mock conjugated Qdot 655 and Qdot 800. Cells with Qdots were incubated for 1 h at 4 °C in PBS containing 1% FBS. Approximately 3.3 pmol of Qdots were used in fluorescence imaging experiments. Cells were then washed twice with PBS (1% FBS) to remove any unbound Qdots. Antibody-conjugated Qdots binding to tumor cells were examined using Maestro *In-vivo* Fluorescence Imaging System (CRI, Inc., Woburn, MA) with a blue filter set (excitation, 445−490 nm; emission, 515 nm long-pass, 515−900 nm). CRI software *Maestro 2p23* was used to analyze the data.

RESULTS

Synthesis and Biophysical Characterization of Anti-HER2 iQdot 655. Anti-HER2 cys-diabody was expressed in mammalian cells and purified successfully. Analysis of the purified proteins on SDS-PAGE showed that the cys-diabody migrated as a monomer consistent with its predicted molecular weight of approximately 25 kDa under reducing conditions and as covalent dimer of 55−60 kDa under nonreducing conditions (Figure 1A). An excess amount of reduced cys-diabody was allowed to react with activated amino PEG CdSe/ZnS Qdot 655 using the heterobifunctional cross-linker EMCS to form anti-HER2 iQdot 655 (Figure 1B).

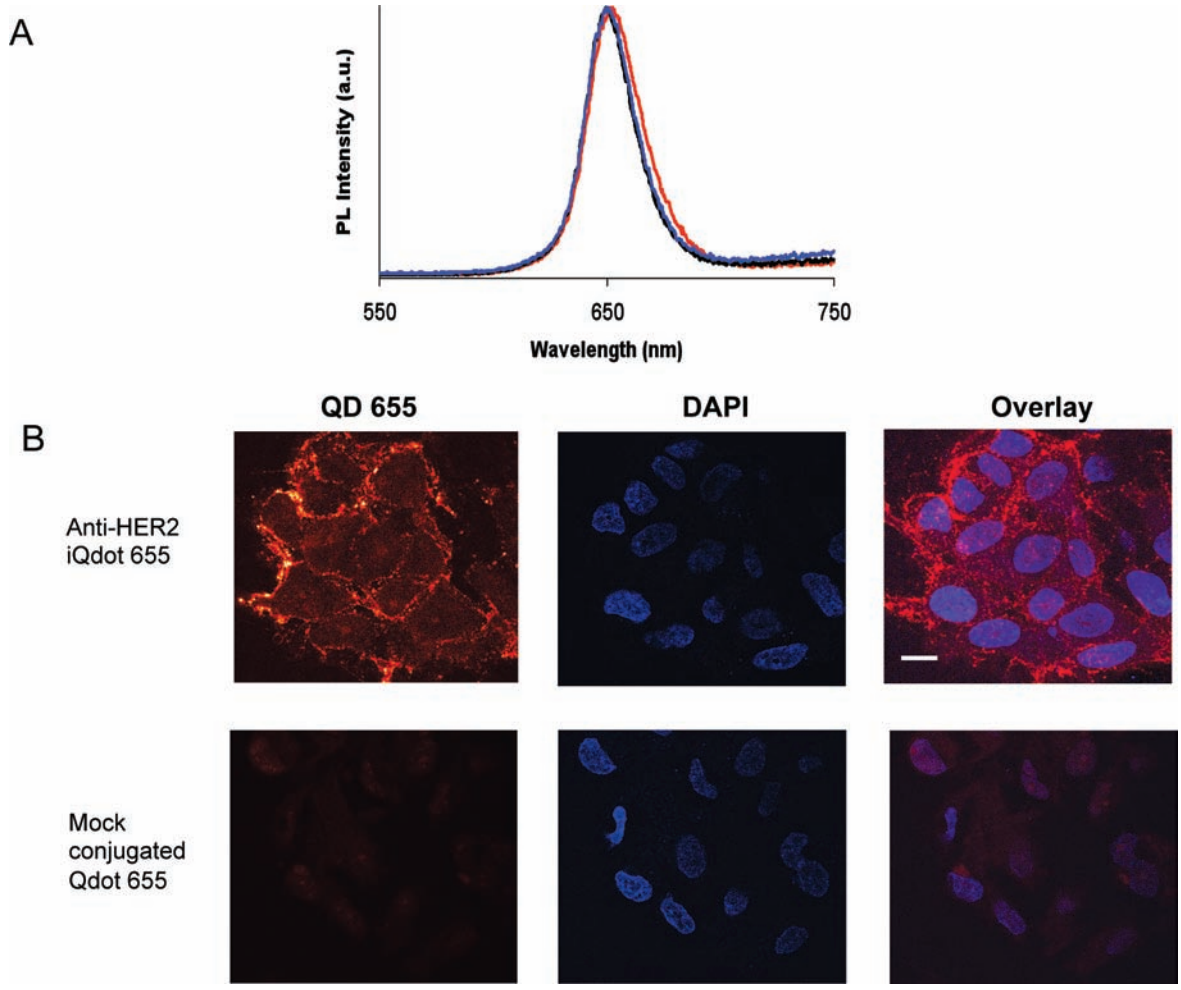

Figure 2. (A) Photoluminescence (emission) spectra of amino PEG Qdot 655 conjugates at excitation wavelength 488 nm. Maximum emission wavelengths are 650.0, 650.5, and 652.5 nm for commercial Qdot 655 (black line), mock conjugated Qdot 655 (blue line), and anti-HER2 iQdot 655 (red line), respectively. All spectra are typically around 30 to 50 nm (full width at half-maximum). (B) Confocal microscopy images of MCF7/HER2 cells stained with anti-HER2 iQdot 655 and mock conjugated Qdot 655. Cell nuclei were counterstained with DAPI and shown in blue. Scale bars: 20 μm.

To visualize the structure of synthesized anti-HER2 iQdot 655, transmission electron microscopy (TEM) was performed on anti-HER2 iQdot 655 and mock conjugated Qdot 655. TEM bright field images revealed that Qdots were uniform in size; prior to and following conjugation, only the inorganic particles are directly visualized at approximately 15 × 5 nm (Supporting Information Figure 1). Negative staining of the conjugates reveals an additional halo, consistent with the conjugation of protein to the particles. Size exclusion chromatography was also performed to evaluate conjugated Qdots. Chromatography on a Superdex 200 HR column showed a single peak eluting at 18.03 min, slightly earlier than that of mock conjugated Qdot 655 (18.28 min) suggesting a relatively uniform preparation without extensive aggregation (Supporting Information Figure 2).

To evaluate whether there was any difference in the photoluminescence (PL) spectrum of Qdots after conjugation to cys-diabody, PL measurements of Qdots were performed by excitation with a 488 nm laser. Figure 2A shows that the spectrum of anti-HER2 iQdot 655 is still symmetrical and almost identical to that of commercial Qdots with only a slight red shift.

Functional Characterization of Anti-HER2 iQdot 655. To determine whether the anti-HER2 iQdot 655 could bind to HER2, HER2 expressing human breast carcinoma MCF7/HER2 cells were incubated with anti-HER2 iQdot 655 and examined by confocal microscopy. The result demonstrated homogeneous surface labeling of the cell membrane with minimal cytoplasmic labeling. Minimal nonspecific binding to the cells was observed with mock conjugated Qdot 655 (Figure 2B).

The anti-HER2 iQdot 655 was also used to assess HER2 expression on MCF7/HER2 cells by flow cytometry. Results showed a strong fluorescent shift of anti-HER2 iQdot 655 with MCF7/HER2 cells (Figure 3A). Control experiments were performed to show the specificity of anti-HER2 iQdot 655. Incubation of MCF7/HER2 cells with mock conjugated Qdot 655 (Figure 3A) or anti-CD20 iQdot 655 (irrelevant iQdot, negative control; data not shown) did not show a shift in fluorescence intensity. Anti-HER2 iQdot 655 also bound efficiently to other HER2 positive cells, i.e., SK-OV-3, ovarian carcinoma cells, and LNCaP/PSCA prostate cancer cells (Figure 3A). No binding was seen to HER2-negative Jurkat cells (Figure 3A).

In order to further evaluate the binding specificity of anti-HER2 iQdot 655, a cell-based competition assay in which Qdot conjugated cys-diabody was incubated simultaneously in the presence of increasing concentrations of competitor, was carried out and analyzed by flow cytometry (Figure 3B). At higher concentrations of the competitor, lower amounts of iQdot were bound. This confirmed that anti-HER2 iQdot 655 retained the same epitope specificity as that of the anti-HER2 antibody fragment.

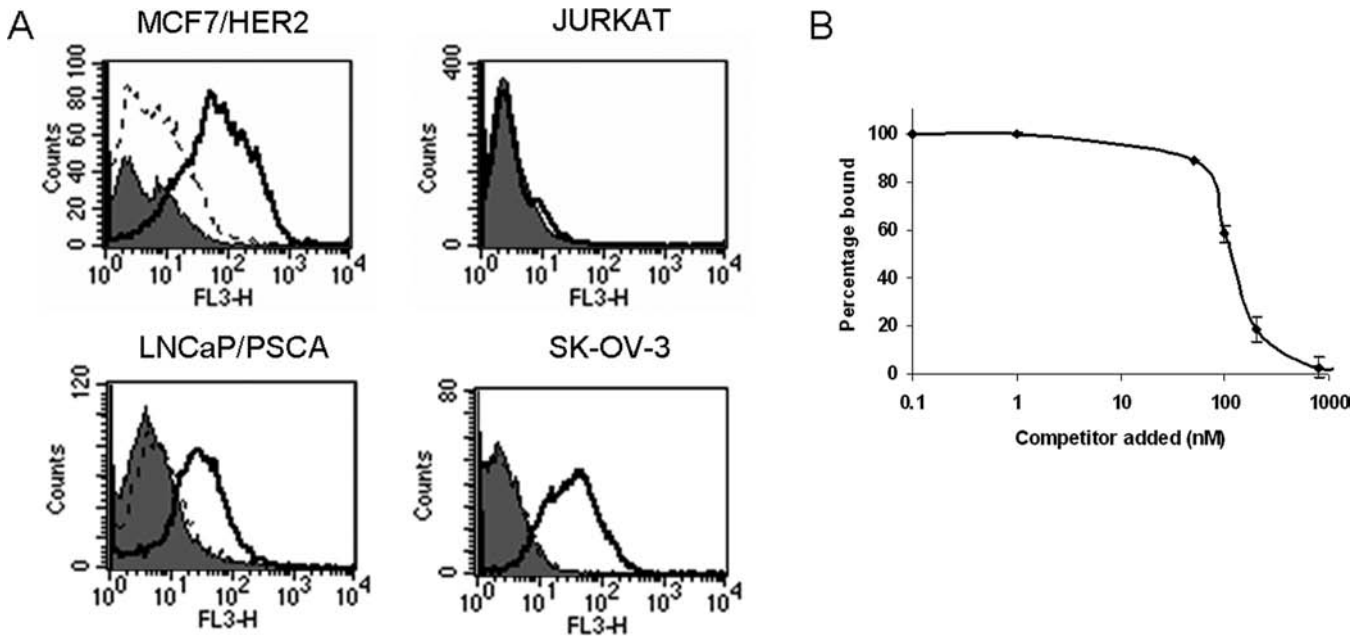

Figure 3. (A) Flow cytometry analysis of cys-diabody conjugated Qdot binding with different tumor cells. Cells were treated with no protein (solid gray), mock conjugated Qdot 655 (dotted black line), and anti-HER2 iQdot 655 (solid black line). FL3 (λ_{em}: 670 nm long pass) was the filter used for Qdot 655. (B) Competitive cell binding assay by flow cytometry. An anti-HER2 antibody fragment, minibody (*29*) was used as competitor. Samples were assayed in triplicate and means ± SEM are shown, normalized to the signal obtained in the absence of competitor.

Functional and Biophysical Characterization of NIR iQdots. In small animals, NIR (700−900 nm) fluorescence imaging is expected to have major utility, because the absorbance spectra for biomolecules reach minima in the NIR region, providing a window for *in vivo* optical imaging. We extended the coupling of anti-HER2 cys-diabody to amino PEG CdSe/ZnS Qdot 800 (emission maximum at 785 nm, anti-HER2 iQdot 800). The specific binding of anti-HER2 iQdot 800 on MCF7/HER2 cells was confirmed by cell binding assay (Figure 4A). In order to demonstrate this oriented thiol-specific coupling of other cys-diabodies specific for cell surface antigens to Qdots, we considered PSCA as an additional target. Applying the same thiol chemistry, we conjugated anti-PSCA cys-diabody with amino PEG Qdot 800 using EMCS (anti-PSCA iQdot 800). Strong binding of anti-PSCA iQdot 800 to LNCaP/PSCA cells was demonstrated by flow cytometry (Figure 4B).

PL measurements of NIR Qdots were performed following excitation with a 532 nm laser. The PL spectra measurements of the Qdots showed maxima at around 785 nm (Figure 4C). There was no significant change observed in mock conjugated and antibody conjugated Qdot spectra.

Duplex Antigen Detection of Prostate Cancer Cells Using Two Colored iQdots. Initially using individual Qdot conjugated cys-diabodies, anti-HER2 iQdot 655 and anti-PSCA iQdot 800, the expression of each target antigen, HER2 and PSCA, was examined on different cancer cells (Table 1). Detection of two individual cancer markers on LNCaP/PSCA prostate cancer cells (which also express HER2) was verified by previous flow cytometry experiments using anti-HER2 iQdot 655 and anti-PSCA iQdot 800 separately (Figure 3A and Figure 4B). Simultaneous detection of the two tumor markers on the same cells was not possible due to lack of proper filters and instrumental settings. To examine the feasibility of multiplex fluorescence imaging, LNCaP/PSCA prostate cancer cells were incubated with two different Qdot conjugates and imaged using a Maestro *In Vivo* optical imaging system (Figure 5A). The spectral analysis shows the presence of two distinct peaks of anti-HER2 iQdot 655 and anti-PSCA iQdot 800 (Figure 5B) verifying that multiplex fluorescence imaging is possible with these iQdots.

DISCUSSION

In this study, we report the site-specific conjugation of engineered antibody fragments with visible/NIR quantum dots for *in vitro* cell labeling and multiplex imaging. A key feature of this approach is the use of cys-diabodies which represent the smallest bivalent antibody fragment that can be generated from intact antibodies. Furthermore, this cys-diabody format enables site-specific, oriented coupling, ideal for applications in nanotechnology. Initial studies showed that Qdots functionalized with anti-HER2 cys-diabody retained antigen-specific cell binding, demonstrated by flow cytometry and fluorescence microscopy. In addition, utilizing the same technique, anti-PSCA cys-diabody was successfully conjugated to Qdots and two-color analysis was possible. The amine modified quantum dots used in this study include a PEG spacer covalently attached to the Qdot surface. We found that the PEG linker gave less nonspecific background compared to the corresponding carboxyl-modified Qdot 655, which does not possess a PEG linker (unpublished data). This characterization is most likely due to the increased hydrophilicity and higher stability resulting from the PEG-coating. The PEGylation reduces the surface charge and as a result, the nonspecific binding is reduced (*16*).

PEGylated Qdots have been used for *in vivo* imaging in mice (*17*). Addition of multiple PEG molecules provides improved biocompatibility and blood retention time. These improved properties of Qdots can facilitate their use as optical imaging probes *in vivo*. Recently, the delivery of Qdot 655 labeled antibody to tumor cells was investigated by *in vivo* real-time tracking (*11*). RGD modified Qdots have also recently been tracked in vasculature by their binding with integrins using intravital microscopy (*36*). PEGylated commercial Qdots had shown slower uptake into liver and spleen and low-level bone uptake in mice compared to un-PEGylated Qdot (*37*), but overall clearance times were still very rapid (6 min vs 2 min).

Use of engineered antibody fragments with Qdots for detection of a specific organic compound, 2,4,6-trinitrotoluene

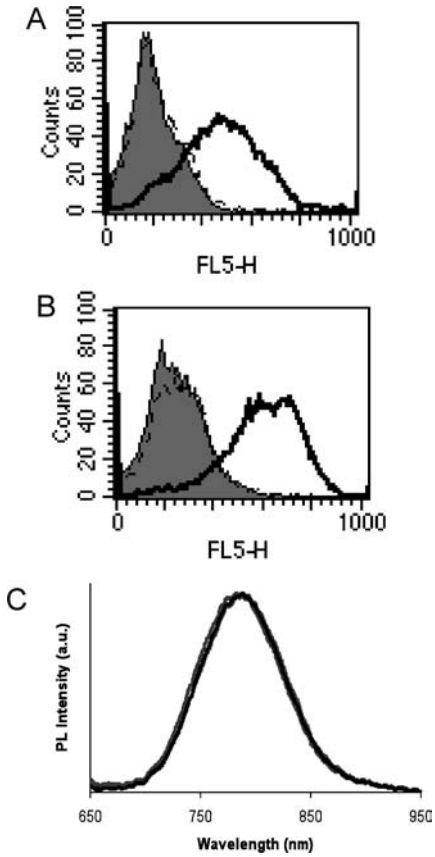

Figure 4. (A) Flow cytometry analysis of cys-diabody conjugated NIR Qdot binding with MCF7/HER2 Cells. Cells were treated with no protein (solid gray), mock conjugated Qdot 800 (dotted black line), and anti-HER2 iQdot 800 (solid black line). (B) LNCaP/PSCA cells stained with no protein (solid gray), mock conjugated Qdot 800 (dotted black line), and anti-PSCA iQdot 800 (solid black line). FL5 (λ_{em}: 740 long pass) was the filter used for Qdot 800. (C) Normalized emission spectra of amino PEG Qdot 800 conjugates. Excitation wavelength was 532 nm. Corresponding emission peaks and associated full-width half-maximum values were 787.9 and 88.95, 785.7 and 89.19, and 789.0 and 89.62 nm for mock conjugated Qdot 655 (black line), anti-HER2 iQdot 800 (red line), and anti-PSCA iQdot 800 (brown line), respectively.

Table 1. Binding Assay of Different ImmunoQdots with Different Tumor Cell Lines

cell line	Anti-HER2 iQdot 655	Anti-PSCA iQdot 800
Jurkat	−	−
MCF7/HER2	+	−
SKW/PSCA	−	+
LNCaP/PSCA	+	+

(TNT) was demonstrated using a scFv fragment (*38*). This study showed the use of luminescent Qdots conjugated to antibody fragments in a solution-phase nanosensor, based on fluorescence resonance energy transfer (FRET) for the specific detection of the explosive TNT in aqueous environments. Attachment of the anti-TNT specific scFv fragments to a hydrophilic Qdot via metal affinity coordination is another example of oriented attachment of small antibody fragments to Qdots. *In vivo* applications may be limited by the size of the overall complexes. In contrast, the present approach to site-specifically label cys-diabodies to any nanoscale particles can be used for *in vitro* as well as *in vivo* applications depending on the size of the conjugated particle.

In contrast to *in vitro* applications, many challenges exist *in vivo*, in particular, when targeting tumor is the goal. Many factors influence the penetration of antibody to areas distal from the blood vessels (*39*). These include antibody affinity, concentrations, antibody size, vascular permeability, and intratumoral pressure. Methodologies for introducing specificities onto Qdots by conjugating intact antibodies specific for HER2 antigen and prostate-specific membrane antigen (PSMA) for *in vivo* study have been developed (*11*, *17*). In mice bearing PSMA expressing tumor xenografts, in addition to tumor uptake, the antibody conjugated Qdots were trapped in the liver and spleen (*17*).

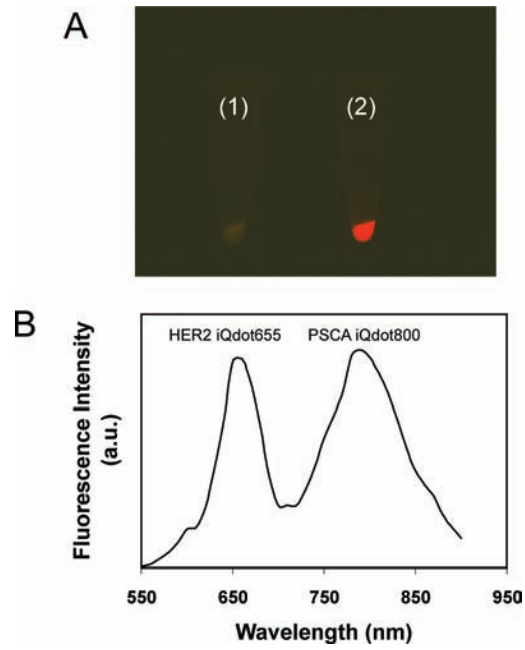

Figure 5. Dual marker Qdot staining of human prostate cancer cells. (A) *In vitro* fluorescence imaging of LNCaP/PSCA cells stained with (1) mock conjugated Qdot 655 and Qdot 800 and (2) anti-HER2 iQdot 655 and anti-PSCA iQdot 800. The raw fluorescence image acquired using a color CCD camera with a 550 to 900 nm filter is shown. (B) Spectral analysis of dual stained cells (sample 2) following background subtraction.

Previous studies of antibodies and antibody fragments have shown rapid and homogeneous tumor penetration by scFv fragments compared to other immunoglobulin forms (*20*). One potential shortcoming of the current Qdot conjugation strategies with biomolecules, especially vis-à-vis *in vivo* applications, is that the Qdot bioconjugates are quite large (∼40−50 nm) once streptavidin or intact antibodies are incorporated. Such large nanoparticles will have difficulty in traversing the endothelium and penetrating into tissues and tumors. In contrast, if smaller antibody fragments such as cys-diabodies are directly labeled to Qdots, the overall smaller size of these iQdots should be more suitable for *in vivo* applications. Further gains can be made by conjugation to even smaller particles such as zwitterionic, cys-coated quantum dots (QD-Cys) having hydrodynamic diameters of about 5.5 nm for rapid and efficient renal clearance and extravasation (*40*). Schipper et al. have further examined the effects of particle size, surface coating, and PEGylation on the biodistribution and clearance of small, near-infrared InAs Qdots, observing a shift toward renal clearance following PEGylation of the smallest, peptide-coated Qdots (*41*).

In conclusion, cys-diabodies are small, bivalent tumor-targeting antibody fragments that retain antigen binding specificity after incorporation of the cysteine-modification at the C-termini. Their small size and favorable pharmacokinetics make them ideal for use in imaging and therapeutic applications. The present study demonstrates site-specific, oriented conjugation of cys-diabodies to commercially available amino PEG quantum dots. The iQdots retain the photoluminescence properties of the unconjugated Qdots as well as the antigen binding

specificity of the cys-diabody. The overall small size of cys-diabody conjugated Qdots should render them suitable for biological applications. The results of Qdot conjugation to cys-diabodies with different tumor specificities opens up new prospects for multiplex imaging in cancer. This thiol-reactive conjugation approach can be used as a generalized platform for site-specific coupling of cys-diabodies with a wide variety of other nanoparticles, such as quantum rods or carbon nanotubes.

ACKNOWLEDGMENT

This work was supported by NIH grants CA119367 (SSG), EB000312 (AMW), CA86306 (AMW), CA092131 (AMW), and CA107399 (AMW). A.M.W. is a member of the Jonsson Comprehensive Cancer Center (CA 16042). We thank the UCLA Brain Research Institute Carol Moss Spivak Cell Imaging Facility for confocal microscopy and the UCLA Jonsson Comprehensive Cancer Center and Center for AIDS Research Flow Cytometry Core Facility.

Supporting Information Available: Experimental methods and results of TEM images and gel filtration chromatography as described in the text. This material is available free of charge via the Internet at http://pubs.acs.org.

LITERATURE CITED

(1) Michalet, X., Pinaud, F. F., Bentolila, L. A., Tsay, J. M., Doose, S., Li, J. J., Sundaresan, G., Wu, A. M., Gambhir, S. S., and Weiss, S. (2005) Quantum dots for live cells, in vivo imaging, and diagnostics. *Science 307*, 538–44.

(2) Xing, Y., Chaudry, Q., Shen, C., Kong, K. Y., Zhau, H. E., Chung, L. W., Petros, J. A., O'Regan, R. M., Yezhelyev, M. V., Simons, J. W., Wang, M. D., and Nie, S. (2007) Bioconjugated quantum dots for multiplexed and quantitative immunohistochemistry. *Nat. Protoc. 2*, 1152–65.

(3) Bruchez, M., Jr., Moronne, M., Gin, P., Weiss, S., and Alivisatos, A. P. (1998) Semiconductor nanocrystals as fluorescent biological labels. *Science 281*, 2013–6.

(4) Chan, W. C., and Nie, S. (1998) Quantum dot bioconjugates for ultrasensitive nonisotopic detection. *Science 281*, 2016–8.

(5) Fountaine, T. J., Wincovitch, S. M., Geho, D. H., Garfield, S. H., and Pittaluga, S. (2006) Multispectral imaging of clinically relevant cellular targets in tonsil and lymphoid tissue using semiconductor quantum dots. *Mod. Pathol. 19*, 1181–91.

(6) Howarth, M., Takao, K., Hayashi, Y., and Ting, A. Y. (2005) Targeting quantum dots to surface proteins in living cells with biotin ligase. *Proc. Natl. Acad. Sci. U.S.A. 102*, 7583–8.

(7) Wu, X., Liu, H., Liu, J., Haley, K. N., Treadway, J. A., Larson, J. P., Ge, N., Peale, F., and Bruchez, M. P. (2003) Immunofluorescent labeling of cancer marker Her2 and other cellular targets with semiconductor quantum dots. *Nat. Biotechnol. 21*, 41–6.

(8) Stroh, M., Zimmer, J. P., Duda, D. G., Levchenko, T. S., Cohen, K. S., Brown, E. B., Scadden, D. T., Torchilin, V. P., Bawendi, M. G., Fukumura, D., and Jain, R. K. (2005) Quantum dots spectrally distinguish multiple species within the tumor milieu in vivo. *Nat. Med. 11*, 678–82.

(9) Jaiswal, J. K., Mattoussi, H., Mauro, J. M., and Simon, S. M. (2003) Long-term multiple color imaging of live cells using quantum dot bioconjugates. *Nat. Biotechnol. 21*, 47–51.

(10) Voura, E. B., Jaiswal, J. K., Mattoussi, H., and Simon, S. M. (2004) Tracking metastatic tumor cell extravasation with quantum dot nanocrystals and fluorescence emission-scanning microscopy. *Nat. Med. 10*, 993–8.

(11) Tada, H., Higuchi, H., Wanatabe, T. M., and Ohuchi, N. (2007) In vivo real-time tracking of single quantum dots conjugated with monoclonal anti-HER2 antibody in tumors of mice. *Cancer Res. 67*, 1138–44.

(12) Medintz, I. L., Clapp, A. R., Mattoussi, H., Goldman, E. R., Fisher, B., and Mauro, J. M. (2003) Self-assembled nanoscale biosensors based on quantum dot FRET donors. *Nat. Mater. 2*, 630–8.

(13) So, M. K., Xu, C., Loening, A. M., Gambhir, S. S., and Rao, J. (2006) Self-illuminating quantum dot conjugates for in vivo imaging. *Nat. Biotechnol. 24*, 339–43.

(14) Kim, S., Lim, Y. T., Soltesz, E. G., De Grand, A. M., Lee, J., Nakayama, A., Parker, J. A., Mihaljevic, T., Laurence, R. G., Dor, D. M., Cohn, L. H., Bawendi, M. G., and Frangioni, J. V. (2004) Near-infrared fluorescent type II quantum dots for sentinel lymph node mapping. *Nat. Biotechnol. 22*, 93–7.

(15) Maysinger, D., Behrendt, M., Lalancette-Hebert, M., and Kriz, J. (2007) Real-time imaging of astrocyte response to quantum dots: in vivo screening model system for biocompatibility of nanoparticles. *Nano Lett.* n/a.

(16) Ballou, B., Lagerholm, B. C., Ernst, L. A., Bruchez, M. P., and Waggoner, A. S. (2004) Noninvasive imaging of quantum dots in mice. *Bioconjugate Chem. 15*, 79–86.

(17) Gao, X., Cui, Y., Levenson, R. M., Chung, L. W., and Nie, S. (2004) In vivo cancer targeting and imaging with semiconductor quantum dots. *Nat. Biotechnol. 22*, 969–76.

(18) Wu, A. M., and Senter, P. D. (2005) Arming antibodies: prospects and challenges for immunoconjugates. *Nat. Biotechnol. 23*, 1137–46.

(19) Kenanova, V., and Wu, A. M. (2006) Tailoring antibodies for radionuclide delivery. *Expert Opin. Drug Delivery 3*, 53–70.

(20) Yokota, T., Milenic, D. E., Whitlow, M., and Schlom, J. (1992) Rapid tumor penetration of a single-chain Fv and comparison with other immunoglobulin forms. *Cancer Res. 52*, 3402–8.

(21) Holliger, P., Prospero, T., and Winter, G. (1993) "Diabodies": small bivalent and bispecific antibody fragments. *Proc. Natl. Acad. Sci. U.S.A. 90*, 6444–8.

(22) Sundaresan, G., Yazaki, P. J., Shively, J. E., Finn, R. D., Larson, S. M., Raubitschek, A. A., Williams, L. E., Chatziioannou, A. F., Gambhir, S. S., and Wu, A. M. (2003) 124I-labeled engineered anti-CEA minibodies and diabodies allow high-contrast, antigen-specific small-animal PET imaging of xenografts in athymic mice. *J. Nucl. Med. 44*, 1962–9.

(23) Wu, A. M., Williams, L. E., and Zieran, L. (1999) Anti-carcinoembryonic antigen (CEA) diabody for rapid tumor targeting and imaging. *Tumor Targeting 4*, 47–58.

(24) Carmichael, J. A., Power, B. E., Garrett, T. P., Yazaki, P. J., Shively, J. E., Raubischek, A. A., Wu, A. M., and Hudson, P. J. (2003) The crystal structure of an anti-CEA scFv diabody assembled from T84.66 scFvs in V(L)-to-V(H) orientation: implications for diabody flexibility. *J. Mol. Biol. 326*, 341–51.

(25) Li, L., Olafsen, T., Anderson, A. L., Wu, A., Raubitschek, A. A., and Shively, J. E. (2002) Reduction of kidney uptake in radiometal labeled peptide linkers conjugated to recombinant antibody fragments. Site-specific conjugation of DOTA-peptides to a Cys-diabody. *Bioconjugate Chem. 13*, 985–95.

(26) Olafsen, T., Cheung, C. W., Yazaki, P. J., Li, L., Sundaresan, G., Gambhir, S. S., Sherman, M. A., Williams, L. E., Shively, J. E., Raubitschek, A. A., and Wu, A. M. (2004) Covalent disulfide-linked anti-CEA diabody allows site-specific conjugation and radiolabeling for tumor targeting applications. *Protein Eng. Des. Sel. 17*, 21–7.

(27) Albrecht, H., Burke, P. A., Natarajan, A., Xiong, C. Y., Kalicinsky, M., DeNardo, G. L., and DeNardo, S. J. (2004) Production of soluble ScFvs with C-terminal-free thiol for site-specific conjugation or stable dimeric ScFvs on demand. *Bioconjugate Chem. 15*, 16–26.

(28) Sirk, S. J., Olafsen, T., Barat, B., Bauer, K. B., and Wu, A. M. (2008) Site-specific, thiol-mediated conjugation of fluorescent probes to cysteine-modified diabodies targeting CD20 or HER2. *Bioconjugate Chem. 19*, 2527–34.

(29) Olafsen, T., Kenanova, V. E., Sundaresan, G., Anderson, A. L., Crow, D., Yazaki, P. J., Li, L., Press, M. F., Gambhir, S. S.,

Williams, L. E., Wong, J. Y., Raubitschek, A. A., Shively, J. E., and Wu, A. M. (2005) Optimizing radiolabeled engineered anti-p185HER2 antibody fragments for in vivo imaging. *Cancer Res. 65*, 5907–16.

(30) Olafsen, T., Gu, Z., Sherman, M. A., Leyton, J. V., Witkosky, M. E., Shively, J. E., Raubitschek, A. A., Morrison, S. L., Wu, A. M., and Reiter, R. E. (2007) Targeting, imaging, and therapy using a humanized antiprostate stem cell antigen (PSCA) antibody. *J. Immunother. (1997) 30*, 396–405.

(31) Bell-Pedersen, D., Dunlap, J. C., and Loros, J. J. (1996) Distinct cis-acting elements mediate clock, light, and developmental regulation of the Neurospora crassa eas (ccg-2) gene. *Mol. Cell. Biol. 16*, 513–21.

(32) Galfre, G., and Milstein, C. (1981) Preparation of monoclonal antibodies: strategies and procedures. *Methods Enzymol. 73*, 3–46.

(33) Slamon, D. J., Clark, G. M., Wong, S. G., Levin, W. J., Ullrich, A., and McGuire, W. L. (1987) Human breast cancer: correlation of relapse and survival with amplification of the HER-2/neu oncogene. *Science 235*, 177–82.

(34) Gu, Z., Thomas, G., Yamashiro, J., Shintaku, I. P., Dorey, F., Raitano, A., Witte, O. N., Said, J. W., Loda, M., and Reiter, R. E. (2000) Prostate stem cell antigen (PSCA) expression increases with high gleason score, advanced stage and bone metastasis in prostate cancer. *Oncogene 19*, 1288–96.

(35) Leyton, J. V., Olafsen, T., Lepin, E. J., Hahm, S., Bauer, K. B., Reiter, R. E., and Wu, A. M. (2008) Humanized radioiodinated minibody for imaging of prostate stem cell antigen-expressing tumors. *Clin. Cancer Res. 14*, 7488–96.

(36) Smith, B. R., Cheng, Z., De, A., Koh, A. L., Sinclair, R., and Gambhir, S. S. (2008) Real-time intravital imaging of RGD-quantum dot binding to luminal endothelium in mouse tumor neovasculature. *Nano Lett 8*, 2599–606.

(37) Schipper, M. L., Cheng, Z., Lee, S. W., Bentolila, L. A., Iyer, G., Rao, J., Chen, X., Wu, A. M., Weiss, S., and Gambhir, S. S. (2007) MicroPET-based biodistribution of quantum dots in living mice. *J. Nucl. Med. 48*, 1511–8.

(38) Goldman, E. R., Medintz, I. L., Whitley, J. L., Hayhurst, A., Clapp, A. R., Uyeda, H. T., Deschamps, J. R., Lassman, M. E., and Mattoussi, H. (2005) A hybrid quantum dot-antibody fragment fluorescence resonance energy transfer-based TNT sensor. *J. Am. Chem. Soc. 127*, 6744–51.

(39) Fujimori, K., Covell, D. G., Fletcher, J. E., and Weinstein, J. N. (1989) Modeling analysis of the global and microscopic distribution of immunoglobulin G, F(ab')2, and Fab in tumors. *Cancer Res. 49*, 5656–63.

(40) Choi, H. S., Liu, W., Misra, P., Tanaka, E., Zimmer, J. P., Itty Ipe, B., Bawendi, M. G., and Frangioni, J. V. (2007) Renal clearance of quantum dots. *Nat. Biotechnol. 25*, 1165–70.

(41) Schipper, M. L., Iyer, G., Koh, A. L., Cheng, Z., Ebenstein, Y., Aharoni, A., Shay, K., Bentolili, L. A., Li, J., Rao, J., Chen, X., Banin, U., Wu, A. M., Sinclair, R., Weiss, S., and Gambhir, S. S. (2009) Particle size, surface coating, and PEGylation influence the biodistribution of quantum dots in living mice. *Small 5*, 126–134.

BC800421F

Supporting Information

Cys-diabody Quantum Dot Conjugates (immunoQdots) for Cancer Marker Detection

TEM Method: Transmission electron microscopy (TEM) specimens were prepared by pipetting 6μl of the sample suspension onto ultrathin Carbon Type-A 400-mesh copper grids (Tedpella Inc., Redding, CA) that had been glow-discharged. After 10 minutes, the grids were rinsed with deionized water to remove any buffer salts that may be present in the samples and wicked to almost dryness with filter paper. Phosphotungstic acid (PTA) of pH 7.0 was then added to the grids to negatively stain the samples. After one minute, the grids were completely dried using filter paper.

All the specimens were analyzed using the Philips CM20 FEG-TEM operating at 200kV. The microscope is also equipped with an energy dispersive x-ray spectrometer (EDS) for compositional analysis.

Size exclusion chromatography: Conjugated Qdots were subjected to size-exclusion chromatography on a Superdex 200 column (GE Healthcare, Piscataway, NJ) in PBS at a flow rate of 0.5 mL/min over one column volume (24 mL) on an AKTA purifier.

Figure 1. (A) TEM and HRTEM images of (Left panel) anti-HER2 iQdot 655 and (Right panel)mock conjugated Qdot 655. **(B)** PTA stained images of (Left panel) anti-HER2 iQdot 655 and (Right panel)mock conjugated Qdot 655.

Figure 2. Size exclusion chromatography of mock conjugated (dotted line) and anti-HER2 iQdot 655 (solid line) on Superdex 200 column.

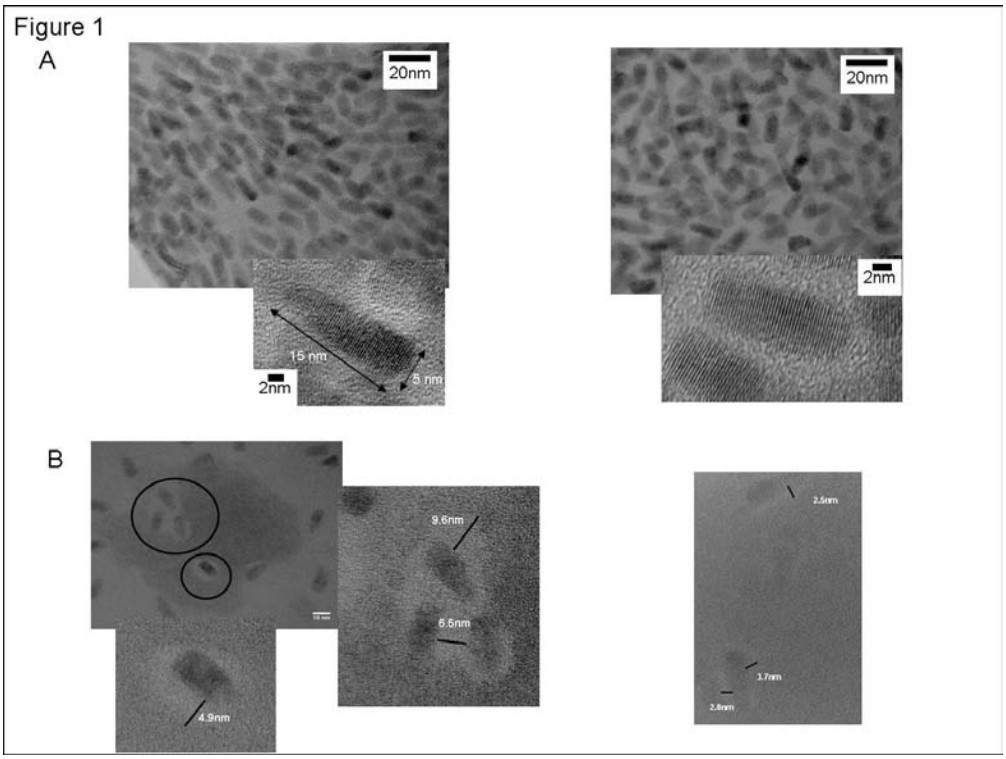

254x190mm (150 x 150 DPI)

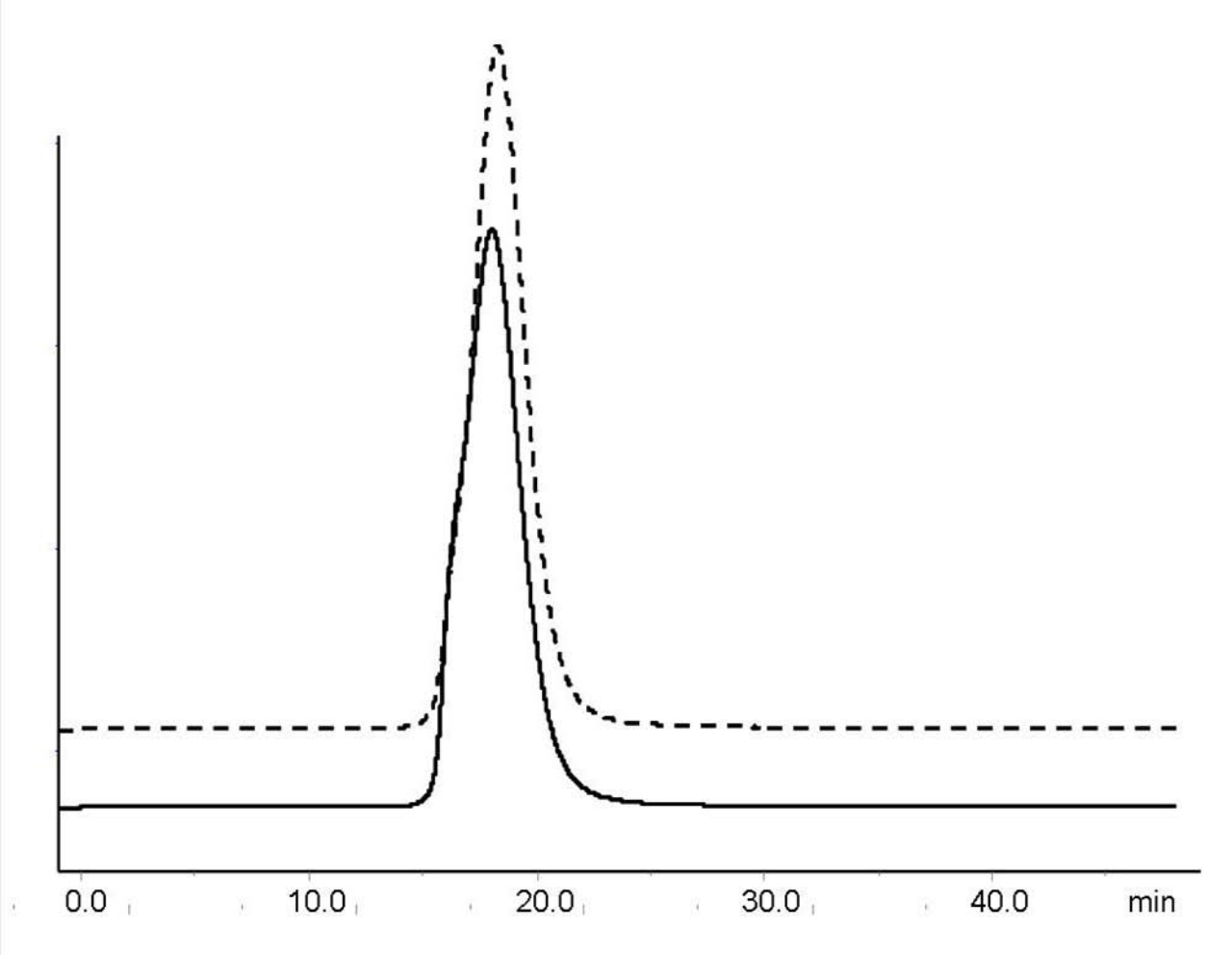
0.0
10.0
20.0
30.0
40.0
min

Site-Specific Labeling of Surface Proteins on Living Cells Using Genetically Encoded Peptides that Bind Fluorescent Nanoparticle Probes

Mark A. Rocco,[†] Jae-Young Kim,[‡] Andrew Burns,[§] Jan Kostecki,[†] Anne Doody,[†] Ulrich Wiesner,[§] and Matthew P. DeLisa*[,†,‡]

Department of Biomedical Engineering, School of Chemical and Biomolecular Engineering, and Department of Materials Science and Engineering, Cornell University, Ithaca, New York 14853. Received January 9, 2009; Revised Manuscript Received July 8, 2009

We report a highly specific, robust, and generic method for noncovalent labeling of cellular proteins with highly fluorescent core−shell silica nanoparticles termed C dots. Our approach uses short genetically engineered peptides with affinity for silica (GEPS) that are site-specifically introduced at the termini or in loops of cellular proteins. Because GEPS are absent from native cell surface proteins, GEPS-tagged recombinant proteins can be selectively and rapidly labeled with fluorescent C dots. To demonstrate the versatility of our method, we targeted 30 nm C dots to two structurally distinct integral outer membrane proteins in *Escherichia coli*, FhuA and OmpX. Efficient labeling was achieved in 15 min or less and was observed to be highly sensitive and specific. This strategy provides a powerful technique, comparable to other chemical and biological labeling strategies, for efficient and quantitative investigation of protein function in live biological cells.

INTRODUCTION

Visualizing the movement and interactions of cellular proteins is fundamental to our understanding of biochemical networks and for elucidating the structure and function of proteins in their native environment. Numerous biophysical probes (e.g., fluorophores, spin labels, etc.) have been developed for labeling cellular proteins with excellent spatiotemporal resolution (*1, 2*). However, a primary factor limiting the use of many such probes is the technological challenge associated with probe conjugation to target proteins. To address this challenge, a number of general labeling strategies have been reported recently that employ special protein or peptide handles for recruitment of biophysical probes to specific sites within proteins on the surface of living cells (*3*−*6*). For instance, Ting and co-workers have developed a two-step conjugation procedure based on enzymatic biotinylation that enables cell surface protein labeling using different probes, including fluorescent semiconductor nanoparticles known as quantum dots (QDs) (*7*). QDs hold great promise as biophysical probes because of their intense fluorescence emission and remarkable photostability (*8, 9*), as well as their ability to be rendered water-soluble and thus used in biological media and other aqueous environments (*10*). However, although QDs exhibit many desirable photophysical properties, they face significant challenges relating to their toxicity and disposal (*11, 12*).

As an alternative to QDs, organic fluorophores can be incorporated into nanoparticles during synthesis (*13*−*16*). For instance, Wiesner and co-workers recently developed a class of monodisperse fluorescent core−shell silica nanoparticles, termed C dots (Figure 1a), by integrating covalently bound dyes in a sol−gel-derived silica matrix (*17*). The particles are assembled in a core−shell architecture via a modified Stöber synthesis (*18*) with the dye molecules (e.g., tetramethylrhodamine isothiocyanate, TRITC) sequestered within the particle core, which in turn is enclosed in a layer of pure silica. This architecture results in a variety of improved properties, such as reduced photobleaching, minimized solvatochromic shift, and increased fluorescence efficiency relative to free dye in aqueous solution and provides particles with sizes down to the 3−5 nm scale (*19, 20*). The C dot design also allows colocalization of multiple fluorophores within a single particle. This significantly increases per-particle brightness and, because the encapsulated dye molecules are decoupled from each other, reduces intermittent blinking under continuous excitation—a limitation that hinders single-emitter systems such as green fluorescent protein (GFP) (*21*) and QDs (*22*). Importantly, C dots have found use in a broad range of biological imaging applications and are non-cytotoxic at biologically relevant concentrations (*17, 23*). Given the vast diversity of organic dye molecules and the exquisite chemical and photophysical tunability of different encapsulation matrices, this approach should enable the development of nanoparticles with a broad range of precisely controlled fluorescence characteristics.

Here, we present a generic method to rapidly and reversibly label proteins on the surface of living cells with highly fluorescent silica nanoparticles. This was accomplished by exploiting short 12-mer peptide sequences, which we term GEPS (genetically engineered peptides for silica), as recognition elements for site-selective labeling of cell surface proteins with 30 nm C dots. Due to the ability of these peptides to bind biogenic silica (*24*), we hypothesized that they could be used to create a noncovalent linkage between the organosilicate exterior matrix of C dots and proteins of interest. Indeed, we demonstrate that these tags can be genetically encoded into regions of a target protein sequence, such as at the termini or in loops, where they do not disturb the protein's structure and function but are accessible to exogenously added C dots.

EXPERIMENTAL PROCEDURES

Synthesis of C Dots. To achieve the core−shell architecture used for the genetically encoded fluorescent silica nanoparticles, a modified Stöber sol−gel process was used as described

* Address all correspondence to: Matthew P. DeLisa, 254 Olin Hall, Cornell University, Ithaca, NY 14853 USA; phone: 607-254-8560; fax: 607-255-9166; e-mail: md255@cornell.edu.

[†] Department of Biomedical Engineering.

[‡] School of Chemical and Biomolecular Engineering.

[§] Department of Materials Science and Engineering.

10.1021/bc9000118 CCC: $40.75 © 2009 American Chemical Society
Published on Web 08/03/2009

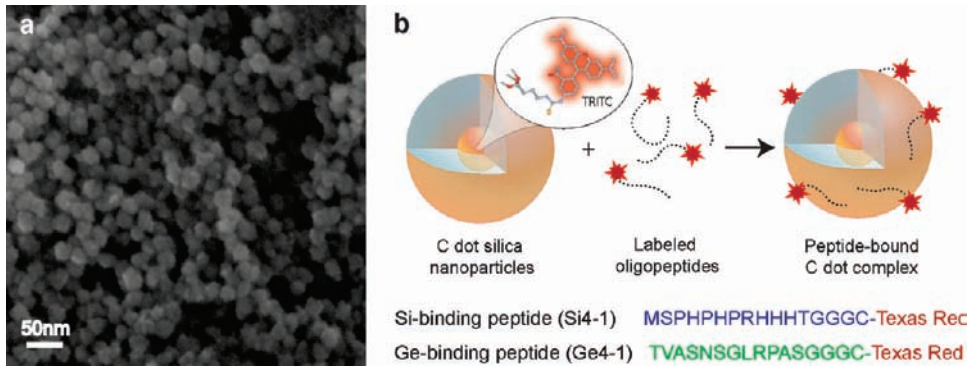

Figure 1. (a) Scanning electron micrograph of 30-nm-diameter TRITC C dots. This size particle was used for all live cell labeling studies. (b) Schematic of binding between C dot and different peptide sequences. Short, purified peptides were used for proof-of-concept binding experiments using orthogonal C dot−peptide pairs. For these experiments, Texas Red conjugated oligopeptides (either silica-binding (Si4−1) or germania-binding (Ge4−1) peptides) were incubated with 60 nm core−shell fluorescent silica nanoparticle C dots that incorporated tetramethylrhodamine isothiocyanate dye (TRITC) as shown.

previously (*17*). Briefly, alkoxysilanes were hydrolyzed and condensed in an aqueous alcohol solution with ammonia acting as catalyst, in the presence of the organic dye TRITC, covalently encapsulating of a silane derivative of the fluorescent dye molecules into the silica matrix (*17, 25, 26*). This dye-rich core formation reaction was followed by a second reaction with further pure silica precursor to form the particle shell. Varying the reaction chemistry allows specific tailoring of the desired nanoparticle size as described (*17*).

Peptide Labeling of C Dots. Proof-of-concept experiments with purified peptides, were performed by incubation of 60 nm C dots with 12-mer oligopeptides (Sigma-Genosys; Ge4−1 - TVASNSGLRPAS and Si4−1 - MSPHPHPRHHHT) conjugated to Texas Red C_2 maleimide (Invitrogen, Inc.) followed by repeated wash steps using water to remove unbound peptide. Following each wash, microcentrifugation was used to pellet the 60 nm particles, and pelleted particles were resuspended in water prior to fluorometric analysis.

Bacterial Strains and Plasmids. *Escherichia coli* strain DH5α (F$^-$ *ϕ80dlacZΔM15 Δ(lacZYA-argF)U169 deoR nupG recA1 endA1 hsdR17*(r_k^-, m_k^+) *phoA glnV44 thi-1 gyrA96 relA1 λ-*) was used for cloning and labeling experiments. *E. coli* strains AB2847 (F$^-$ *aroB thi tsx malT*) and MB97 (as AB2847, but Δ*fhuA*) were used for the albomycin resistance experiments (*27*). All plasmids generated in this study were derivatives of pHIE11 (*28*) or pBAD24. All FhuA constructs were created by inserting DNA encoding the silica- or germania-binding sequences into the *Fse*I-*Not*I multicloning site of plasmid pHIE11 (*28*). This resulted in the placement of each GEPS sequence in extracellular loop 5 of FhuA, just after the proline at position 405. For the OmpX constructs, the *E. coli ompX* gene was PCR-amplified using genomic DNA as template and appended with a C-terminal 6X-histidine tag. The resulting PCR product was cloned in between the *Nco*I and *Sph*I sites of plasmid pBAD24 (*29*) resulting in plasmid pBAD24-OmpX-his. To use extracellular loop 2 in OmpX for the insertion of silica-binding peptides, *Kpn*I and *Spe*I sites were inserted between the serine residues at positions 53 and 54 of OmpX by overlap extension PCR. The resulting PCR product was digested with *Nco*I and *Sph*I and ligated into pBAD24, resulting in pBAD24-OmpX*-his. DNA encoding each of the 12-mer GEPS sequences was cloned in between *Kpn*I and *Spe*I of pBAD24-OmpX*-his. Plasmids pHIE11 and pBAD24-OmpX*-his were modified to include each of the following GEPS primary sequences: Ge4−1 - TVASNSGLRPAS; Si3−3 - APPGHHHWHIHH; Si3−8 - KPSHHHHHTGAN; Si4−8 - APHHHHPHHLSR; and Si4−1 - MSPHPHPRHHHT. All GEPS sequences were codon optimized for expression in *E. coli.* All plasmids were confirmed by sequencing.

Labeling of Living Cells with C Dots. Cells containing FhuA or OmpX plasmids were grown overnight at 37 °C in Luria−Bertani (LB) medium containing appropriate antibiotics (50 μg/mL kanamycin for all FhuA constructs and 100 μg/mL ampicillin for all OmpX constructs). The following day, overnight cells were diluted 10-fold in LB containing antibiotics and allowed to grow for 90 min at 37 °C (OD_{600} ∼0.5). Subcultured cells were induced with 1 mM IPTG for 90 min at 37 °C, at which time the cultures were pelleted via centrifugation for 15 min at 4 °C and 13,200 rpm. Pelleted cells were resuspended in 1 mL of phosphate buffered saline (PBS) and normalized to an OD_{600} of 1.0. Normalized samples were incubated in the dark for 1 h at 4 °C with 30 nm TRITC C dots at a concentration of 8.1×10^8 particles/μL, unless otherwise noted, followed by an additional three washes in PBS.

Fluorescence Microscopy. C dot-labeled cells were imaged using a Carl Zeiss Axioskop 40 optical microscope with a Zeiss 100×/1.30 Oil Plan-NEOFLUAR lens, an EXFO X-Cite Series 120 lamp (Mississauga, Ontario), a TRITC emission filter, and a SPOT FLEX digital camera from Diagnostic Instruments, Inc. (Sterling Heights, MI). A total of 5 μL of live bacterial cells was placed onto a microscope slide and a coverslip placed on top. A drop of oil was added and images were taken using an oil-immersion technique at a magnification of 1000×.

Fluorescence Microplate and Flow Cytometric Analysis. C dot-labeled cells were aliquoted into a 96-well microtiter plate (Corning COSTAR) in triplicate and fluorescence was quantified using a fluorescence microplate reader (Bio-Tek Synergy HT). Cells were excited at a wavelength of 530 nm, and total cell fluorescence was measured at an emission wavelength of 590 nm, parameters that were near-optimal for TRITC (ex, 557 nm; em, 576 nm). Data were reported as an average of three measurements with an error determined as the standard deviation of the mean. For flow cytometric analysis, 5 μL of C dot-labeled cells were diluted into 1 mL of PBS and single-cell fluorescence distributions were measured using a Becton Dickinson FACS-Calibur flow cytometer as described elsewhere (*30*). The excitation/emission filters for this system were configured at 488 and 585 nm, respectively. For TRITC C-dots, a 488 nm excitation wavelength only excites at about 1/6 of the peak absorption and collects at about 80% of the peak emission.

Protein Analysis. To analyze protein expression, soluble fractions were prepared from 10 mL cultures of *E. coli* cells expressing the different FhuA and OmpX constructs as follows. First, cells were pelleted by centrifugation for 15 min at 4 °C and 3500 rpm and then resuspended in 1 mL PBS solution followed by sonication (Branson Sonifier). Then, the sonicant was spun for 15 min at 4 °C and 13,200 rpm, and the resulting supernatant was collected as the soluble fraction. Proteins in

the soluble fractions were separated by SDS-PAGE using 12% Tris−HCl gels (BioRad) and Western blotted as described (*31*). For all pFhuA constructs, anti-FhuA (kindly provided by Dr. Andreas Meinke, InterCell Biomedizinische Forschungs und Entwicklungs AG) was used as the primary antibody at a dilution of 1:100 000 in conjunction with a horseradish peroxidase-conjugated antirabbit secondary antibody (Sigma) diluted 1:5000. For all pOmpX constructs, horseradish peroxidase-conjugated antipolyhistidine antibody (Abcam) was used at a dilution of 1:3000.

Albomycin Resistance Assay. Growth inhibition by albomycin was assayed using a protocol similar to that described by Braun and co-workers (*32*). Briefly, strain MB97 was transformed with plasmids pFhuA, pFhuA-Ge4−1, or pFhuA-Si4−1. Liquid cultures were grown overnight until stationary phase at 37 °C in TY media (1.0% tryptone, 0.5% yeast extract, and 0.5% NaCl). 100 μL of each overnight culture was centrifuged and resuspended in fresh TY media to eliminate any cellular waste and debris. These cells were serial diluted (down to a dilution of 10^6) and spotted on TY/agar plates containing no antibiotics or 25 μg/mL albomycin. Plated cells were grown overnight at 37 °C and subsequently imaged.

RESULTS

Identification of Orthogonal Peptide−Nanoparticle Pairs Using Purified Peptides. The most common approach for targeting QDs and C dots to a protein of interest is to conjugate the nanoparticles with a high-affinity binding protein, such as an immunoglobulin or streptavidin, which mediates binding of the nanoparticle to a specific antigen or biotinylated protein, respectively (*9, 17*). However, the large size of this complex can interfere with membrane protein trafficking and can reduce accessibility of the nanoparticles. Therefore, our goal was to develop a generic method for direct labeling of cell surface proteins with C dots that eliminated the need for bulky binding proteins and provided a genetically encodable linkage between the protein of interest and the C dot. This was accomplished using genetically engineered peptides for silica (GEPS), which are short amino acid sequences that specifically and selectively bind silica. Previous studies using filamentous phage display have isolated genetically engineered peptides that bind to, for example, silica (*24*) and titania (*33*). In the present study, we hypothesized that the silica-binding peptides would electrostatically bind to the surface of C dots. The rationale for this was based on the notion that GEPS selected for strong binding to a specific silica surface of given size and morphology can often bind to another surface of the same material or to a different material but having similar structure or physiochemical properties (*34*).

We first sought to determine whether GEPS sequences that were previously isolated for their ability to bind and precipitate biogenic amorphous silica (*24*) could similarly bind C dots. Proof-of-concept binding experiments were performed to evaluate binding between C dots and different fluorescently labeled peptides (Figure 1b). Specifically, we used two synthetic 12-mer peptides: one with high affinity for silica (Si4−1, MSPHPHPRHHHT) and a second, nonspecific control peptide with affinity for germania (Ge4−1, TVASNSGLRPAS). A GGGC motif was incorporated at the C-terminus of each peptide in order to react the thiol of the C-terminal cysteine with Texas Red C_2 maleimide. Dye-labeled silica- and germania-binding oligopeptides were incubated at various concentrations with 60-nm-diameter TRITC core−shell C dots. Fluorescence spectra and binding curves revealed enhanced binding specificity for the Si4−1 peptides with the silica nanoparticle surface relative to that of the Ge4−1 peptides or to the free dye controls (Figure 2a,b). It should be noted that since silica has its isoelectric point around pH 2−3, at neutral pH the particles are stabilized by eletrostatic repulsive interactions (*19, 20*). At very high salt concentrations (e.g., around 0.1 M aqueous NaCl), these electrostatic repulsions are screened and steric repulsive interactions must be used to stabilize the particles. Hence, the peptide and cell labeling conditions (i.e., PBS at neutral pH) used here are expected to disfavor particle aggregation. It should also be noted that we chose 60 nm C dots for the peptide labeling experiments because of difficulties associated with microcentrifugation of smaller C dots (e.g., 30 nm). In later experiments described below, 30 nm C dots were used because their smaller size was desirable for cell labeling purposes, and due to their specific capture by cells, microcentrifugation was no longer an issue.

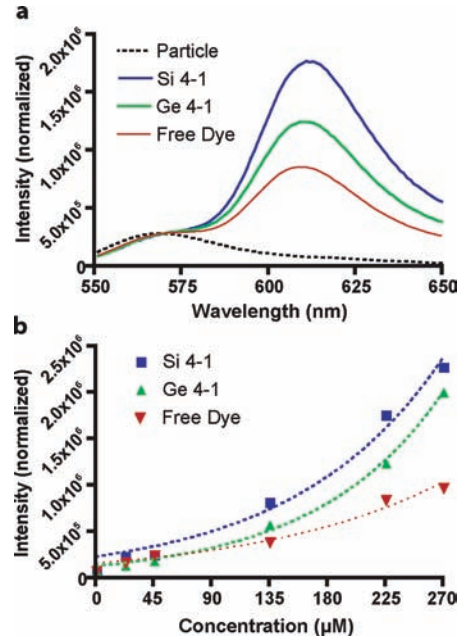

Figure 2. Proof-of-concept binding experiments using C dots and short, fluorescently labeled oligopeptides. (a) Fluorescence spectra and (b) binding curves for the orthogonal C dot−peptide pairs shown in Figure 1b. Texas Red-labeled silica- and germania-binding 12-mer peptides (Si4−1 and Ge4−1, respectively) were incubated with 60 nm TRITC C dot particles and analyzed via a fluorescence spectrometer. Free TRITC dye was used as a control. Data represent the average of three replicate experiments. The standard error in each case was less than 5%.

Rapid, Highly Specific Protein Labeling in Living Cells. We next tested whether the orthogonal C dot−peptide pairs could be used to label cellular proteins. This was achieved by engineering the high- (Si4−1) and low- (Ge4−1) affinity GEPS into a highly exposed extracellular loop of the *E. coli* outer membrane protein, FhuA. FhuA is a ferrichrome and phage T5 receptor that exposes 11 loops to the extracellular milieu and 10 turn regions to the periplasm (*35, 36*). Previous studies demonstrated that extracellular loops 4 and 5 of FhuA are able to tolerate insertions of up to 250 and 166 amino acids, respectively, while still maintaining functionality (*28*). Accordingly, we introduced the Si4−1 and Ge4−1 sequences just after the proline residue at position 405 in the fifth extracellular loop of FhuA (Figure 3a), a site displaying the largest surface area to the extracellular milieu.

To determine the efficacy of this labeling strategy using live cells, the various FhuA constructs were expressed in *E. coli* and analyzed via fluorescence microscopy. Following labeling with 30 nm C dots at a final concentration of 8.1×10^8 particles/μL, cells expressing the FhuA-Si4−1 construct showed a highly fluorescent phenotype, whereas cells expressing FhuA-Ge4−1 or wild-type FhuA with no peptide insert exhibited only minor,

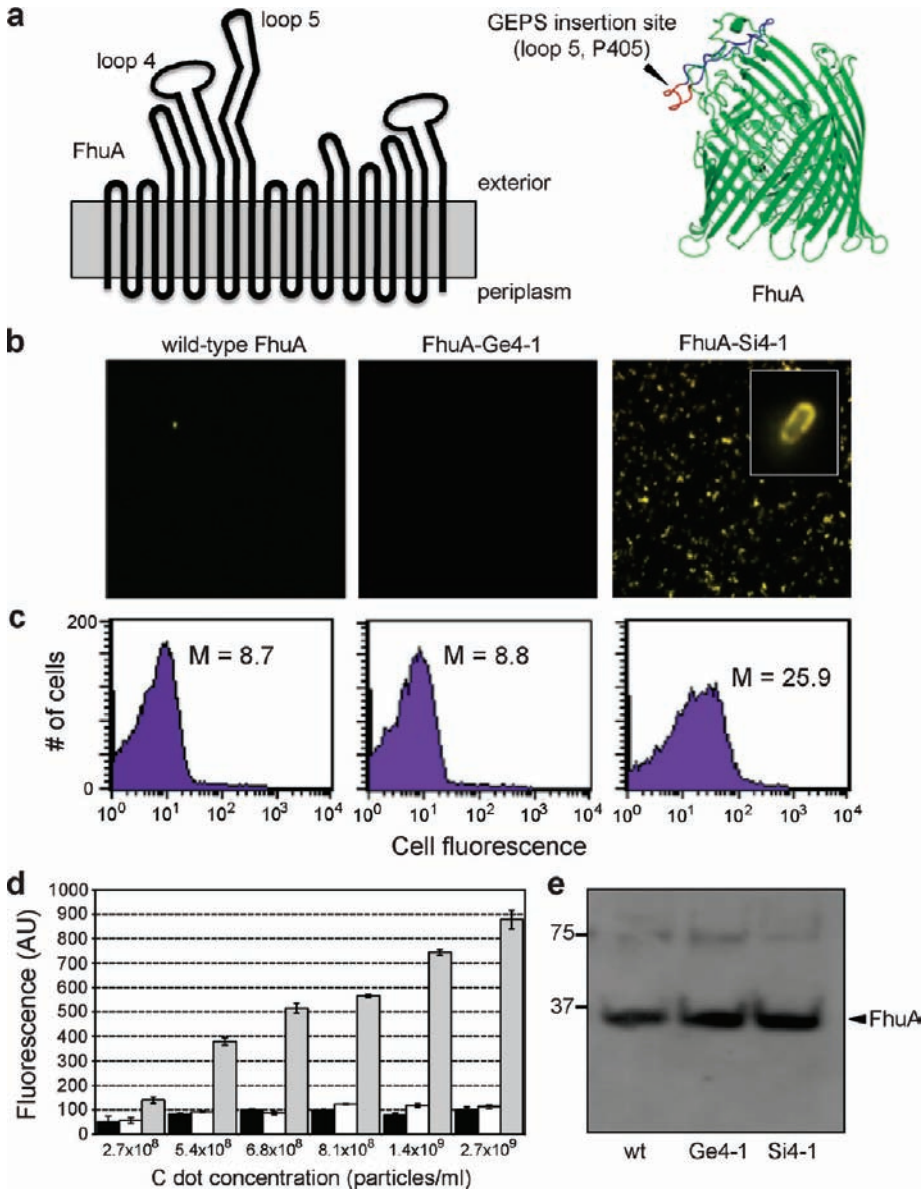

Figure 3. (a) Schematic and three-dimensional structural representations of FhuA depicting the GEPS insertion site in extracellular loop 5, immediately following a proline residue at position 405 (P405). In the FhuA crystal structure (right), loop 5 is highlighted in blue and the GEPS sequence is highlighted in red. (b) Fluorescence microscopy of cells expressing FhuA-Si4−1, FhuA-Ge4−1, or wild-type FhuA with no peptide insert. Following labeling with 30 nm TRITC C dots at a concentration of 8.1×10^8 particles/μL, 5 μL of live bacterial cells were placed onto a microscope slide and a coverslip placed on top. A drop of oil was added and images were taken using an oil immersion technique at a magnification of 1000×. Inset is an enlarged image of a single cell. (c) FACS analysis of the same constructs described in (b). Shown are representative FACS histograms. Mean fluorescence (M) values are the average of three replicate experiments. The error in each case was less than 5%. (d) Quantification of cell fluorescence after C dot labeling. Cells were induced to express FhuA-Si4−1 (gray bars), FhuA-Ge4−1 (white bars), and wild-type FhuA (black bars) and then labeled with a range of C dot concentrations as indicated. Data are the average of three replicate experiments, and error bars represent the standard deviation of the mean. (e) Western blot analysis of soluble fractions generated from cells expressing FhuA-Si4−1, FhuA-Ge4−1, and wild-type FhuA. Soluble proteins from an equivalent number of cells were loaded in each lane and detection was with FhuA antiserum.

static background fluorescence (Figure 3b). Background fluorescence was readily distinguishable from target fluorescence due to both the brightness and localization of the C dots. Characteristic nonspecific background fluorescence appeared as very bright C dot clusters that were not colocalized with *E. coli* cells. In contrast, positive target fluorescence corresponded to a halo-like fluorescent ring that colocalized with the *E. coli* cell body (Figure 3b) and was similar to the fluorescence pattern seen for other cell surface or periplasmic labeling strategies (*37*). The same C dot-treated cells were subjected to fluorescence-activated cell sorting (FACS) analysis. Consistent with the microscopy results, cells expressing FhuA-Si4−1 showed a 3-fold increase in mean cell fluorescence (MF) compared to cells expressing FhuA-Ge4−1 or wild-type FhuA (Figure 3c). When these same cells were analyzed using a fluorescence microplate reader, we observed a 5-fold difference in fluorescence between cells expressing FhuA-Si4−1 and cells expressing FhuA-Ge4−1 or wild-type FhuA (Figure 3d). We attribute the improved signal-to-noise obtained using the microplate reader to the excitation/emission filters (ex, 530; em, 590 nm) of this device, which match the excitation/emission wavelengths of TRITC (ex, 557 nm; em, 576 nm) more closely than our current flow cytometry setup. Moreover, cells expressing FhuA-Si4−1 exhibited a C dot concentration-dependent fluorescence response following labeling with 2.7×10^8 to 2.7×10^9 particles/μL. This was not the case for cells expressing FhuA-Ge4−1 or wild-type FhuA; each of these resulted in only background fluorescence following labeling over the same C dot concentration range (Figure 3d). At the highest concentration of C dots tested (2.7×10^9 particles/μL), the fluorescence signal for FhuA-Si4−1

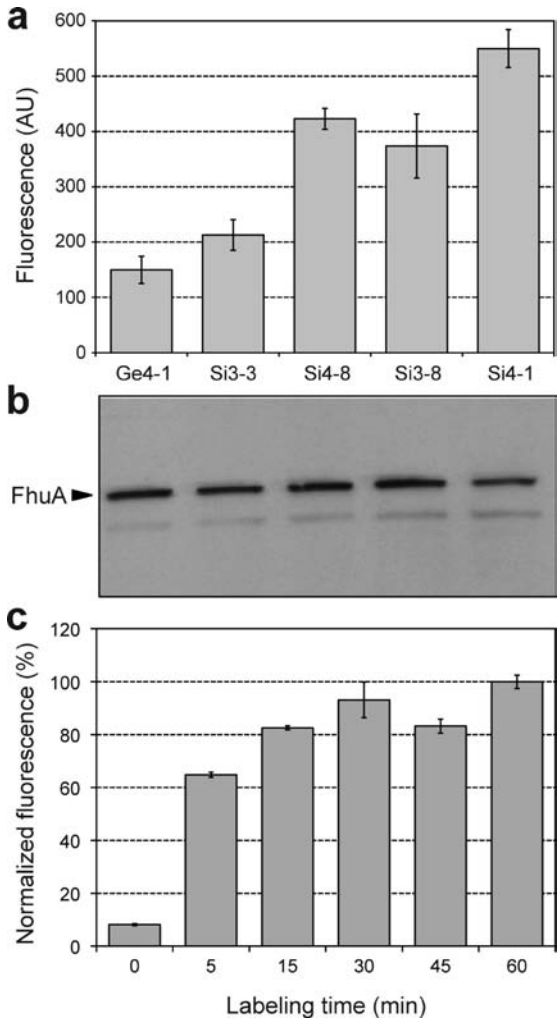

Figure 4. (a) Quantification of cell fluorescence following expression of FhuA constructs modified with different GEPS sequences. All labeling was accomplished with 30 nm particles at a final concentration of 8.1×10^8 particles/mL. Data are the average of three replicate experiments. (b) Western blot analysis of soluble fractions generated from cells expressing the different FhuA constructs as indicated. Soluble proteins from an equivalent number of cells were loaded in each lane and detection was with FhuA antiserum. (c) Effect of C dot incubation time on labeling efficiency. Cells expressing FhuA-Si4−1 were incubated with 30 nm particles at a final concentration of 8.1×10^8 particles/mL for the indicated labeling times. Data are the average of three replicate experiments and are normalized to the florescence signal obtained for FhuA-Si4−1 at 60 min, which was set at 100%. All error bars represent the standard deviation of the mean.

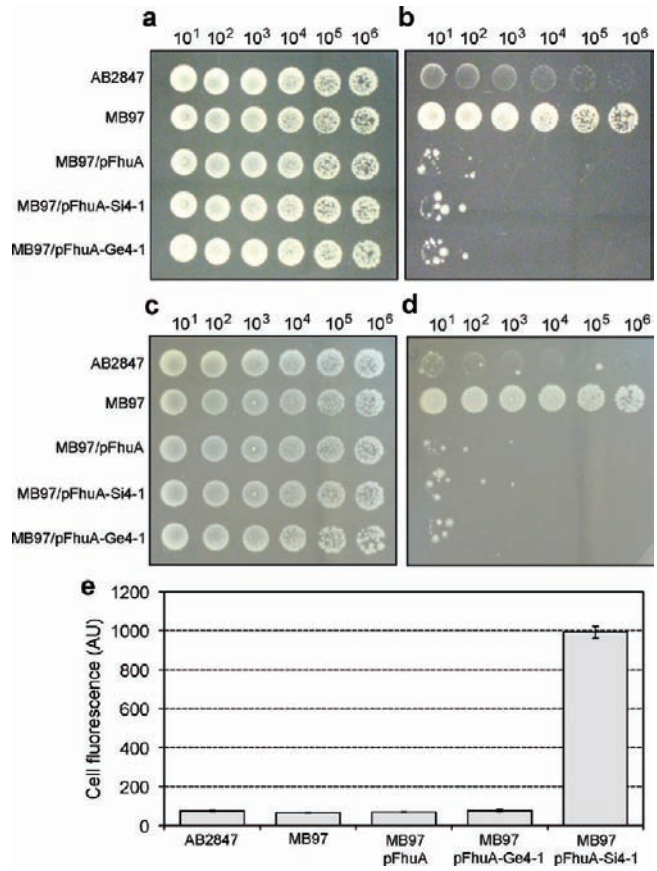

Figure 5. Albomycin resistance phenotype of FhuA-expressing cells. Spot plating of wt AB2847 and isogenic MB97 (Δ*fhuA*) cells on TY/agar plates with (a) no antibiotic or (b) 25 μg/mL albomycin. Plasmid-based complementation of *fhuA* in MB97 cells was from pFhuA, pFhuA-Si4−1, or pFhuA- Ge4−1, as indicated. Spot plating of the same cells in (a,b) following labeling with 30 nm TRITC C dots for 1 h prior to plating on (c) no antibiotic or (d) 25 μg/mL albomycin. Cells were serially diluted as indicated above each panel. (e) Quantification of cell fluorescence after C dot labeling of AB2847 or MB97 cells carrying no plasmids or expressing wild-type FhuA, FhuA-Ge4−1, and FhuA-Si4−1 as indicated. Cells were incubated with 8.1×10^8 C dots/μL for 1 h. Data are the average of three replicate experiments and error bars represent the standard deviation of the mean.

was ∼9× greater than the FhuA-Ge4−1 control, verifying the specificity of the GEPS insert. Finally, it is noteworthy that, even at the highest C dot concentration, there was no measurable growth inhibition for any of the cells tested (data not shown), confirming the biocompatibility of the silica nanoparticles.

We next determined whether the enhanced cellular fluorescence seen for FhuA-Si4−1 versus FhuA-Ge4−1 was due to specificity/affinity of the peptide sequences for the C dots or, instead, differential protein expression. To exclude variations in protein expression, Western blot analysis was performed on samples prepared from cells expressing each of the FhuA constructs. As expected, there was virtually no difference in soluble expression of FhuA-Si4−1 and FhuA-Ge4−1 (Figure 3e), suggesting that the differential fluorescence observed above was attributable to varying degrees of affinity conferred by the peptide inserts. To investigate this in more detail, we constructed several additional FhuA constructs by inserting other silica-specific peptides of varying affinities into extracellular loop 5 of FhuA. These peptides exhibited intermediate binding of silica that was less than the high-affinity Si4−1 clone but greater than the nonspecific Ge4−1 clone, with the relative binding affinity as follows (in order from highest to lowest): Si4−1 ≫ Si3−3 ≈ Si3−8 ≈ Si4−8 ≫ Ge4−1 (*24*). Following C dot labeling of cells, we observed intermediate fluorescence for each of these FhuA constructs that was reproducibly lower than that for FhuA-Si4−1 but significantly higher than that for the FhuA-Ge4−1 construct (Figure 4a). As seen above, similar expression levels were observed for each of these FhuA variants (Figure 4b) indicating that differences in fluorescence were linked to affinity of the displayed peptides for the C dots. A major advantage of this strategy is that high levels of labeling (>80% of the maximum signal) could be achieved in as little as 15 min (Figure 4c).

To determine whether labeling was disruptive to protein function, we next evaluated whether the GEPS-modified FhuA variants retained wild-type activity following labeling with C dots. Native FhuA in the outer membrane of *E. coli* actively transports ferrichrome and the antibiotics albomycin and rifamycin CGP 4832. In the case of albomycin, the antibiotic is internalized through FhuA after which it is cleaved and the antibiotically active moiety is released into the cytoplasm (*27,32*). Cells expressing functional FhuA are sensitive to albomycin,

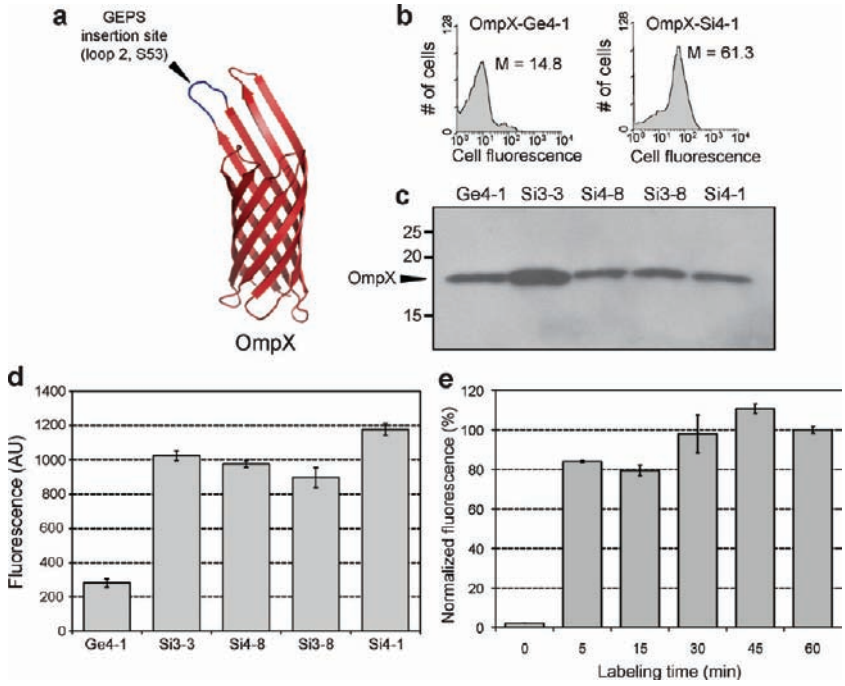

Figure 6. (a) Structural representation of OmpX depicting the GEPS insertion site in extracellular loop 2, immediately after a serine residue at position 53. Loop 2 is highlighted in blue and the GEPS insertion site is indicated by the arrow. (b) FACS analysis of cells induced to express OmpX-Ge4−1 (left) and OmpX-Si4−1 (right) following labeling with 30 nm particles at a final concentration of 8.1×10^8 particles/μL. Shown are representative FACS histograms. Mean fluorescence (*M*) values are the average of three replicate experiments. The error in each case was less than 5%. (c) Western blot analysis of soluble fractions generated from cells expressing different OmpX constructs as indicated. Soluble proteins from an equivalent number of cells were loaded in each lane and detection was with antipolyhistidine antibodies. (d) Quantification of cell fluorescence after C dot labeling of cells expressing OmpX constructs modified with different GEPS sequences. All labeling was accomplished with 30 nm particles at a final concentration of 8.1×10^8 particles/μL. Data are the average of three replicate experiments. (e) Effect of C dot incubation time on labeling efficiency. Cells expressing OmpX-Si4−1 were incubated with 30 nm particles at a final concentration of 8.1×10^8 particles/μL for the indicated labeling times. Data are the average of three replicate experiments and are normalized to the fluorescence signal obtained for FhuA-Si4−1 at 60 min, which was set at 100%. All error bars represent the standard deviation of the mean.

whereas those lacking a functional FhuA protein do not take up albomycin and are resistant to the antibiotic. To determine whether the 12-mer peptide insertions disrupted FhuA function, we evaluated the ability of each FhuA construct to internalize albomycin. As anticipated, AB2847 cells that express an intact copy of wild-type *fhuA* from their genome were highly sensitive to albomycin (Figure 5a,b). In contrast, *E. coli* strain MB97, which carries a complete deletion of the *fhuA* gene (*27*) and thus should not internalize albomycin, grew normally on agar plates supplemented with albomycin. However, when MB97 cells were provided with a plasmid-encoded copy of FhuA, FhuA-Si4−1, or FhuA-Ge4−1, they became highly sensitive to albomycin (Figure 5a,b). Thus, we conclude that the insertion of the peptides in FhuA did not disrupt function because each of the FhuA constructs was capable of internalizing albomycin. Next, to determine whether labeling of FhuA with C dots inhibited function, perhaps by cross-linking FhuA into inactive multimers, we performed a similar experiment as above except now the cells were labeled with C dots for 1 h prior to plating on albomycin. The albomycin resistance behavior of C dot labeled cells was identical to that observed for the same cells that had not been treated with C dots (compare Figure 5c,d with a,b), indicating that C dot labeled FhuA remained functional. It is noteworthy that the fluorescence signal for MB97 cells expressing the FhuA-Si4−1 was nearly 20-fold above the background signal from FhuA-Ge4−1 expressing cells (Figure 5e), which was an improvement over the signal-to-background ratio observed above using DH5α host cells.

Evidence for a Universal Targeting Strategy. To determine whether our C dot binding strategy was generic, we introduced the panel of different GEPS into the *E. coli* integral outer membrane protein OmpX. Like FhuA, OmpX is a β-barrel membrane protein. It contains eight transmembrane β-strands and exposes four extracellular loops (*38*). We introduced each of the different GEPS into extracellular loop 2, just after the serine residue in position 53 (Figure 6a). In agreement with the FhuA results, cells expressing OmpX-Si4−1 were nearly 5 times more fluorescent than their OmpX-Ge4−1-expressing counterparts, as revealed by both FACS and plate reader measurements (Figure 6b,d). Similarly, cells expressing the intermediate peptide sequences exhibited levels of fluorescence that were less than that seen for OmpX-Si4−1 but significantly greater than OmpX-Ge4−1. It is noteworthy that Si3−3 resulted in the lowest fluorescence of the three intermediate binders when inserted in FhuA but was the most fluorescent of the three when cloned in OmpX (Figure 6d). It appears, however, that this unexpectedly high fluorescence was due to a marked increase in OmpX-Si3−3 expression relative to all other OmpX constructs (Figure 6c). For the other two intermediate binders, the relative C dot binding affinity observed with OmpX was the same as FhuA, with Si4−8 showing greater affinity than Si3−8. For these constructs, as well as OmpX-Si4−1 and OmpX-Ge4−1, the soluble expression levels were virtually indistinguishable (Figure 6c), suggesting as above that fluorescence levels were indicative of specificity/affinity for C dots and not gross differences in protein expression levels. Finally, high levels of labeling (>80% of the maximum signal) were observed in as little as 5 min (Figure 6e).

DISCUSSION

In the present study, we report a highly specific, robust, and rapid new method for labeling cell surface proteins with fluorescent nanoparticles, i.e., core−shell silica nanoparticles

referred to as C dots. Our approach uses genetically engineered peptides with affinity for silica (GEPS) as C dot recognition elements that can be site-specifically introduced into cellular proteins. The silica-binding peptides used here were previously isolated for their ability to precipitate silica (*24*) and are enriched in histidine residues, whereas the control germania-binding peptide lacked histidine entirely. Along similar lines, several other groups have reported peptide sequences with affinity for silica and the majority of these appear to be rich in basic and hydroxyl amino acids (*24*, *39*−*41*) as well as proline residues (*40*, *42*). Hence, we believe that C dot binding is due to electrostatic interaction, however, whether other mechanisms are at play cannot be ruled out.

The advantage of GEPS is that they are relatively short peptide sequences that can be genetically encoded at the termini or in loops of proteins without disturbing the protein's structure, function, and subcellular localization. We show here that strategic positioning of GEPS into loops of outer membrane proteins allows for electrostatic capture of 30 nm fluorescent C dots with labeling times as short as 5 min. Because only background fluorescence was observed following C dot labeling of wild-type bacterial cells, we conclude that nonspecific silica-binding activity is largely absent from native cell surfaces. Hence, GEPS-tagged cell surface proteins can be efficiently labeled with fluorescent C dots with signal-to-background ratios of ∼5−20 depending on the target protein, label concentration, and host cell used. It should also be noted that labeling approaches that use peptides rather than proteins are less invasive but typically sacrifice specificity. However, the use of noninvasive silica-binding peptides comprising only 12 residues did not suffer from a lack of specificity as evidenced by the differential binding observed for the different GEPS clones. Since GEPS tags are genetically encodable, we anticipate that the labeling technology described here can be extended to numerous structurally diverse membrane proteins in prokaryotic and also perhaps in eukaryotic cells. Such flexibility should enable visualization of protein dynamics underlying numerous biological processes, especially considering that C dot labeling did not adversely affect protein function. However, a potential concern is that the relatively large 30 nm particles may bind to several genetically modified surface proteins simultaneously in a manner that reduces the mobility of the proteins in the membrane and interferes with dynamic analysis. Therefore, smaller C dot particles may be necessary for performing dynamic analysis. To date, the smallest, stable particles with narrow particle size distributions that we have achieved go down to about 3 nm (*19*).

Interestingly, these peptides not only promoted C dot binding, but different primary sequences resulted in differential binding efficiency. This implies that it may be possible to further optimize GEPS with *increased* affinity for C dots. For instance, cell surface displayed libraries of random Si4−1 variants could be labeled with C dots and screened using FACS to isolate highly fluorescent clones that represent ultrahigh affinity binders. A similar affinity maturation strategy was demonstrated recently by Rozinov and Nolan who used phage display to isolate higher-affinity peptides against small-molecule fluorophores such as Texas Red (*43*). Our studies here show that C dot labeled cells can be visualized with a flow cytometer indicating that FACS could be used to efficiently discriminate binders from nonbinders. Interestingly, while earlier studies reported comparable silica binding for each of these intermediate peptides, our studies show distinct binding differences for these peptides. We suspect that this discrepancy is due to differences in how the peptides were displayed during the binding assays. In the earlier work of Stone and co-workers (*24*), peptides were expressed as unconstrained fusions to the minor coat (pIII) protein of M13 phage, whereas in our studies, the peptides were constrained in the extracellular loops of an outer membrane protein.

A particularly attractive feature of this technology is that it makes possible for the first time a system for genetically tagging cellular proteins with epitopes specific for fluorescent silica nanoparticles. Importantly, the 30 nm diameter variety tested here have already been shown to be 20−30 times brighter on a per particle basis and nearly 20 times more stable than their constituent dyes (*17*, *25*, *44*), offering a robust new avenue for fluorescent labeling. Furthermore, because C dots are multifluorophore systems, at any given time there will still be a portion of the dyes emitting, conferring continuous fluorescence emission. From a practical standpoint, this minimizes the intermittent blinking under continuous excitation suffered by single-emitter systems (*25*). Since many different fluorophores (e.g., TRITC, Oregon Green 488, etc.) and even multiple fluorophores can be localized within a single silica nanoparticle (*25*, *44*), colors and spectral properties, such as peak wavelength and shape, can be chosen at will from a palette of dyes and efficiently coupled to cellular proteins.

In this study, we focused on the integral outer membrane proteins FhuA and OmpX of *E. coli*. These and other β-barrels found in the outer membranes of prokaryotic and eukaryotic organisms constitute an important functional class of proteins. Such proteins play important roles in bacterial pathogenesis, regulating molecular transport, and mitochondrial homeostasis (*45*), and therefore are high-priority targets for structural and functional characterization. For instance, *E. coli* OmpX and its homologues in the human pathogens *Yersinia*, *Enterobacter*, *Klebisiella*, and *Salmonella* promote adherence to and entry into host cells, a key step in the ability of these pathogens to neutralize the host defense system and interfere with the host immune system (*38*, *45*). Thus, we anticipate that site-specific C dot labeling of these membrane proteins in living cells will permit multidimensional time-lapse microscopy and single-molecule analysis of pathogen-host interactions.

ACKNOWLEDGMENT

We thank Dr. Andreas Meinke for plasmid pHIE11 as well as FhuA antiserum. Funding was provided by an NSF CAREER Award CBET-0449080 (to MPD) and a NYSTAR James D. Watson Award (to MPD). We would also like to thank the Cornell Nanobiotechnology Center, an STC Program of the NSF under Agreement No. ECS-9876771 for funding (to UW) and infrastructure.

LITERATURE CITED

(1) Chamberlain, C., and Hahn, K. M. (2000) Watching proteins in the wild: fluorescence methods to study protein dynamics in living cells. *Traffic 1*, 755–62.

(2) Schwille, P., Haupts, U., Maiti, S., and Webb, W. W. (1999) Molecular dynamics in living cells observed by fluorescence correlation spectroscopy with one- and two-photon excitation. *Biophys. J. 77*, 2251–2265.

(3) Chen, I., Howarth, M., Lin, W., and Ting, A. Y. (2005) Site-specific labeling of cell surface proteins with biophysical probes using biotin ligase. *Nat. Methods 2*, 99–104.

(4) Guignet, E. G., Hovius, R., and Vogel, H. (2004) Reversible site-selective labeling of membrane proteins in live cells. *Nat. Biotechnol. 22*, 440–4.

(5) Chen, I., and Ting, A. Y. (2005) Site-specific labeling of proteins with small molecules in live cells. *Curr. Opin. Biotechnol. 16*, 35–40.

(6) Lin, C. W., and Ting, A. Y. (2006) Transglutaminase-catalyzed site-specific conjugation of small-molecule probes to proteins *in vitro* and on the surface of living cells. *J. Am. Chem. Soc. 128*, 4542–3.

(7) Howarth, M., Takao, K., Hayashi, Y., and Ting, A. Y. (2005) Targeting quantum dots to surface proteins in living cells with biotin ligase. *Proc. Natl. Acad. Sci. U.S.A. 102*, 7583–8.

(8) Chan, W. C., Maxwell, D. J., Gao, X., Bailey, R. E., Han, M., and Nie, S. (2002) Luminescent quantum dots for multiplexed biological detection and imaging. *Curr. Opin. Biotechnol. 13*, 40–6.
(9) Dahan, M., Levi, S., Luccardini, C., Rostaing, P., Riveau, B., and Triller, A. (2003) Diffusion dynamics of glycine receptors revealed by single-quantum dot tracking. *Science 302*, 442–5.
(10) Gerion, D., Pinaud, F., Williams, S. C., Parak, W. J., Zanchet, D., Weiss, S., and Alivisatos, A. P. (2001) Synthesis and properties of biocompatible water-soluble silica-coated CdSe/ZnS semiconductor quantum dots. *J. Phys. Chem. B 105*, 8861–8871.
(11) Derfus, A., Chan, W., and Bhatia, S. (2004) Probing the cytotoxicity of semiconductor quantum dots. *Nano Lett. 4*, 11–18.
(12) Kirchner, C., Liedl, T., Kudera, S., Pellegrino, T., Javier, A. M., Gaub, H., Stozle, S., Fertig, N., and Parak, W. (2005) Cytotoxicity of colloidal CdSe and CdSe/ZnS nanoparticles. *Nano Lett. 5*, 331–337.
(13) Erhardt, R., Zhang, M., Böker, A., Zettl, H., Abetz, C., Frederik, P., Krausch, G., Abetz, V., and Müller, A. H. E. (2003) Amphiphilic janus micelles with polystyrene and poly(methacrylic acid) hemispheres. *J. Am. Chem. Soc. 125*, 3260–7.
(14) Minard-Basquin, C., Weil, T., Hohner, A., Rädler, J. O., and Müllen, K. (2003) A polyphenylene dendrimet-detergent complex as a highly fluorescent probe for bioassays. *J. Am. Chem. Soc. 125*, 5832–8.
(15) Nyffenegger, R., Quellet, C., and Ricka, J. (1993) Synthesis of fluorescent, monodisperse, colloidal silica particles. *J. Colloid Interface Sci. 159*, 150–7.
(16) Dullens, R. P. A., Claesson, M., Derks, D., van Blaaderen, A., and Kegel, W. K. (2003) Monodisperse core-shell poly(methyl methacrylate) latex colloids. *Langmuir 19* (15), 5963–6.
(17) Ow, H., Larson, D. R., Srivastava, M., Baird, B. A., Webb, W., and Wiesner, U. (2005) Bright and stable core-shell silica nanoparticles. *Nano Lett. 5*, 113–117.
(18) Stöber, W., Fink, A., and Bohn, E. (1968) Controlled growth of monodisperse silica spheres in the micron size range. *J. Colloid Interface Sci. 26*, 62–69.
(19) Burns, A. A., Vider, J., Ow, H., Herz, E., Penate-Medina, O., Baumgart, M., Larson, S. M., Wiesner, U., and Bradbury, M. (2009) Fluorescent silica nanoparticles with efficient urinary excretion for nanomedicine. *Nano Lett 9*, 442–8.
(20) Larson, D. R., Ow, H., Vishwasrao, H. D., Heikal, A. A., Wiesner, U., and Webb, W. W. (2008) Silica nanoparticle architecture determines radiative properties of encapsulated fluorophores. *Chem. Mater. 20*, 2677–2684.
(21) Dickson, R. M., Cubitt, A. B., Tsien, R. Y., and Moerner, W. E. (1997) On/off blinking and switching behaviour of single molecules of green fluorescent protein. *Nature 388*, 355–8.
(22) Neuhauser, R. G., Shimizu, K. T., Woo, W. K., Empedocles, S. A., and Bawendi, M. G. (2000) Correlation between fluorescence intermittency and spectral diffusion in single semiconductor quantum dots. *Phys. Rev. Lett. 85*, 3301–4.
(23) Choi, J., Burns, A. A., Williams, R. M., Zhou, Z., Fleskes-Nikitin, A., Zipfel, W. R., Wiesner, U., and Nikitin, A. Y. (2007) Core-shell silica nanoparticles as fluorescent labels for nanomedicine. *J. Biomed. Opt. 12*, 064007.
(24) Naik, R. R., Brott, L. L., Clarson, S. J., and Stone, M. O. (2002) Silica-precipitating peptides isolated from a combinatorial phage display peptide library. *J. Nanosci. Nanotechnol. 2*, 95–100.
(25) Burns, A., Ow, H., and Wiesner, U. (2006) Fluorescent core-shell silica nanoparticles: towards "Lab on a Particle" architectures for nanobiotechnology. *Chem. Soc. Rev. 35*, 1028–42.
(26) Herz, E., Burns, A., Lee, S., Sengupta, P., Bonner, D., Ow, H., Liddell, C., Baird, B., and Wiesner, U. (2006) Fluorescent core-shell silica nanoparticles: an alternative radiative materials platform. *Proc. SPIE 6096*, 1–12.
(27) Braun, M., Endriss, F., Killmann, H., and Braun, V. (2003) *In vivo* reconstitution of the FhuA transport protein of *Escherichia coli* K-12. *J. Bacteriol. 185*, 5508–18.
(28) Etz, H., Minh, D. B., Schellack, C., Nagy, E., and Meinke, A. (2001) Bacterial phage receptors, versatile tools for display of polypeptides on the cell surface. *J. Bacteriol. 183*, 6924–35.
(29) Guzman, L. M., Belin, D., Carson, M. J., and Beckwith, J. (1995) Tight regulation, modulation, and high-level expression by vectors containing the arabinose PBAD promoter. *J. Bacteriol. 177*, 4121–30.
(30) DeLisa, M. P., Samuelson, P., Palmer, T., and Georgiou, G. (2002) Genetic analysis of the twin arginine translocator secretion pathway in bacteria. *J. Biol. Chem. 277*, 29825–31.
(31) DeLisa, M. P., Tullman, D., and Georgiou, G. (2003) Folding quality control in the export of proteins by the bacterial twin-arginine translocation pathway. *Proc. Natl. Acad. Sci. U.S.A. 100*, 6115–20.
(32) Braun, V., Gunthner, K., Hantke, K., and Zimmermann, L. (1983) Intracellular activation of albomycin in *Escherichia coli* and *Salmonella typhimurium*. *J. Bacteriol. 156*, 308–15.
(33) Sano, K., and Shiba, K. (2003) A hexapeptide motif that electrostatically binds to the surface of titanium. *J. Am. Chem. Soc. 125*, 14234–5.
(34) Sano, K., Sasaki, H., and Shiba, K. (2005) Specificity and biomineralization activities of Ti-binding peptide-1 (TBP-1). *Langmuir 21*, 3090–5.
(35) Ferguson, A. D., Hofmann, E., Coulton, J. W., Diederichs, K., and Welte, W. (1998) Siderophore-mediated iron transport: crystal structure of FhuA with bound lipopolysaccharide. *Science 282*, 2215–20.
(36) Locher, K. P., Rees, B., Koebnik, R., Mitschler, A., Moulinier, L., Rosenbusch, J. P., and Moras, D. (1998) Transmembrane signaling across the ligand-gated FhuA receptor: crystal structures of free and ferrichrome-bound states reveal allosteric changes. *Cell 95*, 771–8.
(37) Kim, J. Y., Doody, A. M., Chen, D. J., Cremona, G. H., Shuler, M. L., Putnam, D., and DeLisa, M. P. (2008) Engineered bacterial outer membrane vesicles with enhanced functionality. *J. Mol. Biol. 380*, 51–66.
(38) Vogt, J., and Schulz, G. E. (1999) The structure of the outer membrane protein OmpX from *Escherichia coli* reveals possible mechanisms of virulence. *Structure 7*, 1301–9.
(39) Tomczak, M. M., Glawe, D. D., Drummy, L. F., Lawrence, C. G., Stone, M. O., Perry, C. C., Pochan, D. J., Deming, T. J., and Naik, R. R. (2005) Polypeptide-templated synthesis of hexagonal silica platelets. *J. Am. Chem. Soc. 127*, 12577–82.
(40) Coradin, T., and Livage, J. (2001) Effect of some amino acids and peptides on silicic acid polymerization. *Colloids Surf., B 21*, 329–336.
(41) Patwardhan, S. V., Maheshwari, R., Mukherjee, N., Kiick, K. L., and Clarson, S. J. (2006) Conformation and assembly of polypeptide scaffolds in templating the synthesis of silica: an example of a polylysine macromolecular "switch. *Biomacromolecules 7*, 491–7.
(42) Seker, U. O., Wilson, B., Sahin, D., Tamerler, C., and Sarikaya, M. (2009) Quantitative affinity of genetically engineered repeating polypeptides to inorganic surfaces. *Biomacromolecules 10*, 250–7.
(43) Rozinov, M. N., and Nolan, G. P. (1998) Evolution of peptides that modulate the spectral qualities of bound, small-molecule fluorophores. *Chem. Biol. 5*, 713–28.
(44) Burns, A., Sengupta, P., Zedayko, T., Baird, B., and Wiesner, U. (2006) Core-shell fluorescent silica nanoparticles for chemical sensing: moving towards single particle laboratories. *Small 2*, 723–726.
(45) Nikaido, H. (2003) Molecular basis of bacterial outer membrane permeability revisited. *Microbiol. Mol. Biol. Rev. 67*, 593–656.

BC9000118

PEGylated Degradable Composite Nanoparticles Based on Mixtures of PEG-*b*-Poly(γ-benzyl L-glutamate) and Poly(γ-benzyl L-glutamate)

Ma. Elisa Martínez-Barbosa,[†,‡] Sandrine Cammas-Marion,[§] Laurent Bouteiller,[||] Christine Vauthier,[‡] and Gilles Ponchel*[,‡]

UMR CNRS 8612, Laboratoire de Pharmacie et Biopharmacie, Faculté de Pharmacie, Université Paris-Sud, 5 rue J.B. Clément, 92290 Châtenay-Malabry, France, UMR 6226 CNRS-ENSCR, Equipe Chimie Organique et Supramoléculaire, Avenue du Général Leclerc, 35700 Rennes, France, and UMR CNRS 7610, Chimie des Polymères, Université Pierre et Marie Curie, 4 Place Jussieu, 75252, Paris cedex 05, France. Received January 15, 2009; Revised Manuscript Received May 18, 2009

In the present work, the possibility to obtain PEGylated nanoparticles from two PBLG derivatives, PEG-*b*-poly(γ-benzyl L-glutamate), PBLG-PEG-60, and poly(γ-benzyl L-glutamate), PBLG-Bnz-50, by nanoprecipitation has been investigated. Particles were prepared not only from one polymer (PBLG-PEG-60 or PBLG-Bnz-50), but also from mixtures of two PBLG derivatives, PBLG-PEG-60 and PBLG-Bnz-50, in different ratios (90/10, 77/23, and 40/60 wt %). Because of the presence of PEG chains, hydrophilic particles were obtained, which was confirmed by ζ potential measurements (ζ from −13 mV and −21 mV) and by isothermal titration microcalorimetry (ITC). This last technique has shown no heat exchange when BSA was added to PEGylated nanoparticles. Further, complement activation has been evaluated by crossed immuno-electrophoresis demonstrating that the introduction of 77 wt % of PEGylated PBLG chains in the particles was enough to ensure a low complement activation activity. This effect was strongly correlated to the ζ potential of the particles, which decreased with an increase of PEG chains content. Interestingly, such properties are of interest for the preparation of degradable stealth nanocarriers. Moreover, it is suggested that the introduction of a reasonable amount (up to 20 wt %) of a second copolymer in the particle composition can be possible without modifying their stealth character. Moreover, the presence of this second copolymer would help to introduce a second functionality to the particles.

INTRODUCTION

Over the past years, nanoparticulate carriers have been developed in order to improve efficiency and site-specificity of drug delivery (*1, 2*). As a result of their small size, this first generation of nanocarriers can be administrated intravenously. However, such small hydrophobic particles are rapidly (half-time of clearance about 1 min) and efficiently (about 90% uptake) cleared from the circulation due to their recognition by opsonins (*3*−*5*). Therefore, to address these limitations, a second generation of nanocarriers is under development taking into account the various parameters which influence carrier recognition by reticuloendothelial system (*3*−*5*). It has been shown that the coating of hydrophobic nanocarrier surfaces by hydrophilic polymers, such as poly(ethylene glycol) (PEG), induces a significant decrease of the opsonisation process (*6*). The coating has to be dense and flexible in order to reduce all types of interactions with hydrophobic nanocarrier surfaces. Moreover, hydrophilic polymer chains, such as PEG, have to be well anchored on nanoparticles to avoid desorption of chains (*4*). Surface modification on hydrophobic nanoparticulate systems has been carried out. Coating or covalent coupling methods (*7, 8*) have been proposed to introduce hydrophilic chains on nanoparticle surface. Hydrophilic polymers such as poly(ethylene glycol), poly(vinyl alcohol), poloxamers, or dextran have been shown to decrease significantly protein adsorption (*4*). In order to obtain a high density of hydrophilic chains on the surface and an efficient anchoring of these chains in the carrier, core−shell type nanoparticles and macromolecular micelles formed in aqueous media by self-assembly of amphiphilic block copolymers have attracted considerable attention for application as drug delivery systems (*9*−*14*). Besides overcoming the rapid recognition of nanoparticles by the reticuloendothelial system, research has been also focused on overcoming the many-faceted problem of biocompatibility. In this context, efforts have been directed toward the use of natural-like materials such as poly(α-amino acids) (*15*). Poly(γ-benzyl L-glutamate), PBLG, a synthetic polypeptide, has attracted attention for biomedical applications (*15*−*21*) because of the presence of a degradable amide bound in the polymer backbone (*21*) and a carboxylic acid function in the side chain, available after hydrolysis of the lateral benzyl ester. Poly(ethylene oxide)-*block*-poly(γ-benzyl L-glutamate) (*22, 23*) allowed macromolecular micelle formation as a result of their amphiphilic nature (*24, 25*). Recently, in response to the need for targeting systems, poly(γ-benzyl L-glutamate) and poly(ethylene glycol) diblock copolymers end-capped with a galactose moiety have been proposed for site-specific drug delivery (*26*). In this context, we focused our interest on the synthesis of PBLG derivatives using initiators allowing the preparation of biocompatible nanoparticulate systems possessing different specific functionalities. For that, PBLG derivatives were synthesized by ring-opening polymerization (ROP) of γ-benzyl L-glutamate *N*-carboxyanhydride (BLG-NCA) using selected amine-terminated initiators (*27*).

In the present work, we report the possibility to obtain PEGylated nanoparticles from two PBLG derivatives, PBLG-PEG-60 and PBLG-Bnz-50, by nanoprecipitation. Composite nanoparticles with different PBLG-PEG-60/PBLG-Bnz-50 ratio

* Corresponding author. Gilles Ponchel, e-mail: gilles.ponchel@u-psud.fr, Tél: +33 (0)1 46 83 59 19, Fax: +33 (0)1 46 61 93 34.

[†] Present address: Departamento de Investigación en Polímeros y Materiales (DIPM), Universidad de Sonora. Rosales y Blvd. Luis Encinas s/n. C.P. 83000, Hermosillo, Sonora, México.

[‡] UMR CNRS 8612.

[§] UMR 6226 CNRS-ENSCR.

[||] UMR CNRS 7610.

10.1021/bc900017c CCC: $40.75 © 2009 American Chemical Society
Published on Web 07/13/2009

have been prepared and characterized. Interactions of the different nanoparticles with bovine serum albumin (BSA) have been measured by ITC. Moreover, complement activation has been evaluated by crossed immuno-electrophoresis.

MATERIALS AND METHODS

Materials. *N*,*N*-Dimethylformamide (DMF, Acros, 99%) and benzylamine (Janssen Chimica) were distilled under reduced pressure over BaO and KOH, respectively, and stored under argon atmosphere. γ-Benzyl-L-glutamate *N*-carboxyanhydride (γ-BLG-NCA), from ISOCHEM-SNPE, was used as received. Methoxy poly(ethylene glycol) amine (mPEG-NH_2), $\bar{M}w = 5000$ Da from Shearwater Corporation was dried under vacuum over P_2O_5 at 30 °C for 24 h. Bovine serum albumin (BSA) was purchased from Sigma. Water was purified by reverse osmosis (Milli-Q, Millipore). Poloxamer 188 (Lutrol F68), diethyl ether, and other solvents used were analytical grade, and all other chemicals were commercially available reagent grade.

Synthesis and Characterization of PBLG-Derivatives. PBLG-derivatives, PBLG-Bnz-50, and PBLG-PEG-60 were prepared by anionic ring-opening polymerization as described previously (*27*). Briefly, PBLG-Bnz-50 was obtained by anionic ring-opening polymerization of γ-benzyl-L-glutamate *N*-carboxyanhydride initiated by benzylamine in DMF at 30 °C. The reaction mixture was stirred at 30 °C until the characteristic NCA bands disappeared from FT-IR spectrum and then poured into a large volume of cold diethyl ether. The precipitate was dried under vacuum at 35 °C for at least 12 h. This precipitation, purification, and drying procedure was performed twice. The molecular weight of PBLG-Bnz-50 was estimated from intrinsic viscosity measured in DMF at 25 °C using the Mark−Houwink equation for PBLG in DMF at 25 °C (*28*).The molecular weight estimated for the PBLG-Bnz-50 was $\bar{M}w = 45\,000$ g·mol^{-1}. Similarly, PBLG-PEG-60 was obtained by anionic ring-opening polymerization of γ-benzyl-L-glutamate *N*-carboxyanhydride initiated by methoxy poly(ethylene glycol) amine (mPEG-NH_2), average $\bar{M}w = 5000$ g·mol^{-1}, in DMF at 30 °C. The reaction mixture was stirred at 30 °C until the characteristic NCA bands disappeared from FT-IR spectrum and poured into a large volume of cold diethyl ether. The precipitate was filtered, washed with water and diethyl ether, and then dried under vacuum at 35 °C for at least 12 h. A second purification procedure was performed. $\bar{D}Pn$ of the PBLG segment in PBLG-PEG-60 was determined from ^{1}H NMR spectra by the ratio between the peak intensities of methylene protons of the PEG chain, OCH_2CH_2, and the benzyl protons of PBLG chain, $COOCH_2C_6H_5$. A $\bar{D}Pn$ of 231 was found.

Nanoparticles Preparation. Nanoparticles were prepared using a slightly modified nanoprecipitation technique described elsewhere (*29*), in the absence of any surfactant agent, either from one polymer (PBLG-PEG-60 or PBLG-Bnz-50) or from mixtures of these two polymers in different ratios (PBLG-PEG-60/PBLG-Bnz-50 at 90/10, 77/23, and 40/60 wt % ratio and named composite nanoparticles). Briefly, 15 mg of one polymer or a mixture of polymers were dissolved in 5 mL of THF at 30 °C during 18 h, without stirring. The solution was then homogenized under gentle agitation for a few seconds and added, by dripping to 10 mL of Milli-Q water, under magnetic stirring. The mixture was left under magnetic stirring for 15 min and then transferred in a Teflon-coated recipient. The solvent was evaporated, at 30 °C, under a light air flux. In order to eliminate residual solvent, nanoparticles were further diluted with 5 mL of Milli-Q water, and evaporation was carried out to adjust the volume of the nanoparticle suspension to 10 mL. Preparations were kept at 4 °C until characterization.

Nanoparticles Characterization. *Size Distribution.* Mean diameter ($n = 3$) was determined, after suitable dilution of bulk suspensions in Milli-Q water, by dynamic laser light scattering (Nanosizer Coulter N4 Plus, Margency, France).

ζ Potential. ζ potential measurements ($n = 5$) were carried out using a Zetasizer 4, Malvern Instrument after adequate dilution of 200 μL of nanoparticles suspensions into 10 mL of 1 mM KCl filtered through a 0.22 μm filter.

Transmission Electron Microscopy. Nanoparticles were observed by TEM (transmission electron microscope, Philips EM 208). 7 μL of nanoparticles suspension were half-diluted in a 0.125% (w/v) poloxamer solution and placed on a Formvar-carbon film previously coated on a copper grid (400 mesh). After 6 min of deposition at room temperature, nonadherent nanoparticles were eliminated and the sample was stained by phosphotungstic acid (1%) during 30 s. TEM bright field imaging was performed under a 80 kV accelerating voltage.

Isothermal Titration Microcalorimetry (ITC) Studies. ITC experiments were carried out with an VP-ITC, MicrolCal. Interactions between bovine serum albumin (BSA), a model globular protein, and nanoparticles constituted by PBLG-Bnz-50 or PBLG-PEG-60 were evaluated. Solution of BSA at 5.4×10^{-2} mM was placed in a 295 μL continuously rotating (270 rpm) syringe. Nanoparticle suspension at 2.7×10^{-2} mM of polymer was placed in the sample cell of 1.43 mL. A first 2 μL aliquot was injected, without taking into account the observed heat, to remove the effect of solute diffusion across the syringe tip during the equilibration period. Then, injections of 10 μL of the BSA solution were made at intervals of 10 min. Experiments were carried out at 25 °C.

Evaluation of Complement Activation by Crossed Immuno-Electrophoresis. The specific activation of the C3 component of the complement from human serum and induced by the nanoparticle surface was evaluated by comparative measurements of C3 cleavage into C3b. Nanoparticle suspensions (1.5 mg mL^{-1}) were first concentrated by evaporation of part of the water to reach a nanoparticle concentration of 9 mg mL^{-1} or 6 mg mL^{-1} in order to obtain a surface area of 500 cm^2 in a volume $V \leq 100$ μL. The amount of C3 and C3b was measured by crossed immunoelectrophoresis by an adaptation of the method described elsewhere (*7, 30*) after incubation of the nanoparticles with serum. Briefly, human serum obtained from healthy donors was stored at −80 °C until use. Equivalent volumes of nanoparticle suspensions, corresponding to a surface area of 500 cm^2 in 100 μL, were incubated with 50 μL of human serum and 50 μL of veronal-buffered saline containing 0.15 mM Ca^{2+} and 0.5 mM Mg^{2+} in ions (VBS^{2+}), under gentle agitation, for 1 h at 37 °C. Nanoparticle surface area was calculated, assuming that particles were spherical and using the following equations:

$$S = n4\pi r^2 \quad (1)$$

$$V = n4/3\pi r^3 \quad (2)$$

$$\text{leading to} \quad S_{(sp)} = S/V = 6/d\rho \quad (3)$$

where S and V are the surface area and volume, respectively, of n spherical nanoparticles of average radius r. $S_{(sp)}$ is the specific surface area of 1 g of spherical nanoparticles of average diameter d and density ρ (taken as $\rho = 1.2$ g/cm^3 relative to ρ for PBLG).

After incubation with human serum, samples (7 μL) were subjected to a first electrophoresis in 1% agarose gel for about 45 min. The second-dimension electrophoresis was carried out during 18 h with 1% agarose gel on Gelbond films in the presence of a polyclonal antibody to human C3, recognizing both C3 and C3b (complement C3 antiserum developed in goat, Sigma). Buffer used for electrophoresis migration was Tris veronal buffer diluted 1:5 in water and prepared as follow: 44.3 g

Table 1. Physicochemical Characteristics of Nanoparticles Constituted by PBLG-PEG-60 and PBLG-Bnz-50

polymer ratio (wt %)	mean size (nm)[b]	ζ potential (mV)[c]
100/0[a]	58 ± 20	−13.3 ± 0.6
90/10[a]	62 ± 20	−12.6 ± 0.3
77/23[a]	60 ± 21	−13.6 ± 0.3
40/60[a]	54 ± 17	−16.1 ± 0.6
0/100[a]	85 ± 30	−21.1 ± 0.2

[a] PBLG-PEG-60/PBLG-Bnz-50 ratio (in wt %) in the formulation. [b] Measured using dynamic laser light scattering, $n = 3$. [c] Measured using a Zetasizer 4 Instrument, $n = 5$.

of Tris(hydroxy-methyl-amino-methane), 22.4 g of phenobarbital, and 0.53 g of lactate calcium were dissolved in 1 L of water at 50 °C, sodium azide was added to avoid bacterial development, pH was adjusted to pH = 8.6, if necessary. C3 and C3b migration was followed by Coomasie blue staining. The height of the peaks given by the immunoprecipitation of C3 and C3b gave a semiquantitative estimation of the amount of each component in the serum. The complement activation factor (CAF) was expressed as the ratio of the peaks height as follows:

$$\mathrm{CAF} = \mathrm{C3b}/(\mathrm{C3} + \mathrm{C3b}) \quad (4)$$

RESULTS

Nanoparticle Preparation and Characterization. Possibilities to prepare, by nanoprecipitation, nanoparticles, either from one polymer (PBLG-Bnz-50 or PBLG-PEG-60) or from mixtures of these two polymers (composite nanoparticles) in different ratios, have been evaluated. As shown in Table 1, nanoparticles could be easily and reproducibly obtained without any surfactant agents by a slightly modified method described elsewhere (*29*). THF was selected, being both a good solvent of the polymer and miscible to water. Nanoparticle diameter, determined by dynamic laser light scattering, was typically lower than 100 nm. From transmission electron microscopy (Figure 1), it could be seen that nanoparticles prepared from both polymers exhibited ellipsoidal geometries, whose dimensions were compatible with dynamic light scattering measurements. Moreover, it can be seen that particles issued from mixtures of the two polymers were quite homogeneous, suggesting that they formed a single population.

The ζ potential (Table 1) was similar for nanoparticles at 100/0, 90/10, and 77/23 wt % ratio. A weak decrease in the ζ potential was observed for a 40/60 wt % ratio. As expected, the stronger ζ potential value was found for non-PEGylated nanoparticles (0/100 wt % ratio).

Isothermal Titration Microcalorimetry (ITC) Studies. In order to evaluate the capacity of nanoparticles to avoid protein adsorption and, therefore, to confirm the presence of PEG chains at the surface of nanoparticles, isothermal titration microcalorimetry (ITC) has been applied. PEGylated (PBLG-PEG-60) and non-PEGylated (PBLG-Bnz-50) nanoparticle−protein interactions were measured using bovine serum albumin (BSA) as model globular protein. As shown by Figure 2, the interaction of BSA with the nanoparticle surface is an exothermic phenomenon. The area underneath each injection peak is equal to the total heat released for that injection. In the case of nanoparticles constituted by PBLG-Bnz-50 (Figure 2a), signals after each BSA injection were much stronger than signals of nanoparticles constituted by PBLG-PEG-60 (Figure 2b). The corresponding control dilution experiment consisted of BSA injected in water and is shown by Figure 2c.

Evaluation of Complement Activation by Crossed Immuno-Electrophoresis. Figure 3 presents the immuno-electrophoresis patterns of the complement proteins C3 and C3b in serum incubated with the different nanoparticles prepared and of control experiments. The control experiments performed under experimental conditions in the absence of nanoparticles (Figure 3a) showed a major peak of protein C3 and a small peak of protein C3b. It gives the complement activation background under experimental conditions. The CAF value determined for the background activation was 0.16. In the absence of divalent ions (Figure 3b), no C3b peak can be seen on the immuno-electrophoregram in agreement with the fact that activation of the complement system requires divalent cations.

The immuno-electrophoregram of serum incubated with nanoparticles presented both C3 and C3b peaks. The height of the C3b peak was less pronounced for the serum incubated with PEGylated PBLG-PEG-60 nanoparticles (Figure 3d) than the one observed for serum incubated with non-PEGylated PBLG-Bnz-50 nanoparticles (Figure 3c). As reported in Table 2, the CAF was higher for serum incubated with the non-PEGylated nanoparticles (0.40) than the CAF measured for serum incubated with the PEGylated nanoparticles (0.21), indicating that non-PEGylated particles could be rapidly opsonized by serum proteins. The CAF value of the serum incubated with the PEGylated nanoparticles was close to the CAF value of the background activation of the complement under experimental conditions.

The immuno-electrophoresis patterns of the serum incubated with the different composite nanoparticles (Figure 3e,f,g) were very similar to the immuno-electrophoresis pattern shown for PBLG-PEG-60 nanoparticles (Figure 3d). The CAF values reported in Table 2 only showed a slight shift toward a higher value for the serum incubated with the composite nanoparticles containing the lower percentage (40 wt %) of PBLG-PEG-60 polymer. The CAF values obtained for serum incubated with the two other composite nanoparticles were the same than the CAF of serum incubated with nanoparticles prepared with 100 wt % PBLG-PEG-60 polymer.

DISCUSSION

The development of efficient targeting systems necessitates the simultaneous introduction of a set of functionalities within the system itself, regardless of its physical structure. Various polymers have been used to prepare nanoparticles for pharmaceutical applications, and different strategies have been proposed to introduce specific functionalities, e.g., optimized drug encapsulation, controlled release properties, stealthiness in the bloodstream, organ or cell targeting by ligands. It has been shown previously (*27*) that copolymers of poly(γ-benzyl L-glutamate), PBLG, bearing pharmaceutically interesting moieties could be quite easily prepared. Interestingly, mixtures of these copolymers can easily self-associate, which offers a convenient means for introducing by a soft technique desired functionalities within the particles.

In the present work, we investigated the possibility to precisely tune nanoparticle surfaces by introducing an optimal amount of a PEGylated copolymer of PBLG within the structure of nanoparticles. The nanoprecipitation method could be used conveniently to prepare nanoparticles either from one polymer (PBLG-Bnz-50 or PBLG- PEG-60) or from mixtures of these two polymers (composite nanoparticles) in different ratios. Nanoparticles could be easily and reproducibly obtained without any surfactants by a slightly modified method described elsewhere (*29*) as a result of the hydrophobic nature of PBLG. Moreover, DLS and TEM measurements showed that very small particles (lower than 100 nm) could be prepared. In addition, the homogeneous aspect of the particle shapes for the different preparations made from the polymer mixtures suggested that in this case the suspensions were composed of a single population of composite nanoparticles.

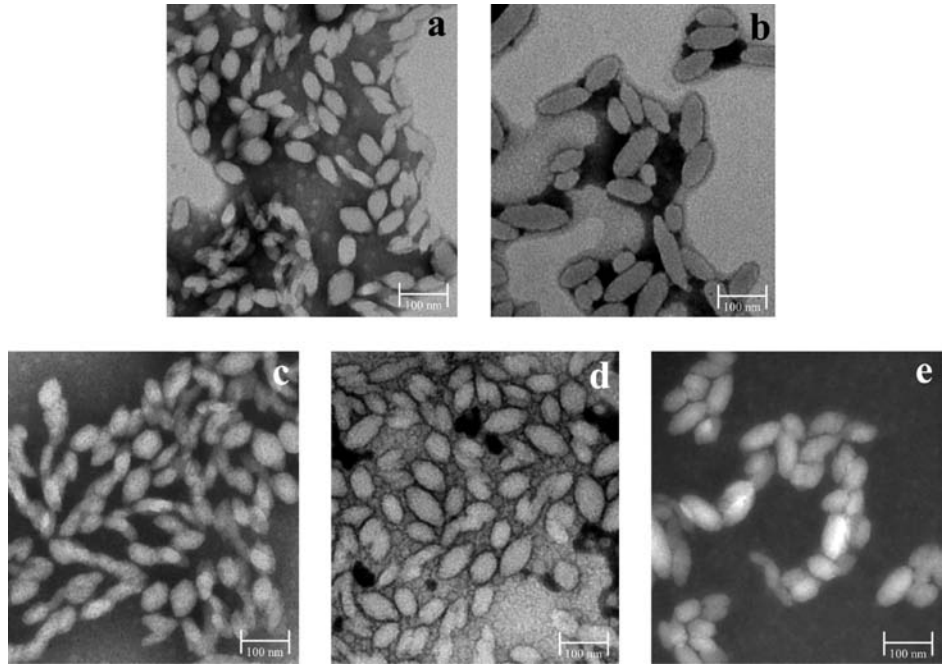

Figure 1. Transmission electron microscope micrographs of the nanoparticles. Simple nanoparticles constituted by (a) PBLG-PEG-60 (100/0 wt %) and (b) PBLG-Bnz-50 (0/100 wt %); Composite nanoparticles constituted by PBLG-PEG-60/PBLG-Bnz-50 at (c) 90/10, (d) 77/23, and (e) 40/60 (wt %), respectively.

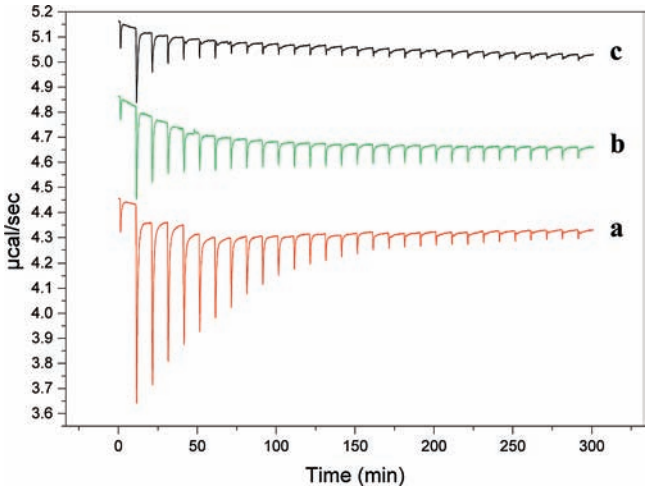

Figure 2. Plots of heat flow vs time of microcalorimetric titration of (a) PBLG-Bnz-50 nanoparticles and (b) PBLG-PEG-60 nanoparticles, by BSA solution. Injections of 10 μL, at 25 °C, of 5.4×10^{-2} mM of BSA solution were made on nanoparticle suspensions (2.7×10^{-2} mM). Control of BSA dilution (c) was carried out by injections of BSA solution in water.

Characterization by ITC of PBLG-PEG-60 or PBLG-Bnz-50 nanoparticle−protein interactions using bovin serum albumin (BSA), a model globular protein, permitted confirmation of the difference in surface properties of PEGylated and non-PEGylated nanoparticle suspensions. Theoretically, PEG chains of PEGylated nanoparticles should avoid or, at least, reduce protein adsorption on the nanoparticle surface as a result of steric repulsions and hydrophilization induced by PEG chains. In the case of nanoparticles constituted by PBLG-Bnz-50 (Figure 2a), signals after each BSA injection were higher than signals observed for nanoparticles constituted by PBLG-PEG-60 (Figure 2b). From this result, it could be concluded that interactions of BSA with nanoparticle surfaces were stronger in the absence of PEG chains.

Quantitative interpretation of observed enthalpy effect after an adsorption process (ΔH_{ads}) could be difficult because various factors can contribute to this effect. For example, Norde and Lyklema (*8*, *31*) took into account several factors while studying adsorption of human plasma albumin and bovin pancreas ribonuclease on negatively charged polystyrene surfaces. Some of these factors were as follows: the structural changes that the protein molecule and other involved molecules (for example, water and electrolyte) can undergo during the adsorption process; the alterations in the hydration state, disruption of the surface/solvent contacts, and simultaneous formation of protein/surface contacts; the modification of protein/solvent interactions due to differences of the chain density between dissolved and adsorbed protein molecules; and the effect of partners dilution.

Because such factors have not yet been elucidated for PBLG-Bnz-50 and PBLG-PEG-60 systems titrated with BSA, interpretation of ΔH_{ads} remains difficult. However, as shown in Figure 2, these studies made possible a qualitative surface characterization of tested nanoparticles. From these results, enthalpies of interactions could be obtained after integration of injection signals and subtraction of control (Figure 2c). Values of $\Delta H_{ads} = 414$ kCal/mol and 83 kCal/mol were obtained for the interaction of BSA with PBLG-Bnz-50 and PBLG-PEG-60 nanoparticles, respectively. Thus, it could be concluded from the existence of this 5-fold factor between adsorption enthalpies that interactions of BSA with non-PEGylated nanoparticles were much important than those observed for PEGylated nanoparticles.

In vitro evaluation of complement activation induced by nanoparticles is a very convenient method that can be used to predict their fate after intravenous injection *in vivo* (*4*, *32*). Indeed, most of the nanoparticles inducing a strong activation of the complement systems are generally rapidly taken up by macrophages of the mononuclear phagocyte systems, while nanoparticles appearing as low or non-activators of the complement systems are not recognized by the macrophages and remain in the bloodstream. In the present work, we have investigated the activation of the complement system induced by both PBLG-PEG-60 nanoparticles and PBLG-Bnz-50 nanoparticles, as well as by composite nanoparticles made from blends of both types of polymers at different composition. The CAF value of PBLG-Bnz-50 nanoparticles was much higher than the CAF value of

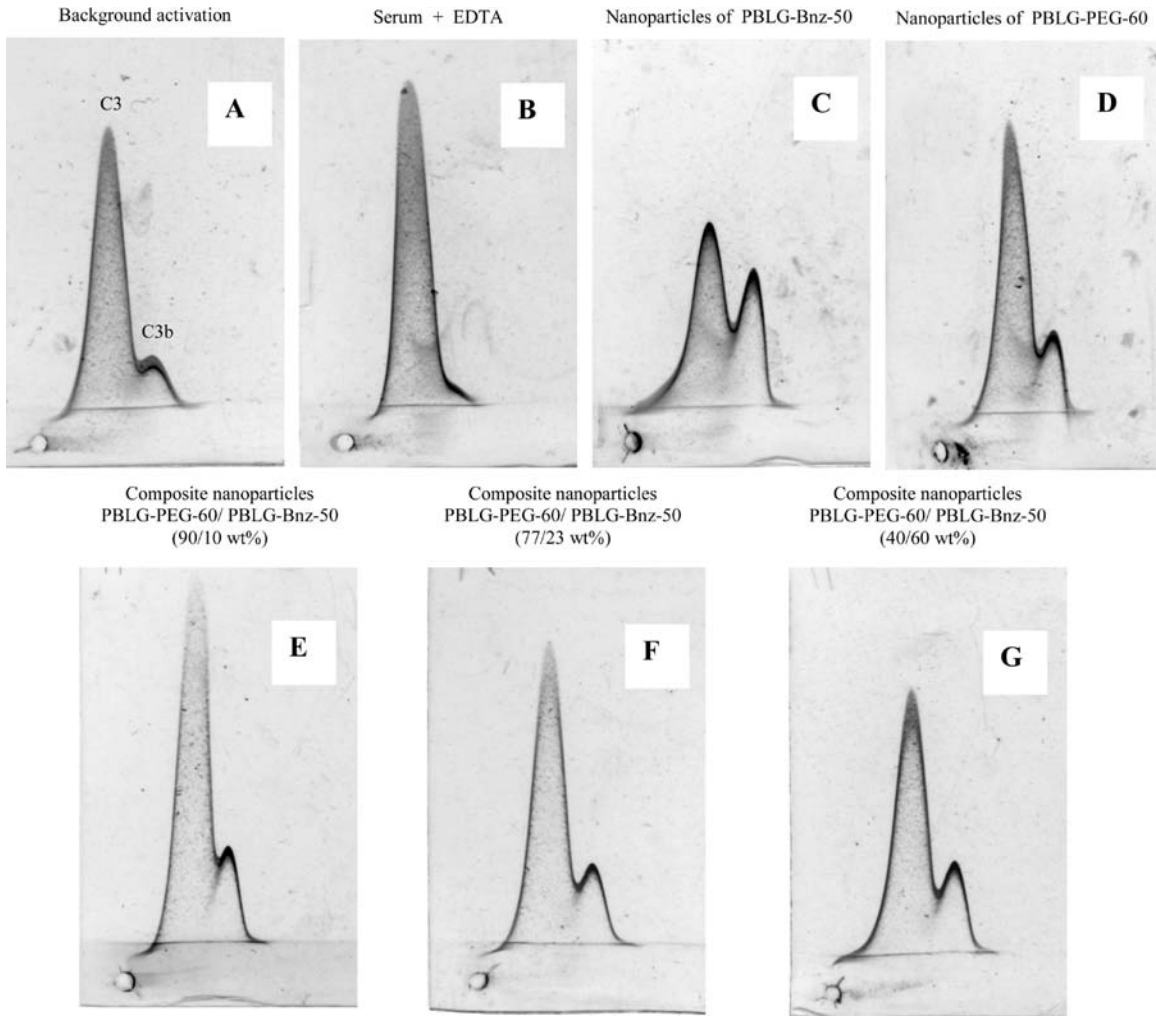

Figure 3. Crossed immunoelectrophoresis of C3 antigens in human serum diluted 1:4 after incubation in the presence of nanoparticles (500 cm^2). (A) Serum/VBS^{2+} (control of complement activation), background. (B) Serum/VBS^{2+}-EDTA (negative control). (C) Serum/VBS^{2+}/PBLG-Bnz-50 nanoparticles. (D) Serum/VBS^{2+}/PBLG-PEG-60 nanoparticles. (E) Serum/VBS^{2+}/(PBLG-PEG-60/PBLG-Bnz-50, 90/10 wt %) nanoparticles. (F) Serum/VBS^{2+}/(PBLG-PEG-60/PBLG-Bnz-50, 77/23 wt %) nanoparticles. (G) Serum/VBS^{2+}/(PBLG-PEG-60/PBLG-Bnz-50, 40/60 wt %) nanoparticles.

Table 2. Relationship between PBLG-PEG-60 Content into the PBLG-PEG-60/PBLG-Bnz-50 Nanoparticles and the Complement Activation Factor

	sample	CAF
controls	background activation	0.16
	serum + EDTA	0.05
nanoparticles polymer ratio (wt%)	100/0	0.21
	90/10	0.21
	77/23	0.21
	40/60	0.25
	0/100	0.40

the PBLG-PEG-60 nanoparticles. This result indicated the tendency of uncoated nanoparticles to activate the complement system contrarily to nanoparticles bearing PEG chains. These nanoparticles which gave a CAF value close to the background activation of the serum under experimental conditions appeared as low complement activating nanoparticles. The results observed here are in good agreement with the literature, which reports that nanoparticles prepared with PEG-containing polymers are generally low complement activators due to the presence of PEG chains at the nanoparticle surface (*4*, *5*). Thus, the results also suggested that the organization of PBLG-PEG-60 polymer chains to form the particle was highly efficient to expose PEG moieties at the surface of nanoparticles, ensuring a coating layer able to avoid complement activation. All these results were also in good agreement with the results obtained from the evaluation of PEGylated and non-PEGylated nanoparticle interactions with BSA. Indeed, the nanoparticles showing the lowest adsorption of BSA were also the lowest complement activators in agreement with the fact that surfaces of such nanoparticles are generally less opsonized as a result of the presence of hydrophilic PEG chains. In contrast, non-PEGylated nanoparticles, which adsorbed higher amounts of BSA, appeared as the highest complement activators in agreement with the fact that they are generally strongly opsonized by seric proteins.

Composite nanoparticles also displayed a low capacity to induce activation of the complement system. It is noteworthy that composite nanoparticles containing 90 and 77 wt % of PBLG-PEG-60 showed identical behavior to nanoparticles composed of 100 wt % of this polymer. The PEG coating formed at the surface of these nanoparticles seemed to have identical properties to the one formed on the surfaces of 100 wt % of PBLG-PEG-60 based nanoparticles. Interestingly, the three types of nanoparticles giving the lowest CAF value also showed identical ζ potential suggesting that they showed similar properties (Figure 4).

The composite nanoparticles containing the lowest amount of PBLG-PEG-60 (40 wt %) showed a slightly higher capacity to induce complement activation as suggested by their CAF,

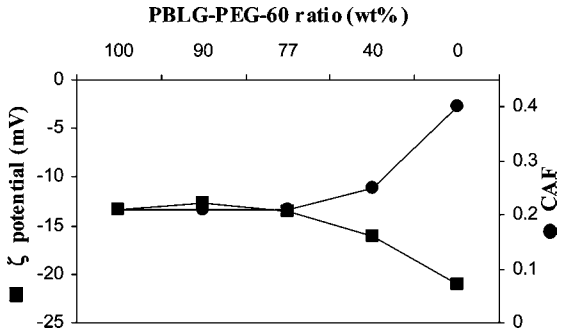

Figure 4. Evolution of ζ potential and complement activation factor as a function of PBLG-PEG-60 ratio (wt %) in nanoparticles constituted of PBLG-PEG-60 and PBLG-Bnz-50. Circle: Complement activation factor. Square symbols: ζ potential.

which was shifted toward higher values. When combining this result with the fact that the ζ potential was also shifted toward the value of the ζ potential measured for nanoparticles composed of 100 wt % non-PEG polymer, it can be suggested that the PEG coating characteristics of the surface of these nanoparticles was modified in such a way that it reduced the effectiveness to prevent complement activation. The lower value of the ζ potential shown by these nanoparticles was in favor of a modification of the surface composition of the nanoparticles, which can be attributed to a decrease in the density of the PEG chains at the nanoparticle surface. Thus, a higher contribution of the core polymer can be associated with the measured ζ potential. This may also contribute to increasing the capacity of inducing complement activation, hence increasing the chance to be taken up by macrophages after intravenous administration in animals.

Finally, from a practical point of view, it is interesting to note that low complement activation characteristics could be obtained with only 77% of PBLG-PEG copolymer chains in the particles, making possible to imagine composite particles containing not only PBLG-PEG copolymer (for ensuring stealth properties in the body), but also other copolymers bearing other chemical moieties, such as recognition ligands, in order to confer simultaneously other properties to the particles.

CONCLUSIONS

The results reported in this contribution permit one to demonstrate that nanoparticles based on PEGylated derivatives of PBLG with a low complement activation pattern can be obtained by nanoprecipitation, an easy and reproducible method. Because of this property, it is strongly expected that these nanoparticles will behave as stealth nanoparticles after *in vivo* administration by the intravenous route. Isothermal titration microcalorimetry and complement activation measurements allowed us to conclude that recognition of PEGylated PBLG-based nanoparticles by proteins is significantly lower than recognition of non-PEGylated nanoparticles. It is worth noting that composite nanoparticles based on a mixture of PBLG-PEG-60 and PBLG polymers have been prepared by nanoprecipitation and present similar properties to PBLG-PEG-60 based nanoparticles, suggesting that it may prove possible to introduce in the particles reasonable amounts of other structurally similar copolymers chains bearing other ligands, without modifying their complement activation properties. This would help to adjunct on demand additional functionalities to the particles.

ACKNOWLEDGMENT

Pr. Denis Labarre is warmly acknowledged for fruitful discussions concerning the discussion of the complement activation experiments. M.EMB would like to thank the CONACyT (Mexico) for the financial support, which enabled her to conduct this study. TEM experiments where performed at the CCME (U. Paris-Sud) facility and authors acknowledge Jeril Degrouard for technical support and fruitful help. The authors would like to acknowledge Laurent Fontaine and Véronique Montembault for their advice and support in the synthesis of the polymers used in the formulation of the nanoparticles.

LITERATURE CITED

(1) Lee, V. H. L. (2004) Nanotechnology: challenging the limit of creativity in targeted drug delivery. *Adv. Drug Delivery Rev. 56*, 1527–1528.

(2) Brannon-Peppas, L., and Blanchette, J. O. (2004) Nanoparticle and targeted systems for cancer therapy. *Adv. Drug Delivery Rev. 56*, 1649–1659.

(3) Illum, L., Hunneyball, I. M., and Davis, S. S. (1986) The effect of hydrophilic coatings on the uptake of colloidal particles by the liver and the peritoneal macrophages. *Int. J. Pharm. 29*, 53–65.

(4) Vonarbourg, A., Passirani, C., Saulnier, P., and Benoit, J.-P. (2006) Parameters influencing the stealthness of colloidal drug delivery systems. *Biomaterials 27*, 4356–4373.

(5) Owens, III, D. E., and Peppas, N. A. (2006) Opsonization, biodistribution, and pharmacokinetics of polymeric nanoparticles. *Int. J. Pharm. 307*, 93–102.

(6) Gref, R., Luck, M., Quellec, P., Marchand, M., Dellacherie, E., Harnisch, S., Blunk, T., and Muller, R. H. (2000) 'Stealth' corona-core nanoparticles surface modified by polyethylene glycol (PEG): influences of the corona (PEG chain length and surface density) and of the core composition on phagocytic uptake and plasma protein adsorption. *Colloids Surf., B 18*, 301–313.

(7) Passirani, C., Barratt, G., Devissaguet, J. P., and Labarre, D. (1998) Interactions of nanoparticles bearing heparin or dextran covalently bound to poly(methyl methacrylate) with the complement system. *Life Sci. 62*, 775–785.

(8) Norde, W., and Lyklema, J. (1978) The adsorption of human plasma albumin and bovine pancreas ribonuclease at negatively charged polystyrene surfaces. V. Microcalorimetry. *J. Colloid Interface Sci. 66*, 295–302.

(9) Gref, R., Minamitake, Y., Peracchia, M. T., Trubetskoy, V., Torchilin, V., and Langer, R. (1994) Biodegradable long-circulating polymeric nanospheres. *Science 263*, 1600–1603.

(10) Kataoka, K., Kwon, G. S., Yokoyama, M., Okano, T., and Sakurai, Y. (1993) Block copolymer micelles as vehicles for drug delivery. *J. Controlled Release 24*, 119–132.

(11) Nah, J. W., Jeong, Y. I., and Cho, C. S. (1998) Clonazepam release from core-shell type nanoparticules composed of poly (γ-benzyl L-glutamate) as the hydrophobic part and poly(ethylene oxide) as the hydrophilic part. *J. Polym. Sci., Part B. 36*, 415–423.

(12) Peracchia, M. T., Gref, R., Minamitake, Y., Domb, A., Lotan, N., and Langer, R. (1997) PEG-coated nanospheres from amphiphilic diblock and multiblock copolymers: investigation of their drug encapsulation and release characteristics. *J. Controlled Release 46*, 223–231.

(13) Kwon, G. S., Yokoyama, M., Okano, T., Sakurai, Y., and Kataoka, K. (1993) Biodistribution of micelle-forming polymer-drug conjugates. *Pharm. Res. 10*, 970–974.

(14) Kwon, G., Naito, M., Yokoyama, M., Okano, T., Sakurai, Y., and Kataoka, K. (1993) Micelles based on AB block copolymers of poly(ethylene oxide) and poly(β-benzyl L-aspartate). *Langmuir 9*, 945–949.

(15) Anderson, J. M., Gibbons, D. F., Martin, R. L., Hiltner, A., and Woods, R. (1974) The potential for poly-α-amino acids as biomaterials. *J. Biomed. Mater. Res. 5*, 197–207.

(16) Yang, J. Z., Antoun, S., Ottembrite, R. M., and Milstein, S. (1996) Amino acid oligomer microspheres as drug delivery systems. I. Synthesis of oligo(amino acids) via NCAs and their

microsphere formation. *J. Bioactive Compat. Polym. 11*, 219–235.
(17) Yang, J. Z., Wang, M., Ottembrite, R. M., and Milstein, S. (1996) Amino acid oligomer microspheres as drug delivery systems. II. Oligomerization of NCAs initiated with L-tyrosine methyl ester. *J. Bioactive Compat. Polym. 11*, 236–247.
(18) Anderson, J. M., Spilizewski, K. L., and Hiltner, A. (1985) *Biocompatibility of Tissue Analogs*, Volume I (Williams, D. F., Ed.) pp 68−88, Chapter *4*, CRC Press, Boca Raton, FL.
(19) Hirayama, C., Ihara, H., Ishimara, S. I., and Imanishi, Y. (1994) Preparation of porous spherical poly(γ-methyl L-glutamate) particles containing β-structure. *Polym. J. 26*, 61–66.
(20) McCormick, T. L. A., Sgouras, D., and Duncan, R. (1989) Poly(amino acid) copolymers as a potential soluble drug delivery system. 2. Body distribution and preliminary biocompatibility testing in vitro and in vivo. *J. Bioactive Compat. Polym. 4*, 252–268.
(21) Hayashi, T., and Iwatsuki, M. (1990) Biodegradation of copoly(L-aspartic acid/L-glutamic acid) in vitro. *Biopolymers 29*, 549–557.
(22) Oh, I., Leek, K., Kwon, H. Y., Lee, Y. B., Shin, S. C., Cho, C. S., and Kim, C. K. (1999) Release of adriamycin from poly(γ-benzyl glutamate)/poly(ethylene oxide) nanoparticles. *Int. J. Pharm. 181*, 107–115.
(23) Cho, C. S., Nah, J. W., Jeong, Y. I., Cheon, J. B., Asayama, S., Ise, H., and Akaike, T. (1999) Conformational transition of nanoparticles composed of poly(γ-benzyl glutamate) as the core and poly(ethylene oxide) as the shell. *Polymer 40*, 6769–6775.
(24) Kwon, G. S., Naito, M., Yokoyama, M., Okano, T., Sakurai, Y., and Kataoka, K. (1995) Physical entrapment of adriamycin in AB block copolymer micelles. *Pharm. Res. 12*, 192–195.
(25) Nah, J. W., Jeong, Y. I., Cho, C. S., and Kim, S. I. (2000) Drug-delivery system based on core-shell-type nanoparticles composed of poly (γ-benzyl-L-glutamate) and poly(ethylene oxide). *J. Appl. Polym. Sci. 75*, 1115–1126.
(26) Jeong, Y. I., Seo, S. J., Park, I. K., Lee, H. C., Kang, I. C., Akaike, T., and Cho, C. S. (2005) Cellular recognition of paclitaxel-loaded polymeric nanoparticles composed of poly(γ-benzyl L-glutamate) and poly(ethylene glycol) diblock copolymer endcapped with galactose moiety. *Int. J. Pharm. 296*, 151–161.
(27) Martínez Barbosa, M. E., Montembault, V., Cammas-Marion, S., Ponchel, G., and, and Fontaine, L. (2007) Synthesis and characterization of novel poly(γ-benzyl L-glutamate) derivatives tailored for the preparation of nanoparticles of pharmaceutical interest. *Polym. Int. 56*, 317–324.
(28) Temyanko, E., Russo, P. S., and Ricks, H. (2001) Study of rodlike homopolypeptides by gel permeation chromatography with light scattering detection: validity of universal calibration and stiffness assessment. *Macromolecules 34*, 582–586.
(29) Thioune, O., Fessi, H., Devissaguet, J. P., and Puisieux, F. (1997) Preparation of pseudolatex by nanoprecipitation: influence of the solvent nature on intrinsic viscosity and interaction constant. *Int. J. Pharm. 146*, 233–238.
(30) Laurell, C. B. (1966) Quantitative estimation of proteins by electrophoresis in agarose gels containing antibodies. *Anal. Biochem. 15*, 45–52.
(31) Norde, W., and Lyklema, J. (1978) The adsorption of human plasma albumin and bovine pancreas ribonuclease at negatively charged polystyrene surfaces. I. Adsorption isotherms. Effects of charge, ionic strength, and temperature. *J. Colloid Interface Sci. 66*, 257–265.
(32) Labarre, D., Vauthier, C., Chauvierre, C., Petri, B., Muller, R., and Chehimi, M. M. (2005) Interactions of blood proteins with poly(isobutylcyanoacrylate) nanoparticles decorated with a polysaccharidic brush. *Biomaterials 26*, 5075–5084.

BC900017C

Inhibition of Herpes Simplex Virus Type 1 Infection by Silver Nanoparticles Capped with Mercaptoethane Sulfonate

Dana Baram-Pinto,[†,‡] Sourabh Shukla,[†] Nina Perkas,[†] Aharon Gedanken,[†] and Ronit Sarid*[,‡]

Department of Chemistry and Kanbar Laboratory for Nanomaterials at Bar-Ilan University Center for Advanced Materials and Nanotechnology, Bar-Ilan University, 52900 Ramat-Gan, Israel, and The Mina and Everard Goodman Faculty of Life Sciences, Bar-Ilan University, 52900 Ramat-Gan, Israel. Received January 22, 2009; Revised Manuscript Received June 6, 2009

Interactions between biomolecules and nanoparticles suggest the use of nanoparticles for various medical interventions. The attachment and entry of herpes simplex virus type 1 (HSV-1) into cells involve interaction between viral envelope glycoproteins and cell surface heparan sulfate (HS). Based on this mechanism, we designed silver nanoparticles that are capped with mercaptoethane sulfonate (Ag−MES). These nanoparticles are predicted to target the virus and to compete for its binding to cellular HS through their sulfonate end groups, leading to the blockage of viral entry into the cell and to the prevention of subsequent infection. Structurally defined Ag−MES nanoparticles that are readily redispersible in water were sonochemically synthesized. No toxic effects of these nanoparticles on host cells were observed. Effective inhibition of HSV-1 infection in cell culture by the capped nanoparticles was demonstrated. However, application of the soluble surfactant MES failed to inhibit viral infection, implying that the antiviral effect of Ag−MES nanoparticles is imparted by their multivalent nature and spatially directed MES on the surface. Our results suggest that capped nanoparticles may serve as useful topical agents for the prevention of infections with pathogens dependent on HS for entry.

INTRODUCTION

The application of nanotechnology in therapeutics, biological imaging, drug delivery, biosensors, and cell labeling is being intensively explored (*1*−*6*). Biologically important entities, such as proteins, antibodies, antigens, and DNA, which possess nanometer size dimensions, may serve as good candidate targets for interactions with such nanoparticles (*1, 7, 8*). Viruses are common nanoelement pathogens that can infect and cause diseases in plants, animals, and humans, while viral diseases present challenging problems with worldwide social and economic implications. Development of antiviral drugs able to target the virus while maintaining host cell viability is challenging (*9, 10*).

Herpes simplex virus type 1 (HSV-1) is a common infectious agent that occurs worldwide and infects humans of all ages (*11*). The outcome of HSV-1 infection includes a wide variety of clinical manifestations, ranging from asymptomatic infection to oral cold sores and severe encephalitis. The HSV-1 virion consists of a 152-kbp double-stranded DNA genome enclosed by an icosahedral capsid, which is surrounded by a lipid bilayer envelope that accommodates 11−12 virally encoded glycoproteins (*11, 12*). The envelope diameter ranges from 170 to 200 nm and contains an array of protruding glycoprotein spikes, making the full diameter of the virion about 225 nm on average. Each virion contains 600−750 spikes, with variable packing densities (*12*). The mechanism of HSV entry into the cell, involving its virus−receptor interaction, is one of the most comprehensively understood routes among members of the Herpesviridae family (*13*). HSV entry occurs when extracellular virions attach to the cell surface via glycoprotein C (gC) and gB, promoting the binding of gD to one of three alternative cellular receptors. In turn, membrane fusion machinery comprised of gB, gH, and gL is activated to mediate fusion with plasma or endocytotic membranes (*11, 14*). During the attachment phase, gC and gB interact independently with cellular heparan sulfate (HS). This reversible interaction likely creates multiple points of adhesion and occurs in both wild-type and laboratory viral strains (*14*). The affinity of the binding of gC to HS is on the order of 10^{-8} M and is considered to be the major binding interaction during attachment (*13*). When gB and gC are absent, viral binding to the cell surface is severely reduced, signifying the important role of this step for viral entry (*11, 15*). Accordingly, cells that are defective in HS exhibit a dramatic reduction in susceptibility to infection (*13*). It is worth noting that the interaction with cell surface HS has been found to be a common pathway for attachment by several other human and animal viruses as well (*15*).

HS is a ubiquitous constituent of cell plasma membranes and extracellular matrices, which mediates various physiological processes, such as development, cell adhesion, tumorigenesis, and viral and bacterial infections (*16*). It is a structurally diverse, highly sulfonated polysaccharide belonging to the family of glycosaminoglycans. HS is composed of alternating sequences of glucosamine and uronic acid. The amino sugars may be N-acetylated or N-sulfated (*17*−*19*). The glucosamine residues may, in some cases, carry O-sulfated groups at C6 or C3, and the uronic acid moieties may be O-sulfated at C2 (*17*). HS is characterized by great structural heterogeneity in terms of chain length and size and the extent of sulfation and epimerization within the modified segments (*19*).

Topical, oral, or intravenous nucleoside derivatives (e.g., acyclovir) have been approved for the treatment of HSV infections and are widely used. However, the emergence of resistant viral strains, mainly after prolonged treatment in immunocompromised patients, is one of the main reasons for the continuous search for new antiviral drugs that can prevent or inhibit infection by both wild-type viruses and drug-resistant strains (*13, 20*). Compounds that mimic HS, such as sulfated polysaccharide (e.g., dextran sulfate, pentosan polysulfate, a

* Corresponding author. Tel: 972-3-5317853. Fax: 972-3-7384058. E-mail: saridr@mail.biu.ac.il.

[†] Department of Chemistry and Kanbar Laboratory for Nanomaterials at Bar-Ilan University Center for Advanced Materials and Nanotechnology.

[‡] The Mina and Everard Goodman Faculty of Life Sciences.

10.1021/bc900215b CCC: $40.75 © 2009 American Chemical Society
Published on Web 07/08/2009

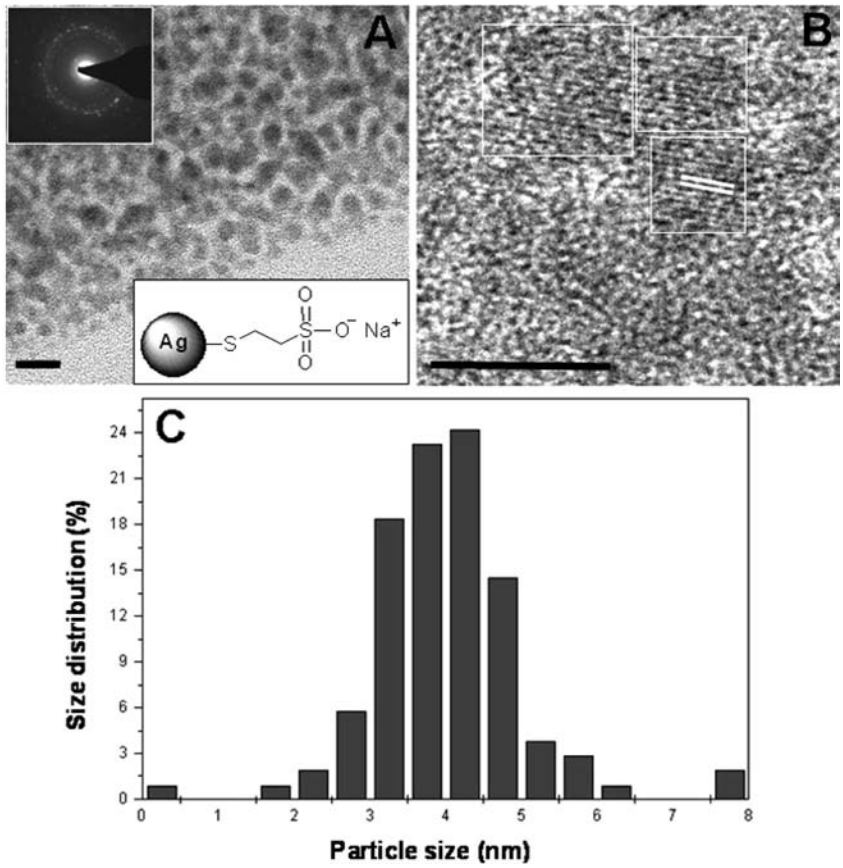

Figure 1. Representative TEM images of Ag−MES nanoparticles. (A, B) with selected area electron diffraction pattern along with the schematic representation of MES binding on the surface of silver nanoparticles (A). The scale bars in TEM images correspond to 10 nm. The size distribution of the Ag−MES nanoparticles was obtained from the TEM analysis and determined by measuring the diameter of 103 Ag−MES nanoparticles (C).

mixture of highly sulfated mannose containing di- to hexasaccharides (PI-88)) and sulfated nonpolysaccharides (e.g., lignin sulfate, poly(sodium 4-styrene sulfonate) (T-PSS)), were shown to inhibit HSV attachment to cells, suggesting that these compounds act via competition with HS chains for the binding to viral post attachment proteins. Interference with post attachment steps by these compounds has also been suggested (*14*, *21*−*24*). Antiviral potencies of candidate compounds are usually enhanced with an increasing degree of sulfation and the size of the oligosaccharide chain. These allow an increased likelihood of successful recognition of the saccharide with the HS-binding domain on the HSV and a simultaneous interaction of the saccharide with numerous copies of viral attachment proteins. Yet, inhibition of HSV during its cell-to-cell spread requires penetration of these compounds into a narrow intercellular space and in this case the size of the inhibitor might be a limiting factor (*14*). Therefore, one should consider the characteristics of the different modes of virus infection and spread during the design of antiviral compounds.

There are only a few reported nanoparticle-based antiviral therapies. Yacaman and co-workers have used silver nanoparticles for the inhibition of human immunodeficiency virus (HIV) infection (*25*), whereas other groups have used modified silver nanoparticles to inhibit monkeypox virus (*26*) and hepatitis B virus (*27*). More recently, Melander and co-workers have used functionalized multivalent gold nanoparticles for the prevention of HIV infection (*28*). Here, we describe the application of a structurally defined aqueous colloidal solution of silver nanoparticles that are capped with mercaptoethane sulfonate group (Ag−MES) as a novel inhibitor of HSV-1 infection. To the best of our knowledge, the antiviral properties of ω-sulfonated nanoparticles remain an undeveloped area, which based on our findings, is of potential medical interest.

EXPERIMENTAL PROCEDURES

Particle Synthesis. Mercaptoethane sulfonate-protected silver nanoparticles (Ag−MES) were synthesized by a modified procedure with a sonochemical reaction based on that described by Zou et al. (*29*). $AgNO_3$ (0.102 g, Aldrich) in 50 mL of ethanol was mixed with 0.25 g of sodium 2-mercaptoethane sulfonate (MES, Fluka Analytical) dissolved in 25 mL of ethanol and 25 mL of a double-distilled water (DDW) solution. After purging the reaction mixture with argon gas for 30 min, sonochemical irradiation (Ti horn from Sonics and Materials VCX 600, 20 kHz, 600 W at 60% efficiency) was applied for 15 min in argon atmosphere. NH_3 (0.1 mL, 25%) was injected into the flask 4 min after the start of the sonication. The reaction was held at a 10 °C, using a water−ice bath.

Characterization of Ag−MES Nanoparticles. The morphology of the nanostructures was characterized with a Philips CM-120 transmission electron microscope (TEM), operating at 120 kV. Images were recorded by a Gatan Ultrascan 1000 2kx2k CCD camera. The nanoparticle size distribution was further characterized using Scion Image software (Alpha 4.0.3.2) based on the TEM images. X-ray photoelectron spectroscopy (XPS) was performed using an Axis HS with monochromatic Al Kα source (Kratos Analytical). Thermogravimetric analysis (TGA) measurements were conducted using a TGA model Q500 (TA Instruments), equipped with a Pt crucible, for the estimation of the amount of the MES surfactant on the surface of the silver nanoparticles.

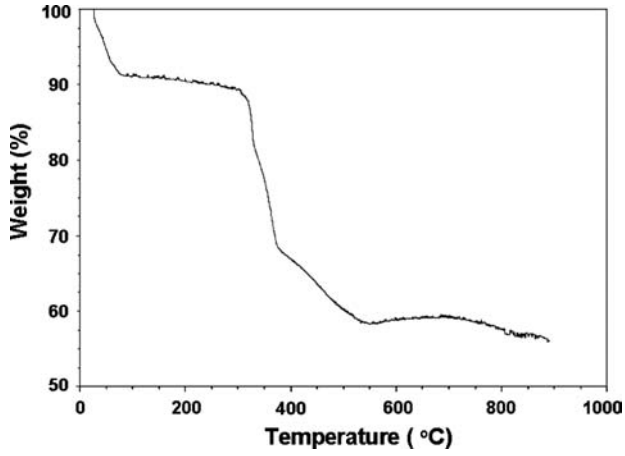

Figure 2. Thermogravimetric analysis (TGA) of Ag−MES nanoparticles depicting percentage weight loss of the sample as a function of temperature.

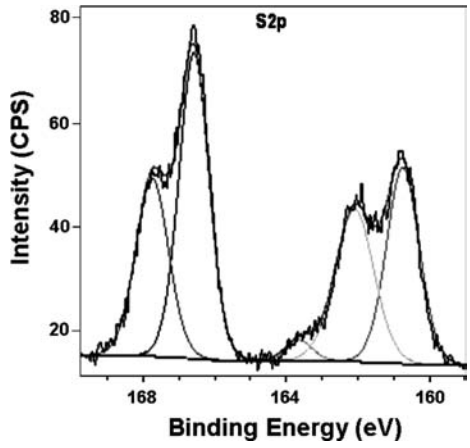

Figure 3. XPS spectra of the S 2p region of Ag−MES nanoparticles. Binding energy (BE) of 161.98 eV corresponds to the thiol group of MES, and BE of 167.77 eV corresponds to the sulfonate group of MES.

Cells and Virus. Vero African green monkey kidney epithelial cells were grown in minimum essential media (MEM)−Eagle's medium (Biological Industries, Israel) supplemented with 10% heat-inactivated fetal calf serum (FCS) (Biological Industries), L-glutamine (Biological Industries), and penicillin−streptomycin−amphotericin (PSA) (Biological Industries). Cells were maintained at 37 °C under 5% CO_2. The virus used was a wild-type HSV-1 McIntyre strain.

Cell Toxicity Assay. The toxicity of the Ag−MES nanoparticles to Vero cells was examined using a cell proliferation kit with an XTT-based colorimetric assay that measures mitochondrial activity, according to the manufacturer's instructions (Biological Industries). Optical density (OD) measurements for calculating cell viability percentage were taken using a TECAN Spectrafluor Plus (NEOTEC Scientific Instrumentation Ltd.) spectrophotometer at 405 nm wavelength.

For the assay, Vero cell monolayers were grown in 96-well plates (2.5×10^4 cells/well) with 5% FCS in MEM−Eagle's medium. Ag−MES nanoparticles were added into each well at different concentrations (25−800 μg/mL in a total volume of 150 μL/well). The control consisted of Vero cell monolayers with no Ag−MES nanoparticles.

HSV-1 in vitro Assays. Viral infection was evaluated by plaque assay on Vero cells. Cells were plated in 24-well dishes (4.5×10^4 cells/well). Confluent monolayers of cells were inoculated with 250 μL of virus suspensions (25, 250, or 2500

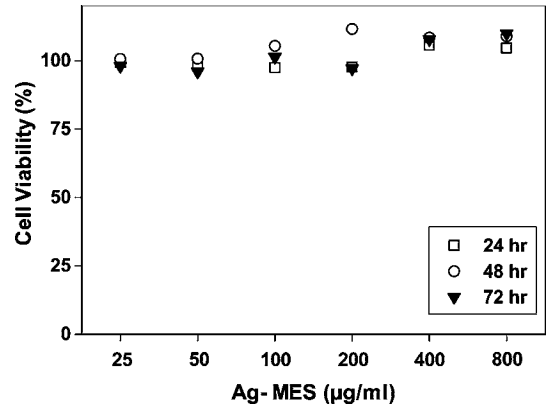

Figure 4. Cell toxicity assay. Cell viability was determined by the XTT assay. The viability of the cells was calculated as percentage relative to control cells, which were not treated with Ag−MES nanoparticles. Average results obtained for control batches were defined as 100% viability, and average values obtained for cells treated with Ag−MES nanoparticles were calculated accordingly. Measurements were taken after 24, 48, and 72 h at different Ag−MES nanoparticle concentrations (25−800 μg/mL). Similar results were obtained in two independent experiments.

plaque forming units (pfu)/well) in the presence of different concentrations of Ag−MES or MES at 37 °C. After 45 min incubation to allow for virus adsorption, the cells were overlaid with 500 μL of MEM−Eagle's medium supplemented with 2% heat-inactivated FCS and 0.1% human γ-globulin (ZLB Behring GmbH, Marburg, Germany) with Ag−MES nanoparticles or MES for maintaining final concentration in each well. Controls included mock-infected cell monolayers with and without Ag−MES nanoparticles or soluble MES. After 2−3 days of incubation, the cell monolayers were stained with Giemsa stain, and the plaques were counted. All determinations were performed in four replicas.

RESULTS AND DISCUSSION

Synthesis and Characterization of Ag−MES Nanoparticles. An aqueous dispersion of silver nanoparticles capped with sodium 2-mercaptoethane sulfonate was synthesized as described in the Experimental Procedures section. Transmission electron microscope (TEM) images of the Ag−MES nanoparticles revealed moderately polydispersed spherical nanoparticles with an average size of 4 ± 1 nm, while the selected area electron diffraction confirmed the presence of metallic silver (Figure 1). MES is expected to bind to the silver surface through the thiol (-SH) group, while the sulfonate end remains free and faces the solvent to target the virus (Figure 1). Thermogravimetric analysis (TGA) measurement on Ag−MES nanoparticles was conducted at a temperature range of 25−900 °C to estimate the amount of the MES on the surface of the silver. Weight loss (%) as a function of the temperature is shown in Figure 2. A total of 10.74% of the initial weight loss was observed over a range of 50−100 °C. We attribute this loss to access of MES molecules that were merely physically adsorbed to the surface of the nanoparticles and to solvent water molecules. A further weight reduction of 30.86% was detected at the temperature range of 320−550 °C. This loss occurred in two main steps: 22% of the weight was lost in the range of 320−370 °C and ~10% between 320 and 550 °C. We assign this weight reduction, at such high temperatures, to the removal of MES molecules that were chemically bonded to the silver core.

Based on the particles size obtained using TEM images and TGA analysis, we calculated that an average single Ag−MES nanoparticle covered with a full monolayer of MES contains 141 MES molecules. These calculations are based on previous

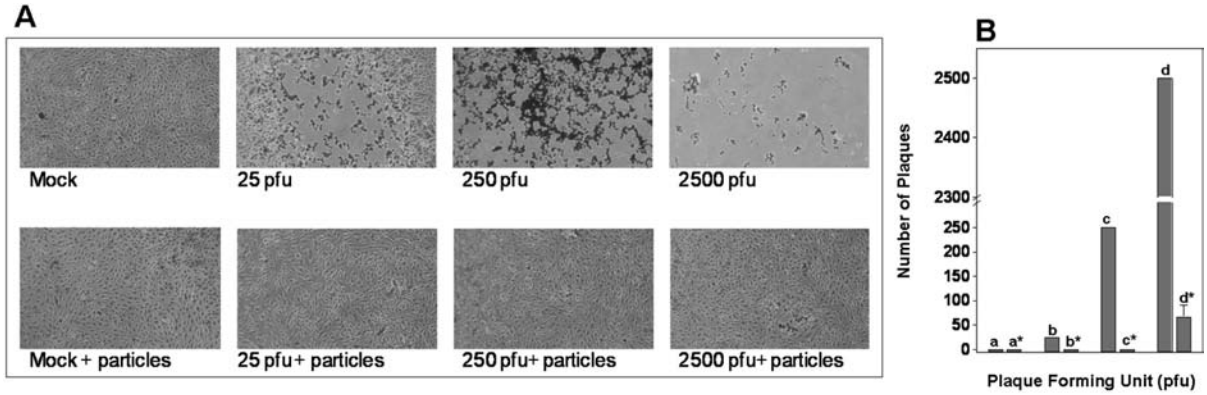

Figure 5. Microscopic and quantitative analysis of effects of Ag−MES nanoparticles toward infection with HSV-1. (A) Optical microscopic image (×10 magnification) demonstrating the effect of Ag−MES nanoparticles on HSV-1 infectivity. Cells were infected with HSV-1 in the absence or the presence of 400 μg/mL Ag−MES nanoparticles. Mock cells were similarly treated, but no virus was added. Pictures were taken 48 h following infection. (B) Quantitative analysis of the Ag−MES inhibition efficiency; a, b, c, and d represent the number of plaques in cell cultures not treated with Ag−MES nanoparticles (mock, 25, 250, and 2500 pfu, respectively); a*, b*, c*, and d* refer to the number of plaques in cell cultures infected with similar viral loads in the presence of 400 μg/mL Ag−MES nanoparticles (mock, 0, 0, and 67 ± 23, respectively).

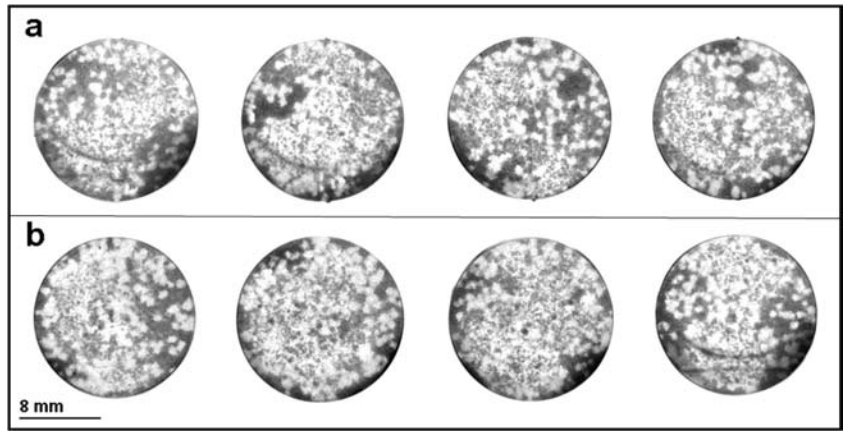

Figure 6. Effect of soluble MES on HSV-1 infection. Cells were infected with HSV-1 in the absence (a) or the presence (b) of 96 μg/mL MES. Pictures were taken 48 h following infection. Results represent four repeats for each condition. A *t* test for the two independent conditions (a and b) showed no significant difference in the diameter of the plaques; $p = 0.372$, $n = 112$.

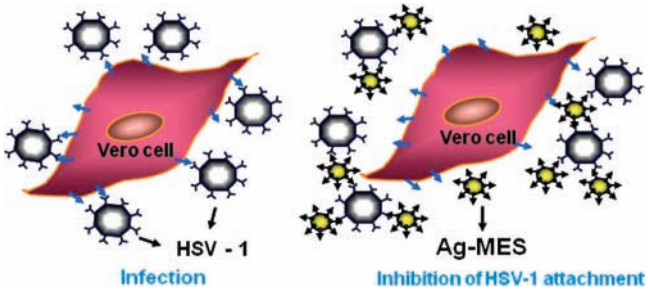

Figure 7. Schematic representation of a proposed mode of HSV-1 inhibition by Ag−MES nanoparticles.

surface coverage measurements carried out with alkanethiolates on metallic nanoclusters (*30*−*32*). The calculated mass percentage of a full MES monolayer on a silver core nanoparticle is therefore 24.1%. TGA measurements showed a 30.86% weight reduction, suggesting that synthesized Ag−MES nanoparticles were fully covered with a MES monolayer.

Figure 3 illustrates the XPS spectrum of S 2p region of Ag−MES nanoparticles. Sulfur appears in two main oxidation states: thiol group binding energy appears as a doublet ($2p_{3/2}$ and $2p_{1/2}$) at 161.98 eV and sulfonate group binding energy appears as a doublet ($2p_{3/2}$ and $2p_{1/2}$) at 167.77 eV. A third, relatively negligible (5.81%), oxidation state appears as well. Assuming that MES molecules were not altered during Ag−MES nanoparticle synthesis, each molecule carries one thiol group and one sulfonate group. Therefore, a 1:1 stoichiometric relation between the two sulfur groups would be expected. However, the XPS spectrum indicates a different ratio, with a larger sulfonate peak area than that of the thiol. This result indicates that most of the MES molecules are bonded to the silver core through thiol groups.

Cytotoxocity Assay. The toxicity of the Ag−MES nanoparticles to mammalian cells was of high concern. We tested the toxicity of the particles on kidney epithelial Vero cells at a concentration range of 25−800 μg/mL using the colorimetric XTT assay. Results were compared with cells that were not treated with Ag−MES nanoparticles (control). Figure 4 presents the results calculated as the percentage of viable cells relative to control cultures for cells incubated with Ag−MES nanoparticles for 24−72 h. As indicated by near 100% cell viability, Ag−MES nanoparticles did not affect the mitochondrial activity of the cells at any time point or concentration.

Inhibition of HSV-1 Infectivity by Ag−MES Nanoparticles. Vero cells show a typical cytopathic effect when infected with HSV-1. Therefore, to evaluate the antiviral activity of the nanoparticles, we used a plaque reduction assay in these cells. Cells were infected with virus suspensions (25−2500 pfu/well) in the absence or presence of different Ag−MES concentrations. Partial inhibition of plaque formation was observed when 200 μg/mL Ag−MES nanoparticles was used. Increased inhibition

was observed in the presence of 400 μg/mL Ag−MES nanoparticles, and no further inhibition was obtained when 800 μg/mL Ag−MES nanoparticles was added. As shown in Figure 5A, infection with HSV-1 was almost completely blocked in the presence of 400 μg/mL nanoparticles. At low virus loads (25 and 250 pfu), infected cell cultures that were treated with Ag−MES nanoparticles demonstrated a similar morphology to control mock infected cells, with no evidence of any plaque formation. In contrast, infected cells that were not treated with Ag−MES nanoparticles demonstrated plaques, with increasing diameters during the experiment. At high virus loads (2500 pfu), very small plaques were observed in cultures treated with Ag−MES nanoparticles, while complete destruction of the culture was observed in the absence of Ag−MES nanoparticles, indicating that Ag−MES nanoparticles act as inhibitors of infection. Figure 5B presents quantitative analysis of the Ag−MES inhibition efficiency calculated according to three independent experiments. The number of plaques was counted in infected cell cultures that were treated with Ag−MES nanoparticles and compared with plaque numbers extrapolated from virus titrations in cell cultures not treated with Ag−MES nanoparticles. It is evident that at low virus loads (25 and 250 pfu), viral infection was completely blocked by the Ag−MES nanoparticles. At higher virus loads (2500 pfu), an average of 67 ± 23 plaques/well was observed, which is nearly a 97% decrease in the number of plaques relative to cell cultures that were not treated with Ag−MES nanoparticles. Furthermore, the observed plaques were tiny compared with the plaques obtained in the absence of Ag−MES nanoparticles. This suggests the efficiency of the Ag−MES particles in blocking HSV-1 infection.

To compare the effect of the soluble MES with that of the nanoparticles, infection was carried out in the presence of 96 μg/mL MES, which is equivalent to the amount of MES incorporated in 400 μg/mL Ag−MES nanoparticles (Figure 6). However, soluble MES was found to be completely ineffective as an HSV-1 inhibitor after 48 or 72 h as indicated by the similarities in the number of plaques and their diameter in comparison to infected cells that were not treated with MES (*t* test for the two independent conditions showed no significant difference in the diameter of the plaques, $p = 0.372$, $n = 112$).

Taken together, using viral plaque reduction assay in Vero cells, we show that infection with HSV-1 was almost completely blocked in the presence of the silver nanoparticles capped with MES. In contrast, equivalent concentration of soluble MES molecules, a clinically approved detoxifying agent for inhibition of hemorrhagic cystitis (*33*), which constitute our nanoparticle capping molecule, was found ineffective in preventing HSV-1 infection.

We believe that the nanoparticles decorated with MES serve as multivalent inhibitors that mimic HS on the host cell membrane and, therefore, that the nanoparticles efficiently interact with HSV-1. This in turn prevents the infection of HSV-1 by blocking viral attachment to the cells as illustrated in Figure 7. Thus, one silver nanoparticle containing numerous functional groups can potentially target more than one virus. This spatial arrangement substantially enhances the effectiveness of the coated nanoparticles. Multivalent particles present the additional advantage of creating a high local concentration of binding molecules, thereby favoring the formation of more virus−particle pairs (*28*, *34*, *35*). In addition, we suggest that the free rotation of the soluble MES considerably reduces the interaction of the sulfonate groups with the target virus, whereas the sulfonate groups in the colloidal solution of the Ag−MES nanoparticles are directed toward the viral glycoproteins. Furthermore, steric effects involving shielding of other viral components that may assist in the attachment process could contribute to the inhibition observed.

The exact inhibitory mechanism will be determined in future studies. Since several pathogens have been shown to exploit cell-surface HS as primary attachment sites during host invasion, Ag−MES nanoparticles may potentially be applied for the topical prevention of other infectious agents, such as genital HSV-2 and HIV. Moreover, alternative nanoparticles constructs, comprised of different core materials and sulfonated surfactants, may be designed based on our prototype and assayed for their antiviral activity.

ACKNOWLEDGMENT

This work will be submitted to Bar Ilan University, Ramat Gan, Israel, by D. Baram-Pinto in partial fulfillment of the degree of Doctor of Philosophy.

LITERATURE CITED

(1) Eugenii, K., and Willner, I. (2004) Integrated nanoparticle-biomolecule hybrid systems: Synthesis, properties, and applications. *Angew. Chem., Int. Ed. 43*, 6042–6108.
(2) De, M., Ghosh, P. S., and Rotello, V. M. (2008) Applications of nanoparticles in biology. *Adv. Mater. 20*, 4225–4241.
(3) Priestly, B. G., Harford, A. J., and Sim, M. R. (2007) Nanotechnology: A promising new technology - but how safe? *Med. J. Aust. 186*, 187–188.
(4) Huang, D. M., Chung, T. H., Hung, Y., Lu, F., Wu, S. H., Mou, C. Y., Yao, M., and Chen, Y. C. (2008) Internalization of mesoporous silica nanoparticles induces transient but not sufficient osteogenic signals in human mesenchymal stem cells. *Toxicol. Appl. Pharmacol. 231*, 208–215.
(5) Prokop, A., and Davidson, J. M. (2008) Nanovehicular intracellular delivery systems. *J. Pharm. Sci. 97*, 3518–3590.
(6) Agui, L., Yanez-Sedeno, P., and Pingarron, J. M. (2008) Role of carbon nanotubes in electroanalytical chemistry: A review. *Anal. Chim. Acta 622*, 11–47.
(7) Willner, I., Basnar, B., and Willner, B. (2007) Nanoparticle-enzyme hybrid systems for nanobiotechnology. *FEBS J. 274*, 302–309.
(8) Allison, R. R., Mota, H. C., Bagnato, V. S., and Sibata, C. H. (2008) Bio-nanotechnology and photodynamic therapy- State of the art review. *Photodiagn. Photodyn. Ther. 5*, 19–28.
(9) Murray, P. R., Rosenthal, K. S., Kobayashi, G. S., Pfaller, M. A. (1998) *Medical microbiology*, 3rd ed., Mosby, St. Louis, MO.
(10) Flint, S. J., Enquist, L. W., Racaniello, V. R., and Skalka, A. M. (2008) Attachment and entry, in *Principles of Virology*, 3rd ed. (Flint, S. J., Enquist, L. W., Racaniello, V. R., and Skalka, A. M., Eds.), Vol. I, Chapter 5, pp 129−166, ASM Press, Washington, DC.
(11) Reske, A., Pollara, G., Krummenacher, C., Chain, B. M., and Katz, D. R. (2007) Understanding HSV-1 entry glycoproteins. *Rev. Med. Virol. 17*, 205–215.
(12) Grunewald, K., Desai, P., Winkler, D. C., Heymann, J. B., Belnap, D. M., Baumeister, W., and Steven, A. C. (2003) Three-dimensional structure of herpes simplex virus from cryo-electron tomography. *Science 302*, 1396–1398.
(13) Campadelli-Fiume, G., and Menotti, L. (2007) Entry of alphaherpesviruses into the cell, in *Human Herpesviruses: Biology, Therapy, and Immunoprophylaxis* (Arvin, A., Campadelli-Fiume, G., Mocarski, E., Moore, P. S., Roizman, B., Whitley, R., and Yamanishi, K., Eds.) Chapter 7, pp 93−111, Cambridge, New York.
(14) Nyberg, K., Ekblad, M., Bergstrom, T., Freeman, C., Parish, C. R., Ferro, V., and Trybala, E. (2004) The low molecular weight heparan sulfate-mimetic, PI-88, inhibits cell-to-cell spread of herpes simplex virus. *Antiviral Res. 63*, 15–24.
(15) Mardberg, K., Trybala, E., Glorioso, J. C., and Bergstrom, T. (2001) Mutational analysis of the major heparan sulfate-binding

domain of herpes simplex virus type 1 glycoprotein C. *J. Gen. Virol. 82*, 1941–1950.
(16) Lu, L. D., Shie, C. R., Kulkarni, S. S., Pan, G. R., Lu, X. A., and Hung, S. C. (2006) Synthesis of 48 disaccharide building blocks for the assembly of a heparin and heparan sulfate oligosaccharide library. *Org. Lett. 8*, 5995–5998.
(17) Lindahl, U. (2007) Heparan sulfate-proteininteractions - A. concept for drug design? *Thromb. Haemost. 98*, 109–115.
(18) Gallagher, J. T., and Walker, A. (1985) Molecular distinctions between heparan sulphate and heparin. *Biochem. J. 230*, 665–674.
(19) Bishop, J. R., Schuksz, M., and Esko, J. D. (2007) Heparan sulphate proteoglycans fine-tune mammalian physiology. *Nature 446*, 1030–1037.
(20) Talarico, L. B., Zibetti, R. G., Faria, P. C., Scolaro, L. A., Duarte, M. E., Noseda, M. D., Pujol, C. A., and Damonte, E. B. (2004) Anti-herpes simplex virus activity of sulfated galactans from the red seaweeds *Gymnogongrus griffithsiae* and *Cryptonemia crenulata*. *Int. J. Biol. Macromol. 34*, 63–71.
(21) Raghuraman, A., Tiwari, V., Zhao, Q., Shukla, D., Debnath, A. K., and Desai, U. R. (2007) Viral inhibition studies on sulfated lignin, a chemically modified biopolymer and a potential mimic of heparin. *Biomacromolecules 8*, 1759–1763.
(22) Piret, J., Lamontagne, J., Bestman-Smith, J., Roy, S., Gourde, P., Desormeaux, A., Omar, R. F., Juhasz, J., and Bergeron, M. G. (2000) In vitro and in vivo evaluations of sodium lauryl sulfate and dextran sulfate as microbicides against herpes simplex and human immunodeficiency. *J. Clin. Microbiol. 38*, 110–119.
(23) Herold, B. C., Bourne, N., Marcellino, D., Kirkpatrick, R., Strauss, D. M., Zaneveld, L. J., Waller, D. P., Anderson, R. A., Chany, C. J., Barham, B. J., Stanberry, L. R., and Cooper, M. D. (2000) Poly(sodium 4-styrene sulfonate): An effective candidate topical antimicrobial for the prevention of sexually transmitted diseases. *J. Infect. Dis. 181*, 770–773.
(24) Ekblad, M., Adamiak, B., Bergefall, K., Nenonen, H., Roth, A., Bergstrom, T., Ferro, V., and Trybala, E. (2007) Molecular basis for resistance of herpes simplex virus type 1 mutants to the sulfated oligosaccharide inhibitor PI-88. *Virology 367*, 244–252.
(25) Elechiguerra, J. L., Burt, J. L., Morones, J. R., Camacho-Bragado, A., Gao, X., Lara, H. H., and Yacaman, M. J. (2005) Interaction of silver nanoparticles with HIV-1. *J. Nanobiotechnol. 3*, 6.
(26) Rogers, J. V., Parkinson, C. V., Choi, Y. W., Speshock, J. L., and Hussain, S. M. (2008) A preliminary assessment of silver nanoparticle inhibition of monkeypox virus plaque formation. *Nanoscale Res. Lett. 3*, 129–133.
(27) Lu, L., Sun, R. W., Chen, R., Hui, C. K., Hui, C. M., Ho, C. M., Luk, J. M., Lau, G. K., and Che, C. M. (2008) Silver nanoparticles inhibit hepatitis B virus replication. *Antiviral Ther. 13*, 253–262.
(28) Bowman, M. C., Ballard, T. E., Ackerson, C. J., Feldheim, D. J., Margolis, D. M., and Melander, C. (2008) Inhibition of HIV fusion with multivalent gold nanoparticles. *J. Am. Chem. Soc. 130*, 6896–6897.
(29) Zou, X., Bao, H., Guo, H., Zhang, L., Qi, L., Jiang, J., Niu, J., and Dong, S. (2006) Mercaptoethane sulfonate protected, water-soluble gold and silver nanoparticles: Syntheses, characterization and their building multilayer films with polyaniline via ion-dipole interactions. *J. Colloid Interface Sci. 295*, 401–408.
(30) Sellers, H., Ulman, A., Shnidman, Y., and Eilers, J. E. (1993) Structure and binding of alkanethiolates on gold and silver surfaces: Implications for self-assembled monolayers. *J. Am. Chem. Soc. 115*, 9389–9401.
(31) Hostetler, M. J., Wingate, J. E., Zhong, C. J., Harris, J. E., Vachet, R. W., Clark, M. R., Londono, J. D., Green, S. J., Stokes, J. J., Wignall, G. D., Glish, G. L., Porter, M. D., Evans, N. D., and Murray, R. W. (1998) Alkanethiolate gold cluster molecules with core diameters from 1.5 to 5.2 nm: Core and monolayer properties as a function of core size. *Langmuir 14*, 17–30.
(32) Templeton, A. C., Wuelfing, W. P., and Murray, R. W. (2000) Monolayer-protected cluster molecules. *Acc. Chem. Res. 33*, 27–36.
(33) Haselberger, M. B., and Schwinghammer, T. L. (1995) Efficacy of mesna for prevention of hemorrhagic cystitis after high-dose cyclophosphamide. *Ann. Pharmacother. 29*, 918–921.
(34) Nicewarner Pena, S. R., Raina, S., Goodrich, S. P., Fedoroff, N. V., and Keating, C. D. (2002) Hybridization and enzymatic extension of Au nanoparticle-bound oligonucleotides. *J. Am. Chem. Soc. 124*, 7314–7323.
(35) Lytton-Jean, A. K., and Mirkin, C. A. (2005) A thermodynamic investigation into the binding properties of DNA functionalized gold nanoparticle probes and molecular fluorophore probes. *J. Am. Chem. Soc. 127*, 12754–12755.

BC900215B

The Role of Ganglioside GM_1 in Cellular Internalization Mechanisms of Poly(amidoamine) Dendrimers

Seungpyo Hong,[†,‡,§,○] Rahul Rattan,[†,▽,○] István J. Majoros,[○] Douglas G. Mullen,[§,○] Jennifer L. Peters,[○] Xiangyang Shi,[○] Anna U. Bielinska,[○] Luz Blanco,[○] Bradford G. Orr,[⊥,○] James R. Baker, Jr.,[▽,○] and Mark M. Banaszak Holl*[,§,||,#,○]

Programs in Macromolecular Science and Engineering and Biophysics, Departments of Physics, Chemistry, and Biomedical Engineering, and Michigan Nanotechnology Institute for Medicine and Biological Sciences, University of Michigan, Ann Arbor, Michigan 48109. Received January 23, 2009; Revised Manuscript Received June 8, 2009

Generation 7 (G7) poly(amidoamine) (PAMAM) dendrimers with amine, acetamide, and carboxylate end groups were prepared to investigate polymer/cell membrane interactions *in vitro*. G7 PAMAM dendrimers were used in this study because higher-generation of dendrimers are more effective in permeabilization of cell plasma membranes and in the formation of nanoscale holes in supported lipid bilayers than smaller, lower-generation dendrimers. Dendrimer-based conjugates were characterized by ^{1}H NMR, UV/vis spectroscopy, GPC, HPLC, and CE. Positively charged amine-terminated G7 dendrimers (G7-NH_2) were observed to internalize into KB, Rat2, and C6 cells at a 200 nM concentration. By way of contrast, neither negatively charged G7 carboxylate-terminated dendrimers (G7-COOH) nor neutral acetamide-terminated G7 dendrimers (G7-Ac) associated with the cell plasma membrane or internalized under similar conditions. A series of *in vitro* experiments employing endocytic markers cholera toxin subunit B (CTB), transferrin, and GM_1-pyrene were performed to further investigate mechanisms of dendrimer internalization into cells. G7-NH_2 dendrimers colocalized with CTB; however, experiments with C6 cells indicated that internalization of G7-NH_2 was not ganglioside GM_1 dependent. The G7/CTB colocalization was thus ascribed to an artifact of direct interaction between the two species. The presence of GM_1 in the membrane also had no effect upon XTT assays of cell viability or lactate dehydrogenase (LDH) assays of membrane permeability.

INTRODUCTION

Polycationic polymers such as poly(lysine)s, poly(ethyleneimine)s, diethylaminoethyl dextrans, and poly(amidoamine) (PAMAM) dendrimers have demonstrated great potential to be exploited as gene transfer and drug delivery vectors (*1*−*9*). Successful *in vitro* biomedical applications of the polycationic polymers have triggered a number of research groups to investigate the internalization mechanism of the macromolecules into cells. Efficient cross-membrane transport and membrane disruption were observed with a strong dependence on size (molecular weight) and surface groups of the polymers, as well as composition of model membranes (*10*−*14*). Among those polycationic polymers, PAMAM dendrimers have attracted great scientific interest in biomedical applications because of their excellent water solubility and well-defined structure, molecular weight, and surface end groups. Demonstrated utility for practical applications, coupled with excellent monodispersity and chemical versatility, make PAMAM dendrimers an ideal material for exploring polymer−membrane interactions in greater detail (*6*, *8*−*10*, *13*, *15*).

The internalization mechanism of amine-terminated PAMAM dendrimers into cells has been explained as polycation-mediated endocytosis or leaky endocytosis (*10*−*14*). In particular, colocalization studies using choleratoxin subunit B (CTB) suggested that ganglioside GM_1 played a major role in the initial interaction with the cell membrane and the subsequent internalization process for EA.hy 926 cells and Chinese hamster ovary (CHO) cells (*16*). Furthermore, inhibition of internalization by methyl-β-cyclodextrin (MβCD) suggested that a lipid-raft mediated process may be a primary pathway for PAMAM dendrimer internalization into the cells. Subsequent studies with HeLa and HepG2 cells did not show an effect from MβCD, but instead, increased uptake and transfection efficiency were observed as a function of caveolin 1 expression (*17*). These results were particularly interesting in light of other studies that had identified an "adsorptive" endocytosis that might involve a specific membrane component for B16f10 melanoma cells (*18*), which are also known to contain GM_1 (*19*). However, the generality of a caveolae-based endocytosis mechanism is called into question by studies on Caco-2 cells which support a clathrin-based mechanism, not a caveolae-mediated mechanism (*20*). In addition, studies on A549 cells indicate that the process is neither clathrin- nor caveolae-based (*21*).

An alternative to endocytic mechanisms of uptake is direct physical disruption of the membrane and the formation of nanoscale holes causing plasma membrane permeability. AFM observations have revealed that polycationic polymers cause nanoscale hole formation, expansion of pre-existing defects, or membrane thinning depending on physical properties of polymers such as structure, size, and terminal groups, as well as

* To whom correspondence should be addressed: Professor Mark M. Banaszak Holl, Programs in Macromolecular Science and Engineering, Applied Physics, Biophysics, and Dept. of Chemistry, University of Michigan, 930 N. University Avenue, Ann Arbor, MI 48109-1055, Phone: (734) 763-2283, Fax: (734) 763-2307, Email: mbanasza@umich.edu.

† These authors made an equal contribution to this work.

‡ Current address: Department of Biopharmaceutical Sciences, University of Illinois, Chicago, IL 60612.

§ Program in Macromolecular Science and Engineering.

|| Program in Biophysics.

⊥ Department of Physics.

Department of Chemistry.

▽ Department of Biomedical Engineering.

○ Michigan Nanotechnology Institute for Medicine and Biological Sciences.

10.1021/bc900029k CCC: $40.75 © 2009 American Chemical Society
Published on Web 07/07/2009

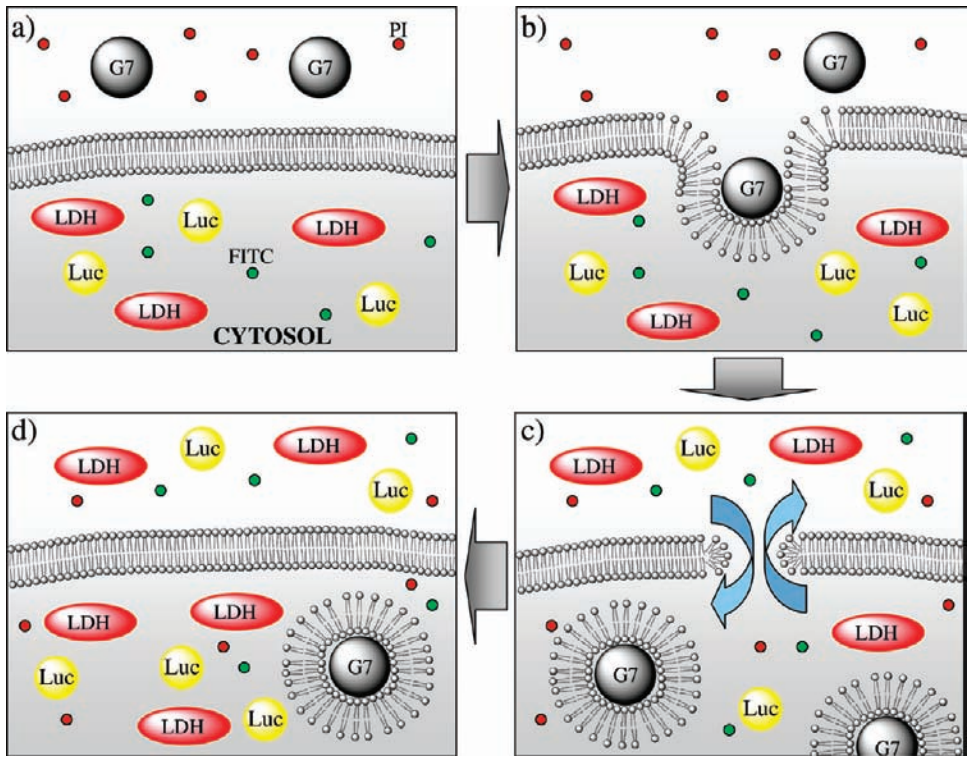

Figure 1. Schematic diagram of the proposed nanoscale hole formation mechanism induced by positively charged PAMAM dendrimers. The data supporting this schematic summary are presented in this paper as well as in our previous reports.

membrane composition and phase (*6, 9, 22*−*25*). Particularly, the efficiency of hole formation in supported lipid bilayers induced by PAMAM dendrimers was concluded to be proportional to molecular weight (G7 > G5 > G3) as well as terminal end groups (amine > acetamide; i.e., charged > uncharged) of the dendrimers. Recent studies across a broad variety of cationic nanomaterials suggests that surface area is the single best correlate (*26*). This observation agrees with *in vivo* studies carried out by Oberdörster et al. (*27*) AFM studies using supported lipid bilayers were consistent with our *in vitro* results exploring cell membrane permeability and dendrimer internalization (*6, 8, 9*). Employing two tumor cell lines, KB and Rat2, cytosolic enzyme (LDH and luciferase) leakage, dendrimer internalization, and small molecule diffusion into and out of the cells were observed as a result of incubation with positively charged G7 PAMAM dendrimers as illustrated in Figure 1. We thus concluded that the cellular-level data for the interaction of cationic PAMAM dendrimers with cell membranes were consistent with induction of nanoscale hole formation and this process may be related to the internalization of these materials into the cell and/or the membrane permeability measured by dye diffusion and LDH assays (*6, 8, 9*).

Considering the recent reports on endocytic internalization (*16*−*21*) and nanoscale hole formation (*6, 8, 9, 26*), we decided to investigate the role of GM_1 in the interaction of PAMAM dendrimers with cells. Experiments were designed probing the roles of GM_1 in endocytosis and/or nanoscale hole formation. Experiments to test other key hypothesis such as clathrin pathways were also explored. For this study, G7 PAMAM conjugates were chosen because of their effectiveness in terms of both endocytosis and cell membrane disruption and because they had been observed to cause membrane permeability even at 4 °C (*6, 8, 9, 28, 29*). Three different types of G7 PAMAM dendrimer−AlexaFluor488 conjugates (amine, acetamide, and carboxylate terminated) were synthesized and characterized (Figure 2). The conjugates were then tested *in vitro* to explore dendrimer−cell interactions. The key findings in this

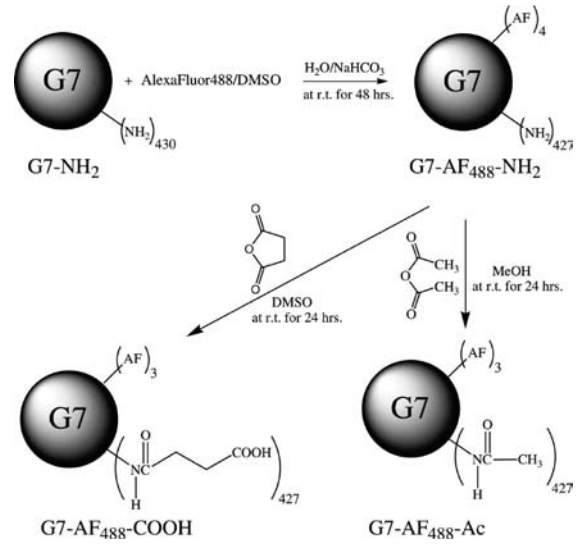

Figure 2. Synthetic routes for G7 PAMAM dendrimer conjugates with various surface end groups.

paper are as follows: (1) no evidence is found for a GM_1 dependence of G7 PAMAM dendrimer with respect to internalization via endocytosis or nanoscale hole formation; (2) the presence of GM_1 in the membrane does not play a role in cell viability assays as measured by XTT; (3) the presence of GM_1 in the membrane does not play a role in plasma membrane permeability assays as measured by LDH.

EXPERIMENTAL SECTION

Materials. G7 and G5 PAMAM dendrimers were synthesized at the Michigan Nanotechnology Institute for Medicine and Biological Sciences and purified using ultrafiltration and dialysis before use. Alexa Fluor488 carboxylated succinimidyl ester (AF488) was supplied by Molecular Probes (Eugene, OR) and

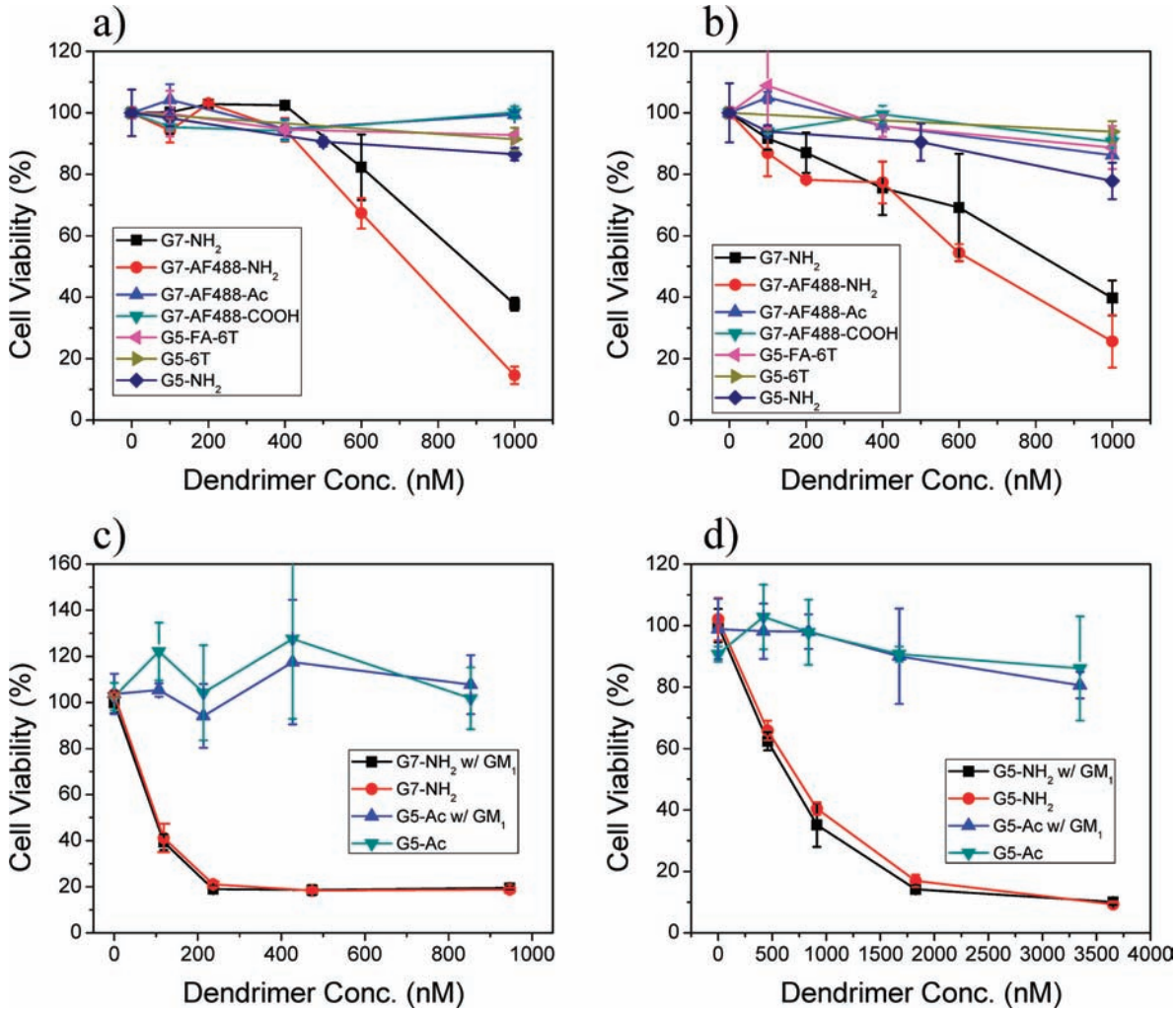

Figure 3. Percentage viability as measured by XTT assay when cells are treated with various G5 and G7 PAMAM dendrimers: (a) KB cells, (b) RAT-2 cells, (c) C6 cells, and (d) C6 cells. FA = folic acid. 6T = 6-Tamra.

used without further purification. Tranferrin from human serum labeled by AlexaFluor546 (TF-AF546), recombinant cholera toxin subunit B-Alexa Fluor647 conjugate (CTB-AF647), and LysoTracker Red DND-99 (LysoTracker) were provided by Molecular Probes. Methyl-β-cyclodextrin (MβCD) and GM_1-pyrene were purchased from Sigma-Aldrich (St. Louis, MO) and used without further purification. Materials for native PAGE were obtained from Invitrogen. All other chemicals were acquired from Aldrich and used as received. Water used in this work was purified by Milli-Q Plus 185 system and had a resistivity higher than 18.0 M$\Omega\cdot$cm.

Preparation of PAMAM Dendrimer Conjugates and Their Surface Modification. Two milligrams of AF488 (6.20 μM, 5× excess to G7) dissolved in 400 μL DMSO were conjugated to 68 mg of the purified G7 PAMAM dendrimers (1.25 μM) under the presence of 2 mL of 1 M $NaHCO_3$ at room temperature for 48 h. The resulting reaction mixture was then dialyzed in water for 2 days and lyophilized for 2 days, followed by 5× ultrafiltration with water using an 80 000 molecular weight cutoff membrane at 21 °C, 5000 rpm, for 30 min each. Sixty milligrams of a yellowish powder (G7-AF488-NH_2) was finally obtained (yield: 86%). The average number of AF488 dye molecules present was determined by ^{1}H NMR and/or GPC. The materials used in these studies varied from 2.4 to 4 AF488 per dendrimer. Twenty-two milligrams of G7-AF488-NH_2 was allowed to react with 12 μL of acetic anhydride (50% mol excess to the conjugate) in 1.5 mL MeOH as a solvent at room temperature for 24 h. The reaction mixture was then purified by ultrafiltration at the same condition above with PBS (w/o Ca^{2+}, Mg^{2+}) and water subsequently 5× each. After lyophilization for 2 days, 16.25 mg of a yellowish powder (G7-AF488-Ac) was obtained (yield: 63%). Twenty milligrams of G7-AF488-NH_2 was also allowed to react with 11 mg succinic anhydride (50% excess to the conjugate) in 1.5 mL DMSO at room temperature for 24 h followed by ultrafiltration and lyophilization at the same condition used for preparation of G7-AF488-Ac. A yellowish powder (18.8 mg) was obtained (G7-AF488-COOH, yield: 67%). The synthetic routes for the three different conjugates are summarized in Figure 2. In addition, G5 PAMAM dendrimers used in the XTT assay (Figure 3) were also conjugated with 6-carboxy-tetramethyl-rhodamine (6-TAMRA) followed by acetylation as described earlier (*30*).

Characterization of the Prepared PAMAM Based Conjugates: UV/vis and ^{1}H NMR Spectroscopy. UV/vis spectra of the G7 PAMAM conjugates were measured on a Perkin-Elmer UV/vis spectrometer Lambda 20 (Wellesley, MA). Molar extinction coefficients of the dendrimer conjugates were also calculated by plotting maximum absorbance values against conjugate concentrations at 20, 40, 60, 80, and 100 μg/mL using the Lambert−Beer law (Table 1). ^{1}H NMR spectra were also taken in D_2O and were used to provide integration values for structural analysis using a Bruker AVANCE DRX 500 instrument (*31*).

Table 1. Molar Extinction Coefficients, Molar Masses, and Polydispersity Indices of the G7 Conjugates

conjugates	molar extinction coeff. ($M^{-1}cm^{-1}$)[a]	theoretical molar mass[b]	molar mass (M_n)[c]	polydispersity (M_w/M_n)	HPLC peak width at half-height[d]
G7-NH_2	N/A	97 020	97 000	1.07 ± 0.02	0.52
G7-AF_{488}-NH_2	171 100	99 137	99 600	1.38 ± 0.03	0.62
G7-AF_{488}-Ac	147 130	116 903	116 300	1.06 ± 0.02	0.49
G7-AF_{488}-COOH	122 520	141 437	138 500	1.08 ± 0.02	0.57

[a] Molar extinction coefficients were obtained from the Lambert−Beer equation by plotting λ_{max} against corresponding concentrations of a conjugate (20, 40, 60, 80, and 100 μg/mL). R^2 values of the linear regressions were 0.9966−0.999. The coefficients were calculated on the basis of UV characteristic peaks of conjugated AF_{488} at 497 nm. [b] Calculated from the measured molecular weight of starting G7-NH_2 by assuming that the G7 PAMAM dendrimers have 4 AF488 moieties per dendrimer and 427 surface terminal groups according to the previously reported curve fit (*30*). [c] Measured by GPC (M_n, Number average molecular weight; M_w, Weight average molecular weight). [d] Obtained from HPLC chromatograms.

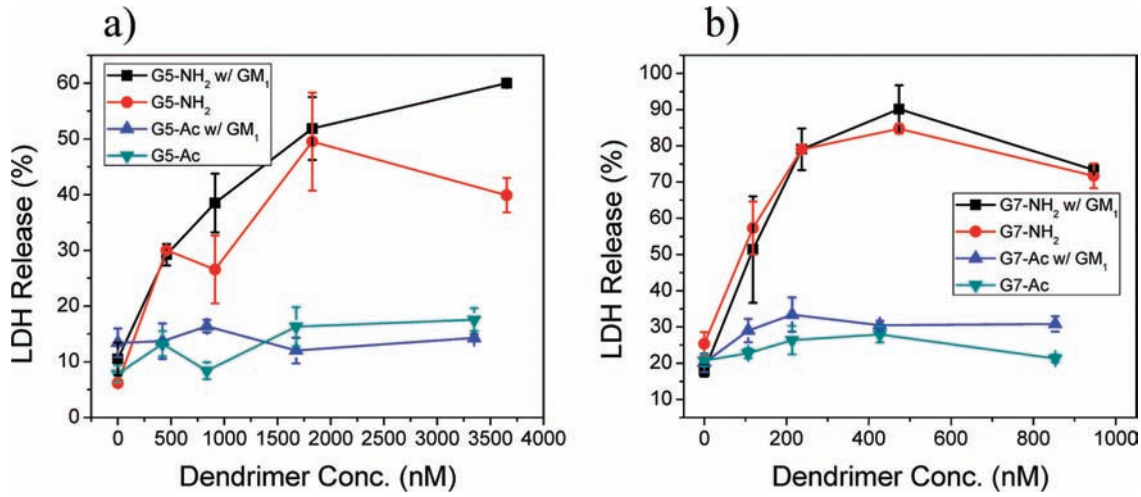

Figure 4. Percentage LDH release of C6 cells when treated with (a) G5 and (b) G7 PAMAM dendrimers.

Characterization of the Prepared PAMAM Based Conjugates: GPC and HPLC. The molar mass moments and molar mass distribution of each polymer sample were measured using gel permeation chromatography (GPC). The number average molecular weight (M_n) and polydispersity index (PDI), a commonly used measure of the breadth of the molar mass distribution defined as the ratio of the weight and number average molecular weights (M_w/M_n), of individual samples are listed in Table 1. GPC experiments were performed using an Alliance Waters 2690 separation module (Waters Corp., Milford, MA) equipped with a Waters 2487 UV absorbance detector (Waters Corp.), a Wyatt Dawn DSP laser photometer (Wyatt Technology Corp., Santa Barbara, CA), an Optilab DSP interferometric refractometer (Wyatt Technology Corp.), and TosoHaas TSK-Gel Guard PHW 06762 (75 × 7.5 mm, 12 μm), G 2000 PW 05761 (300 × 7.5 mm, 10 μm), G 3000 PW 05762 (300 × 7.5 mm, 10 μm), and G 4000 PW (300 × 7.5 mm, 17 μm) columns. A detailed procedure of the GPC measurement was described elsewhere (*9, 31*).

The reverse-phase (RP) HPLC system (Beckman Coulter, Fullerton, CA) consisting of a System GOLD 126 solvent module, a model 507 autosampler equipped with a 100 μL loop, and a model 166 UV detector were used in this study as well. A Jupiter C5 silica-based RP-HPLC column (250 × 4.6 mm, 300 Å) was purchased from Phenomenex (Torrance, CA). Two Phenomenex Widepore C5 safety guards (4 × 3 mm) were also installed ahead of the Jupiter column. The mobile phase for elution of G7-AF488 dendrimer conjugates with different terminal groups was a linear gradient beginning from 100:0 (v/v) water/acetonitrile (ACN) to 50:50 (v/v) water/ACN at a flow rate of 1 mL/min for 40 min. Trifluoroacetic acid (TFA) at 0.14 wt % concentration in water as well as in ACN was used as counterions to make the dendrimer surfaces hydrophobic. All the samples were dissolved into the aqueous mobile phase (water containing 0.14% TFA) at the concentration of 1 mg/mL. The detection of eluted samples was performed at 210 nm. The analysis was performed using Beckman's System GOLD Nouveau software (*32*).

Characterization of the Prepared PAMAM Based Conjugates. *Capillary Electrophoresis (CE).* An Agilent Technologies (Waldbronn, Germany) CE instrument was used in this work. Unmodified quartz capillaries were purchased from Polymicro Technologies (Phoenix, AZ, USA). The voltage was kept at 20 kV. On-capillary UV diode-array detection was used, operating at wavelengths of 210 nm, 250 nm, 280, and 495 nm. Samples were introduced by hydrodynamic injection at a pressure of 50 mbar.

For analysis of G7-AF488 conjugates with amino and acetamide terminal groups, silanized capillaries (i.d. 100 μm) with total length of 48.5 cm and effective length of 40 cm were employed following previous literature (*33*). G7-AF488-NH_2 and G7-AF488-Ac conjugates were dissolved in pH 2.5 phosphate buffer, and the sample solutions were adjusted to pH 2.5 using 0.1 M phosphoric acid to give a concentration of 1 mg/mL. All the conjugates contained 0.05 mg/mL 2,3-diaminopyridine (2,3-DAP) as an internal standard.

For analysis of G7-AF488 conjugate with carboxyl terminal groups, bare silica capillaries (i.d. 75 μm) with total length of 64.5 cm and effective length of 56 cm were used for the characterization of G7-AF488-COOH conjugates. The capillary temperature was maintained at 20 °C. Before use, the uncoated silica capillary was pretreated by rinsing with 1 M NaOH (15 min), deionized water (Purchased from Agilent) (15 min), and running buffer (15 min) (*33*). Before each injection, the capillary was rinsed with a similar sequence of each eluent. Twenty millimolar borate buffer (pH 8.3) was used as the running buffer. G7-AF488-COOH conjugates were dissolved in the running buffer, and the sample's pH was adjusted to 8.3 with 20 mM sodium tetraborate solution to get a final concentration of 1 mg/

mL. 4-Methoxybenzyl alcohol (MBA) (0.05 mg/mL) was used as a neutral marker.

Cell Lines. The KB, Rat2, and C6 cell lines were purchased from the American type Culture Collection (ATCC, Manassas, VA) and grown continuously as a monolayer at 37 °C and 5% CO_2. The KB cells were grown in RPMI 1640 medium (Mediatech, Herndon, VA). The Rat2 and C6 cells were grown in Dulbecco's modified Eagle's medium (DMEM, Gibco, Eggenstein, Germany). The RPMI 1640 and DMEM media were supplemented with penicillin (100 units/mL), streptomycin (100 μg/mL), and 10% heat-inactivated fetal bovine calf serum (FBS) before use.

XTT Cytotoxicity Assay. Cytotoxicity of the dendrimer conjugates used in this study was assessed by the overall activity of mitochondrial dehydrogenase by 2,3-bis(2-methoxy-4-nitro-5-sulfophenyl)-*2H*-tetrazolium-5-carboxanilide (XTT) assay (Cell Proliferation Kit II, Roche Molecular Biochemicals, Mannheim, Germany). KB, Rat2, and C6 cell lines (at a concentration of 5×10^4 cells/well) were prepared as monolayers in 96 well plates, followed by incubation with dendrimers in phosphate buffered saline (PBS) with Ca^{2+} and Mg^{2+} at 37 °C under 5% CO_2 for 4.5 h (2 h for C6 cells). Polymer solutions (supernatants) were then removed, followed by washing with PBS twice. Mitochondrial activities of the cells were spectrophotometrically measured at 492 nm using a Spectra Max 340 ELISA Reader (Molecular Devices, Sunnyvale, CA). Cell viability was then calculated on the basis of optical density (OD) from untreated cells.

LDH Membrane Permeability Assay. Membrane permeability was tested via lactate dehydrogenase (LDH) leakage using the LDH assay kit (Promega, Madison, WI). The activity of LDH in extracellular media is taken as a measure of membrane porosity. C6 cells were seeded at a density of 5×10^4 cells/well in 96 well plates for overnight incubation at 37 °C and 5% CO_2. Dendrimers diluted in 100 μL PBS (w/ Ca^{2+}, Mg^{2+}) were added at specified concentrations into the 96 well plates and incubated at 37 °C and 5% CO_2 for 2 h after which the supernatant was removed and 50 μL was taken for the LDH assay (throughout the experiment boundary wells were not used). LDH activity was spectrophotometrically measured at 490 nm using an ELISA reader.

Confocal Laser Scanning Microscopy (CLSM). A concentration of 1×10^5 cells/mL of KB and Rat2 cells was seeded on MatTek glass bottom Petri dishes (35 mm) and incubated at 37 °C under 5% CO_2 for 24 h. The cell culture medium was removed and 2 mL of each dendrimer-AF488 conjugates in PBS (w/ Ca^{2+}, Mg^{2+}) solution was added into the appropriate dish. The dishes were incubated with added solutions either at 37 °C under 5% CO_2 for 1 h or at 4 °C. For the low-temperature experiment, cells were preincubated at 4 °C for 10 min before adding the dendrimer solutions. The conjugate-containing solutions were removed and the resulting cell monolayer was washed with PBS at least three times. Cells were fixed with 2% formaldehyde in the PBS (w/ Ca^{2+}, Mg^{2+}) at room temperature for 10 min, followed by washing with PBS twice.

For colocalization studies of dendrimers with CTB and transferrin on KB and Rat2 cells, dendrimer solutions were premixed with markers, resulting in final concentrations of 200 nM, 10 μg/mL, and 50 μg/mL for G7-AF488-NH_2, CTB-AF647, and TF-AF546, respectively. The mixed solutions were then added to KB and Rat2 cells, and the cells were incubated at 37 °C, 5% CO_2, for 1 h.

For colocalization studies of CTB and G7-NH_2 dendrimers on C6 cells, cells were seeded in Fisherbrand 2 well microscope cover glass #1.5 at 2.5×10^5 cells/mL density, with 1 mL complete media in each well. Cells were allowed to attach to the surface for 4 h after which wells were washed with PBS (w/ Ca^{2+}, Mg^{2+}) and then overnight incubated with media (w/o serum) containing GM_1-pyrene. Cells were then treated with 5 μg/mL CTB-AF647 for 1 h or 500 nM G7-AF488-NH_2- for 2 h, washed with PBS, and imaged in PBS solution.

For coincubation of KB cells with G7-AF488-NH_2 and fully acetylated G5 PAMAM-6-TAMRA conjugates (G5-6T-Ac) (*34*), KB cells were incubated with 100, 200, and 400 nM G7-AF488-NH_2 at 37 °C for 30 min followed by addition of 1 μM G5-6T-Ac with additional incubation for 30 min.

Confocal and differential interference contrast (DIC) images were taken on an Olympus FV-500 confocal microscope using either a 60×, 1.5 NA, or 100×, 1.4 NA oil immersion objective. For the confocal images using three different AlexaFluors, the 488 nm line of an argon ion laser (for dendrimer conjugates), 543 nm line of a HeNeG laser (for transferrin and LysoTracker), or 633 nm line of a HeNeR laser (for cholera toxin) was used for excitation, and the emission was filtered at 505−525, 560−600, 660 IF nm, respectively. Percentages of overlap between two markers in the confocal images were quantified using Metamorph offline software version 6-3r7 provided by Molecular Devices (Downingtown, PA).

RESULTS

Synthesis and Characterization of G7 PAMAM/AlexaFluor 488 Conjugates with Various Surface End Groups. G7 PAMAM dendrimers were conjugated with AF488 dye to allow confocal laser scanning microscopy (CLSM) studies. AF488 was chosen for this study because this fluorophore is known to exhibit brighter fluorescence and greater photostability than other spectrally similar fluorophores (300% more photostable than fluorescein (FITC) at 90 s exposure) as well as greater pH insensitivity between pH 4.0 and 10.0 (*35*). The synthesis scheme for the conjugates is illustrated in Figure 2. ^{1}H NMR spectra for all three conjugates are provided in the Supporting Information (Figure S1). After conjugation with AF488, characteristic peaks for the conjugated dyes molecules appear in the range of δ 6.8−8.4 ppm. The ^{1}H NMR spectrum of G7-AF488-Ac (Figure S1c) is consistent with the previously published spectra using G5 PAMAM (*31*). UV/vis spectra reveal that maximum absorbance of AF488 shifted from 495 to 497 nm after conjugation with the dendrimer. Calculated molar extinction coefficients decrease with the increase of molecular weights of the conjugates providing a rough guide when the surface modification from primary amine end groups to acetamide and carboxylate end groups is successfully performed (see Table 1).

HPLC chromatograms of the prepared G7 PAMAM dendrimer conjugates are provided in Supporting Information (Figure S2). All the conjugates exhibit a single peak and it is notable that no peak is present for free AF488 in the chromatograms. The peak widths at half-height of all the dendrimers range from 0.49 to 0.62 min indicating that the dendrimer conjugates are relatively monodisperse compared to other types of condensation polymers with molecular weights of >100 000 g/mol. This is consistent with GPC results presented in Table 1 (*32*). In order to provide an even more stringent assessment of polymer homogeneity, the same materials were characterized using CE (*9, 33, 36*−*38*). The G7-NH_2 dendrimer exhibits multiple peaks which persist, with a change in relative magnitude, after conjugation with AF488 (Figure S3b). After surface modification with acetamide and carboxylate groups is performed, the dendrimer conjugates produce sharper peaks, although a multiple peak structure is still apparent for G7-AF488-Ac.

Cytotoxicity of Dendrimer Conjugates as Measured by XTT Assays. The cytotoxicity of the G7 PAMAM conjugates on KB, Rat2, and C6 cells *in vitro* was explored using XTT assay (Figure 3). The KB cell line, a variant of the human HeLa

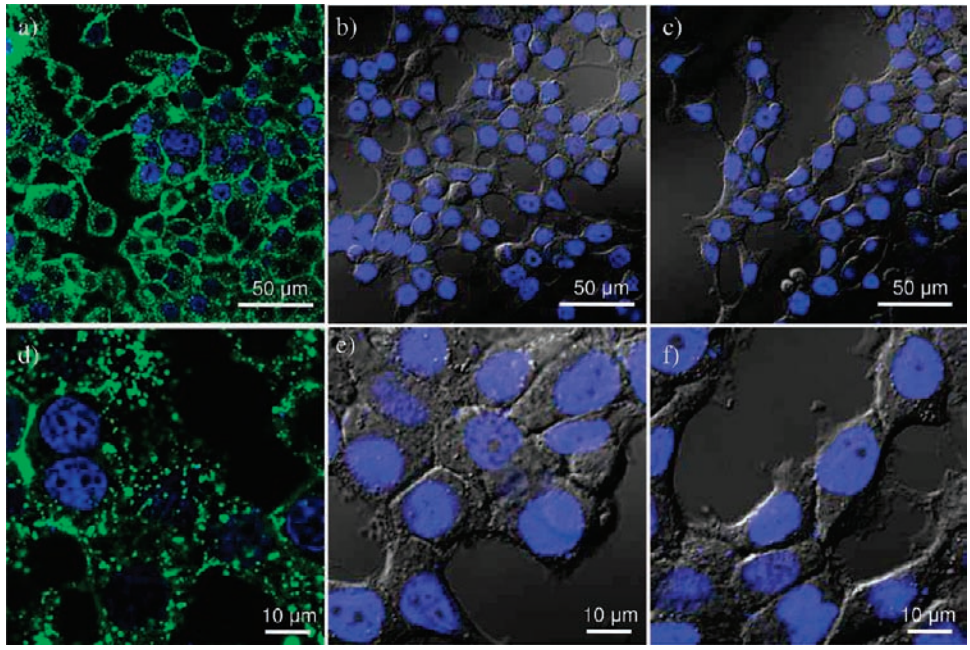

Figure 5. Confocal images of Rat2 cells after exposure to (a) G7-AF488-NH_2, (b) G7-AF488-Ac, and (c) G7-AF488-COOH at 37 °C for 1 h. The concentration of the dendrimer conjugates was at 200 nM. Images e, f, and g are digitally enlarged images of a, b, and c, respectively. Images b, c, e, and f are overlays of confocal and DIC images. Cell nuclei were stained by DAPI resulting in blue fluorescence in the images.

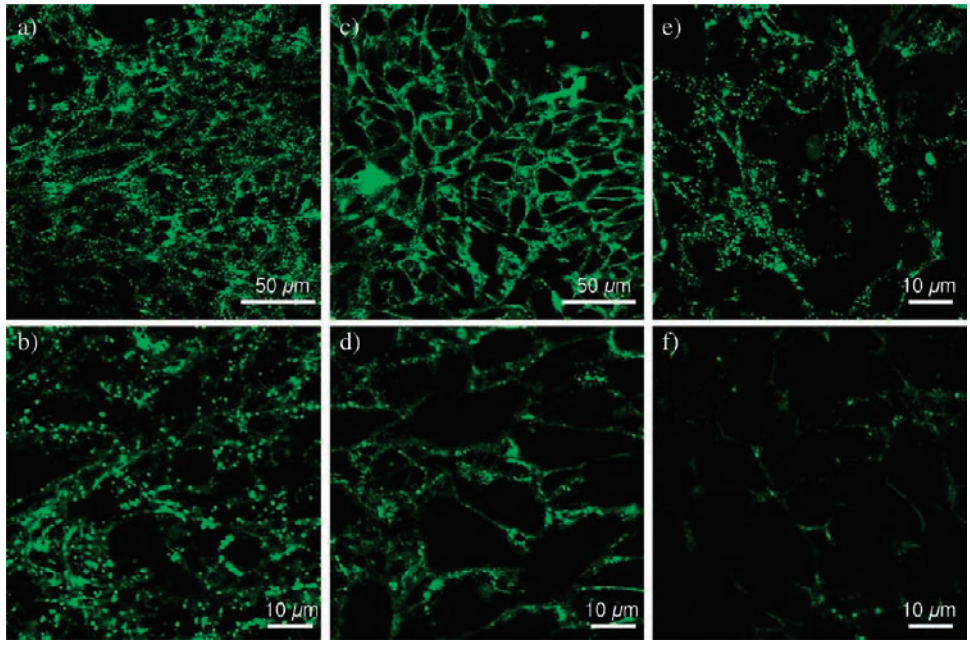

Figure 6. Confocal images of Rat2 cells after incubation with G7-AF488-NH_2 at (a) 37 °C and (c) 4 °C, both for 1 h. Images b and d are enlarged images of a and c, respectively. Concentration of the dendrimer conjugates was 200 nM. Note that G7-AF488-NH_2 penetrates into the cells even at the low temperature. Controls using G5-FITC-NH_2 at (e) 37 °C and (f) 4 °C.

line, and the Rat2 cell line, a dermal fibroblast from Fisher Rat, were selected because they are adherent and robust cell lines enabling us to employ various biological techniques. The C6 cell line was selected because it contains caveolin-1 but lacks GM_1 in the plasma membrane.

Amine-terminated G7 PAMAM dendrimers show a degree of cytotoxicity (~20% toxicity) starting at a concentration of ~400 nM, whereas G5 PAMAMs are not cytotoxic at a concentration as high as 1 μM in both KB and Rat2 cells. These results are consistent with our previous report, which concluded that the cytotoxicity of the PAMAM dendrimers is highly dependent on the size of the macromolecules (9). Surface modification of the starting dendrimers dramatically reduces their cytotoxicity. As shown in Figure 3a,b, G7-AF488-Ac, G7-AF488-COOH, G5-6T-FA (cancer cell targeting dendritic nanodevices), and G5-6T-Ac do not show any significant toxic effect on both cell lines at the concentration range used in the experiment. The effect of the presence of GM_1 in the cell plasma membrane on cytotoxicity was explored using the C6 cell line (Figure 3C,D). The C6 cells exhibited a greater sensitivity to G5-NH_2 and G7-NH_2 exposure, but no differential effect was observed as a function of the presence of GM_1 in the membrane.

Induction of Membrane Permeability as Measured by LDH Assays. The effect of GM_1 on the release of lactate dehydrogenase (LDH) was explored using C6 cells (Figure 4). LDH release was independent of the presence of GM_1 in the

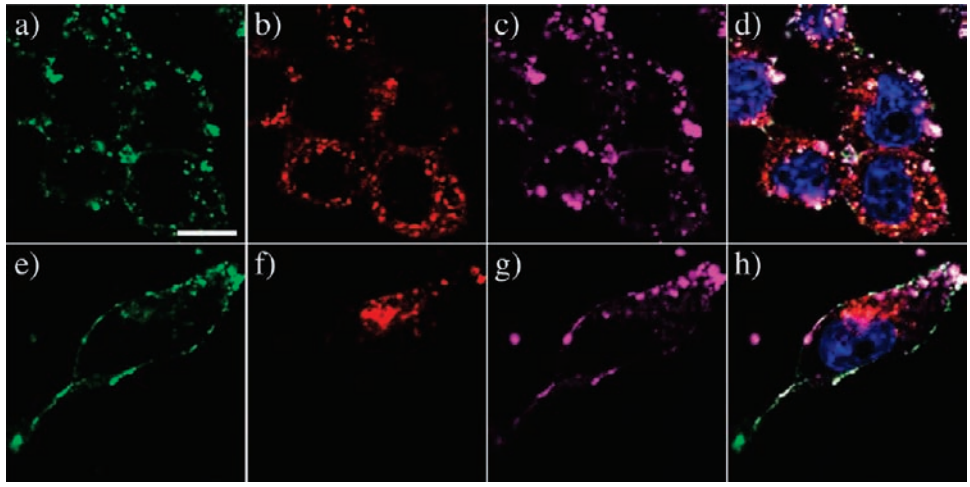

Figure 7. Confocal images of KB cells incubated for 1 h with (a) 200 nM G7-AF488-NH_2, (b) 50 μg/mL transferrin-AlexaFluor 546 (TF-AF546), and (c) 10 μg/mL cholera toxin subunit B-Alexa Fluor 647 (CTB-AF647) conjugates, and (d) a merged image of those. Green, red, and purple fluorescence, respectively, represent G7-AF488-NH_2, TF-AF546, and CTB-AF647. Images e, f, g, and h are a data set of Rat2 cells at the same condition with KB cells. Note that dendrimers are colocalized intracellularly with CTB in both cell lines. Bar: 10 μm.

cell plasma membrane for exposure to G5-NH_2 and G7-NH_2. By way of contrast, the acetylated forms of the dendrimer, G5-Ac and G7-Ac, did not exhibit a concentration-dependent release of LDH.

CLSM Observation: Surface Group Dependence on Dendrimer Internalization. Figure 5 shows confocal images of Rat2 cells after exposure to G7-AF488-NH_2, G7-AF488-Ac, and G7-AF488-COOH at 37 °C, 5% CO_2, for 1 h. The cell nuclei were stained with DAPI and appear as blue fluorescence in the images. Figure 5d,e,f represents digitally enlarged images of Figure 5a,b,c, respectively. As shown in Figure 5a and d, and confirmed by *z*-stack images, G7-AF488-NH_2 readily internalizes into the cells resulting in a punctate distribution of strong green fluorescence. On the other hand, surface-modified dendrimers (G7-AF488-Ac and G7-AF488-COOH) do not interact with the cell membrane or internalize into the cells (Figure 5b,c,e,f). This is consistent with the XTT and LDH assay results shown in Figures 3 and 4 as well as previously published AFM results indicating that G7-NH_2 is the most active with supported lipid bilayers (*24*, *25*). These results stand in stark contrast to CHARM/MD studies that suggest that all three dendrimers should interact strongly with a lipid bilayer (*39*, *40*). To clearly show cell morphology, differential interference contrast (DIC) images of the cells incubated with G7-AF488-Ac and G7-AF488-COOH were overlapped with confocal fluorescence images in those images. Similar results were obtained using KB cells as well (data not shown).

CLSM Observation: Effect of Low-Temperature on G7-NH_2 Internalization. Figure 6 illustrates confocal images of Rat2 cells after incubation with G7-AF488-NH_2 and G5-FITC-NH_2 at both 37 and 4 °C. As shown in Figure 6e,f, G5-FITC-NH_2 penetrates into the cells at 37 °C, whereas they do not internalize but associate with cell plasma membranes at 4 °C, which is in good agreement with previously published images (*9*). Although G7-AF488-NH_2 internalization is reduced at the lowered temperature by ~60% as measured by FACS, the dendrimers internalize into the cells not only at 37 °C, but also at 4 °C as shown in Figure 6a,b. It can be more clearly observed in the enlarged image (Figure 6d). *Z*-stack images of Figure 6d also confirm internalization of the dendrimers (data not shown). The intracellular distribution pattern of fluorescence in Figure 6d is slightly different from that of Figure 6b. Less punctate distribution of the dendrimers in the cytosol is observed in Figure 6d (the low-temperature case) as compared to intracellular distribution of the dendrimers in Figure 6b.

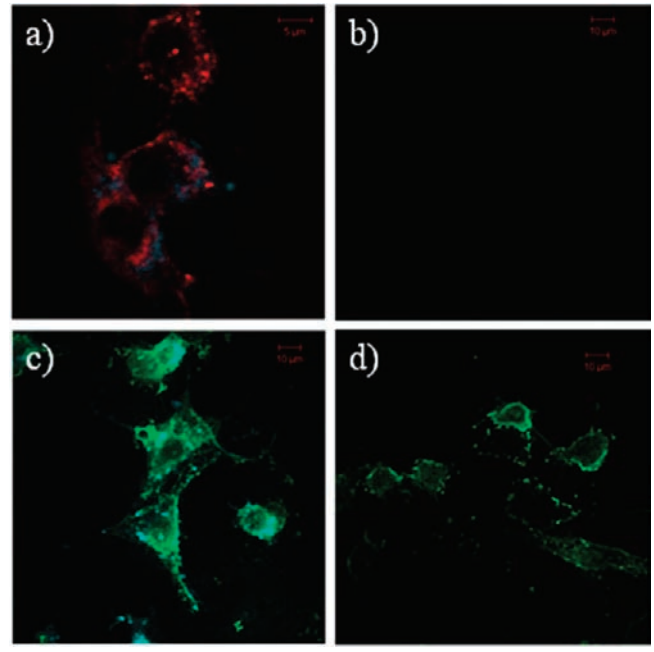

Figure 8. Confocal images of (a) C6 cells having GM_1-pyrene (blue) treated with Cholera toxin subunit B (CTB)-AF647(red), (b) C6 cells without GM_1 treated with CTB, (c) C6 cells having GM_1-pyrene (blue) treated with G7-NH_2-AF488 (green) PAMAM dendrimer, and (d) C6 cells without GM_1 treated with G7 dendrimer. All incubations were for 1 h. CTB is internalized only when GM_1 is present in the cell membrane. G7-NH_2 dendrimer is internalized independent of the presence of GM_1 in the cell membrane.

CLSM Observation: Intracellular Colocalization of G7-NH_2 with Endocytic Markers. The generally reported endocytic pathways for large molecules such as biomedical polymers and cell-penetrating peptides (CPPs) include clathrin-dependent and lipid raft-mediated endocytosis (*2*, *41*). We employed commonly used endocytic markers, transferrin for clathrin-dependent pathways and CTB for lipid raft-mediated endocytosis, to explore the mechanism of dendrimer uptake (*41*, *42*). Direct observation of intracellular localization of the markers using CLSM was enabled by employing markers labeled by different AlexaFluors. As shown in Figure 7, G7-AF488-NH_2 (green fluorescence) is colocalized with CTB-AF647 (purple fluorescence), whereas intracellular localization of TF-AF546 is different from those of dendrimers and CTB in both KB and

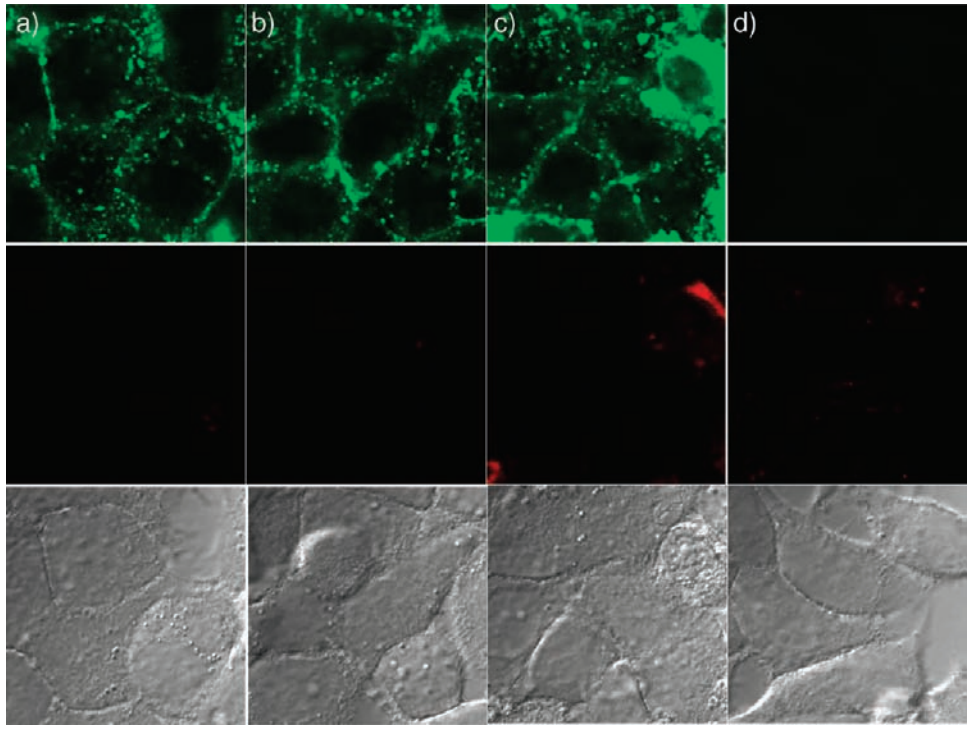

Figure 9. Confocal images of KB cells coincubated for 1 h with (a) 100 nM, (b) 200 nM, and (c) 400 nM G7-AF488-NH_2 and 1 μM G5-6T-Ac. Image d shows KB cells incubated with 1 μM G5−6T-Ac only. Note that red fluorescence should be detected if G7-AF488-NH_2 induces diffusion of G5-6T-Ac into the cells. However, no noticeable signal from G5-6T-Ac is observed. First row, green fluorescence channel detecting G7-AF488-NH_2; second row, red fluorescence channel detecting G5-6T-Ac; and third row, DIC images of each sample. Bar: 50 μm.

Rat2 cells. The quantified pixel counts for overlapped pixels using Metamorph software indicate that the colocalization between G7-AF488-NH_2 and CTB-AF647 is 88% and 68% for KB and Rat2 cells, respectively. In contrast, colocalization as indicated by quantification of overlapped pixels for G7-AF488-NH_2 and TF-AF546 was 10% and 17% for KB and Rat2 cells, respectively.

Colocalization with CTB is commonly taken as evidence for GM_1 interactions and a raft-mediated endocytosis mechanism (*41*). In order to directly test this hypothesis, internalization of CTB and G7-NH_2 was tested using C6 cells. In their native state, these cells contain little GM_1 in the plasma membrane. However, GM_1 can be added to the membrane via incubation. Consistent with previous reports in the literature (*43*), CTB only internalized into C6 cells that had been preincubated with GM_1. However, G7-NH_2 internalized independent of the presence of GM_1 in the plasma membrane (Figure 8). Recall that the results of both the XTT and LDH assays were independent of the presence of GM_1 in the C6 cell plasma membrane (Figures 3 and 4). The interaction of G7-NH_2 dendrimer and CTB was explored using native polyacrylamide gel electrophoresis employing Coommassie blue staining. The band associated with CTB was no longer present upon mixing the dendrimer with the CTB at ratios from 1:5 to 5:1.

CLSM Observation: Diffusion of Neutral Dendrimers into Cell. Neutral dendrimers (G7-Ac and G5-Ac) do not interact with the cell membrane or internalize into the cell as indicated by LDH and XTT assays (Figures 3 and 4) and CLSM experiments (Figure 5). However, if holes of 5−25 nm were created in the membrane, G5-Ac might be expected to enter the cell via passive diffusion processes. Our previous studies have shown that LDH (135−140 kDa, ∼4.3 nm diameter), propidium iodide, and fluorescein all diffuse across the membrane (*6*). However, as illustrated in Figure 9, 100 nM G7-NH_2 is sufficient to give substantial internalization of dendrimer, but 1 μM G5-6T-Ac still gives no detectable internalization. Previous studies indicate the G7-NH_2 should be about 8 nm in diameter and the G5-6T-Ac should be ∼4−7 nm in diameter (*24*, *44*).

DISCUSSION

Dendrimer/Membrane Interactions and Dendrimer Internalization. Amine-terminated (positively charged) G7 PAMAM dendrimers (G7-NH_2) exhibit cytotoxicity (Figure 3), cause LDH leakage (Figure 4), and internalize into cells (Figures 5−8) at <200 nM concentrations whereas charge neutral and negatively charged G7 PAMAM dendrimers do not. This is interesting because negatively charged PAMAM dendrimers (G7-AF488-COOH), suggested as potential drug delivery vectors (*45*), do not bind or internalize into cells at these concentrations (Figure 5c,f). We previously reported that G7-NH_2 PAMAM dendrimers caused more LDH leakage out of cells at 37 °C than G5-NH_2 indicating that G7-NH_2 is more effective in membrane permeabilization or dendroporation. Furthermore, G7-NH_2 induces LDH leakage at 4 °C, whereas G5-NH_2 does not (*9*). Confocal images also illustrate that G7-NH_2 internalizes into the cells at 4 °C but G5-NH_2 does not (Figure 9). One might argue that the enhanced LDH leakage is caused by cell death, since G7-NH_2 appears to be more cytotoxic than G5-NH_2 (Figure 4). In our concentration range (200 nM), however, G7-NH_2 exhibits minimal cytotoxic effects that are ∼100% viability for KB and >80% viability for Rat2. Consequently, the observed LDH assay and confocal data are taken as evidence for membrane permeabilization as opposed to cell death.

Low temperature has been used in a number of studies to investigate energy (or metabolic activities) dependency of proposed internalization mechanisms. Studies have been published for synthetic polymers and for CPPs (*41*, *42*, *46*). The observation of G7-AF488-NH_2 internalization at 4 °C can be explained by a number of possible mechanisms. One would be energy-independent translocation mechanism as previously

proposed for CPP internalization (*47*). However, lowering temperature prevents G5-NH_2 internalization and partially inhibits G7-NH_2 internalization, indicating that dendrimer internalization is an energy-dependent process. A phase change in the cell plasma membrane from the fluid phase (L_α) to low-temperature gel phase (L^*_β) (*48*) would also inhibit nanoscale hole formation. It has recently been demonstrated using supported lipid bilayers that G7-NH_2 dendrimers only cause nanoscale hole formation in fluid-phase membranes (*23*). This is consistent with other reports indicating the membrane fluidity is related to transport properties in epithelial cells (*49*).

There are several energy-dependent pathways proposed for polycationic polymers including endocytosis via clathrin-coated pits (*50, 51*) and endocytosis via lipid rafts or caveolae (*52, 53*). For this study, we employed transferrin which is a commonly used marker for clathrin-mediated endocytosis and CTB which is a commonly used marker for clathrin-independent lipid raft (or caveolae) mediated endocytosis (*41*). G7-AF488-NH_2 did not show substantial colocalization with transferrin (10% and 17% overlapping for KB and Rat2, respectively), indicating that G7-AF488-NH_2 internalization is not related to the clathrin-dependent pathway. Instead, significant colocalization of G7-AF488-NH_2 with CTB-AF647 was observed (88% and 68% overlapping for KB and Rat2, respectively). Colocalization with CTB implies that G7-AF488-NH_2 localizes in the cell with ganglioside GM_1. However, G7-AF488-NH_2 internalized into C6 cells independent of the presence of the GM_1, and G7-AF488-NH_2 did not colocalize with GM_1-pyrene. This indicates that the colocalization observed by us and others (*16*) is probably related to a dendrimer−CTB interaction and is not related to GM_1 interactions or a raft-mediated endocytosis pathway. The LDH assays for C6 cells show no effect upon the presence or absence of GM_1, indicating the GM_1 is also not important for the mechanism of membrane permeabilization and nanoscale hole formation.

A substantial amount of literature exists supporting polycationic endocytosis as a mechanism for the uptake of polycationic polymers into cells (*16, 41, 54−57*). However, many inconclusive and contradictory experiments can be found in the literature, and the details of the internalization mechanisms have remained elusive. In this paper, we provide direct evidence indicating that a GM_1−dendrimer interaction is not involved in G7-AF488-NH_2 internalization. The best evidence supporting raft-mediated endocytosis for dendrimers, colocalization with CTB, is shown to instead result from a CTB−dendrimer interaction. Our results including nanoscale hole formation in supported lipid bilayers (*23−25*), enzyme leakage and small molecule diffusion in and out of cells (*6, 9*), and G7-AF488-NH_2 internalization at 4 °C do provide an alternative mechanism by which polycationic polymers, and nanoparticles more broadly (*26*), may enter cells: the formation of nanoscale holes in the cell plasma membranes (*8*). The data presented here, and published elsewhere by ourselves and others, do not indicate that the nanoscale hole mechanism should be considered as a replacement for endocytosis mechanisms. Rather, it suggests a competitive process in which both mechanisms are operative. The nanoscale hole hypothesis does provide a straightforward explanation for data that is inconsistent with the endocytosis mechanism, both in this paper and in polycationic polymer endocytosis literature more generally.

ACKNOWLEDGMENT

This project was supported by federal funds from the National Institute of Biomedical Imaging and BioEngineering (R01-EB005028).

Supporting Information Available: 1H NMR, HPLC, and CE characterization data for dendrimer conjugates. This material is available free of charge via the Internet at http://pubs.acs.org.

LITERATURE CITED

(1) Abdallah, B., Sachs, L., and Demeneix, B. A. (1995) Non-viral gene transfer: Applications in developmental biology and gene therapy. *Biol. Cell 85*, 1–7.

(2) Nori, A., and Kopecek, J. (2005) Intracellular targeting of polymer-bound drugs for cancer chemotherapy. *Adv. Drug Delivery Rev. 57*, 609–636.

(3) Patri, A. K., Majoros, I. J., and Baker, J. R. (2002) Dendritic polymer macromolecular carriers for drug delivery. *Curr. Opin. Chem. Biol. 6*, 466–471.

(4) Quintana, A., Raczka, E., Piehler, L., Lee, I., Myc, A., Majoros, I., Patri, A. K., Thomas, T., Mule, J., and Baker, J. R. (2002) Design and function of a dendrimer-based therapeutic nanodevice targeted to tumor cells through the folate receptor. *Pharm. Res. 19*, 1310–1316.

(5) Gillies, E. R., and Frechet, J. M. J. (2005) Dendrimers and dendritic polymers in drug delivery. *Drug Discovery Today 10*, 35–43.

(6) Hong, S., Bielinska, A. U., Mecke, A., Keszler, B., Beals, J. L., Shi, X., Balogh, L., Orr, B. G., Baker, J. R., and Banaszak Holl, M. M. (2004) The interaction of polyamidoamine (PAMAM) dendrimers with supported lipid bilayers and cells: hole formation and the relation to transport. *Bioconjugate Chem. 15*, 774–782.

(7) Hong, S., Hessler, J. A., Banaszak Holl, M. M., Leroueil, P. R., Mecke, A., and Orr, B. G. (2006) Physical interactions of nanoparticles with biological membranes: the observation of nanoscale hole formation. *Chemical Health and Safety 13*, 16–20.

(8) Leroueil, P. R., Hong, S. Y., Mecke, A., Baker, J. R., Orr, B. G., and Holl, M. M. B. (2007) Nanoparticle interaction with biological membranes: Does nanotechnology present a janus face? *Acc. Chem. Res. 40*, 335–342.

(9) Hong, S. P., Leroueil, P. R., Janus, E. K., Peters, J. L., Kober, M. M., Islam, M. T., Orr, B. G., Baker, J. R., and Holl, M. M. B. (2006) Interaction of polycationic polymers with supported lipid bilayers and cells: Nanoscale hole formation and enhanced membrane permeability. *Bioconjugate Chem. 17*, 728–734.

(10) Zhang, S. B., Xu, Y. M., Wang, B., Qiao, W. H., Liu, D. L., and Li, Z. S. (2004) Cationic compounds used in lipoplexes and polyplexes for gene delivery. *J. Controlled Release 100*, 165–180.

(11) Hussain, M., Shchepinov, M. S., Sohail, M., Benter, I. F., Hollins, A. J., Southern, E. M., and Akhtar, S. (2004) A novel anionic dendrimer for improved cellular delivery of antisense oligonucleotides. *J. Controlled Release 99*, 139–155.

(12) Jevprasesphant, R., Penny, J., Attwood, D., and D'Emanuele, A. (2004) Transport of dendrimer nanocarriers through epithelial cells via the transcellular route. *J. Controlled Release 97*, 259–267.

(13) Jevprasesphant, R., Penny, J., Attwood, D., McKeown, N. B., and D'Emanuele, A. (2003) Engineering of dendrimer surfaces to enhance transepithelial transport and reduce cytotoxicity. *Pharm. Res. 20*, 1543–1550.

(14) Kopatz, I., Remy, J. S., and Behr, J. P. (2004) A model for non-viral gene delivery: through syndecan adhesion molecules and powered by actin. *J. Gene Med. 6*, 769–776.

(15) Liu, Z. H., Li, M. Y., Cui, D. F., and Fei, J. (2005) Macro-branched cell-penetrating peptide design for gene delivery. *J. Controlled Release 102*, 699–710.

(16) Manunta, M., Tan, P. H., Sagoo, P., Kashefi, K., and George, A. J. T. (2004) Gene delivery by dendrimers operates via a cholesterol dependent pathway. *Nucleic Acids Res. 32*, 2730–2739.

(17) Manunta, M., Nichols, B. J., Tan, P. H., Sagoo, P., Harper, J., and George, A. J. T. (2006) Gene delivery by dendrimers operates via different pathways in different cells, but is enhanced by the presence of caveolin. *J. Immunol. Methods 314*, 134–146.

(18) Seib, F. P., Jones, A. T., and Duncan, R. (2007) Comparison of the endocytic properties of linear and branched PEIs, and cationic PAMAM dendrimers in B16f10 melanoma cells. *J. Controlled Release 117*, 291–300.

(19) Kandyba, A. G., Kozlov, A. M., Somova, O. G., and Dyatlovitskaya, E. V. (2008) A comparative study of sphingolipids in transplanted melanomas with high and low metastatic activity. *Russ. J. Bioorg. Chem. 34*, 230–233.

(20) Kitchens, K. M., Kolhatkar, I. B., Swaan, P. W., and Ghandehari, H. (2008) Endocytosis inhibitors prevent poly(amidoamine) dendrimer internalization and permeability across Ceco-2 cells. *Mol. Pharmaceutics 5*, 364–369.

(21) Perumal, O. P., Inapagolla, R., Kannan, S., and Kannan, R. M. (2008) The effect of surface functionality on cellular trafficking of dendrimers. *Biomaterials 29*, 3469–3476.

(22) Mecke, A., Lee, D. K., Ramamoorthy, A., Orr, B. G., and Banaszak Holl, M. M. (2005) Membrane thinning due to antimicrobial peptide binding - An AFM study of MSI-78 in DMPC bilayers. *Biophys. J. 89*, 4043–4050.

(23) Mecke, A., Lee, D.-K., Ramamoorthy, A., Orr, B. G., and Banaszak Holl, M. M. (2005) Synthetic and natural polycationic polymer nanoparticles interact selectively with fluid-phase domains of DMPC bilayers. *Langmuir 21*, 8588–8590.

(24) Mecke, A., Majoros, I., Patri, A. K., Baker, J. R., Banaszak Holl, M. M., and Orr, B. G. (2005) Lipid bilayer disruption by polycationic polymers: the roles of size and chemical functional group. *Langmuir 21*, 10348–10354.

(25) Mecke, A., Uppuluri, S., Sassanella, T. J., Lee, D. K., Ramamoorthy, A., Baker, J. R., Orr, B. G., and Banaszak Holl, M. M. (2004) Direct observation of lipid bilayer disruption by poly(amidoamine) dendrimers. *Chem. Phys. Lipids 132*, 3–14.

(26) Leroueil, P. R., Berry, S. A., Duthie, K., Han, G., Rotello, V. M., McNerny, D. Q., Baker, J. R., Orr, B. G., and Holl, M. M. B. (2008) Wide varieties of cationic nanoparticles induce defects in supported lipid bilayers. *Nano Lett. 8*, 420–424.

(27) Oberdorster, G., Oberdorster, E., and Oberdorster, J. (2005) Nanotoxicology: An emerging discipline evolving from studies of ultrafine particles. *Environ. Health Perspect. 113*, 823–839.

(28) Karoonuthaisiri, N., Titiyevskiy, K., and Thomas, J. L. (2003) Destabilization of fatty acid-containing liposomes by. polyamidoamine dendrimers. *Colloids Surf., B 27*, 365–375.

(29) Zhang, Z.-Y., and Smith, B. D. (2000) High-generation polycationic dendrimers are unusually effective at disrupting anionic vesicles: membrane bending model. *Bioconjugate Chem. 11*, 805–814.

(30) Patri, A. K., Myc, A., Beals, J., Thomas, T. P., Bander, N. H., and Baker, J. R. (2004) Synthesis and in vitro testing of J591 antibody-dendrimer conjugates for targeted prostate cancer therapy. *Bioconjugate Chem. 15*, 1174–1181.

(31) Majoros, I. J., Keszler, B., Woehler, S., Bull, T., and Baker, J. R. (2003) Acetylation of poly(amidoamine) dendrimers. *Macromolecules 36*, 5526–5529.

(32) Islam, M. T., Shi, X. Y., Balogh, L., and Baker, J. R. (2005) HPLC separation of different generations of poly(amidoamine) dendrimers modified with various terminal groups. *Anal. Chem. 77*, 2063–2070.

(33) Shi, X. Y., Lesniak, W., Islam, M. T., Muniz, M. C., Balogh, L. P., and Baker, J. R. (2006) Comprehensive characterization of surface-functionalized poly (amidoamine) dendrimers with acetamide, hydroxyl, and carboxyl groups. *Colloids Surf., A 272*, 139–150.

(34) Thomas, T. P., Myaing, M. T., Ye, J. Y., Candido, K., Kotlyar, A., Beals, J., Cao, P., Keszler, B., Patri, A. K., Norris, T. B., and Baker, J. R. (2004) Detection and analysis of tumor fluorescence using a two-photon optical fiber probe. *Biophys. J. 86*, 3959–3965.

(35) Banks, P. R., and Paquette, D. M. (1995) Comparison of 3 common amine reactive fluorescent-probes used for conjugation to biomolecules by capillary zone electrophoresis. *Bioconjugate Chem. 6*, 447–458.

(36) Shi, X. Y., Banyai, I., Lesniak, W. G., Islam, M. T., Orszagh, I., Balogh, P., Baker, J. R., and Balogh, L. P. (2005) Capillary electrophoresis of polycationic poly(amidoamine) dendrimers. *Electrophoresis 26*, 2949–2959.

(37) Shi, X. Y., Majoros, I. J., Patri, A. K., Bi, X. D., Islam, M. T., Desai, A., Ganser, T. R., and Baker, J. R. (2006) Molecular heterogeneity analysis of poly(amidoamine) dendrimer-based mono- and multifunctional nanodevices by capillary electrophoresis. *Analyst 131*, 374–381.

(38) Shi, X. Y., Patri, A. K., Lesniak, W., Islam, M. T., Zhang, C. X., Baker, J. R., and Balogh, L. P. (2005) Analysis of poly(amidoamine)-succinamic acid dendrimers by slab-gel electrophoresis and capillary zone electrophoresis. *Electrophoresis 26*, 2960–2967.

(39) Kelly, C. V., Leroueil, P. R., Nett, E. K., Wereszczynski, J. M., Baker, J. R., Orr, B. G., Holl, M. M. B., and Andricioaei, I. (2008) Poly(amidoamine) dendrimers on lipid bilayers I: Free energy and conformation of binding. *J. Phys. Chem. B 112*, 9337–9345.

(40) Kelly, C. V., Leroueil, P. R., Orr, B. G., Holl, M. M. B., and Andricioaei, I. (2008) Poly(amidoamine) dendrimers on lipid bilayers II: Effects of bilayer phase and dendrimer termination. *J. Phys. Chem. B 112*, 9346–9353.

(41) Foerg, C., Ziegler, U., Fernandez-Carneado, J., Giralt, E., Rennert, R., Beck-Sickinger, A. G., and Merkle, H. P. (2005) Decoding the entry of two novel cell-penetrating peptides in HeLa cells: Lipid raft-mediated endocytosis and endosomal escape. *Biochemistry 44*, 72–81.

(42) Richard, J. P., Melikov, K., Vives, E., Ramos, C., Verbeure, B., Gait, M. J., Chernomordik, L. V., and Lebleu, B. (2003) Cell-penetrating peptides - A reevaluation of the mechanism of cellular uptake. *J. Biol. Chem. 278*, 585–590.

(43) Spiegel, S. (1988) Insertion of ganglioside GM_1 into rat glioma C6 cells renders them susceptible to growth-inhibition by the B-subunit of cholera-toxin. *Biochim. Biophys. Acta 969*, 249–256.

(44) Prosa, T. J., Bauer, B. J., Amis, E. J., Tomalia, D. A., and Scherrenberg, R. (1997) A SAXS study of the internal structure of dendritic polymer systems. *J. Polym. Sci., Part B: Polym. Phys. 35*, 2913–2924.

(45) Wiwattanapatapee, R., Carreño-Gómez, B., Malik, N., and Duncan, R. (2000) Anionic PAMAM dendrimers rapidly cross adult rat intestine in vitro: a potential oral delivery system? *Pharm. Res. 17*, 991–998.

(46) Thorén, P. E. G., Persson, D., Esbjorner, E. K., Goksor, M., Lincoln, P., and Norden, B. (2004) Membrane binding and translocation of cell-penetrating peptides. *Biochemistry 43*, 3471–3489.

(47) Wadia, J. S., and Dowdy, S. F. (2002) Protein transduction technology. *Curr. Opin. Biotechnol. 13*, 52–56.

(48) Janiak, M. J., Small, D. M., and Shipley, G. G. (1979) Temperature and compositional dependence of the structure of hydrated dimyristoyl lecithin. *J. Biol. Chem. 254*, 6068–6078.

(49) Le Grimellec, C., Friedlander, G., Elyandouzi, E., Zlatkine, P., and Giocondi, M. C. (1992) Membrane fluidity and transport-properties in epithelia. *Kidney Int. 42*, 825–836.

(50) Vendeville, A., Rayne, F., Bonhoure, A., Bettache, N., Montcourrier, P., and Beaumelle, B. (2004) HIV-1 Tat enters T cells using coated pits before translocating from acidified endosomes and eliciting biological responses. *Mol. Biol. Cell 15*, 2347–2360.

(51) Schmid, S. L. (1997) Clathrin-coated vesicle formation and protein sorting: An integrated process. *Annu. Rev. Biochem. 66*, 511–548.

(52) Simons, K., and Ikonen, E. (1997) Functional rafts in cell membranes. *Nature 387*, 569–572.

(53) Brown, D. A., and London, E. (1998) Functions of lipid rafts in biological membranes. *Annu. Rev. Cell Dev. Biol. 14*, 111–136.
(54) Parton, R. G., and Richards, A. A. (2003) Lipid rafts and caveolae as portals for endocytosis: New insights and common mechanisms. *Traffic 4*, 724–738.
(55) Apodaca, G. (2001) Endocytic traffic in polarized epithelial cells: Role of the actin and microtubule cytoskeleton. *Traffic 2*, 149–159.
(56) Fischer, R., Kohler, K., Fotin-Mleczek, M., and Brock, R. (2004) A stepwise dissection of the intracellular fate of cationic cell-penetrating peptides. *J. Biol. Chem. 279*, 12625–12635.
(57) Bieber, T., Meissner, W., Kostin, S., Niemann, A., and Elsasser, H. P. (2002) Intracellular route and transcriptional competence of polyethylenimine-DNA complexes. *J. Controlled Release 82*, 441–454.

BC900029K

Supplementary Material for

Exploring Membrane Porosity and Cellular Internalization Mechanisms of Poly(amidoamine) Dendrimers: the Role of Sphingolipid GM_1

*Seungpyo Hong,[1,6,†] Rahul Rattan,[5,6,†] István J. Majoros,[6] Douglas G. Mullen,[1,6] Jennifer L. Peters,[6] Xiangyang Shi,[6] Ania Bielinska,[6] Luz Blanco,[6] Bradford G. Orr,[3,6] James R. Baker, Jr.,[5,6] and Mark M. Banaszak Holl[*1,2,4,6]*

Programs in [1]Macromolecular Science and Engineering and [2]Biophysics, Departments of [3]Physics and [4]Chemistry, [5]Biomedical Engineering, and [6]Michigan Nanotechnology Institute for Medicine and Biological Sciences, University of Michigan, Ann Arbor, MI 48109

TITLE RUNNING HEAD: Dendrimer Interaction with Cells

[*]To whom correspondence should be addressed

Professor Mark M. Banaszak Holl
Programs in Macromolecular Science and Engineering, Applied Physics,
Biophysics, and Dept. of Chemistry, University of Michigan
930 N. University Avenue
Ann Arbor, MI 48109-1055
Phone: (734) 763-2283
Fax: (734) 763-2307
Email: mbanasza@umich.edu

† These authors made an equal contribution to this work.

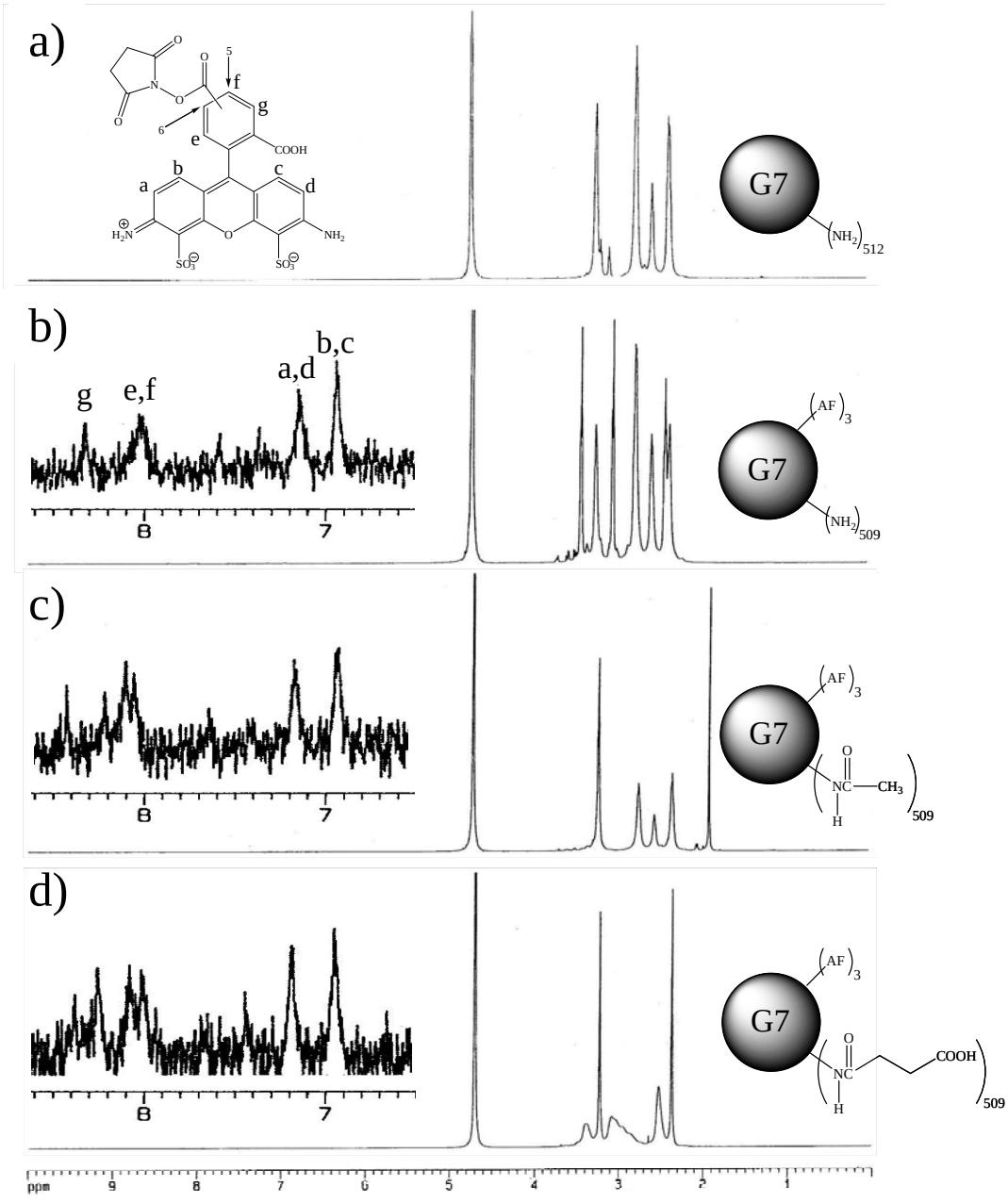

Figure S1. ^{1}H NMR spectra of a) starting G7 PAMAM dendrimers (G7-NH_2), b) G7-AF488 conjugates with amine end groups (G7-AF488-NH_2), c) G7-AF488 conjugates with acetamide end groups (G7-AF488-Ac), and d) G7-AF488 conjugates with carboxylate end groups (G7-AF488-COOH). Inset spectra are enlarged characteristic peaks of AlexaFluor®488.

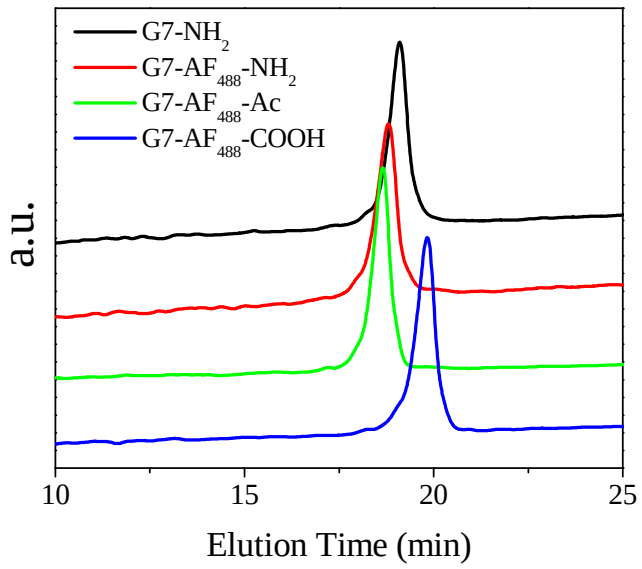

Figure S2. HPLC chromatograms of the dendrimer based conjugates. All the curves are normalized based on the peak intensity of G7-NH_2.

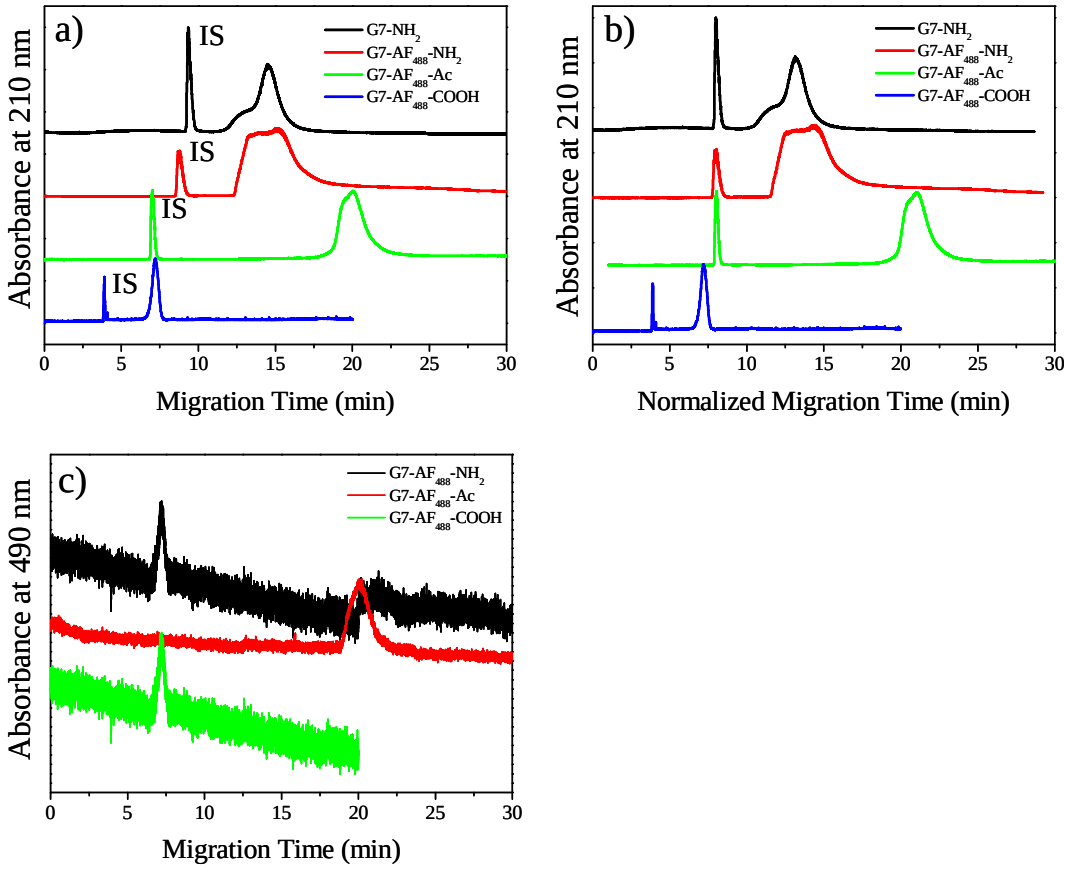

Figure S3. a) CE electropherograms and b) their normalized electropherograms of the dendrimer based conjugates; G7-NH_2, G7-AF488-NH_2, G7-AF488-Ac, and G7-AF488-COOH measured at 210 nm (based on PAMAM dendrimers). Note that 2,3-diaminopyridine (2, 3-DAP) is used as an internal standard (IS) for G7-NH_2, G7-AF488-NH_2, and G7-AF488-Ac. Thus only three curves are normalized in b) based on the IS peak appearance. For G7-AF488-COOH, 4-Methoxybenzyl alcohol (MBA) is used as a neutral marker. Also note that the data of G7-AF488-COOH is shown only up to a 20 min time point because no additional peak was observed thereafter. c) Electropherogram of G7-AF488-NH_2, G7-AF488-Ac, and G7-AF488-COOH measured at 490 nm (based on attached AF488). Peak heights are normalized based on the G7-AF488-NH_2.

Solid Phase 4′-Phosphopantetheinylation: Fungal Thiolation Domains are Targets for Chemoenzymatic Modification

Deirdre Stack, Aisling Frizzell, Karen Tomkins, and Sean Doyle*

National Institute for Cellular Biotechnology, Department of Biology, National University of Ireland Maynooth, Co. Kildare, Ireland. Received February 13, 2009; Revised Manuscript Received June 18, 2009

No data exist on the ability of thiolation domains from fungal non-ribosomal peptide synthetases to undergo 4′-phosphopantetheinylation, using either biotinylated or fluorescently labeled coenzyme A analogues, mediated by 4′-phosphopantetheinyl transferases (PPTase). Yet, this is a key requirement to confirm the amino acid recognition function, and coding potential, of either non-ribosomal peptide synthetases or recombinantly expressed regions of these enzymes (e.g., didomains or modules). Moreover, determination of 4′-phosphopantetheinylation activity remains cumbersome. Here, we demonstrate that a recombinant fungal PPTase catalyzes the solution-phase transfer of either biotin- or fluorescein-labeled 4′-phosphopantetheine region of coenzyme A to a fungal thiolation domain, which is either part of a non-ribosomal peptide synthetase didomain (72 kDa), derived from *Aspergillus fumigatus*, or fused to a non-native protein (glutathione *s*-transferase). Significantly, we demonstrate that this reaction can unexpectedly occur when the target protein (4.4 pmol) is immobilized on a solid surface. These findings (i) confirm that thiolation domains of fungal origin, in native or non-native configuration, can accept modified 4′-phosphopantetheine residues via PPTase-mediated labeling and (ii) illustrate a novel, high-throughput method to determine PPTase activity.

INTRODUCTION

Phosphopantetheinyl transferases (PPTase) catalyze the transfer of 4′-phosphopantetheine from coenzyme A (CoA) to the carrier domain of a range of enzymes involved in non-ribosomal peptide, polyketide, and fatty acid biosynthesis (*1*). Non-ribosomal peptide (NRP) synthetases are produced in the inactive (apo-) form and are post-translationally modified by PPTase to the active (holo-) form by the covalent attachment of CoA-derived 4′-phosphopantetheine to a reactive serine residue in thiolation (T) domains (also referred to as peptidyl carrier protein (PCP)) within the NRP synthetase (*2*). Initial strategies for assaying 4′-phosphopantetheinylation involved the use of [^{3}H]-pantetheine CoA and liquid scintillation counting (*3*), HPLC separation, and analysis of purified proteins (*4*). More recently, the application of protein mass spectrometry for the determination of apoenzyme 4′-phosphopantetheinylation has been reported (*2, 5*). These conventional methods for assaying PPTase activity, however, can be costly and cumbersome and significantly limit high-throughput operations (*6*).

An elegant method of covalently labeling T/PCP domains of NRP synthetases, using biotinylated or fluorescently labeled CoA, and a recombinant *Bacillus subtilis* encoded PPTase, Sfp, in PPTase-mediated reactions has been described (*6*). These authors used Sfp to catalyze modification of carrier proteins with a single fluorescent or affinity reporter, providing a sensitive means of protein visualization, Western blot identification, and affinity purification. This labeling technique also has utility in the identification of carrier protein domains from lysates of native cultures, as a proportion of carrier proteins in the lysate may be present in an unmodified inactive state. Application of the technique to the 6-deoxyerythronolide B synthase (DEBS) pathway from *Saccharapolyspora erythraea* resulted in the identification of a 150 kDa protein indicative of native DEBS (*6*).

The ability of PPTases to post-translationally modify carrier proteins using low molecular mass chemical labels represents a novel and efficient tool for protein labeling and has significant implications in biomolecular research. This approach has been adapted to fluorescence imaging of cellular events involving transferrin-mediated iron uptake (*7*) where the transferrin receptor 1 (TfR1) was fused to a PCP, and the resultant TfR1-PCP fusion specifically labeled with a fluorophore via the action of Sfp. In an independent study, an 11-residue peptide, DSLE-FIASKLA, predicted to be a suitable target for modification by the *B. subtilis* Sfp was fused to the C- and N-termini of target protein and subsequently labeled with a biotin tag by the PPTase (*8*). The majority of reporter labeling of carrier proteins by promiscuous PPTases have been limited to *in vitro* and cell surface protein labeling (*9*−*11*). A chemoenzymatic route to protein modification *in vivo* using a fluorescent marker has also been reported (*12*). This mechanism centered on the ability of native enzymes present in *E. coli*, CoAA, and CoAD and CoAE to sequentially modify a fluorescent pantetheine analogue to result in a fluorescently labeled CoA analogue. Coexpression of the carrier protein *VibB* and the PPTase Sfp in the presence of the fluorescent pantetheine analogue resulted in the fluorescent modification of the VibB carrier protein *in vivo*.

The PPTase-mediated modification of bacterial pyochelin NRP synthetase carrier proteins PchE and PchF using fluorescein (Fl)-CoA analogues has also been reported (*13*). These *in vitro* 4′-phosphopantetheinylation assays used 2 μM *B. subtilis* Sfp, 300 μM Fl-CoA, and PchE/ PchF carrier proteins at concentrations of 10 and 21 μM, respectively. The detection of the modified carrier proteins in this study was enabled by Fourier transform mass spectrometry whereby mass shifts were observed for reporter labeled peptides.

In vitro 4′-phosphopantetheinylation assays have been used to investigate the effect of inhibitors on PPTase activity (*14*).

* Corresponding author. Professor Sean Doyle, National Institute for Cellular Biotechnology, Department of Biology, National University of Ireland Maynooth, Co. Kildare, Ireland. Tel: +353-1-7083858, Fax: +353-1-7083845, E-mail: sean.doyle@nuim.ie.

10.1021/bc900071j CCC: $40.75 © 2009 American Chemical Society
Published on Web 07/23/2009

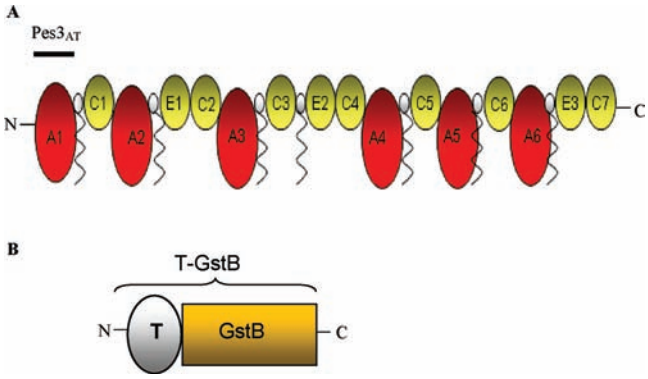

Figure 1. Diagrammatic representation of (A) Pes3 domain architecture, and (B) thiolation (T)-GstB fusion protein. The first adenylation domain and thiolation domain from module 1 of Pes3 ($Pes3_{AT}$) were selected for recombinant protein production. Wavy lines shown in A indicate covalently tethered phosphopantetheine moieties to T domains (shaded). The T-GstB fusion protein is also illustrated showing the Pes3 thiolation domain (T) fused to the GstB protein. The N- and C-termini of both proteins are indicated.

Here, the efficacy of novel anthranilic acid inhibitors of the *B. subtilis* acyl carrier protein synthase (AcpS), which catalyzes the transfer of 4′-phosphopantetheinyl group from CoA onto a conserved serine residue present on an *E. coli* acyl carrier protein (ACP), was assessed and found to exhibit IC_{50} (μM) values of 0.82−32.3. The effect of these inhibitors was determined in a solution phase assay format, which involved incubation of the AcpS (a PPTase) in the presence of a GST-linked ACP carrier protein and a biotin-CoA reporter analogue at room temperature. Detection of the biotin-labeled ACP was achieved by an overnight incubation with streptavidin−allophycocyanin conjugate followed by time-resolved fluorescence detection.

A PPTase from *Aspergillus fumigatus* has recently been expressed in, and purified from, recombinant baculovirus infected *Spodoptera frugiperda*$_9$ (Sf_9) insect cell supernatants. Subsequent mass spectrometric detection of a 4′-phosphopantetheinylated peptide confirmed that this secreted PPTase post-translationally modified a recombinant NRP synthetase T domain from *A. fumigatus* Pes1 in the presence of CoA (*2*). To date, the compatibility of this fungal PPTase has not been demonstrated with modified CoA derivatives; moreover, limited amounts of the secreted PPTase has hindered complete enzyme characterization, and the assay systems for detection of 4′-phosphopantetheinylation are cumbersome and time-consuming.

EXPERIMENTAL METHODS

Bioinformatic Analysis. Preliminary sequence data were obtained from The Institute for Genomic Research Website at http://www.tigr.org. The unannotated genome of *Aspergillus fumigatus* was initially investigated to identify open reading frames corresponding to novel NRP synthetases. One open reading frame, which encoded a putative NRP, was identified and was subsequently termed *pes3* (Figure 1).

Fungal DNA Isolation and PCR Amplification. *A. fumigatus* strain ATCC 26933 was grown (250 mL cultures) at 37 °C in minimal essential medium (MEM) (5% (v/v) containing fetal calf serum (FCS)) for 2 days. Genomic DNA was isolated by crushing fungal mycelia in liquid N_2 followed by phenol/chloroform extraction, washing with 70% (v/v) ethanol and final DNA resuspension in 10 mM Tris-HCl, 1 mM EDTA pH 8.0 (200 μL). PCR was carried out using Accu*Taq* LA polymerase (Sigma) using a total of 5 ng of genomic DNA per PCR reaction. PCR reactions also included 10× Accu*Taq* reaction buffer, 0.25 μM of each dNTP, 1.0 μM forward and reverse primer (Table 1) in a total volume of 20 μL. PCR reactions comprised an initial step of 60 s denaturation at 95 °C, followed by 30 cycles consisting of 60 s at 95 °C, 30 s at 55 °C, 90 s at 72 °C, and finally 360 s at 72 °C. Amplicons were analyzed by agarose gel electrophoresis and visualized using an Eagle-Eye II digital still video system (Stratagene, CA, USA). DNA sequence analysis was carried out on a commercial basis by MWG Biotech (Germany).

Table 1. Oligonucleotide Primers Designed for Directional Cloning of *pes3*$_{AT}$ and *T/PCP* Region Sequences into the pProEx-GstB Expression Vector

gene	(F/R)	primer sequences (5′-3′)	amplicon (bp)
pes3$_{AT}$	F	GAGACTCGAGACATACGCCGAACTGGAA	1800
pes3$_{AT}$	R	GAGAAAGCTTAGTGATCGAGGAACGCAA	
T/PCP	F	GAGAGGATCCCATGGAACGCCGGTTGCGAG	196
T/PCP	R	GAGAGAATTCTGCGAGCTCTGTGATGGA	

Cloning and Expression of the Nonribosomal Peptide Synthetase Gene Fragment, *pes3*$_{AT}$. The *pes3*$_{AT}$ amplicon, which is derived from the 5′ end of the entire *pes3* gene (Figure 1), was initially cloned into the TOPO cloning vector and subsequently cloned into pProEx expression vectors (Invitrogen) according to the manufacturer's instructions. pProEx:*pes3*$_{AT}$, the expression vector containing the region encoding the initial AT didomain of *pes3* (*A. fumigatus pes3*$_{AT}$) (Figure 1), was transformed into *E. coli* according to the manufacturer's guidelines (Invitrogen). Protein expression was induced by the addition of isopropyl β-D-1-thiogalactopyranoside (IPTG; 0.6 mM final concentration) and monitored by SDS-PAGE, Western blot analysis using monoclonal antibody reactivity against a His_6 fusion peptide, and MALDI-ToF mass spectrometry (*15*).

Recombinant $Pes3_{AT}$ Purification and Refolding. Recombinant $Pes3_{AT}$ was purified under denaturing conditions using Ni-NTA metal-chelate affinity chromatography in the presence of 6 M guanidine−HCl. Purified recombinant $Pes3_{AT}$ (250 μg/mL) in 50 mM sodium carbonate pH 9.4 containing 6 M guanidine−HCL was serially dialyzed into 50 mM sodium carbonate pH 9.4 containing 8 M urea, then 4 M urea, followed by dialysis into 50 mM sodium carbonate buffer pH 9.4 to facilitate solubilization.

Generation of Recombinant Fusion Protein (T-GstB) Containing the $Pes3_{AT}$ Derived Thiolation Domain. The region encoding the thiolation (PCP) domain from *pes3*$_{AT}$ was fused to *A. fumigatus* glutathione s-transferase B (*gstB* (*16*)) in order to assess the utility of the domain for non-native protein labeling (Figure 1). PCR cloning primers incorporated *Eco*RI and *Hind*III restriction sites to facilitate PCR amplification and directional subcloning of the T region (Table 1). This amplicon (196 bp) was subsequently digested with *Eco*RI and *Hind*III and ligated to the pProEx-*gstB* expression vector (*16*), which had also been digested with *Eco*RI and *Hind*III. The expression vector containing T-GstB was then transformed into *E. coli* DH5α according to refs 16 and 17. Protein expression was induced by the addition of IPTG (0.6 mM final concentration) and monitored by SDS-PAGE and Western blot analysis. Purification of the T-GstB fusion protein was carried out as previously described (*2*).

PPTase Extraction from Infected (Sf_9) Insect Cells. Sf_9 insect cells (5×10^7), previously infected with recombinant baculovirus encoding PPTase (*2*), were resuspended in Ppant buffer (5 mL; 75 mM Tris-HCl, 5 mM dithiothreitol (DTT), and 10 mM $MgCl_2$ pH 8.0) and sonicated (Bandelin Sonopuls, Progen Scientific Ltd., UK) for 3 × 5 s at a maximum power for 5 min with 30 s second intervals on ice. The resultant cell lysates were centrifuged at 10 000*g* for 10 min at 4 °C. The supernatants were removed and analyzed for the presence of PPTase by Western blot analysis. The concentration of protein present in the cell lysate supernatants was determined by

Bradford analysis and the supernatants divided into 0.5 mL aliquots and stored at −20 °C for further use.

For purification of intracellular PPTase, infected Sf_9 insect cells (5×10^7) were resuspended in lysis buffer (5 mL; 50 mM NaH_2PO_4, 300 mM NaCl, 10 mM imidazole pH 8.0) containing 0.05% (w/v) sodium deoxycholate and sonicated (Bandelin Sonopuls, Progen Scientific Ltd., UK) for 3×5 s at a maximum power for 5 min with 30 s intervals on ice and the resultant lysates centrifuged at 10 000*g* for 10 min at 4 °C. Purification proceeded under native conditions using Ni-NTA metal-chelate affinity chromatography. Optimal protein yields were obtained using an optimized batch purification approach which entailed the incubation of the PPTase lysate to the Ni-NTA resin for 2 h with gentle inversion at 4 °C. Subsequently, the protein/resin complex was packed into a column to facilitate washing and elution steps. Purified PPTase was eluted with 250 mM imidazole and subsequently dialyzed into Ppant buffer.

Coenzyme A Analogue Synthesis and Solution Phase PPTase Activity Analysis. Coenzyme A (CoA) was covalently labeled through an available sulfhydral group by reaction with either maleimido-dPEG$_4$-biotin (MB) (Quanta BioDesign Ltd., Ohio, USA) or 5′-iodoacetamidofluorescein (Sigma-Aldrich) according to ref 6 with modifications (Supporting Information). All reactions were allowed to proceed on ice for 30 min, followed by 10 min incubation at room temperature, and terminated by addition of 1 M DTT (1 μL). 4′-Phosphopantetheinylation reactions using PPTase and recombinant $Pes3_{AT}$ were carried out as follows: Reaction mixtures for the *in vitro* 4′-phosphopantetheinylation assay contained $Pes3_{AT}$ (4.4 μM), PPTase (0.08 μM), biotin-CoA (8.4 μM) in 75 mM Tris-HCL, 5 mM DTT, and 10 mM $MgCl_2$, pH 8.0 (final volume: 100 μL). Reaction mixtures were incubated at 37 °C for 1 h. After incubation, reactions were terminated by the addition of 10% (w/v) trichloroacetic acid (900 μL) and centrifuged at 10 000*g* for 10 min. Pellets were resuspended in 1 M Tris-HCl pH 8.0 and analyzed by SDS-PAGE and Western blot analysis, using direct probing with streptavidin−horseradish peroxidase (HRP) (1/500) and ECL chemiluminescent substrate (Pierce Biotechnology), to visualize biotinylated $Pes3_{AT}$. Fluorescence detection was also undertaken by directly scanning SDS-PAGE gels, when fluorescein-CoA (Fl-CoA) (*6*) was employed instead of biotin-CoA (*6*), using a Typhoon variable mode imager (GE Healthcare) at excitation and emission wavelength at 488 and 520 nm, respectively. Scanned gels were subsequently stained with Coomassie Brilliant Blue R. Alternatively, reaction mixtures were directly added to Nunc Maxisorb microwells (1 h), washed using phosphate buffered saline 0.05% (w/v) Tween-20 (PBST), and fluorescence detected using a plate reader (Bio-Tech, Synergy HT) with excitation and emission values of 490 and 520 nm, respectively.

Microwell Coating with Recombinant $Pes3_{AT}$, T-GstB, or GstB for Use in Solid Phase 4′-Phosphopantetheinylation Assays. Microtiter plates were coated with purified recombinant $Pes3_{AT}$ (2 μg/mL) diluted in 50 mM sodium carbonate buffer pH 9.6 containing 0.01% (w/v) sodium dodecyl sulfate (100 μL/well). Plates were incubated at 37 °C for 2 h and washed twice with PBST (200 μL). Blocking solution (1% (w/v) bovine serum albumin and 10% (w/v) sucrose in 50 mM sodium carbonate buffer pH 9.6; 200 μL/well) was applied to the wells and stored at 4 °C overnight. Blocking solution was decanted from plates, and any residual solution was removed by tapping the plate upside down onto adsorbent paper and transferring the plate to a 37 °C incubator for 1 h prior to use. Microwells were also individually coated with the T-GstB and GstB, respectively (5 μg/mL), for subsequent use in the solid phase 4′-phosphopantetheinylation assays. Microwell coating of T-GstB and GstB and subsequent 4′-phosphopantetheinylation assays were carried out as described for $Pes3_{AT}$.

Table 2. Reagent Preparation for Solid Phase 4′-Phosphopantetheinylation Assay[a]

reagent stock solutions	purified PPTase	PPTase crude cell lysate	control cell lysate	biotin CoA control	buffer control
purified PPTase (0.5 μM)	95 μL	−	−	−	−
PPTase lysate (1.7 mg/mL total cell protein)	−	30 μL	−	−	−
control lysate (1.7 mg/mL total cell protein)	−	−	30 μL	−	−
biotin-CoA (109 μm)	5 μL	5 μL	5 μL	5 μL	−
Ppant buffer	−	55 μL	55 μL	95 μL	100 μL

[a] Final reagent concentrations: Biotin-CoA (5.4 μM), PPTase purified from infected Sf_9 cell supernatants (0.48 μM), PPTase cell lysate obtained from infected Sf_9 insect cells (0.51 mg/mL total cell protein), and as a control, cell lysate obtained from un-infected Sf_9 insect cells (0.51 mg/mL total cell protein).

Table 3. Reagent Preparation for Solid Phase 4′-Phosphopantetheinylation Assay (B)[a]

reagents	purified PPTase	PPTase crude cell lysate	control cell lysate	Fl-CoA control	buffer control
purified PPTase (0.5 μM)	95 μL				
PPTase lysate (1.7 mg/mL total cell protein)	−	30 μL	−	−	−
control lysate (1.7 mg/mL total cell protein)	−	−	30 μL	−	−
Fl-CoA (95 μM)	5 μL	5 μL	5 μL	5 μL	−
Ppant buffer	−	60 μL	60 μL	90 μL	100 μL

[a] Final reagent concentrations; Fl-CoA (3.6 μM), PPTase purified from infected Sf_9 cell supernatants (0.48 μM), PPTase cell lysate obtained from infected Sf_9 insect cells (0.51 mg/mL total cell protein), and as a control, cell lysate obtained from un-infected Sf_9 insect cells (0.51 mg/mL total cell protein).

Solid Phase 4′-Phosphopantetheinylation Using Biotin-CoA. Reactants were prepared in triplicate in 1.5 mL microfuge tubes as outlined in Table 2. Aliquots (100 μL) of each sample were placed in wells of 96-well plates (Nunc Maxisorb) which had been previously coated with $Pes3_{AT}$ (2 μg/mL). Plates were incubated for 1 h at room temperature to facilitate enzymatic reaction. Plates were then washed twice with PBST. Streptavidin−HRP (1/2000 dilution; 100 μL/ well) was added and plates incubated at 37 °C for 1 h. Plates were washed 4 times with PBST. Excess liquid was removed from the wells by tapping the plate out on adsorbent paper. Substrate (3,3′,5,5′-tetramethylbenzidine; TMB; 100 μL/well) was applied to the wells and left to develop for 10 min at room temperature. To terminate the reaction, 1 N H_2SO_4 (100 μL) was added to the wells, and the absorbance values read at 450/630 nm using a plate reader (Bio-Tech, Synergy HT).

Solid Phase 4′-Phosphopantetheinylation Using Fl-CoA. Reactants were prepared in triplicate in 1.5 mL microfuge tubes as outlined in Table 3. Aliquots (100 μL) of each sample were placed in wells of black 96-well plates (Nunc Maxisorb) which had been previously coated with $Pes3_{AT}$ (2 μg/mL). Plates were incubated for 1 h at room temperature in the dark while the enzymatic reaction occurred. Plates were then washed twice with PBST and excess liquid removed by tapping the plates on adsorbent paper. Fluorescence was detected using a plate reader (Bio-Tech, Synergy HT) with excitation and emission values of 490 and 520 nm, respectively.

PPTase Characterization Using Solid Phase 4′-Phosphopantetheinylation Assay. Temperature and pH optima, along with PPTase reaction time, were determined. In addition, the effect of protease inhibitors (phenylmethylsulfonyl fluoride;

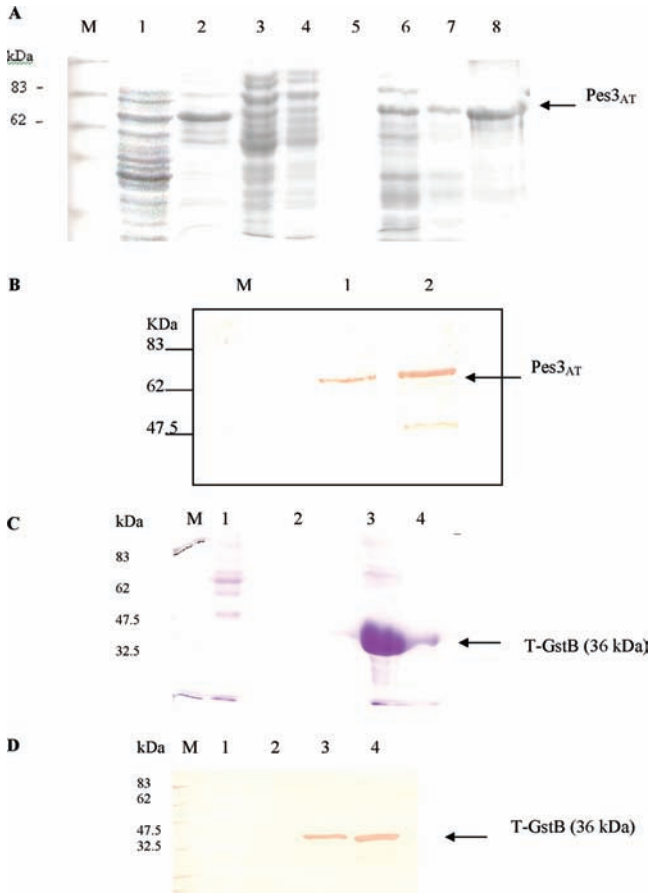

Figure 2. Purification of recombinant $Pes3_{AT}$ and T-GstB by differential extraction. (A) Coomassie stained SDS-PAGE gel of $Pes3_{AT}$ fractions obtained from crude extraction method. Lane M, molecular mass marker; lane 1, unpurified $Pes3_{AT}$; lane 2, cell lysate; lanes 3−5: Triton X-100 washes; lane 6, 2 M urea wash; lane 7, 8 M urea wash; lane 8, purified $Pes3_{AT}$ in 6 M guanidine−HCl. (B) Western blot analysis of $Pes3_{AT}$. Lane M, molecular mass marker; lane 1, unpurified $Pes3_{AT}$; lane 2, $Pes3_{AT}$ purified by differential extraction method. Western blot analysis was carried out using 1/1000 dilution of anti-His_6 monoclonal antibody and 1/1000 dilution of anti-mouse IgG-HRP conjugate. (C) SDS-PAGE analysis of T-GstB fractions obtained from crude extraction method. Lane M, molecular mass marker; lane 1, unpurified T-GstB lysate; lane 2, wash fraction; lane 3, 8 M urea wash (20 μg); lane 4, 8 M urea wash (2 μg). (D) Western blot analysis of purified T-GstB. Lane M, molecular mass marker; lane 1, T-GstB lysate; lane 2, wash fraction; lanes 3 and 4, 8 M urea wash (0.5 and 1 μg/track, respectively) T-GstB.

PMSF) inclusion on PPTase cell lysate stability was investigated. Student's *t* test was used to assess the statistical significance of relevant results. Absorbance values for control lysate (lacking PPTase) were subtracted from PPTase lysates for calculation of relative PPTase activity (%). The mean absorbance value for purified PPTase was set at 100% with all other values (PPTase lysate and biotin-CoA controls) expressed as a percentage of this.

RESULTS

Recombinant Protein Expression, Purification, and Solubilization. $Pes3_{AT}$ was found to be highly insoluble under nondenaturing conditions (data not shown) and was solubilized by addition of 6 M guanidine−HCl containing 1 mM DTT to a final concentration of 30 mg/mL or 5 mg/g cells. SDS-PAGE analysis and Western blot analysis confirmed the required purity of $Pes3_{AT}$ (Figure 2). The 72 kDa $Pes3_{AT}$ band observed on the Coomassie stained gel was excised and subjected to MALDI-ToF mass spectrometry. Resultant tryptic digest peptide monoisotopic *m*/*z* values (Table 4), compared to those of an *in silico* digest of $Pes3_{AT}$, represented 20% sequence coverage thereby providing conclusive confirmation of $Pes3_{AT}$ identity. $Pes3_{AT}$ was solubilized under nondenaturing conditions by dilution into Ppant buffer containing 8 M urea (4 mL) at 0.5 mg/mL $Pes3_{AT}$ followed by serial dialysis into Ppant buffer (final concentration: 0.41 mg/mL (5.75 μM)). This solubilized $Pes3_{AT}$ preparation was aliquoted and stored at −20 °C for subsequent use. The 36 kDa T-GstB fusion protein was purified from *E. coli* cell lysates resulting in a T-GstB yield of 13 mg/mL or 5 mg/g cells (Figure 2).

Table 4. Peptides Identified Following Trypsin Digestion of Recombinant $Pes3_{AT}$ and MALDI-ToF Mass Spectrometry Analysis[a]

m/*z* (Da)	identified peptides
900.39	R Y A D W M A K Y L M V K R
1656.85	K K S V W T M V A M L A I M K
1590.88	K R I L D D T E A P L V I V H R
1523.84	K G I V V P H R S I A T S M R
1930.95	R W N D L A G A M E R L G V N W A K
1288.737	R L L H P E Q V P S L R
1674.8	R Q V G G T L H V V D A G N H D R
1273.61	H R D E D G V L Y H L L G R
1531.66	K V A E H S T D T S AD N E R

[a] The peptides identified represent 20% coverage of the $Pes3_{AT}$ and confirm the identity of the protein.

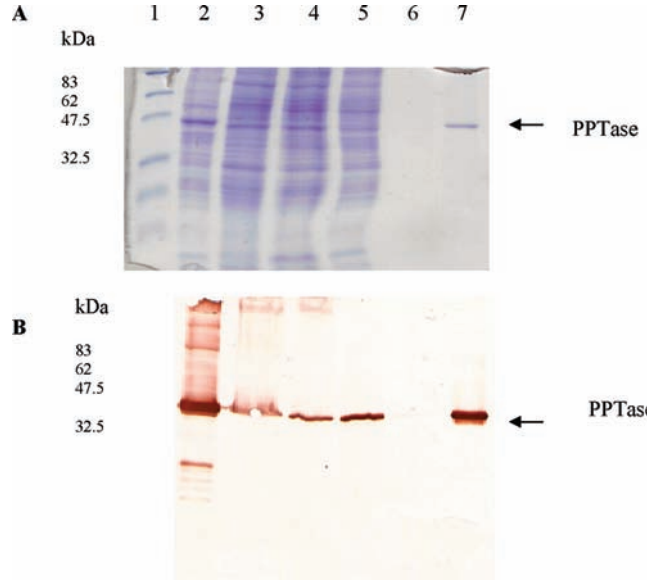

Figure 3. Purification of intracellular PPTase from Sf_9 cell lysate. (A) SDS-PAGE and (B) Western blot analysis of PPTase purification using anti-His_6 monoclonal antibody and 1/1000 dilution of anti-mouse IgG-HRP conjugate. Lane 1, molecular mass markers; lane 2, control PPTase cell lysate; lane 3, PPTase cell lysate 1; lanes 4−6, unbound; lane 7: Ni-NTA affinity column eluate containing purified PPTase.

Following infection with recombinant baculovirus encoding *A. fumigatus* PPTase, *Spodoptera frugiperda* insect cell lysates were prepared by sonication in the presence of 0.05% (w/v) sodium deoxycholate in Ppant diluent. Purified PPTase was obtained by incubation with Ni-NTA affinity resin for 2 h followed by elution with 250 mM imidazole and dialysis into Ppant diluent (yield: 0.33 mg/10^8 cells) (Figure 3).

Labeled CoA Conjugate Synthesis. Biotin-CoA conjugates were prepared by reacting MB with CoA to form a stable thioether-mediated conjugate for subsequent assay development. Prior to addition of free DTT to scavange any unreacted MB, a new method was deployed to determine the efficiency of biotin−CoA conjugate formation, which involved determination of residual CoA using aldrithiol-4 (4,4′-dithiodipyridine) reagent (Supplementary information). This analysis confirmed ef-

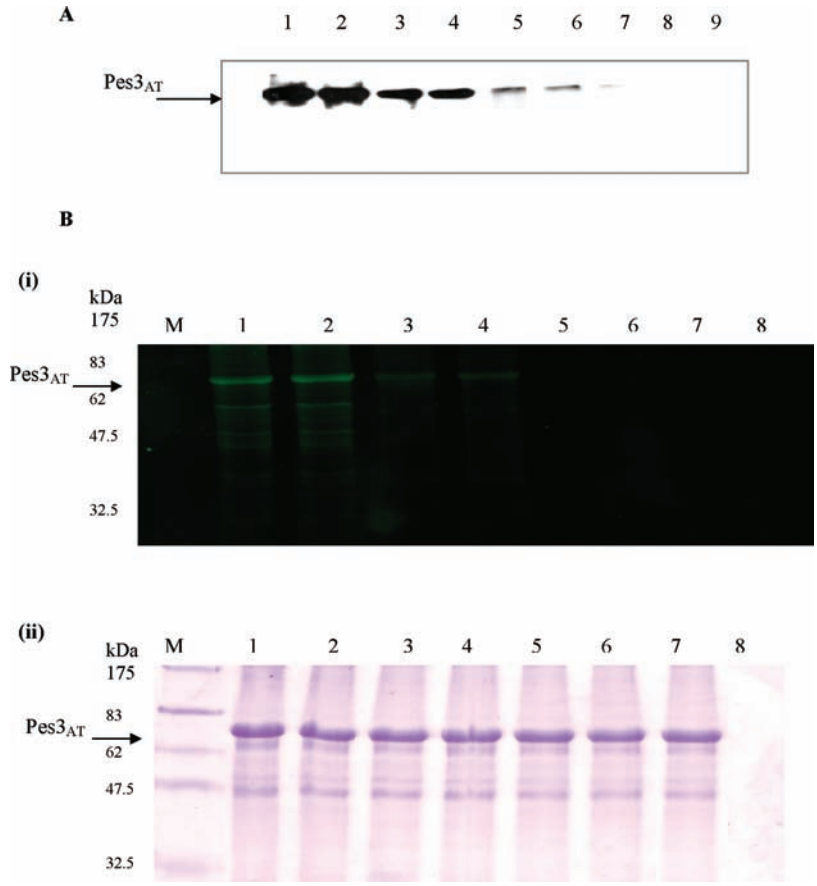

Figure 4. Chemoenzymatic labeling of $Pes3_{AT}$. (A) Western blot showing 4′-phosphopantetheinylation of $Pes3_{AT}$ using a range of PPTase-containing Sf9 cell lysates. Final concentrations of $Pes3_{AT}$ (4.4 μM) and biotin CoA (8.4 μM) were used. Western blots were probed with streptavidin−HRP and developed with ECL substrate. Lanes 1−7, 1.7−0.003 mg/mL, total cell protein; lane 8, $Pes3_{AT}$ negative control; lane 9, Cell lysate negative control. Results shown are representative of duplicate analysis. (B) SDS-PAGE analysis of 4′-phosphopantetheinylation of $Pes3_{AT}$ by PPTase using fluorescein-CoA. (i) Fluorescent analysis was carried out on the Typhoon scanner (Amersham). Lane M, protein marker; lanes 1 and 2, PPTase-containing cell lysate; lanes 3 and 4, purified PPTase (0.08 μM); lanes 5 and 6, PPTase negative control; lane 7, Fl-CoA negative control; lane 8, $Pes3_{AT}$ negative control. (ii) Coomassie staining of the above SDS-PAGE gel showing identical $Pes3_{AT}$ loading (lanes 1−7).

fectively 90%+ efficiency of biotin-CoA conjugate synthesis and extends the utility of aldrithiol-4 and other reagents used for thiol group determination (*18*). Previously, identical biotin-CoA analogues were synthesized, the unincorporated biotin reporter extracted via the use of scavenger resins, and the resultant biotin-CoA reporter subsequently used for the high-sensitivity detection (100 pg) of the biotin labeled recombinant VibB carrier protein domain (*6*). However, we observed minimal background protein modification once DTT was added to biotin-CoA conjugates, which implies that removal of unreacted MB may not always be necessary. A fluorescently linked CoA analogue was also synthesized using 5′-iodoacetamidofluorescein (5′-IAF), which alkylates the sulfhydryl group of CoA. Fluorescent detection offers the potential advantage of direct analysis of labeled proteins without the need for enzyme conjugates and chemiluminescent substrates (*19*). The production of fluorescein-CoA was confirmed by TLC analysis; however, evidence of unreacted 5′-IAF in the fluorescein-CoA sample was also observed (data not shown). As with biotin-CoA conjugates, it was found that subsequent addition of DTT eliminated nonspecific fluorescent labeling of target proteins. In addition, RP-HPLC analysis was also used to detect the production of fluorescein-CoA conjugates with the appearance of a new peak with a lower retention time of 17.0 min for the fluorescein-CoA test specimens which is likely due to the higher polarity of Fl-CoA molecule compared to 5′-IAF (data not shown).

4′-Phosphopantetheinylation of $Pes3_{AT}$ with Biotin- and Fluorescein-CoA is Mediated by PPTase. $Pes3_{AT}$ was subject to specific 4′-phosphopantetheinylation by PPTase present in insect cell lysates (Figure 4a). Here, modification of the $Pes3_{AT}$ (4.4 μM) was clearly detectable using PPTase-containing insect cell lysates (17−1700 μg/mL total protein), with a weak signal, corresponding to specific 4′-phosphopantetheinylation, at 3 μg/mL total cell protein. No 4′-phosphopantetheinylation was detectable in the presence of control insect cell lysate, thereby providing confirmation that modification of $Pes3_{AT}$ with biotin-CoA was mediated specifically by PPTase and not as a result of direct nonspecific labeling of $Pes3_{AT}$ with residual MB. Omission of $Pes3_{AT}$ from the reaction likewise produced a negative result, which confirmed that proteins in the insect cell lysate were not labeled nonspecifically with biotin-CoA (Figure 4a). Replacement of biotin-CoA with fluorescein-CoA as the PPTase substrate also facilitated post-translational modification of $Pes3_{AT}$ (Figure 4b). Here, $Pes3_{AT}$ (4.44 μM) was labeled using both purified PPTase (0.08 μM) and PPTase present in insect cell lysate (34 μg/mL total cell protein). No 4′-phosphopantetheinylation was detectable in the absence of either PPTase or $Pes3_{AT}$. Overall, these observations confirm that the $Pes3_{AT}$ thiolation domain can be post-translationally modified by PPTase with either biotinylated or fluorescently labeled CoA.

High-Throughput Detection of 4′-Phosphopantetheinylation. Reaction mixtures containing combinations of purified PPTase, $Pes3_{AT}$, and fluorescein-CoA were incubated in solution for 1 h and subsequently transferred to black microtiter plates,

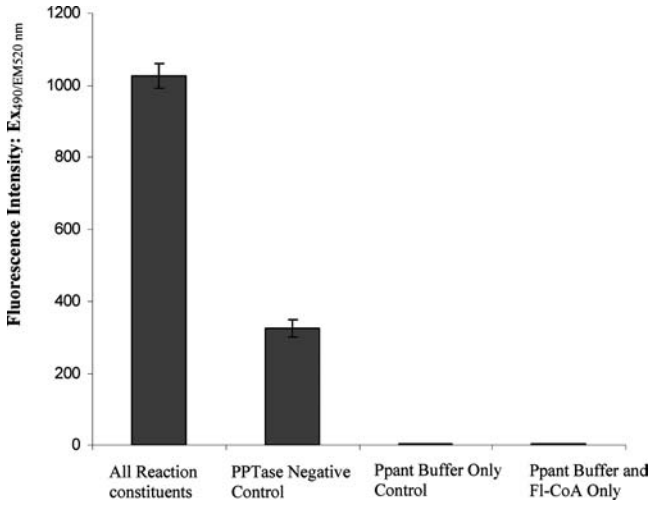

Figure 5. Solid phase 4′-phosphopantetheinylation assay using Fl-CoA. After solution phase incubation, 4′-phosphopantetheinylation reactions (and appropriate controls) were coated on black microtiter plates and subsequently analyzed by fluorescence with excitation and emission at 490 and 520 nm, respectively. Results given represent the mean (±SE) of the experiment performed in triplicate. All reaction constituents: $Pes3_{AT}$; PPTase; Fl-CoA. PPTase negative control: PPTase absent from reactions. Ppant buffer control: Ppant buffer only. Ppant buffer and fluorescein-CoA (Fl-CoA) only: $Pes3_{AT}$ and PPTase absent from reactions.

incubated for a further 1 h, followed by washing with PBST (2×) to remove unbound fluorescein-CoA. Fluorescent analysis at 490/520 nm (ex/em) (Figure 5) indicated that fluorescently labeled $Pes3_{AT}$ had bound to the plate and was detectable by fluorescence analysis. Fluorescence labeling was predominantly mediated by PPTase modification; however, nonspecific labeling was also evident (up to 25%) in the absence of PPTase. No fluorescence was detectable in the absence of $Pes3_{AT}$.

For technical reasons, direct detection of biotinylated $Pes3_{AT}$ on microwells was not possible as described for fluorescent $Pes3_{AT}$ above (data not shown). However, 4′-phosphopantetheinylation was possible using microwells precoated with $Pes3_{AT}$ (4.4 pmol), and stabilized by BSA addition (Figure 6a). To ensure that biotin labeling of the bound $Pes3_{AT}$ protein was the result of PPTase activity and not due to the presence of insect cell proteins present in the crude cell lysate, control reactions were included whereby uninfected insect cell lysates (at identical total protein concentration) were incubated in the $Pes3_{AT}$ coated microwells in the presence of biotin-CoA, and resultant absorbance values compared to those obtained from incubation with PPTase insect cell lysate. Background activity was apparent in uninfected cell lysate controls compared to the biotin-CoA and Ppant buffer controls, but these absorbance values were only 16−25% of those obtained for the wells incubated with PPTase insect cell lysate (mean $A_{450/630\ nm}$: 1.7), thereby confirming that labeling of $Pes3_{AT}$ was due to PPTase present in the insect cell lysate. Consequently, PPTase cell lysate was used for subsequent analysis of PPTase activity using this assay format (Figure 6b). Control insect cell lysate (uninfected cells) was also included in subsequent analysis, and absorbance values obtained for these samples subtracted from the PPTase cell lysate specimens to correct for any nonspecific labeling that may be a result of native insect cell proteins. PPTase-mediated fluorescein-CoA modification of immobilized $Pes3_{AT}$ has also been demonstrated (Figure 6c). Here, nonspecific modification (approximately 25% of the PPTase reaction) was also evident.

Purified PPTase from insect cells lysates also functions in the solid phase 4′-phosphopantetheinylation reaction (Figure 6d). No significant difference was observed between purified PPTase and PPTase cell lysate (at an equivalent dilution; $P = 0.56$), whereas significantly greater 4′-phosphopantetheinylaiton activity was evident compared to biotin-CoA only negative control ($P = 0.00036$).

Fungal Thiolation Domain Facilitates Labeling of Non-Native Substrate Proteins. T-GstB was post-translationally modified by 4′-phosphopantetheinylation with biotinylated 4′-phosphopantetheine when immobilized in microwells (Figure 7). Moreover, background signal arising from GstB negative control was less than 5% of overall T-GstB signal, demonstrating conclusively that the discrete thiolation domain of T-GstB was specifically modified by PPTase activity, even when fused to a non-native protein (i.e., GstB).

Characterization of PPTase Activity. Following the establishment of the *in vitro* 4′-phosphopantetheinylation assay in a solid phase (96 well plate) format using biotin-CoA and PPTase insect cell lysates, temperature, pH optima, and reaction time-course were investigated. Analysis of these data revealed that optimal PPTase activity was evident at 24 °C, with reduced 4′-phosphopantetheinylation observed at 4, 37, and 50 °C (Figure 8a). A statistically significant higher PPTase activity was observed when protease inhibitors were included in the insect cell lysates. This result implies that, in the absence of protease inhibitors, proteases present in the crude insect cell lysate may degrade PPTase and therefore lower the extent of post-translational modification (Figure 8a). The overall affect of pH on PPTase activity is shown in Figure 8b whereby background absorbance values obtained from the insect cell lysate control samples were subtracted from the absorbance values obtained from PPTase lysate reactions. From this analysis, it is clear that pH has an effect on the activity of PPTase with optimal 4′-phosphopantetheinylation occurring at pH 8.0. 4′-Phosphopantetheinylation is 75% complete within 1 h, and complete protein labeling is achieved after 3 h reaction (Figure 8c).

DISCUSSION

Despite recent advances in PPTase-mediated labeling of T/PCP or ACP domains of prokaryotic origin, via biotinylated or fluorescently modified CoA analogues, minimal information on this approach for eukaryotic (fungal) T domain modification is available. Moreover, facile determination of PPTase activity has remained a challenge. Here, data are presented which confirm that T domains of fungal origin can be post-translationally modified, both in solution and when immobilized on a solid surface, using a combination of modified CoA analogues and a functional PPTase. We also demonstrate that T domains can be transferred to a non-native protein (GstB) and that this fusion protein (T-GstB) is also a substrate for PPTase-mediated modification. Finally, it appears that the solid phase assay format presents a new strategy for determination of PPTase activity which is faster than current methods and is compatible with high-throughput functionality.

The gene encoding Pes3 represents the largest NRPS open reading frame in the *A. fumigatus* genome. Here, we have expressed the first AT didomain of Pes3 and a T-GstB fusion protein, in *E. coli* at high yields (5 mg/g cells). We have previously cloned and expressed recombinant PPTase in the baculovirus expression system, purified from PBS washes of intact cells by subsequent Ni-NTA chromatography, and shown it to be capable of transferring the Ppant group from CoA to the T domain derived from a distinct *A. fumigatus* NRPS (*pes1*) (*2*). However, in the present work we utilize PPTase, of intracellular origin, which was extracted in high yields (3.33 mg/10^9 cells) and purified by Ni-NTA affinity chromatography. Interestingly, PPTase activity was detectable in crude cell lysates, indicating that enzyme purification is not always essential.

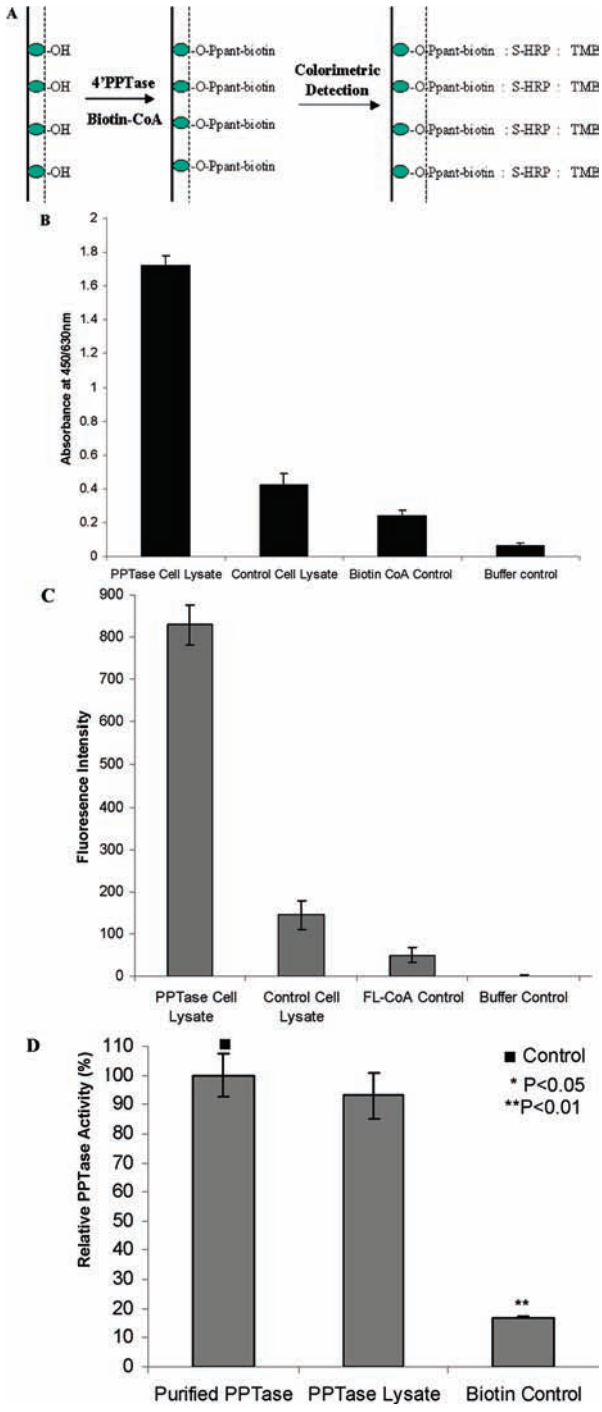

Figure 6. (A) Diagrammatic representation of solid phase 4′-phosphopantetheinylation. Immobilized thiolation domains (e.g., in $Pes3_{AT}$) (green circles) are stabilized by the addition of BSA (dashed line). The reactive serine residue (−OH) on the thiolation domain can then be modified with biotin-CoA in the presence of PPTase. PPTase activity is then indirectly detected by addition of streptavidin−HRP conjugate and TMB substrate. Fluorescein-CoA (Fl-CoA) can be substituted for biotin-CoA followed by subsequent direct fluorescent detection of the labeled thiolation domain. (B) Solid phase 4′-phosphopantetheinylation assay using biotin-CoA. *In vitro* 4′-phosphopantetheinylation assays were carried out on plates coated with $Pes3_{AT}$ (2 μg/mL). Results given represent the mean (±SE) of the experiment performed in triplicate. (C) Solid phase 4′-phosphopantetheinylation assay using fluorescein-CoA. 4′-Phosphopantetheinylation assays were performed in microwells coated with $Pes3_{AT}$ (2 μg/mL). Results given represent the mean (±SE) of the experiment performed in triplicate. (D) Solid phase 4′-phosphopantetheinylation of $Pes3_{AT}$ using purified PPTase (29 μg; 0.7 nmol) and PPTase cell lysate. Results given represent the mean (±SE) of the experiment carried out in triplicate.

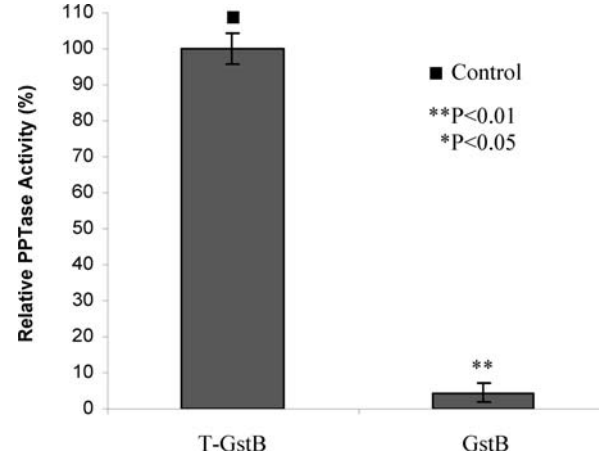

Figure 7. Solid phase 4′-phosphopantetheinylation of T-GstB. Net post-translational modification activity in PPTase cell lysate, toward for T-GstB and GstB, respectively, was calculated by subtracting background signals in control insect cell lysate. Results given represent the mean (±SE) of three individual experiments. Students *t* test was used to calculate *P*-values for the difference between the T-GstB and the GstB ($P = 0.0003$).

To confirm reagent functionality, recombinant $Pes3_{AT}$ was subjected to solution phase biotin- and fluorescein-CoA labeling, respectively, in the presence and absence of PPTase followed by chemiluminescent or direct fluorescence detection (Figure 4). Significantly, $Pes3_{AT}$ (4.4 μM) labeling was observed in all cases in the presence of either purified PPTase or insect cell lysates, which contained impure, but active, preparations of the enzyme. To our knowledge, this is the first demonstration that fungal T domains can be chemoenzymatically labeled with CoA analogues, that crude PPTase preparations can be used to effect *in vitro* 4′-phosphopantetheinylation, and also that the enzyme produced within recombinant baculovirus-infected insect cells is active. Detection of fluorescein-labeled $Pes3_{AT}$ (4.4 μM) was achieved using 7.3 μM fluorescein-CoA and using either 0.08 μM purified PPTase and crude PPTase cell lysate at a concentration of 0.034 mg/mL (estimated to contain 0.92 μM PPTase). Thus, the molar ratios of purified PPTase, carrier protein, and fluorescein-CoA used were approximately 1:55:90. The PPTase mediated modification of the Pyochelin NRP synthetase carrier proteins PchE and PchF using similar fluorescein-CoA analogues has been reported (*13*). The *in vitro* 4′ phosphopantetheinylation assays used in that study, however, used 2 μM *B. subtilis* Sfp, 300 μM fluorescein-CoA, and PchE/PchF carrier proteins at concentrations of 10 and 21 μM, respectively. The molar ratios of PPTase, carrier protein, and fluorescein-CoA in the present study were 1:5−10:150, respectively, similar to fluorescein-CoA-PPTase assay described herein; however, the assay of ref 13 required approximately 5-fold more carrier protein and 25 times more PPTase (Sfp), respectively.

In order to eliminate the time-consuming electrophoretic step associated with labeled carrier protein detection and expedite analysis, we attempted direct immobilization of reaction mixtures to microwells, subsequent to *in vitro* 4′-phosphopantetheinylation followed by visualization and absorbance detection. This approach was unsuitable for use with biotin-CoA reporter analogues as the biotin moiety exhibited high nonspecific binding to microwells thereby masking any possibility of detecting PPTase mediated $Pes3_{AT}$ labeling (data not shown). However, the approach was successfully applied to *in vitro* 4′-phosphopantetheinylation assays using a fluorescein-labeled CoA analogue whereby 3-fold greater fluorescence was detectable in specimens containing PPTase, Fl-CoA and $Pes3_{AT}$ compared to specimens containing Fl-CoA and $Pes3_{AT}$ alone (Figure 5). Although extensive validation of this approach has

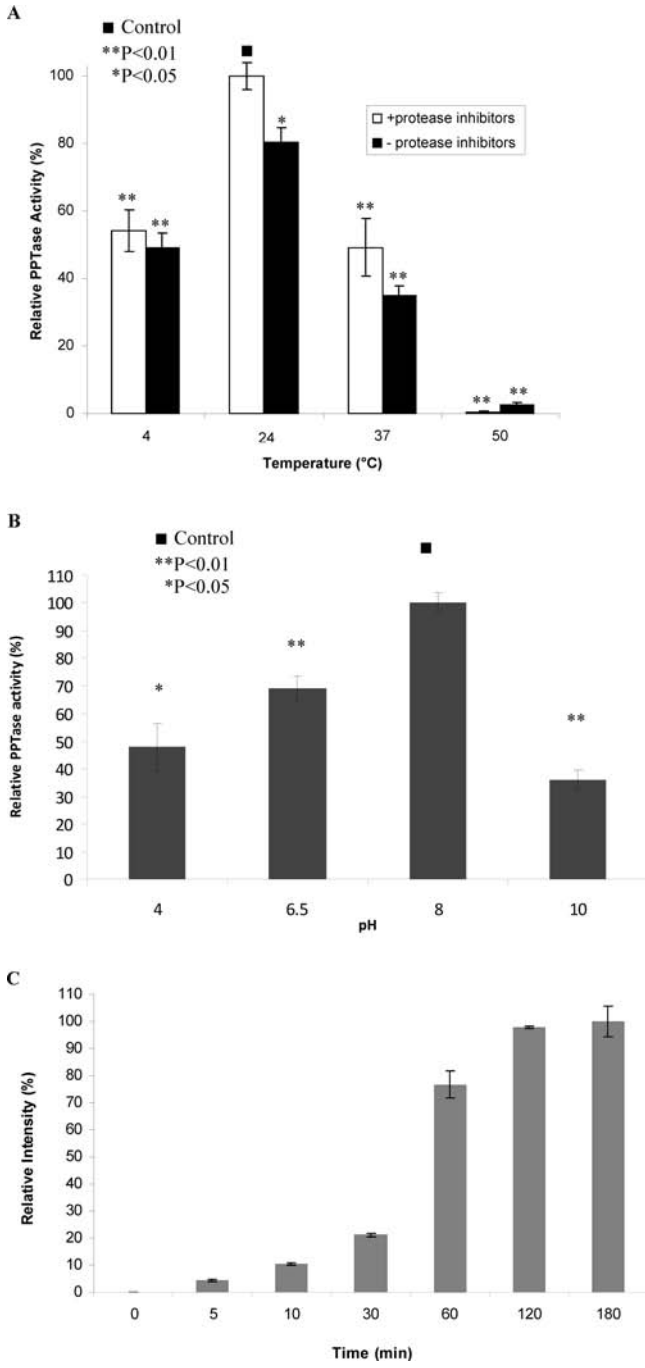

Figure 8. (A) The effect of temperature on PPTase activity in the presence and absence of protease inhibitors. Results given represent the mean (±SE) of three individual experiments. Student's *t* test was used to calculate *P*-values for the difference between the control (24 °C + protease inhibitors) and the following conditions: 4 °C (+/− protease inhibitors ($P = 0.003$; $P = 0.0009$)), 24 °C (− protease inhibitors ($P = 0.03$)), 37 °C (+/− protease inhibitors ($P = 0.005$; $P = 0.0002$)), and 50 °C (± protease inhibitors ($P = 0.00001$; $P = 0.00002$)). (B) The effect of pH on PPTase activity. Results are expressed as percent (%) relative to the highest level, i.e., pH 8.0, and represent the mean (±SE) of three individual experiments. Student's *t* test was used to calculate *P*-values for the difference between the control (pH 8.0) and the following pH conditions: 4.0 ($P = 0.01$), 6.5 ($P = 0.008$), and 10.0 ($P = 0.0003$). (C) The effect of reaction time on PPTase activity. Optimal reaction time is 2 h; however, PPTase-mediated protein modification is up to 75% complete by 1 h.

not been undertaken, we propose that this hybrid assay format, involving solution phase, *in vitro* phosphopantetheinylation and reaction product immobilization for fluorescent detection, may find future application.

A number of groups have confirmed that proteins fused to either T domains of bacterial origin, or peptides derived from phage display, can be covalently tethered to immobilized CoA, and this observation has been proposed as a new strategy for protein array preparation (*9, 20*). However, to date, labeled pantetheine transfer to immobilized T domains, in either native or non-native configuration, has not been demonstrated. The 75 amino acid T domain used in our study is equivalent in size to other fungal and bacterial T domains but considerably longer than ybbR-like tags introduced by other groups (*8*). The use of the T domain of fungal (*A. fumigatus*) origin as a target for C-terminal labeling of $Pes3_{AT}$ and N-terminal labeling of T-GstB, respectively, suggests that domain acceptor function is independent of position in the substrate protein. We have observed that purified $Pes3_{AT}$ or T-GstB can be stably and irreversibly attached to microwells, blocked to minimize nonspecific binding, and followed by PPTase-mediated biotinylation or fluorescent labeling using either biotin-CoA or fluorescein-CoA. This finding represents a new strategy for assessment of both T domain functionality and PPTase activity determination and potentially for the assessment of PPTase/AcpS/Sfp inhibitors, which have been proposed as potential drug targets (*14*).

Our data indicate that 0.33 μg (4.4 pmol) $Pes3_{AT}$ can be detected using 29 μg (0.7 nmol) of recombinant PPTase (in either purified or crude form) in the presence of biotin-CoA via solid phase phosphopantetheinylation. It also suggests that any conformational restriction due to $Pes3_{AT}$ immobilization does not significantly impede phosphopantetheinylation. Moreover, chemoenzymatic detection is statistically significant ($P < 0.05$) over protein labeling in the absence of recombinant PPTase. Importantly, we also demonstrate that the T domain derived from $Pes3_{AT}$ can be fused to an unrelated protein and also be subjected to solid phase phosphopantetheinylation. This confirms the discrete functionality of the T domain and strongly suggests that they can be used as a fusion partners for unrelated proteins to facilitate targeted labeling procedures.

In order to optimise the *in vitro* 4′-phosphopantetheinylation assay and to further characterize PPTase activity, assays were performed at different reaction temperatures. Initial *in vitro* 4′-phosphopantetheinylation assays using the *A. fumigatus* encoded recombinant PPTase (*2*) were carried out at a reaction temperature of 37 °C; however, optimal PPTase activity occurs at 25 °C with 100% increase in the extent of $Pes3_{AT}$ modification observed compared to that at 37 °C. *In vitro* 4′-phosphopantetheinylation assays employing the use of the *B. subtilis* PPTase Sfp, were carried out at room temperature and 30 °C, respectively (*6, 13*). Furthermore, the *in vitro* phosphopantetheinylation assays used to assess the affect of PPTase (AcpS) specific inhibitors on the ability of the *B. subtilis* AcpS to post-translationally modify the ACP carrier protein were also performed at 25 °C (*14*).

Subsequent to determination of optimal PPTase reaction temperature, the effect of pH on PPTase activity was also investigated and revealed that optimal PPTase activity was observed at pH 8.0 (100%), with a significant decrease in PPTase activity to 45%, 65%, and 35% for pH 4.0, pH 6.5, and pH 10.0, respectively. These observations are in accordance with those for the *in vitro* phosphopantetheinylation assays used for *B. subtilis* AcpS type PPTase, which were also carried out at pH 8.0 (*14*). However, a clear pH optimum at pH 6.0 for the *B. subtilis* Sfp type PPTase, with activity reducing to less than 20% of the optimum pH for pH 5.0 and pH 7.0, respectively, has been reported (*3*). Thus, it is clear that optimal reaction conditions should be established for each specific PPTase or equivalent AcpS/Sfp enzyme.

In summary, we have demonstrated that solid phase *in vitro* 4′-phosphopantetheinylation, using either biotin- or fluorescein-CoA substrate analogues, of fungal thiolation domains in native or non-native configuration is possible. Moreover, we have conclusively shown that the solid phase assay format presents a new strategy for determination of PPTase activity, which is superior to current approaches and highly likely to be compatible with high-throughput screening systems for PPTase inhibitor identification. We also suggest that solid phase 4′-phosphopantetheinylation may be compatible with the ongoing search for peptide mimotopes, in part via phage display, of T domain functionality (*21*, *22*).

ACKNOWLEDGMENT

We are grateful to both the Irish Higher Education Authority - Programme for Research in Third Level Institutions (PRTLI-Cycle 3) and Enterprise Ireland Proof of Concept Scheme (EI/PC/2006/379) which provided funding for this work.

Supporting Information Available: Experimental procedures and results relating to the synthesis efficiency of biotin-CoA. This material is available free of charge via the Internet at http://pubs.acs.org.

LITERATURE CITED

(1) Mootz, H. D., Schorgendorfer, K., and Marahiel, M. A. (2002) Functional characterization of 4′-phosphopantetheinyl transferase genes of bacterial and fungal origin by complementation of *Saccharomyces cerevisiae* lys5. *FEMS Microbiol. Lett. 213*, 51–57.

(2) Neville, C. M., Murphy, A., Kavanagh, K., and Doyle, S. (2005) A 4′-phosphopantetheinyl transferase mediates non-ribosomal peptide synthetase activation in *Aspergillus fumigatus*. *ChemBioChem 6*, 679–685.

(3) Quadri, L. E., Weinrab, P. H., Lei, M., Nakano, M. M., Zuber, P., and Walsh, C. T. (1998) Characterization of *Sfp*, a *Bacillus subtilis* phosphopantetheinyl transferase for peptidyl carrier protein domains in peptide synthetases. *Biochemistry 37*, 1585–1595.

(4) Mofid, M. R., Finking, R., and Marahiel, M. A. (2002) Recognition of hybrid peptidyl carrier proteins/acyl carrier proteins in nonribosomal peptide synthetase modules by the 4′-phosphopantetheinyl transferases AcpS and Sfp. *J. Biol. Chem. 277*, 17023–17031.

(5) Weissman, K. J., Hong, H., Oliynyk, M., Siskos, A. P., and Leadlay, P. F. (2004) Identification of a phosphopantetheinyl transferase for erythromycin biosynthesis in *Saccharopolyspora erythraea*. *ChemBioChem 5*, 116–125.

(6) La Clair, J. J., Foley, T. L., Schegg, T. R., Regan, C. M., and Burkart, M. D. (2004) Manipulation of carrier proteins in antibiotic biosynthesis. *Chem. Biol. 11*, 195–201.

(7) Yin, J., Lin, A. J., Buckett, P. D., Wessling-Resnick, M., Golan, D. E., and Walsh, C. T. (2005) Single-cell FRET imaging of transferrin receptor trafficking dynamics by Sfp-catalyzed, site-specific protein labelling. *Chem. Biol. 12*, 999–1006.

(8) Yin, J., Straight, P. D., McLoughlin, S. M., Zhou, Z., Lin, A. J., Golan, D. E., Kelleher, N. L., Kolter, R., and Walsh, C. T. (2005) Genetically encoded short peptide tag for versatile protein labeling by Sfp phosphopantetheinyl transferase. *Proc. Natl. Acad. Sci U.S.A. 102*, 15815–15820.

(9) Yin, J., Liu, F., Xiaohua, L., and Walsh, C. T. (2004) Labeling proteins with small molecules by site-specific postranslational modification. *J. Am. Chem. Soc. 126*, 7754–7755.

(10) Shute, T. S., Matsushita, M., Dickerson, T. J., La Clair, J. J., Janda, K. D., and Burkart, M. D. (2005) A site-specific bifunctional protein labelling system for affinity and fluorescent analysis. *Bioconjugate Chem. 16*, 1352–1355.

(11) Yin, J., Lin, A. J., Golan, D. E., and Walsh, C. T. (2006) Site-specific protein labeling by Sfp phosphopantetheinyl transferase. *Nat. Protoc. 1*, 280–285.

(12) Clarke, K. M., Mercer, A. C., La Clair, J. J., and Burkart, M. D. (2005) In vivo reporter labeling of proteins via metabolic delivery of coenzyme A analogues. *J. Am. Chem. Soc. 127*, 1234–1235.

(13) McLoughlin, S. M., Mazur, M. T., Miller, L. M., Yin, J., Liu, F., Walsh, C. T., and Kelleher, N. L. (2005) Chemoenzymatic approaches for streamlined detection of active site modifications on thiotemplate assembly lines using mass spectrometry. *Biochemistry 44*, 14159–14169.

(14) Joseph-McCarthy, D., Parris, K., Huang, A., Failli, A., Quagliato, D., Dushin, E. G., Novikova, E., Severina, E., Tuckman, M., Petersen, P. J., Dean, C., Fritz, C. C., Meshulam, T., DeCenzo, M., Dick, L., McFadyen, I. J., Somers, W. S., Lovering, F., and Gilbert, A. M. (2005) Use of structure-based drug design approaches to obtain novel anthranilic acid acyl carrier protein synthase inhibitors. *J. Med. Chem. 48*, 7960–7969.

(15) Carberry, S., Neville, C. M., Kavanagh, K. A., and Doyle, S. (2006) Analysis of major intracellular proteins of *Aspergillus fumigatus* by MALDI mass spectrometry: Identification and characterisation of an elongation factor 1B protein with glutathione transferase activity. *Biochem. Biophys. Res. Commun. 341*, 1096–1104.

(16) Burns, C., Geraghty, R., Neville, C., Murphy, A., Kavanagh, K., and Doyle, S. (2005) Identification, cloning, and functional expression of three glutathione transferase genes from *Aspergillus fumigatus*. *Fungal Genet. Biol. 42*, 319–327.

(17) Reeves, E. P., Reiber, K., Neville, C., Scheibner, O., Kavanagh, K., and Doyle, S. (2006) A nonribosomal peptide synthetase (pes1) confers protection against oxidative stress in *Aspergillus fumigatus*. *FEBS J. 273*, 3038–3053.

(18) Hansen, R. E., Østergaard, H., Nørgaard, P., and Winther, J. R. (2007) Quantification of protein thiols and dithiols in the picomolar range using sodium borohydride and 4,4′-dithiodipyridine. *Anal. Biochem. 363*, 77–82.

(19) Haan, C., and Behrmann, I. (2007) A cost effective non-commercial ECL-solution for Western blot detections yielding strong signals and low background. *J. Immunol. Methods 318*, 11–19.

(20) Wong, L. S., Thirlway, J., and Micklefield, J. (2008) Direct site-selective covalent protein immobilization catalyzed by a phosphopantetheinyl transferase. *J. Am. Chem. Soc. 130*, 12456–12464.

(21) Zhou, Z., Koglin, A., Wang, Y., McMahon, A. P., and Walsh, C. T. (2008) An eight residue fragment of an acyl carrier protein suffices for post-translational introduction of fluorescent pantetheinyl arms in protein modification in vitro and in vivo. *J. Am. Chem. Soc. 130*, 9925–9930.

(22) Zhou, Z., Cironi, P., Lin, A. J., Xu, Y., Hrvatin, S., Golan, D. E., Silver, P. A., Walsh, C. T., and Yin, J. (2007) Genetically encoded short peptide tags for orthogonal protein labeling by Sfp and AcpS phosphopantetheinyl transferases. *ACS Chem. Biol. 2*, 337–346.

BC900071J

Supplementary Data

Solid Phase 4'-Phosphopantetheinylation- Fungal Thiolation Domains are Targets for Chemoenzymatic Modification.

Deirdre Stack, Aisling Frizzell, Karen Tomkins and Sean Doyle

National Institute for Cellular Biotechnology, Department of Biology, National University of Ireland Maynooth, Co. Kildare, Ireland.

*Corresponding author:

Professor Sean Doyle,

National Institute for Cellular Biotechnology,

Department of Biology,

National University of Ireland Maynooth,

Co. Kildare,

Ireland.

Tel: +353-1-7083858

Fax: +353-1-7083845

E-mail: sean.doyle@nuim.ie

EXPERIMENTAL METHODS

Determination of thiol availability in Coenzyme A, prior to and post-labeling, using 4,4'-Dithiodipyridine. Coenzyme A solutions were prepared at the following concentrations: 15, 30 and 60 μM. in 50 mM sodium phosphate, 150 mM NaCl, 1 mM EDTA, pH 6.8 (Buffer A). Using Buffer A as a blank at 324 nm, 2 μL aliquot of 4,4'-Dithiodipyridine (11 mg/mL in ethanol) was added to buffer blanks and test specimens respectively. These was slowly mixed by inversion for exactly 1 min and absorbances were determined at 324 nm (A_{324} nm). The same was carried out for labelled CoA preparations (prior to DTT addition). The concentration of thiol (SH) groups was calculated from the A_{324} nm values (Scheme 1). This facilitated the determination of molar ratio of free SH per CoA and this value should theoretically be 1.0. 4,4'-Dithiodipyridine-mediated analysis was also employed to determine residual free thiol groups present in biotin-CoA conjugates (238 μM and 595 μM CoA stock solutions) but diluted to the same CoA concentrations as for free CoA. The molar ratio of free SH per CoA should be 0 assuming conjugation has occurred.

$$[SH]\ (\mu M) = \frac{A_{324}\text{nm (test sample)} - A_{324}\text{nm (blank)}}{0.0198}$$

$$\text{Free SH group per CoA molar ratio} = \frac{\mu M\ SH}{\mu M\ CoA}$$

Scheme 1: Determination of thiol availability in Coenzyme A using 4,4'-Dithiodipyridine.

RESULTS

Biotin-CoA Synthesis and Analysis of the Reaction between Biotin and Coenzyme A. In order to determine biotin-CoA conjugation efficiency, the free thiol group present in CoA was determined. Concentrations of 15 μM, 30 μM and 60 μM

show value approaching 1 free thiol per CoA (Table S1). The same method was used to examine the presence of free thiol groups in biotin-CoA at 1:2 and 1:5 molar ratios of CoA: maleimido-dPEG$_4$-biotin. If 100% conjugation had occurred there should be no free thiol groups present. This was the case for the biotin-CoA at 1:2 and 1:5 molar ratios with reaction efficiency of approximately 95% observed (Table S2; Table S3). Based on the overall results, it appears that the conjugation reaction between maleimido-dPEG$_4$-biotin and CoA is highly efficient, thereby validating the biotin-CoA synthesis method.

Table S1. Determination of thiol/CoA ratio in unconjugated CoA. As expected, one thiol was detectable per CoA.

[CoA]	$A_{324\ nm}$	[SH] (μM)	SH / CoA
60 μm	1.2143	61.32	1.022
30 μm	0.5623	28.39	0.94
15 μm	0.2912	14.70	0.98

Table S2. Determination of thiol/CoA ratio in biotin-CoA prepared with a 1:2 molar ratio of CoA:maleimido-dPEG$_4$-biotin (final CoA concentration: 238 μM). This analysis confirmed 94% efficiency of conjugation.

[CoA]	$A_{324\ nm}$	[SH] (μM)	SH/ Biotin-CoA
60 μm	0.1103	5.57	0.09
30 μm	-0.3581	0	0
15 μm	0.037	1.86	0.1

Table S3 Determination of thiol/CoA ratio in biotin-CoA prepared with a 1:5 molar ratio of CoA:maleimido-dPEG$_4$-biotin (final CoA concentration: 595 μM). This analysis confirmed 92% efficiency of conjugation.

[CoA]	$A_{324\ nm}$	[SH] (μM)	SH/ Biotin-CoA
60 μm	0.087	4.39	0.07
30 μm	0.1003	5.06	0.16
15 μm	-0.3734	0	0

END

Supplementary Data

Solid Phase 4'-Phosphopantetheinylation- Fungal Thiolation Domains are Targets for Chemoenzymatic Modification.

Deirdre Stack, Aisling Frizzell, Karen Tomkins and Sean Doyle

National Institute for Cellular Biotechnology, Department of Biology, National University of Ireland Maynooth, Co. Kildare, Ireland.

*Corresponding author:

Professor Sean Doyle,

National Institute for Cellular Biotechnology,

Department of Biology,

National University of Ireland Maynooth,

Co. Kildare,

Ireland.

Tel: +353-1-7083858

Fax: +353-1-7083845

E-mail: sean.doyle@nuim.ie

EXPERIMENTAL METHODS

Determination of thiol availability in Coenzyme A, prior to and post-labeling, using 4,4'-Dithiodipyridine. Coenzyme A solutions were prepared at the following concentrations: 15, 30 and 60 μM. in 50 mM sodium phosphate, 150 mM NaCl, 1 mM EDTA, pH 6.8 (Buffer A). Using Buffer A as a blank at 324 nm, 2 μL aliquot of 4,4'-Dithiodipyridine (11 mg/mL in ethanol) was added to buffer blanks and test specimens respectively. These was slowly mixed by inversion for exactly 1 min and absorbances were determined at 324 nm (A_{324} nm). The same was carried out for labelled CoA preparations (prior to DTT addition). The concentration of thiol (SH) groups was calculated from the A_{324} nm values (Scheme 1). This facilitated the determination of molar ratio of free SH per CoA and this value should theoretically be 1.0. 4,4'-Dithiodipyridine-mediated analysis was also employed to determine residual free thiol groups present in biotin-CoA conjugates (238 μM and 595 μM CoA stock solutions) but diluted to the same CoA concentrations as for free CoA. The molar ratio of free SH per CoA should be 0 assuming conjugation has occurred.

$$[SH]\ (\mu M) = \frac{A_{324}\text{nm (test sample)} - A_{324}\text{nm (blank)}}{0.0198}$$

$$\text{Free SH group per CoA molar ratio} = \frac{\mu M\ SH}{\mu M\ CoA}$$

Scheme 1: Determination of thiol availability in Coenzyme A using 4,4'-Dithiodipyridine.

RESULTS

Biotin-CoA Synthesis and Analysis of the Reaction between Biotin and Coenzyme A. In order to determine biotin-CoA conjugation efficiency, the free thiol group present in CoA was determined. Concentrations of 15 μM, 30 μM and 60 μM show value approaching 1 free thiol per CoA (Table S1). The same method was used to examine the presence of free thiol groups in biotin-CoA at 1:2 and 1:5 molar ratios of CoA: maleimido-dPEG$_4$-biotin. If 100% conjugation had occurred there should be no free thiol groups present. This was the case for the biotin-CoA at 1:2 and 1:5 molar ratios with reaction efficiency of approximately 95% observed (Table S2; Table S3). Based on the overall results, it appears that the conjugation reaction between maleimido-dPEG$_4$-biotin and CoA is highly efficient, thereby validating the biotin-CoA synthesis method.

Table S1. Determination of thiol/CoA ratio in unconjugated CoA. As expected, one thiol was detectable per CoA.

[CoA]	$A_{324\ nm}$	[SH] (μM)	SH / CoA
60 μm	1.2143	61.32	1.022
30 μm	0.5623	28.39	0.94
15 μm	0.2912	14.70	0.98

Table S2. Determination of thiol/CoA ratio in biotin-CoA prepared with a 1:2 molar ratio of CoA:maleimido-dPEG$_4$-biotin (final CoA concentration: 238 μM). This analysis confirmed 94% efficiency of conjugation.

[CoA]	$A_{324\ nm}$	[SH] (μM)	SH/ Biotin-CoA
60 μm	0.1103	5.57	0.09
30 μm	-0.3581	0	0
15 μm	0.037	1.86	0.1

Table S3 Determination of thiol/CoA ratio in biotin-CoA prepared with a 1:5 molar ratio of CoA:maleimido-dPEG$_4$-biotin (final CoA concentration: 595 μM). This analysis confirmed 92% efficiency of conjugation.

[CoA]	$A_{324\ nm}$	[SH] (μM)	SH/ Biotin-CoA
60 μm	0.087	4.39	0.07
30 μm	0.1003	5.06	0.16
15 μm	-0.3734	0	0

END

A Peptide-Based Dendrimer That Enhances the Splice-Redirecting Activity of PNA Conjugates in Cells

Fatouma Said Hassane,[†] Gabriela D. Ivanova,[‡] Eleonora Bolewska-Pedyczak,[§] Rachida Abes,[†] Andrey A. Arzumanov,[‡] Michael J. Gait,[‡] Bernard Lebleu,[†] and Jean Gariépy*[,§]

UMR 5235 CNRS, Université Montpellier 2, Place Eugene Bataillon, 34095 Montpellier, France, Medical Research Council, Laboratory of Molecular Biology, Hills Road, Cambridge CB2 0QH, United Kingdom, and Department of Medical Biophysics, University of Toronto, 610 University Avenue, Toronto, M5G 2M9, Ontario, Canada. Received February 16, 2009; Revised Manuscript Received June 1, 2009

The full therapeutic potential of oligonucleotide (ON)-based agents has been hampered by cellular delivery challenges. Cell-penetrating peptides (CPP) represent promising delivery vectors for nucleic acids, and their potential has recently been evaluated using a functional splicing redirection assay, which capitalizes on the nuclear delivery of splice-correcting steric-block ON analogues such as peptide nucleic acids (PNA). Despite encouraging in vitro and in vivo data with arginine-rich CPP-steric block conjugates, mechanistic studies have shown that entrapment within the endosome/lysosome compartment after endocytosis remains a limiting factor. Previous work from our group has shown that CPP oligomerization greatly improves cellular delivery and increases transfection of plasmid DNA. We now report the chemical synthesis and the evaluation of multivalent CPP−PNA constructs incorporating monomeric ($p53^{mono}$) and dendrimer-like tetrameric ($p53^{tet}$) forms of the p53 tetramerization domain containing peptide, a 10 arginine CPP domain (R10), and a splice redirecting PNA (PNA705). These CPP−PNA conjugates were termed $R10p53^{tet}$-PNA705 and $R10p53^{mono}$-PNA705, referring to their oligomerization state. The present study demonstrates that the splicing redirection efficiency of PNA705 is much greater in the context of the tetrameric $R10p53^{tet}$-PNA705 construct than for the monomeric and occurs at nanomolar concentrations, demonstrating that multivalency is an important factor in delivering PNA into cells.

INTRODUCTION

Oligonucleotide (ON)-based agents have shown great potential in regulating gene expression and are routinely used to carry out functional genomics analyses. However, neither natural nucleic acids nor their chemically modified homologues are taken up efficiently by most cell types. While this challenge is easily circumvented through the use of transfection techniques in cultured cells, the systemic delivery of ONs in experimental animals remains a major limitation. Likewise, clinical trials with antisense ONs have resulted in mixed successes (*1*). Even very potent agents such as siRNAs have led to few clinical trials so far, due to a lack of efficient and nontoxic delivery vectors. Cell-penetrating peptides (CPP) represent good candidates for the intracellular delivery of nucleic acids with short oligoarginine motifs and peptides derived from the HIV Tat protein (Tat 48−60) and the Antennapedia homeodomain (Penetratin) being the most widely cited CPPs. The evaluation of CPPs in delivering functional ONs can best be achieved using the splicing redirection assay proposed by Kole (*2*). The assay is based on the splicing alteration in the β-globin gene in thalassemia. Intronic mutations (such as mutation 705 in intron 2) activate cryptic splice sites in this gene leading to a nonfunctional mRNA. This mutated intron has been introduced into the coding region of a reporter luciferase gene, and the construct has been stably transfected into HeLa cells. Masking the 705 mutated site with an antisense ON results in the reorientation of the splicing machinery toward intron elimination and to luciferase expression. The assay is easy to implement (assessing splicing by luminescence or by RT-PCR) and provides signals covering a high dynamic range. It has now been adopted by many groups in the field of drug delivery as a convenient way to compare the performance of various CPP carriers in delivering ON analogues (*3*−*6*). A broad range of ON analogues has been synthesized to date that do not recruit RNase H. However, peptide nucleic acids (PNA) and phosphorodiamidate morpholino oligomer (PMO) analogues are particularly suited as therapeutic agents since they are RNase H incompetent, are metabolically stable, and hybridize to RNA with high affinity and specificity. Initial assays with a panel of CPPs including Tat 48−60, Penetratin, oligo-Arg, or oligo-Lys have been disappointing, since no efficient splicing correction could be demonstrated in the absence of endosomolytic agents at submicromolar CPP−ON conjugate concentrations. By contrast, encouraging data have been obtained with an arginine-rich peptide named $(RXR)_4$-PNA or -PMO (where X stands for an unnatural aminohexanoyl moiety) (*7*), with R_6-Penetratin-PNA (in which an Arg-rich tail has been appended to Penetratin) (*8*), and with the subsequent serum-stable Pip-PNAs (*9*). Dose-dependent and sequence-specific splicing correction has been achieved at micromolar or slightly lower concentrations in the absence of endosomolytic agents. Importantly, these PMO and PNA conjugates of Arg-rich CPPs also lead to splicing redirection in murine models of Duchenne muscular dystrophy (DMD) (*10*, *11*). Such peptides are being evaluated for clinical applications, such as DMD, but it remains unclear at present whether the CPP-PMO doses required to be administered to humans will avoid potential liver and other toxic effects.

As far as mechanisms are concerned, it is now generally considered that CPP-PNA and PMO conjugates are taken up by endocytosis after binding to cell surface heparan sulfates.

* Corresponding author. Jean Gariepy, Ph.D., professor, Tel: 416-946-2967; fax: 416-946-6529; E-mail: gariepy@uhnres.utoronto.ca.
[†] UMR 5235 CNRS.
[‡] Medical Research Council, Laboratory of Molecular Biology.
[§] University of Toronto.

10.1021/bc900075p CCC: $40.75 © 2009 American Chemical Society
Published on Web 07/10/2009

Structure activity (SAR) and mechanistic studies currently in progress with conjugates based on both $(RXR)_4$ and Pip CPP types have confirmed that entrapment within endocytic vesicles remains a major limitation. Studies of $(RXR)_4$-PMO intracellular distribution, in particular, clearly demonstrated that splicing redirection activity was due to the low amount of material that escaped from entrapment within endocytic vesicles.

The multivalent display of peptides harboring arginine- or lysine-containing CPP import sequences has been shown to dramatically enhance the cellular uptake levels of associated cargoes (*12*, *13*). Specifically, synthetic branched peptides incorporating CPP sequences (loligomers) (*12*, *14*, *15*) as well as recombinant peptide constructs containing a self-assembling motif such as the p53 tetramerization domain (*13*, *16*) have been shown to carry more efficiently drugs and chromophores into cells than the equivalent concentration of monomeric CPP homologues (*15*). Similarly, the condensation of such multivalent CPP dendrimers with plasmids results in particle complexes displaying excellent efficiency in entering targeted cells (*14*). In this report, we discuss the chemical assembly and evaluation of multivalent CPP−PNA constructs incorporating monomeric and tetrameric forms of a $p53^{tet}$ domain containing peptide ($p53^{tet}$), a 10 arginine CPP domain (R10), and a splice redirecting PNA (PNA705). These CPP−PNA conjugates were termed R10$p53^{tet}$-PNA705 and R10$p53^{mono}$-PNA705 constructs, referring to their oligomerization state. The present study demonstrates that multivalency is an important factor in delivering PNA into cells.

EXPERIMENTAL PROCEDURES

Synthesis of PNA. The N-terminal nitropyridyl (Npys) cysteine-containing PNA705 (NH_2-Cys(NPys)-Lys-CCTCTTACCTCAGTTACA-Lys-amide) was synthesized on a Liberty microwave peptide synthesizer (CEM) by the Fmoc/Bhoc solid-phase method as previously described using monomers obtained from Link Technologies Ltd. (Lanarkshire, Scotland) or Panagene Inc. (Daejeon, Korea), purified by HPLC, and analyzed by MALDI-TOF mass spectrometry on a Voyager DE Pro BioSpectrometry workstation as previously described (*9*, *17*).

Synthesis and Characterization of R10p53 Peptides. The peptides R10$p53^{tet}$ (R_{10}GEYFTLQIRGRERFEMFRELNEALELKDAQAGCGH$_6$) and R10$p53^{mono}$ (R_{10}GEYFTLQIRGRERFEMFREPNEALELKDAQAGCGH$_6$) were assembled by Fmoc solid-phase peptide synthesis as previously described (*16*). A single mutation of Leucine 344 to Proline (underlined residue) prevents tetramerization. A single cysteine residue was also introduced at their C-terminal end for the subsequent directional coupling of PNA. Peptides were purified to homogeneity by reverse-phase HPLC, and their sequences were confirmed by MALDI-TOF masses: R10$p53^{tet}$, calculated 6363.3, found 6361.2; R10$p53^{mono}$, calculated 6347.2, found 6345.2. The oligomerization status of R10p53 peptides was confirmed by cross-linking these peptides with glutaraldehyde followed by SDS-PAGE, which reveals the presence of a distinctive ladder of protein bands (monomer, dimer, and oligomers of p53 peptides) in the case of tetrameric $p53^{tet}$-containing peptides (Figure 1) as described elsewhere (*18*).

Peptide−PNA Conjugates. Single cysteine residues were inserted in both PNA 705 and R10p53 peptides to covalently link peptide and PNA via a disulfide bond (Table 1) as previously described, using a 2.5-fold excess of peptide component over NPys PNA component. Conjugate purifications were carried out by reverse-phase HPLC and analyzed by MALDI-TOF mass spectrometry as described elsewhere (*9*, *17*). MALDI-TOF masses: R10$p53^{tet}$-PNA705, calculated 11487.3, found 11485.4; R10$p53^{mono}$, calculated 11471.3, found 11467.0.

Cells and Cell Culture. HeLa pLuc705 cells were stably transfected with pLuc/705 plasmid in which the coding sequence of the luciferase gene is interrupted by the mutated intron 2 of the human β globin gene. Cells were cultured at 37 °C, 5% CO_2, as exponentially growing subconfluent monolayers in DMEM medium (Gibco, Cergy-Pontoise, France) supplemented with 10% fetal bovine serum (FBS).

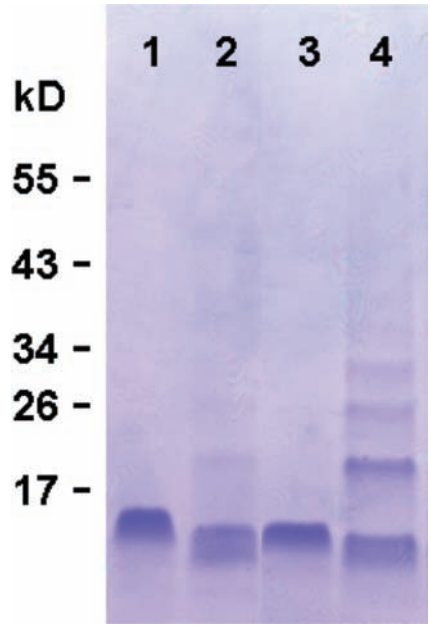

Figure 1. Glutaraldehyde cross-linking of monomeric and tetrametic p53 peptides demonstrating the presence of R10p53 peptide oligomers only for the tetrameric R10$p53^{tet}$ peptide. Coomassie-stained SDS PAGE gel highlights a single protein band migration pattern for unmodified monomeric R10p53 peptide analogue (harboring a L344P mutation; lane 1, $p53^{mono}$) or cross-linked with 0.2% glutharaldehyde for 20 min (lane 2). The unmodified form of the tetrameric R10p53 analogue (lane 3) generates a comparable single band pattern, while the presence of glutaraldehyde results in a characteristic ladder of protein bands associated with the presence of R10$p53^{tet}$ domain oligomers in solution.

Table 1. Sequences of PNA Conjugates

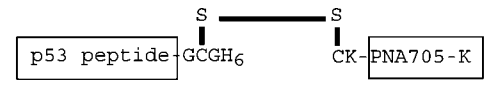

$p53^{mono}$=R_{10}GEYFTLQIRGRERFEMFRELNEALELKDAQA

$p53^{tet}$=R_{10}GEYFTLQIRGRERFEMFREPNEALELKDAQA

PNA 705=cctcttacctcagttaca

Splicing Redirection Assay. The PNA conjugates incorporating either monomeric or tetrameric R10p53 or $(RXR)_4$ were incubated for 1 h at 37 °C in 1 mL optiMEM with exponentially growing HeLa pLuc 705 cells (1.75×10^5 cells/well seeded and cultivated overnight in 24 well plates). Cells were then washed twice with ice-cold PBS and incubation continued for 23 h in complete DMEM supplemented with 10% FBS. Cells were washed twice with ice-cold PBS and lysed with Reporter Lysis Buffer (Promega, Madison, WI, USA). The same protocol was used for HeLa pLuc 705 cells treated with 100 μM chloroquine (Figure 4B). Luciferase activity was measured using a Berthold Centro LB 960 luminometer (Berthold Technologies, Bad Wildbad, Germany) using the Luciferase Assay System substrate (Promega, Madison, WI, USA). Cellular protein concentrations were measured with the BCAProtein Assay Kit (Pierce, Rockford, IL, USA) and read using an ELISA plate reader (Dynatech MR 5000, Dynatech Laboratories, Chantilly,

VA, USA) at 550 nm. Luciferase activities were expressed as relative luminescence units (RLU) per μg protein. All experiments were performed in triplicate. Each data point represents the average of three replicates.

RT-PCR Analysis of Splicing Redirection. Total RNA was extracted from cellular lysates obtained as described in the previous paragraph using the Tri-Reagent kit (Sigma, St. Quentin Fallavier, France) according to manufacturer's instructions. The extracted RNA was amplified by RT-PCR (MJ Research PTC 200 Peltier Thermal Cycler) with forward primer 5′TTG ATA TGT GGA TTT CGA GTC GTC3′ and reverse primer 5′TGT CAA TCA GAG TGC TTT TGG CG3′. The products were analyzed by electrophoresis on a 2% agarose gel.

Saponin Cell Permeabilization. Exponentially growing HeLa pLuc705 cells (1.75×10^5 cells seeded and grown overnight in 24 well plates) were coincubated with the PNA conjugate and with 20 μg/mL of saponin for 30 min. The cells were then washed and incubation continued for 24 h in complete medium (DMEM plus 10% FBS). Cells were washed twice with ice-cold PBS, lysed with reporter lysis buffer, and processed as described above.

RESULTS

Design and Characterization of p53^{tet} Domain-Based PNA Delivery Peptides. As described in the Introduction, the human p53^{tet} tetramerization domain (residues 325−355; GEYFTLQIRGRERFEMFRELNEALELKDAQA) is able to self-assemble into a well-defined tetramer in solution and to enhance the cellular import of conjugated cationic CPPs, as compared to its monomeric counterpart (*13*, *16*). Importantly, the condensation of NLS-R10-p53^{tet} with luciferase reporter plasmid DNA led to complexes that increased the levels of luciferase expression in cells when compared to p53^{mono} constructs (*16*). In terms of designing CPP vectors better able to deliver steric-block ON analogues into cells, we have synthesized a new CPP construct in which an arginine-rich motif (R10) has been attached to the tetramerization domain (residues 325−355) of the human p53 protein. A cysteine was inserted near its C-terminus to covalently attach a PNA, while a short His_6 tag was added for purification purposes (Table 1).

The synthetic peptide was chemically conjugated to a splice-redirecting 18-base-long PNA complementary to the 705 splice site (PNA 705), which we have used extensively in conjugation with other CPPs (*9*). In contrast to our previous CPP-p53^{tet} conjugates designed for plasmid delivery, no nuclear localization signal was included in the construct, since the molecular mass of the conjugate should be small enough to allow diffusion from the cytoplasm to the nuclei through the nuclear pores. R10p53^{tet}-PNA705 conjugates were constructed by forming a disulfide bond between unique cysteine thiol groups present in the p53 peptide and the PNA705 (Table 1) (*17*). A monomeric PNA705 conjugated to a R10p53^{mono} peptide was also synthesized to serve as a control. The monomeric form of the p53 tet domain was generated by introducing a single mutation (L344P) within its sequence: a modification that is known to block tetramer formation (*16*). Both conjugates were purified by reverse-phase HPLC and characterized by MALDI-TOF mass spectral analysis. The oligomerization state of each peptide was confirmed following glutaraldehyde cross-linking experiments with only the tetrameric peptide R10p53^{tet} giving rise to a characteristic ladder of peptide oligomers on SDS PAGE (*18*) (Figure 1). The sequences of the PNA conjugates are presented in Table 1. Light scattering experiments in aqueous solution for the R10p53^{tet}-PNA705 conjugate suggested some level of aggregation, whereas no such signal was observed for the R10p53^{mono}-PNA705 conjugate (data not shown). The exposure of cells to these 10R-p53 peptides did not lead to cell toxicity even at concentrations of up to 25 μM (the highest concentration tested; ref 16).

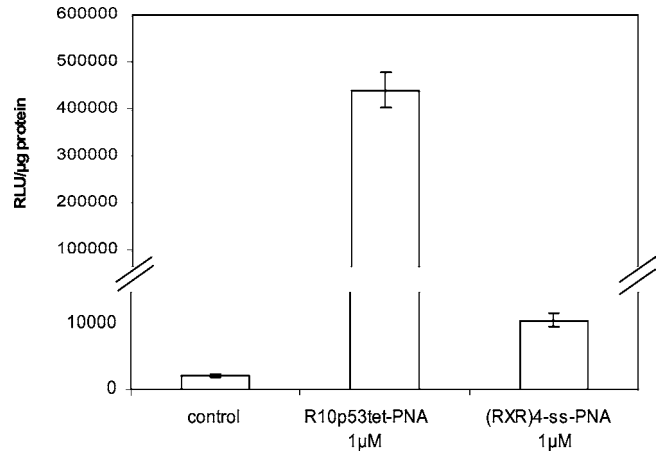

Figure 2. Comparison of R10p53^{tet}-PNA705 with $(RAhxR)_4$-PNA705 in the luciferase assay. Hela pLuc 705 cells were incubated for 4 h with either R10p53^{tet}-PNA705 or $(RAhxR)_4$ PNA705 conjugate at the concentration of 1 μM. After treatment, cells were washed twice with 500 μL PBS, and incubation was continued for 20 h in the presence of complete medium (10% FBS plus DMEM). Luciferase expression was measured 20 h later and was expressed as RLU/μg protein. The control histogram bar represents cells untreated with peptide−PNA conjugates. Each histogram bar represents the averaged RLU/μg protein value with its associated standard deviation derived from experiments performed in triplicate.

R10p53^{tet}-PNA Is Very Effective at Correcting a Defective Luciferase Reporter Gene Located Inside Cells. Our first objective was to establish if the construct R10p53^{tet}-PNA705 CPP could enter HeLa pLuc705 cells and perform the splicing redirection function expected of the conjugated steric-block PNA705 oligomer leading to the expression of active luciferase (*2*). This construct was evaluated and compared to the PNA705 conjugate with the cationic CPP $(RXR)_4$ (data not shown). The conjugate was prepared in OptiMEM medium to avoid technical issues arising from the absorption or proteolytic degradation of CPP peptides in serum. Specifically, the presence of serum has been shown by us and others to generally reduce the in vitro efficiency of CPP conjugates (*5*, *6*, *19*), an effect that does not correlate with their in vivo performance. For instance, $(RAhxR)_4$ PMO conjugates performed poorly in vitro when prepared in serum-containing medium but have been used successfully in vivo in a murine model of Duchenne muscular dystrophy (*9*).

As presented in Figure 2, the treatment of HeLa pLuc705 cells with R10p53^{tet}-PNA705 at 1 μM concentration in the absence of any transfection agent gave rise to an approximately 45-fold higher increase in luciferase signal when compared to the $(RXR)_4$-PNA705 conjugate. In order to monitor whether the increased efficiency of R10p53^{tet}-PNA was due to peptide-based tetramerization, R10p53^{tet}-PNA705 was also compared to its monomeric R10p53^{mono}-PNA counterpart in a dose−response experiment. As expected, the tetrameric form was 10-fold more active in the redirection of luciferase splicing than its monomeric form at nanomolar concentrations (Figure 3A,B). Both peptide conjugates were soluble in the transfection media (OptiMEM), and no signs of toxicity were observed under the tested conditions, as assessed in terms of cell viability and protein levels (data not shown). Using the same experimental samples, it was also demonstrated that the cellular delivery of R10p53^{tet}-PNA705 and R10p53^{mono}-PNA705 constructs at submicromolar concentrations into HeLa pLuc705 cells resulted in

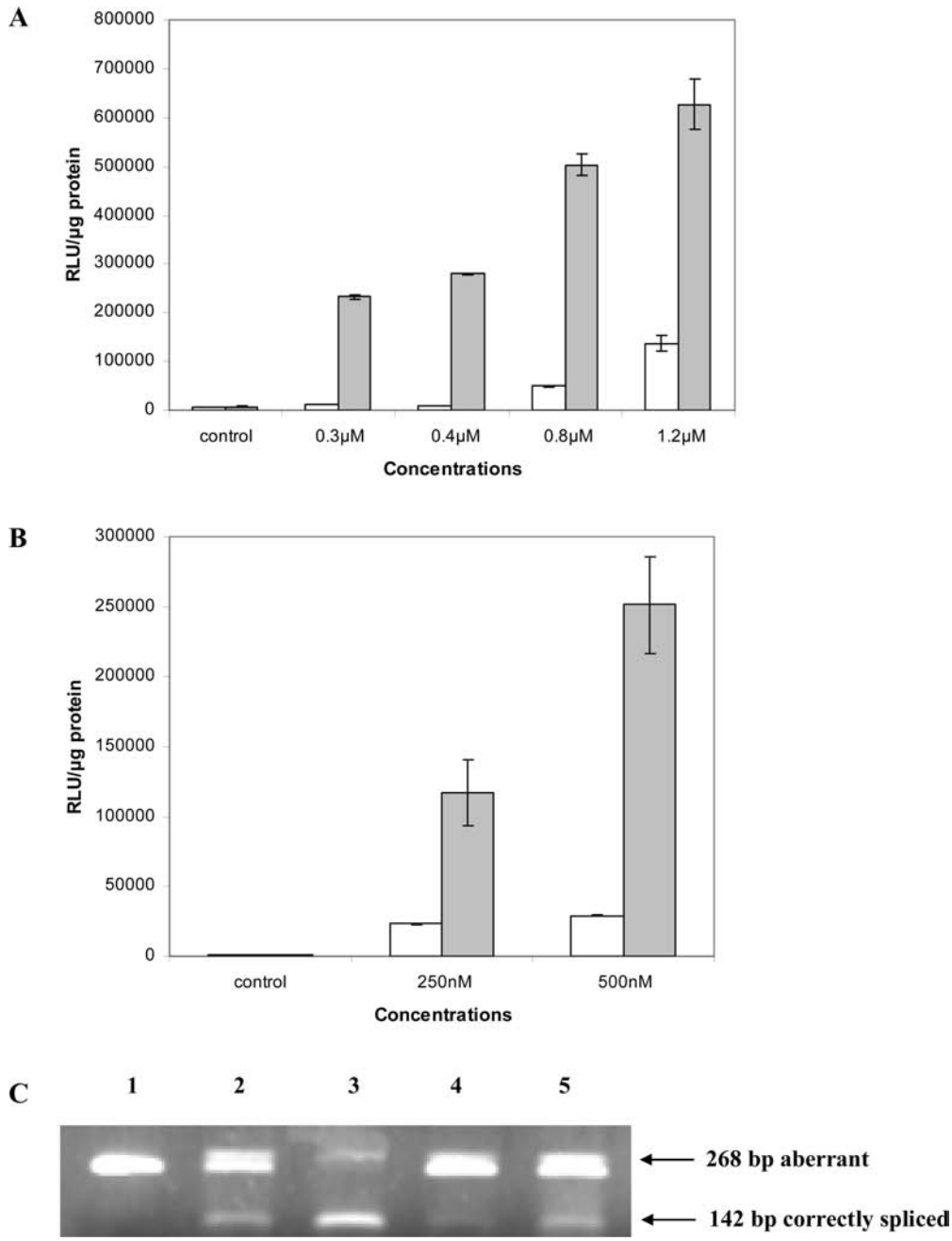

Figure 3. Effect of peptide−PNA concentration on cellular gene correction event. Panels A and B. Dependency of cellular luciferase activity on extracellular peptide−PNA concentration as derived from two separate experiments. HeLa pLuc 705 cells were incubated for 1 h in medium containing R10p53^{tet}-PNA705 (gray bars) or R10p53^{mono}-PNA705 (white bars) conjugates at the indicated concentrations. Luciferase expression was measured 20 h later and expressed as RLU/μg protein. Each histogram bar represents the averaged RLU/μg protein value with its associated standard deviation derived from experiments performed in triplicate. Panel C. RT-PCR detection of correctly spliced transcripts in HeLa pLuc 705 cells at nanomolar concentrations of R10p53-PNA constructs. Lane 1, Nontreated cells (control); Lane 2, R10p53^{tet}-PNA705 250 nM; Lane 3, R10p53^{tet}-PNA705 500 nM; Lane 4, R10p53^{mono}-PNA705 250 nM; Lane 5, R10p53^{mono}-PNA705 500 nM. The RT-PCR experiment was performed with cellular lysates used for generating panel B. The upper band corresponds to the aberrantly spliced luciferase mRNA and the lower band to the correctly spliced mRNA.

the correct splicing of the luciferase transcript at the RNA level (Figure 3C). In brief, treated cells were lysed, and aliquots were processed either for the luciferase luminescence assay or for an RT-PCR assay where the two forms (aberrant and correctly spliced) of luciferase mRNA were amplified. The appearance of the correctly spliced mRNA was dose-dependent and matched the decrease of the aberrantly spliced mRNA. Again, the splicing redirection event was significantly more pronounced for the tetrameric conjugate when compared to its monomeric counterpart.

Mechanism of Cellular Uptake. The mechanism by which cationic CPP−cargo conjugates enter cells is defined by the CPP valency/aggregation state within complexes (*13*, *16*) and the concentration of the CPP/cargoes complexes outside cells. At extracellular CPP concentrations in the 5−100 μM range, cationic CPPs can enter cells via both endocytic and membrane-active mechanisms, which explains the co-observation of both energy-dependent endocytotic and energy-independent entry pathway(s) (*20*). However, the practicality of using CPPs in vivo as delivery vectors would favor their

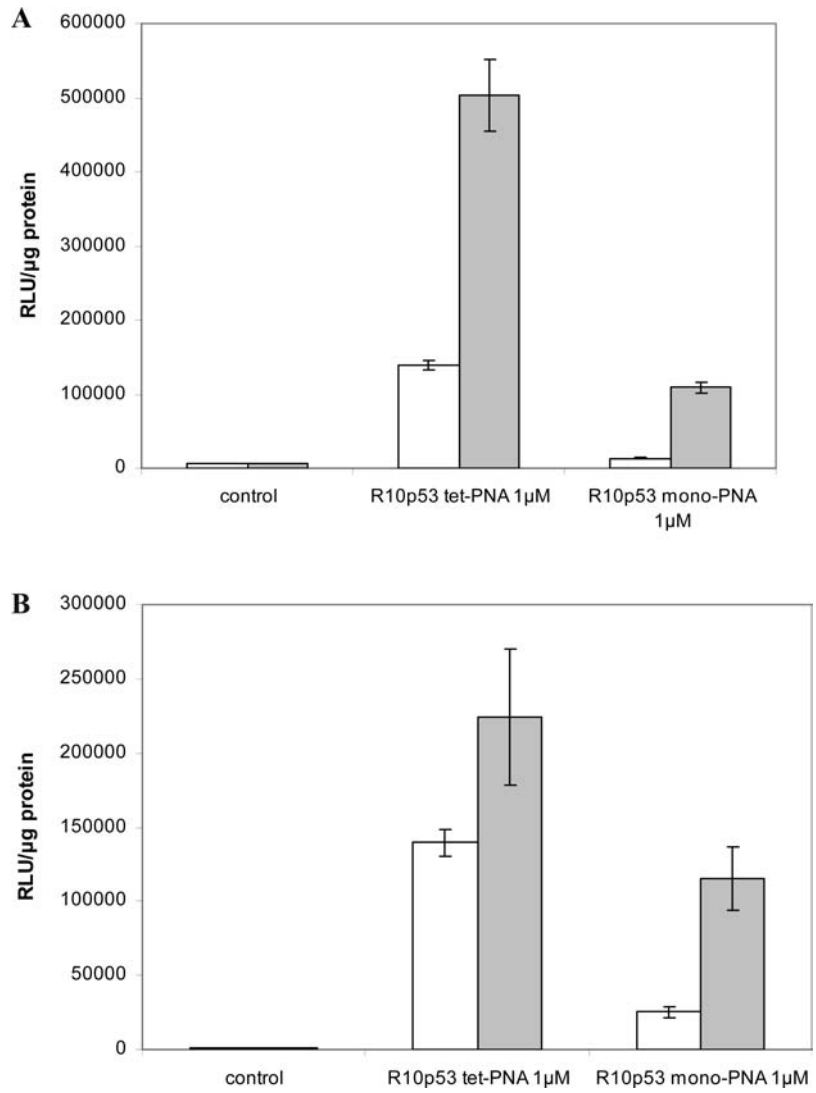

Figure 4. Mechanism of peptide−PNA internalization. Panel A: R10p53^{tet}-PNA and R10p53^{mono}-PNA conjugates are internalized by an energy-dependent mechanism. The splicing correction assay was used to assess the effect of temperature (energy dependency) on peptide−PNA delivery into cells. HeLa pLuc 705 cells were preincubated for 30 min at 4 °C (white bars) or at 37 °C (gray bars) and subsequently exposed to R10p53-PNA conjugates (1 μM) for 1 h under the same conditions. Panel B: Effect of chloroquine on the cytosolic delivery of peptide−PNA constructs leading to luciferase gene correction in HeLa pLuc 705 cells. Cells were incubated for 1 h with either R10p53^{tet} -PNA705 or R10p53^{mono}-PNA705 conjugates (1 μM) in the absence (white bars) or presence (gray bars) of 100 μM chloroquine. Luciferase expression was measured 23 h later and expressed as RLU/μg protein. Each histogram bar represents the averaged RLU/μg protein value with its associated standard deviation derived from experiments performed in triplicate.

use at low micromolar to submicromolar concentrations where their membrane active properties are not observed. Thus, a comparison of the mechanism of cell entry of the tetrameric and monomeric R10p53-PNA705 constructs seemed worthwhile. Therefore, cells were first preincubated at 37 °C or at 4 °C (i.e., at a temperature that prevents any form of endocytosis) before being treated with the conjugates under the same conditions for 1 h. The results (Figure 4A) show a much-reduced splicing redirection activity (as measured by the level of luciferase activity) at low temperature for both monomeric and tetrameric constructs, which suggests an endocytotic mechanism of internalization occurring at a 1 μM concentration.

Since endosomal sequestration remains the principal limitation for the cellular delivery of ONs conjugated to CPPs that pass through the endocytotic route, we incubated cells with each form of R10p53-PNA705 in the presence or absence of chloroquine, a well-known endosomolytic agent (*21, 22*). The splicing redirection efficiency of the PNA conjugate was found to be significantly enhanced (7-fold) in relation to the monomeric conjugate (Figure 4B), which supports the model that entrapment in endocytic vesicles is a limiting step in the cytoplasmic and nuclear release of such conjugates. Interestingly, chloroquine treatment was found to have a much smaller effect on splicing redirection in the case of R10p53^{tet}-PNA705.

Effect of Saponin Treatment. To circumvent the endocytotic pathway, cells were treated under mild conditions with saponin (20 μg/mL), a detergent which transiently permeabilizes the plasma membrane without damaging cells (*23*). Coincubation of R10p-53^{mono}-PNA705 conjugate with saponin gave the expected substantial augmentation of the splicing redirection activity (Figure 5) consistent with other cationic CPP−PNAs previously tested (*7*). However, the observed luciferase expression level remained lower than the value obtained for the tetrameric conjugate without permeabilization. The effect of saponin treatment on the cellular delivery of R10p53^{tet}-PNA705 led to a lower splicing redirection activity comparable to splicing levels observed for the monomeric conjugate. One possible explanation for this result is that the tetrameric conjugate dissociates when coincubated with detergent (loss of valency), behaving the same way as the monomeric

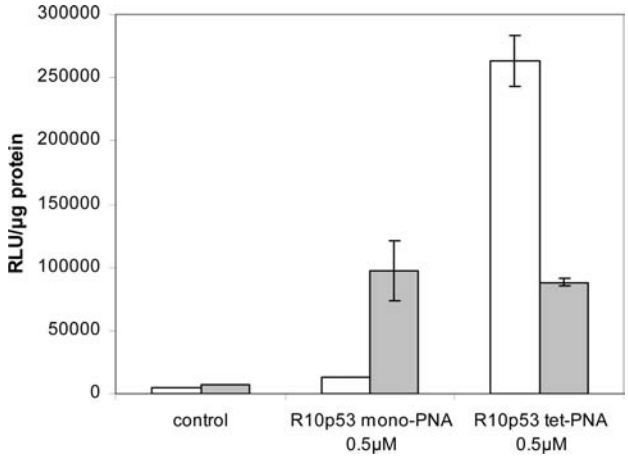

Figure 5. Effect of saponin on delivering peptide−PNA constructs into HeLa pLuc 705 cells. HeLa pLuc705 cells were coincubated with either R10p53^{tet} -PNA705 or R10p53^{mono}-PNA705 conjugates (0.5 μM) in the absence (gray bars) or presence (white bars) of saponin for 30 min. The expression of properly corrected luciferase gene product in HeLa pLuc705 cells was measured as previously described. Each histogram bar represents the averaged RLU/μg protein value with its associated standard deviation derived from experiments performed in triplicate.

conjugate. As shown in Figure 1 (lane C), detergents such as SDS do dissociate the tetramer.

DISCUSSION

Previous work has established that CPP oligomerization through the construction of peptide dendrimers can significantly improve cellular uptake and cytoplasmic delivery of arginine-rich CPPs. The potential of displaying multiple CPPs and their cargoes in the context of the p53 tetramerization domain was evaluated here using a well-characterized splicing redirection assay. The R10p53^{tet}-PNA construct was approximately 45 times more efficient than $(RXR)_4$PNA (Figure 2) and even more active than the Pip2b-PNA construct (ref 9 and data not shown). These results are important, since the Pip series represented until now the most efficient cationic CPP-based PNA delivery vectors.

In order to verify whether the increased efficiency of the R10p53^{tet}-PNA was effectively due to its tetrameric configuration, a monomeric version (R10p53^{mono}-PNA) was engineered through the replacement of leucine 344 by a proline residue, a mutation known to prevent the tetramerization of p53 peptide. Splicing redirection was reduced by a factor of about 10 in keeping with the reduced transfection of a plasmid DNA previously reported by Kawamura and her co-workers (*16*). However, notable differences between the constructs used in these studies should be pointed out. First, the R10p53^{tet}- and R10p53^{mono}- conjugates used in this study do not include a nuclear localization signal (NLS), in contrast to the NLS-10R-P53^{tet} constructs used to condense and transfect luciferase and β-galactosidase reporter plasmids. Also, the number of NLS-10R-p53^{tet} or NLS-10R-p53^{mono} peptides complexed to a single plasmid was not defined in our previous study (*16*). Specifically, the CPP-mediated delivery of DNA plasmids requires that cationic CPPs fulfill more than one role: first, by acting to neutralize the anionic character of plasmid DNA and, second, by condensing the resulting complexes into particles that retain the capacity of CPPs to cause cellular import. By contrast, the role of the present 10Rp53 peptides is limited to the cellular internalization and trafficking of an uncharged PNA cargo. Specifically, the single 18-base-long PNA705 was chemically conjugated to the CPP moiety such that the resulting monomers and tetramers obtained are simple, well-defined structures. Altogether, the present study provides a more direct evaluation of the potential of oligomerization on the nuclear delivery of a cargo.

As highlighted in Figures 2−5, the tetrameric R10p53^{tet}-PNA705 construct represents by far the most effective peptide-PNA705 construct to date in terms of correcting the genetic defect present in HeLa pLuc705 cells. This construct was able to deliver an effective dose of the PNA705 peptide nucleic acid to the cytosol of these cells when present outside HeLa pLuc705 cells at nanomolar concentrations. Somewhat unexpectedly, the R10p53^{mono}-PNA construct remained slightly more active than the $(RXR)_4$PNA conjugate. Clues as to why both R10p53-PNAs are more effective in delivering PNA705 to cells than the $(RXR)_4$PNA conjugate may be linked to two parameters. First, the spacial presentation of CPPs on a p53^{tet} scaffold (branched display where CPPs are equivalently presented) is not identical to that of the $(RXR)_4$PNA conjugate (single CPP consisting of a linear sequence of short internal diarginyl-containing peptide motifs). Second, the p53 constructs possess a higher arginine content (4 × 10 Arg; p53^{tet} scaffold and 10 Arg for the monomeric form) than in the case of the (RXR)4-ss-PNA (4 × 2 Arg) construct. Finally, the presence of the hexahistidine tag in the p53 constructs may also be consequential.

Further studies will be required to identify what features of the p53 peptide and $(His)_6$ domains (see Table 1 for the complete sequence) have a positive impact on PNA delivery.

The mechanism by which CPP−cargo conjugates enter cells remains in part dependent on the steady-state levels of CPP concentration outside cells. Mechanisms involving a direct energy-independent translocation (*20, 23*) as well as various endocytotic pathways (*24*−*27*) have been proposed. Dominance of one or another internalization pathways appears to be linked to the concentration of CPP-conjugates experienced by cells with high local (membrane-bound) concentration of CPP-conjugates (high micromolar range) favoring the aggregation and membrane-active properties of cationic peptides allowing for their direct cell translocation, whereas low CPP concentrations lead to internalization via proteoglycan binding and to endocytic pathways (*28, 29*). As an in vivo drug delivery strategy, CPP concentrations needed to achieve energy-independent translocation are too high (>10 μM) to be effective and may result in cell cytotoxicity.

Internalization of both the tetramer and the monomer R10p53-PNA constructs is energy dependent as previously demonstrated for R10p53 peptides (*16*) and in our functional assay when R10p53 peptides deliver their PNA705 cargo. Specifically, the exposure of HeLa pLuc705 cells to low temperature reduces the expression of functional luciferase driven by the presence of either R10p53 constructs in the medium (Figure 4A). These findings are in accordance with previous work reporting a clathrin-mediated endocytotic pathway of cell uptake for fluorescein-tagged 10R-p53^{tet} peptides (*16*).

Taken together, these observations do not point to differences in the cellular entry mechanism as an explanation for the increased efficiency of R10p53^{tet}-PNA as compared to its monomeric analogue or to $(RXR)_4$PNA. A significant fraction of R10p53 peptides remains trapped in endosomes. As expected, chloroquine treatment, which is known to promote endosomal release of entrapped CPP−cargo conjugates (*30*), indeed causes a significantly more pronounced increase in splicing correction for R10p53^{mono}-PNA compared to R10p53^{tet}-PNA (Figure 4B). Whether this increased ability to escape endocytic vesicles is the only determinant of the increased splice redirecting activity of R10p53^{tet}-PNA as compared to the monomeric form cannot be ascertained on this basis. The presence of chloroquine is thus not essential for cellular delivery using the R10p53^{tet}-PNA

construct. Interestingly, $(RAhxR)_4$ PMO conjugates have been used in vivo (in the absence of the lysosomotropic amine agent chloroquine) and were able to promote exon skipping in the *mdx* mouse model of Duchenne muscular dystrophy (*9*). The constructs used in the present study are more efficient in vitro than these $(RAhxR)_4$ PMO constructs when compared in the same assay in the absence of chloroquine. Thus, we expect that they might be more efficient in vivo in the absence of chloroquine.

We thus attempted to deliberately bypass endocytosis by submitting cells to a brief saponin treatment under mild conditions, known to transiently permeabilize the plasma membrane with minimal alteration of cell physiology (*23*). As expected and in line with previous data from our group for other CPP−PMO/PNA conjugates (*7*), splicing correction by $R10p53^{mono}$-PNA was increased in saponin-treated cells but did not reach the efficiency achieved by $R10p53^{tet}$-PNA in untreated cells. One of the many possible explanations could be that the more bulky $R10p53^{tet}$-PNA construct more efficiently masks the cryptic splice site and reorients the splicing machinery. Unexpectedly, splicing redirection was less efficient in saponin-treated cells for the $R10p53^{tet}$-PNA construct. It might be due to a conversion of the tetrameric form into the monomeric form upon saponin treatment.

Altogether, our results confirm the potential of CPP oligomerization as a strategy to enhance the delivery of conjugated cargoes into cells. Specifically, the cellular delivery and splicing activity of PNA705 observed at nanomolar concentrations for the tetrameric R10p53-PNA construct is remarkable when compared to all other CPP strategies tested to date. This study provides a proof-of-concept for exploiting multivalent CPP strategies in the context of in vivo applications. Future work by our group will include the grafting of CPPs and cargoes onto simpler synthetic dendrimeric scaffolds.

ACKNOWLEDGMENT

This work was funded by IFCPAR (contract 3205-A) and AFM (contract 13345) grants to BL and by grants from the Canadian Breast Cancer Research Alliance in collaboration with the Canadian Cancer Society to JG. R. Abes is recipient of a predoctoral LNFCC fellowship and F. Said Hassane of a post doctoral AFM fellowship.

LITERATURE CITED

(1) Rayburn, R. E., and Zhang, R. (2008) Antisense, RNAi, and gene silencing strategies for therapy: mission possible or impossible? *Drug Discovery Today 13*, 513–521.

(2) Kang, S. H., Cho, M. J., and Kole, R. (1998) Up-regulation of luciferase gene expression with antisense oligonucleotides: implications and applications in functional assay development. *Biochemistry 37*, 6235–6239.

(3) Abes, R., Arzumanov, A. A., Moulton, H. M., Abes, S., Ivanova, G. D., Iversen, P. L., Gait, M.J., and Lebleu, B. (2007) Cell-penetrating-peptide-based delivery of oligonucleotides: an overview. *Biochem. Soc. Trans. 35*, 775–779.

(4) El Andaloussi, S., Guterstam, P., and Langel, U. (2007) Assessing the delivery efficacy and internalization route of cell-penetrating peptides. *Nat. Protoc. 2*, 2043–2047.

(5) Wu, R. P., Youngblood, D. S., Hassinger, J. N., Lovejoy, C. E., Nelson, M. H., Iversen, P. L., and Moulton, H. M. (2007) Cell-penetrating peptides as transporters for morpholino oligomers: effects of amino acid composition on intracellular delivery and cytotoxicity. *Nucleic Acids Res. 35*, 5182–5191.

(6) Koppelhus, U., Shiraishi, T., Zachar, V., Pankratova, S., and Nielsen, P. E. (2008) Improved cellular activity of antisense peptide nucleic acids by conjugation to a cationic peptide-lipid (CatLip) domain. *Bioconjugate Chem. 19*, 1526–1534.

(7) Abes, R., Moulton, H. M., Clair, P., Yang, S. T., Abes, S., Melikov, K., Prevot, P., Youngblood, D. S., Iversen, P. L., Chernomordik, L. V., and Lebleu, B. (2008) Delivery of steric block morpholino oligomers by (R-X-R)4 peptides: structure-activity studies. *Nucleic Acids Res. 36*, 6343–6354.

(8) Abes, S., Turner, J. J., Ivanova, G. D., Owen, D., Williams, D., Arzumanov, A., Clair, P., Gait, M. J., and Lebleu, B. (2007) Efficient splicing correction by PNA conjugation to an R6-Penetratin delivery peptide. *Nucleic Acids Res. 35*, 4495–4502.

(9) Ivanova, G. D., Arzumanov, A., Abes, R., Yin, H., Wood, M. J., Lebleu, B., and Gait, M. J. (2008) Improved cell-penetrating peptide-PNA conjugates for splicing redirection in HeLa cells and exon skipping in mdx mouse muscle. *Nucleic Acids Res. 36*, 6418–6428.

(10) Yin, H., Lu, Q., and Wood, M. (2008) Effective exon skipping and restoration of dystrophin expression by peptide nucleic acid antisense oligonucleotides in mdx mice. *Mol. Ther. 16*, 38–45.

(11) Yin, H., Moulton, H. M., Seow, Y., Boyd, C., Boutilier, J., Iverson, P., and Wood, M. J. (2008) Cell-penetrating peptide-conjugated antisense oligonucleotides restore systemic muscle and cardiac dystrophin expression and function. *Hum. Mol. Genet. 17*, 3909–3918.

(12) Sheldon, K., Liu, D., Ferguson, J., and Gariépy, J. (1995) Loligomers: design of de novo peptide-based intracellular vehicles. *Proc. Natl. Acad. Sci. U.S.A. 92*, 2056–2060.

(13) Sung, M., Poon, G. M., and Gariépy, J. (2006) The importance of valency in enhancing the import and cell routing potential of protein transduction domain-containing molecules. *Biochim. Biophys. Acta, Biomembr. 1758*, 355–363.

(14) Singh, D., Bisland, S. K., Kawamura, K., and Gariépy, J. (1999) Peptide-based intracellular shuttle able to facilitate gene transfer in mammalian cells. *Bioconjugate Chem. 10*, 745–754.

(15) Bisland, S. K., Singh, D., and Gariépy, J. (1999) Potentiation of chlorin e6 photodynamic activity in vitro with peptide-based intracellular vehicles. *Bioconjugate Chem. 10*, 982–992.

(16) Kawamura, K. S., Sung, M., Bolewska-Pedyczak, E., and Gariépy, J. (2006) Probing the impact of valency on the routing of arginine-rich peptides into eukaryotic cells. *Biochemistry 45*, 1116–1127.

(17) Turner, J. J., Ivanova, G. D., Verbeure, B., Williams, D., Arzumanov, A. A., Abes, S., Lebleu, B., and Gait, M. J. (2005) Cell-penetrating peptide conjugates of peptide nucleic acids (PNA) as inhibitors of HIV-1 Tat-dependent trans-activation in cells. *Nucleic Acids Res. 33*, 6837–6849.

(18) Poon, G. M., Brokx, R. D., Sung, M., and Gariépy, J. (2007) Tandem dimerization of the human p53 tetramerization domain stabilizes a primary dimer intermediate and dramatically enhances its oligomeric stability. *J. Mol. Biol. 365*, 1217–1231.

(19) Abes, S., Williams, D., Prevot, P., Thierry, A., Gait, M. J., and Lebleu, B. (2006) Endosome trapping limits the efficiency of splicing correction by PNA-oligolysine conjugates. *J. Controlled Release 110*, 595–604.

(20) Ter-Avetisyan, G., Tunnemann, G., Nowak, D., Nitschke, M., Herrmann, A., Drab, M., and Cardoso, M. C. (2009) Cell entry of arginine-rich peptides is independent of endocytosis. *J. Biol. Chem. 284*, 3370–3378.

(21) Ciftci, K., and Levy, R. J. (2001) Enhanced plasmid DNA transfection with lysosomotropic agents in cultured fibroblasts. *Int. J. Pharm. 218*, 81–92.

(22) Abes, S., Williams, D., Prevot, P., Thierry, A., Gait, M. J., and Lebleu, B. (2006) Endosome trapping limits the efficiency of splicing correction by PNA-oligolysine conjugates. *J. Controlled Release 110*, 595–604.

(23) Hudder, A., Nathanson, L., and Deutscher, M. P. (2003) Organization of mammalian cytoplasm. *Mol. Cell. Biol. 23*, 9318–9326.

(24) Duchardt, F., Fotin-Mleczek, M., Schwarz, H., Fischer, R., and Brock, R. (2007) A comprehensive model for the cellular

uptake of cationic cell-penetrating peptides. *Traffic (Oxford, U.K.) 8*, 848–866.
(25) Richard, J. P., Melikov, K., Vives, E., Ramos, C., Verbeure, B., Gait, M. J., Chernomordik, L. V., and Lebleu, B. (2003) Cell-penetrating peptides. A reevaluation of the mechanism of cellular uptake. *J. Biol. Chem. 278*, 585–590.
(26) Richard, J. P., Melikov, K., Brooks, H., Prevot, P., Lebleu, B., and Chernomordik, L. V. (2005) Cellular uptake of unconjugated TAT peptide involves clathrin-dependent endocytosis and heparan sulfate receptors. *J. Biol. Chem. 280*, 15300–15306.
(27) Kaplan, I. M., Wadia, J. S., and Dowdy, S. F. (2005) Cationic TAT peptide transduction domain enters cells by macropinocytosis. *J. Controlled Release 102*, 247–253.
(28) Fretz, M. M., Penning, N. A., Al-Taei, S., Futaki, S., Takeuchi, T., Nakase, I., Storm, G., and Jones, A. T. (2007) Temperature-, concentration- and cholesterol-dependent translocation of L- and D-octa-arginine across the plasma and nuclear membrane of CD34+ leukaemia cells. *Biochem. J. 403*, 335–342.
(29) Poon, G. M., and Gariépy, J. (2007) Cell-surface proteoglycans as molecular portals for cationic peptide and polymer entry into cells. *Biochem. Soc. Trans. 35*, 788–793.
(30) Abes, S., Moulton, H. M., Clair, P., Prevot, P., Youngblood, D. S., Wu, R. P., Iversen, P. L., and Lebleu, B. (2006) Vectorization of morpholino oligomers by the (R-Ahx-R)4 peptide allows efficient splicing correction in the absence of endosomolytic agents. *J. Controlled Release 116*, 304–313.

BC900075P

TAT Peptide and Its Conjugates: Proteolytic Stability

Jacob Grunwald,[¶,†] Tomas Rejtar,[‡] Rupa Sawant,[†] Zhouxi Wang,[‡,§] and Vladimir P. Torchilin*[,†]

Department of Pharmaceutical Sciences and Center for Pharmaceutical Biotechnology and Nanomedicine, Barnett Institute and Department of Chemistry and Chemical Biology, Northeastern University, Boston, Massachusetts 02115. Received February 20, 2009; Revised Manuscript Received June 19, 2009

The proteolytic cleavage of TATp, TATp-PEG_{1000}-PE conjugate (TATp-conjugate), and TATp as TATp-conjugate in mixed micelles made of TATp-conjugate and PEG_{5000}-PE (2.5% mol of TATp-conjugate, TATp-Mic) were studied by HPLC with fluorescent detection using fluorenylmethyl chloroformate (FMOC) labeling and by MALDI-TOF MS analysis. The cleavage kinetics were analyzed in human blood plasma and in trypsin-containing phosphate buffered saline (PBS), pH 7.4, to simulate the proteolytic activity of human plasma. The trypsinolysis of free TATp, TATp-conjugate, and TATp-Mic revealed that the main initial fragmentation is an endocleavage at the carboxyl terminus resulting in an Arg-Arg (RR) dimer. The trypsinolysis followed pseudo-first-order kinetics. The cleavage of the free TATp was relatively fast with a half-life of a few minutes ($t_{1/2} \sim 3.5$ min). The TATp-conjugate showed more stability with about a 3-fold increase in half-life ($t_{1/2} \sim 10$ min). TATp in TATp-Mic was highly protected against proteolysis with an over 100-fold increase in half-life ($t_{1/2} \sim 430$ min). The shielding of TATp by PEG moieties in the proposed TATp-Mic is of great importance for its potential use as a cell-penetrating moiety for multifunctional "smart" drug delivery systems with detachable PEG.

INTRODUCTION

Cell-penetrating peptides (CPPs) are molecules commonly of a polycationic nature. They readily cross the hydrophobic cell membrane (*1–5*) and can facilitate intracellular delivery of conjugated macromolecules and nanoparticles. The mechanism of their activity is not yet completely elucidated (*6–11*), although it is assumed that CPPs themselves and CPPs with a small-sized cargo cross the cell membrane via a combination of hydrophobic and electrostatic interactions (*12*), while CPPs with a large-sized cargo enter cells via macropinocytosis with subsequent escape from endosomes (*13*). In the past decade, numerous works have been published on the use of CPPs for successful *in vitro* and *in vivo* intracellular delivery of biologically active macromolecules (*14–16*), enzymes (*3*), antibodies (*15*), DNA (*17–19*), liposomes (*20–22*), and imaging probes (*3, 23–25*). The most intensively studied CPP is the transactivating transcriptional activator peptide (TATp) derived from the protein transduction domain (PTD) of HIV-1 (*1, 2, 26, 27*) extending from residues 47 to 57 (YGRKKRRQRRR). The composition of TATp is unique for its predominant content of the positively charged amino acids arginine and lysine. This distinct composition makes it highly susceptible to proteolysis by tryptic enzymes. As pointed out in a recent review (*6*), TATp has six potential trypsin cleavage sites. Since the cell penetration property relies on the integrity of the highly basic TATp sequence (*6, 7*), it is clear that the potential of TATp or similar peptides as mediators of intracellular delivery of therapeutic molecules and drug delivery systems *in vivo* could be significantly limited by their cleavage with proteolytic enzymes (*28–31*).

Despite the enormous number of publications on the use of TATp as a mediator of intracellular delivery, only a few authors have investigated the *in vivo* instability of TATp (*28*) that results from its proteolytic cleavage (*28, 29*). To obtain stable CPPs, an all D-enantiomer peptide was suggested (*30, 31*); another approach offered to overcome proteolytic degradation (*32, 33*) was the replacement of the amino acids, which are particularly susceptible to degradation, with their stable synthetic mimics.

In the study specifically dedicated to the enzymatic cleavage of TATp (*28*), the investigation of furin cleavage of HIV-1 TATp showed that cleavage takes place at the carboxyl terminus and greatly reduces its transactivation activity. However, no studies have been done to determine the kinetics of the proteolysis of TATp or fragment identification by MS.

Our aim was to study the exact pattern of TATp proteolysis and compare the stability against proteolysis (trypsinolysis) of different forms of TATp: native TATp, TATp conjugated with poly(ethylene glycol)-phosphatidyl ethanolamine block copolymer (TATp-PEG-PE), and TATp as TATp-PEG-PE incorporated into PEG-PE micelles with the PEG block in the PEG-PE longer than the PEG block in TATp-PEG-PE conjugate. The kinetics of the proteolytic cleavage of TATp in these forms were investigated using HPLC with fluorescent labeling and MALDI-TOF-MS.

EXPERIMENTAL SECTION

Chemicals. TATp (11-mer: TyrGlyArgLysLysArgArgGlnArgArgArg; molecular mass 1560 Da) and TAT-cysteine peptide (TATp-Cys 12-mer: CysTyrGlyArgLys-LysArgArgGlnArgArgArg; molecular mass 1663 Da, one reactive thiol group) were synthesized by the Tufts University Core Facility (Boston, MA). 1,2-Dioleoyl-*sn*-glycero-3-phosphoethanolamine (DOPE) and 1,2-dioleoyl-*sn*-glycero-3-phosphoethanolamine-*N*-[methyl(poly(ethylene glycol))-5000] (PEG_{5000}-PE) were purchased from Avanti Polar Lipids Inc. (Alabaster, AL), NHS-PEG_{1000}-maleimide was purchased from Quanta Biodesign (Powell, OH), and

* Corresponding author. Dr. Vladimir P. Torchilin, Department of Pharmaceutical Sciences, Northeastern University, Mugar Building, Room 312, 360 Huntington Avenue, Boston, MA 02115. tel 617-373-3206; fax 617-373-8886, e-mail: v.torchilin@neu.edu.

¶ While on leave from Israel Institute for Biological Research, Ness Ziona, Israel.

† Department of Pharmaceutical Sciences and Center for Pharmaceutical Biotechnology and Nanomedicine.

‡ Barnett Institute.

§ Department of Chemistry and Chemical Biology.

10.1021/bc900081e CCC: $40.75 © 2009 American Chemical Society
Published on Web 07/14/2009

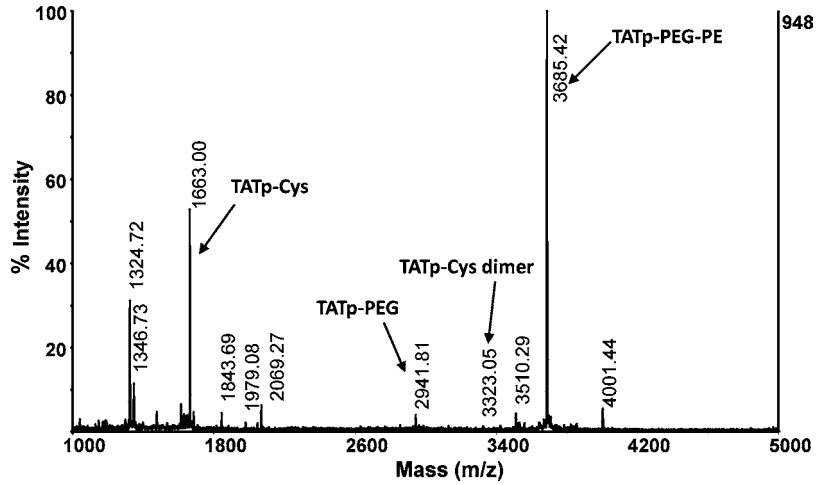

Figure 1. MS spectra of the purified TATp-PEG_{1000}-PE conjugate. The main peak $m/z = 3685.42$ was identified as the conjugate (theoretical $[M+H]^+ = 3685.21$).The intensities of MS peaks do not represent a quantitative ratio. The relative concentration of TATp-Cys did not exceed 7% as determined by HPLC analysis.

TATp-PEG_{1000}-PE (TATp-conjugate) was synthesized in-house (see below). 9-Fluorenylmethyl chloroformate (FMOC-Cl) was purchased from Fluka (Switzerland). Trypsin from porcine pancreas (type IX-S, 13 000−20 000 units/mg), and lyophilized human plasma reconstituted by adding the specified volume of deionized water were purchased from Sigma (St. Louis, MO). All other chemicals and solvents were of analytical grade.

Synthesis of TATp-PEG_{1000}-PE (TATp-Conjugate). TATp-PEG_{1000}-PE conjugate was synthesized as described previously in ref 34 with some modifications. Briefly, an approximately 1.5-fold molar excess of NHS-PEG_{1000}-maleimide was reacted with DOPE-NH_2 by stirring for 4 h in chloroform under argon at room temperature with a 3-fold molar excess of triethylamine. A 2-fold molar excess of TATp-Cys was then added, and the reaction was continued with stirring under argon for an additional 12 h. The excess of TATp-Cys was separated from the product by gel filtration chromatography. The solvent was evaporated, and the product was freeze−dried overnight. The dried product was dissolved in 0.5 mL of water and loaded onto a Sephadex G25 column (length, 10−15 cm; diameter, 0.5−1 cm). The product was eluted with water. Fractions of 0.5−1 mL were collected and monitored by TLC using silica plates and a mobile phase of chloroform/methanol (80:20% v/v). TATp-PEG-PE was visualized by iodine, phosphomolybdic acid, and Dragendorff spray reagents.

The resulting product was freeze−dried, dissolved in chloroform, and stored at −80 °C. The final purified product was identified by MALDI-TOF MS (Figure 1), and its purity as determined by HPLC was above 90%.

Preparation of TATp-Micelles. PEG-PE micelles containing 2.5 mol % of TATp-PEG-PE (TATp-Mic) were prepared as follows: 0.5 mL of PEG_{5000}-PE (10 mg/mL in chloroform) was mixed with 40 μL of TATp-PEG_{1000}-PE (2 mg/mL in chloroform); a PEG-PE film was formed on the bottom of the glass test tube by evaporating the solvent with nitrogen and lyophilization overnight. The film was hydrated in 0.5 mL of PBS, pH 7.4, and vortexed for 2−3 min to yield a clear micelle solution.

A solution of TATp-PEG_{1000}-PE was prepared by a similar procedure, by taking an appropriate volume of the pure TATp-conjugate solution in chloroform (2 mg/mL), evaporating the solvent, and hydrating the residue in PBS, pH 7.4. The hydration required occasional heating to 37 °C and vortexing. Solutions with a conjugate concentration of 0.1 or 1.0 mg/mL were prepared.

Table 1. Summary of the Main Fragments Resulting from Free TATp (0.1 mg/mL) Incubated in Human Plasma at 37 °C, as Identified by MALDI-TOF MS Analysis

incubation time (min)	residual intact TATp YGRKKRRQRRR	main fragments
10	25%	GRKKRRQ**RRR**
		GRKKRRQ**RR**
		GRKKRRQ**R**
		YGRKKRRQ**R**
30	12%	GRKKRRQ**RRR**
		GRKKRRQ**RR**
		GRKKRRQ**R**
		YGRKKRRQ**RR**
		YGRKKRRQ**R**

TATp Proteolysis in Human Plasma. Plasma samples (100 μL) were spiked with 10 μL of TATp (1 mg/mL, in deionized water) and incubated at 37 °C. To follow the kinetics of TATp proteolysis, the incubation was terminated at specified time points by adding 100 μL of acetone with 2% (v/v) of formic acid. The precipitated proteins were separated by centrifugation (10 000 rpm/10 min); the clear supernatant was lyophilized, dissolved in 100 μL of 0.1% formic acid, and filtered through Amicon centrifugal filters (5 kDa MWCO). The resulting filtrate was transferred for MS analysis. The initial concentration of the intact TATp (at time = 0) was determined by adding 10 μL of the same stock (1 mg/mL) of TATp to plasma in which the proteolytic activity was totally inhibited by phenylmethylsulfonyl fluoride (PMSF).

Trypsinolysis of TATp, TATp-PE-PE, and TATp-Mic. Five microliters of trypsin (0.002 mg/mL, 1.5−1.8 total units) was added to a sample of 100 μL of TATp, TATp-PEG-PE, or TATp-Mic in PBS, pH 7.4, and incubated at 37 °C. The concentration of the different forms of TATp was adjusted to be equivalent to 0.05 mg/mL of TATp (3×10^{-5} M), while the final trypsin concentration was 1×10^{-4}mg/mL (5×10^{-9} M). At prescheduled time intervals, 10 μL aliquots were withdrawn from the sample and immediately used for FMOC-Cl derivatization (see below). It was confirmed that trypsin was completely deactivated by the derivatization conditions, (raising the pH to 10 and 1:1 dilution with FMOC-Cl in acetonitrile). The proteolysis kinetics were determined with HPLC analysis by following the increase in the concentration of the main digest product, the RR fragment.

MS Analysis. The samples resulting from the HPLC or plasma filtrates were spiked with human Glu-fibrinopeptide B to serve as an internal standard for the normalization of signal

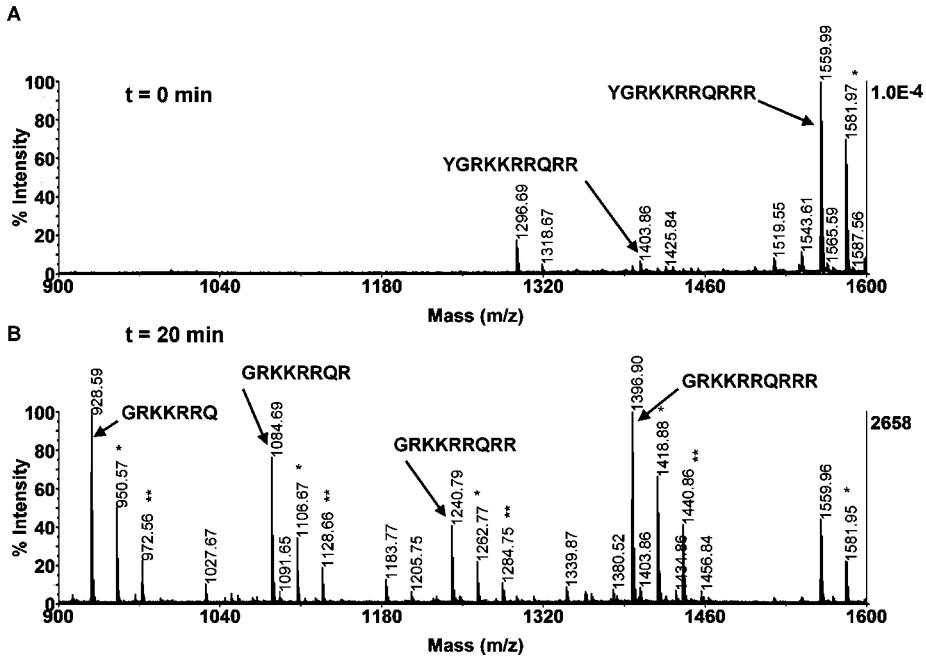

Figure 2. MS spectra of TATp fragments resulting from the incubation of TATp in human plasma at 37 °C. Symbols: * $[M + Na]^+$ and ** $[M + 2Na - H]^+$. (A) $t = 0$ min (determined by spiking TATp into plasma, in which the proteolytic activity was completely inhibited). (B) $t = 20$ min (small peptide fragments were not identified, as they could not be distinguished from the background plasma peptides).

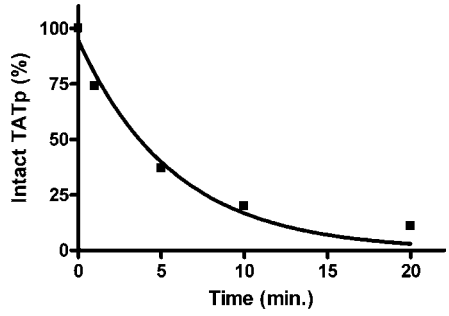

Figure 3. The kinetic of TATp proteolysis in human plasma, described by pseudo-first-order kinetics; $y = 94.84e^{-0.173t}$ (y = % of residual intact TATp); $R^2 = 0.975$.

intensities. Samples were analyzed by MALDI-TOF-MS in a positive reflectron mode with an AB 4700 instrument (Applied Biosystems, Framingham, MA) using 7 mg/mL α-cyano-4-hydroxycinnamic acid or 2,5-dihydroxybenzoic acid in 50% acetonitrile with 0.1% trifluoroacetic acid in water as a matrix solution. The intensity of TATp signal was expressed as a ratio of TATp peak height over the peak height of the spiked standard. For the identification of the chromatographic peaks by MALDI-TOF-MS analysis, the appropriate fractions were collected, lyophilized, and redissolved in 10 μL of 0.1% formic acid.

TATp Derivatization with FMOC-Cl. Samples of TATp, TATp-PEG-PE, TATp-Mic (10 μL), or their trypsin digests in PBS, pH 7.4, were added to a microcentrifuge tube (0.6 mL) containing 2.5 μL of borate buffer (0.4 M, pH 10) followed by addition of 12.5 μL of FMOC-Cl (0.02−0.4 mg/mL) in acetonitrile, then vortexed and incubated for 10 min at room temperature to complete the derivatization. The FMOC-Cl concentration was adjusted in proportion to that of TATp to reach a molar ratio of 1.2–5. Higher excess of FMOC-Cl should be avoided, as highly derivatized TATp tends to aggregate. The 0.4 mg/mL solution of FMOC-Cl was used with trypsin digest samples. Following the fluorescent labeling, the TATp samples were analyzed by HPLC.

HPLC Analysis. The HPLC analysis was performed on a Hitachi Elite Lachrom system (Tokyo, Japan) composed of the

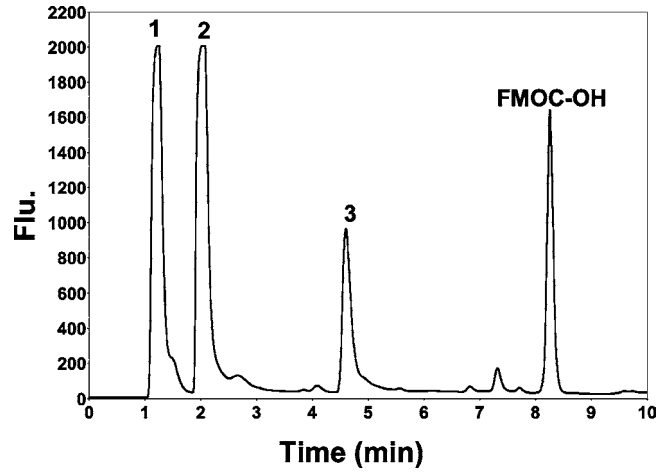

Figure 4. HPLC chromatogram of TATp following FMOC-Cl derivatization. The three separate peaks represent a different extent of derivatization as identified by MALDI-TOF MS (see Figure 5).

following units: a quaternary pump, model L-2130; an automatic sample injector model L-2200; a fluorescence detector, model L-2485, and a Teledyne ISCO fraction collector, Foxy Jr (Lincoln, NE). *EZChrom Elite* (Agilent, Pleasanton, CA) data software was used for the system operation and data processing. The chromatographic separation was performed on a reverse-phase column (Symmetry C18 5 μm, 4.6 × 150 mm, Waters, Milford, MA) using a binary gradient elution. Mobile phase A consisted of 0.1% formic acid in acetonitrile, and B consisted of 0.1% formic acid in deionized water. A constant flow rate of 1 mL/min was used to increase phase A from 30% to 90% within 10 min; this composition (90% A) was held for 5 min and then changed back to the initial composition (30% A). A wait for an additional 5 min was allowed for the column to equilibrate to the initial eluent composition. The FMOC-Cl derivatized samples were diluted 20- to 100-fold with deionized water, and 10 μL volumes were injected for analysis. The

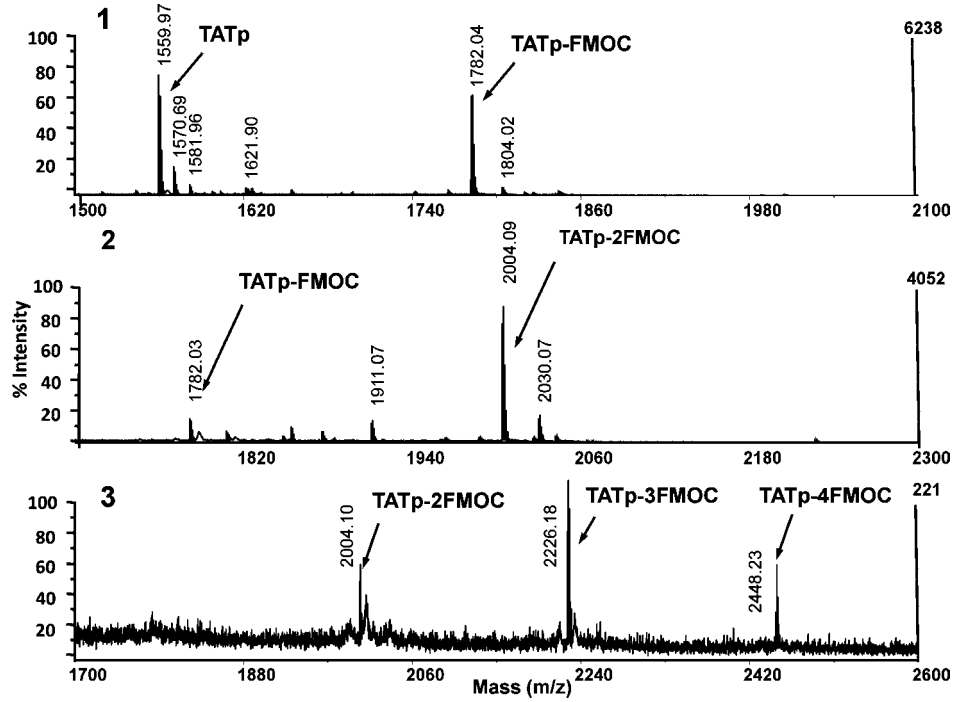

Figure 5. MS identification of the relevant peaks 1−3 (see Figure 4) resulting from FMOC derivatization of TATp. 1, TATp-FMOC and nonderivatized TATp; 2, TATp-2FMOC and traces of TATp-FMOC; 3, TATp-3FMOC and traces of TATp-2FMOC and TATp-4FMOC.

precolumn labeled analytes were detected by the fluorescence detector (ex 263 nm, em 314 nm).

RESULTS

TATp Proteolysis in Human Plasma. The kinetics of TATp proteolysis in human plasma were studied by MALDI-TOF-MS analysis. The main fragments resulting from TATp cleavage were identified as depicted in Figure 2 and summarized in Table 1. The same main fragments were found after 10 and 30 min of plasma incubation, but there was a pronounced change in their relative intensities. The ratio between the most intense fragment resulting from the N-terminal cleavage (GRKKRRQR-RR) and the fragment resulting from C-terminal cleavage (YGRKKRRQRR) increased by 3-fold after 30 min. There was also an increase in the intensity of the smaller fractions with incubation time.

The kinetics of TATp proteolysis were determined by MS analysis by following the decrease in the concentration of the intact TATp as a function of time. As found in other works on peptide proteolysis (*33*), the resulting kinetics (Figure 3) followed a pseudo-first-order rate, described by the following equation: $y = b \cdot e^{-kt}$, where y is the normalized concentration (percentage) of the residual intact peptide at time t; b, the initial peptide concentration; k, the pseudo-first-order rate constant, and t, the incubation time in minutes. The half-life ($t_{1/2}$) calculated from the resulting rate constant equaled 3.5 min. This result points out that the expected lifetime of nonprotected TATp *in vivo* should be on the scale of few minutes.

HPLC Method for TATp Analysis. The analytical method based on HPLC we have developed, with the use of precolumn FMOC derivatization (*35*), RP-chromatography, and fluorescence detection, proved to be a fast and highly sensitive analytical tool to study the proteolytic digestion of TATp.

TATp contains four functional groups which can readily react with FMOC-Cl, three primary amino groups—one at the N-terminal and two at the R-chains of lysine—and the phenol group on tyrosine. As a result, several derivatization products are expected. We found such products separated by HPLC into three peaks (Figure 4) and identified by MS as containing one, two, three, and four FMOC labels per TATp molecule (Figure 5). The FMOC labeling extent could be controlled by adjusting the quantity of the FMOC-Cl used for the derivatization. High molar excesses of FMOC-Cl should be avoided since the highly derivatized peptide tends to aggregate.

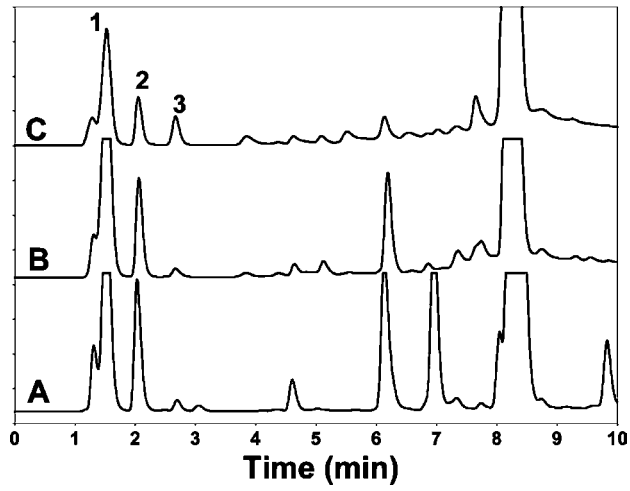

Figure 6. HPLC chromatograms of TATp fragments resulting from the trypsinolysis (1.5 trypsin unit/mL) for 20 min in PBS, pH 7.4, at 37 °C. For the proteolysis of TATp-Mic, 100-fold higher concentration of trypsin was used. Fractions of peaks 1, 2, and 3 were collected and identified by MS. The chromatograms represent free TATp (A), TATp-conjugate (B), TATp-Mic (C).

We found the main derivatization product to be TATp-FMOC, when a molar ratio (FMOC/TATp) of 1.2 was used, and TATp-3FMOC, when a molar ratio of 4.8 was used.

TATp Trypsinolysis in PBS, pH 7.4. For the *in vitro* studies of the proteolysis kinetics of TATp, TATp-conjugate, and TATp-Mic, a solution of trypsin (1×10^{-4} mg/mL, 1.5−1.8 units/mL) in PBS, pH 7.4, was used. This trypsin concentration allowed for TATp proteolysis kinetics similar to those found in human plasma. By using the HPLC analysis to follow the proteolysis of TATp, the same main peptide fragments, peaks

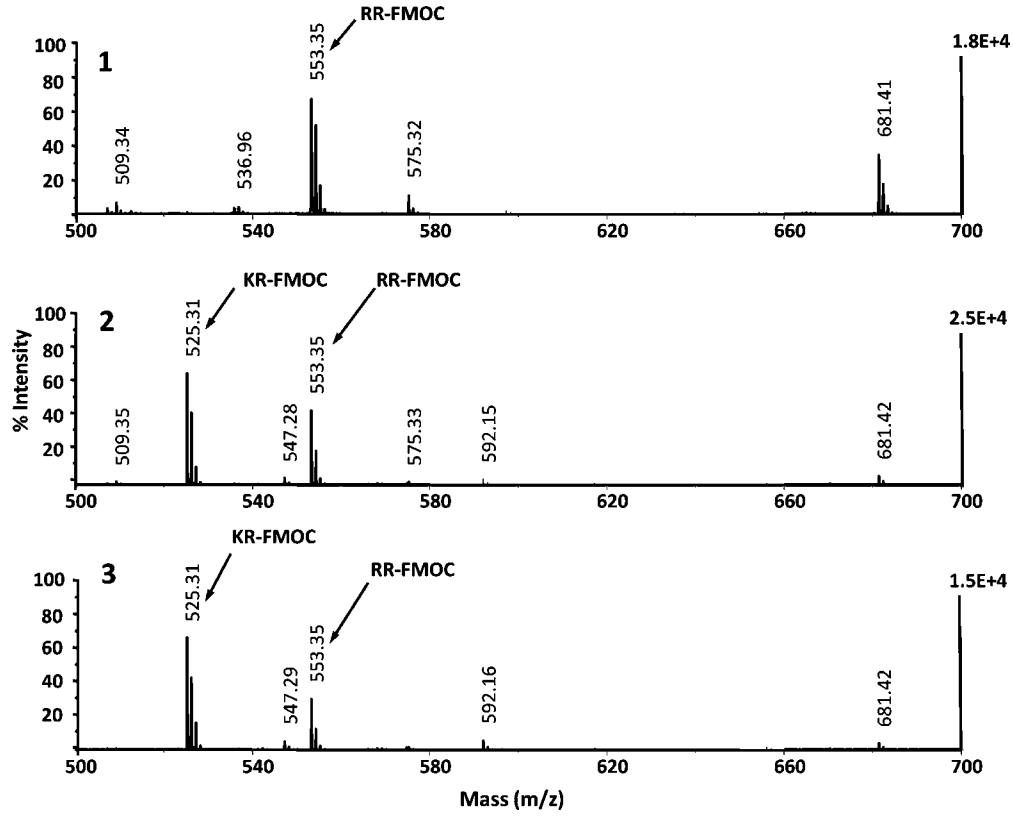

Figure 7. MS identification of the three main fractions (1−3) resulting from TATp proteolysis: (1) RR-FMOC, (2) KR-FMOC, (3) KR-FMOC. The two separate chromatographic peaks of KR-FMOC might result from the two different positions of FMOC labeling: N-terminal or ε-amino group of lysine.

1, 2, and 3 (Figure 6) were detected for the three (A,B,C) different forms of TATp used in this study. The fractions were identified by MS (Figure 7), fraction 1 as RR, and fractions 2 and 3 as KR with individual chromatographic peaks for KR resulting from different positions of FMOC labeling (at N-terminus or ε-amino groups). The RR dimer was the predominant initial proteolysis fragment, which is believed to result from the endocleavage at the carboxyl terminus (YGRKKRRQR↓RR). This finding is in agreement with the cleavage of TATp by furin (*28*).

We found that the chromatographic peak of the RR fragment was the most suitable for the proteolysis kinetics studies since it was the most intense initial fragment and thus easy to detect and analyze quantitatively.

The proteolysis kinetics of TATp were studied either by following the decrease in intact TATp as a function of the incubation time or by following the increase in the main digest fragment (RR). Similar kinetic rates were obtained with both methods (Figure 8). We preferred, however, the method based on the RR fragment, since the same peptide fragment (RR) was found to be the main proteolysis product for all three forms of TATp used in this study. This enabled us to use precisely the same HPLC method for the proteolysis kinetics determination of all the different forms of TATp.

The proteolysis kinetics as determined for the different forms of TATp (Figure 9) fit pseudo-first-order kinetics (R^2 = 0.94−0.98) well, although with quite different proteolysis rates as expressed by the half-lives of TATp: 3.5, 10, and 430 min for TATp, TATp-conjugate, and TATp-Mic, respectively.

DISCUSSION

The studies of the proteolysis of TATp represented in the present work are based on highly precise analytical tools: MALDI-TOF-MS and HPLC. We believe it was important to develop an HPLC method for this study in addition to the MS since most laboratories do not have free access to costly MS instruments. The HPLC analysis developed in this work proved to be a straightforward, highly sensitive, and accurate analytical tool to study the proteolysis kinetics of TATp and TATp conjugates incorporated into PEGylated micelles.

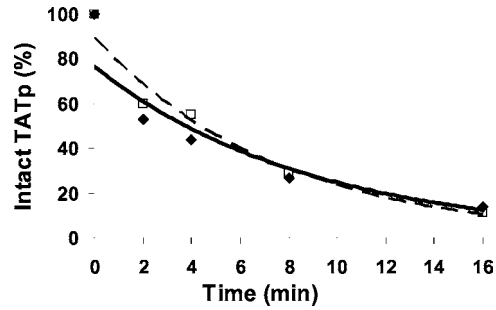

Figure 8. The kinetics of TATp proteolysis by trypsin (1.5 units/mL) in PBS, pH 7.4, at 37 °C. The kinetics was followed by the HPLC based on two different monitoring methods: 1. (—) By determining the decrease in the concentration of the intact TATp. 2. (---) By determining the increase of the RR-fragment normalized to % of the residual intact TATp using the following equation: % Intact TATp = $[A_\infty - A_t/A_\infty] \times 100$; A_∞ = RR concentration at the end of proteolysis; At = RR concentration at time t. The kinetics as determined by both methods fit first-order kinetics (as specified in Figure 2) resulting in a similar half-life ($t_{1/2}$ = ca. 3.5 min).

These kinetics results point out that the expected lifetime *in vivo* of the nonprotected TATp should be on the scale of a few minutes, while highly protected TATp in TATp-Mic can be expected to have a lifetime of several hours. The pronounced differences in the stability against proteolysis among TATp, TATp-conjugate, and TATp-Mic are quite understandable when their structural differences in aqueous medium are taken into

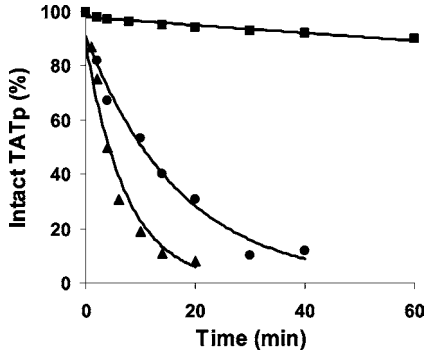

Figure 9. Proteolysis kinetics of different forms of TATp by trypsin (1.5 units/mL) in PBS, pH 7.4, 37 °C, following the RR fragment (as specified in Figure 8). TATp (▲), TATp-conjugate (•), TATp-Mic (■).

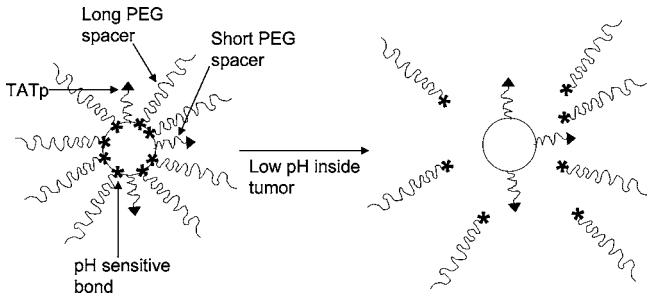

Figure 10. The principal scheme for the action of stimuli-sensitive nanocarriers. The surface of the nanocarrier is modified with TATp (or other CPP) via a relatively short PEG spacer. The TATp is shielded with longer PEG chains, which are attached to the nanocarrier surface via pH-sensitive bonds. The whole system is stable in the blood with TATp moieties protected against proteolytic degradation, and the carrier accumulates in the tumor via the EPR effect. Inside the tumor, protective PEG chains are detached from the surface by rapid hydrolysis of pH-sensitive bonds at the lower intratumoral pH; intact TATp becomes exposed and allows TATp-mediated intracellular delivery.

account. Free TATp can be attacked easily by trypsin and degraded rapidly. The TATp-PEG-PE conjugate, a clearly amphiphilic molecule, can exist in solution as an individual molecule or can form micelles similar to PEG-PE (we did not study the detailed properties of these micelles), but both in free form and in such micelles, the TATp moiety is exposed to the water phase and can still be attacked by trypsin. To some extent, certain steric hindrances for such attacks are created by the presence of PEG or by the micelle surface and will slow down the degradation rate (half-life increased from 3 min for free TATp to 10 min for the TATp-conjugate). By contrast, in TATp-Mic, where the TATp-PEG_{1000}-PE conjugate is located between PEG_{5000}-PE chains, the extended PEG_{5000} chains sterically protect the TATp moiety hidden inside the hydrophilic corona of the mixed micelle from the enzymatic attack and result in a greatly increased lifetime of TATp in TATp-Mic.

These attempts being made to construct "smart" drug delivery systems involve a TATp function hidden under a PEG-based shield, which could be removed, exposing their cell-penetrating function only when the system was in the vicinity of target cells (*22*, *34*, *36*) as depicted in Figure 10. The findings presented clearly show that the hidden TATp function can be well preserved within such "smart" structures for the time required for drug delivery into a target.

CONCLUSIONS

The HPLC analysis based on the FMOC-Cl fluorescent labeling developed in this work is a straightforward, accurate analytical tool for studying the proteolysis kinetics of TATp and TATp conjugates incorporated into PEGylated micelles.

The proteolytic cleavage of free TATp in human plasma or in trypsin-containing medium is relatively fast, with a half-life of approximately 3.5 min. TATp modification with PEG-PE moieties stabilizes TATp only slightly against proteolytic degradation ($t_{1/2}$ = 10 min). High stability of TATp against proteolysis ($t_{1/2}$ > 400 min) can be achieved by incorporating TATp as TATp-PEG-PE conjugates into polymeric micelles formed by PEG-PE if the size of a PEG block is bigger than the PEG fragment in TATp-PEG-PE. Protection of TATp against proteolysis is of great importance for its potential use as a cell-penetrating moiety in multifunctional smart drug delivery systems.

ACKNOWLEDGMENT

This study was supported by the NIH grants RO1 CA121838 and RO1 CA128486 to VPT. W.C. Hartner is gratefully acknowledged for his help during this manuscript preparation.

LITERATURE CITED

(1) Frankel, A. D., and Pabo, C. O. (1988) Cellular uptake of the tat protein from human immunodeficiency virus. *Cell 55*, 1189–1193.

(2) Fawell, S., Seery, J., Daikh, Y., Moore, C., Chen, L. L., Pepinsky, B., and Barsoum, J. (1994) Tat-mediated delivery of heterologous proteins into cells. *Proc. Natl. Acad. Sci. U.S.A. 91*, 664–668.

(3) Schwarze, S. R., Ho, A., Vocero-Akbani, A., and Dowdy, S. F. (1999) In vivo protein transduction: delivery of a biologically active protein into the mouse. *Science 285*, 1569–1572.

(4) Ryser, H. J., and Hancock, R. (1965) Histones and basic polyamino acids stimulate the uptake of albumin by tumor cells in culture. *Science 150*, 501–503.

(5) Goun, E. A., Pillow, T. H., Jones, L. R., Rothbard, J. B., and Wender, P. A. (2006) Molecular transporters: synthesis of oligoguanidinium transporters and their application to drug delivery and real-time imaging. *ChemBioChem 7*, 1497–1515.

(6) Chauhan, A., Tikoo, A., Kapur, A. K., and Singh, M. (2007) The taming of the cell penetrating domain of the HIV Tat: myths and realities. *J. Controlled Release 117*, 148–162.

(7) Fischer, R., Kohler, K., Fotin-Mleczek, M., and Brock, R. (2004) A stepwise dissection of the intracellular fate of cationic cell-penetrating peptides. *J. Biol. Chem. 279*, 12625–12635.

(8) Dathe, M., Schumann, M., Wieprecht, T., Winkler, A., Beyermann, M., Krause, E., Matsuzaki, K., Murase, O., and Bienert, M. (1996) Peptide helicity and membrane surface charge modulate the balance of electrostatic and hydrophobic interactions with lipid bilayers and biological membranes. *Biochemistry 35*, 12612–12622.

(9) Ryser, H. J. (1968) Uptake of protein by mammalian cells: an underdeveloped area. The penetration of foreign proteins into mammalian cells can be measured and their functions explored. *Science 159*, 390–396.

(10) Fuchs, S. M., and Raines, R. T. (2004) Pathway for polyarginine entry into mammalian cells. *Biochemistry 43*, 2438–2444.

(11) Ignatovich, I. A., Dizhe, E. B., Pavlotskaya, A. V., Akifiev, B. N., Burov, S. V., Orlov, S. V., and Perevozchikov, A. P. (2003) Complexes of plasmid DNA with basic domain 47−57 of the HIV-1 Tat protein are transferred to mammalian cells by endocytosis-mediated pathways. *J. Biol. Chem. 278*, 42625–42636.

(12) Rothbard, J. B., Jessop, T. C., Lewis, R. S., Murray, B. A., and Wender, P. A. (2004) Role of membrane potential and hydrogen bonding in the mechanism of translocation of guanidinium-rich peptides into cells. *J. Am. Chem. Soc. 126*, 9506–9507.

(13) Wadia, J. S., Stan, R. V., and Dowdy, S. F. (2004) Transducible TAT-HA fusogenic peptide enhances escape of TAT-fusion proteins after lipid raft macropinocytosis. *Nat. Med. 10*, 310–315.
(14) Silhol, M., Tyagi, M., Giacca, M., Lebleu, B., and Vives, E. (2002) Different mechanisms for cellular internalization of the HIV-1 Tat-derived cell penetrating peptide and recombinant proteins fused to Tat. *Eur. J. Biochem. 269*, 494–501.
(15) Stein, S., Weiss, A., Adermann, K., Lazarovici, P., Hochman, J., and Wellhoner, H. (1999) A disulfide conjugate between anti-tetanus antibodies and HIV (37−72)Tat neutralizes tetanus toxin inside chromaffin cells. *FEBS Lett. 458*, 383–386.
(16) De Coupade, C., Fittipaldi, A., Chagnas, V., Michel, M., Carlier, S., Tasciotti, E., Darmon, A., Ravel, D., Kearsey, J., Giacca, M., and Cailler, F. (2005) Novel human-derived cell-penetrating peptides for specific subcellular delivery of therapeutic biomolecules. *Biochem. J. 390*, 407–418.
(17) Lee, H. J., and Pardridge, W. M. (2001) Pharmacokinetics and delivery of tat and tat-protein conjugates to tissues in vivo. *Bioconjugate Chem. 12*, 995–999.
(18) Torchilin, V. P., Levchenko, T. S., Rammohan, R., Volodina, N., Papahadjopoulos-Sternberg, B., and D'Souza, G. G. (2003) Cell transfection in vitro and in vivo with nontoxic TAT peptide-liposome-DNA complexes. *Proc. Natl. Acad. Sci. U.S.A. 100*, 1972–1977.
(19) Ziegler, A., and Seelig, J. (2007) High affinity of the cell-penetrating peptide HIV-1 Tat-PTD for DNA. *Biochemistry 46*, 8138–8145.
(20) Torchilin, V. P., Rammohan, R., Weissig, V., and Levchenko, T. S. (2001) TAT peptide on the surface of liposomes affords their efficient intracellular delivery even at low temperature and in the presence of metabolic inhibitors. *Proc. Natl. Acad. Sci. U.S.A. 98*, 8786–8791.
(21) Gupta, B., Levchenko, T. S., and Torchilin, V. P. (2007) TAT peptide-modified liposomes provide enhanced gene delivery to intracranial human brain tumor xenografts in nude mice. *Oncol. Res. 16*, 351–359.
(22) Kale, A. A., and Torchilin, V. P. (2007) "Smart" drug carriers: PEGylated TATp-modified pH-sensitive liposomes. *J. Liposome Res. 17*, 197–203.
(23) Koch, A. M., Reynolds, F., Kircher, M. F., Merkle, H. P., Weissleder, R., and Josephson, L. (2003) Uptake and metabolism of a dual fluorochrome Tat-nanoparticle in HeLa cells. *Bioconjugate Chem. 14*, 1115–1121.
(24) Ruan, G., Agrawal, A., Marcus, A. I., and Nie, S. (2007) Imaging and tracking of tat peptide-conjugated quantum dots in living cells: new insights into nanoparticle uptake, intracellular transport, and vesicle shedding. *J. Am. Chem. Soc. 129*, 14759–14766.
(25) Endres, P. J., Macrenaris, K. W., Vogt, S., Allen, M. J., and Meade, T. J. (2006) Quantitative imaging of cell-permeable magnetic resonance contrast agents using x-ray fluorescence. *Mol. Imaging 5*, 485–497.
(26) Vives, E., Brodin, P., and Lebleu, B. (1997) A truncated HIV-1 Tat protein basic domain rapidly translocates through the plasma membrane and accumulates in the cell nucleus. *J. Biol. Chem. 272*, 16010–16017.
(27) Siomi, H., Shida, H., Maki, M., and Hatanaka, M. (1990) Effects of a highly basic region of human immunodeficiency virus Tat protein on nucleolar localization. *J. Virol. 64*, 1803–1807.
(28) Tikhonov, I., Ruckwardt, T. J., Berg, S., Hatfield, G. S., and David Pauza, C. (2004) Furin cleavage of the HIV-1 Tat protein. *FEBS Lett. 565*, 89–92.
(29) Trehin, R., Nielsen, H. M., Jahnke, H. G., Krauss, U., Beck-Sickinger, A. G., and Merkle, H. P. (2004) Metabolic cleavage of cell-penetrating peptides in contact with epithelial models: human calcitonin (hCT)-derived peptides, Tat(47−57) and penetratin(43−58). *Biochem. J. 382*, 945–956.
(30) Elmquist, A., and Langel, U. (2003) In vitro uptake and stability study of pVEC and its all-D analog. *Biol. Chem. 384*, 387–393.
(31) Schorderet, D. F., Manzi, V., Canola, K., Bonny, C., Arsenijevic, Y., Munier, F. L., and Maurer, F. (2005) D-TAT transporter as an ocular peptide delivery system. *Clin. Experiment. Ophthalmol. 33*, 628–635.
(32) Achilefu, S., Srinivasan, A., Schmidt, M. A., Jimenez, H. N., Bugaj, J. E., and Erion, J. L. (2003) Novel bioactive and stable neurotensin peptide analogues capable of delivering radiopharmaceuticals and molecular beacons to tumors. *J. Med. Chem. 46*, 3403–3411.
(33) Meng, H., and Kumar, K. (2007) Antimicrobial activity and protease stability of peptides containing fluorinated amino acids. *J. Am. Chem. Soc. 129*, 15615–15622.
(34) Kale, A. A., and Torchilin, V. P. (2007) Enhanced transfection of tumor cells in vivo using "Smart" pH-sensitive TAT-modified pegylated liposomes. *J. Drug Targeting 15*, 538–545.
(35) Lewis, J. R., Morley, J. S., and Venn, R. F. (1993) Analysis of human beta-endorphin 28−31 (melanotropin potentiating factor) and analogues by high-performance liquid chromatography of their 9-fluorenylmethoxycarbonyl derivatives. *J. Chromatogr. 615*, 37–45.
(36) Sawant, R. M., Hurley, J. P., Salmaso, S., Kale, A., Tolcheva, E., Levchenko, T. S., and Torchilin, V. P. (2006) "SMART" drug delivery systems: double-targeted pH-responsive pharmaceutical nanocarriers. *Bioconjugate Chem. 17*, 943–949.

BC900081E

Distance Dependent Interhelical Couplings of Organic Rods Incorporated in DNA 4-Helix Bundles

Casper S. Andersen,[†] Martin M. Knudsen,[†] Rahul Chhabra,[‡] Yan Liu,[‡] Hao Yan,*[,‡] and Kurt V. Gothelf*[,†]

Danish National Research Foundation, Centre for DNA Nanotechnology, Department of Chemistry and Interdisciplinary Nanoscience Center at Aarhus University, Langelandsgade 140, 8000 Aarhus C, Denmark, and Department of Chemistry and Biochemistry and The Biodesign Institute, Arizona State University, Tempe, Arizona 85287. Received March 1, 2009; Revised Manuscript Received May 29, 2009

The synthesis of a conjugated linear organic module containing terminal salicylaldehyde groups and a central activated ester, designed for conjugation to amino-modified oligonucleotides, is presented. The organic module has a phenylene−ethynylene backbone and is highly fluorescent. It is conjugated to oligonucleotide sequences and incorporated into specific locations in a well-defined DNA 4-helix bundle (4-HB). The DNA-nanostructure offers precise location control of the organic modules which allows for selective interhelical coupling reactions. In this study, metal-salen formation as well as dihydrazone formation are used to covalently interlink the organic modules. Both coupling reactions are highly dependent on the distances between the organic modules in the 4-HB. Neighboring modules dimerize easier, whereas more distanced modules are less prone to react, even when the linkers are extended. The dimeric products are characterized by denaturing polyacrylamide gel electrophoresis (PAGE), high performance liquid chromatography (HPLC), and matrix assisted laser desorption/absorption ionization time-of-flight (MALDI TOF) mass spectrometry.

INTRODUCTION

The area of DNA-nanotechnology has evolved over the last 15 years, and an increasing number of impressive two-dimensional (2D) and three-dimensional (3D) nanostructures formed by DNA self-assembly have been described (*1*−*5*). The majority of these self-assembled structures are made of DNA alone; however, convincing results have been reported for the DNA controlled assembly of other materials (*6*). For example, DNA-nanostructures have been used to arrange nanoparticles (*7*−*11*), proteins (*12*−*14*), and RNA (*15*). The use of DNA-programmed assembly of organic building blocks has also been reported (*16*−*21*), but in these cases, only less complex DNA-scaffolds have been applied to template a chemical reaction.

DNA-directed chemistry is a method that offers exclusive control of chemical reactions (*22, 23*). By attachment of functional groups to oligodeoxynucleotides (ODN), the chemical reaction between two or more of such conjugates can be controlled by the ability of the ODNs to self-assemble. The functional groups of choice will typically spontaneously react with each other at millimolar concentrations; however, at micro- to nanomolar concentrations, reactions only happen when DNA-hybridization leads to the formation of a high local concentration, i.e., a pseudointramolecular reaction. Several classical chemical reactions have been applied in DNA-directed chemistry (*22*−*28*). Our interest in DNA-directed chemistry has mainly been in assembling conjugated organic rods into potentially conducting oligomers. We have reported on the direct self-assembly and coupling of ODN−rod conjugates (*29*−*34*) and recently demonstrated DNA-templated assembly of organic rods along the axis of a DNA helix (*35*). These methods were applied to the assembly and coupling of up to four modules; however, they could not be applied to preparing larger structures.

In our continued search for DNA structures that can serve as templates for directed assembly and coupling of organic building blocks, we have investigated interhelical couplings in a DNA 4-helix bundle (4-HB). To the best of our knowledge, the only example of DNA-directed interhelical coupling relies on a short distance amide formation (*36*), and the only two examples of longer distance couplings within the same helix are from Seeman et al. (*27*). and our laboratories (*35*). Furthermore, Mao et al. has described a triplex controlled regioselective formation of an amide (*37*). On the basis of our previous reports on the DNA-directed assembly of organic rods into potentially conducting oligomers (*38*−*41*), we explore the incorporation of organic modules in a 4-HB as a template for organic reactions (*42*).

EXPERIMENTAL DETAILS

General Methods. All organic solvents used in experiments were of high performance liquid chromatography (HPLC) grade purity. THF and triethylamine were distilled over sodium and CaH_2, respectively. Flash chromatography was performed using Merck silica gel 60 (230−400 mesh). Analytical thin layer chromatography (TLC) was performed using precoated aluminum-backed plates (Merck Kieselgel 60 F254) and visualized by ultraviolet irradiation. NMR spectra were acquired on a Varian AS 400 spectrometer, running at 400, 100, and 376 MHz for ^{1}H, ^{13}C and ^{19}F, respectively. Chemical shifts (δ) are reported in ppm relative to solvent signals ($CHCl_3$ at 7.26 ppm for ^{1}H NMR and $CDCl_3$ at 77.0 ppm for ^{13}C NMR). ^{13}C NMR spectra were acquired on a broadband decoupled mode. High resolution mass spectra (HRMS) were recorded on a MicromassLCT spectrometer using electrospray (ES^+) ionization techniques. Matrix assisted laser desorption/absorption ionization time-of-flight (MALDI-TOF) mass spectrometry experiments were performed using a Bruker Daltonics Autoflex spectrometer, an AnchorChip target plate, and one of the following matrixes: saturated dihydroxybenzoic acid (DHB) in methanol for organic

* To whom correspondence should be addressed. Tel: +45 89423907. Fax: +45 8619 6199. E-mail: hao.yan@asu.edu (H.Y.); kvg@chem.au.dk (K.V.G.).

[†] Interdisciplinary Nanoscience Center at Aarhus University.

[‡] Arizona State University.

10.1021/bc900078c CCC: $40.75 © 2009 American Chemical Society
Published on Web 07/02/2009

compounds and a 4:1 ratio of 3-hydroxypiccolinic acid (HPA) and diammoniumcitrate (DAC) 10 g/L in water for oligonucleotide containing compounds. The organic compounds were analyzed using a reflective positive mode, and oligonucleotide samples were analyzed using linear negative mode. Water used in oligonucleotide containing experiments was triple distilled. UV−vis absorption spectra were recorded on a Nanodrop ND 1000 spectrophotometer. HPLC analyses were accomplished on a Hewlett-Packard Agilent 1100 series using a Phenomenex Clarity 3u oligo-RP (50 × 4.60 mm 3 μm) column. Oligonucleotides were purchased from DNA technology A/S, Risskov in Denmark and IDT, Coralville, USA.

*Compound **4***. A flame-dried Schlenk flask charged with a magnet, 2-(1,3-dioxan-2-yl)-4-iodophenyl acetate (**3**) (691 mg, 2,79 mmol), $Pd(PPh_3)_2Cl_2$ (98 mg, 5 mol %), and CuI (26 mg, 5 mol %) was left under vacuum for 30 min. Upon turning to an argon atmosphere, we added THF (20 mL), NEt_3 (5 mL), and TMS-acetylene (820 mg, 1.16 mL, 8.36 mmol), and the mixture was stirred at rt overnight. The crude product was concentrated by rotary evaporation and purified by flash chromatography on silica gel (1:1 pentane/CH_2Cl_2) to yield compound **2** as a clear oil (552 mg, 1,73 mmol, 62%).

HRMS $[M + Na]^+$ calc, 341.1185; found, 341.1188. ^{1}H NMR (400 MHz, $CDCl_3$) δ 7.77 (s, 1H), 7.44 (d, J = 8.4, 1H), 7.02 (d, J = 8.4, 1H), 5.54 (s, 1H), 4.24 (dd, J = 4.8, 11.0, 2H), 3.93 (t, J = 11.3, 2H), 2.29 (s, 3H), 2.25 − 2.11 (m, 1H), 1.43 (d, J = 13.5, 1H), 0.22 (s, 9H). ^{13}C NMR (101 MHz, CDCl3) δ 168.8, 147.9, 133.0, 131.3, 130.5, 122.7, 121.1, 104.1, 97.3, 94.3, 67.4, 25.6, 20.8, −0.1.

*Compound **5***. A round-bottomed flask with compound **4** (550 mg, 2.57 mmol) in THF (5 mL) was cooled to 0 °C, and TBAF in THF (2.8 mL of 1 M solution) was added dropwise. After 10 min, the mixture was poured into CH_2Cl_2 (40 mL), and the organic phase was washed twice with water (15 mL). The organic phase was dried with Na_2SO_4 (s) and evaporated to dryness by rotary evaporation of the solvent. The crude product was treated with acetyl chloride (0.5 mL) in THF (10 mL) and pyridine (1 mL) for 10 min at rt. The mixture was poured into CH_2Cl_2 (40 mL) and washed with $NaHCO_3$ (aq, sat., 15 mL) and twice with water (15 mL). The organic phase was dried with Na_2SO_4 and evaporated to dryness by rotary distillation. Compound **5** was obtained by flash chromatography on silica gel (1:1 pentane/CH_2Cl_2) as a light yellow crystalline compound (383 mg, 1.56 mmol, 61%).

Mp 93−96 °C, HRMS $[M + Na]^+$ calc, 269.0790; found, 269.0786. ^{1}H NMR (400 MHz, $CDCl_3$) δ 7.80 (s, 1H), 7.47 (d, J = 8.2, 1H), 7.04 (d, J = 8.3, 1H), 5.54 (s, 1H), 4.22 (dd, J = 4.6, 11.2, 2H), 3.92 (t, J = 11.5, 2H), 3.05 (s, 1H), 2.29 (s, 3H), 2.25 − 2.11 (m, 1H), 1.40 (d, J = 13.5, 1H). ^{13}C NMR (101 MHz, $CDCl_3$) δ 168.65, 148.07, 133.15, 131.33, 130.62, 122.80, 119.86, 97.07, 82.56, 77.26, 67.27, 25.43, 20.67. Anal. Calcd for $C_{14}H_{14}O_4$: C, 68.28; H, 5.73. Found: C, 67.44; H 5.93. FTIR (KBr, cm^{-1}): 3271 s, 2849−2961 m, 2110 w, 1773 s, 1756 s, 1608 w, 1486 s.

*Compound **1***. A flame-dried Schlenk flask containing a magnet, pentafluorophenyl-2,5-diiodobenzoate (**7**) (199 mg, 0.37 mmol), $Pd(PPh_3)_2Cl_2$ (8 mg, 2.5 mol %), CuI (2.2 mg, 2.5 mol %), and Cs_2CO_3 (240 mg, 0.74 mmol) was left under vacuum for 30 min. Upon turning to argon atmosphere, we added THF (10 mL) and compound **5** (200 mg, 0.81 mmol), and the mixture was stirred for 1 h at rt. The solvent was removed by rotary distillation, and product **1** was obtained by flash chromatography on silica gel (1:50 Et_2O/ CH_2Cl_2) as a white crystalline product (210 mg, 270 mmol, 73%).

Mp 147−152 °C. HRMS $[M + Na]^+$ calc, 799.1579; found, 799.1591. ^{1}H NMR (400 MHz, $CDCl_3$) δ 8.32 (dd, J = 0.5, 1.6, 1H), 7.88 (d, J = 2.1, 1H), 7.81 (d, J = 2.1, 1H), 7.72 (dd, J = 1.7, 8.1, 1H), 7.68 (dd, J = 0.5, 8.1, 1H), 7.57 − 7.50 (m, 2H), 7.10 (d, J = 8.4, 1H), 7.07 (d, J = 8.4, 1H), 5.59 (s, 1H), 5.55 (s, 1H), 4.32 − 4.15 (m, 5H), 4.03 − 3.86 (m, 5H), 2.32 (s, 3H), 2.30 (s, 4H), 2.29 − 2.13 (m, 3H), 1.51 − 1.37 (m, 3H). ^{13}C NMR (101 MHz, $CDCl_3$) δ 168.75, 168.73, 161.04, 148.38, 148.26, 135.78, 134.53, 134.40, 133.05, 132.78, 131.17, 131.12, 130.87, 130.78, 128.21, 124.48, 123.35, 123.06, 123.03, 120.51, 120.28, 97.25, 97.17, 96.93, 91.88, 89.13, 87.64, 87.28, 67.43, 67.40, 25.58, 25.55, 20.79. ^{19}F NMR (376 MHz, $CDCl_3$) δ −152.11 − −152.27 (m, 1H), −158.36 (t, J = 21.8, 0H), −162.61 (dt, J = 11.1, 22.1, 1H). Anal.: Calcd for $C_{41}H_{29}F_5O_{10}$: C, 63.41; H, 3.76. Found: C, 63.39; H, 3.58. FTIR (KBr, cm^{-1}): 2850−2924 m, 2849 m, 2225 w, 1762 s, 1653 w, 1521 s, 1505 s.

*Compound **8***. Compound **8** was synthesized according to a modified literature procedure as follows (*43*). Hydrazine dihydrochloride (5 g, 48 mmol), 1,6-dichlorohexane (1.47 g, 9 mmol), and NaOH (4.2 g, 2.2 equiv) were dissolved in ethanol (40 mL) and heated to reflux for 3 h. The product was obtained upon extraction into EtOAc (40 mL), washing twice with water (20 mL), drying with Na_2SO_4, and evaporating to dryness by rotary evaporation of the solvent. The product was analyzed with ^{1}H NMR, which showed signals identical to those in the literature procedure.

General Procedure for ODNs O1, O2, O3, O4, O7a, O7b, O8a, and O8b. In an Eppendorf tube, a solution of compound **1** in DMF (10 μL, 25 mM) and an aqueous solution of the amino-modified oligonucleotide (10 μL, 0.5 mM) were mixed. Acetonitrile (20−25 μL) was added to produce a clear solution, and finally, NEt_3 (1 μL) was added, and the mixture was left for 2 h at room temperature. The solution was treated with an aqueous solution of ammonia (50 μL, 35% NH_3 in H_2O) for 30 min, and then all solvents were removed on a Speed Vac. A buffer (100 μL, 10% acetic acid adjusted with NEt_3 to pH 4) was added to the dry sample, and the mixture was vortexed carefully and was left at 60 °C for 2 h. Upon centrifugation (13000 rpm) for 1 min, we carefully removed the aqueous phase and injected it into a RP-HPLC column. The column was eluated with TEAA (100 mM, pH 7) and an increasing percentage of acetonitrile. The pure conjugate were eluted from the column with approximately 35% acetonitrile.

Formation of 4-HBs. Each ODN was dissolved in water and diluted to a final concentration of 10 μM. The 9 ODN strands, needed for the 4-HB, were mixed at equimolar concentration. To the resulting solution was added MES-buffer (pH 6.5, 100 mM) and NaCl (aq, 4 M) to a final concentration of 10 mM and 400 mM, respectively. The resulting solution was annealed in a PCR tube cooling from 90 to 25 °C over 2 h, and they were then ready for the coupling reactions.

General Procedure for Ni−Salen Coupling. The coupling was achieved by the addition of $NiCl_2$ and EDA to the 4-HBs obtaining a final concentration of 1 mM and 2 mM, respectively. The mixtures were left to react for 4 h at room temperature. The crude reaction was analyzed by PAGE without further purification.

General Procedure for Dihydrazone Coupling. The coupling was achieved by the addition of dihydrazine (60 mM in a MES buffer (100 mM, pH 5)) to the 4-HBs to obtain a final concentration of 6 mM. The mixtures were left to react for 3 h at room temperature. The crude reaction was analyzed by PAGE without further purification.

RESULTS AND DISCUSSION

The incorporation of organic modules into DNA-nanostructures requires a rational geometrical design to enable the coupling reactions. As illustrated in Figure 1, we aim for a setup where the termini of a 4-HB is functionalized with organic modules. The four DNA helices in the bundle are arranged in

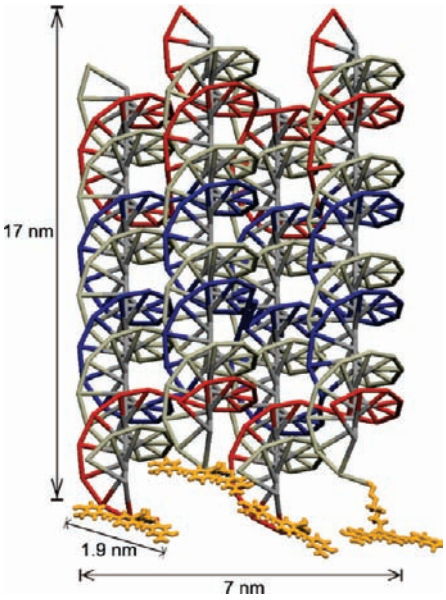

Figure 1. Schematic representation of a 4-HB with four organic modules (yellow) incorporated.

Scheme 1. Synthesis of Organic Module 1[a]

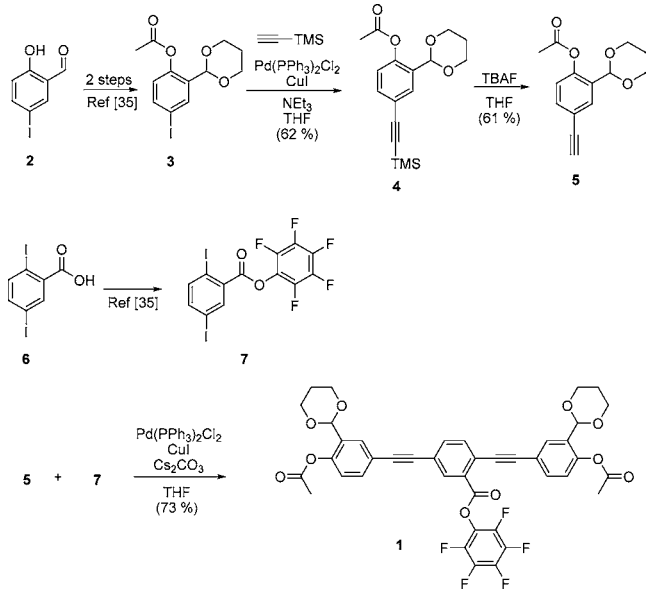

[a] TMS, trimethylsilyl; NEt_3, triethylamine; THF, tetrahydrofuran; TBAF, tetrabutylammonium-fluoride.

parallel, and each helix is coupled to its neighbor with a double crossover giving the 4-HB a well-defined shape. The attachment of organic modules in specific positions allows the 4-HB to serve as a scaffold at which the organic modules are positioned. The organic modules are linked to the 4-HB via spacers that allow the modules to rotate and define the space in which the modules move.

Organic module **1** (Scheme 1) is related to the module applied in a recent report by our laboratories (*35*), however, in a shorter version that fits with an interhelical coupling. It is based on a phenylene−ethynylene backbone with diprotected terminal salicylaldehydes and a central activated pentafluorophenyl ester. The latter functional group allows for the conjugation to amino-modified ODNs. The module has the required solubility in polar media, which is needed for the conjugation to ODNs.

The synthesis of **1**, shown in Scheme 1, is based on 5-iodosalicylaldehyde (**2**) and 2,5-diiodobenzoic acid (**6**).

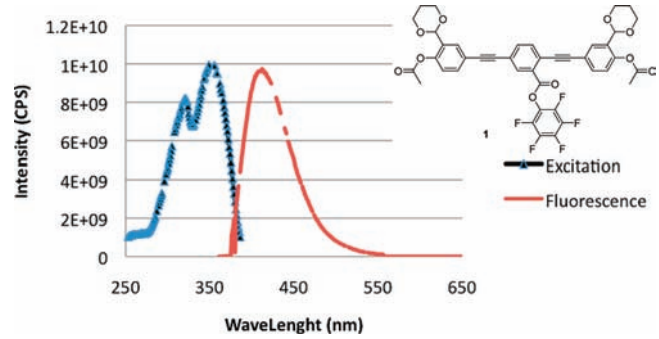

Figure 2. Excitation (blue) and emission (red) spectrum of organic module **1**. The spectra are measured with a solution of 1.66×10^{-4} mg/mL of **1** in 96% ethanol.

The aldehyde in **2** was acetal-protected followed by acetyl-protection of the phenol moiety (*35*). The resulting diprotected 5-iodosalicylaldehyde (**3**) was then ethynylated in a Sonogashira coupling (*44*) by reaction with trimethylsilyl-acetylene to obtain compound **4**. After the TMS group was removed, **5** was obtained in a moderate overall yield. The central aryl moiety (**7**) was prepared from 2,5-diiodobenzoic acid (**6**) by activation of the acid with pentafluorophenol in the presence of dicyclohexyl-carbodiimide (DCC) (*35*). To prevent hydrolysis or cleavage of the labile pentafluoroester (**7**), the final Sonogashira coupling between **5** and **7** was performed using anhydrous Cs_2CO_3 as a base instead of the more common use of secondary or tertiary amines. The coupling reaction gave the desired product **1** in 73% yield.

The excitation and emission spectra of product **1** were measured in ethanol at a concentration of 1.66×10^{-4} mg/mL (2.1×10^{-7} M). The module has two excitation peaks at 321 and 348 nm (Figure 2). After conjugation to an ODN and removal of the protecting groups, the peak at 321 nm disappears (see Supporting Information, Figure S1). When the compound excites at 348 nm, an emission maximum at 412 nm is obtained. It is clear that the organic module is highly fluorescent, and hence, it can be used to track ODNs conjugated to organic module **1**.

The reactive pentafluoroester in **1** serves as a handle for attachment of amino-modified ODNs. As illustrated in Scheme 2, we attached compound **1** to 8 different amino-modified ODNs by mixing the components in a mixture of 25% water, 25% DMF, and 1% triethylamine in acetonitrile. The desired amides were formed within 2 h. It is important that the ratio of water and organic solvent is well balanced since water content that is too high causes the organic module to precipitate, whereas water content that is too low makes the ODN insoluble. After conjugation, the acetyl protecting groups were removed by treatment with aqueous ammonia for 30 min. After evaporation of all solvents, the conjugate could be dissolved in a 10% acetic acid buffer at pH 4. This treatment has a dual purpose: it removes the acetal protecting group, and it causes unreacted organic modules to precipitate, which makes it easy to remove by simple centrifugation.

The conjugates were purified by preparative reverse phase (RP) HPLC. The RP-HPLC chromatograms for the conjugation reaction are shown in the Supporting Information (Figure S1). The product is easily identified because the organic module has a unique absorption peak at 348 nm. Furthermore, the relative height between the calculated extension coefficient of the ODN at 260 nm and the measured extension coefficient of the organic module at 348 nm can verify that exactly one organic module per ODN is present. For all eight conjugates, the product was further characterized by MALDI-TOF mass spectroscopy (see Supporting Information, Figure S2).

Scheme 2. Attachment of Organic Module 1 to Amino-Modified ODNs Followed by Deprotection

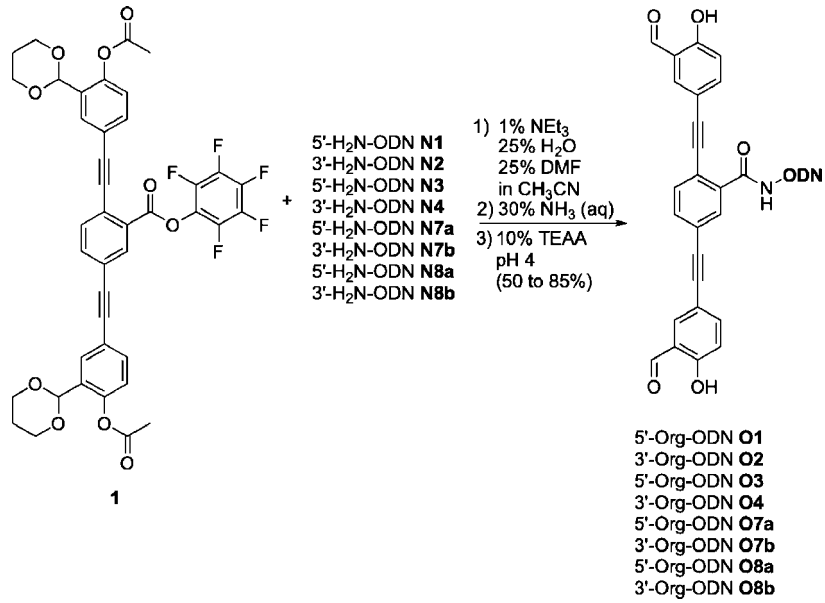

Table 1. Sequences of All 17 Different ODNs Used in the Study[a]

oligo name	sequence
ODN 1	TGT TCG GAC TAC TAA TCG TCT GAA CGG GAC AAC ACT CCA AC
ODN 2	CGA GCC TGC TAC CTG TAA CCG AGA TCC TGA TCC CTG AGT CG
ODN 3	CTA GCG GAC CAG GGA CGG AAC GAG TAG GAC TAT GGA CAT CG
ODN 4	GAT GGG AAA TGC CTG TGT CAT ACC GTA AGA ACC CTG TCC TC
ODN 5	GTT GCG TGG ATC TCG GTT ACA CCC GTT CAG ACG ATT AGT AGT GGG ATC ACC CTG GTG GGT TCT TAC GGT ATG ACA CAC CTA CTC
ODN 6	CGA TGT GGC TCG
ODN 7	CGA CTC ACC GAA CA
ODN 8	GAG GAC ACC GCT AG
ODN 9	GTT GGA GTG TTG TGG TAG CAC CAT AGT GGC ATT TCC CAT C
ODN O1	Org-CONH-C6-T TGT TCG GAC TAC TAA TCG TCT GAA CGG GAC AAC ACT CCA AC
ODN O2	CGA GCC TGC TAC CTG TAA CCG AGA TCC TGA TCC CTG AGT CGT TT-C6-HNCO-Org
ODN O3	Org-CONH-C6-TCTA GCG GAC CAG GGA CGG AAC GAG TAG GAC TAT GGA CAT CG
ODN O4	GAT GGG AAA TGC CTG TGT CAT ACC GTA AGA ACC CTG TCC TCT TT-C6- NHCO-Org
ODN O7a	Org-CONH-C6-TCGA CTC ACC GAA CA
ODN O7b	CGA CTC ACC GAA CAT TT-C6- NHCO-Org
ODN O8a	Org-CONH-C6-TGAG GAC ACC GCT AG
ODN O8b	GAG GAC ACC GCT AGT TT-C6- NHCO-Org

[a] Org, conjugated organic module; C6, C_6H_{12} spacer.

The 4-HB applied in this study is built up by 9 DNA strands and is a modification of a 4-HB structure designed by Yan and co-workers (*42*). In the original layout, the 4-HB contained sticky ends for wire formation; however, in this study the sticky ends are omitted. We have, furthermore, applied eight T1-C6 or T3-C6 amino-modified linkers to the organic module, which in different combinations were incorporated into the 4HB bundle. A list of all ODN sequences can be seen in Table 1. Permutations of the oligonucleotides in the 4-HB allow for the construction of 144 possible 4-HBs of which a representative number was prepared.

We have focused on three different designs. The first design has only 3′-modified ODNs, the second has two 3′- and two 5′-modified ODNs, and the third design has alternating 5′- and 3′ modified ODNs (see Figure 3).

All 5′-modified ODNs have one thymine (T) nucleotide (nt) and a C6 linker between the ODN and the organic module. If it is assumed that distance from the 4-HB to the terminal of the organic module is 2.3 nm (measured in ChemDraw 3D), the module can occupy a volume of 26 nm^3, and the concentration in this volume will be 130 mM (two salicylaldehydes in 26 nm^3). The 3′-modified conjugates have three Ts and one C6 linker, and the distance from the last hybridized nucleotide to the terminal position of the organic module is estimated to be 3.5 nm. The volume is calculated to be 90 nm^3 and the concentration of aldehydes 36 mM. The maximum bridging distances will then theoretically be 4.6 and 7.0 nm, respectively. Relating this to the dimensions of the 4-HB dimension reveals that when at least one 3′-modified ODN is incorporated, it should be possible to bridge all the way from the first to the fourth helix and form a dimer. However, if we use the 5′-modified ODNs we have a large actual concentration but a smaller overlapping volume where the two organic compounds can react. Using the long spacer gives a smaller actual concentration but a larger overlapping volume (see Figure 4). However, it should be taken into consideration that the calculated distances are based on the assumption that the 4-HB is rigid and DNA hybridization irreversible. This is of course not the correct picture since DNA is a soft and flexible material that can breathe. Nevertheless, the 4-HB will induce a great increase in the local concentration of the organic module, and the position of the organic modules in the 4-HB highly affects the plausibility for coupling reactions to occur.

The 4-HBs were assembled by heating the nine ODNs of choice to 90 °C followed by cooling to room temperature over 2 h in a MES-buffer (pH 6.5, 10 mM) containing 400 mM NaCl.

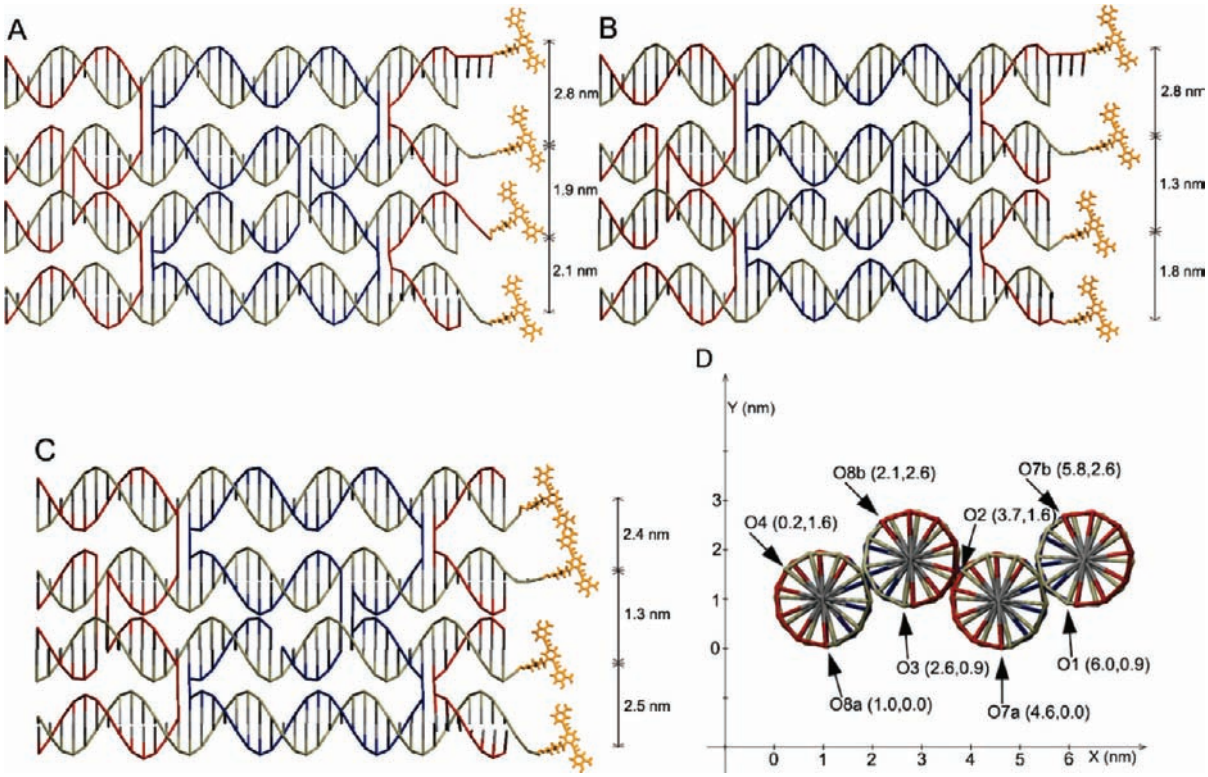

Figure 3. (A) 4-HB with **ODN O7b**, **O2**, **O8b**, and **O4** (all 3′-modified ODNs). (B) 4-HB with **ODN O7b**, **O2**, **O3**, and **O8a** (two 3′- and two 5′-modified ODNs). (C) 4-HB with **ODN O1**, **O2**, **O3**, and **O4** (alternating 5′- and a 3′-modified ODNs). (D) Model of the 4-HB illustrates the position of the eight different organic modified ODNs.

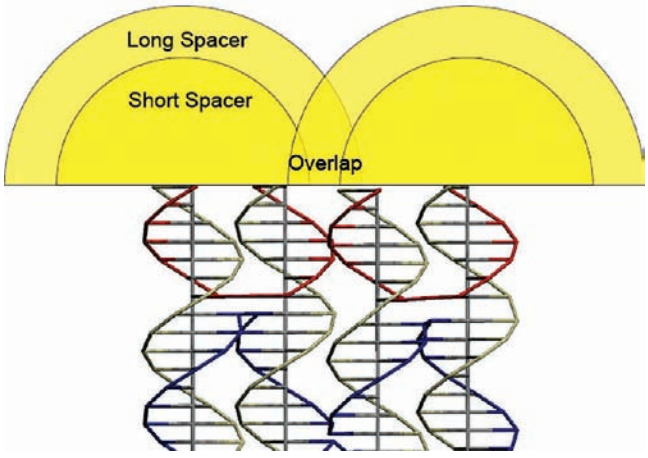

Figure 4. Top of the 4-HB is shown. The yellow spheres placed at helices 1 and 4 indicate the actual volume occupied by the organic modules. The small spheres refer to the short spacer (1 T), and the large spheres refer to the long spacer (3 T). The overlap indicates the chance for coupling.

The resulting 4-HB was analyzed by native polyacrylamide gel electrophoresis (PAGE). As mentioned above, the organic module is highly fluorescent. This enables imaging of the gel without staining with ethidium bromide or other DNA interchelators. Only structures containing the labeled DNA strand are visible, and this greatly simplifies gel analysis. Figure 5a illustrates the stepwise assembly of a 4-HB containing **ODN O1**, and Figure 5b illustrates fully assembled 4-HBs with one or more organic modules incorporated. The fully assembled 4-HBs with one or more organic modules incorporated migrate similarly since the modules constitute a very small fraction of the total molecular mass. The migration of the 4-HBs containing 189 base pairs corresponds to the migration of a linear dsDNA strand of 250 base pairs. The bulk and rigidity of the bundle retards its mobility compared to that of a linear DNA helix.

In this study, we have used two different approaches to perform the interhelical chemical coupling reactions of the terminal salicylaldehydes of the modules. In the first approach, a Ni(II)−salen complex is formed by reaction of Ni(II) chloride and ethylenediamine with two salicylaldehydes (Scheme 3) (*35*). In the other approach, dihydrazine **8**, synthesized according to a modified literature procedure (*43*), reacts with the two salicylaldehydes to form a hydrazone bridge.

In the first approach, the 4-HBs containing organic modules were treated with 1 mM Ni(II) chloride ($NiCl_2$) and 2 mM ethylenediamine (EDA) for 4 h. The products were analyzed with denaturing PAGE. Since two oligonucleotides are covalently coupled, the product of the chemical reactions migrates corresponding to the additive number of nucleotide in the conjugates that react, i.e., as a slower migrating band. We find that product is only observed in cases where the organic modules are incorporated at the right positions in the 4-HB and if structures have been treated with $NiCl_2$ and EDA. A typical denaturing 9% PAGE analysis for the reaction is shown in Figure 6. As Ni−salen complexes have been reported to quench fluorescence (*45*−*47*), the gel has to be stained with ethidium bromide before imaging by UV-light irradiation. Lane 3 is a control, containing a 4-HB with four different organic modified ODNs but without coupling reagents, and as expected, no higher-order structures are observed. In lanes 2 and 5, products arising from the coupling of **ODN O2** and **ODN O3** are observed. The band corresponds well with the 86 nt's of the dimeric product. In lane 2, it is also possible to form other products, but the dimer between helices 2 and 3 seems to be favored. Lanes 1 and 4 illustrate experiments where two shorter dimers containing two organic modules and 59 nt's should be formed. However, this product is not observed in the denaturing PAGE gel, although we do observe the disappearance of starting

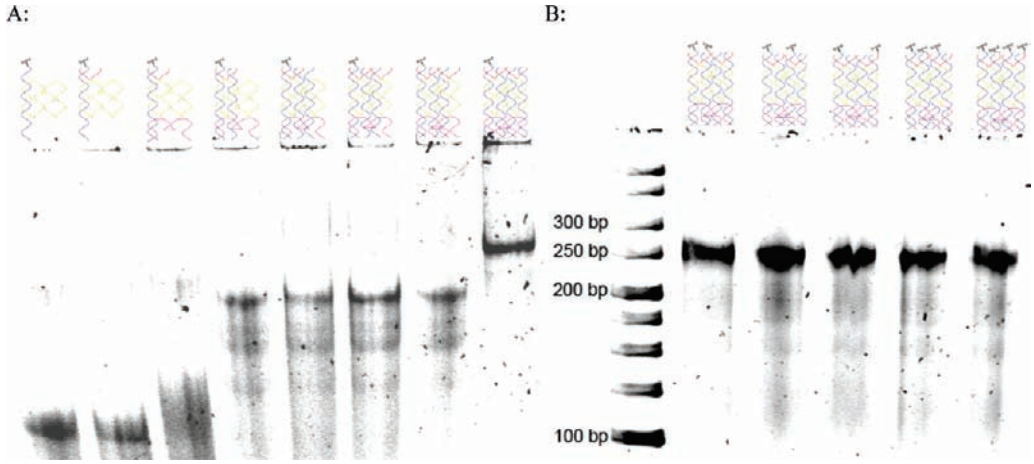

Figure 5. (A) Stepwise assembly of 4-HB. The conjugated DNA strand **ODN O1** is used as the fluorescent probe, and no staining is performed. PAGE (75 V, 2.5 h, 7.5% acrylamide). Lane 1 (**ODN 5** + **ODN O1**), lane 2 (lane 1+ **ODN 7**), lane 3 (lane 2+ **ODN 9**), lane 4 (lane 3+ **ODN 2**), lane 5 (lane 4+ **ODN 3**), lane 6 (lane 5+ **ODN 8**), lane 7 (lane 6+ **ODN 6**), and lane 8 (lane 7+ **ODN 4**). The gel is imaged by UV-irradiation. (B) 4-HBs with one or more organic modules incorporated. PAGE (75 V, 2.5 h, 7.5% acrylamide). The gel is stained with ethidium bromide before imaging. Lane 1 (marker), lane 2 (4-HB with **O1** and **O7a**), lane 3 (**O1** and **O3**), lane 4 (**O1** and **O8a**), lane 5 (**O1**, **O7a**, and **O3**), and lane 6 (**O1**, **O7a**, **O3**, and **O8a**).

Scheme 3. Two Different Approaches for Interhelical Couplings[a]

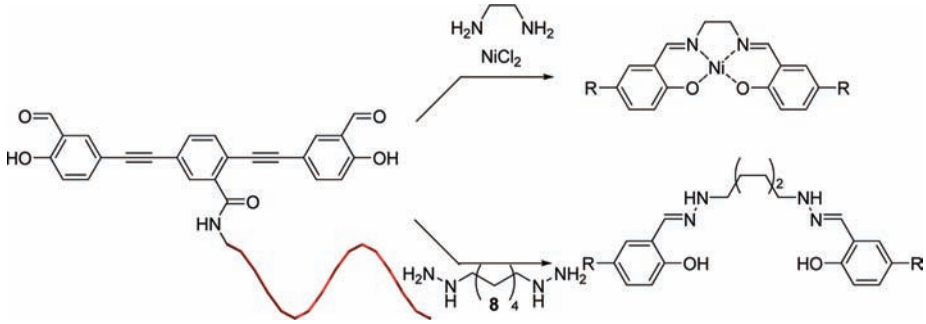

[a] Top: aldehyde reacts with dihydrazine to form a dihydrazone. Bottom: salicylaldehydes react with ethylenediamine and Ni^{2+} to form a Ni−salen complex.

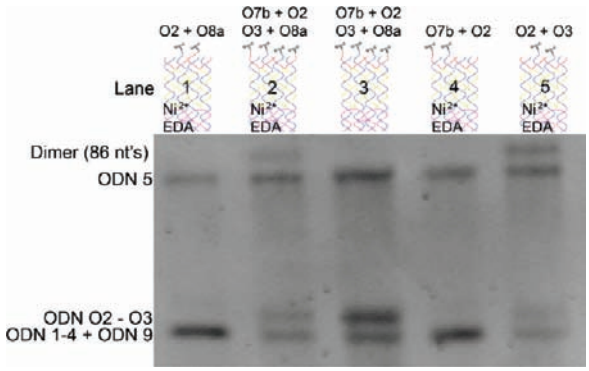

Figure 6. Ethidium bromide stained 9% denaturing PAGE. The 4-HBs with the incorporated organic modules are illustrated on the top of each well. Lane 1 (4-HB with **ODN O2** and **O8b**) treated with Ni^{2+} and ethylene diamine (EDA), lane 2 (4-HB with **ODN O7b**, **O2**, **O3**, and **O8a**) treated with Ni^{2+} and EDA, lane 3 (4-HB with **ODN O7b**, **O2**, **O3**, and **O8b**) not treated with Ni^{2+} and EDA, lane 4 (4-HB with **ODN O7b** and **O2**) treated with Ni^{2+} and EDA, and lane 5 (4-HB with **ODN O2** and **O3**) treated with Ni^{2+} and EDA. The dimer products of the Ni−salen dimer between **ODN O2** and **ODN O3** (organic dimer + 86 nt) are observed. The smaller dimer as well as trimers and tetramer are not observed.

material. We believe that the reason for this is fluorescence quenching by the Ni−salen complex (*45*−*47*). The existence of the small dimer was, however, observed by a number of other techniques. Accumulating the 4-HBs on filter cups before loading onto the polyacrylamide gel gave a weak and smeared dimer band according to PAGE analysis. We also analyzed the reaction mixture by RP-HPLC. The HPLC fractions were analyzed with UV−vis, PAGE analysis and MALDI-TOF mass spectrometry, and the existence of the short dimeric product was confirmed (see Supporting Information, Figure S3). We attribute, in part, the weakness of the bands containing the Ni complexes to be caused by quenching of the ethidium bromide emission (*45*−*47*).

For a further analysis of interhelical Ni−salen couplings, we used 4-HBs containing **ODN O1**−**O4** (42−44 nt) in order to obtain dimers containing at least 84 nt's. We performed PAGE analysis of 8 different 4-HBs, treated with Ni(II) chloride and ethylenediamine, testing the possibility to form interhelical couplings between neighboring helices, across one helix, across two helices, and attempting to form trimers and tetramers. The results are shown in Figure 7. Lane 1 shows the formation of dimer product between helices 1 and 2 (**ODN O1** and **O2**). Lanes 2, 3, and 4 show attempts to form trimer and tetramers, but we only observe increasing amounts of dimer. Lanes 5 and 6 show dimer bands formed between helices 2 and 3 and between helices 3 and 4. Lane 7 shows an attempt to form a dimer across one helix from helix 1 to helix 3. The linker size has only little influence on this result.

Since quenching of ethidium bromide fluorescence by the Ni−salen and other Ni complexes seems to be a serious problem for determining the yields of the experiments, alternative strategies had to be considered. Aldehydes are known to react

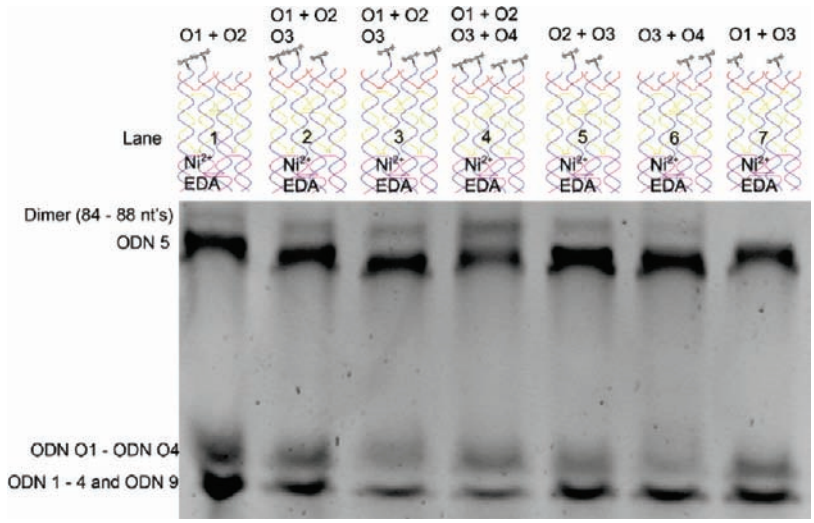

Figure 7. Ethidium bromide stained 9% denaturing PAGE. The 4-HBs with the incorporated organic modules are illustrated on the top of each well. Lane 1 (4-HB with **ODN O1** and **O2**) treated with Ni^{2+} and EDA, lane 2 (4-HB with **ODN O1**, **O2**, and **O3**) treated with Ni^{2+} and EDA, lane 3 (4-HB with **ODN O2**, **O3**, and **O4**) treated with Ni^{2+} and EDA, lane 4 (4-HB with **ODN O1**, **O2**, **O3**, and **O4**) treated with Ni^{2+} and EDA, lane 5 (4-HB with **ODN O2** and **O3**) treated with Ni^{2+} and EDA, lane 6 (4-HB with **ODN O3** and **O4**) treated with Ni^{2+} and EDA, lane 7 (4-HB with **ODN O1** and **O3**) treated with Ni^{2+} and EDA, and lane 8 (4-HB with **ODN O1** and **O4**) treated with Ni^{2+} and EDA. The Ni−salen dimer products of **ODN O1, ODN O2**, **ODN O3**, or **ODN O4** (organic dimer + 84−88 nt) are clearly observed.

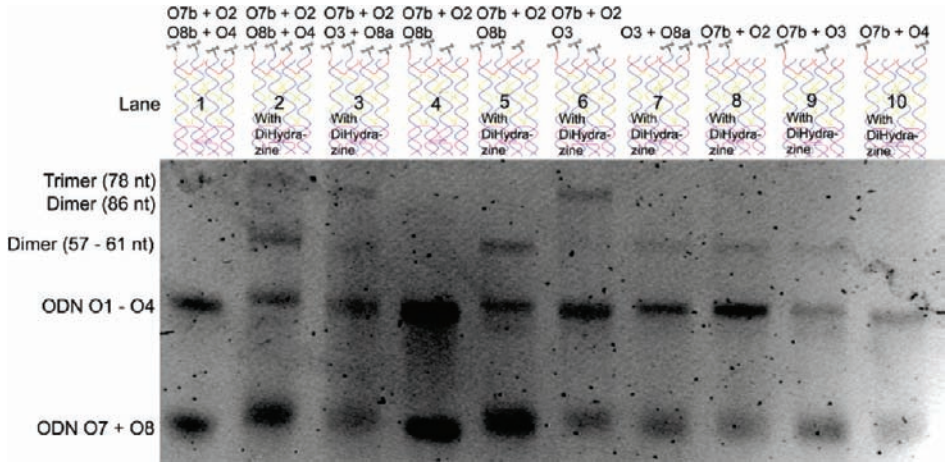

Figure 8. Unstained 9% denaturing PAGE. The 4-HBs with the incorporated organic modules are illustrated on the top of each well. Lane 1 (4-HB with **ODN O7b**, **O2**, **O8b**, and **O4**) with no dihydrazine treatment, lane 2 (4-HB with **ODN O7b**, **O2**, **O8b**, and **O4**) with dihydrazine, lane 3 (4-HB with **ODN O7b**, **O2**, **O3**, and **O8a**) with dihydrazine, lane 4 (4-HB with **ODN O7b**, **O2**, and **O8b**) with no dihydrazine, lane 5 (4-HB with **ODN O7b**, **O2**, and **O8b**) with dihydrazine, lane 6 (4-HB with **ODN O7b**, **O2**, and **O3**) with dihydrazine, lane 7 (4-HB with **ODN O3** and **O8a**) with dihydrazine, lane 8 (4-HB with **ODN O7b** and **O2**) with dihydrazine, lane 9 (4-HB with **ODN O7b** and **O3**) with dihydrazine, and lane 10 (4-HB with **ODN O7b** and **O4**) with dihydrazine. We observe clear dimer bands of both 59−61 nt (dimer 1) and 86 nt (dimer 2), and in lane 2, we observe a trimer with 78 nt.

with hydrazines to form stable hydrazones, and therefore, we developed an approach which is based on this. First, we synthesized the dihydrazine (**8**, Scheme 3) by reacting 1,6-dichlorohexane with hydrazine according to a modified literature procedure (*43*). The modified 4-HB was then treated with 5 mM of the dihydrazine (**8**), which allows the formation of interhelical couplings. Figure 8 illustrates a representative gel, denaturing 9% PAGE, for this approach. One great advantage of this approach is that it allows one to image the gel without staining, which implies that only ODNs with conjugated organic modules are observed, whereas bare ODNs not are visible.

From the PAGE analysis in Figure 8, both the small dimer (with ca. 59 nt) and the large dimer (with 86 nt) are observed in lanes 2, 3, and 5−9. A weak trimeric product is observed in lane 2. Furthermore, it can be seen that no dimer or higher ordered structures are formed in the absence of the dihydrazine (lanes 1 and 4). Important information about the distance dependence can also be derived from this gel image. When the distance between organic modules is increased, the product yield decreases. We do observe a weak band for the coupling between modules attached to helix 1 and helix 3 (across one helix, lane 9).

It is notable that the interhelical couplings are highly specific and rely on the 4-HB template. Both the Ni−salen and the dihydrazone coupling reactions were tested for unspecific couplings where modified ODNs were treated with coupling reagents without the ODNs required for the formation of 4-HB. Here, PAGE analysis (see Supporting Information, Figure S5) revealed that no coupling product was formed, which implies that the interhelical couplings exclusively occur in the 4-HB.

To compare the Ni−salen and the hydrazone couplings, we have repeated the Ni−salen experiments shown in Figure 7, using the same 4-HB and conjugates but applying the dihydrazone coupling instead (see Figure S4, Supporting Information). It is assumed that the results obtained by the Ni−salen couplings shown in Figure 7 are better than they appear from the gel image

since Ni-complexes quench the emission from ethidium bromide (*45*−*47*). The conjugates which have not participated in the formation of a dimer will also react with the diamine and form a complex with nickel (*48*). If it is assumed that the quenching of dimer and the other salicylaldehyde-containing sequences is comparable, then the relative intensities of the **ODN O1**−**O4** and dimer bands in Figure 7 indicate the formation in up to or above 50% yield. For the results obtained for the dihydrazone coupling reactions shown in Figure S4 (Supporting Information), we assume that all aldehyde groups are converted to hydrazones, and therefore, the potential quenching of the starting materials and the dimer is the same. The yields obtained for the dihydrazone couplings appears to be lower than that for the corresponding Ni−salen couplings, but the relative intensity distribution for the different setups are almost identical in the two experiments. The highest dimer yield is obtained when all four organic modules are present, and the lowest yields are obtained when the organic modules are places with a larger distance in between. We also attempted to form trimers and tetramers by placing 3 or 4 modules on 4 neighboring helices. The results from these attempts were in general disappointing since no tetramer was identified. It was possible to form the trimer as verified by PAGE in the dihydrazine reactions, but yields were low.

On the basis of the results presented in Figures 6−8, a consistent picture of the dimerization reactions can be drawn. The efficiency of the coupling reactions is moderate with a maximal yield of around 50% as estimated from relative intensities in the gels. We and others have previously observed that DNA-directed metal−salen couplings can proceed in high yields when the salicylaldehyde moieties are positioned in close proximity (*30, 49*). However, we have also previously observed that increased distance, between the attachment points of the organic module at the DNA-structure, in this case, 3.5 nm, corresponding to one helical turn in a B-DNA helix, gives rise to significantly lower yields. In the 4-HB, the length of the organic module is 1.9 nm and the length distance between neighboring helices around 2 nm, depending on the position of the attachment point in the helix. It is clearly demonstrated that the most favorable positioning of modules for the formation of dimers is where the organic modules are placed closest to a module at neighboring DNA helices (between helices 2 and 3).

CONCLUSIONS

Organic module **1** has been synthesized from 5-iodosalicylaldehyde (**2**) and 2,5-diiodobenzoic acid (**6**) in six synthetic steps closely related to a previously developed compound (*35*). Module **1** was conjugated to 8 different amino-modified oligonucleotides which were applied for the formation of 4-HBs. The stability of the modified DNA-nanostructure has been proved by native PAGE analysis. It is shown for the first time that a more complex DNA-nanostructure (4-HB) is applied to control the formation of a variety of different dimers formed by interhelical coupling of the modules. The bis(salicylaldehyde) terminated molecular rods in the 4-HBs were coupled either by Ni−salen formation or by a dihydrazone linkage developed for this study. The products were analyzed with denaturing PAGE analysis, and a single dimer has also been analyzed with MALDI-TOF analysis (additional gels and MALDI-TOF spectrum are shown in Supporting Information). The yields of the Ni−salen dimers are highly distance dependent. Even though we have designed the modules to be able to couple across one or two helices, we did not observe these long distance coupling. Even at neighboring helices, we observe a significant higher yield when the modules are placed in close proximity. We did not see full conversion of the modified ODNs, but no nontemplated coupling is observed. The dihydrazone coupling is less distance dependent, and the products are much easier to characterize since the fluorescence of the organic modules can be used to images the gel bands. We accomplished coupling across one helix to produce a trimer by this method. In the future, we will aim at improving the yields of interhelical couplings of organic modules and thereby enable the formation of monodisperse macromolecular networks templated by 2D DNA structures.

ACKNOWLEDGMENT

We thank the Danish National Research Foundation for financial support. Hao Yan acknowledges funding support by NSF, NIH, ONR, AFOSR, and ARO from US.

Supporting Information Available: HPLC chromatograms, UV−vis spectra, MALDI-TOF MS, additional PAGE analysis, and NMR spectra. This material is available free of charge via the Internet at http://pubs.acs.org.

LITERATURE CITED

(1) Seeman, N. C. (2003) DNA in a material world. *Nature 421*, 33–37.
(2) Simmel, F. C. (2008) Three-dimensional nanoconstruction with DNA. *Angew. Chem., Int. Ed. 47*, 5884–5887.
(3) Rothemund, P. W. K. (2006) Folding DNA to create nanoscale shapes and patterns. *Nature 440*, 297–302.
(4) Feldkamp, U., and Niemeyer, C. M. (2006) Rational design of DNA nanoarchitectures. *Angew. Chem. Int. Ed. 45*, 1856–1876. (e) Seeman, N. C., and Lukeman, P. S. (2005) Nucleic acid nanostructures: bottom-up control of geometry on the nanoscale. *Rep. Prog. Phys. 68*, 237–270.
(5) Gothelf, K. V., and LaBean, T. H. (2005) DNA-programmed assembly of nanostructures. *Org. Biomol. Chem. 3*, 4023–4037.
(6) Aldaye, F. A., Palmer, A. L., and Sleiman, H. F. (2008) Assembling Materials with DNA as the Guide. *Science 321*, 1795–1799.
(7) Sharma, J., Chhabra, R., Cheng, A., Brownell, J., Liu, Y., and Yan, H. (2009) Control of self-assembly of DNA tubules through integration of gold nanoparticles. *Science 323*, 112–116.
(8) Sharma, J., Ke, Y., Lin, C., Chhabra, R., Wang, Q., Nangreave, J., Liu, Y., and Yan, H. (2008) DNA-tile-directed self-assembly of quantum dots into two-dimensional nanopatterns. *Angew. Chem., Int. Ed. 47*, 5157–5159.
(9) Sharma, J., Chhabra, R., Andersen, C. S., Gothelf, K. V., Yan, H., and Liu, Y. (2008) Toward reliable gold nanoparticle patterning on self-assembled DNA nanoscaffold. *J. Am. Chem. Soc. 130*, 7820–7821.
(10) Beyer, S., Nickels, P., and Simmel, F. C. (2005) Periodic DNA nanotemplates synthesized by rolling circle amplification. *Nano Lett. 5*, 719–722.
(11) Aldaye, F. A., and Sleiman, H. F. (2006) Sequential self-assembly of a DNA hexagon as a template for the organization of gold nanoparticles. *Angew. Chem., Int. Ed. 45*, 2204–2209.
(12) Niemeyer, C. M. (2000) Self-assembled nanostructures based on DNA: towards the development of nanobiotechnology. *Curr. Opin. Chem. Biol. 4*, 609.
(13) Yan, H., Park, S. H., Finkelstein, G., Reif, J. H., and LaBean, T. H. (2003) DNA-templated self-assembly of protein arrays and highly conductive nanowires. *Science 301*, 1882–1884.
(14) Rinker, S., Ke, Y., Liu, Y., and Yan, H. (2008) Self-assembled DNA nanostructures for distance-dependent multivalent ligand-protein binding. *Nat. Nanotechnol. 3*, 418–422.
(15) Ke, Y., Lindsay, S., Chang, Y., Liu, Y., and Yan, H. (2008) Self-assembled water-soluble nucleic acid probe tiles for label-free RNA hybridization assays. *Science 319*, 180–183.
(16) Yang, H., and Sleiman, H. F. (2008) Templated Synthesis of Highly Stable, Electroactive, and Dynamic Metal-DNA Branched Junctions. *Angewandte Chem. Int. Ed. 47*, 2443–2447.

(17) Abdalla, M. A., Bayer, J., Rädler, J. O., and Müllen, K. (2004) Synthesis and self-assembly of perylenediimide-oligonucleotide conjugates. *Angew. Chem., Int. Ed. 43*, 3967–3970.
(18) Waybright, S. M., Singleton, C. P., Wachter, K., Murphy, C. J., and Bunz, U. H. (2001) Oligonucleotide-directed assembly of materials: defined oligomers. *J. Am. Chem. Soc. 123*, 1828–1833.
(19) Mitra, D., Cesare, N. D., and Sleiman, H. F. (2004) Self-assembly of cyclic metal-DNA nanostructures using ruthenium tris(bipyridine)-branched oligonucleotides. *Angew. Chem., Int. Ed. 43*, 5804–5808.
(20) Choi, J. S., Kang, C. W., Jung, K., Yang, J. W., Kim, Y. G., and Han, H. Y. (2004) Synthesis of DNA triangles with vertexes of bis(terpyridine)iron(II) complexes. *J. Am. Chem. Soc. 126*, 8606–8607.
(21) Xu, J., Fogleman, E. A., and Craig, S. L. (2004) Structure and properties of DNA-based reversible polymers. *Macromolecules 37*, 1863–1870.
(22) Li, X., and Liu, D. R. (2004) DNA-templated organic synthesis: nature's strategy for controlling chemical reactivity applied to synthetic molecules. *Angew. Chem., Int. Ed. 43*, 4848–4870.
(23) Gothelf, K. V., and Brown, R. S. (2005) A modular approach to DNA-programmed self-assembly of macromolecular nanostructures. *Chem.—Eur. J. 11*, 1062–1069.
(24) Rozenman, M. M., and Liu, D. R. (2006) DNA-templated synthesis in organic solvents. *ChemBioChem 7*, 253–256.
(25) Snyder, T. M., and Liu, D. R. (2005) Ordered multistep synthesis in a single solution directed by DNA templates. *Angew. Chem., Int. Ed. 44*, 7379–7382.
(26) Liu, Y., Sha, R., Wang, R., Ding, L., Canary, J. W., and Seeman, N. C. (2008) 2′,2′-Ligation demonstrates the thermal dependence of DNA-directed positional control. *Tetrahedron 64*, 8417–8422.
(27) Liu, Y., Kuzuya, A., Sha, R., Guillaume, J., Wang, R., Canary, J. W., and Seeman, N. C. (2004) Coupling across a DNA helical turn yields a hybrid DNA/organic catenane doubly tailed with functional termini. *J. Am. Chem. Soc. 130*, 10882–10883.
(28) Gartner, Z. J., Tse, B. N., Grubina, R., Doyon, J. B., Snyder, T. M., and Liu, D. R. (2004) DNA-templated organic synthesis and selection of a library of macrocycles. *Science 305*, 1601–1605.
(29) Gothelf, K. V., Thomsen, A. H., Nielsen, M., Cló, E., and Brown, R. S. (2004) Modular DNA-programmed assembly of linear and branched conjugated nanostructures. *J. Am. Chem. Soc. 126*, 1044–1046.
(30) Nielsen, M., Thomsen, A. H., Cló, E., Kirpekar, F., and Gothelf, K. V. (2004) Synthesis of linear and tripoidal phenylacetylene-based organic modules for application in DNA-programmed assembly. *J. Org. Chem. 69*, 2240–2250.
(31) Brown, R. S., Nielsen, M., and Gothelf, K. V. (2004) Self-assembly of aluminium-salen coupled nanostructures from encoded modules with cleavable disulfide DNA-linkers. *Chem. Commun.* 1464–1465.
(32) Blakskjær, P., and Gothelf, K. V. (2006) Synthesis of an elongated linear oligo(phenylene ethynylene)-based building block for application in DNA-programmed assembly. *Org. Biomol. Chem. 4*, 3442–3447.
(33) Nielsen, M., Dauksaite, V., Kjems, J., and Gothelf, K. V. (2005) DNA-directed coupling of organic modules by multiple parallel reductive aminations and subsequent cleavage of selected DNA sequences. *Bioconjugate Chem. 16*, 681–685.
(34) Weigelt, S., Busse, C., Bombis, C., Knudsen, M. M., Gothelf, K. V., Lægsgaard, E., Besenbacher, F., and Linderoth, T. R. (2008) Synthesis of polymeric nanostructures on surfaces imaged by UHV-STM. *Angew. Chem., Int. Ed. 47*, 4406–4410.
(35) Andersen, C. S., Yan, H., and Gothelf, K. V. (2008) Bridging one helical turn in dsDNA by dimerization of molecular rods. *Angew. Chem., Int. Ed. 67*, 5569–5571.
(36) Chhabra, R., Sharma, J., Liu, Y., and Yan, H. (2006) Addressable molecular tweezers for DNA-templated coupling reactions. *Nano Lett. 6*, 978–983.
(37) Chen, Y., and Mao, C. (2004) Reprogramming DNA-directed reactions on the basis of a DNA conformational change. *J. Am. Chem. Soc. 126*, 13240–13241.
(38) Smits, E. C. P., Mathijssen, S. G. J., Hal, P. A. v., Setayesh, S., Geuns, T. C. T., Mutsaers, K. A. H. A., Cantatore, E., Wondergem, H. J., Werzer, O., Resel, R., Kemerink, M., Kirchmeyer, S., Muzafarov, A. M., Ponomarenko, S. A., Boer, B. d., Blom, P. W. M., and Leeuw, D. M. d. (2008) Bottom-up organic integrated circuits. *Nature 455*, 956–959.
(39) James, D. K., and Tour, J. M. (2006) Organic Synthesis and Device Testing for Molecular Electronics. *Aldrichimica Acta 39*, 47–56.
(40) Donhauser, Z. J., Mantooth, B. A., Kelly, K. F., Buum, L. A., Monnell, J. D., Stapleton, J. J., Price, Jr, D. W., Rawlett, A. M., Allara, D. L., Tour, J. M., and Weiss, P. S. (2001) Conductance switching in single molecules through, conformational changes. *Science 292*, 2303–2307.
(41) Kubatkin, S., Danilov, A., Hjort, M., Cornil, J., Bredas, J.-L., Hansen, N. S., Hedegaard, P., and Bjornholm, T. (2003) Single-electron transistor of a single organic molecule with access to several redox states. *Nature 425*, 698–701.
(42) Ke, Y., Liu, Y., Zhang, J., and Yan, H. (2006) A study of DNA tube formation mechanisms using 4-, 8-, and 12-helix DNA nanostructures. *J. Am. Chem. Soc. 128*, 4414–4421.
(43) Daneiker, H. U., and Druey, J. (1957) Heilmittelchemische Studien in der heterocyclischen Reihe. 18. Mitteilung. Über Polymethylen-bis-sydnone und Polymethylen-bis-hydrazine. *Helv. Chim. Acta 40*, 918–932.
(44) Sonogashira, K., Tohda, Y., and Hagihara, N. (1975) A convenient synthesis of acetylenes: catalytic substitutions of acetylenic hydrogen with bromoalkenes, iodoarenes and bromopyridines. *Tetrahedron Lett. 16*, 4467–4470.
(45) Kang, J., Wang, X., and Dong, S. (2006) Mechanism of DNA strand cleavage induced by hexaaza macrocyclic nickel (II) complex. *Toxicol. Mech. Methods 16*, 515–523.
(46) Liu, G.-D., Liao, J.-P., Huang, S.-S., Shen, G.-L., and Yu, R.-Q. (2001) Fluorescence spectral study of interaction of water-soluble metal complexes of Schiff-base and DNA. *Anal. Sci. 17*, 1031–1036.
(47) Liu, G.-D., Yang, X., Chen, Z.-P., Shen, G.-L., and Yu, R.-Q. (2000) Interaction of metal complexes of bis(salicylidene)-ethylenediamine with DNA. *Anal. Sci. 16*, 1255–1259.
(48) Elder, R. C. (1978) Tridentate and unsymmetrical tetradentate Schiff-base ligands from salicylaldehydes and diamines - their monomeric and dimeric nickel(II) complexes. *Aust. J. Chem. 31*, 35–45.
(49) Czlapinski, J. L., and Sheppard, T. L. (2001) Nucleic acid template-directed assembly of metallosalen-DNA conjugates. *J. Am. Chem. Soc. 123*, 8618–8619.

BC900078C

Distance Dependent Interhelical Couplings of Organic Rods Incorporated in DNA 4-Helix Bundles

Casper S. Andersen,[§] Martin M. Knudsen,[§] Rahul Chhabra,[‡] Yan Liu,[‡] Hao Yan,[‡] and Kurt V. Gothelf*[,§]*

[§]Danish National Research Foundation: Centre for DNA Nanotechnology, Department of Chemistry and Interdisciplinary Nanoscience Center at Aarhus University, Langelandsgade 140, 8000 Aarhus C, Denmark. Fax: +45 8619 6199 ; Tel: +45 89423907; Homepage: http://www.cdna.dk

‡ Department of Chemistry and Biochemistry & The Biodesign Institute, Arizona State University, Tempe, Az, 85287 (USA)

Contents:

Title page	S1
HPLC chromatograms of all DNA conjugates (Figure S1)	S2 – S3
MALDI-TOF of all DNA conjugates (Figure S2)	S4 – S7
Supporting data for the formation of a Ni-salen dimer (Figure S3)	S8 – S9
Dihydrazone-coupling in the 4-HBs, used in Figure 7 (Figure S4)	S10
Test for unspecific couplings (Figure S5)	S11 – S12
NMR spectra of organic compounds	S13 – S16

Figure S1. HPLC chromatograms and UV-VIS spectra of DNA conjugates.

A) Conjugate **O2**

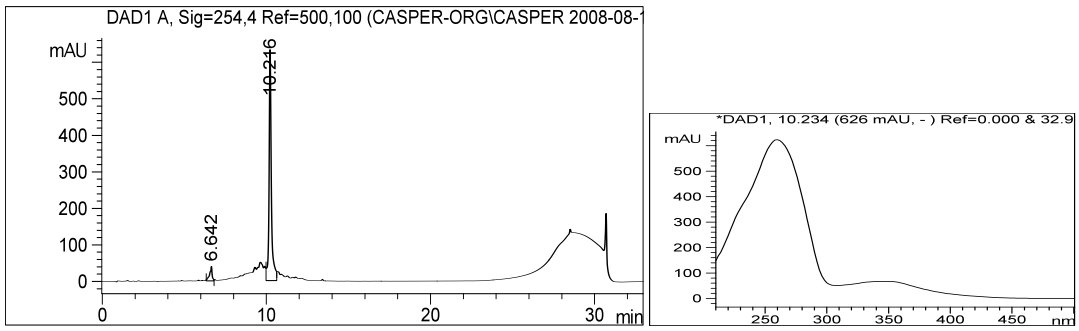

B) Conjugate **O4**

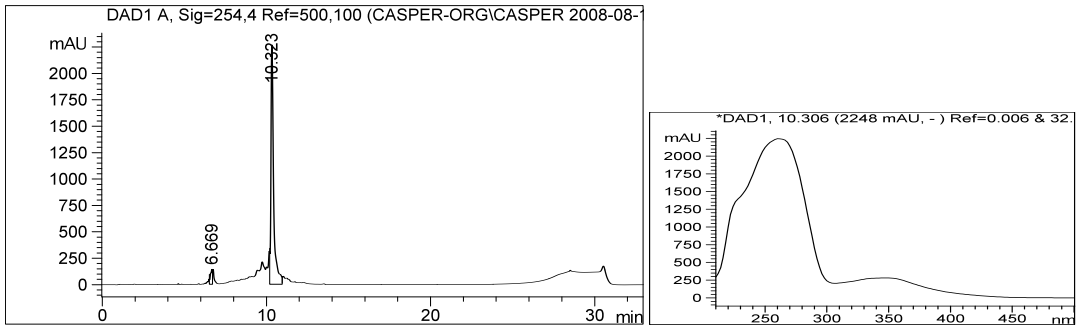

C) Conjugate **O7b**

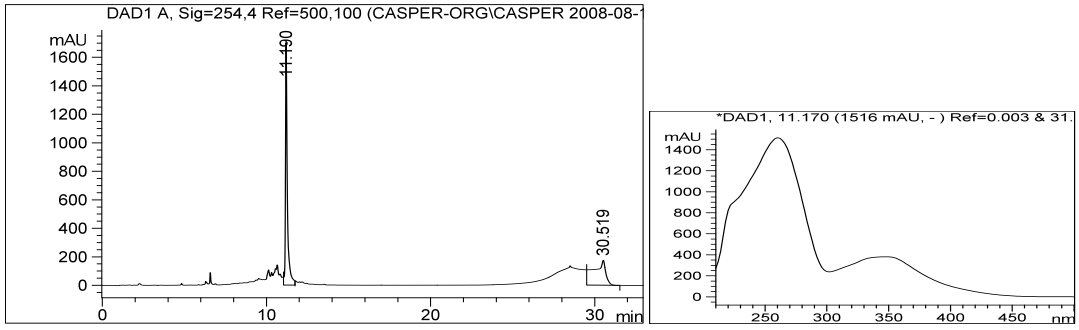

D) Conjugate **O8b**

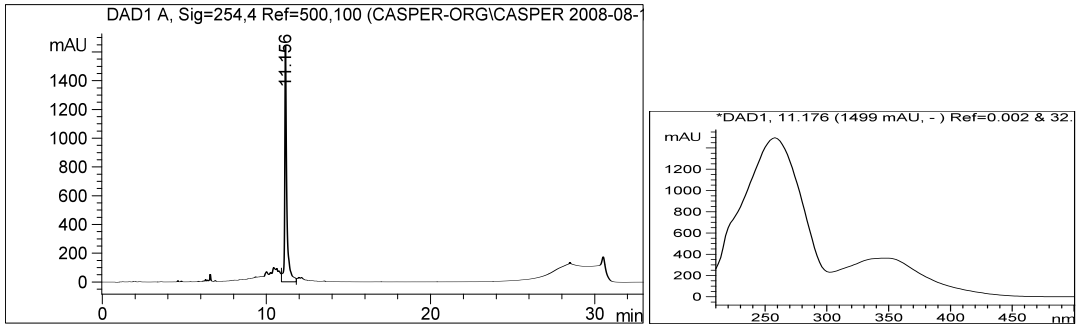

E) Conjugate **O1**

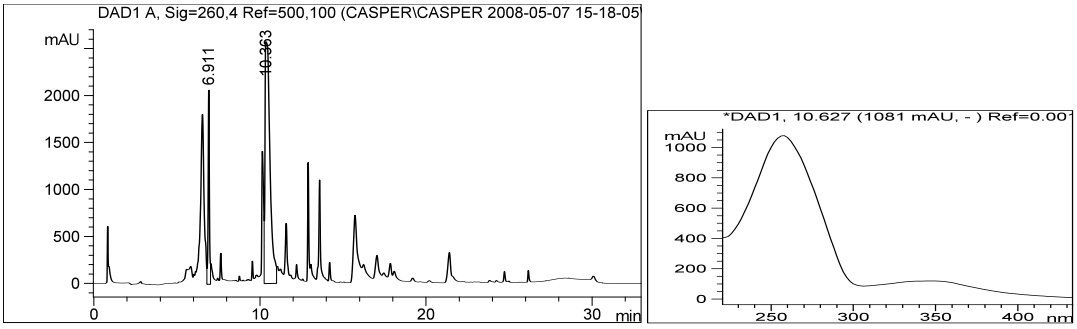

F) Conjugate **O3**

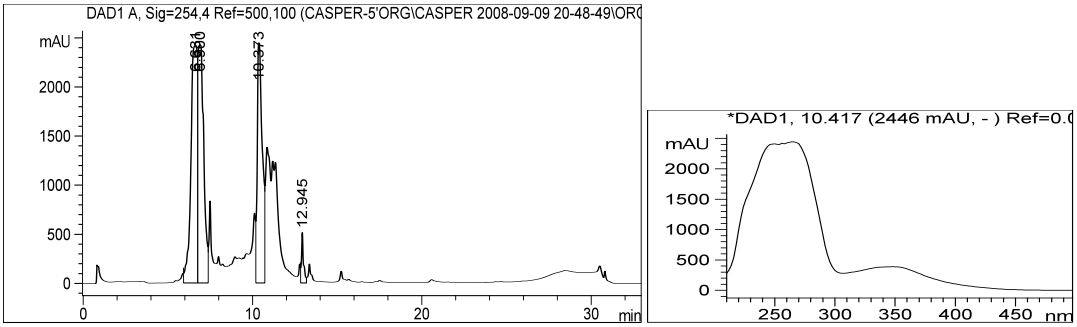

G) Conjugate **O7a**

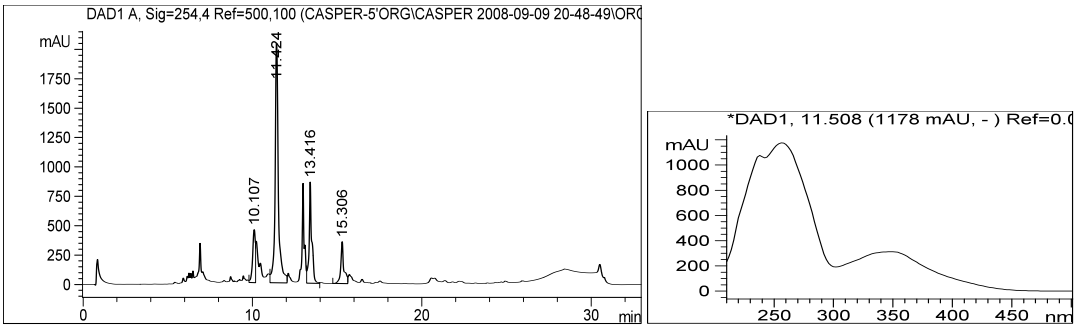

H) Conjugate **O8a**

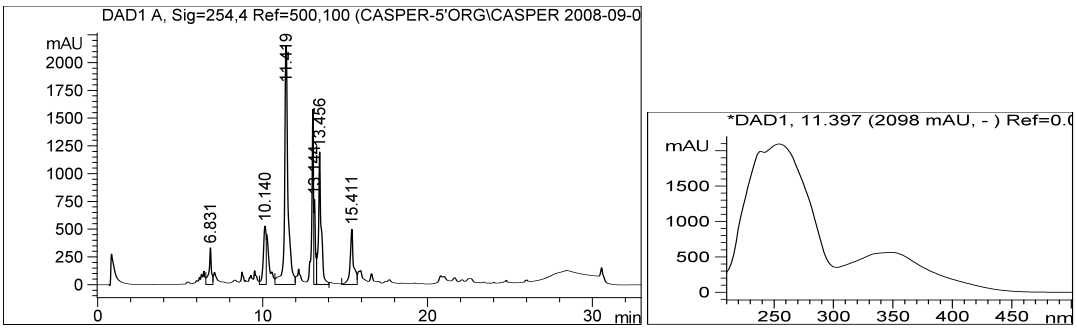

Figure S2. MALDI-TOF MS of the HPLC purified modified ODNs.

A) Conjugate **O2**: Calcd 14010 Found 14015

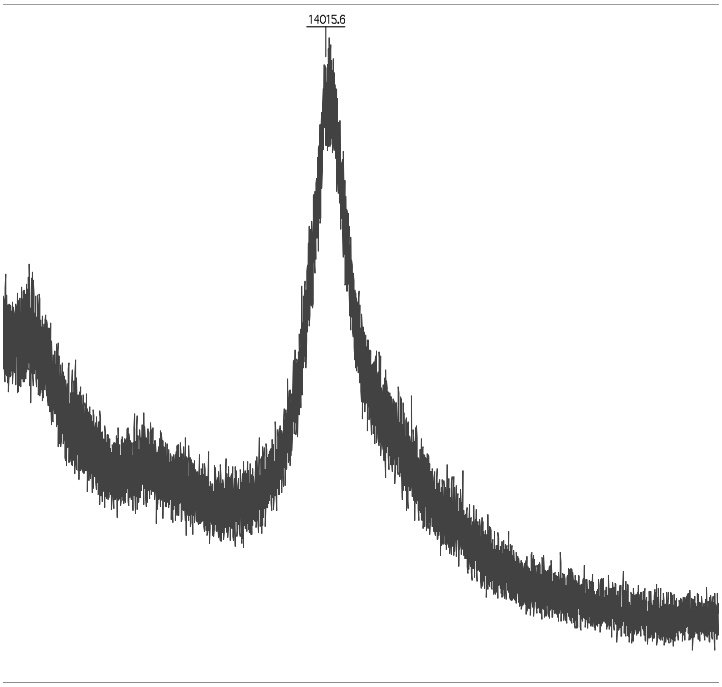

B) Conjugate **O4**: Calcd 14070 Found 14057

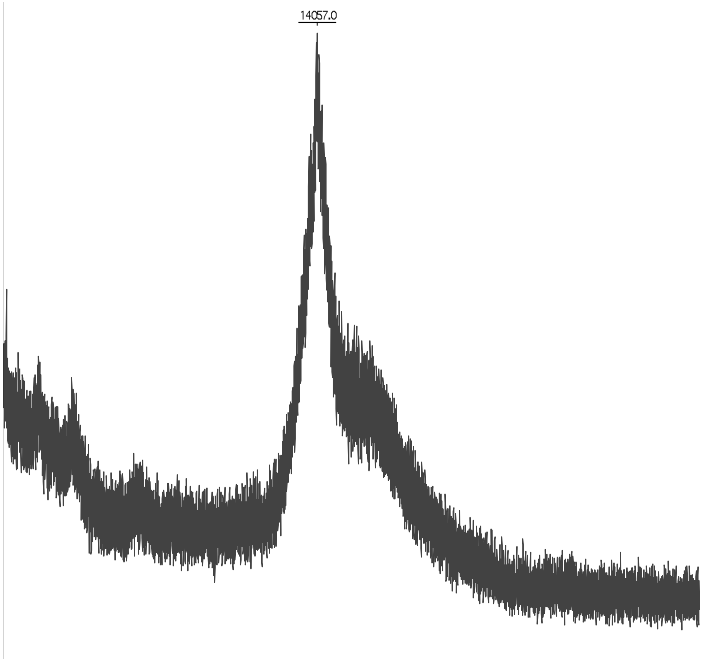

C) Conjugate **O7b**: Calcd 5986 Found 5985. The peak at [M+138] corresponds to the product + one matrix molecule.

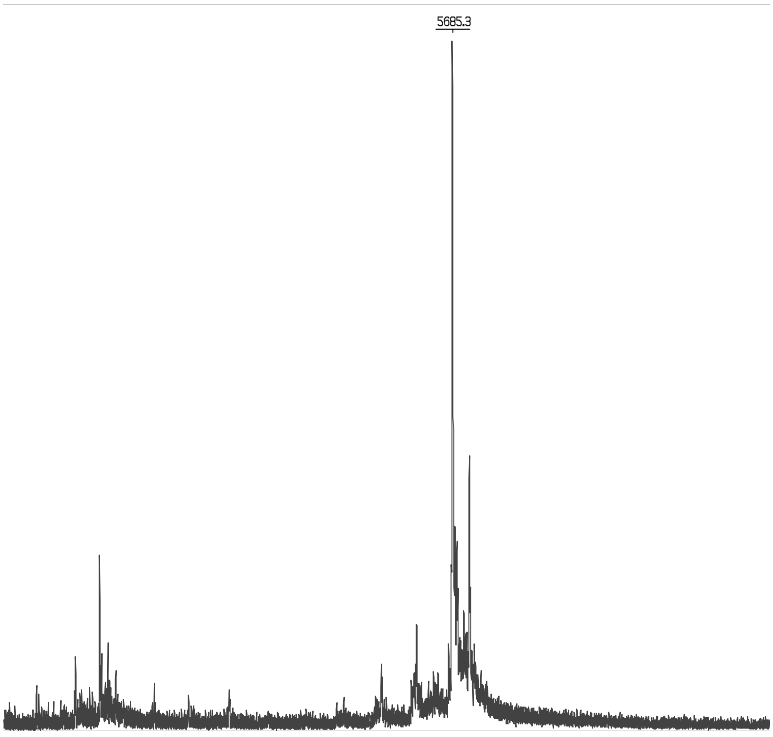

D) Conjugate **O8b**: Calcd 5782 Found 5773. The peak at [M+138] corresponds to the product + one matrix molecule.

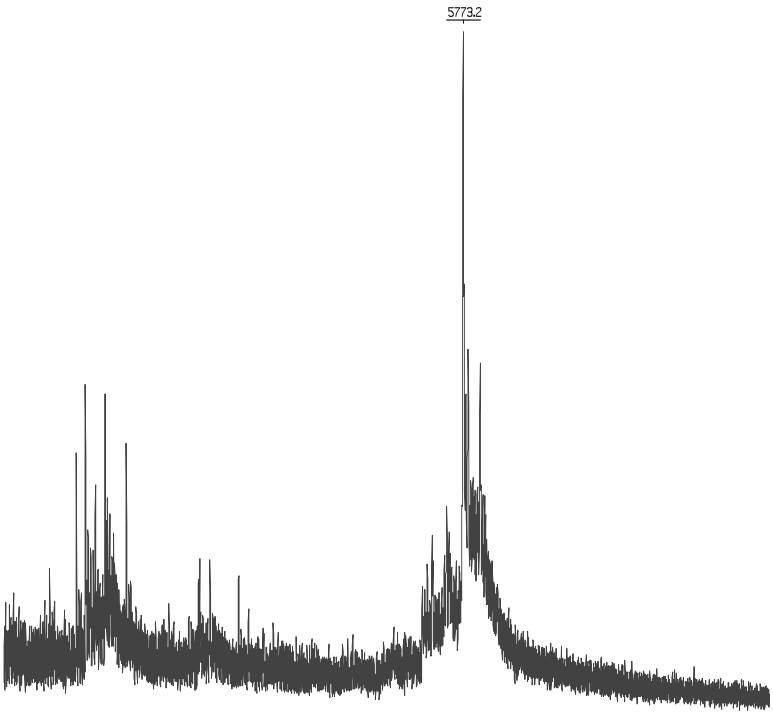

E) Conjugate **O1**: Calcd 13414 Found 13410.

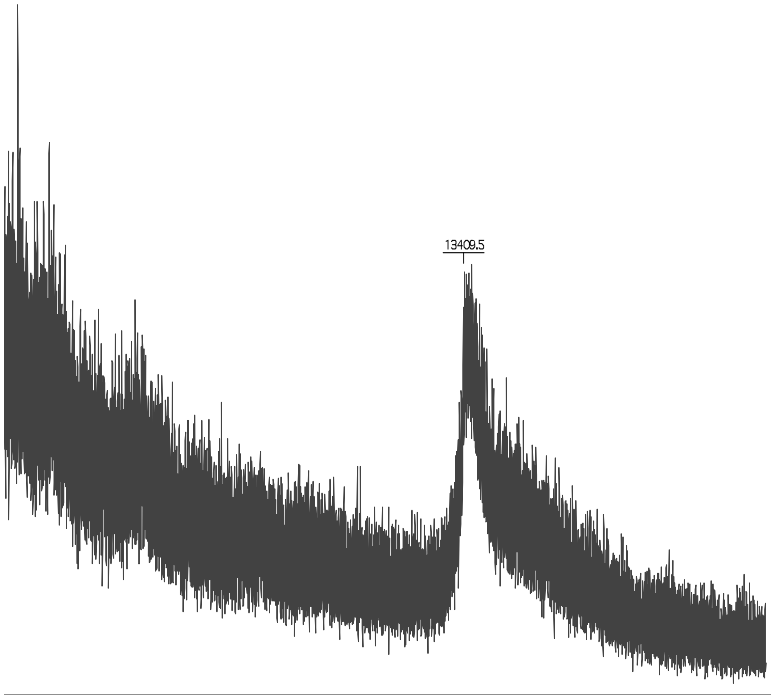

F) Conjugate **O3**: Calcd 13634 Found 13634

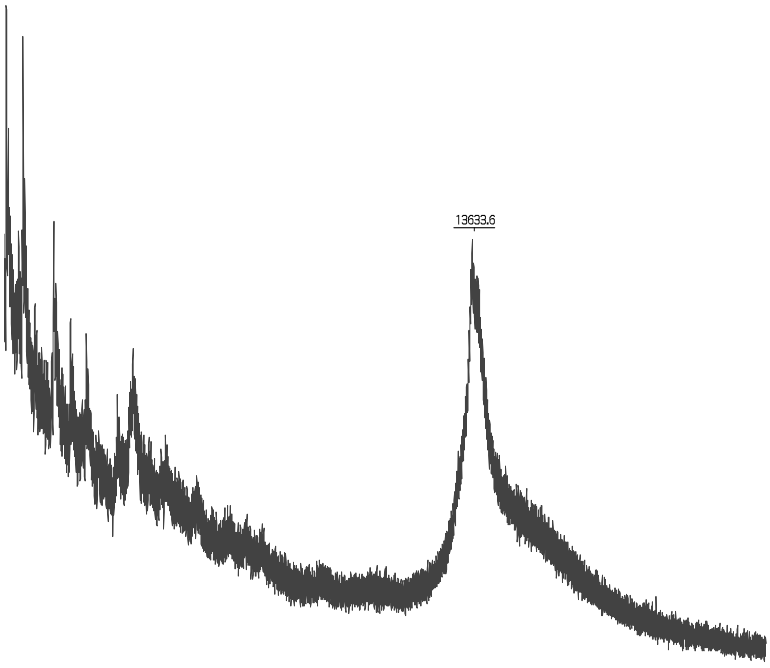

G) Conjugate **O7a**: Calcd 5162 Found 5167. The peak at [M+138] corresponds to the product + one matrix molecule.

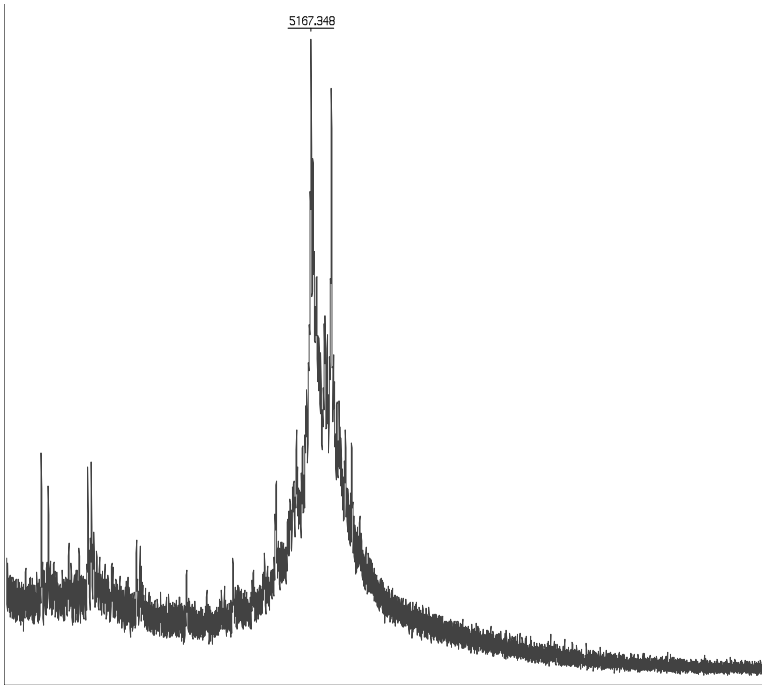

H) Conjugate **O8a**: Calcd 5258 Found 5258. The peak at [M+138] corresponds to the product + one matrix molecule.

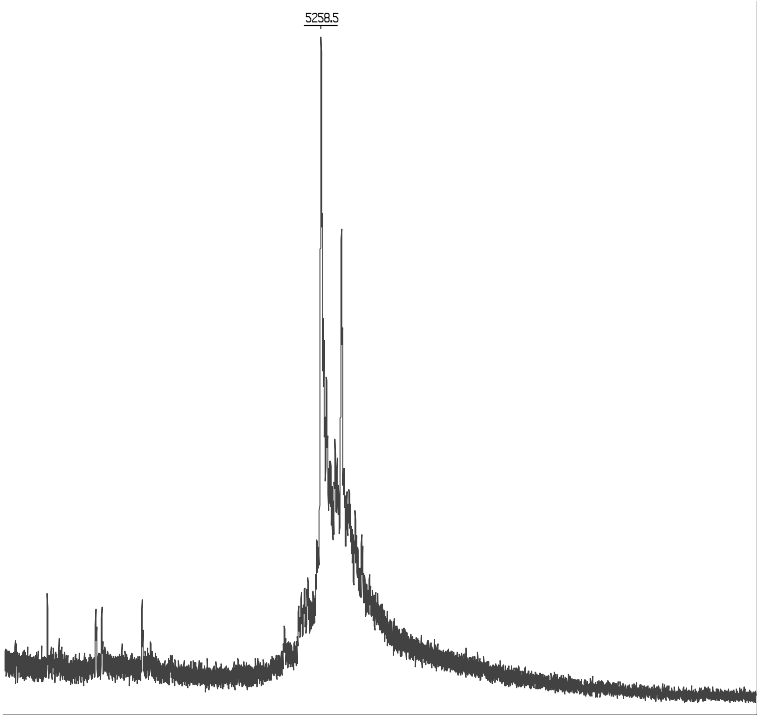

Figure S3. 4-HB templated nickel-salen couplings. (A) 9% denaturative PAGE analysis of 4-HBs, accumulated to one fifth of the original volume on filter cups before gel loading. (B) RP-HPLC chromatogram of the 4-HB with **O1** and **O7a** treated with nickel(II)chloride and EDA. (C) MALDI-TOF analysis of the partly purified dimer. (D) PAGE analysis of the partly purified dimer.

A) Lane 1 (unmodified 4-HB). Lane 2 (4-HB with **ODN O1** and **O7a** without coupling reagents). Lane 3 (4-HB with **ODN O1** and **O7a** without coupling reagents). Lane 4 (4-HB with **ODNO1** and **O7a** with coupling reagents).

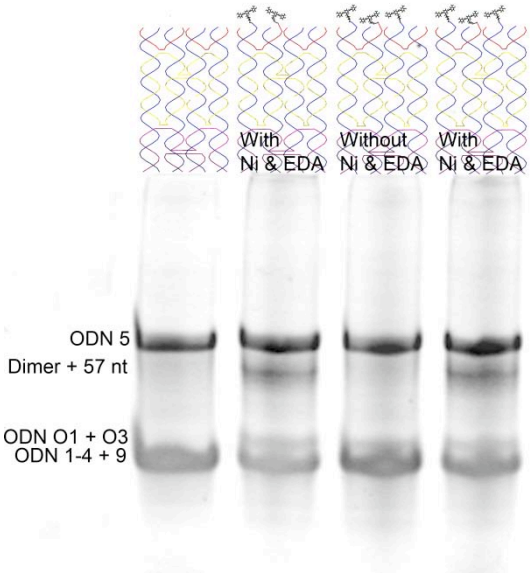

B) RP-HPLC chromatogram of a 4-HB with **ODN O1** and **ODN O7a** treated with nickel(II)chloride and EDA for 4 hours. The initial eluent is pure 0.1 M TEAA and is changed stepwise to separate the unmodified DNA strands (elutes from 7 to 10 minutes) from the organic modified DNA strands (eluted at 13 minutes). The peak at 13 minutes contains a mixture of monomers and the dimer. The UV-VIS spectrum of the collected sample at 13 minutes is shown. The purpose with this stepwise procedure is to remove all unmodified DNA strands and thereby enable the identification of the dimer. The fraction at 13 minutes is analyzed with MALDI-TOF MS and PAGE analysis (see Figure S3C and D)

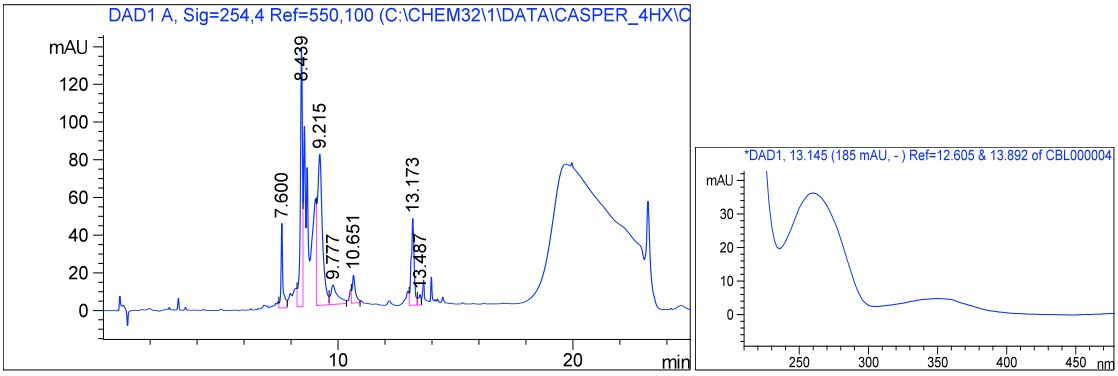

The stepwise method: The acetonitrile percentage is increased from 0 to 20% in the first 10 minutes. From 10 to 17 minutes is the acetonitrile percentage held constant at 70%.

C) MALDI-TOF analysis of the HPLC fraction collected at 13 minutes, according to the HPLC spectrum in Figure S3B. The peak is very broad and it is therefore difficult to find an exact mass. Expected mass of the **O1**-**O7a** dimer: 18573. Found: 18633.

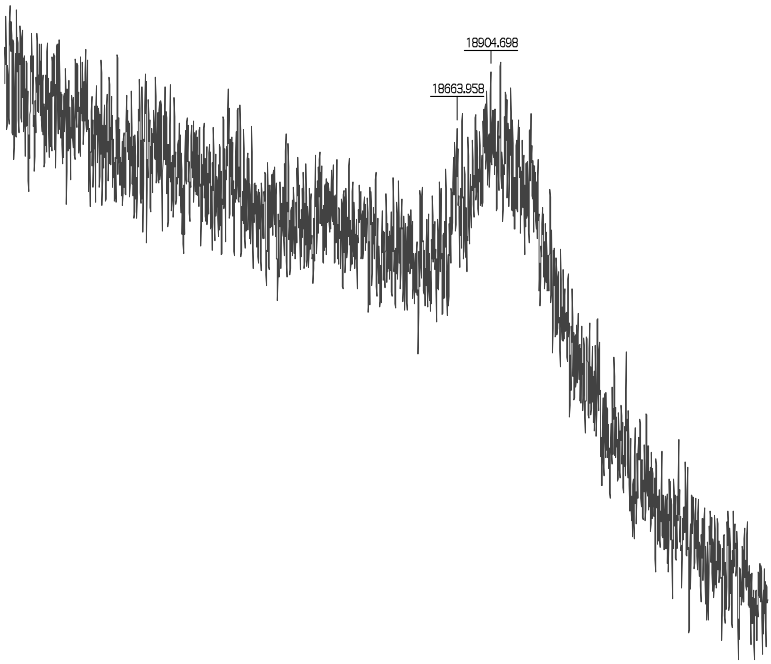

D) PAGE analysis. An 4-HB with **ODN O1** and **ODN O7a** that has not been treated with coupling reagents was purified by the same stepwise method as described in Figure S3B. Lane 1 contains the resulting fraction at 13 minutes (containing the organic modified DNA strands). Lane 2 contains the fraction at 13 minutes according to the HPLC spectrum in Figure S3B. The short dimer is easily observed because all the unmodifed DNA strand are removed and the SYBr gold stained gel can be images by integrating the fluorescent light for 4 seconds.

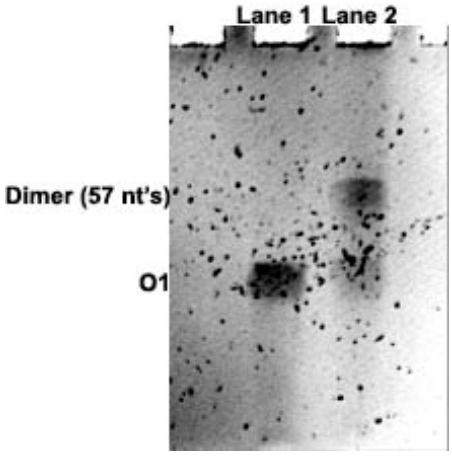

Figure S4. Non-stained 9% denaturing PAGE similar to the gel in Figure 7, but with the dihydrazine as the coupling reagent. The 4-HB incorporating **ODN O1**, **O2**, **O3** and **O4**. Lane 1 (4-HB with **ODN O1**, **O2**, **O3** and **O4** without dihydrazine treatment). Lane 2 (4-HB with **ODNO1** and **O2** treated with dihydrazine). Lane 3 (4-HB with **ODN O1**, **O2** and **O3** treated with dihydrazine). Lane 4 (4-HB with **ODN O2**, **O3** and **O4** treated with dihydrazine). Lane 5 (4-HB with **ODN O1**, **O2**, **O3** and **O4** treated with dihydrazine). Lane 6 (4-HB with **ODN O2** and **O3** treated with dihydrazine). Lane 7 4-HB with **ODN O3** and **O4** treated with dihydrazine). Lane 8 (4-HB with **ODN O1** and **O3** treated with dihydrazine). Lane 9 (4-HB with **ODN O1** and **O4** treated with dihydrazine). The hydrazone dimer consisting of **ODN O1, O2, O3** or **O4** (organic dimer with 84-88 nt) is clearly observed.

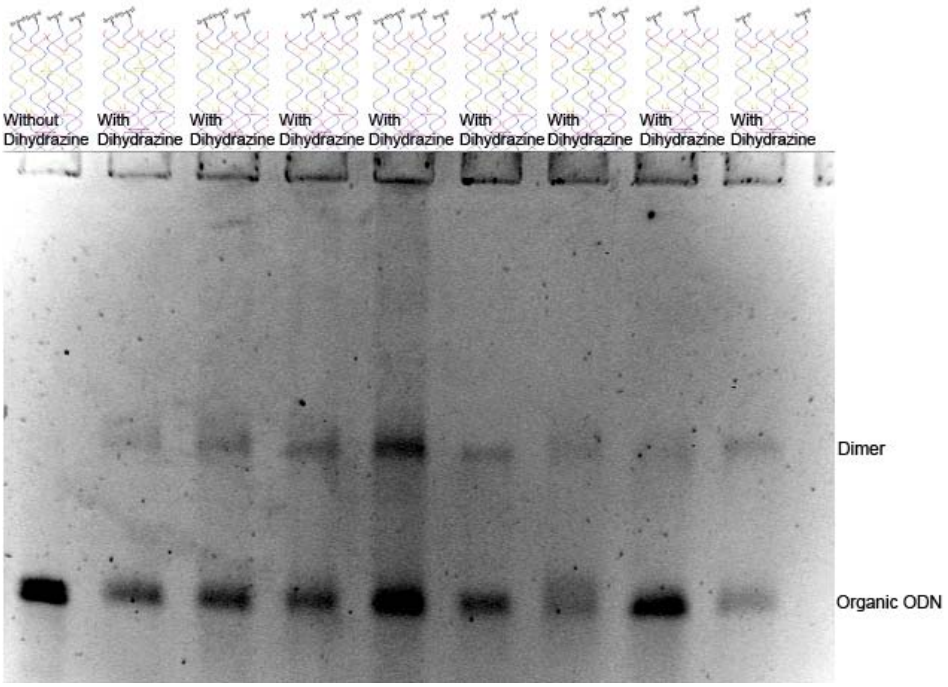

Figure S5. Tests for unspecific couplings in, (A) nickel-salen formation and (B) for dihydrazone formation. (A) Lane 1 (**ODN 1**). Lane 2 (**ODN O1**). Lane 3 (**ODN O1** and **O3**). Lane 4 (**ODN 5**). Lane 5 (4-HB with **O1**). Lane 6 (4-HB). Prior to gel loading was all solutions treated with nickel(II)chloride and EDA. The gel clearly verifies that no intermolecular couplings are observed.

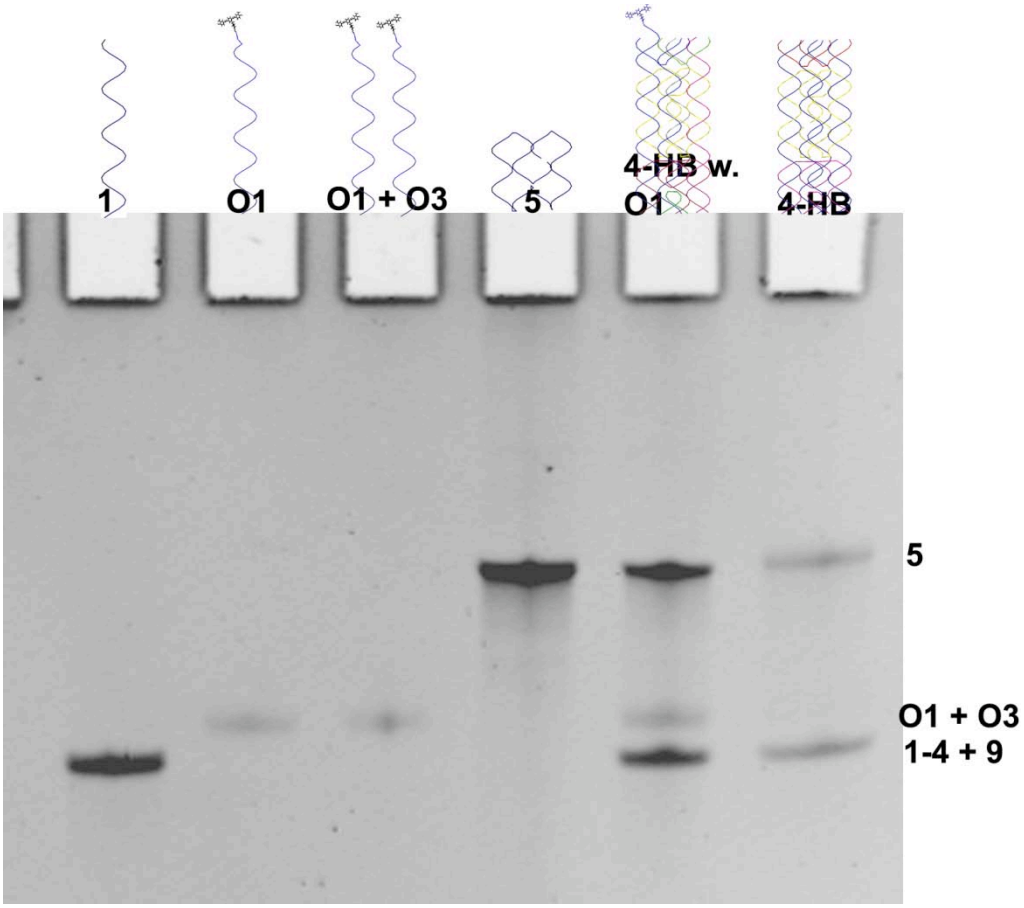

(B) Lane 1 (**ODN 1**). Lane 2 (**ODN O7a**). Lane 3 (**ODN O1** and **O3**). Lane 4 (**ODN O7a** and **O8a**). Lane 5 (4-HB with **O7a**). Prior to gel loading was all solutions treated with dihydrazine for two hours. The gel clearly verifies that no intermolecular couplings are observed.

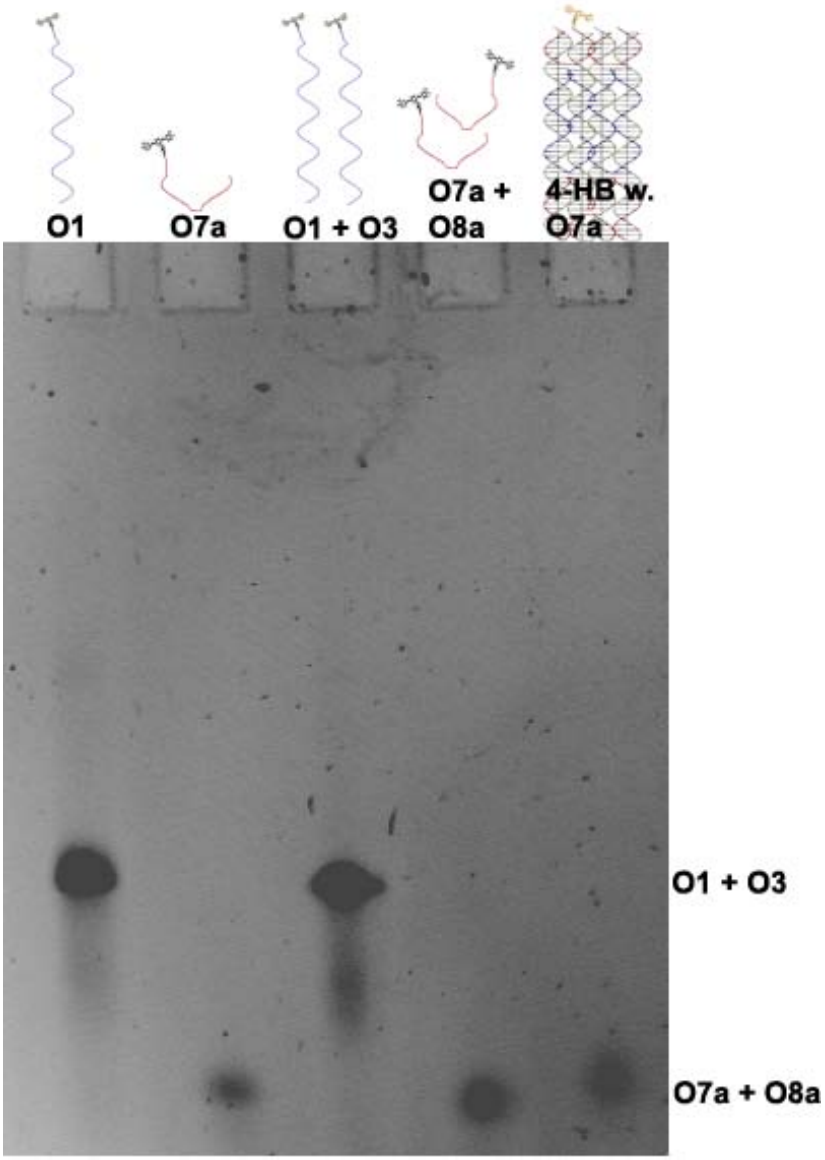

NMR spectra

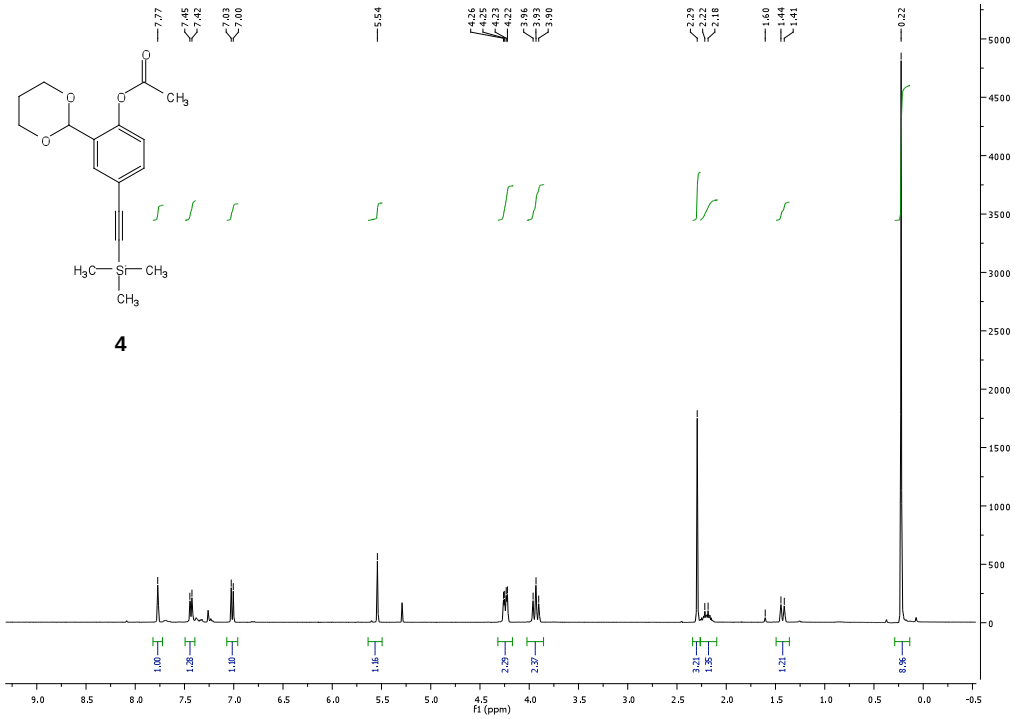

4

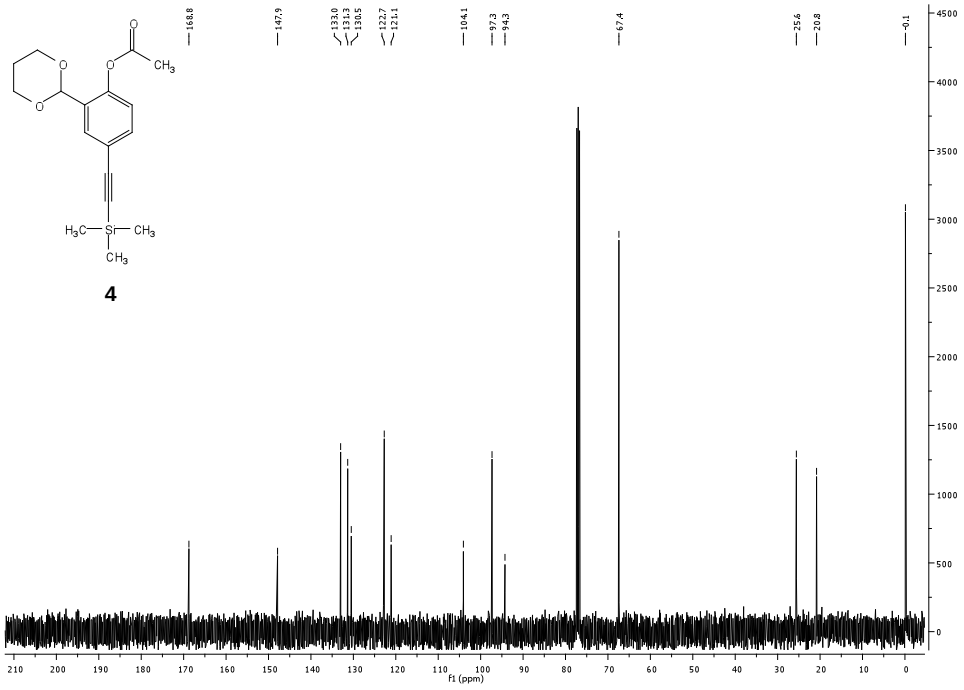

4

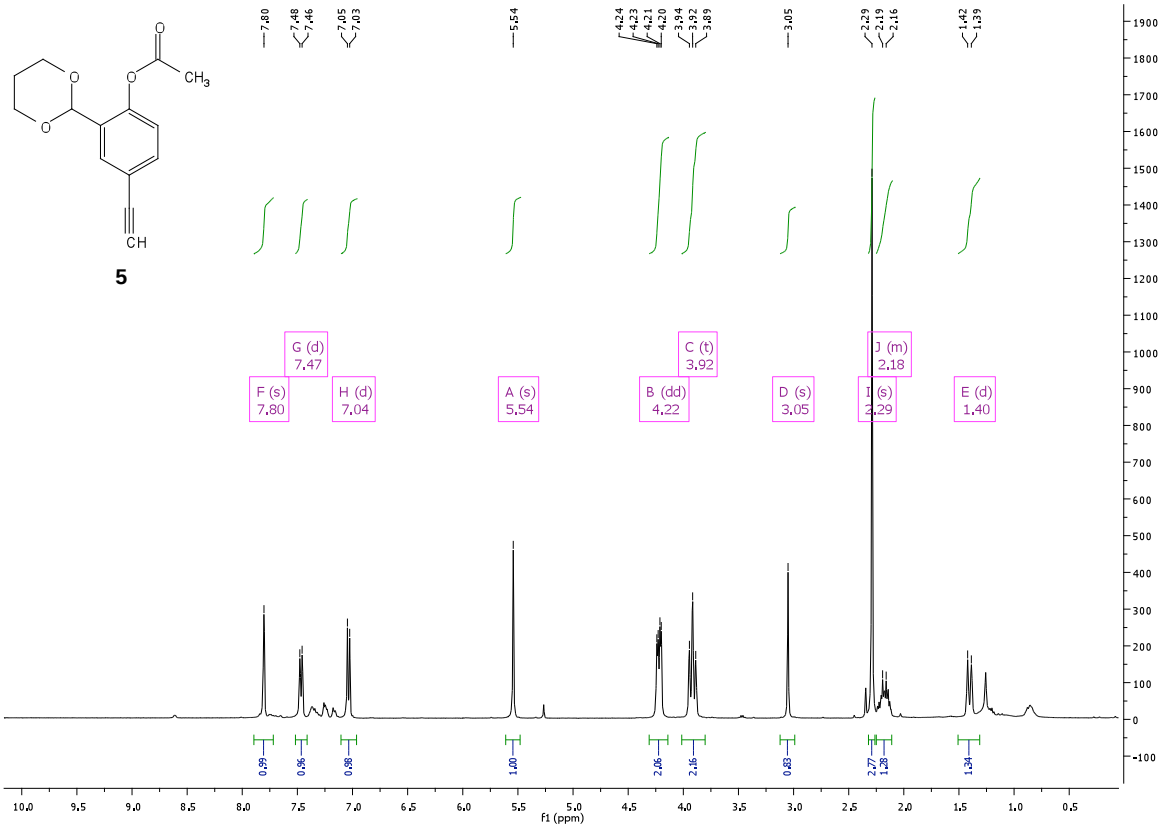
5
F (s) 7,80
G (d) 7,47
H (d) 7,04
A (s) 5,54
B (dd) 4,22
C (t) 3,92
D (s) 3,05
I (s) 2,29
J (m) 2,18
E (d) 1,40
f1 (ppm)

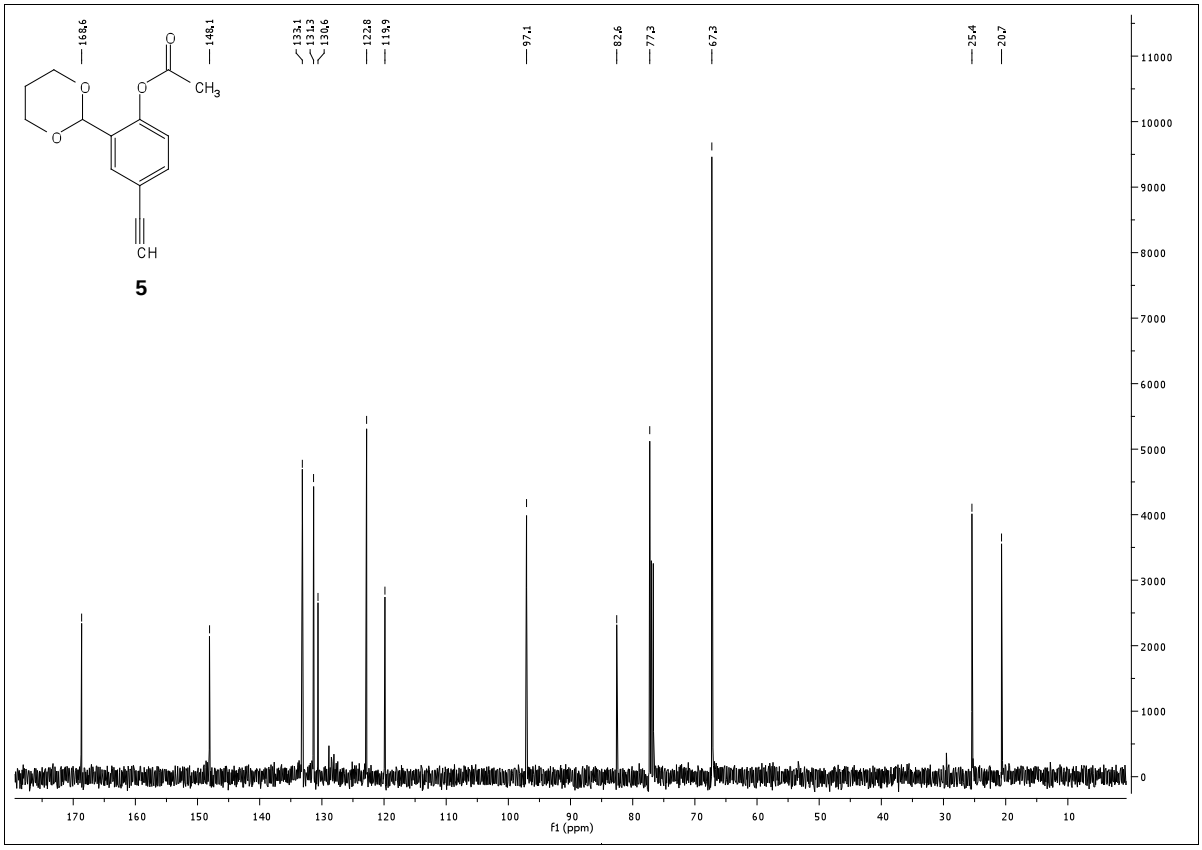
5
f1 (ppm)

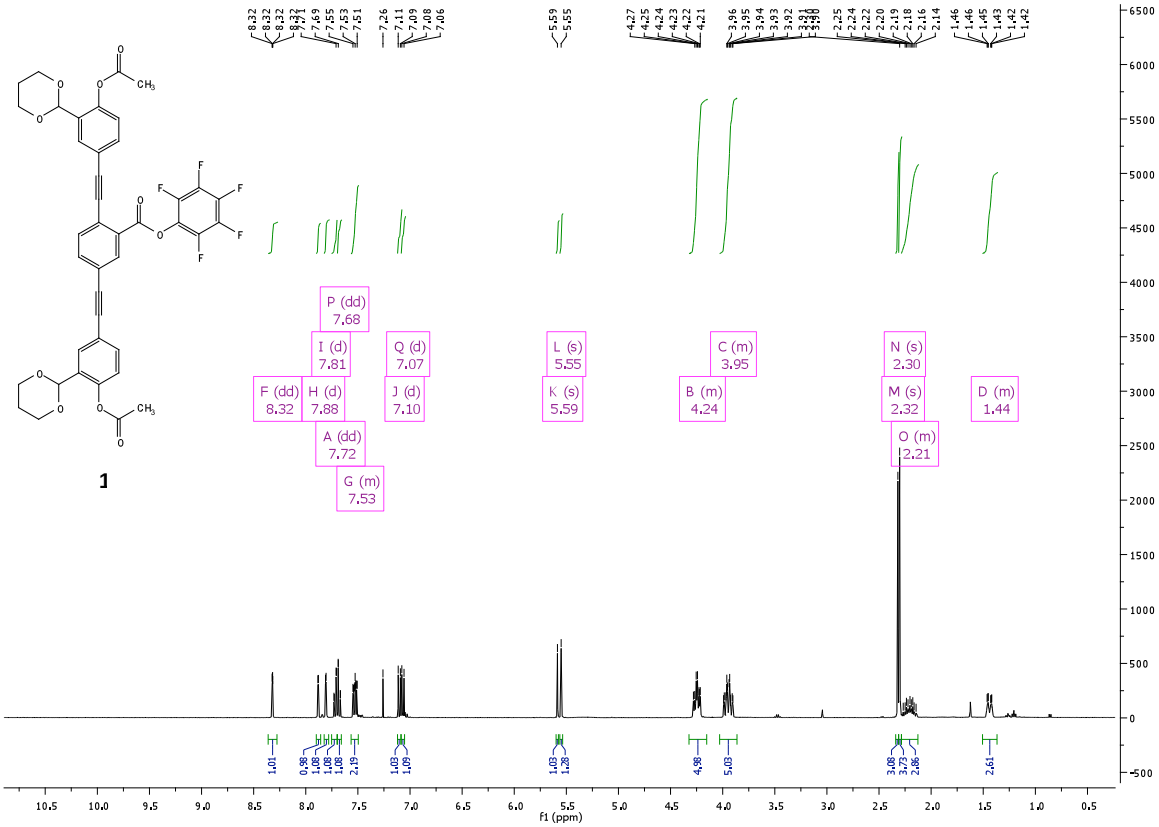
P (dd) 7.68
I (d) 7.81
Q (d) 7.07
L (s) 5.55
C (m) 3.95
N (s) 2.30
F (dd) 8.32
H (d) 7.88
J (d) 7.10
K (s) 5.59
B (m) 4.24
M (s) 2.32
D (m) 1.44
A (dd) 7.72
O (m) 2.21
G (m) 7.53
f1 (ppm)

1

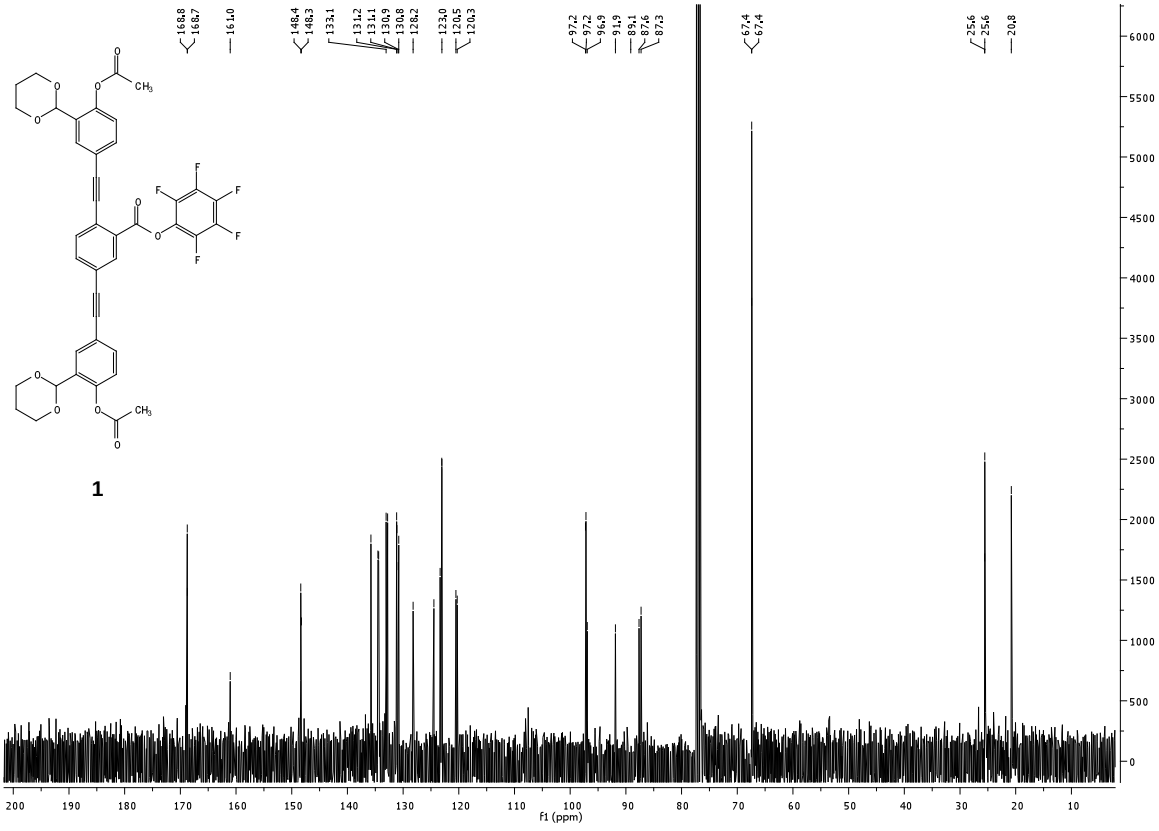
f1 (ppm)

1

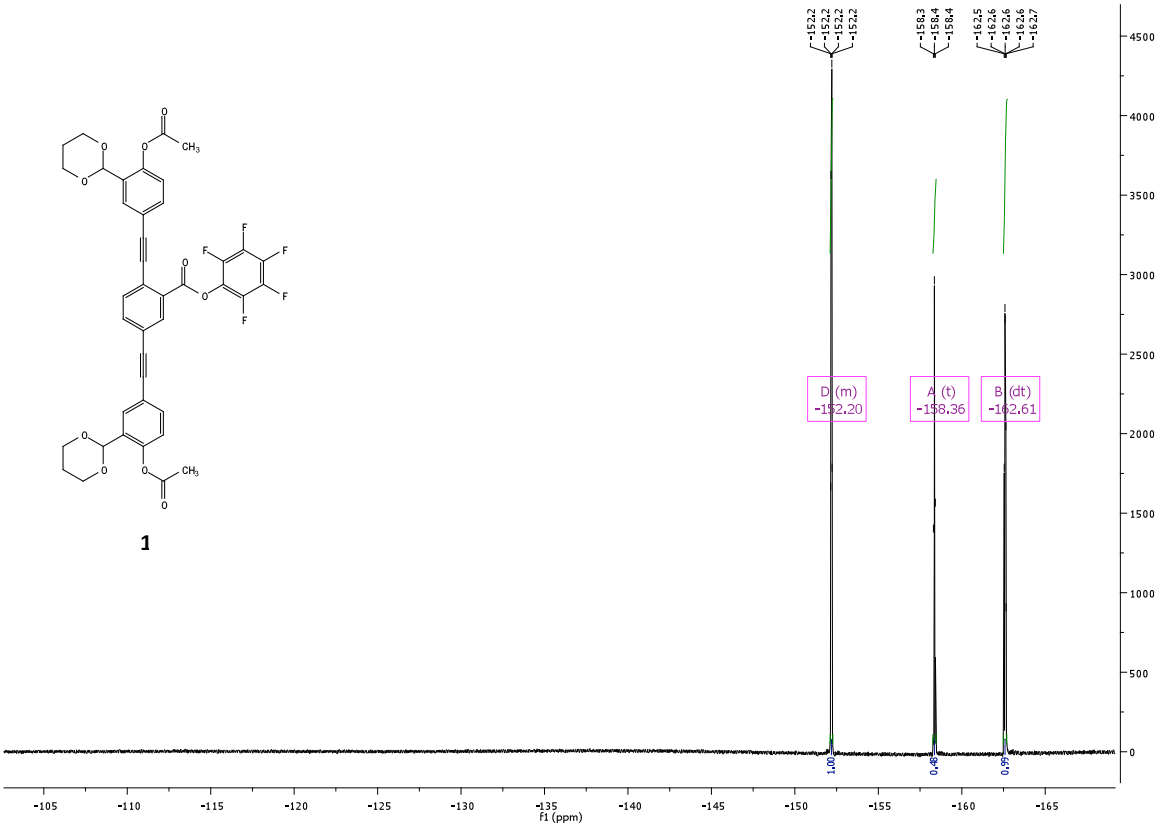

1

Optimal ^{99m}Tc Radiolabeling and Uptake of Glucosamine Sulfate by Cartilage. A Potential Tracer for Scintigraphic Detection of Osteoarthritis

Grazyna Sobal,* Johannes Menzel,† and Helmut Sinzinger*

University Clinic of Nuclear Medicine and Institute of Immunology, Medical University of Vienna, Vienna, Austria. Received March 3, 2009; Revised Manuscript Received May 26, 2009

Glucosamine sulfate (GS) is used in treatment of human osteoarthritis, but no data for ^{99m}TcGS scintigraphy are available. Radiolabeling of GS was performed using the $^{99m}TcO_4^-$/tin method. We applied two procedures for separation of free ^{99m}Tc using PD10 and G10 columns. In each eluted fraction, GS content was estimated by the Elson/Morgan method. For optimal radiolabeling, we varied the amount of GS, tin, ^{99m}Tc activity, and pH. For uptake age matched human rib cartilage (males, 78 and 63 years old) and 5−10 μCi/well of ^{99m}TcGS were used. Uptake was monitored up to 72 h. Also, washout of the tracer 3 h and 24 h after uptake was investigated. At pH 2, using PD10 column, the uptake of ^{99m}TcGS amounted to 100.8 ± 2.9%, $n = 6$ at saturation time of 72 h. Uptake was age-dependent; at pH 5, it amounted to 99.8% as compared to 66.1% at 78 vs 63 years old. When the amount of tin was varied at pH 2, the tracer uptake amounted to 21.37% (1 mg) vs 45.99% (2.5 mg) at saturation. At pH 7, the amount of needed tin was much lower and amounted to 42.50 ± 2.50% using 0.1 mg vs 25.11 ± 1.90% using 0.05 mg. Although the uptake at pH 7 (0.1 mg tin) is comparable with that at pH 2 (2.5 mg tin), the washout of the tracer amounted only to 4.10 ± 1.25% and 2.05 ± 0.65% after 3 h and 24 h, respectively. During degeneration of cartilage, incorporation of ^{99m}TcGS is high and could therefore be a promising tracer not only to target osteoarthritis but also to monitor the effects of therapy.

INTRODUCTION

Glucosamine (GA) is a natural sugar and a key component of the extracellular matrix of cartilage. These monomeric sugars possess charged side chains, which absorb water and provide lubrication for cartilage that covers the bones in the joints. With aging or under pathological conditions, GA, like other sugars, declines in concentration and loses the ability to absorb water. Treatment with GA affects the symptoms but not the disease, since after ingestion, GA has been shown to be absorbed in the joints as a component of the cellular matrix of cartilage. Glucosamine sulfate (GS) is the sulfate derivative of the naturally occurring aminomonosaccharide, GA.

GA and chontroitin sulfate (CS) are widely used drugs for treatment of osteoarthritis (*1*−*4*) as symptomatic slow-acting drugs for osteoarthritis (SYSADOA). Osteoarthritis (OA) represents an advanced stage of disease caused in part by injury, loss of cartilage structure, and function and is an inflammatory process. The results of an in vitro study (*5*) indicated that GS and CS can regulate gene expression and synthesis of nitric oxide (NO) and prostaglandin PGE_2, thereby modulating anti-inflammatory activity.

Bone scintigraphy is generally regarded as very sensitive but nonspecific. Because of their sensitivity and advantage over MRI (*6, 7*), noninvasive isotopic methods including SPECT and PET (*8, 9*) play an important role in clinical studies of arthritis. Although imaging techniques using radiolabeled polyphosphonates have been a major clinical tool for imaging osteoblastic activity and tumor involvement of the skeleton during the past decades, radiolabeled probes specific for the pathophysiology of synovium and articular cartilage are just at the early stages of exploration. For this reason, more specific probes for articular cartilage disease would be preferable. GS as an endogenous cartilage component is one of these candidates. GS is widely used for the treatment of human osteoarthritis, but no data on GS labeling with ^{99m}Tc or studies of radiolabeled ^{99m}Tc GS in the cartilage are available.

The aim of this study was to elaborate the optimal radiolabeling of ^{99m}Tc GS for future SPECT analysis by providing the optimal radiolabeling method, quality control of the tracer, its stability, and evaluation of uptake of radiolabeled compound by cartilage and to verify the degree of GS internalization.

EXPERIMENTAL PROCEDURES

Materials. GS was provided by Rottapharm, Monza, Italy. Radiolabeling of GS was performed using $^{99m}TcO_4^-$/stannous chloride according to the methods (*8, 10*) analogous to chondroitin sulfate labeling. We found that, because of colloid formation, pH is a limiting factor for the labeling procedure and tracer uptake.

Radiolabeling Procedure. Briefly, 25 mg of GS was dissolved in 0.75 mL of 0.3 M HCl, pH 2; then, 1 mg of stannous chloride was added followed by the addition of 1−3 mCi (37−121 MBq) of $^{99m}TcO_4^-$/(0.25 mL). We also performed experiments by buffering final reaction mixture with 0.50 M sodium acetate buffer at pH 5.0 or 0.01 M sodium citrate buffer at pH 7 to obtain more physiological conditions. The reaction mixture was gently stirred and incubated for 1 h at room temperature. Thereafter, the radiolabeled product was applied to the Sephadex PD10 chromatography column (Bio-Rad, California, USA) for separation from free technetium. The radiolabeled GS was eluted from the column with 0.3 M HCl in 10% ethanol or buffer in the void volume (3−5 mL), while free technetium was eluted from the column with the total volume (6−10 mL). In parallel, we measured ^{99m}Tc activity in each fraction to obtain the elution profile from the column. For

* Address all correspondence and reprint requests to Dr. G. Sobal, Department of Nuclear Medicine, Medical University of Vienna, A-1090 Vienna, Währinger Gürtel 18-20, Austria. Tel. +431/40400-5558, Fax +431 /40400-5552, E-mail: Grazyna.Sobal@meduniwien.ac.at.

† Institute of Immunology.

10.1021/bc9000883 CCC: $40.75 © 2009 American Chemical Society
Published on Web 07/17/2009

optimal radiolabeling, we varied the amount of GS (2.5 mg versus 25 mg), tin (1−5 mg), and also ^{99m}Tc activity (1.5−4 mCi, 55.5−148 MBq). We also applied two different procedures for separation of free ^{99m}Tc after radiolabeling by using PD10 and G10 (self-prepared, 15 mL) columns. In each eluted fraction after labeling, GS content was estimated by the Elson and Morgan method (*11*). For each of the radiolabeling variations, the radiolabeling efficiency, maximal uptake, and washout of the tracer were estimated.

Uptake Studies. For uptake studies, human rib cartilage (males, 78 and 63 years old, post mortem) cut into pieces of about 5 mg wet weight was used. For uptake, we incubated with 5−10 μCi/well of ^{99m}TcGS. Uptake was monitored every 10−30 min, and thereafter every few hours until saturation was achieved (up to 72 h).

After each incubation period, the tissue was separated from incubation medium by simple differential centrifugation and rapidly washed twice with PBS buffer. The net (after subtraction of residual activity and activity related to adhesion of tracer to the tubes) cellular uptake of ^{99m}TcGS in vitro was measured by a gamma counter (Packard, Meridien, CT, USA). Also, washout of the tracer after uptake was investigated. The washout of the tracer was performed by incubation of tissue after uptake experiments (3 h and 24 h) with PBS buffer for different times (10 min to 3 h).

Derivatisation of GS. GS measurement was perfomed according to the modified method by Elson and Morgan (*11*). Briefly, 1 mL of column eluent containing GS was mixed with 1 mL of the acetylacetone reagent (2 mL of acetylacetone dissolved in 98 mL of 1 N sodium carbonate) and closed with a cap. The tubes were then placed in a water bath at 90 °C for 45 min. Thereafter, they were cooled in running water. Then, 4 mL of ethanol (95%) was added and tubes were vortexed. Finally, 1 mL of PDMAB (*p*-dimethylaminobenzaldehyde) for derivatization was added. After mixing again, the tubes were allowed to stand at room temperature for 1 h, getting a characteristic pink color. The absorbance was read at 540 nm. GS content of the samples was calculated using a standard curve with defined GS amount (5−50 μg/mL).

Statistical Analysis. The results are expressed as mean values ± SD. Statistical analysis was performed using one-way ANOVA; $p < 0.05$ was considered statistically significant.

RESULTS

Radiolabeling Procedure and Uptake Studies. The radiolabeling yield was strongly influenced by pH because of colloid formation. At higher pH 5, the labeling efficiency was very low (10.1−12.5%) and the colloid content high (31.6−89.9%), detected on Sephadex PD10 chromatography column by separation after labeling. In contrast, at pH 2.0 almost no colloid or only a few percent of colloid was formed (maximal 4.5%; data not shown), and a very high labeling efficiency (72.0−95.6%) was achieved.

During the incubation with ^{99m}TcGS, we observed continuously increasing uptake of tracer over the time up to saturation. At pH 2, after separation on a PD10 column, uptake was very high, amounting to 100.8 ± 2.9%, $n = 6$, at saturation of 72 h (Figure 1A). This means that the obtained saturation of the tracer at this pH was achieved when the total of introduced ^{99m}Tc GS tracer was completely taken up into the cartilage. At pH 5, the uptake was much lower, but increasing with time until saturation amounting to 50.1 ± 5.5%, $n = 6$ (Figure 1A).

After 3 h uptake, the washout of the tracer from cartilage at pH 2 amounted to 45.7 ± 2.5% and was completed after 30 min. After 24 h uptake, the washout was unchanged at 44.1 ± 7.5%, but it was completed after 3 h (Figure 1B). These results indicate that in both experiments more that 55% of the

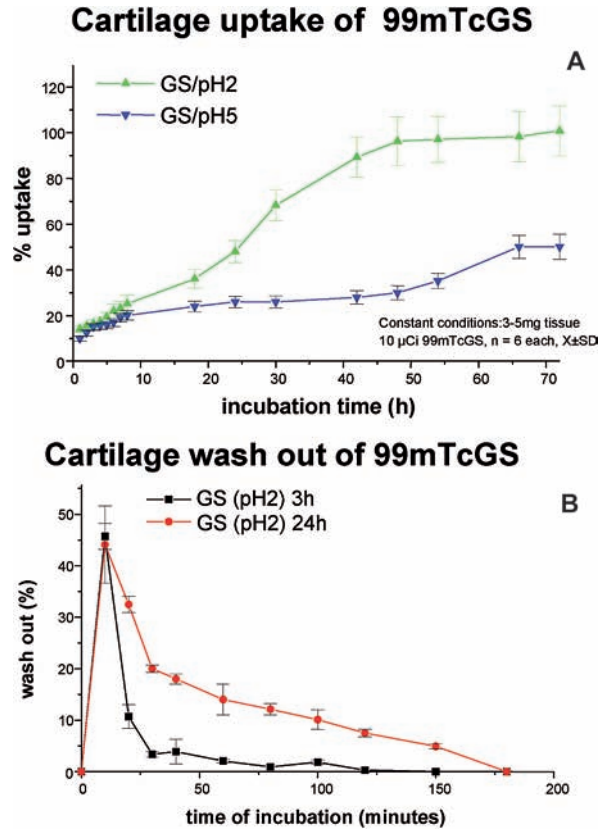

Figure 1. Uptake of ^{99m}TcGS after separation on PD10 column as a function of time, at different pH values (A). The washout of ^{99m}TcGS from cartilage at pH 2, after 3 h and 24 h of uptake as a function of time (B). Each point represents the mean value of three radiolabeling experiments with two measurements each.

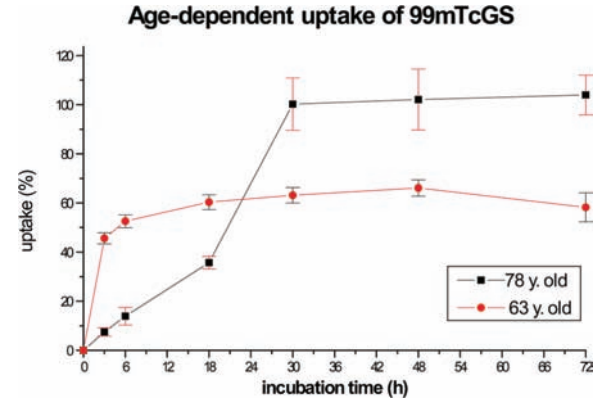

Figure 2. Age-dependent uptake of ^{99m}TcGS at ph 2. Each point represents the mean value of three radiolabeling experiments from two specimens.

introduced tracer is retained in the cartilage and is not eluted. Uptake was age-dependent and amounted to 99.8% as compared to 66.1% at 78- vs 63-year-old individuals at saturation by 72 h (Figure 2). The nonspecific uptake in the presence of a 50-fold excess of cold GS in all experiments increased with time up to a maximum of 12−15% at saturation by 72 h.

Because of similar molecular weights of both components (GS and pertechnetate), the separation of free ^{99m}Tc after radiolabeling by a chromatography column or ITLC-SG chromatography was difficult. For radiolabeling of GS using $^{99m}TcO_4^-$/1 mg tin method at pH 2, we evaluated the separation by PD10 and G10 columns. By estimation of GS content in

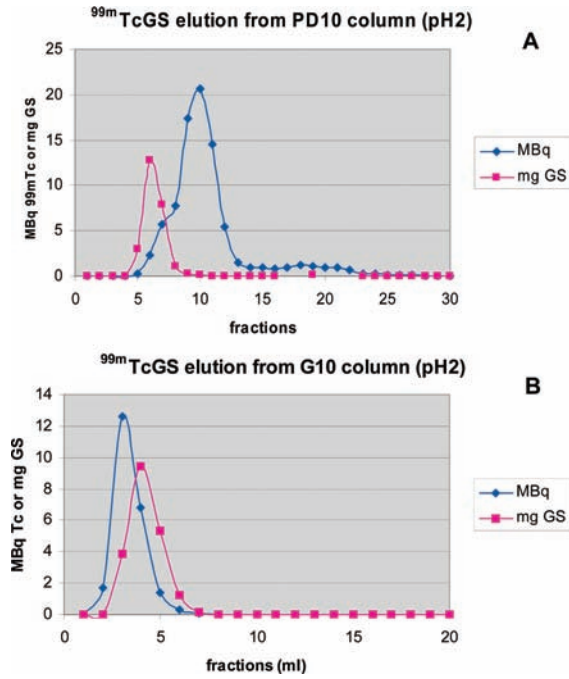

Figure 3. Chromatography procedure on PD10 vs G10 column, after radiolabeling at pH 2. In parallel, GS content in each eluted fraction was estimated.

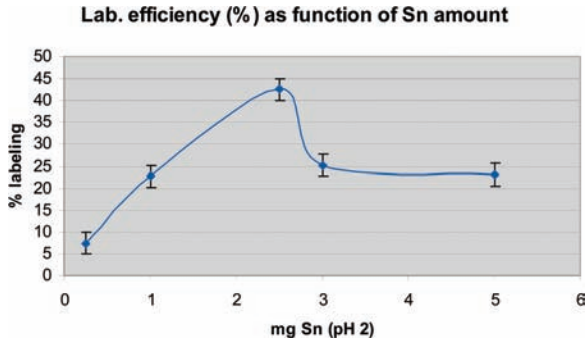

Figure 4. Dose-dependent (tin) estimation of radiolabeling efficiency at pH 2. Each point represents the mean value of three radiolabeling experiments with two measurements each.

each eluted fraction, we found a shift between the maximum of GS content peak and the radioactivity peak by PD10 (Figure 3A); therefore, we applied a G10 column for more precise separation of components after radiolabeling (Figure 3B).

Varying the amount of tin (0.1−5 mg), at pH 2 and using G10 column for separation, we found the optimal conditions at 2.5 mg tin and 25 mg of GS, 4 mCi, for radiolabeling. This factor not only influences the labeling efficiency (22.95−42.73%, 1 mg vs 2.5 mg tin) (Figure 4), but also the ^{99m}TcGS uptake in cartilage. While tracer uptake using 1 mg tin for labeling achieved a maximum of 21.37% at saturation (72 h), in contrast using 2.5 mg tin the maximal uptake amounted to 45.99% at saturation (Figure 5A). However, using 3−5 mg of tin the labeling efficiency and uptake could not be further increased and achieved a comparable amount to that using 1 mg, amounting to 28.13% at saturation at 72 h. Tracer washout after 3 h incubation using 2.5 mg tin for radiolabeling amounted to a maximum of 17.44 ± 6.60% and after 24 h to 4.94 ± 3.60%, respectively (Figure 5B).

Finally, we found that buffering of the radiolabeling mixture with 0.01 M citrate at pH 7, reflecting more closely physiological

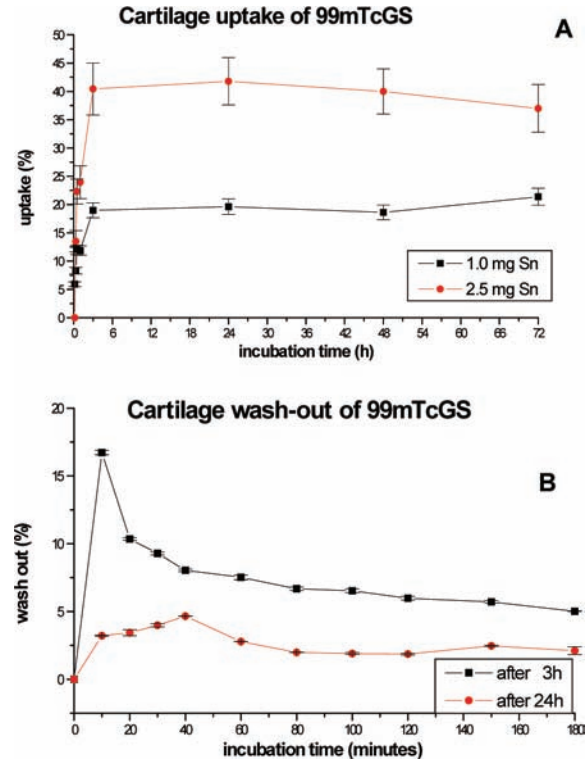

Figure 5. Dose-dependent uptake of ^{99m}TcGS at pH 2 (A) and washout of the tracer 3 h vs 24 h after uptake (B), at constant condition: pH 2, 2.5 mg tin. Each point represents the mean value of three radiolabeling experiments with two measurements each.

conditions, gave the best results of highest labeling efficiency and specific activity of 1.6 MBq/mg GS. However, the amount of tin was much lower than at pH 2. Using 0.1 mg tin for radiolabeling, we get the highest labeling efficiency and specific activity (Figure 6A), followed by 0.05 mg tin, getting slightly worse results (Figure 6B).

Also, the corresponding uptake at this pH 7 (0.1 mg tin) showed a higher uptake (42.50 ± 2.50%) than using 0.05 mg tin for radiolabeling (25.11 ± 1.90%) (Figure 7A). Although the uptake at this pH 7 (0.1 mg thin) is comparable to that at the uptake at pH 2 (2.5 mg tin) (Figure 5A), the washout of the tracer at pH 7 was much lower, amounting only to (4.10 ± 1.25%) and 2.05% ± 0.65%), after 3 h and 24 h, respectively (Figure 7B).

DISCUSSION

GA is an endogenous component of cartilage and is a monomeric part of glucosaminoglycans in cartilage matrix and synovial fluid (*12*). Chondrocytes use it for CS proteoglycan synthesis. GS has been found to be of benefit in OA in a number of studies (*13*−*15*) for the symptomatic treatment beneficially affecting the radiographic progression of OA (*16*−*19*). Therefore, ^{99m}Tc GS could be such a specific tracer for uptake in articular cartilage.

The mechanism of action of GS has not been fully elucidated yet. Cartilage-unrelated effects such as inhibition of superoxide-radical generation (*20*) or the inhibition of nitric oxide synthesis (*21*) have been suggested to explain the fast onset of action on symptoms reported even in short-term clinical trials (*22*). In contrast, the long-term effects of GS reported effects on cartilage metabolism are by stimulation of anabolic activities on proteoglycan synthesis (*23, 24*) and depression of catabolic activity, such as the effect of metalloproteases (*24, 25*).

Clinical studies have shown that GS is fairly safe (*22, 26, 27*) and definitely far more safe than standard nonsteroidal anti-

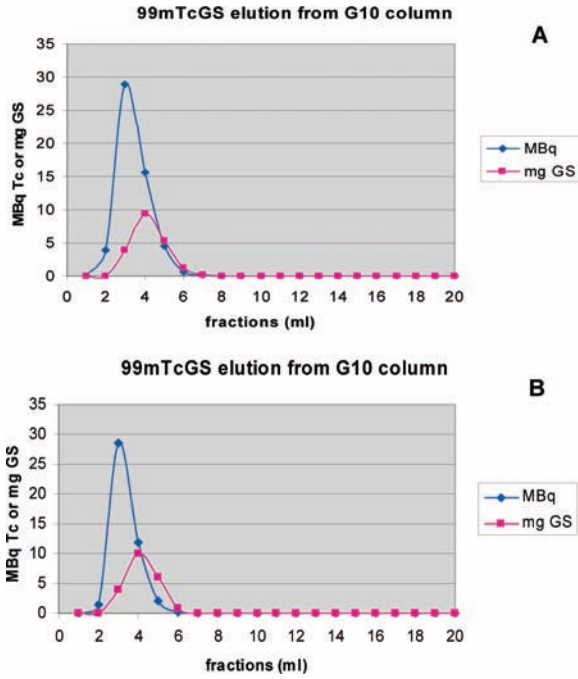

Figure 6. Radiolabeling of GS at pH 7 using 0.1 mg tin (A), as compared to 0.05 mg tin (B). Each point represents the mean value of three radiolabeling experiments with two measurements each.

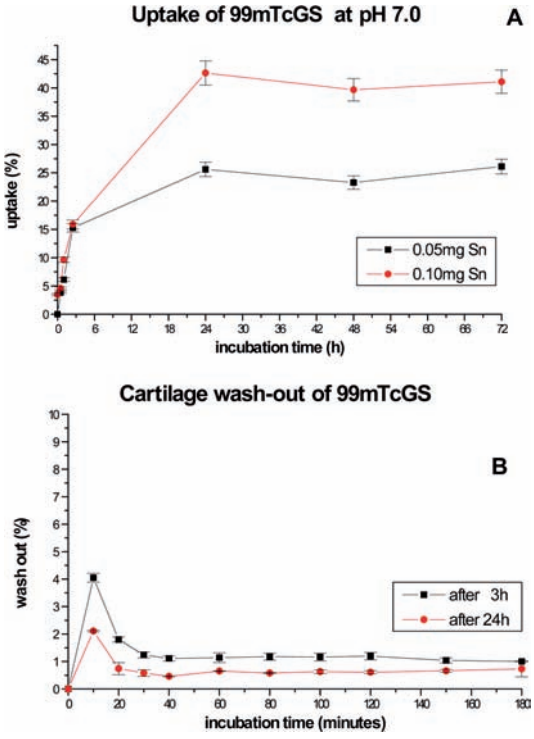

Figure 7. Uptake of ^{99m}TcGS at pH 7 using 0.1 mg tin vs 0.05 mg tin (A) and corresponding minimal washout of the tracer (0.1 mg tin) 3 h vs 24 h after uptake. Each point represents the mean value of three radiolabeling experiments with two measurements each.

inflammatory drugs (NSAIDs), especially concerning the gastrointestinal side effects (*26, 27*). Short-term studies indicate that a daily dose of 1.5 g GS for at least 7 days is sufficient to achieve significant improvement in OA symptoms, being as effective as a 400 mg daily dose of ibuprofen (*27*). Of course, the treatment with GS results in only mild side effects, if any, as compared to ibuprofen. In addition, although the improvements occurred more rapildy with ibuprofen, a more persistent benefit was achieved in patients receiving GS (*28*).

Many studies report that GS is significantly more effective than placebo and even as effective as NSAIDs (*17*). Other studies show that GS has an even significantly greater influence on pain reduction than ibuprofen itself (*18, 19*). In accordance with these findings, a meta-analysis revealed a 40.2% benefit from GS treatment concerning global pain scores or Lequesne's index as compared to placebo (*28*).

Due its low molecular weight, radiolabeling of GS is difficult, as is the separation after radiolabeling from ^{99m}Tc, which also has low molecular weight; in contrast to other GAGs, e.g., chondroitin sulfate with much higher molecular weight. For this reason, it was very important to elaborate the optimal radiolabeling condition considering labeling efficiency, uptake of ^{99m}TcGS in degenerated cartilage itself, and washout of the tracer with time to estimate the net uptake.

It was important and interesting for us to evaluate the in vitro uptake of ^{99m}TcGS by cartilage itself. We found a very high persistent cartilage uptake. The age-dependent uptake of ^{99m}TcGS might reflect the changes in pathologically affected cartilage by dynamic stress during life span. In healthy cartilage, chondrocytes are able to maintain a dynamic equilibrium between anabolic and catabolic processes. However, with increasing age and degeneration this equilibrium is seriously unbalanced causing a dramatic decrease of matrix material, especially of the PG fraction. The major source of structural variation in PG is due to glycosaminoglycan (GAG) chains. They become extended with highly negative charged sulfate and carboxylate groups. With progressing age and degeneration, the number of main and side chains as well as their length and sulfation pattern varies (*29*). This results in a loss of negative charge density and can increase charge-mediated diffusion of GS to compensate this negative charge deficiency. This tendency was also observed in our uptake studies. Of course, this needs to be proven in a higher number of samples.

Apparently, pH plays a very important role not only for the radiolabeling yield, but also with respect to later ^{99m}Tc GS uptake by cartilage. While the radiolabeling at pH 5.0 resulted in very high colloid formation and lower uptake of the tracer, in contrast, at pH 2.0 only few percent colloid were formed and the uptake was very high. The obtained saturation of the tracer at pH 2.0 was achieved when all the ^{99m}Tc GS was completely incorporated into the cartilage. This means that GS has a high tropism for cartilage.

At the physiological condition of pH 7.0, the uptake is comparable to that at pH 2, but the washout is decreased, amounting only to a maximum of 4%. Only experiments undertaken at pH 7.0 are representative for in vivo conditions. The amount of Sn^{2+} influences the labeling procedure of GS. The reason for the highly different uptake depending on the labeling conditions is more complex. For each pH value and each Sn^{2+} amount, there seems to be an optimal reduction state of Tc^{7+} in pertechnetate to $Tc^{+5,+4,+3}$ and the ability to form a more or less stable complex with GS. At pH 7.0, the higher amount of tin (0.1 mg versus 0.05 mg) as a reducing agent influences most likely the efficiency to create the most stable complex with high availability of negatively charged GAG-moieties of cartilage proteoglycans.

Our study supports other findings (*23, 24*) indicating effects of GS on cartilage metabolism including stimulation of anabolic activities such as synthesis of proteglycans. Experimental evidence indicates that GS and CS have a particular effect on cartilage where they serve as substrates in the biosynthesis of glycosaminoglycans (GAGs) (*30*). GS stimulates chondrocytes to synthesize the cartilage GAGs and proteoglycans (PGs), but

also inhibits lysosomal enzymes degrading cartilage (*31*). Animal and human studies have shown that GS after oral administration rapidly appears in the articular cartilage and is retained there for long time periods (*32*−*35*). These findings indicate that endogenous GS has an affinity for cartilage as a substrate for PG biosynthesis. Also, in this respect ^{99m}Tc GS could be used for scintigraphy of joints to monitor effects of therapy by pre- and post-therapy scintigraphy.

CONCLUSION

Using 0.1 mg tin for radiolabeling, at pH 7 (G10 column for separation), we found the highest radiolabeling efficiency and specific activity of GS, a quite high uptake of the tracer, and only a very small washout, resulting in a high "net" uptake of tracer into the degenerated cartilage. Due to high incorporation into cartilage,^{99m}Tc-GS could become a promising tracer to target osteoarthritis, to detect cartilage degeneration, and also to monitor therapeutic effects.

ACKNOWLEDGMENT

The authors would like to thank Rottapharm, Monza, Italy, for providing of glucosamine sulfate.

LITERATURE CITED

(1) Baker, C. L., Jr., and Ferguson, C. M. (2005) Future treatment of osteoarthritis. *Orthopedics 28*, 227–234.
(2) Fajardo, M., and Di Cesare, P. E. (2005) Disease-modifying therapies for osteoarthritis: current status. *Drugs Aging 22*, 141–161.
(3) Palmieri, L., Conte, A., Giovannini, L., Lualdi, P., and Ronca, G. (1990) Metabolic fate of exogenous chondroitin sulfate in the experimental animal. *Arzneimittelforsch. Drug Res. 40*, 319–323.
(4) Ronca, F., Palmieri, L., Pinicucci, P., and Ronca, G. (1998) Anti-inflammatory activity of chondroitin sulfate. *Osteoarthritis Cartilage 6S A*, 14–21.
(5) Chan, P. S., Caron, J. P., Rosa, G. J., and Orth, M. W. (2005) Glucosamine and chondroitin sulfate regulate gene expression and synthesis of nitric oxide and prostaglandin E(2) in articular cartilage explants. *Osteoarthritis Cartilage 13*, 387–394.
(6) Trattnig, S., Ba-Ssalamah, A., Puig, S., and Imhof, H. (2000) Magnetic resonance imaging of articular cartilage and evaluation of cartilage disease. *Invest. Radiol. 35*, 595–601.
(7) Hanly, J. G., Mitchell, M. J., Barnes, D. C., and MacMillan, L. (1994) Early recognition of sacroiliitis by magnetic resonance imaging and single photon emission computed tomography. *J. Rheumatol. 21*, 2088–2095.
(8) Dupuy, J. C., Harmand, M. F., and Blanquet, P. (1976) ACS marque au ^{99m}Tc et scintigraphie du cartilage. *Isotopes Radioactivite Clin. Recherch. 12*, 183–191.
(9) Palmer, W. E., Schoenberg, O. I., Fischman, A. J., Rosenthall, D. I., and Polisson, R. P. (1994) FDG metabolism in the wrist during treatment of inflammatory arthritis: Quantitation with PET and correlation with clinical response (abstr.). *J. Nucl. Med. 35*, 45P.
(10) Sobal, G., Menzel, E. J., and Sinzinger, H. (2008) Radiolabeling procedure, quality control and stability of 99mTc-labeled chondroitin sulfate: A new approach of targeting osteoarthritis. *Appl. Radiat. Isotopes 66*, 415–420.
(11) Elson, L. A., and Morgan, W. T. (1933) A colorimetric method for the determination of glucosamine and chondrosamine. *Biochem. J. 27*, 1824–1828.
(12) Hamerman, D. (1989) The biology of osteoarthritis. *N. Engl. J. Med. 320*, 1322–1330.
(13) Lequesne, M., Brandt, K., Bellamy, N., Moskowitz, R., Menkes, C. J., Pelletier, J. P., and Altman, R. (1994) Guidelines for testing slow acting drugs in osteoarthritis. *J. Rheumatol. 21*, 65–73.
(14) Piperno, M., Hellio Le Graverand, M. P., Conrozier, T., Bochu, M., Mathieu, P., and Vignon, E. (1998) Quantitative evaluation of joint space width infemorotibial osteoarthritis: comparison of three radiographic views. *Osteoarthritis Cartilage 6*, 252–259.
(15) Mazzuca, S. A., Brandt, K. D., and Katz, B. P. (1997) Is conventional radiography suitable for evaluation of a disease-modifying drug in patients with knee osteoarthritis? *Osteoarthritis Cartilage 5*, 217–226.
(16) Crolle, G., and D'Este, E. (1980) Glucosamine sulphate for the management of arthrosis: a controlled clinical investigation. *Curr. Med. Res. Opin. 7*, 104–109.
(17) Reichelt, A., Forster, K. K., Fischer, M., Rovati, L. C., and Setnikar, I. (1994) Efficacy and safety of intramuscular glucosamine sulfate in osteoarthritis of the knee. A randomised, placebo-controlled, double-blind study. *Arzneimittelforschung 44*, 75–80.
(18) Thie, N. M., Prasad, N. G., and Major, P. W. (2001) Evaluation of glucosamine sulfate compared to ibuprofen for the treatment of temporomandibular joint osteoarthritis: a randomized double blind controlled 3 month clinical trial. *J Rheumatol. 28*, 1347–1355.
(19) Qiu, G. X., Gao, S. N., Giacovelli, G., Rovati, L., and Setnikar, I. (1998) Efficacy and safety of glucosamine sulfate versus ibuprofen in patients with knee osteoarthritis. *Arzneimittelforschung 48*, 469–474.
(20) Setnikar, I., Cereda, R., Pacini, M. A., and Revel, L. (1991) Antireactive properties of glucosamine sulfate. *Arzneimittelforschung 41*, 157–161.
(21) Shikhman, A. R., Kuhn, K., Alaaeddine, N., and Lotz, M. (2001) N-acetylglucosamine prevents IL-1 beta-mediated activation of human chondrocytes. *J. Immunol. 166*, 5155–5160.
(22) Rovati, L. C. (1997) The clinical profile of glucosamine sulfate as a selective symptom modifying drug in and osteoarthritis: current data and perspectives. *Osteoarthritis Cartilage 5* (suppIA), 72.
(23) Bassleer, C., Rovati, L., and Franchimont, P. (1998) Stimulation of proteoglycan production by glucosamine sulfate in chondrocytes isolated from human osteoarthritic articular cartilage in vitro. *Osteoarthritis Cartilage 6*, 427–434.
(24) Dodge, G. R., Hawkins, D., Boesler, E., Sakai, L., and Jimenez, S. A. (1998) Production of cartilage oligomeric matrix protein (COMP) by cultured human dermal and synovial fibroblasts. *Osteoarthritis Cartilage 6*, 435–440.
(25) Sandy, J. D., Thompson, V., Verscharen, C., and Gamett, D. (1999) Chondrocyte-mediated catabolism of aggrecan: evidence for a glycosylphosphatidylinositol-linked protein in the aggrecanase response to interleukin-1 or retinoic acid. *Arch. Biochem. Biophys. 367*, 258–264.
(26) Noack, W., Fischer, M., Forster, K. K., Rovati, L. C., and Setnikar, I. (1994) Glucosamine sulfate in osteoarthritis of the knee. *Osteoarthritis Cartilage 2*, 51–59.
(27) Muller-Fassbender, H., Bach, G. L., Haase, W., Rovati, L. C., and Setnikar, I. (1999) Glucosamine sulfate compared to ibuprofen in osteoarthritis of the knee. *Osteoarthritis Cartilage 2*, 61–69.
(28) McAlindon, T. E., LaValley, M. P., Gulin, J. P., and Felson, D. T. (1999) Glucosamine and chondroitin for treatment of osteoarthritis: a systematic quality assessment and meta-analysis. *JAMA 283*, 1469–1475.
(29) Hardingham, T. E., and Fosang, A. J. (1992) Proteoglycans: many forms and many functions. *FASEB J. 6*, 861–870.
(30) de los Reyes, G. C., Koda, R. T., and Lien, E. J. (2000) Glucosamine and chondroitin sulfates in the treatment of osteoarthritis: a survey. *Prog. Drug Res. 55*, 81–103.
(31) Verbruggen, G., Goemaere, S., and Veys, E. (1998) Chondroitin sulfate: S/DMOAD (structure/disease modifying anti-osteoarthritis drug) in the treatment of finger joint OA. *Osteoarthritis Cartilage 6*, 37–38.
(32) Setnikar, I., Giacchetti, C., and Zanolo, G. (1986) Pharmacokinetics of glucosamine in the dog and in man. *Arzneimittelforschung 36*, 729–735.

(33) Setnikar, I., Giacchetti, C., and Zanolo, G. (1984) Absorption, distribution and excretion of radioactivity after a single intravenous or oral administration of [14C] glucosamine to the rat. *Pharmatherapeutica 3*, 538–550.

(34) Fosang, A. J., and Little, C. B. (2008) Drug insight: aggrecanases as therapeutic targets for osteoarthritis. *Clin. Pract. Rheumatol. 4*, 420–427.

(35) Wang, L., and Detamore, M. S. (2009) Effects of growth factors and glucosamine on porcine mandibular condylar cartilage cells and hyaline cartilage cells for tissue engineering applications. *Arch. Oral. Biol. 54*, 1–5.

BC9000883

Effect of PEGylation of N-WASP181-200 on the Inhibitory Potency for Renal Aminoglycoside Accumulation

Kenji Fujii, Junya Nagai, Takeshi Sawada, Ryoko Yumoto, and Mikihisa Takano*

Department of Pharmaceutics and Therapeutics, Graduate School of Biomedical Sciences, Hiroshima University, 1-2-3 Kasumi, Minami-ku, Hiroshima 734-8553, Japan. Received March 4, 2009; Revised Manuscript Received May 18, 2009

We previously showed that a 20-residue basic peptide, N-WASP181-200 (NISHTKEKKKGKAKKKRLTK), inhibits renal accumulation of aminoglycoside antibiotics such as gentamicin and arbekacin. The aim of this study is to determine whether PEGylation of N-WASP181-200 enhances its inhibitory potency for renal accumulation of aminoglycosides. N-terminally PEGylated peptide (PEG1k-N-W) was synthesized by conjugating N-WASP181-200 with PEG of approximately 1 kDa using the Fmoc protection/deprotection method. PEG1k-N-W decreased gentamicin binding to isolated rat renal brush-border membrane in a concentration-dependent manner, but the in vitro inhibitory potency of PEG1k-N-W was weaker than that of N-WAP181-200. On the other hand, under in vivo conditions, PEG1k-N-W decreased the renal accumulation of arbekacin more potently than N-WASP181-200. When injected intravenously, PEG1k-N-W showed a 1.7-fold longer plasma half-life relative to N-WASP181-200. In addition, the stability of N-WASP181-200 in renal brush-borer membrane suspension was found to be increased by PEGylation. Our findings suggest that PEGylation of N-WASP181-200 is a useful strategy for reducing dosage of the concomitant with which to decrease renal accumulation in the kidney, leading to prevention of aminoglycoside-induced nephrotoxicity.

INTRODUCTION

Aminoglycoside antibiotics such as gentamicin, amikacin, and arbekacin are widely used for the treatment of Gram-positive and Gram-negative infectious diseases. Aminoglycosides are not metabolized in the body, and most of the injected dose is excreted into the urine. However, a fraction is selectively accumulated in the renal cortex. The concentration of aminoglycoside accumulated in the renal cortex amounts to several times higher than in the plasma. Aminoglycoside taken up by the renal proximal tubular cells stays there with a long-half-life, leading to renal damage such as structural changes and functional impairments (*1*−*3*).

Aminoglycoside binding receptors such as acidic phospholipids and/or megalin are a potential target for preventing aminoglycoside-induced nephrotoxicity (*3, 4*). Early studies reported that acidic phospholipids of the plasma membrane of the proximal tubular cells are the initial binding site (*5, 6*). Subsequently, aminoglycosides including gentamicin were shown to be ligands of megalin (*7*). Megalin (alias LRP-2; low-density lipoprotein receptor-related protein-2) is a multiligand, enodcytic receptor abundantly expressed in the renal proximal tubule (*8, 9*). It was reported that there was little accumulation of gentamicin in the kidney in mice lacking megalin (*10*). In a previous report, we demonstrated that coadministration of cytochrome c, a ligand of megalin, decreased not only renal accumulation of gentamicin but also gentamicin-induced nephrotoxicity (*11*). In addition, several basic peptide fragments with pI values from 10.30 to 11.72, which reportedly bind to phosphoinositides (*12*−*14*), inhibited renal accumulation of gentamicin injected intravenously. Among those peptide fragments examined, a 20-amino-acid peptide N-WASP181-200 from neural Wiskott-Aldrich syndrome protein (N-WASP) was found to be the most effective antagonist under in vitro conditions (*11*).

On the other hand, under in vivo conditions, the inhibitory effect of N-WASP181-200 on renal accumulation of aminoglycosides was much weaker than was expected from the in vitro inhibitory effect; the 50% inhibitory concentration (IC_{50}) value of N-WASP181-200 for gentamicin binding to renal brush-border membrane in vitro (0.041 mM) was much lower than that of cytochrome c (3.20 mM) (*15*), while its IC_{50} value for renal arbekacin accumulation in vivo (19.6 μmol/kg) was found to be higher than that of cytochrome c (1.23 μmol/kg) (*16*). We speculated that one of the main reasons for the apparent inconsistency between in vitro and in vivo studies may be the rapid degradation in the plasma and/or extensive binding to various tissues after intravenous injection of N-WASP181-200.

A number of studies have demonstrated that chemical modification with poly(ethylene glycol) (PEG), PEGylation, is an effective means of improving the in vivo biological potencies of various pharmaceutical peptides/proteins (*17, 18*). The technique is one of the useful strategies to prolong the half-lives of unstable peptides/proteins in the body by reducing proteolysis and renal clearance. In addition, increase in the apparent molecular weight by PEGylation leads to an altered pattern of body distribution of peptide/protein drugs. Furthermore, PEGylation effectively reduces immunogenicity/antigenicity and toxicity, which are caused by injection of peptides/proteins (*17, 18*).

The purpose of this study was to investigate whether PEGylation enhances the in vivo inhibitory effect of N-WASP181-200 on renal accumulation of arbekacin. In addition, the plasma half-life of PEGylated N-WASP181-200 (PEG1k-N-W) intravenously injected was compared with those of N-WASP181-200 and arbekacin. Furthermore, the stabilities of N-WASP181-

* Corresponding author. Mikihisa Takano, Department of Pharmaceutics and Therapeutics, Graduate School of Biomedical Sciences, Hiroshima University, 1-2-3 Kasumi, Minami-ku, Hiroshima 734-8553, Japan, Tel. +81-82-257-5315; Fax. +81-82-257-5319; E-Mail: takanom@hiroshima-u.ac.jp.

10.1021/bc900094g CCC: $40.75 © 2009 American Chemical Society
Published on Web 07/02/2009

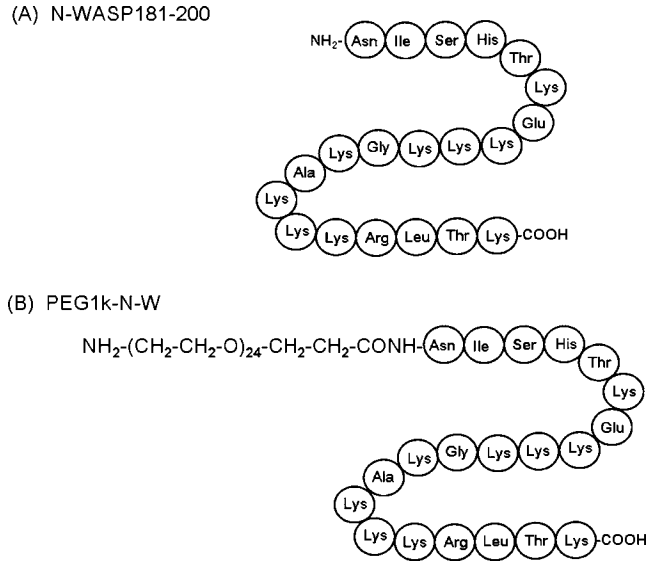

Figure 1. Primary structures of N-WASP181-200 (A) and its PEGylated peptide, PEG1k-N-W (B).

200 and PEG1k-N-W in the plasma and renal brush-border membrane suspension were evaluated.

MATERIALS AND METHODS

Materials. N-Fmoc-amido-dPEG$_{24}$ acid was purchased from Quanta Biodesign (Powell, OH, USA). [^{3}H]Gentamicin sulfate (7.4 GBq/g) was obtained from American Radiolabeled Chemicals, Inc. (St. Louis, MO, USA). Arbekacin sulfate was from Meiji Seika Kaisha, Ltd. (Tokyo, Japan). Gentamicin sulfate and 2,4,6,-trinitrobenzene sulfonic acid sodium salt were obtained from Nacalai Tesque (Kyoto, Japan). Trifluoroacetic acid was purchased from Sigma Chemical Co. (St. Louis, MO, USA). All other chemicals used for the experiments were of the highest purity available.

Preparation of N-WASP181-200 and Its PEGylated Peptide. N-WASP181-200 (NISHTKEKKKGKAKKKKRLTK) and its N-terminally PEGylated peptide (PEG1k-N-W) were synthesized chemically with the peptide synthesizer (PSSM-8, Shimadzu, Kyoto, Japan) (Figure 1). For N-terminal PEGylation of N-WASP181-200, N-Fmoc-amido-dPEG$_{24}$ acid with molecular weight of 1368.59 was used. After deprotection of the side chain protecting groups, the peptides were precipitated with ice-cold diethyl ether and isolated by centrifugation at 4000 rpm for 5 min. This procedure was repeated twice. The precipitate was dissolved with 0.1% trifluoroacetic acid (TFA) and chromatographed on a Sephadex G-15 column equilibrated with 0.1% TFA. Elution fractions containing peptide were pooled and dialyzed overnight at 4 °C. After lyophilization, the obtained peptides were stored at −30 °C until analysis.

Matrix-Assisted Laser Desorption Ionization Time-of-Flight Mass Spectrometry. The compounds prepared by the synthesizer were confirmed by matrix-assisted laser desorption ionization time-of-flight (MALDI-TOF) mass spectrometry (PerSeptive Biosystems, Tokyo, Japan). Freeze−dried peptides were dissolved with the matrix solution, a saturated solution of α-cyano-4-hydroxycinnamic acid (α-CHCA) in 50% acetonitrile in water with 0.1% TFA. The spectra were recorded with the analyzer in the linear mode at an accelerating voltage of 20 kV.

Preparation of Brush-Border Membrane from Rat Kidney. Experiments with animals were performed in accordance with the Guide for Animal Experimentation, Hiroshima University, and the Committee of Research Facilities for Laboratory Animal Sciences, Graduate School of Biomedical Sciences, Hiroshima University. Renal brush-border membrane (BBM) was isolated from the renal cortex of male Wistar albino rats (190−220 g). The isolation procedure of BBM was based on the Mg/EGTA precipitation method as described previously (*15*). The isolated membranes were suspended in a buffer comprising 100 mM mannitol and 10 mM HEPES/Tris (pH7.5), and stored in liquid nitrogen until use (usually less than 1 month).

Binding Studies Using BBM. [^{3}H]Gentamicin binding to BBM was measured by a rapid filtration technique. In brief, BBM (20 μL) were suspended in a buffer comprising 300 mM mannitol and 10 mM HEPES, adjusted to pH 7.5 with KOH (buffer A). The reaction was initiated by the addition of buffer A (20 μL) containing 20 μM [^{3}H]gentamicin without or with competitor into the membrane suspension at 4 °C. At 60 min, incubation was stopped by diluting the reaction mixture with 1 mL of ice-cold buffer A. The contents of the tube were immediately poured onto Millipore filters (HAWP, 0.45 μm, 2.5 cm diameter), and then the filters were washed once with 5 mL of the ice-cold buffer A. The radioactivity on the filter was determined by liquid scintillation counting. Nonspecific binding was estimated by the addition of unlabeled gentamicin at 1000-fold concentration (10 mM) of [^{3}H]gentamicin. Then, specific binding of gentamicin was determined by subtracting the nonspecific binding from the total binding.

The half-maximal inhibitory concentration (IC_{50}) values of competitors were determined by the Hill equation, as described previously (*15*). The values of the dissociation constant (K_d) and the maximum amounts of the binding (B_{max}) were estimated from the linear regression lines using the double reciprocal analysis based on Klotz equation, as described previously (*15*).

In Vivo Renal Accumulation Study. Male ddy mice weighting 26−33 g were administered arbekacin at a dose of 0.25 mg/kg alone or in combination with the indicated compound via the tail vein. At 24 h after administration, kidneys were excised. The tissues were weighed and then homogenized with an IKA T25 Basic dispenser (IKA Labortechnik, Germany) in 2 mL of 30 mM phosphate buffer (pH 7.5). After shaking for 20 min, the homogenate was mixed with 400 μL of 20% trichloroacetic acid and was further shaken for 40 min. After centrifugation at 3000 rpm for 10 min, arbekacin concentration in the supernatant was determined by HPLC as described below.

In Vivo Pharmacokinetic Study. Male ddy mice (20−30 g) were anesthetized by intraperitoneal injection of pentobarbital. A blood sample was withdrawn through the jugular vein at a stated time after a bolus administration of N-WASP181-200 (100 mg/kg), PEG1k-N-W (100 mg/kg), or arbekacin (4 mg/kg) via the tail vein. Plasma was separated immediately by centrifugation at 10 000 rpm for 5 min. A 100 μL aliquot of plasma sample was mixed with 20 μL of 20% trichloroacetic acid. After centrifugation at 10 000 rpm for 5 min, the concentration of each compound in the supernatant was determined by HPLC as described below.

Proteolytic Stabilities of N-WASP181-200 and PEG1k-N-W. The proteolytic stabilities of N-WASP181-200 and PEG1k-N-W were examined in rat plasma and rat renal brush-border membrane (BBM) suspension. Rat plasma was obtained by centrifuging blood from male Wistar rats. BBM was prepared as described above. For plasma stability assay, 10 mg/mL N-WASP181-200 or PEG1k-N-W (30 μL) were incubated with rat plasma (270 μL) at 37 or 4 °C for 30 min. The incubation was terminated by the addition of 60 μL 20% trichloroacetic acid (TCA). After centrifugation at 10 000 rpm for 10 min, the concentration of N-WASP181-200 or PEG1k-N-W in the supernatant was determined by HPLC as described below. For BBM stability assay, BBM suspension (54 μL) was mixed with a buffer comprising 300 mM mannitol and 10 mM HEPES, adjusted to pH 7.5 with KOH (buffer A). The reaction was initiated by the addition of buffer A (6 μL) containing 10 mg/

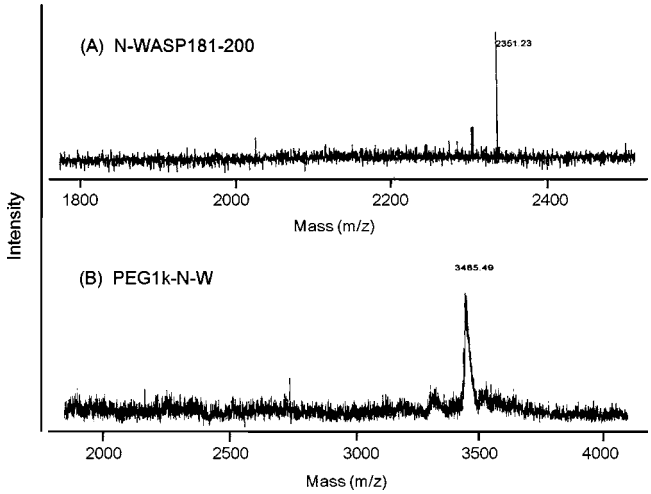

Figure 2. MALDI-TOF mass spectra of N-WASP181-200 (A) and PEG1k-N-W (B).

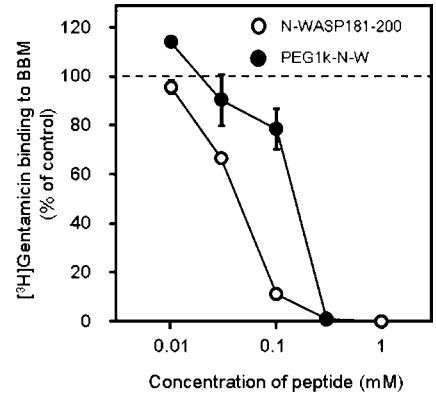

Figure 3. Effects of N-WASP181-200 and PEG1k-N-W on [^{3}H]gentamicin binding to rat renal brush-border membrane (BBM). BBM was incubated for 60 min at 4 °C with the substrate mixture (pH 7.5) including 10 μM [^{3}H]gentamicin with various concentrations of N-WASP181-200 (open circle) or PEG1k-N-W (closed circle). Each symbol represents the mean ± SE of three determinations.

mL N-WASP181-200 and PEG1k-N-W at 37 or 4 °C. At 5, 10, or 15 min, the incubation was terminated by the addition of 12 μL 20% TCA. After centrifugation at 10 000 rpm for 5 min, the concentration of N-WASP181-200 or PEG1k-N-W in the supernatant was determined by HPLC as described below.

HPLC Analysis. Quantitative determinations of N-WASP181-200, PEG1k-N-W, and arbekacin were performed by using high-performance liquid chromatography (PU-980, Jasco, Tokyo, Japan) equipped with an ultraviolet spectrophotometric detector (UV-970, Jasco) with a TSK gel ODS-80TM (4.6 × 100 mm, Tosoh, Tokyo, Japan). For the assay of N-WASP181-200 and PEG-N-W, the mobile phase consisted of 0.1% trifluoroacetic acid (TFA) in distilled water (solvent A) and 0.1% TFA in acetonitrile (solvent B). The mobile phase was run with a linear gradient from 0% to 100% solvent B over 40 min at a flow rate of 1.0 mL/min, and the absorbance of the eluent was monitored at 210 nm at room temperature. For the assay of arbekacin, an isocratic HPLC assay was performed after derivatization of the drug by reaction with 2,4,6-trinitrobenzenesulfonic acid. The conditions were as follows: mobile phase 0.03 M phosphate buffer (pH 7.5)/acetonitrile/methanol (v/v) = 1.1:2:1; flow rate 1.0 mL/min; and room temperature. The absorbance of the eluent was monitored at 350 nm.

Analytical Methods. The elimination rate constant k value was calculated based on the first-order equation. The elimination half-life ($t_{1/2}$) was determined based on the equation $t_{1/2} = 0.693/k$. The *KaleidaGraph* program (version 3.08, Synergy Software, PA, USA) was used for the curve-fitting. Protein concentration was measured by the method of Bradford (*19*) with bovine serum albumin as a standard.

RESULTS

Characterization of PEGylated N-WASP181-200. N-WASP181-200 and its N-terminally PEGylated peptide (PEG1k-N-W) were synthesized using the Fmoc protection/deprotection method. These peptides were identified by mass spectroscopy using MALDI-TOF (Figure 2). The molecular mass of PEG1k-N-W was detected to be 3485 Da, which would be equivalent to N-WASP181-200 (2351 Da) conjugated with 1 unit of $dPEG_{24}$ where the Fmoc group was removed (1368.59 Da as N-Fmoc-amido-$dPEG_{24}$ acid according to the product sheet obtained from the supplier).

In Vitro Inhibitory Efficacy on Gentamicin Binding to Isolated Rat Renal Brush-Border Membrane. To analyze the inhibitory potency of PEG1k-N-W under in vitro conditions, we examined the effect of PEG1k-N-W on [^{3}H]gentamicin binding to isolated rat renal brush-border membrane (BBM). PEG1k-N-W decreased the binding of gentamicin to BBM in a concentration-dependent manner (Figure 3). However, the concentration−response curve of PEG1k-N-W was shifted to the right, compared to that of N-WASP181-200. The IC_{50} value of PEG1k-N-W was 0.128 mM, which was 3.1-fold greater than that of N-WASP181-200 (0.041 mM).

Previously, we showed that N-WASP181-200 inhibits gentamicin binding to BBM in a competitive manner (*15*). In this study, to analyze the nature of the inhibitory effect of PEG1k-N-W on gentamicin binding to BBM, the binding activity at various concentrations of gentamicin was examined at 4 °C in the absence or presence of 200 μM PEG1k-N-W (Figure 4). The double reciprocal plot analysis of the data indicated that the maximum amounts of gentamicin binding (B_{max}) in the absence and presence of PEG1k-N-W were estimated to be 8.4 and 3.3 nmol/mg protein, respectively. In addition, the calculated dissociation constants (K_d) in the absence and presence of PEG1k-N-W were 39.8 μM and 260.1 μM, respectively. Thus, the results of the kinetic analysis (decreased binding capacity and affinity) indicated that PEG1k-N-W gave a mixed-type inhibition against gentamicin binding to BBM.

In Vivo Inhibitory Efficacy on Renal Arbekacin Accumulation in Mice. Next, to analyze the inhibitory potency of PEG1k-N-W under in vivo conditions, the effect of coadministration of PEG1k-N-W on renal accumulation of arbekacin in mice was examined and compared with that of N-WASP181-200 (Figure 5). The accumulation of arbkacin in mouse kidney was inhibited by coadministration of PEG1k-N-W in a dose-dependent fashion, and its dose−response curve was shifted to the left, compared to that of N-WASP181-200. The calculated IC_{50} value of PEG1k-N-W was 17.8 mg/kg, which was 2.6-fold lower than that of N-WASP181-200 (46.1 mg/kg).

Pharmacokinetics of N-WASP181-200 and PEG1k-N-W in Mice. The pharmacokinetics of N-WASP181-200 and PEG1k-N-W were investigated in mice. Figure 6 shows the plasma concentration−time profiles of N-WASP181-200 and PEG1k-N-W after an intravenous bolus injection at a dose of 100 mg/kg into mice. The plasma concentrations of N-WASP181-200 and PEG1k-N-W declined exponentially with time, resulting in half-lives of 2.7 and 4.6 min, respectively. The volumes of distribution of N-WASP181-200 and PEG1k-N-W were 0.40 ± 0.03 L/kg and 0.46 ± 0.03 L/kg, respectively. Figure 7 shows the plasma concentration−time profile of arbekacin after an intravenous bolus injection at 4 mg/kg. The calculated half-life and volume of distribution were 32.4 min and 0.60 ± 0.03 L/kg, respectively.

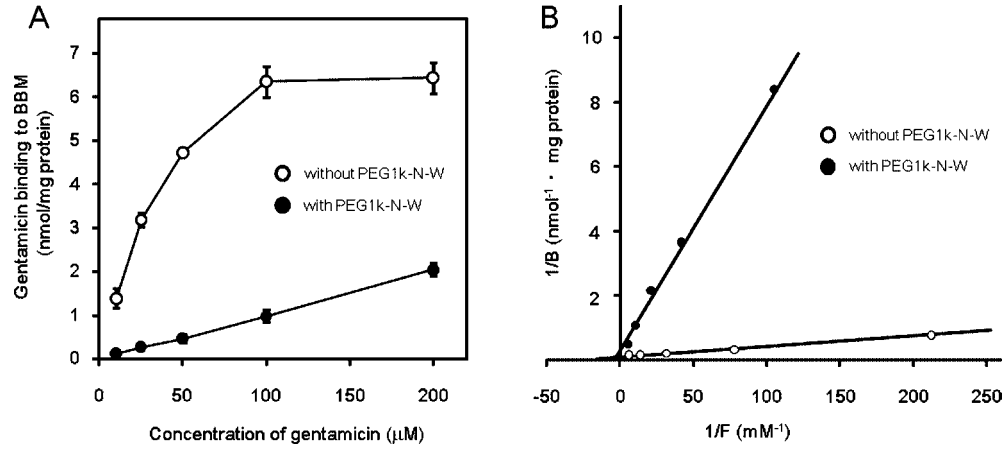

Figure 4. Gentamicin binding to rat renal BBM at various concentrations of gentamicin without or with PEG1k-N-W (A) and its double reciprocal plots (Klotz plots) (B). The BBM binding of various concentrations of [^{3}H]gentamicin in the absence (open circle) or presence (closed circle) of 200 μM PEG1k-N-W was measured as described in Figure 3. Each symbol represents the mean ± SE of three determinations. Abbreviations are as follows: B, the amount of bound gentamicin to BBM; F, the concentration of free gentamicin in the incubation buffer.

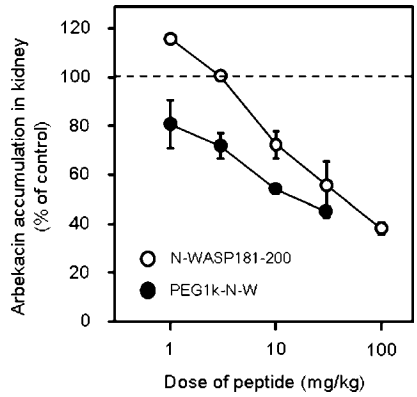

Figure 5. Effect of coadministration of N-WASP181-200 or PEG1k-N-W on arbekacin accumulation. Mice were administered arbekacin alone or in combination with N-WASP181-200 (open circle, 1−100 mg/kg) or PEG1k-N-W (closed circle, 1−30 mg/kg). Each symbol represents the mean ± SE of three mice.

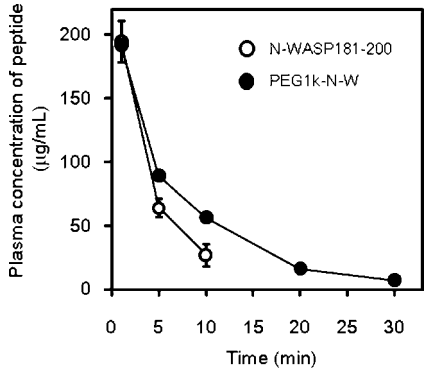

Figure 6. Plasma concentration−time profiles of N-WASP181-200 (open circle) and PEG1k-N-W (closed circle) given intravenously at a dose of 100 mg/kg in mice. Each symbol represents the mean ± SE of three to four mice.

Metabolic Stability. The effect of PEGylation on the stability of N-WASP181-200 was examined in rat plasma and renal brush-border membrane suspension. First, we compared the stability of 1 mg/mL N-WASP181-200 in the plasma between 37 and 4 °C. The concentrations of N-WASP181-200 after 30 min incubation at 37 and 4 °C were 0.76 mg/mL and 0.75 mg/mL, respectively. Thus, it is likely that there was little enzymatic degradation of N-WASP181-200 in the plasma because no

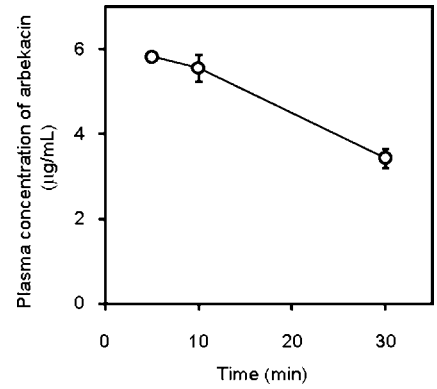

Figure 7. Plasma concentration−time profile of arbekacin given intravenously at a dose of 4 mg/kg in mice. Each symbol represents the mean ± SE of three mice.

temperature-dependent degradation was observed. The decreases in concentration of N-WASP181-200 that were observed at both temperatures might be due to coprecipitation of N-WASP181-200 with plasma proteins during the deproteinization process. Next, the stability of N-WASP181-200 and PEG1k-N-W in renal brush-border membrane suspension was analyzed at 37 or 4 °C (Figure 8). At 37 °C, N-WASP181-200 was rapidly degraded in renal brush-border membrane suspension with a half-life of 6.7 min. The degradation rate of PEG1k-N-W at 37 °C was slower than that of N-WASP181-200, showing an approximately 2-fold longer half-life (12.9 min). At 4 °C, neither N-WASP181-200 nor PEG1k-N-W was degraded up to 15 min incubation.

DISCUSSION

In a previous paper, we found that N-WASP181-200 had a 78-fold higher in vitro inhibitory potency for gentamicin binding to rat renal brush-border membrane than a low molecular weight protein, cytochrome c, when their IC_{50} values were compared (*15*). However, the in vivo inhibitory potency of N-WASP181-200 was 16-fold as low as that of cytochrome c when their IC_{50} values were compared (*16*). One of the main reasons for this disagreement between in vitro and in vivo studies was expected to be a poor delivery of N-WASP181-200 into the renal proximal tubule, where aminoglycosides are taken up. It has been shown that about 90% of the injected dose of cytochrome c was accumulated in the kidney, in particular in the proximal tubular cells through a luminal reabsorption mechanism possibly involving megalin-mediated endocytosis (*20, 21*). Therefore, we

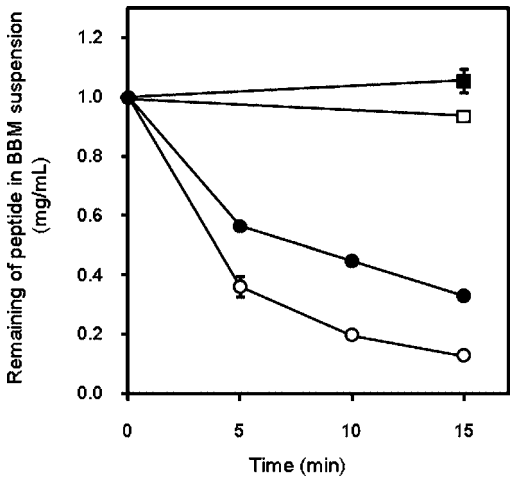

Figure 8. Degradation profiles of N-WASP181-200 and PEG1k-N-W incubated with rat renal brush-border membrane suspension. N-WASP181-200 (open circle and square) and PEG1k-N-W (closed circle and square) were incubated with rat renal brush-border membrane suspension at 37 °C (open and closed circles) or 4 °C (open and closed squares).

expected that more efficient delivery of N-WASP181-200 into the renal proximal tubule might improve the in vivo inhibitory potency for renal accumulation of aminoglycosides. In this study, we tried to investigate whether PEGylation is useful for enhanced delivery of N-WASP181-200 into the renal proximal tubule, resulting in reduced dose requirement of the concomitant for prevention of renal accumulation/toxicity of aminoglycosides.

Since aminoglycosides are taken up in the renal proximal tubular cells after filtration through the glomerulus, a PEGylated compound also needs to be filtered through the glomerulus in order to compete with aminoglycosides for its binding site(s) in the apical membrane of the renal proximal tubule. It has been reported that the ultrafiltration of PEG with molecular size lower than 8 kDa is not restricted, whereas the elimination of PEG in the range 8−30 kDa is governed by the molecular size (*17*, *22*). The elimination of PEG with the molecular sizes exceeding 30 kDa is dramatically decreased, possibly because of molecular sizes beyond the glomerular filtration cutoff (*17*, *22*). Therefore, we selected N-Fmoc-amido-dPEG$_{24}$ acid with a molecular size of 1368.59 Da, which is small enough to be filtered through the glomerulus, for the conjugation with N-WASP181-200. In addition, PEGylation with N-Fmoc-amido-dPEG$_{24}$ acid by the Fmoc solid-phase peptide synthesis had no contamination of unconjugated PEG in the synthesized compound. Furthermore, there was no PEGylation on the ε-amino groups of lysine residues in N-WASP181-200, which would affect the in vitro inhibitory potency for gentamicin binding to renal brush-border membrane (*15*), since N-Fmoc-amido-dPEG$_{24}$ acid is selectively attached to the N-terminal residue of N-WASP181-200 (asparagine). In this study, the purity of the N-terminally mono-PEGylated N-WASP181-200 (PEG1k-N-W) was identified by MALDI-TOF MS analysis.

It is reported that the bioactivities of peptides and proteins in vitro can be reduced by PEGylation (*18*, *23*, *24*). Therefore, we first examined whether or not the inhibitory potency for gentamicin binding to renal brush-border membrane is retained after PEGylation. The in vitro binding study showed that PEGylation decreased the in vitro inhibitory potency by about 3-fold. The reason for the decreased in vitro inhibitory potency by PEGylation is not clear at present, but the steric hindrance effect induced by the flexible PEG chain around the binding site of aminoglycosides may be responsible for a decrease in in vitro inhibitory potency of PEG1k-N-W.

Though PEGylation decreased the in vitro inhibitory potency of N-WASP181-200, it enhanced the in vivo inhibitory potency. To clarify the mechanisms underlying the enhancement of in vivo inhibitory potency by PEGylation, the plasma concentration−time profiles of N-WASP181-200 and PEG1k-N-W after intravenous injection were examined in mice. The plasma half-life of PEG1k-N-W was prolonged by 1.7-fold, as compared to that of N-WASP181-200. There was little change in the distribution volumes between N-WASP181-200 and PEG1k-N-W. However, it is likely that the observed prolongation of the plasma half-life by PEGylation was not due to increased proteolytic resistance in the plasma, since temperature-dependent degradation of N-WASP181-200 in the plasma was not observed. The difference in half-life between N-WASP181-200 and PEG1k-N-W may be due to that inefficiency of glomerular filtration, resulting from small but significantly different molecular sizes (N-WASP181-200, 2351 Da; PEG1k-N-W, 3485 Da). In addition, there might be another possibility that a decrease in nonrenal clearance including hepatic extraction is associated with the prolonged plasma half-life by PEGylation.

The prolongation of plasma half-life was not enough to explain the enhanced in vivo potency by PEGylation, because the plasma half-life of arbekacin was 32.4 min, which is much longer than that of PEG1k-N-W (4.59 min). It has been reported that the membrane-bound peptidases including aminopeptidase A, aminopeptidase M, γ-glutamyltransferase, and dipeptidyl peptidase IV are localized in the brush-border of the renal proximal tubule (*25*, *26*). Therefore, we speculated on the possibility of an increased proteolytic resistance by PEGylation against the peptidases expressed in the renal brush-border membrane, which is the target site for the inhibition of aminoglycoside binding in vivo. Incubation of N-WASP181-200 in renal brush-border membrane suspension at 37 °C induced a disappearance of its peptide with a half-life of 6.7 min, but there was no degradation of N-WASP181-200 when incubation was performed at 4 °C, the temperature at which brush-border enzymes would not work. Thus, the temperature-dependent disappearance indicates the enzymatic degradation of N-WASP181-200 by peptidase(s) in renal brush-border membrane, but not nonenzymatic decomposition. Furthermore, the half-life of PEG1k-N-W for degradation in bush-border membrane suspension at 37 °C was 1.9-fold longer compared to N-WASP181-200. Thus, the resistance to proteolysis in the renal brush-border membrane may be, at least in part, involved in the enhanced in vivo inhibitory effect by PEGylation.

In conclusion, PEGylation enhanced the in vivo inhibitory potency of N-WASP181-200 for renal accumulation of arbekacin in spite of the reduced in vitro inhibitory potency for binding of gentamicin to renal brush-border membrane. Therefore, PEGylation technique is expected to be a useful means with which to develop a more potent peptidic protectant against aminoglycoside-induced nephrotoxicity.

ACKNOWLEDGMENT

This work was supported in part by a Grant-in-Aid for Scientific Research from the Ministry of Education, Culture, Sports, Science and Technology of Japan. We also thank the Analysis Center of Life Science, Hiroshima University, for the use of their facilities.

LITERATURE CITED

(1) Chambers, H. F. (2001) The aminoglycosides, *Goodman & Gilman's The Pharmacological Basis of Therapeutics*, 10th ed. (Hardman, J. G., Limbird, L. E., and Gilman, A. G., Eds.) pp 1219−1238, McGraw-Hill, New York.

(2) Mingeot-Leclercq, M. P., and Tulkens, P. M. (1999) Aminoglycosides: nephrotoxicity. *Antimicrob. Agents Chemother. 43*, 1003–1012.
(3) Nagai, J., and Takano, M. (2004) Targeted prevention of renal accumulation and toxicity of gentamicin by aminoglycoside binding receptor antagonists. *Drug Metab. Pharmacokin. 19*, 159–170.
(4) Nagai, J., Tanaka, H., Nakanishi, N., Murakami, T., and Takano, M. (2001) Role of megalin in renal handling of aminoglycosides. *Am. J. Physiol. Renal Physiol. 281*, F337−F344.
(5) Schacht, J. (1979) Isolation of an aminoglycoside receptor from guinea pig inner ear tissues and kidney. *Arch. Otorhinolaryngol. 224*, 129–134.
(6) Sastrasinh, M., Knauss, T. C., Weinberg, J. M., and Humes, H. D. (1982) Identification of the aminoglycoside binding site in rat renal brush border membranes. *J. Pharmacol. Exp. Ther. 222*, 350–358.
(7) Moestrup, S. K., Cui, S., Vorum, H., Bregengård, C., Bjørn, S. E., Norris, K., Gliemann, J., and Christensen, E. I. (1995) Evidence that epithelial glycoprotein 330/megalin mediates uptake of polybasic drugs. *J. Clin. Invest. 96*, 1404–1413.
(8) Saito, A., Pietromonaco, S., Loo, A. K., and Farquhar, M. G. (1994) Complete cloning and sequencing of rat gp330/"megalin," a distinctive member of the low density lipoprotein receptor gene family. *Proc. Natl. Acad. Sci. U.S.A. 91*, 9725–9729.
(9) Christensen, E. I., and Birn, H. (2002) Megalin and cubilin: multifunctional endocytic receptors. *Nat. Rev. Mol. Cell Biol. 3*, 256–266.
(10) Schmitz, C., Hilpert, J., Jacobsen, C., Boensch, C., Christensen, E. I., Luft, F. C., and Willnow, T. E. (2002) Megalin deficiency offers protection from renal aminoglycoside accumulation. *J. Biol. Chem. 277*, 618–622.
(11) Watanabe, A., Nagai, J., Adachi, Y., Katsube, T., Kitahara, Y., Murakami, T., and Takano, M. (2004) Targeted prevention of renal accumulation and toxicity of gentamicin by aminoglycoside binding receptor antagonists. *J. Controlled Release 95*, 423–433.
(12) Janmey, P. A., Lamb, J., Allen, P. G., and Matsudaira, P. T. (1992) Phosphoinositide-binding peptides derived from the sequences of gelsolin and villin. *J. Biol. Chem. 267*, 11818–11823.
(13) Yu, F. X., Johnston, P. A., Südhof, T. C., and Yin, H. L. (1990) gCap39, a calcium ion- and polyphosphoinositide-regulated actin capping protein. *Science 250*, 1413–1415.
(14) Prehoda, K. E., Scott, J. A., Mullins, R. D., and Lim, W. A. (2000) Integration of multiple signals through cooperative regulation of the N-WASP-Arp2/3 complex. *Science 290*, 801–806.
(15) Nagai, J., Saito, M., Adachi, Y., Yumoto, R., and Takano, M. (2006) Inhibition of gentamicin binding to rat renal brush-border membrane by megalin ligands and basic peptides. *J. Controlled Release 112*, 43–50.
(16) Murakami, S., Nagai, J., Fujii, K., Yumoto, R., and Takano, M. (2008) Influences of dosage regimen and co-administration of low-molecular weight proteins and basic peptides on renal accumulation of arbekacin in mice. *J. Antimicrob. Chemother. 61*, 658–664.
(17) Caliceti, P., and Veronese, F. M. (2003) Pharmacokinetic and biodistribution properties of poly(ethylene glycol)-protein conjugates. *Adv. Drug Delivery Rev. 55*, 1261–1277.
(18) Veronese, F. M., and Pasut, G. (2005) PEGylation, successful approach to drug delivery. *Drug Discov. Today 10*, 1451–1458.
(19) Bradford, M. M. (1976) A rapid and sensitive method for the quantitation of microgram quantities of protein utilizing the principle of protein-dye binding. *Anal. Biochem. 72*, 248–254.
(20) Haas, M., Moolenaar, F., Meijer, D. K., and de Zeeuw, D. (2002) Specific drug delivery to the kidney. *Cardiovasc. Drugs Ther. 16*, 489–496.
(21) Haas, M., de Zeeuw, D., van Zanten, A., and Meijer, D. K. (1993) Quantification of renal low-molecular-weight protein handling in the intact rat. *Kidney Int. 43*, 949–954.
(22) Yamaoka, T., Tabata, Y., and Ikada, Y. (1994) Distribution and tissue uptake of poly(ethylene glycol) with different molecular weights after intravenous administration to mice. *J. Pharm. Sci. 83*, 601–606.
(23) Bailon, P., Palleroni, A., Schaffer, C. A., Spence, C. L., Fung, W. J., Porter, J. E., Ehrlich, G. K., Pan, W., Xu, Z. X., Modi, M. W., Farid, A., Berthold, W., and Graves, M. (2001) Rational design of a potent, long-lasting form of interferon: a 40 kDa branched polyethylene glycol-conjugated interferon alpha-2a for the treatment of hepatitis C. *Bioconjugate Chem. 12*, 195–202.
(24) Lee, S. H., Lee, S., Youn, Y. S., Na, D. H., Chae, S. Y., Byun, Y., and Lee, K. C. (2005) Synthesis, characterization, and pharmacokinetic studies of PEGylated glucagon-like peptide-1. *Bioconjugate Chem. 16*, 377–382.
(25) Jedrzejewski, K., and Kugler, P. (1982) Peptidases in the kidney and urine of rat after castration. *Histochemistry 74*, 63–84.
(26) Kugler, P., Wolf, G., and Scherberich, J. (1985) Histochemical demonstration of peptidases in the human kidney. *Histochemistry 83*, 337–341.

BC900094G

2-Mercaptoacetylglycylglycyl (MAG_2) as a Bifunctional Chelator for ^{99m}Tc-Labeling of Cyclic RGD Dimers: Effect of Technetium Chelate on Tumor Uptake and Pharmacokinetics

Jiyun Shi,[†] Young-Seung Kim,[†] Sudipta Chakraborty,[†] Bing Jia,[‡] Fan Wang,[‡] and Shuang Liu*[,†]

School of Health Sciences, Purdue University, Indiana 47907, and Medical Isotopes Research Center, Peking University, Beijing 100191, China. Received March 4, 2009; Revised Manuscript Received June 10, 2009

This report describes the synthesis of MAG_2-PEG_4-E[c(RGDfK)]$_2$ (MAG_2-P-RGD_2: MAG_2 = *S*-benzoylmercaptoacetylglycylglycyl; PEG_4 = 15-amino-4,7,10,13-tetraoxapentadecanoic acid) and MAG_2-PEG_4-E[PEG_4-c(RGDfK)]$_2$ (MAG_2-3P-RGD_2), and the evaluation of ^{99m}TcO(MAG_2-P-RGD_2) and ^{99m}TcO(MAG_2-3P-RGD_2) as new radiotracers for tumor imaging in the athymic nude mice bearing U87MG human glioma xenografts. We found that MAG_2 is such an efficient bifunctional chelating agent that ^{99m}TcO(MAG_2-P-RGD_2) and ^{99m}TcO(MAG_2-3P-RGD_2) could be prepared in high yield (>90%) with high specific activity (~5 Ci/μmol) using a kit formulation. ^{99m}TcO(MAG_2-P-RGD_2) and ^{99m}TcO(MAG_2-3P-RGD_2) have very high solution stability in the kit matrix. Biodistribution data in athymic nude mice bearing U87MG human glioma xenografts indicated that replacing the highly charged [^{99m}Tc(HYNIC = 6-hydrazinonicotinyl and TPPTS = trisodium triphenylphosphine-3,3′,3″-trisulfonate) with smaller ^{99m}TcO(MAG_2) resulted in a significant increase in the radiotracer uptake in the tumor and normal organs most likely due to the higher lipophilicity of ^{99m}TcO(MAG_2-3P-RGD_2) (log $P = -3.15 \pm 0.10$) than that for [^{99m}Tc(HYNIC-3P-RGD_2)(tricine)(TPPTS)] (^{99m}Tc-3P-RGD_2: log $P = -3.96 \pm 0.05$). Even though ^{99m}TcO(MAG_2-3P-RGD_2) has better tumor uptake (15.36 ± 2.17 %ID/g at 60 min postinjection (p.i.)) than ^{99m}Tc-3P-RGD_2 (9.15 ± 2.13 %ID/g at 60 min p.i.), its tumor-to-background (*T*/B) ratios (tumor/blood = 13.52 ± 4.57; tumor/liver = 4.25 ± 0.88; tumor/lung = 3.17 ± 0.60; and tumor/muscle = 8.34 ± 2.34) are not as good as those of ^{99m}Tc-3P-RGD_2 (tumor/blood = 36.0 ± 11.5; tumor/liver = 5.14 ± 1.46; tumor/lung = 4.36 ± 0.54; and tumor/muscle = 13.70 ± 2.21) at 60 min p.i. On the basis of these results, we believe that ^{99m}Tc-3P-RGD_2 remains a better radiotracer because of its higher T/B ratios.

INTRODUCTION

Radiolabeled cyclic RGD (Arg-Gly-Asp) peptides represent a new class of radiotracers that target the integrin $\alpha_v\beta_3$ overexpressed on both tumor cells and endothelial cells of neovasculature during tumor growth, invasion, and metastasis (*1*−*12*). Many radiolabeled cyclic RGD peptides have been evaluated for imaging integrin $\alpha_v\beta_3$-positive tumors by single photon emission computed tomography (SPECT) or positron emission tomography (PET) over the last several years (*13*−*49*). Among the RGD peptide radiotracers evaluated in different tumor-bearing animal models, [^{18}F]-AH111585, the core peptide sequence discovered from a phage display library (such as ACDRGDCFCG) (*50, 51*), and [^{18}F]Galacto-RGD (2-[^{18}F]fluoropropanamide c(RGDfK(SAA)): SAA = 7-amino-L-glyero-L-galacto-2,6-anhydro-7-deoxyheptanamide) (*52*−*54*) are currently under clinical investigation for noninvasive visualization of integrin $\alpha_v\beta_3$ expression in cancer patients. The imaging studies show that the ^{18}F-labeled RGD peptides are able to target integrin $\alpha_v\beta_3$-positive tumors (*51*−*54*). However, the low tumor uptake, high cost, and lack of preparation modules for ^{18}F-labeled cyclic RGD peptides impose a significant challenge on their continued clinical applications.

To improve integrin $\alpha_v\beta_3$ binding affinity and radiotracer tumor uptake, multimeric cyclic RGD peptides, such as E-[c(RGDfK)]$_2$ and E{E[c(RGDfK)]$_2$}$_2$, were used as targeting biomolecules to carry radionuclide (e.g., ^{99m}Tc, ^{18}F, ^{64}Cu, and ^{111}In) to the integrin $\alpha_v\beta_3$ on tumor cells and endothelial cells of the tumor neovasculature (*20*−*22, 30*−*35, 37*−*49*). The results from in vitro assays, ex vivo biodistribution, and in vivo imaging studies clearly demonstrate that the radiolabeled (^{99m}Tc, ^{18}F, ^{64}Cu, and ^{111}In) multimeric cyclic RGD peptides, such as E{E[c(RGDxK)]$_2$}$_2$ and E[c(RGDxK)]$_2$ (x = f and y), have better tumor targeting capability as evidenced by their higher integrin $\alpha_v\beta_3$ binding affinity and better tumor uptake with longer tumor retention times than their monomeric counterparts (*20*−*22, 30*−*35, 37*−*49*). However, the uptake of radiolabeled (^{99m}Tc, ^{18}F, ^{64}Cu, and ^{111}In) multimeric cyclic RGD peptides in the kidneys and liver is also increased as the peptide multiplicity increases.

Recently, we reported the evaluation of the complex [^{99m}Tc-(HYNIC-3P-RGD_2)(tricine)(TPPTS)] (Figure 1: ^{99m}Tc-3P-RGD_2; HYNIC = 6-hydrazinonicotinyl; TPPTS = trisodium triphenylphosphine-3,3′,3″-trisulfonate; 3P-RGD_2 = PEG_4-E[PEG_4-c(RGDfK)]$_2$ and PEG_4 = 15-amino-4,7,10,13-tetraoxapentadecanoic acid) as radiotracers for imaging integrin $\alpha_v\beta_3$ expression in athymic nude mice bearing U87MG glioma and MDA-MB-435 breast cancer xenografts (*55*). The PEG_4 linkers are used to increase the distance between two cyclic RGD motifs from 6 bonds (excluding side arms of K-residues) in E-[c(RGDfK)]$_2$ to 38 bonds in 3P-RGD_2 so that they are able to achieve the simultaneous integrin $\alpha_v\beta_3$ binding in a bivalent fashion, and to improve radiotracer excretion kinetics from noncancerous organs. Results from the $\alpha_v\beta_3$ integrin binding assay show that the addition of PEG_4 linkers between two cyclic RGD motifs makes it possible for 3P-RGD_2 to become bivalent

* To whom correspondence should be addressed. School of Health Sciences, Purdue University, 550 Stadium Mall Drive, West Lafayette, IN 47907. Phone: 765-494-0236; Fax 765-496-1377; Email: lius@pharmacy.purdue.edu.

[†] Purdue University.

[‡] Peking University.

10.1021/bc9001739 CCC: $40.75 © 2009 American Chemical Society
Published on Web 07/15/2009

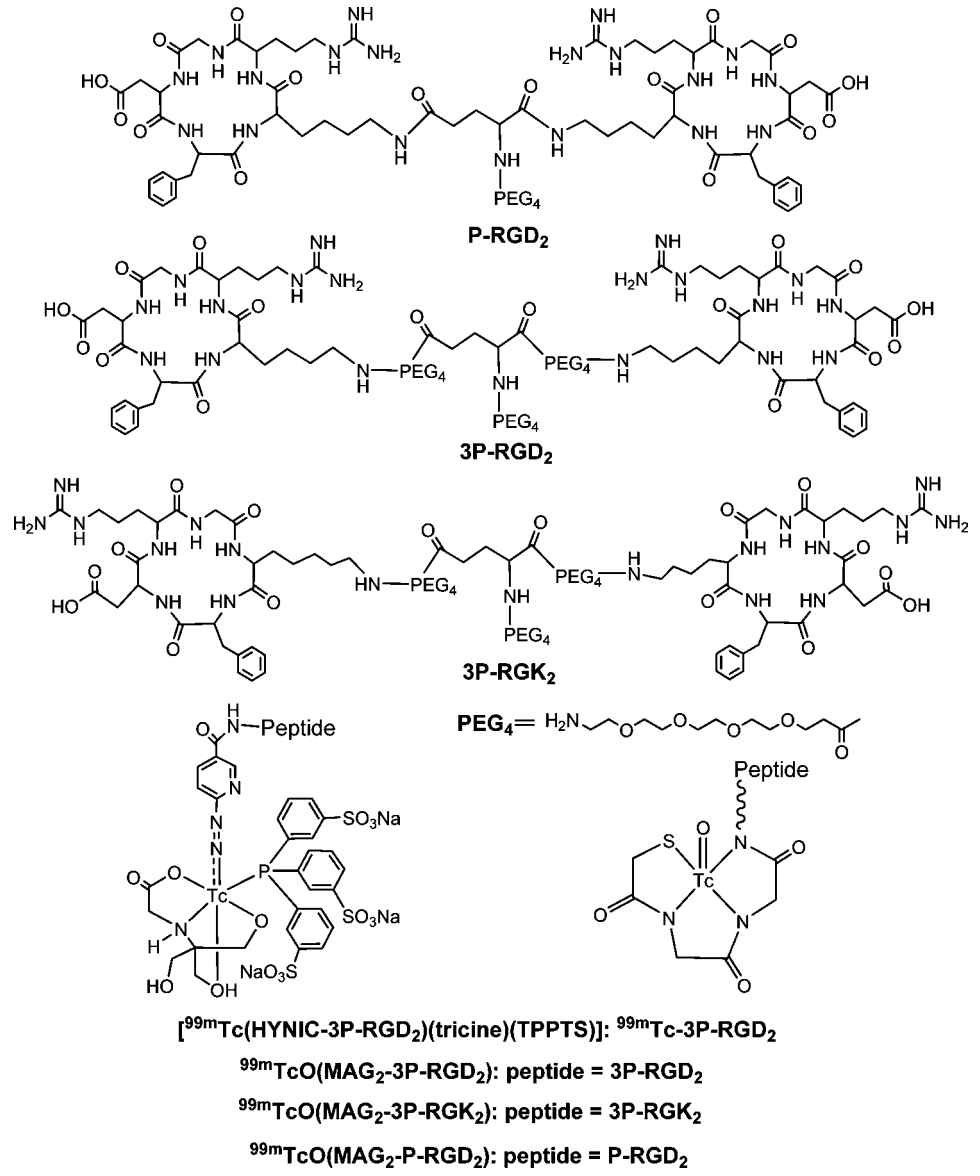

Figure 1. Structures of bivalent cyclic RGD dimers (P-RGD$_2$ and 3P-RGD$_2$) and their ^{99m}Tc complexes: [^{99m}Tc(HYNIC-3P-RGD$_2$)(tricine)(TPPTS)] (^{99m}Tc-3P-RGD$_2$), ^{99m}TcO(MAG$_2$-P-RGD$_2$), and ^{99m}TcO(MAG$_2$-3P-RGD$_2$).

in binding to the integrin $\alpha_v\beta_3$. The results from biodistribution studies clearly demonstrate that PEG$_4$ and G$_3$ linkers are useful for improving the tumor uptake and clearance kinetics of ^{99m}Tc radiotracers from noncancerous organs (*55*, *56*). Similar results were also obtained for [^{99m}Tc(HYNIC-3G-RGD$_2$)(tricine)-(TPPTS)] (^{99m}Tc-3G-RGD$_2$: 3G-RGD$_2$ = G$_3$-E[G$_3$-c(RGDfK)]$_2$ and G$_3$ = Gly-Gly-Gly) (*56*), ^{64}Cu(DOTA-3P-RGD$_2$) (DOTA = 1,4,7,10-tetraazacyclo-dodecane-1,4,7,10-tetracetic acid) and ^{64}Cu(DOTA-3G-RGD$_2$) (*57*).

As a continuation of our interest in radiolabeled cyclic RGD peptides as radiotracers for tumor imaging (*41*−*44*, *55*, *56*), we prepared two novel cyclic RGD conjugates, MAG$_2$-PEG$_4$-E[c(RGDfK)]$_2$ (MAG$_2$-P-RGD$_2$: MAG$_2$ = S-benzoylmercaptoacetylglycylglycyl) and MAG$_2$-3PEG$_4$-E[PEG$_4$-c(RGDfK)]$_2$ (MAG$_2$-3P-RGD$_2$), and their ^{99m}Tc complexes (Figure 1: ^{99m}TcO(MAG$_2$-P-RGD$_2$) and ^{99m}TcO(MAG$_2$-3P-RGD$_2$). MAG$_2$ is of our particular interest as the bifunctional chelator (BFC) because it forms the ^{99m}TcO(MAG$_2$) chelate (molecular weight (MW) ~300 Da) that is much smaller than the bulky and highly charged [^{99m}Tc(HYNIC)(tricine)(TPPTS)] (MW ~900 Da). The integrin $\alpha_v\beta_3$ binding affinities of MAG$_2$-P-RGD$_2$ and MAG$_2$-3P-RGD$_2$ were determined using a displacement assay against ^{125}I-c(RGDyK) bound to U87MG glioma cells. Biodistribution characteristics of ^{99m}TcO(MAG$_2$-P-RGD$_2$) and ^{99m}TcO(MAG$_2$-3P-RGD$_2$) were evaluated in the athymic nude mice bearing U87MG glioma xenografts. The main objective of this study is to demonstrate the usefulness of MAG$_2$ as a BFC for ^{99m}Tc-labeling of small biomolecules and to assess the impact of ^{99m}Tc chelates (^{99m}TcO(MAG$_2$) vs [^{99m}Tc(HYNIC)(tricine)(TPPTS)]) on both tumor uptake and tumor-to-background (*T*/*B*) ratios.

EXPERIMENTAL SECTION

Materials. Chemicals were purchased from Sigma-Aldrich (St. Louis, MO), and were used without further purification. Cyclic RGD peptides, PEG$_4$-E[PEG$_4$-c(RGDfK)]$_2$ (3P-RGD$_2$) and PEG$_4$-E[PEG$_4$-c(RGKfD)]$_2$ (3P-RGK$_2$: a scrambled nonsense peptide), were custom-made by the Peptides International, Inc. (Louisville, KY). MAG$_2$ (*S*-benzoylmercaptoacetylglycylglycine) and PEG$_4$-E[c(RGDfK)]$_2$ (P-RGD$_2$) were prepared according to the literature methods (*43*, *58*). Na^{99m}TcO$_4$ was obtained from a commercial DuPont Pharma ^{99}Mo/^{99m}Tc generator (North Billerica, MA). The ESI (electrospray ionization) mass spectral data were collected on a Finnigan LCQ classic mass spectrometer, School of Pharmacy, Purdue University.

HPLC Methods. HPLC method 1 used a LabAlliance HPLC system equipped with a UV/vis detector (λ = 254 nm) and Zorbax C_{18} semiprep column (9.4 nm × 250 mm, 100 Å pore size; Agilent Technologies, Santa Clara, CA). The flow rate was 2.5 mL/min with the mobile phase starting from 90% A (25 mM NH_4OAc, pH = 6.8) and 10% B (acetonitrile) at 0 min, followed by a gradient mobile phase going from 85% A and 15% B at 5 min to 65% A and 35% B at 30 min. The radio-HPLC method (method 2) used the LabAlliance HPLC system equipped with a β-ram IN/US detector (Tampa, FL) and Zorbax C_{18} column (4.6 mm × 250 mm, 300 Å pore size; Agilent Technologies, Santa Clara, CA). The flow rate was 1 mL/min. The mobile phase was isocratic with 90% A (25 mM NH_4OAc, pH = 6.8) and 10% B (acetonitrile) at 0−2 min, followed by a gradient mobile phase going from 10% B at 2 min to 15% B at 5 min and to 20% B at 20 min. The radio-ITLC method used GelmanSciences silica-gel paper strips and a 1:1 mixture of acetone and saline as eluant. By this method, ^{99m}Tc-labeled cyclic RGD peptides migrate to the solvent front, while $^{99m}TcO_4^-$ and [^{99m}Tc]colloid remain at the origin.

MAG_2-OSu. To a solution of MAG_2 (310 mg, 1 mmol) and *N*-hydroxysuccinimide (130 mg, 1.1 mmol) in DMF (5 mL) was added dicyclcohexylcarbodiimide (DCC: 230 mg, 1.1 mmol). The mixture was stirred at room temperature for 24 h. After addition of 0.3 mL acetic acid, the resulting mixture was stirred at room temperature for another 5 h. The precipitate was filtered and discarded. The filtrate was evaporated to dryness on a rotary evaporator. The residue was dissolved in dichloromethane (10 mL). After filtration, the filtrate was concentrated to ~2 mL. The solution was added dropwise into diethyl ether (20 mL) to give an off-white precipitate. The solid product was collected, washed with diethyl ether, and dried under vacuum. The yield was 340 mg (83%). ^{1}H NMR ($CDCl_6$, chemical shifts in ppm relative to TMS): 2.81 (s, 4H, $COCH_2CH_2CO$); 3.78 (s, 2H, SCH_2CO); 4.03 (d, 2H, CH_2CO); 4.38 (d, 2H, CH_2CO); 7.13 (dt, 2H, aromatic); 7.47 (t, 2H, aromatic); 7.61 (t, H, aromatic); and 7.96 (d, 2H, NHCO). ESI-MS: m/z = 408.50 for $[M+H]^+$ (408 calcd. for $[C_{17}H_{18}N_3O_7S]^+$).

MAG_2-P-RGD_2. MAG_2-OSu (5.8 mg, 14.2 μmol) and P-RGD_2 (5.4 mg, 3.45 μmol) were dissolved in DMF (2 mL). To the mixture above was added diisopropylethylamine (DIEA, 2 drops). The solution was stirred at room temperature for 2 h. After addition of water (2 mL), the pH was adjusted to 3.0−4.0. The product was separated from the reaction mixture by HPLC (method 1). Fractions at 17.5 min were collected. Lyophilization of combined collections afforded the crude product MAG_2-P-RGD_2 (~75% purity by HPLC), which was then further purified by HPLC (method 1). The yield was 2.7 mg (42%). ESI-MS: m/z = 1858.43 for (1857 calcd for $[C_{83}H_{121}N_{22}O_{25}S]^+$).

MAG_2-3P-RGD_2. MAG_2-3P-RGD_2 was prepared in a similar fashion to that for MAG_2-P-RGD_2 using MAG_2-OSu (4 mg, 9.7 μmol) and 3P-RGD_2 (5 mg, 2.43 μmol). The product was purified by HPLC (method 1). Fractions at ~16 min were collected. Lyophilization of the combined collections afforded the crude product MAG_2-3P-RGD_2 (~77% purity by HPLC), which was further purified by HPLC (method 1). Lyophilization of the combined collections at 20 min afforded MAG_2-3P-RGD_2 with >95% HPLC purity. The yield was 2.0 mg (35%). ESI-MS: m/z = 2351.79 for (2352 calcd. for $[C_{105}H_{163}N_{24}O_{35}S]^+$).

MAG_2-PEG_4-E[PEG_4-c(RGKfD)]$_2$ (MAG_2-3P-RGK_2). MAG_2-3P-RGK_2 was prepared according to the same procedure used for MAG_2-PEG_4-dimer using MAG_2-OSu (12.5 mg, 40 μmol) and 3P-RGK_2 (15 mg, 7.29 μmol). The product was separated from the reaction mixture by HPLC (method 1). Fractions at 16 min were collected. Lyophilization of the combined collections afforded the crude product MAG_2-3P-RGK_2 (~70% purity by HPLC), which was then further purified by HPLC (method 1). Lyophilization of the combined collections at 19 min afforded MAG_2-3P-RGK_2 with >95% HPLC purity. The yield was 6.2 mg (36%). ESI-MS: m/z = 2351.76 for (2351 calcd. for $[C_{105}H_{163}N_{24}O_{35}S]^+$).

^{99m}Tc-Labeling. To a lyophilized vial containing 2.28 mg of NaH_2PO_4, 11.5 mg of Na_2HPO_4, 50 mg of α-D-glucoheptonic acid, 50 μg of $SnCl_2 \cdot 2H_2O$, and 25 μg of the MAG_2-conjugate (MAG_2-P-RGD_2, MAG_2-3P-RGD_2, or MAG_2-3P-RGD_2) was added 1.0 mL of $Na^{99m}TcO_4$ solution (10−50 mCi/mL). The vial was heated at 100 °C for 20−25 min in a lead-shielded water bath. After heating, the vial was placed back into the lead pig and allowed to stand at room temperature for ~10 min. A sample of the resulting solution was analyzed by radio-HPLC (method 2) and radio-ITLC. The radiochemical purity (RCP) was >95% for all three radiotracers, ^{99m}TcO(MAG_2-P-RGD_2), ^{99m}TcO(MAG_2-3P-RGD_2), and ^{99m}TcO(MAG_2-3P-RGK_2), with less than 0.5% of [^{99m}Tc]colloid.

Dose Preparation. For the ex vivo biodistribution studies, the ^{99m}Tc radiotracers were first prepared and then purified by HPLC (method 2). Volatiles in the HPLC mobile phases were removed under vacuum. The dose solution was prepared by dissolving the purified radiotracer in saline to a concentration of 10−25 μCi/mL. In the blocking experiment, E[c(RGDfK)]$_2$ was dissolved in the dose solution to ~3.5 mg/mL. For imaging studies, ^{99m}TcO(MAG_2-3P-RGD_2) was prepared in high yield (RCP > 95%). Doses were made by dissolving the reconstituted kit solution to a concentration of 5 mCi/mL. The solution was filtered with a 0.20 μ Millex-LG filter to remove any particle or precipitate. Each tumor-bearing mouse was injected with ~0.1 mL of the filtered dose solution.

Determination of Log *P* Values. Log P values of were determined using the following procedure: the ^{99m}Tc radiotracer was purified by HPLC. Volatiles were removed completely under vacuum. The residue was dissolved in a equal volume (3 mL/3 mL) mixture of *n*-octanol and 25 mM phosphate buffer (pH = 7.4). After stirring vigorously for ~20 min, the mixture was centrifuged at a speed of 8000 rpm for 5 min. Samples (in triplets) from *n*-octanol and aqueous layers were counted in a Perkin-Elmer Wizard 1480 γ-counter (Shelton, CT). The log *P* value was measured three different times and reported as an average of three independent measurements plus the standard deviation.

In vitro Whole-Cell Integrin $\alpha_v\beta_3$ Binding Assay. The in vitro integrin binding affinity of cyclic RGD peptides were assessed by a displacement assay using ^{125}I-c(RGDyK) as the integrin $\alpha_v\beta_3$-specific radioligand. Experiments were performed on U87MG human glioma cells by slight modification of a method previously described (*28, 30*). Briefly, U87MG glioma cells were grown in Gibco's Dulbecco's medium supplemented with 10% fetal bovine serum (FBS), 100 IU/mL penicillin, and 100 μg/mL streptomycin (Invitrogen Co, Carlsbad, CA), at 37 °C in humidified atmosphere containing 5% CO_2. Filter multiscreen DV plates were seeded with 10^5 cells in binding buffer and incubated with ^{125}I-c(RGDyK) in the presence of increasing concentrations of cyclic RGD peptides. After removing the unlabeled c(RGDyK), hydrophilic PVDF filters were collected and the radioactivity was determined using a gamma counter (Packard, Meriden, CT). The IC_{50} values were calculated by fitting the data by nonlinear regression using *GraphPad Prism* (GraphPad Software, Inc., San Diego, CA), and reported as an average plus the standard deviation. Comparison between two radiotracers was made using the two-way ANOVA test (*GraphPad Prism 5.0*, San Diego, CA). The level of significance was set at $p < 0.05$.

Animal Model. Biodistribution studies were performed using the athymic nude mice bearing U87MG human glioma xenografts in compliance the NIH animal experiment guidelines

(Principles of Laboratory Animal Care, NIH Publication No. 86−23, revised 1985). The protocol was approved by Purdue University Animal Care and Use Committee (PACUC). The U87MG human glioma cells were grown at 37 °C in Minimal Essential Medium (Alpha Modification) containing 3.7 g of sodium bicarbonate/L, 10% fetal bovine serum v/v, and 5% penicillin streptomycin (GIBCO, Grand Island, NY) in a humidified atmosphere of 5% carbon dioxide. Female athymic nu/nu mice were purchased from NCI at 4−5 weeks of age. The mice were implanted subcutaneously with ~8 × 10^6 U87MG human glioma cells into the upper left flanks. All procedures will be performed in a laminar flow cabinet using aseptic technique. Two to three weeks after inoculation, the tumor size was 0.1−0.4 g, and animals were used for biodistribution and imaging studies.

Biodistribution Protocol. Fifteen tumor-bearing mice (20 − 25 g) were randomly divided into four groups. Each animal was administered with ^{99m}Tc radiotracer (~2.5 μCi in 0.1 mL saline) via tail vein. Five animals were euthanized by sodium pentobarbital overdose (100−200 mg/kg) at 30, 60, and 120 min postinjection (p.i.). Blood samples were withdrawn from the heart. The tumor and normal organs (brain, eyes, heart, intestine, kidneys, liver, lungs, muscle, and spleen) were excised, washed with saline, dried with absorbent tissue, weighed, and counted on a γ-counter (Perkin-Elmer Wizard 1480). The organ uptake was calculated as the percentage of injected dose per gram of organ tissue (%ID/g). For the blocking experiment to demonstrate the radiotracer integrin $\alpha_v\beta_3$ specificity, each animal was administered ~2 μCi of ^{99m}TcO(MAG_2-3P-RGD_2) along with ~350 μg of E[c(RGDfK)]$_2$ (~14 mg/kg). At 1 h p.i., five animals were sacrificed by sodium pentobarbital overdose (100 mg/kg) for organ biodistribution. The organ uptake (%ID/g) was compared to that obtained in the absence of excess E-[c(RGDfK)]$_2$ at the same time point. For the experiment to demonstrate the radiotracer RGD-specific, each animal was administered with ~2 μCi of ^{99m}TcO(MAG_2-3P-RGD_2) along with ~350 μg of E[c(RGDfK)]$_2$ (~14 mg/kg). At 1 h p.i., five animals were sacrificed by sodium pentobarbital overdose (100 mg/kg) for organ biodistribution. The organ uptake (%ID/g) was compared to that obtained in the absence of excess E[c(RGD-fK)]$_2$ at the same time point.

Scintigraphic Imaging. Three athymic nude mice bearing U87MG glioma xenografts were used for planar imaging studies. Each glioma-bearing mouse was intravenously administered with ~500 μCi of ^{99m}TcO(MAG_2-3P-RGD_2) via tail vein. The animals were anesthetized with intramuscular injection of ketamine (80 mg/kg) and xylazine (19 mg/kg). The animal was placed prone on a single head mini γ-camera (Diagnostic Services Inc., NJ) equipped with a parallel-hole, low-energy, and high-resolution collimator. Static images were acquired at 15, 30, 60, and 120 min p.i. and were stored digitally in a 128 × 128 matrix. The acquisition count limits were set at 500 K. After imaging, the animals were euthanized by sodium pentobarbital overdose (100−200 mg/kg).

Metabolism. Three glioma-bearing mice were used for the in vivo metabolic stability study of ^{99m}TcO(MAG_2-3P-RGD_2), which was intravenously administered at the dose of ~100 μCi per mouse via tail vein. At 120 min p.i., the urine samples were collected and were mixed with equal volume of 20% acetonitrile aqueous solution. The mixture was centrifuged at 8000 rpm for 5 min. The supernatant was collected and filtered through a 0.20 μ Millex-LG filter unit. The feces samples were collected at 120 min p.i. and suspended in a mixture of 20% acetonitrile aqueous solution (2 mL). The resulting mixture was vortexed for 10 min. After centrifuging at 8000 rpm for 5 min, the supernatant was collected and passed through a 0.20 μ Millex-LG filter unit to remove any particles or precipitate. Both the urine and feces samples were analyzed by radio-HPLC (method 2). The tumor, kidney, and liver tissues were harvested at 120 min p.i., counted in a Perkin-Elmer Wizard 1480 γ-counter (Shelton, CT) for total radioactivity, and then homogenized. The homogenate was mixed with 2 mL of 20% acetonitrile aqueous solution. After centrifuging at 8000 rpm for 5 min, the supernatant was collected and counted on a γ-counter to determine the percentage of radioactivity recovery in each organ. After filtration through a 0.20 μm Millex-LG filter unit to remove foreign particles or precipitate, the filtrate was then analyzed by radio-HPLC (method 2).

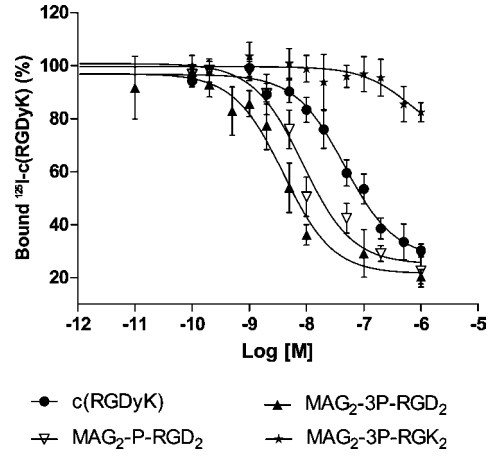

Figure 2. The in vitro inhibition curve of ^{125}I-c(RGDyK) bound to integrin $\alpha_v\beta_3$ on U87MG human glioma cells by c(RGDyK), MAG_2-P-RGD_2, MAG_2-3P-RGD_2, and MAG_2-3P-RGK_2. Their IC_{50} values were calculated to be 46.6 ± 4.5, 8.6 ± 2.8, 3.9 ± 0.4, and 711 ± 128 nM, respectively.

Data and Statistical Analysis. The biodistribution data and target-to-background (*T*/*B*) ratios are reported as an average plus the standard variation based on results from four tumor-bearing mice at each time point. Comparison between two different ^{99m}Tc radiotracers was made using the two-way ANOVA test (*GraphPad Prism 5.0*, San Diego, CA). The level of significance was set at $p < 0.05$.

RESULTS

MAG_2 Conjugate Synthesis. Synthesis of new cyclic RGD peptide conjugates (MAG_2-P-RGD_2 and MAG_2-3P-RGD_2) was straightforward. They were prepared by conjugation of P-RGD_2 and 3P-RGD_2, respectively, with excess MAG_2-NHS in DMF in the presence of a base, such as DIEA. MAG_2-3P-RGK_2 contains two c(RGKfD) motifs instead of c(RGDfK) motifs in MAG_2-3P-RGD_2 and was prepared as a "negative control" to demonstrate the RGD-specificity of ^{99m}TcO(MAG_2-3P-RGD_2). All new peptide conjugates were purified twice by HPLC (method 1) and characterized by ESI-MS. Their HPLC purity was >95% before being used for ^{99m}Tc-labeling and determination of their integrin $\alpha_v\beta_3$ binding affinity.

Integrin $\alpha_v\beta_3$ Binding Affinity. The integrin $\alpha_v\beta_3$ binding affinities of c(RGDyK), MAG_2-3P-RGD_2 and MAG_2-3P-RGD_2 and MAG_2-3P-RGK_2 were determined by a competitive displacement assay. Their IC_{50} values were obtained from curve fitting from Figure 2 and calculated to be 46.6 ± 4.5, 8.6 ± 2.8, 3.9 ± 0.4, and 711 ± 128 nM, respectively.

Radiochemistry. ^{99m}TcO(MAG_2-P-RGD_2) and ^{99m}TcO(MAG_2-3P-RGD_2) were prepared by reacting MAG_2-P-RGD_2 and MAG_2-3P-RGD_2, respectively, with $^{99m}TcO_4^-$ at pH ~8.5 in the presence of excess D-glucoheptonic acid (~50 mg per vial) and stannous chloride. ^{99m}Tc-labeling was accomplished by heating the reaction mixture at 100 °C for 15−20 min. D-Glucoheptonic acid was used to stabilize $SnCl_2$ and the

Table 1. HPLC Retention Time and Log *P* Values for ^{99m}Tc-Labeled Cyclic RGD Peptides

compound	RCP (%)	RT (min)	Log *P*
^{99m}TcO(MAG$_2$-P-RGD$_2$)	>95	17.0	-3.30 ± 0.13
^{99m}TcO(MAG$_2$-3P-RGD$_2$)	>90	16.9	-3.19 ± 0.15
^{99m}TcO(MAG$_2$-3P-RGK$_2$)	>90	17.3	-2.40 ± 0.14
^{99m}Tc-3P-RGD$_2$	>90	16.9	-4.35 ± 0.10[a]

[a] The log *P* value of -3.96 ± 0.05 was reported in our previous communication (*55*). These two values seem to be statistically significant, but they are within the experimental error of the assay.

Table 2. Biodistribution Data of ^{99m}TcO(MAG$_2$-P-RGD$_2$) in Athymic Nude Mice ($n = 5$) Bearing U87MG Human Glioma Xenografts

	30 min	60 min	120 min
blood	1.50 ± 0.64	0.85 ± 0.42	0.11 ± 0.02
brain	0.45 ± 0.29	0.54 ± 0.55	0.09 ± 0.01
eyes	2.21 ± 0.80	2.14 ± 0.55	0.94 ± 0.14
heart	2.51 ± 1.13	1.60 ± 0.54	0.71 ± 0.10
intestine	9.39 ± 2.92	5.25 ± 1.08	3.27 ± 1.14
kidney	16.61 ± 5.52	9.95 ± 3.90	3.92 ± 0.60
liver	4.25 ± 1.53	2.75 ± 0.76	1.47 ± 0.15
lungs	5.41 ± 1.62	2.65 ± 0.57	2.28 ± 0.72
muscle	3.33 ± 0.77	2.53 ± 1.10	1.12 ± 0.26
spleen	3.52 ± 1.13	3.04 ± 1.09	1.25 ± 0.12
U87MG	9.63 ± 1.39	11.95 ± 1.90	5.90 ± 0.35
tumor/blood	8.53 ± 3.72	12.58 ± 2.60	46.62 ± 4.17
tumor/kidney	0.59 ± 0.08	1.15 ± 0.05	1.49 ± 0.28
tumor/liver	2.54 ± 0.68	2.98 ± 0.29	3.69 ± 0.58
tumor/lungs	1.95 ± 0.40	3.25 ± 1.13	2.93 ± 0.68
tumor/muscle	2.98 ± 0.35	4.20 ± 0.75	4.79 ± 0.54

Table 3. Biodistribution Data of ^{99m}TcO(MAG$_2$-3P-RGD$_2$) in Athymic Nude Mice ($n = 5$) Bearing U87MG Human Glioma Xenografts

%ID/gram	30 min	60 min	120 min
blood	1.62 ± 0.69	1.16 ± 0.78	0.42 ± 0.29
brain	0.26 ± 0.07	0.21 ± 0.06	0.17 ± 0.07
eyes	2.47 ± 1.34	1.40 ± 0.65	1.48 ± 0.77
heart	2.40 ± 0.97	1.79 ± 0.45	1.05 ± 0.18
intestine	10.99 ± 1.95	9.26 ± 1.50	6.58 ± 1.62
kidney	16.35 ± 5.53	11.79 ± 3.98	6.07 ± 1.12
liver	4.35 ± 1.51	3.45 ± 0.86	2.30 ± 0.23
lungs	6.15 ± 1.93	4.17 ± 1.35	2.78 ± 0.49
muscle	2.17 ± 0.35	1.82 ± 0.83	0.97 ± 0.24
spleen	3.41 ± 1.12	3.02 ± 0.56	1.98 ± 0.14
U87MG	15.49 ± 5.55	15.36 ± 2.17	14.02 ± 2.20
tumor/blood	9.15 ± 2.51	13.52 ± 4.57	31.54 ± 10.23
tumor/kidney	0.98 ± 0.30	1.25 ± 0.36	2.01 ± 0.12
tumor/liver	3.49 ± 1.13	4.25 ± 0.88	5.81 ± 0.65
tumor/lung	2.51 ± 0.62	3.17 ± 0.60	4.95 ± 1.00
tumor/muscle	6.60 ± 1.25	8.34 ± 2.34	12.19 ± 1.07

$[^{99m}TcO]^{3+}$ core and to prevent formation of [^{99m}Tc]colloid during radiolabeling. Their radiochemical purity was >90% with <0.5% of [^{99m}Tc]colloid. In general, 20−25 μg MAG$_2$-3P-RGD$_2$ was sufficient for successful radiolabeling of 50 mCi of $^{99m}TcO_4^-$. The specific activity for ^{99m}TcO(MAG$_2$-3P-RGD$_2$) was ~2.0 mCi/μg (~5 Ci/μmol). ^{99m}TcO(MAG$_2$-3P-RGD$_2$) was stable in the kit matrix for >6 h. All ^{99m}Tc radiotracers were analyzed by the same HPLC method, and their retention times were listed in Table 1. The log *P* values for ^{99m}TcO(MAG$_2$-P-RGD$_2$), ^{99m}TcO(MAG$_2$-3P-RGD$_2$), and ^{99m}TcO(MAG$_2$-3P-RGK$_2$) were determined to be -3.30 ± 0.13, -3.19 ± 0.10, and -2.40 ± 0.14, respectively.

Biodistribution Characteristics. The biodistribution data for ^{99m}TcO(MAG$_2$-P-RGD$_2$) and ^{99m}TcO(MAG$_2$-3P-RGD$_2$) were listed in Tables 2 and 3, respectively. ^{99m}TcO(MAG$_2$-P-RGD$_2$) had the tumor uptake of 9.63 ± 1.39 and 11.95 ± 1.90%ID/g at 30 and 60 min, respectively, but it decreased to 5.90 ± 0.35%ID/g at 120 min p.i. It also had a high kidney uptake with a fast clearance (16.61 ± 5.52 and 3.93 ± 0.60%ID/g at 30 and 120 min p.i., respectively). The liver uptake of ^{99m}TcO(MAG$_2$-P-RGD$_2$) was 4.25 ± 1.53, 2.75 ± 0.76 and 1.47 ± 0.15%ID/g while its tumor/liver ratios were 2.54 ± 0.68, 2.98 ± 0.29 and 3.69 ± 0.58 at 30, 60 and 120 min p.i., respectively. ^{99m}TcO(MAG$_2$-3P-RGD$_2$) also had a high tumor uptake (15.49 ± 5.55, 15.36 ± 2.17 and 14.02 ± 2.20%ID/g at 30, 60 and 120 min p.i., respectively). Its kidney uptake was 16.35 ± 2.20, 11.79 ± 3.98 and 6.07 ± 1.12%ID/g at 30, 60 and 120 min p.i. respectively. Its liver uptake was 4.35 ± 1.51%ID/g at 30 min p.i. and 2.30 ± 0.23%ID/g at 120 min p.i., and its tumor/liver ratio increased steadily from 3.49 ± 1.13 at 30 min p.i. to 5.81 ± 0.65 at 120 min p.i.

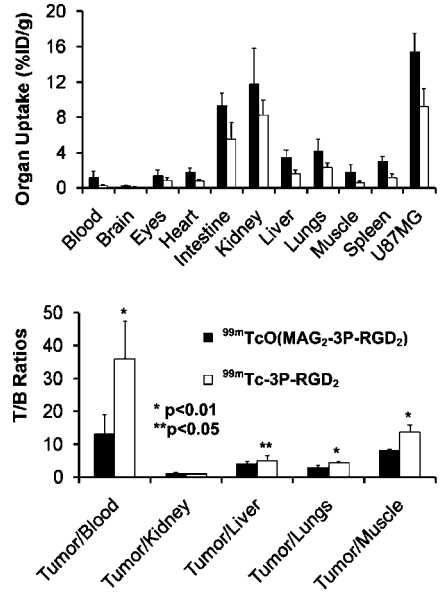

Figure 3. Comparison of the biodistribution data (top) and selected *T*/*B* ratios (bottom) of ^{99m}TcO(MAG$_2$-3P-RGD$_2$) and ^{99m}Tc-3P-RGD$_2$ at 60 min p.i. in the athymic nude mice ($n = 5$) bearing U87MG glioma xenografts.

Effects of Technetium Chelate. To assess the impact of ^{99m}Tc chelates (^{99m}TcO(MAG$_2$) vs [^{99m}Tc(HYNIC)(tricine)-(TPPTS)]) on the radiotracer tumor uptake and T/B ratios, we also obtained the 60-min biodistribution data of ^{99m}Tc-3P-RGD$_2$ using the same animal model with similar tumor size. Figure 3 compares the organ uptake and *T*/*B* ratios for ^{99m}TcO(MAG$_2$-3P-RGD$_2$) and ^{99m}Tc-3P-RGD$_2$ at 60 min p.i. Replacing [^{99m}Tc-(HYNIC)(tricine)(TPPTS)] with the much smaller ^{99m}TcO-(MAG$_2$) resulted in a significant increase in the tumor and normal organ uptake. For example, ^{99m}TcO(MAG$_2$-3P-RGD$_2$) had the 60-min uptake of 15.36 ± 2.17, 1.16 ± 0.78, 9.26 ± 1.50, 11.79 ± 3.98, 3.45 ± 0.86 and 4.17 ± 1.35%ID/g in the tumor, blood, intestine, kidneys, liver and lungs, respectively, while the uptake of ^{99m}Tc-3P-RGD$_2$ in the same organs was 9.15 ± 2.13%ID/g, 0.27 ± 0.08%ID/g, 5.25 ± 1.92%ID/g, 8.22 ± 1.99%ID/g, 1.69 ± 0.46%ID/g, and 2.10 ± 0.54%ID/g at the same time point.

Integrin $\alpha_v\beta_3$ Specificity. Figure 4A compares the organ uptake of ^{99m}TcO(MAG$_2$-3P-RGD$_2$) in the absence/presence of E[c(RGDfK)]$_2$ at 60 min p.i. Coinjection of excess E[c-(RGDfK)]$_2$ almost completely blocked its tumor uptake (0.31 ± 0.07%ID/g with E[c(RGDfK)]$_2$ vs 15.36 ± 2.17%ID/g without E[c(RGDfK)]$_2$). The normal organ uptake of ^{99m}TcO-(MAG$_2$-3P-RGD$_2$) was also almost completely blocked by coinjection of excess E[c(RGDfK)]$_2$.

RGD Specificity. Figure 4B compares the 60 min organ uptake values for ^{99m}TcO(MAG$_2$-3P-RGK$_2$) and ^{99m}TcO(MAG$_2$-3P-RGD$_2$). This experiment was designed to demonstrate the RGD specificity of ^{99m}TcO(MAG$_2$-3P-RGD$_2$). ^{99m}TcO(MAG$_2$-3P-RGK$_2$) had much lower tumor uptake (0.70 ± 0.09%ID/g)

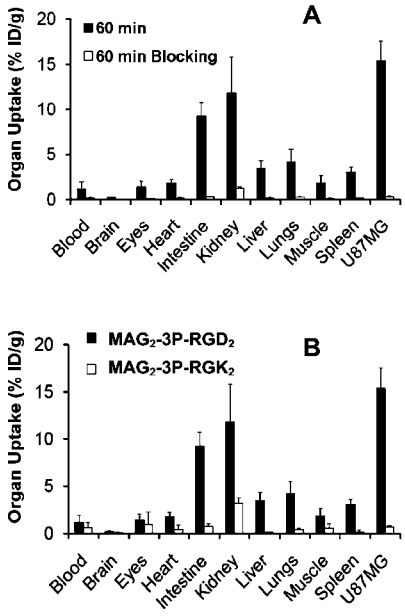

Figure 4. (A) Biodistribution data of ^{99m}TcO(MAG$_2$-3P-RGD$_2$) in athymic nude mice ($n = 5$) bearing U87MG human glioma xenografts in the absence/presence of excess E[c(RGDfK)]$_2$ (14 mg/kg or ~350 μg/mouse) at 60 min p.i. (B) Direct comparison of biodistribution characteristics between ^{99m}TcO(MAG$_2$-3P-RGD$_2$) and ^{99m}TcO(MAG$_2$-3P-RGK$_2$) in athymic nude mice ($n = 5$) bearing U87MG human glioma xenografts at 60 min p.i.

than ^{99m}TcO(MAG$_2$-3P-RGD$_2$) (15.36 ± 2.17%ID/g). It also had significantly ($p < 0.01$) lower uptake in normal organs than ^{99m}TcO(MAG$_2$-3P-RGD$_2$). As a result, the radioactivity was excreted much more rapidly (more urine activity at the same time point) from the renal route in the tumor-bearing mice administered with ^{99m}TcO(MAG$_2$-3P-RGK$_2$).

Tumor Size vs Tumor Uptake. In this study, we used a total of 14 glioma-bearing mice to explore the relationship between the tumor size and %ID uptake of ^{99m}TcO(MAG$_2$-3P-RGD$_2$) at 120 min p.i. As illustrated in Figure 5A, there was a linear relationship between the tumor size (0.08−0.4 g; $n = 14$) and the %ID glioma uptake of ^{99m}TcO(MAG$_2$-3P-RGD$_2$) with $R^2 = 0.9226$. Obviously, the %ID tumor uptake of ^{99m}TcO(MAG$_2$-3P-RGD$_2$) increased in a linear fashion as the tumor size became larger.

Planar Imaging. Figure 5B illustrates representative static images of the glioma-bearing mice ($n = 3$) administered with ^{99m}TcO(MAG$_2$-3P-RGD$_2$) at 15, 30, 60, and 120 min p.i. The tumor was clearly seen with excellent contrast as early as 15 min p.i. The tumor radioactivity remained relatively steady over the 2 h study period. The radioactivity accumulation in the blood and muscle disappeared almost completely by 120 min p.i. The most visible organs were tumor, gallbladder, kidneys, and bladder. Because of the radioactivity accumulation in the abdominal region, it was difficult to accurately determine the tumor/kidney and tumor/liver ratios on the basis of planar imaging.

Metabolic Properties. Metabolism studies were performed on ^{99m}TcO(MAG$_2$-3P-RGD$_2$) using athymic nude mice bearing U87MG glioma xenografts. The percentage of radioactivity recovery in the urine and feces samples was very high (>90%); but it was only 45−55% from the homogenates of the tumor, kidney, and liver tissues. Figure 6 shows radio-HPLC chromatograms of ^{99m}TcO(MAG$_2$-3P-RGD$_2$) in saline before injection, in the extracts of urine and feces samples, and in the homogenates from tumor, kidneys, and liver at 120 min p.i. There was no significant metabolism for ^{99m}TcO(MAG$_2$-3P-RGD$_2$) during its excretion from renal and hepatobiliary routes and in the tissues from tumor, liver, and kidneys.

DISCUSSION

In this study, we prepared two cyclic RGD dimer conjugates (MAG$_2$-P-RGD$_2$ and MAG$_2$-3P-RGD$_2$). It is found that both ^{99m}TcO(MAG$_2$-P-RGD$_2$) and ^{99m}TcO(MAG$_2$-3P-RGD$_2$) can be obtained in high yield (>90%) and with high specific activity (~5 Ci/μmol) using a kit formulation, and have very high solution stability in the kit matrix. There are advantages of using small peptides, such as MAG$_2$ (the smallest N_3S triamidethiol chelating unit when conjugated to the peptide), as BFCs. The attachment of BFC can be easily incorporated into solid-phase peptide synthesis. The N_3S chelating units form stable Tc complexes with the $[Tc{=}O]^{3+}$ core. The hydrophilicity of the Tc chelate can be tuned by changing the glycine residues with more hydrophilic amino acids, such as aspartic and glutamic acids.

The integrin $\alpha_v\beta_3$ binding affinity follows the order MAG$_2$-3P-RGD$_2$ ($IC_{50} = 3.9 \pm 0.4$ nM) > MAG$_2$-P-RGD$_2$ ($IC_{50} = 8.6 \pm 2.8$ nM) > c(RGDfK) ($IC_{50} = 46.6 \pm 4.5$ nM), suggesting that bivalency is most likely responsible for the higher integrin $\alpha_v\beta_3$ binding affinity of MAG$_2$-3P-RGD$_2$ as compared to that of MAG$_2$-P-RGD$_2$. This conclusion is well supported by the significantly ($p < 0.01$) higher tumor uptake (Figure 3) of ^{99m}TcO(MAG$_2$-3P-RGD$_2$) than that of ^{99m}TcO(MAG$_2$-P-RGD$_2$). If they were bound to integrin $\alpha_v\beta_3$ in the same fashion, MAG$_2$-3P-RGD$_2$ and MAG$_2$-P-RGD$_2$ would have had the same integrin $\alpha_v\beta_3$ binding affinity, whereas ^{99m}TcO(MAG$_2$-3P-RGD$_2$) and ^{99m}TcO(MAG$_2$-P-RGD$_2$) would have shared the similar tumor uptake in the same tumor-bearing animal model.

The integrin $\alpha_v\beta_3$ binding affinity of MAG$_2$-3P-RGD$_2$ ($IC_{50} = 3.9 \pm 0.4$ nM) is very similar to that of HYNIC-3P-RGD$_2$ ($IC_{50} = 4.1 \pm 0.3$ nM), respectively, suggesting that replacing HYNIC with MAG$_2$ has little impact on the integrin $\alpha_v\beta_3$ binding affinity of 3P-RGD$_2$. It must be noted that this comparison is between the cyclic RGD conjugates, not their ^{99m}Tc radiotracers, the integrin $\alpha_v\beta_3$ binding affinity and biodistribution characteristic of which could be altered significantly depending on the size of ^{99m}Tc chelates (Figure 1: ^{99m}TcO(MAG$_2$) vs [^{99m}Tc(HYNIC)(tricine)(TPPTS)]). ^{99m}TcO-(MAG$_2$) has a molecular weight of ~300 Da and is expected to have minimal impact on integrin $\alpha_v\beta_3$ binding affinity of 3PEG$_4$-dimer. In contrast, [^{99m}Tc(HYNIC)(tricine)(TPPTS)] has a molecular weight of ~1000 Da due to the presence of tricine and TPPTS coligands, and is expected to have much more significant impact on the integrin $\alpha_v\beta_3$ binding affinity of 3P-RGD$_2$. This assumption seems to be supported by the significantly ($p < 0.01$) higher tumor uptake of ^{99m}TcO(MAG$_2$-3P-RGD$_2$) (15.36 ± 2.17%ID/g at 60 min p.i.) than that of ^{99m}Tc-3P-RGD$_2$ (9.15 ± 2.13%ID/g at 60 min p.i.).

Replacing [^{99m}Tc(HYNIC)(tricine)(TPPTS)] with ^{99m}TcO-(MAG$_2$) results in >10× higher lipophilicity for ^{99m}TcO(MAG$_2$-3P-RGD$_2$) ($\log P = -3.19 \pm 0.13$) as compared to ^{99m}Tc-3P-RGD$_2$ ($\log P = -4.35 \pm 0.10$), which is most likely responsible for its higher uptake in tumor, blood, and normal organs (Figure 3: top). For example, the blood radioactivity for ^{99m}TcO(MAG$_2$-3P-RGD$_2$) is 1.16 ± 0.78%ID/g at 60 min p.i. while it is only 0.27 ± 0.08%ID/g for ^{99m}Tc-3P-RGD$_2$ at the same time point. The liver uptake of ^{99m}TcO(MAG$_2$-3P-RGD$_2$) is 3.45 ± 0.86%ID/g whereas ^{99m}Tc-3P-RGD$_2$ has the liver uptake of 2.92 ± 0.77%ID/g at 60 min p.i. ^{99m}TcO(MAG$_2$-3P-RGD$_2$) has the kidney uptake of 11.79 ± 3.98%ID/g while ^{99m}Tc-3PEG$_4$-dimer has the kidney uptake of 8.62 ± 1.99%ID/g at 60 min p.i. The lung uptake is 4.17 ± 1.35%ID/g for ^{99m}TcO(MAG$_2$-3P-RGD$_2$) and 2.10 ± 0.54%ID/g for ^{99m}Tc-3P-RGD$_2$ at 60 min p.i. the tumor/blood, tumor/liver, tumor/lung, and tumor/liver ratios for

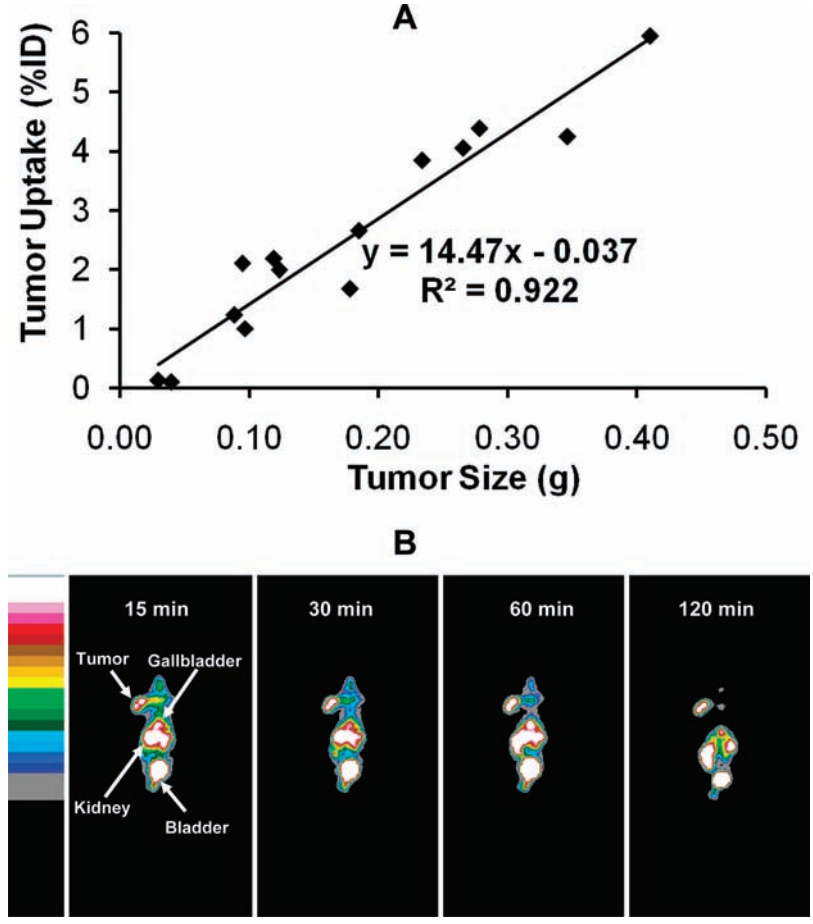

Figure 5. (A) Relationship between tumor size and tumor uptake for ^{99m}TcO(MAG$_2$-3P-RGD$_2$) at 120 min p.i. in the athymic nude mice (n = 14) bearing the U87MG glioma xenografts. The linear relationship between the tumor size and %ID tumor uptake suggests that ^{99m}TcO(MAG$_2$-3P-RGD$_2$) has the potential for noninvasive monitoring of tumor growth or shrinkage during antiangiogenic therapy. (B) Planar images of the athymic nude mice (bearing U87MG glioma xenografts) administered with ~500 μCi of ^{99m}TcO(MAG$_2$-3P-RGD$_2$) at 15, 30, 60, and 120 min p.i. Arrows indicate the presence of the tumor, gallbladder, kidneys, and bladder.

^{99m}TcO(MAG$_2$-3P-RGD$_2$) are not as good as those for ^{99m}Tc-3P-RGD$_2$ (Figure 4: bottom). On the basis of these data, we believe that ^{99m}Tc-3P-RGD$_2$ remains a better SPECT radiotracer for noninvasive imaging of integrin $\alpha_v\beta_3$-positive tumors.

The integrin $\alpha_v\beta_3$-specificity of ^{99m}TcO(MAG$_2$-3P-RGD$_2$) has been demonstrated by the "blocking experiment" (Figure 4A). The blockage of its tumor uptake indicates that ^{99m}TcO(MAG$_2$-3P-RGD$_2$) is integrin $\alpha_v\beta_3$-specific. The uptake blockage in the eyes, heart, intestine, lungs, liver, and spleen suggests that its accumulation in these organs is also integrin $\alpha_v\beta_3$-mediated. This conclusion is supported by the immunohistopathological studies (*34, 35*), which showed a strong positive staining of endothelial cells of small glomeruli vessels in the kidneys and weak staining in branches of the hepatic portal vein. The RGD-specificity of ^{99m}TcO(MAG$_2$-3P-RGD$_2$) is demonstrated by the lower integrin $\alpha_v\beta_3$ binding affinity of MAG$_2$-3P-RGK$_2$ (IC_{50} = 711 ± 128 nM) than that of MAG$_2$-3P-RGD$_2$ (IC_{50} = 3.9 ± 0.4 nM), and the lower tumor uptake of ^{99m}TcO(MAG$_2$-3P-RGK$_2$) than that of ^{99m}TcO(MAG$_2$-3P-RGD$_2$) (Figure 4B). In addition, ^{99m}TcO(MAG$_2$-3PEG$_4$-dimer) is able to maintain its chemical integrity during excretion from both renal and hepatobiliary routes, and in the tumor and liver tissues (Figure 6).

The ability to noninvasively quantify the integrin $\alpha_v\beta_3$ level provides new opportunities to select appropriate patients for antiangiogenic treatment of integrin $\alpha_v\beta_3$-positive cancer patients (*59, 60*). The %ID tumor uptake reflects the total integrin $\alpha_v\beta_3$ level, while the %ID/g tumor uptake reflects the integrin $\alpha_v\beta_3$ density. When tumor is small (<0.05 g or 50 m^3), there is little angiogenesis with low blood flow. As a result, ^{99m}TcO(MAG$_2$-3P-RGD$_2$) has low %ID tumor uptake (Figure 5A). As the tumor grows, the integrin $\alpha_v\beta_3$ level becomes higher, and the %ID tumor uptake of ^{99m}TcO(MAG$_2$-3P-RGD$_2$) increases (Figure 5A). The linear relationship between the tumor size and %ID tumor uptake strongly suggests that ^{99m}TcO-(MAG$_2$-3P-RGD$_2$) has the potential for monitoring the integrin $\alpha_v\beta_3$ expression levels during antiangiogenic therapy. It is important to note that the integrin $\alpha_v\beta_3$ expression is not homogeneous in the tumor tissue. Parts of the tumor tissue may become necrotic when its size is >10 mm in diameter. Therefore, the radiotracer %ID/g uptake values in tumors of different sizes are scattered as previously reported for ^{99m}Tc-3P-RGD$_2$ (*55*), ^{99m}Tc-3G-RGD$_2$ (*56*), and ^{64}Cu(DOTA-3P-RGD$_2$) (*57*).

We must be concerned that the subcutaneous glioma-bearing model used in this study may not reflect the real tumor growth rate in glioma cancer patients, since the tumor growth is too fast in the athymic nude mice bearing U87MG glioma xenografts. However, this tumor-bearing animal model as a screening tool should provide us with sufficient biodistribution data to select an optimal radiotracer for more preclinical evaluations in the future. In addition, we also noticed that the tumor growth rate is largely dependent on the number of U87MG human glioma cells implanted in each animal, and the radiotracer tumor uptake may vary significantly with the tumor growth rate. Whenever possible, the comparison between different radiotracers should be made by using their biodistribution data obtained from the same groups of tumor-bearing

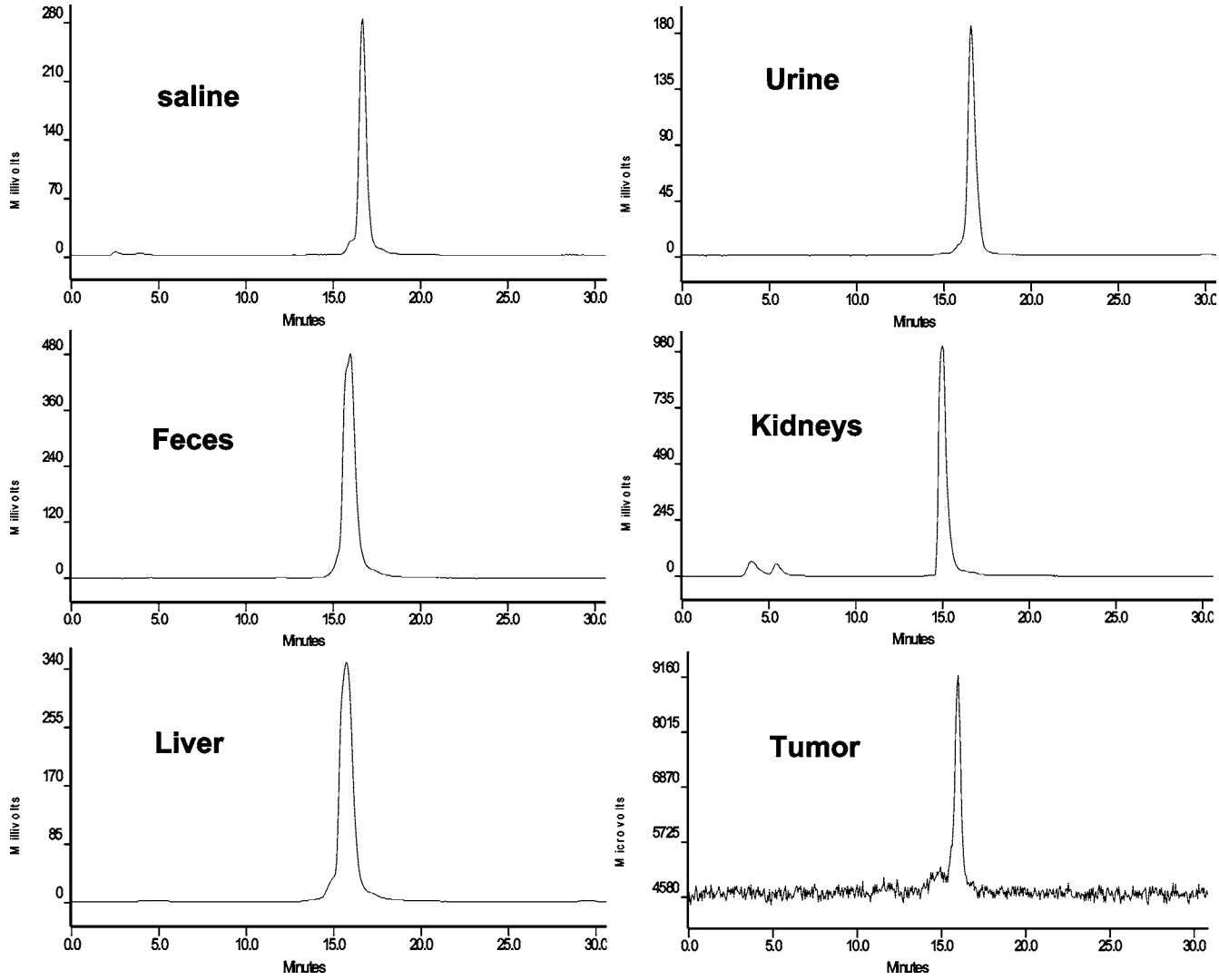

Figure 6. Typical radio-HPLC chromatograms of ^{99m}TcO(MAG$_2$-3P-RGD$_2$) in saline before injection, urine, feces, kidney, liver, and tumor at 120 min p.i. Slight variation in HPLC retention time was probably caused by the presence of 20% acetonitrile in the organ extract.

mice with similar tumor size. That is why in this study we obtained the 60 min biodistribution data of ^{99m}Tc-3PEG$_4$-dimer, instead of using those reported in our previous studies (*55*), to demonstrate the impact of ^{99m}Tc chelates (^{99m}TcO(MAG$_2$) vs [^{99m}Tc(HYNIC)(tricine)(TPPTS)]) on radiotracer tumor uptake and *T*/*B* ratios.

CONCLUSION

In this study, we presented the synthesis of two cyclic RGD peptide conjugates, MAG$_2$-P-RGD$_2$ and MAG$_2$-3P-RGD$_2$, and evaluated ^{99m}TcO(MAG$_2$-P-RGD$_2$) and ^{99m}TcO(MAG$_2$-3P-RGD$_2$) as new radiotracers for noninvasive imaging of integrin $\alpha_v\beta_3$ expression in athymic nude mice bearing U87MG glioma xenografts. The key findings are as follows: (1) MAG$_2$ is such an efficient BFC that ^{99m}TcO(MAG$_2$-3P-RGD$_2$) could be readily prepared in high yield with high specific activity using a single-vial kit formulation; (2) replacing [^{99m}Tc(HYNIC)(tricine)-(TPPTS)] with ^{99m}TcO(MAG$_2$) results in a significant increase in the radiotracer uptake in the tumor, blood, and normal organs due to the increased lipophilicity of ^{99m}TcO(MAG$_2$-3P-RGD$_2$). Even though ^{99m}TcO(MAG$_2$-3P-RGD$_2$) has the better tumor uptake, its tumor/blood, tumor/liver, tumor/lung, and tumor/liver ratios are not as good as those for ^{99m}Tc-3P-RGD$_2$. On the basis of these results, we believe that future research should be directed toward BFC with highly charged amino acid residues, such as aspartic and glutamic acids, instead of glycine in MAG$_2$.

ACKNOWLEDGMENT

This work is supported, in part, by Purdue University and research grants: R01 CA115883 A2 (S.L.) from National Cancer Institute (NCI), R21 HL083961-01 (S.L.) from the National Heart, Lung, and Blood Institute (NHLBI), and DE-FG02-08ER64684 (S.L.) from the Department of Energy, and NSF-30780728 (F.W.) from the National Science Foundation of China.

LITERATURE CITED

(1) Weber, W. A., Haubner, R., Vabuliene, E., Kuhnast, B., Webster, H. J., and Schwaiger, M. (2001) Tumor angiogenesis targeting using imaging agents. *Q. J. Nucl. Med. 45*, 179–182.

(2) Liu, S., and Edwards, D. S. (2002) Fundamentals of receptor-based diagnostic metalloradiopharmaceuticals. *Top. Curr. Chem. 222*, 259–278.

(3) Van de Wiele, C., Oltenfreiter, R., De Winter, O., Signore, A., Slegers, G., and Dieckx, R. A. (2002) Tumor angiogenesis pathways: related clinical issues and implications for nuclear medicine imaging. *Eur. J. Nucl. Med. 29*, 699–709.

(4) Liu, S., Robinson, S. P., and Edwards, D. S. (2003) Integrin $\alpha_v\beta_3$ directed radiopharmaceuticals for tumor imaging. *Drugs Future 28*, 551–564.
(5) Haubner, R., and Wester, H. J. (2004) Radiolabeled tracers for imaging of tumor angiogenesis and evaluation of antiantiogenic therapies. *Curr. Pharmaceut. Des. 10*, 1439–1455.
(6) D'Andrea, L. D., Del Gatto, A., Pedone, C., and Benedetti, E. (2006) Peptide-based molecules in angiogenesis. *Chem. Biol. Drug Des. 67*, 115–126.
(7) Meyer, A., Auremheimer, J., Modlinger, A., and Kessler, H. (2006) Targeting RGD recognizing integrins: drug development, biomaterial research, tumor imaging and targeting. *Curr. Pharmaceut. Des. 12*, 2723–2747.
(8) Chen, X. (2006) Multimodality imaging of tumor integrin $\alpha_v\beta_3$ expression. *Mini-Rev. Med. Chem. 6*, 227–234.
(9) Liu, S. (2006) Radiolabeled multimeric cyclic RGD peptides as integrin $\alpha_v\beta_3$-targeted radiotracers for tumor imaging. *Mol. Pharm. 3*, 472–487.
(10) Cai, W., and Chen, X. (2008) Multimodality molecular imaging of tumor angiogenesis. *J. Nucl. Med. 49*, 113S–128S.
(11) Cai, W., Niu, G., and Chen, X. (2008) Imaging of integrins as biomarkers for tumor angiogenesis. *Curr. Pharmaceut. Des. 14*, 2943–2973.
(12) Hsu, A., and Chen, X. (2008) Advances in anatomic, functional, and molecular imaging of angiogenesis. *J. Nucl. Med. 49*, 511–514.
(13) Van Hagen, P. M., Breeman, W. A. P., Bernard, H. F., Schaar, M., Mooij, C. M., Srinivasan, A., Schmidt, M. A., Krenning, E. P., and de Jong, M. (2000) Evaluation of a radiolabeled cyclic DTPA-RGD analog for tumor imaging and radionuclide therapy. *Int. J. Cancer (Radiat. Oncol. Invest.) 90*, 186–198.
(14) Huabner, R., Wester, H. J., Senekowitsch-Schmidtke, R., Diefenbach, B., Kessler, H., Stöcklin, G., and Schwaiger, M. (1997) RGD-peptides for tumor targeting: biological evaluation of radioiodinated analogs and introduction of a novel glycosylated peptide with improved biokinetics. *J. Labelled Compd. Radiopharm. 40*, 383–385.
(15) Sivolapenko, G. B., Skarlos, D., Pectasides, D., Stathopoulou, E., Milonakis, A., Sirmalis, G., Stuttle, A., Courtenay-Luck, N. S., Konstantinides, K., and Epenetos, A. A. (1998) Imaging of metastatic melanoma utilizing a technetium-^{99m} labeled RGD-containing synthetic peptide. *Eur. J. Nucl. Med. 25*, 1383–1389.
(16) Haubner, R., Wester, H. J., Weber, W. A., Mang, C., Ziegler, S. I., Goodman, S. L., Senekowisch-Schmidtke, R., Kessler, H., and Schwaiger, M. (2001) Noninvasive imaging of $\alpha_v\beta_3$ integrin expression using ^{18}F-labeled RGD-containing glycopeptide and positron emission tomography. *Cancer Res. 61*, 1781–1785.
(17) Haubner, R., Wester, H. J., Reuning, U., Senekowisch-Schmidtke, R., Diefenbach, B., Kessler, H., Stöcklin, G., and Schwaiger, M. (1999) Radiolabeled $\alpha_v\beta_3$ integrin antagonists: a new class of tracers for tumor imaging. *J. Nucl. Med. 40*, 1061–1071.
(18) Haubner, R., Wester, H. J., Burkhart, F., Senekowisch-Schmidtke, R., Weber, W., Goodman, S. L., Kessler, H., and Schwaiger, M. (2001) Glycolated RGD-containing peptides: tracer for tumor targeting and angiogenesis imaging with improved biokinetics. *J. Nucl. Med. 42*, 326–336.
(19) Haubner, R., Bruchertseifer, F., Bock, M., Schwaiger, M., and Wester, H. J. (2004) Synthesis and biological evaluation of ^{99m}Tc-labeled cyclic RGD peptide for imaging the $\alpha_v\beta_3$ expression. *Nuklearmedizin 43*, 26–32.
(20) Thumshirn, G., Hersel, U., Goodman, S. L., and Kessler, H. (2003) Multimeric cyclic RGD peptides as potential tools for tumor targeting: solid-phase peptide synthesis and chemoselective oxime ligation. *Chem. Eur. J. 9*, 2717–2725.
(21) Poethko, T., Schottelius, M., Thumshirn, G., Herz, M., Haubner, R., Henriksen, G., Kessler, H., Schwaiger, M., and Wester, H. J. (2004) Chemoselective pre-conjugate radiohalogenation of unprotected mono- and multimeric peptides via oxime formation. *Radiochim. Acta 92*, 317–327.
(22) Poethko, T., Schottelius, M., Thumshirn, G., Hersel, U., Herz, M., Henriksen, G., Kessler, H., Schwaiger, M., and Wester, H. J. (2004) Two-step methodology for high yield routine radiohalogenation of peptides: ^{18}F-labeled RGD and octreotide analogs. *J. Nucl. Med. 45*, 892–902.
(23) Alves, S., Correia, J. D. G., Gano, L., Rold, T. L., Prasanphanich, A., Haubner, R., Rupprich, M., Alberto, R., Decristoforo, C., Snatos, I., and Smith, C. J. (2007) In vitro and in vivo evaluation of a novel ^{99m}Tc(CO)$_3$-pyrazolyl conjugate of *cyclo*-(Arg-Gly-Asp-D-Tyr-Lys). *Bioconjugate Chem. 18*, 530–537.
(24) Fani, M., Psimadas, D., Zikos, C., Xanthopoulos, S., Loudos, G. K., Bouziotis, P., and Varvarigou, A. D. (2006) Comparative evaluation of linear and cyclic ^{99m}Tc-RGD peptides for targeting of integrins in tumor angiogenesis. *Anticancer Res. 26*, 431–434.
(25) Su, Z. F., Liu, G., Gupta, S., Zhu, Z., Rusckowski, M., and Hnatowich, D. J. (2002) In vitro and in vivo evaluation of a technetium-^{99m}-labeled cyclic RGD peptide as specific marker of $\alpha_v\beta_3$ integrin for tumor imaging. *Bioconjugate Chem. 13*, 561–570.
(26) Decristoforo, C., Faintuch-Linkowski, B., Rey, A., vo Guggenberg, E., Rupprich, M., Hernandez-Gonzales, I., Rodrigo, T., and Haubner, R. (2006) [^{99m}Tc]HYNIC-RGD for imaging integrin $\alpha_v\beta_3$ expression. *Nucl. Med. Biol. 33*, 945–952.
(27) Chen, X., Park, R., Tohme, M., Shahinian, A. H., Bading, J. R., and Conti, P. S. (2004) MicroPET and autoradiographic imaging of breast cancer α_v-integrin expression using ^{18}F- and ^{64}Cu-labeled RGD peptide. *Bioconjugate Chem. 15*, 41–49.
(28) Chen, X., Park, R., Shahinian, A. H., Tohme, M., Khankaldyyan, V., Bozorgzadeh, M. H., Bading, J. R., Moats, R., Laug, W. E., and Conti, P. S. (2004) ^{18}F-labeled RGD peptide: initial evaluation for imaging brain tumor angiogenesis. *Nucl. Med. Biol. 31*, 179–189.
(29) Chen, X., Park, R., Shahinian, A. H., Bading, J. R., and Conti, P. S. (2004) Pharmacokinetics and tumor retention of 125I-labeled RGD peptide are improved by PEGylation. *Nucl. Med. Biol. 31*, 11–19.
(30) Chen, X., Liu, S., Hou, Y., Tohme, M., Park, R., Bading, J. R., and Conti, P. S. (2004) MicroPET imaging of breast cancer α_v-integrin expression with ^{64}Cu-labeled dimeric RGD peptides. *Mol. Imaging Biol. 6*, 350–359.
(31) Chen, X., Tohme, M., Park, R., Hou, Y., Bading, J. R., and Conti, P. S. (2004) MicroPET imaging of breast cancer α_v-integrin expression with ^{18}F-labeled dimeric RGD peptide. *Mol. Imaging 3*, 96–104.
(32) Wu, Y., Zhang, X., Xiong, Z., Cheng, Z., Fisher, D. R., Liu, S., Gambhir, S. S., and Chen, X. (2005) MicroPET imaging of glioma integrin $\alpha_v\beta_3$ expression using ^{64}Cu-labeled tetrameric RGD peptide. *J. Nucl. Med. 46*, 1707–1718.
(33) Zhang, X., Xiong, Z., Wu, Y., Cai, W., Tseng, J. R., Gambhir, S. S., and Chen, X. (2006) Quantitative PET imaging of tumor integrin $\alpha_v\beta_3$ expression with ^{18}F-FRGD2. *J. Nucl. Med. 47*, 113–121.
(34) Wu, Z., Li, Z., Chen, K., Cai, W., He, L., Chin, F. T., Li, F., and Chen, X. (2007) Micro-PET of tumor integrin $\alpha_v\beta_3$ expression using ^{18}F-labeled PEGylated tetrameric RGD peptide (^{18}F-FPRGD4). *J. Nucl. Med. 48*, 1536–1544.
(35) Zhang, X., and Chen, X. (2007) Preparation and characterization of ^{99m}Tc(CO)$_3$-BPy-RGD complex as $\alpha_v\beta_3$ integrin receptor-targeted imaging agent. *Appl. Radiat. Isot. 65*, 70–78.
(36) Li, Z. B., Chen, K., and Chen, X. (2008) ^{68}Ga-labeled multimeric RGD peptides for microPET imaging of integrin $\alpha_v\beta_3$ expression. *Eur. J. Nucl. Med. Mol. Imaging 35*, 1100–1108.
(37) Liu, S., Cheung, E., Rajopadyhe, M., Ziegler, M. C., and Edwards, D. S. (2001) ^{90}Y- and ^{177}Lu-labeling of a DOTA-conjugated vitronectin receptor antagonist for tumor therapy. *Bioconjugate Chem. 12*, 559–568.
(38) Janssen, M., Oyen, W. J. G., Massuger, L. F. A. G., Frielink, C., Dijkgraaf, I., Edwards, D. S., Rajopadyhe, M., Corsten, F. H. M., and Boerman, O. C. (2002) Comparison of a monomeric and dimeric radiolabeled RGD-peptide for tumor targeting. *Cancer Biother. Radiopharm. 17*, 641–646.
(39) Janssen, M., Oyen, W. J. G., Dijkgraaf, I., Massuger, L. F. A. G., Frielink, C., Edwards, D. S., Rajopadyhe, M.,

Boonstra, H., Corsten, F. H. M., and Boerman, O. C. (2002) Tumor targeting with radiolabeled integrin $\alpha_v\beta_3$ binding peptides in a nude mice model. *Cancer Res. 62*, 6146–6151.

(40) Janssen, M. L., Frielink, C., Dijkgraaf, I., Oyen, W. J., Edwards, D. S., Liu, S., Rajopadhye, M., Massuger, L. F., Corstens, F. H. M., and Boerman, O. C. (2004) Improved tumor targeting of radiolabeled RGD-peptides using rapid dose fractionation. *Cancer Biother. Radiopharm. 19*, 399–404.

(41) Liu, S., Hsieh, W. Y., Kim, Y. S., and Mohammed, S. I. (2005) Effect of coligands on biodistribution characteristics of ternary ligand ^{99m}Tc complexes of a HYNIC-conjugated cyclic RGDfK dimer. *Bioconjugate Chem. 16*, 1580–1588.

(42) Jia, B., Shi, J., Yang, Z., Xu, B., Liu, Z., Zhao, H., Liu, S., and Wang, F. (2006) ^{99m}Tc-labeled cyclic RGDfK dimer: initial evaluation for SPECT imaging of glioma integrin $\alpha_v\beta_3$ expression. *Bioconjugate Chem. 17*, 1069–1076.

(43) Liu, S., He, Z. J., Hsieh, W. Y., Kim, Y. S., and Jiang, Y. (2006) Impact of PKM linkers on biodistribution characteristics of the ^{99m}Tc-labeled cyclic RGDfK dimer. *Bioconjugate Chem. 17*, 1499–1507.

(44) Liu, S., Hsieh, W. Y., Jiang, Y., Kim, Y. S., Sreerama, S. G., Chen, X., Jia, B., and Wang, F. (2007) Evaluation of a ^{99m}Tc-labeled cyclic RGD tetramer for noninvasive imaging integrin $\alpha_v\beta_3$-positive breast cancer. *Bioconjugate Chem. 18*, 438–446.

(45) Dijkgraaf, I., Liu, S., Kruijtzer, J. A. W., Soede, A. C., Oyen, W. J. G., Liskamp, R. M. J., Corstens, F. H. M., and Boerman, O. C. (2007) Effects of linker variation on the in vitro and in vivo characteristics of an 111 In-labeled RGD peptide. *Nucl. Med. Biol. 34*, 29–35.

(46) Dijkgraaf, I., John, A. W., Kruijtzer, J. A. W., Liu, S., Soede, A., Oyen, W. J. G., Corstens, F. H. M., Liskamp, R. M. J., and Boerman, O. C. (2007) Improved targeting of the $\alpha_v\beta_3$ integrin by multimerization of RGD peptides. *Eur. J. Nucl. Med. Mol. Imaging 34*, 267–273.

(47) Liu, S., Kim, Y. S., Hsieh, W. Y., and Sreerama, S. G. (2008) Coligand effects on solution stability, biodistribution and metabolism of ^{99m}Tc-labeled cyclic RGDfK tetramer. *Nucl. Med. Biol. 35*, 111–121.

(48) Jia, B., Liu, Z., Shi, J., Yu, Z. L., Yang, Z., Zhao, H. Y., He, Z. J., Liu, S., and Wang, F. (2008) Linker effects on biological properties of 111 In-labeled DTPA conjugates of a cyclic RGDfK dimer. *Bioconjugate Chem. 19*, 201–210.

(49) Wang, J. J., Kim, Y. S., and Liu, S. (2008) ^{99m}Tc-labeling of HYNIC-conjugated cyclic RGDfK dimer and tetramer using EDDA as coligand. *Bioconjugate Chem. 19*, 634–642.

(50) Morrison, M. S., Ricketts, S. A., Barnett, J., Cuthbertson, A., Jean Tessier, J., and Wedge, S. R. (2009) Use of a novel Arg-Gly-Asp radioligand, ^{18}F-AH111585, to determine changes in tumor vascularity after antitumor therapy. *J. Nucl. Med. 50*, 116–122.

(51) Kenny, L. M., Coombes, R. C., Oulie, I., Contractor, K. B., Miller, M., Spinks, T. J., McParland, B., Cohen, P. S., Hui, A., Palmieri, C., Osman, S., Glaser, M., Turton, D., Al-Nahhas, A., and Anoagye, E. O. (2008) Phase I trial of the positron-emitting Arg-Gly-Asp (RGD) peptide radioligand ^{18}F-AH111585 in breast cancer patients. *J. Nucl. Med. 49*, 879–886.

(52) Beer, A. J., Haubner, R., Goebel, M., Luderschmidt, S., Spilker, M. E., Webster, H. J., Weber, W. A., and Schwaiger, M. (2005) Biodistribution and pharmacokinetics of the $\alpha_v\beta_3$-selective tracer ^{18}F-Galacto-RGD in cancer patients. *J. Nucl. Med. 46*, 1333–1341.

(53) Haubner, R., Weber, W. A., Beer, A. J., Vabulience, E., Reim, D., Sarbia, M., Becker, K. F., Goebel, M., Hein, R., Wester, H. J., Kessler, H., and Schwaiger, M. (2005) Noninvasive visualization of the activiated $\alpha_v\beta_3$ integrin in cancer patients by positron emission tomography and [^{18}F]Galacto-RGD. *PLOS Med. 2: e70*, 244–252.

(54) Beer, A. J., Grosu, A. L., Carlsen, J., Kolk, A., Sarbia, M., Stangier, I., Watzlowik, P., Wester, H. J., Haubner, R., and Schwaiger, M. (2007) [^{18}F]Galacto-RGD positron emission tomography for imaging of $\alpha_v\beta_3$ expression on the neovasculature in patients with squamous cell carcinoma of the head and neck. *Clin. Cancer Res. 13*, 6610–6616.

(55) Wang, L., Kim, Y. S., Shi, J., Zhai, S., Jia, B., Liu, Z., Zhao, H., Wang, F., Chen, X., and Liu, S. (2009) Improving tumor targeting capability and pharmacokinetics of ^{99m}Tc-labeled cyclic RGD dimers with PEG_4 linkers. *Mol. Pharm. 6*, 231–245.

(56) Shi, J., Wang, L., Kim, Y. S., Zhai, S., Liu, Z., Chen, X., and Liu, S. (2008) Improving tumor uptake and excretion kinetics of ^{99m}Tc-labeled cyclic Arginine-Glycine-Aspartic (RGD) dimers with triglycine linkers. *J. Med. Chem. 51*, 7980–7990.

(57) Shi, J., Wang, L., Kim, Y. S., Zhai, S., Liu, Z., Chen, X., Liu, S. Improving tumor uptake and pharmacokinetics of ^{64}Cu-labeled cyclic RGD dimers with triglycine and PEG_4 Linkers. *Bioconjugate Chem.* Accepted.

(58) Liu, S., Edwards, D. S., Looby, R. J., Harris, A. R., Poirier, M. J., Rajopadhye, M., Bourque, J. P., and Carroll, T. R. (1996) Labeling cyclic glycoprotein IIb/IIIa receptor antagonists with ^{99m}Tc by the preformed chelate approach: Effects of chelators on properties of ^{99m}Tc-chelator-peptide conjugates. *Bioconjugate Chem. 7*, 196–202.

(59) Cai, W., Rao, J., Gambhir, S. S., and Chen, X. (2006) How molecular imaging is speeding up antiangiogenic drug development? *Mol. Cancer Ther. 5*, 2624–2633.

(60) Niu, G., and Chen, X. (2008) Has molecular and cellular imaging enhanced drug discovery and drug development? *Drugs R&D 9*, 351–368.

BC9001739

Epidermal Growth Factor Tethered through Coiled-Coil Interactions Induces Cell Surface Receptor Phosphorylation

Cyril Boucher,[†,‡] Benoît Liberelle,[†] Mario Jolicoeur,[†] Yves Durocher,[‡] and Gregory De Crescenzo*[,†]

Department of Chemical Engineering, Groupe de Recherche en Sciences et Technologie Biomédicales (GRSTB), Bio-P^2 Research Unit, École Polytechnique de Montréal, P.O. Box 6079, succ. Centre-Ville, Montréal (Qc), Canada H3C 3A7, and Animal Cell Technology Group, Bioprocess Sector, Biotechnology Research Institute, National Research Council Canada, Montréal (Qc), Canada H4P 2R2. Received March 13, 2009; Revised Manuscript Received June 1, 2009

We have elaborated and validated a novel approach for the oriented tethering of proteins such as the epidermal growth factor (EGF) on aminated surfaces. The grafting reactions were optimized to generate a dense and homogeneous EGF layer. Impact of EGF orientation on A-431 cellular response was investigated. Our results demonstrate that, in sharp contrast to responses obtained with soluble EGF supply or with randomly grafted EGF, oriented immobilization of EGF via a de novo designed coiled-coil capture system leads to a sustained phosphorylation of A-431 cell surface EGF receptors. Our results thus indicate that oriented protein immobilization via coiled-coil interactions is an efficient and versatile method to control tethering of bioactive molecules for future applications in the field of regenerative medicine and tissue engineering.

INTRODUCTION

The development of new materials with potential to serve as two- and three-dimensional scaffolds for tissue engineering and regenerative medicine purposes has undergone rapid expansion (*1*). Advances in surface chemistry, much of it propelled by plasma-based polymer modification (*2, 3*) and chemical modification methodologies (*3, 4*) have opened interesting avenues for controlling protein binding as well as cell adhesion and differentiation (*5*). Another level of tailoring may also be added to this new class of materials by tethering specific macromolecules including peptides (*6*) or proteins (*7*) in order to synergistically enhance material intrinsic properties.

In that endeavor, immobilization of the epidermal growth factor (EGF) has already been reported (*7*−*14*). EGF is known to promote the oligomerization and activation of EGF receptors (EGFR) present at the cell surface (*15*), which ultimately leads in a broad spectrum of phenotypic responses such as the proliferation and differentiation of many cell types, including epithelial and mesenchymal cells. The role of soluble EGF in neovascularization and chemotaxis in the wound healing processes has also been documented (*16*). Recently, EGF has also been proposed as a promising candidate for ex vivo expansion of mesenchymal stem cells as well as neuronal stem cells, two attractive cell sources for tissue engineering applications (*12, 17*). Of interest, EGF immobilization has been demonstrated to enhance the EGF mitogenic effect on CHO cells when compared to its soluble form (*18*). On the same note, tethered EGF gradient surfaces were also shown to induce accelerated and polarized migration of keratinocytes, a key issue in the wound closure mechanism (*14*).

The most frequently used method for tethering human or murine EGF on solid supports relies on covalent immobilization through the reactive amine groups present at the EGF N-terminus or on its lysine side chain (at positions 28 and 48 for human EGF; no lysine in murine EGF) or by photoimmobilization. Although unambiguous effects on cell growth and phenotype have been reported with these approaches, it is likely that these immobilization methods are not efficiently transposable to growth factors harboring multiple lysine residues. That is, random amine coupling may not be optimal, since it may negatively impact protein internal conformation, relative molecular orientation, and spatial homogeneity, leading to diminished or even totally abrogated bioactivity (*7*). These concerns have led to the development of alternative strategies for oriented tethering of proteins on various substrates (*11, 19*). For EGF, most of them rely on the design of an EGF fusion protein comprising the Fc region of immunoglobulin G (IgG) or a His tag for their capture onto solid supports that have been previously functionalized with protein A/G or nitrilotriacetate (NTA), respectively (*11, 17*). The use of a hydrophobic tag has also been reported for EGF immobilization on hydrophobic supports (*8*).

In a previous study (*20*), we highlighted the potential of a new capture system based on de novo designed peptides, i.e., the E and K coils (*21, 22*). These two distinct and unstructured 35 amino acid peptides form a stable heterodimeric E/K coiled-coil complex upon binding (*22*). This coiled-coil system was demonstrated to be efficient for the stable and oriented capture of coil tagged proteins (*22*), including fully bioactive N-terminally coil-tagged EGF that had been produced in mammalian cells (*20*) or in bacteria (*23*).

The aim of this work was to further investigate the extent to which coiled-coil oriented immobilization of EGF would promote EGFR activation and, in turn, modulate cell response. Silicon surfaces with native oxide overlayer (Si/SiO_2) harboring primary amines through 3-aminopropyltriethoxysilane (APTES) functionalization were used to characterize and optimize the oriented covalent immobilization of Kcoil peptides and the subsequent capture of Ecoil-tagged EGF proteins (Ecoil-EGF). Dry thickness and water contact angle measurements were achieved to evaluate the amount of end-grafted molecules and the macroscopic homogeneity of the grafted layer, respectively. The optimized experimental conditions were then applied to cell culture-compatible amino-coated glass surfaces. Our study was

* To whom correspondence should be addressed. E-mail: gregory.decrescenzo@polymtl.ca; Tel: (514) 340-4711 (#7428); Fax: (514) 340-2990.

[†] École Polytechnique de Montréal.

[‡] National Research Council Canada.

10.1021/bc9001147 CCC: $40.75 © 2009 American Chemical Society
Published on Web 07/09/2009

then complemented by culturing A-431 cells on these Ecoil-EGF derivatized surfaces. This cell line was selected as a model system since A-431 response to EGF is well-documented. Our in vitro cellular assays demonstrated that oriented EGF immobilization leads to a strong and sustained EGFR autophosphorylation as compared to that observed with randomly immobilized or soluble EGF. Altogether, our results demonstrated that the E/K coiled-coil system is an interesting alternative for the oriented immobilization of EGF, and by extension, of any growth factor, for future applications in the fields of tissue engineering and regenerative medicine.

MATERIALS AND METHODS

Chemicals and Reagents. Native silicon wafers (Prime Si P/Boron) were obtained from University Wafer (South Boston, MA), and amino-coated glass slides (10×10 mm^2) were from Erie Scientific Co. (Portsmouth, NH). Anhydrous 3-aminopropyltriethoxysilane (APTES, 99% purity), ethylenediamine, cysteine (99+% purity), glutaric anhydride (95% purity), and sodium chloride (99.99% purity) were purchased from Sigma-Aldrich Canada Ltd. (Oakville, ON). Succinimidyl 6-[30-(2-pyridyldithio)-propionamido]hexanoate (LC-SPDP, 95+% purity) was obtained from Pierce Biotechnology, Inc. (Rockford, IL). Hydrogen peroxide (30% v/v), chlorhydric acid (37% v/v), chloroform (99.8% purity), sulfuric acid (98% purity), dimethylsulfoxide (DMSO, 99+% purity), and toluene (99.5% purity) were purchased from VWR International Inc. (Mont-Royal, Qc). All solvents were distilled under strict anhydrous conditions prior to use. Milli-Q quality water (18.2 MΩ.cm; total organic compounds (TOC) = 4 ppb) was generated with a Millipore Gradient A 10 purification system. Cysteine-tagged Kcoil peptides were synthesized as previously described (*22*). Untagged human EGF was purchased from R&D Systems (Minneapolis, MN). All the surface plasmon resonance (SPR) experiments were performed using a Biacore 3000 instrument (GE Healthcare, Baie d'Urfe, Qc). CM4 sensor chips and the amine coupling kit containing *N*-hydroxysuccinimide (NHS), ethyl-*N*′-(3-dimethylaminopropyl) carbodiimide hydrochloride (EDC), and ethanolamine were also purchased from GE Healthcare.

Cell Culture. A human embryonic kidney (HEK) 293 cell line stably expressing EBNA1 (293−6E) was maintained in shake flasks (110 rpm) in F17 medium (Invitrogen, Burlington, ON) supplemented with glutamine (4 mM), Geneticin (25 μg/mL) and pluronic acid (0.1%) in a humidified incubator at 37 °C with 5% CO_2. The A-431 cells were maintained in 175 cm^2 flasks in Dulbecco's modified Eagle's medium (GIBCO/BRL, Burlington, ON) supplemented with 10% fetal bovine serum (Invitrogen, Burlington, ON) in 5% CO_2 incubator until 85−90% confluence.

E/Kcoil-EGF Production. As previously described (*20*), Ecoil and Kcoil-EGF were produced in HEK 293-6E cells and purified by immobilized metal ion affinity chromatography (IMAC). Protein concentration was determined by the Bradford method and analyzed by SDS-PAGE. Purified Ecoil-EGF was then stored at −80 °C until use. Note that the bioactivity of Ecoil-EGF was assayed in solution as described in (*20*) and was found to be equal to that of untagged EGF.

Surface Preparation. All glassware was carefully cleaned by overnight immersion in a bath of KOH-saturated isopropyl alcohol followed by intensive rinsing with Milli-Q water. Glassware was dried in a clean oven at 120 °C under atmospheric pressure. Prior to layer grafting, silicon and amino-coated glass surfaces were washed to remove any adsorbed organic compounds. The silicon surfaces (10×10 mm^2) were cleaned according to the Piranha procedure, i.e., the surfaces were immersed in a 3:1 mixture of sulfuric acid and hydrogen peroxide for 10 min at 100 °C. After intensive rinsing with Milli-Q water, the surfaces were dried in air at room temperature and then introduced in a dried Schlenk. To ensure anhydrous conditions, two cycles of vacuum/dry argon were performed in the Schlenk. The amino-coated glass surfaces (10×10 mm^2) were cleaned in an ultrasonic bath for 1 min in distilled chloroform and then dried in air at room temperature.

Grafting Procedures. *APTES Grafting on Silicon Surfaces.* APTES layers were generated on silicon surfaces using a silanization procedure as previously reported (*24*). Briefly, APTES was first dissolved in anhydrous toluene at a concentration of 10 mM. The solution was injected through a 0.2 μm PTFE filter in dry Schlenk tubes, each containing one silicon surface. After a reaction time of 3 h at room temperature, the surfaces were taken out from the Schlenk tubes, dried in air for 1 min, and placed in an oven at 120 °C for 1.5 h. Then, the surfaces were rinsed by soaking them in freshly distilled toluene for 5 min.

Kcoil Peptides Grafting on APTES-Coated Silicon and Glass Surfaces. Kcoil peptides were immobilized onto APTES-coated surfaces via LC-SPDP linker (*9*). The surfaces were covered with 150 μL of 2 mM LC-SPDP in 100 mM phosphate buffer (10% DMSO) for 2 h at room temperature. The surfaces were rinsed by soaking them in Milli-Q water for 5 min. Then, the thiol-reactive surfaces were covered with 150 μL of 10 μM cysteine-tagged Kcoil peptides (5 heptad repeats (*22*)) in 10 mM phosphate buffer for 2 h at room temperature. The surfaces were finally rinsed by soaking them in 10 mM phosphate buffer (pH 7.4) and in Milli-Q water. Unreacted LC-SPDP sites were blocked using 150 μL of 50 mM cysteine solution (1 M NaCl in 0.1 M sodium acetate, pH 4.0) followed by rinsing with Milli-Q water.

Ecoil-EGF Grafting and Degrafting. To immobilize the Ecoil-EGF on covalently attached Kcoil peptides, the Kcoil-grafted surfaces were covered with 150 μL of 600 nM Ecoil-EGF for 2 h at room temperature. The surfaces were finally rinsed by soaking them in 10 mM phosphate buffer (pH 7.4) and Milli-Q water for 5 min. The detachment of the coil-tagged EGF from the surface was performed by soaking the surfaces in a 5 M guanidium hydrochloride solution, followed by rinses in 10 mM phosphate buffer (pH 7.4) and Milli-Q water for 5 min each.

Nonoriented EGF Grafting. Untagged EGF was covalently grafted onto APTES-coated surfaces using disuccinimide glutarate (DSG) as linker. A glutaric acid solution was prepared by dissolving glutaric anhydride in 10 mM phosphate buffer (pH 7.4) to reach a final concentration of 0.1 mM. Reactive DSG molecules were obtained by mixing 200 μL of 200 mM EDC and 200 μL of 50 mM NHS in 2 mL of the glutaric acid solution. 150 μL of the freshly prepared reactive DSG solution was then deposited on the APTES-coated surfaces for 45 min at room temperature. The surfaces were rinsed in Milli-Q water for 5 min, dried in air, and reacted with 150 μL of 600 nM untagged EGF in Milli-Q water (pH 5.5) for 2 h at room temperature.

SPR Assays. SPR experiments were conducted at 25 °C using HBS-T (10 mM HEPES pH 7.4, 150 mM NaCl, 3.4 mM EDTA, 0.05% Tween 20) as running buffer.

Kcoil Immobilization on Sensorchip. All the steps of the immobilization procedure were carried out at a flow rate of 5 μL/min. The carboxylic groups of CM4 sensorchips were activated by the injection of 50 μL of a mixture containing 0.05 M NHS and 0.2 M EDC. The NHS ester groups were reacted with 50 μL of 1 M ethylenediamine to introduce amino groups on the sensorchip surface (thus mimicking amino-coated glass surfaces). Remaining reactive NHS ester groups were blocked by injecting ethanolamine (50 μL of 1 M ethanolamine). The amino groups were reacted with LC-SPDP (50 μL of 2 mM in

100 mM phosphate buffer, 10% DMSO) to end-graft cysteine-tagged Kcoil (30 μL of 10 μM Kcoil in 100 mM phosphate buffer). Finally, freshly prepared cysteine solution (150 μL of 50 mM cysteine in 0.1 M sodium acetate, 1 M NaCl, pH 4.0) was injected to block any unreacted LC-SPDP sites.

E/Kcoil-EGF Immobilization. Ecoil-EGF proteins were injected 3 times at 10 nM, 100 nM, and 500 nM for 2 min at a flow rate of 10 μL/min. Regeneration of the sensorchip (i.e., removal of Ecoil-EGF) was accomplished by 2 pulses of guanidium hydrochloride (50 μL, 100 μL/min, 5 M). Finally, 100 nM Kcoil-EGF was injected for 2 min at 10 μL/min (control).

Contact Angle Measurements. Contact angle measurements were performed using a FTA200 Dynamic Contact Angle Analyzer (First Ten Angstrom Inc., Portsmouth, VA). All measurements were carried out in equilibrium static mode using Milli-Q quality water as the probe liquid. Equilibrium contact angles θ correspond to the mean values of measurements performed at three different locations on at least two different surfaces. Data analysis was performed using the FTA32 Video software.

Ellipsometric Measurements. Thickness measurements on silicon surfaces were performed with an automatic M2000 ellipsometer (J.A. Woollam Co. Inc., Lincoln, NE). Data were acquired in the wavelength range 245−1650 nm. All measurements were carried out at an angle of incidence of 75°, with air as the ambient medium, at room temperature, and at a normal relative humidity (ca. 50%). The assumed refractive index of the grafted films was $n = 1.465$ (*25*). Effective thickness was computed as the difference between the thickness of modified and unmodified surface. Three measurements were taken on each surface and repeated for at least two samples to obtain average values.

Immobilized EGF Quantification. MicroBCA protein assay kit (Pierce Biotechnology Inc., Rockford, IL) was used to determine the EGF surface density by comparing the EGF concentration in the solution before and after immobilization. The microBCA reaction mixture (50 μL) was added to protein solution (50 μL) in a 96-well plate. Absorbance was measured using a Victor v3 spectrophotometer (562 nm, Perkin-Elmer, Woodbridge, ON) after a 2 h incubation at 37 °C. Bovine serum albumin was used as standard.

Stimulation of A-431 Cells. EGF is known to induce a rapid tyrosine phosphorylation of EGF receptor present at the A-431 cell surface (*26*). To test physiological activity of immobilized EGF, 5 h before experiment, A-431 cells were washed with DMEM medium without serum. Cells were then trypsinized for 5 min at 37 °C, washed by centrifugation, and resuspended in DMEM. A-431 cells were distributed in 24-well plates containing one glass surface at 0.3×10^6 cells/mL, 1 mL/well, and kept at 37 °C in a 5% CO_2 incubator. Five hours after inoculation, Ecoil-EGF was added at 4 nM in the wells corresponding to unmodified glass surfaces (control). This soluble Ecoil-EGF concentration was selected since we previously demonstrated that the EC_{50} related to the phosphorylation of A-431 cell surface EGFR by soluble untagged and Ecoil-tagged EGF was close to 4 nM (*20*).

Adhesion Assays. Medium was removed 5 h after inoculation and immobilized cells were washed 3 times with DMEM (serum-free). Cells were observed using inverted microscope Axiovert S100TV (Carl Zeiss Canada, North York, ON). Images were processed with a QICAM Fast 1394 camera (QImaging), and cell count was operated using Northern Eclipse image acquisition software (Empix imaging).

Phosphorylation Assays by Western Blot. DMEM medium was removed and A-431 cells were washed three times with PBS supplemented with sodium-orthovanadate (1 mM, Sigma) and extracted with lysis buffer (50 mM HEPES pH 7.4), 150 mM NaCl, 1% Thesit, 0.5% Na Deoxycholate, Complete protease inhibitor cocktails (Roche, Laval, QC)) supplemented with 0.1 mM Na_3VO_4, 20 mM β-glycerophosphate, 10 mM $Na_4P_2O_7 \cdot 10H_2O$ and 0.5 μM microcystin) 5 min, 2 h, 3 h, and 4 h after inoculation for wells corresponding to unmodified glass surfaces and 2 h, 3 h, 4 h, and 5 h for wells corresponding to EGF-functionalized surfaces. Insoluble material was removed by centrifugation at $10\,000 \times g$ for 5 min at 4 °C. Western blotting experiments were then performed as previously described (*20*). Briefly, samples were mixed with 4× NuPAGE sample buffer (Invitrogen) containing 50 mM DTT and heated to 70 °C for 10 min. Electrophoresis was performed at 200 V and proteins transferred to nitrocellulose membranes (Schleicher & Schuell) for 1 h at 300 mA. Membranes were incubated in blocking reagent (Roche Diagnostics, Indianapolis, IN), and then probed with phosphotyrosine (PY99) (Santacruz, CA) for 1 h. Detection was performed using BM Chemiluminescence Blotting Substrate (Roche Diagnostics) with a Kodak Digital Science Image Station 440cf equipped with Kodak Digital Science 1D image analysis software version 3.0 (Eastman Kodak, NY).

Statistical Analysis. Values are given as mean value ± standard deviation. Statistical analysis was performed by independent two-sample *t* test with equal variances. Values of $P < 0.05$ and $P < 0.001$ was considered to be statistically significant and are identified by * and **, respectively.

RESULTS

Immobilization of EGF on Surfaces. Silicon substrates with native oxide overlayer (Si/SiO_2), whose surface chemistry is comparable to that of glass, were used to optimize the grafting reactions since high optical contrast at the Si/SiO_2 interface improved the sensitivity of ellipsometric thickness and contact angle measurements. Once optimized on silicon wafers, the experimental conditions for the grafting reactions were then applied to commercially available amino-coated glass surfaces.

Our oriented EGF immobilization strategy consisted of end-grafting cysteine-tagged Kcoil peptides on APTES-coated surfaces using a LC-SPDP linker (Figure 1). Ecoil-EGF proteins were then captured to the Kcoil-modified surface via reversible coiled-coil interaction (*20*).

The APTES, LC-SPDP, and Kcoil layers that were successively grafted on silicon surfaces were each characterized using ellipsometric and contact angle measurements as reported in Figure 2. APTES was self-assembled in solution under strict anhydrous conditions to avoid cross-polymerization of the ethoxysilane groups that might have led to surface heterogeneities and multilayer formation. APTES-deposited layers were heated to promote condensation reactions with the surface and cross-linking of monolayer film. Grafted APTES layers appeared thin and homogeneous with an ellipsometric thickness of 0.9 ± 0.1 nm and a water contact angle of 50 ± 2° (Figure 2, condition a). The bifunctional LC-SPDP linker was then grafted onto the surface via a chemical reaction between its amine-reactive *N*-hydroxysuccinimide ester and the free amino groups of APTES to form a stable amide bond. The resulting films displayed a thickness of 1.2 ± 0.1 nm and a water contact angle of 61 ± 1° (Figure 2, condition b). The other extremity of the LC-SPDP linking agent was terminated in a pyridyl disulfide group that was reacted with thiol groups of cysteine-tagged Kcoil peptides to form a disulfide bond. In order to maximize the Kcoil grafting density, the influence of the pH of the reaction (from 3.0 to 8.5) was studied (Figure 2, conditions c−g). Maximal dry thickness and contact angle values were obtained for Kcoil peptides reacted at pH 7.4 (Figure 2). Of interest, when the same reaction was performed in the absence of LC-SPDP linker, a minor variation of the surface characteristics was observed when

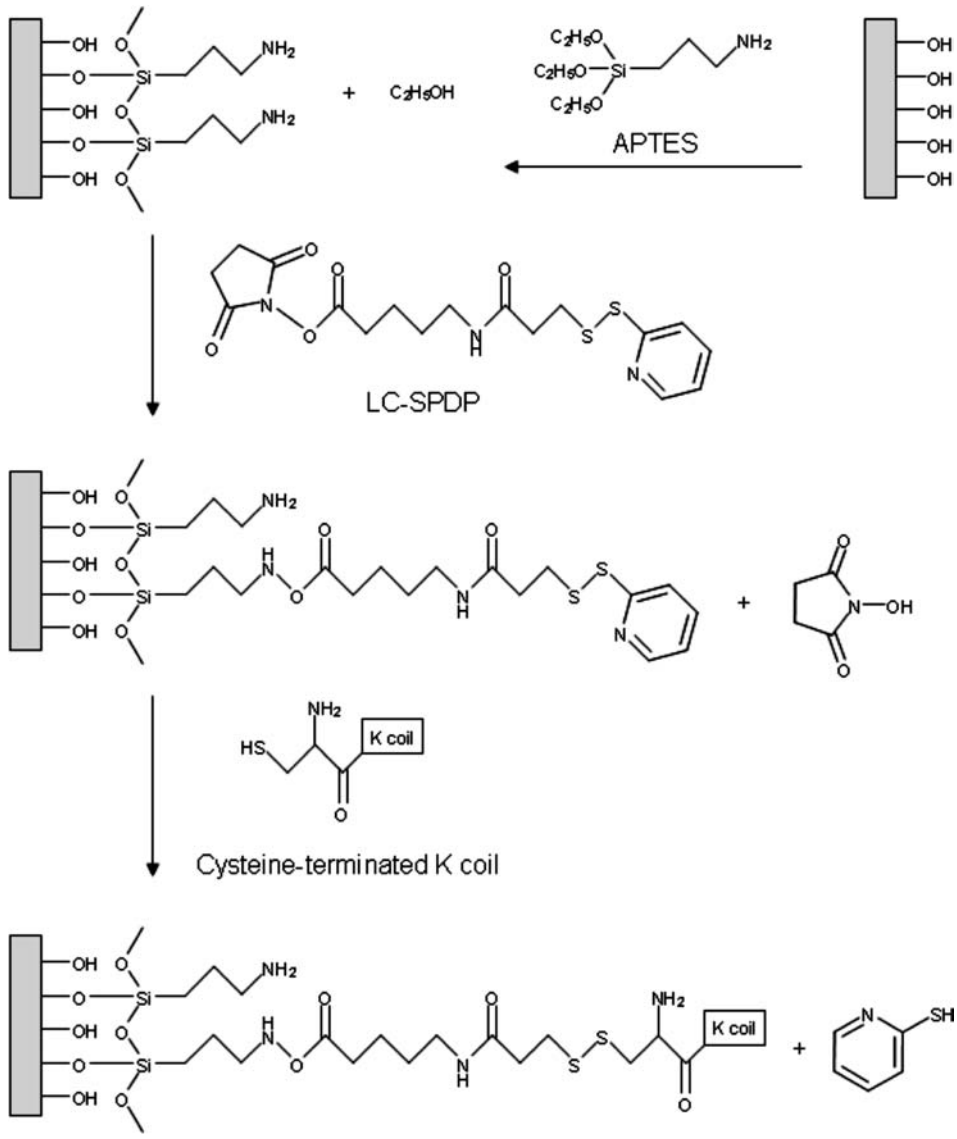

Figure 1. Schematic illustration of the chemical grafting procedure. End-grafting of APTES on silicon surfaces was followed by chemical immobilization of cysteine-tagged Kcoil peptides on APTES-coated surfaces using LC-SPDP as linker.

compared to the APTES layer (+0.1 nm and +1° for dry thickness and contact angle measurements, respectively, Figure 2; compare conditions a and h). This strongly suggested that nonspecific adsorption of Kcoil peptides on the surface was negligible.

After Kcoil grafting, cysteine was used to block the unreacted pyridyl disulfide group of LC-SPDP in order to prevent the attachment of undesired molecules containing thiol groups. No significant changes in the thickness and the water contact angle were observed after cysteine-mediated LC-SPDP deactivation (Figure 2, compare conditions b and f with Figure 3, conditions e and a, respectively). Kcoil-functionalized surfaces were shown to be able to recruit Ecoil-EGF (Figure 3). The resulting film was characterized by a net thickness increase of 0.8 nm and a water contact angle of 61°. The reversibility of the E−K coiled-coil interaction was demonstrated by washing bound Ecoil-EGF with 5 M guanidium hydrochloride. This lead to total thickness and contact angle measurements varying from 3.7 nm and 61° to 3.2 nm and 68°, respectively (Figure 3, conditions b and c). The high specificity of Ecoil-EGF binding to Kcoil surfaces was also demonstrated, since Kcoil-EGF addition onto Kcoil-functionalized surfaces did not lead to any thickness or contact angle variations (Figure 3, condition d). Finally, cysteine-tagged Kcoil or Ecoil-EGF were incubated on LC-SPDP layers previously blocked by cysteine molecules, as reported in Figure 3 (conditions f and g). In both cases, thickness and contact angle values were similar to those measured prior each incubation (Figure 3, condition e), once again demonstrating that nonspecific adsorption was negligible.

The efficiency of the grafting procedure was also evaluated by using a surface plasmon resonance instrument (Figure 4). In order to further demonstrate the adequacy of our chemical strategy, carboxymethylated dextran sensorchip surfaces (CM4) were first chemically modified to present amine groups at their surface (hence mimicking amine groups present on our glass surfaces). Cysteine-tagged Kcoil was covalently immobilized (950 arbitrary resonance units, RUs) on these surfaces using LC-SPDP linker. After Kcoil-oriented covalent coupling, Ecoil-EGF was then injected three times (10 nM, 100 nM, and 500 nM) on Kcoil-functionalized and mock (no immobilized Kcoil on amines) surfaces. This resulted in the net accumulation of 90, 420, and 870 RUs of proteins, respectively. As expected, SPR experiments also demonstrated that the Ecoil-EGF/Kcoil complexes were stable, as almost no dissociation occurred during each buffer injection following each Ecoil-EGF injection. The kinetic profile corresponding to the first Ecoil-EGF injection was found comparable to that already observed when the Kcoil had been covalently coupled using standard thiol-coupling

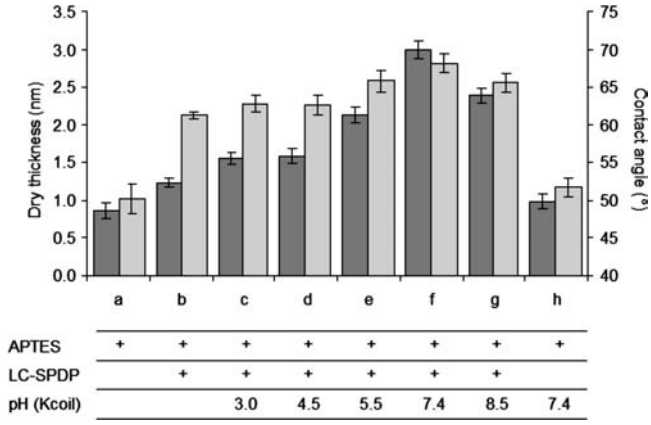

Figure 2. Characterization of the (a) APTES, (b) LC-SPDP, and Cysteine-tagged Kcoil layers grafted on silicon surfaces as illustrated in Figure 1. The dark and light gray bars correspond to dry thickness and contact angle measurements, respectively. The cysteine-tagged Kcoil peptides were reacted on LC-SPDP-coated surfaces at (c) pH 3.0, (d) pH 4.5, (e) pH 5.5, (f) pH 7.4, and (g) pH 8.5. As a comparison, the characterization of Kcoil incubation on APTES-coated surfaces (without LC-SPDP addition), at pH 7.4 is also presented (h). The reference was set as (0 nm, 0°) for a cleaned silicon surface. The successive grafting reactions were performed as described in the Materials and Methods section.

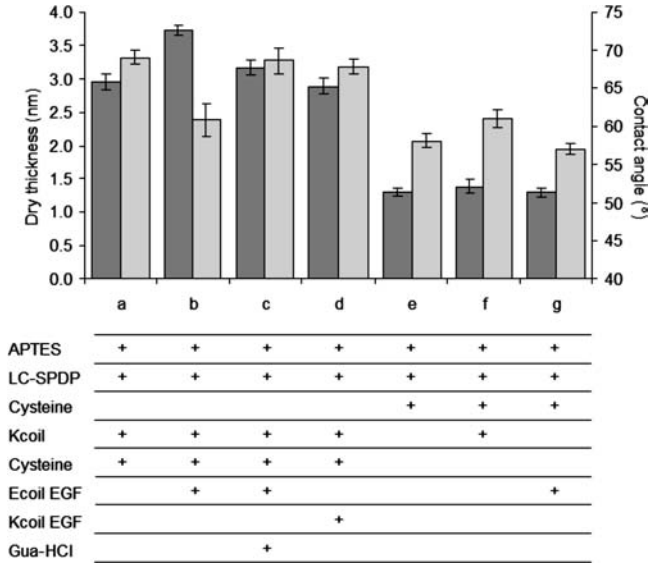

Figure 3. Sequential grafting of Ecoil-EGF via coiled-coil interactions. The dark and the light gray bars correspond to dry thickness and contact angle measurements, respectively. (a) APTES + LC-SPDP + Kcoil + Cysteine, pH 7.4; (b) Ecoil-EGF capture on (a); (c) Ecoil-EGF removal after capture (as in b) with guanidium hydrochloride (5 M). In contrast to Ecoil-EGF, (d) Kcoil-EGF does not bind to Kcoil-functionalized surface (a). As negative controls, the deposition of (f) cysteine-tagged Kcoil peptides and (g) Ecoil-EGF proteins on (e) LC-SPDP layers that had been blocked by cysteine are reported. The reference was set as (0 nm, 0°) for a cleaned silicon wafer surface. The successive grafting reactions were performed as described in the Materials and Methods section.

chemistry (*20*). After Ecoil-EGF dissociation (promoted by injections of guanidium hydrochloride), no Kcoil-EGF binding was observed. This absence of interaction between Kcoil and Kcoil-EGF cannot be attributed to any damage to surface-bound Kcoil by guanidium hydrochloride, since we already demonstrated that guanidium hydrochloride promoted E/K coiled-coil dissociation without affecting surface-bound Kcoil capacity to subsequently recruit Ecoil-tagged proteins (*20*). This once again confirmed the high specificity of the E/K coiled-coil interaction (Figure 4). Altogether, these results unambiguously demonstrated that Ecoil-EGF had been immobilized on APTES-coated surface via stable and specific E/K coiled-coil interactions.

In order to further validate our coiled-coil-based strategy and to compare its efficiency to that of random coupling procedures, EGF proteins were also immobilized on APTES-coated silicon surfaces using disuccinimide glutarate (DSG) as linker. This leads to thickness and contact angle measurements varying from 1.0 ± 0.1 nm and 30 ± 2° (after DSG treatment) to 3.0 ± 0.1 nm and 55 ± 2° (after EGF coupling).

Quantification of Immobilized EGF. 600 nM of Ecoil-EGF were incubated on a Kcoil-coated silicon wafer surface, resulting in the stable capture of 115 ± 8 pmol/cm^2 of Ecoil-EGF (surface density was quantified in a MicroBCA assay). This surface density is at least two times higher than what was previously reported with other protocols for oriented EGF immobilization (*11*, *19*). Combined with dry protein thickness measurements, we then estimated the variation of Ecoil-EGF surface density induced by varying Ecoil-EGF concentration during incubation (Figure 5). Assuming that the Ecoil-EGF/Kcoil interaction followed a Langmuirian isotherm, an apparent thermodynamic dissociation constant (K_D) of 13 nM was determined for the Ecoil-EGF/Kcoil interaction (Figure 5). In parallel, covalent coupling of untagged EGF was performed on APTES-coated silicon wafer surface using DSG as linker. This resulted in the covalent capture of 330 ± 87 pmol/cm^2 of untagged EGF.

EGF Receptor Phosphorylation Assays. EGF mediates its biological effects by binding to EGF receptors (EGFR). Ligand/receptor complex formation leads to cell surface receptor tyrosine autophosphorylation (*27*). Levels of EGFR phosphorylation were assayed for A-431 cells, at different times, by Western Blot analysis. Results corresponding to cells that had been grown on different Kcoil-coated surfaces or on native glass surfaces are presented in Figure 6. As expected, no phosphorylation of EGFR was observed for native surfaces or for Kcoil-functionalized surfaces to which Ecoil peptide had been captured (Figure 6). Of salient interest, we observed that Ecoil-EGF, when immobilized via coiled-coil interactions, induced a sustained phosphorylation of EGFR for at least 5 h (Figure 6). This observation sharply contrasted with EGFR phosphorylation induced by soluble Ecoil-EGF (autophosphorylation was not detectable after 3 h; Figure 6). The influence of EGF orientation, i.e., random versus coiled-coil-oriented, on EGFR phosphorylation was also demonstrated (Figure 6) since EGFR phosphorylation was more intense with coiled-coil oriented EGF compared to randomly coupled EGF.

In Vitro Adhesion Assays. The effect of immobilized EGF on A-431 cell adhesion was also assayed. A-431 cells were incubated on native or Kcoil-coated surfaces (in the presence or absence of soluble EGF), on Ecoil peptides or Ecoil-EGF that had been tethered on Kcoil-coated surfaces, and on covalently immobilized EGF surfaces (random immobilization; Figure 7). An increase of the cell adhesion (+ ca. 65%) was observed for coiled-coil immobilized Ecoil-EGF, whereas a lower increase was observed in the presence of soluble Ecoil-EGF (+ ca. 35%). In contrast, no significant differences from the negative control were observed for surfaces harboring randomly immobilized EGF (Figure 7). These results demonstrate that modified glass surfaces on which Ecoil-EGF had been immobilized via coiled-coil interactions promoted initial A-431 cell adhesion.

DISCUSSION

The development of biocompatible surfaces to promote and sustain tissue regeneration is of great interest for many biomedical applications, including the promotion of the wound healing processes around stent grafts after endovascular aneurysm repair (*5*) or the attachment of epithelial cells to polymeric corneal

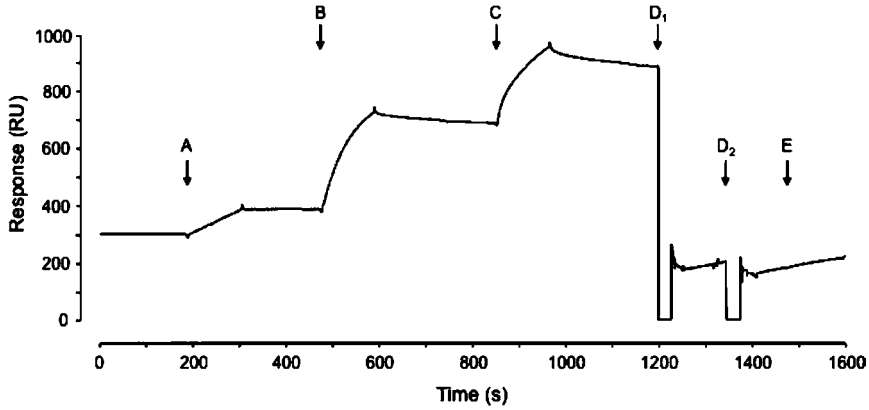

Figure 4. Control-corrected sensograms corresponding to Ecoil-EGF capture via E/K coiled-coil interactions by SPR. Kcoil peptides were immobilized on CM4 sensorchips using the same chemistry strategy (i.e., LC-SPDP as linker) as for silicon wafers and glass surfaces. Ecoil-EGF was then injected three times at 10 nM (A), 100 nM (B), and 500 nM (C). After surface regeneration with 2 pulses of guanidium hydrochloride ($D_{1,2}$), 100 nM Kcoil-EGF were injected (E).

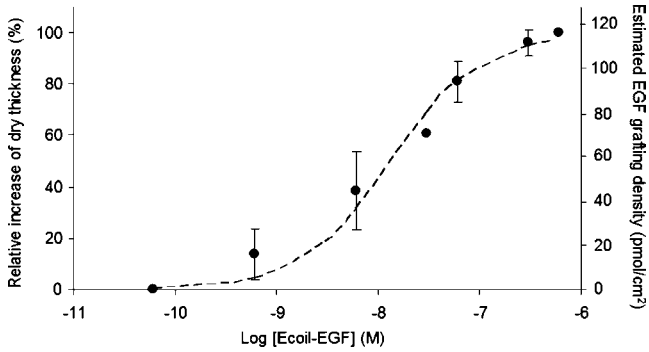

Figure 5. Variation of captured Ecoil-EGF density with Ecoil-EGF concentration during incubation. Various concentrations of Ecoil-EGF ranging from 60 pM to 600 nM were incubated on Kcoil-coated silicon wafer surfaces, as described in the Materials and Methods section, before dry thickness measurements. Surface density (pmol/cm^2) was deduced from the maximum Ecoil-EGF value determined using MicroBCA assay (see text for details). Each black dot corresponds to values obtained for 3 independent measurements while the dotted line corresponds to data fitting using a simple Langmuirian isotherm (K_D = 13 nM).

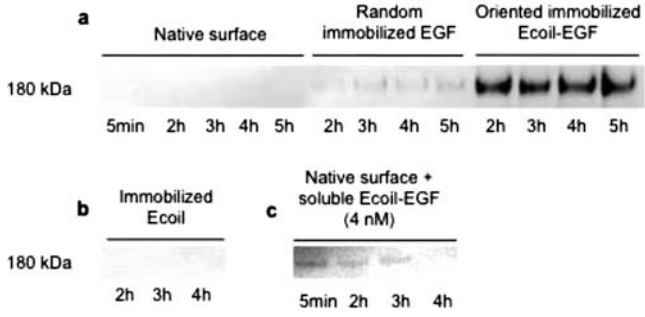

Figure 6. Phosphorylation of A-431 cell surface EGF receptors. The phosphorylation of EGF receptors on A-431 cells was monitored at different times by Western blot (A) on native surface, random immobilized EGF, and oriented immobilized Ecoil-EGF (same membrane); (B) on immobilized Ecoil peptide; and (C) on native surfaces with soluble Ecoil-EGF. The 180 kDa band immunoreactive to anti-pTyr antibody (corresponding to EGFR) was captured using a Kodak 440cf imager.

devices (*10*). Immobilization of specific proteins, such as growth factors, is now acknowledged to improve the potential of these engineered surfaces in stimulating the recruitment of cells and their adhesion and proliferation (*6, 9, 11, 19*). In that context, we have developed a versatile and cell culture-compatible strategy for the oriented immobilization of proteins on surfaces harboring primary amine functionalities. Our experimental approach takes advantage of a de novo designed heterodimerizing peptide system composed of the Ecoil and Kcoil pair. This grafting system has already been used as a tool for different biotechnology applications such as protein capture on biosensor surfaces (*28*), controlled protein dimerization (*17, 29*), or virus targeting (*23*). For the first time, we provide the proof of concept that the E/K coiled-coil system can be used for protein capture, aiming at enhancing material properties with the ultimate goal of developing tailored materials for tissue engineering and regenerative medicine applications.

In that effort, we first optimized Kcoil covalent and oriented immobilization on APTES-functionalized silicon wafers and characterized using dry thickness and water contact angle measurements. Low standard deviations in the measurements indicate that the successive grafted layers are homogeneous and that our protocols are highly reproducible (Figure 2). Nonspecific adsorption on Kcoil-functionalized surfaces was negligible (Figures 2 and 3). Therefore, as previously described (*22*), the protein immobilization via E/K coiled-coil interactions is highly specific, mostly due to the importance of both ionic and hydrophobic interactions during E/K coiled-coil complex formation. Furthermore, additional SPR experiments on sensorchips mimicking the functionalities displayed on our surfaces unambiguously demonstrates that covalently immobilized Kcoil is able to recruit Ecoil-EGF in a highly stable fashion (Figure 4), once again, in excellent agreement with previous studies in which we applied a different Kcoil coupling chemistry (*30, 31*).

Our optimized grafting conditions were then successfully applied to glass surfaces for cell culture. The amount of immobilized EGF was quantified for surfaces supporting the highest EGF grafting density, i.e., 115 and 330 pmol/cm^2 for the coiled-coil oriented capture and nonoriented covalent immobilization, respectively. Dry thicknesses of EGF layers for the corresponding surfaces were 0.7 and 2.0 nm as measured on silicon wafers (Figure 3), thus supporting that dry thickness is directly related to the amount of immobilized EGF (*32*). Ellipsometric measurements were performed on Kcoil-grafted silicon wafers in order to evaluate the influence of soluble Ecoil-EGF concentration upon EGF surface density during the grafting process (Figure 5). Our results underline that varying the concentration of added soluble Ecoil-EGF allows for the controllable modulation of EGF density on Kcoil-derivatized surfaces. The apparent thermodynamic dissociation constant (K_D) between grafted Kcoil peptides and Ecoil-tagged EGF proteins was in the low nanomolar range, in good agreement with previously reported K_D (*28*).

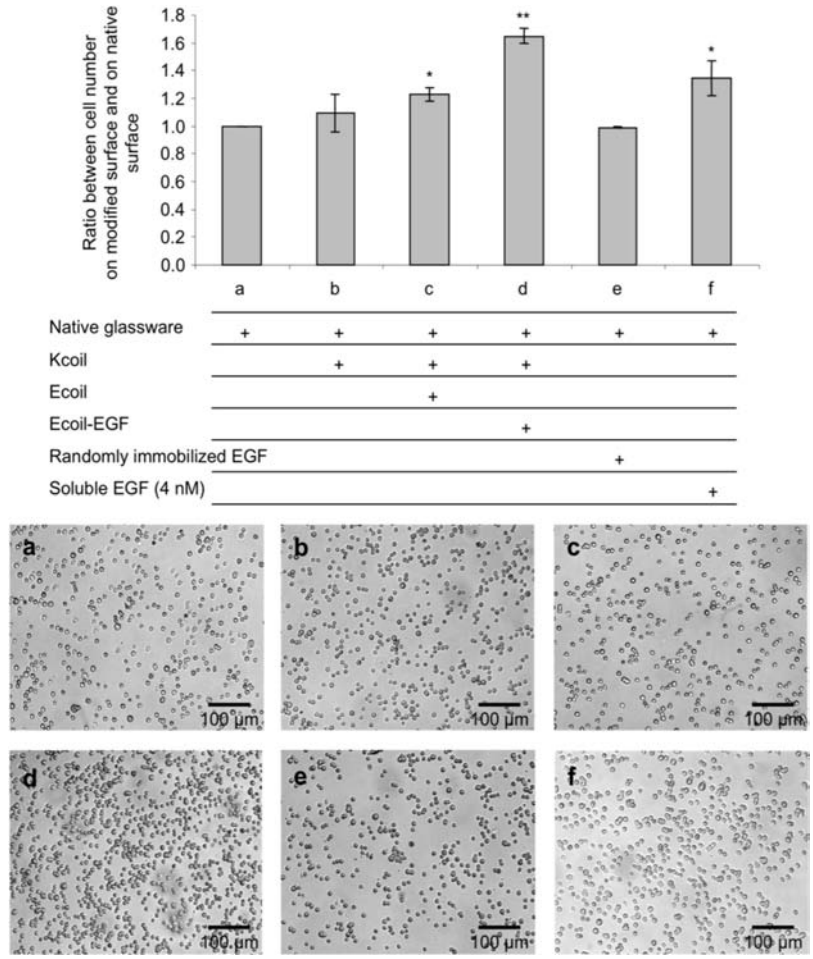

Figure 7. Images of attached cells after 5 h of incubation for adhesion assays. A-431 cells were incubated during 5 h on glass surfaces harboring (a) native amino groups, or coated with (b) grafted Kcoil peptide layer, (c) Ecoil peptides bound to grafted Kcoil peptide layer, (d) Ecoil-EGF bound to grafted Kcoil peptide layer, (e) randomly immobilized EGF layer, and (f) native amino groups with an injection of soluble Ecoil-EGF (4 nM). Differences were significant for $p < 0.05$ (*) and $p < 0.001$ (**).

In order to evaluate the full potential of our grafting strategy, in vitro cellular assays were performed with A-431 cell line. Of interest, after 5 h of incubation with A-431 cells, we noticed an increase of ca. 10%, 20%, and 65% for A-431 cell adhesion for surfaces derivatized with Kcoil alone, Kcoil/Ecoil complexes, and Kcoil/Ecoil-EGF, respectively. In contrast, no increase in cell adhesion was observed for randomly grafted EGF (Figure 7), more likely due to the loss of EGF bioactivity that may have resulted from the random coupling procedure and the absence of linker, as already reported by Kuhl and colleagues (*7*). Altogether, our results suggest that our immobilization strategy per se has a positive effect on cell attachment, a desirable property in tissue engineering. Our results are also in excellent agreement with previous observations by Ogiwara et al. that cultivated 3T3 cells and A-431 cells on surfaces where (i) bioactive EGF fused to the Fc region of an antibody (EGF-Fc) had been photoimmobilized (*11*) and (ii) EGF had been chemically immobilized via an engineered *p*-azido-phenylalanine at its C-terminus, respectively (*13*). More specifically, in both studies, cell adhesion was observed to moderately increase with soluble EGF supply (when compared to negative control), while immobilized EGF surfaces were shown to further increase cell adhesion in an integrin-independent fashion. Of interest, the authors noticed differences in A-431 cell phenotype whether EGF receptors were activated with soluble or tethered EGFs. Cells adhering to tethered EGF were characterized by filipodia structures, whereas cells exposed to soluble EGF displayed lamellipodia structures, hence suggesting that the signal transduction pathways activated in both cases were slightly different.

Cell exposure to immobilized EGF has been reported to sustain EGF-induced autophosphorylation of cell surface EGFR when compared to soluble EGF (*13, 33*). This effect has been attributed to ligand internalization impediment and/or to limited degradation of the EGF-EGFR complexes. Our results support these conclusions and further illustrate the advantage of oriented EGF capture. Indeed, a more intense EGFR autophosphorylation is observed with coiled-coil-captured EGF (oriented approach, 115 pmol/cm^2) when compared to that corresponding to EGF that has been covalently immobilized in a random fashion (330 pmol/cm^2) (Figure 6).

Altogether, our results demonstrate that our coiled-coil based capture approach offers several advantages when compared to previously reported systems for oriented protein immobilization, in terms of protein bioactivity, surface density, and grafting process. First, coil tags do not affect EGF bioactivity, since soluble N- or C-terminally coil-tagged EGF were shown to be behave as EGF in various in vitro cell assays (*17, 23*). This sharply contrasts with the negative effect of an Fc tag that totally abrogated EGF bioactivity when positioned at the N-terminus of EGF (*20*). Second, we observed a maximal EGF surface density for tethered Ecoil-EGF of 115 pmol/cm^2 (Figure 5); this is at least two times higher than previously reported values for tagged EGF grafting, i.e., 16 pmol/cm^2 for immobilization via the Fc portion of immunoglobulin G and 52 pmol/cm^2 for immobilization via polyhistidine tags (*11, 19*). Oriented protein layers may thus be generated over a wider range of surface density with our coiled-coil-based strategy. Furthermore, the length of the coiled-coil motif, in combination with that of LC-

SPDP, provides coiled-coil tethered EGF with enough mobility, a critical factor for optimal EGF signaling (*7, 20*). This is likely dictated by the 2:2 overall stoichiometry of the signaling-competent ligand/receptor complex (*15, 17*).

At last, our coiled-coil-based approach is sequential and versatile: stable Kcoil layers can be produced several days before grafting with any Ecoil-tagged protein. As opposed to protein A or G, Kcoil-derivatized surfaces can be treated with strong acidic, basic, or chaotropic solutions, as Kcoil on its own is unstructured and can thus withstand these treatments (*22*). Moreover, our proposed strategy is simple in its implementation and allows for the oriented immobilization of every coil-tagged protein on any aminated surface.

CONCLUSION

We report a new approach for oriented immobilization of growth factors on aminated surfaces based on a coiled-coil interaction. This method relies on a sequential grafting process based on the covalent grafting of a homogeneous Kcoil peptide layer and on the subsequent capture of Ecoil-tagged proteins. The first step can be realized in dry and nonsterile environment several days before protein immobilization, whereas the second step allows for a specific and stable immobilization of the Ecoil-tagged protein over a wide range of grafting density. Consequently, this easy and versatile approach could be applied to specifically tailor any type of biomaterial.

ACKNOWLEDGMENT

This work was supported by the Canada Research Chair on Protein-Enhanced Biomaterials (G.D.C.), the Canada Research Chair in Applied Metabolic Engineering (M.J.), by the Natural Sciences and Engineering Research Council of Canada (G.D.C., M.J.), and by GRSTB (postdoctoral fellowship to B.L.).

LITERATURE CITED

(1) Little, L., Healy, K. E., and Schaffer, D. (2008) Engineering biomaterials for synthetic neural stem cell microenvironments. *Chem. Rev. 108*, 1787–96.

(2) Merrett, K., Griffith, C. M., Deslandes, Y., Pleizier, G., Dube, M. A., and Sheardown, H. (2003) Interactions of corneal cells with transforming growth factor beta 2-modified poly dimethyl siloxane surfaces. *J. Biomed. Mater. Res., Part A 67*, 981–93.

(3) Vallieres, K., Petitclerc, E., and Laroche, G. (2007) Covalent grafting of fibronectin onto plasma-treated PTFE: influence of the conjugation strategy on fibronectin biological activity. *Macromol. Biosci. 7*, 738–45.

(4) Nakajima, M., Ishimuro, T., Kato, K., Ko, I. K., Hirata, I., Arima, Y., and Iwata, H. (2007) Combinatorial protein display for the cell-based screening of biomaterials that direct neural stem cell differentiation. *Biomaterials 28*, 1048–60.

(5) Lerouge, S., Major, A., Girault-Lauriault, P. L., Raymond, M. A., Laplante, P., Soulez, G., Mwale, F., Wertheimer, M. R., and Hebert, M. J. (2007) Nitrogen-rich coatings for promoting healing around stent-grafts after endovascular aneurysm repair. *Biomaterials 28*, 1209–17.

(6) Hadjizadeh, A., Doillon, C. J., and Vermette, P. (2007) Bioactive polymer fibers to direct endothelial cell growth in a three-dimensional environment. *Biomacromolecules 8*, 864–73.

(7) Kuhl, P. R., and Griffith-Cima, L. G. (1996) Tethered epidermal growth factor as a paradigm for growth factor-induced stimulation from the solid phase. *Nat. Med. 2*, 1022–1027.

(8) Elloumi, I., Kobayashi, R., Funabashi, H., Mie, M., and Kobatake, E. (2006) Construction of epidermal growth factor fusion protein with cell adhesive activity. *Biomaterials 27*, 3451–58.

(9) Ichinose, J., Morimatsu, M., Yanagida, T., and Sako, Y. (2006) Covalent immobilization of epidermal growth factor molecules for single-molecule imaging analysis of intracellular signaling. *Biomaterials 27*, 3343–3350.

(10) Klenkler, B. J., Griffith, M., Becerril, C., West-Mays, J. A., and Sheardown, H. (2005) EGF-grafted PDMS surfaces in artificial cornea applications. *Biomaterials 26*, 7286–96.

(11) Ogiwara, K., Nagaoka, M., Cho, C. S., and Akaike, T. (2005) Construction of a novel extracellular matrix using a new genetically engineered epidermal growth factor fused to IgG-Fc. *Biotechnol. Lett. 27*, 1633–1637.

(12) Fan, V. H., Tamama, K., Au, A., Littrell, R., Richardson, L. B., Wright, J. W., Wells, A., and Griffith, L. G. (2007) Tethered epidermal growth factor provides a survival advantage to mesenchymal stem cells. *Stem cells (Dayton, Ohio) 25*, 1241–51.

(13) Ogiwara, K., Nagaoka, M., Cho, C. S., and Akaike, T. (2006) Effect of photo-immobilization of epidermal growth factor on the cellular behaviors. *Biochem. Biophys. Res. Commun. 345*, 255–9.

(14) Stefonek, T. J., and Masters, K. S. (2007) Immobilized gradients of epidermal growth factor promote accelerated and directed keratinocyte migration. *Wound repair and regeneration: official publication of the Wound Healing Society [and] the European Tissue Repair Society 15*, 847–55.

(15) Ogiso, H., Ishitani, R., Nureki, O., Fukai, S., Yamanaka, M., Kim, J. H., Saito, K., Sakamoto, A., Inoue, M., Shirouzu, M., and Yokoyama, S. (2002) Crystal structure of the complex of human epidermal growth factor and receptor extracellular domains. *Cell 110*, 775–787.

(16) Barrientos, S., Stojadinovic, O., Golinko, M. S., Brem, H., and Tomic-Canic, M. (2008) Growth factors and cytokines in wound healing. *Wound repair and regeneration: official publication of the Wound Healing Society [and] the European Tissue Repair Society 16*, 585–601.

(17) Nakaji-Hirabayashi, T., Kato, K., and Iwata, H. (2009) Surface-anchoring of spontaneously dimerized epidermal growth factor for highly selective expansion of neural stem cells. *Bioconjugate Chem. 20*, 102–10.

(18) Chen, G., Ito, Y., and Imanishi, Y. (1997) Photo-immobilization of epidermal growth factor enhances its mitogenic effect by artificial juxtacrine signaling. *Biochim. Biophys. Acta 1358*, 200–208.

(19) Nakaji-Hirabayashi, T., Kato, K., Arima, Y., and Iwata, H. (2007) Oriented immobilization of epidermal growth factor onto culture substrates for the selective expansion of neural stem cells. *Biomaterials 28*, 3517–29.

(20) Boucher, C., St-Laurent, G., Loignon, M., Jolicoeur, M., Crescenzo, G. D., and Durocher, Y. (2008) The bioactivity and receptor affinity of recombinant tagged EGF designed for tissue engineering applications is defined by the nature and position of the tags. *Tiss. Eng., Part A 14*, 2069–2077.

(21) Chao, H., Houston, M. E., Jr., Grothe, S., Kay, C. M., O'Connor-McCourt, M., Irvin, R. T., and Hodges, R. S. (1996) Kinetic study on the formation of a de novo designed heterodimeric coiled-coil: use of surface plasmon resonance to monitor the association and dissociation of polypeptide chains. *Biochemistry 35*, 12175–12185.

(22) De Crescenzo, G., Litowski, J. R., Hodges, R. S., and O'Connor-McCourt, M. D. (2003) Real-time monitoring of the interactions of two-stranded de novo designed coiled-coils: effect of chain length on the kinetic and thermodynamic constants of binding. *Biochemistry 42*, 1754–1763.

(23) Le, P. U., Lenferink, A. E. G., Pinard, M., Baardsnes, J., Massie, B., and O'Connor-McCourt, M. D. (2009) *Escherichia coli* expression and refolding of E/K-coil-tagged EGF generates fully bioactive EGF for diverse applications. *Protein Express. Purif.*, in press.

(24) Liberelle, B., Banquy, X., and Giasson, S. (2008) Stability of silanols and grafted alkylsilane monolayers on plasma-activated mica surfaces. *Langmuir 24*, 3280–3288.

(25) Wettero, J., Askendal, A., Bengtsson, T., and Tengvall, P. (2002) On the binding of complement to solid artificial surfaces in vitro. *Biomaterials 23*, 981–991.

(26) Hunter, T., and Cooper, J. A. (1981) Epidermal growth factor induces rapid tyrosine phosphorylation of proteins in A431 human tumor cells. *Cell 24*, 741–752.

(27) Schlessinger, J. (2002) Ligand-induced, receptor-mediated dimerization and activation of EGF receptor. *Cell 110*, 669–672.

(28) De Crescenzo, G., Pham, P. L., Durocher, Y., and O'Connor-McCourt, M. D. (2003) Transforming growth factor-beta (TGF-beta) binding to the extracellular domain of the type II TGF-beta receptor: receptor capture on a biosensor surface using a new coiled-coil capture system demonstrates that avidity contributes significantly to high affinity binding. *J. Mol. Biol. 328*, 1173–1183.

(29) De Crescenzo, G., Pham, P. L., Durocher, Y., Chao, H., and O'Connor-McCourt, M. D. (2004) Enhancement of the antagonistic potency of transforming growth factor-beta receptor extracellular domains by coiled coil-induced homo- and heterodimerization. *J. Biol. Chem. 279*, 26013–26018.

(30) Tripet, B., De Crescenzo, G., Grothe, S., O'Connor-McCourt, M., and Hodges, R. S. (2002) Kinetic analysis of the interactions between troponin C and the C-terminal troponin I regulatory region and validation of a new peptide delivery/capture system used for surface plasmon resonance. *J. Mol. Biol. 323*, 345–362.

(31) Tripet, B., Yu, L., Bautista, D. L., Wong, W. Y., Irvin, R. T., and Hodges, R. S. (1996) Engineering a de novo-designed coiled-coil heterodimerization domain off the rapid detection, purification and characterization of recombinantly expressed peptides and proteins. *Protein Eng. 9*, 1029–42.

(32) Liberelle, B., and Giasson, S. (2007) Chemical end-grafting of homogeneous polystyrene monolayers on mica and silica surfaces. *Langmuir 23*, 9263–70.

(33) Ito, Y., Li, J. S., Takahashi, T., Imanishi, Y., Okabayashi, Y., Kido, Y., and Kasuga, M. (1997) Enhancement of the mitogenic effect by artificial juxtacrine stimulation using immobilized EGF. *J. Biochem. 121*, 514–20.

BC9001147

"Four-Potential" Ferrocene Labeling of PNA Oligomers via Click Chemistry

Nina Hüsken, Gilles Gasser, S. David Köster, and Nils Metzler-Nolte*

Lehrstuhl für Anorganische Chemie I - Bioanorganische Chemie, Fakultät für Chemie und Biochemie, Ruhr-Universität Bochum, Universitätsstrasse 150, D-44801 Bochum, Germany. Received March 20, 2009; Revised Manuscript Received June 4, 2009

The scope of the Cu(I)-catalyzed [2 + 3] azide/alkyne cycloaddition (CuAAC, click chemistry) as a key reaction for the conjugation of ferrocene derivatives to N-terminal functionalized PNA oligomers is explored herein (PNA: peptide nucleic acid). The facile solid-phase synthesis of N-terminal azide or alkyne-functionalized PNA oligomer precursors and their cycloaddition with azidoferrocene, ethynylferrocene, and *N*-(3-ethylpent-1-yn-3-yl)ferrocenecarboxamide (DEPA−ferrocene) on the solid phase are presented. While the click reaction with azidomethylferrocene worked equally well, the ferrocenylmethyl group is lost from the conjugate upon acid cleavage. However, the desired product was obtained via a post-SPPS conversion of the alkyne−PNA oligomer with azidomethylferrocene in solution. The synthesis of all ferrocene−PNA conjugates (trimer t_3-PNA, **3**, **4**, **5**, **6**; 12mer PNA, **10** - t c t a c a a g a c t c, **11** - t c t a c c g t a c t c) succeeded with excellent yields and purities, as determined by mass spectrometry and HPLC. Electrochemical studies of the trimer Fc−PNA conjugates **3**, **4**, **5**, and **6** with four different ferrocene moieties revealed quasi-reversible redox processes of the ferrocenyl redox couple $Fc^{0/+}$ and electrochemical half-wave potentials in a range of $E_{1/2} = -20$ mV to +270 mV vs $FcH^{0/+}$ (Fc: ferrocenyl, $C_{10}H_9Fe$). The observed potential differences $\Delta E_{1/2}{}^{min}$ are always greater than 60 mV for any given pair of Fc−PNA conjugates, thus allowing a reliable differentiation with sensitive electrochemical methods like e.g. square wave voltammetry (SWV). This is the electrochemical equivalent of "four-color" detection and is hence denoted "four-potential" labeling. Preparation and electrochemical investigation of the set of four structurally different and electrochemically distinguishable ferrocenyl groups conjugated to PNA oligomers, as exemplified by the conjugates **3**, **4**, **5**, and **6**, demonstrates the scope of the azide/alkyne cycloaddition for the labeling of PNA with electrochemically active ferrocenyl groups. Furthermore, it provides a PNA-based system for the electrochemical detection of single-nucleotide polymorphism (SNP) in DNA/RNA.

INTRODUCTION

Peptide nucleic acid (PNA) are nucleic acids analogues. In PNA, the negatively charged deoxyribose phosphodiester backbone of DNA and RNA is replaced by a neutral, pseudopeptide backbone of repeating *N*-(2-aminoethyl)glycine units (*1*−*9*). PNA have outstanding properties including faster hybridization with RNA, DNA, and PNA as well as higher binding affinity, mismatch sensitivity, and greater chemical and biological stability compared to natural nucleic acid oligomers (*10, 11*). These exceptional characteristics make PNA attractive for medicinal, biological, and analytical applications such as antigene/antisense therapy (*12, 13*), drug discovery (*14*), or molecular recognition of nucleic acids (*15*).

Promising and relatively new is the application of PNA as electrochemical biosensors for DNA or RNA (*16, 17*). A major advantage of using PNA for this purpose is their ability to reliably discriminate and therefore detect single-base mismatches in oligonucleotide sequences (*18*). Monolayers of PNA-modified transducer surfaces serve as the recognition device, while a reversible redox-active metal complex bound to the PNA sequence serves as the electrochemical probe. This type of biosensor offers the opportunity to monitor and detect the event of hybridization with various electroanalytical methods (*19*). A remaining challenge in the synthesis of an electrochemical PNA biosensor is the linkage of the electroactive metal complex to the PNA strand. In the past years, various examples of label-free electrochemical DNA detection with PNA were reported (*20*−*26*). In these studies, a charged metal complex or charged polymer interacts ionically with the negatively charged DNA backbone of the resulting PNA/DNA duplex. However, this method is limited by the lack of a defined bonding situation, which is crucial for the significance of the obtained electrochemical signal. In this perspective, a facile method to covalently conjugate a metal complex to a PNA strand is needed. Our group already presented the coupling of ferrocene carboxylic acid to the N-terminus of PNA oligomers on the solid phase (*27, 28*). Although this coupling method is efficient, it is limited to carboxylic acid functionalized metal complexes. An enhanced flexibility in the choice of organometallic starting materials would be very attractive, since not every metal complex can be

* Corresponding author. Fax: +49 (0)234 32 14378; Tel: +49 (0)234 32 28152; E-mail: Nils.Metzler-Nolte@ruhr-uni-bochum.de.

[1]Abbreviations: A, adenine; Ahx, amino hexanoic acid; DCM, dichloromethane; DMF, *N*,*N*-dimethyl formamide; DPV, differential pulse voltammetry; Bhoc, benzhydryloxycarbonyl; Boc, *tert*-butyloxycarbonyl; C, cytosine; CV, cyclic voltammetry; DEPA, diethylpropargylamine; DIPEA, diisopropylethylamine; ESI, electrospray ionization; Fc, ferrocenyl ($C_5H_5FeC_5H_4$); FcH, ferrocene (dicyclopentadienyl iron, Cp_2Fe, $(C_5H_5)_2Fe$); Fmoc, fluorenylmethoxycarbonyl; G, guanine; HATU, 2-(1*H*-7-azabenzotriazole-1-yl)-1,1,3,3-tetramethyluronium hexafluorophosphate; HOBt, 1-hydroxy-1*H*-benzotriazole; HPLC, high performance liquid chromatography; MALDI-TOF, matrix assisted laser desorption/ionization−time-of-flight; MOPS, 3-(*N*-morpholino)propanesulfonic acid; MS, mass spectrometry; RP, reversed phase; R_t, retention time; PDA, photodiode array; SPPS, solid-phase peptide (or PNA) synthesis; PHB, photochemical hole burning; T, thymine; TBTU, 2-(1*H*-benzotriazole-1-yl)-1,1,3,3,-tetramethyluronium tetrafluoroborate; TFA, trifluoroacetic acid; TIS, triisopropyl silane; Trt, trityl. The common three-letter code for amino acids is used throughout. Nucleobases are denoted by their usual abbreviations in DNA; small letters however indicate PNA monomers.

10.1021/bc9001272 CCC: $40.75 © 2009 American Chemical Society
Published on Web 07/08/2009

functionalized with a carboxylic acid, hence limiting the number of organometallic/metal complex PNA bioconjugates.

In order to provide new metal−PNA conjugates with different electrochemical potentials, we searched for an alternative method for the labeling of PNA with various ferrocene derivatives on the solid phase. We rapidly turned our attention to the so-called click chemistry methodology. "Click chemistry" describes a group of reactions that proceed with high yield and chemical specificity (*29*−*33*). The prototype "click reaction" is a Huisgen [2 + 3] dipolar azide/alkyne cycloaddition, and its Cu-catalyzed variant is valued as a key reaction for bioconjugation, since it is chemoselective, reliable, and takes places under mild conditions (*34*−*40*). For metal bioconjugates, this method enlarges the spectrum of metal complex starting materials to be possibly used, as the reagents may be azide- and alkyne-functionalized derivatives. We recently reported the use of click chemistry to generate peptide-functionalized self-assembled monolayers on Au surfaces, which are highly proteophobic (*41*). Furthermore, the first example of (multi)insertion by click chemistry of azidoferrocene into a PNA oligomer containing a new alkyne functionalized PNA monomer synthon was also presented recently (*42*).

In this paper, we report the facile N-terminal functionalization of PNA with azide or alkyne functionalities on the solid phase, and their subsequent conversion by click chemistry with a range of different alkynyl and azido ferrocene derivatives to give a small library of ferrocene−PNA bioconjugates. The metal complexes were chosen such that four readily discernible potentials result, and we therefore speak of "four-potential" labeling. In effect, this will provide the electrochemical equivalent of "four-color" detection, which is evidently important for sequencing applications and single nucleotide polymorphism (SNP) analysis. Hence, this study is of fundamental relevance for the development of new electrochemical DNA biosensors.

EXPERIMENTAL PROCEDURES

General Experimental Conditions. All reagents and HPLC-grade solvents were purchased from Acros (Geel, Belgium), Aldrich/Sigma/Fluka (Deisenhofen, Germany), E. Merck (Darmstadt, Germany), Novabiochem (Laufelfingen, Switzerland), and IRIS Biotech (Marktredwitz, Germany) and were used without further purification. The preloaded polystyrene resins were purchased from Rapp Polymers (Tübingen, Germany). Only L-amino acids were used throughout. PNA monomers were purchased from Link Technologies (Edinburgh, Scotland) and ASM (Hannover, Germany). All solutions were freshly prepared before use. HPLC[1] fractions of all products were frozen in liquid nitrogen and lyophilized using an Edwards Modulyo freeze−dryer. The preparation and handling of azide materials was performed at all stages on the smallest possible amounts and with routine precautions in order to minimize the risk of possible decomposition and explosions. Higher temperatures were avoided generally, and light was excluded during all stages of the handling of azidoferrocene.

General Analytical Procedures. MALDI-TOF mass spectra were measured on a Bruker Daltonics Autoflex in linear mode with positive polarity using sinapic acid as the matrix. ESI mass spectra were recorded on a Bruker Esquire 6000.

HPLC Analysis and Purification. HPLC analysis and purification was performed on a customized Varian ProStar 210 System, equipped with a PDA detector and auto sampler, using Varian DynaStar C-18 reverse-phase columns for analytical (250 × 4 mm, 8 μm) and preparative (250 × 21 mm, 8 μm) runs. Analytical (flow rate: 1.0 mL min^{-1}) and semipreparative (flow rate: 4.7 mL min^{-1}) runs were performed with a linear gradient of A (Millipore water containing 0.1% v/v TFA) and B (acetonitrile (Baker HPLC-grade), containing 0.1% v/v TFA. Analytical runs: t = 0 min 5% B, t = 20 min 80% B, t = 25 min 5% B. Preparative runs: t = 0 min 5% B, t = 12 min 15% B, t = 32 min 40% B, t = 50 min 80% B, t = 60 min 5% B. All samples were filtered before injection using a 0.22 μm syringe filter. Spectra were recorded at 254 nm and 25 °C; retention times (t_R [min]) were noted in each case.

Electrochemical Studies. Cyclic voltammetry and differential pulse voltammetry were performed on a Princeton Applied Research BES potentiostat operated by Princeton Applied Research MS DOS software M270. The measurements were perfomed with a home-made three-electrode microvolume electrochemical cell (*43*), placed in a Faraday cage consisting of copper hole sheet metal. For the measurements, a glassy carbon electrode with a geometric diameter of 2 mm was used as the stationary working electrode, a platinum wire was used as the counter electrode, and Ag/AgCl in 3 M KCl was used as the reference electrode. The Ag/AgCl reference electrode was permanently stored in aq KCl solution (3 M) if not in use. Measurements were carried out in a 1:1 (v/v) mixture of acetonitrile and MOPS buffer (0.15 M) at pH 7.4. Sodium perchlorate (0.2 M) was used as the supporting electrolyte. Solutions were degassed and filtered before use. The working electrode was polished with moistened carpet material before each measurement until DPV[1] of the pure electrolyte solution revealed a clean electrode surface. Ferrocene with the reversible redox couple $FcH^{0/+}$ was used as internal (**4**, **6**) or external (**3**, **5**) reference. To this end, ferrocene was measured three times before and after the respective measurement. Half-wave potentials $E_{1/2}$ and peak separation values ΔE_p were determined as described in Table 2. Return-to-forward peak current ratios I_{pc}/I_{pa} were determined according to the Nicholson procedure (*44*) on individual cyclic voltammograms by applying the following equation:

$$I_{pc}/I_{pa} = (I_{pc})_0/I_{pa} + 0.485(I_{pc})_0/I_{pa} + 0.086$$

Solid-Phase PNA Synthesis. SPPS was performed manually in 5 mL polypropylene one-way syringes as reaction vessels, which were equipped with a frit at the bottom. They were filled with 50 mg of polystyrene resin beads TentaGel R PHB Cys(Trt)Fmoc (0.18 mmol/g) or TentaGel S RAM Lys(Boc)-Fmoc (0.20 mmol/g). The resin was swollen in DMF before use for 1 h. All reactions were performed on a mechanical shaker with 400 rpm, soaking approximately 3−4 mL of freshly prepared solutions into the syringe. Fmoc/Bhoc protected PNA monomers (5 equiv) were preactivated in Eppendorf tubes before every coupling step for 2 min with HATU (4.5 equiv) in DMF, adding DIPEA and 2,6-lutidine (10 equiv each) (A(bhoc)-PNA-monomer, 5 min; C(bhoc)-PNA-monomer, 7 min). The amino acids Fmoc-Ahx and Fmoc-Lys(Boc)-OH were preactivated in an analogous manner with TBTU and HOBt·H_2O (4.5 equiv each). For each coupling step, the resin beads were treated with the activated acid under agitation (50 °C, 20 min) and subsequently washed with DMF. The coupling step was monitored with the Kaiser test. Double Fmoc deprotection was performed with piperidine (20%, v/v) in DMF (2 min + 10 min). The resin beads were then washed successively with DMF, DCM, and DMF. The whole procedure (deprotection, coupling, monitoring) was repeated for every PNA monomer until the PNA sequence was completed. The resin was washed and shrunk with methanol (30 min) and dried under vacuum. Final cleavage of the PNA oligomer from the resin and the deprotection of all Bhoc, Boc and Trt side chain protecting groups were simultaneously performed in TFA/TIS/phenol (85/5/10, v/v/v) (2 h + 1 h). Following the removal of TFA under reduced pressure, the crude product was precipitated with ice-cold diethyl ether, washed twice with ice-cold diethyl ether,

and each time centrifuged (10 min, 8000 rpm). The thus-produced crude oligomer was lyophilized in acetonitrile/water and analyzed by analytical HPLC, showing good purities already (90−98%) for all oligomers. For characterization with analytical HPLC and ESI or MALDI-TOF mass spectrometry, small oligomer quantities were purified by preparative HPLC. All yields given in the following are crude yields, with products likely containing at least traces of excess solvents, TFA, and salts.

Azide/Alkyne-Functionalized Carboxylic Acids and Ferrocene Derivatives. Propynoic acid as well as the ferrocene derivatives ethynylferrocene, ferrocene carboxylic acid, and ferrocenylmethanol were purchased from Acros (Geel, Belgium). All other ferrocene derivatives, namely azidoferrocene, DEPA−ferrocene, azidomethylferrocene, and 2-azidoacetic acid, were synthesized according to known and published synthetic routes. Analytical data of all compounds matched the previously reported data.

Preparation of Azide/Alkyne-Functionalized PNA Oligomers. N-Terminal azide and alkyne functionalizations of PNA oligomers were performed on polystyrene resins, which were preloaded with the respective PNA sequence, synthesized according to the general SPPS procedure. The solid-phase coupling of 2-azidoacetic acid and propynoic acid to the N-terminus of a PNA oligomer followed the Fmoc deprotection of the last PNA monomer of the respective PNA sequence.

Preparation of Propynoic Acid Functionalized PNA Oligomers 1 and 8. 50 mg (**1**, 10 μmol; **8**, 9 μmol) of a polystyrene resin, which was preloaded with the respective PNA sequence (**1**, H-t t t $LysNH_2$; **8**, H-t c t a c a a g a c t c Lys Ahx $CysNH_2$), was successively treated with a solution of DIPEA and 2,6-lutidine (each 10 equiv) in DMF (2 min) and then with a solution of propynoic acid (5 equiv) and HATU (4.5 equiv) in DMF at ambient temperature under agitation for 15 min. The resin was washed after each step with DMF, and the whole process was repeated eight times. When coupling was completed (monitoring with Kaiser test), the resin was washed successively with DMF, DCM, and DMF. The propynoic acid functionalized PNA oligomers were cleaved from the resin following the general procedure.

*Oligomer **1***. TentaGel S RAM Lys(Boc)Fmoc (0.20 mmol/g) was used. **1** was obtained as a white solid. Yield: 86% (8.6 mg, 8.6 μmol). HPLC: t_R = 4.8 min. ESI-MS: *m*/*z* = 996.3 $[M+H]^+$ (100), 498.7 $[M+2H]^{2+}$ (71).

Oligomer **8.** TentaGel R RAM Cys(Trt)Fmoc (0.18 mmol/g) was used. **8** was obtained as a white solid. Yield: 79% (25.6 mg, 7.1 μmol). MALDI-TOF MS: *m*/*z* (%) = 3613.5 $[M+H]^+$ (100).

Preparation of 2-Azidoacetic Acid Functionalized PNA Oligomers 2 and 9. 2-Azidoacetic acid (5 equiv) was preactivated for 3 min in an Eppendorf tube with TBTU and HOBt·H_2O (4.5 equiv each) in DMF, with DIPEA and 2,6-lutidine (10 equiv each). 50 mg (**2**, 10 μmol; **9**, 9 μmol) of a polystyrene resin, which was preloaded with the respective PNA sequence (**2**, H-t t t $LysNH_2$; **9**, H-t c t a c c g t a c t c Lys Ahx $CysNH_2$), was treated with the activated acid under agitation at ambient temperature for 1 h. The resin was then successively washed with DMF, DCM, and DMF. The azide-functionalized PNA oligomer was cleaved from the resin following the general procedure.

*Oligomer **2***. TentaGel S RAM Lys(Boc)Fmoc (0.20 mmol/g) was used. **2** was obtained as a white solid. Yield: 83% (8.6 mg, 8.3 μmol). ESI-MS: *m*/*z* (%) = 1027.3 $[M+H]^+$ (100), 514.2 $[M+2H]^{2+}$ (91).

*Oligomer **9***. TentaGel R RAM Cys(Trt)Fmoc (0.18 mmol/g) was used. **9** was obtained as a white solid. Yield: 80% (26.0 mg, 7.2 μmol). MALDI-TOF MS: *m*/*z* (%) = 3609.6 $[M+H]^+$ (100).

Preparation of Fc-PNA Conjugate 7. The conjugation of ferrocene via peptide coupling was performed on 50 mg (10 μmol) of the resin TentaGel R PHB, which was preloaded with the 12-mer PNA sequence H-t c t a c g a g a c t c Lys Ahx $CysNH_2$, and follows the Fmoc deprotection of the last PNA monomer of this sequence. Ferrocenecarboxylic acid (5 equiv) was preactivated for 3 min in an Eppendorf tube adding HATU and HOBt·H_2O (4.5 equiv each) in DMF, with DIPEA and 2,6-lutidine (10 equiv each). The resin was treated with the activated ferrocenecarboxylic acid under agitation (20 min, 50 °C). The resin was then successively washed with DMF, DCM, and DMF. Cleavage from the resin following the general procedure yielded Fc-PNA conjugate **7** as a yellowish solid. Yield: 83% (31.3 mg, 8.3 μmol). HPLC: t_R = 12.5 min, 100%. MALDI-TOF MS: *m*/*z* (%) = 3785.5 $[M+H]^+$ (100).

Preparation of Fc-PNA-Conjugate 3. 2.00 mg (2.0 μmol) of PNA oligomer **1** was dissolved in an Eppendorf tube in 150 μL of a 1:1 (v/v) mixture of acetonitrile/water containing 10 equiv of DIPEA and 10 equiv of 2,6-lutidine. Successively, the following 1% solutions were added under nitrogen flow: 0.73 mg (3.0 μmol) of azidomethylferrocene in a 1:1 (v/v) mixture of acetonitrile/water, 1.2 mg (6.1 μmol) of sodium L-ascorbate in water, and 0.29 mg (2.0 μmol) of copper(I) bromide in acetonitrile. The reaction mixture was shaken for 2 days. Subsequently, acetonitrile was removed under reduced pressure. The remaining residue was treated with ice-cold diethyl ether, and the supernatant was removed from the resulting precipitate. After washing three times with diethyl ether and air-drying, **3** was obtained as a yellowish solid. Yield: 73% (1.8 mg, 1.5 μmol). MALDI-TOF MS: *m*/*z* (%) = 1279.0 $[M+H+CH_3CN]^+$ (100).

Preparation of Fc-PNA Conjugates 4, 5, 6, 10, 11. Conjugation of ferrocene via [2 + 3]-azide/alkyne cycloaddition was performed on polystyrene resins, which were preloaded with an alkyne or azide functionalized PNA oligomer under inert conditions. All solvents were taken out of crown cap bottles and Eppendorf tubes were flushed with nitrogen before use. Following the synthesis of the azide/alkyne-functionalized PNA oligomers, the resin beads were washed and shrunk with methanol (30 min) and completely dried under reduced pressure. The syringe was then flushed with nitrogen, and the resin was washed and swollen for 1 h with dry DMF. The following solutions were prepared: DIPEA and 2,6-lutidine (each 10 equiv) in DMF, 1% of an azide or alkyne functionalized ferrocene derivative (5 equiv) in DMF, and 1% copper(I) bromide (1 equiv) in acetonitrile. These solutions were successively introduced into the syringe containing the preloaded resin. This reaction mixture was shaken for the given reaction time at ambient temperature. Subsequently, the resin was successively washed with DMF, CH_2Cl_2, CH_3CN, CH_2Cl_2, and DMF. All ferrocene-labeled PNA oligomers were cleaved from the resin following the general procedure.

Preparation of Fc-PNA Conjugate 4. 50 mg (10 μmol) of the resin TentaGel S RAM (0.20 mmol/g), which was preloaded with the propynoic acid functionalized PNA oligomer **1**, was converted according to the general procedure with 11.4 mg (50 μmol, 5 equiv) of azidoferrocene in 2 days. Cleavage from the resin yielded **4** as a yellowish solid. Yield: 78% (8.6 mg, 7.0 μmol). HPLC: t_R = 13.7 min. ESI-MS: *m*/*z* (%) = 1223.2 $[M+H]^+$ (41), 612.2 $[M+2H]^{2+}$ (100).

Preparation of Fc-PNA Conjugate 5. 50 mg (10 μmol) of the resin TentaGel S RAM (0.20 mmol/g), which was preloaded with the azide-functionalized PNA oligomer **2**, was converted

according to the general procedure with 10.5 mg (50 μmol, 5 equiv) of ethynylferrocene in two days. Cleavage from the resin yielded **5** as a yellowish solid. Yield: 88% (10.9 mg, 8.8 μmol). HPLC: t_R = 13.2 min. ESI-MS: *m*/*z* (%) = 1237.2 $[M+H]^+$ (25), 619.2 $[M+2H]^{2+}$ (100).

Preparation of Fc-PNA Conjugate 6. 50 mg (10 μmol) of the resin TentaGel S RAM (0.20 mmol/g), which was preloaded with the azide-functionalized PNA oligomer **2**, was converted according to the general procedure with 16.2 mg (50 μmol, 5 equiv) of DEPA−ferrocene in two days. Cleavage from the resin following the general procedure yielded **6** as a yellowish solid. Yield: 91% (12.3 mg, 9.1 μmol). HPLC: t_R = 13.1 min, 100%. ESI-MS: *m*/*z* (%) = 1350.3 $[M+H]^+$ (22), 675.7 $[M+2H]^{2+}$ (100).

Preparation of Fc-PNA Conjugate 10. 50 mg (9 μmol) of the resin TentaGel R PHB Cys(Trt)Fmoc (0.18 mmol/g), which was preloaded with the propynoic acid functionalized PNA oligomer **8**, was converted according to the general procedure with 10.2 mg (45 μmol, 5 equiv) of azidoferrocene in 2 days. Cleavage from the resin following the general procedure yielded **10** as a yellowish/greenish solid. Yield: 74% (25.7 mg, 6.7 μmol). HPLC: t_R = 14.8 min, 100%. MALDI-TOF MS: *m*/*z* = 3841.1 $[M+H]^+$ (100).

Preparation of Fc-PNA Conjugate 11. 50 mg (9 μmol) of the resin TentaGel R PHB Cys(Trt)Fmoc (0.18 mmol/g), which was preloaded with the azide-functionalized PNA oligomer **9**, was converted according to the general procedure with 9.45 mg (45 μmol, 5 equiv) of ethynylferrocene in 2 days. Cleavage from the resin following the general procedure yielded **11** as a yellowish/greenish solid. Yield: 76% (26.1 mg, 6.8 μmol). HPLC: t_R = 13.7 min, 100%. MALDI-TOF MS: *m*/*z* (%) = 3819.8 $[M+H]^+$ (100).

RESULTS AND DISCUSSION

As a proof of principle, all synthetic reactions and electrochemical studies were first undertaken on a trimer PNA model sequence H-t-t-t-Lys-NH_2. Selected reactions were subsequently carried out on 12mer bacterial PNA sequences to verify the compatibility of the key reactions with mixed-sequence PNA oligomers and various protecting groups.

Synthesis of Azide- or Alkyne-Functionalized PNA Oligomers 1, 2, 8, 9. All PNA oligomers were synthesized by manual standard solid-phase synthesis using Fmoc-protected PNA monomers (see Table 1 for a summary of the sequences synthesized in this work and Schemes 1 and 2 for synthesis details). Oligomers with the trimer model sequence H-t-t-t-Lys-NH_2 were synthesized on Fmoc-Lys(Boc) preloaded TentaGel S RAM resin, while 12mer oligomers were synthesized on Fmoc-Cys(Trt) preloaded TentalGel R PHB resin. Additionally, the Fmoc-protected amino acids lysine (with Boc-side chain protection) and aminohexanoic acid were introduced to increase the solubility of PNAs and as a spacer molecule, respectively. For the synthesis of **2** and **9**, an azide function was introduced by coupling 2-azidoacetic acid (*45*) to the Fmoc-deprotected N-terminus of the PNA oligomer. Correspondingly, for the synthesis of **1** and **8**, an alkyne function was introduced by peptide coupling of propynoic acid to the *N*-terminus. The coupling of 2-azidoacetic acid proceeded under conditions analogous to those for the coupling of α-amino acids and therefore offers the possibility of automation. On the contrary, the coupling of propynoic acid under standard conditions had to be repeated several times until complete conversion was achieved as shown by a negative Kaiser test (*46*). Cleavage from the resin with TFA/TIS/phenol 85:5:10 (v/v/v), precipitation with diethyl ether followed by centrifugation gave products **1**, **2**, **8**, and **9** in good yield and purity. The ESI mass spectra of compounds **1** and **2** show both the $[M+H]^+$ and $[M+2H]^{2+}$ peaks, while the MALDI spectra of **8** and **9** show only the monocationic $[M+H]^+$ peak. Mass spectrometry of the crude products only revealed product mass peaks and no peaks corresponding to truncated sequence fragments. This, in combination with clean HPL chromatograms, proves that all reactions including the coupling of the alkynyl and azido carboxylic acids occurred with nearly complete conversion. However, comparison of mass spectra and analytical HPL chromatograms show that the azide-functionalized PNA oligomers **2** and **9** are not completely stable toward our routine HPL chromatography conditions.

Table 1. Sequences and MS Data of PNA Oligomers 1−11

PNA	Sequence	M_{calc}	M_{found}
1	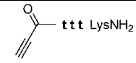	995.4	996.3[a]
2	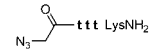	1026.4	1027.3[a]
3	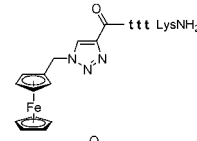	1237.1	1279.0[b]
4	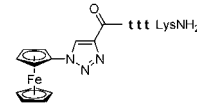	1222.4	1223.2[a]
5	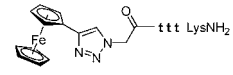	1236.5	1237.2[a]
6	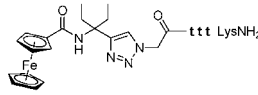	1349.5	1350.3[a]
7	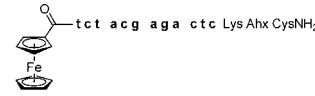	3785.6	3785.5[b]
8	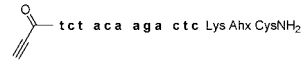	3609.6	3613.5[b]
9	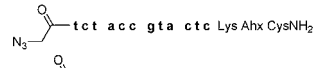	3607.6	3609.6[b]
10	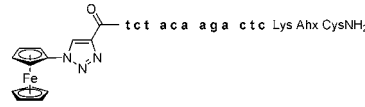	3836.6	3841.2[b]
11	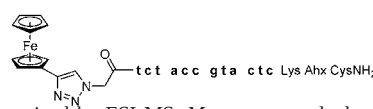	3817.6	3819.8[b]

[a] Determined by ESI MS. M_{calc} corresponds the calculated monoisotopic mass. [b] Determined by MALDI-TOF MS. M_{calc} corresponds to the calculated average mass.

Synthesis of Fc-PNA Conjugates 3−7, 10, 11. The conversion of the azide or alkyne functionalized PNA oligomers **1**, **2**, **8**, and **9** in a [2 + 3] azide/alkyne cycloaddition was performed with different alkyne or azide functionalized ferrocene derivatives, namely, the commercially available ferrocene derivative ethynylferrocene and the synthesized derivatives azidoferrocene (*47*), azidomethylferrocene (*48*), and the diethylpropargylamine ferrocene derivative *N*-(3-ethylpent-1-yn-3-yl)ferrocene-carboxamide (DEPA−ferrocene) (*49*). The cycloaddition reactions with ethynylferrocene, azidoferrocene, and DEPA−ferrocene were performed on the solid support, starting from the synthesized azide or alkyne functionalized PNA oligomers **1**, **2**, **8**, or **9** (Schemes 1 and 2). The reactions were carried out in syringes with a frit at the bottom under argon in thoroughly dried solvents using similar reaction conditions to those recently reported by our group for the synthesis of mono- and multiferrocene-

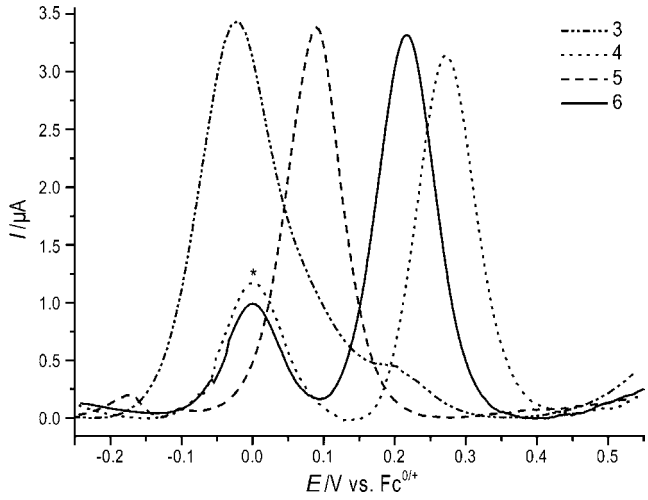

Figure 1. Overlay of differential pulse voltammograms (anodic scan; background subtracted) of Fc conjugates of PNA trimers **3**, **4**, **5**, and **6** at a glassy carbon electrode in 1:1 (v/v) mixture of CH_3CN and MOPS-buffer (0.15 M, pH 7.4) containing $NaClO_4$ as the supporting electrolyte (0.2 M). The experiments were undertaken at a scan rate of 4 mV/s with ferrocene as internal reference for **4** and **6** (smaller signals around 0 V, marked by an asterisk) and as external reference for **3** and **5**.

containing peptides (*50*) and PNA oligomers (*42*). Hence, the preloaded resins were treated with a reagent mixture containing copper(I) bromide as the catalyst and the respective ferrocene derivative. The reactions were carried out in DMF with small amounts of acetonitrile as cosolvent to achieve complete solubility of copper(I) bromide. After cleavage of the oligomer from the resin with TFA/TIS/phenol 85:5:10 (v/v/v), precipitation with ice-cold diethyl ether and lyophilization of the acetonitrile/water solutions, the crude products of **4**, **5**, **6**, **10**, and **11** were obtained as slightly orange powders.

The ESI mass spectra of products **4**, **5**, and **6** show the molecular peak $[M+H]^+$ with low intensity and the calculated peak $[M+2H]^{2+}$ as the base peak. ESI-MS of the crude products only revealed product peaks and not even trace signals of the azide or alkyne functionalized PNA precursors. This, again in combination with HPL chromatography of the crude products, proves that all cycloadditions occurred with practically complete conversion. Furthermore, it indicates that all synthesized Fc-PNA bioconjugates **4**, **5**, and **6** are completely stable to the fairly harsh (for organometallic compounds) cleavage conditions. MALDI-TOF spectra of 12mer Fc-PNA conjugates **10** and **11** reveal as well only peaks $[M+H]^+$ of the clicked products, as found during our previous investigations (*42*). No peaks originating from the azide and alkyne precursors could be detected. HPLC purification was performed to reduce the salt content of the crude products. An overall comparison of the trimer models **4**, **5**, and **6** with analytical data for the 12mer PNA conjugates **10** and **11** did not show any general difference in conversion, purity, or yield. This underscores that the solid-phase conversion of azide- or alkyne-functionalized PNA oligomers in a [2 + 3] cycloaddition with the chosen alkyne or azide ferrocene derivatives, respectively, is compatible with all four PNA monomers and qualified for the ferrocene labeling of even longer mixed-sequence PNA oligomers.

The synthesis of Fc-PNA conjugate **7** succeeded according to the literature procedure (*51*). Comparison of MALDI-TOF spectra and HPL chromatograms of the crude product **7** with those of the crude products **10** and **11** shows that the conjugation of a ferrocene moiety by click chemistry (**10**, **11**) yields comparable conversion and purity like the known conjugation of ferrocene carboxylic acid by peptide coupling (**7**). Click

Table 2. Half-Wave Potentials ($E_{1/2}$), Peak Separation Values (ΔE_p), and Peak Current Ratios (I_{pc}/I_{pa}) of Fc-PNA Trimer Conjugates 3, 4, 5, and 6 as Determined by Cyclic Voltammetry[a]

no.	scan rate/ mVs^{-1}	$E_{1/2}$ vs $FcH^{0/+}$/ mV	ΔE_p/ mV	I_{pa}/ μA	I_{pc}/ μA	I_{sp}/ μA	I_{pc}/I_{pa}
3	250	−14	+114	−9.45	+5.83	−9.14	1.17
4	250	+269	+87	−3.73	+1.22	−3.05	0.81
5	250	+97	+79	−5.41	+2.88	−3.39	0.92
6	250	+208	+80	−2.66	+1.40	−1.88	0.96
FcH	250	0	+72	−10.67	+7.17	−4.98	0.99

[a] Data for ferrocene (FcH) measured under identical conditions are included for comparison. E_{pa} = anodic peak potential; E_{pc} = cathodic peak potential; half-wave potential $E_{1/2} = (E_{pa} + E_{pc})/2$; I_{pa} = anodic peak current; I_{pc} = cathodic peak current; peak separation value $\Delta E_p = E_{pa} - E_{pc}$; I_{sp} = current at switching potential; peak current ratios I_{pc}/I_{pa} determined as described in experimental section.

Table 3. Peak Potentials (E_p), Peak Currents (I_p), and Peak Widths ($w_{1/2}$) of Fc-PNA Trimer Conjugates 3, 4, 5, and 6 as Determined by Differential Pulse Voltammetry[a]

no	ΔE_p vs $FcH^{0/+}$ /mV	I_p /μA	$w_{1/2}$ /mV
3	−20	−3.92	131
4	+272	−3.14	103
5	+89	−8.46	90
6	+212	−3.32	100

[a] Scan rate 4 mVs^{-1}; voltage range 0−800 mV; modulation amplitude 10 mV; pulse width = 50 ms.

chemistry is even superior to the more traditional peptide coupling procedure in that it allows conjugation of a larger range of chemically diverse, commercially available, or easy-to-synthesize ferrocene derivatives. Furthermore, identical procedures and reagent concentrations for the click chemistry labeling with ethynylferrocene, azidoferrocene, and DEPA−ferrocene offer the possibility for automation. This flexibility is crucial for the preparation of PNA biosensors, since it allows the synthesis of metal−PNA conjugates with different electrochemical potentials.

Besides the successful introduction of azidoferrocene, ethynylferrocene, and DEPA−ferrocene, also an N-terminal labeling by click chemistry with azidomethyl ferrocene was attempted on a resin which was preloaded with the alkynyl functionalized PNA oligomer **1**. After cleavage and precipitation with cold ether, the product was characterized by ESI-MS. A major peak at m/z = 1039.3 corresponds to the PNA t_3-trimer, carrying a triazole ring at the N-terminus but *without* an attached ferrocene moiety. We thus conclude that the click reaction had taken place but yielded a product that is not stable to the relatively harsh PNA cleavage conditions as recently reported by Spiccia et al. in their endeavor to synthesize a ferrocenyl PNA monomer (see above and Experimental Procedures) (*52, 53*). We assume that the acidic cleavage conditions first cause a protonation of triazole N-3. In the presence of nucleophiles, the N−C bond is then cleaved with formation of the relatively stable ferrocenyl methyl cation, which finally forms ferrocenylmethanol. Following this line of argument, it is only the strongly acidic cleavage conditions that cause decomposition of the desired oligomer **3**. To exclude the possibility of inherent instability of **3**, the click reaction of azidomethyl ferrocene with the PNA trimer **1** was performed in solution as a postsynthetic labeling strategy. This finally succeeded and gave Fc-PNA conjugate **3** in good yield and purity. The MALDI-TOF mass spectrum of **3** after precipitation and washing revealed just one major peak corresponding to the $[M+H+CH_3CN]^+$ molecular ion. This synthetic work thus reveals the scope of click chemistry for the labeling of PNA oligomers with organometallic complexes. Since an instability toward harsh reaction conditions, e.g., the strong acidic PNA cleavage conditions, is a characteristic of many classes of metal complexes, click chemistry as a key reaction

Scheme 1. Synthesis of Fc-PNA Trimer Conjugates 3, 4, 5, and 6 and Corresponding Azide- and Alkyne-Functionalized PNA Precursors 1 and 2[a]

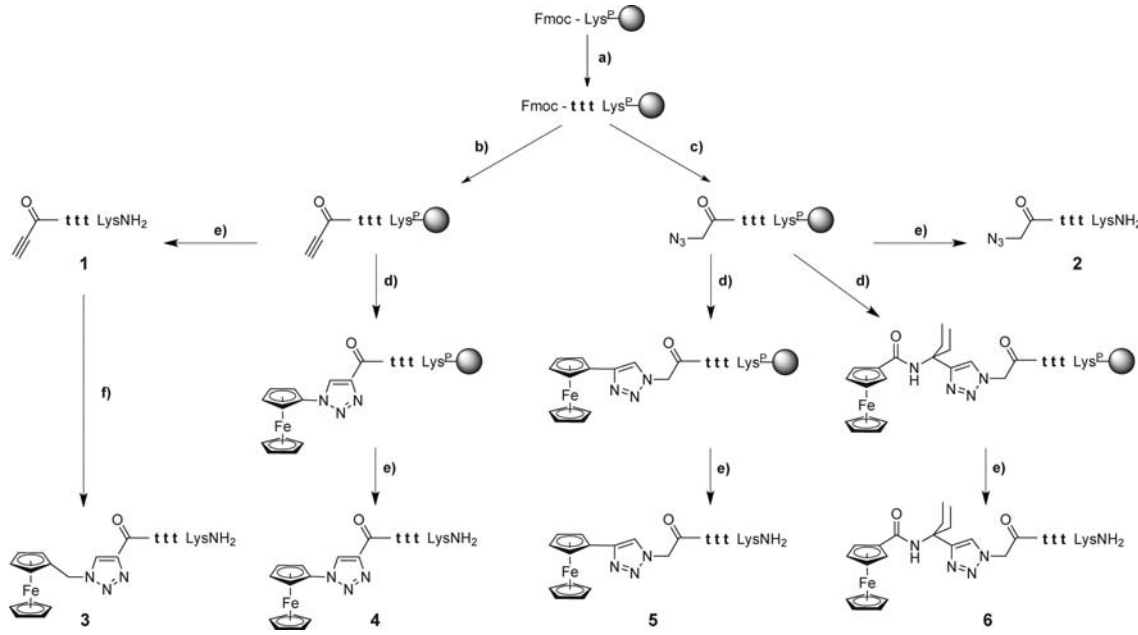

[a] (a) Standard Fmoc solid-phase PNA synthesis. (b) Coupling of propynoic acid, HATU, DIPEA, 2,6-lutidine in DMF. (c) Coupling of 2-azidoacetic acid, TBTU, HOBt·H_2O, DIPEA, 2,6-lutidine in DMF. (d) Click reaction on solid support: Ferrocene derivative (**4**, azidoferrocene; **5**, ethynylferrocene; **6**, DEPA−ferrocene), DIPEA, 2,6-lutidine in DMF; CuBr in CH_3CN. (e) Cleavage: TFA/TIS/Phenol. (f) Click reaction in solution: Azidomethylferrocene, DIPEA, 2,6-lutidine, CuBr in H_2O/CH_3CN. See experimental section for details, "Lys^P" denotes N-Boc protected lysine.

in the synthesis of metal-PNA conjugates is not just applicable as part of the solid-phase synthesis scheme but furthermore offers a reliable alternative as a postsynthetic labeling strategy, effectively yielding the same products.

Electrochemical Studies. The electrochemical behavior of the Fc-PNA conjugates **3**, **4**, **5**, and **6** with the trimer model sequence H-t-t-t-Lys-NH_2 was examined by cyclic voltammetry (CV) and differential pulse voltammetry (DPV). Each of these four compounds contains a ferrocene moiety that was attached to the N-terminus of the t_3-PNA sequence via one of the four specific click reactions described above. Fc-PNA trimer conjugates **3**, **4**, **5**, and **6** present structurally comparable compounds that only show differences in the chemical environment of the ferrocene moiety. An electrochemical microvolume cell with a stationary glassy carbon working electrode, Ag/AgCl in aq KCl (3 M) as reference electrode, and a platinum wire as counter electrode was used. All electrochemical measurements were undertaken with 80 μL of 0.8 mM solutions of the respective Fc-PNA bioconjugate in a 1:1 (v/v) mixture of acetonitrile and MOPS buffer (0.15 M, pH = 7.4) with $NaClO_4$ (0.2 M) as the supporting electrolyte. CV and DPV of ferrocene were performed in the same electrolyte solution, and the electrochemical half-wave potential $E_{1/2}$ of the redox couple ferrocene/ferrocenium $FcH^{0/+}$ vs Ag/AgCl ($E_{1/2}$ = 270 mV) was set to 0 mV as the reference potential for all measurements. Ferrocene was used as an internal reference for the DPV measurements of **4** and **6**. For the DPV measurements of **3** and **5** and for all CV measurements, ferrocene was used as an external reference to avoid an overlap of the corresponding redox processes (Figure 1).

Cyclic voltammograms of all Fc-PNA conjugates revealed one-electron waves with quasi-reversible Nernst behavior. Peak separations ΔE_p between +80 mV and +114 mV were observed, which are 8 to 42 mV higher than the ΔE_p value obtained with the same electrochemical setup for the fully reversible redox couple $FcH^{0/+}$(ΔE_p = +72 mV). Fc-PNA conjugates **5** and **6** yield current ratios I_p^{ox}/I_p^{red} close to unity, while conjugate **3** shows a higher value of 1.17 and conjugate **4** shows a lower value of 0.81, both still being sufficiently close to unity for practical biosensor applications.

The electrochemical half-wave potentials $E_{1/2}$ (vs $FcH^{0/+}$) are determined by CV and spread over 280 mV, ranging from $E_{1/2}$ = −14 mV for compound **3** to $E_{1/2}$ = +269 mV for compound **4**. These electrochemical potentials could be confirmed with DPV. Oligomer **6** revealed a half-wave potential of $E_{1/2}$ = +208 mV vs. $FcH^{0/+}$. This value corresponds well to the literature

Scheme 2. Azide- and Alkyne-Functionalized PNA Oligomers 8 and 9 and Fc-PNA Conjugates 10 and 11 with Bacterial 12mer PNA Sequences[a]

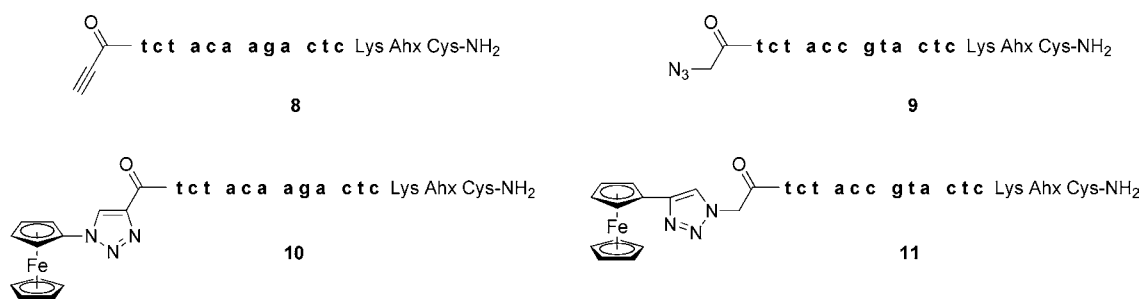

[a] See experimental section for details of the syntheses.

values for PNA with a peptidic bound ferrocene moiety (*51*), which was expected, since oligomer **6** is derived from a propargylamido ferrocene derivative and therefore contains a Cp-bound carboxamido function. Compound **4** reveals a potential of $E_{1/2} = +269$ mV vs $FcH^{0/+}$, showing a shift to positive potentials of 61 mV compared to **6**. In contrast, a potential of $E_{1/2} = +97$ mV vs $FcH^{0/+}$ was determined for oligomer **5**, a shift of 111 mV to negative potentials compared to **6**. Both conjugates **4** and **5** contain ferrocene moieties carrying the triazole structure in α-position to the Cp ring. The ferrocene moiety of **4** is bound to a nitrogen atom (N-1), whereas the ferrocene moiety of **5** is bound to a C_{sp2} atom (C-4) of the respective triazole ring. Independent of any effects of a possible Cp/triazole-conjugation, it can be assumed that differences in the electronegativity of the respective Cp-bound triazole ring atoms have a strong influence on the determined differences in the half-wave potentials of **4** and **5** (*54*). In contrast, the ferrocene moiety of oligomer **3** is disconnected from the triazole ring via a methylene bridge. The determined half-wave potential of **3** just exhibits a small shift to negative potentials compared to ferrocene/ferrocenium ($E_{1/2} = -14$ mV vs $FcH^{0/+}$), which is comparable to literature values for methyl or methylene substituted ferrocene derivatives (*55*).

The minimum differences in the electrochemical half-wave potentials $\Delta E_{1/2}^{min}$ of all Fc-PNA trimer conjugates **3**, **4**, **5**, and **6** were determined from Table 2. Conjugates **4** and **6** show a minimum value of $\Delta E_{1/2}^{min}$ (4, 6) = 61 mV, whereas conjugates **6** and **5** as well as **5** and **3** reveal values of $\Delta E_{1/2}^{min}$ (5, 6) = 111 mV (= $\Delta E_{1/2}^{min}$ (3, 5)). An overlay of differential pulse voltammograms of the four Fc-PNA trimer conjugates **3**, **4**, **5**, and **6** nicely demonstrates the differences in the electrochemical potentials (Figure 1). Generally, potential differences in this range are significant for a reliable resolution with sensitive electrochemical methods like differential pulse voltammetry (DPV) or square wave voltammetry (SWV). Figure 1 reveals that, even with consideration of the respective peak width $w_{1/2}$, ranging from 90 mV for **5** to 131 mV for **3** (see Table 3), a good resolution of the electrochemical potentials is possible, and therefore, a reliable distinction of the Fc-PNA conjugates **3**, **4**, **5**, and **6** with DPV is ensured.

CONCLUSIONS

In summary, the facile, reliable, and high-yielding preparation of new Fc-containing PNA oligomers was accomplished in this work using the click chemistry methodology. In contrast to all earlier work which had used ferrocene carboxylic acid as an electroactive label for PNA oligomers (*56*−*59*), the synthetic method used here allows the formation of a small library of new ferrocenyl PNA bioconjugates through the use of different ferrocenyl starting materials, but employing the same "click" chemistry. Accordingly, different electrochemical potentials could be encoded into PNA oligomer sequences by using one and the same type of reaction. Using the same conditions for the introduction of different labels is a bonus for automation, e.g., for an on-chip or parallel library synthesis. A similar approach was utilized by Seela et al. for the labeling of all four nucleobases with coumarin dyes by click chemistry (*60*). Our electrochemical analysis shows that the four ferrocenyl−triazole PNA oligomers described exhibit electrochemical potentials with potential differences bigger than 60 mV, which can be reliably distinguished by electrochemical methods like DPV. This is unprecedented and of significant interest for a potential application of PNA as electrochemical nucleic acid biosensors. In principle at least, the use of four different potentials in electrochemical labels (called "four-potential" labeling) corresponds to the "four-color" detection with four different dyes in classical DNA analysis. Kuhr and co-workers were the first to show a related electrochemical "four-potential" detection scheme with ferrocene-labeled DNA (*61*, *62*). Apart from the fact that different chemistry had to be used in Kuhr's work for the introduction of all four ferrocene labels into the DNA oligomers, PNA clearly has advantages for DNA biosensors because of its higher affinity and superior mismatch discrimination. Investigations of the electrochemical responses of these oligomers with (non)cDNA/RNA sequences is currently underway in our laboratories and will be published in due course.

ACKNOWLEDGMENT

N.H. is the recipient of a Ruhr-University Research School fellowship for doctoral students. G.G. thanks the Alexander von Humboldt Foundation for a research fellowship. The authors thank Prof. Mallayan Palaniandavar for helpful discussions on the electrochemical measurements and Prof. Wolfgang Schuhmann and his co-workers for experimental help and assistance in the preparation of the glassy carbon electrodes and the microvolume electrochemical cell.

Supporting Information Available: ESI-MS and MALDI-MS data for all oligomers, HLPC, cyclic voltammograms. This material is available free of charge via the Internet at http://pubs.acs.org.

LITERATURE CITED

(1) Nielsen, P. E., Egholm, M., Berg, R. H., and Buchardt, O. (1991) Sequence-selective recognition of DNA by strand displacement with a thymine-substituted polyamide. *Science 254*, 1497–1500.

(2) Egholm, M., Nielsen, P. E., Buchardt, O., and Berg, R. H. (1992) Recognition of guanine and adenine in DNA by cytosine and thymine containing peptide nucleic acids (PNA). *J. Am. Chem. Soc. 114*, 9677–9678.

(3) Egholm, M., Buchardt, O., Nielsen, P. E., and Berg, R. H. (1992) Peptide nucleic acids (PNA). Oligonucleotide analogs with an achiral peptide backbone. *J. Am. Chem. Soc. 114*, 1895–1897.

(4) Uhlmann, E., Will, D. W., Breipohl, G., Peyman, A., Langner, D., Knolle, J., and O'Malley, G. (1997) Synthesis of polyamide nucleic acids (PNAs), PNA/DNA-chimeras and phosphonic ester nucleic acids (PHONAs). *Nucleosides Nucleotides 16*, 603–608.

(5) Uhlmann, E. (1998) Peptide nucleic acids (PNA) and PNA-DNA chimeras. From high binding affinity towards biological function. *Biol. Chem. 379*, 1045–1052.

(6) Larsen, H. J., Bentin, T., and Nielsen, P. E. (1999) Antisense properties of peptide nucleic acid. *Biochim. Biophys. Acta 1489*, 159–166.

(7) Soomets, U., Hällbrink, M., and Langel, Ü. (1999) Antisense properties of peptide nucleic acids. *Front. Bioscience 4*, d782–786.

(8) Koppelhus, U., and Nielsen, P. E. (2003) Cellular delivery of peptide nucleic acid (PNA). *Adv. Drug. Delivery Rev. 55*, 267–280.

(9) Metzler-Nolte, N. (2006) Conjugates of peptides and PNA with organometallic complexes: syntheses and applications. *Bioorganometallics* (Jaouen, G., Ed.) pp 125−179, Wiley-VCH, Weinheim.

(10) Ratilainen, T., Holmén, A., Tuite, E., Haaima, G., Christensen, L., Nielsen, P. E., and Nordén, B. (1998) Hybridization of peptide nucleic acid. *Biochemistry 37*, 12331–12342.

(11) Ratilainen, T., Holmén, A., Tuite, E., Nielsen, P. E., and Nordén, B. (2000) Thermodynamics of sequence-specific binding of PNA to DNA. *Biochemistry 39*, 7781–7791.

(12) Wang, G., and Xu, X. S. (2004) Peptide nucleic acid (PNA) binding-mediated gene regulation. *Cell Res. 14*, 111–116.

(13) Knudsen, H., and Nielsen, P. E. (1996) Antisense properties of duplex- and triplex-forming PNAs. *Nucleic Acids Res. 24*, 494–500.

(14) Good, L., and Nielsen, P. E. (1997) Progress in developing PNA as a gene-targeted drug. *Antisense Nucl. Acid Drug Dev. 7*, 431–437.
(15) Wang, J., Palecek, E., Nielsen, P. E., Rivas, G., Cai, X., Shiraishi, H., Dontha, N., Luo, D., and Farias, P. A. M. (1996) Peptide nucleic acid probes for sequence-specific DNA biosensors. *J. Am. Chem. Soc. 118*, 7667–7670.
(16) Wang, J. (1998) DNA biosensors based on peptide nucleic acid (PNA) recognition layers. A review. *Biosens. Bioelectron. 13*, 757–762.
(17) Wang, J. (1999) PNA biosensors for nucleic acid detection. *Peptide Nucleic Acids* (Nielsen, P. E., Egholm, M., Ed.) pp 155−161, Horizon Scientific Press, Wymondham.
(18) Mateo-Martí, E., Briones, C., Pradier, C. M., and Martín-Gago, J. A. (2007) A DNA biosensor based on peptide nucleic acids on gold surfaces. *Biosens. Bioelectron. 22*, 1926–1932.
(19) Wang, J. (1999) PNA biosensors for nucleic acid detection. *Curr. Issues Mol. Biol. 1*, 117–122.
(20) Steichen, M., Decrem, Y., Godfroid, E., and Buess-Herman, C. (2007) Electrochemical DNA hybridization detection using peptide nucleic acids and $[Ru(NH_3)_6]^{3+}$ on gold electrodes. *Biosens. Bioelectron. 22*, 2237–2243.
(21) Aoki, H., and Umezawa, Y. (2002) High sensitive ion-channel sensors for detection of oligonucleotides using PNA modified gold electrodes. *Electroanalysis 14*, 1405–1410.
(22) Degefa, T. H., and Kwak, J. (2008) Electrochemical impedance sensing of DNA at PNA self assembled monolayer. *J. Electroanal. Chem. 612*, 37–41.
(23) Liu, J., Tian, S., Nielsen, P. E., and Knoll, W. (2005) In situ hybridization of PNA/DNA studied label-free by electrochemical impedance spectroscopy. *Chem. Commun.* 2969–2971.
(24) Le Floch, F., Ho, H.-A., Harding-Lepage, P., Bédard, M., Neagu-Plesu, R., and Leclerc, M. (2005) Ferrocene-functionalized cationic polythiophene for the label-free electrochemical detection of DNA. *Adv. Mater. 17*, 1251–1254.
(25) Wang, Y., Li, C., Li, X., Li, Y., and Kraatz, H.-B. (2008) Unlabeled hairpin-DNA probe for the detection of single-nucleotide mismatches by electrochemical impedance spectroscopy. *Anal. Chem. 80*, 2255–2260.
(26) Li, X., Lee, J. S., and Kraatz, H.-B. (2006) Electrochemical detection of single-nucleotide mismatches using an electrode microarray. *Anal. Chem. 78*, 6096–6101.
(27) Hess, A., and Metzler-Nolte, N. (1999) Transition metal labels on peptide nucleic acid (PNA) monomers. *Chem. Commun.* 885–886.
(28) Verheijen, J. C., van der Marel, G. A., van Boom, J. H., and Metzler-Nolte, N. (2000) Transition metal derivatives of peptide nucleic acid (PNA) oligomers-synthesis, characterization, and DNA binding. *Bioconjugate Chem. 11*, 741–743.
(29) Kolb, H. C., Finn, M. G., and Sharpless, K. B. (2001) Click chemistry: diverse chemical function from a few good reactions. *Angew. Chem., Int. Ed. 40*, 2004–2021.
(30) Huisgen, R. (1963) 1,3-Dipolar cycloadditions. *Angew. Chem. 75*, 604–637.
(31) Rostovtsev, V. V., Green, L. G., Fokin, V. V., and Sharpless, K. B. (2002) A stepwise Huisgen cycloaddition process: copper(I)-catalyzed regioselective "ligation" of azides and terminal alkynes. *Angew. Chem., Int. Ed. 41*, 2596–2599.
(32) Tornøe, C. W., Christensen, C., and Meldal, M. (2002) Peptidotriazoles on solid phase: [1,2,3]-triazoles by regiospecific copper(I)-catalyzed 1,3-dipolar cycloadditions of terminal alkynes to azides. *J. Org. Chem. 67*, 3057–3064.
(33) Moses, J. E., and Moorhouse, A. D. (2007) The growing applications of click chemistry. *Chem. Soc. Rev. 36*, 1249–1262.
(34) van Berkel, S. S., Dirks, A. J., Debets, M. F., van Delft, F. L., Cornelissen, J. J. L. M., Nolte, R. J. M., and Rutjes, F. P. J. T. (2007) Metal-free triazole formation as a tool for bioconjugation. *ChemBioChem 8*, 1504–1508.
(35) Laughlin, S. T., Baskin, J. M., Amacher, S. L., and Bertozzi, C. R. (2008) In vivo imaging of membrane-associated glycans in developing zebrafish. *Science 320*, 664–667.
(36) Gramlich, P. M. E., Warncke, S., Gierlich, J., and Carell, T. (2008) Click-click-click: single to triple modification of DNA. *Angew. Chem., Int. Ed. 47*, 3442–3444.
(37) Gramlich, P. M. E., Wirges, C. T., Manetto, A., and Carell, T. (2008) Postsynthetic DNA modification through the copper-catalyzed azide-alkyne cycloadditon reaction. *Angew. Chem., Int. Ed. 47*, 8350–8358.
(38) Wang, Q., Chan, T. R., Hilgraf, R., Fokin, V. V., Sharpless, K. B., and Finn, M. G. (2003) Bioconjugation by copper(I)-catalyzed azide-alkyne [3 + 2] cycloaddition. *J. Am. Chem. Soc. 125*, 3192–3193.
(39) Aucagne, V., and Leigh, D. A. (2006) Chemoselective formation of successive triazole linkages in one pot: "click-click" chemistry. *Org. Lett. 8*, 4505–4507.
(40) Speers, A. E., and Cravatt, B. F. (2004) Profiling enzyme activities in vivo using click chemistry methods. *Chem. Biol. 11*, 535–546.
(41) Chelmowski, R., Köster, S. D., Kerstan, A., Prekelt, A., Grunwald, C., Winkler, T., Metzler-Nolte, N., Terfort, A., and Wöll, C. (2008) Peptide-based SAMs that resist the adsorption of proteins. *J. Am. Chem. Soc. 130*, 14952–14953.
(42) Gasser, G., Hüsken, N., Köster, S. D., and Metzler-Nolte, N. (2008) Synthesis of organometallic PNA oligomers by click chemistry. *Chem. Commun.* 3675–3677.
(43) Habermüller, K., and Schuhmann, W. (1998) A low-volume electrochemical cell for the deposition of conducting polymers and entrapment of enzymes. *Electroanalysis 10*, 1281–1284.
(44) Nicholson, R. S. (1965) Theory and application of cyclic voltammetry for measurement of electrode reaction kinetics. *Anal. Chem. 37*, 1351–1355.
(45) Alvarez, S. G., and Alvarez, M. T. (1997) A practical procedure for the synthesis of alkyl azides at ambient temperature in dimethyl sulfoxide in high purity and yield. *Synthesis* 413–414.
(46) Kaiser, E., Colescott, R. L., Bossinger, C. D., and Cook, P. I. (1970) Color test for detection of free terminal amino groups in the solid-phase synthesis of peptides. *Anal. Biochem. 34*, 595–598.
(47) Sheinker, Y. N., Senyavina, L. B., and Zheltova, V. N. (1965) Position and intensity of the absorption band due to antisymmetric valence vibration of the N_3 group in the infrared spectra of organic azides. *Dokl. Akad. Nauk SSSR 160*, 1339–1342.
(48) Casas-Solvas, J. M., Vargas-Berenguel, A., Capitán-Vallvey, L. F., and Santoyo-González, F. (2004) Convenient methods for the synthesis of ferrocene-carbohydrate conjugates. *Org. Lett. 6*, 3687–3690.
(49) Brosch, O., Weyhermüller, T., and Metzler-Nolte, N. (2000) A two-step palladium-catalyzed coupling scheme for the synthesis of ferrocene-labeled amino acids. *Eur. J. Inorg. Chem.* 323–330.
(50) Köster, S. D., Dittrich, J., Gasser, G., Hüsken, N., Henao Castañeda, I. C., Jios, J. L., Della Védova, C. O., and Metzler-Nolte, N. (2008) Spectroscopic and electrochemical studies of ferrocenyl triazole amino acid and peptide bioconjugates synthesized by click chemistry. *Organometallics 27*, 6326–6332.
(51) Maurer, A., Kraatz, H.-B., and Metzler-Nolte, N. (2005) Synthesis and electrochemical characterization of metallocene-PNA oligomers. *Eur. J. Inorg. Chem.* 3207–3210.
(52) Gasser, G., Belousoff, M. J., Bond, A. M., and Spiccia, L. (2006) Facile synthesis and detailed characterization of a new ferrocenyl uracil peptide nucleic acid monomer. *J. Org. Chem. 71*, 7565–7573.
(53) Gasser, G., and Spiccia, L. (2008) Synthesis of a ferrocenyl uracil PNA monomer for insertion into PNA sequences. *J. Organomet. Chem. 693*, 2478–2482.
(54) Batterjee, S. M., Marzouk, M. I., Aazab, M. E., and El-Hashash, M. A. (2003) The electrochemistry of some ferrocene

derivatives: redox potential and substituent effects. *Appl. Organomet. Chem. 17*, 291–297.

(55) Gubin, S. P. (1970) Application of electrochemical methods in the organometallic chemistry of transition metal p-complexes. *Pure Appl. Chem. 23*, 463–487.

(56) Salmain, M., Metzler-Nolte, N. (2008) *The bioorganometallic chemistry of ferrocene. Ferrocenes* (Stepnicka, P., Ed.) pp 499−639, John Wiley & Sons, Chichester.

(57) van Staveren, D. R., and Metzler-Nolte, N. (2004) Bioorganometallic chemistry of ferrocene. *Chem. Rev. 104*, 5931–5985.

(58) Metzler-Nolte, N. (2006) Bioorganometallic Chemistry. *Comprehensive Organometallic Chemistry III* (Parkin, G., Ed.) pp 883−920, Elsevier, Amsterdam.

(59) Metzler-Nolte, N. (2004) Modifizierte DNA, PNA und ihre Anwendungen in der Medizin und Biotechnologie. *Molekulare Biotechnologie* (Wink, M., Ed.) pp 579−593, Wiley-VCH, Weinheim.

(60) Seela, F., Sirivolu, V. R., and Chittepu, P. (2008) The modification of DNA with octadiynyl side chains: synthesis, base pairing and formation of fluorescent coumarin dye conjugates of four nucleobases by the alkyne-azide "click" reaction. *Bioconjugate Chem. 19*, 211.

(61) Brazill, S. A., Kim, P. H., and Kuhr, W. G. (2001) Capillary gel electrophoresis with sinusoidal voltammetric detection: a strategy to allow four-"color" DNA sequencing. *Anal. Chem. 73*, 4882–4890.

(62) Brazill, S. A., and Kuhr, W. G. (2002) A single base extension technique for the analysis of known mutations utilizing capillary gel electrophoresis with electrochemical detection. *Anal. Chem. 74*, 3421–3428.

BC9001272

Supporting Information

"Four-potential" Ferrocene Labelling of PNA oligomers via Click Chemistry

Nina Hüsken, Gilles Gasser, S. David Köster and Nils Metzler-Nolte.

Table of Content

I. MALDI-TOF mass spectra (12mer PNA sequences)
- a) Alkyne-functionalized PNA oligomer
- b) Azido-functionalized PNA oligomer
- c) Ferrocene-PNA conjugates

II. ESI mass spectra (3mer PNA sequences)
- a) Alkyne-functionalized PNA oligomer
- b) Azido-functionalized PNA oligomer
- c) Ferrocene-PNA conjugates

III. HPL chromatograms
- a) Ferrocene-PNA conjugates (12mer)

IV. Cyclovoltammograms
- a) Ferrocene-PNA conjugates with model sequence H-t t t LysNH_2
- b) Ferrocene-PNA conjugates with 12mer bacterial sequences

I. MALDI-TOF mass spectra

a) Alkyne-functionalized PNA oligomers

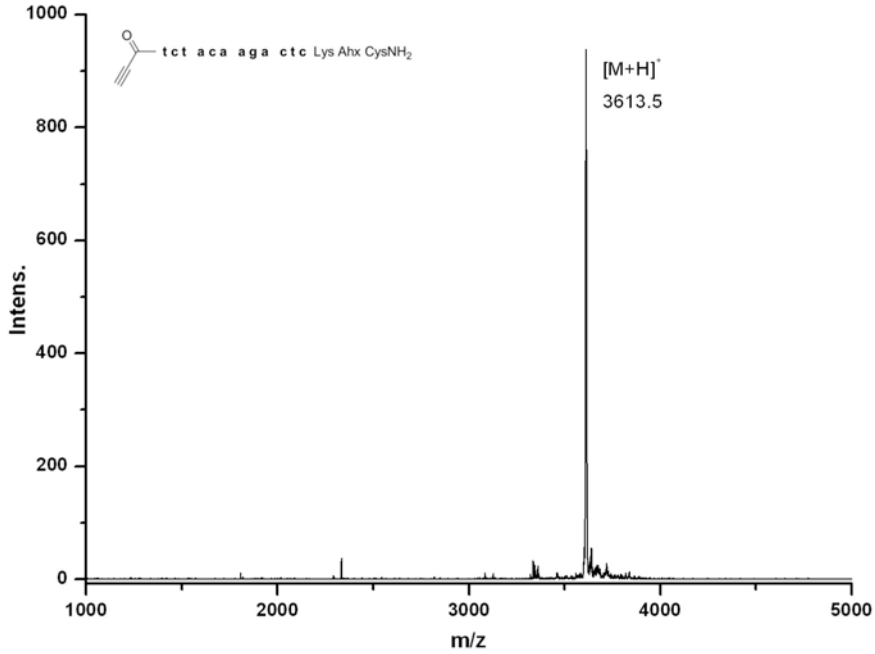

Fig. S1: MALDI-TOF mass spectrum of **8**.

b) Azide-functionalized PNA oligomer

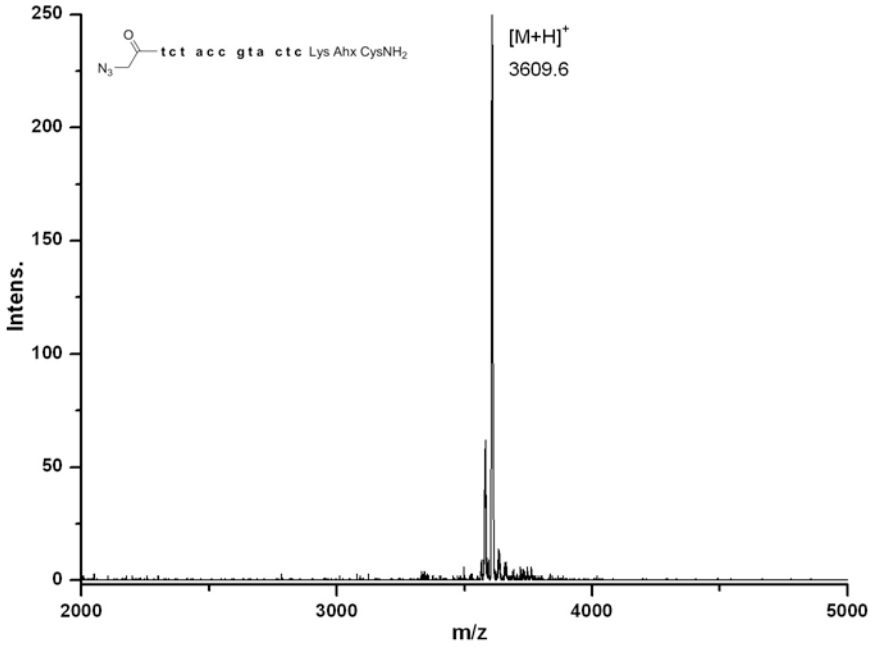

Fig. S2: MALDI-TOF mass spectrum of **9**.

c) Fc-PNA conjugates

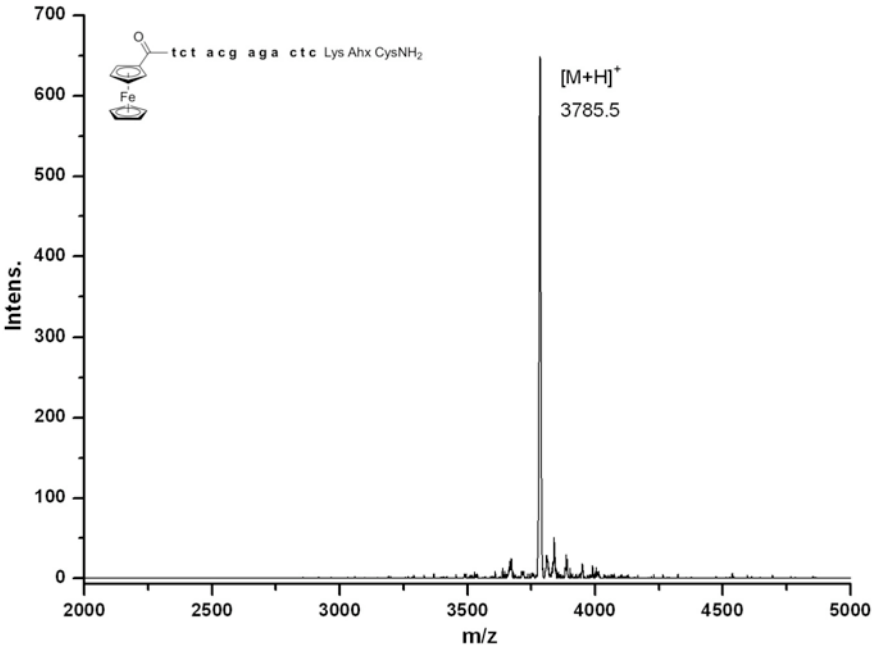

Fig. S3: MALDI-TOF mass spectrum of **7**.

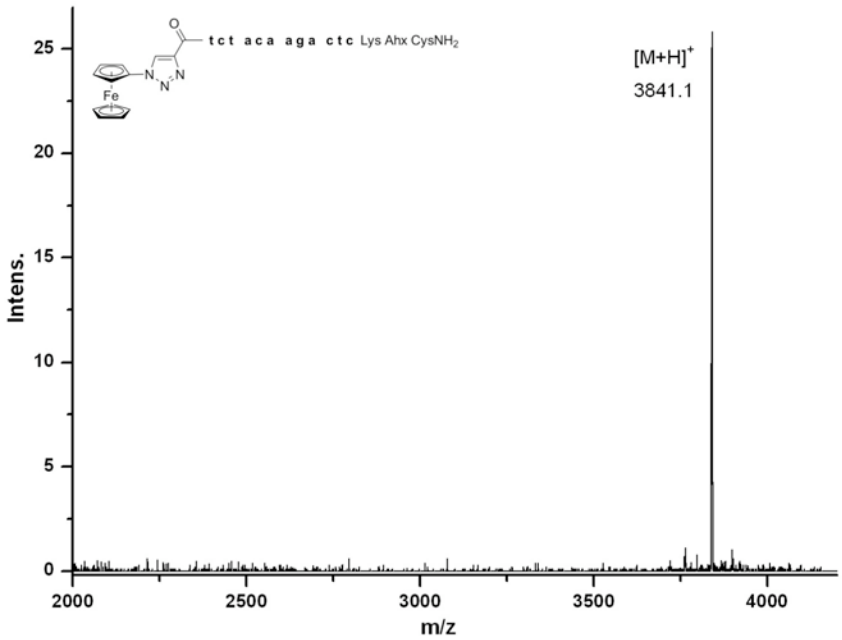

Fig. S4: MALDI-TOF mass spectrum of **10**.

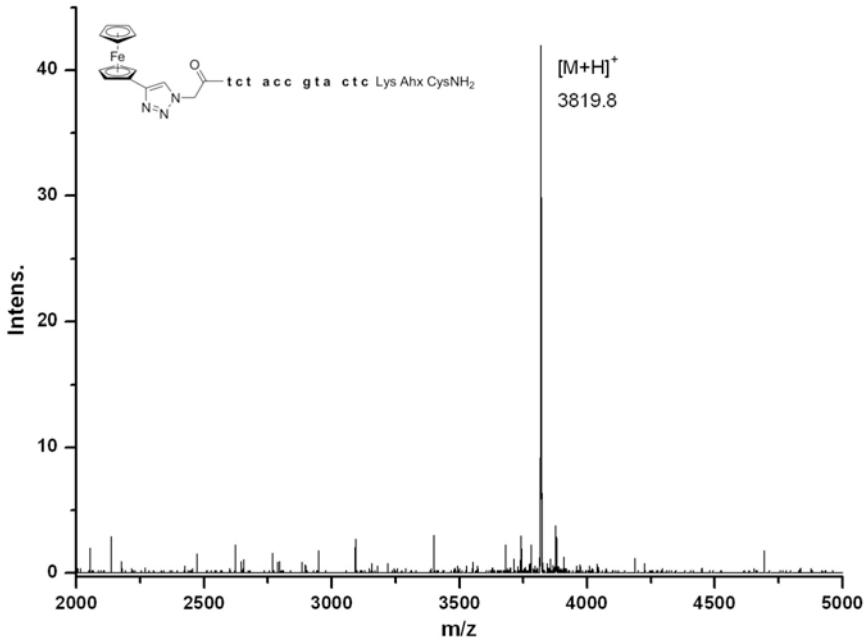

Fig. S5: MALDI-TOF mass spectrum of **11**.

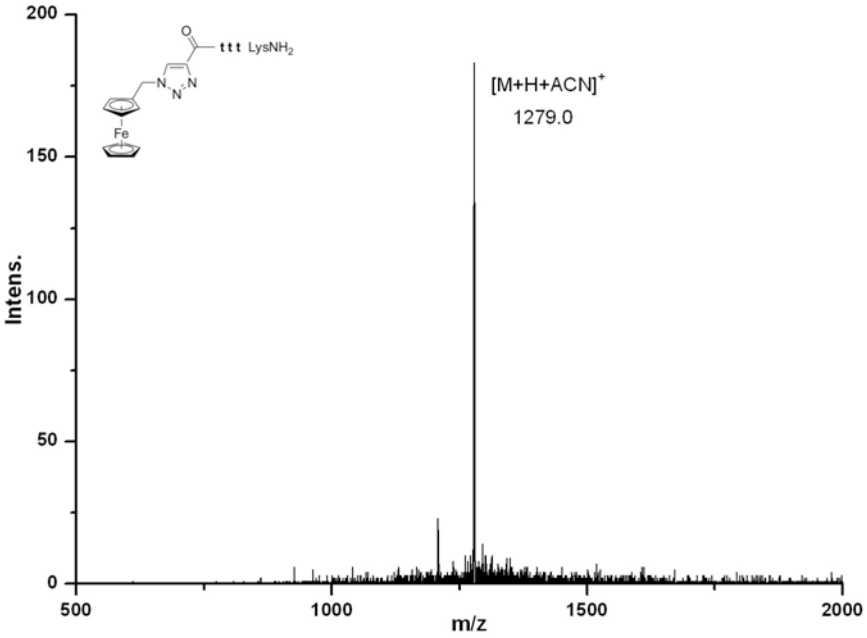

Fig. S6: MALDI-TOF mass spectrum of **3**.

II. ESI mass spectra

a) Alkyne-functionalized PNA oligomer **1**

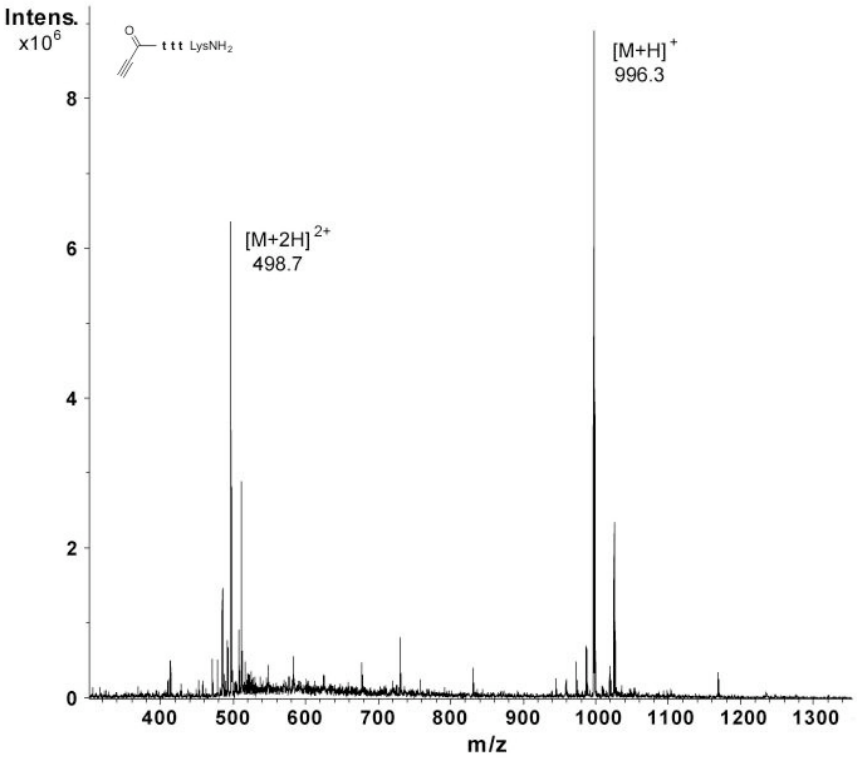

Fig. S7: ESI mass spectrum of **1**.

b) Azide-functionalized PNA oligomer **2**

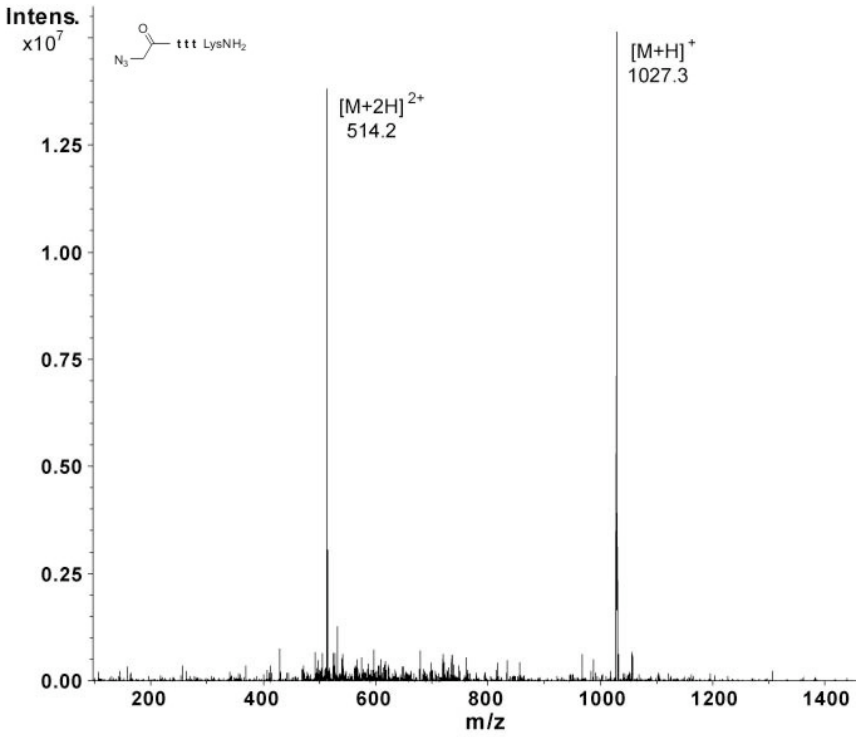

Fig. S8: ESI mass spectrum of **2**.

c) Fc-PNA conjugates **4**, **5** and **6**

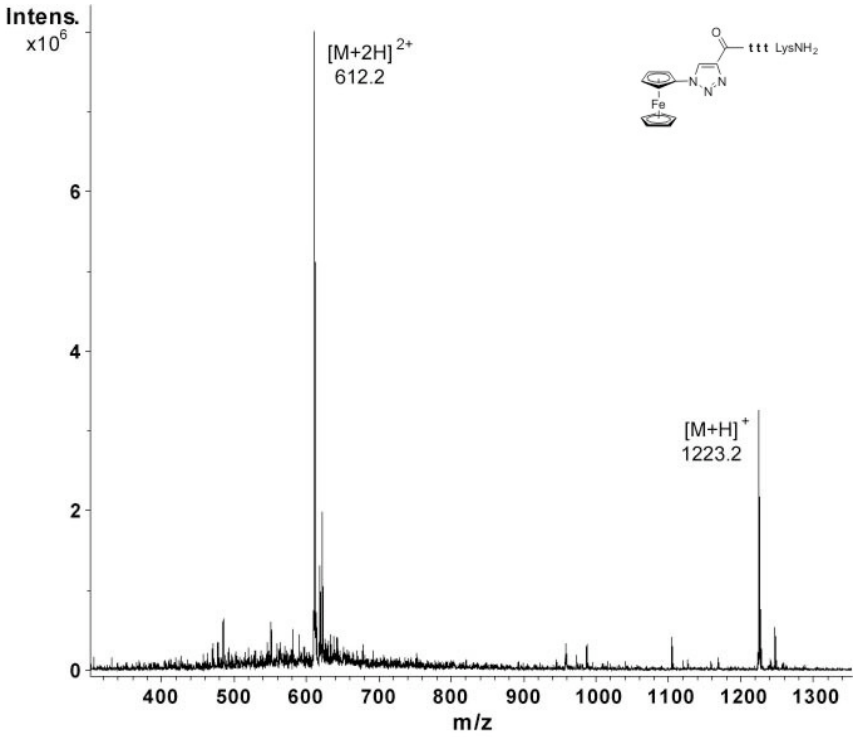

Fig. S9: ESI mass spectrum of **4**.

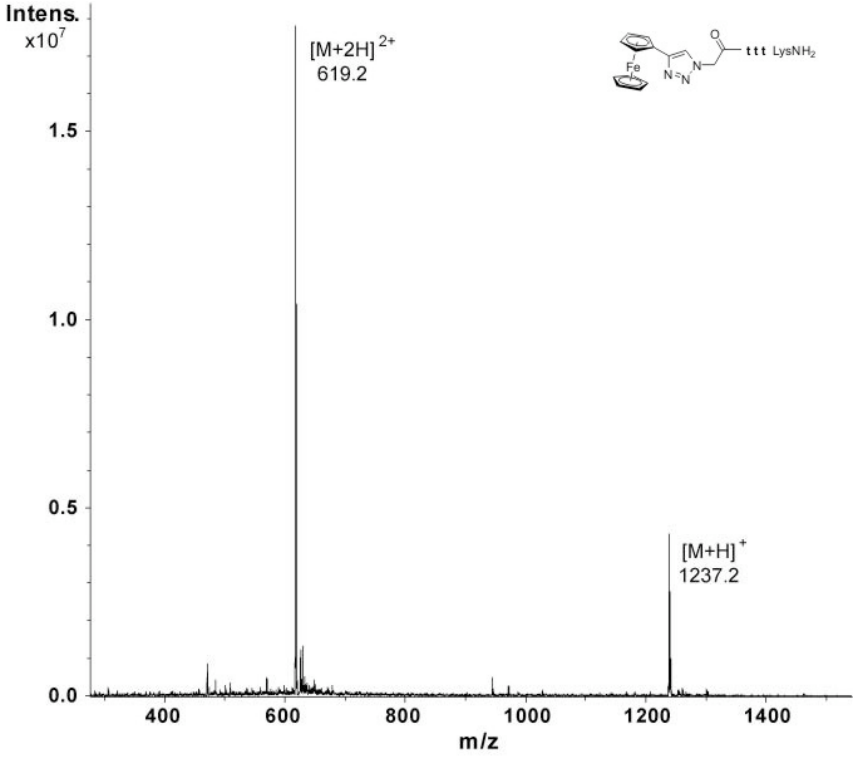

Fig. S10: ESI mass spectrum of **5**.

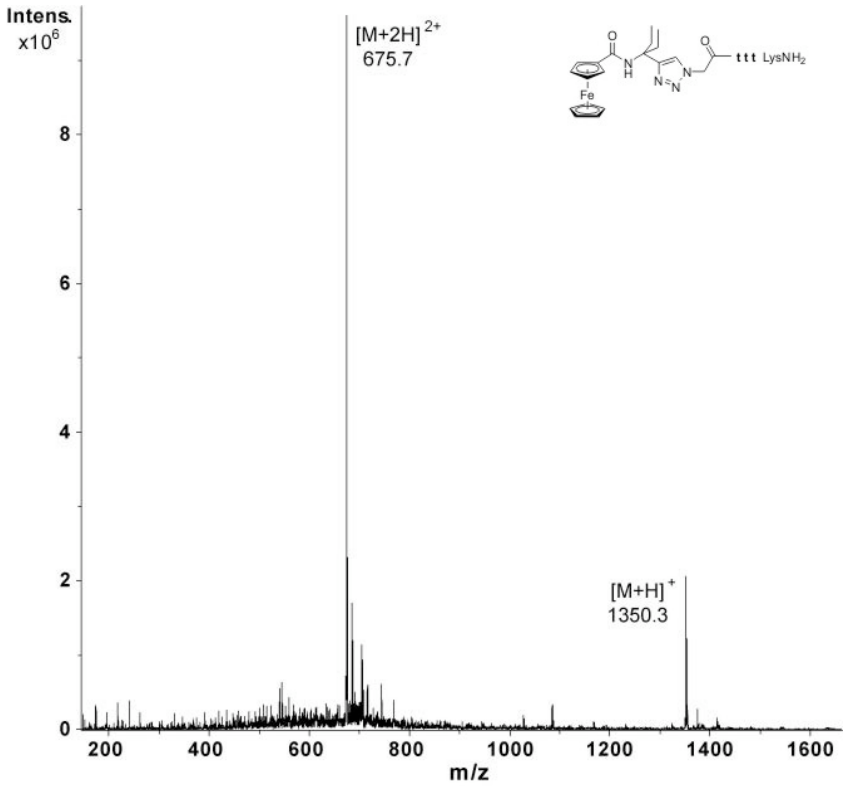

Fig. S11: ESI mass spectrum of **6**.

III. HPL chromatograms

a) 12mer Fc-PNA conjugates

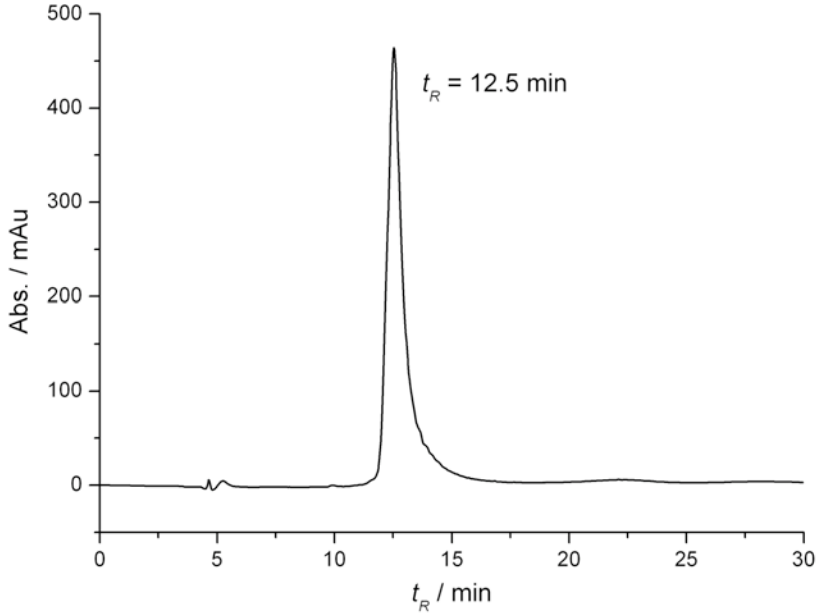

Fig. 12: HPL chromatogram of Fc-PNA conjugate **7**.

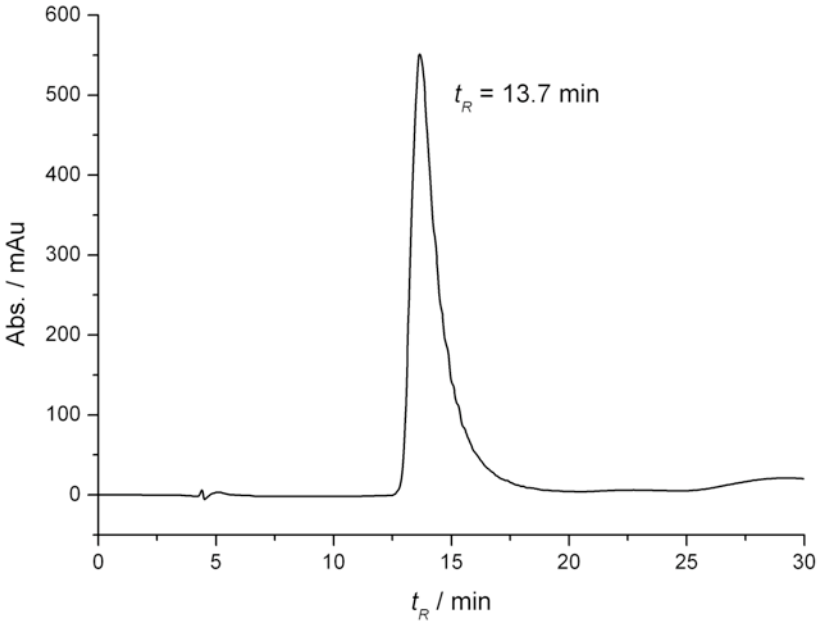

Fig. S13: HPL chromatogram of Fc-PNA conjugate **11**.

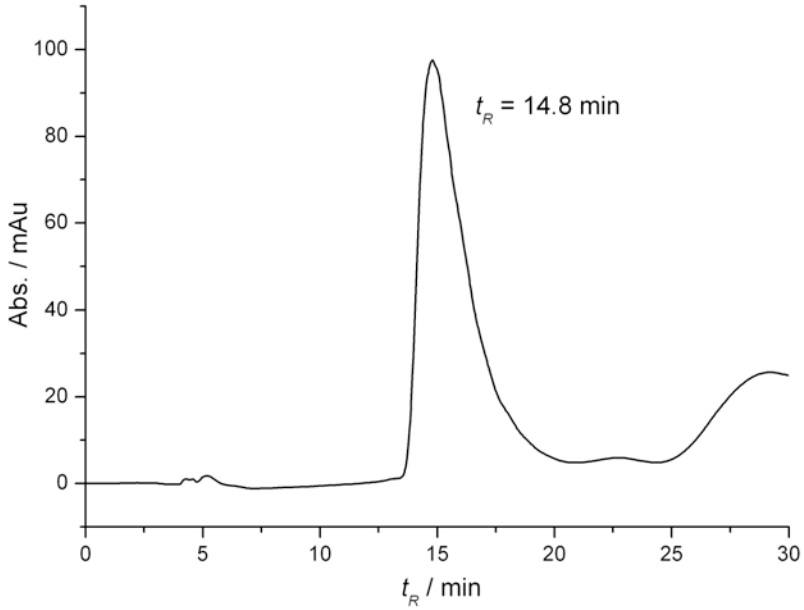

Fig. S14: HPL chromatogram of Fc-PNA conjugate **10**.

IV. Cyclic Voltammetry

a) Fc-PNA conjugates with model sequence H-t t t LysNH$_2$

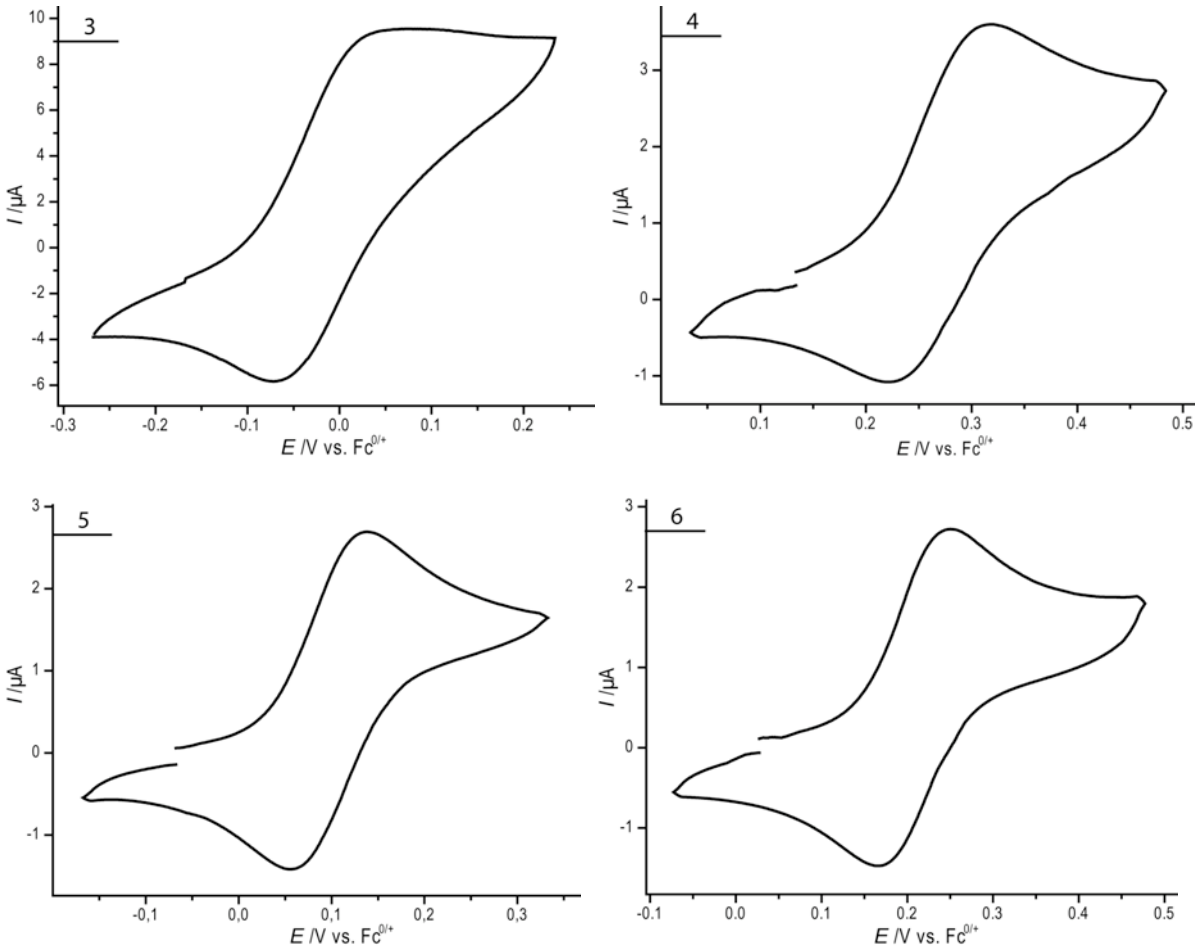

Fig. S15. Cyclic voltammograms of Fc-PNA conjugates **3**, **4**, **5** and **6** at a scan rate of 0.25 Vs^{-1} at a glassy carbon working electrode in 0.15 MOPS buffer in a 1:1 (v/v) mixture of CH_3CN/H_2O containing $NaOCl_4$ as the supporting electrolyte. Ag/AgCl in KCl (3M) served as reference electrode and a platinum wire as counter electrode.

Eradication of CD19$^+$ Leukemia by Targeted Calicheamicin θ

Kathrin M. Bernt,[‡] Aram Prokop,[§] Nicole Huebener,[‡] Gerhard Gaedicke,[†,‡] Wolfgang Wrasidlo,[†,||] and Holger N. Lode*[,‡]

Charité Universitätsmedizin Berlin, Department of Pediatrics, Experimental Oncology, Berlin, Germany, Department of Pediatric Hematology/Oncology, Berlin, Germany, and Moore's Cancer Center, University of California, San Diego, California. Received March 24, 2009; Revised Manuscript Received May 18, 2009

Children with relapsed and refractory acute lymphoblastic leukemia (ALL) still face a critical prognosis. We tested the hypothesis that targeted calicheamicin theta (θ) using an anti-CD19-immunoconjugate may provide an effective treatment strategy for CD19$^+$ ALL. Calicheamicin θ is a rationally designed prodrug of the natural enediyene calicheamicin γ, obtained by total synthesis. It offers the advantage of increased in vivo stability and 1000-fold higher antitumor potency over calicheamicin γ. First, we demonstrate efficacy of calicheamicin θ against primary pre-B leukemic cells and multidrug-resistant leukemia cell lines ($IC_{50} = 10^{-9}$ to 10^{-12} M). Second, conjugation of calicheamicin θ to an internalizing murine anti-CD19 monoclonal antibody was demonstrated to affect neither calicheamicin θ mediated cytotoxicity nor binding of the antibody to the target molecule. Third, anti-CD19-calicheamicin θ immunoconjugate revealed a maximum tolerated dose of 10 μg/kg and CD19-specific and long-lasting eradication of established leukemia was demonstrated in a xenograft model. Finally, we show that the antileukemic effect of anti-CD19-calicheamicin θ is mediated by induction of apoptosis proceeding through the caspase-mediated mitochondrial pathway. On the basis of these results, we conclude that anti-CD19-calicheamicin θ immunoconjugates may offer a novel and effective approach for the treatment of relapsed CD19$^+$ ALL.

INTRODUCTION

The treatment success of pediatric patients with newly diagnosed acute lymphoblastic leukemia (ALL) has dramatically inproved over the last decades and overall cure rates are above 70% (*1*, *2*). However, one of the limitations remains a relapse rate of nearly 30% (*3*) as described in stratified and randomized multicenter trials such as ALL-REZ BFM 85 (*4*). Although the overall second complete remission (CR) rate was 92%, the probability of event-free survival (EFS) at 6 years was only 0.31 ± 0.04. Thus, the proposed treatment regimen can induce long-lasting second remissions in about one-third of patients even after intensive front-line treatment. However, the majority of patients still face a critical prognosis particularly subsequent to early relapse.

Alternative treatment approaches to B-cell malignancies were established by using a monoclonal antibody directed against the common B-cell differentiation antigen CD20. Efficacy of adjuvant immunotherapy using anti-CD20 in low-grade B-cell lymphoma has been clearly demonstrated (*5*, *6*) suggesting that anti-CD20 therapy is also effective in more aggressive, high-grade B-cell malignancies such as Burkitts and diffuse large-cell lymphoma (*7*−*10*). The mechanism of action mediated by anti-CD20 is a combination of humoral and cellular immune responses (*11*) and the induction of apoptosis in cells targeted by the antibody (*12*), which can be further improved by labeling the antibody with radioisotopes (*13*). However, the use of this anti-CD20 antibodies in pediatric leukemias is limited by the fact that pre-B cell leukemias do not express CD20. This is in contrast to CD19, an earlier differentiation marker in B-cell differentiation. CD19 expression is induced at the point of B lineage commitment during the differentiation of the hematopoietic stem cell, and its expression continues through preB and mature B cell differentiation until it is finally down-regulated during terminal differentiation into plasma cells. CD19 expression is maintained in B-lineage cells that have undergone neoplastic transformation, and therefore, CD19 is a useful target in leukemia and lymphoma thearpy using monoclonal antibodies (*14*, *15*). CD19 is highly expressed by the majority of relapsed ALL leukemic cells and immunotoxins targeted to CD19 were shown to mediate apoptosis also in rituximab-resistant hematologic malignancies (*16*).

Since induction of apoptosis is one important mechanism of action mediated by anti-CD19 antibodies (*14*), we intended to amplify the mode of action by fusing an anti-CD19 antibody to the enediyene calicheamicin θ. Enediyenes are a group of cytotoxic compounds identified from a broth extract of a soil microorganism, *Micromonospora echinospora calichensis*, which were termed calicheamicins. These compounds were later identified as members of a class of antibiotics incorporating the enediyne moiety which include the esperamicins, dynemicins, and neocarzinostatin (*17*) which were found to exert impressive potencies in a screen for DNA damaging agents (*18*) that exceeded the cytotoxic potency of substances such as CN-MRA (*19*) and ricin (*20*), which have been claimed as some of the most toxic substances known at the time. Within this group of enediyene antibiotics, calicheamicin γ was the most potent compound, which was found to bind in the minor groove of DNA, and the resulting sequence-specific DNA-cleavage has been described (*21*). A novel biologically active and selective enediyene molecule calicheamicin θ was rationally designed on the basis of the mechanism of action of the naturally occurring calicheamicin γ. Unlike its natural counterpart, calicheamicin θ contains structural variations that facilitate molecular triggering to form the active compound under mild

* Holger N. Lode, Charité Universitätsmedizin Berlin, Experimental Oncology, Forum 4, R 2.0407, Augustenburger Platz 1, 13353 Berlin, Germany, E-mail: holger.lode@charite.de. Tel.: + 49 30 450 566233, Fax: +49 30 450 566916.

[‡] Department of Pediatrics, Experimental Oncology.

[§] Department of Pediatric Hematology/Oncology.

[†] Charité Universitätsmedizin Berlin.

[||] University of California.

10.1021/bc900128h CCC: $40.75 © 2009 American Chemical Society
Published on Web 07/02/2009

Table 1. Effect of Calicheamicin θ against Primary Patients ALL and Leukemia Cell Lines[a]

cell line[b]	cell type	calicheamicin θ IC_{50} [M][c]
Molt-3	T-cell	2.0×10^{-12}
Molt-4	T-cell	1.5×10^{-13}
MOVP-3	T-cell	4.5×10^{-11}
TCAF	T-cell	1.1×10^{-11}
HL60	Promyelocytic	3.6×10^{-11}
L1210	Lymphocytic Leukemia[d]	1.8×10^{-10}
P-388	Lymphocytic Leukemia[d]	4.5×10^{-9}
Nalm-6	pre B-cell	9.0×10^{-13}
Reh	pre B-cell	1.5×10^{-12}
Patient I	ALL	4.8×10^{-12}
Patient II	ALL	1.9×10^{-10}
Patient III	ALL	5.2×10^{-10}

[a] The IC_{50} concentration of calicheamicin θ was determined against ALL blasts and leukemia cell lines using the XTT assay. [b] Cells used for calicheamicin θ drug sensitivity testing were human and murine cell lines. [c] Values represent the means of experiments in triplicate. Standard deviations were below 10%. [d] Cells of murine origin.

Table 2. Cytotoxicity of Chemotherapeutic Agents on NALM-6 Cells

drug[a]	target	IC_{50} [M][b]
Calicheamicin θ	DNA minor groove (TCCT)	5×10^{-13}
Doxorubicin	topoisomerase II	3×10^{-10}
Camptothecan	topoisomerase I	4×10^{-9}
Paclitaxel	tubulin, microtubles	1×10^{-10}
Etoposide	topoisomerase II	1×10^{-8}
Melphalan	alkylation of DNA	4×10^{-8}
Methotrexate	dihydrofolate reductase	6×10^{-8}
Vinblastine	microtuble depolymerization	2×10^{-6}
Genistein	Src kinase family blocker	6×10^{-6}
Calicheamicin θ -anti CD19	CD19	2×10^{-13}
Doxo-anti-CD19	CD19	1×10^{-9}
Doxo-anti-CD20	CD20	3×10^{-9}
Doxo-anti-CD22	CD22	8×10^{-10}
AntiCD19, 20, 22	CD19, CD20, CD22	$>1 \times 10^{-4}$
Calicheamicin θ -anti CD19[c]	$CD19^+$ (NALM-6)	5×10^{-11}
Calicheamicin θ -anti CD19[c]	$CD19^-$ (Molt-3)	6×10^{-8}

[a] The IC_{50} concentration of indicated chemotherapeutic agents was determined against NALM-6 B-cell lymphoblastic leukemia using the XTT assay. [b] Values represent the means of experiments in triplicate. Standard deviations were below 10%. [c] The IC_{50} concentration of Calicheamicin θ -anti CD19 immunotoxin was determined in CD19 positive and negative cells using a short exposure experiments as described in Materials and Methods.

basic conditions (*22*, *23*). This modification led to a further increase in cytotoxicity over the natural compound when tested against a large number of different human cancer cell lines as determined by the decrease in the concentration at which 50% of cell viability was observed (*22*, *23*). The small size of calicheamicins with molecular weights of approximately 1500 Da combined with their unique mode of action and the extreme potency of calicheamicin θ suggest that this compound might be a good candidate for targeted chemotherapy. In fact, we demonstrated the use of calicheamicin θ for targeted therapy of neuroblastoma using antiganglioside GD2 antibodies (*24*). Here, we expand these findings and establish for the first time efficacy and mechanism of an antibody drug conjugate between a murine monoclonal anti-CD19 mAb and calicheamicin θ that suppresses growth and dissemination of leukemic cells in a Nalm-6 pre B-cell leukemia model.

MATERIALS AND METHODS

Cell Lines and Patient Cells. NALM-6, Reh, Molt-3, Molt-4, TCAF, TCAF-Dox, HL60, L1210, and P-388 cell lines were purchased from ATCC. Cells were maintained in RPMI with 10% fetal bovine serum. Control vector and FADD-dn-transfected BJAB cells expressing a dominant negative FADD mutant lacking the N-terminal death receptor domain have been described earlier (*25*). Leukemic cells from patients were isolated from bone marrow samples at initial diagnosis. Mononuclear cells were prepared by Ficoll centrifugation and characterized by flow cytometry. Patient cells were maintained in RPMI with 20% fetal bovine serum and gentamicin (50 μg/mL).

Mice. Female FOX CHASE C.B-17/lcrCrl-scid BR mice were obtained at 8 weeks of age from Charles River Laboratories, Sulzfeld, Germany. They were housed in the pathogen-free mouse colony at our institution in groups of 8 mice. Mice were fed ad libitum on standard mouse laboratory chow. Animal experiments were performed according to the German guide for the care and use of laboratory animals, i.e., "Tierschutzgesetz".

Cytostatic Agents, Antibodies, and Reagents. Anti-CD19 (mouse IgG2a) was obtained from CellGenics (Freiburg, Germany) and anti-CD19 (mouse IgG2b, clone HID-9703) and anti-CD20 (mouse IgG1, clone L-27) from Baxter (Unterschleissheim, Germany). Human-mouse chimeric antiganglioside GD2 antibody ch14.18 (*26*) was used as a negative control. Conjugation of mAbs with fluorescein isothiocyanate (FITC) was accomplished at pH 9.0 using 20 μL FITC solution (5 mg/mL in DMSO) per mg mAb (1 mg/mL). After 2 h, the pH was lowered to pH 7.4 and FITC-labeled antibody was purified over PD-10 columns (Amersham-Pharmacia, Freiburg, Germany).

Calicheamicin θ (MW 1464 g/mol) was obtained by total synthesis as previously described (*23*). Succinimidyl 6-(3-[2-pyridyldithio]-propionamido)hexanoate (LC-SPDP) and iminothiolane were obtained from PIERCE (Rockford, IL). Doxorubicin, camptothecan, paclitaxel, etoposide, melphalan, methotrexate, vinblastine, genistein, 2,3-bis(2-methoxy-4-nitro-5-sulfophenyl)-5-[(phenylamino)carbonyl]-2*H*-tetrazolium hydroxide (XTT), organic solvents, and phenazine methosulfate (PMS) were obtained from Sigma-Aldrich (Deisenhofen, Germany). All cytotoxic agents were dissolved in DMSO or DMF, and 10 mM stock solutions were stored at −20 °C until use. Cell culture reagents, restriction enzymes, and other molecular biology reagents were from Life Technologies (Karlsruhe, Germany).

Conjugation of Calicheamicin θ. The conjugation of calicheamicin θ to anti-CD19, anti-CD20, and anti-GD2 mAb involved the activation of the sugar amino groups with LC-SPDP, using 4-dimethylaminopyridine (DMAP, Aldrich, Munich, Germany) as a catalyst, followed by disulfide exchange with iminothiolane-modified anti-CD19 and anti-GD2 mAb. For activation, 1 mg calicheamicin θ (1 mg/mL in DMF) was reacted with a 2-fold molar excess of LC-SPDP (succinimidyl 6-(3-[2-pyridyldithio]-propionamido)hexanoate) (37 μL of 20 mM LC-SPDP in DMSO) at 4 °C for 6 h and stored in small aliquots at −80 °C until further use. Sulfhydryl groups were introduced in mAbs (2 mg in 2 mL PBS, pH 8.3) by adding 10 μL iminothiolane (4.4 mg dissolved in 1 mL DMF) for 1 h under nitrogen. The iminothiolane-modified antibody was purified by size exclusion chromatography using a NAP-5 column (Amersham-Pharmacia, Freiburg, Germany) preequilibrated with PBS. The conjugation of activated drugs with thiolated mAb was done at RT for 1 h under nitrogen, using a 5:1 molar ratio followed by size exclusion chromatography. Finally, solutions were filter sterilized. The purity was checked by HPLC analysis (G200 size exclusion column, PBS elution buffer, 0.5 mL/min flow). The number of drug molecules per mAb was on the average two, calculated from the absorption ratios at A333/A280 for calicheamicin in the HPLC spectrum. Free calicheamicin was not detectable in these preparations. The dosage of the conjugate for cytotoxicity experiments was calculated on the basis of the molar concentration of drug on the antibody.

CD19 Expression Analysis. For the analysis of CD19 expression on Nalm-6, Reh and Molt-3 (negative control) anti-CD19-FITC was used. Cells were blocked with PBS (0.1% BSA in PBS, pH 7.4) and incubated with anti-CD19-FITC (1 μg/10^6 cells) or a mouse IgG2a isotype control (PharMingen, La Jolla,

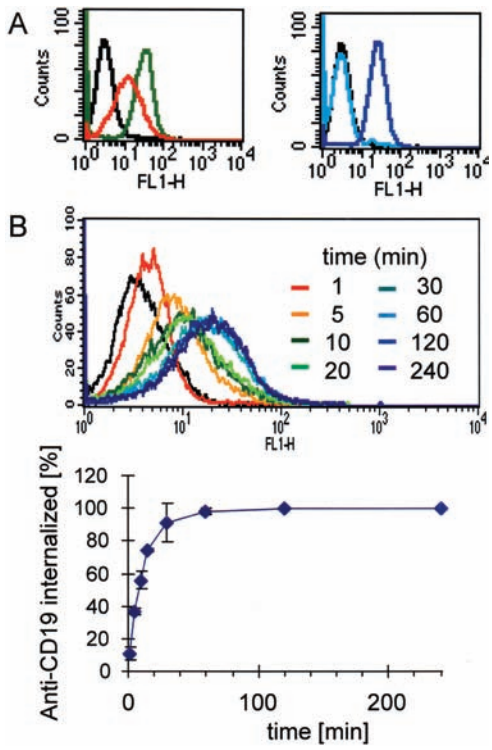

Figure 1. Internalization kinetics of anti-CD19 mAb. (A) Investigation of antibody internalization comparing two different anti-CD19 antibodies. Internalization of anti-CD19 (clone HID-9703) into Nalm-6 leukemia cells was demonstrated as indicated by an increase in fluorescence over background (red signal, left panel). Internalization was absent for anti-CD19 (IgG2a, Cell Genix) (light blue signal, right panel). Two control samples were incubated at 0 °C in the presence of 0.01% NaN_3 in order to block internalization. The first control sample (0 °C; 0.01% NaN_3) was stripped of bound antibody (black signals, left and right panels) and served as a negative control. The second control sample (0 °C; 0.01% NaN_3) was not stripped (green and dark blue signals, left and right panels) and was used as a positive control. All experiments were done in triplicate. (B) Internalization kinetics of anti-CD19 (clone HID-9703) into Nalm-6 leukemia cells over time. Mean fluoresence signals obtained from histograms (top) were used to calculate the percentage of internalized antibody (bottom). 100% equals the signal obtained with Nalm-6 cells incubated with anti-CD19-FITC antibody under non-internalizing conditions (0 °C in the presence of 0.01% NaN_3). Internalization (37 °C) was investigated over time by analysis of fluorescence signals resulting from internalization after stripping cells from non-internalized membrane-bound anti-CD19 antibody as described in Materials and Methods. Data represent mean ± sd ($n = 3$).

CA) for 20 min on ice, washed twice, and analyzed by FACSscan (Becton Dickinson, Franklin Lakes NJ).

Internalization Assay of anti-CD-19-FITC. Cells were washed twice and blocked with PBS + 0.1% BSA on ice. Anti-CD19-FITC (1 μg/10^6 cells) was added on ice. Aliquots were subsequently transferred to 37 °C to allow for internalization. Negative control samples were incubated at 0 °C in the presence of 0.01% NaN_3, conditions which block internalization. An aliquot of each condition was retained at different time points to determine the total amount of bound and internalized antibody. At each time point, a second aliquot was stripped of noninternalized antibody with RPMI titered to pH 2.0 with HCl and adjusted to high salt (1 M NaCl, 2×, 15 min), and washed briefly in PBS (0.1% BSA, pH 7.4) before analysis. The quality of the stripping was assured by the total removal of all antibodies from control cells incubated under non-internalizing conditions. For the integration time course, experimental samples were incubated at 37 °C for the indicated time spans. The amount of integrated antibody in percent total integration was calculated as follows: MFI (time point)/MFI (4 h) × 100. The binding of calicheamicin conjugates was determined by indirect staining using a FITC-conjugated goat-anti mouse IgG secondary antibody (ParMingen), and secondary antibody only as control.

Cytotoxicity Assay. Cytotoxicity was determined by the XTT tetrazolium/formazan assay as previously described (*27*). Briefly, cells were seeded in 96 flat-bottomed well plates at a density of 10^4/well in 100 μL media, incubated overnight, and exposed to drug concentrations ranging from 10^{-6} to 10^{-16} M for calicheamicin θ or calicheamicin θ immunoconjugates and from 10^{-4} to 10^{-14} for all other drugs. In short exposure experiments, plates were washed (×2) by centrifugation after 1 h exposure to calicheamicin θ anti-CD19 immunoconjugates. Cell viability was assessed after 72 h by adding 50 μL XTT-reagent (1 mg/mL in RPMI) activated with 0.2% v/v PMS (1.53 mg/mL in PBS) incubated at 37 °C for 4 h. Plates were analyzed in a Thermomax (Molecular Devices) microplate reader at 450 nm. OD values were plotted as a function of drug concentration and the curves were integrated using the softmax software to obtain the IC_{50} concentration values. In experiments with BJAB cells, the cytotoxicity of calicheamicin θ immnunoconjugate was determined by the release of lactate dehydrogenase (LDH) using a detection kit from Boehringer-Mannheim (Mannheim, Germany).

Nalm-6 Xenograft Model. The Nalm-6 xenograft model was used as previously described (*28*). Briefly, leukemia was induced by injection of 1×10^6 Nalm-6 cells in 100 μL PBS (pH 7.4) into the tail vein of each SCID mouse. Mice ($n = 6$) were treated by intraperitoneal injection of PBS (pH 7.4), anti-CD19-calicheamicin θ and anti-GD2-calicheamicin θ immunoconjugates (1.0, 3.0, and 10.0 μg/kg linked calicheamicin θ; MW 1464 g/mol; 2 molecules per antibody) and anti-CD19 antibody (50, 150, and 500 μg/kg) (MW 150 000 g/mol) in a total volume of 200 μL. Each mouse received a total of 2 injections on days 5 and 7. Event-free survival of mice was followed over time. An event was defined by the development of central nervous system leukemia as indicated by presence paraplegia in individual mice.

Processing of Caspase 3, DNA Fragmentation, and Mitochondrial Permeability Transition. Processing of caspase 3, DNA fragmentation, and mitochondrial permeability transition was determined as previously described (*29*). Processing of caspase 3 was determined by Western blot using 30 μg of cytosolic protein probed with polyclonal rabbit antihuman caspase 3 antibody (1:2000). DNA fragmentation was investigated by flow cytometry of fixed cells after incubation with 50 μg/mL propidium iodide in PBS (pH 7.4), and data are expressed as percent of hypoploidy (subG1), reflecting the percentage of apoptotic cells. Mitochondrial permeability transition was analyzed by staining the cells with JC1 (Molecular Probes, Leiden, Netherlands). Determination of cells with decreased fluorescence signals consistent with mitochondria displaying a lower membrane potential was accomplished by flow cytometry. Data are expressed in percent of cells with low $\Delta\Psi_m$, which reflects the number of cells undergoing mitochondrial apoptosis.

Statistics. The statistical significance of differential findings between experimental groups of animals and control groups and between experimental and control samples was determined by two-tailed Student's *t* test. Findings were regarded as significant if two-tailed *p* values were <0.01.

RESULTS

Determination of the Efficacy of Calicheamicin θ against ALL Cells. The efficacy of calicheamicin θ against ALL cells was determined using a panel of cell lines and primary blasts from bone marrow of ALL patients (Table 1). The IC_{50} concentration for calicheamicin θ was in the picomolar range ($IC_{50} < 10^{-9}$ M) for the majority of ALL cells tested, including T-ALL and multidrug-resistant ALL, as well as the patients cells,

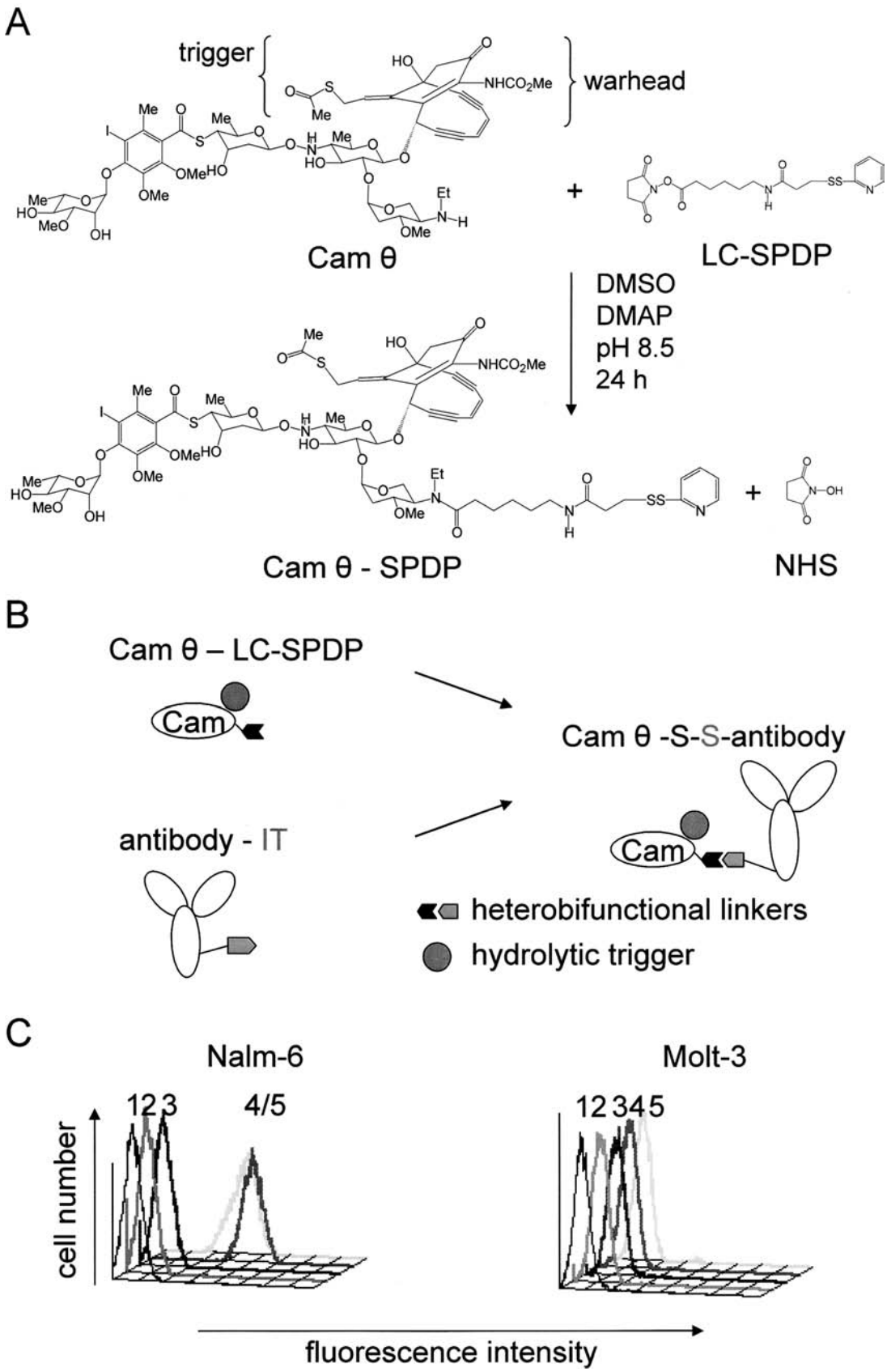

Figure 2. Synthesis and binding of anti-CD19 calicheamicin θ immunoconjugate. (A) Structures and reaction conditions of calicheamicin θ with the LC-SPDP linker to form calicheamicin θ-LC-SPDP. (B) Conjugation of calicheamicin θ-LC-SPDP with iminothiolane (IT) activated anti-CD19 (clone HID-9703) to form anti-CD19 calicheamicin θ immunotoxin. (C) Binding of anti-CD19 calicheamicin θ immunotoxin to CD19 positive Nalm-6 cells (left panel) in contrast to CD19-negative Molt-3 controls (right panel). 1, no antibody; 2, secondary antibody only; 3, anti-CD20; 4, anti-CD19; 5, anti-CD19 calicheamicin θ immunotoxin. All experiments were done in triplicate.

except for P-388 mouse lymphoblastic leukemia. In some cell lines (Molt-4, Nalm-6), the efficacy was even in the femtomolar range ($IC_{50} < 10^{-12}$ M). In order to further evaluate these results, we compared the efficacy of calicheamicin θ with other

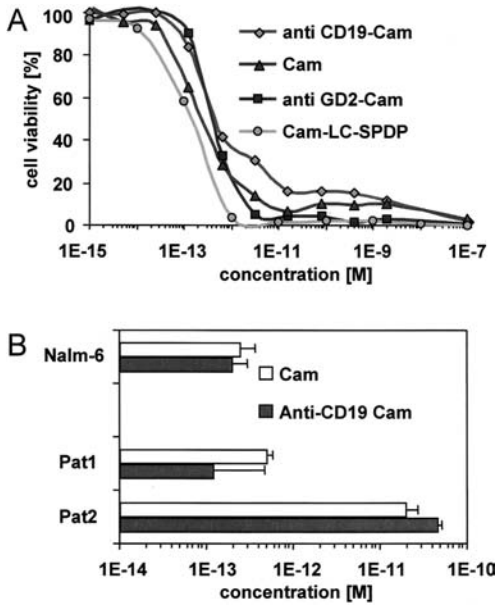

Figure 3. Cytotoxic effect of anti-CD19 calicheamicin θ immunoconjugate in vitro. A) The concentration dependent cytotoxic effects of calicheamicin θ, calicheamicin θ - LC-SPDP, anti-CD19 calicheamicin θ immunoconjugate and anti-GD2 calicheamicin θ immunoconjugate were determined on Nalm-6 cells. Data represent mean values of triplicate experiments. B) Cytotoxic effects of calicheamicin θ and anti-CD19 calicheamicin θ immunoconjugate against blasts obtained from relapsed ALL patients compared to Nalm-6 cells. Data represent IC50 concentrations (mean ± sd, $n = 3$).

established chemotherapeutic compounds used for ALL therapy on Nalm-6 cells (Table 2). Results revealed the lowest IC_{50} concentration for calicheamicin θ ($IC_{50} = 5 \times 10^{-13}$ M) in contrast to all other drugs tested, which were at best 1000-fold less active (i.e., doxorubicin $= 3 \times 10^{-10}$ M). These findings clearly demonstrate the excellent cytotoxic potential of calicheamicin θ for the generation of an immunotoxin for targeted therapy.

Generation and Characterization of an Anti-CD19 Calicheamicin θ Immunotoxin. The selection of the CD19 specific monoclonal antibody for the generation of a calicheamicin θ immunotoxin was based on antibody internalization experiments (Figure 1). Results indicate that the anti-CD19 antibody (Baxter) showed rapid internalization that was nearly complete after 60 min.

Therefore, this anti-CD19 antibody was selected for the conjugation to calicheamicin θ using the heterobifunctional linker LC-SPDP (Figure 2). The conjugation of the linker to calicheamicin θ is complicated by the highly unstable "trigger" and "warhead" portions of calicheamicin θ (Figure 2A). However, the conjugation of the activated NHS ester end of the LC-SPDP linker to the secondary amine of calicheamicin θ to form calicheamicin θ-LC-SPDP was accomplished in organic solvent at pH 8.5, without affecting the cytotoxic potential of calicheamicin θ (Figure 3). The 2-pyridylthiol group at the other end of the LC-SPDP linker was reacted with sulfhydryl residues in the anti-CD19 antibody to form a disulfide linkage (Figure 2B). Binding of the purified immunotoxin to CD19-positive Nalm-6 cells was demonstrated in contrast to CD19-negative Molt-3 cells used as negative controls (Figure 2C). The cytotoxic effect of anti-CD19-calicheamicin θ-immunotoxin was compared to that of free calicheamicin θ, calicheamicin θ-LC-SPDP and anti-GD2 calicheamicin θ (Figure 3A). Results indicate that the level of calicheamicin θ mediated cytotoxicity remained unchanged after conjugation to LC-SPDP and to a monoclonal antibody as determined in one ALL cell line and ALL blasts

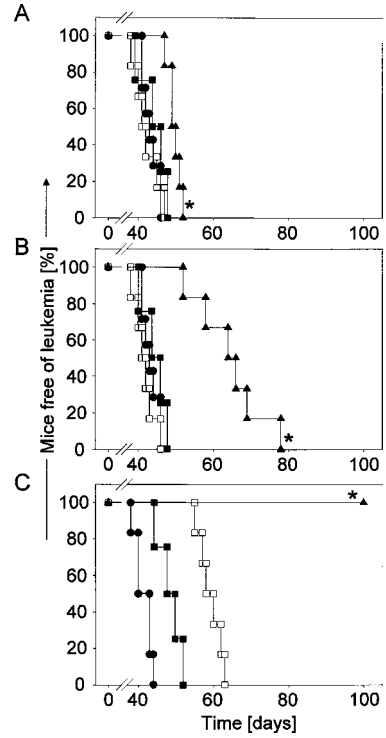

Figure 4. Effect of CD19 targeted calicheamicin θ in vivo. The effect of anti-CD19 calicheamicin θ immunotoxin against CD19-positive leukemia was determined in a xenograft model. Mice ($n = 6$ per group) were injected i.v. with 1×10^6 Nalm-6 cells. Treatment was initiated by two intraperitoneal injections on days 5 and 7 of 1.0 (A), 3.0 (B), and 10.0 μg/kg (C) with anti-CD19 calicheamicin θ immunotoxin (dose indicates linked calicheamicin θ) (closed triangle) and anti-GD2 calicheamicin θ immunotoxin control (open square). Controls received an equivalent amount of unconjugated anti-CD19 abtibody (500, 150, and 50 μg/kg) (closed square). Untreated control groups of animals received PBS injections (closed circles). Data represent the percentage of mice free of leukemia. The difference between groups of mice treated with anti-CD19 calicheamicin θ immunotoxin and all control groups was statistically significant (* $p < 0.01$).

from bone marrow aspirates of two ALL patients (Figure 3B). We could also demonsrate an antigen-specific cytotoxic effect mediated by the anti-CD19-calicheamicin θ-immunotoxin in vitro since the IC_{50} on $CD19^-$ Molt 3 cells is 1000× higher than on $CD19^+$ Nalm-6 cells (Table 2). In summary, we could demonstrate that the conjugation affected neither antigen binding of the anti-CD19 portion of the immunotoxin nor the cytotoxicity of calicheamicin θ, resulting in an immunotoxin with antigen-specific cytotoxic potential similar to free calicheamicin θ.

Effect of Anti-CD19 Calicheamicin θ Immunotoxin in a Leukemia Xenograft Model. The efficacy of CD19-targeted calicheamicin θ therapy was evaluated in a leukemia xenograft model. For this purpose, CD19-positive Nalm-6 B-cell leukemia was established in SCID mice by intravenous injection (1×10^6 Nalm-6 cells). Treatment was initiated 5 days after tumor cell inoculation by two intraperitoneal injections of anti-CD19 calicheamicin θ immunotoxin per mouse (10, 3, and 1 μg/kg; dose indicates linked calicheamicin θ) on days 5 and 7. Controls received an equivalent amount of nonspecific anti-GD2 calicheamicin θ immunotoxin, unconjugated anti-CD19 antibody (500, 150, and 50 μg/kg), and PBS. A control group with free calicheamicin θ was not included, based on previous reports demonstrating high toxicity when used at an equivalent amount to 10 μg/kg calicheamicin θ immunotoxin (all animals died) and lack of activity when used at lower doses (*24*, *30*). We selected the highest dose of 10 μg/kg calicheamicin θ immu-

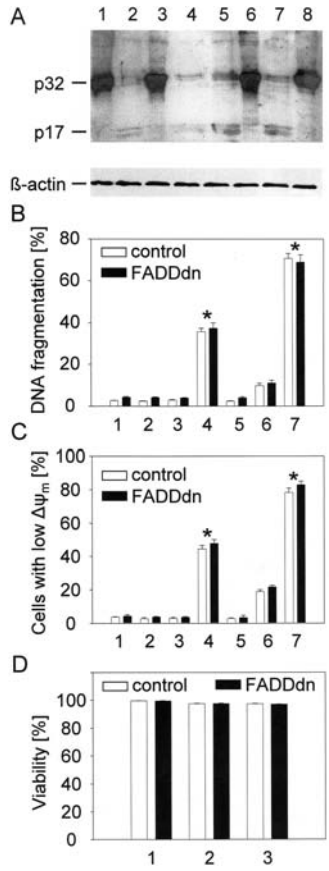

Figure 5. Apoptotic pathway induced by CD19 targeted calicheamicin θ. (A) The effect of anti-CD19 calicheamicin θ immunotoxin on processing of caspase 3 was determined in CD19-positive cALL lymphoblasts of a relapsed patient by Western blot. Procaspase 3 (p32) and activated caspase 3 fragment (p17) are indicated. 1, control (untreated); 2, anti-CD19 calicheamicin θ immunoconjugate (2 pmol/L); 3, anti-CD19 (2 pmol/L); 4, calicheamicin θ (2 pmol); 5, anti-CD19 calicheamicin θ immunoconjugate (20 pmol/L); 6, anti-CD19 (20 pmol/L); 7, calicheamicin θ (20 pmol/L); 8, control (untreated BJAB cells). Induction of DNA fragmentation after treatment for 72 h (B) and loss of mitochondrial membrane potential after treatment for 48 h (C) with anti-CD19 calicheamicin θ immunotoxin was investigated in CD19-positive BJAB cells in the presence (closed bars) and absence (open bars) of dominant negative FADD death receptor expression. 1, control; 2, anti-CD19 (1 pmol/L); 3, calicheamicin θ (1 pmol/L); 4, anti-CD19 calicheamicin θ immunotoxin (1 pmol/L); 5, anti-CD19 (10 pmol/L); 6, calicheamicin θ (10 pmol/L); 7, anti-CD19 calicheamicin θ immunotoxin (10 pmol/L). Data represent mean ± SD ($n = 3$). The difference between anti-CD19 calicheamicin θ immunotoxin and all controls was statistically significant (* $p < 0.01$). (D) Cytotoxic effects of calicheamicin θ immunotoxin were analyzed at concentrations levels with established proapoptotic effect. 1, control; anti-CD19 calicheamicin θ immunotoxin 2, 1 pmol/L; 3, 10 pmol/L. Data represent mean ± SD ($n = 3$).

notoxin based on previous reports demonstrating no toxicity at this level (*24*).

Treatment of mice ($n = 6$/group) with established CD19-positive leukemia using 10 μg/kg anti-CD19 calicheamicin θ immunotoxin (2×, days 5 and 7 after tumor cell inoculation) induced a 3-fold prolongation of the life span with all animals alive at the end of the experiment (Figure 4). Specificity of this therapy was demonstrated, since mice treated with an equivalent amount of anti-GD2 calicheamicin θ immunotoxin used as nonspecific control was far less effective at the 10 μg/kg dose and ineffective at the 3 and 1 μg/kg doses, respectively. Similarly, the use of unconjugated anti-CD19 antibody at dose levels of 3 and 1 μg/kg was ineffective. There was a small effect by unconjugated anti-CD19 antibody at the dose level of 10 μg/kg, related to antibody-mediated immunological effector functions. However, the anti-CD19 calicheamicin θ immunotoxin was far more effective. The treatment was well-tolerated, since none of the mice receiving 10, 3, and 1 μg/kg calicheamicin θ immunotoxin presented with a drop in body weight of >20% as shown by weight loss measurements (data not shown). The antileukemia effect following anti-CD19 calicheamicin θ immunotoxin therapy was dose-dependent and highly significant in all treatment groups ($p < 0.01$).

Mechanism of Antileukemic Effects Mediated by Anti-CD19 Calicheamicin θ Immunotoxin. The mechanism of antileukemic effects mediated by the anti-CD19 calicheamicin θ immunotoxin was determined on CD19-positive primary ALL blasts and CD19-positive BJAB cells in vitro. We could demonstrate that the anti-CD19 calicheamicin θ immunotoxin induced apoptosis in CD19-positive leukemia cells (Figure 5). Induction of apoptosis by anti-CD19 calicheamicin θ immunotoxin involves processing of caspase 3 as indicated by a decrease in procaspase 3 and increase in 17 kDa active caspase subunit (p17) signals. Interestingly, the level of DNA fragmentation and loss of mitochondria membrane potential was more than 5× higher than that observed with an equivalent amount of free calicheamicin θ (Figure 5B,C), consistent with rapid internalization of the anti-CD19 antibody immunotoxin. The induction of apoptosis was demonstrated to be independent from death-receptor/FADD-mediated signals, since the immunotoxin was as effective in induction of apoptosis parameters in BJAB/FADD-dn cells with dominant negative death receptor domains as in BJAB control cells (Figure 5B,C). Results of control experiments with Fas ligand and anti-CD95 mAb for validation of experiments with BJAB/FADD-dn cells shown here were previously reported (*29*). Importantly, these proapoptotic effects were observed under time and concentration conditions with no effect on cell viability (Figure 5D).

DISCUSSION

In order to solve the problem of poor outcome in relapsed pediatric ALL patients, targeting of CD19 constitutes an appealing approach based on the following considerations. The cell surface glycoprotein of the immunoglobulin superfamily CD19 is absent from hematopoietic stem cells, and in healthy individuals, its presence is exclusively restricted to the B-cell lineage and follicular dendritic cells. Furthermore, CD19 is not shed from the cell surface and is rarely lost during neoplastic transformation (*31*). The antigen is expressed on most B-cell malignancies, including cells from patients with acute lymphoblastic leukemia (ALL) (*32*). Importantly, CD19 is consistently expressed on B-precursor and mature B-ALLs, whereas CD20 is frequently absent on B-precursor ALLs. Furthermore, high levels of CD19 expression remains unchanged as shown in diagnostic and relapse flow cytometry phenotypes in childhood ALL (*33*).

The use of CD19-specific antibody conjugates has been evaluated for immunotherapy of B-lineage malignancies with promising results (*34*−*40*). This also applies to anti-CD19 immunotoxins with idarubicin, ricin A, blocked ricin (dose range 20−50 μg/kg) (*34, 35, 41*), deglycosylated ricin A chain (MTD 16 mg/m^2 = 320 μg/kg) (*36*) and genistein (dose range 100−320 μg/kg) (*37*), which showed efficacy in vivo. Here, we report for the first time construction, effect, and mechanism of a novel anti-CD19 immunotoxin using calicheamicin θ (Figures 1−4). The efficacy over the reported immunotoxins was improved, since a dosage of 10 μg/kg was sufficient to eradicate CD19 leukemia in mice (Figure 4). This is mainly a result of the highly potent calicheamicin θ (Tables 1 and 2), a synthetic derivative of calicheamicin γ.

The use of calicheamicin in the treatment of adult and pediatric B-cell malignancies is well-established (*37, 42, 43*). In fact, calicheamicin γ, which is up to 3 logs less potent than calicheamicin θ {Nicolaou, 1994 174 /id}, is currently used as

the cytotoxic component of an immunotoxin targeting CD33 (gemtuzumab ozogamicin, CMA-676, Mylotarg). Efficacy and tolerability of gemtuzumab ozogamicin has been evaluated in children with relapsed or refractory myeloid leukemia, with a promising response rate of 25% (*42*). An important aspect for the efficacy of the gemtuzumab ozogamicin is rapid internalization and subsequent induction of cell death (*44*). We could also demonstrate rapid internalization of the anti-CD19 antibody used for the calicheamicin θ anti-CD19 immunotoxin (Figure 1). This translated into excellent efficacy and specificity in a xenograft model of CD19-positive leukemia in mice (Figure 4). Specifically, mice treated with 10 μg/kg anti-CD19 calicheamicin θ immunotoxin were free of leukemia in contrast to controls treated with an equivalent dose of a nonspecific control immunotoxin (anti-GD2 calicheamicin θ immunotoxin). This control immunotoxin showed a minor nonspecific antileukemic effect at the highest dose level (10 μg/kg) (Figure 4) most likely due to a prolonged half-life of calicheamicin θ as a result of its conjugation to a monoclonal antibody. Importantly, induction of death receptor independent apoptosis proceeding through the mitochondrial pathway in a caspase 3 dependent mechanism was demonstrated for the anti-CD19 calicheamicin θ immunotoxin (Figure 5). The apoptotic pathways observed with anti-CD19 calicheamicin θ immunotoxin were no different from those delineated for unconjugated calicheamicin θ (*29*). Importantly, these effects were observed at picomolar concentrations and were over 5-fold higher than effects observed with free calicheamicin θ (Figure 5), indicating the important role of internalization in this process. These findings establish proof of concept that targeting of CD19 using a calicheamicin θ immunotoxin may be effective against CD19-positive malignancies. Considering established work with calicheamicin γ immunotoxin (gemtuzumab ozogamicin) and in view of the advantages of calicheamicin θ over calicheamicin γ, this study provides an important baseline for the clinical development of an anti-CD19 calicheamicin θ immunotoxin.

ACKNOWLEDGMENT

We would like to thank Anne Strandsby for excellent technical assistance. This work was supported by the Deutsche Forschungsgemeinschaft, Emmy-Noether Program, Lo 635/2-1 (H.N.L) and Kinderkrebs Neuroblastomforschung e.V. Kinderleben e.V. Berlin (A.P.) and AIP fellowships from the Charité (K.B.).

LITERATURE CITED

(1) Schrappe, M., Reiter, A., Ludwig, W. D., Harbott, J., Zimmermann, M., Hiddemann, W., Niemeyer, C., Henze, G., Feldges, A., Zintl, F., Kornhuber, B., Ritter, J., Welte, K., Gadner, H., and Riehm, H. (2000) Improved outcome in childhood acute lymphoblastic leukemia despite reduced use of anthracyclines and cranial radiotherapy: results of trial ALL-BFM 90. German-Austrian-Swiss ALL-BFM Study Group. *Blood 95*, 3310–3322.

(2) Pui, C. H., Sandlund, J. T., Pei, D., Rivera, G. K., Howard, S. C., Ribeiro, R. C., Rubnitz, J. E., Razzouk, B. I., Hudson, M. M., Cheng, C., Raimondi, S. C., Behm, F. G., Downing, J. R., Relling, M. V., and Evans, W. E. (2003) Results of therapy for acute lymphoblastic leukemia in black and white children. *JAMA 290*, 2001–2007.

(3) Pui, C. H., Relling, M. V., Campana, D., and Evans, W. E. (2002) Childhood acute lymphoblastic leukemia. *Rev. Clin. Exp. Hematol. 6*, 161–180.

(4) Henze, G., Fengler, R., Hartmann, R., Kornhuber, B., Janka-Schaub, G., Niethammer, D., and Riehm, H. (1991) Six-year experience with a comprehensive approach to the treatment of recurrent childhood acute lymphoblastic leukemia (ALL-REZ BFM 85). A relapse study of the BFM group. *Blood 78*, 1166–1172.

(5) Cheson, B. D. (2006) Monoclonal antibody therapy for B-cell malignancies. *Semin. Oncol. 33*, S2–14.

(6) Griffin, T. C., Weitzman, S., Weinstein, H., Chang, M., Cairo, M., Hutchison, R., Shiramizu, B., Wiley, J., Woods, D., Barnich, M., and Gross, T. G. (2009) A study of rituximab and ifosfamide, carboplatin, and etoposide chemotherapy in children with recurrent/refractory B-cell (CD20+) non-Hodgkin lymphoma and mature B-cell acute lymphoblastic leukemia: a report from the Children's Oncology Group. *Pediatr. Blood Cancer 52*, 177–181.

(7) de Vries, M. J., Veerman, A. J., and Zwaan, C. M. (2004) Rituximab in three children with relapsed/refractory B-cell acute lymphoblastic leukaemia/Burkitt non-Hodgkin's lymphoma. *Br. J. Hamaetol. 125*, 414–415.

(8) Thomas, D. A., Faderl, S., O'Brien, S., Bueso-Ramos, C., Cortes, J., Garcia-Manero, G., Giles, F. J., Verstovsek, S., Wierda, W. G., Pierce, S. A., Shan, J., Brandt, M., Hagemeister, F. B., Keating, M. J., Cabanillas, F., and Kantarjian, H. (2006) Chemoimmunotherapy with hyper-CVAD plus rituximab for the treatment of adult Burkitt and Burkitt-type lymphoma or acute lymphoblastic leukemia. *Cancer 106*, 1569–1580.

(9) Gisselbrecht, C. (2008) Use of rituximab in diffuse large B-cell lymphoma in the salvage setting. *Br. J. Hamaetol. 143*, 607–621.

(10) Martin, A., Conde, E., Arnan, M., Canales, M. A., Deben, G., Sancho, J. M., Andreu, R., Salar, A., Garcia-Sanchez, P., Vazquez, L., Nistal, S., Requena, M. J., Donato, E. M., Gonzalez, J. A., Leon, A., Ruiz, C., Grande, C., Gonzalez-Barca, E., and Caballero, M. D. (2008) R-ESHAP as salvage therapy for patients with relapsed or refractory diffuse large B-cell lymphoma: the influence of prior exposure to rituximab on outcome. A GEL/TAMO study. *Haematologica 93*, 1829–1836.

(11) Hilchey, S. P.; Hyrien, O.; Mosmann, T. R.; Livingstone, A. M.; Friedberg, J. W.; Young, F.; Fisher, R. I.; Kelleher; R. J., Jr., Bankert, R. B.; Bernstein, S. H. (2009) Rituximab immunotherapy results in the induction of a lymphoma idiotype-specific T-cell response in patients with follicular lymphoma: support for a "vaccinal effect" of rituximab. *Blood*.

(12) Bonavida, B. (2007) Rituximab-induced inhibition of anti-apoptotic cell survival pathways: implications in chemo/immunoresistance, rituximab unresponsiveness, prognostic and novel therapeutic interventions. *Oncogene 26*, 3629–3636.

(13) Hagenbeek, A., and Lewington, V. (2005) Report of a European consensus workshop to develop recommendations for the optimal use of (90)Y-ibritumomab tiuxetan (Zevalin) in lymphoma. *Ann. Oncol. 16*, 786–792.

(14) Scheuermann, R. H., and Racila, E. (1995) CD19 antigen in leukemia and lymphoma diagnosis and immunotherapy. *Leuk. Lymphoma 18*, 385–397.

(15) Herrera, L., Stanciu-Herrera, C., Morgan, C., Ghetie, V., and Vitetta, E. S. (2006) Anti-CD19 immunotoxin enhances the activity of chemotherapy in severe combined immunodeficient mice with human pre-B acute lymphoblastic leukemia. *Leuk. Lymphoma 47*, 2380–2387.

(16) Gerber, H. P., Kung-Sutherland, M., Stone, I., Morris-Tilden, C., Miyamoto, J., McCormick, R., Alley, S. C., Okeley, N., Hayes, B., Hernandez-Ilizaliturri, F. J., McDonagh, C. F., Carter, P. J., Benjamin, D., Grewal, I. S. (2009) Potent antitumor activity of the anti-CD19 auristatin antibody-drug conjugate hBU12-vcMMAE against rituximab sensitive and resistant lymphomas. *Blood*.

(17) Zein, N., Sinha, A. M., McGahren, W. J., and Ellestad, G. A. (1988) Calicheamicin gamma 1I: an antitumor antibiotic that cleaves double-stranded DNA site specifically. *Science 240*, 1198–1201.

(18) Lee, M. D., Manning, J. K., Williams, D. R., Kuck, N. A., Testa, R. T., and Borders, D. B. (1989) Calicheamicins, a novel family of antitumor antibiotics. 3. Isolation, purification and characterization of calicheamicins beta 1Br, gamma 1Br, alpha 2I, alpha 3I, beta 1I, gamma 1I and delta 1I. *J. Antibiot. 42*, 1070–1087.

(19) Acton, E. M., Tong, G. L., Mosher, C. W., and Wolgemuth, R. L. (1984) Intensely potent morpholinyl anthracyclines. *J. Med. Chem. 27*, 638–645.

(20) Raso, V., Ritz, J., Basala, M., and Schlossman, S. F. (1982) Monoclonal antibody-ricin A chain conjugate selectively cytotoxic for cells bearing the common acute lymphoblastic leukemia antigen. *Cancer Res. 42*, 457–464.

(21) Zein, N., Poncin, M., Nilakantan, R., and Ellestad, G. A. (1989) Calicheamicin gamma 1I and DNA: molecular recognition process responsible for site-specificity [published erratum appears in Science 1989 Jun 9;244(4909):following 1128]. *Science 244*, 697–699.

(22) Nicolaou, K. C., Dai, W. M., Tsay, S. C., Estevez, V. A., and Wrasidlo, W. (1992) Designed enediynes: a new class of DNA-cleaving molecules with potent and selective anticancer activity. *Science 256*, 1172–1178.

(23) Nicolaou, K. C., Li, T., Nakada, M., Hummel, C. W., and Wrasidlo, W. (1994) Calicheamicin θ^{I}_{1}: a rationally designed molecule with extremely potent and selective DNA cleaving properties and apoptosis inducing activity. *Angew. Chem., Int. Ed. Engl. 33*, 183–186.

(24) Lode, H. N., Reisfeld, R. A., Handgretinger, R., Nicolaou, K. C., Gaedicke, G., and Wrasidlo, W. (1998) Targeted therapy with a novel enediyene antibiotic calicheamicin theta(I)1 effectively suppresses growth and dissemination of liver metastases in a syngeneic model of murine neuroblastoma. *Cancer Res. 58*, 2925–2928.

(25) Wieder, T., Essmann, F., Prokop, A., Schmelz, K., Schulze-Osthoff, K., Beyaert, R., Dorken, B., and Daniel, P. T. (2001) Activation of caspase-8 in drug-induced apoptosis of B-lymphoid cells is independent of CD95/Fas receptor-ligand interaction and occurs downstream of caspase-3. *Blood 97*, 1378–1387.

(26) Lode, H. N., Xiang, R., Varki, N. M., Dolman, C. S., Gillies, S. D., and Reisfeld, R. A. (1997) Targeted interleukin-2 therapy for spontaneous neuroblastoma metastases to bone marrow. *J. Natl. Cancer Inst. 89*, 1586–1594.

(27) Scudiero, D. A., Shoemaker, R. H., Paull, K. D., Monks, A., Tierney, S., Nofziger, T. H., Currens, M. J., Seniff, D., and Boyd, M. R. (1988) Evaluation of a soluble tetrazolium/formazan assay for cell growth and drug sensitivity in culture using human and other tumor cell lines. *Cancer Res. 48*, 4827–4833.

(28) Gunther, R., Chelstrom, L. M., Tuel-Ahlgren, L., Simon, J., Myers, D. E., and Uckun, F. M. (1995) Biotherapy for xenografted human central nervous system leukemia in mice with severe combined immunodeficiency using B43 (anti-CD19)-pokeweed antiviral protein immunotoxin. *Blood 85*, 2537–2545.

(29) Prokop, A., Wrasidlo, W., Lode, H., Herold, R., Lang, F., Henze, G., Dorken, B., Wieder, T., and Daniel, P. T. (2003) Induction of apoptosis by enediyne antibiotic calicheamicin thetaII proceeds through a caspase-mediated mitochondrial amplification loop in an entirely Bax-dependent manner. *Oncogene 22*, 9107–9120.

(30) Knoll, K., Wrasidlo, W., Scherberich, J. E., Gaedicke, G., and Fischer, P. (2000) Targeted therapy of experimental renal cell carcinoma with a novel conjugate of monoclonal antibody 138H11 and calicheamicin thetaI1. *Cancer Res. 60*, 6089–6094.

(31) Scheuermann, R. H., and Racila, E. (1995) CD19 antigen in leukemia and lymphoma diagnosis and immunotherapy. *Leuk. Lymphoma 18*, 385–397.

(32) Uckun, F. M., Jaszcz, W., Ambrus, J. L., Fauci, A. S., Gajl-Peczalska, K., Song, C. W., Wick, M. R., Myers, D. E., Waddick, K., and Ledbetter, J. A. (1988) Detailed studies on expression and function of CD19 surface determinant by using B43 monoclonal antibody and the clinical potential of anti-CD19 immunotoxins. *Blood 71*, 13–29.

(33) Borowitz, M. J., Pullen, D. J., Winick, N., Martin, P. L., Bowman, W. P., and Camitta, B. (2005) Comparison of diagnostic and relapse flow cytometry phenotypes in childhood acute lymphoblastic leukemia: implications for residual disease detection: a report from the children's oncology group. *Cytometry B Clin. Cytom. 68*, 18–24.

(34) Grossbard, M. L., Multani, P. S., Freedman, A. S., O'Day, S., Gribben, J. G., Rhuda, C., Neuberg, D., and Nadler, L. M. (1999) A Phase II study of adjuvant therapy with anti-B4-blocked ricin after autologous bone marrow transplantation for patients with relapsed B-cell non-Hodgkin's lymphoma. *Clin. Cancer Res. 5*, 2392–2398.

(35) Grossbard, M. L., Gribben, J. G., Freedman, A. S., Lambert, J. M., Kinsella, J., Rabinowe, S. N., Eliseo, L., Taylor, J. A., Blattler, W. A., and Epstein, C. L. (1993) Adjuvant immunotoxin therapy with anti-B4-blocked ricin after autologous bone marrow transplantation for patients with B-cell non-Hodgkin's lymphoma. *Blood 81*, 2263–2271.

(36) Stone, M. J., Sausville, E. A., Fay, J. W., Headlee, D., Collins, R. H., Figg, W. D., Stetler-Stevenson, M., Jain, V., Jaffe, E. S., Solomon, D., Lush, R. M., Senderowicz, A., Ghetie, V., Schindler, J., Uhr, J. W., and Vitetta, E. S. (1996) A phase I study of bolus versus continuous infusion of the anti-CD19 immunotoxin, IgG-HD37-dgA, in patients with B-cell lymphoma. *Blood 88*, 1188–1197.

(37) Uckun, F. M., Messinger, Y., Chen, C. L., O'Neill, K., Myers, D. E., Goldman, F., Hurvitz, C., Casper, J. T., and Levine, A. (1999) Treatment of therapy-refractory B-lineage acute lymphoblastic leukemia with an apoptosis-inducing CD19-directed tyrosine kinase inhibitor. *Clin. Cancer Res. 5*, 3906–3913.

(38) Chen, C. L., Levine, A., Rao, A., O'Neill, K., Messinger, Y., Myers, D. E., Goldman, F., Hurvitz, C., Casper, J. T., and Uckun, F. M. (1999) Clinical pharmacokinetics of the CD19 receptor-directed tyrosine kinase inhibitor B43-Genistein in patients with B-lineage lymphoid malignancies. *J. Clin. Pharmacol. 39*, 1248–1255.

(39) Messmann, R. A., Vitetta, E. S., Headlee, D., Senderowicz, A. M., Figg, W. D., Schindler, J., Michiel, D. F., Creekmore, S., Steinberg, S. M., Kohler, D., Jaffe, E. S., Stetler-Stevenson, M., Chen, H., Ghetie, V., and Sausville, E. A. (2000) A phase I study of combination therapy with immunotoxins IgG-HD37-deglycosylated ricin A chain (dgA) and IgG-RFB4-dgA (Combotox) in patients with refractory CD19(+), CD22(+) B cell lymphoma. *Clin. Cancer Res. 6*, 1302–1313.

(40) Gekeler, V., Boer, R., Uberall, F., Ise, W., Schubert, C., Utz, I., Hofmann, J., Sanders, K. H., Schachtele, C., Klemm, K., and Grunicke, H. (1996) Effects of the selective bisindolylmaleimide protein kinase C inhibitor GF 109203X on P-glycoprotein-mediated multidrug resistance. *Br. J. Cancer 74*, 897–905.

(41) Szatrowski, T. P., Dodge, R. K., Reynolds, C., Westbrook, C. A., Frankel, S. R., Sklar, J., Stewart, C. C., Hurd, D. D., Kolitz, J. E., Velez-Garcia, E., Stone, R. M., Bloomfield, C. D., Schiffer, C. A., and Larson, R. A. (2003) Lineage specific treatment of adult patients with acute lymphoblastic leukemia in first remission with anti-B4-blocked ricin or high-dose cytarabine: Cancer and Leukemia Group B Study 9311. *Cancer 97*, 1471–1480.

(42) Brethon, B., Auvrignon, A., Galambrun, C., Yakouben, K., Leblanc, T., Bertrand, Y., Leverger, G., and Baruchel, A. (2006) Efficacy and tolerability of gemtuzumab ozogamicin (anti-CD33 monoclonal antibody, CMA-676, Mylotarg) in children with relapsed/refractory myeloid leukemia. *BMC Cancer 6*, 172.

(43) Arceci, R. J., Sande, J., Lange, B., Shannon, K., Franklin, J., Hutchinson, R., Vik, T. A., Flowers, D., Aplenc, R., Berger, M. S., Sherman, M. L., Smith, F. O., Bernstein, I., and Sievers, E. L. (2005) Safety and efficacy of gemtuzumab ozogamicin in pediatric patients with advanced CD33+ acute myeloid leukemia. *Blood 106*, 1183–1188.

(44) van, D. V. V., te Marvelde, J. G., Hoogeveen, P. G., Bernstein, I. D., Houtsmuller, A. B., Berger, M. S., and Van Dongen, J. J. (2001) Targeting of the CD33-calicheamicin immunoconjugate Mylotarg (CMA-676) in acute myeloid leukemia: in vivo and in vitro saturation and internalization by leukemic and normal myeloid cells. *Blood 97*, 3197–3204.

BC900128H

A General Methodology Toward Drug/Dye Incorporated Living Copolymer−Protein Hybrids: (NIRF Dye-Glucose) Copolymer−Avidin/BSA Conjugates as Prototypes

Wei Shi,[†,§] Sukanta Dolai,[†,§] Saadyah Averick,[§] Suraj S. Fernando,[§] Jose A. Saltos,[§] William L'Amoreaux,[#] Probal Banerjee,[§] and Krishnaswami Raja*[,§]

The City University of New York at College of Staten Island, NewYork. Received April 2, 2009; Revised Manuscript Received June 15, 2009

Azide-terminated poly(*tert*-butyl acrylate) was synthesized via atom transfer radical polymerization (ATRP). Subsequent deprotection was performed to yield poly(acrylic acid) (PAA) possessing a reactive chain-end. A one-pot sequential amidation of the PAA with the amine derivatives of a near-infrared fluorescent dye (ADS832WS) and glucose produced NIRF dye-incorporated water-soluble copolymers. End-group modifications were performed to produce alkyne/biotin-terminated copolymers which were further employed to generate dye-incorporated polymer−protein hybrids via the biotin−avidin interaction with avidin or "click" bioconjugation with azide-modified BSA. We have overcome two fundamental limitations in the synthesis of bioconjugates: (a) the basic restriction in the diversity of copolymers which can be synthesized for producing bioconjugates, (b) the limitation in the number of dyes/drug molecules that can be attached per protein molecule. The copolymers possessed enhanced optical properties compared to the dye due to increased solubility in water. Potential utility of these copolymers and conjugates in multiwell plate based assays, cell surface imaging and in vivo animal imaging were explored.

INTRODUCTION

Polymer−protein hybrids are a newly emerging class of bioconjugates with several applications in biotechnology, biopharmaceutical chemistry, and other life science areas (*1*−*4*). There are, however, some fundamental limitations in the current methodologies available for the synthesis of these hybrids: (a) Using current technologies, the number of copies of cytotoxic drugs/dyes that can be chemically conjugated to a protein (antibody, avidin/streptavidin, etc.) is limited. (b) There is a basic limitation in the diversity of copolymers that can be synthesized for bioconjugation. The former limitation arises from the fact that extensive modification of proteins with several copies of a drug/dye would cause deactivation of the active sites and because of the limited numbers of functional groups available per protein molecule for bioconjugation. The latter limitation (in the diversity of copolymers synthesized for bioconjugation) arises from (a) widely different reactivity between monomers and (b) the lack of reactivity of many biologically relevant acrylates (e.g., an acrylate derivative of the anticancer drug candidate curcumin can be synthesized but will not polymerize since the molecule is a radical quencher) (*5*). Biological properties (e.g., bioactivity and self-assembly) of polymer−protein hybrids demands the synthesis of well-defined polymers for bioconjugation (*6*−*8*). In the early embodiments, the polymer component of the conjugates was synthesized via uncontrolled free radical polymerization (*9*).

The synthesis of well-defined polymer−protein hybrids in which the polymers are synthesized via controlled radical polymerization methods (such as atom transfer radical polymerization [ATRP] or reversible addition−fragmentation polymerization [RAFT] is a rich newly emerging field of research (*10*−*19*). The synthesis of living polymer−protein hybrid materials has, however, been restricted to a few acrylate/methacrylate monomers such as poly(ethylene glycol) acrylate/methacrylate and poly(*N*-isopropyl) acrylamide; the recently reported streptavidin conjugates with biotinylated polymers serve as examples (*10, 12, 13*).

Herein, we present a general methodology for significantly increasing the number of dye/drug molecules that can be attached per protein molecule. The diversity of copolymers that can be synthesized for bioconjugation to proteins has also been considerably expanded. The synthesis of poly(acrylic acid)-based near infrared fluorescence (NIRF) dye and glucose incorporated novel copolymers that were further employed for bioconjugation to avidin and bovine serum albumen (BSA) demonstrates this breakthrough. It should be noted that near-infrared (NIR)-absorbing dyes have opened new avenues in optical imaging with direct applications in pharmacology, cellular biology, and diagnostics as living subjects can be monitored with safe, noninvasive optical imaging/contrasting techniques (*20*−*23*). In vitro and in vivo imaging with cyanine-based NIRF dyes are advantageous due to significant reduction of background absorption, enhanced fluorescence, the availability of low-cost sources of irradiation, the versatility of different reporter probes, large molar extinction coefficients, and moderate-to-high fluorescence quantum yields (*24*−*26*).

MATERIALS AND METHODS

Synthesis. Detailed information on the materials used, synthetic procedures, and compound characterization data are provided in the Supporting Information. A few representative experiments are presented here.

* Author to whom correspondence should be addressed: Dr. Krishnaswami Raja, Department of Chemistry, College of Staten Island, 2800 Victory Boulevard, Staten Island, NY 10314. Ph: 718-982-4091, Fax: 718-982-3910, Email:raja@mail.csi.cuny.edu.

[§] Department of Chemistry.

[#] Department of Biology.

[†] Both authors contributed equally to this work.

10.1021/bc900142y CCC: $40.75 © 2009 American Chemical Society
Published on Web 07/09/2009

Synthesis of Azide-Terminated Poly(*tert*-butyl acrylate) (2). A 100 mL flask fitted with a stopcock was flame-dried under vacuum and allowed to cool at ambient temperature under argon. The flask was charged with CuBr (115 mg, 0.8 mmol). Under positive pressure of argon, a solution of 2-bromo-2-methylpropionic acid 2-[2-(2-azidoethoxy)ethoxy] ethyl ester (118 mg, 0.36 mmol) dissolved in *tert*-butyl acrylate (4 mL, 27.55 mmol) was added via syringe, followed by the addition of 1,1,4,7,7-pentamethyldiethylenetriamine (PMDETA) (0.17 mL, 0.8 mmol). Following three freeze−pump−thaw degassing cycles, the reaction was allowed to stir for 2 h 10 min at 60 °C. The polymerization was quenched by submerging the flask in liquid nitrogen; the mixture was allowed to warm to ambient temperature and diluted with tetrahydrofuran. CupriSorb was added and stirred ca. 30 min to remove copper complex. After filtration, the mixture was poured into a 15% methanol, deionized water solution, and a white solid product was precipitated. The polymer was further purified via reprecipitation and dried under vacuum; isolated yield was 2.18 g (47%). DPn = 64, M_n = 8586 g/mol, M_w/M_n = 1.21. ^{1}H NMR (600 MHz, $CDCl_3$): δ (ppm) 4.19 (s, 2H), 3.55−3.75 (m, 6H), 3.39 (t, 2H), 2.18−2.30 (bm), 1.85 (s), 1.28−1.62 (bm), 1.15 (s, 6H), 0.89 (m). FTIR (film, cm^{-1}): 3433, 2977, 2289, 2113 (azide), 1727, 1619, 1450, 1367, 1255, 1153, 845, 752.

Synthesis of Biotin-Terminated Poly(glucosamine)-Poly-(NIRF dye) Copolymer (6). The biotinylated poly(acrylic acid) polymer (**5**) (76 mg, 1.055 mmol of COOH), Near-infrared absorption dye (ADS832WS) (200 mg, 0.213 mmol), EDC·HCl (213 mg, 1.11 mmol), and HOBt (153 mg, 1.148 mmol) were dissolved in DMF (1.5 mL) in a r.b. followed by the addition of triethylamine (0.15 mL, 1.08 mmol). After stirring for 2 days at room temperature, D-(+)-glucosamine (230 mg, 1.067 mmol) (in water (2 mL) and DMF (1 mL) mixture solution) was added. EDC·HCl (200 mg, 1.043 mmol) was also added, and the mixture was stirred for another 3 days at room temperature. After stopping the reaction, the solution was transferred into a dialysis bag (MWCO 3.5 KDa), and the solution was dialyzed against a continuous flow of deionized water for 24 h. The dialyzed reaction mixture was filtered and lyophilized to yield greenish-brown crude product. The crude product was further purified with Sephadex LH-20 size-exclusion column with deionized water as eluent and lyophilized. Isolated yield: 249 mg. GPC (H_2O): M_n = 23 259 g/mol, M_w/M_n = 1.48. ^{1}H NMR (600 MHz, CD_3OD) δ (ppm) 8.98 (d), 7.18−8.34 (bm), 6.68 (m), 6.37 (m), 5.27 (d), 4.63 (s), 4.30 (s), 3.31−3.96 (m), 3.19 (m), 3.12 (m), 2.99−3.02 (m), 2.86−2.91 (m), 2.79 (s), 1.35−2.22 (m), 1.61 (d), 1.19−1.32 (m), 1.08 (m).

Synthesis of Alkyne-Terminated Poly(glucosamine)-Poly-(NIRF dye) Copolymer (10). Poly(glucosamine)-poly(NIRF dye) copolymer (60 mg, 3 μmol) was dissolved in 3 mL of *t*-BuOH/THF/H_2O (1:1:1) and stirred with propargyl ether (9.14 mg, 10 μL, 31.5 equiv), $CuSO_4 \cdot 5H_2O$ (5 mg, 0.02 mmol), Sodium ascorbate (4 mg, 0.02 mmol) in a r.b. flask under N_2 atmosphere at room temperature for 24 h. The reaction was stopped, and the reaction mixture was dialyzed extensively in deionized water using 10 kD MWCO membrane. The dialyzed mixture was further purified via Sephadex-LH 20 size exclusion chromatography and lyophilized. Yield: 42 mg (70%). GPC (H_2O): M_n = 19 988, M_w/M_n = 1.40. ^{1}H NMR (600 MHz, D_2O) δ (ppm): 1.03 (bs), 1.52−1.75 (bd), 2.01 (bs), 2.58 (s), 2.81 (s), 2.94 (s), 3.36 (s), 3.66−3.73 (bd), 5.06−5.23 (bm), 7.15−8.33 (m). FT-IR (cm^{-1}): 3299, 2928, (No N_3 peak ~2100), 1648, 1536, 1429, 1389, 1351, 1232, 1155, 1113.

Conjugation of Biotin-Terminated Copolymer 6 and Avidin. Avidin (1 mg) was dissolved in 0.25 mL of PBS buffer, pH 7.4. Polymer **6** (5.5 mg) was dissolved in 0.65 mL PBS buffer and slowly added. After 1.5 h at room temperature, the solution was extensively dialyzed using a 50 KDa MWCO membrane in deionized water, and the modified protein was analyzed by fast protein liquid chromatography (FPLC) and SDS-PAGE.

Synthesis of Protein−Polymer Conjugate; BSA-"Clicked"-Poly(glucosamine)-Poly(NIRF dye) Copolymer (14). BSA-azide (5 mg, approximately 1.5 μmol in azide) was incubated with alkyne-poly(glucosamine)-poly(NIRF dye) polymer (20 mg, 1 μmol) in Tris buffer (1800 μL, 0.1 M, pH 8) in the presence of TCEP (4 mM), "click" ligand (4 mM, dissolved in 200 μL of DMF) and copper sulfate (2 mM) for 16 h at 4 °C. The ligand was added before the addition of copper sulfate. The reaction mixture was then dialyzed using Spectra Por 6 dialysis membrane (MWCO 50 KDa) in PBS pH 7.4 for 48 h to remove excess of copper and ligand. The conjugate was further characterized via SDS-PAGE and Fast Protein Liquid Chromatographic system (Akta Purifier, Amarsham Bio-Science's) using HiPrep 26/10 Sephacryl S-200HR (GE Healthcare) size-exclusion column in PBS pH 7.4 as eluent buffer.

UV−vis−NIR and Fluorescence Spectroscopy of NIRF Dye and Polymer 9. NIRF dye (ADS832WS) (2.8 mg) was dissolved in 10 mL of deionized water to prepare a stock solution of 3 μM. Azide-terminated poly(glucosamine)-poly(NIRF dye) polymer **9** (11.7 mg; 5 dye molecule per polymer chain) was dissolved in 10 mL of deionized water to prepare a solution of 0.3 mM of effective dye concentration. The stock solution of NIRF dye was further diluted to 0.3 μM. The UV−vis−NIR spectra were obtained on an Agilent Technologies 845× UV−vis System using deionized water as blank. The fluorescence spectra of both the dye and the dye-incorporated polymer **9** were obtained on JobinYvon Horiba FluoroMax-3 instrument using the solutions containing 0.3 μM effective dye concentration.

Detection of Binding Affinity of Biotinylated Copolymers to Streptavidin-Coated Wells. Control poly(glucosamine)-poly(NIRF dye) polymer, biotin-terminated poly(acrylic acid)-poly (NIRF dye) polymer (**6a**), and biotin-terminated poly(glucosamine)-poly(NIRF dye) copolymer (**6**). All samples were prepared at a starting effective molar dye concentration of 0.2 mM in PBS (pH = 7.4); then, each of the three samples was successively diluted 10-fold to final concentrations of 0.02, 2.0 × 10^{-3}, and 2.0 × 10^{-4} mM. 50 μL of each solution was then added to the wells and incubated overnight at 4 °C. Then, the wells were washed four times with PBS containing 0.05% Tween 20. Finally, the wells were then visualized using the Odyssey imaging system (LI-COR, Lincoln, NE) at 800 nm.

Test of the Utility of NIRF Dye-Incorporated Polymer in Noninvasive Imaging in Mice. Each of two female, six-month-old mice were injected with 200 μL of the NIRF dye, and the biotin-terminated poly(glucosamine)-poly(NIRF dye) polymer **6** (0.2 mM effective dye concentration in both cases) via the tail vein. Each mouse was then anaesthetized using a mixture of 15 μL Xylezene mixed with 54 μL Ketamine to reach a dose of 10 mg/kg body weight of Xylezene and 90 mg/kg bodyweight of Ketamine per mouse, and then scanned using a Odyssey scanner (Near IR) at wavelength 800 nm. To investigate the extent of fluorescence and the extent of catabolism of the polymer, the mice were scanned after 1 and 4 h. Another female six-month-old mouse (control mouse) was anaesthetized with the same mixture and then scanned to eliminate background fluorescence.

In Vitro Imaging Using Retinal Epithelial Cells. Retinal pigment epithelial cells were divided onto four wells and then allowed to grow for three days with regular feeding; the cells were then fixed using 2% PFA, then rinsed three times for five minutes each using PBS (pH = 7.4). The nonspecific binding sites were then blocked using a blocking buffer and incubated overnight. The blocking buffer was then removed, and well (**a**)

Scheme 1. Schematic Synthesis of NIRF Dye Incorporated Synthetic Polymer−Protein Hybrid via Biotin−Avidin Interaction

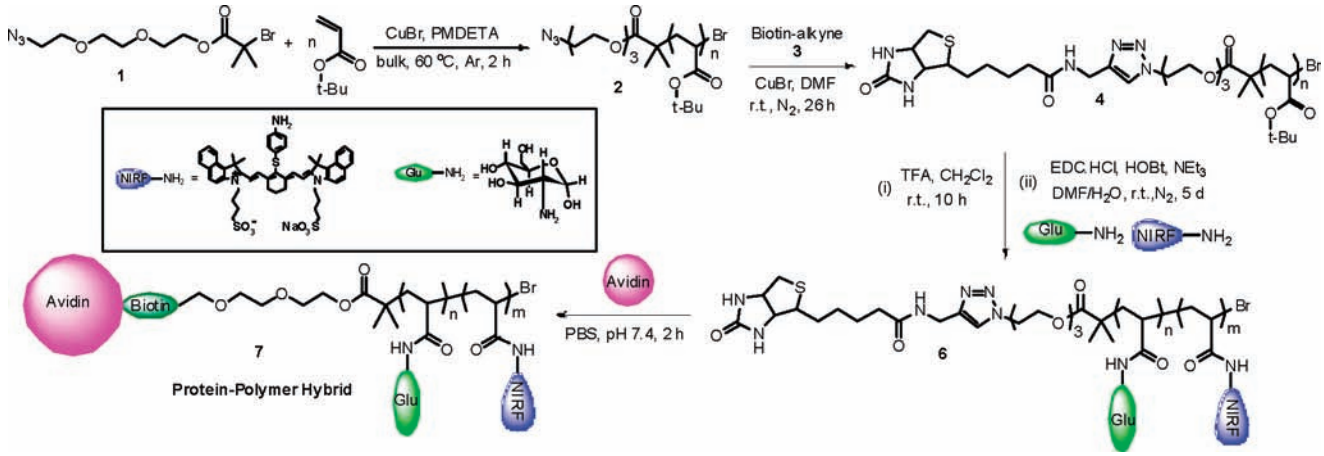

Scheme 2. Synthetic Representation of Protein−Polymer Hybrid via Bio-Orthogonal "Click" Reaction with NIRF Dye Incorporated Living Copolymer and BSA

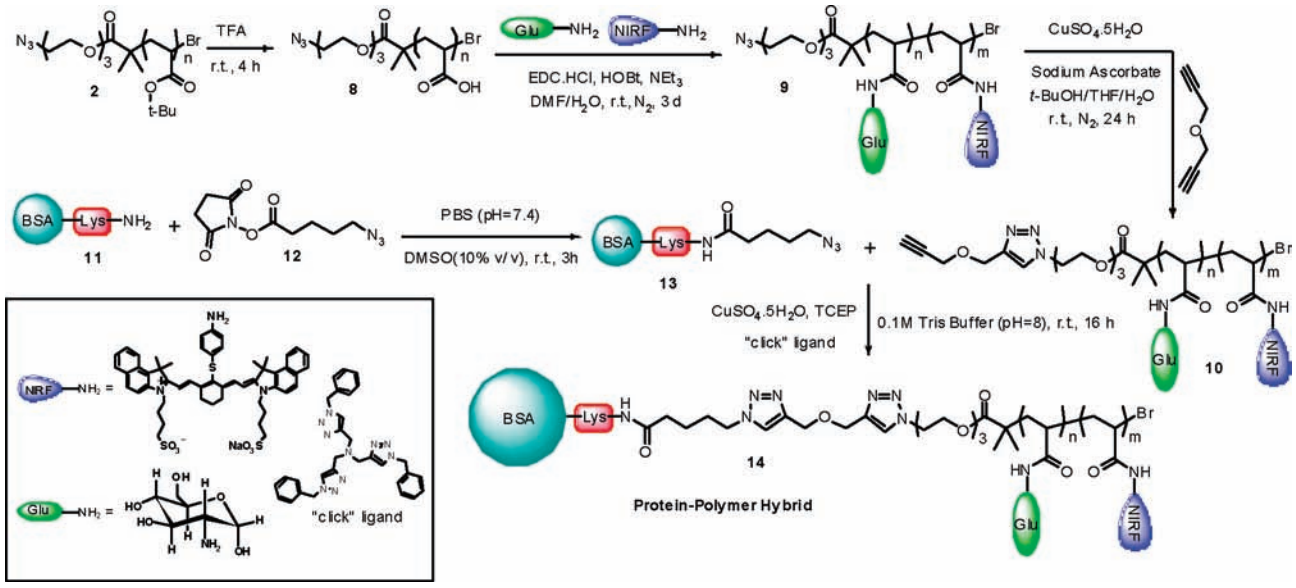

only was incubated with the primary antibody and incubated overnight at 4 °C. The primary antibody was then rinsed 3 × 5 min each, and then the biotinylated secondary antibody was added to wells (a,b) and incubated overnight at 4 °C. Rinsing was performed for the excess secondary antibody using the same technique used for the primary antibody; then, 500 μL of Avidin (1 mg/mL) was added to each of wells (a,b,c) and incubated overnight at 4 °C, and excess avidin was washed off with PBS (pH = 7.4) 3 × 5 min each. Finally, 500 μL of poly(glucosamine)-poly(NIRF dye) copolymer **6** (0.1 mg/mL) was added to each of the wells (a,b,c,d) and incubated 2 h at 37 °C in a controlled temperature chamber. Excess polymer was washed off using PBS (pH = 7.4) 3 × 5 min each; fresh PBS was then added to the wells and scanned using Odyssey imaging system (LI-COR, Lincoln, NE) with detection in the NIR region at 800 nm.

RESULTS AND DISCUSSION

Our approach to these polymer−protein conjugates involved three steps: (1) the synthesis of well-defined living polymers containing reactive chain end and functional side chain pendant groups in which the chain end and side chain possesses orthogonal reactivity, (2) the attachment of a number of water-soluble, biocompatible moieties and imaging/therapeutic agents to the functional polymer side chains, and (3) the attachment of the polymers (via the reactive polymer chain end) with proteins to produce the final bioconjugates. Two parallel synthetic designs were employed to establish the feasibility of this concept. In the first design, poly(acrylic acid) with a single reactive biotin chain end was synthesized; straightforward post-polymerization modification of the polymer yielded the final NIRF dye-glucose copolymers for bioconjugation (Scheme 1). The biotinylated copolymers were employed to produce conjugates with avidin via the biotin−avidin interaction ($K_d \sim 10^{15}$) (*27*). In the second embodiment, an alkyne-terminated NIRF dye-glucose copolymer was synthesized and further conjugated to azide linker-modified BSA via the azide−alkyne triazole forming "click" bioconjugation reaction (*28*). The representation of both the copolymer-avidin (Scheme 1) and the copolymer-BSA (Scheme 2) hybrids portray the synthetic breakthrough that has been achieved: a copolymer composed of several copies of an imaging agent/drug displayed in a side chain polymer architecture is attached via a single link to avidin or BSA. Hence, on a per protein molecule basis a larger number of dyes/drugs are being attached using this strategy. In this Article, we also present the potential applications of representative polymers and conjugates in multiwell plate-based bioassays and in in vitro and in vivo imaging. To the best of our knowledge, this is the

first report describing the synthesis of well-defined NIRF dye incorporated living copolymer−protein hybrids.

Polymer−Protein Hybrids via Biotin−Avidin Interaction. The synthesis involved the polymerization of *tert*-butyl acrylate via ATRP (*29*) using an azide-incorporated initiator **1** to produce poly(*tert*-butyl acrylate) **2** (Scheme 1). The intact nature of the azide group in the polymer was confirmed by the presence of the azide peak at 2113 cm^{-1} in the IR spectrum of the polymer (see Supporting Information). The resulting polymer was reacted with an alkyne derivative of biotin **3** under [3 + 2] azide−alkyne triazole forming "click" conditions to produce a polymer with a single biotin chain end **4** (Scheme 1). Peaks arising from the biotin moiety (*14*) at 4.48 ppm and 4.31 ppm were observed in the ^{1}H NMR of **4**; peaks at 7.68 (s) and 7.44 (s) arising from the triazole protons (*30*) were also observed (see Supporting Information). Polymer **4** was treated with trifluoroacetic acid (TFA) to produce poly(acrylic acid) (PAA) with a single biotin chain end **5**. The rationale for synthesizing PAA with a single chain end is based on the facts that (a) PAA is FDA approved and is generally regarded as safe (GRAS); (b) amine derivatives of a broad spectrum of dyes and a wide range of therapeutic agents are readily available commercially and can be employed using amidation chemistry with PAA to produce copolymers; and (c) azidotriethylene glycol and the ATRP initiator with the azide group employed for the polymerizations are safe (many short chain azides are explosive). The amine derivatives, NIRF-NH_2 (ADS832WS) and Glu-NH_2 (D-(+)-glucosamine) were grafted to the PAA polymer **5** using standard amide coupling reagents 1-ethyl-3-(3-dimethyllaminopropyl)carbodiimide hydrochloride (EDC·HCl) and *N*-hydroxybenzotriazole (HOBt) in DMF to produce **6**. The polymers synthesized were characterized via ^{1}H NMR, gel permeation chromatography (GPC), and FT-IR spectroscopy (see Supporting Information).

On the basis of the GPC results, comparing the molecular weights of **4** and **6**, the percentage of the NIRF dye in the polymer **6** was determined to be ~17% per polymer chain (see Supporting Information). Polymers with higher dye loading numbers and a control polymer **6a** (PAA with dye alone) were also synthesized; however, those polymers were not readily soluble in water. Therefore, copolymer **6** was chosen for further studies due to its better solubility in water. It should be noted that, recently, side chain poly(alkyne) polymers were synthesized and various azide molecules were attached to the polymer backbone via "click" chemistry (*31*). The approach is restricted to a few azides because many small azides are potentially explosive (*31*). The copolymer−protein hybrid **7** was synthesized by incubating the copolymer **6** with avidin. The formation of a conjugate was indicated by higher molecular weight bands in SDS PAGE; the conjugate band which glowed when imaged using a NIRF imager was also visible following Coomassie staining indicating the presence of both polymer and protein at the same position (Figure 1B). The formation of the conjugate was further confirmed via size exclusion fast protein liquid chromatography (FPLC) where conjugate **7** eluted earlier (due to its higher molecular weight) in comparison to the synthetic polymer **6** and the control avidin sample (Figure 1A).

Polymer−Protein Hybrids via "Click" Reaction. In the second synthetic methodology (Scheme 2), the azide-terminated polymer **2** was treated with TFA to produce PAA with azide chain end **8**. The pendant carboxylic acid side chains of polymer **8** were grafted with NIRF-NH_2 and Glu-NH_2 via amide-coupling (EDC·HCl and HOBt) in DMF to produce poly(glucosamine)-poly(NIRF dye) copolymer **9**. In a separate reaction, BSA was modified by incubating with NHS-azide or NHS-alkyne heterobifunctional linkers to produce either azide-labeled BSA **13** or alkyne-labeled BSA **13a**, respectively. MALDI-TOF spectroscopy was used to estimate the average number of lysine residue modifications of the BSA (please note that BSA contains 65 lysine groups). Results indicate that on an average BSA was modified with ~35 alkyne or ~45 azide groups (see Supporting Information). Polymer **9** with a reactive azide chain end was incubated with alkyne-modified BSA **13a** under "click" bioconjugation conditions (*11*) but unfortunately without any success (lack of reaction confirmed via SDS-PAGE; data not shown). Earlier reports support the reduced/lack of reactivity of alkyne modified proteins in "click" bioconjugation reactions (*12*). To circumvent the above-mentioned problem, copolymer **9** was reacted with a large excess of dipropargyl ether under "click" condition to convert the azide-terminated copolymer to an alkyne-terminated poly(glucosamine)-poly(NIRF dye) copolymer **10**. The absence of the azide peak (~2100 cm^{-1}) in the FT-IR spectra confirmed the conversion of all the azide end groups to alkyne (see Supporting Information). The incubation of azide-linker modified BSA **13** with alkyne-terminated copolymer **10** finally produced the desired polymer−protein hybrid **14**. The formation of the conjugate was confirmed via FPLC (Figure 2) and SDS-PAGE (Figure 3). The conjugate **14** eluted earlier than both copolymer **10** and modified BSA **13** in the FPLC experiment. The unmodified BSA **11** eluted at the same volume as the modified BSA **13**; hence, it was not shown in the chromatogram (Figure 2). The SDS-PAGE gels were consistent with the FPLC results; the bands which glowed at 800 nm (lanes 4 and 8) also appeared when stained with

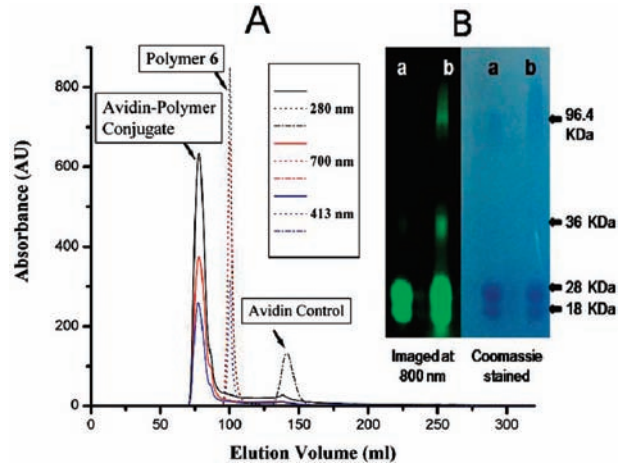

Figure 1. A. Size-exclusion FPLC (Hiprep 26/60 Sephacryl S-200 HR column) of avidin (dashed line), copolymer **6** (dotted line), and conjugate **7** (solid line). B. SDS-PAGE of avidin (lane a) and conjugate **7** (lane b).

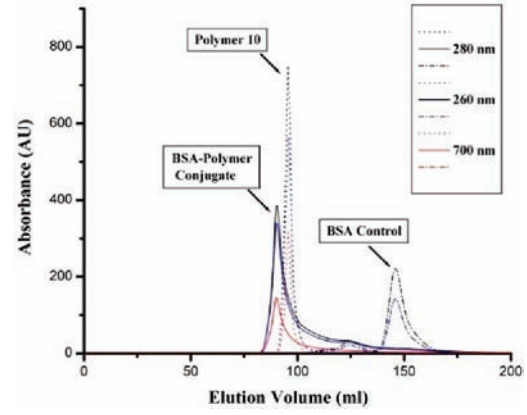

Figure 2. Size-exclusion FPLC (Hiprep 26/60 Sephacryl S-200 HR column) of azide-modified BSA **13** (dashed line), copolymer **10** (dotted line), and conjugate **14** (solid line).

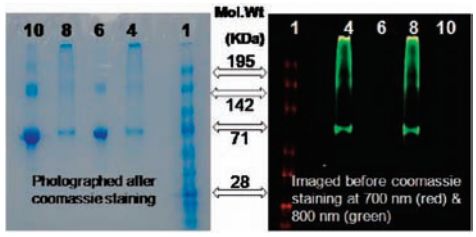

Figure 3. SDS-PAGE of conjugate **14** (lanes 4,8), mixture of azide modified BSA **13** and copolymer **10** without "click" reagents (lane 6), and unmodified BSA (lane 10).

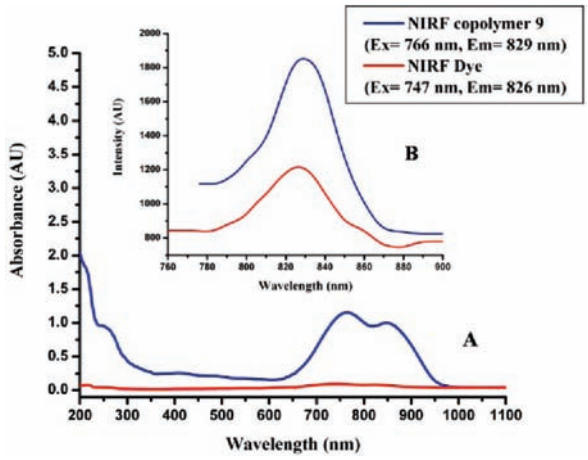

Figure 4. UV/vis/NIR absorption spectra (A) and fluorescence emission spectra (B) of NIRF copolymer **9** (blue line), NIRF dye (red line) in water at 25 °C. The effective dye concentrations in both the cases are identical (0.3 μM).

Coomassie (but the control lanes 6 and 10 did not glow at 800 nm). This confirmed the presence of both protein and polymer at the same ordinate in the conjugate samples. To confirm that copolymer **10** was indeed chemically bonded to the protein, we incubated the mixture of copolymer **10** and modified BSA **13** in the same ratio but without the "click" reagents and dialyzed the mixture with a 50 KDa MWCO membrane; in this case, no higher molecular weight conjugate bands were observed (lane 6).

UV and Fluorescence Study. We have investigated the absorbance and fluorescence emission profiles for the NIRF dye (ADS832WS) and the poly(glucosamine)-poly(NIRF dye) copolymer **9** (Figure 4). Copolymer **9** had superior solubility in water compared to the dye molecule. As a result, higher absorbance values were observed in the case of the polymer sample even though both solutions contained the same effective dye concentration of 0.3 μM (Figure 4A). A red shift of 19 nm (from 747 to 766 nm) in the absorbance maxima (λ_{max}) of the dye was also observed. Although the fluorescence emission intensity of copolymer **9** was higher than that of the dye as expected, the dye displayed larger Stokes shift (79 nm) compared to copolymer **9** (63 nm) (Figure 4B).

Multiwell Plate Binding Assay. Immobilization of the synthesized biotinylated neoglycopolymer was performed on streptavidin-coated multiwell plates where the plates were incubated with a 10-fold serial dilution of (a) nonbiotinylated poly(glucosamine)-poly(NIRF dye) copolymer control (b) polymer **6a** and (c) copolymer **6**. The wells were washed with PBS buffer to avoid nonspecific binding and scanned using an NIRF imaging system; see Figure 5A. The result indicated that the control polymer did not bind to the plates (low fluorescence intensity), whereas the biotin-terminated polymers remained bound to the streptavidin-coated plates, thereby resulting in

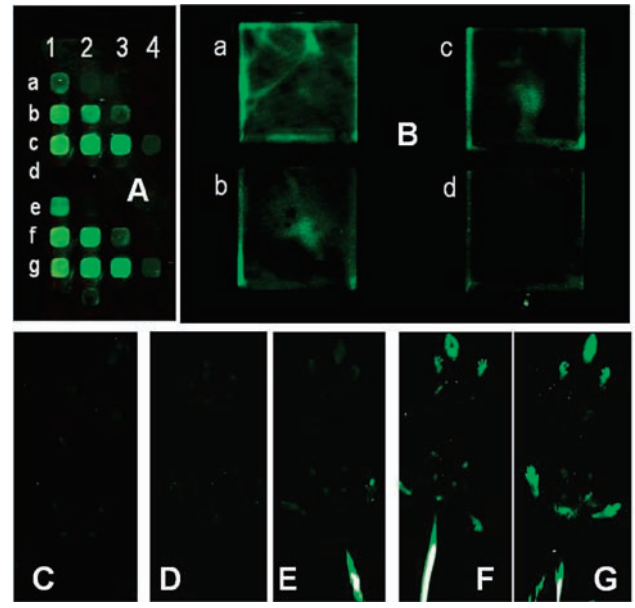

Figure 5. A. Streptavidin-coated multiwell plates treated with nonbiotinylated copolymer control (a,e), polymer **6a** (b,f), and copolymer **6** (c,g). Wells 1−4 correspond to a 10-fold serial dilution of the polymers. B. Fixed retinal pigment epithelial cells (ARPE-19) labeled using copolymer **6**. Slide a was incubated with primary, biotinylated secondary antibody, avidin, and copolymer **6** and imaged. Primary antibody was omitted in slide b; in slide c, the primary and biotinylated secondary antibodies were omitted; in slide d, the primary, biotinylated secondary antibodies and avidin were omitted prior to the copolymer **6** treatment step. C. The control mouse without an imaging agent. D,E. Mouse scanned 1 and 4 h after tail-vein injection with the NIRF dye, respectively. F,G. Mouse scanned 1 and 4 h after tail-vein injection with copolymer **6**, respectively. All the images were scanned using an odyssey NIRF imager at 800 nm.

higher fluorescence intensity. In the case of **6**, the fluorescence intensity was significantly higher than that of **6a** presumably because of the superior water/buffer solubility of **6**. The resulting immobilized neoglycopolymers can interact with complementary cell surface receptors/lectins (*32*). Hence, one can potentially create a convenient platform to study carbohydrate−receptor interactions; by varying the carbohydrates in the polymer and by using dye-modified lectins/cell receptors, which are fluorescence resonance energy transfer (FRET) (*33*) partners for the NIRF dye on the polymers, a range of lectins/cell receptor interactions can be explored.

In Vitro Imaging Study. The utility of copolymer **6** in in vitro imaging cells was also evaluated using retinal pigment epithelial cells. The cells were fixed and treated with primary antibody (2B-α5 rabbit polyclonal IgG), biotinylated secondary antibody, avidin, and poly(glucosamine)-poly(NIRF dye) copolymer **6** (Figure 5B). Slide a was incubated with primary, secondary antibodies, avidin, and copolymer **6**; in slide b, the primary antibody was omitted; in slide c, the primary and secondary antibodies were omitted; in slide d, the primary, secondary antibodies, and avidin were omitted prior to the copolymer **6** treatment step. Slides b, c, and d serve as controls. The results indicate that only slide a showed maximum fluorescence, while control slides show minimal fluorescence.

In Vivo Imaging Study. Polymer **6** also showed considerable promise in noninvasive in vivo imaging of mice: mice injected with the polymer could be imaged more efficiently than mice injected with the small molecule NIRF-NH_2 dye (Figure 5C−G; please note that since the mice were not shaved only the hairless body parts of mice were clearly visible). The polymer is superior for imaging mice compared to the low molecular weight dye probably because of the superior solubility of poly(glucosamine)-

poly(NIRF dye) copolymer **6** in water/blood/serum compared to the dye and because it is not cleared from the blood rapidly via kidney filtration. Employing the copolymer to produce conjugates (with antibodies) for tissue-specific targeted imaging is being currently pursued; this is beyond the scope of the current article.

CONCLUSION

In this study, we have overcome two fundamental limitations in the synthesis of bioconjugates: (a) the basic restriction in the diversity of copolymers which can be synthesized for producing bioconjugates and (b) the limitation that only a small number of dyes/drug molecules can be attached per protein molecule. To demonstrate our synthetic strategy, poly(glucosamine)-poly(NIRF dye) copolymers with reactive chain ends were synthesized via a one-pot amidation of poly(acrylic acid) with NIRF-NH_2 and Glu-NH_2. The copolymers were further employed to produce bioconjugates via (a) biotin−avidin interaction and (b) covalent linkage with BSA (triazole link, "click" bioconjugation reaction) and successfully characterized via NMR, FT-IR, GPC, FPLC, and SDS-PAGE techniques. The synthesized NIRF dye-based copolymers possessed enhanced optical properties compared to their monomeric counterparts. The copolymers were successfully immobilized for potential multiwell plate based assay experiments and utilized for in vitro and in vivo imaging. We are currently exploiting this general synthetic methodology to produce a range of bioactive copolymers and protein/antibody conjugates for applications ranging from tissue-specific imaging to targeted drug delivery.

ACKNOWLEDGMENT

This work was supported by NSF (CHE-0723028) and PSC−CUNY. We sincerely would like to thank Dr. K. B. Sharpless for providing us the "click" ligand and Mrs. Narmandakh Mijid Taylor, Ms. Samar Rizk, and Ms. Francoise Sidime for helping us with experiments.

Supporting Information Available: Experimental details and characterization data of synthesized compounds and bioconjugates. This material is available free of charge via the Internet at http://pubs.acs.org.

LITERATURE CITED

(1) Hermenson, G. T. (2008) *Bioconjugate Techniques*, 2nd ed., Academic Press, San Diego, CA.

(2) Wu, A. M., and Senter, P. D. (2005) Arming antibodies: prospects and challenges for immunoconjugates. *Nat. Biotechnol. 23*, 1137–1146.

(3) Raja, K., McDonald, R., Tuck, S., Rodriguez, R., Milley, B., and Traquina, P. (2007) One-pot synthesis, purification, and formulation of bionanoparticle-CpG oligodeoxynucleotide hepatitis B surface antigen conjugate vaccine via tangential flow filtration. *Bioconjugate Chem. 18*, 285–288.

(4) Raja, K. S., Wang, Q., Gonzalez, M. J., Manchester, M., Johnson, J. E., and Finn, M. G. (2003) Hybrid virus-polymer materials. 1. Synthesis and properties of PEG-decorated cowpea mosaic virus. *Biomacromolecules 4*, 472–476.

(5) Shi, W., Dolai, S., Rizk, S., Hussain, A., Tariq, H., Averick, S., L'Amoreaux, W., El Idrissi, A., Banerjee, P. and, and Raja, K. S. (2007) Synthesis of monofunctional curcumin derivatives, clicked curcumin dimer, and a PAMAM dendrimer curcumin conjugate for therapeutic applications. *Org. Lett. 9*, 5461–5464.

(6) Hannink, J. M., Cornelissen, J. J., Farrera, J. A., Foubert, P., De Schryver, F. C., Sommerdijk, N. A., and Nolte, R. J. (2001) Protein-polymer hybrid amphiphiles. *Angew. Chem., Int. Ed. Engl. 40*, 4732–4734.

(7) Velonia, K., Rowan, A. E., and Nolte, R. J. (2002) Lipase polystyrene giant amphiphiles. *J. Am. Chem. Soc. 124*, 4224–4225.

(8) Kochendoerfer, G. G., Chen, S.-Y., Mao, F., Cressman, S., Traviglia, S., Shao, H., Hunter, C. L., Low, D. W., Cagle, E. N., Carnevali, M., Gueriguian, V., Keogh, P. J., Porter, H., Stratton, S. M., Wiedeke, M. C., Wilken, J., Tang, J., Levy, J. J., Miranda, L. P., Crnogorac, M. M., Kalbag, S., Botti, P., Schindler-Horvat, J., Savatski, L., Adamson, J. W., Kung, A., Kent, S. B. H., and Bradburne, J. A. (2003) Design and chemical synthesis of a homogeneous polymer-modified erythropoiesis protein. *Science 299*, 884–887.

(9) Lewis, J. D., Kovar, M., Strohalm, J., Etrych, T., Ulbrich, K., and Rihova, B. (2002) Star structure of antibody-targeted HPMA copolymer-bound doxorubicin: a novel type of polymeric conjugate for targeted drug delivery with potent antitumor effect. *Bioconjugate Chem. 13*, 206–215.

(10) Kulkarni, S., Schilli, C., Grin, B., Mueller, A. H. E., Hoffman, A. S., and Stayton, P. S. (2006) Controlling the aggregation of conjugates of streptavidin with smart block copolymers prepared via the RAFT copolymerization technique. *Biomacromolecules 7*, 2736–2741.

(11) Sengupta, S., Raja, K. S., Kaltgrad, E., Strable, E., and Finn, M. G. (2005) Virus-glycopolymer conjugates by copper(I) catalysis of atom transfer radical polymerization and azide-alkyne cycloaddition. *Chem. Commun. 34*, 4315–4317.

(12) Sengupta, S., Kuzelka, J., Singh, P., Lewis, W. G., Manchester, M., and Finn, M. G. (2005) Accelerated bioorthogonal conjugation: a practical method for the ligation of diverse functional molecules to a polyvalent virus scaffold. *Bioconjugate Chem. 16*, 1572–1579.

(13) Hou, S., Sun, X. L., Dong, C. M., and Chaikof, E. L. (2004) Facile synthesis of chain-end functionalized glycopolymers for site-specific bioconjugation. *Bioconjugate Chem. 15*, 954–959.

(14) Vazquez-Dorbatt, V., and Maynard, H. D. (2006) Biotinylated glycopolymers synthesized by atom transfer radical polymerization. *Biomacromolecules 7*, 2297–2302.

(15) Lele, B. S., Murata, H., Matyjaszewski, K., and Russell, A. J. (2005) Synthesis of uniform protein-polymer conjugates. *Biomacromolecules 6*, 3380–3387.

(16) De, P., Li, M., Gondi, S. R., and Sumerlin, B. S. (2008) Temperature-regulated activity of responsive polymer-protein conjugates prepared by grafting-from via RAFT polymerization. *J. Am. Chem. Soc. 130*, 11288–11289.

(17) Bontempo, D., Heredia, K. L., Fish, B. A., and Maynard, H. D. (2004) Cysteine-reactive polymers synthesized by atom transfer radical polymerization for conjugation to proteins. *J. Am. Chem. Soc. 126*, 15372–15373.

(18) Bontempo, D., and Maynard, H. D. (2005) Streptavidin as a macroinitiator for polymerization: in situ protein-polymer conjugate formation. *J. Am. Chem. Soc. 127*, 6508–6509.

(19) Li, M., De, P., Gondi, S. R., and Sumerlin, B. S. (2008) Responsive polymer-protein bioconjugates prepared by RAFT polymerization and copper-catalyzed azide-alkyne click chemistry. *Macromol. Rapid Commun. 29*, 1172–1176.

(20) Fabian, J., Nakazumi, H., and Matsuoka, M. (1992) Near-infrared absorbing dyes. *Chem. Rev. (Washington, DC, U. S.) 92*, 1197–1226.

(21) Mishra, A., Behera, R. K., Behera, P. K., Mishra, B. K., and Behera, G. B. (2000) Cyanines during the 1990s: a review. *Chem. Rev. (Washington, DC, U. S.) 100*, 1973–2012.

(22) Law, K.-Y. (1993) Organic photoconductive materials: recent trends and developments. *Chem. Rev. (Washington, DC, U. S.) 93*, 449–486.

(23) Zhao, W., and Carreira, E. M. (2005) Conformationally restricted aza-bodipy: a highly fluorescent, stable, near-infrared-absorbing dye. *Angew. Chem., Int. Ed. Engl. 44*, 1677–1679.

(24) Patonay, G., Salon, J., Sowell, J., and Strekowski, L. (2004) Noncovalent labeling of biomolecules with red and near-infrared dyes. *Molecules 9*, 40–49.

(25) Tung, C.-H. (2004) Fluorescent peptide probes for in vivo diagnostic imaging. *Biopolymers 76*, 391–403.

(26) Zaheer, A., Lenkinski, R. E., Mahmood, A., Jones, A. G., Cantley, L. C., and Frangioni, J. V. (2001) In vivo near-infrared fluorescence imaging of osteoblastic activity. *Nat. Biotechnol. 12*, 1148–1154.
(27) Weber, P. C., Ohlendorf, D. H., Wendoloski, J. J., and Salemme, F. R. (1989) Structural origins of high-affinity biotin binding to streptavidin. *Science 243*, 85–88.
(28) Rostovtsev, V. V., Green, L. G., Fokin, V. V., and Sharpless, K. B. (2002) A stepwise Huisgen cycloaddition process: copper(I)-catalyzed regioselective "ligation" of azides and terminal alkynes. *Angew. Chem., Int. Ed. Engl. 41*, 2596–2599.
(29) Wang, J. S., and Matyjaszewski, K. (1995) Controlled/"living" radical polymerization. atom transfer radical polymerization in the presence of transition-metal complexes. *J. Am. Chem. Soc. 117*, 5614–5615.
(30) Luxenhofer, R., and Jordan, R. (2006) Click chemistry with poly(2-oxazoline)s. *Macromolecules 39*, 3509–3516.
(31) Geng, J., Mantovani, G., Tao, L., Nicolas, J., Chen, G., Wallis, R., Mitchell, D. A., Johnson, B. R. G., Evans, S. D., and Haddleton, D. M. (2007) Site-directed conjugation of "clicked" glycopolymers to form glycoprotein mimics: binding to mammalian lectin and induction of immunological function. *J. Am. Chem. Soc. 129*, 15156–15163.
(32) Kiessling, L. L., Gestwicki, J. E., and Strong, L. E. (2006) Synthetic ligands as probes of signal transduction. *Angew. Chem., Int. Ed. Engl. 45*, 2348–2368.
(33) Andrews, D. L. (2008) Mechanistic principles and applications of resonance energy transfer. *Can. J. Chem. 86*, 855–870.

BC900142Y

SUPPORTING INFORMATION

A GENERAL METHODOLOGY TOWARDS DRUG/DYE INCORPORATED LIVING COPOLYMER-PROTEIN HYBRIDS: (NIRF DYE-GLUCOSE) COPOLYMER-AVIDIN/BSA CONJUGATE AS PROTOTYPES.

Wei Shi, Sukanta Dolai, Saadyah Averick, Suraj S. Fernando, Jose A. Saltos, William L'Amoreaux, Probal Banerjee and Krishnaswami Raja*

Department of Chemistry and Biology, The City University of New York at College of Staten Island, 2800 Victory Blvd., Staten Island, New York, 10314.

*Corresponding Author: (phone) 718-982-4091 (fax) 718-982-3910
(Email) raja@mail.csi.cuny.edu

CONTENTS **PAGE #**

GENERAL INFORMATION **S2**

SYNTHETIC PROTOCOLS **S3**

SPECTRAL DATA (^{1}H NMR, ^{13}C NMR, FT-IR) **S28**

GENERAL INFORMATION: Reagent-grade acetone, HPLC grade tetrahydrofuran, methylene chloride, N,N-dimethylformamide, methanol, ethylacetate were used without further purification. Solvents used for reactions were purified using *Puresolv*^{TM} system. 2-(2-(2-chloroethoxy)ethoxy)ethanol, 2-bromoisobutyryl bromide, *tert*-butyl acrylate, 1,1,4,7,7-pentamethyldiethylenetriamine, trifluoroacetic acid, D(+)-glucosamine, N-Hydroxybenzotriazole (HOBt), Copper (II) Sulfate pentahydrate and sodium ascorbate were obtained from Sigma-Aldrich. D(+)-Biotin was obtained from Acros Organics. 1-Ethyl-3-(3-dimethyllaminopropyl)carbodiimide hydrochloride (EDC.HCl) and Avidin were obtained from Pierce Biotechnology. Streptavidin coated 96-Well Plates were obtained from Sigma. NIRF-Dye (ADS832WS) was obtained from American Dye Source, Inc. CupriSorb® was obtained from Seachem Laboratories Inc. Silica gel 60 F 254 plates for thin-layer chromatography (TLC) were purchased from Fisher Scientific. Column chromatographic separations were performed using silica gel (Fisher) with a particle size of 0.040-0.063 mm. Nuclear magnetic resonance (NMR) spectra were recorded on Oxford NMR 600 (600 MHz), Varian Unity (200 MHz) and Varian Unity (300 MHz) spectrometers. Mass spectra (ESI-MS) were recorded using an Agilent LC/MS mass spectrometer. FPLC analysis was performed using an AKTA explorer from GE Biosciences. The Near Infrared images were taken using Odyssey Imaging system (LI-COR, Lincoln, NE). The Mol. Wt. of polymers were determined using Waters HPLC system equipped with either PLgel 5µm Mixed-D or PLaquagel-OH Mixed 8µm columns and Breeze software. Poly(methyl methacrylate) and poly(ethylene glycol) standards were used for organic soluble and water soluble polymers respectively. Agilent Technologies 845x UV-Vis spectrophotometer equipped with ChemStation Rev. A.10.01 software was used to record the UV/Vis/NIR spectra. Fluorescence was recorded on Jobin Yvon Horiba FluoroMax-3 and the data was analyzed with DataMax software. Bruker Daltonics- microflex™ series-MALDI-TOF MS instrument equipped with FlexAnalysis software was used to record the MS of proteins (samples were prepared by mixing the protein with Sinapinic acid (matrix) in apporx. 1:10 molar ratio).

SYNTHETIC PROTOCOLS:

1. SYNTHESIS OF *2-(2-(2-Azidoethoxy)ethoxy)ethanol* (1')

Protocol followed from: Sengupta, S., Raja, K. S., Kaltgrad, E., Strable, E. and Finn, M. G. (2005) Virus-glycopolymer conjugates by copper(I) catalysis of atom transfer radical polymerization and azide-alkyne cycloaddition. *Chem. Comm. 34*, 4315-4317.

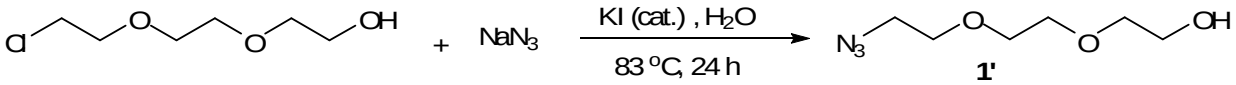

A mixture of 2-(2-(2-chloroethoxy)ethoxy)ethanol (7.04 g, 41.72 mmol), sodium azide (13.65 g, 209.94 mmol) and potassium iodide (1.87 g, 11.25 mmol) in water (72 mL) was stirred at 83 ^{0}C for 24 h. The reaction mixture was extracted with ether, and the organic layer was washed with brine and then dried over anhydrous Na_2SO_4. The solvent was evaporated and the product was dried under vacuum to give colourless oil. The product was purified via column chromatography, CH_2Cl_2:MeOH, 95:5 was used as the eluent. Yield: 62%. ^{1}H NMR (600 MHz, $CDCl_3$): δ(ppm) 2.85-2.87 (t, 2H), 3.29-3.31 (t, 2H), 3.50-3.51 (m, 2H), 3.57-3.64 (m, 6H). ^{13}C NMR (150 MHz, $CDCl_3$): δ(ppm) 46.58, 57.58, 65.96, 66.31, 66.57, 68.55. ESI-MS m/z = 198.1 (M+Na); IR (KBr, cm^{-1}) 2104.

2. SYNTHESIS OF *2-Bromo-2-methylpropionic acid 2-[2-(2-Azidoethoxy)ethoxy] ethyl ester* (1)

Protocol followed from: Sengupta, S., Raja, K. S., Kaltgrad, E., Strable, E. and Finn, M. G. (2005) Virus-glycopolymer conjugates by copper(I) catalysis of atom transfer radical polymerization and azide-alkyne cycloaddition. *Chem. Comm. 34*, 4315-4317.

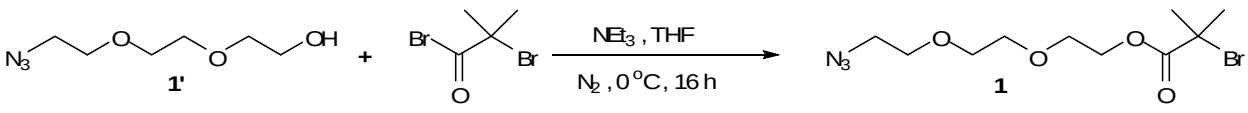

A solution of 2-bromoisobutyryl bromide (4.58 g, 19.9 mmol) and triethylamine (2.18 g, 21.5 mmol) in THF (5 mL) was cooled to 0 °C in a 2-necked round-bottomed flask. A solution of 2-[2-(2-azidoethoxy)ethoxy]ethanol (3 g, 17.1 mmol) in THF (5 mL) was added dropwise with stirring. The reaction mixture was then stirred under N_2 at room temperature for 16 h, filtered, and the solvent was removed by rotatory evaporator. The crude product was added to a cooled (ice bath) 5% aqueous (Na_2CO_3) solution and the resulting mixture was extracted with ethyl acetate (3 x 50 mL). The combined organic layers were washed with brine, dried over anhydrous (Na_2SO_4), and evaporated to provide **1** as dark-yellow oil. Yield: 5 g (90 %). ^{1}H NMR (600 MHz, $CDCl_3$): δ(ppm) 1.88 (s, 6H), 3.56-3.58 (t, 2H), 3.63 (s, 4H), 3.69-3.70 (t, 4H), 4.26-4.28 (t, 2H). ^{13}C NMR (150 MHz, $CDCl_3$): δ(ppm) 30.53, 42.57, 55.54, 64.89, 68.58, 68.60, 70.43, 70.48, 71.15, 171.37. ESI-MS m/z = 346.10 (M+Na)

3. SYNTHESIS OF *Azide terminated Poly(tert-butyl acrylate)* (2)

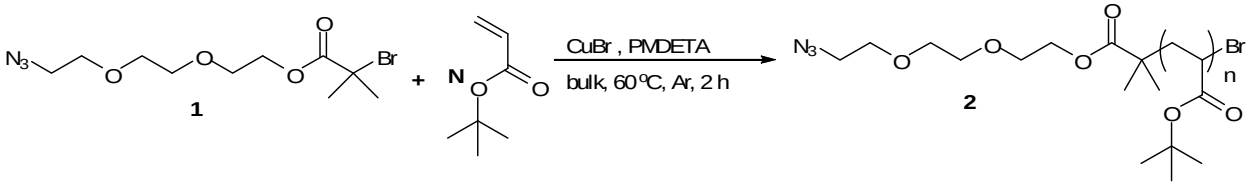

A 100 mL flask fitted with a stopcock was flame-dried under vacuum and allowed to cool at ambient temperature under Argon. The flask was charged with CuBr (115 mg, 0.8 mmol). Under positive pressure of Argon, a solution of 2-Bromo-2-methylpropionic acid 2-[2-(2-Azidoethoxy)ethoxy] ethyl ester (118 mg, 0.36 mmol) dissolved in tert-butyl acrylate (4 mL, 27.55 mmol) was added via syringe, followed by the addition of 1,1,4,7,7-pentamethyldiethylenetriamine (PMDETA) (0.17 mL, 0.8 mmol). Following three freeze-pump-thaw degassing cycles, the reaction was allowed to stir for 2 hour 10 minutes at 60 ^{0}C. The polymerization was quenched by submerging the flask in liquid N_2, the mixture was allowed to warm to ambient temperature, and diluted with tetrahydrofuran. CupriSorb® was added and

stirred ca. 30 minutes for removing copper complex. After filtration, the mixture was poured into a 15% methanol, deionized water solution, white solid product was precipitated. The polymer was further purified via reprecipitation and dried under vacuum; isolated yield was 2.18 g (47%), DPn= 64. M_n=8586 g/mol, M_w/M_n=1.21. (calculated using poly(methyl methacrylate) standards and THF as mobile phase). ^{1}H NMR (600 MHz, $CDCl_3$): δ(ppm) 4.19 (s, 2H), 3.55-3.75 (m, 6H), 3.39 (t, 2H), 2.18-2.30 (bm), 1.85 (s), 1.28-1.62 (bm), 1.15 (s, 6H), 0.89 (m). FTIR (film, cm^{-1}): 3433, 2977, 2289, 2113 (azide), 1727, 1619, 1450, 1367, 1255, 1153, 845, 752.

4. SYNTHESIS OF *5-(2-oxooctahydropyrrolo[3,4-d]imidazol-4-yl)-N-(prop-2-ynyl)pentanamide (Biotin-Alkyne)* (3)

D(+)-biotin (186 mg, 0.76 mmol) was dissolved in 7 mL DMF and a solution of propargylamine (76 mg, 1.37 mmol) in CH_2Cl_2 (7 mL) was added to it followed by EDC.HCl (. After being stirred under N_2 for 24 h at room temperature, the reaction mixture was concentrated in vacuum and diluted by 30 mL of CH_2Cl_2 and the organic layer was washed by water (10 mL×3), dried over Na_2SO_4 and then concentrated in vacuum. The crude product was purified by flash column chromatography (MeOH/CH_2Cl_2=5/95-15/85) to obtain the product 160 mg (75%). ^{1}H NMR (600 MHz, CD_3OD): δ(ppm) 4.48-4.50 (dd, 1H), 4.29-4.31 (dd, 1H), 3.94 (d, 2H), 3.19-3.22 (dt, 1H), 2.91-2.94 (dd, 1H), 2.69-2.41 (d, 2H), 2.58-2.59 (t, 1H), 2.20-2.23 (t, 2H), 1.58-1.74 (m, 4H), 1.42-1.46 (q, 2H); ^{13}C NMR (150 MHz, CD_3OD): δ(ppm) 173.6, 164.1, 78.7, 70.1, 61.3, 59.6, 55.0, 39.1, 34.5, 27.7, 27.4, 24.7. ESI-MS m/z = 282.10 (M+H).

5. SYNTHESIS OF *Biotin Terminated poly(tert-butyl acrylate)* (4)

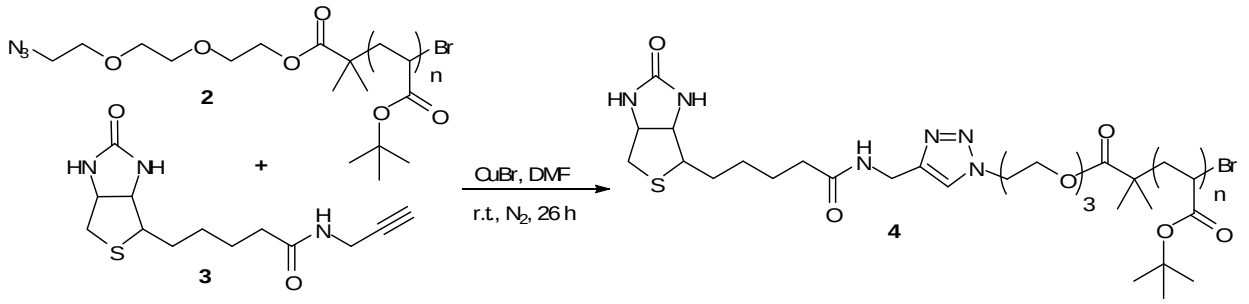

The azide-containing polymer (**2**) (565 mg, 0.073 mmol of azide groups), biotin-alkyne (25 mg, 0.087 mmol), CuBr (35 mg, 0.024 mmol), and 1,1,4,7,7-pentamethyldiethylenetriamine PMDETA (5.2 µL, 0.025 mmol) were placed in a round-bottom flask. The flask was closed with rubber septum and degassed with N_2. Deoxygenated DMF (3 mL) was added with an argon-purged syringe, and the reaction was stirred for 26 h at room temperature. The mixture was diluted with tetrahydrofuran, and CupriSorb® was added stirred ca. 30 minutes to remove copper complex. Solid residue was filtered off and the mixture was poured into a 15% methanol, deionized water solution where white solid product was precipitated. The product was further purified by re precipitation and dried over vacuum. Yield: 537 mg (92%). M_n=8850 g/mol, M_w/M_n=1.30. (calculated using poly(methyl methacrylate) standards and THF as mobile phase). ^{1}H NMR (600 MHz, $CDCl_3$): δ(ppm) 7.68 (s), 7.44 (s), 4.48 (s), 4.31 (s), 4.19 (s), 4.00 (s), 3.3803.64 (m), 3.11 (m), 2.73 (d), 2.18-2.30 (bm), 1.79 (s), 1.28-1.62 (bm), 1.10 (s), 0.89 (m). FTIR (film, cm^{-1}): 3433, 2977, 2932, 2720, 2360, 1991, 1728, 1479, 1449, 1392, 1367, 1256, 1150, 1037, 845, 734.

6. SYNTHESIS OF *Biotin Terminated poly(acrylic acid)* (5)

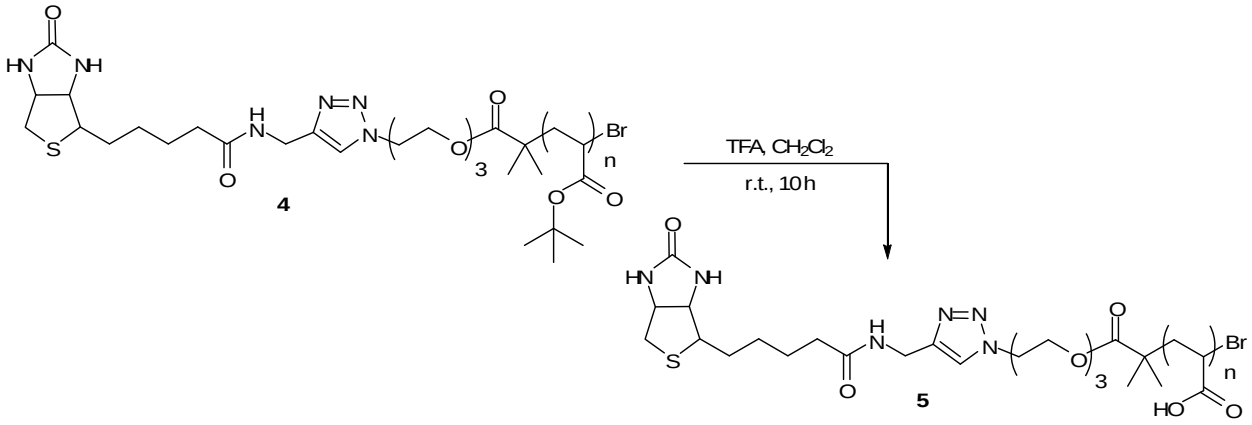

The polymer (**4**) (489 mg, 0.061 mmol) was dissolved in a solution of trifluoroacetic acid (1.5 mL, 19.5 mmol) in dichloromethane (13 mL). The reaction was allowed to stir at ambient temperature for 10 h. The solvent was removed under vacuum, and the resulting solid was dissolved in deionized water. The solution was transferred to a dialysis bag (MWCO 3.5 KDa), and dialyzed against a continuous flow of deionized water for overnight. The final polymer was isolated by lyophilization: Isolated yield 238 mg, (87%). ^{1}H NMR (600 MHz, $CDCl_3$): δ(ppm) 12.23 (bs), 7.85 (s), 7.78 (s), 4.47 (t), 4.26-4.30 (m), 4.04 (b), 3.38-3.82, (bm), 3.23-3.25 (t), 3.08 (s), 2.87 (d), 2.80-2.83 (t), 2.68-2.74 (m), 2.19 (bs), 2.07 (t), 1.74 (bm), 1.22-1.60 (bm), 1.07 (bm), 0.88 (m).

7. SYNTHESIS OF *Biotin Terminated poly(glucosamine)-poly(NIRF dye) copolymer* (6)

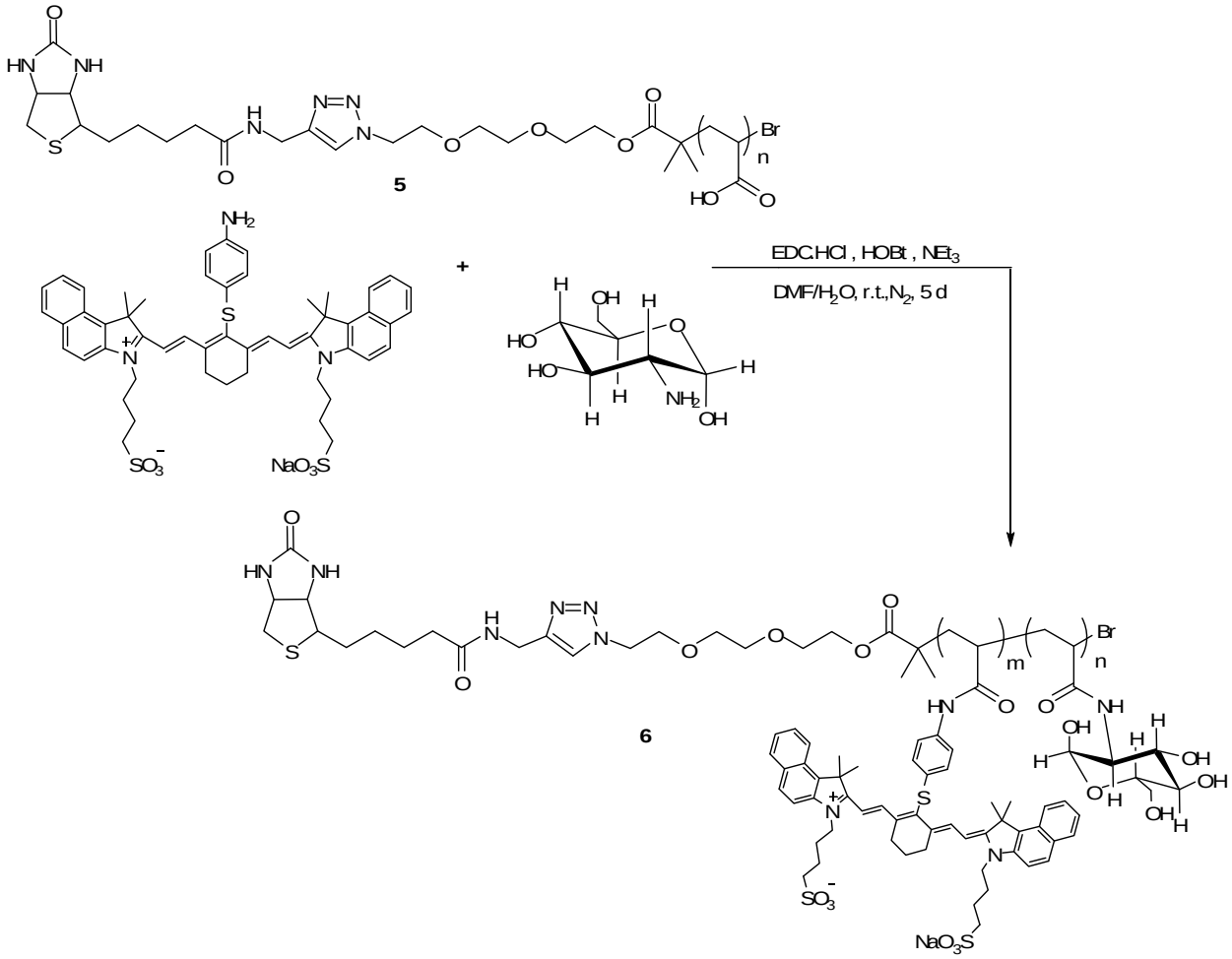

M_n=23259 g/mol, M_w/M_n=1.48. (calculated using poly(ethylene glycol) standards and 0.25 M $NaNO_3$, 0.01 M NaH_2PO_4, pH = 7 buffer as mobile phase). ^{1}H NMR (600 MHz, CD_3OD) δ(ppm) 8.98 (d), 7.18-8.34 (bm), 6.68 (m), 6.37 (m), 5.27 (d), 4.63 (s), 4.30 (s), 3.31-3.96 (m), 3.19 (m), 3.12 (m), 2.99-3.02 (m), 2.86-2.91 (m), 2.79 (s), 1.35-2.22 (m), 1.61 (d), 1.19-1.32 (m), 1.08 (m).

Comparing the *Mn*=8850 of polymer **4** and *Mn*=23259 of polymer **6,** the percent of dyes per polymer chain were calculated: subtracting the mol.wt. of the chain-end groups from *Mn* of polymer **4**, the number of repeat units in polymer **4** was calculated to be 64, this number was used as the total number of repeat units in the copolymer **6**, employing the following equation

the number of dye repeat unit per polymer chain was calculated: $ax + b(64 - x) = (Mn - c)$. Where x = number of dyes per polymer chain, a, b & c are mol.wts. of dye repeat unit, sugar repeat unit and chain-ends respectively, and the number percentage of dyes per polymer chain(please note that there are 64 repeat units per polymer chain) was calculated to be ~17%.

The quantity of different compositions in the copolymer was further quantified by comparing the peaks area of the protons from dye ADS832WS at 7.35-8.40 ppm, glucosamine at 2.89-3.73 ppm, and that of -C*H*$_2$-C*H*- protons from main chain of polymer at 1.82-2.10 ppm. Results showed the loading number of dye ADS832WS and glucosamine were 15.92% and 81.97% respectively.

8. SYNTHESIS OF *Biotin Terminated Poly(acrylic acid)-poly(NIRF dye)* (6A)

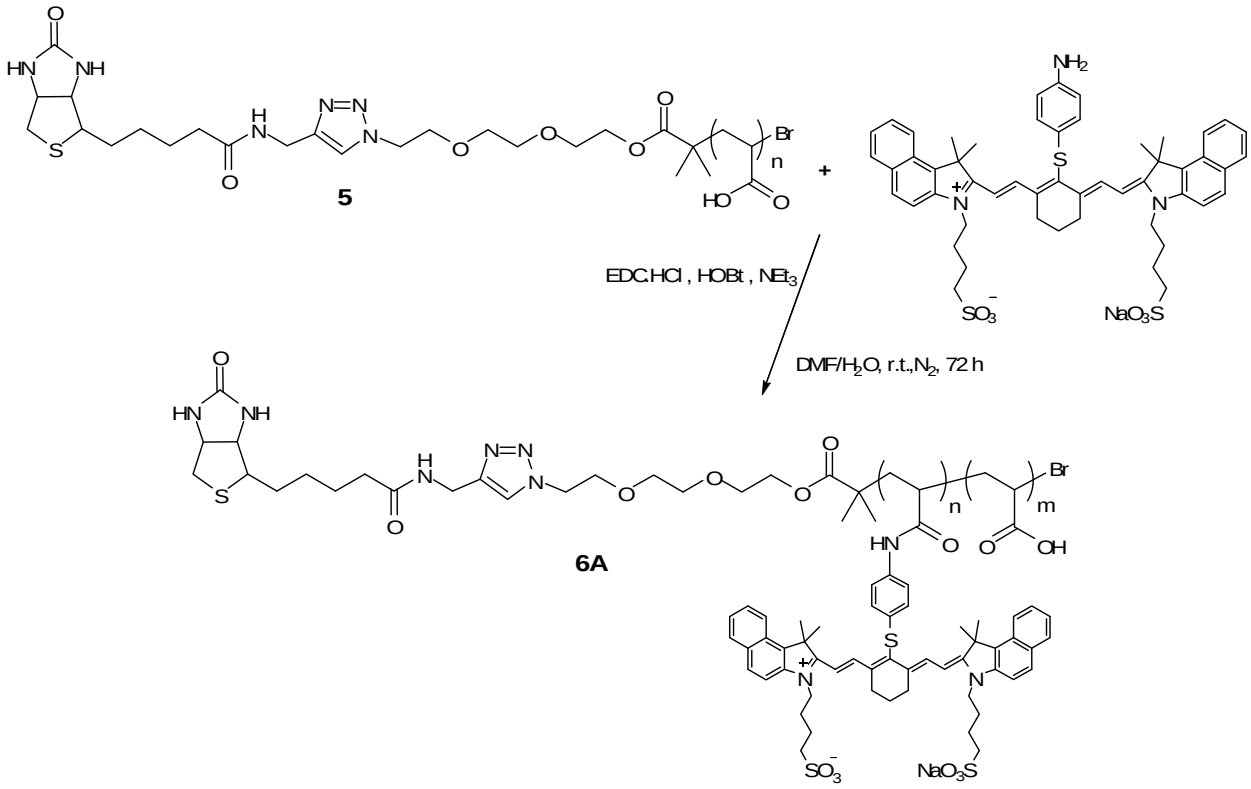

The polymer (**5**) (76 mg, 1.055 mmol), Near infrared absorption dye (ADS832WS) (498 mg, 0.531 mmol), EDC·HCl (213 mg, 1.11 mmol), and HOBt (153 mg, 1.148 mmol) were

dissolved in DMF (1.5 mL) in a r.b. followed by the addition of Triethylamine (0.03 mL, 0.17 mmol). The mixture was stirred 72 h at room temperature under N_2. After stopping of the reaction, the solution was transferred into a dialysis bag (MWCO 3.5 KDa), and the solution was dialyzed against 10 exchanges of deionized water for 24 h. The dialyzed reaction mixture was filtered and lyophilized to yield dark purple cotton shaped crude product. The crude product was further purified with Sephadex^{TM} LH-20 size-exclusion column with deionized water as eluent. Yield: 40 mg. ^{1}H NMR (600 MHz, CD_3OD): δ(ppm) 8.83 (b), 7.13-8.23 (bm), 6.35 (b), 4.04-4.34 (b), 3.09-3.19 (bm), 2.55-3.07 (bm), 1.02-2.48 (bm).

9. SYNTHESIS OF *Azide Terminated Poly(Acrylic acid)* (8)

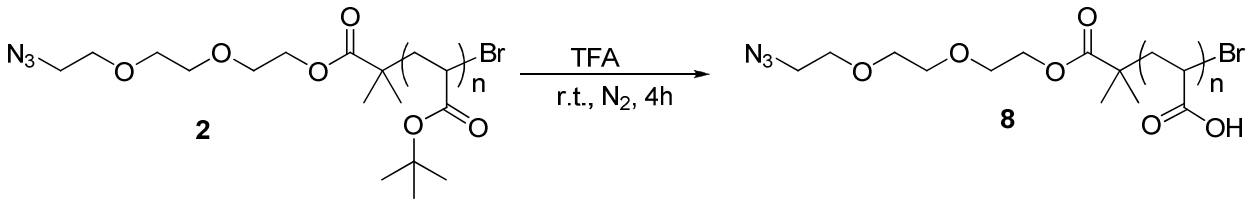

Trifluro acetic acid (2 ml, 27 mmol) of was added dropwise to a round bottom flask containing poly(*tert*-Butyl Acrylate) (0.3 g , 0.02 mmol). The reaction was stirred under N_2 for 4 hours. The reaction mixture was dialyzed using 3500 MWCO membrane in distilled water with several exchanges and finally the lyophilization yielded the polymer as white powder. Yield: 97% ^{1}H NMR (600 MHz, D_2O), δ (ppm): 1.14-1.18 (m, 8 H), 1.40 (s, 4 H), 1.61 (s, 46 H), 1.73 (s, 112 H), 1.90 (s, 40 H), 2.36 (s, 104 H), 3.67-4.17 (m, 12 H). FT-IR (cm^{-1}): 3022, 2117 (N_3), 1681, 1454.

10. SYNTHESIS OF *Azide Terminated poly(glucosamine)-poly(NIRF dye) copolymer* (9)

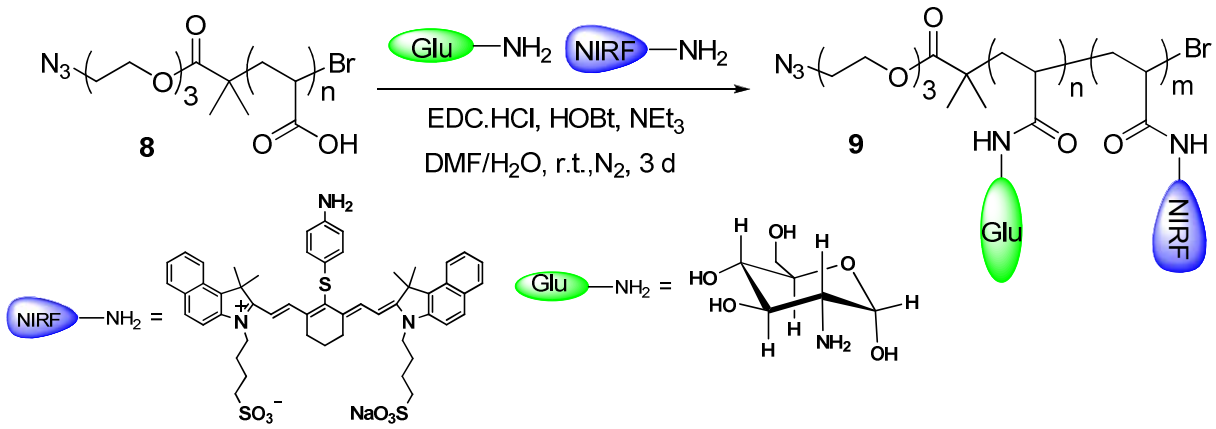

Azide terminated poly(acrylic acid) (72 mg, 0.96 mmol of COOH), NIRF dye (ADS832WS) (100 mg, 0.106 mmol), D(+)-Glucosamine (190 mg, 0.9 mmol), EDC.HCl (575 mg, 3.0 mmol) and HOBt (460 mg, 3.0 mmol) were dissolved in 10 ml of DMF in a round bottom flask and was degassed with N_2 and followed by dropwise addition of Et_3N (0.42 ml, 5 mmol). The reaction mixture was stirred at room temperature for 3 days. The reaction mixture was dialyzed extensively using 10K MWCO membrane and then purified by passing through a Sephadex LH20 column. Finally the product was isolated as dark purple colored fluffy powder after lyophilization. Yield: 76 %. ^{1}H NMR (600 MHz, D_2O), δ (ppm): 1.03 (bs), 1.52-1.66 (bd), 1.76 (s), 2.01(bs), 2.57(s), 2.80 (s), 2.93 (bs), 3.59 (s), 3.65 (s), 3.75 (s), 5.09-5.22 (bm). FT-IR (cm^{-1}): 3431, 2935, 2111 (N_3), 1714, 1538, 1504, 1443, 1393, 1353, 1266, 1233, 1166, 1140, 1115. GPC (H_2O): Mn= 19469, Mw= 25074, PDI= 1.28. (calculated using poly(ethylene glycol) standards and 0.25 M $NaNO_3$, 0.01 M NaH_2PO_4, pH = 7 buffer as mobile phase).

Comparing the *Mn*=8586 of polymer **2** and *Mn*=19469 of polymer **9,** the percent of dyes per polymer chain were calculated: subtracting the mol.wt. of the chain-end groups from *Mn* of polymer **2**, the number of repeat units in polymer **2** was calculated to be 64, this number was used as the total number of repeat units in the copolymer **9**, employing the following equation

the number of dye repeat unit per polymer chain was calculated: $ax + b(64 - x) = (Mn - c)$. Where x = number of dyes per polymer chain, a, b & c are mol.wts. of dye repeat unit, sugar repeat unit and chain-ends respectively, and the number percentage of dyes per polymer chain (please note that there are 64 repeat units per polymer chain) was calculated to be ~8%.

The quantity of different compositions in the copolymer was further quantified by comparing the peak area of the protons from dye ADS832WS at 7.38-8.40 ppm, glucose at 3.36-3.73 ppm to that of -C*H*$_2$-C*H*- protons from main chain of polymer at 1.52-2.09 ppm, and results showed the loading number of dye ADS832WS and glucose was 8.10% and 90.12% respectively.

11. SYNTHESIS OF *Alkyne terminated poly(glucosamine)-poly(NIRF dye) copolymer* (10)

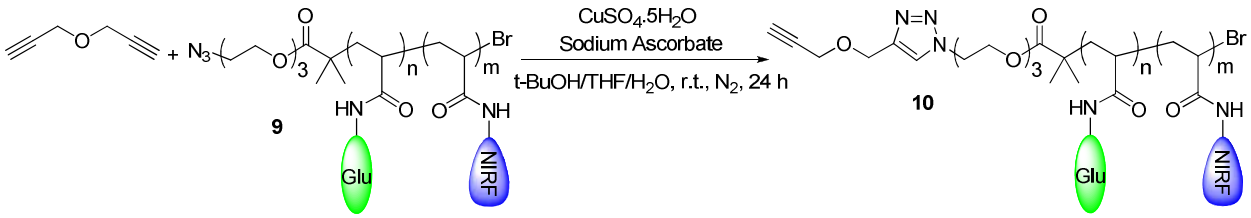

^{1}H NMR (600 MHz, D_2O), δ (ppm): 1.03 (bs), 1.52-1.75 (bd), 2.01(bs), 2.58 (s), 2.81 (s), 2.94 (s), 3.36 (s), 3.66-3.73 (bd), 5.06-5.23 (bm), 7.15-8.33 (m) . GPC: Mn= 19988, Mw= 28168, PDI= 1.40. (calculated using poly(ethylene glycol) standards and 0.25 M $NaNO_3$, 0.01 M NaH_2PO_4, pH = 7 buffer as mobile phase). FT-IR (cm^{-1}): 3299, 2928, (no N_3 peak ~2100), 1648, 1536, 1429, 1389, 1351, 1232, 1155, 1113. The absence of the azide peak (~2100 cm^{-1}) in the FT-IR spectra confirmed that all of the azide-end groups were reacted with dipropargyl ether. The polymer was used for further conjugation as it was.

The calculated dye loading was ~9% by number per polymer chain (please note that there are 64 repeat units per polymer chain) via the subtraction method. The quantity of different compositions in the copolymer was further quantified by comparing the peak area of the protons from dye ADS832WS at 7.38-8.40 ppm, glucose at 3.36-3.73 ppm to that of -CH_2-C*H*- protons from main chain of polymer at 1.52-2.09 ppm, and results showed the loading number of dye ADS832WS and glucose was 8.62% and 89.22% respectively.

12. ***Synthesis of Methyl-5-azido valerate***

Protocol followed from: Seo, T. S.; Li, Z.; Ruparel, H. an Ju, J. (2003) Click Chemistry to Construct Fluorescent Oligonucleotides for DNA Sequencing. *J. Org. Chem. 68*, 609-612.

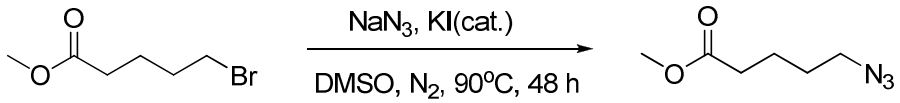

Methyl-5-bromovalerate (2.18 ml, 15.38 mmol) and Sodium azide (10 g, 10 eq) were dissolved in 20 ml DMSO in a round bottom flask and a pinch of KI was added. The mixture was stirred at 90 ^{O}C under N_2 atmosphere for 48 h. The reaction was cooled, diluted with water and extracted with hexanes. Organic layers were combined and dried over anhydrous Na_2SO_4. Solvent was evaporated to yield oily liquid. Yield: 2.2 g (91%); ^{1}H NMR (600 MHz, $CDCl_3$, 25°C): δ = 1.56-1.59 (m, 2H; CH_2), 1.65-1.67 (m, 2H; CH_2), 2.30 (t, *J* =12 Hz, 2H; CH_2), 3.24 (t, *J* =12 Hz, 2H; CH_2), 3.62 (s, 3H; CH_3); ^{13}C NMR (150 MHz, $CDCl_3$, 25°C): δ = 18.0, 24.2, 29.3, 47.0, 47.5, 169.5.

13. SYNTHESIS OF *5-Azido valeric acid*

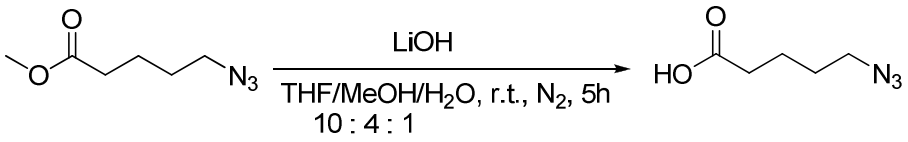

Methyl-5-azido valerate (2g, 12.73 mmol) was dissolved in 150 ml THF/MeOH/H_2O (10:4:1) mixture and LiOH (3.05 g, 10 eq) was added. The mixture was stirred at room temperature for 5h. The reaction was stopped and acidified to pH =2 with H_2SO_4 and extracted with ethyl acetate. Organic layers were combined, dried over anhydrous Na_2SO_4, and finally the solvent was evaporated to yield oily product. Yield:1.1 g (60%); ^{1}H NMR (600 MHz, $CDCl_3$, 25°C): δ = 1.25 (t, *J* = 12 Hz, 1H), 1.64-1.67 (m, 2H; CH_2), 1.70-1.73 (m, 2H; CH_2), 2.40 (t, *J* =11 Hz, 2H; CH_2), 3.30 (t, *J* =11 Hz, 2H; CH_2); ^{13}C NMR (150 MHz, $CDCl_3$, 25°C): δ = 15.5, 23.2, 29.5, 34.9, 52.4, 180.8.

14. SYNTHESIS OF *NHS-Azide* (12)

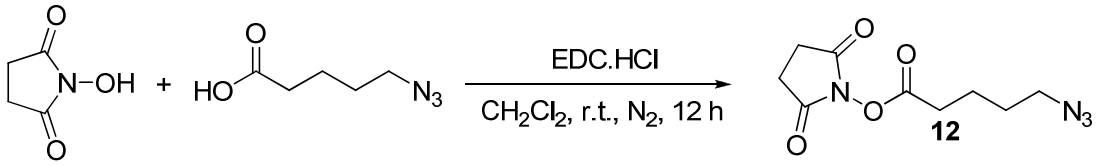

5-Azidovaleric acid (0.8 g, 5.6 mmol) and EDC.HCl (1.61 g, 1.5 mmol) were dissolved in 10 ml dry DCM and *N*-Hydroxysuccinimide (0.65 g, 1.01 mmol) was added. The reaction was stirred at room temperature under N_2 atmosphere for 12 h. The reaction was stopped, diluted with water and extracted with EtOAc. The organic layers were combined and washed with brine and dried over anhydrous Na_2SO_4. Finally the solvent was evaporated to yield white sticky

product. Yield: 1.2 g (90%); ^{1}H NMR (600 MHz, $CDCl_3$, 25°C): δ = 1.68-1.71 (m, 2H; CH_2), 1.80-1.84 (m, 2H; CH_2), 2.64 (t, *J* =12 Hz, 2H; CH_2), 2.81 (s, 4H; CH_2), 3.32 (t, *J* =11 Hz, 2H; CH_2); ^{13}C NMR (150 MHz, $CDCl_3$, 25°C): δ = 17.8, 21.6, 23.9, 26.4, 46.8, 164.2, 165.1. ESI-MS m/z = 241.10 (M+H)

15. ***Synthesis of 5-oxo-5-(prop-2-ynylamino)pentanoic acid***

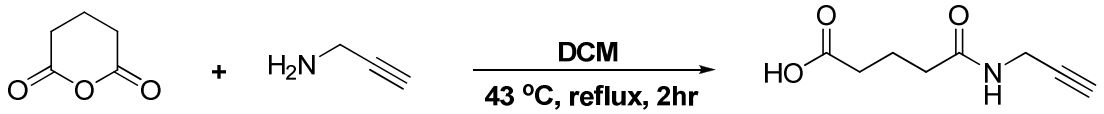

Glutaric anhydride (2.34 g, 0.2 mmol) was dissolved in 100 ml dry DCM in a round bottom flask and degassed with Argon. Propargyl amine (1.4 ml, 20 mmol) was added and the reaction mixture was refluxed at 43 ^{o}C for 2 hours and then stirred at room temperature for 2 hours. The solvent was evaporated and the crude product was purified by column chromatography using 95:5 CH_2Cl_2/ MeOH. Yield: 75%. ^{1}H NMR ($CDCl_3$, 200 MHz) δ (ppm): 1.67-1.76 (m, 2H), 2.09-2.26 (m, 4H), 2.38-2.41 (m, 1H), 3.75-3.76 (d, 2H).

16. ***Synthesis of 2,5-dioxopyrrolidin-1-yl-5-oxo-5-(prop-2-ynylamino)pentanoate (NHS-Alkyne)(12a)***

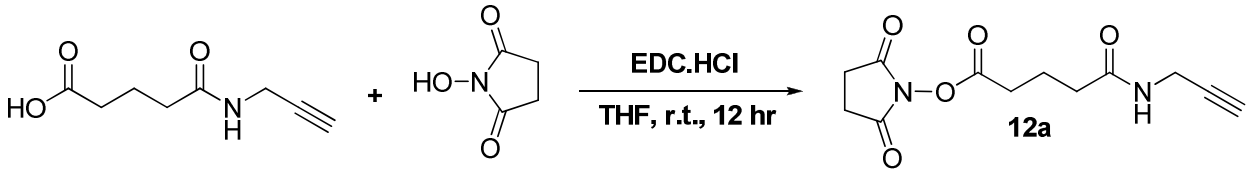

N-Hydroxy succinimide (0.93 g, 8.05 mmol), 5-oxo-5-(prop-2-ynylamino) pentanoic acid (1.01 g, 6 mmol) and EDC.HCl (1.22 g, 6.4 mmol) were dissolved in 50 ml of THF in a round

bottom flask and degassed with Ar. The mixture was stirred at room temperature for 12 hrs and then the solvent was evaporated. Further the crude reaction mixture was dissolved in DCM and washed thoroughly with water, saturated $NaHCO_3$, and brine. The organic layer was collected and dried over Na_2SO_4 and finally the solvent was evaporated to produce the product as white powder. Yield: 71 %. ^{1}H NMR ($CDCl_3$, 300 MHz) δ (ppm): 2.12-2.19 (m, 2H), 2.23-2.25 (t, 1H), 2.34-2.38 (t, 2H), 2.69-2.75 (m, 2H), 2.89 (s, 4H), 4.06-4.89 (m, 2H), 6.22 (bs, 1H). ESI-MS m/z = 267.10 (M+H), 289.10 (M+Na).

17. *Synthesis of Alkyne modified BSA* (13A)

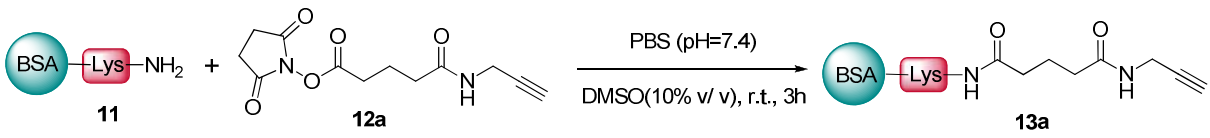

BSA (5mg, 5mg/ml in PBS, pH 7.4) was incubated with NHS-Alkyne **12A** (6 mg in 100 µl DMSO, 10 eq to each modifiable lysine group) at room temperature for 3 h and then dialyzed against 0.1 M Tris buffer, pH 8.0 for 48 h to remove excess of alkyne linker. The dialyzed product was characterized via FPLC, MALDI-TOF and used for further bioconjugation. Comparing the Mol. Wt. of unmodified BSA **11** and alkyne-modified BSA **13A**, it was calculated that about 35 lysine groups were modified by NHS-Alkyne bifunctional linker (see Supplementary Figure S1).

18. *Synthesis of Azide modified BSA* (13)

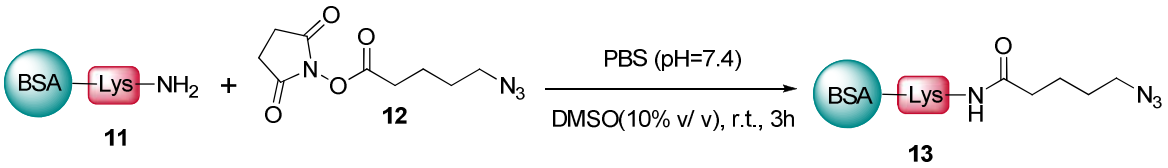

BSA (5mg, 5mg/ml in PBS, pH 7.4) was incubated with NHS-Azide **12** (5mg in 100 µl DMSO, 10 eq to each modifiable lysine group) at room temperature for 3 h and then dialyzed against 0.1 M Tris buffer, pH 8.0 for 48 h to remove excess of azide linker. The dialyzed product was characterized via FPLC, MALDI-TOF and used for further bioconjugation. Comparing the Mol. Wt. of unmodified BSA **11** and azide-modified BSA **13**, it was calculated that about 45 lysine groups were modified by NHS-Azide hetero-bifunctional linker (see Supplementary Figure S1).

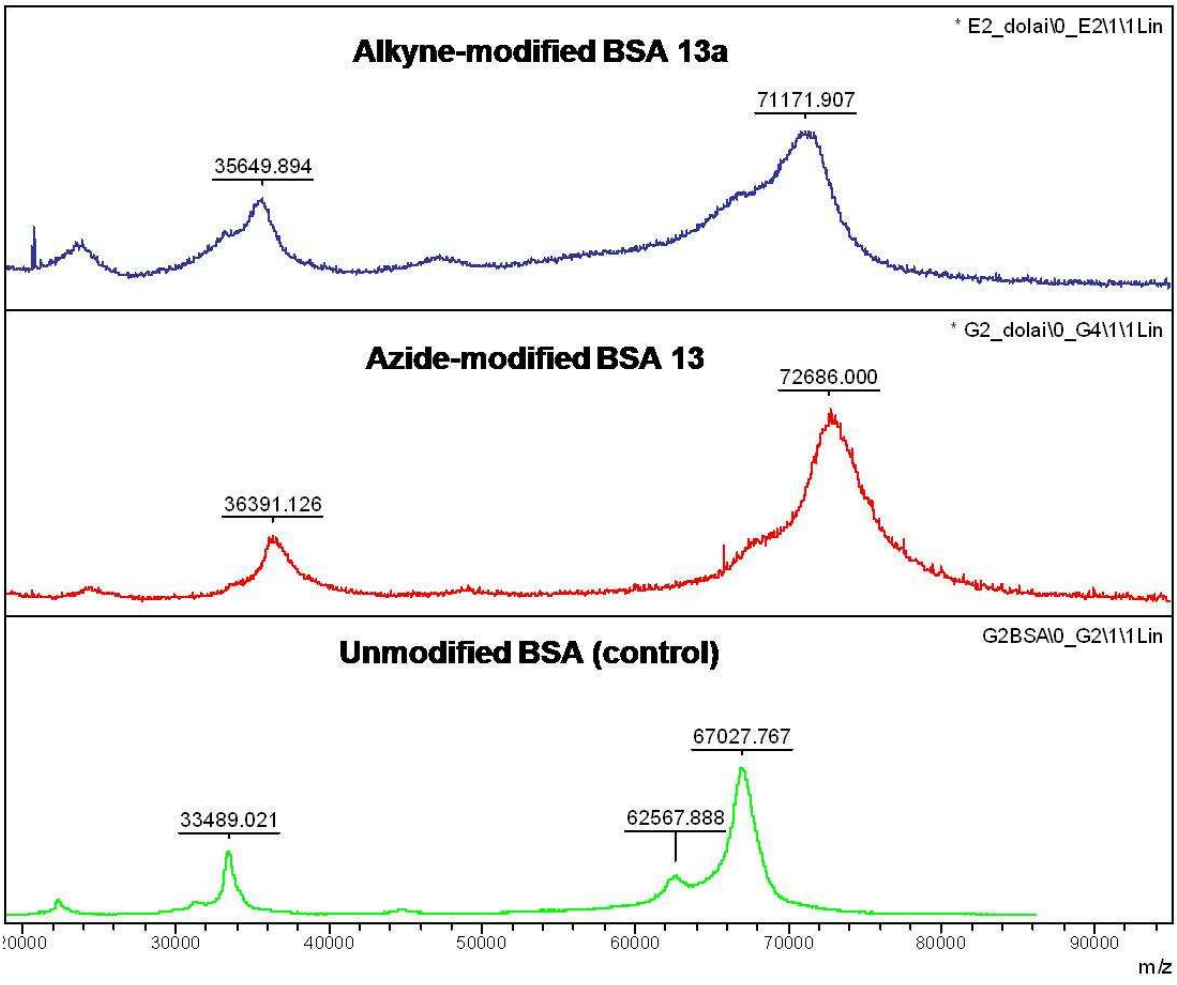

SUPPLEMENTARY FIGURE S1. MALDI-TOF Data comparison of alkyne modified BSA **13A** (red line), azide modified BSA **13** (blue line), unmodified BSA (green line).

19. CONJUGATION OF *Biotin Terminated Polymer (6) and Avidin.*

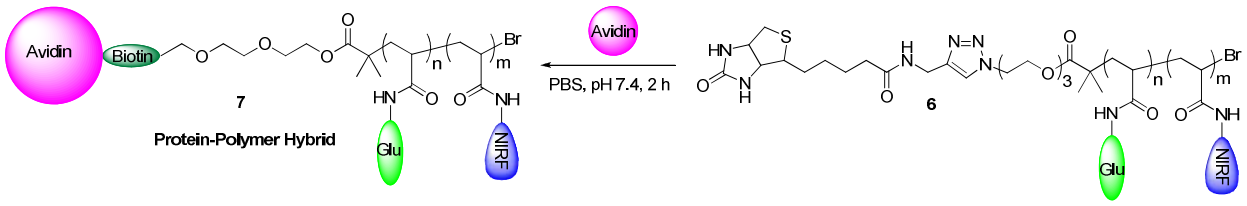

Avidin (1 mg) was dissolved in 0.25 mL of PBS buffer, pH 7.4. Poly(glucosamine)-poly(NIRF dye) copolymer **6** (5.5 mg) was dissolved in 0.65 ml PBS buffer, and slowly added. After 2 h at room temperature, the solution was extensively dialyzed using a 50 KDa MWCO membrane in deionized water, and the modified protein was analyzed by fast protein liquid chromatography (FPLC) and SDS-PAGE.

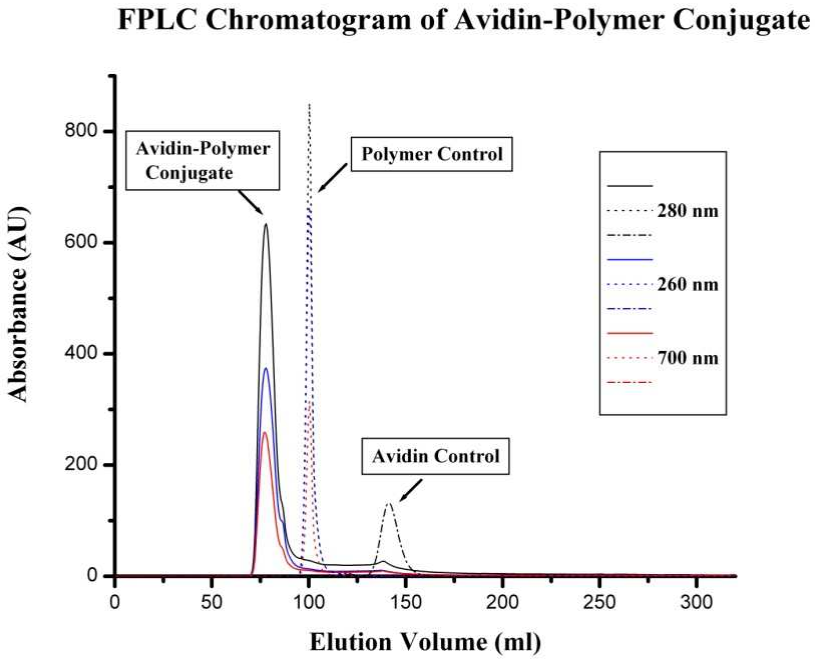

SUPPLEMENTARY FIGURE S2. Size exclusion FPLC (Hiprep 26/60™ Sephacryl™ S-200 HR column) of Avidin, biotin terminated poly(glucosamine)-poly(NIRF dye) copolymer **6**, and Avidin-polymer (**6**) conjugate .

SDS PAGE

Sodium dodecylsulfate-polyacrylamide gel electrophoresis (SDS-PAGE) was performed by forming a complex of avidin with the polymer, and then avidin alone as a control. First a mixture of avidin with the polymer in the ratio of 1:20 was incubated in PBS overnight on a rocking platform at 4 ºC, then the samples were heated and loaded onto 10-20% PAGEgel SDS Cassette Gel 17-Well. The avidin, and the avidin binding complex were visualized using Odyssey imaging system (LI-COR, Lincoln, NE) in the NIR at 800 nm, then detected after protein staining with coomassie.

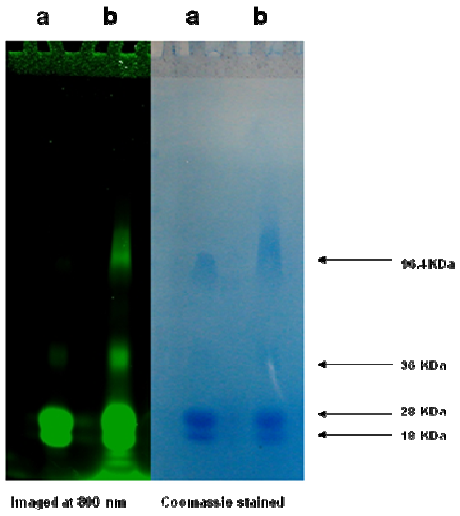

SUPPLEMENTARY FIGURE S13 SDS PAGE of control Avidin and Avidin-polymer **6** conjugate. The conjugate has two higher molecular weight bands imaged using an Odyssey imaging system (LI-COR, Lincoln, NE) with detection in the NIR at 800 nm (left) and after coomassie staining (right).

20. ***Synthesis of Protein-Polymer Conjugate; BSA-"clicked"- poly(glucosamine)-poly(NIRF dye) copolymer*** **(14)**

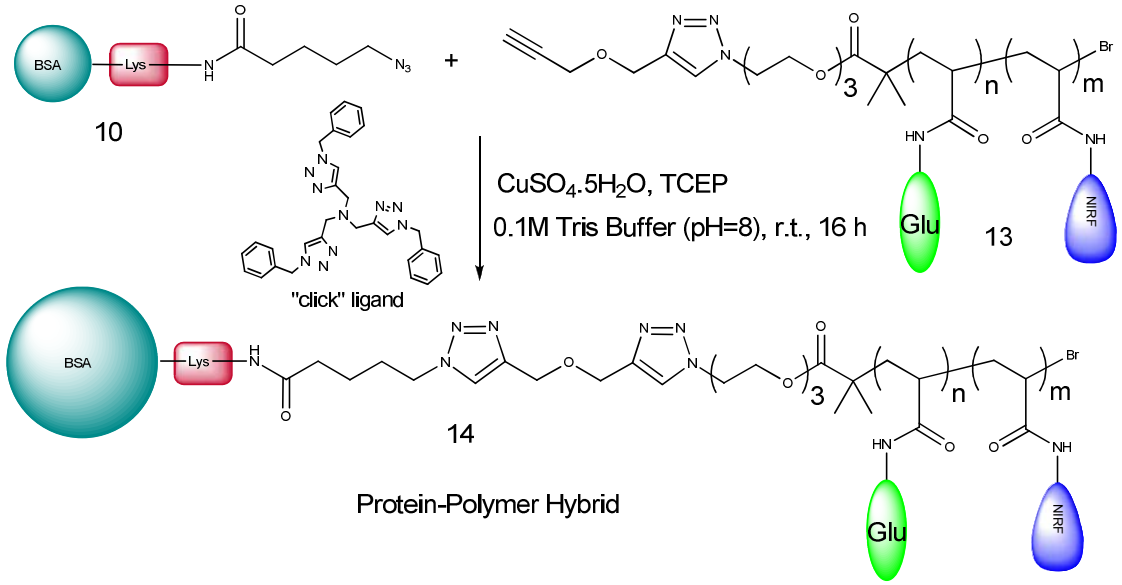

BSA-azide **13** (5 mg, approx. 1.5 µmol in azide) was incubated with alkyne-poly(glucosamine)-poly(NIRF dye) copolymer **10** (20 mg, 1 µmol) in Tris buffer (1800 µL, 0.1 M, pH 8) in the presence of TCEP (4 mM), "click" ligand (TBTA) (4 mM, dissolved in 200 µL of DMF) and copper sulfate (2mM) for 16 h at 4 ^{o}C. The ligand was added before the addition of copper sulfate. The reaction mixture was then dialyzed using Spectra Por 6 dialysis membrane (MWCO 50 KDa) in PBS pH 7.4 for 48 h to remove excess of Copper and ligand. The conjugate was further characterized via Fast Protein Liquid Chromatographic system (Akta Purifier, Amarsham Biosciences) using HiPrep 26/10 Sephacryl S-200HR (GE Healthcare) size-exclusion column in PBS pH 7.4 as eluent buffer. The conjugate was also characterized via SDS PAGE.

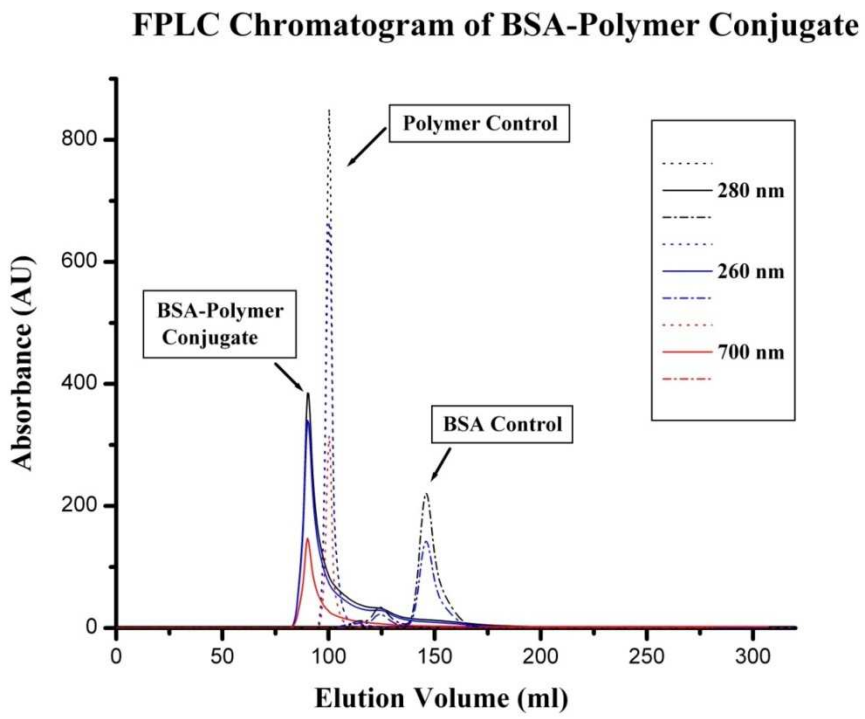

SUPPLEMENTARY FIGURES S4. exclusion FPLC (Hiprep 26/60™ Sephacryl™ S-200 HR column) of azide modified BSA **13** (dashed line), copolymer **10** (dotted line), and "clicked" conjugate **14** (solid line).

SDS PAGE

Sodium dodecylsulfate-polyacrylamide gel electrophoresis (SDS-PAGE) was performed with BSA-polymer conjugate **14** and alkyne-terminated poly(glucosamine)-poly(NIRF dye) copolymer **10**, modified BSA **13** as controls using a 10-20% PAGEgel SDS Cassette Gel. To confirm that the copolymer **10** was indeed chemically bonded to the protein, the mixture of copolymer **10** and modified BSA **13** was incubated at 4 ^{o}C for 16h in the same ratio but without the "click" reagents and dialyzed the mixture with a 50 KD MWCO membrane. The gel cassette was visualized using Odyssey imaging system (LI-COR, Lincoln, NE) in the NIR at 800 nm, then detected after protein staining with coomassie.

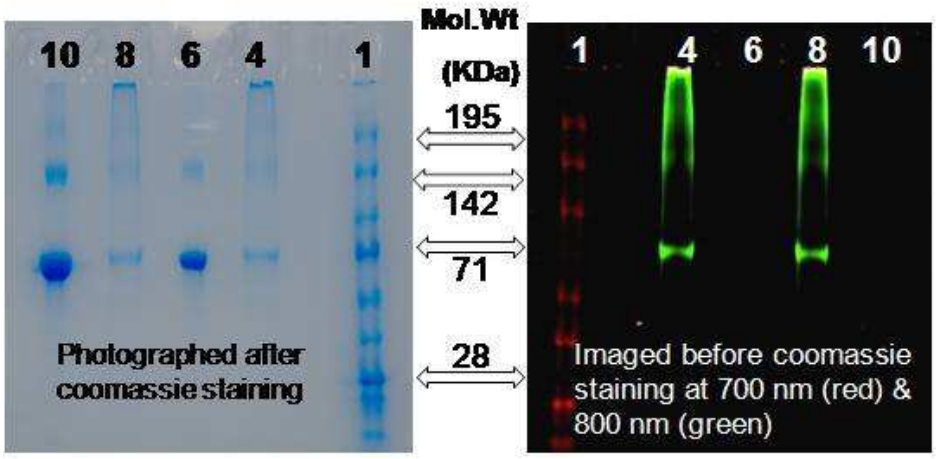

SUPPLEMENTARY FIGURE S5. SDS-PAGE of conjugate **14** (lane 4&8), mixture of azide modified BSA **13** & copolymer **10** without "click" reagents (lane 6) and unmodified BSA (lane 10).

21. UV-VIS-NIR AND FLUORESCENCE SPECTROSCOPY OF NIRF DYE AND COPOLYMER 9.

NIRF dye (ADS832WS) (2.8 mg) was dissolved in 10 ml of deionized water to prepare a stock solution of 3 µM. Azide terminated poly(glucosamine)-poly(NIRF dye) copolymer **9** (11.7 mg; 5 dye molecule per polymer chain) was dissolved in 10 ml of deionized water to prepare a solution of 0.3 mM of effective dye concentration. The stock solution of NIRF dye was further diluted to 0.3 µM. The UV-VIS-NIR spectra were obtained on an Agilent Technologies 845x UV-Vis System using deionized water as blank. The fluorescence spectra of both the dye and the dye incorporated copolymer **9** were obtained on JobinYvon Horiba FluoroMax-3 instrument using the solutions containing 0.3 µM effective dye concentration.

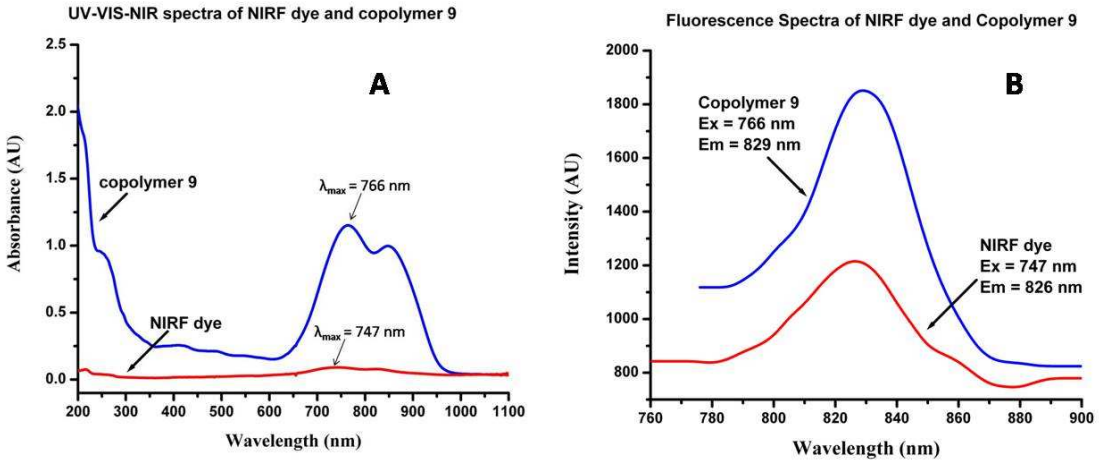

SUPPLEMENTARY FIGURE S6. **A.** Visible/NIR absorption spectra, **B.** Fluorescence emission spectra of poly(glucosamine)-poly(NIRF dye) copolymer **9** (blue line) and NIRF dye (red line) in water at 25 ^{o}C. The effective dye concentrations in both the cases are identical (0.3 µM).

22. TEST OF THE UTILITY OF PROTEIN-POLYMER HYBRID IN NON INVASIVE IMAGING IN MICE.

Each of two female, six months old mice were injected with 200 µL of the NIRF dye, and the biotin terminated poly(glucosamine)-poly(NIRF dye) copolymer **6** (0.2 mM effective dye concentration in both cases) via the tail vein. Each mouse was then anaesthetized using mixture of 15 µL Xylezene mixed with 54 µL Ketamine to reach a dose of 10 mg/kg body weight of Xylezene, and 90 mg/kg bodyweight of Ketamine per mouse, and then scanned using a Odyssey scanner (Near IR) at wavelength 800 nm. To investigate the extent of fluorescence, and the extent of catabolism of the polymer the mice were scanned after one hour and four hours. Another female six months old mouse (control mouse) was anaesthetized with the same anesthetic mixture and then scanned to eliminate background fluorescence.

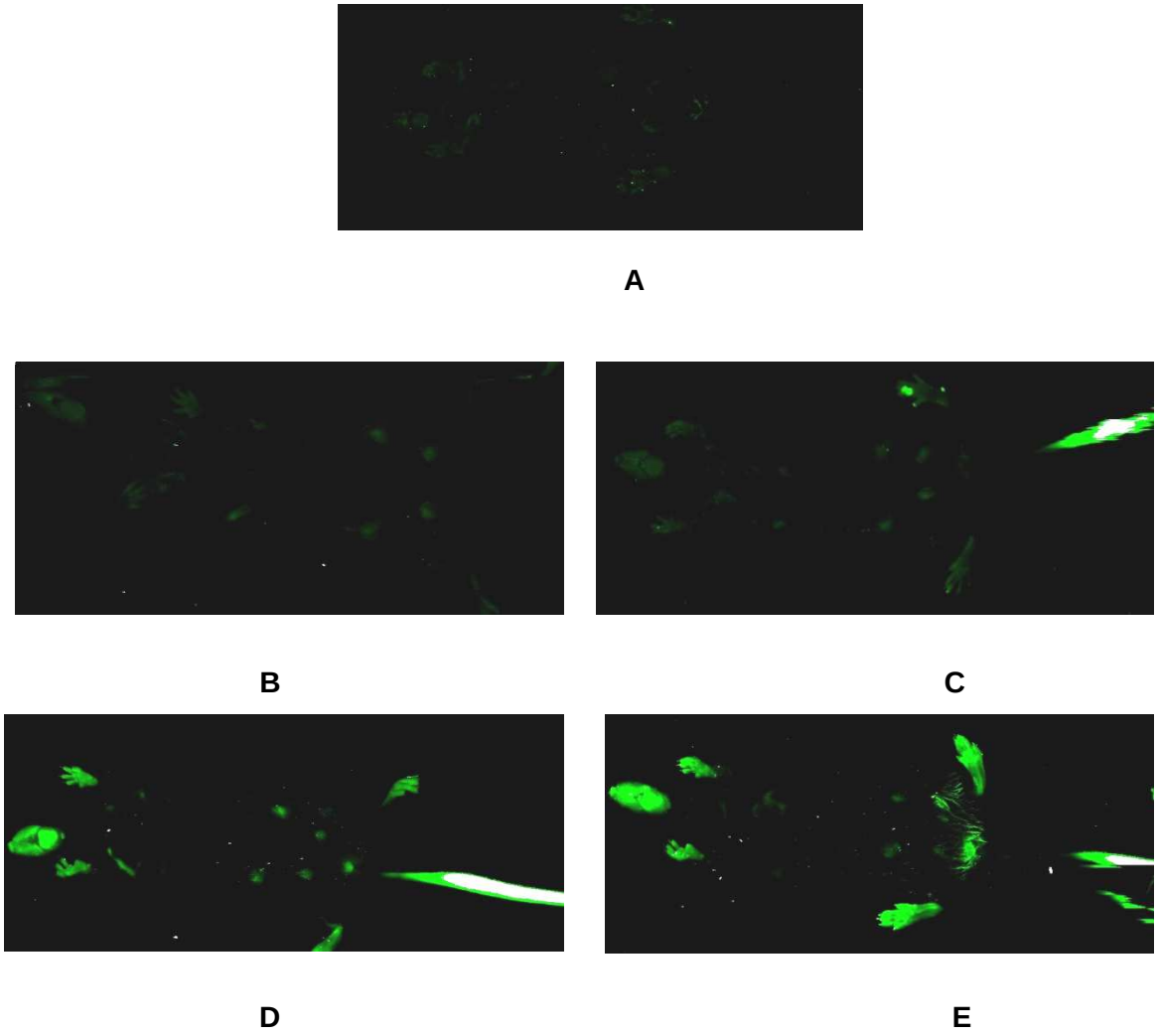

SUPPLEMENTARY FIGURE S7. Picture **A** shows the control mouse without an imaging agent. Pictures **B** & **C** show mouse scanned one, and four hours after injection with the NIRF dye respectively. Pictures **D** & **E** show mouse scanned one, and four hours after injection with the copolymer **6** respectively.

23. DETECTION OF BINDING OF BIOTINYLATED COPOLYMERS TO STREPTAVIDIN COATED WELLS.

Control poly(glucosamine)-poly(NIRF dye) copolymer, biotin terminated poly(acrylic acid)-poly (NIRF Dye) polymer **6A**, and biotin terminated poly(glucosamine)-poly(NIRF dye) copolymer **6**. All samples were prepared at a starting effective molar dye concentration of 0.2

mM in PBS (pH=7.4), then each of the three samples were successively diluted ten-fold to final concentrations of 0.02, 2.0 x 10^{-3}, 2.0 x 10^{-4} mM. 50 µL of each solution was then added to the wells, and incubated overnight at 4 degrees Celsius. Then the wells were washed four times with PBS containing 0.05% Tween-20. Finally, the wells were then visualized using the Odyssey imaging system (LI-COR, Lincoln, NE) at 800 nm.

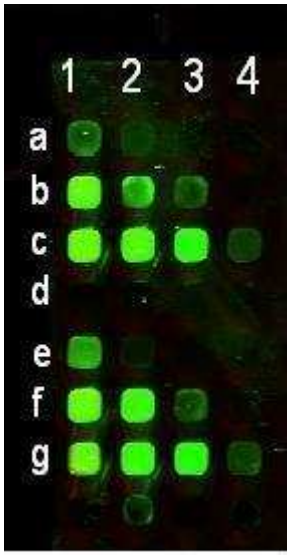

SUPPLEMENTARY FIGURE 58. Image for Streptavidin coated wells taken by Odyssey imaging system using the 800 nm channel detector where lanes (**A** through **C**) and (**E** through **G**) are the same experiment performed as a duplicate. Lanes **A-C** are samples control poly(glucosamine)-poly(NIRF dye) copolymer, biotin terminated poly(acrylic acid)-poly(NIRF dye) polymer **6A**, and biotin terminated poly(glucosamine)-poly(NIRF dye) copolymer **6** respectively.

24. THE UTILITY OF PROTEIN-POLYMER HYBRID IN IMAGING USING RETINAL EPITHELIAL CELLS.

Retinal pigment epithelial cells were divided onto four wells, and then allowed to grow for three days with regular feeding; the cells were then fixed using 2% PFA, then rinsed three times for five minutes each using PBS (pH=7.4). The nonspecific binding sites were then blocked using a blocking buffer and incubated for overnight. The blocking buffer was then removed, and

well (**A**) only was incubated with the primary antibody, and incubated for overnight at 4 ^{o}C. The primary antibody was then rinsed three times five minutes each, and then the biotinylated secondary antibody was added to wells (**A** & **B**), and incubated for overnight at 4 ^{o}C. Rinsing was performed for the excess secondary antibody using the same technique used for the primary antibody, then 500 µL of Avidin (1 mg/ml) was added to each of wells (**A**,**B** & **C**) and incubate for overnight at 4 ºC, and excess of avidin was washed off with PBS (pH=7.4) three times five minutes each. Finally 500 µL of poly(glucosamine)-poly(NIRF dye) copolymer **6** (0.1 mg/ml) was added to each of the wells (**A**,**B**,**C** & **D**) and incubated for two hours at 37 ºC at a controlled temperature chamber. Excess polymer was washed off using PBS (pH=7.4) three times five minutes each, fresh PBS was then added to the wells and scanned using Odyssey imaging system (LI-COR, Lincoln, NE) with detection in the NIR region at 800 nm.

Blocking solution:

4% Normal goat serum (NGS)

2% BSA

0.05% Tween 20

Antibody dilution buffer:

2% NGS

1% BSA

0.05% Tween 20

50% blocking buffer in PBS was used to prepare the Antibody Dilution Buffer

Preparation of Antibodies:

Primary antibody: (2B- α5 Rabbit polyclonal IgG)

1: 200 preparation of the antibody in 2% ADB without Tween (not to permeate the cells).

Secondary antibody: (GtxRb secondary Lot: 0507003644)

1:200 preparartion of the antibody in 2% ADB without Tween (not to permeate the cells).

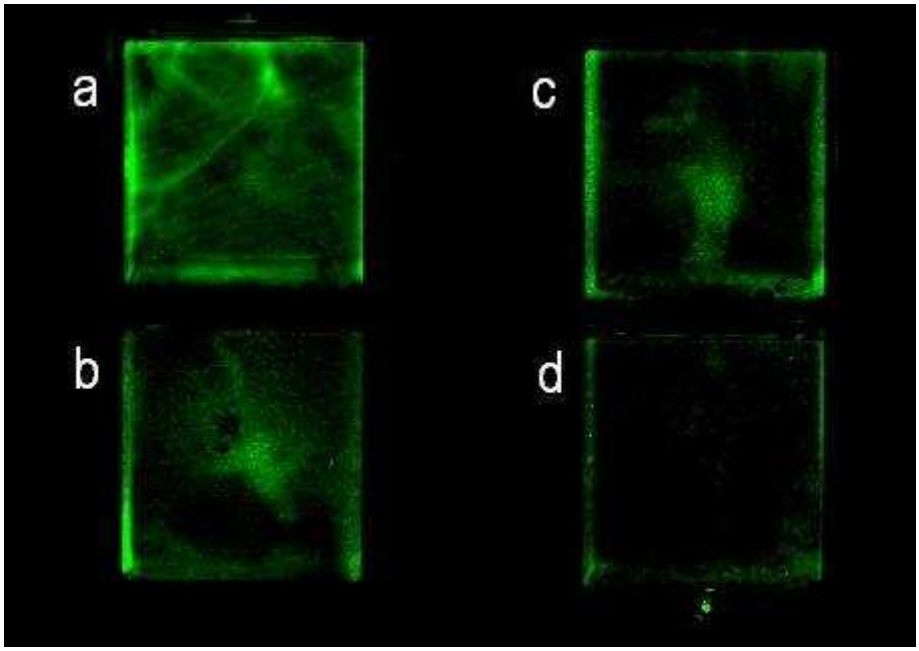

SUPPLEMENTARY FIGURE 59. Images taken by Odyssey at 800 nm of the pigment epithelial cells. The well which was incubated with primary & biotinylated secondary antibodies, Avidin, and copolymer **6** (well **A**) showed maximum fluorescence, while wells (**B**, **C**, and **D**) showed very little fluorescence relative to (well **A**) and that fluorescence is due to non specific binding to the antigens on the cell surface.

SPECTRAL DATA (^1H NMR, ^13C NMR, FT-IR):

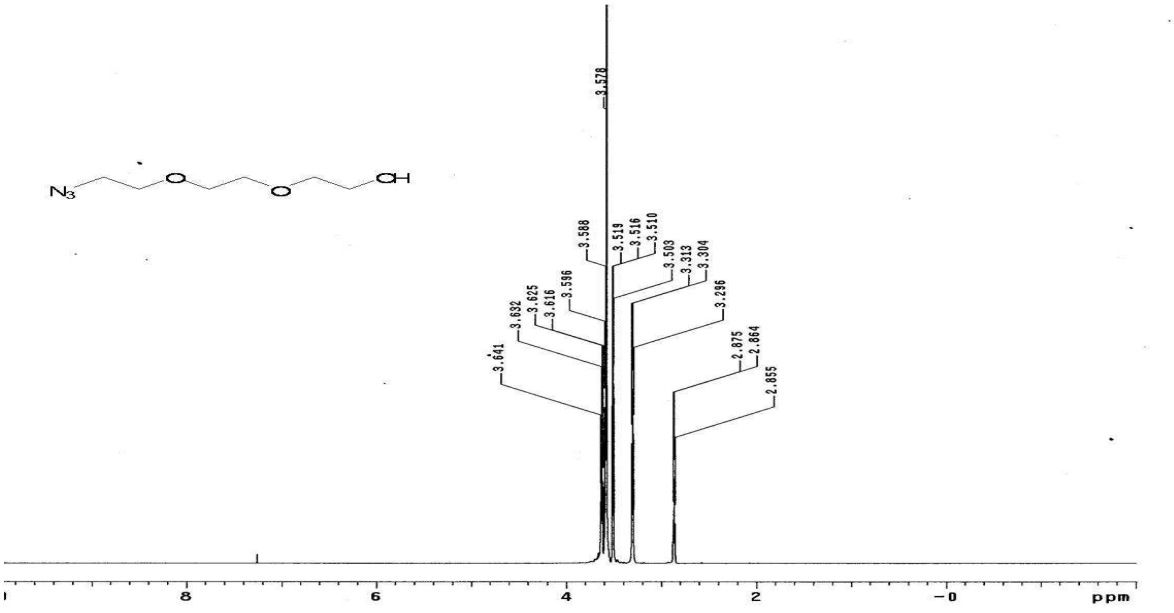

^1H NMR OF 1'

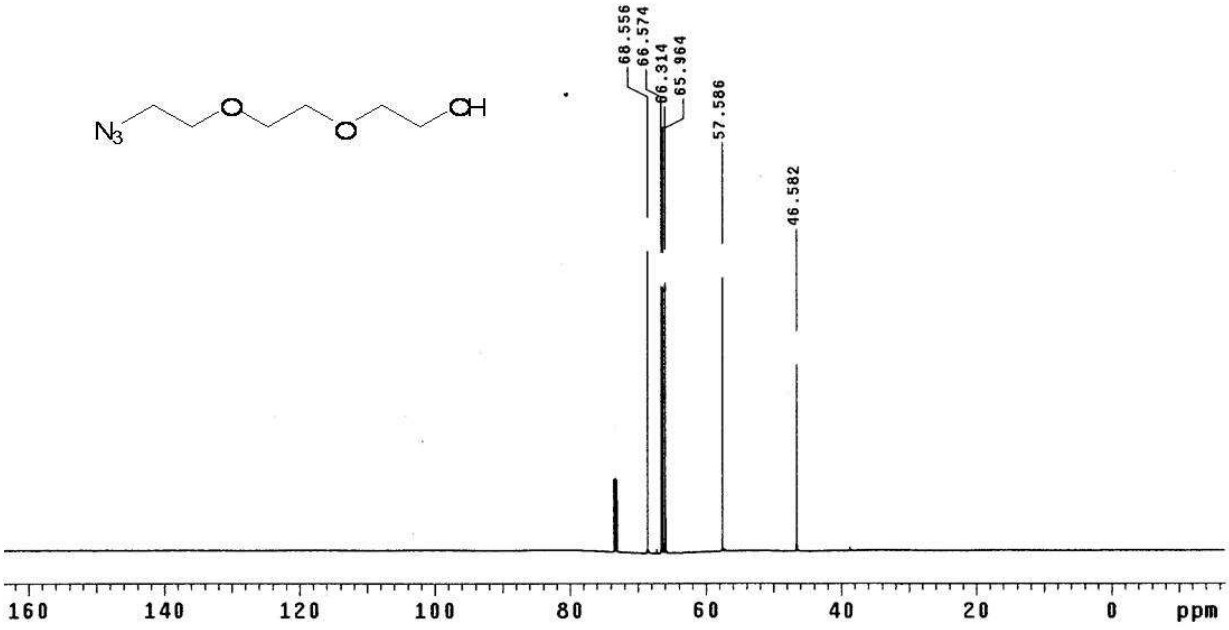

^13C NMR OF 1'

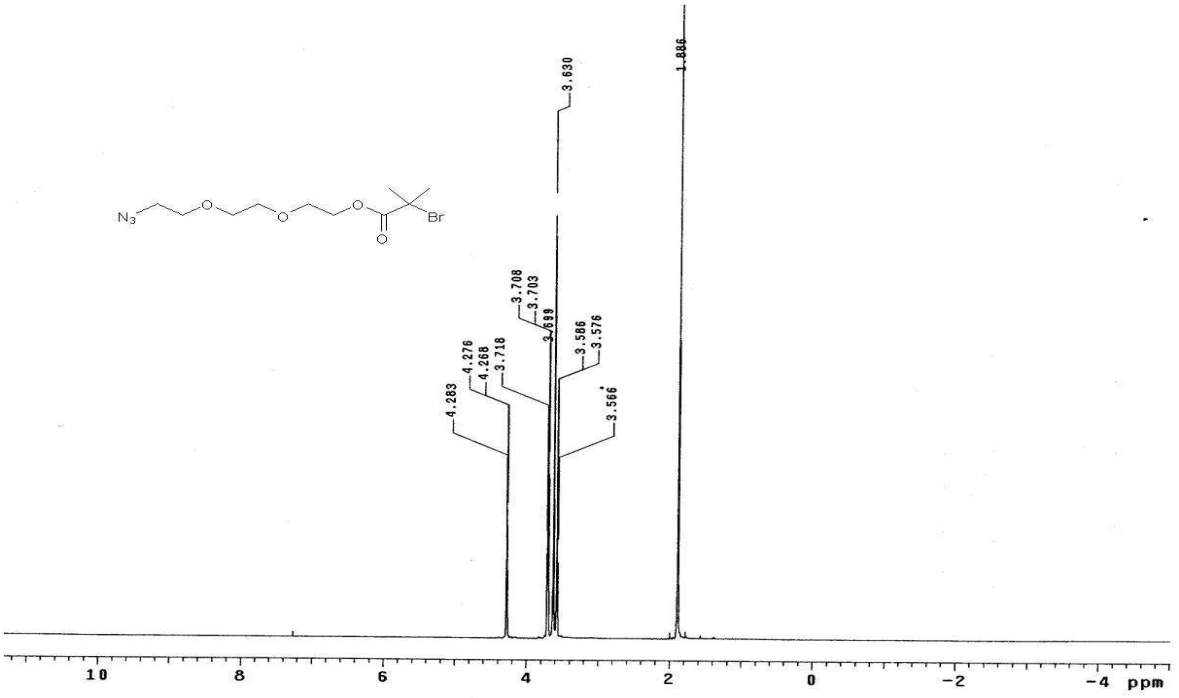

^{1}H NMR OF 1

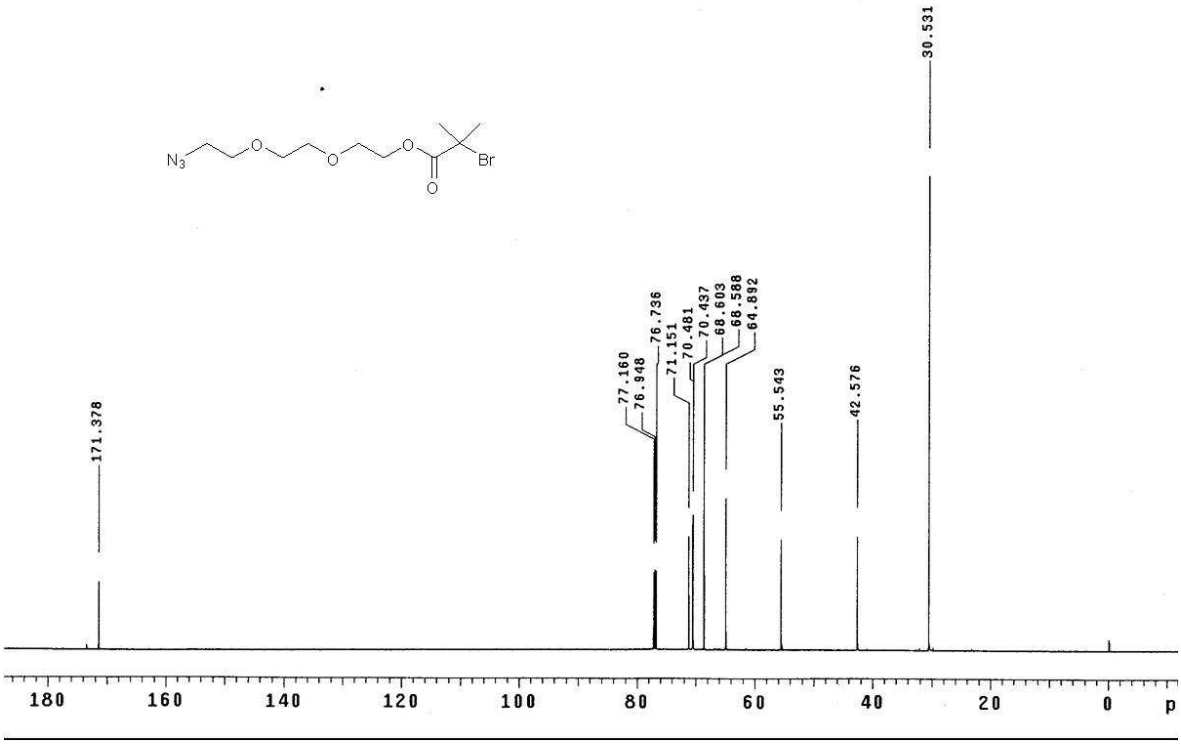

^{13}C NMR OF 1

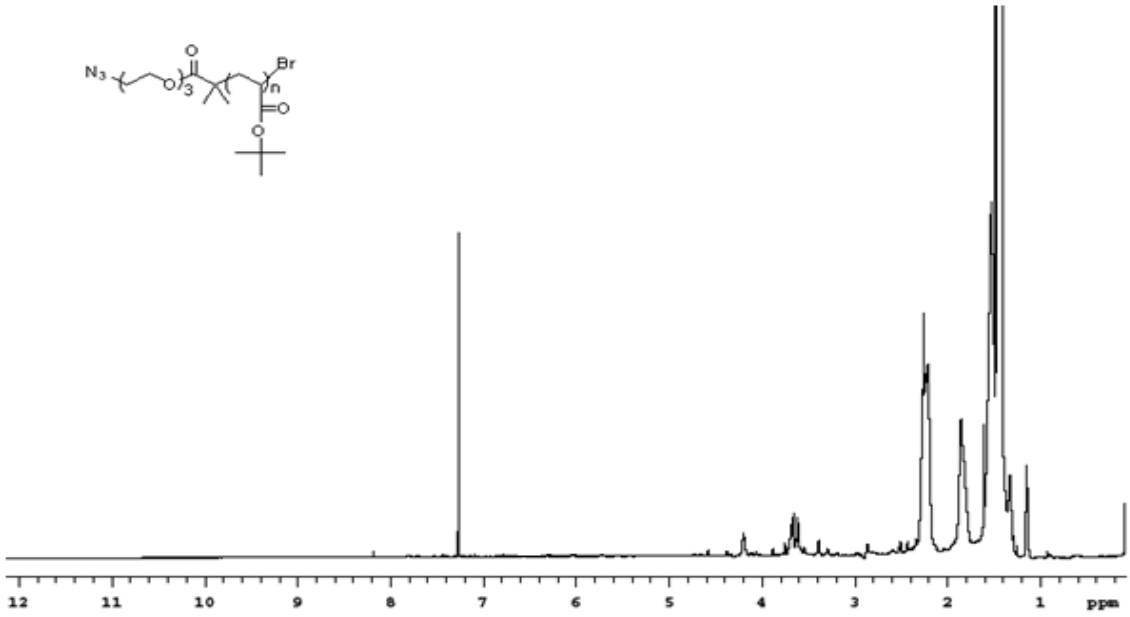

^{1}H NMR OF 2

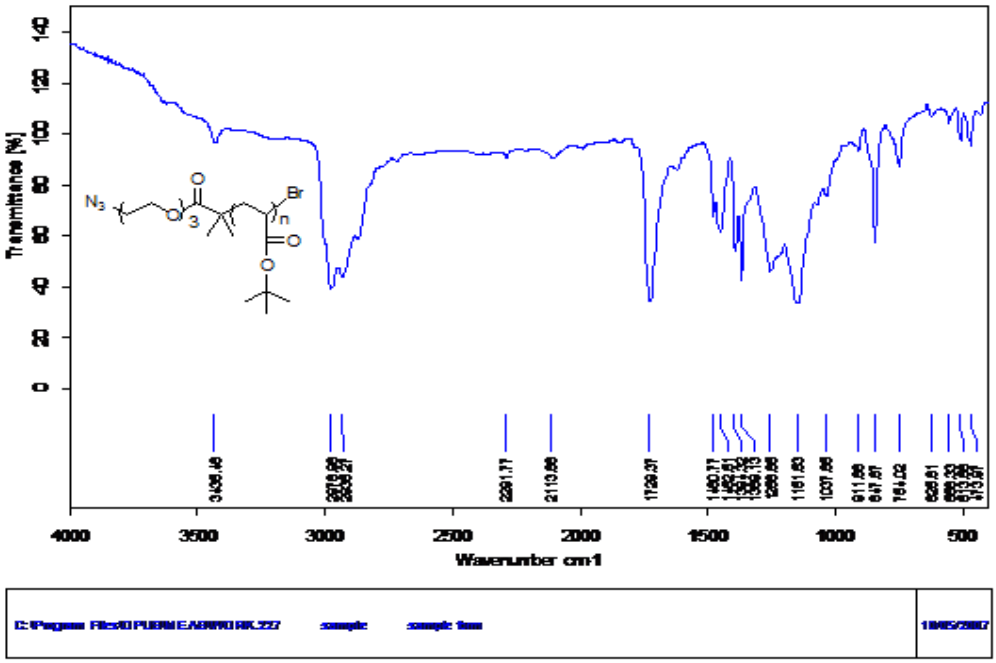

FTIR OF 2

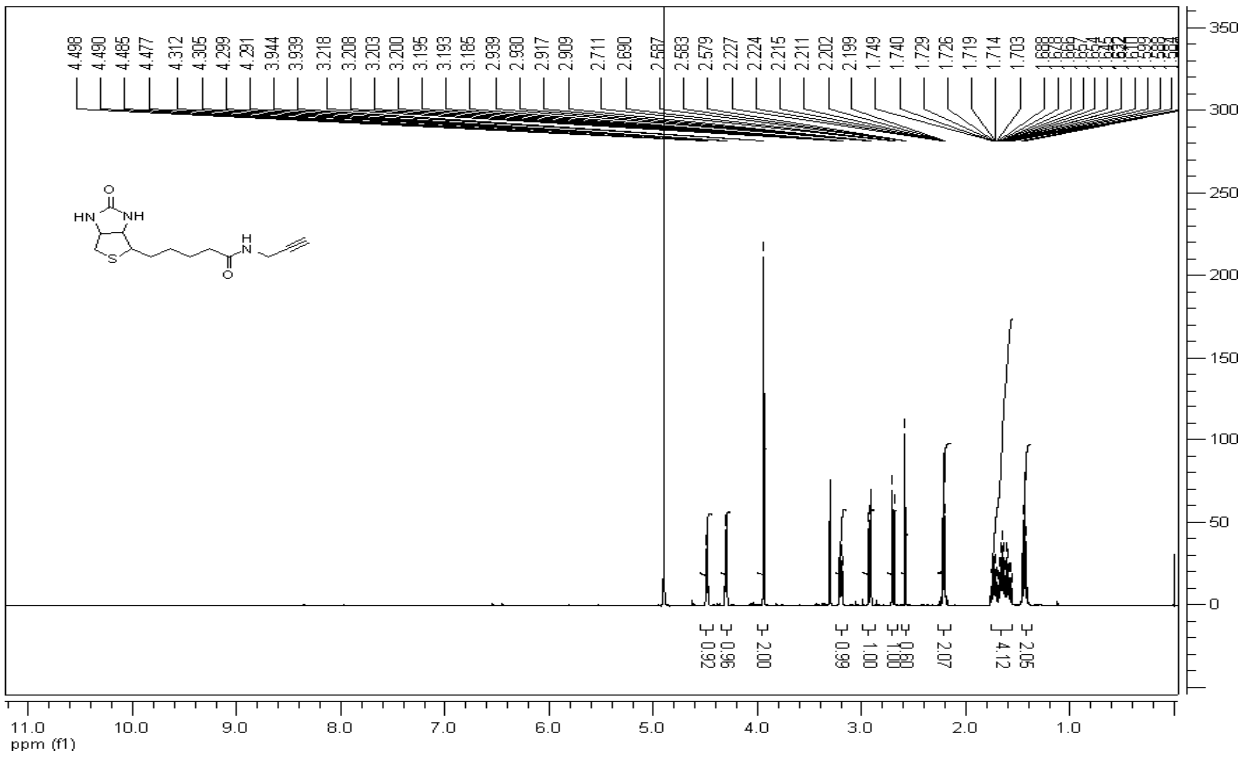

^{1}H NMR OF 3

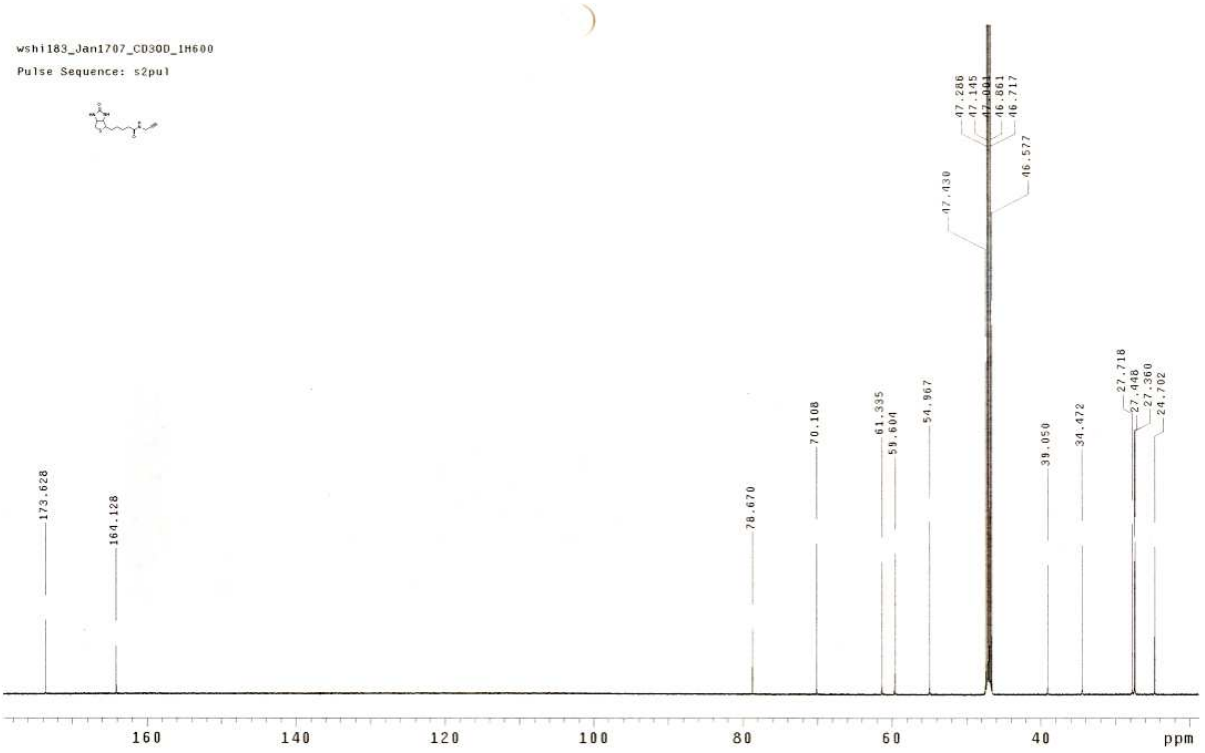

^{13}C NMR OF 3

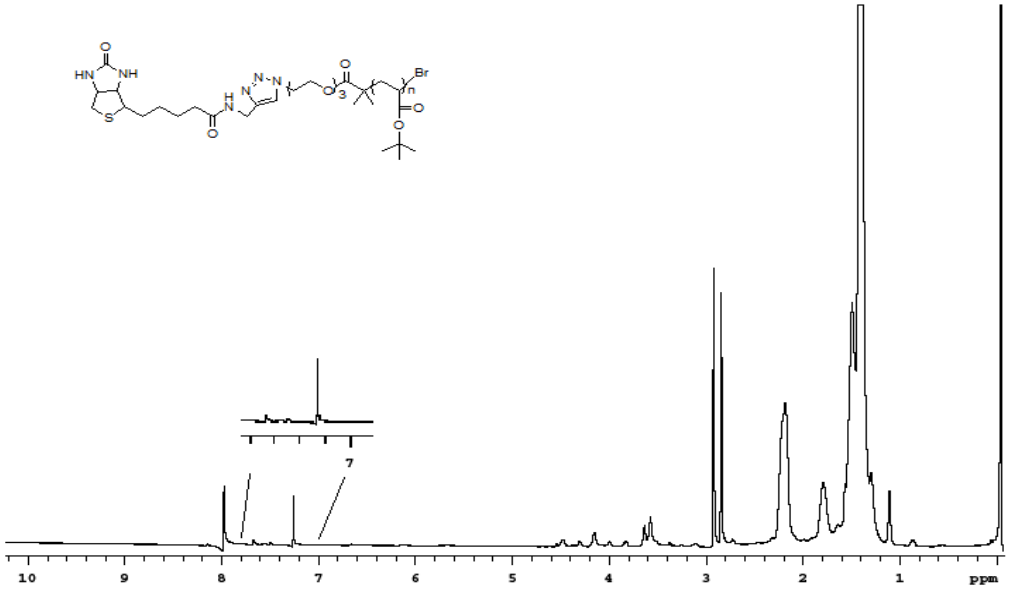

^{1}H NMR OF 4

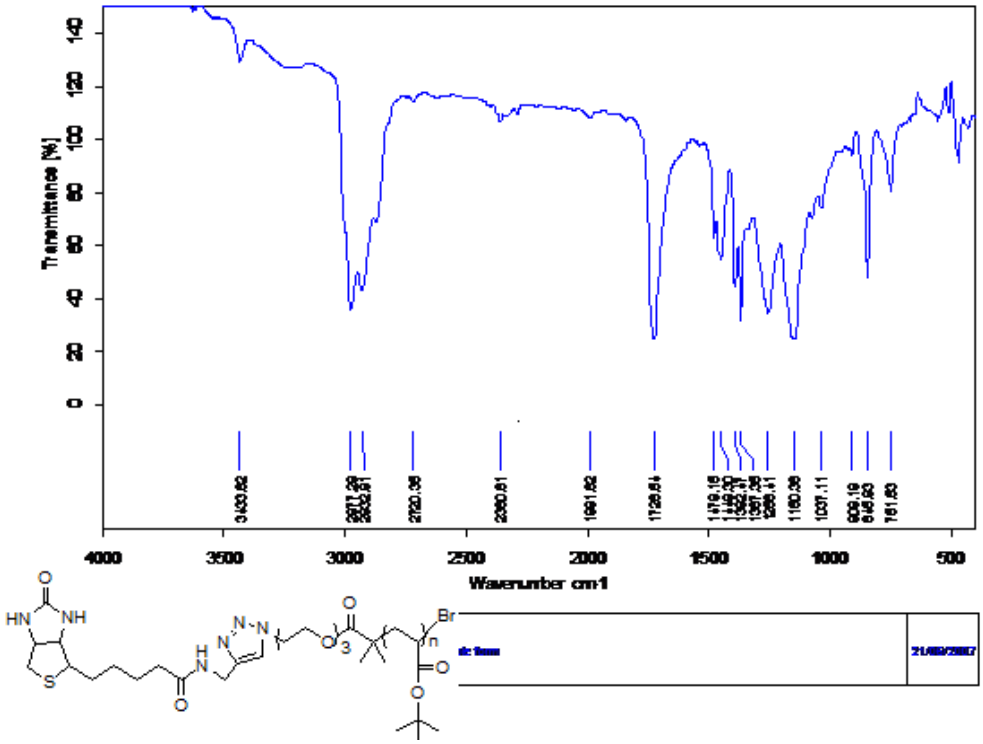

FTIR OF 4

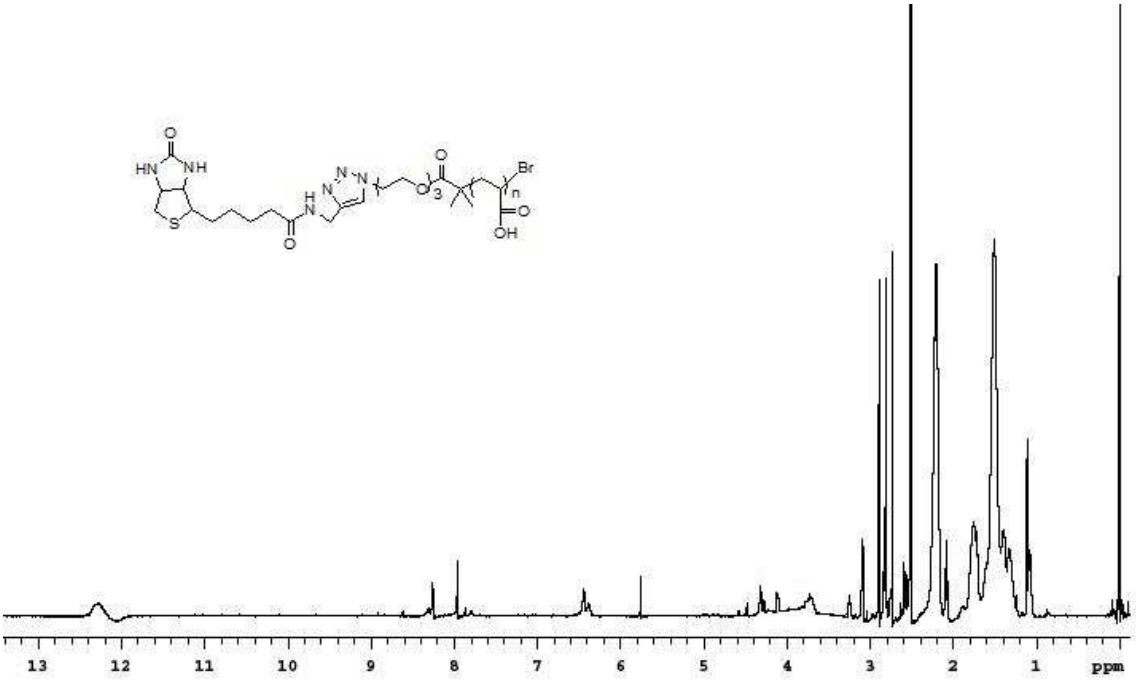

^{1}H NMR OF 5

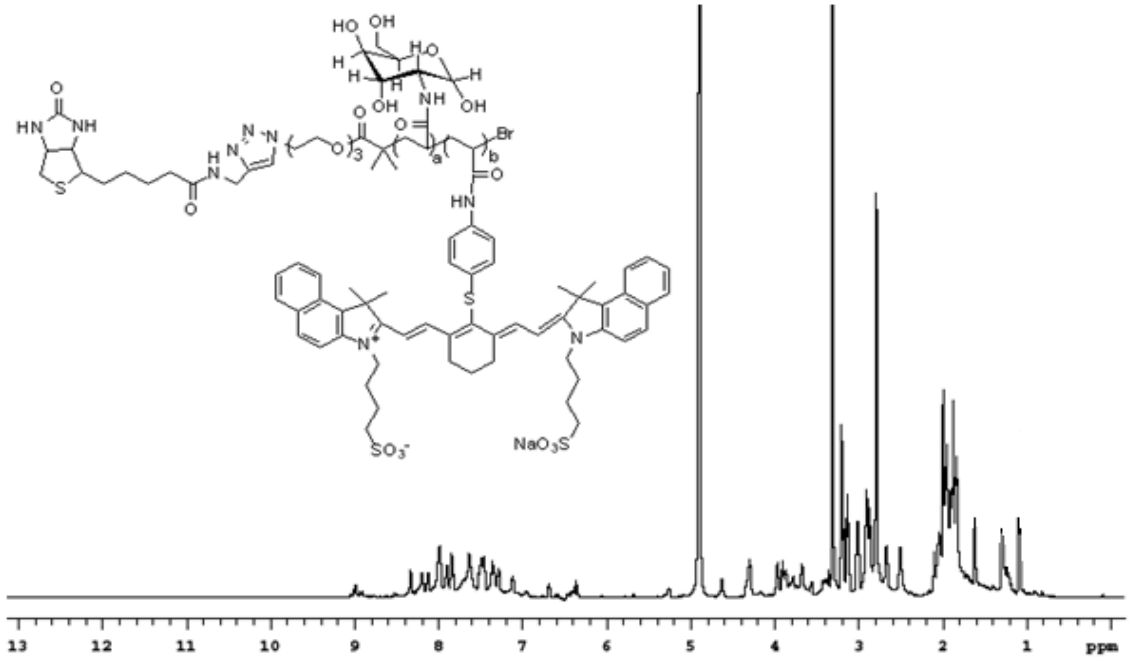

^{1}H NMR OF 6

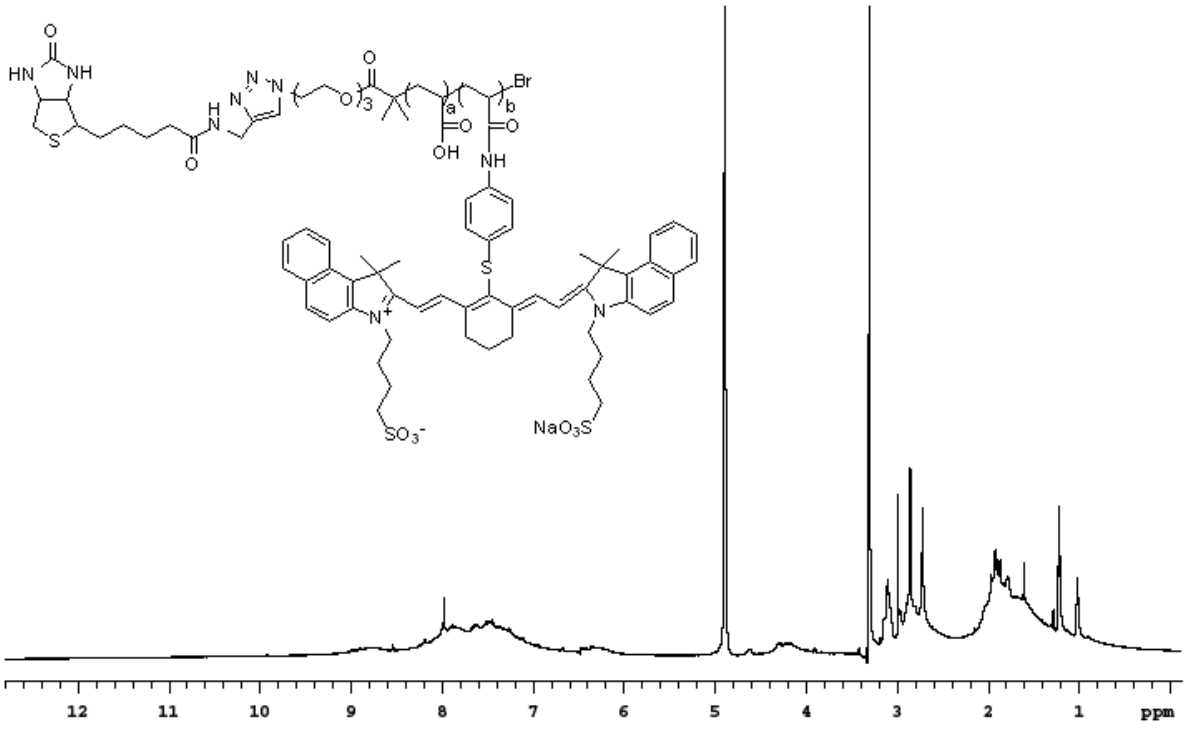

^{1}H NMR OF 6A

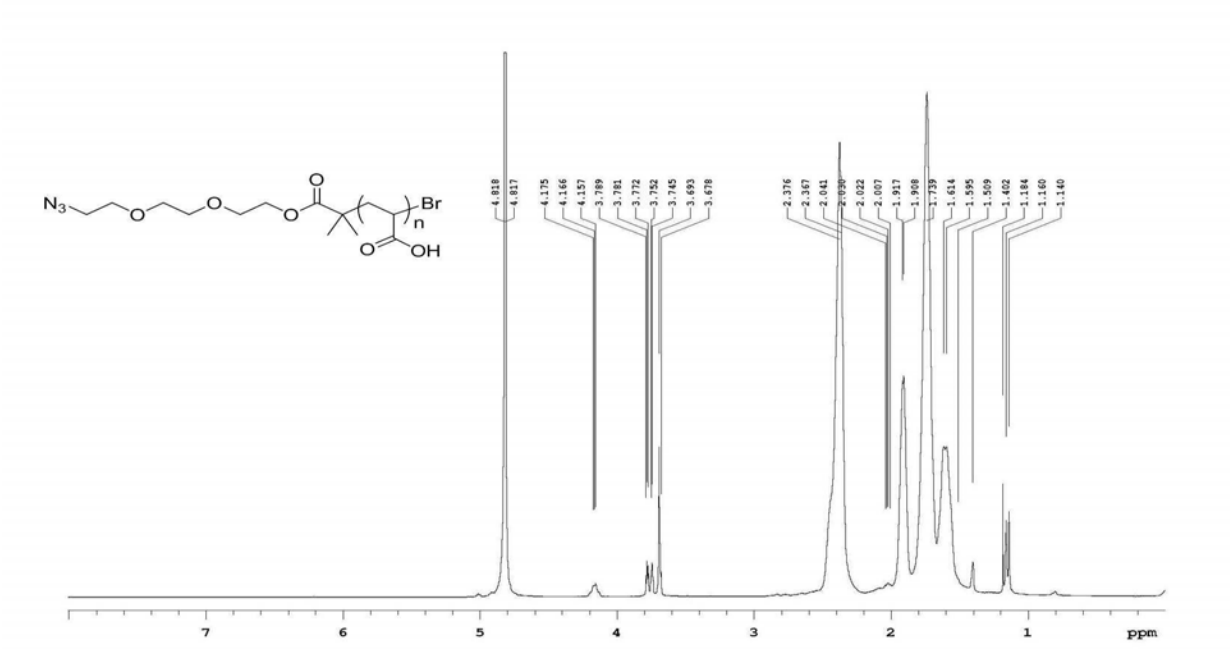

^{1}H NMR OF 8

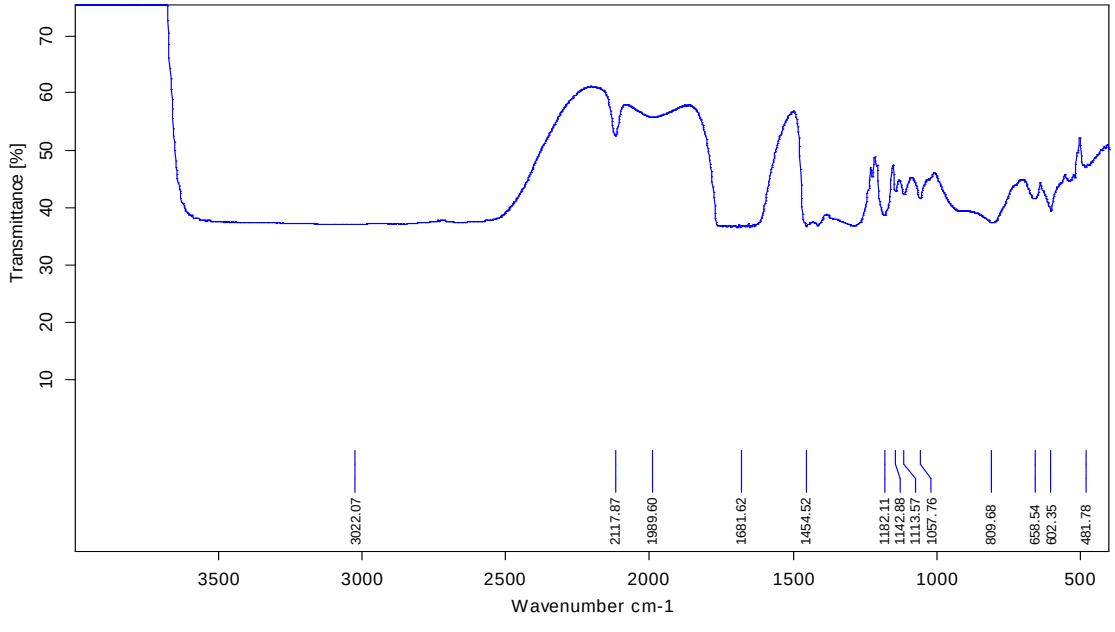

FTIR OF 8

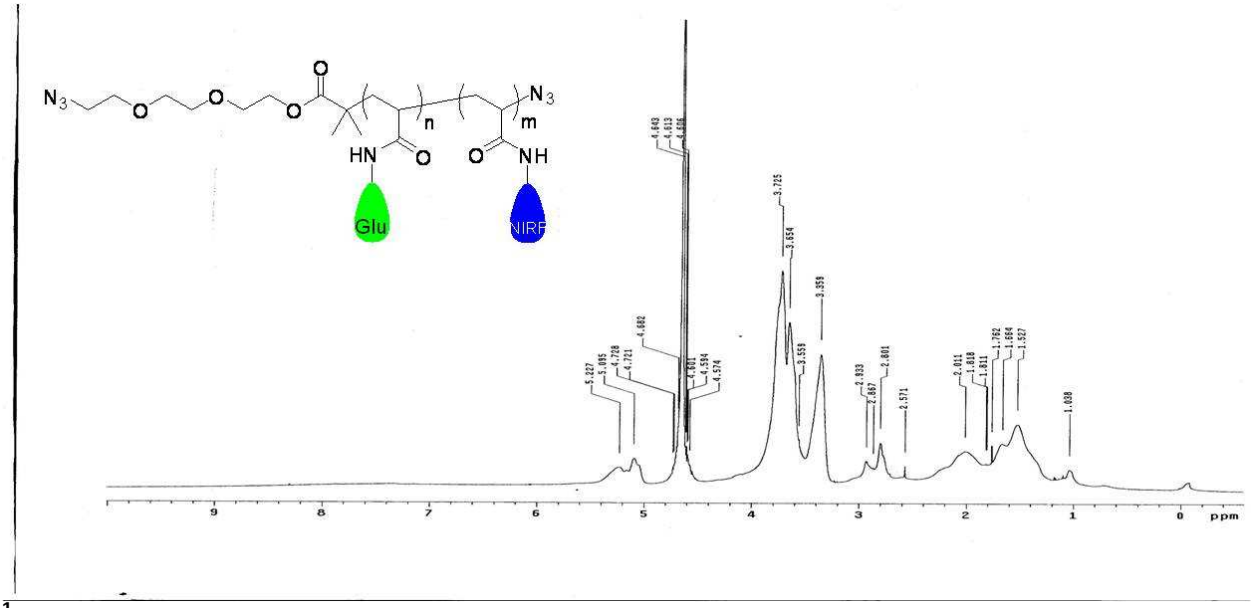

^{1}H NMR OF 9

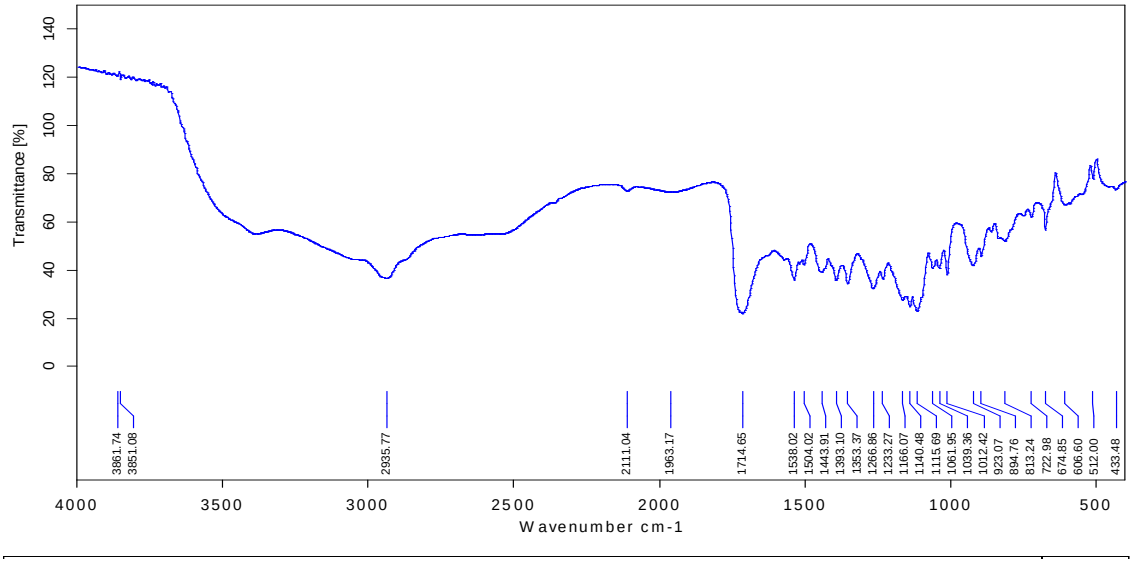

FTIR OF 9

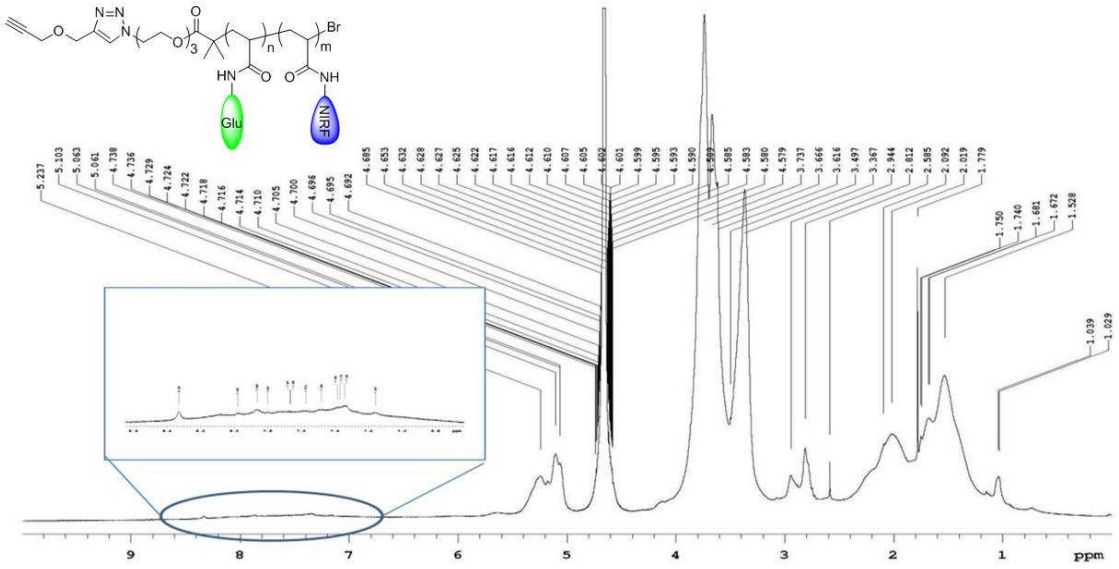

^{1}H NMR OF 10

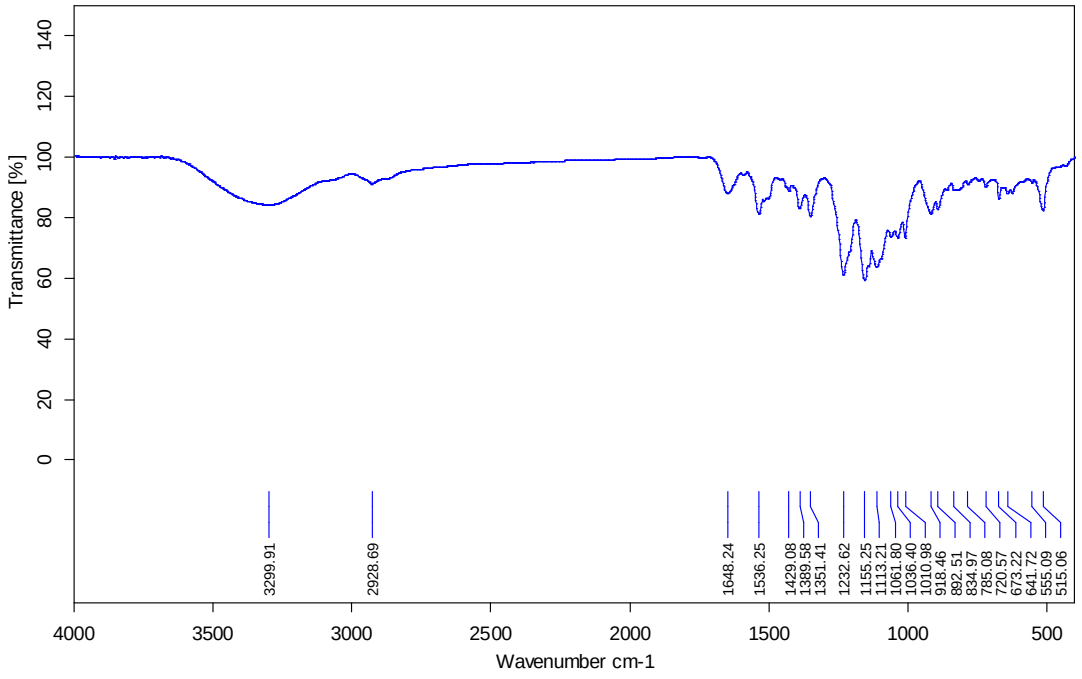

FTIR OF 10

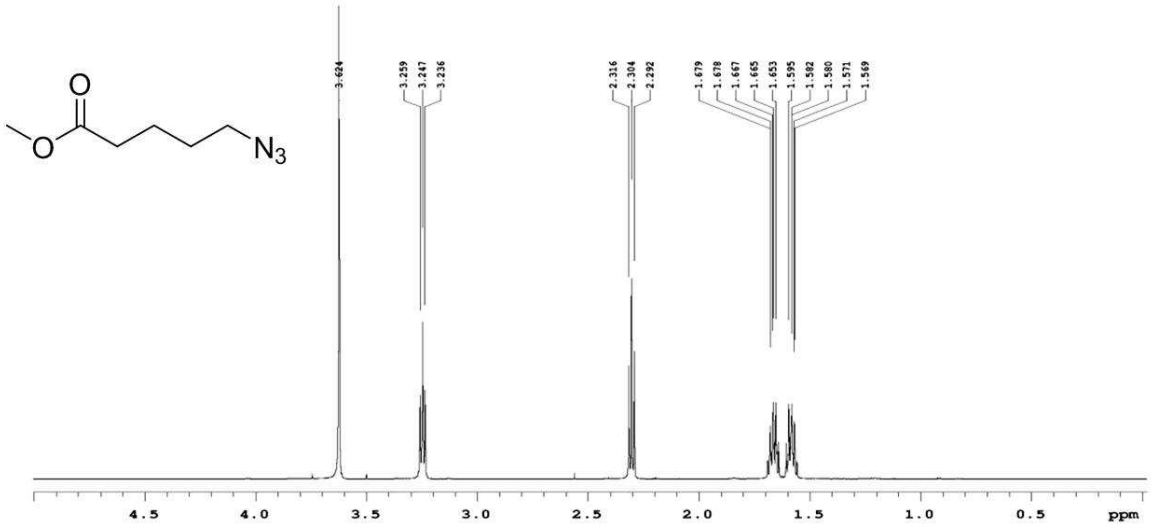

^{1}H NMR

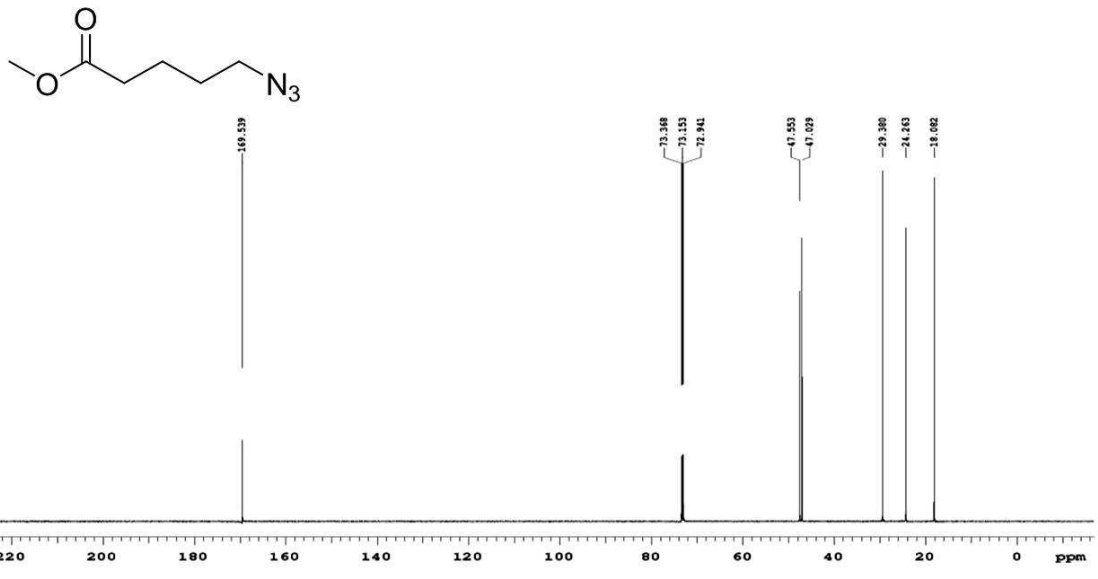

^{13}C NMR

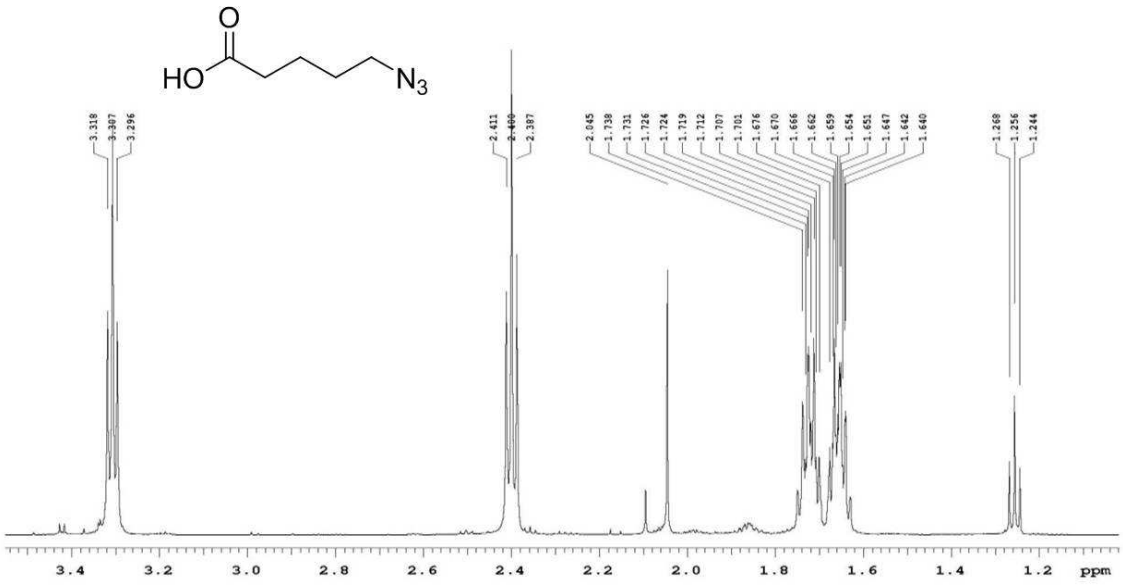

^{1}H NMR

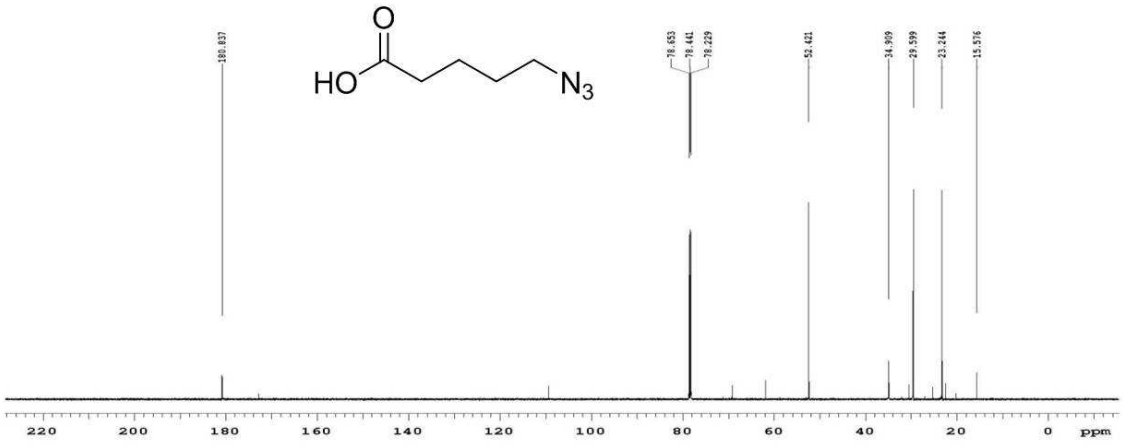

^{13}C NMR

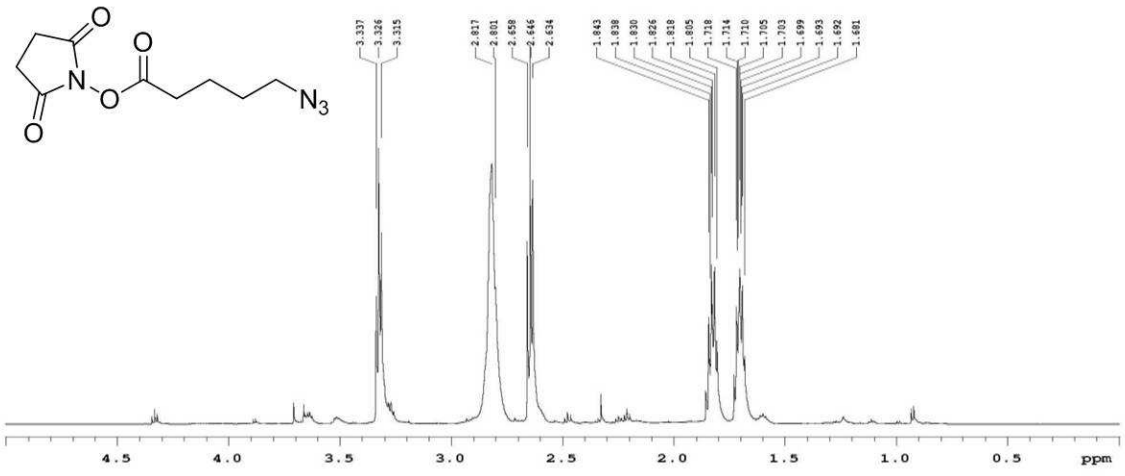

^{1}H NMR

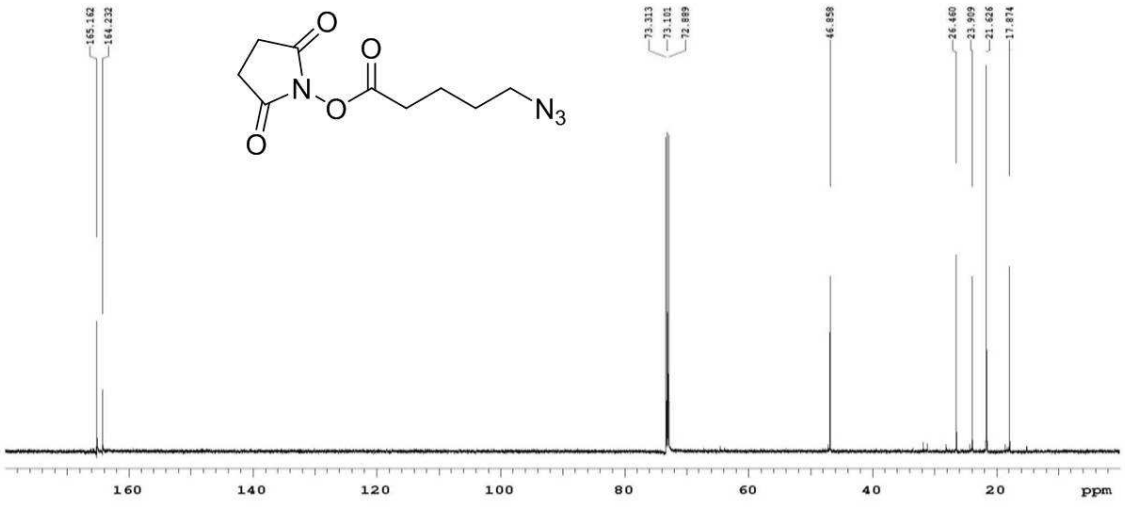

^{13}C NMR

Novel Neurotensin Analogues for Radioisotope Targeting to Neurotensin Receptor-Positive Tumors

Faisal Alshoukr,[†,‡,§] Cedric Rosant,[†,‡,§] Veronique Maes,[⊥] Jallane Abdelhak,[†,‡,§] Olivier Raguin,[†,‡,§] Samuel Burg,[†,‡,§] Laure Sarda,[†,‡,§] Jacques Barbet,[§,∥] Dirk Tourwé,[⊥] Didier Pelaprat,[†,‡,§] and Anne Gruaz-Guyon*[,†,‡,§]

Inserm, U773, team 11, Paris, F-75018, France, Université Denis Diderot-Paris 7, UMR S773 Paris, F-75018, France, CNRS, GDR Antibodies and therapeutic targeting 3260, Tours, F-37032, France, Centre de Recherche en Cancérologie de Nantes-Angers, Inserm, Université de Nantes, U892, Nantes, F-44000, France, and Department of Organic Chemistry, Vrije Universiteit Brussel, Pleinlaan 2, B-1050 Brussels, Belgium. Received April 6, 2009; Revised Manuscript Received June 19, 2009

The increased expression of the neurotensin (NT) receptor NTS1 by different cancer cells, such as pancreatic adenocarcinoma and ductal breast cancer cells, as compared to normal epithelium, offers the opportunity to target these tumors with radiolabeled neurotensin analogues for diagnostic or therapeutic purposes. The aim of the present study was to design and synthesize new neurotensin radioligands and to select a lead molecule with high in vivo tumor selectivity for further development. Two series of neurotensin analogues bearing DTPA were tested: a series of NT(8−13) analogues, with DTPA coupled to the α-NH_2, sharing the same peptide sequence with analogues previously developed for radiolabeling with technetium or rhenium, as well as an NT(6−13) series in which DTPA was coupled to the ε-NH_2 of Lys^6. Changes were introduced to stabilize the bonds between Arg^8-Arg^9, Pro^{10}-Tyr^{11}, and Tyr^{11}-Ile^{12} to provide metabolic stability. Structure−activity studies of NT analogues have shown that the attachment of DTPA induces an important loss of affinity unless the distance between the chelator and the NT(8−13) sequence, which binds to the NTS1 receptor, is increased. The doubly stabilized DTPA-NT-20.3 exhibits a high affinity and an elevated stability to enzymatic degradation. It shows specific tumor uptake and high tumor to blood, to liver, and to intestine activity uptake ratios and affords high-contrast planar and SPECT images in an animal model. The DTPA-NT-20.3 peptide is a promising candidate for imaging neurotensin receptor-positive tumors, such as pancreatic adenocarcinoma and invasive ductal breast cancer. Analogues carrying DOTA are being developed for yttrium-90 or lutetium-177 labeling.

INTRODUCTION

Pancreatic adenocarcinoma, the tenth most common human cancer, grows extremely rapidly, disseminates early, and occult metastases are frequent. Noninvasive staging modalities have shown limited ability to detect local invasion or small volume metastatic disease. ^{18}F-labeled 2-deoxy-2-fluoro-D-glucose (^{18}F-FDG), which has greatly improved the diagnosis and staging of numerous tumors, does not significantly increase the accuracy of the preoperative determination of resectability of pancreatic adenocarcinoma (*1*). Therefore, a noninvasive method to improve preoperative staging would be extremely useful. It has been shown that 75−88% of ductal pancreatic adenocarcinomas express neurotensin (NT) receptors (*2, 3*). These receptors have been proposed as new markers for this tumor, since they were not detected in normal pancreas and chronic pancreatitis (*2*). NT receptors were also identified in other tumor cells as, for example, Ewing's sarcoma, meningiomas, small cell lung carcinoma, and colon adenocarcinoma (*4*−*6*). In patients with invasive ductal breast cancers, 91% of tumors are positive for the neurotensin high-affinity receptor (NTS1), while it is poorly expressed or absent in normal cells (*7*). This recent work suggests that neurotensin contributes to human breast cancer progression and points out to the therapeutic potential of molecules targeting NTS1 receptor.

Three NT receptor subtypes have been cloned to date. Most NT biological effects are mediated by NTS1. NT(8−13) is the minimal sequence that mimics the effects of full-length NT (*8*). Numerous neurotensin analogues containing the (N^{α}His)Ac chelator and labeled with ^{99m}Tc or ^{188}Re have been synthesized (*9*−*15*). Since neurotensin is rapidly degraded in vivo by peptidases, changes were introduced to protect the three major sites of enzymatic cleavage, the Arg^8-Arg^9, Pro^{10}-Tyr^{11}, and Tyr^{11}-Ile^{12} bonds (*9*), to stabilize these molecules. The recently reported analogue NT-XIX with the three enzymatic cleavage sites stabilized displayed the highest tumor uptake described in the literature for radiolabeled neurotensin analogues, with low uptake in normal organs and particularly in kidneys (*12, 13*). Very encouraging therapy results of 50% reduction of tumor growth were obtained in nude mice with ^{188}Re-labeled NT-XIX. Significant activity detected in the intestines may nevertheless be a source of radiotoxicity (*12*). Peptides and proteins coupled to diethylenetriaminepentaacetic acid (DTPA) have been used successfully to deliver indium-111, gallium-67, and gallium-68 for imaging applications (SPECT and TEP) (*16*−*18*). By contrast, yttrium-90 needs macrocyclic chelators such as 1,4,7,10-tetraazacyclododecane-*N*,*N*′,*N*″,*N*‴-tetraacetic acid (DOTA) to prevent leakage and bone marrow toxicity in targeted radionuclide therapy (*19*). Lutetium-177 has also

* To whom correspondence should be addressed: Anne Gruaz-Guyon, Inserm, U773, Faculté de Médecine Xavier Bichat, 16 rue Henri Huchard, BP 416, F-75018, France; E-mail: anne.gruaz-guyon@inserm.fr, Phone: (33) 1 57 27 75 55, Fax (33) 1 57 27 83 21.

† Inserm, U773.

‡ Université Denis Diderot-Paris 7.

§ CNRS, GDR Antibodies and therapeutic targeting 3260.

⊥ Vrije Universiteit Brussel.

∥ Centre de Recherche en Cancérologie de Nantes-Angers, Inserm, Université de Nantes.

10.1021/bc900151z CCC: $40.75 © 2009 American Chemical Society
Published on Web 07/17/2009

Table 1. Peptide Sequence and Analytical Data

peptide	sequence	% purity	M+H$^+$ MALDI-TOF	M+H$^+$ calculated
	NT(1−13) Analogues			
NT	pGlu-Leu-Tyr-Glu-Asn-Lys-Pro-Arg-Arg-Pro-Tyr-Ile-Leu-OH			
[Lys^6(DTPA)]-NT	pGlu-Leu-Tyr-Glu-Asn-Lys(DTPA)-Pro-Arg-Arg-Pro-Tyr-Ile-Leu-OH	>95[b]	2048.16[b]	2048.32[b]
	NT(8−13) Analogues			
NT(8−13)	H-Arg-Arg-Pro-Tyr-Ile-Leu-OH			
DTPA-NT(8−13)	DTPA-Arg-Arg-Pro-Tyr-Ile-Leu-OH	>96	1192.23	1192.62
DTPA-NT-VI	DTPA-Lys-Ψ(CH_2-NH)-Arg-Pro-Tyr-Ile-Leu-OH	95	1150.12	1150.65
DTPA-NT-XI	DTPA-Lys-Ψ(CH_2-NH)-Arg-Pro-Tyr-Tle-Leu-OH	97	1150.33	1150.65
DTPA-Ahx-NTXII[a]	DTPA-Ahx-Arg-Me-Arg-Pro-Tyr-Tle-Leu-OH	92	1319.11	1318.73
DTPA-Ahx-NT-XIX[a]	DTPA-Ahx-Arg-Me-Arg-Pro-Dmt-Tle-Leu-OH	97	1346.50	1346.76
	NT(6−13) Analogues			
NT-20.1	Ac-Lys-Pro-Arg-Arg-Pro-Tyr-Ile-Leu-OH			
NT-20.2	Ac-Lys-Pro-Arg-Arg-Pro-Tyr-Tle-Leu-OH			
NT-20.3	Ac-Lys-Pro-Me-Arg-Arg-Pro-Tyr-Tle-Leu-OH			
DTPA-NT-20.1	Ac-Lys(DTPA)-Pro-Arg-Arg-Pro-Tyr-Ile-Leu-OH	>99	1459.78	1459.78
DTPA-NT-20.2	Ac-Lys(DTPA)-Pro-Arg-Arg-Pro-Tyr-Tle-Leu-OH	>97	1459.77	1459.78
DTPA-NT-20.3	Ac-Lys(DTPA)-Pro-Me-Arg-Arg-Pro-Tyr-Tle-Leu-OH	>99	1473.83	1473.80

[a] Ahx: aminohexanoic acid. [b] Results already described (*22*).

been used with DOTA-substituted peptides and antibodies. However, with previously described DTPA/DOTA neurotensin analogues, tumor uptake was limited and accumulation of radioactivity in kidneys resulted in low tumor to kidney uptake ratios (*20*−*22*). In the present study, since DTPA is a suitable chelator for ^{111}In scintigraphy, new neurotensin analogues carrying DTPA have been synthesized to further investigate the peptide structural parameters influencing tumor targeting and normal tissue uptake and to select a lead molecule for further development. They were evaluated with regard to binding affinity, stability to enzymatic degradation, internalization rate, and biodistribution. Their properties were compared to those of a reference peptide [Lys^6(DTPA(^{111}In))]-NT in which DTPA was coupled to the Lys^6 ε-NH_2 of NT (*22*).

MATERIALS AND METHODS

Cells. Experiments were performed with the human colorectal carcinoma cell line HT29 (ATCC, Rockville, USA). Cells were grown in DMEM (Gibco, France) supplemented with 10% fetal calf serum, 2 mM glutamine, and 50 μg/mL gentamycin at 37 °C in 5% CO_2.

Synthesis of the DTPA-NT Analogues. All reagents used for the synthesis were obtained from Sigma-Aldrich (Saint Quentin Fallavier, France, or Bornem, Belgium), Novabiochem (Läufelfingen, Switzerland), Bachem (Bubendorf, Switzerland), and RSP (Shirley, USA). The purity of the compounds was checked by HPLC on a Nucleosil C_{18} (5 μm, 100 Å, Shandon, France) reverse-phase column or on a DiscoveryBIO SUPELCO Wide Pore (5 μm, 300 Å, Sigma-Aldrich) column with a gradient of A, water (0.05% TFA), and B, CH_3CN (0.05% TFA), at a flow rate of 1 mL/min on a Waters apparatus. The NT(8−13), NT-VI, NT-XI, NT-XII, and NT-XIX peptides (Table 1) were prepared by solid-phase peptide synthesis as described in detail elsewhere (*10*, *13*, *23*). Tris-*t*Bu-DTPA (3 equiv) (*24*) was coupled to the resin-bound neurotensin analogue in a mixture of DMF/CH_2Cl_2 using 2−1*H*(benzotriazol-1-yl)-1,1,3,3-tetramethylureum tetrafluoroborate (TBTU), 1-hydroxybenzotriazole (HOBt), and diisopropylethylamine (DIPEA) during 4 h. The acetylated NT(6−13) analogues were synthesized by NeoMPS (Strasbourg, France) and DTPA was coupled to the lysine ε-NH_2 as already described (*25*).

Radiolabeling. The DTPA-NT analogues were labeled with indium-111 ($^{111}InCl_3$, 60 or 180 MBq, CIS bio International, France) in 100 mM acetate, 10 mM citrate, buffer pH 5, for 22 h at room temperature, and then free DTPA groups were saturated with nonradioactive $InCl_3$ as already described (*26*).

Determination of the NTS1 Binding Affinities of the DTPA-NT Analogues. *Binding to HT29 Cell Membranes.* Cell membranes (60 μg protein) were incubated for 45 min at room temperature in 250 μL buffer (50 mM Tris HCl, 5 mM $MgCl_2$, 0.8 mM 1,10-phenanthroline, 0.2% BSA, pH 7.4) in the presence of 50 pM ^{125}I-Tyr^3-neurotensin (Perkin-Elmer) and increasing concentrations of nonradioactive DTPA(In)-NT analogues. Membrane-bound activity was recovered by filtration onto Whatman GF/B filters presoaked for 1 h with polyethyleneimine (0.2% in water) and rinsed twice with buffer. Nonspecific binding was evaluated in the presence of 10^{-6} M neurotensin. Radioactivity was counted, and results were analyzed with GraphPad Prism (GraphPad Software, Inc., San Diego, CA). All experiments were performed three times.

Binding to Living HT29 Cells and Internalization. IC_{50} values for the binding to living HT29 cells were determined from competition experiments between [Lys^6(DTPA(^{111}In))]-NT (150 pM) and the peptides without DTPA or DTPA(In)-Ahx-NT-XIX. For the other peptides, IC_{50} was evaluated using the labeled DTPA(^{111}In)-peptide and increasing concentrations of the corresponding nonradioactive DTPA(In)-peptide. Cells were rinsed with 500 μL DMEM and 0.2% BSA, and incubated with DTPA(^{111}In)-NT analogue (0.15×10^{-9} M, 300 μL DMEM, 0.2% BSA, 0.8 mM 1,10-phenanthroline, 60 min, 37 °C) in the presence of increasing concentrations of nonradioactive DTPA(In)-NT analogue. After washing the wells twice with ice-cold DMEM 0.2% BSA, cells were lysed in 500 μL 0.1 N NaOH, and radioactivity was counted. Nonspecific binding was evaluated in the presence of 10^{-6} M neurotensin. Competition curves were analyzed with the *Equilibrium Expert* software (*27*). All experiments were performed three times.

Incubation for internalization studies was performed with 0.15×10^{-9} M DTPA(^{111}In)-NT analogue as above except for the use of twelve-well plates (600 μL). At selected times, the total binding was evaluated as above. To determine the amount of internalized radioactivity, wells were incubated in DMEM/0.2% BSA, pH 2.0, for 15 min at 4 °C, to dissociate the surface-bound ligand. Internalized activity was then counted after washing. Nonspecific binding and internalization were evaluated in the presence of 10^{-6} M neurotensin. Results are expressed as the ratio between internalized and specifically bound radioactivity.

Metabolic Stability. *In Human Serum.* Serum from healthy donors (100 μL) was incubated with the DTPA(^{111}In) analogues

(2 pmol, 37 °C). Samples were collected at different time points, and proteins were precipitated with methanol and filtered. Then, methanol was evaporated under vacuum, and the sample was analyzed by C_{18} RP-HPLC as described above. Detection was performed with a radioactivity detector (HERM LB 500, Berthold, France). Elution was performed using, after 5 min 0% B, a linear 10 min gradient from 0% to 35% B and a linear 25 min gradient from 35% to 50%, flow rate 1.5 mL/min. The sample was also coinjected with the radioactive control to identify the peak corresponding to intact peptide.

In Vivo Stability. Female BALB/c mice were injected in the tail vein with ^{111}In-labeled DTPA-NT analogues (25 pmol). The mice were sacrificed 15 min after injection. Plasma and urine samples (50 μL) were added to 200 μL methanol and treated as above.

Biodistribution and Imaging Studies. All in vivo experiments were performed in compliance with the French guidelines for experimental animal studies and fulfill the UKCCCR guidelines for the welfare of animals in experimental neoplasia.

HT29 cells (6.7×10^5 cells) were injected subcutaneously in the flank of 6−8 week old athymic nu/nu mice (Harlan, France). Two weeks later, mice were i.v. injected with ^{111}In-labeled-DTPA-NT analogues (20−25 pmol in 100 μL PBS) and sacrificed at different times. Blood, organs, and tumors were collected, weighed, and radioactivity counted. Injected activity was corrected for losses by subtraction of noninjected and subcutaneously injected material (remaining in the animal tail). In blocked experiments, each mouse received a coinjection of the labeled peptide and of its unlabeled counterpart (60 nmol of NT or 180 nmol of NT-20.3). Statistical analysis of differences in the tissue uptake values was performed using unpaired *t* test for comparison between two groups, or ANOVA variance analysis followed by Newman-Keuls' test for multiple comparisons. Differences of $p < 0.05$ were considered significant.

Scintigraphic imaging was performed under pentobarbital anesthesia after i.v. injection with DTPA(^{111}In)-NT-20.3 (30−50 pmol, 9−13 MBq) using a dedicated small animal Gamma Imager-S/CT system (Biospace Mesures) equipped with parallel collimators (matrix 128 × 128, with 15% energy windows centered on both indium-111 peaks at 171 and 245 KeV). A planar anterior acquisition was performed from 0 to 60 min postinjection, and a dynamic series of images of 5 min each were computed from the recorded scintigraphy data. At 2 h postinjection, SPECT images (1 h acquisition) were obtained after volume reconstruction using an iterative algorithm. Tumor to background activity (evaluated in a ROI symmetrical to that of the tumor, counts per mm^2) ratio was evaluated on planar images. Radioactivity excretion in urine was determined from activity at 1 h postinjection in the bladder.

RESULTS

Synthesis of DTPA-NT Analogues. We synthesized two series of DTPA-bearing neurotensin analogues that were stabilized against enzymatic degradation at the bonds between Arg^8 and Arg^9, Pro^{10} and Tyr^{11}, or Tyr^{11} and Ile^{12} by changes introduced in the peptide sequence (Table 1). DTPA-NT-VI, DTPA-NT-XI, DTPA-Ahx-NT-XII, and DTPA-Ahx-NT-XIX are DTPA-NT(8−13) analogues. They share the same peptide sequence with analogues carrying (Nα-His)Ac for radiolabeling with technetium or rhenium described in the literature (*9*−*11,13,15*). These analogues were prepared by solid-phase synthesis as described previously, and tris-*t*Bu-DTPA was coupled to their N-terminus, followed by resin cleavage and HPLC purification.

We also synthesized analogues of the 6−13 sequence of [Lys^6(DTPA)]-NT, which provided encouraging in vivo tumor targeting results in earlier studies (*22*). The N terminal end was acetylated in order to decrease the positive charge that favors renal accumulation of radiometals (*28, 29*) and to protect it against amino-peptidases. These analogues were obtained by coupling DTPA to the free ε-NH$_2$ group of Lys. Coupling yields were approximately 80% except for DTPA-NT-20.2 (48%). All DTPA-peptides were purified to at least 92% purity (92−99%) and identified by mass spectrometry (Table 1).

Table 2. Affinity of Peptides

peptide	K_i (nM) membranes	IC_{50} (nM) cells
NT	0.28 ± 0.05	1.67 ± 0.40
[Lys^6(DTPA(In))]-NT	1.77 ± 0.39	17.3 ± 4.3
NT(8−13)	0.044 ± 0.009	0.68 ± 0.04
DTPA(In)-NT(8−13)	1.36 ± 0.39	21.7 ± 5.1
DTPA(In)-NT-VI	3.20 ± 0.81	14.7 ± 1.6
DTPA(In)-NT-XI	8.11 ± 1.03	101 ± 17
DTPA(In)-Ahx-NTXII	5.26 ± 1.24	132 ± 44
DTPA(In)-Ahx-NT-XIX	67 ± 11	626 ± 30
NT-20.1	0.072 ± 0.019	0.82 ± 0.08
NT-20.2	0.26 ± 0.07	2.46 ± 0.79
NT-20.3	0.16 ± 0.03	2.20 ± 0.31
DTPA(In)-NT-20.1	0.66 ± 0.1	6.73 ± 0.31
DTPA(In)-NT-20.2	1.55 ± 0.42	41.2 ± 6.2
DTPA(In)-NT-20.3	2.24 ± 0.21	15.9 ± 1.7

Radiolabeling. ^{111}In-labeling of all DTPA-NT was performed with >90% indium-111 incorporation. Specific activities between 220 and 260 MBq/nmol could be obtained and were used for in vitro and imaging studies. Lower specific activities were used for biodistribution studies.

Binding Affinity Profile. Affinity of the peptides for NTS1 was evaluated using HT29 cells. These cells from which NTS1 has been first cloned (*30*) have been used to evaluate most labeled NT analogues described in the literature. K_i values for binding to membranes and IC_{50} values for binding to cells were used to evaluate affinity. K_i values for binding to HT29 membranes were, for most peptides, about 10 times lower (5−27) than the IC_{50} for the binding to HT29 cells (Table 2). This can be attributed to the decreased affinity for binding to the NTS1 induced by sodium (*31*) and to the effects of internalization and externalization of radioactivity in cells. Nevertheless, the affinities of the different peptides for membranes and living cells show a similar rank order.

Shortening the NT(1−13) sequence increased the affinity of the N^{α}-acetyl-NT(6−13) analogue NT-20.1 as already reported for N^{α}-acetyl-Lys^6(acetyl)-NT(6−13) (*8*).

DTPA(In) coupled to the NH$_2$-α of NT(8−13) induced an important decrease in the affinity for membranes and for cells (by a factor of 31 and 32, respectively) as compared to NT(8−13). This loss of affinity is less important when the distance between the receptor-binding (8−13) sequence and DTPA is larger. When coupling DTPA to the ε-NH$_2$ of Lys^6 of NT, the affinity loss is only a factor of 6 for membranes and 10 for cells. Similarly, the affinity loss in DTPA(In)-NT-20.1 is only a factor of 9 and 8 as compared to NT-20.1. A lower decrease in affinity (by a factor of 3) was observed in a larger peptide described in previous studies: DTPA(In)-(Gly^0-Glu^1-[AcLys^6]NT) (*22*). As a result, the affinity of DTPA(In)-NT-20.1 was 2-fold higher than that of DTPA(In)-NT(8−13), even though NT(8−13) displayed an affinity slightly higher than that of NT-20.1.

In the NT(8−13) series containing the stabilized Lys-Ψ(CH$_2$-NH)-Arg bond (*13*), introduction of a tertiary leucine (Tle^{12}) reduced the affinity by a factor of 3 for membranes and 7 for living HT29 cells, resulting in the lower affinity of DTPA(In)-NT-XI.

N-Methylation of the Arg^8-Arg^9 bond and introduction of an aminohexanoic acid spacer between DTPA and the 8−13 receptor binding sequence did not improve the affinity of DTPA(In)-Ahx-NT-XII as compared to DTPA(In)-NT-XI.

Table 3. In Vitro and in Vivo Stability of Peptides

peptide	in vitro stability ($t_{1/2}$ h)[a]	in vivo stability (% intact peptide)[b]
[Lys^6(DTPA(In))]-NT	25 ± 2	4 (3−5)
DTPA(In)-NT-VI	ND	10 (5−15)
DTPA(In)-NT-XI	ND	47 (40−53)
DTPA(In)-NT-20.1	0.4 ± 0.02	0.8 (0.8−0.8)
DTPA(In)-NT-20.2	4.4 ± 0.6	10 (6−14)
DTPA(In)-NT-20.3	257 ± 71	26.5 (26−27)

[a] In vitro stability is expressed as the degradation half-life in human serum at 37 °C. [b] In vivo stability is expressed as the % intact peptide (mean (individual values)) recovered in plasma 15 min after tracer injection.

Replacement of Tyr^{11} by 2′,6′-dimethyltyrosine in DTPA(In)-Ahx-NT-XIX led to an additional loss of affinity.

Introduction of a Tle^{12} in the NT(6−13) series induced a decrease in affinity similar to that observed in the DTPA(In)-NT(8−13) series. N-Methylation of the Pro^7-Arg^8 bond had little effect on affinity. Because the affinity of NT-20.1 was higher than that of NT, DTPA coupling and sequence modifications to the doubly stabilized DTPA(In)-NT-20.3 analogue resulted in a high affinity, for membranes and for living cells, similar to those of the reference peptide [Lys^6(DTPA(In))]-NT.

The peptides exhibiting the highest affinities, [Lys^6(DTPA(In))]-NT, DTPA(In)-NT-VI, DTPA(In)-NT-XI, DTPA(In)-NT-20.1, DTPA(In)-NT-20.2, and DTPA(In)-NT-20.3, were further evaluated for stability and tumor targeting in vivo.

In Vivo and in Vitro Peptide Catabolism. The fraction of radioactivity associated to the intact DTPA(^{111}In)-peptide in serum and in urine was determined 15 min after iv injection to BALB/c mice (Table 3). Samples were analyzed by C_{18} RP-HPLC chromatography. Metabolites eluted at shorter retention times than the full-length radioactive peptide. The nonstabilized peptides [Lys^6(DTPA(In))]-NT and DTPA(^{111}In)-NT-20.1 were rapidly catabolized (Figure 1, Table 3). Protection of Arg^8-Arg^9 (DTPA(^{111}In)-NT-VI) or Tyr^{11}-Ile^{12} (DTPA(^{111}In)-NT-20.2) bonds improved slightly the stability. Doubly stabilized peptides were much more resistant. Higher amounts of intact tracer were recovered in serum and about 20% of the intact peptide was excreted in urine.

The in vitro stability in human serum was also evaluated for ^{111}In-labeled NT(6−13) analogues and for the reference peptide (Figure 2, Table 3). In agreement with the in vivo results, the unprotected peptide DTPA(^{111}In)-NT-20.1 was very rapidly degraded and DTPA(^{111}In)-NT-20.3 was more stable than DTPA(^{111}In)-NT-20.2. These results confirmed the stabilizing effect of the two modifications. By contrast to the rapid degradation observed in vivo, the unprotected [Lys^6(DTPA(^{111}In))]-NT displayed an in vitro stability higher than that of the monostabilized DTPA(^{111}In)-NT-20.2. These results point out the discrepancies that could occur between in vitro and in vivo degradation even when low tracer amounts are used in vitro in order to avoid saturation of peptidases (*9*).

In Vitro Internalization. As shown in Figure 3, DTPA(^{111}In)-NT-20.3 internalized rapidly in HT29 cells, reaching a 86 ± 3% plateau with a $t_{1/2}$ of 2.1 ± 0.4 min. Similar internalization curves were obtained with [Lys^6(DTPA(^{111}In))]-NT ($t_{1/2}$ 4.2 ± 1.1 min, plateau: 88 ± 6%) and DTPA(^{111}In)-NT-VI ($t_{1/2}$: 3.8 ± 1.2 min, plateau: 82 ± 6%).

Biodistribution and Imaging Studies. The results of biodistribution studies performed in female nude mice grafted with HT29 cells are presented in Tables 4 and 5. They are expressed as the percentage of injected dose per gram of tissue (%ID/g). DTPA(^{111}In)-NT-20.3 displayed the highest tumor uptake, about 3-fold higher than that of [Lys^6(DTPA(^{111}In))]-NT at 1 h (3.3 ± 0.2 vs 1.0 ± 0.3%ID/g, $P < 0.001$) and at 3 h (2.4 ± 0.2 vs 0.7 ± 0.2%ID/g, $P < 0.001$). The difference observed between

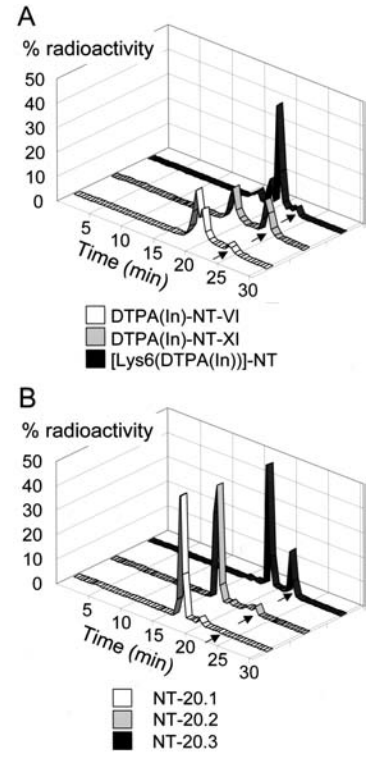

Figure 1. In vivo serum stability of DTPA(^{111}In)-peptides: representative C18 HPLC chromatograms of plasma samples collected 15 min postinjection to mice. (A) reference peptide and NT(8−13) analogues, (B) NT(6−13) analogues. Arrows show the intact peptide retention time identified by a coinjection of the sample with the radioactive control. Results are expressed as the fraction of radioactivity (%) which eluted with the intact peptide.

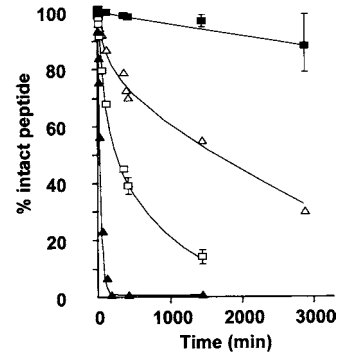

Figure 2. Degradation kinetics of DTPA(^{111}In)-peptides in human serum. Peptides (2 pmol) were incubated with human serum (100 μL) at 37 °C: Δ, [Lys6(DTPA(In))]-NT; ▲, DTPA(In)-NT-20.1; □, DTPA(In)-NT-20.2; ■, DTPA(In)-NT-20.3 (mean ± sem, three independent experiments).

tumor retention at 1 h and 3 h postinjection for DTPA(^{111}In)-NT-20.3 was not statistically significant, indicating a slow washout of radioactivity from the tumor, confirmed by the 0.33 ± 0.04%ID/g tumor uptake observed 100 h postinjection (Figure 4). Radioactivity uptake of other peptides in tumor was lower than that of [Lys^6(DTPA(^{111}In))]-NT, but the difference was not significant.

Tumor uptake of [Lys^6(DTPA(^{111}In))]-NT or DTPA(^{111}In)-NT-20.3 was receptor mediated, since it was significantly reduced by coinjection of their unlabeled counterpart (78% reduction, $P = 0.02$; and 94% reduction, $P < 0.0001$; respectively).

Radioactivity in blood at 1 h postinjection was significantly higher for DTPA(^{111}In)-NT-20.3 and [Lys^6(DTPA(^{111}In))]-NT

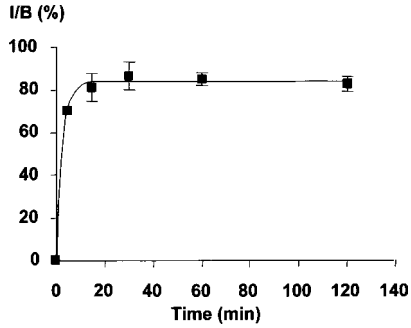

Figure 3. Internalization of DTPA(^{111}In)-NT20.3 in HT29 cells. Results are expressed as the ratio between internalized and specifically bound radioactivity (*I*/*B*, mean ± SEM, 3 experiments in triplicate).

than for other peptides. It decreased rapidly with time for both peptides. Radioactivity excretion in urine was fast and amounted to 69 ± 4% of the injected dose 1 h after injection for DTPA(^{111}In)-NT-20.3. Low activity accretion was observed in normal tissues for all peptides except in kidneys and, particularly for DTPA(^{111}In)-NT-20.3, in gastrointestinal tract. Nevertheless, for DTPA(^{111}In)-NT-20.3, high uptake ratios were obtained between tumor and stomach (7.2 ± 1.7 at 1 h and 30 ± 7 at 3 h), small intestine (1.8 ± 0.2 at 1 h and 3.5 ± 0.6 at 3 h), and colon (8.3 ± 0.8 at 1 h and 3.0 ± 0.5 at 3 h).

We investigated the basis of the gastrointestinal uptake of DTPA(^{111}In)-NT-20.3 (Table 5). In contrast to colon uptake, which was significantly decreased by coinjection of the unlabeled analogue ($P = 0.004$), stomach and small intestine uptakes were not significantly reduced by the coinjection, despite the expression of NTS1 in these organs. Most of the activity was associated to the content of the organs (stomach 68 ± 4%, small intestine 59 ± 6%, colon 73 ± 6%) indicating an elimination by the gastrointestinal route. When organ content was removed, coinjection of DTPA(^{111}In)-NT-20.3 with its unlabeled counterpart significantly decreased uptake at 3 h postinjection in stomach ($P = 0.04$), in small intestine ($P = 0.001$), and in colon ($P = 0.0002$). These results suggest that some uptake in these tissues is receptor mediated, but most of the activity comes from gastrointestinal elimination.

Kidney uptake of DTPA(In)-NT-20.3 in female nude mice was significantly lower than that of [Lys^6(DTPA(In))]-NT and significantly higher than that of other tested peptides at 1 and 3 h postinjection, with the exception of DTPA(^{111}In)-NT-XI for which the difference was not significant. As already reported in the literature for labeled octreotide analogues (*32*), kidney uptake of DTPA(^{111}In)-NT-20.3 was lower in males than in females. The difference was not significant at 6 h (2.8 ± 0.3% ID/g vs 3.6 ± 0.4%) but was highly significant at 100 h (0.83 ± 0.05% ID/g vs 0.48 ± 0.08, $P = 0.002$) (Figure 4). Therefore, tumor to kidney uptake ratio was higher in male than in female mice: at 6 h post injection (0.72 ± 0.09 vs 0.45 ± 0.03) and at 100 h (0.86 ± 0.13 vs 0.40 ± 0.04). DTPA(^{111}In)-NT-20.1 displayed the lowest renal accretion of the peptides tested in this study with 1.4 ± 0.25%ID/g as soon as 1 h post injection, but tumor uptake was also lower.

For DTPA(^{111}In)-NT-20.3, tumor to normal tissues uptake ratios were elevated for most organs; in particular, tumor/pancreas ratio was 17.5 ± 0.8 and 68.2 ± 6.5 at 1 and 3 h postinjection, respectively. They were markedly improved as compared to [Lys^6(DTPA(^{111}In))]-NT, particularly tumor/blood (60.5 ± 6.8 vs 10.9 ± 1.7 $P < 0.0001$ at 3 h postinjection), tumor/liver (19.1 ± 1.5 vs 9.3 ± 0.8 $P < 0.0001$), and tumor/muscle (91.6 ± 8.6 vs 33.1 ± 4.1 $P < 0.0001$) ratios. Tumor to kidney uptake ratio was also improved about 5-fold (0.49 ± 0.04 vs 0.11 ± 0.01 $P < 0.0001$, 3 h postinjection) as a result of higher activity uptake in tumor and lower accretion in kidney for DTPA(^{111}In)-NT-20.3.

Accumulation of DTPA(^{111}In)-NT-20.3 was clearly observed in tumors in planar at early (30 to 60 min, Figure 5) and late time points, 24, 48, and 100 h (not shown), postinjection, and in tomographic images recorded in male mice (Figure 6). Kidneys and bladder were the only other sites of activity accumulation. Tumor to background ratio increased with time reaching 2.8 ± 0.7 at 1 h and 4.5 ± 1.0 at 24 h. At 24 h, the activity ratio between tumor and kidneys was 1.3 ± 0.4 (tumor weight: 0.428 ± 0.095 g).

DISCUSSION

For imaging and therapy of neuroendocrine tumors, indisputable successes have been obtained with somatostatin analogues labeled with radiometals, such as ^{111}In, ^{68}Ga, ^{90}Y, or ^{177}Lu, PET imaging with ^{68}Ga potentially providing higher diagnostic efficacy than SPECT (*33*, *34*) and therapy with ^{90}Y or ^{177}Lu affording symptomatic improvement, prolonged survival, and better quality of life in some instances (*35*−*37*). NTS1 ligands bearing polyamino polycarboxylate chelators such as DTPA or macrocyclic chelators such as DOTA have also been developed (*20*−*22*). DTPA is considered a very powerful binder of indium-111 for single-photon emission computed tomography (SPECT), and no data suggest any superiority of macrocyclic ligands for imaging with this radionuclide. By contrast, yttrium-90 has been shown to leak out of DTPA too rapidly for therapeutic applications (*19*). Macrocyclic polyamino polycarboxylates such as DOTA are suitable chelators for ^{90}Y and ^{177}Lu, which afford promising treatment options for patients with inoperable or metastasized neuroendocrine tumors using DOTA-substituted somatostatin analogues (*35*−*37*). The situation with gallium is less clear: DTPA was used as a chelating agent in different gallium-labeled molecules (*16*−*18*). In vitro, the exchange of ^{111}In and ^{67}Ga from DTPA-albumin to transferrin occurs at approximately the same rate, which would be insignificant in studies with ^{68}Ga, a short half-life (68 min) isotope (*17*). In addition, the DTPA-albumin gallium-68 complex was found stable enough in vivo over the time span of studies possible with ^{68}Ga, since only 2% ^{68}Ga is transferred to transferrin 1 h after injection (*17*). Nevertheless, gallium-labeled DTPA-octreotide provided somewhat disappointing results (*38*). Many publications also deal with gallium-labeled DOTA-substituted somatostatin analogues (*38*) prepared for therapeutic application with yttrium-90 in the first place.

The aim of the present study was to design new polyamino polycarboxylic acid-substituted neurotensin radioligands providing higher tumor uptake and higher tumor to normal tissue uptake ratios, particularly for kidneys, than DTPA or DOTA neurotensin analogues previously described in the literature. To achieve this goal, intermediate objectives were (i) to better understand structure−activity relationships, particularly the effect on affinity induced by coupling the chelating agent and by amino-acid sequence modifications and (ii) to evaluate the relative impacts of affinity and stability on in vivo tumor uptake. In a first step, DTPA was the chelating agent since high radiolabeling efficiency under mild conditions can be obtained (*19*) and little difference is usually observed in terms of affinity, biodistribution, tumor accretion and tumor to nontumor uptake ratios between DTPA and DOTA-carrying peptides, when labeled with indium-111 (*21*). We synthesized a series of DTPA-peptides with the same sequence as the ^{99m}Tc- or ^{188}Re-labeled (N$^{\alpha}$His)Ac-NT(8−13) derivatives, which have already been described and which have shown promising targeting properties and encouraging preclinical therapy results (*10*−*13*). We also synthesized analogues of the C-terminal (6−13) part of [Lys^6-(DTPA(In))]-NT, which provided encouraging in vivo tumor

Table 4. Tissue Distributions of [Lys^6(DTPA(^{111}In))]-NT and the DTPA(^{111}In)-NT(8−13) Analogues in Female Nude Mice Grafted with HT29 Cells

	[Lys6(DTPA(^{111}In))]-NT			DTPA(^{111}In)-NT-VI	DTPA(^{111}In)-NT-XI
uptake (%ID/g)[a]	1 h $n = 6$	3 h $n = 9$	3 h blocked[b] $n = 8$	1 h $n = 3$	1 h $n = 3$
blood	0.63 ± 0.12	0.06 ± 0.01	0.04 ± 0.01	0.24 ± 0.13	0.28 ± 0.02
lungs	0.44 ± 0.06	0.07 ± 0.01	0.07 ± 0.01	0.21 ± 0.06	0.37 ± 0.02
liver	0.22 ± 0.03	0.16 ± 0.07	0.09 ± 0.01	0.14 ± 0.06	0.19 ± 0.02
spleen	0.19 ± 0.02	0.07 ± 0.01	0.45 ± 0.37	0.10 ± 0.02	0.18 ± 0.01
stomach[c]	2.46 ± 2.01	0.26 ± 0.15	0.15 ± 0.09	0.06 ± 0.02	0.14 ± 0.02
small intestine[c]	0.69 ± 0.09	0.59 ± 0.30	0.20 ± 0.09	0.28 ± 0.05	0.38 ± 0.07
large intestine[c]	0.16 ± 0.02	0.71 ± 0.16	1.05 ± 0.47	0.17 ± 0.04	0.19 ± 0.04
muscle	0.14 ± 0.03	0.03 ± 0.01	0.03 ± 0.01	0.11 ± 0.04	0.16 ± 0.08
bone	0.13 ± 0.03	0.06 ± 0.01	0.03 ± 0.01	0.17 ± 0.05	0.13 ± 0.03
tumor	1.02 ± 0.26	0.71 ± 0.18	0.22 ± 0.02	0.62 ± 0.06	0.52 ± 0.23
kidney	12.50 ± 1.63	9.28 ± 0.73	7.18 ± 0.48	2.80 ± 0.37	3.90 ± 0.59
			Tumor(T)/Organ		
T/blood	3.3 ± 2.1	10.9 ± 1.7	5.7 ± 0.5	4.9 ± 2.5	2.0 ± 0.9
T/liver	5.8 ± 2.3	9.3 ± 0.8	2.8 ± 0.6	6.2 ± 2.3	3.0 ± 1.4
T/muscle	10.4 ± 4.8	33.1 ± 4.1	8.9 ± 1.3	9.6 ± 5.6	3.4 ± 1.6
T/kidney	0.08 ± 0.02	0.11 ± 0.01	0.03 ± 0.01	0.20 ± 0.04	0.16 ± 0.07

[a] Uptake is expressed as the percentage of injected dose per gram of tissue (%ID/g). [b] Blocked animals received a coinjection of the labeled peptide with neurotensin (60 nmol). [c] Organ with its content.

Table 5. Tissue Distributions of the DTPA(^{111}In)-NT(6−13) Analogues in Female Nude Mice Grafted with HT29 Cells

	DTPA(^{111}In)-NT-20.1		DTPA(^{111}In)-NT-20.2		DTPA(^{111}In)-NT-20.3		
uptake (%ID/g)[a]	1 h $n = 3$	3 h $n = 6$	1 h $n = 5$	3 h $n = 5$	1 h $n = 6$	3 h $n = 15$	3 h blocked[b] $n = 4$
blood	0.19 ± 0.03	0.03 ± 0.00	0.31 ± 0.06	0.02 ± 0.01	0.70 ± 0.09	0.04 ± 0.01	0.04 ± 0.01
lungs	0.17 ± 0.01	0.04 ± 0.01	0.30 ± 0.04	0.10 ± 0.04	0.73 ± 0.04	0.17 ± 0.03	0.12 ± 0.01
liver	0.11 ± 0.01	0.06 ± 0.01	0.14 ± 0.01	0.07 ± 0.01	0.39 ± 0.04	0.17 ± 0.05	0.08 ± 0.01
spleen	0.08 ± 0.01	0.05 ± 0.01	0.12 ± 0.01	0.06 ± 0.01	0.31 ± 0.01	0.11 ± 0.01	0.09 ± 0.01
stomach (with content)	0.13 ± 0.04	0.02 ± 0.01	0.42 ± 0.17	0.04 ± 0.01	0.66 ± 0.19	0.17 ± 0.04	0.14 ± 0.04
small intestine (with content)	0.53 ± 0.20	0.18 ± 0.04	1.07 ± 0.44	0.16 ± 0.02	1.90 ± 0.22	1.30 ± 0.46	0.18 ± 0.05
large intestine (with content)	0.09 ± 0.01	1.65 ± 0.99	0.11 ± 0.02	0.46 ± 0.09	0.42 ± 0.05	1.03 ± 0.14	0.15 ± 0.04
stomach (without content)	ND	ND	ND	ND	ND	0.21 ± 0.03	0.09 ± 0.02
small intestine (without content)	ND	ND	ND	ND	ND	0.78 ± 0.10	0.10 ± 0.03
large intestine (without content)	ND	ND	ND	ND	ND	0.45 ± 0.04	0.09 ± 0.01
muscle	0.07 ± 0.01	0.01 ± 0.01	0.07 ± 0.01	0.01 ± 0.01	0.16 ± 0.01	0.03 ± 0.01	0.04 ± 0.01
bone	0.07 ± 0.01	0.03 ± 0.01	0.43 ± 0.22	0.03 ± 0.01	0.22 ± 0.05	0.11 ± 0.02	0.28 ± 0.11
tumor	0.46 ± 0.06	0.49 ± 0.12	0.93 ± 0.32	0.46 ± 0.09	3.27 ± 0.21	2.38 ± 0.21	0.14 ± 0.03
kidney	1.44 ± 0.25	1.36 ± 0.10	2.55 ± 0.24	1.97 ± 0.26	7.49 ± 0.54	4.85 ± 0.25	4.81 ± 0.63
				Tumor(T)/Organ			
T/blood	2.5 ± 0.3	18.8 ± 4.7	4.6 ± 2.8	19.4 ± 3.7	5.6 ± 1.5	60.5 ± 6.8	3.7 ± 0.8
T/liver	4.3 ± 0.4	8.5 ± 1.7	6.6 ± 2.1	6.5 ± 0.9	8.8 ± 0.6	19.1 ± 1.5	1.7 ± 0.2
T/muscle	7.1 ± 1.9	35.6 ± 8.3	14.8 ± 6.7	34.0 ± 8.0	20.8 ± 1.4	91.6 ± 8.6	4.2 ± 1.0
T/pancreas	ND	ND	ND	ND	17.5 ± 0.8	68.2 ± 6.5	ND
T/kidney	0.32 ± 0.02	0.37 ± 0.04	0.35 ± 0.08	0.23 ± 0.01	0.44 ± 0.03	0.49 ± 0.04	0.03 ± 0.01

[a] Uptake is expressed as the percentage of injected dose per gram of tissue (%ID/g). [b] Blocked animals received a coinjection of the labeled peptide with NT-20.3 (180 nmol).

targeting. The α-NH_2 was acetylated to protect against aminopeptidases and to lower the number of positive charges, which may increase renal uptake (*28, 29*).

By contrast to the 5-fold affinity increase for HT29 cells provided by the introduction of [^{99m}Tc(CO)$_3$]-(Nα-His)Ac at the N-terminal end of NT(8−13) (*39*), DTPA(In) coupling led to an important loss of affinity, which was minimized by increasing the distance between DTPA and the NT(8−13) sequence. This observation may be attributed to steric hindrance due to the DTPA(In) complex, but also to structural changes induced by DTPA: it was recently reported that coupling DOTA to a 13 aminoacid peptide induced an α-helix structure, which was not observed in the free peptide (*40*). This possibility remains to be explored with NT analogues.

In the DTPA(In)-NT(8−13) series, the influence on affinity of most of the sequence modifications is in agreement with previously reported results for the [^{99m}Tc(CO)$_3$]-(Nα-His)Ac-NT(8−13) analogues (*10, 12, 13*). On the contrary, the loss of affinity induced by a Tle^{12} substitution, also observed in the NT (6−13) peptides and already reported in the literature for DTPA analogues (*20*), was not observed with the ^{99m}Tc-labeled NT(8−13) derivatives. As a result of the effect of DTPA coupling and Tle^{12} substitution, DTPA-NT-XIX displayed a low affinity, in opposition to its [^{99m}Tc(CO)$_3$]-(Nα-His)Ac counterpart (*13*). Since the affinity of NT-20.1 was higher than that of NT, the double-stabilized DTPA(In)-NT-20.3 exhibited an affinity in the low nanomolar range despite DTPA coupling and sequence modifications.

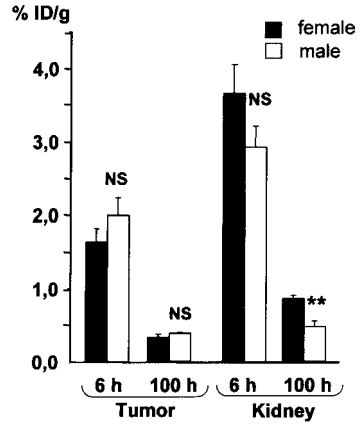

Figure 4. Tumor and kidney uptake in female and male nude mice, grafted with HT29 cells, after iv injection of DTPA((111In)-NT-20.3. Uptake is expressed as the percentage of injected dose per gram of tissue (%ID/g, mean ± SEM). **: $P < 0.005$.

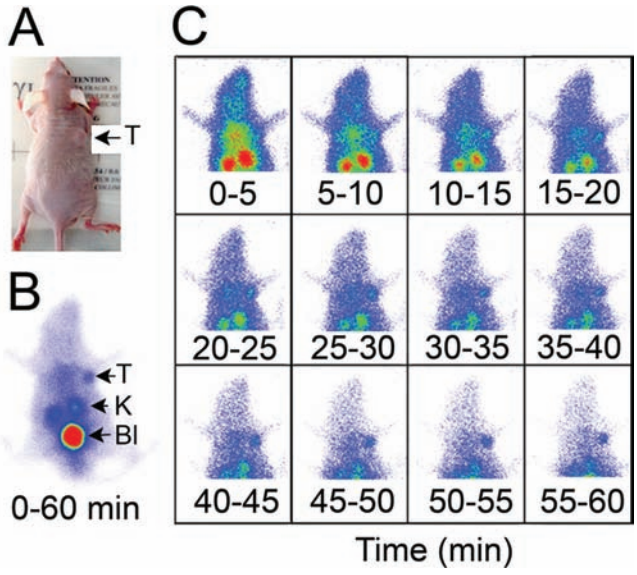

Figure 5. DTPA(111In)-NT-20.3 planar images of a male nude mice grafted with HT29 cells. (A) photograph, (B) planar image, (C) 5 min frames, acquisition from 0 to 60 min postinjection under anesthesia. Bl, bladder; K, kidney; T, tumor. Tumor weight: 240 mg.

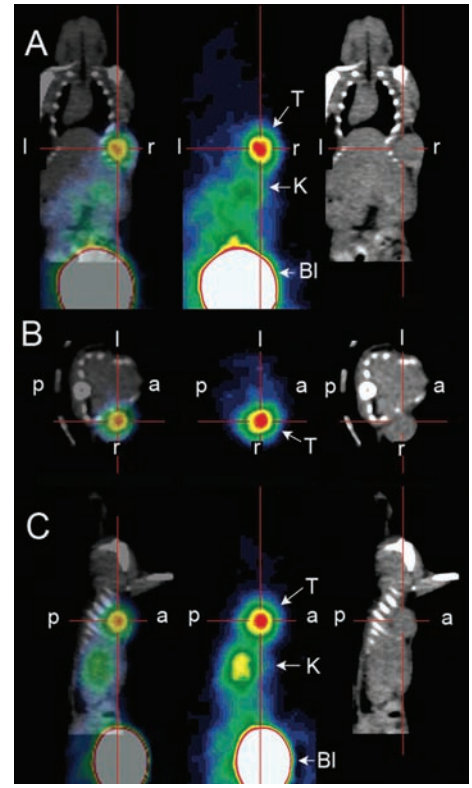

Figure 6. SPECT/CT imaging of a male nude mice grafted with HT29 cells in the right flank 2.5 h postinjection of DTPA(111In)-NT-20.3. Left, CT; center, SPECT; right, SPECT/CT fused images. Frames: A, coronal; B, axial; C, sagittal. Abbreviations as in Figure 5 and r, right; l, left; a, anterior; p, posterior. Tumor weight: 498 mg.

As expected, sequence modifications increased the in vitro and in vivo stability to enzymatic degradation and the peptides with two protected bonds were the most resistant. In vivo, increased stability had a major impact on tumor uptake in the DTPA-NT(6−13) series as already reported in the literature for bombesin analogues (*41*). Nevertheless, higher in vivo stability associated to lower affinity of DTPA(In)-NT-XI led to much lower tumor uptake as compared to DTPA(In)-NT-20.3.

Charge and charge distribution of radiolabeled peptides may produce various effects on renal uptake, but in general, it is increased by positive charges (*28, 29*). One objective of the present study was to lower kidney uptake as compared to the reference peptide. [Lys^6(DTPA(111In))]-NT may, after cleavage in the 1−6 N-terminal end, release labeled metabolites with a free positively charged α-NH_2, which could contribute to the high kidney uptake. To avoid the formation of these metabolites, we deleted the 1−6 N-terminal part of the molecule and acetylated its N-terminal end to neutralize the positive charge. The difference between the remarkably low renal accretion of DTPA(111In)-NT-20.1, compared to DTPA(111In)-NT-20.3, cannot be related to their charge or charge distribution at physiological pH which are identical. It may not be attributed to differences of hydrophobicity, as all peptides eluted with approximately the same acetonitrile percentage in HPLC (data not shown), indicative of similar hydrophobicity (*29*). It may only be ascribed to reabsorption and accumulation of metabolites. Cleavage of DTPA(111In)-NT-20.1 at the Arg^8-Arg^9 bond may produce labeled metabolites with only one positive charge (Arg^8). The same is true for DTPA(111In)-NT-20.2, which also exhibits low renal uptake. In DTPA(111In)-NT-20.3, the Arg^8-Arg^9 bond is stabilized, and it may be hypothesized that metabolites with two positively charged Arg are released that induce higher renal accumulation of radioactivity.

CONCLUSION

In summary, structure−activity studies of new NT analogues carrying DTPA have shown that this polyamino polycarboxylate chelating agent induces an important loss of affinity unless the distance between the chelating agent and the NT(8−13) sequence that binds to the NTS1 receptor is increased. Altogether, it was not possible to design a peptide with both the lowest kidney retention and highest tumor uptake, but DTPA(111In)-NT-20.3 is a good compromise with improved uptake ratio between tumor and kidneys, superior to previously published DTPA and DOTA neurotensin analogues. In spite of some excretion of activity by the gastrointestinal route and some receptor-mediated binding of the tracer to stomach, small intestine and colon, ratios between uptakes in the tumor and in these organs was high. The tumor to intestines ratio was higher than that of the ^{99m}Tc-labeled analogue NT-XIX described in the literature (*12*). In spite of a relatively high uptake in kidneys, DTPA(111In)-NT-20.3 showed specific tumor uptake and afforded high-

contrast planar and SPECT tumor images in nude mice. It may be considered as a promising candidate for imaging neurotensin receptor positive tumors, such as pancreatic adenocarcinoma and invasive ductal breast cancer. If therapeutic application of this neurotensin analogue is developed, infusion of basic amino acids, gelofusin, and albumin fragments may be considered to prevent nephrotoxicity, as with radiolabeled somatostatin analogues (*42*, *43*). Thus, an analogue carrying DOTA is being developed for therapy with ^{90}Y or ^{177}Lu. ^{68}Ga PET imaging with DOTA- and DTPA-NT20.3 will be evaluated.

ACKNOWLEDGMENT

The authors are grateful to E. Treca, S. Mendes, H Medjoudoum, A Darbois, and A. Augereau for help in affinity determination and to Pr. M. A. Pocidalo for providing human serum. This work was supported by Inserm, by the Association pour la Recherche sur le Cancer (ARC), by the Cancéropole Ile de France and by the Fund for Scientific Research Flanders (FWO). V. M. is a postdoctoral researcher of the Fund for Scientific Research-Flanders (FWO). We thank the Syrian government for awarding a research fellowship to F. A.

LITERATURE CITED

(1) Parsons, C. M., Sutcliffe, J. L., and Bold, R. J. (2008) Preoperative evaluation of pancreatic adenocarcinoma. *J. Hepatobil. Pancreat. Surg. 15*, 429–435.

(2) Reubi, J. C., Waser, B., Friess, H., Buchler, M., and Laissue, J. (1998) Neurotensin receptors: a new marker for human ductal pancreatic adenocarcinoma. *Gut 42*, 546–550.

(3) Ehlers, R. A., Kim, S., Zhang, Y., Ethridge, R. T., Murrilo, C., Hellmich, M. R., Evans, D. B., Townsend, C. M., Jr., and Mark Evers, B. (2000) Gut peptide receptor expression in human pancreatic cancers. *Ann. Surg. 231*, 838–848.

(4) Reubi, J. C., Waser, B., Schaer, J. C., and Laissue, J. A. (1999) Neurotensin receptors in human neoplasms: high incidence in Ewing's sarcomas. *Int. J. Cancer 82*, 213–218.

(5) Bossard, C., Souaze, F., Jarry, A., Bezieau, S., Mosnier, J. F., Forgez, P., and Laboisse, C. L. (2007) Over-expression of neurotensin high-affinity receptor 1 (NTS1) in relation with its ligand neurotensin (NT) and nuclear beta-catenin in inflammatory bowel disease-related oncogenesis. *Peptides 28*, 2030–2035.

(6) Pelosi, G., Volante, M., Papotti, M., Sonzogni, A., Masullo, M., and Viale, G. (2006) Peptide receptors in neuroendocrine tumors of the lung as potential tools for radionuclide diagnosis and therapy. *Q. J. Nucl. Med. Mol. Imaging 50*, 272–287.

(7) Souaze, F., Dupouy, S., Viardot-Foucault, V., Bruyneel, E., Attoub, S., Gespach, C., Gompel, A., and Forgez, P. (2006) Expression of neurotensin and NT1 receptor in human breast cancer: a potential role in tumor progression. *Cancer Res. 66*, 6243–6249.

(8) Granier, C., van Rietschoten, J., Kitabgi, P., Poustis, C., and Freychet, P. (1982) Synthesis and characterization of neurotensin analogues for structure/activity relationship studies. Acetyl-neurotensin-(8−13) is the shortest analogue with full binding and pharmacological activities. *Eur. J. Biochem. 124*, 117–124.

(9) Garcia-Garayoa, E., Allemann-Tannahill, L., Blauenstein, P., Willmann, M., Carrel-Remy, N., Tourwe, D., Iterbeke, K., Conrath, P., and Schubiger, P. A. (2001) In vitro and in vivo evaluation of new radiolabeled neurotensin(8−13) analogues with high affinity for NT1 receptors. *Nucl. Med. Biol. 28*, 75–84.

(10) Bruehlmeier, M., Garayoa, E. G., Blanc, A., Holzer, B., Gergely, S., Tourwe, D., Schubiger, P. A., and Blauenstein, P. (2002) Stabilization of neurotensin analogues: effect on peptide catabolism, biodistribution and tumor binding. *Nucl. Med. Biol. 29*, 321–327.

(11) Buchegger, F., Bonvin, F., Kosinski, M., Schaffland, A. O., Prior, J., Reubi, J. C., Blauenstein, P., Tourwe, D., Garcia Garayoa, E., and Bischof Delaloye, A. (2003) Radiolabeled neurotensin analog, 99mTc-NT-XI, evaluated in ductal pancreatic adenocarcinoma patients. *J. Nucl. Med. 44*, 1649–1654.

(12) Garcia-Garayoa, E., Blauenstein, P., Blanc, A., Maes, V., Tourwe, D., and Schubiger, P. A. (2009) A stable neurotensin-based radiopharmaceutical for targeted imaging and therapy of neurotensin receptor-positive tumours. *Eur. J. Nucl. Med. Mol. Imaging 36*, 37–47.

(13) Maes, V., Garcia-Garayoa, E., Blauenstein, P., and Tourwe, D. (2006) Novel 99mTc-labeled neurotensin analogues with optimized biodistribution properties. *J. Med. Chem. 49*, 1833–1836.

(14) Maina, T., Nikolopoulou, A., Stathopoulou, E., Galanis, A. S., Cordopatis, P., and Nock, B. A. (2007) [99mTc]Demotensin 5 and 6 in the NTS1-R-targeted imaging of tumours: synthesis and preclinical results. *Eur. J. Nucl. Med. Mol. Imaging 34*, 1804–1814.

(15) Garcia-Garayoa, E., Maes, V., Blauenstein, P., Blanc, A., Hohn, A., Tourwe, D., and Schubiger, P. A. (2006) Double-stabilized neurotensin analogues as potential radiopharmaceuticals for NTR-positive tumors. *Nucl. Med. Biol. 33*, 495–503.

(16) Moerlein, S. M., Daugherty, A., Sobel, B. E., and Welch, M. J. (1991) Metabolic imaging with gallium-68 and indium-111-labeled low-density lipoprotein. *J. Nucl. Med. 32*, 300–307.

(17) Wagner, S. J., and Welch, M. J. (1979) Gallium-68 labeling of albumin and albumin microspheres. *J. Nucl. Med. 20*, 428–433.

(18) Fani, M., Andre, J. P., and Maecke, H. R. (2008) ^{68}Ga-PET: a powerful generator-based alternative to cyclotron-based PET radiopharmaceuticals. *Contr. Med. Mol. Imaging 3*, 67–77.

(19) Liu, S. (2008) Bifunctional coupling agents for radiolabeling of biomolecules and target-specific delivery of metallic radionuclides. *Adv. Drug. Delivery Rev. 60*, 1347–1370.

(20) Achilefu, S., Srinivasan, A., Schmidt, M. A., Jimenez, H. N., Bugaj, J. E., and Erion, J. L. (2003) Novel bioactive and stable neurotensin peptide analogues capable of delivering radiopharmaceuticals and molecular beacons to tumors. *J. Med. Chem. 46*, 3403–3411.

(21) de Visser, M., Janssen, P. J., Srinivasan, A., Reubi, J. C., Waser, B., Erion, J. L., Schmidt, M. A., Krenning, E. P., and de Jong, M. (2003) Stabilised 111In-labelled DTPA- and DOTA-conjugated neurotensin analogues for imaging and therapy of exocrine pancreatic cancer. *Eur. J. Nucl. Med. Mol. Imaging 30*, 1134–1139.

(22) Hillairet De Boisferon, M., Raguin, O., Thiercelin, C., Dussaillant, M., Rostene, W., Barbet, J., Pelegrin, A., and Gruaz-Guyon, A. (2002) Improved tumor selectivity of radiolabeled peptides by receptor and antigen dual targeting in the neurotensin receptor model. *Bioconjugate Chem. 13*, 654–662.

(23) Bergmann, R., Scheunemann, M., Heichert, C., Mading, P., Wittrisch, H., Kretzschmar, M., Rodig, H., Tourwe, D., Iterbeke, K., Chavatte, K., Zips, D., Reubi, J. C., and Johannsen, B. (2002) Biodistribution and catabolism of (18)F-labeled neurotensin(8−13) analogs. *Nucl. Med. Biol. 29*, 61–72.

(24) Achilefu, S., Wilhelm, R. R., Jimenez, H. N., Schmidt, M. A., and Srinivasan, A. (2000) A new method for the synthesis of tri-tert-butyl diethylenetriaminepentaacetic acid and its derivatives. *J. Org. Chem. 65*, 1562–1565.

(25) Janevik-Ivanovska, E., Gautherot, E., Hillairet de Boisferon, M., Cohen, M., Milhaud, G., Tartar, A., Rostene, W., Barbet, J., and Gruaz-Guyon, A. (1997) Bivalent hapten-bearing peptides designed for iodine-131 pretargeted radioimmunotherapy. *Bioconjugate Chem. 8*, 526–533.

(26) Raguin, O., Fournie-Zaluski, M. C., Romieu, A., Pelegrin, A., Chatelet, F., Pelaprat, D., Barbet, J., Roques, B. P., and Gruaz-Guyon, A. (2005) A labeled neutral endopeptidase inhibitor as a potential tool for tumor diagnosis and prognosis. *Angew. Chem., Int. Ed. Engl. 44*, 4058–4061.

(27) Raguin, O., Gruaz-Guyon, A., and Barbet, J. (2002) Equilibrium expert: an add-in to Microsoft Excel for multiple binding

equilibrium simulations and parameter estimations. *Anal. Biochem. 310*, 1–14.
(28) Akizawa, H., Arano, Y., Mifune, M., Iwado, A., Saito, Y., Mukai, T., Uehara, T., Ono, M., Fujioka, Y., Ogawa, K., Kiso, Y., and Saji, H. (2001) Effect of molecular charges on renal uptake of ^{111}In-DTPA-conjugated peptides. *Nucl. Med. Biol. 28*, 761–768.
(29) Froidevaux, S., Calame-Christe, M., Tanner, H., and Eberle, A. N. (2005) Melanoma targeting with DOTA-alpha-melanocyte-stimulating hormone analogs: structural parameters affecting tumor uptake and kidney uptake. *J. Nucl. Med. 46*, 887–895.
(30) Vita, N., Laurent, P., Lefort, S., Chalon, P., Dumont, X., Kaghad, M., Gully, D., Le Fur, G., Ferrara, P., and Caput, D. (1993) Cloning and expression of a complementary DNA encoding a high affinity human neurotensin receptor. *FEBS Lett. 317*, 139–142.
(31) Kitabgi, P. (2006) Functional domains of the subtype 1 neurotensin receptor (NTS1). *Peptides 27*, 2461–2468.
(32) Melis, M., Krenning, E. P., Bernard, B. F., de Visser, M., Rolleman, E., and de Jong, M. (2007) Renal uptake and retention of radiolabeled somatostatin, bombesin, neurotensin, minigastrin and CCK analogues: species and gender differences. *Nucl. Med. Biol. 34*, 633–641.
(33) Gabriel, M., Decristoforo, C., Kendler, D., Dobrozemsky, G., Heute, D., Uprimny, C., Kovacs, P., Von Guggenberg, E., Bale, R., and Virgolini, I. J. (2007) ^{68}Ga-DOTA-Tyr3-octreotide PET in neuroendocrine tumors: comparison with somatostatin receptor scintigraphy and CT. *J. Nucl. Med. 48*, 508–518.
(34) Kowalski, J., Henze, M., Schuhmacher, J., Macke, H. R., Hofmann, M., and Haberkorn, U. (2003) Evaluation of positron emission tomography imaging using [^{68}Ga]-DOTA-D Phe(1)-Tyr(3)-Octreotide in comparison to [^{111}In]-DTPAOC SPECT. First results in patients with neuroendocrine tumors. *Mol. Imaging Biol. 5*, 42–48.
(35) de Visser, M., Verwijnen, S. M., and de Jong, M. (2008) Update: improvement strategies for peptide receptor scintigraphy and radionuclide therapy. *Cancer Biother. Radiopharm. 23*, 137–157.
(36) Kwekkeboom, D. J., de Herder, W. W., Kam, B. L., van Eijck, C. H., van Essen, M., Kooij, P. P., Feelders, R. A., van Aken, M. O., and Krenning, E. P. (2008) Treatment with the radiolabeled somatostatin analog [^{177} Lu-DOTA 0, Tyr3]octreotate: toxicity, efficacy, and survival. *J. Clin. Oncol. 26*, 2124–2130.
(37) Krenning, E. P., Teunissen, J. J., Valkema, R., deHerder, W. W., deJong, M., and Kwekkeboom, D. J. (2005) Molecular radiotherapy with somatostatin analogs for neuro-endocrine tumors. *J. Endocrinol. Invest. 28*, 146–150.
(38) Maecke, H. R., Hofmann, M., and Haberkorn, U. (2005) (68)Ga-labeled peptides in tumor imaging. *J. Nucl. Med. 46* (Suppl 1), 172S–178S.
(39) Schubiger, P. A., Allemann-Tannahill, L., Egli, A., Schibli, R., Alberto, R., Carrel-Remy, N., Willmann, M., Blauenstein, P., and Tourwe, D. (1999) Catabolism of neurotensins. Implications for the design of radiolabeling strategies of peptides. *Q. J. Nucl. Med. 43*, 155–158.
(40) Mier, W., Zitzmann, S., Kramer, S., Reed, J., Knapp, E. M., Altmann, A., Eisenhut, M., and Haberkorn, U. (2007) Influence of chelate conjugation on a newly identified tumor-targeting peptide. *J. Nucl. Med. 48*, 1545–1552.
(41) Garcia Garayoa, E., Ruegg, D., Blauenstein, P., Zwimpfer, M., Khan, I. U., Maes, V., Blanc, A., Beck-Sickinger, A. G., Tourwe, D. A., and Schubiger, P. A. (2007) Chemical and biological characterization of new Re(CO)/[^{99}mTc](CO)$_3$ bombesin analogues. *Nucl. Med. Biol. 34*, 17–28.
(42) de Jong, M., Rolleman, E. J., Bernard, B. F., Visser, T. J., Bakker, W. H., Breeman, W. A., and Krenning, E. P. (1996) Inhibition of renal uptake of indium-111-DTPA-octreotide in vivo. *J. Nucl. Med. 37*, 1388–1392.
(43) Vegt, E., van Eerd, J. E., Eek, A., Oyen, W. J., Wetzels, J. F., de Jong, M., Russel, F. G., Masereeuw, R., Gotthardt, M., and Boerman, O. C. (2008) Reducing renal uptake of radiolabeled peptides using albumin fragments. *J. Nucl. Med. 49*, 1506–1511.

BC900151Z

Functionalized Cyclic RGD Peptidomimetics: Conjugable ligands for $\alpha_v\beta_3$ Receptor Imaging

Daniela Arosio,*,† Leonardo Manzoni,*,† Elena M. V. Araldi,# Andrea Caprini,§ Eugenia Monferini,§ and Carlo Scolastico‡

CNR-Istituto di Scienze e Tecnologie Molecolari (ISTM), Via Fantoli 16/15, I-20138, Milan, Italy, Università di Milano, Dipartimento di Chimica Organica e Industriale, Via Venezian 21 and Centro Interdipartimentale Studi Biomolecolari e Applicazioni Industriali (CISI), Via Fantoli 16/15, I-20138, Milano, Italy, and CISI scrl, Via Fantoli 16/15, I-20138, Milano, Italy. Received April 8, 2009; Revised Manuscript Received May 29, 2009

The $\alpha_v\beta_3$ integrin is an adhesion molecule involved in physiological and pathological angiogenesis as well as in tumor invasion and metastasis, and therefore, there is a strong interest in developing novel agents interacting with this molecule. We report the synthesis and characterization of fluorescent $\alpha_v\beta_3$ integrin probes and their use to visualize integrin $\alpha_v\beta_3$ expression on human normal and cancer cells. The fluorescent probes we describe here may be of use for noninvasive imaging of $\alpha_V\beta_3$ integrin expression also *in vivo*.

INTRODUCTION

Integrins are heterodimeric transmembrane proteins expressed at the cell surface and involved in cellular adhesion to the extracellular matrix (*1*). A deregulated expression and/or function of integrins contributes to the progression of lethal pathologies including cancer (*2*, *3*). Among the integrin superfamily, the $\alpha_v\beta_3$ integrin has been the focus of considerable attention because of its expression in a restricted number of normal and malignant cell types such as platelets (*4*), osteoclasts (*5*), melanoma (*6*), glioblastoma (*7*), and osteosarcoma cells (*8*), and its elevated expression on activated endothelial cells during physiological and pathological angiogenesis (*9*). The $\alpha_v\beta_3$ integrin interacts with specific proteins of the extracellular matrix such as fibronectin, vitronectin, von Willebrand factor, and fibrinogen through the tripeptide Arg-Gly-Asp (RGD) sequence (*10*, *11*). Therefore, RGD-containing peptides targeting the $\alpha_v\beta_3$ integrin are attractive for studying and managing diseases related to its overexpression. Many research groups have in fact focused on developing RGD peptides and analogous compounds for biomedical studies (*12*−*16*).

Linear peptide sequences containing the RGD motif are known to bind integrins, and these have been used as cell-targeting agents (*17*). Due to the low affinity and promiscuity of such linear peptides, however, their utility for selective cell targeting is limited. Peptide derivatives, such as cyclo(RGDfV) or Cilengitide have been used as tumor-homing agents due to their selectivity for $\alpha_v\beta_3$ integrin (*18*, *19*).

Our group previously reported a library of cyclic RGD pentapeptide mimics based on 1-aza-2-oxobicyclo[*X.3.0*]alkane amino acids as dipeptide analogues (*20*, *21*). The replacement of the D-Phe-Val dipeptide in the lead structure cyclo(RGDfV) with such azabicycloalkane scaffolds showing different reverse-turn mimetic properties constrains the RGD sequence into different conformations and provides the required activity and selectivity for integrin antagonism. This library was found to contain specific high-affinity ligands for $\alpha_v\beta_3$ integrin, which are currently under evaluation as very promising antiangiogenic drugs. One of the peptides tested, **ST1646**, displayed the highest affinity to $\alpha_v\beta_3$, inhibiting echistatin binding to $\alpha_v\beta_3$ with an IC_{50} of 3.7 ± 0.6 nM (Figure 1).

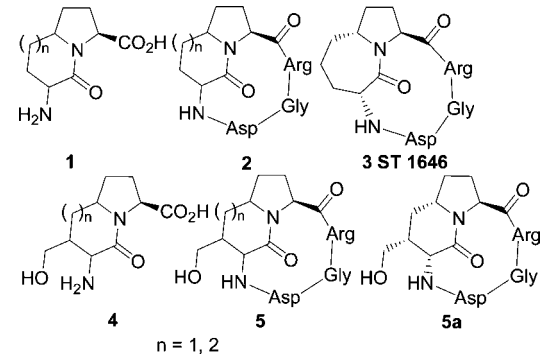

Figure 1. Integrin inhibitors and scaffolds for their preparation.

The functionalization of such azabicycloalkane scaffolds with heteroalkyl substituents enabled us to conjugate different diagnostic or therapeutic entities. Our group has recently reported an efficient and simple synthesis of functionalized azabicycloalkane amino acids mimicking a homoSer-Pro dipeptide (*22*) and their use in the preparation of cyclic RGD compounds (**5**, Figure 1) (*23*). These mimics present a heteroalkyl side chain ending with a hydroxy group that can easily be converted into other suitable functional groups (i.e., azide, amine, etc.) or directly used for conjugations (*23*, *24*). Such molecules are then attractive tools for the homing of drugs and biological tracers in cells highly expressing $\alpha_v\beta_3$ integrin. To this end, we explored the possibility to use these compounds as "markers" of the $\alpha_v\beta_3$ integrin expression in human cells. We selected the green fluorescent dye Fluorescein as a probe, because it is approved for human use in diagnostic techniques such as retinal angiography (*25*). Fluorescein is therefore advantageous because of its known safety profile in humans. Furthermore, the use of a RGD peptide−fluorescein conjugate in a fluorescent polarization assay has recently been reported (*26*), a technique that is often applied for high-throughput

* Corresponding authors. Tel.: +39 02 50320906, Fax: +39 02 50320945, E-mail: leonardo.manzoni@istm.cnr.it, Tel.: +39 02 50320907, Fax: +39 02 50320945, E-mail: daniela.arosio@istm.cnr.it.

† CNR-ISTM.

‡ CISI scrl.

§ University of Milano and CISI.

University of Milano and CISI, Doctorate School of Molecular Medicine.

10.1021/bc900155j CCC: $40.75 © 2009 American Chemical Society
Published on Web 07/22/2009

screening in the drug discovery process. During the preparation of this paper, the work of the Li group has been published on a photostable fluorescent probe for imaging of tumor cells possessing integrin $\alpha_v\beta_3$ (*27*).

We report here the conjugation of cyclic RGD compounds containing the conformationally constrained homoSer-Pro dipeptide unit with the fluorescein probe, the study of their binding properties, and the biological effects of these compounds on human cell cultures. We demonstrate that such fluorescent compounds could be useful for $\alpha_v\beta_3$ integrin imaging, thus suggesting their possible use in diagnostic techniques.

MATERIALS AND METHODS

General. All chemicals and solvents were of reagent grade and were used without further purification. Solvents were dried by standard procedures and reactions requiring anhydrous conditions were performed under nitrogen or argon atmosphere. ^{1}H and ^{13}C NMR spectra were recorded at 300 K on a Bruker AVANCE-400 and 600 MHz. Chemical shifts δ are expressed in ppm relative to internal Me_4Si as standard. Mass spectra were obtained with an ESI apparatus Bruker Esquire 3000 plus. Column chromatography was carried out with the Biotage SP1 or SP4 systems using the Biotage cartridges.

*Compound **11***. A solution of c-RGD-N_3 **7** (498 mg, 0.56 mmol) in MeOH (25 mL) containing a catalytic amount of Pd/C 10% was stirred overnight under hydrogen atmosphere. After reaction completion (monitored by TLC: CH_2Cl_2/MeOH 9:1), the mixture was filtered through a pad of Celite and washed with MeOH. The collected organic phase was evaporated under reduced pressure. The crude was dissolved in dry DMF (5 mL) and mixed, under N_2 atmosphere and at room temperature, with a solution of spacer **10** (253 mg, 0.742 mmol), HATU (282 mg, 0.742 mmol), HOAt (94 mg, 0.689 mmol), and DIPEA (0.37 mL, 2.12 mmol) in dry DMF (5 mL). The reaction mixture was stirred overnight, and after reaction completion, the solvent was evaporated under reduced pressure. The pure product was obtained after reverse-phase column chromatography on a Biotage C_{18} 25+M cartridge eluting with water/acetonitrile (95:5 → 10:90). Yield: 85% (white solid). ^{1}H NMR (400 MHz, acetone-d_6): δ 1.31 (s, 6H, $C(CH_3)_2$ Pmc), 1.36 (m, 1H, *H*-5), 1.43 (s, 9H, $C(CH_3)_3$), 1.43−1.55 (m, 2H, *Hγ* Arg, *Hβ* Arg), 1.55−1.61 (m, 2H, *Hγ* Arg, *H*-7), 1.84 (t, 2H, J = 6.8 Hz, CH_2CH_2Ar Pmc), 1.99 (m, 1H, *H*-8), 2.07−2.25 (m, 4H, CH_3 Pmc, *Hβ* Arg), 2.33−2.48 (m, 3H, *H*-5, *H*-7, *H*-8), 2.52−2.64 (m, 7H, *Hβ* Asp, 2 CH_3 Pmc), 2.67 (t, 2H, J = 6.6 Hz, CH_2CH_2Ar Pmc), 2.80 (m, 1H, *H*-4), 3.03 (dd, 1H, J = 16.8 Hz, J = 6.8 Hz, *Hβ* Asp), 3.12−3.29 (m, 4H, 2 *Hδ* Arg, $NHCH_2$), 3.29−3.40 (m, 2H, NCH_2CH_2O), 3.45 (d, 1H, J = 13.6 Hz, *Hα* Gly), 3.57 (m, 2H, NCH_2CH_2O), 3.60−3.80 (m, 8H, 4 OCH_2), 3.90 (s, 2H, OCH_2CO), 4.16 (m, 1H, *H*-6), 4.19−4.36 (m, 3H, *Hα* Gly, *H*-9, *H*-3), 4.50−4.62 (m, 2H, *Hα* Arg, *Hα* Asp), 5.09 (s, 2H, CH_2Ph), 6.20−6.75 (m, 4H, $(NH)_2C{=}NH$, *NH*Cbz), 7.23 (m, 1H, $NHCH_2$), 7.28−7.45 (m, 6H, 5 *Aromatic protons*, N*H* bicycle.), 7.51 (m, 1H, N*H* Arg), 7.60 (m, 1H, N*H* Gly), 8.40 (m, 1H, N*H* Asp). ^{13}C NMR (100.6 MHz, acetone-d_6): δ 173.2, 171.5, 171.2, 170.3, 170.2, 170.0, 169.8, 156.4, 152.9, 137.6, 135.6, 135.0, 134.6, 128.3, 127.8, 127.7, 123.1, 117.8, 80.0, 73.4, 70.8, 70.2, 70.1, 70.0, 69.6, 65.6, 62.5, 55.7, 53.5, 51.3, 42.7, 40.7, 40.5, 39.8, 36.3, 35.0, 33.3, 32.6, 30.1, 28.2, 27.4, 26.1, 25.9, 21.1, 17.9, 16.8, 11.4. MS (ESI^+) m/z: 1183.7 $(M+H)^+$.

*Compound **12***. A solution of compound **11** (260 mg, 0.22 mmol) in MeOH (13 mL) containing a catalytic amount of Pd/C 10% was stirred for 3 h under hydrogen atmosphere. After reaction completion (monitored by TLC: CH_2Cl_2/MeOH 9:1), the mixture was filtered through a pad of Celite and washed with MeOH. The collected organic phase was evaporated under reduced pressure and submitted to the following deprotection step without any further purification.

A solution of protected compound (0.040 mmol) in TFA/thioanisole/1,2-ethanedithiol/anisole 90:5:3:2 (2 mL) was stirred at room temperature for 2 h. The solvent was evaporated under reduced pressure, and then the crude was dissolved in H_2O and washed with iPr$_2$O. The aqueous phase was evaporated under reduced pressure and the crude purified by HPLC (Atlantis C_{18} OBD 5 μm 19 mm × 10 cm, flow 20 mL/min, gradient 100% A for 1 min, from 100% A to 85% A over 8 min, from 85% A to 0% A over 8 min. A H_2O + 0.1% TFA, B CH_3CN + 0.1% TFA). Yield: 70%. White foam. ^{1}H NMR (400 MHz, D_2O): δ 1.23 (m, 1H, *H*-5), 1.44−1.70 (m, 4H, 2 *Hγ* Arg, *Hβ* Arg, *H*-7), 1.85 (m, 1H, *H*-8), 2.04 (m, 1H, *Hβ* Arg), 2.36−2.50 (m, 3H, *H*-8, *H*-7, *H*-5), 2.71 (dd, 1H, J = 7.1 Hz, J = 17.0 Hz, *Hβ* Asp), 2.39 (m, 1H, *H*-4), 3.07 (dd, 1H, J = 7.5 Hz, J = 17.0 Hz, *Hβ* Asp), 3.10−3.24 (m, 6H, 2 *Hδ* Arg, $NH_2CH_2CH_2O$, CH_2NH), 3.48 (d, 1H, J = 14.6 Hz, *Hα* Gly), 3.63−3.75 (m, 10H, 4 CH_2O, $NH_2CH_2CH_2O$), 3.90−4.06 (m, 3H, *H*-6, OCH_2CO), 4.20−4.30 (m, 2H, *H*-9, *Hα* Gly), 4.38 (m, 1H, *H*-3), 4.48−4.60 (m. 2H, *Hα* Asp, *Hα* Arg). ^{13}C NMR (100.6 MHz, D_2O): 174.8, 174.5, 174.1, 173.1, 172.6, 171.6, 170.1, 156.8, 70.3, 69.7, 69.6, 69.5, 69.4, 66.4, 62.2, 56.0, 53.1, 51.7, 51.4, 42.6, 40.5, 40.2, 39.2, 35.7, 33.3, 32.9, 32.6, 27.1, 24.5. MS (ESI^+) m/z: 727.1 $(M+H)^+$, 364.0 $(M+2H)^{2+}$.

*Compound **8***. A solution of protected compound **7** (324 mg, 0.365 mmol) in TFA/thioanisole/1,2-ethanedithiol/anisole 90:5:3:2 (15 mL) was stirred at room temperature for 2 h. The solvent was evaporated under reduced pressure, and then the crude was dissolved in H_2O and washed with iPr$_2$O. The aqueous phase was evaporated under reduced pressure. The crude was purified by HPLC (Atlantis C_{18} OBD 5 μm 19 mm × 10 cm, flow 20 mL/min, gradient from 5% A to 15% A over 10 min, A CH_3CN + 0.1% HCOOH, B H_2O + 0.1% HCOOH). Yield: 97%. White foam. ^{1}H NMR (400 MHz, D_2O): δ 1.32 (m, 1H, *H*-5), 1.43−1.61 (m, 3H, 2 *Hγ* Arg, *Hβ* Arg), 1.66 (m, 1H, *H*-7), 1.83 (m, 1H, *H*-8), 2.03 (m, 1H, *Hβ* Arg), 2.34−2.47 (m, 3H, *H*-8, *H*-7, *H*-5), 2.69 (dd, 1H, J = 7.1 Hz, J = 16.9 Hz, *Hβ* Asp), 2.78 (m, 1H, *H*-4), 3.05 (dd, 1H, J = 7.5 Hz, J = 16.9 Hz, *Hβ* Asp), 3.09−3.20 (m, 2H, 2 *Hδ* Arg), 3.32−3.42 (m, 2H, CH_2N_3), 3.47 (d, 1H, J = 14.7 Hz, *Hα* Gly), 3.96 (m, 1H, *H*-6), 4.20−4.32 (m, 3H, *Hα* Gly, *H*-9, *H*-3), 4.48−4.58 (m. 2H, *Hα* Asp, *Hα* Arg). ^{13}C NMR (100.6 MHz, D_2O): 175.0, 174.8, 174.1, 173.0, 171.6, 170.6, 156.7, 62.2, 56.0, 52.8, 52.0, 51.6, 51.3, 42.4, 40.4, 35.5, 33.2, 32.7, 30.1, 27.0, 24.4. MS (ESI^+) m/z: 564.1 $(M+H)^+$.

*Compound **13***. FITC (3.0 mg, 0.0075 mmol) dissolved in DMSO (0.4 mL) was mixed with compound **12** (6.0 mg, 0.0063 mmol) dissolved in sodium borate buffer pH = 9 (0.4 mL) in the dark and at room temperature. After stirring for ca. 18 h, the reaction was complete. The solvent was removed and the crude was purified by HPLC (Ascentis RPAMIDE 150 × 21.1 mm column, guard cartridge, RPAMIDE 20 × 4 mm; 12 mL/min flow; gradient 100% A for 2 min, from 100% A to 70% A over 3 min, from 70% A to 50% A over 20 min, from 50% A to 20% A over 5 min, then from 20% A to 0% A over 2 min A, H_2O + 0.2% TFA; B, CH_3CN + 0.2% TFA). Yield: 70%. Yellow foam. ^{1}H NMR (600 MHz, D_2O): δ 1.00 (m, 1H, *H*-5), 1.24−1.50 (m, 4H, 2 *Hγ* Arg, *Hβ* Arg, *H*-7), 1.65 (m, 1H, *H*-8), 1.87 (m, 1H, *Hβ* Arg), 2.13−2.28 (m, 3H, *H*-8, *H*-7, *H*-5), 2.48−2.62 (m, 2H, *Hβ* Asp, *H*-4), 2.77−2.91 (m, 3H, *Hβ* Asp, CH_2NH), 2.91−3.02 (m, 2H, 2 *Hδ* Arg), 3.25 (d, 1H, J = 15.6 Hz, *Hα* Gly), 3.42−3.69 (m, 12H, 5 CH_2O, $NH_2CH_2CH_2O$), 3.69−3.83 (m, 3H, OCH_2CO, *H*-6), 4.03−4.11 (m, 2H, *H*-9, *Hα* Gly), 4.18 (d, 1H, J = 8.4 Hz, *H*-3), 4.28 (m, 1H, *Hα* Asp), 4.36 (m. 1H, *Hα* Arg), 6.63. (m, 2H, *fluorescein protons*), 6.77 (m, 2H, *fluorescein protons*), 8.87−7.16 (m, 3H, *fluorescein*

protons), 7.56 (m, 1H, *fluorescein proton*), 7.95 (m, 1H, *fluorescein proton*). ^{13}C NMR HETCOR (600 MHz, D_2O): 130.7, 129.9, 122.8, 116.2, 102.5, 70.2, 69.4, 69.1, 61.8, 55.7, 52.7, 51.4, 51.3, 44.0, 42.1, 40.2, 39.9, 35.5, 33.0, 32.5, 29.8, 26.8, 24.3. MS (ESI^+) *m/z*: 1116.4 $(M+H)^+$, 558.8 $(M+2H)^{2+}$.

General Procedure for Click Reaction. To a solution of compound **8** (0.02 mmol) and the opportune alkynyl derivative (**14** or 1-hexyne) (0.02 mmol) in H_2O/*t*-BuOH 1:1 (500 μL.), a 0.9 M solution of sodium ascorbate (9 μL, 0.008 mmol, 0.4 mol equiv) and a 0.3 M solution of $Cu(OAc)_2$ (13 μL, 0.004 mmol, 0.2 mol eq) were added. The reaction was stirred at r.t. for ca. 18 h.

After reaction completion, compounds **15** or **16** were purified by HPLC (Waters X-Terra PR 18 19 × 50 mm, 5 μm column; 3.5 mL/min flow; gradient from 20% B to 35% B over 11 min, then washed 60% B for 1 min; A, 97% H_2O/3% CH_3CN + 0.1% TFA; B, CH_3CN + 0.1% TFA).

*Compound **15**.* Yield: 60%. White foam. ^{1}H NMR (600 MHz, D_2O): δ 1.10 (m, 1H, *H*-5), 1.41 (m, 2H, *H*γ Arg), 1.44 (m, 1H, *H*-7), 1.46 (m, 1H *H*β Arg), 1.49 (m, 2H, CH_2 spacer), 1.58 (m, 2H, CH_2 spacer), 1.69 (m, 2H, CH_2 spacer), 1.72 (m, 1H, *H*-8), 1.85 (m, 2H, CH_2 spacer), 1.95 (m, 1H, *H*β Arg), 2.19 (m, 1H, *H*-5), 2.23 (m, 1H, *H*-7), 2.31 (m, 1H, *H*-8), 2.56 (m, 1H, *H*β Asp), 2.91 (m, 1H, *H*β Asp), 3.03 (m, 1H, *H*δ Arg), 3.07 (m, 1H, *H*-4), 3.09 (m, 1H, *H*δ Arg), 3.24−3.55 (m, 8H, OCH_2 spacer), 3.29 (m, 1H, NHC*H* spacer), 3.36 (m, 1H, *H*α Gly), 3.44 (m, 1H, NHC*H* spacer), 3.84 (m, 1H, *H*6), 3.91 (m, 1H, COCH_2O), 3.99 (m, 1H, COCH_2O), 3.95 (m, 1H, HC*H*N), 4.07 (m, 1H, *H*-9), 4.11 (m, 1H, NHC*H* spacer), 4.15 (m, 1H, *H*α Gly), 4.28 (m, 1H, *H*-3), 4.30 (m, 1H, *H*α Asp), 4.32 (m, 2H, NCH_2=), 4.46 (m, 1H, *H*α Arg). ^{13}C NMR HETCOR (400 MHz, DMSO-d_6): 69.7, 68.9, 62.0, 55.5, 52.6, 51.1, 42.2, 40.1, 37.9, 35.9, 33.8, 33.3, 32.5, 32.2, 29.9, 28.0, 27.0, 24.3. δ MS (ESI^+) *m/z*: 1295.6 $(M+H)^+$, 648.3 $(M+2H)^{2+}$.

*Compound **16**.* Yield: 80%. White foam. ^{1}H NMR (400 MHz, D_2O): δ 0.82 (m, 3H, C$H_3CH_2CH_2CH_2C$=), 1.17−1.33 (m, 3H, *H*-5, $CH_3CH_2CH_2CH_2C$=), 1.41−1.66 (m, 6H, 2 *H*γ Arg, *H*β Arg, $CH_3CH_2CH_2CH_2C$=, *H*-7), 1.82 (m, 1H, *H*-8), 2.00 (m, 1H, *H*β Arg), 2.32−2.46 (m, 3H, *H*-8, *H*-7, *H*-5), 2.60−2.71 (m, 3H, *H*β Asp, $CH_3CH_2CH_2CH_2C$=), 2.99 (m, 1H, *H*β Asp), 3.06−3.19 (m, 2H, 2 *H*δ Arg), 3.25 (m, 1H, *H*-4), 3.46 (m, 1H, *H*α Gly), 3.99 (m, 1H, *H*-6), 4.10−4.30 (m, 3H, *H*-9, HC*H*N, *H*α Gly), 4.31−4.43 (m, 3H, *H*α Asp, HC*H*N, *H*-3), 4.54 (m. 1H, *H*α Arg), 7.80 (s, 1H, *H* triazole). ^{13}C NMR (100.6 MHz, D_2O): 174.6, 174.0, 173.0, 171.6, 170.8, 156.7, 148.1, 124.4, 62.2, 55.8, 52.9, 51.8, 51.6, 51.2, 42.4, 40.4, 36.1, 33.2, 32.7, 32.2, 30.6, 30.0, 27.0, 24.4, 23.7, 21.4, 13.0. MS (ESI^+) *m/z*: 646.2 $(M+H)^+$.

Solid-Phase Receptor-Binding Assay. Purified $\alpha_v\beta_3$ and $\alpha_v\beta_5$ receptors (Chemicon International, Inc., Temecula, CA) were diluted to 0.5 μg/mL in coating buffer containing 20 mmol/L Tris-HCl (pH 7.4), 150 mmol/L NaCl, 1 mmol/L $MnCl_2$, 2 mmol/L $CaCl_2$, and 1 mmol/L $MgCl_2$. An aliquot of diluted receptors (100 μL/well) was added to 96-well microtiter plates (NUNC MW 96F MEDISORP STRAIGHT) and incubated overnight at 4 °C. The plates were then incubated with blocking solution (coating buffer plus 1% bovine serum albumin (Sigma) for additional 2 h at room temperature to block nonspecific binding followed by 3 h incubation at room temperature with various concentrations (10^{-10}−10^{-5} M) of test compounds in the presence of 1 μg/mL Vitronectin biotinylated using EZ-Link Sulfo-NHS-Biotinylation kit (Pierce, Rockford, IL). After washing, the plates were incubated for 1 h at room temperature with streptavidin−biotinylated peroxidase complex (Amersham Biosciences, Uppsala, Sweden) followed by 30 min incubation with 100 μL Substrate Reagent Solution (R&D Systems, Minneapolis, MN) before stopping the reaction by addition of 50 μL of 1 N H_2SO_4. Absorbance at 415 nm was read in a Synergy HT Multi-Detection Microplate Reader (BioTek Instruments, Inc.). Each data point is the result of the average of triplicate wells and was analyzed by nonlinear regression analysis with the *Prism GraphPad* program.

Reagents for Cellular Experiments. All reagents were purchased from Sigma-Aldrich (unless otherwise indicated). For all our tests, phosphate buffer saline supplemented with calcium and magnesium (Euroclone) was used.

Cell Lines and Culture. Human umbilical vein vascular endothelial cells (HUVECs) were obtained from Promocell GmbH (cat. no C-12200; Heidelberg, Germany) and were routinely cultured on tissue flasks (BD Biosciences, Franklin Lakes, NJ, USA) coated with 0.1% gelatin (Gibco) in medium M199 supplemented with 20% fetal calf serum (FCS), 2 mM L-glutamine, penicillin (100 U/mL), streptomycin (100 μg/mL), 100 μg/mL porcine heparin, and 10 ng/mL endothelial cells growth factor (ECGF). HUVEC cells were used until 5−6 passages. ECV-304 human bladder carcinoma cells were kindly provided by Prof. M. L. Villa (University of Milan, Italy). ECV-304 cells were grown on tissue flasks in medium M199 supplemented with 10% FCS, 2 mM L-glutamine, penicillin (100 U/mL), and streptomycin (100 μg/mL). MDA-MB-231 human breast adenocarcinoma cells, T98G human glioblastoma multiforme cells, and PC3 human prostate cancer cells were purchased from Istituto Zooprofilattico Sperimentale della Lombardia e dell'Emilia (cat. nos BS TCL 223, BS TCL 175, and BS TCL 197, respectively; Brescia, Italy) and were grown on tissue flasks in medium RPMI supplemented with 10% FCS, 2 mM L-glutamine, penicillin (100 U/mL), and streptomycin (100 μg/mL). Caki-1 human renal clear cell carcinoma cells were purchased from the American type Culture Collection (ATCC) (cat. no HTB-46) and were grown on tissue flasks in medium RPMI supplemented with 10% FCS, 2 mM L-glutamine, penicillin (100 U/mL), and streptomycin (100 μg/mL). All cell lines were maintained at 37 °C in an atmosphere of 95% air and 5% CO_2.

Immunofluorescence on Adherent Cells. For $\alpha_v\beta_3$ staining, cells were washed in PBS and fixed in 4% paraformaldehyde (Fluka) for 10 min at room temperature. Cells were then washed and permeabilized with 0.1% Triton-X100 (Fluka) for 3 min at 4 °C. Blocking was performed in PBS with 5% bovine serum albumin (BSA) for 1 h at room temperature. We incubated cells with anti-$\alpha_V\beta_3$ antibody (clone LM609, Chemicon, Temecula, California) diluted in PBS + 5% BSA at a final concentration of 10 μg/mL, overnight at 4 °C. Cells were then extensively washed in PBS + 5% BSA and incubated with 3.75 μg/mL donkey-antimouse cy3-conjugated secondary antibody (Jackson Immunoresearch Laboratories Inc., UK) diluted in PBS + 5% BSA, for 1 h at RT in the dark. Nuclei were counterstained for 5 min at room temperature with 0.25 μg/mL 4′,6-diamidino-2-phenylindole (DAPI) diluted in PBS. Cells were finally mounted with Vectashield mounting medium and visualized with Zeiss Axio Observer A1 microscope (Carl Zeiss Inc., Chester, VA, USA). All fuorescence microscopy scans were acquired with Zeiss AxioCam MRm (Carl Zeiss Inc., Chester, VA, USA).

Treatment of Cells with Compounds and Analysis. Cells (1.6×10^4/cm^2) were seeded and allowed to adhere overnight in complete medium on glass slides. Cells were treated 4 h at 37 °C with selected compounds diluted in fresh medium supplemented with 0.1% FCS. After incubation, cells were extensively washed in PBS and fixed in 4% paraformaldehyde for 10 min at room temperature. Nuclei were then counterstained with 0.25 μg/mL DAPI diluted in PBS for 5 min at room

Scheme 1. Synthesis of the RGD Derivatives 8 and 12[a]

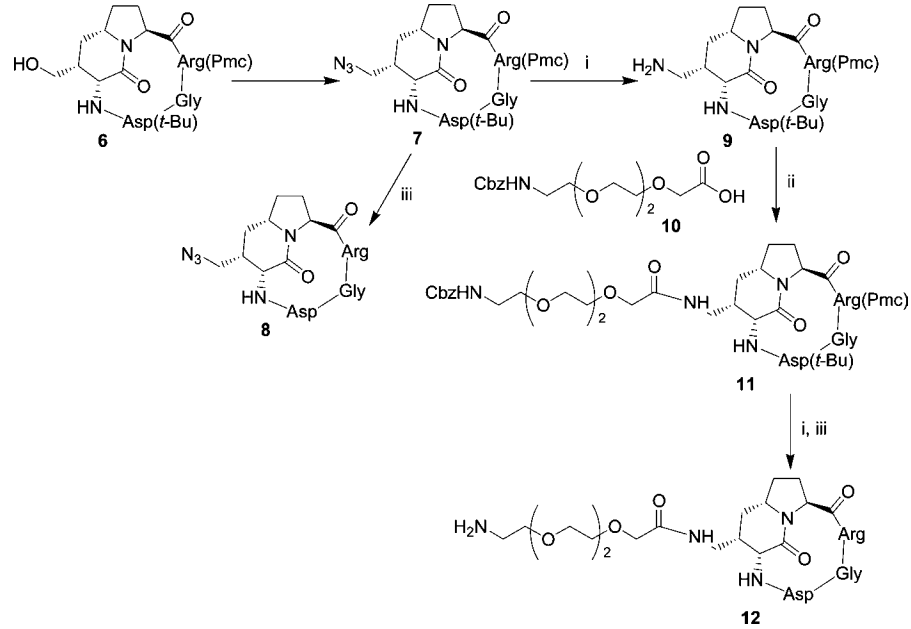

[a] Reagents: i. H_2, Pd/C, MeOH; ii. HATU, HOAt, DIPEA, DMF, 85% over two steps; iii. TFA, thioanisole, 1,2-ethanedithiol, anisole, 90:5:3:2, (**8**) 97%, (**12**) 70% over two steps.

Scheme 2. FITC Conjugation

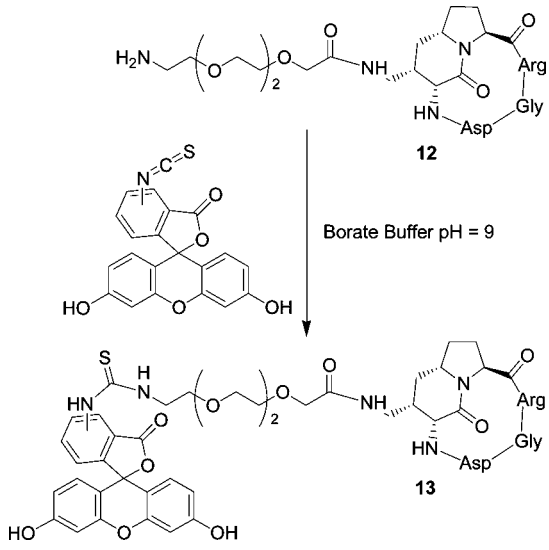

temperature. Cells were finally mounted and visualized as previously described. Experiments were repeated in triplicate.

RESULTS

Chemistry. Among a small collection of functionalized cyclic RGD (**5**, Figure 1) (*23*), we chose compound **5a** (Scheme 1) that showed the highest affinity for $\alpha_v\beta_3$ integrin in an *in vitro* binding assay (IC_{50} of 53.7 ± 17.3 nM) as a good candidate for fluorescein conjugation.

The fluorescent dye can be directly conjugated to the suitably fuctionalized RGD derivative, but, in order to avoid a decrease in the affinity due to steric hindrance, a spacer was introduced.

We decided to use two different synthetic strategies for conjugation. The first one involves the functionalization of the RGD cyclopeptide with a short poly(ethylene glycol) spacer armed with a terminal amine that can be reacted with fluoresceine isothiocyanate (FITC). The second approach involves the preparation of a fluorescein spacer derivative that can be directly reacted with an azide bearing RGD peptide through the copper-catalyzed click reaction (*28*, *29*).

The hydroxyl group of the pseudopentapeptide **6** was easily transformed into the azide using a reported procedure (*23*). The standard hydrogenation procedure was used to reduce the azide into amine **9**. After the coupling with spacer **10**, carried out using standard coupling procedure (HATU, HOAt, DIPEA), the Cbz was removed by hydrogenation, while the side-chain protecting groups (Pmc and *t*Bu) were cleaved by TFA in the presence of ion scavengers. Compounds **8** and **12** were obtained, after HPLC purification, in good yields.

Fluoresceine 5(6)-isothiocyanate (FITC) was used for direct conjugation to the amine derivative **12**. The reaction was performed dissolving compound **12** in sodium borate buffer (pH = 9) and adding FITC dissolved in DMSO. The obtained compound **13** was purified by HPLC.

The fluorescein-spacer derivative **14** was prepared by adding commercially available 5(6)-carboxyfluorescein-*N*-hydroxysuccinimide ester to a basic solution of the spacer (*24*). The 1,3-dipolar cycloaddition between compounds **8** and **14** was performed using $Cu(OAc)_2$ and Na ascorbate as catalysts in *t*-BuOH/H_2O 1:1 (Scheme 3). The reaction proceeded overnight at room temperature, and the desired product **15** was isolated after HPLC purification in good yield.

Compound **16** was synthesized in an analogous way to that reported above in order to evaluate the influence of the triazole moiety on the biological activity.

Receptor Binding Assay. The derivatives **13**, **15**, and **16** were examined *in vitro* for their abilities to inhibit the binding of biotinylated vitronectin to the isolated, immobilized $\alpha_v\beta_3$ integrin (Table 1). Affinities of commercially available compound c(RGDfV) and our compound ST1646 were determined as references, in the same assays. The functionalized cyclic pentapeptide **5a** displayed a lower binding affinity toward $\alpha_v\beta_3$ integrin when compared to the low nanomolar reference ligand ST1646. Nevertheless, the affinities in the nanomolar range toward $\alpha_v\beta_3$ integrin suggested that the functionalization of the scaffold does not influence the binding activity and it could be a suitable platform for targeted imaging. In order to evaluate the influence of a triazole moiety near the RGD sequence, we have

Scheme 3. Synthetic Pathway for Conjugate RGD Derivative with Click Reaction

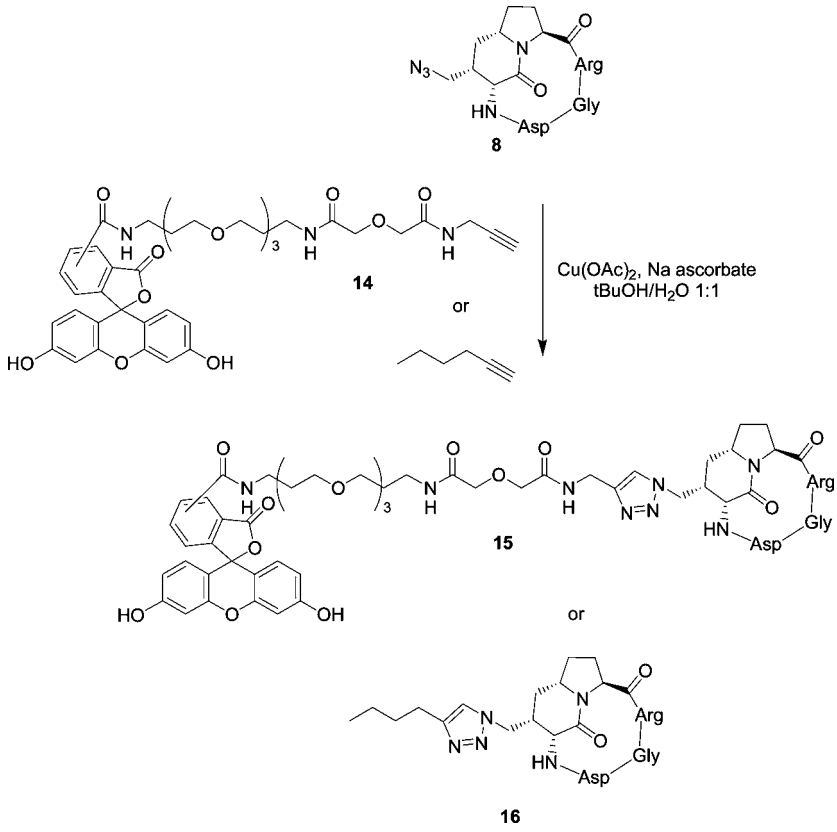

Table 1. Compound-Mediated Inhibition of Vitronectin Binding to $\alpha_v\beta_3$ Integrin[a]

entry	compound	IC_{50} (nM) ± SD for $\alpha_v\beta_3$
1	Vitronectin	47.1 ± 10.0
2	c(RGDfV)	3.2 ± 1.3
3	ST1646	1.0 ± 0.5
4	**5a**	53.7 ± 17.3
5	**13**	142 ± 6
6	**15**	207 ± 85
7	**16**	465 ± 297

[a] IC_{50} values were calculated as the concentration of compound required for 50% inhibition of biotinylated vitronectin binding as estimated by *Prism GraphPad* program. All values are the mean (±standard deviation) of triplicate determinations.

synthesized compound **16**, which showed a slightly lower affinity to $\alpha_v\beta_3$ compared with the compound **5a**, probably due the increased steric hindrance of the triazole. However, the affinity in the nanomolar range toward integrin receptors suggested that the "click reaction" could be a suitable method for the conjugation of molecules of biological interest. Compound **13** compared with **15** showed a slightly better binding affinity for the receptor; this could be due to the presence of a less hindered amide bond instead of triazole and also to a different length of the spacer between the RGD sequence and the fluoresceine moiety.

Fluorescein Detection in Human Cell Lines. The above results demonstrate that compounds **13** and **15** have a high affinity for the $\alpha_v\beta_3$ integrin; this prompted us to test their possible use as tracers of cells highly expressing $\alpha_V\beta_3$ integrin.

For this purpose, we tested each compound on cells highly expressing $\alpha_v\beta_3$ integrin, namely, human umbilical vein endothelial cells (HUVECs), and on a panel of cell lines deriving from solid tumors in which $\alpha_v\beta_3$ overexpression is reported (ECV304 bladder cancer cells, T98G glioblastoma multiforme cells, PC3 prostate cancer cells, Caki-1 renal clear cell carcinoma cells). We included also a cell line derived from human breast adenocarcinoma (MDA-MB-231 cells) as a control, because this cell line is known to express very low amounts of $\alpha_v\beta_3$ integrin (*31*). We first verified and confirmed by immunofluorescence that HUVECs and all tumor-derived cells highly expressed $\alpha_v\beta_3$ integrin, apart from MDA-MB-231 cells with very little expressed $\alpha_v\beta_3$ integrin (Figure 2).

All cell lines were exposed to scalar concentrations of compounds **13** and **15** for different incubation times. We found that a 4 h incubation with 10 μM of both compounds determined a good detection threshold for the fluorescein signal in vascular endothelial cells and all tumor-derived cells expressing $\alpha_v\beta_3$ integrin (Figure 3). In particular, compound **13** gave a signal stronger than that of compound **15**. Each compound displayed a fluorescence distributed both at the cell surface and in putative cytosolic vesicles, suggesting that both compounds were internalized upon binding with $\alpha_v\beta_3$ integrin. Moreover, the morphological analysis of cells showed no signs of toxicity or stress after 4 or 24 h incubation with 10 μM of either compound **13** or **15** (data not shown). Notably, breast adenocarcinoma cells subjected to the treatment previously described did not show any sign of fluorescence (Figure 3), suggesting that both compounds were highly specific for $\alpha_v\beta_3$ integrin.

DISCUSSION

The diagnostic approaches based on modern imaging techniques are important tools to prevent and cure lethal pathologies such as cardiovascular diseases and cancer. In this paper, we describe the characterization, the synthesis, and the biological activity of RGD-containing peptides conjugated with the fluorescent probe fluorescein as tracers for $\alpha_v\beta_3$ integrin expression on cells.

Using the solid-phase receptor binding assay, we demonstrated that compounds **13** and **15** were able to efficiently inhibit the binding of biotinylated vitronectin to immobilized $\alpha_v\beta_3$

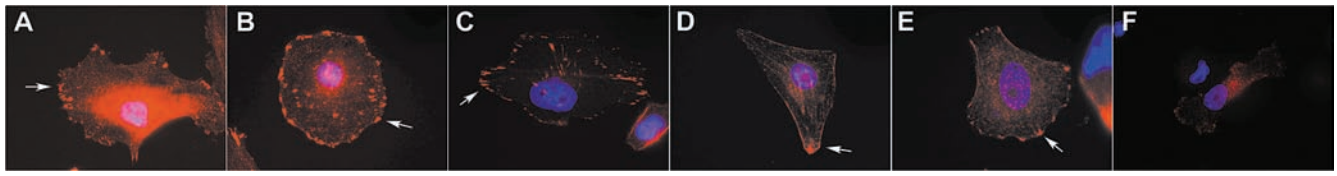

Figure 2. Expression of the $\alpha_v\beta_3$ integrin in the cell panel. HUVEC (A), ECV-304 (B), T98G (C), PC3 (D), Caki-1 (E), and MDA-MB-231 (F) cells were subjected to immunofluorescence staining for $\alpha_v\beta_3$ integrin (red). Nuclei were counterstained with DAPI (blue). (A,B,C,D,E) HUVEC, ECV-304, T98G, PC3, and Caki-1 cells showed high amounts of the $\alpha_v\beta_3$ integrin, which was predominantly clustered at focal contacts (arrows). (F) MDA-MB-231 cells expressed lower amounts of $\alpha_v\beta_3$ integrin, which was mainly diffused on the cell surface. Original magnification 63×.

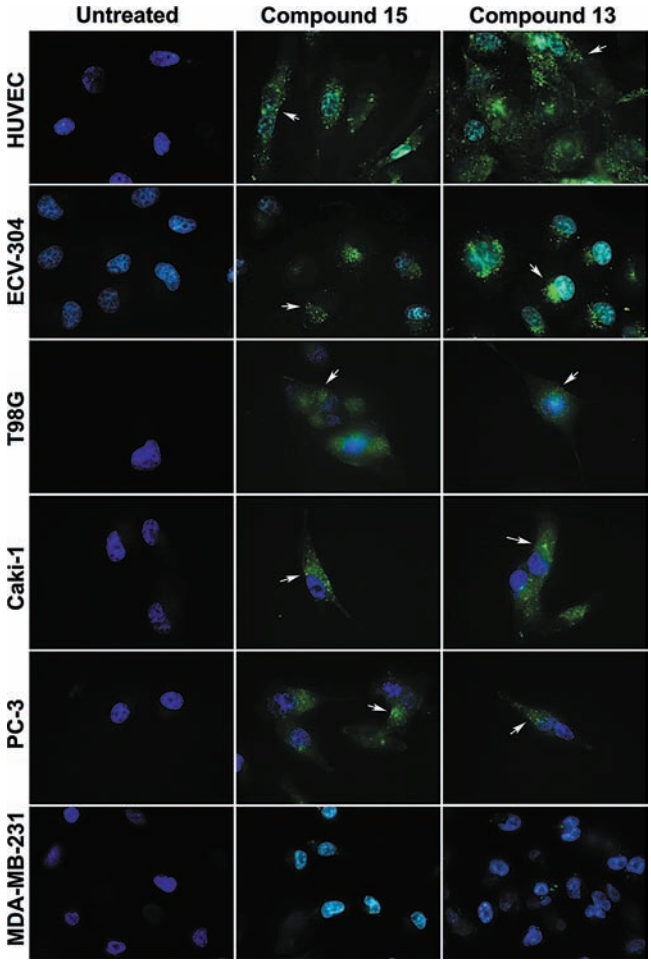

Figure 3. HUVEC, ECV-304, T98G, Caki-1, PC3, and MDA-MB-231 cells were incubated 4 h with treatment medium alone (left column), 10 μM compound **15** (middle column, green), or **13** (right column, green). Nuclei were counterstained with DAPI (blue). HUVEC, ECV304, T98G, Caki-1, and PC3 cells were positively stained after treatment with either compound **13** or **15**, even if the signal provided by compound **13** is stronger. In particular, the signal was highly detectable and located both at the cell surface and in putative cytosolic vescicles (arrows). Differently, MDA-MB-231 cells did not display any staining after treatment with either compound **13** or compound **15**. All three cell lines incubated with treatment medium alone displayed no fluorescence at all. Original magnification 63×.

integrin. Although we found that the binding affinity of both compounds for this integrin was less potent than the low nanomolar values of ST1646, their affinities in the nanomolar range prompted us to explore the possibility to use them as suitable platforms for $\alpha_v\beta_3$-targeted imaging. Therefore, we generated compounds **13** and **15** conjugated with the fluorescent probe fluorescein. We demonstrated that, after *in vitro* treatment with these two conjugated compounds, the fluorescein probe was detectable in a panel of cell lines highly expressing the $\alpha_v\beta_3$ integrin, namely, primary endothelial cells (HUVEC) and several human cell lines derived from solid tumors (bladder cancer, glioblastoma multiforme, prostate cancer, and renal clear cell carcinoma). According to the results of the solid-phase receptor binding assay, compound **13** gave a fluorescent signal stronger than that of compound **15** on cells. In both cases, the pattern of the detected fluorescence also suggested that the two compounds were dynamically internalized by cells. Notably, cancer cells expressing very faint levels of $\alpha_v\beta_3$ integrin (such as breast carcinoma cells) could not be visualized with these compounds. Moreover, treated cells retained their viability, making both molecules attractive as tools for the imaging of both angiogenic vessels and tumor masses specifically and highly expressing $\alpha_v\beta_3$ integrin.

In summary, the described fluorescent probes are able to efficiently target and "visualize" the $\alpha_v\beta_3$ integrin on human cells *in vitro*, suggesting their possible future use for a noninvasive imaging of the $\alpha_v\beta_3$ integrin expression also *in vivo*.

ACKNOWLEDGMENT

The authors thank CNR and MUR (FIRB RBNE03LF7X and PRIN 2006030449 research projects) for financial support. Elena M.V. Araldi was supported by a fellowship of the Doctorate School of Molecular Medicine, University of Milan.

LITERATURE CITED

(1) Giancotti, F., and Ruoslahti, E. (1999) Integrin signaling. *Science 285*, 1028–1032.
(2) Felding-Habermann, B. (2003) Integrin adhesion receptors in tumor metastasis. *Clin. Exp. Metastasis 20*, 203–213.
(3) Guo, W., and Giancotti, F. G. (2004) Integrin signalling during tumor progression. *Nat. Rev. Mol. Cell. Biol. 5*, 816–826.
(4) Kasirer-Friede, A., Kahn, M. L., and Shattil, S. J. (2007) Platelet integrins and immunoreceptors. *Immunol. Rev. 218*, 247–264.
(5) Nakamura, I., and Jimi, E. (2004) Role of alphavbeta3 integrins in osteoclast function. *Recent Res. Dev. Immunol. 6*, 79–94.
(6) Kuphal, S., Bauer, R., and Bosserhoff, A.-K. (2005) Integrin signaling in malignant melanoma. *Cancer Metastasis Rev. 24*, 195–222.
(7) Ding, Q., Stewart, J., Jr., Olman, M. A., Klobe, M. R., and Gladson, C. L. (2003) The pattern of enhancement of Src kinase activity on platelet-derived growth factor stimulation of glioblastoma cells is affected by the integrin engaged. *J. Biol. Chem. 278*, 39882–39891.
(8) Duan, X., Jia, S. F., Zhou, Z., Langley, R. R., Bolontrade, M. F., and Kleinerman, E. S. (2004) Association of alphaVbeta3 integrin expression with the metastatic potential and migratory and chemotactic ability of human osteosarcoma cells. *Clin. Exp. Metastasis 21*, 747–753.
(9) Rüegg, C., and Mariotti, A. (2003) Vascular integrins: pleiotropic adhesion and signaling molecules in vascular homeostasis and angiogenesis. *Cell. Mol. Life Sci. 60*, 1135–1157.
(10) Horton, M. A. (1997) The alpha V beta 3 integrin "vitronectin receptor". *Int. J. Biochem. Cell Biol. 29*, 721–725.
(11) Arnaout, M. A., Goodman, S. L., and Xiong, J. P. (2002) Coming to grips with integrin binding to ligands. *Curr. Opin. Cell. Biol. 14*, 641–651.

(12) Huveneers, S., Truong, H., and Danen, E. H. J. (2007) Integrins: signalling, disease and therapy. *Int. J. Radiat. Biol. 83*, 743–751.

(13) Haubner, R., Wester, H. J., Burkhart, F., Senekowitsch-Schmidtke, R., Weber, W., Goodman, S. L., Kessler, H., and Schwaiger, M. (2001) Glycosylated rgd-containing peptides, tracer for tumor targeting and angiogenesis imaging with improved biokinetics. *J. Nucl. Med. 42*, 326–336.

(14) Haubner, R., Kuhnast, B., Mang, C., Weber, W. A., Kessler, H., Wester, H. J., and Schwaiger, M. (2004) F-18 galacto-rgd: Synthesis, radiolabeling, metabolic stability, and radiation dose estimates. *Bioconjugate Chem. 15*, 61–69.

(15) Nisato, R. E., Tille, J. C., Jonczyk, A., Goodman, S. L., and Pepper, M. S. (2003) Alphav beta 3 and alphav beta 5 integrin antagonists inhibit angiogenesis in vitro. *Angiogenesis 6*, 105–119.

(16) Kessler, T., Bieker, R., Padro, T., Schwoppe, C., Persigehl, T., Bremer, C., Kreuter, M., Berdel, W. E., and Mesters, R. M. (2005) Inhibition of tumor growth by rgd peptide-directed delivery of truncated tissue factor to the tumor vasculature. *Clin. Cancer Res. 11*, 6317–6324.

(17) D'Andrea, L. D., Del Gatto, A., Pedone, C., and Benedetti, E. (2006) Peptide-based molecules in angiogenesis. *Chem. Biol. Drug Des. 67*, 115–126.

(18) Haubner, R., Gratias, R., Diefenbach, B., Goodman, S. L., Jonczyk, A., and Kessler, H. (1996) Structural and functional aspects of RGD-containing cyclic pentapeptides as highly potent and selective integrin alphavbeta3 antagonists. *J. Am. Chem. Soc. 118*, 7461–7472.

(19) Smith, J. W. (2003) Cilengitide Merck. *Curr. Opin. Investig. Drugs 4*, 741–745.

(20) Belvisi, L., Bernardi, A., Checchia, A., Manzoni, L., Potenza, D., Scolastico, C., Castorina, M., Cupelli, A., Giannini, G., Carminati, P., and Pisano, C. (2001) Potent integrin antagonist from a small library of RGD-including cyclic pseudopeptides. *Org. Lett.* 1001–1004.

(21) Belvisi, L., Riccioni, T., Marcellini, M., Chiarucci, I., Efrati, D., Vesci, L., Potenza, D., Scolastico, C., Manzoni, L., Lombardo, K., Stasi, M. A., Nico, B., Ribatti, D., Presta, M., Carminati, P., and Pisano, C. (2005) Biological and molecular properties of a new $\alpha v\beta 3/\alpha v\beta 5$ integrin antagonist. *Mol. Cancer Therapeut. 4*, 1670–1680.

(22) Manzoni, L., Arosio, D., Belvisi, L., Bracci, A., Colombo, M., Invernizzi, D., and Scolastico, C. (2005) Functionalized azabicycloalkane amino acids by nitrone 1,3-dipolar intramolecular cycloaddition. *J. Org. Chem. 70*, 4124–4132.

(23) Manzoni, L., Belvisi, L., Arosio, D., Civera, M., Pilkington-Miksa, M., Potenza, D., Caprini, A., Araldi, E. M. V., Monferini, E., Mancino, M., Podestà, F., and Scolastico, C. (2009) Cyclic RGD-including functionalized azabicycloalkane amino acids as potent integrin antagonists for tumor targeting, *ChemMedChem* DOI: 10.1002/cmdc.200800422.

(24) Manzoni, L., Arosio, D., Bertoli, M., and Scolastico, C. (2006) Click chemistry to functionalize peptidomimetics. *Tetrahedron Lett. 47*, 3697–3700.

(25) Ciardella, A. P., Prall, F. R., Borodoker, N., and Cunningham, E. T. Jr. (2004) Imaging techniques for posterior uveitis. *Curr. Opin. Ophtalmol. 15*, 519–530.

(26) Wang, W., Wu, Q., Pasuelo, M., McMurray, J. S., and Li, C. (2005) Probing for integrin avb3 binding of RGD peptide using fluorescent polarization. *Bioconjugate Chem. 16*, 729–734.

(27) Xiong, L., Yu, M., Cheng, M., Zhang, M., Zhang, X., Xu, C., and Li, F. (2009) A photostable fluorescent probe for targeted imaging of tumour cells possessing integrin avb3. *Mol. BioSyst. 5*, 241–243.

(28) Kolb, H. C., Finn, M. G., and Sharpless, K. B. (2001) Click chemistry: diverse chemical function from a few good reactions. *Angew. Chem., Int. Ed. 40*, 2004–2021.

(29) Rostovtsev, V. V., Green, L. G., Fokin, V. V., and Sharpless, K. B. (2002) A stepwise Huisgen cycloaddition process: copper(I)-catalyzed regioselective "ligation" of azides and terminal alkynes. *Angew. Chem., Int. Ed. 41*, 2596–2599.

(30) Genersch, E., Ferletta, M., Virtanen, I., Haller, H., and Ekblom, P. (2003) Integrin alphavbeta3 binding to human alpha5-laminins facilitates FGF-2- and VEGF-induced proliferation of human ECV304 carcinoma cells. *Eur. J. Cell Biol. 82*, 105–117.

(31) Ramos, O. H. P., Kauskot, A., Cominetti, M. R., Bechyne, I., Salla Potes, C. L., Chareyre, F., Manent, J., Vassy, R., Giovannini, M., Legrand, C., Selistre-de-Araujo, H., Crépin, M., and Bonnefoy, A. (2008) A novel alpha(v)beta (3)-blocking disintegrin containing the RGD motive, DisBa-01, inhibits bFGF-induced angiogenesis and melanoma metastasis. *Clin. Exp. Metastasis 25*, 53–64.

BC900155J

Facile Preparation of Fluorescent Neoglycoproteins Using *p*-Nitrophenyl Anthranilate as a Heterobifunctional Linker

Anthony Luyai, Yi Lasanajak, David F. Smith, Richard D. Cummings, and Xuezheng Song*

Department of Biochemistry, Emory University School of Medicine, Atlanta, Georgia 30322. Received April 23, 2009; Revised Manuscript Received June 10, 2009

A facile preparation of neoglycoconjugates has been developed with a commercially available chemical, *p*-nitrophenyl anthranilate (PNPA), as a heterobifunctional linker. The two functional groups of PNPA, the aromatic amine and the *p*-nitrophenyl ester, are fully differentiated to selectively conjugate with glycans and other biomolecules containing nucleophiles. PNPA is efficiently conjugated with free reducing glycans via reductive amination. The glycan−PNPA conjugates (GPNPAs) can be easily purified and quantified by UV absorption. The active *p*-nitrophenyl ester in the GPNPA conjugates readily reacts with amines under mild conditions, and the resulting conjugates acquire strong fluorescence. This approach was used to prepare several fluorescent neoglycoproteins. The neoglycoproteins were covalently printed on activated glass slides and were bound by appropriate lectins recognizing the glycans.

INTRODUCTION

Glycoconjugates including glycoproteins, glycolipids, and proteoglycans play important roles in many biological systems (*1*). Neoglycoconjugates, including neoglycolipids and neoglycoproteins as artificial mimics of natural glycoconjugates (*2*−*6*), have found many applications in various areas. One of the major applications is the development of carbohydrate-based vaccines and drugs (*7*−*11*).

To prepare neoglycoconjugates, and specifically neoglycoproteins, usually one or both of the molecules (glycan and protein) are derivatized with an appropriate functional group and then covalently linked. Theoretically, the linkages could be built through many different chemical reactions. Practically, however, derivatization is limited by several critical requirements. First, since glycans from natural sources or expensive synthetic approaches are often available only in small quantities, the glycan incorporation reaction should be highly efficient. Second, the reaction conditions should ideally be in aqueous buffer under physiological pH to avoid altering the glycan or denaturation of proteins, which might affect the solubility and immunogenicity of the conjugate. Third, the linkage itself should not decrease the immunogenicity of the conjugate and should be of minimal toxicity and antigenicity. There have been numerous methods developed for protein−carbohydrate conjugation, or neoglycoprotein synthesis, based on heterobifunctional or homobifunctional cross-linkers (*12*, *13*). Stowell et al. used 2-imino-2-methoxyethyl 1-thioglycosides to link glycans to proteins (*14*, *15*). Diethyl squarate has been used for efficient conjugation of proteins and carbohydrates; however, the potential immune response of the linker itself has impeded its application in vaccine development (*16*). Click chemistry (*17*) as well as a number of other protein− or peptide−carbohydrate conjugation methods have been employed for carbohydrate bioconjugation (*18*−*21*). Activated dicarboxylic acids can be used as homobifunctional linkers, but usually, no intermediate glycan derivatives can be separated. Wu et al. utilized bis-*p*-nitrophenylesters (*22*) to conjugate glycans and proteins. The intermediates can be separated and purified; however, the glycans need to be premodified to possess an active amine. Reductive amination has also been used in the conjugation of free reducing glycans (*23*) or ninhydrin-treated glycopeptides (*24*) to proteins; however, the reaction conditions are relatively harsh: they require large quantities of glycan and often the yields are very low.

Here, we describe a simple and efficient method to conjugate free reducing glycans with proteins using a commercially available chemical linker (Figure 1). The linker, *p*-nitrophenyl anthranilate (PNPA)[1], has two different functional groups: an aryl amine that can react with free reducing glycans by reductive amination and an active *p*-nitrophenyl ester that can react with nucleophiles. We show that this bifunctional linker is a useful reagent for preparing fluorescent neoglycoproteins from naturally occurring complex glycans. Moreover, the neoglycoconjugates acquire fluorescence upon linking, thus providing a ready means of following the reaction and quantifying the products.

EXPERIMENTAL PROCEDURES

Free reducing glycans were purchased from V-LABS and stored at −20 °C until use. All chemicals were purchased from Sigma-Aldrich and used without further purification. HPLC solvents were purchased from Fisher Scientific. An Ultraflex-II TOF/TOF system from Bruker Daltonics was used for MALDI-TOF mass spectrometry analysis of glycan conjugates.

Glycan−PNPA Conjugation. The conjugation of glycan with PNPA was carried out using the common reductive amination procedure for free glycan labeling with modifications on sample purification. Briefly, to a free reducing glycan (0.1

* Send correspondence to: Xuezheng Song, Ph.D., Assistant Professor, Department of Biochemistry, Emory University School of Medicine, O. Wayne Rollins Research Center, 1510 Clifton Road, Room 4031, Atlanta, GA 30322. Tel: 404-727-0592; Fax: 404-727-2738, E-mail: xsong2@emory.edu.

[1]Abbreviations: AAL, *Aleuria aurantia* lectin; AEAB, 2-amino-*N*-(2-aminoethyl)-benzamide; GBP, glycan binding protein; GPNPA, Glycan-PNPA conjugate; HPLC, high performance liquid chromatography; LNFIII, lacto-*N*-fucopentaose III; LNnT, lacto-*N*-neotetraose; LSTc, lacto-*N*-sialyltetraose c; NHS, *N*-hydroxysuccinimide; PNPA, *p*-nitrophenyl anthranilate; RCA I, *Ricinus communis* Agglutinin I; RFU, relative fluorescence unit; SNA, *Sambucus nigra* lectin.

10.1021/bc900189h CCC: $40.75 © 2009 American Chemical Society
Published on Web 07/22/2009

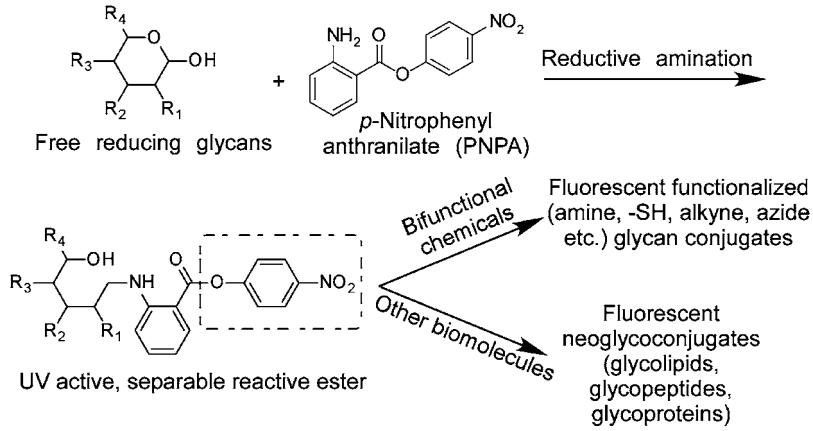

Figure 1. General strategy for using *p*-nitrophenyl anthranilate (PNPA) as a heterobifunctional linker to make neoglycoconjugates and other potential applications.

to 1 mg), freshly prepared PNPA solution (0.35 M in DMSO/AcOH = 7:3 (v/v), 25−50 μL) and an equal volume $NaCNBH_3$ solution (1 M in DMSO/AcOH = 7:3 (v/v)) were added. The mixture was heated at 65 °C for 2 h. The reaction mixture was quenched by addition of acetonitrile (0.5 to 1 mL). The mixture was cooled at −20 °C for 2 h and centrifuged at 10 000 *g* for 5 min. The supernatant was discarded and the pellet subjected to either C18 Sep-pak for desalting or C18 HPLC for direct purification. For reaction with ethylenediamine, LNnT-PNPA (0.1 to 1 mg) was dissolved in 20−200 μL 10% ethylenediamine, and the solution was kept at room temperature for 30 min and subjected to HPLC analysis.

HPAEC-PAD and High-Performance Liquid Chromatography (HPLC). High-performance anion-exchange chromatography with pulsed amperometric detection (HPAEC-PAD) analysis was carried out with a Dionex ICS-3000 system with a Carbpac PA-100 column. The eluent gradient was set to 0−125 mM sodium acetate over 50 min in sodium hydroxide (100 mM).

A Shimadzu HPLC CBM-20A system was used for HPLC analysis and separation of glycan−PNPA conjugates. For reverse-phase HPLC, it was coupled with a Vydec C18 HPLC column and a UV detector SPD-20A. UV absorptions at 330 and 280 nm were used to detect and quantify GPNPAs and BSA−GPNPA conjugates. The mobile phase was acetonitrile and water with 0.1% trifluoroacetic acid (TFA). The concentration of acetonitrile increased from 1% to 90% in 30 min with a linear gradient. For SEC-HPLC, a Biobasic-60 SEC column was used. The eluent was ammonium acetate (10 mM) at pH 4.5. The flow rate was set at 1 mL/min for all HPLC runs.

Conjugation of Proteins with GPNPAs. Protein conjugation with GPNPAs was carried out in various buffers as described above. Protein concentration was kept at 5 mg/mL. Aqueous buffer with 1% DMSO was used. The protein conjugates were purified by SEC by collecting the eluent with strong absorption at UV 280 nm. Lyophilized fractions were dissolved in water or suitable buffer for MALDI-TOF characterization and printing.

Printing, Binding Assay, and Scanning. The printing of protein−glycan conjugates on NHS-activated slides and epoxy slides was carried out according to previous procedure (*25*). Biotinylated lectins were used in the binding assay, and the bound lectins were detected by a secondary incubation with cyanine 5-streptavidin. The slides were scanned with a Perkin-Elmer ProScanArray microarray scanner equipped with 4 lasers covering an excitation range from 488 to 633 nm. The scanned images were analyzed with the *ScanArray Express* software. For cyanine 5 fluorescence, 649 nm (Ex) and 670 nm (Em) were used. All the images obtained from the scanner were in grayscale and colored for easy discrimination.

RESULTS

Derivatization of Free Reducing Sugars with PNPA by Reductive Amination. The preliminary study of PNPA conjugation with free reducing glycans was carried out using lactoneotetraose (LNnT) (Galβ1−4GlcNAcβ1−3Galβ1−4Glc) as the model compound. The conjugation reaction is shown in Figure 2a. The reaction time was optimized by analyzing free LNnT and the product mixture after various reaction times using HPAEC-PAD (Figure 2b). The conversion of LNnT did not significantly increase after 2 h of heating at 65 °C, when >80% yield was obtained. The reaction mixture was precipitated in 10 volumes of acetonitrile, and the supernatant and precipitate were analyzed using RP-HPLC (Figure 2c). Most of the excess PNPA remained in the supernatant, and the LNnT−PNPA conjugate was precipitated in high yield (>90%). The major product peak was collected from RP-HPLC and analyzed by ESI-MS (Figure 2d), which showed an expected mass at 950.3237 [$M+H^+$] (calc. 950.3248) and confirmed the successful derivatization of the reducing glycan. Interestingly, the behavior of the LNnT-PNPA conjugate on MALDI-TOF-MS was quite different from ESI-MS. Although the expected molecular ion peak at 972.61 [$M+Na^+$] (calc. 972.3068) is evident in the spectrum, the most intense peak occurs at 958.63, along with other fragmentation peaks at 956.62 and 942.63 (Figure 2e). The fragmentation ions of −14, −16, and −30 Da caused by radical reactions on the nitro group (*26*) further confirmed the installation of PNPA. The pattern is highly reproducible and serves as an indicator for all glycan−PNPA conjugates in mass spectrometry analysis (Figure 2e).

Reaction of Glycan−PNPA (GPNPA) Conjugates with Nucleophiles. The reactivity of the GPNPAs toward nucleophiles was tested with ethylenediamine. This mild reaction at room temperature transforms the electrophilic *p*-nitrophenyl ester into a nucleophilic amino group (Figure 3a). Addition of 10% ethylenediamine at room temperature for 30 min quantitatively converted LNnT−PNPA to the expected LNnT−AEAB as shown by RP-HPLC (Figure 3b). The major product was purified by HPLC and characterized by MALDI-TOF (Figure 3c). This confirmed the formation of LNnT−AEAB conjugate, and therefore demonstrated the general reactivity of *p*-nitrophenyl ester toward alkylamines. The minor peak that eluted at 11.2 min with the reaction products matched the *p*-nitrophenol standard, confirming the PNPA conjugation with glycans and its reactivity toward amines (nucleophiles) as an active ester.

Conjugation of Proteins with GPNPAs. The conjugation of GPNPA with proteins was evaluated with BSA and

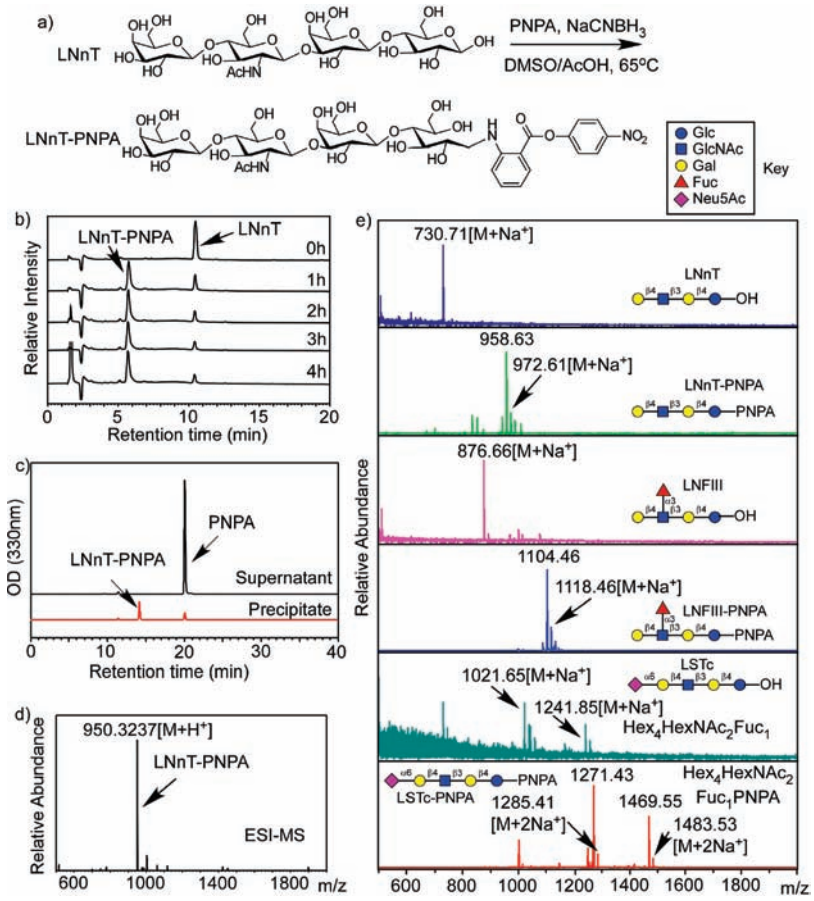

Figure 2. The PNPA derivatization of LNnT: (a) the chemical reaction equation; (b) Dionex profiles of LNnT−PNPA conjugation over a time course; (c) RP-HPLC profiles of supernatant and precipitate after precipitation of the LNnT−PNPA conjugation with acetonitrile; (d) ESI-MS of the HPLC purified LNnT−PNPA showing the expected mass; (e) MALDI TOF of the starting material and the product of several compounds, showing the expected masses and fragmented major peaks.

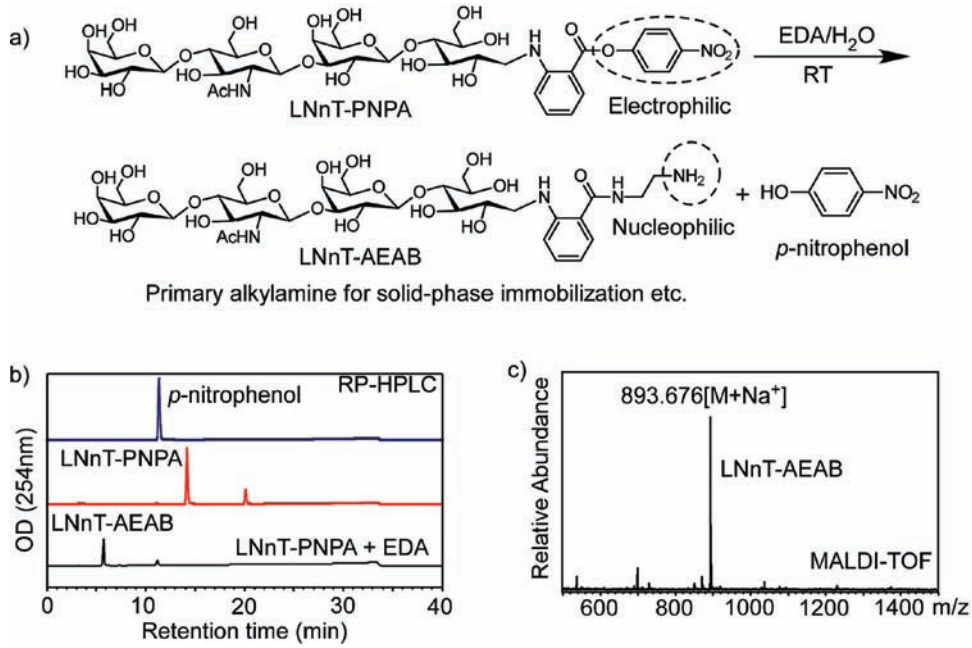

Figure 3. (a) The reaction of LNnT−PNPA with ethylenediamine; (b) HPLC profile of *p*-nitrophenol, LNnT−PNPA, and its product after reaction with ethylenediamine; (c) MALDI-TOF of HPLC purified product of LNnT−PNPA and ethylenediamine.

LNnT−PNPA. To optimize the conjugation, various buffers and temperatures were tested (Figure 4 and Table 1). Figure 4a is a schematic representation of the reaction between GPNPA and proteins. Lysine residues in proteins can attack the active *p*-nitrophenol ester to form a stable amide bond. In this reaction, glycan and protein are thus linked through a small fluorescent anthranilamide moiety. Figure 4b shows the MALDI-TOF analyses that compare the conjugation of LNnT−PNPA with

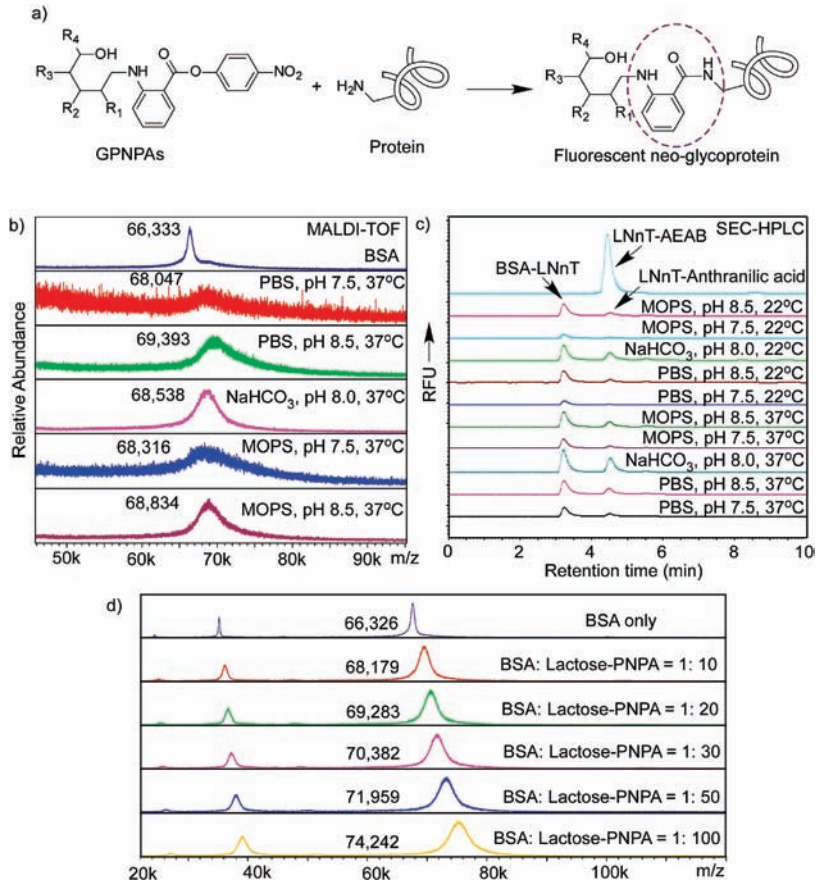

Figure 4. BSA conjugation with LNnT−PNPA: (a) the general equation of protein conjugation with GPNPAs; (b) overlay of MALDI-TOF profiles of BSA conjugation with LNnT−PNPA at 37 °C in various buffers; (c) fluorescent SEC-HPLC profiles of BSA conjugation with LNnT−PNPA at different temperatures and buffers; (d) overlay of MALDI-TOF profiles of BSA conjugation with lactose−PNPA at different ratios.

BSA in various buffers at 37 °C. The starting molar ratio of LNnT−PNPA and BSA was 10:1. While significant conjugation occurred in all buffers, reactions were faster in more basic conditions (pH 8.5 over pH 7.5). There was no significant conjugation difference seen in phosphate, MOPS, and carbonate buffers based on analysis by mass spectrometry. The conjugation efficiencies were estimated to be 2−3.5 glycans/protein molecule based on the MALDI-TOF peak values, indicating a yield of 20−35%. Figure 4c shows the fluorescent SEC-HPLC profiles of the conjugations in different buffers. The protein−glycan conjugates are fluorescent as expected (Ex 330 nm, Em 420 nm), and the intensity of the fluorescence can be directly correlated to the conjugation efficiency. Apparently, a relatively higher temperature (37 °C over 22 °C) and pH (8.5 over 7.5) significantly increased the conjugation efficiency. More interestingly, the fluorescence of the LNnT−BSA conjugate generated in carbonate buffer is stronger than those in PBS or MOPS buffer, suggesting a faster reaction. It is worthwhile to note that another fluorescent peak eluting at the same time as LNnT−AEAB is observed. This is presumably the hydrolysis product of LNnT−PNPA (LNnT-anthranilic acid, MW 828.77), which has a similar size to LNnT−AEAB (870.85). This peak is of significantly lower intensity than the protein peak, indicating that hydrolysis of GPNPA under these conditions is not seriously affecting the protein−glycan conjugation. To further evaluate the conjugation of GPNPAs with proteins, we tested the conjugation of lactose−PNPA (Galβ1−4Glc-PNPA) with BSA at different molar ratios (Figure 4d and Table 1). The increased amount of lactose−PNPA, as expected, increased the average number of lactose−PNPA conjugated per BSA molecule. At 100:1 ratio, ∼17−18 lactose/BSA were conjugated.

Table 1. Conjugation of BSA with Glycan−PNPA Conjugates in Different Buffers, pH, and Molar Ratios

glycan PNPA	temp (°C)	buffer	pH	starting molar ratio (glycan/BSA)	product molar ratio (glycan/BSA)
LNnT	37	PBS	7.5	10	2.1
LNnT	37	PBS	8.5	10	3.8
LNnT	37	$NaHCO_3$	8.0	10	2.7
LNnT	37	MOPS	7.5	10	2.4
LNnT	37	MOPS	8.5	10	3.1
LNnT	22	PBS	7.5	10	0.5
LNnT	22	PBS	8.5	10	2.2
LNnT	22	$NaHCO_3$	8.0	10	2.0
LNnT	22	MOPS	7.5	10	0.0
LNnT	22	MOPS	8.5	10	1.5
lactose	37	$NaHCO_3$	8.0	10	4.1
lactose	37	$NaHCO_3$	8.0	20	6.6
lactose	37	$NaHCO_3$	8.0	30	9.1
lactose	37	$NaHCO_3$	8.0	50	12.6
lactose	37	$NaHCO_3$	8.0	100	17.7

Printing and Recognition of Glycan−BSA Conjugates on Microarray Slides. To validate the structural integrity of glycans after conjugation with proteins, we conjugated several GPNPAs (LNnT, LNFIII, and LSTc) with BSA using a 5:1 molar ratio of glycan/protein. The conjugates were purified by SEC-HPLC. The MALDI-TOF profiles in Figure 5a show the mass shifts compared to BSA alone, indicating that 1.5−2 glycans/protein molecule were conjugated. The purified BSA−glycan conjugates were printed on epoxy and NHS-activated glass slides and interrogated with several plant lectins. All three lectins showed expected bindings on both epoxy and NHS-activated slides (Figure 5b). AAL, a fucose binding lectin (*27*), bound to BSA−LNFIII conjugates. RCA I, a plant lectin that recognizes

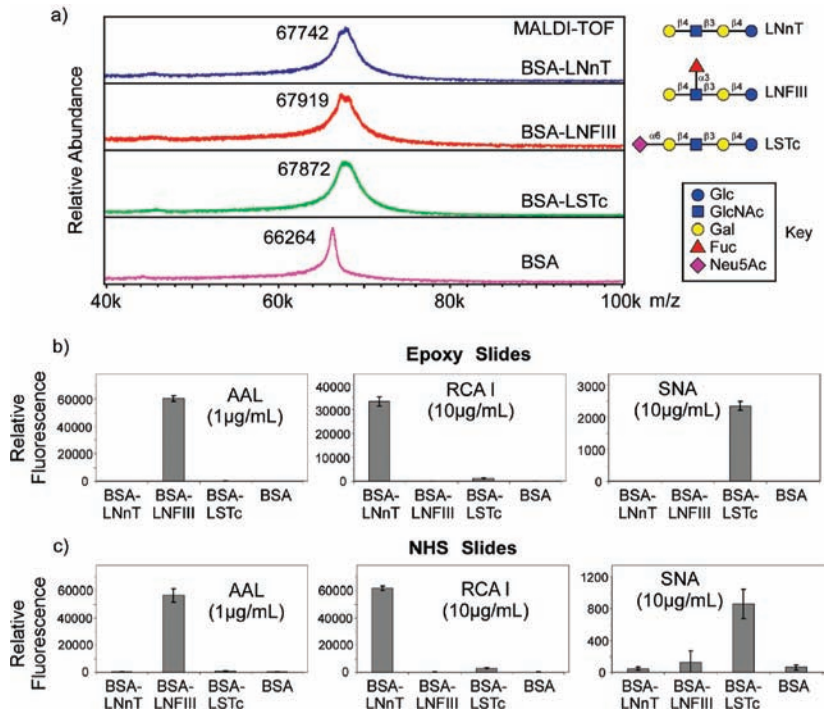

Figure 5. (a) MALDI-TOF of conjugates of BSA with LNnT−PNPA, LNFIII−PNPA, and LSTc−PNPA. (b,c) The conjugates of BSA−LNnT, −LNFIII, and −LSTc, and BSA alone printed on epoxy slides (b) and NHS slides (c) and interrogated with the lectins AAL, RCA I, and SNA. The glycan structures are indicated along with a key to the symbols.

β1,4-linked galactose residues (*28*) bound to BSA−LNnT conjugates and also to BSA−LSTc conjugates, weakly, since α2,6-sialylation does not fully abolish its binding to Galβ1,4-R moieties. SNA, a plant lectin that binds α2,6-linked sialic acid residues (*29*), bound to BSA-LSTc conjugates, as expected.

DISCUSSION

p-Nitrophenyl ester is known to be an active ester due to the strong electronegativity of the nitro group. This active ester, however, is well-tolerated by the aromatic amine group in PNPA, which is a nucleophile. The existence of two opposing but tolerant functional groups makes PNPA a promising heterobifunctional linker under finely tuned conjugation conditions. Reductive amination of PNPA with free reducing glycans does not interfere with the *p*-nitrophenyl ester, as shown by HPAEC, HPLC, and MALDI-TOF (Figure 2b−d). Although this reaction does not go to completion under the commonly used conditions, it is still highly efficient (>80% yield) and nonselective toward many glycans, as shown by LNnT, LNFIII, and LSTc conjugation profiles (Figure 2e). Furthermore, GPNPAs can be easily separated from unconjugated free glycans by C18 Sep-pak due to the strong hydrophobicity of the linker. The high conjugation efficiency, nonselectivity, and easy separation make this approach appropriate for extracting natural glycans as active esters for neoglycoconjugate preparation. We have noticed that, by direct reductive amination with glycans, the reducing end ring structure is opened. This is of concern in situations where the whole glycan structures are considered epitopes, such as conjugation of mono- and disaccharides or structures with epitopes close to the reducing end. In most cases, we are more interested in the terminal moieties as epitopes, which should not be affected by this strategy. Under these circumstances, the ability to utilize complex natural glycans directly without laborious synthesis is of more importance than the reducing end structural variation. On the other hand, this strategy could also be applied to any biomolecules with an aldehyde group, which could be installed at the glycan reducing end without breaking the ring structures (*30*).

It is worthwhile to note the interesting behavior of GPNPAs on MALDI-TOF. While ESI-MS clearly showed the molecular ion, MALDI-TOF of GPNPAs showed a reproducible fragmentation pattern besides the molecular ion. This radical reaction related pattern is specific to the nitro group. While it might complicate mass spectra to a certain extent, it could also serve as a fingerprint for confirming glycan−PNPA conjugates in mass spectrometry analysis. Nevertheless, this does not interfere with the reactivity of GPNPAs for conjugation with other molecules, as shown in Figure 3. LNnT−PNPA quickly reacts with ethylenediamine to form LNnT−AEAB. The electrophile (ester) of LNnT−PNPA is easily transformed to a nucleophile (amine), enabling its direct conjugation with electrophilic molecules such as epoxy and NHS esters. We have demonstrated the use of AEAB conjugation with glycans for generation of fluorescent natural glycan arrays (*31*), providing an alternative for this application. Although AEAB and PNPA are all heterobifunctional linkers that can be used to conjugate free reducing glycans with other biomolecules or solid surfaces, they are complementary in terms of the reactivity. GAEABs have a nucleophilic alkylamine, while GPNPAs have a good leaving group that is reactive toward nucleophiles. Application of both conjugations offers more flexibility in the design and preparation of bioconjugates.

Protein−carbohydrate conjugation has become an important route for generating glycan-related antibodies. Many methods have been developed, most of which focus on conjugating synthetic glycans through bifunctional linkers. In our effort to develop carbohydrate-based vaccines against schistosomiasis and other pathogens (*32*), we sought to conjugate complex glycans extracted from natural sources, which are usually very complicated to synthesize with appropriate linkers attached. Therefore, we needed an effective method to efficiently conjugate free reducing glycans with protein carriers. Although there are a number of methods developed for protein−carbohydrate conjugations, most of them are not targeting naturally occurring complex glycans, which are difficult to obtain through synthesis. Although direct coupling of glycans with proteins by reductive

amination has been used, the yields are often disappointing. To obtain homogeneous natural glycans is also a major challenge. PNPA, as a heterobifunctional linker, can react efficiently and selectively with glycans and proteins. GPNPAs can be easily prepared and purified from natural sources based on their UV absorbance. The GPNPAs can be efficiently conjugated with BSA, as shown by MALDI-TOF and HPLC (Figure 4). MALDI-TOF is the most common method used to determine the protein−carbohydrate conjugation efficiency based on the mass shift before and after conjugation. However, with more glycans and linkers added, the MALDI-TOF peak broadens quickly so that the peak value does not accurately represent the average molecular weight of protein conjugates. The protein−glycan conjugates prepared with the GPNPA strategy are fluorescent, which can greatly facilitate the quantification of conjugated glycans even at a minimal level (Figure 4c). Furthermore, with appropriate UV range fluorescence detection methods, this fluorescence could be used to detect small amounts of protein in purification steps and bioassays. On the basis of the mass and fluorescence of the conjugates, we confirmed that various glycans such as lactose, LNnT, and LSTc can be reproducibly conjugated to proteins. The molar ratio of glycans versus glycan−protein conjugates can be driven by increasing the molar ratio of glycans to proteins, reaching 17−18 glycans/conjugate at 100:1 glycan/protein molar ratio.

Upon conjugation of glycans to proteins, it is difficult to validate that the structures of glycans are not affected during the glycan−protein conjugation process. Therefore, we conjugated and printed several glycan−protein conjugates on activated glass slides and interrogated them with various lectins. The conjugation of LNnT, LNFIII, and LSTc GPNPAs to BSA showed similar mass shifts (Figure 5a), indicating the general applicability of this approach to different glycans. This is especially useful for sialylated structures, as the sialic acid is not compatible with many conjugation approaches relying on carboxylic acid activation. With *p*-nitrophenyl ester incorporated onto the glycan reducing end by reductive amination, sialylated glycans can be conjugated to proteins as easily as other glycans. When the BSA conjugates of LNnT, LNFIII, and LSTc were printed on activated glass slides (epoxy and NHS) and assayed with three lectins, AAL, RCA I, and SNA, expected specific binding was observed for each lectin. These results show that the glycan structures are presented after the conjugation process in a manner that is consistent with their predicted recognition, which implies that such conjugates can be used to explore biological functions of glycans. It is also worth noting that this approach provides an alternative platform for natural glycan microarray printing. While suitably derivatized glycans (*25*, *31*, *33*, *34*) can be directly printed on NHS or epoxy slides for successful carbohydrate binding protein screening, printing of protein−glycan conjugates presents the glycan structures in the context of protein. This somewhat addresses concerns about nonspecific surface interactions related to microarray slide presentation and may provide a desirable alternative presentation strategy under certain circumstances. The fact that the protein−glycan conjugates are fluorescent is also a major advantage when quantifiable microscale material is used in microarray printing.

One general issue in using protein−carbohydrate conjugates as potential vaccines is that the linker itself is sometimes immunogenic or alters immunogenic potential of the glycan. While no testing is yet available on the immunogenicity of anthranilamide derivatives, the fluorescent anthranilamide is generally considered safe as a chemical, and the closely related anthranilic acid is the precursor of the amino acid tryptophan. Thus, while not yet tested in vivo, we expect this linker to have minimal immunogenicity and toxicity.

In conclusion, we have developed a novel approach utilizing a commercially available chemical as a convenient fluorescent linker for protein−carbohydrate conjugation. The ease and efficiency, the ability to utilize natural glycans, and the acquired fluorescence of the final conjugates make this approach very promising in the development of carbohydrate antibodies and carbohydrate-based vaccines.

ACKNOWLEDGMENT

Supported in part by a Collaboration Planning Grant from the Georgia Research Alliance and NIH Grant GM085448 (RDC, DFS). We thank Dr. Jamie Heimburg-Molinaro for manuscript editing and review.

LITERATURE CITED

(1) Varki, A., Cummings, R. D., Esko, J. D., Freeze, H. H., Stanley, P., Bertozzi, C. R., Hart, G. W., Etzler, M. E. (2009) *Essentials of Glycobiology*, 2nd ed., Cold Spring Harbor Press, New York.
(2) Wong, S. Y. C. (1995) Neoglycoconjugates and their applications in glycobiology. *Curr. Opin. Struct. Biol. 5*, 599–604.
(3) Lee, R. T., and Lee, Y. C. (1997) Neoglycoconjugates. *Glycosciences* 55–77.
(4) Bovin, N. V. (2003) Neoglycoconjugates as probes in glycobiology. *NATO Sci. Seri., II 129*, 207–225.
(5) Davis, B. G. (2002) Synthesis of glycoproteins. *Chem. Rev. 102*, 579–602.
(6) Pratt, M. R., and Bertozzi, C. R. (2005) Synthetic glycopeptides and glycoproteins as tools for biology. *Chem. Soc. Rev. 34*, 58–68.
(7) Slovin, S. F., Keding, S. J., and Ragupathi, G. (2005) Carbohydrate vaccines as immunotherapy for cancer. *Immunol. Cell. Biol. 83*, 418–28.
(8) Ouerfelli, O., Warren, J. D., Wilson, R. M., and Danishefsky, S. J. (2005) Synthetic carbohydrate-based antitumor vaccines: challenges and opportunities. *Expert Rev. Vaccines 4*, 677–85.
(9) Lloyd, K. O. (2000) Carbohydrate vaccines for the immunotherapy of cancer. *Drug News Perspect. 13*, 463–70.
(10) Ada, G., and Isaacs, D. (2003) Carbohydrate-protein conjugate vaccines. *Clin. Microbiol. Infect. 9*, 79–85.
(11) Roy, R. (2004) New trends in carbohydrate-based vaccines. *Drug Discovery Today: Technologies 1*, 327–336.
(12) Stowell, C. P., and Lee, V. C. (1980) Neoglycoproteins: the preparation and application of synthetic glycoproteins. *Adv. Carbohydr. Chem. Biochem. 37*, 225–81.
(13) Macmillan, D., and Bertozzi, C. R. (2000) New directions in glycoprotein engineering. *Tetrahedron 56*, 9515–9525.
(14) Stowell, C. P., and Lee, Y. C. (1982) Preparation of neoglycoproteins using 2-imino-2-methoxyethyl 1-thioglycosides. *Methods Enzymol. 83*, 278–88.
(15) Stowell, C. P., and Lee, Y. C. (1980) Preparation of some new neoglycoproteins by amidination of bovine serum albumin using 2-imino-2-methoxyethyl 1-thioglycosides. *Biochemistry 19*, 4899–904.
(16) Mawas, F., Niggemann, J., Jones, C., Corbel, M. J., Kamerling, J. P., and Vliegenthart, J. F. (2002) Immunogenicity in a mouse model of a conjugate vaccine made with a synthetic single repeating unit of type 14 pneumococcal polysaccharide coupled to CRM197. *Infect. Immun. 70*, 5107–14.
(17) Wang, Q., Chan, T. R., Hilgraf, R., Fokin, V. V., Sharpless, K. B., and Finn, M. G. (2003) Bioconjugation by copper(I)-catalyzed azide-alkyne [3 + 2] cycloaddition. *J. Am. Chem. Soc. 125*, 3192–3.
(18) Crich, D., and Yang, F. (2008) Synthesis of neoglycoconjugates by the desulfurative rearrangement of allylic disulfides. *J. Org. Chem. 73*, 7017–7027.
(19) Kubler-Kielb, J., and Pozsgay, V. (2005) A new method for conjugation of carbohydrates to proteins using an aminooxy-thiol heterobifunctional linker. *J. Org. Chem. 70*, 6987–90.

(20) Wong, S. Y., Guile, G. R., Dwek, R. A., and Arsequell, G. (1994) Synthetic glycosylation of proteins using N-(beta-saccharide) iodoacetamides: applications in site-specific glycosylation and solid-phase enzymic oligosaccharide synthesis. *Biochem. J. 300* (Pt 3), 843–50.
(21) Shao, M. C., Chen, L. M., and Wold, F. (1990) Complex neoglycoproteins. *Methods Enzymol. 184*, 653–9.
(22) Wu, X., Ling, C. C., and Bundle, D. R. (2004) A new homobifunctional p-nitro phenyl ester coupling reagent for the preparation of neoglycoproteins. *Org. Lett. 6*, 4407–10.
(23) Gildersleeve, J. C., Oyelaran, O., Simpson, J. T., and Allred, B. (2008) Improved procedure for direct coupling of carbohydrates to proteins via reductive amination. *Bioconjugate Chem. 19*, 1485–90.
(24) Mencke, A. J., Cheung, D. T., and Wold, F. (1987) Attachment of oligosaccharide-asparagine derivatives to proteins: activation of asparagine with ninhydrin and coupling to protein by reductive amination. *Methods Enzymol. 138*, 409–13.
(25) Song, X., Xia, B., Lasanajak, Y., Smith, D. F., and Cummings, R. D. (2008) Quantifiable fluorescent glycan microarrays. *Glycoconjugate J. 25*, 15–25.
(26) Ueda, K., Katagiri, T., Shimada, T., Irie, S., Sato, T. A., Nakamura, Y., and Daigo, Y. (2007) Comparative profiling of serum glycoproteome by sequential purification of glycoproteins and 2-nitrobenzensulfenyl (NBS) stable isotope labeling: a new approach for the novel biomarker discovery for cancer. *J. Proteome Res. 6*, 3475–83.
(27) Yamashita, K., Kochibe, N., Ohkura, T., Ueda, I., and Kobata, A. (1985) Fractionation of L-fucose-containing oligosaccharides on immobilized Aleuria aurantia lectin. *J. Biol. Chem. 260*, 4688–93.
(28) Green, E. D., Brodbeck, R. M., and Baenziger, J. U. (1987) Lectin affinity high-performance liquid chromatography. Interactions of N-glycanase-released oligosaccharides with Ricinus communis agglutinin I and Ricinus communis agglutinin II. *J. Biol. Chem. 262*, 12030–9.
(29) Shibuya, N., Goldstein, I. J., Broekaert, W. F., Nsimba-Lubaki, M., Peeters, B., and Peumans, W. J. (1987) The elderberry (Sambucus nigra L.) bark lectin recognizes the Neu5Ac(alpha 2−6)Gal/GalNAc sequence. *J. Biol. Chem. 262*, 1596–601.
(30) Munoz, F. J., Perez, J., Rumbero, A., Santos, J. I., Canada, F. J., Andre, S., Gabius, H. J., Jimenez-Barbero, J., Sinisterra, J. V., Hernaiz, M. J. (2009) Glycan tagging to produce bioactive ligands for a surface plasmon resonance (SPR) study via immobilization on different surfaces, *Bioconjugate Chem. 20*, 673−682.
(31) Song, X., Xia, B., Lasanajak, Y., Stowell, S. R., Smith, D. F., Cummings, R. D. (2009) Novel fluorescent glycan microarray strategy reveals ligands for galectins. *Chem. Biol. 16*, 36−47.
(32) Nyame, A. K., Kawar, Z. S., and Cummings, R. D. (2004) Antigenic glycans in parasitic infections: implications for vaccines and diagnostics. *Arch. Biochem. Biophys. 426*, 182–200.
(33) Blixt, O., Head, S., Mondala, T., Scanlan, C., Huflejt, M. E., Alvarez, R., Bryan, M. C., Fazio, F., Calarese, D., Stevens, J., Razi, N., Stevens, D. J., Skehel, J. J., van Die, I., Burton, D. R., Wilson, I. A., Cummings, R., Bovin, N., Wong, C. H., and Paulson, J. C. (2004) Printed covalent glycan array for ligand profiling of diverse glycan binding proteins. *Proc. Natl. Acad. Sci. U.S.A. 101*, 17033–8.
(34) de Boer, A. R., Hokke, C. H., Deelder, A. M., and Wuhrer, M. (2007) General microarray technique for immobilization and screening of natural glycans. *Anal. Chem. 79*, 8107–13.

BC900189H

Comprehensive Radiolabeling, Stability, and Tissue Distribution Studies of Technetium-99m Single Amino Acid Chelates (SAAC)

Kevin P. Maresca,[†] Shawn M. Hillier,[†] Frank J. Femia,[†] Craig N. Zimmerman,[†] Murali K. Levadala,[‡] Sangeeta R. Banerjee,[‡] Justin Hicks,[§] Chitra Sundararajan,[§] John Valliant,[§] Jon Zubieta,[‡] William C. Eckelman,[†] John L. Joyal,[†] and John W. Babich*[,†]

Molecular Insight Pharmaceuticals, Inc., 160 Second Street, Cambridge, Massachusetts 02142, Department of Chemistry, Syracuse University, Syracuse, New York 13244, and Department of Chemistry, McMaster University, Hamilton, Canada ON L8S4MI. Received April 24, 2009; Revised Manuscript Received May 27, 2009

Technetium tricarbonyl chemistry has been a subject of interest in radiopharmaceutical development over the past decade. Despite the extensive work done on developing chelates for Tc(I), a rigorous investigation of the impact of changing donor groups and labeling conditions on radiochemical yields and/or distribution has been lacking. This information is crucially important if these platforms are going to be used to develop molecular imaging probes. Previous studies on the coordination chemistry of the $\{M(CO)_3\}^+$ core have established alkylamine, aromatic nitrogen heterocycles, and carboxylate donors as effective chelating ligands. These observations led to the design of tridentate ligands derived from the amino acid lysine. Such amino acid analogues provide a tridentate donor set for chelation to the metal and an amino acid functionality for conjugation to biomolecules. We recently developed a family of single amino acid chelates (SAAC) that serve this function and can be readily incorporated into peptides via solid-phase synthesis techniques. As part of these continuing studies, we report here on the radiolabeling with technetium-99m (^{99m}Tc) and stability of a series of SAAC analogues of lysine. The complexes studied include cationic, neutral, and anionic complexes. The results of tissue distribution studies with these novel complexes in normal rats demonstrate a range of distribution in kidney, liver, and intestines.

INTRODUCTION

Advances in molecular imaging and targeted radiotherapy of cancer are intimately dependent on technological advancements in radiochemistry. Recent reports show significant clinical benefit of targeted radiotherapeutics for the treatment of cancer; however, the arsenal of available compounds is limited despite the significant unmet clinical need (*1*−*4*). In addition, the desire to produce high specific activity radiopharmaceuticals for both imaging and therapy that bind to low-density, molecular targets has been clearly demonstrated (*5*).

The ability to incorporate readily available radionuclides with optimal decay characteristics into targeting molecules has been the foremost consideration in developing diagnostic radiopharmaceuticals. In this respect, ^{99m}Tc has become the mainstay of diagnostic nuclear medicine and in some chemical form is used in more than 85% of the diagnostic scans performed each year in hospitals (*6*). The preferential use of ^{99m}Tc radiopharmaceuticals reflects the ideal nuclear properties of the isotope, as well as its convenient availability from commercial generator columns. ^{99m}Tc emits a 140 keV γ-ray with 89% abundance which is close to optimal for imaging with commercial gamma cameras. The minimal tissue-damaging linear energy transfer radiation allows the injection of activities of more than 1 GBq with low radiation exposure to the patient. The six-hour half-life is sufficiently long for pharmaceutical preparation and *in vivo* accumulation in the target, yet short enough to minimize radiation dose to the patient or environmental repercussions. Furthermore, the combination of the medically useful radionuclides, ^{99m}Tc and rhenium-186/188 ($^{186/188}$Re), is attractive for developing molecular imaging and molecular radiotherapeutics due to the similarities in their coordination chemistry and their excellent physical decay characteristics, which enable imaging and therapy, respectively. The coordination chemistries of ^{99m}Tc and $^{186/188}$Re are remarkably similar in regard to the $\{M(CO)_3L_3\}^+$ core, where the coordination complexes of ^{99m}Tc and $^{186/188}$Re are isostructural (*7*−*9*).

Radiopharmaceuticals may be classified into two broad categories: (i) those with biological distribution determined strictly by blood flow, or perfusion, which target high capacity systems such as glomerular filtration, phagocytosis, hepatocyte clearance and bone absorption, and (ii) those with biological distribution determined by specific enzymatic or receptor mediated binding interactions, i.e., low-density sites. The latter approach, which necessitates high specific activity complexes, is achieved using two methods to chelate ^{99m}Tc in a receptor specific molecule, the conjugate/pendent approach and the integrated approach.

The conjugate or pendant approach, Scheme 1, involves tethering a ^{99m}Tc chelate moiety to a species known to possess high affinity binding to a receptor (*10*−*13*). This strategy has an inherent disadvantage in that incorporation of the metal chelate complex often decreases the affinity of the "native" biomolecule, requiring optimization of both the chelator and the physical−chemical properties of the tether to regain affinity, often at the expense of a favorable pharmacokinetic profile. The very nature of the bifunctional chelate is constructed from three independent components adding complexity to the optimization process: a side arm for linkage to the bioactive molecule, the tether between the side arm linker and the donor groups, and a set of appropriate ligand donor groups for coordination to the metal site, in this case, ^{99m}Tc. The "bifunctional" ligand serves two purposes. First, it complexes the metal (M) radionuclide securely, holding it to the radiopharmaceutical without leakage

* Corresponding author. E-mail JBabich@molecularinsight.com.
[†] Molecular Insight Pharmaceuticals, Inc.
[‡] Syracuse University.
[§] McMaster University.

10.1021/bc900192b CCC: $40.75 © 2009 American Chemical Society
Published on Web 07/02/2009

Scheme 1. Representation of the Pendant Approach for the Design of Radiopharmaceutical and Radioimaging Agents

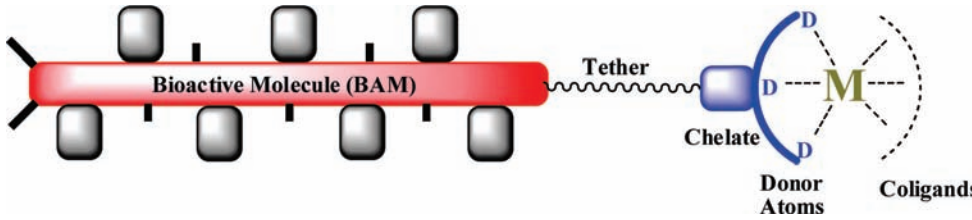

in vivo, and second, it provides a side arm for antibody, peptide, or small molecule attachment while maintaining maximal integrity of the bioactive molecule (BAM). The bifunctional chelators must be capable of conjugation under rapid, mild, preferably aqueous conditions reasonably close to physiological pH, with minimal need for purification. In addition, the moiety that chelates the ^{99m}Tc must demonstrate significant kinetic stability under biological conditions.

Conversely, the integrated approach replaces a portion of the high affinity receptor ligand with a ^{99m}Tc chelate, so as to preserve the binding affinity (*14*−*16*). The SAAC system is an example of the integrated approach which simplifies the process of identifying the appropriate combination of linker and chelator. By combining the tether and chelator into one molecule, SAAC systems transform this from a two variable to a one variable challenge. In the case of the lysine SAAC systems (Figure 1), the components consist of constant functionalities (B,C,D) for conjugation to the biomolecules of interest and a set of functional donor groups (A). One advantage of this approach is that the SAAC systems can be tailored to produce desired pharmacokinetic profiles in a more straightforward manner, via modification of the chelator (A) since B, C, and D are held constant in lysine. Furthermore, SAAC ligands are compatible with solid-phase peptide synthesis and to this end have been successfully exploited to created vast libraries of SAAC-containing peptides to enable high-throughput screening. The fluorescent SAAC analogue, rhenium tricarbonyl 2-amino-6-(bis(quinolin-2-ylmethyl)amino)hexanoic acid (Re-DqK), has been successfully integrated into the chemotactic peptide sequence fMLFK which has been used for imaging bacterial infection (*17*), and into the *trans*-activating transcriptional activator (TAT) peptide for imaging neuronal stem cells (*18*).

The most stable and readily accessible oxidation states are often characterized by chemically robust core structures which may be exploited as platforms for the development of radiopharmaceutical reagents. The most extensively developed core structure is $\{Tc(V)O\}^{3+}$, particularly with tetradentate ligands of the $N_xS_{(4-x)}$ type. Past research has focused primarily on attachment of the bifunctional chelators for complexation of the $\{Tc(V)O\}^{+3}$ core into small tripeptides and tetrapeptides (*19*−*22*). This has been accomplished predominantly using N_3S and N_4 ligands. Other structural subunits which have attracted attention include the $\{TcN\}^{2+}$, $\{TcO_2\}^{+}$, and technetium 6-hydrazinonicotinic acid $\{Tc(HYNIC)_x\}^{3+}$ (where $x = 1$ or 2) cores. More recently, the Tc(I) core, technetium tricarbonyl $\{Tc(CO)_3\}^{+}$ has been shown to provide an ideal geometry for the labeling of chelators of the $\{Tc(CO)_3\}^{+}$ core with high specific activity. The Tc(I)-tricarbonyl core offers a number of advantages for the design of novel radiopharmaceuticals: (i) a facile route exists to the important intermediate $[M(H_2O)_3(CO)_3]^{+}$ through the work of Alberto and co-workers (*23*, *24*); (ii) $[M(H_2O)_3(CO)_3]^{+}$ is water-soluble and the water molecules readily undergo ligand exchange with appropriate donor ligands; (iii) the complexes containing the $\{Tc(CO)_3\}^{+}$ core are chemically robust and maintain their integrity under the most forcing conditions. Complex formation is facilitated by the facile substitution chemistry at the aqua sites of the $\{M(CO)_3(H_2O)_3\}^{+}$ (M = Tc, Re) and $\{Re(CO)_3X\ (H_2O)_2\}$ (where X = Cl, Br) intermediate species, and the coordination preferences of Tc(I) and Re(I) for nitrogen and oxygen donors.

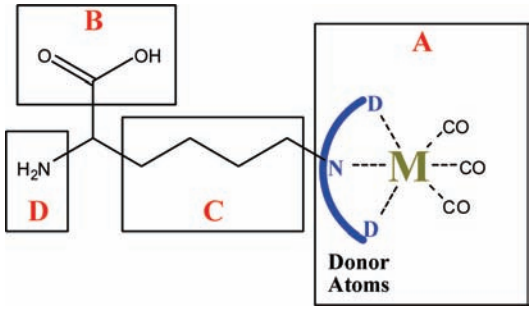

Figure 1. Components of the lysine SAAC analogues binding the group (VII) metals (M = Re or Tc).

Research in our laboratories focused on the derivatization of a single amino acid (L-lysine) for incorporation of the $\{Tc(CO)_3\}^{+}$ core. The advantages of this strategy include (i) decreased size and complexity of the chelator due to the ability to modify a single amino acid terminus, a feature which should minimize perturbations of the peptide receptor targeting small molecule or peptide by reducing the molecular weight and steric constraints of the bifunctional unit; (ii) the ease of derivatization of the amino acid or amino acid analogue; (iii) the use of a robust Tc-core, $\{Tc(CO)_3\}^{+}$, which is readily available from the $[Tc(CO)_3(H_2O)]^{+}$ precursor and undergoes substitution reactions at the aqua ligand sites with donor ligands (*25*−*28*). By reducing the size of the bifunctional unit, the lipophilicity of the complexes may be minimized, leading to diminished liver and gastrointestinal uptake and accumulation. These novel chelators should lead to ^{99m}Tc-radiopharmaceuticals with improved whole body clearance and thus enhanced image quality especially in the abdominal regions.

The use of $\{^{99m}Tc(CO)_3(H_2O)_3\}^{+}$ as the starting material leads to readily formed complexes of the *fac*-$[^{99m}Tc(CO)_3(L)_3]^{+}$ core. Recent work has demonstrated the high affinity of the $\{Tc(CO)_3\}^{+}$ core for this chelator system (*29*−*32*). The thermodynamic stability of the $\{Tc(I)(CO)_3\}^{+}$ core also adds *in vivo* stability, limiting complicating presence of metabolites and side products that may negatively effect the imaging properties of the final complexes and negate the true tracer characteristics.

We recently synthesized and characterized a series of bifunctional chelators derivatized from the ε-amine of L-lysine as stable, low molecular weight chelates for ^{99m}Tc and rhenium, including bis(2-pyridine), bis(dithiazole), bis(*o*-phenols), and 2-pyridine monoacetic acid (*33*) with the goal of investigating the impact of donor groups and labeling conditions on radiochemical yields and/or distribution that could be readily inserted into a solid-phase peptide synthesizer. Modification of the chelating moieties presents a facile way to vary the structural and physiochemical properties of our SAAC systems. The chelators prepared led to cationic, neutral and anionic complexes. Herein, are described the $\{^{99m}Tc(I)(CO)_3^{+}\}$ SAAC systems: $[^{99m}Tc(CO)_3(\eta^3$-{2-amino-6-(bis(pyridin-2-ylmethyl)amino)hexanoic acid}] (**7**), $[^{99m}Tc(CO)_3(\eta^3$-{2-amino-6-(bis(thiazol-2-

ylmethyl)amino)hexanoic acid}] (**8**), [^{99m}Tc(CO)$_3$(η^3-{2-amino-6-((carboxymethyl)(pyridin-2-ylmethyl)amino)hexanoic acid}] (**9**), and [^{99m}Tc(CO)$_3$(η^3-{6-[bis(2-hydroxy-benzyl)amino]-2-(9*H*-fluoren-9-ylmethoxycarbonylamino)hexanoic acid}] (**10**). All the ligands were evaluated for radiolabeling optimization, stability, and in addition, ligands **7**−**9** were evaluated for tissue distribution studies in normal rats providing crucial data relating characteristics of the chelates to pharmacokinetic profiles.

EXPERIMENTAL SECTION

General Methods. All reactions were carried out in dry glassware under an atmosphere of argon unless otherwise noted. Reactions were purified by column chromatography, under medium pressure using a Biotage SP4 or by preparative high-pressure liquid chromatography using a Varian Prostar 210 preparative HPLC system equipped with a semipreparative Vydac C18 reverse-phase column (250 mm × 10 mm × 5 μm) connected to a Varian Prostar model 320 UV−visible detector and monitored at a wavelength of 254 nm. The final product purifications were achieved using a binary solvent gradient of 5−95% B over 21 min (A = triethyl ammonium phosphate (TEAP) pH 3, B = methanol). Analytical HPLC of the radioiodinated compounds was performed using the same method with an analytical Vydac C18 reverse-phase column (250 mm × 4.6 mm × 5 μm). Microwave reactions were performed in a Biotage Initiator 60 microwave using 10 mL reactor vials. ^{1}H NMR spectra were obtained on a Bruker 400 MHz instrument. Spectra are reported as ppm and are referenced to the solvent resonances in $CDCl_3$, DMSO-d_6, or methanol-d_4. Elemental analysis was performed by Prevalere Life Sciences, Inc. High-resolution mass spectra were determined by M-Scan Inc. using positive ion electrospray with a Q-Tof API US hybrid quadrupole/time-of-flight mass spectrometer. ^{99m}Tc was used as a Na^{99m}TcO$_4$ solution in saline, as a commercial ^{99}Mo/^{99m}Tc generator eluant (Cardinal Health). The ^{99m}Tc-containing solutions were always kept behind sufficient lead shielding. The use of [^{99m}Tc(CO)$_3$(H$_2$O)$_3$]$^+$ was prepared from commercially available Isolink kits (Mallinckrodt). The synthesis of the [ε-{*N*,*N*-di(pyridyl-2-methyl)}-α-(Fmoc)lysine], [ε-{*N*,*N*-di(thiazole-2-methyl)}-α-(Fmoc)lysine], and [ε-{*N*-(pyridyl-2-methyl)-*N*-(acetic acid}-α-(Fmoc)lysine] were reported previously by our group (*33*). All solvents were purchased from Sigma Aldrich. Reagents were purchased from Sigma Aldrich (St. Louis, MO), Bachem (Switzerland), Akaal (Long Beach, CA), or Anaspec (San Jose, CA). The following abbreviations are used: Fmoc = Fluorenylmethyloxycarbonyl, DMAP = *N*, *N*-dimethylaminopyridine, DMF = *N*,*N* -dimethylformamide, DCM = dichloromethane, NaOH = sodium hydroxide, ID/g = injected dose per gram, PBS = phosphate buffered saline, RCP = radiochemical purity, RCY = radiochemical yield.

SYNTHESIS

All ligands were prepared using standard reductive amination techniques and have been described previously by Zubieta et al. (*33*)

2-Amino-6-(bis(pyridin-2-ylmethyl)amino)hexanoic Acid (DpK) (1). In a 100 mL round-bottom flask was placed 2-(9*H*-fluoren-9-ylmethoxycarbonylamino)-6-(bis(pyridin-2-ylmethyl)-amino)hexanoic acid (0.20 g, 0.36 mmol) and an equal molar amount of DMAP. The solids were dissolved in 5 mL of DMF and 1 mL of methanol. The reaction mixture was allowed to stir at room temperature for 12 h. The crude reaction was concentrated and purified by column chromatography (SiO_2) (20% methanol/methylene chloride as eluent) to afford the final product as an off-white solid (100 mg, 0.30 mmol, 83% yield). ^{1}H NMR ($CDCl_3$) δ 8.64 (d, 2H). 8.24 (t, 2H), 7.80 (d, 2H), 7.72 (t, 2H), 4.31 (s, 2H), 3.20 (m, 2H), 3.14 (s, 9H), 3.04 (m, 2H), 2.25 (m, 2H),1.30 (m, 2H). ESMS *m*/*z*: 328 $(M+H)^+$. Anal. ($C_{18}H_{24}N_4O_2$) C, H, N.

2-Amino-6-(bis(thiazol-2-ylmethyl)amino)hexanoic Acid (DtK) (2). In a 100 mL round-bottom flask was placed 2-(9*H*-fluoren-9-ylmethoxycarbonylamino)-6-(bis(thiazol-2-ylmethyl)-amino)hexanoic acid (0.050 g, 0.089 mmol) and an equal molar amount of DMAP. The solids were dissolved in 5 mL of DMF and 1 mL of methanol. The reaction mixture was allowed to stir at room temperature for 12 h. The crude reaction was concentrated and purified by column chromatography (SiO_2) (0−40% methanol/methylene chloride as eluent) to afford the final product as an off-white solid (18 mg, 0.053 mmol, 60% yield). ^{1}H NMR (D_2O) δ 7.73 (d, 2H). 7.57 (d, 2H), 4.09 (s, 4H), 3.69 (t, H), 2.63 (t, 2H), 1.81 (m, 2H), 1.61 (m, 2H), 1.35 (m, 2H). ESMS *m*/*z*: 340 $(M+H)^+$. Anal. ($C_{14}H_{20}N_4O_2$) C, H, N.

2-Amino-6-((carboxymethyl)(pyridin-2-ylmethyl)amino)-hexanoate (PAMA-K) (3). In a 100 mL round-bottom flask was placed *t*-butyl 2-(9*H*-fluoren-9-ylmethoxycarbonylamino)-6-pyridin-2-ylmethyl)amino)hexanoate (0.070 g, 0.122 mmol) and an equal molar amount of DMAP. The solids were dissolved in 5 mL of DMF and 1 mL of methanol. The reaction mixture was allowed to stir at room temperature for 12 h. The crude reaction was concentrated and purified by column chromatography (SiO_2) (0−40% methanol/ methylene chloride as eluent). Subsequently, the *t*-butyl-6-pyridin-2-ylmethyl)amino)hexanoate was dissolved in 4 mL dichloromethane and 4 mL of trifluoroacetic acid. The reaction mixture was allowed to stir at room temperature for 1.5 h. The solution was blown dry under a stream of nitrogen. The crude reaction was purified by column chromatography (SiO_2) (0−40% methanol/ methylene chloride as eluent) to afford the final product as an off-white solid. (21 mg, 0.068 mmol, 55% yield). ^{1}H NMR ($CDCl_3$) ^{1}H NMR (d_6-DMSO) δ 8.62 (d, H), 8.15 (s, 2H), 7.92 (m, H), 7.56 (d, H), 7.47 (m, H), 4.40 (d, 2H), 3.87 (m, 2H), 3.01 (m, H), 2.50 (m, 2H), 1.75 (m, 2H), 1.62 (m, 2H), 1.39 (m, 2H). ESMS *m*/*z*: 295 $(M+H)^+$. Anal. ($C_{14}H_{21}N_3O_4$) C, H, N.

2-Amino-6-(bis-(2-hydroxybenzyl)amino)hexanoic Acid (Diphenol-K) (4). In a 100 mL round-bottom flask was placed 2-(9*H*-fluoren-9-ylmethoxycarbonylamino)-6-[bis-(2-hydroxybenzyl)amino]-hexanoic acid (0.050 g, 0.086 mmol), and an equimolar amount of DMAP and 5 mL of DMF and 1 mL of methanol was added. The reaction mixture was allowed to stir at room temperature for 12 h. The crude reaction was purified by column chromatography (SiO_2) (0−40% methanol/methylene chloride as eluent) to afford the final product as an off-white solid (16 mg, 0.047 mmol, 52% yield). ^{1}H NMR ($CDCl_3$) δ 7.10 (m, 4H), 6.90 (m, 4H), 4.20 (d, 2H), 3.92 (m, 2H), 3.0 (m, H), 2.50 (m, 2H), 1.78 (m, 2H), 1.55 (m, 2H), 1.42 (m, 2H). ESMS *m*/*z*: 358 $(M+H)^+$. Anal. ($C_{20}H_{26}N_2O_4$) C, H, N.

2,2′-(pyridin-2-ylmethylazanediyl)diacetic Acid (PADA) (5). In a 100 mL round-bottom flask was placed pyridin-2-ylmethanamine (1.0 g, 9.26 mmol) dissolved in 20 mL of toluene. The solution was placed in an ice bath for dropwise addition of ethyl bromo acetate. The reaction was allowed to stir at 0 °C for 30 min. The crude reaction was concentrated and purified by column chromatography (SiO_2) (10% methanol/ methylene chloride as eluent) to afford the diethyl 2,2′-(pyridin-2-ylmethylazanediyl)diacetate (0.40 g, 1.42 mmol). The diethyl 2,2′-(pyridin-2-ylmethylazanediyl)diacetate (0.40 g, 0.142 mmol) was dissolved in 5 mL of methanol and 5 mL of 2 N NaOH. The reaction was refluxed for 18 h. The crude reaction was purified by column chromatography (SiO_2) (0−40% methanol/ methylene chloride) to afford the final product as an off-white solid. (310 mg, 0.138 mmol, 96% yield). ^{1}H NMR (d_6-DMSO) δ 8.10 (s, H), 7.84 (dd, H), 7.60 (d, H), 7.47 (m, H), 4.30 (d,

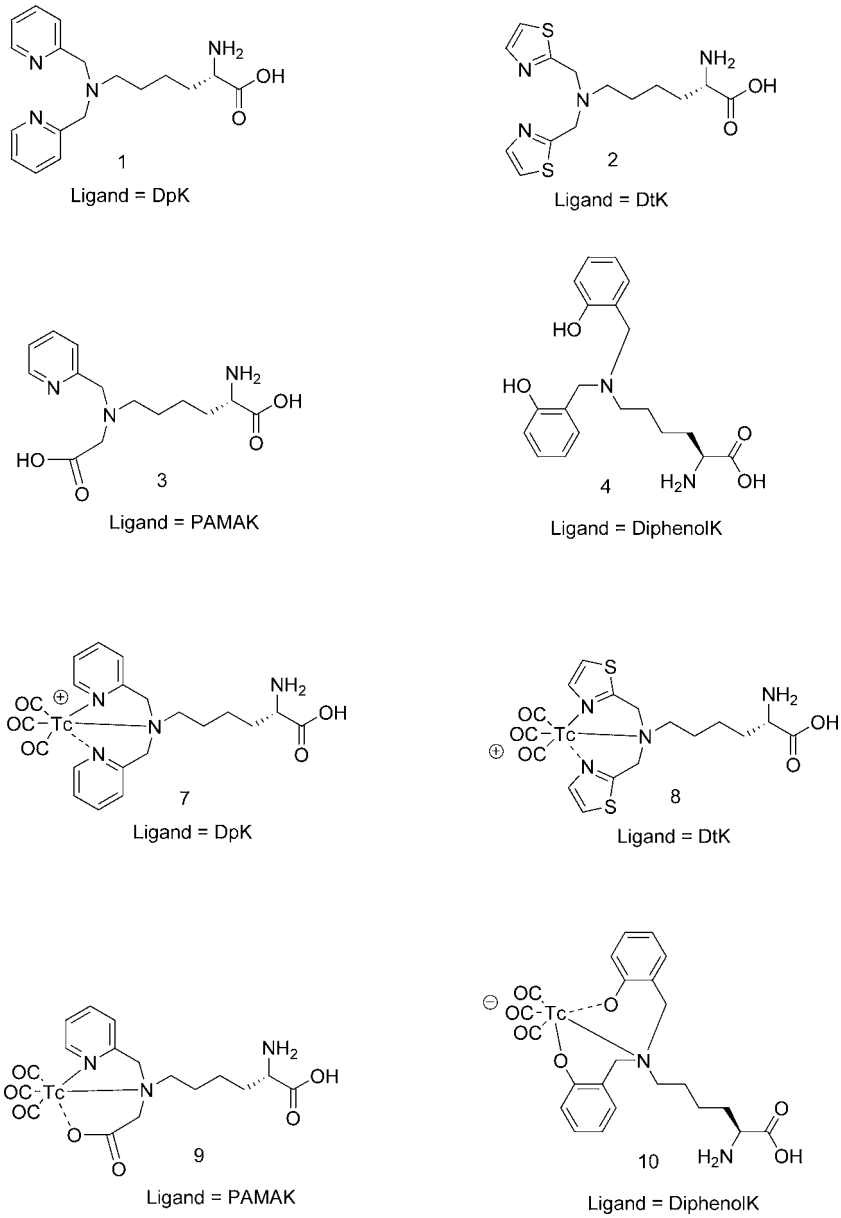

Figure 2. The SAAC ligands (**1**−**4**) and their respective ^{99m}Tc-SAAC complexes (**7**−**10**) prepared and evaluated for radiolabeling yield, stability, and lipophilicity.

2H), 3.45 (m, 4H). LCMS *m*/*z*: 224 $(M+H)^+$. Anal. ($C_{10}H_{12}N_2O_4$) C, H, N.

General Preparation of ^{99m}Tc-Complexes. The $\{^{99m}Tc(I)(CO)_3\}^+$ labeling was accomplished in two steps using commercially available IsoLink kits (Covidien) to form the $[^{99m}Tc(CO)_3(H_2O)_3]^+$ intermediate, which was heated at 75 °C for 30 min with the appropriate SAAC (Figure 2) (10^{-4} to 10^{-6} M, pH 2−9, 75−100 °C) to form complexes $[^{99m}Tc(CO)_3(\eta^3$-{2-amino-6-(bis(pyridin-2-ylmethyl)amino)hexanoic acid}] = $[^{99m}Tc(CO)_3(DpK)]^+$ (**7**), $[^{99m}Tc(CO)_3(\eta^3$-{2-amino-6-(bis(thiazol-2-ylmethyl)amino)hexanoic acid}] = $[^{99m}Tc(CO)_3(DtK)]^+$ (**8**), $[^{99m}Tc(CO)_3(\eta^3$-{2-amino-6-((carboxymethyl)(pyridin-2-ylmethyl)amino)hexanoic}] = $[^{99m}Tc(CO)_3(PAMA\text{-}K)]$ (**9**), and $[^{99m}Tc(CO)_3(\eta^3$-{6-[bis(2-hydroxy-benzyl)amino]-2-(9*H*-fluoren-9-ylmethoxycarbonylamino)hexanoic acid}]=$[^{99m}Tc(CO)_3$(diphenol-K)]$^-$ (**10**). Likewise, the control ligands PADA and L-histidine (Figure 3) were labeled in a similar manner (10^{-6} M, pH 7, 75 °C) to form their ^{99m}Tc-complexes. Upon cooling, the reactions were purified by preparatory reverse-phase (RP) HPLC and the purity assessed by analytical RP-HPLC.

Microwave Preparation of $[^{99m}Tc(CO)_3(DpK)]^+$ (7). The $\{^{99m}Tc(I)(CO)_3\}^+$ labeling was accomplished in two steps using the $[^{99m}Tc(CO)_3(H_2O)_3]^+$ intermediate, which was heated at 100 °C for 5 min with 2-amino-6-(bis(pyridin-2-ylmethyl)amino)-hexanoic acid (DpK) (**1**) (10^{-4} M, PBS pH 7.4) in 10 mL reactor tubes within the Biotage Initiator 60 microwave to form the complex $[^{99m}Tc(CO)_3(\eta^3$-{2-amino-6-(bis(pyridin-2-ylmethyl)-amino)hexanoic acid}] = $[^{99m}Tc(CO)_3(DpK)]^+$ (**7**).

Determination of the Optimal pH for the Radiolabeling. The effect of pH on the radiochemical yield (RCY) of the radiolabeling reactions was investigated at a constant temperature, concentration, and reaction time. Solutions of the ligands at a concentration of 10^{-6} M were radiolabeled at a temperature of 75 °C and analyzed for RCY at pH = 2, 5, 6, 7, 8, and 9 using sodium acetate and phosphate buffers. The optimal pH for all of the individual chelators was determined from the RCY at 30 min.

Determination of Complex Stability. The stability of the HPLC purified final complexes was assessed by simultaneous incubation with cysteine and histidine (final ligand concentration

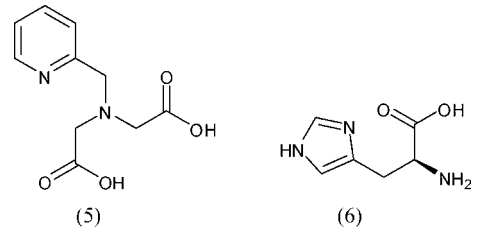

Figure 3. Structure of control ligands PADA (*5*) and histidine (*6*).

10^{-5} M) at pH = 7.4 and 37 °C at 1, 4, and 18 h. The complexes were prepared, purified by RP-HPLC to achieve carrier free complexes, and then incubated with an excess of cysteine and histidine. A solution of the ^{99m}Tc-SAAC complex was incubated under identical reaction conditions in the absence of cysteine and histidine as a control.

Determination of Log *P* Values. The Log *P* values of the ^{99m}Tc(I)-complexes were determined as follows. The ^{99m}Tc-SAAC complexes were prepared and purified by RP-HPLC. The desired peak was collected, and the sample was evaporated under a stream of nitrogen. The residue was dissolved in 25 μL of saline and placed in an equal volume of *n*-octanol (3 mL) and 25 mM pH = 7.4 phosphate buffer (3 mL). The samples were mixed under vortex for 20 min and centrifuged at 8000 rpm for 5 min, and three 100 μL aliquots were removed from both the aqueous and the organic layers for analysis on a gamma counter (Wallac 1282). Subsequently, 1 mL of the phosphate buffer-Tc-complex solution was removed, and the process was repeated with fresh *n*-octanol, for a total number of six extractions to ensure full extraction of all the organic components. The partition coefficients were calculated using the equation: P = (activity concentration in *n*-octanol)/(activity concentration in aqueous layer). The Log *P* values reported were calculated from the average of the different measurements.

Rat Tissue Distribution Studies. The distribution and pharmacokinetics of selected ^{99m}Tc-SAAC complexes (*7*−*10*) were evaluated in normal male Sprague−Dawley rats (180−200 g) administered via the tail vein as a bolus injection (approximately 10 μCi/rat) in a constant volume of 0.1 mL. The animals (n = 5 per time point) were euthanized by asphyxiation with carbon dioxide at 5, 30, 60, and 120 min post injection. Tissues (blood, heart, lungs, liver, spleen, kidneys, adrenals, stomach, intestines (with contents), testes, skeletal muscle, bone, and brain) were dissected, excised, weighed wet, and counted in an automated γ-counter (LKB Model 1282, Wallac Oy, Finland). Tissue time−radioactivity levels expressed as percent injected dose per gram of tissue (%ID/g) were determined.

RESULTS AND DISCUSSION

The novel tridentate ligands possess a unique primary amine which allows for the facile synthesis of large numbers of structural variants with diverse physiochemical properties. The synthetic ease of preparation of *N*-substituted derivatives allowed for the preparation of SAAC ligands with the potential to form neutral, cationic, and anionic ^{99m}Tc complexes. The chemistry utilized to prepare the bifunctional SAAC chelators was based on the use of the reductive alkylation reaction (*34*, *35*). The compounds were purified by column chromatography using silica gel to afford the pure prototype SAAC ligands, 2-amino-6-(bis(pyridin-2-ylmethyl)amino)hexanoic acid (**1**), 2-amino-6-(bis(thiazol-2-ylmethyl)amino)hexanoic acid (**2**), 2-amino-6-((carboxymethyl)(pyridin-2-ylmethyl)amino)hexanote (**3**), and 2-amino-6-(bis-(2-hydroxybenzyl)amino)hexanoic acid (**4**) in fair to moderate yields.

Radiolabeling of ^{99m}Tc-SAAC. Radiolabeling of SAAC systems was accomplished to form **7**−**10** on either the free

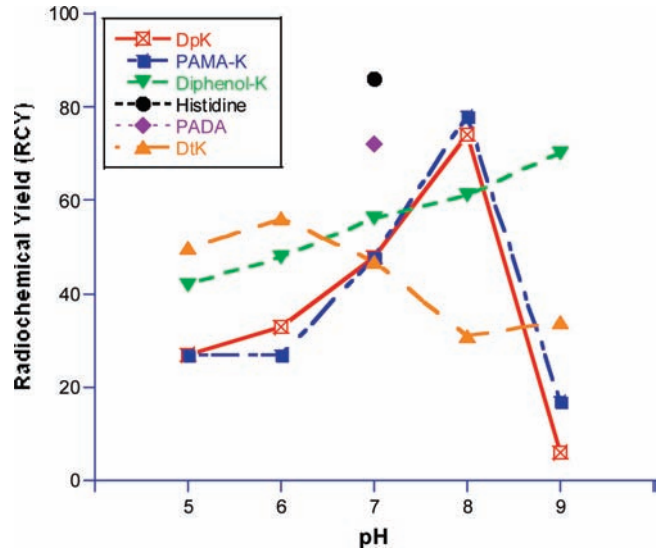

Figure 4. RCY as a function of pH for the formation of ^{99m}Tc-SAAC complexes at 75 °C for 30 min at a concentration of 10^{-6} M.

α-amino acids or as the appropriately *N*-protected amino acid derivative utilizing similar methodology, demonstrating the ease of preparation and the flexibility in the design of the SAAC systems. The ^{99m}Tc(I)$(CO)_3^+$ radiolabeling was accomplished in two steps using the commercially available IsoLink kits (Covidien) to form the $[^{99m}Tc(CO)_3(H_2O)_3]^+$ intermediate, which was reacted with the appropriate SAAC ligand (10^{-6} to 10^{-4} M) in an equal volume mixture of 1:1 acetonitrile and phosphate buffer. The sealed vial was heated at 100 °C for 30 min. Upon cooling, the reaction was analyzed for purity via RP-HPLC. The radiochemical purity (RCP) after HPLC purification, resulting in "carrier-free" products, was determined via HPLC and shown to be consistently ≥95%. Although initial results demonstrated radiolabeling at concentrations as low as 10^{-6} M, the RCY was ≤80%. To achieve a RCY of >95% at 75 °C, the reaction concentration needed to be increased to 10^{-4} M.

Microwave Radiolabeling of $[^{99m}Tc(CO)_3(DpK)]^+$ (7). Heating with a Biotage Initiator 60 microwave was explored as an alternative to conventional heating, with the goal of reducing the time necessary to produce the ^{99m}Tc-SAAC complex in the highest yields. The conditions to produce **7** in >95% RCY were achieved (>97% RCY; n = 5) by employing microwave heating at 100 °C for 5 min at a concentration of 10^{-4} M in PBS, pH 7.4 (data not shown). The RCY decreased to <60% using lower concentrations (10^{-5} M and 10^{-6} M) under the same reaction conditions. These results represent a significant improvement in the radiolabeling time and warrant further studies using microwave heating to optimize the process.

pH Optimization. The RCY of the various chelators depended on the pH at which the radiolabeling reaction was conducted. The results shown in Figure 4, demonstrated that performing the radiolabeling at pH = 8 afforded higher yields for ligands **1** and **3** when compared to radiolabeling at higher (pH > 8) or lower (pH < 8) pH values where the RCY decreased significantly; however, for ligands **2** and **4**, slightly acidic and slightly basic reaction conditions were favored, respectively.

Further evaluation demonstrated that the starting material $[^{99m}Tc(CO)(H_2O)]^+$ is extremely stable at pH > 6 but undergoes significant (∼20%) degradation upon heating at temperatures required for effective radiolabeling (75−100 °C at ≤pH 5. When the radiolabeling was conducted at pH <5 the RCY for all the chelators studied was poor (<10%). Due to differences in the heterocyclic donating atoms of the chelating ligands, the optimal pH for effective radiolabeling varied for each of the SAAC

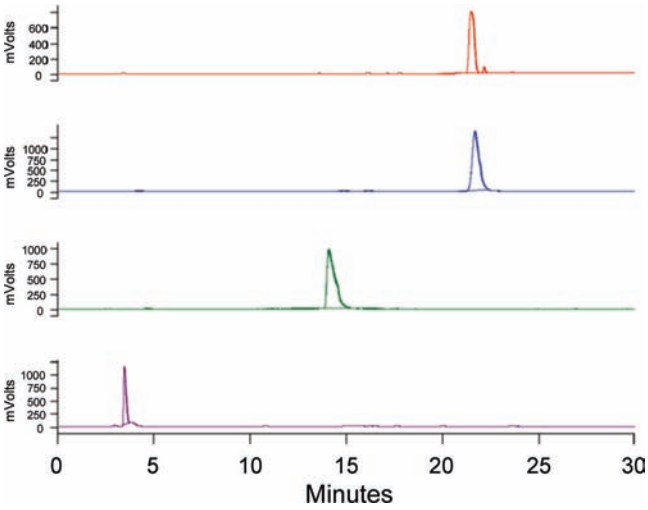

Figure 5. RP-HPLC chromatograms of (from top to bottom) $[Re(CO)_3(Fmoc\text{-}DpK)]^+$ (UV−vis chromatogram), $[^{99m}Tc(CO)_3(Fmoc\text{-}DpK)]^+$ (radiochromatogram), $[^{99m}Tc(CO)_3(DpK)]^+$ (**7**) (radiochromatogram), and the metal-free chelating agent DpK (**1**) (UV−vis chromatogram).

ligands studied. The pyridine-containing SAAC ligands, **1** and **3**, were labeled more efficiently at pH = 8. In contrast to the slightly basic optimal pH for radiolabeling of the pyridine containing SAAC ligands, the dithiazole containing SAAC ligand (**2**) produced a higher yield when the radiolabeling was conducted at a slightly acidic pH, pH = 6. The diphenol SAAC ligand (**4**), whose donating atoms are the phenolic oxygens, gave the highest yield when the radiolabeling was conducted at a slightly basic pH (pH = 9). The RCY of the SAAC ligands studied were only fair to good when the radiolabeling was performed at a concentration of 10^{-6} M (RCY ≤ 60%). The results were comparable for the two control ligands studied, 2,2′-(pyridin-2-ylmethylazanediyl)diacetic acid **(**PADA) (**5**) and L-histidine (**6**) which demonstrated similar results (RCY = 70−86%) at pH = 7.

The radiolabeling of the SAAC ligands could be accomplished on the Fmoc-protected ligand or on the unprotected free amine of the SAAC ligand utilizing identical reaction conditions, an advantage of the SAAC system compared to other chelators reported in the literature (see Figure 5). The complexes were analyzed by RP-HPLC and demonstrated >90% RCY when the radiolabeling was performed at a concentration of the SAAC ligand of $\geq 10^{-4}$ M and >50% RCY (at optimal pH) when the amount of SAAC ligand used was 10^{-6} M. The identities of the ^{99m}Tc-complexes were readily confirmed by RP-HPLC analysis after coinjection with the nonradioactive rhenium analogues as shown in Figure 5.

^{99m}Tc Challenge Experiments. The ^{99m}Tc-SAAC complexes were analyzed by RP-HPLC for stability against ligand challenge with excess histidine (100 mM) and cysteine (100 mM) in PBS, pH = 7.4 at 37 °C for 18 h. The ^{99m}Tc-SAAC complexes (carrier-free) demonstrated no degradation by HPLC analysis (see Figure 6) for **7**. In contrast, the negatively charged ^{99m}Tc-Diphenol-K complex proved to be much less stable, with significant degradation encountered upon purification by RP-HPLC, and therefore it was excluded from the tissue distribution study.

Determination of Lipophilicity (Log *P* Values). Log *P* values of the complexes were determined using the HPLC-purified ^{99m}Tc-SAAC complexes in *n*-octanol and 25 mM phosphate buffer (pH = 7.4). The Log *P* values (Table 1) demonstrated similar partition coefficients for all three of the stable complexes evaluated. The Log *P* values ranged from −1.80 to −2.20 regardless of differences in charge on the metal center or the heterocycle employed.

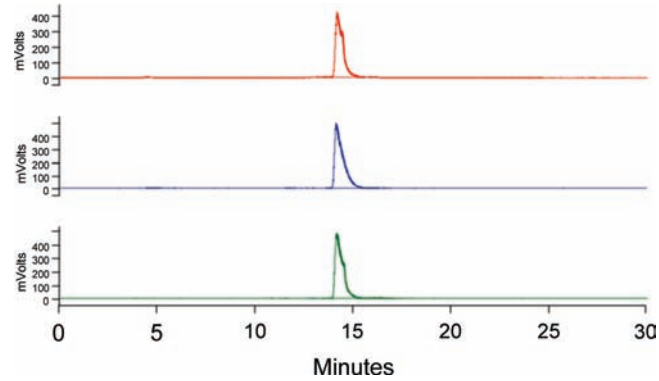

Figure 6. Radiochromatogram of HPLC purified $[^{99m}Tc(CO)_3(DpK)]$ (**7**) after 18 h incubation at 37 °C in PBS at pH = 7.4 (top), incubation at 37 °C with cysteine (100 mM) at pH = 7.4 (middle), and incubation at 37 °C with histidine (100 mM) at pH = 7.4 (bottom).

Table 1. Comparisons of the Partition Coefficients (Log *P*) and HPLC Retention Times for the ^{99m}Tc-SAAC Complexes

^{99m}Tc-complex	HPLC R_t [min]	Log *P*
7	13.5	−1.9
8	13	−2.2
9	14	−1.8
10	17.2	n.d.[a]
^{99m}Tc-Histidine	10.2	n.d.[a]
^{99m}Tc-PADA	16.6	n.d.[a]

[a] n.d. = not determined.

Rat Tissue Distribution Studies. Animal tissue distribution studies were performed on three of the SAAC complexes, $[^{99m}Tc(CO)_3\{\eta^3\text{-}(DpK)\}]$ (**7**), $[^{99m}Tc(CO)_3\{\eta^3\text{-}(DtK)\}]$ (**8**), and $[^{99m}Tc(CO)_3\{\eta^3\text{-}(PAMAK)\}]$ (**9**). A summary of the results for all three complexes in selected organs is shown in Table 2. Each SAAC complex demonstrated a unique hepatobiliary or renal clearance profile.

Tissue distribution studies with complexes **7**, Figure 7, and **9**, Figure 9, demonstrated rapid clearance from the blood and primary excretion through the kidneys and liver. The activity decreased in all tissues as a function of time, except in the gastrointestinal (GI) tract. There was no prolonged retention of radioactivity in any of the other organs analyzed. Qualitatively, $[^{99m}Tc(CO)_3\{\eta^3\text{-}(PAMAK)\}]$ (**9**) cleared more rapidly from the kidney and liver, while $[^{99m}Tc(CO)_3\{\eta^3\text{-}(DpK)\}]$ (**7**) cleared more rapidly from the blood. In contrast, the blood clearance of $[^{99m}Tc(CO)_3\{\eta^3\text{-}(DtK)\}]$ (**8**) (2.33 ± 0.26%ID/g at 30 min) was significantly slower than both **7**, 0.07 ± 0.01%ID/g at 30 min ($p < 0.001$), and **9**, 0.18 ± 0.02%ID/g at 30 min ($p < 0.001$). In contrast to complexes **7** and **9**, which were efficiently cleared, for $[^{99m}Tc(CO)_3\{\eta^3\text{-}(DtK)\}]$ (**8**), Figure 8, the radioactivity was retained in both the liver and kidneys throughout the time course of the experiment. In addition, $[^{99m}Tc(CO)_3\{\eta^3\text{-}(DtK)\}]$ (**8**) was retained longer in most nontarget organs as shown in Figure 8. Overall, $[^{99m}Tc(CO)_3\{\eta^3\text{-}(PAMAK)\}]$ (**9**) demonstrated lower hepatobiliary uptake at 30 min, 1.45 ± 0.21%ID/g, compared to 2.75 ± 0.11%ID/g for **7** ($p < 0.001$) and 1.93 ± 0.15%ID/g for **8** ($p < 0.015$).

The cationic complexes, $[^{99m}Tc(CO)_3\{\eta^3\text{-}(DpK)\}]$ (**7**) and $[^{99m}Tc(CO)_3\{\eta^3\text{-}(DtK)\}]$ (**8**), demonstrated increased clearance through the liver and GI compared to the neutral complex, $[Tc(CO)_3\{\eta^3\text{-}(PAMAK)\}]$ (**9**). For example at 120 min, $[^{99m}Tc(CO)_3\{\eta^3\text{-}(DpK)\}]$ (**7**) and $[^{99m}Tc(CO)_3\{\eta^3\text{-}(DtK)\}]$ (**8**) both exhibited approximately 10-fold more radioactivity in the liver 2.12 ± 0.06% ID/g ($p < 0.001$) and 1.74 ± 0.12% ID/g ($p < 0.001$), respectively, compared to the uncharged complex $[^{99m}Tc(CO)_3\{\eta^3\text{-}(PAMAK)\}]$ (**9**) 0.20 ± 0.03% ID/g, which suggests increased lipophilic character of the cationic **7** and **8**.

Table 2. Comparison of the Rat Tissue Distribution Results of ^{99m}Tc-SAAC Complexes in Blood and Excretory Tissues, Expressed as Average %ID/g ± SEM

		time (min)			
compound	tissue	5	30	60	120
7	Blood	0.58 ± 0.05	0.07 ± 0.01	0.025 ± 0.005	0.013 ± 0.001
	Liver	3.36 ± 0.44	2.75 ± 0.11	2.59 ± 0.08	2.12 ± 0.06
	Kidney	6.05 ± 1.03	4.95 ± 0.11	4.93 ± 0.43	3.89 ± 0.42
	GI	0.49 ± 0.08	0.89 ± 0.07	1.46 ± 0.09	2.73 ± 0.57
8	Blood	3.32 ± 0.82	2.33 ± 0.26	1.4 ± 0.07	0.76 ± 0.12
	Liver	1.7 ± 0.42	1.93 ± 0.15	2.05 ± 0.41	2.61 ± 0.31
	Kidney	3.26 ± 1.04	4.71 ± 0.41	4.78 ± 0.14	4.83 ± 0.41
	GI	0.3 ± 0.15	0.59 ± 0.13	0.73 ± 0.29	0.87 ± 0.2
9	Blood	0.63 ± 0.12	0.18 ± 0.02	0.071 ± 0.003	0.034 ± 0.012
	Liver	1.26 ± 0.27	1.45 ± 0.21	0.56 ± 0.1	0.2 ± 0.06
	Kidney	6.4 ± 1.4	3.25 ± 0.47	1.14 ± 0.27	0.47 ± 0.09
	GI	0.18 ± 0.04	1.14 ± 0.23	1.82 ± 0.35	2.44 ± 1.18

It is unclear whether the increased hepatobiliary clearance is the result of the second heterocyclic ring (pyridine or thiazole) or the positively charged technetium metal center. Although the clearance of **7** is primarily via the hepatobiliary route, its clearance from the blood is the most rapid of the three SAAC complexes studied 0.013 ± 0.001% ID/g in the blood at 2 h compared to 1.09 ± 0.04% ID/g for **8** ($p < 0.001$) and 0.03 ± 0.01% ID/g for **9** ($p < 0.01$).

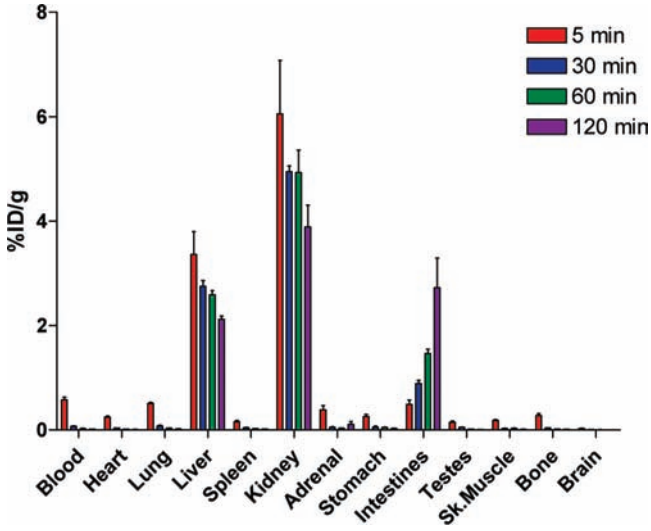

Figure 7. Tissue distribution results of [^{99m}Tc(CO)$_3${η^3-(DpK)}](**7**) expressed as average %ID/g.

One goal of the SAAC labeling technology is to design complexes that preferentially clear the body via renal excretion. It was anticipated that the lipophilicity of the ^{99m}Tc-SAAC complexes would influence the route of clearance. Therefore, the Log *P* values of the ^{99m}Tc-SAAC complexes were measured as an independent assessment of the lipophilic nature of the complexes to gain insight into the impact of overall lipophilicity of the metal complex on tissue pharmacokinetics and how it may effect future bioconjugates. The experimentally determined Log *P* values suggested that the complexes were very hydrophilic, **7** (Log $P = -1.9$), **8** (Log $P = -2.2$), and **9** (Log $P = -1.8$), were surprisingly very similar, and did not predict the differences in clearance described above. This lack of correlation between the Log *P* values and the clearance pathway suggests that the partition coefficient alone may be insufficient to assess the behavior of the ^{99m}Tc-SAAC complexes *in vivo*. Furthermore, this implies that differences in tissue distribution, pharmacokinetics, and clearance may be governed by parameters other than lipophilicity, such as the overall charge of the complex, complex sterics, the basicity of the nitrogen donor and/or the other properties of the heterocyclic rings themselves.

These studies suggest the physicochemical properties of the chelator portion of the SAAC complex affects the overall pharmacokinetics of the SAAC systems. While the impact of the chelator on the tissue pharmacokinetics of the biomolecule complex is anticipated to have a greater influence on small molecules and small peptides compared to larger peptides and proteins, it may be exploited in the design of chelators that, when incorporated into bioconjugates, offer preferred tissue distribution, pharmacokinetics, and clearance profiles. Impor-

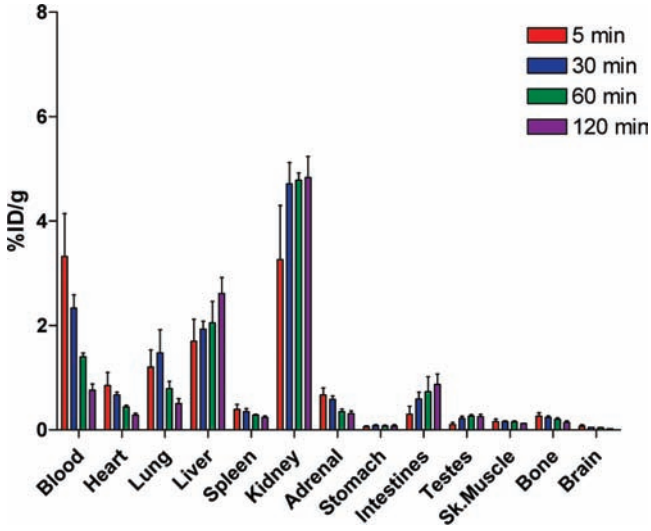

Figure 8. Tissue distribution results of [^{99m}Tc(CO)$_3${η^3-(DtK)}] (**8**), expressed as average %ID/g.

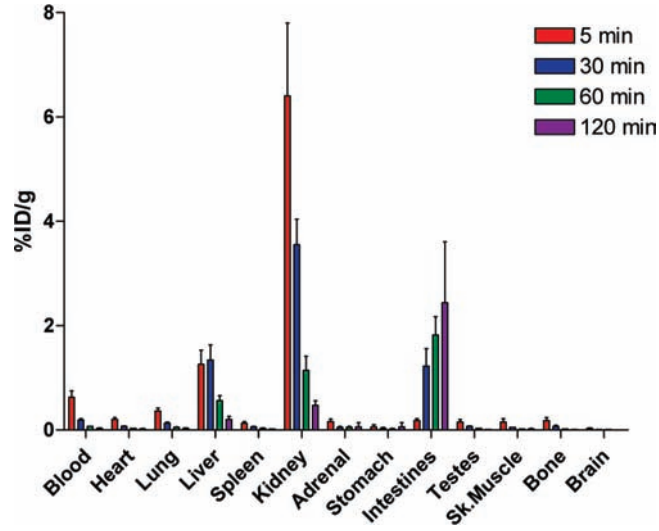

Figure 9. Tissue distribution results of [Tc(CO)$_3${η^3-(PAMAK)}] (**9**), expressed as average %ID/g.

tantly, the ability to modify the pharmacokinetic properties of a SAAC-conjugate through chelator selection should provide an advantage in the design and development of novel radiopharmaceuticals.

In summary, an examination of a set of SAAC ligands where the final technetium complex was neutral, cationic, or anionic at the metal center was accomplished. The SAAC systems could be efficiently radiolabeled in high yields with the $\{^{99m}Tc(CO)_3\}^+$ core to produce robust neutral or cationic ^{99m}Tc-SAAC complexes. The stability and optimal pH radiolabeling conditions were explored. The complexes were easily purified and are compatible with standard solid-phase peptide synthesis chemistries. The three stable SAAC complexes, cationic [^{99m}Tc(CO)$_3${η^3-(DpK)}] (**7**) and [^{99m}Tc(CO)$_3${η^3-(DtK)}] (**8**), neutral [^{99m}Tc(CO)$_3${η^3-(PAMAK)}] (**9**), and their role in the uptake, retention, and clearance in normal rats was evaluated; however, the anionic complex, [^{99m}Tc(CO)$_3${η^3-(Di-phenolK)}] (**10**), was unstable over time and was therefore eliminated from the rat tissue distribution studies. The pharmacokinetics of the complexes varied for each of the three stable complexes evaluated, with **9** demonstrating the most promise as a chelator for future technetium radiopharmaceuticals based on the efficient radiolabeling, high RCY, and favorable pharmacokinetic properties.

The advantageous pharmacokinetic profiles included rapid blood clearance for both **7** and **9** with decreased radioactivity in all background tissues (excluding GI tract) as a function of time. These experiments suggest that the SAAC systems, particularly those that clear rapidly, like [^{99m}Tc(CO)$_3${η^3-(PAMAK)}] (**9**) should serve well as a novel radiolabeling strategy for peptide library synthesis and radiolabeling of other important biomolecules.

ACKNOWLEDGMENT

This work was supported in part by grants (J.W.B.) from the Department Of Energy, grant no D2-FG02-99ER62791 and the National Institutes of Health, grant no 1R41A1054080-01.

Supporting Information Available: Elemental analysis data for compounds **1**−**4**. This material is available free of charge via the Internet at http://pubs.acs.org.

LITERATURE CITED

(1) Park, S. I., and Press, O. W. (2007) Radioimmunotherapy for treatment of B-cell lymphomas and other hematologic malignancies. *Curr. Opin. Hematol. 14* (6), 632–8.

(2) Matthay, K. K., Yanik, G., Messina, J., Quach, A., Huberty, J., Cheng, S. C., Veatch, J., Goldsby, R., Brophy, P., Kersun, L. S., Hawkins, R. A., and Maris, J. M. (2007) Phase II study on the effect of disease sites, age, and prior therapy on response to iodine-131-meta-iodobenzylguanidine therapy in refractory neuroblastoma. *J. Clin. Oncol. 25* (9), 1054–60.

(3) Fitzgerald, P. A., Goldsby, R. E., Huberty, J. P., Price, D. C., Hawkins, R. A., Veatch, J. J., De la Cruz, F., Jahan, T. M., Linker, C. A., Damon, L., and Matthay, K. K. (2006) Malignant pheochromocytomas and paragangliomas: a phase II study of therapy with high-dose I-131-metaiodobenzylguanidine (I-131-MIBG). *Ann. N.Y. Acad. Sci. 1073*, 465–90.

(4) Frilling, A., Weber, F., Saner, F., Bockisch, A., Hofmann, M., Mueller-Brand, J., and Broelsch, C. E. (2006) Treatment with (90)Y- and (177)Lu-DOTATOC in patients with metastatic neuroendocrine tumors. *Surgery 140* (6), 968–76.

(5) Boyd, M., Ross, S., Owens, J., Hunter, D., Babich, J., Zalutsky, M. R., Hamilton, T. G., Bell, S., and Mairs, R. J. (2004) Preclinical evaluation of no-carrier-added [131I] meta-iodobenzyl guanidine, for the treatment of tumours transfected with the noradrenaline transporter gene. *Lett. Drug Des. Discovery 1* (1), 50–57.

(6) Mariani, G., Nicolini, M., and Wagner, H. W. (1983) *Technetium in Chemistry and Nuclear Medicine*, p 131, Vol 1, Cortina International, Verona.

(7) Heeg, M. J., and Jurisson, S. (1999) The role of inorganic chemistry in the development of radiometal agents for cancer therapy. *Acc. Chem. Res. 32* (12), 1053–1060.

(8) Nicolini, M., Bandoli, G., and Mazzi, U., Eds. (2006) *Technetium, Rhenium and Other Metals in Chemistry and Nuclear Mediciine*, Vol 7, New York.

(9) Jurisson, S. S., and Lyden, J. D. (1999) Potential technetium small molecule radiopharmaceuticals. *Chem. Rev. 99*, 2205.

(10) Liu, S., Edwards, D. S., Harris, A. R., Heminway, S. J., and Barrett, J. A. (1999) Technetium complexes of a hydrazinonicotinamide-conjugated cyclic peptide and 2-hydrazinopyridine: synthesis and characterization. *Inorg. Chem. 38* (6), 1326–1335.

(11) Schweinsberg, C., Maes, V., Brans, L., Blauenstein, P., Tourwe, D. A., Schubiger, P. A., Schibli, R., and Garayoa, E. G. (2008) Novel glycated [99mTc(CO)3]-labeled bombesin analogues for improved targeting of gastrin-releasing peptide receptor-positive tumors. *Bioconjugate Chem. 19* (12), 2432–2439.

(12) Femia, F. J., Maresca, K. P., Hillier, S. M., Zimmerman, C. N., Joyal, J. L., Barrett, J. A., Aras, O., Dilsizian, V., Eckelman, W. C., and Babich, J. W. (2008) Synthesis and evaluation of a series of ^{99m}Tc(CO)$_3$+ lisinopril complexes for in vivo imaging of angiotensin-converting enzyme expression. *J. Nucl. Med. 49* (6), 970–977.

(13) Chen, X., Dou, S., Liu, G., Liu, X., Wang, Y., Chen, L., Rusckowski, M., and Hnatowich, D. J. (2008) Synthesis and in vitro characterization of a dendrimer-MORF conjugate for amplification pretargeting. *Bioconjugate Chem. 19* (8), 1518–1525.

(14) Hom, R. K., and Katzenellenbogen, J. A. (1997) Technetium-99m-labeled receptor-specific small-molecule radiopharmaceuticals: recent developments and encouraging results. *Nucl. Med. Biol. 24* (6), 485–498.

(15) Fitzsimmons, J. M., and Lever, S. Z. (2004) *Synthesis and characterization of metal complexes designed to retain affinity for the sigma receptor, Abstracts of Papers*, 228th ACS National Meeting, Philadelphia, PA, United States, August 22−26, NUCL-002.

(16) Katzenellenbogen, J. A., Welch, M. J., and Dehdashti, F. (1997) The development of estrogen and progestin radiopharmaceuticals for imaging breast cancer. *Anticancer Res. 17* (3B), 1573–1576.

(17) James, S., Maresca, K., Babich, J., Valliant, J., Doering, L., and Zubieta, J. (2006) Isostructural Re and 99mTc complexes of biotin derivatives for fluorescence and radioimaging studies. *Bioconjugate Chem. 17* (3), 590–596.

(18) Bursavich, M. G., and Rich, D. H. (2002) Designing non-peptide peptidomimetics in the 21st century: inhibitors targeting conformational ensembles. *J. Med. Chem. 45* (3), 541–58.

(19) Hirschmann, R., Nicolaou, K. C., Pietranico, S., Leahy, E. M., Salvino, J., Arison, B., Cichy, M. A., Spoors, P. G., Shakespeare, W. C., Sprengeler, P. A., Hamley, P., Smith III, A. B., Reisine, T., Raynor, K., Maechler, L., Donaldson, C., Vale, W., Freidinger, R. M., Cascieriand, M. R., and Strader, C. D. (1993) De novo design and synthesis of somatostatin non-peptide peptidomimetics utilizing &D-glucose as a novel scaffolding. *J. Am. Chem. Soc. 115*, 12550–12568.

(20) Rajagopalan, R., Grummon, G. D., Bugaj, J., Hallemann, L. S., Webb, E. G., Marmion, M. E., Vanderheyden, J. L., and Srinivasan, A. (1997) Preparation, characterization, and biological evaluation of technetium(V) and rhenium(V) complexes of novel heterocyclic tetradentate N_3S ligands. *Bioconjugate Chem. 8* (3), 407–415.

(21) Pollak, A., Roe, D. G., Pollock, C. M., Lu, L. F., and Thornback, J. R. (1999) A convenient method of preparing high specific activity technetium complexes using thiol-containing chelators adsorbed on gold. *J. Am. Chem. Soc. 121* (49), 11593–11594.

(22) Zhu, Z., Wang, Y., Zhang, Y., Liu, G., Liu, N., Rusckowski, M., and Hnatowich, D. J. (2001) A novel and simplified route to the synthesis of N_3S chelators for ^{99m}Tc labeling. *Nucl. Med. Biol. 28* (6), 703–708.

(23) Alberto, R., Schlibi, R., Egli, A., and Schubiger, A. P. (1998) A novel organometallic aqua complex of technetium for the

labeling of biomolecules: synthesis of $[^{99m}Tc(OH_2)_3(CO)_3]^+$ from $[^{99m}TcO_4]^-$ in aqueous solution and its reaction with a bifunctional ligand. *J. Am. Chem. Soc. 120*, 7987.

(24) Alberto, R., Schibli, R., Waibel, R., Abram, U., and Schubiger, A. P. (1999) Basic aqueous chemistry of $[M(OH_2)_3(CO)_3]+$ (M = Re, Tc) directed towards radiopharmaceutical application. *Coord. Chem. Rev. 190*−*192*, 901–919.

(25) Schibil, R., La Bella, R., Alberto, R., Garcia-Garayoa, E., Ortner, K., Abram, U., and Schubiger, P. A. (2000) Influence of the denticity of ligand systems on the in vitro and in vivo behavior of 99mTc(I)-tricarbonyl complexes: a hint for the future functionalization of biomolecules. *Bioconjugate Chem. 11*, 345–351.

(26) Garcia-Garayoa, E., Schweinsberg, C., Maes, V., Brans, L., Blauenstein, P., Tourwe, D. A., Schibli, R., and Schubiger, P. A. (2008) Influence of the molecular charge on the biodistribution of bombesin analogues labeled with the $[^{99m}Tc(CO)_3]^+$ core. *Bioconjugate Chem. 19* (12), 2409–2416.

(27) Liu, G., Dou, S., He, J., Vanderheyden, J., Rusckowski, M., and Hnatowich, D. J. (2004) Preparation and properties of $[^{99m}Tc(CO)_3]^+$ labeled N,N-bis(2-pyridylmethyl)-4-aminobutyric acid. *Bioconjugate Chem. 15* (6), 1441–1446.

(28) Lipowska, M., Marzilli, L. G., and Taylor, A. T. (2009) 99mTc(CO)3-nitrilotriacetic acid: a new renal radiopharmaceutical showing pharmacokinetic properties in rats comparable to those of 131I-OIH. *J. Nucl. Med. 50*, 454–460.

(29) Bartholomae, M., Valliant, J., Maresca, K. P., Babich, J. W., and Zubieta, J. (2009) Single amino acid chelates: a strategy for the design of technetium and rhenium radiopharmaceuticals. *Chem. Commun. 5*, 493–512.

(30) Stephenson, K. A., Zubieta, J., Banerjee, S. R., Levadala, M. K., Taggart, L., Ryan, L., McFarlane, N., Boreham, D. R., Maresca, K. P., Babich, J. W., and Valliant, J. F. (2004) A new strategy for the preparation of peptide-targeted radiopharmaceuticals based on an Fmoc-lysine-derived single amino acid chelate (SAAC). Automated solid-phase synthesis, NMR characterization, and in vitro screening of fMLF(SAAC)G and fMLF[(SAAC-Re(CO)3)+]G. *Bioconjugate Chem. 15* (1), 128–136.

(31) Stephenson, K. A., Banerjee, S. R., Besanger, T., Sogbein, O. O., Levadala, M. K., McFarlane, N., Lemon, J. A., Boreham, D. R., Maresca, K. P., Brennan, J. D., Babich, J. W., Zubieta, J., and Valliant, J. F. (2004) Bridging the gap between in vitro and in vivo imaging: isostructural Re and ^{99m}Tc complexes for correlating fluorescence and radioimaging studies. *J. Am. Chem. Soc. 126* (28), 8598–8599.

(32) Maresca, K. P., Kronauge, J. F., Zubieta, J., and Babich, J. W. (2007) Novel ether-containing ligands as potential ^{99m}technetium(I) heart agents. *Inorg. Chem. Commun. 10* (12), 1409–1412.

(33) Levadala, M. K., Banerjee, S. R., Maresca, K. P., Babich, J. W., and Zubieta, J. (2004) Direct reductive alkylation of amino acids: Synthesis of bifunctional chelates for nuclear imaging. *Synthesis 11*, 1759–1766.

(34) Matos, K., Pichlmair, S., and Burkhardt, E. R. (2007) Boron reagents for reductive amination. *Chim. Oggi. 25* (1), 17–20.

(35) Maresca, K. P., Hillier, S. M., Femia, F. J., Keith, D., Barone, C., Joyal, J. L., Zimmerman, C. N., Kozikowski, A. P., Barrett, J. A., Eckelman, W. C., and Babich, J. W. (2009) A series of halogenated heterodimeric inhibitors of prostate specific membrane antigen (PSMA) as radiolabeled probes for targeting prostate cancer. *J. Med. Chem. 52* (2), 347–357.

BC900192B

Supplemental Information

Comprehensive Radiolabeling, Stability, and Tissue Distribution Studies of Technetium-99m Single Amino Acid Chelates (SAAC)

Kevin P. Maresca [1], Shawn M. Hillier [1], Frank J. Femia [1], Craig N. Zimmerman [1], Murali K. Levadala [2], Sangeeta R. Banerjee [2], Justin Hicks [3], Chitra Sundararajan [3], John Valliant [3], Jon Zubieta [2], William C. Eckelman [1], John L. Joyal,[1] and John W. Babich[1*]

[1]Molecular Insight Pharmaceuticals, Inc., 160 Second Street, Cambridge, MA 02142

[2]Department of Chemistry, Syracuse University, Syracuse, NY 13244.

[3]Department of Chemistry, McMaster University, Hamilton, Canada ON L8S4MI.

* To whom correspondence should be addressed: Phone: 617-492-5554. Fax: 617-492-5664. Email: jbabich@molecularinsight.com

Elemental Analysis C, H, N

COMPOUND	%C (Expected) %C (Found)	%H (Expected) %H (Found)	%N (Expected) %N (Found)
1	65.83 65.63	7.37 7.26	17.06 17.30
2	49.39 49.24	5.92 5.66	16.46 16.86
3	56.94 56.86	7.17 7.23	14.23 14.12
4	67.02 67.20	7.31 7.59	7.82 7.48

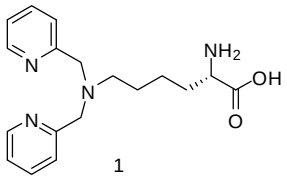

1

Ligand = DpK

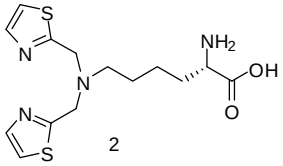

2

Ligand = DtK

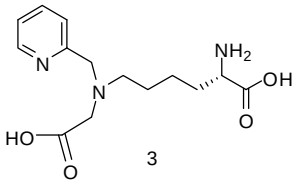

3

Ligand = PAMAK

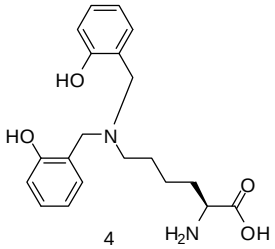

4

Ligand = DiphenolK

Evaluation of a Novel Arg-Gly-Asp-Conjugated α-Melanocyte Stimulating Hormone Hybrid Peptide for Potential Melanoma Therapy

Jianquan Yang,[†] Haixun Guo,[†] Fabio Gallazzi,[⊥] Marianne Berwick,[‡,§] R. Steven Padilla,[§,||] and Yubin Miao*[,†,§,||]

College of Pharmacy, Department of Internal Medicine, Cancer Research Treatment Center, and Department of Dermatology, University of New Mexico, Albuquerque, New Mexico 87131, and Department of Biochemistry, University of Missouri, Columbia, Missouri 65211. Received April 28, 2009; Revised Manuscript Received June 5, 2009

The purpose of this study was to determine whether Arg-Gly-Asp (RGD)-conjugated α-melanocyte stimulating hormone (α-MSH) hybrid peptide could be employed to target melanocortin-1 (MC1) receptor for potential melanoma therapy. Methods: The RGD motif {cyclic(Arg-Gly-Asp-DTyr-Asp)} was coupled to [$Cys^{3,4,10}$, $DPhe^{7}$, Arg^{11}]α-MSH_{3-13} {(Arg^{11})CCMSH} to generate RGD-Lys-(Arg^{11})CCMSH hybrid peptide. The MC1 receptor binding affinity of RGD-Lys-(Arg^{11})CCMSH was determined in B16/F1 melanoma cells. The internalization and efflux, melanoma targeting and pharmacokinetic properties and single photon emission computed tomography/CT (SPECT/CT) imaging of ^{99m}Tc-RGD-Lys-(Arg^{11})CCMSH were determined in B16/F1 melanoma cells and melanoma-bearing C57 mice. Clonogenic cytotoxic effect of RGD-Lys-(Arg^{11})CCMSH was examined in B16/F1 melanoma cells. Results: RGD-Lys-(Arg^{11})CCMSH displayed 2.1 nM MC1 receptor binding affinity. ^{99m}Tc-RGD-Lys-(Arg^{11})CCMSH showed rapid internalization and extended retention in B16/F1 cells. The cellular uptake of ^{99m}Tc-RGD-Lys-(Arg^{11})CCMSH was MC1 receptor-mediated. ^{99m}Tc-RGD-Lys-(Arg^{11})CCMSH exhibited high tumor uptake (14.83 ± 2.94% ID/g 2 h postinjection) and prolonged tumor retention (7.59 ± 2.04% ID/g 24 h postinjection) in B16/F1 melanoma-bearing mice. Nontarget organ uptakes were generally low except for the kidneys. Whole-body clearance of ^{99m}Tc-RGD-Lys-(Arg^{11})CCMSH was rapid, with approximately 62% of the injected radioactivity cleared through the urinary system by 2 h postinjection. Flank melanoma tumors were clearly imaged by small animal SPECT/CT using ^{99m}Tc-RGD-Lys-(Arg^{11})CCMSH as an imaging probe 2 h postinjection. Single treatment (3 h incubation) with 100 nM of RGD-Lys-(Arg^{11})CCMSH significantly ($p < 0.05$) decreased the clonogenic survival of B16/F1 cells by 65% compared to the untreated control cells. Conclusion: Favorable melanoma targeting property of ^{99m}Tc-RGD-Lys-(Arg^{11})CCMSH and remarkable cytotoxic effect of RGD-Lys-(Arg^{11})CCMSH in B16/F1 cells warranted the further evaluation of ^{188}Re-labeled α-MSH hybrid peptides as novel therapeutic peptides for melanoma treatment once the strategies of amino acid coinjection or structural modification of peptide sequence substantially reduce the renal uptake.

INTRODUCTION

Malignant melanoma is the most lethal form of skin cancer and the most commonly diagnosed malignancy among young adults with an increasing incidence. It was predicted that 62 480 cases would be diagnosed and 8420 fatalities would occur in the year 2008 (*1*). Melanoma metastases are very aggressive, and the survival time for patients with metastatic melanoma averages 3−15 months (*2, 3*). Unfortunately, no curative treatment exists for metastatic melanoma due to its resistance to current chemotherapy and immunotherapy regimens (*4*). Novel and effective treatment approaches are urgently needed to improve the effectiveness of melanoma treatment. The overexpression of melanocortin-1 (MC1) receptor on human and mouse melanoma cells (*5*−*9*) makes the MC1 receptor a distinct molecular target for developing novel diagnostic and therapeutic radiopharmaceuticals for melanoma (*10*−*17*). Radiolabeled α-melanocyte stimulating hormone (α-MSH) peptides can specifically bind the MC1 receptors with nanomolar binding affinities, can be rapidly internalized upon binding the MC1 receptors, and can selectively deliver the diagnostic and therapeutic radionuclides to melanoma tumor cells for imaging and therapy (*10*−*17*). The very promising preclinical therapeutic efficacies of ^{177}Lu-, ^{188}Re-, and ^{212}Pb-labeled metal-cyclized α-MSH peptides in melanoma-bearing mice demonstrated their potential as effective therapeutic agents for melanoma treatment (*15*−*17*).

Integrin receptors are involved in tumor metastasis and angiogenesis and mediate a variety of cell adhesion activities. Arg-Gly-Asp (RGD) peptide is recognized by many of the integrin receptors and is an important structural component of extracellular matrices that control physiological cell functions (*18*−*21*). Antagonists of $\alpha_v\beta_3$ integrin receptors promote tumor regression by inducing apoptosis of newly spouting blood vessels in the tumor (*20*). Besides the $\alpha_v\beta_3$ integrin receptors, several cytoplasmic members of the procaspase family of apoptosis genes, such as procaspase-1 and procaspase-3, contain RGD binding motif as well (*22*). It was reported that the RGD-containing peptide could induce cell apoptosis through activating cytoplasmic procaspase-3 directly after the RGD-containing peptide entering the cells without any requirement for integrin-mediated cell clustering or signals (*22*), highlighting the novel concept of using the RGD motif as an intracellular apoptosis inducer. Recently, the RGD motif has been used as an intracellular apoptosis inducer and been coupled to a somatostatin peptide (targeting somatostatin receptor-2) to examine

* Yubin Miao, 2502 Marble NE, MSC09 5360, College of Pharmacy, University of New Mexico, Albuquerque, NM 87131-0001. Phone: (505) 925-4437; Fax: (505) 272-6749; E-mail: ymiao@salud.unm.edc.

[†] College of Pharmacy, University of New Mexico.

[‡] Department of Internal Medicine, University of New Mexico.

[§] Cancer Research Treatment Center, University of New Mexico.

[||] Department of Dermatology, University of New Mexico.

[⊥] University of Missouri.

10.1021/bc9001954 CCC: $40.75 © 2009 American Chemical Society
Published on Web 06/24/2009

the cytotoxic effect of the hybrid somatostatin peptide {RGD-Lys-(^{111}In-DTPA)-Tyr^3-Octreotate} (*23*−*26*). RGD-Lys(^{111}In-DTPA)-Tyr^3-octreotate exhibited enhanced tumoricidal effects than ^{111}In-DTPA-Tyr^3-octreotate and ^{111}In-DTPA-RGD due to elevated tumor cell apoptosis (*23*), demonstrating the feasibility of employing the receptor-targeting peptides to target the RGD motif (as an intracellular apoptosis inducer) to cancer cells to enhance the synergistic therapeutic effectiveness of the radiolabeled hybrid peptides.

Favorable properties of radiolabeled α-MSH peptides, such as nanomolar MC1 receptor binding affinities, rapid internalization, and extended retention, underscore the potential to employ the α-MSH peptides as effective delivery vehicles. We hypothesized that the unique metal-cyclized α-MSH peptide could serve as an effective delivery vehicle to specifically transport the RGD motif into melanoma cells to induce apoptosis. In this study, we synthesized and evaluated a novel RGD-conjugated α-MSH hybrid peptide {RGD-Lys-(Arg^{11})CCMSH} to examine our hypothesis. The RGD motif {cyclic(Arg-Gly-Asp-DTyr-Asp)} was coupled to [Cys^{3,4,10}, DPhe^7, Arg^{11}]α-MSH$_{3-13}$ {(Arg^{11})CCMSH} through Lys to generate RGD-Lys-(Arg^{11})-CCMSH. We determined the internalization and efflux, melanoma targeting and pharmacokinetic properties, SPECT/CT imaging of ^{99m}Tc-labeled RGD-Lys-(Arg^{11})CCMSH in B16/F1 melanoma cells and B16/F1 melanoma-bearing mice. Furthermore, we examined clonogenic cytotoxic effect of RGD-Lys-(Arg^{11})CCMSH in B16/F1 melanoma cells.

EXPERIMENTAL PROCEDURES

Chemicals and Reagents. Amino acid and resin were purchased from Advanced ChemTech Inc. (Louisville, KY) and Novabiochem (San Diego, CA). $^{99m}TcO_4^-$ was purchased from Cardinal Health (Albuquerque, NM). ^{125}I-Tyr^2-[Nle^4, DPhe^7]-α-MSH {^{125}I-(Tyr^2)-NDP-MSH} was obtained from PerkinElmer, Inc. (Shelton, CT). All other chemicals used in this study were purchased from Thermo Fischer Scientific (Waltham, MA) and used without further purification. B16/F1 murine melanoma cells were obtained from American Type Culture Collection (Manassas, VA).

Peptide Synthesis. Intermediate scaffold of H_2N-Arg-(Pbf)-Gly-Asp(OtBu)-DTyr(tBu)-Asp(*O*-2-phenylisopropyl)-Lys(Boc)-Cys(Trt)-Cys(Trt)-Glu(OtBu)-His(Trt)-DPhe-Arg(Pbf)-Trp(Boc)-Cys(Trt)-Arg(Pbf)-Pro-Val was synthesized on Sieber amide resin using standard 9-fluorenylmethyloxycarbonyl (Fmoc) chemistry by an Advanced ChemTech multiple-peptide synthesizer (Louisville, KY). The protecting group of 2-phenylisopropyl was removed, and the peptide was cleaved from the resin treating with a mixture of 2.5% of trifluoroacetic acid (TFA) and 5% of triisopropylsilane. After the precipitation with ice-cold ether and characterization by liquid chromatography−mass spectroscopy (LC-MS), the protected peptide was dissolved in H_2O/CH_3CN (50:50) and lyophilized to remove the reagents such as TFA and triisopropylsilane. The protected peptide was further cyclized by coupling the carboxylic group from the Asp with the α-amino group from the Arg at the N-terminus. The cyclization reaction was achieved by overnight reaction in dimethylformamide (DMF) using benzotriazole-1-yl-oxy-tris-pyrrolidino-phosphonium-hexafluorophosphate (PyBOP) as a coupling agent in the presence of *N*,*N*-diisopropylethylamine (DIEA). After characterization by LC-MS, the cyclized protected peptide was dissolved in H_2O/CH_3CN (50:50) and lyophilized to remove the reagents such as PyBOP and DIEA. The protecting groups were totally removed by treating with a mixture of trifluoroacetic acid (TFA), thioanisole, phenol, water, ethanedithiol, and triisopropylsilane (87.5:2.5:2.5:2.5:2.5:2.5) for 2 h at room temperature (25 °C). The peptide was precipitated and washed with ice-cold ether for four times, purified by reverse-phase high-performance liquid chromatography (RP-HPLC) and characterized by LC-MS.

In Vitro Competitive Binding Assay. The IC_{50} value of RGD-Lys-(Arg^{11})CCMSH was determined according to our previously published procedure (*27*). B16/F1 cells were harvested and seeded into a 24-well cell culture plate (5×10^5/well) and incubated at 37 °C overnight. After being washed with binding medium [modified Eagle's medium with 25 mM *N*-(2-hydroxyethyl)-piperazine-*N*′-(2-ethanesulfonic acid), pH 7.4, 0.2% bovine serum albumin (BSA), 0.3 mM 1,10-phenathroline], the cells were incubated at room temperature (25 °C) for 2 h with approximately 40 000 counts per minute (cpm) of ^{125}I-(Tyr^2)-NDP-MSH in the presence of increasing concentrations (10^{-12} to 10^{-5} M) of RGD-Lys-(Arg^{11})CCMSH in 0.3 mL of binding medium. The reaction medium was aspirated after the incubation. The cells were rinsed twice with 0.5 mL of ice-cold pH 7.4, 0.2% BSA/0.01 M phosphate buffered saline (PBS) and lysed in 0.5 mL of 1 N NaOH for 5 min. The activities associated with cells were measured in a Wallac 1480 automated gamma counter (PerkinElmer, NJ). The IC_{50} value for the peptide was calculated using *Prism* software (GraphPad Software, La Jolla, CA).

Peptide Radiolabeling. RGD-Lys-(Arg^{11})CCMSH was radiolabeled with ^{99m}Tc via a glucoheptonate transchelation reaction using methods described previously (*7*). Briefly, 100 μL of 2 mg/mL $SnCl_2$ in 0.2 M glucoheptonate aqueous solution and 200 μL of fresh $^{99m}TcO_4^-$ solution (37−148 MBq) were added into a reaction vial and incubated at room temperature (25 °C) for 20 min to form ^{99m}Tc-glucoheptonate. Then, 10 μL of 1 mg/mL RGD-Lys-(Arg^{11})CCMSH aqueous solution was added into the reaction vial, and the pH of the reaction mixture was adjusted to 8.5 with 0.1 M NaOH. The reaction mixture was incubated at 75 °C for 40 min. The radiolabeled peptide was purified to single species by Waters RP-HPLC (Milford, MA) on a Grace Vydac C-18 reverse-phase analytic column (Deerfield, IL) using a 20 min gradient of 16−26% acetonitrile in 20 mM HCl aqueous solution at a flow rate of 1 mL/min. The purified peptide sample was purged with N_2 gas for 20 min to remove the acetonitrile. The pH of the final solution was adjusted to 5 with 0.1 N NaOH and normal saline for animal studies. The stability of ^{99m}Tc-RGD-Lys-(Arg^{11})CCMSH was determined by incubation in mouse serum at 37 °C according to the published procedure (*27*) for various time periods, and monitored for degradation by RP-HPLC.

Cellular Internalization and Efflux of ^{99m}Tc-RGD-Lys-(Arg^{11})CCMSH. Cellular internalization and efflux of ^{99m}Tc-RGD-Lys-(Arg^{11})CCMSH were evaluated in B16/F1 cells as previously described by Miao et al. (*27*). After being washed once with binding medium, B16/F1 cells in 24-well cell culture plates were incubated at 25 °C for 20, 40, 60, 90, and 120 min ($n = 4$) in the presence of approximately 200 000 cpm of HPLC purified ^{99m}Tc-RGD-Lys-(Arg^{11})CCMSH. After incubation, the reaction medium was aspirated and the cells were rinsed twice with 0.5 mL of ice-cold pH 7.4, 0.2% BSA/0.01 M PBS. Cellular internalization of ^{99m}Tc-RGD-Lys-(Arg^{11})CCMSH was assessed by washing the cells with acidic buffer [40 mM sodium acetate (pH 4.5) containing 0.9% NaCl and 0.2% BSA] to remove the membrane-bound radioactivity. The remaining internalized radioactivity was obtained by lysing the cells with 0.5 mL of 1 N NaOH for 5 min. Membrane-bound and internalized ^{99m}Tc activities were counted in a gamma counter. Cellular efflux of ^{99m}Tc-RGD-Lys-(Arg^{11})CCMSH was determined by incubating B16/F1 cells with ^{99m}Tc-RGD-Lys-(Arg^{11})CCMSH for 2 h at 25 °C, removing nonspecific-bound radioactivity with 2 × 0.5 mL of ice-cold pH 7.4, 0.2% BSA/0.01 M PBS rinse, and monitoring radioactivity released into cell culture medium. At time points of 20, 40, 60, 90, and 120

min, the radioactivities in medium, on cell surface, and in cells were separately collected and counted in a gamma counter.

Specificity of Cellular Uptake of ^{99m}Tc-RGD-Lys-(Arg^{11})-CCMSH. The specificity of cell binding was determined by incubating ^{99m}Tc-RGD-Lys-(Arg^{11})CCMSH with or without nonradioactive peptides. After being washed once with binding media, B16/F1 cells in 24-well cell culture plates were incubated with approximately 200 000 cpm of HPLC purified ^{99m}Tc-RGD-Lys-(Arg^{11})CCMSH at 25 °C for 120 min ($n = 4$) in the presence of 0.1 μM of RGD-Lys-(Arg^{11})CCMSH, NDP-MSH, (Arg^{11})CCMSH, or RGD peptide (Peptides International Inc., Louisville, KY) in 0.5 mL of binding media, respectively. The reaction medium was aspirated after the incubation. The cells were rinsed twice with 0.5 mL of ice-cold pH 7.4, 0.2% BSA/0.01 M PBS, and lysed in 0.5 mL of 1 N NaOH for 5 min. The activities associated with cells were measured in a gamma counter.

Biodistribution Studies. All the animal studies were conducted in compliance with Institutional Animal Care and Use Committee approval. The pharmacokinetics of ^{99m}Tc-RGD-Lys-(Arg^{11})CCMSH was determined in B16/F1 melanoma-bearing C57 female mice (Harlan, Indianapolis, IN). C57 mice were subcutaneously inoculated on the right flank with 1×10^6 B16/F1 cells. The weight of tumors reached approximately 0.2 g 10 days post cell inoculation. Each melanoma-bearing mouse was injected with 0.037 MBq of ^{99m}Tc-RGD-Lys-(Arg^{11})CCMSH via the tail vein. Groups of 5 mice were sacrificed at 0.5, 2, 4, and 24 h postinjection, and tumors and organs of interest were harvested, weighed, and counted. Blood values were taken as 6.5% of the whole-body weight.

The MC1 receptor specificity of the tumor uptake was determined at 2 h postinjection by coinjecting ^{99m}Tc-RGD-Lys-(Arg^{11})CCMSH with 10 μg (6.1 nmol) of unlabeled NDP-MSH. The $\alpha_v\beta_3$ integrin specificity of the tumor uptake was also determined by coinjecting ^{99m}Tc-RGD-Lys-(Arg^{11})CCMSH with 3.5 μg (6.1 nmol) of RGD peptide 2 h postinjection.

Imaging Melanoma with ^{99m}Tc-RGD-Lys-(Arg^{11})CCMSH. A B16/F1 melanoma-bearing C57 mouse was injected with 10.4 MBq of ^{99m}Tc-RGD-Lys-(Arg^{11})CCMSH via the tail vein. The mouse was anesthetized with 1.5% isoflurane for small animal SPECT/CT (Nano-SPECT/CT, Bioscan) imaging 2 h postinjection. The 9 min CT imaging was immediately followed by the SPECT imaging of whole-body. The SPECT scans of 24 projections were acquired, and total acquisition time was approximately 45 min. After the SPECT imaging, the mouse was euthanized with CO_2 inhalation. Reconstructed data from SPECT and CT were visualized and coregistered using InVivoScope (Bioscan, Washington, DC).

Urinary Metabolites of ^{99m}Tc-RGD-Lys-(Arg^{11})CCMSH. Urinary metabolites of ^{99m}Tc-RGD-Lys-(Arg^{11})CCMSH were determined by injecting 3.7 MBq of ^{99m}Tc-RGD-Lys-(Arg^{11})-CCMSH into a B16/F1 melanoma-bearing C57 mouse through the tail vein. At 2 h after dose administration, the mouse was euthanized and the urine was collected. The radioactive metabolites in the urine were analyzed by injecting aliquots of urine into HPLC. A 20 min gradient of 16−26% acetonitrile/20 mM HCl was used for the urine analysis.

Clonogenic Cytotoxicity of RGD-Lys-(Arg^{11})CCMSH. Clonogenic cytotoxic effect of RGD-Lys-(Arg^{11})CCMSH was examined in B16/F1 melanoma cells according to the published procedure with slight modification (*23*). The B16/F1 cells were seeded in a 6 well plate (200 cells/well) and incubated at 37 °C overnight. After being washed once with culture medium (RPMI 1640 medium), the cells were incubated in the culture medium at 37 °C for 3 h in the presence of 0.1 μM of RGD-Lys-(Arg^{11})CCMSH, (Arg^{11})CCMSH, or RGD, respectively. Control cells were only incubated in the culture medium. After the incubation, the cells were washed with PBS twice and allowed to form colonies over 6 days in the culture medium. The medium was changed every other day. After 6 days, the cells were fixed with methanol/glacial acetic acid (3:1), stained with hematoxylin, and visually examined under microscope for survival. Colonies contained more than 50 cells were scored as survivors.

Statistical Methods. Statistical analysis was performed using the Student's *t* test for unpaired data to determine the significant differences between the groups in the studies of specificity of cellular uptake, biodistribution, and clonogenic cytotoxicity described above. Differences at the 95% confidence level ($p < 0.05$) were considered significant.

RESULTS

RGD-Lys-(Arg^{11})CCMSH was synthesized, purified by RP-HPLC, and the identity of peptide was confirmed by electrospray ionization mass spectrometry. RGD-Lys-(Arg^{11})CCMSH displayed greater than 95% purity with 30% overall synthetic yield. The synthetic scheme is presented in Figure 1. The competitive binding curve of RGD-Lys-(Arg^{11})CCMSH is shown in Figure 2A. The IC_{50} value of RGD-Lys-(Arg^{11})CCMSH was 2.1 nM in B16/F1 cells. The peptide was readily labeled with ^{99m}Tc using a glucoheptonate transchelation reaction with greater than 95% radiolabeling yield. ^{99m}Tc-RGD-Lys-(Arg^{11})CCMSH was completely separated from its excess nonlabeled peptide by RP-HPLC. The specific activity of ^{99m}Tc-RGD-Lys-(Arg^{11})CCMSH was 8.514×10^9 MBq/g. ^{99m}Tc-RGD-Lys-(Arg^{11})CCMSH showed greater than 98% radiochemical purity after the HPLC purification. The retention time of ^{99m}Tc-RGD-Lys-(Arg^{11})-CCMSH was 12.2 min. ^{99m}Tc-RGD-Lys-(Arg^{11})CCMSH was stable in mouse serum at 37 °C for 24 h.

Cellular internalization and efflux of ^{99m}Tc-RGD-Lys-(Arg^{11})CCMSH was evaluated in B16/F1 cells. Figure 2 (B and C) illustrate cellular internalization and efflux of ^{99m}Tc-RGD-Lys-(Arg^{11})CCMSH. ^{99m}Tc-RGD-Lys-(Arg^{11})CCMSH exhibited rapid cellular internalization and extended cellular retention. There was 76.28 ± 1.36% of the ^{99m}Tc-RGD-Lys-(Arg^{11})-CCMSH activity internalized in the B16/F1 cells 40 min postincubation. There was 85.93 ± 1.22% of the ^{99m}Tc-RGD-Lys-(Arg^{11})CCMSH activity internalized in the cells after 2 h incubation. Cellular efflux results demonstrated that 68.57 ± 3.77% of the ^{99m}Tc-RGD-Lys-(Arg^{11})CCMSH activity remained inside the cells 2 h after incubating cells in culture medium.

Specificity of cellular uptake of ^{99m}Tc-RGD-Lys-(Arg^{11})-CCMSH was examined in B16/F1 cells. The results are presented in Figure 3. The cellular uptake of ^{99m}Tc-RGD-Lys-(Arg^{11})CCMSH was MC1 receptor-mediated rather than $\alpha_v\beta_3$ integrin-mediated. Compared to the cellular uptake of ^{99m}Tc-RGD-Lys-(Arg^{11})CCMSH without peptide blockade, the cellular uptakes of ^{99m}Tc-RGD-Lys-(Arg^{11})CCMSH decreased 88.1%, 90.5%, and 88.1% with 0.1 μM of RGD-Lys-(Arg^{11})CCMSH, NDP-MSH and (Arg^{11})CCMSH as blockades, respectively. Incubation of ^{99m}Tc-RGD-Lys-(Arg^{11})CCMSH with 0.1 μM of RGD did not reduce the cellular uptake of ^{99m}Tc-RGD-Lys-(Arg^{11})CCMSH in B16/F1 cells.

The melanoma targeting and pharmacokinetic properties of ^{99m}Tc-RGD-Lys-(Arg^{11})CCMSH were determined in B16/F1 melanoma-bearing C57 mice. The biodistribution results of ^{99m}Tc-RGD-Lys-(Arg^{11})CCMSH are shown in Table 1. ^{99m}Tc-RGD-Lys-(Arg^{11})CCMSH exhibited rapid and high tumor uptake in melanoma-bearing mice. The tumor uptake value was 11.06 ± 1.41% ID/g 0.5 h postinjection. ^{99m}Tc-RGD-Lys-(Arg^{11})CCMSH reached its peak tumor uptake value of 14.83 ± 2.94% ID/g 2 h postinjection. There was 12.57 ± 2.53% ID/g of the ^{99m}Tc-RGD-Lys-(Arg^{11})CCMSH activity remained in the tumors 4 h postinjection. The tumor uptake value of ^{99m}Tc-RGD-Lys-(Arg^{11})CCMSH gradually decreased to 7.59 ± 2.04%

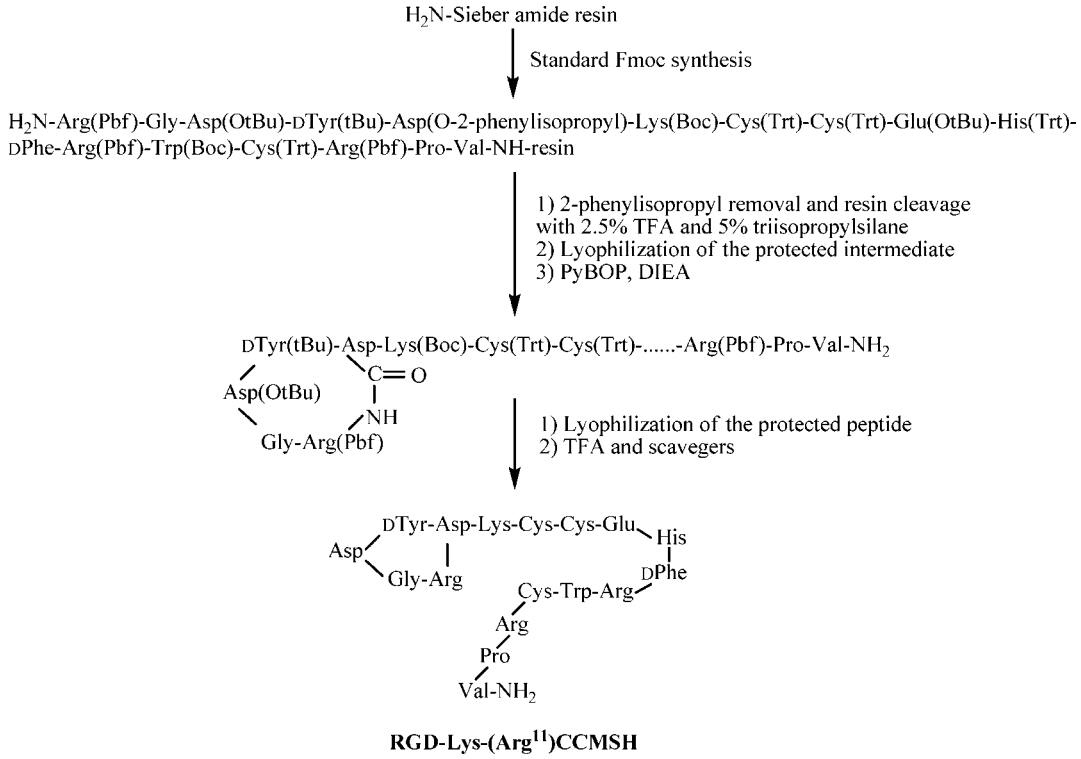

Figure 1. Synthetic scheme of RGD-Lys-(Arg^{11})CCMSH.

ID/g 24 h postinjection. In melanoma uptake blocking studies, the tumor uptake of ^{99m}Tc-RGD-Lys-(Arg^{11})CCMSH with 10 μg (6.1 nmol) of nonradiolabeled NDP-MSH coinjection was only 12.2% of the tumor uptake without NDP-MSH coinjection at 2 h after dose administration ($p < 0.01$), demonstrating that the tumor uptake was specific and MC1 receptor-mediated. Compared to the tumor uptake of ^{99m}Tc-RGD-Lys-(Arg^{11})-CCMSH, coinjection of ^{99m}Tc-RGD-Lys-(Arg^{11})CCMSH with 3.5 μg (6.1 nmol) of RGD decreased 29.2% of the tumor uptake value, demonstrating that the tumor uptake was $\alpha_v\beta_3$ integrin receptor-mediated as well. Whole-body clearance of ^{99m}Tc-RGD-Lys-(Arg^{11})CCMSH was rapid, with approximately 62% of the injected radioactivity cleared through the urinary system by 2 h postinjection (Table 1). Normal organ uptakes of ^{99m}Tc-RGD-Lys-(Arg^{11})CCMSH were generally low (<3.2% ID/g) except for the kidneys after 2 h postinjection. High tumor/blood and tumor/muscle uptake ratios were demonstrated as early as 0.5 h postinjection (Table 1). The renal uptake of ^{99m}Tc-RGD-Lys-(Arg^{11})CCMSH reached its peak value of 69.37 $\pm$ 5.37% ID/g 0.5 h postinjection. The renal uptake decreased to 40.26 $\pm$ 10.83% ID/g 24 h postinjection.

One B16/F1 melanoma-bearing C57 mouse was injected with ^{99m}Tc-RGD-Lys-(Arg^{11})CCMSH through the tail vein to visualize the tumors 2 h after dose administration. The whole-body SPECT/CT image is presented in Figure 4A. Flank melanoma tumors were visualized clearly by ^{99m}Tc-RGD-Lys-(Arg^{11})-CCMSH 2 h postinjection. ^{99m}Tc-RGD-Lys-(Arg^{11})CCMSH exhibited high tumor to normal organ uptake ratios except for the kidney. Radioactivity in the bladder demonstrated the urinary clearance of ^{99m}Tc-RGD-Lys-(Arg^{11})CCMSH, which was coincident with the biodistribution results. In view of the substantial renal uptake values of ^{99m}Tc-RGD-Lys-(Arg^{11})-CCMSH in the biodistribution results, the urinary metabolites of ^{99m}Tc-RGD-Lys-(Arg^{11})CCMSH were analyzed by RP-HPLC 2 h postinjection. The urinary HPLC profile of ^{99m}Tc-RGD-Lys-(Arg^{11})CCMSH is shown in Figure 4B. Approximately 68% of ^{99m}Tc-RGD-Lys-(Arg^{11})CCMSH remained intact, while 32% of ^{99m}Tc-RGD-Lys-(Arg^{11})CCMSH was transformed to two more lipophilic metabolites 2 h postinjection.

Clonogenic cytotoxic effect of RGD-Lys-(Arg^{11})CCMSH hybrid peptide was examined in B16/F1 melanoma cells. The results are presented in Figure 5. The clonogenic survival percentages of peptide-treated groups were normalized taking the clonogenic survival percentage of untreated group (in culture medium) as 100%. RGD-Lys-(Arg^{11})CCMSH exhibited remarkable cytotoxic effect in B16/F1 melanoma cells, with 65% decrease ($p < 0.05$) in clonogenic survival compared to that of the untreated group. In comparison with untreated cells, incubation with (Arg^{11})CCMSH and RGD peptides reduced 11% and 7% of clonogenic survival, respectively. However, the differences were not significant ($p > 0.05$).

DISCUSSION

Metastatic melanoma is very aggressive and is resistant to current available chemotherapy and immunotherapy. High mortality of malignant melanoma is associated with the occurrence of melanoma metastases. Hence, it is urgent to develop novel and effective therapeutic approaches to improve the therapeutic effectiveness of melanoma treatment. Peptide-targeted radionuclide therapy is a novel and effective treatment approach for melanoma. MC1 receptor-avid α-MSH peptides are employed as effective delivery vehicles to selectively and specifically target cytotoxic radiation generated from radionuclides to tumor cells, resulting in tumor cell death (*28*). In comparison with external beam radiation therapy and chemotherapy, peptide-targeted radionuclide therapy can specifically deliver the cytotoxic radiation to tumor cells, while sparing the normal tissues and organs. Unique metal-cyclized α-MSH peptides were labeled with various therapeutic radionuclides with low-energy β-emission (^{177}Lu), high-energy β-emission (^{188}Re), and high-energy α-emission (^{212}Pb, parent radionuclide of high-energy α-emitter ^{212}Bi) to examine their therapeutic efficacies in B16/F1 melanoma-bearing mice (*15*−*17*). ^{177}Lu-, ^{188}Re-, and ^{212}Pb-labeled metal-cyclized α-MSH peptides ex-

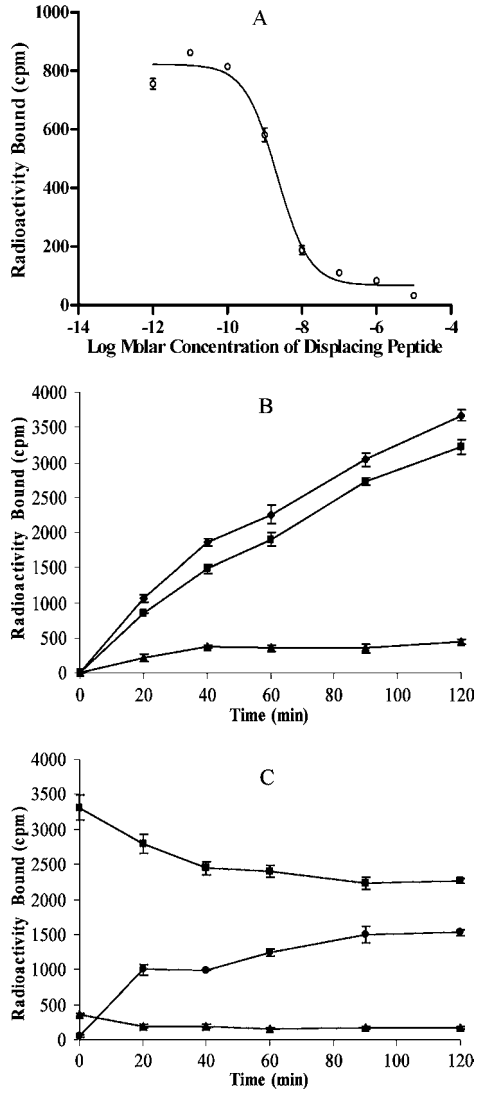

Figure 2. The competitive binding curve (A) of RGD-Lys-(Arg^{11})CCMSH in B16/F1 melanoma cells. The IC_{50} value of RGD-Lys-(Arg^{11})CCMSH was 2.1 nM. Cellular internalization (B) and efflux (C) of ^{99m}Tc-RGD-Lys-(Arg^{11})CCMSH in B16/F1 melanoma cells at 25 °C. Total bound radioactivity (◆), internalized activity (■), cell membrane activity (▲), and cell culture medium activity (•) were presented as counts per minute (cpm).

hibited very promising therapeutic effects in preclinical melanoma-bearing mouse models (*15*−*17*), demonstrating the potential of peptide-targeted radionuclide therapy for human melanoma treatment. The findings of that RGD-containing peptide could induce cell apoptosis through activating cytoplasmic procaspase-3 directly after the peptide entering the cells (*22*) opened the avenue of using the RGD motif as an intracellular apoptosis inducer for cancer therapy. RGD-Lys(^{111}In-DTPA)-Tyr^3-Octreotate exhibited enhanced tumoricidal effects than ^{111}In-DTPA-Tyr^3-octreotate due to elevated tumor cell apoptosis (*23*), demonstrating the feasibility of coupling the RGD motif to the receptor-targeting peptides to enhance the synergistic therapeutic effectiveness of the radiolabeled hybrid peptides. In this study, we designed and synthesized a novel RGD-Lys-(Arg^{11})CCMSH hybrid peptide to examine whether the unique metal-cyclized α-MSH peptide [^{99m}Tc-(Arg^{11})CCMSH] could be used as an effective delivery vehicle to specifically transport the RGD motif into melanoma cells to induce apoptosis.

Synthetic hybrid RGD-Lys-(Arg^{11})CCMSH exhibited 2.1 nM MC1 receptor binding affinity (Figure 2), whereas (Arg^{11})-CCMSH displayed 1.7 nM MC1 receptor binding affinity (*8*), demonstrating that the coupling of the RGD motif did maintain the nanomolar MC1 receptor binding affinity of the hybrid peptide. ^{99m}Tc-RGD-Lys-(Arg^{11})CCMSH was easily prepared and was stable in mouse serum for 24 h. The coordination of ^{99m}Tc with three cysteines presented in the RGD-Lys-(Arg^{11})CCMSH simultaneously cyclized the hybrid peptide, making ^{99m}Tc-RGD-Lys-(Arg^{11})CCMSH stable against proteolytic degradation in vivo . As we anticipated, ^{99m}Tc-RGD-Lys-(Arg^{11})CCMSH exhibited rapid internalization and extended efflux in B16/F1 cells (Figure 2), warranting effective transportation of the RGD motif into the melanoma cells, as well as subsequent long-lasting apoptotic effect generated from the RGD motif after entering the melanoma cells. The cellular uptake of ^{99m}Tc-RGD-Lys-(Arg^{11})CCMSH was MC1 receptor-mediated rather than $\alpha_v\beta_3$ integrin-mediated, since approximately 90% of the cellular uptake of ^{99m}Tc-RGD-Lys-(Arg^{11})CCMSH was blocked by RGD-Lys-(Arg^{11})CCMSH, (Arg^{11})CCMSH, or NDP-MSH (rather than RGD) (Figure 3). The MC1 receptor-mediated cellular uptake of ^{99m}Tc-RGD-Lys-(Arg^{11})CCMSH was consistent with the published immunohistochemical results that RGD-HuMab only localized at the endothelium of B16/F10 melanoma tumor rather than B16/F10 melanoma cells (*30*). Nanomolar MC1 receptor binding affinity, rapid internalization, and extended retention of the hybrid RGD-Lys-(Arg^{11})CCMSH in melanoma cells warranted further evaluation on melanoma targeting and pharmacokinetic properties of ^{99m}Tc-RGD-Lys-(Arg^{11})CCMSH in melanoma-bearing mice.

^{99m}Tc-RGD-Lys-(Arg^{11})CCMSH exhibited a rapid high B16/F1 melanoma uptake value of 11.06 ± 1.41% ID/g 0.5 h postinjection and reached its peak tumor uptake value of 14.83 ± 2.94% ID/g 2 h postinjection (Table 1). Meanwhile, ^{99m}Tc-RGD-Lys-(Arg^{11})CCMSH displayed prolonged retention in melanoma tumors. The tumor uptake value was 12.57 ± 2.53% ID/g 4 h postinjection, which was 85% of the tumor uptake value 2 h postinjection. Even 24 h postinjection, the tumor uptake value was 7.59 ± 2.04% ID/g, which was 51% of the tumor uptake value 2 h postinjection. The majority of melanoma uptake of ^{99m}Tc-RGD-Lys-(Arg^{11})CCMSH was MC1 receptor-mediated demonstrated by the fact that 87.8% of the tumor uptake of ^{99m}Tc-RGD-Lys-(Arg^{11})CCMSH was blocked by 6.1 nmol of NDP-MSH (Table 1), whereas 29.2% of the tumor uptake of ^{99m}Tc-RGD-Lys-(Arg^{11})CCMSH was blocked by 6.1 nmol of RGD (Table 1). A minority of $\alpha_v\beta_3$ integrin-mediated melanoma uptake was likely due to the presence of $\alpha_v\beta_3$ integrin receptors in the B16/F1 tumor vasculature. It was reported that $\alpha_v\beta_3$ integrin receptors were overexpressed in B16/F10 tumor vasculature (*30*). The B16/F1 melanoma tumors consist of highly vascularized dense gelatinous masses. Interestingly, ^{99m}Tc-RGD-Lys-(Arg^{11})CCMSH showed a comparable tumor uptake value to ^{99m}Tc-(Arg^{11})CCMSH 4 h postinjection and longer tumor retention than ^{99m}Tc-(Arg^{11})CCMSH 24 h postinjection in the same B16/F1 melanoma-bearing mouse model (*13*). The tumor uptake values of ^{99m}Tc-RGD-Lys-(Arg^{11})CCMSH were 1.1 and 2.3 times the tumor uptake values of ^{99m}Tc-(Arg^{11})CCMSH 4 and 24 h postinjection, respectively. The improved melanoma retention of ^{99m}Tc-RGD-Lys-(Arg^{11})CCMSH are attributed to the introduction of the RGD motif in ^{99m}Tc-RGD-Lys-(Arg^{11})CCMSH. It was likely that the RGD motif in hybrid ^{99m}Tc-RGD-Lys-(Arg^{11})CCMSH bound to the $\alpha_v\beta_3$ integrin receptors presented on blood vessels in B16/F1 tumors, contributing the prolonged tumor retention of ^{99m}Tc-RGD-Lys-(Arg^{11})CCMSH. Technetium-99m and ^{188}Re are matched-pair diagnostic and therapeutic radionuclides, sharing similar coordination chemistry. Hence, from the therapeutic point of view, high melanoma uptake and prolonged retention of ^{99m}Tc-RGD-Lys-(Arg^{11})CCMSH warranted long-lasting synergistic therapeutic effects of apoptosis and targeted radiation from ^{188}Re-

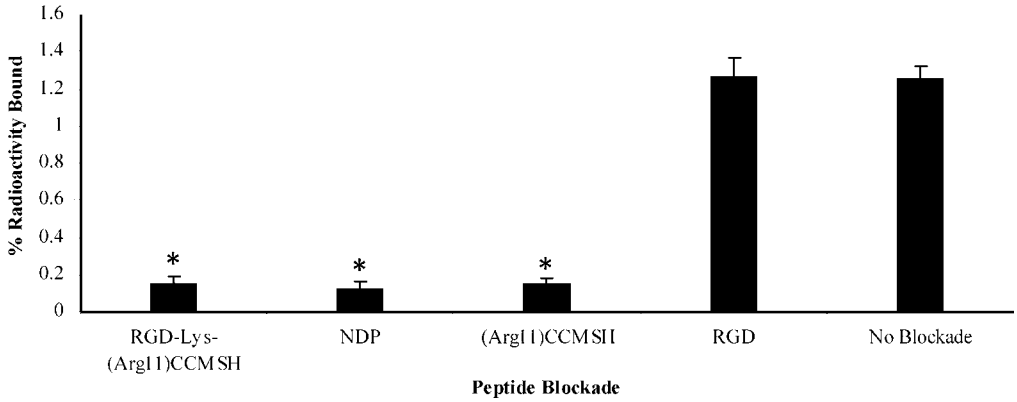

Figure 3. Blocking studies of cellular uptake of ^{99m}Tc-RGD-Lys-(Arg^{11})CCMSH in B16/F1 murine melanoma cells. The cells were incubated with ^{99m}Tc-RGD-Lys-(Arg^{11})CCMSH in the presence of 0.1 μM of RGD-Lys-(Arg^{11})-CCMSH, NDP-MSH, (Arg^{11})CCMSH, RGD, or no peptide blockade. * $p < 0.001$.

Table 1. Biodistribution of ^{99m}Tc-RGD-Lys-(Arg^{11})CCMSH in B16/F1 Murine Melanoma-Bearing C57 Mice[a]

tissue	0.5 h	2 h	2 h NDP blockade	2 h RGD blockade	4 h	24 h
			Percentage Injected Dose/gram (% ID/g)			
tumor	11.06 ± 1.41	14.83 ± 2.94	1.81 ± 0.64[b]	10.50 ± 1.18[b]	12.57 ± 2.53	7.59 ± 2.04
brain	0.13 ± 0.03	0.12 ± 0.03	0.06 ± 0.02[b]	0.03 ± 0.01[b]	0.07 ± 0.04	0.06 ± 0.01
blood	3.18 ± 0.51	0.96 ± 0.87	0.32 ± 0.34	0.53 ± 0.17	0.50 ± 0.27	0.11 ± 0.07
heart	2.10 ± 0.41	0.85 ± 0.16	0.47 ± 0.18[b]	0.37 ± 0.23[b]	0.62 ± 0.31	0.39 ± 0.14
lung	5.31 ± 0.53	1.26 ± 0.32	1.31 ± 0.47	1.12 ± 0.10	1.07 ± 0.42	0.94 ± 0.45
liver	4.02 ± 0.42	3.17 ± 1.43	2.89 ± 0.25	2.27 ± 0.23	2.91 ± 0.80	1.73 ± 0.33
skin	4.53 ± 0.88	1.52 ± 0.66	1.14 ± 0.38	0.81 ± 0.13	1.17 ± 0.61	0.78 ± 0.19
spleen	2.18 ± 0.88	1.23 ± 0.62	0.75 ± 0.37	0.94 ± 0.30	1.14 ± 0.16	0.88 ± 0.30
stomach	7.61 ± 1.98	2.57 ± 0.38	2.43 ± 0.80	2.64 ± 0.10	2.46 ± 1.39	0.91 ± 0.67
kidneys	69.37 ± 5.37	67.12 ± 8.79	59.53 ± 9.98	54.24 ± 15.11	69.29 ± 14.34	40.26 ± 10.83
muscle	0.38 ± 0.17	0.34 ± 0.29	0.21 ± 0.12	0.15 ± 0.06	0.13 ± 0.07	0.23 ± 0.19
pancreas	1.48 ± 1.24	0.72 ± 0.53	0.44 ± 0.37	0.35 ± 0.19	0.52 ± 0.41	0.25 ± 0.06
bone	1.53 ± 0.75	1.05 ± 0.31	0.78 ± 0.65	0.37 ± 0.42[b]	0.98 ± 0.67	0.71 ± 0.39
			Percentage Injected Dose (% ID)			
intestines	3.27 ± 0.13	3.14 ± 1.20	1.97 ± 0.17	1.88 ± 0.16	2.95 ± 0.62	1.13 ± 0.18
bladder	46.92 ± 2.54	62.26 ± 8.16	75.86 ± 1.75	75.09 ± 3.69	68.69 ± 2.06	78.25 ± 5.29
			Uptake Ratio of Tumor/Normal Tissue			
tumor/blood	3.48	15.45	5.66	19.81	25.14	69.00
tumor/kidneys	0.16	0.22	0.03	0.19	0.18	0.19
tumor/lung	2.08	11.77	1.38	9.38	11.75	8.07
tumor/liver	2.75	4.68	0.63	4.63	4.32	4.39
tumor/muscle	29.11	43.62	8.62	70.00	96.69	33.00

[a] The data was presented as percent injected dose/gram or as percent injected dose (mean ± SD, $n = 5$). [b] $p < 0.05$, significance comparison between ^{99m}Tc-RGD-Lys-(Arg^{11})CCMSH with or without blockade peptide.

labeled hybrid CCMSH peptide. Flank B16/F1 melanoma tumors were clearly visualized by SPECT/CT imaging using ^{99m}Tc-RGD-Lys-(Arg^{11})CCMSH as an imaging probe 2 h postinjection (Figure 4). ^{99m}Tc-RGD-Lys-(Arg^{11})CCMSH displayed high tumor to normal organ uptake ratios except for the kidneys, which was coincident with the biodistribution results (Table 1).

The RGD motif was attached to the somatostatin-2 receptor-targeting Tyr^3-octreotate via Lys to yield hybrid RGD-Lys(^{111}In-DTPA)-Tyr^3-octreotate. DTPA was attached to the amino group on the side chain of Lys for ^{111}In labeling (*24*). In this study, The RGD motif was conjugated to (Arg^{11})CCMSH via Lys to generate RGD-Lys-(Arg^{11})CCMSH. The advantage of using Lys as a linker to connect the RGD motif with the (Arg^{11})CCMSH moiety was that the amino group on the side chain of Lys could be used to attach DOTA for coordination with a variety of therapeutic radionuclides (i.e., ^{177}Lu, ^{90}Y, and ^{212}Pb) to generate synergistic therapeutic effects of targeted radiation from the therapeutic radionuclides and apoptosis from the RGD motif. The coupling of the RGD motif to the Tyr^3-octreotate through Lys increased the renal uptake value of RGD-Lys(^{111}In-DTPA)-Tyr^3-octreotate compared to ^{111}In-DOTA-Tyr^3-octreotate (*24*). The renal uptake value of RGD-Lys(^{111}In-DTPA)-Tyr^3-octreotate was 3.3 times the renal uptake value of ^{111}In-DOTA-Tyr^3-octreotate in CA20948 and AR42J tumor-bearing Lewis rats 24 h postinjection (*24*). Surprisingly, the renal uptake value of ^{99m}Tc-RGD-Lys-(Arg^{11})CCMSH was 12.5 times the renal uptake value of ^{99m}Tc-(Arg^{11})CCMSH in B16/F1 melanoma-bearing mice 4 h postinjection. Considering the structural difference between the ^{99m}Tc-RGD-Lys-(Arg^{11})CCMSH and ^{99m}Tc-(Arg^{11})CCMSH, the substantial increased renal uptake of ^{99m}Tc-RGD-Lys-(Arg^{11})CCMSH was due to the introduction of the RGD-Lys moiety. Further biodistribution comparison revealed that the renal uptake value of ^{99m}Tc-RGD-Lys-(Arg^{11})CCMSH was only 1.2 times the renal uptake value of ^{188}Re-dLys-(Arg^{11})CCMSH (*31*), indicating that the Lys between the RGD motif and the (Arg^{11})CCMSH moiety played an important role in high renal uptake value of ^{99m}Tc-RGD-Lys-(Arg^{11})CCMSH. It is necessary to note that the amino group on the side chain of the Lys was available in ^{99m}Tc-RGD-Lys-(Arg^{11})CCMSH and added a positive charge to the overall charge of ^{99m}Tc-RGD-Lys-(Arg^{11})CCMSH, that might contribute to the high renal uptake value of ^{99m}Tc-RGD-Lys-(Arg^{11})CCMSH due to the electrostatic interaction between positively charged peptide

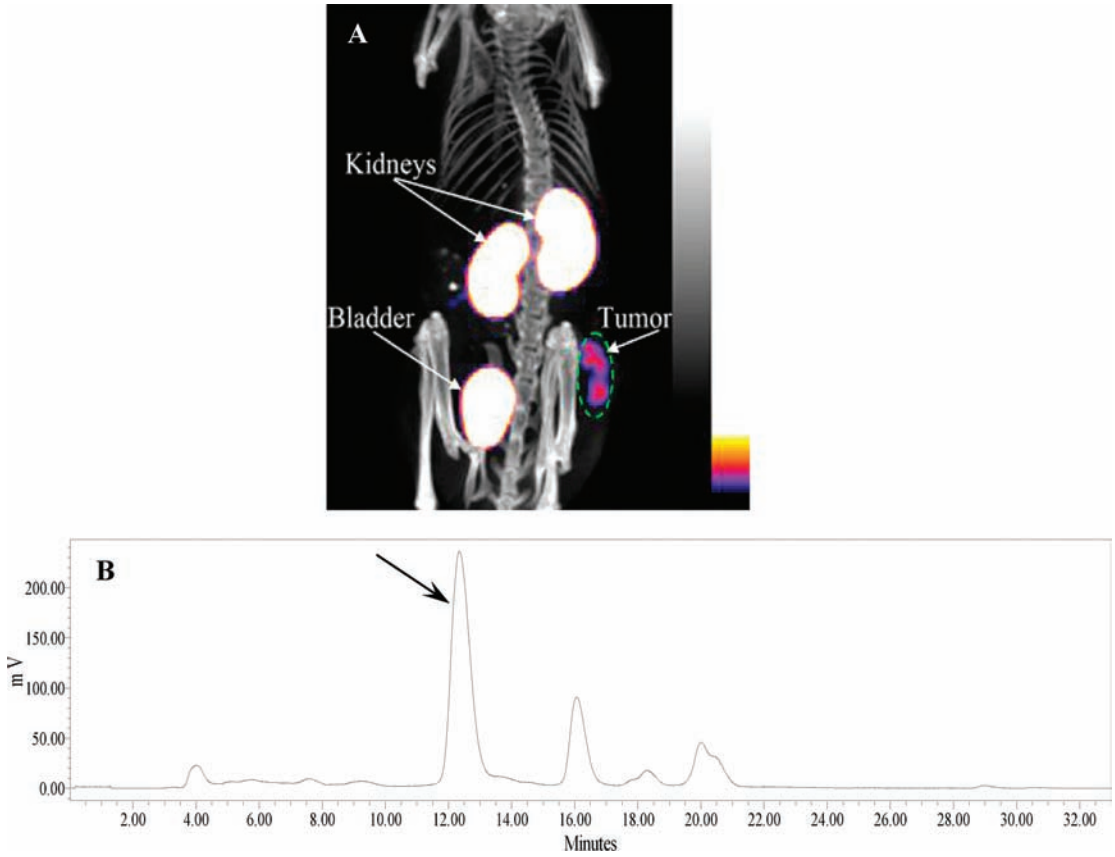

Figure 4. Whole-body SPECT/CT image (A) of ^{99m}Tc-RGD-Lys-(Arg^{11})CCMSH in a B16/F1 melanoma-bearing C57 mouse at 2 h postinjection; HPLC profile (B) of radioactive urine sample of a B16/F1 murine melanoma-bearing C57 mouse at 2 h postinjection of ^{99m}Tc-RGD-Lys-(Arg^{11})CCMSH. Black arrow indicates the retention time of the original compound of ^{99m}Tc-RGD-Lys-(Arg^{11})CCMSH prior to the tail vein injection.

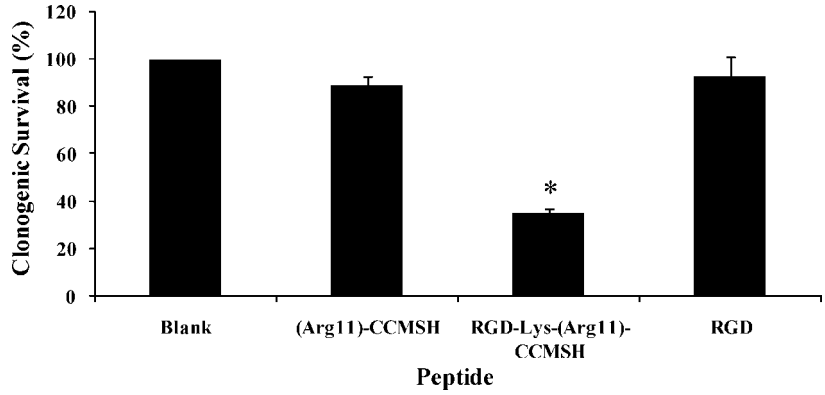

Figure 5. Clonogenic cytotoxic effect of RGD-Lys-(Arg^{11})CCMSH in B16/F1 melanoma cells. The cells were visually examined under microscope for survival. Colonies contained more than 50 cells were scored as survivors. * $p < 0.05$, significance comparison between RGD-Lys-(Arg^{11})CCMSH treated cells and untreated cells (blank).

molecules and negatively charged tubule cells. A direct way to shield this electrostatic interaction is to conjugate DOTA to RGD-Lys-(Arg^{11})CCMSH through the amino group on the side chain of the Lys. Conjugation of DOTA to the amino group on the side chain of the Lys in RGD-Lys-(Arg^{11})CCMSH can reduce the overall positive charge of radiolabeled hybrid CCMSH peptide, as well as provide an excellent metal chelator for the coordination of therapeutic radionuclides such as ^{177}Lu (low-energy β-emitter), ^{90}Y (high-energy β-emitter), and ^{212}Pb (parent radionuclide of high-energy α-emitter ^{212}Bi). Furthermore, strategies of coinjection of positively charged amino acid and structurally introduction of negatively charged amino acid into peptide sequence will also be options to employ to decrease the renal uptakes of the radiolabeled hybrid CCMSH peptides. Coinjection of lysine or arginine has effectively reduced the renal uptakes of ^{188}Re-labeled metal-cyclized CCMSH by 50% (*8*). Introduction of a negatively charged Glu at second position of metal-cyclized CCMSH peptide decreased 72% of the renal uptake values of ^{177}Lu- and ^{90}Y-DOTA-Re(Arg^{11})CCMSH 4 h postinjection (*32, 33*).

It will be attractive to determine the synergistic therapeutic effects of apoptosis and targeted radiation of ^{188}Re-labeled α-MSH hybrid peptides for melanoma once the strategies of amino acid coinjection or structural modification of peptide sequence substantially reduce the renal uptake. Targeted radionuclide therapy with ^{188}Re-(Arg^{11})CCMSH exhibited

therapeutic effects in both human and murine melanoma-bearing mice (*15*). Nonradioactive hybrid RGD-Lys-(Arg^{11})CCMSH showed very promising cytotoxic effect in B16/F1 cells in this report (Figure 5). Single treatment (3 h incubation) with 100 nM of RGD-Lys-(Arg^{11})CCMSH decreased 65% of the clonogenic survival of B16/F1 cells compared to untreated control cells (in culture medium) 6 days post-treatment (Figure 5). On the other hand, neither treatment with 100 nM of (Arg^{11})CCMSH nor that with 100 nM of RGD peptide reduced the clonogenic survival of B16/F1 cells significantly ($p > 0.05$), demonstrating that the cytotoxic effect of RGD-Lys-(Arg^{11})CCMSH hybrid peptide was due to the apoptotic effect of the RGD motif coupled to the hybrid peptide. The remarkable clonogenic cytotoxic effect of RGD-Lys-(Arg^{11})CCMSH warranted the further evaluation of ^{188}Re-labeled α-MSH hybrid peptides for melanoma treatment. Combination therapy of $\alpha_v\beta_3$ integrin receptor antagonist and ^{90}Y-DOTA-peptide ChL6 exhibited increased synergistic (apoptosis and targeted radiation) therapeutic effects in breast cancer xenografts without increased toxicity (*34*). RGD-Lys(^{111}In-DTPA)-Tyr^3-Octreotate displayed more profound tumoricidal effects than ^{111}In-DTPA-Tyr^3-octreotate and ^{111}In-DTPA-RGD due to elevated tumor cell apoptosis (*23*), highlighting the potential enhanced synergistic therapeutic effectiveness of ^{188}Re-labeled α-MSH hybrid peptides for melanoma in future studies.

CONCLUSIONS

Novel RGD-Lys-(Arg^{11})CCMSH showed 2.1 nM MC1 receptor binding affinity. ^{99m}Tc-RGD-Lys-(Arg^{11})CCMSH exhibited MC1 receptor-mediated rapid cellular internalization and extended retention. Furthermore, ^{99m}Tc-RGD-Lys-(Arg^{11})CCMSH displayed rapid high melanoma uptake and prolonged tumor retention in B16/F1 melanoma-bearing mice. Single treatment (3 h incubation) with 100 nM of RGD-Lys-(Arg^{11})CCMSH significantly ($p < 0.05$) decreased the clonogenic survival of B16/F1 melanoma cells by 65%. Technetium-99m and ^{188}Re are matched-pair diagnostic and therapeutic radionuclides, sharing similar coordination chemistry. Hence, favorable melanoma targeting property of ^{99m}Tc-RGD-Lys-(Arg^{11})CCMSH and remarkable cytotoxic effect of RGD-Lys-(Arg^{11})CCMSH warranted the further evaluation of ^{188}Re-labeled α-MSH hybrid peptides as novel MC1 receptor-targeting therapeutic peptides for melanoma treatment once the strategies of amino acid coinjection or structural modification of peptide sequence substantially reduce the renal uptake.

ACKNOWLEDGMENT

We appreciate Drs. Scott W. Burchiel and Larry A. Sklar for their valuable insights. We thank Mr. Benjamin M. Gershman for his technical assistance. This work was supported in part by the Southwest Melanoma SPORE Developmental Research Program (Y. Miao) and the DOD grant W81XWH-09-1-0105 (Y. Miao). The image in this article was generated by the Keck-UNM Small Animal Imaging Resource established with funding from the W.M. Keck Foundation and the University of New Mexico Cancer Research and Treatment Center (NIH P30 CA118100).

LITERATURE CITED

(1) Jemal, A., Siegel, R., Ward, E., Hao, Y., Xu, J., Murray, T., and Thun, M. J. (2008) Cancer statistics, 2008. *CA. Cancer J. Clin. 58*, 71–96.

(2) Marghoob, A. A., Slade, J., Salopek, T. G., Kopf, A. W., Bart, R. S., and Rigel, D. S. (1995) Basal cell and squamous cell carcinomas are important risk factors for cutaneous malignant melanoma. *Cancer 75*, 707–714.

(3) Balch, C. M., Soong, S. J., Gershenwald, J. E., Thompson, J. F., Reintgen, D. S., Cascinelli, N., Urist, M., McMasters, K. M., Ross, M. I., Kirkwood, J. M., Atkins, M. B., Thompson, J. A., Coit, D. G., Byrd, D., Desmond, R., Zhang, Y., Liu, P. Y., Lyman, G. H., and Morabito, A. (2001) Prognostic factors analysis of 17,600 melanoma patients: validation of the American Joint Committee on Cancer melanoma staging system. *J. Clin. Oncol. 19*, 3622–3634.

(4) Anderson, C. M., Buzaid, A. C., and Legha, S. S. (1995) Systemic treatments for advanced cutaneous melanoma. *Oncology 9*, 1149–1158.

(5) Tatro, J. B., and Reichlin, S. (1987) Specific receptors for alpha-melanocyte-stimulating hormone are widely distributed in tissues of rodents. *Endocrinology 121*, 1900–1907.

(6) Siegrist, W., Solca, F., Stutz, S., Giuffre, L., Carrel, S., Girard, J., and Eberle, A. N. (1989) Characterization of receptors for alpha-melanocyte-stimulating hormone on human melanoma cells. *Cancer Res. 49*, 6352–6358.

(7) Chen, J., Cheng, Z., Hoffman, T. J., Jurisson, S. S., and Quinn, T. P. (2000) Melanoma-targeting properties of ^{99m}Technetium-labeled cyclic alpha-melanocyte-stimulating hormone peptide analogues. *Cancer Res. 60*, 5649–5658.

(8) Miao, Y., Owen, N. K., Whitener, D., Gallazzi, F., Hoffman, T. J., and Quinn, T. P. (2002) In vivo evaluation of ^{188}Re-labeled alpha-melanocyte stimulating hormone peptide analogs for melanoma therapy. *Int. J. Cancer 101*, 480–487.

(9) Miao, Y., Whitener, D., Feng, W., Owen, N. K., Chen, J., and Quinn, T. P. (2003) Evaluation of the human melanoma targeting properties of radiolabeled alpha-melanocyte stimulating hormone peptide analogues. *Bioconjugate Chem. 14*, 1177–1184.

(10) Giblin, M. F., Wang, N., Hoffman, T. J., Jurisson, S. S., and Quinn, T. P. (1998) Design and characterization of alpha-melanotropin peptide analogs cyclized through rhenium and technetium metal coordination. *Proc. Natl. Acad. Sci. U.S.A. 95*, 12814–12818.

(11) Froidevaux, S., Calame-Christe, M., Tanner, H., Sumanovski, L., and Eberle, A. N. (2002) A novel DOTA-alpha-melanocyte-stimulating hormone analog for metastatic melanoma diagnosis. *J. Nucl. Med. 43*, 1699–1706.

(12) Froidevaux, S., Calame-Christe, M., Schuhmacher, J., Tanner, H., Saffrich, R., Henze, M., and Eberle, A. N. (2004) A gallium-labeled DOTA-alpha-melanocyte- stimulating hormone analog for PET imaging of melanoma metastases. *J. Nucl. Med. 45*, 116–123.

(13) Miao, Y., Benwell, K., and Quinn, T. P. (2007) ^{99m}Tc- and ^{111}In-labeled alpha-melanocyte-stimulating hormone peptides as imaging probes for primary and pulmonary metastatic melanoma detection. *J. Nucl. Med. 48*, 73–80.

(14) Miao, Y., Figueroa, S. D., Fisher, D. R., Moore, H. A., Testa, R. F., Hoffman, T. J., and Quinn, T. P. (2008) ^{203}Pb-labeled alpha-melanocyte-stimulating hormone peptide as an imaging probe for melanoma detection. *J. Nucl. Med. 49*, 823–829.

(15) Miao, Y., Owen, N. K., Fisher, D. R., Hoffman, T. J., and Quinn, T. P. (2005) Therapeutic efficacy of a ^{188}Re-labeled alpha-melanocyte-stimulating hormone peptide analog in murine and human melanoma-bearing mouse models. *J. Nucl. Med. 46*, 121–129.

(16) Miao, Y., Hylarides, M., Fisher, D. R., Shelton, T., Moore, H., Wester, D. W., Fritzberg, A. R., Winkelmann, C. T., Hoffman, T., and Quinn, T. P. (2005) Melanoma therapy via peptide-targeted α-radiation. *Clin. Cancer Res. 11*, 5616–5621.

(17) Miao, Y., Shelton, T., and Quinn, T. P. (2007) Therapeutic efficacy of a ^{177}Lu-labeled DOTA conjugated alpha-melanocyte-stimulating hormone peptide in a murine melanoma-bearing mouse model. *Cancer Biother. Radiopharm. 22*, 333–341.

(18) Brooks, P. C., Clark, R. A., and Cheresh, D. A. (1994) Requirement of vascular integrin $\alpha_v\beta_3$ for angiogenesis. *Science 264*, 569–571.

(19) Hood, J. D., and Cheresh, D. A. (2002) Role of integrins in cell invasion and migration. *Nat. Rev. Cancer 2*, 91–100.

(20) Brooks, P. C., Montgomery, A. M., Rosenfeld, M., Reisfeld, R. A., Hu, T., Klier, G., and Cheresh, D. A. (1994) Integrin α_v β_3 antagonists promote tumor regression by inducing apoptosis of angiogenic blood vessels. *Cell 79*, 1157–1164.

(21) Mitjans, F., Meyer, T., Fittschen, C., Goodman, S., Jonczyk, A., Marshall, J. F., Reyes, G., and Piulats, J. (2000) In vivo therapy of malignant melanoma by means of antagonists of α_v integrins. *Int. J. Cancer 87*, 716–723.

(22) Buckley, C. D., Pilling, D., Henriquez, N. V., Parsonage, G., Threlfall, K., Scheel-Toellner, D., Simmons, D. L., Akbar, A. N., Lord, J. M., and Salmon, M. (1999) RGD peptides induce apoptosis by direct caspase-3 activation. *Nature 397*, 534–539.

(23) Capello, A., Krenning, E. P., Bernard, B. F., Breeman, W. A., van Hagen, M. P., and de Jong, M. (2004) Increased cell death after therapy with an Arg-Gly-Asp-linked somatostatin analog. *J. Nucl. Med. 45*, 1716–1720.

(24) Bernard, B., Capello, A., van Hagen, M., Breeman, W., Srinivasan, A., Schmidt, M., Erion, J., van Gameren, A., Krenning, E., and de Jong, M. (2004) Radiolabeled RGD-DTPA-Tyr^3-octreotate for receptor-targeted radionuclide therapy. *Cancer Biother. Radiopharm. 19*, 173–180.

(25) Hofland, L. J., Capello, A., Krenning, E. P., de Jong, M., and van Hagen, M. P. (2005) Induction of apoptosis with hybrids of Arg-Gly-Asp molecules and peptides and antimitotic effects of hybrids of cytostatic drugs and peptides. *J. Nucl. Med. 46 Suppl 1* 191S–198S.

(26) Capello, A., Krenning, E. P., Bernard, B. F., Breeman, W. A., Erion, J. L., and de Jong, M. (2006) Anticancer activity of targeted proapoptotic peptides. *J. Nucl. Med. 47*, 122–129.

(27) Miao, Y., Gallazzi, F., Guo, H., and Quinn, T. P. (2008) ^{111}In-labeled lactam bridge-cyclized alpha-melanocyte stimulating hormone peptide analogues for melanoma imaging. *Bioconjugate Chem. 19*, 539–547.

(28) Heppeler, A., Froidevaux, S., Eberle, A. N., and Maecke, H. R. (2000) Receptor targeting for tumor localisation and therapy with radiopeptides. *Curr. Med. Chem. 7*, 971–994.

(29) Fung, S., and Hruby, V. J. (2005) Design of cyclic and other templates for potent and selective peptide alpha-MSH analogues. *Curr. Opin. Chem. Biol. 9*, 352–358.

(30) Schraa, A. J., Kok, R. J., Moorlag, H. E., Bos, E. J., Proost, J. H., Meijer, D. K., de Leij, L. F., and Molema, G. (2002) Targeting of RGD-modified proteins to tumor vasculature: a pharmacokinetic and cellular distribution study. *Int. J. Cancer 102*, 469–475.

(31) Miao, Y., Hoffman, T. J., and Quinn, T. P. (2002) Optimizing the tumor to kidney uptake ratio of ^{188}Re labeled alpha-melanocyte stimulating hormone peptide analogs through chemical modification. *Technetium, Rhenium and other Metals in Chemistry and Nuclear Medicine 6* (Nicolini, M., and Mazzi, U., Eds.) pp 567−570, Servizi Grafici Editoriali, Padova, Italy.

(32) Miao, Y., Hoffman, T. J., and Quinn, T. P. (2005) Tumor-targeting properties of ^{90}Y- and ^{177}Lu-labeled alpha-melanocyte stimulating hormone peptide analogues in a murine melanoma model. *Nucl. Med. Biol. 32*, 485–493.

(33) Miao, Y., Fisher, D. R., and Quinn, T. P. (2006) Reducing renal uptake of ^{90}Y- and ^{177}Lu-labeled alpha-melanocyte stimulating hormone peptide analogues. *Nucl. Med. Biol. 33*, 723–733.

(34) Burke, P. A., DeNardo, S. J., Miers, L. A., Lamborn, K. R., Matzku, S., and DeNardo, G. L. (2002) Cilengitide targeting of α_v β_3 integrin receptor synergizes with radioimmunotherapy to increase efficacy and apoptosis in breast cancer xenografts. *Cancer Res. 62*, 4263–4272.

BC9001954

Efficient Guest Inclusion by β-Cyclodextrin Attached to the Ends of DNA Oligomers upon Hybridization to Various DNA Conjugates

Akinori Kuzuya,*,† Toshiyuki Ohnishi,† Tsugutoshi Wasano,‡ Suguru Nagaoka,† Jun Sumaoka,† Toshihiro Ihara,*,‡ Akinori Jyo,‡ and Makoto Komiyama*,†

Research Center for Advanced Science and Technology, The University of Tokyo, 4-6-1 Komaba, Meguro, Tokyo, 153-8904 Japan, and Department of Applied Chemistry and Biochemistry, Graduate School of Science and Technology, Kumamoto University, 2-39-1 Kurokami, Kumamoto 860-8555, Japan. Received May 4, 2009; Revised Manuscript Received June 15, 2009

Two types of 5′-β-CyD-DNA conjugates were synthesized using two different strategies and were hybridized with cDNA conjugates bearing various possible guest compounds at the 3′ ends. One of the β-CyD conjugates was synthesized on the basis of solid-phase postmodification of DNA with a monoamino-β-CyD derivative on a synthesis column for automated DNA synthesis. The other β-CyD conjugate was synthesized by the solution-phase coupling of DNA with a monomercapto-β-CyD derivative using a heterobifunctional cross-coupling reagent. When these 5′-β-CyD-DNA conjugates were hybridized with cDNA conjugates bearing 1-adamantaneacetic acid at the 3′ ends, significant stabilization of the duplexes was observed as compared with the control duplex without β-CyD. Duplexes of 5′-β-CyD-DNA conjugates and complementary 3′-dansyl-glycine-DNA conjugates were also moderately stabilized. Thermodynamic measurements revealed that the host−guest inclusion interactions between β-CyD and 1-adamantaneacetic acid or dansyl-glycine are roughly as strong as those found in bulk solution even if they are tethered to the ends of the DNA.

INTRODUCTION

Cyclodextrins (CyDs) are cyclic oligosaccharides composed of five or more α-D-glucopyranosides and are important players in supramolecular and molecular-recognition chemistry, as a result of their unique host−guest inclusion capabilities (*1*−*3*). Due to their rigid and well-defined ring structure, CyDs bind various small guest molecules in their hydrophobic inner cavity. β-CyD is composed of seven glucopyranosides and has an inner cavity of 7 Å diameter. Interactions between CyDs and various guest molecules such as adamantane have been widely studied, particularly for β-CyD, and many interesting applications of these inclusion phenomena have been proposed to date (*4*). For example, dansyl-modified cyclodextrins have been applied as a fluorescent probe, which can detect guest molecules based on the fluorescence change of the dansyl moiety (*5*−*9*).

Nucleic acids are another interesting subject of supramolecular chemistry, mainly due to their accurate complementary base-pairing and regularly formed double-helical structure. Recent progress with DNA and RNA modification techniques has widened the scope of their application in various research fields such as life science (*10, 11*), analytical chemistry (*12, 13*), and even nanotechnology (*14*−*16*). The conjugation of β-CyD and DNA should encourage further progress. However, few papers have been published on the actual synthesis of β-CyD−DNA conjugates (*17*−*19*), and almost no detailed studies have been undertaken regarding their guest inclusion capabilities. DNA bears many hydrophobic nucleobases, which are all possible guest compounds of β-CyD. The formation of a rotaxane-type complex between β-CyD and the linker moiety may also prevent desired guest inclusion by β-CyD. Thus, a clear-cut proof of guest inclusion by β-CyD-DNA conjugates is necessary.

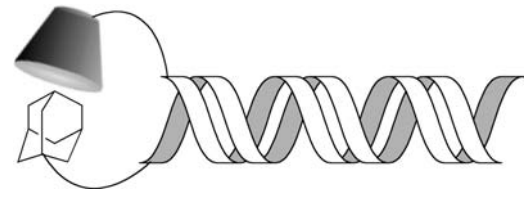

Figure 1. Schematic illustration of the present system. β-CyD is attached to the 5′ end of DNA, and possible guest molecules are attached to the 3′ end of the complementary strand such that they are placed in front of the β-CyD over the duplex.

In this study, we have synthesized two types of β-CyD−DNA conjugates that bear β-CyD at their 5′ ends via different linkers in order to evaluate the guest inclusion ability of β-CyD on DNA duplexes (Figure 1). In the measurements of melting profiles obtained using a variety of complementary strands modified with possible guest compounds at the opposite site, significant stabilization was observed for the duplexes of both of the two β-CyD−DNA conjugates (Figure 2) and their cDNA conjugates bearing 1-adamantane at the 3′ ends (Figure 3). Thermodynamic analyses revealed that the host−guest inclusion interaction between β-CyD and 1-adamantane is as strong as that observed in a bulk solution even if they are tethered to the ends of the DNA. Moderate stabilization was also observed for the duplexes between the β-CyD−DNA conjugate and complementary 3′-dansyl-glycine-DNA conjugates, which showed significant fluorescence enhancement upon hybridization.

EXPERIMENTAL PROCEDURES

MALDI-TOF mass spectra were measured on a Bruker Daltonics AutoFLEX MALDI TOF-MS spectrometer (Billerica, MA, USA). *N*-Succinimidyl 3-(2-pyridyldithio)propionate (SPDP) was purchased from Dojindo Laboratories (Kumamoto, Japan). All of the phosphoramidite monomers for DNA modification were purchased from Glen Research (Sterling, VA, USA).

Synthesis of Monotosylated-β-CyD (5). β-CyD (0.50 g, 0.43 mmol) was dissolved in 4.3 mL of dried pyridine under an argon

* E-mail of Makoto Komiyama: komiyama@mkomi.rcast.u-tokyo.ac.jp.
† The University of Tokyo.
‡ Kumamoto University.

10.1021/bc900200c CCC: $40.75 © 2009 American Chemical Society
Published on Web 07/08/2009

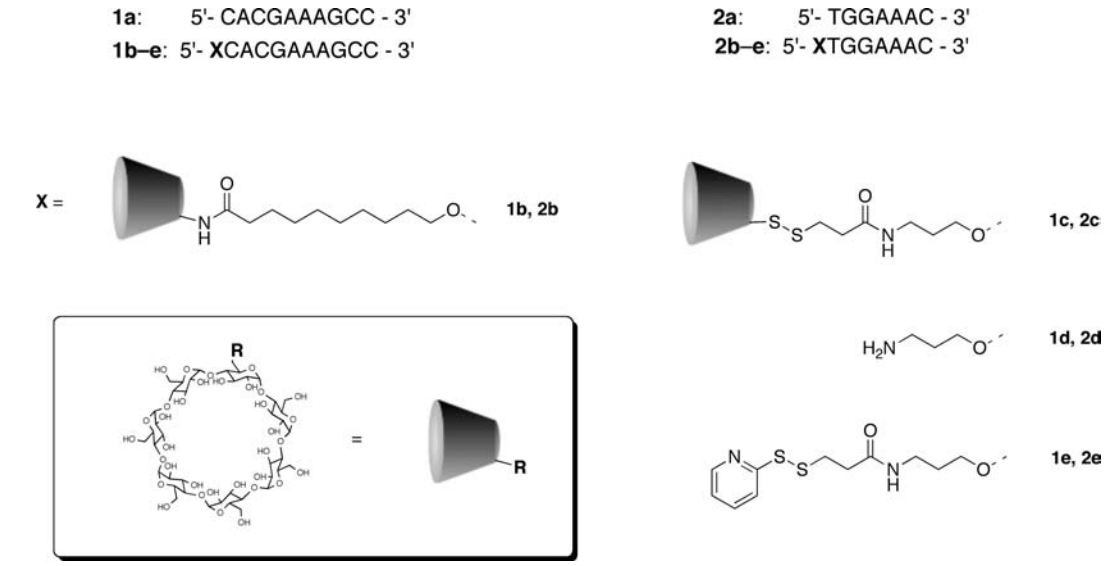

Figure 2. Structures of β-CyD−DNA conjugates and their controls used in this study.

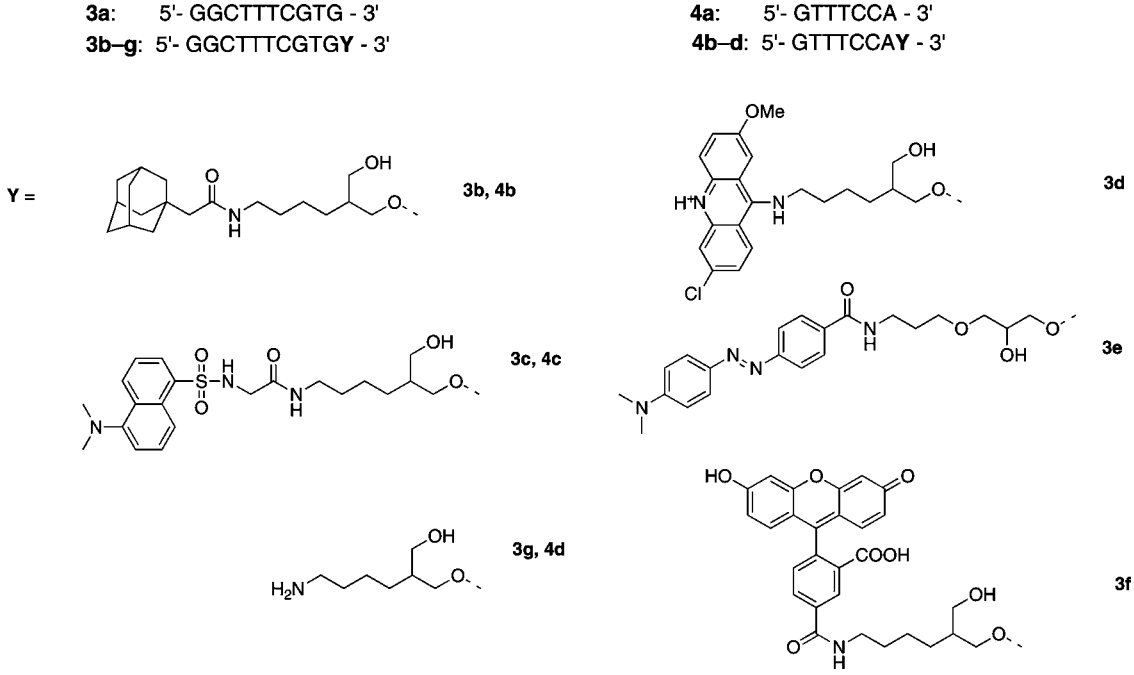

Figure 3. Structures of the complementary strands bearing possible guest molecules.

atmosphere. To the solution, *p*-toluenesulfonyl chloride (0.16 g, 0.85 mmol) was added in an ice bath and then stirred at room temperature. The progress of the reaction was intermittently monitored by thin-layer chromatography (TLC) (1-buthanol/ethanol/water = 5/4/3; indicator: *p*-anisaldehyde). The reaction was quenched by the addition of 0.35 mL of water after 3 h. Analysis by TLC indicated the presence of three spots for β-CyD (R_f = 0.30), monotosylated-β-CyD (0.48), and ditosylated-β-CyD (0.57) of almost the same density. The solution was concentrated to half of the volume in vacuo and poured into 8.5 mL of acetone with vigorous stirring. The resulting white solid was collected and repeatedly recrystallized from water.

White solid: 72 mg (12.7%). ^{1}H NMR (DMSO-d_6, 399.65 MHz) δ 2.43 (s, 3H), 3.10−3.45 (m, 14H), 3.45−3.66 (m, 28H), 4.10−4.60 (m, 6H), 4.76 (s, br, 2H), 4.83 (s, br, 5H), 5.60−5.85 (m, 14H), 7.42 (d, 2H, J = 8.3 Hz), 7.74 (d, 2H, 8.3 Hz) ppm.

Synthesis of Mono(6-amino-6-deoxy)-β-CyD (6). Mono(6-amino-6-deoxy)-β-CyD (**6**) was synthesized from **5** using sodium azide and aqueous ammonia according to a previous report (*20*).

Synthesis of Mono(6-deoxy-6-mercapto)-β-CyD (7). Compound **5** (0.50 g, 0.39 mmol) and thiourea (0.50 g, 6.6 mmol) were dissolved in 25 mL of 80% aqueous methanol and refluxed for 72 h. The solution was evaporated in vacuo. The resulting solid was suspended in 7.6 mL of methanol and stirred for 1 h at room temperature. The solid was then filtered and dissolved in 17 mL of a 10% aqueous solution of NaOH and stirred for 5 h at 50 °C. After the solution was acidified with 1 M HCl to pH 2, 1.2 mL of trichloroethylene was added to the solution. After stirring overnight, the precipitate was filtered and washed with water. Evaporation of trichloroethylene in vacuo was followed by repeated recrystallization from water, resulting in a white solid.

Table 1. MALDI-TOF/MS Analyses of the Conjugates

	calcd. *m/z* $[M+H]^+$	found
1b	4373.2	4370.1
1c	4379.2	4378.4
1e	3339.3	3336.9
2b	3495.7	3495.1
2c	3501.9	3502.0
2e	2463.5	2464.0
3b	3432.6	3432.3
3c	3547.1	3547.5
3d	3497.5	3498.7
3e	3510.1	3512.0
3f	3618.5	3617.8
4b	2453.9	2449.3
4c	2568.9	2564.4

White solid: 0.27 g (59.4%). TLC (silica): one spot (R_f = 0.23, CH_3CO_2Et/*n*-PrOH/H_2O, 7/7/5). MALDI-TOF/MS calcd for $[M+H]^+$: 1150.54; found: 1150.06.

Attachment of 6 to DNA. In the final coupling cycle for the synthesis of **1b**, 5′-Carboxy-Modifier C10 phosphoramidite, which is activated with *N*-hydroxysuccinimide ester, was attached. The CPG column was removed from the synthesizer and filled with 1 M solution of **6** in pyridine/water (3:1) using two 1 mL glass syringes on both sides of the column. After incubating the column overnight at room temperature, it was washed three times with 1 mL of water and with acetonitrile (1 mL × 3). The conjugate **1b** was detached from the support and deprotected with conc. aqueous ammonia at 55 °C for 8 h. The 7-mer conjugate **2b** was synthesized in the same manner.

Syntheses of DNA Conjugates Bearing Acridine (3d), Dabcyl (3e), and Fluorescein (3f). The conjugates bearing acridine (**3d**), dabcyl (**3e**), and fluorescein (**3f**) at the 3′ end were synthesized using the corresponding CPG supports purchased from Glen Research on an automated DNA synthesizer with standard phosphoramidite chemistry. Cleavage from the supports and deprotection of the conjugates were performed with conc. aqueous ammonia at 55 °C for 8 h for **3e** and **3f**, and 0.4 M methanolic NaOH (4:1 MeOH/H_2O) was used for **3d** at room temperature and allowed to react for 16 h (*21*). The crude mixtures were desalted with Poly-Pak cartridges (Glen Research) and evaporated to dryness for further purification as described below.

Purification and Characterization of 1b, 2b, and 3d-f. The conjugates **1b**, **2b**, and **3d-f** were purified using 20% denaturing polyacrylamide gel electrophoresis (PAGE) and then by reverse-phase HPLC (RP-HPLC) equipped with an RP-C18 column (Cica-Merck LiChroCART 125−4; room temperature; linear gradient 5−25% acetonitrile in 50 mM ammonium formate for 20 min; flow rate 0.5 mL/min). These were characterized by MALDI-TOF/MS in the positive ion mode (Table 1).

Syntheses of DNA Conjugates Bearing an Adamantane (3b, 4b) or Dansyl-Glycine (3c, 4c) Residue at the 3′ End. A DNA conjugate bearing a 3′-amino group (**3g** or **4d**) was synthesized with standard phosphoramidite chemistry using 3′-Amino-Modifier C7 CPG and purified using 20% denaturing PAGE and RP-HPLC, as described above. The activated 1-adamantaneacetic acid (for **3b** and **4b**) or dansyl-glycine (for **3c** and **4c**) was obtained by treating the corresponding carboxylic acid (0.1 mmol) with *N*,*N*′-dicyclohexylcarbodiimide (0.1 mmol) and *N*-hydroxysuccinimide (0.1 mmol) in DMSO (0.5 mL) overnight at room temperature. The supernatant of the above reaction mixture (20 μL) was added to the solution of **3g** (or **4d**, 10 nmol) in a pH 9.0 $NaHCO_3$ buffer (0.1 M, 100 μL); it was then allowed to react overnight at 37 °C, and 400 μL of water was added to the mixture. The desired conjugates were isolated by RP-HPLC after filtration and fully characterized using MALDI-TOF/MS.

Attachment of 7 to DNA. The purified aminopropyl-bearing DNA **1d** (100 nmol) was dissolved in 100 μL of pH 9.3 $NaHCO_3$ buffer (0.5 M). SPDP (1.5 mg, 4.6 μmol), dissolved in 50 μL of DMSO, was added to this solution. The resulting suspension was stirred overnight at room temperature. The solution was diluted to 400 μL with water. The resulting SPDP−DNA conjugate **1e** was purified by RP-HPLC (Wakosil-II 5C18 RS column; room temperature; linear gradient 5−30% acetonitrile in 0.1 M triethylammonium acetate for 30 min; flow rate 1.0 mL/min).

To the solution of **1e** (50 nmol) in 100 μL of pH 7.2 Na_2HPO_4/NaH_2PO_4 buffer (10 mM) was added **7** (5.8 mg, 5.0 μmol) dissolved in 60 μL of DMSO. The resulting suspension was stirred overnight at room temperature. The solution was diluted to 400 μL with water. The mixture was purified by RP-HPLC as described above and fully characterized using MALDI-TOF/MS. The 7-mer conjugate **2c** was synthesized in the same manner.

Measurement of Melting Temperature (T_m). The melting profiles of the duplexes were obtained with a JASCO V-530 spectrometer at 260 nm in a quartz cell with a 1-cm path length. The specimens contained the DNA conjugates (1−20 μM), Na_2EDTA (10 mM), and NaCl (1.0 M) in a pH 7 Na_2HPO_4/NaH_2PO_4 buffer (10 mM). The heating rate was 1.0 °C/min. Thermodynamic parameters of each duplex were calculated by plotting the reciprocals of the T_m values for various DNA concentrations according to a previous report (*22*).

Fluorescence Measurements. Fluorescence changes in the dansyl groups upon hybridization were obtained with a JASCO FP-6500 spectrofluorometer in a quartz cell at 25 °C for the **1**/**3c** combination and 10 °C for the **2**/**4c** combination. The specimens (50 μL) contained the DNA conjugates (5 μM each) and NaCl (1.0 M) in a pH 7 Na_2HPO_4/NaH_2PO_4 buffer (10 mM). The excitation wavelength was 343 nm.

RESULTS AND DISCUSSION

Syntheses of DNA Conjugates. Two different types of DNA conjugates bearing β-CyD at the 5′ end were synthesized on the basis of two distinct strategies. The conjugates **1b** and **2b** were synthesized using a solid-phase DNA postmodification technique on a synthesis column for an automated DNA synthesizer. First, mono(6-amino-6-deoxy)-β-CyD (**6**) was prepared as described in the literature (*20*) (Scheme 1). Then, **6** was reacted with the activated carboxylic acid tethered to the 5′ end of DNA through a nonyl-linker to form an amide linkage between β-CyD and the DNA (Scheme 2). The resulting β-CyD−DNA conjugates were detached from the support and deprotected by a standard method with conc. aqueous ammonia at 55 °C for 8 h. The conjugates were further purified using 20% denaturing PAGE and RP-HPLC.

The other conjugates, **1c** and **2c**, were synthesized by the solution-phase coupling of DNA and thiolated β-CyD (Scheme 3). For example, the amino-modified DNA **1d** was first reacted with a heterobifunctional cross-coupling reagent, SPDP. The resulting dithio-functionalized DNA **1e** then reacted with mono(6-deoxy-6-mercapto)-β-CyD (**7**), prepared from mono-tosylated-β-CyD (*23*, *24*). The products in each step were purified by RP-HPLC.

The complementary conjugates bearing possible guest compounds at the 3′ end were also synthesized in two different ways. The conjugates bearing acridine (**3d**), dabcyl (**3e**), and fluorescein (**3f**) at the 3′ end were synthesized using commercially available corresponding CPG supports on an automated DNA synthesizer with standard phosphoramidite chemistry, and were purified using 20% denaturing PAGE and RP-HPLC in the same way as **1b**. The conjugates bearing 1-adamantaneacetic acid (**3b** and **4b**) and dansyl-glycine (**3c** and **4c**), by contrast, were

Scheme 1

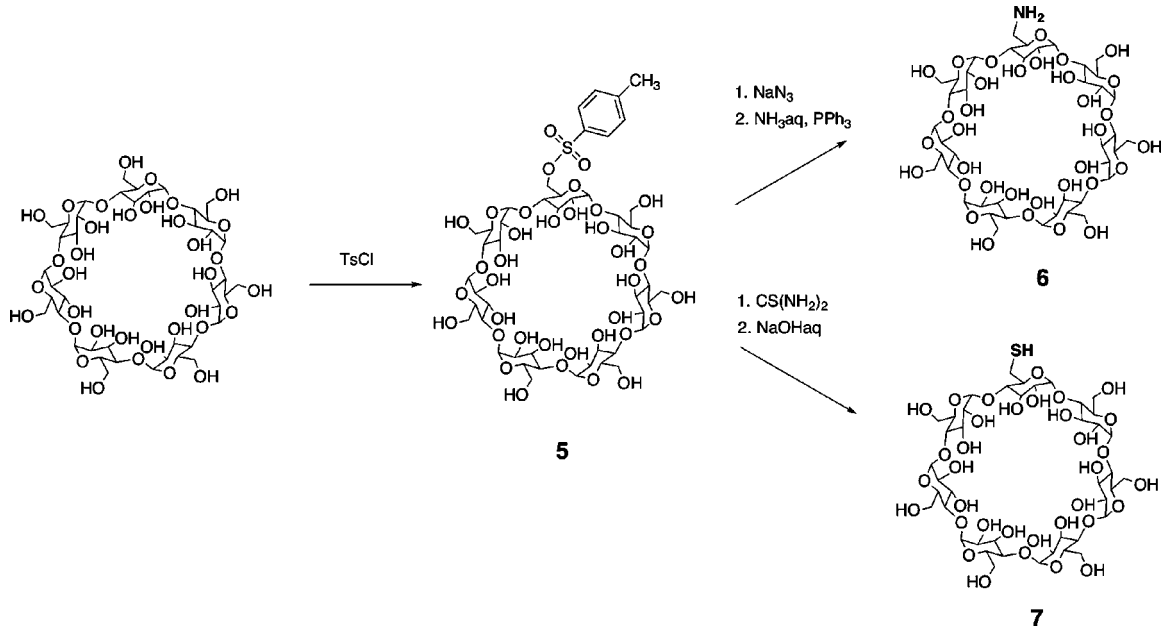

Scheme 2

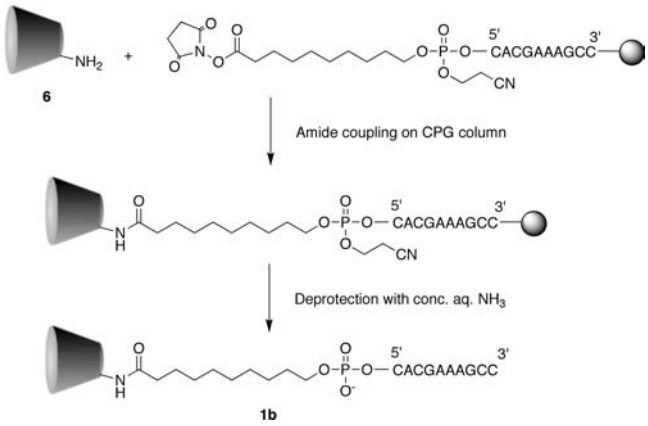

obtained by the solution-phase coupling of prepurified amino-modified DNA and corresponding activated esters. All of the conjugates used in this study were fully characterized with MALDI-TOF/MS (Table 1).

Thermodynamic Properties. To evaluate the strength of the interaction between β-CyD in the conjugates and possible guest compounds attached to the opposite position in the cDNA, the melting temperatures of the duplexes of the **1**/**3** (Table 2) and **2**/**4** (Table 3) combinations were measured. For the duplexes of unmodified **1a** and its complements (**3a**−**3f**), the attachment of possible guests did not significantly alter the stability of the duplexes, except for **3d**, which bears an acridine moiety (Table 2). This acridine has a positive charge on its aromatic nitrogen atom under neutral conditions and is known to stabilize duplexes by intercalation (*25, 26*). The β-CyD−DNA conjugate **1b**, in which β-CyD is connected to the linker portion via an amide bond, was used in place of **1a** and provided significant stabilization of the duplex between **1b** and its adamantane-modified complement **3b**. The difference in melting temperature was as high as 11 °C, when comparing the T_m values of **1b**/**3b** (62.0 °C) and **1a**/**3b** (51.3 °C). For other conjugates bearing aromatic rings (i.e., **3c**, **3d**, **3e**, and **3f**), the differences in the T_m values between the duplexes of **1b**/**3** and **1a**/**3** were very slight, although it has been reported that, in a bulk solution, the dansyl group in **3c** and the methyl red group, which has a ring structure identical to the dabcyl group in **3e**, are included in β-CyD cavities with significant binding constants (*27*−*30*).

More drastic T_m changes were observed for the duplexes of **1c**/**3b**, in which β-CyD is connected to the DNA via a disulfide bond. The T_m value of the duplex formed by the adamantane conjugate **3b** and **1c** was 73.9 °C, which is nearly 23 °C higher than that of the duplex of **3b** and unmodified **1a** (51.3 °C). Similarly, but in contrast to the **1b**/**3** series, a significant increase in the T_m values was observed for the duplexes of **1c**/**3c** (β-CyD/dansyl, $\Delta\Delta T_m$ = 2.4 °C), **1c**/**3e** (β-CyD/dabcyl, 9.1 °C), and **1c**/**3f** (β-CyD/FAM, 6.1 °C) combinations.

The above tendency was also observed for the shorter 7-mer duplexes of the **2**/**4** series with completely different sequences from the **1**/**3** series (Table 3). The T_m value of **2c**/**4b** (β-CyD/adamantane, 55.1 °C) is elevated by as much as 34.0 °C, as compared to that of **2c**/**4a** (β-CyD/unmodified, 21.1 °C), and by 36.8 °C, as compared to that of **2a**/**4b** (unmodified/adamantane, 18.3 °C); the T_m of **2c**/**4c** (β-CyD/dansyl, 29.7 °C) is 8.6 °C higher than that of **2c**/**4a** (β-CyD/unmodified, 21.1 °C) and is higher than the T_m of **2a**/**4c** (unmodified/dansyl, 19.4 °C) by 10.3 °C. The T_m elevations for the **2b**/**4** combinations, on the other hand, are both smaller than those of the **2c**/**4** combinations.

Previous studies have shown that adamantane is one of the best guest molecules for β-CyD, with an association constant of $\sim 10^5$ M^{-1}, due to its hydrophobic nature and because its size matches that of the cavity (*27, 31, 32*). The strong stabilization observed in the present study of the duplexes is presumably attributable to the strong interaction between the adamantane and β-CyD attached to the ends of the DNA strands. To more accurately evaluate the interaction between β-CyD and the possible guests on the complementary strand, the thermodynamic parameters of duplex formation for the **1**/**3** (Table 4) and **2**/**4** (Table 5) combinations were estimated. Differences in the ΔG_{37} values corresponding to adamantane incorporation are −8.1 kcal/mol for the duplex of **1c**/**3b**, −8.3 kcal/mol for **2c**/**4b**, −5.8 kcal/mol for **1b**/**3b**, and −4.3 kcal/mol for **2b**/**4b**. These values are in good accordance with, or even larger than, the values previously obtained in bulk solution by various measurements such as competitive reaction inhibition, proton uptake, competitive spectral displacement, and microcalorimetry (*27*). It has been noted that the binding of guest molecules in

Scheme 3

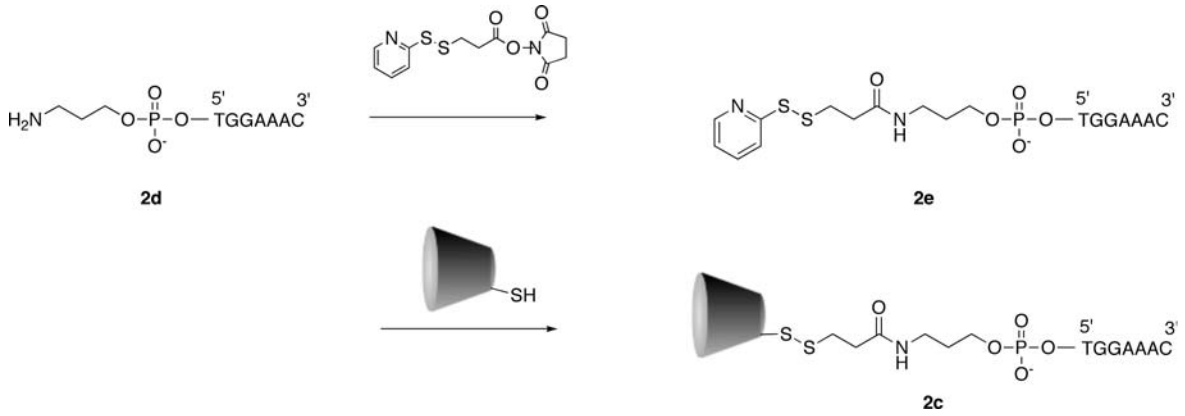

Table 2. Melting Temperatures of the Duplexes of the 10-mer DNA (1) and Their Complementary Strands at 1.25 μM

	1a		1b			1c		
	T_m (°C)	ΔT_m (°C)[a]	T_m (°C)	ΔT_m (°C)[a]	$\Delta\Delta T_m$ (°C)[b]	T_m (°C)	ΔT_m (°C)[a]	$\Delta\Delta T_m$ (°C)[b]
3a	49.7	–	49.3	–	–	51.8	–	–
3b	51.3	1.6	62.0	12.7	11.1	73.9	22.1	20.5
3c	51.1	1.4	51.0	1.7	0.3	55.6	3.8	2.4
3d	54.6	4.9	54.2	4.9	0	57.1	5.3	0.4
3e	51.5	1.8	52.6	3.3	1.5	62.7	10.9	9.1
3f	47.9	−1.8	49.8	0.5	2.3	56.1	4.3	6.1

[a] Difference in T_m from that of the duplex involves **3a**. [b] Difference in ΔT_m from that of the duplex involves **1a**.

Table 3. Melting Temperatures of the Duplexes of the 7-mer DNA (2) and Their Complementary Strands at 1.25 μM

	2a		2b			2c		
	T_m (°C)	ΔT_m (°C)[a]	T_m (°C)	ΔT_m (°C)[a]	$\Delta\Delta T_m$ (°C)[b]	T_m (°C)	ΔT_m (°C)[a]	$\Delta\Delta T_m$ (°C)[b]
4a	15.2	–	15.3	–	–	21.1	–	–
4b	18.3	3.1	40.7	25.4	22.3	55.1	34.0	30.9
4c	19.4	4.2	20.7	5.4	1.2	29.7	8.6	4.4

[a] Difference in T_m from that of the duplex involves **4a**. [b] Difference in ΔT_m from that of the duplex involves **2a**.

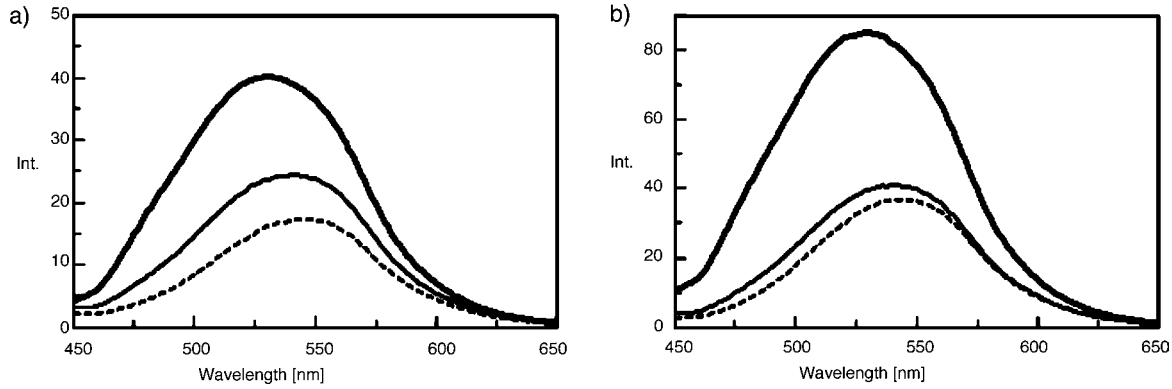

Figure 4. Emission spectra of the fluorescence from the dansyl group in the duplexes with and without β-CyD. (a) **1a**/**3c** (broken line); **1b**/**3c** (regular line); **1c**/**3c** (bold line). (b) **2a**/**4c** (broken line); **2b**/**4c** (regular line); **2c**/**4c** (bold line).

cyclodextrin cavities is usually enthalpy-driven, since van der Waals forces (negative $\Delta H°$; negative $\Delta S°$) dominantly contribute to the binding more than the classical hydrophobic effect (near-zero $\Delta H°$; positive $\Delta S°$) (*1, 32*). The parameters obtained for the above conjugates agree well with this argument (see Supporting Information Tables 2−4 for the $\Delta\Delta H$ and $\Delta\Delta S$ values). The binding mode of a β-CyD/adamantane complex formed on a DNA duplex is thus expected to be almost the same as that in bulk solution.

For the duplexes of the **1b**/**3** combinations, dansyl-modified **3c** generated the largest ΔG_{37} change among the dye−DNA conjugates (**3c**−**f**) investigated in this study, although little change in T_m was observed. Differences in the ΔG_{37} values in the presence of a dansyl group (**1**/**3c** and **2**/**4c**) are all around −1 to −2 kcal/mol, as compared to the absence of the dansyl

Table 4. Thermodynamic Parameters of the 10-Mer Duplexes (1/3)

	1a		1b		1c	
	ΔG_{37} (kcal/mol)	$\Delta\Delta G_{37}$[a] (kcal/mol)	ΔG_{37} (kcal/mol)	$\Delta\Delta G_{37}$[a] (kcal/mol)	ΔG_{37} (kcal/mol)	$\Delta\Delta G_{37}$[a] (kcal/mol)
3a	−12.8	–	−11.7	–	−12.5	–
3b	−13.1	−0.3	−17.5	−5.8	−20.6	−8.1
3c	−13.8	−1.0	−12.9	−1.2	−13.6	−1.1
3d	−12.8	0	−12.5	−0.8	−15.5	−3.0
3e	−12.8	0	−12.0	−0.3	−15.6	−3.1
3f	−12.4	0.4	−11.5	0.2	−13.2	−0.7

[a] Difference in ΔG_{37} from that of the duplex involves **3a**.

Table 5. Thermodynamic Parameters of the 7-Mer Duplexes (2/4)

	2a		2b		2c	
	ΔG_{37} (kcal/mol)	$\Delta\Delta G_{37}{}^{a}$ (kcal/mol)	ΔG_{37} (kcal/mol)	$\Delta\Delta G_{37}{}^{a}$ (kcal/mol)	ΔG_{37} (kcal/mol)	$\Delta\Delta G_{37}{}^{a}$ (kcal/mol)
4a	−5.9	−	−5.3	−	−5.6	−
4b	−6.4	−0.6	−9.6	−4.3	−13.9	−8.3
4c	−5.9	0	−7.1	−1.8	−7.5	−1.9

[a] Difference in ΔG_{37} from that of the duplex involves **4a**.

in the duplexes (**1**/**3a** and **2**/**4a**). This is also in good agreement with the previous $\Delta G^{\circ} = -2$ to -3 kcal/mol calculated in a fluorimetric study (*28*). In contrast, significant stabilization of the duplex was observed in the presence of acridine (−3.0 kcal/mol) and dabcyl (−3.1 kcal/mol) in the duplexes involving the other β-CyD−DNA conjugate, **1c**.

Fluorescence Change of Dansyl Group upon Hybridization. The fluorescence of the dansyl group is significantly enhanced when the dye is included in the hydrophobic cavity of β-CyD, since it is protected from quenching by water (*5*−*9*). A slight but reproducible free energy decrease was observed, which suggests a weak interaction between the dansyl group and β-CyD on the conjugates, leading to an investigation of the fluorescence change in the dansyl groups upon hybridization. Figure 4 shows emission spectra of the dansyl groups in the duplexes with and without β-CyD. For 10-mer duplexes, the emission at 548 nm of **1b**/**3c** was 39% greater than that of **1a**/**3c**, and a 6 nm blue shift in the emission maximum wavelength from 548 to 542 nm was observed (Figure 4a). These changes were significantly larger for **1c**/**3c**, for which the enhancement of the emission was 115% and the blue shift was 18 nm. These are both typical changes that have been observed in previous systems of dansyl groups included in β-CyD cavities (*5*−*9*). Thus, it is strongly suggested that the dansyl group in **3c** is in fact included in the β-CyD units in **1b** and **1c**, even though the extent of interaction is somewhat different, depending upon the structure of the linker that connects β-CyD with the DNA.

A similar observation was made for the **2**/**4c** combinations (Figure 4b). The emission at 545 nm of the dansyl in **2c**/**4c** was 115% larger than that of **2a**/**4c**, and the blue shift was 16 nm, whereas the emission enhancement was only 10% with a 4 nm blue shift for the **2b**/**4c** combination.

Overall, the β-CyD in **1c** and **2c** showed superior inclusion ability, as compared to that in **1b** and **2b**. This may be due to an unoptimized linker structure in **1b** and **2b**. The linker portion in these conjugates consists solely of a hydrophobic alkyl chain, and β-CyD is directly connected to this chain via a rigid amide bond. Thus, the movement of β-CyD in the conjugates is expected to be somewhat limited, particularly in water, and the resulting unfavorable alignment of β-CyD and guest molecules over the DNA duplex prevents efficient guest inclusion. This may also be a factor in the failure of dabcyl inclusion in the **1b**/**3e** system (ΔG° in bulk is around −4 to −5 kcal/mol (*29*)).

In conclusion, β-CyD attached to the 5′ end of DNA forms inclusion complexes when adamantane or dansyl groups are attached to the opposite position in the complementary strand. These interactions are roughly equivalent to those of the systems in bulk solution, although the linker structure affects the interaction. The present findings should strongly encourage the development of versatile applications of β-CyD−DNA conjugates in a variety of research fields. Because the free energy changes estimated from duplex stability are comparable to those estimated in bulk solution, DNA could be used as a supporting device for measurements of binding interactions between β-CyD and rare biological compounds at low concentrations around the micromolar to nanomolar range.

ACKNOWLEDGMENT

This work was partially supported by a Grant-in-Aid for Specially Promoted Scientific Research (18001001) and a Grant-in-Aid for Scientific Research (B) (20350038) from the Ministry of Education, Culture, Sports, Science and Technology, Japan, and by the Global COE Program for Chemistry Innovation. The support from PRESTO, JST, is also acknowledged.

Supporting Information Available: Thermodynamic parameters for the duplexes that do not involve β-CyD (Supporting Table 1), the duplexes of the β-CyD−DNA conjugate (**1b**) and its complementary strands (**3**) (Supporting Table 2), the duplexes of the β-CyD−DNA conjugate (**1c**) and its complementary strands (**3**) (Supporting Table 3), and the 7-mer duplexes (Supporting Table 4). This material is available free of charge via the Internet at http://pubs.acs.org.

LITERATURE CITED

(1) Bender, M. L., Komiyama, M. (1978) *Cyclodextrin Chemistry*, Springer-Verlag, Berlin.
(2) Harada, A. (1996) Cyclodextrins. *Large Ring Molecules* (Semlyen, J. A. , Ed.) pp 407−432, Wiley, Chichester, UK.
(3) Harada, A. (2001) Cyclodextrin-based molecular machines. *Acc. Chem. Res. 34*, 456–464.
(4) Ogoshi, T., and Harada, A. (2008) Chemical sensors based on cyclodextrin derivatives. *Sensors 8*, 4961–4982.
(5) Ueno, A., Minato, S., Suzuki, I., Fukushima, M., Ohkubo, M., Osa, T., Hamada, F., and Murai, K. (1990) Host-guest sensory system of dansyl-modified β-cyclodextrin for detecting steroidal compounds by dansyl fluorescence. *Chem. Lett.* 605–608.
(6) Wang, Y., Ikeda, T., Ikeda, H., Ueno, A., and Toda, F. (1994) Dansyl-β-cyclodextrins as fluorescent sensors responsive to organic compounds. *Bull. Chem. Soc. Jpn. 67*, 1598–1607.
(7) Corradini, R., Dossena, A., Marchelli, R., Panagia, A., Sartor, G., Saviano, M., Lombardi, A., and Pavone, V. (1996) A modified cyclodextrin with a fully encapsulated dansyl group: self-inclusion in the solid state and in solution. *Chem.−Eur. J. 2*, 373–381.
(8) Pagliari, S., Corradini, R., Galaverna, G., Sforza, S., Dossena, A., Montalti, M., Prodi, L., Zaccheroni, N., and Marchelli, R. (2004) Enantioselective fluorescence sensing of amino acids by modified cyclodextrins: role of the cavity and sensing mechanism. *Chem.−Eur. J. 10*, 2749–2758.
(9) Matsumura, S., Sakamoto, S., Ueno, A., and Mihara, H. (2000) Construction of α-helix peptides with β-cyclodextrin and dansyl units and their conformational and molecular sensing properties. *Curr. Chem.−Eur. J. 64*, 1781–1788.
(10) Crooke, S. T. (2000) Progress in antisense technology: the end of the beginning. *Methods Enzymol. 313*, 3–45.
(11) Hannon, G. J. (2002) RNA interference. *Nature 418*, 244–251.
(12) Ihara, T., Maruo, Y., Takenaka, S., and Takagi, M. (1996) Ferrocene-oligonucleotide conjugates for electrochemical probing of DNA. *Nucleic Acids Res. 24*, 4273–4280.
(13) Kitamura, Y., Ihara, T., Tsujimura, Y., Osawa, Y., Sasahara, D., Yamamoto, M., Okada, K., Tazaki, M., and Jyo, A. (2008) Template-directed formation of luminescent lanthanide complexes: Versatile tools for colorimetric identification of single nucleotide polymorphism. *J. Inorg. Biochem. 102*, 1921–1931.
(14) Seeman, N. C. (1982) Nucleic acid junctions and lattices. *J. Theor. Biol. 99*, 237–247.
(15) LaBean, T. H., and Li, H. (2007) Constructing novel materials from DNA. *Nano Today 2*, 26–35.
(16) Kuzuya, A., Numajiri, K., and Komiyama, M. (2008) Accommodation of a single protein guest in nanometer scale wells embedded in a "DNA Nanotape". *Angew. Chem., Int. Ed. 47*, 3400–3402.
(17) Habus, I., Zhao, Q., and Agrawal, S. (1995) Synthesis, hybridization properties, nuclease stability, and cellular uptake

of the oligonucleotide-amino-β-cyclodextrins and adamantane conjugates. *Bioconjugate Chem. 6*, 327–331.
(18) Fujimoto, K., Muto, Y., and Inouye, M. (2008) A DNA duplex-based, tailor-made fluorescent Sensor for porphyrin derivatives. *Bioconjugate Chem. 19*, 1132–1134.
(19) Ihara, T., Uemura, A., Futamura, A., Shimizu, M., Baba, N., Nishizawa, S., Teramae, N., and Jyo, A. (2009) Cooperative DNA probing using a β-cyclodextrin-DNA conjugate and a nucleobase-specific fluorescent ligand. *J. Am. Chem. Soc. 131*, 1386–1387.
(20) Osawa, T., Shirasaka, K., Matsui, T., Yoshihara, S., Akiyama, T., Hishiya, T., Asanuma, H., and Komiyama, M. (2006) Importance of the position of vinyl group on β-cyclodextrin for the effective imprinting of amino acid derivatives and oligopeptides in water. *Macromolecules 39*, 2460–2466.
(21) Nelson, P. S., Kent, M., and Muthini, S. (1992) Oligonucleotide labeling methods 3. Direct labeling of oligonucleotides employing a novel, non-nucleosidic, 2-aminobutyl-1,3-propandiol backbone. *Nucleic Acids Res. 20*, 6253–6259.
(22) Sugimoto, N., Kierzek, R., Freier, S. M., and Turner, D. H. (1986) Energetics of internal GU mismatches in ribooligonucleotide helixes. *Biochemistry 25*, 5755–5759.
(23) Melton, L. D., and Slessor, K. N. (1971) Synthesis of monosubstituted cyclohexaamyloses. *Carbohydr. Res. 18*, 29–37.
(24) Fujita, K., Ueda, T., Imoto, T., Tabushi, I., Toh, N., and Koga, T. (1982) Guest-induced conformational change of β-cyclodextrin capped with an environmentally sensitive chromophore. *Bioorg. Chem. 11*, 72–84.
(25) Kuzuya, A., Machida, K., Mizoguchi, R., and Komiyama, M. (2002) Conjugation of various acridines to DNA for site-selective RNA scission by lanthanide ion. *Bioconjugate Chem. 13*, 365–369.
(26) Kuzuya, A., Machida, K., and Komiyama, M. (2002) A highly acidic acridine for efficient site-selective activation of RNA leading to an eminent ribozyme mimic. *Tetrahedron Lett. 43*, 8249–8252.
(27) Rekharsky, M. V., and Inoue, Y. (1998) Complexation thermodynamics of cyclodextrins. *Chem. Rev. 98*, 1875–1917.
(28) Kinoshita, T., Iinuma, F., and Tsuji, A. (1974) Microanalysis of proteins and peptides. I. Enhancement of the fluorescence intensity of dansyl amino acids and dansyl proteins in aqueous media and its application to assay of amino acids and proteins. *Chem. Pharm. Bull. 22*, 2413–2420.
(29) Tawarah, K. M., and Khouri, S. J. (1993) An equilibrium study of p-Methyl Red inclusion complexes with α- and β-cyclodextrins. *Carbohydr. Res. 245*, 165–173.
(30) Ueno, A., Kuwabara, T., Nakamura, A., and Toda, F. (1992) A modified cyclodextrin as a guest responsive colour-change indicator. *Nature 356*, 136–137.
(31) Komiyama, M., and Bender, M. L. (1978) Importance of apolar binding in complex formation of cyclodextrins with adamantanecarboxylate. *J. Am. Chem. Soc. 100*, 2259–2260.
(32) Eftink, M. R., Andy, M. L., Bystrom, K., Perlmutter, H. D., and Kristol, D. S. (1989) Cyclodextrin inclusion complexes: Studies of the variation in the size of alicyclic guests. *J. Am. Chem. Soc. 111*, 6765–6772.

BC900200C

Supporting Information for

"Efficient Guest Inclusion by β-Cyclodextrin Attached to the Ends of DNA Oligomers upon Hybridization to Various DNA Conjugates"

Akinori Kuzuya,* Toshiyuki Ohnishi, Tsugutoshi Wasano, Suguru Nagaoka,

Jun Sumaoka, Toshihiro Ihara,* Akinori Jyo, and Makoto Komiyama*

Supporting Table 1. Thermodynamic parameters of the duplexes that do not involve β-CyD.

Supporting Table 2. Thermodynamic parameters of the duplexes of β-CyD–DNA conjugate (**1b**) and its complementary strands (**3**).

Supporting Table 3. Thermodynamic parameters of the duplexes of β-CyD–DNA conjugate (**1c**) and its complementary strands (**3**).

Supporting Table 4. Thermodynamic parameters of the 7-mer duplexes.

Supporting Table 1. Thermodynamic parameters of the duplexes that do not involve β-CyD.

	ΔH (kcal/mol)	$\Delta\Delta H$ (kcal/mol)	ΔS (cal/mol·K)	$\Delta\Delta S$ (cal/mol·K)	ΔG_{37} (kcal/mol)	$\Delta\Delta G_{37}$ (kcal/mol)
1a/3a	-98.3		-275.6		-12.8	
1a/3b	-97.6	0.7	-272.5	3.1	-13.1	-0.3
1a/3c	-113.4	-15.1	-321.3	-45.7	-13.8	-1.0
1a/3d	-77.5	20.8	-208.2	67.4	-12.9	-0.1
1a/3e	-97.2	1.0	-271.3	4.4	-13.1	-0.3
1a/2f	-92.4	5.9	-257.4	18.3	-12.6	0.2

Supporting Table 2. Thermodynamic parameters of the duplexes of β-CyD–DNA conjugate (**1b**) and its complementary strands (**3**).

	ΔH (kcal/mol)	$\Delta\Delta H$ (kcal/mol)	ΔS (cal/mol·K)	$\Delta\Delta S$ (cal/mol·K)	ΔG_{37} (kcal/mol)	$\Delta\Delta G_{37}$ (kcal/mol)
1b/3a	-76.6	-	-209.2	-	-11.7	-
1b/3b	-116.3	-39.7	-318.8	-109.6	-17.5	-5.8
1b/3c	-93.0	-16.4	-258.2	-49.0	-12.9	-1.2
1b/3d	-71.3	5.3	-189.5	19.7	-12.5	-0.8
1b/3e	-67.9	8.7	-180.2	29.0	-12.0	-0.3
1b/3f	-68.5	8.1	-183.9	25.3	-11.5	0.2

Supporting Table 3. Thermodynamic parameters of the duplexes of β-CyD–DNA conjugate (**1c**) and its complementary strands (**3**).

	ΔH (kcal/mol)	$\Delta\Delta H$ (kcal/mol)	ΔS (cal/mol·K)	$\Delta\Delta S$ (cal/mol·K)	ΔG_{37} (kcal/mol)	$\Delta\Delta G_{37}$ (kcal/mol)
1c/3a	-79.5	-	-216.1	-	-12.5	-
1c/3b	-111.2	-31.7	-292.3	-76.2	-20.6	-8.1
1c/3c	-84.4	-4.9	-228.7	-12.6	-13.6	-1.0
1c/3d	-110.7	-31.2	-95.2	120.9	-15.5	-3.0
1c/3e	-89.1	-9.6	-237.2	-21.1	-15.6	-3.1
1c/3f	-75.5	4.0	-201.0	15.1	-13.2	-0.7

Supporting Table 4. Thermodynamic parameters of the 7-mer duplexes.

	ΔH (kcal/mol)	ΔS (cal/mol·K)	ΔG_{37} (kcal/mol)
2a/4a	-39.3	-107.9	-5.9
2a/4b	-36.8	-316.5	-6.4
2a/4c	-48.2	-136.6	-5.9
2b/4a	-45.5	-129.5	-5.3
2b/4b	-67.6	-187.2	-9.6
2b/4c	-19.2	-39.0	-7.1
2c/4a	-59.3	-173.2	-5.6
2c/4b	-90.0	-245.6	-13.9
2c/4c	-55.0	-153.3	-7.5

Enhanced Potency of Nucleotide−Dendrimer Conjugates as Agonists of the $P2Y_{14}$ Receptor: Multivalent Effect in G Protein-Coupled Receptor Recognition

Arijit Das,[†] Yixing Zhou,[‡] Andrei A. Ivanov,[+,†] Rhonda L. Carter,[‡] T. Kendall Harden,[‡] and Kenneth A. Jacobson*[,†]

Laboratory of Bioorganic Chemistry, National Institute of Diabetes and Digestive and Kidney Diseases, National Institutes of Health, Bethesda, Maryland 20892, and Department of Pharmacology, University of North Carolina School of Medicine, Chapel Hill, North Carolina 27599. Received May 7, 2009; Revised Manuscript Received June 3, 2009

The $P2Y_{14}$ receptor is a G protein-coupled receptor activated by uridine-5′-diphosphoglucose and other nucleotide sugars that modulates immune function. Covalent conjugation of $P2Y_{14}$ receptor agonists to PAMAM (polyamidoamine) dendrimers enhanced pharmacological activity. Uridine-5′-diphosphoglucuronic acid (UDPGA) and its ethylenediamine adduct were suitable functionalized congeners for coupling to several generations (G2.5−6) of dendrimers (both terminal carboxy and amino). Prosthetic groups, including biotin for avidin complexation, a chelating group for metal complexation (and eventual magnetic resonance imaging), and a fluorescent moiety, also were attached with the eventual goals of molecular detection and characterization of the $P2Y_{14}$ receptor. The activities of conjugates were assayed in HEK293 cells stably expressing the human $P2Y_{14}$ receptor. A G3 PAMAM conjugate containing 20 bound nucleotide moieties (UDPGA) was 100-fold more potent (EC_{50} 2.4 nM) than the native agonist uridine-5′-diphosphoglucose. A molecular model of this conjugate docked in the human $P2Y_{14}$ receptor showed that the nucleotide-substituted branches could extend far beyond the dimensions of the receptor and be available for multivalent docking to receptor aggregates. Larger dendrimer carriers and greater loading favored higher potency. A similar conjugate of G6 with 147 out of 256 amino groups substituted with UDPGA displayed an EC_{50} value of 0.8 nM. Thus, biological activity was either retained or dramatically enhanced in the multivalent dendrimer conjugates in comparison with monomeric $P2Y_{14}$ receptor agonists, depending on size, degree of substitution, terminal functionality, and attached prosthetic groups.

INTRODUCTION

G protein-coupled receptors (GPCRs)[1] are cell membrane-spanning receptors that respond to extracellular signaling molecules to control cell function via specific signaling pathways. Direct or indirect modulation of GPCRs serves as the basis of many disease treatments (*1*). The P2 receptors for purine and pyrimidine nucleotides have diverse biological roles (*2*−*4*). P2 receptors are divided into two structurally unrelated subfamilies—the P2X receptors, which are ligand-gated ion channels (*5*), and the P2Y receptors (*2*), which are GPCRs. P2Y receptors are divided into two subgroups. The first subgroup consisting of the $P2Y_1$, $P2Y_2$, $P2Y_4$, $P2Y_6$, and $P2Y_{11}$ receptors activate G_q and promote phospholipase C (PLC)-dependent inositol lipid signaling. The second consists of $P2Y_{12}$, $P2Y_{13}$, and $P2Y_{14}$ receptors, which preferentially activate G_i and inhibit adenylyl cyclase (*2*). P2Y receptors are activated by adenine and/or uracil nucleotides, while P2X receptors are principally activated by adenine nucleotides. P2Y receptors are widely distributed, for example, in the immune system (and widely distributed on hematopoietic cells), cardiovascular system, central and peripheral nervous system, endocrine system, and the renal and pulmonary systems (*3*−*10*).

Chart 1. Structures of a Native Agonist of the $P2Y_{14}$ Receptor 1 and a Carboxylic Acid Derivative 2 Suitable for Covalent Coupling to Carriers while Preserving Biological Activity

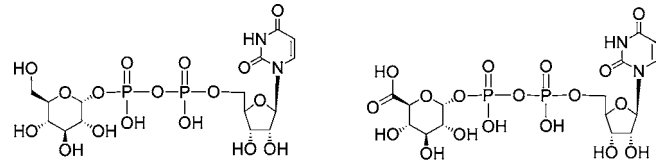

UDPG, 1 UDPGA, 2

The $P2Y_{14}$ receptor is activated by uridine-5′-diphosphoglucose (UDPG) **1** (Chart 1) and other UDP-sugars (*11, 12*). The $P2Y_{14}$ receptor affects immune function, but the physiological function of the receptor is not clearly established (*13, 14*). Extracellular **1** also acts as a weak full agonist at the $P2Y_2$ receptor (EC_{50} 10 μM) (*15*). We have studied the SAR of nucleotide derivatives at this receptor, which is among the most structurally restrictive of the P2Y family (*15*−*18*). Activity of synthetic analogues of **1** at the $P2Y_{14}$ receptor has been followed through the stimulation of phosphoinositide hydrolysis by coexpression in COS-7 cells of a PLC-activating chimeric G protein that responds to G_i-coupled receptors (*18*).

* Corresponding author. Molecular Recognition Section, Laboratory of Bioorganic Chemistry, National Institute of Diabetes and Digestive and Kidney Diseases, National Institutes of Health, Bethesda, Maryland 20892, USA; E-mail: kajacobs@helix.nih.gov.

[†] National Institutes of Health.

[‡] University of North Carolina School of Medicine.

[+] Current address: Emory University School of Medicine, Department of Biochemistry, Atlanta, GA 30322.

[1] Abbreviations: DTPA, diethylenetriaminepentaacetic acid; EDC, *N*-ethyl-*N*′-dimethylaminopropylcarbodiimide; GPCR, G protein-coupled receptor; HEK, human embryonic kidney; IBMX, 3-isobutyl-1-methylxanthine; MES, 2-(*N*-morpholino)ethanesulfonic acid; MRI, magnetic resonance imaging; NHS, *N*-hydroxysuccinimide; PAMAM, polyamidoamine; SAR, structure activity relationship; p-SCN-Bn-DTPA, 2-(4-isothiocyanatobenzyl)-diethylenetriaminepentaacetic acid; UDPG, uridine-5′-diphosphoglucose; UDPGA, uridine-5′-diphosphoglucuronic acid.

10.1021/bc900206g CCC: $40.75 © 2009 American Chemical Society
Published on Web 07/02/2009

Dendrimers are tree-like polymeric macromolecular nanostructures, which can serve as nanocarriers for drug delivery (*19*−*21*). Dendrimer chemistry offers versatility in the control of the component functional groups and in feasibility for conjugation of multiple functional units at both the periphery and interior. Dendrimers recently have attracted considerable attention in biomedical research in the context of drug delivery (targeted/controlled release, encapsulation, or covalent/electrostatic attachment) (*22*−*24*), protein−carbohydrate interactions (multivalent effect) (*25*−*30*), medical diagnostics (signal amplification) (*31, 32*), and tissue engineering (*33, 34*).

Polyamidoamine (PAMAM) dendrimers have well-defined chemical structures in which a core is surrounded by successively added (and bifurcating) layers of methyl acrylate and ethylenediamine, which form each dendrimeric shell (or "generation") of the polymer. Different generations of PAMAM dendrimers have either primary amine (integral generations) or carboxylic acid (half-integral generations) groups on their surface, and the number of surface groups for conjugation to multiple functional units depends on the generation of the dendrimer. PAMAM dendrimers are relatively biocompatible, which allows many applications in biomedicine (*35*−*38*).

We recently reported the first example of application of dendrimers to multivalent GPCR-promoted signal transduction in a study of adenosine receptor-targeted dendrimers (*39*−*41*). Various adenosine receptor agonists were attached covalently to PAMAM dendrimers, and the resulting nucleoside conjugates displayed distinct biological properties, including potent inhibition of platelet aggregation.

Here, we report the first example of application of PAMAM dendrimers to covalently conjugate a P2Y receptor ligand resulting in the enhancement of its pharmacological activity. The $P2Y_{14}$ receptor agonist uridine-5′-diphosphoglucuronic acid (UDPGA) **2** and its ethylenediamine adduct **3a** were utilized as appropriately functionalized congeners to couple with several generations of PAMAM dendrimers with the goal of modulating pharmacological interaction with this receptor. We also attached prosthetic groups, such as biotin, AlexaFluor488, and the metal chelating group diethylenetriaminepentaacetic acid (DTPA) on the dendrimer-nucleotide conjugates for targeting the $P2Y_{14}$ receptor in vivo. Our long-term goal is to initiate the genesis of receptor probes that lead to improved biomedical diagnostics and possibly to novel conjugates for drug treatment.

EXPERIMENTAL PROCEDURES

Chemical Synthesis. *Materials and Methods.* All reactions were carried out under a nitrogen atmosphere. G2.5 PAMAM (10 wt % solution in methanol), G3 PAMAM (20 wt % solution in methanol), G5.5 PAMAM (5 wt % solution in methanol), and G6 PAMAM (5 wt % solution in methanol), dendrimer with an ethylenediamine core, EDC, UDPGA, $Gd(OAc)_3$, and ethylenediamine were purchased from Aldrich. Sulfo-NHS-LC-biotin was purchased from Pierce (Rockford, IL), and AlexaFluor488-carboxylic acid 2,3,5,6-tetrafluorophenyl ester (AlexaFluor488−5-TFP) was purchased from Invitrogen Corp. (Carlsbad, CA) and 2-(4-isothiocyanatobenzyl)-diethylenetriaminepentaacetic acid (*p*-SCN-Bn-DTPA) purchased from Macrocyclic (Dallas, TX). Dialysis membranes (Spectra/Pore Membrane, MWCO 3500, flat width 18 mm) were purchased from Spectrum Laboratories, Inc. (Rancho Dominguez, CA).

Nuclear magnetic resonance (NMR) spectra were recorded on a Bruker DRX-600 spectrometer using D_2O as a solvent. The chemical shifts are expressed as relative ppm from HOD (4.80).

The electrospray ionization mass spectrometry (ESI MS) and matrix-assisted laser desorption ionization time-of-flight (MALDI-TOF) MS experiments were performed on a Waters LCT Premier mass spectrometer at the Mass Spectrometry Facility, NIDDK, NIH.

*Synthesis of G3 or G6 PAMAM-UDPGA Conjugates **8**, **9**, and **12.*** A commercial solution of G3 PAMAM **5** (100 μL, 2 μmol) or G6 PAMAM **7** (167 μL, 0.11 μmol) was added to a round-bottom flask, and the methanol was evaporated using a rotary evaporator. The dendrimer was treated with EDC-HCl (2.1 mg, 5.5 equiv for compound **8**; 13.8 mg, 36 equiv for compound **9**; and 5.4 mg, 256 equiv for compound **12**) and then dissolved with minimum volume of 0.1 M 2-(*N*-morpholino)ethanesulfonic acid (MES), pH 5 (1 mL). The reaction mixture was stirred and UDPGA **2** (7.7 mg, 6 equiv for compound **8**; 82.7 mg, 64 equiv for compound **9**; and 27.2 mg, 384 equiv for compound **12**) was added. The pH of the reaction was adjusted to the range 4.5−5.0 using 0.1 M HCl. The reaction mixture was stirred at room temperature under nitrogen atmosphere for 2 days and then diluted with water (1 mL). After that, the product was purified by extensive dialysis in water. The mixture was then lyophilized to give the pure product of the conjugates **8**, **9**, and **12**.

*G3 PAMAM-UDPGA Conjugate **8** (Low Loading).* Compound **8** (13.5 mg, 71%) was obtained as a white solid following the general procedure. The product was analyzed by NMR and MALDI-TOFF MS, which indicated approximately 4.3 UDPGA moieties attached per dendrimer. ^{1}H NMR (D_2O) δ 7.84 (d, J = 8.8 Hz, 4.3 H), 5.91 (d, J = 5.7 Hz, 8.6 H), 5.53 (m, 4.3 H), 4.28 (m, 8.6 H), 4.17 (m, 8.6 H), 4.08 (m, 8.6 H), 3.85 (m, 4.3 H), 3.63 (m, 8.6 H), 3.44 (m, 180 H), 3.3 (m, 120 H), 3.14 (m, 60 H), 2.72 (m, 120 H); *m/z* (M^+ ESI MS) found 9848.0; calc 9519.0.

*G3 PAMAM-UDPGA Conjugate **9** (High Loading).* Compound **9** (26 mg, 68%) was obtained as a white solid following the general procedure. The product was analyzed by NMR and MALDI-TOFF MS, which indicated approximately 20.1 UDPGA moieties attached per dendrimer. ^{1}H NMR (D_2O) δ 7.88 (d, J = 7.4 Hz, 20.1 H), 5.81 (d, J = 5.4 Hz, 40.2 H), 5.51 (dd, J = 3.3, 6.1 Hz, 20.1 H), 4.3 (m, 40.2 H), 4.2 (m, 40.2 H), 4.1 (m, 40.2 H), 3.65 (m, 20.1 H), 3.52 (m, 40.2 H), 3.41 (m, 180 H), 3.3 (m, 120 H), 3.14 (m, 60 H), 2.72 (m, 120 H); *m/z* (M^+ ESI MS) found 18721.4; calc 19113.7.

*G6 PAMAM-UDPGA Conjugate **12.*** Compound **12** (9.86 mg, 61%) was obtained as a white solid following the general procedure. The product was analyzed by NMR and MALDI-TOFF MS, which indicated approximately 147 UDPGA moieties attached per dendrimer. ^{1}H NMR (D_2O) δ 7.87 (d, J = 7.5 Hz, 147 H), 5.89 (d, J = 5.4 Hz, 294 H), 5.51 (m, 147 H), 4.29 (m, 294 H), 4.17 (m, 294 H), 4.09 (m, 294 H), 3.81 (m, 147 H), 3.7 (m, 294 H), 3.51 (m, 512 H), 3.41 (m, 512 H), 3.28 (m, 1020 H) 3.12 (m, 504 H), 3.07 (m, 504 H), 2.78 (m, 1020 H). The molecular weight was unable to be determined using ESI or MALDI-TOF MS, possibly due to stacking of the PAMAM dendrimer or because of the high molecular weight.

*Synthesis of G2.5 or G5.5 PAMAM−UDPGA Conjugates **10** and **11**.* A commercial solution of G2.5 PAMAM **4** (13.76 μL, 0.2 μmol) or G5.5 PAMAM **6** (115 μL, 0.1 μmol) was added to a round-bottom flask, and the methanol was evaporated. EDC-HCl (1.4 mg, 36 equiv, for compound **8**; and 1.9 mg, 100 equiv for compound **9**) was added to the residue, and then the mixture was dissolved in a minimum volume of 0.1 M MES, pH 5 (0.5 mL), and stirred under a nitrogen atmosphere. UDPGA-ethylenediamine (**3a**) was added to the reaction mixture (6.5 mg, 50 equiv, for compound **10**; and 13.1 mg, 200 equiv, for compound **11**). The pH of the reaction mixture was maintained within the range 4.5−5.0 using 0.1 M HCl. After 48 h, the small molecule impurities were removed by extensive dialysis in water. After dialysis, the mixture was lyophilized to give conjugate **10** or **11**.

*G2.5 PAMAM-UDPGA Conjugate **10.*** Compound **10** (2.4 mg, 66%) was obtained as a white solid following the general procedure. The product was analyzed by NMR and MALDI-TOF MS, which indicated approximately 17.3 UDPGA moieties attached per dendrimer. ^{1}H NMR (D_2O) δ 7.82 (d, $J = 7.7$ Hz, 17.34 H), 5.84 (d, $J = 5.5$ Hz, 34.68 H), 5.51 (dd, $J = 3$, 5.1 Hz, 17.34 H), 4.29 (m, 52.0 H), 4.15 (m, 52.0 H), 3.7 (m, 17.34 H), 3.51 (m, 98.7 H), 3.41 (m, 120 H), 3.31 (m, 90.7 H), 3.14 (m, 60 H), 2.68 (m, 34.7 H), 2.51 (m, 56 H); *m*/*z* (M^+ESI MS) found 18151.4, calc 18477.9.

*G5.5 PAMAM-UDPGA Conjugate **11.*** Compound **11** (4.5 mg, 63%) was obtained as a white solid following the general procedure. The product was analyzed by NMR and MALDI-TOF MS, which indicated approximately 29.9 UDPGA moieties attached per G5.5 dendrimer. ^{1}H NMR (D_2O) δ 7.85 (d, $J =$ 8.3 Hz, 29.94 H), 5.88 (d, $J = 6.5$ Hz, 59.9 H), 5.57 (dd, $J =$ 3.1, 5.7 Hz, 29.9 H), 4.26 (m, 89.8 H), 4.14 (m, 89.8 H), 3.72 (m, 29.94 H), 3.44 (m, 571 H), 3.23 (m, 1075.88 H), 2.84 (m, 504 H), 2.67 (m, 508 H), 2.48 (m, 564 H); *m*/*z* (M^+ESI MS) found 72626, calc 71651.

*Synthesis of G3 PAMAM-UDPGA-Biotin Conjugate **13**.* A mixture of G3 PAMAM complex **9** (20 mg, 1.04 μmol) and Sulfo-NHS-LC-Biotin **17** (361 μg, 0.65 μmol) in a flask was dissolved in bicarbonate buffer (1 mL, pH 8.5, 0.002 M Na_2CO_3, 0.048 M $NaHCO_3$, 0.15 M NaCl). After 48 h of stirring at room temperature, the reaction mixture was diluted with 1 mL water, and the product was purified by dialysis against water. The solution was then lyophilized, which provided G3 PAMAM-botin **13** (14.4 mg, 67%) as a white solid. The product was analyzed by NMR and MALDI-TOF MS, which indicated that approximately 4.87 biotin moieties attached per dendrimer. ^{1}H NMR (D_2O) δ 7.87 (d, $J = 7.4$ Hz, 20.1 H), 5.82 (d, $J = 5.4$ Hz, 40.2 H), 5.51 (m 20.1 H),4.55 (m, 9.74 H) 4.28 (m, 40.2 H), 4.18 (m, 40.2 H), 4.09 (m, 40.2 H), 3.67 (m, 20.1 H), 3.53 (m, 40.2 H), 3.42 (m, 180 H), 3.28 (m, 135 H), 3.11 (m, 60 H), 2.91(m, 9.74 H) 2.71 (m, 120 H), 2.12 (m, 19.5 H), 1.52 (m, 39.0 H), 1.27 (m, 19.5 H); *m*/*z* (M^+ESI MS) found 21114.0, calc 20767.0.

*Synthesis of G3 PAMAM-UDPGA-AlexaFluor488 Conjugate **14**.* G3 PAMAM complex **9** (20 mg, 1.04 μmol) was reacted with AlexaFluor488-5-TFP **18** (575 μg, 0.65 μmol) in bicarbonate buffer (1 mL, pH 8.5, 0.002 M Na_2CO_3, 0.048 M $NaHCO_3$, 0.15 M NaCl). The reaction mixture was stirred for 2 days at room temperature and then diluted with 1 mL of water. The mixture was purified by dialysis with water. Lyophilization of the solution gave the G3 PAMAM−AlexaFluor488 complex **14** (13.4 mg, 62%) as a red solid. The product was analyzed by NMR and MALDI-TOFF MS, which indicated approximately 2.3 AlexaFluor488 moieties attached per dendrimer. ^{1}H NMR (D_2O) δ 8.28 (m, 2.3 H), 8.01 (d, $J = 7.4$ Hz, 20.1 H), 7.85 (m, 4.6 H), 6.1 (m, 2.3 H), 6.9 (m, 2.3 H), 5.9 (d, $J = 5.4$ Hz, 40.2 H), 5.75 (m, 2.3 H), 5.53 (dd, $J = 3.1$, 5.9 Hz, 20.1 H), 5.3 (m, 2.3 H), 4.32 (m, 40.2 H), 4.21 (m, 40.2 H), 4.18 (m, 40.2 H), 3.94 (m, 40.2 H), 3.68 (m, 20.1 H), 3.43 (m, 180 H), 3.28 (m, 120 H), 3.15 (m, 60 H), 2.63 (m, 120 H); *m*/*z* (M^+ESI MS) found 22336.0, calc 20766.3.

*Synthesis of G3 PAMAM-UDPGA-DTPA Conjugate **15** and G3 PAMAM-UDPGA-DTPA-Gd Conjugate **16.*** G3 PAMAM complex **9** (20 mg, 1.04 μmol) was stirred with *p*-SCN-Bn-DTPA **19** (351 μg, 0.65 μmol) in bicarbonate buffer (1 mL, pH 8.5, 0.002 M Na_2CO_3, 0.048 M $NaHCO_3$, 0.15 M NaCl). The reaction mixture was stirred for 48 h, at room temperature, and then the small molecule impurities were removed by extensive dialysis in water followed by lyophilization to yield the G3 PAMAM-DTPA complex **15** (15.2 mg, 68%) as a white solid. The product was analyzed by NMR and MALDI-TOF MS, which indicated approximately 4.5 DTPA moieties attached per dendrimer. ^{1}H NMR (D_2O) δ 7.89 (d, $J = 7.4$ Hz, 20.1 H), 7.21 (m, 9 H), 7.31 (m, 9 H), 5.85 (d, $J = 5.4$ Hz, 40.2 H), 5.53 (dd, $J = 3.3$, 6.1 Hz, 20.1 H), 4.31 (m, 40.2 H), 4.24 (m, 40.2 H), 4.15 (m, 80.4 H), 3.71 (m, 20.1 H), 3.64 (m, 49.5 H), 3.44 (m, 180 H), 3.33 (m, 120 H), 3.16 (m, 69 H), 2.63 (m, 120 H), 2.66 (m, 27 H); *m*/*z* (M^+ESI MS) found 22744.0, calc 21546.1.

The chelating prosthetic group on conjugate **15** was used to complex Gd(III) by addition of $Gd(OAc)_3$. G3 PAMAM-UDPGA-DTPA **15** (10 mg, 0.46 μmol), Gd $(OAc)_2$ (94 μg, 0.28 μmol) were dissolved in 0.3 M citrate buffer (1 mL, pH 4.5). The mixture was stirred at room temperature for 48 h in dark. The mixture was dialyzed sequentially with 0.1 M NH_4OAc (pH 7.0) to remove the uncomplexed Gd(III) and then extensively against water. Lyophilization of the solution gave the product **16** (7.5 mg, 74%). Since the compound **16** contains Gd(III), we could not analyze the NMR spectra. We assume that all the DTPA moieties would complex with Gd(III), because we reacted **15** with excess $Gd(OAC)_3$ in this theoretically quantitative reaction. So, we assumed that compound G3 PAMAM-UDPGA-DTPA-Gd(III) **16** contained approximately 4.5 Gd(III) moieties attached per dendrimer based on the stoichiometry of the precursor, which was comparable to mass spectral data. *m*/*z* (M^+ESI MS) found 24175.0, calc 22311.2.

Biological Methods. *Materials.* IBMX was purchased from SigmaAldrich (St. Louis, MO). Compounds **1** and **2** were manufactured by Fluka and were purchased from SigmaAldrich (St. Louis, MO). [^{3}H]Adenine was purchased from American Radiolabeled Chemicals (St. Louis, MO). All cell culture media and sera were from Gibco (Invitrogen, Carlsbad, CA).

Cell Culture. Human embryonic kidney-293 cells stably expressing the human $P2Y_{14}$-R ($P2Y_{14}$−HEK293 cells) were generated as previously described by Fricks et al. (*46*). $P2Y_{14}$−HEK293 cells were grown in Dulbecco's Modified Eagle Medium (DMEM) supplemented with 10% fetal bovine serum (FBS), 1% genticin (Gibco), and 1% antibiotic−antimocotic (Gibco) at 37 °C in a 5% CO_2 environment.

Cyclic AMP Accumulation. $P2Y_{14}$−HEK293 cells were grown in 24-well plates and incubated with 1 μCi [^{3}H]adenine/well in serum-free DMEM for at least 2 h prior to assay. Assays were initiated by addition of HEPES-buffered, serum-free DMEM containing 200 μM 3-isobutyl-1-methyl-xanthine (IBMX) and 30 μM forskolin, with or without drugs, and incubation continued for 15 min at 37 °C. Incubations were terminated by aspiration of the medium and addition of 450 μL ice-cold 5% trichloroacetic acid. [^{3}H]Cyclic AMP was isolated by sequential Dowex and alumina chromatography and quantified by liquid scintillation counting as previously described by Harden et al. (*55*).

Data Analysis. The concentrations of the dendrimer−ligand complexes were measured by the concentration of the dendrimer, not the attached ligand. EC_{50} values were determined using *Prism* software (GraphPad, San Diego, CA) and are presented as mean ± SE. All experiments were repeated at least three times.

RESULTS

Chemical Synthesis. We recently investigated the SAR (structure−activity relationship) of analogues of UDPG **1** at the $P2Y_{14}$ receptor (*15*, *16*), but few of the ligands displayed comparable pharmacological properties to those of the native ligand, and nearly all modifications of the uracil and ribose moieties abolished activity. We also reported that functionalized congeners of UDPGA **2** in which an amide-linked chain was extended from the terminal carboxylic acid group via *N*-acetylethylenediamine (e.g., **3b**) or *N*-(*t*-butyloxycarbonyl)ethylenediamine moieties did not significantly differ from **1** in their

Scheme 1. Covalent Coupling of the Carboxylic Acid Functionalized Congener UDPGA 2 to PAMAM Dendrimers of Integral Generations 3 and 6, by Carbodiimide Condensation with the Surface Amino Groups of the Dendrimer

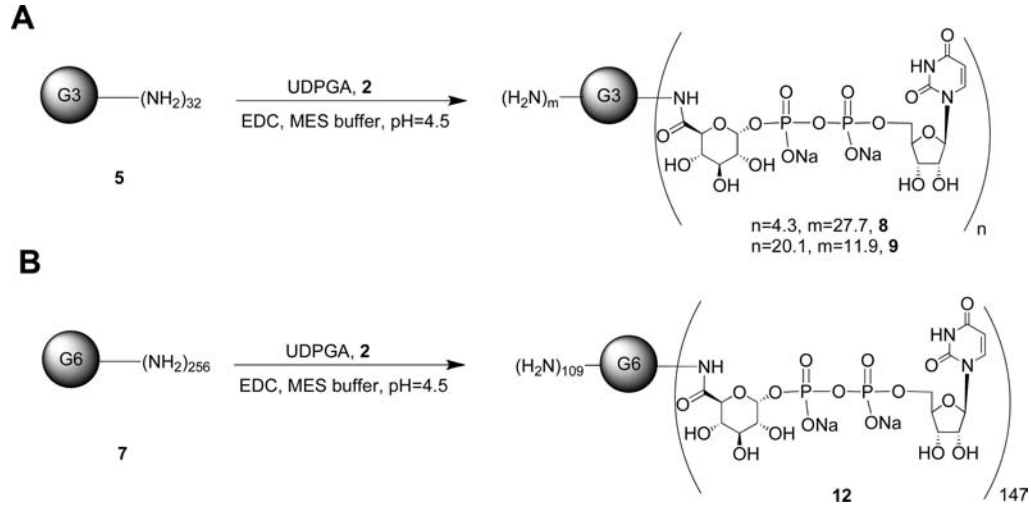

pharmacological activity (*15*). This suggests that it is possible to incorporate structural modifications of the carboxylic acid chain in **2** that do not substantively affect interaction with the $P2Y_{14}$ receptor.

In this study, we first coupled **2** with the peripheral amino groups of a third-generation (G3) PAMAM dendrimer to yield **8** and **9** and to a sixth-generation (G6) PAMAM dendrimer to yield **12**. The coupling conditions used were the water-soluble carbodiimide reagent EDC in aqueous medium at pH 4.5 in 0.1 M MES buffer and under a nitrogen atmosphere (Scheme 1). The degree of substitution of the G3 dendrimer was varied to determine how the fraction of drug loading on the PAMAM surface would affect the pharmacological activity. Compound **8** contained an average of 4.3 bound nucleotide moieties (**2**) per dendrimer, and compound **9** an average of 20.1 bound nucleotide moieties per dendrimer, out of a theoretical 32. The degree of substitution was calculated using mass spectroscopy and integration of the 600 MHz ^{1}H NMR spectra. For compound **12**, we added excess nucleotide monomer to derivatize the maximum number of nucleotide moieties on the surface of a G6 dendrimer, in which the average number of drug moieties attached was found to be an average of 147 out of a theoretical 256. Following the coupling reaction, we removed all residual compound **2** that remained unreacted by extensive dialysis in water. Thus, we successively varied the number of covalently attached ligands, determined to be an average of 4.3, 20.1, and 147 per dendrimer in compounds **8**, **9**, and **12**, respectively.

A G3 PAMAM-biotin conjugated UDPGA complex **13** also was prepared. Since biotin and its amide derivatives are known to bind strongly with the tetrameric protein avidin, compound **13** was designed as a multifunctional chemical probe of the $P2Y_{14}$ receptor. For the preparation of compound **13**, PAMAM-UDPGA **9** was reacted with a water-soluble *N*-hydroxysuccinimide (NHS) ester of a chain-elongated biotin **17** in bicarbonate buffer at pH 8.5 (Scheme 2) and the product **13** was subjected to dialysis in water. From the ^{1}H NMR and mass spectra, we confirmed that the average number of biotin units attached in compound **13** was 4.9 per dendrimer.

With the eventual goal of direct microscopic visualization of the $P2Y_{14}$ receptor in biological systems, we prepared a fluorescent dendrimer−UDPGA derivative **14**. Compound **14** was synthesized by reaction of **9** and an equimolar amount of 5-carboxy tetrafluorophenyl ester of AlexaFluor488 **18** in the presence of triethylamine in a minimum volume of water. AlexaFluor488 was chosen, because although its fluorescent properties are similar to fluorescein, it exhibits higher photostability, pH insensitivity, and good water solubility (*42*). We subjected compound **14** to dialysis in water to remove low MW impurities. The conjugated product was analyzed by ^{1}H NMR and mass spectroscopy, which showed that the average number of AlexaFluor488 units attached per dendrimer molecule was 2.3.

PAMAM dendrimers recently were used for magnetic resonance imaging (MRI) (*43*). MRI is one of the fastest growing diagnostic methods in medical technology because of its effectiveness in visualizing soft tissues with good resolution. Ionic gadolinium is a widely used reagent for MRI, and a chelated Gd(III) complex recently was covalently attached to PAMAM dendrimers for molecular imaging (*44*). As such, we derivatized the PAMAM−UDPGA conjugate **9** with the same MRI-active reagent for chelation of Gd(III). Compound **9** was reacted with an electrophilic reactive derivative (aryl isothiocyanate) of diethylenetriaminepentaacetic acid (DTPA) **19** in bicarbonate buffer at pH = 8.5 for two days to obtain compound **15**, which was purified by dialysis in water. The molecular weight of **15** was >10 000 D, and ^{1}H NMR and mass spectroscopic analyses revealed that the average number of DTPA moieties attached in compound **15** was 4.5 per dendrimer. We subsequently reacted compound **15** with excess $Gd(OAc)_3$ in the presence of 0.3 M citrate buffer (pH = 4.5) to obtain compound **16**, which was subjected to dialysis using 0.1 M ammonium acetate to remove low MW impurities. It was not possible to obtain a ^{1}H NMR spectrum for compound **16**, so we have assumed that the number of Gd(III) ions in compound **16** was 4.5 based on quantitative complexation of the attached DTPA with excess ionic Gd. We used $Gd(OAc)_3$ as a biological control to ensure that Gd(III) does not exhibit activity in the system examined and to anticipate eventual replacement of nonradioactive $Gd(OAc)_3$ with radioactive $Gd(OAc)_3$ for in vivo imaging.

The unreacted dendrimer surface in compounds **8**, **9**, and **12**−**16** contains amino groups, which are known to be associated with cell toxicity (*45*). Therefore, we also produced conjugates of carboxylic acid-containing PAMAM dendrimers by coupling an amine-functionalized congener of UDPGA **3a** to G2.5 (**4**) and G5.5 (**6**) PAMAM dendrimers to form compounds **10** and **11**. Compound **3a** was further purified by a subsequent HPLC step for subsequent biological testing. Compound **3a** was reacted with PAMAM dendrimer G2.5 **4** and G5.5 **6** by EDC coupling in 0.1 M MES buffer under a nitrogen atmosphere and at pH 4.5 to 5.0 to form products **10** and **11**, respectively. Each polymeric product was subjected to dialysis in water to remove

Scheme 2. Multiple Functionalization of a Covalent Conjugate 9 of UDPGA 2 on a PAMAM G3 Dendrimer, For the Purpose of Fluorescent Detection (14), Avidin Binding (13), and Chelation with Heavy Metal Gadolinium (16)

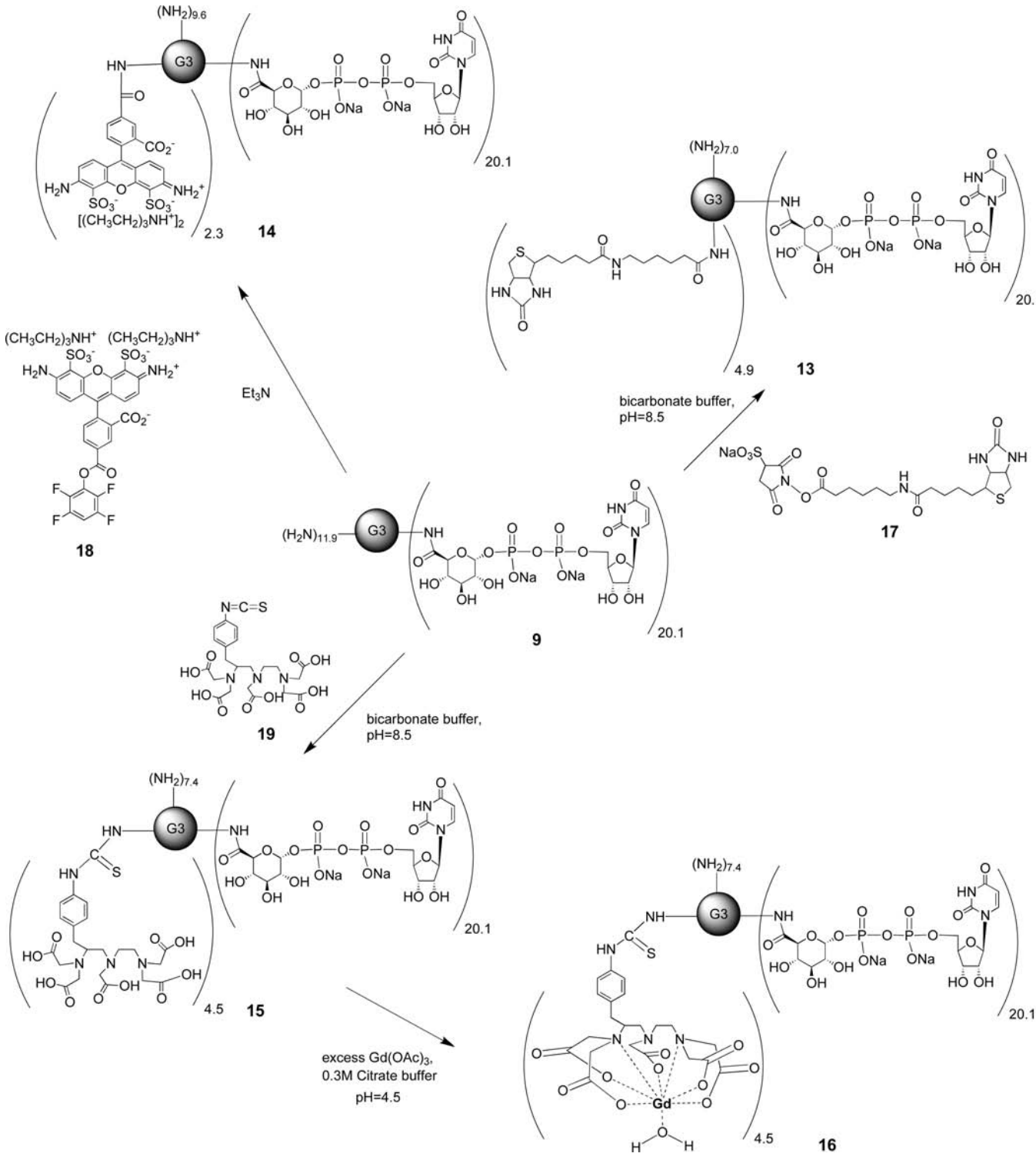

low MW impurities. Compounds **10** and **11** were analyzed by ^{1}H NMR and mass spectroscopy, which showed that the average number of monomers **3a** in compounds **10** and **11** was 17.3 and 29.9 per dendrimer, respectively.

Biological Activity. The activities of dendrimer conjugates were tested in human embryonic kidney (HEK293) cells stably expressing the human $P2Y_{14}$ receptor. Concentration effect curves were generated as previously described (*46*) comparing the relative capacities of UDPG **1** and the denrimer conjugates to inhibit forskolin (30 μM)-stimulated cyclic AMP accumulation. Neither compound **1** (*46*) nor any of the dendrimers tested (data not shown) exhibited activity in wild-type HEK293 cells.

The control dendrimers **4** and **5** were inactive in this test system. In contrast, compound **9**, derived from the G3 dendrimer and containing free residual amino groups, was a very potent agonist that exhibited an EC_{50} of 2.4 nM at the $P2Y_{14}$ receptor (Figure 1). This potency was approximately 100-fold greater than that of the native agonist UDPG **1**, which had an EC_{50} of 261 nM. UDPGA **2** was approximately equipotent to **1** in this assay. The corresponding dendrimer **8** (Figure 1), which had a

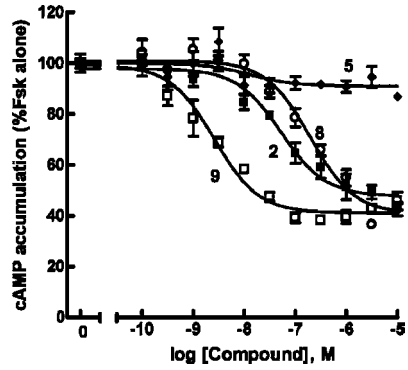

Figure 1. Comparison of G3 dendrimer conjugates as agonists at the human $P2Y_{14}$ receptor. The capacities of UDPGA **2** (■) and the G3 dendrimer conjugates **5** (◆), **8** (○), and **9** (□) to inhibit forskolin (30 μM) stimulated cyclic AMP accumulation were quantified in $P2Y_{14}$−HEK293 cells as described in Methods. Assays were carried out in triplicate, and all experiments were repeated at least three times. Data were pooled and normalized using forskolin-stimulated cyclic AMP accumulation as 100% and the phosphodiesterase inhibitor IBMX alone as 0%.

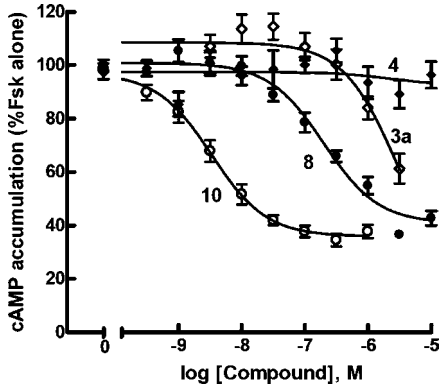

Figure 2. Comparison of G2.5 dendrimer conjugates as agonists at the human $P2Y_{14}$ receptor. The capacities of G2.5 dendrimer conjugates **3a** (◇), **4** (◆), **8** (●), and **10** (○) to inhibit forskolin (30 μM) stimulated cyclic AMP accumulation were quantified in $P2Y_{14}$−HEK293 cells as described in Methods. Assays were carried out in triplicate, and all experiments were repeated at least three times. Data were pooled and normalized using forskolin-stimulated cyclic AMP accumulation as 100% and IBMX alone as 0%.

lower degree of loading of the nucleotide on a G3 dendrimer, was considerably less potent than **9**, but similar in potency to **1**. Therefore, a distinct multivalent effect occurs in these compounds.

Compounds **10** and **11**, both of which were derived from half-integral dendrimers and contain free residual carboxylate groups, were very potent at the $P2Y_{14}$ receptor with EC_{50} values of 3.2 and 3.1 nM, respectively (Figure 2). The corresponding amine derivative **3a** of UDPGA, which also served as the synthetic precursor of conjugates **10** and **11**, was considerably less potent.

The higher molecular weight G6 dendrimer conjugate **12** was similar in relative composition to the smaller conjugate **9**, which had a high degree of loading of nucleotide. Compound **12** (EC_{50} = 0.8 nM) was significantly more potent than **9** (Figure 3). Both **9** and **12** contain significant fractions (but less than 50%) of residual amino groups.

The G3 dendrimer conjugates **13** and **15** were equivalent to the precursor dendrimer conjugate **12**, except that they both contain covalently attached prosthetic groups in addition to the nucleotide. Each of these dendrimers was essentially as potent as **9**. The G3 dendrimer conjugate **14**, which had approximately two covalently attached AlexaFluor488 moieties, was 17-fold less potent than the corresponding **9** but 7-fold more potent than

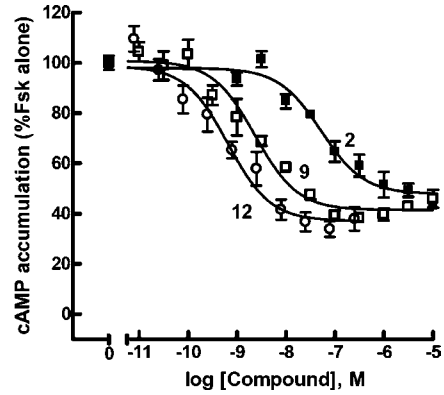

Figure 3. Comparison of larger dendrimer conjugates as agonists at the human $P2Y_{14}$ receptor. The capacities of UDPGA **2** (■), G3 dendrimer conjugate **9** (□), and G6 dendrimer conjugate **12** (○) to inhibit forskolin (30 μM)-stimulated cyclic AMP accumulation were quantified in $P2Y_{14}$−HEK293 cells as described in Methods. Assays were carried out in triplicate, and all experiments were repeated at least three times. Data were pooled and normalized using forskolin-stimulated cyclic AMP accumulation as 100% and IBMX alone as 0%.

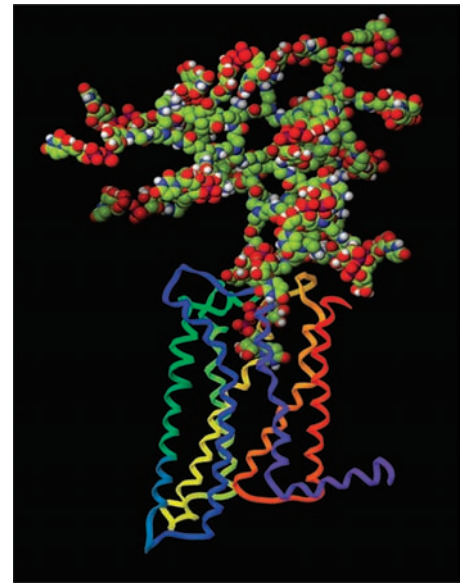

Figure 4. Molecular model of compound **9** docked in the human $P2Y_{14}$ receptor, obtained after docking to the receptor homology model built based on the crystal structure of the A_{2A} adenosine receptor (*47*). The receptor helices are colored by residue position: N-terminus in red, TM 1 in orange, TM 2 in ochre, TM 3 in yellow, TM 4 in green, TM 5 in cyan, TM 6 in blue, and TM 7 and C-terminus in purple.

compound **1**. However, when the DTPA conjugate **15** was complexed with gadolinium, the potency was greatly reduced, to the level of **1**, the native agonist.

Molecular Modeling. A molecular model of compound **3b** docked to the human $P2Y_{14}$ receptor recently was constructed on the basis of the crystal structure of the human A_{2A} adenosine receptor (*15, 47*). This model was utilized to build a complex of the $P2Y_{14}$ receptor bound to a PAMAM G3 dendrimer using the same approach as reported for the docking of a polyvalent dendrimer−nucleoside conjugate to the human A_{2A} adenosine receptor (*48*). In particular, our published model of the conjugate of PAMAM (G3) with an A_{2A} receptor agonist (2-[*p*-(2-carboxyethyl)phenyl-ethylamino]-5′-*N*-ethylcarboxamidoadenosine, CGS21680) was utilized to build a model of dendrimer−nucleotide conjugate **9**, which was partially substituted with nucleotide moieties. Initially, all fragments of the carboxylic acid CGS21680 were removed from the model of PAMAM-

Scheme 3. Synthesis of an Amine-Functionalized Congener UDPGA 3a and Its Covalent Coupling to PAMAM Dendrimers of Half-Generations 2.5 and 5.5, by Carbodiimide Condensation with the Surface Carboxylic Groups of the Dendrimer

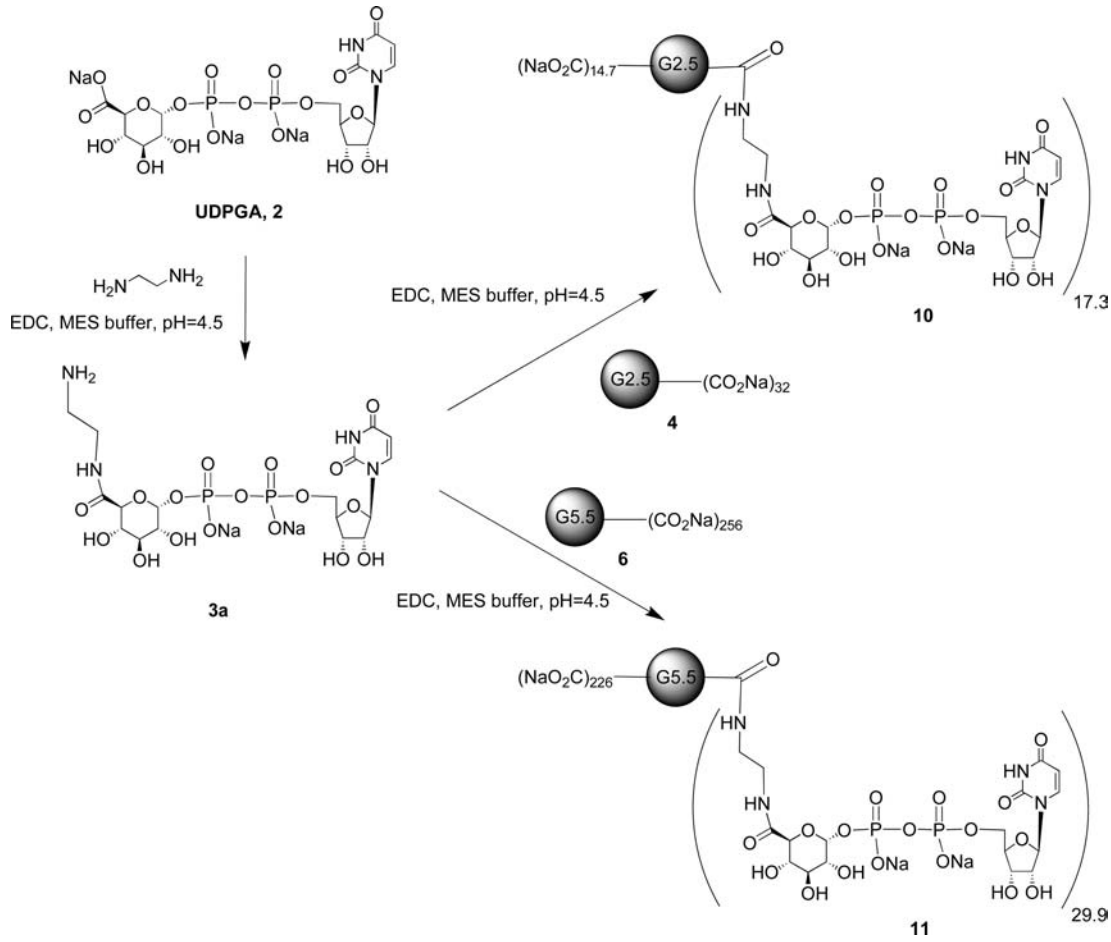

CGS21680, and hydrogen atoms were added to the remaining PAMAM structure. Twenty moieties of UDPGA **2** then were coupled to randomly selected amino groups of the PAMAM chains. The remaining 12 unacylated chains of the dendrimer were substituted with protonated amino groups.

The model of **9** was minimized in the OPLS2005 force field. The Polak−Ribier conjugate gradient (PRCG) minimization method with a maximum of 5000 iterations and with a convergence threshold of 0.05 $kJ \cdot mol^{-1} \cdot Å^{-1}$ was applied. One randomly selected UDPGA moiety attached to the dendrimer then was removed from the PAMAM model, and the UDPGA docked to the $P2Y_{14}$ receptor was attached to the dendrimer. Thus, an initial complex of **9** docked to the $P2Y_{14}$ receptor was obtained. The orientation of a few UDPGA moieties was manually adjusted to avoid overlays with the amino acid residues of the $P2Y_{14}$ receptor. The model was subjected to geometry optimization using the same protocol as mentioned above. After minimization, the binding mode of the UDPGA moiety located inside the $P2Y_{14}$ receptor was found to be similar to the binding mode of **1** itself (*15*). The ethylenediamine chain of PAMAM connected to the receptor-bound UDPGA moiety was located between extracellular loops of $P2Y_{14}$ receptor. In particular, the nucleotide moiety was surrounded by Ile173 (EL2), and Leu175 (EL2), Arg274 (EL3), and Lys277 (7.35). In addition, Lys277 formed an H-bond with the amide oxygen atom of the chain of PAMAM. The molecular model of compound **9** docked in the human $P2Y_{14}$ receptor (Figure 4) showed that the nucleotide-substituted branches of the dendrimer extended far beyond the dimensions of the receptor protein and thus would be available for multivalent docking to receptor dimers and higher-order aggregates (*49*).

DISCUSSION

A functionalized ethylenediamine-containing chain was incorporated in agonists of the human $P2Y_{14}$ receptor, and this chain provided a conjugation strategy for coupling nucleoside agonists to PAMAM dendrimer carriers. Uridine-5′-diphosphoglucuronic acid and its ethylenediamine adduct were suitable functionalized congeners (*50*) for coupling to several generations (G2.5−6) of dendrimers (both terminal carboxy and amino) to modulate potency of the intact conjugates. The observed biological activity of the dendrimer conjugates was clearly $P2Y_{14}$ receptor-dependent; the control dendrimers **4** and **5** lacking nucleotides were inactive. A G3 PAMAM conjugate containing 20 bound nucleotide moieties was 100-fold more potent than the native agonist **1**. Larger dendrimer carriers and those with greater loading favored higher potency as $P2Y_{14}$ receptor agonists. All of the dendrimer−nucleotide conjugates were full agonists at the receptor.

The molecular mechanism whereby these dendrimers exhibit increased activity relative to the native cognate agonist UDPG is unclear. One possible explanation is that these multivalent compounds may bridge multiple $P2Y_{14}$ receptor binding sites simultaneously. Molecular modeling has indicated this possibility for an analogous G3 PAMAM dendrimer conjugate of an A_{2A} adenosine receptor agonist (*48*). The dramatic enhancement in potency, especially in the more heavily substituted dendrimer derivatives, is highly suggestive of a multivalent effect. The ability to span multiple receptor binding sites would be further

Table 1. In Vitro Pharmacological Data for Various Nucleotides and Their Complexes with PAMAM Dendrimers

compound	name/composition	molecular weight (kD)	EC_{50} at $hP2Y_{14}$ receptor, nM
1	UDPG	0.61	261 ± 53
2	UDPGA	0.65	370 ± 70
3a	UDPGA-ethylenediamine	0.82	2590 ± 1590
3b	UDPGA-(*N*-Ac-ethylenediamine)	0.87	496 ± 67
4	G2.5 dendrimer	6.27	NE[a]
5	G3 dendrimer	6.91	NE
8	$G3\text{-}(UDPGA)_{4.3}$	9.52	159 ± 14
9	$G3\text{-}(UDPGA)_{20.1}$	19.11	2.4 ± 0.1
10	$G2.5\text{-}(UDPGA\text{-}ethylenediamine)_{17.3}$	18.48	3.2 ± 1.4
11	$G5.5\text{-}(UDPGA\text{-}ethylenediamine)_{29.9}$	71.65	3.1 ± 0.8
12	$G6\text{-}(UDPGA)_{147}$	147.31	0.8 ± 0.4
13	$G3\text{-}(UDPGA)_{20.1}\text{-}(Biotin)_{4.9}$	20.77	3.4 ± 0.8
14	$G3\text{-}(UDPGA)_{20.1}\text{-}(AlexaFluor488)_{2.3}$	20.77	39.8 ± 7.4
15	$G3\text{-}(UDPGA)_{20.1}\text{-}(DTPA)_{4.5}$	21.55	4.1 ± 1.2
16	$G3\text{-}(UDPGA)_{20.1}\text{-}(DTPA\text{-}Gd(III))_{4.5}$	22.31	421 ± 104

[a] NE, no effect.

promoted by the possible aggregation of dendrimer derivatives (*56*). Nanomolar and subnanomolar potencies have been achieved, which are unprecedented for any monomeric nucleotides acting at the $P2Y_{14}$ receptor. Dendrimer conjugates **10** and **11**, which are both more than half substituted with nucleotide moieties, are more than 800-fold more potent than a corresponding monomer, i.e., the ethylenediamine analogue **3a**. Lower loading of the same dendrimer with nucleotides resulted in a conjugate (compound **9**) that exhibited relatively lower potency. Variability of the potency depending on degree of loading will be the subject of future systematic studies. Such studies also might benefit from quantification of the relative activities of these compounds across a wide range of receptor expression levels in the same cell system.

It is possible that conjugation to dendrimers might protect the nucleotides against enzymatic degradation, but this is not the basis for the enhancement of potency in cAMP-inhibition with the multivalent dendrimers. Our earlier studies (*51*) indicated that little metabolism of extracellular **1** occurs under the conditions of these assays. Moreover, the concentration effect curve of **1** for decreasing cyclic AMP levels is similar whether quantified at times of <5 min or times up to 30 min.

Dendrimers containing several different prosthetic groups also were synthesized. Dendrimer conjugate **14**, which is tagged with AlexaFluor488, potentially will be useful for receptor visualization. Although the potency of **14** was 17-fold lower than that of the corresponding dendrimer lacking the fluorescent group (i.e., **9**), the EC_{50} of approximately 40 nM was comparable to previously introduced fluorescent ligand probes for other GPCRs (*52*). A similar approach in a previous study, using a fluorescent AlexaFluor488-tagged G3 PAMAM dendrimer, was used to detect the expression of the A_3 adenosine receptor in cultured cells (*41*). Gd(III) is a paramagnetic ion that is used for magnetic resonance imaging (*44*). Dendrimer conjugate **15**, which is tagged with the chelating group DTPA, is substantially less potent as its Gd(III) complex, thus limiting the potential utility of this derivative. The in vivo application of dendrimer conjugates is normally limited to i.p. or i.v. injection, but novel approaches for gaining greater bioavailability of dendrimers by other routes of administration have been discussed (*53*, *54*).

In conclusion, we have identified a site on a nucleotide agonist of the $P2Y_{14}$ receptor for chemical tethering to a macromolecular carrier without losing the ability to activate the receptor. Moreover, we have shown that the potency of the native ligand is greatly enhanced in these multivalent ligands. These biologically active drug conjugates do not require cleavage or cellular internalization for their action at the GPCR; in fact, these processes would reduce activity. Covalent conjugation of $P2Y_{14}$ receptor agonists to PAMAM dendrimers qualitatively altered their pharmacological activity. Thus, potency was either retained or dramatically enhanced in the multivalent dendrimer conjugates in comparison to the monomeric $P2Y_{14}$ receptor agonists, depending on size, degree of substitution, terminal functionality, and attached prosthetic groups. The ability to modulate the potency of a given GPCR ligand by the mode and stoichiometry of attachment to dendrimer carriers promises to have general applicability to this therapeutically important class of receptor proteins.

ACKNOWLEDGMENT

This research was supported in part by the Intramural Research Program of the NIH, NIDDK, and by NIH grant GM38213 to T.K.H. We thank Dr. Herman Yeh and Dr. Athena M. Keene-Klutz of NIDDK for helpful advice on the NMR experiments and chemical synthesis. We thank Dr. John Lloyd (NIDDK) for mass spectral measurements.

Supporting Information Available: ^1H NMR and MALDI spectra. This material is available free of charge via the Internet at http://pubs.acs.org.

LITERATURE CITED

(1) Bridges, T. M., and Lindsley, C. W. (2008) G-protein-coupled receptors: from classical modes of modulation to allosteric mechanisms. *ACS Chem. Biol. 3*, 530–541.

(2) Abbracchio, M. P., Burnstock, G., Boeynaems, J. M., Barnard, E. A., Boyer, J. L., Kennedy, C., Fumagalli, M., King, B. F., Gachet, C., Jacobson, K. A., and Weisman, G. A. (2006) International Union of Pharmacology. Update of the P2Y G protein-coupled nucleotide receptors: from molecular mechanisms and pathophysiology to therapy. *Pharmacol. Rev. 58*, 281–341.

(3) Gachet, C. (2006) Regulation of platelet functions by P2 receptors. *Annu. Rev. Pharmacol. Toxicol. 46*, 277–300.

(4) Burnstock, G. (2008) Purinergic signalling and disorders of the central nervous system. *Nat. Rev. Drug Discovery 7*, 575–590.

(5) Idzko, M., Hammad, H., van Nimwegen, M., Kool, M., Willart, M. A., Muskens, F., Hoogsteden, H. C., Luttmann, W., Ferrari, D., Di Virgilio, F., Virchow, J. C., and Lambrecht, B. N. (2007) Extracellular ATP triggers and maintains asthmatic airway inflammation by activating dendritic cells. *Nat. Med. 13*, 913–919.

(6) Shin, A., Toy, T., Rothenfusser, S., Robson, N., Vorac, J., Dauer, M., Stuplich, M., Endres, S., Cebon, J., Maraskovsky, E., and Schnurr, M. (2008) P2Y receptor signaling regulates phenotype and IFN-alpha secretion of human plasmacytoid dendritic cells. *Blood 111*, 3062–3069.

(7) Malin, S. A., Davis, B. M., Richard, K. H., Reynolds, I. J., Albers, K. M., and Molliver, D. C. (2008) Thermal nociception and TRPV1 function are attenuated in mice lacking the nucleotide receptor $P2Y_2$. *Pain 138*, 484–496.

(8) Lugo-Garcia, L., Filhol, R., Lajoix, A. D., Gross, R., Petit, P., and Vignon, J. (2007) Expression of purinergic P2Y receptor subtypes by INS-1 insulinoma beta-cells: a molecular and binding characterization. *Eur. J. Pharmacol. 568*, 54–60.

(9) Lazarowski, E. R., Tarran, R., Grubb, B. R., van Heusden, C. A., Okada, S., and Boucher, R. C. (2004) Nucleotide release provides a mechanism for airway surface liquid homeostasis. *J. Biol. Chem. 279*, 36855–36864.

(10) Müller, T., Bayer, H., Myrtek, D., Ferrari, D., Sorichter, S., Ziegenhagen, M. W., Zissel, G., Virchow, J. C., Luttmann, W., Norgauer, J., Di Virgilio, F., and Idzko, M. (2005) The $P2Y_{14}$ receptor of airway epithelial cells coupling to intracellular Ca^{2+} and IL-8 secretion. *Am. J. Respir. Cell Mol. Biol. 33*, 601–609.

(11) Chambers, J. K., Macdonald, L. E., Sarau, H. M., Ames, R. S., Freeman, K., Foley, J. J., Zhu, Y., McLaughlin, M. M., Murdock, P., McMillan, L., Trill, J., Swift, A., Aiyar, N., Taylor, P., Vawter, L., Naheed, S., Szekeres, P., Hervieu, G., Scott, C., Watson, J. M., Murphy, A. J., Duzic, E., Klein, C., Bergsma, D. J., Wilson, S., and Livi, G. P. (2000) A G protein-coupled receptor for UDP-glucose. *J. Biol. Chem. 275*, 10767–10771.

(12) Abbracchio, M. P., Boeynaems, J.-M., Barnard, E. A., Boyer, J. L., Kennedy, C., Miras-Portugal, M. T., King, B. F., Gachet, C., Jacobson, K. A., Weisman, G. A., and Burnstock, G. (2003) Characterization of the UDP-glucose receptor (re-named here the $P2Y_{14}$ receptor) adds diversity to the P2Y receptor family. *Trends Pharmacol. Sci. 24*, 52–55.

(13) Scrivens, M., and Dickenson, J. M. (2006) Functional expression of $P2Y_{14}$ receptor in human neutrophils. *Eur. J. Pharmacol. 543*, 166–173.

(14) Bassil, A. K., Bourdu, S., Townson, K. A., Wheeldon, A., Jarvie, E. M., Zebda, N., Abuin, A., Grau, E., Livi, G. P., Punter, L., Latcham, J., Grimes, A. M., Hurp, D. P., Downham, K. M., Sanger, G. J., Winchester, W. J., Morrison, A. D., and Moore, G. B. T. (2009) UDP-glucose modulates gastric function through $P2Y_{14}$ receptor-dependent and -independent mechanisms. *Am. J. Physiol. Gastrointest. Liver Physiol. 296*, G923−G930.

(15) Ko, H., Das, A., Carter, R. L., Fricks, I. P., Zhou, Y., Ivanov, A. A., Melman, A., Joshi, B. V., Kováč, P., Hajduch, J., Kirk, K. L., Harden, T. K., and Jacobson, K. A. Molecular recognition in the $P2Y_{14}$ receptor: Probing the structurally permissive terminal sugar moiety of UDP-glucose. *Bioorg. Med. Chem.*, DOI: 10.1016/j.bmc. 2009.05.024.

(16) Ko, H., Fricks, I., Ivanov, A. A., Harden, T. K., and Jacobson, K. A. (2007) Structure activity relationship of uridine 5′-diphosphoglucose (UDP-Glucose) analogues as agonists of the human $P2Y_{14}$ receptor. *J. Med. Chem. 50*, 2030–2039.

(17) Ivanov, A. A., Fricks, I., Harden, T. K., and Jacobson, K. A. (2007) Molecular dynamics simulation of the $P2Y_{14}$ receptor. Ligand docking and identification of a putative binding site of the distal hexose moiety. *Bioorg. Med. Chem. Lett. 17*, 761–766.

(18) Fricks, I., Maddiletti, S., Carter, R., Lazarowski, E. R., Nicholas, R. A., Jacobson, K. A., and Harden, T. K. (2008) UDP is a competitive antagonist at the human $P2Y_{14}$ receptor and a full agonist at the rat $P2Y_{14}$ receptor. *J. Pharm. Exp. Therap. 325*, 588–594.

(19) Tomalia, D. A., Reyna, L. A., and Svenson, S. (2007) Dendrimers as multi-purpose nanodevices for oncology drug delivery and diagnostic imaging. Cellular delivery of therapeutic macromolecules. *Biochem. Soc. Trans. 35*, 61–67.

(20) Lee, C. C., MacKay, J. A., Fréchet, J. M. J., and Szoka, F. C. (2005) Designing dendrimers for biological applications. *Nat. Biotechnol. 23*, 1517–1526.

(21) Zeng, F., and Zimmerman, S. C. (1997) Dendrimers in supramolecular chemistry: from molecular recognition to self-assembly. *Chem. Rev. 97*, 1681–1712.

(22) Gillies, E. R., and Fréchet, J. M. J. (2005) Dendrimers and dendritic polymers in drug delivery. *Drug Discovery Today 10*, 35–43.

(23) D'Emanuele, A., and Attwood, D. (2005) Dendrimer-drug interactions. *Adv. Drug Delivery Rev. 57*, 2147–2162.

(24) Patri, A. K., Majoros, I. J., and Baker, J. R. (2002) Dendritic polymer macromolecular carriers for drug delivery. *Curr. Opin. Chem. Biol. 6*, 466–471.

(25) Woller, E. K., Walter, E. D., Morgan, J. R., Singel, D. J., and Cloninger, M. J. (2003) Altering the strength of lectin binding interactions and controlling the amount of lectin clustering using mannose/hydroxyl-functionalized dendrimers. *J. Am. Chem. Soc. 125*, 8820–8826.

(26) Woller, E. K., and Cloninger, M. J. (2002) The lectin-binding properties of six generations of mannose-functionalized dendrimers. *Org. Lett. 4*, 7–10.

(27) Jayaraman, N., Nepogodiev, S. A., and Stoddart, J. F. (1997) Synthetic carbohydrate-containing dendrimers. *Chem.—Eur. J. 3*, 1193–1199.

(28) Page, D., and Roy, R. (1997) Synthesis and biological properties of mannosylated starburst poly(amidoamine) dendrimers. *Bioconjugate Chem. 8*, 714–723.

(29) Kieburg, C., and Lindhorst, T. K. (1997) Glycodendrimer synthesis without using protecting groups. *Tetrahedron Lett. 38*, 3885–3888.

(30) Mammen, M., Choi, S.-K., and Whitesides, G. M. (1998) Polyvalent interactions in biological systems: implications for design and use of multivalent ligands and inhibitors. *Angew. Chem., Int. Ed. 37*, 2754–2794.

(31) Stiriba, S.-E., Frey, H., and Haag, R. (2002) Dendritic polymers in biomedical applications: from potential to clinical use in diagnostics and therapy. *Angew. Chem., Int. Ed. 41*, 1329–1334.

(32) Krause, W., Hackmann-Schlichter, N., Maier, F. K., and Müller, R. (2000) Dendrimers in diagnostics. *Top. Curr. Chem. 210*, 261–308.

(33) Wathier, M., Jung, P. J., Carnahan, M. A., Kim, T., and Grinstaff, M. W. (2004) Dendritic macromers as in situ polymerizing biomaterials for securing cataract incisions. *J. Am. Chem. Soc. 126*, 12744–12745.

(34) Grinstaff, M. W. (2002) Biodendrimers: New Polymeric Biomaterials for Tissue Engineering. *Chem.—Eur. J. 8*, 2838–2846.

(35) Lee, H., Baker, J. R., and Larson, R. G. (2006) Molecular dynamics studies of the size, shape, and internal structure of 0% and 90% acetylated fifth-generation polyamidoamine dendrimers in water and methanol. *J. Phys. Chem. B 110*, 4014–4019.

(36) Maiti, P. K., Çağın, T., Wang, G., and Goddard, W. A. (2004) Structure of PAMAM dendrimers: generations 1 through 11. *Macromolecules 37*, 6236–6254.

(37) Lee, I., Athey, B. D., Wetzel, A. W., Meixner, W., and Baker, J. R. (2002) Structural molecular dynamics studies on polyamidoamine dendrimers for a therapeutic application: effects of pH and generation. *Macromolecules 35*, 4510–4520.

(38) Esfand, R., and Tomalia, D. A. (2001) Poly(amidoamine) (PAMAM) dendrimers: from biomimicry to drug delivery and biomedical applications. *Drug Discovery Today 6*, 427–436.

(39) Kim, Y., Hechler, B., Klutz, A., Gachet, C., and Jacobson, K. A. (2008) Toward multivalent signaling across G protein-coupled receptors from poly(amidoamine) dendrimers. *Bioconjugate Chem. 19*, 406–411.

(40) Kim, Y., Klutz, A. M., Hechler, B., Gao, Z. G., Gachet, C., and Jacobson, K. A. (2008) Application of the functionalized congener approach to dendrimer-based signaling agents acting through A_{2A} adenosine receptors. *Purinergic Signalling 5*, 39–50.

(41) Klutz, A. M., Gao, Z. G., Lloyd, J., Shainberg, A., and Jacobson, K. A. (2008) Enhanced A_3 adenosine receptor selectivity of multivalent nucleoside-dendrimer conjugates. *J. Nanobiotechnol. 6*, 12.

(42) Haugland, R. P. (2002) *Handbook of Fluorescent Probes and Research Products*, 9th ed., pp 20−35, Molecular Probes, Invitrogen.

(43) Kobayashi, H., and Brechbiel, M. W. (2004) Dendrimer-based nanosized MRI contrast agents. *Curr. Pharm. Biotechnol. 5*, 539–549.

(44) Longmire, M., Choyke, P. L., and Kobayashi, H. (2008) Dendrimer-based contrast agents for molecular imaging. *Curr. Topics Med. Chem. 8*, 1180–1186.

(45) Kim, Y., Klutz, A. M., and Jacobson, K. A. (2008) Systematic investigation of polyamidoamine dendrimers surface-modified with poly(ethylene glycol) for drug delivery applications: Synthesis, characterization, and evaluation of cytotoxicity. *Bioconjugate Chem. 19*, 1660–1672.

(46) Fricks, I. P., Carter, R. L., Lazarowski, E. R., and Harden, T. K. (2009) Gi-dependent cell signaling responses of the human $P2Y_{14}$-receptor in model cell systems. *J. Pharmacol. Exp. Therap.* DOI:10.1124/jpet.109.150730.

(47) Jaakola, V.-P., Griffith, M. T., Hanson, M. A., Cherezov, V., Chien, E. Y. T., Lane, J. R., IJzerman, A. P., and Stevens, R. C. (2008) The 2.6 Å crystal structure of a human A_{2A} adenosine receptor bound to an antagonist. *Science 322*, 1211–1217.

(48) Ivanov, A. A., and Jacobson, K. A. (2008) Molecular modeling of a PAMAM-CGS21680 dendrimer bound to an A_{2A} adenosine receptor homodimer. *Bioorg. Med. Chem. Lett. 18*, 4312–4315.

(49) Gandia, J., Galino, J., Amaral, O., Soriano, A., Lluís, C., Franco, R., and Ciruela, F. (2008) Detection of higher-order G protein-coupled receptor oligomers by a combined BRET-BiFC technique. *FEBS Lett. 582*, 2979–2984.

(50) Jacobson, K. A. (2009) Functionalized congener approach to the design of ligands for G protein-coupled receptors (GPCRs). *Bioconjugate Chem.* doi: 10.1021/bc9000596

(51) Lazarowski, E. R., Shea, D. A., Boucher, R. C., and Harden, T. K. (2003) Release of cellular UDP-glucose as a potential extracellular signaling molecule. *Mol. Pharmacol. 63*, 1190–1197.

(52) Cordeaux, Y., Briddon, S. J., Alexander, S. P., Kellam, B., and Hill, S. J. (2008) Agonist occupied A_3 adenosine receptors exist within heterogeneous microdomains of individual living cells. *FASEB J. 22*, 850–860.

(53) Kitchens, K. M., El-Sayed, M. E. H., and Ghandehari, H. (2005) Transepithelial and endothelial transport of poly (amidoamine) dendrimers. *Adv. Drug Delivery Rev. 57*, 2163–2176.

(54) Duncan, R., and Izzo, L. (2005) Dendrimer biocompatibility and toxicity. *Adv. Drug Delivery Rev. 57*, 2215–2237.

(55) Harden, T. K., Scheer, A. G., and Smith, M. M. (1982) Differential modification of the interaction of cardiac muscarinic cholinergic and beta-adrenergic receptors with a guanine nucleotide binding component(s). *Mol. Pharmacol. 21*, 570–580.

(56) Nourse, A., Millar, D. B., and Minton, A. P. (2000) Physicochemical characterization of generation 5 polyamidoamine dendrimers. *Biopolymers 53*, 316–328.

BC900206G

Supporting Information for:

Enhanced Potency of Nucleotide-Dendrimer Conjugates as Agonists of the $P2Y_{14}$ Receptor: Multivalent Effect in G Protein-Coupled Receptor Recognition

Arijit Das,[a] Yixing Zhou,[b] Rhonda Carter,[b] T. Kendall Harden,[b] and Kenneth A. Jacobson[a*]

Table of Contents

Figure S1. ^{1}H NMR spectrum of compound **9**.	p. S2
Figure S2. ^{1}H NMR spectrum of compound **12**.	p. S3
Figure S3. MALDI MS of PAMAM dendrimer complex **8**.	p. S4
Figure S4. MALDI MS of PAMAM dendrimer complex **9**.	p. S5
Figure S5. MALDI MS of PAMAM dendrimer complex **10**.	p. S6
Figure S6. MALDI MS of PAMAM dendrimer complex **11**.	p. S7
Figure S7. MALDI MS of PAMAM dendrimer complex **15**.	p. S8

Figure S1. ^{1}H NMR spectrum of PAMAM-UDPGA conjugate **9**.

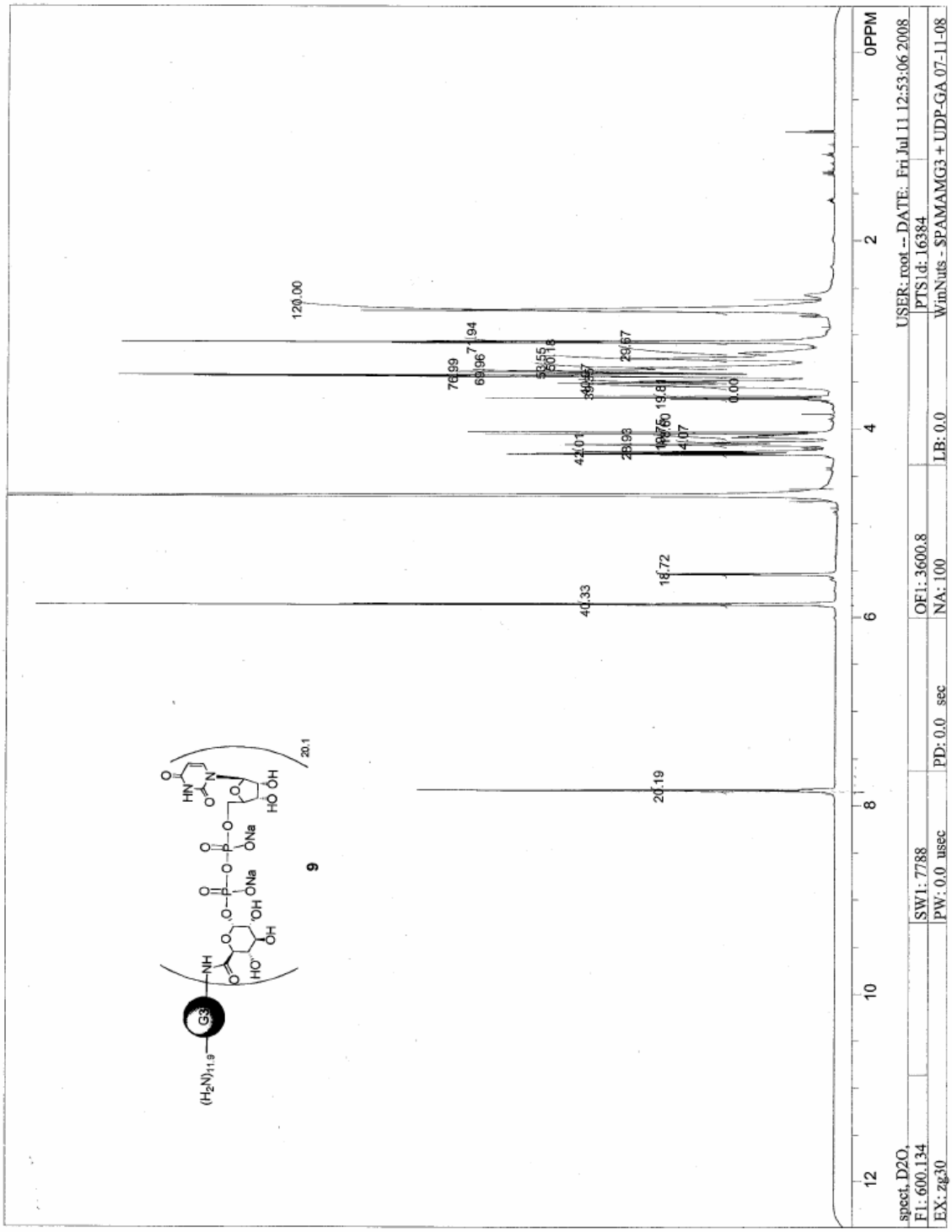

Figure S2. ^{1}H NMR spectrum of PAMAM-UDPGA conjugate **12**.

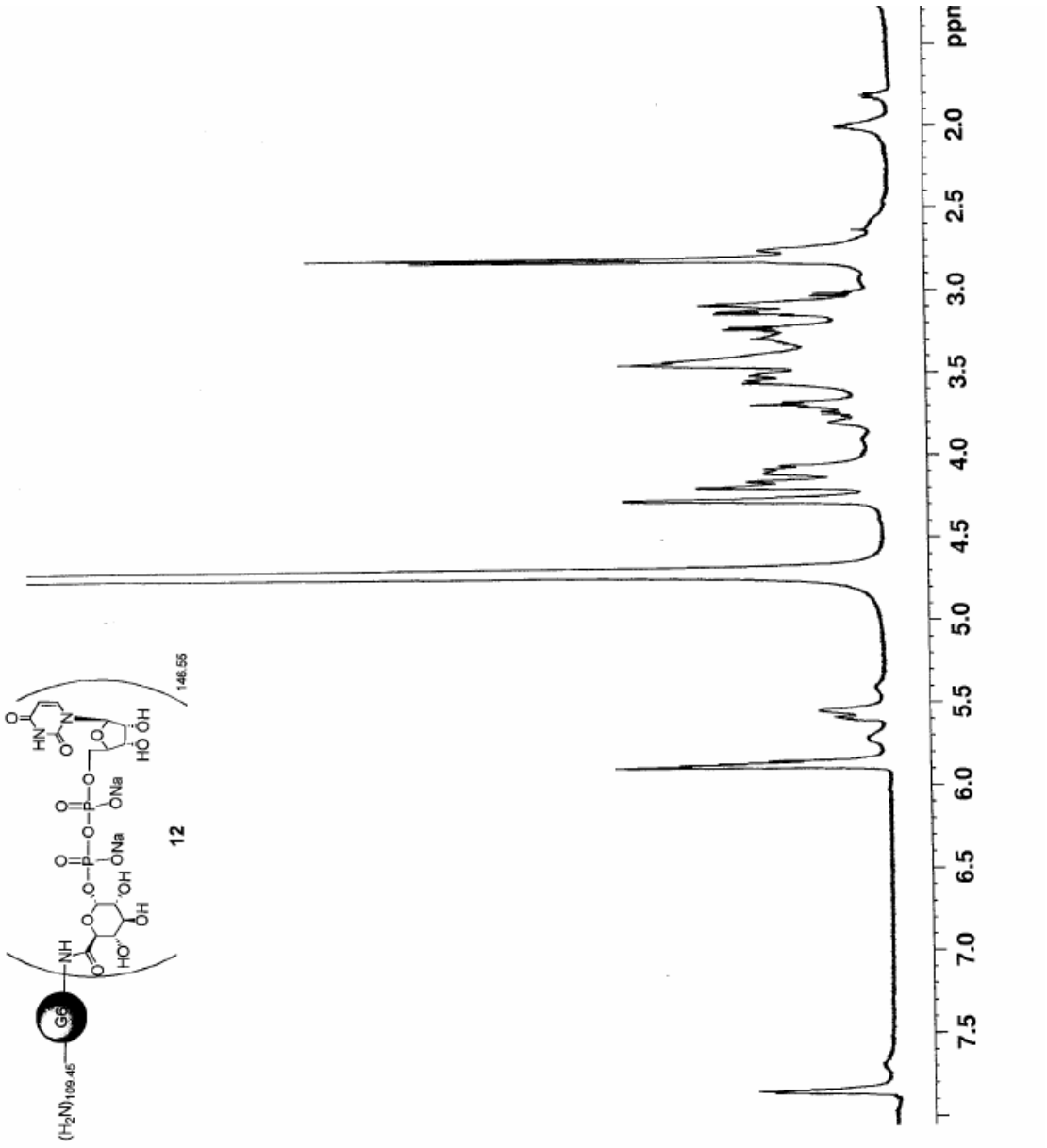

Figure S3. MALDI MS of PAMAM dendrimer complex **8.**

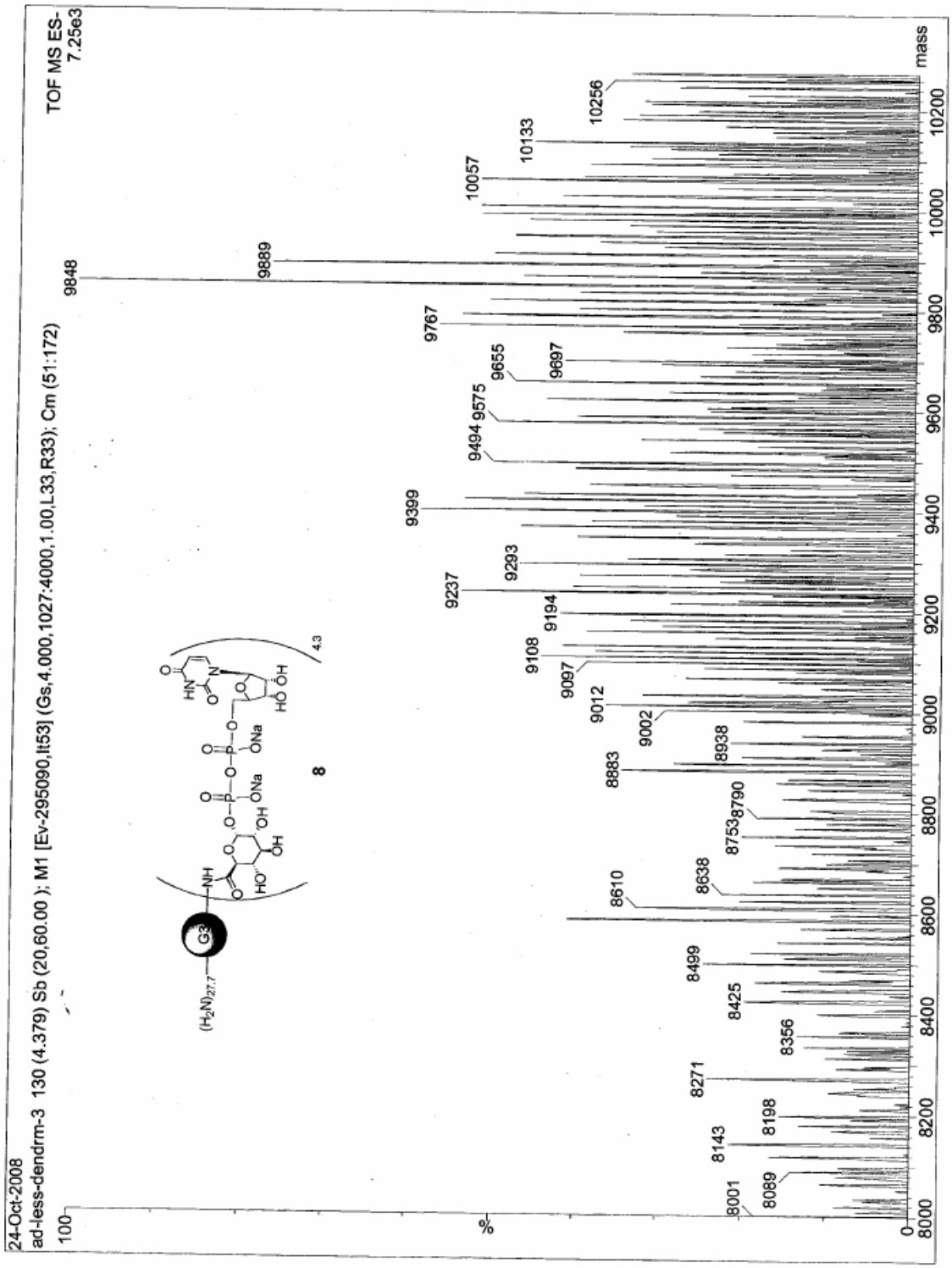

Figure S4. MALDI MS of PAMAM dendrimer complex **9**.

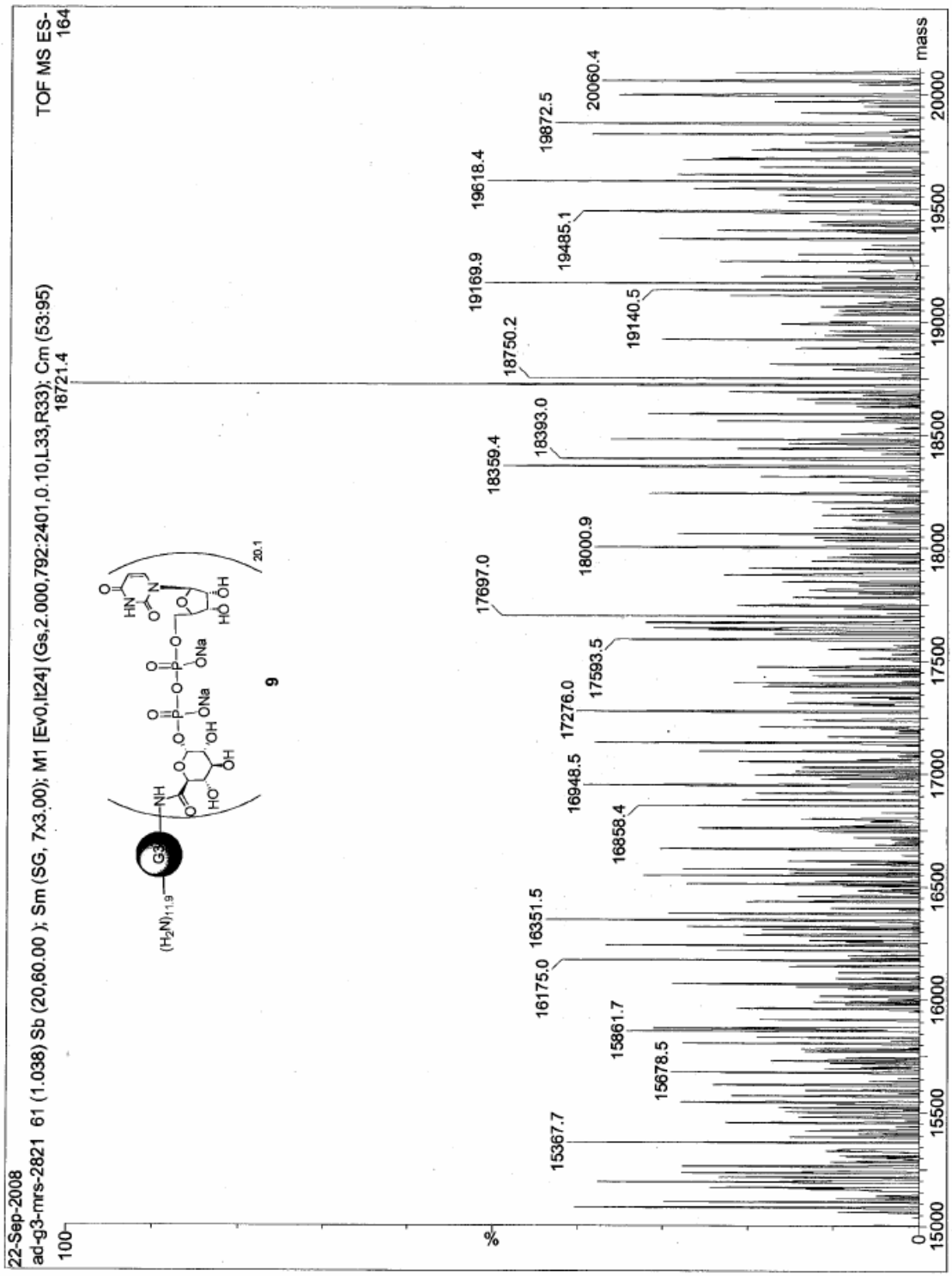

Figure S4. MALDI MS of PAMAM dendrimer complex **10**.

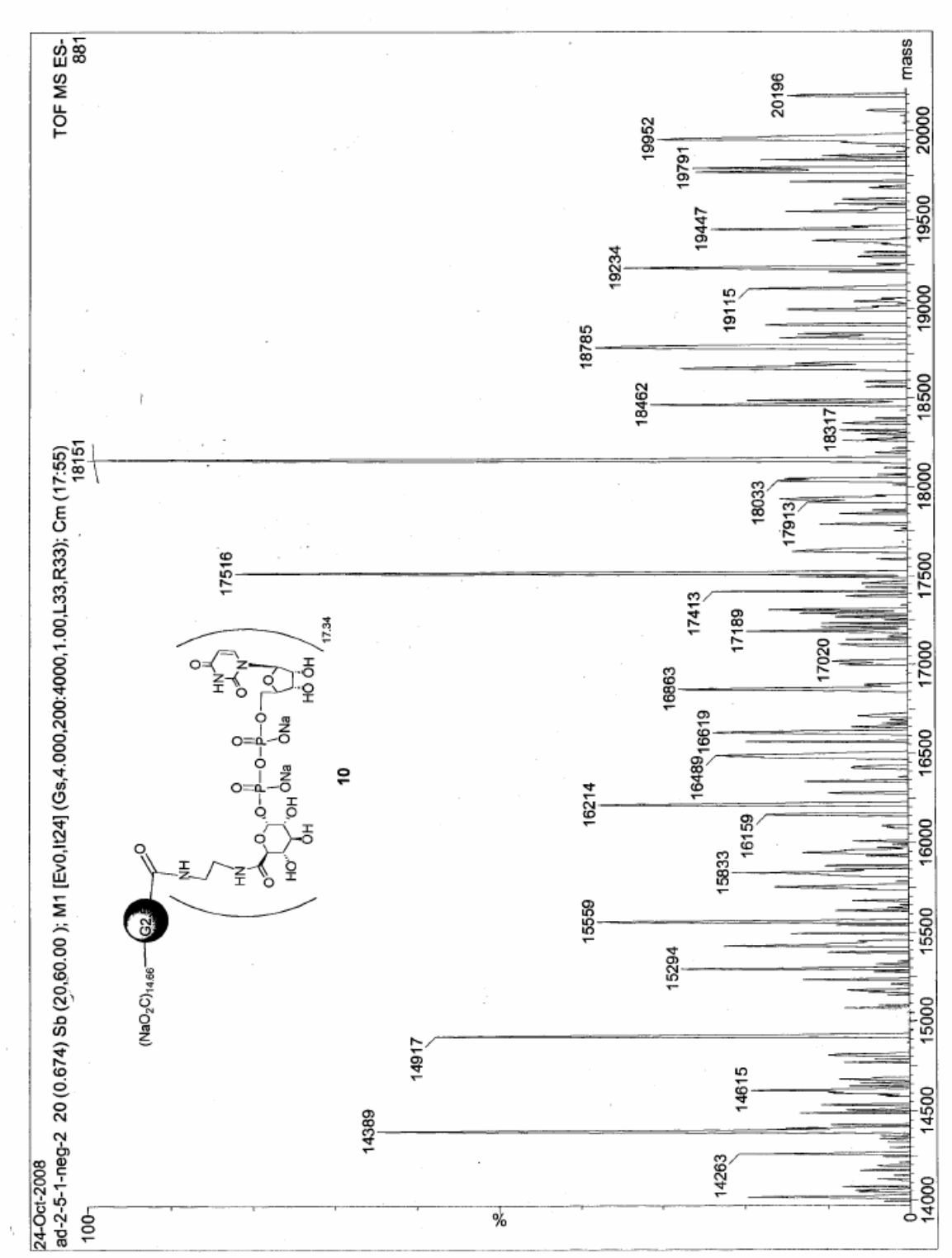

Figure S6. MALDI MS of PAMAM dendrimer complex **11**.

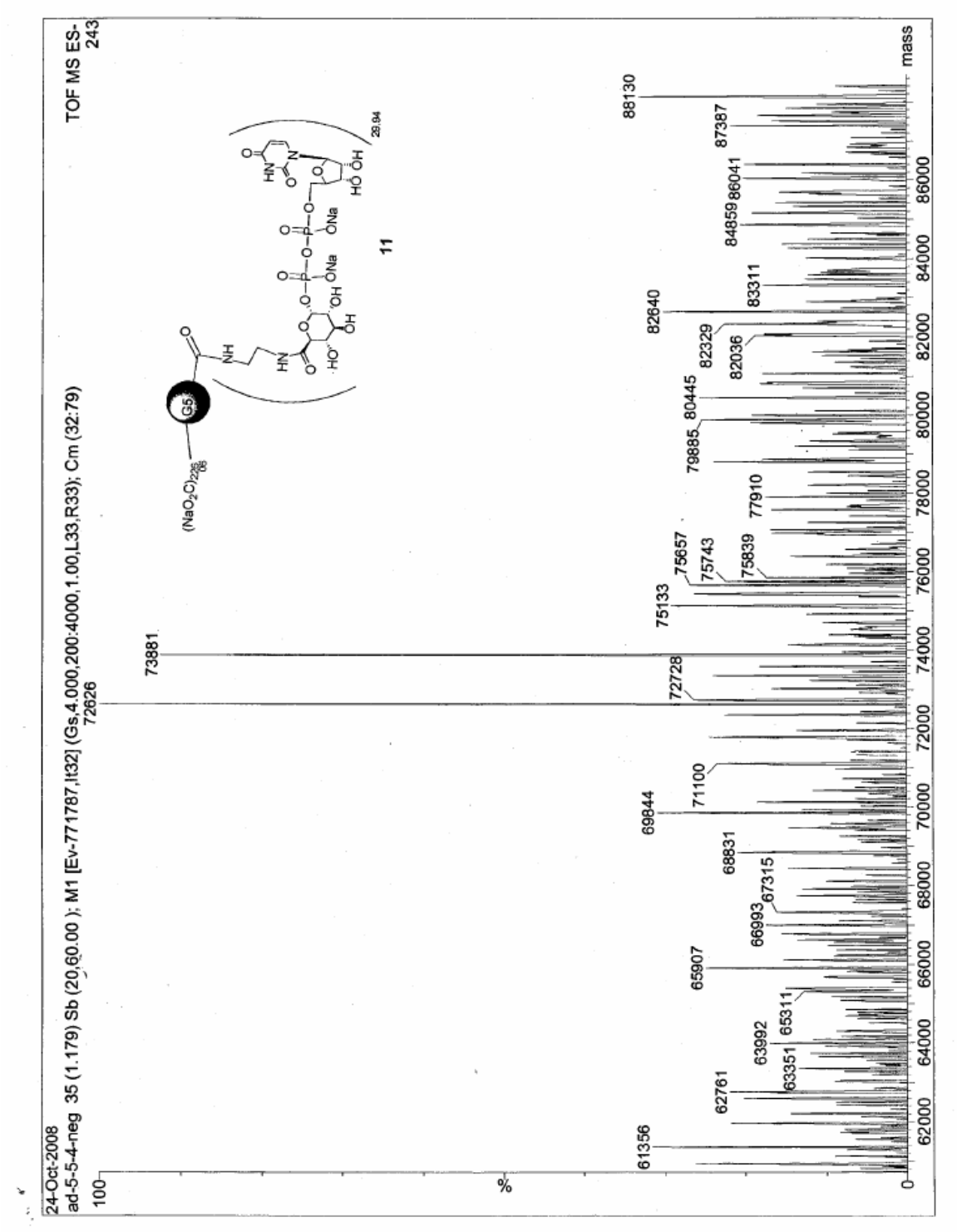

Figure S7. MALDI MS of PAMAM dendrimer complex **15**.

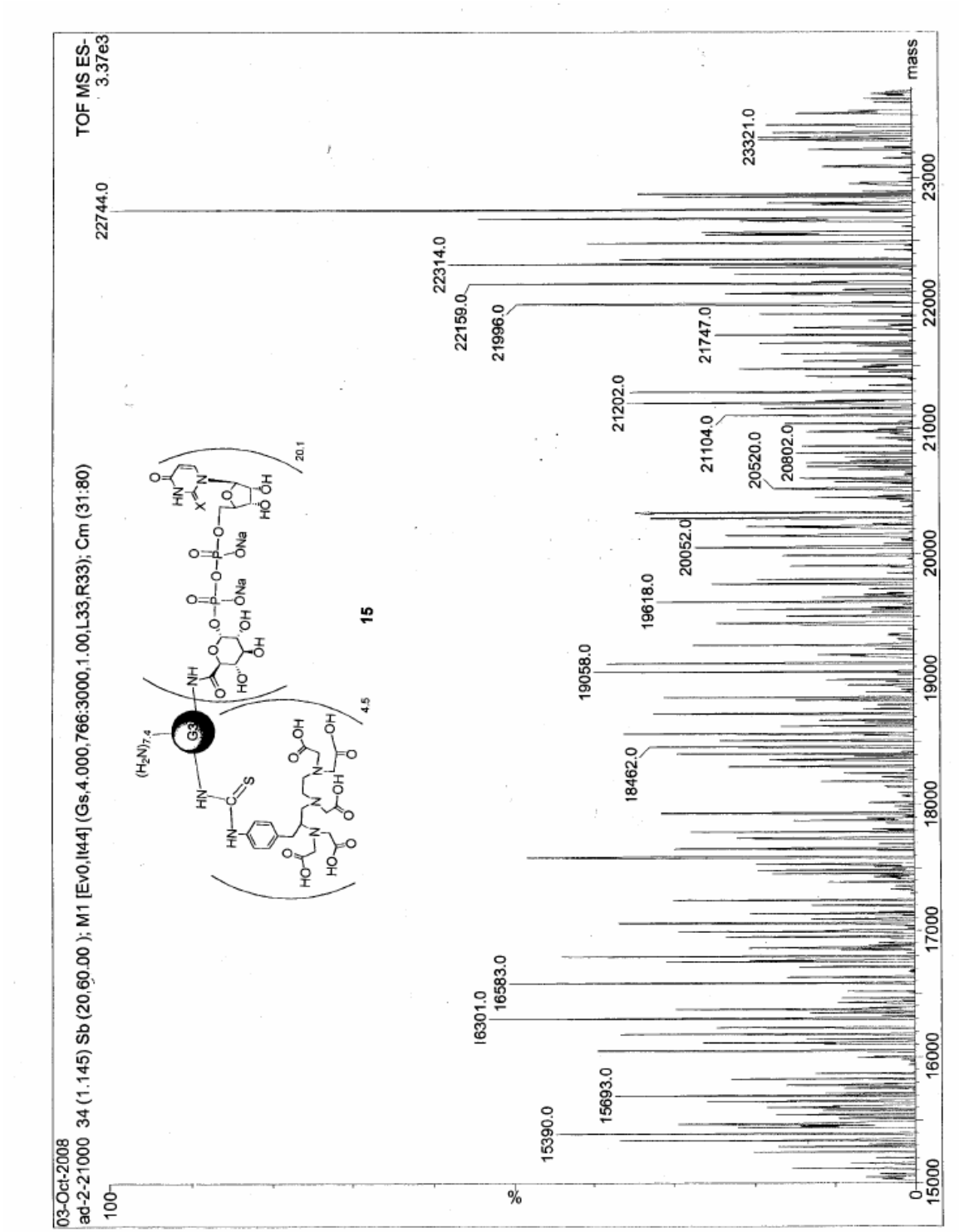

In Vivo Bioluminescence Imaging of Furin Activity in Breast Cancer Cells Using Bioluminogenic Substrates

Anca Dragulescu-Andrasi, Gaolin Liang, and Jianghong Rao*

Department of Radiology, Molecular Imaging Program at Stanford, Bio-X Program, and Cancer Biology Program, Stanford University School of Medicine, 1201 Welch Road, Stanford, California 94305. Received June 5, 2009; Revised Manuscript Received July 13, 2009

Furin, a proprotein convertases family endoprotease, processes numerous physiological substrates and is overexpressed in cancer and inflammatory conditions. Noninvasive imaging of furin activity will offer a valuable tool to probe furin function over the course of tumor growth and migration in the same animals in real time and directly assess the inhibition efficacy of drugs in vivo. Here, we report successful bioluminescence imaging of furin activity in xenografted MBA-MB-468 breast cancer tumors in mice with bioluminogenic probes. The probes are conjugates of furin substrate, a consensus amino acid motif R-X-K/R-R (X, any amino acid), with the firefly luciferase substrate D-aminoluciferin. In the presence of the luciferase reporter, the probes are unable to produce bioluminescent emission without furin activation. Blocking experiments with a furin inhibitor and control experiments with a scrambled probe showed that the bioluminescence emission in the presence of firefly luciferase is furin-dependent and specific. After furin activation, a 30-fold increase in the bioluminescent emission was observed in vitro, and on average, a 7−8-fold contrast between the probe and control was seen in the same tumor xenografts in mice. Direct imaging of furin activity may facilitate the study of furin function in tumorigenicity and the discovery of new drugs for furin-targeted cancer therapy.

INTRODUCTION

In vivo bioluminescence imaging (BLI) uses luciferase enzymes (such as firefly luciferase, *Renilla* luciferase, and green or red click beetle luciferase) as reporters to generate light emission during the catalytic oxidation of their substrates for noninvasive imaging of biological targets and processes in intact cells and living animals (*1*−*3*). Because of its extremely high sensitivity and relatively simple instrument setup, BLI has been extensively used as a molecular imaging technique in small animals, particularly for cancer imaging research. For example, BLI is used to measure the mass and location of implanted cells in animals (*4*), to evaluate the efficacy of anticancer drugs (*5*−*7*), and to detect protein−protein interactions in living cancer cells (*8*, *9*).

BLI employs both the enzyme and substrate to generate light emission, and many strategies have been developed to regulate the activity of the reporter enzyme at various levels (transcriptional, post-transcriptional, translational, and post-translational) for molecular imaging (*10*). Alternatively, the substrates may be chemically converted into an inactive caged form that can be activated by certain biological targets to generate the original substrates for imaging. For example, the substrates of firefly luciferase have been conjugated to a caspase-3 peptide substrate and β-lactam to produce bioluminogenic probes for imaging caspase-3 (*11*, *12*) and β-lactamase activity (*13*). Herein, we report the design of luminogenic probes based on D-aminoluciferin for imaging furin activity in breast cancer cells in vivo.

Furin, one of the seven endoproteases that belong to the proprotein convertases family, is ubiquitously expressed in mammalian cells processing and activating a wide variety of proprotein substrates (*14*). The physiological substrates of furin include growth factors and hormones (e.g., pro-β-NGF and TGF-β), receptors such as insulin proreceptor, plasma proteins, and as well as proteases such as membrane type 1-matrix metalloproteinase (MT1-MMP) and matrix metalloproteinases (*15*). Upregulation of furin mRNA was identified in head and neck tumors, breast tumors, and lung cancer by means of reverse transcription polymerase chain reaction (RT-PCR) and in situ hybridization (*16*). Recent reports have indicated that furin is a target of hypoxia-inducible factor 1 (HIF-1) and that hypoxia induces elevated levels of furin, leading to more aggressive tumors (*17*). It has been demonstrated that furin inhibition correlates with decreased invasiveness and tumorigenicity of several human cancer cells in vivo (*18*, *19*). Considering the vital role of furin in tumor formation and invasion, the ability to image its activity in vivo will offer a valuable tool to probe furin function over the course of tumor growth and migration in the same animals in real time and provide a means to assess the in vivo inhibition efficacy of drugs. However, no probes are currently available for noninvasive imaging of furin activity in living animals.

Furin performs a calcium-dependent proteolytic cleavage at the *C*-terminus of a consensus amino acid motif R-X-K/R-R (X, any amino acid) (*20*). This tetrapeptide motif provides sufficient specificity to bind the active furin (*21*). To take advantage of the high sensitivity of BLI, we developed bioluminogenic furin probes by conjugating the furin substrate to the luciferase substrate D-aminoluciferin. Here, we show that these bioluminogenic probes are specifically activated by furin and produce bioluminescence emission in the presence of firefly luciferase in vitro, in living breast cancer cells, and in breast cancer tumor xenografts in mice.

MATERIALS AND METHODS

Probe Syntheses. All peptides were synthesized using standard Fmoc-protocol on a trityl chloride resin (Novabiochem). After sequence completion, the peptides were cleaved from the solid support without removing the protecting groups of the amino acids (Pbf for Arg, Boc for Lys, and *t*Bu for Tyr)

* Corresponding author. Phone: 650-736-8563. Fax: 650-736-7925. E-mail: jrao@stanford.edu.

10.1021/bc9002508 CCC: $40.75 © 2009 American Chemical Society
Published on Web 07/31/2009

Scheme 1. Schematic of Bioluminogenic Probes for Detecting Furin Activity and Their Chemical Structures

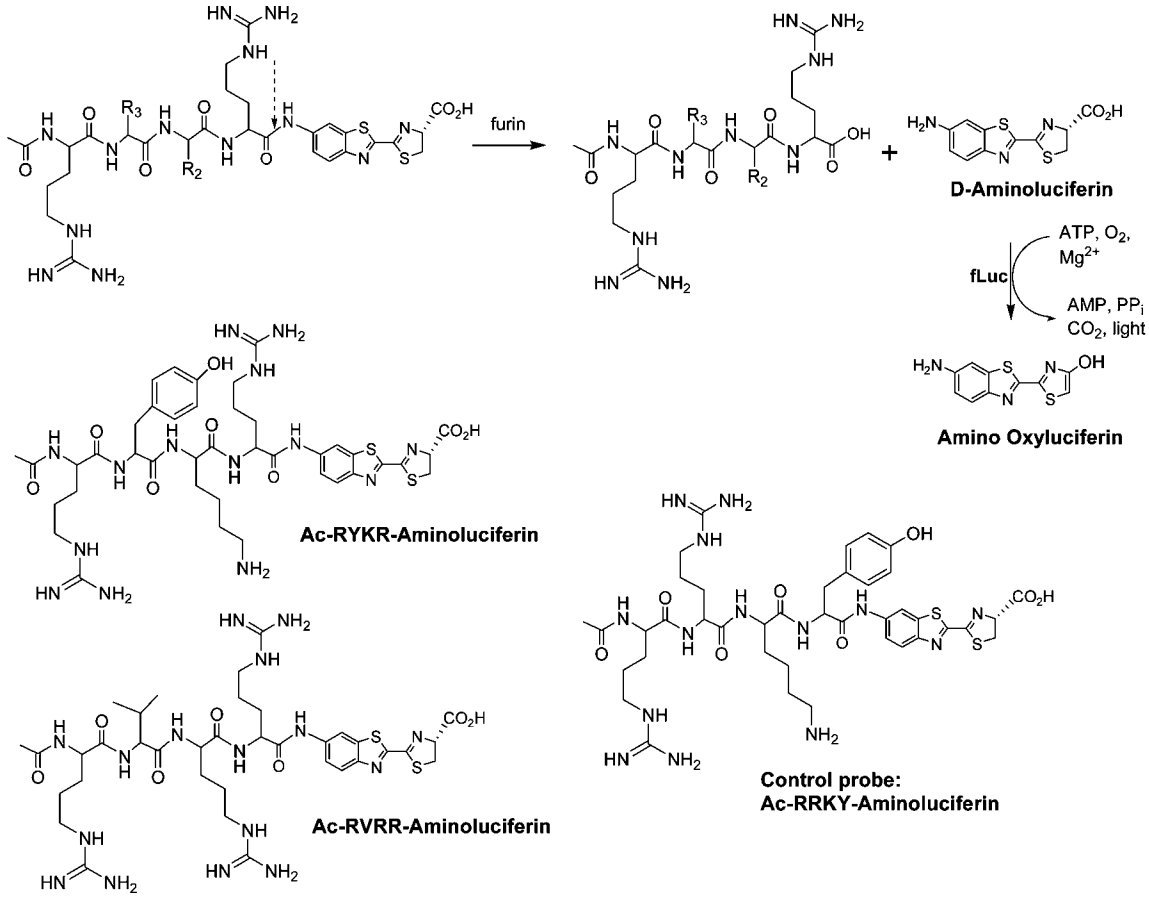

using 1% trifluoroacetic acid (TFA) in dichloromethane. 2-Cyano-6-aminobenzothiazole (CABT) was synthesized as previously described (*22*). All aminoluciferin−peptide conjugates were obtained using a three-step postsynthetic protocol as described below.

First, CABT was coupled to the *C*-terminal carboxylic acid group using the following procedure: Ac-R(Pbf)VR(Pbf)R(Pbf)-COOH (300 mg, 0.22 mmol) was dissolved in dry tetrahydrofuran (THF) (3 mL). *N*-Methylmorpholine (65 μL, 0.56 mmol) and isobutyl chloroformate (32 μL, 0.27 mmol) were added. The reaction mixture was stirred at room temperature for 30 min. Afterward, CABT (60 mg, 0.34 mmol) was added, and the reaction mixture was stirred at room temperature overnight. The CABT−peptide conjugate was purified by RP-HPLC, and then the solvent was removed by rotary evaporation and dried.

Second, the protection groups were removed using 95% TFA, 2.5% water, and 2.5% triisopropylsilane (TIPS), and then the peptide was precipitated with ether, washed, dried, and used for the next step without further purification.

Third, the yellow solid was dissolved in PBS (1 mL). D-Cysteine hydrochloride monohydrate (38 mg, 0.22 mmol) was dissolved in water, adjusted at pH 8.5 with sodium carbonate, and added to the CABT−peptide solution. The reaction mixture was further adjusted to pH 8 and stirred at room temperature for 20 min. The product, Ac-RVRR-AmLuc, was purified by RP-HPLC and lyophilized to give a light-yellow foamy solid (total yield: 21%). The final identity of the products was confirmed with mass spectroscopic analyses (Supporting Information).

Cell Culture and Tumor Xenograft Generation. All cell culture reagents were purchased from Invitrogen unless otherwise noted. MDA-MB-468 (human breast adenocarcinoma) cells, transduced with a retrovirus (pMSCV/L2G) to express a dual reporter containing firefly luciferase (Fluc) and green fluorescent protein (GFP), were kindly supplied by Dr. Christopher Contag (Stanford University). MDA-MB-468 Fluc$^+$ cells were cultured in Dulbecco's modified Eagle's medium (DMEM) (high glucose, 4500 mg/L D-glucose, and 110 mg/L sodium pyruvate) supplemented with 10% fetal bovine serum (FBS) and penicillin−streptomycin (100 units/mL) at 37 °C in a humidified atmosphere in a 5% CO_2 incubator. To generate tumor xenografts in mice, MDA-MB-468 Fluc$^+$ cells (10×10^6) were implanted subcutaneously in the mid-dorsal region of each 4-weeks-old female nude mouse (*Nu/Nu*, Charles River). Tumors were allowed to grow for 10 days and reach sizes between 5−7 mm before imaging.

In Vitro Bioluminescence Measurements. Probes were diluted to a final concentration of 50 μM in Dulbecco's phosphate buffered saline (DPBS) containing Ca^{2+} and Mg^{2+}, and incubated for 1 h at room temperature with or without 4 U of furin (New England BioLabs). Subsequently, 20 μL of luciferase assay buffer (Promega) and 1 μL of QuantiLum recombinant luciferase solution (Promega), diluted to a concentration of 0.13 mg/mL in 1 mg/mL BSA solution in PBS, were added. The luminescence was immediately measured using a 20/20^n Single Tube Luminometer (Turner BioSystems) at a 1 s integration time every 5 min for 1 h.

Cell Bioluminescence Imaging. MDA-MB-468 Fluc$^+$ cells were grown in 60 mm dishes to reach 80−90% confluence. After washing twice with PBS, cells were detached using a plastic cell scraper, diluted in 2 mL of PBS, and counted. Next, cells were centrifuged down, dissolved in DPBS (containing Mg^{2+} and Ca^{2+}), and placed in the 96-well plate at 3×10^5 cells/well. The furin probes were added immediately before imaging. In the inhibition experiments, 300 μM furin inhibitor (Decanoyl-RVKR-CMK, CalBiochem) was added. Biolumi-

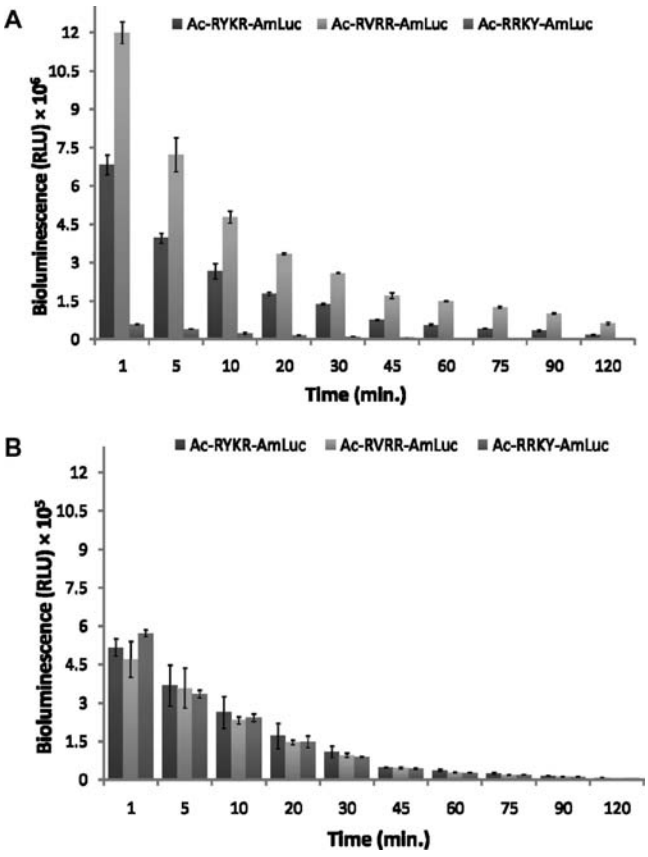

Figure 1. In vitro detection of furin activity. All substrates were incubated with (A) or without 4 U (B) of furin at room temperature for 1 h. Luciferase buffer and enzyme were added, and the bioluminescence signal was measured and plotted as a function of time.

nescence images were acquired every 5 min for 2 h using an optical imaging system (IVIS 200; Xenogen Corp.) at a 50 s integration time. Circular regions of interest (ROI) were drawn over each well and quantified using Living Image software (Xenogen Corp). The background of an empty well was subtracted from the total signal. The results were reported as total photon flux within an ROI in photons per second.

Fluorescence Immunostaining. MDA-MB-468 $Fluc^+$ cells were plated on glass coverslips in 24-well plates at 70% confluence and fixed with 4% paraformaldehyde for 20 min the next day. Subsequently, fixed cells were washed 3 times with DPBS and permeabilized with 1% Triton X-100/PBS for 20 min, followed by blocking with 1% nonfat milk solution in PBS for 20 min at room temperature. After blocking, cells were incubated with primary antibody (1:100, antifurin rabbit polyclonal antibody (Biomol International), diluted with 1% nonfat milk PBS solution) for 1 h at 37 °C. After washing three times with PBS and once with 1% nonfat milk, cells were incubated with secondary antibody (1: 100, goat polyclonal antirabbit IgG rhodamine conjugate) for 30 min at 37 °C. After washing with PBS and distilled water, the final samples were mounted on a glass slide with mounting media containing DAPI. Images were acquired using an Axiovert 200 M fluorescence microscope (MicroImaging, Inc., Thornwood, NY) equipped with a 63× objective. Acquisition time was 150 ms for 4′,6′-diamidino-2-phenylindole (DAPI) and 600 ms for the rhodamine channel. For MDA-MB-468 tumor tissue staining, tumors were sectioned at a thickness of 10 μm, placed on glass slides, and fixed with acetone on ice for 10 min. The same staining protocol for fixed cells applied to them for furin imaging.

In Vivo Bioluminescence Imaging. Animal handling was performed in accordance with Stanford University, Animal Research Committee guidelines. Prior to imaging, all mice bearing MDA-MB-468$Fluc^+$ subcutaneous tumors were anesthetized using isoflurane gas (2% isoflurane in oxygen, 1 L/min) during all injection and imaging procedures. Mice were imaged in a light-tight chamber using an in vivo optical imaging system (IVIS 200; Xenogen Corp.) equipped with a cooled charge-coupled device (CCD) camera. Mice were imaged 1 min after tail vein injection of 100 μL of 10 mM probe solution with an acquisition time of 1 min, and a gray scale reference image was obtained before the acquisition of a bioluminescence image. The pseudocolored bioluminescence images (in photons/s/cm2/steradian) were superimposed over the gray scale photographs of the animals. Circular ROIs were drawn over the tumor areas and quantified using Living Image software, version 3.0 (Xenogen Corp.). The results were reported as total photon flux within an ROI in photons per second.

RESULTS

Luminogenic Probes Specifically Detect Furin Activity in Vitro. D-Aminoluciferin, an analogue of D-luciferin, is a bioluminescent substrate for the luciferase enzyme. Derivatization of its amino group with amino acids renders D-aminoluciferin a poor substrate for luciferase with drastically decreased photon production efficiency presumably due to the steric hindrance at the active site of firefly luciferase (*23*). We therefore designed our bioluminogenic furin probes by coupling D-aminoluciferin to the *C*-terminus of furin recognition peptide sequences, such as previously reported furin substrates RVRR and RYKR (*24, 25*), affording two bioluminogenic furin probes: Acetyl-RVRR-aminoluciferin (Ac-RVRR-AmLuc) and Acetyl-RYKR-aminoluciferin (Ac-RYKR-AmLuc) (Scheme 1). Because furin cleaves at the C-terminal to the last arginine residue, small molecules at this site such as 7-amino-4-methylcoumarin can be attached at this position, and the resulting conjugate can still be recognized and processed by furin (*26*). Both probes should be poor substrates for firefly luciferase and would produce little light emission. In the presence of furin, the probes will be hydrolyzed to remove the peptide caging group and generate free D-aminoluciferin which will subsequently produce light emission in the presence of firefly luciferase. Therefore, the activity of furin can be measured from the firefly luciferase based bioluminescence assay. As a control, we synthesized another conjugate with a scrambled amino acid sequence that should not be recognized by furin, Acetyl-RRKY-aminoluciferin (Ac-RRKY-AmLuc) (Scheme 1).

First, we evaluated our probes in vitro by measuring the bioluminescent signal as a function of time in the presence or absence of furin. As shown in Figure 1A, Ac-RVRR-AmLuc and Ac-RYKR-AmLuc were incubated with furin for 1 h at room temperature, and upon the addition of luciferase, both produced an initial burst of bioluminescence resulting from free D-aminoluciferin generated during the incubation with furin, followed by a gradual decrease of the signal over time. At each time point, Ac-RVRR-AmLuc produced a higher bioluminescent signal than Ac-RYKR-AmLuc. In the absence of furin, both bioluminogenic probes generated negligible levels of bioluminescence (for example, at 1 min, for Ac-RVRR-AmLuc, 4.5×10^5 R.L.U., which is 3.8% of the signal observed in the presence of furin) demonstrating that both probes are stable and furin-specific (Figure 1B). The initial signals observed with three probes in the absence of furin are likely due to the trace amounts of D-aminoluciferin still present in the probes even after HPLC purification. This signal decreased with time as the trace D-aminoluciferin was consumed by the luciferase enzyme. At 30 min after the luciferase addition, the bioluminescent signal of Ac-RVRR-AmLuc in the presence of furin was 30-fold higher than that without furin. In contrast, the control probe Ac-RRKY-

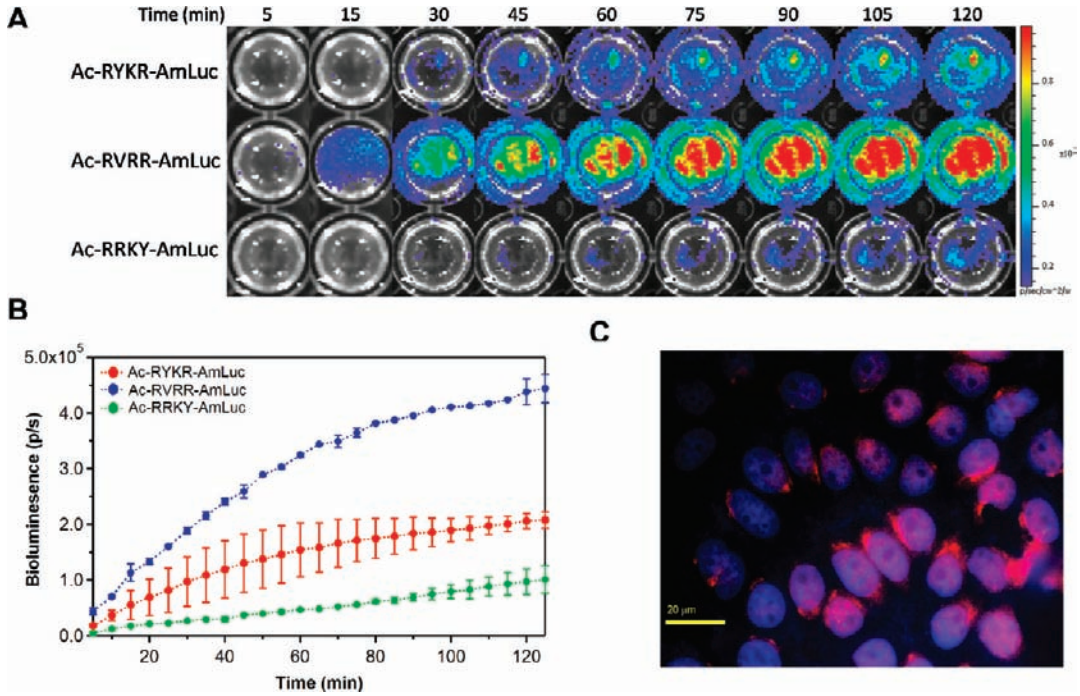

Figure 2. Furin activity detection in MDA-MB-468Fluc$^+$ cells. (A) Bioluminescence imaging of cells incubated with Ac-RYKR-AmLuc, Ac-RVRR-AmLuc, and Ac-RRKY-AmLuc at 2 μM. (B) Quantification of the bioluminescence signal; ROIs were drawn over individual wells, and the total flux in photon/s was plotted vs time for each probe. (C) Furin fluorescence immunostaining of MDA-MB-468 Fluc$^+$ cells. Red, furin (rhodamine-conjugated secondary antibody); blue, nucleus (DAPI).

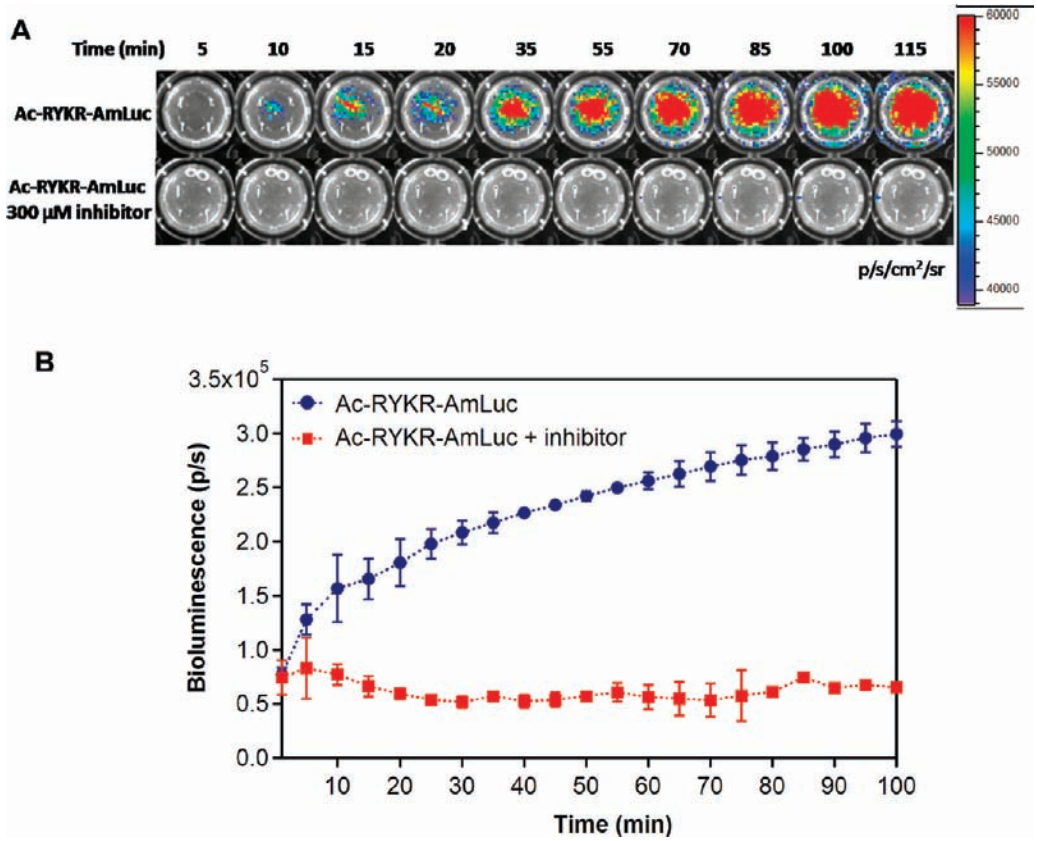

Figure 3. Imaging the furin inhibition in MDA-MB-468Fluc$^+$ cells. (A) Bioluminescence imaging of cells incubated with 20 μM Ac-RYKR-AmLuc in the absence or presence of 300 μM furin inhibitor. (B) Quantification of the bioluminescence signal; ROIs were drawn over individual wells, and the total flux in photon/s was plotted vs time.

AmLuc generated negligible light emission under identical conditions regardless of the presence of furin: 5.8×10^5 R.L.U at 1 min in the presence of furin and 5.6×10^5 R.L.U. in the absence of furin.

Bioluminescence Imaging of Furin Activity in Live Breast Cancer Cells. Next, we evaluated the capacity of the probes for detecting furin activity in live cells. It has been established that the majority of human breast cancer cells

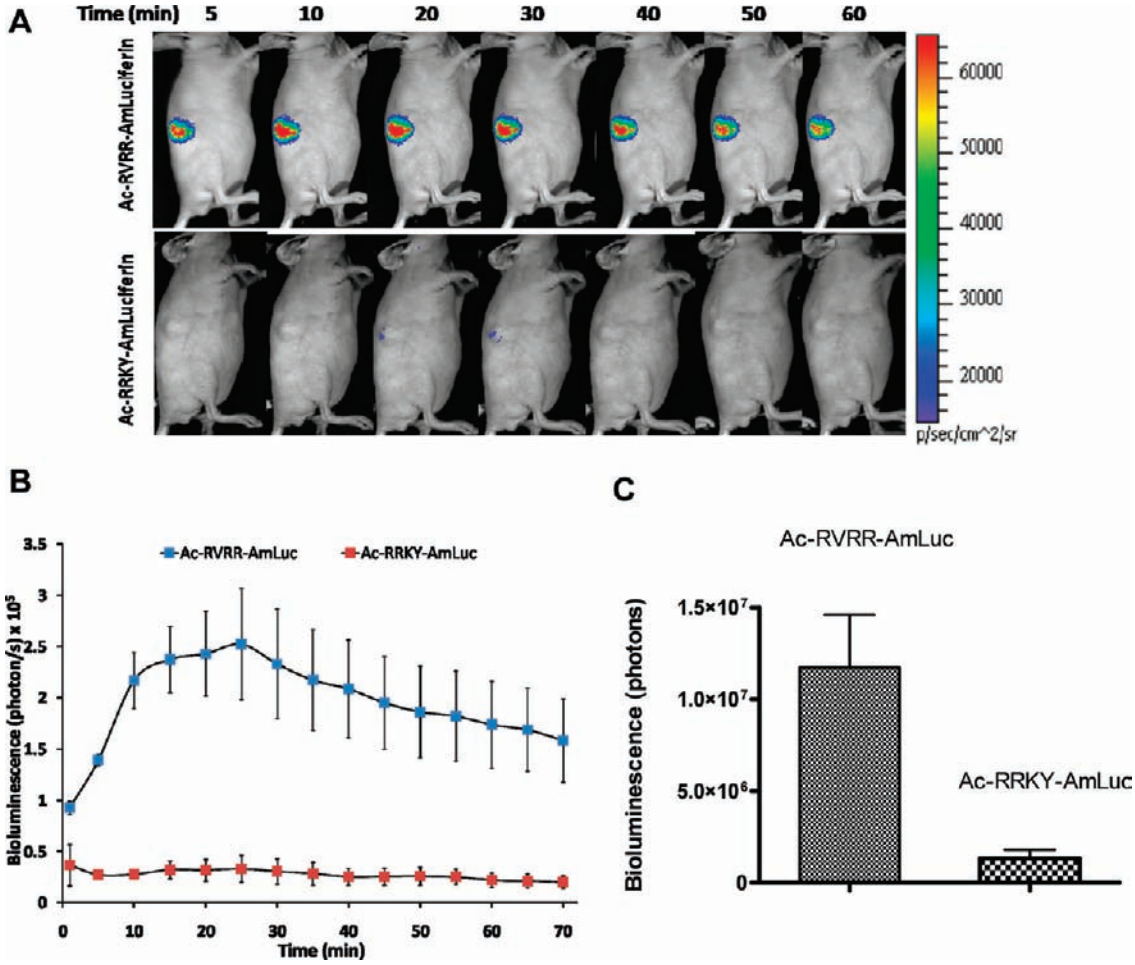

Figure 4. Bioluminescence imaging of furin activity in xenografted tumors in nude mice. (A) Representative bioluminescence imaging of furin activity in the implanted MDA-MB-468Fluc+ cells ($n = 4$). Images were acquired 1 min after tail vain injection of 100 μL (10 mM) of Ac-RVRR-AmLuc (top panel). After two days, the same protocol was applied with injecting Ac-RRKY-AmLuc in the same mice (lower panel). (B) Quantification of the total flux (photon/s) from the tumor area for Ac-RVRR-AmLuc and negative control, Ac-RRKY-AmLuc. (C) Integrated bioluminescence emission for mice injected with Ac-RVRR-AmLuc and Ac-RRKY-AmLuc; $p = 0.017$.

overexpress furin (*16*). We confirmed the expression of furin in breast cancer MDA-MB-468Fluc$^+$ cells by fluorescence immunostaining (Figure 2C), which showed strong furin staining predominantly in the trans-Golgi network, in agreement with previous reports (*27*). Consequently, we thus used this cell line to evaluate the probes for imaging furin activity. MDA-MB-468-Fluc$^+$ cells (3×10^5) were imaged at an interval of 5 min for 2 h after probe addition (2 μM) (Figure 2A). The signal from each well was quantified as photons/s and plotted as a function of time for each probe (Figure 2B). For both Ac-RVRR-AmLuc and Ac-RYKR-AmLuc, strong bioluminescent signals were detected, which gradually increased over time and nearly reached a plateau in 2 h. In contrast, the control probe showed just the background level of bioluminescence, which increased slightly in 2 h. After 60 min, Ac-RRVR-AmLuc generated ~6-fold higher bioluminescence signals in live cells than the control probe. This result correlates with the in vitro data observed with the probes, demonstrating that our probes are cell-permeable and can detect furin activity in live cells.

To further examine the kinetics of the probes in imaging furin activity in live cells, MDA-MB-468-Fluc$^+$ cells (3×10^5) were imaged for approximately 2 h starting immediately after the addition of 2, 10, or 20 μM Ac-RYKR-AmLuc (Figure 3A and Figure S6A, Supporting Information). The kinetics at 10 and 20 μM shared the same pattern with a fast increase in first 10 min followed by a slow increase, and the signal intensity was also similar, suggesting that intracellular furin was saturated at 10 μM of the probe (Figure 3B and Figure S6B, Supporting Information). At 2 μM, the bioluminescence signal gradually increased for 2 h and as expected, the intensity was lower than that at 10 or 20 μM (Figure S6B, Supporting Information).

Imaging the Inhibition of Furin Activity in Live Breast Cancer Cells. To demonstrate that the observed bioluminescent signal can be blocked by the furin inhibitor, we performed the same cell imaging study with Ac-RYKR-AmLuc in the presence of the inhibitor Decanoyl-RVKR-CMK (300 μM). The bioluminescence emission decreased significantly; for example, at 30 min, the bioluminescent signal for 20 μM of Ac-RYKR-AmLuc was 4-fold higher than that in the presence of the furin inhibitor (Figure 3A and B). This result further confirms that the bioluminogenic probe is specific to furin activity in MBA-MD-468 cells.

Imaging Furin Activity in Living Mice. Our in vitro and cell imaging data have indicated that the bioluminogenic probe Ac-RVRR-AmLuc produced a higher signal than Ac-RYKR-AmLuc; thus, Ac-RVRR-AmLuc was chosen for in vivo imaging of furin activity in tumor xenografts in nude mice. Ac-RVRR-AmLuc and the control Ac-RRKY-AmLuc were injected via the tail vain (100 μL of 10 mM probe in PBS) in the same tumor-bearing mice but two days apart. After injection, the animals were imaged every 5 min for 1 h (Figure 4A). For Ac-RVRR-AmLuc, the signal at the tumor site increased significantly at 10 min, peaked at 25 min, and then decreased slowly within 60 min (Figure 4B). In contrast, the control probe showed

low bioluminescence signals at the tumor site constantly over time (Figure 4B). The contrast between the two probes on average ($n = 4$ mice) reached 7.8-fold at 10 min and 7.6-fold between 25−35 min; at the same time point (25 min), the observed contrast between the two probes was 30-fold in vitro (Figure 1), and 7.1-fold in cell culture (Figure 2). Total emission from the tumors (substrates and control) was integrated over 1 h for all mice, and on average, the emission for Ac-RVRR-AmLuc was 8.7-fold higher than that of the control Ac-RRKY-AmLuc ($p = 0.017$) (Figure 4C). Histological staining of tumor dissections validated the expected expression of furin (Figure S7, Supporting Information). These results demonstrate that our bioluminogenic probes can specifically image furin activity in xenografted breast cancer tumors in mice.

DISCUSSION

Proteases as an important class of enzymes play vital roles in many biological processes such as cell replication, growth, differentiation, viral infection, tumor formation, and metastasis, and thus, extensive efforts have been made toward developing probes for imaging their activity in vivo (*28*−*30*). A generally used method is fluorescence-based by taking advantage of the enzymatic function of cleaving the amide bond between two adjacent amino acid residues to create smart or activatable probes through modulation of the fluorescence emission. It can be a specific peptide substrate sequence labeled by a fluorescent emitter at one side of the enzyme cleavage site and a light absorber (or fluorescent acceptor) at the other side of the cleavage site (*31, 32*), or fluorochromes attached to a polymer backbone via a specific peptide substrate (*33*−*35*). Because of fluorescence resonance energy transfer or proximity-based self-quenching, these probes emitted little fluorescence before encountering the target proteases, but enhanced fluorescent emission was observed from proteolytic activity. A similar concept has been applied to the bioluminescence-based method for imaging protease activity in vivo (*11, 12*). As shown in this work, it typically involves a conjugate between the substrate of a bioluminescent protein such as firefly luciferase and a synthetic peptide substrate. In comparison to fluorescence-based in vivo imaging, bioluminescence imaging offers greater sensitivity (*36*), although it requires the expression of luciferases at the target site.

After the initial demonstration of the commercially available DEVD-aminoluciferin substrate for imaging caspase-3 activity (*11, 12*), there have been few further reports of this method in the literature (*13*). The bioluminogenic probes we developed here for imaging furin activity represent a latest addition and further demonstrate the value and general applicability of this approach for imaging protease activity in vivo.

We have chosen the tetrapeptidyl substrates of furin over hexapeptidyl substrates even though hexapeptidyl substrates generally display more efficient hydrolytic kinetics because of the substrate inhibition observed with hexapeptidyl but not with tetrapeptidyl substrates (*37*). Between the two tetrapeptidyl probes we designed, Ac-RVRR-AmLuc showed higher activity than Ac-RYKR-AmLuc both in vitro and in vivo. Interestingly, similar substrates such as Boc-RVRR-MCA (Boc, *N-t*-butoxycarbonyl; MCA, methylcoumarinamide) have been reported to show less efficient kinetics (k_{cat}/K_m of 3.57×10^3 s^{-1} M^{-1} for furin purified from CHO cells) (*25, 26*) than Acetyl-RYKR-MCA (k_{cat}/K_m of 5.2×10^5 s^{-1} M^{-1} for human furin) (*24*), suggesting that the aminoluciferin group may have different effects than the coumarin moiety on the conjugate kinetics.

Furin has a strikingly diverse collection of physiological substrates from growth factors, hormones, receptors, and even other proteases, and plays crucial roles in development, homeostasis, and diseases ranging from anthrax, Ebola fever, Alzheimer's disease, and cancer (*15*). The previous fluorogenic substrate Boc-RVRR-MCA is just not useful to noninvasively image furin activity in vivo. Our bioluminogenic probes now fill in the gap and make the in vivo monitoring of furin activity in the same animals in real time feasible.

In summary, we report here caged bioluminogenic probes for imaging furin activity in vivo. The probes can be specifically activated by furin and produce bioluminescence emission in the presence of firefly luciferase in vitro, in living breast cancer cells, and in breast cancer tumor xenografts in mice. Noninvasive imaging of furin activity could provide a platform for in vivo assessment of furin-based prodrugs and screening of therapeutic furin inhibitors (*19*). Moreover, these bioluminogenic probes could allow for investigating the role of furin in hypoxia in vivo and provide a means for in vivo imaging of tumor hypoxia.

ACKNOWLEDGMENT

This work was supported by an IDEA award from Department of Defense Breast Cancer Research Program (W81XWH-09-1-0057) and the NCI's Small Animal Imaging Resource Program (SAIRP R24CA92862). We thank Dr. Contag (Stanford Medical School) for providing the MDA-MB-468 $Fluc^+$ cell line.

Supporting Information Available: Mass spectra of peptide amino-luciferin conjugates, imaging the furin inhibition in MDA-MB-468$Fluc^+$ cells (at 2 and 10 μM Ac-RYKR-AmLuc in the absence or presence of 300 μM furin inhibitor), and furin immunohistochemistry staining of tumor tissues. This material is available free of charge via the Internet at http://pubs.acs.org.

LITERATURE CITED

(1) Contag, C. H., and Bachmann, M. H. (2002) Advances in in vivo bioluminescence imaging of gene expression. *Annu. Rev. Biomed. Eng. 4*, 235–260.

(2) Contag, P. R., Olomu, I. N., Stevenson, D. K., and Contag, C. H. (1998) Bioluminescent indicators in living mammals. *Nat. Med. 4*, 245–247.

(3) Bhaumik, S., and Gambhir, S. S. (2002) Optical imaging of *Renilla* luciferase reporter gene expression in living mice. *Proc. Natl. Acad. Sci. U.S.A. 99*, 377–382.

(4) Drake, J. M., Gabriel, C. L., and Henry, M. D. (2005) Assessing tumor growth and distribution in a model of prostate cancer metastasis using bioluminescence imaging. *Clin. Exp. Metastasis 22*, 674–684.

(5) Rehemtulla, A., Stegman, L. D., Cardozo, S. J., Gupta, S., Hall, D. E., Contag, C. H., and Ross, B. D. (2000) Rapid and quantitative assessment of cancer treatment response using in vivo bioluminescence imaging. *Neoplasia 2*, 491–495.

(6) Shah, K., Jacobs, A., Breakefield, X. O., and Weissleder, R. (2004) Molecular imaging of gene therapy for cancer. *Gene Ther. 11*, 1175–1187.

(7) Pichler, A., Prior, J., and Piwnica-Worms, D. (2004) Imaging reversal of multidrug resistance in living mice with bioluminescence: MDR1 P-glycoprotein transports coelenterazine. *Proc. Natl. Acad. Sci. U.S.A. 101*, 1702–1707.

(8) De, A., and Gambhir, S. S. (2005) Noninvasive imaging of protein-protein interactions from live cells and living subjects using bioluminescence resonance energy transfer. *FASEB J. 19*, 2017–2019.

(9) Luker, G. D., Sharma, V., Pica, C. M., Dahlheimer, J. L., Li, W., Ochesky, J., Ryan, C. E., Piwnica-Worms, H., and Piwnica-Worms, D. (2002) Noninvasive imaging of protein-protein interactions in living animals. *Proc. Natl. Acad. Sci. U.S.A. 99*, 6961–6966.

(10) Gross, S., and Piwnica-Worms, D. (2005) Spying on cancer: molecular imaging in vivo with genetically encoded reporters. *Cancer Cell 7*, 5–15.
(11) Shah, K., Tung, C. H., Breakefield, X. O., and Weissleder, R. (2005) In vivo imaging of S-TRAIL-mediated tumor regression and apoptosis. *Mol. Ther. 11*, 926–931.
(12) Liu, J. J., Wang, W., Dicker, D. T., and El-Deiry, W. S. (2005) Bioluminescent imaging of TRAIL-induced apoptosis through detection of caspase activation following cleavage of DEVD aminoluciferin. *Cancer Biol. Ther. 4*, 885–892.
(13) Yao, H., So, M.-K., and Rao, J. (2007) A bioluminogenic substrate for in vivo imaging of beta-lactamase activity. *Angew. Chem., Intl. Ed. 46*, 7031–7034.
(14) Bassi, D. E., Fu, J., de Cicco, R. L., and Klein-Szanto, A. J. P. (2005) Proprotein convertases: "master switches" in the regulation of tumor growth and progression. *Mol. Carcinog. 44*, 151–161.
(15) Thomas, G. (2002) Furin at the cutting edge: from protein traffic to embryogenesis and disease. *Nat. Rev. Mol. Cell Biol. 3*, 753–766.
(16) Cheng, M., Watson, P. H., Paterson, J. A., Seidah, N., Chretien, M., and Shiu, R. P. (1997) Pro-protein convertase gene expression in human breast cancer. *Int. J. Cancer 71*, 966−971.
(17) McMahon, S., Grondin, F., McDonald, P. P., Richard, D. E., and Dubois, C. M. (2005) Hypoxia-enhanced expression of the proprotein convertase furin is mediated by hypoxia-inducible factor-1. *J. Biol. Chem. 280*, 6561–6569.
(18) Bassi, D. E., De Cicco, R. L., Mahloogi, H., Zucker, S., Thomas, G., and Klein-Szanto, A. J. P. (2001) Furin inhibition results in absent or decreased invasiveness and tumorigenicity of human cancer cells. *Proc. Natl. Acad. Sci. U.S.A. 98*, 10326–10331.
(19) Coppola, J. M., Bhojani, M. S., Ross, B. D., and Rehemtulla, A. (2008) A small-molecule furin inhibitor inhibits cancer cell motility and invasiveness. *Neoplasia 10*, 363–370.
(20) Hosaka, M., Nagahama, M., Kim, W. S., Watanabe, T., Hatsuzawa, K., Ikemizu, J., Murakami, K., and Nakayama, K. (1991) Arg-X-Lys/Arg-Arg motif as a signal for precursor cleavage catalyzed by furin within the constitutive secretory pathway. *J. Biol. Chem. 266*, 12127–12130.
(21) Henrich, S., Cameron, A., Bourenkov, G. P., Kiefersauer, R., Huber, R., Lindberg, I., Bode, W., and Than, M. E. (2003) The crystal structure of the proprotein processing proteinase furin explains its stringent specificity. *Nat. Struct. Biol. 10*, 520–526.
(22) White, E. H., Worther, H., Seliger, H. H., and McElroy, W. D. (1966) Amino analogs of firefly luciferase and biological activity thereof. *J. Am. Chem. Soc. 88*, 2015–2019.
(23) Shinde, R., Perkins, J., and Contag, C. H. (2006) Luciferin derivatives for enhanced in vitro and in vivo bioluminescence assays. *Biochemistry 45*, 11103–11112.
(24) Krysan, D. J., Rockwell, N. C., and Fuller, R. S. (1999) Quantitative characterization of furin specificity. *J. Biol. Chem. 274*, 23229–23234.
(25) Hatsuzawa, K., Nagahama, M., Takahashi, S., Takada, K., Murakami, K., and Nakayama, K. (1992) Purification and characterization of furin, a Kex2-like processing endoprotease, produced in Chinese hamster ovary cells. *J. Biol. Chem. 267*, 16094–16099.
(26) Molloy, S. S., Bresnahan, P. A., Leppla, S. H., Klimpel, K. R., and Thomas, G. (1992) Human furin is a calcium-dependent serine endoprotease that recognizes the sequence Arg-X-X-Arg and efficiently cleaves anthrax toxin protective antigen. *J. Biol. Chem. 267*, 16396–16402.
(27) Shapiro, J., Sciaky, N., Lee, J., Bosshart, H., Angeletti, R. H., and Bonifacino, J. S. (1997) Localization of endogenous furin in cultured cell lines. *J. Histochem. Cytochem. 45*, 3–12.
(28) Funovics, M., Weissleder, R., and Tung, C. H. (2003) Protease sensors for bioimaging. *Anal. Bioanal. Chem. 377*, 956–963.
(29) Tung, C. H. (2004) Fluorescent peptide probes for in vivo diagnostic imaging. *Biopolymers 76*, 391–403.
(30) Law, B., and Tung, C. H. (2009) Proteolysis: A biological process adapted in drug delivery, therapy, and imaging. *Bioconjugate Chem.* [Online early access], DOI: 10.1021/bc800500a, published online Mar 9, 2009.
(31) Pham, W., Choi, Y., Weissleder, R., and Tung, C. H. (2004) Developing a peptide-based near-infrared molecular probe for protease sensing. *Bioconjugate Chem. 15*, 1403–1407.
(32) Lee, S., Park, K., Lee, S. Y., Ryu, J. H., Park, J. W., Ahn, H. J., Kwon, I. C., Youn, I. C., Kim, K., and Choi, K. (2008) Dark quenched matrix metalloproteinase fluorogenic probe for imaging osteoarthritis development in vivo. *Bioconjugate Chem. 19*, 1743–1747.
(33) Weissleder, R., Tung, C. H., Mahmood, U., and Bogdanov, A. (1999) In vivo imaging of tumors with protease-activated near-infrared fluorescent probes. *Nat. Biotechnol. 17*, 375–378.
(34) Bremer, C., Tung, C. H., and Weissleder, R. (2001) In vivo molecular target assessment of matrix metalloproteinase inhibition. *Nat. Med. 7*, 743–748.
(35) Law, B., Curino, A., Bugge, T. H., Weissleder, R., and Tung, C. H. (2004) Design, synthesis, and characterization of urokinase plasminogen-activator-sensitive near-infrared reporter. *Chem. Biol. 11*, 99–106.
(36) Troy, T., Jekic-McMullen, D., Sambucetti, L., and Rice, B. (2004) Quantitative comparison of the sensitivity of detection of fluorescent and bioluminescent reporters in animal models. *Mol. Imaging 3*, 9–23.
(37) Rockwell, N. C., Krysan, D. J., Komiyama, T., and Fuller, R. S. (2002) Precursor processing by Kex2/furin proteases. *Chem. Rev. 102*, 4525–4538.

BC9002508

Supplementary Information

In vivo bioluminescence imaging of furin activity in breast cancer cells using luminogenic substrates

Anca Dragulescu-Andrasi, Gaolin Liang, and Jianghong Rao

Department of Radiology, Molecular Imaging Program at Stanford, Bio-X Program, and Cancer Biology Program, Stanford University School of Medicine, Stanford, California

1. Figures S1-S5. Mass spectra of peptide amino-luciferin conjugates.

2. Figure S6. Imaging the furin inhibition in MDA-MB-468Fluc+ cells.

3. Figure S7. Furin immunohistochemistry staining of tumor tissues.

1. Supplementary Figures S1-S5. Mass spectra of peptide amino-luciferin conjugates.

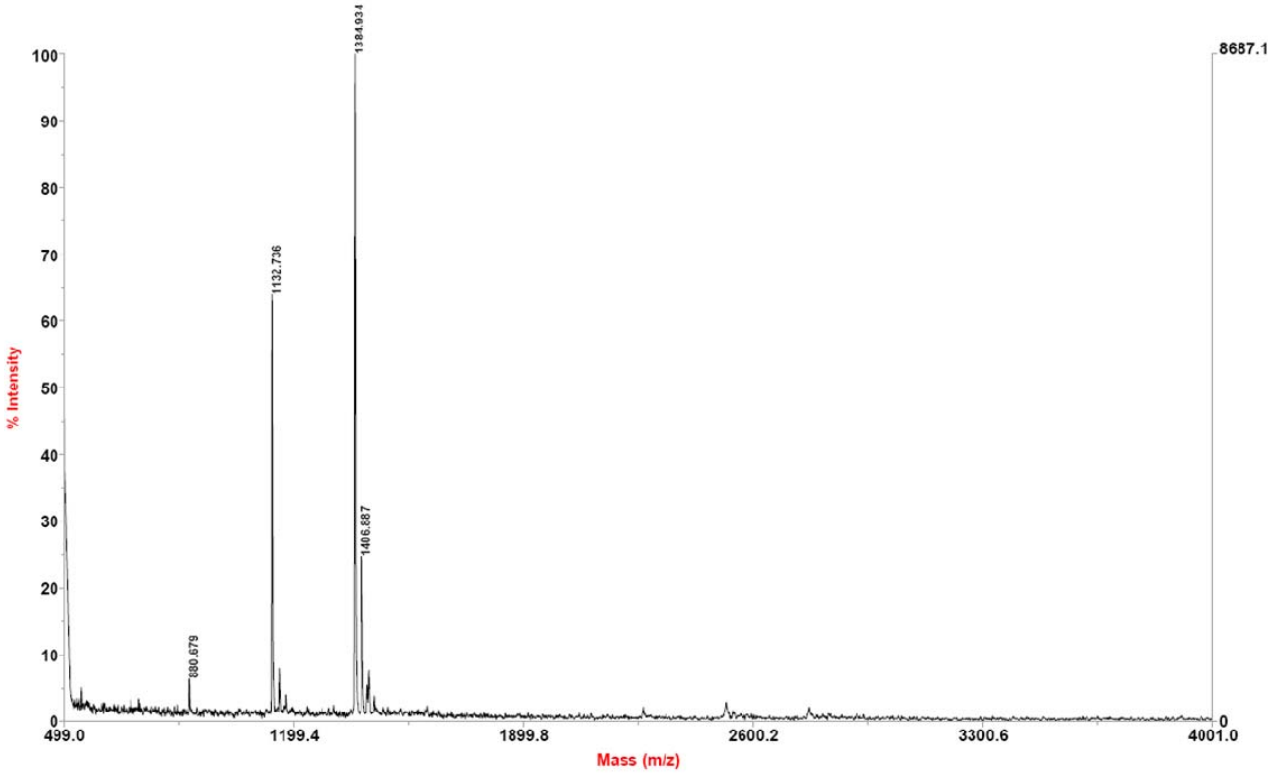

S1. MALDI-MS for Ac-R(Pbf)VR(Pbf)R(Pbf)-COOH. Calculated $[M+H]^+$: 1384.64 Observed $[M+H]^+$: 1384.93 and $[M\text{-}Pbf]^+$:1132.73.

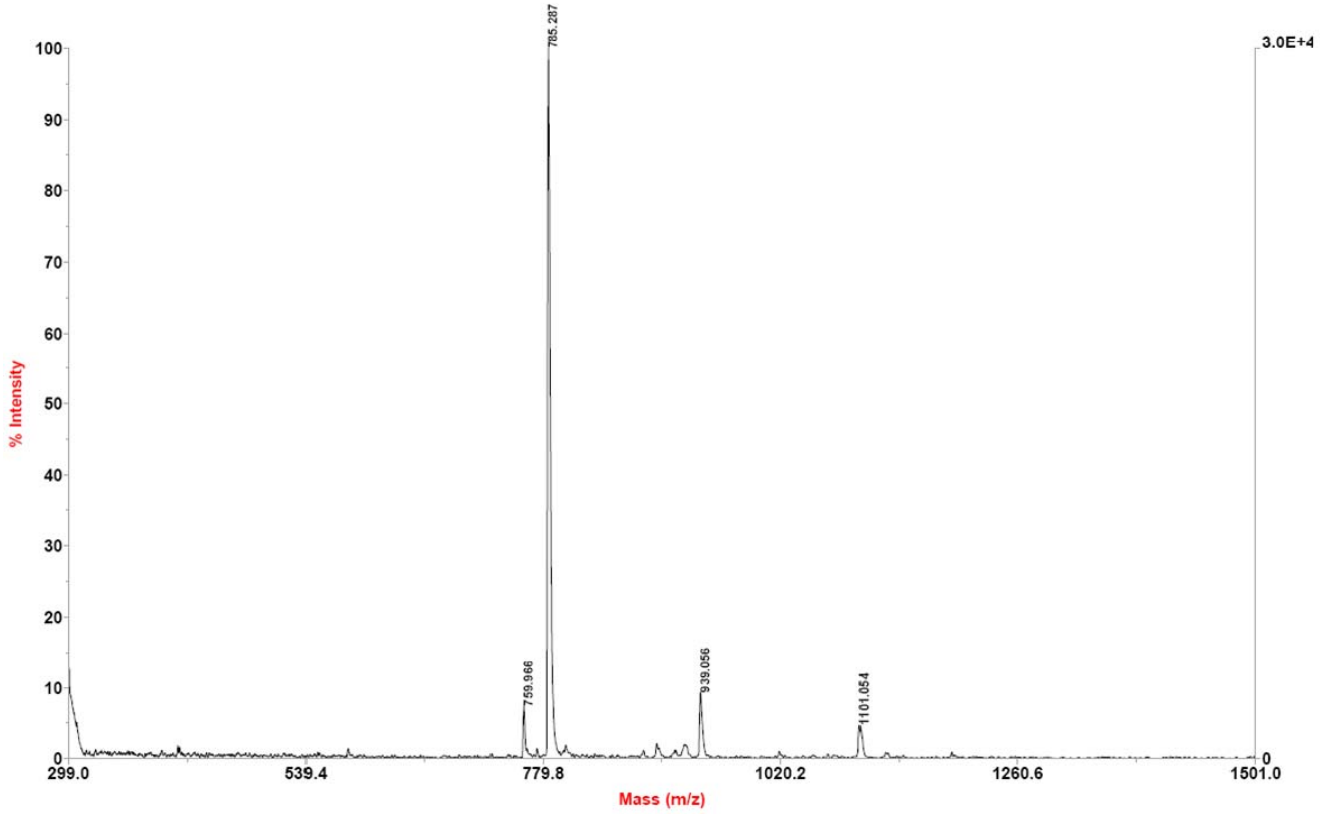

S2. MALDI-MS for Ac-RVRR-CABT. Calculated $[M+H]^+$: 785.4 Observed $[M+H]^+$: 785.3.

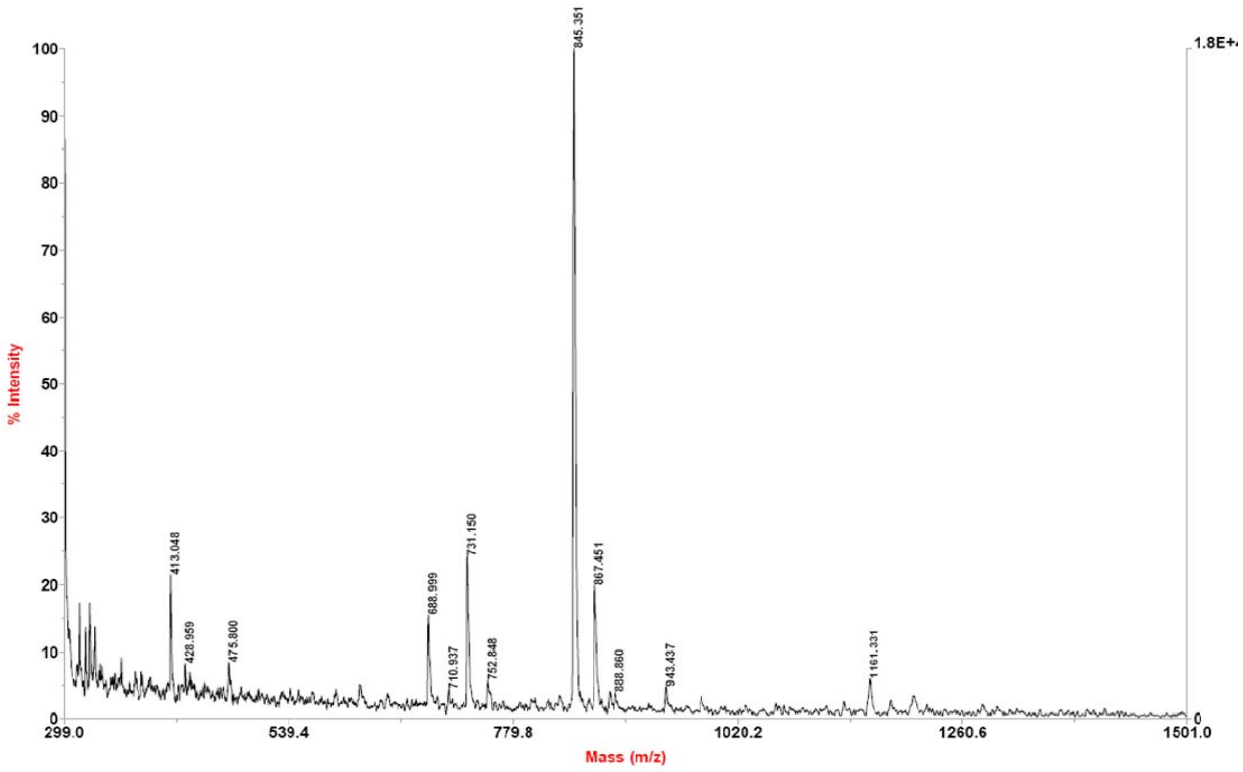

S3. MALDI-MS for Ac-RVRR-AmLuc. Calculated $[M\text{-}CO_2]^+$: 845.41 Observed $[M\text{-}CO_2]^+$: 845.35.

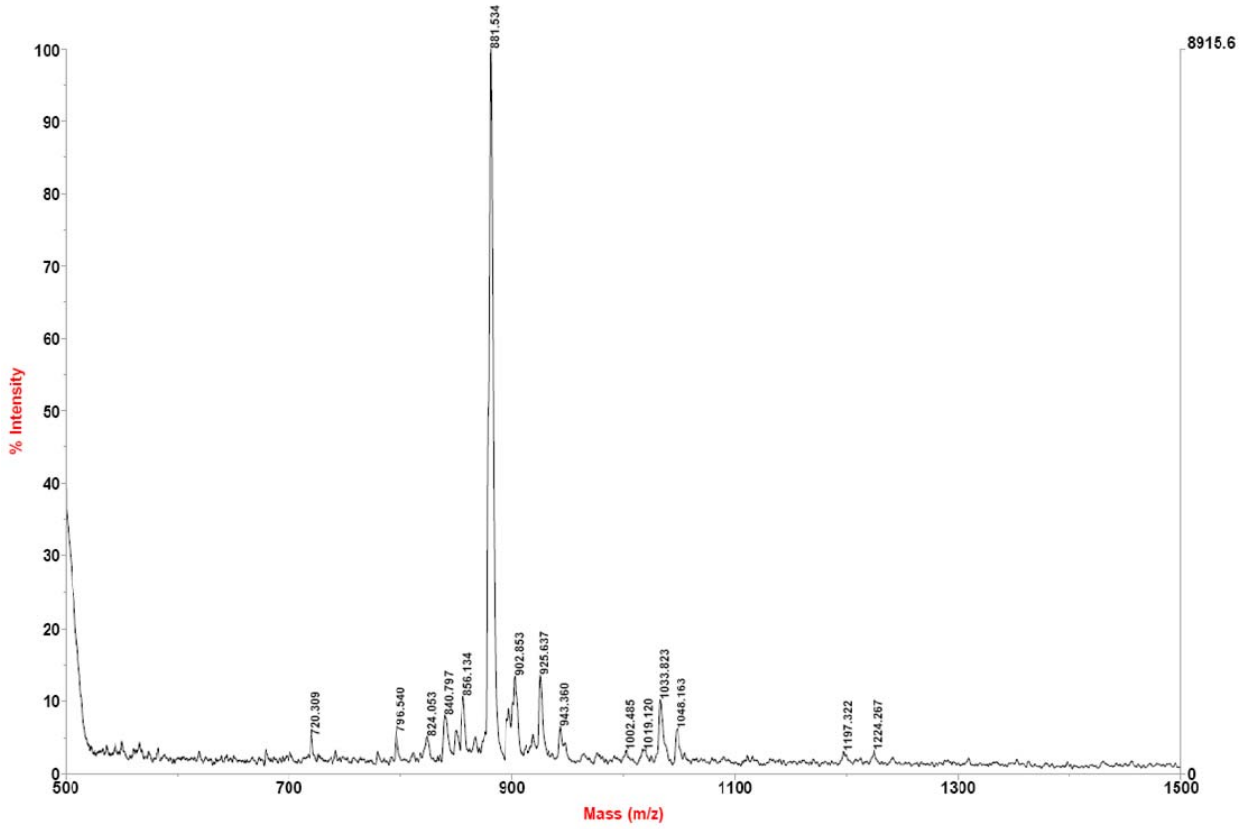

S4. MALDI-MS for Ac-RYKR-AmLuc. Calculated $[M\text{-}CO_2]^+$: 881.39 Observed $[M\text{-}CO_2]^+$: 881.53.

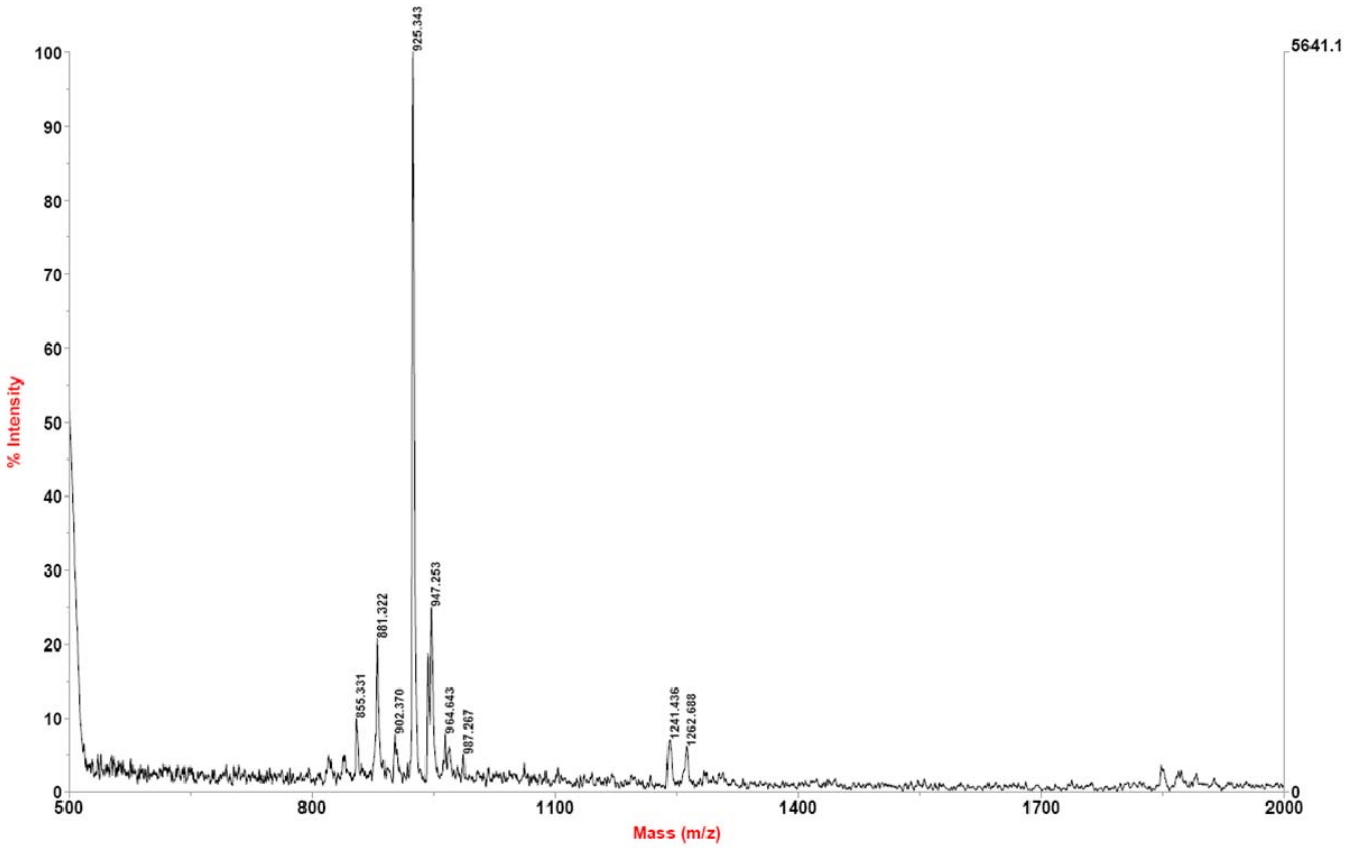

S5. MALDI-MS for Ac-RRKY-AmLuc. Calculated $[M+H]^+$: 925.38 Observed $[M+H]^+$: 925.34.

2. Figure S6. Imaging the furin inhibition in MDA-MB-468Fluc+ cells. *A*. Bioluminescence imaging of cells incubated with 2 and 10 μM of Ac-RYKR-AmLuc in the absence and in the presence of 300 μM furin inhibitor. *B*. Quantification of the bioluminescence signal; ROIs were drawn over individual wells and the total flux in photon/s was plotted vs. time.

A.

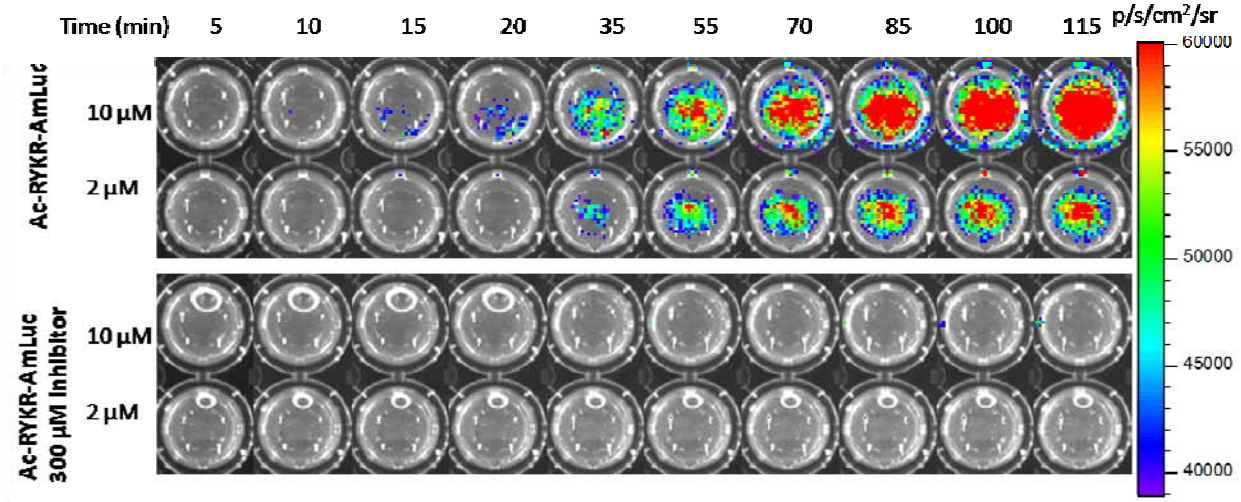

B.

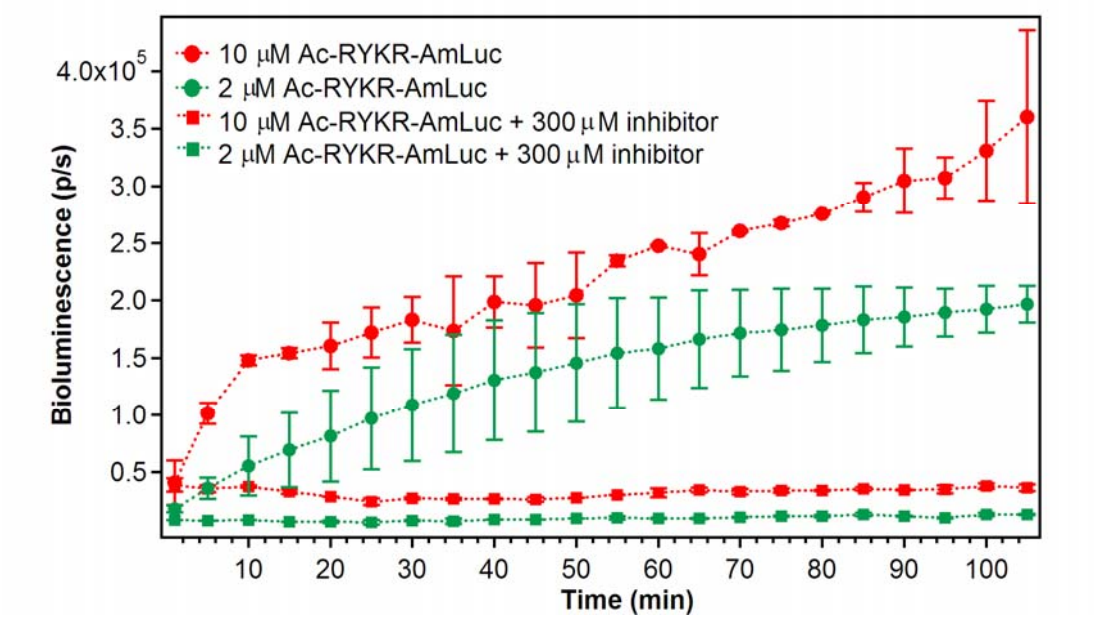

3. Figure S7. Furin immunohistochemistry staining of tumor tissues with anti-furin rabbit polyclonal antibody followed by anti-rabbit polyclonal goat IgG antibody conjugated with rhodamine (red). The nucleus was stained with DAPI (blue). Size bar represents 20 μm.

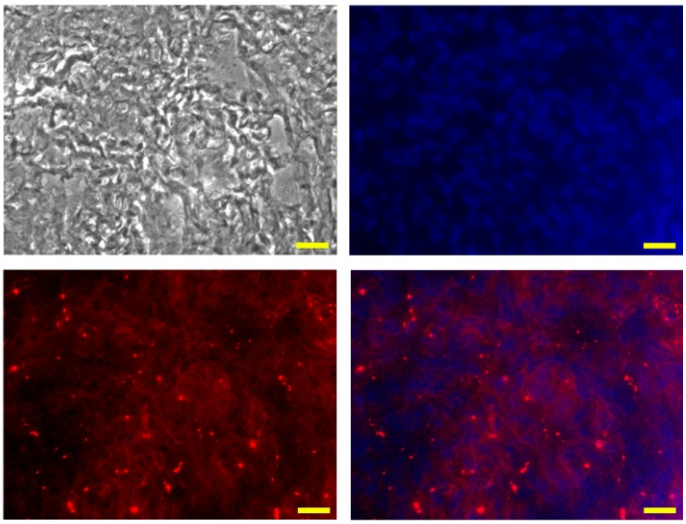

Tris-Nitrilotriacetic Acids of Subnanomolar Affinity Toward Hexahistidine Tagged Molecules

Zhaohua Huang,[†] Peter Hwang,[‡] Douglas S. Watson,[†] Limin Cao,[†] and Francis C. Szoka, Jr.*[,†]

Department of Bioengineering and Therapeutic Sciences, University of California, San Francisco, California 94143-0912, and Department of Biochemistry and Biophysics, University of California, San Francisco, California 94143-2240. Received July 13, 2009

Nitrilotriacetic acid (NTA) has moderate affinity (10 μM) for hexahistidine (His6) and is widely used in the purification of His6-tagged proteins. The affinity can be increased significantly (10 nM) through multivalency such as using a tris-NTA. We show that the binding affinity of tris-NTA is dependent on the flexibility and length of the spacer between the mono-NTA and the scaffold: the shorter the spacer, the higher the affinity. A series of biotinylated tris-NTA having different spacers were synthesized and used to prepare tris-NTA sensor chips for surface plasmon resonance measurement of binding affinity. Subnanomolar affinity can be achieved with a short spacer. The new high-affinity tris-NTA enables the formation of stable complexes with hexahistidine containing molecules and provides a convenient method to noncovalently attach proteins to various surfaces.

INTRODUCTION

Nitrilotriacetic acid (NTA) and its derivatives have broad applications in the manipulation of hexahistidine (His6) tagged proteins such as in immobilized metal affinity chromatography (*1*, *2*), crystallization on lipid template (*3*), fluorescent labeling (*4*−*7*), and surface immobilization (*8*). The advantages of the NTA-His6 interaction are reversibility and selectivity. However, the relatively weak affinity (equilibrium dissociation constant $K_D \sim 10$ μM) between mono-NTA and His6 makes such technology unsuitable for applications where high affinity is required. Recent studies from Lata (*9*), van Broekhoven (*10*), and Huang (*11*) have demonstrated that a significant increase of binding affinity of NTA with His6-tagged proteins can be achieved through multivalency. For example, tris-NTA has a K_D around 10 nM toward His6-tagged proteins. Furthermore, the development of multifunctional tris-NTA provides a useful toolbox for the analysis and modification of His6-tagged proteins.

An important issue that has not been addressed is the influence of tris-NTA structure on the binding affinity. It remains a challenge to accurately predict the best scaffold and linker for a multivalent molecule (*12*). In the synthesis of tris-NTA, Lata used a tetraaza cyclam scaffold and glutamic acid spacer resulting in a K_D of 20 nM (*9*). We employed a dendritic lysine scaffold and a lysine spacer leading to a similar K_D (5−20 nM depending on the structure of His6-tagged protein) (*11*). Although the current generation of tris-NTAs exhibit high affinity, the interaction between the tris-NTA and His6 may not be strong enough to keep the conjugate intact in the biological environment, especially at a low concentration. Thus, it would be of interest to determine if higher-affinity multi-NTA molecules can be obtained by changing the spacer between the scaffold and the mono-NTA (Figure 1). Here, we report the structure−affinity relationship on modified tris-NTA and the realization of subnanomolar affinity with shorter spacers.

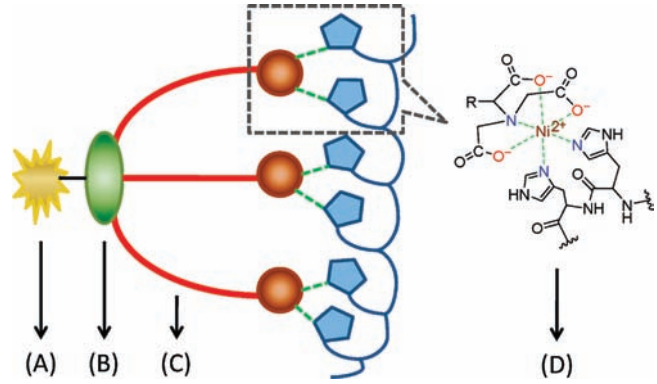

Figure 1. Schematic illustration of tris-NTA/His6 tag binding pair. (A) Functional unit. (B) Scaffold. (C) Spacer. (D) Structure of NTA/Ni^{2+}/His2. The flexibility and the length of the spacer play an important role in the overall binding affinity of tris-NTA toward His6 tag.

EXPERIMENTAL PROCEDURES

Materials and Methods. H-Lys(Z)-OtBu.HCl and H-Orn(Z)-OtBu.HCl were from BACHEM (Torrance, CA). N-CBZ-amido-dPEG4-acid was from QuantaBioDesign (Powell, OH). Other reagents were from Aldrich (Milwaukee, WI). ^{1}H NMR (400 MHz) spectra were recorded on a Varian 400 MHz instrument. Chemical shifts are expressed as parts per million using tetramethylsilane as internal standard. *J* values are in hertz. MALDI-TOF mass spectra were obtained at the Mass Spectrometry Facility, University of California, San Francisco. TLC analyses were performed on 0.25 mm silica gel F_{254} plates. High-performance flash chromatography (HPFC) was carried out on a Biotage (Charlottesville, VA) Horizon system with prepacked silica gel columns (60 Å, 40−63 μm). Unless noted otherwise, the ratios describing the composition of solvent mixtures represent relative volumes.

General Chemistry. Biotin−tris-NTAs (**6a**−**e**) were synthesized according to the previously published method for **6b** (*11*). The general synthetic route was outlined in Scheme 1. Various spacers were introduced in *tert*-butyl protected amino-

* To whom correspondence should be addressed. Tel: (415) 476-3895; Fax: (415) 476-0688; E-mail: szoka@cgl.ucsf.edu.
[†] Department of Bioengineering and Therapeutic Sciences.
[‡] Department of Biochemistry and Biophysics.

10.1021/bc900309n CCC: $40.75 © 2009 American Chemical Society
Published on Web 08/03/2009

Scheme 1. General Synthetic Route for Biotin−tris-NTA

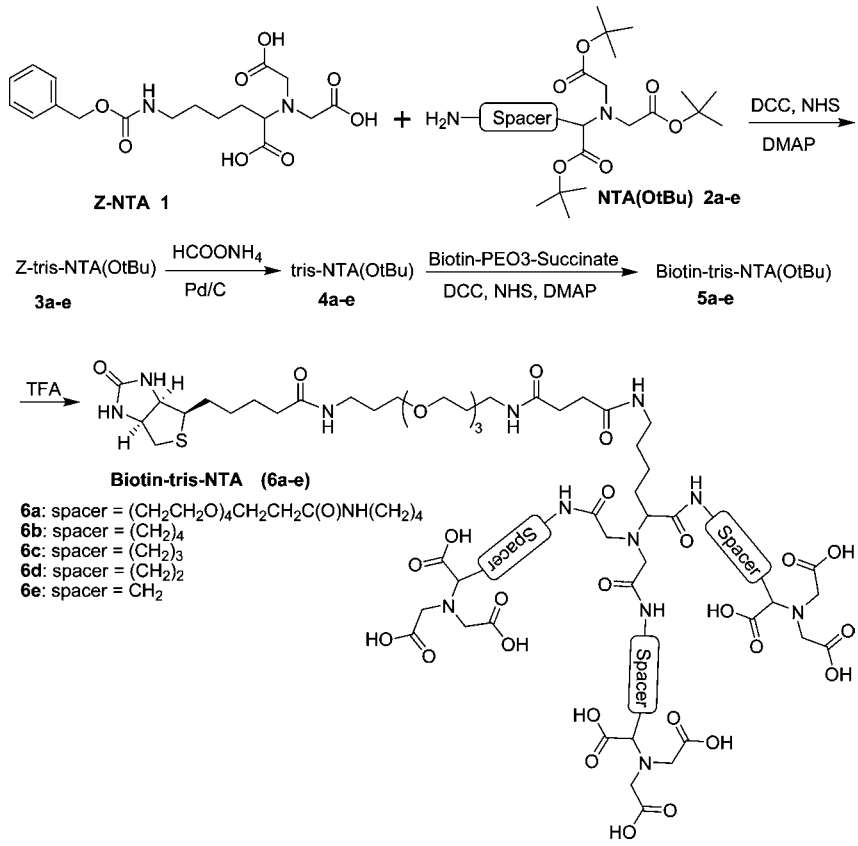

Scheme 2. Synthesis of Amino-NTA(O-tBu)[a]

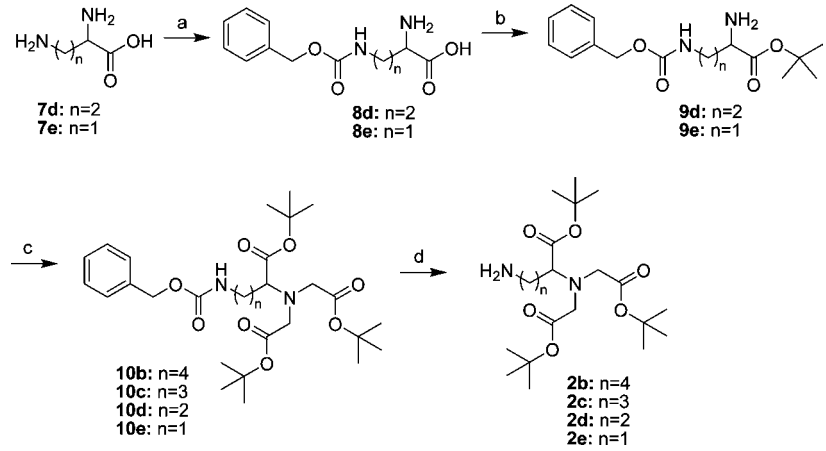

[a] (a) Benzyl chloroformate (1 equiv), pH 7.0 phosphate buffer, r.t.; (b) 2-methylpropene, conc H_2SO_4, dioxane, r.t.; (c) *tert*-butyl bromoacetate (4 equiv), DIPEA, DMF, 55 °C; (d) HCO_2NH_4 (6 equiv), 10% Pd/C, 90% methanol, 40 °C.

mono-NTA (**2a**−**e**) by using different amino acids as the starting material. Compounds **2b**,**c** were synthesized by using commercially available H-Lys(Z)-OtBu.HCl and H-Orn(Z)-OtBu.HCl, respectively. For the synthesis of compounds **2d**,**e**, 2,4-diaminobutyric acid and 2,3-diaminopropionic acid were selectively protected by the carbobenzyloxy (Z) group and *tert*-butyl group first, then converted to amino-mono-NTA by the same method as **2b** (Scheme 2). Compound **2a** was obtained by the coupling of N-CBZ-amido-dPEG4-acid to **2b** followed by the removal of the Z group (Scheme 3).

*2-Amino-3-(benzyloxycarbonylamino)propanoic Acid (**8e**) (13).* 2,3-Diaminopropanoic acid (10 g, 71.1 mmol) was dissolved in 150 mL pH 7 phosphate buffer. The pH of the solution dropped to 5.5 initially and was adjusted to 6.8 with 1 M sodium hydroxide. A solution of benzyl chloroformate (10.2 mL, 71.1 mmol) in 10 mL toluene was added dropwise into the reaction mixture with vigorous stirring at 0 °C over 80 min. The pH of the mixture was monitored with a pH meter and maintained between 6.7 and 7.0 by addition of 1 M sodium hydroxide. The mixture was kept at 0 °C for another 4 h after the completion of addition, then 8 h reaction at room temperature. The white precipitate was collected by filtration and washed with water and ether consecutively. The white solid was recrystallized from water. Yield: 12.8 g, 71%.

*tert-Butyl 2-amino-3-(benzyloxycarbonylamino)propanoate (**9e**) (14).* Compound **8e** (5 g, 21 mmol) was suspended in anhydrous dioxane (40 mL) in a 150 mL pressure vessel. After the addition of 4 mL conc H_2SO_4, the suspension turned clear.

Scheme 3. Synthesis of 2a[a]

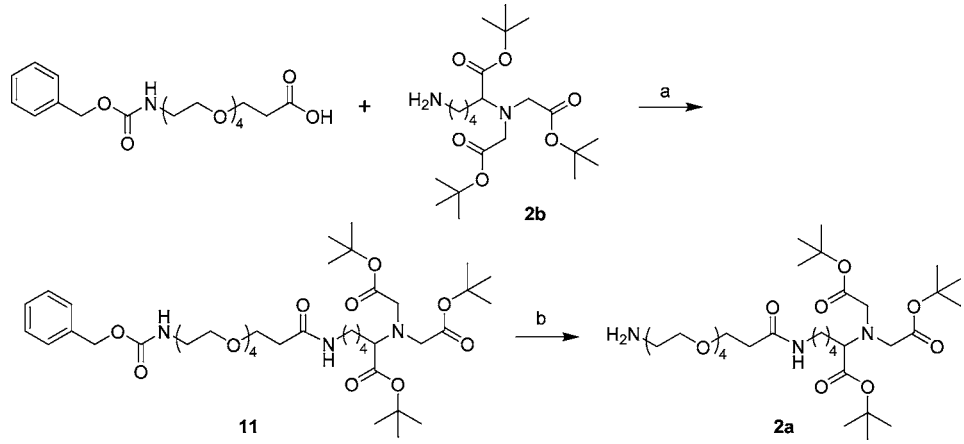

[a] (a) DCC (1.2 equiv), DMAP, dry $CHCl_3$, r.t.; (b) HCO_2NH_4 (6 equiv), 10% Pd/C, 90% methanol, 40 °C.

Isobutene (ca. 50 mL, cooled by dry ice−acetone bath) was poured into the solution, and the vessel was sealed. After 16 h reaction at room temperature, the cap of the vessel was carefully loosened and the pressure was released slowly. The reaction mixture was poured into a mixture of cold ether and 1 M NaOH (150 mL/210 mL) in a separation funnel and shaken well. The ether layer was collected. The aqueous layer was washed with 100 mL cold ether. The ether layers were combined and dried over anhydrous sodium sulfate, evaporated under reduced pressure, and placed under high vacuum. Yield: 5.0 g. TLC: R_f = 0.52 in $CHCl_3$−MeOH (6:1). ^{1}H NMR ($CDCl_3$) δ: 1.46 (s, 9H); 3.29 (m, 2H); 3.48 (m, 1H); 5.08 (s, 2H); 5.92 (br, 1H); 7.33 (m, 5H).

*Compound **10e.*** Compound **10e** was synthesized according to the method of **10b** (*11*). ^{1}H NMR ($CDCl_3$) δ: 1.45 (s, 9H); 1.47 (s, 18H); 3.08 (m, 1H); 3.40 (m, 1H); 3.44 (m, 4H); 5.12 (s, 2H); 6.42 (br, 1H); 7.33 (m, 5H).

*Compound **2e.*** Compound **2e** was synthesized according to the method of **2b**. ^{1}H NMR ($CDCl_3$) δ: 1.45 (s, 9H); 1.47 (s, 18H); 2.86 (m, 1H); 3.36 (m, 5H); 3.72 (m, 1H); 4.9 (br, 2H).

*Compound **11.*** To a solution of N-CBZ-amido-dPEG4-COOH (1 g, 2.5 mmol) and **2b** (1.08 g, 2.5 mmol) in dry chloroform were added dimethylaminopyridine (cat.) and dicyclohexylcarbodimide (0.62 g, 3 mmol). The mixture was stirred at room temperature for 48 h. White precipitate was filtered off, and the filtrate was concentrated and applied to HPFC. The crude product was purified on a silica gel flash column with a gradient elution (1−5% methanol in chloroform). Yield: 1.7 g. TLC: R_f = 0.77 in $CHCl_3$−MeOH (9:1). ^{1}H NMR ($CDCl_3$) δ: 1.45 (s, 9H); 1.47 (s, 18H); 1.51 (m, 3H), 1.64 (m, 3H); 2.45 (t, J = 4.5, 2H); 3.22 (m, 2H); 3.28 (m, 1H); 3.40 (m, 2H), 3.44 (s, 2H), 3.46 (s, 2H); 3.60 (m, 14H), 3.71 (t, J = 4.2, 2H); 5.11 (s, 2H); 5.41 (br, 1H); 6.47 (br, 1H); 7.35 (m, 5H).

*Compound **2a.*** To a solution of **11** (1.58 g, 1.95 mmol) in methanol (35 mL) under nitrogen were added 10% Pd/C (0.2 g) and ammonium formate (1.4 g, 22 mmol) solution in 1 mL water and 9 mL methanol sequentially. The reaction mixture was vigorously stirred for 4 h under nitrogen at 40 °C. Pd/C was filtered off over Celite 545, and the filtrate was evaporated under reduced pressure. The residual was azeotropically dried with toluene. The crude product was purified by HPFC (10−18% methanol in chloroform). Yield: 1.2 g, 90% wrt **11**. TLC: R_f = 0.1 in chloroform−methanol (9:1). ^{1}H NMR confirmed the removal of CBZ group from **11**.

*Compound **6a.*** Compound **6a** was synthesized according to the method of **6b**. ^{1}H NMR ($CDCl_3$) δ: 1.32−1.78 (m, 34H); 2.38 (m, 6H); 2.52 (m, 4H); 2.62 (m, 2H); 2.80 (m, 2H); 3.14−3.30 (m, 18H); 3.37−3.63 (m, 45H); 3.76 (br, 26H); 4.22 (m, 1H); 4.41 (m, 1H).

*Compounds **6c−e.*** Compounds **6c−e** were synthesized according to the method of **6b**. Their ^{1}H NMR spectra were similar to that of **6b**. The mass of all biotin−tris-NTA (**6a−e**) were confirmed by MALDI-MS using 2,5-dihydroxybenzoic acid as matrix.

Synthesis of His6-peptide. His6-peptide (N−C sequence: GWGGHHHHHHG) was synthesized on an ABI 433A automated peptide synthesizer (Applied Biosystems) by solid-phase 9*H*-fluoren-9-ylmethoxycarbonyl chemistry according to standard Fastmoc procedures (*15*). The peptide was cleaved from the resin with 94% trifluoroacetic acid in the presence of water, ethanedithiol, and triisopropylsilane. The free peptide was separated from the resin by filtration followed by precipitation in cold diethyl ether. Peptide synthesis reagents were obtained from Novabiochem. The molecular weight of His6-peptide was confirmed by MALDI mass spectrometry (Voyager DE, Applied Biosystems) using α-cyano-4-hydroxycinnamic acid as matrix (Calcd 1254.3, found 1255.4). Lyophilized peptide was stored at −20 °C until use.

Peptide stock solutions of 1 to 5 mM were prepared by dissolution of lyophilized powders in ultrapure water (Milli-Q, Millipore) and filtration through 0.2 μm PTFE membranes (Whatman). Stock concentrations were determined by tryptophan absorbance at 280 nm as described by Pace (*16*). Each concentration measurement represented the mean of three dilutions, each providing absorbance values between 0.1 and 1.1. Prior to the SPR experiment, His6-peptide was further diluted to working concentrations in the SPR running buffer.

Surface Plasmon Resonance Experiment. Preparation of tris-NTA sensor chip (Figure 2A): A Series S Sensor Chip SA (Biacore, Piscataway, NJ) was pretreated with two injections of 50 mM NaOH in 1 M NaCl (20 μL/min, 60 s), then washed with pH 7.4 HBS-P running buffer until the baseline was stabilized. Flow cell #1 was reserved as blank; the remaining flow cells (#2−4) were coated with biotin−tris-NTA having specific spacers by injection of 20 μL 100 nM biotin−tris-NTA (10 μL/min for 2 min) to capture a 50 RU response. These low-density tris-NTA chips were used for the binding kinetics experiments. High-density tris-NTA chips (ca. 300 RU) were prepared by saturating the streptavidin chip surface with biotin−tris-NTA and were used for the immobilization of His6 protein on the surface.

Binding kinetics (Figure 2B): Various concentrations of the His-tagged molecules were injected to flow over the tris-NTA surfaces, according to the programmed cycles of the following sequence: (1) activation of tris-NTA with 5 mM $NiCl_2$, (2)

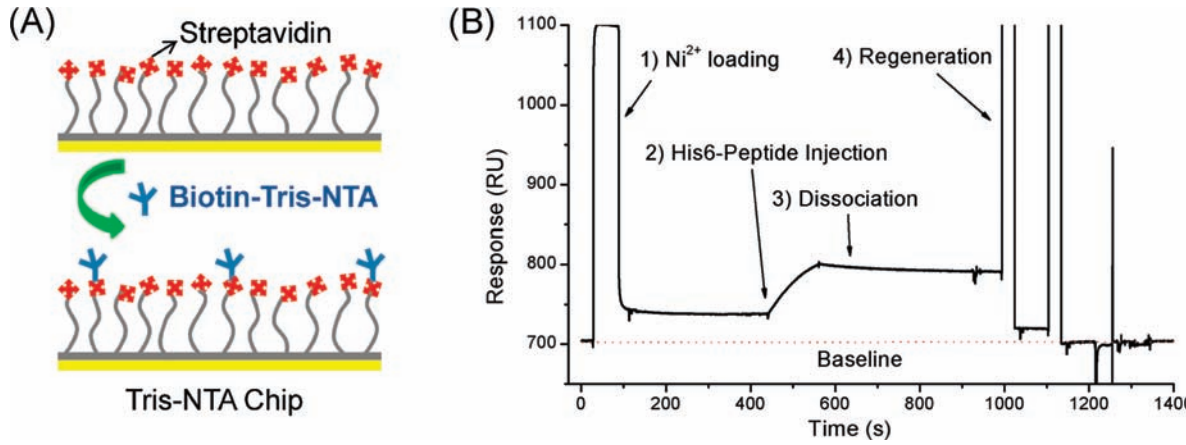

Figure 2. Measurement of binding kinetics by surface plasmon resonance using a tris-NTA chip. (A) Tris-NTA chip was prepared by coating a streptavidin chip with biotin−tris-NTA at low surface density. (B) Representative kinetics experiment cycle.

protein injection, (3) Ni(II) removal with 0.3 M EDTA, (4) rinse with 0.25% SDS and 0.5 M NaCl for baseline regeneration and stabilization. Both sample and control measurements were run in duplicate. The raw data were processed with *Biaevaluation T100* software, and the kinetic parameters were obtained by globally fitting the experimental curves with a 1:1 Langmuir binding model. The quality of the fitting was estimated by the *T* value and the residue (χ^2). $T(k) = k/\mathrm{SE}(k)$, where k is a fitted parameter such as ka and SE(k) is the standard error of k. A good fit should have a small residue and a large *T* value (*17*).

RESULTS

Synthesis of Biotin−tris-NTA. Biotin−tris-NTAs were synthesized according to previously published method (*11*) (Scheme 1). Briefly, the amino group of NTA *tert*-butyl ester (**2**) having various spacers was coupled to carboxyl acids of benzyloxycarbonyl-protected lysine NTA scaffold (**1**). Biotin was conjugated to tris-NTA after the removal of the benzyloxycarbonyl group so that the final product (**6**) can be immobilized on a streptavidin sensor chip for the surface plasmon resonance (SPR) measurement. In addition to the original lysine spacer (**6b**), four variants were introduced by either reducing the number of methylene groups (**6c**−**e**) or extending the lysine spacer with a flexible polyethylene oxide chain (**6a**). These alterations have the effect of varying the distance between adjacent mono-NTAs in the cluster.

Binding Parameters. The binding kinetics of tris-NTA/His6 complex were measured on a Biacore T100 SPR instrument. A customized tris-NTA chip was prepared by coating a Biacore streptavidin chip with biotin−tris-NTA at low surface density (around 50 response units, about 1/6 of the chip surface capacity, illustrated in Figure 2a). The surface density of tris-NTA was kept low to avoid the avidity effect but high enough to allow a good measurement (*18*). The mass transport effect on measured affinity was suppressed by using relatively high flow rate (50 μL/min) and was automatically isolated by the *Biaevaluation T100* program. Typical SPR sensorgrams of the tris-NTA/His6 complex are shown in Figure 3. All the data fit a simple 1:1 binding model well with negligible residue and satisfactory *T* values (>100). The binding parameters of tris-NTA with His6-tagged molecules are summarized in Table 1.

The kinetics data (Table 1) showed that the length of the spacer in tris-NTA has a significant effect on the binding affinity. The general trend is higher affinity and lower instant-off rate for the shorter spacer. The apparent binding affinity toward the same tris-NTA varies for different His6-tagged proteins and His6-peptides, which may relate to the accessibility of the His6-tag. Subnanomolar affinity was reached by **6d**, and no further improvement was achieved by **6e**.

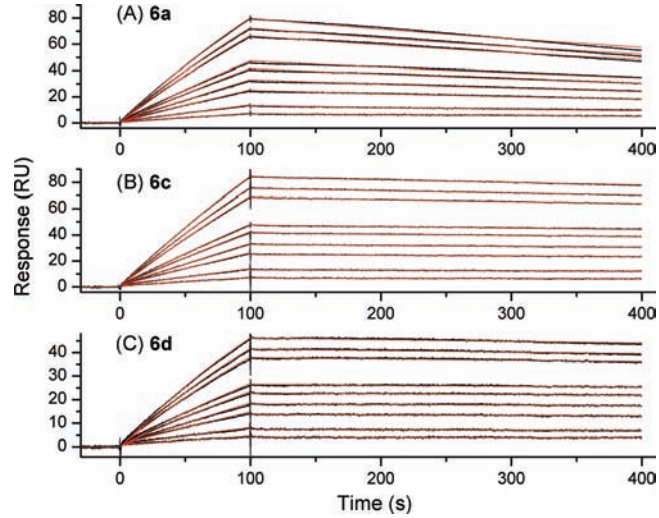

Figure 3. Double-referenced SPR sensorgrams of His6-mKate binding to tris-NTA having various spacer at a series of concentrations (1−10 nM at 1 nM increment excluding 7 nM). Experimental data were globally fitted with a 1:1 binding model. Black line, experimental data; red line, fitted data. The precision of the fitting was estimated by the *T* value that can be interpreted as the signal-to-noise ratio. A *T* value of 100 corresponds to 1% uncertainty. (A) mKate/**6a**, *T* (ka), 100; *T* (kd), 110. (B) mKate/**6c**, *T* (ka), 180; *T* (kd), 240. (C) mKate/**6d**, *T* (ka), 150; *T* (kd), 150.

DISCUSSION

We synthesized a series of biotin−tris-NTA to study the effect of a spacer on the binding affinity of tris-NTA nickel(II) complex toward His6-tagged molecules. The introduction of the biotin moiety in the tris-NTA conjugate allows the preparation of a customized low surface density tris-NTA chip for SPR measurement of the binding kinetics. SPR is a powerful and valid technique to measure molecular interactions in real time (*19*). We have used SPR in a previous study to measure the interaction between tris-NTA and His6-tagged proteins; the binding affinity was consistent with the data determined by the isothermal titration calorimetry (*9, 11*).

To quantify the interaction between multivalent binding pairs, it is important to keep the surface density low to avoid the avidity effect since the apparent affinity of His6 with mono-NTA was dependent on the surface density (*20*). The advantage of a tris-NTA surface over a mono-NTA surface is that tris-

Table 1. Binding Parameters of Tris-NTA/His6 Complexes[a]

Tris-NTA	AR-NTD[c]			yCD[d]			TSG6[e]			His6-Peptide[f]			mKate[g]		
(spacer)[b]	k_a[h]	k_d[i]	K_D[j]	k_a	k_d	K_D	k_a	k_d	K_D	k_a	k_d	K_D	k_a	k_d	K_D
6a (>4)[k]	0.94	1.29	13.7	3.11	12.3	39.4	6.89	4.84	7.03	3.09	3.97	12.8	5.38	1.53	2.84
6b (4)	0.81	1.40	17.3	1.19	0.83	6.97	19.4	5.78	3.0	1.86	1.85	9.95	ND	ND	ND
6c (3)	1.44	0.27	1.87	1.97	0.59	3.02	3.92	0.008	0.02	2.19	0.72	3.29	10.6	0.43	0.40
6d (2)	ND	ND	ND	ND	ND	ND	ND	ND	ND	35.8	0.64	0.18	10.3	0.20	0.21
6e (1)	ND	ND	ND	ND	ND	ND	ND	ND	ND	33.8	0.62	0.18	ND	ND	ND

[a] Measurements were carried out at 25 °C on a Biacore T100 SPR machine, and were repeated at least once. Data were analyzed by *Biaevaluation T100* software with a global fit of 1:1 binding model. All fitted curves had low residue and satisfactory *T* value (>100). All protein ligands tested have a C-terminal His6-tag. [b] Number of methylene groups in the spacer. [c] Androgen receptor N-terminal domain, MW: 21 Kda. [d] Yeast cytosine deaminase (*22*), MW: 19.7 Kda. [e] Tumor necrosis factor α-stimulated gene-6 (*22*), MW: 13.5 Kda. [f] His6-tagged peptide: GWGGHHHHHHG. [g] Monomeric Katushka, a far-red fluorescent protein (*23*), MW: 27 Kda. [h] k_a: Instant association rate constant, 10^5 M^{-1} S^{-1}. [i] k_d: Instant dissociation rate constant, 10^{-3} S^{-1}. [j] K_D: Equilibrium dissociation constant, 10^{-9} M. [k] Spacer:$(CH_2CH_2O)_4CH_2CH_2C(O)NH(CH_2)_4$.

NTA can provide a local high "effective concentration" even at low surface density. In our experiment, the surface density is about one-sixth of the total capacity of the chip and the experimental kinetics data can be globally fitted by a simple 1:1 binding model with very low residue and satisfactory *T* values (>100, indicating less than 1% uncertainty of the calculated data). In addition to low surface density, low analyte concentration is also required to minimize the undesired multisite interactions such as two His6 tags binding to one tris-NTA. Thus, a concentration that leads to maximum signal is not suitable for the 1:1 binding kinetics study on a multivalent binding pair as tris-NTA and His6. After systematic evaluation of the SPR conditions, we determined that 1−10 nM was a good concentration range for the kinetics study. Although quantification of multivalent interactions is still a challenge, we acquired kinetic data as accurate as possible through the combination of a sensitive instrument (Biacore T100) and careful experiment design: this included low surface density, low analyte concentration, and high flow rate.

The focus of current research is to investigate the influence of the spacer length on the binding affinity. We have synthesized tris-NTAs having five different spacers and included five His6-tagged molecules in order to determine if there is a general trend. Although the K_d value varies for different His6-tagged molecules, the trend is clear: as the spacer gets shorter, the affinity is higher. Different proteins have different binding affinities: these differences may arise from the extent of exposure of the His6 tag and other nonspecific interactions that are idiosyncractic for each protein. For example, TSG6 had an abnormally high affinity (0.02 nM, exceeded the detection limit of Biacore T100) toward **6c**. This cannot simply be attributed to the His6/tris-NTA interaction but is probably caused by other structural features of the protein in the vicinity of the local structure of the His6.

The His6-peptide may provide a closer model of the binding between His6 and tris-NTA. The high affinity of **6d** may be partly attributed to the short spacer that results in less conformational entropic cost of association than the flexible long spacers. When the spacer gets even shorter, such as in **6e**, the enthalpy of binding may become less favorable due to the increased steric hindrance and may offset the entropic effect. Thermodynamic studies of the tris-NTA/His6 binding by SPR at various temperatures (data not shown) were inconclusive, and we were unable to determine whether the entropy or enthalpy of binding was the predominant factor leading to the increased affinity. These measurements are most certainly complicated by the conformational change of the His6-tagged protein at different temperatures. Thus, it is difficult to quantify entropy and enthalpy changes of binding in such a complex system by the SPR technique. Nevertheless, it is clear the binding affinity of tris-NTA to His6 tag can be substantially improved by employing a shorter spacer.

Formation of a stable complex is essential to the broad applications of tris-NTA/His6 technology. One major problem in protein−protein interaction studies using the commercial SPR NTA chip is fast baseline drift due to the dissociation of protein immobilized on the surface through mono-NTA/His6 interaction. The new high-density tris-NTA chip (such as coated with **6e**) enables reversible yet stable immobilization of His6-tagged protein with a stable baseline. The high-density tris-NTA is now broadly used by researchers at University of California San Francisco for SPR analysis of various proteins (*21*). Derivatives of high-affinity tris-NTA can also be used to attach His6-tagged molecules to nanoparticles such as carbon nanotubes, gold particles, liposomes, magnetic particles, micelles, and quantum dots.

In conclusion, we have demonstrated that subnanomolar affinity to a His6 tag can be achieved by tris-NTA where the individual NTAs are separated by short spacers. The development of these high-affinity binding pairs opens the avenue to broader applications of His6-tagged molecules with enhanced stability.

ACKNOWLEDGMENT

This work was supported by NIH R01 CA107268 and RS10 RR023443. Thanks are also extended to the UCSF Mass Spectrometry Facility (A.L. Burlingame, Director) supported by NIH NCRR RR01614.

LITERATURE CITED

(1) Janknecht, R., de Martynoff, G., Lou, J., Hipskind, R. A., Nordheim, A., and Stunnenberg, H. G. (1991) Rapid and efficient purification of native histidine-tagged protein expressed by recombinant vaccinia virus. *Proc. Natl. Acad. Sci. U.S.A. 88*, 8972–6.

(2) Porath, J., Carlsson, J., Olsson, I., and Belfrage, G. (1975) Metal chelate affinity chromatography, a new approach to protein fractionation. *Nature 258*, 598–599.

(3) Thompson, D. H., Zhou, M. K., Grey, J., and Kim, H. K. (2007) Design, synthesis, and performance of NTA-modified lipids as templates for histidine-tagged protein crystallization. *Chem. Lett. 36*, 956–975.

(4) Kim, S. H., Jeyakumar, M., and Katzenellenbogen, J. A. (2007) Dual-mode fluorophore-doped nickel nitrilotriacetic acid-modified silica nanoparticles combine histidine-tagged protein purification with site-specific fluorophore labeling. *J. Am. Chem. Soc. 129*, 13254–13264.

(5) Lata, S., Gavutis, M., Tampe, R., and Piehler, J. (2006) Specific and stable fluorescence labeling of histidine-tagged proteins for dissecting multi-protein complex formation. *J. Am. Chem. Soc. 128*, 2365–2372.

(6) Goldsmith, C. R., Jaworski, J., Sheng, M., and Lippard, S. J. (2006) Selective labeling of extracellular proteins containing polyhistidine sequences by a fluorescein-nitrilotriacetic acid conjugate. *J. Am. Chem. Soc. 128*, 418–9.

(7) Kapanidis, A. N., Ebright, Y. W., and Ebright, R. H. (2001) Site-specific incorporation of fluorescent probes into protein: hexahistidine-tag-mediated fluorescent labeling with (Ni(2+): nitrilotriacetic Acid (n)-fluorochrome conjugates. *J. Am. Chem. Soc. 123*, 12123–12125.

(8) Cheng, F., Gamble, L. J., and Castner, D. G. (2008) XPS, TOF-SIMS, NEXAFS, and SPR characterization of nitrilotriacetic acid-terminated self-assembled monolayers for controllable immobilization of proteins. *Anal. Chem. 80*, 2564–2573.

(9) Lata, S., Reichel, A., Brock, R., Tampe, R., and Piehler, J. (2005) High-affinity adaptors for switchable recognition of histidine-tagged proteins. *J. Am. Chem. Soc. 127*, 10205–10215.

(10) van Broekhoven, C. L., and Altin, J. G. (2005) The novel chelator lipid 3(nitrilotriacetic acid)-ditetradecylamine (NTA(3)-DTDA) promotes stable binding of His-tagged proteins to liposomal membranes: potent anti-tumor responses induced by simultaneously targeting antigen, cytokine and costimulatory signals to T cells. *Biochim. Biophys. Acta 1716*, 104–116.

(11) Huang, Z. H., Park, J. I., Watson, D. S., Hwang, P., and Szoka, F. C. (2006) Facile synthesis of multivalent nitrilotriacetic acid (NTA) and NTA conjugates for analytical and drug delivery applications. *Bioconjugate Chem. 17*, 1592–1600.

(12) Mammen, M., Choi, S. K., and Whitesides, G. M. (1998) Polyvalent interactions in biological systems: Implications for design and use of multivalent ligands and inhibitors. *Angew. Chem., Int. Ed. 37*, 2755–2794.

(13) Mokotoff, M., and Logue, L. W. (1981) Potential inhibitors of L-asparagine biosynthesis. 5. Electrophilic amide analogues of (S)-2,3-diaminopropionic acid. *J. Med. Chem. 24*, 554–9.

(14) Roeske, R. (1963) Preparation of t-butyl esters of free amino acids. *J. Org. Chem. 28*, 1251–1253.

(15) Wyman, T. B., Nicol, F., Zelphati, O., Scaria, P. V., Plank, C., and Szoka, F. C., Jr. (1997) Design, synthesis, and characterization of a cationic peptide that binds to nucleic acids and permeabilizes bilayers. *Biochemistry 36*, 3008–17.

(16) Pace, C. N., Vajdos, F., Fee, L., Grimsley, G., and Gray, T. (1995) How to measure and predict the molar absorption coefficient of a protein. *Protein Sci. 4*, 2411–23.

(17) Onell, A., and Andersson, K. (2005) Kinetic determinations of molecular interactions using Biacore--minimum data requirements for efficient experimental design. *J. Mol. Recognit. 18*, 307–17.

(18) Myszka, D. G. (1999) Improving biosensor analysis. *J. Mol. Recognit. 12*, 279–284.

(19) Rich, R. L., and Myszka, D. G. (2008) Survey of the year 2007 commercial optical biosensor literature. *J. Mol. Recognit. 21*, 355–400.

(20) Nieba, L., Nieba-Axmann, S. E., Persson, A., Hamalainen, M., Edebratt, F., Hansson, A., Lidholm, J., Magnusson, K., Karlsson, A. F., and Pluckthun, A. (1997) BIACORE analysis of histidine-tagged proteins using a chelating NTA sensor chip. *Anal. Biochem. 252*, 217–28.

(21) Sablin, E. P., Woods, A., Krylova, I. N., Hwang, P., Ingraham, H. A., and Fletterick, R. J. (2008) The structure of corepressor Dax-1 bound to its target nuclear receptor LRH-1. *Proc. Natl. Acad. Sci. U.S.A. 105*, 18390–5.

(22) Park, J. I., Cao, L., Platt, V. M., Huang, Z., Stull, R. A., Dy, E. E., Sperinde, J. J., Yokoyama, J. S., and Szoka, F. C. (2009) Antitumor therapy mediated by 5-fluorocytosine and a recombinant fusion protein containing TSG-6 hyaluronan binding domain and yeast cytosine deaminase. *Mol. Pharm. 6*, 801–12.

(23) Shcherbo, D., Merzlyak, E. M., Chepurnykh, T. V., Fradkov, A. F., Ermakova, G. V., Solovieva, E. A., Lukyanov, K. A., Bogdanova, E. A., Zaraisky, A. G., Lukyanov, S., and Chudakov, D. M. (2007) Bright far-red fluorescent protein for whole-body imaging. *Nat. Methods 4*, 741–6.

BC900309N

TECHNICAL NOTES

Practical Synthesis of Isomerically Pure 5- and 6-Carboxytetramethylrhodamines, Useful Dyes for DNA Probes

Maksim V. Kvach,[†] Irina A. Stepanova,[‡] Igor A. Prokhorenko,[‡] Aleksander P. Stupak,[§] Dmitry A. Bolibrukh,[||] Vladimir A. Korshun,*[,‡] and Vadim V. Shmanai*[,†]

Institute of Physical Organic Chemistry, Surganova 13, 220072 Minsk, Belarus, Shemyakin-Ovchinnikov Institute of Bioorganic Chemistry, Miklukho-Maklaya 16/10, 117997 Moscow, Russia, Institute of Physics, Nezavisimosti av. 70, 220072 Minsk, Belarus, and Institute of Bioorganic Chemistry, Kuprevicha 5/2, 220141, Minsk, Belarus. Received January 29, 2009; Revised Manuscript Received June 21, 2009

Simple and scalable synthesis of 5- and 6-carboxytetramethylrhodamines (TAMRAs) is reported. Acylation of 3-dimethylaminophenol with 1,2,4-benzenetricarboxylic anhydride afforded a mixture of 4-dimethylamino-2-hydroxy-2′,4′(5′)-dicarboxybenzophenones, which can be easily separated into individual compounds upon recrystallization from methanol and acetic acid. Individual benzophenones were reacted with 3-dimethylaminophenol to give 5- or 6-carboxytetramethylrhodamines. The dyes were converted into hydroxyprolinol-based phosphoramidite reagents suitable for oligonucleotide synthesis. 5- and 6-TAMRA isomers on oligonucleotides showed similar absorption and emission spectra. Fluorescence quantum yield of the dyes correlates with the presence of dG nucleosides in the adjacent region of oligonucleotide sequence. Several energy transfer primers containing on their 5′-termini (6-FAM)dT$_n$(6-TAMRA) dye system (n = 0, 2, 4, 6, 8, 10, 12, 14) were prepared, and their spectral properties were studied.

INTRODUCTION

Xanthene fluorescent dye tetramethylrhodamine (TMR, TAMRA) is extremely popular for covalent labeling of various types of biomolecules (*1*−*3*), especially oligonucleotides for various formats of DNA analysis (*4*−*6*). The most convenient compounds for bioconjugation are 5- and 6-carboxy derivatives of tetramethylrhodamine. The mixture of isomers, easily prepared from 3-dimethylaminophenol and trimellitic anhydride (*7*), can be separated by chromatography (*8*) to give individual 5- and 6-isomers suitable for labeling of biomolecules, e.g., DNA (*9*), PNA (*10*), and peptides (*11*). TAMRA-labeled peptide substrates were used for determination of caspase-3 (*12*) and protein kinase (*13*) activity. Recent study showed that TAMRA conjugate with one of the sodium-dependent glucose cotransporter 2 (SGLT2) inhibitors is a 10-fold more potent agent than phlorizin (*14*).

However, more diverse applications have tetramethylrhodamine dye in the field of nucleic acids. Fluorescent properties of TAMRA-labeled oligonucleotides were thoroughly studied (*15*−*18*). The dye attached to the terminal position of an oligonucleotide showed little influence on the duplex stability (*19*). Changes in fluorescence polarization and intensity of singly TAMRA-labeled oligonucleotide probes were used for the monitoring of DNA−protein interactions (*20*−*25*). Fluorescence resonance energy transfer (FRET) dye pair fluorescein−tetramethylrhodamine on oligonucleotides can be used for the measurement of ribonuclease activity (*26*), hydroxyl radical detection (*27*), and in DNA−protein binding studies (*28, 29*). In DNA-related FRET investigations and applications, TAMRA was used as donor (*30*−*32*), acceptor (*33*−*38*), or energy bridge (*39*−*42*). The dye is an important label in four-color DNA sequencing (*43*−*48*). Many real-time PCR platforms have spectral channels suitable for TAMRA (*49*), and it is a standard reporter (*50*−*52*) or quencher (*53, 54*) dye for real-time PCR probes.

The widespread popularity of tetramethylrhodamine dye requires highly producible and easy scalable methods for the preparation of isomerically pure carboxytetramethylrhodamines. These would be suitable for the preparation of phosphoramidite reagents that can be automatically incorporated into oligonucleotides. Although several 5′-TAMRA and TAMRA-dT phosphoramidites for terminal and internal labeling are commercially available (*55, 56*), only two TAMRA phosphoramidite reagents have been described in the literature in detail (*57, 58*). Their disadvantage is that they are terminal, i.e., can be attached exclusively to the 5′-position of an oligonucleotide. On the other hand, phosphoramidites and solid supports derived from (3*R*,5*S*)-5-hydroxymethyl-3-hydroxypyrrolidine (*trans*-L-4-hydroxyprolinol) allow one to introduce modification into any position of an oligonucleotide (*59*−*72*). Hence, the aims of the present work are the development of a simple and easily scalable procedure for the synthesis of 5- and 6-carboxytetramethylrhodamines, the synthesis of phosphoramidite reagents from both isomers using

* Corresponding authors. V.A.K.: E-mail: korshun@mail.ibch.ru, Tel/Fax: +7-495-330-6738. V.V.S.: E-mail: shmanai@ifoch.bas-net.by, Tel: +375-17-284-2055, Fax: +375-17-284-2539.

[†] Institute of Physical Organic Chemistry.

[‡] Shemyakin-Ovchinnikov Institute of Bioorganic Chemistry.

[§] Institute of Physics.

[||] Institute of Bioorganic Chemistry.

10.1021/bc900037b CCC: $40.75 © 2009 American Chemical Society
Published on Web 07/16/2009

trans-L-4-hydroxyprolinol as a scaffold, and the study of spectral and photophysical properties of TAMRA-labeled oligonucleotides.

EXPERIMENTAL PROCEDURES

General. Reagents and solvents obtained from commercial suppliers were used without further purification. CH_2Cl_2 was used freshly distilled from CaH_2. HPLC-grade DMF was distilled under reduced pressure and stored over 4 Å molecular sieves under argon. Other solvents were used as received. *N*,*N*-Diisopropylamino-2-cyanoethoxychlorophosphine (*73, 74*), trimethylsilyl polyphosphate solution in chloroform (*75*), and (3*R*,5*S*)-5-[(4,4′-dimethoxytrityl)oxymethyl]-3-hydroxypyrrolidine (*69*) were prepared as described. 500 MHz ^{1}H, 125.7 MHz ^{13}C, and 202.4 MHz ^{31}P NMR spectra were recorded on a Bruker DRX-500 or Bruker Avance 500 spectrometers and referenced to $CDCl_3$ (7.26 ppm for ^{1}H and 77.1 ppm for ^{13}C), DMSO-d_6 (2.50 ppm for ^{1}H and 39.5 ppm for ^{13}C), CD_3CN (1.94 ppm for ^{1}H and 118.3 ppm for ^{13}C) (*76*), and 85% aq H_3PO_4 (0.00 ppm for ^{31}P). ^{1}H NMR coupling constants are reported in hertz (Hz) and refer to apparent multiplicities. High-resolution mass spectra (HRMS) were recorded in positive-ion mode using an IonSpec FT ISR mass spectrometer (MALDI) or PE SCIEX QSTAR pulsar mass spectrometer (ESI). Melting points were determined using a Boetius heating table and are uncorrected. Analytical thin-layer chromatography was performed on Kieselgel 60 F_{254} precoated aluminum plates (Merck); spots were visualized under UV light (254 nm). Silica gel column chromatography was performed using Merck Kieselgel 60 0.040−0.063 mm. The oligonucleotide synthesis was carried out on a BiosSet ASM-800 instrument on a 200 nmol scale using standard manufacturer's protocols. Oligonucleotides were isolated using electrophoresis in 20% denaturing (7 M urea) PAGE in Tris-borate buffer, pH 8.3, and desalted by gel filtration on a Sephadex G-25 column in 1×10^{-5} M Tris-HCl buffer, pH 7.5 ("saltless" buffer). MALDI-TOF mass spectra of oligonucleotide conjugates were recorded in positive-ion mode on a Bruker Ultraflex spectrometer. UV absorption spectra were recorded using a Varian Cary 500 spectrophotometer in 0.1 M bicarbonate buffer (pH 8.5). Fluorescence studies in the same buffer were performed using a Solar CM 2203 spectrofluorometer. Rhodamine 6G (R6G) in ethanol was used as a quantum yield standard. The fluorescence quantum yields (Φ_f) were calculated using the relative method according to the equation

$$\Phi_f = \Phi_{f(\mathrm{R6G})} \times \frac{I}{I_{\mathrm{R6G}}} \times \frac{A_{\mathrm{R6G}}}{A} \times \frac{n^2}{n_{\mathrm{R6G}}{}^2}$$

where $\Phi_{f(\mathrm{R6G})}$ is rhodamine 6G quantum yield in ethanol ($\Phi_{f(\mathrm{R6G})} = 0.94$ (*77*)); I and I_{R6G} are integrated intensities of sample and R6G dye solutions, respectively; A and A_{R6G} are optical densities of sample and R6G dye solutions, respectively; n and n_{R6G} are refractive indexes of ethanol and 0.1 M bicarbonate buffer, 1.3591 and 1.3340 at 20 °C, respectively. The measurements were performed at an angle of 90° to the exciting light beam. The optical density of the solutions in the 1 cm quartz cell at the excitation wavelength did not exceed 0.05. The samples used in quantum yield measurements were not degassed.

4-Dimethylamino-2-hydroxy-2′,4′(5′)-dicarboxy-benzophenones (1a,b). Freshly distilled 3-dimethylaminophenol (13.70 g, 0.10 mol) was dissolved in toluene (300 mL), heated to 60 °C, and pounded trimellitic anhydride (23.04 g, 0.12 mol) was added with magnetic stirring. The mixture was refluxed for 24 h and cooled. The residue was filtered off, washed with toluene (3×50 mL), dissolved in MeOH (300 mL), and refluxed for 10 min. Then, acetic acid (100 mL) was added and the mixture was evaporated to dryness. Crystalline solid was refluxed with MeOH (200 mL) for 2 h and kept at 4 °C overnight. The crystals formed were filtered off and washed with MeOH (50 mL) to give pure **1a** as brown crystalline solid (5.16 g, 16%). The mother liquid was evaporated to dryness, refluxed 1 h with acetic acid (150 mL), and stored at room temperature overnight. Crystals were filtered off and dried *in vacuo* at 115−120 °C to give mixture **1a**,**b** (9.66 g). This was recrystallized twice from acetic acid to give pure **1b** as a yellow crystalline solid (3.35 g, 10%). Filtered solutions can be combined, evaporated, and recrystallized succesively from MeOH and AcOH as above to give further amounts of individual **1a** and **1b**.

*4-Dimethylamino-2-hydroxy-2′,4′-dicarboxy-benzophenone (**1a**).* R_f 0.34 (Et_3N−MeOH−$CHCl_3$ 5:20:75 v/v/v); dec. >250 °C (MeOH). ^{1}H NMR (DMSO-d_6) δ = 13.44 (br s, 2H, CO_2H), 12.38 (s, 1H, O*H*), 8.49 (d, 1H, $^4J_{3',5'}$ = 1.7 Hz, H-3′), 8.20 (dd, 1H, $J_{5',6'}$ = 7.9 Hz, $^4J_{3',5'}$ = 1.7 Hz, H-5′), 7.52 (d, 1H, $J_{5',6'}$ = 7.9 Hz, H-6′), 6.80 (d, 1H, $J_{5,6}$ = 9.2 Hz, H-6), 6.20 (dd, 1H, $J_{5,6}$ = 9.2 Hz, $^4J_{3,5}$ = 2.5 Hz, H-5), 6.11 (d, 1H, $^4J_{3,5}$ = 2.5 Hz, H-3), 3.00 (s, 6H, CH_3). ^{13}C NMR (DMSO-d_6) δ = 197.66 (*C*O), 166.14 (2C, *C*O_2H), 164.24 (C2), 155.83 (C4), 143.76 (C1′), 133.82 (C6), 132.71 (C5′), 131.66 (C2′ or C4′), 130.73 (C3′), 130.03 (C2′ or C4′), 128.28 (C6′), 109.46 (C1), 104.52 (C5), 97.03 (C3), 39.63 (2C, *C*H_3). HRMS (MALDI+): *m*/*z* $[M+H]^+$ calcd for $C_{17}H_{16}NO_6^+$ 330.0972; found 330.0975.

*4-Dimethylamino-2-hydroxy-2′,5′-dicarboxy-benzophenone (**1b**).* R_f 0.52 (Et_3N−MeOH−$CHCl_3$ 5:20:75 v/v/v); mp 244−245 °C (AcOH). ^{1}H NMR (DMSO-d_6) δ = 13.46 (br s, 2H, CO_2H), 12.41 (s, 1H, O*H*), 8.14 (dd, 1H, $J_{3',4'}$ = 8.3 Hz, $^4J_{4',6'}$ = 1.7 Hz, H-4′), 8.06 (d, 1H, $J_{3'4'}$ = 8.3 Hz, H-3′), 7.83 (d, 1H, $^4J_{4',6'}$ = 1.7 Hz, H-6′), 6.86 (d, 1H, $J_{5,6}$ = 9.3 Hz, H-6), 6.22 (dd, 1H, $J_{5,6}$ = 9.3 Hz, $^4J_{3,5}$ = 2.5 Hz, H-5), 6.11 (d, 1H, $^4J_{3,5}$ = 2.5 Hz, H-3), 3.01 (s, 6H, CH_3). ^{13}C NMR (DMSO-d_6) δ = 197.40 (*C*O), 166.53 (2′-*C*O_2H), 166.10 (5′-*C*O_2H), 164.40 (C2), 155.87 (C4), 140.10 (C1′), 133.93 (C6), 133.73 (C2′), 133.65 (C5′), 130.42 (C3′), 130.23 (C4′), 128.25 (C6′), 109.43 (C1), 104.56 (C5), 97.08 (C3), 39.62 (2C, *C*H_3). HRMS (MALDI+): *m*/*z* $[M+H]^+$ calcd for $C_{17}H_{16}NO_6^+$ 330.0972; found 330.0970.

Carboxytetramethylrhodamines (*2a,b*); General Procedure. Benzophenone **1a**(**1b**) (3.29 g, 10.00 mmol) was mixed with 3-dimethylaminophenol (1.78 g, 13.00 mmol) and dissolved in DMF (80 mL). Trimethylsilylpolyphosphate solution in chloroform (20 mL) was added, and the mixture was refluxed for 3 h. Solvents were removed *in vacuo*; the residue was dissolved in 5% NaOH (70 mL) and stirred at room temperature overnight. Then, the solution was diluted with water (150 mL), and rhodamine was precipitated with concentrated hydrochloric acid (ca. 5 mL). The solid was filtered off, washed with water (50 mL), and dried *in vacuo* at 150 °C. Yields: 4.25 g, 99% of **2a**, or 4.27 g, 99% of **2b**. Carboxytetramethylrhodamines **2a**,**b** were used in the next step without additional purification. Analytical samples were purified on preparative silica gel TLC in Et_3N−MeOH−$CHCl_3$ 5:15:80 v/v/v as a mobile phase and characterized as triethylammonium salts.

*3,6-Bis(dimethylamino)-9-[2,4-dicarboxylatephenyl]xanthylium, Triethylammonium Salt (4-Carboxytetramethylrhodamine, Triethylammonium Salt) (**2a**·Et$_3$N).* R_f 0.14 (Et_3N−MeOH−$CHCl_3$ 5:20:75 v/v/v). ^{1}H NMR (CD_3OD), open chain numbering, δ = 8.73 (br s, 1H, H-3′), 8.18 (d, 1H, $J_{5',6'}$ = 7.5 Hz, H-5′), 7.28 (d, 1H, $J_{5',6'}$ = 7.5 Hz, H-6′), 7.25 (d, 2H, $J_{1,2} = J_{7,8}$ = 9.3 Hz, H-1,8), 6.98 (dd, 2H, $J_{1,2} = J_{7,8}$ = 9.3 Hz, $^4J_{2,4} = {}^4J_{5,7}$ = 1.7 Hz, H-2,7), 6.83 (d, 2H, $^4J_{2,4} = {}^4J_{5,7}$ = 1.7 Hz, H-4,5), 3.23 (br s, 12H, NCH_3), 3.13 (q, 6H, J = 7.4 Hz, NCH_2), 1.25 (t, 9H, J = 7.4 Hz, CH_2CH_3). ^{13}C NMR (CD_3OD) δ = 173.42 (4′-*C*O_2^-), 173.06 (2′-*C*O_2^-), 160.64 (C9), 158.75 (2C, C4a,10a), 158.40 (2C, C3,6), 140.82 (C2′ or 4′), 140.47 (C2′ or 4′), 136.30 (C1′), 132.66 (2C, C1,8), 131.81 (C3′), 131.38 (C5′), 129.96

(C6′), 114.73 (2C, C2,7), 114.65 (2C, C8a,9a), 97.35 (2C, C4,5), 47.33 (3C, *C*H_2CH$_3$), 40.81 (4C, N*C*H$_3$), 9.07 (3C, CH$_2$*C*H$_3$). HRMS (MALDI+): *m*/*z* [M+H]$^+$ calcd for $C_{25}H_{23}N_2O_5^+$ 431.1601; found 431.1597.

*3,6-Bis(dimethylamino)-9-[2,5-dicarboxylatephenyl]xanthylium, Triethylammonium Salt (5-Carboxytetramethylrhodamine, Triethylammonium Salt) (**2b**·Et$_3$N).* R_f 0.25 (Et$_3$N−MeOH−CHCl$_3$ 5:20:75 v/v/v). ^{1}H NMR (CD$_3$OD), open chain numbering, δ = 8.23 (d, 1H, $J_{3',4'}$ = 8.0 Hz, H-4′), 8.11 (d, 1H, $J_{3',4'}$ = 8.0 Hz, H-3′), 7.97 (br s, 1H, H-6′), 7.27 (d, 2H, $J_{1,2} = J_{7,8}$ = 9.3 Hz, H-1,8), 6.96 (dd, 2H, $J_{1,2} = J_{7,8}$ = 9.3 Hz, $^4J_{2,4} = {}^4J_{5,7}$ = 2.4 Hz, H-2,7), 6.84 (d, 2H, $^4J_{2,4} = {}^4J_{5,7}$ = 2.4 Hz, H-4,5), 3.22 (br s, 12H, NC*H*$_3$), 3.09 (q, 6H, *J* = 7.4 Hz, NC*H*$_2$), 1.21 (t, 9H, *J* = 7.4 Hz, CH$_2$C*H*$_3$). ^{13}C NMR (CD$_3$OD) δ = 173.02 (2C, 2′-*C*O$_2^-$, 4′-*C*O$_2^-$), 162.71 (C9), 158.85 (2C, C4a,10a), 158.49 (2C, C3,6), 142.85 (C2′), 140.21 (C5′), 133.49 (C1′), 132.84 (2C, C1,8), 131.51 (C4′), 131.38 (C6′), 130.57 (C3′), 114.95 (2C, C8a,9a), 114.78 (2C, C2,7), 97.38 (2C, C4,5), 47.39 (3C, *C*H_2CH$_3$), 40.82 (4C, N*C*H$_3$), 9.09 (3C, CH$_2$*C*H$_3$). HRMS (MALDI+): *m*/*z* [M+H]$^+$ calcd for $C_{25}H_{23}N_2O_5^+$ 431.1601; found 431.1595.

Amides *3a,b*; General Procedure. To a solution of carboxytetramethylrhodamine **2a**(**2b**) (1.72 g, 4.00 mmol) in DMF (22 mL), benzotriazol-1-yloxy-tris(pyrrolidino)phosphonium hexafluorophosphate (PyBOP, 2.08 g, 4.00 mmol) was added, followed by DIEA (8.00 mmol, 1.39 mL), and the mixture was stirred for 5 min. A solution of (3*R*,5*S*)-5-[(4,4′-dimethoxytrityl)oxymethyl]-3-hydroxypyrrolidine (1.68 g, 4.00 mmol) in DMF (8 mL) was added in one portion, and the stirring was continued for 2 h. The mixture was diluted with ethyl acetate (350 mL), washed with 5% NaHCO$_3$ (350 mL) and brine (200 mL), dried over MgSO$_4$, evaporated, and chromatographed on silica gel column in 1% Et$_3$N in acetone as a mobile phase to give the dark red amorphous foam.

*1-{3′,6′-Bis(dimethylamino)-3-oxo-spiro[isobenzofuran-1(3H),9′-[9H]xanthene]-5-yl-carbonyl}-(3R,5S)-5-[(4,4′-dimethoxytrityl)-oxymethyl]-3-hydroxypyrrolidine (**3a**).* Yield 1.98 g (60%). R_f 0.25 (Et$_3$N-MeOH-acetone 2:20:78 v/v/v). ^{1}H NMR (CDCl$_3$), spirolactone form numbering, δ = 8.14 (br s, 1H, H-4′), 7.79 (d, 1H, $J_{6',7'}$ = 7.8 Hz, H-6′), 7.43 (d, 2H, $J_{2'''',3''''} = J_{5'''',6''''}$ = 7.4 Hz, H-2′′′′,6′′′′), 7.31 (m, 4H, H-2′′′,6′′′), 7.27 (m, 2H, H-3′′′′,5′′′′), 7.18 (m, 2H, H-7′,4′′′′), 6.81 (m, 4H, H-3′′′,5′′′), 6.75−6.66 (m, 2H, H-1′′,8′′), 6.49 (m, 2H, H-4′′,5′′), 6.44 (m, 2H, H-2′′,7′′), 4.72 (m, 1H, H-3), 4.49 (m, 1H, H-5), 3.82−3.54 (m, 9H, OC*H*$_3$, OC*H*$_2$, H-2a), 3.30 (m, 1H, H-2b), 2.98 (m, 12H, NC*H*$_3$), 2.34−2.26 (m, 1H, H-4a), 2.15−2.08 (m, 1H, H-4b). ^{13}C NMR (CDCl$_3$) δ = 169.20 (*C*O), 169.06 (*C*O), 158.50 (2C, C4′′′), 153.77 (2C, C4a′′,10a′′), 153.04 (2C, C3′′,6′′), 150.94 (C7a′), 145.10 (C1′′′′), 138.34 (C3a′ or C5′), 136.24 (C1′′′), 136.16 (C1′′′), 133.21 (C6′), 130.08 (5C, C2′′′,6′′′, C5′ or C3a′), 129.38 (2C, C1′′,8′′), 128.16 (2C, C3′′′′,5′′′′), 127.92 (2C, C2′′′′,6′′′′), 126.87 (C4′′′′), 125.34 (C7′), 124.91 (C4′), 113.21 (4C, C3′′′,5′′′), 109.67 (2C, C2′′,7′′), 107.55 (2C, C8a′′,9a′′), 98.16 (C4′′ or C5′′), 98.10 (C4′′ or C5′′), 85.94 (Ar$_3$*C* (Dmt)), 70.59 (C5), 63.49 (C2), 59.08 (O*C*H$_2$), 56.19 (C3), 55.27 (2C, O*C*H$_3$), 40.37 (4C, N*C*H$_3$), 36.75 (C4). HRMS (MALDI+): *m*/*z* [M+H]$^+$ calcd for $C_{51}H_{50}N_3O_8^+$ 832.3592; found 832.3595.

*1-{3′,6′-Bis(dimethylamino)-3-oxo-spiro[isobenzofuran-1(3H),9′-[9H]xanthene]-6-yl-carbonyl}-(3R,5S)-5-[(4,4′-dimethoxytrityl)-oxymethyl]-3-hydroxypyrrolidine (**3b**).* Yield 1.52 g (46%). R_f 0.16 (Et$_3$N-MeOH-acetone 2:20:78 v/v/v). ^{1}H NMR, spirolactone form numbering, (CDCl$_3$) δ = 8.01 (d, 1H, $J_{4',5'}$ = 8.0 Hz, H-4′), 7.76 (d, 1H, $J_{4',5'}$ = 8.0 Hz, H-5′), 7.34 (m, 2H, H-2′′′′,6′′′′), 7.27 (br s, 1H, H-7′), 7.26−7.19 (m, 4H, H-2′′′,6′′′), 7.15−7.05 (m, 3H, H-3′′′′,4′′′′,5′′′′), 6.80−6.70 (m, 6H, H-1′′,8′′,3′′′,5′′′), 6.51−6.41 (m, 4H, H-2′′,4′′,5′′,7′′), 4.60 (m, 1H, H-3), 4.39 (m, 1H, H-5), 3.78−3.40 (m, 9H, OC*H*$_3$, OC*H*$_2$, H-2a), 3.21 (m, 1H, H-2b), 2.96 (m, 12H, NC*H*$_3$), 2.16 (m, 1H, H-4a), 2.04 (m, 1H, H-4b). ^{13}C NMR (CDCl$_3$) δ = 169.30 (O*C*O), 169.07 (N*C*O), 158.45 (C4′′′), 158.39 (C4′′′), 154.29 (C4a′′ or C10a′′), 154.24 (C4a′′ or C10a′′), 153.43 (2C, C3′′,6′′), 147.40 (C7a′), 144.99 (C1′′′′), 141.58 (C6′), 136.44 (C1′′′), 135.93 (C1′′′), 130.15 (4C, C2′′′,6′′′), 130.08 (C3a′), 129.88 (2C, C1′′,8′′), 129.03 (C5′), 128.05 (2C, C3′′′′,5′′′′), 127.82 (2C, C2′′′′,6′′′′), 126.77 (C4′′′′), 126.68 (C4′), 124.59 (C7′), 113.11 (4C, C3′′′,5′′′), 110.32 (C2′′ or C7′′), 110.24 (C2′′ or C7′′), 108.38 (C8a′′ or C9a′′), 108.31 (C8a′′ or C9a′′), 97.91 (2C, C4′′,5′′), 85.78 (Ar$_3$*C* (Dmt)), 70.35 (C5), 63.58 (C2), 58.90 (O*C*H$_2$), 56.21 (C3), 55.22 (2C, O*C*H$_3$), 40.36 (4C, N*C*H$_3$), 36.53 (C4). HRMS (MALDI+): *m*/*z* [M+H]$^+$ calcd for $C_{51}H_{50}N_3O_8^+$ 832.3592; found 832.3594.

Phosphoramidites *4a,b*; General Procedure. Amide **3a**(**3b**) (0.83 g, 1.0 mmol) was evaporated with dry CH$_2$Cl$_2$ (2 × 50 mL), dissolved in dry CH$_2$Cl$_2$ (100 mL), and diisopropylammonium tetrazolide (0.26 g, 1.5 mmol) was added, followed by addition of bis(*N*,*N*-diisopropylamino)-2-cyanoethoxyphosphine (476 μL, 1.5 mmol). The mixture was half-evaporated and stirred under argon for 1 h. After conversion of the starting compound was complete (monitoring by TLC, 2% Et$_3$N in Me$_2$CO v/v), the mixture was diluted with CH$_2$Cl$_2$ (100 mL) and washed with 5% NaHCO$_3$ (100 mL) and brine (100 mL). Organic layer was dried over Na$_2$SO$_4$ during 2 h, evaporated to dryness, and the residue was purified by chromatography on a silica gel column with 1% Et$_3$N in acetone (v/v) as the mobile phase. Fractions containing product were combined and evaporated. The resulting phosphoramidite was dissolved in CH$_2$Cl$_2$ (2 mL) and precipitated into hexane (100 mL). The solid was filtered off, dissolved in dry CH$_2$Cl$_2$ (20 mL), and evaporated to dryness to afford compounds **4a**(**4b**) as red amorphous solids.

*1-{3′,6′-Bis(dimethylamino)-3-oxo-spiro[isobenzofuran-1(3H),9′-[9H]xanthene]-5-yl-carbonyl}-(3R,5S)-5-[(4,4′-dimethoxytrityl)-oxymethyl]-3-(N,N-diisopropylamino-2-cyanoethoxyphosphinyl-oxy)pyrrolidine (**4a**).* Yield 0.75 g (73%). R_f 0.60 (1% Et$_3$N in acetone). ^{1}H NMR (MeCN-d_3), spirolactone form numbering, δ = 8.05 (br s, 1H, H-4′), 7.82 (m, 1H, H-6′), 7.46 (m, 2H, H-2′′′′,6′′′′), 7.36−7.18 (m, 8H, H-7′,2′′′,6′′′,3′′′′,4′′′′,5′′′′), 6.84 (m, 4H, H-3′′′,5′′′), 6.75−6.62 (m, 2H, H-1′′,8′′), 6.51 (m, 4H, H-2′′,4′′,5′′,7′′), 4.55 (m, 2H, H-3,5), 4.15−3.45 (m, 13H, OC*H*$_3$, POC*H*$_2$, DmtOC*H*$_2$, NC*H*, H-2a), 3.21 (m, 1H, H-2b), 2.98 (m, 12H, NC*H*$_3$), 2.75 (t, 1H, *J* = 5.9 Hz, C*H*$_2$CN), 2.63 (m, 1H, C*H*$_2$CN), 2.37−2.20 (m, 2H, H-4), 1.17−1.04 (m, 12H, CHC*H*$_3$). ^{13}C NMR (MeCN-d_3) δ = 169.56 (*C*O), 169.50 (*C*O), 159.55 (2C, C4′′′), 154.14 (2C, C4a′′,10a′′), 153.85 (2C, C3′′,6′′), 153.09 (C7a′), 146.33 (C1′′′′), 139.54 (0.5C, C5′ or C3a′), 139.37 (0.5C, C5′ or C3a′), 137.09 (2C, C1′′′), 134.45 (m, C6′), 130.90 (m, 4C, C2′′′,6′′′), 129.86 (m, 3C, C3a′ or C5′, C1′′,8′′), 128.90 (2C, C2′′′′,6′′′′), 128.78 (2C, C3′′′′,5′′′′), 127.74 (C4′′′′), 125.63 (C7′), 125.08 (m, C4′), 119.44 (m, *C*N), 113.99 (4C, C3′′′,5′′′), 110.30 (2C, C2′′,7′′), 107.75 (2C, C8a′′,9a′′), 98.77 (2C, C4′′,5′′), 86.56 (Ar$_3$*C* (Dmt)), 73.64 (m, C5), 64.12 (m, C2), 59.50−58.60 (m, 2C, *C*H$_2$ODmt, PO*C*H$_2$), 56.91 (m, C3), 55.82 (2C, O*C*H$_3$), 43.96 (m, 2C, *C*HCH$_3$), 40.49 (4C, N*C*H$_3$), 36.35 (C4), 23.09 (m, 4C, CH*C*H$_3$), 20.94 (m, 2C, *C*H$_2$CN). ^{31}P NMR (MeCN-d_3) δ = 147.35, 147.22 (diastereomers). HRMS (ESI+): *m*/*z* [M+Na]$^+$ calcd for $C_{60}H_{66}N_5NaO_9P^+$ 1054.4490; found 1054.4492.

*1-{3′,6′-Bis(dimethylamino)-3-oxo-spiro[isobenzofuran-1(3H),9′-[9H]xanthene]-6-yl-carbonyl}-(3R,5S)-5-[(4,4′-dimethoxytrityl)-oxymethyl]-3-(N,N-diisopropylamino-2-cyanoethoxyphosphinyl-oxy)pyrrolidine (**4b**).* Yield 0.48 g (47%). R_f 0.35 (1% Et$_3$N in acetone). ^{1}H NMR (MeCN-d_3), spirolactone form numbering, δ = 8.01 (m, 1H, H-4′), 7.74 (m, 1H, H-5′), 7.40−7.04 (m, 10H, H-7′,2′′′,6′′′,2′′′′,3′′′′,4′′′′,5′′′′,6′′′′), 6.86−6.62 (m, 6H,

Chart 1. Tetramethylrhodamine Dye in Zwitterionic Open-Chain Form (left) and Spirolactone Form (right)

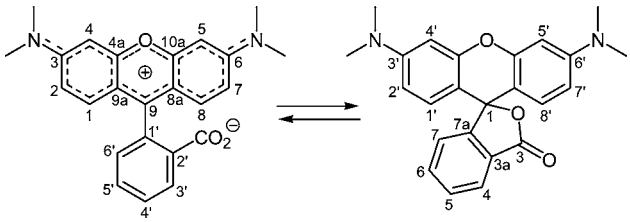

H-1″,8″,3‴,5‴), 6.51−6.41 (m, 4H, H-2″,4″,5″,7″), 4.54−4.39 (m, 2H, H-3,5), 3.79−3.39 (m, 14H, OCH_3, POCH_2, DmtOCH_2, NC*H*, H-2), 3.03−2.86 (m, 13H, NCH_3, CH_2CN), 2.57 (t, 1H, J = 5.9 Hz, CH_2CN), 2.36−2.19 (m, 2H, H-4), 1.21−0.86 (m, 12H, CHCH_3). ^{13}C NMR (MeCN-d_3) δ = 169.59 (*C*O), 169.20 (*C*O), 159.50 (C4‴), 159.43 (C4″), 154.00−153.00 (m, 4C, C3″,4a″,10a″), 146.03 (C1‴), 144.28 (C6′), 137.26 (C1″), 136.66 (C1‴), 130.96 (2C), 130.67 (2C) (C2‴,6‴), 129.93 (C5′), 129.51 (m, 3C, C3a′,1″,8″), 128.70 (m, 4C, C2‴,3‴,5‴,6‴), 127.62 (C4‴), 125.92 (m, C4′), 123.73 (0.5C), 123.57 (0.5C) (C7′), 113.85 (4C, C3‴,5‴), 109.85 (m, 2C, C2″,7″), 107.05 (2C, C8a″,9a″), 98.97 (m, 2C, C4″,5″), 86.37 (Ar$_3$*C* (Dmt)), 73.50−73.00 (m, C5), 63.54 (m, C2), 59.16 (m, PO*C*H$_2$), 58.45 (m, *C*H$_2$ODmt), 56.79 (m, C3), 55.79 (2C, O*C*H$_3$), 43.84 (m, 2C, *C*HCH$_3$), 40.39 (4C, N*C*H$_3$), 35.89 (C4), 24.75 (m, 4C, CH*C*H$_3$), 20.86 (m, 2C, *C*H$_2$CN). ^{31}P NMR (MeCN-d_3) δ = 147.39, 146.55 (diastereomers). HRMS (ESI+): m/z [M+Na]$^+$ calcd for $C_{60}H_{66}N_5NaO_9P^+$ 1054.4490; found 1054.4494.

RESULTS AND DISCUSSION

Like others rhodamine dyes, tetramethylrhodamine can exist in two tautomeric open-chain and lactone forms (Chart 1).

The fluorescent open-chain structure prevails in polar protic media, whereas in aprotic solvents, the dye becomes nonfluorescent switching to spirolactone form. It is worth noting that the alteration in tautomeric structure changes the numbering system. The major ring system in the open-chain form is xanthene changing to isobenzofuran in the lactone form (Chart 1). Thus, carboxyrhodamines derived from trimellitic anhydride are usually known as 5(6)-derivatives corresponding to spirolactone form. Actually, in cases these dyes exist in open-chain form: their correct name is 4′(5′)-derivatives.

Carboxytetramethylrhodamines can be easily obtained as a mixture of 5- and 6- isomers. However, in many analytical applications individual isomers are preferred. In a previous communication (*78*), we described an easy method for chromatographic separation of multigram quantities of 5(6)-carboxyfluorescein derivatives. The chromatographic technique (*8*) for the separation of 5(6)-carboxytetramethylrhodamines in our hands turned out to be ineffective: we were able to separate less than 1 g of isomeric mixture in one run. We found the method hardly scalable and not applicable for multigram synthesis of single TAMRA isomers.

In the present paper, we report a convenient procedure for the synthesis of isomerically pure carboxytetramethylrhodamines using a two-step approach (Scheme 1) with crystallization as a key stage leading to separation of isomers.

Benzophenones **1a**,**b** are easily available from trimellitic anhydride and 3-dimethylaminophenol by refluxing in toluene (*79*). After filtration, the crude mixture of benzophenones was obtained as an amorphous solid. Dissolving it in methanol and evaporation with addition of acetic acid promoted crystallization. The solubilities of benzophenones **1a** and **1b** in methanol differ significantly: **1a** is slightly soluble, whereas **1b** dissolves well. In that way, the major part of benzophenone **1a** was separated from the mixture by simple extraction **1b** with methanol. Evaporation of extract enriched with **1b** followed by double crystallization of the residue from acetic acid afforded pure 5′-carboxy substituted benzophenone **1b**. The simple, direct method using inexpensive starting compounds gives 16% of **1a** and 10% of **1b** together with mixture **1a**+**1b** (ca. 20%), suitable for further fractional crystallization. The procedure can be scaled up several times without difficulty.

The structures of isomeric benzophenones **1a**,**b** were determined using 2D ^{1}H−^{13}C HSQC and HMBC NMR techniques. Here, we consider signal assignment for benzophenone **1b** (the resulting ^{13}C NMR shifts assignment is shown in Chart 2). There are signals of two 1,2,4-trisubstituted benzene systems seen in the proton NMR spectrum of this compound (Figure 1A): one has signals at 6.11, 6.22, and 6.86 ppm with constants ^3J = 9.3 Hz and ^4J = 2.5 Hz; another one has shifts 7.83, 8.03, and 8.15 ppm and constants ^3J = 8.3 Hz and ^4J = 1.7 Hz. The direct correlation HSQC (Figure 1B) shows carbons attached to protons. The next step is the assignment of phenolic ring carbons. In the HMBC spectrum, the phenolic proton O*H* at 12.41 displays cross-peaks with carbon signals at 97.08, 109.43, and 164.40, which apparently belong to carbons 1, 2, and 3 (Figure 1C). Only the carbon at 97.08 is bound to a proton, evidently being C3. Thus, the high field proton system belongs to the phenolic ring, and the low field system is protons of the phthalic acid. From HSQC (Figure 1B), the assignment of C5 and C6 is clear. HMBC correlation of protons 3 and 5 shows that the signal at 109.43 originates from C1 (Figure 1D). Therefore, the signal at 164.40 belongs to C2. HMBC correlation of methyl protons (data not shown) allows assignment of C4. The assignment of C2 and C4 is confirmed by cross-peaks from H6 (Figure 1E). Thus, the assignment of carbon signals of the phenolic ring is complete. The carbonyl signal at 197.40 in HMBC spectrum gives cross-peaks with H6 and H6′ (Figure 1F). The assignment of C3′ and C4′ arises from the HSQC spectrum (Figure 1B). The assignment of closely located signals at 133.65 and 133.73 is carried out using the HMBC spectrum (Figure 1G). The signal at 133.73 displays cross-peaks with protons H4′ and H6′ thus coming from C2′. The signal at 133.65 gives a cross-peak with H3′ and is therefore C5′. Hence, the substitution pattern in the benzene ring is unambiguous: carboxyl groups are located in 2′- and 5′-positions. The assignment of carboxylic carbons is performed using cross-peaks in HMBC spectrum (Figure 1E): the carboxyl signal at 166.10 gives cross-peaks with H4′ and H6′ thus arising from 5′-carboxyl. The signal at 166.53 shows a cross-peak with H3′ and is therefore assigned as 2′-carboxyl.

The core of tetramethylrhodamine was assembled by refluxing **1a** or **1b** with an additional equivalent of 3-dimethylaminophenol in DMF using trimethylsilylpolyphosphate as a dehydrating agent and weak acid catalyst (*80, 81*). The resulting pure isomers of tetramethylrhodamine were obtained in almost quantitative yields and were used without additional purification. Thus, the two-step assembly method of tetramethylrhodamines allows us to obtain multigram quantities of isomerically pure dye in one run avoiding column chromatography. Carboxytetramethylrhodamines can be converted further into various useful derivatives: oxysuccinimide, maleimide, biotin, acetylene, azide, and so forth.

To demonstrate the utility of isomerically pure tetramethylrhodamines, two phosphoramidite reagents for the labeling of oligonucleotides in automated solid-phase synthesis were prepared. Acids **2a**,**b** were reacted with (3*R*,5*S*)-5-[(4,4′-dimethoxytrityl)oxymethyl]-3-hydroxypyrrolidine (*69*) using benzotriazol-1-yloxy-tris(pyrrolidino)phosphonium hexafluorophosphate (PyBOP) as a coupling reagent to afford amides **3a**,**b** in satisfactory yields. The phosphitylation of secondary alcohols **3a**,**b** with bis(*N*,*N*-diisopropylamino)-2-cyanoethoxyphosphine

Scheme 1[a]

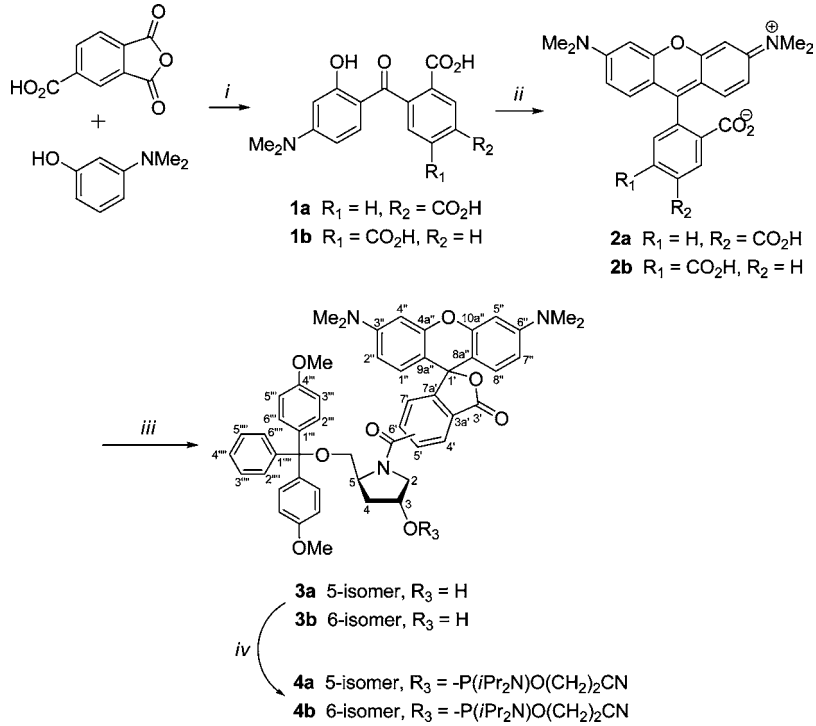

[a] Reagents and conditions. *i*, PhMe, reflux, 24 h, 16% (**1a**), 10% (**1b**); *ii*, 3-dimethylaminophenol, trimethylsilylpolyphosphate, DMF, reflux, 3 h, 99% (**2a**), 99% (**2b**); *iii*, (3*R*,5*S*)-5-[(4,4′-dimethoxytrityl)oxymethyl]-3-hydroxypyrrolidine, PyBOP, DIEA, DMF, 2 h, 60% (**3a**), 46% (**3b**); *iv*, bis(*N*,*N*-diisopropylamino)-2-cyanoethoxyphosphine, diisopropylammonium tetrazolide, CH_2Cl_2, 1 h, 73% (**4a**), 47% (**4b**). For compounds **3a**,**b** and **4a**,**b**, the shown numbering is used for NMR assignments.

Chart 2. ^{13}C NMR Shifts in Benzophenone 1b (solvent DMSO-d_6)

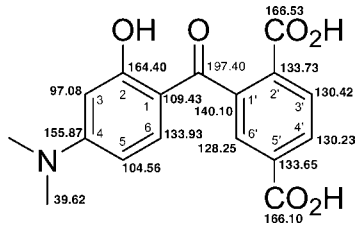

in the presence of diisopropylammonium tetrazolide gave the desired phosphoramidites **4a**,**b**. The structures of the compounds were confirmed by ^{1}H, ^{13}C, and ^{31}P NMR spectra and by high-resolution mass spectra (HRMS). For the tetramethylrhodamine derivatives **2**−**4**, the assignment of ^{1}H and ^{13}C signals in NMR spectra was accomplished using 2D ^{1}H−^{1}H COSY and ^{1}H−^{13}C HSQC and HMBC techniques. In ^{13}C spectra, we observed the signal of C1-atom in compounds **2a**,**b** at ∼160 ppm (when dissolved in polar d_4-MeOD); however, it completely disappears (in compounds **3** and **4**) when dissolving in aprotic solvents $CDCl_3$, CD_3CN, or DMSO-d_6 due to the fast equilibrium process between lactone and open-chain forms (Chart 1).

Reagents **4a**,**b** were tested in automated oligonucleotide synthesis. TAMRA phosphoramidites **4a**,**b** are readily soluble in dry acetonitrile and were used as 0.1 M solutions. They reacted well with hydroxy groups of a growing oligonucleotide in tetrazole-assisted coupling conditions. The reaction time for **4a**,**b** was increased from 20 s to 7.5 min to achieve maximum coupling yield. After capping and oxidizing steps, the last dimethoxytrityl group was removed and coupling yield was estimated to be >95%. Using phosphoramidites **4a**,**b** oligonucleotides **ON1**−**ON4** carrying tetramethylrhodamines on 5′-terminus (Table 1) were synthesized. Reagent **4b** was also applied for the synthesis of the oligomer **ET**- and energy transfer oligonucleotides **ET0**−**ET14** carrying 6-TAMRA label in internal position and 6-FAM label (*78*) on the 5′ terminus (Chart 3). Similar energy transfer probes with poly-T linker between donor and acceptor dyes can be applied for construction of wavelength-shifting molecular beacons (*82*, *83*). Oligonucleotides were cleaved from solid support and deprotected by "TAMRA-cocktail"—*t*BuNH$_2$/MeOH/H$_2$O 1:1:2 mixture (*84*). Conjugates obtained were purified by PAGE and characterized by MALDI-TOF, UV−vis, and fluorescence spectra (Tables 1, 2, and Figures 2, 3).

Previous study of fluorescein-labeled oligonucleotides (*78*) showed that absorption spectra of 5- and 6-FAM-labeled oligonucleotides do not differ significantly, whereas in fluorescence spectra, the 5-isomer displays a 3−5 nm red shift against 6-isomer and emission band in the spectrum of 5-FAM is substantially broader. Like FAM-labeled oligonucleotides, different isomers of TAMRA show differences in fluorescence spectra but they are not so evident. 5-TAMRA on an oligonucleotide displays only 1−3 nm red shift vs 6-isomer. The emission band in the spectrum of 5-TAMRA is slightly broader (Figure 2).

Fluorescence quantum yield of the dye in TAMRA-labeled oligonucleotides is sequence dependent (Table 1). It is well-known that guanine residues quench fluorescence if they are near fluorescent label (*85*, *86*), this is also the case for TAMRA (*17*, *18*). Data show that quantum yield of TAMRA-labeled oligonucleotides **ON1**−**ON4** correlates with the presence or absence of guanine residues in proximity to the TAMRA label. The highest quantum yield (0.69) is observed for conjugate **ON1b** with no neighbor guanine. The conjugate **ON2b** with three closely located adjacent guanines shows decreased quantum yield (0.29). There are no significant differences in quantum yields between 5- and 6-isomers of carboxytetramethylrhodamines on oligonucleotides.

The synthesis of energy transfer primers **ET0**−**ET14** (Chart 3) demonstrates the internal labeling of oligonucleotides. The conjugates are 5′-labeled with the combined fluorophore (6-FAM)-(dT)$_n$(6-TAMRA) and their formal Stokes shift is ca. 85 nm (Table

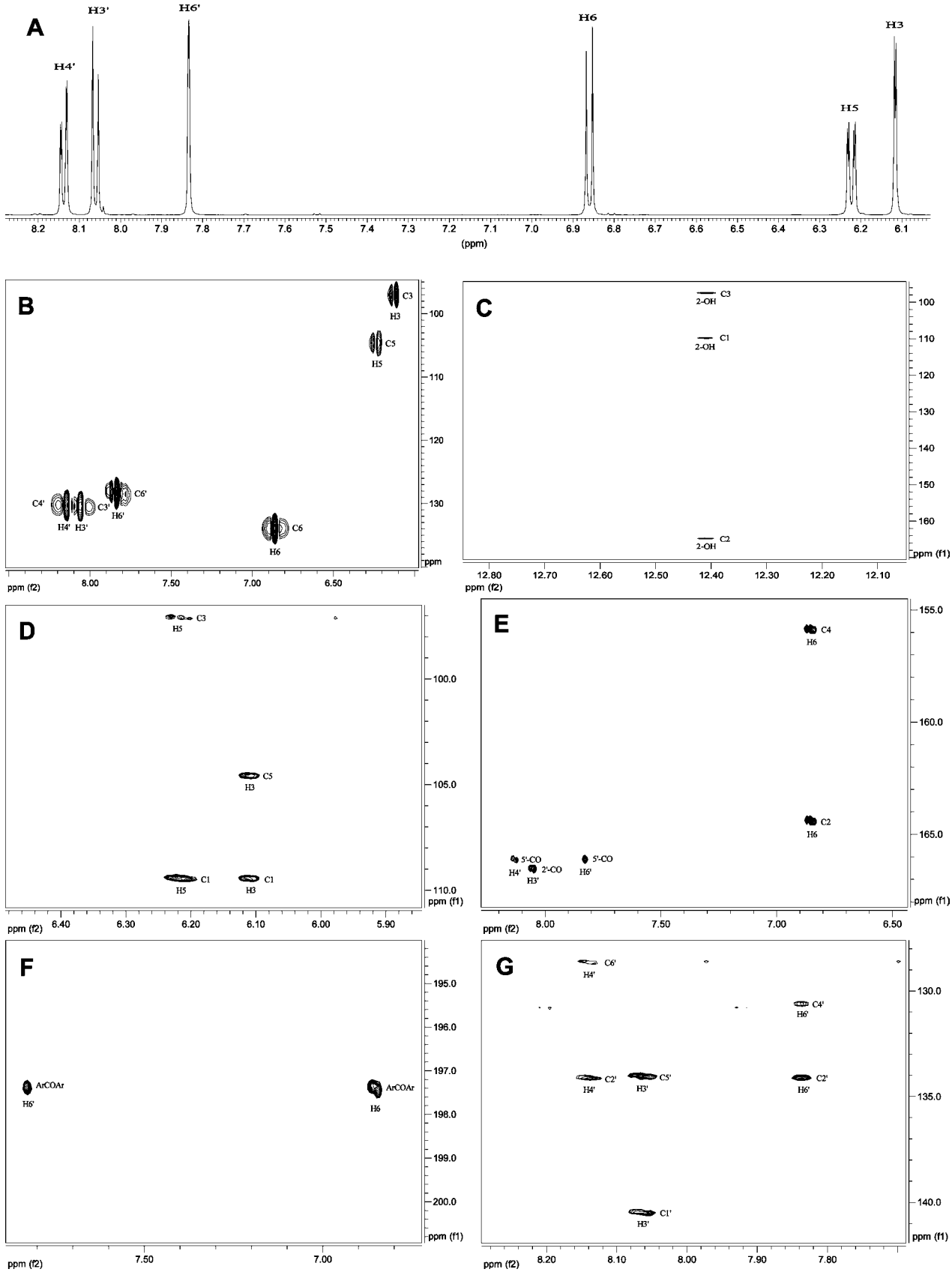

Figure 1. NMR spectra of benzophenone **1b**. (A) Proton spectrum of aromatic region; (B) $^{1}H-^{13}C$ HSQC spectrum of the aromatic region; (C−G) fragments of $^{1}H-^{13}C$ HMBC spectrum.

2). For detection purposes, FAM dye is usually excited at 480 nm; thus, the difference between FAM excitation and TAMRA emission (580−583 nm) for **ET** conjugates is about 100 nm.

The efficiency of energy transfer from donor to acceptor depends on the spacing between them (*37*, *87*, *88*). Increasing the length of the oligo-dT spacer decreases the quenching of the FAM label,

Table 1. Spectroscopic and Photophysical Properties of TAMRA-Labeled Oligonucleotides[a]

#	sequence, 5′ → 3′	MALDI-TOF, $[M+H]^+$, found/calcd	λ^{abs}_{max}, nm	λ^{fl}_{max}, nm	Φ_f
ON1a	**5-TAMRA**-aataatcagtatgtgacttggattga	8640.4/8639.8[b]	561	588	0.66
ON1b	**6-TAMRA**-aataatcagtatgtgacttggattga	8638.5/8639.8[b]	561	586	0.69
ON2a	**5-TAMRA**-tgggctctgtaaagaatagtg	7115.8/7114.3[c]	562	589	0.32
ON2b	**6-TAMRA**-tgggctctgtaaagaatagtg	7116.5/7114.3[c]	561	585	0.29
ON3a	**5-TAMRA**-aaataaaattaggcatatttacaagc	8584.1/8585.8[b]	561	588	0.63
ON3b	**6-TAMRA**-aaataaaattaggcatatttacaagc	8584.9/8585.8[b]	560	586	0.62
ON4a	**5-TAMRA**-aggcttgaggccaaccatcag	7032.3/7029.3[c]	561	586	0.65
ON4b	**6-TAMRA**-aggcttgaggccaaccatcag	7031.4/7029.3[c]	562	585	0.58

[a] **5-TAMRA**-modified oligonucleotides were prepared using phosphoramidite **4a**; **6-TAMRA**-modified oligonucleotides were prepared using phosphoramidite **4b**; absorption and fluorescence spectra were measured in 0.1 M bicarbonate buffer (pH 8.5) using rhodamine 6G as a reference (see Experimental Procedures). [b] Average mass. [c] Monoisotopic mass.

Chart 3. Structures of Energy Transfer Oligonucleotides

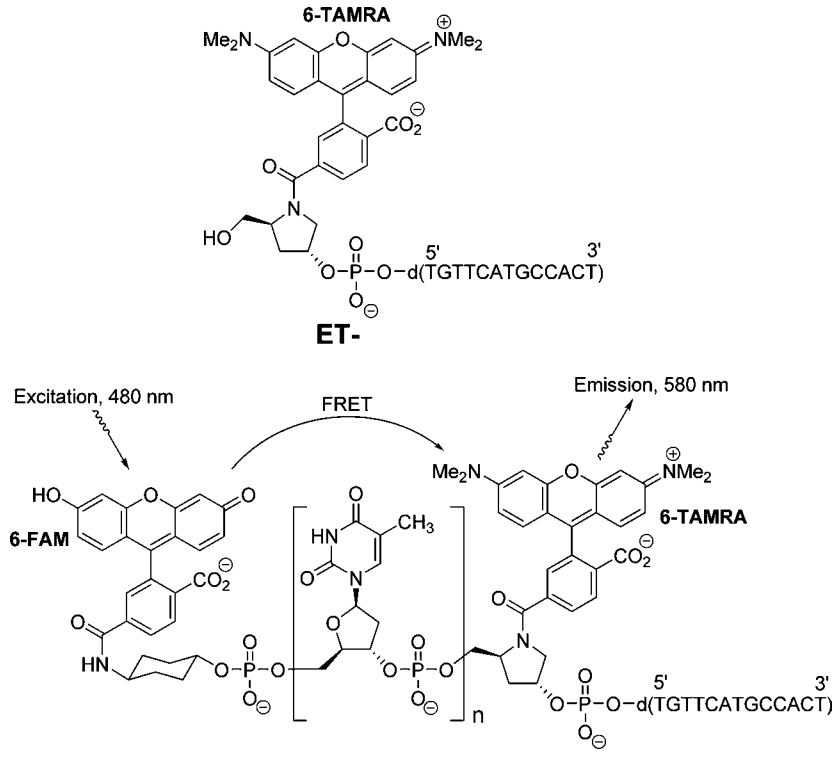

Table 2. Spectroscopic Properties of 6-FAM-6-TAMRA-Labeled Oligonucleotides ET[a]

#	*n*	MALDI-TOF, $[M+H]^+$, found/calcd	donor (6-FAM) $\lambda_{max}{}^{abs}$, nm	acceptor (6-TAMRA) $\lambda_{max}{}^{fl}$, nm	$I_{(TAMRA)}/I_{ET\text{-}(TAMRA)}$[b]	$I_{(TAMRA)}/I_{(FAM)}$[c]
ET-	–	4490.6/4490.9[d]	–	583	1.0	–
ET0	0	5024.8/5026.0[d]	497	583	2.9	5.2
ET2	2	5432.0/5634.1[d]	493	583	11.8	7.9
ET4	4	6241.2/6242.2[d]	494	581	14.9	4.2
ET6	6	6848.8/6850.3[d]	495	581	16.5	2.8
ET8	8	7459.9/7458.4[d]	495	581	16.3	2.0
ET10	10	8071.1/8069.5[e]	495	581	16.3	1.7
ET12	12	8679.0/8677.9[e]	495	580	14.5	1.2
ET14	14	9289.1/9286.3[e]	495	580	14.6	1.0

[a] Structures of energy transfer oligonucleotides **ET** are shown in Chart 3; for conditions, see Figure 3a. [b] See Figure 3a. [c] See Figure 3b. [d] Monoisotopic mass. [e] Average mass.

and its emission at 519 nm rises nearly linearly from **ET0** to **ET14** (Figure 3a). The behavior of the emission intensity of TAMRA label is more complicated. The spacer is very important for the intensity of TAMRA fluorescence: the insertion of $(dT)_2$ between dyes increases the acceptor emission of **ET2** four times in comparison to **ET0**. Maximal values of TAMRA emission are observed for conjugates **ET6**, **ET8**, and **ET10**—their emission is 16 times more intense as compared to single TAMRA label excited at 480 nm in conjugate **ET-** (Table 2, Figure 3a). The values are higher than expected, because the combined chromophore absorbance at the excitation wavelength 480 nm increases only ca. 10 times ($\varepsilon_{480(FAM)} + \varepsilon_{480(TAMRA)}/\varepsilon_{480(TAMRA)} = 10.5$).

The highest TAMRA/FAM (581 nm/519 nm) emission intensity ratio was observed for **ET2**, not for **ET0** (7.9 vs 5.2). The same behavior of the acceptor intensity was mentioned in other investigations when donor−acceptor distances were too close (*37, 87*). When two dyes appear in proximity, a contact quenching occurs, and the emission of both the donor and the acceptor diminishes. However, the insertion of a few nucleosides between two dyes prevents such a contact quenching; even with a spacer of two

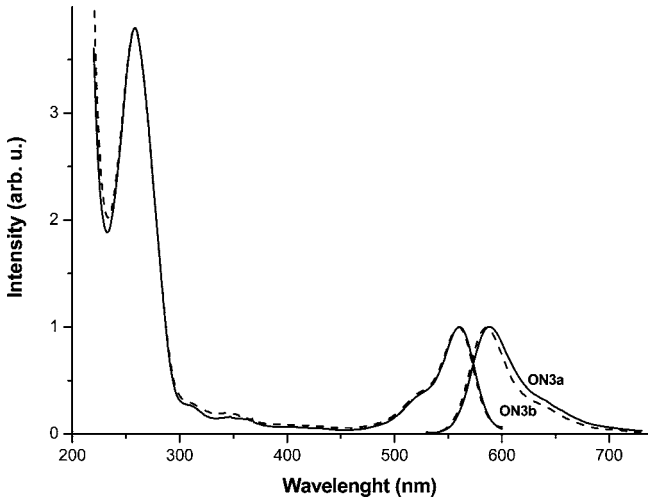

Figure 2. Normalized absorption (left) and fluorescence (right) spectra of conjugates **ON3a** (straight lines) and **ON3b** (dashed lines) in 0.1 M bicarbonate buffer (pH 8.5), excitation at $\lambda = 525$ nm.

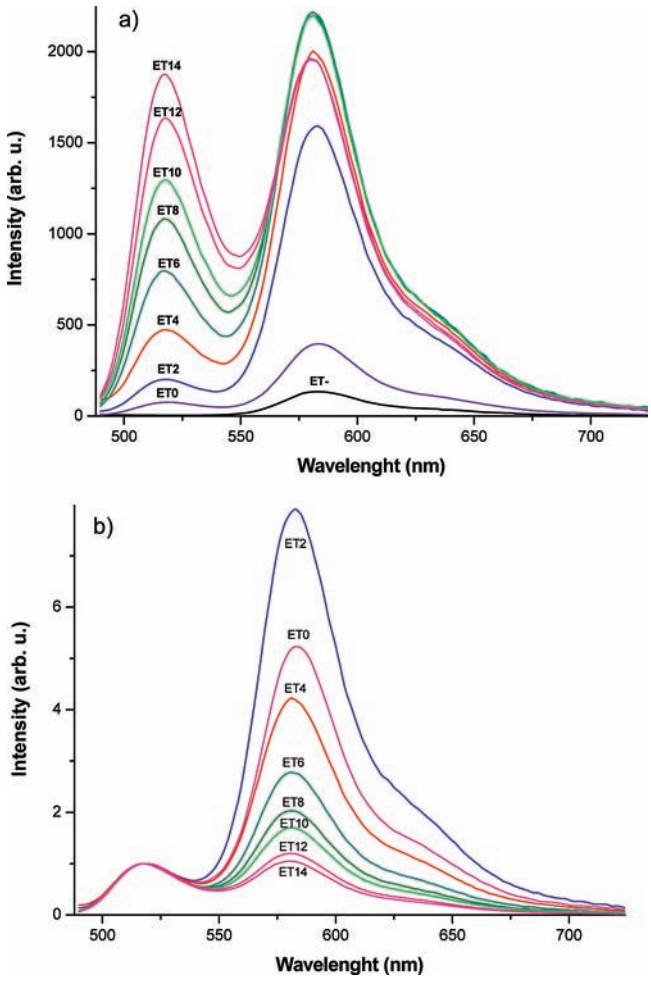

Figure 3. (a) Fluorescence spectra of oligonucleotides **ET-** and **ET0...ET14** in 0.1 M bicarbonate buffer (pH 8.5), excitation at $\lambda = 480$ nm, concentration 6×10^{-7} M; (b) fluorescence spectra of oligonucleotides **ET0...ET14** normalized to 6-FAM fluorescence maximum (519 nm).

nucleosides, no other interaction than dipole−dipole was observed within the donor−acceptor dye pair (*88*).

The TAMRA/FAM intensity ratio decreases rapidly in the series **ET2...ET14** (Table 2, Figure 3b). Conjugate **ET2** emits 90% of the integral light energy in the TAMRA fluorescence band (550−650 nm), and 10% in the FAM band (500−550 nm). However, the overall emission efficiency of the absorbed light (FAM emission + TAMRA emission) decreases in the series **ET14** > **ET12** ≈ **ET10** > **ET8** > **ET6** > **ET4** > **ET2** ≫ **ET0** (Figure 3a). Thus, conjugates **ET6**−**ET10** showed highest TAMRA emission, **ET14** the highest FAM+TAMRA overall emission, and **ET2** the highest TAMRA/FAM emission intensity ratio. The data may appear useful for design of energy transfer primers and probes.

To conclude, we have developed a simple and scalable procedure for the preparation of individual isomers of carboxytetramethylrhodamines, described hydroxyprolinol-based TAMRA phosphoramidite reagents containing individual dye isomers, prepared a series of oligonucleotides 5′- and internal labeled with carboxytetramethylrhodamines, and compared spectral and photophysical spectra of TAMRA−oligonucleotide conjugates. We also showed that in energy transfer primers the optimal spacer between donor (FAM) and acceptor (TAMRA) dyes for maximum acceptor fluorescence should contain 6−10 dT nucleotides.

ACKNOWLEDGMENT

The research was supported by BFBR (project B06R-004) and RFBR (projects 06-04-81019 and 08-03-90900). We thank Primetech ltd. (Minsk, Belarus) for the synthesis of labeled oligonucleotides, Alexander Peregudov for NMR spectra, Alexander Baranovsky and Alexey Ustinov for helpful discussion, and anonymous referees for their useful comments.

LITERATURE CITED

(1) Mason, W. T., Ed. (1999) *Fluorescent and Luminescent Probes for Biological Activity. A Practical Guide to Technology for Quantitative Real-Time Analysis*, 2nd ed., Academic Press, London, San Diego.

(2) Haugland, R. P. (2005) *The Handbook. A Guide to Fluorescent Probes and Labelling Technologies*, 10th ed., Invitrogen/Molecular Probes, Eugene, OR (web edition: http://probes.invitrogen.com/handbook/).

(3) Lakowicz, J. R. (2006) *Principles of Fluorescence Spectroscopy*, 3th ed., Springer, Singapore.

(4) Ranasinghe, R. T., and Brown, T. (2005) Fluorescence based strategies for genetic analysis. *Chem. Commun.* 5487–5502.

(5) Asseline, U. (2006) Development and applications of fluorescent oligonucleotides. *Curr. Org. Chem. 10*, 491–518.

(6) Weisbrod, S. H., and Marx, A. (2008) Novel strategies for site-specific covalent labelling of nucleic acids. *Chem. Commun.* 5675–5685.

(7) Khanna, P. L., and Ullman, E. F. (1980) 4′,5′-Dimethoxy-6-carboxyfluorescein: a novel dipole-dipole coupled fluorescence energy transfer acceptor useful for fluorescence immunoassays. *Anal. Biochem. 108*, 156–161.

(8) Edmundson, A. B., Ely, K. R., and Herron, J. N. (1984) A search for site-filling ligands in the Mcg Bence-Jones dimer: crystal binding studies of fluorescent compounds. *Mol. Immunol. 21*, 561–576.

(9) Vinayak, R. (1999) A convenient, solid-phase coupling of rhodamine dye acids to 5′ amino-oligonucleotides. *Tetrahedron Lett. 40*, 7611–7613.

(10) Mayfield, L. D., and Corey, D. R. (1999) Enhancing solid phase synthesis by a noncovalent protection strategy-efficient coupling of rhodamine to resin-bound peptide nucleic acids. *Bioorg. Med. Chem. Lett. 9*, 1419–1422.

(11) Brunner, A., Minamitake, Y., and Göpferich, A. (1998) Labelling peptides with fluorescent probes for incorporation into degradable polymers. *Eur. J. Pharm. Biopharm. 45*, 265–273.

(12) Mizukami, S., Kikuchi, K., Higuchi, T., Urano, Y., Mashima, T., Tsuruo, T., and Nagano, T. (1999) Imaging of caspase-3 activation in HeLa cells stimulated with etoposide using a novel fluorescent probe. *FEBS Lett. 453*, 356–360.

(13) Viht, K., Vaasa, A., Raidaru, G., Enkvist, E., and Uri, A. (2005) Fluorometric TLC assay for evaluation of protein kinase inhibitors. *Anal. Biochem. 340*, 165–170.

(14) Lansdell, M. I., Burring, D. J., Hepworth, D., Strawbridge, M., Graham, E., Guyot, T., Betson, M. S., and Hart, J. D. (2008) Design and synthesis of fluorescent SGLT2 inhibitors. *Bioorg. Med. Chem. Lett. 18*, 4944–4947.

(15) Edman, L., Mets, Ü., and Rigler, R. (1996) Conformational transitions monitored for single molecules in solution. *Proc. Natl. Acad. Sci. U.S.A. 93*, 6710–6715.

(16) Vámosi, G., Gohlke, C., and Clegg, R. M. (1996) Fluorescence characteristics of 5-carboxytetramethylrhodamine linked covalently to the 5′ end of oligonucleotides: multiple conformers of single-stranded and double-stranded dye-DNA complexes. *Biophys. J. 71*, 972–994.

(17) Eggeling, C., Fries, J. R., Brand, L., Günther, R., and Seidel, C. A. M. (1998) Monitoring conformational dynamics of a single molecule by selective fluorescence spectroscopy. *Proc. Natl. Acad. Sci. U.S.A. 95*, 1556–1561.

(18) Wang, L., Gaigalas, A. K., Blasic, J., and Holden, M. J. (2004) Spectroscopic characterization of fluorescein- and tetramethylrhodamine-labeled oligonucleotides and their complexes with a DNA template. *Spectrochim. Acta, Part A 60*, 2741–2750.

(19) Moreira, B. G., You, Y., Behlke, M. A., and Owczarzy, R. (2005) Effects of fluorescent dyes, quenchers, and dangling ends on DNA duplex stability. *Biochem. Biophys. Res. Commun. 327*, 473–484.

(20) Stern, J. C., and Schildbach, J. F. (2001) DNA Recognition by F factor TraI36: highly sequence-specific binding of single-stranded DNA. *Biochemistry 40*, 11586–11595.

(21) Harley, M. J., Toptygin, D., Troxler, T., and Schildbach, J. F. (2002) R150A mutant of F TraI relaxase domain: reduced affinity and specificity for single-stranded DNA and altered fluorescence anisotropy of a bound labeled oligonucleotide. *Biochemistry 41*, 6460–6468.

(22) Harley, M. J., and Schildbach, J. F. (2003) Swapping single-stranded DNA sequence specificities of relaxases from conjugative plasmids F and R100. *Proc. Natl. Acad. Sci. U.S.A. 100*, 11243–11248.

(23) Larkin, C., Datta, S., Harley, M. J., Anderson, B. J., Ebie, A., Hargreaves, V., and Schildbach, J. F. (2005) Inter- and intramolecular determinants of the specificity of single-stranded DNA binding and cleavage by the F factor relaxase. *Structure 13*, 1533–1544.

(24) Unruh, J. R., Gokulrangan, G., Lushington, G. H., Johnson, C. K., and Wilson, G. S. (2005) Orientational dynamics and dye-DNA interactions in a dye-labeled DNA aptamer. *Biophys. J. 88*, 3455–3465.

(25) Anderson, B. J., Larkin, C., Guja, K., and Schildbach, J. F. (2008) Using fluorophore-labeled oligonucleotides to measure affinities of protein-DNA interactions. *Methods Enzymol. 450*, 253–272.

(26) Kelemen, B. R., Klink, T. A., Behlke, M. A., Eubanks, S. R., Leland, P. A., and Raines, R. T. (1999) Hypersensitive substrate for ribonucleases. *Nucleic Acids Res. 27*, 3696–3701.

(27) Soh, N., Makihara, K., Sakoda, E., and Imato, T. (2004) A ratiometric fluorescent probe for imaging hydroxyl radicals in living cells. *Chem. Commun.* 496–497.

(28) Dragan, A. I., Liu, Y., Makeyeva, E. N., and Privalov, P. L. (2004) DNA-binding domain of GCN4 induces bending of both the ATF/CREB and AP-1 binding sites of DNA. *Nucleic Acids Res. 32*, 5192–5197.

(29) Dragan, A. I., and Privalov, P. L. (2008) Use of fluorescence resonance energy transfer (FRET) in studying protein-induced DNA bending. *Methods Enzymol. 450*, 185–199.

(30) Dietrich, A., Buschmann, V., Müller, C., and Sauer, M. (2002) Fluorescence resonance energy transfer (FRET) and competing processes in donor-acceptor substituted DNA strands: a comparative study of ensemble and single-molecule data. *Rev. Mol. Biotechnol. 82*, 211–231.

(31) Wu, Z.-S., Jiang, J.-H., Fu, L., Shen, G.-L., and Yu, R.-Q. (2006) Optical detection of DNA hybridization based on fluorescence quenching of tagged oligonucleotide probes by gold nanoparticles. *Anal. Biochem. 353*, 22–29.

(32) Dolghih, E., Roitberg, A. E., and Krause, J. L. (2007) Fluorescence resonance energy transfer in dye-labeled DNA. *J. Photochem. Photobiol. A: Chem. 190*, 321–327.

(33) Clegg, R. M., Murchie, A. I. H., Zechel, A., and Lilley, D. M. J. (1993) Observing the helical geometry of double-stranded DNA in solution by fluorescence resonance energy transfer. *Proc. Natl. Acad. Sci. U.S.A. 90*, 2994–2998.

(34) Vámosi, G., and Clegg, R. M. (1998) The helix-coil transition of DNA duplexes and hairpins observed by multiple fluorescence parameters. *Biochemistry 37*, 14300–14316.

(35) Mergny, J.-L. (1999) Fluorescence energy transfer as a probe for tetraplex formation: the i-motif. *Biochemistry 38*, 1573–1581.

(36) Horsey, I., Furey, W. S., Harrison, J. G., Osborne, M. A., and Balasubramanian, S. (2000) Double fluorescence resonance energy transfer to explore multicomponent binding interactions: a case study of DNA mismatches. *Chem. Commun.* 1043–1044.

(37) Marras, S. A. E., Kramer, F. R., and Tyagi, S. (2002) Efficiencies of fluorescence resonance energy transfer and contact-mediated quenching in oligonucleotide probes. *Nucleic Acids Res. 30*, e122.

(38) Chen, L., Lee, S., Lee, M., Lim, C., Choo, J., Park, J. Y., Lee, S., Joo, S.-W., Lee, K.-H., and Choi, Y.-W. (2008) DNA hybridization detection in a microfluidic channel using two fluorescently labelled nucleic acid probes. *Biosens. Bioelectron. 23*, 1878–1882.

(39) Shchepinov, M. S., and Korshun, V. A. (2001) Design of multidye systems for FRET-based applications. *Nucleosides Nucleotides Nucleic Acids 20*, 369–374.

(40) Tong, A. K., Jockusch, S., Li, Z., Zhu, H.-R., Akins, D. L., Turro, N. J., and Ju, J. (2001) Triple fluorescence energy transfer in covalently trichromophore-labeled DNA. *J. Am. Chem. Soc. 123*, 12923–12924.

(41) Haustein, E., Jahnz, M., and Schwille, P. (2003) Triple FRET: a tool for studying long-range molecular interactions. *ChemPhysChem 4*, 745–748.

(42) Martí, A. A., Li, X., Jockusch, S., Stevens, N., Li, Z., Raveendra, B., Kalachikov, S., Morozova, I., Russo, J. J., Akins, D. L., Ju, J., and Turro, N. J. (2007) Design and characterization of two-dye and three-dye binary fluorescent probes for mRNA detection. *Tetrahedron 63*, 3591–3600.

(43) Smith, L. M., Sanders, J. Z., Kaiser, R. J., Hughes, P., Dodd, C., Connell, C. R., Heiner, C., Kent, S. B. H., and Hood, L. E. (1986) Fluorescence detection in automated DNA sequence analysis. *Nature 321*, 674–678.

(44) Lee, L. G., Connell, C. L., Woo, S. L., Cheng, R. D., McArdle, B. F., Fuller, C. W., Halloran, N. D., and Wilson, R. K. (1992) DNA sequencing with dye-labeled terminators and T7 DNA polymerase: effect of dyes and dNTPs on incorporation of dye-terminators and probability analysis of termination fragments. *Nucleic Acids Res. 20*, 2471–2483.

(45) Ju, J., Ruan, C., Fuller, C. W., Glazer, A. N., and Mathies, R. A. (1995) Fluorescence energy transfer dye-labeled primers for DNA sequencing and analysis. *Proc. Natl. Acad. Sci. U.S.A. 92*, 4347–4351.

(46) Lee, L. G., Spurgeon, S. L., Heiner, C. R., Benson, S. C., Rosenblum, B. B., Menchen, S. M., Graham, R. J., Constantinescu, A., Upadhya, K. G., and Cassel, J. M. (1997) New energy transfer dyes for DNA sequencing. *Nucleic Acids Res. 25*, 2816–2822.

(47) Rosenblum, B. B., Lee, L. G., Spurgeon, S. L., Khan, S. H., Menchen, S. M., Heiner, C. R., and Chen, S. M. (1997) New dye-lebeled terminators for improved DNA sequencing patterns. *Nucleic Acids Res. 25*, 4500–4504.

(48) Nampalli, S., Khot, M., and Kumar, S. (2000) Fluorescence resonance energy transfer terminators for DNA sequencing. *Tetrahedron Lett. 41*, 8867–8871.

(49) Gibson, N. J. (2006) The use of real-time PCR methods in DNA sequence variation analysis. *Clin. Chim. Acta 363*, 32–47.
(50) Nasarabadi, S., Milanovich, F., Richards, J., and Belgrader, P. (1999) Simultaneous detection of TaqMan® probes containing Fam and Tamra reporter fluorophores. *BioTechniques 27*, 1116–1118.
(51) De Baar, M. P., Timmermans, E. C., Bakker, M., de Rooij, E., van Gemen, B., and Goudsmit, J. (2001) One-tube real-time isothermal amplification assay to identify and distinguish human immunodeficiency virus type 1 subtypes A, B, and C and circulating recombinant forms AE and AG. *J. Clin. Microbiol. 39*, 1895–1902.
(52) Ameziane, N., Seguin, C., Borgel, D., Fumeron, F., Moatti, D., Alhenc-Gelas, M., Grandchamp, B., Aiach, M., Emmerich, J., and de Prost, D. (2002) The−33T→C polymorphism in intron 7 of the TFPI gene influences the risk of venous thromboembolism, independently of the factor V Leiden and prothrombin mutations. *Thromb. Haemost. 88*, 195–199.
(53) Lee, L. G., Connell, C. R., and Bloch, W. (1993) Allelic discrimination by nick-translation PCR with fluorgenic probes. *Nucleic Acids Res. 21*, 3761–3766.
(54) Daum, L. T., Ye, K., Chambers, J. P., Santiago, J., Hickman, J. R., Barnes, W. J., Kruzelock, R. P., and Atchley, D. H. (2004) Comparison of TaqMan and Epoch Dark Quenchers during real-time reverse transcription PCR. *Mol. Cell. Probes 18*, 207–209.
(55) www.glenres.com.
(56) www.biosearchtech.com.
(57) Lyttle, M. H., Carter, T. G., Dick, D. J., and Cook, R. M. (2000) A tetramethyl rhodamine (Tamra) phosphoramidite facilitates solid-phase-supported synthesis of 5′-Tamra DNA. *J. Org. Chem. 65*, 9033–9038.
(58) Woo, S. L., Menchen, S. M., and Fung, S. (1993) Rhodamine phosphoramidite compounds. U.S. Pat. 5,231,191.
(59) Reed, M. W., Meyer, R. B., Jr., Petrie, C. R., and Tabone, J. C. (1995) Solid support for synthesis of 3′-tailed oligonucleotides. U.S. Pat. 5,419,966.
(60) Cheng, Y., Lukhtanov, E. A., Meyer, R. B., Jr., Pai, B. S., Reed, M. W., and Zhou, J. H. (1997) Sterol modified oligonucleotide duplexes having anticancer activity. U.S. Pat. 5,646,126.
(61) Reed, M. W., Adams, A. D., Nelson, J. S., and Meyer, R. B., Jr. (1991) Acridine- and cholesterol-derivatized solid supports for improved synthesis of 3′-modified oligonucleotides. *Bioconjugate Chem. 2*, 217–225.
(62) Gamper, H. B., Reed, M. W., Cox, T., Virosco, J. S., Adams, A. D., Gall, A. A., Scholler, J. K., and Meyer, R. B., Jr. (1993) Facile preparation of nuclease resistant 3′ modified oligodeoxynucleotides. *Nucleic Acids Res. 21*, 145–150.
(63) Reed, M. W., Lukhtanov, E. A., Gorn, V. V., Lucas, D. D., Zhou, J. H., Pai, S. B., Cheng, Y., and Meyer, R. B., Jr. (1995) Structure-activity relationships of cytotoxic cholesterol-modified DNA duplexes. *J. Med. Chem. 38*, 4587–4596.
(64) Balakin, K. V., Korshun, V. A., Esipov, D. S., Mikhalev, I. I., and Berlin, Y. A. (1999) Perylene-labeled oligonucleotide as a probe in homogeneous hybridization assay. *Nucleosides Nucleotides 18*, 1279–1280.
(65) Acevedo, O. L., Hebert, N. (1998) Pyrolidine-containing monomers and oligomers. U.S. Pat. 5,714,606.
(66) Hebert, N. (2001) Combinatorial libraries having aminodiol monomer dubunits. U.S. Pat. 6,184,389.
(67) Lukhtanov, E. A., Vorobiev, A. V., Reed, M. W., Vermeulen, N. M. J. (2005) Compounds and methods for fluorescent labeling. U.S. Pat. 6,972,339.
(68) Reed, M. W., Lukhtanov, E. A., Gall, A. A., Dempcy, R. O., Vermeulen, N. M. J. (2006) Fluorescent quenching detection reagents and methods. U.S. Pat. Appl. 2006/0292589.
(69) Hébert, N., Davis, P. W., DeBaets, E. L., and Acevedo, O. L. (1994) Synthesis of N-substituted hydroxyprolinol phosphoramidites for the preparation of combinatorial libraries. *Tetrahedron Lett. 35*, 9509–9512.
(70) Prokhorenko, I. A., Korshun, V. A., Petrov, A. A., Gontarev, S. V., and Berlin, Y. A. (1995) Incorporation of a pyrene nucleoside analogue into synthetic oligonucleotides using a nucleoside-like synthon. *Bioorg. Med. Chem. Lett. 5*, 2081–2084.
(71) Ceulemans, G., Van Aerschot, A., Wroblowski, B., Rozenski, J., Hendrix, C., and Herdewijn, P. (1997) Oligonucleotide analogues with 4-hydroxy-N-acetylprolinol as sugar substitute. *Chem.—Eur. J. 3*, 1997–2010.
(72) Verheijen, J. C., van Roon, A.-M. M., Meeuwenoord, N. J., Stuivenberg, H. R., Bayly, S. F., Chen, L., van der Marel, G. A., Torrence, P. F., and van Boom, J. H. (2000) Incorporation of a 4-hydroxy-*N*-acetylprolinol nucleotide analogue improves the 3′-exonuclease stability of 2′−5′-oligoadenylate-antisense conjugates. *Bioorg. Med. Chem. Lett. 10*, 801–804.
(73) Bannwarth, W., and Trzeciak, A. (1987) A simple and effective chemical phosphorylation procedure for biomolecules. *Helv. Chim. Acta 70*, 175–186.
(74) Caruthers, M. H., Barone, A. D., Beaucage, S. L., Dodds, D. R., Fisher, E. F., McBride, L. J., Matteucci, M., Stabinsky, Z., and Tang, J.-Y. (1987) Chemical synthesis of deoxyoligonucleotides by the phosphoramidite method. *Methods Enzymol. 154*, 287–313.
(75) Yokoyama, M., Yoshida, S., and Imamoto, T. (1982) Organic reactions using trimethylsilyl polyphosphate (PPSE): a convenient synthesis of nitriles from carboxamides. *Synthesis* 591–592.
(76) Gottlieb, H. E., Kotlyar, V., and Nudelman, A. (1997) NMR chemical shifts of common laboratory solvents as trace impurities. *J. Org. Chem. 62*, 7512–7515.
(77) Fischer, M., and Georges, J. (1996) Fluorescence quantum yield of rhodamine 6G in ethanol as a function of concentration using thermal lens spectrometry. *Chem. Phys. Lett. 260*, 115–118.
(78) Kvach, M. V., Tsybulsky, D. A., Ustinov, A. V., Stepanova, I. A., Bondarev, S. L., Gontarev, S. V., Korshun, V. A., and Shmanai, V. V. (2007) 5(6)-Carboxyfluorescein revisited: new protecting group, separation of isomers, and their spectral properties on oligonucleotides. *Bioconjugate Chem. 18*, 1691–1696.
(79) Hughes, N., Renfrew, A. H. M. (1976) Colour formers. G.B. Pat. 1,427,318.
(80) Corrie, J. E. T., and Craik, J. S. (1994) Synthesis and characterisation of pure isomers of iodoacetamidotetramethylrhodamine. *J. Chem. Soc., Perkin Trans. I* 2967–2973.
(81) Munasinghe, V. R. N., and Corrie, J. E. T. (2006) Optimised synthesis of 6-iodoacetamidotetramethylrhodamine. *ARKIVOC* 143–149.
(82) Tyagi, S., Marras, S. A. E., and Kramer, F. R. (2000) Wavelenght-shifting molecular beacons. *Nat. Biotechnol. 18*, 1191–1196.
(83) Li, X., Li, Z., Martí, A. A., Jockusch, S., Stevens, N., Akins, D. L., Turro, N. J., and Ju, J. (2006) Combinatorial fluorescence energy transfer molecular beacons for probing nucleic acid sequences. *Photochem. Photobiol. Sci. 5*, 896–902.
(84) Mullah, B., and Andrus, A. (1997) Automated synthesis of double dye-labeled oligonucleotides using tetramethylrhodamine (TAMRA) solid supports. *Tetrahedron Lett. 38*, 5751–5754.
(85) Kelley, S. O., and Barton, J. K. (1999) Electron transfer between bases in double helical DNA. *Science 283*, 375–381.
(86) Torimura, M., Kurata, S., Yamada, K., Yokomaku, T., Kamagata, Y., Kanagawa, T., and Kurane, R. (2001) Fluorescence-quenching phenomenon by photoinduced electron transfer between a fluorescent dye and a nucleotide base. *Anal. Sci. 17*, 155–160.
(87) Heller, M. J., and Jablonski, E. J. (1987) Fluorescent stokes shift probes for polynucleotide hybridization assays. EP pat. 229,943.
(88) Mergny, J.-L., Boutorine, A. S., Garestier, T., Belloc, F., Rougee, M., Bulychev, N. V., Koshkin, A. A., Bourson, J., Lebedev, A. V., Valeur, B., Thuong, N. T., and Hélène, C. (1994) Fluorescence energy transfer as a probe for nucleic acid structures and sequences. *Nucleic Acids Res. 22*, 920–928.

BC900037B

SEPTEMBER 2009
Volume 20, Number 9

© *Copyright 2009 by the American Chemical Society*

Bioconjugate Chemistry

REVIEWS

Proteolysis: A Biological Process Adapted in Drug Delivery, Therapy, and Imaging

Benedict Law*,† and Ching-Hsuan Tung‡

Department of Pharmaceutical Sciences, North Dakota State University, Fargo, North Dakota 58105, and The Methodist Hospital Research Institute, Weill Cornell Medical College, Houston, Texas 77030. Received November 19, 2008; Revised Manuscript Received January 15, 2009

In many diseases, protease expressions are found deregulated when compared with them at the healthy states. The unique ability to hydrolyze protein amide bonds has made those deregulated proteases attractive biological triggers in drug development. Proteolysis has been widely applied in pro-drug design to achieve favorable pharmacokinetics. Controlled drug delivery systems are also reported by incorporating protease-sensitive motifs onto bio-, inorganic-, or organic- materials. In addition, protease responsive molecular probes are developed for in vitro bioanalysis and in vivo diagnostic imaging. This review focuses on various proteolysis-dependent approaches to drug delivery, therapy, and imaging. References are selected to illustrate the concepts and demonstrate the potentials of these enzyme-responsive strategies.

INTRODUCTION

Proteolysis is a simple hydrolytic process that separates two adjacent amino acid residues at the amide bond, aided by proteases (or proteinase). Without the catalytic assistance of protease, protein hydrolysis is a very slow process. Proteolytic activities are tightly regulated through various mechanisms. For example, intracellular proteolysis is regulated by segregation within organelles such as lysosomes. Some proteases are expressed as pro-enzymes, while others are complexed with natural enzyme−inhibitors. Their enzymatic properties can be restored only when they are in demand. As disease initiated, misregulation of enzymatically active proteases or launching of new foreign proteases can occur, resulting in various host responses.

Diseases can be controlled by stopping or slowing disease-associated abnormal proteolysis. Protease inhibitors have a long history as therapeutic agents. Synthetic inhibitors targeting various proteases have been developed and clinically used in treating a large variety of diseases (*1*). Cancer is a well-known example. Protease inhibitors against matrix metalloproteinases (MMP) have been proposed to control tumor growth; unfortunately, the outcomes were not as originally expected (*2*). Beyond cancer, protease inhibitors have been applied or proposed for treating diseases such as thrombosis (*3*), hypertension (*4*), diabetes (*5*), cognitive disorders (*6*), infectious diseases (*7*), and others. Clinically approved protease inhibitors have supported

* Benedict Law, Ph.D., Department of Pharmaceutical Sciences, 1401 Albrecht Blvd, Sudro Hall 116, North Dakota State University, Fargo, ND 58105. E-mail: Shek.law@ndsu.edu. Ching H. Tung, Ph.D., Department of Radiology, The Methodist Hospital Research Institute, Weill Medical College of Cornell University, 6565 Fannin Street, #B5-022 Houston, TX 77030. Email: ctung@tmhs.org.
† North Dakota State University.
‡ Weill Cornell Medical College.

10.1021/bc800500a CCC: $40.75 © 2009 American Chemical Society
Published on Web 03/09/2009

Table 1. Examples of Amino Acid and Peptide Caged Prodrugs That Are Activated by Their Target Proteases[a]

active drug metabolite	conjugated peptide-substrate	target protease	disease
Doxorubicin	L (*13*)	cathepsin B	cancer
Methotrexate	A (*20*)	carboxypeptidase	cancer
Methotrexate	Pyroglutamyl (*21*)	aminopeptidase	cancer
Amiloride	LFGGGG (*143*)	enkephalinase	ischemia
Cyclopamine	SSKYQ (*144*)	PSA	cancer
Doxorubicin	BLAL (*25*)	TOP	cancer
	PLGL (*32*)	MMP-2, MMP-9	cancer
		plasmin	cancer
	aFK (*145*)		
Fluorodeoxyuridine	HSSKLQL (*34*)	PSA	cancer
Gentamicin	GfPRGFPAGG (*70*)	thrombin	infection
Methotrexate	Pyr (*21*)	PYA	cancer
	aFKK (*146*)	cathepsin, plasmin	arthritis
Paclitaxel	aFK, vLK (*38*)	plasmin	cancer
Thapsigargin	HSSKLQL (*35*)	PSA	cancer
Vinblastine	Hyp-SS-Chg-QSSP (*33*)	PSA	cancer

[a] Note: The small letters in the peptide sequences indicate that particular amino acids are in D-configuration. All amino acid derivatives are shown by a group of three italics. Abbreviations: Chg, L-cyclohexylglycine; Hyp, trans-4-hydroxy-L-proline; PSA, prostate specific antigen; PYA, pyrogluatmate aminopeptidase; Pyr, L-pyroglutamic acid; TOP, thimet oligopeptidase.

the original hypothesis that active site blocking could relieve, correct, or slow disease progress.

In contrast, since upregulated proteolysis is often seen during disease progression, instead of blocking its catalytic property, proteolysis has been proposed as a unique in vivo process to assist therapy and diagnosis. Numerous approaches based on proteolysis have been crafted to manage diseases; for example, prodrugs are designed to be activated by proteases, delivery systems are constructed to release drugs in a controllable manner, and molecular reporters are prepared to be protease sensitive for disease detection and imaging.

APPLICATIONS OF PROTEOLYSIS

Protease-Activatable Prodrug. The rationale behind prodrug design is to improve bioactivity and/or bioavailability of a therapeutic agent. A prodrug generally has minimal pharmacological effect in its native form, but can be converted to its active pharmacophore when triggered in vivo. The concept of prodrugs is not new. For example, enalapril, an antihypertensive precursor of enalaprilat, was chemically modified to improve its absorption from the gastrointestinal tract (*8*), and capecitabine was designed to reduce the adverse effects of its cytotoxic metabolite, 5′-fluorouracil (FU) (*9*). Rational prodrug design requires an extensive knowledge of chemical entities that are likely to alter resulting pharmacokinetic properties. In addition, a profound understanding of disease molecular pathologies and their heterogeneities versus normal health states helps to identify potential activators. As mentioned, excessive proteolysis is involved in many diseases such as cancer, cardiovascular injury, and inflammation; thus, disease-associated proteases are attractive targets for pro-drug developments. In fact, numerous protease-activatable prodrugs have been reported (*10*, *11*), while the majority have been developed for cancer treatment (*12*) (Table 1).

Amino Acid Caged Prodrugs. To design a protease-activatable prodrug, a single amino acid or a dipeptide can simply be attached to a free drug via the formation of an amide bond; the resulting conjugate (prodrug) with significantly reduced potency can be hydrolyzed by selective aminopeptidase later to generate clinically effective metabolite (Figure 1A). L-Leucyl-doxorubicin is an early example developed in the 1980s (Figure 1B) (*13*). It is four times less toxic than its parent doxorubicin and has been shown to reduce cardiotoxicity in preclinical studies (*14*−*16*). Several studies of human breast, lung, and ovarian tumor

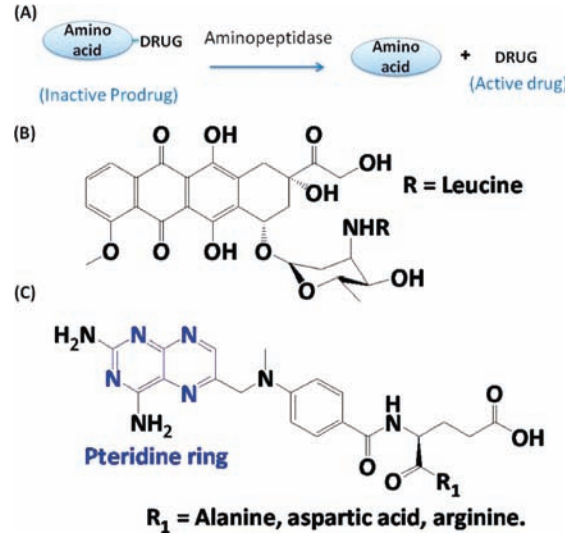

Figure 1. (A) Schematic presentation of an amino acid−drug conjugate activated by aminopeptidase. (B) The chemical structure of L-leucyl-doxorubicin. Leucine is covalently conjugated to the aminoglycoside portion of doxorubicin (*13*). (C) The chemical structure of various 2-α-carboxyl methotrexate derivatives (*21*).

xenografts demonstrated that L-leucyl-doxorubicin had not only a better therapeutic index, but also a greater efficacy than doxorubicin (*17*, *18*). A high concentration of active metabolite doxorubicin was found in tumor cells, suggesting that the enzymatic cleavage of L-leucyl-doxorubicin takes place either on the surface inside of the tumor cells. Tissue peptidases such as cathepsin B have been proposed to be the responsible activators (*19*). Prodrugs with a similar strategy have also been described for methotrexate (*20*). Amino acids such as alanine, aspartic acid, and arginine were conjugated to the α-carboxyl of methotrexate via an amide linkage (Figure 1C). Ex vivo studies indicated that the resulting alanine-conjugate was 100 times less toxic than its parent drug. On the other hand, cytotoxicity was greatly enhanced by carboxypeptidase activation. Protease selectivity could be altered by modifying a different position on methotrexate (*21*). A series of 2-L-leucyl, 2-L-valyl, 2-L-isoleucyl, and 2-L-pyroglutamyl methotrexate conjugates were synthesized by attaching the corresponding amino acids to the NH_2-group at the 2-position of the pteridine ring (*21*). Among all of these, 2-L-pyroglutamyl analogue was considered the best drug candidate, as it can be selectively activated by pyroglutamate aminopeptidase but is resistant to nonspecific enzymatic degradation in serum.

Peptide Caged Prodrugs. Although the amino acid caging approach shows promise, the prepared prodrugs are not stable enough in circulation. With L-leucyl-doxorubicin as an example, pharmacokinetic studies have shown that leucyl-doxorubicin was rapidly converted into free doxorubicin in plasma compartment (*19*). Its superior therapeutic efficacy over doxorubicin is most likely due to the higher accumulation of this metabolite (free doxorubicin) in tumor than in normal tissue. To design a more stable prodrug, a tetrapeptide conjugate, BLAL-doxorubicin (B = β-alanine), was synthesized (Figure 2) (*22*). The β-alanine at the N-terminus was incorporated to improve stability in blood. In vitro and in vivo studies with a similar prodrug analogue, *N*-(succinyl)-BLAL-doxorubicin (CPI-0004Na), have shown that extracellular activation is a multistep process (*22*−*24*): (1) The prodrug was first hydrolyzed extracellularly into AL-doxorubicin. This process was also proven to be the rate-limiting step; (2) AL-doxorubicin was subsequently cleaved into leucyl-doxorubicin; and (3) it finally entered the cell and was converted into fully active doxorubicin. Thimet oligopeptidase (TOP) and

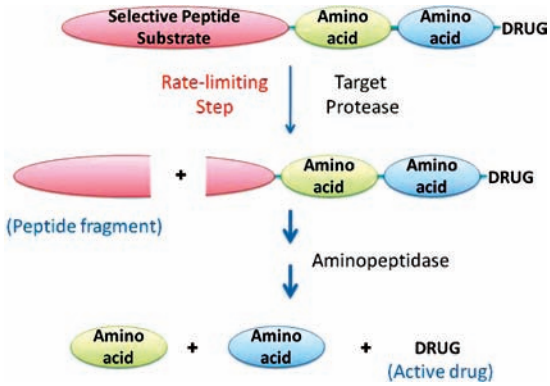

Figure 2. Schematic presentation of a peptide−prodrug conjugate activated by multiple proteases. Prodrug acylated with a specific peptide substrate is cleaved by its target protease, and the remaining peptide−drug intermediates can be further digested by different aminopeptidases to release the free drug.

neprilysin (CD10) were identified as the responsible initial activators (*25*, *26*).

However, the choice between aminopeptidase and carboxypeptidase is limited; more sequence selectivity would be favored to achieve disease-specific prodrug activation. Using the same construct as shown in Figure 2, conjugating longer specific peptide substrates recognized by endopeptidases to an active pharmacophore has been done to obtain better protease selectivity. Peptide-caged prodrugs activated by plasmin (*27*−*29*), MMPs (*30*−*32*), and prostate-specific antigen (PSA) (*33*−*36*) have all been reported.

In some cases, proteases do not accept a complex pharmacophore directly attached to the end of a peptide sequence. For example, in the early 1980s, vLK-doxorubicin prodrug was developed to treat cancer, but it turned out to be a poor substrate for plasmin, resulting in an unfavorable therapeutic effect, probably because of steric hindrance. To overcome this problem, self-immolative linkers were inserted between the peptide substrate and the drug molecule (*37*). Two types of self-immolative systems are known: electronic cascade spacers and cyclization spacers. Paclitaxel prodrugs prepared with both spacers have been reported (*38*). *p*-Aminobenzyl oxycarbonyl (PABC) and monomethylated ethylene diamine (MED) were employed as electronic cascade and cyclization spacers, respectively (Figure 3). Both conjugated prodrugs, which have significantly decreased cytotoxicity, could be readily activated by plasmin, followed by spontaneous spacer elimination and subsequent release of free paclitaxel. Interestingly, the two systems have distinct pharmacokinetic properties. Prodrug incorporated with the PABC spacer had a slower enzymatic hydrolysis (42 min vs 3.5 min) but a faster spacer elimination rate (instantaneous vs 23 h) than with the MED spacer (Figure 3).

Alternatively, a nonremovable enhancer can be covalently attached through an irreversible spacer to the drug molecule for better efficacy. The enhancer molecule to which the parent drug connects is carefully chosen to avoid significant loss of drug potency. For example, thapsigargin (TG) is an apoptotic agent with $LD_{50} = 30$ nM in TSU-Pr1 prostate cancer cell (*39*). Covalent attachment of a 12-aminododecanoyl linker yielded an analogue (L12ADT) that retains the same efficacy as TG (Figure 4) and can be further conjugated with a PSA substrate (HSSKLQ). The resulting prodrug is nontoxic to normal cells, because the attached peptide substrate prevents it from entering the cells (*35*). The prodrug has demonstrated selective cytotoxicity in PSA-producing LNCaP cells, while remaining nontoxic to PSA-negative HCT-116 cell lines.

Antibody−Drug Conjugates. Traditional anticancer drugs are highly toxic and have limited specificity to cancer cells. In

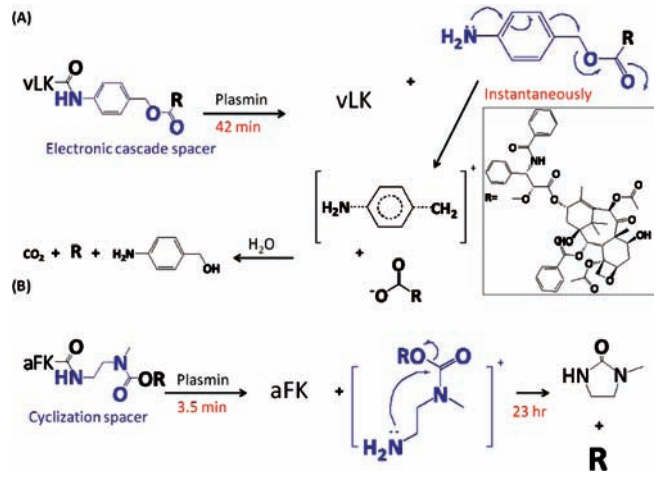

Figure 3. Example of paclitaxel prodrug derivatives incorporated with self-immolative spacers. (A) Paclitaxel prodrug analogues were designed by incorporating PABC to paclitaxel via a 2′-carbonate. PABC is inserted between the peptide substrate (vLK) and paclitaxel. The prodrug is proteolyzed by plasmin, followed by spontaneous solvolysis. (B) The paclitaxel-2′-carbamate derivative consisting of a MED spacer and tripeptide (aFK) is hydrolyzed, followed by spontaneous cyclization reaction to yield the pentacyclic urea (*38*).

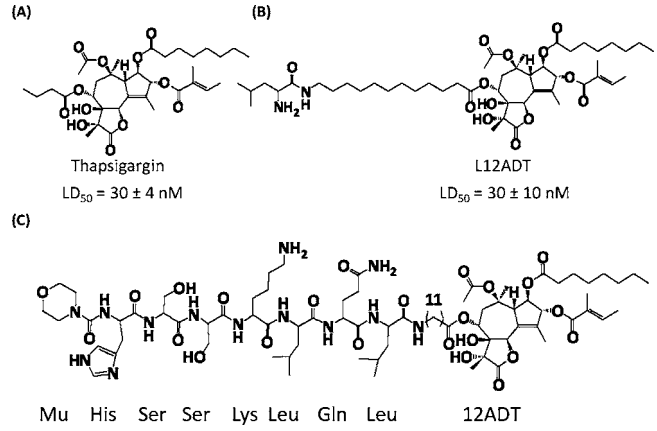

Figure 4. Chemical structures of (A) thapsigargin (TP), (B) 8-*O*-(12-[L-leucinoylamino]dodecanoyl)-8-*O*-debutanoylthapsigargin (L12ADT), and (C) a PSA substrate (HSSKLQL) conjugated with 12ADT (*35*).

contrast, monoclonal antibodies (mAbs) can selectively bind to tumor cells via specific surface markers, but only display moderate antitumor activity. Antibody−drug conjugates (ADCs) have been designed by covalently attaching cytotoxic agents to mAbs. This tumor-targeting technology utilizes the fact that mAbs can help to deliver the nonspecific toxic agents to the tumor sites, thus greatly reduce their undesired systemic toxicity. Moreover, the mAbs can also synergic elucidate the tumor cells. To design an ADC, a linker is required to connect the cytotoxic agent and the mAb. This linker should be stable in blood circulation but readily cleaved or disconnected to release the cytotoxic drugs. Various linkers have been designed and synthesized to enhance drug releases upon cellular internalization. These include the hydrazone-based or ester linkers that can be hydrolyzed in the acidic environment of lysosomes (*40*−*45*) and the disulfide exchange or self-immolative disulfide linkers that can be reduced by glutathione inside the cells (*46*−*48*). Peptide substrates have also been employed for designing ADCs; the resulting conjugates can be hydrolyzed by lysosomal proteases such as cathepsin B to release the active drugs (*45*, *49*, *50*). For example, *n*-butyl diacetate derivative of doxorubicin has been synthesized and attached to both the anti-CD70 and anti-CD30 mAbs via a dipeptide linker. A self-immolative PABC

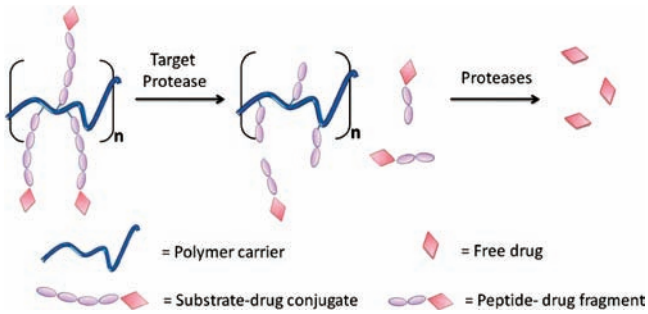

Figure 5. Schematic presentation of a prodrug−polymer.

Table 2. Examples of Polymeric Drug Carriers That Are Activated by Target Proteases[a]

polymer carrier	active drug	peptide linker	target protease	indication
CM-Dextran-PA	Exatecan (*147*)	GGFG	Cathepsin B	anticancer
Dextran	Methotrexate (*58*)	PVGLIG	MMP-2, MMP-9	anticancer
HPMA	Thapsigargin (*148*)	SSKYQL	PSA	anticancer
HPMA	TNP-470 (*149*)	GFLG	Cathepsin B	anticancer
L-PG	Paclitaxel (*150*)	EE	Cathepsin B	anticancer
PEG	Camptothecin (*56*)	GLFG	Cathepsin B	anticancer
PGC	Porphyrin (*110*)	KK	Cathepsin B	anticancer

[a] Abbreviations: CM-Dextran-PA, carboxymethyldextran polyalcohol; L-PG, polyglutamic acid; PEG, poly(ethylene glycol); PGC, poly-(L-lysine) grafted with monomethoxy-poly(ethylene glycol) copolymer; TPN-470, O-(chloracetyl-carbamoyl) fumagillol.

spacer was further introduced in between the dipeptide linker (valine-citrulline) and the daunosamine nitrogen of the doxorubicin derivative. Upon proteolysis, 2-pyrrolinodoxorubicin was self-eliminated as the active metabolite. The ADCs were >70-fold more potent than doxorubicin and also demonstrated >40-fold specificity when evaluated against their corresponding antigen negative cell lines (*51*).

Besides aiming for intracellular delivery of cytotoxic agents, peptide linkers can be employed to improve the therapeutic index of radio-immunotherapy by accelerating the liver clearance of radiometals from their immunoconjugates (ICs) (*52*), since cathepsin degradation of the peptide linkers could release the chelated radiometals into the circulation and subsequently eliminated by renal clearance. Cathepsin-degradable peptide-linked radio-ICs (RICs) and their corresponding 2-iminothiolane (2IT) nondegradable linked RICs have been designed to compare their pharmacokinetics in HBT-3488 human breast adenocarcinoma xenografts (*53*). The results indicated that the cumulative activities of peptide-linked RICs in liver were significantly lower (reduced from 59% to 68%) than their corresponding 2IT-linked RICs.

Protease-Responsive Carriers and Biomatrices. *Polymeric Carriers.* To extend the in vivo half-life of a therapeutic agent, multiple drugs can be covalently attached to the backbone of a polymer via peptide substrates. In general, drug−peptide conjugates are covalently attached to a synthetic polymer. In the presence of a target protease, the prodrug−polymer releases multiple peptide−drug fragments that subsequently hydrolyze into active metabolites (Figure 5). Various protease substrates have been reported as the linkers (examples in Table 2). The advantages of employing polymers as drug carriers are that they can be biocompatible, biodegradable, and soluble. Polymer−drug conjugation has become a popular approach to cancer delivery, as polymers with high molecular weights tend to accumulate at tumor sites via the enhanced permeability and retention (EPR) effect, or so-called passive targeting (*54, 55*). For example, 10-amino-7-ethylcamptothecin (SN-392) was conjugated to a linear methoxypoly(ethylene glycol) (mPEG) through a tetrapeptide (GLFG) spacer (*56*). The resulting polymeric conjugate had higher antitumor activity than free SN-392 in a Meth A fibrosarcoma (solid tumor) model. Another example is dextran-PVGLIG-methrotrexate conjugate. The prodrug was cleaved by both MMP-2 and MMP-9 (*57*), which could release a sufficient number of peptidyl methotrexate fragments to inhibit tumor growth (*58*). However, the tumor targeting mechanism relied predominantly on EPR. The same approach has been applied to other diseases, such as choroidal neovascularization (CNV) (*59*) and myocardial infarction (*60*), because the affected tissues also exhibit the similar anatomical characteristics to those of a tumor (i.e., hyperpermeable vessels and lack of effective lymphatic drainage).

Biomatrices. Hydrogels have been extensively developed for drug delivery and tissue engineering. They are usually three-dimensional networks formed by polymeric chains cross-linking via hydrophobic, electrostatic, and/or covalent interactions; for example, naturally derived polymers such as dextrans and gelatin have been used for protein delivery (*61, 62*). The state of the art in tissue engineering is to optimize matrix degradation for tissue regeneration processes, while allowing healing and remodeling to take place. Some of the employed matrices are natural and can be intrinsically digested by proteases. For example, the release of vascular endothelial growth factor (VEGF) from heparinized collagen matrices appeared to be controlled by both the presence of heparin from the matrices and the proteinases that are secreted from the fibroblasts (*63*). To modulate (increase or decrease) the rates of matrix degradations, reagents such as glutaraldehyde (*64*), polyepoxy compounds (*65, 66*), and carbodiimides (*67*) have been employed to cross-link the collageneous materials. Alternatively, the amino acid side chains on the collagen could be capped to prohibit cross-linking. For example, the lysine and arginine amino acid side chains on collagen were chemically modified by *n*-butylglycidyl ether and methylglyoxal, respectively (*68*). The modified collagen had a significant reduction in swelling property, but an increased solubilization when treated with proteases such as trypsin, acetyltrypsin, and cathepsin B, which was attributed to disruption of the collagen structure by chemical modifications.

Depending on the desired applications, environmentally sensitive hydrogels can be designed by chemically modifying their polymer components (*69*). Therapeutic molecules can be attached, encapsulated, or absorbed onto these matrices. Of particular importance, external stimuli such as temperature, electric fields, light, pH, or enzymes can be exploited to control their release rates. Various matrices that are sensitive to proteases have also been developed. An early example was the development of polyvinyl alcohol (PVA) hydrogels for bacterial prophylaxis (*70*). This approach was similar to that for polymeric−peptide conjugate, except an insoluble PVA matrix was grafted to gentamicin through multiple thrombin substrates (GfPRGFPAGG). Gentamicin molecules were selectively released from the matrix when incubated with thrombin-expressed *Staphylococcus aureus* infected wound fluid, while no biologically active antibiotic was released with noninfected wound fluid (*71*). Further evaluation in animals showed that the matrix was potent and specific for treating *Staphylococcus aureus* infected wounds (*70*). MMPs-activatable wafers were developed for local delivery of chemotherapeutic agent (*72*). Cisplatin complexed with an MMP substrate (CGLDD) was incorporated into poly(ethylene glycol) diacrylate hydrogel wafers. Drug release was dependent on MMPs expressed in a conditioned U-87 MG cell culture media.

A protease-responsive hydrogel based on the KLD-12 peptide (Ac-KLDLKLDLKLDL) was reported to control release of cytotoxic peptide (*73*). The peptide was able to form a self-

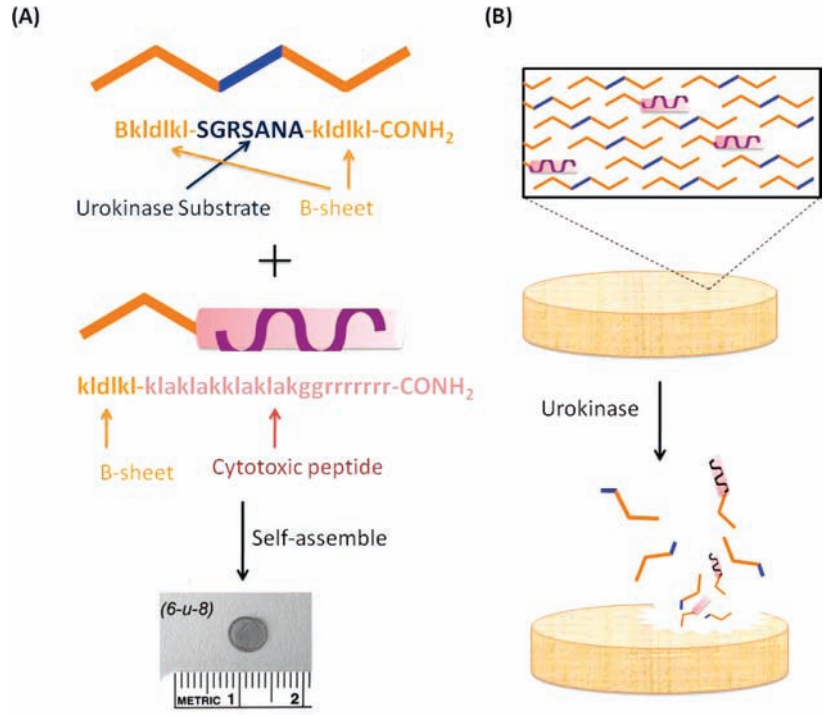

Figure 6. The design of a urokinase activatable hydrogel. (A) A self-assembling peptide (KLD-12) inserted with urokinase substrate was complexed with a cytotoxic peptide (kldlkl-r7-kla) to form a hydrogel system. (B) Upon addition of the targeted protease, the enzyme digests the preparations at the substrate cleavage site resulting in release of gel fragments and therapeutic peptides (*77*).

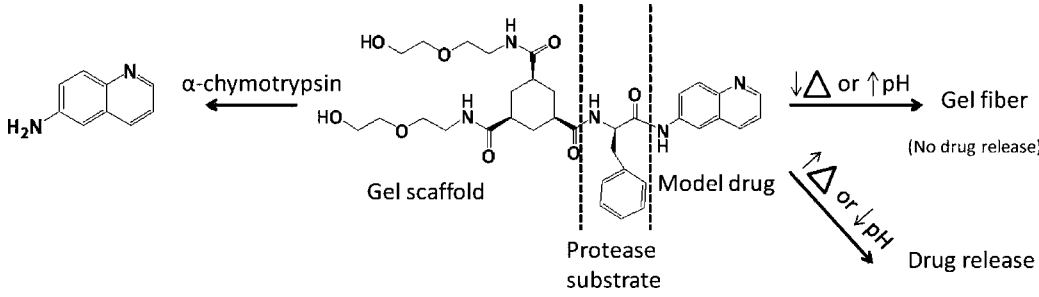

Figure 7. The design of a protease-cleavable LMWG−(model) drug conjugate system. Gel fiber formation is completely reversible by temperature and pH (*79*).

assembled matrix via β-sheet stacking (*74, 75*). An urokinase substrate sequence (SGRSANA) (*76*) was inserted between the assembling motifs with D-configuration, thus creating a uPA-responsive formulation when assembled (Figure 6). Cleavage of the protease substrate from the assembled matrix fragmented the building blocks, which in turn weakened the β-sheet interactions and caused matrix degradation. Further anchoring a cytotoxic peptide (r7-kla) into the matrix demonstrated that drug release was triggered by urokinase (*77*).

Recently, a recombinant gelatin (HU4) containing part of the amino acid sequence of the α1-chain from human type I collagen was synthesized as the polymeric construct for hydrogel (*78*). The HU4 gelatin was further modified with methacrylate residues, thus enabling chemical cross-linking and gel formation by radical polymerization. The assembled hydrogels were degraded by MMP-1. In addition to polymer gel based systems, drug delivery based on low molecular weight gelator (LMWG) has been synthesized (*79*). A model protease-activatable prodrug, L-phenylalanyl-amidoquinoline, and two ethylene glycol chains were conjugated to a cyclohexane trisamide gelator (Figure 7). The gel fiber system demonstrated a two-stage enzyme-mediated drug release mechanism. At room temperature, the assembled gel fibers protected the prodrug molecules from protease cleavage. When the temperature was raised (from 25 to 45 °C), the gel-to-solution transition equilibrium was shifted, and relaxed gelators became available for α-chymotrypsin cleavage to release the free 6-aminoquinoline.

Protease-Sensitive Imaging Probes. Immunohistological analysis showed high regional expression of disease-associated proteases in many disease tissues. Compared with adjacent normal tissues, the difference is significant; for example, in the case of colon adenoma, upregulated cathepsin B was observed in early phase tumor (*80*). Labeled antibodies against enzymes are suitable for ex vivo tissue analysis, but for in vivo detection of proteases, a more sensitive sensing approach would be favored. Since the proteases are catalytic enzymes, one protease could specifically activate tens, hundreds, or even thousands of its substrates. Amplification of the signal could be expected if the molecular probes are designed to be the substrates of their target proteases (*81*). The ability to repeatedly and noninvasively map protease expressions in real time in vivo can be an important tool for disease diagnosis (*82*). Recently, three major types of activatable fluorescent probes have been developed to report protease activity in living biological systems (Figure 8) (*83*). To distinguish background signal from true signal, in general, the principle mechanism of activation is based on quenching−dequenching upon enzymatic cleavage. The molecular probes are typically designed to be maximally quenched

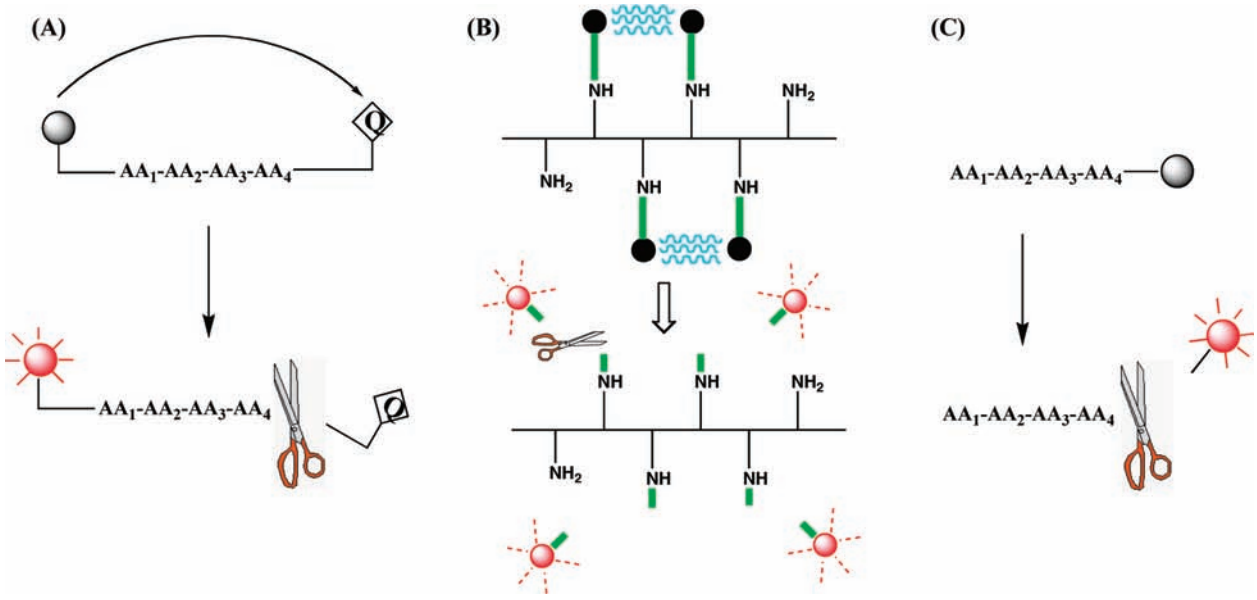

Figure 8. Schematic diagram of protease-activatable fluorescence probes. (A) Peptide-based enzyme sensitive probe. The molecular probe has a fluorescent donor at one end of the peptide substrate and a light absorber at the other end, (B) Self-quenched enzyme sensitive probe. Fluorochromes were covalently coupled to a polymer backbone via a synthetic peptide substrate (green line). Due to the proximity of the fluorochromes, self-quenching occurs so that almost no fluorescent signal can be detected in the nonactivated state. After designated enzyme cleavage of the peptide spacer, fluorochromes are released from the carrier and become brightly fluorescent. (C) Fluorogenic enzyme-sensitive probe. Fluorescence signal will be switched on when the probe is proteolytically activated.

in their native states and to brightly fluoresce in their cleaved states. On the basis of this quenching design, the background signal can be maintained at a minimum.

The first approach (Figure 8A) to producing a proteolysis-activatable probe is to flank an enzyme substrate with a fluorophore and a spectrally matched "quenching" molecule that effectively absorbs the energy from the fluorophore via fluorescence resonance energy transfer (FRET) (*84*). The second type (Figure 8B) of design is also based on energy transfer, but between the same types of fluorochromes. High numbers of fluorochromes were anchored onto a polymer template through cleavable peptide substrate sequences, which brought in protease selectivity. Loading the polymer with a large number of fluorochromes, typically 20−30 fluorochromes, results in nearly completely quenched fluorescence. The third type of protease-sensitive probe has the simplest design (Figure 8C). Only one fluorogenic reporter is needed for the probe. Typically, the intact probe emits no fluorescence until the amide bond between the peptide substrate and the dye is clipped.

Peptide-Based Molecular Probes. Various fluorochrome and quencher pairs have been selected for the best fluorescence energy transfer (Figure 8A). By linkage through a peptide substrate sequence, molecular probes could be selectively activated. A near-infrared fluorochrome Cy5.5 pairing with an absorber NIRQ820 was developed for MMP-7 imaging. Up to a 7-fold increase in fluorescence signal was observed when treated with MMP-7 (*85*). A recent example with Cy5.5/BHQ-3 pair was prepared to image osteoarthritis associated MMP-13 activity and to monitor therapeutic response in living animals (*86*).

Different from an optical quenching approach, a cell retention strategy was designed by integrating proteolysis and cell penetration signals (*87*). A polyarginine-based, cell-penetrating peptide was linked to a polyglutamate through an MMP-2/9 linker. Because of the intramolecular charge interaction, the cell-penetrating property was blocked until tumor-associated MMP-2/9 degraded the linker and then exposed the cell-penetrating peptide, which was able to direct the optical reporter into high MMP expressing tumors, reporting the location of the tumor. In addition to imaging, the same approach can be applied to provide site-selective drug delivery.

In a separate approach, regional proteolysis was applied to change the solubility of an imaging probe, resulting in local deposition of reporter (*88*). An MMP-7 substrate peptide was tethered with a chelated gadolinium (Gd) and a hydrophilic PEG chain. Upon proteolytic degradation, the PEG solubility enhancer was eliminated, causing solubility to drop in the Gd-containing peptide fragment. In vivo MR imaging indicated that Gd deposition correlated with MMP-7 expression and a protease inhibition effect by therapeutic inhibitor could be conveniently imaged by MR imaging.

Polymeric−Peptide Conjugate. The first protease-activatable optical contrast agent developed for in vivo imaging was reported in the late 1990s (*89*). The probe was a protected grafted copolymer (PGC) composed of a poly(L-lysine) backbone (PL) conjugated with multiple mPEGs and near-infrared fluorophores (Cy5.5). The fluorophores were enclosed in proximity resulting in significant quenching in their fluorescence emissions. Broad-spectrum proteases including cathepsin B and L could digest the polymeric backbone through the remaining free lysine residues, release the polymeric fragments, and subsequently initiate a dequenching process (i.e., fluorescent amplification). The approach was employed to image diseases such as cancer (*89*), arthritis (*90*), and atherosclerosis (*91*). To target different proteases, selective peptide substrates have been inserted between the fluorophores and the PGC (Figure 9). Simply by replacing the peptides, imaging probes were developed for detecting other disease-associated proteases such as cathepsins (*92*, *93*), MMPs (*94*, *95*), caspases (*96*), and thrombin (*97*). For example, a peptide substrate (GGSGRSANA) was employed for a uPA-sensitive probe (*98*). When the probe was tested in HT-1080 breast fibrosarcoma tumor-bearing mice, the observed fluorescence signals at the tumor sites were correlated with uPA activity (*99*).

Recently, self-assembled nanofibers have been designed to sense uPA activities (*100*). Their basic assembly constructs comprise (1) a peptide sequence (kldlkldlkldl) reported to form stable β-sheet platform; (2) a uPA substrate motifs (SGRSANA); (3) a nontoxic

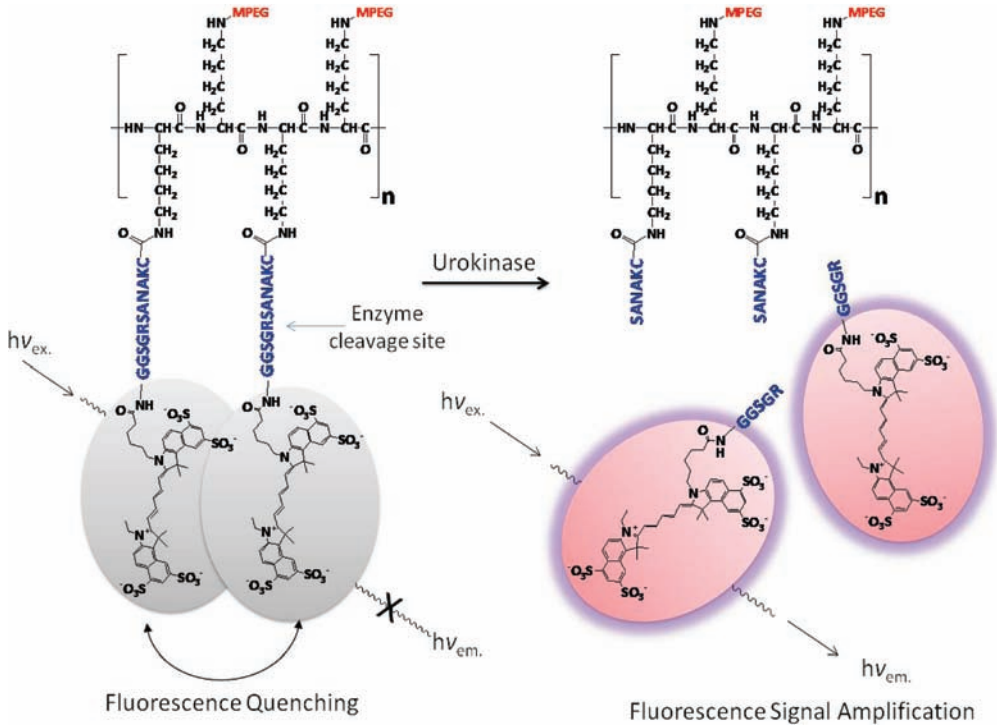

Figure 9. Schematic presentation of a urokinase-selective probe. The Cy5.5-peptide substrates (Cy5.5-GGSGRSANAKC) are attached to a PGC. The close spatial proximity of these multiple conjugates leads to fluorescence quenching. Upon urokinase cleavage, the released peptide fragments result in fluorescence signal amplification (*98*).

MPEG attached at the peptide N-terminus; and (4) a fluorescein as the optical reporter. Upon addition of proteases, the enzymes digest the nanofibers via their substrate cleavage sites, causing the release of hydrophilic fluorescent fragments and resulting in fluorescence emission. Interestingly, these nanofibers have the ability to compensate for the loss of intrinsic hydrophilicity; the remaining digested or partially cleaved nanofibers undergo morphological changes with time (*101*).

Fluorogenic Probes. On the basis of delocalization of the lone pair electrons, fluorogenic probes can be extremely simple (Figure 8C). Amino-4-methylcoumarin (AMC) is a widely used fluorogenic dye in measurements of protease activity. For in vivo applications, fluorophores having the excitation and emission at near-infrared (NIR) region (700−1000 nm) are generally preferred, since they have less interference from endogenous chromophores and also have deeper tissue penetrations while imaging. A series of fluorogenic dyes with benzo[*a*]phenoxazine core structure have been synthesized and evaluated (*102, 103*). Among them, 9-di-3-sulfonyl-propylaminobenzo[*a*]phenoxazonium perchlorate (2SBPO) has the best solubility and optical properties. Thus, it was selected as a scaffold to synthesize a panel of enzyme substrates, sensitive to amino peptidase (*103*), other proteases (*104*), and galactosidases (*105*). The assembled probes are nonfluorescent but display strong fluorescent emission at 670 nm following proteolytic release of 2SBPO. Bioluminogenic probe is another type of optical imaging agent designed by using the same concept as fluorogenic substrate. Peptide substrate was added to amino-luciferin, which was derived from the natural substrate of fire fly luciferase, D-luciferin. Because of steric hindrance, luciferase cannot recognize the peptide-modified luciferin. After proteolytic hydrolysis of the peptide, free luciferin was released and utilized by luciferase in situ. We have used a commercially available DEVD-luciferin substrate to study treatment effect of anticancer gene therapy (*106*). Expressed anticancer protein induced apoptosis of tested tumor cells, triggering caspase-3 expression. A bioluminescence signal was found associated with the gene therapy effect.

Protease-Mediated Photodynamic therapy. Photodynamic therapy (PDT) is currently used to treat several types of cancer. Regional therapeutic effect can be achieved only by combining photosensitizer (PS), light, and oxygen. Each component is harmless by itself, but when all three components get together, light excitation of a PS will locally generate highly cytotoxic singlet oxygen, $^1O_2$, which induces cell death and tumor ablation (*107*). Most PSs are porphyrin analogues that absorb light energy and then transfer to oxygen or emitted fluorescence. It has been reported that singlet oxygen generation is closely correlated with fluorescence intensity (*108*). When a PS is in a fluorescent quenched state, its ability to generate singlet oxygen is also reduced.

Using the same PGC platform used in imaging probes, a pro-PDT agent was synthesized by replacing Cy5.5 with a photosensitive agent, chlorin e6 (Ce6). When the assembled agent was in its native state, both the fluorescence and the singlet oxygen generation (SOG) of the anchored Ce6 were depopulated by energy transfer (Figure 10). The resulting pro-PDT agent had a lower toxicity (13%) than the free Ce6, but the hidden phototoxicity could be recovered after proteolysis (*109*). In an animal experiment with one single low dose of pro-PDT agent, tumor growth was slowed by 50% (*110*). In addition, local Ce6 concentrations could be simultaneously monitored by fluorescence imaging. A similar polymer-induced quenching approach was also reported, using pheophorbide-a as the PS (*111*). Phototoxicity was recovered when treated with a model protease, trypsin. Using the same concept as previously described for peptide-based molecular probes, short peptide-based protease-mediated PDT agents were also developed with a pyropheophorbide-a photosensitizer and a BHQ-3 quencher pair (*112*). Protease-mediated phototoxicity of target enzymes, caspase-3 and MMP-7, was demonstrated in vitro and in vivo (*112, 113*).

Protease and Nanoparticles. Particle sizes under 100 nm are unlikely to be eliminated by renal filtration but rather cleared by the liver and spleen or phagocytized by macrophages (*114*). Similar to polymeric carriers, nanoparticles ranging in size from

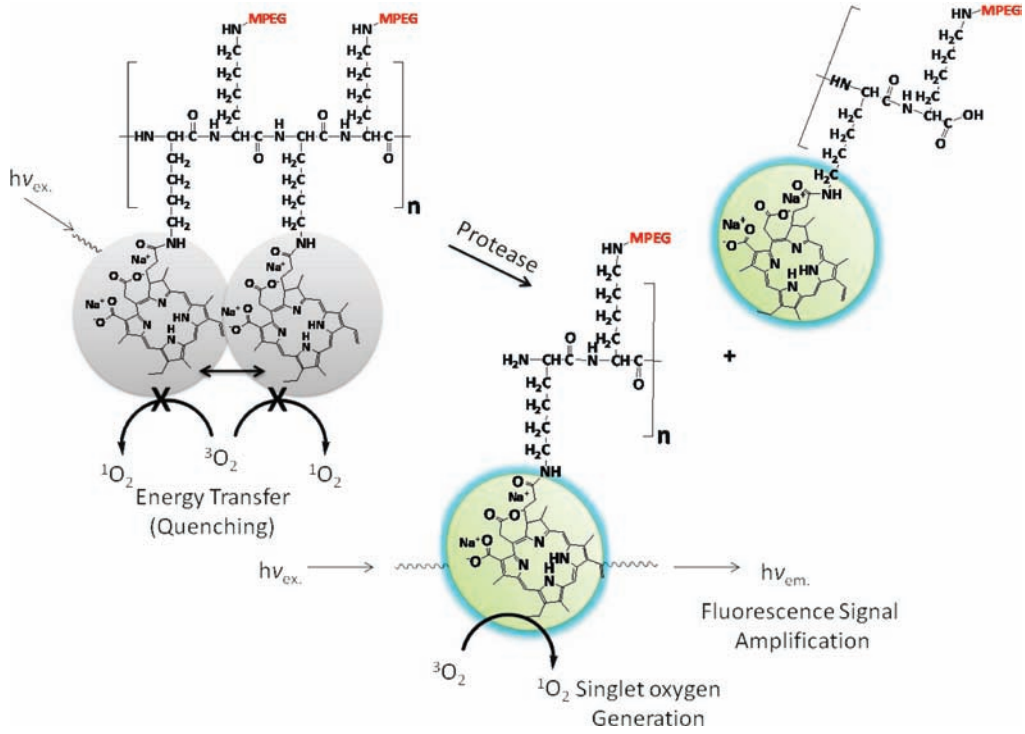

Figure 10. Schematic presentation of a protease-sensitive photodynamic therapeutic agent. Multiple photosensitizers (Ce6s) are attached to a PGC. Intramolecular energy transfer between the closely positioned Ce6 molecules contributes to a significant quenching of fluorescence emission and singlet oxygen generation. Following enzymatic cleavage of the poly(L-lysine) backbone, the released Ce6s-polymeric fragments regain their fluorescent properties and SOG (*110*).

20 to 150 nm tend to accumulate in tumor tissues via EPR effect (*54*). Nanomaterials such as nanofibers (*115*), carbon nanotubes (*116*), superparamagnetic iron oxide crystals (*117*), quantum dots (*118*), dendrimers (*119*), polymeric micelles (*32*), liposomes (*120*), nanospheres (*121*), and polyplexes (*122*) have been engineered as therapeutic carriers. Efficient drug delivery can be achieved by incorporating therapeutic agents into these inherent carriers (*55*). Some of them are designed to be degraded by natural proteases. For example, paclitaxel-loaded gelatin nanoparticles were developed for intravesical therapy of superficial bladder cancer (*123*). The particles are rapidly degraded by Pronase to release the free drug molecules.

To promote cellular internalization, protease-activatable liposomes were designed by conjugating an acetylated dipeptide substrate (N-Ac-AA) through its carboxyl terminus to the amino group of 1,2-dioleoyl-*sn*-glycero-3-phosphoethanolamine (DOPE) (*124*). The resulting peptide−lipid (*N*-Ac-AA-DOPE), together with dioleoyl trimethylammonium propane (DOTAP) and phosphatidyl-ethanolamine (PE), were assembled into nonfusogenic liposomes. The liposomes were activated by elastase or proteinase K to become fusogenic for enhanced intracellular delivery (Figure 11).

In another study, a pegylated MMP-2 substrate (GPLGIAGQ) was conjugated to the amino group of DOPE (*125*). When assembled with disteraoyl phosphatidylcholine (DSPC), cholesteryl chloroformate, and cholesten-5-yloxy-*N*-(4-((1-imino-2-,*β*-D-thiogalactosylethyl)amino)butyl)formamide (Gal-C4-Chol) (*126*), the resulting liposomes (Gal-PEG-PD) were composed of (1) active targeting ligands (galactose moieties) recognized by the hepatic cell surface asialoglycoprotein receptors; and (2) a pegylated peptide substrate cleaved by MMP-2 (Figure 12). In the absence of enzymes, Gal-PEG-PD-liposomes could not be taken up by normal hepatocytes because of steric shielding of the targeting ligands. With the addition of MMP-2, the enzyme removed the bulky mPEGs, thus exposing the galactose ligands for targeting. The cytotoxicity of *N* (*4*)-

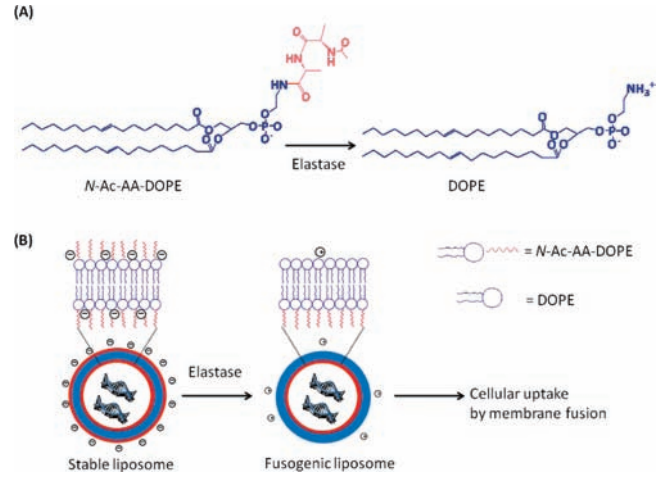

Figure 11. (A) Chemical structure of *N*-Ac-AA-DOPE. The lipid−peptide substrate can be converted into DOPE by elastase (*124*). (B) Activation of a non-fusogenic liposome. The liposome is stable with negatively charges. Removal of *N*-Ac-AA by elastase results in charge reversal, thus enhancing the ability to fuse with the plasma membrane for drug delivery.

octadecyl-1-*β*-D-arabinofuranosylcytosine (NOAC) incorporated Gal-C4-PD liposomes were significantly enhanced in cultured HepG2 cells after pretreatment with purified human MMP-2.

Quantum dots (QDs) that are activated by MMP-2 and MMP-7 were developed for cellular imaging (*127*). The QDs were attached with a peptide consisting of (1) a cationic tetraarginine as the transporter for intracellular delivery; (2) an anionic tetraglutamic acid as the blocker to inhibit cellular uptake; and (3) a peptide substrate sequence (PLVGR). Once the blockers are removed by MMPs, resurfaced tetraarginine signals direct QDs into cells. FRET pairs composed of QDs are also designed to sense protease activities (*128, 129*). Quenchers such as gold nanoparticles (*128*), organic fluoro-

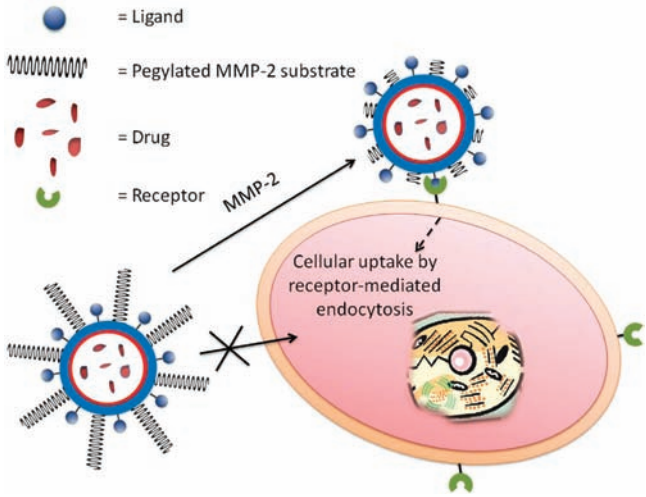

Figure 12. Schematic presentation of MMP-2 activatable targeting liposome (*126*). Cell-specific delivery was initiated when the masking PEG chain was eliminated by MMP-2.

phores (*129*), or fluorescent proteins (*130*) have been attached to the QDs via peptide substrates. QD photoluminescence was quenched through FRET. Protease cleavage of the peptide linkers released the quenchers, which subsequently recovered the QD luminescence emissions. This approach has been applied to study the protease activity in HTB126 cancer cell line (*131*).

A low nanometer-sized dendritic molecular probe having Cy5.5 as fluorescence reporter and AF750 as an internal reference was prepared for tumor detection (*132*). The AF750 was attached to a dendrimer directly, while Cy5.5 was linked through an MMP-7 spacer. In animal experiments, a bright Cy5.5 signal switched on by intestinal adenoma-associated MMP-7 was found in microsized adenomas. In another dendrimer example, anticancer agent Pt^{2+}-complex was attached to first-generation dendrimers through a cathepsin B releasable linker (*133*). Cell culture experiments confirmed the potential of applying this dendritic drug in anticancer therapy.

Organic nanoparticles have been formed by a "hydrophobic collapse-like" construct (*134*). In aqueous solution, a hydrophobic core was formed by multiple deoxycholic acids and was attached to a branched polyethyleneimine (PEI) chain. Multiple fluorescence-labeled caspase-3 substrates were then tethered to the surface of spherical particles, forming 80−100 nm organic nanoparticles. Because of a self-quenching mechanism, the fluorescence signal was shielded until the particle was recognized by target proteases. The described nanoprobe has been applied to following the apoptotic process under a fluorescence microscope.

CONCLUSION AND PROSPECTS

Proteolysis is a simple reaction that cleaves the peptide amide bond, but its applications have been proved enormous. Taking advantage of disease associated proteolysis, numerous prodrugs, biomaterials, and probes have been developed. Pharmacophores and reporters are first restrained or masked by various smart designs. Subsequent proteolysis by target proteases releases the active ingredients chemically or physically, regaining the desired therapeutic activity or imaging sensitivity in situ. Another advantage of proteolysis in drug development is catalytic capability. Operating like a self-propelled machine, one protease could potentially release a large number of drugs. Moreover, the catalytic function is a kind of in vivo PCR reaction that amplifies signal outputs and improves the detection limit significantly, which may have tremendous potential medical applications including disease detection and diagnosis.

In this brief review, only proteolysis was summarized, but it is not the only enzyme candidate used in drug engineering. Other natural enzymes have also been proposed, studied, and applied. For example, lactamase-responsive prodrugs (*135*), hydrogel biomaterials (*136*), and imaging probes (*137*) have all been reported. Another good example is transglutaminase, a type of enzyme usually found at the site of tissue healing and blood coagulation. It cross-links proteins through glutamate and lysine side chains. On the basis of this unique chemical linking property, transglutaminases are often used to increase toughness of hydrogels that can be applied to drug delivery systems or implants for tissue regeneration (*138, 139*). Imaging probes deposited by transglutaminase were also developed to understand healing and blood clotting processes (*140−142*). Many more enzymes have been identified but are waiting for creative twists, directing their enzymatic capability to assist in diagnosis and therapy.

Since disease-associated enzymatic activities vary during disease progression and between individuals, an enzyme-responsive delivery system potentially could provide an in situ self-regulated medicine, paving the way to personalized medicine. It can be envisioned that more and more intelligently designed enzyme-responsive systems will be developed for their environmental sensitivity. To achieve the ultimate goal, treating individual patients with personalized medicine, a more profound understanding of enzyme structure, mechanisms, distribution, and regulation in vivo is required.

ACKNOWLEDGMENT

This research was supported in part by RO1-CA099385 and RO1-CA135312 to CT, and North Dakota EPSCoR Program (FAR0014970) to B.L.

LITERATURE CITED

(1) Southan, C. (2001) A genomic perspective on human proteases as drug targets. *Drug. Discovery Today 6*, 681–688.
(2) Overall, C. M., and Kleifeld, O. (2006) Tumour microenvironment - opinion: validating matrix metalloproteinases as drug targets and anti-targets for cancer therapy. *Nat. Rev. Cancer 6*, 227–39.
(3) Bunnage, M. E., and Owen, D. R. (2008) Tafia inhibitors in the treatment of thrombosis. *Curr. Opin. Drug Discovery Dev. 11*, 480–6.
(4) Frank, J. (2008) Managing hypertension using combination therapy. *Am. Fam. Physician 77*, 1279–86.
(5) VanDeKoppel, S., Choe, H. M., and Sweet, B. V. (2008) Managed care perspective on three new agents for type 2 diabetes. *J. Manag. Care Pharm. 14*, 363–80.
(6) Mannisto, P. T., Venalainen, J., Jalkanen, A., and Garcia-Horsman, J. A. (2007) Prolyl oligopeptidase: a potential target for the treatment of cognitive disorders. *Drug News Perspect. 20*, 293–305.
(7) Maresso, A. W., and Schneewind, O. (2008) Sortase as a target of anti-infective therapy. *Pharmacol. Rev. 60*, 128–41.
(8) Tabacova, S. A., and Kimmel, C. A. (2001) Enalapril: pharmacokinetic/dynamic inferences for comparative developmental toxicity. a review. *Reprod. Toxicol. 15*, 467–78.
(9) Walko, C. M., and Lindley, C. (2005) Capecitabine: a review. *Clin. Ther. 27*, 23–44.
(10) de Groot, F. M., Damen, E. W., and Scheeren, H. W. (2001) Anticancer prodrugs for application in monotherapy: targeting hypoxia, tumor-associated enzymes, and receptors. *Curr. Med. Chem. 8*, 1093–122.
(11) Atkinson, J. M., Siller, C. S., and Gill, J. H. (2008) Tumour endoproteases: the cutting edge of cancer drug delivery? *Br. J. Pharmacol. 153*, 1344–52.

(12) Kratz, F., Muller, I. A., Ryppa, C., and Warnecke, A. (2008) Prodrug strategies in anticancer chemotherapy. *ChemMedChem 3*, 20–53.

(13) Baurain, R., Masquelier, M., Deprez-De Campeneere, D., and Trouet, A. (1980) Amino acid and dipeptide derivatives of daunorubicin. 2. Cellular pharmacology and antitumor activity on L1210 leukemic cells in vitro and in vivo. *J. Med. Chem. 23*, 1171–4.

(14) de Jong, J., Klein, I., Bast, A., and van der Vijgh, W. J. (1992) Analysis and pharmacokinetics of N-L-leucyldoxorubucin and metabolites in tissues of tumor-bearing Balb/C mice. *Cancer Chemother. Pharmacol. 31*, 156–60.

(15) Deprez-de Campeneere, D., Baurain, R., and Trouet, A. (1982) Accumulation and metabolism of new anthracycline derivatives in the heart after iv injection into mice. *Cancer Chemother. Pharmacol. 8*, 193–7.

(16) Zbinden, G., DeCampeenere, D., and Baurain, R. (1991) Preclinical assessment of the cardiotoxic potential of anthracycline antibiotics: N-L-leucyl-doxorubicin. *Arch. Toxicol. Suppl. 14*, 107–17.

(17) Boven, E., Hendriks, H. R., Erkelens, C. A., and Pinedo, H. M. (1992) The anti-tumour effects of the prodrugs N-L-leucyl-doxorubicin and vinblastine-isoleucinate in human ovarian cancer xenografts. *Br. J. Cancer 66*, 1044–7.

(18) Breistol, K., Hendriks, H. R., Berger, D. P., Langdon, S. P., Fiebig, H. H., and Fodstad, O. (1998) The antitumour activity of the prodrug N-L-leucyl-doxorubicin and its parent compound doxorubicin in human tumour xenografts. *Eur. J. Cancer 34*, 1602–6.

(19) Breistol, K., Hendriks, H. R., and Fodstad, O. (1999) Superior therapeutic efficacy of N-L-leucyl-doxorubicin versus doxorubicin in human melanoma xenografts correlates with higher tumour concentrations of free drug. *Eur. J. Cancer 35*, 1143–9.

(20) Kuefner, U., Lohrmann, U., Montejano, Y. D., Vitols, K. S., and Huennekens, F. M. (1989) Carboxypeptidase-mediated release of methotrexate from methotrexate alpha-peptides. *Biochemistry (Mosc). 28*, 2288–97.

(21) Smal, M. A., Dong, Z., Cheung, H. T., Asano, Y., Escoffier, L., Costello, M., and Tattersall, M. H. (1995) Activation and cytotoxicity of 2-alpha-aminoacyl prodrugs of methotrexate. *Biochem. Pharmacol. 49*, 567–74.

(22) Trouet, A., Passioukov, A., Van derpoorten, K., Fernandez, A. M., Abarca-Quinones, J., Baurain, R., Lobl, T. J., Oliyai, C., Shochat, D., and Dubois, V. (2001) Extracellularly tumor-activated prodrugs for the selective chemotherapy of cancer: application to doxorubicin and preliminary in vitro and in vivo studies. *Cancer Res. 61*, 2843–6.

(23) Dubois, V., Dasnois, L., Lebtahi, K., Collot, F., Heylen, N., Havaux, N., Fernandez, A. M., Lobl, T. J., Oliyai, C., Nieder, M., Shochat, D., Yarranton, G. T., and Trouet, A. (2002) Cpi-0004na, a new extracellularly tumor-activated prodrug of doxorubicin: in vivo toxicity, activity, and tissue distribution confirm tumor cell selectivity. *Cancer Res. 62*, 2327–31.

(24) Fernandez, A. M., Van Derpoorten, K., Dasnois, L., Lebtahi, K., Dubois, V., Lobl, T. J., Gangwar, S., Oliyai, C., Lewis, E. R., Shochat, D., and Trouet, A. (2001) N-Succinyl-(beta-alanyl-L-leucyl-L-alanyl-L-leucyl)doxorubicin: an extracellularly tumor-activated prodrug devoid of intravenous acute toxicity. *J. Med. Chem. 44*, 3750–3.

(25) Dubois, V., Nieder, M., Collot, F., Negrouk, A., Nguyen, T. T., Gangwar, S., Reitz, B., Wattiez, R., Dasnois, L., and Trouet, A. (2006) Thimet oligopeptidase (Ec 3.4.24.15) activates Cpi-0004na, an extracellularly tumour-activated prodrug of doxorubicin. *Eur. J. Cancer 42*, 3049–56.

(26) Pan, C., Cardarelli, P. M., Nieder, M. H., Pickford, L. B., Gangwar, S., King, D. J., Yarranton, G. T., Buckman, D., Roscoe, W., Zhou, F., Salles, A., Chen, T. H., Horgan, K., Wang, Y. H., Nguyen, T., and Bebbington, C. R. (2003) Cd10 is a key enzyme involved in the activation of tumor-activated peptide prodrug Cpi-0004na and novel analogues: implications for the design of novel peptide prodrugs for the therapy of Cd^{10+} tumors. *Cancer Res. 63*, 5526–31.

(27) Carl, P. L., Chakravarty, P. K., Katzenellenbogen, J. A., and Weber, M. J. (1980) Protease-activated "prodrugs" for cancer chemotherapy. *Proc. Natl. Acad. Sci. U.S.A. 77*, 2224–8.

(28) Chakravarty, P. K., Carl, P. L., Weber, M. J., and Katzenellenbogen, J. A. (1983) Plasmin-activated prodrugs for cancer chemotherapy. 1. synthesis and biological activity of peptidylacivicin and peptidylphenylenediamine mustard. *J. Med. Chem. 26*, 633–8.

(29) Balajthy, Z., Aradi, J., Kiss, I. T., and Elodi, P. (1992) Synthesis and functional evaluation of a peptide derivative of 1-beta-D-arabinofuranosylcytosine. *J. Med. Chem. 35*, 3344–9.

(30) Albright, C. F., Graciani, N., Han, W., Yue, E., Stein, R., Lai, Z., Diamond, M., Dowling, R., Grimminger, L., Zhang, S. Y., Behrens, D., Musselman, A., Bruckner, R., Zhang, M., Jiang, X., Hu, D., Higley, A., Dimeo, S., Rafalski, M., Mandlekar, S., Car, B., Yeleswaram, S., Stern, A., Copeland, R. A., Combs, A., Seitz, S. P., Trainor, G. L., Taub, R., Huang, P., and Oliff, A. (2005) Matrix metalloproteinase-activated doxorubicin prodrugs inhibit Ht1080 xenograft growth better than doxorubicin with less toxicity. *Mol. Cancer Ther. 4*, 751–60.

(31) Timar, F., Botyanszki, J., Suli-Vargha, H., Babo, I., Olah, J., Pogany, G., and Jeney, A. (1998) The antiproliferative action of a melphalan hexapeptide with collagenase-cleavable site. *Cancer Chemother. Pharmacol. 41*, 292–8.

(32) Kline, T., Torgov, M. Y., Mendelsohn, B. A., Cerveny, C. G., and Senter, P. D. (2004) Novel antitumor prodrugs designed for activation by matrix metalloproteinases-2 and−9. *Mol. Pharm. 1*, 9–22.

(33) DeFeo-Jones, D., Brady, S. F., Feng, D. M., Wong, B. K., Bolyar, T., Haskell, K., Kiefer, D. M., Leander, K., McAvoy, E., Lumma, P., Pawluczyk, J. M., Wai, J., Motzel, S. L., Keenan, K., Van Zwieten, M., Lin, J. H., Garsky, V. M., Freidinger, R., Oliff, A., and Jones, R. E. (2002) A prostate-specific antigen (psa)-activated vinblastine prodrug selectively kills psa-secreting cells in vivo. *Mol. Cancer Ther. 1*, 451–9.

(34) Mhaka, A., Denmeade, S. R., Yao, W., Isaacs, J. T., and Khan, S. R. (2002) A 5-fluorodeoxyuridine prodrug as targeted therapy for prostate cancer. *Bioorg. Med. Chem. Lett. 12*, 2459–61.

(35) Denmeade, S. R., Jakobsen, C. M., Janssen, S., Khan, S. R., Garrett, E. S., Lilja, H., Christensen, S. B., and Isaacs, J. T. (2003) Prostate-specific antigen-activated thapsigargin prodrug as targeted therapy for prostate cancer. *J. Natl. Cancer Inst. 95*, 990–1000.

(36) Kumar, S. K., Williams, S. A., Isaacs, J. T., Denmeade, S. R., and Khan, S. R. (2007) Modulating paclitaxel bioavailability for targeting prostate cancer. *Bioorg. Med. Chem. 15*, 4973–84.

(37) Devy, L., de Groot, F. M., Blacher, S., Hajitou, A., Beusker, P. H., Scheeren, H. W., Foidart, J. M., and Noel, A. (2004) Plasmin-activated doxorubicin prodrugs containing a spacer reduce tumor growth and angiogenesis without systemic toxicity. *FASEB J. 18*, 565–7.

(38) de Groot, F. M., Loos, W. J., Koekkoek, R., van Berkom, L. W., Busscher, G. F., Seelen, A. E., Albrecht, C., de Bruijn, P., and Scheeren, H. W. (2001) Elongated multiple electronic cascade and cyclization spacer systems in activatible anticancer prodrugs for enhanced drug release. *J. Org. Chem. 66*, 8815–30.

(39) Jakobsen, C. M., Denmeade, S. R., Isaacs, J. T., Gady, A., Olsen, C. E., and Christensen, S. B. (2001) Design, synthesis, and pharmacological evaluation of thapsigargin analogues for targeting apoptosis to prostatic cancer cells. *J. Med. Chem. 44*, 4696–703.

(40) Kaneko, T., Willner, D., Monkovic, I., Knipe, J. O., Braslawsky, G. R., Greenfield, R. S., and Vyas, D. M. (1991) New hydrazone derivatives of adriamycin and their immunoconjugates--a correlation between acid stability and cytotoxicity. *Bioconjugate Chem. 2*, 133–41.

(41) Guillemard, V., and Saragovi, H. U. (2001) Taxane-antibody conjugates afford potent cytotoxicity, enhanced solubility, and tumor target selectivity. *Cancer Res. 61*, 694–9.

(42) Safavy, A., Bonner, J. A., Waksal, H. W., Buchsbaum, D. J., Gillespie, G. Y., Khazaeli, M. B., Arani, R., Chen, D. T., Carpenter, M., and Raisch, K. P. (2003) Synthesis and biological evaluation of paclitaxel-C225 conjugate as a model for targeted drug delivery. *Bioconjugate Chem. 14*, 302–10.

(43) Greenfield, R. S., Kaneko, T., Daues, A., Edson, M. A., Fitzgerald, K. A., Olech, L. J., Grattan, J. A., Spitalny, G. L., and Braslawsky, G. R. (1990) Evaluation in vitro of adriamycin immunoconjugates synthesized using an acid-sensitive hydrazone linker. *Cancer Res. 50*, 6600–7.

(44) Wu, A. M., and Senter, P. D. (2005) Arming antibodies: prospects and challenges for immunoconjugates. *Nat. Biotechnol. 23*, 1137–46.

(45) Doronina, S. O., Toki, B. E., Torgov, M. Y., Mendelsohn, B. A., Cerveny, C. G., Chace, D. F., DeBlanc, R. L., Gearing, R. P., Bovee, T. D., Siegall, C. B., Francisco, J. A., Wahl, A. F., Meyer, D. L., and Senter, P. D. (2003) Development of potent monoclonal antibody auristatin conjugates for cancer therapy. *Nat. Biotechnol. 21*, 778–84.

(46) Erickson, H. K., Park, P. U., Widdison, W. C., Kovtun, Y. V., Garrett, L. M., Hoffman, K., Lutz, R. J., Goldmacher, V. S., and Blattler, W. A. (2006) Antibody-maytansinoid conjugates are activated in targeted cancer cells by lysosomal degradation and linker-dependent intracellular processing. *Cancer Res. 66*, 4426–33.

(47) Chari, R. V. (2008) Targeted cancer therapy: conferring specificity to cytotoxic drugs. *Acc. Chem. Res. 41*, 98–107.

(48) Ojima, I. (2008) Guided molecular missiles for tumor-targeting chemotherapy--case studies using the second-generation taxoids as warheads. *Acc. Chem. Res. 41*, 108–19.

(49) Sutherland, M. S., Sanderson, R. J., Gordon, K. A., Andreyka, J., Cerveny, C. G., Yu, C., Lewis, T. S., Meyer, D. L., Zabinski, R. F., Doronina, S. O., Senter, P. D., Law, C. L., and Wahl, A. F. (2006) Lysosomal trafficking and cysteine protease metabolism confer target-specific cytotoxicity by peptide-linked anti-Cd30-auristatin conjugates. *J. Biol. Chem. 281*, 10540–7.

(50) Francisco, J. A., Cerveny, C. G., Meyer, D. L., Mixan, B. J., Klussman, K., Chace, D. F., Rejniak, S. X., Gordon, K. A., DeBlanc, R., Toki, B. E., Law, C. L., Doronina, S. O., Siegall, C. B., Senter, P. D., and Wahl, A. F. (2003) Cac10-vcmmae, an anti-Cd30-monomethyl auristatin E conjugate with potent and selective antitumor activity. *Blood 102*, 1458–65.

(51) Jeffrey, S. C., Nguyen, M. T., Andreyka, J. B., Meyer, D. L., Doronina, S. O., and Senter, P. D. (2006) Dipeptide-based highly potent doxorubicin antibody conjugates. *Bioorg. Med. Chem. Lett. 16*, 358–62.

(52) Li, M., and Meares, C. F. (1993) Synthesis, metal chelate stability studies, and enzyme digestion of a peptide-linked dota derivative and its corresponding radiolabeled immunoconjugates. *Bioconjugate Chem. 4*, 275–83.

(53) DeNardo, G. L., DeNardo, S. J., Peterson, J. J., Miers, L. A., Lam, K. S., Hartmann-Siantar, C., and Lamborn, K. R. (2003) Preclinical evaluation of cathepsin-degradable peptide linkers for radioimmunoconjugates. *Clin. Cancer Res. 9*, 3865S–72S.

(54) Maeda, H., Fang, J., Inutsuka, T., and Kitamoto, Y. (2003) Vascular permeability enhancement in solid tumor: various factors, mechanisms involved and its implications. *Int. Immunopharmacol. 3*, 319–28.

(55) Reddy, L. H. (2005) Drug delivery to tumours: recent strategies. *J. Pharm. Pharmacol. 57*, 1231–42.

(56) Guiotto, A., Canevari, M., Orsolini, P., Lavanchy, O., Deuschel, C., Kaneda, N., Kurita, A., Matsuzaki, T., Yaegashi, T., Sawada, S., and Veronese, F. M. (2004) Synthesis, characterization, and preliminary in vivo tests of new poly(ethylene glycol) conjugates of the antitumor agent 10-amino-7-ethylcamptothecin. *J. Med. Chem. 47*, 1280–9.

(57) Chau, Y., Tan, F. E., and Langer, R. (2004) Synthesis and characterization of dextran-peptide-methotrexate conjugates for tumor targeting via mediation by matrix metalloproteinase II and matrix metalloproteinase IX. *Bioconjugate Chem. 15*, 931–41.

(58) Chau, Y., Dang, N. M., Tan, F. E., and Langer, R. (2006) Investigation of targeting mechanism of new dextran-peptide-methotrexate conjugates using biodistribution study in matrix-metalloproteinase-overexpressing tumor xenograft model. *J. Pharm. Sci. 95*, 542–51.

(59) Kimura, H., Yasukawa, T., Tabata, Y., and Ogura, Y. (2001) Drug targeting to choroidal neovascularization. *Adv. Drug Delivery Rev. 52*, 79–91.

(60) Lukyanov, A. N., Hartner, W. C., and Torchilin, V. P. (2004) Increased accumulation of PEG-PE micelles in the area of experimental myocardial infarction in rabbits. *J. Controlled Release 94*, 187–93.

(61) Cadee, J. A., de Groot, C. J., Jiskoot, W., den Otter, W., and Hennink, W. E. (2002) Release of recombinant human interleukin-2 from dextran-based hydrogels. *J. Controlled Release 78*, 1–13.

(62) Ikada, Y., and Tabata, Y. (1998) Protein release from gelatin matrices. *Adv. Drug Delivery Rev. 31*, 287–301.

(63) Yao, C., Roderfeld, M., Rath, T., Roeb, E., Bernhagen, J., and Steffens, G. (2006) The impact of proteinase-induced matrix degradation on the release of vegf from heparinized collagen matrices. *Biomaterials 27*, 1608–16.

(64) Cheung, D. T., and Nimni, M. E. (1982) Mechanism of crosslinking of proteins by glutaraldehyde II. reaction with monomeric and polymeric collagen. *Connect. Tissue Res. 10*, 201–16.

(65) Lee, J. M., Pereira, C. A., and Kan, L. W. (1994) Effect of molecular structure of poly(glycidyl ether) reagents on crosslinking and mechanical properties of bovine pericardial xenograft materials. *J. Biomed. Mater. Res. 28*, 981–92.

(66) Tu, R., Shen, S. H., Lin, D., Hata, C., Thyagarajan, K., Noishiki, Y., and Quijano, R. C. (1994) Fixation of bioprosthetic tissues with monofunctional and multifunctional polyepoxy compounds. *J. Biomed. Mater. Res. 28*, 677–84.

(67) Olde Damink, L. H., Dijkstra, P. J., van Luyn, M. J., van Wachem, P. B., Nieuwenhuis, P., and Feijen, J. (1996) Cross-linking of dermal sheep collagen using a water-soluble carbodiimide. *Biomaterials 17*, 765–73.

(68) Gratzer, P. F., Santerre, J. P., and Lee, J. M. (2007) The effect of chemical modification of amino acid side-chains on collagen degradation by enzymes. *J. Biomed. Mater. Res. B Appl. Biomater. 81*, 1–11.

(69) Qiu, Y., and Park, K. (2001) Environment-sensitive hydrogels for drug delivery. *Adv Drug. Delivery Rev. 53*, 321–39.

(70) Tanihara, M., Suzuki, Y., Nishimura, Y., Suzuki, K., Kakimaru, Y., and Fukunishi, Y. (1999) A novel microbial infection-responsive drug release system. *J. Pharm. Sci. 88*, 510–4.

(71) Suzuki, Y., Tanihara, M., Nishimura, Y., Suzuki, K., Kakimaru, Y., and Shimizu, Y. (1997) A novel wound dressing with an antibiotic delivery system stimulated by microbial infection. *ASAIO J. 43*, M854–7.

(72) Tauro, J. R., and Gemeinhart, R. A. (2005) Matrix metalloprotease triggered delivery of cancer chemotherapeutics from hydrogel matrixes. *Bioconjugate Chem. 16*, 1133–9.

(73) Law, B., Weissleder, R., and Tung, C. H. (2006) Peptide-based biomaterials for protease-enhanced drug delivery. *Biomacromolecules 7*, 1261–5.

(74) Kisiday, J., Jin, M., Kurz, B., Hung, H., Semino, C., Zhang, S., and Grodzinsky, A. J. (2002) Self-assembling peptide hydrogel fosters chondrocyte extracellular matrix production and cell division: implications for cartilage tissue repair. *Proc. Natl. Acad. Sci. U.S.A. 99*, 9996–10001.

(75) Xiong, H., Buckwalter, B. L., Shieh, H. M., and Hecht, M. H. (1995) Periodicity of polar and nonpolar amino acids is the major determinant of secondary structure in self-assembling oligomeric peptides. *Proc. Natl. Acad. Sci. U.S.A. 92*, 6349–53.

(76) Ke, S. H., Coombs, G. S., Tachias, K., Corey, D. R., and Madison, E. L. (1997) Optimal subsite occupancy and design of a selective inhibitor of urokinase. *J. Biol. Chem. 272*, 20456–62.

(77) Law, B., Quinti, L., Choi, Y., Weissleder, R., and Tung, C. H. (2006) A mitochondrial targeted fusion peptide exhibits remarkable cytotoxicity. *Mol. Cancer Ther. 5*, 1944–9.

(78) Sutter, M., Siepmann, J., Hennink, W. E., and Jiskoot, W. (2007) Recombinant gelatin hydrogels for the sustained release of proteins. *J. Controlled Release 119*, 301–12.

(79) van Bommel, K. J., Stuart, M. C., Feringa, B. L., and van Esch, J. (2005) Two-stage enzyme mediated drug release from LMWG hydrogels. *Org. Biomol. Chem. 3*, 2917–20.

(80) Marten, K., Bremer, C., Khazaie, K., Sameni, M., Sloane, B., Tung, C. H., and Weissleder, R. (2002) Detection of dysplastic intestinal adenomas using enzyme-sensing molecular beacons in mice. *Gastroenterology 122*, 406–14.

(81) Funovics, M., Weissleder, R., and Tung, C. H. (2003) Protease sensors for bioimaging. *Anal.Bioanal. Chem. 377*, 956–63.

(82) Scherer, R. L., McIntyre, J. O., and Matrisian, L. M. (2008) Imaging matrix metalloproteinases in cancer. *Cancer Metastasis Rev. 27*, 679–90.

(83) Tung, C. H. (2004) Fluorescent peptide probes for in vivo diagnostic imaging. *Biopolymers 76*, 391–403.

(84) Wang, G. T., Matayoshi, E., Huffaker, H. J., and Krafft, G. A. (1990) Design and synthesis of new fluorogenic HIV protease substrates based on resonance energy transfer. *Tetrahedron Lett. 31*, 6493–6.

(85) Pham, W., Choi, Y., Weissleder, R., and Tung, C. H. (2004) Developing a peptide-based near-infrared molecular probe for protease sensing. *Bioconjugate Chem. 15*, 1403–7.

(86) Lee, S., Park, K., Lee, S. Y., Ryu, J. H., Park, J. W., Ahn, H. J., Kwon, I. C., Youn, I. C., Kim, K., and Choi, K. (2008) Dark quenched matrix metalloproteinase fluorogenic probe for imaging osteoarthritis development in vivo. *Bioconjugate Chem. 19*, 1743–7.

(87) Jiang, T., Olson, E. S., Nguyen, Q. T., Roy, M., Jennings, P. A., and Tsien, R. Y. (2004) Tumor imaging by means of proteolytic activation of cell-penetrating peptides. *Proc. Natl. Acad. Sci. U.S.A. 101*, 17867–72.

(88) Lepage, M., Dow, W. C., Melchior, M., You, Y., Fingleton, B., Quarles, C. C., Pepin, C., Gore, J. C., Matrisian, L. M., and McIntyre, J. O. (2007) Noninvasive detection of matrix metalloproteinase activity in vivo using a novel magnetic resonance imaging contrast agent with a solubility switch. *Mol. Imaging 6*, 393–403.

(89) Weissleder, R., Tung, C. H., Mahmood, U., and Bogdanov, A. (1999) In vivo imaging of tumors with protease-activated near-infrared fluorescent probes. *Nat. Biotechnol. 17*, 375–8.

(90) Lai, W. F., Chang, C. H., Tang, Y., Bronson, R., and Tung, C. H. (2004) Early diagnosis of osteoarthritis using cathepsin B sensitive near-infrared fluorescent probes. *Osteoarthritis Cartilage 12*, 239–44.

(91) Chen, J., Tung, C. H., Mahmood, U., Ntziachristos, V., Gyurko, R., Fishman, M. C., Huang, P. L., and Weissleder, R. (2002) In vivo imaging of proteolytic activity in atherosclerosis. *Circulation 105*, 2766–71.

(92) Tung, C. H., Mahmood, U., Bredow, S., and Weissleder, R. (2000) In vivo imaging of proteolytic enzyme activity using a novel molecular reporter. *Cancer Res. 60*, 4953–8.

(93) Jaffer, F. A., Kim, D. E., Quinti, L., Tung, C. H., Aikawa, E., Pande, A. N., Kohler, R. H., Shi, G. P., Libby, P., and Weissleder, R. (2007) Optical visualization of cathepsin K activity in atherosclerosis with a novel, protease-activatable fluorescence sensor. *Circulation 115*, 2292–8.

(94) Bremer, C., Bredow, S., Mahmood, U., Weissleder, R., and Tung, C. H. (2001) Optical imaging of matrix metalloproteinase-2 activity in tumors: feasibility study in a mouse model. *Radiology 221*, 523–9.

(95) Bremer, C., Tung, C. H., and Weissleder, R. (2001) In vivo molecular target assessment of matrix metalloproteinase inhibition. *Nat. Med. 7*, 743–8.

(96) Messerli, S. M., Prabhakar, S., Tang, Y., Shah, K., Cortes, M. L., Murthy, V., Weissleder, R., Breakefield, X. O., and TungC. H. (2004) A novel method for imaging apoptosis using a caspase-1 near-infrared fluorescent probe. *Neoplasia 6*, 95–105.

(97) Jaffer, F. A., Tung, C. H., Gerszten, R. E., and Weissleder, R. (2002) In vivo imaging of thrombin activity in experimental thrombi with thrombin-sensitive near-infrared molecular probe. *Arterioscler. Thromb. Vasc. Biol. 22*, 1929–35.

(98) Law, B., Curino, A., Bugge, T. H., Weissleder, R., and Tung, C. H. (2004) Design, synthesis, and characterization of urokinase plasminogen-activator-sensitive near-infrared reporter. *Chem. Biol. 11*, 99–106.

(99) Hsiao, J. K., Law, B., Weissleder, R., and Tung, C. H. (2006) In-vivo imaging of tumor associated urokinase-type plasminogen activator activity. *J. Biomed. Opt. 11*, 34013.

(100) Law, B., Weissleder, R., and Tung, C. H. (2007) Protease-sensitive fluorescent nanofibers. *Bioconjugate Chem. 18*, 1701–4.

(101) Law, B., and Tung, C. H. (2008) Structural modification of protease inducible preprogrammed nanofiber precursor. *Biomacromolecules 9*, 421–5.

(102) Ho, N.-H., Weissleder, R., and Tung, C.-H. (2006) Development of water-soluble far-red fluorogenic dyes for enzyme sensing. *Tetrahedron 62*, 578–585.

(103) Ho, N. H., Weissleder, R., and Tung, C. H. (2006) Development of a dual fluorogenic and chromogenic dipeptidyl peptidase IV substrate. *Bioorg. Med. Chem. Lett. 16*, 2599–602.

(104) Lai, K. S., Ho, N. H., Cheng, J. D., and Tung, C. H. (2007) Selective fluorescence probes for dipeptidyl peptidase activity-fibroblast activation protein and dipeptidyl peptidase IV. *Bioconjugate Chem. 18*, 1246–50.

(105) Ho, N. H., Weissleder, R., and Tung, C. H. (2007) A self-immolative reporter for beta-galactosidase sensing. *ChemBioChem 8*, 560–6.

(106) Shah, K., Tung, C. H., Breakefield, X. O., and Weissleder, R. (2005) In vivo imaging of S-trail-mediated tumor regression and apoptosis. *Mol. Ther. 11*, 926–31.

(107) Castano, A. P., Mroz, P., and Hamblin, M. R. (2006) Photodynamic therapy and anti-tumour immunity. *Nat. Rev. Cancer 6*, 535–45.

(108) Hamblin, M. R., Miller, J. L., Rizvi, I., and Ortel, B. (2002) Degree of substitution of chlorin E6 on charged poly-L-lysine chains affects their cellular uptake, localization and phototoxicity towards macrophages and cancer cells. *J. X-Ray Sci. Technol. 10*, 139–152.

(109) Choi, Y., Weissleder, R., and Tung, C. H. (2006) Protease-mediated phototoxicity of a polylysine-chlorin(E6) conjugate. *ChemMedChem 1*, 698–701.

(110) Choi, Y., Weissleder, R., and Tung, C. H. (2006) Selective antitumor effect of novel protease-mediated photodynamic agent. *Cancer Res. 66*, 7225–9.

(111) Gabriel, D., Campo, M. A., Gurny, R., and Lange, N. (2007) Tailoring protease-sensitive photodynamic agents to specific disease-associated enzymes. *Bioconjugate Chem. 18*, 1070–7.

(112) Zheng, G., Chen, J., Stefflova, K., Jarvi, M., Li, H., and Wilson, B. C. (2007) Photodynamic molecular beacon as an activatable photosensitizer based on protease-controlled singlet oxygen quenching and activation. *Proc. Natl. Acad. Sci. U.S.A. 104*, 8989–94.

(113) Stefflova, K., Chen, J., Marotta, D., Li, H., and Zheng, G. (2006) Photodynamic therapy agent with a built-in apoptosis sensor for evaluating its own therapeutic outcome in situ. *J. Med. Chem. 49*, 3850–6.

(114) Moghimi, S. M., Hunter, A. C., and Murray, J. C. (2001) Long-circulating and target-specific nanoparticles: theory to practice. *Pharmacol. Rev. 53*, 283–318.

(115) Silva, G. A., Czeisler, C., Niece, K. L., Beniash, E., Harrington, D. A., Kessler, J. A., and Stupp, S. I. (2004) Selective differentiation of neural progenitor cells by high-epitope density nanofibers. *Science 303*, 1352–5.

(116) Klumpp, C., Kostarelos, K., Prato, M., and Bianco, A. (2006) Functionalized carbon nanotubes as emerging nanovectors for the delivery of therapeutics. *Biochim. Biophys. Acta 1758*, 404–12.
(117) Jaffer, F. A., and Weissleder, R. (2004) Seeing within: molecular imaging of the cardiovascular system. *Circ. Res. 94*, 433–45.
(118) Santra, S., Dutta, D., Walter, G. A., and Moudgil, B. M. (2005) Fluorescent nanoparticle probes for cancer imaging. *Technol. Cancer Res. Treat. 4*, 593–602.
(119) Morgan, M. T., Carnahan, M. A., Immoos, C. E., Ribeiro, A. A., Finkelstein, S., Lee, S. J., and Grinstaff, M. W. (2003) Dendritic molecular capsules for hydrophobic compounds. *J. Am. Chem. Soc. 125*, 15485–9.
(120) Moghimi, S. M., and Szebeni, J. (2003) Stealth liposomes and long circulating nanoparticles: critical issues in pharmacokinetics, opsonization and protein-binding properties. *Prog. Lipid Res. 42*, 463–78.
(121) Sahoo, S. K., and Labhasetwar, V. (2003) Nanotech approaches to drug delivery and imaging. *Drug Discovery Today 8*, 1112–20.
(122) Kodama, K., Katayama, Y., Shoji, Y., and Nakashima, H. (2006) The features and shortcomings for gene delivery of current non-viral carriers. *Curr. Med. Chem. 13*, 2155–61.
(123) Lu, Z., Yeh, T. K., Tsai, M., Au, J. L., and Wientjes, M. G. (2004) Paclitaxel-loaded gelatin nanoparticles for intravesical bladder cancer therapy. *Clin. Cancer Res. 10*, 7677–84.
(124) Pak, C. C., Ali, S., Janoff, A. S., and Meers, P. (1998) Triggerable liposomal fusion by enzyme cleavage of a novel peptide−lipid conjugate. *Biochim. Biophys. Acta 1372*, 13–27.
(125) Terada, T., Iwai, M., Kawakami, S., Yamashita, F., and Hashida, M. (2006) Novel PEG-matrix metalloproteinase-2 cleavable peptide-lipid containing galactosylated liposomes for hepatocellular carcinoma-selective targeting. *J. Controlled Release 111*, 333–42.
(126) Kawakami, S., Munakata, C., Fumoto, S., Yamashita, F., and Hashida, M. (2001) Novel galactosylated liposomes for hepatocyte-selective targeting of lipophilic drugs. *J. Pharm. Sci. 90*, 105–13.
(127) Zhang, Y., So, M. K., and Rao, J. (2006) Protease-modulated cellular uptake of quantum dots. *Nano Lett. 6*, 1988–92.
(128) Chang, E., Miller, J. S., Sun, J., Yu, W. W., Colvin, V. L., Drezek, R., and West, J. L. (2005) Protease-activated quantum dot probes. *Biochem. Biophys. Res. Commun. 334*, 1317–21.
(129) Medintz, I. L., Clapp, A. R., Brunel, F. M., Tiefenbrunn, T., Uyeda, H. T., Chang, E. L., Deschamps, J. R., Dawson, P. E., and Mattoussi, H. (2006) Proteolytic activity monitored by fluorescence resonance energy transfer through quantum-dot-peptide conjugates. *Nat. Mater. 5*, 581–9.
(130) Suzuki, M., Husimi, Y., Komatsu, H., Suzuki, K., and Douglas, K. T. (2008) Quantum dot fret biosensors that respond to pH, to proteolytic or nucleolytic cleavage, to DNA synthesis, or to a multiplexing combination. *J. Am. Chem. Soc. 130*, 5720–5.
(131) Shi, L., De Paoli, V., Rosenzweig, N., and Rosenzweig, Z. (2006) Synthesis and application of quantum dots fret-based protease sensors. *J. Am. Chem. Soc. 128*, 10378–9.
(132) Scherer, L. J., VanSaun, M. N., McIntyre, J. O., and Matrisian, L. M. (2008) Optical imaging of matrix metalloproteinase-7 activity in vivo using a proteolytic nanobeacon. *Mol. Imaging 7*, 118–131.
(133) Fuchs, S., Otto, H., Jehle, S., Henklein, P., and Schluter, A. D. (2005) Fluorescent dendrimers with a peptide cathepsin B cleavage site for drug delivery applications. *Chem. Commun. (Cambridge)* 1830–2.
(134) Kim, K., Lee, M., Park, H., Kim, J. H., Kim, S., Chung, H., Choi, K., Kim, I. S., Seong, B. L., and Kwon, I. C. (2006) Cell-permeable and biocompatible polymeric nanoparticles for apoptosis imaging. *J. Am. Chem. Soc. 128*, 3490–1.
(135) Ruddle, C. C., and Smyth, T. P. (2007) Exploring the chemistry of penicillin as a beta-lactamase-dependent prodrug. *Org. Biomol. Chem. 5*, 160–8.
(136) Yang, Z., Ho, P. L., Liang, G., Chow, K. H., Wang, Q., Cao, Y., Guo, Z., and Xu, B. (2007) Using beta-lactamase to trigger supramolecular hydrogelation. *J. Am. Chem. Soc. 129*, 266–7.
(137) Gao, W., Xing, B., Tsien, R. Y., and Rao, J. (2003) Novel fluorogenic substrates for imaging beta-lactamase gene expression. *J. Am. Chem. Soc. 125*, 11146–7.
(138) Broderick, E. P., O'Halloran, D. M., Rochev, Y. A., Griffin, M., Collighan, R. J., and Pandit, A. S. (2005) Enzymatic stabilization of gelatin-based scaffolds. *J. Biomed. Mater. Res. B Appl. Biomater. 72*, 37–42.
(139) Ehrbar, M., Rizzi, S. C., Schoenmakers, R. G., Miguel, B. S., Hubbell, J. A., Weber, F. E., and Lutolf, M. P. (2007) Biomolecular hydrogels formed and degraded via site-specific enzymatic reactions. *Biomacromolecules 8*, 3000–7.
(140) Tung, C. H., Ho, N. H., Zeng, Q., Tang, Y., Jaffer, F. A., Reed, G. L., and Weissleder, R. (2003) Novel factor XIII probes for blood coagulation imaging. *ChemBioChem 4*, 897–9.
(141) Kim, D. E., Schellingerhout, D., Jaffer, F. A., Weissleder, R., and Tung, C. H. (2005) Near-infrared fluorescent imaging of cerebral thrombi and blood-brain barrier disruption in a mouse model of cerebral venous sinus thrombosis. *J. Cereb. Blood Flow Metab. 25*, 226–33.
(142) Nahrendorf, M., Hu, K., Frantz, S., Jaffer, F. A., Tung, C. H., Hiller, K. H., Voll, S., Nordbeck, P., Sosnovik, D., Gattenlohner, S., Novikov, M., Dickneite, G., Reed, G. L., Jakob, P., Rosenzweig, A., Bauer, W. R., Weissleder, R., and Ertl, G. (2006) Factor XIII deficiency causes cardiac rupture, impairs wound healing, and aggravates cardiac remodeling in mice with myocardial infarction. *Circulation 113*, 1196–202.
(143) Palandoken, H., By, K., Hegde, M., Harley, W. R., Gorin, F. A., and Nantz, M. H. (2005) Amiloride peptide conjugates: prodrugs for sodium-proton exchange inhibition. *J. Pharmacol. Exp. Ther. 312*, 961–7.
(144) Kumar, S. K., Roy, I., Anchoori, R. K., Fazli, S., Maitra, A., Beachy, P. A., and Khan, S. R. (2008) Targeted inhibition of hedgehog signaling by cyclopamine prodrugs for advanced prostate cancer. *Bioorg. Med. Chem. 16*, 2764–8.
(145) de Groot, F. M., Broxterman, H. J., Adams, H. P., van Vliet, A., Tesser, G. I., Elderkamp, Y. W., Schraa, A. J., Kok, R. J., Molema, G., Pinedo, H. M., and Scheeren, H. W. (2002) Design, synthesis, and biological evaluation of a dual tumor-specific motive containing integrin-targeted plasmin-cleavable doxorubicin prodrug. *Mol. Cancer Ther. 1*, 901–11.
(146) Fiehn, C., Kratz, F., Sass, G., Muller-Ladner, U., and Neumann, E. (2008) Targeted drug delivery by in vivo coupling to endogenous albumin: an albumin-binding prodrug of methotrexate (MTX) is better than MTX in the treatment of murine collagen-induced arthritis. *Ann. Rheum. Dis. 67*, 1188–91.
(147) Shiose, Y., Ochi, Y., Kuga, H., Yamashita, F., and Hashida, M. (2007) Relationship between drug release of DE-310, macromolecular prodrug of Dx-8951f, and cathepsins activity in several tumors. *Biol. Pharm. Bull. 30*, 2365–70.
(148) Chandran, S. S., Nan, A., Rosen, D. M., Ghandehari, H., and Denmeade, S. R. (2007) A prostate-specific antigen activated N-(2-hydroxypropyl) methacrylamide copolymer prodrug as dual-targeted therapy for prostate cancer. *Mol. Cancer Ther. 6*, 2928–37.
(149) Satchi-Fainaro, R., Puder, M., Davies, J. W., Tran, H. T., Sampson, D. A., Greene, A. K., Corfas, G., and Folkman, J. (2004) Targeting angiogenesis with a conjugate of HPMA copolymer and TNP-470. *Nat. Med. 10*, 255–61.
(150) Li, C. (2002) Poly(L-glutamic acid)--anticancer drug conjugates. *Adv. Drug Delivery Rev. 54*, 695–713.

BC800500A

COMMUNICATIONS

Blood Circulation and Tissue Biodistribution of Lipid−Quantum Dot (L-QD) Hybrid Vesicles Intravenously Administered in Mice

Wafa' T. Al-Jamal,[†] Khuloud T. Al-Jamal,[†] Andrew Cakebread,[‡] John M. Halket,[‡] and Kostas Kostarelos*[,†]

Nanomedicine Lab, Centre for Drug Delivery Research, The School of Pharmacy, University of London, London WC1N 1AX, and Department of Forensic Science & Drug Monitoring, Kings College London, London SE1 9NH, United Kingdom. Received February 5, 2009; Revised Manuscript Received June 25, 2009

The present work describes the pharmacokinetics of recently developed liposome−quantum dot (L-QD) hybrid vesicles in nude mice following systemic administration. Hydrophobic QD were incorporated into different bilayer compositions, and the serum stability of such hybrid vesicles was evaluated using turbidity and carboxyfluorescein release measurements. L-QD hybrid blood profile and organ biodistribution were also determined by elemental (cadmium) analysis. Following intravenous administration, different tissue biodistribution profiles and tissue affinities were observed depending on the L-QD lipid bilayer characteristics. Immediate blood clearance was observed with cationic (DOTAP/DOPE/Chol) hybrid with rapid lung accumulation, while incorporation of PEG at the surface of zwitterionic vesicles dramatically prolonged their blood circulation half-life after systemic administration. Overall, the L-QD hybrid vesicle system is considered a viable platform that allows QD delivery to different tissues through facile modulation of the hybrid vesicle characteristics. In addition, L-QD offers many opportunities for the development of combinatory therapeutic and imaging (theranostic) modalities by incorporating both drug molecules and QD within the different compartments of a single vesicle.

INTRODUCTION

Quantum dots (QD) are being intensively explored as fluorescent probes for long-term and multimodal imaging purposes *in vitro* and *in vivo* (*1*). However, the low hydrophilicity of QD is considered a major obstacle that impedes their widespread use in biology. Many strategies have been developed to improve the poor hydrophilicity, therefore biocompatibility, of QD, including attachment of hydrophilic moieties to their surface (*2, 3*), encapsulation within amphiphilic copolymer micelles (*4*), phospholipid micelles (*5*), silica polymers (*6*), emulsions (*7*), and polystyrene particles (*8*). These different coating strategies minimize QD nanocrystal aggregation (*9, 10*), protect the QD fluorescence character (*11*), and have also been reported to reduce their cytotoxicity (*2*). We have recently explored an alternative strategy by the self-assembly of lipids and quantum dots (L-QD) into hybrid bilayers, leading to the formation of nanoscale vesicles (*12*). The embedding of QD into the bilayers rendered nonfunctionalized QD compatible with the aqueous environment and enhanced the QD photostability, and most importantly, the L-QD vesicles labeled tumor cells efficiently *in vitro* and *in vivo*. L-QD hybrid vesicles are considered relevant for clinical use since their vesicular morphology allows loading of their internal aqueous phase with therapeutic molecules, in this way constituting a potential combinatory (theranostic) system for the simultaneous delivery of therapeutic and diagnostic agents.

In this work, we explored the use of various types of L-QD hybrid vesicles as delivery systems for *in vivo* systemic circulation applications. Their stability and release profiles in mouse serum were evaluated by turbidimetry and by using vesicle-encapsulated carboxyfluorescein. Further, the blood circulation and tissue biodistribution profiles of the different L-QD hybrid vesicles following intravenous (i.v.) administration in mice were determined, in comparison to the more widely used (and commercially available) poly(ethylene glycol) (PEG)-coated functionalized QD.

RESULTS

L-QD hybrids were prepared following the thin lipid film hydration protocol as previously described (*12*). Briefly, 5.6×10^{14} p/mL CdSe/ZnS QD (960 pmol/mL) were mixed with 8 μmol phospholipid molecules in chloroform, and vesicles were formed following film hydration and sonication, resulting in L-QD hybrid vesicles of 80−100 nm average diameter (Figure 1). The surface charge characteristics of the L-QD hybrid vesicles were in accordance with the characteristics of the lipid molecules used to form the bilayers. L-QD hybrids containing cationic (DOTAP[1]) and PEGylated (DSPE-PEG_{2000}) lipids exhibited surface charges of +47.5 mV and −20 mV, respectively (Figure 1). Also, the characteristics of the bilayers were dependent on the lipid composition selected, namely, fusogenic,

* To whom correspondence should be addressed. Phone: ++44-207-753-5861, Fax: + +44-207-753-5942, E-mail: kostas.kostarelos@pharmacy.ac.uk.

[†] University of London.

[‡] Kings College London.

[1]Abbreviations: DOPC, dioleoylphosphatidylcholine; DOPE, dioleoylphosphatidylethanolamine; DOTAP, 1,2-dioleoyl-3-trimethylammonium-propane; DSPC, distearoylphosphatidylcholine; Chol, cholesterol; DSPE-PEG_{2000}, distearoylphosphatidylethanolamine-poly(ethylene glycol) of molecular weight 2000; CdSe, cadmium selenide; ZnS, zinc sulfide; ICP-MS, inductively coupled plasma mass spectroscopy.

10.1021/bc900047n CCC: $40.75 © 2009 American Chemical Society
Published on Web 08/05/2009

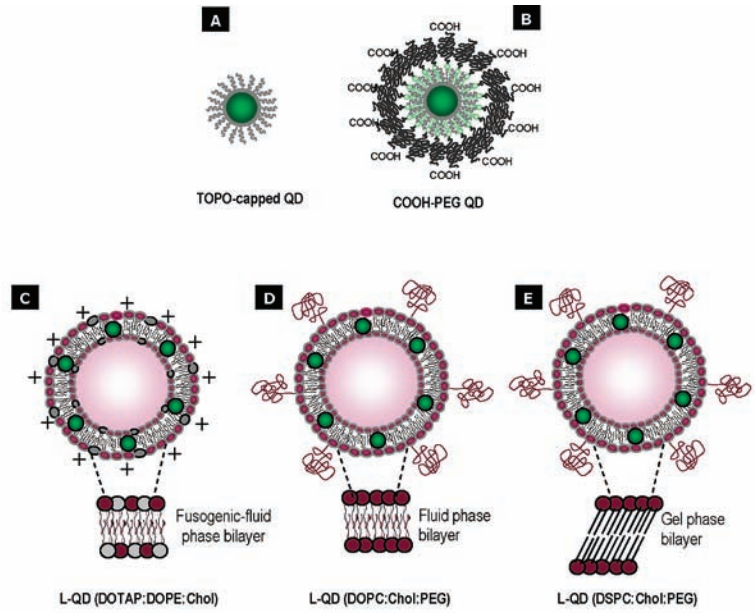

QD Nanoparticle Type	Hydrodynamic Diameter (nm) ±S.D [a]	Polydispersity Index ±S.D [a]	Zeta potential (mV) ±S.D [a]
TOPO-capped QD	2.2 [b]	n/a	n/a
COOH-PEG QD	39.0 (0.00827)	0.167 (0.013)	-7.63 (2.02)
DOTAP:DOPE:Chol (2:1:1.5)	88.8 (0.865)	0.269 (0.005)	+47.5 (1.51)
DOPC:Chol:DSPE-PEG$_{2000}$ (1.8:1:0.2)	104 (0.727)	0.220 (0.010)	-24.0 (1.51)
DSPC:Chol:DSPE-PEG$_{2000}$ (1.8:1:0.2)	111 (0.959)	0.220 (0.001)	-19.5 (0.282)

[a] Mean ±standard deviation; n=3, [b] QD core size according to the manufacturer , n/a: not applicable

Figure 1. A schematic diagram showing a simplified structure of (a) TOPO-capped QD, (b) COOH-PEG QD, and the L-QD hybrids consisting of (c) DOTAP/DOPC/Chol (2:1:1.5), (d) DOPC/Chol/DSPE-PEG$_{2000}$ (1.8:1:0.2) and (e) DSPC/Chol/DSPE-PEG$_{2000}$ (1.8:1:0.2) (diagrams are not drawn to scale). The size, polydispersity index, and zeta potential of COOH-PEG QD and L-QD hybrids used in this study were obtained by dynamic light scattering using Nanosizer ZS.

fluid-phase using DOTAP/DOPE/Chol; fluid-phase using DOPC/Chol/DSPE-PEG$_{2000}$; and gel-phase using DSPC/Chol/DSPE-PEG$_{2000}$.

To evaluate the stability of L-QD hybrid vesicles in physiological conditions, 200 μL (1.6 μmol) of plain liposomes or L-QD vesicles in 5% dextrose were incubated with 1 mL 50% (v/v) CD-1 mouse serum at 37 °C to mimic the *in vivo* environment (approximately half of the volume of complete blood is serum (*13*)). The effect of serum on plain liposomes and L-QD vesicles was monitored by measuring the changes in the turbidity and mean vesicle diameter. Samples were incubated at 37 °C and analyzed at 2, 5, 10, 30, and 60 min using a Beckman DU 640 spectrophotometer (USA). Turbidity was measured at 400 nm with the corresponding amount of serum alone used as a reference. The mean vesicle diameter was measured by dynamic light scattering using the NanoZS (Malvern, UK). All samples were incubated for 60 min in serum.

Figure 2 depicts the stability of L-QD hybrid vesicles incubated in 50% (v/v) CD-1 mouse serum at 37 °C over time. Turbidity increased sharply for both liposomes (diamonds Figure 2a) and L-QD vesicles (diamonds Figure 2b) of the cationic DOTAP/DOPE/Chol lipid composition and was found to be constant over 60 min and 24 h (data not shown), similar to previous observations with cationic systems (*13*). Cationic vesicle aggregation was confirmed by light scattering, as evidenced by increases in the mean diameter from 100 nm to more than 300 nm after 60 min serum incubation (black bars, Figure 2c,d). To determine if changes in cationic vesicle size were due to incubation at 37 °C, all vesicle systems were also incubated in 5% dextrose under the same conditions; however, no changes in size were observed (white bars, Figure 2c,d). PEGylated (sterically stabilized) liposomes and L-QD vesicles (those containing DSPE-PEG$_{2000}$) showed no changes in turbidity (Figure 2a,b) and size (Figure 2c,d) due to the presence of PEG polymer on the vesicle surface (Figure 1) that reduces interactions with serum proteins (*14*). On the basis of these results, only sterically stabilized formulations were used further to determine the release profile of the vesicles.

In order to evaluate the integrity of L-QD vesicles in serum, a high concentration (0.2 M) of the aqueous marker carboxyfluorescein (CF) was encapsulated in the vesicles and free CF was removed by size exclusion chromatography. Release from plain liposomes and L-QD hybrid vesicles were studied by monitoring the increase in the CF fluorescence signal. Rapid release was observed from the L-QD (DOPC/Chol/DSPE-PEG$_{2000}$) vesicles that released 30% of encapsulated CF after 5 min and 50−70% between 0.5 and 4 h (□, Figure 3a). Similar results were obtained for the equivalent liposome system (■, Figure 3a), suggesting that the presence of QD in this vesicle bilayer did not dramatically change the bilayer characteristics that could lead to increased CF leakage.

Modification of the vesicle bilayer by substitution of the fluid-phase DOPC bilayer (Figure 1d) with the "rigid" DSPC (high phase transition lipid in gel phase at 37 °C) (Figure 1d,e),

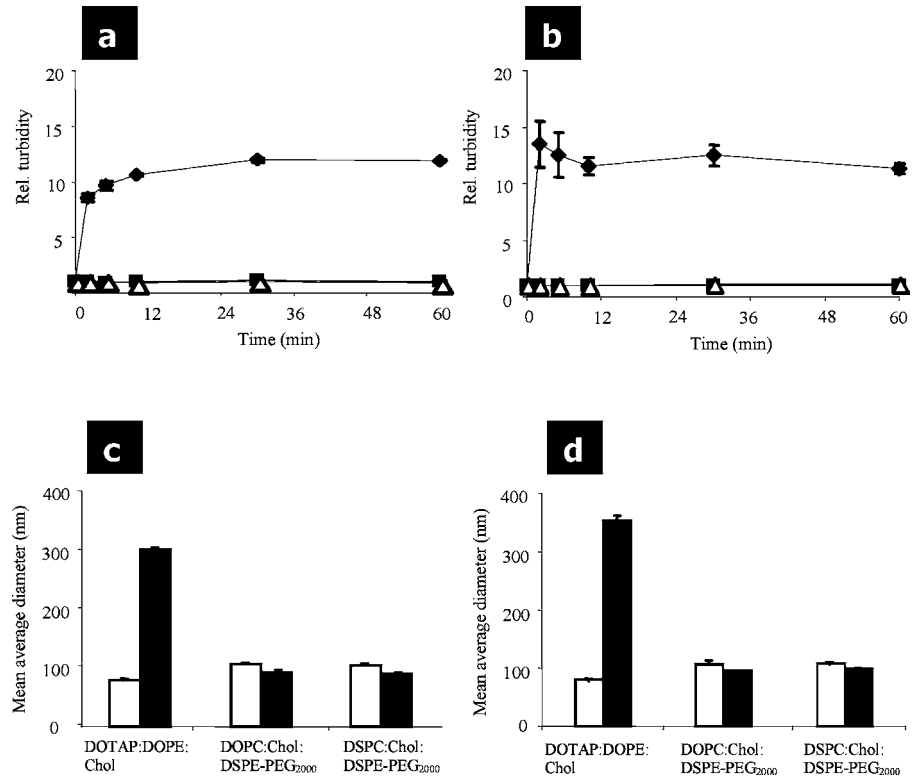

Figure 2. Stability of L-QD vesicles incubated in 50% mouse serum. Relative turbidity at 400 nm of (a) liposomes and (b) L-QD hybrid vesicles consisting of (◆) DOTAP/DOPE/Chol (2:1:1.5); (■) DOPC/Chol/DSPE-PEG$_{2000}$ (1.8:1:0.2); and (Δ) DSPC/Chol/DSPE-PEG$_{2000}$ (1.8:1:0.2); incubated for 2, 5, 10, 30, and 60 min in 50% mouse serum at 37 °C. Mean diameter (nm) of the (c) liposomes and (d) L-QD hybrids after 60 min incubation in 5% dextrose (white bars) and 50% mouse serum (black bars) at 37 °C. Data represent the mean ± S.D.(n = 3).

retarded the CF release from liposomes by a factor of 2, as described previously (*15*). The percentage of CF released from "rigid" [DSPC/Chol/DSPE-PEG$_{2000}$] liposome vesicles was 30−40% after 9 h incubation in serum (▲, Figure 3b). The presence of QD in the DSPC/Chol/DSPE-PEG$_{2000}$ bilayer almost completely prevented CF release up to 72 h (white bars, Figure 3c), indicating the dramatically improved stability of these PEGylated L-QD hybrids at physiological conditions. More biophysical studies are warranted to further elucidate the effect of QD embedding within the lipid bilayer and the interactions at the molecular level between the lipids and the hydrophobic QD self-assembling into vesicles.

We have previously reported that L-QD made of cationic and fusogenic lipid bilayers were capable of effectively labeling cancer cells *in vivo* following intratumoral administration (*12*). To investigate the behavior of L-QD hybrid vesicles in a living animal further, we studied their blood clearance and tissue biodistribution following intravenous (tail vein) administration compared to PEGylated, functionalized QD (COOH-PEG-QD). All pharmacokinetic and biodistribution data in this study were generated by detecting the amount of Cd atoms in the animal tissues using ICP-MS (Supporting Information for details).

Cationic L-QD hybrid vesicles (DOTAP/DOPE/Chol) exhibited rapid clearance from blood circulation with 20% and 1% of the injected dose (% ID) circulating in the blood after 2 and 10 min, respectively (Figure 4a, circles). The rapid clearance is due to transient lung accumulation, where more than 70% of ID was found after 10 min compared to 25% in the liver and spleen (Figure 4b, black bars). At 24 h, redistribution of the cationic L-QD led to their localization mainly in the liver (90% ID) and to a lesser extent in the spleen (5% ID), leaving only 4% in the lung (Figure 4c, black bars). Transient lung accumulation after systemic administration has been described previously for a variety of positively charged nanoparticles (*16*) and is thought to be due to the cationic L-QD interacting with the lung capillaries—the first capillary bed encountered following tail vein administration (*17*−*21*). At later time points, adsorption of negatively charged plasma proteins on the surface of the cationic vesicles hinders the nonspecific interaction with the pulmonary endothelium, leading to their redistribution to liver and spleen (at 24 h) (*17*−*22*). Similar observations have been previously reported for cationic liposome/plasmid DNA complexes (lipoplexes) (*23, 24*).

The blood circulation and tissue biodistribution of sterically stabilized L-QD hybrid vesicles containing 10 mol % of DSPE-PEG$_{2000}$ (*25*) was studied next. PEGylated L-QD (DOPC:Chol: DSPE-PEG$_{2000}$) vesicles exhibited 5−10-fold increase in blood circulation during the first 60 min (Figure 4a, empty diamonds) compared to cationic L-QD (Figure 4a, circles). However, only 10% ID could be detected in the blood after 10 min due to almost complete (>90%) and rapid liver uptake (Figure 4b, white bars). Substitution of DOPC for DSPC to form "rigid" L-QD vesicles (DSPC/Chol/DSPE-PEG$_{2000}$) exhibited up to 30-fold increase in blood circulation during the first 60 min (Figure 4a, squares) compared to DOPC/Chol/DSPE-PEG$_{2000}$ and cationic (DOTAP/DOPE/Chol) L-QD vesicles, with lower RES uptake (Figure 4b, gray bars) as has been previously reported for liposomes (*26*). However, the retention in the blood compartment of these "rigid" L-QD vesicles could not be maintained over time, with only 3% ID detected in the blood after 240 min (Figure 4a, squares).

The pharmacokinetic behavior of L-QD hybrid vesicles was also compared to that of commercially available hydrophilic QD (at 192 pmol—same concentration of QD used throughout) using carboxyl-functionalized poly(ethylene glycol) coated QD (COOH-PEG QD) (Evident Technologies, USA). The hydrodynamic diameter and surface charge of this material were found to be 39 nm and −7.6 mV (Figure 1) injected without further modification via the mouse tail vein. COOH-PEG QD showed prolonged blood circulation (Figure 4a, filled diamonds) as 90%

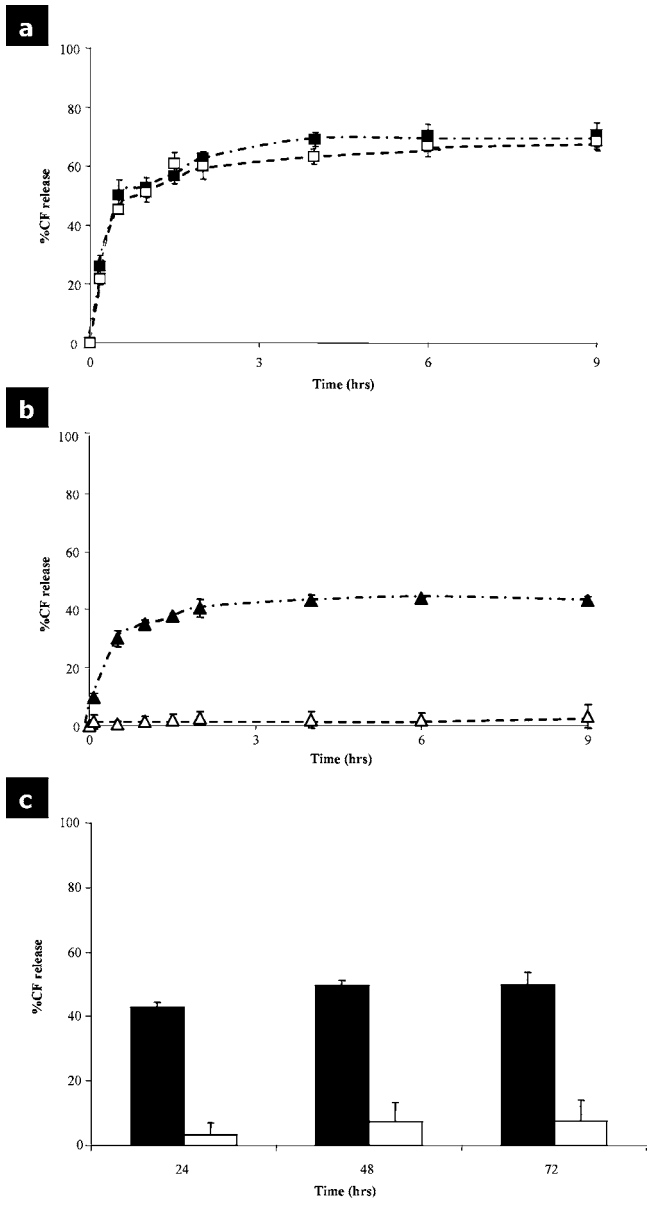

Figure 3. CF release profile from liposomes and L-QD hybrid vesicles incubated in 50% mouse serum. Percentage of CF release from (a) plain (■) and L-QD DOPC/Chol/DSPE-PEG_{2000} (1.8:1:0.2) (□) vesicles; (b) plain (▲) and L-QD DSPC/Chol/DSPE-PEG_{2000} (1.8:1:0.2) (Δ) vesicles incubated in 50% mouse serum at 37 °C for 9 h; and (c) 72 h (plain liposomes, black bars; and L-QD, white bars). Data represent the mean ± SD ($n = 3$).

ID and 20% ID were detected in the blood after 10 min and 24 h (Figure 4c, hatched bars). The tissue biodistribution of COOH-PEG QD was found to be sharply different from that of the L-QD hybrids at the early time point (10 min) with only 4% ID in the liver and spleen. At 24 h postinjection, the COOH-PEG QD concentration in the blood decreased due to accumulation primarily in the liver. No significant accumulation in the kidney, brain, and heart was obtained with either COOH-PEG QD or L-QD hybrids in this study, consistent with previous reports using COOH-PEG QD (*11, 27*).

DISCUSSION

QD have been previously investigated for *in vivo* imaging to visualize tumors, angiogenic endothelium, and lymph nodes in living animals (*1, 11, 28*−*30*). Better understanding of QD structure, surface, and elemental content on their pharmacological behavior *in vivo*, such as their blood circulation and organ biodistribution, is needed. Polymer-coated QD are the most relevant for clinical applications due to their stability *in vivo* and low toxicity (*2, 11*). Moreover, consistent with findings described here, decorating the QD surface with PEG_{2000} can significantly improve their blood circulation ($t_{1/2} = 4-5$ h) (Figure 4a) and reduce their recognition by the liver and spleen (Figure 4b,c) (*1, 11, 29*). We recently described an alternative approach to solubilize organic QD by engineering self-assembled liposome-QD (L-QD) hybrid vesicles that were capable of successful labeling of tumor cells *in vitro* and *in vivo* (*12*). One of the key advantages offered by the L-QD hybrid system is the versatility of potential structural and surface characteristics by selection of different lipid components with minimal manipulation of the QD nanocrystal. Also, they offer the possibility to encapsulate therapeutic agents (e.g., doxorubicin) in their internal aqueous phase for the construction of multimodal (therapeutic and diagnostic) delivery devices. In this study, we explored this versatility by constructing different types of L-QD by rational selection of different molecular (lipid) components (Figure 1) and correlated their composition with their stability *in vitro* and their pharmacokinetic profile *in vivo*.

Our *in vitro* investigations indicated that L-QD hybrids of cationic surface character and a fluid-phase bilayer were not stable in serum and released encapsulated carboxyfluorescein rapidly (Figures 2 and 3). On the other hand, L-QD hybrids consisting of a "rigid", gel-phase lipid bilayer (DSPC) and cholesterol exhibited longer blood circulation (Figure 4a) and slower accumulation in liver (Figure 4b,c) compared to fluid-bilayer or cationic formulations, which is in agreement with earlier observations regarding the effect of liposome compositions on their behavior *in vivo* (*25, 26*). L-QD hybrids with PEG on their surface exhibited higher serum stability (Figure 2), indicating that such L-QD hybrids could offer a platform for systemic multimodal applications (*31*). However, on systemic (i.v.) administration sterically stabilized, PEGylated L-QD showed rapid blood clearance compared to previous reports on similar liposome-alone systems (*25, 26*).

The rapid blood clearance of these hybrids, despite PEG surface coating, can be due to (a) translocation of the hydrophobic QD from the hybrid bilayer to the plasma proteins leading to subsequent uptake by the liver; (b) suboptimal PEGylation of the vesicles containing QD leading to rapid clearance of this vesicle population only (*25*). More work on improving the steric stabilization of L-QD vesicles and their pharmacological profile is warranted by using different lipid molar ratios, PEG of different molecular weights, and optimization of the PEG surface conformation (mushroom or brush) on the L-QD surface (*32*). On the basis of the pharmacokinetic data obtained, L-QD hybrid systems will not be suitable candidates as blood-pool imaging agents due to their rapid clearance from systemic circulation.

Several studies have reported the effect of QD surface coating on QD behavior *in vivo* (*27, 28*). Surface coating determines the overall QD size; therefore, high molecular weight polymers or organic coatings lead to considerable increases in QD diameter that accelerate QD blood clearance and liver entrapment. Such effects have been previously reported by Fischer et al. who observed remarkable differences in the blood profile of 25 nm mercaptoundecanoic acid cross-linked with lysine-QD (LM-QD) ($t_{1/2} = 60$ min), compared to 80 nm bovine serum albumin coated QD (BSA-QD) ($t_{1/2} = 38$ min) (*27*). In addition, QD surface charge was also found to significantly affect QD tissue biodistribution. The cationic LM-QD accumulated significantly in the lung and kidney compared to the zwitterionic BSA-QD that accumulated predominantly (99% ID) in the liver (*27*). More

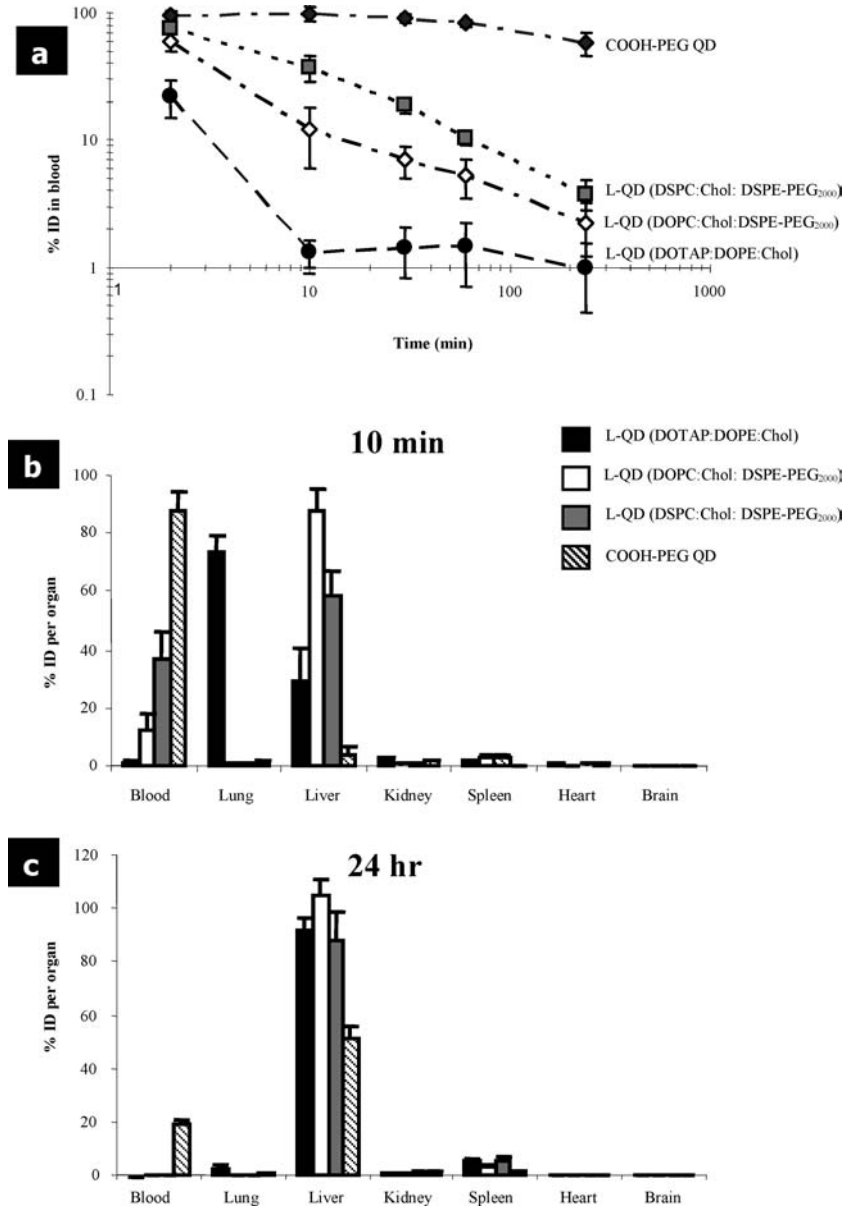

Figure 4. Biodistribution of different QD nanoparticles in CD-1 nude mice after intravenous administration. (a) Blood clearance profile of L-QD DOTAP/DOPE/Chol (2:1:1.5, circles), L-QD DOPC/Chol/DSPE-PEG_{2000} (1.8:1:0.2, empty diamonds), L-QD DSPC/Chol/DSPE-PEG_{2000} (1.8:1:0.2, squares), and COOH-PEG QD (filled diamonds) in CD-1 nude mice after intravenous administration. Organ biodistribution in CD-1 nude mice of L-QD DOTAP/DOPE/Chol (2:1:1.5, black bars), L-QD DOPC/Chol/DSPE-PEG_{2000} (1.8:1:0.2, white bars), L-QD DSPC/Chol/DSPE-PEG_{2000} (1.8:1:0.2, gray bars), and COOH-PEG QD (hatched bars) nanoparticles (b) 10 min and (c) 24 h after tail vein injection. Data represent the mean $\pm$ SD ($n = 4$).

recently, Frangioni et al. reported that the QD surface charge had a profound effect on the ensuing size of QD under physiological conditions. Purely negative or positive QD surface character was associated with an overall increase in the QD hydrodynamic diameter above 15 nm, due to interaction with serum proteins. This increased QD size did not allow their renal excretion and enhanced their accumulation in the liver. That study indicated that only neutral organic coatings (e.g., cysteine) that maintained the QD size in the blood below 5.5 nm were rapidly excreted in the urine and eliminated from the body (*29*, *33*).

The pharmacological profiles of sterically stabilized QD using different molecular weight PEG have also been studied. QD conjugated to low molecular weight PEG (PEG_{750}) exhibited short blood circulation ($t_{1/2} < 12$ min) with predominant uptake in the liver, spleen, lymph nodes, and bone marrow (*28*). Increasing PEG molecular weight to 2000 and 5000 Da significantly reduced macrophage recognition and consequently increased their blood circulation $t_{1/2}$ to an average of 5 and 18.5 h, respectively (*11*, *29*, *34*). Interestingly, similar observations in relation to the size of PEG on the QD surface have also been illustrated after conjugation of ligands (such as epidermal growth factor and RGD) at the distal end of the PEG-coated QD to improve their systemic tumor targeting (*35*, *36*). It would be interesting to explore any differences in the pharmacokinetic profile of the L-QD systems after conjugation of targeting ligands on their lipid bilayer.

In the present study, cationic L-QD (DOTAP/DOPE/Chol) hybrid vesicles exhibited a different *in vivo* profile compared to previously reported 25 nm, cationic mercaptoundecanoic acid cross-linked with lysine-QD (*27*). Cationic L-QD hybrids cleared very rapidly from blood circulation after injection (2 min) (Figure 4b) and ~80% ID resided in the lung compared to 2%

ID of lysine-QD localized in the lung between 15 and 90 min. The low lung accumulation of lysine-QD can be explained by their small size (*37*) and lower cationic surface charge (*38*) compared to the highly positively charged L-QD hybrid vesicles (+47.5 mV). On the basis of this pharmacological profile, improvements in the dynamics of cellular uptake of cationic L-QD by the pulmonary endothelium by inclusion of an appropriate ligand may offer even more effective and specific delivery of QD to the lung tissue for imaging and tracking purposes.

CONCLUSION

In this work, we rationally modulated the surface and bilayer characteristics of the recently developed L-QD hybrid vesicles and correlated them to blood stability (*in vitro* and *in vivo*) and tissue biodistribution in mice after intravenous administration. Sterically stabilized L-QD hybrid vesicles have shown high serum stability *in vitro* comparable to corresponding liposome-alone systems. The *in vivo* profiles obtained for the different L-QD hybrid systems (by monitoring Cd atom deposition in blood and tissues) showed identical behavior between cationic L-QD and previously described cationic nanoparticles. However, in the case of PEGylated L-QD much shorter blood circulation times were observed compared to PEGylated liposomes of the same lipid composition. Such findings indicate that liposome−nanoparticle hybrid systems should not be expected to behave pharmacologically similarly to liposome-alone systems. Eventually (time points at 24 h or later), both the L-QD and functionalized QD accumulated primarily in the liver, which may cause toxicological concerns that will have to be overcome before further clinical development. Overall, the L-QD hybrid vesicle system in comparison to functionalized QD is considered a viable platform that allows the facile modulation of the hybrid vesicle characteristics for the rational design of QD delivery to different tissues such as the lung, particularly if therapeutic agents are encapsulated in the L-QD internal aqueous phase.

ACKNOWLEDGMENT

This work was partially supported by The School of Pharmacy, University of London. The authors thank Lipoid Co. (Germany) for the lipid samples and Evident Technologies (New York, USA) for the collaborative agreement on the provision of quantum dots. W.T.A.-J. is a recipient of the Overseas Research Student Award Scheme (ORSAS) from the University of London and K.T.A.-J. is a recipient of the Maplethorpe Fellowship, The University of London.

Supporting Information Available: L-QD hybrid vesicle preparation, serum stability, carboxyfluorescein release, L-QD biodistribution *in vivo*, and quantification in organs. This material is available free of charge via the Internet at http://pubs.acs.org.

LITERATURE CITED

(1) Akerman, M. E., Chan, W. C., Laakkonen, P., Bhatia, S. N., and Ruoslahti, E. (2002) Nanocrystal targeting in vivo. *Proc. Natl. Acad. Sci. U.S.A. 99*, 12617–12621.

(2) Derfus, A. M., Chan, W. C., and Bhatia, S. N. (2003) Probing the cytotoxicity of semiconductor quantum dots. *Nano Lett. 4*, 11–18.

(3) Michalet, X., Pinaud, F. F., Bentolila, L. A., Tsay, J. M., Doose, S., Li, J. J., Sundaresan, G., Wu, A. M., Gambhir, S. S., and Weiss, S. (2005) Quantum dots for live cells, in vivo imaging, and diagnostics. *Science 307*, 538–544.

(4) Gao, X., Yang, L., Petros, J. A., Marshall, F. F., Simons, J. W., and Nie, S. (2005) In vivo molecular and cellular imaging with quantum dots. *Curr. Opin. Biotechnol. 16*, 63–72.

(5) Dubertret, B., Skourides, P., Norris, D. J., Noireaux, V., Brivanlou, A. H., and Libchaber, A. (2002) In vivo imaging of quantum dots encapsulated in phospholipid micelles. *Science 298*, 1759–1762.

(6) Gerion, D., Pinaud, F., Williams, S. C., Parak, W. J., Zanchet, D., Weiss, S., and Alivisatos, A. P. (2001) Synthesis and properties of biocompatible water-soluble silica-coated CdSe/ZnS semiconductor quantum dots. *J. Phys. Chem. B 105*, 8861–8871.

(7) Liu, S., Lee, C. M., Wang, S., and Lu, D. R. (2006) A new bioimaging carrier for fluorescent quantum dots: phospholipid nanoemulsion mimicking natural lipoprotein core. *Drug Delivery 13*, 159–164.

(8) Joumaa, N., Korgel, B. A., Theretz, A., Elaissari, A., Sukhanova, A., Artemyev, M., Nabiev, I., and Cohen, J. H. (2006) Synthesis of quantum dot-tagged submicrometer polystyrene particles by miniemulsion polymerization. *Langmuir 22*, 1810–1816.

(9) Alivisatos, P. (2004) The use of nanocrystals in biological detection. *Nat. Biotechnol. 22*, 47–52.

(10) Derfus, A. M., Chan, W. C., and Bhatia, S. N. (2004) Intracellular delivery of quantum dots for live cell labeling and organelle tracking. *Adv. Mater. 16*, 961–966.

(11) Gao, X., Cui, Y., Levenson, R. M., Chung, L. W., and Nie, S. (2004) In vivo cancer targeting and imaging with semiconductor quantum dots. *Nat. Biotechnol. 22*, 969–976.

(12) Al-Jamal, W. T., Al-Jamal, K. T., Tian, B., Lacerda, L., Bomans, P. H., Frederik, P. M., and Kostarelos, K. (2008) Lipid-quantum dot (L-QD) bilayer vesicles enhance tumor cell uptake & retention in vitro and in vivo. *ACS Nano 2*, 408–418.

(13) Zhang, Y., and Anchordoquy, T. J. (2004) The role of lipid charge density in the serum stability of cationic lipid/DNA complexes. *Biochim. Biophys. Acta 1663*, 143–157.

(14) Han, H. D., Shin, B. C., and Choi, H. S. (2006) Doxorubicin-encapsulated thermosensitive liposomes modified with poly(N-isopropylacrylamide-co-acrylamide): drug release behavior and stability in the presence of serum. *Eur. J. Pharm. Biopharm. 62*, 110–116.

(15) Senior, J., and Gregoriadis, G. (1982) Stability of small unilamellar liposomes in serum and clearance from the circulation: the effect of the phospholipid and cholesterol components. *Life Sci. 30*, 2123–2136.

(16) le Masne de Chermont, Q., Chaneac, C., Seguin, J., Pelle, F., Maitrejean, S., Jolivet, J. P., Gourier, D., Bessodes, M., and Scherman, D. (2007) Nanoprobes with near-infrared persistent luminescence for in vivo imaging. *Proc. Natl. Acad. Sci. U.S.A. 104*, 9266–9271.

(17) Barron, L. G., Gagne, L., and Szoka, F. C., Jr. (1999) Lipoplex-mediated gene delivery to the lung occurs within 60 minutes of intravenous administration. *Hum. Gene Ther. 10*, 1683–1694.

(18) Ishiwata, H., Suzuki, N., Ando, S., Kikuchi, H., and Kitagawa, T. (2000) Characteristics and biodistribution of cationic liposomes and their DNA complexes. *J. Control. Rel. 69*, 139–148.

(19) Liu, F., Qi, H., Huang, L., and Liu, D. (1997) Factors controlling the efficiency of cationic lipid-mediated transfection in vivo via intravenous administration. *Gene Ther. 4*, 517–523.

(20) Mahato, R. I., Anwer, K., Tagliaferri, F., Meaney, C., Leonard, P., Wadhwa, M. S., Logan, M., French, M., and Rolland, A. (1998) Biodistribution and gene expression of lipid/plasmid complexes after systemic administration. *Hum. Gene Ther. 9*, 2083–2099.

(21) Nicolazzi, C., Mignet, N., de la Figuera, N., Cadet, M., Ibad, R. T., Seguin, J., Scherman, D., and Bessodes, M. (2003) Anionic polyethyleneglycol lipids added to cationic lipoplexes increase their plasmatic circulation time. *J. Control. Rel. 88*, 429–443.

(22) Brigger, I., Morizet, J., Laudani, L., Aubert, G., Appel, M., Velasco, V., Terrier-Lacombe, M. J., Desmaele, D., d'Angelo, J., Couvreur, P., and Vassal, G. (2004) Negative preclinical results with stealth nanospheres-encapsulated Doxorubicin in an orthotopic murine brain tumor model. *J. Control. Rel. 100*, 29–40.

(23) Litzinger, D. C., Brown, J. M., Wala, I., Kaufman, S. A., Van, G. Y., Farrell, C. L., and Collins, D. (1996) Fate of cationic liposomes and their complex with oligonucleotide in vivo. *Biochim. Biophys. Acta 1281*, 139–149.

(24) Li, S., Tseng, W. C., Stolz, D. B., Wu, S. P., Watkins, S. C., and Huang, L. (1999) Dynamic changes in the characteristics of cationic lipidic vectors after exposure to mouse serum: implications for intravenous lipofection. *Gene Ther. 6*, 585–594.

(25) Papahadjopoulos, D., Allen, T. M., Gabizon, A., Mayhew, E., Matthay, K., Huang, S. K., Lee, K. D., Woodle, M. C., Lasic, D. D., and Redemann, C. (1991) Sterically stabilized liposomes: improvements in pharmacokinetics and antitumor therapeutic efficacy. *Proc. Natl. Acad. Sci. U.S.A. 88*, 11460–11464.

(26) Gabizon, A., and Papahadjopoulos, D. (1998) Liposome formulations with prolonged circulation time in blood and enhanced uptake by tumors. *Proc. Natl. Acad. Sci. U.S.A. 85*, 6949–6953.

(27) Fischer, H. C., Liu, L. C., Pang, K. S., and Chan, W. C. W. (2006) Pharmacokinetics of nanoscale quantum dots: In vivo distribution, sequestration, and clearance in the rat. *Adv. Funct. Mater. 16*, 1299–1305.

(28) Ballou, B., Lagerholm, B. C., Ernst, L. A., Bruchez, M. P., and Waggoner, A. S. (2004) Noninvasive imaging of quantum dots in mice. *Bioconjugate Chem. 15*, 79–86.

(29) Cai, W., Shin, D. W., Chen, K., Gheysens, O., Cao, Q., Wang, S. X., Gambhir, S. S., and Chen, X. (2006) Peptide-labeled near-infrared quantum dots for imaging tumor vasculature in living subjects. *Nano Lett. 6*, 669–676.

(30) Larson, D. R., Zipfel, W. R., Williams, R. M., Clark, S. W., Bruchez, M. P., Wise, F. W., and Webb, W. W. (2003) Water-soluble quantum dots for multiphoton fluorescence imaging in vivo. *Science. 300*, 1434–1436.

(31) Torchilin, V. P. (2005) Recent advances with liposomes as pharmaceutical carriers. *Nat. Rev. Drug Discovery 4*, 145–160.

(32) Washington, C., King, S. M., and Heenan, R. K. (1996) Structure of block copolymers adsorbed to perfluorocarbon emulsions. *J. Phys. Chem. 100*, 7603–7609.

(33) Liu, W., Howarth, M., Greytak, A. B., Zheng, Y., Nocera, D. G., Ting, A. Y., and Bawendi, M. G. (2008) Compact biocompatible quantum dots functionalized for cellular imaging. *J. Am. Chem. Soc. 130*, 1274–1284.

(34) Yang, R. S., Chang, L. W., Wu, J. P., Tsai, M. H., Wang, H. J., Kuo, Y. C., Yeh, T. K., Yang, C. S., and Lin, P. (2007) Persistent tissue kinetics and redistribution of nanoparticles, quantum dot 705, in mice: ICP-MS quantitative assessment. *Environ. Health Perspect. 115*, 1339–1343.

(35) Cai, W., Chen, K., Li, Z. B., Gambhir, S. S., and Chen, X. (2007) Dual-function probe for PET and near-infrared fluorescence imaging of tumor vasculature. *J. Nucl. Med. 48*, 1862–1870.

(36) Diagaradjane, P., Orenstein-Cardona, J. M., Colon-Casasnovas, E., Deorukhkar, A., Shentu, S., Kuno, N., Schwartz, D. L., Gelovani, J. G., and Krishnan, S. (2008) Imaging epidermal growth factor receptor expression in vivo: pharmacokinetic and biodistribution characterization of a bioconjugated quantum dot nanoprobe. *Clin. Cancer Res. 14*, 731–741.

(37) Tranchant, I., Thompson, B., Nicolazzi, C., Mignet, N., and Scherman, D. (2004) Physicochemical optimisation of plasmid delivery by cationic lipids. *J. Gene Med. 6* (Suppl 1), S24–S35.

(38) Bragonzi, A., Boletta, A., Biffi, A., Muggia, A., Sersale, G., Cheng, S. H., Bordignon, C., Assael, B. M., and Conese, M. (1999) Comparison between cationic polymers and lipids in mediating systemic gene delivery to the lungs. *Gene Ther. 6*, 1995–2004.

BC900047N

Supporting Information

Blood circulation and Tissue Biodistribution of Lipid-Quantum Dot (L-QD) Hybrid Vesicles Intravenously Administered in Mice

*Wafa' T. Al-Jamal[†], Khuloud T. Al-Jamal[†], Andrew Cakebread[‡], John M. Halket[‡] and Kostas Kostarelos[†]**

[1] Nanomedicine Lab, Centre for Drug Delivery Research, The School of Pharmacy, University of London, London WC1N 1AX, United Kingdom

[2] Mass-Spectroscopy, Department of Forensic Science & Drug Monitoring, Kings College London London SE1 9NH, United Kingdom

Materials: CdSe/ZnS core/shell TOPO-capped quantum dots (QD), supplied in toluene with a reported CdSe core size of 2.2 nm in diameter, and with overall size of 4-5 nm including 1-2 nm thickness of the organic coat (TOPO and ZnS) [1-3]; carboxyl functionalized polyethylene glycol-lipid coated QD (COOH-PEG QD) (Evident Technologies, USA). QD exhibited an absorption peak at 502 nm and an emission peak at 517 nm, which agree with their core size as described earlier by Peng et al.[4]. Dioleoylphosphatidylcholine (DOPC 98%); distearoylphosphatidylcholine (DSPC 98%); 1,2-distearoyl-sn-glycero-3-phosphoethanolamine-N-[methoxy(polyethyleneglycol)-2000] (ammonium salt) (DSPE-PEG_{2000} 98%) (Lipoid GmbH, Germany), 1,2-dioleoyl-*sn*-glycero-3-phosphoethanolamine (DOPE 99%); 1,2-dioleoyl-3-trimethylammonium-propane (chloride salt) (DOTAP 99%) (Avanti Polar Lipid, USA), cholesterol (Chol); dextrose (Sigma, USA)

L-QD preparation*:* $5.6x10^{14}$ p/mL CdSe/ZnS QD (960 pmol/mL) were mixed with 8 μmol phospholipid molecules (DOTAP:DOPE:Chol, 2:1:1.5; DOPC:Chol:DSPE-PEG_{2000}, 1.8:1:0.2 and DSPC:Chol:DSPE-PEG_{2000}, 1.8:1:0.2) in chloroform and vesicles were formed following the lipid film hydration methodology as previously described [5]. After evaporation of the solvent in a rotary evaporator, a thin QD-containing lipid film was formed, effluxed with a stream of N_2 and kept until further use. Upon hydration of the L-QD lipid film with 1 mL 5% dextrose, multilamellar vesicles (MLV) were self-assembled, incorporating the QD into their lipid bilayers. Sonication using an ultrasonic bath (Ultrasonic cleaner, VWR) for 10-15 min at 30 °C and 50 °C with high phase transition formulation (DSPC), led to formation of QD-containing small unilamellar vesicles, so-called L-QD hybrids. Samples were flushed

with N_2 and left to anneal overnight. Dynamic light scattering (DLS) and surface charge were measured with Zetasizer Nano ZS (Malvern, UK, He-Ne laser).

CF-loaded vesicle preparation: Lipid films were hydrated with 0.2 M 5, 6-carboxyfluorescein (CF) (Fluka, USA) solution prepared in PBS buffer pH 7.4. The hydration was carried out gradually using 200µl aliquot of CF solution accompanied with votex mixing to achieve better hydration and higher CF entrapment. Unentrapped CF was removed with Sepharose CL-2B size exclusion chromatography column (5*1.5cm) (Sigma, USA). Liposomes were eluted by PBS buffer pH 7.4, and SUV-containing fractions were collected and diluted samples were concentrated to the original volumes using Vivaspin 4 concentrators MWCO 5000 (Vivascience, Sartorus, Germany) by centrifugation at 3000 rpm for 2 hr. The CF encapsulation efficiency for liposomes was identical to L-QD vesicles at 6mmol.

CF release experiment: CF release from plain liposomes and L-QD vesicles were studied by monitoring the increase in the fluorescence signal of CF during the release from the liposomes. At high concentration as encapsulated in the vesicles, CF is quenched. As CF is diluted (released to the surrounding medium) self-quenching decreases and fluorescence signals increases. To simulate the ensuing dilution in the blood plasma expected upon injection of 0.2 mL volume for 25g body weight, 100 µl of CF-loaded vesicles were diluted in 500 µl of 50% (v/v) CD-1 mouse serum (Sera Laboratories International, UK) in PBS and incubated at 37 $^{\circ}$C with gentle shaking. At different time points, 10 µl samples were withdrawn further diluted with PBS for fluorescence intensity measurement. Fluorescence measurements were carried out in quartz cuvette using PerkinElmer luminescence spectrometer (LS50B). The samples

were excited at 495 nm and the emission was read at 520 nm, with excitation and emission slit width of 2.5 nm and integration time of 2 seconds. CF release was determined by normalizing the intensity of the fluorescence signals:

$$\%CF\ release = (I_{(t)} - I_{\circ}) / (I_{\infty} - I_{\circ}) \times 100$$

Where $I_{\circ}$ is the initial signal, $I_{(t)}$ is the fluorescence signals at definite time point and I_{∞} is the CF signal after disrupting the liposomes with 10µl of 10% Triton X-100 solution and mixing for few seconds.

Intravenous administration of L-QD vesicle: All animal experiments were performed in compliance with the UK Home Office Code of Practice for the Housing and Care of Animals used in Scientific Procedures. 1.6 µmol/200 µl of L-QD hybrids (equivalents to 196 pmol QD) were injected in 14-16 weeks old female CD-1 nude mice (Charles River Laboratories, UK) via the tail vein. At different time points, the mice were anesthetized by inhalation isoflurane and bled by the tail vein puncture at 2, 10, 30, 60 min, 4 and 24 hr post injection and 50 µl blood was collected. Blood withdrawn did not exceed 10% of the mouse blood volume. The mice were killed after 10 min and 24 hr by cervical dislocation and dissected. In addition to blood, organs were collected, weighted and analyzed for Cd element by Inductively Coupled Plasma Mass Spectrometry (ICP-MS) as described elsewhere [6]. The total Cd concentration in the blood was determined by assuming the total blood volume was 7.3% of the body weight [7]. The percentage of injected dose (%ID) was expressed per organ. (n= 4 ± S.D).

Quantification of quantum dots in organs: Blood, liver, lung, kidney, spleen, heart and brain were collected. Mice organs (150-200 mg) were incubated in 500 µl lysate

buffer (1% SDS, 0.1 M NaCl, 0.05 M tris(hydroxylmethyl)aminomethane, Tris, pH 8) over night. The samples rendered soluble by the addition of 1 mL 70% nitric acid (HNO_3) (Fluka, UK). All the samples were prepared in disposal 10 mm *7.5-mL glass culture tubes that were fitted with polyethylene “snap cap”. With punctured cap, acid digestion of the samples was carried out by heating them in an oil bath at 115°C for 2-3hrs. Later on, the cooled samples were filtered using 0.45 μm pore poly (vinylidene fluoride) membrane syringe filter (VWR, UK). The filtrate was re-diluted to 5 mL by deionized water and transferred to 15 mL polypropylene centrifuge tubes for storage prior for the measurement. For all Inductively Coupled Plasma Mass Spectrometry (ICP-MS) measurements (PerkinElmer SCIEX ICP mass spectrometer, ELAN DRC 6100, USA) nitric acid blank, blank tissue samples, spiked samples with known QD for calibration curve and Cd standards were prepared and tested concurrently with test samples.

References

(1) Gao, X., Cui, Y., Levenson, R. M., Chung, L. W., Nie, S. (2004) In vivo cancer targeting and imaging with semiconductor quantum dots, *Nat. Biotechnol. 22*, 969-976 .

(2) Luccardini, C., Tribet, C., Vial, F., Marchi-Artzner, V., Dahan, M. (2006) Size, charge, and interactions with giant lipid vesicles of quantum dots coated with an amphiphilic macromolecule, *Langmuir. 22*, 2304-2310 .

(3) Pons, T., Uyeda, H. T., Medintz, I. L., Mattoussi, H. (2006) Hydrodynamic dimensions, electrophoretic mobility, and stability of hydrophilic quantum dots, *J. Phys. Chem. B Condens. Matter Mater. Surf. Interfaces. Biophys. 110*, 20308-20316 .

(4) Yu, W. W., Qu, L., Guo, W., Peng, X. (2003) Experimental determination of the extinction coefficient of CdTe, CdSe, and CdS nanocrystals, *Chem. Mater. 15*, 2854-2860 .

(5) Al-Jamal, W. T., Al-Jamal, K. T., Tian, B., Lacerda, L., Bomans, P. H., Frederik, P. M., Kostarelos, K. (2008) Lipid-Quantum Dot (L-QD) bilayer vesicles enhance tumor cell uptake & retention in vitro and in vivo, *ACS Nano. 2*, 408-418 .

(6) Fischer, H. C., Liu, L. C., Pang, K. S., Chan, W. C. W. (2006) Pharmacokinetics of nanoscale quantum dots: In vivo distribution, sequestration, and clearance in the rat, *Adv. Funct. Mater. 16*, 1299-1305 .

(7) Nicolazzi, C., Mignet, N., de la Figuera, N., Cadet, M., Ibad, R. T., Seguin, J., Scherman, D., Bessodes, M. (2003) Anionic polyethyleneglycol lipids added to cationic lipoplexes increase their plasmatic circulation time, *J. Control. Rel. 88*, 429-443 .

Construction of Oligonucleotide Microarrays (Biochips) via Thioether Linkage for the Detection of Bacterial Meningitis

S. Mahajan,[†] D. Sethi,[†] S. Seth,[†] A. Kumar,[†] P. Kumar,[†] and K. C. Gupta*[,†,‡]

Institute of Genomics and Integrative Biology (CSIR), Mall Road, Delhi University Campus, Delhi-110 007, India, and Indian Institute of Toxicology Research (CSIR), Mahatma Gandhi Marg, Lucknow-226001, Uttar Pradesh, India. Received April 10, 2009; Revised Manuscript Received July 21, 2009

Oligonucleotide-based arrays are increasingly becoming useful tools for the analysis of gene expression and single-nucleotide polymorphism. Here, we report a method that allows the direct immobilization of thiolated oligonucleotides onto an epoxy-activated glass surface via a stable thioether linkage under microwaves. The described chemistry efficiently immobilizes the probes via terminal thiol groups with uniform spot morphology. The thioether linkage could endure repeated PCR-like heat cycling with only 2.5% loss after 20 cycles, indicating that the chemistry can be used in integrated PCR/microarray devices. The highlighting feature of the proposed method is that the detection limit for the probe concentration can be reduced to 0.25 μM with 20-mer oligonucleotides. The efficiency of the projected method (~33%) indicates its advantage over the existing standard methods, viz., NTMTA (~9.8%), epoxide-amine (~9.8%) and disulfide (~1.7%). The constructed microarrays were validated through the detection of base mismatches and bacterial meningitis. These features make the projected strategy ideal for manufacturing oligonucleotide arrays and detection of mismatches and bacterial diseases.

INTRODUCTION

Oligonucleotide microarrays have lately emerged into the academic and commercial arena owing to their usefulness in high-throughput, parallel gene expression, SNP analysis, and comparative genome hybridization (*1*−*4*).

DNA microarrays can be produced essentially in two different ways: (i) by direct chemical synthesis on the solid surface using photolithography technique (*5*, *6*); (ii) by immobilization of presynthesized oligonucleotides on selected surfaces (*7*−*10*). An example of the first approach is the Affymetrix method, which involves stepwise synthesis of oligonucleotides using photocleavable protecting groups. It is advantageous in generating high-density (10^6 sequences/cm^2) microarrays but lacks flexibility and economy. There are also some practical limits to the length of oligonucleotides to be synthesized. The immobilization method allows the tethering of long as well as modified base-incorporated oligonucleotide sequences and flexibility of a variety of ligands to be fixed on a surface of choice. That is why patterning of presynthesized oligonucleotides is preferred in research laboratories and commercial applications, where low to medium density arrays are required. In addition to the chemistry involved in fixing oligonucleotides to the polymer surface, the choice of polymer matrix, particularly glass, plays an important role in influencing the quality of the constructed microarrays.

Since oligonucleotides bind poorly to virgin glass, a number of methods for noncovalent and covalent immobilization of oligonucleotides on modified glass have been reported (*11*−*23*). The simplest is electrostatic adsorption of probes on polylysine and aminopropyl-coated microslides (*10*), but it results in low hybridization efficiency, as ionic interactions encourage the probes to lay flat on the surface. Therefore, a single terminal covalent attachment is preferred for short oligonucleotides, as it allows the entire oligonucleotide to be available for hybridization. Some common combinations of surface/oligonucleotide modifications that have been demonstrated include the following: carboxyl−amine, thiol−disulfide, amine−aldehyde, aldehyde−oxyamine, biotin−streptavidin, gold−thiol, zirconylated-surface−phosphate, epoxide−amine, and so forth. In addition, there are strategies employing heterobifunctional reagents, such as *N*-(2-trifluoroethanesulfonatoethyl)-*N*-(methyl)-triethoxysilylpropyl-3-amine (NTMTA) and *N*-(3-trifluoroethanesulfonyloxypropyl)anthraquinone-2-carboxamide (NTPAC), previously reported from the authors' laboratory (*7*), for construction of oligonucleotide microarrays. These methods make use of single terminal attachment of oligonucleotides on modified glass surfaces. In some cases, immobilization was also realized by photochemical methods (single or multipoint contact). All of the above-mentioned approaches have their own limitations with respect to factors like involvement of multisteps for the introduction of functional groups on either the oligomer or glass surface, time-consuming reactions to realize immobilization with low to moderate immobilization efficiency, low thermal and chemical stability, and so forth.

Recently, Bocking et al. (*9*) have reported the immobilization of thiolated oligonucleotides on epoxylated silicon (111) surface. The method involves a one-step DNA immobilization; however, the functionalization of silicon (111) to generate epoxy groups is quite tedious and requires a multistep reaction scheme. Similarly, Preininger et al. (*16*) have generated high-capacity epoxy surfaces by coating 1% epoxy resin using different methods for achieving signal enhancement and immobilized amine- and thiol-modified oligonucleotides. However, reproducibility of the coating process and enhanced background signals limit the viability of the protocol. In search of a simple and efficient immobilization method, which would overcome the limitations of the existing ones, we explored the thioether linkage for microarray fabrication.

In this Communication, we propose the covalent attachment of thiol-modified probes to epoxy-activated glass slides under microwaves, where it takes only 12 min for immobilization with

* Tel.: +91 11 27662491; Fax: +91 11 27667471; E-mail: kcgupta@igib.res.in.

[†] Institute of Genomics and Integrative Biology, Delhi.

[‡] Indian Institute of Toxicology Research, Lucknow.

10.1021/bc900162u CCC: $40.75 © 2009 American Chemical Society
Published on Web 08/13/2009

Table 1. List of Oligonucleotide Sequences Synthesized with Their Deprotection Conditions and Yields

no.	oligonucleotide sequence	deprotection conditions	yield (A_{260})
1.	TET-d (TCT GTA TGT CTA TTC TCG TT)-$OPO_3(CH_2)_6$-SH	Aq. NH_4OH (30%) containing 0.1 M DTT, 16 h, 55 °C.	24.3
2.	TET-d (TCT GTA TGT CTA TTC TCG TT)	Aq. NH_4OH (30%), 16 h, 55 °C.	27.1
3.	TET-d (AAC GAT CGA TTT GCT TAC GT)	Aq. NH_4OH (30%), 16 h, 55 °C.	25.1
4.	TET-d (TAC GAC CGT CTA TGC CGA)	Aq. NH_4OH (30%), 16 h, 55 °C.	23.1
5.	HS-$(CH_2)_6$-OPO_3-d (ACG TAA GCA AAT CGA TCG TT)	Aq. NH_4OH (30%) containing 0.1 M DTT, 16 h, 55 °C.	24.3
6.	HS-$(CH_2)_6$-OPO_3-d (ACG TAA GCA AAT CGA TCG GT)	Aq. NH_4OH (30%) containing 0.1 M DTT, 16 h, 55 °C.	24.6
7.	HS-$(CH_2)_6$-OPO_3-d (ACG TAA GCA AAT CGA TCA GT)	Aq. NH_4OH (30%) containing 0.1 M DTT, 16 h, 55 °C.	22.1
8.	HS-$(CH_2)_6$-OPO_3-d (TTT TTT TTT TTT TTT TTT TT)	Aq. NH_4OH (30%) containing 0.1 M DTT, 16 h, 55 °C.	23.2
9.	HS-$(CH_2)_6$-OPO_3-d (TCG ACG AAC TGA TCA TCC)	Aq. NH_4OH (30%) containing 0.1 M DTT, 16 h, 55 °C.	23.6
10.	HS-$(CH_2)_6$-OPO_3-d (CGT CGA GTT GTT CAT CTC GCA).	Aq. NH_4OH (30%) containing 0.1 M DTT, 16 h, 55 °C.	24.5
11.	H_2N-$(CH_2)_5$-OPO_3-d (ACG TAA GCA AAT CGA TCG TT)	Aq. NH_4OH (30%), 16 h, 55 °C	25.3
12.	TET-d(TCG ACG AAC TGA TCA TCC) Forward primer	Aq. NH_4OH (30%), 16 h, 55 °C	23.1
13.	TET-d(TCG GCA TAG ACG GTC GTA) Reverse primer	Aq. NH_4OH (30%), 16 h, 55 °C	22.5

~24% immobilization efficiency. A major advantage of the projected method is that it requires neither a coupling reagent nor chemical manipulations for the immobilization of prefabricated oligonucleotides. The proposed strategy is demonstrated with respect to pH and thermal stabilities, immobilization efficiency, functional availability of the probes for hybridization, and detection of mismatches. Also, it has been compared with the standard methods, viz., NTMTA, epoxide−amine, and disulfide approaches, to highlight its advantages over the existing ones. Subsequently, the oligonucleotide-based biochip was validated for detection of bacterial meningitis in human samples.

EXPERIMENTAL PROCEDURES

Materials. Virgin glass microslides (75 × 22 mm^2), *N*-methylimidazole, and 3-glycidyloxypropyltrimethoxy silane (GOPTS) were procured from Sigma-Aldrich Chemical Co., St. Louis, MO. Tetrachlorocarboxyfluorescein (TET) phosphoramidite was obtained from Applied Biosystems Inc., Foster City, CA. Other reagents and chemicals were of analytical grade and used as received from commercial sources, unless indicated.

Buffers. Reaction buffer: 0.1 M *N*-methylimidazole containing DMSO (10%), pH 8.0. Hybridization buffer: 125 mM sodium citrate containing 750 mM NaCl, pH 7.0. Capping buffer: 0.1 M Tris containing 50 mM ethanolamine, pH 9.0.

Glass Silanization. *Step 1: Glass Cleaning.* Glass microslides were cleaned by immersing them in NaOH (1.0 M) for 2 h at 35 °C followed by rinsing with Milli Q water (2 × 100 mL). The slides were then subjected to treatment with a solution of hydrochloric acid (2.0 M) for 30 min, followed by rinsing with Milli Q water (3 × 100 mL), and finally submerged in ~95% ethanol for 1 h. The slides were dried under vacuum and stored in an inert atmosphere.

Step 2: Silanization of the Slides. The precleaned slides were immersed in a solution of GOPTS (2%, v/v) in toluene (75 mL) for 4−5 h at 50 °C, followed by washings with toluene (2 × 75 mL) and ethanol (2 × 75 mL), and dried under vacuum. Finally, these were baked for 1 h at 100 °C and stored in an inert atmosphere.

Oligonucleotide Synthesis and Purification. Oligonucleotides and their thiol-modified analogues (*23*) were synthesized at 0.2 μmol scale on a Pharmacia Gene Assembler Plus using the standard phosphoramidite approach following the manufacturer's protocol (Gene Assembler Plus Manual, Uppsala, Sweden, 1988). The oligonucleotide sequences were assembled, and their deprotection conditions and yields are given in Table 1. The ammoniacal solution of oligomers was concentrated in a speed vac concentrator; the residue obtained was redissolved in water (200 μL) and applied onto a desalting column (reverse-phase ODS-silica gel column). The oligomers were eluted with 30% acetonitrile in water, concentrated in a speed vac, purified on RP-HPLC, and stored at 4 °C.

Determination of Optimal pH Required for Immobilization of Thiolated Oligomers on Epoxy-Activated Glass Surface. In order to study the effect of pH on immobilization of thiolated oligonucleotides on epoxylated polymer surface, the attachment of the probe was carried out at different pH values ranging 6−12. Briefly, a labeled oligomer, viz., TET-d (TCT GTA TGT CTA TTC TCG TT)-OPO_3-$(CH_2)_6$-SH, dissolved in the reaction buffer of different pH, was spotted onto a functionalized glass microslide and incubated in a humid chamber for 12 h, followed by capping of the residual epoxy functionalities with the capping buffer for 15 min at 50 °C. The slide was subjected to washings with 1× SSC buffer (4 × 50 mL), pH 7.0, for 20 min, and Milli Q water (2 × 50 mL), dried under vacuum and scanned under a laser scanner.

Determination of Optimal Time Required for Immobilization of Thiolated Oligomers on Epoxy-Activated Glass Surface. The optimal time required for immobilization of 3′-thiolated oligonucleotide onto epoxylated surface was evaluated by spotting an oligomer sequence, TET-d (TCT GTA TGT CTA TTC TCG TT)-OPO_3-$(CH_2)_6$-SH (40 μM), onto functionalized glass surface in duplicates using a 2 μL micropipet. The slides were then subjected to microwave irradiation up to 20 min (120 × 10 s) in a domestic microwave oven operating at 800 W (with no exposure longer than 10 s in a humid chamber, after each exposure, the slide was cooled in an ice−water mixture to room temperature). The microslides were removed at different time intervals (4, 8, 12, 16, and 20 min), followed by capping and washings as mentioned above. After drying, the spots were visualized under a laser scanner.

Similarly, to find out the optimal time required for immobilization under thermal conditions, the slides were spotted with a labeled oligomer as mentioned above and kept at 35 °C, followed by their withdrawal at different time intervals (2, 4, 6, 8, and 20 h) and subjected to capping, washings, and scanning, as described above.

Determination of Threshold Concentration of Oligonucleotides Required for Fluorescence Detection. In order to arrive at the optimal probe concentration required for visualization of spotted oligonucleotides under a laser scanner, a kinetic study was undertaken to immobilize a labeled oligomer at different concentrations under microwaves. Briefly, a labeled oligomer, viz., TET-d (TCT GTA TGT CTA TTC TCG TT)-OPO_3-$(CH_2)_6$-SH, was serially diluted to concentrations (20, 10, 5, 2.5, 1.0, 0.75, 0.5, 0.25 μM) and spotted (0.5 μL) onto the functionalized glass slide. The slide was then subjected to microwave irradiation for 12 min (72 × 10 s). After capping and usual washings, the slide was visualized under a laser scanner and the spots were quantified using *QuantArray* software (Packard Biosciences, USA).

The extent of involvement of exocyclic amino groups of heterocyclic base (guanosine) and backbone phosphodiesters in reaction with epoxy functions on glass surfaces was evaluated

by immobilizing 5′-labeled-3′-thiolated and 5′-labeled-3′-OH oligonucleotides at 5 μM concentration on an epoxy-coated slide under microwaves, followed by usual washings and drying. The slide was then subjected to a laser scanner followed by quantification.

Thermal and pH Stabilities. To evaluate the thermal stability of the immobilization chemistry, a microarray was prepared by tethering a TET-labeled oligomer at 0.5 μM to a functionalized glass slide under microwaves, as mentioned above. The slide was then subjected to PCR-like conditions and 0, 5, 10, 15, and 20 cycles were performed. PCR parameters were as follows: 94 °C for 30 s (denaturing step), 54 °C for 30 s (annealing step), and 72 °C for 30 s (extension step). After thermocycling, the slide was thoroughly washed and scanned under a laser scanner.

In an analogous way, vulnerability of the projected chemistry was evaluated at different pHs by subjecting the constructed microarrays to washings (4 × 15 min) with buffers of different pH values, ranging 7−9.

Hybridization Assay. To study the hybridization kinetics, two glass slides, each one spotted (0.5 μL) with 5 μM concentration of probe, viz., HS-$(CH_2)_6$-OPO_3-d (ACG TAA GCA AAT CGA TCG TT), were subjected to microwave irradiation for 12 min (72 × 10s) and 12 h at 35 °C, respectively. After the usual capping, washings, and drying, the microarrays were hybridized with 40 μL of complementary labeled oligonucleotide sequence, TET-d (AAC GAT CGA TTT GCT TAC GT) (40 μM), under a coverslip. The slides were then kept in a humidified chamber for 1 h at 45 °C and overnight at 35 °C. After hybridization, the coverslips were gently removed and the slides were successively washed with 2× SSC (2 × 15 min) and 1× SSC buffers (1 × 5 min), followed by drying under vacuum. The slides were scanned under a laser scanner and fluorescence intensity of the spots was quantified.

Detection of Mismatches. To investigate the sensitivity of the system, four oligonucleotides, viz., HS-$(CH_2)_6$-OPO_3-d (ACG TAA GCA AAT CGA TCG TT), HS-$(CH_2)_6$-OPO_3-d (ACG TAA GCA AAT CGA TCG GT), HS-$(CH_2)_6$-OPO_3-d (ACG TAA GCA TAT CGA TCG GT), and HS-$(CH_2)_6$-OPO_3-d (TTT TTT TTT TTT TTT TTT TT) having zero, one, and two base mismatches, and a noncomplementary sequence, respectively, were spotted at 5 μM onto an epoxy-coated glass slide followed by capping and usual washings. Subsequently, the microslide was subjected to hybridization experiment with a labeled oligomer, TET-d (AAC GAT CGA TTT GCT TAC GT), and washed with the hybridization buffer, as mentioned above. After drying under vacuum, the slides were subjected to a laser scanner.

Detection of Bacterial Meningitis. *PCR-Amplification.* Amplification of 430bp fragment of *Transposase* gene (*Neisseria meningitidis*; serogroup C) was performed by taking labeled forward primer TET-d (TCG ACG AAC TGA TCA TCC), labeled reverse primer TET-d (TCG GCA TAG ACG GTC GTA), genomic DNA, and Taq polymerase following a reported protocol (*22*). Analysis of the resulting PCR-amplicons was carried out on agarose gel electrophoresis.

Hybridization with PCR Amplicons. Two oligonucleotide sequences, HS-$(CH_2)_6$-OPO_3-d (TCG ACG AAC TGA TCA TCC) (probe) and HS-$(CH_2)_6$-OPO_3-d (CGT CGA GTT GTT CAT CTC GCA) (control) were immobilized on the glass slide, as described above. Amplicons were hot denatured (5 min, 95 °C), cooled on ice (10 min), and used for carrying out the hybridization assay. After usual washings and drying, the slide was subjected to laser scanning.

Signal Detection and Data Analysis. The arrays were imaged on a Scan Array Lite Scanner (GSI Lumonics) fitted with a Cy3 optical filter with 30 μm resolution. The laser power and PMT voltage were set accordingly to obtain optimum signal intensity. *QuantArray* software (Packard Bioscience) was used for analysis of intensity of the original images and the graphs were plotted in MS *Excel*. The fluorescence intensities in color images of slides were color coded, varying from blue (low) to green, yellow, and then white (saturation).

Scheme 1. Strategy for the Immobilization of Thiolated Oligonucleotides onto Epoxy-Activated Glass Microslides

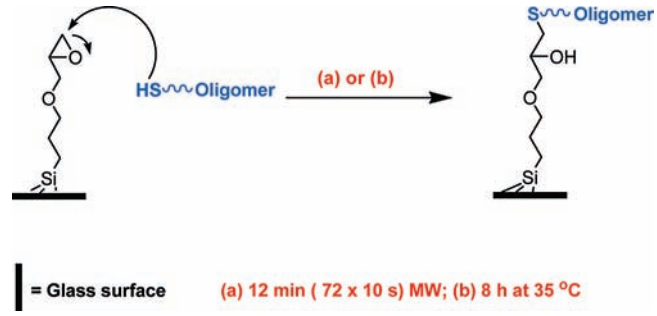

DNA Quantification. In an attempt to quantify the density of immobilized oligonucleotides, varying amounts (0.0125, 0.025, 0.05, 0.1, 0.2, 0.3, 0.4, and 0.5 pmol) of an oligomer sequence, TET-d (TCT GTA TGT CTA TTC TCG TT)-OPO_3-$(CH_2)_6$-SH were spotted on a virgin glass microslide. After drying, the slide was scanned and the spots were quantified to obtain a standard calibration curve by plotting fluorescence intensity (A.U.) as a function of amount of the spotted probe (pmol) (Figure S1, Supporting Information).

For each experimental condition tested on the microarrays, oligomers were spotted in duplicates and the experiment was repeated at least three times. The immobilization and hybridization data presented are the averages of these repetitions, and the error bars represent the percentage error observed on this average.

RESULTS AND DISCUSSION

The use of oligonucleotide arrays is expanding beyond their high-profile role in genome sequencing to other fundamental applications like nucleic acid-ligand binding studies and medical diagnostics. The high-throughput screening technology enables researchers to rapidly profile the expression of thousands of genes simultaneously. Reports have shown that oligonucleotides immobilized through end-specific covalent linkage increase the availability of the immobilized probes for hybridization. Therefore, active groups are often introduced at either the 3′- or 5′-end (usually amino or thiol) of the oligonucleotides to allow end-specific immobilization onto the activated glass surface. For a new chemical method to be useful for the construction of microarrays, the functionalities on the surface should be compatible with the reactive groups on the probe molecules and the immobilization chemistry should be fast and reproducible and offer low background noise during detection. Holistic development of efficient chemistries for the manufacture of oligonucleotide arrays is essential to garner the potential of biochip technology. Microwave (MW) activation, as a nonconventional energy source, has become a very popular and useful technology in organic chemistry. A large number of articles describe significant acceleration in the reaction rates for a wide range of organic reactions, reducing the reaction time from hours to minutes with improved yields and reproducibility (*24, 25*). In contrast to thermal/photochemical reactions, the use of microwaves to construct oligonucleotide arrays has largely remained unexplored. We now present a method for covalent immobilization of 3′/5′-thiolated oligonucleotides onto an epoxy-activated glass surface under microwaves as illustrated in Scheme 1. The optimal pH for reaction, immobilization kinetics,

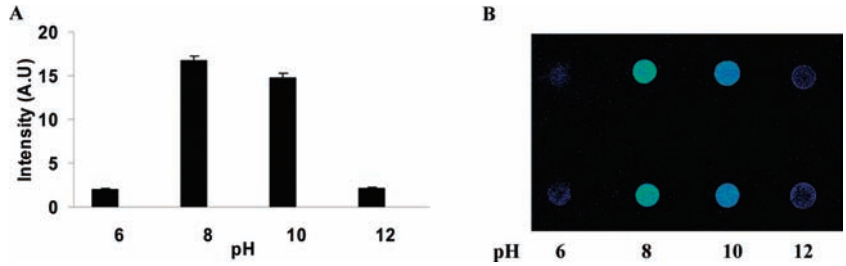

Figure 1. (a) A graph representing the influence of pH on the immobilization reaction of thiolated probes with epoxy-activated surface. (b) Fluorescence map obtained by immobilization of 5′-labeled, 3′-thiolated probe in the pH range 6−12.

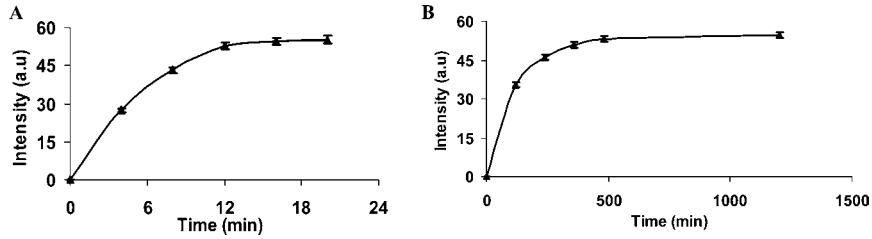

Figure 2. Time kinetics to determine the optimal time required for immobilization of thiolated probes under (a) microwave; (b) thermal condition (35 °C).

stability (thermal and pH), effect of probe, and target concentrations on hybridization efficiency have been optimized.

Immobilization of Thiolated Oligonucleotide onto Epoxy-Activated Glass Microslides. The optimal condition required for effective immobilization of thiol-modified oligonucleotides via thioether linkage was determined by spotting a labeled probe (at 1 μM) on epoxy-functionalized glass surface under different pH conditions, as mentioned in the Experimental Procedures. The results showed that maximum immobilization was achieved at pH 8.0 possibly through the availability of thiol groups in their anionic form (Figure 1A,B). As the pH was increased from 8 to 12, the fluorescence intensity decreased, which might have resulted due to partial oxidation of thiol functions at higher pH values, whereas the reason for lower attachment density attained at pH 6 could be due to the lower reactivity of thiol functionality at slightly acidic pH. On the basis of these findings, immobilization of thiol-modified probes was carried out at pH 8.0 for the rest of the experiments.

The kinetics of thioether linkage formation under both microwaves and thermal conditions were investigated by spotting a large excess of 3′-thiolated oligomer onto an epoxy-functionalized glass surface. The results show that the reaction between the thiolated probe and epoxy groups is essentially completed in 12 min under microwaves, while it takes ∼8 h at 35 °C under thermal conditions (Figure 2A,B). Therefore, the rest of the experiments were conducted for 12 min under microwaves for the immobilization of thiol-modified probes onto the functionalized glass surface. Similarly, to find the highest density of oligonucleotide attachment on the surface, a kinetics study of the probe immobilization at various amounts (0.125−10 pmol) was undertaken (Figure 3). It can be deduced from the results that the attachment density increases upon increasing the concentration of the probe, and the highest fluorescence intensity was obtained at 10 pmol in the spotting buffer (Figure 3). Subsequently, the immobilization efficiency was determined using a standard calibration curve (Figure 3, Lane 2) (Table S1, Supporting Information).

With the aim to determine the extent of involvement of terminal thiol groups of the probe with epoxy functions of glass surface, a microarray was prepared by spotting 5′-labeled oligonucleotides (5 μM) with and without thiol modification at 3′-terminus. After treatment with the capping buffer and usual

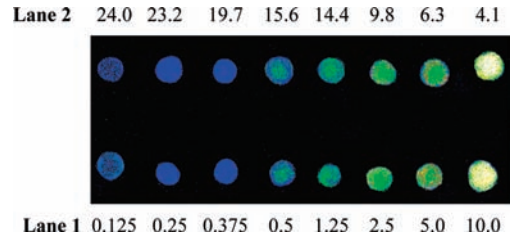

Figure 3. Threshold amount of probe, viz., TET-d (TCT GTA TGT CTA TTC TCG TT)-OPO_3-$(CH_2)_6$-SH, required for detection under a laser scanner. Lane 1: Amount of the spotted probe (pmol). Lane 2: Immobilization efficiency (%).

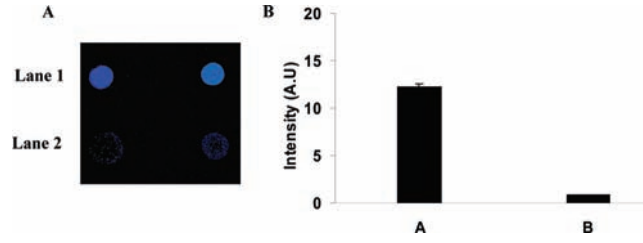

Figure 4. (a) Fluorescence map showing immobilization of TET-d (TCT GTA TGT CTA TTC TCG TT)-OPO_3-$(CH_2)_6$-SH (lane 1) and TET-d (TCT GTA TGT CTA TTC TCG TT) (lane 2) on epoxy-functionalized glass surface. (b) A graph representing the comparison of fluorescence intensity obtained by spotting thiol-modified (A) and unmodified oligomer (B) on epoxy-activated surface.

washings, the slide was visualized under a laser scanner (Figure 4A). The fluorescence intensity from spots of the unmodified oligonucleotide was found to be ∼6.5% of that measured from the probe with a 3′-thiol modification, implying specific binding of the terminal thiol groups to the epoxy-activated surface (Figure 4B). The low amount of fluorescent signal obtained with unmodified oligonucleotide could have arisen from weaker binding of internucleotidic phosphate groups and exocyclic amino groups of guanosine moieties in the probe with the epoxy-activated surface. Although nonspecific binding of the unmodified probe is small, a measurable fluorescent signal still resulted, indicating that the same interactions may result from the

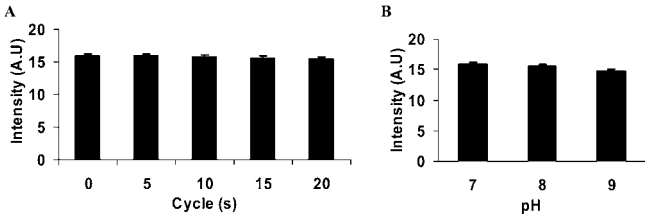

Figure 5. (a) Thermal stability of thioether linkage under PCR-like conditions and comparison of the fluorescent signal obtained after 0, 5, 10, 15, and 20 cycles; (b) stability of the constructed microarrays under a pH range of 7−9.

complementary targets during hybridization, leading to significant background and artifacts. This was eliminated by treating the spotted slides with a capping buffer to deactivate the residual epoxy functions.

Thermal and pH Stability. The heat stability of the constructed microarray was evaluated by submitting it to 0, 5, 10, 15, and 20 PCR-like heating cycles. The fluorescent signal of the heat-treated microarrays was found to be decreased by only ~1.4% after 10 cycles and ~2.5% after 20 cycles. Figure 5A shows a histogram obtained by comparing the fluorescent signal of heat-treated and pretreated microarray. This shows that the oligonucleotides immobilized on the activated glass surface following the projected strategy are sufficiently stable to be used in biological research.

In order to find the vulnerability of the constructed microarrays toward different pHs, the constructed microarrays were subjected to washings (4 × 15 min) with buffers of different pH, ranging 7−9. The quantification results reveal that the fluorescence intensity decreased by only 2.0% at pH 8.0 and 4.4% at pH 9.0 in comparison to that obtained at pH 7.0 (Figure 5B). Thus, the fabricated microarray can be used over a wide range of pH safely without significant change in its performance.

Hybridization Assay. The accessibility and specificity of the surface-bound probes during hybridization have been the major concern while preparing microarrays. In order to investigate these parameters, two microarrays were prepared by immobilizing oligonucleotide under microwaves (12 min) and thermal conditions (~8 h) (Scheme 1). After the hybridization experiment, the spots were visualized under a laser scanner as shown in Figure 6A,B. Negligible fluorescence was obtained during hybridization with the noncomplementary oligonucleotide, demonstrating that nonspecific hybridization did not occur. The signal-to-noise ratio was on average 96, as calculated from signals obtained from complementary hybridized spots and nonhybridized spots.

To demonstrate the dynamics of microarray hybridization, the kinetics of hybridization reaction for different target oligonucleotide concentrations was followed. The results showed that, in the initial stage, the hybridization signal increases on increasing the target concentration, then reaches a steady state between 40 and 60 μM (Figure 7A). The results of kinetics of hybridization for different probe concentrations are shown in Figure 7B. The plot of hybridization efficiency (efficiency defined as percent of covalently attached oligonucleotides that participated in duplex formation) for different amounts of immobilized probes reveals that it reaches a maximum (~33%) for an optimal immobilized probe concentration of 5 μM (Table S1, Supporting Information). Above this concentration, the efficiency did not increase, even if the concentration of the immobilized probe was increased, as the overloading of the surface with probe may cause a crowding effect that can lower the accessibility of the surface-bound probe molecules. In addition, the efficiency of hybridization depends on many factors like the number of epoxy groups on the surface accessible to

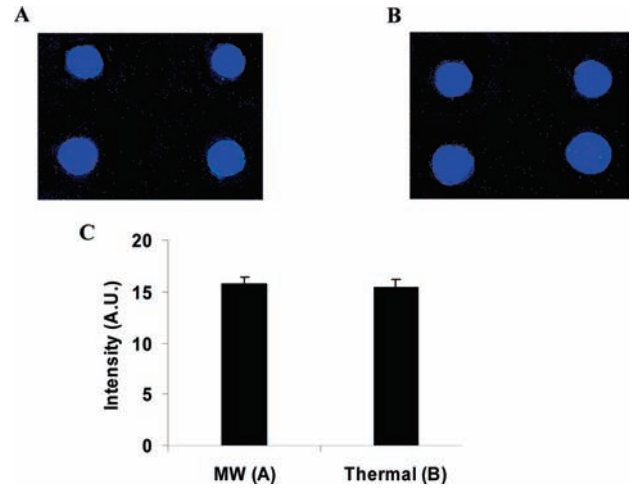

Figure 6. Fluorescence maps obtained after hybridization of HS-$(CH_2)_6$-OPO_3-d (ACG TAA GCA AAT CGA TCG TT) immobilized at 5 μM with target, TET-d (AAC GAT CGA TTT GCT TAC GT) (40 μM). Oligonucleotide is immobilized (A) under microwaves for 12 min (72 × 10s) at 800 W; (B) under thermal condition at 35 °C for ~8 h. (C) Quantification representation of hybridization results of the two methods, A and B.

the 5′-thiolated oligonucleotides, attachment efficiency of oligonucleotides to the epoxy-activated surface, and availability of immobilized probes to the target oligomer.

Specificity of Immobilization Chemistry for Detection of Mismatches. In order to demonstrate the specificity of the system, four oligonucleotides were immobilized onto an epoxy-functionalized glass microslide at 5 μM concentration of each probe as mentioned in the Experimental Procedures. After treatment with the capping buffer, the microslide was subjected to a hybridization step with a labeled oligomer (complementary to zero mismatch sequence). Figure 8 clearly shows the base mismatches. The perfectly matched sequence gave the maximum intensity (lane 1), while the spots having one (lane 2) and two (lane 3) showed fluorescence intensity in decreasing order. No measurable nonspecific hybridization signal from the noncomplementary control was detected. This may be because the residual epoxy groups on the surface got masked during treatment with the capping buffer to exclude nonspecific interactions with the target oligonucleotides.

Quantification and Surface Coverage of the Immobilized Oligonucleotides. Quantification of the microarrays prepared following the proposed method was carried out by using a standard calibration curve plotted between fluorescence intensity (a.u.) and amount of the spotted probe (pmol), as mentioned in the Experimental Procedures. Surface coverage of the immobilized probe was calculated from the following formula (*9b*):

$$\text{surface coverage (molecules/}\mu\text{m}^2) = \frac{\text{amt. of immobilized probe (pmol)} \times 6.023 \times 10^{23}}{\text{area of spot } (\mu\text{m}^2)}$$

(spotting vol.: 0.5 μL)

Comparison of the Proposed Method with the Standard Methods. The projected method for microarray preparation was compared with the three existing standard methods, viz., NTMTA (*7*), epoxide-amine (*21*), and disulfide (*19*) approach (Scheme 2). For comparison purposes, an equal concentration of the appropriate oligonucleotide was used. However, different reaction times, as reported therein, were employed in all the three methods. After immobilization, the spots were hybridized with the complementary labeled oligonucleotide, and the mi-

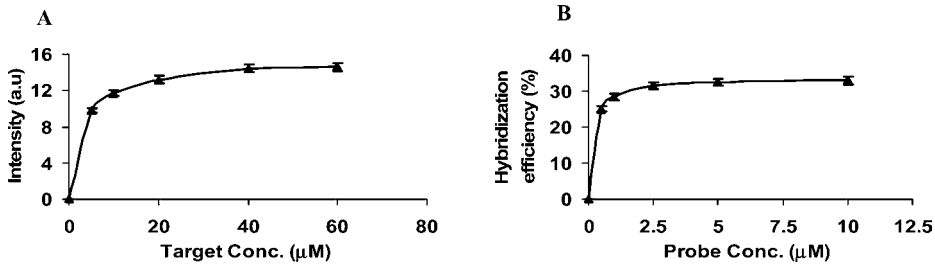

Figure 7. (a) Measurement of optimal target concentration for steady hybridization at 5 μM concentration of immobilized 5′-thiolated probe. (b) Hybridization efficiency obtained, by varying the amount of probes immobilized (0.5, 1, 2.5, 5, and 10 μM) onto epoxy-functionalized glass surfaces upon hybridization with a complementary strand (TET-labeled).

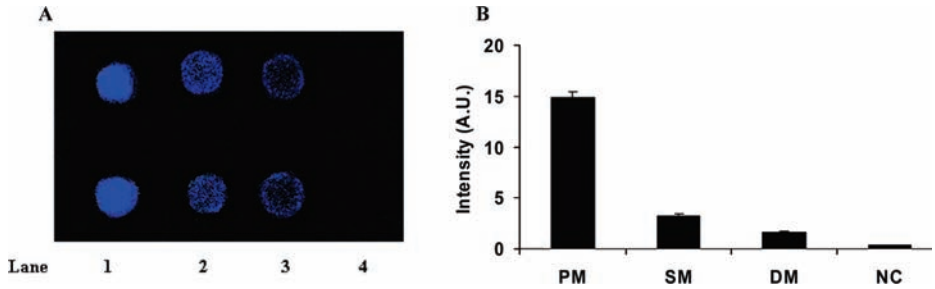

Figure 8. Detection of nucleotide mismatches and specificity of immobilization via hybridization with labeled oligonucleotide, viz., TET-d (AAC GAT CGA TTT GCT TAC GT) (complementary to zero mismatch). (A) Lane 1, HS-$(CH_2)_6$-OPO_3-d (ACG TAA GCA AAT CGA TCG TT). Lane 2, HS-$(CH_2)_6$-OPO_3-d (ACG TAA GCA AAT CGA TCG GT). Lane 3, HS-$(CH_2)_6$-OPO_3-d (ACG TAA GCA AAT CGA TCA GT). Lane 4, HS-$(CH_2)_6$-OPO_3-d (TTT TTT TTT TTT TTT TTT TT). (B) Quantitative representation of the results of nucleotide mismatches. PM: Perfect match. SM: Single mismatch. DM: Double mismatch. NC: Noncomplemenatry.

Scheme 2. Comparison of the Proposed Strategy with the Standard Methods

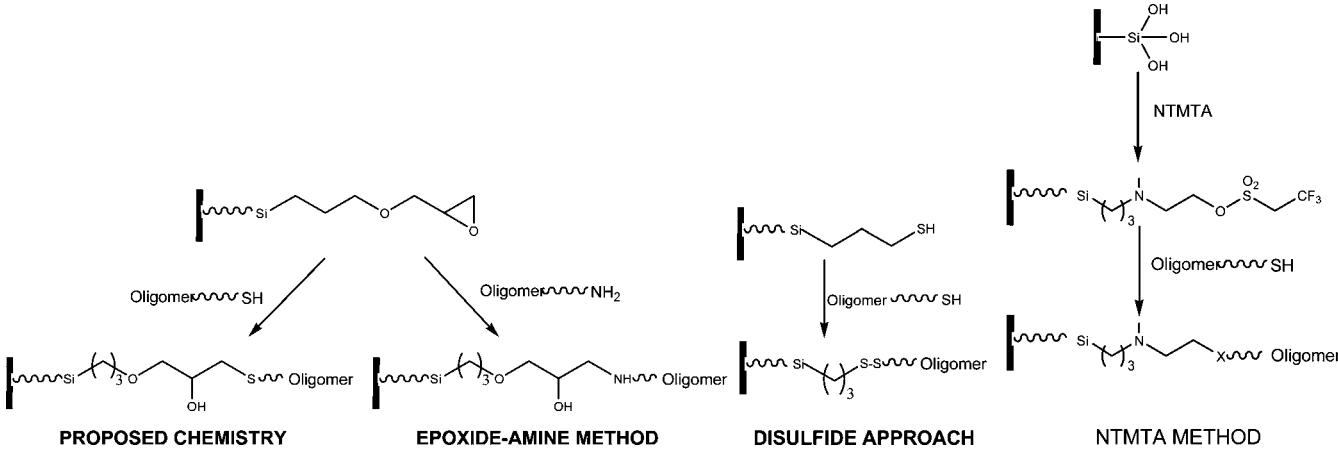

croslides were visualized under a laser scanner for quantification of spots (Table S2, Supporting Information). The hybridization efficiency of the proposed method (∼33%) is much higher than the method employing NTMTA reagent (∼9.8%), epoxide-amine immobilization chemistry (∼9.8%), and disulfide approach (1.7%), as shown in Figure 9.

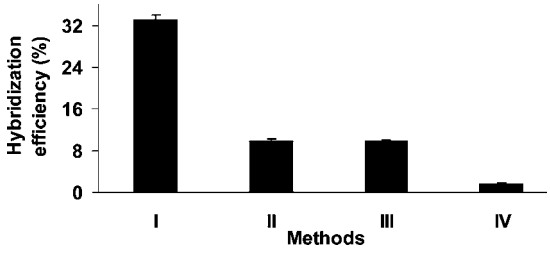

Figure 9. Comparison of hybridization efficiency of proposed method (I) with standard ones, viz., (II) = NTMTA, (III) = epoxide-amine, and (IV) = disulfide method.

Detection of Bacterial Meningitis. In order to demonstrate the ability of the constructed biochip to detect bacterial infection, a specific probe of the *Transposase* gene and a noncomplementary probe, as control, were immobilized onto an epoxylated glass slide, and after the usual washings, the spots on the glass surface were subjected to hybridization with the labeled PCR

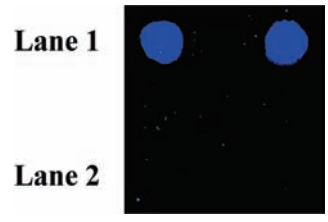

Figure 10. Detection of bacterial meningitis. Lane 1: Probe sequence, HS-$(CH_2)_6$-OPO_3-d (TCG ACG AAC TGA TCA TCC). Lane 2: Control sequence, HS-$(CH_2)_6$-OPO_3-d (CGT CGA GTT GTT CAT CTC GCA).

amplicons. After washings and drying, the slide was visualized under a laser scanner (Figure 10). Spots pertaining to probe sequence specific to *Transposase* gene of bacteria (*N. Meningitidis*, Serogroup C) showed fluorescence, while spots pertaining to the control did not fluoresce at all, signifying the specificity of the system to prepare biochips for the detection of bacterial meningitis in humans.

CONCLUSIONS

A simple and efficient method for preparation of oligonucleotide microarrays via a stable thioether linkage is established with rapid immobilization of thiolated oligomers onto epoxylated surface under microwaves with excellent immobilization efficiency (~24%), stable over a wide pH range and thermocyclic conditions, suggesting that the biochip could be integrated with PCR. The proposed chemistry enables the immobilized probes to be highly accessible to targets during hybridization with remarkable efficiency (~33%) and negligible background noise (signal-to-noise ratio 96). It also successfully discriminates the base mismatches and can detect bacterial diseases thus promising for other biomolecules and chemicals for diagnostic purposes.

ACKNOWLEDGMENT

This work is supported by the Deparment of Biotechnology, New Delhi and CSIR NWP013. D.S. thanks the University Grants Commission, New Delhi, India, for the award of a Senior Research Fellowship. Authors are also thankful to Drs. S. Gupta and S. Khare, NICD, Delhi, India for providing patient samples and facilities.

Supporting Information Available: Standard calibration curve for quantification, surface coverage data of immobilized probe and captured target and comparison data of the proposed method with the standard methods. This material is available free of charge via the Internet at http://pubs.acs.org.

LITERATURE CITED

(1) Drobyshev, A. N., Mologina, N., Shick, V., Pobedimskaya, D., Yershov, G., and Mirzabekov, A. D. (1997) Sequence analysis by hybridization with oligonucleotide microchip: identification of β-thalassemia mutations. *Gene 188*, 45–52.

(2) Hacia, J. G., Brody, L. C., Chee, M. S., Fodor, S. P. A., and Collins, F. S. (1996) Detection of heterozygous mutations in *BRCA1* using high density oligonucleotide arrays and two-colour fluorescence analysis. *Nat. Genet. 14*, 441–447.

(3) Yershov, G., Barsky, V., Belgovskiy, A., Kirillov, E., Kreindlin, E., Ivanov, I., Parinov, S., Guschin, D., Drobishev, A., Dubiley, S., and Mirzabekov, A. D. (1996) DNA analysis and diagnostics on oligonucleotide microchips. *Proc. Natl. Acad. Sci. U.S.A. 93*, 4913–18.

(4) Cho, R. J., Fromont-Racine, M., Wodicka, L., Feierbach, B., Stearns, T., Legrain, P., Lockhart, D. J., and Davis, R. (1998) Parallel analysis of genetic selections using whole genome oligonucleotide arrays. *Proc. Natl. Acad. Sci. U.S.A. 95*, 3752–57.

(5) Fodor, S. A., Rava, R., Huang, X. C., Pease, A. C., Holmes, C. P., and Adams, C. L. (1991) Light-directed, spatially addressable parallel chemical synthesis. *Science 251*, 767–773.

(6) Schena, M., Shalon, D., Davis, R. W., and Brown, P. O. (1995) Quantitative monitoring of gene expression patterns with a complementary DNA microarray. *Science 270*, 467–470.

(7) Choithani, J., Vaijayanthi, B., Kumar, P. Gupta, K. C. (2007) Construction of oligonucleotide microarrays (Biochip) using heterobifunctional reagents, In *Methods in Molecular Biology, Vol. 381: Microarrays, Second Edition: Vol. 1, Synthesis Methods*, (Rampal, J. B., Ed.) pp 133−164, Humana Press, Totowa.

(8) Mahajan, S., Vaijayanthi, B., Rembhotkar, G., Gupta, K. C. Kumar, P. (2007) Choice of polymer matrix, its functionalization and estimation of functional group density for preparation of biochips, In *Methods in Molecular Biology, Vol. 381: Microarrays, Second Edition: Vol. 1, Synthesis Methods*, (Rampal, J. B., Ed.) pp 165−188, Humana Press, Totowa.

(9) (a) Bocking, T., Kilian, K. A., Gaus, K., and Gooding, J. J. (2006) Single-step DNA immobilization on antifouling self-assembled monolayers covalently bound to silicon (111). *Langmuir 22*, 3494–3496. (b) Fixe, F., Dufva, M., Telleman, P., and Christensen, C. B. V. (2004) Functionalization of poly(methyl methacrylate) (PMMA) as a substrate for DNA microarrays. *Nucleic Acids Res. 32*, e9.

(10) Belosludtsev, Y., Iverson, B., Lemeshko, S., Eggers, R., Wiese, R., Lee, S., Powdrill, T., and Hogan, M. (2001) DNA microarrays based on noncovalent oligonucleotide attachment and hybridization in two dimensions. *Anal. Biochem. 292*, 250–256.

(11) Broude, N. E., Woodward, K., Cavallo, R., Cantor, C. R., and Englert, D. (2001) DNA microarrays with stem-loop DNA probes: Preparation and Applications. *Nucleic Acids Res. 29*, e92.

(12) (a) Mahajan, S., Kumar, P., and Gupta, K. C. (2006) Oligonucleotide microarrays: Immobilization of phosphorylated oligonucleotides on epoxylated surface. *Bioconjugate Chem. 17*, 1184–1189. (b) Mahajan, S., Kumar, P., and Gupta, K. C. (2006) An efficient and versatile approach for the construction of oligonucleotide microarrays. *BioMed. Chem., Lett. 16*, 5654–5658.

(13) Burns, N. L., Van Alstine, J. M., and Harris, J. M. (1995) Poly(ethylene glycol) grafted to quartz: analysis in terms of a site-dissociation model of electroosmotic fluid flow. *Langmuir 11*, 2768–2776.

(14) Guschin, D., Yershov, G., Zaslavsky, A., Gemmell, A., Shick, V., Proudnikov, D., Arenkov, P., and Mirzabekov, A. D. (1997) Manual manufacturing of oligonucleotide, DNA, and protein microchips. *Anal. Biochem. 250*, 203–211.

(15) Kamisetty, N. K., Pack, S. P., Nonogawa, M., Yamada, K., Yoshido, Y., Kodaki, T., and Makino, K. (2009) Stabilization of the immobilized linkers and DNA probes for DNA microarray fabrication by end-capping of the remaining unreacted silanol on the glass. *J. Biotechnol. 140*, 242–245.

(16) Preininger, C., Sauer, U., Dayteg, J., and Pichler, R. (2005) Optimizing processing parameters for signal enhancement of oligonucleotide and protein arrays on ARChip epoxy. *Bioelectrochemistry 67*, 155–162.

(17) Pack, S. P., Kamisetty, N. K., Nonogawa, M., Devarayapalli, K. C., Ohtani, K., Yamada, K., Yoshida, Y., Kodaki, T., and Makino, K. (2007) Direct immobilization of DNA oligomers onto the amine-functionalized glass surface for DNA microarray fabrication through the activation-free reaction of oxanine. *Nucleic Acids Res. 35*, e110.

(18) Lockett, M. R., Phillips, M. F., Jarecki, J. L., Peelen, D., and Smith, L. M. (2008) A tetrafluorophenyl activated ester self-assembled monolayer for immobilization of amine-modified oligonucleotides. *Langmuir 24*, 69–75.

(19) Rogers, Y.-H., Jiang-Baucom, P., Huang, Z.-J., Bogdanov, V., Anderson, S., and Boyce-Jacino, M. T. (1999) Immobilization of oligonucleotides onto a glass support via disulfide bonds: A method for preparation of DNA microarrays. *Anal. Biochem. 266*, 23–30.

(20) Nonglaton, G., Benitez, I. O., Guisle, I., Pipelier, M., Léger, J., Dubreuil, D., Tellier, C., Talham, D. R., and Bujoli, B. (2004) New approach to oligonucleotide microarrays using zirconium phosphonate-modified surfaces. *J. Am. Chem. Soc. 126*, 1497–1502.

(21) Lamture, J. B., Beattie, K. L., Burke, B. E., Eggers, M. D., Ehrlich, D. J., Fowler, R., Hollis, M. A., Kosicki, B. B., Reich, R. K., and Smith, S. R. (1994) Direct detection of nucleic acid

hybridization on the surface of a charged coupled device. *Nucleic Acids Res. 22*, 2121–2125.

(22) Sethi, D. S., Kumar, A., Gupta, K. C., and Kumar, P. (2008) A facile method for the construction of oligonucleotide microarrays. *Bioconjugate Chem. 19*, 2136–43.

(23) Ghosh, P. K., Kumar, P., and Gupta, K. C. (2000) Recent advances in synthesis of modified oligonucleotides. *J. Ind. Chem. Soc. 77*, 109–132.

(24) Kappe, C. O. (2004) Controlled microwave heating in modern organic synthesis. *Angew. Chem., Int. Ed. 43*, 6250–6284.

(25) Padmanabhan, S., Coughlin, J. E., and Iyer, R. P. (2005) Microwave-assisted functionalization of solid supports: application in the rapid loading of nucleosides on controlled-pore-glass (CPG). *Tetrahedron Lett. 46*, 343–347.

BC900162U

SUPPORTING INFORMATION

Construction of oligonucleotide microarrays (biochips) via thioether linkage for the detection of bacterial meningitis

S. Mahajan, D. Sethi, S. Seth, A. Kumar, P. Kumar and K.C. Gupta*
Institute of Genomics and Integrative Biology, Mall Road, Delhi University Campus, Delhi-110 007, India. Tel.: +91 11 27662491; Fax : +91 11 27667471; Email : kcgupta@igib.res.in;

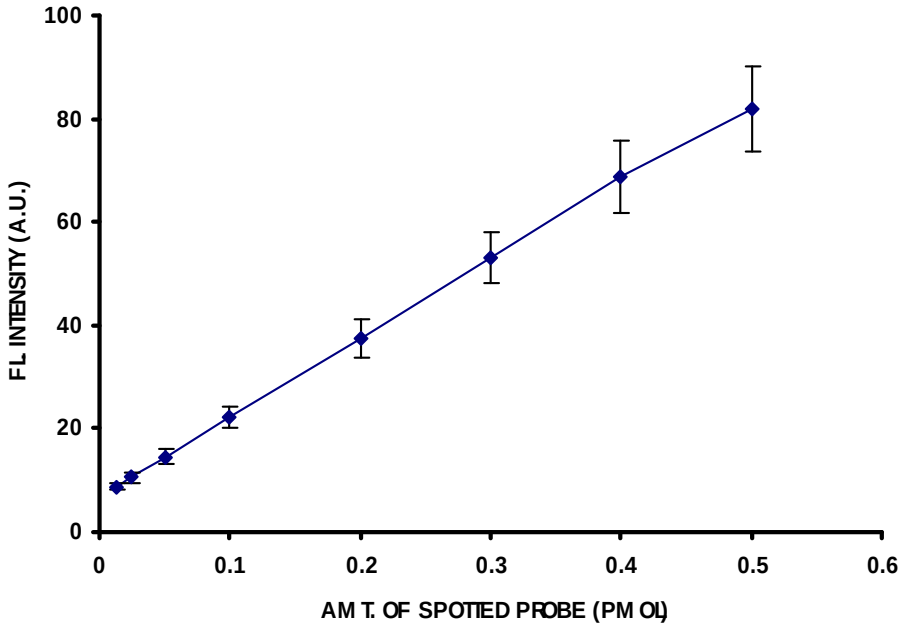

Fig. S1: A calibration curve plotted between fluorescence intensity (A.U.) and the amount of spotted probe (pmol)

Table S1: Surface coverage data of immobilized probe and captured target

S. No.	Amount of spotted probe (pmol) **X**	Fl. Intensity (A.U.) **A**	Amount of immobilized probe (pmol) **Y**	Immobilization efficiency (%) **Y/X**	Surface coverage of immobilized probe (molecules/μm^2) x 10^3	Intensity after hybridization (A.U.) **B**	Hybridization efficiency (%) **B/A**	Surface coverage of captured target (molecules/μm^2) x 10^3
1	0.125	11.45	0.030	24.0	4.933 ± 0.888	---	---	----
2	0.25	16.01	0.058	23.2	9.537 ± 1.717	4.01	25.04	2.388 ± 0.430
3	0.375	18.63	0.074	19.7	12.168 ± 2.191	---	---	----
4	0.5	19.20	0.078	15.6	12.825 ± 2.303	5.46	28.43	3.646 ± 0.656
5	1.25	35.17	0.180	14.4	29.597 ± 5.329	11.15	31.7	9.382 ± 1.689
6	2.5	45.69	0.245	9.8	40.285 ± 7.253	14.85	32.5	13.093 ± 2.357
7	5.0	55.56	0.314	6.3	51.630 ± 9.296	18.31	32.95	17.012 ± 3.063
8	10	70.82	0.413	4.1	67.909 ± 12.226	23.44	33.09	22.471 ± 4.046

Table S2: Comparison of the proposed method with the standard methods

Method	**Fl. Intensity (A.U.)**	**Intensity after hybridization (A.U.)**	**Hybridization efficiency (%)**	**Surface coverage** (molecules/μm^2) x 10^3
Epoxide-Thiol	45.69	14.85	32.5	13.093 ± 2.357
Epoxide-NTMTA	32.43	3.17	9.78	2.798 ± 0.504
Epoxide-Amine	34.28	3.37	9.84	2.977 ± 0.556
Disulfide	24.86	0.43	1.72	0.376 ± 0.068

$$\text{Surface coverage (molecules/}\mu m^2) = \frac{\text{Amount of immobilized probe (pmol)} \times 6.022 \times 10^{23}}{\text{Area of spot } (\mu m^2)}$$

(Spotting vol.: 0.5 µl)

A Fine Line Between Molecular Umbrella Transport and Ionophoric Activity

Wen-Hua Chen,[†] Vaclav Janout,[†] Masaharu Kondo,[†] Arevik Mosoian,[‡] Goar Mosoyan,[‡] Ravil R. Petrov,[†] Mary E. Klotman,[‡] and Steven L. Regen*[,†]

Department of Chemistry, Lehigh University, Bethlehem, Pennsylvania 18015 and Department of Infectious Diseases, Mount Sinai School of Medicine, New York, New York 10029. Received June 5, 2009; Revised Manuscript Received July 7, 2009

A persulfated molecular umbrella derived from one spermine, four lysine, and eight deoxycholic acid molecules was found to exhibit ionophoric activity, as shown by pH discharge and Na^+ and Cl^- transport experiments. In sharp contrast, a moderately more hydrophilic analogue derived from cholic acid showed no such ionophoric activity. Both molecular umbrellas crossed liposomal membranes by passive transport with experimental rates that were similar. These findings show how the interactions between such amphomorphic molecules and phospholipid bilayers are a sensitive function of the umbrella's hydrophilic/lipophilic balance (HLB). They also raise the possibility of exploiting molecular umbrellas in fundamentally new ways.

Molecular umbrellas are a unique class of conjugates made from two or more facial amphiphiles that have been covalently attached to a central scaffold (*1*). Such molecules are "amphomorphic" in the sense that they can produce a hydrophobic or hydrophilic exterior when exposed to a hydrophobic or hydrophilic environment, respectively. Because molecular umbrellas are capable of crossing lipid bilayers, even when strongly hydrophilic agents are coupled to them (e.g., oligonucleotides), they hold promise as drug carriers (*2*−*4*).

In previous work, we showed that highly sulfated molecular umbrellas, themselves, have interesting biological properties. Specifically, we showed that a bioconjugate derived from one spermine, four lysine, and eight cholic acid groups, having all of its hydroxyl groups sulfated (i.e., **1**), exhibits significant anti-HIV and anti-HSV activity (Figure 1) (*5*, *6*). In a related investigation, we showed that a fluorescently labeled analogue of **1** readily enters live HeLa cells and provided evidence that passive transport may be playing a significant role in this internalization process (*7*).

In the present study, we sought to test the feasibility of enhancing the membrane transport activity of a persulfated molecular umbrella by increasing its lipophilicity. Our motivation for this work was based on the presumption that, if molecules of this type could cross the blood-brain barrier, they could have therapeutic value as anti-HIV and anti-HSV agents (*8*). With this aim in mind, we investigated more lipophilic analogues of **1**. According to the classic solution-diffusion model for bilayer transport, the permeability coefficient (*P*) of a permeant is directly proportional to its water−membrane partition coefficient (*K*) and its diffusion coefficient (*D*), but inversely proportional to the thickness (*x*) of the bilayer (*1*, *9*, *10*). Since $P = (K \times D)/x$, any increase in lipophilicity is expected to increase *P* by increasing *K*, although exceptions to this model have already been noted for certain molecular umbrella−fluorophore conjugates (*11*). As documented in this paper, we have discovered that a moderate increase in the lipophilicity of a persulfated molecular umbrella does not enhance its transport activity but, instead, leads to *ionophoric activity*; that is, a "fine line" exists between umbrella transport and ionophoric activity based on the umbrella's hydrophilic/lipophilic balance.

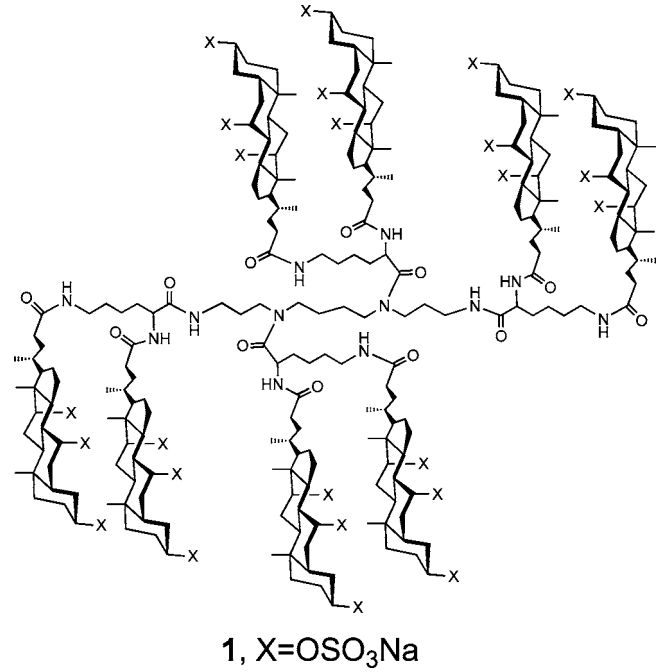

Figure 1. Molecular structure of a persulfated molecular umbrella having significant anti-HIV and anti-HSV activity.

Two specific molecular umbrellas that were chosen as synthetic targets for this work were **2** and **3** (Figure 2). Thus, replacement of all of the secondary amide groups with *N*-methylated amide units (i.e., **2**) was expected to result in a modest increase in lipophilicity. In contrast, removal of one sulfate group per sterol (i.e., **3**) was expected to lead to a more moderate increase in lipophilicity. As a control for umbrella-mediated transport, we chose a sulfonated polymer that was similar in size and charge to **1**, **2**, and **3**, but devoid of facial amphiphilicity, that is, a β-naphthalene sulfonate/formaldehyde condensation polymer (PRO 2000) (*12*). This synthetic polymer, which is currently in clinical trials as an anti-HIV microbicide, was a gift from Indevus Pharmaceuticals (Lexington, MA).

* slr0@lehigh.edu.
[†] Lehigh University.
[‡] Mount Sinai School of Medicine.

10.1021/bc900246u CCC: $40.75 © 2009 American Chemical Society
Published on Web 08/18/2009

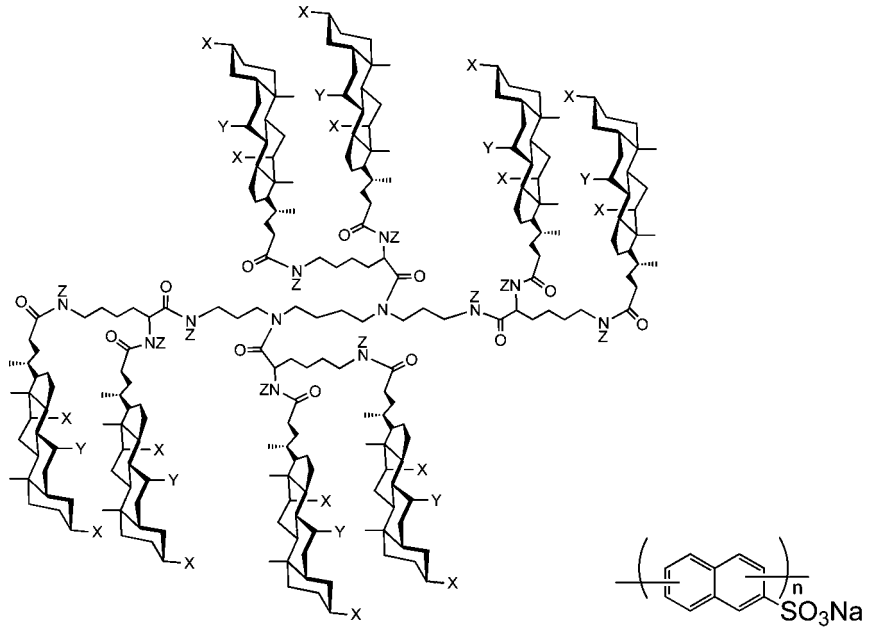

Figure 2. Molecular structures of **2** and **3** having a modest and moderate increase in lipophilicity, respectively, relative to **1**.

Umbrella **3** was synthesized using methods analogous to those previously described for the preparation of **1**. In this case, deoxycholic acid was used in place of cholic acid. Umbrella **2** was prepared in a similar way except that *N*-methylated derivatives of L-lysine-dicholamide (i.e., **8**) and spermine (i.e., **9**) were employed (Figure 3) (*5, 13, 14*). Relative lipophilicities were determined by measuring the affinity of each agent toward liposomes (200 nm, extrusion) derived from 1-palmitoyl-2-oleyol-*sn*-glycero-3-phosphocholine (POPC)/1-palmitoyl-2-oleoyl-*sn*-glycero-3-phosphatidylglycerol (POPG) (95/5, mol/mol). Partition coefficients, *K*, that are reported in Table 1 were calculated using the nonsaturable partitioning model (*10*). Thus, if C_o is the equilibrium concentration of the conjugate in solution as measured in the absence of liposomes, and *C* is the concentration in the presence of liposomes, then the partition coefficient is calculated as $K = [(C_o - C) \times W]/[C(L/2)]$. Here, $L/2$ is the concentration of the lipids in the external half of the bilayer with a weighted average molecular weight of 649 and *W* is the concentration of water, 55.5 M. If the inner leaflet contributes to binding, the true *K* values could be lower by a factor of 2. The efflux rate for each molecular umbrella obeyed first-order kinetics; experimental rate constants, k_{obsd}, are also reported in Table 1.

The increase in lipophilicity on going from **1** to **2** proved to be so modest that it could not be detected by binding measurements. In contrast, the increase in lipophilicity of **3** was substantial. For PRO 2000, even stronger affinity to these lipid membranes was observed. Despite this variation in lipophilicities, the observed efflux rates for all three molecular umbrellas were similar. With PRO 2000, no efflux could be detected after 250 h. An *in vitro* examination of **1** and **2** revealed that both molecular umbrellas had similar anti-HIV activity (Figure 4). In addition, neither of these agents showed any evidence of cytotoxicity at 1000 μg/mL. In sharp contrast, **3** was found to have significant cytotoxicity at 10 μg/mL. Because of its high toxicity, no attempt was made to determine the anti-HIV activity of **3**. On the basis of its relatively high lipophilicity, we hypothesized that the cytotoxicity associated with **3** was due to membrane-disrupting properties, possibly by acting as an ionophore (*9*). To test for membrane permeabilization, we carried out a series of pH discharge experiments using liposomes made from POPC/POPG (95/5, mol/mol) containing 0.1 mM of entrapped pyranine in 25 mM HEPES buffer (pH 7.0, 50 mM NaCl) (*15, 16*). After raising the pH of the external aqueous phase to 8.0, subsequent addition of 0.006 mol % of **3** led to a rapid increase in fluorescence intensity (Figure 5). A control experiment confirmed that exposure to **3** did not release any (i.e., <2%) of the dye from the aqueous interior of the liposomes within 4.5 h. Retention of this dye was quantified using an equilibrium dialysis cell, where the concentrations of dye in the source (i.e., liposome) and receiving sides were measured after 4.5 h. Taken together, these results show that **3** discharges the pH gradient across these liposomal membranes. Under similar conditions, **1**, **2**, and PRO 2000 showed no permeabilization activity; that is, their fluorescence profiles were the same as that found in the absence of an added umbrella. Increasing the concentration of **1** by 2 orders of magnitude (i.e., using 0.6 mol %) still showed no evidence of permeabilization activity.

To determine whether **3** might be creating pores or channels in these lipid bilayers, we examined its ability to promote the transport of Na^+ and Cl^- ions across liposomal membranes. Using established procedures, a paramagnetic shift reagent $[Dy(P_3O_{10})_2Na_7]$ plus NaCl was added to liposomal dispersions that were prepared from POPC (200 nm, extrusion) and 150 mM KCl (*17*). Subsequent addition of **3** resulted in an internalization of Na^+, which could be monitored by $^{23}Na^+$ NMR (Figure 6). The biphasic nature of this kinetic profile is a likely consequence of the use of substoichiometric amounts of umbrella, which are expected to be distributed according to binomial statistics. Thus, the fast phase is presumed to be due to those liposomes that contain one or more umbrella molecules, and the slow phase due to a redistribution of the molecular umbrellas among the liposomes. Under similar conditions, **1** had no detectable Na^+ transport activity (not shown). To test for Cl^- transport, we first attempted to monitor the kinetics of chloride ion influx

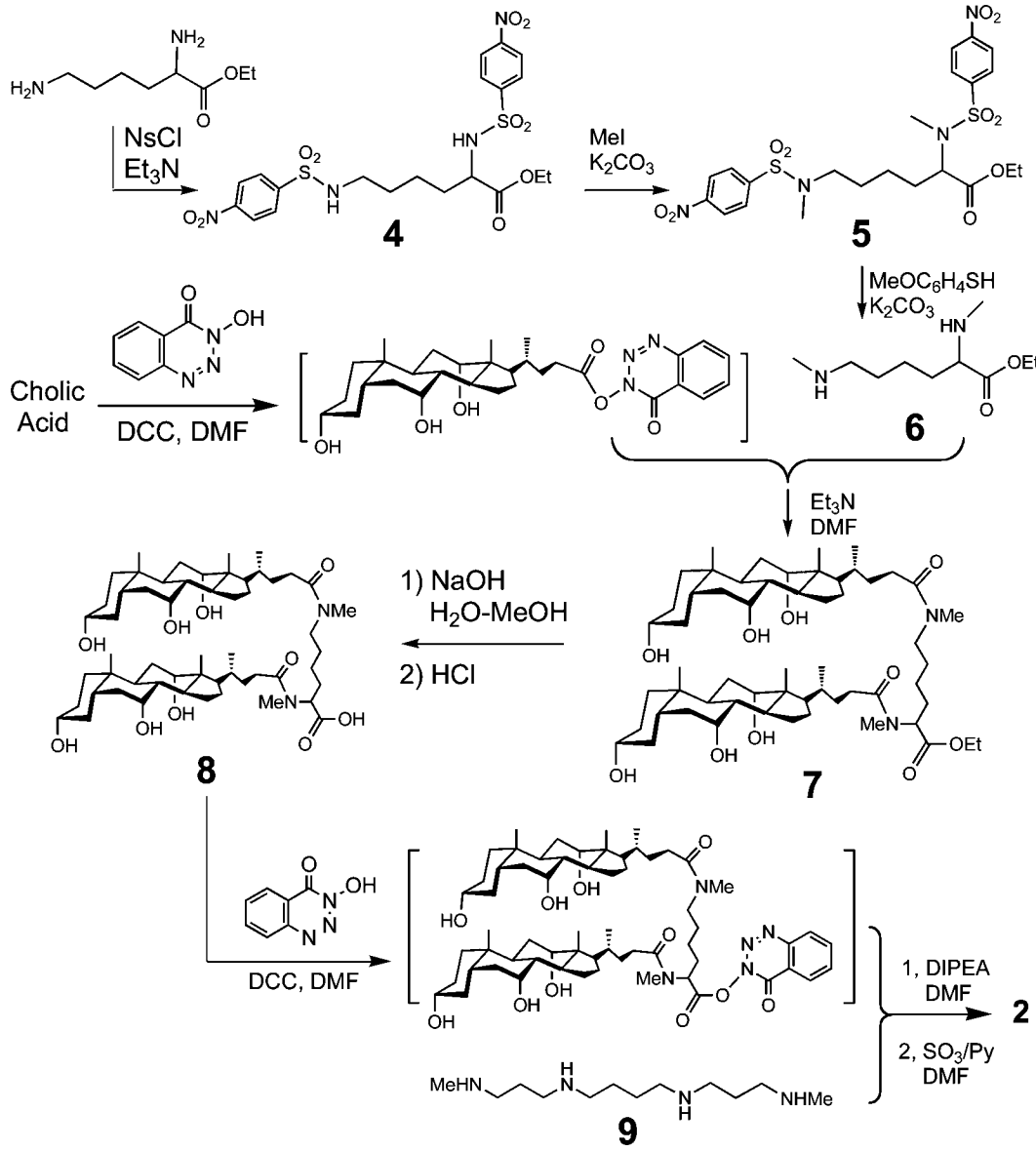

Figure 3. Synthetic approach used for the synthesis of **2**.

Table 1. Binding and Efflux Data[a]

entrapped permeant	binding (%)	K^b	$10^3 k_{obsd}{}^c$ (h^{-1})
1	3.4	590	12.1
2	2.8	490	7.7
3	19	4000	9.8
PRO 2000	74	41000	0.0

[a] Measurements were at 24 °C using POPC/POPG (95/5, mol/mol). [b] In all cases, equilibrium was reached within 24 h. [c] Experimental first-order rate constant for efflux.

using a liposome-entrapped chloride-sensitive dye (i.e., lucigenin) as a sensor. Such methods have previously been employed by other researchers (*18*). For our system, however, we found that the addition of **3** led to the complete release of the dye, as determined by equilibrium dialysis measurements. Because of this release, we chose an alternate approach, where we measured the efflux of chloride ion upon addition of **3**. Thus, a similar liposomal dispersion was first prepared from POPC and 100 mM NaCl in 10 mM sodium phosphate (pH 6.7). Subsequent dialysis against 100 mM $NaNO_3$ in 10 mM sodium phosphate (pH 6.7), followed by addition of 0.006 mol % of **3**, resulted in (61 ± 2)% release of the entrapped chloride ion after a 12 h at 23 °C (see Supporting Information). In the absence of **3**, only (18 ± 2)% of the entrapped chloride ion was released over this same time period. The fact that **3** promotes the transport of Cl^- ions rules out a simple carrier mechanism, since chloride ion and the molecular umbrella are both negatively charged. Rather, it lends support for **3** acting as a pore- or channel-forming agent. The fact that two distinct resonances are observed for Na^+ further indicates that these openings are too small to permit the passage of the paramagnetic shift reagent but large enough to allow for a flow of Na^+ ions. The difference between **1** and **3**, in terms of their interactions with phospholipid bilayers, is striking. One possible explanation for this difference is that **3**, being more lipophilic, prefers to reside within and across the bilayer, which leads to pore formation. In contrast, the more hydrophilic analogue, **1**, may favor binding to the inner and outer surfaces of the membrane, and its presence in the hydrocarbon interior is only transient as it crosses from one leaflet to the adjoining one. The strong dependency of molecular umbrella−lipid bilayer interactions on an umbrella's hydrophilic/lipophilic balance that we have discovered shows that a "fine line" exists between

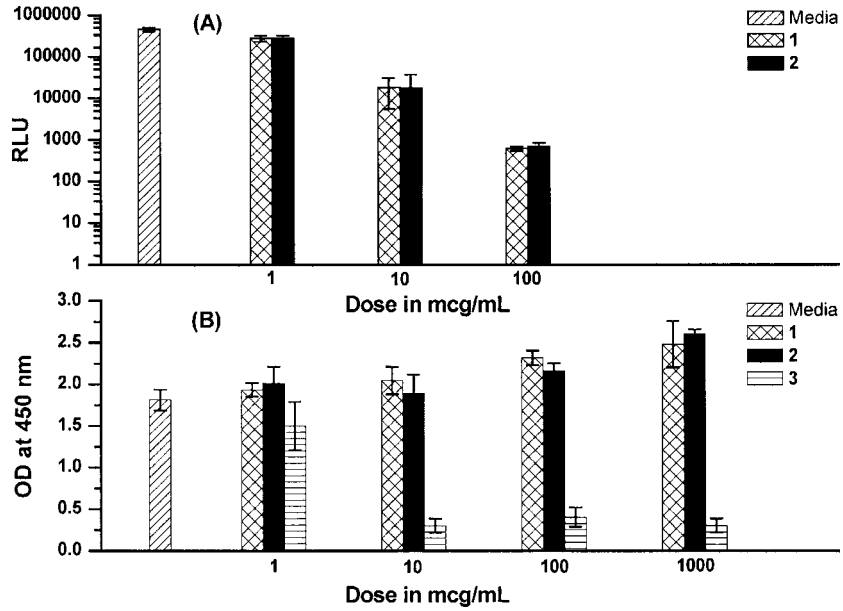

Figure 4. Dose-dependent inhibition of HIV-1 gene expression in U87 cells by different drugs. (A) U87 $CD4^+$ $CCR5^+$ cells pretreated with indicated concentrations of different drugs for 1 h followed by infection with JRFL envelope pseudotyped replication-defective HIV-1. Luciferase quantitation was performed on cell lysates 48 h post infection and is reported as relative light units (RLUs). (B) Cytotoxicity of compounds **1**, **2**, and **3** was done on U87 cells treated with different concentrations of the compounds. Cells were treated for 1 h with different drugs, and then compounds were aspirated and replaced with control medium and cultured for additional 3 days. This was followed by addition of 20 uL of MTS/PMS solution and incubation for 2 to 4 h. Optical densities (OD) were read at 450 nm.

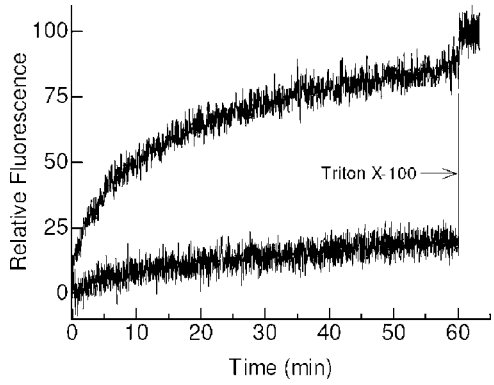

Figure 5. Fluorescence intensity as a function of time (23 °C) in liposomal dispersions made from POPC/POPG (95/5, mol/mol) in the absence (lower trace) and presence of 0.006 mol % of **3** (upper trace). An excess of Triton X-100 was used to destroy the liposomes by forming mixed micelles.

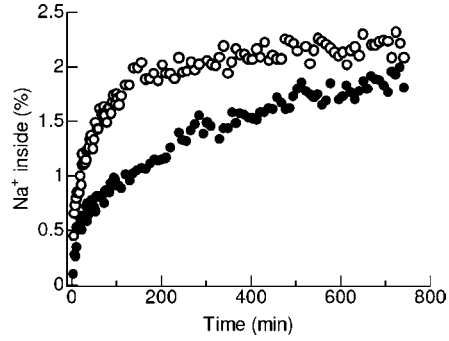

Figure 6. Entry of Na^+ into liposomes made from POPC as a function of time at 35 °C after addition of (●) 0.002 mol % and (○) 0.004 mol % of **3**. In the absence of **3**, there was no detectable entry of Na^+ after 12 h (not shown).

umbrella transport and ionophoric activity—a line that must not be crossed if such conjugates are to be used for drug delivery. At the same time, this finding raises the possibility of exploiting such molecules in fundamentally new ways, e.g., as biogenic ionophores and as cytotoxic drugs.

ACKNOWLEDGMENT

We are grateful to the National Institutes of Health (PHS Grant GM51814) for support of this research.

Supporting Information Available: Experimental procedures. This material is available free of charge via the Internet at http://pubs.acs.org.

LITERATURE CITED

(1) Janout, V., and Regen, S. L. (2009) Bioconjugate-based molecular umbrellas. *Bioconjugate Chem. 20*, 183–192.
(2) Janout, V., DiGiorgio, C., and Regen, S. L. (2000) Molecular umbrella-assisted transport of a hydrophilic peptide across a phospholipid membrane. *J. Am. Chem. Soc. 122*, 2671–2672.
(3) Janout, V., Jing, B., and Regen, S. L. (2005) Molecular umbrella-assisted transport of an oligonucleotide across cholesterol-rich phospholipid bilayers. *J. Am. Chem. Soc. 127*, 15862–15870.
(4) Janout, V., Staina, I. V., Bandyopadhyay, P., and Regen, S. L. (2001) Evidence for an umbrella mechanism of bilayer transport. *J. Am. Chem. Soc. 123*, 9926–9927.
(5) Jing, B., Janout, V., Herold, B. C., Klotman, M. E., Heald, T., and Regen, S. L. (2004) Persulfated molecular umbrellas as anti-HIV and anti-HSV agents. *J. Am. Chem. Soc. 126*, 15930–15931.
(6) Madan, R. P., Mesquita, P. M.M., Cheshenko, N., Jing, B., Shende, V., Guzman, E., Heald, T., Keller, M. J., Regen, S. L., Shattock, R. J., and Herold, B. C. (2007) Molecular umbrellas: a novel class of candidate topical microbicides to prevent human immunodeficiency virus and herpes simplex virus infections. *J. Virol. 81*, 7636–7646.
(7) Mehiri, M., Jing, B., Ringhoff, D., Janout, V., Cassimeris, L., and Regen, S. L. (2008) Cellular entry and nuclear targeting by a highly anionic molecular umbrella. *Bioconjugate Chem. 19*, 1510–1513.

(8) Enting, R. H., Hoetelemans, R. M. W., Lange, J. M. A., Burger, D. M., Beijnen, J. H., and Portegies, P. (1998) Antiretroviral drugs and the central nervous system. *AIDS 12*, 1941–1955.

(9) Stein, W. D. (1986) *Transport and Diffusion Across Cell Membranes*, Academic Press, San Diego, CA.

(10) Romanowski, M., Zhu, X., Ramanswami, V., Misicka, A., Lipkowski, A. W., Hruby, V. J., and O'Brien, D. F. (1997) Interaction of a highly potent dimeric enkephalin analog, biphalin, with model membranes. *Biochim. Biophys. Acta 1329*, 245–258.

(11) Mehiri, M., Chen, W.-H., Janout, V., and Regen, S. L. (2009) Molecular umbrella transport: exceptions to the classic size/lipophilicity rule. *J. Am. Chem. Soc. 131*, 1338–1339.

(12) Keller, M. J., Zerhouni-Layachi, B., Cheshenko, N., John, M., Hogarty, K., Kasowitz, A., Goldberg, C. L., Wallenstein, S., Profy, A. T., Klotman, M. E., and Herold, B. C. (2006) PRO 2000 gel inhibits HIV and herpes simplex virus infection following vaginal application: a double-blind placebo-controlled trial. *J. Infect. Dis. 193*, 27–35.

(13) Bergeron, R. J., Neims, A. H., McManis, J. S., Hawthorne, T. R., Vinson, J. R., Bortell, R., and Ingeno, M. J. J. (1988) Synthetic polyamine analogs as antineoplastics. *J. Med. Chem. 31*, 1183–1190.

(14) Bergeron, R. J., Feng, Y., Weimar, W. R., McManis, J. S., Dimova, H., Porter, C. W., Raisler, B., and Phanstiel, O. (1997) A comparison of structure-activity relationships between spermidine and spermine analogue antineoplastics. *J. Med. Chem. 40*, 1475–1494.

(15) Kano, K., and Fendler, J. H. (1978) Pyrene as a sensitive pH probe for liposome interiors and surfaces: pH gradients across phospholipid vesicles. *Biochim. Biophys. Acta 509*, 289–299.

(16) Clement, N. R., and Gould, J. M. (1981) Pyanine (8-hydroxy-1,3,6-pyrenetrisulfonate) as a probe of internal aqueous hydrogen ion concentration in phospholipid vesicles. *Biochemistry 20*, 1534–1538.

(17) Zhang, J., Jing, B., and Regen, S. L. (2003) Kinetic evidence for the existence, and mechanism of formation, of a barrel stave structure from pore-forming dendrimers. *J. Am. Chem. Soc. 125*, 13984–13987.

(18) McNally, B. A., Koulov, A. V., Lambert, T. N., Smith, B. D., Jooss, J.-B., Sisson, A. L., Clare, J. P., Sgarlata, V., Judd, L. W., Magro, G., and Davis, A. P. (2008) Structure-activity relationships in cholapo anion carriers: enhanced transmembrane chloride transport through subsituent tuning. *Chem.—Eur. J. 14*, 9599–9606.

BC900246U

A Fine Line Between Molecular Umbrella Transport and Ionophoric Activity

Wen-Hua Chen, Vaclav Janout, Masaharu Kondo, Arevik Mosoian, Goar Mosoyan, Ravil R. Petrov, Mary E. Klotman and Steven L. Regen

Department of Chemistry, Lehigh University, Bethlehem, Pennsylvania 18015 and Department of Infectious Diseases, Mount Sinai School of Medicine, New York, New

SUPPORTING INFORMATION

EXPERIMENTAL PROCEDURES

General Methods. ^{1}H NMR spectra were recorded in CD_3OD, DMSO-d_6 or $CDCl_3$ using a Bruker 500 spectrometer, and the solvent as a reference. HR-ESI mass spectra were recorded on an Agilent 6210 LCMS spectrometer. Silica gel 60 (EMD, particle size 0.063-0.200 mm, 70-230 mesh) was used for all column chromatographic purifications. Thin-layer chromatography (TLC) was performed on glass plates that were precoated with silica gel containing a fluorescence indicator (Whatman). Detection on TLC was made by use of 10% sulfuric acid in water, iodine, ninhydrin solution and UV (254 or 365 nm). All reagents and chemicals were obtained from commercial sources and used as received unless noted otherwise. Bioconjugate **1**, was prepared using established procedures.[1,2] A bis-N-methylated spermine (**9**) was synthesized using literature procedures.[3,4] Experimental methods that were used to measure binding constants and efflux rates constants, which are described below, were similar to those previously reported.[5] PRO 2000 was a gift from Indevus Pharmaceuticals (Lexington, MA) and was >99.3% pure, as indicated by the supplier.

Scheme 1

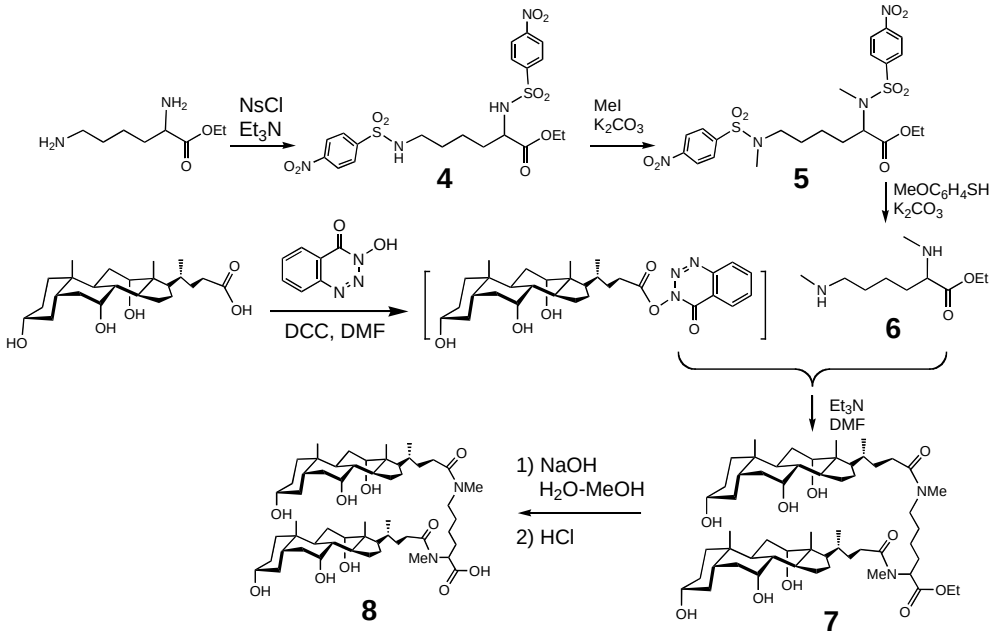

Scheme 2

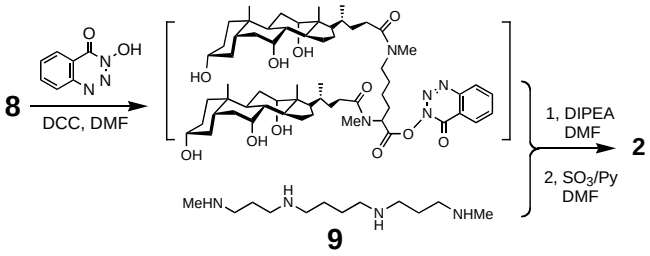

Synthesis of *L*-Lysine-dideoxycholamide. The procedure used for the synthesis of *L*-lysine-dideoxycholamide was similar to that previously used to prepare *L*-lysine-dicholamide.[2] Thus, DCC (1.97 g, 9.55 mmol) was added to a solution of deoxycholic acid (2.5 g, 6.37 mmol) and *N*-hydroxysuccinimide (0.84 g, 7.30 mmol) in anhydrous THF (40 mL). The resulting mixture was stirred at room temperature for 4 h, and then filtered to remove the insoluble urea. The filtrate was then added, dropwise, to a solution of *L*-lysine (445 mg, 3.04 mmol) and triethylamine (2.9 mL) in H_2O (10 mL), and stirred overnight. The reaction mixture was concentrated under reduced pressure and poured into

1 M hydrochloride acid (250 mL). The resulting solid was collected by filtration and purified by chromatography on a silica-gel column, eluting with $CHCl_3$/MeOH/H_2O (40/10/1, v/v/v) to afford *L*-lysine-dideoxycholamide (1.88 g, 69%) having ^{1}H NMR (500 MHz, CD_3OD, 296 K) δ 4.35 (m, 1 H), 3.95 (s, 2 H), 3.52 (m, 2 H), 3.23 (t, *J* = 5.75 Hz, 2 H), 2.38-2.27 (m, 2 H), 2.24-2.15 (m, 2 H), 1.92 (m, 66 H), 0.70 (s, 6 H); and HR-ESI MS for $C_{54}H_{91}N_2O_8$ ($[M+H]^+$) calcd: 895.6781; found: 895.6792.

Synthesis of 3. To a solution of *L*-lysine-dideoxycholamide (750 mg, 0.838 mmol) and 3-hydroxy-1,2,3-benzotriazine-4(3*H*)-one (DHBT) (157 mg, 0.96 mmol) in anhydrous DMF (10 mL) was added DCC (260 mg, 1.26 mmol). After the mixture was stirred for 4 h, a solution of spermine (34 mg, 0.17 mmol), and 4-dimethylaminopyridine (164 mg, 1.34 mmol) in anhydrous DMF (1.0 mL) was added. The reaction mixture was stirred at room temperature overnight, concentrated under reduce pressure, and poured into a 5% ammonia solution (200 mL). The resulting precipitate was collected by filtration and purified by chromatography on a silica-gel column, eluting with $CHCl_3$/CH_3OH/H_2O (40/10/1, v/v/v) to give the hydroxylated precursor to **3** (515 mg, 83%) having ^{1}H NMR (500 MHz, CD_3OD, 296 K) δ 4.73 (m, 2 H), 4.24 (m, 2 H), 3.94 (s, 8 H), 3.52 (m, 8 H), 3.47-3.36 (m, 8 H), 3.15 (m, 12 H), 2.37-2.04 (m, 16 H), 1.93-0.92 (m, 272 H), 0.70 (s, 24 H); and HR-ESI MS for $C_{226}H_{378}N_{12}O_{28}$ (M^+) Calcd: 3708.8524; found: 3708.8372.

Sulfation was then carried out by dissolving this hydroxylated precursor **(**204 mg, 0.06 mmol) in DMF (3 mL) at 0°C, followed by direct addition of sulfur trioxide/pyridine complex (560 mg, 3.52 mmol). After stirring overnight at room temperature, 2 mL of cold water was added, followed by addition of sodium carbonate until the pH of the

mixture was 10. The combined solvents were then removed under reduced pressure, and the resulting residue was purified by dialysis (MWCO 500) against water (250 mL) to give **3** (210 mg, 71%) as its sodium salt having ^{1}H NMR (500 MHz, DMSO-d_6, 296 K) δ 4.57 (br, 2 H), 4.35 (s, 8 H), 4.11 (br, 2 H), 3.92 (s, 8 H), 3.40-3.03 (m, 8 H), 2.95 (m, 12 H), 2.10-0.83 (m, 288 H), 0.61 (s, 24 H); and HR-ESI MS for $C_{226}H_{362}N_{12}O_{76}Na_{16}S_{16}$ (M^-) Calcd: 5339.8725; found: 5339.8843.

Synthesis of 4. A solution of 4-nitrobenzenesulfonyl chloride (2.70 g, 12.18 mmol) in CH_2Cl_2 (15 mL) was added dropwise to a mixture of *L*-lysine ethyl ester dihydrochloride (1.50 g, 6.07 mmol) and triethyl amine (5.0 mL, 35.9 mmol) in CH_2Cl_2 (20 mL). The resulting mixture was stirred at room temperature for 4 h, diluted with $CHCl_3$ (100 mL) and washed with water (150 mL, pH 1.0). The organic layer was dried over anhydrous Na_2SO_4 and concentrated under reduced pressure. The resulting residue was purified by chromatography on a silica-gel column [$CHCl_3$/MeOH, 20/1 (v/v)] to afford compound **4** (3.13 g, 95%) having ^{1}H NMR (500 MHz, $CDCl_3$, 296 K) δ 8.34 (d, *J* = 7.96 Hz, 2 H), 8.32 (d, *J* = 7.93 Hz, 2 H), 8.04 (d, *J* = 7.90 Hz, 2 H), 8.01 (d, *J* = 7.90 Hz, 2 H), 5.80 (br, 2 H), 5.32 (unresolved, 1 H), 3.93 (q, 2 H), 2.97 (t, *J* = 6.11 Hz, 2 H), 1.77-1.70 (m, 1 H), 1.64-1.57 (m, 1 H), 1.55-1.43 (m, 2 H), 1.42-1.36 (m, 2 H), 1.08 (t, 3 H), and HR-ESI for $C_{20}H_{25}N_4O_{10}S_2$ ($[M+H]^+$) Calcd: 545.1007. Found: 545.1001.

Synthesis of 5. Iodomethane (1.08 mL, 17.31 mmol) was added to a mixture of compound **4** (3.10 g, 5.69 mmol) and potassium carbonate (2.36 g, 17.08 mmol) in anhydrous DMF (20 mL). The resulting mixture was stirred overnight at room temperature, and then diluted with $CHCl_3$ (150 mL) and washed with water (150 mL). The organic layer was dried over anhydrous Na_2SO_4 and concentrated under reduced

pressure. The obtained residue was purified by chromatography on a silica-gel column, eluting with $CHCl_3$/MeOH (50/1, [v/v)]) to give compound **5** (3.03 g, 93%) having ^{1}H NMR (500 MHz, $CDCl_3$, 296 K) δ 8.37 (d, *J* = 8.88 Hz, 2 H), 8.33 (d, *J* = 8.91 Hz, 2 H), 7.97 (d, *J* = 9.13 Hz, 2 H), 7.96 (d, *J* = 9.01 Hz, 2 H), 4.61-4.58 (m, 1 H), 3.99-3.89 (m, 2 H), 3.11-3.01 (m, 2 H), 282 (s, 3 H), 2.77 (s, 3 H), 1.95-1.87 (m, 1 H), 1.80-1.68 (m, 2 H), 1.60-1.52 (m, 1 H), 1.51-1.35 (m, 2 H), 1.08 (t, 3 H), and HR-ESI for $C_{22}H_{29}N_4O_{10}S_2$([M+H]$^+$) Calcd: 573.1320. Found: 573.1320.

Synthesis of 6. Solid potassium carbonate (3.42 g, 24.74 mmol) was added to a solution of compound **5** (2.64 g, 4.61 mmol) and 4-methoxybenzenethiol (2.59 g, 18.47 mmol) in DMF (10 mL).[6] The resulting heterogeneous mixture was stirred vigorously at room temperature for 3 h. Then the reaction mixture was added, dropwise, into ethanol (150 mL) and filtered. The filtrate was concentrated under reduced pressure, and the residue was purified by chromatography on a silica-gel column, eluting with MeOH/$NH_3{\cdot}H_2O$ (10/1, v/v) to afford compound **6** (797 mg, 85%) having ^{1}H NMR (500 MHz, CD_3OD, 296 K) δ 4.19 (q, 2 H), 3.16 (t, *J* = 6.60 and 6.64 Hz, 1 H), 2.80 (t, *J* = 7.58 and 7.70 Hz, 2 H), 2.55 (s, 3 H), 2.30 (s, 3 H), 1.70-1.58 (m, 4 H), 1.42-1.36 (m, 2 H), 1.27 (t, *J* = 7.12 and 7.13 Hz, 3 H), and HR-ESI for $C_{10}H_{23}N_2O_2$ ([M+H]$^+$) Calcd: 203.1754. Found: 203.1748.

Synthesis of 7. DCC (2.55 g, 12.36 mmol) was added to a solution of cholic acid (3.36 g, 8.22 mmol) and DHBT (1.54 g, 9.44 mmol) in anhydrous DMF (10 mL). The resulting reaction mixture was stirred at room temperature for 4 h and then added, dropwise, into a solution of dimethylated *L*-lysine **6** (793 mg, 3.92 mmol) and triethylamine (2.2 mL) in anhydrous DMF (5.0 mL). The reaction mixture was then

stirred overnight. After being concentrated to ca. 10 mL, the reaction mixture was poured into water (250 mL), and the resulting precipitate was collected by filtration. The solid precipitate was purified by chromatography on a silica-gel column [$CHCl_3$/MeOH, 6/1 (v/v)] to afford compound **7** (2.63 g, 68%) having ^{1}H NMR (500 MHz, CD_3OD, 292 K) δ 5.04-4.96 (m) and 4.63-4.57 (m) (1 H), 4.22-4.10 (m, 2 H), 3.96 (unresolved, 2 H), 3.79 (unresolved, 2 H), 3.39-3.34 (m, 4 H), 3.04-3.03 and 2.89-2.88 (3 H), 3.00-2.99 and 2.78-2.77 (3 H), 2.51-2.23 (m, 8 H), 2.03-0.91 (m, 61 H), 0.72 and 0.71 (ss, 6 H), and HR-ESI MS for $C_{58}H_{99}N_2O_{10}$ ($[M+H]^+$) Calcd: 983.7294. Found: 983.727.

Synthesis of 8. A solution of sodium hydroxide (1.07 g, 26.75 mmol) in water (10.0 mL) was added to a solution of compound **7** (2.63 g, 2.67 mmol) in MeOH (40 mL). The resulting mixture was stirred at room temperature until the starting material disappeared. After being concentrated to ca. 10 mL under reduced pressure, the reaction mixture was added, dropwise, to water (500 mL), and the pH was adjusted with diluted HCl to ca. 1. The resulting precipitate was collected by filtration and dried under vacuum to afford compound **8** (2.41 g, 95%) having ^{1}H NMR (500 MHz, CD_3OD, 296 K) δ 5.10-5.04 (m) and 4.58-4.52 (m) (1 H), 3.95 (unresolved, 2 H), 3.79 (unresolved, 2 H), 3.41-3.33 (m, 4 H), 3.05 and 2.91-2.90 (3 H), 2.99-2.98 and 2.80-2.79 (3 H), 2.52-2.22 (m, 8 H), 2.03-0.91 (m, 58 H), 0.71 (s, 6 H), and HR-ESI MS for $C_{56}H_{95}N_2O_{10}$ ($[M+H]^+$) Calcd: 955.6981. Found: 955.6958.

Synthesis of 2. DCC (165 mg, 0.80 mmol) was added to a solution of **8** (508 mg, 0.53 mmol) and DHBT (100 mg, 0.61 mmol) in anhydrous DMF (3.0 mL). After stirring for 3 h, a solution of **9** (24.5 mg, 0.11 mmol) and DIPEA (300 μL, 1.75 mmol) in anhydrous DMF (1.0 mL) was added to the reaction mixture. The obtained reaction mixture was

stirred at room temperature overnight, and then concentrated under reduced pressure. The resulting residue was purified by chromatography on a silica-gel column eluting with $CHCl_3$/MeOH/H_2O (50/10/1, v/v/v) to afford a hydroxylated precursor of **2** (213 mg, 50%) having ^{1}H NMR (500 MHz, CD_3OD, 296 K) δ 5.42 (br, 4 H), 3.95 (s, 8 H), 3.79 (s, 8 H), 3.40-3.25 (m, 28 H), 3.04-3.01 (m, 12 H), 2.94 (s, 12 H), 2.89 (s, 6 H), 2.48-0.91 (m, 272 H), 0.71 (s, 24 H), and HR-ESI MS for $C_{236}H_{398}N_{12}O_{36}$ (M^+) Calcd: 3976.9682. Found: 3976.8472.

Sulfation was then carried out by dissolving the hydroxylated precursor **(**108 mg, 0.027 mmol) in DMF (2.0 mL) at 0°C (ice cooling), followed by direct addition of sulfur trioxide/pyridine complex (415 mg, 2.61 mmol). The resulting solution was allowed to warm gradually to room temperature and stirred at room temperature overnight. Then, cold water (1.0 mL) was added, followed by addition of sodium carbonate until the pH of the mixture reached 10. The combined solvents were then removed under reduced pressure, and the resulting residue was purified by chromatography on a silica-gel column eluting with $CHCl_3$/MeOH/H_2O (4/4/1, v/v/v), followed by dialysis (MWCO 500) against water (500 mL), to give **2** (152 mg, 87%) as its sodium salt having ^{1}H NMR (500 MHz, CD_3OD, 296 K) δ 5.40 (br, 4 H), 4.66 (s, 8 H), 4.44 (s, 8 H), 4.12 (m, 8 H), 3.50-3.19 (m, 20 H, overlapping with solvent), 3.04-2.88 (m, 30 H), 2.45-0.93 (m, 272 H), 0.76 (s, 24 H), and HR-ES-MS for $C_{236}H_{374}N_{12}Na_{24}O_{108}S_{24}$ (M^-) Calcd: 6423.4983. Found: 6423.4253.

Anti-HIV Activity and Cytotoxicity. U87 glioblastoma cells were obtained from the NIH AIDS Research and Reference Reagent Program (Rockville, MD) and cultured in DMEM (Invitrogen Canada) supplemented with 15% fetal bovine serum (FBS), 1 μg/mL

puromycin, and 300 μg/mL G418. Approximately 6 x 10^4 cells were plated in triplicate in 96-well plates, and then treated with the different concentrations of compounds **1**, **2** and **3** for 1 h followed by infection with replication incompetent HIV_{JRFL} for 48 h. Control samples did not receive any treatment. After 48 h, luciferase assay was performed on lysed cell extracts.

Pseudotyped, replication-defective virus HIV_{JRFL} was generated in 293T cells using a three-plasmid cotransfection system.[7] These three plasmids include the packaging construct pCMVΔR8.2, the HIV-1 reporter construct pNL4-3.Luc.R-E with firefly luciferase gene inserted into the pNL4-3 *nef* gene, and the HIV-1 envelope-expressing construct, pJRFL. Transfection was performed in 75-cm^2 culture flasks using Lipofectamine 2000 (Invitrogen).

U87 cells were pretreated for 1 h with compounds **1**, **2** and **3**, followed by infection with replication incompetent HIV_{JRFL} for 3 h, and then virus was replaced with fresh growth medium. Viral infection was determined by quantifying luciferase activity using Luciferase Assay Substrate (Promega, Madison, WI).

Drug toxicity assays were done as previously described.[8] Thus, to determine the cytotoxicity of a giving compound, 50 × 10^3 U87 cells were plated in a 96-well plate, followed by treatment with varying concentrations of the drug. A standard colorimetric assay was then used for measuring the activity of enzymes that reduce MTT + PMS to formazan, according to the protocol, Promega, CellTiter 96 Non-radioactive Proliferation Assay (MTT). Here, yellow MTT (3-(4,5-Dimethylthiazol-2-yl)-2,5-diphenyltetrazolium bromide, a tetrazole) is reduced to purple formazan in the presence of phenazine

methosulfate (PMS), which produces a water-soluble formazan in living cells. The absorbance of this colored solution was then quantified by measuring the absorption at 570 nm. The amount of purple formazan produced by cells that were treated with a given concentration of compound was then compared with the amount of formazan produced by untreated control cells. The cytotoxicity of each compound was determined in triplicate.

Statistics Data are expressed as mean ± SD. Student *t*-test was used to compare the means of different samples (treated vs. control). $P < 0.05$ was considered to be statistically significant.

Liposome Formation and pH Discharge Experiments. Typically, 1-palmitoyl-2-oleoyl-*sn*-glycero-3-phospho-choline (POPC) and 1-palmitoyl-2-oleoyl-*sn*-glycero-3-phosphatidylglycerol (POPG) (a 20 mg mixture of POPC/POPG (95/5, mol/mol) in choloroform was transferred to a Pyrex test tube. While rotating the tube, the organic solvent was removed under a stream of argon, resulting in a thin lipid film. The last traces of solvent were then removed under reduced pressure (25 °C, 12 h, <0.2 Torr). To the dried film was added 1.0 mL of 0.1 mM pyranine in 25 mM HEPES buffer (pH 7.0, 50 mM NaCl), and the mixture vortexed for 1 min. The dispersion was then incubated for 5 min, followed by another 1 min of vortexing and 20 min of incubation at ambient temperature. The sample was subjected to five freeze/thaw cycles (77 K/325 K), followed by sequential extrusion through a 400 nm Nuclepore membrane (10 times) and a 200 nm membrane (10 times). After extrusion, the dispersion was incubated at room temperature for 1.25 h. The non-entrapped pyranine was then removed by gel filtration (Sephadex G-

25, 1 x 20 cm), eluting with 25 mM HEPES buffer (pH 7.0, 50 mM NaCl)). The concentration of lipid in the vesicle dispersion was calculated from volume after gel filtration.

To 0.3 mL of the above liposome dispersion was added 1.7 mL of a 25 mM HEPES buffer (pH 8.0, 50 mM NaCl) that contained 0.006 mol% of a given agent (relative to the total phospholipid to which it was added). The fluorescence intensity was monitored as a function of time (λ_{ex} 460 nm, λ_{em} 510 nm, slit width $\lambda_{ex}/\lambda_{em}$ 2.5 nm/2.5 nm) using a Perkin-Elmer Luminescence Spectrometer LS50B. Complete pH discharge was made by destroying the vesicles and forming mixed micelles after 60 min via the addition of 50 µL of aqueous solution of Triton X-100 (5 wt %).

Sodium Ion Transport. Typically, 2.5 mL of a 20 mg/mL solution of 1-palmitoyl-2-oleoyl-2-*sn*-glycero-3-phosphocholine (POPC) in chloroform was transferred to a pyrex test tube. While rotating the tube, the organic solvents were removed under a stream of nitrogen, resulting in a thin lipid film. The last traces of solvent were then removed under reduced pressure (25°C, 12 h, <0.2 Torr). To the dried film was added 1.0 mL of a 150 mM KCl solution that was 10% in D_2O and 90% in H_2O, and the mixture was vortexed for 1 min. The dispersion was then incubated for 5 min, followed by another 1 min of vortexing and 20 min of incubation at ambient temperature. The sample was subjected to five freeze/thaw cycles (77 K/325 K), followed by sequential extrusion through a 400 nm Nuclepore membrane (10 times) and a 200 nm membrane (10 times). After extrusion, the dispersion was incubated at room temperature for 1.25 h. In a quartz NMR tube, 1.5 mL of a 150 mM NaCl solution in 10% D_2O plus 90% H_2O was mixed with 0.3 mL of a shift reagent solution (10 mM $DyCl_3$; 30 mM $Na_5P_3O_{10}$ in 10% D_2O plus 90% H_2O) and the

desired amount of umbrella. To this solution was added 0.75 mL of the vesicle dispersion, and the resulting mixture was vortexed for 30 s. ^{23}Na NMR spectra were recorded continuously at 35°C overnight on a Bruker AMX 500 MHz NMR instrument.

Chloride Ion Transport. Typically, 9.0 mL of 1-palmitoyl-2-oleoyl-*sn*-glycero-3-phosphocholine (POPC) in chloroform (20 mg/mL) was transferred to a Pyrex test tube. While rotating the tube, the organic solvent was removed under a stream of argon, resulting in a thin lipid film. The last traces of solvent were then removed under reduced pressure (25 °C, 12 h, <0.2 Torr). To the 180 mg of dried film was added 3.60 mL of 100 mM NaCl in 10 mM sodium phosphate (pH 6.7), and the mixture was vortex mixed for 1 min. The dispersion was then incubated for 5 min, followed by another 1 min of vortex mixing and 20 min of incubation at ambient temperature. The sample was subjected to five freeze/thaw cycles (77 K/325 K), followed by sequential extrusion through a 400 nm Nuclepore membrane (10 times) and a 200 nm membrane (10 times). After extrusion, the dispersion was dialyzed (Nucleopore membrane, pore diameter 100 nm) using a equilibrium dialysis cell against same volume of 100 mM $NaNO_3$ in 10 mM sodium phosphate (pH 6.7) (10 times 1/2 h for each dialysis) to remove external NaCl. Four aliquots of 0.200 mL of the resulting vesicle dispersion were used to determine captured chloride ion.

Four Cl^- efflux experiments were then run simultaneously. Two experiments were carried out in presence of **3** and two control experiments were carried out in absence of **3**. Thus a 0.200 mL portion of the above liposomal dispersion was mixed in test tube with 30 μL of compound **3** (9.36×10^{-5} M) in 100 mM $NaNO_3$/10 mM sodium phosphate (pH 6.7). Thus, the concentration of **3** relative to POPC was 0.006 mol%. The resulting

mixture was gently shaken (Environ shaker, 150 rpm) for 12 h and placed in dialysis cell and dialyzed at room temperature against 0.73 mL of 100 mM $NaNO_3$ in 10 mM sodium phosphate (pH 6.7) for 30 min. The solution from the receiving side (0.400 mL) was then mixed with 220 μL of lucigenin (12.54×10^{-6} M) in 100 mM $NaNO_3$/10 mM sodium phosphate (pH 6.7), and the fluorescence intensity at 505 nm was used to determine concentration of chloride ion (λ_{ex} 368 nm, slit ex/em 3.0/3.0 nm. A calibration curve. was constructed in an similar way using standard solutions of NaCl (0.500 mM-10.00 mM in 10 mM phosphate buffer, pH 6.7. Experiments that were carried out in the absence of **3** were conducted in a similar way.

To determine the total amount of NaCl that was entrapped in POPC vesicles, 0.200 mL of the above liposome dispersion was mixed with water solution of 0.300 mL 5%w Triton X 100. To the resulting clear solution was added 0.360 mL of lucigenin (12.54×10^{-6} M) and maximum fluorescence intensity at 505 nm was used to determine the chloride concentration. This analysis was run two times for each experiment. Calibration curve was constructed in a similar way using standard solutions of NaCl ([NaCl]= 2-20 mM).

Efflux Measurements. A thin lipid film was formed on the inside walls of a glass test tube using a chloroform solution that contained 40.0 mg of POPC/POPG (95/5, mol/mol). Removal of solvent was carried out under a stream of argon. The resulting film was then hydrated with 2.0 mL of an aqueous buffer [PBS, pH 7.4], which was 0.50 mM in a given persulfated molecular umbrella**.**. The contents of the tube was then mixed via vortexing at room temperature for 30 min, and was subjected to six freeze-thaw cycles -192/40°C.

Subsequent extrusion through two Nuclepore membranes 0.4 mm (10 times) and 0.2 mm (15 times) afforded a dispersion, which was dialyzed against 300 mL of buffer for 18 h, using dialysis tubing with a MW cutoff of 100 000. This dialysis was then repeated using fresh buffer for another 18 h, and finally one additional dialysis for 16 h, again using fresh buffer. After this time, the percent capture of the umbrella was then monitored as a function of time.

To determine the amount of umbrella that was retained by the liposomes, typically, a 200 μL aliquot of the liposome dispersion was concentrated to dryness via freeze-drying (18 h). The lipids were then redissolved in 40 μL of mixture $CHCl_3$/MeOH/H_2O, 10/10/1, v/v/v with the aid of vortex mixing. An exact volume of the resulting solution (2-5 μL) was withdrawn and analyzed by TLC (5 × 10 cm thin layer chromatography plate, silica gel, 0.25 mm, J.T. Baker). The same volume of two or three standard solutions of given umbrellas (0.450 mM, 0.400mM, 0.250mM, 0.100mM, 0.050mM) was always co-deposited for calibration purposes. A mixture of $CHCl_3$/MeOH/H_2O (65/25/4, (v/v/w) was used as a eluent. After the plate was dried for 10 min at rt, it was sprayed with 10% H_2SO_4 and carefully heated with a heat gun to maintain uniformity of the background. The resulting spots were then quantitatively analyzed via densitometry. The density of each spot (the area that was measured for each spot was constant) was quantified by use of Scion Image Beta 4.02 for Windows 95 to XP software, which was available from the Internet (http://www.scioncorp.com/pages/download_now.htm). The intensity of each spot was determined in triplicate.

LITERATURE

1. Jing, B.; Janout, V.; Herold, B.C.; Klotman, M.E.; Heald, T.; Regen, S. L. *J. Am. Chem. Soc.*, **2004**, *126*, 15930-15931.
2. Chen, W.H.; Shao, X.B.; Regen, S. L., *J. Am. Chem. Soc*., **2005**, *127*, 12727-12735.
3. Bergeron, R. J.; Neims, A. H.; McManis, J. S.; Hawthorne, T. R.;. Vinson, J. R ; Bortell, R.; Ingeno, M. J. *J. Med. Chem.*, **1988**, *31*, 1183-1190.
4. Bergeron, R. J. ; Feng, Y. ; Weimar, W. R.; McManis, J. S.; Dimova, H.; Porter, C. W.; Raisler, B.; Phanstiel, O. *J. Med. Chem.*, **1997**, *40*, 1475-1494.
5. Mehiri, M.; Chen, W-H.; Janout, V.; Regen, S. L. *J. Am. Chem. Soc*., **2009**, *131*, 1338-1339.
6. Narayan, R. S.; VanNieuwenhze, M. S.; *Org. Lett.* **2005**, *7*, 2655-2658.
7. Mosoian, A.; Teixeira, A.; High, A. A.; Christian, R. E.; Hund, D. F.; Shabanowitz, J.; Liu, X.; Klotman, M. *J. of Virol*., **2006**, *18*, 9200-9206.
8. Mosoian, A.; Teixeira, A.; Burns, C. S.; Khitrov, G.; Zhang, W.; Gusella, L.; Klotman, P; Klotman, M. *Ann. N.Y. Acad. Sci*., **2007**, *1112*, 269-285.

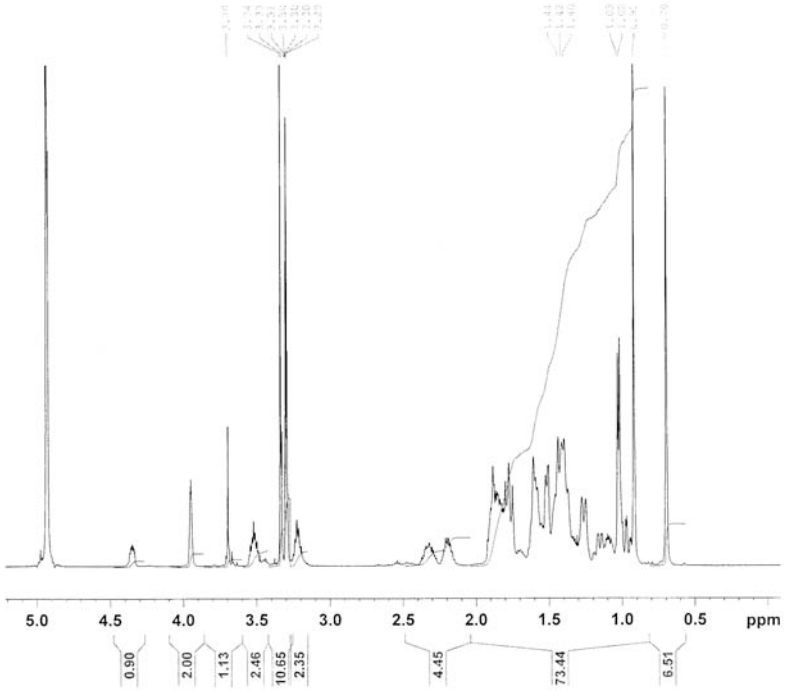

Figure SI 1. ^{1}H NMR (500 MHz, CD_3OD, 296 K) of *L*-Lysine-dideoxycholamide.

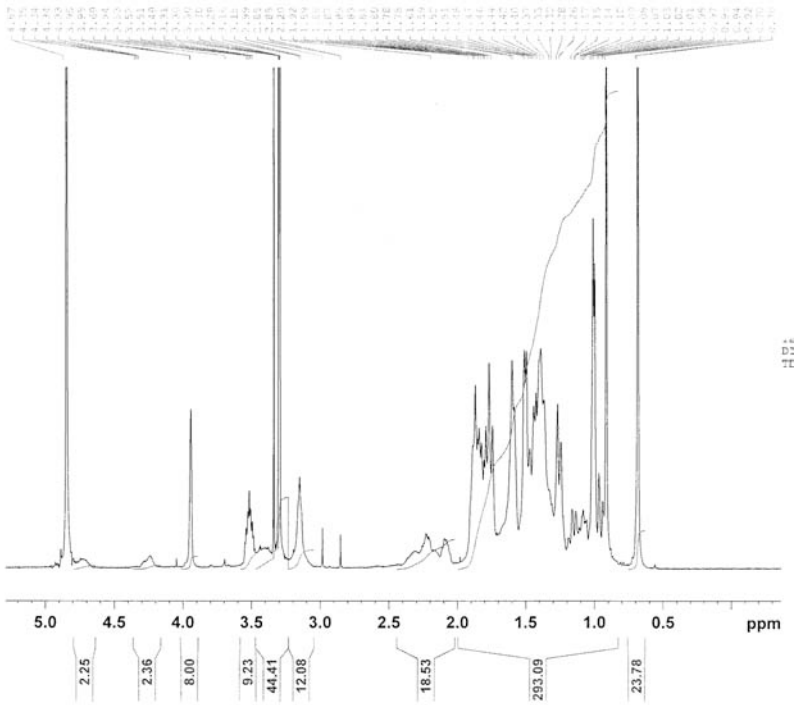

Figure SI 2. ^{1}H NMR (500 MHz, CD_3OD, 296 K) of hydroxylated precursor to **3**.

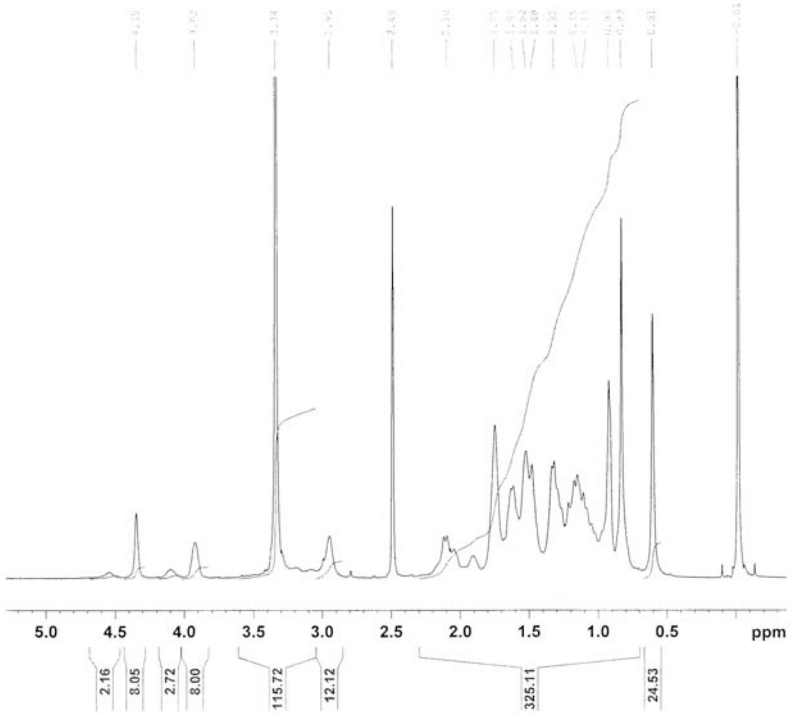

Figure SI 3. ^{1}H NMR (500 MHz, DMSO-d_6, 296 K) of **3**.

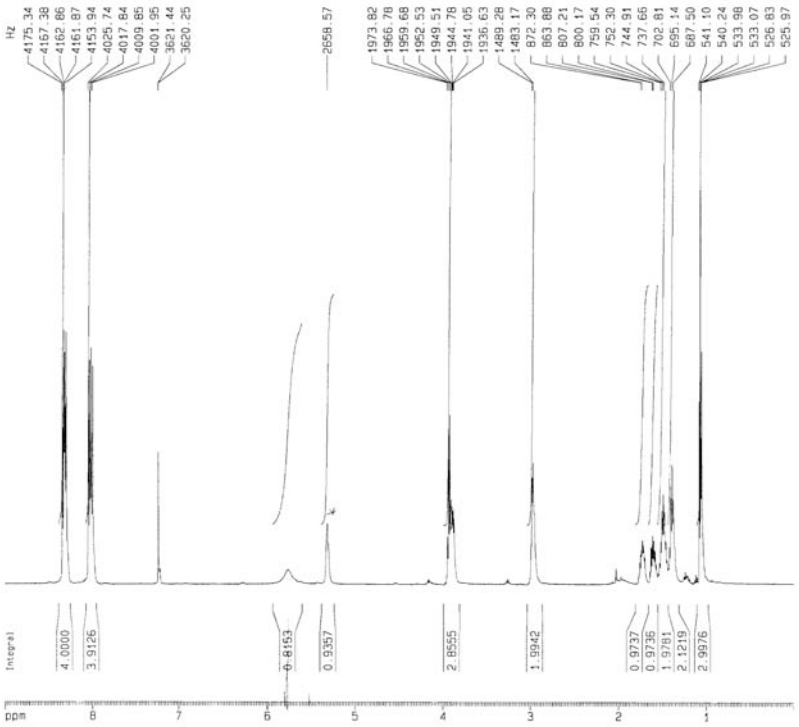

Figure SI 4. ^{1}H NMR (500 MHz, $CDCl_3$, 296 K) of **4**.

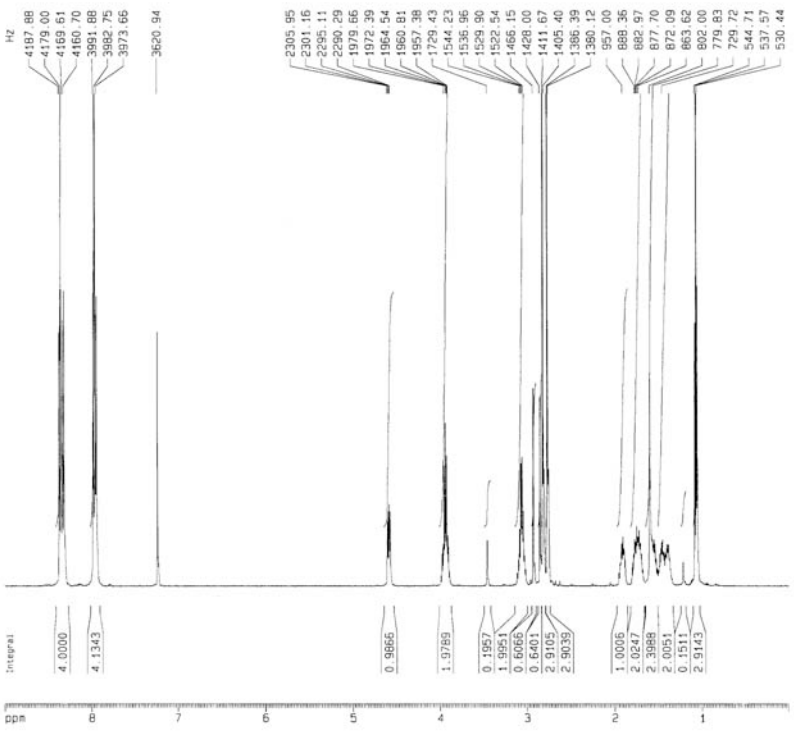

Figure SI 5. ^{1}H NMR (500 MHz, $CDCl_3$, 296 K) of **5**.

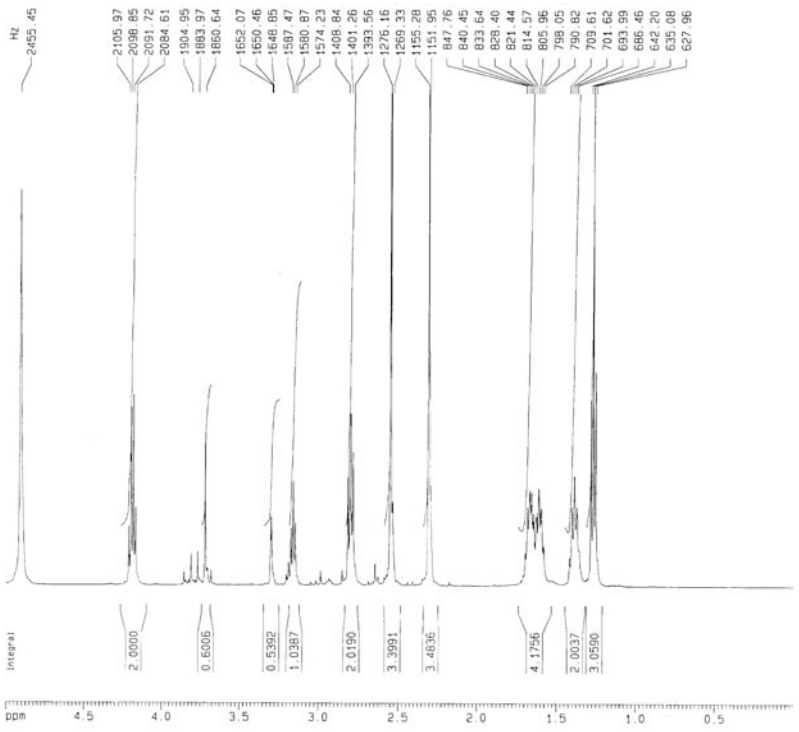

Figure SI 6. ^{1}H NMR (500 MHz, CD_3OD, 298 K) of **6**.

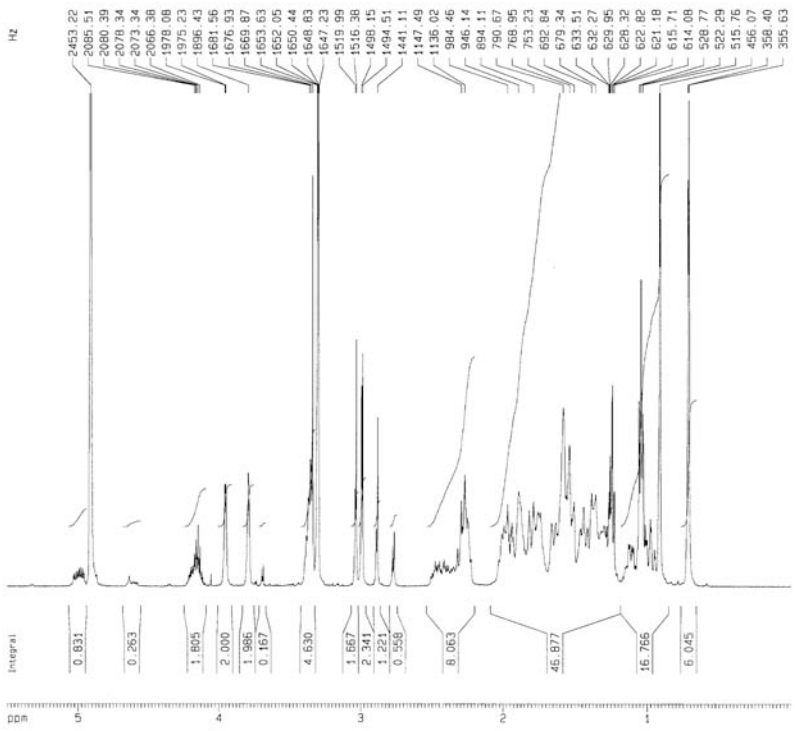

Figure SI 7. ^{1}H NMR (500 MHz, CD_3OD, 292 K) of **7**.

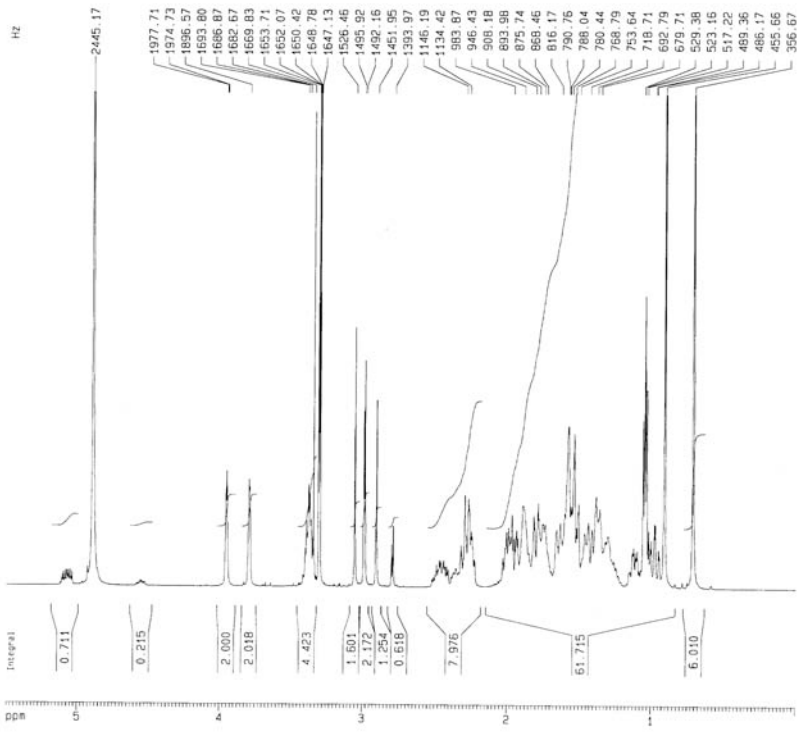

Figure SI 8. ^{1}H NMR (500 MHz, CD_3OD, 296 K) of **8**.

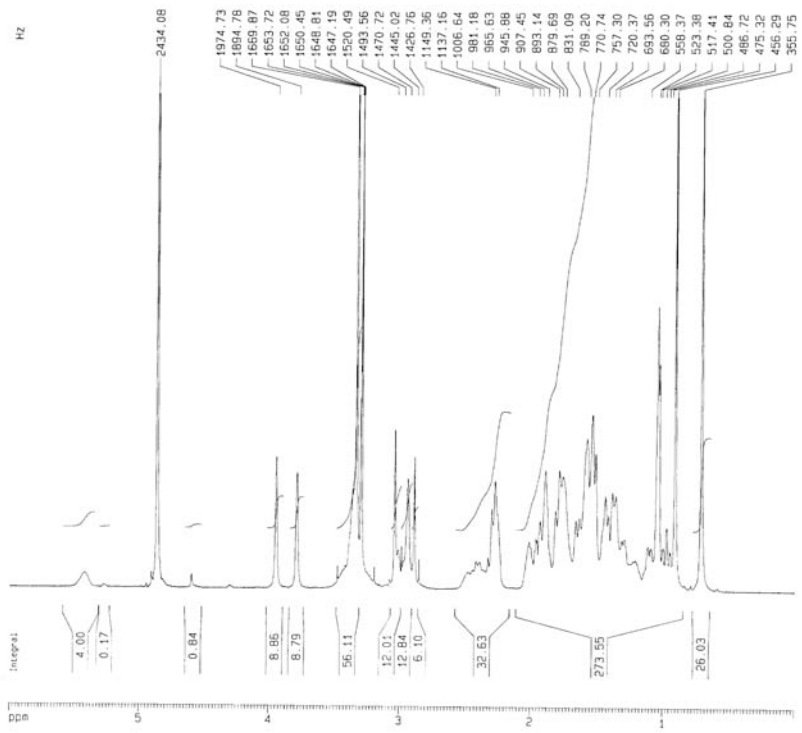

Figure SI 9. ^{1}H NMR (500 MHz, CD_3OD, 296 K) of the hydroxylated precursor of **2**.

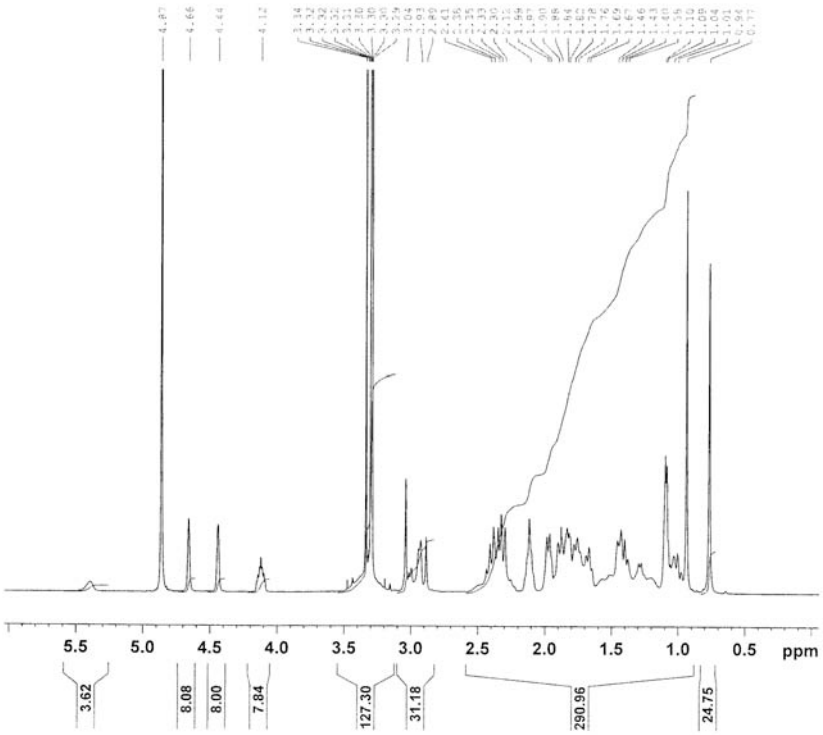

Figure SI 10. ^{1}H NMR (500 MHz, CD_3OD, 296 K) of **2**.

ARTICLES

Carbamate-Linked Lactose: Design of Clusters and Evidence for Selectivity to Block Binding of Human Lectins to (Neo)Glycoproteins with Increasing Degree of Branching and to Tumor Cells

Sabine André,[†] Daniel Specker,[‡,||] Nicolai V. Bovin,[§] Martin Lensch,[†] Herbert Kaltner,[†] Hans-Joachim Gabius,*[,†] and Valentin Wittmann*[,‡]

Institut für Physiologische Chemie, Tierärztliche Fakultät, Ludwig-Maximilians-Universität, Veterinärstraße 13, 80539 München, Germany, Fachbereich Chemie, Universität Konstanz, Universitätsstr. 10, 78457 Konstanz, Germany, and Shemyakin and Ovchinnikov Institute of Bioorganic Chemistry, Russian Academy of Sciences, ul. Miklukho-Maklaya 16/10, 117997 Moscow, Russia. Received October 29, 2008; Revised Manuscript Received June 26, 2009

Various pathogenic processes are driven by protein(lectin)-glycan interactions, especially involving β-galactosides at branch ends of cellular glycans. These emerging insights fuel the interest to design potent inhibitors to block lectins. As a step toward this aim, we prepared a series of ten mono- to tetravalent glycocompounds with lactose as a common headgroup. To obtain activated carbonate for ensuing carbamate formation, conditions for the facile synthesis of pure isomers from anomerically unprotected lactose were identified. To probe for the often encountered intrafamily diversity of human lectins, we selected representative members from the three subgroups of adhesion/growth-regulatory galectins as receptors. Diversity of the glycan display was accounted for by using four (neo)glycoproteins with different degrees of glycan branching as matrices in solid-phase assays. Cases of increased inhibitory potency of lactose clusters compared to free lactose were revealed. Extent of relative inhibition was not directly associated with valency in the glycocompound and depended on the lectin type. Of note for screening protocols, efficacy of blocking appeared to decrease with increased degree of glycan branching in matrix glycoproteins. Binding to tumor cells was impaired with selectivity for galectins-3 and -4. Representative compounds did not impair growth of carcinoma cells up to a concentration of 5 mM of lactose moieties (valence-corrected value) per assay. The reported bioactivity and the delineation of its modulation by structural parameters of lectins and glycans set instructive examples for the further design of selective inhibitors and assay procedures.

INTRODUCTION

A salient route of biological information transfer starts from glycan determinants of cellular glycoconjugates (*1*). These sugar-encoded signals act as ligands for target-specific receptors (lectins) (*1*, *2*). Physiologically, this interaction is involved in disease manifestation, e.g., during chronic inflammation, heart failure, or malignancy. Thus, the design of glycoclusters blocking target recognition of lectins has become an active research area (*2*−*4*). In view of their role as markers for unfavorable prognosis in human tumors (*5*−*7*), we focus here on the family of adhesion/growth-regulatory galectins.

Galectins share the specificity for β-galactosides at branch ends of glycans so that glycoclusters can conveniently be loaded with lactose as a common headgroup (*8*). Of note, the spatial presentation of lectin sites differs within this family (*2*). Thus, it is mandatory to examine at least one member of each subgroup in a comparative study. Hence, the following representatives were chosen: the homodimeric (prototype) galectin-1, the chimera-type galectin-3 with the ability for pentamerization in the presence of suitable ligands, the tandem-repeat-type galectin-4 with its two domains connected by a linker, and galectin-5 with its low degree of oligomer formation. Aside from the panel of lectins, it is equally important to take account of the local density of ligand. As work with different (neo)glycoproteins has revealed (*9*, *10*), lectin affinity and selectivity can be modulated by glycan substitutions and branching.

In detail, four different types of binding partner for the lectins were thus tested: lactosylated bovine serum albumin (LacBSA), a neoglycoprotein with rather random and widely spaced presentation of lactose units, and three glycoproteins with either biantennary (serum amyloid P component: SAP), triantennary (asialofetuin: ASF), or tetra-antennary N-glycans (α_1-acid glycoprotein: AGP). The listed (neo)glycoproteins were adsorbed to microtiter plate wells to serve as lectin binders. With these surfaces, solid-phase assays were carried out to determine inhibition of binding of the lectins to the surfaces by lactose or synthetic lactose clusters. Natural ligands on cell surfaces are known to be present in more complex form than these lactose derivatives (*11*, *12*). Since it is an open question whether the glycoclusters are capable of impairing the binding of lectins to cell surfaces, we performed fluorimetric binding assays with

* Corresponding author. H.-J.G.: e-mail gabius@tiph.vetmed.uni-muenchen.de; fax (+49) 89-2180-2508. V.W.: e-mail mail@valentin-wittmann.de; fax (+49) 7531-88-4573.

[†] Ludwig-Maximilians-Universität.

[‡] Universität Konstanz.

[§] Russian Academy of Sciences.

[||] New address: Polymer Research - Polymer Colloids, BASF SE, 67056 Ludwigshafen, Germany.

10.1021/bc900152w CCC: $40.75 © 2009 American Chemical Society
Published on Web 08/28/2009

human tumor cells. In addition to the galectins, a toxic plant lectin akin to ricin, i.e., the galactoside-specific mistletoe lectin (*Viscum album* agglutinin, VAA) with β-trefoil folding and two fully accessible lectin sites 87 Å apart in the dimer (*13*), was also tested.

The lactose derivatives that were tested for their potency to inhibit the lectin−matrix interaction varied in valency from one to four lactose moieties per inhibitor. However, the valency of the ligands is not the only factor that determines avidity. Case studies on selectins with a lipid anchor (i.e., 2-tetradecylhexadecyl) attached to the glycan, the cholera toxin B pentamer with spacered *p*-nitrophenyl galactopyranoside, and galectins with thiourea-linked ligands on calix[*n*]arenes showed that the spacer portion can notably contribute to the inhibitor's performance (*14*−*16*). Variations in this part can add to selectivity, because the vicinity of the lectin sites is quite divergent in galectins (*12*, *17*). Therefore, we employed two series of lactose clusters differing in the absence or presence of a butene diol linker leading to varied lactose spacing. Lactosyl carbamates were conveniently synthesized by coupling an activated lactosyl carbonate to a set of amines. Therefore, we first had to resolve the problem of finding conditions to produce the glycosyl carbonate from anomerically deprotected lactose as pure isomer.

Our report, combining synthesis of ten mono- to tetravalent lactose derivatives with biochemical/cell biological testing on plant/human lectins, will answer the following questions: (1) Which conditions are suitable to gain fast and easy access to pure isomers of activated lactosyl carbonates? (2) Will the inhibitory potency of conjugated lactose relative to free lactose be enhanced? (3) How will the structure and valency of the lactose clusters and the degree of glycan branching in the (neo)glycoprotein matrix influence inhibition in solid-phase assays? (4) Will lectin binding to cells be inhibited by the lactose derivatives? (5) Will potent lactose derivatives lack cytotoxicity?

EXPERIMENTAL PROCEDURES

General Methods. Analytical thin layer chromatography was performed using silica gel 60 F_{254} aluminum sheets from Merck (Darmstadt, Germany); compound spots were visualized by quenching of fluorescence and/or by charring after treatment with cerium molybdophosphate. Preparative flash column chromatography (FC) was carried out on Merck silica gel 60 (40−63 μm). ^{1}H NMR and ^{13}C NMR spectra were recorded on a Bruker Avance DRX 600 instrument at a temperature of 300 K. ^{1}H Chemical shifts are referenced to residual protic solvent ($CDCl_3$, $\delta_H = 7.26$; D_2O, $\delta_H = 4.63$). ^{13}C Chemical shifts are referenced to the solvent signal ($CDCl_3$, $\delta_C = 77.0$) or in the case of D_2O to internal standard CD_3CN ($\delta_C = 1.32$ ppm). Assignments of proton and carbon signals were carried out by the aid of DQF-COSY, HMQC, and ROESY experiments. MALDI mass spectra were obtained on a Bruker Biflex III instrument with α-cyano-4-hydroxycinnamic acid as the matrix (positive mode). Elemental analyses were performed by the microanalytical facility at the Universität Konstanz.

4-Nitrophenyl-[2,3,4,6-tetra-*O*-acetyl-β-D-galactopyranosyl-(1→4)-2,3,6-tri-*O*-acetyl-α-D-glucopyranosyl] Carbonate (*18*) (α-3). Lactose derivative **1** (*19*) (100 mg, 0.16 mmol) was dissolved in CH_3CN (3.5 mL). A solution of *p*-nitrophenyl chloroformate **2** (48 mg, 0.24 mmol) in CH_3CN (0.5 mL) and 4-(dimethylamino)-pyridine (29 mg, 0.24 mmol) was added and the mixture was stirred for 30 min. The solvent was evaporated, and the remainder was dissolved in ethyl acetate and washed with water, 1 M HCl, and brine. The organic layer was dried (Na_2SO_4), concentrated, and purified by FC (petroleum ether/ethyl acetate 1:1→1:2) to yield α-**3** (122 mg, 95%) as a white solid: $R_f = 0.45$ (petroleum ether/ethyl acetate 1:2). ^{1}H NMR (600 MHz, $CDCl_3$): δ = 8.30−8.28 (m, 2 H, Ar), 7.43−7.42 (m, 2 H, Ar), 6.20 (d, J = 3.6 Hz, 1 H, H-1^{Glc}), 5.54 (dd, J = 10.1 Hz, J = 9.5 Hz, 1 H, H-3^{Glc}), 5.35 (dd, J = 3.3 Hz, J = 0.7 Hz, 1 H, H-4^{Gal}), 5.12 (dd, J = 10.4 Hz, J = 7.9 Hz, 1 H, H-2^{Gal}), 5.07 (dd, J = 10.3 Hz, J = 3.6 Hz, 1 H, H-2^{Glc}), 4.96 (dd, J = 10.4 Hz, J = 3.5 Hz, 1 H, H-3^{Gal}), 4.53−4.51 (m, 2 H, H-6^{Glc}, H-1^{Gal}), 4.17−4.06 (m, 4 H, H-5^{Glc}, H-6′^{Glc}, H-6^{Gal}, H-6′^{Gal}), 3.91−3.87 (m, 2 H, H-4^{Glc}, H-5^{Gal}), 2.15 (s, 3 H, C(O)CH_3), 2.13 (s, 3 H, C(O)CH_3), 2.07 (s, 3 H, C(O)CH_3), 2.05 (s, 3 H, C(O)CH_3), 2.04 (s, 3 H, C(O)CH_3), 2.04 (s, 3 H, C(O)CH_3), 1.95 (s, 3 H, C(O)CH_3). ^{13}C NMR (150 MHz, $CDCl_3$): δ = 170.2, 170.1, 170.0, 170.0, 169.7, 169.4, 168.9 (*C*(O)CH_3), 154.9 (OC(O)O), 150.7, 145.6, 125.4, 121.4 (Ar), 101.0 (C-1^{Gal}), 94.0 (C-1^{Glc}), 75.2 (C-4^{Glc}), 71.3 (C-5^{Glc}), 70.9 (C-3^{Gal}), 70.7 (C-5^{Gal}), 79.3 (C-2^{Glc}), 69.1 (C-3^{Glc}), 69.0 (C-2^{Gal}), 66.5 (C-4^{Gal}), 61.1 (C-6^{Glc}), 60.7 (C-6^{Gal}), 20.7−20.4 (C(O)*C*H). MALDI-MS: calcd *m*/*z* 824.2 [M + Na^+], 840.2 [M + K^+], found 824.0, 839.9. Anal. calcd for $C_{33}H_{39}NO_{22}$: C 49.44, H 4.90, N 1.75, found: C 49.24, H 4.98, N 1.76.

4-Nitrophenyl-[2,3,4,6-tetra-*O*-acetyl-β-D-galactopyranosyl-(1→4)-2,3,6-tri-*O*-acetyl-β-D-glucopyranosyl] Carbonate (*18*) (β-3). Lactose derivative **1** (*19*) (8.6 g, 13.5 mmol) was dissolved in CH_3CN (430 mL) and cooled to 0 °C. A solution of *p*-nitrophenyl chloroformate **2** (2.89 g, 14.3 mmol) in CH_3CN (20 mL) and 2,6-lutidine (1.66 mL, 14.3 mmol) was added, and the mixture was stirred overnight. The solvent was evaporated, and the remainder was dissolved in ethyl acetate and washed with water, 1 M HCl, and brine. The organic layer was dried (Na_2SO_4), concentrated, and crystallized from ethyl acetate/petroleum ether to yield β-**3** (5.40 g, 50%) as a white solid: R_f = 0.47 (petroleum ether/ethyl acetate 1:2). ^{1}H NMR (600 MHz, $CDCl_3$): δ = 8.30−8.28 (m, 2 H, Ar), 7.42−7.40 (m, 2 H, Ar), 5.63 (d, J = 7.8 Hz, 1 H, H-1^{Glc}), 5.35 (dd, J = 3.4 Hz, J = 0.8 Hz, 1 H, H-4^{Gal}), 5.26 (t, J = 9.0 Hz, 1 H, H-3^{Glc}), 5.15−5.10 (m, 2 H, H-2^{Glc}, H-2^{Gal}), 4.96 (dd, J = 10.4 Hz, J = 3.2 Hz, 1 H, H-3^{Gal}), 4.53−4.49 (m, 2 H, H-6^{Glc}, H-1^{Gal}), 4.16−4.06 (m, 3 H, H-6′^{Glc}, H-6^{Gal}, H-6′^{Gal}), 3.94−3.88 (m, 2 H, H-4^{Glc}, H-5^{Gal}), 3.83−3.81 (m, 1 H, H-5^{Glc}), 2.16 (s, 3 H, C(O)CH_3), 2.13 (s, 3 H, C(O)CH_3), 2.09 (s, 3 H, C(O)CH_3), 2.07 (s, 3 H, C(O)CH_3), 2.05 (s, 3 H, C(O)CH_3), 2.04 (s, 3 H, C(O)CH_3), 1.97 (s, 3 H, C(O)CH_3). ^{13}C NMR (150 MHz, $CDCl_3$): δ = 170.4, 170.2, 170.1, 169.6, 169.4, 169.0 (*C*(O)CH_3), 154.7 (OC(O)O), 150.7, 145.7, 125.4, 121.6 (Ar), 101.0 (C-1^{Gal}), 95.7 (C-1^{Glc}), 75.3 (C-4^{Glc}), 73.7 (C-5^{Glc}), 72.6 (C-3^{Glc}), 71.0 (C-3^{Gal}), 70.7 (C-5^{Gal}), 70.2 (C-2^{Glc}), 69.0 (C-2^{Gal}), 66.5 (C-4^{Gal}), 61.4 (C-6^{Glc}), 60.8 (C-6^{Gal}), 20.8−20.5 (C(O)*C*H$_3$). MALDI-MS: calcd *m*/*z* 824.2 [M + Na^+], 840.2 [M + K^+], found 824.1, 840.0. Anal. calcd for $C_{33}H_{39}NO_{22}$: C 49.44, H 4.90, N 1.75, found: C 48.98, H 5.22, N 1.82.

4-Hydroxy-(*Z*)-but-2-enyl 2,3,4,6-tetra-*O*-acetyl-β-D-galactopyranosyl-(1→4)-2,3,6-tri-*O*-acetyl-β-D-glucopyranoside (6). Under argon Ag_2CO_3 (2.7 g, 9.7 mmol), $CaSO_4 \cdot 0.5\ H_2O$ (6.5 g, 45 mmol), an iodine crystal, and (*Z*)-but-2-ene-1,4-diol **5** (26 mL, 322 mmol) were stirred for 15 min at room temperature. Acetobromolactose **4** (*20*, *21*) (3 g, 4.3 mmol) was added and the mixture was stirred for further 24 h. After addition of CH_2Cl_2 (100 mL), the mixture was filtered through Celite. To the biphasic filtrate water (100 mL) was added, and the aqueous phase was separated and extracted with CH_2Cl_2 (50 mL). The combined organic layers were washed with water (3 × 100 mL) and brine and dried over Na_2SO_4. The solvent was evaporated and the remainder purified by FC (petroleum ether/ethyl acetate 1:2) to give **6** (1.85 g, 61%): $R_f = 0.25$ (petroleum ether/ethyl acetate 1:2). ^{1}H NMR (600 MHz, $CDCl_3$): δ = 5.85−5.81 (m, 1 H, H^{vinyl}), 5.63−5.59 (m, 1 H, H^{vinyl}), 5.34 (d, J = 3.0 Hz, 1 H, H-4^{Gal}), 5.19 (d, J = 9.3 Hz, 1 H, H-3^{Glc}), 5.10 (dd, J = 10.4 Hz, J = 7.9 Hz, 1 H, H-2^{Gal}), 4.95 (dd, J = 10.4 Hz, J = 3.5 Hz, 1 H, H-3^{Gal}), 4.90 (dd, J = 9.4 Hz, J = 8.0 Hz, 1 H,

H-2^{Glc}), 4.53−4.50 (m, 2 H, H-1^{Glc}, H-6^{Glc}), 4.49 (d, J = 7.9 Hz, 1 H, H-1^{Gal}), 4.28 (ddd, J = 19.9 Hz, J = 12.6 Hz, J = 6.7 Hz, 2 H, H^{allyl}), 4.18 (bd, J = 6.2 Hz, 2 H, H^{allyl}), 4.14−4.06 (m, 3 H, H-6′^{Glc}, H-6^{Gal}, H-6′^{Gal}), 3.87 (bt, J = 6.7 Hz, 1 H, H-5^{Gal}), 3.79 (t, J = 9.5 Hz, 1 H, H-4^{Glc}), 3.61 (ddd, J = 9.8 Hz, J = 5.0 Hz, J = 2.0 Hz, 2 H, H-5^{Glc}), 2.14 (s, 3 H, C(O)CH$_3$), 2.13 (s, 3 H, C(O)CH$_3$), 2.05 (s, 3 H, C(O)CH$_3$), 2.04 (s, 9 H, C(O)CH$_3$), 1.96 (s, 3 H, C(O)CH$_3$). ^{13}C NMR (150 MHz, CDCl$_3$): δ = 170.4, 170.3, 170.1, 170.0, 169.7, 169.7, 169.0 (*C*(O)CH$_3$), 133.3, 126.8 (CH^{olefin}), 125.3, 121.7 (Ar), 101.0 (C-1^{Gal}), 99.1 (C-1^{Glc}), 76.2 (C-4^{Glc}), 72.8 (C-3^{Glc}), 72.7 (C-5^{Glc}), 71.6 (C-2^{Glc}), 71.0 (C-3^{Gal}), 70.7 (C-5^{Gal}), 69.1 (C-2^{Gal}), 66.6 (C-4^{Gal}), 64.3 (CH$_2^{allyl}$), 61.9 (C-6^{Glc}), 60.8 (C-6^{Gal}), 58.5 (CH$_2^{allyl}$), 20.8−20.5 (C(O)*C*H$_3$).

4-(*p*-Nitrophenoxycarbonyloxy)-(*Z*)-but-2-enyl 2,3,4,6-tetra-*O*-acetyl-β-D-galactopyranosyl-(1→4)-2,3,6-tri-*O*-acetyl-β-D-glucopyranoside (7). Compound **6** (1.72 g, 2.43 mmol) was dissolved in CH$_3$CN (80 mL). A solution of *p*-nitrophenyl chloroformate **2** (0.59 g, 2.92 mmol) in CH$_3$CN (5 mL) and pyridine (0.24 mL, 2.92 mmol) were added, and the mixture was stirred for 1 h. The solvent was evaporated and the remainder was dissolved in ethyl acetate and washed with water, 1 M HCl, and brine. The organic layer was dried (Na$_2$SO$_4$), concentrated, and purified by FC (petroleum ether/ethyl acetate 1:1→1:2) to yield **7** (1.84 g, 87%) as a white solid: R_f = 0.50 (petroleum ether/ethyl acetate 1:2). ^{1}H NMR (600 MHz, CDCl$_3$): δ = 8.29−8.28 (m, 2 H, Ar), 7.39−7.37 (m, 2 H, Ar), 5.83−5.78 (m, 2 H, H^{vinyl}), 5.34 (d, J = 3.0 Hz, 1 H, H-4^{Gal}), 5.19 (d, J = 9.3 Hz, 1 H, H-3^{Glc}), 5.09 (dd, J = 10.4 Hz, J = 7.9 Hz, 1 H, H-2^{Gal}), 4.95 (dd, J = 10.4 Hz, J = 3.4 Hz, 1 H, H-3^{Gal}), 4.90 (dd, J = 9.4 Hz, J = 8.0 Hz, 1 H, H-2^{Glc}), 4.87−4.79 (m, 2 H, H^{allyl}), 4.52 (d, J = 7.8 Hz, 1 H, H-1^{Glc}), 4.51 (dd, J = 11.8 Hz, J = 2.1 Hz, 1 H, H-6^{Glc}), 4.48 (d, J = 7.9 Hz, 1 H, H-1^{Gal}), 4.34 (ddd, J = 18.6 Hz, J = 13.3 Hz, J = 4.2 Hz, 2 H, H^{allyl}), 4.14−4.05 (m, 3 H, H-6′^{Glc}, H-6^{Gal}, H-6′^{Gal}), 3.86 (bt, J = 6.9 Hz, 1 H, H-5^{Gal}), 3.80 (t, J = 9.4 Hz, 1 H, H-4^{Glc}), 3.60 (ddd, J = 9.8 Hz, J = 4.7 Hz, J = 2.0 Hz, 1 H, H-5^{Glc}), 2.14 (s, 3 H, C(O)CH$_3$), 2.11 (s, 3 H, C(O)CH$_3$), 2.05 (s, 3 H, C(O)CH$_3$), 2.04 (s, 3 H, C(O)CH$_3$), 2.03 (s, 3 H, C(O)CH$_3$), 2.01 (s, 3 H, C(O)CH$_3$), 1.96 (s, 3 H, C(O)CH$_3$). ^{13}C NMR (150 MHz, CDCl$_3$): δ = 170.3, 170.3, 170.1, 170.0, 169.7, 169.6, 169.0 (*C*(O)CH$_3$), 155.4 (OC(O)O), 152.3, 145.5 (Ar), 130.8, 126.0 (Olefin CH), 125.3, 121.7 (Ar), 101.1 (C-1^{Gal}), 99.2 (C-1^{Glc}), 76.2 (C-4^{Glc}), 72.9 (C-3^{Glc}), 72.7 (C-5^{Glc}), 71.5 (C-2^{Glc}), 70.9 (C-3^{Gal}), 70.7 (C-5^{Gal}), 69.1 (C-2^{Gal}), 66.5 (C-4^{Gal}), 64.5, 64.4 (CH$_2^{allyl}$), 61.8 (C-6^{Glc}), 60.7 (C-6^{Gal}), 20.8−20.5 (C(O)*C*H$_3$). MALDI-MS: calcd *m*/*z* 894.2 [M + Na$^+$], 910.2 [M + K$^+$], found 894.0, 910.0. Anal. calcd for C$_{37}$H$_{45}$NO$_{23}$: C 50.98, H 5.20, N 1.61, found: C 50.80, H 5.23, N 1.61.

General Procedure 1 (GP 1) for Coupling of *p*-Nitrophenyl Carbonates to Primary Amines. The amine and *i*-Pr$_2$NEt (1 equiv per amino group) were added to a solution of activated carbonate β-**3** or **7** (1.1−1.3 equiv per amino group) in dry CH$_2$Cl$_2$ (3−10 mL per mmol of activated carbonate). After complete reaction (usually after few minutes), the solvent was removed under reduced pressure and the product was purified by FC.

General Procedure 2 (GP 2) for Deacetylation with NaOMe/MeOH. The acetylated compound was dissolved in MeOH (10−30 mL per mmol) and a 0.5 M solution of NaOMe in MeOH (0.05−0.25 mL per mL of reaction mixture) was added. After complete reaction, any precipitate formed was dissolved by addition of water or MeOH. The solution was neutralized by addition of acidic ion-exchange resin (Dowex 50W-X8 or Amberlite IRC-86, H$^+$ form) and filtered. The filtrate was concentrated and lyophilized.

General Procedure 3 (GP 3) for Deacetylation with EtNMe$_2$/MeOH. The acetylated compound was stirred with a 1:5 mixture of EtNMe$_2$/MeOH (10−30 mL per mmol). After complete reaction, the mixture was concentrated and the remaining product was then dried under vacuum and lyophilized.

(2,3,4,6-Tetra-*O*-acetyl-β-D-galactopyranosyl-(1→4)-2,3,6-tri-*O*-acetyl-β-D-glucopyranosyloxycarbonyl)benzylamine (Ac-A). According to GP 1, β-**3** (115 mg, 0.15 mmol) and benzylamine **8** (14 mg, 0.13 mol) were reacted in CH$_2$Cl$_2$ (3 mL). Purification by FC (petroleum ether/ethyl acetate 1:1) gave Ac-**A** (100 mg, 99%) as a white foam: R_f = 0.45 (petroleum ether/ethyl acetate 1:2). ^{1}H NMR (600 MHz, CDCl$_3$): δ = 7.35−7.27 (m, 5 H, Ar), 5.67 (d, J = 8.3 Hz, 1 H, H-1^{Glc}), 5.35 (d, J = 2.3 Hz, 1 H, H-4^{Gal}), 5.25 (t, J = 9.0 Hz, 1 H, H-3^{Glc}), 5.17−5.10 (m, 2 H, H-2^{Gal}, NHC(O)), 5.02 (t, J = 8.7 Hz, 1 H, H-2^{Glc}), 4.95 (dd, J = 10.4 Hz, J = 3.4 Hz, 1 H, H-3^{Gal}), 4.48−4.45 (m, 2 H, H-6^{Glc}, H-1^{Gal}), 4.38−4.36 (m, 2 H, CH$_2^{Bn}$), 4.17−4.07 (m, 3 H, H-6′^{Glc}, H-6^{Gal}, H-6′^{Gal}), 3.88−3.83 (m, 2 H, H-4^{Glc}, H-5^{Gal}), 3.78−3.76 (m, 1 H, H-5^{Glc}), 2.16 (s, 3 H, C(O)CH$_3$), 2.12 (s, 3 H, C(O)CH$_3$), 2.07 (s, 3 H, C(O)CH$_3$), 2.05 (s, 6 H, C(O)CH$_3$), 2.02 (s, 3 H, C(O)CH$_3$), 1.97 (s, 3 H, C(O)CH$_3$), 1.97 (s, 3 H, C(O)CH$_3$). ^{13}C NMR (150 MHz, CDCl$_3$): δ = 170.3, 170.2, 170.1, 169.7, 169.5, 169.0 (*C*(O)CH$_3$), 153.7 (OC(O)N), 137.4, 128.8, 127.8, 127.6 (Ar), 101.0 (C-1^{Gal}), 92.8 (C-1^{Glc}), 75.8 (C-4^{Glc}), 73.3 (C-5^{Glc}), 72.6 (C-3^{Glc}), 71.0 (C-3^{Gal}), 70.7 (C-5^{Gal}), 70.6 (C-2^{Glc}), 69.0 (C-2^{Gal}), 66.6 (C-4^{Gal}), 61.8 (C-6^{Glc}), 60.8 (C-6^{Gal}), 45.2 (CH$_2^{Bn}$), 20.9−20.5 (C(O)*C*H$_3$). MALDI-MS: calcd *m*/*z* 792.2 [M + Na$^+$], 808.2 [M + K$^+$], found 792.4, 808.4. Anal. calcd for C$_{34}$H$_{43}$NO$_{19}$: C 53.05, H 5.63, N 1.82, found: C 53.03, H 5.66, N 1.83.

(β-D-Galactopyranosyl-(1→4)-β-D-glucopyranosyloxycarbonyl)benzylamine (A). According to GP 2, Ac-**A** (100 mg, 0.13 mmol) was deacetylated with 0.5 M NaOMe solution (0.25 mL) in MeOH (3 mL) to give **A** (61 mg, 99%) as a white solid. ^{1}H NMR (600 MHz, D$_2$O): δ = 7.33−7.25 (m, 5 H, Ar), 5.36 (d, J = 8.2 Hz, 1 H, H-1^{Glc}), 4.35 (d, J = 7.9 Hz, 1 H, H-1^{Gal}), 4.26 (m, 2 H, CH$_2^{Bn}$), 3.86−3.82 (m, 2 H, H-4^{Gal}, H-6^{Glc}), 3.73−3.56 (m, 8 H, H-3^{Glc}, H-3^{Gal}, H-4^{Glc}, H-5^{Glc}, H-5^{Gal}, H-6′^{Glc}, H-6^{Gal}, H-6′^{Gal}), 3.47−3.40 (m, 2 H, H-2^{Glc}, H-2^{Gal}). ^{13}C NMR (150 MHz, D$_2$O): δ = 156.6 (OC(O)N), 138.2, 128.8, 127.5, 127.1 (Ar), 102.9 (C-1^{Gal}), 94.8 (C-1^{Glc}), 77.8, 75.4, 75.3, 74.1, 72.5 (C-3^{Glc}, C-3^{Gal}, C-4^{Glc}, C-5^{Glc}, C-5^{Gal}), 71.7 (C-2^{Glc}), 70.9 (C-2^{Gal}), 68.6 (C-4^{Gal}), 61.0 (C-6^{Glc}), 59.8 (C-6^{Gal}), 44.2 (CH$_2^{Bn}$). MALDI-MS: calcd *m*/*z* 498.2 [M + Na$^+$], 514.2 [M + K$^+$], found 498.1, 514.1.

***N*,*N*′-Bis-(2,3,4,6-tetra-*O*-acetyl-β-D-galactopyranosyl-(1→4)-2,3,6-tri-*O*-acetyl-β-D-glucopyranosyloxycarbonyl)-*m*-xylylenediamine (Ac-B).** According to GP 1, β-**3** (123 mg, 0.15 mmol) and α,α′-diamino-*m*-xylene **9** (9.5 mg, 0.07 mmol) were reacted in CH$_2$Cl$_2$ (3 mL). Purification by FC (petroleum ether/ethyl acetate 1:2) gave Ac-**B** (102 mg, 99%) as a white foam: R_f = 0.18 (petroleum ether/ethyl acetate 1:2). ^{1}H NMR (600 MHz, CDCl$_3$): δ = 7.27−7.25 (m, 1 H, Ar), 7.15−7.11 (m, 3 H, Ar), 5.62 (m, 4 H, H-1^{Glc}, NHC(O)), 5.33 (bs, 2 H, H-4^{Gal}), 5.23 (t, J = 9.1 Hz, 2 H, H-3^{Glc}), 5.09 (t, J = 9.4 Hz, 2 H, H-2^{Gal}), 5.00 (t, J = 8.7 Hz, 2 H, H-2^{Glc}), 4.94 (bd, J = 10.2 Hz, 2 H, H-3^{Gal}), 4.49−4.38 (m, 6 H, H-6^{Glc}, H-1^{Gal}, CH$_2^{Bn}$), 4.26 (dd, J = 14.9 Hz, J = 4.5 Hz, 2 H, CH$_2^{Bn}$), 4.18−4.03 (m, 6 H, H-6′^{Glc}, H-6^{Gal}, H-6′^{Gal}), 3.88−3.86 (m, 4 H, H-4^{Glc}, H-5^{Gal}), 3.73−3.72 (m, 2 H, H-5^{Glc}), 2.14 (s, 6 H, C(O)CH$_3$), 2.04 (s, 6 H, C(O)CH$_3$), 2.03 (s, 18 H, C(O)CH$_3$), 2.00 (s, 6 H, C(O)CH$_3$), 1.95 (s, 6 H, C(O)CH$_3$). ^{13}C NMR (150 MHz, CDCl$_3$): δ = 170.4, 170.3, 170.1, 170.0, 169.8, 169.5, 169.0, (*C*(O)CH$_3$), 153.9 (OC(O)N), 138.4, 129.0, 126.7, 125.7 (Ar), 100.9 (C-1^{Gal}), 92.8 (C-1^{Glc}), 75.7 (C-4^{Glc}), 73.4 (C-5^{Glc}), 72.7 (C-3^{Glc}), 71.0 (C-3^{Gal}), 70.6 (C-5^{Gal}), 70.6 (C-2^{Glc}), 69.0 (C-2^{Gal}), 66.5 (C-4^{Gal}), 61.6 (C-6^{Glc}),

60.6 (C-6^{Gal}), 44.8 (CH_2^{Bn}), 20.7−20.5 (C(O)CH_3). MALDI-MS: calcd *m/z* 1483.4 [M + Na^+], 1499.4 [M + K^+], found 1483.4, 1499.7. Anal. calcd for $C_{62}H_{80}N_2O_{38}$: C 50.96, H 5.52, N 1.92, found: C 50.80, H 5.70, N 1.88.

***N,N′*-Bis-(*β*-D-galactopyranosyl-(1→4)-*β*-D-glucopyranosyloxycarbonyl)-*m*-xylylenediamine (B).** According to GP 2, Ac-**B** (102 mg, 0.07 mmol) was deacetylated with 0.5 M NaOMe solution (0.5 mL) in MeOH (2 mL) to give **B** (61 mg, quant) as a white solid. ^{1}H NMR (600 MHz, D_2O): δ = 7.30−7.28 (m, 1 H, Ar), 7.18−7.16 (m, 3 H, Ar), 5.35 (d, *J* = 8.2 Hz, 2 H, H-1^{Glc}), 4.36 (d, *J* = 7.7 Hz, 2 H, H-1^{Gal}), 4.25 (bs, 4 H, CH_2^{Bn}), 3.85−3.82 (m, 4 H, H-4^{Gal}, H-6^{Glc}), 3.72−3.60 (m, 14 H, H-3^{Glc}, H-4^{Glc}, H-5^{Glc}, H-5^{Gal}, H-6′^{Glc}, H-6^{Gal}, H-6′^{Gal}), 3.57−3.55 (m, 2 H, H-3^{Gal}), 3.46−3.40 (m, 4 H, H-2^{Glc}, H-2^{Gal}). ^{13}C NMR (150 MHz, D_2O): δ = 156.6 (OC(O)N), 138.6, 129.1, 126.1, 126.0 (Ar), 102.9 (C-1^{Gal}), 94.9 (C-1^{Glc}), 77.8, 75.4, 75.4, 74.1, 72.5 (C-3^{Glc}, C-3^{Gal}, C-4^{Glc}, C-5^{Glc}, C-5^{Gal}), 71.7 (C-2^{Glc}), 71.0 (C-2^{Gal}), 68.6 (C-4^{Gal}), 61.1 (C-6^{Gal}), 59.8 (C-6^{Glc}), 44.0 (CH_2^{Bn}). MALDI-MS: calcd *m/z* 895.3 [M + Na^+], 911.3 [M + K^+], found 895.2, 911.1.

1,4-Bis-(3-(2,3,4,6-tetra-*O*-acetyl-*β*-D-galactopyranosyl-(1→4)-2,3,6-tri-*O*-acetyl-*β*-D-glucopyranosyloxycarbonylaminopropyloxy)butane (Ac-C). According to GP 1, *β*-**3** (148 mg (0.188 mmol) and 1,4-bis-(3-aminopropoxy)butane **11** (16 *μ*L, 0.075 mmol) were reacted in CH_2Cl_2 (4 mL). Purification by FC (petroleum ether/ethyl acetate 1:3, then ethyl acetate) gave Ac-**C** (114 mg, 99%) as a white solid: R_f = 0.38 (ethyl acetate). ^{1}H NMR (600 MHz, $CDCl_3$): δ = 5.62 (d, *J* = 8.1 Hz, 2 H, H-1^{Glc}), 5.36−5.34 (m, 4 H, H-4^{Gal}, NHC(O)), 5.25 (t, *J* = 9.2 Hz, 2 H, H-3^{Glc}), 5.09 (t, *J* = 8.1 Hz, 2 H, H-2^{Gal}), 5.00 (t, 2 H, *J* = 8.8 Hz,, H-2^{Glc}), 4.94 (dd, 2 H, *J* = 10.1 Hz, *J* = 2.5 Hz, H-3^{Gal}), 4.48−4.43 (m, 4 H, H-1^{Gal}, H-6^{Glc}), 4.15−4.05 (m, 6 H, H-6′^{Glc}, H-6^{Gal}, H-6′^{Gal}), 3.87−3.83 (m, 4 H, H-4^{Glc}, H-5^{Gal}), 3.75 (m, 2 H, H-5^{Glc}), 3.47 (bs, 4 H, OCH_2CH$_2$), 3.41 (bs, 4 H, CH$_2$CH_2O), 3.28 (bs, 4 H, CH$_2$CH_2NH), 2.15 (s, 6 H, C(O)CH_3), 2.11 (s, 6 H, C(O)CH_3), 2.06 (s, 6 H, C(O)CH_3), 2.04 (s, 12 H, C(O)CH_3), 2.02 (s, 6 H, C(O)CH_3), 1.96 (s, 6 H, C(O)CH_3), 1.76 (bs, 4 H, CH$_2$CH_2CH$_2$), 1.59 (bs, 4 H, CH_2CH$_2$O). ^{13}C NMR (150 MHz, $CDCl_3$): δ = 170.3, 170.1, 170.0, 169.7, 169.6, 169.0 (*C*(O)CH_3), 153.6 (OC(O)N), 100.9 (C-1^{Gal}), 92.6 (C-1^{Glc}), 75.7 (C-4^{Glc}), 73.2 (C-5^{Glc}), 72.8 (C-3^{Glc}), 71.0 (C-3^{Gal}), 70.8 (CH$_2$*C*H$_2$O), 70.7 (C-5^{Gal}), 70.6 (C-2^{Glc}), 69.0 (C-2^{Gal}), 68.9 (O*C*H$_2$CH$_2$), 66.6 (C-4^{Gal}), 61.8 (C-6^{Glc}), 60.8 (C-6^{Gal}), 39.4 (CH$_2$*C*H$_2$NH), 29.3 (CH$_2$*C*H$_2$CH$_2$), 26.3 (*C*H$_2$CH$_2$O), 20.9−20.5 (C(O)*C*H$_3$). MALDI-MS: calcd *m/z* 1551.5 [M + Na^+], 1567.5 [M + K^+], found 1551.2, 1567.1. Anal. calcd for $C_{64}H_{92}N_2O_{40}$: C 50.26, H 6.06, N 1.83, found: C 49.88, H 6.05, N 1.90.

1,4-Bis-(3-(*β*-D-galactopyranosyl-(1→4)-*β*-D-glucopyranosyloxycarbonylaminopropyloxy)butane (C). According to GP 2, Ac-**C** (93 mg, 0.061 mmol) was deacetylated with 0.5 M NaOMe solution (0.1 mL) in MeOH (2 mL) to give **C** (58 mg, quant) as a white solid. ^{1}H NMR (600 MHz, D_2O): δ = 5.31 (d, *J* = 8.2 Hz, 2 H, H-1^{Glc}), 4.35 (d, *J* = 7.8 Hz, 2 H, H-1^{Gal}), 3.85−3.81 (m, 4 H, H-4^{Gal}, H-6^{Glc}), 3.74−3.60 (m, 14 H, H-3^{Glc}, H-4^{Glc}, H-5^{Glc}, H-5^{Gal}, H-6′^{Glc}, H-6^{Gal}, H-6′^{Gal}), 3.55 (dd, *J* = 10.0 Hz, *J* = 3.3 Hz, 2 H, H-3^{Gal}), 3.46−3.38 (m, 12 H, H-2^{Glc}, H-2^{Gal}, OCH_2CH$_2$), 3.16−3.10 (m, 4 H, CH$_2$CH_2NH), 1.71−1.66 (m, 4 H, CH$_2$CH_2CH$_2$), 1.51 (bs, 4 H, OCH$_2$CH_2). ^{13}C NMR (150 MHz, D_2O): δ = 156.4 (OC(O)N), 102.9 (C-1^{Gal}), 94.7 (C-1^{Glc}), 77.8, 75.4, 75.3 (C-4^{Glc}, C-5^{Glc}, C-5^{Gal}), 74.1 (C-3^{Glc}), 72.5 (C-3^{Gal}), 71.7 (C-2^{Glc}), 71.0 (C-2^{Gal}), 70.4 (O*C*H$_2$CH$_2$), 68.6 (C-4^{Gal}), 67.7 (O*C*H$_2$CH$_2$), 61.1 (C-6^{Gal}), 59.8 (C-6^{Glc}), 37.6 (CH$_2$*C*H$_2$NH), 28.6 (CH$_2$*C*H$_2$CH$_2$), 25.3 (OCH$_2$C*H*$_2$). MALDI-MS: calcd *m/z* 963.4 [M + Na^+], 979.3 [M + K^+], found 963.4, 979.1.

***N,N′*-Bis-(2,3,4,6-tetra-*O*-acetyl-*β*-D-galactopyranosyl-(1→4)-2,3,6-tri-*O*-acetyl-*β*-D-glucopyranosyloxycarbonyl)-4,7,10-trioxa-1,13-tridecanediamine (Ac-D).** According to GP 1, *β*-**3** (150 mg (0.190 mmol) and 4,7,10-trioxa-1,13-tridecanediamine **12** (17 *μ*L, 0.078 mmol) were reacted in CH_2Cl_2 (4 mL). Purification by FC (ethyl acetate) gave Ac-**D** (106 mg, 89%) as a white solid. R_f = 0.36 (ethyl acetate). ^{1}H NMR (600 MHz, $CDCl_3$): δ = 5.62 (d, *J* = 8.2 Hz, 2 H, H-1^{Glc}), 5.54 (t, *J* = 5.3 Hz, 2 H, NHC(O)), 5.35 (bs, 2 H, H-4^{Gal}), 5.24 (t, *J* = 9.4 Hz, 2 H, H-3^{Glc}), 5.10 (t, *J* = 8.2 Hz, 2 H, H-2^{Gal}), 5.00 (t, 2 H, *J* = 8.8 Hz, H-2^{Glc}), 4.94 (dd, 2 H, *J* = 10.0 Hz, *J* = 2.9 Hz, H-3^{Gal}), 4.48−4.44 (m, 4 H, H-1^{Gal}, H-6^{Glc}), 4.15−4.07 (m, 6 H, H-6′^{Glc}, H-6^{Gal}, H-6′^{Gal}), 3.88−3.84 (m, 4 H, H-4^{Glc}, H-5^{Gal}), 3.76−3.75 (m, 2 H, H-5^{Glc}), 3.61 (bs, 4 H, OCH_2CH$_2$O), 3.58 (bs, 4 H, OCH$_2$CH_2O), 3.54 (bs, 4 H, OCH_2CH$_2$), 3.29 (bs, 4 H, CH$_2$CH_2NH), 2.15 (s, 6 H, C(O)CH_3), 2.11 (s, 6 H, C(O)CH_3), 2.06 (s, 6 H, C(O)CH_3), 2.04 (s, 12 H, C(O)CH_3), 2.03 (s, 6 H, C(O)CH_3), 1.96 (s, 6 H, C(O)CH_3), 1.79 (bs, 4 H, CH$_2$CH_2CH$_2$). ^{13}C NMR (150 MHz, $CDCl_3$): δ = 170.3, 170.1, 170.1, 169.7, 169.6, 169.0 (*C*(O)CH_3), 153.7 (OC(O)N), 100.9 (C-1^{Gal}), 92.5 (C-1^{Glc}), 75.7 (C-4^{Glc}), 73.2 (C-5^{Glc}), 72.8 (C-3^{Glc}), 71.0 (C-3^{Gal}), 70.7 (C-5^{Gal}), 70.6 (C-2^{Glc}), 70.5 (O*C*H$_2$CH$_2$O), 70.2 (OCH$_2$*C*H$_2$O), 69.4 (O*C*H$_2$CH$_2$), 69.0 (C-2^{Gal}), 66.6 (C-4^{Gal}), 61.8 (C-6^{Glc}), 60.8 (C-6^{Gal}), 39.3 (CH$_2$*C*H$_2$NH), 29.1 (CH$_2$*C*H$_2$CH$_2$), 20.8−20.5 (C(O)*C*H$_3$). MALDI-MS: calcd *m/z* 1567.5 [M + Na^+], 1583.5 [M + K^+], found 1567.9, 1583.9. Anal. calcd for $C_{64}H_{92}N_2O_{41}$: C 49.74, H 6.00, N 1.81, found: C 49.58, H 6.18, N 1.81.

***N,N'*-Bis-(*β*-D-galactopyranosyl-(1→4)-*β*-D-glucopyranosyloxycarbonyl)-4,7,10-trioxa-1,13-tridecanediamine (D).** According to GP 2, Ac-**D** (100 mg, 0.065 mmol) was deacetylated with 0.5 M NaOMe solution (0.5 mL) in MeOH (2 mL) to give **D** (58 mg, 94%) as a white solid. ^{1}H NMR (600 MHz, D_2O): δ = 5.33 (d, *J* = 8.3 Hz, 2 H, H-1^{Glc}), 4.36 (d, *J* = 7.8 Hz, 2 H, H-1^{Gal}), 3.86−3.83 (m, 4 H, H-4^{Gal}, H-6^{Glc}), 3.74−3.56 (m, 24 H, H-3^{Glc}, H-3^{Gal}, H-4^{Glc}, H-5^{Glc}, H-5^{Gal}, H-6′^{Glc}, H-6^{Gal}, H-6′^{Gal}, OCH_2CH$_2$O, OCH$_2$CH_2O), 3.51−3.44 (m, 6 H, H-2^{Gal}, OCH_2CH$_2$), 3.40 (t, *J* = 8.6 Hz, 2 H, H-2^{Glc}), 3.15 (bs, 4 H, CH$_2$CH_2NH), 1.73−1.69 (m, 4 H, CH$_2$CH_2CH$_2$). ^{13}C NMR (150 MHz, D_2O): δ = 156.4 (OC(O)N), 102.9 (C-1^{Gal}), 94.7 (C-1^{Glc}), 77.8, 75.4, 75.3, 74.1, 72.5 (C-3^{Glc}, C-3^{Gal}, C-4^{Glc}, C-5^{Glc}, C-5^{Gal}), 71.7 (C-2^{Glc}), 70.9 (C-2^{Gal}), 69.6 (O*C*H$_2$CH$_2$O), 69.3(OCH$_2$*C*H$_2$O), 68.6 (C-4^{Gal}), 68.3(O*C*H$_2$CH$_2$), 61.1 (C-6^{Gal}), 59.8 (C-6^{Glc}), 37.6 (CH$_2$*C*H$_2$NH), 28.5 (CH$_2$*C*H$_2$CH$_2$). MALDI-MS: calcd *m/z* 979.4 [M + Na^+], 995.4 [M + K^+], found 979.4, 995.3.

1,7-Bis-(2,3,4,6-tetra-*O*-acetyl-*β*-D-galactopyranosyl-(1→4)-2,3,6-tri-*O*-acetyl-*β*-D-glucopyranosyloxycarbonyl)diethylenetriamine (Ac-E). According to GP 1, *β*-**3** (202 mg, 0.252 mmol) and diethylenetriamine **13** (11 *μ*L, 0.102 mmol) were reacted in CH_2Cl_2 (2 mL). Purification by FC (CH_2Cl_2/MeOH 15:1) gave Ac-**E** (105 mg, 71%) as a colorless syrup. ^{1}H NMR (600 MHz, $CDCl_3$): δ = 5.76 (t, *J* = 5.1 Hz, 2 H, NHC(O)), 5.58 (d, *J* = 8.3 Hz, 2 H, H-1^{Glc}), 5.31 (d, *J* = 2.8 Hz, 2 H, H-4^{Gal}), 5.21 (t, *J* = 9.1 Hz, 2 H, H-3^{Glc}), 5.06 (dd, *J* = 9.9 Hz, *J* = 8.3 Hz, 2 H, H-2^{Gal}), 4.98 (t, *J* = 8.9 Hz, 2 H, H-2^{Glc}), 4.91 (dd, *J* = 10.4 Hz, *J* = 2.9 Hz, 2 H, H-3^{Gal}), 4.48−4.42 (m, 4 H, H-1^{Gal}, H-6^{Glc}), 4.11−4.09 (m, 2 H, H-6′^{Glc}, H-6^{Gal}), 4.05−4.02 (m, 2 H, H-6′^{Gal}), 3.86−3.84 (m, 4 H, H-4^{Glc}, H-5^{Gal}), 3.73−3.71 (m, 2 H, H-5^{Glc}), 3.40−3.18 (m, 4 H, CH$_2$CH_2NH), 2.76−2.71 (m, 4 H, CH_2CH$_2$NH), 2.11 (s, 6 H, C(O)CH_3), 2.07 (s, 6 H, C(O)CH_3), 2.02 (s, 6 H, C(O)CH_3), 2.01 (s, 6 H, C(O)CH_3), 2.00 (s, 6 H, C(O)CH_3), 1.99 (s, 6 H, C(O)CH_3), 1.95 (s, 6 H, C(O)CH_3). ^{13}C NMR (150 MHz, $CDCl_3$): δ = 170.3, 170.2, 170.0, 170.0, 169.5, 168.9 (*C*(O)CH_3), 154.0 (OC(O)N), 100.8 (C-1^{Gal}), 92.6 (C-1^{Glc}), 75.5 (C-4^{Glc}), 73.2 (C-5^{Glc}), 72.6 (C-3^{Glc}), 70.9 (C-3^{Gal}), 70.5 (C-5^{Gal}), 70.5 (C-2^{Glc}), 68.9 (C-2^{Gal}), 66.5 (C-4^{Gal}), 61.6

(C-6^{Glc}), 60.6 (C-6^{Gal}), 48.0 (CH_2CH_2NH), 40.3 (CH_2CH_2NH), 20.8−20.5 (C(O)CH_3). MALDI-MS: calcd *m*/*z* 1450.5 [M + Na^+], 1466.5 [M + K^+], found 1449.6, 1466.0.

1,7-Bis-(β-D-galactopyranosyl-(1→4)-β-D-glucopyranosyloxycarbonyl)diethylenetriamine (E). According to GP 3, Ac-**E** (67 mg, 0.047 mmol) was deacetylated in EtNMe$_2$/MeOH 1:5 (2.4 mL) to give **E** (39 mg, 99%) as a white solid. ^{1}H NMR (600 MHz, D_2O): δ = 5.34 (d, J = 8.2 Hz, 2 H, H-1^{Glc}), 4.35 (d, J = 7.5 Hz, 2 H, H-1^{Gal}), 3.85−3.82 (m, 4 H, H-4^{Gal}, H-6^{Glc}), 3.72−3.54 (m, 16 H, H-3^{Glc}, H-3^{Gal}, H-4^{Glc}, H-5^{Glc}, H-5^{Gal}, H-6′^{Glc}, H-6^{Gal}, H-6′^{Gal}), 3.45−3.39 (m, 4 H, H-2^{Gal}, H-2^{Glc}), 3.20−3.13 (bs, 4 H, CH_2CH_2NH), 2.78 (bs, 4 H, CH_2CH_2NH). ^{13}C NMR (150 MHz, D_2O): δ = 156.6 (OC(O)N), 102.9 (C-1^{Gal}), 94.8 (C-1^{Glc}), 77.8, 75.4, 75.3, 74.1 (C-3^{Glc}, C-4^{Glc}, C-5^{Glc}, C-5^{Gal}), 72.6 (C-3^{Gal}), 71.6 (C-2^{Glc}), 71.0 (C-2^{Gal}), 68.6 (C-4^{Gal}), 61.1 (C-6^{Gal}), 59.7 (C-6^{Glc}), 47.2 (CH_2CH_2NH), 38.9 (CH_2CH_2NH).

Tris-(2-(2,3,4,6-tetra-*O*-acetyl-β-D-galactopyranosyl-(1→4)-2,3,6-tri-*O*-acetyl-β-D-glucopyranosyloxycarbonylamino)ethyl)amine (Ac-F). According to GP 1, β-**3** (144 mg, 0.18 mmol) and tris-(2-aminoethyl)amine **14** (8 μL, 0.053 mmol) were reacted in CH_2Cl_2 (4 mL). Purification by FC (petroleum ether/ethyl acetate 1:1, then ethyl acetate) gave Ac-**F** (111 mg, 97%) as a white solid. R_f = 0.32 (ethyl acetate). ^{1}H NMR (600 MHz, $CDCl_3$): δ = 5.61 (d, J = 8.0 Hz, 3 H, H-1^{Glc}), 5.49 (bs, 3 H, NHC(O)), 5.34 (s, 3 H, H-4^{Gal}), 5.25 (t, J = 9.1 Hz, 3 H, H-3^{Glc}), 5.10 (t, J = 9.2 Hz, 3 H, H-2^{Gal}), 5.03−4.94 (m, 6 H, H-2^{Glc}, H-3^{Gal}), 4.50−4.45 (m, 6 H, H-1^{Gal}, H-6^{Glc}), 4.15−4.05 (m, 9 H, H-6′^{Glc}, H-6^{Gal}, H-6′^{Gal}), 3.89−3.84 (m, 6 H, H-4^{Glc}, H-5^{Gal}), 3.75 (m, 3 H, H-5^{Glc}), 3.33 (bs, 3 H, CH_2CH_2NH), 3.23 (bs, 3 H, CH_2CH_2NH), 2.77 (bs, 6 H, CH_2CH_2NH), 2.15 (s, 9 H, C(O)CH_3), 2.11 (s, 18 H, C(O)CH_3), 2.06 (s, 9 H, C(O)CH_3), 2.05 (s, 9 H, C(O)CH_3), 2.04 (s, 9 H, C(O)CH_3), 1.96 (s, 9 H, C(O)CH_3). ^{13}C NMR (150 MHz, $CDCl_3$): δ = 170.4, 170.1, 170.1, 169.8, 169.6, 169.0 (*C*(O)CH_3), 154.0 (OC(O)N), 100.9 (C-1^{Gal}), 92.7 (C-1^{Glc}), 75.6 (C-4^{Glc}), 73.3 (C-5^{Glc}), 72.7 (C-3^{Glc}), 71.0 (C-3^{Gal}), 70.7 (C-5^{Gal}), 70.6 (C-2^{Glc}), 69.0 (C-2^{Gal}), 66.6 (C-4^{Gal}), 61.8 (C-6^{Glc}), 60.7 (C-6^{Gal}), 48.2 (CH_2CH_2NH), 40.6 (CH_2CH_2NH), 20.9−20.5 (C(O)CH_3). MALDI-MS: calcd *m*/*z* 2155.7 [M + Na^+], found 2155.2. Anal. calcd for $C_{87}H_{120}N_4O_{57}$: C 48.97, H 5.67, N 2.63, found: C 49.14, H 5.84, N 2.59.

Tris-(2-(β-D-galactopyranosyl-(1→4)-β-D-glucopyranosyloxycarbonylamino)ethyl)amine (F). According to GP 3, Ac-**F** (67 mg, 0.031 mmol) was deacetylated in EtNMe$_2$/MeOH 1:5 (1.8 mL) to give **F** (38 mg, 97%) as a white solid. ^{1}H NMR (600 MHz, D_2O): δ = 5.33 (d, J = 8.2 Hz, 3 H, H-1^{Glc}), 4.34 (d, J = 7.8 Hz, 3 H, H-1^{Gal}), 3.85−3.81 (m, 6 H, H-4^{Gal}, H-6^{Glc}), 3.72−3.60 (m, 21 H, H-3^{Glc}, H-4^{Glc}, H-5^{Glc}, H-5^{Gal}, H-6′^{Glc}, H-6^{Gal}, H-6′^{Gal}), 3.55 (dd, J = 10.0 Hz, J = 3.4 Hz, 3 H, H-3^{Gal}), 3.43 (dd, J = 9.7 Hz, J = 8.1 Hz, 3 H, H-2^{Gal}), 3.40 (t, J = 8.1 Hz, 3 H, H-2^{Glc}), 3.20−3.13 (bs, 6 H, CH_2CH_2NH), 2.63 (bs, 6 H, CH_2CH_2NH). ^{13}C NMR (150 MHz, D_2O): δ = 156.4 (OC(O)N), 102.9 (C-1^{Gal}), 94.7 (C-1^{Glc}), 77.7, 75.4, 75.3, 74.1 (C-3^{Glc}, C-4^{Glc}, C-5^{Glc}, C-5^{Gal}), 72.5 (C-3^{Gal}), 71.6 (C-2^{Glc}), 70.9 (C-2^{Gal}), 68.5 (C-4^{Gal}), 61.0 (C-6^{Gal}), 59.7 (C-6^{Glc}), 52.5 (CH_2CH_2NH), 38.1 (CH_2CH_2NH). MALDI-MS: calcd *m*/*z* 1273.4 [M + Na^+], 1289.4 [M + K^+], found 1273.4, 1289.4.

***N*,*N*′-Bis-(4-(2,3,4,6-tetra-*O*-acetyl-β-D-galactopyranosyl-(1→4)-2,3,6-tri-*O*-acetyl-β-D-glucopyranosyloxy)-(*Z*)-but-2-enyloxycarbonyl)-*m*-xylylenediamine (Ac-G).** According to GP 1, **7** (171 mg, 0.196 mmol) and α,α′-diamino-*m*-xylene **9** (12 mg, 0.088 mmol) were reacted in CH_2Cl_2 (3 mL). Purification by FC (petroleum ether/ethyl acetate 1:2 → 1:3) gave Ac-**G** (135 mg, 95%) as a white foam. R_f = 0.15 (petroleum ether/ethyl acetate 1:2). ^{1}H NMR (600 MHz, $CDCl_3$): δ = 7.33−7.30 (m, 1 H, Ar), 7.21−7.18 (m, 3 H, Ar), 5.75−5.64 (m, 4 H, H^{vinyl}), 5.35 (dd, J = 3.3 Hz, J = 0.7 Hz, 2 H, H-4^{Gal}), 5.20 (bs, 2 H, NHC(O)), 5.16 (t, J = 9.3 Hz, 2 H, H-3^{Glc}), 5.10 (dd, J = 10.4 Hz, J = 7.9 Hz, 2 H, H-2^{Gal}), 4.95 (dd, J = 10.4 Hz, J = 3.5 Hz, 2 H, H-3^{Gal}), 4.89 (dd, J = 9.4 Hz, J = 8.0 Hz, 2 H, H-2^{Glc}), 4.69 (dd, J = 13.0 Hz, J = 6.9 Hz, 2 H, H^{allyl}), 4.57 (dd, J = 13.1 Hz, J = 5.7 Hz, 2 H, H^{allyl}), 4.52−4.50 (m, 4 H, H-1^{Glc} H-6^{Glc}), 4.48 (d, J = 7.9 Hz, 2 H, H-1^{Gal}), 4.35 (d, J = 5.9 Hz, 4 H, H^{benzyl}), 4.31 (d, J = 6.2 Hz, 4 H, H^{allyl}), 4.14−4.11 (m, 2 H, H-6^{Gal}), 4.09−4.06 (m, 4 H, H-6′^{Glc}, H-6′^{Gal}), 3.87 (bt, J = 6.8 Hz, 2 H, H-5^{Gal}), 3.79 (t, J = 9.5 Hz, 2 H, H-4^{Glc}), 3.61−3.59 (m, 2 H, H-5^{Glc}), 2.15 (s, 6 H, C(O)CH_3), 2.11 (s, 6 H, C(O)CH_3), 2.06 (s, 6 H, C(O)CH_3), 2.04 (s, 6 H, C(O)CH_3), 2.04 (s, 6 H, C(O)CH_3), 2.02 (s, 6 H, C(O)CH_3), 1.96 (s, 6 H, C(O)CH_3). ^{13}C NMR (150 MHz, $CDCl_3$): δ = 170.4, 170.3, 170.1, 170.0, 169.8, 169.7, 169.1 (*C*(O)CH_3), 156.2 (OC(O)N), 137.1, 129.1 (Ar), 128.9, 128.5 (CH^{olefin}), 128.5,126.6 (Ar), 101.1 (C-1^{Gal}), 99.0 (C-1^{Glc}), 76.3 (C-4^{Glc}), 72.9 (C-3^{Glc}), 72.6 (C-5^{Glc}), 71.6 (C-2^{Glc}), 71.0 (C-3^{Gal}), 70.7 (C-5^{Gal}), 69.1 (C-2^{Gal}), 66.6 (C-4^{Gal}), 64.3 (CH_2^{allyl}), 62.0 (C-6^{Glc}), 60.8 (C-6^{Gal}), 60.5 (CH_2^{allyl}), 44.9 (CH_2^{benzyl}), 20.9−20.5 (C(O)CH_3). MALDI-MS: calcd *m*/*z* 1623.5 [M + Na^+], 1639.5 [M + K^+], found 1623.6, 1639.6. Anal. calcd for $C_{70}H_{92}N_2O_{40}$: C 52.50, H 5.79, N 1.75, found: C 51.92, H 5.81, N 1.84.

***N*,*N*′-Bis-(4-(β-D-galactopyranosyl-(1→4)-β-D-glucopyranosyloxy)-(Z)-but-2-enyloxycarbonyl)-*m*-xylylenediamine (G).** According to GP 2, Ac-**G** (130 mg, 0.081 mmol) was deacetylated with 0.5 M NaOMe solution (0.5 mL) in MeOH (2 mL) to give **G** (81 mg, 98%) as a white solid. ^{1}H NMR (600 MHz, D_2O): δ = 7.29−7.27 (m, 1 H, Ar), 7.14−7.12 (m, 3 H, Ar), 5.73−5.71 (m, 4 H, H^{vinyl}), 4.60−4.54 (m, 4 H, H^{allyl}), 4.38−4.28 (m, 8 H, H-1^{Glc}, H-1^{Gal}, H^{allyl}), 4.20 (s, 4 H, H^{benzyl}), 3.84−3.82 (m, 4 H, H-4^{Gal}, H-6^{Glc}), 3.70−3.60 (m, 8 H, H-5^{Gal}, H-6′^{Glc}, H-6^{Gal}, H-6′^{Gal}), 3.57−3.48 (m, 6 H, H-3^{Glc}, H-3^{Gal}, H-4^{Glc}), 3.45−3.42 (m, 4 H, H-2^{Gal}, H-5^{Glc}), 3.20 (t, J = 8.3 Hz, 2 H, H-2^{Glc}). ^{13}C NMR (150 MHz, D_2O): δ = 158.4 (OC(O)N), 139.2, 129.0 (Ar), 128.9, 128.5 (CH^{olefin}), 125.9, 125.3 (Ar), 102.9 (C-1^{Gal}), 100.9 (C-1^{Glc}), 78.3 (C-4^{Glc}), 75.4 (C-5^{Gal}), 74.8 (C-5^{Glc}), 74.4 (C-3^{Glc}), 72.8 (C-3^{Gal}), 72.6 (C-2^{Glc}), 71.0 (C-2^{Gal}), 68.6 (C-4^{Gal}), 64.8 (CH_2^{allyl}), 61.0 (C-6^{Gal}), 61.0 (CH_2^{allyl}), 60.0 (C-6^{Glc}), 43.9 (CH_2^{Bn}). MALDI-MS: calcd *m*/*z* 1035.4 [M + Na^+], found 1035.4.

***N*,*N*′-Bis-(4-(2,3,4,6-tetra-*O*-acetyl-β-D-galactopyranosyl-(1→4)-2,3,6-tri-*O*-acetyl-β-D-glucopyranosyloxy)-(*Z*)-but-2-enyloxycarbonyl)-*p*-xylylenediamine (Ac-H).** According to GP 1, **7** (157 mg, 180 mmol) and α,α′-diamino-*p*-xylene **10** (12 mg, 0.088 mmol) were reacted in CH_2Cl_2 (3 mL). Purification by FC (petroleum ether/ethyl acetate 1:2 → 1:3) gave Ac-**H** (130 mg, 92%) as a white foam. R_f = 0.10 (petroleum ether/ethyl acetate 1:2). ^{1}H NMR (600 MHz, $CDCl_3$): δ = 7.27 (s, 4 H, Ar), 5.75−5.64 (m, 4 H, H^{vinyl}), 5.35 (d, J = 2.9 Hz, 2 H, H-4^{Gal}), 5.17 (t, J = 9.3 Hz, 2 H, H-3^{Glc}), 5.10 (dd, J = 10.4 Hz, J = 7.9 Hz, 2 H, H-2^{Gal}), 4.96 (dd, J = 10.4 Hz, J = 3.5 Hz, 2 H, H-3^{Gal}), 4.89 (dd, J = 9.4 Hz, J = 8.0 Hz, 2 H, H-2^{Glc}), 4.68 (dd, J = 12.6 Hz, J = 7.1 Hz, 2 H, H^{allyl}), 4.57 (dd, J = 13.1 Hz, J = 5.8 Hz, 2 H, H^{allyl}), 4.51−4.48 (m, 6 H, H-1^{Glc}, H-1^{Gal}, H-6^{Glc}), 4.35 (d, J = 5.9 Hz, 4 H, H^{benzyl}), 4.32 (d, J = 6.3 Hz, 4 H, H^{allyl}), 4.15−4.12 (m, 2 H, H-6^{Gal}), 4.10−4.07 (m, 4 H, H-6′^{Glc}, H-6′^{Gal}), 3.87 (bt, J = 6.7 Hz, 2 H, H-5^{Gal}), 3.79 (t, J = 9.5 Hz, 2 H, H-4^{Glc}), 3.62−3.60 (m, 2 H, H-5^{Glc}), 2.15 (s, 6 H, C(O)CH_3), 2.11 (s, 6 H, C(O)CH_3), 2.06 (s, 6 H, C(O)CH_3), 2.05 (s, 6 H, C(O)CH_3), 2.04 (s, 6 H, C(O)CH_3), 2.03 (s, 6 H, C(O)CH_3), 1.97 (s, 6 H, C(O)CH_3). ^{13}C NMR (150 MHz, $CDCl_3$): δ = 170.3, 170.3, 170.1, 170.0, 169.7, 169.6, 169.0 (*C*(O)CH_3), 156.7 (OC(O)N), 136.9 (Ar), 128.8, 128.5 (CH^{olefin}), 127.7 (Ar), 101.1 (C-1^{Gal}), 98.9 (C-1^{Glc}), 76.3 (C-4^{Glc}), 72.9 (C-3^{Glc}), 72.6 (C-5^{Glc}), 71.6 (C-2^{Glc}), 71.0 (C-3^{Gal}), 70.7 (C-5^{Gal}), 69.1 (C-2^{Gal}), 66.6 (C-4^{Gal}), 64.7 (CH_2^{allyl}), 62.0 (C-6^{Glc}), 60.8 (C-6^{Gal}), 60.5 (CH_2^{allyl}), 44.3 (CH_2^{benzyl}), 20.8−20.5

(C(O)CH_3). MALDI-MS: calcd *m/z* 1623.5 [M + Na^+], 1639.5 [M + K^+], found 1623.4, 1639.4. Anal. calcd for $C_{70}H_{92}N_2O_{40}$: C 52.50, H 5.79, N 1.75, found: C 52.21, H 5.72, N 1.72.

***N,N′*-Bis-(4-(β-D-galactopyranosyl-(1→4)-β-D-glucopyranosyloxy)-(*Z*)-but-2-enyloxycarbonyl)-*p*-xylylenediamine (H).** According to GP 2, Ac-**H** (125 mg, 0.078 mmol) was deacetylated with 0.5 M NaOMe solution (0.5 mL) in MeOH (2 mL) to give **H** (76 mg, 96%) as a white solid. ^{1}H NMR (600 MHz, D_2O): δ = 7.21 (s, 4 H, Ar), 5.74−5.72 (m, 4 H, H^{vinyl}), 4.60−4.53 (m, 4 H, H^{allyl}), 4.39−4.29 (m, 8 H, H-1^{Glc}, H-1^{Gal}, H^{allyl}), 4.20 (s, 4 H, H^{benzyl}), 3.85−3.83 (m, 4 H, H-4^{Gal}, H-6^{Glc}), 3.71−3.66 (m, 6 H, H-6′^{Glc}, H-6^{Gal}, H-6′^{Gal}), 3.65−3.61 (m, 2 H, H-5^{Gal}), 3.58−3.49 (m, 6 H, H-3^{Glc}, H-3^{Gal}, H-4^{Glc}), 3.46−3.43 (m, 4 H, H-2^{Gal}, H-5^{Glc}), 3.21 (t, *J* = 8.5 Hz, 2 H, H-2^{Glc}). ^{13}C NMR (150 MHz, D_2O): δ = 158.4 (OC(O)N), 135.4 (Ar), 128.9, 128.5 (CH^{olefin}), 127.9 (Ar), 102.9 (C-1^{Gal}), 100.9 (C-1^{Glc}), 78.3 (C-4^{Glc}), 75.4 (C-5^{Gal}), 74.8, 74.4, 72.8, 72.6, 71.0, 68.6, (C-2^{Glc}, C-2^{Gal}, C-3^{Gal}, C-3^{Glc}, C-4^{Gal}, C-5^{Glc}), 64.7 (CH_2^{allyl}), 61.0 (C-6^{Gal}), 61.0 (CH_2^{allyl}), 60.0 (C-6^{Glc}), 43.8 (CH_2^{Bn}). MALDI-MS: calcd *m/z* 1035.4 [M + Na^+], found 1034.9.

***N,N′*-Bis-(4-(2,3,4,6-tetra-*O*-acetyl-β-D-galactopyranosyl-(1→4)-2,3,6-tri-*O*-acetyl-β-D-glucopyranosyloxy)-(*Z*)-but-2-enyloxycarbonyl)-4,7,10-trioxa-1,13-tridecanediamine (Ac-I).** According to GP 1, **7** (140 mg, 0.178 mmol) and 4,7,10-trioxa-1,13-tridecanediamine **12** (16 μL, 0.073 mmol) were reacted in CH_2Cl_2 (3 mL). Purification by FC (petroleum ether/ethyl acetate 1:3, then ethyl acetate) gave Ac-**I** (120 mg, 98%) as a white solid. R_f = 0.27 (ethyl acetate). ^{1}H NMR (600 MHz, $CDCl_3$): δ = 5.72−5.62 (m, 4 H, H^{vinyl}), 5.35 (dd, *J* = 3.4 Hz, *J* = 0.8 Hz, 2 H, H-4^{Gal}), 5.18 (t, *J* = 9.3 Hz, 2 H, H-3^{Glc}), 5.10 (dd, *J* = 10.4 Hz, *J* = 7.9 Hz, 2 H, H-2^{Gal}), 4.95 (dd, *J* = 10.4 Hz, *J* = 3.5 Hz, 2 H, H-3^{Gal}), 4.89 (dd, *J* = 9.5 Hz, *J* = 8.0 Hz, 2 H, H-2^{Glc}), 4.63−4.47 (m, 10 H, H-1^{Glc}, H-1^{Gal}, H-6^{Glc}, H^{allyl}), 4.33−4.26 (m, 4 H, H^{allyl}), 4.15−4.12 (m, 2 H, H-6^{Gal}), 4.13−4.06 (m, 4 H, H-6′^{Glc}, H-6′^{Gal}), 3.87 (bt, *J* = 6.8 Hz, 2 H, H-5^{Gal}), 3.79 (t, *J* = 9.5 Hz, 2 H, H-4^{Glc}), 3.65−3.59 (m, 10 H, H-5^{Glc}, OCH_2CH$_2$, OCH$_2$CH_2), 3.55 (t, *J* = 5.8 Hz, 4 H, OCH_2CH_2CH$_2$), 3.29−3.26 (m, 4 H, CH$_2$CH_2NH), 2.15 (s, 6 H, C(O)CH_3), 2.12 (s, 6 H, C(O)CH_3), 2.06 (s, 6 H, C(O)CH_3), 2.05 (s, 6 H, C(O)CH_3), 2.04 (s, 12 H, C(O)CH_3), 1.96 (s, 6 H, C(O)CH_3), 1.79−1.75 (m, 4 H, CH$_2$CH_2CH$_2$). ^{13}C NMR (150 MHz, $CDCl_3$): δ = 170.4, 170.3, 170.1, 170.0, 169.8, 169.7, 169.1 (*C*(O)CH_3), 156.2 (OC(O)N), 128.8, 128.5 (CH^{olefin}), 101.1 (C-1^{Gal}), 99.1 (C-1^{Glc}), 76.3 (C-4^{Glc}), 72.9 (C-3^{Glc}), 72.6 (C-5^{Glc}), 71.6 (C-2^{Glc}), 71.0 (C-3^{Gal}), 70.7 (C-5^{Gal}), 70.5 (OCH_2CH$_2$O), 70.2 (OCH$_2$CH_2O), 69.6 (OCH_2CH$_2$), 69.1 (C-2^{Gal}), 66.6 (C-4^{Gal}), 65.5 (Allyl CH_2), 62.0 (C-6^{Glc}), 60.8 (C-6^{Gal}), 60.2 (Allyl CH_2), 39.3 (CH$_2$CH_2NH), 29.4 (CH$_2$CH_2CH$_2$), 20.9−20.5 (C(O)CH_3). MALDI-MS: calcd *m/z* 1707.6 [M + Na^+], 1723.6 [M + K^+], found 1707.2, 1723.2. Anal. calcd for $C_{72}H_{104}N_2O_{43}$: C 51.30, H 6.22, N 1.66, found: C 51.38, H 5.96, N 1.83.

***N,N′*-Bis-(4-(β-D-galactopyranosyl-(1→4)-β-D-glucopyranosyloxy)-(*Z*)-but-2-enyloxycarbonyl)-4,7,10-trioxa-1,13-tridecanediamine (I).** According to GP 2, Ac-**I** (114 mg, 0.068 mmol) was deacetylated with 0.5 M NaOMe solution (0.5 mL) in MeOH (2 mL) to give **I** (73 mg, 99%) as a white solid. ^{1}H NMR (600 MHz, D_2O): δ = 5.72 (bs, 4 H, H^{vinyl}), 4.60−4.53 (m, 4 H, H^{allyl}), 4.41 (d, *J* = 8.0 Hz, 2 H, H-1^{Glc}), 4.38−4.29 (m, 6 H, H-1^{Gal}, H^{allyl}), 3.87 (dd, *J* = 12.4 Hz, *J* = 1.5 Hz, 2 H, H-6^{Glc}) 3.82 (d, *J* = 2.9 Hz, H-4^{Gal}), 3.73−3.61 (m, 8 H, H-5^{Gal}, H-6′^{Glc}, H-6^{Gal}, H-6′^{Gal}), 3.56−3.52 (m, 14 H, H-3^{Gal}, OCH_2CH$_2$, OCH$_2$CH_2, OCH$_2$CH_2O), 3.49−3.42 (m, 8 H, H-2^{Gal}, H-3^{Glc}, H-4^{Glc}, H-5^{Glc}), 3.22 (t, *J* = 8.4 Hz, 2 H, H-2^{Glc}), 3.01 (t, *J* = 6.2 Hz, 4 H, CH$_2$CH_2NH), 1,69 (p, *J* = 6.3 Hz, 4 H, CH$_2$CH_2CH$_2$). ^{13}C NMR (150 MHz, D_2O): δ = 158.2 (OC(O)N), 128.8, 128.6 (CH^{olefin}), 102.9 (C-1^{Gal}), 101.0 (C-1^{Glc}), 78.3 (C-4^{Glc}), 75.4 (C-5^{Gal}), 74.8, 74.5, 72.8, 72.6, 71.0, 69.6 68.6 (C-2^{Glc}, C-2^{Gal}, C-3^{Gal}, C-3^{Glc}, C-5^{Glc}, OCH_2CH$_2$), 68.4 (C-4^{Gal}), 68.3 (OCH_2CH$_2$), 64.8 (CH_2^{allyl}), 61.0 (C-6^{Gal}), 61.0 (CH_2^{allyl}), 60.8, 60.0 (C-6^{Glc}), 37.6 (CH$_2$CH_2NH), 28.7 (CH$_2$CH_2CH$_2$). MALDI-MS: calcd *m/z* 1119.4 [M + Na^+], 1135.4 [M + K^+], found 1119.3, 1135.3.

Tetrakis-(4-(2,3,4,6-tetra-*O*-acetyl-β-D-galactopyranosyl-(1→4)-2,3,6-tri-*O*-acetyl-β-D-glucopyranosyloxy)-(*Z*)-but-2-enyloxycarbonylaminomethyl)methane (Ac-J). According to GP 1, **7** (240 mg, 0.275 mmol) and tetra(aminomethyl)methane **15** (*22*) (8 mg, 0.056 mmol) were reacted in CH_2Cl_2 (2 mL). Purification by FC (petroleum ether/ethyl acetate 1:2 → 1:3 → 1:4) gave Ac-**J** (70 mg, 53%) as a white solid. R_f = 0.20 (petroleum ether/ethyl acetate 1:3). ^{1}H NMR (600 MHz, $CDCl_3$): δ = 6.36 (t, *J* = 6.6 Hz, 4 H, NH), 5.73−5.65 (m, 8 H, H^{vinyl}), 5.34 (d, *J* = 3.3 Hz, 4 H, H-4^{Gal}), 5.18 (d, *J* = 9.3 Hz, 4 H, H-3^{Glc}), 5.09 (dd, *J* = 10.4 Hz, *J* = 7.9 Hz, 4 H, H-2^{Gal}), 4.95 (dd, *J* = 10.4 Hz, *J* = 3.4 Hz, 4 H, H-3^{Gal}), 4.89 (dd, *J* = 9.4 Hz, *J* = 8.0 Hz, 4 H, H-2^{Glc}), 4.62−4.56 (m, 8 H, H^{allyl}), 4.51−4.48 (m, 12 H, H-1^{Glc}, H-1^{Gal}, H-6^{Glc}), 4.34 (dd, *J* = 12.8 Hz, *J* = 5.2 Hz, 4 H, H^{allyl}), 4.22 (dd, *J* = 12.8 Hz, *J* = 6.2 Hz, 4 H, H^{allyl}), 4.14−4.06 (m, 12 H, H-6′^{Glc}, H-6^{Gal}, H-6′^{Gal}), 3.87 (bt, *J* = 6.9 Hz, 4 H, H-5^{Gal}), 3.80 (t, *J* = 9.4 Hz, 4 H, H-4^{Glc}), 3.60 (ddd, *J* = 9.7 Hz, *J* = 4.9 Hz, *J* = 2.0 Hz, 4 H, H-5^{Glc}), 2.81 (d, *J* = 4.2 Hz, 8 H, CCH_2NH), 2.15 (s, 12 H, C(O)CH_3), 2.12 (s, 12 H, C(O)CH_3), 2.06 (s, 12 H, C(O)CH_3), 2.04 (s, 24 H, C(O)CH_3), 2.03 (s, 12 H, C(O)CH_3), 1.96 (s, 12 H, C(O)CH_3). ^{13}C NMR (150 MHz, $CDCl_3$): δ = 170.3, 170.3, 170.1, 170.0, 169.7, 169.6, 169.0 (*C*(O)CH_3), 157.8 (OC(O)N), 128.7, 128.2 (CH^{olefin}), 101.1 (C-1^{Gal}), 99.4 (C-1^{Glc}), 76.2 (C-4^{Glc}), 72.9 (C-3^{Glc}), 72.7 (C-5^{Glc}), 71.6 (C-2^{Glc}), 71.0 (C-3^{Gal}), 70.7 (C-5^{Gal}), 69.1 (C-2^{Gal}), 66.6 (C-4^{Gal}), 64.7 (CH_2^{allyl}), 62.0 (C-6^{Glc}), 61.0 (CH_2^{allyl}), 60.8 (C-6^{Gal}), 39.8 (C*C*H$_2$NH), 20.8−20.5 (C(O)*C*H$_3$). MALDI-MS: calcd *m/z* 3084.0 [M + Na^+], 3100.0 [M + K^+], found 3083.9, 3099.9. Anal. calcd for $C_{129}H_{176}N_4O_{80}$: C 50.59, H 5.79, N 1.83, found: C 50.77, H 5.94, N 1.79.

Tetrakis-(4-(β-D-galactopyranosyl-(1→4)-β-D-glucopyranosyloxy)-(*Z*)-but-2-enyloxycarbonylaminomethyl)methane (J). According to GP 2, Ac-**J** (78 mg, 0.025 mmol) was deacetylated with 0.5 M NaOMe solution (0.5 mL) in MeOH (2 mL) to give **J** (48 mg, quant) as a white solid. ^{1}H NMR (600 MHz, D_2O): δ = 5.77−5.72 (m, 8 H, H^{vinyl}), 4.61−4.56 (m, 8 H, H^{allyl}), 4.43−4.30 (m, 16 H, H-1^{Glc}, H-1^{Gal}, H^{allyl}), 3.88 (d, *J* = 8.3 Hz, 4 H, H-6^{Glc}), 3.83 (d, *J* = 3.0 Hz, 4 H, H-4^{Gal}), 3.73−3.62 (m, 16 H, H-5^{Gal}, H-6′^{Glc}, H-6^{Gal}, H-6′^{Gal}), 3.58−3.53 (m, 12 H, H-3^{Glc}, H-3^{Gal}, H-4^{Glc}), 3.49−3.43 (m, 8 H, H-2^{Gal}, H-5^{Glc}), 3.23 (t, *J* = 8.3 Hz, 4 H, H-2^{Glc}), 2.95 (bs, 8 H, CCH_2NH). ^{13}C NMR (150 MHz, D_2O): δ = 158.3 (OC(O)N), 128.8, 128.5 (CH^{olefin}), 102.9 (C-1^{Gal}), 100.9 (C-1^{Glc}), 78.4 (C-4^{Glc}), 75.4 (C-5^{Gal}), 74.8 (C-5^{Glc}), 74.4 (C-3^{Glc}), 72.8 (C-3^{Gal}), 72.5 (C-2^{Glc}), 71.0 (C-2^{Gal}), 68.5 (C-4^{Gal}), 64.7 (CH_2^{allyl}), 61.1 (CH_2^{allyl}), 61.0 (C-6^{Gal}), 60.0 (C-6^{Glc}), 38.8 (C*C*H$_2$NH). MALDI-MS: calcd *m/z* 1907.7 [M + Na^+], found 1908.4.

Lectins and (Neo)glycoproteins. Purification of VAA and of the galectins (human galectins-1, -3, and -4 as well as rat galectin-5) started from extracts of dried leaves and bacteria harboring the respective expression vector. One-step isolation used lactosylated Sepharose 4B, which was prepared after activation by divinyl sulfone and elution with 0.2 M lactose (*23*). The purity of the proteins was tested by one- and two-dimensional gel electrophoresis on 10% running gels and mass spectrometry by nanoESI-MS/MS on a QTOF instrument Q-Tof2 (Waters Micromass, Manchester, UK) (*24*). Their quaternary structure was analyzed on a Superose 12 HR 10/30 column (GE Healthcare, Munich, Germany), and lectin activity was tested in 2-fold dilutions by hemagglutination with trypsinized, glutaraldehyde-fixed rabbit erythrocytes (*25*−*27*). Biotinylation with the *N*-hydroxysuccinimide ester derivative

of biotin (Sigma, Munich, Germany) under activity-preserving conditions followed by mass spectrometric product analysis to quantify label incorporation was performed as described (*24*). Proteolytic truncation of human galectin-3 required 300 μg collagenase D from *Clostridium histolyticum* (Roche Diagnostics, Mannheim, Germany) in Tris-buffered saline with 10 mM $CaCl_2$ at pH 7 for 2 h at 37 °C and 1 mg lectin as substrate (*24*). The neoglycoprotein with average ligand density of 28 units attached as *p*-isothiocyanatophenyl derivatives was based on bovine serum albumin as carrier; the glycoproteins serum amyloid P component, asialofetuin, and α_1-acid glycoprotein were prepared as outlined (*28*−*30*).

Inhibition Assays. Adsorption of (neo)glycoproteins to the surface of microtiter plate wells from phosphate-buffered saline (50 μL) at 4 °C overnight established the ligand-bearing matrix. Residual sites for binding proteins were saturated with bovine serum albumin free of contaminating glycoproteins (Biomol, Hamburg, Germany; 100 μL, 1% w/v) for 1 h at 37 °C. The incubation with lectin-containing solution in the absence and presence of lactose and the glycocompounds lasted 1 h at 37 °C, and the extent of bound lectin was determined after thorough washing steps with aliquots of the indicator conjugate streptavidin−peroxidase (0.5 μg mL^{-1}; Sigma, Munich, Germany) and then with *o*-phenylenediamine (1 mg mL^{-1})/H_2O_2 (1 μL mL^{-1}) as chromogenic substrates (*31*). Cell assays were performed with the human B-lymphoblastoid line Croco II, the T-lymphoblast line MOLT-4 (T-ALL), the human pancreatic carcinoma line Capan-1, with reconstituted expression of the tumor suppressor $p16^{INK4a}$, which enhances galectin-binding capacity linked to susceptibility to anoikis (*32*; kindly provided by K. M. Detjen, Berlin, Germany), and the colon adenocarcinoma line SW480 in Dulbecco's phosphate-buffered saline (9.2 mM Na_2HPO_4, 1.5 mM KH_2PO_4, 137 mM NaCl, and 2.7 mM KCl at pH 7.4) using standard conditions with lectin incubation for 30 min at 4 °C to minimize uptake and streptavidin/R-phycoerythrin as fluorescent indicator (1:40; Sigma, Munich, Germany). FACScan analysis and processing of data from fluorescence detection yielded the percentage of positive cells and the mean fluorescence intensity (*15*, *32*). Cell proliferation in the absence/presence of test compound in aliquots of cell suspension was monitored after 48 h by using the blue chromogen MTT (5 mg mL^{-1}; 3-(4,5-dimethyl-thiozol-2-yl)-2,5-diphenyltetrazolium bromide) (*33*).

RESULTS AND DISCUSSION

Synthesis of the Glycocompounds. A convergent strategy with lactose derivatives activated as *p*-nitrophenyl carbonates was set up, taking advantage of (a) the fast reaction of *p*-nitrophenyl carbonates with amines, (b) the high yields of resulting carbamates, and (c) the versatile nature of the reaction with a variety of amino-substituted scaffolds (*34*, *35*). To delineate any influence of sugar spacing on lectin binding, we synthesized two series of ligands with the carbamate either directly connected to the anomeric center (*O*-glycosyl carbamates **A**−**F**) or separated from the pyranose ring by a butene diol linker (**G**−**J**). The synthesis of *O*-glycosyl carbamates by addition of anomerically unprotected carbohydrates to isocyanates is, with few exceptions (*36*), not stereoselective (*37*−*39*) and requires extensive product purification and identification, especially if several carbohydrate moieties are attached in one step. Activated glycosyl carbonates and 1-imidazolylcarbonyl glycosides, on the other hand, are excellent precursors of *O*-glycosyl carbamates—provided they are available as pure isomers—because they react under retention of configuration at the anomeric center. However, the preparation of glycosyl carbonates and 1-imidazolylcarbonyl glycosides from anomerically unprotected carbohydrates usually leads to α/β mixtures,

Scheme 1. Synthesis of Lactosyl Carbonate 3

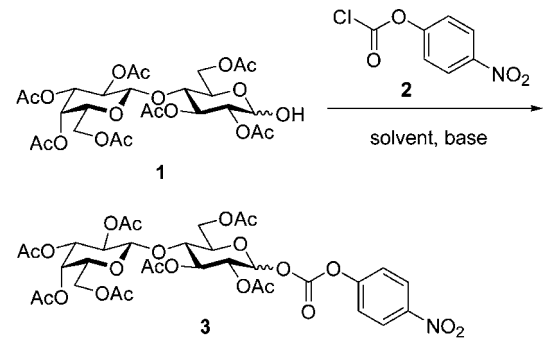

Table 1. Synthesis of lactosyl carbonate 3 under various reaction conditions according to Scheme 1

solvent	base	α/β ratio[a]	yield (%)[b]
toluene	K_2CO_3	1:2	80
	NaH	1:1	60
	Et_3N	1:1	70
	pyridine	1:4	80
	2,6-lutidine	1:1	85
CH_2Cl_2	K_2CO_3	n.d.[e]	<10
	NaH	1:1.5	80
	Et_3N	1:1	80
	pyridine	2:1	80
	DMAP	2:1	80
	2,6-lutidine	1:4	90
THF	K_2CO_3	n.d.	<10
	Et_3N	1:2.5	80
	pyridine	1:1	80
	DMAP	2.5:1	80
	2,6-lutidine	1:7	30
CH_3CN	K_2CO_3	1:1	90
	Et_3N	1.5:1	90
	pyridine	3:1	90
	KO*t*-Bu	1:2.5	35
	DMAP	>19:1	95[c]
	2,6-lutidine	1:>10	50[d]

[a] Determined by ^{1}H NMR spectroscopy of crude product. [b] Determined by ^{1}H NMR spectroscopy of crude product unless otherwise stated. [c] Yield of isolated α-**3**. [d] Yield of isolated β-**3**. [e] n.d. = not determined.

too (*18*, *40*−*45*). Leenders et al. reported high β-selectivity by hydrolysis of an intermediate anomeric silyl ether and immediate condensation of the resulting β-hydroxy group with succinimidyl chloroformate in an overall yield of 38% (*46*). When we applied this strategy to lactosyl carbonates, we also experienced a low overall yield (30−40%). Therefore, we searched for conditions that gain fast and easy access to pure isomers of activated lactosyl carbonates to answer the first question given in the Introduction.

Scheme 1 and Table 1 summarize our results for the stereoselective preparation of lactosyl carbonate **3**. From anomeric *O*-alkylation reactions, it is well-established that solvent and base have a tremendous influence on the selectivity at the anomeric center (*47*, *48*). To explore the effect of these parameters on stereoselective *O*-acylation, we reacted anomerically deprotected lactose **1** (*19*) and *p*-nitrophenyl chloroformate **2** in different base/solvent combinations. With K_2CO_3, NaH, Et_3N, and pyridine, only modest degrees of selectivity were observed regardless of the solvent. Similar results had been reported with CH_2Cl_2/pyridine (α/β = 2/1, 72%) and dimethoxyethane/NaH (α/β = 1/1, 55%) (*18*). In acetonitrile, however, 4-(dimethylamino)pyridine (DMAP) led to a remarkable α/β-selectivity of >19:1, and it was possible to isolate α-**3** in a yield of 95%. In contrast, the sterically hindered base 2,6-lutidine gave an α/β-mixture of 1:>10, from which β-**3** could be purified in a yield of 50%. Attempts to improve the yield with

Scheme 2. Synthesis of Activated Carbonate 7

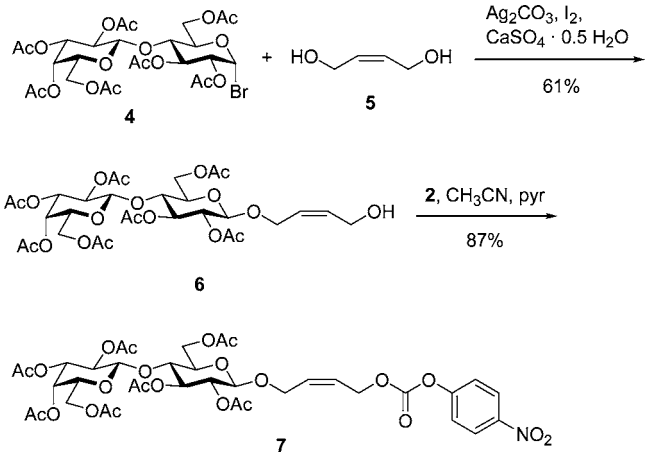

conservation of the β-selectivity by prolonging reaction times, however, were unsuccessful. We also observed that the concentration of the reaction mixture is crucial for product generation. Increasing the concentration from 0.03 M (the concentration at which all reactions had been carried out) to 0.4 M gave quantitative turnover, but with complete loss of selectivity ($\alpha/\beta = 1/1$). At lower concentrations (0.003 M) no products were found.

The synthesis of spacer-separated carbonate **7** is depicted in Scheme 2. Acetobromolactose **4** (*20*, *21*) and excess (*Z*)-butenediol **5** were reacted under Koenigs−Knorr conditions to give the β-glycoside **6**. Treatment with chloroformate **2** and pyridine in acetonitrile resulted in *p*-nitrophenyl carbonate **7** with 87% yield. The activated carbonates β-**3** and **7** were coupled to a series of amines shown in Figure 1 to give the peracetylated lactosides Ac-**A**−Ac-**J**. These were deacetylated to the mono- to tetravalent lactose derivatives **A**−**J** in a straightforward manner (Schemes 3 and 4), completing the synthesis. These compounds were next tested for their potency relative to lactose to inhibit the binding of labeled lectins to the (neo)glycoproteins.

Solid-Phase Inhibition Assays. Commonly, solid-phase inhibition assays are performed with a single type of matrix. To address the issue of whether the inhibitory activity of glycoclusters depends on local density of glycans in the (neo)glycoprotein matrix, we employed four types of matrices. The (neo)glycoproteins (LacBSA, SAP, ASF, and AGP, respectively) were adsorbed to the surface of plastic wells of microtiter plates. In each experimental series, the binding of the lectins to the (neo)glycoproteins was saturable and inhibitable by blocking the carbohydrate-binding site of the lectins. Their concentration was adjusted to yield signal intensity in the linear range in each case. To assess the inhibitory profiles lectin incubation was carried out in the presence of different concentrations of lactose and the synthesized lactose derivatives **A**−**J**, respectively. Figure 2 shows examples for inhibition of the binding of biotinylated VAA to AGP and human galectin-4 to LacBSA, respectively, by lactose and lactose derivatives **B**, **D**, and **F**. From these inhibition curves, we determined the concentration of inhibitor leading to inhibition of bound lectin of 50% (IC_{50}). All IC_{50} values of multivalent ligands were calculated per lactose moiety contained; i.e., they were valency-corrected, leading to lower inhibitory potencies of some compounds (for example, trivalent **F**, Figure 2) compared to free lactose. Relative inhibitory potencies compared to free lactose (set to 1) were plotted for each type of matrix, test substance, and lectin (Figure 3A−D). Only data for inhibitors with values above 1 are given.

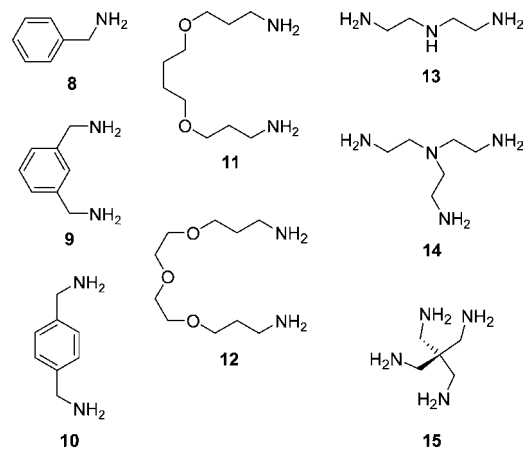

Figure 1. Amines used for preparation of **A**−**J**.

The inhibition tests revealed that conjugation of lactose to an aglycon by carbamate formation can increase inhibitory potency. Some selectivity of the bivalent lactose derivatives for certain galectins could be detected. The highest relative inhibitory potency (65 per lactose moiety), e.g., was observed for inhibition of binding of galectin-1 to the LacBSA surface by bivalent **E**. The insertion of the spacer (direct comparison for the pairs **B/G** and **D/I**) had favorable consequences only rarely. On average, these glycoclusters were more active than lysine-based compounds and surpass the activity of Tris- or aspartate-glycine-based compounds with 6-aminohexyl spacers in several cases (*31*, *49*).

Comparison of the different (neo)glycoprotein matrices revealed interesting insight into the dependence of the inhibitory activity of the lactose clusters on the local density of glycans in the matrix. For example, relative inhibition was generally lowered with increased degree of glycan branching, except for the chimera-type galectin-3 (Figure 3A−D). Since this lectin is a substrate for proteolytic processing by matrix metalloproteinases-3/-9 *in vivo* with impact for its activity in biosignaling (*50*, *51*), we tested the truncated version along with full-length galectin-3. Conspicuous selectivity for full-length galectin-3 but not its proteolytically processed derivative was observed for several ligands (**B**, **C**, **E**, **F**) with short spacers when the degree of glycan branching on the matrix was high (Figure 3D). This feature resembles the activity of 1,3,5-triiodobenzene-based inhibitors with rigidified 2-propynyl lactoside with its 7.6-fold enhancement relative to lactose and of an octavalent poly(amidoamine) starburst glycodendrimer (*52*, *53*). Under this special condition, even the monovalent compound **A** showed high activity with remarkable selectivity for galectin-3 (Figure 3D). As detailed comparison among the four panels A−D reveals, relative potency is a factor of ligand display on the matrix (see **E** in Figure 3A−D as instructive example). Inhibitory capacity should thus not be regarded as an absolute measure. Its emerging context-dependent nature confers some uncertainty to predictions for the impact on binding under physiological conditions, i.e., to cell surfaces. It is thus an obligatory step to determine whether the lactose derivatives can interfere with the binding of lectins to cells, using established tumor cells as model.

Cell-Binding Inhibition Assays. In these assays, biotinylated lectins were incubated with cells of different lines. The extent of binding of lectins to cells was measured by using fluorescently labeled streptavidin as second-step reagent. As described in the preceding part, concentration dependence of lectin binding was first determined to plot the linear range and plateau levels in each combination. Then, sugar specificity and constant reactivity of cells were ascertained in each case. An example for the carbohydrate dependence of lectin binding is given in Figure

Scheme 3. Synthesis of Lactosyl Carbamates A−F[a]

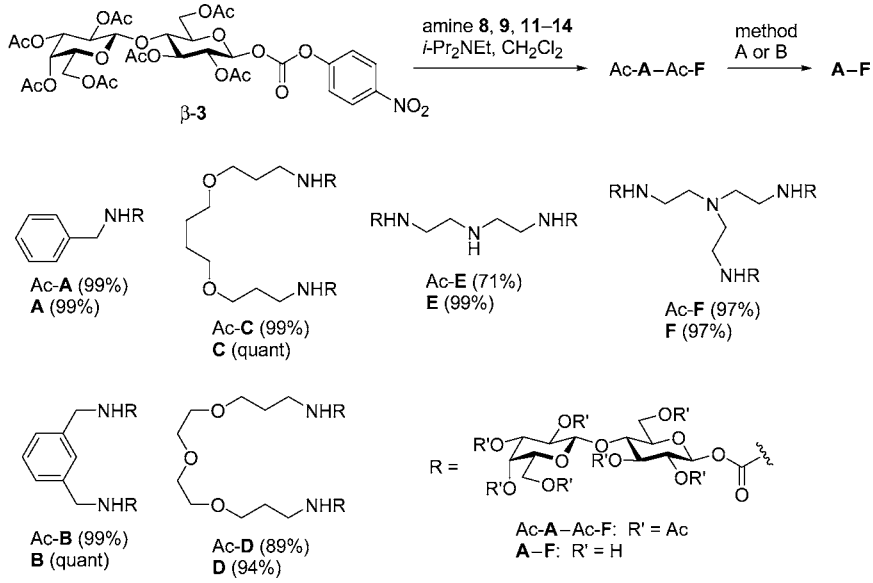

[a] Method A: NaOMe, MeOH (used for **A**−**D**). Method B: $EtNMe_2$, MeOH (used for **E**, **F**).

Scheme 4. Synthesis of Lactosyl Carbamates G−J

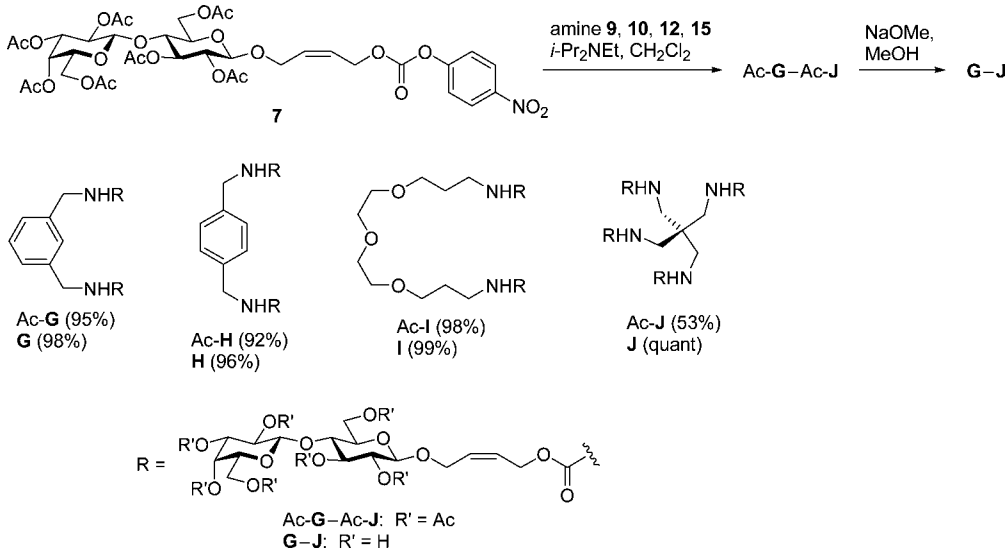

4. To preclude an impact of any variability in the cells' reactivity due to length of culture time during the passage, comparative measurements were performed with aliquots of cell batches in the same series. The obtained data, expressed in percentage of positive cells that show fluorescence above the control and mean fluorescence intensity (*F*), confirms that the test substances can

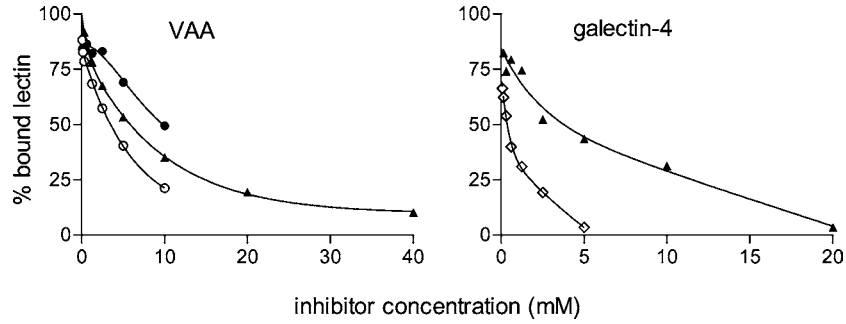

Figure 2. Inhibition of binding of biotinylated VAA (7.5 μg mL^{-1}; left) and human galectin-4 (5 μg mL^{-1}; right) to glycans of a (neo)glycoprotein-presenting matrix by a glycocompound and free lactose for comparison. The matrix presenting the lectin ligands was AGP (0.5 μg/well; left) and the neoglycoprotein LacBSA (0.25 μg/well; right). Lactose (▲) was used as control, and the bivalent compounds **D** (○) and **B** (◇) and the trivalent compound **F** (•) as inhibitors. The concentration of inhibitor is calculated with respect to its lactose contents present in the inhibition assay to normalize data.

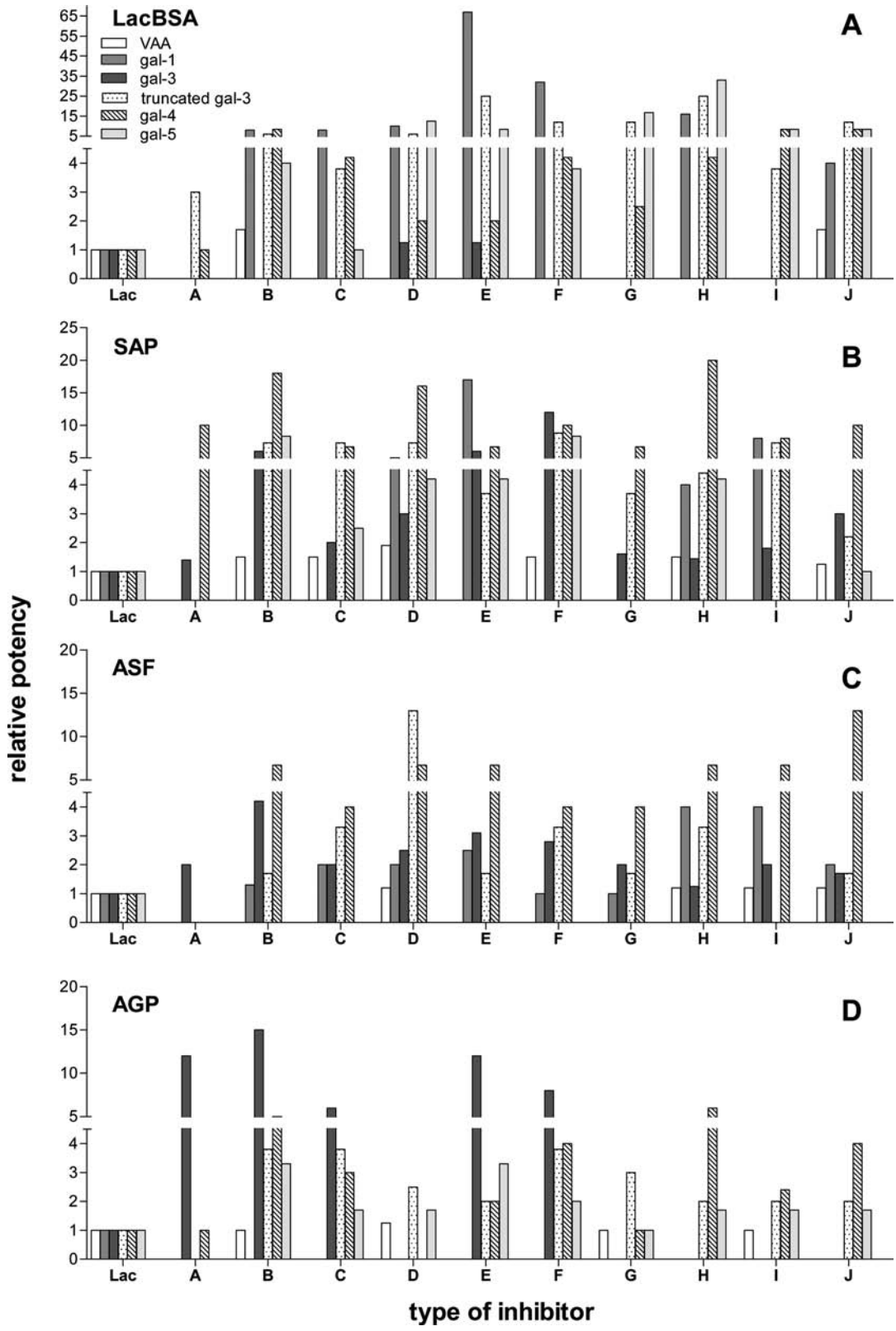

Figure 3. Relative potency of the panel of the synthetic lactose-containing compounds **A**−**J** (for structures, see Schemes 3 and 4; designations of lectins are given in the top panel) as inhibitor of lectin binding. The IC_{50} values are based on the lactose concentration with free lactose as standard (set to 1) and they were determined in each case by systematic inhibition assays (for an example, see Figure 2). Experiments were repeated up to six times; the standard deviation did not exceed 11%. All cases better than free lactose are given. The optimal conditions were as follows: (A) 0.25 μg/well neoglycoprotein (lactosylated bovine serum albumin: LacBSA) and 0.5 μg mL^{-1} VAA, 30 μg mL^{-1} galectin-1, 15 μg mL^{-1} galectin-3 (both versions), 5 μg mL^{-1} galectin-4, and 35 μg mL^{-1} galectin-5; (B) 0.5 μg/well serum amyloid P component (SAP) and 2 μg mL^{-1} VAA, 2.5 μg mL^{-1} galectin-1, 5 μg mL^{-1} full-length galectin-3, 30 μg mL^{-1} truncated galectin-3, 5 μg mL^{-1} galectin-4, and 15 μg mL^{-1} galectin-5; (C) 0.25 μg/well asialofetuin (ASF) and 0.5 μg mL^{-1} VAA, 5 μg mL^{-1} galectin-1, full-length galectin-3 and galectin-4, 30 μg mL^{-1} truncated galectin-3, and 10 μg mL^{-1} galectin-5; (D) 0.5 μg/well α_1-acid glycoprotein (AGP) and 7.5 μg mL^{-1} VAA, 30 μg mL^{-1} galectin-1, 10 μg mL^{-1} full-length galectin-3, 60 μg mL^{-1} truncated galectin-3, 20 μg mL^{-1} galectin-4, and 25 μg mL^{-1} galectin-5.

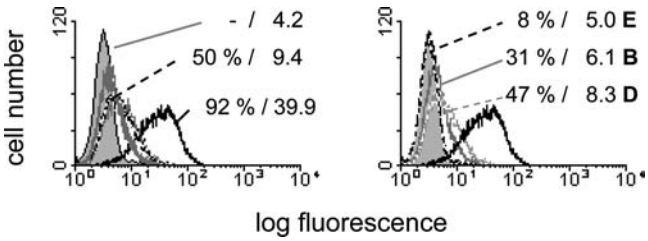

Figure 4. Semilogarithmic representation of the fluorescent surface staining of T-lymphoblast cells MOLT-4 (T-ALL) by labeled full-length galectin-3 (10 μg mL^{-1}). The control value representing staining by the second-step reagent in the absence of lectin is given as the shaded area; the peak for lectin binding in the absence of any inhibitor as the black line. Quantitative data on the percentage of positive cells that show fluorescence above the control and mean fluorescence intensity are given. The left diagram illustrates the inhibition curves obtained by increasing concentrations of lactose of 1 mM, 2 mM, 4 mM, 8 mM, and 10 mM. Given values are for the control (background staining without lectin), 2 mM lactose, and maximal lectin binding without inhibitor. Right diagram: inhibition curves obtained by glycocompounds **E**, **B**, and **D** at a concentration of 2 mM of lactose residues (i.e., a concentration of bivalent inhibitors of 1 mM).

act as inhibitors of lectin binding to cells. As shown in Figure 4, compound **E** at a concentration of 2 mM of lactose residues (i.e., a concentration of bivalent **E** of 1 mM) reduces binding of galectin-3 to the MOLT-4 T-lymphoblast cells from 92% (*F* 39.9) to 8% (*F* 5.0). In comparison, a 2 mM solution of free lactose leads to a reduction to 50% (*F* 9.4). This compound distinguishes the full-length lectin from its truncated derivative and is only rather weakly reactive with galectins-1 and -5. In general, none of the lactose clusters surpasses lactose as inhibitor for galectin-1. Compound **D**, at a concentration of 2 mM in lactose moieties reduces binding of truncated galectin-3 to MOLT-4 T-lymphoblasts from 53% (*F* 9.0) to 28% (*F* 9.0) and binding of galectin-5 to the colon adenocarcinoma line SW480 from 89% (*F* 50.8) to 60% (*F* 16.7). A 2 mM solution of lactose correspondingly leads to a reduction to 32% (*F* 7.6) and 69% (*F* 20.2), respectively. Binding of galectin-4 to the p16^{INK4a}-expressing pancreatic carcinoma line Capan-1 is impaired best by the bivalent compound **B**, a strongly active reagent in the solid-phase assays, with a reduction from 60% (*F* 47.0) to 16% (*F* 7.6) at a concentration of lactose residues of 4 mM. Here, even a 20 mM lactose solution results in a reduction to only 44% (*F* 24.5). To examine the influence of cell type, we tested galectin-3 binding also with pancreatic carcinoma cells. In this system, compound **F** was the best inhibitor with a nearly 4-fold enhancement relative to lactose. Similar results on influence of cell type were obtained with the plant toxin, with compound **D** yielding the best results at a nearly 2-fold increase (not shown).

Having delineated the activity of the lactose derivatives in lectin binding to tumor cells, any further consideration for potential applications will crucially depend on their lack of cytotoxicity. To answer this last question, we monitored cell proliferation over a period of 48 h in the presence of lactose as control and lactose clusters selected to represent the scaffolds all at the same concentration of sugar in parallel. Compounds **D**, **F**, **G**, and **I** did not influence the growth of SW480 colon adenocarcinoma cells at a concentration of lactose residues of 2 mM; compound **F** was also tested on Capan-1 pancreatic carcinoma cells at 5 mM without influence on proliferation.

CONCLUSIONS

In summary, we investigated inhibition of binding of adhesion/growth-regulatory galectins and a plant toxin to a series of immobilized (neo)glycoproteins and to tumor cells by mono- to tetravalent lactose derivatives. Our experiments enabled us to answer the five questions given at the end of the Introduction: (1) Synthetically, we developed conditions to stereoselectively produce activated lactosyl carbonates from the anomerically unprotected disaccharide. These derivatives have general application for the attachment of lactosyl residues to amino-substituted scaffolds yielding lactosyl carbamates. (2) In systematic solid-phase screening, bioactivity was found to increase by more than 1 order of magnitude relative to free lactose (valence-corrected values) for galectins. (3) Individual scaffold structure was more important than valency of lactose in the glycocompounds, and introduction of butene diol to extend the spacer's length led to enhancements only rarely. However, the inhibitory activity showed selectivity for lectin type (plant toxin vs galectins) and among galectins. In addition, the nature of the matrix glycans ranging from bi- to tetraantennary N-glycans and including the neoglycoprotein LacBSA also had a strong impact on inhibitory potency and selectivity. Interestingly, rather low activity was noted with the AGP matrix having the highest degree of branching except for the chimera-type galectin-3, an effector in cardiac dysfunction (*54*). This is why test series should routinely include cell assays to gauge potential for lectin blocking in a physiological context. (4) Strong inhibition of cell binding was detected for galectins-3 and -4 with distinct lactose-bearing compounds, and (5) we could show that representative examples of our compounds are not cytotoxic, emphasizing the suitability of carbamate-linked lactose derivatives in a lectin blocking approach.

Evidently, it is a reasonable long-term aim to tailor scaffolds adorned with lectin ligands for the ability to distinguish lectin groups or even members of a family based on reactivity. Due to arising evidence for functional antagonism among lectins, e.g., for galectins-1 and -3 in tumor growth regulation (*50*), such a discriminatory capacity is desirable. However, the impact of glycan branching revealed herein precludes immediate extrapolations from data in a single system. The measured relative reduction in inhibitory potency in cell assays could be compensated by tailoring the glycan part to the lectin. Extended structures such as histo-blood group ABH epitopes or other natural ligands will enhance affinity and selectivity (*9, 11, 55*−*57*).

ACKNOWLEDGMENT

We gratefully acknowledge the generous financial support by the research initiative LMU*excellent*, the Deutsche Forschungsgemeinschaft (FOR 434 "Oligosaccharide and DNA Chips - Analysis of Secondary Gene Products"), the Verein zur Förderung des biologisch-technologischen Fortschritts in der Medizin e.V. (Heidelberg, Germany), and an EC Marie Curie Research Training Network grant (contract no. MCRTN-2005-19561), the inspiring discussions with Drs. B. Friday and S. Namirha, the helpful advice and remarkable diligence of the reviewers as well as the expert technical assistance by B. Hofer and L. Mantel.

LITERATURE CITED

(1) Gabius, H.-J., Ed. (2009) *The Sugar Code. Fundamentals of Glycosciences*, Wiley-VCH, Weinheim.
(2) Gabius, H.-J., Siebert, H.-C., André, S., Jiménez-Barbero, J., and Rüdiger, H. (2004) Chemical biology of the sugar code. *ChemBioChem 5*, 740–764.
(3) Yamazaki, N., Kojima, S., Bovin, N. V., André, S., Gabius, S., and Gabius, H.-J. (2000) Endogenous lectins as targets for drug delivery. *Adv. Drug Delivery Rev. 43*, 225–244.
(4) Roy, R. (2003) A decade of glycodendrimer chemistry. *Trends Glycosci. Glycotechnol. 15*, 291–310.
(5) Rorive, S., Belot, N., Decaestecker, C., Lefranc, F., Gordower, L., Micik, S., Maurage, C.-A., Kaltner, H., Ruchoux, M.-M., Danguy, A., Gabius, H.-J., Salmon, I., Kiss, R., and Camby, I.

(2001) Galectin-1 is highly expressed in human gliomas with relevance for modulation of invasion of tumor astrocytes into the brain parenchyma. *Glia 33*, 241–255.

(6) Nagy, N., Legendre, H., Engels, O., André, S., Kaltner, H., Wasano, K., Zick, Y., Pector, J.-C., Decaestecker, C., Gabius, H.-J., Salmon, I., and Kiss, R. (2003) Refined prognostic evaluation in colon carcinoma using immunohistochemical galectin fingerprinting. *Cancer 97*, 1849–1858.

(7) Langbein, S., Brade, J., Badawi, J. K., Hatzinger, M., Kaltner, H., Lensch, M., Specht, K., André, S., Brinck, U., Alken, P., and Gabius, H.-J. (2007) Gene-expression signature of adhesion/growth-regulatory tissue lectins (galectins) in transitional cell cancer and its prognostic relevance. *Histopathology 91*, 681–690.

(8) Dam, T. K., Gabius, H.-J., André, S., Kaltner, H., Lensch, M., and Brewer, C. F. (2005) Galectins bind to the multivalent glycoprotein asialofetuin with enhanced affinities and a gradient of decreasing binding constants. *Biochemistry 44*, 12564–12571.

(9) Wu, A. M., Singh, T., Wu, J. H., Lensch, M., André, S., and Gabius, H.-J. (2006) Interaction profile of galectin-5 with free saccharides and mammalian glycoproteins: probing its fine specificity and the effect of naturally clustered ligand presentation. *Glycobiology 16*, 524–537.

(10) André, S., Kožár, T., Schuberth, R., Unverzagt, C., Kojima, S., and Gabius, H.-J. (2007) Substitutions in the N-glycan core as regulators of biorecognition: the case of core-fucose and bisecting GlcNAc moieties. *Biochemistry 46*, 6984–6995.

(11) Siebert, H.-C., André, S., Lu, S.-Y., Frank, M., Kaltner, H., van Kuik, A., Korchagina, E. Y., Bovin, N. V., Tajkhorshid, E., Kaptein, R., Vliegenthart, J. F. G., von der Lieth, C.-W., Jiménez-Barbero, J., Kopitz, J., and Gabius, H.-J. (2003) Unique conformer selection of human growth-regulatory lectin galectin-1 for ganglioside GM_1 versus bacterial toxins. *Biochemistry 42*, 14762–14773.

(12) Wu, A. M., Singh, T., Liu, J.-H., Krzeminski, M., Russwurm, R., Siebert, H.-C., Bonvin, A. M. J. J., André, S., and Gabius, H.-J. (2007) Activity-structure correlations in divergent lectin evolution: fine specificity of chicken galectin CG-14 and computational analysis of flexible ligand docking for CG-14 and the closely related CG-16. *Glycobiology 17*, 165–184.

(13) Jiménez, M., André, S., Siebert, H.-C., Gabius, H.-J., and D. Solís, D. (2006) AB-type lectin (toxin/agglutinin) from mistletoe: differences in affinity of the two galactoside-binding Trp/Tyr-sites and regulation of their functionality by monomer/dimer equilibrium. *Glycobiology 16*, 926–937.

(14) Tsujishita, H., Hiramatsu, Y., Kondo, N., Ohmoto, H., Kondo, H., Kiso, M., and Hasegawa, A. (1997) Selectin-ligand interactions revealed by molecular dynamics simulation in solution. *J. Med. Chem. 40*, 362–369.

(15) André, S., Sansone, F., Kaltner, H., Casnati, A., Kopitz, J., Gabius, H.-J., and Ungaro, R. (2008) Calix[n]arene-based glycoclusters: bioactivity of thiourea-linked galactose/lactose moieties as inhibitors of binding of medically relevant lectins to a glycoprotein and cell-surface glycoconjugates and selectivity among human adhesion/growth-regulatory galectins. *ChemBioChem 9*, 1649–1661.

(16) Liu, J., Begley, D., Mitchell, D. D., Verlinde, C. L. M. J., Varani, G., and Fan, E. (2008) Multivalent drug design and inhibition of cholera toxin by specific and transient protein-ligand interactions. *Chem. Biol. Drug Des. 71*, 408–419.

(17) André, S., Kaltner, H., Lensch, M., Russwurm, R., Siebert, H.-C., Fallsehr, C., Tajkhorshid, E., Heck, A. J. R., von Knebel Doeberitz, M., Gabius, H.-J., and Kopitz, J. (2005) Determination of structural and functional overlap/divergence of five prototype galectins by analysis of the growth-regulatory interaction with ganglioside GM_1 in silico and in vitro on human neuroblastoma cells. *Int. J. Cancer 114*, 46–57.

(18) Azoulay, M., Escriou, V., Florent, J.-C., and Monneret, C. (2001) Synthesis of new galactosyl and lactosyl carbamate-containing glycolipids. *J. Carbohydr. Chem. 20*, 841–853.

(19) Renaudet, O., and Dumy, P. (2001) Expedient synthesis of aminooxylated carbohydrates for chemoselective access of glycoconjugates. *Tetrahedron Lett. 42*, 7575–7578.

(20) Dale, J. K. (1916) Preparation of bromoacetylglucose and certain other bromoacetyl sugars. *J. Am. Chem. Soc. 38*, 2187–2188.

(21) Hudson, C. S., and Kunz, A. (1925) Relations between rotatory power and structure in the sugar group. X. The chloro-, bromo- and iodo-acetyl derivatives of lactose. *J. Am. Chem. Soc. 47*, 2052–2055.

(22) Feldman, K. S., and Masters, K. M. (1999) Facile preparation of tetra(2-aminoethyl)methane and tetra(3-aminopropyl)methane: novel tetravalent monomers for materials synthesis. *J. Org. Chem. 64*, 8945–8947.

(23) Gabius, H.-J. (1990) Influence of type of linkage and spacer on the interaction of β-galactoside-binding proteins with immobilized affinity ligands. *Anal. Biochem. 189*, 91–94.

(24) Kübler, D., Hung, C.-W., Dam, T. K., Kopitz, J., André, S., Kaltner, H., Lohr, M., Manning, J. C., He, L., Wang, H., Middelberg, A., Brewer, C. F., Reed, J., Lehmann, W.-D., and Gabius, H.-J. (2008) Phosphorylated human galectin-3: facile large-scale preparation of active lectin and detection of structural changes by CD spectroscopy. *Biochim. Biophys. Acta 1780*, 716–722.

(25) Gabius, H.-J., Engelhardt, R., Cramer, F., Bätge, R., and Nagel, G. A. (1985) Pattern of endogenous lectins in a human epithelial tumor. *Cancer Res. 45*, 253–257.

(26) Jiménez, M., Sáiz, J. L., André, S., Gabius, H.-J., and Solís, D. (2005) Monomer/dimer equilibrium of the AB-type lectin from mistletoe enables combination of toxin/agglutinin activities in one protein: analysis of native and citraconylated proteins by ultracentrifugation/gel filtration and cell biological consequences of dimer destabilization. *Glycobiology 15*, 1386–1395.

(27) Lensch, M., Lohr, M., Russwurm, R., Vidal, M., Kaltner, H., André, S., and Gabius, H.-J. (2006) Unique sequence and expression profiles of rat galectins-5 and -9 as a result of species-specific gene divergence. *Int. J. Biochem. Cell Biol. 38*, 1741–1758.

(28) Gabius, H.-J., Bodanowitz, S., and Schauer, A. (1988) Endogenous sugar-binding proteins in human breast tissue and benign and malignant breast lesions. *Cancer 61*, 1125–1131.

(29) Shiyan, S. D., and Bovin, N. V. (1997) Carbohydrate composition and immunomodulatory activity of different glycoforms of α_1-acid glycoprotein. *Glycoconj. J. 14*, 631–638.

(30) André, S., Kaltner, H., Furuike, T., Nishimura, S.-I., and Gabius, H.-J. (2004) Persubstituted cyclodextrin-based glycoclusters as inhibitors of protein-carbohydrate recognition using purified plant and mammalian lectins and wild-type and lectin-gene-transfected tumor cells as targets. *Bioconjugate Chem. 15*, 87–98.

(31) André, S., Frisch, B., Kaltner, H., Desouza, D. L., Schuber, F., and Gabius, H.-J. (2000) Lectin-mediated drug targeting: selection of valency, sugar type (Gal/Lac), and spacer length for cluster glycosides as parameters to distinguish ligand binding to C-type asialoglycoprotein receptors and galectins. *Pharm. Res. 17*, 985–990.

(32) André, S., Sanchez-Ruderisch, H., Nakagawa, H., Buchholz, M., Kopitz, J., Forberich, P., Kemmner, W., Böck, C., Deguchi, K., Detjen, K. M., Wiedenmann, B., von Knebel-Doeberitz, M., Gress, T. M., Nishimura, S.-I., Rosewicz, S., and Gabius, H.-J. (2007) Tumor suppressor $p16^{INK4a}$ - modulator of glycomic profile and galectin-1 expression to increase susceptibility to carbohydrate-dependent induction of anoikis in pancreatic carcinoma cells. *FEBS J. 274*, 3233–3256.

(33) Gabius, H.-J., Darro, F., Remmelink, M., André, S., Kopitz, J., Danguy, A., Gabius, S., Salmon, I., and Kiss, R. (2001) Evidence for stimulation of tumor proliferation in cell lines and histotypic cultures by clinically relevant low doses of the galactoside-binding mistletoe lectin, a component of proprietary extracts. *Cancer Invest. 19*, 114–126.

(34) Wittmann, V., and Seeberger, S. (2000) Combinatorial solid-phase synthesis of multivalent cyclic neoglycopeptides. *Angew. Chem., Int. Ed. 39*, 4348–4352.
(35) Wittmann, V., and Seeberger, S. (2004) Spatial screening of cyclic neoglycopeptides: identification of polyvalent wheat-germ agglutinin ligands. *Angew. Chem., Int. Ed. 43*, 900–903.
(36) Leenders, R. G. G., Ruytenbeek, R., Damen, E. W. P., and Scheeren, H. W. (1996) Highly diastereoselective synthesis of anomeric β-*O*-glycopyranosyl carbamates from isocyanates. *Synthesis* 1309–1312.
(37) Kunz, H., and Zimmer, J. (1993) Glycoside synthesis via electrophile-induced activation of N-allyl carbamates. *Tetrahedron Lett. 34*, 2907–2910.
(38) Gum, A. G., Kappes-Roth, T., and Waldmann, H. (2000) Enzyme-labile protecting groups in peptide synthesis: development of glucose- and galactose-derived urethanes. *Chem.—Eur. J. 6*, 3714–3721.
(39) Knoben, H.-P., Schlüter, U., and Redlich, H. (2004) Synthesis of N-unsubstituted, mono- and disubstituted carbohydrate-1-O-carbamates and their behaviour in glycoside syntheses. *Carbohydr. Res. 339*, 2821–2833.
(40) Ford, M. J., and Ley, S. V. (1990) A simple, one-pot, glycosidation procedure via 1-O-(1-imidazolylcarbonyl)glycoses and zinc bromide. *Synlett* 255–256.
(41) Iimori, T., Shibazaki, T., and Ikegami, S. (1996) A novel intramolecular decarboxylative glycosidation via mixed carbonate. *Tetrahedron Lett. 37*, 2267–2270.
(42) Scheffler, G., and Schmidt, R. R. (1997) Decarboxylative glycosidation reaction - intramolecular versus intermolecular reaction course. *Tetrahedron Lett. 38*, 2943–2946.
(43) Azumaya, I., Niwa, T., Kotani, M., Iimori, T., and Ikegami, S. (1999) An efficient synthesis of mixed β-carbonates of acyl-protected sugars and their decarboxylative glycosidation promoted by trimethylsilyl trifluoromethanesulfonate. *Tetrahedron Lett. 40*, 4683–4686.
(44) Fernández, C., Nieto, O., Fontenla, J. A., Rivas, E., de Ceballos, M. L., and Fernández-Mayoralas, A. (2003) Synthesis of glycosyl derivatives as dopamine prodrugs: interaction with glucose carrier glut-1. *Org. Biomol. Chem. 1*, 767–771.
(45) Cai, T. B., Lu, D., Tang, X., Zhang, Y., Landerholm, M., and Wang, P. G. (2005) New glycosidase activated nitric oxide donors: glycose and 3-morphorlinosydnonimine conjugates. *J. Org. Chem. 70*, 3518–3524.
(46) Leenders, R. G. G., Scheeren, H. W., Houba, P. H. J., Boven, E., and Haisma, H. J. (1995) Synthesis and evaluation of novel daunomycin-phosphate, -sulfate, -β-glucuronide and -β-glucoside prodrugs for application in ADEPT. *Bioorg. Med. Chem. Lett. 5*, 2975–2980.
(47) Schmidt, R. R. (1996) The anomeric *O*-alkylation and the trichloroacetimidate method - versatile strategies for glycoside bond formation. *Modern Methods in Carbohydrate Synthesis* (Khan, S. H., and O'Neill, R. A., Eds.) pp 20−54, Harwood Academic Publishers, Amsterdam.
(48) Tamura, J. (2000) Glycosylation methods: alkylations of reducing sugars. *Carbohydrates in Chemistry and Biology* (Ernst, B., Hart, G. W., and Sinaÿ, P., Eds.) pp 177−193, Wiley-VCH, Weinheim.
(49) Lee, R. T., Gabius, H.-J., and Lee, Y. C. (1992) Ligand binding characteristics of the major mistletoe lectin. *J. Biol. Chem. 267*, 23722–23727.
(50) Kopitz, J., von Reitzenstein, C., André, S., Kaltner, H., Uhl, J., Ehemann, V., Cantz, M., and Gabius, H.-J. (2001) Negative regulation of neuroblastoma cell growth by carbohydrate-dependent surface binding of galectin-1 and functional divergence from galectin-3. *J. Biol. Chem. 276*, 35917–35923.
(51) Lohr, M., Kaltner, H., Lensch, M., André, S., Sinowatz, F., and Gabius, H.-J. (2008) Cell-type-specific expression of murine multifunctional galectin-3 and its association with follicular atresia/luteolysis in contrast to pro-apoptotic galectins-1 and -7. *Histochem. Cell Biol. 130*, 567–581.
(52) André, S., Ortega, P. J. C., Perez, M. A., Roy, R., and Gabius, H.-J. (1999) Lactose-containing starburst dendrimers: influence of dendrimer generation and binding-site orientation of receptors (plant/animal lectins and immunoglobulins) on binding properties. *Glycobiology 9*, 1253–1261.
(53) André, S., Liu, B., Gabius, H.-J., and Roy, R. (2003) First demonstration of differential inhibition of lectin binding by synthetic tri- and tetravalent glycoclusters from cross-coupling of rigidified 2-propynyl lactoside. *Org. Biomol. Chem. 1*, 3909–3916.
(54) Liu, Y.-H., D'Ambrosio, M., Liao, T.-D., Peng, H., Rhaleb, N.-E., Sharma, U., André, S., Gabius, H.-J., and Carretero, O. A. (2009) N-acetyl-seryl-aspartyl-lysyl-proline prevents cardiac remodeling and dysfunction induced by galectin-3, a mammalian adhesion/growth-regulatory lectin. *Am. J. Physiol. Heart Circ. Physiol. 296*, H404–H412.
(55) Wu, A. M., Wu, J. H., Liu, J.-H., Singh, T., André, S., Kaltner, H., and Gabius, H.-J. (2004) Effects of polyvalency of glycotopes and natural modifications of human blood group ABH/Lewis sugars at the Galβ1-terminated core saccharides on the binding of domain I of recombinant tandem-repeat-type galectin-4 from rat gastrointestinal tract (G4-N). *Biochimie 86*, 317–326.
(56) André, S., Kojima, S., Prahl, I., Lensch, M., Unverzagt, C., and Gabius, H.-J. (2005) Introduction of extended LEC14-type branching into core-fucosylated biantennary N-glycan. *FEBS J. 272*, 1986–1998.
(57) Gabius, H.-J. (2008) Glycans: bioactive signals decoded by lectins. *Biochem. Soc. Trans. 36*, 1491–1496.

BC900152W

Phospholipid Conjugate for Intracellular Delivery of Peptide Nucleic Acids

Gang Shen, Huafeng Fang, Yinyin Song, Agata A. Bielska, Zhenghui Wang, and John-Stephen A. Taylor*

Department of Chemistry, Washington University in St. Louis, One Brookings Drive, St. Louis, Missouri 63130. Received January 31, 2009; Revised Manuscript Received July 18, 2009

Peptide nucleic acids (PNAs) have a number of attractive features that have made them an ideal choice for antisense and antigene-based tools, probes, and drugs, but their poor membrane permeability has limited their application as therapeutic or diagnostic agents. Herein, we report a general method for the synthesis of phospholipid-PNAs (LP-PNAs) and compare the effect of noncleavable lipids and bioreductively cleavable lipids (L and LSS) and phospholipid (LP) on the splice-correcting bioactivity of a PNA bearing the cell penetrating Arg9 group (PNA-R9). While the three constructs show similar and increasing bioactivity at 1−3 μM, the activity of **LP-PNA-R9** continues to increase from 4−6 μM, while the activity of **L-PNA-R9** remains constant and that of **LSS-PNA-R9** decreases rapidly in parallel with their relative cytotoxicity. The activity of both **LP-PNA-R9** and **L-PNA-R9** dramatically increased in the presence of chloroquine, as expected for an endocytotic entry mechanism. The constructs were also found to have CMC values of 1.0 and 4.5 μM, respectively, in 150 mM NaCl, pH 7 water, suggesting that micelle formation may play a hitherto unrecognized role in modulating toxicity and/or facilitating endocytosis.

INTRODUCTION

Compared to conventional drug inhibitors that target enzymes by a complex set of interactions, antisense and antigene agents such as oligonucleotides (ODNs), peptide nucleic acids (PNAs), and siRNA target nucleic acids by sequence-specific Watson−Crick base pairing, making them more easily programmable (*1*−*4*). Peptide nucleic acids contain repeating *N*-(2-aminoethyl)glycine units with the nucleobases attached through methylenecarbonyl linkers which mimic natural deoxyribose phosphate backbone of DNA (*5, 6*). Due to their non-native peptide backbone, PNAs have a number of attractive features for the development of probes, tools, and drugs (*7*−*9*). They exhibit higher binding affinity and specificity for RNA and DNA and can invade regions of secondary structure. They also do not activate RNaseH degradation of a target mRNA and are highly resistant to enzymatic degradation by nuclease and proteases. Therefore, PNAs have emerged as promising candidates for the development of antisense and antigene therapeutics and diagnostics.

Because of their size and polar nature, PNAs are not very membrane permeable and require attachment of cell penetrating groups or complexation with cationic lipid-based transfection agents to enter cells (*10*−*14*). Cationic peptides, such as Arg9 or the Tat peptide, have been found to facilitate entry of PNAs into cells via macropinocytosis, though a significant amount appears to be trapped in endosomes (*15*−*22*). PNAs have been hybridized to short ODNs to impart negative charge to the PNA to enable electrostatic delivery by cationic transfection agents (*11, 17, 23*), but the toxicity of these agents has limited their use *in vivo* (*13, 24*). More recently, a cationic nanoparticle has been developed that can deliver PNAs into cells with greater efficiency and less toxicity than cationic liposomes (*25*). As of yet, an efficient and nontoxic PNA delivery system for *in vivo* PNA delivery remains elusive.

It was reported recently that attachment of a phospholipid to an anti-telomerase thiophosphoramidate greatly improved its activity in cell culture (*26*−*28*). Subsequently, it was shown that attachment of a fatty acid to the N-terminus of PNAs bearing cell penetrating peptides also enhanced their bioactivity (*29, 30*), but nothing is known about the effect of attaching a phospholipid. We hypothesized that the phosphodiester group might be important for bioactivity, because it could function either as a part of a recognition element for some membrane mediated intracellular delivery mechanism or as a cleavable linker to release the PNA from the membrane once inside the cell. Herein, we report that a phospholipid conjugated to a PNA bearing an Arg9 cell penetrating peptide exhibits better bioactivity and lower cytotoxicity than the corresponding conjugates with a lipid or a bioreductively cleavable lipid in the 4−6 μM range.

EXPERIMENTAL PROCEDURES

General Procedures. All reactions were performed under an argon or nitrogen atmosphere unless otherwise specified. All commercially available materials were used without further purification unless otherwise noted. Anhydrous solvents for reactions, such as DMF, DCM, and acetonitrile were either used as obtained from Sigma-Aldrich or distilled from an appropriate drying agent. ^{1}H NMR, ^{13}C NMR, and ^{31}P NMR spectra were recorded on VarianUnityPlus-300. Trimethyl phosphate was used as the external reference for ^{31}P NMR. All PNAs and conjugates were purified by reversed-phase high-performance liquid chromatography (HPLC) on a Beckman System Gold instrument equipped with a UV−vis array detector. HPLC fractions were collected and concentrated under vacuum in a SpeedVac (Savant). Concentrations of PNAs were determined by UV absorption on a Bausch and Lomb Spectronic1001 spectrophotometer or on a Varian Cary 100 Bio UV−vis spectrophotometer using standard extinction coefficients. Fluorescence spectra were measured on a Varian Cary Eclipse fluorescence spectrophotometer. The PNAs were characterized by MALDI-TOF on a PerSpective Voyager MALDI-TOF mass spectrometer in linear mode using insulin as the internal reference.

2-Cyanoethyl 3-((4-methoxyphenyl)diphenylmethylamino) propyl Diisopropyl-Phosphoramidite (1). 3-((4-Methoxyphenyl)diphenylmethylamino)propan-1-ol (0.74 g, 2.33 mmol) was

* To whom correspondence should be addressed. Department of Chemistry, Campus Box 1134, Washington University, One Brookings Drive, St. Louis, MO 63130, Email: taylor@wustl.edu.

10.1021/bc900048y CCC: $40.75 © 2009 American Chemical Society
Published on Web 08/13/2009

dissolved in freshly distilled CH_2Cl_2 (23 mL). *N*,*N*-Diisopropylethylamine (1.63 mL, 9.34 mmol) was added, followed by 2-cyanoethyl *N*,*N*-diisopropylchlorophosphoramidite (1.04 mL, 4.67 mmol). The mixture was stirred at room temperature for 8 h before addition of saturated aqueous NH_4Cl solution (100 mL). The aqueous layer was extracted with EtOAc (3 × 100 mL). The combined organic extracts were dried (Na_2SO_4), filtered, and concentrated. The residue was used directly in the next step.

2,5-Dioxopyrrolidin-1-yl 12-((2-cyanoethyl)(3-((4-methoxyphenyl)diphenylmethyl-amino)propyl)phosphoryloxy)dodecanoate (3). Compound **1** from the previous step was dissolved in freshly distilled CH_2Cl_2 (9 mL) and CH_3CN (9 mL). 2,5-Dioxopyrrolidin-1-yl 12-hydroxydodecanoate (0.75 g, 2.38 mmol) was added, followed by diisopropylammonium tetrazolide (0.41 g, 2.38 mmol). The mixture was stirred at room temperature for 12 h before addition of *tert*-butyl hydroperoxide (5 M, 1.83 mL). The reaction was quenched after 2 h with saturated aqueous $NaHCO_3$ solution (100 mL). The aqueous layer was extracted with EtOAc (3 × 100 mL). The combined organic extracts were dried (Na_2SO_4), filtered, and concentrated. The oil was purified by chromatography (SiO_2, 50% EtOAc in hexanes) to afford **3** (0.75 g, 42%) as pale yellow oil: ^{1}H NMR (CD_2Cl_2, 300 MHz) δ 7.54 (m, 4H), 7.42 (m, 2H), 7.36 (m, 4H), 7.26 (m, 2H), 6.87 (m, 2H), 4.26 (m, 2H), 4.14 (m, 2H), 4.06 (m, 2H), 3.85 (s, 3H), 2.83 (s, 4H), 2.73 (t, J = 6.2 Hz, 2H, $\underline{CH_2}CN$), 2.65 (t, J = 7.5 Hz, 2H,$\underline{CH_2}CONHS$), 2.28 (m, 2H), 1.93 (m, 2H), 1.78 (m, 4H), 1.35 (m, 14H); ^{13}C NMR (CD_2Cl_2, 75 MHz) δ 169.6, 169.1, 158.3, 146.7, 130.0, 128.7, 128.0, 126.5, 117.0, 113.3, 70.6, 68.5, 66.6, 66.5, 62.0, 55.4, 40.0, 31.6, 31.1, 30.5, 29.7, 29.6, 29.3, 29.0, 25.9, 25.6, 24.9, 19.9; ^{31}P NMR (CD_2Cl_2, 121.4 MHz) δ −0.1; HRMS (ES^+) *m*/*z* 776.3684 (M^+ + H, $C_{42}H_{55}N_3O_9P$ requires *m*/*z* 776.3676).

***tert*-Butyl 3-((2-Cyanoethoxy)(diisopropylamino)phosphinooxy)propylcarbamate (2).** *tert*-Butyl 3-hydroxypropylcarbamate (0.13 g, 0.75 mmol) was dissolved in freshly distilled CH_2Cl_2. 2-Cyanoethyl *N*,*N*,*N*′,*N*′-tetraisopropylphosphoramidite (0.29 g, 0.97 mmol) in dry CH_3CN (4 mL) was added, followed by *N*,*N*-diisopropylammonium tetrazolide (0.15 g, 0.90 mmol). The mixture was stirred at room temperature for 8 h before addition of saturated aqueous NH_4Cl solution (80 mL). The aqueous layer was extracted with EtOAc (3 × 100 mL). The combined organic extracts were dried (Na_2SO_4), filtered, and concentrated. The residue was used directly in the next step.

***tert*-Butyl 3-(((2-Cyanoethoxy)(2,5-dioxopyrrolidin-12-yl)-dodecanoate)phosphoryl-oxy)propylcarbamate (4).** Compound **2** (0.18 g, 0.48 mmol) from the previous step was dissolved in freshly distilled CH_2Cl_2 (2.5 mL) and CH_3CN (2.5 mL). 2,5-Dioxopyrrolidin-1-yl 12-hydroxydodecanoate (0.10 g, 0.62 mmol) was added, followed by *N*,*N*-diisopropylammonium tetrazolide (0.04 g, 0.58 mmol). The mixture was stirred at room temperature for 12 h before addition of *tert*-butyl hydroperoxide (5 M, 0.5 mL). The reaction was quenched after 2 h with saturated aqueous $NaHCO_3$ solution (100 mL). The aqueous layer was extracted with EtOAc (3 × 100 mL). The combined organic extracts were dried (Na_2SO_4), filtered, and concentrated. The oil was purified by chromatography (SiO_2, 50% EtOAc in hexanes) to afford **4** (178 mg, 61%) as a colorless oil: ^{1}H NMR (CD_2Cl_2, 300 MHz) δ 5.05 (broad, NH), 4.26 (m, 2H), 4.12 (m, 4H), 3.24 (m, 2H), 2.84 (s, 4H), 2.80 (m, 2H), 2.63 (t, J = 7.5 Hz, 2H, $\underline{CH_2}CONHS$), 1.89 (m, 2H), 1.73 (m, 4H), 1.55 (m, 23H); ^{13}C NMR (CD_2Cl_2, 75 MHz) δ 169.6, 169.1, 156.1, 117.0, 79.1, 68.7, 65.8, 62.1, 37.0, 30.7, 30.5, 30.4, 29.6, 29.5, 29.3, 29.2, 28.9, 28.4, 25.9, 25.6, 24.8, 20.0, 19.9; ^{31}P NMR (CD_2Cl_2, 121.4 MHz) δ −3.6; HRMS (ES^+) *m*/*z* 626.2797 (M^+ + Na, $C_{27}H_{46}N_3O_{10}PNa$ requires *m*/*z* 626.2819).

2,5-Dioxopyrrolidin-1-yl palmitate (5). Palmitic acid (2.0 g, 7.8 mmol), *N*-hydroxy-succinimide (0.94 g, 8.2 mmol), and *N*,*N*′-dicyclohexylcarbodiimide (1.69 g, 8.2 mmol) were dissolved in dry 1,4-dioxane (30 mL). The mixture was stirred at room temperature for 12 h. The precipitate was filtered, and the resulting residue was washed with saturated aqueous $NaHCO_3$ (3 × 100 mL). The aqueous layer was extracted with EtOAc (3 × 100 mL). The combined organic extracts were dried (Na_2SO_4), filtered, and concentrated to afford **5** (1.88 g, 81%) as a white solid: ^{1}H NMR ($CDCl_3$, 300 MHz) δ 2.86 (s, 4H), 2.63 (t, J = 7.5 Hz, 2H, $\underline{CH_2}CONHS$), 1.77 (m, 2H), 1.29 (m, 24H), 0.91 (t, J = 6.5 Hz, 3H, $CH_2\underline{CH_3}$); ^{13}C NMR ($CDCl_3$, 75 MHz) δ 169.4, 169.0, 32.2, 31.2, 29.9, 29.8, 29.6, 29.3, 29.1, 25.9, 24.8, 23.0, 14.4; HRMS (ES^+) *m*/*z* 354.2659 (M^+ + H, $C_{20}H_{36}NO_4$ requires *m*/*z* 354.2644).

***N*-(3-Hydroxypropyl)palmitamide (6).** 3-Amino-1-propanol (0.47 g, 6.3 mmol), palmitic acid (1.2 g, 4.2 mmol), and *N*-(3-dimethylaminopropyl)-*N*′-ethylcarbodiimide hydrochloride (0.81 g, 4.2 mmol) were dissolved in freshly distilled CH_2Cl_2 (46 mL) and pyridine (23 mL) at 0 °C. The mixture was then stirred at room temperature for 12 h before addition of 1 N HCl (250 mL). The aqueous layer was extracted EtOAc (3 × 50 mL); the combined organic extracts was dried (Na_2SO_4), filtered, and concentrated. The residue was purified by chromatography (SiO_2, 40% EtOAc in hexanes) to afford **6** (1.11 g, 76%) as a white solid: ^{1}H NMR ($CDCl_3$, 300 MHz) δ 5.77 (broad, NH), 3.65 (m, 2H), 3.47 (m, 2H), 3.26 (broad, 1H), 2.23 (s, 2H), 1.72 (m, 4H), 1.29 (m, 24H), 0.91 (t, J = 7.2 Hz, 3H, $CH_2\underline{CH_3}$); ^{13}C NMR ($CDCl_3$, 75 MHz) δ 174.9, 59.3, 37.0, 36.3, 32.7, 32.2, 29.9 (3), 29.7, 29.6 (2), 26.1, 22.9, 14.1; HRMS (ES^+) *m*/*z* 314.3050 (M^+ + H, $C_{19}H_{40}NO_2$ requires *m*/*z* 314.3059).

General Procedures for the Synthesis of PNA and Its Conjugates. All PNAs and conjugates were synthesized on an Expedite 8900 PNA synthesizer (Applied Biosystems) on 2 μmol Fmoc-PAL-PEG-PS resin following the standard automated Fmoc PNA synthesis procedure with commercially available monomers (Panagene Inc., Korea). For nonautomated steps, the resin was removed from the column and transferred to a glass vial to which solvent and reagents were added and shaken. After the specified time, the resin was filtered, washed and dried, by filtering the suspension through the original column by drawing the solvent through the bottom with an attached syringe, and then washed with dry DMF (2 × 3 mL) and dry CH_2Cl_2 (2 × 3 mL), followed by drying under a stream of N_2. Final cleavage of the PNA from the resin and deprotection was carried out by transferring washed and dried resin to a vial and treating with trifluoroacetic acid (300 μL) and *m*-cresol (100 μL) at room temperature for 2 h. The solution was filtered from the resin and added into ice-cold Et_2O (5 mL) and kept in an ice bath for 1 h. The resulting precipitate was collected by centrifugation and purified by reverse-phase gradient HPLC with solvent A [0.1% TFA in H_2O] and solvent B [0.1% TFA in CH_3CN] on Varian Microsorb-MV column (C-18, 5 μm, 300 Å pore size, 4.6 × 250 mm) at 1 mL/min. HPLC method A: 40 min 0−40% B in A, 45 min 40−100% B in A. Method B: 15 min 0−40% B in A, 40 min 40−60% B in A. The desired PNAs eluted as single HPLC peaks, which were broader and tended to tail for lipidated PNAs (see Supporting Information). The HPLC fractions were collected, concentrated to dryness, and redissolved in water. PNA solutions were characterized by UV−vis, and their concentration was determined from their absorbance at 260 nm. PNAs were also characterized by MALDI-TOF analysis with insulin as an internal standard, and showed a single major molecular ion peak corresponding to the desired product (see Supporting Information).

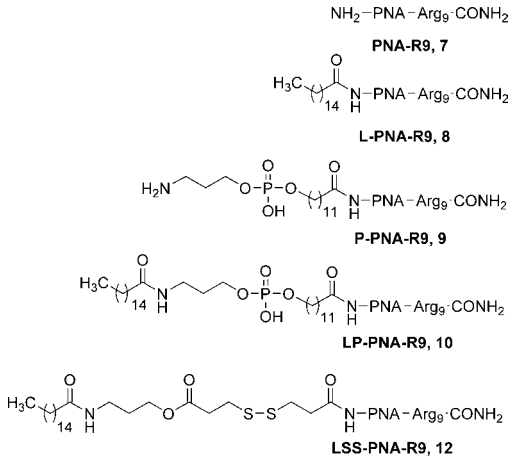

Figure 1. Structures of the PNA conjugates.

PNA-R9 (7). The PNA-R9 H-CCTCTTACCTCAGTTAC-ARRRRRRRRR-NH_2 was synthesized and purified by the general procedure described above using HPLC Method A. MALDI-TOF (matrix: α-cyano-4-hydroxy-cinnamic acid (CHCA)): average $[M+H]^+$ expected 6171.2, found 6172.9.

L-PNA-R9 (8). Following automated PNA synthesis of H-CCTCTTACCTCAGTTACARRRRRRRRR-NH_2 and washing and drying, but prior to cleavage and deprotection, the resin was removed from the column and shaken with piperidine (1 mL) and dry DMF (4 mL) in a vial for 30 min and then filtered, washed, and dried. The resin was then shaken for 12 h with palmitic acid (5.1 mg), *N*,*N*′-dicyclohexylcarbodiimide (4.1 mg), and 4-dimethylaminopyridine (2.4 mg) in dry DMF (100 μL) in a vial and then filtered, washed, and dried. The PNA was then cleaved from the resin, deprotected, and purified by HPLC method B. MALDI-TOF (matrix: CHCA): average $[M+H]^+$ expected 6409.7, found 6410.1.

P-PNA-R9 (9). Following automated PNA synthesis of H-CCTCTTACCTCAGTTACARRRRRRRRR-NH_2 and washing and drying, but prior to cleavage and deprotection, the resin was removed from the column and shaken with piperidine (1 mL) and dry DMF (4 mL) for 30 min in a vial and then filtered, washed, and dried. The resin was then shaken for 12 h with **4** (10 μmol, 11.5 mg) and *N*,*N*-diisopropylethylamine (10 μmol, 1.7 μL) in dry DMF (100 μL) in a vial and then filtered, washed, and dried. The resin was then shaken with pyridine (1.6 μL) and triethylamine (2.8 μL) in DMF (100 μL) for 20 h and then filtered, washed, and dried. The PNA was cleaved from the resin, deprotected, and purified by HPLC Method A. MALDI-TOF (matrix: CHCA): average $[M+H]^+$ expected 6506.6, found 6506.4.

LP-PNA-R9 (10). Following automated PNA synthesis of H-CCTCTTACCTCAGTTACARRRRRRRRR-NH_2 and washing, but prior to cleavage and deprotection, the resin was removed from the column and shaken with piperidine (1 mL) and dry DMF (4 mL) for 30 min in a vial and then filtered, washed, and dried. The resin was then shaken for 12 h with **3** (20 μmol, 15.5 mg) and *N*,*N*-diisopropylethylamine (20 μmol, 3.5 μL) in dry DMF (100 μL) in a vial and filtered, washed, and dried. The resin was then treated with 1% TFA in CH_2Cl_2 (2 × 3 mL) for 10 min in a vial and then filtered, washed, and dried. The resin was then shaken for 20 h with **5** (20 μmol, 7.1 mg) and *N*,*N*-diisopropylethylamine (40 μmol, 7.0 μL) in dry DMF (100 μL) in a vial and then filtered, washed, and dried. The resin was then shaken for 20 h with pyridine (1.6 μL) and triethylamine (2.8 μL) in DMF (100 μL) in a vial and then filtered, washed, and dried. The PNA was then cleaved from the resin, deprotected, and purified by HPLC method B. MALDI-TOF (matrix: CHCA): average $[M+H]^+$ expected 6744.9, found 6744.4.

LP-sPNA-R9 (11). This PNA was prepared by the same procedure used to prepare LP-PNA-R9 **10** except that the scrambled sequence ACATCACTTGTTACCCCT was used. MALDI-TOF (matrix: CHCA): average $[M+H]^+$ expected 6744.9, found 6745.3.

LSS-PNA-R9 (12). Following automated PNA synthesis of H-CCTCTTACCTCAGTTACARRRRRRRRR-NH_2 and washing, but prior to cleavage and deprotection, the resin was removed from the column and shaken in piperidine (1 mL) and dry DMF (4 mL) for 30 min in a vial and then filtered, washed, and dried. The resin was then shaken for 12 h with 3,3′-dithiodipropionic acid (5.1 mg), *N*,*N*′-dicyclohexylcarbodiimide (4.1 mg), and 4-dimethylaminopyridine (2.4 mg) in dry DMF (100 μL) in a vial and then filtered, washed, and dried. The resin was then shaken for 12 h with **6** (2.9 mg), *N*,*N*′-dicyclohexylcarbodiimide (4.1 mg), and 4-dimethylaminopyridine (2.4 mg) in dry DMF (100 μL) in a vial and then filtered, washed, and dried. The PNA was then cleaved from the resin, deprotected, and purified by HPLC method B. MALDI-TOF (matrix: α-cyano-4-chloro-cinnamic acid): average $[M+H]^+$ expected 6660.0, found 6659.4.

Cell Culture. pLuc705 HeLa cells were maintained in DMEM containing 10% FBS, streptomycin (100 μg/mL), penicillin (100 units/mL), G418 (100 μg/mL), and hygromycin B (100 μg/mL) at 37 °C in a humidified atmosphere with 5% CO_2.

Splice Correction Assay. pLuc705 HeLa cells were seeded in a 96-well microtiter plate at a density of 1×10^4 cells/well and cultured for 24 h in 100 μL DMEM containing 10% FBS. At the time of transfection, the medium was replaced with 80 μL fresh medium, and then a solution of PNA in 20 μL OPTI-MEM was added. After 24 h incubation, 100 μL Steady-Glo Luciferase assay reagent was added to each well. The contents were mixed and allowed to incubate at room temperature for 10 min to stabilize luminescence. Signals were recorded on a Luminoskan Ascent luminometer (Thermo Scientific) with an integration time of 1 s per well. For experiments requiring disulfide cleavage, the PNA was preincubated with DTT (10 mM) for 10 min before adding to the plate. For experiments requiring chloroquine, the chloroquine (Sigma-Aldrich Co.) was added 6 h after PNA addition to give a final concentration of 100 μM.

Cytotoxicity Assays. The cytotoxicity of the PNAs was evaluated by the CellTiter-Glo Luminescent Cell Viability Assay (Promega Co.). HeLa cells were seeded in a 96-well plate at a density of 1×10^4 cells/well and cultured for 24 h in 100 μL DMEM containing 10% FBS. Thereafter, the medium was replaced with 100 μL fresh medium containing various concentrations of the PNAs, Polyfect (positive controls), or no additive (negative control). After 24 h incubation at 37 °C, 100 μL of CellTiter-Glo reagent were added. The contents were mixed, and the plate was allowed to incubate at room temperature for 10 min to stabilize the luminescence signals. Luminescence intensities were recorded on a Luminoskan Ascent luminometer (Thermo Scientific) with an integration time of 1 s per well. The relative cell viability was calculated as the ratio of the luminescence in the presence and absence of PNA and fit to LC50 values using the Hill-Slope model (% viability $= 100/(1 + ([PNA]/LC50)^{slope})$.

Determination of Critical Micelle Concentration (CMC). Pyrene was purified by silica gel chromatography with cyclohexane to give a pale yellow solid. Stock solutions of **L-PNA-R9** (45.5 μM) and **LP-PNA-R9** (18.1 μM) were diluted in water to different concentrations. Pyrene in 1% methanol/water (50 μL, 10 μM) was added to each concentration of PNA (450 μL).

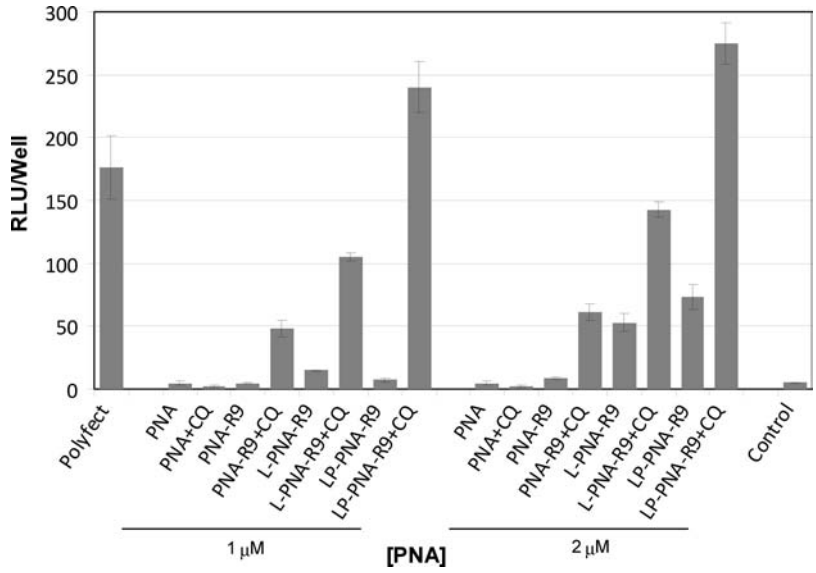

Figure 2. Luciferase splice-correcting bioactivity for 1 and 2 μM **PNA**, **PNA-R9**, **L-PNA-R9**, **LP-PNA-R9**, with and without 100 μM chloroquine (CQ), using a blank as a control.

Scheme 1. Synthesis of Phosphodiester Building Blocks for Phospholipid PNA Synthesis

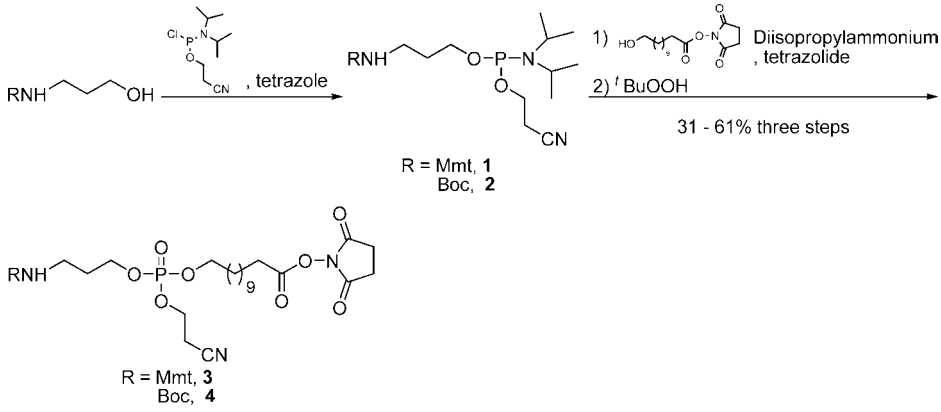

L-PNA-R9 and **LP-PNA-R9** were also diluted in a buffer (150 mM NaCl, 5 mM Tris, pH 7) to different concentrations. Pyrene in 1.4% methanol/buffer solution (50 μL, 10 μM) was added to each concentration of PNA (450 μL). Fluorescence emission spectra were obtained by exciting the pyrene at 332 nm. The ratio of intensity of the first (373 nm) and third (384 nm) emission peaks was plotted against PNA concentration to determine the CMC from the breakpoint in a bilinear fit to the data.

RESULTS AND DISCUSSION

Building Block Synthesis. L-PNA-R9, **LSS-PNA-R9**, and **LP-PNA-R9** (Figure 1) were synthesized to study the effect of adding a lipid, a bioreductively cleavable lipid, and a phospholipid on the bioactivity of **PNA-R9**, a splice-correcting PNA linked to the well-studied cell penetrating peptide, D-Arg$_9$ (Figure 1) (*19, 31*). The unnatural D-enantiomer of arginine has been shown to affect membrane permeability in the same way as the L-enantiomer, and was used to minimize enzymatic degradation by proteases and increase the lifetime of the PNA construct (*32*). The PNAs were synthesized by a combination of standard solid-phase automated Fmoc peptide synthesis (*33*), and by on column and postsynthetic modification (*34*). The phosphotriester building blocks **3** and **4** were synthesized by treating *N*-methoxytrityl (Mmt) or *N*-Boc propanolamine with 2-cyanoethyl *N*,*N*-diisopropylchlorophosphoramidite in the presence of 1*H*-tetrazole, respectively. The resulting phosphites were then treated with the NHS ester of 12-hydroxydodecanoic acid in the presence of diisopropylammonium tetrazolide and oxidized with *tert*-butyl hydroperoxide, to give **3** and **4** in good yields (Scheme 1).

PNA-R9 was first synthesized in a 2 μmol scale by automated Fmoc PNA synthesis on an Fmoc-PAL-PEG-PS resin with Bhoc-protected monomers on ABI 8909 solid-phase PNA synthesis machine. The phosphate building block **3** was coupled to the amino terminus of the PNA on the resin and deprotected with 1% TFA in DCM to remove the Mmt protecting group. The resulting primary amine was coupled with succinimidyl palmitate, and the cyanoethyl protecting group was removed with pyridine/triethylamine. **LP-PNA-R9** was precipitated from cold ether after it was cleaved from the resin and deprotected with TFA/*m*-cresol (Scheme 2). It is worth noting that initial attempts to use Boc instead of Mmt as an amino-protecting ligand proved to be problematic because of competitive cleavage from the resin. Both 10% TFA/DCM and 10% v/v concentrated sulfuric acid/1,4-dioxane only gave the desired product in very low yields (*35*). It is likely that the TFA was not concentrated enough to efficiently deprotect Boc after treatment for 12 h, while the 10% sulfuric acid in 1,4-dioxane appeared to cause premature cleavage of PNA from the resin. **P-PNA-R9** (Figure

Scheme 2. Synthesis of Phospholipid PNA, LP-PNA-R9

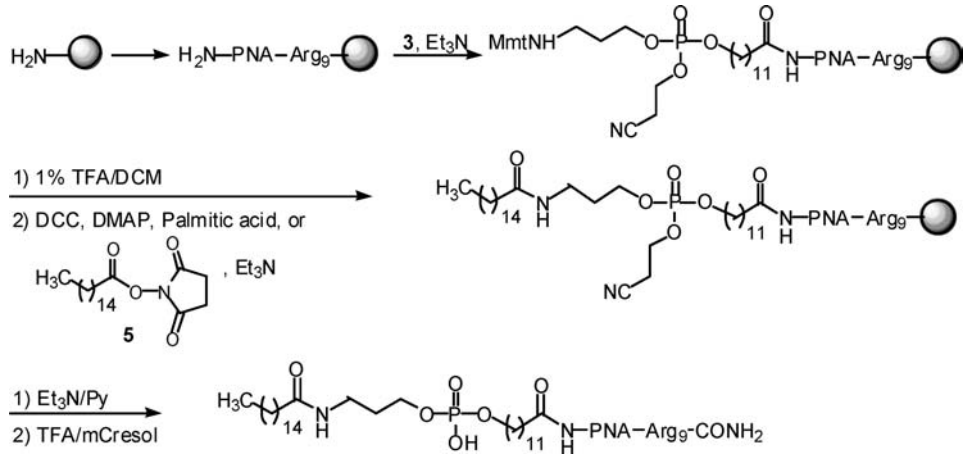

Scheme 3. Synthesis of Lipid-Disulfide-PNA, LSS-PNA-R9

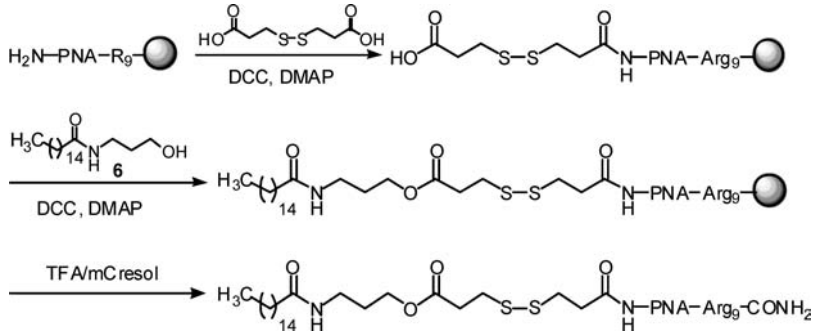

1) was prepared using the Boc-protected building block **4** and used for comparison to **LP-PNA-R9**, which has an additional lipid attached.

The disulfide-linked lipid−PNA **LSS-PNA-R9** (Figure 1) was designed and synthesized to compare the bioactivity of a bioreductively cleavable (*19, 36, 37*) lipid−PNA with that of **L-PNA-R9** and **LP-PNA-R9**. The synthesis was carried out on column by sequentially coupling with 3,3′-dithiodipropionic acid and then the building block **6** (Scheme 3).

MALDI-TOF Mass Spectrometry of the PNA Conjugates. In general, the standard MALDI matrix material, CHCA, gave good MALDI-TOF spectra for most PNAs. It was difficult, however, to get molecular ions for **LSS-PNA-R9** with CHCA. After an investigation of different matrices, the recently reported α-cyano-4-chloro-cinnamic acid (*38*) was found to be a good matrix for this PNA.

Luciferase Splice Correcting Bioactivity. The PNA sequence of **PNA-R9** corresponds to that of PNA-705, which has been used in a positive assay for the presence of intracellular, and more specifically, intranuclear PNA in a splice correction assay (*13, 39*). PNA-705 restores correct splicing of a luciferase transcript in HeLa pLuc cells by blocking splicesome assembly at the mis-splicing site, thereby resulting in functional luciferase and quantifiable light emission in the presence of luciferin. The bioactivity of 1 and 2 μM **PNA**, **PNA-R9**, **L-PNA-R9**, **P-PNA-R9**, and **LP-PNA-R9** was compared to that of 1 μM 2′-methoxy phosphorothioate ODN-705 transfected with Polyfect by incubating them with pLuc705 cells for 24 h and then assaying for luciferase activity (Figure 2). At 1 μM, **L-PNA-R9**, and **LP-PNA-R9** exhibit slightly higher bioactivity than **PNA-R9** and **P-PNA-R9**, but the difference in activity increased 7- and 10-fold respectively, when the concentrations were doubled to 2 μM.

To probe the mechanism of entry, we examined the effect of adding 100 μM chloroquine (CQ), which is known to enhance escape of PNA cell penetrating peptide conjugates from endosomes (*18, 20*). The concentration of chloroquine used is half that reported to result in an 18% loss in viability of HeLa cells and was therefore expected to have minimal toxicity (*40*). As expected for an endocytosis mechanism, CQ enhanced the bioactivity of 1 μM **PNA-Arg9** 10-fold and **L-PNA-R9** 7-fold, while the bioactivity of 1 μM **LP-PNA-R9** increased 33-fold (Figure 2). At 2 μM concentration, chloroquine increased their bioactivity about 7.4, 2.7, and 3.7 times, respectively. Furthermore, the relative bioactivity of the PNA derivatives in the presence of chloroquine increased for **PNA-R9**, **L-PNA-R9**, and **LP-PNA-R9** in the order 1:2.2:5.0 at 1 μM PNA and 1:2.3:4.5 at 2 μM PNA. The greater bioactivity of **LP-PNA-R9** suggested that more **LP-PNA-R9** had entered the endosomes and/or that it was better able to exit in the presence of chloroquine. One possibility is that the phosphate group is functioning as a recognition element for entry and/or is acting as cleavable linker to release it from the endosomal membrane. Addition of 100 μM sodium palmitate did not affect the amount of bioluminescence, suggesting that there were no palmitate-specific transporters involved in uptake of the lipid or phospholipid−PNAs.

Concentration Dependence of Splice-Correcting Bioactivity. We then examined the concentration dependence of the bioactivity of the various PNA conjugates over a larger concentration range. We found that **L-PNA-R9**, **LSS-PNA-R9**, and **LP-PNA-R9** had similar bioactivity that rapidly increased in the 1−3 μM range, in contrast to that of **PNA-R9** and **P-PNA-R9**, which had much lower activity and showed very little increase in this concentration range. The higher activity of the lipidated PNAs suggested that the lipid portion was aiding in binding to the cell membrane and/or facilitating endocytosis and endosomal release. When **LSS-PNA-R9** was preincubated with 10 mM DTT to precleave the disulfide bond, the bioactivity dropped more than 2-fold at 4 μM (data not shown), suggesting

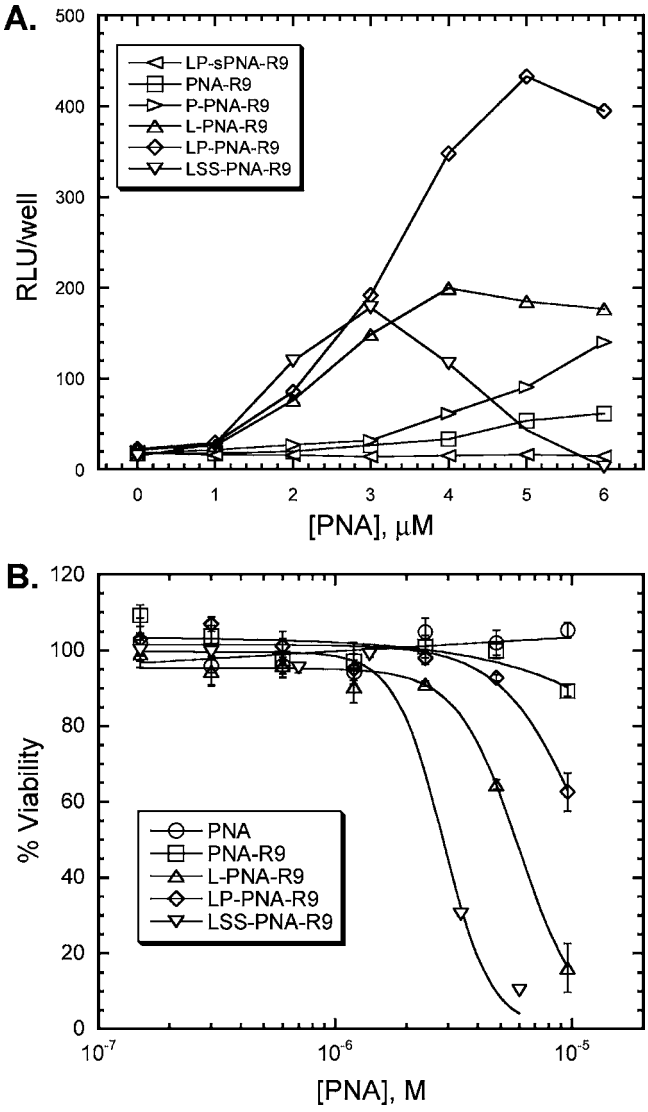

Figure 3. PNA concentration dependence of (a) splicing correction bioactivity and (b) cell viability as measured by the CellTiter-Blue cell viability assay and fit to a Hill-Slope model.

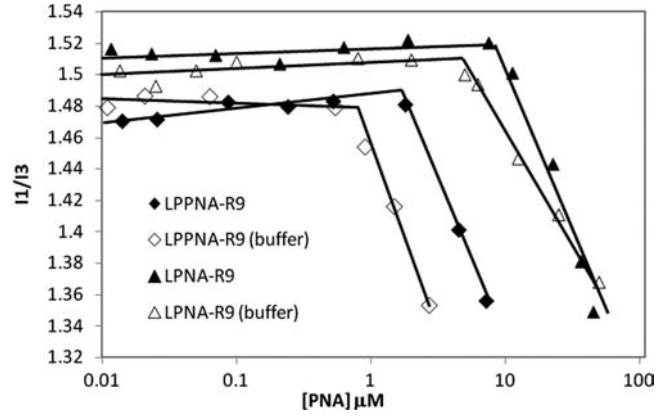

Figure 4. Determination of the critical micelle concentrations of **L-PNA-R9** and **LP-PNA-R9** (in water and in 150 mM NaCl, 5 mM Tris pH 7 buffer) from the break point in a bilinear plot of the ratio of the first (373 nm) and second (384 nm) emission bands of pyrene (I1/I3).

that the lipid chain did facilitate cellular uptake. The lower than expected decrease in activity might be the result of incomplete cleavage or some sort of thiol-facilitated entry mechanism. The similar activity of **L-PNA-R9**, **LP-PNA-R9**, and **LSS-PNA-R9**, which all had different linkers between the lipid and the PNA, at 1−3 μM suggested that the cleavability of the linker was not an important contributor to the bioactivity in this concentration range.

On increasing the concentration from 3 to 5 μM, the bioactivity of **LP-PNA-R9** increased more than 2-fold, while that of **L-PNA-R9** leveled off, and **LSS-PNA-R9** decreased dramatically (Figure 3a). In contrast, the bioactivities of **PNA-R9** and **P-PNA-R9** remained essentially the same from 1−3 μM and then increased with concentration from 4−6 μM. Interestingly, **P-PNA-R9** reached almost the same level of activity at 6 μM that was observed for **LP-**, **L-**, and **LSS-PNA**s at 3 μM and was almost 2-fold higher than PNA-R9 at 6 μM. It may be that the undecane linker between the PNA and the phosphodiester group imparts a sufficient amount of lipophilicity to enhance endocytosis. The scrambled **LP-sPNA-R9** did not show any significant bioactivity at any concentration, demonstrating that the observed bioluminescence was PNA sequence-specific and not related to other features of the constructs.

Cytotoxicity of the PNAs. The leveling off and decrease in bioactivity of some of the PNA constructs with increasing concentration suggested that they might have different cytotoxicities at higher concentrations. In accord with this idea, **L-PNA-R9** and **LSS-PNA-R9** showed the greatest cytotoxicity resulting in a 90% loss of viability at 9.6 μM and 6 μM, respectively, while **LP-PNA-R9** at 9.6 μM resulted in only a 33% loss (Figure 3b). From curve fitting, the LC50 values for **LSS-PNA-R9**, **L-PNA-R9**, and **LP-PNA-R9** were estimated to be 2.9 $\pm$ 0.2, 6 $\pm$ 0.2, and 11.7 $\pm$ 1.2 μM, respectively. **PNA** and **PNA-R9** were the least cytotoxic at 9.6 μM, resulting in zero and 10% loss in viability, respectively. The higher cytotoxicity of **L-PNA-R9** compared to **PNA-R9** might be due to its ability to anchor to the membrane, which might then disrupt membrane function at higher concentrations. The lower cytotoxicity of the **LP-PNA-R9** compared to **L-PNA-R9** might then be explained by enzymatic hydrolysis of the phosphodiester group of **LP-PNA-R9**, which would release the **PNA-R9** from the membrane. While **LSS-PNA-R9** should also be cleaved, at least internally, it is much more cytotoxic, possibly because it can undergo disulfide exchange with membrane proteins and interfere with their function, or because of some other toxic effect of the thiolipid.

Micelle Formation. Because the lipidated PNAs have hydrophobic tails and charged head groups and are therefore amphiphilic, it seemed likely that they would form micelles, which might explain their better uptake into cells through endocytosis or membrane fusion (*41*). Alternatively, micelle formation might reduce the cytotoxicity of lipids at higher concentrations by sequestering them. By using a pyrene-based fluorescence assay (Figure 4) (*42*), we determined that **LP-PNA-R9** has a critical micelle concentration (CMC) of 1.7 μM in water, while **L-PNA-R9** has a CMC of 9.2 μM. Because the positively charged Arg9 groups would be expected to repel each other in a micelle, we expected that CMC would be lower in the presence of salt. Indeed, addition of 150 mM NaCl in 5 mM Tris pH 7 caused the CMC of **L-PNA-R9** to drop to 4.5 μM and that of **LP-PNA-R9** to decrease to 1.0 μM. Though the CMCs are in the range in which **L-PNA-R9** and **LP-PNA-R9** show bioactivity, they do not correlate directly with the bioactivity or the cytotoxicity. We have yet to determine the role of micelle formation in facilitating cell uptake of the lipidated PNAs or their

cytotoxicity, though it appears that the spherical shape of a micelle may be optimal for macropinocytosis (*43*, *44*).

CONCLUSION

In conclusion, we find that conjugating a phospholipid to a luciferase splice-correcting PNA increases its bioactivity more than does a lipid or disulfide-linked lipid in the 4−6 μM range. Part of the higher bioactivity of the phospholipid PNA in this concentration range can be ascribed to its lower cytotoxicity, possibly because the lipid tail can be removed by enzymatic phosphodiester hydrolysis to yield less toxic products. We also find that lipidated PNAs form micelles which may also play a role in facilitating cell entry and/or lowering cytotoxicity, suggesting that altering the lipid portion to change the size, shape, and stability of the micellular form might lead to better and less toxic cell-penetrating PNAs. Further studies are in progress to study this novel PNA delivery system.

ACKNOWLEDGMENT

This work was supported in part by the National Heart Lung and Blood Institute of the National Institutes of Health as a Program of Excellence in Nanotechnology (NHLBI-PEN HL080729) and by NIH PO1 CA 104457. We also acknowledge support from grants to the Washington University NIH Mass Spectrometry Resource (grant no. P41 RR000954) and Washington University NMR facility (grant no. RR1571501). We also thank Cindy Fogal of Dr. Kranz's group for help with the luminometer, and Dr. R. Kole (University of North Carolina, Chapel Hill, NC) for the pLuc705 HeLa cell line.

Supporting Information Available: ^{1}H NMR, ^{13}C NMR, ^{31}P NMR spectra of building blocks and HPLC and MALDI of PNAs. This material is available free of charge via the Internet at http://pubs.acs.org.

LITERATURE CITED

(1) Alvarez-Salas, L. M. (2008) Nucleic acids as therapeutic agents. *Curr. Top. Med. Chem. 8*, 1379–404.

(2) Eckstein, F. (2007) The versatility of oligonucleotides as potential therapeutics. *Expert Opin. Biol. Ther. 7*, 1021–34.

(3) Sahu, N. K., Shilakari, G., Nayak, A., and Kohli, D. V. (2007) Antisense technology: a selective tool for gene expression regulation and gene targeting. *Curr. Pharm. Biotechnol. 8*, 291–304.

(4) Karkare, S., and Bhatnagar, D. (2006) Promising nucleic acid analogs and mimics: characteristic features and applications of PNA, LNA, and morpholino. *Appl. Microbiol. Biotechnol. 71*, 575–86.

(5) Nielsen, P. E., Egholm, M., Berg, R. H., and Buchardt, O. (1991) Sequence-selective recognition of DNA by strand displacement with a thymine-substituted polyamide. *Science 254*, 1497–1500.

(6) Egholm, M., Buchardt, O., Nielsen, P. E., and Berg, R. H. (1992) Peptide nucleic acids (PNA). Oligonucleotide analogues with an achiral peptide backbone. *J. Am. Chem. Soc. 114*, 1895–1897.

(7) Nielsen, P. E. (2004) PNA Technology. *Mol. Biotechnol. 26*, 233–48.

(8) Porcheddu, A., and Giacomelli, G. (2005) Peptide nucleic acids (PNAs), a chemical overview. *Curr. Med. Chem. 12*, 2561–99.

(9) Lundin, K. E., Good, L., Stromberg, R., Graslund, A., and Smith, C. I. (2006) Biological activity and biotechnological aspects of peptide nucleic acid. *Adv. Genet. 56*, 1–51.

(10) Hamilton, S. E., Simmons, C. G., Kathiriya, I. S., and Corey, D. R. (1999) Cellular delivery of peptide nucleic acids and inhibition of human telomerase. *Chem. Biol. 6*, 343–51.

(11) Braasch, D. A., and Corey, D. R. (2002) Lipid-mediated introduction of peptide nucleic acids into cells. *Methods Mol. Biol. 208*, 211–23.

(12) Zhilina, Z. V., Ziemba, A. J., and Ebbinghaus, S. W. (2005) Peptide nucleic acid conjugates: synthesis, properties and applications. *Curr. Top. Med. Chem. 5*, 1119–31.

(13) Rasmussen, F. W., Bendifallah, N., Zachar, V., Shiraishi, T., Fink, T., Ebbesen, P., Nielsen, P. E., and Koppelhus, U. (2006) Evaluation of transfection protocols for unmodified and modified peptide nucleic acid (PNA) oligomers. *Oligonucleotides 16*, 43–57.

(14) Resina, S., Abes, S., Turner, J. J., Prevot, P., Travo, A., Clair, P., Gait, M. J., Thierry, A. R., and Lebleu, B. (2007) Lipoplex and peptide-based strategies for the delivery of steric-block oligonucleotides. *Int. J. Pharm. 344*, 96–102.

(15) Simmons, C. G., Pitts, A. E., Mayfield, L. D., Shay, J. W., and Corey, D. R. (1997) Synthesis and membrane permeability of PNA-peptide conjugates. *Bioorg. Med. Chem. Lett. 7*, 3001–3006.

(16) Bergstrom, R. C., Mayfield, L. D., and Corey, D. R. (2001) A bridge between the RNA and protein worlds? Accelerating delivery of chemical reactivity to RNA and DNA by a specific short peptide (AAKK)(4). *Chem. Biol. 8*, 199–205.

(17) Braasch, D. A., and Corey, D. R. (2001) Synthesis, analysis, purification, and intracellular delivery of peptide nucleic acids. *Methods 23*, 97–107.

(18) Shiraishi, T., and Nielsen, P. E. (2006) Enhanced delivery of cell-penetrating peptide-peptide nucleic acid conjugates by endosomal disruption. *Nat. Protoc. 1*, 633–6.

(19) Bendifallah, N., Rasmussen, F. W., Zachar, V., Ebbesen, P., Nielsen, P. E., and Koppelhus, U. (2006) Evaluation of cell-penetrating peptides (CPPs) as vehicles for intracellular delivery of antisense peptide nucleic acid (PNA). *Bioconjugate Chem. 17*, 750–8.

(20) Abes, S., Williams, D., Prevot, P., Thierry, A., Gait, M. J., and Lebleu, B. (2006) Endosome trapping limits the efficiency of splicing correction by PNA-oligolysine conjugates. *J. Controlled Release 110*, 595–604.

(21) Abes, S., Turner, J. J., Ivanova, G. D., Owen, D., Williams, D., Arzumanov, A., Clair, P., Gait, M. J., and Lebleu, B. (2007) Efficient splicing correction by PNA conjugation to an R6-Penetratin delivery peptide. *Nucleic Acids Res. 35*, 4495–502.

(22) Ivanova, G. D., Arzumanov, A., Abes, R., Yin, H., Wood, M. J., Lebleu, B., and Gait, M. J. (2008) Improved cell-penetrating peptide-PNA conjugates for splicing redirection in HeLa cells and exon skipping in mdx mouse muscle. *Nucleic Acids Res. 36*, 6418–28.

(23) Nastruzzi, C., Cortesi, R., Esposito, E., Gambari, R., Borgatti, M., Bianchi, N., Feriotto, G., and Mischiati, C. (2000) Liposomes as carriers for DNA-PNA hybrids. *J. Controlled Release 68*, 237–49.

(24) Lv, H., Zhang, S., Wang, B., Cui, S., and Yan, J. (2006) Toxicity of cationic lipids and cationic polymers in gene delivery. *J. Controlled Release 114*, 100–9.

(25) Fang, H., Zhang, K., Shen, G., Wooley, K. L., and Taylor, J. S. (2009) Cationic shell-cross-linked Knedel-like (cSCK) nanoparticles for highly efficient PNA delivery. *Mol. Pharm. 6*, 615–26.

(26) Herbert, B. S., Gellert, G. C., Hochreiter, A., Pongracz, K., Wright, W. E., Zielinska, D., Chin, A. C., Harley, C. B., Shay, J. W., and Gryaznov, S. M. (2005) Lipid modification of GRN163, an N3′-->P5′ thio-phosphoramidate oligonucleotide, enhances the potency of telomerase inhibition. *Oncogene 24*, 5262–8.

(27) Gellert, G. C., Dikmen, Z. G., Wright, W. E., Gryaznov, S., and Shay, J. W. (2006) Effects of a novel telomerase inhibitor, GRN163L, in human breast cancer. *Breast Cancer Res. Treat. 96*, 73–81.

(28) Agarwal, M., Pandita, S., Hunt, C. R., Gupta, A., Yue, X., Khan, S., Pandita, R. K., Pratt, D., Shay, J. W., Taylor, J. S., and Pandita, T. K. (2008) Inhibition of telomerase activity enhances hyperthermia-mediated radiosensitization. *Cancer Res. 68*, 3370–8.

(29) Hu, J., and Corey, D. R. (2007) Inhibiting gene expression with peptide nucleic acid (PNA)-peptide conjugates that target chromosomal DNA. *Biochemistry 46*, 7581–9.

(30) Koppelhus, U., Shiraishi, T., Zachar, V., Pankratova, S., and Nielsen, P. E. (2008) Improved cellular activity of antisense peptide nucleic acids by conjugation to a cationic peptide-lipid (CatLip) domain. *Bioconjugate Chem. 19*, 1526–34.

(31) Mitchell, D. J., Kim, D. T., Steinman, L., Fathman, C. G., and Rothbard, J. B. (2000) Polyarginine enters cells more efficiently than other polycationic homopolymers. *J. Pept. Res. 56*, 318–25.

(32) Wender, P. A., Mitchell, D. J., Pattabiraman, K., Pelkey, E. T., Steinman, L., and Rothbard, J. B. (2000) The design, synthesis, and evaluation of molecules that enable or enhance cellular uptake: peptoid molecular transporters. *Proc. Natl. Acad. Sci. U.S.A. 97*, 13003–13008.

(33) Thomson, S. A., Josey, J. A., Cadilla, R., Gaul, M. D., Hassman, C. F., Luzzio, M. J., Pipe, A. J., Reed, K. L., Ricca, D. J., Wiethe, R. W., and Noble, S. A. (1995) Fmoc mediated synthesis of peptide nucleic acids. *Tetrahedron 51*, 6179–94.

(34) Oquare, B. Y., and Taylor, J. S. (2008) Synthesis of peptide nucleic acid FRET probes via an orthogonally protected building block for post-synthetic labeling of peptide nucleic acids at the 5-position of uacil. *Bioconjugate Chem. 19*, 2196–2204.

(35) Trivedi, H. S., Anson, M., Steel, P. G., and Worley, J. (2001) A method for selective N-Boc deprotection on Wang resin. *Synlett.* 1932–1934.

(36) Koppelhus, U., Awasthi, S. K., Zachar, V., Holst, H. U., Ebbesen, P., and Nielsen, P. E. (2002) Cell-dependent differential cellular uptake of PNA, peptides, and PNA-peptide conjugates. *Antisense Nucleic Acid Drug Dev. 12*, 51–63.

(37) Reshetnyak, Y. K., Andreev, O. A., Lehnert, U., and Engelman, D. M. (2006) Translocation of molecules into cells by pH-dependent insertion of a transmembrane helix. *Proc. Natl. Acad. Sci. U.S.A. 103*, 6460–5.

(38) Jaskolla, T. W., Lehmann, W. D., and Karas, M. (2008) 4-Chloro-alpha-cyanocinnamic acid is an advanced, rationally designed MALDI matrix. *Proc. Natl. Acad. Sci. U.S.A. 105*, 12200–5.

(39) Kang, S. H., Cho, M. J., and Kole, R. (1998) Up-regulation of luciferase gene expression with antisense oligonucleotides: implications and applications in functional assay development. *Biochemistry 37*, 6235–9.

(40) Cheng, J., Zeidan, R., Mishra, S., Liu, A., Pun, S. H., Kulkarni, R. P., Jensen, G. S., Bellocq, N. C., and Davis, M. E. (2006) Structure-function correlation of chloroquine and analogues as transgene expression enhancers in nonviral gene delivery. *J. Med. Chem. 49*, 6522–31.

(41) Torchilin, V. P. (2007) Micellar nanocarriers: pharmaceutical perspectives. *Pharm. Res. 24*, 1–16.

(42) Goddard, E. D., Turro, N. J., and Kuo, P. L. (1985) Fluorescence probes for critical micelle concentration determination. *Langmuir 1*, 352–5.

(43) Swanson, J. A. (2008) Shaping cups into phagosomes and macropinosomes. *Nat. Rev. Mol. Cell. Biol. 9*, 639–649.

(44) Zhang, K., Fang, H., Chen, Z., Taylor, J.-S. A., and Wooley, K. L. (2008) Shape effects of nanoparticles conjugated with cell-penetrating peptides (HIV Tat PTD) on CHO cell uptake. *Bioconjugate Chem. 19*, 1880–1887.

BC900048Y

Supporting Information for:

Phospholipid conjugate for intracellular delivery of peptide nucleic acids

Gang Shen, Huafeng Fang, Yinyin Song, Agata Bielska, Zhenghui Wang, and John-Stephen A. Taylor*

Department of Chemistry, Washington University in St. Louis, One Brookings Drive, St. Louis, MO 63130

*To whom correspondence should be addressed:

Department of Chemistry
Campus Box 1134
Washington University
One Brookings Drive
St. Louis, MO 63130
email: taylor@wustl.edu

	Page
Figure S1. ^{1}H NMR spectrum of **3**.	S2
Figure S2. ^{13}C NMR spectrum of **3**.	S3
Figure S3. ^{31}P NMR spectrum of **3**.	S4
Figure S4. ^{1}H NMR spectrum of **4**.	S5
Figure S5. ^{13}C NMR spectrum of **4**.	S6
Figure S6. ^{31}P NMR spectrum of **4**.	S7
Figure S7. ^{1}H NMR spectrum of **5**.	S8
Figure S8. ^{13}C NMR spectrum of **5**.	S9
Figure S9. ^{1}H NMR spectrum of **6**.	S10
Figure S10. ^{13}C NMR spectrum of **6**.	S11
Figure S11. HPLC purification and MALDI-TOF analysis of **PNA-R9, 7**.	S12
Figure S12. HPLC purification and MALDI-TOF analysis of **L-PNA-R9, 8**.	S13
Figure S13. HPLC purification and MALDI-TOF analysis of **P-PNA-R9, 9**.	S14
Figure S14. HPLC purification and MALDI-TOF analysis of **LP-PNA-R9, 10**.	S15
Figure S15. HPLC purification and MALDI-TOF analysis of **LP-sPNA-R9, 11**	S16
Figure S16. HPLC purification and MALDI-TOF analysis of **LSS-PNA-R9, 12**.	S17

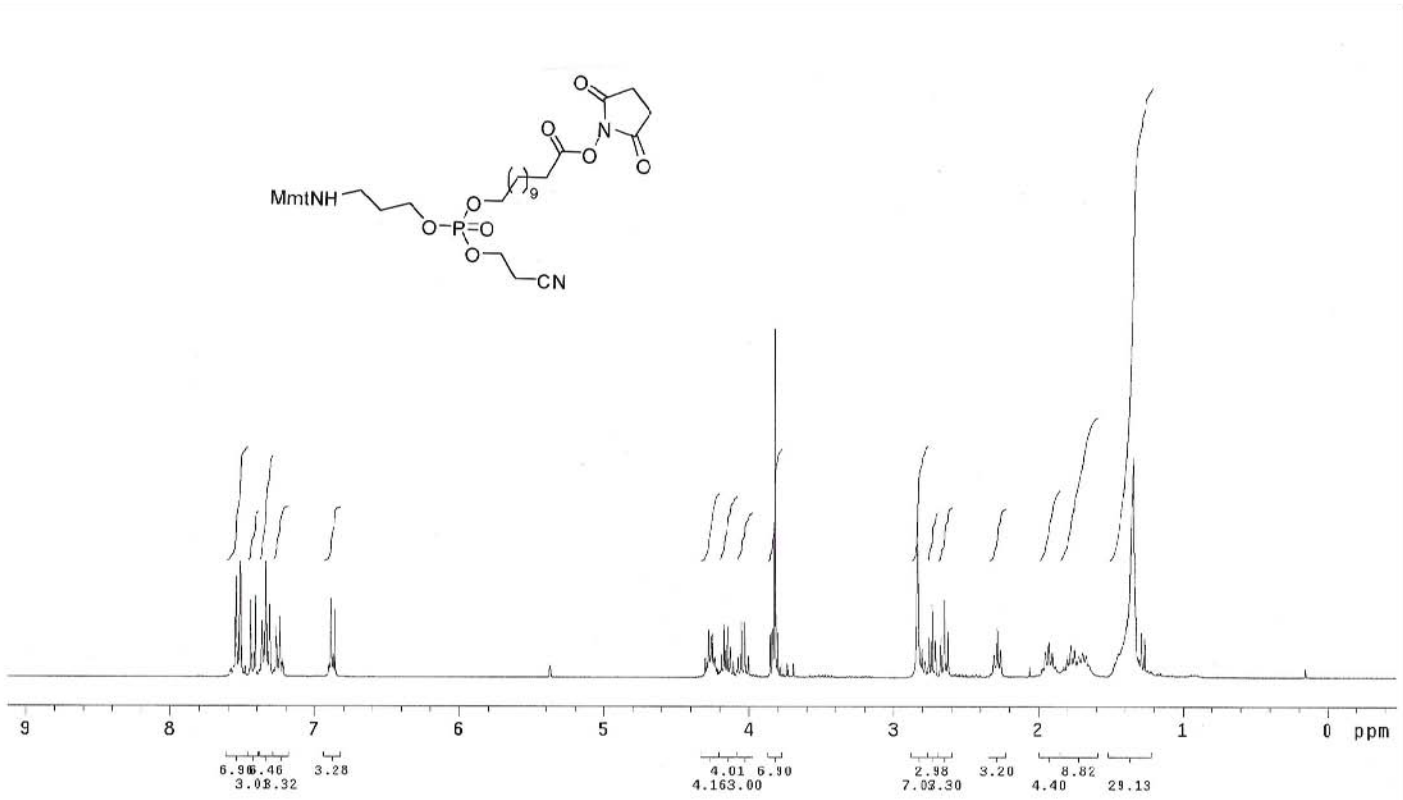

Figure S1. ^{1}H NMR spectrum of **3**.

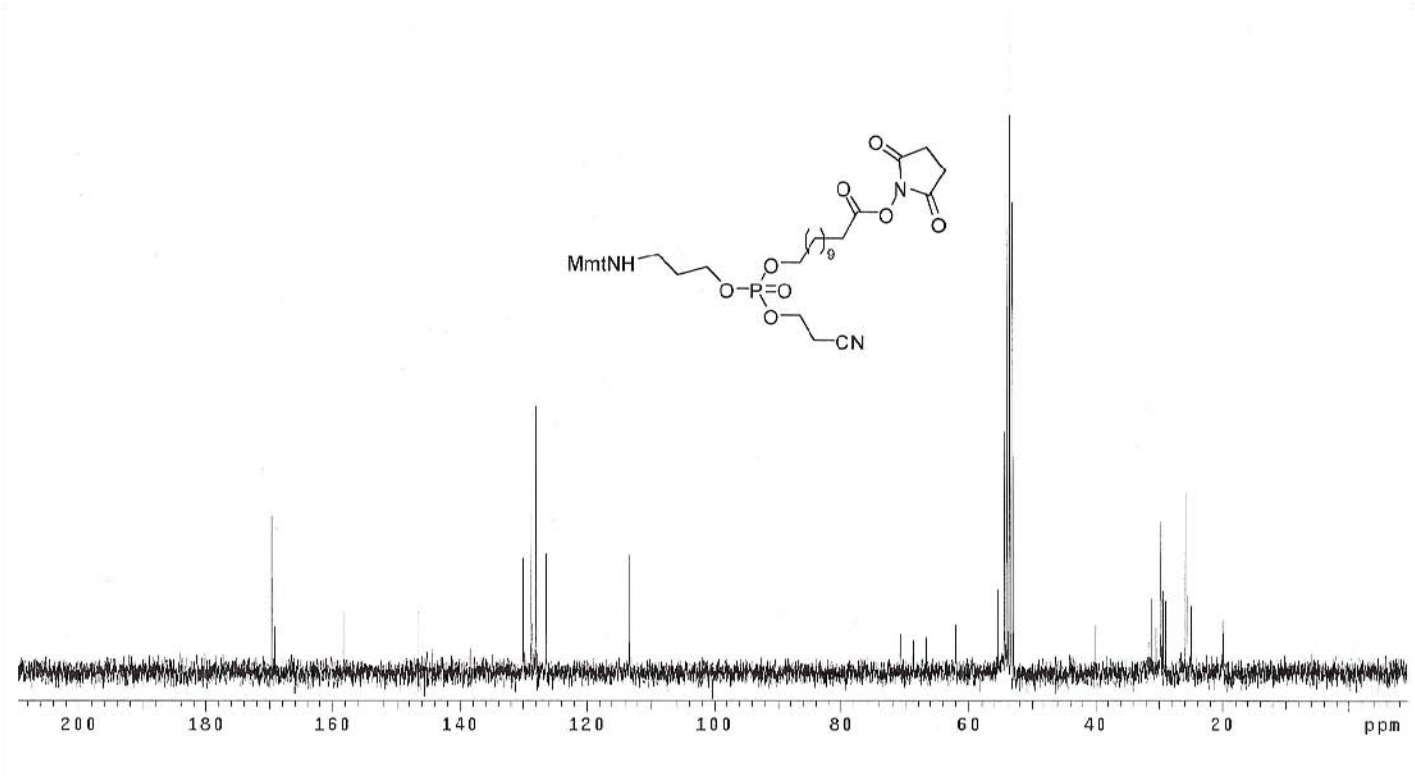

Figure S2. ^{13}C NMR spectrum of **3**.

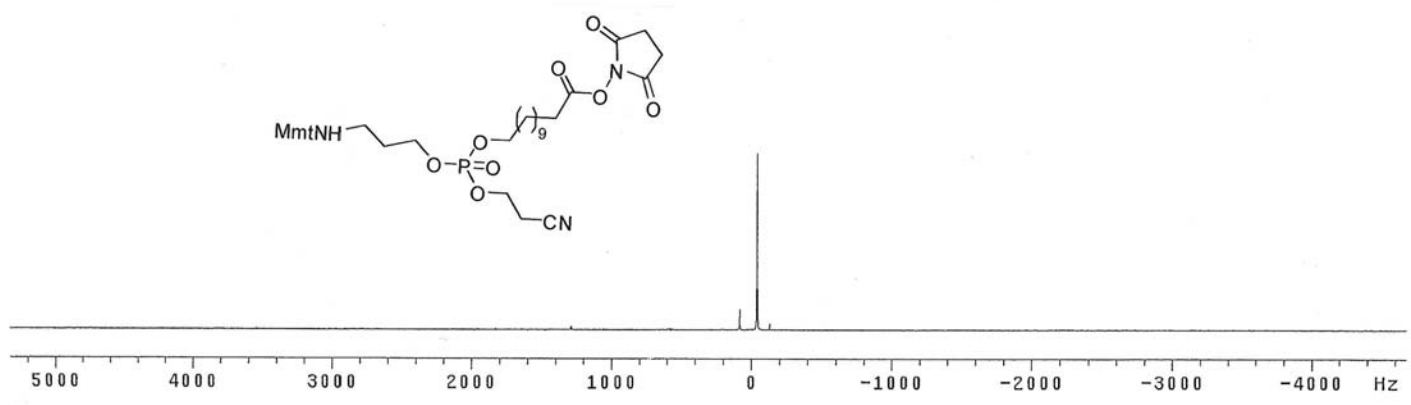

Figure S3. ^{31}P NMR spectrum of **3**.

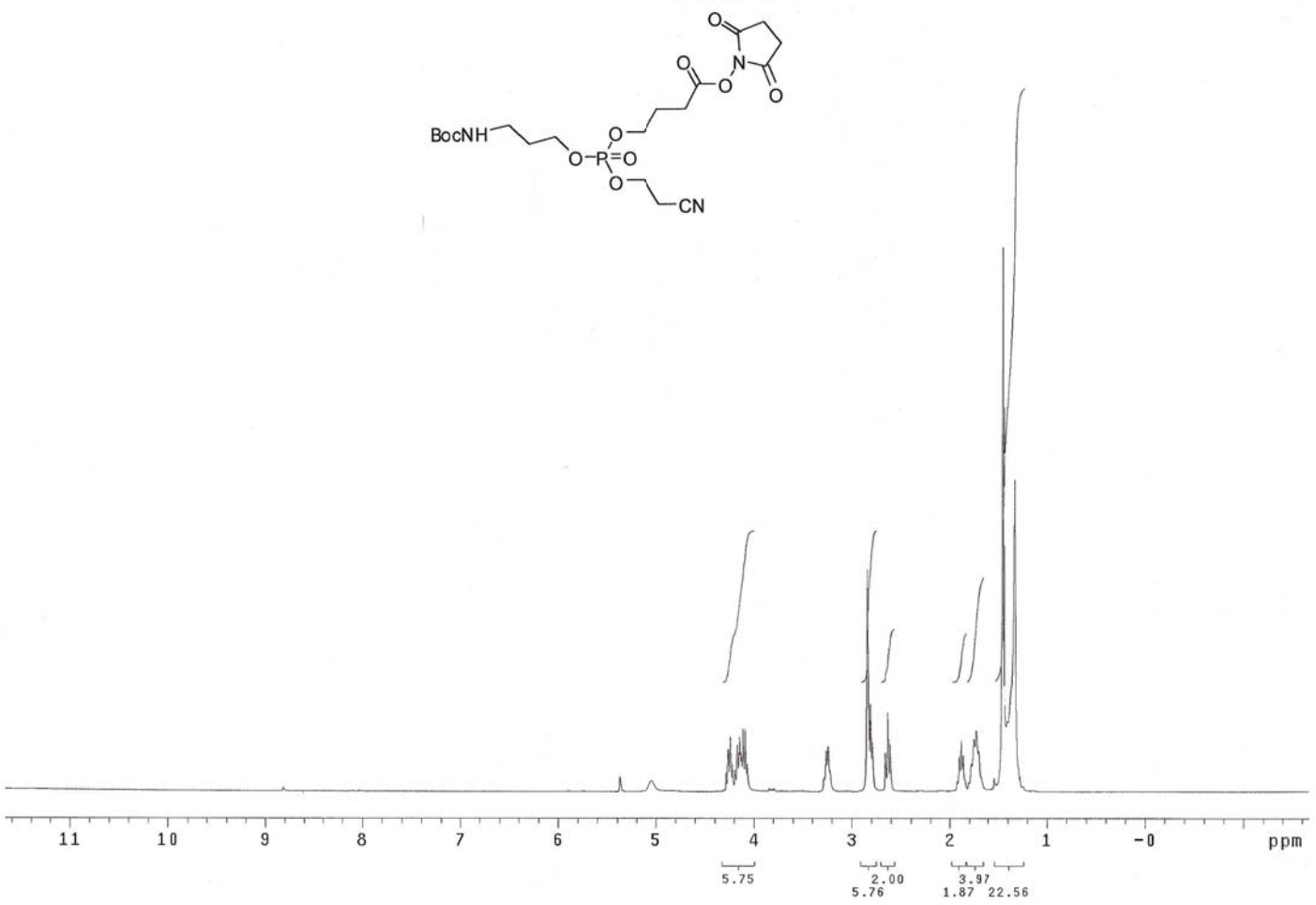

Figure S4. ^{1}H NMR spectrum of **4**.

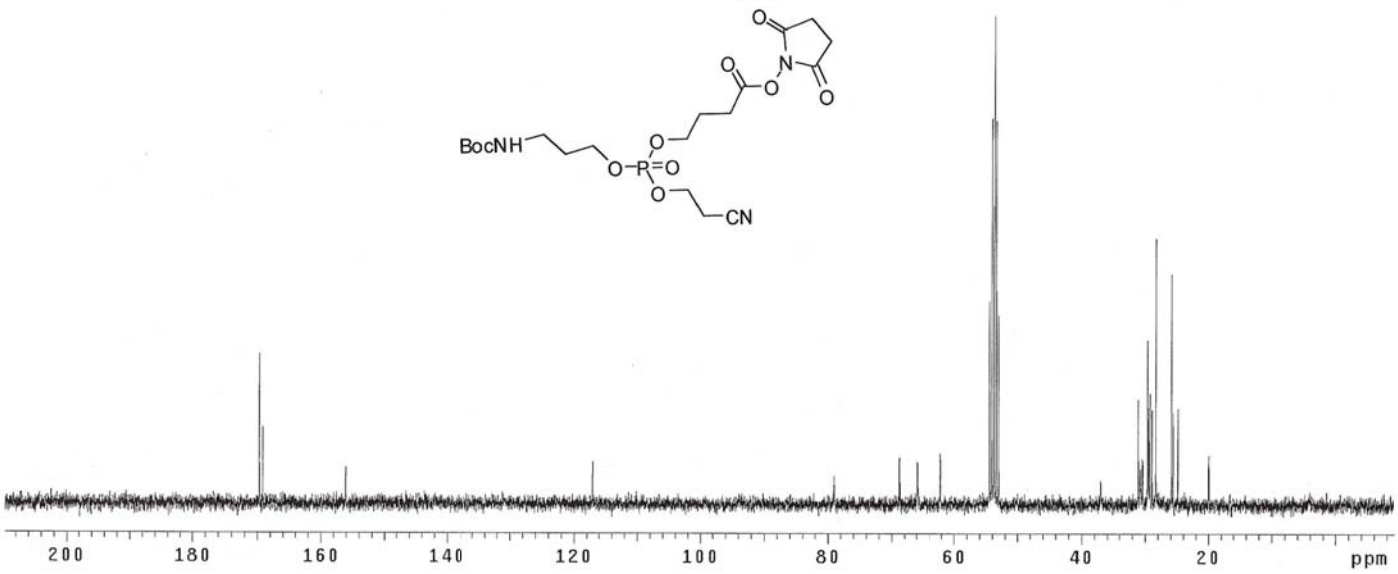

Figure S5. ^{13}C NMR spectrum of **4**.

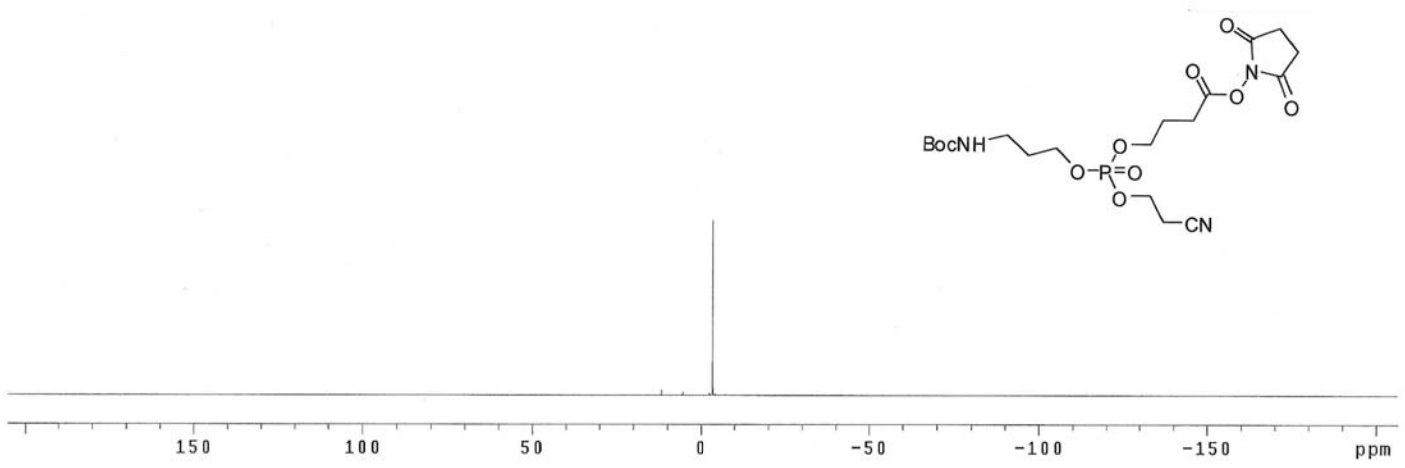

Figure S6. ^{31}P NMR spectrum of **4**. 1

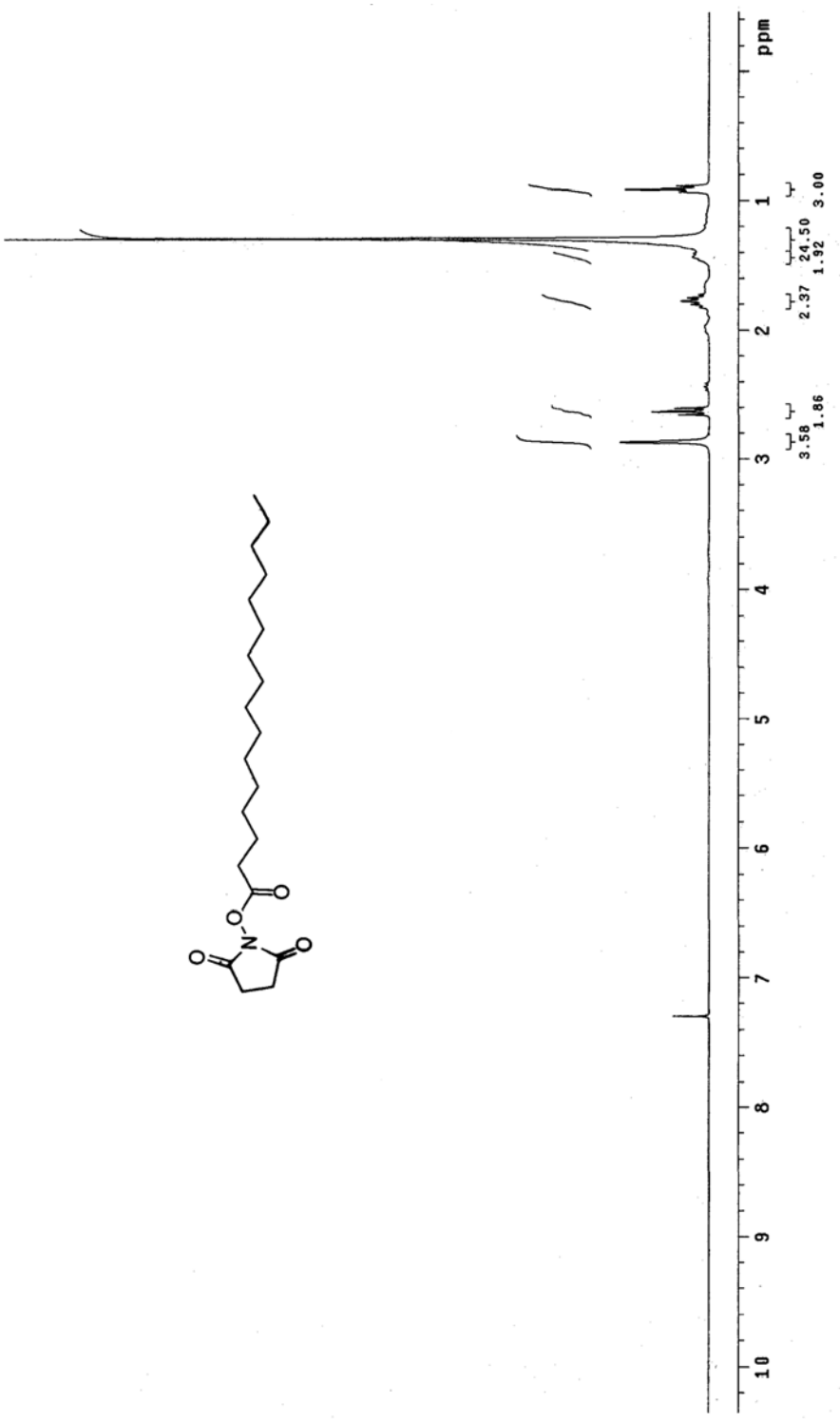

Figure S7. ^{1}H NMR spectrum of **5**.

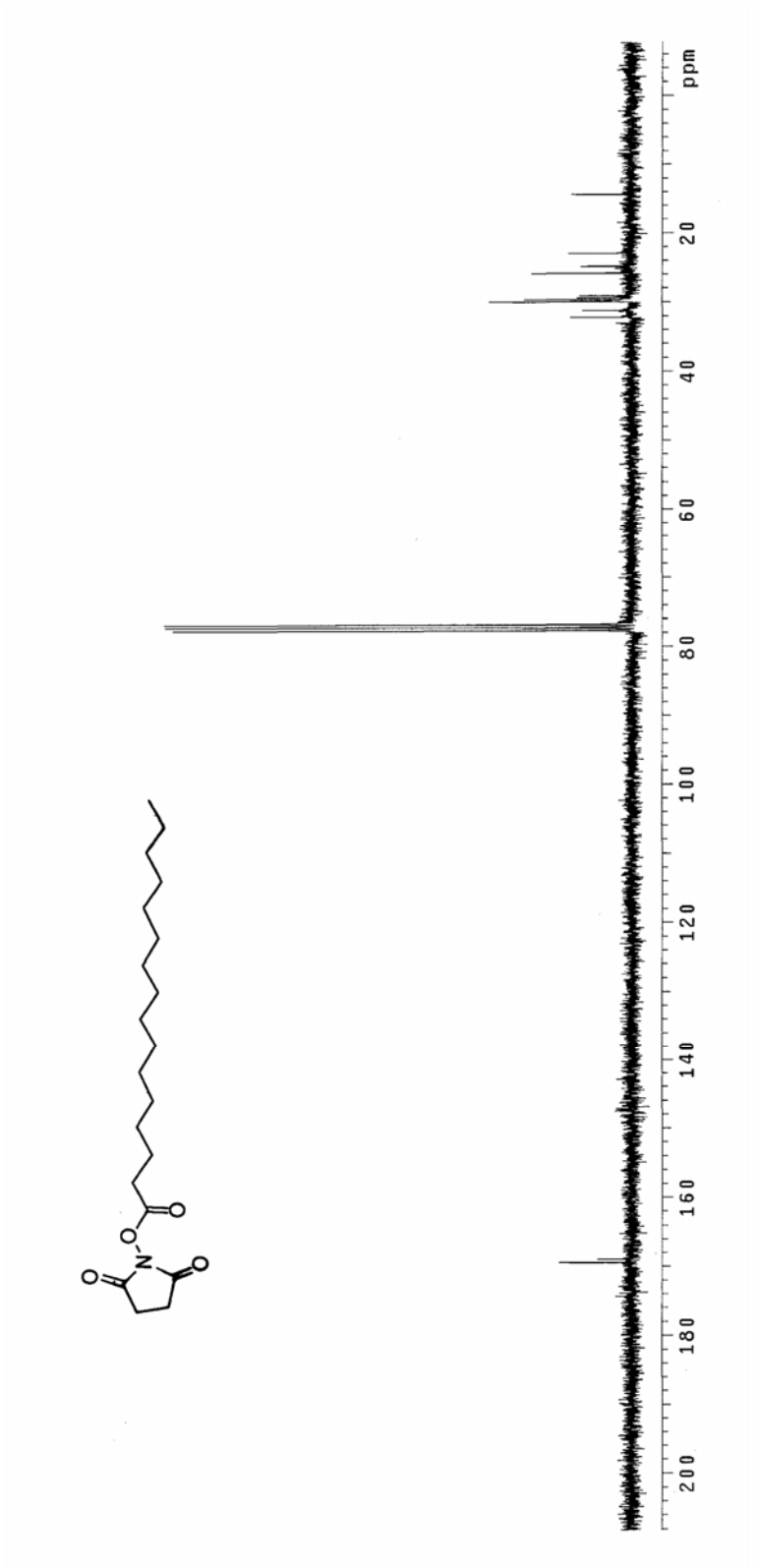

Figure S8. ^{13}C NMR spectrum of **5**.

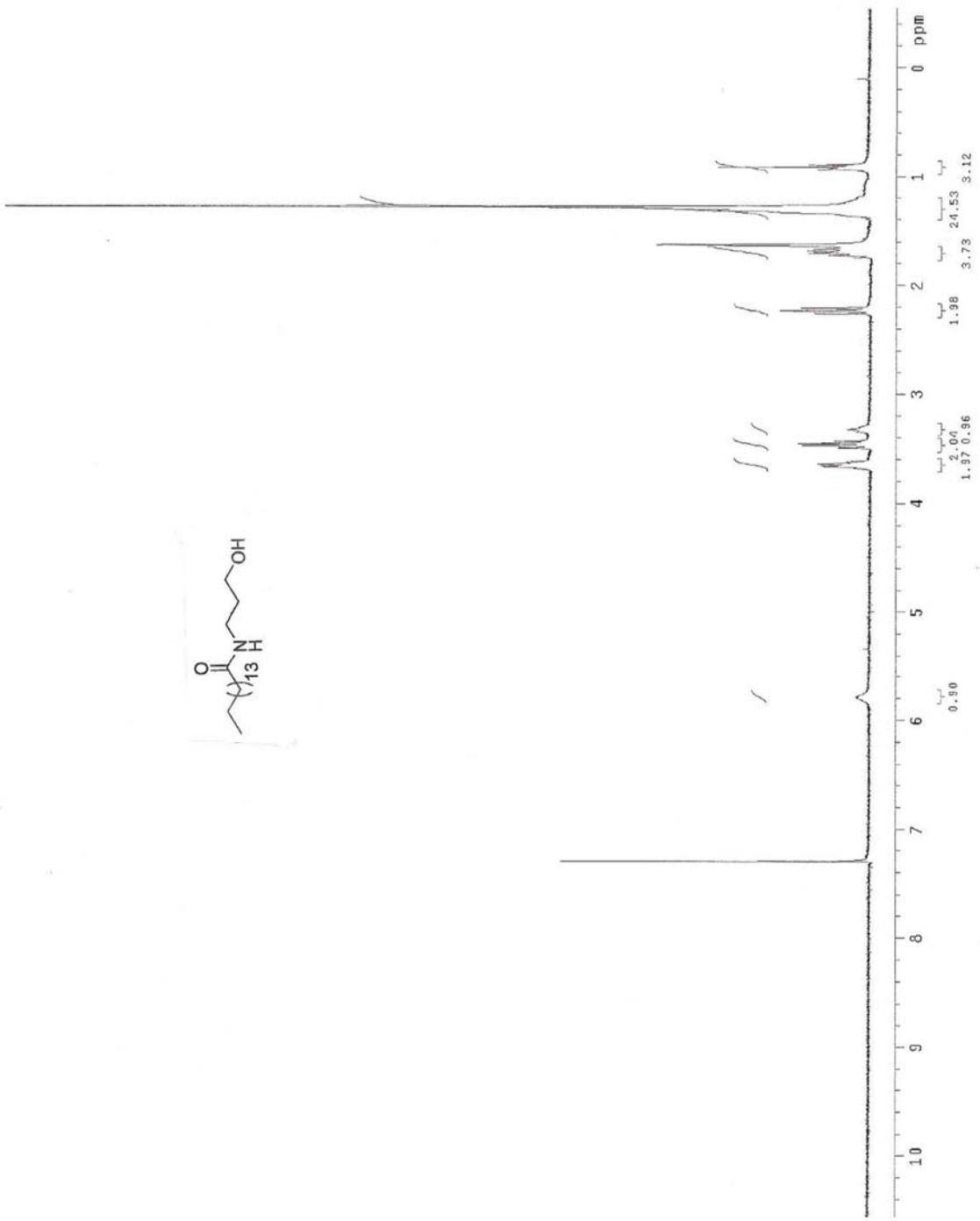

Figure S9. ^{1}H NMR spectrum of **6**.

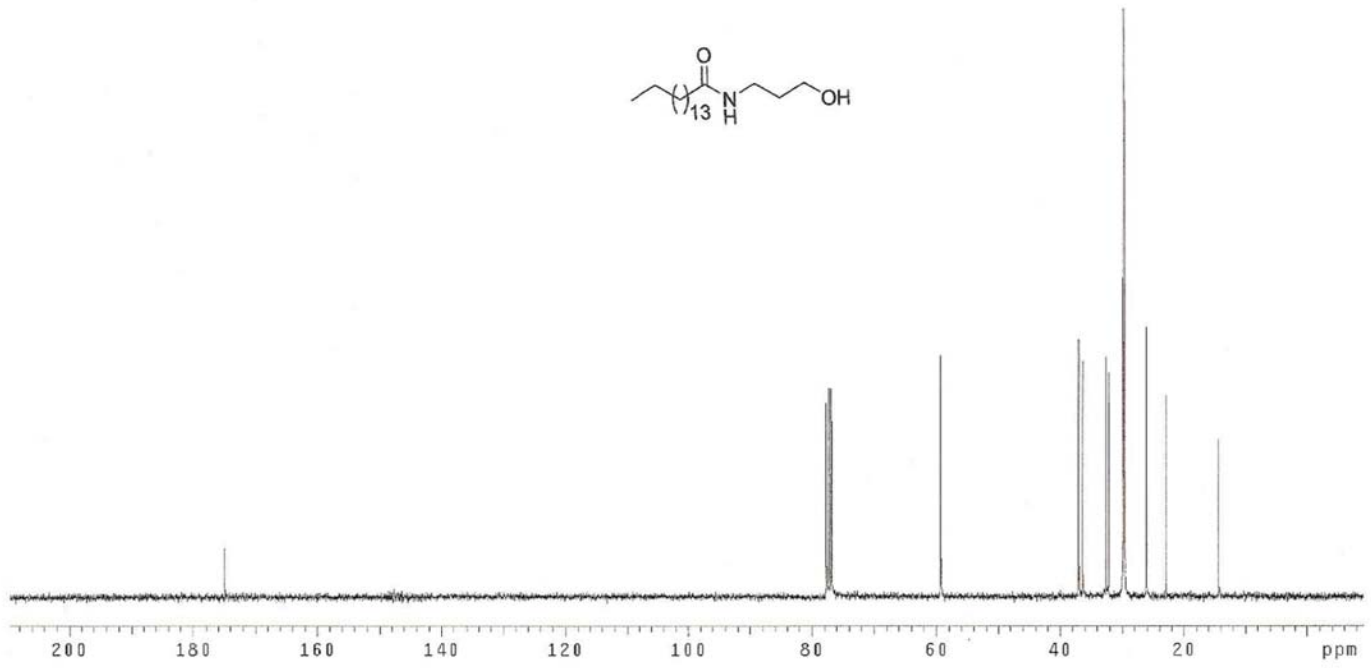

Figure S10. ^{13}C NMR spectrum of **6**.

A)

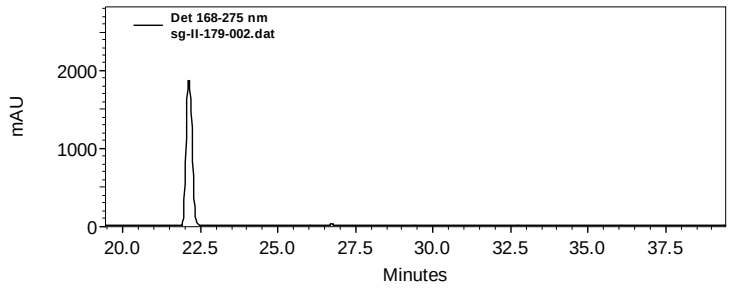

B)

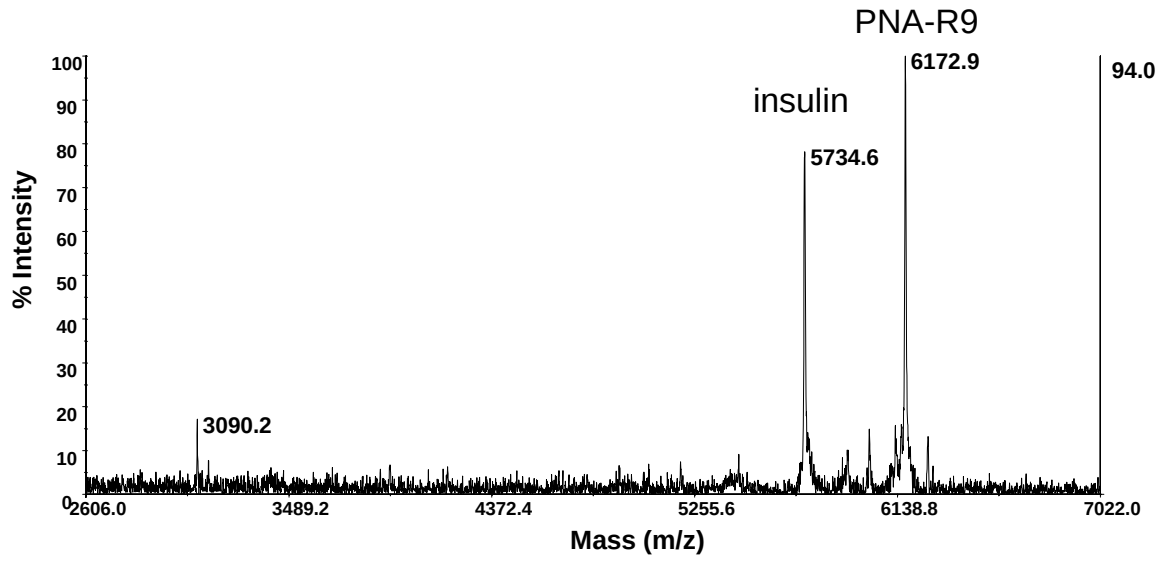

Figure S11. HPLC purification and MALDI-TOF analysis of **PNA-R9**, **7.** A) Reverse-phase HPLC with Method A. B) MALDI-TOF with α-cyano-4-hydroxy-cinnamic acid matrix, average $[M+H]^+$ expected 6171.2, found 6172.9. Insulin (average $[M+H]^+$ assigned to 5734.6) was the internal reference.

A)

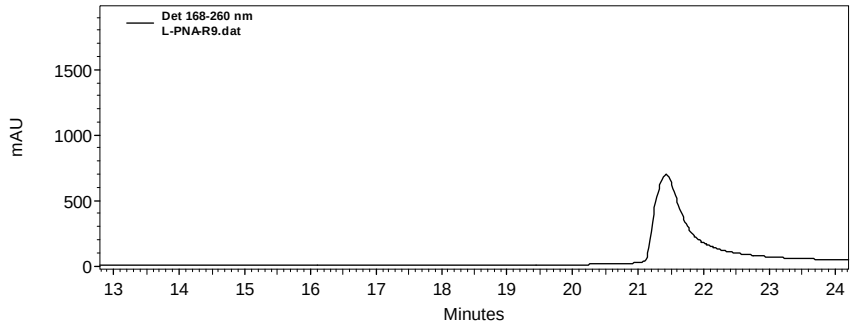

B)

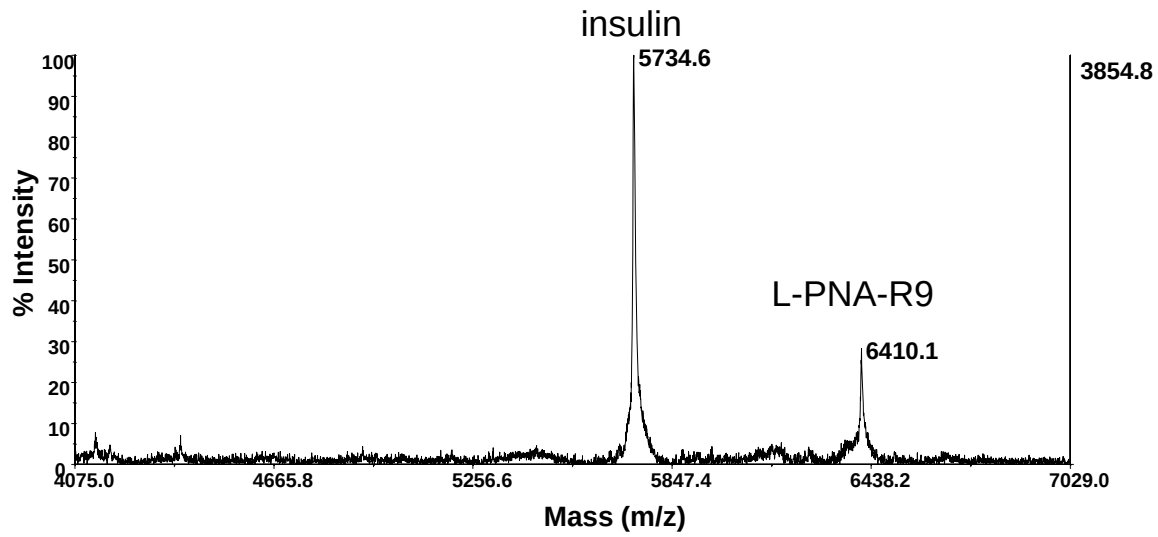

Figure S12. HPLC purification and MALDI-TOF analysis of **L-PNA-R9**, **8.** A) Reverse-phase HPLC with Method B. B) MALDI-TOF with α-cyano-4-hydroxy-cinnamic acid matrix, average $[M+H]^+$ expected 6409.7, found 6410.1. Insulin (average $[M+H]^+$ assigned to 5734.6) was the internal reference.

A)

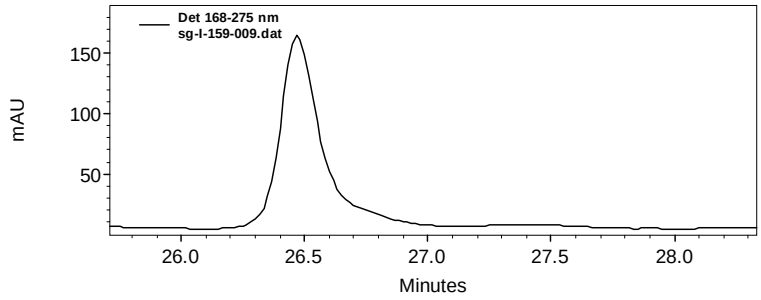

B)

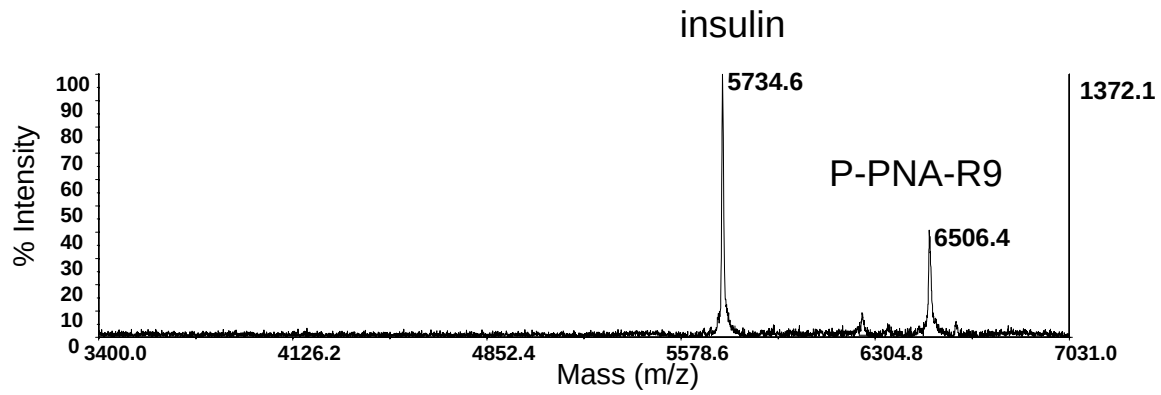

Figure S13. HPLC purification and MALDI-TOF analysis of **P-PNA-R9 (9).** A) Reverse-phase HPLC with Method A. B) MALDI-TOF with α-cyano-4-hydroxy-cinnamic acid matrix, average $[M+H]^+$ expected 6506.6, found 6506.4. Insulin (average $[M+H]^+$ assigned to 5734.6) was the internal reference.

A)

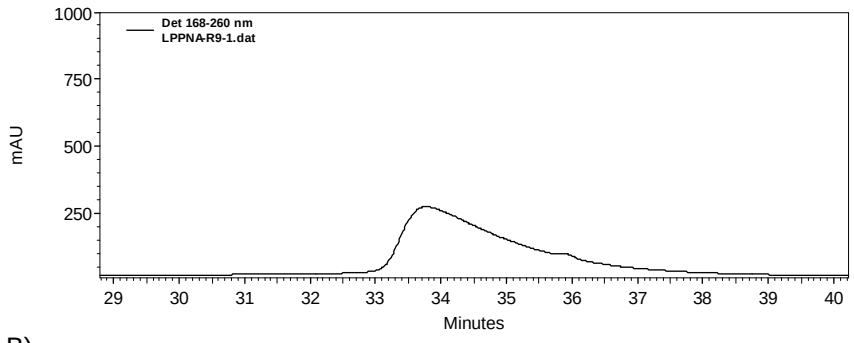

B)

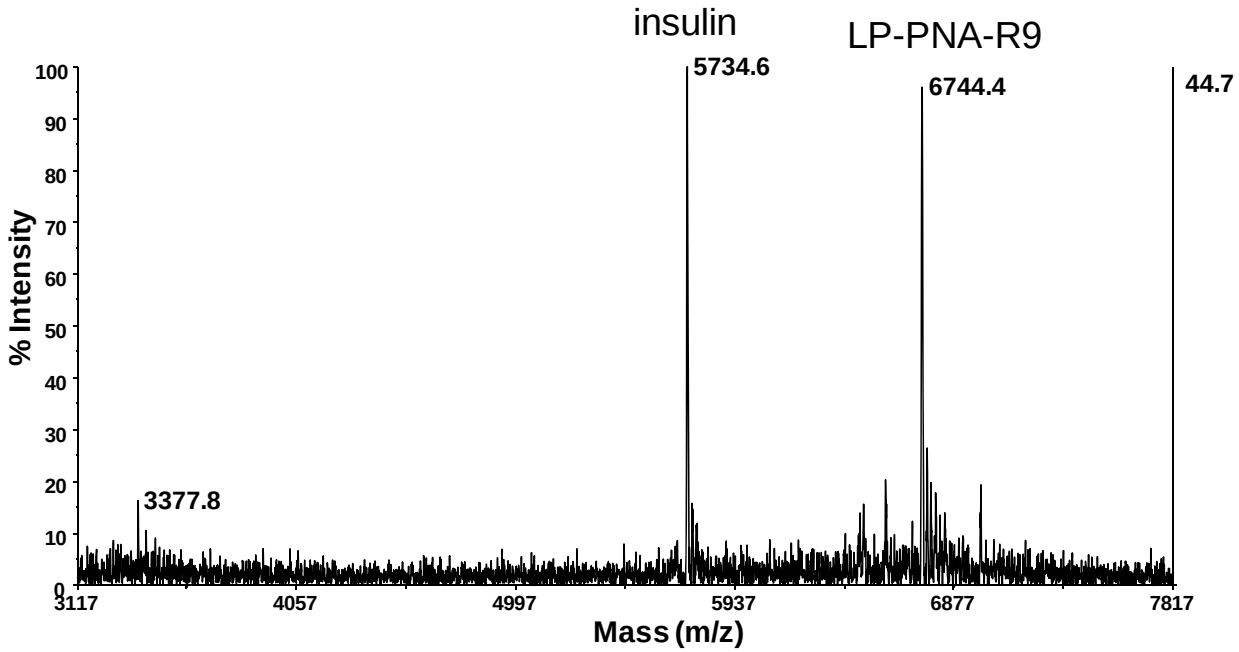

Figure S14. HPLC purification and MALDI-TOF analysis of **LP-PNA-R9 (10).** A) Reverse-phase HPLC with Method B. B) MALDI-TOF with α-cyano-4-hydroxy-cinnamic matrix, average $[M+H]^+$ expected 6744.9, found 6744.4. Insulin (average $[M+H]^+$ assigned to 5734.6) was the internal reference.

A)

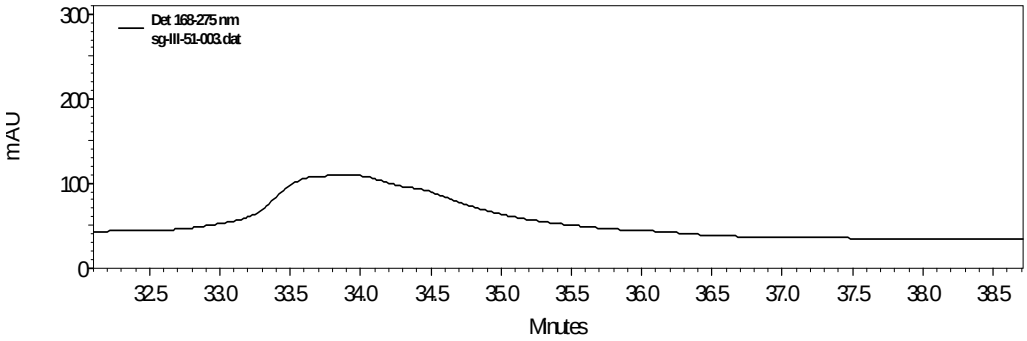

B)

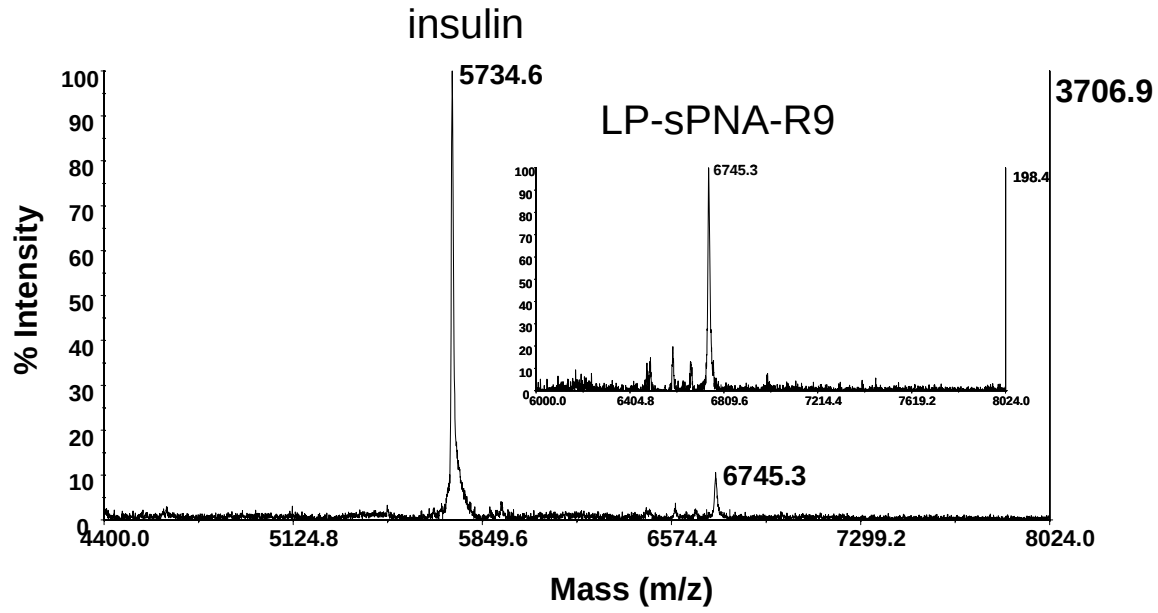

Figure S15. HPLC purification and MALDI-TOF analysis of **LP-sPNA-R9 (11).** A) Reverse-phase HPLC with Method B. B) MALDI-TOF with α-cyano-4-hydroxy-cinnamic acid matrix, average $[M+H]^+$ expected 6744.9, found 6745.3. Insulin (average $[M+H]^+$ assigned to 5734.6) was the internal reference.

A)

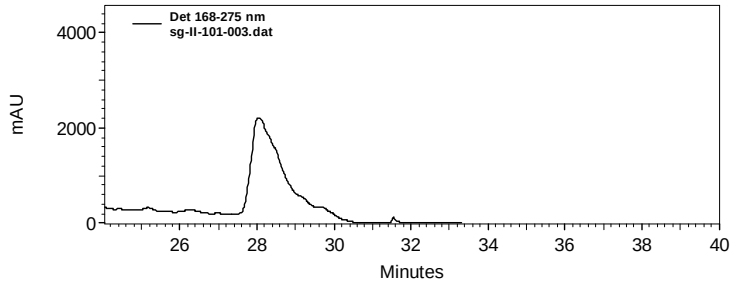

B)

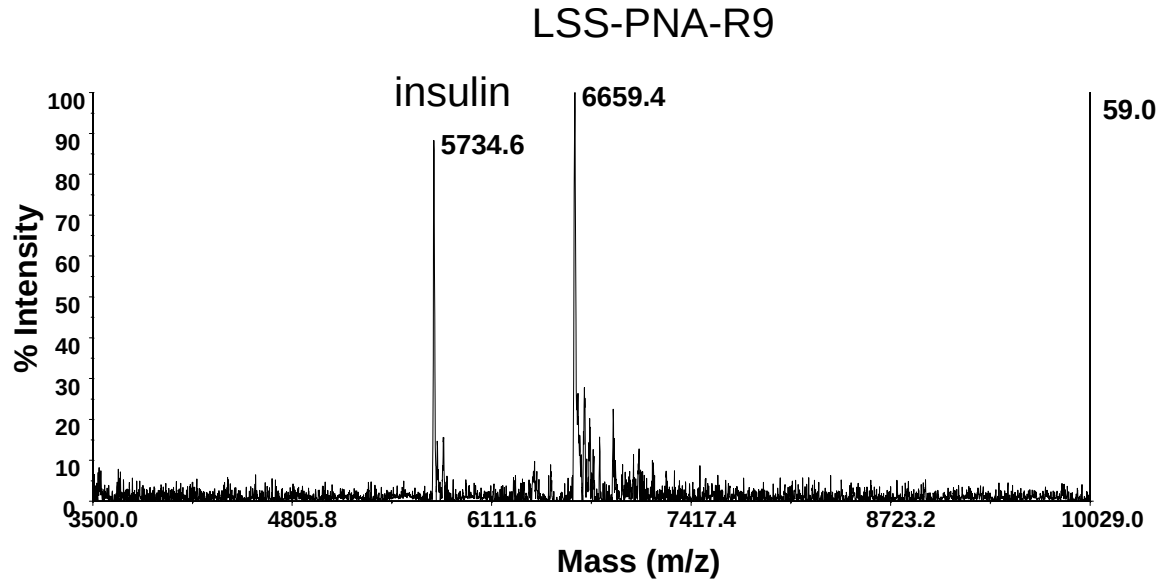

Figure S15. HPLC purification and MALDI-TOF analysis of **LSS-PNA-R9 (12).** A) Reverse-phase HPLC with Method B. B) MALDI-TOF with α-cyano-4-chloro-cinnamic acid matrix, average $[M+H]^+$ expected 6660.0, found 6659.4. Insulin (average $[M+H]^+$ assigned to 5734.6) was the internal reference.

Synthesis and in Vitro and in Vivo Evaluation of a Series of Dihydroisocoumarin Derivatives Conjugated with Fatty Acids, Alcohols, and Amines as Potential Anticancer Agents

Catherine A. Higgins,*[,†] Zoica Delbederi,[‡] Kelly McGarel,[‡] Timothy Mills,[‡] Owen McGrath,[†] Stephanie Feutren-Burton,[‡] William Watters,[‡] Paul Armstrong,[‡] Patrick G. Johnston,[†] David Waugh,[†] and Hendrik van den Berg[§]

Centre for Cancer Research and Cell Biology (CCRCB), Queens University Belfast, 97 Lisburn Road, Belfast, Northern Ireland, BT9 7BL, Almac Sciences, Almac House, 20 Seagoe Industrial Estate, Craigavon, Northern Ireland, BT63 5QD, United Kingdom, and Medicine and Therapeutics, School of Medicine, Queens University Belfast, U Floor, Belfast City Hospital, Belfast, Northern Ireland, BT9 7AB, United Kingdom. Received March 19, 2009; Revised Manuscript Received July 7, 2009

In this paper, we report the synthesis and biological activity of a series of dihydroisocoumarin analogues conjugated with fatty acids, alcohols, or amines, of varying hydrocarbon chain length and degree of unsaturation, to the dihydroisocoumarins, kigelin and mellein, at the C-7 and C-8 positions on the core dihydroisocoumarin structure. These compounds were evaluated for their antiproliferative activity against human breast cancer (MCF-7 and MDA-MB-468) and melanoma cells (SK-MEL-28 and Malme-3M) using the 3-(4,5-dimethylthiazol-2-yl)-2,5-diphenyl-2*H*-tetrazolium bromide (MTT) assay. Two compounds conjugated with γ-linolenyl alcohol (18:3 n-6) demonstrated potent antiproliferative activity in vitro with one of these 4-hydroxy-3-oxo-1,3-dihydro-isobenzofuran-5-carboxylic acid octadeca-6,9,12-trienyl ester, demonstrating significant antitumor activity in vivo in a number of human tumor xenograft models.

INTRODUCTION

Isocoumarins represent an important class of naturally occurring lactones, isolated from a diverse range of natural organisms, including fungi, plants, and insects, that display a wide range of biological activities (*1*−*8*). Isocoumarins can be classified as secondary metabolites structurally related to coumarins but with an inverted lactone ring, and it is anticipated that substituents to the basic isocoumarin skeleton may influence their biological activity. Reported activities include protease inhibitory properties, antifungal, cytotoxic, antimicrobial, antiallergic, and antimalarial effects (*9*−*11*). Dihydroisocoumarins, lacking the double bond between the 3- and 4-positions present on the isocoumarin structure, have also been previously isolated in a limited number of studies. Dihydroisocoumarins in themselves are an important class of naturally occurring biologically active lactones, originating from a variety of natural sources, with multiple biological activities described ranging from antibacterial, antimalarial, antifungal, and anticancer activity in addition to their use as sweetening agents (*12*−*15*).

We previously identified the dihydroisocoumarins, kigelin and demethylkigelin, in extracts of the fruits of *Kigelia pinnata*, which in part accounted for some of the observed antiproliferative activity of extracted material from this tree against human cancer cells in vitro (*16*). Synthetic versions of the active isolated dihydroisocoumarin compounds failed to demonstrate the same degree of antiproliferative activity as their extracted counterparts. The presence of trace amounts of several fatty acids was noted in extracted material from the plant, suggesting that these minor contaminants may be acting in synergy with other components of the fruit extracts. Accordingly, such an interaction would explain the difference in biological activity observed between the extracted and synthesized compounds.

Several polyunsaturated fatty acids (PUFAs) containing 18 or more carbons are known. PUFAs have exhibited in vitro direct anticancer activity against numerous cancer cell lines, and their antitumor activity has been evaluated in preclinical and clinical studies (*17*−*22*). It is known that PUFAs are taken up avidly by tumor cells presumably for use as biochemical precursors and energy sources. In addition, PUFAs are known to be readily incorporated into lipid bilayers of cells, which can result in the disruption of both membrane structure and fluidity, factors which have been suggested to increase intracellular drug accumulation (*23*−*25*). All these factors strongly suggest the benefit of PUFAs in specifically targeting drugs to the tumor cells. Importantly, a number of PUFAs have been shown to selectively inhibit tumor cell proliferation and are significantly less toxic to normal cells (*26*). Several mechanisms of action have been proposed to account for the anticancer activity of PUFAs including alteration in gene expression, modulation of cellular proliferation, differentiation and apoptosis, increase in drug transport across the cell membrane, generation of free oxygen radicals, and lipid peroxidation (*27*).

One way to improve upon the therapeutic index of chemotherapy drugs is conjugation to fatty acids (*28*). Chemotherapy drugs conjugated to fatty acids have been shown to enhance tumor targeting and deliver prodrugs for intratumoral activation. Taxoprexin, a novel synthetic small molecule linking paclitaxel to the fatty acid docosahexaenoic (DHA) acid, demonstrated significantly enhanced tumor distribution and antitumor activity in various tumor models as compared with paclitaxel alone after equitoxic or equimolar doses (*29, 30*). In a lung cancer mouse model and in preclinical human studies, treatment with DHA−paclitaxel demonstrated better pharmacokinetic properties and a more favorable toxicity profile than that seen with

* To whom correspondence should be addressed. Tel: +44 (0) 28 90 97 2779. Fax: +44 (0) 28 90 97 2776. E-mail: c.a.higgins@qub.ac.uk.

† CCRCB, Queens University Belfast.

‡ Almac Sciences.

§ Medicine and Therapeutics, Queens University Belfast.

10.1021/bc900122g CCC: $40.75 © 2009 American Chemical Society
Published on Web 08/26/2009

paclitaxel alone. In a number of preclinical models, data indicate that such conjugates are preferentially taken up by tumor cells compared to normal cells (*29*). A number of studies have also demonstrated an enhanced anticancer activity when PUFAs are given with conventional chemotherapeutic agents (*31*). Specific long-chain omega-3 PUFAs have been shown to enhance the cytotoxicity of paclitaxel, doxorubicin, and cyclophosphamide in cancer cells in vitro (*32, 33*). In addition, lipid aminoalcohols and diamines have been reported in the literature to have several biological activities including their anti-inflammatory activities and their cytotoxicity toward neoplastic cells (*34*−*36*).

Initially, we evaluated the biological activity of a number of fatty acids in combination with kigelin, a dihydroisocoumarin compound we had previously isolated from fruit extracts of *K. pinnata*. We previously noted that simple modifications to the dihydroisocoumarin core structure could alter the biological activity of this class of compounds and significantly enhance the antiproliferative activity observed (*16*). As a result, a synthetic chemistry program was undertaken to further study the structure−activity relationship (SAR) of this class of compounds. In this paper, we report the synthesis and biological activity of a series of dihydroisocoumarin analogues conjugated with fatty acids, alcohols, or amines, of varying hydrocarbon chain length and degree of unsaturation, to the dihydroisocoumarins, kigelin and mellein, at the C-7 and C-8 positions on the core dihydroisocoumarin structure. The antiproliferative activity of these compounds was assessed by MTT assay in two breast cancer cell lines, MCF-7 and MDA-MB-468, and two melanoma cell lines, SK-MEL-28 and Malme-3M. Further in vitro and in vivo activity of a highly active compound, 4-hydroxy-3-oxo-1,3-dihydro-isobenzofuran-5-carboxylic acid octadeca-6,9,12-trienyl ester **36** identified in the initial MTT screen, is also reported.

EXPERIMENTAL PROCEDURES

Materials and Instrumentation. UV spectra were recorded on two HPLC systems. System 1: Waters 2690, photodiode array detector (PDA) 996. System 2: Waters 2695, PDA 2996. IR spectra were recorded on a Perkin-Elmer FT-IR spectrometer SN, 50267; PO, 1118−5248. ^{1}H NMR (400 MHz) and ^{13}C NMR (100 MHz) were recorded on a Bruker 400 MHz Avance NMR spectrometer equipment (ID: BZH 299/400/70F D207/54−3914) (the chemical shifts are reported as ppm (δ) relative to TMS as internal standard). Mass spectra were obtained with a Finnigan LCQ DUO SN LDU 00253 mass spectrometer. In chromatographic fractionations, thin layer chromatographs (TLC) were run on silica gel 60F254 aluminum sheets (Merck). The reagent used for visualization was a solution of 10% phosphomolybdic acid in ethanol. For column chromatography, silica gel (Davisil grade 633, particle size 35−75 μM and/or Merck grade 9385, particle size 40−63 μM)) was used. All starting materials were commercially available. Solvents and reagents were used without further purification. γ-Linolenic acid (GLA; 18:3 n-6), oleic acid (OA; 18:1 n-9), linoleic acid (LA; 18:2 n-6), α-linolenic acid (ALA; 18:3 n-3), and docosahexanoic acid (DHA; 22:6 n-3) were purchased from Sigma Chemical.

Synthesis of Fatty Acid Conjugates at the C-8 Position of Racemic Kigelin (2−5) (Scheme 1). Under nitrogen atmosphere, the corresponding acid (100 mg; 1 equiv) was charged and dissolved in dichloromethane (4 mL) (for C21, a mixture of DCM/THF 1/1 was used as a solvent due to poor solubility of the acid in DCM only). To this solution were added dicyclohexyl carbodiimide (DCC; 1 equiv) and 4-*N*,*N*′-dimethylaminopyridine (DMAP; 1 equiv). The reaction mixture was cooled to 0 °C. Kigelin **1** (1 equiv) was added, and the reaction mixture stirred for 2 h at 0 °C. The precipitated dicyclohexyl urea was filtered, and the solvent was removed under reduced pressure. The residue was purified by column chromatography using hexane/ether (70/30) as eluent. The concentration of the appropriate fractions gave an oily residue, which was taken up in diethyl ether and washed 2−3 times with aqueous NaOH (2 M; 25 mL portions) to remove unreacted starting materials. The organic phase was separated, dried over magnesium sulfate, and the solvent concentrated under reduced pressure to give the fatty acid esters of (±)-kigelin.

Scheme 1. Synthesis of Fatty Acid Esters of Racemic Kigelin (2−5)

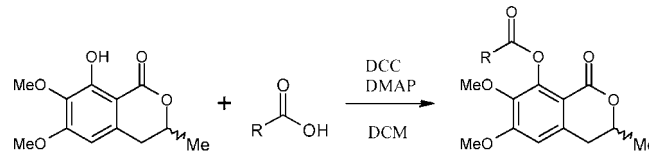

(+/-)-Kigelin 1 2 - 5

Racemic Kigelin Oleyl Ester (2). Racemic kigelin oleyl ester (**2**) was prepared from (±)-kigelin **1** and oleic acid. Yield = 80 mg (45%). ^{1}H NMR ($CDCl_3$, 400 MHz) δ 6.54 (1H, s, ArH), 5.27 (2H, t, *J* 4.6 Hz, CH═CH), 4.50 (1H, m, CH−CH_3 lactone), 3.85 (3H, s, OCH_3), 3.73 (3H, s, OCH_3), 2.77 (2H, m, CH_2), 2.62 (2H, t, *J* 7.6 Hz, CH_2−CO), 1.95 (4H, d, br, CH_2), 1.72 (2H, m, CH_2), 1.38 (3H, d, *J* 6.3 Hz, CH_3 on lactone ring), 1.26−1.19 (20H, m, CH_2 acid), 0.80 (3H, t, *J* 6.8 Hz, CH_3 acid).^{13}C NMR ($CDCl_3$, 100 MHz): 171.9, 161.9, 157.5, 146.1, 141.3, 136.8, 129.9, 129.8, 111.1, 107.8, 74.2, 61.1, 56.2, 35.6, 34.7, 31.9, 30.3, 29.8, 29.7, 29.5, 29.3 (2 × C), 29.3, 29.2, 29.1, 27.2, 24.6, 22.7, 20.7, 14.1.

Racemic Kigelin Linoleyl Ester (3). Racemic kigelin linoleyl ester (**3**) was prepared from (±)-kigelin **1** and linoleic acid. Yield = 55 mg (31%). ^{1}H NMR ($CDCl_3$, 400 MHz) δ 6.54 (1H, s, ArH), 5.34 (4H, m, CH═CH), 4.57 (1H, m, CH−CH_3 lactone), 3.92 (3H, s, OCH_3), 3.80 (3H, s, OCH_3), 2.86 (2H, m, CH_2), 2.77 (2H, t, *J* 6.4 Hz, CH_2), 2.68 (2H, t, *J* 7.6 Hz, CH_2−CO), 2.05 (4H, m, CH_2), 1.77 (2H, m, CH_2), 1.41 (3H, d, *J* 6.3 Hz CH_3 on lactone ring), 1.34−1.27 (14H, m, CH_2 acid), 0.87 (3H, t, *J* 6.8 Hz, CH_3 acid).

Racemic Kigelin α-Linolenyl Ester (4). Racemic kigelin **1** α-linolenyl ester (**4**) was prepared from (±)-kigelin and α-linolenic acid. Yield = 68 mg (38%). ^{1}H NMR ($CDCl_3$, 400 MHz) δ 6.61 (1H, s, ArH), 5.38 (6H, m, 3 × CH═CH), 4.60 (1H, m, CH−CH_3 lactone), 3.92 (3H, s, OCH_3), 3.81 (3H, s, OCH_3), 2.84 (2H, m, CH_2), 2.81 (2H, t, *J* 6.4 Hz, CH_2), 2.69 (2H, t, *J* 7.6 Hz, CH_2−CO), 2.10 (4H, m, CH_2), 1.80 (2H, m, CH_2), 1.45 (3H, d, *J* 6.3 Hz, CH_3 on lactone ring), 1.36 (10H, m, CH_2 acid), 0.98 (3H, t, *J* 6.8 Hz, CH_3 acid). ^{13}C NMR ($CDCl_3$, 100 MHz) 171.9, 161.9, 157.5, 146.1, 141.3, 136.8, 131.9, 130.3, 128.3, 128.3, 127.7, 127.1, 111.1, 107.8, 102.0, 71.2, 61.1, 56.2, 35.6, 34.1, 29.6, 29.2, 29.1, 27.0, 25.6, 25.5, 24.6, 20.7, 20.5, 14.3.

Racemic Kigelin γ-Linolenyl Ester (5). Racemic kigelin **1** γ-linolenyl ester (**5**) was prepared from (±)-kigelin and γ-linolenic acid. Yield = 29 mg (16%). ^{1}H NMR ($CDCl_3$, 400 MHz) δ 6.61 (1H, s, ArH), 5.43−5.32 (6H, m, 3 × CH═CH), 4.60 (1H, m, CH−CH_3 lactone), 3.93 (3H, s, OCH_3), 3.81 (3H, s, OCH_3), 2.84 (4H, m, CH_2), 2.71 (2H, t, *J* 6.4 Hz, CH_2−CO), 2.14 (2H, m, CH_2), 2.05 (2H, m, CH_2), 1.82 (2H, m, CH_2), 1.53 (2H, m, CH_2), 1.46 (3H, d, *J* 6.3 Hz, CH_3 on lactone ring), 1.38−1.25 (8H, m, CH_2 acid), 0.88 (3H, t, *J* 6.8 Hz CH_3 acid).

Synthesis of Fatty Acid Conjugates at C-8 Position of Racemic Mellein (7−10) (Scheme 2). Under nitrogen atmosphere, the corresponding acid (100 mg; 1 equiv) was charged and dissolved in dichloromethane (4 mL) (for C21 a mixture of DCM/THF 1/1 was used as a solvent due to poor solubility of the acid in DCM only). To this solution were added

Scheme 2. Synthesis of Fatty Acid Esters of Racemic Mellein (7−10)

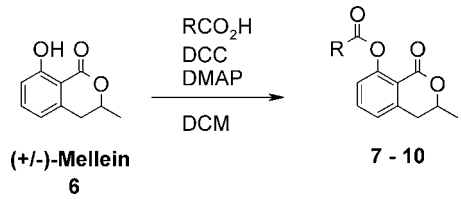

dicyclohexyl carbodiimide (DCC; 1 equiv) and 4-*N*,*N*′-dimethylaminopyridine (DMAP; 1 equiv). The reaction mixture was cooled to 0 °C. Mellein **6** (1 equiv) was added and the reaction mixture stirred for 2 h at 0 °C. The precipitated dicyclohexyl urea was filtered and the solvent was removed under reduced pressure. The residue was purified by column chromatography using hexane/ether (90/10) as eluent. The concentration of the appropriate fractions gave an oily residue, which was taken up in diethyl ether and washed 2−3 times with aqueous NaOH (2 M; 25 mL portions) to remove unreacted starting materials. The organic phase was separated, dried over magnesium sulfate, and the solvent concentrated under reduced pressure to give the fatty acid esters of (±)-mellein.

Racemic Mellein Oleyl Ester (7). Racemic mellein oleyl ester (**7**) was prepared from (±)-mellein **6** and oleic acid. Yield = 50 mg (40%). ^{1}H NMR ($CDCl_3$, 400 MHz) δ 7.51 (1H, t, *J* 7.9 Hz, ArH), 7.12 (1H, d, *J* 7.6 Hz ArH), 7.03 (1H, d, *J* 7.9 Hz, ArH), 5.36 (2H, t, *J* 4.6 Hz, CH═CH), 4.63 (1H, m, CH−CH_3 lactone), 2.93 (2H, m, CH_2 lactone), 2.64 (2H, t, *J* 7.6 Hz, CH_2−CO), 2.02 (4H, m, CH_2), 1.76 (2H, m, CH_2), 1.48 (3H, d, *J* 6.3 Hz, CH_3 on lactone ring), 1.44−1.27 (20H, m, CH_2 acid), 0.88 (3H, t, *J* 6.9 Hz, CH_3 acid). ^{13}C NMR ($CDCl_3$, 100 MHz) δ 172.4, 162.1, 152.0, 141.2, 134.2, 129.7, 129.8, 125.0, 122.9, 118.0, 77.2, 74.6, 35.4, 34.2, 31.9, 29.8, 29.7, 29.5, 29.3, 29.2, 29.1, 27.2, 27.2, 24.4, 22.7, 20.6, 14.1.

Racemic Mellein Linoleyl Ester (8). Racemic mellein linoleyl ester (**8**) was prepared from (±)-mellein **6** and linoleic acid. Yield = 102 mg (65%). ^{1}H NMR ($CDCl_3$, 400 MHz) δ 7.51 (1H, t, *J* 7.8 Hz, ArH), 7.11 (1H, d, *J* 7.6 Hz, ArH), 7.02 (1H, d, *J* 8.1 Hz, ArH), 5.36 (4H, m, 2 × CH═CH), 4.62 (1H, m, CH−CH_3 lactone), 2.92 (2H, m, CH_2 lactone), 2.78 (2H, t, *J* 6.3 Hz, CH_2), 2.65 (2H, t, *J* 7.6 Hz, CH_2−CO), 2.05 (4H, m, CH_2−CH═CH), 1.78 (2H, m, CH_2), 1.47 (3H, d, *J* 6.3 Hz, CH_3 on lactone ring), 1.35−1.24 (14H, m, CH_2 acid), 0.89 (3H, t, *J* 6.8 Hz, CH_3 acid). ^{13}C NMR ($CDCl_3$, 100 MHz) δ 172.4, 162.1, 151.9, 141.2, 134.2, 130.2, 130.1, 128.0, 127.9, 125.0, 122.9, 118.0, 74.6, 35.4, 34.2, 32.8, 31.5, 29.6, 29.3, 29.2, 29.1, 27.2, 27.2, 25.6, 24.4, 22.6, 20.6, 14.1.

Racemic Mellein α-Linolenyl Ester (9). Racemic mellein α-linolenyl ester (**9**) was prepared from (±)-mellein **6** and α-linolenic acid. Yield = 88 mg (56%). ^{1}H NMR ($CDCl_3$, 400 MHz) δ 7.51 (1H, t, *J* 7.8 Hz, ArH), 7.11 (1H, d, *J* 7.6 Hz, ArH), 7.02 (1H, d, *J* 8.0 Hz, ArH), 5.35 (6H, m, 3 × CH═CH), 4.62 (1H, m, CH−CH_3 lactone), 2.92 (2H, d, *J* 7.0 Hz, CH_2 lactone), 2.81 (2H, t, *J* 5.9 Hz, CH_2), 2.65 (2H, t, *J* 7.6 Hz CH_2−CO), 2.06 (4H, m, CH_2), 1.75 (2H, m, CH_2), 1.47 (3H, d, *J* 6.3 Hz, CH_3 on lactone ring), 1.44−1.32 (10H, m, CH_2 acid), 0.97 (3H, t, *J* 7.5 Hz, CH_3 acid). ^{13}C NMR ($CDCl_3$, 100 MHz) δ 172.4, 162.1, 151.9, 141.2, 134.2, 131.9, 130.3, 128.3, 128.3, 127.7, 127.1, 125.0, 122.9, 118.0, 74.6, 35.4, 34.2, 29.6, 29.2, 29.1, 29.1, 27.2, 25.6, 25.5, 25.4, 24.4, 20.6, 14.3.

Racemic Mellein γ-Linolenyl Ester (10). Racemic mellein γ-linolenyl ester (**10**) was prepared from (±)-mellein **6** and γ-linolenic acid. Yield = 79 mg (50%). ^{1}H NMR ($CDCl_3$, 400 MHz) δ 7.51 (1H, t, *J* 7.9 Hz, ArH), 7.12 (1H, d, *J* 7.6 Hz, ArH), 7.02 (1H, d, *J* 8.0 Hz, ArH), 5.45−5.31(6H, m, 3 × CH═CH), 4.62 (1H, m, CH−CH_3 lactone), 2.93 (2H, d, *J* 6.8 Hz, CH_2 lactone), 2.82 (4H, m, CH_2), 2.67 (2H, t, *J* 7.5 Hz, CH_2−CO), 2.13 (2H, q, *J* 7.0 Hz, CH_2), 2.06 (2H, q, *J* 6.9 Hz, CH_2), 1.82 (2H, m, CH_2), 1.53 (2H, m, CH_2), 1.47 (3H, d, *J* 6.3 Hz, CH_3 on lactone ring), 1.39−1.25 (6H, m, CH_2 acid), 0.90 (3H, t, *J* 7.1 Hz, CH_3 acid). ^{13}C NMR ($CDCl_3$, 100 MHz) δ 172.2, 162.1, 151.9, 141.2, 134.2, 130.4, 129.7, 128.4, 128.2, 127.6, 125.0, 122.9, 117.9, 74.6, 35.4, 34.1, 31.5, 29.3, 29.3, 29.1, 27.2, 26.9, 25.8 (2 × C), 22.6, 20.6, 14.1.

Preparation of 8-Hydroxy-3-methyl-1-oxo-isochroman-7-carboxylic Acid (14) (Scheme 3): Dimethyl 2-Hydroxy-4-methylbenzene-1,3-dicarboxylate (12). To a suspension of sodium methoxide (26.0 g, 0.48 mol, 1.12 equiv) in anhydrous THF (250 mL) under nitrogen at 0 °C was added dropwise a solution of ethyl formate (31.89 g, 0.43 mol, 1.0 equiv) and acetone (25.00 g, 0.43 mol, 1.0 equiv), maintaining the temperature at <5 °C. The reaction was stirred at 0 °C for 15 min then warmed to ambient temperature, at which it was then stirred for 15 min. The reaction was evaporated to dryness, to afford crude sodium formyl acetone **11**, which was dissolved in methanol (500 mL) under nitrogen. Dimethyl 1,3-acetonedicarboxylate (71.21 g, 0.41 mol, 0.95 equiv) was added dropwise, maintaining the temperature at <25 °C. The reaction mixture was stirred for 16 h at room temperature. The reaction was concentrated to dryness. The residue was diluted with 2 M HCl and extracted into ethyl acetate. The combined organic extracts were washed with saturated brine, dried over $MgSO_4$, filtered, and concentrated in vacuo. Purification by vacuum distillation (∼0.1 mbar, bp ∼115−120 °C) afforded dimethyl 2-hydroxy-4-methylbenzene-1,3-dicarboxylate **12** as a pale yellow oil, which solidified upon standing. Yield = 21.76 g (24%). ^{1}H NMR ($CDCl_3$, 400 MHz) δ 7.74 (1H, d, *J* 8.2 Hz, ArH), 6.72 (1H, d, *J* 8.2 Hz, ArH), 3.94 (3H, s, OCH_3), 3.91 (3H, s, OCH_3), 2.33 (3H, s, CH_3).

8-Hydroxy-3-methyl-1-oxo-isochroman-7-carboxylic Acid Methyl Ester (13). To a solution of LDA (54.5 mL, 1.8 M solution, 98.1 mmol, 2.2 equiv) in anhydrous THF (180 mL) under nitrogen cooled to −78 °C was added dropwise a solution of dimethyl 2-hydroxy-4-methylbenzene-1,3-dicarboxylate **12** (10.00 g, 44.6 mmol, 1 equiv) in anhydrous THF (20 mL) at −78 °C. After stirring for 20 min, acetaldehyde (6.12 g, 139.0 mmol, 3.1 equiv) was added dropwise at −78 °C. The reaction was stirred at −78 °C for 30 min, then warmed to 0 °C, and then stirred for 45 min. The reaction was quenched at 0 °C by the addition of acetic acid (5.15 mL) and then warmed to ambient temperature. The reaction was diluted with 2 M HCl and extracted into ethyl acetate. The combined organic extracts were washed with brine, dried over $MgSO_4$, filtered, and concentrated in vacuo. The residue was recrystallized from hexane/ethyl acetate to afford 8-hydroxy-3-methyl-1-oxo-isochroman-7-carboxylic acid methyl ester **13** as a beige solid. Yield = 5.12 g (49%). ^{1}H NMR ($CDCl_3$, 400 MHz) δ 8.04 (1H, d, *J* 7.9 Hz, ArH), 6.76 (1H, d, *J* 7.9 Hz, ArH), 4.72 (1H, m, OCH), 3.94 (3H, s, OCH_3), 2.97 (2H, d, *J* 7.2 Hz, CH_2), 1.54 (3H, d, *J* 6.3 Hz, CH_3); ESIMS *m*/*z* (M−1) = 235.

8-Hydroxy-3-methyl-1-oxo-isochroman-7-carboxylic Acid (14). To a suspension of 8-hydroxy-3-methyl-1-oxo-isochroman-7-carboxylic acid methyl ester **13** (4.75 g, 20.1 mmol, 1 equiv) in ethanol (75 mL) was added 10 w/v % sodium hydroxide aqueous solution (15 mL, 37.5 mmol, 1.9 equiv). The mixture was refluxed for 1 h and then cooled to ambient temperature. The reaction mixture was concentrated in vacuo. The residue was diluted with water and washed with ethyl acetate. The organic layer was discarded. The aqueous layer was adjusted to pH 1 with 2 M HCl, saturated with NaCl, and extracted with ethyl acetate. The combined organic extracts were dried over $MgSO_4$, filtered, and concentrated in vacuo. The solid was slurried in methanol to afford 8-hydroxy-3-methyl-1-oxo-

Scheme 3. Synthesis of 13 and 14[a]

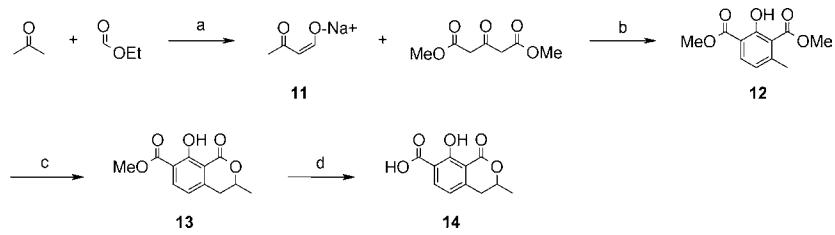

[a] Reagents and Conditions: (a) NaOMe, Et_2O; (b) MeOH; (c) acetaldehyde, LDA, THF; (d) NaOH, EtOH.

Scheme 4. Synthesis of Fatty Alcohol Conjugates at C-7 Position

isochroman-7-carboxylic acid **14** as an off-white solid. Yield = 3.46 g (77%). ^{1}H NMR (MeOD, 400 MHz) δ 7.97 (1H, d, *J* 8.0 Hz, ArH), 6.89 (1H, d, *J* 8.0 Hz, ArH), 4.72 (1H, m, OCH), 2.91 (2H, m, CH_2), 1.40 (3H, d, *J* 6.3 Hz, CH_3). ^{13}C NMR (MeOD, 100 MHz) δ 168.8, 165.4, 161.8, 146.7, 136.5, 117.8, 115.7, 110.8, 74.8, 34.4, 20.2. ESIMS *m/z* (M+1) = 223.

Synthesis of Ester Linked Fatty Alcohol Conjugates at C-7 Position of Racemic Mellein (15−24) (Scheme 4). To the reaction vessel were charged 8-hydroxy-3-methyl-1-oxo-isochroman-7-carboxylic acid **14** (250 mg, 1.13 mmol, 1.0 equiv), the alcohol (1.0 equiv), DMAP (151 mg, 1.24 mmol, 1.1 equiv), and anhydrous DCM (10 mL) under nitrogen. To this was added DCC (255 mg, 1.24 mmol, 1.1 equiv), and the reaction mixture was stirred at room temperature overnight. The mixture was filtered through Celite and the filtrate concentrated in vacuo. The crude material was purified by column chromatography using hexane/EtOAc to afford pure 8-hydroxy-3-methyl-1-oxo-isochroman-7-carboxylic acid ester.

Ochratoxin Acid Hexyl Ester (15). Yield = 100 mg (41%). ^{1}H NMR ($CDCl_3$, 400 MHz) δ 8.02 (1H, d, *J* 8.3 Hz, ArH), 6.75 (1H, d, *J* 8.3 Hz, ArH), 4.71 (1H, m, CH), 4.34 (2H, t, *J* 6.7 Hz, CH_2), 2.96 (2H, d, *J* 7.2 Hz, CH_2), 1.77 (2H, q, *J* 7.1 Hz, CH_2), 1.53 (3H, d, *J* 6.3 Hz, CH_3), 1.44 (2H, m, CH_2), 1.34 (4H, m, CH_2), 0.89 (3H, t, *J* 6.3 Hz, CH_3). ^{13}C NMR ($CDCl_3$, 100 MHz) δ 167.7, 166.2, 162.7, 145.2, 137.6, 117.4, 117.2, 110.3, 75.3, 65.6, 35.2, 31.4, 28.6, 25.6, 22.5, 20.7, 14.0. ESIMS *m/z* (M+1) = 307.

Ochratoxin Acid Dodecyl Ester (16). Yield = 300 mg (68%). ^{1}H NMR ($CDCl_3$, 400 MHz) δ 8.02 (1H, d, *J* 7.9 Hz, ArH), 6.74 (1H, d, *J* 7.9 Hz, ArH), 4.71 (1H, m, CH), 4.33 (2H, t, *J* 6.7 Hz, CH_2), 2.96 (2H, d, *J* 7.2 Hz, CH_2), 1.77 (2H, m, CH_2), 1.53 (3H, d, *J* 6.3 Hz, CH_3), 1.44 (1H, m, CH), 1.32 (17H, m, br), 0.88 (3H, t, *J* 6.8 Hz, CH_3). ^{13}C NMR ($CDCl_3$, 100 MHz) δ 167.7, 166.2, 162.7, 145.2, 137.6, 117.4, 117.1, 110.3, 75.3, 65.6, 35.2, 31.9, 29.6, 29.6, 29.6, 29.5, 29.3, 29.3, 28.6, 25.9, 22.7, 20.6, 14.1. ESIMS *m/z* (M+1) = 391.

Ochratoxin Acid Oleyl Ester (17). Ochratoxin Yield = 319 mg (60%). ^{1}H NMR ($CDCl_3$, 400 MHz) δ 8.02 (1H, d, *J* 7.9 Hz, ArH), 6.74 (1H, d, *J* 7.9 Hz, ArH), 5.34 (2H, m, CH=CH), 4.71 (1H, m, CH), 4.33 (2H, t, *J* 6.7 Hz, CH_2), 2.96 (2H, d, *J* 7.0 Hz, CH_2), 2.02 (4H, m, CH_2), 1.76 (2H, m, CH_2), 1.53 (3H, d, *J* 6.4 Hz, CH_3), 1.47−1.22 (22H, m, 11 × CH_2), 0.88 (3H, t, *J* 6.9 Hz, CH_3). ESIMS *m/z* (M+1) = 473.

Ochratoxin Acid Linoleyl Ester (18). Yield = 191 mg (60%). ^{1}H NMR ($CDCl_3$, 400 MHz) δ 8.02 (1H, d, *J* 7.9 Hz, ArH), 6.74 (1H, d, *J* 7.9 Hz, ArH), 5.36 (4H, m, 2 × CH=CH), 4.71 (1H, m, CH), 4.33 (2H, t, *J* 6.7 Hz, CH_2), 2.96 (2H, d, *J* 7.2 Hz, CH_2), 2.77 (2H, t, *J* 6.5 Hz, CH_2), 2.05 (4H, m, CH_2), 1.76 (2H, m, CH_2), 1.53 (3H, d, *J* 6.3 Hz, CH_3), 1.49−1.25 (16H, m, 8 × CH_2), 0.88 (3H, t, *J* 6.9 Hz, CH_3). ESIMS *m/z* (M+1) = 471.6.

Ochratoxin Acid Eicosadienyl Ester (19). Yield = 225 mg (67%). ^{1}H NMR ($CDCl_3$, 400 MHz) δ 8.02 (1H, d, *J* 7.9 Hz, ArH), 6.74 (1H, d, *J* 7.9 Hz, ArH), 5.35 (4H, m, 2 × CH=CH), 4.70 (1H, q, *J* 6.4 Hz, CH), 4.33 (2H, t, *J* 6.7 Hz, CH_2), 2.96 (2H, d, *J* 7.1 Hz, CH_2), 2.77 (2H, t, *J* 6.5 Hz, CH_2), 2.05 (4H, m, CH_2), 1.76 (2H, m, CH_2), 1.53 (3H, d, *J* 6.3 Hz, $CHCH_3$), 1.47−1.24 (20H, m, 10 × CH_2), 0.89 (3H, t, *J* 6.9 Hz, CH_3). ESIMS *m/z* (M+1) = 500.2.

Ochratoxin Acid γ-Linolenyl Ester (20). Yield = 70 mg (40%). ^{1}H NMR ($CDCl_3$, 400 MHz) δ 8.02 (1H, d, *J* 7.9 Hz, ArH), 6.74 (1H, d, *J* 7.9 Hz, ArH), 5.36 (6H, m, 3 × CH=CH), 4.71 (1H, m, CH), 4.34 (2H, t, *J* 6.7 Hz, CH_2), 2.96 (2H, d, *J* 7.1 Hz, CH_2), 2.81 (4H, m, CH_2), 2.08 (4H, m, CH_2), 1.76 (2H, m, CH_2), 1.55 (3H, d, *J* 6.3 Hz CH_3), 1.49−1.25 (10H, m, 5 × CH_2), 0.88 (3H, t, *J* 6.3 Hz, CH_3).

Ochratoxin Acid α-Linolenyl Ester (21). Yield = 183 mg (58%). ^{1}H NMR ($CDCl_3$, 400 MHz) δ 8.02 (1H, d, *J* 7.9 Hz, ArH), 6.74 (1H, d, *J* 7.9 Hz, ArH), 5.35 (6H, m, 3 × CH=CH), 4.70 (1H, q, *J* 6.8 Hz, CH), 4.33 (2H, t, *J* 6.7 Hz, CH_2), 2.96 (2H, d, *J* 7.2 Hz, CH_2), 2.80 (4H, t, *J* 6.0 Hz, CH_2), 2.07 (4H, m, CH_2), 1.77 (2H, q, *J* 7.1 Hz, CH_2), 1.55 (3H, d, *J* 6.3 Hz, $CHCH_3$), 1.54−1.33 (10H, m, 5 × CH_2), 0.97 (3H, t, *J* 6.3 Hz, CH_3). ESIMS *m/z* (M+1) = 469.6.

Ochratoxin Acid Docosatetraenyl Ester (22). Yield = 75 mg (46%). ^{1}H NMR ($CDCl_3$, 400 MHz) δ 8.02 (1H, d, *J* 7.9 Hz, ArH), 6.74 (1H, d, *J* 7.9 Hz, ArH), 5.40 (8H, m, 4 × CH=CH), 4.70 (1H, m, CH), 4.33 (2H, t, *J* 6.7 Hz, CH_2), 2.96 (2H, d, *J* 7.1 Hz, CH_2), 2.82 (4H, m, CH_2), 2.06 (4H, m, CH_2), 1.76 (2H, m, CH_2), 1.53 (3H, d, *J* 6.3 Hz, $CHCH_3$), 1.49−1.24 (12H, m, 6 × CH_2), 0.89 (3H, t, *J* 6.3 Hz CH_3). ESIMS *m/z* (M+1) = 523.5.

Ochratoxin Acid Docosapentaenyl Ester (23). Yield = 38 mg (23%). ^{1}H NMR ($CDCl_3$, 400 MHz) δ 8.02 (1H, d, *J* 7.9 Hz, ArH), 6.74 (1H, d, *J* 7.9 Hz, ArH), 5.36 (10H, m, 5 × CH=CH), 4.71 (1H, m, CH), 4.33 (2H, t, *J* 6.7 Hz, CH_2), 2.96 (2H, d, *J* 8.0 Hz, CH_2), 2.80 (4H, m, CH_2), 2.06 (2H, m, CH_2), 1.74 (2H, m, CH_2), 1.53 (3H, d, *J* 6.3 Hz, $CHCH_3$), 1.55−1.24 (8H, m, 4 × CH_2), 0.95 (3H, t, *J* 6.3 Hz, CH_3). ESIMS *m/z* (M+1) = 521.5.

Ochratoxin Acid Docosahexenyl Ester (24). Yield = 43 mg (26%). ^{1}H NMR ($CDCl_3$, 400 MHz) δ 8.02 (1H, d, *J* 7.9 Hz ArH), 6.74 (1H, d, *J* 7.9 Hz, ArH), 5.47−5.27 (12H, m, 6 × CH=CH), 4.71 (1H, q, *J* 5.6 Hz, CH), 4.35 (2H, t, *J* 6.5 Hz, CH_2), 2.96 (2H, d, *J* 7.1 Hz, CH_2), 2.80 (10H, m, CH_2), 2.24 (2H, q, *J* 6.8 Hz, CH_2), 2.08 (2H, q, *J* 7.3 Hz, CH_2), 1.86 (2H, q, *J* 7.0 Hz, CH_2), 1.53 (3H, d, *J* 6.3 Hz, $CHCH_3$), 0.97 (3H, t, *J* 7.5 Hz CH_3). ESIMS *m/z* (M+1) = 519.2.

Synthesis of Amide Linked Fatty Amine Conjugates at C-7 Position of Racemic Mellein (25−30) (Scheme 5). To a stirred solution of 8-hydroxy-3-methyl-1-oxo-isochroman-7-carboxylic acid **14** (250 mg, 1.12 mmol, 1.0 equiv) in dry DMF (10 mL) under nitrogen at room temperature was added solid

Scheme 5. Synthesis of Fatty Amine Conjugates at C-7 Position

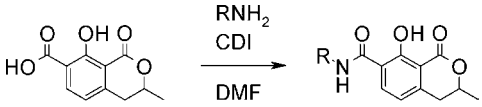

14 **25 - 30**

N,N-carbonyl diimidazole (192 mg, 1.18 mmol, 1.05 equiv) and the reaction monitored by TLC. Once the reaction was judged complete (~1 h), the amine (1.0 equiv) was added and the reaction stirred further until TLC indicated that the reaction was complete. The crude mixture was then evaporated to dryness in vacuo. The residual oil was taken up into EtOAc or $CHCl_3$, washed with water, dried ($MgSO_4$), and evaporated to dryness to afford the amide of 8-hydroxy-3-methyl-1-oxo-isochroman-7-carboxylic acid.

Methyl Amide (25). Methyl amide **25** was prepared from **14**. The residual solid was taken up into chloroform and stirred with Amberlite IR-120+ resin, filtered off resin, dried ($MgSO_4$), and evaporated to dryness to afford the amide as a white solid. Yield = 161 mg (61%). ^{1}H NMR ($CDCl_3$, 400 MHz) δ 12.7−12.6 (1H, s, br, OH), 8.31 (1H, d, *J* 7.9 Hz, ArH), 7.96 (1H, s, br, NH), 6.76 (1H, d, *J* 7.9 Hz, ArH), 4.75−4.66 (1H, m, CH), 2.95−2.86 (5H, m, CH_2 and CH_3), 1.48 (3H, d, *J* 6.4 Hz, CH_3). ^{13}C NMR ($CDCl_3$, 100 MHz) δ 170.5, 164.6, 160.1, 143.1, 138.9, 119.8, 118.5, 108.6, 77.3, 34.6, 26.5, 20.6. ESIMS *m/z* (M+1) = 236.1.

Hexyl Amide (26). Yield = 120 mg (35%) as a yellow solid. ^{1}H NMR ($CDCl_3$, 400 MHz) δ 12.7−12.6 (1H, s, br, OH), 8.32 (1H, d, *J* 8.0 Hz, ArH), 8.00 (1H, s, br, NH), 6.76 (1H, d, *J* 8.0 Hz, ArH), 4.74−4.66 (1H, m, CH), 3.39 (2H, q, *J* 6.6 Hz, CH_2), 2.96−2.90 (2H, m, CH_2), 1.58−1.51 (2H, m, CH_2), 1.48 (3H, d, *J* 6.3 Hz, CH_3), 1.47−1.30 (6H, m, 3 × CH_2), 0.86−0.75 (3H, t, *J* 6.3 Hz, CH_3). ^{13}C NMR ($CDCl_3$, 100 MHz) δ 170.5, 163.8, 160.2, 143.0, 139.0, 120.0, 118.5, 108.6, 76.4, 39.9, 34.6, 31.5, 29.4, 26.7, 22.5, 20.6, 14.0; ESIMS *m/z* (M+1) = 306.2.

***N*-Methyl-*N*-hexyl Amide (27).** Yield = 150 mg (52%) as a colorless oil. **27** was a 1:1 mixture of unassigned rotamers. ^{1}H NMR ($CDCl_3$, 400 MHz) δ 11.37 (0.5H, s, OH), 11.35 (0.5H, s, OH), 7.45 (0.5H, d, *J* 7.6 Hz, ArH), 7.41 (0.5H, d, *J* 7.6 Hz, ArH), 6.75 (1H, d, *J* 7.6 Hz, ArH), 4.77−4.71 (1H, m, CH), 3.55 (1H, m, CH_2), 3.18 (1H, m, CH_2), 3.09 (1.5H, s, CH_3), 2.96−2.94 (2H, m, CH_2), 2.90 (1.5H, s, CH_3), 1.70−1.63 (1H, m, CH_2), 1.63−1.51 (3H, d, *J* 6.3 Hz, CH_3), 1.40−1.10 (7H, m, CH_2), 0.94−0.81 (3H, m, CH_3). ^{13}C NMR ($CDCl_3$, 100 MHz) δ 169.7, 169.7, 167.6, 167.4, 157.9, 140.5, 140.4, 134.9, 134.7, 125.6, 125.3, 118.1, 118.0, 108.5, 108.4, 76.2, 50.8, 47.3, 36.0, 34.5, 32.4, 31.6, 31.3, 28.0, 26.9, 26.4, 26.0, 22.6, 22.4, 20.7, 14.0, 13.9. ESIMS *m/z* (M+1) = 320.3.

Dodecyl Amide (28). Yield = 298 mg (63%) as a yellow waxy solid. ^{1}H NMR ($CDCl_3$, 400 MHz) δ 8.42 (1H, d, *J* 8.0 Hz, ArH), 8.07 (1H, s, br, NH), 6.85 (1H, d, *J* 8.0 Hz, ArH), 4.78 (1H, m, CH), 3.47 (2H, q, *J* 6.6 Hz, CH_2), 2.99 (2H, m, CH_2), 1.64−1.55 (9H, m, 4 × CH_2 and CH_3), 1.26 (14H, m, br), 0.88 (3H, t, *J* 6.3 Hz, CH_3). ESIMS *m/z* (M+1) = 390.3.

Oleyl Amide (29). Yield = 172 mg (32%). ^{1}H NMR ($CDCl_3$, 400 MHz) δ 8.42 (1H, d, *J* 8.0 Hz, ArH), 8.07 (1H, s, br, NH), 6.85 (1H, d, *J* 8.0 Hz, ArH), 5.35 (2H, m, CH=CH), 4.78 (1H, m, CH), 3.46 (2H, q, *J* 6.6 Hz, CH_2), 2.99 (2H, m, CH_2), 2.01 (4H, m, 2 × CH_2), 1.66−1.55 (8H, m, CH_2 and CH_3), 1.41−1.20 (19H, m, CH_2), 0.86 (3H, t, *J* 6.3 Hz, CH_3). ESIMS *m/z* (M+1) = 472.4.

γ-Linolenyl Amide (30). Yield = 75 mg (21%). ^{1}H NMR ($CDCl_3$, 400 MHz) δ 8.33 (1H, d, *J* 7.9 Hz, ArH), 8.01 (1H, s, br, NH), 6.77 (1H, d, *J* 7.9 Hz, ArH), 5.36−5.24 (6H, m, 3 × CH=CH), 4.70 (1H, m, CH), 3.40 (2H, q, *J* 6.6 Hz, CH_2), 2.92 (2H, m, CH_2), 2.73 (4H, t, *J* 5.6 Hz, CH_2), 1.98 (4H, m, CH_2), 1.55 (2H, m, CH_2), 1.48 (3H, d, *J* 6.3 Hz, CH_3), 1.37−1.18 (10H, m, 5 × CH_2), 0.82 (3H, t, *J* 6.8 Hz, CH_3). ^{13}C NMR ($CDCl_3$, 100 MHz) δ 170.5, 163.9, 160.2, 143.0, 139.1, 130.4, 130.0, 128.3, 128.2, 128.0, 127.6, 120.1, 118.5, 108.6, 76.4, 39.8, 34.6, 31.5, 30.9, 29.4, 29.3, 27.2, 27.1, 26.7, 25.6, 22.6, 20.7, 14.1. ESIMS *m/z* (M+1) = 468.4.

Synthesis of 4-Hydroxy-3-oxo-1,3-dihydro-isobenzofuran-5-carboxylic Acid Octadeca-6,9,12-trienyl Ester (36) (Scheme 6): 2-Prop-2-ynyloxy-tetrahydropyran (31). *p*-Toluenesulfonic acid monohydrate (20 mg, 0.1 mmol) was added to 3,4-dihydro-2*H*-pyran (33 g, 0.39 mol), and the mixture was stirred for 10 min. Propargyl alcohol (20 g, 0.36 mol) was added dropwise over 30 min. The reaction was stirred for 10 min, prior to the addition of sodium hydrogencarbonate (2.24 g, 27 mmol). The reaction was stirred overnight at room temperature. Filtration of the reaction mixture afforded 2-prop-2-ynyloxy-tetrahydropyran **31**. Yield = 49.40 g (99%). ^{1}H NMR ($CDCl_3$, 400 MHz) δ 4.82 (1H, t, *J* 3.3 Hz, CH), 4.25 (2H, m, CH_2), 3.84 (1H, m, CHH), 3.53 (1H, m, CHH), 2.47 (1H, t, *J* 3.8 Hz, CH), 1.64−1.89 (6H, m, CH_2). ^{13}C NMR ($CDCl_3$, 100 MHz) δ 96.7, 79.7, 74.0, 61.9, 53.9, 30.1, 25.5, 19.1.

4-Tetrahydropyran-2-yloxy-but-2-ynal (32). *n*-Butyl lithium solution (2.1 M solution in hexanes, 83 mL, 0.175 mol, 1.05 equiv) was added dropwise to a solution of 2-prop-2-ynyloxy-tetrahydropyran **31** (23.3 g, 0.167 mol, 1.0 equiv) in dry THF (350 mL) under nitrogen at −45 °C at such a rate so as to ensure that the temperature remained below −35 °C. Upon complete addition, the mixture was stirred for a further 10 min before the dropwise addition of neat DMF (26 mL, 0.33 mol) again added at a rate ensuring the reaction temperature remained below 35 °C. After complete addition, the Dewar cooling bath was removed and the reaction was allowed to warm to ambient. The reaction mixture was then poured into a cooled (~0 °C) vigorously stirred biphasic solution of aqueous KH_2PO_4 (91 g, 0.67 mol, 4.0 equiv dissolved in 1 L water) and MTBE (1 L). The mixture was separated and the aqueous layer retained. The ethereal extracts were washed with water (2 × 600 mL). All aqueous layers were then combined and back-extracted with MTBE (500 mL). The organic extracts were combined, dried ($MgSO_4$), filtered, and evaporated to dryness to afford crude 4-tetrahydropyran-2-yloxy-but-2-ynal **32** as a brown oil, which was sufficiently pure to be reacted immediately in the next step. Yield = 23.7 g (85%). ^{1}H NMR ($CDCl_3$, 400 MHz) δ 9.24 (1H, s, CHO), 4.82−4.80 (1H, m, CH), 4.46−4.42 (2H, m, CH_2), 3.86−3.75 (1H, m, CHH), 3.59−3.54 (1H, m, CHH), 1.86−1.71 (2H, m, CH_2), 1.67−1.55 (4H, m, CH_2).

2-Hydroxy-4-(tetrahydropyran-2-yloxymethyl)isophthalic Acid Dimethyl Ester (33). A concentrated solution of dimethyl 1, 3-acetone dicarboxylate (24.2 g, 0.14 mol, 1.0 equiv) in dry THF (30 mL) was added dropwise to a stirred suspension of NaH (6.76 g, 0.17 mol, 1.2 equiv) in dry THF (120 mL) under nitrogen at 0 °C. After complete addition, the reaction was allowed to stir for a further 20 min before the slow, dropwise addition at ~0 °C of a solution of crude 4-tetrahydropyran-2-yloxy-but-2-ynal **32** dissolved in dry THF (100 mL) over approximately 1 h. The reaction mixture was allowed to warm to ambient temperature overnight. The crude reaction was then poured onto 2 M HCl (200 mL), separated, and then extracted with ethyl acetate (3 × 250 mL). All organic layers were combined and washed with brine, dried (Na_2SO_4), filtered, and evaporated to dryness. The oil was then preabsorbed onto silica and purified by column chromatography using 9:1 v/v hexanes/ethyl acetate to afford 2-hydroxy-4-(tetrahydropyran-2-yloxymethyl)-isophthalic acid dimethyl ester **33** as a yellow oil. Yield = 18.1 g (40%). ^{1}H NMR ($CDCl_3$, 400 MHz) δ 11.22 (1H, s, OH), 7.88 (1H, d, *J* 8.2 Hz, ArH), 7.01 (1H, d, *J* 8.2 Hz, ArH),

Scheme 6. Synthesis of Hydroxy-phthalide-6-carboxylic Acid γ-Linolenyl Ester 36[a]

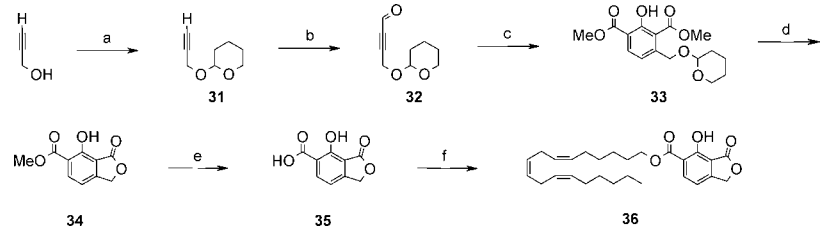

[a] Reagents and Conditions: (a) 3,4-dihydro-2*H*-pyran, r.t., 30 min; (b) n-BuLi, DMF, −45°C; (c) dimethyl 1, 3-acetone dicarboxylate, NaH, THF, 0 °C; (d) p-TSA·H_2O, MeOH, r.t., 30 min; (e) NaOH, dioxane, reflux, 3 h; (f) γ-linolenyl alcohol, EDC·HCl, HOBt, DIPEA, DMF.

Table 1. Cytotoxic Activity of Fatty Acids

	IC_{50} (μg/mL)			
	MCF-7	MDA-MB-468	SK-MEL-28	Malme-3M
heneicosanoic acid (C21:0)	>200	>200	93.5 ± 2.1	90 ± 0.0
oleic acid (C18:1, n-9)	62.5 ± 0.7	67.5 ± 0.7	77.5 ± 7.8	65 ± 0.0
linoleic acid (C18:2, n-6)	>200	>200	>200	>200
α-linolenic acid (C18:3, n-3)	65 ± 0.0	64 ± 0.0	69 ± 1.4	60.5 ± 0.7
γ-linolenic acid (C18:3, n-6)	54 ± 8.5	48 ± 14.7	64.5 ± 0.7	39.5 ± 2.1

[a] Data represent the mean IC_{50} ± SD (the concentration of each compound that inhibited 50% of the growth of the corresponding cancer cell line) of the tested compounds screened in an MTT assay against human breast cancer (MCF-7 and MDA-MB-468) and melanoma cells (SK-MEL-28 and Malme-3M).

4.82 and 4.58 (2 × 1H, d(AB), *J* 13.6 Hz, CHH), 4.65−4.63 (1H, t, *J* 3.5 Hz), 3.96 (3H, s, OCH_3), 3.94 (3H, s, OCH_3), 3.88−3.82 (1H, m), 3.55−3.50 (1H, m), 1.86−1.83 (1H, m), 1.75−1.65 (1H, m), 1.64−1.51 (4H, m, CH_2). ^{13}C NMR ($CDCl_3$, 100 MHz) δ 169.9, 167.0, 158.9, 144.8, 131.3, 121.4, 118.4, 112.1, 98.0, 66.4, 62.1, 52.5, 52.3, 30.3, 25.3, 19.1. ESIMS *m*/*z* $(M-1)^-$ 323.4.

7-Hydroxyphthalide-6-carboxylic Acid Methyl Ester (34). Solid *p*-toluenesulfonic acid monohydrate (1.0 g, 5.6 mmol, 0.1 equiv) was added to a stirred solution of 2-hydroxy-4-(tetrahydropyran-2-yloxymethyl)isophthalic acid dimethyl ester **33** dissolved in methanol (180 mL) and stirred for ∼30 min. The white precipitate that had formed was filtered off and dried in air to afford 7-hydroxyphthalide-6-carboxylic acid methyl ester **34** as a white powder. Yield = 8.16 g (70%). ^1H NMR ($CDCl_3$, 400 MHz) δ 11.7 (1H, s, OH), 8.16 (1H, d, *J* 8.0 Hz, ArH), 6.97 (1H, d, *J* 8.0 Hz, ArH), 5.27 (2H, s, CH_2), 4.01 (3H, s, OCH_3). ^{13}C NMR ($CDCl_3$, 100 MHz) δ 169.8, 167.9, 160.9, 155.3, 136.6, 113.5, 113.1, 112.5, 68.8, 52.9. ESIMS *m*/*z* (M−1) 207.4.

7-Hydroxyphthalide-6-carboxylic Acid (35). Sodium hydroxide solution (10 wt %, ∼8 mL) was added to a stirred suspension of 7-hydroxyphthalide-6-carboxylic acid methyl ester **34** (1.84 g, 8.8 mmol) in dioxane (20 mL) before heating to reflux under nitrogen for 3 h, at which time TLC analysis indicated complete conversion. The reaction mixture was evaporated to dryness. The residual oil was taken up into water (25 mL) and extracted with ethyl acetate (25 mL), The aqueous layer was then acidified to pH 1 with 2 M HCl, and the precipitate that formed was stirred for ∼10 min. The solid was isolated by filtration, washed with water (5 mL), dried in air, collected, and dried in a vacuum oven at 40 °C (over P_4O_{10}) to afford 7-hydroxyphthalide-6-carboxylic acid **35** as a white powder. Yield = 1.54 g (90%); mp 277 °C. ^1H NMR (d_6-DMSO, 400 MHz) δ 8.12 (1H, d, *J* 8.0 Hz, ArH), 7.11 (1H, d, *J* 8.0 Hz, ArH), 5.34 (2H, s, CH_2). ^{13}C NMR (d_6-DMSO, 100 MHz) δ 171.6, 167.5, 160.3, 156.0, 136.7, 113.1, 112.9, 112.3, 68.9. ESIMS *m*/*z* (M+1) 195.

7-Hydroxyphthalide-6-carboxylic Acid γ-Linolenyl Ester (36). To a mixture of 7-hydroxyphthalide-6-carboxylic acid **35** (2.30 g, 11.8 mmol), hydroxybenzotriazole (1.68 g, 12.5 mmol, 1.05 equiv) in anhydrous DMF (50 mL) under nitrogen and cooled to 0 °C was added diisopropylethylamine (2.52 g, 19.5 mmol, 1.7 equiv) followed by EDC·HCl (3.58 g, 18.7 mmol, 1.6 equiv). The reaction was stirred at 0 °C for 1 h and then warmed to room temperature. After stirring for 20 min, γ-linolenyl alcohol (3.13 g, 11.8 mmol, 1.0 equiv) was added, and the reaction stirred at room temperature overnight. The DMF was removed in vacuo. The residue was dissolved in $CHCl_3$ (100 mL) and washed sequentially with 10% citric acid solution (2 × 100 mL), sat. $NaHCO_3$ (2 × 100 mL) and brine (100 mL), dried over $MgSO_4$, and concentrated in vacuo to afford a yellow semisolid. Purification by flash chromatography on silica using hexane/EtOAc afforded 7-hydroxyphthalide-6-carboxylic acid γ-linolenyl ester **36**. Yield = 2.90 g (56%). ^1H NMR ($CDCl_3$, 400 MHz) δ 11.87 (1H, s OH), 8.16 (1H, d, *J* 8.0 Hz, ArH), 6.97 (1H, d, *J* 8.0 Hz ArH), 5.53−5.29 (6H, m, 3 × CH═CH), 5.27 (2H, s, CH_2), 4.40 (2H, t, *J* 6.3 Hz, CH_2), 2.81 (4H, m, CH_2), 2.02−2.12 (4H, m, CH_2), 1.82 (2H, m, CH_2), 1.47 (4H, m, CH_2), 1.31 (6H, m, CH_2), 0.89 (3H, t, *J* 6.1 Hz CH_3). ^{13}C NMR ($CDCl_3$, 100 MHz) δ 169.4, 167.9, 161.0, 155.2, 136.5, 130.5, 129.7, 128.4, 128.2, 128.0, 127.5, 113.5, 113.3, 112.4, 77.2, 68.8, 66.2, 31.5, 29.3, 29.2, 28.4, 27.2, 27.0, 25.7, 25.5, 22.6, 14.1. ESIMS *m*/*z* (M+1) 441.2.

Cell Culture. The cell lines used in this study were human breast adenocarcinoma cell lines, MCF-7 and MDA-MB-468, human melanoma cells, SK-MEL-28 and Malme-3M, human colorectal cancer cell lines, HT-29 and RKO, human lung adenocarcinoma cell lines, NCI-H23 and NCI-H157, and human prostate cancer cell lines (PC3 and LnCap). All cell lines used were originally obtained from the American Tissue Culture Collection and routinely maintained as monolayer cultures in RPMI 1640 supplemented with 10% fetal calf serum (GIBCO, Grand Island, NY) and 2 mmol/L L-glutamine at 37 °C in a humidified atmosphere of 5% CO_2. To remove the adherent cells from the flask for passaging and counting, cells were incubated with 0.25% trypsin−EDTA solution (GIBCO, Grand Island, NY) for 5 min. All experiments were performed using cells in exponential cell growth phase.

Cytotoxicity Assay (MTT Assay). The MTT assay is a widely used colorimetric assay for assessing the antiproliferative activity and determining the cytotoxic effects of novel therapeutic agents. 3-(4,5-Dimethylthiazol-2-yl)-2,5-diphenyltetrazolium bromide (MTT), a thiazolyl blue tetrazolium salt, is reduced from a yellow material to an insoluble purple formazan in the mitochondria of living metabolically active cells (*37*). Cells were maintained in RPMI 1640 containing 1% penicillin−streptomycin and 10% fetal calf serum (Gibco, Grand Island, NY) at 37 °C in a humidified atmosphere of 5% CO_2. 180 μL of cells was seeded at 1 × 10^3 cells per well in 96 well plates with 6 replicates for each drug concentration. Following the attachment period, cells were treated with appropriate drug concentrations (20 μL added per well). Chemically synthesized compounds

Table 2. Structure and Cytotoxic Activity of Kigelin Compounds Conjugated with Fatty Acids at C-8 Position against Human Cancer Cells[a]

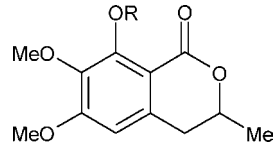

		IC_{50} (μM)			
	R	MCF-7	MDA-MB-468	SK-MEL-28	Malme-3M
1.	-H	>200	>200	>200	>200
2	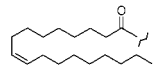	>200	>200	>200	>200
3	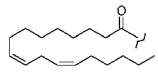	150.9 ± 1.6	99.9 ± 0.1	>200	>200
4	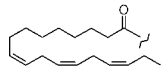	42.6 ± 24.9	62.6 ± 39.0	>200	>200
5	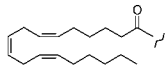	22.1 ± 3.54	31.3 ± 26.6	>200	106.0 ± 62.1

[a] Data represents the mean IC_{50} (the concentration of each compound that inhibited 50% of the growth of the corresponding cancer cell line) ± std dev of the tested compounds screened in an MTT assay against human breast cancer (MCF-7 and MDA-MB-468) and melanoma cells (SK-MEL-28 and Malme-3M).

Table 3. Structure and Cytotoxic Activity of Mellein Compounds Conjugated with Fatty Acids at C-8 Position against Human Cancer Cells[a]

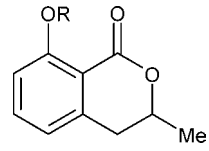

		IC_{50} (μM)			
	R	MCF-7	MDA-MB-468	SK-MEL-28	Malme-3M
6	H	>200	>200	>200	>200
7	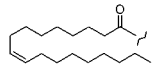	>200	>200	>200	>200
8	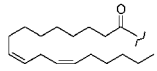	>200	>200	>200	>200
9	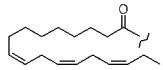	>200	>200	>200	>200
10	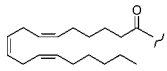	>200	>200	>200	>200

[a] Data represent the mean IC_{50} (the concentration of each compound that inhibited 50% of the growth of the corresponding cancer cell line) of the tested compounds screened in an MTT assay against human breast cancer (MCF-7 and MDA-MB-468) and melanoma cells (SK-MEL-28 and Malme-3M).

were dissolved in DMSO. 10 mmol/L stock solutions of all test compounds were prepared in DMSO and stored in aliquots at −20 °C. Further dilutions were made in medium when required. Wells containing medium only were used as blanks. Cells were maintained at 37 °C 5% CO_2 for 96 h. MTT was added to the cells, and after 4 h, the MTT medium was removed and 100 μL DMSO added per well. Plates were agitated on an orbital mixer platform (Stuart Scientific) for 10 min. Absorbance was measured at 570 nm on a Biotrak II (Amersham Bioscience) plate reader. IC_{50} values were calculated comparing control and drug-treated cells. The IC_{50} value was defined as the concentration of samples that produced a 50% reduction in cell viability and calculated with GraphPad *Prism* software. Data for combination treatments examining multiple drug effects were analyzed using the Chou and Talalay method, based on the median effect principle, with the software calcusyn to examine the nature of interaction between drugs (*38*). Combination index (CI) values were calculated; briefly, CI values of less than 1 indicate synergy (and the smaller the value the greater the degree of synergy), values above 1 indicate antagonism, and values equal to 1 indicate additive effects.

Cell Counts. The effects of **20** and **36** treatment were also assessed by performing daily cell counts in the human breast cancer cell line, MDA-MB-468. Cells were seeded at 100 cells per well in 24 well plates and following an attachment period were treated with various concentrations of the compound to

Table 4. Structure and Cytotoxic Activity of Mellein Compounds Conjugated with Fatty Alcohols at C-7 Position with Ester Linkage against Human Cancer Cells[a]

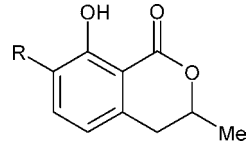

		IC_{50} (μM)			
	R	MCF-7	MDA-MB-468	SK-MEL-28	Malme-3M
15	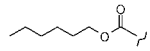	36.2 ± 19.7	27.8 ± 13.4	74.5 ± 59.2	61.4 ± 34.8
16	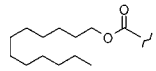	158.1 ± 48.1	114.5 ± 73.5	193.1 ± 89.2	216.5 ± 164.7
17	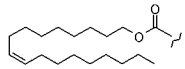	>200	>200	>200	>200
18	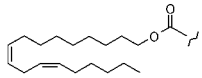	32.6 ± 12.2	21.9 ± 9.1	123.7 ± 58.4	129.6 ± 62.6
19	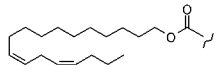	>200	144.0 ± 62.2	>200	>200
20	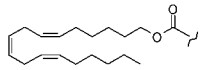	4.2 ± 2.2	5.9 ± 2.9	23.9 ± 11.8	15.4 ± 8.5
21	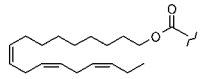	10.1 ± 3.7	7.2 ± 1.8	63.0 ± 25.5	66.4 ± 26.8
22	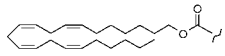	7.3 ± 0.4	8.0 ± 2.2	14.1 ± 4.4	11.9 ± 2.0
23	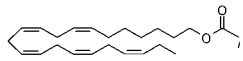	7.6 ± 1.3	8.8 ± 2.5	19.9 ± 7.0	14.9 ± 3.4
24	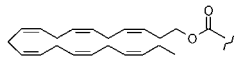	8.0 ± 2.2	8.0 ± 2.2	25.9 ± 9.8	15.9 ± 4.8

[a] Data represents the mean IC_{50} (the concentration of each compound that inhibited 50% of the growth of the corresponding cancer cell line) of the tested compounds screened in an MTT assay against human breast cancer (MCF-7 and MDA-MB-468) and melanoma cells (SK-MEL-28 and Malme-3M).

be tested. Cell counts were determined on a Coulter counter daily for 5 days post-treatment. All treatments were performed in triplicate.

Cell Survival. Cells were seeded at 100 cells per well in 24 well plates and allowed to attach overnight. The following day, dilutions of the test compounds were added in medium to the appropriate wells and cells incubated for 96 h at 37 °C in a humidified atmosphere of 5% CO_2. Medium was then removed and replaced by fresh drug-free medium and cultured for a further 96 h. Cells were subsequently washed with phosphate buffered saline (PBS) solution, fixed with ice cold 70% ethanol for 5 min, and stained with a 2% crystal violet solution for 20 min. After staining, cells were thoroughly washed with water and allowed to dry. Crystal violet was resorbed using 0.1 M sodium citrate solution and the absorbance of the solution measured at 570 nm. Each treatment was performed in triplicate.

Cell Cycle Analysis. Cell cycle analysis was analyzed by propidium iodide staining. Briefly, exponentially growing cells were treated with different doses of the drug for 72 h. At the end of each treatment time, cells were collected by scraping the cells off the flask and washed with PBS containing 1% FCS after centrifugation at 1000 rpm for 5 min. Cells were resuspended in PBS and washed. Cells were subsequently fixed in ice-cold 70% ethanol overnight at 4 °C. Ethanol was removed following centrifugation at 1000 rpm for 5 min and the cells washed twice in PBS to remove residual ethanol. For cell cycle analysis, the cells were suspended in 1 mL of PBS containing 0.02 mg/mL of propidium iodide and 0.5 mg/mL RNase A and incubated at 37 °C for 30 min. Cell cycle profiles were obtained using A FACScan flow cytometer (Becton Dickinson, San Jose, CA), which measured the fluorescence emitted from the propidium iodide−DNA complex.

Human Tumor Xenografts. Female athymic nude (*nu*/*nu*) mice (Charles River) were used for in vivo testing of the test compounds. The animals were fed ad libitum and kept in isolators in air-conditioned rooms at 20 ± 2 °C with a 12 h light−dark cycle. Animal care and procedures were carried out in agreement with Home Office guidelines and approved by Queens University Belfast Ethics Committee. MCF-7, MDA-MB-468, or HT29 cells were inoculated s.c. in both flanks of female athymic nude mice (1×10^6 cells/flank) under asceptic conditions. Equal volumes of cell solution and matrigel was used in the cell suspension. Tumor growth was assessed every 2−3 days with digital calipers recording length and width of tumors. Tumor volume was determined according to the following formula: shortest tumor diameter^2 × longest tumor diameter × 0.5. Tumors were allowed to grow to an average volume of 100 mm^3 prior to randomization to the control and

Table 5. Structure and Cytotoxic Activity of Mellein Compounds Conjugated with Fatty Amines at C-7 Position with Amide Linkage against Human Cancer Cells[a]

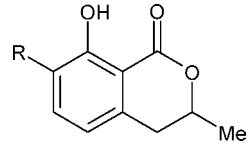

		IC_{50} (μM)			
	R	MCF-7	MDA-MB-468	SK-MEL-28	Malme-3M
25		>200	>200	>200	191.3
26	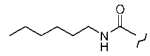	12.3 ± 12.9	1.8 ± 1.3	59.9 ± 38.9	37.5 ± 24.3
27	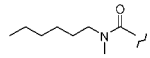	60.4 ± 42.9	38.7 ± 29.3	94.9 ± 64.9	73.5 ± 50.9
28	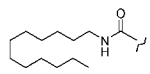	11.4 ± 1.9	9.9 ± 0.6	25.7 ± 10.9	20.1 ± 7.9
29	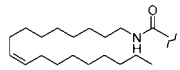	17.3 ± 5.4	12.1 ± 0.8	184.4 ± 84	39.4 ± 19.0
30	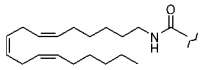	8.1 ± 3.7	6.0 ± 3.6	22.2 ± 10.9	13.0 ± 5.7

[a] Data represent the mean IC_{50} (the concentration of each compound that inhibited 50% of the growth of the corresponding cancer cell line) of the tested compounds screened in an MTT assay against human breast cancer (MCF-7 and MDA-MB-468) and melanoma cells (SK-MEL-28 and Malme-3M).

Table 6. Comparison of γ-Linolenyl Ester Linked Compounds 20 and 36 in a Panel of Human Cancer Cell Lines[a,b]

	20	**36**
	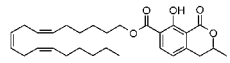	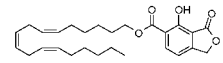
Cell Line	**IC50μM**	
MCF-7	42	4.9
MDA-MB-468	5.9	2.5
ZR-75-1	6.4	4.8
SK-MEL-28	23.9	12.4
Malme-3M	15.4	10.4
HT29	18.7	4.5
RKO	10.7	2.3
NCI-H23	2.1	1.9
NCI-H157	NT	12.5
PC3	9.6	7.3
LnCap	10.7	4.1

[a] Data represents the mean IC_{50} (the concentration of each compound that inhibited 50% of the growth of the corresponding cancer cell line) of the tested isolated compounds screened in an MTT assay against human breast cancer (MCF-7 and MDA-MB-468) and melanoma cells (SK-MEL-28 and Malme-3M). [b] NT, compounds not tested.

treatment groups. Following randomization to treatment groups, animals (8−10 animals per group) received daily intraperitoneal (i.p.) injections of test compound (80 mg/kg) or solvent control for the duration of the study. Animal weights were also recorded every 2−3 days throughout the study. All animals were also monitored daily for signs of treatment toxicity or mortality. On autopsy, tumors and vital organs (heart, liver, lungs, kidney, and spleen) were collected and fixed in 10% neutral buffered formalin for subsequent pathological examination.

Statistics. Statistical analysis and *P* value determination were performed by two-tailed paired *t* test with a confidence interval of 95% for the determination of the significance difference between treatment groups. $P < 0.05$ was considered to be significant. ANOVA was used to test for significance among groups. *Prism* software was used for statistical analysis. Values are expressed as means ± SD.

RESULTS

The synthesis of all compounds tested are described in Schemes 1−6 and the structures contained within Tables 2−6. Racemic kigelin **1** and mellein **6** were synthesized from commercially available starting materials as previously described (*16*). Fatty acid esters of racemic kigelin (compounds **2** to **5**) and racemic mellein (**7** to **10**) were prepared by coupling with *N*,*N*′-dicyclohexylcarbodiimide (DCC) and 4-dimethylaminopy-

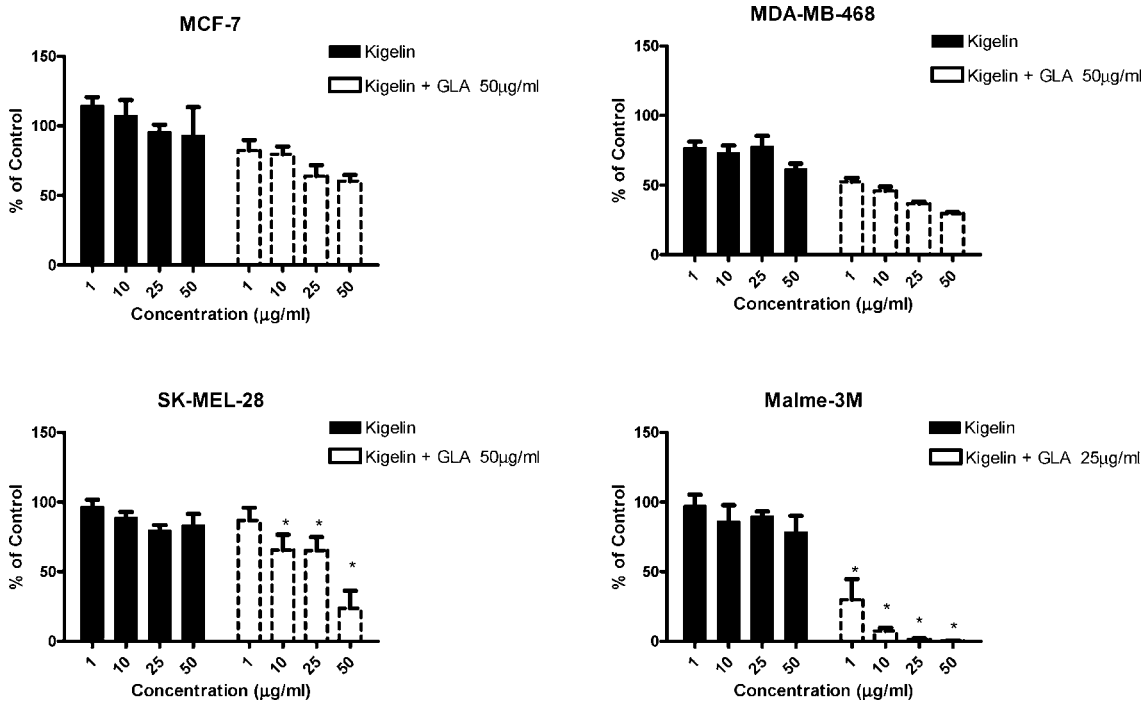

Figure 1. Cytotoxic activity of cells treated with kigelin **1** and the combination of kigelin and γ-linolenic acid (GLA). Data represent the mean values ± standard deviation of 3 replicates treated for 96 h and assessed using an MTT assay against human breast cancer (MCF-7 and MDA-MB-468) and melanoma cells (SK-MEL-28 and Malme-3M) expressed as the % of control untreated cells. * Indicates synergistic effect as determined using combination index values for drug interaction between kigelin and γ-linolenic acid. *a* indicates effect of GLA alone; MCF-7 50 μg/mL 97.28 ± 27.3%; MDA-MB-468 50 μg/mL 59.02 ± 11.84%; SK-MEL-28 50 μg/mL 91.95 ± 12.77%; Malme-3 M 25 μg/mL 78.28 ± 18.22%. Data for combination treatments examining multiple drug effects were analyzed using the Chou and Talalay method, based on the median effect principle, with the software *Calcusyn* to examine the nature of interaction between drugs (*38*). Combination index (CI) values were calculated; briefly, CI values of <1 indicate synergy.

ridine (DMAP) according to the general method described in Schemes 1 and 2, respectively.

Acid **14** and ester **13** were prepared on the basis of modifications of the previously reported synthetic sequence illustrated in Scheme 3 (*39*). Acetone and ethyl formate were reacted in the presence of sodium methoxide. The resulting intermediate **11** was then reacted with dimethyl 1,3-acetone dicarboxylate to yield 2-hydroxy-4-methylbenzene-1,3-dicarboxylate **12** in 24% yield over two steps. Deprotonation of **12** with LDA followed by reaction with acetaldehyde then cyclization under acidic conditions afforded ester **13**. Finally, saponification with aqueous sodium hydroxide in dioxane provided acid **14** in 9% overall yield. Esters (**15** to **24**) were then synthesized by coupling **14** with the corresponding fatty alcohol in presence of DCC and DMAP in dichloromethane according to the general conditions outlined in Scheme 4. Amides (**25** to **30)** were synthesized by coupling acid **14** with the corresponding fatty amine in the presence of *N,N′*-carbonyl diimidazole in dimethylformamide according to the general conditions outlined in Scheme 5.

36 was prepared as illustrated in Scheme 6. Propargyl alcohol was first protected with 3,4-dihydro-2*H*-pyran. Intermediate **31** was then reacted with dimethylformamide to yield aldehyde **32** in 85% yield. Reaction of **32** with dimethyl 1, 3-acetone dicarboxylate afforded intermediate **33** in 40% yield. Cyclization to **34** was effected under acidic conditions with *p*-toluene sulfonic acid monohydrate. Saponification with sodium hydroxide in dioxane afforded acid **35** in 21% overall yield. Finally, coupling with γ-linolenyl alcohol gave **36**.

In a previous study, kigelin **1**, a dihydroisocoumarin, was identified in extracts from the fruits of *Kigelia pinnata*, which demonstrated antiproliferative activity against human melanoma cells in vitro (*16*). Subsequently, kigelin was synthesized; however, the synthetic version did not demonstrate as potent an activity as observed with the extracted compound. Further fractionation and scaleup of the extraction process revealed the presence of trace amounts of fatty acids, both saturated and unsaturated, in their free form and as glycerol esters in some of the active fractions. A preliminary investigation of the antiproliferative activity of a number of fatty acids (oleic acid, heneicosanoic acid, linoleic acid (LA), α-linolenic acid (ALA), and γ-linolenic acid (GLA)) was carried out to determine if these had any direct effect on cell proliferation. The choice of the fatty acids was made to contain 0, 1, 2, or 3 double bonds of *cis*-configuration, since the majority of the unsaturated fatty acids occurring in the cell surface are of *cis*-configuration rather than the *trans* form and the *cis*-acid esters are assumed to be more favorably taken up into the cell (*40*−*44*).

The human breast cancer cell lines, MCF-7 and MDA-MB-468, and the melanoma cell lines, SkMel28 and Malme-3M, were selected for the preliminary screening of the panel of fatty acids (FAs) using the 3-(4,5-dimethylthiazol-2-yl)-2,5-diphenyltetrazolium bromide (MTT) assay to determine cell growth inhibition. Individual FAs demonstrated varying degrees of antiproliferative activity against the cell lines tested with GLA demonstrating the most potent activity against all four cancer cell lines. Neither heneicosanoic or linoleic acid demonstrated any activity in the breast cancercell lines (Table 1). We further investigated the effect of cotreating cells with kigelin and GLA to observe whether any synergistic activity could be observed in vitro. All cell lines with the exception of Malme-3 M were cotreated with 50 μg/mL GLA for combination experiments. As Malme-3 M cells were more sensitive to the effects of GLA, a lower dose of 25 μg/mL was used. Combination index values, a quantitative measurement of the degree of drug interactions, were calculated using the software *Calcusyn* (<0.9 synergy, 0.90−1.10 nearly additive, >1 antagonism) (*38*). As shown in

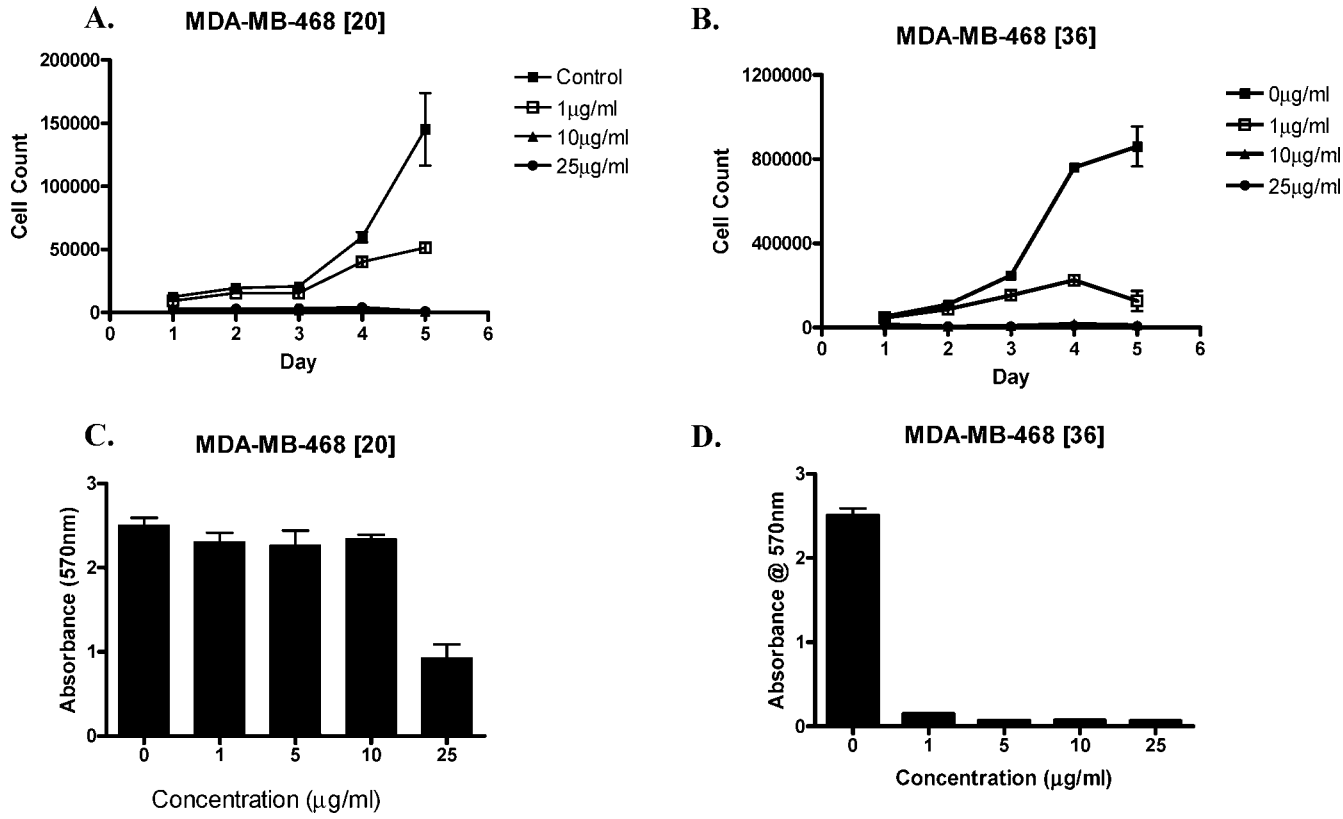

Figure 2. Antiproliferative effects of **20** and **36** treated MDA-MB-468 human breast cancer cells. (A) Five day cell counts for cells treated with **20** at indicated concentrations. (B) Five day cell counts for cells treated with **36** at indicated concentrations. (C) Cell survival assay for cells treated with **20** at indicated concentrations. (D) Cell survival assay for cells treated with **36** at indicated concentrations. Each value represents the mean ± standard deviation from triplicate treatments.

Figure 1, combining the GLA with kigelin did result in a synergistic interaction in each of the melanoma cell lines tested.

A number of compounds were synthesized by conjugating fatty acids, alcohols, or amines to dihydroisocoumarins, at either the C-7 or C-8 position by ester or amide linkages. The antiproliferative activity of all compounds synthesized was evaluated using the MTT assay in the human breast cancer cell lines, MCF-7 and MDA-MB-468, and melanoma cell lines, SK-MEL-28 and Malme-3 M (Tables 2−6).

Substitution of oleic, linoleic, α-linolenic, or γ-linolenic acid to kigelin at the C-8 position of the dihydroisocoumarin core structure generally increased the antiproliferative activity of the compounds against the breast cell lines, MCF-7 and MDA-MB-468, and the Malme-3 M melanoma cell line. There were no apparent antiproliferative effects observed in the SK-MEL-28 cell line treated with these compounds at the concentration range tested. γ-Linolenic acid conjugated to kigelin (**5**) and containing 3 double bonds on the hydrocarbon chain was the most potent of this series of compounds. Increasing the number of double bonds in the hydrocarbon chain was also observed to enhance the antiproliferative activity in these cells. The difference in potency observed between γ-linolenic and α-linolenic acid conjugated kigelin indicates that not only is the degree of saturation important but also the position of the starting double bond (Table 2).

Substitution of oleic, linoleic, α-linolenic, or γ-linolenic acid to mellein at the 8-position of the dihydroisocoumarin core structure did not significantly alter the antiproliferative activity of these compounds against the breast cell lines, MCF-7 and MDA-MB-468, or the melanoma cell lines SK-MEL-28 and Malme-3M, with all compounds not demonstrating an antiproliferative activity at the concentration range tested (Table 3).

A further series of compounds were synthesized conjugating fatty alcohols of increasing hydrocarbon chain length and number of double bonds by ester linkages at the C-7 position of mellein. The most potent antiproliferative activity was observed with compounds containing long hydrocarbon chains with three or more double bonds. The most potent compound, against the two breast cancer cell lines, was the γ-linolenyl ester compound (**20**) (IC_{50}s 4.2−23.9 μM). Generally, the breast cancer cell lines were more sensitive to this series of compounds than the melanoma cells. The difference in potency observed between γ-linolenyl and α-linolenyl alcohol conjugated mellein again indicates that not only is the degree of saturation important but also the position of the starting double bond (Table 4).

A similar series of compounds were also synthesized linking fatty amines at the C-7 position by an amide linkage rather than the ester linkage previously used. In this series of compounds, increasing the length of the hydrocarbon chain clearly increased the antiproliferative activity in three of the four cell lines tested. The most potent analogue in this series was the γ-linolenyl amide linked compound (**30**) in MCF-7, SK-MEL-28, and Malme-3 M cells with observed IC_{50}s ranging from 6.0 to 22.2 μM (Table 5).

As the γ-linolenyl compounds were the most potent compounds in all the series, we conjugated the γ-linolenyl alcohol to a 5-membered lactone as opposed to the 6-membered dihydroisocoumarin. This compound, 4-hydroxy-3-oxo-1,3-dihydro-isobenzofuran-5-carboxylic acid octadeca-6,9,12-trienyl ester (**36**), was subsequently tested. Both **20** and **36** were further evaluated against a panel of cancer cell lines including prostate and colon cancer cell lines (Table 6). In general, **36** was slightly more potent against all the cancer cell lines tested in the panel than the corresponding 6-membered lactone **20**. The most potent

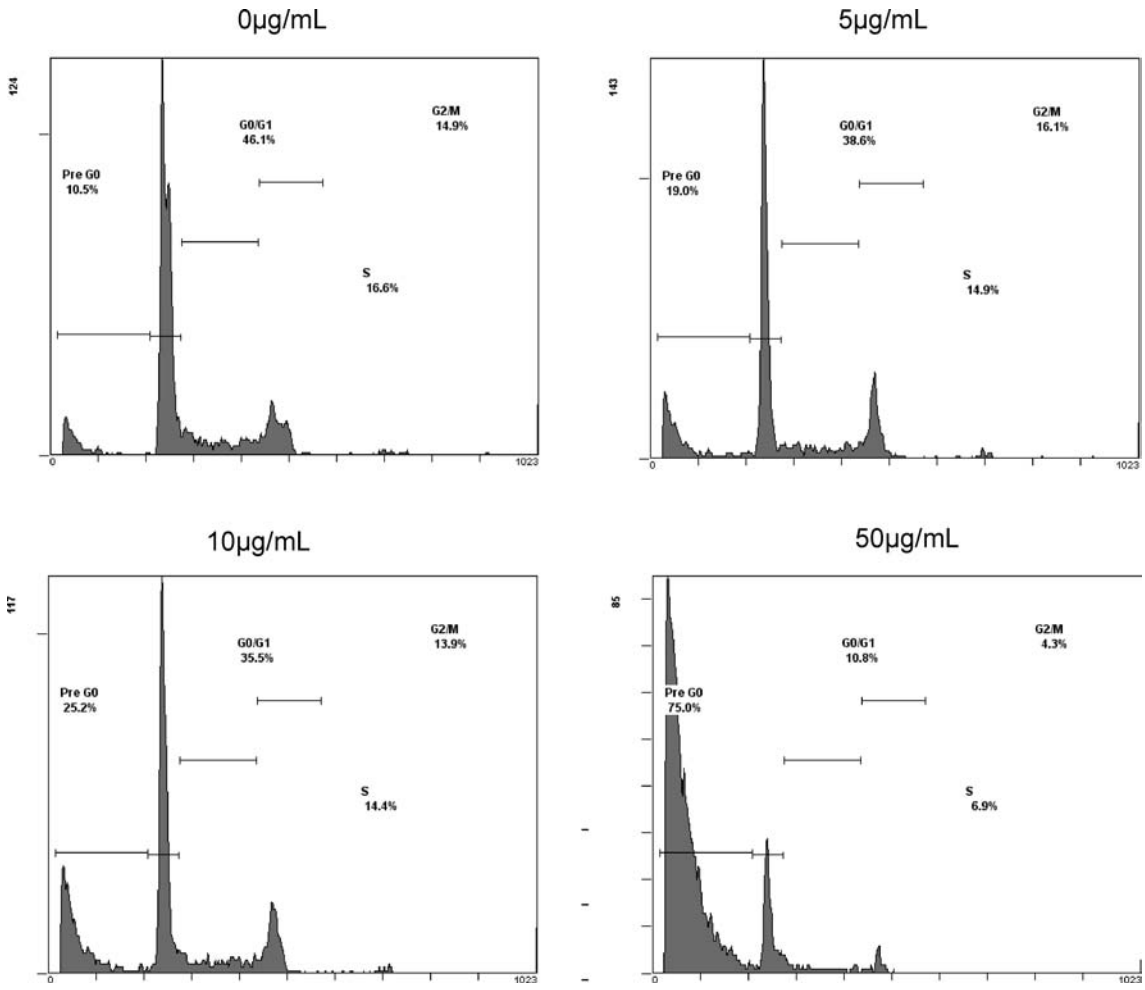

Figure 3. Flow cytometric analysis of the cell cycle profiles of MDA-MB-468 cells treated with **36** at the indicated concentrations. Cells were exposed for 72 h, stained with propidium iodide, and analyzed for perturbation in the cell cycle.

antiproliferative activity observed with **36** was against the breast cancer cell lines (IC_{50}s 2.5−4.9 μM). Both **20** and **36** were further evaluated for their antiproliferative activity using cell counts and cell survival assays (Figure 2). A clear difference in the effect on cell survival was observed between the two compounds with cells failing to recover from treatment with the drug. Flow cytometry analysis of MDA-MB-468 cells treated with increasing doses of **36** (0−50 μg/mL) over a 72 h period demonstrated a dose-dependent increase in cells in pre G0 phase of the cell cycle as assessed with propidium iodide staining (Figure 3) (% pre G0 cells: 0 μg/mL, 10.5%; 1 μg/mL, 19.6%; 5 μg/mL, 19.0; 10 μg/mL, 25.2%; 25 μg/mL, 41.0%; 50 μg/mL, 75.0%).

A preliminary MDA-MB-468 breast cancer xenograft study examined the in vivo antitumor efficacy of two compounds, **36** and **20**, selected on the basis of their potency in the original MTT screen. Following daily i.p. injections (80 mg/kg) of both compounds, **36**, clearly exhibited an antitumor effect in vivo. **20** failed to demonstrate an in vivo effect at the concentration tested in the MDA-MB-468 human xenograft model. A delay in tumor growth was observed with **36** from day 8 post-treatment and was maintained for the duration of the study. **36** was further evaluated in a HT29 colorectal cancer xenograft model and an MCF-7 human breast cancer xenograft model and demonstrated antitumor activity in both cases (Figure 4). In the MCF-7 and HT29 model, a significant delay in tumor growth was observed from day 6 and day 16, respectively. Both compounds demonstrated no toxicity in vivo, determined by monitoring of body weight and pathological evaluation of major organs (heart, liver, lung, spleen, and kidneys) at autopsy. The combined effect on tumor growth observed with compound **36** and its apparent lack of toxicity in tumor-bearing mice support further investigation of this compound for use as an anticancer agent.

DISCUSSION

In conclusion, these studies have demonstrated a synergistic interaction of the fatty acid, γ-linolenic acid and the dihydroisocoumarin kigelin, in their antiproliferative activity against cancer cell lines. We have demonstrated that the fatty acid GLA is capable of acting in synergy with kigelin, a dihydroisocoumarin identified from natural products, to increase the antiproliferative activity of this class of compounds against human melanoma and breast cancer cells in vitro.

In addition, we have described simple synthetic approaches to generate a series of dihydroisocoumarins linked to a long hydrocarbon chain of varying length and degree of unsaturation. We have described the synthesis and biological activity relating to the antiproliferative effect of this novel series of potential anticancer agents. Synthetic dihydroisocoumarin compounds conjugated with fatty alcohols or amines through an acid function demonstrated varying degrees of antiproliferative activity on the cancer cell lines tested. Ester-linked fatty alcohols, with three or more double bonds in the hydrocarbon chain, conjugated to intermediate **14** at the C-7 position were the most active of the series tested. The most potent compound tested, **36**, demonstrated both in vitro antiproliferative effects and in vivo activity against both breast and colon cancer human

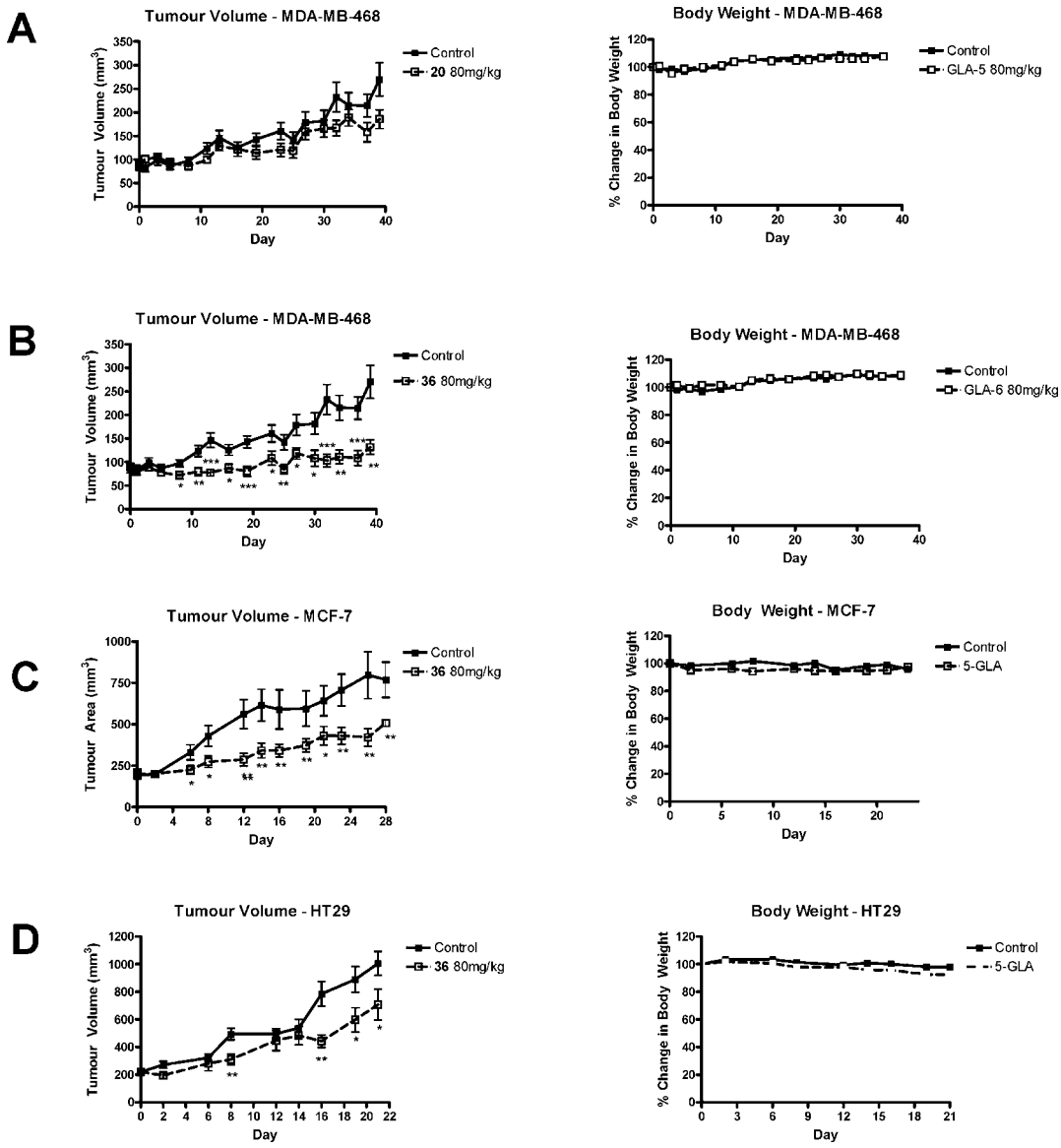

Figure 4. Growth of human tumor xenograft models and body weight. (A) MDA-MB-468 xenograft model treated with **20** (80 mg/kg, i.p.daily). (B) MDA-MB-468 xenograft model treated with **36** (80 mg/kg, i.p. daily). (C) MCF-7 xenograft model treated with **36** (80 mg/kg, i.p. daily). (D) HT29 xenograft model treated with **36** (80 mg/kg, i.p daily). Athymic nude mice implanted with MDA-MB-468, MCF-7, or HT29 cells as indicated were randomly assigned to treatment groups and injected intraperitonealy (i.p.) daily following establishment of tumors. Values represent the tumor volume (mean ± SD) for each group. Differences between treatment groups were determined using Students *t* test and by calculating subsequent p values. * $p < 0.05$, ** $P < 0.01$, *** $p < 0.005$.

xenograft models. This compound, containing a 5-membered lactone ring, showed superior in vivo activity compared to the corresponding 6-membered lactone ring compound **20**. The growth inhibitory activity of the compounds in cells and animal studies clearly support their promise as potential anticancer agents. The apparent lack of toxicity observed in vivo is also promising.

The data indicate that **36** may be suitable for further investigation as a possible therapeutic agent for the treatment of cancer. Since the early 1980s, it has been established that highly unsaturated fatty acids, including γ-linolenic acid, can be toxic to tumor cells while demonstrating much lower toxicity toward normal cells (*42*). The ability of fatty acids to increase the cytotoxic activity of some anticancer drugs has also previously been documented (*45*−*49*). Gamma linolenic acid (GLA) has been shown to inhibit tumor cell growth and tumor invasion in several studies across a diverse range of tumor types including prostate, melanoma, colon, liver, pancreatic, and lung cancer both in vitro and in vivo. GLA is believed to exert its antitumor effects by enhancing the formation of lipid peroxides and possibly the production of eicosanoids, themselves cytotoxic, generated from GLA supplementation. GLA has also been shown to enhance free radical generation such as superoxide and H_2O_2 generation in tumor cells but not normal cells. In an in vivo glioma model GLA has been shown to induce tumor regression and preserve the surrounding normal brain tissue (*19*). The lithium salt of GLA has being evaluated in phase II and III clinical trials for a variety of tumors (*18*, *46*). Intratumoral injection of GLA has been shown to induce significant reduction of glioma without any significant side effects. Agents that preferentially kill tumor cells without adversely affecting normal cells would clearly be of benefit for cancer treatment. Chemotherapy drugs conjugated to fatty acids have also been shown to enhance tumor targeting and deliver prodrugs for intratumoral activation (*28*−*30*).

Our study indicates that γ-linolenyl hydrocarbon side chain conjugated to dihydroisocoumarins clearly has potential for further investigation as potential anticancer drugs. Whether

esterification with γ-linolenyl alcohol is having a direct cytotoxic effect on the cancer cells or is facilitating the passage of the dihydroisocoumarin compound through the cell membrane and/or increasing the tumor delivery of the compound is currently unknown.

ACKNOWLEDGMENT

This work was supported by funding from Northern Ireland HSPSS (Cancer Research Recognised Group) and the McClay Trust. Dr. Lioe Tong is also acknowledged for his assistance and pathological evaluation of the in vivo studies.

LITERATURE CITED

(1) Magid, A. A., Voutquenne-Nazabadioko, L., Moroy, G., Moretti, C., and Lavaud, C. (2007) Dihydroisocoumarin glucosides from stem bark of *Carvocar glabrum*. *Phytochemistry 68*, 2439–2443.

(2) Perez Baz, J., Canedo, L. M., Fernandez Puentes, J. L., and Silva Elipe, M. V. (1997) Thiocoraline, a novel depsipeptide with antitumor activity produced by a marine Micromonospora. II Physio-chemical properties and structure determination. *J. Antibiot. 50*, 738–741.

(3) Huang, Y. F., Li, L. H., Tian, L., Qiao, L., Hua, H. M., and Pei, Y. H. (2006) Sg17−1-4, a novel isocoumarin from a marine fungus Alternia tenuis Sg17−1. *J. Antibiot. 59*, 355–357.

(4) Devienne, K. F., Raddi, G., Coelho, R. G., and Vilegas, W. (2005) Structure-antimicrobial activity of some natural isocoumarins and their analogues Int. *J. Phytother. Phytopharm. 12*, 378–381.

(5) Di Stasi, L. C., Camuesco, D., Nieto, A., Vilegas, W., Zarzuelo, A., and Galvez, J. (2004) Intestinal antiinflammatory activity of paepalantine, an isocoumarin isolated from the capitula of *Paepalanthus bromelioides*, in the trinitrobenzenesulphonic acid model of rat colitis. *Planta Medica 70*, 315–330.

(6) Kostova, I. (2005) Synthetic and natural coumarins as cytotoxic agents. *Curr. Med. 5*, 29–46.

(7) Hill, R. A. (1986) Naturally occurring isocoumarins. *Chem. Org. Naturst. Fortschr. 49*, 1–D78.

(8) Okamoto, T., Kobayashi, T., and Yoshida, S. (2005) Chemical aspects of coumarin compounds for the prevention of hepatocellular carcinomas. *Curr. Med. Chem. 5*, 47–51.

(9) Ozcan, S., Sahin, E., and Balci, M. (2007) The synthesis of unusual isocoumarin derivatives: the chemistry of homophthalic acid. *Tetrahed. Lett. 48*, 2151–2154.

(10) Petit, A., Pasini, A., Alves Da Costa, C., Ayral, E., Hernandez, J. F., Dumanchin-Njock, C., Phiel, C. J., Marambaud, P., Wilk, S., Farzan, M., Fulcrand, P., Martinez, J., Andrau, D., and Checler, F. (2003) JLK isocoumarin inhibitors: selective gamma-secretase inhibitors that do not interfere with notch pathway in vitro or in vivo. *J. Neurosci. Res. 74*, 370–377.

(11) Petit, A., Bihel, F., Alvès da Costa, C., Pourquié, O., Checler, F., and Kraus, J. L. (2001) New protease inhibitors prevent gamma-secretase-mediated production of Abeta 40/42 without affecting Notch cleavage. *J. Nat. Cell Biol. 3*, 507–511.

(12) Endringer, D. C., Guimaraes, K. G., Kondratyuk, T. P., Pezzuto, J. M., and Braga, F. C. (2008) Selective inhibition of aromatase by a dihydroisocoumarin from Xyris pterygoblephara. *J. Nat. Prod. 71*, 1082–1084.

(13) Bogdanov, M. G., Kandinska, M. I., Dimitrova, D. B., Gocheva, B. T., and Palamareva, M. D. (2007) Preliminary evaluation of antimicrobial activity of diastereomeric cis/trans-3-aryl(heteroaryl)-3,4-dihydroisocooumarin-4-carboxylics. *Naturforsch. 62*, 477–482.

(14) Wu, M., Harvey, K. A., Ruzmetov, N., Welch, Z. R., Sech, L., and Jackson, K. (2005) Omega-3 polyunsaturated fatty acids attenuate breast cancer growth through activation of a neutral sphingomyelinase-mediated pathway. *Int. J. Cancer 117*, 340–348.

(15) Kongsaeree, P., Prabpai, S., Sriubolmas, N., Vongvein, C., and Wiyakrutta, S. (2003) Antimalarial dihydroisocoumarins produced by *Geotrichum* sp., an endophytic fungus of *Crassocephalum crepidioides*. *J. Nat. Prod. 66*, 709–711, 3.

(16) Higgins, C. A., Bell, T., Delbederi, Z., Feutren-Burton, S., McClean, P., O'Dowd, C.; Watters, W., Armstrong, P., Johnston, P. G., Waugh, D. van den Berg H. (2009) Characterization of the antiproliferative activities of constituents of Kigelia pinnata and some derivatives against two human melanoma cells. Manuscript pending.

(17) McIllmurray, M. B., and Turkie, W. (1987) Controlled trial of gamma linolenic acid in Duke's C colorectal cancer. *Br. Med. J. 294*, 1260.

(18) Fearon, K. C., Falconer, J. S., Ross, J. A., Carter, D. C., Hunter, J. O., Reynolds, P. D., and Tuffnell, O. (1996) An open-label phase I/II dose escalation study of the treatment of pancreatic cancer using lithium gammalinolenate. *Anticancer Res. 16*, 867–874.

(19) Das, U. N. (2007) Gamma-linolenic acid therapy of human glioma-a review of in vitro, in vivo and clinical studies. *J. Expert Clin. Res. 13*, 119–131.

(20) Das, U. N., Prasad, V. V., and Reddy, D. R. (1995) Local application of gamma-linolenic acid in the treatment of human gliomas. *Cancer Lett. 94*, 147–155.

(21) Harries, M., O'Donnell, A., Scurr, M., Reade, S., Cole, C., and Judson, I. (2004) Phase I/II study of DHA-paclitaxel in combination with carboplatin in patients with advanced malignant solid tumors. *Br. J. Cancer 91*, 1651–1655.

(22) Jiang, W. G., Bryce, R. P., Horrobin, D. F., and Mansel, R. E. (1998) gamma-Linolenic acid blocks cell cycle progression by regulating phosphorylation of p27kip1 and p57kip2 and their interactions with other cycle regulators in cancer cells. *Int. J. Oncol. 13*, 611–617.

(23) Jaracz, S., Chen, J., Kuznetsova, L. V., and Ojima, I. (2005) Recent advances in tumor-targeting anticancer drug conjugates. *Bioorg. Med. Chem. 13*, 5043–5054.

(24) Begin, M. E., Ells, G., Das, U. N., and Horrobin, D. F. (1986) Differential killing of human carcinoma cells supplemented with n-3 and n-6 polyunsaturated fatty acids. *J. Natl. Cancer Inst. 77*, 1053–1062.

(25) Bougnoux, P., Germain, E., Lavillonniere, F., Cognault, S., Jourdan, M. L., and Chajes, V. (1999) Polyunsaturated fatty acids and breast cancer. *Lipids 34*, S99.

(26) Das, U. N. (2006) Essential fatty acids — a review. *Curr. Pharm. Biotechnol. 7*, 467–482.

(27) Maheo, K., Vibet, S., Steghens, J. P., Dartigeas, C., Lehman, M., and Bougnoux, P. (2005) Differential sensitization of cancer cells to doxorubicin by DHA: a role for lipoperoxidation. *Free Rad. Biol. Med. 39*, 742–751.

(28) Harries, M. O., Donnell, A., Scurr, M., Reade, S., Cole, C., Judson, I., Greystoke, A., Twelves, C., and Kaye, S. (2004) Phase I/II study of DHA-paclitaxel in combination with carboplatin in patients with advanced malignant solid tumors. *Br. J. Cancer 91*, 1651–1655.

(29) Bradley, M. O., Swindell, C. S., Anthony, F. H., Witman, P. A., Devanesan, P., and Webb, N. L. (2001) Tumor targeting by conjugation of DHA to paclitaxel. *J. Controlled Release 74*, 233–236.

(30) Wolff, A. C., Donehower, R. C., Carducci, M. K., Carducci, M. A., Brahmer, J. R., and Zabelina, Y. (2003) Phase I study of docosohexaenoic acid-paclitaxel: a taxane-fatty acid conjugate with a unique pharmacology and toxicity profile. *Clin. Cancer Res. 9*, 3589–3597.

(31) Menendez, J. A., Ropero, S., del Barbacid, M. M., Montero, S., Solanas, M., and Escrich, E. (2002) Synergistic interaction between vinorelbine and gamma-linolenic acid in breast cancer cells. *Breast Cancer Res. Treatment 72*, 203–219.

(32) Menendez, J. A., del Mar Barbacid, M., Montero, S., Sevilla, E., Escrich, E., and Solanas, M. (2001) Effects of gamma-linolenic acid and oleic acid on paclitaxel cytotoxicity in human breast cancer cells. *Eur. J. Canc. 37*, 402–413.

(33) Fite, A., Goua, M., Wahle, K. W., Schofield, A. C., Hutcheon, A. W., and Heys, S. D. (2007) Potentiation of the anti-tumor effect of docetaxel by conjugated linoleic acids in breast cancer cells in vitro. *Prostagland. Leuk. Ess. Fatty Acids 77*, 87–96.

(34) Padron, J. M., Martin, V. S., Hadjipavlou-Litina, D., Noula, C., Constantinou-Kokotou, V., Peters, G., and Kokotos, G. (1999) Synthesis, in vitro cytotoxicity and in vivo anti-inflammatory activity of long chain 3-amino-1,2-diols. *Bioorg. Med. Chem. Lett. 9*, 821–826.

(35) Del Olmo, E., Macho, A., Alves, M., Lopez, J. L., el Banoua, F., Munoz, E., and San Feliciano, A. (2002) Long-chain amino, alcohol and diamine derivatives induce apoptosis through a caspase-3 dependent pathway. *Bioorg. Med. Chem. Lett. 12*, 2621–2626.

(36) Lucas, R., Ubeda, A., Paya, M., Alves, M., del Olmo, E., Lo' pez, J. L., and San Feliciano, A. (2000) Synthesis and enzyme inhibitory activities of a series of lipidic, diamine and aminoalcoholderivatives on cytosolic and secretory phospholipases A2. *Bioorg. Med. Chem. Lett. 10*, 285–288.

(37) Mosmann, T. J. (1983) Rapid colorimetric assay for cell growth and survival: application to proliferation and cytotoxicity assays. *Immunol. Methods 65*, 55–63.

(38) Chou, T. C., and Talalay, P. (1984) Quantitative analysis of dose-effect relationships: the combined effects of multiple drugs or enzyme inhibitors. *Adv. Enz. Reg. 22*, 27–55.

(39) Kraus, G. A. (1982) Synthesis of ochratoxins. U.S. Patent 4,346,039.

(40) You, Y. J., Kim, Y., Nam, N. H., and Ahn, B. Z. (2003) Antitumor activity of unsaturated fatty acid esters of 4′-demethyldeoxypodophyllotoxin. *Bioorg. Med. Chem. Lett. 13*, 2629–2632.

(41) Igarashi, M., and Miyazawa, T. (2000) Newly recognized cytotoxic effect of conjugated trienoic fatty acids on cultured human tumor cells. *Cancer Lett. 148*, 173–179.

(42) Zhu, Y. P., Su, Z. W., and Li, C. H. (1989) Growth-inhibition effects of oleic acid, linoleic acid and their methyl esters on transplanted tumors in mice. *J. Natl. Cancer Inst. 81*, 1302–1326.

(43) Bradley, M. O., Webb, N. L., Anthony, F. H., Devanesan, P., Witman, P. A., and Hemamalini, S. (2001) Tumor targeting by covalent conjugation of a natural fatty acid to paclitaxel. *Clin. Cancer Res. 7*, 3229–3238.

(44) Jiang, W. G., Bryce, R. P., and Horrobin, D. F. (1998) Essential fatty acids: molecular and cellular basis of their anti-cancer action and clinical implications. *Crit. Rev. Oncol./ Hematol. 27*, 179–209.

(45) Germain, E., Chajes, V., Cognault, S., Lhuillery, C., and Bougnoux, P. (1998) Enhancement of doxorubicin cytotoxicity by polyunsaturated fatty acids in the human breast tumor cell line MDA-MB-231: relationship to lipid peroxidation. *Int. J. Canc. 75*, 578–583.

(46) Shao, Y., Pardini, L., and Pardini, R. S. (1995) Dietary menhaden oil enhances mitomycin C antitumor activity toward human mammary carcinoma MX-1. *Lipids 30*, 1035–1045.

(47) Timmer-Bosscha, H., Hospers, G. A., Meijer, C., Mulder, N. H., Muskiet, F. A., and Martini, I. A. (1989) Influence of docosahexaenoic acid on cisplatin resistance in a human small cell lung carcinoma cell line. *J.N.C.I. 81*, 1069–1075.

(48) Zijlstra, J. G., de Vries, E. G., Muskiet, F. A., Martini, I. A., Timmer-Bosscha, H., and Mulder, N. H. (1987) Influence of docosahexaenoic acid in vitro on intracellular adriamycin concentration in lymphocytes and human adriamycin-sensitive and —resistant small cell lung cancer cell lines and on cytotoxicity in the tumor cell lines. *Int. J. Cancer 40*, 850–856.

(49) Van der Merwe, C. F., Booyens, J., and Katzeff, I. E. (1987) Oral gamma-linolenic acid in 21 patients with untreatable malignancy. An ongoing pilot open clinical trial. *Br. J. Clin. Pract. 41*, 907–915.

BC900122G

Surface Coating Directed Cellular Delivery of TAT-Functionalized Quantum Dots

Yifeng Wei, Nikhil R. Jana,*,† Shawn J. Tan, and Jackie Y. Ying*

Institute of Bioengineering and Nanotechnology, 31 Biopolis Way, The Nanos, Singapore 138669. Received September 6, 2008; Revised Manuscript Received June 18, 2009

TAT peptide functionalized shell−core ZnS-CdSe quantum dots (QDs) have been prepared by three different methods, direct ligand exchange with cysteine-terminated TAT (TAT-$QD_{lig\ exch}$), and covalent conjugation to QDs coated with silanes (TAT-QD_{silica}) and polyacrylate derivatives (TAT-$QD_{polyacrylate}$). The silica and polyacrylate coatings incorporated multiple primary and secondary amines, introducing positive surface charges onto the QDs, providing high water solubility and sites for peptide conjugation, while inducing the "proton sponge effect". The different coating methods produced particles of different sizes, surface charges, and colloidal stability; these factors jointly influenced the cellular uptake and subcellular localization of these particles. As the particle size increased, (TAT-$QD_{lig\ exch}$ (6 nm) < TAT-QD_{silica} (10 nm) < $QD_{polyacrylate}$ (25 nm)), both the particle surface charge and cellular uptake increased. The smaller TAT-$QD_{lig\ exch}$ and TAT-QD_{silica} particles were localized mainly in the perinuclear regions, while the larger TAT-$QD_{polyacrylate}$ particles were localized in both the perinuclear regions and the lysosomes. Compared to the other TAT-QDs, TAT-$QD_{lig\text{-}exch}$ has a lower colloidal stability and was more cytotoxic due to the weak binding of the ligands.

INTRODUCTION

QDs are of interest to cell imaging due to their bright, sharp, stable, and tunable fluorescence, which can be excited by UV and visible light (*1*−*4*). Current research efforts are focused on greener QD syntheses (*5*), cadmium-free QDs (*6*), biocompatible coatings that allow for QD-bioconjugates (*7*−*13*), reduction of nonspecific binding (*14*), and bioaffinity molecules attachment to improve the labeling specificity and cellular trafficking of QDs (*15*−*19*). Although there have been many examples of QD-based labeling of fixed cells and tissues and of cell surface proteins, there has been limited success with live cell imaging using QDs (*3, 4*). One major difficulty is the delivery of QD-bioconjugates into live cells intact, as QDs usually either aggregate within the cytoplasm due to the instability of their coating (*9*) or are trafficked to vesicles or endosomes (*3, 4*). Thus, there is a need to develop coatings that can protect QDs from aggregation within cells and facilitate endosomal escape (*12*).

Cationic cell-penetrating peptides are widely used as cell transfection reagents for delivering macromolecules, nanoparticles, and QDs (*20*−*36*). Commonly used peptides include TAT peptide (a nuclear localization signal (NLS) peptide derived from the HIV-1 transcriptional activator protein TAT), SV40 NLS peptide, and oligoarginine or other variants (*20*−*36*). There are various ways to prepare peptide-functionalized QDs (*31*−*36*), e.g., biotin−streptavidin linkage (*33, 36*), covalent coupling with a terminal cysteine residue (*34*), self-assembly of terminal oligohistidine (*35*), or ligand exchange with cysteine-terminated peptide (*32*). The self-assembly and ligand-exchange methods are simple and produce smaller particles (<10 nm), but the weak binding of the peptides results in QDs with poor colloidal stability. In comparison, the biotin−streptavidin or covalent coupling approaches produce larger particles (10−50 nm), but the peptides are tightly bound and the resulting particles have a greater colloidal stability (*33, 34, 36*). This difference in size and colloidal stability affects the QDs' performance in cell labeling and subcellular localization. For example, QDs functionalized with TAT and mitochondrial localization signal peptide, which are prepared via the ligand-exchange method, target the respective cell organelles when delivered by microinjection (bypassing endocytosis), but undergo aggregation in lysosomes when subjected to direct incubation (*32*). QDs functionalized with SV40 NLS peptide, which are prepared via biotin−streptavidin linkage with silica-coated QDs, target the nucleus and perinuclear region when introduced by endocytosis (*33*). TAT-QDs, which are prepared from covalent linkage with silica-coated QDs, label rat brain tissue when delivered intra-arterially (*34*). TAT peptide coated QDs, which are prepared by biotin−streptavidin linkage with polyacrylate-coated QDs, are internalized via macropinocytosis and localized in the perinuclear region (*36*). These examples illustrate that the coating method and peptide conjugation strategy have a strong influence on the cell labeling applications of QDs.

We have developed various coatings that could protect nanoparticles with either multidentate ligands or a cross-linked shell, encapsulating each particle within a covalent polymeric network (*37*−*43*). These shell−core particles were very stable under physiological conditions, such as in the presence of a high salt concentration and competitive ligands. They further allowed for the synthesis of a variety of bioconjugates using different linking chemistry. For cellular delivery applications, *N*-(3-aminopropyl) methacrylamide and [3-(2-aminoethylamino)propyl]trimethoxysilane have been used as coating precursors to produce water-soluble cationic particles. The polymeric backbones consisted of multiple primary and secondary amines, which could provide a "proton sponge effect" as in polyethyleneimine (PEI) (*12, 44*−*48*). Zeta potential measurement showed that these types of coatings provided positive surface charge over a wide range of pHs; the particle surface charge continuously increased as the pH decreased from 7 to 4, suggesting that the coatings induced a "proton sponge effect" (*39, 43*). Such coatings

* Corresponding authors. E-mail: jyying@ibn.a-star.edu.sg (J. Y. Y.) and camnrj@iacs.res.in (N. R. J.).

† Present Address: Centre for Advanced Materials, Indian Association for the Cultivation of Science, Kolkata-700032, India.

10.1021/bc8003777 CCC: $40.75 © 2009 American Chemical Society
Published on Web 08/14/2009

were used in this work to derive TAT-QD conjugates for cell imaging. We prepared the QDs functionalized with TAT peptides by three different methods, direct ligand exchange of cysteine-TAT (TAT-$QD_{lig\ exch}$), and covalent conjugation of TAT with silica-coated QD (TAT-QD_{silica}) and polyacrylate-coated QD (TAT-$QD_{polyacrylate}$). Cellular interaction, uptake, and subcellular delivery varied significantly for the three TAT-QD systems. The smaller and less cationic TAT-$QD_{lig\ exch}$ showed significantly lower cellular uptake than TAT-QD_{silica} and TAT-$QD_{polyacrylate}$. TAT-$QD_{lig\ exch}$ and TAT-QD_{silica} were localized mainly in the perinuclear region, but TAT-$QD_{polyacrylate}$ did not display such specificity. This study demonstrated that particle size and surface coating played significant roles in the cell labeling with QDs.

EXPERIMENTAL SECTION

Materials. Igepal CO-520 (Sigma), *N*-(3-aminopropyl) methacrylamide hydrochloride (Polysciences), poly(ethylene glycol) monomethacrylate (cat no 16712, Polysciences), *N*,*N*′-methylene bisacrylamide (Alfa Aesar), ammonium persulfate (Alfa Aesar), *N*,*N*,*N*′,*N*′-tetramethylethylenediamine (Alfa Aesar), and PEG thiol (MW = 5000, NEKTAR) were used as received. [3-(2-Aminoethylamino)propyl]trimethoxysilane (AEAPS) (Merck) and 2-[methoxy(polyethyleneoxy)propyl]trimethoxysilane (PEG silane) (Gelest) were used as received. Succinimidyl-[(*N*-maleimidopropionamido)tetraethylene glycol] ester (NHS-PEO_4-MAL) (Pierce) was used as received. TAT peptide with terminal cysteine group (CGRKKRRQRRR) with 95% purity was purchased from GenScript.

Synthesis of QDs. Shell−core ZnS-CdSe QDs were synthesized according to published procedures with minor modifications (*5*). The ZnS shell was grown at 220 °C in octadecene via the alternate injection of Zn stearate in octadecene and elemental S dissolved in octadecene. The QDs were purified of free ligands by repeated precipitation with ethanol and redispersion in toluene. They were finally redispersed in either toluene or a reverse micellar solution of Igepal in cyclohexane.

Synthesis of TAT-QDs by Ligand Exchange. 5−10 mg of purified QDs were dissolved in 2 mL of a reverse micellar system, which was prepared by mixing 1 mL of Igepal CO-520 with 9 mL of cyclohexane. Next, 50 μL of aqueous TAT peptides (10 mg/mL) were added, followed by 50 μL of aqueous tetramethylammonium hydroxide (0.1 M) to induce the ligand exchange. After 1 min of sonication and 5 min of vortexing, ethanol (1−2 mL) was added to disrupt the reverse micellar system, and the TAT-QDs were collected by centrifugation. The precipitate was washed twice with the reverse micellar solution and three times with ethanol, and then redispersed in pH 7.0 tris(hydroxymethyl)aminomethane (Tris) buffer. A similar ligand-exchange approach was used to prepare the PEG thiol coated QDs.

Synthesis of TAT-QDs from Silica-Coated QDs. Silica-coated QDs were prepared according to our earlier protocol (*39*) with two significant modifications. First, 3-mercaptopropyltrimethoxysilane, used as a linker silane earlier, was removed to prevent interparticle cross-linking by NHS-PEO_4-MAL during the peptide conjugation step. Second, the silanization medium was changed from pure toluene to a toluene−methanol mixture (volume ratio = 1:1) to ensure effective coating in the absence of 3-mercaptopropyltrimethoxysilane. Typically, 1 mL of toluene solution of QDs was mixed with 1 μL of AEAPS, 10 μL of PEG silane, and 1 mL of tetramethylammonium hydroxide in methanol (0.01 M). The resulting solution was stirred at 80 °C for 1 h. The particles were precipitated with toluene, washed several times with toluene and chloroform, and redispersed in pH 9.5 borate buffer (0.1 M).

For peptide conjugation, 1 mg of NHS-PEO_4-MAL was dissolved in 100 μL of *N*,*N*′-dimethylformamide (DMF), which was immediately added to the QDs and incubated at room temperature for 1 h. The product was purified using a desalting column (Sephadex G25), followed by the addition of 20 μL of 5 mg/mL of TAT peptides and overnight incubation at 4 °C. Finally, the particles were purified by overnight dialysis against deionized water using a membrane of 12−14 kDa molecular weight cutoff (MWCO). The solution of peptide-conjugated QDs was diluted with Tris buffer (pH 7.0) and stored at 4 °C.

Synthesis of TAT-QDs from Polyacrylate-Coated QDs. Ten milliliters of QD solution in a reverse micellar system of 1 mL of Igepal CO-520 and 9 mL of cyclohexane were prepared. The QD concentration was adjusted using the absorbance value of ∼0.5 at the first absorption maximum. *N*-(3-Aminopropyl) methacrylamide hydrochloride (17 mg dissolved in 100 μL of water), 60 μL of poly(ethylene glycol) monomethacrylate, and methylene bisacrylamide (3 mg dissolved in 200 μL of water with 10 min of sonication) were added and mixed with the QD solution. Next, 50−100 μL of tetramethyl ethylene diamine was added as a basic catalyst. The solution was optically clear. It was placed in a 50 mL three-necked flask and purged with nitrogen for 10 min. An ammonium persulfate solution (3 mg dissolved in 100 μL of water) was injected to initiate the polymerization, which was continued at room temperature for 1 h. The polyacrylate-coated QDs were then precipitated with a few drops of ethanol, washed with chloroform and ethanol, and redispersed in deionized water.

For peptide conjugation, the polymer-coated QDs were diluted with pH 9.5 borate buffer. The QD absorbance at the first absorption maxima was ∼0.2. Next, a freshly prepared DMF solution of NHS-PEO_4-MAL (1 mg dissolved in 100 μL of DMF) was added to the QDs and incubated at room temperature for 1 h. The product was purified using a desalting column (Sephadex G25), followed by the addition of 100 μL of 1 mg/mL of TAT peptide and overnight incubation at 4 °C. Finally, the particles were purified from free peptide by overnight dialysis against deionized water, using a membrane of 12−14 kDa MWCO. The solution of peptide-conjugated QDs was diluted with Tris buffer (pH 7.0) and stored at 4 °C.

Cell Labeling. The human hepatocellular carcinoma line HepG2 was cultured on 24-well plates in 0.5 mL/well of Dulbecco's Modified Eagle's Medium (DMEM) with 10% (v/v) fetal bovine serum (FBS) overnight. 10−100 μL of TAT-QD solution was added. After 2−24 h of incubation at 37 °C, cells were gently washed twice with phosphate buffered saline (PBS), and fresh cell culture medium was added. Cells were then observed with fluorescence microscopy (Olympus microscope IX71 with DP70 camera) using blue excitation. For confocal microscopy, the cells were cultured on glass cover slides placed at the bottom of the wells.

Flow Cytometry. Cells were first labeled with QDs after 1 h of incubation with different TAT-QDs. Cell were then washed with PBS and trypsinized to detach from the well plate. Next, cells were transferred into 15 mL centrifuge tubes containing ∼2 mL of complete media for trypsin inactivation. Cells were then separated by centrifuging at 1000 rpm for 5 min. Precipitated cells were collected after removing the supernatant and again resuspended in 2 mL of PBS for washing. The suspended cells were centrifuged again at 1000 rpm for 5 min. The cells precipitated were collected, resuspended in 1 mL of PBS, and used for flow cytometry analysis.

Cell Viability Study by MTT Assay. HepG2 cells were trypsinized and resuspended in DMEM culture medium. The cells were seeded to 96-well flat-bottom microplate in 100−200 μL of full DMEM culture medium and kept overnight at 37 °C and 5% CO_2. Next, various TAT-QDs of different concentrations were loaded to each well. After incubation for 20 h, 20 μL of MTT solution (5 mg/mL) were added to each well and incubated

Scheme 1. Synthetic Approaches Used in Preparing Three Different TAT-QD Systems

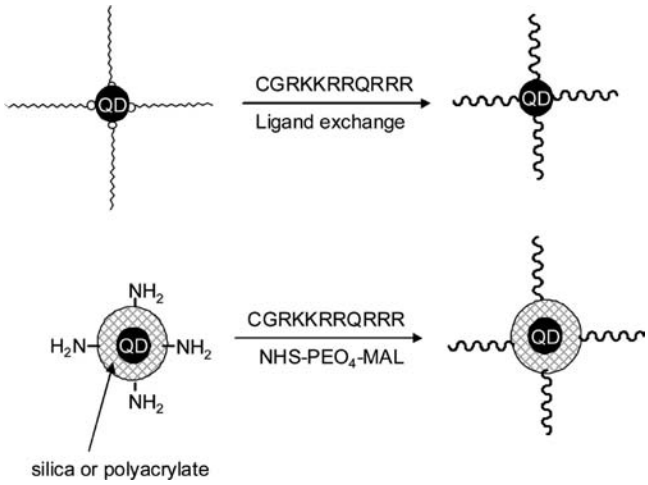

for 4 h. The medium was discarded by aspiration, and the formazan obtained was dissolved with 200 μL of dimethylsulfoxide (DMSO). The plates were read for absorbance at 550 nm. The optical density was directly correlated with cell quantity, and the cell viability was calculated by assuming 100% viability in the control set without any QDs.

Instrumentation. UV−vis absorption spectra were collected with Agilent 8453 spectrophotometer in a 1 cm quartz cell. Fluorescence spectra were obtained with Jobin Yvon Horiba Fluorolog fluorescence spectrometer. Dynamic light scattering (DLS) samples were first filtered through a Millipore syringe filter (0.2 μm pores) and then characterized with model BI-200SM instrument (Brookhaven Instrument Corporation). Particle surface charge was analyzed by ZetaPALS zeta potential analyzer (Brookhaven Instrument Corporation). Cell imaging was performed using Olympus microscope IX71 with DP70 digital camera. Confocal fluorescence imaging was performed using an Olympus Fluoview 300 confocal laser scanning system with 488 nm laser excitation. BD FACSCalibur flow cytometer (with four-color basic modular flow) was used to quantify cellular uptake. About 10 000−20 000 cells were examined for each sample.

RESULTS AND DISCUSSION

Synthesis and Characterization of TAT-QD Conjugate. Three methods were used to prepare TAT-conjugated QDs (see Scheme 1). In the ligand-exchange method, the hydrophobic ligands of the QDs were replaced by cysteine-terminated TAT peptide. To facilitate the ligand exchange, a reverse micellar medium was used to dissolve both the hydrophobic QDs and hydrophilic peptides, and ligand exchange took place smoothly and with minimal aggregation. The resulting particles were water-soluble, cationic, and stable in pH 7.0 Tris and PBS buffers for more than a week. However, partial precipitation was observed upon longer storage.

The silica- and polyacrylate-coated QDs were synthesized according to our earlier protocols (*39, 43*). For the silica coating, a mixture of AEAPS and PEG silane was polymerized in a toluene−methanol mixture in the presence of the hydrophobic QDs, replacing the hydrophobic ligands on the QDs with a thin, cross-linked and hydrophilic silica shell. A similar approach was used to prepare polyacrylate-coated QDs (*43*). The monomers *N*-(3-aminopropyl) methacrylamide, poly(ethylene glycol) monomethacrylate, and methylene bisacrylamide were dissolved in a reverse micellar solution of hydrophobic QDs, and polymerization was initiated with ammonium persulfate in an oxygen-free atmosphere, replacing the hydrophobic surfactant with a cross-linked hydrophilic polyacrylate shell. The particles prepared via both methods were water-soluble, buffer-stable, and cationic due to the amines on their surfaces. The TAT peptides were conjugated to the silica- and polyacrylate-coated QDs using a bifunctional NHS-PEG-MAL reagent. The NHS ester reacted with the primary amines on the silica and polyacrylate coatings, while MAL reacted with the thiol of the terminal cysteine of the peptide.

Figure 1 and Table 1 show the sizes of the three different TAT-QD systems. Transmission electron microscopy (TEM) reflected minimal particle aggregation after the coating, ligand exchange, and peptide conjugation processes. It illustrated that the QD core size remained the same (~4 nm) for all three TAT-QD systems. DLS showed a significant variation in their hydrodynamic diameters due to the different coating thicknesses. The low molecular weight TAT ligand increased the diameter of the QD by only 2−3 nm. In contrast, the particle diameter was increased by 6 and 21 nm due to the silica coating and polyacrylate coating, respectively. Particle size distribution was broadened after the silica coating and polyacrylate coating. Surface charge was positive for all three TAT-QD systems. It was lowest for TAT-$QD_{lig\ exch}$ and highest for TAT-$QD_{polyacrylate}$. The difference in surface charge was due to the combined effect of particle size, nature of coating, and number of TAT ligands bound to each QD. The lower positive surface charge of $QD_{lig\ exch}$ was possibly due to the lower surface area available for TAT adsorption on this smaller QD. In contrast, silica and polyacrylate coatings introduced positive surface charges (from amine functional groups) and provided access for multiple TAT conjugation on each QD, which further increased the overall surface charge. From our earlier work (fluorescamine titration to estimate the number of primary amines per particle (*38*)), 50−100 primary amines were estimated per particle (for silica- and polyacrylate-coated QDs), and only a fraction of these would be used for peptide conjugation (since conjugation was not 100% efficient). For ligand-exchanged QDs, several tens of peptides were estimated per particle, assuming that thiolated peptides were adsorbed on the surface of the 4 nm QDs.

The cell viability of various TAT-QDs was tested using HepG2 cells via standard MTT assay. We found that at QD concentrations of 20−40 nM, the cell viability (after 24 h) was up to 75% for silica- and polyacrylate-coated QDs, but was only 20% for ligand-exchanged QDs.

Cell Labeling with TAT-QDs. The cell labeling was studied using the human hepatocellular carcinoma line, HepG2. Different experimental conditions such as temperature, QD concentration, and incubation time were tested in order to optimize the labeling conditions. As QD uptake was very low at 4 °C, all uptake experiments were conducted at 37 °C. TAT functionalization significantly increased QD uptake for three types of coated QDs (Figures 2−5). We also found that the surface coating affected the internalization traffics. All three types of TAT-QDs attached to the cell surface within 15 min began to enter the cytoplasm in the next 1−2 h, and were trafficked to the endosome. In the next 2−8 h, the ligand-exchanged QDs and silica-coated QDs (Figure 4) entered the perinuclear region. However, the polyacrylate-coated QDs did not show further movements.

A quantitative study of cellular interaction was performed with flow cytometry (Figure 2). Control experiments were conducted with QDs without TAT conjugation, i.e., PEG thiol coated QD ($QD_{lig\ exch}$), silica-coated QD, and polyacrylate-coated QD. Control QDs were tested over a wide range of concentrations (5−100 nM). QDs without any surface-bound TAT displayed a significantly lower uptake, irrespective of the coating type. This was likely due to the presence of PEG on the QD

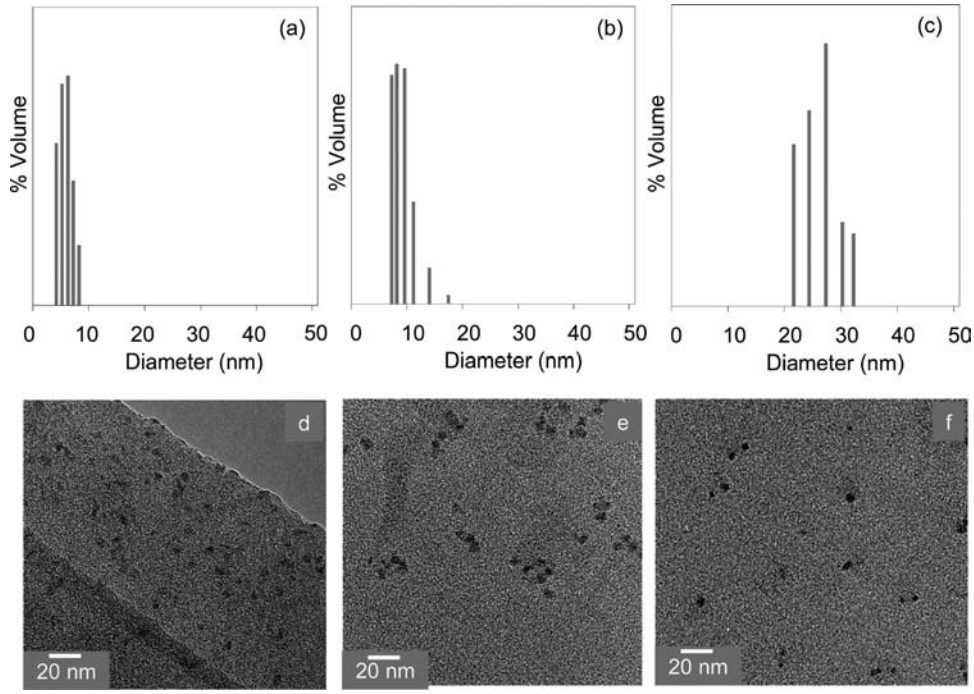

Figure 1. (a−c) DLS analyses and (d−f) TEM images of (a,d) TAT-$QD_{lig\ exch}$, (b,e) TAT-QD_{silica}, and (c,f) TAT-$QD_{polyacrylate}$.

Table 1. Characteristics of Three Different TAT-QD Systems

TAT-QD System	DLS particle size (TEM QD Size) (nm)	surface charge (mV)	cellular uptake (subcellular localization)
TAT-$QD_{lig\ exch}$	6 ± 2 (4 ± 1)	+8	low (perinuclear region)
TAT-QD_{silica}	10 ± 3 (4 ± 1)	+16	moderate (perinuclear region)
TAT-$QD_{polyacrylate}$	25 ± 5 (4 ± 1)	+35	high (perinuclear region and lysosome)

surface. Nonspecific uptake increased at higher QD concentrations; thus, subsequent experiments were performed in the concentration range of 5−40 nM.

Although TAT functionalization increased the cellular interaction and uptake of QDs, the percentage uptake and subcellular localization varied for different TAT-QD systems. The uptake of TAT-QDs increased from 5% to 50−90% as the QD concentration increased from 5 nM to 40 nM. TAT-$QD_{polyacrylate}$ and TAT-$QD_{lig\ exch}$ showed the highest uptake and the lowest uptake, respectively, at a given QD concentration.

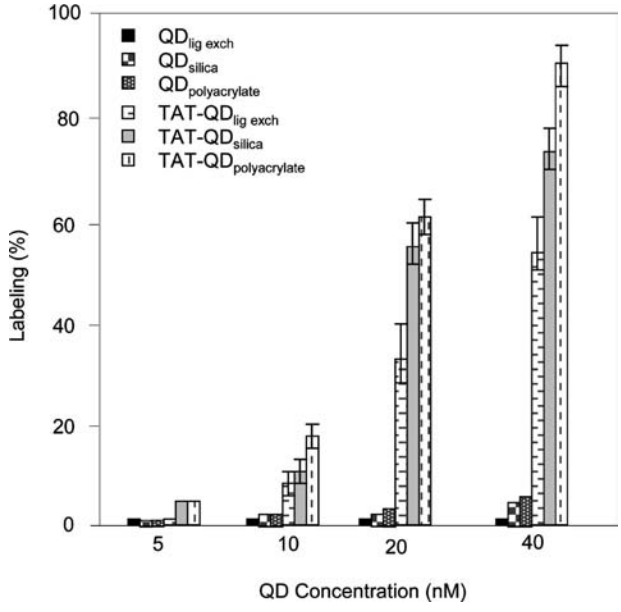

Figure 2. Flow cytometry quantification of the labeling of HepG2 cells by QDs and TAT-QDs.

Subcellular localization of QDs was investigated using confocal microscopy, and colocalization was studied with the nuclear Hoechst dye and the lysosomal dye lysotracker red, where necessary. The colocalization study was performed after overnight incubation of QDs with cells, followed by 5−10 min of incubation with Hoechst dye and lysotracker red. Subcellular localization clearly varied for different TAT-QD systems (Figures 3−5). TAT-$QD_{lig\ exch}$ and TAT-QD_{silica} were localized mainly in the perinuclear region, but TAT-$QD_{polyacrylate}$ was localized in both the lysosome and the perinuclear region. In addition, we observed that TAT-$QD_{lig\ exch}$ was more toxic, and since perinuclear labeling required longer incubation time (8−24 h), such labeling was difficult to achieve with the toxic TAT-$QD_{lig\ exch}$. In contrast, the less toxic TAT-QD_{silica} could be used for perinuclear labeling with >80% labeling efficiency.

Effect of Coating on QD-based Cell Labeling. TAT peptide has been used in the intracellular delivery of macromolecules, nanoparticles, and QDs (*22*−*36*). It generally enhances the cargo uptake and, in certain cases, causes it to localize in the perinuclear region. The delivery process starts with the binding of TAT to the plasma membrane due to its highly cationic nature associated with the arginine and lysine residues (*20, 28*). Arginine differs from other cationic amino acids, as it can make strong bidentate hydrogen bonds with sulfate, phosphate, and carboxylate anions via its guanidium group (*20, 28*). This feature leads to many possible interactions of TAT with the cell membrane, such as with the acidic regions of proteins, sulfated glycans, membrane phospholipid head groups, or a combination of these. Such interactions are responsible for the enhanced cellular interaction of TAT-QDs, as well as their membrane translocation.

We noted that the uptake of TAT-QDs was significantly reduced at 4 °C, as observed for other TAT-conjugated cargos,

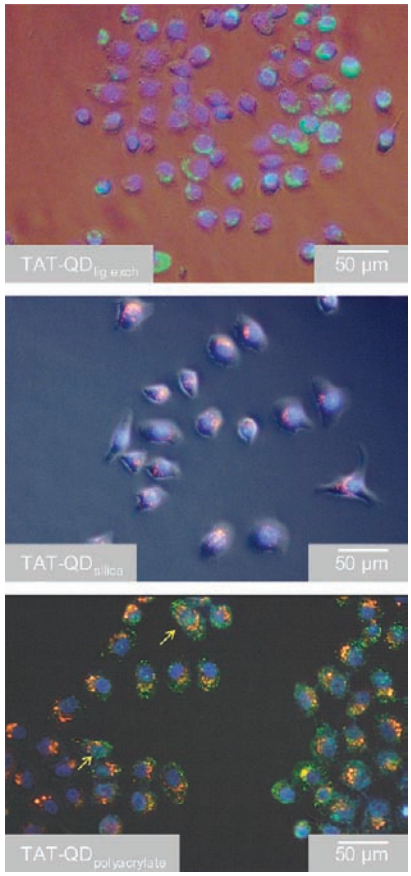

Figure 3. Fluorescence micrographs of TAT-QD labeled HepG2 cells. Green QDs were used for the TAT-QD$_{lig\ exch}$ and TAT-QD$_{polyacrylate}$ systems, and orange QDs were used for the TAT-QD$_{silica}$ system. Cell nucleus was colocalized with Hoechst 33342 dye (blue) in all cases. For TAT-QD$_{polyacrylate}$, the lysotracker red was used to label lysosome, in addition to the Hoechst dye. A QD concentration of 20 nM and an incubation time of 12 h were employed for all cases.

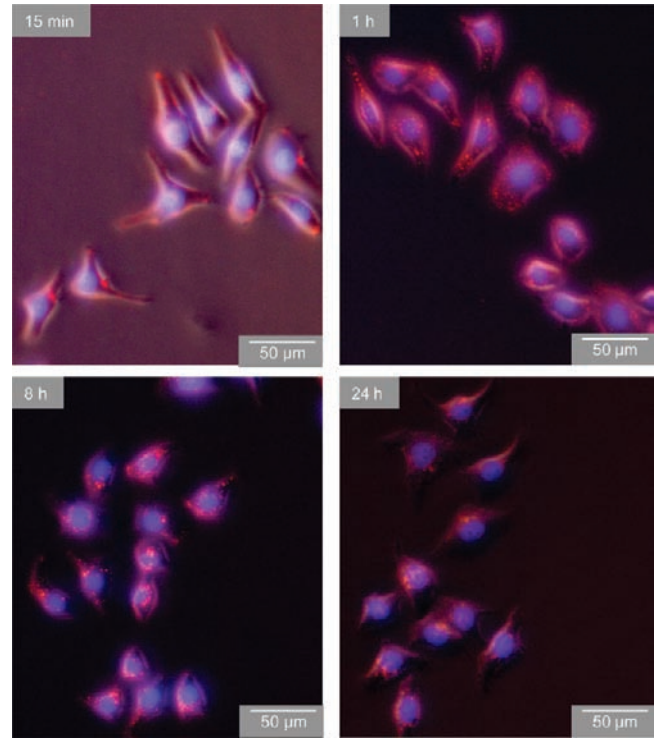

Figure 4. Fluorescence micrographs of TAT-QD$_{silica}$ labeled HepG2 cells, showing the time-dependent migration of QDs toward the nucleus. Cell nucleus was colocalized with Hoechst 33342 dye (blue) in all cases. A QD concentration of 20 nM was employed.

suggesting that the uptake was an active process (*28*). A variety of endocytic routes has been suggested earlier for TAT-mediated cargo delivery, such as caveolae-mediated endocytosis of TAT-protein and localization in the perinuclear region via actin cytoskeleton-mediated mechanism (*25*), clathrin-mediated endocytosis of TAT-peptide (*27*), lipid raft dependent macropinocytosis of TAT-protein (*26*), and macropinocytosis-directed uptake of TAT-QD via vesicle generation from plasma membrane, followed by active transport of QD-containing vesicle from cell periphery to the perinuclear region (*36*).

The cargo size and nature, surface charge of TAT-cargo conjugate, and nature of cell are important factors determining the endocytic pathway taken. Earlier studies showed that the endocytosis mechanism is particle size dependent (*49*, *50*). Clathrin- and caveolin-dependent endocytosis usually occurs with <200-nm-sized particles, while macropinocytosis takes place with larger particles (*50*). This is because of the larger size of macropinosomes compared to other endocytic vesicles (*28*,*49*). Size effect is also reported for TAT-mediated cargo delivery. For example, TAT-conjugated proteins of <10 nm have access to cytoplasm and would eventually enter the cell nucleus (*25*). In contrast, TAT-conjugated gold nanoparticles and QDs of >10 nm are trapped in vesicles, and their entry to nuclei is significantly restricted (*30*, *36*). Our results demonstrated that particle size has a significant role in cellular uptake and subcellular delivery. The three coating methods led to three different particle sizes with different overall surface charges. With increase in particle size from 6 to 25 nm, the surface charge also increased. This resulted in a combined effect in cellular uptake and subcellular delivery. The TAT-QD$_{lig\ exch}$ has a low positive charge and, thus, a lower cell uptake, but it could successfully reach the perinuclear region due to its smaller particle size. However, TAT-QD$_{lig\ exch}$ has less colloidal stability due to the weak adsorption of the peptide, and appeared more cytotoxic. TAT-QD$_{silica}$ has a higher positive charge, and thus a stronger cell interaction and a higher cell uptake; it could also reach the perinuclear region due to its small particle size. In contrast, TAT-QD$_{polyacrylate}$ has the highest positive charge, and thus a very strong interaction with the cell surface and a very high cell uptake. However, it was mostly trapped in the endosome and could not reach the perinuclear region. It was difficult to conclude how far the coating helped in the endosomal escape for TAT-QD$_{silica}$. Although most of the earlier studies showed that QDs were trafficked to endosomes and limited subcellular targeting (*3*, *4*), our TAT-QD$_{silica}$ successfully reached the perinuclear region. The time-dependent labeling study showed that TAT-QD$_{silica}$ was aggregated within the cell in 1 h and later migrated to the perinuclear region (Figure 4). This suggested a slow release mechanism of QD via endosomal escape, which might be affected by the coating. While TAT-QD$_{polyacrylate}$ was coated similarly, its larger size might have hindered the release of its aggregates.

CONCLUSION

We have synthesized TAT-functionalized QDs by different coating approaches, ligand exchange, silica coating, and polyacrylate coating, for cell labeling. The cellular uptake and subcellular localization were coating-dependent. Different coating methods produced TAT-QDs of different sizes and surface charges, which affected their cellular interaction and delivery. Smaller particles have lower cationic surface charge and cell uptake but a significant subcellular targeting specificity. In contrast, larger particles have a highly positive surface charge

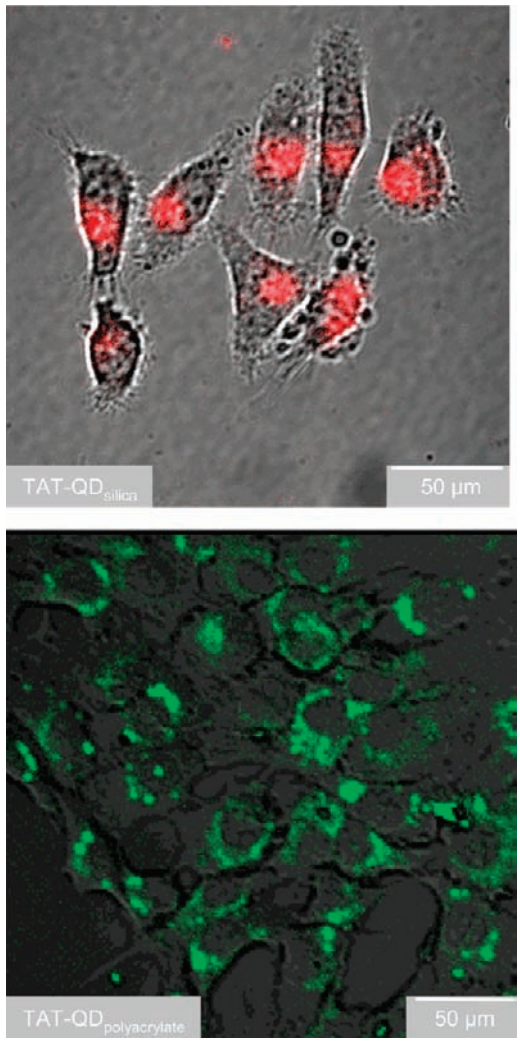

Figure 5. Confocal micrographs of HepG2 cells labeled with TAT-QD$_{silica}$ (top panel) and TAT-QD$_{polyacrylate}$ (bottom panel), showing different subcellular localization of QDs. A QD concentration of 20 nM and an incubation time of 12 h were employed for both cases.

and a high cell uptake, but a lower nuclear localization due to significant endosomal trafficking.

ACKNOWLEDGMENT

The authors would like to thank Dr. Jiang Jiang for TEM characterization. This work was supported by the Institute of Bioengineering and Nanotechnology (Biomedical Research Council, Agency for Science, Technology and Research, Singapore).

Supporting Information Available: Fluorescence micrograph of TAT-QD labeled HepG2 cells (not merged), colocalization study of HepG2 cells labeled by TAT-QD$_{silica}$, time-dependent migration of TAT-QD$_{lig\ exch}$ and TAT-QD$_{polyacrylate}$ in HepG2 cells, and confocal micrographs of HepG2 cells labeled with TAT-QD$_{silica}$. This material is available free of charge via the Internet at http://pubs.acs.org.

LITERATURE CITED

(1) Bruchez, M., Moronne, M., Gin, P., Weiss, S., and Alivisatos, A. P. (1998) Semiconductor nanocrystals as fluorescent biological labels. *Science 281*, 2013–2016.

(2) Chan, W. C., and Nie, S. (1998) Quantum dot bioconjugates for ultrasensitive nonisotopic detection. *Science 281*, 2016–2018.

(3) Michalet, X., Pinaud, F. F., Bentolila, L. A., Tsay, J. M., Doose, S., Li, J. J., Sundaresan, G., Wu, A. M., Gambhir, S. S., and Weiss, S. (2005) Quantum dots for live cells, in vivo imaging, and diagnostics. *Science 307*, 538–544.

(4) Medintz, I. L., Uyeda, H. T., Goldman, E. R., and Mattoussi, H. (2005) Quantum dot bioconjugates for imaging, labelling and sensing. *Nat. Mater. 4*, 435–446.

(5) Li, J. J., Wang, Y. A., Guo, W., Keay, J. C., Mishima, T. D., Johnson, M. B., and Peng, X. (2003) Large-scale synthesis of nearly monodisperse CdSe/CdS core/shell nanocrystals using air-stable reagents via successive ion layer adsorption and reaction. *J. Am. Chem. Soc. 125*, 12567–12575.

(6) Pradhan, N., Goorskey, D., Thessing, J., and Peng, X. (2005) An alternative of CdSe nanocrystal emitters: Pure and tunable impurity emissions in ZnSe nanocrystals. *J. Am. Chem. Soc. 127*, 17586–17587.

(7) Gerion, D., Pinaud, F., Williams, S. C., Parak, W. J., Zanchet, D., Weiss, S., and Alivisatos, A. P. (2001) Synthesis and properties of biocompatible water-soluble silica-coated CdSe/ZnS semiconductor quantum dots. *J. Phys. Chem. B 105*, 8861–8871.

(8) Guo, W., Li, J. J., Wang, Y. A., and Peng, X. (2003) Luminescent CdSe/CdS core/shell nanocrystals in dendron boxes: Superior chemical, photochemical and thermal stability. *J. Am. Chem. Soc. 125*, 3901–3909.

(9) Aldana, J., Lavelle, N., Wang, Y., and Peng, X. (2005) Size-dependent dissociation pH of thiolate ligands from cadmium chalcogenide nanocrystals. *J. Am. Chem. Soc. 127*, 2496–2504.

(10) Smith, A. M., Duan, H., Rhyner, M. N., Ruan, G., and Nie, S. (2006) A systematic examination of surface coatings on the optical and chemical properties of semiconductor quantum dots. *Phys. Chem. Chem. Phys. 8*, 3895–3903.

(11) Yu, W. W., Chang, E., Falkner, J. C., Zhang, J., Al-Somali, A. M., Sayes, C. M., Johns, J., Drezek, R., and Colvin, V. L. (2007) Forming biocompatible and nonaggregated nanocrystals in water using amphiphilic polymers. *J. Am. Chem. Soc. 129*, 2871–2879.

(12) Duan, H., and Nie, S. (2007) Cell-penetrating quantum dots based on multivalent and endosome-disrupting surface coatings. *J. Am. Chem. Soc. 129*, 3333–3338.

(13) Susumu, K., Uyeda, H. T., Medintz, I. L., Pons, T., Delehanty, J. B., and Mattoussi, H. (2007) Enhancing the stability and biological functionalities of quantum dots via compact multifunctional ligands. *J. Am. Chem. Soc. 129*, 13987–13996.

(14) Bentzen, E. L., Tomlinson, I. D., Mason, J., Gresch, P., Warnement, M. R., Wright, D., Sanders-Bush, E., Blakely, R., and Rosenthal, S. J. (2005) Surface modification to reduce nonspecific binding of quantum dots in live cell assays. *Bioconjugate Chem. 16*, 1488–1494.

(15) Wu, X., Liu, H., Liu, J., Haley, K. N., Treadway, J. A., Larson, J. P., Ge, N., Peale, F., and Bruchez, M. P. (2003) Immunofluorescent labeling of cancer marker Her2 and other cellular targets with semiconductor quantum dots. *Nat. Biotechnol. 21*, 41–46.

(16) Gao, X., Cui, Y., Levenson, R. M., Chung, L. W. K., and Nie, S. (2004) In vivo cancer targeting and imaging with semiconductor quantum dots. *Nat. Biotechnol. 22*, 969–976.

(17) van Tilborg, G. A. F., Mulder, W. J. M., Chin, P. T. K., Storm, G., Reutelingsperger, C. P., Nicolay, K., and Strijkers, G. J. (2006) Annexin A5-conjugated quantum dots with a paramagnetic lipidic coating for the multimodal detection of apoptotic cells. *Bioconjugate Chem. 17*, 865–868.

(18) Courty, S., Luccardini, C., Bellaiche, Y., Cappello, G., and Dahan, M. (2006) Tracking individual kinesin motors in living cells using single quantum-dot imaging. *Nano Lett. 6*, 1491–1495.

(19) Chakraborty, S. K., Fitzpatrick, J. A. J., Phillippi, J. A., Andreko, S., Waggoner, A. S., Bruchez, M. P., and Ballou, B. (2007) Cholera toxin B conjugated quantum dots for live cell labeling. *Nano Lett. 7*, 2618–2626.

(20) Pujals, S., Fernandez-Carneado, J., Lopez-Iglesias, C., Kogan, M. J., and Giralt, E. (2006) Mechanistic aspects of CPP-mediated intracellular drug delivery: Relevance of CPP self-assembly. *Biochem. Biophys. Acta 1758*, 264–279.

(21) Patel, L. N., Zaro, J. L., and Shen, W.-C. (2007) Cell penetrating peptides: Intracellular pathways and pharmaceutical perspectives. *Pharm. Res. 24*, 1977–1992.

(22) Nori, A., Jensen, K. D., Tijerina, M., Kopeckova, P., and Kopecek, J. (2003) Tat-conjugated synthetic macromolecules facilitate cytoplasmic drug delivery to human ovarian carcinoma cells. *Bioconjugate Chem. 14*, 44–50.

(23) Jensen, K. D., Nori, A., Tijerina, M., Kopeckova, P., and Kopecek, J. (2003) Cytoplasmic delivery and nuclear targeting of synthetic macromolecules. *J. Controlled Release 87*, 89−105.

(24) Vives, E. (2003) Cellular uptake of the Tat peptide: An endocytosis mechanism following ionic interactions. *J. Mol. Recognit. 16*, 265–271.

(25) Fittipaldi, A., Ferrari, A., Zoppe, M., Arcangeli, C., Pellegrini, V., Beltram, F., and Giacca, M. (2003) Cell membrane lipid rafts mediate caveolar endocytosis of HIV-1 Tat fusion proteins. *J. Biol. Chem. 278*, 34141–34149.

(26) Wadia, J. S., Stan, R. V., and Dowdy, S. F. (2004) Transducible TAT-HA fusogenic peptide enhances escape of TAT-fusion proteins after lipid raft macropinocytosis. *Nat. Med. 10*, 310–315.

(27) Richard, J. P., Melikov, K., Brooks, H., Prevot, P., Lebleu, B., and Chernomordik, L. V. (2005) Cellular uptake of unconjugated TAT peptide involves clathrin-dependent endocytosis and heparan sulfate receptors. *J. Biol. Chem. 280*, 15300–15306.

(28) Gump, J. M., and Dowdy, S. F. (2007) TAT transduction: The molecular mechanism and therapeutic prospects. *Trends Mol. Med. 13*, 443–448.

(29) Josephson, L., Tung, C.-H., Moore, A., and Weissleder, R. (1999) High-efficiency intracellular magnetic labeling with novel superparamagnetic-Tat peptide conjugates. *Bioconjugate Chem. 10*, 186–191.

(30) Tkachenko, A. G., Xie, H., Liu, Y., Coleman, D., Ryan, J., Glomm, W. R., Shipton, M. K., Franzen, S., and Feldheim, D. L. (2004) Cellular trajectories of peptide-modified gold particle complexes: Comparison of nuclear localization signals and peptide transduction domains. *Bioconjugate Chem. 15*, 482−490.

(31) Lagerholm, B. C., Wang, M., Ernst, L. A., Ly, D. H., Liu, H., Bruchez, M. P., and Waggoner, A. S. (2004) Multicolor coding of cells with cationic peptide coated quantum dots. *Nano Lett. 4*, 2019–2022.

(32) Derfus, A. M., Chan, W. C. W., and Bhatia, S. N. (2004) Intracellular delivery of quantum dots for live cell labeling and organelle tracking. *Adv. Mater. 16*, 961–966.

(33) Chen, F., and Gerion, D. (2004) Fluorescent CdSe/ZnS nanocrystal-peptide conjugates for long-term, nontoxic imaging and nuclear targeting in living cells. *Nano Lett. 4*, 1827–1832.

(34) Santra, S., Yang, H., Stanley, J. T., Holloway, P. H., Moudgil, B. M., Walter, G., and Mericle, R. A. (2005) Rapid and effective labeling of brain tissue using TAT-conjugated CdS: Mn/ZnS quantum dots. *Chem. Commun.* 3144–3146.

(35) Delehanty, J. B., Medintz, I. L., Pons, T., Brunel, F. M., Dawson, P. E., and Mattoussi, H. (2006) Self-assembled quantum dot-peptide bioconjugates for selective intracellular delivery. *Bioconjugate Chem. 17*, 920–927.

(36) Ruan, G., Agrawal, A., Marcus, A. I., and Nie, S. (2007) Imaging and tracking of Tat peptide-conjugated quantum dots in living cells: New insights into nanoparticle uptake, intracellular transport, and vesicle shedding. *J. Am. Chem. Soc. 129*, 14759–14766.

(37) Selvan, S. T., Tan, T. T., and Ying, J. Y. (2005) Robust, non-cytotoxic, silica-coated CdSe quantum dots with efficient photoluminescence. *Adv. Mater. 17*, 1620–1625.

(38) Jana, N. R., Yu, H. H., Ali, E. M., Zheng, Y., and Ying, J. Y. (2007) Controlled photostability of luminescent nanocrystalline ZnO solution for selective detection of aldehydes. *Chem. Commun.* 1406–1408.

(39) Jana, N. R., Earhart, C., and Ying, J. Y. (2007) Synthesis of water-soluble and functionalized nanoparticles by silica coating. *Chem. Mater. 19*, 5074–5082.

(40) Jana, N. R., and Ying, J. Y. (2008) Synthesis of functionalized Au nanoparticles for protein detection. *Adv. Mater. 20*, 430–434.

(41) Nandanan, E., Jana, N. R., and Ying, J. Y. (2008) Functionalization of gold nanospheres and nanorods by chitosan oligosaccharide derivatives. *Adv. Mater. 20*, 2068–2073.

(42) Jana, N. R., Nandanan, E., Jiang, J., and Ying, J. Y. Cysteine-functionalized polyaspartic acid: A polymer for coating and bioconjugation of nanoparticles and quantum dots. submitted.

(43) Jana, N. R., and Ying, J. Y. Functionalized nanoparticles and quantum dots with polyacrylate or polyacrylamide coating. *U. S. Pat. Appl. pending.*

(44) Boussif, O., Lezoualc'h, F., Zanta, M. A., Mergny, M. D., Scherman, D., Demeneix, B., and Behr, J.-P. (1995) A versatile vector for gene and oligonucleotide transfer into cells in culture and in vivo: Polyethylenimine. *Proc. Natl. Acad. Sci. U.S.A. 92*, 7297–7301.

(45) Sonawane, N. D., Szoka, F. C., Jr., and Verkman, A. S. (2003) Chloride accumulation and swelling in endosomes enhances DNA transfer by polyamine-DNA polyplexes. *J. Biol. Chem. 278*, 44826–44831.

(46) Akinc, A., Thomas, M., Klibanov, A. M., and Langer, R. (2005) Exploring polyethylenimine-mediated DNA transfection and the proton sponge hypothesis. *J. Gene Med. 7*, 657–663.

(47) Nimesh, S., Goyal, A., Pawar, V., Jayaraman, S., Kumar, P., Chandra, R., Singh, Y., and Gupta, K. C. (2006) Polyethylenimine nanoparticles as efficient transfecting agents for mammalian cells. *J. Controlled Release 110*, 457–468.

(48) Hattori, Y., and Maitani, Y. (2007) Low-molecular-weight polyethylenimine enhanced gene transfer by cationic cholesterol-based nanoparticle vector. *Biol. Pharm. Bull. 30*, 1773–1778.

(49) Conner, S. D., and Schmid, S. L. (2003) Regulated portals of entry into the cell. *Nature 422*, 37–44.

(50) Rejman, J., Oberle, V., Zuhorn, I. S., and Hoekstra, D. (2004) Size-dependent internalization of particles via the pathways of clathrin- and caveolae-mediated endocytosis. *Biochem. J. 377*, 159–169.

BC8003777

Supporting Information

Surface Coating Directed Cellular Delivery of TAT-Functionalized Quantum Dots

Yifeng Wei, Nikhil R. Jana,*† Shawn Tan, and Jackie Y. Ying*

Institute of Bioengineering and Nanotechnology,
31 Biopolis Way, The Nanos, Singapore 138669

* Corresponding authors. E-mail: jyying@ibn.a-star.edu.sg (J. Y. Y.) and camnrj@iacs.res.in (N. R. J.).

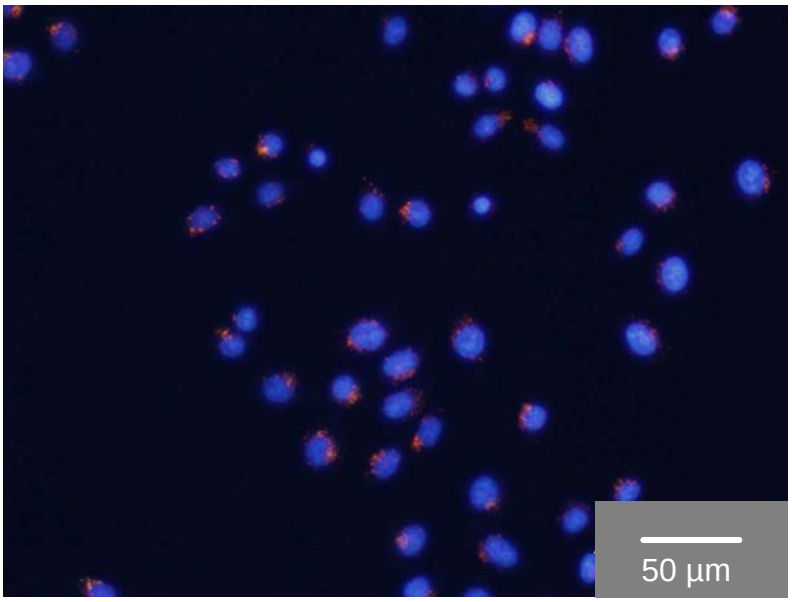

Figure S1. Fluorescence micrographs (not merged) of HepG2 cells labeled by TAT-QD_{silica} (red), showing that most QDs were located at the perinuclear region. Cell nucleus was co-localized with Hoechst 33342 dye (blue). A QD concentration of 20 nM and an incubation time of 12 h were employed.

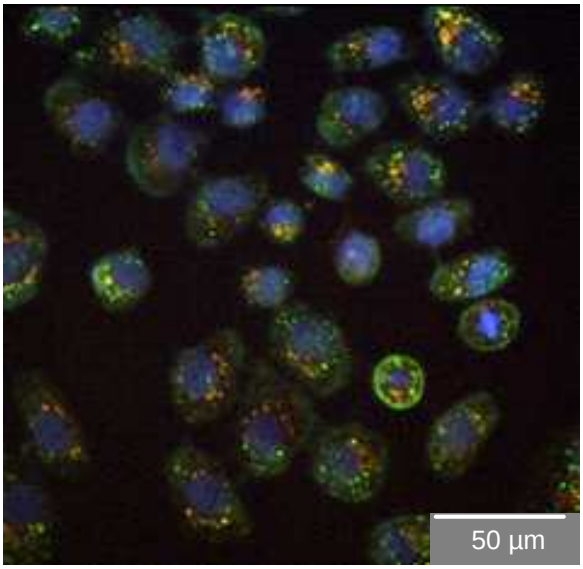

Figure S2. Fluorescence micrographs of co-localization study of HepG2 cells labeled by TAT-QD_{silica} (green) after 1 h of incubation, showing that most QDs were localized at the lysosomes. Cell nucleus was co-localized with Hoechst 33342 dye (blue), and lysotracker red was used to label lysosome. A QD concentration of 20 nM was employed.

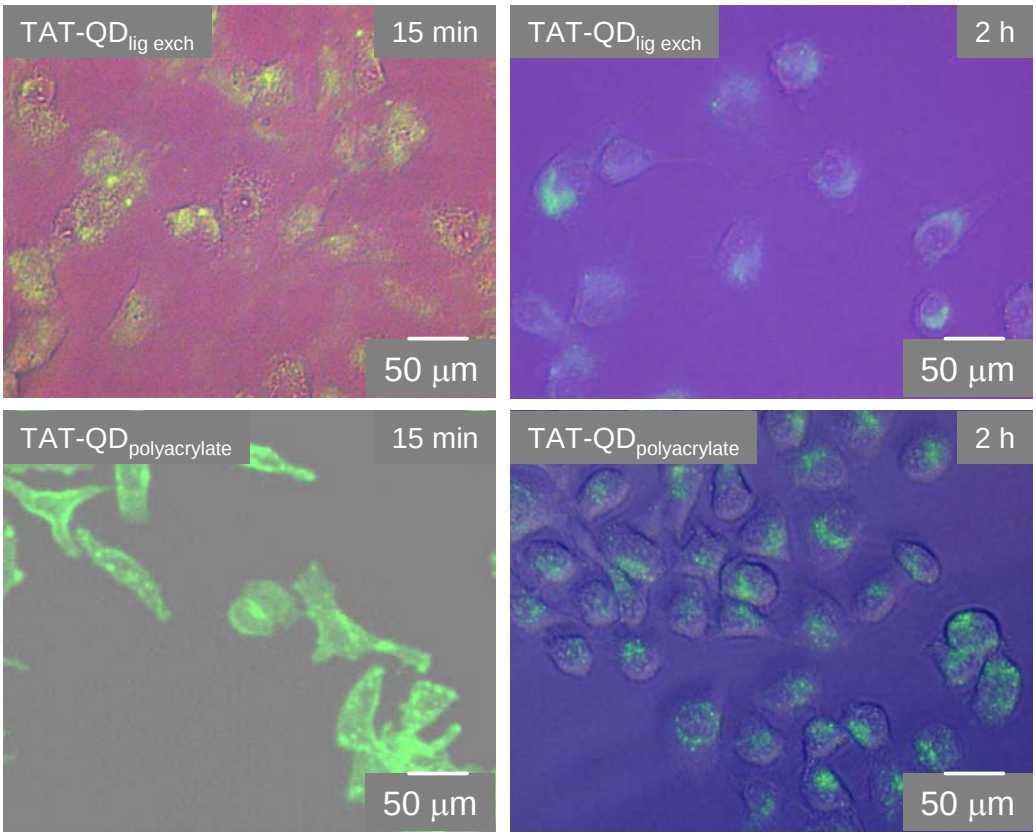

Figure S3. Fluorescence micrographs of HepG2 cells labeled by TAT-$QD_{lig\ exch}$ and TAT-$QD_{polyacrylate}$ after 15 min and 2 h of incubation, showing the time-dependent migration of the TAT-QDs. A QD concentration of 20 nM was employed.

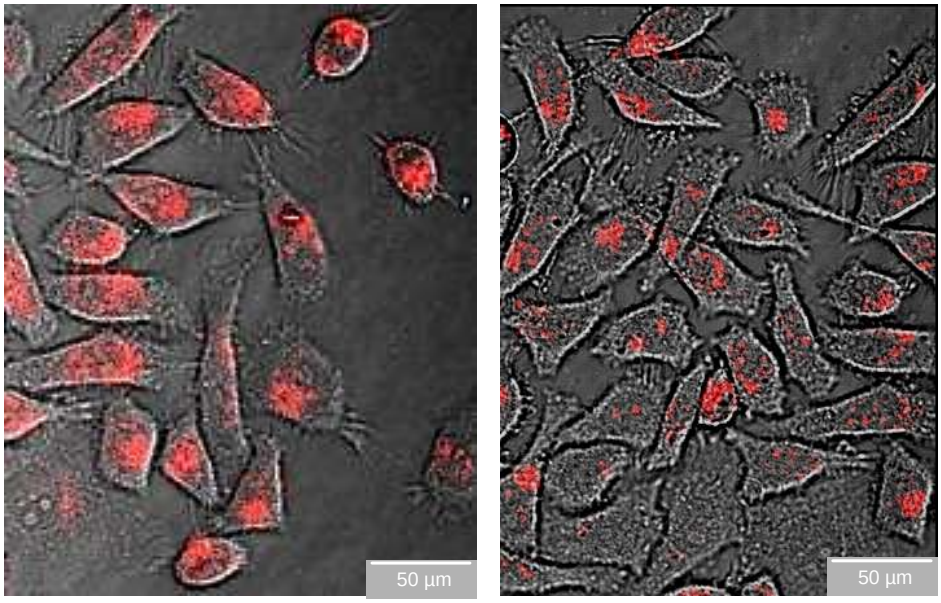

Figure S4. Confocal micrographs of HepG2 cells labeled with TAT-QD_{silica}. Different areas of the slide were imaged to illustrate the differences in distribution of TAT-QD_{silica}. A QD concentration of 20 nM and an incubation time of 12 h were employed (as in Figure 5 (top panel)).

Promotion of Angiogenesis by an Artificial Extracellular Matrix Protein Containing the Laminin-1-Derived IKVAV Sequence

Makiko Nakamura,[†] Kumiko Yamaguchi,[‡] Masayasu Mie,[†] Makoto Nakamura,[§] Keiichi Akita,[‡] and Eiry Kobatake*,[†]

Department of Biological Information, Graduate School of Bioscience and Biotechnology, Tokyo Institute of Technology, Graduate School of Medicine and Dentistry, Tokyo Medical and Dental University, and Department of Biomedical Engineering, University of Toyama. Received March 20, 2009; Revised Manuscript Received July 7, 2009

The laminin-1-derived IKVAV sequence is known for its angiogenic function. We previously developed artificial extracellular matrix (ECM) proteins containing the IKVAV sequence. They were designed to have collagen-binding activity and active functional units that promote network formation of vascular endothelial cells. The resultant fusion protein, called EREI2CBD, was confirmed to bind to collagen type I and promote tubular network formation of endothelial cells cultured in collagen gel *in vitro*. In this study, EREI2CBD was applied to the chick chorioallantoic membrane (CAM) assay to investigate *in vivo* angiogenic activity. The CAM assay results showed that EREI2CBD caused the number and area of vascular branches to be increased. The constructed fusion protein and the engineering strategy of designing multifunctional ECM proteins support current tissue engineering techniques.

INTRODUCTION

In recent years, much attention has been focused on tissue engineering techniques to provide artificial tissue substitutes as an alternative for donor tissue and organs. Scaffold material is one of the essential factors for tissue engineering to support cell attachment and provide necessary signals for cell growth and organization.

In a previous study, we developed artificial extracellular matrix (ECM) proteins designed to have a stable structural unit and active functional units that promote cell attachment and network formation of vascular endothelial cells (*1*). To achieve that purpose, we constructed new fusion proteins with multiple activities of (i) cell adhesion, (ii) promoting tubular network formation, (iii) structural support, and (iv) affinity to collagen. As a functional part of these fusion proteins, the Ile-Lys-Val-Ala-Val (IKVAV) peptide sequence, located in the laminin α1 chain, was chosen as it has a variety of activities including promoting cell adhesion, neurite outgrowth (*2*), and angiogenesis (*3, 4*). An elastin-derived (APGVGV) motif was also adapted to produce a stable matrix protein. This polypeptide module had been studied in our laboratory as an artificial matrix protein and enabled the short active peptides such as IKVAV or GRGDS to work efficiently as a scaffold protein (*5*−*7*). The resultant protein was illustrated in Figure 1, shown as EREI2. The EREI2 fusion protein was constructed with recombinant DNA technology to conjugate the functional peptide sequences and the rigid poly (APGVGV) module. EREI2 was designed to be two repeats of $(APGVGV)_{12}$, RGD, $(APGVGV)_{12}$, and the IKVAV sequence because the activity of the smaller molecule (EREI) was shown to be less than EREI2 (*1*). As the GRGDS-IKVAV conjugated peptide was reported to have stronger cell-adhesive property than the IKVAV sequence (*8*),

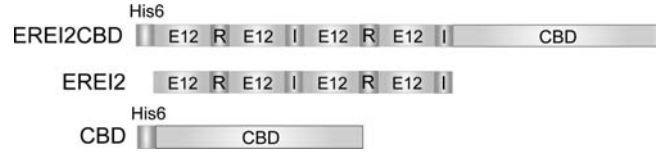

Figure 1. Construction of artificial ECM. (A) E12 means 12 repeats of the elastin-derived APGVGV sequence. R and I indicate the GRGDS sequence derived from fibronectin and the laminin-derived CS-RARKQAASIKVAVSADR sequence, respectively. Collagen-binding domain (CBD) was derived from fibronectin and fused to the C-terminus of the engineered protein. CBD and CBD-fused EREI2 had a histidine tag on their N-terminus.

GRGDS sequence was incorporated into EREI2 to enhance the interaction between cells and the scaffold. Furthermore, we introduced collagen-binding activity into the designed ECMs in order to enable the accumulation of ECM onto specific scaffold materials. Since collagen is biocompatible and is easily processed into several shapes such as membrane, gel, or sponge, it is considered to be a useful material for tissue engineering. Collagen-immobilized forms of engineered ECMs have the potential to provide a safe and functional angiogenesis model for enhancing the activity of necessary signals locally and effectively.

Here, we focused on the collagen-binding domain (CBD) of fibronectin (*9*). CBD sequences are widely used as fusion partners for chimera proteins, as they provide the option for localized application on collagen (*10*−*12*). The resultant collagen-specific, immobilized fusion ECM, called EREI2CBD, promoted angiogenic properties in a collagen type I gel model (*1*). Therefore, EREI2CBD promoted capillary formation of endothelial cells and revealed its potential to produce multifunctional artificial ECM. However, the *in vivo* angiogenesis process was dissimilar to an *in vitro* collagen gel model, and therefore, the application of EREI2CBD under *in vivo* conditions required further investigation.

In the present study, the angiogenic activity of EREI2CBD was determined using a chick chorioallantoic membrane (CAM) assay. The CAM assay is a simple technique for investigating

* Author for correspondence. 4259 Nagatsuta, Midori-ku, Yokohama 226-8501, Japan. Tel.: +81-45-924-5760; Fax: +81-45-924-5779; E-mail: ekobatak@bio.titech.ac.jp.

[†] Tokyo Institute of Technology.

[‡] Tokyo Medical and Dental University.

[§] University of Toyama.

10.1021/bc900126b CCC: $40.75 © 2009 American Chemical Society
Published on Web 08/18/2009

angiogenic behavior *in vivo* (*13*−*15*). EREI2CBD was immobilized on a permeable collagen membrane and the membrane was applied onto CAMs with a glass coverslip. Angiogenic activity, that is, growth of capillary vessels, was then investigated.

EXPERIMENTAL PROCEDURES

Materials. The artificial fusion ECMs, EREI2, EREI2CBD, and CBD were prepared as described in a previous study (*1*). The 19-mer peptide, CSRARKQAASIKVAVSADR, which we refer to as the IKVAV peptide, was synthesized by a solid-phase method using Fmoc. Permeable atelocollagen membrane (MEN-01) was purchased from Koken Co. Ltd. (Tokyo, Japan). All other chemicals were of analytical grade.

Preparation of Artificial Proteins Immobilized on a Collagen Membrane. Permeable atelocollagen membrane was cut into appropriate sizes, soaked with phosphate buffered saline (PBS), and put onto 13-mm-diameter glass coverslips (Thermo Fisher Scientific Inc.). After drying at room temperature, 2 μg of artificial proteins in PBS was added onto the membrane and dried again at room temperature. For the experiment described in the Results section "Concentration-dependent angiogenic behavior of EREI2CBD", EREI2CBD was applied at 0.5−2 μg. Negative control samples contained 20 μL of PBS only. Membranes adhering onto coverslips were stored at 4 °C until use.

Determination of Diffusion of CBD-Fused ECMs from the Collagen Membrane. Atelocollagen membranes immobilized with artificial proteins such as EREI2 and EREI2CBD were prepared as described above. Membrane-adhering coverslips were placed into each well of 24-well culture plates (Falcon), and 300 μL of PBS was added. After 3 h of incubation at 37 °C, 150 μL of supernatant PBS was sampled. Whole protein concentrations desorbed into bulk PBS were determined with the micro BCA protein assay kit (Pierce). Concentrations were calculated after subtraction of negative control membranes soaked with PBS only. Each assay was repeated three times.

Chick Chorioallantoic Membrane Assay. The chick chorioallantoic membrane (CAM) assay was performed using embryonated eggs. On embryonic day 3, 4 mL of ovalbumin was removed from each egg. After opening windows on embryonic day 10, glass coverslips with the protein-treated atelocollagen membrane were placed membrane side face-down onto the surface of the CAM and photographed. Two days later, glass coverslips were cut off together with egg membranes and photographed after washing with PBS. The mortality rate of the embryos supplied with each sample was calculated as the ratio of dead embryos to the sum of three repeated experiments. Quantitative evaluation of vessel areas was performed by determining the number of black pixels per field using Scion image software (Scion Corp.) and by manually counting the number of vessel branches. These numbers were calculated from the whole area of glass coverslips pictured at 0 and 48 h. Each assay was repeated three times using 8 to 12 eggs for each treatment.

Statistical Evaluation. Statistical significance of the results was determined using Student's *t* test. A value of $P < 0.05$ was considered to be significant. Mean ± standard deviation (s.d.) values of three experiments are presented.

RESULTS

Immobilization of CBD-Fused ECM to a Collagen Membrane. The previously constructed artificial ECM proteins (*1*) are illustrated in Figure 1. The EREI2 fusion protein consisted of two repeats of $(APGVGV)_{12}$, RGD, $(APGVGV)_{12}$, and the IKVAV sequence. Fibronectin-derived collagen-binding domain (CBD) and CBD-fused EREI2 were designed to immobilize the fusion construct onto the collagen-based material. CBD-fused ECM and CBD also contain a histidine tag sequence (His6) at their N terminals to aid purification.

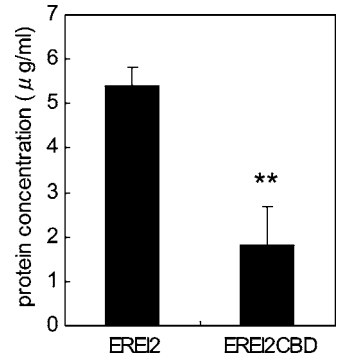

Figure 2. Determination of diffusion of ECMs from the atelocollagen membrane. Two micrograms of constructed ECMs were air-dried onto atelocollagen membranes and incubated in PBS for 3 h at 37 °C. Results show the diffused protein concentration into PBS. Each experiment was repeated 3 times. Error bars represent the standard deviation of the mean. $^{**}P < 0.01$.

Table 1. Mortality Rate of Chick Embryos Treated with Engineered Proteins

	amount (μg)	mortality rate
PBS		0/33
IKVAV pep.	2	0/26
CBD	2	1/26
EREI2CBD	0.5	2/33
	1	1/29
	2	0/31
	5	8/30

To confirm the localization of CBD-fused ECM on collagen membranes, EREI2 and EREI2CBD were fixed onto the membrane by air-drying, and then the amount diffused from the membranes was determined after 3 h of incubation in PBS. The results are shown in Figure 2. A higher protein concentration was detected in PBS from the EREI2-immobilized membrane than that of EREI2CBD, suggesting that more EREI2CBD remained fixed onto the collagen membrane than EREI2. We then confirmed EREI2CBD binding to the collagen membrane and determined its potential to function locally under *in vivo* conditions.

Concentration-Dependent Angiogenic Behavior of EREI2CBD. For the assessment of angiogenic behavior of EREI2CBD, serial amounts were immobilized on the collagen membrane and applied to the CAM assay. The CAM assay was performed as described in previous reports with some modifications for the collagen membrane (*16, 17*). The mortality rate of chick embryos supplemented with EREI2CBD is shown in Table 1. Since the negative control PBS samples survived the 2 day incubation, it was confirmed that our CAM assay protocol itself did not influence chick embryo survival. Table 1 also indicates that EREI2CBD did not significantly affect embryo mortality at concentrations ranging from 0.5 μg to 2 μg. In contrast, when 5 μg of EREI2CBD was applied, nearly 30% of embryos died after 2 days. The mortality table shows that high amounts of EREI2CBD could not be applied to our CAM assay and 5 μg of EREI2CBD was the limit for chick embryo survival. All subsequent experiments on capillary vessel formation were performed at concentrations ranging from 0.5 μg to 2 μg.

In our present study, angiogenesis was evaluated with two indexes, the vessel area and the number of vessel branches. The results are shown in Figure 3. Increases of vessel area in chick embryos were calculated from the black pixel ratio at 48 h compared to 0 h (Figure 3A). This indicated that 0.5 and 2 μg of EREI2CBD significantly increased vessel area. Vascular

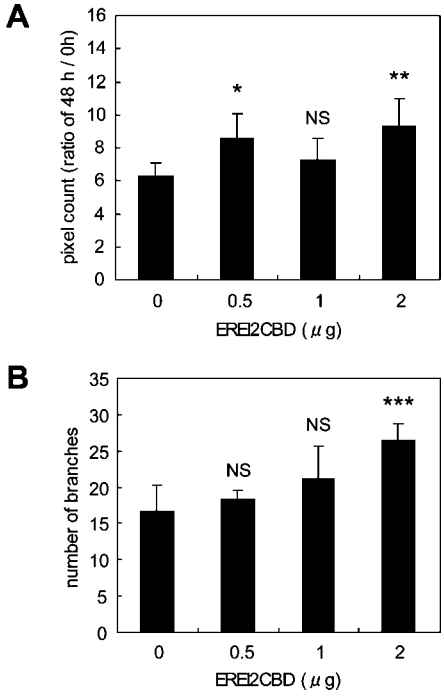

Figure 3. Angiogenic behavior of EREI2CBD. EREI2CBD was air-dried at the indicated concentrations onto atelocollagen membranes and applied to the CAM assay. Zero means the control sample with PBS alone. (A) Quantitative evaluation of vessel areas by determining the number of black pixels per field. The number of black pixels was calculated within the whole area of glass coverslips imaged at 0 and 48 h. Results show the ratio of pixel counts at 0 to 48 h. (B) The number of vessel branches after 48 h of incubation. Each experiment was repeated 3 times. Error bars represent the standard deviation of the mean. NS, not significant; $*P < 0.05$, $**P < 0.01$; $***P < 0.001$ compared to the PBS control sample (referred to as zero).

sprouting, an important factor for the angiogenic process, was evaluated by counting the number of vessel branches. The number of branches after 2 days was increased in a concentration-dependent manner and was significantly increased in the case of 2 μg EREI2CBD (Figure 3B). Therefore, EREI2CBD promoted vascular sprouting in an angiogenesis assay.

From the results of Table 1 and Figure 3, the angiogenic properties of EREI2CBD were confirmed in the CAM assay. The optimal amount of EREI2CBD was determined to be 2 μg, as this concentration did not significantly affect survival of the chick embryos but induced angiogenic activity. In the subsequent experiments, 2 μg of EREI2CBD was applied for further determination of angiogenic ability.

Determination of the Angiogenic Activity of EREI2CBD. The angiogenic activity of EREI2CBD was compared using the same amounts of CBD protein or IKVAV synthetic peptide. Two micrograms of CBD protein or IKVAV synthetic peptide were shown to be harmless to chick embryos (Table 1). Figure 4A indicated that the capillary vessel network was more complex when EREI2CBD was applied to CAM. The morphology of vessels was similar in PBS and IKVAV peptide treated CAMs. CBD caused an increase of vascular thickness, but EREI2CBD showed the greatest increase in the number of vascular branches. Quantitative results of angiogenic activity are shown in Figure 4B,C, and these corresponded to the above observations. The vessel areas of CBD- or EREI2CBD-treated CAMs were greatly increased compared to PBS and IKVAV peptide-treated CAMs (Figure 4B). CBD also increased the number of vascular branches compared to PBS. EREI2CBD further increased vascular branching, and this was significantly more than CBD-treated CAMs (Figure 4C).

Throughout the results, the angiogenic activity of EREI2CBD was confirmed. Although CBD showed some angiogenic properties such as increased vessel area, EREI2CBD was superior to CBD in promoting vessel sprouting. Therefore, the CBD-fused form of EREI2 is a promising approach for promotion of angiogenesis.

DISCUSSION

In the present study, we have determined the angiogenic properties of an artificial multifunctional extracellular matrix (ECM) protein. This novel ECM protein, referred to as EREI2CBD, was previously constructed by fusing functional peptide sequences derived from existing ECM proteins (*1*). We arranged two well-known active sequences with $(APGVGV)_{12}$ to construct ECMs that had strong cell-adhesive properties and the ability to induce cellular network signals. The sequences we focused on were GRGDS and CSRARKQAASIKVAVSADR. The latter IKVAV-containing sequence was reported to promote endothelial cell migration and tubular network formation (*3, 4*) through the interaction of an unknown receptor on the cellular surface. EREI2CBD also had a collagen-binding domain (CBD) fused to its C-terminus, and the CBD part enabled the fusion protein to be immobilized onto collagen. Since fixed forms of functional proteins such as growth factors could function locally, they have been recently reported to work more efficiently than their free forms (*12*). Furthermore, collagen is a well-known biocompatible material that has given satisfactory results for tissue regeneration (*18, 19*). Therefore, we focused on the collagen-immobilized form of the designed fusion protein for construction of an efficiently functioning ECM protein. We used atelocollagen-based material as it is free of immunogenicity as terminus telopeptides have been digested (*20, 21*). The CAM assay was performed with an EREI2CBD-immobilized atelocollagen membrane for assessment of angiogenesis *in vivo*.

Collagen-specific binding of EREI2CBD was confirmed by an ELISA assay using collagen type I-coated microplates in our previous study (*1*). Here, it was determined whether EREI2CBD could be fixed onto collagen membranes for *in vivo* applications. By determining the amount of atelocollagen diffused from the membrane into PBS (Figure 2), it was revealed that more EREI2CBD remained on the membrane than EREI2. After 3 h of incubation, only 0.6 μg of EREI2CBD (30% of the applied amount) was detected in PBS while 1.8 μg of EREI2 (90% of the applied amount) was released. The diffusion rate of EREI2CBD was much lower than EREI2, and EREI2CBD was confirmed to be immobilized onto the atelocollagen membrane. Therefore, the CBD part of the constructed ECM functioned as an anchor to atelocollagen-based material, and EREI2CBD was determined to have the potential to work efficiently in its localized form.

Next, EREI2CBD was applied to an *in vivo* angiogenic model, the CAM assay, and the optimized amount to evaluate its angiogenic ability was determined. The CAM assay is a well-known angiogenic model (*13*−*15*). Kleinman et al. introduced the CAM assay for assessment of anticancer drugs such as functional peptides (*16, 17*). Along with these previous reports, we examined the angiogenic properties of EREI2CBD using the CAM assay. Our first concern was biocompatibility of EREI2CBD. The designed fusion protein, EREI2CBD, was produced by means of recombinant DNA technology and *E. coli* fermentation. According to the related work reported by Urry et al. (*22*), high levels of purification were required so that *E. coli*-expressed recombinant proteins could be used *in vivo*. They tried to remove trace amounts of *E. coli* proteins by a series of purification steps. In contrast (*22*), EREI2CBD was purified with a simple single step. The mortality table (Table 1) indicated that a high concentration of EREI2CBD was fatal

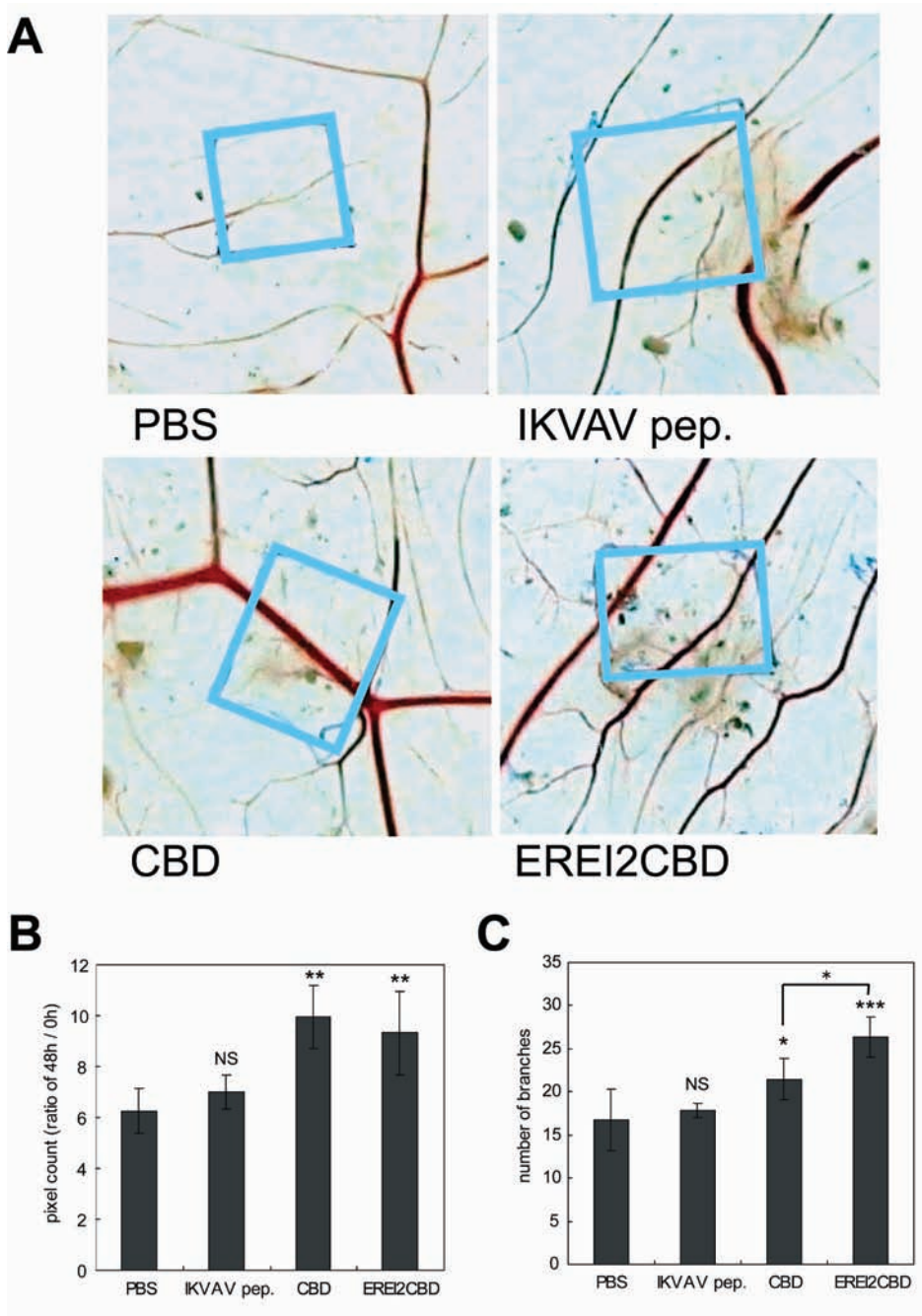

Figure 4. Angiogenic activity of EREI2CBD. Two micrograms of IKVAV synthetic peptide, CBD, or EREI2CBD were air-dried onto atelocollagen membranes and applied to the CAM assay. (A) Morphologies of capillary vessels treated with each sample. The squares indicate the position of the atelocollagen membrane. Each photo was pictured after 48 h of incubation. (B) Quantitative evaluation of vessel areas. The number of black pixels was calculated within the whole areas of glass coverslips imaged at 0 and 48 h. Results show the ratio of pixel counts at 0 to 48 h. (C) The number of vessel branches after 48 h incubation. Each experiment was repeated 3 times. Error bars represent the standard deviation of the mean. NS, not significant; $*P < 0.05$, $**P < 0.01$; $***P < 0.001$ compared to the PBS sample.

to chick embryos, which might be due to remaining harmful substances derived from *E. coli* cell lysates such as endotoxins (*23*). Table 1 showed that EREI2CBD should be applied at concentrations less than 5 μg. In the future, high levels of purity are required before pharmaceutical use of EREI2CBD.

To determine the angiogenic behavior of EREI2CBD, two semiquantitative methods were used (Figure 3). One was to determine the number of black pixels per field, a value that represented the vessel area of samples. The other method was to count the number of capillary vessel branches to evaluate the development of a vascular network. From the results of Figure 3B, the increase in the number of vessel branches was dependent on EREI2CBD concentration. EREI2CBD promoted cardiovascular sprouting and generation of neovessels. The laminin-1-derived IKVAV sequence included in EREI2CBD has been reported to affect endothelial migration, which is the first important process of angiogenesis (*3, 4*). Therefore, the CAM assay results suggested that EREI2CBD could retain the angiogenic properties of the functional peptide sequence in *in vivo* conditions. Furthermore, promotion of vessel sprouting caused an increase in vessel area, especially when 2 μg of EREI2CBD was added (Figure 3A). Figure 3 results showed the angiogenic function of EREI2CBD, and 2 μg was applied to all subsequent experiments.

To further analyze EREI2CBD angiogenic activity, EREI2CBD was compared to the IKVAV synthetic peptide and CBD protein

(Figure 4). For the IKVAV peptide, no effect was observed in either vessel area or the number of branches compared to a PBS control. Previous reports showed angiogenic activity of the IKVAV sequence using concentrations of 200 μg (*3, 4*), while only 2 μg was used in our present study. Therefore, the concentration of synthetic IKVAV peptide was too low to affect angiogenic activity. Since short IKVAV peptide sequences included in EREI2CBD were stably supported with a rigid $(APGVGV)_{12}$ scaffold and localized onto a collagen membrane, they may interact with the cellular surface more efficiently. Furthermore, the poly(APGVGV) sequence itself was reported to promote cell migration and may enhance the angiogenic effect of the IKVAV peptide (*24, 25*). Therefore, the EREI2CBD peptide was superior to synthetic IKVAV peptides for inducing angiogenesis, and our collagen-binding artificial ECMs were functional at lower concentrations than synthetic peptides, as expected.

In contrast to the IKVAV peptide, CBD itself showed some angiogenic effects compared with the PBS control. Vessel area was increased by the CBD protein at the same ratio as EREI2CBD, although the increase of vessel branches by CBD was inferior to that of EREI2CBD. CBD was determined to have cell adhesive activity and promoted tube formation of endothelial cells *in vitro* in our previous study (*1*). Those results suggested that CBD increased the thickness of capillary vessels through promotion of endothelial cell attachment and migration. The CBD sequence adopted here was Ala260-Trp 599 of fibronectin (*9*), and recently, Schor et al. reported that some Ile-Gly-Asp (IGD) peptide motifs included in this CBD sequence had cell adhesive ability and motogenic activity (*26, 27*). These reports correspond with our results and suggest that CBD plays some role in the cellular signaling pathway in addition to its collagen-binding property. Further analysis is required to determine the angiogenic function of CBD. However, our experiments (Figure 4) revealed that the angiogenic activities of CBD did not compete with EREI2CBD. Rather, EREI2CBD was superior to CBD in increasing the number of vessel branches, which suggests a specific effect for the designed ECM domain EREI2 that includes the IKVAV sequence.

In conclusion, the artificially designed fusion ECM protein, EREI2CBD, was shown to have angiogenic activity using an *in vivo* CAM assay. EREI2CBD could be immobilized onto atelocollagen membranes and increase vessel area, especially the number of capillary vessel branches. Our design strategy for constructing fusion proteins produced stable, functional ECM proteins that worked more efficiently than synthetic peptides. Atelocollagen-based material and collagen-binding engineered ECM proteins hold potential for generating functional tissues by tissue engineering.

ACKNOWLEDGMENT

This work was supported by Grant-in-Aid for Japan Society for the Promotion of Science (JSPS) Fellows, and the Ministry of Education, Culture, Sports, Science & Technology (MEXT), Japan.

LITERATURE CITED

(1) Nakamura, M., Mie, M., Mihara, H., Nakamura, M., and Kobatake, E. (2008) Construction of multi-functional extracellular matrix proteins that promote tube formation of endothelial cells. *Biomaterials 29*, 2977–2986.

(2) Tashiro, K., Sephel, G. C., Weeks, B., Sasaki, M., Martin, G. R., Kleinman, H. K., and Yamada, Y. (1989) A synthetic peptide containing the IKVAV sequence from the A chain of laminin mediates cell attachment, migration, and neurite outgrowth. *J. Biol. Chem. 264*, 16174–16182.

(3) Grant, D. S., Kinsella, J. L., Fridman, R., Auerbach, R., Piasecki, B. A., Yamada, Y., Zain, M., and Kleinman, H. K. (1992) Interaction of endothelial cells with a laminin A chain peptide (SIKVAV) in vitro and induction of angiogenic behavior in vivo. *J. Cell. Phys. 153*, 614–625.

(4) Malinda, K. M., Nomizu, M., Chung, M., Delgado, M., Kuratomi, Y., Yamada, Y., Kleinman, H. K., and Ponce, M. L. (1999) Identification of Laminin α1 and β1 chain peptides active for endothelial cell adhesion, tube formation, and aortic sprouting. *FASEB J. 13*, 53–62.

(5) Kobatake, E., Onoda, K., Yanagida, Y., and Aizawa, M. (2000) Design and gene engineering synthesis of an extremely thermostable protein with biological activity. *Biomacromolecules 1*, 382–386.

(6) Elloumi, I., Kobayashi, R., Funabashi, H., Mie, M., and Kobatake, E. (2006) Construction of epidermal growth factor fusion protein with cell adhesive activity. *Biomaterials 27*, 3451–3458.

(7) Hannachi, I. E., Nakamura, M., Mie, M., and Kobatake, E. (2009) Construction of multifunctional proteins for tissue engineering: epidermal growth factor with collagen binding and cell adhesive activities. *J. Biotechnol. 139*, 19–25.

(8) Kasai, S., Ohga, Y., Mochizuki, M., Nishi, N., Kadoya, Y., and Nomizu, M. (2004) Multifunctional peptide fibrils for biomedical materials. *Biopolymers 76*, 27–33.

(9) Owens, R. J., and Baralle, F. E. (1986) Mapping of the collagen-binding site of human fibronectin by expression in Escherichia coli. *EMBO J. 5*, 2825–2830.

(10) Ishikawa, T., Terai, H., and Kitajima, T. (2001) Production of a biologically active epidermal growth factor fusion protein with high collagen affinity. *J. Biochem. 129*, 627–633.

(11) Ishikawa, T., Eguchi, M., Wada, M., Iwami, Y., Tono, K., Iwaguro, H., Masuda, H., Tamaki, T., and Asahara, T. (2006) Establishment of a functionally active collagen-binding vascular endothelial growth factor fusion protein in situ. *Arterioscler. Thromb. Vasc. Biol. 26*, 1998–2004.

(12) Kitajima, T., Terai, H., and Ito, Y. (2007) A fusion protein of hepatocyte growth factor for immobilization to collagen. *Biomaterials 28*, 1989–1997.

(13) Leng, T., Miller, J. M., Bilbao, K. V., Palanker, D. V., Huie, P., and Blumenkranz, M. P. (2004) The chick chorioallantoic membrane as a model tissue for surgical retinal research and simulation. *Retina 24*, 427–434.

(14) Auerbach, R., Lewis, R., Shinners, B., Kubai, L., and Akhtar, N. (2003) Angiogenesis assays: a critical overview. *Clin. Chem. 49*, 32–40.

(15) Norrby, K. (2006) In vivo models of angiogenesis. *J. Cell. Mol. Med. 10*, 588–612.

(16) Ponce, M. L., Hibino, S., Lebioda, A. M., Mochizuki, M., Nomizu, M., and Kleinman, H. K. (2003) Identification of a potent peptide antagonist to an active laminin-1 sequence that blocks angiogenesis and tumor growth. *Cancer Res. 63*, 5060–5064.

(17) Hibino, S., Shibuya, M., Engbring, J. A., Mochizuki, M., Nomizu, M., and Kleinman, H. K. (2004) Identification of an active site on the laminin α5 chain globular domain that binds to CD44 and inhibits malignancy. *Cancer Res. 64*, 4810–4816.

(18) Lee, C. H., Singla, A., and Lee, Y. (2001) Biomedical applications of collagen. *Int. J. Pharm. 221*, 1–22.

(19) Horch, R. E., Kopp, J., Kneser, U., Beier, J., and Bach, A. D. (2005) Tissue engineering of cultured skin substitutes. *J. Cell. Mol. Med. 9*, 592–608.

(20) Sano, A., Maeda, M., Nagahara, S., Ochiya, T., Honma, K., Itoh, H., Miyata, T., and Fujioka, K. (2003) Atelocollagen for protein and gene delivery. *Adv. Drug Delivery Rev. 55*, 1651–1677.

(21) Lynn, A. K., Yannas, I. V., and Bonfield, W. (2004) Antigenicity and immunogenicity of collagen. *J. Biomed. Mater. Res. B 71*, 343–354.

(22) Urry, D. W., Pattanaik, A., Xu, J., Woods, T. C., McPherson, D. T., and Parker, T. M. (1998) Elastic protein-based polymers

in soft tissue augmentation and generation. *J. Biomater. Sci. Polym. Ed. 9*, 1015–1048.

(23) Rietschel, E. T., Kirikae, T., Schade, F. U., Mamat, U., Schmidt, G., Loppnow, H., Ulmer, A. J., Zahringer, A., Seydel, U., Padova, F. D., Schreier, C., and Brade, H. (1994) Bacterial endotoxin: molecular relationships of structure to activity and function. *FASEB J. 8*, 217–225.

(24) Long, M. M., King, V. J., Prasad, K. U., Freeman, B. A., and Urry, D. W. (1989) Elastin repeat peptides as chemoattractants for bovine aortic endothelial cells. *J. Cell. Phys. 140*, 512–518.

(25) Robinet, A., Fahem, A., Cauchard, J. H., Huet, E., Vincent, L., Lorimier, S., Antonicelli, F., Soria, C., Crepin, M., Hornebeck, W., and Bellon, G. (2005) Elastin-derived peptides enhance angiogenesis by promoting endothelial cell migration and tubulogenesis through upregulation of MT1-MMP. *J. Cell Sci. 118*, 343–356.

(26) Schor, S. L., Ellis, I., Banyard, J., and Schor, A. M. (1999) Motogenic activity of IGD-containing synthetic peptides. *J. Cell Sci. 112*, 3879–3888.

(27) Millard, C. J., Ellis, I. R., Pickford, A. R., Schor, A. M., Schor, S. L., and Campbell, I. D. (2007) The role of the fibronectin IGD motif in stimulating fibroblast migration. *J. Biol. Chem. 282*, 35530–35535.

BC900126B

Anionic Nucleotide−Lipids for *In Vitro* DNA Transfection

Salim Khiati,[†,‡] Nathalie Pierre,[†,‡] Soahary Andriamanarivo,[†,‡] Mark W. Grinstaff,[||] Nessim Arazam,[§] Frédéric Nallet,[§] Laurence Navailles,[§] and Philippe Barthélémy*[,†,‡]

INSERM U869, Bordeaux, F-33076, France, Université Victor Segalen Bordeaux 2, Bordeaux, F-33076, France, Université Bordeaux-1 CNRS, Centre de Recherche Paul Pascal, 115 avenue A. Schweitzer, F-33600 Pessac, France, and Departments of Biomedical Engineering, Metcalf Center for Science and Engineering, Boston University, Boston, Massachusetts 02215.
Received April 10, 2009; Revised Manuscript Received July 20, 2009

A family of new anionic nucleotide based lipids featuring thymidine-3′-monophosphate as nucleotide and 1,2-diacyl-*sn*-glycerol as lipid moiety for *in vitro* delivery of nucleic acids is described. The nucleotide lipids were prepared in three steps starting from 1,2-diacyl-*sn*-glycerols and 2′-deoxythymidine-3′-phosphoramidite. Gel electrophoresis experiments show that nucleotide-based lipid−DNA complexes are observed at Ca^{2+} concentration higher than 1 mM. The transfection experiments carried out on mammalian Hek cell lines clearly demonstrate that the nucleotide moiety enhances the transfection efficacy of the natural anionic DPPA and DPPG lipids. SAXS studies indicate that the enhancement in transfection for nucleotide-based lipid formulations compared to those of the abasic natural derivative (DPPA) is likely due to the presence of the 2D columnar inverted hexagonal phase (H_{II}) with a unit cell parameter $a = 69.1$ Å in the nucleotide lipid formulations. The cytotoxicity studies of lipoplexes, evaluated against Hek cells using an MTS assay, revealed that palmitoyl nucleotide derivative complexes were not toxic even after 4 h of incubation, thus indicating that the anionic nucleotide lipids presented in this work offer an alternative to cationic transfection reagents.

INTRODUCTION

Therapies ± using natural or synthetic nucleic acids have emerged as promising strategies for developing cures against inherited and acquired disorders or diseases, including cancer (*1, 2*). One of the significant advantages of nucleic acid based drugs over low molecular weight pharmaceutical drugs is their selectivity for their biological target and their specificity of ± action (*3*). To be effective, nucleic acid based therapies require the use of vector platforms for delivering various genetic materials into cells. The earliest synthetic DNA delivery systems, first introduced in the 1980s (*4, 5*), were based on cationic lipids. Today, cationic lipids are still important transfecting tools for research, likely because of the researchers' ability to control their chemical and physical properties (*6*). However, most of these cationic systems exhibit specific problems outlined by Burgess et al. (*7*), including cytotoxicity, inactivation in the presence of serum, and inefficiency *in vivo*, that scientists are attempting to address (*8*−*12*). To overcome these limitations, alternative cationic synthetic vectors ± are currently under investigation by a number of research groups (*13*−*16*). In ± recent years, there has also been intense research activity in the development of various innovative lipid systems, including pH-sensitive fusiogenic polymer-modifed liposomes (*17*), pH-sensitive pegylated lipoplexes (*18*), nucleolipoplexes (*19*−*21*), imidazole (*22*) and charge reversal lipids (*23, 24*), lipopolythiourea (*25*), lipophilic peptides (*26*), zwitterionic lipids (*27*), and glycosylated lipids (*28*). Additionally, amphiphiles possessing a nucleoside as a lipid headgroup and lipophilic alkyl chains have been identified as promising tools for gene delivery into cells (*19*−*21*) (*28*−*30*) and for self-assembling nucleic acid−nucleolipid supramolecular systems (*31*−*40*).

Examples of anionic amphiphiles for gene delivery are rare. Recently, an anionic amphiphile (1,2-dioleoyl-*sn*-glyerol-3-[phospho-*rac*-(1-glycerol] sodium salt), zwitterionic amphiphile (DOPE), and Ca^{2+} system have been reported that exhibited transfection efficiencies similar to the cationic lipid lipofectamine (*7*) (*41*). To our knowledge, no reports of anionic nucleotide based amphiphiles for gene transfection have been reported.

Within this context, we hypothesized that an anionic amphiphile possessing a nucleotide polar head for DNA−lipid association would enable formation of lipoplexes in the presence of Ca^{2+} and afford *in vitro* tranfection. For this purpose, we synthesized a series of anionic nucleotide−lipids with a thymidine nucleotide polar head and various 1,2-diacyl-*sn*-glycerol of C_{12}, C_{14}, and C_{16} chain length as hydrophobic species. The potential of these novel anionic nucleotide based lipids for DNA delivery and expression was investigated. Herein, we report the synthesis, physicochemical studies, cytotoxicity, and *in vitro* transfection results of these new anionic nucleotide based lipids (Scheme 1).

EXPERIMENTAL PROCEDURES

Materials. *General Experiments and Analytical Conditions.* Unless noted otherwise, all starting materials and solvents were obtained from Aldrich, Bachem, Genzyme, and Glen Research and were used without further purification. All compounds were characterized using standard analytical and spectroscopic techniques such as ^{1}H, ^{13}C, and ^{31}P spectroscopy (apparatus Bruker Avance DPX-300, ^{1}H at 300.13 MHz, ^{13}C at 75.46 MHz, and ^{31}P at 121.49 MHz) and mass spectrometry (Instrument JEOL SX 102, NBA matrix). The NMR chemical shifts are reported in ppm relative to tetramethylsilane using the deuterium signal of the solvent ($CDCl_3$) as a heteronuclear reference for ^{1}H. The ^{1}H NMR coupling constants, *J*s, are reported in Hz. TEM microscopy experiments were performed

* Corresponding author. philippe.Barthelemy@inserm.fr.
† INSERM U869.
‡ Université Victor Segalen Bordeaux 2.
|| Boston University.
§ Université Bordeaux-1 CNRS.

10.1021/bc900163s CCC: $40.75 © 2009 American Chemical Society
Published on Web 08/27/2009

Scheme 1. Chemical Structure of an Anionic Nucleotide−Lipid Used in This Study, the Thymidine 3′-(1,2-dipalmitoyl-*sn*-glycero-3-phosphate) (di c_{16}dT) and Non-Nucleotide−Lipids DPPA and DPPG

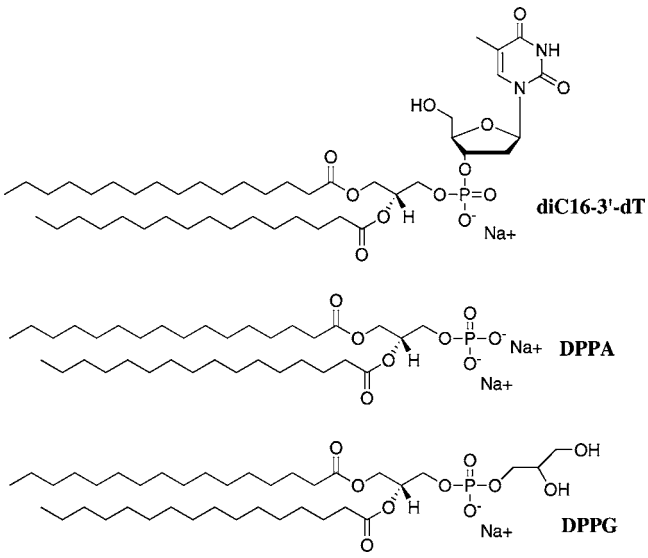

with a Hitachi H 7650 (negative staining with uranyl acetate 1% in water, nickel carbon coated grids). Fluorescence microscopy experiments were performed on a Zeiss axiovert 200. Silica gel 60 (particle size: 45 μm) was used for flash chromatography (Biotage). Thin layer chromatograms were performed with aluminum plates coated with silica gel 60 F_{254} (Merck). The revealing solution for TLC is an anisaldehyde solution (85 mL ethanol, 10 mL acetic acid, 5 mL sulfuric acid, and 0.5 mL *p*-anisaldehyde).

Synthesis. *Thymidine 3′-(1,2-Dilauroyl-sn-glycero-3-phosphate), diC_{12}-3′-dT, Compound* **1.** 5′-*O*-(4,4′-Dimethoxytrityl)-2′-deoxythymidine-3′-[(2-cyano-ethyl)-*N*,*N*-diisopropyl)] phosphoramidite (0.500 g, 1 equiv, 0.67 mmol), 1,2-dilauroyl-*sn*-glycerol (0.398 g, 1.3 equiv, 0.87 mmol/dissolved in 3 mL of THF) and a tetrazole solution in acetonitrile (0.45 M, 2 mL, 1,3 equiv, 0,87 mmol) were dissolved in 3 mL of dry acetonitrile under argon. The reaction mixture was stirred for 7 h at room temperature followed by oxidation with 40 mL of a solution of I_2 (0.02 M in THF/Pyr/H_2O). After 12 h at room temperature, the solvent was evaporated under high vacuum to yield intermediate products. The contents of the reaction flask were dissolved in 10 mL of methylene chloride and then washed first with 3 × 10 mL of HCl (0.1 N) and second with 3 × 10 mL of a saturated solution of $Na_2S_2O_3$. Product **1** (160 mg) was isolated after purification on silica gel (DCM/MeOH/TEA from 98:2:1 to 50:49:1). Yield: 33% R_f = 0.5 (DCM/MeOH 7:3).

^{1}H NMR (300 MHz, $CDCl_3$): δ in ppm 0.83 (t, 6H, J = 6.8 Hz, $2CH_3$), 1.21 (m, 32H, $16CH_2$), 1.54 (m, 4H, $2CH_2$), 1.86 (s, 3H, Me base), 2.25 (m, 4H, $2CH_2$), 3.04 (t, 2H), 3.7−4.4 (m, 7H, $2CH_2$(glycerol), H4′, H5′), 5.28 (m, 1H, CH glycerol), 6.21 (t, 1H, J = 6.5 Hz, H1′), 7.61 (s,1H, H base).

^{13}C NMR (75 MHz, $CDCl_3$): δ in ppm 12.5 (CH_3 base), 14.0 (CH_3 chain), 19.6 (CH_2), 19.7 (CH_2), 22.6 (CH_2), 24.8 (CH_2), 29.0−29.5 (CH_2), 31.9 (CH_2), 33.9 (CH_2), 34.1 (CH_2), 61.5 (CH_2), 61.7 (CH_2), 62.5 (CH_2), 62.6 (CH_2), 66.1 (CH_2), 66.2 (CH_2), 69.1 (CH), 78.8 (CH), 85.5 (CH), 86.1 (CH), 110.7 (C base), 136.2 (CH base), 150.5 (C═O base), 164.0 (C═O base), 172.9 (C═O chain), 173.3 (C═O chain).

^{31}P NMR (121 MHz, $CDCl_3$): δ 2.1 ppm. High-resolution ESI MS^- $[M-H]^-$, theorical m/z = 759.4197, observed m/z = 759.4182.

Thymidine 3′-(1,2-Dimyristoyl-sn-glycero-3-phosphate) diC_{14}-3′-dT, Compound **2.** A procedure similar to that used for compound **1** was followed here. 5′-Dimethoxytrityl-2′-deoxythymidine, 3′-[(2-cyanoethyl)-*N*,*N*-diisopropyl)]-phosphoramidite (500 mg, 1 equiv, 0.67 mmol), 1,2-dimyristoyl-*sn*-glycerol (447 mg, 1.3 equiv, 0.87 mmol), and a tetrazole solution 0.45 M in acetonitrile (2 mL, 0.87 mmol) were dissolved in dry acetonitrile under argon. Product **2** (160 mg) was isolated after purification on silicagel (DCM/MeOH/TEA from 98:2:1 to 50:49:1). Yield: 17% R_f = 0.6 (DCM/MeOH 7:3).

^{1}H NMR (300 MHz, $CDCl_3$): δ in ppm 0.86 (t, 6H, J = 6.9 Hz, $2CH_3$), 1.24 (m, 40H, $16CH_2$), 1.57 (m, 4H, $2CH_2$), 1.90 (s, 3H, Me base), 2.28 (m, 4H, $2CH_2$), 2.98 (t, 2H), 3.7−4.4 (m, 7H, $2CH_2$(glycerol), H4′, H5′), 5.22 (m, 1H, CH glycerol), 6.22 (t, 1H, J = 6.5 Hz, H1′), 7.61 (s,1H, H base).

^{13}C NMR (75 MHz, $CDCl_3$): δ in ppm 12.5 (CH_3 base), 14.0 (CH_3 chain), 22.6 (CH_2), 24.8 (CH_2), 29.1−29.6 (CH_2), 31.8 (CH_2), 34.0 (CH_2), 34.2 (CH_2), 39.0 (CH_2), 39.1 (CH_2), 61.8 (CH_2), 62.5 (CH_2), 63.4 (CH_2), 63.5 (CH_2), 70.1 (CH), 74.3 (CH), 84.6 (CH), 85.8 (CH), 110.8 (C base), 136.2 (CH base), 150.4 (C═O base), 164.0 (C═O base), 173.0 (C═O chain), 173,4 (C═O chain).

^{31}P NMR (121 MHz, $CDCl_3$): δ 2.5 ppm.

High-resolution ESI MS^- $[M-H]^-$, theorical m/z = 815.4823, observed m/z = 815.4819.

Thymidine-3′-(1,2-dipalmitoyl-sn-glycero-3-phosphate) diC_{16}-3′-dT, Compound **3.** A procedure similar to that used for compound **1** was followed here. 5′-Dimethoxytrityl-2′-deoxythymidine, 3′-[(2-cyanoethyl)-*N*,*N*-diisopropyl)]-phosphoramidite (1 g, 1 equiv, 1.34 mmol), 1,2-dipalmitoyl-*sn*-glycerol (992 mg, 1.3 equiv, 1,75 mmol), and a tetrazole solution 0.45 M in acetonitrile (4 mL, 1.75 mmol) were dissolved in dry acetonitrile under argon. Product **3** (552 mg) was isolated after purification on silica gel (DCM/MeOH/TEA from 98:2:1 to 50:49:1). Yield: 47% R_f = 0.3 (DCM/MeOH 8:2).

^{1}H NMR (300 MHz, $CDCl_3$): δ in ppm 0.88 (t, 6H, J = 6.9 Hz, $2CH_3$), 1.25 (m, 48H, $16CH_2$), 1.42 (dd, 4H, J_1 = 8.4 Hz, J_2 = 15.6 Hz, $2CH_2$), 1.90 (s, 3H, Me base), 2.33 (m, 4H, $2CH_2$), 2.83 (t, 2H J = 5.6 Hz, H2′), 3.84 (m, 1H, H3′), 4.09−4.35 (m, 7H, $2CH_2$ (glycerol), H4′, H5′), 5.27 (s, 1H, CH glycerol), 6.21 (t, 1H, J = 6.7 Hz, H1′), 7.54 (s,1H, H base).

^{13}C NMR (75 MHz, $CDCl_3$): δ in ppm 12.4 (CH_3 base), 14.1 (CH_3 chain), 19.6 (CH_2), 19.7 (CH_2), 22.6 (CH_2), 24.8 (CH_2), 29.1−29.6 (CH_2), 31.9 (CH_2), 33.9 (CH_2), 34.1 (CH_2), 61.5 (CH_2), 61.7 (CH_2), 62.5 (CH_2), 62.6 (CH_2), 66.1 (CH_2), 66.2 (CH_2), 69.1 (CH), 78.8 (CH), 85.5 (CH), 86.1 (CH), 111.3 (C base), 136.8 (CH base), 150.5 (C═O base), 164.1 (C═O base), 173.0 (C═O chain), 173.5 (C═O chain).

^{31}P NMR (121 MHz, $CDCl_3$): δ 2.1 ppm.

ESI MS^- $[M-H]^-$, theorical m/z = 871.5449, observed m/z = 871.5473.

Preparation of Liposomes. Liposomes were prepared from binary mixtures of the negatively charged lipid nucleolipids (NL) and neutral lipid DOPE. Stock solutions of DOPE and (NL) (10 mg/mL in chloroform) were mixed at the desired ratio and placed in glass tubes. The mixture was dried under dry N_2 and then desiccated under vacuum overnight. Milli-Q Water was added to the dried lipids to obtain liposome solutions (1 mg/mL). This was followed by five thaw−sonication cycles using a water bath at 55 °C and an ultrasonic bath. The resultant solution was extruded at room temperature through a 50 nm pore-size nucleopore polycarbonate filter.

Preparation of Plasmid DNA. Plasmid containing a GFP reporter gene under the cytomegalovirus promoter, pE-GFP, was propagated in transformed *Escherichia coli* cells. *E. coli* cells were grown in standard luria Bertani medium at pH 7.0. Cells were harvested by centrifugation, and the plasmid DNA was

extracted and purified using a Qiagen Plasmid Maxi Kit (Qiagen, Santa Clarita, CA) as per the manufacturer's recommended protocols.

Preparation of Anionic Lipoplexes. DNA (250 μg/mL), liposomes (1 mg/mL), and divalent salt ($CaCl_2$ $2H_2O$, 200 mM) samples were mixed to yield anionic lipoplexes at different global salt concentrations. The DNA to lipid charge stoichiometry (*D*/*L* ratio) was defined as the total charge of DNA divided by the total charge of anionic nucleolipides.

Particle Size Determination. Anionic liposomes and lipoplexes were prepared as described above. Particle size was determined using Zetasizer 3000 HAS Malvern. All measurements were conducted at 25 °C.

Electrophoresis Studies. Electrophoresis studies were conducted in 0.8% agarose gels containing ethidium bromide in 0.5 Tris-borate without EDTA buffer. Anionic lipoplexes were prepared as described above. For this purpose, 20 μL of each sample was mixed with 4 μL loading buffer (glycerol 30% (v/v), bromophenol blue 0.25% (w/v), and xylene cyanol 0.25 (w/v)) and subjected to agarose gel electrophoresis for 35 min at 100 V. The electrophoresis gel was visualized and digitally photographed using a G.BOX camera.

Transmission Electronic Microscopy (TEM). Anionic liposomes and lipoplexes were prepared as described above and were visualized by negative staining microscopy. Ten microliters of liposomes (1 mg/mL) was transferred to a carbon-coated grid for 10 min. The sample was then dried and stained with 1% (W/W) of uranyl acetate for 30 s. The specimens were observed with a Hitachi H 7650 electron microscope.

Transfection Assays. Cell lines (Hek 293 human embryo kidney) were cultured in Dulbecco's Modified Eagle's Medium (D-MEM, Invitrogen) and supplemented with 10% fetal bovine serum (FBS, invitrogen) and 1% not essence AA and 1% L-glutamine at 37 °C in a 5% CO_2 atmosphere. Cells were split every 3−4 days to maintain monolayer coverage.

The day before transfection, cells were seeded in 24 well plates (50 000 cells/well). On the day of transfection, the medium containing serum was removed from the well plates and replaced with 200 μL of transfection medium without serum.

Lipoplexes were prepared by adding 4 μL of plasmid (250 ng/μL) in 50 μL of medium without serum and 42 μL of anionic liposome dispersions (1 mg/mL). Anionic lipoplex formation was achieved by the addition of various amounts of a calcium chloride solution (200 mM). These complexes were left at room temperature for 15 min before being added to the cells. In the case of fluorescence microscopy samples, a similar procedure was followed. In that case, an oligonucleotide fluorescein (random sequence, 18mers) was mixed with the DNA fraction and added to the sample. 50 μL of medium without serum, 42 μL of liposomes (1 mg/mL), and 3 μL DNA (250 μg/mL) + 1 μL oligonucleotide−fluorescein (250 μg/mL) were mixed. The complex formation was achieved by adding Ca^{2+} (final concentration 15 mM).

The cells were incubated with lipoplexes in a media without serum for 2 or 4 h to permit transient transfection. Afterward, the complex-containing suspension was removed and replaced by 200 μL of the complete growth medium. GFP expression was analyzed after 48 h and measured with flow cytometry. Lipofectamine transfections were performed, as per the manufacturer's instructions, using 2 μL of lipofectamine and an identical amount of plasmid 4 μL (250 ng/μL).

Flow Cytometry Studies. Cells were assayed for GFP expression 48 h after being exposed to the transfection agents. Cells in the well plates were rinsed with PBS, treated using 100 μL trypsine EDTA, and incubated for 5 min (37 °C) in 5% CO_2 incubator. The cell suspension was then diluted to 200 μL using PBS, pH 7,4. The cells were then assayed for expression of GFP. GFP expression was analyzed using a FACS Canto dual laser flow cytometry.

Toxicity Assay. The toxicity of the thymidine-3′-(1,2-diacyl-*sn*-glycero-3-phosphate) (compounds **1**, **2**, **3**) for the cells was determined 48 h after exposure to the transfection agents using the MTS tetrazolium. Cells in the well plates were treated using 50 μL of MTS tetrazolium and incubated for 2−4 h (37 °C) in a 5% CO_2 incubator. Once coloring developed, the absorbance of 200 μL of each sample was analyzed at 490 nm.

X-ray Diffraction. SAXS measurements were carried out on the Bruker Nanostar apparatus at the Centre de Recherche Paul Pascal (Pessac, France). The wavelength of the incident beam was $\lambda = 1.54$ Å, and the sample-to-detector distance was 0.25 m (q range investigated from 0.05 $Å^{-1}$ to 0.6 $Å^{-1}$). The diffraction patterns were recorded by a 2D multiwire gas-filled detector. Anionic membranes formulated with the negatively charged nucleolipids (NL) and the neutral lipid (DOPE) were mixed with deionized water to obtain solutions with a concentration of 10 mg/mL. A plasmid−DNA solution in water was prepared (300 mg/mL) and added to the membrane solution in order to get the molar ratio NL/DNA = 2. The complex formation was achieved by adding divalent salt ($CaCl_2$ $2H_2O$, 200 mM) with a final concentration $[Ca^{2+}] = 15$ mM. The suspension was held in a 1.5 mm size glass capillary and then centrifuged for a few minutes in order to locally concentrate the complex on the bottom of the capillary. The capillary was sealed and inserted in a sample holder at room temperature (25 °C). The collected 2D diffraction spectra were angularly integrated to get a 1D intensity vs q pattern.

RESULTS AND DISCUSSION

In this study, we hypothesized that anionic lipid−nucleic acid complexes could take advantage of lipid polar head groups featuring nonionic interactions such as hydrogen-bonding and base $\pi-\pi$ stacking. These additional interactions would likely influence the lipid−DNA associations and enhance the transfection efficacy of the natural anionic lipids previously reported (*7*). To demonstrate this hypothesis, the following constituting natural building blocks were selected to prepare the anionic nucleotide based lipids: thymidine (nucleotide polar head) and 1,2-diacyl-*sn*-glycerol (lauroyl, myristoyl, and palmitoyl acyl chains). Both moieties, the diacyl-*sn*-glycerol motif and the thymidine as a nucleotide polar head, were selected on the basis of their natural occurrence in biological systems. In this contribution, we report the synthesis of a family of thymidine-3′-(1,2-diacyl-*sn*-glycero-3-phosphate), the formation of lipoplexes between DNA and nucleotide based lipids in the presence of Ca^{2+}, SAXS studies, cytotoxicity, and successful *in vitro* gene delivery.

Synthesis. In order to evaluate the impact of the lipid structure on the transfection properties, a series of nucleotide derivatives composed of thymidine 3′-phosphates bearing natural 1,2-diacyl-*sn*-glycerol as hydrophobic building blocks was prepared. Although, to the best of our knowledge, nucleoside-5′-monophosphate lipids structures have been reported by Baglioni, Berti, and co-workers (*31*, *32*), no double-chain nucleoside-3′-monophosphate amphiphile has been described so far. The double-chain nucleoside-3′-monophosphate lipids were synthesized by using a recently published (*37*) synthetic approach for single-chain nucleolipids (Scheme 2). Coupling reactions between 5′-DMT protected commercial phosphoramidite (5′-dimethoxytrityl-2′-deoxythymidine,3′-[(2-cyanoethyl)-*N*,*N*-diisopropyl)]-phosphoramidite) and lipophilic 1,2-diacyl-*sn*-glycerol were undertaken in acidic conditions (tetrazole) similar to those found in oligonucleotide synthesis. The resulting phosphite intermediates were then oxidized with iodine in a THF/pyridine/water mixture at room temperature under argon to provide the

Scheme 2. Synthetic Route to Anionic Nucleotide−Lipids[a]

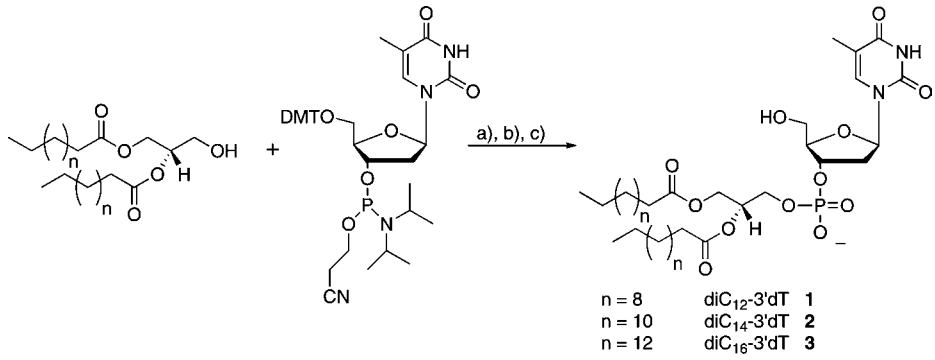

[a] (a) 0.45 M tetrazole in acetonitrile RT 7 h; (b) 0.02 M I_2 pyidine/H_2O/THF RT 12 h; (c) 0.1 N HCl.

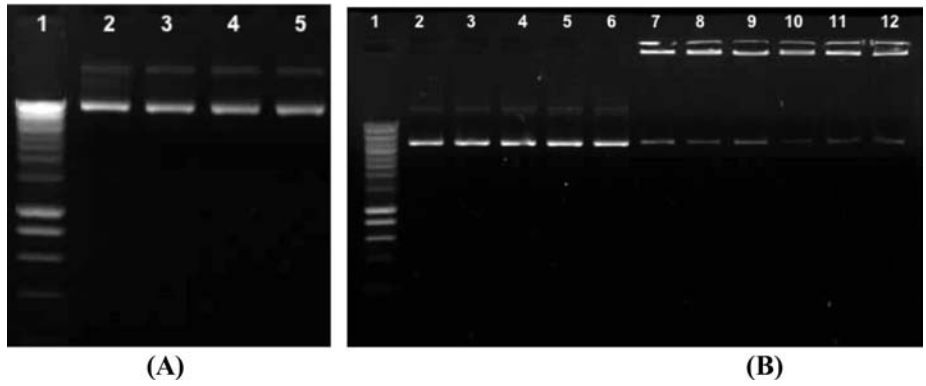

Figure 1. Effect of Ca^{2+} on the electrophoretic mobility of (A) Ca^{2+}−DNA complexes and (B) anionic lipoplexes (anionic liposome−Ca^{2+}−DNA) diC16T/DOPE (mol ratio 10/90). (A) The lanes represent control DNA ladder (1); plasmid DNA (2); and Ca^{2+}−DNA complexes at Ca^{2+} concentrations of 10 mM (3), 30 mM (4), and 50 mM (5). (B) The lanes represent control DNA ladder (1); plasmid DNA (2); plasmid DNA and empty anionic liposomes (3); anionic lipoplexes at Ca^{2+} concentrations of 1, 50, and 100 μM, and 1, 5, 10, 15, 30, and 60 mM (7−12).

cyanoethyl-protected phosphates. Removal of the DMT group led to the production of compounds **1**, **2**, and **3**, which were fully characterized by ^1H, ^{13}C, ^{31}P NMR, and HRMS. The cyanoethyl protecting group was removed via an elimination reaction under basic conditions (TEA). Importantly, the synthetic strategy developed allowed easy access to the expected thymidine-3′-(1,2-diacyl-*sn*-glycero-3-phosphate) in four steps from the commercially available starting materials.

Complexation Studies. Next, to determine whether or not the nucleotide based lipids **1**, **2**, and **3** complex nucleic acids, we performed a standard electrophoresis gel shift assay with plasmid−DNA for the assessment of DNA complexation. Since the lipid polar head bears an anionic charge, just as was the case for the previous anionic delivery vectors (*7*), the formation of lipid−DNA complexes was evaluated in the presence of different concentrations of divalent calcium. Standard agarose gel electrophoresis revealed two bands for naked DNA (supercoil, nonsupercoil forms, high and low mobility, respectively) (Figure 1A, lane 2). As a control, the addition of Ca^{2+} to the plasmid DNA samples in the absence of anionic liposomes did not affect the mobility of the plasmid DNA (Figure 1A, lanes 3−5). On the contrary, the presence of anionic liposomes and Ca^{2+} dramatically affected plasmid−DNA migration (Figure 1B). On the basis of the hypothesis that the nucleolipid/DNA stability depends on calcium concentration, we also evaluated the threshold Ca^{2+} concentration for complexation. Interestingly, we found that nucleolipid−DNA complexes are observed above a concentration of 1 mM (Figure 1B, lane 7), which is higher than the intracellular calcium concentration ([Ca^{2+}] 1 μM) indicating that the lipoplexes can release the DNA inside the cells. Next, we investigated the optimum ratio of nucleolipid−DOPE. As shown in Figure 2, based upon the lack of free DNA, an optimal ratio of 10/90 (diC16T/DOPE) was determined.

Nucleolipid−Ca^{2+}−DNA Lipoplexes. The hydrated mixtures of DOPE/diC$_{16}$-3′-dT in aqueous solution were investigated without plasmid−DNA by transmission electronic microscopy (TEM) and zetasizer (3000 HAS Malvern instrument). As was expected, the extruded mixtures were found to self-assemble at room temperature into liposome-like structures in aqueous solutions. Under these conditions, at room temperature, the DOPE/diC$_{16}$-3′-dT were in a "fluid" state. As seen in TEM images (Figure 3), in the absence of both nucleic acids and Ca^{2+} and after extrusion with a 50 nm filter, different sizes of liposomes ranging from 40 to 80 nm were observed. These sizes are consistent with the average sizes of the same samples measured by dynamic light scattering (hydrodynamic diameter: 84 nm polydispersity index 0.38). Interestingly, in the presence of DNA and Ca^{2+}, the mean aggregates size was increased from 84 to 128 nm, indicating the formation of larger aggregates. Dried samples of these aggregates investigated by TEM revealed objects possessing a nonvesicular morphology (data not shown). It is noteworthy that no modification of size was noticed for the samples containing liposomes in the presence of DNA without Ca^{2+}.

It should also be noted that the presence of anionic nucleolipids in DOPE/diC$_{16}$-3′-dT mixtures enhanced the hydration phenomenon during the preparation of liposomes, which resulted in much more homogeneous colloidal suspensions compared to DOPE/DPPA samples. This unexpected hydration behavior is likely due to the hydrophilic nucleotide polar head inserted in the molecular structure.

SAXS Studies. Next, to further characterize the molecular organization within the DOPE−NL−Ca^{2+}−DNA lipoplexes, small-angle X-ray scattering (SAXS) experiments were performed. Figure 4 shows the diffraction patterns of the DOPE−DPPA samples with (curve 2) and without (curve 1)

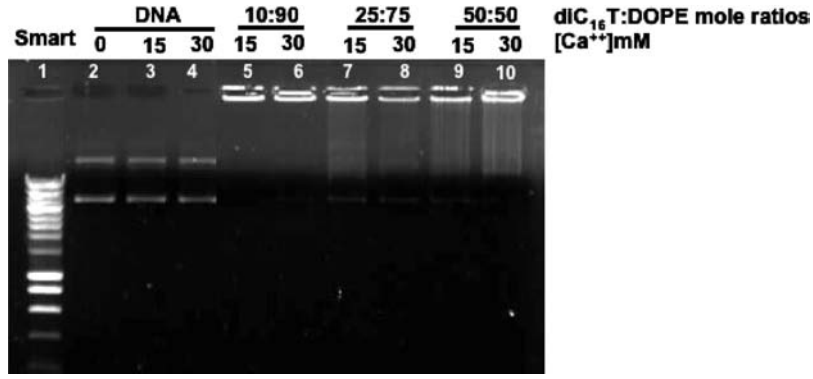

Figure 2. Electrophoretic mobility of different formulations and Ca^{2+} concentrations. The lanes represent control DNA ladder (1); plasmid DNA with different concentrations of Ca^{2+} (2−4); lipoplexes (anionic nucleotide lipid−Ca^{2+}−DNA) diC16T/DOPE mol ratios of 10/90 (5,6), 25/75 (7,8), and 50/50 (9,10) with $[Ca^{2+}] = 15$ and 30 mM, respectively.

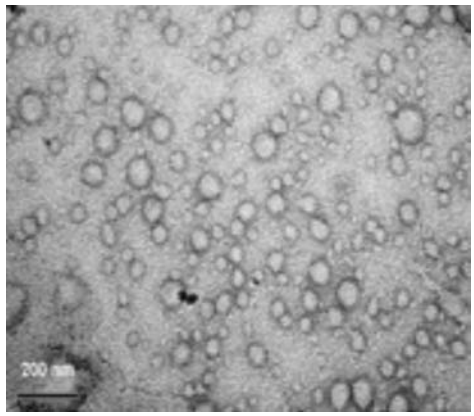

Figure 3. Transmission electron microscopic (TEM) images of anionic DOPE/diC$_{16}$-3′-dT liposomes (mol ratio of 10/90) in water with uranyl acetate (1%) as negative stainer. Scale bars, 200 nm.

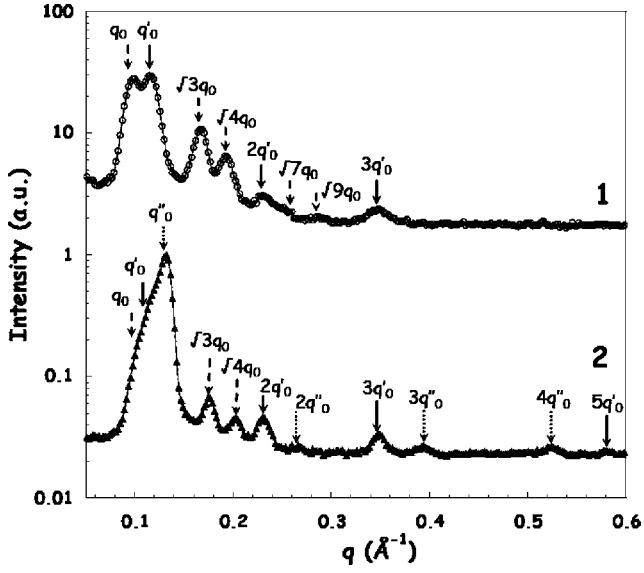

Figure 4. SAXS patterns of DOPE−DPPA−Ca^{2+} system without plasmid DNA (curve 1) and with plasmid DNA (curve 2).

the plasmid DNA. For the system without plasmid DNA, two distinct sets of peaks are identified. A 2D hexagonal lattice (q_0) with a unit cell spacing of $a = 72.6$ Å can be indexed. This pattern corresponds to the well-known 2D columnar inverted hexagonal phase (H_{II}). The second set of Bragg peaks can be attributed to a lamellar structure with a stacking period $d = 54$ Å. Bragg peaks up to the fifth and third order are observed for

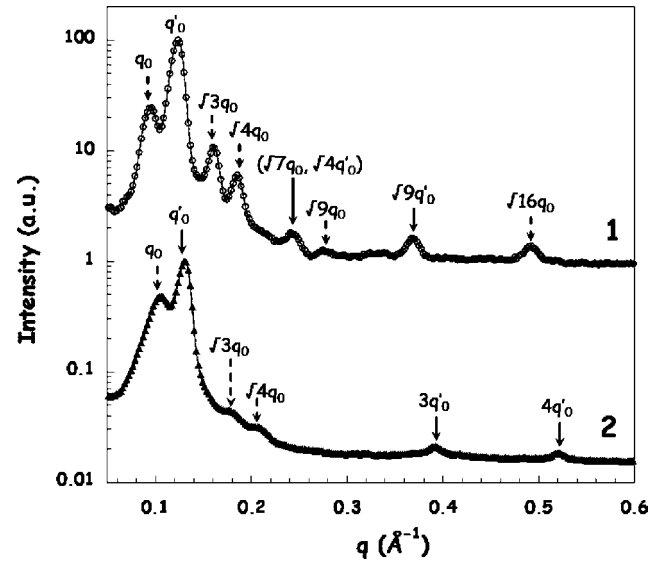

Figure 5. SAXS patterns of DOPE−diC$_{16}$-3′-dT−Ca^{2+} system without plasmid DNA (curve 1) and with plasmid DNA (curve 2).

the hexagonal and lamellar phases, respectively. The lamellar structure unambiguously corresponds to the lamellar phase observed (data not shown) for the pure DPPA system. On the other hand, the 2D hexagonal lattice seems to be very similar to that noticed for the pure DOPE system (*42*). These results suggest a very weak miscibility of the DPPA lipid in the DOPE membrane. The sample with plasmid DNA exhibits a more complicated pattern (empty circles) with a three-phase coexistence domain. We can identify the two phases previously observed for the free plasmid DNA system with a 2D hexagonal lattice (q_0) $a = 71.8$ Å and with a lamellar structure (q'_0) with a stacking period $d = 54$ Å. Interestingly, in the presence of plasmid DNA, a new lamellar phase (q''_0) can be indexed with a lamellar periodicity $d = 48$ Å. This new lamellar phase can be identified as lamellar complex made from DNA Ca^{2+} and DOPE (data not shown).

Figure 5 shows the diffraction patterns of the DOPE−diC$_{16}$-3′-dT samples with (curve 2) and without (curve 1) the plasmid DNA. For the system without plasmid DNA, two distinct sets of peaks are identified which can be indexed on a 2D hexagonal lattice (q_0 and q'_0) with different unit cell spacing, namely, $a = 77$ Å and $a' = 59$ Å. The sample with plasmid DNA also reveals two sets of peaks. The first set of peaks (q_0) corresponds to a H_{II} phase with a unit cell spacing with $a = 69.1$ Å. The second set of peaks (q'_0) can be indexed for a lamellar phase with a stacking period $d = 48$ Å. This lamellar structure is similar to that observed in the DOPE−DPPA−plasmid DNA sample. The

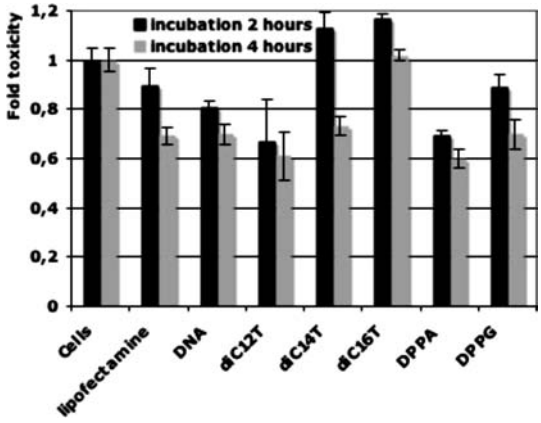

Figure 6. Cytotoxicities of anionic lipoplexes composed of nucleolipids ($diC_{12,14,16}T$), DPPA or DPPG and DOPE (10:90 mol ratio)−Ca^{2+} (15 mM)−DNA compared to lipofectamine and DNA with 15 mM Ca^{2+} and untreated cells.

differences for the structural parameters observed for the samples with and without plasmid DNA strongly suggest the presence of DNA inside the two phases H_{II} and L_α and a good miscibility of DOPE with the nucleotide lipid (diC_{16}-3′-dT). These results prove that the structure of the various complexes is formulation-dependent. In particular, the presence of the nucleotide lipid enhances the existence of a 2D inverse hexagonal phase (a = 69.1 Å) which does not occur in the nucleotide free lipid system (DOPE−DPPA−plasmid−DNA−Ca^{2+}), while the lamellar phase with a stacking period d = 48 Å is present in both systems.

Cell Proliferation. The effect on the proliferation of mammalian cell lines of the nucleolipid−Ca^{2+}−DNA lipoplexes was compared to a commercially available transfectant, lipofectamine and Ca^{2+}-DNA binary mixtures. The *in vitro* lipoplex cytotoxicity was evaluated against Hek cells using an MTS assay. The proliferation of cells is expressed as percentages of nontreated cells. As shown in Figure 6, after 2 h of incubation, the proliferation of Hek cells was not affected in the presence of myristoyl (DOPE/diC_{14}-3′-dT-Ca^{2+}-DNA) or palmitoyl derivatives (DOPE/diC_{16}-3′-dT-Ca^{2+}-DNA), since the cellular growth responses were essentially higher or the same as the negative controls (nontreated Hek cells). Note, furthermore, that no toxicity was observed even after 4 h of incubation for the palmitoyl derivative. In contrast, Hek cell viability decreased in the presence of lipofectamine, DOPE/DPPG−Ca^{2+}−DNA, and Ca^{2+}−DNA mixtures for both 2 and 4 h of incubation. The cytotoxic effect was much stronger for ternary mixtures featuring non-nucleotide lipid (DOPE/DPPA−Ca^{2+}−DNA) than for dipalmitoyl nucleolipid (diC_{16}-3′-dT), because the cell viability was reduced by 30% and 40% for 2 and 4 h, respectively. A similar cytotoxicity effect was observed with DOPE/diC_{12}-3′-dT-Ca^{2+}-DNA samples, indicating that an optimal chain length of C_{16} is required to avoid toxicity. Toxic effects of dilauroyl derivatives were previously reported for cationic lipids bearing 1,3-diamino-2-propanol backbone (*43*).

Fluorescence Microscopy Studies. We next used fluorescence microscopy to determine whether the DOPE/diC_{16}-3′-dT-Ca^{2+}-DNA complexes penetrated the cultured eukaryotic cells. For this purpose, DOPE/diC_{16}-3′-dT liposomes and a mixture of nucleic acids containing plasmid DNA (0.75 μg) and oligonucleotide−fluorescein (0.25 μg) were mixed. The complex formation was realized by adding Ca^{2+} (final concentration 15 mM). Hek cells were incubated later with the fluorescein-labeled complexes for 2 h at 37 °C. As shown in Figure 7 (left), the fluorescein-labeled complexes were internalized at 37 °C, indicating that anionic lipoplexes can transfer DNA into cells.

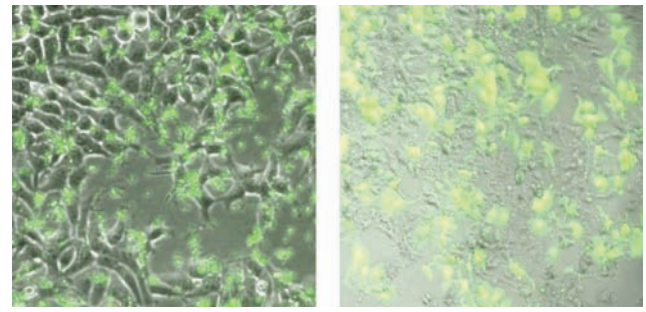

Figure 7. Fluorescence microscopy images of anionic lipoplexes ([Ca^{2+}] = 15 mM) carrying DNA fluorescein labeled (left) and transfected Hek cells (GFP expression) (right).

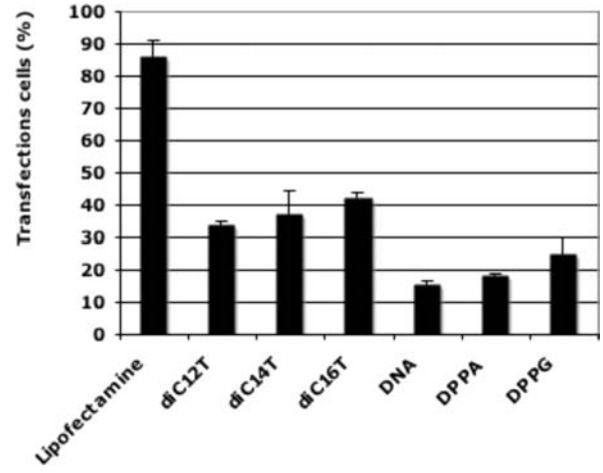

Figure 8. Transfection efficiencies of anionic lipoplexes composed of nucleolipids/DOPE (10:90 mol ratio) ($diC_{12,14,16}T$), DPPA/DOPE (10:90 mol ratio)−Ca^{2+}(15 mM)−DNA), DPPG/DOPE (10:90 mol ratio)−Ca^{2+}(15 mM)−DNA), compared with lipofectamine and DNA with 15 mM Ca^{2+}.

It is important to note that Hek cells incubated in the presence of anionic lipoplexes—prepared without fluorescein-labeled oligonucleotides—(DOPE/diC_{16}-3′-dT-Ca^{2+}-DNA), where the DNA is an expression vector (pEGFP) encoding GFP, confirm the release and the expression of the anionic lipoplexes from the GFP-plasmid DNA. (Figure 7 right).

Transfection. To investigate the efficiency of the anionic nucleotide based lipids to deliver DNA into cells, we performed a transient transfection assay of mammalian cell lines (Hek 293 human embryo kidney). The transfected DNA is an expression vector (pEGFP) encoding GFP, which enables the detection of fluorescence by FACS. Different formulations of anionic nucleolipids were mixed with 1 μg of pEGFP, and then lipoplexes were incubated with Hek cells. Single-cell suspensions were analyzed by FACS Canto dual laser flow cytometry. The GFP negative and positive gates were defined using the control experiment carried out in the absence of lipoplex. In each experiment, 50 000 cells were sorted, and the results are shown in Figure 8. Anionic lipoplexes are efficient for transfection at a concentration of liposomes (42 μg, DOPE/diC_n-3′-dT-Ca^{2+}-DNA) per well. As control experiments, the transfection capability of lipofectamine−DNA and calcium−DNA mixtures were evaluated. As expected for this cell line, lipofectamine appeared to be the most efficient transfecting reagent, whereas calcium salts alone remained less effective in transfecting EGFP. Likewise, with only 18% and 24% of transfection after 2 h of incubation, the DPPA−Ca^{2+}−DNA and DPPG−Ca^{2+}−DNA lipoplexes, respectively, exhibited weak transfecting activity. On the contrary, the nucleolipids exhibited higher transfecting efficacies. With a level of transfection higher

than 40%, the DOPE/diC$_{16}$-3′-dT-Ca^{2+}-DNA lipoplex shows the best efficacy among the anionic systems. Note that this level was increased to 55% after incubating the Hek cells in the presence of this complex for 4 h (data not shown). An explanation for the lower activity of dilauroyl derivatives could be found in the early work of Minsky and co-workers (*44*). They have suggested that fatty acid chains of 12 carbons are not long enough to create the hydrophobic environment required for efficient DNA compaction. Therefore, it appears that the anionic nucleotide lipids are more efficient compared to both DPPA−Ca^{2+}−DNA and Ca^{2+}−DNA transfecting systems, demonstrating that the nucleotide moiety influences the lipid−DNA associations and enhances the transfection efficacy of the natural anionic DPPA lipid.

CONCLUSION

In this study, we synthesized a new series of nucleotide-based lipids featuring thymidine-3′-monophosphate as nucleotide and 1,2-diacyl-*sn*-glycerol as hydrophobic moieties for *in vitro* delivery of nucleic acids. The amphiphilic structures were prepared in three steps from commercially available starting materials: 1,2-diacyl-*sn*-glycerols and 2′-deoxythymidine-3′phosphoramidite. Gel electrophoresis experiments indicate that nucleotide-based lipid−DNA complexes are observed above a concentration of 1 mM, which is higher than the intracellular calcium concentration ([Ca^{2+}] 1 μM) indicating that DNA can be released inside the cells. Electronic microscopy and dynamic light scattering investigations reveal that extrusion of DOPE −diC$_{16}$-3′-dT mixtures provide homogeneous liposomes, whereas larger aggregates are observed in the presence of DNA and Ca^{2+} confirming the formation of complexes.

SAXS studies indicate that the structure of the complexes is strongly dependent on the formulation. Different multiphase systems can be obtained for the DOPE−diC$_{16}$-3′-dT and DOPE−DPPA samples with and without plasmid DNA. The transfection experiments carried out on mammalian Hek cell lines clearly demonstrate that the nucleotide moiety enhances the transfection efficacy of the natural anionic DPPA and DPPG lipids. The SAXS studies also indicate that the enhancement in transfection is likely due to the presence of the 2D columnar inverted hexagonal phase (H_{II}) with a unit cell parameter a = 69.1 Å, which does not occur in the nucleotide free lipid system (DOPE−DPPA). These results confirm the interest of using anionic species (*45*) such as nucleotide lipids in formulations to optimize transfection efficacy.

The issue of transfection reagent cytotoxicity is particularly important in protocols that attempt to modulate gene function *in vitro* an/or *in vivo*. As nontoxic and efficient transfection reagents, the anionic nucleotide lipids presented in this work offer an alternative to cationic species, which can be, in some instances, especially toxic (*46*). These investigations further support the need for the synthesis and evaluation of nucleotide-based lipids as nucleotide acids delivery vehicles. *In fine*, nucleotide-based lipids further extend the possibilities of modulating the interactions between nucleic acids and lipids. Depending upon the nature of both partners, nucleotide lipids may offer new alternatives to lipids, and could be exploited in the case of small therapeutic oligonucleotides, for example.

ACKNOWLEDGMENT

This research was supported by the Region d'Aquitaine. P.B. acknowledges financial support from the Army Research Office. The authors thank the SERCOMI Centre for technical assistance during TEM observations and G. Sigaud for physicochemical experiments.

LITERATURE CITED

(1) Guinn, B. A., and Mulherkar, R. (2008) International progress in cancer gene therapy. *Cancer Gene Ther. 12*, 765–75.
(2) El-Aneed, A. (2003) An overview of current delivery systems in cancer gene therapy. *J. Controlled Release 94*, 1–14.
(3) Patil, S. D., Rhodes, D. G., and Burgess, D. J. (2005) DNA-based therapeutics and DNA delivery systems: a comprehensive review. *AAPS J. 7*, 61–77.
(4) Felgner, P. L., Gadek, T. R., Holm, M., Roman, R., Chan, H. W., Wenz, M., Northrop, J. P., Ringold, G. M., and Danielsen, M. (1987) Lipofection: a highly efficient, lipid-mediated DNA-transfection procedure. *Proc. Natl. Acad. Sci. U.S.A. 84*, 7413–7.
(5) Behr, J. P., Demeneix, B., Loeffler, J. P., and Perez-Mutul, J. (1989) Efficient gene transfer into mammalian primary endocrine cells with lipopolyamine-coated DNA. *Proc. Natl. Acad. Sci. U.S.A. 86*, 6982–6.
(6) Caracciolo, G., Pozzi, D., Caminiti, R., Marchini, C., Montani, M., Amici, A., and Amenitsch, H. (2008) Enhanced transfection efficiency of multicomponent lipoplexes in the regime of optimal membrane charge density. *J. Phys. Chem. B 112*, 11298–11304.
(7) Patil, S. D., Rhodes, D. G., and Burgess, D. J. (2004) Anionic liposomal delivery system for DNA transfection. *AAPS. J. 6*, e29.
(8) Putnam, D. (2006) Polymers for gene delivery across length scales. *Nat. Mater. 5*, 439–451.
(9) Dan Luo, W., and Mark, Saltzman. (2000) Synthetic DNA delivery systems. *Nat. Biotechnol. 18*, 33–37.
(10) Bello-Roufaï, M., Lambert, O., and Pitard, B. (2007) Relationships between the physicochemical properties of an amphiphilic triblock copolymers/DNA complexes and their intramuscular transfection efficiency. *Nucleic Acids Res. 35*, 728–39.
(11) Pomel, C., Leborgne, C., Cheradame, H., Scherman, D., Kichler, A., and Guegan, P. (2008) Synthesis and evaluation of amphiphilic poly(tetrahydrofuran-β-ethylene oxide) copolymers for DNA delivery into skeletal muscle. *Pharm. Res. 25*, 2963–71.
(12) Pitard, B., Pollard, H., Agbulut, O., Lambert, O., Vilquin, J. T., Cherel, Y., Abadie, J., Samuel, J. L., Rigaud, J. L., Menoret, S., Anegon, I., and Escande, D. (2002) A nonionic amphiphile agent promotes gene delivery in vivo to skeletal and cardiac muscles. *Hum. Gene Ther. 13*, 1767–75.
(13) Neu, M., Fischer, D., and Kissel, T. (2005) Recent advances in rational gene transfer vector design based on poly(ethylene imine) and its derivatives. *J. Gene. Med. 7*, 992–1009.
(14) Midoux, P. and Pichon, C. (2002) Peptide-based gene delivery systems. In *Pharmaceutical Perspectives of Nucleic Acid-Based Therapeutics*, (Kim, S. W., Ed.) pp 334−366, Taylor & Francis, London.
(15) Zhou, J., Wu, J., Hafdi, N., Behr, J. P., Erbacher, P., and Peng, L. (2006) PAMAM dendrimers for efficient siRNA delivery and potent gene silencing. *Chem. Commun. 22*, 2362–4.
(16) Mennesson, E., Erbacher, P., Kuzak, M., Kieda, C., Midoux, P., and Pichon, C. (2006) DNA/cationic polymer complex attachment on a human vascular endothelial cell monolayer exposed to a steady laminar flow. *J. Controlled Release 114*, 389–97.
(17) Yuba, E., Kojima, C., Sakaguchi, N., Harada, A., Koiwai, K., and Kono, K. (2008) Gene delivery to dendritic cells mediated by complexes of lipoplexes and pH-sensitive fusogenic polymer-modified liposomes. *J. Controlled Release 130*, 77–83.
(18) Mignet, N., Richard, C., Seguin, J., Largeau, C., Bessodes, M., and Scherman, D. (2008) Anionic pH-sensitive pegylated lipoplexes to deliver DNA to tumors. *Int. J. Pharm. 361*, 194–201.
(19) Chabaud, P., Camplo, M., Payet, D., Serin, G., Moreau, L., Barthélémy, P., and Grinstaff, M. W. (2006) Cationic nucleoside lipids for gene delivery. *Bioconjugate Chem. 17*, 466–472.
(20) Banchelli, M., Berti, D., and Baglioni, P. (2007) Molecular recognition drives oligonucleotide binding to nucleolipid self-assemblies. *Angew. Chem., Int. Ed. 46*, 3070–3.

(21) Ceballos, C., Prata, C. A., Giorgio, S., Garzino, F., Payet, D., Barthélémy, P., Grinstaff, M. W., and Camplo, M. (2009) Cationic nucleoside lipids based on a 3-nitropyrrole universal base for siRNA delivery. *Bioconjugate Chem. 20*, 193–6.

(22) Mével, M., Neveu, C., Gonçalves, C., Yaouanc, J. J., Pichon, C., Jaffrès, P. A., and Midoux, P. (2008) Novel neutral imidazole-lipophosphoramides for transfection assays. *Chem. Commun. 27*, 3124–6.

(23) Prata, C. A., Li, Y., Luo, D., McIntosh, T. J., Barthélémy, P., and Grinstaff, M. W. (2008) A new helper phospholipid for gene delivery. *Chem. Commun. 13*, 1566–8.

(24) Prata, C. A., Zhao, Y., Barthélémy, P., Li, Y., Luo, D., McIntosh, T. J., Lee, S. J., and Grinstaff, M. W. (2004) Charge-reversal amphiphiles for gene delivery. *J. Am. Chem. Soc. 126*, 12196–12197.

(25) Leblond, J., Mignet, N., Largeau, C., Seguin, J., Scherman, D., and Herscovici, J. (2008) Lipopolythiourea transfecting agents: lysine thiourea derivatives. *Bioconjugate Chem. 19*, 306–14.

(26) Prata, C. A., Zhang, X. X., Luo, D., McIntosh, T. J., Barthélémy, P., and Grinstaff, M. W. (2008) Lipophilic peptides for gene delivery. *Bioconjugate Chem. 19*, 418–20.

(27) McManus, J. J., Rädler, J. O., and Dawson, K. A. (2003) Does calcium turn a zwitterionic lipid cationic? *J. Phys. Chem. B 107*, 9869–9875.

(28) Arigon, J., Prata, C. A., Grinstaff, M. W., and Barthélémy, P. (2005) Nucleic acid complexing glycosyl nucleoside-based amphiphile. *Bioconjugate Chem. 16*, 864–72.

(29) Moreau, L., Barthélémy, P., Li, Y., Luo, D., Prata, C. A., and Grinstaff, M. W. (2005) Nucleoside phosphocholine amphiphile for in vitro DNA transfection. *Mol. Biosyst. 1*, 260–264.

(30) Barthélémy, P. (2009) Nucleoside-based lipids at work: From supramolecular assemblies to biological applications. *C. R. Chimie 12*, 171–179, and references herein.

(31) Milani, S., Bombelli, F. B., Berti, D., and Baglioni, P. (2007) Nucleolipoplexes: a new paradigm for phospholipid bilayer-nucleic acid interactions. *J. Am. Chem. Soc. 129*, 11664–5.

(32) Milani, S., Berti, D., Dante, S., Hauss, T., and Baglioni, P. (2009) Intercalation of single-strand oligonucleotides between nucleolipid anionic membranes: a neutron diffraction study. *Langmuir 25*, 4084–4092.

(33) Barthélémy, P., Lee, S. J., and Grinstaff, M. W. (2005) Supramolecular assemblies with DNA. *Pure Appl. Chem. 77*, 2133–2148.

(34) Moreau, L., Barthélémy, P., El Maataoui, M., and Grinstaff, M. W. (2004) Supramolecular assemblies of nucleoside phosphocholine amphiphiles. *J. Am. Chem. Soc. 126*, 7533–7539.

(35) Barthélémy, P., Prata, C. A., Filocamo, S. F., Immoos, C. E., Maynor, B. W., Hashmi, S. A., Lee, S. J., and Grinstaff, M. W. (2005) Supramolecular assemblies of DNA with neutral nucleoside amphiphiles. *Chem. Commun. 10*, 1261–1263.

(36) Moreau, L., Ziarelli, F., Grinstaff, M. W., and Barthélémy, P. (2006) Self-assembled microspheres from f-block elements and nucleoamphiphiles. *Chem. Commun. (Camb.) 15*, 1661–1663.

(37) Campins, N., Dieudonné, P., Grinstaff, M. W., and Barthélémy, P. (2007) Nanostructured assemblies from nucleotide-based amphiphiles. *New J. Chem. 31*, 1928–1934.

(38) Gissot, A., Camplo, M., Grinstaff, M. W., and Barthélémy, P. (2008) Nucleoside, nucleotide and oligonucleotide based amphiphiles: a successful marriage of nucleic acids with lipids. *Org. Biomol. Chem. 6*, 1324–1333.

(39) Bestel, I., Campins, N., Marchenko, A., Fichou, D., Grinstaff, M. W., and Barthélémy, P. (2008) Two-dimensional self-assembly and complementary base-pairing between amphiphile nucleotides on graphite. *J. Colloid Interface Sci. 323*, 435–440.

(40) Moreau, L., Camplo, M., Wathier, M., Taib, N., Laguerre, M., Bestel, I., Grinstaff, M. W., and Barthélémy, P. (2008) Real time imaging of supramolecular assembly formation via programmed nucleolipid recognition. *J. Am. Chem. Soc. 130*, 14454–14455.

(41) Srinivasan, C., and Burgess, D. J. (2009) Optimization and characterization of anionic lipoplexes for gene delivery. *J. Controlled Release 136*, 62–70.

(42) Tate, M. W., and Gruner, S. M. (1989) Temperature dependence of the structural dimensions of the inverted hexagonal (HII) phase of phosphatidylethanolamine-containing membranes. *Biochemistry. 28*, 4245–53.

(43) Sheikh, M., Feig, J., Gee, B., Li, S., and Savva, M. (2003) In vitro lipofection with novel series of symmetric 1,3-dialkoylamidopropane-based cationic surfactants containing single primary and tertiary amine polar head groups. *Chem. Phys. Lipids 124*, 49–61.

(44) Ghirlando, R., Wachtel, E. J., Arad, T., and Minsky, A. (1992) DNA packaging induced by micellar aggregates: a novel in vitro DNA condensation system. *Biochemistry. 31*, 7110–9.

(45) Liang, H., Harries, D., and Wong, G. C. (2005) Polymorphism of DNA-anionic liposome complexes reveals hierarchy of ion-mediated interactions. *Proc. Natl. Acad. Sci. U.S.A. 102*, 11173–8.

(46) Masotti, A., Mossa, G., Cametti, C., Ortaggi, G., Bianco, A., Grosso, N. D., Malizia, D., and Esposito, C. (2008) Comparison of different commercially available cationic liposome-DNA lipoplexes: Parameters influencing toxicity and transfection efficiency. *Colloids Surf., B 68*, 136–44.

BC900163S

Nucleic Acid Therapeutic Carriers with On-Demand Triggered Release

Siddarth Venkatesh,[†] Jacek Wower,*[,‡] and Mark E. Byrne*[,†]

Biomimetic and Biohybrid Materials, Biomedical Devices, and Drug Delivery Laboratories, Department of Chemical Engineering, and Department of Animal Sciences, Auburn University, Auburn, Alabama. Received April 23, 2009; Revised Manuscript Received July 28, 2009

Biohybrid platforms such as synthetic polymer networks engineered from artificial and natural materials hold immense potential as drug and gene delivery vehicles. Here, we report the synthesis and characterization of novel polymer networks that release oligonucleotide sequences via enzymatic and physical triggers. Chemical monomers and acrylated oligonucleotides were copolymerized into networks, and phosphoimaging revealed that 70% of the oligonucleotides were incorporated into the networks. We observed that the immobilized oligonucleotides were readily cleaved when the networks were incubated with the type II restriction enzyme *Bam*HI. The diffusion of the cleaved fragments through the macromolecular chains resulted in relatively constant release profiles very close to zero-order. To our knowledge, this is the first study which harnesses the sequence-specificity of restriction endonucleases as triggering agents for the cleavage and release of oligonucleotide sequences from a synthetic polymer network. The polymer networks exhibited an oligonucleotide diffusion coefficient of 5.6×10^{-8} cm^2/s and a diffusional exponent of 0.92. Sigmoidal temperature responsive characteristics of the networks matched the theoretical melting temperature of the oligonucleotides and indicated a cooperative melting transition of the oligonucleotides. The networks were also triggered to release a RNA-cleaving deoxyribozyme, which degraded a HIV-1 mRNA transcript *in vitro*. To tailor release profiles of the oligonucleotides, we controlled the structure of the macromolecular architecture of the networks by varying their cross-linking content. When incubated with DNase I, networks of cross-linking content 0.15%, 0.22%, and 0.45% exhibited oligonucleotide diffusion coefficients of 1.67×10^{-8}, 7.65×10^{-9}, and 2.7×10^{-9} cm^2/s, and diffusional exponents of 0.55, 0.8, and 0.8, respectively. The modular nature of our platform promises to open new avenues for the creation and optimization of a rich toolbox of novel drug and gene delivery platforms. We anticipate further inquiry into nucleic acid based programmable on-demand switches and modulatory devices of exquisite sensitivity and control.

INTRODUCTION

It is now a well-established paradigm that molecular therapeutics can be used for the pharmacological intervention of many diseases (*1*−*3*). Nucleic acids are emerging as important drug targets and versatile therapeutic agents, because they perform critical enzymatic activities and regulate gene expression (*4*−*6*). Nucleic acids are also attractive for nanotechnology because they can be programmed to bind metals, small organic compounds, nucleic acids, proteins, and even entire cells via SELEX (*7, 8*). Efforts are underway to design novel drug agents such as siRNA cocktails and double-stranded miRNA mimetics and antagonists, that interfere with the processing and functioning of endogenous coding and noncoding transcripts (*9*). Equally imperative is the parallel development of devices and shuttles that enable precise delivery of such novel therapeutics to the diseased tissue or cells at therapeutically relevant concentrations, and with controlled release rates (*10, 11*). Off-targeting, toxicity, reduced *in vivo* potency, and interferon responses are pressing concerns for the clinical viability of novel therapies such as RNAi therapeutics (*12*). Bottom-up synthesis of conjugates of synthetic polymers, lipids, and RNAi therapeutics can lower toxicity and could be remodeled into recognizable epitopes in order to pacify the immune response. These molecular therapeutics could be targeted to specific receptors and markers using their cognate ligands (*13, 14*).

Biohybrid platforms, particularly synthetic polymers engineered from artificial and natural materials, hold immense potential as controlled release vehicles (*15*−*17*). They possess striking properties such as biocompatibility, greater flexibility in their bottom-up design, and well-studied synthetic protocols. Polymer networks synthesized purely from artificial monomers such as methacrylic acid, acrylamide, and N-isopropylacrylamide demonstrate phase or volume transitions on varying pH (*18*), temperature (*19*−*21*), light (*22*), and electric field (*23*−*25*). Conjugates of polymers and biomolecules immobilized within the network transduce either a local physical or ionic stimulus into changes in tertiary structure and controllable macroscopic transitions (*26*−*30*). Novel synthetic networks cross-linked by peptides and recombinant proteins have gained significant attention (*31*−*33*), because they translate temperature- and pH-sensitive biomolecular conformation switches into observable volume transitions at the macromolecular level. In particular, the focus is either on networks whose cross-links are selectively hydrolyzed by enzymes or on chemically cross-linked polymer networks that carry pendant enzyme-sensitive moieties (*32, 34*−*37*). Affinity-based delivery systems consisting of bidentate peptides have been used to sequester proteins within fibrin matrices (*38*−*42*). One domain of the peptide consists of a transglutaminase substrate and facilitates cross-linking of the peptide into the matrix. The other domain has a heparin-binding domain and immobilizes heparin via

* Corresponding authors. Auburn University, Auburn, AL 36849 U.S.A., Tel: (334) 844-2862, Fax: (334) 844-2063, E-mail: byrneme@eng.auburn.edu and wowerja@auburn.edu.

[†] Biomimetic and Biohybrid Materials, Biomedical Devices, and Drug Delivery Laboratories, Department of Chemical Engineering.

[‡] Department of Animal Sciences.

10.1021/bc900187b CCC: $40.75 © 2009 American Chemical Society
Published on Web 08/11/2009

electrostatic interactions. Heparin, in turn, binds various proteins and can be triggered to release them via enzymatic triggers or by passive diffusion. Such a system has been shown to control the release of growth factors such as NGF, BDNF, and NT-3.

Much progress is being made in the development of biohybrid platforms for the intracellular delivery of RNAi therapeutics (*5, 10*). Conventional thinking leans toward the delivery of double-stranded RNAs from which siRNAs are derived by the enzymatic activity of Dicer, the direct delivery of artificial siRNAs, and the construction of miRNA or shRNA mimetics and antagonists (*43*). A variety of strategies to express siRNAs using viral vector-based cassettes have been developed (*44*−*46*). Furthermore, siRNAs have been rendered resistant to nucleases via modifications and have been conjugated to ligands such as folic acid, galactosamine, or transferrin, to enhance specificity (*12, 47*). Respiratory, urogenital, and ocular tissues can take up siRNAs after topical application or direct injection of naked siRNAs alone or in complexes with cationic lipids used for *in vitro* transfection, but most other tissues are refractory to the direct uptake of siRNAs (*48, 49*). Gold nanoparticles of sizes ranging 2−30 nm are readily taken up by cells without eliciting immune responses, although the exact mechanism of uptake remains unclear (*50*−*53*). Thus, biohybrid platforms composed of lipids, polymers, and RNA therapeutics are generating much excitement due to their multiple modalities and selective delivery properties (*17, 54*−*60*).

Branched DNA molecules with strategically programmed sticky ends have been assembled into hydrogels via the action of T4 DNA ligase (*61*). Nucleic acid sequences have also been used to cross-link polymer networks (*62, 63*). What has remained unresolved is whether the vast array of enzymes used for DNA cloning and analysis could be exploited for catalytic activity within synthetic polymer networks. To answer this question, we synthesized and characterized novel synthetic polymer networks that release oligonucleotide sequences in response to physical and enzymatic triggers. To our knowledge, this is the first study which harnesses the sequence-specificity of restriction endonucleases as triggering agents for the cleavage and release of oligonucleotide sequences from a synthetic polymer network. By remodeling our construct to include an anti-HIV deoxyribozyme, i.e., an oligonucleotide sequence bearing catalytic properties, we showed *in vitro* degradation of a HIV-1 Tat/Rev mRNA upon triggered release of the deoxyribozyme from the network. We further tailored the release rates by structurally controlling the macromolecular architecture of the synthetic polymer networks. The modules of our biohybrid platform, i.e., the macromolecular architecture, the oligonucleotide sequences, and the triggering agent can be individually optimized in order to obtain a rich toolbox of novel drug and gene delivery platforms.

EXPERIMENTAL PROCEDURES

Materials. The chemical monomers, acrylamide (AM), bisacrylamide, and 2-hydroxyethylmethacrylate (HEMA), were purchased from Sigma-Aldrich (Milwaukee, WI). Poly(ethylene glycol) (200) dimethacrylate (PEG200DMA) and poly(ethylene glycol) (600) dimethacrylate (PEG600DMA) was purchased from Polysciences, Inc. (Warrington, PA). T4 RNA ligase, DNA polymerase I (Klenow fragment), and restriction enzymes *Bam*HI and *Eco*RI were obtained from New England BioLabs. T4 polynucleotide kinase (3′ phosphatase-free) was purchased from Roche Diagnostics. SUPERase-In was obtained from Ambion. Modified oligonucleotides were synthesized by Operon Biotechnologies. All radiochemicals were purchased from ICN Biochemicals, Inc. Ribonucleoside triphosphates (rNTPs) were from Amersham. NAP-5 columns were from GE Healthcare.

All buffers were prepared according to standard recipes: TE buffer: 10 mM Tris-HCl (pH 7.5) and 1 mM EDTA. PNK buffer: 50 mM Tris-HCl (pH 7.5), 10 mM $MgCl_2$, and 5 mM dithiothreitol. TBE buffer: 100 mM Tris-100 mM H_3BO_4 (pH 8.3) and 2.5 mM EDTA. Hybridization buffer: 10 mM Tris-HCl (pH 7.5) and 5 mM $MgCl_2$. T7 RNA polymerase buffer: 20 mM Tris-HCl (pH 8), 3 mM $MgCl_2$, 5 mM dithiothreitol, and 1 mM spermidine. DNA/RNA extraction buffer: 500 mM CH_3COONH_4, 10 mM $(CH_3COO)_2Mg$, 0.1 mM EDTA, and 0.1% SDS.

***In Vitro* Hybridization and Restriction Enzyme Digestion of Oligonucleotides.** The anchoring 5′ acrydite-modified oligonucleotide (ANC, Figure 1a) and its complementary oligonucleotide (COMP-ANC, Figure 1a) were resuspended to 1 mM final concentration in TE buffer. The COMP-ANC oligonucleotide was labeled at its 5′ end with [γ-^{32}P]ATP and T4 polynucleotide kinase. Reaction mixtures consisted of 2 μL of the oligonucleotide (1 mM), 4.3 μL of TE buffer (pH 7.5), 1 μL of 10X PNK buffer, 2 μL of [γ-^{32}P]ATP (4500 Ci/mmol), and 0.7 μL of enzyme (10 U/μL). After incubation for 30 min at 37 °C, the ^{32}P-labeled oligonucleotide was purified on a denaturing 12% polyacrylamide gel in TBE buffer and 8 M urea, and visualized by autoradiography. The ^{32}P-labeled oligonucleotide was extracted from the gel using 400 μL of DNA/RNA extraction buffer, desalted on a NAP-5 column according to the manufacturer's specifications, and concentrated by freeze−drying in an Integrated SpeedVac System (Savant Instruments, Inc.).

Electrophoretic mobility shift assay was used to confirm annealing of oligonucleotides. Increasing amounts of ANC oligonucleotide (0, 100, 200, 300, and 500 pmoles) were added to aliquots of ^{32}P-labeled COMP-ANC oligonucleotide (5000 cpm). Reaction mixtures consisted of 5 μL of ANC oligonucleotide, 5 μL of COMP-ANC oligonucleotide, and 1.1 μL of 10× hybridization buffer. A negative control reaction mixture consisted of 5 μL of RNase-free water, 5 μL of COMP-ANC oligonucleotide, and 1.1 μL of 10× hybridization buffer. All hybridization reaction mixtures were heated for 3 min at 90 °C, cooled on ice, and analyzed by electrophoresis on a non-denaturing 12% polyacrylamide gel at 4 °C. Annealed oligonucleotides were quantified using Typhoon 9410 phosphoimager and *ImageQuant* software (Amersham Biosciences).

The annealed oligonucleotides were digested with restriction enzyme *Bam*HI for 1 h at 37 °C, as per the manufacturer's instructions. Digestion reactions consisted of 9.4 μL of the annealed oligonucleotides, 1.1 μL of 10× NEBuffer 3, and 0.6 μL of *Bam*HI enzyme. The digested products were fractionated on a non-denaturing 12% polyacrylamide gel and analyzed by autoradiography. Autoradiograms were quantified using Typhoon 9410 phosphoimager and *ImageQuant* software.

Synthesis and Characterization of Networks Conjugated with Oligonucleotides. Poly(AM-*co*-bisacrylamide-*co*-acrylated DNA), poly(AM-*co*-PEG200DMA-*co*-acrylated DNA), poly(HEMA-*co*-PEG600DMA-*co*-acrylated DNA) networks of varying cross-linking content were prepared via redox polymerization at 25 °C in the loading wells of a non-denaturing 12% polyacrylamide gel. Typically, 10 μL of acrylamide and bisacrylamide were copolymerized with 10 μL of the annealed oligonucleotides. When the poly(AM-*co*-PEG200DMA-*co*-acrylated DNA) and poly(HEMA-*co*-PEG600DMA-*co*-acrylated DNA) networks were synthesized, homogeneous mixtures of HEMA and PEG(200/600)DMA were prepared first and then copolymerized with 10 μL of the annealed oligonucleotides. After polymerization, the unreacted annealed oligonucleotides and unhybridized ^{32}P-labeled oligonucleotides were removed by

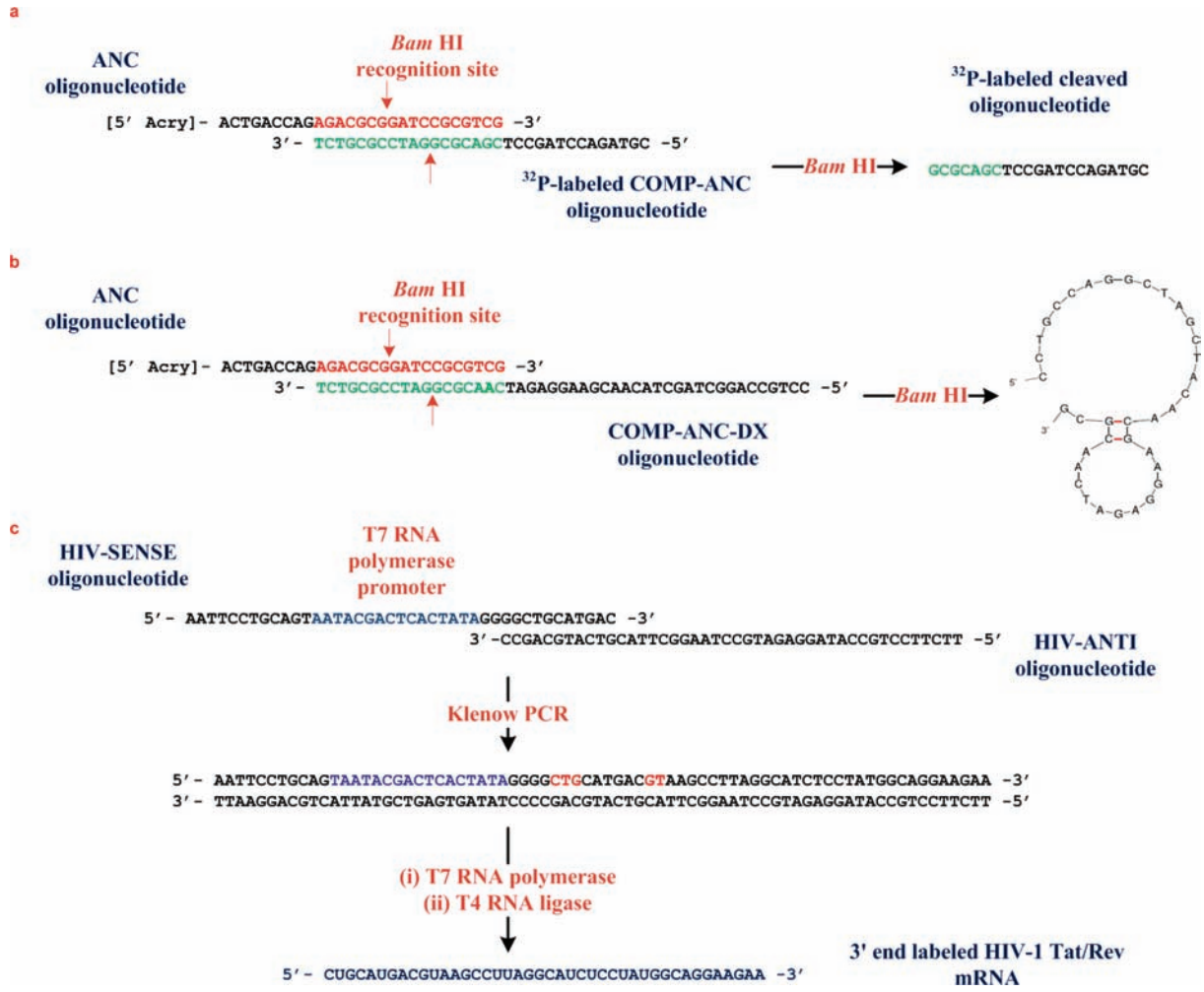

Figure 1. Oligonucleotide constructs used in this study. (a) The annealed ANC and ^{32}P-labeled COMP-ANC oligonucleotides were readily cleaved and yielded ^{32}P-labeled single-stranded fragments when the networks were incubated with *Bam*HI. (b) The annealed ANC and COMP-ANC-DX oligonucleotides released an anti-HIV-1 deoxyribozyme when the networks were incubated with *Bam*HI. (c) *In vitro* transcription and 3′ end labeling of the HIV-1 Tat/Rev mRNA.

electrophoresis. The polymer networks were cut out from the loading wells and incubated in 10 mM Tris-HCl buffer, pH 7.5. The efficiency of the polymerization reaction was determined by scanning the polyacrylamide gel in a Typhoon 9410 phosphoimager.

***In Vitro* Kinetic Release of Oligonucleotides upon Restriction Enzyme and Temperature Triggers.** Kinetic release studies of ^{32}P-labeled oligonucleotides from poly(AM-*co*-PEG200DMA-*co*-acrylated DNA) networks were conducted by incubating the networks with *Bam*HI in NEBuffer 3. The release of the DNA fragments was monitored by Cerenkov counting. The networks were incubated in reaction mixtures of 8 μL of 10× NEBuffer 3, 70 μL of 10 mM Tris-HCl buffer at pH 7.5, and 2 μL of *Bam*HI enzyme. In control experiments, the networks were incubated either without *Bam*HI or with *Eco*RI, a restriction endonuclease that does not cut DNA at the *Bam*HI recognition site. Temperature-responsive release characteristics of melted oligonucleotides were investigated between 30 and 85 °C.

The Stokes radii of the enzymes were determined using a calibration curve of standard proteins of known Stokes' radii: bovine thyroglobulin (85 Å), horse spleen ferritin (61 Å), bovine liver catalase (52.2 Å), rabbit muscle aldolase (48.1 Å), bovine serum albumin (35.5 Å), ovalbumin (30.5 Å), bovine pancreas chymotrypsinogen A (20.9 Å), and bovine pancreas ribonuclease A (16.4 Å).

***In Vitro* Kinetic Release of Oligonucleotides upon Deoxynuclease I Trigger.** Kinetic release studies of ^{32}P-labeled DNA from poly(HEMA-*co*-PEG600DMA-*co*-acrylated DNA) networks were conducted by incubating the networks with DNase I (a nonspecific endonuclease). The release of the cleaved fragments was monitored by Cerenkov counting. The effect of the macromolecular architecture of the polymer network on the diffusion of oligonucleotides was investigated using networks of varying cross-linking content (0.15%, 0.22%, and 0.45%). Cross-linking content was calculated on an acrylate DNA-free basis.

Analysis of the Release of Oligonucleotides upon Enzymatic Triggers. Diffusion of oligonucleotides from a thin polymer network was approximated to a plane sheet. Because geometries with aspect ratios (exposed surface length/thickness) greater than 10 edge effects could be ignored, the problem could be modeled as a one-dimensional process.

By using Fick's Law, the following partial differential equation, initial conditions, and boundary conditions were used to model the one-dimensional planar release from a synthetic polymer network (*64*, *65*).

$$\frac{\partial C}{\partial t} = D\frac{\partial^2 C}{\partial x^2} \qquad (1)$$

$$t = 0 \quad C(x, t) = C_0 \tag{2}$$

$$t > 0 \quad x = 0 \quad \frac{\partial C}{\partial x} = 0 \tag{3}$$

$$t > 0 \quad x = \pm L \quad C = C_s \tag{4}$$

where C_o represents the initial DNA concentration (assumed to be uniform in the homogeneous gel), x represents the distance from the center of the sample to the surface, C_s represents the surface concentration, C is the concentration of the DNA within the gel, D represents a diffusion coefficient independent of position and concentration, t is time, and $2L$ is the thickness of the network.

Using integral transform techniques, the solution of the PDE is given by

$$\frac{C - C_0}{C_s - C_0} = 1 - \frac{4}{\pi}\sum_{n=0}^{\infty}\frac{(-1)^n}{2n+1} \times \exp[-(2n+1)^2\pi^2 D/4L^2]t \cos\frac{(2n+1)\pi x}{2L} \tag{5}$$

If M_t is the total cumulative radioactive counts of DNA released at time t, and M_∞ is the total cumulative radioactive counts of DNA released at infinite time, M_t/M_∞ represents the fractional release of DNA with respect to the value at infinite time.

$$\frac{M_t}{M_\infty} = 1 - \sum_{n=0}^{\infty}\frac{8}{(2n+1)^2\pi^2}\exp[-(2n+1)^2\pi^2 D/4L^2]t \tag{6}$$

The above expression is cumbersome to estimate a value of the diffusion coefficient, and hence, a solution is obtained in terms of error functions.

$$\frac{M_t}{M_\infty} = 4\left[\frac{Dt}{L^2}\right]^{1/2}\left[\frac{1}{\pi^{1/2}} + 2\sum_{n=1}^{\infty}(-1)^n i\,\mathrm{erfc}\left(\frac{nL}{2\sqrt{Dt}}\right)\right] \tag{7}$$

The integral complementary error function vanishes for short times (as $t \rightarrow 0$), and an expression is obtained for short times of diffusion.

$$\frac{M_t}{M_\infty} = 4\left[\frac{Dt}{\pi L^2}\right]^{1/2} \tag{8}$$

As indicated by eq 8, Fickian diffusional release is characterized by an initial $t^{0.5}/L$ dependence of the DNA released. This short time approximation is generally valid for the first 60% of the DNA released. For each synthetic polymer network, the fractional release of DNA *vs* ($t^{0.5}/L$) was plotted and the diffusion coefficient was calculated from the slope.

Most release processes are typically intermediates of Fickian and non-Fickian mechanisms (*66*, *67*). The fractional release of DNA with respect to the value at infinite time

$$\frac{M_t}{M_\infty} = kt^n \tag{9}$$

where k is a constant incorporating characteristics of the synthetic polymer network and DNA, and n is the diffusional exponent, which is indicative of the transport mechanism. For a thin slab, Fickian diffusion is defined by $n = 0.5$, non-Fickian diffusion is defined by $n > 0.5$, and zero-order release is defined by $n = 1$.

Validation of the Platform by the *in Vitro* Degradation of HIV-1 Tat/Rev mRNA. The COMP-ANC oligonucleotide sequence was modified to encode a deoxyribozyme that degrades HIV-1 Tat/Rev mRNA (COMP-ANC-DX, Figure 1b). It was hybridized with the ANC oligonucleotide, and copolymerized with acrylamide and bisacrylamide as described earlier.

The HIV-1 mRNA was synthesized *in vitro* by runoff transcription of synthetic DNA templates (*68*, *69*). The DNA templates were constructed from two DNA strands 41 and 44 nucleotides in length, having an 11-bp overlap region (HIV-SENSE and HIV-ANTI, Figure 1c). HIV-SENSE contained the T7 RNA polymerase promoter and encoded the 5′ region of the mRNA, while HIV-ANTI encoded the complement of the 3′ region. Full-length templates were generated by extension of the annealed HIV-SENSE and HIV-ANTI oligonucleotides with the Klenow fragment of DNA polymerase I. Reaction mixtures consisted of 2 μL of oligonucleotides (100 μM), 5 μL of 10× Klenow buffer (New England BioLabs), 5 μL of dNTPs (4 mM), 37.5 μL of water, and 0.5 μL of the enzyme.

In vitro transcription reaction mixtures consisted of 10 μL of 2× T7 RNA polymerase buffer, 5.1 μL of rNTPs (10 mM), 1.9 μL of water, 2 μL of DNA templates (4 μM), 0.5 μL of T7 RNA polymerase, and 0.5 μL of SUPERase-In (20 U/ μL) for 2 h at 37 °C.

The transcripts were labeled at their 3′ ends using [5′-^{32}P]pCp and T4 RNA ligase (*70*, *71*) and purified on a denaturing 12% polyacrylamide gel. The 3′-end labeled HIV-1 Tat/Rev mRNA was incubated with the poly(AM-*co*-bisacrylamide-*co*-acrylated DNA) networks and *Bam*HI in NEBuffer 3. Reaction products were fractionated on a denaturing 12% polyacrylamide gel and visualized by autoradiography. Autoradiograms were quantified using Typhoon phosphoimager and *ImageQuant* software.

RESULTS AND DISCUSSION

We reasoned that oligonucleotide sequences covalently immobilized in synthetic polymer networks would be amenable to the action of their cognate enzymes used in conventional DNA cloning and gene manipulation (Figure 2a). Observing that chemical cross-linking of modified oligonucleotides into interpenetrating poly(acrylic acid) and poly(allylamine) chains resulted in inefficient gelation and poor mechanical characteristics of polymer networks (data not shown), we designed all oligonucleotide constructs with 5′-acrydite functionality. This would incorporate the oligonucleotides into the backbone of the propagating chains during redox polymerization (*72*).

Our first construct was formed by hybridizing the ANC and ^{32}P-labeled COMP-ANC oligonucleotides (Figure 1a). The double-stranded region of the annealed oligonucleotides contained the recognition site of the restriction endonuclease *Bam*HI. We chose a type II restriction endonuclease as our model enzyme, because these enzymes have tight sequence specificity for DNA (*73*) and are used widely in genomic mapping, DNA cloning, and restriction fragment length polymorphism (RFLP) analysis.

In vitro hybridization conditions were optimized in various concentrations of Tris-HCl buffer (pH 7.5) and water. Hybridization was inefficient in water (Figure 2b, lane 2) and 20 mM Tris-HCl buffer (Figure 2b, lane 3). Magnesium was determined to be critical for hybridization of the oligonucleotides (Figure 2b, lane 4). About 10% of ^{32}P-labeled COMP-ANC oligonucleotides self-annealed. The chemical monomers used for polymer synthesis had no effect on hybridization efficiency (data not shown). The annealed oligonucleotides were readily digested by *Bam*HI (Figure 2c, lane 4). In the absence of *Bam*HI, the annealed oligonucleotides remained stable on ice (Figure 2c, lane 2) and at 37 °C (Figure 2c, lane 3). In control experiments,

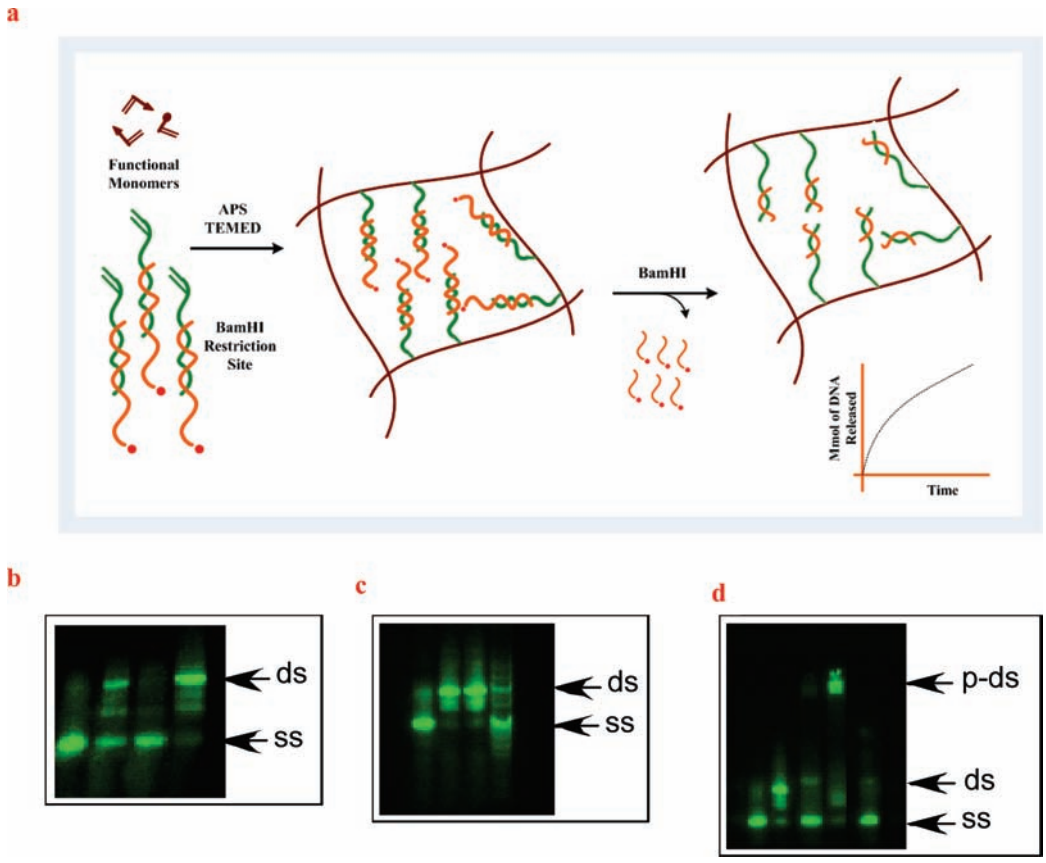

Figure 2. Synthesis and characterization of networks conjugated with oligonucleotides. (a) Redox copolymerization of chemical monomers and annealed oligonucleotides yields novel networks with pendant DNA helices. Restriction enzyme *Bam*HI specifically cleaves the sequence and releases an oligonucleotide from the network. (b) Mg^{2+} ions are critical for efficient hybridization of the acrylated DNA. (c) *Bam*HI cleaves the DNA double helix (lane 4). Single-stranded DNA is shown in lane 1. Single- and double-stranded DNA are denoted ss and ds, respectively. (d) Incorporation of the acrylated oligonucleotides and elution of single- and double stranded DNA by electrophoresis (lane 4). ^{32}P-labeled COMP-ANC elutes due to the absence of ANC oligonucleotide (lane 3). ^{32}P-labeled COMP-ANC (ss) and hybridized duplexes (ds) (lanes 1 and 2, respectively), were used as controls. p-ds is covalently incorporated ds DNA.

we verified that NEBuffer 3 did not disrupt the annealed oligonucleotides.

We synthesized poly(AM-*co*-bisacrylamide-*co*-acrylated DNA), poly(AM-*co*-PEG200DMA-*co*-acrylated DNA), poly(HEMA-*co*-PEG600DMA-*co*-acrylated DNA) networks by copolymerizing the relevant chemical monomers with the annealed oligonucleotides. During the polymerization reaction, unreacted single and double strands get entangled in the propagating macromolecular chains, and interfere with further analysis. The networks were synthesized in the loading wells of non-denaturing 12% polyacrylamide gels, in order to remove unreacted DNA by electrophoresis. A number of control experiments were performed to characterize the process. In order to test if the anchoring of the annealed oligonucleotides was due to the acrydite modification, the ^{32}P-labeled COMP-ANC oligonucleotide was copolymerized with acrylamide and bisacrylamide. The oligonucleotide eluted readily from the network during electrophoresis (Figure 2d, lane 3). On the other hand, the annealed oligonucleotides were polymerized into the backbone of the macromolecular chains (Figure 2d, lane 4). Phosphoimaging revealed that 70% of the annealed oligonucleotides were incorporated into the networks. To conclusively demonstrate that Watson−Crick pairing, and not physical entanglement, is responsible for the incorporation of DNA, acrylamide, and bisacrylamide were copolymerized with the ANC oligonucleotide and a ^{32}P-labeled oligonucleotide whose sequence was not complementary to it. As expected, the ^{32}P-labeled oligonucleotide eluted from the network during electrophoresis, as annealing did not occur between the two strands (Figure 2d, lane 5).

The poly(AM-*co*-bisacrylamide-*co*-acrylated DNA) networks were then incubated with *Bam*HI *in vitro* to evaluate their potential as controlled-release vehicles. We observed that the DNA helices were readily cleaved and diffusion of the ^{32}P-labeled cleaved fragments through the macromolecular chains resulted in relatively constant release profiles very close to zero-order (Figure 3a). The networks exhibited an oligonucleotide diffusion coefficient of 5.6×10^{-8} cm^2/s, and a diffusional exponent of 0.92. The release of the oligonucleotides depends on multiple steps: diffusion of the enzyme; binding, distortion, and cleaving of oligonucleotides by the enzyme; and diffusion of the cleaved oligonucleotide fragments. These processes are reflected in a lag time between the enzyme dosage and the initial detection of the ^{32}P-labeled cleaved oligonucleotides. We hypothesize that the rate-limiting step of the release process is the slow diffusion of the large enzyme molecule within the macromolecular structure.

In control experiments, we evaluated the specificity of restriction endonucleases within the macromolecular architecture of synthetic polymer networks. Incubating the networks in the absence of *Bam*HI did not result in DNA release (Figure 3a). Furthermore, *Eco*RI, a restriction endonuclease which does not recognize the *Bam*HI recognition site, did not trigger DNA release. It is important to note that *Eco*RI (M_r 31 057 Da, Stokes radius of 23.85 Å) has dimensions similar to *Bam*HI (M_r 24 569, Stokes radius of 22.22 Å), and

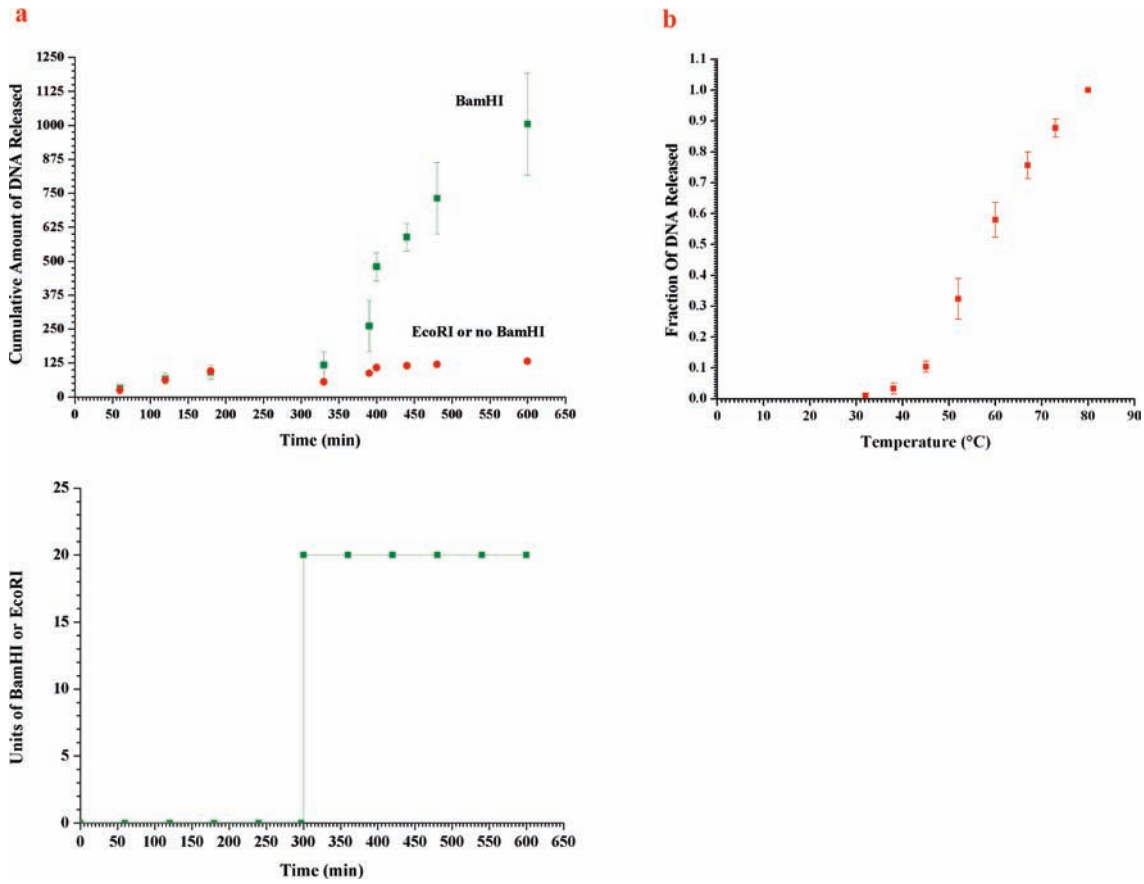

Figure 3. Dynamic tunable release profiles of oligonucleotides from synthetic polymer networks by enzymatic or temperature triggers. (a) Tailored release of oligonucleotides (top panel) by incubating the gels with *Bam*HI (green filled square, lower panel) as compared to incubating in buffer only (red filled circle). (b) Sigmoidal temperature dependent release of DNA (red filled square). $N = 5 \pm$ SD.

that these two globular enzymes are among the most efficient restriction enzymes known. The efficiency of these enzymes is enhanced by flanking sequences, which increase the binding affinity of the enzyme to the recognition site, and the stability of the ensuing interaction (*74*). Our findings suggest that release profiles could be delayed further by using restriction enzymes of lower efficiency or by modifying sequences flanking their recognition sites. In order to control the star activity of these enzymes, i.e., the relaxation of sequence specificity under extreme conditions, our experiments were carried out under tightly controlled pH conditions, low concentrations of glycerol and enzyme, and the absence of organic solvents or divalent cations such as Mn^{2+}, Cu^{2+}, or Zn^{2+}.

Incubation of annealed oligonucleotides at the melting temperature results in the separation of the DNA strands. Figure 3b illustrates the release characteristics of a poly(AM-*co*-bisacrylamide-*co*-acrylated DNA) network in response to a linear temperature gradient. The sigmoidal nature of the release indicated a cooperative melting transition of the immobilized oligonucleotides. The temperature gradient had no effect on the structural integrity of the network. The melting temperature of an oligonucleotide can be estimated from its sequence by the nearest-neighbor method (*75*). The observed melting temperature matched the estimated value of 58 °C. Hence, sequence can be used to tailor the temperature of release from this platform.

We next remodeled the oligonucleotide construct to encode an RNA-cleaving deoxyribozyme that possesses the catalytic 10−23 motif (*76*, *77*) and cleaves the overlapping sequences of the Tat and Rev exons (*78*, *79*). These genes are essential for viral replication and pathogenesis, and hence their mRNAs are attractive targets for gene therapy (*1*). The resulting poly(AM-*co*-bisacrylamide-*co*-acrylated DNA) networks were incubated with *Bam*HI and the HIV-1 Tat/Rev mRNA, which was transcribed *in vitro*. We hypothesized that *Bam*HI would trigger the release of the deoxyribozyme and degrade the HIV-1 Tat/Rev mRNA by trans-esterification (Figure 4a,b). As expected, incubation of the HIV-1 Tat/Rev mRNA along with the deoxyribozyme-loaded network and *Bam*HI resulted in specific cleavage (Figure 4c, lane 3). In control experiments, we incubated a network lacking the deoxyribozyme construct with *Bam*HI. The HIV-1 Tat/Rev mRNA was not degraded, demonstrating that catalytic activity of the deoxyribozyme is necessary for degradation of the transcript (Figure 4c, lane 2). Our data suggest that such platforms could be useful for developing delivery systems for siRNAs, aptamers, and ribozymes. Intriguingly, the oligonucleotide release could be triggered *in vivo* by endogenous nucleases such as RNase P (*80*−*82*), RNase L (*83*, *84*), and RNase 4 (*85*, *86*). These enzymes could be recruited by incorporating their cognate recognition sites in the constructs. This would enhance the targeting efficacy and specificity.

We hypothesized that macromolecular structure could affect oligonucleotide diffusion rates. To test this, we synthesized poly(HEMA-*co*-PEG600DMA-*co*-acrylated DNA) networks of varying cross-linking content (0.15%, 0.22%, and 0.45%). The release of oligonucleotides from these networks was triggered by the nonspecific endonuclease DNase I. Figure 5a,b illustrates the release characteristics of such networks. Our results suggest that cross-linking content, which is correlated with molecular parameters such as mesh

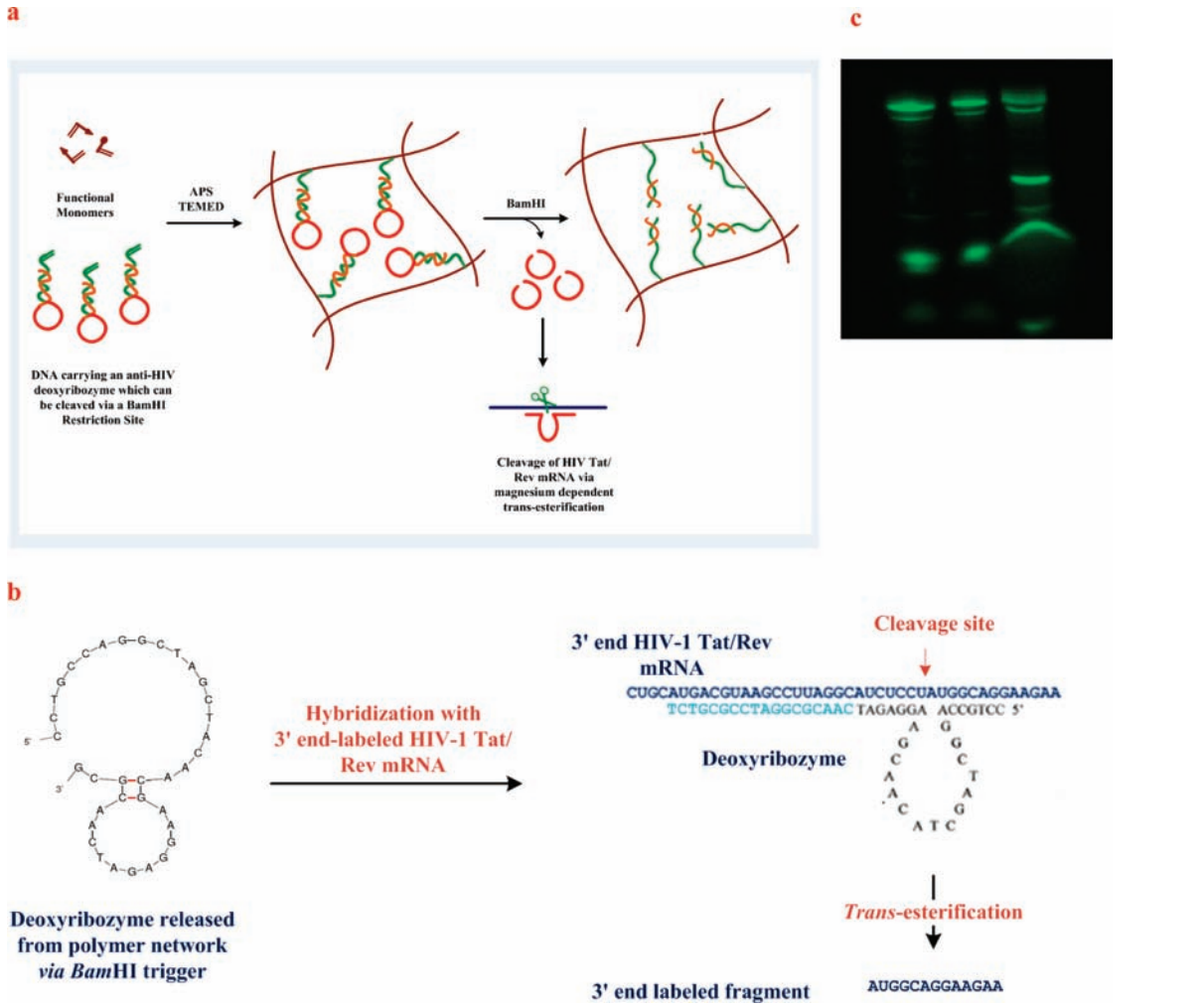

Figure 4. Degradation of a HIV-1 Tat/Rev mRNA by a deoxyribozyme released from a synthetic polymer network via a specific enzymatic trigger. (a) *Bam*HI cleaves the construct and releases the deoxyribozyme encoded in the loop of the hairpin. The deoxyribozyme then binds and cleaves the HIV-1 Tat/Rev mRNA. (b) Cleavage of the HIV-1 Tat/Rev mRNA via trans-esterification. (c) Degradation of HIV-1 Tet/Rev mRNA by deoxyribozyme released from a synthetic polymer network via *Bam*HI trigger (lane 3). No degradation is observed when *Bam*HI is incubated with a network lacking deoxyribozyme (lane 2). pCp-labeled HIV-A Tat-Rev mRNA was used as control (lane 1).

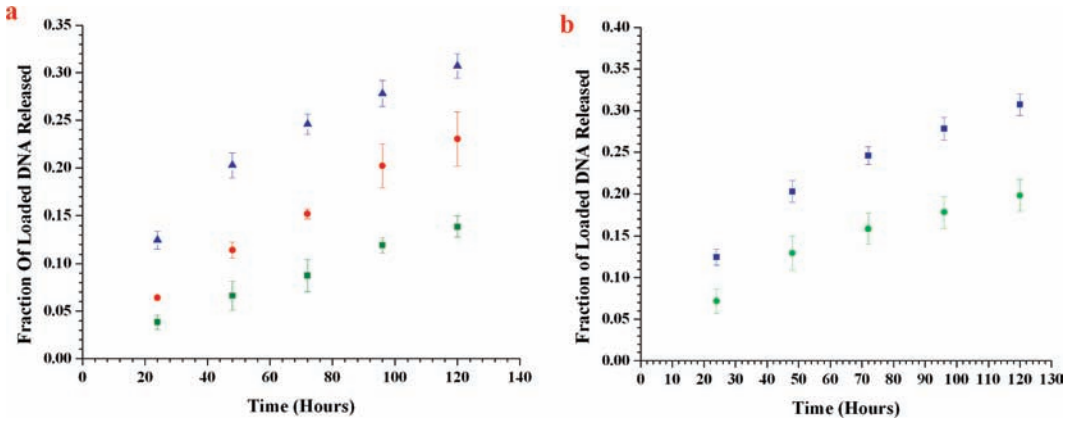

Figure 5. Tunable release profiles of oligonucleotides from synthetic polymer networks by controlling macromolecular architecture and enzymatic triggers. (a) Tailored release of oligonucleotides by incubating the poly(HEMA-*co*-PEG600DMA-*co*-acrylated DNA) networks of varying cross-linking content in DNase I. Cross-linking content of the networks, calculated on an acrylate DNA-free basis, were 0.15% (blue triangle), 0.22% (red circle), and 0.45% (green square). $N = 3 \pm$ SD. (b) Tailored release of oligonucleotides by incubating a gel of weak cross-linking content (0.15%) in DNase I at physiological conditions (blue square) as compared to incubating in buffer only (green circle).

size (*87*), can be used to tailor release rates. The networks of cross-linking content 0.15%, 0.22%, and 0.45% exhibited oligonucleotide diffusion coefficients of 1.67×10^{-8}, 7.65×10^{-9}, and 2.7×10^{-9} cm^2/s, respectively, and diffusional exponents of 0.55, 0.8, and 0.8, respectively. Our findings suggest that diffusion of oligonucleotides through the networks is Fickian at lower cross-linking content and moves closer to zero-order as cross-linking content is increased. The switch from Fickian to zero-order transport on increasing the cross-linking content occurs due to the following reasons:

hindrance of polymer chains to the diffusing enzyme, a decrease in the ratio between the polymer mesh size and the hydrodynamic radius of the enzyme, and decrease in the free volume available for diffusional transport (*87*). Further optimization of the polymer network structure can be performed to obtain desired release rates.

CONCLUSIONS

In summary, we have synthesized and characterized novel synthetic polymer networks that are versatile, programmable platforms for the controlled delivery of oligonucleotides via both enzymatic and physical triggers. We observed that the immobilized oligonucleotides were readily cleaved when the networks were incubated with the type II restriction enzyme *Bam*HI, and diffusion of the cleaved fragments through the macromolecular chains resulted in relatively constant release profiles very close to zero-order. The networks were triggered to release a RNA-cleaving deoxyribozyme, which degraded a HIV-1 mRNA transcript *in vitro*. Furthermore, the structural characteristics of the macromolecular polymer networks were controlled in order to tailor release profiles of the oligonucleotides. We envision that biohybrid platforms of oligonucleotide sequences and biodegradable synthetic polymers could be utilized for the intracellular delivery of multiple drugs from the same vehicle and as injectable systems targeted to specific cells using functionalized ligands such as folic acid.

ACKNOWLEDGMENT

We are grateful to I. Wower and S. Palani for insightful discussions and advice. The authors acknowledge funding by Auburn University VPR Office (MEB) and the Upchurch Fund for Excellence (JW).

LITERATURE CITED

(1) Stevenson, M. (2003) Dissecting HIV-1 through RNA interference. *Nat. Rev. Immunol. 3*, 851–858.
(2) Vane, J. R. (1976) The mode of action of aspirin and similar compounds. *J. Allergy Clin. Immunol. 58*, 691–712.
(3) Black, J. W., and Prichard, B. N. (1973) Activation and blockade of beta adrenoceptors in common cardiac disorders. *Br. Med. Bull. 29*, 163–7.
(4) Fedor, M. J., and Williamson, J. R. (2005) The catalytic diversity of RNAs. *Nat. Rev. Mol. Cell Biol. 6*, 399–412.
(5) Kim, D. H., and Rossi, J. J. (2007) Strategies for silencing human disease using RNA interference. *Nat. Rev. Genet. 8*, 173–84.
(6) Serganov, A., and Patel, D. J. (2007) Ribozymes, riboswitches and beyond: regulation of gene expression without proteins. *Nat. Rev. Genet. 8*, 776–90.
(7) Tuerk, C., and Gold, L. (1990) Systematic evolution of ligands by exponential enrichment: RNA ligands to bacteriophage T4 DNA polymerase. *Science 249*, 505–10.
(8) Ellington, A. D., and Szostak, J. W. (1990) In vitro selection of RNA molecules that bind specific ligands. *Nature 346*, 818–22.
(9) Krutzfeldt, J., Rajewsky, N., Braich, R., Rajeev, K. G., Tuschl, T., Manoharan, M., and Stoffel, M. (2005) Silencing of microRNAs in vivo with 'antagomirs'. *Nature 438*, 685.
(10) Castanotto, D., and Rossi, J. J. (2009) The promises and pitfalls of RNA-interference-based therapeutics. *Nature 457*, 426–33.
(11) Whitehead, K. A., Langer, R., and Anderson, D. G. (2009) Knocking down barriers: advances in siRNA delivery. *Nat. Rev. Drug Discovery 8*, 129–38.
(12) Bumcrot, D., Manoharan, M., Koteliansky, V., and Sah, D. W. Y. (2006) RNAi therapeutics: a potential new class of pharmaceutical drugs. *Nat. Chem. Biol. 2*, 711–719.
(13) Choi, Y., Thomas, T., Kotlyar, A., Islam, M. T., and Baker, J. R., Jr. (2005) Synthesis and functional evaluation of DNA-assembled polyamidoamine dendrimer clusters for cancer cell-specific targeting. *Chem. Biol. 12*, 35–43.
(14) Zhang, K., Wang, Q., Xie, Y., Mor, G., Sega, E., Low, P. S., and Huang, Y. (2008) Receptor-mediated delivery of siRNAs by tethered nucleic acid base-paired interactions. *RNA 14*, 577–83.
(15) Langer, R., and Peppas, N. A. (2003) Advances in biomaterials, drug delivery, and bionanotechnology. *AlChE J. 49*, 2990–3006.
(16) Venkatesh, S., Byrne, M. E., Peppas, N. A., and Hilt, J. Z. (2005) Applications of biomimetic systems in drug delivery. *Exp. Opin. Drug Delivery 2*, 1085–96.
(17) Pack, D. W., Hoffman, A. S., Pun, S., and Stayton, P. S. (2005) Design and development of polymers for gene delivery. *Nat. Rev. Drug Discovery 4*, 581–93.
(18) Tanaka, T., Fillmore, D., Sun, S.-T., Nishio, I., Swislow, G., and Shah, A. (1980) Phase transitions in ionic gels. *Phys. Rev. Lett. 45*, 1636–9.
(19) Chen, G., and Hoffman, A. S. (1995) Graft copolymers that exhibit temperature-induced phase transitions over a wide range of pH. *Nature 373*, 49–52.
(20) Yoshida, R., Uchida, K., Kaneko, Y., Sakai, K., Kikuchi, A., Sakurai, Y., and Okano, T. (1995) Comb-type grafted hydrogels with rapid de-swelling response to temperature changes. *Nature 374*, 240–2.
(21) Stayton, P. S., Shimoboji, T., Long, C., Chilkoti, A., Chen, G., Harris, J. M., and Hoffman, A. S. (1995) Control of protein-ligand recognition using a stimuli-responsive polymer. *Nature 378*, 472–4.
(22) Suzuki, A., and Tanaka, T. (1990) Phase transition in polymer gels induced by visible light. *Nature 346*, 345–347.
(23) Kwon, I. C., Bae, Y. H., and Kim, S. W. (1991) Electrically erodible polymer gel for controlled release of drugs. *Nature 354*, 291–3.
(24) Osada, Y., Okuzaki, H., and Hori, H. (1992) A polymer gel with electrically driven motility. *Nature 355*, 242–4.
(25) Tanaka, T., Nishio, I., Sun, S. T., and Ueno-Nishio, S. (1982) Collapse of gels in an electric field. *Science 218*, 467–9.
(26) Miyata, T., Asami, N., and Uragami, T. (1999) A reversibly antigen-responsive hydrogel. *Nature 399*, 766–9.
(27) Petka, W. A., Hardin, J. L., McGrath, K. P., Wirtz, D., and Tirrell, D. A. (1998) Reversible hydrogels from self-assembling artificial proteins. *Science 281*, 389–392.
(28) Wang, C., Stewart, R. J., and Kopecek, J. (1999) Hybrid hydrogels assembled from synthetic polymers and coiled-coil protein domains. *Nature 397*, 417–420.
(29) Ehrick, J. D., Deo, S. K., Browning, T. W., Bachas, L. G., Madou, M. J., and Daunert, S. (2005) Genetically engineered protein in hydrogels tailors stimuli-responsive characteristics. *Nat. Mat. 4*, 298–302.
(30) Obaidat, A. A., and Park, K. (1996) Characterization of glucose dependent gel-sol phase transition of the polymeric glucose-concanavalin A hydrogel system. *Pharm. Res. 13*, 989–995.
(31) Schneider, J. P., Pochan, D. J., Ozbas, B., Rajagopal, K., Pakstis, L., and Kretsinger, J. (2002) Responsive Hydrogels from the Intramolecular Folding and Self-Assembly of a Designed Peptide. *J. Am. Chem. Soc. 124*, 15030–15037.
(32) Collier, J. H., Hu, B.-H., Ruberti, J. W., Zhang, J., Shum, P., Thompson, D. H., and Messersmith, P. B. (2001) Thermally and photochemically triggered self-assembly of peptide hydrogels. *J. Am. Chem. Soc. 123*, 9463–9464.
(33) Nowak, A. P., Breedveld, V., Pakstis, L., Ozbas, B., Pine, D. J., Pochan, D., and Deming, T. J. (2002) Rapidly recovering hydrogel scaffolds from self-assembling diblock copolypeptide amphiphiles. *Nature 417*, 424–428.
(34) Sperinde, J. J., and Griffith, L. G. (1997) Synthesis and characterization of enzymically-crosslinked poly(ethylene glycol) hydrogels. *Macromolecules 30*, 5255–5264.

(35) Sperinde, J. J., and Griffith, L. G. (2000) Control and prediction of gelation kinetics in enzymatically cross-linked poly(ethylene glycol) hydrogels. *Macromolecules 33*, 5476–5480.
(36) Hu, B.-H., and Messersmith, P. B. (2003) Rational design of transglutaminase substrate peptides for rapid enzymatic formation of hydrogels. *J. Am. Chem. Soc. 125*, 14298–14299.
(37) Collier, J. H., and Messersmith, P. B. (2003) Enzymatic modification of self-assembled peptide structures with tissue transglutaminase. *Bioconjugate Chem. 14*, 748–755.
(38) Sakiyama-Elbert, S. E., and Hubbell, J. A. (2000) Controlled release of nerve growth factor from a heparin-containing fibrin-based cell ingrowth matrix. *J. Controlled Release 69*, 149–158.
(39) Wood, M. D., and Sakiyama-Elbert, S. E. (2008) Release rate controls biological activity of nerve growth factor released from fibrin matrices containing affinity-based delivery systems. *J. Biomed. Mater. Res. 84*, 300–12.
(40) Willerth, S. M., and Sakiyama-Elbert, S. E. (2007) Approaches to neural tissue engineering using scaffolds for drug delivery. *Adv. Drug Delivery Rev. 59*, 325–38.
(41) Taylor, S. J., and Sakiyama-Elbert, S. E. (2006) Effect of controlled delivery of neurotrophin-3 from fibrin on spinal cord injury in a long term model. *J. Controlled Release 116*, 204–10.
(42) Sakiyama-Elbert, S. E., and Hubbell, J. A. (2000) Development of fibrin derivatives for controlled release of heparin-binding growth factors. *J. Controlled Release 65*, 389–402.
(43) Stevenson, M. (2004) Therapeutic potential of RNA interference. *New Engl. J. Med. 351*, 1772–1777.
(44) Raoul, C., Abbas-Terki, T., Bensadoun, J. C., Guillot, S., Haase, G., Szulc, J., Henderson, C. E., and Aebischer, P. (2005) Lentiviral-mediated silencing of SOD1 through RNA interference retards disease onset and progression in a mouse model of ALS. *Nat. Med. 11*, 423–8.
(45) Raoul, C., Barker, S. D., and Aebischer, P. (2006) Viral-based modelling and correction of neurodegenerative diseases by RNA interference. *Gene Ther. 13*, 487–95.
(46) Carlson, M. E., Hsu, M., and Conboy, I. M. (2008) Imbalance between pSmad3 and Notch induces CDK inhibitors in old muscle stem cells. *Nature 454*, 528–32.
(47) Morrissey, D. V., Lockridge, J. A., Shaw, L., Blanchard, K., Jensen, K., Breen, W., Hartsough, K., Machemer, L., Radka, S., Jadhav, V., Vaish, N., Zinnen, S., Vargeese, C., Bowman, K., Shaffer, C. S., Jeffs, L. B., Judge, A., MacLachlan, I., and Polisky, B. (2005) Potent and persistent in vivo anti-HBV activity of chemically modified siRNAs. *Nat. Biotechnol. 23*, 1002–1007.
(48) Dykxhoorn, D. M., Chowdhury, D., and Lieberman, J. (2008) RNA interference and cancer: endogenous pathways and therapeutic approaches. *Adv. Exp. Med. Biol. 615*, 299–329.
(49) Dykxhoorn, D. M., and Lieberman, J. (2006) Knocking down disease with siRNAs. *Cell 126*, 231–5.
(50) Mirkin, C. A., Letsinger, R. L., Mucic, R. C., and Storhoff, J. J. (1996) A DNA-based method for rationally assembling nanoparticles into macroscopic materials. *Nature 382*, 607–609.
(51) Rosi, N. L., Giljohann, D. A., Thaxton, C. S., Lytton-Jean, A. K. R., Han, M. S., and Mirkin, C. A. (2006) Oligonucleotide-modified gold nanoparticles for intracellular gene regulation. *Science 312*, 1027–1030.
(52) Hurst, S. J., Lytton-Jean, A. K. R., and Mirkin, C. A. (2006) Maximizing DNA loading on a range of gold nanoparticle sizes. *Anal. Chem. 78*, 8313–8318.
(53) Kim, E.-Y., Stanton, J., Vega, R. A., Kunstman, K. J., Mirkin, C. A., and Wolinsky, S. M. (2006) A real-time PCR-based method for determining the surface coverage of thiol-capped oligonucleotides bound onto gold nanoparticles. *Nucleic Acids Res. 34*, e54/1−e54/7.
(54) Akinc, A., Thomas, M., Klibanov, A. M., and Langer, R. (2005) Exploring polyethylenimine-mediated DNA transfection and the proton sponge hypothesis. *J. Gene Med. 7*, 657–63.
(55) Palliser, D., Chowdhury, D., Wang, Q. Y., Lee, S. J., Bronson, R. T., Knipe, D. M., and Lieberman, J. (2006) An siRNA-based microbicide protects mice from lethal herpes simplex virus 2 infection. *Nature 439*, 89–94.
(56) Rozema, D. B., Lewis, D. L., Wakefield, D. H., Wong, S. C., Klein, J. J., Roesch, P. L., Bertin, S. L., Reppen, T. W., Chu, Q., Blokhin, A. V., Hagstrom, J. E., and Wolff, J. A. (2007) Dynamic polyconjugates for targeted in vivo delivery of siRNA to hepatocytes. *Proc. Natl. Acad. Sci. U.S.A. 104*, 12982–7.
(57) Wolff, J. A., and Rozema, D. B. (2008) Breaking the bonds: non-viral vectors become chemically dynamic. *Mol. Therapeutics 16*, 8–15.
(58) Akinc, A., Zumbuehl, A., Goldberg, M., Leshchiner, E. S., Busini, V., Hossain, N., Bacallado, S. A., Nguyen, D. N., Fuller, J., Alvarez, R., Borodovsky, A., Borland, T., Constien, R., de Fougerolles, A., Dorkin, J. R., Narayanannair Jayaprakash, K., Jayaraman, M., John, M., Koteliansky, V., Manoharan, M., Nechev, L., Qin, J., Racie, T., Raitcheva, D., Rajeev, K. G., Sah, D. W., Soutschek, J., Toudjarska, I., Vornlocher, H. P., Zimmermann, T. S., Langer, R., and Anderson, D. G. (2008) A combinatorial library of lipid-like materials for delivery of RNAi therapeutics. *Nat. Biotechnol. 26*, 561–9.
(59) Zimmermann, T. S., Lee, A. C., Akinc, A., Bramlage, B., Bumcrot, D., Fedoruk, M. N., Harborth, J., Heyes, J. A., Jeffs, L. B., John, M., Judge, A. D., Lam, K., McClintock, K., Nechev, L. V., Palmer, L. R., Racie, T., Rohl, I., Seiffert, S., Shanmugam, S., Sood, V., Soutschek, J., Toudjarska, I., Wheat, A. J., Yaworski, E., Zedalis, W., Koteliansky, V., Manoharan, M., Vornlocher, H. P., and MacLachlan, I. (2006) RNAi-mediated gene silencing in non-human primates. *Nature 441*, 111–4.
(60) Zintchenko, A., Philipp, A., Dehshahri, A., and Wagner, E. (2008) Simple modifications of branched PEI lead to highly efficient siRNA carriers with low toxicity. *Bioconjugate Chem. 19*, 1448–55.
(61) Um, S. H., Lee, J. B., Park, N., Kwon, S. Y., Umbach, C. C., and Luo, D. (2006) Enzyme-catalysed assembly of DNA hydrogel. *Nat. Mat. 5*, 797–801.
(62) Nagahara, S., and Matsuda, T. (1996) Hydrogel formation via hybridization of oligodeoxyribonucleotides derivatized in water-soluble vinyl polymers. *Polym. Gels Networks 4*, 111–127.
(63) Lin, D. C., Yurke, B., and Langrana, N. A. (2004) Mechanical properties of a reversible, DNA-crosslinked polyacrylamide hydrogel. *J. Biomech. Eng. 126*, 104–10.
(64) Crank, J. (1975) *The Mathematics of Diffusion*, 2nd ed., Oxford University Press, Oxford.
(65) Ali, M., Horikawa, S., Venkatesh, S., Saha, J., Hong, J. W., and Byrne, M. E. (2007) Zero-order therapeutic release from imprinted hydrogel contact lenses within in vitro physiological ocular tear flow. *J. Controlled Release 124*, 154–62.
(66) Ritger, P. L., and Peppas, N. A. (1987) A simple equation for description of solute release. I. Fickian and non-Fickian release from non-swellable devices in the form of slabs, spheres, cylinders or disks. *J. Controlled Release 5*, 23–36.
(67) Ritger, P. L., and Peppas, N. A. (1987) A simple equation for description of solute release. II. Fickian and anomalous release from swellable devices. *J. Controlled Release 5*, 37–42.
(68) Holowachuk, E. W., and Ruhoff, M. S. (1995) Efficient gene synthesis by Klenow assembly/extension-Pfu polymerase amplification (KAPPA) of overlapping oligonucleotides. *PCR Methods Appl. 4*, 299–302.
(69) Sherlin, L. D., Bullock, T. L., Nissan, T. A., Perona, J. J., Lariviere, F. J., Uhlenbeck, O. C., and Scaringe, S. A. (2001) Chemical and enzymatic synthesis of tRNAs for high-throughput crystallization. *RNA 7*, 1671–8.
(70) England, T. E., and Uhlenbeck, O. C. (1978) 3′-Terminal labelling of RNA with T4 RNA ligase. *Nature 275*, 560–1.
(71) England, T. E., Bruce, A. G., and Uhlenbeck, O. C. (1980) Specific labeling of 3′ termini of RNA with T4 RNA ligase. *Methods Enzymol. 65*, 65–74.
(72) Rehman, F. N., Audeh, M., Abrams, E. S., Hammond, P. W., Kenney, M., and Boles, T. C. (1999) Immobilization of acrylamide-modified oligonucleotides by co-polymerization. *Nucleic Acids Res. 27*, 649–655.

(73) Nathans, D., and Smith, H. O. (1975) Restriction endonucleases in the analysis and restructuring of DNA molecules. *Annu. Rev. Biochem. 44*, 273–93.
(74) Engler, L. E., Sapienza, P., Dorner, L. F., Kucera, R., Schildkraut, I., and Jen-Jacobson, L. (2001) The energetics of the interaction of *Bam*HI endonuclease with its recognition site GGATCC. *J. Mol. Biol. 307*, 619.
(75) SantaLucia, J., Jr., and Hicks, D. (2004) The thermodynamics of DNA structural motifs. *Annu. Rev. Biophys. Biomol. Struct. 33*, 415–40.
(76) Santoro, S. W., and Joyce, G. F. (1997) A general purpose RNA-cleaving DNA enzyme. *Proc. Natl. Acad. Sci. U.S.A. 94*, 4262–6.
(77) Santoro, S. W., and Joyce, G. F. (1998) Mechanism and utility of an RNA-cleaving DNA enzyme. *Biochemistry 37*, 13330–42.
(78) Unwalla, H., and Banerjea, A. C. (2001) Novel mono- and di-DNA-enzymes targeted to cleave TAT or TAT-REV RNA inhibit HIV-1 gene expression. *Antiviral Res. 51*, 127–39.
(79) Unwalla, H., and Banerjea, A. C. (2001) Inhibition of HIV-1 gene expression by novel macrophage-tropic DNA enzymes targeted to cleave HIV-1 TAT/Rev RNA. *Biochem. J. 357*, 147–55.
(80) Kim, K., and Liu, F. (2007) Inhibition of gene expression in human cells using RNase P-derived ribozymes and external guide sequences. *Biochim. Biophys. Acta Gene Struct. Expression 1769*, 603.
(81) Yuan, Y., and Altman, S. (1994) Selection of guide sequences that direct efficient cleavage of mRNA by human ribonuclease P. *Science 263*, 1269–73.
(82) Ma, M., Benimetskaya, L., Lebedeva, I., Dignam, J., Takle, G., and Stein, C. A. (2000) Intracellular mRNA cleavage induced through activation of RNase P by nuclease-resistant external guide sequences. *Nat. Biotechnol. 18*, 58–61.
(83) Floyd-Smith, G., Slattery, E., and Lengyel, P. (1981) Interferon action: RNA cleavage pattern of a (2′−5′)oligoadenylate-dependent endonuclease. *Science 212*, 1030–2.
(84) Wreschner, D. H., McCauley, J. W., Skehel, J. J., and Kerr, I. M. (1981) Interferon action-sequence specificity of the ppp(A2′p)nA-dependent ribonuclease. *Nature 289*, 414–7.
(85) Shapiro, R., Fett, J. W., Strydom, D. J., and Vallee, B. L. (1986) Isolation and characterization of a human colon carcinoma-secreted enzyme with pancreatic ribonuclease-like activity. *Biochemistry 25*, 7255–64.
(86) Hofsteenge, J., Moldow, C., Vicentini, A. M., Zelenko, O., Jarai-Kote, Z., and Neumann, U. (1998) A single amino acid substitution changes ribonuclease 4 from a uridine-specific to a cytidine-specific enzyme. *Biochemistry 37*, 9250.
(87) Peppas, N. A., Bures, P., Leobandung, W., and Ichikawa, H. (2000) Hydrogels in pharmaceutical formulations. *Eur. J. Pharm. Biopharm. 50*, 27–46.

BC900187B

Activity-Linked Labeling of Enzymes by Self-Immolative Polymers

Roy Weinstain,[†] Phil S. Baran,[‡] and Doron Shabat*[,†]

School of Chemistry, Raymond and Beverly Sackler Faculty of Exact Sciences, Tel Aviv University, Tel Aviv 69978 Israel, and Department of Chemistry, The Scripps Research Institute, 10550 North Torrey Pines Road, La Jolla, California 92037. Received May 6, 2009; Revised Manuscript Received July 26, 2009

The development and application of tools that allow labeling of proteins *in vitro* and *in vivo* is a highly active and interdisciplinary area of research. Self-immolative polymers (SIPs) are a unique type of molecules that respond to external stimuli by undergoing head-to-tail disassembly through a self-immolative fragmentation. We have demonstrated how these polymers can be applied as activity-linked labeling probes for proteins with catalytic activity. A real-time detection of the protein labeling can be monitored due to a change in the fluorescence emission wavelength of the probe during the polymer disassembly process. The SIP-based labeling approach showed considerable conservation of catalytic activity of the labeled protein and significant preference toward labeling of the activating protein.

INTRODUCTION

The vital roles played by proteins in many cellular processes make studies of protein dynamics, localization, and interactions crucial. Fluorophore-labeled proteins allow such studies using fluorescent imaging (*1, 2*). In recent years, chemical labeling utilizing small molecules emerged as a powerful technique for *in vivo* and *in vitro* studies of cellular proteins, circumventing some problems presented by genetic encoding of large fluorescent proteins (*3, 4*). Various strategies have been developed in order to achieve specific labeling of proteins in their native competitive environment. These include the use of protein targeting sequences (*5*−*7*), peptide targeting sequences (*8*−*12*), unnatural amino acids (*13, 14*), and others (*15*−*18*). More recently, a new strategy for specific labeling of proteins is being explored. This strategy takes advantage of the protein's specific activity to achieve its selective labeling (*19, 20*). Nagano and co-workers developed an enzyme activity-based labeling probe, with a quinone-methide species generated by the catalytic activity of the enzyme (*21*). Quinone-methide chemistry has also been proven useful for chemical modification of cellular components such as nucleotides and proteins (*22*−*24*). A short time ago, we introduced novel "smart" polymers that respond to external stimuli by undergoing head-to-tail disassembly through self-immolative fragmentation (*25*). We have demonstrated the applicability of these self-immolative polymers (SIPs)[1] for signal amplification and controlled drug release (*26*). The disassembly of SIPs under aqueous conditions releases azaquinone-methide intermediates that react with water to generate fluorescent molecules. However, if the external stimulus that initiates the SIP disassembly is generated by an enzyme, the azaquinone-methide units can be trapped by a nucleophilic residue of the protein, thereby generating a labeled protein. Here, we report the use of SIPs as activity-linked fluorescent labeling agents for proteins.

* Corresponding author. Doron Shabat, Department of Organic Chemistry, School of Chemistry, Faculty of Exact Sciences, Tel Aviv University, Tel Aviv 69978, Israel, Tel: +972 (0) 3 640 8340, Fax: +972 (0) 3 640 9293, E-mail: chdoron@post.tau.ac.il.

[†] Tel Aviv University.

[‡] The Scripps Research Institute.

[1]Abbreviations: SIP, Self-Immolative Polymer; DCM, Dichloromethane; DMF, Dimethylformamide; EtOAc, Ethyl acetate; Hex, *n*-Hexanes; PBS, Phosphate buffer saline; THF, Tetrahydrofuran; ACN, Acetonitrile; MeOH, Methanol; NaOH, Sodium hydroxide; AcOH, Acetic acid; DMSO, Dimethylsulfoxide; DIBAL-H, Diisobutylaluminium hydride; DBTL, Dibutyltin dilaurate; TFA, Trifluoroacetic acid; PNA, *p*-Nitroaniline; TBSCl, *tert*-butyldimethylsilyl chloride; PGA, Penicillin G-amidase; Ab38C2, Antibody 38C2.

MATERIALS AND METHODS

All reactions requiring anhydrous conditions were performed under an Ar or N_2 atmosphere. All reactions were carried out at room temperature unless stated otherwise. Chemicals and solvents were either A.R. grade or purified by standard techniques. Thin layer chromatography (TLC): silica gel plates Merck 60 F_{254}; compounds were visualized by irradiation with UV light. Flash chromatography (FC): silica gel Merck 60 (particle size 0.040−0.063 mm), eluent given in parentheses. ^{1}H NMR spectra were measured using Bruker Avance operated at 200 or 400 MHz as mentioned. ^{13}C NMR spectra were measured using Bruker Avance instrument operated at 50 or 100 MHz as mentioned. The chemical shifts are expressed in δ relative to TMS ($\delta = 0$ ppm) and the coupling constants J in Hz. The spectra were recorded in $CDCl_3$ as solvent at room temperature unless stated otherwise. All fluorescence and absorbance measurements were performed in a 96-well ELISA plate using a Molecular Devices SPECTRAmaxM2 plate reader. All general reagents, including salts and solvents, were purchased from Sigma-Aldrich. Antibody 38C2 was kindly obtained from the Scripps Research Institute.

Synthesis. The synthesis, including detailed procedures, synthetic schemes and full characterization of all new compounds presented in the manuscript, is described in the Supporting Information.

Competition Behavior between Morpholine and Methanol: The Concentration Ratio of MeOH to Morpholine is 900 to 1. Compound **4** (25 mg, 0.047 mmol) was dissolved in MeOH (10 mL, 900 equiv), morpholine (30 μL, 0.34 mmol, 1 equiv) was added, and the reaction was monitored to completion (2 h) by TLC (EtOAc/Hex 3:7). The solvent was removed under reduced pressure and the residue taken in EtOAc (30 mL). The organic phase was washed twice with saturated NH_4Cl solution, dried over $MgSO_4$, then filtered, and the solvent was removed under reduced pressure. The crude products were purified by column chromatography on silica gel (EtOAc/Hex 3:7) to give

10.1021/bc9002037 CCC: $40.75 © 2009 American Chemical Society
Published on Web 08/18/2009

compound **4c** (3 mg, 20%) as a yellow oil (see characterization of **4c** in Supporting Information) and compound **4b** (9 mg, 72%) as a yellow oil (see characterization of **4b** in Supporting Information).

Competition Behavior between Morpholine and Methanol: The Concentration Ratio of MeOH to Morpholine is 90 to 1. Compound **4** (25 mg, 0.047 mmol) was dissolved in MeOH (10 mL, 312.5 mmol, 90 equiv), and morpholine (300 μL, 3.44 mmol, 1 equiv) was added. The reaction was monitored to completion (1 h) by TLC (EtOAc/Hex 3:7). The solvent was removed under reduced pressure and the residue taken in EtOAc (30 mL). The organic phase was washed twice with saturated NH_4Cl solution, dried over $MgSO_4$, then filtered, and the solvent was removed under reduced pressure. The crude product was purified by column chromatography on silica gel (EtOAc/Hex 3:7) to give compound **4c** (12 mg, 79%) as a yellow oil.

Competition Behavior between Z-Lys(Boc)-OH and Methanol: The Concentration Ratio of MeOH to Z-Lys(Boc)-OH is 950 to 1. Compound **4** (35 mg, 0.066 mmol) was dissolved in MeOH (10 mL, 950 equiv), and Z-Lys-OEt **15** (102 mg, 0.33 mmol, 1 equiv) was added. The reaction was stirred at room temperature and monitored to completion (8 h) by TLC (EtOAc/Hex 1:3). After concentration to dryness, the residue was taken in EtOAc (30 mL) and washed twice with water. The organic phase was dried with $MgSO_4$, filtered, and the solvent removed under reduced pressure. The crude product was purified by column chromatography on silica gel (EtOAc/Hex 15:85) to give compound **4b** (8 mg, 46%) as a yellow oil.

Competition Behavior between Z-Lys(Boc)-OH and Methanol: The Concentration Ratio of MeOH to Z-Lys(Boc)-OH is 75 to 1. To a solution of Z-Lys-OEt **15** (12 mg, 0.04 mmol, 1 equiv) in methanol (95 μL, 3 mmol, 75 equiv) was added 5 μL of compound **4** (from stock solution of 10 mM in DMSO) and the reaction monitored to completion (6 h) by RP-HPLC-MS. Two major products were formed (not including the released *p*-nitroaniline) and characterized according to their recorded masses (see Supporting Information).

Fluorescence Emission of Probe 5 upon Activation with PGA. To a 95 μL solution of PGA (0.5 mg/mL) in PBS pH 7.4 was added 5 μL of probe **5** (from 10 mM stock solution in DMSO) for a final concentration of 250 μM. Fluorescence spectra (λ_{ex} = 270 nm) were recorded every 3 min. Small molecules were removed by means of column chromatography over Sephadex G-25 (eluent: PBS pH 7.4). The protein concentration in the eluted solution was assessed using a standard BCA kit (bicinchoninic acid kit, Pierce, USA). In all cases, more than 95% of the protein's initial amount was present in the eluted solution. Fluorescence (λ_{ex} = 270 nm, λ_{em} = 510 nm) was measured for 100 μL solution of the purified protein (28 μg).

Labeling Procedure of PGA. To a 0.5 mL solution of PGA (1 mg) in PBS pH 7.4 was added 12.5 μL of polymer **7** (from stock solution of 10 mM in DMSO) for a final concentration of 250 μM. The solution was kept at room temperature for 3 h, then diluted with 2 mL PBS pH 7.4, and small molecules were removed by means of column chromatography over Sephadex G-25 (eluent: PBS pH 7.4). The protein concentration in the eluted solution was assessed using a standard BCA kit (bicinchoninic acid kit, Pierce, USA). In all cases, more than 95% of the initial amount of the protein was present in the eluted solution. Fluorescence (λ_{ex} = 270 nm, λ_{em} = 510 nm) was measured for 100 μL solution of the purified protein (0.285 mg/mL).

Labeling Procedure of Ab38C2. To a 0.5 mL solution of Ab38C2 (1 mg) in PBS pH 7.4 was added 12.5 μL of polymer **8** (from stock solution of 10 mM in DMSO) for a final concentration of 250 μM. The solution was kept at room temperature for 14 h, then diluted with 2 mL PBS pH 7.4, and small molecules were removed by means of column chromatography over Sephadex G-25 (eluent: PBS pH 7.4). The protein concentration in the eluted solution was assessed using a standard BCA kit (bicinchoninic acid kit, Pierce, USA). In all cases, more than 95% of the initial amount of the protein was present in the eluted solution. Fluorescence (λ_{ex} = 270 nm, λ_{em} = 510 nm) was measured for 100 μL solution of the purified protein (0.285 mg/mL).

MS Measurements for Labeled and Nonlabeled Ab38C2. To a 0.5 mL solution of Ab38C2 (0.5 mg) in PBS pH 7.4 was added 0, 12.5, or 25 μL of polymer **8** (from stock solution of 10 mM in DMSO) for a final concentration of 0, 250, or 500 μM, respectively. The solution was kept at room temperature for 14 h and dialyzed against 2 L of deionized water in a dialysis cassette (Slide-A-Lyzer 10K, Pierce, USA) to remove excess monomers and salts. Samples were analyzed by MALDI-TOF-MS.

Enzymatic Activity of Labeled and Nonlabeled PGA. The relative enzymatic activity of labeled vs unlabeled PGA was tested for the cleavage of PGA-probe **25** (see Supporting Information) by monitoring the absorbance at λ = 378 nm.

Procedure: To a 190 μL solution of labeled or unlabeled PGA (0.285 mg/mL) in PBS pH 7.4 was added 10 μL of compound **25** (from stock solution of 5 mM in DMSO) to give a final concentration of 250 μM. The absorbance at λ = 378 nm was monitored every 20 s.

Enzymatic Activity of Labeled and Nonlabeled Ab38C2. The relative enzymatic activity of labeled vs unlabeled of Ab38C2 was tested for the *retro*-aldol reaction with methodol according to a published assay (*29*).

Procedure: To a 190 μL solution of labeled or unlabeled Ab38C2 (0.285 mg/mL) in PBS pH 7.4 was added 10 μL of methodol (from stock solution of 5 mM in ACN) to give a final concentration of 250 μM. Fluorescence (λ_{ex} = 355 nm, λ_{em} = 460 nm) was measured every 1 min.

Comparison of the Labeling Characters for Monomeric (10), Trimeric (11), and SIP (8) Probes. The labeling of Ab38C2 was performed for three aza-quinone methide concentrations, 3.5 mM, 2.1 mM, and 1.05 mM (see Supporting Information). All labeling experiments were performed on 1 mg Ab38C2 in 0.5 mL PBS 7.4. After the addition of the labeling probe (either **10**, **11**, or **8**) at the appropriate concentration, the solution was kept at room temperature for 14 h, then diluted with 2 mL PBS pH 7.4, and small molecules were removed by means of column chromatography over Sephadex G-25 (eluent: PBS pH 7.4). Fluorescence (λ_{ex} = 270 nm, λ_{em} = 510 nm) was measured for 100 μL solution of the purified protein (0.285 mg/mL).

Protein Labeling with Polymer 12 and Hydrogen Peroxide. To 1 mg Ab38C2 in 0.45 mL PBS pH 7.4 and polymer **12** (500 μM) (25 μL from stock solution of 10 mM in DMSO), hydrogen peroxide [1 mM] was added (50 μL from stock solution of 10 mM in PBS 7.4). The solution was kept at room temperature for 14 h, then diluted with 2 mL PBS pH 7.4, and small molecules were removed by means of column chromatography over Sephadex G-25 (eluent: PBS pH 7.4). Fluorescence (λ_{ex} = 270 nm, λ_{em} = 510 nm) was measured for 100 μL solution of the purified protein (0.285 mg/mL).

Selective Protein Labeling in the Presence of Nonactivating Protein. To a 0.5 mL solution of Ab38C2 or PGA (0.5 mg) and β-casein (0.5 mg) in PBS pH 7.4 was added 12.5 μL of polymer **8** or **7**, respectively, (from stock solution of 10 mM in DMSO) for a final concentration of 250 μM. The solution was kept at room temperature for 14 h and dialyzed against 2 L of PBS pH 7.4 in a dialysis cassette (Slide-A-Lyzer 10K, Pierce, USA) (PBS was replaced once during this time) to

Scheme 1. Proposed Labeling Pathway of Proteins by Self-Immolative Polymers

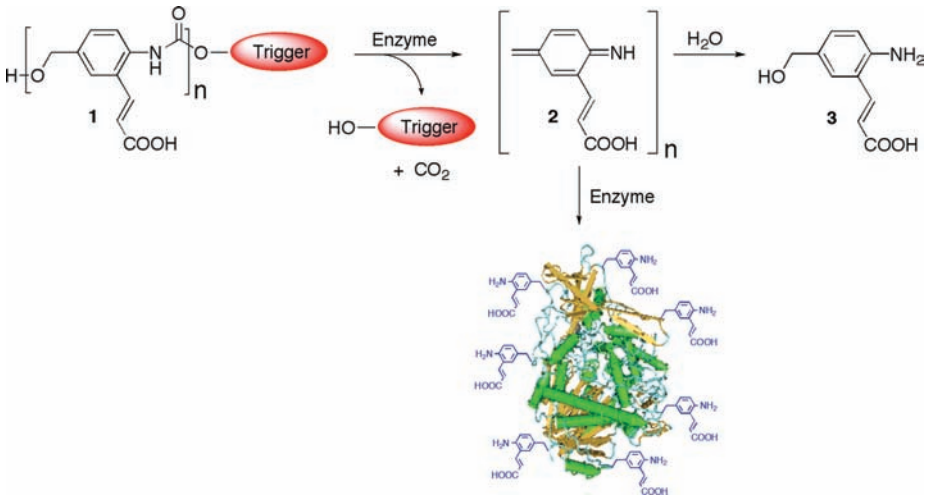

remove excess monomers. The protein solution was then put in an Amicon Microcon centrifuge tube with a 30 kDa cutoff membrane and centrifuged at 12 000 rpm for 7 min, until all fluids had passed through the membrane. This step was repeated twice. The described procedure should result in the permeation of the small β-casein (23 kDa) through the membrane, leaving the larger Ab38C2 (150 kDa) or PGA (85 kDa) on the membrane surface. The resulting protein slurry on the membrane surface was redissolved in 0.5 mL PBS pH 7.4. The presence of protein in the filtrate was confirmed using a standard BCA kit (bicinchoninic acid kit, Pierce, USA). Fluorescence (λ_{ex} = 270 nm, λ_{em} = 510 nm) was measured for 100 μL solution of the separated proteins.

Quantum Yield Calculations. The quantum yield of molecule **3** was calculated in comparison to 1-naphthylamine in ethanol (Φ_F = 0.43). For each compound, the absorbance at λ_{max} and the integrated fluorescence intensity were measured in various concentrations using a Molecular Devices SPECTRAmaxM2 plate reader. For 1-naphthylamine, the absorbance (OD) was measured for λ_{max} = 313 nm and the integrated fluorescence intensity was measured for λ_{ex} = 313 in the range 360−630 nm. For molecule **3**, the absorbance (OD) was measured for λ_{max} = 270 nm and the integrated fluorescence intensity was measured for λ_{ex} = 270 in the range 400−680 nm.

RESULTS AND DISCUSSION

The fragmentation of SIPs, such as **1**, generates multiple azaquinone-methide (**2**) units (Scheme 1). These reactive intermediates are rapidly entrapped by nearby nucleophiles, usually a solvent molecule like water, to give compound **3**. When a SIP-disassembly is triggered by an enzyme, azaquinone−methide **2** can react with nucleophilic residues of the enzyme, resulting in a covalent conjugation of **2** with the activating protein. An activity-linked fluorescent labeling probe, like **1**, has fluorescent building blocks (compound **3**) and an enzyme substrate as a trigger at the head of the polymer. The fluorescence generated by the released monomers during the fragmentation significantly differs from that of the unactivated probe (*25*) and could therefore facilitate real-time detection of the labeling process. The acrylic acid side-chain of the polymer's building block **3** adds aqueous solubility and generates a fluorescent chromophore through conjugation with the aromatic amine (*25*).

To verify the feasibility of the labeling pathway proposed in Figure 1, we initially evaluated the ability of a triggering nucleophile to trap the released azaquinone−methide in the presence of a polar solvent that can also act as a nucleophile. For this purpose, we designed and synthesized molecule **4** with *p*-nitroaniline as reporter and 4-alkoxide butanone as a trigger (Scheme 2). Removal of the trigger by morpholine, through a β-elimination reaction and spontaneous decarboxylation, results in the release of *p*-nitroaniline and the formation of azaquinone−methide **4a**. We incubated monomeric probe **4** with various concentrations of morpholine in a methanol solution. The morpholine served both as trigger-activator and as a nucleophile, which can attack the generated azaquinone−methide **4a**. When

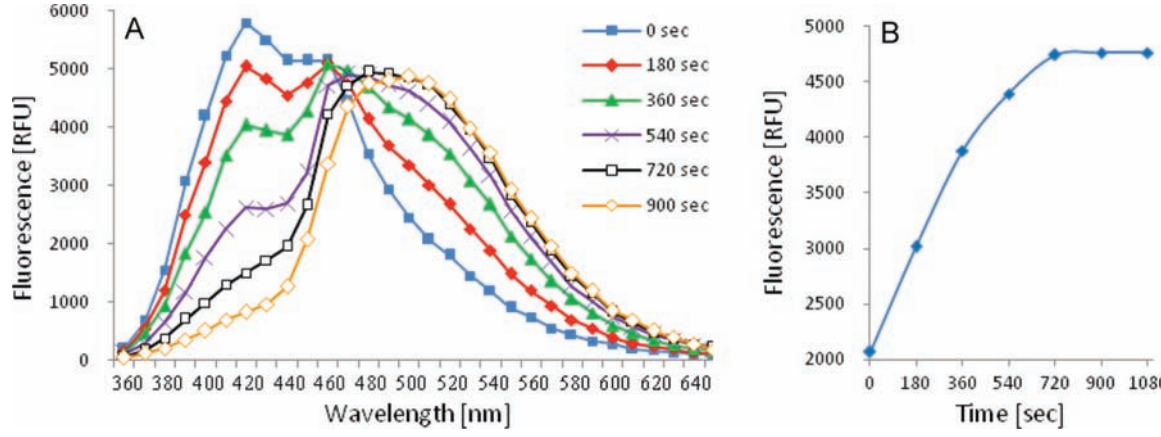

Figure 1. (A) Emission spectra of trimer **5** (final concentration 250 μM) when added to a solution of PGA (0.5 mg/mL) in PBS (pH 7.4, final volume 100 μL) at room temperature. Fluorescence emission spectra were measured every 3 min, λ_{ex} = 270 nm. (B) Fluorescence emission (λ_{ex} = 270 nm, λ_{em} = 510 nm) upon activation of trimer **5** (250 μM) with PGA (0.5 mg/mL) as a function of time.

Scheme 2. Disassembly Pathway of Monomeric Probe 4 through β-Elimination with Morpholine

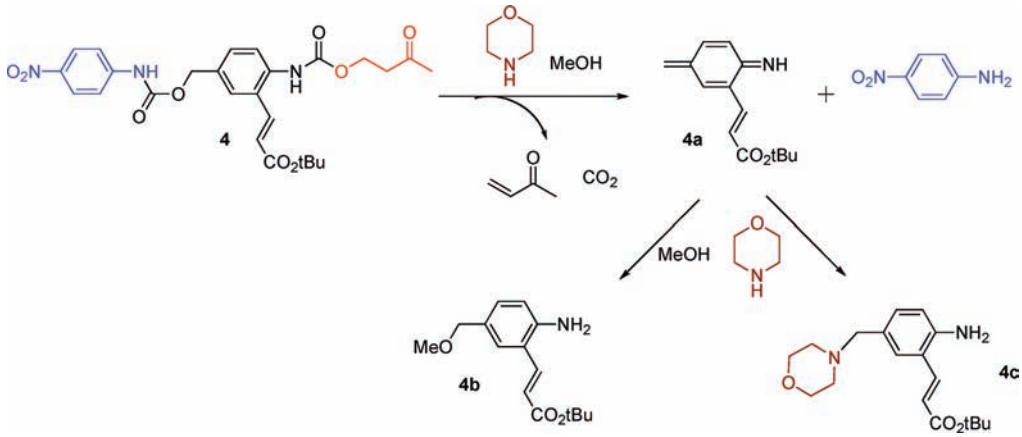

Scheme 3. Labeling Pathway of PGA by Self-Immolative Trimeric Probe 5

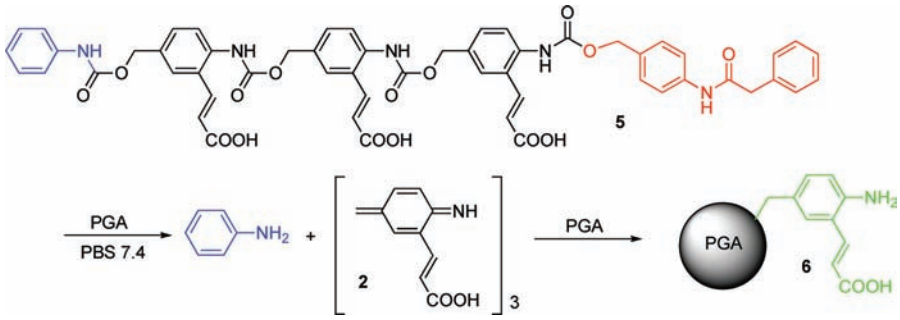

the equivalent ratio of solvent to morpholine was 900:1, the major product of the reaction was the solvent-trapped azaquinone−methide **4b**. However, when the ratio was reduced to 90:1, the sole product was the morpholine-trapped azaquinone−methide **4c**. This observation indicates that nucleophilic species such as amine residues can react with the azaquinone−methide intermediate in the presence of a polar solvent.

When the labeling probe is activated by an enzyme, the entrapment of the released azaquinone−methide (**2**) should occur through one of the nucleophilic amino acid residues of the activating protein. To evaluate the capability of an amino acid nucleophilic side residue to entrap the formed azaquinone−methide, we have synthesized Z-lysine-OEt (see Supporting Information). This amino acid derivative has a free ε-amine functional group that can serve as an activating base, for the β-elimination of the trigger of probe **4**, and as a nucleophilic side-residue, which can be labeled by the azaquinone−methide. Therefore, probe **4** was incubated with Z-Lysine-OEt in methanol at various ratios of methanol to Z-Lysine-OEt. When the ratio was 950:1 (respectively), the sole product of the reaction was the methanol-trapped azaquinone−methide. However, when the ratio of solvent to amino acid was decreased to 75:1, the major product was the lysine-trapped azaquinone−methide (see Supporting Information). The formation of lysine derivative with the azaquinone−methide product demonstrates the feasibility of protein labeling by nucleophilic residues of an activating enzyme.

In order to evaluate the potential of our SIPs as probes that enable monitoring of the labeling process in real time, we synthesized a simple model of water-soluble self-immolative trimer (compound **5**). The trimer was equipped with a phenylacetamide trigger that is designed for cleavage by Penicillin-G-Amidase (PGA). Incubation of trimer **5** with PGA will result in the generation of three azaquinone−methide units from each trimer molecule (Scheme 3). Reaction of nucleophilic residues from the enzyme with azaquinone−methide units (**2**) should afford the labeled protein **6**.

To follow the labeling process of the enzyme by self-immolative trimer **5**, the probe was incubated with PGA in PBS (pH 7.4) and the fluorescence emission spectrum was recorded every 3 min (Figure 1A). The spectral changes over 12 min included a decrease in intensity at 410 nm and an increase at 510 nm. The fluorescence intensity at 510 nm is plotted vs time in Figure 1B.

Upon completion of the labeling process (12 min, as determined by following fluorescence emission), the enzyme was subjected to dialysis and purification by Sephadex G25 column. The fluorescence emitted (λ_{ex} = 270 nm, λ_{em} = 510 nm) by the purified enzyme was compared to that of native PGA. An 8-fold increase in fluorescence emitted by the protein that underwent the labeling process was observed (see Supporting Information). These results suggest that the labeling process can be detected in real time when using labeling probes such as **5**.

Next, we addressed the applicability of SIPs for labeling of proteins. We synthesized SIP probe **7** with a trigger that is cleaved by PGA (Scheme 4). Polymer **7** was incubated for 90 min in PBS (pH 7.4) in the presence of PGA (0.5 mg/mL). The enzyme was then purified over a Sephadex G-25 column and its labeling was quantified by determining emitted fluorescence. The fluorescence emission at 510 nm was increased with increasing initial concentrations of polymer **7** (Figure 2A). The fluorescence emission spectrum of the unlabeled protein is compared to that of the labeled protein in Figure 2B. In a control experiment, PGA was incubated with a SIP bearing a trigger that cannot be cleaved by PGA. The enzyme purified after the incubation showed no increase in its emitted fluorescence compared to that of the unlabeled enzyme (data not shown). These results indicate that fluorescent labeling of PGA was achieved using SIP **7** as a labeling probe.

Scheme 4. Activity-Linked Labeling of PGA with SIP Probe 7

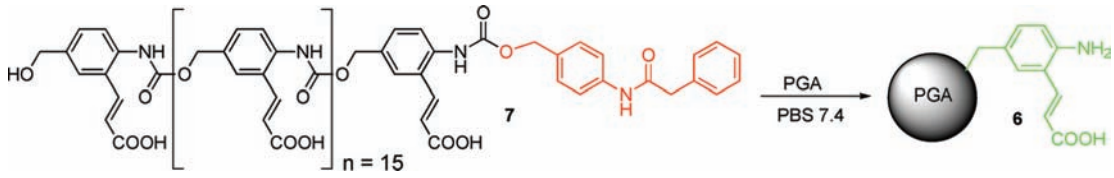

To broaden the scope of this polymer-based labeling technique, we evaluated the labeling of catalytic antibody 38C2 (Ab38C2) using the same approach. We synthesized polymer **8** with a trigger designed for activation by the catalytic antibody 38C2 through a *retro*-Michael reaction (Scheme 5) (*27*, *28*). Removal of the trigger by the catalytic antibody should initiate the polymer disassembly to generate multiple azaquinone−methide units that will react with nucleophilic residues of the antibody to afford the labeled antibody **9**.

Similar labeling experiments, as described above for PGA, were performed with Ab38C2. The results showed an increase in fluorescence when a constant amount of Ab38C2 was incubated with growing concentrations of polymer **8** (Figure 3A). The number of labeling molecules per antibody was determined by MALDI-MS analysis. The average mass of Ab38C2 increased as the concentration of probe **8** in the reaction was increased (Figure 3B). Nine molecules of labeling agent per antibody were obtained at the highest concentration of probe evaluated. These results support our assumption that the degree of labeling corresponds to the concentration of labeling agent present. The MALDI-MS analysis also confirmed that the bond between the protein and the fluorescent molecule is indeed covalent. These observations confirm the labeling of Ab38C2, demonstrating the generality of the method and suggesting that other proteins can be labeled by this technique upon introduction of appropriate trigger at the head of the polymer.

It is critical that the activity of the labeled protein be retained in order to allow evaluation of behavior and function in the native environment. Therefore, we determined the catalytic activities of labeled PGA and Ab38C2. To evaluate the activity of labeled PGA, we synthesized a simple chromogenic probe constructed of *p*-nitroaniline linked to phenylacetamide (see Supporting Information). Cleavage of the amide bond by PGA leads to the release of *p*-nitroaniline and a notable shift in the UV spectrum (from $\lambda_{max} = 317$ nm to $\lambda_{max} = 378$ nm) that can be detected with a spectrophotometer. The probe was incubated with labeled and unlabeled PGA, and the absorbance at wavelength of 378 nm was monitored. As shown in Figure 4A, the activity of highly labeled PGA was comparable to that of the unlabeled enzyme.

The activity of labeled Ab38C2 was evaluated using the fluorogenic substrate methodol (*29*). This substrate undergoes *retro*-aldol reaction with the antibody to release the fluorescent compound 6-methoxy-2-naphthaldehyde. In contrast to labeled PGA, the activity of labeled Ab38C2 was decreased as the concentration of probe in the labeling reaction was increased (Figure 4B). The loss of activity of Ab38C2 upon labeling is probably associated with reaction of azaquinone−methide released by the probe with the nucleophilic lysine in the antibody's catalytic site. This lysine is involved with the catalytic activity of the antibody, and its alkylation leads to inactivation of the antibody. Nevertheless, the antibody preserved about 50% of its catalytic activity when moderately labeled. The difference in catalytic activity retained by PGA and Ab38C2 upon labeling is probably derived from the different amino acids responsible for each protein catalytic activity. The ε-amino lysine inside the active site of Ab38C2 is an efficient nucleophile for alkylation by the formed azaquinone−methides. On the other hand, the hydroxy serine functional group responsible for the catalytic activity of PGA (*30*, *31*) is a weaker nucleophile, thus less susceptible for the alkylation that inactivates the enzyme.

In general, labeling of proteins using the azaquinone−methide-based labeling approach can be achieved with large polymers, short oligomers, or even monomeric probes. Thus, we sought

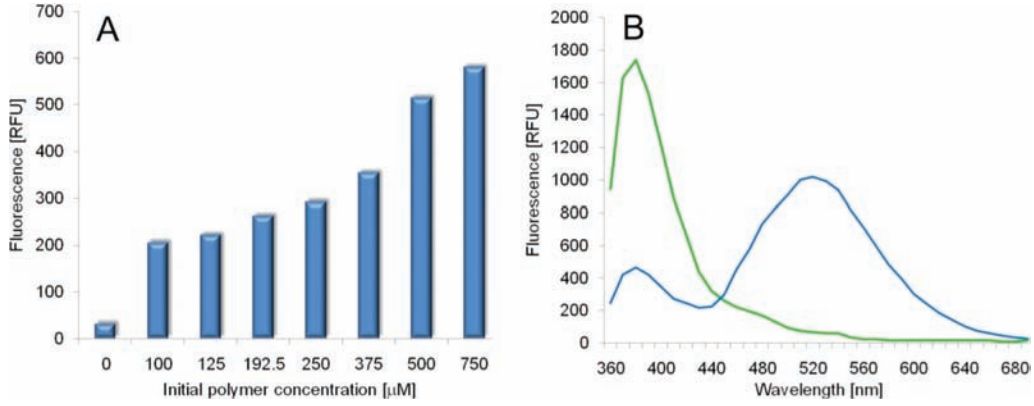

Figure 2. (A) Emitted fluorescence ($\lambda_{ex} = 270$ nm, $\lambda_{em} = 510$ nm) of PGA (28 μg) after incubation with indicated concentrations of polymer **7** in 100 μL PBS (pH 7.4). (B) Fluorescence emission spectra ($\lambda_{ex} = 270$ nm) of (▲) PGA (42 μg) and (■) purified labeled PGA (42 μg).

Scheme 5. Activity-Linked Labeling of Ab38C2 with SIP Probe 8

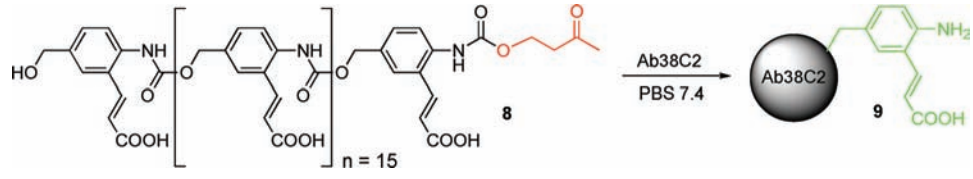

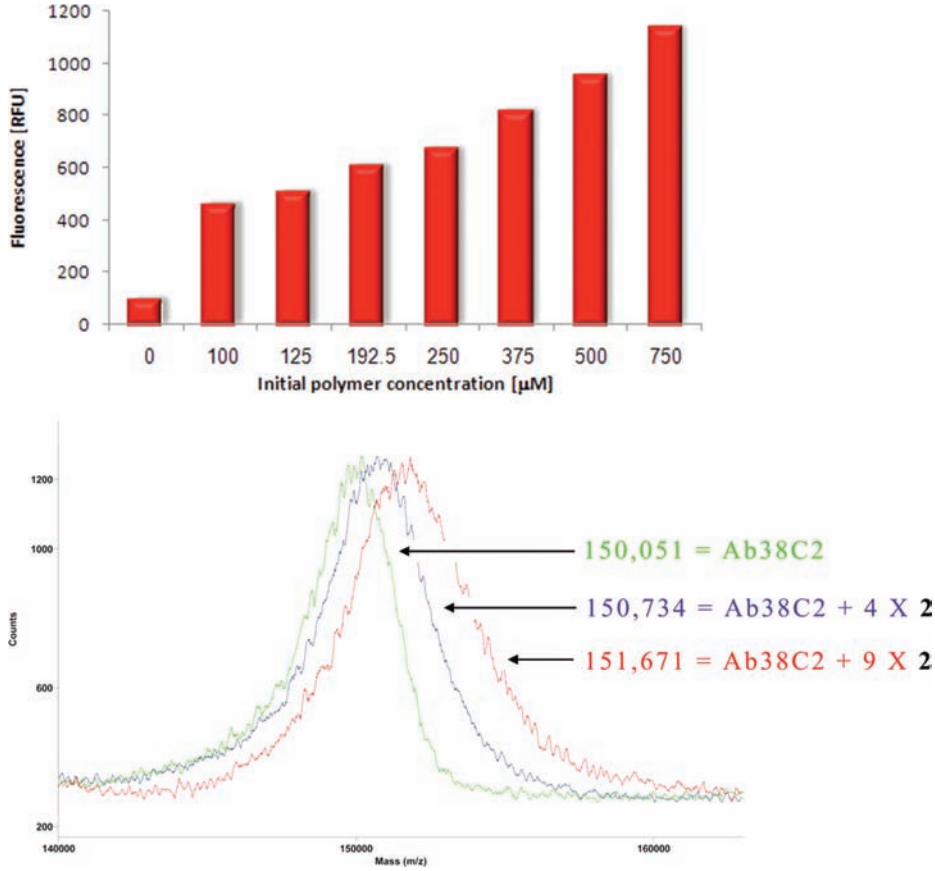

Figure 3. (A) Emitted fluorescence (λ_{ex} = 270 nm, λ_{em} = 510 nm) of Ab38C2 (28 μg) after incubation with indicated concentrations of polymer **8**, in 100 μL PBS (pH 7.4). (B) Mass spectra of Ab38C2 after incubation in PBS (pH 7.4) with polymer **8** at (green trace) 0 μM, (blue trace) 250 μM, and (red trace) 500 μM polymer.

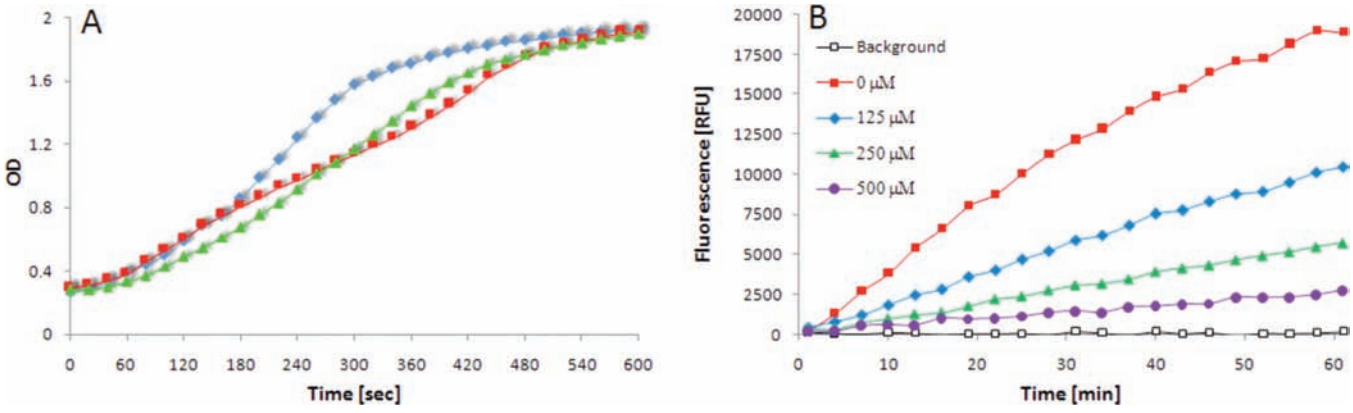

Figure 4. (A) Absorbance at 378 nm of PGA-probe (250 μM) in 200 μL PBS (pH 7.4) upon incubation with (♦) unlabeled PGA (28 μg), (■) moderately labeled PGA (28 μg), and (▲) heavily labeled PGA (28 μg) indicates that PGA retains enzymatic activity when labeled. (B) Fluorescence (λ_{ex} = 355 nm, λ_{em} = 460 nm) of methodol (250 μM) in 200 μL PBS (pH 7.4) upon incubation with Ab38C2 (28 μg) labeled with indicated concentrations of polymer **8**, indicates that catalytic activity is reduced at the extent of labeling degree.

to evaluate the efficiency of labeling with the SIP probe to that of monomeric (**10**) and trimeric (**11**) probes (Scheme 6). For this, Ab38C2 was incubated with monomeric, trimeric, and polymeric (**8**) labeling probes at equivalent concentrations per azaquinone−methide units expected to be released. Complete activation of each labeling probe should result in the formation of identical azaquinone−methide concentrations. This experiment was performed with increasing azaquinone−methide concentrations, as presented in Figure 5A.

The emitted fluorescence of the antibody labeled with polymer **8** was significantly higher than the fluorescence of the antibody labeled with either monomeric (**10**) or trimeric (**11**) probes (Figure 5A). This indicates that a higher degree of labeling was achieved using the polymer-based probe **8** than probes **10** or **11**. In addition, the degree of labeling obtained using polymer **8** was significantly increased when the probe concentration was increased, whereas labeling with monomeric and trimeric probes showed very little concentration dependence. Interestingly, when the catalytic activity of the labeled antibodies was evaluated, the polymer-labeled antibody, although labeled to a higher degree, had the highest activity of the three (Figure 5B). The monomer-labeled antibody, which was labeled to a very low degree, showed significantly reduced catalytic activity compared to the polymer-labeled antibody.

The reduction of catalytic activity observed after labeling with probes **10** and **11** is probably a result of alkylation of the

Scheme 6. Chemical Structures of Monomeric (10) and Trimeric (11) Self-Immolative Probes for Labeling of Ab38C2

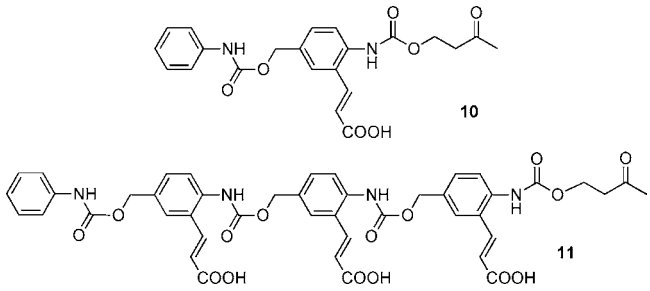

ε-amino lysine in the antibody active site by the released azaquinone−methide. Such alkylation also explains the extremely low degree of labeling by probes **10** and **11**, since rapid inactivation of the antibody's catalytic activity will inhibit the labeling process at an early stage. The ability of SIP **8** to achieve a high degree of labeling, while preserving much of the catalytic activity of the antibody, may be explained by the following hypothesis. Since the probe fragmentation process occurs within seconds to minutes (*25*), the polymer molecules can diffuse away from the antibody's active site after their activation. Therefore, it is likely that only the first azaquinone−methides released from the polymer chain have the possibility to react with the ε-amino lysine inside the catalytic site of the antibody. Most of the azaquinone−methides are probably generated far from the catalytic site, thus reacting with nucleophilic residues of the protein surface or with water. Each trigger activation results in the formation of an azaquinone−methide unit near the catalytic ε-amino lysine, increasing the likelihood for its alkylation. For the complete activation of all the monomeric probes, the antibody is required to perform 15 times more cleavages (on average) than for the polymeric probe. Therefore, the antibody is about 15 times less inclined for inactivation when using the polymeric probe over a monomeric one. This effect rationalizes both the higher labeling degree achieved by the polymeric probe and the better retention of catalytic activity upon labeling, demonstrating a major advantage for the use of such polymers as labeling probes.

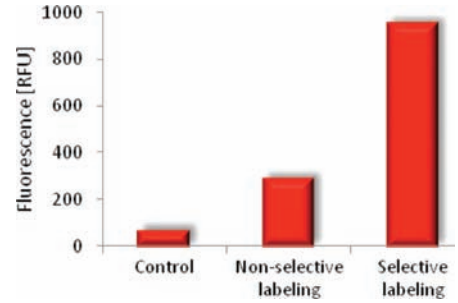

Figure 6. Emitted fluorescence (λ_{ex} = 270 nm, λ_{em} = 510 nm) of Ab38C2 (28 μg) in 100 μL PBS (pH 7.4) after incubation with polymer **8** (500 μM) (selective labeling), polymer **12** [500 μM] in the presence of H_2O_2 (nonselective labeling), or PBS (pH 7.4) (control).

Selective labeling of a specific enzyme in an environment containing other proteins, as in living cells, while preserving the enzyme catalytic activity, is highly valuable. Therefore, we investigated whether labeling of a protein will still occur when it is not involved in the activation process of a SIP probe. For this, we have designed and synthesized a SIP with a boronic ester trigger (compound **12**) that can be cleaved by hydrogen peroxide (*32*, *33*) (Scheme 7).

Ab38C2 was incubated for 5 h in PBS pH 7.4 solution of SIP **12** in the presence of hydrogen peroxide. Then, the antibody was purified and its emitted fluorescence was recorded. The labeling degree of the antibody in this experiment was found to be about four times less than the labeling level measured when activity-linked probe **8** was used (Figure 6). We assume that, when SIP **12** is activated, the protein is not necessarily positioned in close proximity to the generated azaquinone−methides, and therefore, they are mostly trapped by water molecules. Whereas when activity-linked probe **8** is applied, the antibody is placed close to the activated polymer, raising the likelihood for reaction of its nucleophilic residues with formed azaquinone−methides. This result suggests that, although some nonspecific labeling might still take place, specific labeling through a SIP probe activation could be achieved to a certain level.

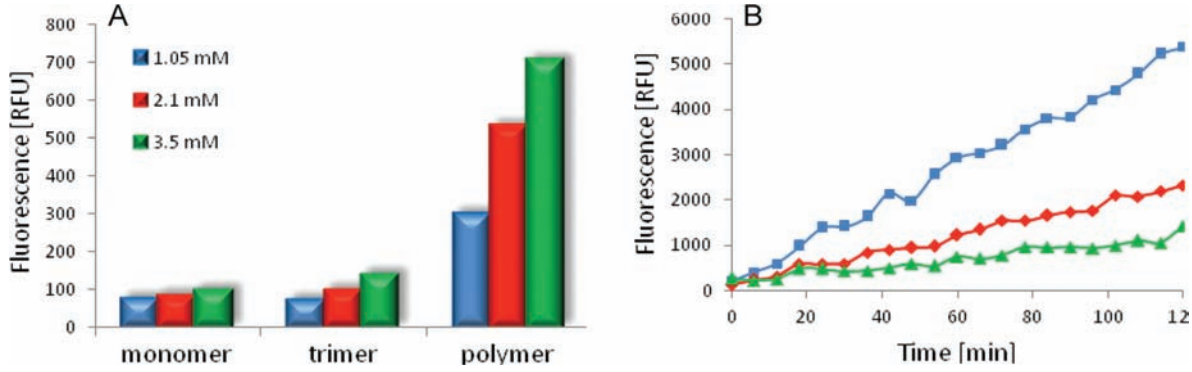

Figure 5. (A) Emitted fluorescence (λ_{ex} = 270 nm, λ_{em} = 510 nm) of Ab38C2 (14 μg) after incubation with monomeric (**10**), trimeric (**11**), and polymeric (**8**) labeling probes, at indicated monomer concentrations in 100 μL PBS (pH 7.4). (B) To evaluated the catalytic activity of the labeled antibodies, (■) polymer-labeled Ab38C2, (♦) trimer-labeled Ab38C2, and (▲) monomer-labeled Ab38C2 were incubated with methodol. The catalytic activities were monitored by measuring fluorescence (λ_{ex}= 355 nm, λ_{em}= 460 nm).

Scheme 7. Hydrogen Peroxide Initiated Disassembly of SIP 12 to Release Multiple Azaquinone−Methide Units

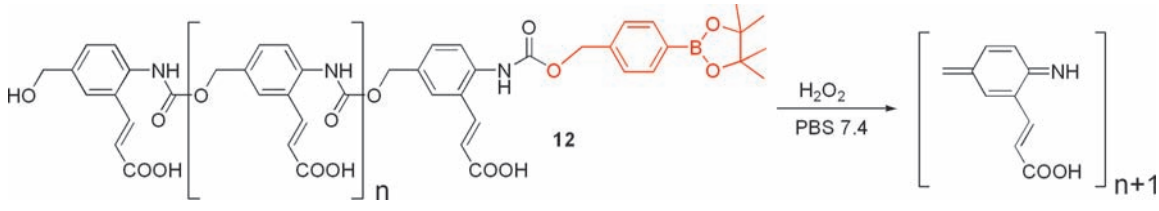

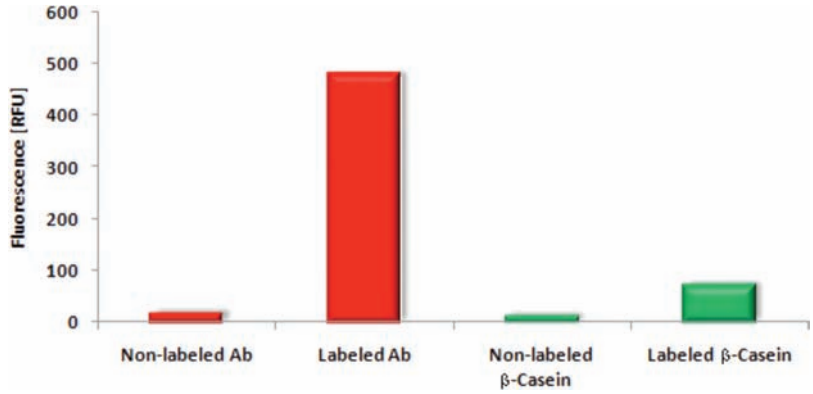

Figure 7. Fluorescence measurements (λ_{ex} = 270 nm, λ_{em} = 510 nm) of Ab38C2 and β-casein after labeling with polymer **8** (250 μM) in PBS (pH 7.4).

To investigate the labeling of SIPs in a more competitive environment, we evaluated the labeling specificity of polymer **8** in a solution containing an activating protein and a nonactivating protein. We incubated polymer **8** with both Ab38C2 (1 mg/mL) and the protein β-casein (1 mg/mL). After 14 h, the solution was dialyzed and the proteins were separated by size-exclusion apparatus (see Supporting Information). The emitted fluorescence of each protein was measured separately at identical concentration (Figure 7).

The extent of labeling observed for Ab38C2 was about eight times higher than that observed for β-casein, although both proteins were present in the initial solution at the same concentration. This suggests that the high reactivity of the azaquinone−methide units is sufficient to allow some labeling specificity. When polymer **8** was incubated with PGA in the presence of β-casein, preferential labeling of PGA was observed (see Supporting Information). The results of these experiments imply that SIPs could be used to achieve some specificity in labeling in a competitive environment. We chose to use β-casein only as a model protein. The labeling specificity observed by SIPs is most probably a consequence of a proximity effect between the polymer and the activating protein. Thus, structural differences in other inert proteins (like molecular weight and amino acid composition) should not significantly influence the specificity achieved by SIPs. Therefore, we anticipate that all inert proteins should be labeled to a much lesser degree in comparison with the triggering protein.

In order to efficiently visualize the labeling process by imaging techniques *in vivo*, the emitted fluorescence must preferably be at a wavelength of above 600 nm (near IR). The low quantum yield of fluorescent amine **3** (Φ_F =0.043 ± 10%, see Supporting Information) and its emission wavelength (λ_{em} = 510 nm) indicate that SIPs built of monomer **3** would be unsuitable for application in living cells. However, the activity-linked labeling polymer presented herein can be improved by using monomers with different fluorogenic characteristics, which will enable their use under physiological conditions. We are currently developing a SIP probe based on coumarin monomers that have significantly stronger fluorescence.

CONCLUSIONS

In summary, we have successfully demonstrated that self-immolative polymers can be used as activity-linked labeling probes to label enzymes such as PGA and Ab38C2. The synthetic strategy used allows introduction of various activating triggers, thereby allowing wide scope of enzymes to be labeled. A real-time detection of the enzyme labeling process is possible due to the change in fluorescence emission wavelength of the probe during the polymer disassembly process. In the SIP-based labeling approach, much of the catalytic activity of the labeled enzymes was conserved. Moreover, a significant preference toward labeling of the activating protein was observed in the presence of another protein, indicating that it is possible to achieve selective enzyme labeling. Although spectroscopic characteristics of the labeling fluorophore presented here are not suitable for *in vivo* study, it should be possible to construct SIPs from monomers with more desirable fluorogenic behavior and thereby to image specific intracellular labeling of the proteins. Current studies are focused on improving the fluorescent characteristics of the labeling agent to enable the use of SIPs in living cells.

ACKNOWLEDGMENT

D.S. thanks the Israel Science Foundation (ISF) and the Binational Science Foundation (BSF) for financial support.

Supporting Information Available: Full experimental details, characterization data of all new compounds. This material is available free of charge via the Internet at http://pubs.acs.org.

LITERATURE CITED

(1) Lichtman, J. W., and Conchello, J.-A. (2005) Fluorescence microscopy. *Nat. Methods 2*, 910–919.
(2) Marks, K. M., and Nolan, G. P. (2006) Chemical labeling strategies for cell biology. *Nat. Methods 3*, 591–596.
(3) Andresen, M., Schmitz-Salue, R., and Jakobs, S. (2004) Short tetracysteine tags to beta -tubulin demonstrate the significance of small labels for live cell imaging. *Mol. Biol. Cell 15*, 5616–5622.
(4) Lisenbee, C. S., Karnik, S. K., and Trelease, R. N. (2003) Overexpression and mislocalization of a tail-anchored GFP redefines the identity of peroxisomal ER. *Traffic 4*, 491–501.
(5) Farinas, J., and Verkman, A. S. (1999) Receptor-mediated targeting of fluorescent probes in living cells. *J. Biol. Chem. 274*, 7603–7606.
(6) George, N., Pick, H., Vogel, H., Johnsson, N., and Johnsson, K. (2004) Specific labeling of cell surface proteins with chemically diverse compounds. *J. Am. Chem. Soc. 126*, 8896–8897.
(7) Keppler, A., Gendreizig, S., Gronemeyer, T., Pick, H., Vogel, H., and Johnsson, K. (2003) A general method for the covalent labeling of fusion proteins with small molecules in vivo. *Nat. Biotechnol. 21*, 86–89.
(8) Chen, I., Howarth, M., Lin, W., and Ting, A. Y. (2005) Site-specific labeling of cell surface proteins with biophysical probes using biotin ligase. *Nat. Methods 2*, 99–104.
(9) Fernandez-Suarez, M., Baruah, H., Martinez-Hernandez, L., Xie, K. T., Baskin, J. M., Bertozzi, C. R., and Ting, A. Y. (2007) Redirecting lipoic acid ligase for cell surface protein labeling with small-molecule probes. *Nat. Biotechnol. 25*, 1483–1487.

(10) Griffin, B. A., Adams, S. R., and Tsien, R. Y. (1998) Specific covalent labeling of recombinant protein molecules inside live cells. *Science 281*, 269–72.
(11) Guignet, E. G., Hovius, R., and Vogel, H. (2004) Reversible site-selective labeling of membrane proteins in live cells. *Nat. Biotechnol. 22*, 440–444.
(12) Marks, K. M., Rosinov, M., and Nolan, G. P. (2004) In vivo targeting of organic calcium sensors via genetically selected peptides. *Chem. Biol. 11*, 347–356.
(13) Deiters, A., Cropp, T. A., Mukherji, M., Chin, J. W., Anderson, J. C., and Schultz, P. G. (2003) Adding amino acids with novel reactivity to the genetic code of *Saccharomyces cerevisiae*. *J. Am. Chem. Soc. 125*, 11782–11783.
(14) Zhang, Z., Smith, B. A. C., Wang, L., Brock, A., Cho, C., and Schultz, P. G. (2003) A new strategy for the site-specific modification of proteins in vivo. *Biochemistry 42*, 6735–6746.
(15) Chen, G., Heim, A., Riether, D., Yee, D., Milgrom, Y., Gawinowicz, M. A., and Sames, D. (2003) Reactivity of functional groups on the protein surface: Development of epoxide probes for protein labeling. *J. Am. Chem. Soc. 125*, 8130–8133.
(16) Dutton, A., and Singer, S. J. (1975) Crosslinking and labeling of membrane proteins by transglutaminase-catalyzed reactions. *Proc. Natl. Acad. Sci. U.S.A. 72*, 2568–71.
(17) Mao, H., Hart, S. A., Schink, A., and Pollok, B. A. (2004) Sortase-mediated protein ligation: a new method for protein engineering. *J. Am. Chem. Soc. 126*, 2670–2671.
(18) Soh, N. (2008) Selective chemical labeling of proteins with small fluorescent molecules based on metal-chelation methodology. *Sensors 8*, 1004–1024.
(19) Mizukami, S., Watanabe, S., Hori, Y., and Kikuchi, K. (2009) Covalent protein labeling based on noncatalytic beta -lactamase and a designed FRET substrate. *J. Am. Chem. Soc. 131*, 5016–5017.
(20) Tsukiji, S., Miyagawa, M., Takaoka, Y., Tamura, T., and Hamachi, I. (2009) Ligand-directed tosyl chemistry for protein labeling in vivo. *Nat. Chem. Biol. 5*, 341–343.
(21) Komatsu, T., Kikuchi, K., Takakusa, H., Hanaoka, K., Ueno, T., Kamiya, M., Urano, Y., and Nagano, T. (2006) Design and synthesis of an enzyme activity-based labeling molecule with fluorescence spectral change. *J. Am. Chem. Soc. 128*, 15946–15947.
(22) Janda, K. D., Lo, L.-C., Lo, C.-H. L., Sim, M.-M., Wang, R., Wong, C.-H., and Lerner, R. A. (1997) Chemical selection for catalysis in combinatorial antibody libraries. *Science 275*, 945–948.
(23) Kurogochi, M., Nishimura, S.-I., and Lee, Y. C. (2004) Mechanism-based fluorescent labeling of beta -galactosidases: an efficient method in proteomics for glycoside hydrolases. *J. Biol. Chem. 279*, 44704–44712.
(24) Wang, Q., Dechert, U., Jirik, F., and Withers, S. G. (1994) Suicide inactivation of human prostatic acid phosphatase and a phosphotyrosine phosphatase. *Biochem. Biophys. Res. Commun. 200*, 577–83.
(25) Sagi, A., Weinstain, R., Karton, N., and Shabat, D. (2008) Self-immolative polymers. *J. Am. Chem. Soc. 130*, 5434–5.
(26) Weinstain, R., Sagi, A., Karton, N., and Shabat, D. (2008) Self-immolative comb-polymers: multiple-release of side-reporters by a single stimulus event. *Chem.—Eur. J. 14*, 6857–61.
(27) Shabat, D., Rader, C., List, B., Lerner, R. A., and Barbas, C. F., 3rd. (1999) Multiple event activation of a generic prodrug trigger by antibody catalysis. *Proc. Natl. Acad. Sci. U.S.A. 96*, 6925–30.
(28) Wagner, J., Lerner, R. A., and Barbas, C. F., III. (1995) Efficient aldolase catalytic antibodies that use the enamine mechanism of natural enzymes. *Science 270*, 1797–800.
(29) List, B., Barbas, C. F., 3rd., and Lerner, R. A. (1998) Aldol sensors for the rapid generation of tunable fluorescence by antibody catalysis. *Proc. Natl. Acad. Sci. U.S.A. 95*, 15351–5.
(30) Duggleby, H. J., Tolley, S. P., Hill, C. P., Dodson, E. J., Dodson, G., and Moody, P. C. E. (1995) Penicillin acylase has a single-amino-acid catalytic center. *Nature 373*, 264–8.
(31) Slade, A., Horrocks, A. J., Lindsay, C. D., Dunbar, B., and Virden, R. (1991) Site-directed chemical conversion of serine to cysteine in penicillin acylase from Escherichia coli ATCC 11105. Effect on conformation and catalytic activity. *Eur. J. Biochem. 197*, 75–80.
(32) Kuivila, H. G., and Armour, A. G. (1957) Electrophilic displacement reactions. IX. Effects of substituents on rates of reactions between hydrogen peroxide and benzeneboronic acids. *J. Am. Chem. Soc. 79*, 5659–62.
(33) Lo, L.-C., and Chu, C.-Y. (2003) Development of highly selective and sensitive probes for hydrogen peroxide. *Chem. Commun.* 2728–2729.

BC9002037

Supporting Information

Activity-Linked Labeling of Enzymes by Self-Immolative Polymers

Roy Weinstain[a], Phil S. Baran[b] and Doron Shabat[a]*

[a]School of Chemistry, Raymond and Beverly Sackler Faculty of Exact Sciences, Tel-Aviv University, Tel Aviv 69978 Israel. [b]Department of Chemistry, The Scripps Research Institute, 10550 North Torrey Pines Road, La Jolla, CA 92037.

Synthetic schemes and experimental procedures S2 – S21

Spectral data of relevant compounds S22 – S23

Synthesis of monomeric labeling probe 13

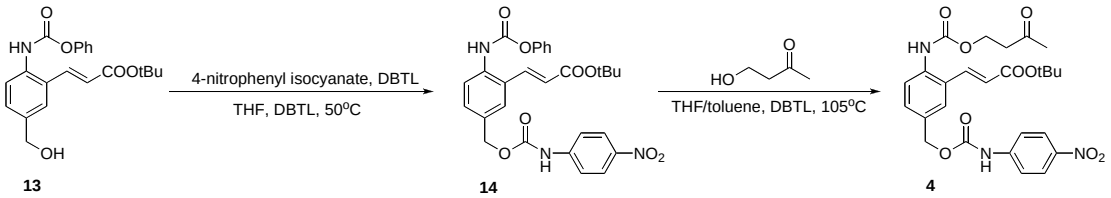

Compound 13. Compound **13** was synthesized and characterized according to published procedure.(25)

Compound 14. To a solution of compound **13** (400 mg, 1.08 mmol, 1 eq) in THF (5 mL), 4-nitrophenyl isocyanate (178 mg, 1.08 mmol, 1 eq) and DBTL (32 μL, 0.054 mmol, 0.05 eq) were added. The reaction was heated to 50°C and monitored to completion (15 minutes) by TLC (EtOAc:Hex 3:7). The solvent was removed under reduced pressure and the crude product was purified by column chromatography on silica gel (EtOAc:Hex 1:3) to give compound **14** (510 mg, 88%) as a white solid.

^{1}H NMR (400 MHz, DMSO-d^{6}): δ = 10.36 (1H, s), 9.27 (1H, s), 8.17 (2H, d, *J* = 7.0 Hz), 7.74 (1H, d, *J* = 15.7 Hz), 7.63-7.70 (3H, m), 7.52 (1H, s), 7.09-7.13 (5H, m), 6.66 (1H, d, *J* = 8.3 Hz), 6.24 (1H, d, *J* = 15.7 Hz), 4.98 (2H, s), 1.44 (9H, s). ^{13}C NMR (100 MHz, DMSO-d^{6}): δ = 166.4, 157.7, 153.7, 153.4, 148.7, 146.2, 146.0, 142.2, 142.0, 130.1, 129.8, 129.0, 123.7, 119.1, 118.4, 117.8, 116.7, 115.1, 80.4, 67.2, 28.4. MS (ESI): calculated for [M^{+}] $C_{28}H_{27}N_3O_8$ 533.2; found 533.2.

Compound 4. Compound **14** (240 mg, 0.45 mmol, 1 eq) was dissolved in a mixture of THF:toluene (10 mL, ratio 3:7), preheated to 105°C. 4-Hydroxy-2-butanoe (240 μL, 2.72 mmol, 6 eq) was added, followed by DBTL (15 μL, 0.022 mmol, 0.05 eq) and the reaction was monitored to completion (45 minutes) by TLC (EtOAc:Hex 4:6). The solvent was removed under reduced pressure and the crude product purified by column chromatography on silica gel (EtOAc:Hex 4:6) to give compound **4** (205 mg, 85%) as a yellow solid.

^{1}H NMR (200 MHz, DMSO-d^{6}): δ = 10.50 (1H, s), 9.45 (1H, s), 8.20 (2H, d, *J* = 7.2 Hz), 7.89 (1H, s), 7.66-7.74 (3H, m), 7.37-7.48 (2H, m), 6.45 (1H, d, *J* = 15.8 Hz),

5.17 (2H, s), 4.25 (2H, t, *J* = 6.2 Hz), 2.82 (2H, t, *J* = 6.2 Hz), 2.14 (3H, s), 1.48 (9H, s). ^{13}C NMR (50 MHz, DMSO-d^{6}): δ = 206.8, 166.3, 154.8, 153.6, 148.7, 146.1, 142.0, 139.8, 133.6, 128.9, 126.7, 121.0, 118.0, 117.6, 116.7, 80.4, 67.2, 60.2, 42.5, 30.4, 28.3. MS (ESI): calculated for [M^{+}] $C_{26}H_{29}N_3O_9$ 527.2; found 527.2.

Competition behavior between a triggering nucleophile and polar solvent

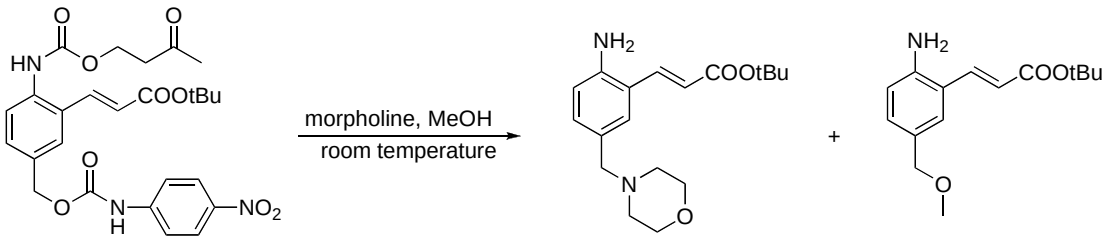

4 **4c** **4b**

Compound 4b. ^{1}H NMR (200 MHz, $CDCl_3$): δ = 7.72 (1H, d, *J* = 15.8 Hz), 7.31 (1H, s), 7.14 (1H, d, *J* = 8.3 Hz), 6.69 (1H, d, *J* = 8.3 Hz), 6.32 (1H, d, *J* = 15.8 Hz), 4.34 (2H, s), 3.36 (3H, s), 1.44 (9H, s). ^{13}C NMR (50 MHz, $CDCl_3$): δ = 166.5, 147.0, 144.9, 130.3, 128.4, 124.4, 123.9, 120.3, 116.6, 80.4, 74.3, 57.7, 29.6. MS (FAB^{+}): calculated for $C_{15}H_{21}NO_3$ [M^{+}]: 263.1; found: 263.1.

Compound 4c. ^{1}H NMR (200 MHz, $CDCl_3$): δ = 7.71 (1H, d, *J* = 15.8 Hz), 7.30 (1H, s), 7.11 (1H, d, *J* = 8.2 Hz), 6.65 (1H, d, *J* = 8.2 Hz), 6.30 (1H, d, *J* = 15.8 Hz), 3.92 (2H, s), 3.69 (4H, t, *J* = 4.7 Hz), 3.38 (2H, s), 2.42 (4H, t, *J* = 4.7 Hz), 1.47 (9H, s). ^{13}C NMR (50 MHz, $CDCl_3$): 166.8, 144.5, 138.8, 132.1, 130.3, 128.9, 126.8, 120.1, 116.5. MS (FAB^{+}): calculated for [M+H^{+}] $C_{18}H_{26}N_2O_3$: 319.2; found: 319.2.

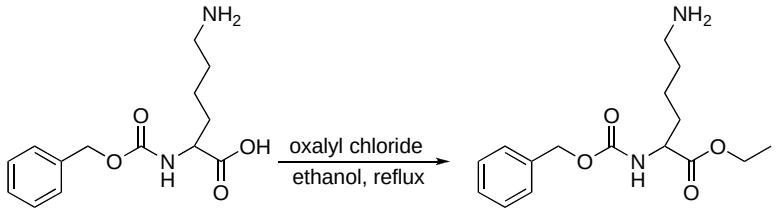

15

Compound 15. Z-Lys-OH (250 mg, 0.89 mmol, 1 eq) was suspended in ethanol (25 mL) and brought to reflux. Oxalyl-chloride (117 μL, 1.34 mmol, 1.5 eq) was added and the reaction was stirred for 45 minutes. After concentration to dryness, the residue was taken in EtOAc (100 mL) and washed with 1M NaOH. The organic phase was dried with $MgSO_4$, filtered and the solvent removed under reduced pressure to give compound **15** (257 mg, 93%) as yellowish oil.

^{1}H NMR (400 MHz, $CDCl_3$): δ = 7.29-7.35 (5H, m), 5.42 (1H, d, *J* = 7.1 Hz), 5.10 (2H, s), 4.34 (1H, q, *J* = 7.1 Hz), 4.18 (2H, q, *J* = 7.0 Hz), 2.66 (2H, t, *J* = 6.4 Hz), 1.79-1.88 (1H, m), 1.60-1.71 (1H, m), 1.30-1.56 (6H, m), 1.26 (3H, t, *J* = 7.0 Hz). ^{13}C NMR (100 MHz, $CDCl_3$): δ = 172.5, 155.9, 136.3, 128.8, 128.7, 128.3, 127.9, 127.6, 66.9, 61.4, 53.8, 41.8, 33.1, 32.5, 22.5, 14.4. MS (FAB^+): calculated for [$M+H^+$] $C_{16}H_{24}N_2O_4$: 309.2; found: 309.1.

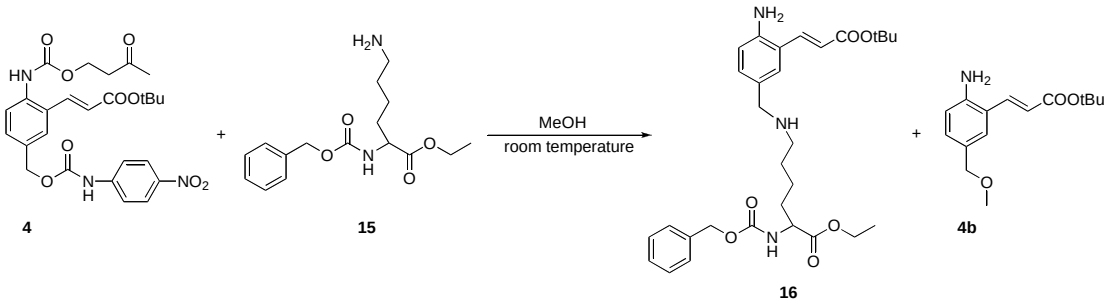

RP-HPLC-MS chromatogram and analysis of competition between Z-Lys(Boc)-OH and MeOH (ratio 75:1).

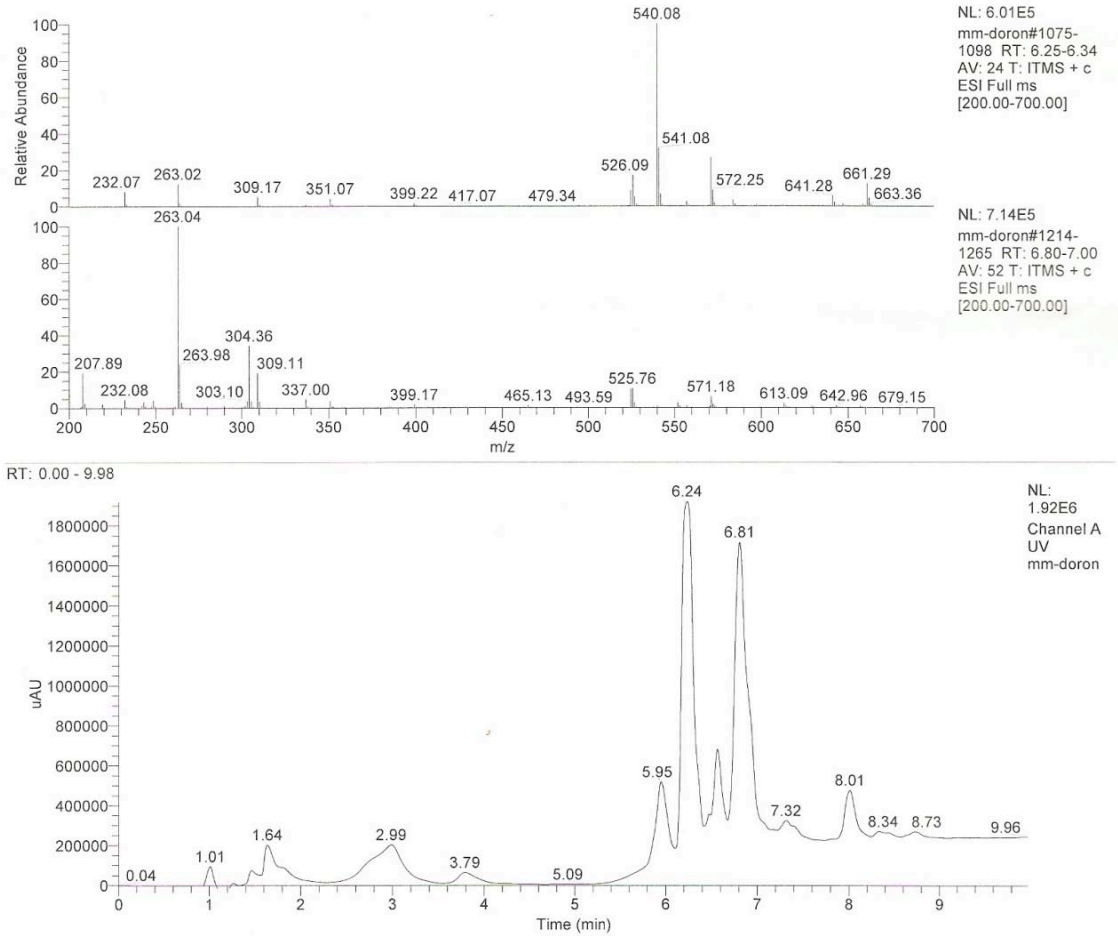

Figure 1S: RP-HPLC-MS chromatogram of compound **4** after incubated with Z-lys-OEt **15** in MeOH for 6 hours at Z-lys-OEt:MeOH ratio of 1:75. MS spectra of the peaks at 6.24 and 6.81 minutes are presented abouve.

	Retention time [minutes]	**Chemical formula**	**Calculated mass**	**Recorded mass**
Compound **16**	6.24	$C_{30}H_{41}N_3O_6$	539.30	540.08 [M+H$^+$]
Compound **4b**	6.81	$C_{15}H_{21}NO_3$	263.15	263.04 [M$^+$]

Table 1S: Analysis of RP-HPLC-MS chromatogram.

In order to validate these results, we have independently synthesized and fully characterized molecule **4b**. The retention time observed for the synthesized molecule **4b**, under the same separation condition in RP-HPLC, was 6.81 minutes. Furthermore, when Z-lys-OEt's initial concentration was increased or decreased, the peak at 6.24 minutes grew or shrunk accordingly.

Synthesis of trimeric labeling probe 5

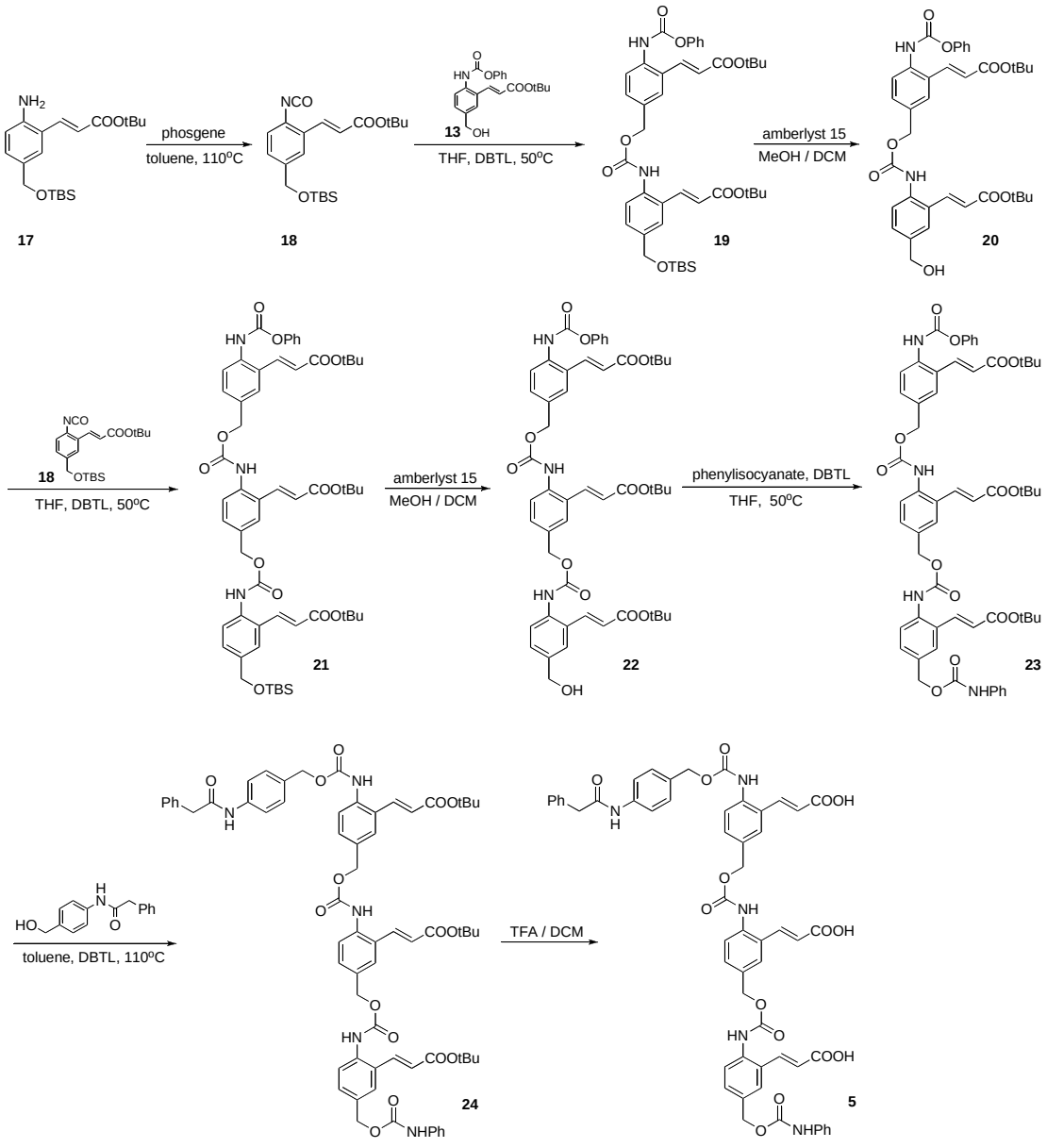

Compound 17. Compound **17** was synthesized and characterized according to published procedure.(25)

Compound 19. Compound **17** (750 mg, 2.06 mmol, 1 eq), dissolved in toluene (5 mL), was added drop-wise into a solution of refluxed phosgene in toluene (10.3 mL, 10.30 mmol, 5 eq) over 10 minutes. The reaction was stirred for 15 minutes and the solvent removed under reduced pressure yielding the corresponding isocyanate as brownish oil (**18**). Isocyanate **18** was re-dissolved in dry THF (5 mL) at 50°C. Compound **13** (760 mg, 2.06 mmol, 1 eq) was added, followed by DBTL (61 μL, 0.103 mmol, 0.05 eq) and the reaction was monitored to completion (20 minutes) by TLC (EtOAc:Hex 15:85). The solvent was then removed under reduced pressure and the crude product purified by column chromatography on silica gel (EtOAc:Hex 15:85) to give compound **19** (1.12 g, 72%) as a yellow solid.

^{1}H NMR (400 MHz, DMSO-d^{6}): δ = 9.32-9.38 (2H, m), 7.68-7.83 (5H, m), 7.35-7.50 (4H, m), 7.14-7.18 (2H, m), 6.68-6.76 (2H, m), 6.35-6.40 (2H, m), 5.14 (2H, s), 4.70 (2H, s), 1.46 (18H, s), 0.9 (9H, s), 0.08 (6H, s). ^{13}C NMR (100 MHz, DMSO-d^{6}): δ = 166.4, 165.9, 157.7, 150.2, 149.4, 148.0, 145.7, 141.9, 137.6, 137.5, 129.8, 128.8, 128.4, 127.9, 127.1, 122.5, 121.1, 119.9, 118.3, 116.5, 116.3, 115.3, 80.3, 79.8, 65.8, 62.7, 28.3, 28.2, 26.2, 18.4, -4.8. MS (MALDI-TOF): calculated for [M+Na^{+}] $C_{42}H_{54}N_2O_9Si$ 781.3; found 781.3.

Compound 20. Compound **19** (1.12 g, 1.47 mmol) was dissolved in MeOH:DCM mixture (3:1), amberlyst 15 was added and the reaction was monitored to completion (30 minutes) by TLC (EtOAc:Hex 4:6). The amberlyst 15 beads were filtered out, the solvent removed under reduced pressure and the crude product purified by column chromatography on silica gel (EtOAc:Hex 4:6) to give compound **20** (935 mg, 98%) as a white solid.

^{1}H NMR (400 MHz, $CDCl_3$): δ = 9.32-9.36 (2H, m), 7.69-7.80 (5H, m), 7.34-7.51 (4H, m), 7.14-7.18 (2H, m), 6.69-6.78 (2H, m), 6.37-6.41 (2H, m), 5.13 (2H, s), 4.49 (2H, d, *J* = 4.8 Hz), 1.47 (18H, s). ^{13}C NMR (100 MHz, DMSO-d^{6}): δ = 166.4, 166.0, 157.8, 150.2, 149.4, 148.0, 145.7, 141.9, 137.6, 137.5, 129.8, 128.8, 128.4, 127.9, 127.1, 122.5, 121.1, 119.9, 118.3, 116.5, 116.3, 115.6, 80.3, 79.8, 65.8, 64.1, 28.3, 28.2. MS (MALDI-TOF): calculated for [M+Na^{+}] $C_{36}H_{40}N_2O_9$ 667.2; found 667.2.

Compound 21. Compound **17** (545 mg, 1.50 mmol, 1 eq), dissolved in toluene (5 mL), was added drop-wise into a solution of refluxed phosgene in toluene (7.5 mL, 7.50 mmol, 5 eq) over 10 minutes. The reaction was stirred for 15 minutes and the solvent removed under reduced pressure yielding the corresponding isocyanate as brownish oil (**18**). Isocyanate **18** was re-dissolved in dry THF (5 mL) at 50^{o}C. Compound **20** (905 mg, 1.4 mmol, 0.9 eq) was added, followed by DBTL (45 μL, 0.07 mmol, 0.05 eq) and the reaction was monitored to completion (20 minutes) by TLC (EtOAc:Hex 2:8). The solvent was then removed under reduced pressure and the crude product purified by column chromatography on silica gel (EtOAc:Hex 2:8) to give compound **21** (908 mg, 63%) as a yellow solid.

^{1}H NMR (400 MHz, $CDCl_3$): δ = 9.48-9.51 (2H, m), 9.32 (1H, s), 7.70-7.84 (6H, m), 7.37-7.52 (6H, m), 7.14-7.18 (2H, m), 6.70-6.77 (3H, m), 6.37-6.41 (3H, m), 5.13 (4H, s), 4.70 (2H, s), 1.47 (27H, s), 0.91 (9H, s), 0.08 (6H, s). ^{13}C NMR (100 MHz, DMSO-d^{6}): δ =166.1, 165.9, 157.7, 155.0, 148.6, 147.5, 139.9, 139.6, 139.4, 139.1, 137.1, 136.0, 134.3, 134.1, 132.3, 130.0, 129.8, 128.8, 128.5, 128.3, 126.8, 126.6, 124.6, 124.3, 120.9, 120.7, 119.2, 117.8, 117.4, 117.0, 116.8 ,115.6, 80.4, 79.8, 66.7, 65.8, 64.2, 28.3, 28.2, 26.2, 18.4, -4.8. MS (MALDI-TOF): calculated for [M+Na^{+}] $C_{57}H_{71}N_3O_{13}Si$ 1056.4; found 1056.4.

Compound 22. Compound **21** (600 mg, 0.61 mmol) was dissolved in MeOH:DCM mixture (3:1), amberlyst 15 was added and the reaction was monitored to completion (45 minutes) by TLC (EtOAc:Hex 1:1). The amberlyst 15 beads were filtered out, the solvent removed under reduced pressure and the crude product purified by column chromatography on silica gel (EtOAc:Hex 1:1) to give compound **22** (512 mg, 90%) as a white solid.

^{1}H NMR (400 MHz, $CDCl_3$): δ = 9.44-9.56 (2H, m), 9.28 (1H, s), 7.67-7.83 (6H, m), 7.32-7.47 (6H, m), 7.11-7.22 (2H, m), 6.68-6.73 (3H, m), 6.35-6.39 (3H, m), 5.12 (4H, s), 4.45 (2H, d, *J* = 5.6 Hz), 1.47 (27H, s). ^{13}C NMR (100 MHz, DMSO-d^{6}): δ = 166.4, 165.9, 157.7, 155.0, 148.6, 147.5, 139.9, 139.6, 139.5, 139.1, 137.1, 135.8, 134.3, 134.1, 132.3, 130.0, 129.8, 128.9, 128.5, 128.3, 126.8, 126.6, 124.6, 124.3, 121.0, 120.6, 119.2, 117.8, 117.6, 117.0, 116.8 ,115.6, 80.3, 79.9, 66.8, 65.8, 62.7,

28.3, 28.2. MS (MALDI-TOF): calculated for [M+Na^+] $C_{51}H_{57}N_3O_{13}$ 942.3; found 942.3.

Compound 23. Compound **22** (477 mg, 0.52 mmol, 1 eq) was dissolved in dry THF (5 mL), preheated to 50°C. Phenylisocyanate (57 μL, 0.52 mmol, 1 eq) was added, followed by DBTL (16 μL, 0.026 mmol, 0.05 eq) and the reaction was monitored to completion (10 minutes) by TLC (EtOAc:Hex 1:3). The solvent was removed under reduced pressure and the crude product purified by column chromatography on silica gel (EtOAc:Hex 2:8) to give compound **23** (416 mg, 77%) as a white solid.

^{1}H NMR (400 MHz, DMSO-d^6): δ = 10.01 (1H, s), 9.71 (1H, s), 9.64 (1H, s), 9.28 (1H, s), 7.71-7.87 (6H, m), 7.39-7.47 (9H, m), 7.22-7.26 (5H, m), 6.95 (1H, t, *J* = 7.4 Hz), 6.70-6.74 (1H, m), 6.40-6.45 (3H, m), 5.10 (6H, s), 1.45 (27H, s). ^{13}C NMR (100 MHz, DMSO-d^6): δ = 166.4, 165.9, 157.7, 155.0, 154.9, 153.7, 148.6, 139.9, 137.0, 134.3, 134.1, 132.4, 130.6, 130.3, 130.0, 129.8, 129.5, 129.2, 128.9, 127.1, 127.0, 124.3, 122.8, 121.1, 121.0, 119.2, 118.7, 118.5, 117.6, 116.8, 115.7, 80.4, 79.9, 66.8, 65.9, 65.6, 28.3, 28.2. MS (MALDI-TOF): calculated for [M+Na^+] $C_{58}H_{62}N_4O_{14}$ 1061.4; found 1061.4.

Compound 24. Compound **23** (150 mg, 0.14 mmol, 1 eq) was dissolved in toluene (7 mL), preheated to 110°C. PGA substrate (155 mg, 0.64 mmol, 4.4 eq) was added, followed by DBTL (9.5 μL, 0.014 mmol, 0.1 eq) and the reaction was monitored to completion (1 hour) by TLC (EtOAc:Hex 6:4). The solvent was removed under reduced pressure and the crude product purified by column chromatography on silica gel (EtOAc:Hex 6:4) to give compound **24** (120 mg, 70%) as a white solid.

^{1}H NMR (200 MHz, $CDCl_3$): δ = 10.20 (1H, s), 9.73 (1H, s), 9.56 (1H, s), 9.51 (1H, s), 9.46 (1H, s), 7.81 (2H, s), 7.75 (1H, t, *J* = 3.2 Hz), 7.71 (1H, t, *J* = 3.2 Hz), 7.68 (2H, s), 7.58-7.61 (4H, m), 7.41-7.42 (6H, m), 7.19-7.33 (9H, m), 6.36-6.43 (3H, m), 5.17 (1H, t, *J* = 5.6 Hz), 5.05-5.10 (8H, m), 3.62 (2H, s), 1.44 (27H, s). ^{13}C NMR (50 MHz, DMSO-d^6): δ = 169.6, 165.9, 155.0, 154.9, 140.5, 139.9, 139.7, 139.5, 137.0, 136.9, 136.4, 135.8, 134.4, 134.3, 131.6, 130.6, 130.2, 129.8, 129.6, 129.5, 129.2,

129.0, 128.9, 128.4, 127.2, 127.0, 126.8, 125.4, 125.1, 124.9, 124.6, 121.3, 121.0, 120.6, 119.8, 119.5, 119.3, 119.0, 80.4, 80.3, 66.3, 65.9, 65.8, 62.7, 60.2, 43.7, 28.3, 28.1. MS (MALDI-TOF): calculated for $[M+Na^+]$ $C_{60}H_{66}N_4O_{14}$ 1208.5; found 1028.5.

Compound 5. Compound **24** (5 mg) was dissolved in a 1:1 mixture of TFA and DCM, stirred for 5 minutes and the solvents removed under reduced pressure. The obtained compound **5** was used without further purification.

^{1}H NMR (200 MHz, DMSO-d^6): δ = 10.11 (1H, s), 9.74 (1H, s), 9.62 (1H, s), 9.53 (1H, s), 9.46 (1H, s), 7.80 (2H, s), 7.75 (1H, t, *J* = 3.0 Hz), 7.70 (1H, t, *J* = 3.0 Hz), 7.68 (2H, s), 7.55-7.62 (4H, m), 7.40-7.45 (6H, m), 7.19-7.36 (9H, m), 6.36-6.43 (3H, m), 5.16 (1H, t, *J* = 5.6 Hz), 5.06-5.13 (8H, m), 3.62 (2H, s).

Fluorescence emission of PGA upon labeling with trimeric probe 5

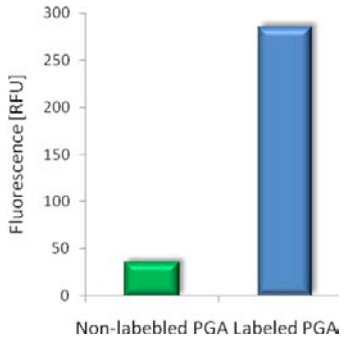

Figure 2S: Emitted fluorescence (λ_{ex} = 270 nm, λ_{em} = 510 nm) of PGA (28 μg) in PBS pH 7.4 (non-labeled PGA) and after treatment with trimer probe **5** [250 μM] (labeled PGA).

Synthesis of SIP labeling probe 7

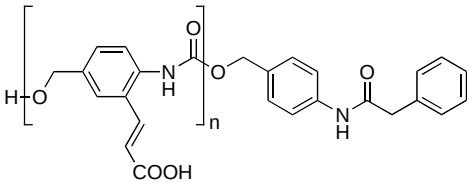

7

Polymer 7. Polymer **7** was synthesized and characterized according to published procedure.(25) The formed polymer was constructed of 14 monomers in average (determined by ^{1}H-NMR).

Synthesis of SIP labeling probe 8

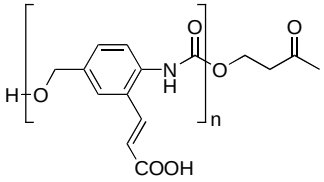

8

Polymer 8. Polymer **8** was synthesized and characterized according to published procedure.(25) The formed polymer was constructed of 15 monomers in average (determined by ^{1}H-NMR).

To exclude fluorescence increase due to flawed purification process, resulting in presence of free monomers in the purified PGA or Ab38C2 solution, we have incubated different amounts of protein with a fixed concentration of polymer **7** or **8**, correspondingly. Since in this experiment the same polymer concentration is used, if a certain percentage of monomers do pass through the purification process, a similar rise in fluorescence for all experiments would be expected. However, an increase in the fluorescence was observed upon growing amount of protein (Figure 3S), suggesting that presence of unattached monomers is not responsible for fluorescence change.

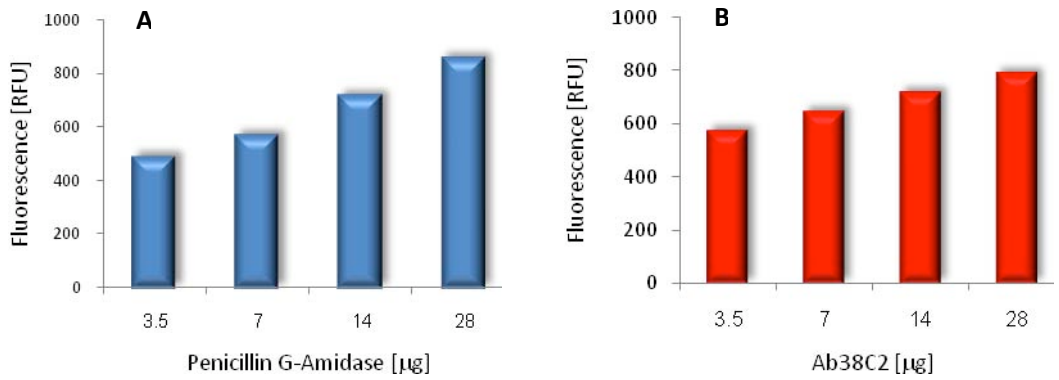

Figure 3S: Fluorescence measurements (λ_{ex} = 270 nm, λ_{em} = 510 nm) of increasing amounts of A) PGA after incubation with polymer **7** [250 µM], in 100 µL PBS pH 7.4. B) Ab38C2 after incubation with polymer **8** [250 µM], in 100 µL PBS pH 7.4.

Relative enzymatic activity of PGA

Synthesis of PGA probe 25

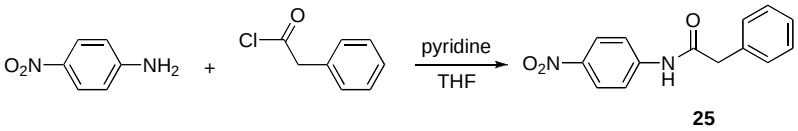

25

Compound 25. Pyridine (161 µL, 1.99 mmol, 1.1 eq) was added to a solution of 4-nitroaniline (250 mg, 1.81 mmol, 1 eq) dissolved in THF (5 mL) at 0°C and the mixture was stirred for 10 minutes. Then, phenacetylchloride (239 µL, 1.81 mmol, 1 eq) was added. The reaction was warmed to room temperature and monitored to completion (10 hours) by TLC (EtOAc:Hex 3:7). Upon completion, the reaction mixture was diluted with EtOAc (50 mL) and washed with saturated solution of NH_4Cl and brine. The solvents were removed under reduced pressure and the crude product purified by column chromatography on silica gel (EtOAc:Hex 3:7) to give compound **25** (428 mg, 92%) as a yellow solid.

^{1}H NMR (200 MHz, DMSO-d^6): δ = 9.74 (1H, s), 8.16 (2H, d, *J* = 7.3 Hz), 7.79 (2H, d, *J* = 7.3 Hz), 7.22-7.30 (5H, m), 3.67 (2H, s). ^{13}C NMR (50 MHz, DMSO-d^6): δ = 170.5, 145.7, 142.6, 135.7, 129.6, 128.7, 127.1, 125.3, 119.2, 43.7. MS (FAB$^+$): calculated for $C_{14}H_{12}N_2O_3$ [M$^+$]: 256.1; found: 256.1.

Absorbance of activated and inactivated PGA-probe 25

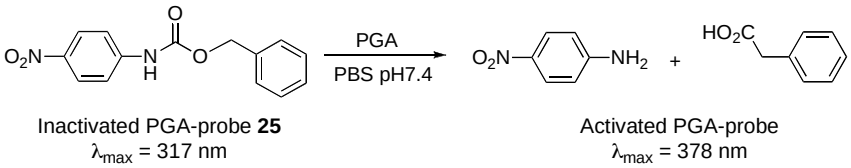

Inactivated PGA-probe **25**
λ_{max} = 317 nm

Activated PGA-probe
λ_{max} = 378 nm

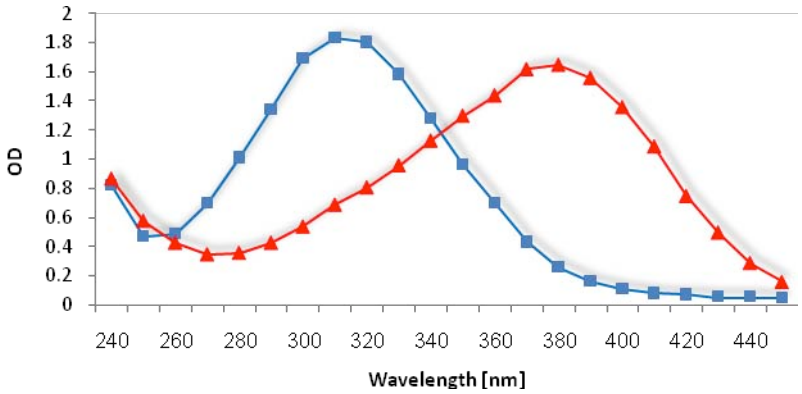

Figure 4S: UV absorbance spectra of (■) inactivated and (▲) activated PGA-probe **25** [250 μM].

Relative enzymatic activity of Ab38C2

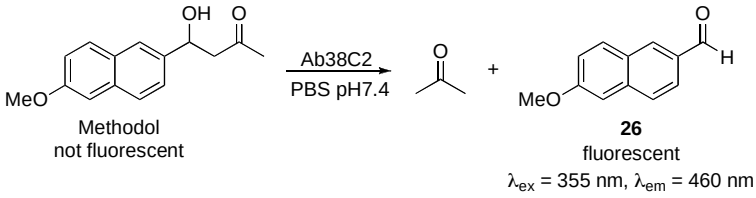

Methodol
not fluorescent

26
fluorescent
λ_{ex} = 355 nm, λ_{em} = 460 nm

The relative enzymatic activity of labeled and unlabeled of Ab38C2 was tested for the *retro*-aldol reaction with methodol according to a published assay.(29) When used as a substrate for *retro*-aldol reaction, methodol disintegrates into acetone and the fluorescent aldehyde 6-methoxy-2-naphthaldehyde (**26**) (λ_{ex} = 355 nm, λ_{em} = 460 nm). Experiments were conducted in a 96-wells fluorescence measuring plate and fluorescence was monitored using a Molecular Devices SPECTRAmaxM2 plate reader.

Comparison of the labeling characterizations for monomeric (10), trimeric (11) and SIP (8) probes

Synthesis of monomeric labeling probe 10

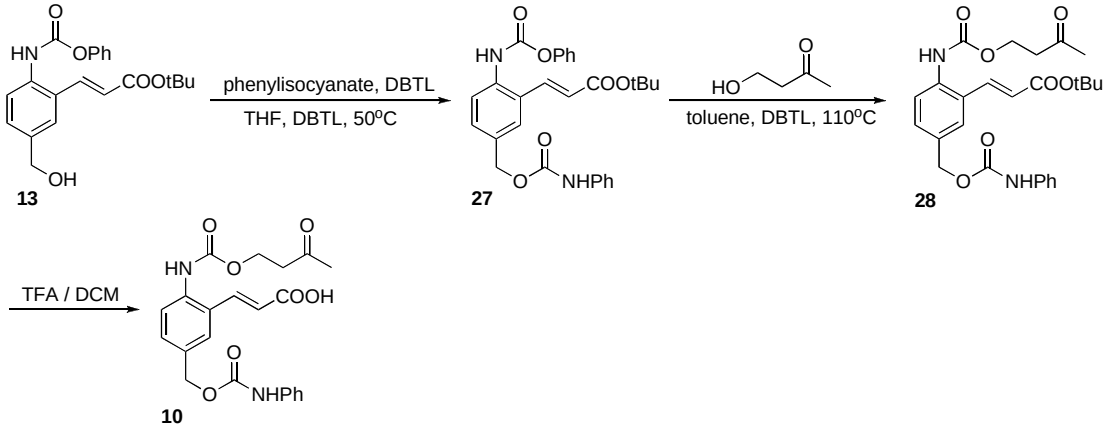

Compound 27. Compound **13** (250 mg, 0.68 mmol, 1 eq) was dissolved in dry THF (5 mL), preheated to 50°C. Phenylisocyanate (78 μL, 0.71 mmol, 1.05 eq) was added, followed by DBTL (22 μL, 0.033 mmol, 0.05 eq) and the reaction was monitored to completion (10 minutes) by TLC (EtOAc:Hex 1:3). The solvent was removed under reduced pressure and the crude product purified by column chromatography on silica gel (EtOAc:Hex 2:8) to give compound **27** (345 mg, 95%) as a white solid.

^{1}H NMR (400 MHz, $CDCl_3$): δ = 7.85 (1H, s), 7.89 (1H, d, *J* = 15.7 Hz), 7.56 (1H, s), 7.37-7.42 (5H, m), 7.27-7.32 (2H, m), 7.26 (1H, d, *J* = 1.6 Hz), 7.20-7.25 (2H, m), 6.80 (1H, s), 6.40 (2H, d, *J* = 15.7 Hz), 5.17 (2H, s), 1.56 (9H, s). ^{13}C NMR (100 MHz, $CDCl_3$): δ = 165.8, 153.2, 152.0, 150.5, 137.6, 137.2, 235.5, 132.8, 130.8, 129.5, 129.4, 127.2, 123.8, 121.8, 121.6, 121.3, 119.5, 118.7, 81.2, 66.2, 28.4. MS (MALDI-TOF): calculated for [M+Na^+] $C_{28}H_{28}N_2O_6$ 511.1; found 511.1.

Compound 28. Compound **27** (200 mg, 0.41 mmol, 1 eq) was dissolved in toluene (4 mL), preheated to 110°C. 4-Hydroxy-2-butanoe (108 μL, 1.23 mmol, 3 eq) was added, followed by DBTL (25 μL, 0.041 mmol, 0.1 eq) and the reaction was monitored to completion (30 minutes) by TLC (EtOAc:Hex 4:6). The solvent was removed under reduced pressure and the crude product purified by column

chromatography on silica gel (EtOAc:Hex 4:6) to give compound **28** (142 mg, 72%) as a white solid.

^{1}H NMR (400 MHz, DMSO-d^{6}): δ = 9.69 (1H, s), 9.38 (1H, s), 7.79 (1H, d, *J* = 1.2 Hz), 7.65 (1H, d, *J* = 15.9 Hz), 7.33-7.42 (4H, m), 7.23 (2H, t, *J* = 7.4 Hz), 6.95 (1H, t, 7.4 Hz), 6.39 (1H, d, *J* = 15.9 Hz), 5.08 (2H, s), 4.21 (2H, t, *J* = 6.2 Hz), 2.77 (2H, t, *J* = 6.2 Hz), 2.09 (3H, s), 1.44 (9H, s). ^{13}C NMR (100 MHz, DMSO-d^{6}): δ = 206.8, 166.0, 154.9, 153.7, 139.6, 139.4, 136.8, 134.4, 129.5, 129.2, 129.0, 126.8, 123.1, 121.0, 118.8, 80.6, 65.6, 60.3, 42.4, 30.3, 28.4. MS (MALDI-TOF): calculated for [M+Na^{+}] $C_{26}H_{30}N_2O_7$ 505.2; found 505.2.

Compound 10. Compound **28** (5 mg) was dissolved in a 1:1 mixture of TFA and DCM, stirred for 5 minutes and the solvents removed under reduced pressure. The obtained compound **10** was used without further purification.

^{1}H NMR (400 MHz, DMSO-d^{6}): δ = 9.71 (1H, s), 9.38 (1H, s), 7.79 (1H, s), 7.65 (1H, d, *J* = 15.8 Hz), 7.33-7.42 (4H, m), 7.23 (2H, t, *J* = 7.4 Hz), 6.95 (1H, t, 7.4 Hz), 6.39 (1H, d, *J* = 15.8 Hz), 5.09 (2H, s), 4.20 (2H, t, *J* = 6.3 Hz), 2.75 (2H, t, *J* = 6.3 Hz), 2.10 (3H, s).

Synthesis of trimeric labeling probe 11

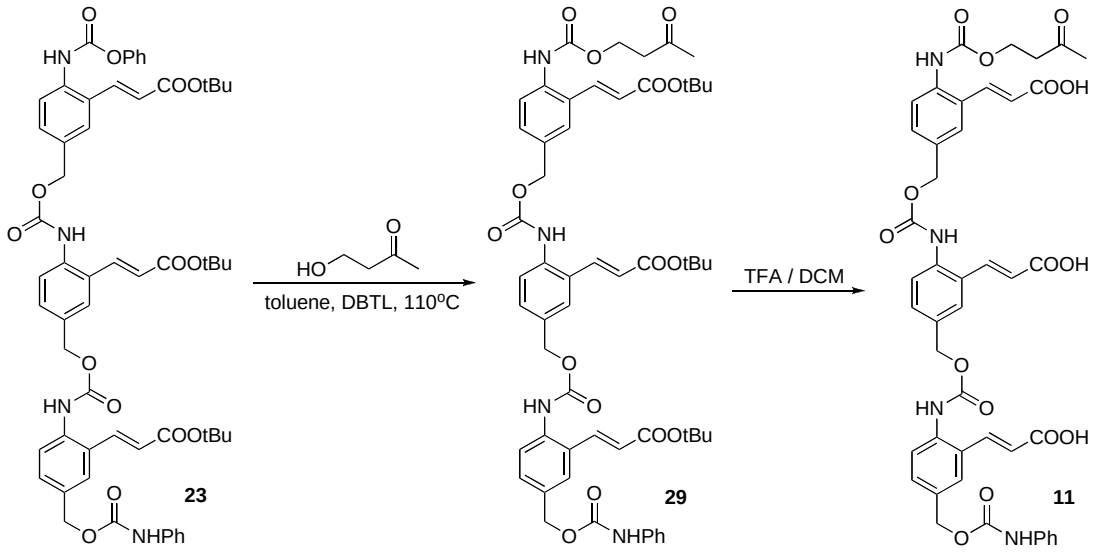

Compound 29. Compound **23** (150 mg, 0.14 mmol, 1 eq) was dissolved in toluene (6 mL), preheated to 110°C. 4-Hydroxy-2-butanoe (80 μL, 0.86 mmol, 6 eq) was added, followed by DBTL (10 μL, 0.014 mmol, 0.1 eq) and the reaction was monitored to completion (45 minutes) by TLC (EtOAc:Hex 4:6). The solvent was removed under reduced pressure and the crude product purified by column chromatography on silica gel (EtOAc:Hex 4:6) to give compound **29** (134 mg, 93%) as a white solid.

^{1}H NMR (200 MHz, DMSO-d^{6}): δ = 9.74 (1H, s), 9.54 (2H, s), 9.47 (1H, s), 7.67-7.87 (6H, m), 7.37-7.48 (8H, m), 7.27 (2H, t, *J* = 7.5 Hz), 7.00 (1H, t, *J* = 7.5 Hz), 6.39-6.50 (3H, m), 5.13 (6H, s), 4.25 (2H, t, *J* = 6.2 Hz), 2.82 (2H, t, *J* = 6.2 Hz), 2.14 (3H, s), 1.46 (27H, s). ^{13}C NMR (50 MHz, DMSO-d^{6}): δ = 206.8, 166.3, 165.8, 155.0, 154.8, 153.7, 148.5, 139.9, 139.4, 137.6, 137.1, 136.9, 134.3, 134.1, 132.2, 130.6, 130.3, 129.1, 128.9, 128.8, 128.4, 126.7, 124.3, 122.8, 121.1, 118.6, 117.7, 117.6, 116.7, 80.4, 79.8, 66.7, 65.9, 65.5, 28.2. MS (MALDI-TOF): calculated for [M+Na^{+}] $C_{56}H_{64}N_{4}O_{15}$ 1055.4; found 1055.4.

Compound 11. Compound **29** (5 mg) was dissolved in a 1:1 mixture of TFA and DCM, stirred for 5 minutes and the solvents removed under reduced pressure. The obtained compound **11** was used without further purification.

^{1}H NMR (400 MHz, DMSO-d^{6}): δ = 9.77 (1H, s), 9.52 (2H, s), 9.45 (1H, s), 7.65-7.89 (6H, m), 7.33-7.50 (8H, m), 7.26 (2H, t, *J* = 7.5 Hz), 7.00 (1H, t, *J* = 7.5 Hz), 6.36-6.49 (3H, m), 5.14 (6H, s), 4.21 (2H, t, *J* = 6.2 Hz), 2.83 (2H, t, *J* = 6.2 Hz), 2.14 (3H, s).

Labeling experiments

The labeling of Ab38C2 was performed for three final aza-quinone methide concentrations, as presented in Table 2S.

Final aza-quinone methide concentration	SIP 8[a] concentration	Trimer 11[b] concentration	Molecule 10[c] concentration
3.5 mM	250 μM	1.16 mM	3.5 mM
2.1 mM	150 μM	700 μM	2.1 mM
1.05 mM	75 μM	350 μM	1.05 mM

Table 2S: [a] SIP **8** is constructed of 15 monomers (on average), therefore, each polymer molecule is expected to release 14 aza-quinone methides. [b] Trimer **11** is constructed of 3 monomers, therefore, each trimer molecule is expected to release 3 aza-quinone methides. [c] Molecule **10** is constructed of one monomer, therefore, each molecule is expected to release one aza-quinone methide.

Synthesis of hydrogen-peroxide-activated SIP labeling probe 12

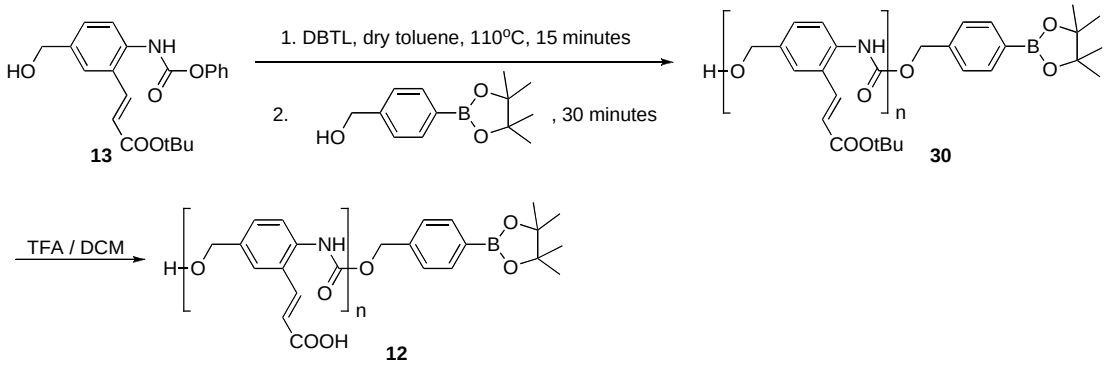

Polymer 30. Compound **13** (150 mg, 0.40 mmol, 1 eq) and DBTL (13 μL, 0.02 mmol, 0.05 eq) were dissolved in dry toluene (400 μL), preheated to 110°C, under

argon atmosphere. The reaction was stirred for 15 minutes and 4-(Hydroxymethyl)benzeneboronic acid pinacol ester (56 mg, 0.24 mmol, 0.6 eq) was then added. The reaction mixture was stirred for additional 30 minutes and then allowed to cool to room temperature. The polymer was precipitated from methanol, filtered and dried under reduced pressure for three hours. Polymer **30** (85 mg) was obtained as a white powder. The formed polymer was constructed of 15 monomers in average (determined by ^{1}H-NMR).

^{1}H NMR (400 MHz, DMSO-d^{6}): δ = 9.60 (15H, s), 7.86 (15H, s), 7.77 (17H, d, *J* = 15.6 Hz), 7.35 (30H, s), 7.30 (2H, s), 6.45 (15H, d, *J* = 15.6 Hz), 5.14 (30H, s), 4.49 (2H, s), 1.47 (135 H, s), 1.29 (12H, s).

Polymer 12. Polymer **30** (5 mg) was dissolved in a 1:1 mixture of TFA and DCM, stirred for 5 minutes and the solvents were then removed under reduced pressure. The obtained polymer **12** was used without further purifications.

^{1}H NMR (400 MHz, DMSO-d^{6}): δ = 9.59 (15H, s), 7.75-7.86 (32H, m), 7.29-7.36 (32H, m), 6.45 (15H, d, *J* = 15.7 Hz), 5.14 (30H, s), 4.47 (2H, s), 1.30 (12H, s).

Comparative quantum yield calculations

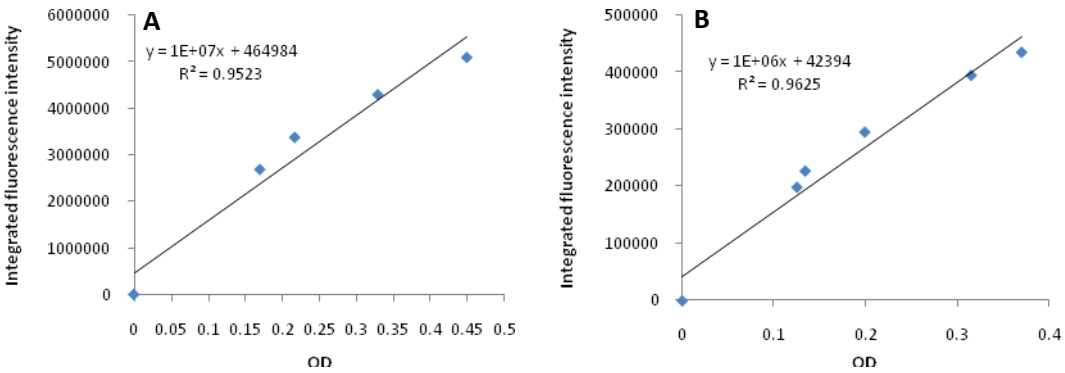

Figure 5S: Integrated fluorescence intensity *vs* absorbance at λ_{max} for: A) 1-naphtylamin and B) molecule **3**.

$$\Phi_X = \Phi_{ST} \cdot \left(\frac{Grad_X}{Grad_{ST}} \right) \left(\frac{\eta_X{}^2}{\eta_X{}^2} \right)$$

Equation 1: The subscripts ST and X denote standard and test respectively, Φ is the fluorescence quantum yield, *Grad* the gradient from the plot of integrated fluorescence intensity *vs* absorbance at λ_{max}, and η the refractive index of the solvent.

Since ethanol was used as solvent in all measurements, the influence of the refractive index of the solvent was dismissed and the quantum yield was calculated based on the results presented above using equation 1. The quantum yield found for molecule **3** in ethanol was $\Phi_F = 0.043 \pm 10\%$.

Spectral data of new SIPs

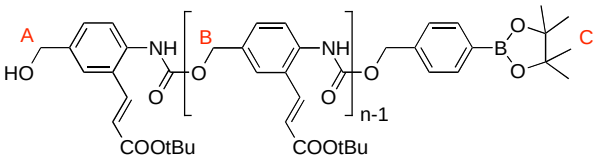

30

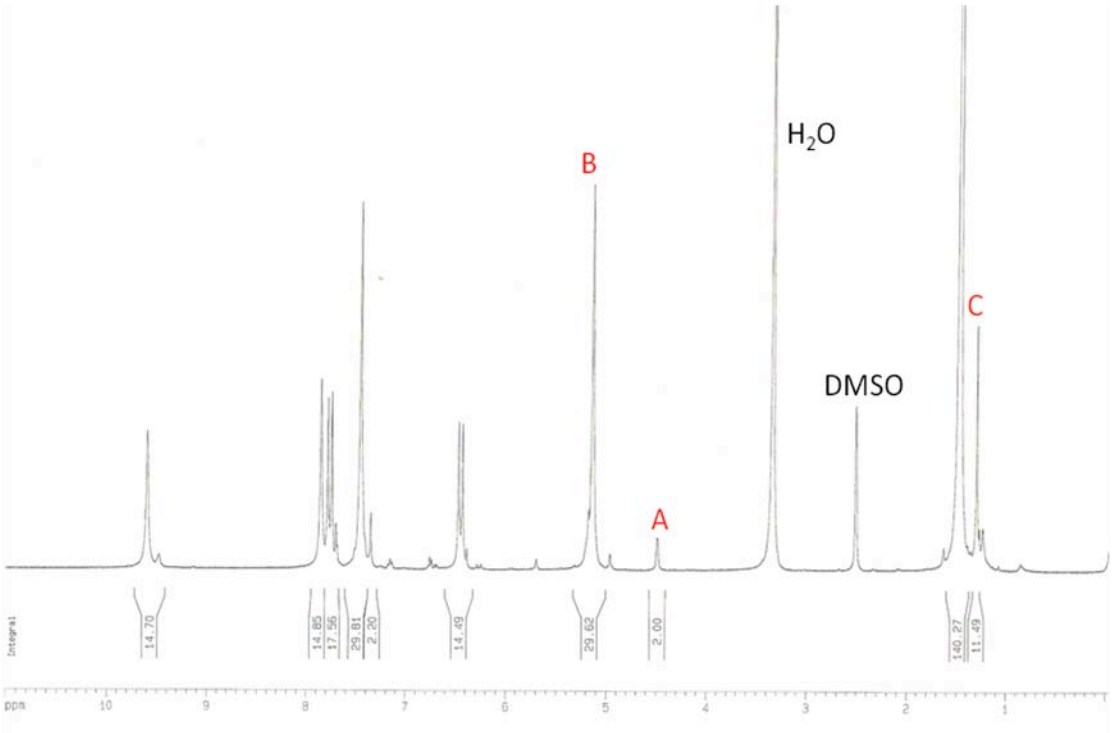

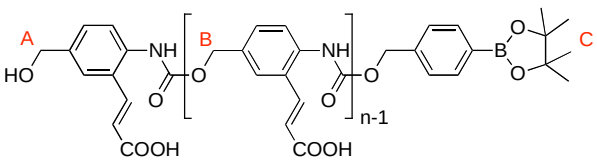
A
HO
NH
B
O
O
NH
O
O
n-1
COOH
COOH
B
O
O
C

12

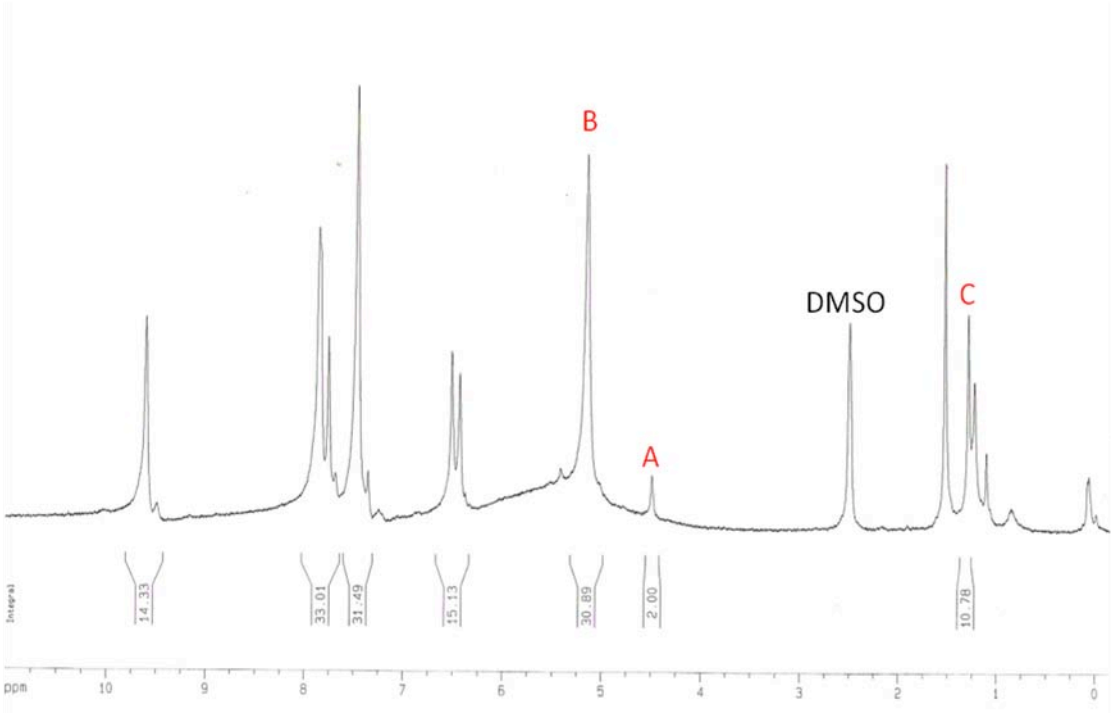
B
DMSO
C
A
14.33
33.01
31.49
15.13
30.89
2.00
10.78
ppm
10
9
8
7
6
5
4
3
2
1
0

pH-Sensitive Radical-Containing-Nanoparticle (RNP) for the L-Band-EPR Imaging of Low pH Circumstances

Toru Yoshitomi,[†] Rie Suzuki,[†] Takashi Mamiya,[‖,#] Hirofumi Matsui,[§,‖,#] Aki Hirayama,[§,▽] and Yukio Nagasaki*[,†,‡,§,‖,⊥]

Graduate School of Pure and Applied Sciences, University of Tsukuba, Tsukuba Research Center for Interdisciplinary Materials Science (TIMS), University of Tsukuba, Center for Tsukuba Advanced Research Alliance (TARA), University of Tsukuba, Master's School of Medical Sciences, Graduate School of Comprehensive Human Sciences, University of Tsukuba, Satellite Laboratory, International Center for Materials Nanoarchitectonics (MANA), National Institute for Materials Science (NIMS), Division of Gastroenterology, Graduate School of Comprehensive Human Sciences, University of Tsukuba, Tennoudai 1-1-1, Tsukuba, 305-8573, Ibaraki, Center for Integrative Medicine, Tsukuba Universiy of Technology, Kasuga 4-12-7, Tsukuba, 305-8521, Ibaraki, Japan. Received May 15, 2009; Revised Manuscript Received July 24, 2009

For the imaging of low pH circumstances *in vivo*, a pH-sensitive radical-containing-nanoparticle (RNP), which has an intense electron paramagnetic resonance (EPR) signal, was designed and developed using a self-assembling amphiphilic block copolymer (PEG-*b*-PCTEMPO) composed of a hydrophilic poly(ethylene glycol) (PEG) segment and a hydrophobic poly(chloromethylstyrene) (PCMS) segment in which the chloromethyl groups were converted to 2,2,6,6-tetramethylpiperidinyloxys (TEMPOs) via the amination of PEG-*b*-PCMS block copolymer with 4-amino-TEMPO. This RNP formed core−shell-type micelles in the physiological environment, and the cumulant average diameter of the RNP was about 50 nm. The cytotoxicity and acute toxicity studies for the RNP revealed that the median inhibitory concentration (IC_{50}) of TEMPO radicals in RNP core and median lethal dose (LD_{50}) of RNP were >8 mmol N(TEMPO)/L and >600 mg/kg (>960 μmol N(TEMPO)/kg), respectively, indicating fairly low toxicity. The blood circulation of the RNP was evaluated using ICR mice. Contrary to the rapid clearance of low-molecular-weight TEMPO derivatives such as 4-hydroxy-TEMPO (TEMPOL) from the bloodstream, the EPR signal of the RNP remained for a fairly long period of time. Actually, the signal was observed in the blood for more than 2 h, as monitored by EPR spectroscopy. The compartmentalization of the TEMPO radicals in the RNP core improved the stability in the bloodstream. Since an amino group was introduced in each repeating unit of the PCTEMPO segment, the disintegration of the RNP was caused by the protonation of the amino groups in response to the acidic pH environment (pH < 6.0), as confirmed by the dynamic light scattering (DLS) measurements. In addition, a drastic change in the EPR spectra from broad to sharp triplet was observed, accompanying the disintegration. This change was based upon the mobility of the TEMPO moieties covalently conjugated in the hydrophobic segment, which was confirmed by the rotational correlation time of the TEMPO moieties on the PCTEMPO segment. Note that the peak intensity of the EPR signal increased at around the phase transition point (ca. pH = 6.0). When pH-sensitive RNP solutions at pH values 5.6 and 7.4 were visualized using an L-band EPR imaging system, the phantom images showed a remarkable on−off regulation in response to the acidic pH environment. These results demonstrate that pH-sensitive RNPs are expected to serve as nanoprobes for the *in vivo* EPR imaging of low pH circumstances.

INTRODUCTION

Recently, the non-invasive *in vivo* imaging of low pH circumstances has attracted attention as a new means of detecting disease and response to clinical treatment. Low pH circumstances, which are an aberration of normal pH homeostasis, are caused by ischemia (*1, 2*), infection (*3*) or inflammation (*4*), extracellular acidosis in tumors (*5, 6*), wound healing (*7*), and so forth. However, there is currently no clinical tool available to capture an image of low pH circumstances *in vivo*. In order to image acidic pH regions *in vivo*, various molecular probes have been developed so far for magnetic resonance imaging (MRI) (*8*−*10*), positron emission tomography (PET) (*11*), and optical imaging (*12*). Under *in vivo* conditions, however, the diagnostic efficiency of such probes is still controversial. A more desirable design criterion for the imaging of acidic pH regions *in vivo* is believed to be the development of nanoprobes capable of the on−off regulation of the signal in response to the acidic pH environment (*8*, *12*).

Nitroxyl radicals, such as 2,2,6,6-tetramethylpiperidinyloxy (TEMPO), are organic molecules that have a stable radical and are therefore susceptible to electron paramagnetic resonance (EPR). Recently, the research on *in vivo* EPR imaging has been stepped up by several groups (*13, 14*). Some groups have reported on pH-sensitive nitroxyl radicals of the imidazolidine type or the imidazoline type for the noninvasive measurement of pH (*15, 16*) Under *in vivo* conditions, however, such low-molecular-weight nitroxyl radicals pose several problems, such as nonspecific accumulation in normal tissues, preferential renal

* yukio@nagalabo.jp.
[†] Graduate School of Pure and Applied Sciences, University of Tsukuba.
[‡] TIMS, University of Tsukuba.
[§] TARA, University of Tsukuba.
[‖] Master's School of Medical Sciences, Graduate School of Comprehensive Human Sciences, University of Tsukuba.
[⊥] MANA, NIMS.
[#] Division of Gastroenterology, Graduate School of Comprehensive Human Sciences, University of Tsukuba.
[▽] Center for Integrative Medicine, Tsukuba Universiy of Technology.

10.1021/bc900214f CCC: $40.75 © 2009 American Chemical Society
Published on Web 08/17/2009

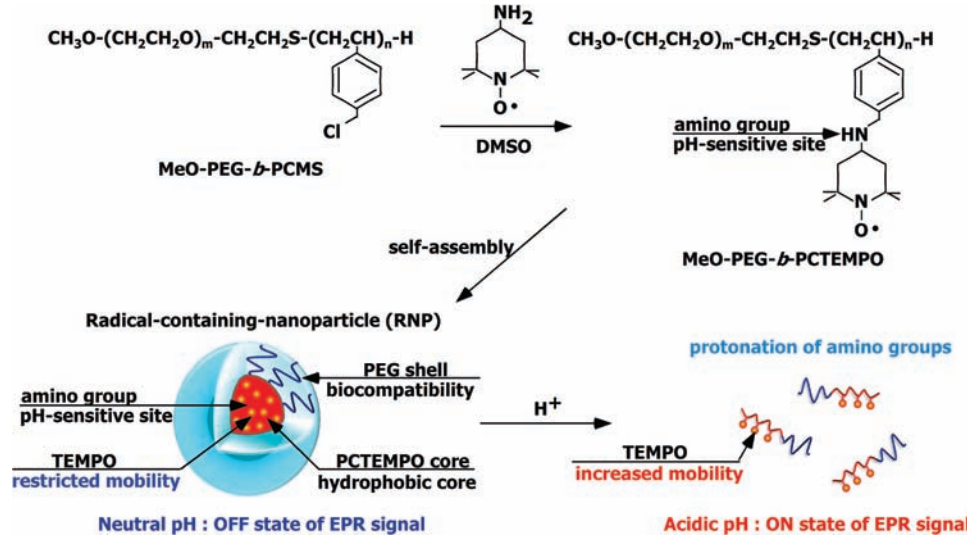

Figure 1. Schematic illustration of the pH-sensitive radical-containing-nanoparticle (RNP) prepared from PEG-*b*-PCTEMPO for the *in vivo* EPR imaging of low pH circumstances.

clearance, and rapid reduction of the nitroxyl radical form to the corresponding hydroxylamine form (*17*, *18*).

To solve these difficulties, we have designed and developed a radical-containing-nanoparticle (RNP) using a self-assembling amphiphilic block copolymer (PEG-*b*-PCTEMPO) composed of a hydrophilic poly(ethylene glycol) (PEG) segment and a hydrophobic poly(chloromethylstyrene) (PCMS) segment in which the chloromethyl groups were converted to TEMPOs via the amination of PEG-*b*-PCMS block copolymer with 4-amino-TEMPO (Figure 1) (*19*). This RNP formed core−shell-type micelles in the physiological environment; the cumulant average diameter of the RNP was about 50 nm, and the RNP emitted an intense EPR signal. We have previously reported that the TEMPO radicals in the core of the RNP showed fairly high resistance against reducing reactions compared with low-molecular-weight 4-hydroxyl-TEMPO (TEMPOL) even in the presence of 3.5 mM ascorbic acid (*19*). Thus, this RNP is anticipated to serve as a high-performance bionanoparticle which can be used *in vivo*. In this study, we evaluated the toxicity and the blood circulation of the RNP in view of its use *in vivo*. Since an amino group was introduced into each repeating unit on the PCTEMPO segment, the RNP emitted pH-sensitive EPR signals in response to the acidic pH environment due to the protonation of the amino groups. We demonstrated the drastic change in the EPR signal of the RNP as a function of pH. A pH-dependent phantom study of the RNP for the *in vivo* EPR imaging of low pH circumstances using L-band EPR spectroscopy is also described herein.

EXPERIMENTAL PROCEDURES

Synthesis of MeO-PEG-*b*-PCTEMPO. MeO-PEG-*b*-PCMS was synthesized by the radical telomerization of chloromethylstyrene (CMS) using MeO-PEG-SH ($M_n = 5000$) as a telogen, according to procedure described in the previous report (*19*) (see Supporting Information Scheme S1 and Figure S1). After the synthesis of PEG-*b*-PCMS, the chloromethyl groups on the PCMS segment of the block copolymer MeO-PEG-*b*-PCMS were converted to stable radicals via the amination of MeO-PEG-*b*-PCMS with 4-amino-TEMPO in DMSO (see Supporting Information Scheme S1 and Figure S2).

Preparation of the RNP. The RNP was prepared from MeO-PEG-*b*-PCTEMPO by the dialysis method described previously (*19*). Briefly, 400 mg of MeO-PEG-*b*-PCTEMPO was dissolved in 100 mL of DMF, and the polymer solution was transferred into a membrane tube (Spectra/Por, molecular-weight cutoff size 3500; Spectrum, USA) and then dialyzed for 24 h against 2 L of water, which was changed after 2, 5, 8, and 20 h. Dynamic light scattering (DLS) measurement was carried out to determine the diameter of the obtained RNP after dialysis. In order to adjust the concentration of the RNP solution, the obtained RNP solution was concentrated by a centrifugal evaporator (~60 mg/mL), followed by DLS measurement of the concentrated RNP to confirm the size of the RNP after the concentration.

Cytotoxicity Studies. Cell viability was determined by a quantitative colorimetric assay using WST-8 (DOJINDO Laboratories, Kumamoto, Japan). Briefly, 1×10^4 cells were seeded per well on a 96-well flat-bottom plate. At 24 h after treatment, 10 μL of WST-8 reagent was added to each well containing 100 μL of medium, according to the manufacturer's instructions. The plate was incubated for 1 h at 37 °C and read at an absorbance of 450 nm by a plate reader.

Median Lethal Dose (LD_{50}) Studies. Male ICR mice (5 weeks old, ca. 25 g) were purchased from Charles River Japan, Inc. The LD_{50} value of the RNP was determined by injecting the RNP saline solution with increasing doses into the ICR mice via the tail vein. There were five mice in each dose group. The doses of intravenous administration were elevated as follows: 75, 150, 300, and 600 mg/kg mouse body weight. The mice in all groups were observed for 2 weeks, and the number of surviving mice was recorded.

Blood Circulation of the RNP. The blood circulation of the RNP was examined as follows: after anesthesia with pentobarbital sodium (40 mg/kg), 200 μL of RNP saline solution (12 mg/mL) were injected into the tail vein of male ICR mice (ca. 25 g), and then blood samples were collected at 2 min, 10 min, 30 min, 1 h, and 3 h. Plasma samples were obtained by centrifugation (6200 rpm, 2000 × *g*, 10 min) of the blood. It was confirmed that no EPR signal was observed in the blood cell precipitates after centrifugation. The EPR signal intensities in these plasma samples were measured by an X-band EPR spectrometer (JES-TE25X, JEOL, Tokyo, Japan) at room temperature. In the case of the EPR intensities at 0 min, 50 μL of the RNP solution (12 mg/mL) was added to the blood (500 μL), followed by centrifugation (6200 rpm, 2000 × *g*, 10 min) of the blood and EPR measurement, assuming that the total blood volume in mice is 80 mL/kg. A free-TEMPOL saline solution with the same spin concentration as the RNP was used as a control. The EPR measurements were carried out under

the following conditions: frequency, 9.41 GHz; power, 8.00 mW; field, 333.8 ± 5 mT; sweep time, 1.0 min; modulation, 0.1 mT; time constant, 0.1 s. All procedures and animal care were approved by the Committee on the Ethics of Animal Experimentation of the University of Tsukuba, and were conducted according to the Guidelines for Animal Experimentation of the University of Tsukuba.

Potentiometric Titrations. An aqueous solution of RNP (1.0 mL: 20 mg/mL) was added to a solution of 0.01 M HCl (4.0 mL), followed by the adjustment of the NaCl concentration to 0.15 M (40 mL). The resulting RNP solution (40 mL) was titrated with 0.01 M NaOH containing 0.15 M NaCl at 25 °C. An automatic titrator (DL-25, Mettler) was used for the titration. In this case, the titrant was added in quantities of 0.05 mL after the pH values were stabilized (minimal interval: 30 s), and the titration curves in the pH range from about 3 to about 10 were recorded.

Dynamic Light Scattering (DLS) Experiments and X-Band Electron Paramagnetic Resonance (EPR) Experiments as a Function of pH. The light scattering intensities of the pH-sensitive RNP were measured as a function of pH using a light scattering spectrometer (Nano ZS, ZEN3600, Malvern Instruments, Ltd., U.K.) equipped with a He−Ne laser that produces vertically polarized incident beams at a detection angle of 173° at 25 °C. Briefly, 3.5 mg/mL of the RNP solution was prepared as stock solution A after the formation of the RNPs by the dialysis method. Britton-Robinson buffers (100 μL each) with various pH values, which were prepared from a stock solution containing 1 M phosphoric acid, 1 M boric acid, and 1 M acetic acid and by adjusting the pH value with NaOH, were added to stock solution A (400 μL). The mixtures with various pH values were transferred to the cells immediately, followed by DLS measurement. A nanoparticle (CMS-NP: CNP) prepared from PEG-*b*-PCMS was used as a control.

After DLS measurement, the samples were transferred to a capillary tube, followed by EPR measurement. To measure the EPR spectra of the pH-sensitive RNP as a function of pH, the EPR spectra were recorded at room temperature on a JEOL JES-TE25X spectrometer. The EPR measurements were carried out under the following conditions: frequency, 9.4190 GHz; power, 8.00 mW; field, 333.8 ± 50 mT; sweep time, 2.0 min; modulation, 0.1 mT; time constant, 0.1 s.

Phantom EPR Imaging. Phantom images were obtained using a capillary glass tube (1.2 mm i.d.) containing 80 mg/mL of RNP solution at pH 5.6 or 7.4. 2D spatial images perpendicular to the axes of the tubes using an L-band EPR spectrometer manufactured by JEOL (Tokyo, Japan), consisting of a 1 GHz microwave unit and a bridged four-gap loop-gap resonator (38 mm in diameter and 28 mm in length), were obtained in this study. The EPR conditions for these phantom studies were as follows: magnetic field, 370.0 ± 5.0 mT; modulation width, 2.0 mT; time constant, 0.03 s; microwave power, 0.25 mW; scanning time, 30 s. EPR images were constructed on 256 points × 256 points.

RESULTS AND DISCUSSION

Synthesis of the Polymer and Preparation of the RNP. As described in the previous report (*19*), MeO-PEG-*b*-PCMS was synthesized by the radical telomerization of CMS using MeO-PEG-SH as a telogen, as shown in Supporting Information Scheme S1. The molecular weight distribution of MeO-PEG-*b*-PCMS was evaluated by size exclusion chromatography (SEC), as shown in Supporting Information Figure S1a. The SEC profile of MeO-PEG-*b*-PCMS and the molecular weight of the PCMS segment after polymerization were almost the same as those of acetal-PEG-*b*-PCMS reported previously (*19*). The polymer backbone of PEG-*b*-PCMS consisted of PEG with a molecular weight of 5000 g/mol for the hydrophilic segment and 20 repeating units of PCMS for the hydrophobic segment (MW = 3300), as determined by the ^{1}H NMR data based on the M_n of PEG (see Supporting Information Figure S1b). MeO-PEG-*b*-PCTEMPO was synthesized by the substitution of the chloromethyl groups of the PCMS segment of MeO-PEG-*b*-PCMS with amino-TEMPO via amination in DMSO. After the purification of the obtained PEG-*b*-PCTEMPO, the substitution ratio of the modified TEMPO moieties per repeating unit of PCMS was 80%, as determined by EPR spectroscopy using the standard curve of free-amino-TEMPO in chloroform. The thus-obtained PEG-*b*-PCTEMPO was dialyzed against water to obtain the RNP. As shown in Supporting InformationFigure S3, the RNP after dialysis showed a unimodal distribution in the histogram analysis. The average diameter and polydispersity factor (μ_2/Γ^2), as determined by the cumulant method, were about 50 nm and 0.133, respectively.

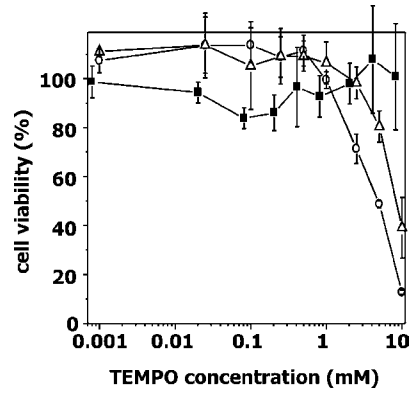

Figure 2. Cell viability against RNP (closed square), TEMPO (open triangle), and 4-amino-TEMPO (open circle) in colon cells (WST assay). The plotted data represent the average ± SEM of three experiments.

Toxicity Study of the RNP. TEMPO derivatives are known as biologically active substances (*20, 21*). Suy et al. have reported that the promotion of apoptosis by TEMPO is one of its physiological activities in cancer cells (*22*). Since each RNP carries several thousand TEMPO moieties (stable radicals) in its core, it is interesting to investigate the behavior of RNP *in vivo*. The cytotoxicity of the RNP was investigated by subjecting colon cells to the WST assay. As shown in Figure 2, the dose-dependent cell viabilities were observed in colon cells treated with TEMPO, 4-amino-TEMPO, and the RNP. The number on the horizontal axis of the figure indicates the concentration of TEMPO radical, as determined by EPR spectroscopy. The colon cell viabilities were progressively reduced after 24 h with increasing concentrations of low-molecular-weight TEMPO and amino-TEMPO. The median inhibitory concentrations (IC_{50}) of TEMPO and 4-amino-TEMPO were 8.3 mM and 4.8 mM, respectively. Because amino groups generally show high toxicity, the cytotoxicity of 4-amino-TEMPO might be higher than that of TEMPO. In contrast, the RNP induced no change in cell viability regardless of the concentration of RNP up to the concentration of 8 mmol N(TEMPO)/L. The extremely low toxicity of RNP is probably because the outer PEG layer constitutes an excellent stealth shield around the amino-TEMPO moieties in the RNP core. The median lethal dose (LD_{50}) of the RNP in ICR mice was then evaluated. For the evaluation of the LD_{50} value, RNP solution at a concentration of 60 mg/mL was employed, because the size of the RNP did not change up to this concentration (data not shown). 250 μL of RNP saline solution (0, 7.5, 15.0, 30.0, 60.0 mg/mL, which correspond to 0, 75, 150, 300, 600 mg/kg-dose, respectively) were intravenously administered to ICR mice (ca. 25 g).

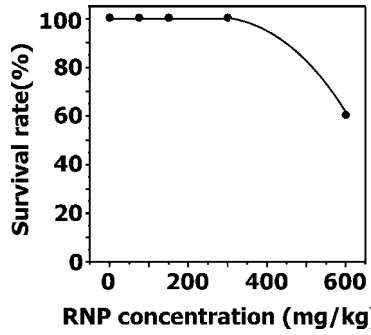

Figure 3. Survival rate of ICR mice injected with RNP. The RNP doses of the intravenous injections were gradually increased as follows: 0, 75, 150, 300, 600 mg/kg mouse body weight.

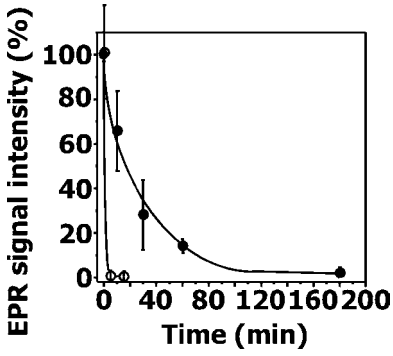

Figure 4. Blood circulation of the RNP (closed circle) and TEMPOL (open circle). The EPR intensity changes in the blood were measured at 2, 5, 30, 60, and 180 min after injecting RNP saline solution into the mice.

As shown in Figure 3, no dead mice were observed for 2 weeks after the administration of the RNP (0−300 mg/kg). Even at 600 mg/kg (concentration of amino-TEMPO moieties: 960 μmol N(TEMPO)/kg), 60% of the mice lived. Stefano et al. have reported that the LD_{50} of poly(L-lysine) with a molecular weight of 28 000−42 000 (polymerization degree = 135−203) was between 15 and 30 mg/kg (concentration of amino groups: 72.5−145 μmol N/kg) (*23*). The extremely low toxicity of RNP, viz., IC_{50} > 8 mmol N(TEMPO)/L and LD_{50} > 600 mg/kg (>960 μmol N(TEMPO)/kg), is considered to be due to the confinement of the polyamine segment of the block copolymer in the RNP core. The antioxidant character of the RNP might also have contributed to the reduced toxicity.

Blood Circulation of Nitroxyl Radicals. In order to obtain information on the circulation of nitroxyl radicals in the bloodstream, an EPR study was carried out. Figure 4 shows the time course of the spin concentration of the RNP in the blood after intravenous injection. When low-molecular-weight TEMPOL was administered, almost no EPR signals was observed even after 2 min in the bloodstream. The half-life of TEMPOL in blood is reported to be about 15 s (*24*). It is interesting to note, in contrast, that the EPR signal in the bloodstream was observed even 2 h after tail-vein injection of the RNP. The half-life of the RNP was 60 times longer (15 min) than that of low-molecular-weight TEMPOL. The rapid clearance of low-molecular-weight TEMPOL from the bloodstream was probably due to preferential renal clearance and the rapid reduction of the TEMPO radical form to the corresponding hydroxylamine form in the blood. We have previously reported that the TEMPO radicals in the RNP core showed high reduction resistance in the presence of 3.5 mM ascorbic acid (*19*). The compartmentalization of the TEMPO radicals in the RNP core resulted in the reduced reactivity of the TEMPO radicals toward ascorbic acid. The increased reduction resistance of the RNP must be one of the reasons for the prolonged blood circulation time. Since the observed EPR signals were broad singlet in blood (data not shown), it is considered that the TEMPO moieties are still located in the solid core of the RNP. Thus, slow dissociation is one of the important factors to improve blood circulation of nitroxyl radicals in bloodstream.

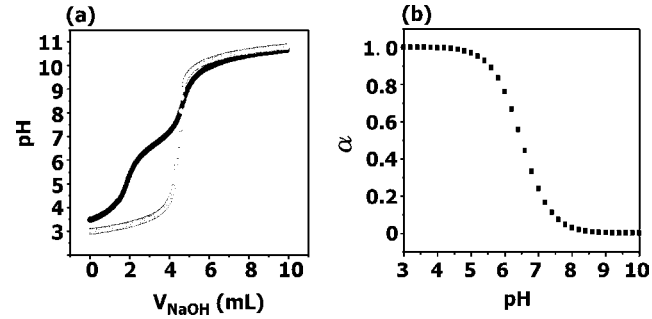

Figure 5. (a) Experimental titration curve obtained for aqueous solutions of CNP prepared from PEG-*b*-PCMS (open circle) and RNP prepared from PEG-*b*-PCTEMPO (closed circle) using 0.01 M NaOH. (b) The degree of protonation (α) as a function of solution pH for the pH-sensitive RNP prepared from PEG-*b*-PCTEMPO.

pH Response of the RNP. *Potentiometric Titration and Dynamic Light Scattering (DLS) Measurements.* Polyamine with the appropriate hydrophobicity is known to show phase transition as a function of pH (*25*, *26*). For example, the poly[2-(*N*,*N*-diethylamino)ethyl methacrylate] (PEAMA) homopolymer exhibits precipitation above pH 7.5 owing to the deprotonation of the amino groups of the PEAMA (*27*). It is reported that the self-assembly structure of block copolymer micelles can be controlled by the environmental pH when PEAMA is used as one of the segments in the block copolymer (*28*, *29*). Because the PCTEMPO segment possesses an amino group in each repeating unit, a similar phenomenon is anticipated in response to acidic pH environments due to the protonation of the amino groups. In order to confirm the pH-response of the RNP, potentiometric measurement of the RNP was performed. As shown in Figure 5a, the CNP, prepared as a control from PEG-*b*-PCMS (no amino groups), did not show buffer action at all, while the titration curve of the RNP showed a clear inflection point at pH 6−8, which was regarded as a buffer action. From the obtained titration curves, the pK_a of RNP was confirmed to be 6.5. The α-pH curves calculated using the Henderson-Hasselbach equation indicated that the amino groups on the PCTEMPO segment were almost completely protonated at pH values below 5.0, as shown in Figure 5b. In order to investigate the effect of the protonation of the PCTEMPO segment on the self-assembly structure of the RNP, the light scattering intensities of RNP solutions were measured as a function of pH. As shown in Figure 6, the light scattering intensity of CNP prepared from PEG-*b*-PCMS (no amino groups) did not change at all, whereas it drastically decreased at pH values below 6.0 in the case of RNP prepared from the PEG-*b*-PCTEMPO block copolymer. According to the Rayleigh approximation ($I \propto d^6$, where I is the scattering intensity and d is the particle size) (*30*), it is clear that the RNP disintegrated at pH values below 6.0. These results suggest that the PCTEMPO segment cannot form the hydrophobic core of the RNP due to the increased solubility of the PCTEMPO segment, which may be due to the protonation of the amino groups. On the basis of the obtained data, viz., titration and DLS measurements, it is concluded that the disintegration of the RNP at around pH = 6.0 was due to the protonation of the amino groups on the PCTEMPO segment and the molecular dissolution of the PEG-*b*-PCTEMPO copolymer in the acidic solution.

Electron Paramagnetic Resonance (EPR) Measurement. EPR spectra are known to give information on the local environment

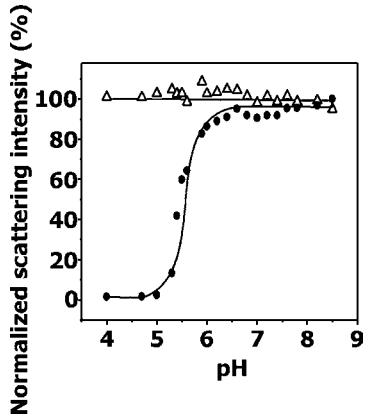

Figure 6. Effect of pH on the light scattering intensity of RNP prepared from PEG-*b*-PCTEMPO (closed circle) and CNP prepared from PEG-*b*-PCMS (open triangle). The normalized scattering intensity (%) is expressed as the value relative to that at pH 8.2.

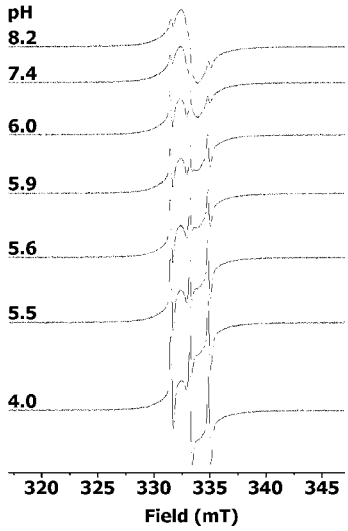

Figure 7. X-band EPR spectra of the RNP as a function of pH, at pH 4.0, 5.5, 5.6, 5.9, 6.0, 7.4, and 8.2, in Britton-Robinson buffer prepared from a stock solution containing 1 M phosphoric acid, 1 M boric acid, and 1 M acetic acid, and by adjusting the pH value with NaOH.

around the spin probe (*31*). The EPR measurement of the polymers carrying nitroxyl radicals thus gives us the dynamics of the polymer chain (*32*, *33*). Since the assembly of PEG-*b*-PCTEMPO depends on the protonation of the amino groups, as described above, the EPR spectra must be influenced by the environmental pH. In order to obtain detailed information on the EPR signals, the EPR measurement of the RNP under various pH conditions was carried out using an X-band EPR spectrometer. Figure 7 shows the EPR spectra of the RNP under various pH conditions, from pH = 4.0 to 8.2. Contrary to the clear triplet signals of low-molecular-weight TEMPO derivatives resulting from the interaction between the ^{14}N nuclei and the unpaired electron in the dilute solution (*19*), broad signals of the RNP were observed at pH values above 6.0, in same manner as the EPR signal after the dialysis. The EPR spectra of the RNP at pH values above 6.0 are due to the confinement of the TEMPO radicals in the solid core of the RNP. With decreasing pH, the EPR signals gradually changed, and typical triplet signals were observed under acidic pH (pH < 6.0) conditions, which is consistent with the disintegration region of the RNP. Since the spin probe is covalently conjugated in the PCTEMPO segment of the PEG-*b*-PCTEMPO block copolymer, the relative anisotropy observed in the EPR spectrum is directly related to the rotational mobility of the probe. In order to confirm the

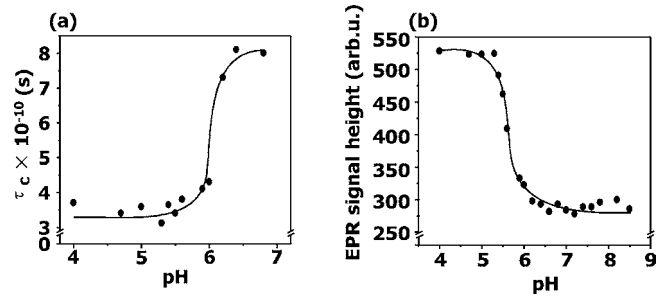

Figure 8. (a) Rotational correlation times (τ_c) of the TEMPO moieties on the PCTEMPO segment of RNP as a function of pH, which were calculated using eq 1 (see Supporting Information Figure S4).(b) EPR signal height of RNP as a function of pH.

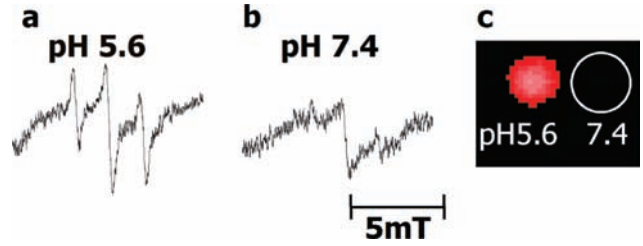

Figure 9. Phantom images of the RNP obtained by L-band EPR spectroscopy at pH 5.6 and 7.4. EPR spectrum of the RNP at pH 5.6 (a) and pH 7.4 (b). (c) Phantom images of the RNP at pH 5.6 (left) and pH 7.4 (right).

change in the rotational mobility factor, the rotational correlation time, τ_c (see Supporting Information Figure S4), was determined as a function of the environmental pH (Figure 8a). Under neutral conditions, the τ_c was about 8.0×10^{-10} s. Its abrupt decrease was observed again at around the phase transition region (ca. pH = 6.0). Actually, the τ_c was about $(3-4) \times 10^{-10}$ s at pH values below 6.0. The lower τ_c indicates the higher mobility of the TEMPO moieties, which is certainly correlated with the disintegration of the RNP. Crucially, the mobility of the TEMPO moieties as side chains of the PCTEMPO segments increased along with the disintegration of the RNP core, and the distance between the TEMPO radicals increased due to the electrostatic repulsion between the protonated amino groups. In conjunction with the phase transition, a change in the EPR signal height was observed, as shown in Figure 8b. Indeed, a significant increase in signal height was observed at pH values below 6.0, which confirms that the RNP shows a phase transition at a specific pH (around pH = 6.0). If this phenomenon is also observed in the L-band EPR spectra, low pH circumstances might be visualized by *in vivo* EPR imaging. L-band EPR imaging systems operating in the lower-frequency microwave bands (less than 1.2 GHz), where the dielectric losses are lower, have been developed and utilized for the *in vivo* imaging of animals using a spin probe (*34*). After two different RNP samples (80 mg/mL) were transferred to a capillary glass tube at pH values 5.6 and 7.4, phantom images were obtained using the L-band EPR imaging system. Figure 9a,b shows the EPR spectra of the RNP at pH values 5.6 and 7.4, as measured by L-band EPR spectroscopy. The EPR spectrum of the RNP at pH 5.6 showed a clear triplet signal due to the disintegration of the RNP, in the same manner as the X-band EPR spectroscopy (Figure 9a). On the other hand, almost no narrow-line-width EPR signals were observed at pH 7.4 (Figure 9b). The signal-to-noise (*S*/*N*) ratios of the spectra at pH values 5.6 and 7.4 were about 12.5 and 7.8, respectively. The improvement of the *S*/*N* ratios in response to the acidic pH environment is remarkable. Figure 9c shows phantom images of the RNPs at pH values 5.6 and 7.4. The appropriate threshold (cutoff: 40%)

was used for de-noising. The phantom images clearly show a remarkable on−off regulation in the capillary glass tube. If the RNP is able to accumulate in low pH circumstances *in vivo*, then the RNP might disintegrate and emit strong EPR signals. This is our strategy for imaging of low pH circumustances using pH-sensitive RNP. From these results, the RNP might be used as a nanoprobe for the *in vivo* EPR imaging of low pH circumstances.

CONCLUSIONS

We have developed an EPR-imaging nanoprobe based on a pH-sensitive radical-containing-nanoparticle (RNP), which consists of PEG-*b*-PCTEMPO block copolymer. The RNP was confirmed to attain long-term spin circulation in the blood compared with low-molecular-weight TEMPOL. The RNP was also confirmed to show extremely low toxicity due to the confinement of the amino-TEMPO moieties in the RNP core. It is interesting to note that the disintegration and drastic change in the EPR signal of the RNP were observed at pH values below 6.0; this change was caused by the protonation of the amino groups on the PCTEMPO segments in response to the acidic pH environment. The phantom images indicate that the RNP can implement a remarkable on−off regulation of the EPR signal in response to acidic pH environments (pH < 6.0). These results demonstrate that pH-sensitive RNPs are expected to serve as an EPR imaging nanoprobes, which can image low pH circumstances *in vivo*.

ACKNOWLEDGMENT

We appreciate Dr. Kazuko Toh of the University of Tsukuba for her helpful assistance in this study. This work was partly supported by a Grant-in-Aid for Scientific Research A (21240050) and the World Premier International Research Center Initiative (WPI Initiative) on Materials Nanoarchitronics of the Ministry of Education, Culture, Sports, Science and Technology (MEXT) of Japan.

Supporting Information Available: The SEC diagram and ^{1}H NMR spectrum of MeO-PEG-*b*-PCMS and MeO-PEG-*b*-PCTEMPO and the size distribution of the RNP are provided. Also, the materials and calculation method for the rotational correlation time (τ_c) are described. This material is available free of charge via the Internet at http://pubs.acs.org.

LITERATURE CITED

(1) Zweier, J. L., Wang, P., Samouilov, A., and Kuppusamy, P. (1995) Enzyme-independent formation of nitric oxide in biological tissues. *Nat. Med. 1*, 804–809.

(2) Bond, J. M., Chacon, E., Herman, B., and Lemasters, J. J. (1993) Intracellular pH and Ca2+ homeostasis in the pH paradox of reperfusion injury to neonatal rat cardiac myocytes. *Am. J. Physiol. 265*, C129–C137.

(3) Ferrari, L. A., and Giannuzzi, L. (2005) Clinical parameters, postmortem analysis and estimation of lethal dose in victims of a massive intoxication with diethylene glycol. *Forensic Sci. Int. 153*, 45–51.

(4) Issberner, U., Reeh, P. W., and Steen, K. H. (1996) Pain due to tissue acidosis: a mechanism for inflammatory and ischemic myalgia? *Neurosci. Lett. 208*, 191–194.

(5) Raghunand, N., and Gillies, R. J. (2000) pH and drug resistance in tumors. *Drug Resist. Update 3*, 39–47.

(6) Deborah, M., Prescott, H., Cecil, C., Jean, M. P., Rodney, L. P., Donald, E. T., Zeljko, V., and Mark, W. D. (2000) The relationship between intracellular and extracellular pH in spontaneous canine tumors. *Clin. Cancer Res. 6*, 2501–2505.

(7) Greener, B., Hughes, A. A., Bannister, N. P., and Douglass, J. (2005) Proteases and pH in chronic wounds. *J. Wound Care 14*, 59–61.

(8) Oishi, M., Sumitani, S., and Nagasaki, Y. (2007) On-off regulation of 19F magnetic resonance signals based on pH-sensitive PEGylated nanogels for potential tumor-specific smart 19F MRI probes. *Bioconjugate Chem. 18*, 1379–1382.

(9) van Sluis, R., Bhujwalla, Z. M., Raghunand, N., Ballesteros, P., Alvarez, J., Cerdan, S., Galons, J. P., and Gillies, R. J. (1999) In vivo imaging of extracellularpH using 1H MRSI. *Magn. Reson. Med. 41*, 743–750.

(10) Gillies, R. J., Liu, Z., and Bhujwalla, Z. (1994) 31P-MRS measurements of extracellular pH of tumors using 3-aminopropylphosphonate. *Am. J. Physiol. 267*, C195–C203.

(11) Rottenberg, D. A., Ginos, J. Z., Kearfott, K. G., Junck, L., Dhawan, V., and Jarden, J. O. (1985) In vivo measurement of brain tumor pH using [^{11}C]DMO and positron emission tomography. *Ann. Neurol. 17*, 70–79.

(12) Urano, Y., Asanuma, D., Hama, Y., Koyama, Y., Barrett, T., Kamiya, M., Nagano, T., Watanabe, T., Hasegawa, A., Choyke, P., and Kobayashi, H. (2009) Selective molecular imaging of viable cancer cells with pH-activatable fluorescence probes. *Nat. Med. 15*, 104–109.

(13) Utsumi, H., Yamada, K., Ichikawa, K., Sakai, K., Kinoshita, Y., Matsumoto, S., and Nagai, M. (2006) Simultaneous molecular imaging of redox reactions monitored by Overhauser-enhanced MRI with 14N- and 15N-labeled nitroxyl radicals. *Proc. Natl. Acad. Sci. U.S.A. 103*, 1463–1468.

(14) He, G., Deng, Y., Li, H., Kuppusamy, P., and Zweier, J. L. (2002) EPR/NMR co-imaging for anatomic registration of free-radical images. *Magn. Reson. Med. 47*, 571–578.

(15) Gallez, B., Mader, K., and Swartz, H. M. (1996) Noninvasive measurement of the pH inside the gut by using pH-sensitive nitroxides. An in vivo EPR study. *Magn. Reson. Med. 36*, 694–697.

(16) Potapenko, D. I., Foster, M. A., Lurie, D. J., Kirilyuk, I. A., Hutchison, J. M. S., Grigor'ev, I. A., Bagryanskaya, E. G., and Khramtsov, V. V. (2006) Real-time monitoring of drug-induced changes in the stomach acidity of living rats using improved pH-sensitive nitroxides and low-field EPR techniques. *J. Magn. Reson. 182*, 1–11.

(17) Yoshioka, H., Tanizawa, H., Ogata, T., and Kazama, S. (1995) A novel spin probe with prolonged life for ESR imaging. *Biol. Pharm. Bull. 18*, 1572–1575.

(18) Saito, K., Kazama, S., Tanizawa, H., Ito, T., Tada, M., Ogata, T., and Yoshioka, H. (2001) ESR imaging on a solid-tumor-bearing mouse using spin-labeled dextran. *Biosci. Biotechnol. Biochem. 65*, 787–794.

(19) Yoshitomi, T., Miyamoto, D., and Nagasaki, Y. (2009) Design of core-shell-type nanoparticles carrying stable radicals in the core. *Biomacromolecules 10*, 596–601.

(20) Soule, B. P., Hyodo, F., Matsumoto, K., Simone, N. L., Cook, J. A., Krishna, M. C., and Mitchell, J. B. (2007) The chemistry and biology of nitroxide compounds. *Free Radical Biol. Med. 42*, 1632–1650.

(21) Gariboldi, M. B., Terni, F., Ravizza, R., Meschini, S., Marra, M., Condello, M., Arancia, G., and Monti, E. (2006) The nitroxide Tempol modulates anthracycline resistance in breast cancer cells. *Free Radical Biol. Med. 40*, 1409–1418.

(22) Suy, S., Mitchell, J. B., Samuni, A., Mueller, S., and Kasid, U. (2005) Nitroxide tempo, a small molecule, induces apoptosis in prostate carcinoma cells and suppresses tumor growth in athymic mice. *Cancer 103*, 1302–1313.

(23) Stefano, G. D., Busi, C., Maitioli, A., and Fiume, L. (1995) Selective delivery to the liver of antiviral nucleoside analogs coupled to a high molecular mass lactosaminated poly-L-lysine and administered to mice by intramuscular route. *Biochem. Pharmacol. 49*, 1769–1775.

(24) Takechi, K., Tamura, H., Yamaoka, K., and Sakurat, H. (1997) Pharmacokinetic analysis of free radicals by in vivo BCM (blood

circulation monitoring)-ESR method. *Free Rad. Res. 26*, 483–496.
(25) Lee, A. S., Gast, A. P., Butun, V., and Armes, S. P. (1999) Characterizing the structure of pH dependent polyelectrolyte block copolymer micelles. *Macromolecules 32*, 4302–4310.
(26) Addison, T., Cayre, O. J., Biggs, S., Armes, S. P., and York, D. (2008) Incorporation of block copolymer micelles into multilayer films for use as nanodelivery systems. *Langmuir 24*, 13328–13333.
(27) Asayama, S., Maruyama, A., Cho, C., and Akaike, T. (1997) Design of comb-type polyamine copolymers for a novel pH-sensitive DNA carrier. *Bioconjugate Chem. 8*, 833–838.
(28) Xu, P., Van Kirk., E. A., Murdoch, W. J., Zhan, Y., Isaak, D. D., Radosz, M., and Shen, Y. (2006) Anticancer efficacies of cisplatin-releasing pH-responsive nanoparticles. *Biomacromolecules 7*, 829–835.
(29) Jiang, X., Luo, S., Armes, S. P., Shi, W., and Liu, S. (2006) UV irradiation-induced shell cross-linked micelles with pH-responsive cores using ABC triblock copolymers. *Macromolecules 39*, 5987–5994.
(30) Huh, K. M., Min, H. S., Lee, S. C., Lee, H. J., Kim, S., and Park, K. (2008) A new hydrotropic block copolymer micelle system for aqueous solubilization of paclitaxel. *J. Controlled Release 126*, 122–129.
(31) Kobayashi, H., Ueda, T., Miyakubo, K., Eguchi, T., and Tani, A. (2007) Spin-spin interaction of TEMPO molecular chains formed in an organic one-dimensional nanochannel as studied by electron spin resonance (ESR). *Bull. Chem. Soc. Jpn. 80*, 711–720.
(32) Ranby, B., and Rabek, J. F. (1977) ESR Spectroscopy in Polymer Research, *Polymers/Properties and Applications 1* (Cantow, H. J., Harwood, H. J., Kennedy, J. P., Meibner, J., Okamura, S., and Olive, S., Eds.) pp 305−311, Chapter 11, Springer-Verlag, Berlin.
(33) Yoshida, E., and Tanaka, T. (2006) Oxidation-induced micellization of a diblockcopolymer containing stable nitroxyl radicals. *Colloid Polym. Sci. 285*, 135–144.
(34) Yoshimura, T., Yokoyama, H., Fujii, S., Takayama, F., Oikawa, K., and Kamada, L. (1996) In vivo EPR detection and imaging of endogenous nitric oxide in lipopolysaccharide-treated mice. *Nat. Biotechnol. 14*, 992–994.

BC900214F

pH-Sensitive Radical-Containing-Nanoparticle (RNP) for the L-Band-EPR Imaging of Low pH Circumstances

Toru Yoshitomi[1], Rie Suzuki[1], Takashi Mamiya[4,6], Hirofumi Matsui[3,4,6], Aki Hirayama[3,7], and Yukio Nagasaki[1-5]

[1]Graduate School of Pure and Applied Sciences, University of Tsukuba, [2]Tsukuba Research Center for Interdisciplinary Materials Science (TIMS), University of Tsukuba, [3]Center for Tsukuba Advanced Research Alliance (TARA), University of Tsukuba, [4]Master's School of Medical Sciences, Graduate School of Comprehensive Human Sciences, University of Tsukuba, [5]Satellite Laboratory, International Center for Materials Nanoarchitectonics (MANA), National Institute of Materials Science (NIMS), [6]Division of Gastroenterology, Graduate School of Comprehensive Human Sciences, University of Tsukuba, Tennoudai 1-1-1, Tsukuba, 305-8573, Ibaraki, [7]Center for Integrative Medicine, Tsukuba Universiy of Technology, Kasuga 4-12-7, Tsukuba, 305-8521, Ibaraki

S1. Materials

2,2'-Azobisisobutyronitrile (AIBN) (Kanto Chemical Co., Inc., Tokyo, Japan) was purified by recrystallization from methanol. Chloromethylstyrene (CMS) was kindly provided by Seimi Chemical Co., Ltd. (Kanagawa, Japan) and purified on a silica gel column to remove the inhibitor, followed by vacuum distillation under a nitrogen atmosphere. 2,2,6,6-Tetramethylpiperidinyloxy (TEMPO), 4-amino-TEMPO, 4-hydroxy-TEMPO (TEMPOL) (Aldrich Chemical Co., Inc., U.S.A.), 2-propanol, diethyl ether, dimethyl sulfoxide (DMSO) and N,N-dimethylformamide (DMF) (Wako Pure Chemical Industries, Ltd., Osaka, Japan) were used without further purification. PEG possessing a methoxy group at the α-chain end and a sulfanyl group at the □-chain end (MeO-PEG-SH) (NOF CORPORATION Co., Ltd., Japan) was used without further purification.

S2. Synthesis of MeO-PEG-*b*-PCMS

Method: After 0.2 mmol (1 g) of MeO-PEG-SH (Mn = 5,000) and 0.1 mmol of AIBN were weighed into a flask, the inside of the reactor was degassed and filled with nitrogen gas. The degassing-N_2-purge cycle was repeated three times. Ten millimoles (1.38 mL) of CMS and 10 mL of benzene were then added to the flask. Polymerization was conducted for 24 h at 60 °C in an oil bath. The reaction mixture was recovered by precipitation into 40 mL of hexane, followed by freeze-drying with benzene. The reacted polymer was washed with diethyl ether three times in order to eliminate the PCMS homopolymer, followed by freeze-drying with benzene. The yield of the obtained MeO-PEG-*b*-PCMS copolymer was 87.5% (1.4 g).

Results: MeO-PEG-*b*-PCMS was prepared by the radical telomerization of CMS using MeO-PEG-SH (Mn = 5,000) as a telogen, according to the previous report, as shown in Scheme 1. The molecular weight distribution of the MeO-PEG-*b*-PCMS thus prepared was evaluated by SEC, as shown in Figure S1a. The SEC profile of MeO-PEG-*b*-PCMS after polymerization showed a bimodal distribution similar to that of previously reported acetal-PEG-*b*-PCMS. In the previous study, ^{1}H NMR analysis performed after the two peaks were separated by SEC fractionation showed that the composition ratios of PEG to PCMS in the two fractions were almost the same. The Mn

value of PCMS was determined by the ^{1}H NMR data based on the Mn of PEG (Mn = 5,000). From the SEC profile, it can be seen that the number-average molecular weight (Mn) of the first fraction was two times higher than that of the second fraction. Based on the Mn value of PEG as determined by SEC, the Mn values of the PCMS segments for the two fractions were determined to be 3,300 and 6,600, respectively. The products were a mixture of di-block and tri-block copolymers possessing the same composition, as reported previously. The ratios of di-block to tri-block copolymer were determined to be 59 % and 41 %, respectively, based on the chromatogram.

S3. Synthesis of the radical-containing blockcopolymer (MeO-PEG-*b*-PCTEMPO)
Method: After 177 μmol (1.25 g) of the obtained MeO-PEG-*b*-PCMS (Mn = 8,000) were weighed into a 100 mL flask, a DMSO solution (40 mL) of 4-amino-TEMPO (17.7 mmol, 3 g) was added to the flask and stirred for 12 h at room temperature. The reacted polymer was recovered by precipitation into 80 mL of cold 2-propanol (-15 °C) and centrifugation for 30 min at 5,000 rpm (4,500 × *g*). In order to purify the obtained polymer, the precipitation-centrifugation cycle was repeated three times, followed by freeze-drying with benzene. The yield of the obtained MeO-PEG-*b*-PCTEMPO copolymer was 74.4 % (1.26 g).

Results: The chloromethyl groups in the PCMS segment of the block copolymer MeO-PEG-*b*-PCMS were converted to stable radicals via the amination of MeO-PEG-*b*-PCMS with 4-amino-TEMPO in DMSO (Scheme S1). When PEG-*b*-PCMS was reacted with 4-amino-TEMPO, the CH_2Cl signal of the PCMS segment in the ^{1}H NMR spectrum disappeared. After the TEMPO radicals were reduced by phenylhydrazine, the entire ^{1}H NMR spectrum was examined, as shown in Figure S2b. After the reducing reaction, it was confirmed that the signal for the methylene protons of the chloromethyl group in the PCMS unit at 4.5 ppm completely disappeared. On the basis of these results, it was confirmed that the TEMPOs were successfully introduced into the polymer.

S4. Preparation of the RNP
Results: The size of the obtained RNP after dialysis was estimated by DLS measurement. As shown in Figure S3, the RNP thus obtained showed a unimodal distribution in the histogram analysis. The average diameter and polydispersity factor (μ_2/Γ^2), as determined by the cumulant method, were about 50 nm and 0.133, respectively.

S5. Calculation method for the rotational correlation time, τ_c

The rotational correlation time, τ_c (s), which is the time taken for the axis of the nitroxyl group to rotate one radian, is highly sensitive to the motion of the TEMPO radicals on the PCTEMPO segment, and is calculated using the following equation[1]:

---

[1] Yoshioka, H., Haga, H., Kubota, M., Sakai, Y., and Yoshioka, H. (2006) Interaction of (+)-Catechin with a Lipid Bilayer Studied by the Spin Probe Method. *Biosci. Biotechnol. Biochem. 70*, 395-400.

$$\tau_c = B \times \Delta H_{(m=+1)}[(I_{m=+1} / I_{m=-1})^{1/2} - 1] \quad (1)$$

Here, B is a constant determined from the principal values of A and the g factor; the value of 6.6×10^{-10} s/Gauss is used. $\Delta H_{(m+1)}$ is the peak-to-peak width in gauss of the low-field lines, as shown in Figure S4. $I_{(m=+1)}$ and $I_{(m=-1)}$ are the peak-to-peak heights in arbitrary units of the low- and high-field lines, respectively. The value of τ_c reflects the mobility of the probe and the rigidity of the surroundings of the probe. An increase in τ_c means that the motion of the probe is suppressed.

Scheme S1

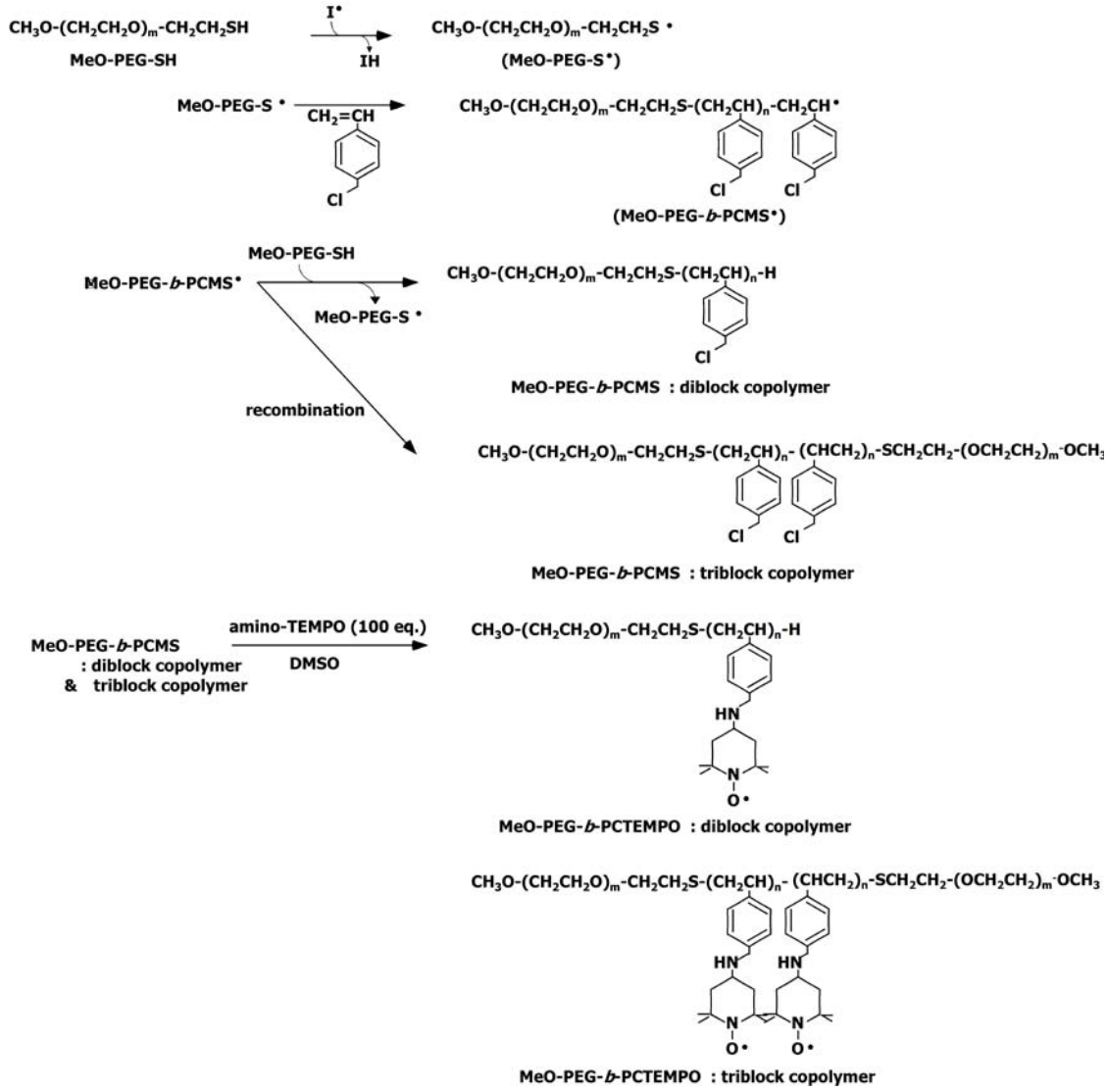

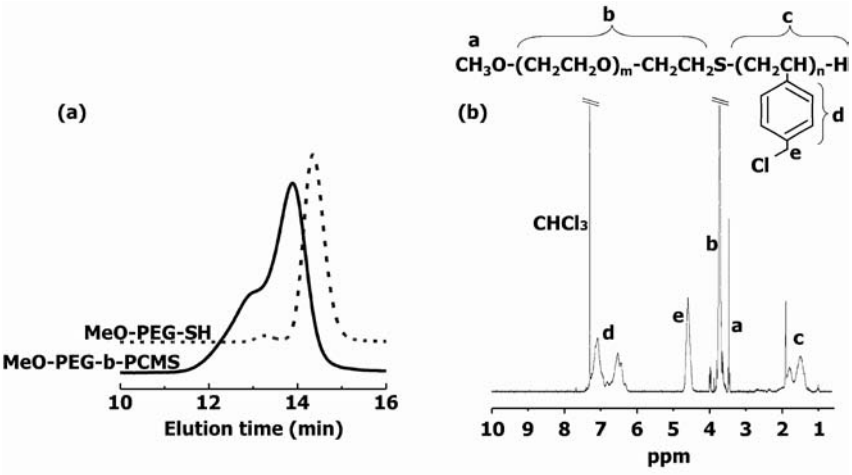

Figure S1. SEC diagram (a) and ^{1}H NMR spectrum (b) of MeO-PEG-*b*-PCMS. (SEC apparatus, TOSOH HLC-8120GPC; detector, RI; column, TOSOH SUPER HZ4000+3000; solvent, THF (containing 2 w% triethylamine); flow rate, 0.35 mL/min; calibration, standard PEGs.

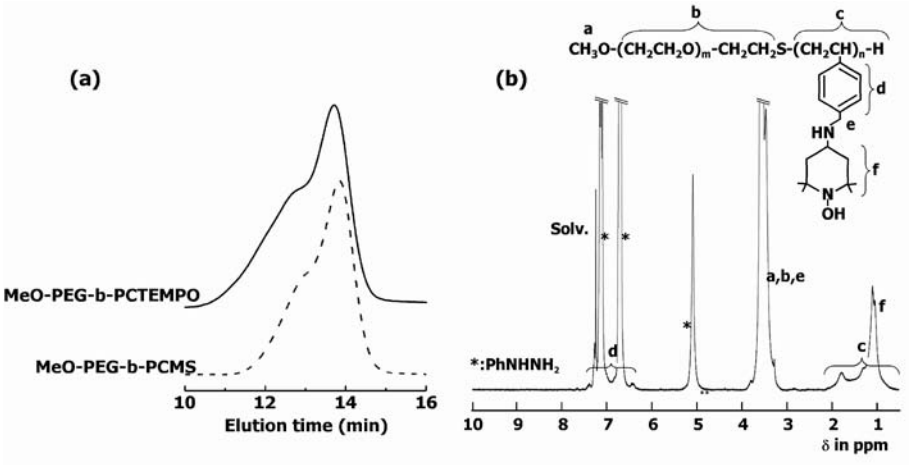

Figure S2. SEC diagram (a) and ^{1}H NMR spectrum (b) of MeO-PEG-*b*-PCTEMPO. (SEC apparatus, TOSOH HLC-8120GPC; detector, RI; column, TOSOH SUPER HZ4000+3000; solvent, THF (containing 2 w% triethylamine); flow rate, 0.35 mL/min; calibration, standard PEGs.)

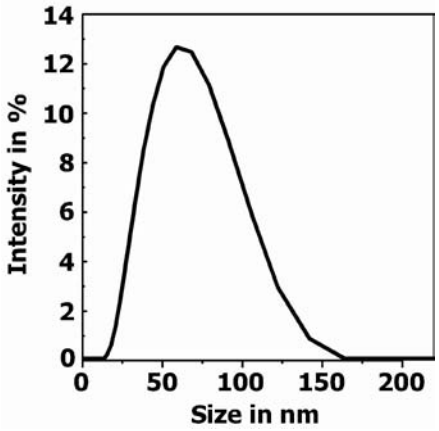

Figure S3. Size distribution of the RNP analyzed by DLS.

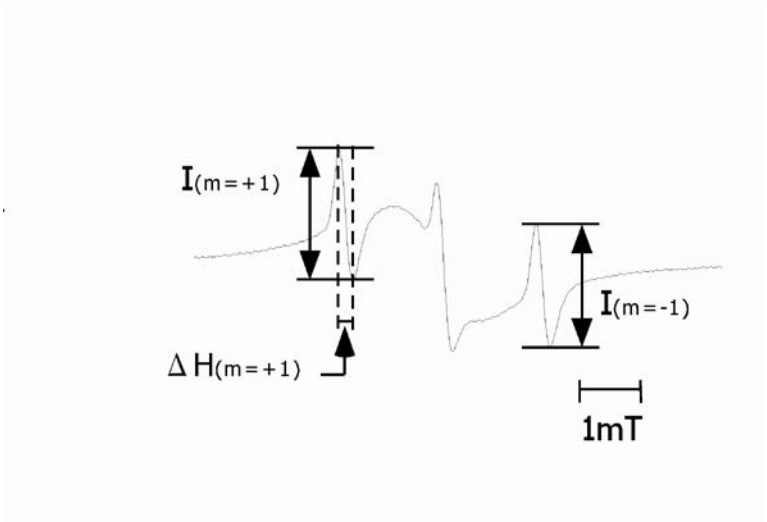

Figure S4. EPR spectrum of the RNP at pH 5.5 and the peak-to-peak height and width of line.

Triazine Dendrimers as Nonviral Gene Delivery Systems: Effects of Molecular Structure on Biological Activity

Olivia M. Merkel,[†,‡] Meredith A. Mintzer,[†,§] Johannes Sitterberg,[‡] Udo Bakowsky,[‡] Eric E. Simanek,[§] and Thomas Kissel*[,‡]

Department of Pharmaceutics and Biopharmacy, Philipps-Universität, Marburg, Germany, and Department of Chemistry, Texas A&M University, College Station, Texas 77843-3255. Received June 4, 2009; Revised Manuscript Received July 23, 2009

A family of generation 1, 2, and 3 triazine dendrimers differing in their core flexibility was prepared and evaluated for their ability to accomplish gene transfection. Dendrimers and dendriplexes were analyzed by their physicochemical and biological properties such as condensation of DNA, size, surface charge, morphology of dendriplexes, toxic and hemolytic effects, and ultimately transfection efficiency in L929 and MeWo cells. Flexibility of the backbone was found to play an important role with generation 2 dendrimer displaying higher transfection efficiencies than 25 kDa poly(ethylene imine) or SuperFect at a lower cytotoxicity level. This result is surprising, as PAMAM dendrimers require generations 4 or 5 to become effective transfection reagents. The ability to delineate effects of molecular structure and generation of triazine dendrimers with biological properties provides valuable clues for further modifying this promising class of nonviral delivery system.

INTRODUCTION

Gene therapy has gained importance in recent years due to its potential for targeting genetic diseases and inhibiting tumor growth. However, clinical application is limited by numerous biological barriers to delivering plasmid DNA (*1*). Both viral and nonviral vector systems have been developed to overcome these hurdles. Viral delivery systems, which include retroviruses, lentiviruses, and adenoviruses, have encountered potential safety problems such as recombination, insertional mutagenesis, and immunogenicity, as well as scale-up difficulties (*2*). Therefore, synthesis and evaluation of nonviral vector systems becomes increasingly important in spite of their comparatively lower transfection efficiency (*3*).

Nonviral vectors such as cationic liposomes, linear and branched polycations, and dendrimers have been shown to be effective transfection agents and offer advantages over viral vectors regarding safety and manufacturing. Several nonviral gene delivery systems based on poly(amidoamine) (PAMAM) (*4*−*6*), poly(propylene imine) (PPI) (*7, 8*), and poly(ethylene imine) (PEI) (*9, 10*) have yielded efficient transfection *in vivo* with relatively low toxicity. The potential of triazine dendrimers as gene delivery systems is largely unexplored, but has been described by us in a study involving generation 2 rigid structures (*11*), which reveal an optimized peripheral group for further study. These dendrimers may be attractive candidates, as they can be synthesized in high yields via a divergent strategy that creates multiple surface functionalities in a completely monodisperse manner (*12*). In addition, triazine dendrimers show low toxicity, both *in vitro* and *in vivo*: mice tolerate i.p. doses up to 40 mg/kg (*13*). This level of toxicity is comparable to PAMAM (*14*) suggesting that triazine dendrimers could be considered as a platform for transfection studies. Here, the physicochemical properties, cytotoxicities, and transfection efficiencies of a panel of triazine dendrimers were evaluated to establish structure−function relationships. The effect of dendrimer size (generations) as well as core structure is probed in an attempt to maximize transfection efficiency. Increasing generation increases size and the number of available cations. Changing the composition of the core affords dendrimers that differ in flexibility, a characteristic that is thought to influence interactions with p-DNA (*6*). The dendrimers used in this study are shown in Figure 1. Here, we present results from the synthesis, physicochemical and biological *in vitro* evaluation of a panel of five triazine dendrimers, and compare them to commercially available PAMAM dendrimers of different generations to define structural parameters such as generation and core flexibility for the design of triazine dendrimers as nonviral gene delivery systems.

EXPERIMENTAL SECTION

Materials. Poly(ethylene imine) (Polymin, 25 kDa) was a gift from BASF (Ludwigshafen, Germany); PAMAM (ethylenediamine core, amino surface) second and third generations were bought from Sigma-Aldrich Laborchemikalien GmbH, Seelze, Germany, and SuperFect from Qiagen, Hilden, Germany. All chemicals used for synthesis were obtained from Sigma-Aldrich (St. Louis, MO).

Synthesis. The synthesis of all dendrimers used in this study proceeded via a divergent strategy originating from cyanuric chloride. The rigid, first-generation dendrimer was synthesized by reacting a tris(piperazyl) triazine core with **MCT1**, followed by deprotection. The rigid, second-generation dendrimer, **G2-1**, was synthesized as previously described (*11*). To form the third-generation rigid dendrimer, **G3-1**, the rigid, deprotected G1-dendrimer, **G1-C**, was reacted with di(Boc-piperazyl)monochlorotriazine. This second generation structure was deprotected and reacted with **MCT1** to form the protected third-generation compound, which was deprotected using HCl (Supporting Information). A detailed description of the synthesis is provided in the Supporting Information.

The flexible core dendrimer, **F2-1**, was synthesized by reacting cyanuric chloride with mono-Boc-protected *O*,*O*′-bis(3-aminopropyl)di(ethylene glycol). This core was deprotected with

* Corresponding author. Thomas Kissel, Philipps-University Marburg, Dept. Pharmaceutics and Biopharmacy, Ketzerbach 63, D-35032 Marburg, Germany. Phone: +49-6421-282 5881. FAX: +49-6421-282 7016. E-mail kissel@staff.uni-marburg.de.

[†] Both authors contributed equally to this work.

[‡] Philipps-Universität.

[§] Texas A&M University.

10.1021/bc900243r CCC: $40.75 © 2009 American Chemical Society
Published on Web 08/27/2009

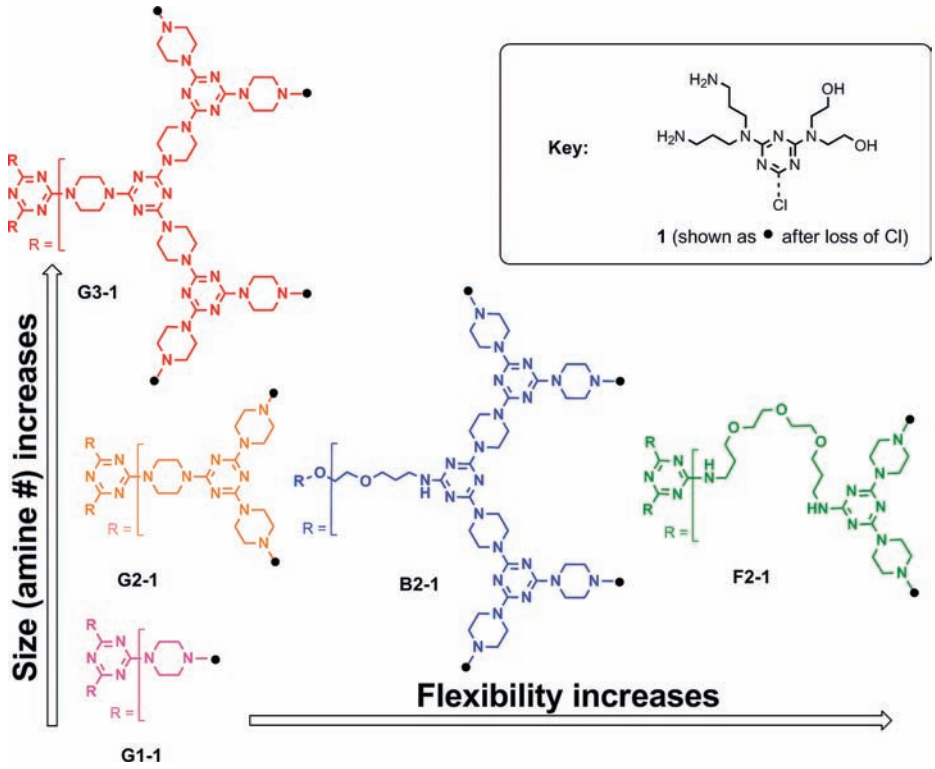

Figure 1. The dendrimer panel is given as chemical structures and sketches in a color code used throughout the study. Structure−activity relationships of the dendrimers in Table 1 were investigated in a two-dimensional approach: By variation of the generation (vertical arrows) and the core structure (horizontal arrows), influences of both parameters were investigated.

Table 1. Summary of Properties of the Screened Dendrimers Concerning *in Vitro* Parameters

	generation-1 rigid	generation-2 rigid	generation-3 rigid	generation-2 flexible	generation-2 bow tie
primary amines	6	12	24	12	16
amine density [Da/N atom]	211.27	245.30	262.20	262.32	262.20
DNA condensation at plateau [%]	48.0	30.2	4.2	36.4	5.9
size [nm]	338.3	154.8	230.2	426.3	882.0
zeta potential [mV]	−0.05	22.6	17.7	−7.5	3.1
hemolysis [%]	12.6	10.9	12.9	6.11	13.0
toxicity (IC_{50}) [μg/mL]	501.2	64.3	20.1	22.8	115.3
transfection efficiency (N/P 5, MeWo) [RLU/s]	2480.0	4948.3	7087.3	44184.0	4487.0

HCl, reacted with Boc-piperazyl-dichlorotriazine, and capped with Boc-piperazine. After removal of the protecting groups with HCl, the compounds were reacted with **MCT1** and deprotected to form the flexible, second-generation dendrimer, **F2-1** (Supporting Information). A detailed description of the synthesis is provided in the Supporting Information.

Finally, the second-generation bow tie structure, **B2-1**, was synthesized by reacting di(Boc-piperazyl)monochlorotriazine with *O*,*O*′-bis(3-aminopropyl)di(ethylene glycol). This core structure was deprotected with HCl and reacted with di(Boc-piperazyl)monochlorotriazine to form a first-generation bow-tie structure. This structure was deprotected, reacted with **MCT1**, and deprotected again to afford the dendrimer **B2-1** (Supporting Information). A detailed description of the synthesis is provided in the Supporting Information.

Cell Culture. L929 murine fibroblasts and MeWo human melanoma cells were purchased from LG Promochem, Wesel, Germany, and maintained in DMEM low or high glucose (PAA Laboratories, Cölbe, Germany), respectively, and supplemented with 10% fetal calf serum (Cytogen, Sinn, Germany) in humidified atmosphere with 5% CO_2 at 37 °C.

Preparation of Dendriplexes. Dendriplexes were formed by adding 25 μL of a calculated concentration depending on "protonable unit" and N/P ratio) of dendrimer to an equal volume of the DNA solution (pCMV-Luc, Plasmid Factory, Bielefeld, Germany) and then mixing the two components before letting them mature for 20 min. The final concentration of pDNA in the dendriplex solution was 0.02 μg/μL. Both pDNA and dendrimers were diluted with 10 mM HEPES buffer, pH 7.4, and the appropriate amount of dendrimer was calculated by considering the desired N/P ratio and the "protonable unit" of each dendrimer, which represents the mass of dendrimer per protonable nitrogen atom. For comparison, standard transfection reagents, including poly(ethylene imine) (PEI 25 kDa), second- and third-generation PAMAM (ethylenediamine core, amino surface), and SuperFect (Qiagen, Hilden, Germany) were used. Polyplexes with PEI 25 kDa and dendriplexes with PAMAMs of second and third generation were formed as described above, whereas dendriplexes with SuperFect were prepared as recommended by the manufacturer.

Ethidium Bromide Quenching Assay. To quantify condensation efficiency of the dendrimers, an indirect dye-quenching assay was performed as previously reported (*15*). Briefly, 4 μg of herring testes DNA (Sigma-Aldrich Chemie GmbH, Schnelldorf, Germany) was complexed with increasing amounts of dendrimer in a final volume of 280 μL 10 mM HEPES buffer. After incubation for 20 min at room temperature, 20 μL of a 0.1 mg/mL ethidium bromide solution (Carl Roth GmbH, Karlsruhe, Germany) was added and incubated for 20 min in the dark following intensive mixing. Intercalation-caused fluorescence was quantified using a fluorescence plate reader (LS 50 B, Perkin-Elmer, Rodgau-Jügesheim, Germany) at 518 nm

excitation and 605 nm emission wavelengths. Results are given as relative fluorescence intensity values where intercalation of free DNA represents 100% fluorescence and non-intercalating ethidium bromide in buffer represents 0% remaining fluorescence. Results are given as means of triplicate measurements ± standard deviation (SD).

Dynamic Light Scattering and Zeta Potential Analysis. Polyplex size and zeta potential were determined as previously reported (*15*). Briefly, dendriplexes of 0.6 μg pCMV-Luc and the corresponding amount of dendrimer were prepared as described above. Complexes were incubated for 20 min and then diluted to a total volume of 800 μL with 10 mM HEPES buffer, pH 7.4, to be measured using a Zetasizer Nano ZS, Malvern, Herrenberg, Germany. Position and attenuator were optimized by the device. The accuracy of the size measurements was routinely checked using reference polymer particles (Nanosphere Size Standards; 50, 100, and 200 nm; Duke Scientific Corp., Palo Alto, CA, USA), and the zeta potential values were calibrated with the Zeta Potential Transfer Standard (Malvern Instruments, Herrenberg, Germany). The data was analyzed using a high-resolution mulitmodal algorithm. All measurements were conducted in triplicate. For better characterization of the size distributions, in addition to *Z* average, the PDI of the distribution is given as the mean value of three independent measurements ± SD.

Atomic Force Microscopy. The size and morphology of dried dendriplexes were analyzed by atomic force microscopy as previously described for polyplexes (*16*). Briefly, dendriplexes were prepared by mixing 1 μg pCMV-Luc and a dendrimer at an N/P ratio of 5 as described above, incubating for 20 min, and drying on silicon chips. Microscopy was performed on a NanoWizard (JPK instruments, Berlin, Germany). Commercial NSC16 AlBS-tips (Micromasch, Estonia) on an I-type cantilever with a length of 230 μm and a nominal force constant of 40 N/m were used. All measurements were performed in tapping mode to avoid damage to the sample surface. The scan frequency was 0.6 Hz and scan size was 5×5 μm^2. Multiple images were recorded, of which one representative topograph is presented.

Erythrocyte Aggregation and Hemolysis. Unspecific cell interaction was visualized by erythrocyte aggregation and quantified by the measurement of hemolysis according to previously described procedures (*17*). Briefly, human erythrocytes were isolated from fresh citrated blood from healthy volunteers by centrifugation, washed with PBS buffer, and diluted to 500 000 000 cells/mL. Dendriplexes of 0.1 μg pDNA per mL were prepared at N/P 5, and 50 μL aliquots of dendriplex solutions, 1% Triton-X 100 (100% lysis) or PBS (0% lysis) were mixed with 50 μL erythrocyte suspension. After incubation for 30 min at 37 °C, samples were centrifuged at 850 *g*. Hemolysis was measured by VIS-absorption of supernatants at 541 nm and the data are given as a mean percentage ($n = 3$) of the released hemoglobin ± SD, normalized to total hemolysis induced by 1% Triton-X 100. Pelleted erythrocytes were resuspended in 50 μL PBS and microscopically examined to determine erythrocyte aggregation.

Cell Viability. The cytotoxicity of the dendrimers was investigated using an MTT assay (*15*). Murine L929 fibroblasts were seeded on 96-well plates at a density of 8000 cells per well approximately 24 h before they were treated with dendrimer solutions of increasing concentrations in the range 0.001−1 mg/mL. Another 24 h later, the medium was changed. MTT solution was added into fresh serum-free medium and incubated for 4 h. The remaining mitochondrial enzyme activity as compared to untreated cells was determined by measuring the absorbance of enzymatically formed formazane at 580 nm with 690 nm background corrections after cell lysis in 200 μL DMSO. The results are given as mean values of a replicate of 4 ± SD.

Transfection Experiments. To compare transfection efficiency in different cell lines, murine 3T3 fibroblasts (L929) and human melanoma cells (MeWo) were seeded in 96 well plates at a seeding density of 8000 cells per well. Approximately 24 h later, the cells were transfected with dendriplexes consisting of 0.25 μg pCMV-Luc per well and the amount of dendrimer calculated to be N/P 2.5, 5, or 7.5. Branched PEI of 25 kDa, second- and third-generation PAMAM, and fourth-generation SuperFect were used as standards and free plasmid was used as a negative control.

Polyplexes were added to full serum-containing medium, and cells were incubated for 4 h before the medium was changed. Another 44 h later, the cells were washed with PBS, lysed with CCLR (Promega, Mannheim, Germany), and assayed for luciferase expression using a commercial luciferase assay kit (Promega, Mannheim, Germany) on a BMG LUMIstar OPTIMA luminometer plate reader (BMG Labtech, Offenburg, Germany). Transfection assays were performed in triplicate and the mean values ± SD are given.

RESULTS AND DISCUSSION

Nomenclature Adopted. Throughout the manuscript, the targets are named to reflect common and disparate features in structure with the core/generation-surface groups identified. The cores increase in flexibility from **G** (standard) to **B** (bow tie) to **F** (flexible), and the effect of size is determined over three (**1**, **2**, **3**) generations using the standard core structure. Each dendrimer contains a common surface group (**1**) that was previously reported to avoid obtaining variations in transfection efficiency that result from the peripheral functionalities (*11*).

Synthesis and Design Criteria. As the products of multistep organic syntheses, triazine dendrimers allow us access to well-defined structures to investigate structure−activity relationships such as the influence of size and backbone structure on transfection efficiency and cytotoxicity. For this purpose, a preliminary panel of dendrimers was synthesized consisting of different generations (**G1**, **G2**, **G3**) with a rigid backbone and a common surface group (**1**), yielding 6, 12, or 24 amino groups in the periphery. With each increase in generation number, the number of primary amino groups presented in the periphery doubles.

In addition to generation number, the flexibility of the core could hypothetically affect transfection efficiency by influencing the distribution and accessibility of the peripheral groups for interacting with p-DNA (*18*). The role of flexibility has been supported experimentally by Szoka who showed enhanced transfection efficiency resulting from fragmentation of PAMAM dendrimers (*6*). In this study, this effect was investigated with second-generation triazine dendrimers, each having differing core flexibilities (**G2-1**, **F2-1**, **B2-1**). Synthetic yields and NMR data are provided within the Supporting Information.

The composition of the panel is summarized in Figure 1 and Table 1. Branched poly(ethylene imine) of 25 kDa (PEI 25 kDa) was used as a control. The transfection efficiencies of the triazine dendriplexes were additionally compared to SuperFect, a commercially available fourth-generation fractured PAMAM dendrimer, and to second- and third-generation PAMAM as dendrimer standards.

Condensation Properties of Triazine Dendrimers. The formation of dendriplexes results from electrostatic interactions between polycationic dendrimers and negatively charged DNA. The quantification of condensation properties was performed using an ethidium bromide quenching assay (*15*), which reveals the fraction of uncomplexed DNA that is accessible for intercalation with ethidium bromide at a given N/P ratio.

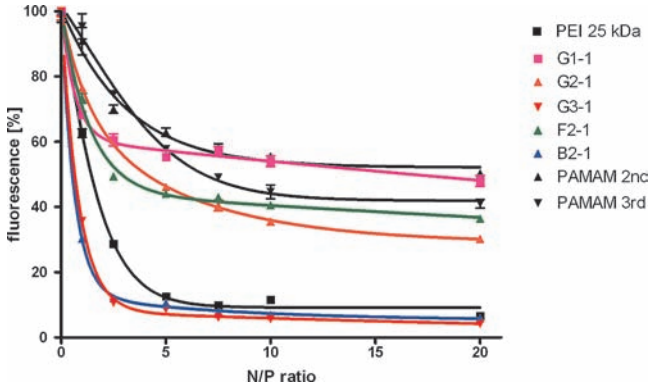

Figure 2. DNA condensation efficiency was quantified by ethidium bromide quenching assays and compared to PAMAMs of the same generations and PEI 25 kDa.

PAMAM dendrimers of generations 2 and 3 showed significant residual fluorescence leading to a plateau around N/P 7.5 (compare Figure 2). A similar trend was seen for several triazine dendrimers, including **G1-1**, **G2-1**, and **F2-1**. The third-generation triazine dendrimer, **G3-1**, yielded higher condensation than PEI, even at low N/P ratios. Interestingly, the bow tie dendrimer **B2-1** showed better DNA condensation than PEI, with a condensation profile comparable to that of the third-generation rigid dendrimer **G3-1**.

Similar to PAMAM, triazine dendrimers showed an increase in condensation efficiency with increasing generation. The first-generation dendrimer **G1-1** condensed DNA less effectively than the second-generation analogue, **G2-1**, which in turn was less efficient than the third-generation dendrimer, **G3-1**. However, the effect of the core structure on condensation efficiency seems minimal. This may result from the type of amines present in the triazine core. The reason that more flexible dendrimers are thought to complex with DNA more effectively than rigid analogues has been attributed to the increased capacity of flexible dendrimers to interact with DNA, as all amine groups, both inside the core and at the surface, contributed to the electrostatic interactions for binding (*19*). This increased availability of internalized amines in flexible structures results in the formation of more compact complexes (*7*, *20*, *21*). However, in the case of triazine dendrimers, the nitrogen atoms in the core are part of a delocalized electron system and hence not available for protonation under physiologic conditions (pH 7.4). Therefore, only the primary amino functional groups at the dendrimer periphery contribute to DNA condensation due to their accessibility to protonation (*22*). As the perhipheral groups are identical and the triazine core amines remain unprotonated at physiological pH, the trend of increased condensation efficiency for more flexible structures is not apparent; the semiflexible bow tie dendrimer **B2-1** more effectively condenses DNA than either the rigid **G2-1** or flexible **F2-1** analogues.

Dendriplex Sizes and Surface Charges. Polyplexes with diameters <200 nm in size are internalized by most cell lines (*23*), while larger particles can sediment more rapidly leading to enhanced transfection efficiency under *in vitro* conditions (*24*). A positive surface charge generally facilitates endocytosis, whereas negatively charged particles are often repelled by the negatively charged cell surface. Previous studies have shown that the complexation of DNA with PEI decreases polyplex sizes for increasing N/P ratios up to 20 (*25*). This trend could not be observed for the triazine dendrimers (data not shown). In the case of triazine dendriplexes, there seems to be an optimal N/P ratio at which minimal sizes can be achieved. When this N/P ratio is exceeded, larger dendriplexes (and possibly aggregates) form. By comparing rigid **G1-1**, **G2-1**, and **G3-1** dendrimers (Figure 3A), no clear trend between dendriplex sizes and the

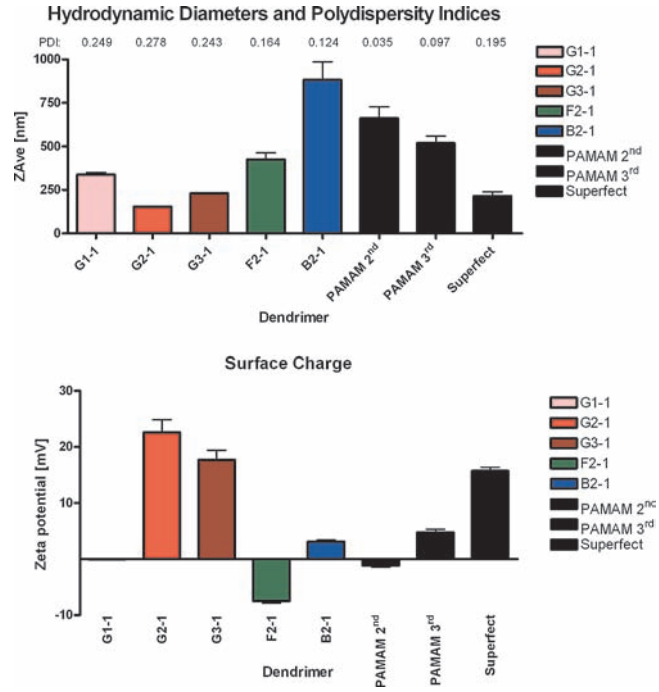

Figure 3. Hydrodynamic diameters and polydispersity indices (PDI) (A) and zeta potentials (B) of various dendriplexes at an N/P of 5 were determined in 10 mM HEPES buffer, pH 7.4.

generation number emerges. Generally, dendrimers with a higher number of primary amines on the periphery tend to form smaller polyplexes with DNA, as shown for PAMAM in this study. This behavior is not observed for the rigid triazine dendrimers, **G2-1**, **G2-1**, and **G3-1**. Our findings indicated that the rigid second-generation dendrimer, **G2-1**, forms the smallest complexes. This may be due to the "nitrogen density" (*26*) or "charge density" (*27*, *28*), a parameter that is known to influence the interaction of polycations with pDNA. This parameter is defined as the density of protonable amines in the polycation per molecular weight and can also be called the "protonable unit". The protonable unit can therefore be measured in g/mol N and helps to characterize polycations. The charge density of PEI, where every third atom is a nitrogen atom, is 43.1 g/mol N (*29*), which is a comparably high charge density considering that the charge density in our triazine dendrimers is about 200 g/mol N: **G1-1** has a density of primary amines of 211.27 Da/N atom, **G2-1** has a density of 245.3 Da/N atom, and **G3-1** has a density of 262.2 Da/N atom. Therefore, **G2-1** may form smaller complexes as compared to **G3-1** because of the difference in charge density. However, despite the lower charge density of **G2-1**, **G2-2** formed smaller complexes, which can be explained by the 2-fold increase in primary amines per molecule. The formation of large dendriplexes using the flexible dendrimer, **F2-1**, and the bow tie dendrimer, **B2-1**, may result partially from the low charge densities of these dendrimers (**F2-1**, 262.32 Da/N atom; **B2-1**, 262.2 Da/N atom). These values may be too low for the formation of very small complexes. Additionally, the sizes of dendriplexes formed with the flexible dendrimer, **F2-1,** were much larger than those of **G2-1**, suggesting that loose structures were obtained, in accordance with data from ethidium bromide quenching assay. The bow tie dendrimer **B2-1** formed the largest dendriplexes despite its DNA condensation efficiency, possibly caused by the formation of interdendriplex aggregates (*7*). The dendriplex size distributions were monomodal but showed polydispersity indices around 0.2 (Figure 3A) as reported previously for dendriplexes (*30*−*32*).

Zeta potentials of the PAMAM dendriplexes generally increased as particle size decreased. For example, the PAMAM

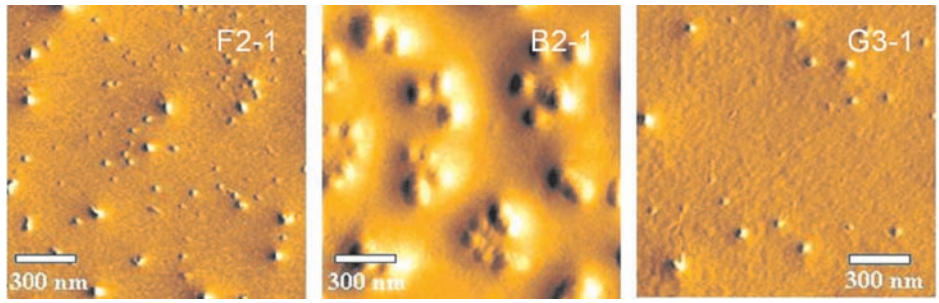

Figure 4. Morphology and density of dendriplexes were investigated by AFM revealing spherically shaped nanoplexes. Differing polyplex sizes as measured by dynamic light scattering are probably due to sample preparation (drying).

second generation dendrimer did not condense DNA efficiently, as illustrated by a negative zeta potential and large complexes sizes. As the number of primary amines on the periphery (generation) increases, the PAMAM dendrimers condensed DNA more efficiently (Figure 2) due to their very high number of primary amines (PAMAM G4 = SuperFect: 64 surface amines) and charge density (PAMAM G4: 222.10 Da/N atom). The rigid triazine dendrimers (**G1-1**, **G2-1**, and **G3-1**) did not show a clear generation-dependent trend for surface charge. **G1-1** exhibited a zeta potential of −0.0513 mV. The zeta potential of **G2-1** dendriplexes, which had proven to form the smallest particles among the rigid dendrimers, was observed to be strongly positive. By further increasing the generation of the rigid dendrimer, not only did sizes increase (Figure 3A), but the zeta potential decreased also (Figure 3B). Taken together, third-generation dendrimers condense and protect DNA (Figure 2) efficiently, but may result in larger aggregates in solution. It is possible that, due to their rather low charge density at the same N/P ratio and molecular composition, **G3-1** dendrimers do not shield the negative charge of DNA effectively, which results in lower electrostatic repulsion and stronger aggregation of dendriplexes. According to the data acquired in the ethidium bromide assay (Figure 2B), the flexible dendrimer **F2-1** only loosely bound DNA and was not able to fully protect the complex. Therefore, it seems reasonable to assume that the net negative charge measured for **F2-1** dendriplexes was caused by segments of free DNA which were not incorporated into any particle but were only bound to the surface of the flexible polycation. The dendriplexes formed with the bow tie dendrimer **B2-1** exhibited a low but positive surface charge, which can again be explained by interdendriplex interaction.

Atomic Force Microscopy. Although dynamic light scattering is an effective method for measuring particle size, the method is limited because it assumes spherically shaped particles. Therefore, atomic force microscopy (AFM) was used to characterize the morphology and heterogeneity of dendriplexes (*33*). The broad polydispersities observed with the dynamic light scattering experiments were also reflected in the AFM micrographs (Figure 4). The flexible core dendrimer, **F2-1**, produced two populations or particles: very small complexes (<50 nm) as well as larger ones (>100 nm). The bow tie dendrimer, **B2-1**, formed clusters of aggregates, which supports the assumption of interdendriplex interactions (*7*). The third-generation dendrimer **G3-1** showed the most uniform distribution.

Both the formation of clusters and the discrepancy between size measurement of dried particles and complexes in solution are not surprising: Similar observations have been made for PAMAM dendriplexes (*21*). The sizes measured for **F2-1** and **G3-1** dendriplexes by DLS are confirmed by AFM. In AFM, a distribution of 20−100 nm (**F2-1**) and narrow size distribution of particles of 100 nm (**G3-1**) could be observed. The larger sizes measured by DLS can be explained by the high number of short ethylene glycol chains that might be hydrated in solution but carry no weight after drying the sample for AFM. The picture of the **B2-1** dendriplex-clusters confirmed the DLS determined size of ∼900.

Erythrocyte Aggregation and Hemolysis. Red blood cells can be used to visualize and quantify the membrane interactions of dendriplexes by determining erythrocyte aggregation or hemolysis. Positive surface charges can lead to unspecific binding, membrane interactions, and the cytotoxicity associated with amino groups (*34*). The concentration-dependent hemolysis and perturbation of red blood cells after incubation with PAMAM, diaminobutane (DAB), diamonoethane (DAE), and poly(ethylene oxide) (PEO) grafted carbosilane (CSi-PEO) was reported previously (*35*). Generation-dependent hemolysis similar to PAMAM was seen with triazine dendrimers as well, though not as pronounced (Figure 5A). The hemolytic activity of triazine dendrimers seems to depend on their core structure, as hemolysis of the flexible dendrimer, **F2-1**, was markedly decreased compared to the rigid analogue, **G2-1**. However, dendriplexes formed from the bow tie dendrimer, **B2-1**, caused hemolytic effects comparable to **G3-1** dendriplexes. A possible explanation is the strong aggregation of **B2-1** dendriplexes, which could facilitate electrostatic interactions with cells. The extent of hemolytic activity of a dendriplex was clearly shown to be influenced by the zeta potential.

Cytotoxicity. Cell viability or cytotoxicity can routinely be measured by quantification of mitochondrial enzyme activity using an MTT assay. In order to mimic the "worst case scenario", murine fibroblasts (L929) were incubated with various concentrations of free dendrimer, ranging from 0.001 to 1 mg/mL (Figure 6). The half enzyme inhibitory concentrations (IC_{50}) were determined. While PEI 25 kDa exhibited the strongest toxic effects for the panel investigated, there was a clear trend between cytotoxicity and generation number for the rigid triazine dendrimers. For **G1-1**, we determined an IC_{50} value of 501.2 μg/mL, which is about 100-fold higher than the IC_{50} value of PEI 25 kDa (4.9 μg/mL; compare Figure 6). The IC_{50} values decreased with increased generation among the rigid dendrimers, which can be explained by the increasing number of peripheral primary amino groups. Nontheless, **G3-1**, the dendrimer that contains the highest number of primary amines per molecule, was approximately 5-fold less toxic than PEI 25 kDa and showed a 2.5-fold lower IC_{50} value than the third-generation PAMAM (*35*). The **F2-1** dendrimer showed a higher toxicity profile than **G2-1**, which can be explained as resulting from an increased accessibility of both the core and the terminal amine groups, although the hemolytic activity we measured for **F2-1**/DNA complexes was comparably low. The effect on remaining cell viability, on the other hand, which is expressed in the IC_{50} values, can have various causes. Highly surface active substances are expected to strongly impede the phospholipids double layer, leading to decreased cell viability and cell death. However, substances that do not exhibit strong membrane toxicity can still alter cellular mechanisms, leading to decreased

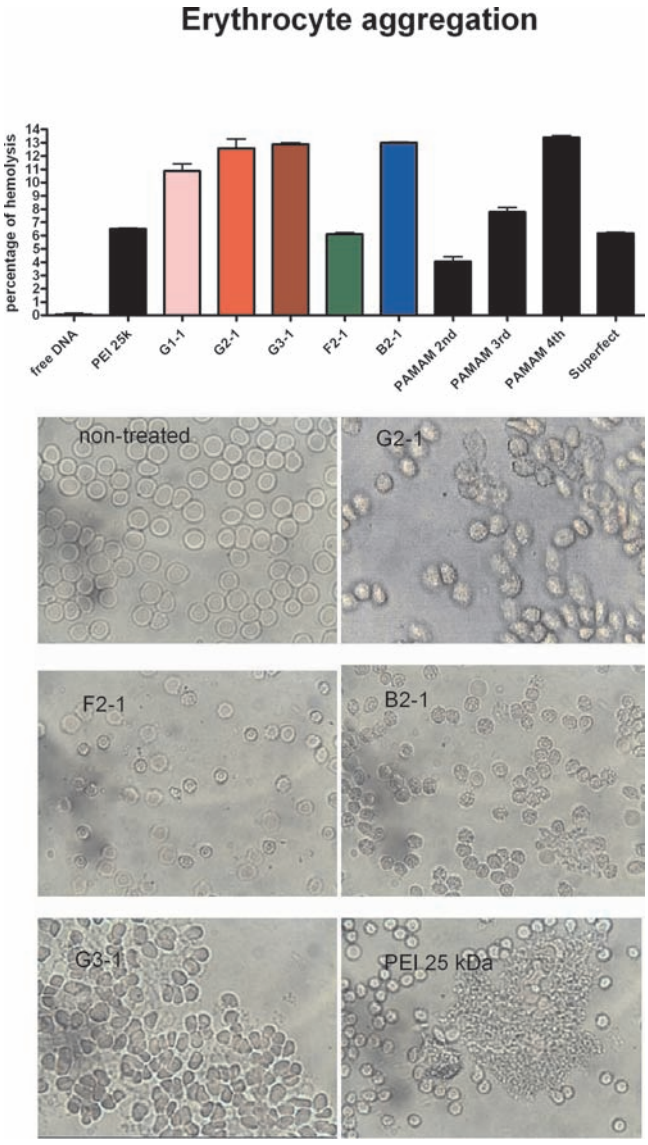

Figure 5. (A) Hemolysis after incubation with dendriplexes at an N/P of 5 was UV-metrically quantified and (B) morphologic changes of erythrocytes were microscopically captured. Hemolysis depended strongly on the core structure, whereas erythrocyte aggregation increased by generation.

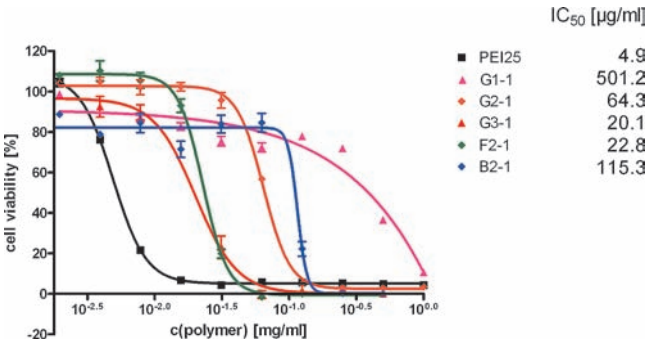

Figure 6. Toxicity profiles of all the dendrimers according to the MTT assays were compared to that of PEI 25 kDa, and for clarity, IC_{50} values are given.

cell viability. It is therefore not surprising that **F2-1**, which shows comparably low hemolysis, is more toxic than **G2-1** and **B2-1**, which have higher hemolytic potentials.

The bow tie dendrimer **B2-1**, on the other hand, exhibited lower toxicity than the rigid dendrimer **G2-1**, despite causing

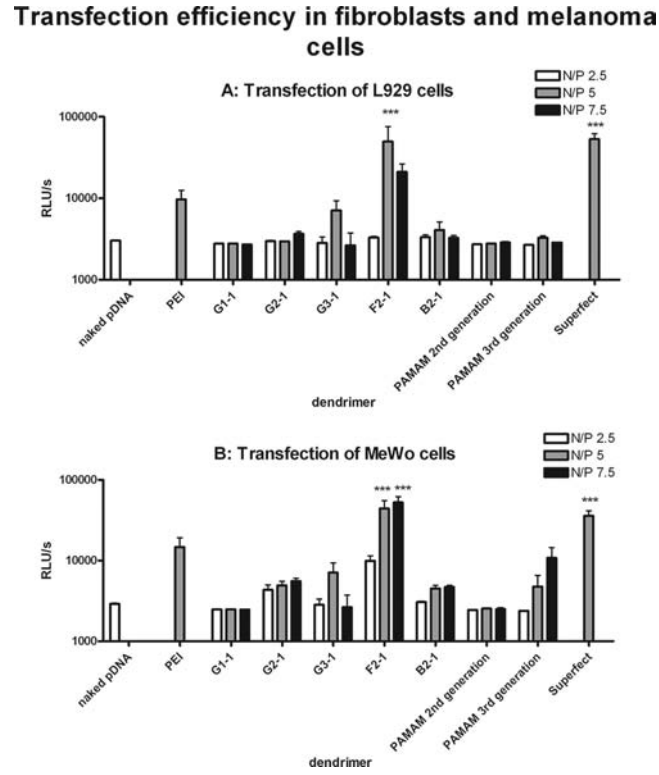

Figure 7. Transfection efficiency of the dendrimers at various N/P ratios in (A) L929 and (B) MeWo cells are given as relative light units detected by luciferase assay. **F2-1** and Superfect exhibited significantly (***$p < 0.01$) higher transgene expression than PEI 25 kDa and all other dendrimers.

comparable hemolytic effects. For all of the triazine dendrimers, our cytotoxicity results are in line with an earlier report (*13*) revealing an IC_{50} value of 0.1 mg/mL for a related melamine structure. Triazine dendrimers seem to be less toxic than PEI and therefore more suitable for possible *in vivo* studies. Moreover, cytotoxicity strongly depends on the core structure and can be significantly reduced by dendriplex formation.

Transfection Efficiency. The primary interest for nonviral vectors is the efficiency of transfection. This property was studied using a luciferase-expressing plasmid in two different cell lines, namely, murine L929 fibroblasts (Figure 7A) and human MeWo (Figure 7B) melanoma cells. The transfection efficiency of dendriplexes at different N/P ratios was quantified using a commercial luciferase assay and was compared to the transfection efficiencies of PEI 25 kDa, SuperFect, and second- and third-generation PAMAM.

PAMAM (second and third generation) dendrimers showed little transfection efficiency with increasing N/P ratios, as reported in the literature (*5*). An increase in transfection efficiency with increasing generation was revealed for rigid triazine dendrimers (**G1-1**, **G2-1**, and **G3-1**). The lowest-generation dendrimer, **G1-1**, did not induce transgene expression in L929 or MeWo cells, while **G2-1** successfully transfected MeWo and L929 at N/P ratio of >7.5. Interestingly, **G3-1** yielded a maximum luciferase expression at N/P 5 in both cell lines. The reduced transfection efficiency at a higher N/P ratio for the higher-generation dendrimer may be caused by cytotoxic effects. In both cell lines, **F2-1** achieved the highest transgene expression, even higher than the expression of PEI 25 or SuperFect. The bow tie dendrimer, **B2-1**, exhibited moderate transfection efficiency at N/P ratio of 5 in L929 and at N/P 5 and 7.5 in MeWo cells.

These results demonstrate that triazine dendrimers could provide a promising platform for gene delivery systems as they induce transfection at generation two, while established transfection reagents such as PAMAM are ineffective at that size. Similarly, the phosphorus-containing dendrimers of Majoral show a transfection optimum at generation 5 (*36*). Higher-generation, flexible triazine dendrimers are therefore under investigation with the goal of providing more efficient transfection reagents.

Because the flexible dendrimer, **F2-1**, formed larger complexes than the third-generation dendrimer, **G3-1**, it presumably sedimented more rapidly (*24*). This could have contributed to the higher transfection efficiency seen for this dendriplex. However, this route of endocytosis may not prove viable for *in vivo* applications, but also, a higher availability to RNA polymerase inside the nucleus of DNA in these less compact dendriplexes, as reported by Yamagata et al. (*37*), might be an explanation. Hence, the colloidal stability and the systematic variation of the triazine dendrimer surface are further goals for synthetic modifications.

CONCLUSION

Efforts to optimize the triazine dendrimers will require consideration of a number of lessons learned from these studies. The first-generation rigid dendrimer, **G1-1**, yielded very low condensation efficiency, and although the structure had a good biocompatibility profile, it did not show any transfection efficiency. The second-generation rigid dendrimer **G2-1** showed improved DNA condensation, formed small dendriplexes, and was less toxic but more hemolytic than PEI. However, it showed intermediate transfection efficiency. The **G3-1** dendrimer condensed DNA well, formed small particles within a narrow size distribution, but exhibited erythrocyte aggregation. Transfection efficiency of this dendrimer was possibly limited by toxic effects at higher N/P ratios.

The change in core structure had the most profound impact on physicochemical as well as biologic properties of the triazine dendrimers. While the rigid, second-generation dendrimer, **G2-1**, formed comparably small dendriplexes, both **B2-1** and **F2-1** assembled DNA into larger complexes with lower or even negative surface charge. DNA condensation was affected differently: DNA condensation with **F2-1** and **G2-1** was similar, whereas **B2-1** protected DNA even better than PEI 25 kDa. The flexible dendrimer **F2-1** was most effective in transfection experiments. The low-density particles exhibited the lowest hemolytic effect and almost no erythrocyte aggregation.

The bow tie dendrimer, **B2-1**, caused the most pronounced hemolytic effects, which are attributed to the formation of aggregates and clusters as observed with DLS and AFM. Due to their large size, **B2-1** dendriplexes were not effectively taken up by L929 or MeWo cells, leading to low transfection efficiency. We remain optimistic that triazine dendrimers demonstrate a promising platform for nonviral delivery systems, meriting further investigations, while our most important result is that flexible triazine dendrimers that are biocompatible may be highly efficient vectors for nonviral gene delivery at comparably low generations. This is especially true for the flexible dendrimer **F2-1**, which exhibits higher transfection efficacy than SuperFect.

ACKNOWLEDGMENT

We thank Eva Mohr and Sandra Engel (DPB, Marburg, Germany) for their support in the cell culture lab and Michael Dutescu (Dept. of Clinical Chemistry, Marburg, Germany) for providing us with fresh blood samples. E.E.S. acknowledges support of the NIH (NIGMS R01 45640).

Supporting Information Available: Detailed descriptions of the syntheses of all dendrimers and precursors as well as yields and ^{1}H NMR and MS (MALDI) data. This material is available free of charge via the Internet at http://pubs.acs.org.

LITERATURE CITED

(1) Anderson, W. F. (1998) Human gene therapy. *Nature 392*, 25–30.

(2) Verma, I. M., and Somia, N. (1997) Gene therapy -- promises, problems and prospects. *Nature 389*, 239–42.

(3) Mintzer, M. A., and Simanek, E. E. (2009) Nonviral vectors for gene delivery. *Chem. Rev, 109*, 259–302.

(4) Haensler, J., and Szoka, F. C., Jr. (1993) Polyamidoamine cascade polymers mediate efficient transfection of cells in culture. *Bioconjugate Chem. 4*, 372–9.

(5) Kukowska-Latallo, J. F., Bielinska, A. U., Johnson, J., Spindler, R., Tomalia, D. A., and Baker, J. R., Jr. (1996) Efficient transfer of genetic material into mammalian cells using Starburst polyamidoamine dendrimers. *Proc. Natl. Acad. Sci. U.S.A. 93*, 4897–902.

(6) Tang, M. X., Redemann, C. T., and Szoka, F. C., Jr. (1996) In vitro gene delivery by degraded polyamidoamine dendrimers. *Bioconjugate Chem. 7*, 703–14.

(7) Zinselmeyer, B. H., Mackay, S. P., Schatzlein, A. G., and Uchegbu, I. F. (2002) The lower-generation polypropylenimine dendrimers are effective gene-transfer agents. *Pharm. Res. 19*, 960–7.

(8) Hollins, A. J., Benboubetra, M., Omidi, Y., Zinselmeyer, B. H., Schatzlein, A. G., Uchegbu, I. F., and Akhtar, S. (2004) Evaluation of generation 2 and 3 poly(propylenimine) dendrimers for the potential cellular delivery of antisense oligonucleotides targeting the epidermal growth factor receptor. *Pharm. Res. 21*, 458–66.

(9) Fischer, D., Bieber, T., Li, Y., Elsasser, H. P., and Kissel, T. (1999) A novel non-viral vector for DNA delivery based on low molecular weight, branched polyethylenimine: effect of molecular weight on transfection efficiency and cytotoxicity. *Pharm. Res. 16*, 1273–9.

(10) Kunath, K., von Harpe, A., Fischer, D., Petersen, H., Bickel, U., Voigt, K., and Kissel, T. (2003) Low-molecular-weight polyethylenimine as a non-viral vector for DNA delivery: comparison of physicochemical properties, transfection efficiency and in vivo distribution with high-molecular-weight polyethylenimine. *J. Controlled Release 89*, 113–25.

(11) Mintzer, M. A., Merkel, O. M., Kissel, T., and Simanek, E. (2009) Polycationic triazine-based dendrimers: Effect of peripheral groups on transfection efficiency. *New J. Chem.* . doi: 10.1039/b908735d.

(12) Lim, J., Guo, Y., Rostollan, C. L., Stanfield, J., Hsieh, J. T., Sun, X., and Simanek, E. E. (2008) The role of the size and number of polyethylene glycol chains in the biodistribution and tumor localization of triazine dendrimers. *Mol. Pharm. 5*, 540–7.

(13) Neerman, M. F., Zhang, W., Parrish, A. R., and Simanek, E. E. (2004) In vitro and in vivo evaluation of a melamine dendrimer as a vehicle for drug delivery. *Int. J. Pharm. 281*, 129–32.

(14) Roberts, J. C., Bhalgat, M. K., and Zera, R. T. (1996) Preliminary biological evaluation of polyamidoamine (PAMAM) Starburst dendrimers. *J. Biomed. Mater. Res. 30*, 53–65.

(15) Germershaus, O., Mao, S., Sitterberg, J., Bakowsky, U., and Kissel, T. (2008) Gene delivery using chitosan, trimethyl chitosan or polyethylenglycol-graft-trimethyl chitosan block copolymers: establishment of structure-activity relationships in vitro. *J. Controlled Release 125*, 145–54.

(16) Germershaus, O., Merdan, T., Bakowsky, U., Behe, M., and Kissel, T. (2006) Trastuzumab-polyethylenimine-polyethylene

glycol conjugates for targeting Her2-expressing tumors. *Bioconjugate Chem. 17*, 1190–9.
(17) Germershaus, O., Neu, M., Behe, M., and Kissel, T. (2008) HER2 targeted polyplexes: the effect of polyplex composition and conjugation chemistry on in vitro and in vivo characteristics. *Bioconjugate Chem. 19*, 244–53.
(18) Han, M., Chen, P., and Yang, X. (2005) Molecular dynamics simulation of PAMAM dendrimer in aqueous solution. *Polymer 46*, 3481–3488.
(19) Kabanov, V. A., Sergeyev, V. G., Pyshkina, O. A., Zinchenko, A. A., Zezin, A. B., Joosten, J. G. H., Brackman, J., and Yoshikawa, K. (2000) Interpolyelectrolyte complexes formed by DNA and astramol Poly(propylene imine) dendrimers. *Macromolecules 33*, 9587–9593.
(20) Gebhart, C. L., and Kabanov, A. V. (2001) Evaluation of polyplexes as gene transfer agents. *J. Controlled Release 73*, 401–16.
(21) Tang, M. X., and Szoka, F. C. (1997) The influence of polymer structure on the interactions of cationic polymers with DNA and morphology of the resulting complexes. *Gene Ther. 4*, 823–32.
(22) Wolfert, M. A., Dash, P. R., Nazarova, O., Oupicky, D., Seymour, L. W., Smart, S., Strohalm, J., and Ulbrich, K. (1999) Polyelectrolyte vectors for gene delivery: influence of cationic polymer on biophysical properties of complexes formed with DNA. *Bioconjugate Chem. 10*, 993–1004.
(23) Wood, K. C., Little, S. R., Langer, R., and Hammond, P. T. (2005) A family of hierarchically self-assembling linear-dendritic hybrid polymers for highly efficient targeted gene delivery. *Angew. Chem., Int. Ed. Engl. 44*, 6704–8.
(24) Mahato, R. I., Rolland, A., and Tomlinson, E. (1997) Cationic lipid-based gene delivery systems: pharmaceutical perspectives. *Pharm. Res. 14*, 853–9.
(25) Erbacher, P., Bettinger, T., Belguise-Valladier, P., Zou, S., Coll, J. L., Behr, J. P., and Remy, J. S. (1999) Transfection and physical properties of various saccharide, poly(ethylene glycol), and antibody-derivatized polyethylenimines (PEI). *J. Gene Med. 1*, 210–22.
(26) Kim, T. I., Seo, H. J., Choi, J. S., Jang, H. S., Baek, J. U., Kim, K., and Park, J. S. (2004) PAMAM-PEG-PAMAM: novel triblock copolymer as a biocompatible and efficient gene delivery carrier. *Biomacromolecules 5*, 2487–92.
(27) Akinc, A., Thomas, M., Klibanov, A. M., and Langer, R. (2005) Exploring polyethylenimine-mediated DNA transfection and the proton sponge hypothesis. *J. Gene Med. 7*, 657–63.
(28) Wittmar, M., Ellis, J. S., Morell, F., Unger, F., Schumacher, J. C., Roberts, C. J., Tendler, S. J. B., Davies, M. C., and Kissel, T. (2005) Biophysical and transfection studies of an amine-modified poly(vinyl alcohol) for gene delivery. *Bioconjugate Chem. 16*, 1390–1398.
(29) Kunath, K., von Harpe, A., Petersen, H., Fischer, D., Voigt, K., Kissel, T., and Bickel, U. (2002) The structure of PEG-modified poly(ethylene imines) influences biodistribution and pharmacokinetics of their complexes with NF-kappaB decoy in mice. *Pharm. Res. 19*, 810–7.
(30) Khandare, J. J., Jayant, S., Singh, A., Chandna, P., Wang, Y., Vorsa, N., and Minko, T. (2006) Dendrimer versus linear conjugate: Influence of polymeric architecture on the delivery and anticancer effect of paclitaxel. *Bioconjugate Chem. 17*, 1464–72.
(31) Patil, M. L., Zhang, M., Betigeri, S., Taratula, O., He, H., and Minko, T. (2008) Surface-modified and internally cationic polyamidoamine dendrimers for efficient siRNA delivery. *Bioconjugate Chem. 19*, 1396–403.
(32) Zhou, J., Wu, J., Hafdi, N., Behr, J. P., Erbacher, P., and Peng, L. (2006) PAMAM dendrimers for efficient siRNA delivery and potent gene silencing. *Chem. Commun. (Camb.)* 2362–4.
(33) Manunta, M., Tan, P. H., Sagoo, P., Kashefi, K., and George, A. J. (2004) Gene delivery by dendrimers operates via a cholesterol dependent pathway. *Nucleic Acids Res. 32*, 2730–9.
(34) Braun, C. S., Vetro, J. A., Tomalia, D. A., Koe, G. S., Koe, J. G., and Middaugh, C. R. (2005) Structure/function relationships of polyamidoamine/DNA dendrimers as gene delivery vehicles. *J. Pharm. Sci. 94*, 423–36.
(35) Malik, N., Wiwattanapatapee, R., Klopsch, R., Lorenz, K., Frey, H., Weener, J. W., Meijer, E. W., Paulus, W., and Duncan, R. (2000) Dendrimers: relationship between structure and biocompatibility in vitro, and preliminary studies on the biodistribution of ^{125}I-labelled polyamidoamine dendrimers in vivo. *J. Controlled Release 65*, 133–48.
(36) Padié, C., Maszewska, M., Majchrzak, K., Nawrot, B., Caminade, A.-M., and Majoral, J.-P. (2009) Polycationic phosphorus dendrimers: synthesis, characterization, study of cytotoxicity, complexation of DNA, and transfection experiments. *New J. Chem. 33*, 318.
(37) Yamagata, M., Kawano, T., Shiba, K., Mori, T., Katayama, Y., and Niidome, T. (2007) Structural advantage of dendritic poly(L-lysine) for gene delivery into cells. *Bioorg. Med. Chem. 15*, 526–32.

BC900243R

Supplementary Material:

Synthesis of Triazine Dendrimers:

Monochlorotriazine 1 (MCT1). Cyanuric chloride (0.9220g, 5.000 mmol) and Boc-protected 3,3'-bisaminopropylamine (1.6575g, 5.00 mmol) were each dissolved in 60 mL tetrahydrofuran and cooled to 0 °C. The Boc-protected triamine was added dropwise to cyanuric chloride followed by the addition of DIPEA (1.75 mL, 10.046 mmol). After 3 hours, diethanolamine (0.5276g, 5.018 mmol) and DIPEA (1.75 mL, 10.046 mmol) were dissolved in 60 mL tetrahydrofuran, cooled to 0 °C, and added dropwise to the reaction mixture. The mixture was allowed to warm to room temperature. After 20 hours the solvent was evaporated under reduced pressure. The crude product was dissolved in dichloromethane and the salt byproducts were extracted with distilled water. The organic layer was condensed and the product purified by column chromatography (10:1 CH_2Cl_2:ethyl acetate) to yield MCT1 (2.4937g, 91%). ^{1}H NMR (300 MHz, $CDCl_3$) δ: 5.76 (b, 1H, O**H**) 5.36 (t, 2H, N**H**Boc), 3.77 (d, 4H, C**H**$_2$OH), 3.67 (d, 4H, NC**H**$_2$CH$_2$OH), 3.51-3.43 (br, 4H, NC**H**$_2$CH$_2$CH$_2$), 3.01 (m, 4H, C**H**$_2$NHBoc), 1.79-1.67 (m, 4H, CH$_2$C**H**$_2$CH$_2$), 1.37 (s, 18H, C(C**H**$_3$)$_3$). ^{13}C NMR (300 MHz, $CDCl_3$) δ: 168.4 (C_3N_3), 165.0 (C_3N_3), 164.1 (C_3N_3), 156.3 (CO), 79.3 (O**C**(CH$_3$)$_3$), 61.7 (**C**H$_2$OH), 51.7 (NC**H**$_2$CH$_2$OH), 44.6 (NC**H**$_2$CH$_2$CH$_2$), 38.0 (**C**H$_2$NHBoc), 28.2 (C(**C**H$_3$)$_3$), 27.7 (CH$_2$**C**H$_2$CH$_2$). MS (ESI): calcd 547.29 (M^+); found 548.30 ($M + H^+$).

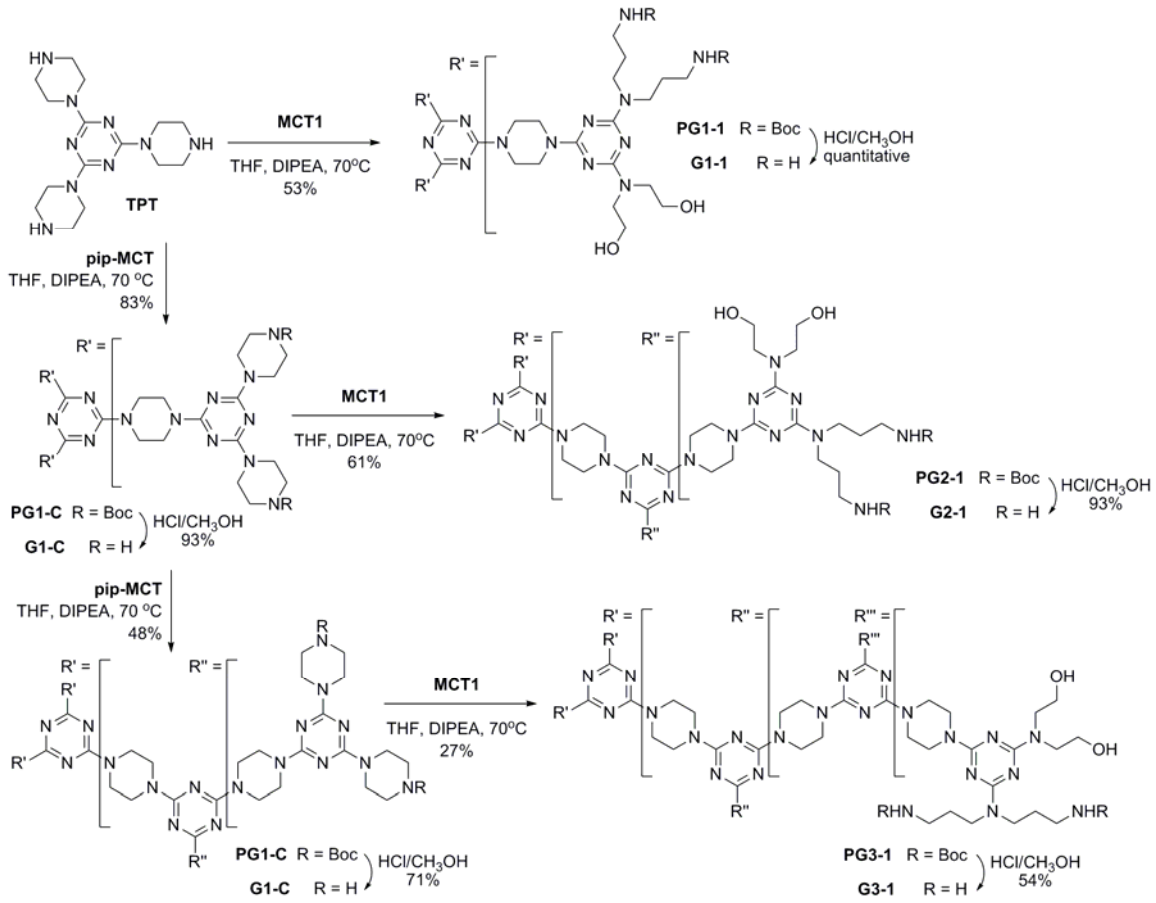

Scheme S1: Synthesis of rigid generation 1-3 dendrimers (G1-1, G2-1, G3-1)

Protected G1-1 Dendrimer (P-G1-1). Tris(piperazyl)triazine (TPT) (0.1837g, 0.551 mmol) and MCT1 (0.9071g, 1.655 mmol) were dissolved separately in 10 mL dichloromethane. The monochlorotriazines solution was added to the solution containing TPT followed by the addition of DIPEA (0.6mL, 3 mmol), and the mixture was heated to reflux. After two days reaction mixture was washed three times with H_2O, condensed under reduced pressure, and purified by column chromatography (1:1 CH_2Cl_2:ethyl acetate with 4% CH_3OH → 1:1 CH_2Cl_2:ethyl acetate with 20% CH_3OH) to afford G1-1

in 53% yield. ^{1}H NMR (300 MHz, $CDCl_3$) δ: 5.68 (s, 3H, O**H**) 5.10 (s, 6H, N**H**Boc), 3.85 (br, 12H, C**H**$_2$OH), 3.80 (br, 24H, piperazine), 3.75 (br, 12H, NC**H**$_2$CH$_2$OH), 3.59-3.48 (br, 12H, NC**H**$_2$CH$_2$CH$_2$), 3.08-3.15 (br, 12H, C**H**$_2$NHBoc), 1.73 (br, 12H, CH$_2$C**H**$_2$CH$_2$), 1.42 (s, 54H, C(C**H**$_3$)$_3$). ^{13}C NMR (300 MHz, $CDCl_3$) δ: 167.2 (C_3N_3), 164.6 (C_3N_3), 164.6 (C_3N_3), 156.1 (CO), 79.3 (O**C**(CH$_3$)$_3$), 63.0 (**C**H$_2$OH), 51.3 (NC**H**$_2$CH$_2$OH), 44.1 (NC**H**$_2$CH$_2$CH$_2$), 43.5 (piperazine), 38.1 (**C**H$_2$NHBoc), 28.6 (C(**C**H$_3$)$_3$), 27.8 (CH$_2$**C**H$_2$CH$_2$). MS (MALDI): calcd 1867.17 (M^+); found 1869.07 (M + H^+).

G1-1. P-G1-1 (0.3326g, 0.178 mmol) was dissolved in 3 M HCl:CH_3OH. After 2 days, the reaction was condensed and neutralized with $NaCO_3$ to pH=7. NaCl byproduct was removed from the mixture using an Amicon apparatus and a millipore membrane with NMWL = 1,000 under 35 psi N_2. The water that was pushed through the membrane was tested for Cl^- using $AgNO_3$. When no AgCl precipitate formed from the filtrate, the solution remaining inside the Amicon vessel was condensed *in vacuo* to afford G1-1 (0.5276 g, 129%). MS (MALDI): calcd 1267.59 (M^+); found 1267.91 (M + H^+).

Protected G2-1 (P-G2-1). MCT1 (0.5686g, 1.037 mmol) and G1-C (0.1826g, 0.1698 mmol) were each dissolved in 10mL of 9:1 CH_2Cl_2:CH_3OH. The solutions were mixed at room temperature followed by the addition of DIPEA (0.5mL, 2.8704 mmol). The reaction mixture was heated to 70 °C. After 10 days the reaction mixture was condensed, re-dissolved in dichloromethane, and washed with distilled water. The organic layer was condensed and purified by column chromatography (4:1 CH_2Cl_2:ethyl acetate with 1 → 3% CH_3OH) to yield P-G2-1 (0.4267g, 61%). ^{1}H NMR (300 MHz, $CDCl_3$) δ: 5.64 (s,

12H, O**H**) 5.09 (s, 12H, N**H**Boc), 3.87 (br, 24H, C**H**$_2$OH), 3.81 (br, 72H, piperazine), 3.77 (br, 24H, NC**H**$_2$CH$_2$OH), 3.61 (br, 24H, NC**H**$_2$CH$_2$CH$_2$), 3.11 (br, 24H, C**H**$_2$NHBoc), 1.67 (br, 24H, CH$_2$C**H**$_2$CH$_2$), 1.44 (s, 108H, C(C**H**$_3$)$_3$). ^{13}C NMR (300 MHz, $CDCl_3$) δ: 165.6 (C_3N_3), 165.5 (C_3N_3), 156.2 (CO), 79.2 (O**C**(CH$_3$)$_3$), 62.0 (**C**H$_2$OH), 51.3 (NC**H**$_2$CH$_2$OH), 44.2 (NC**H**$_2$CH$_2$CH$_2$), 43.6 (piperazine), 38.2 (**C**H$_2$NHBoc), 28.7 (C(**C**H$_3$)$_3$), 27.9 (CH$_2$**C**H$_2$CH$_2$). MS (MALDI): calcd 4142.57 (M^+); found 4142.71 ($M + H^+$).

G2-1. P-G2-1 was dissolved in 3 M HCl:CH_3OH. After 2 days the reaction was condensed and neutralized with $NaCO_3$ to pH=7. NaCl byproduct was removed from the mixture using an Amicon apparatus and a millipore membrane with NMWL = 1,000 under 35 psi N_2. The water that was pushed through the membrane was tested for Cl^- using $AgNO_3$. When no AgCl precipitate formed from the filtrate, the solution remaining inside the Amicon vessel was condensed *in vacuo* to afford G2-1 (0.2463g, 93%). MS (MALDI): calcd 2941.94 (M^+); found 4142.90 ($M + H^+$). HPLC (2:1 H_2O with 0.14% TFA:acetonitrile): 3.196 min.

Protected G3-1 (P-G3-1). G2-C (0.0408g, 0.016 mmol) and MCT1 (0.1053g, 0.192 mmol) were each dissolved in 1 mL of 9:1 $CHCl_3$:CH_3OH. The monochlorotriazine solution was added to the G2-C solution at room temperature. The reaction was heated to 70 ºC. After 6 days the reaction mixture was condensed, dissolved in chloroform and washed with distilled water. The organic layer was condensed and purified by column chromatography (10:1 CH_2Cl_2:EtOAc → 1:1 CH_2Cl_2:EtOAc) to yield P-G3-1 (0.0374g, 27%). ^{1}H NMR (300 MHz, $CDCl_3$) δ: 5.01-5.69 (s, 24H, N**H**), 3.82 (br, 192H, C**H**$_2$OH,

piperazine), 3.75 (br, 48H, NC**H**$_2$CH$_2$OH), 3.47-3.57 (br, 48H, NC**H**$_2$CH$_2$CH$_2$), 3.09 (br, 48H, C**H**$_2$NHBoc), 1.71 (br, 48H, CH$_2$C**H**$_2$CH$_2$), 1.43 (s, 216H, C(C**H**$_3$)$_3$). ^{13}C NMR (300 MHz, $CDCl_3$) δ: 167.0 (**C**$_3$N$_3$), 165.7 (**C**$_3$N$_3$), 164.6 (**C**$_3$N$_3$), 164.4 (**C**$_3$N$_3$), 156.2 (**C**O), 79.3 (**C**(CH$_3$)$_3$), 63.0 (**C**H$_2$OH), 51.4 (N**C**H$_2$CH$_2$OH), 46.0 (N**C**H$_2$CH$_2$CH$_2$NHBoc), 43.0 - 43.3 (N**C**H$_2$**C**H$_2$N), 38.2 (**C**H$_2$NHBoc), 28.7 (C(CH$_3$)$_3$), 27.9 (NCH$_2$**C**H$_2$CH$_2$NHBoc). MS (MALDI): calcd 8693.4 (M^+); found 8700.1 (M + H^+).

G3-1. P-G3-1 (0.0330g, 0.004 mmol) was dissolved in 3 mL CH_3OH. Concentrated HCl (2 mL) was added to the solution. After 24 hours the reaction was condensed and neutralized using NaOH. NaCl byproduct was removed from the solution using an Amicon apparatus and a millipore membrane with NMWL = 3,000 under 25 psi N_2. The filtrate was tested for Cl^- using $AgNO_3$. When no AgCl precipitate formed the solution remaining inside the Amicon vessel was condensed *in vacuo* to afford G3-1 (0.0129g, 54%).

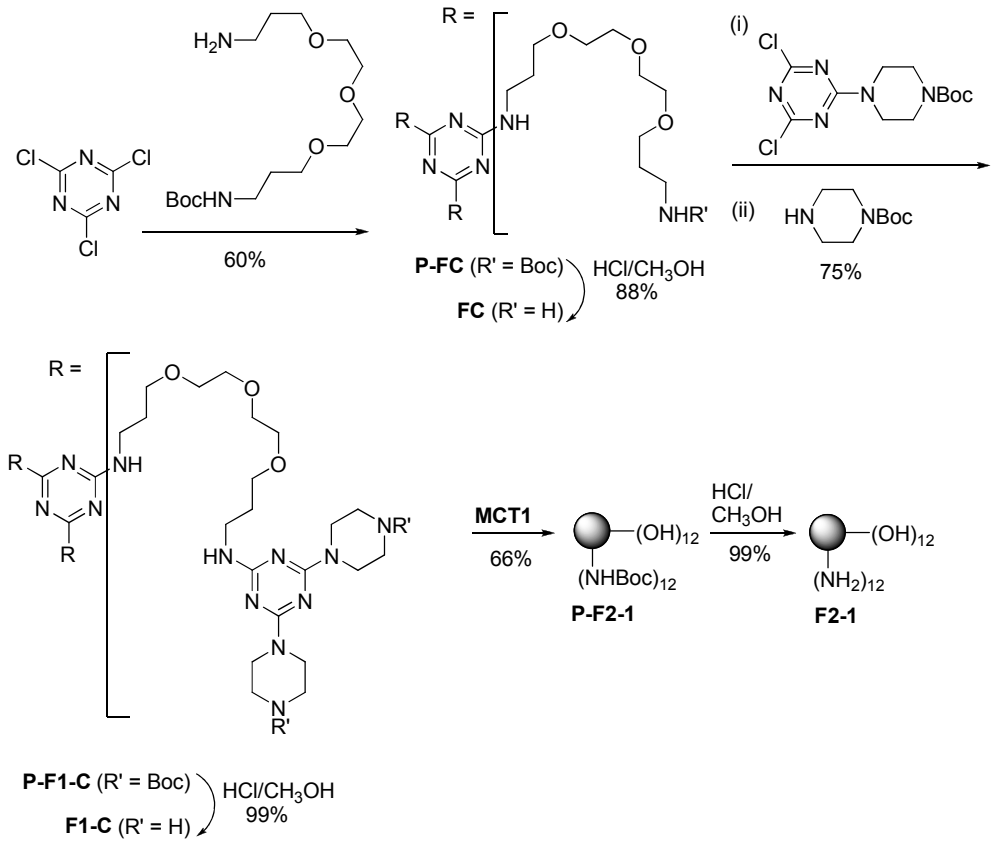

Scheme S2: Synthesis of second generation flexible dendrimer (F2-1)

Protected Flexible Core (P-FC). Cyanuric chloride (0.1596g, 0.866 mmol) and N-Boc-4,7,10-trioxa-1,13-tridecanediamine (0.9512g, 2.769 mmol) were each dissolved in 15 mL THF. The N-Boc-diamine solution was added to the cyanuric chloride solution and the mixture was heated to 70 ºC. After 4 days the reaction mixture was condensed, dissolved in dichloromethane, and washed three times with distilled water. The organic layer was collected, condensed, and purified by column chromatography (30:1 CH_2Cl_2:CH_3OH → 10:1 CH_2Cl_2:CH_3OH) to yield P-FC (0.5338g, 60%). ^{1}H NMR (300 MHz, $CDCl_3$) δ: 5.09 (s, 4H, NH), 3.45-3.62 (m, 36H, C**H$_2$**OC**H$_2$**C**H$_2$**OC**H$_2$**C**H$_2$**OC**H$_2$**), 3.41 (q, 6H, NHC**H$_2$**), 3.20 (q, 6H, C**H$_2$**NHBoc),1.81 (m, 6H, NHCH$_2$C**H$_2$**), 1.73 (m, 6H, C**H$_2$**CH$_2$NHBoc), 1.41 (s, 27H, C(C**H$_3$**)$_3$). ^{13}C NMR (300 MHz, $CDCl_3$) δ: 165.9

(**C**$_3$N$_3$), 156.2 (**C**O), 79.0 (**C**(CH$_3$)$_3$), 70.7-70.8 (**C**H$_2$O**C**H$_2$), 70.4-70.5 (**C**H$_2$CH$_2$OCH$_2$**C**H$_2$), 69.6-69.7 (NHCH$_2$CH$_2$**C**H$_2$O), 39.1 (NH**C**H$_2$), 38.7 (**C**H$_2$NHBoc), 29.8 (**C**H$_2$CH$_2$NHBoc), 29.0 (NH**C**H$_2$**C**H$_2$). (N**C**H$_2$**C**H$_2$NBoc), 28.6 (C(**C**H$_3$)$_3$). MS (MALDI): calcd 1035.7 (M^+); found 1036.7 ($M + H^+$).

Flexible Core (FC). P-FC (0.5332g, 0.5166 mmol) was dissolved in 7.5 mL CH$_3$OH. Concentrated HCl (2.5 mL was added to the solution. After 24 hours, the reaction mixture was condensed, and 5 M NaOH was added to obtain a basic solution (pH=14). The product was extracted from the aqueous solution with dichloromethane. The organic fractions were condensed to yield FC (0.3331g, 88%). ^{1}H NMR (300 MHz, CDCl$_3$) δ: 5.15 (s, 3H, NH), 3.52-3.62 (m, 36H, C**H$_2$**OC**H$_2$**C**H$_2$**OC**H$_2$**C**H$_2$**OC**H$_2$**), 3.41 (q, 6H, NHC**H$_2$**), 2.76 (q, 6H, C**H$_2$**NHBoc),1.79 (m, 6H, NHCH$_2$C**H$_2$**), 1.69 (m, 6H, C**H$_2$**CH$_2$NHBoc), 1.58 (s, 6H, NH$_2$). ^{13}C NMR (300 MHz, CDCl$_3$) δ: 166.3 (**C**$_3$N$_3$), 70.7-70.8 (**C**H$_2$O**C**H$_2$), 70.3-70.4 (**C**H$_2$CH$_2$OCH$_2$**C**H$_2$), 69.5-69.6 (NHCH$_2$CH$_2$**C**H$_2$O), 39.8 (**C**H$_2$NH$_2$), 38.3 (**C**H$_2$NH), 33.5 (CH$_2$CH$_2$NH$_2$), 29.8 (**C**H$_2$CH$_2$NH). MS (MALDI): calcd 735.5 (M^+); found 736.8 ($M + H^+$).

Protected, Flexible G1 Core (P-F1-C). FC (0.3069g, 0.417mmol) and Boc-piperazyldichlorotriazine were each dissolved in 10 mL THF and cooled to 0 ºC. The dichlorotriazine solution was added dropwise to the FC solution followed by the addition of DIPEA (0.7 mL, 4.019 mmol). The mixture was allowed to warm to room temperature, and 1M K$_2$CO$_3$ was added to the solution. After 16 hours, Boc-piperazine was added to reaction, and the solution was heated to 70 ºC. After 24 hours the reaction

was condensed, dissolved in dichloromethane, and washed three times with distilled water. The organic layer was purified by column chromatography (30:1 CH_2Cl_2:CH_3OH → 15:1 CH_2Cl_2:CH_3OH) to yield P-F1-C (0.6529g, 75%). ^{1}H NMR (300 MHz, $CDCl_3$) δ: 5.23 (s, 6H, NH), 3.71 (s, 24H, NC**H$_2$**CH_2NBoc), 3.53-3.63 (m, 36H, C**H$_2$**OC**H$_2$**C**H$_2$**OC**H$_2$**C**H$_2$**OC**H$_2$**), 3.42 (br, 36H, NHC**H$_2$**, CH_2C**H$_2$**NBoc), 1.82 (m, 12H, C**H$_2$**NH), 1.46 (s, 54H, C(C**H$_3$**)$_3$). ^{13}C NMR (300 MHz, $CDCl_3$) δ: 166.5 (**C**$_3$N$_3$), 165.4 (**C**$_3$N$_3$), 155.0 (**C**O), 80.1(**C**$(CH_3)_3$), 70.78 (**C**H_2O**C**H_2), 70.4 (**C**$H_2CH_2OCH_2$**C**H_2), 69.5 ($NHCH_2CH_2$**C**H_2O), 43.1 (piperazine), 38.3 (**C**H_2NH), 29.8 (**C**H_2CH_2NH), 28.6 (C(**C**$H_3)_3$). MS (MALDI): calcd 2077.3 (M^+); found 2078.6 ($M + H^+$).

Flexible G1 Core (F1-C). P-F1-C (0.6295g, 0.303 mmol) was dissolved in 7.5 mL CH_3OH. Concentrated HCl (2.5 mL) was added to the solution. After 24 hours, the reaction mixture was condensed and the solution was made basic by adding 5 M NaOH. The product was extracted with dichloromethane to yield F1-C (0.4438g, 99%). ^{1}H NMR (300 MHz, $CDCl_3$) δ: 5.23-5.33 (s, 6H, NH), 3.69 (s, 24H, NC**H$_2$**CH_2NBoc), 3.53-3.63 (m, 36H, C**H$_2$**OC**H$_2$**C**H$_2$**OC**H$_2$**C**H$_2$**OC**H$_2$**), 3.41 (br, 12H, NHC**H$_2$**, CH_2C**H$_2$**NBoc), 2.83 (s, 24H, NCH_2C**H$_2$**NH), 1.80 (m, 12H, C**H$_2$**NH). ^{13}C NMR (300 MHz, $CDCl_3$) δ: 166.5 (**C**$_3$N$_3$), 165.3 (**C**$_3$N$_3$), 70.73 (**C**H_2O**C**H_2), 70.4 (**C**$H_2CH_2OCH_2$**C**H_2), 69.4-69.5 ($NHCH_2CH_2$**C**H_2O), 46.1 ((CH_2**C**$H_2)_2NH$), 44.3 ((**C**$H_2CH_2)_2NH$), 38.3 (**C**H_2NH), 29.8 (CH_2**C**H_2CH_2NH). MS (MALDI): calcd 1477.0 (M^+); found 1478.2 ($M + H^+$).

Protected F2-1 (P-F2-1). MCT1 (0.2804g, 0.512 mmol) and P-F1-C (0.1006g, 0.068 mmol) were each dissolved in 5mL dichloromethane. The MCT1 solution was added to

the solution containing F1-C followed by the addition of DIPEA (0.2 mL, 1.148 mmol). The mixture was heated to 70 ºC. After two days the reaction mixture was washed three times with distilled water. The organic layer was condensed and purified by column chromatography (30:1 CH_2Cl_2:CH_3OH → 4:1 CH_2Cl_2:CH_3OH) to yield P-F2-1 (0.2058g, 66%). ^{1}H NMR (300 MHz, $CDCl_3$) δ: 5.68 (s, 6H, NH), 5.23 (s, 12H, NH), 3.84 (br, 24H, C**H$_2$**OH), 3.75 (s, 72H, NC**H$_2$**CH_2OH, piperazine), 3.59 (br, 60H, C**H$_2$**OC**H$_2$**C**H$_2$**OC**H$_2$**C**H$_2$**OC**H$_2$**, NC**H$_2$**CH_2CH_2NHBoc), 3.45 (br, 48H, piperazine), 3.08-3.14 (br, 24H, NCH_2CH_2C**H$_2$**NHBoc), 1.80 (m, 12H, C**H$_2$**NH), 1.72 (br, 24H, NCH_2C**H$_2$**CH_2NHBoc), 1.42 (s, 108H, C(C**H$_3$**)$_3$). ^{13}C NMR (300 MHz, $CDCl_3$) δ: 167.1 (**C**$_3N_3$), 166.5 (**C**$_3N_3$), 165.3 (**C**$_3N_3$), , 164.6 (**C**$_3N_3$), 164.4 (**C**$_3N_3$), 156.5 (**C**O), 79.2 (**C**$(CH_3)_3$), 70.8 (**C**H_2O**C**H_2), 70.4 (**C**$H_2CH_2OCH_2$**C**H_2), 69.4 ($NHCH_2CH_2$**C**H_2O), 62.4 (**C**H_2OH), 51.3 (N**C**H_2CH_2OH), 43.5 (N**C**$H_2CH_2CH_2$NHBoc), 43.0 (piperazine), 38.3 (**C**H_2NH), 37.5 (**C**H_2NHBoc), 29.8 (**C**H_2CH_2NH), 28.7 (C(**C**$H_3)_3$), 27.9 (NCH_2**C**H_2CH_2NHBoc). MS (MALDI): calcd 4544.9 (M^+); found 4546.5 ($M + H^+$).

F2-1. P-F2-1 (0.2056g, 0.045 mmol) was dissolved in 7.5 mL methanol. Concentrated HCl (2.5 mL) was added to the solution. After 24 hours the reaction was condensed and neutralized with NaOH. NaCl byproduct was removed from the solution using an Amicon apparatus and a millipore membrane with NMWL = 1,000 under 35 psi N_2. The filtrate was tested for Cl^- using $AgNO_3$. When no AgCl precipitate formed the solution remaining inside the Amicon vessel was condensed *in vacuo* to afford F2-1 (0.1506g, 99%).

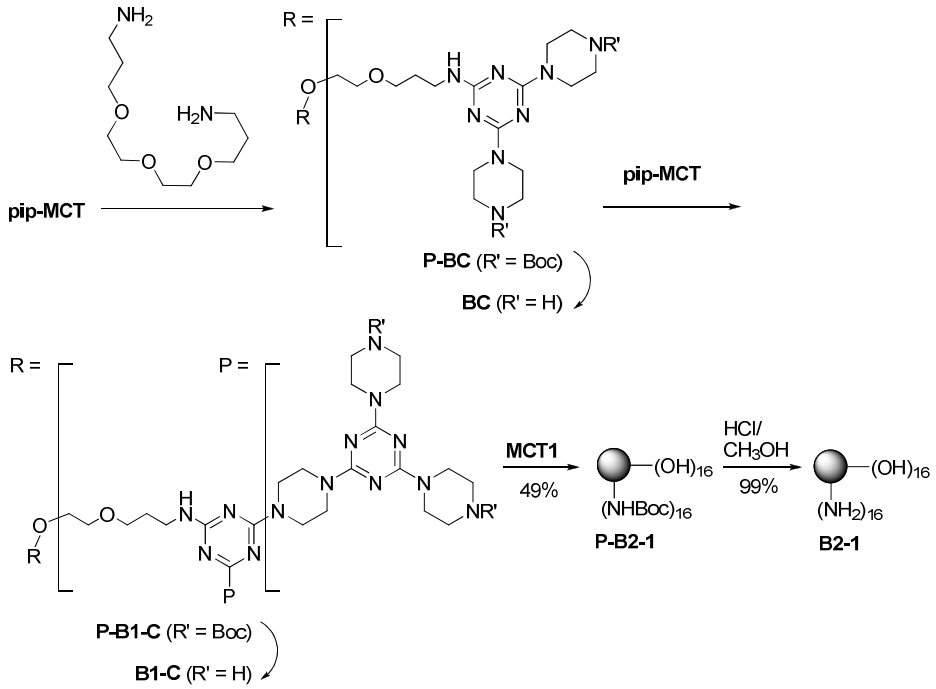

Scheme S3: Synthesis of second generation bow-tie dendrimer (B2-1)

Protected Bow-tie core (P-BC). Pip-MCT (0.9713g, 2.007 mmol) and 4,7,10-trioxa-1,13-tridecanediamine (0.2009g, 0.912 mmol) were each dissolved in 7.5 mL THF. The monochlorotriazine solution was added to the diamine solution, and the mixture was heated to 70 ºC. After 24 hours the reaction mixture was condensed and purified by column chromatography (10:1 CH_2Cl_2:EtOAc → 1:1 CH_2Cl_2:EtOAC) to yield P-BC (0.5802g, 91%). ^{1}H NMR (300 MHz, $CDCl_3$) δ: 5.09 (t, 2H, NH), 3.71 (s, 16H, NC**H$_2$**CH_2NBoc), 3.53-3.66 (m, 12H, C**H$_2$**OC**H$_2$**C**H$_2$**OC**H$_2$**C**H$_2$**OC**H$_2$**), 3.43 (br, 20H, NHC**H$_2$**, CH_2C**H$_2$**NBoc), 1.82 (m, 4H, C**H$_2$**CH_2NH), 1.46 (s, 36H, C(C**H$_3$**)$_3$). ^{13}C NMR (300 MHz, $CDCl_3$) δ: 166.5 (**C**$_3$N$_3$), 165.4 (**C**$_3$N$_3$), 155.0 (**C**O), 80.1(**C**$(CH_3)_3$), 70.8 (**C**H_2O**C**H_2), 70.4 (**C**$H_2CH_2OCH_2$**C**H_2), 69.6 (NHCH_2CH_2**C**H_2O), 43.1 (piperazine), 38.5

(**C**H_2NH), 29.8 (**C**H_2CH_2NH), 28.6 (C(**C**H_3)$_3$). MS (MALDI): calcd 1114.7 (M^+); found 1115.6 ($M + H^+$).

Bow-tie Core (BC). P-BC (0.2384g, 0.214 mmol) was dissolved in 7.5 mL methanol. Concentrated HCl (2.5 mL) was added to the solution. After 24 hours the reaction was condensed and NaOH was added until the solution was at pH 14. The product was extracted from solution using dichloromethane to yield BC (0.0896g, 59%). ^{1}H NMR (300 MHz, $CDCl_3$) δ: 5.03 (t, 2H, N**H**CH_2), 3.70 (s, 16H, NC**H$_2$**CH_2NBoc), 3.53-3.63 (m, 12H, C**H$_2$**OC**H$_2$**C**H$_2$**OC**H$_2$**C**H$_2$**OC**H$_2$**), 3.41 (q, 4H, NHC**H$_2$**), 2.84 (s, 16H, NCH_2C**H$_2$**NH), 1.82 (m, 4H, C**H$_2$**CH_2NH), 1.57 (br, 4H, N**H**). ^{13}C NMR (300 MHz, $CDCl_3$) δ: 166.6 (**C**$_3N_3$), 165.4 (**C**$_3N_3$), 70.8 (**C**H_2O**C**H_2), 70.5 (**C**$H_2CH_2OCH_2$**C**H_2), 69.6 ($NHCH_2CH_2$**C**H_2O), 46.2 ((CH_2**C**$H_2)_2$NH), 44.4 ((**C**$H_2CH_2)_2$NH), 38.4 (**C**H_2NH), 29.8 (CH_2**C**H_2CH_2NH).

Protected G1 Bow-tie Core (P-B1-C). BC (0.0778g, 0.109 mmol) and pip-MCT (0.2158g, 0.446 mmol) were each dissolved in 2 mL 9:1 $CHCl_3$:CH_3OH. Pip-MCT solution was added to the core solution followed by the addition of DIPEA (1.4 mL, 8.037 mmol). The solution was heated to 70 ºC. After 24 hours the reaction was condensed, dissolved in chloroform and washed three times with distilled water. The organic layer was condensed and purified by column chromatography (30:1 CH_2Cl_2:CH_3OH) to yield P-B1-C (0.2017g, 74%). ^{1}H NMR (300 MHz, $CDCl_3$) δ: 5.12 (t, 2H, N**H**CH_2), 3.77 (s, 32H, NC**H$_2$**C**H$_2$**N), 3.74 (s, 32H, C**H$_2$**CH_2NBoc), 3.53-3.63 (m, 12H, C**H$_2$**OC**H$_2$**C**H$_2$**OC**H$_2$**C**H$_2$**OC**H$_2$**), 3.43 (q, 36H, NHC**H$_2$**, NCH_2C**H$_2$**NBoc), 1.85 (m, 4H, C**H$_2$**CH_2NH), 1.47 (s, 72H, C(C**H$_3$**)$_3$). ^{13}C NMR (300 MHz, $CDCl_3$) δ: 166.6

(**C**$_3$N$_3$), 165.5 (**C**$_3$N$_3$), 155.0 (**C**O), 80.1 (**C**(CH$_3$)$_3$), 70.8 (**C**H$_2$O**C**H$_2$), 70.5 (**C**H$_2$CH$_2$OCH$_2$**C**H$_2$), 69.6 (NHCH$_2$CH$_2$**C**H$_2$O), 43.2-44.0 (piperazine), 38.4 (**C**H$_2$NH), 29.9 (CH$_2$**C**H$_2$CH$_2$NH), 28.6 (C(**C**H$_3$)$_3$). MS (MALDI): calcd 2503.5 (M^+); found 2504.8 ($M + H^+$).

G1 Bow-tie Core (B1-C). P-B1-C (0.1794g, 0.072 mmol) was dissolved in 4 mL methanol. Concentrated HCl (2 mL) was added to the solution. After 24 hours the reaction mixture was condensed, and the product was precipitated using 5 M NaOH. The precipitate was dissolved in chloroform and washed with 1 M NaOH. The organic layer was condensed to yield P-B1-C (0.1201g, 98%). ^{1}H NMR (300 MHz, $CDCl_3$) δ: 5.12 (t, 2H, N**H**CH$_2$), 3.76 (s, 32H, NC**H$_2$**C**H$_2$**N), 3.73 (s, 32H, NC**H$_2$**CH$_2$NH), 3.55-3.65 (m, 12H, C**H$_2$**OC**H$_2$**C**H$_2$**OC**H$_2$**C**H$_2$**OC**H$_2$**), 3.46 (q, 4H, NHC**H$_2$**), 2.85 (s, 32H, NCH$_2$C**H$_2$**NH), 1.83 (m, 4H, C**H$_2$**CH$_2$NH). ^{13}C NMR (300 MHz, $CDCl_3$) δ: 166.6 (**C**$_3$N$_3$), 165.6 (**C**$_3$N$_3$), 70.8 (**C**H$_2$O**C**H$_2$), 70.5 (**C**H$_2$CH$_2$OCH$_2$**C**H$_2$), 69.6 (NHCH$_2$CH$_2$**C**H$_2$O), 46.2 (NCH$_2$**C**H$_2$NH), 44.5 (N**C**H$_2$CH$_2$NH), 43.3 (N**C**H$_2$**C**H$_2$NH), 38.4 (**C**H$_2$NH), 29.9 (CH$_2$**C**H$_2$CH$_2$NH). MS (MALDI): calcd 1703.1 (M^+); found 1704.2 ($M + H^+$).

Protected B2-1. MCT1 (0.1138g, 0.208 mmol) and B1-C (0.0294g, 0.017 mmol) were each dissolved in 3 mL 10:1 $CHCl_3$:CH_3OH. The MCT1 solution was added to the core solution followed by the addition of DIPEA (0.1 mL, 0.574 mmol). The solution was heated to 70 ºC. After three days the reaction was condensed, dissolved in chloroform, and washed three times with distilled water. The chloroform solution was condensed and

purified by column chromatography (30:1 CH_2Cl_2:CH_3OH → 9:1 CH_2Cl_2:CH_3OH) to yield P-B2-1 (0.0492g, 49%). ^{1}H NMR (300 MHz, $CDCl_3$) δ: 5.12 (t, 16H, N**H**Boc), 3.83 (s, 32H, C**H$_2$**OH), 3.77 (s, 128H, NC**H$_2$**C**H$_2$**N, NC**H$_2$**CH_2OH), 3.67 (s, 32H, NC**H$_2$**CH_2CH_2NHBoc), 3.58 (m, 12H, C**H$_2$**OC**H$_2$**C**H$_2$**OC**H$_2$**C**H$_2$**OC**H$_2$**), 3.47 (q, 4H, NHC**H$_2$**), 3.07-3.15 (br, 32H, NCH_2CH_2C**H$_2$**NHBoc), 1.85 (m, 4H, C**H$_2$**CH_2NH), 1.72 (s, 32H, NCH_2C**H$_2$**CH_2NHBoc), 1.42 (s, 144H, C(C**H$_3$**)$_3$). ^{13}C NMR (300 MHz, $CDCl_3$/CD_3OD) δ: 167.0 (**C**$_3N_3$), 165.4 (**C**$_3N_3$), 164.4 (**C$_3$**N_3), 156.2-156.5 (**C**O), 79.2-79.3 (**C**$(CH_3)_3$), 70.8 (**C**H_2O**C**H_2), 70.4 (**C**$H_2CH_2OCH_2$**C**H_2), 69.5 ($NHCH_2CH_2$**C**H_2O), 62.4-63.1(**C**H_2OH), 51.3 (N**C**H_2CH_2OH), 44.2 (N**C**$H_2CH_2CH_2$NHBoc), 43.0-43.5 (N**C**H_2**C**H_2N), 38.2 (**C**H_2NH), 37.5 (**C**H_2NHBoc), 29.8 (OCH_2**C**H_2CH_2NH), 28.7 (C(**C**$H_3)_3$), 27.9 (NCH_2**C**H_2CH_2NHBoc). MS (MALDI): calcd 5793.6 (M^+); found 5794.9 ($M + H^+$).

B2-1. P-B2-1 (0.0453g, 0.008 mmol) was dissolved in 7 mL methanol. Concentrated HCl (2.5 mL) was added to the solution. After 24 hours the solution was condensed and neutralized with sodium hydroxide. NaCl byproduct was removed from the solution using an Amicon apparatus and a millipore membrane with NMWL = 1,000 under 35 psi N_2. The filtrate was tested for Cl^- using $AgNO_3$. When no AgCl precipitate formed the solution remaining inside the Amicon vessel was condensed *in vacuo* to afford B2-1 (0.0365g, 99%).

TECHNICAL NOTES

Seta-633 - A NIR Fluorescence Lifetime Label for Low-Molecular-Weight Analytes

Yevgen A. Povrozin,[†] Olga S. Kolosova,[†] Olena M. Obukhova,[†] Anatoliy L. Tatarets,[†] Vadim I. Sidorov,[†] Ewald A. Terpetschnig,*[,‡,§] and Leonid D. Patsenker[†,‡]

SSI "Institute for Single Crystals" of the National Academy of Sciences of Ukraine, 60 Lenin Avenue, Kharkov 61001, Ukraine, SETA BioMedicals, 2014 Silver Court East, Urbana, Illinois 61802, and ISS, Inc., 1602 Newton Drive, Champaign, Illinois 61822. Received June 4, 2009; Revised Manuscript Received July 3, 2009

We describe the photophysical properties of Seta-633, a commercially available near-infrared (NIR) dye, and its use as a fluorescent label to study the interaction between low-molecular-weight analytes and proteins using fluorescence lifetime as the readout parameter. In a model assay, we demonstrate that a biotinylated Seta-633 tracer binds to antibiotin with high specificity. Importantly, the lifetime of Seta-633−biotin increases about 1.8-fold upon binding to a specific antibody (antibiotin, MW = 160 kDa), while the titration with bovine serum albumin (BSA) or nonspecific antibody does not result in a noticeable change in lifetime. This behavior is contrary to that of fluorescent tracers like Cy5 or Alexa 647, which typically exhibit much smaller lifetime changes upon binding to antibodies.

INTRODUCTION

Fluorescence detection is widely used in biomedical research applications (*1*−*3*). A majority of these applications are based on the use of extrinsic labels (*4*−*8*). Red and near-infrared (NIR) dyes exhibit advantages over short-wavelength absorbing and emitting dyes due to reduced autofluorescence from biological samples beyond 600 nm. Among these labels, the cyanine-based labels of the Cy, Alexa, Atto, and Dy series are the most common ones used for bioanalytical applications (*5*−*13*).

Seta dyes are another group of commercially available dyes based on squaraines (*14, 15*). Squaraines are 1,3-disubstituted squaric acid derivatives. They show high extinction coefficients ($e > 200\,000$ L mol^{-1} cm^{-1}) in the red region, display high photostability, and allow the introduction of reactive functional groups such as *N*-hydroxysuccinimide (NHS) esters (*16*). As previously reported (*14*−*18*), these dyes exhibit shorter lifetime in aqueous solutions but increased lifetimes upon covalent or noncovalent binding to proteins (BSA, antibodies, and avidin). The phenomena of quantum yield and lifetime increases of squaraine dyes upon noncovalent binding to BSA and covalent binding to an antibody were thouroughly investigated and desribed in detail earlier (*14, 17*). Briefly, squaraines are considered more polar molecules as compared to open-chain cationic cyanines (*19*) (e.g., Cy5 or Alexa 647), and therefore, the quantum yields and fluorescence lifetimes of squaraines are significantly decreased in polar, protic solvents such as water or aqueous buffers (*15*) and substantially increase in hydrophobic microenvironments (e.g., upon binding to proteins (BSA, IgG)) (*16, 17*) or in aprotic solvents (*15*).

Fluorescence lifetime is one of the most robust readout parameters available for fluorescence detection (*20*). It is mostly independent of the fluorophore concentration, and therefore to some degree unaffected by changes in the probe volume and photobleaching effects (*20*).

In frequency domain (FD) measurements, the intensity of the excitation light is sinusoidally modulated at a specific frequency (*21*). Upon excitation of a fluorescent molecule with modulated light, the emitted fluorescence will also be modulated with the same frequency. However, depending on the frequency of the excitation and the lifetime of the fluorescent molecule, the modulation depth of the emitted light vs the excitation light will be decreased. In addition, the phase will be shifted in the emitted light. This phase and modulation change is then used to calculate the lifetime based on ref 21

$$\omega\tau = \tan \Phi = (1/M^2 - 1)^{1/2} \qquad (1)$$

where ω is the angular modulation frequency (2π times modulation frequency); τ is the lifetime; θ is the phase angle; and M is the modulation. To recover the fluorescence decay parameters from the signal response of the emission, a nonlinear least-squares fitting procedure is performed (*21*).

Here, we discuss the use of Seta-633 as a lifetime label for tracing the interaction of small molecules with proteins, wherein the interaction is accompanied by a change in the fluorescence lifetime. We use the biotin/antibiotin interaction as a model system and demonstrate that binding of proteins to the Seta-633−biotin is accopanied by a distinct increase in lifetime that could be easily measured with inexpensive instrumentation such as a light source modulated at a fixed wavelength and a long-in amplifier. Single label assays that are based on a lifetime readout

* Corresponding author. SETA BioMedicals, 2014 Silver Court East, Urbana IL 61802, USA. Phone: +1 217 417 2160, Fax: +1 217 689 4237. E-mail: ewaldte@juno.com.

[†] SSI "Institute for Single Crystals" of the National Academy of Sciences of Ukraine.

[‡] SETA BioMedicals.

[§] ISS, Incorporated.

10.1021/bc9002458 CCC: $40.75 © 2009 American Chemical Society
Published on Web 08/21/2009

are preferred, as they are not limited by factors such as size or distance of binding partners.

EXPERIMENTAL PROCEDURES

Chemicals, Proteins, and Media. Seta-633 (catalog no: K8−1663), a reactive dye containing one NHS ester group, is commercially available from SETA Biomedicals, Urbana, IL (http://www.setabiomedicals.com) and was used as is. Cy5 and Alexa Fluor 647 are commercially available from GE Healthcare and Invitrogen.

Bovine serum albumin (BSA, essentially fatty acid free), immunoglobulin G (IgG) from bovine serum (reagent grade, ≥95%), biotin, approximately 99% TLC, biotin-NHS, anti-biotin antibody produced in goat, affinity isolated antibody, Sephadex G25, and Sephadex G50 are commercially available from Sigma; all other chemicals and solvents were from Aldrich. All chemicals were used without further purification.

Phosphate buffer pH 7.4 (PB) (67 mM) was prepared by mixing of 808 mL of $Na_2HPO_4 \cdot 2H_2O$ (11.876 g L^{-1}) and 192 mL of KH_2PO_4 (9.078 g L^{-1}). Bicarbonate buffer of pH 9.0 (50 mM) was obtained by dissolving 2.1 g of $NaHCO_3$ in 500 mL of distilled water.

General Protein Labeling Procedures and Dye-to-Protein Ratios. Protein labeling reactions were carried out using 50 mM bicarbonate buffer (pH 9.0). A stock solution of 1 mg of dye in 200 μL of anhydrous DMF was prepared; 5 mg of BSA or 3 mg of immunoglobulin G (IgG) protein were dissolved in 1 mL of a 50 mM bicarbonate buffer pH 9.0, and various amounts of dye from the stock solution were added, and the mixture was allowed to stir for 2 h at room temperature.

Unconjugated dye was separated from the labeled proteins using gel permeation chromatography with Sephadex G25 for BSA conjugates or Sephadex G50 for IgG (1.5 cm × 20 cm column) and a 67 mM phosphate buffer solution of pH 7.4 as the eluent. The first colored fraction containing the dye−protein conjugate is isolated, while the blue or bluish-green band with a much higher retention time (free label) is discarded. A series of labeling reactions as described above were set up to obtain different dye-to-protein ratios.

The molar dye-to-protein ratio (degree of labeling) (*22*) for each purified dye conjugate was calculated as the molarity of dye divided by the molarity of protein. The dye concentration of the conjugate was determined according to Lambert−Beer's law from the absorbance of the dye at the absorption maximum. The protein concentration was assessed by measurement of the absorption of the protein at 278 nm. The dye-to-protein ratios (*D*/*P*) were calculated using the following formula (with the assumption that the extinction coefficients for the free and conjugated dyes are about the same) (*22*−*24*)

$$D/P = \frac{A_{\mathrm{conj}(\lambda\mathrm{max})}\varepsilon_{\mathrm{p}}}{(A_{\mathrm{conj}(278)} - xA_{\mathrm{conj}(\lambda\mathrm{max})})\varepsilon_{\mathrm{dye}}} \qquad (2)$$

where $A_{\mathrm{conj}(\lambda\mathrm{max})}$ and $A_{\mathrm{conj}(278)}$ are the absorbances at absorption maxima and at 278 nm of the dye−protein conjugate, respectively; $\varepsilon_{\mathrm{dye}}$ is the extinction coefficient of the dye at λ_{max}, ε_{p} is the extinction coefficient of the protein at 278 nm: for BSA, ε_{p} = 45 540 M^{-1} cm^{-1}, and for IgG, ε_{p} = 201 700 M^{-1} cm^{-1}. The factor x in the denominator accounts for dye absorption at 278 nm ($A_{\mathrm{dye}(278)}$), which is a percent of the absorption of the dye at its maximum absorption ($A_{\mathrm{dye}(\lambda\mathrm{max})}$) ($x = A_{\mathrm{dye}(278)}/A_{\mathrm{dye}(\lambda\mathrm{max})}$).

Absorption Spectra and Extinction Coefficients. Absorption spectra were measured at room temperature on a Perkin-Elmer Lambda 35 UV/vis spectrophotometer. Absorption maxima were recorded with an accuracy of 0.5 nm.

For determination of the extinction coefficients, each dye (7−10 mg) was dissolved in 50 mL of phosphate buffer pH 7.4 (PB). The stock solution was diluted (1:2000) and the absorbance (A) was measured in a 5 cm standard quartz cell. All dye concentrations were between 0.1 and 0.2 μM. The extinction coefficients were calculated according to Lambert−Beer's law. The reproducibility for determining the extinction coefficients was 1000 M^{-1} cm^{-1}.

Emission Spectra and Quantum Yields. Emission spectra and quantum yields of the dyes, dye-BSA, and dye-IgG conjugates were measured in PB at room temperature on a Varian Cary Eclipse spectrofluorometer in a standard 1 cm quartz cell. All dyes were excited with an excitation slit width of 5 nm and emission slit width of 2.5 nm. The spectra were corrected. All concentrations of the fluorophores were chosen to be between 0.1 and 0.2 μM.

For the determination of the quantum yields (QY), the integrated relative intensities of the dyes or dye−protein conjugates were measured against Cy5 as the reference. All absorbances at the excitation wavelength (λ_{exc}) were in the range 0.12−0.18 (when measured in a 5 cm cell). The fluorescence spectra of the solutions were measured and the QYs were determined relative to Cy5 (QY = 27% (*25*)) using the formula (*26*)

$$\mathrm{QY} = \mathrm{QY}_{\mathrm{Cy5}}\left(\frac{F}{F_{\mathrm{Cy5}}}\right)\left(\frac{A_{\mathrm{Cy5}}}{A}\right) \qquad (3)$$

where $\mathrm{QY}_{\mathrm{Cy5}}$ is the quantum yield of Cy5, F_{Cy5} and F are the integrated areas of the fluorescence spectra ($F = \int I(\lambda)\, d\lambda$), and A_{Cy5} and A are the absorbencies at the excitation wavelength of Cy5 and the fluorophore under examination, respectively.

The QY of each sample was independently measured 3−4 times, and the average value was calculated. The QYs of the dye−BSA conjugates were measured for various D/P ratios, and then, the QYs for $D/P = 1$ were determined by a nonlinear interpolation.

Fluorescence Lifetime Measurements. Fluorescence lifetime measurements were acquired on ChronosFD − the laser-diode based frequency domain instrument produced by ISS Inc., Champaign, IL, USA. A 635 nm laser diode was used as the excitation source. Two synthesizers (model IFR2023) providing modulation frequencies in the range from 9 kHz to 1.2 GHz were utilized for the measurements. Data analysis was done with Vinci - Multidimensional Fluorescence Spectroscopy − a comprehensive software package for the analysis of time-resolved data from ISS. The analysis of the time-resolved fluorescence data was carried out using the traditional nonlinear least-squares method. This method evaluates how close a model selected by the user matches the data acquired with the instrument; the Marquardt−Levenberg algorithm was utilized for the minimization routine of the χ^2-function that compares the selected model with the experimental data. In all lifetime measurements, the dye concentration in PB (pH 7.4) was between 0.1 and 1 μM.

Mass Spectrum. The mass spectrum of *N*-[2-(D-biotinylamino)ethyl]amine was recorded on a Varian 1200 L mass spectrometer system using the electron ionization (EI) method.

Photostability. Photostability measurements were performed in aqueous solutions with Cy5, Alexa Fluor 647, and Seta-633 and their IgG conjugates. The optical density of the long-wavelength maximum was controlled to be between 0.09 and 0.10, and all measurements were carried out in 1 cm cells. These solutions were placed at the distance of approximately 30 cm from a 500 W lamp and irradiated with occasional stirring. The absorption and emission spectra of the solutions were measured before irradiation and during light exposure. The relative photostabilities were calculated as the ratio between (i) the measured absorbances at the longwavelength maximum before

Table 1. Spectral Properties for Seta-633 and Seta-633 Conjugates

dye or dye conjugate	λ_{max} (abs) (nm)	ε ($M^{-1}\cdot cm^{-1}$)	λ_{max} (em) (nm)	QY (%)	Stokes' shift ($\Delta\nu$) (cm^{-1})
Seta-633	633	250 000	644	7	270
Seta-633-BSA	646		656	53	240
Seta-633-IgG	637		647	26	240

and after exposure (A/A_0) and (ii) the relative fluorescence intensities before and after exposure (I/I_0), and the corresponding plots were generated.

Biotin Conjugation. *N-[2-(D-Biotinylamino)ethyl]amine.* To a stirred solution of 63 mg (0.18 mmol) of D-biotin-NHS in 1.5 mL DMF were added 500 μL (7.48 mmol) of ethylenediamine, and stirring was continued for 1 h at room temperature. The product was precipitated with the addition of 50 mL diethyl ether, filtered, and dried under vacuum. Yield: 49 mg (93%).

^{1}H NMR (200 MHz, DMSO-d_6), δ, ppm: 8.00 (1H, s), 7.91−7.67 (2H, m), 6.40 (2H, d, 13.3 Hz), 4.36−4.24 (1H, m), 4.18−4.06 (1H, m), 3.17−2.92 (5H, m), 2.82 (1H, dd, 5.0, 12.6 Hz), 2.57 (1H, d, 12.2 Hz), 2.06 (2H, t, 7.2 Hz), 1.69−1.15 (6H, m). MS-EI spectrum (m/z 40−600): calcd mass using formula $C_{12}H_{22}N_4O_2S$, $[M+H]^+$ 287.15; found m/z 287.

Seta-633-CONH-$(CH_2)_2$NH-biotinyl. A mixture of 20 mg (19.8 mmol) of Seta-633, 8.1 mg (28.3 mmol) of *N*-[2-(D-biotinylamino)ethyl]amine, and 5 μL (28.7 mmol) of DIPEA in 1 mL of DMF was stirred for 2 h at room temperature. The reaction was monitored by HPLC (Discovery Bio Wide Pore C18, gradient from 0.05% trifluoroacetic acid (TFA) in water to 50:50 (0.05% TFA in water:0.05% TFA in acetonitrile). The reaction mixture was diluted with 20 mL of water and then purified by column chromatography (Lichroprep RP-18, MeOH−water (1:9, v/v) as eluent) to give Seta-633-mono-CONH-$(CH_2)_2$NH-biotinyl as a dark-blue solid with yield 18.7 mg (79%). The purity of Seta-633-CONH-$(CH_2)_2$NH-biotinyl was 89.3% by HPLC. The structure of Seta-633-CONH-$(CH_2)_2$NH-biotinyl was confirmed by ^{1}H NMR (200 MHz, DMSO-d_6) spectroscopy. The corresponding signals of the biotin moiety which can be found at 7.88 (2H, broad s), 6.41 (2H, d, 11.8 Hz), 4.37−4.23 (1H, m), 2.82 (1H, dd, 5.0, 12.6 Hz), 2.57 (1H, d, 12.1 Hz) are visible. All other proton signals of the biotin moiety overlap with dye proton signals.

Immunoassay. The immunoassay experiments included a titration of Seta-633−biotin with specific (antibiotin antibody produced in goat, affinity isolated antibody, Sigma) and nonspecific (IgG from bovine serum (reagent grade, ≥95%, Sigma) antibodies. A 0.6 μM solution of Seta-633−biotin was prepared in PB pH 7.4.

During each titration step, 0.06 μM of the antibody was added to the labeled biotin solution. After each addition of the antibodies, the solution containing the labeled antigen and antibodies was incubated at 37 °C for 5 min in the dark, followed by measurement of the fluorescence lifetime.

RESULTS AND DISCUSSION

Absorption, Emission Spectra, and Stokes' Shifts. The spectral characteristics of Seta-633 and their BSA- and IgG-conjugates in PB pH 7.4 are given in Table 1; a representative absorption and emission spectrum of Seta-633 is shown in Figure 1.

The absorption and emission maximum of Seta-633 (Table 1) makes it perfectly suited for use with the 635 nm diode laser. Covalent binding of Seta-633 to BSA produces a red-shift of both the absorption (13 nm) and emission (12 nm) maxima, while the red-shift for the IgG conjugates is substantially smaller (4 and 3 nm, respectively).

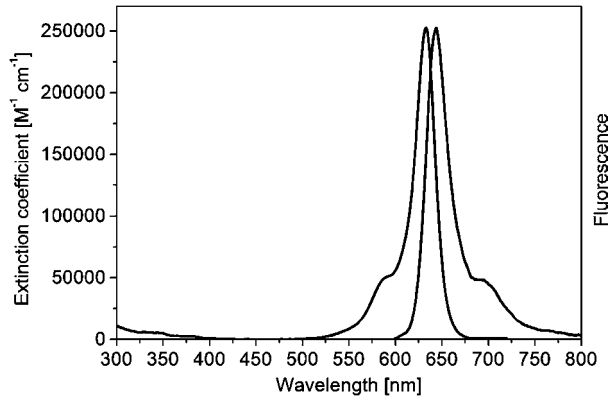

Figure 1. Absorption and emission spectrum of Seta-633.

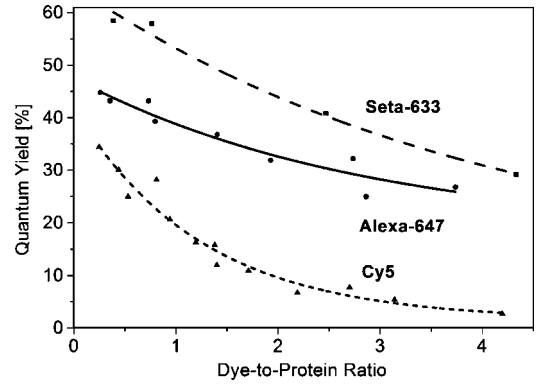

Figure 2. Quantum yield vs dye-to-protein ratio of dye−BSA conjugates in PB pH 7.4.

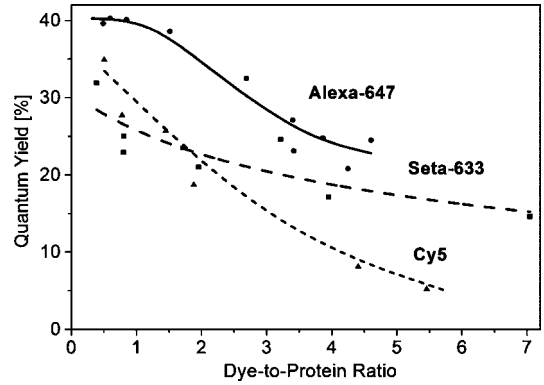

Figure 3. Quantum yield vs dye-to-protein ratio of dye−IgG conjugates in PB pH 7.4.

Seta-633 exhibits a lower quantum yield in aqueous solutions, but these quantum yields (QYs) substantially increase after binding to proteins. The QYs of the Seta-633-BSA conjugates are as high as 50% and generally exceed those of Cy5-BSA and Alexa Fluor 647-BSA conjugates for the same dye-to-protein ratios (Figure 2). The QY increase is less pronounced upon binding to proteins such as IgG (Figure 3, Table 1).

Photostability. The photostability of dyes plays important role for their practical use. We investigated the photostabilities of Seta-633 and its IgG conjugates and compared them to Cy5 and Alexa Fluor 647. These measurements were carried out in PB pH 7.4. The relative photostabilities for the free dyes and the IgG conjugates are presented in Figure 4a and b. Figure 4b clearly demonstrates reduced photobleaching for Seta-633-IgG conjugates upon prolonged exposure to light.

Fluorescence Lifetimes. As expected, the mean fluorescence lifetime (τ_{mean}) of Seta-633 measured in PB 7.4 is shorter than

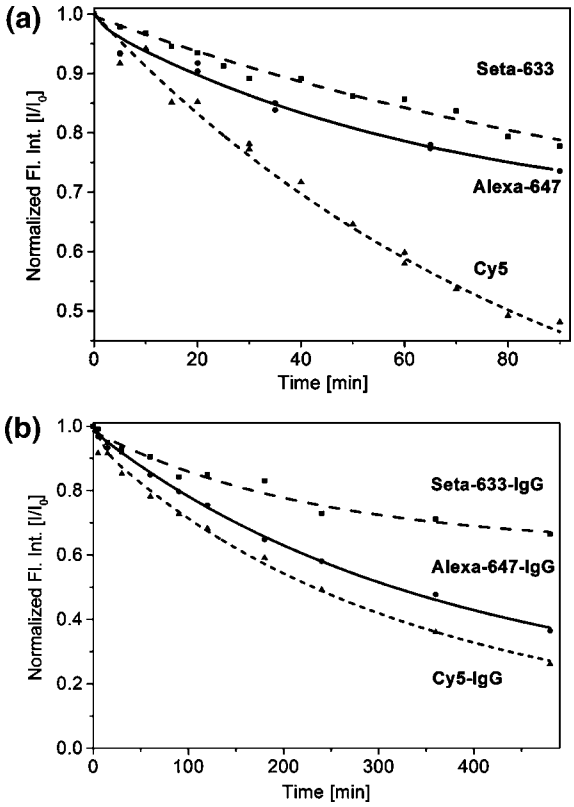

Figure 4. a. Normalized fluorescence intensity changes for free dyes upon exposure to light from a halogen lamp (500 W). b. Normalized fluorescence intensity changes for dye-conjugates upon exposure to light from a halogen lamp (500 W).

Table 2. Dye-to-Protein Ratios, Lifetimes, and Fractional Contributions for Selected Dyes and Dye-Conjugates

dye or dye conjugate	*D/P*	τ_1 (ns)	f_1	τ_2 (ns)	f_2	χ^2	τ_{mean} (ns)
Cy5	—	1.00	1.00	—	—	1.20	1.00
Cy5-BSA	0.94	0.28	0.10	1.88	0.90	1.49	1.72
Cy5-IgG	1.90	0.28	0.23	1.47	0.77	1.95	1.20
Alexa 647	—	1.17	1.00	—	—	1.99	1.17
Alexa 647-BSA	0.90	0.33	0.07	1.91	0.93	0.63	1.80
Alexa 647-IgG	1.83	0.31	0.20	1.29	0.80	1.87	1.09
Seta-633	—	0.12	0.61	0.46	0.39	0.58	0.25
Seta-633-biotin	—	0.27	0.33	0.87	0.67	1.22	0.66
Seta-633-BSA	0.90	0.56	0.05	2.93	0.95	0.94	2.81
Seta-633-IgG	1.10	0.40	0.26	1.88	0.74	1.19	1.49

those for Cy5 and Alexa Fluor 647 (Table 2), which is because polar compounds are quenched in polar solvents and squaraine dyes can be considered more polar than cyanine dyes (*17*). While the intensity decays for Cy5 and Alexa Fluor 647 are well-fitted with monoexponential curves, the decays for Seta-633 are better fitted with a biexponential decay curve (*15*). The observed biexponential decay times for Seta-633 and Seta-633−biotin are most probably due to dye−solvent effects (*27*).

The fluorescence lifetime of Seta-633 as well as Seta-633-biotin increase several-fold after binding to proteins. Covalent binding of Seta-633 to BSA leads to an 10-fold lifetime increase from 250 ps to 2.81 ns, while the average lifetime increase between the free and IgG-bound Seta-633 is about 6-fold. This is in contrast to cyanine-based labels, which show less pronounced fluorescence lifetime changes upon labeling to proteins − especially antibodies (Table 2).

The observed large fluorescence lifetime changes between Seta-633 free in solution and coupled to IgG were instrumental to our decision to evaluate Seta-633 in a lifetime-based immunoassay. We intentionally chose the immunoassay format

Scheme 1. Synthesis of Seta-633−Biotin

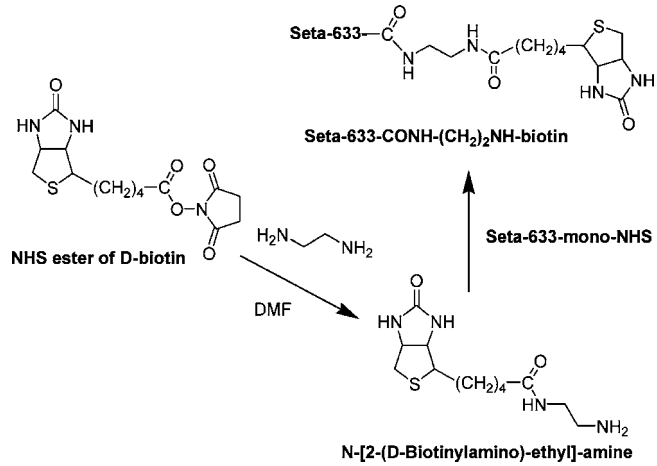

over the biotin−avidin/streptavidin interaction because of its broader applicability. In general, biotin could be replaced by any other low-molecular-weight antigen.

Model Immunoassay. For the model immunoassay, a labeled biotin-conjugate of Seta-633 as shown in Scheme 1 was synthesized. Coupling between D-biotin and Seta-633 was facilitated by introducing an ethylenediamine linker into biotin (*28*). *N*-[2-(D-Biotinylamino)ethyl]amine was synthesized analogously to a literature procedure but by using biotin-NHS instead of biotin and CDI (1,1′-carbonyldiimidazole) (*29*). Dimer formation was prohibited by using an excess of ethylenediamine. Subsequently, the amino-group of *N*-[2-(D-biotinylamino) ethyl]amine was conjugated to Seta-633 to yield Seta-633-CONH-$(CH_2)_2$NH-biotin (see Biotin Conjugation).

The introduction of the biotin-ethylenediamine moiety into Seta-633 causes an increase in the average lifetime from 0.25 to 0.66 ns (Table 2). Titration of the small-molecular-weight tracer with its specific antibody (antibiotin, MW = 160 kDa) leads to a steady increase of the fluorescence lifetime to a maximum value of 1.82 ns, a 176% increase compared to the unbound tracer. Importantly, no change is observed when the tracer was titrated with nonspecific antibody or BSA, indicating that the nonspecific interactions due to hydrophobic binding of are minimal (Figures 5 and 6).

We also made an attempt to demonstrate a competitive lifetime-based phase-modulation assay with the biotin/antibiotin model system. In this competitive assay, fixed concentrations of 0.65 μM Seta-633−biotin tracer and antibiotin (ratio = 1:1) were incubated with increasing concentrations of free biotin.

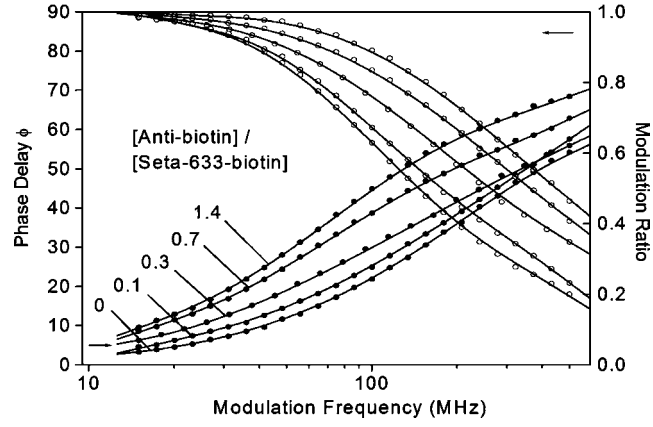

Figure 5. Frequency response curves (phase angle and modulation ratio vs modulation frequency) of Seta-633−biotin (0.65 μM) upon titration with antibiotin (specific antibody).

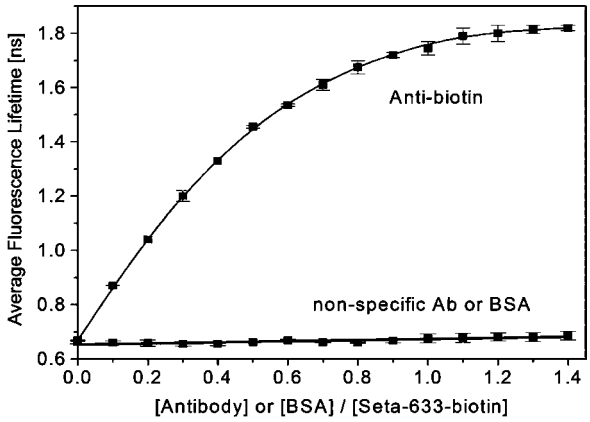

Figure 6. Average fluorescence lifetime changes of Seta-633−biotin (0.65 μM) upon titration with antibiotin (specific), (nonspecific) human IgG, or BSA.

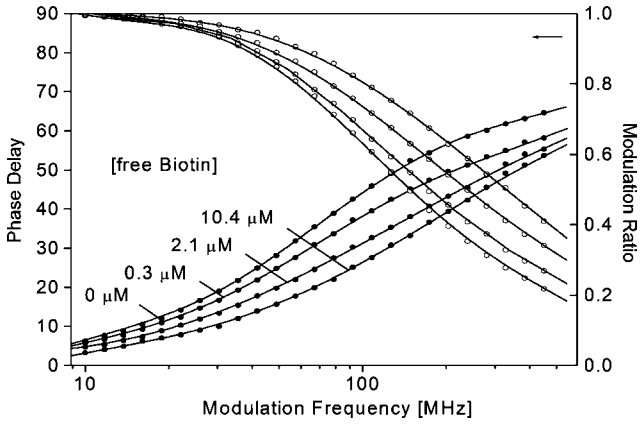

Figure 7. Frequency response curves for the titration of the Seta-633−biotin−antibiotin complex with free biotin (competitive reaction).

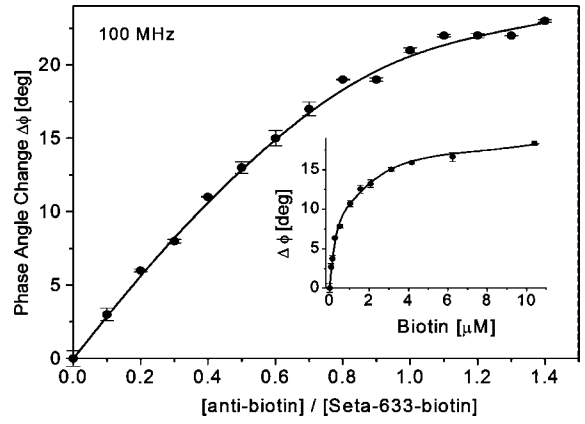

Figure 8. Changes in phase angle upon titration of Seta-633−biotin (0.65 μM) with antibiotin (specific antibody), measured at 100 MHz. The inset shows phase angle changes of a mixture of 0.65 μM Seta-633−biotin and 0.65 μM antibiotin (ratio of 1) upon titration with free biotin, measured at 100 MHz.

Replacement of the labeled biotin tracer by free biotin leads to a shift of the frequency response curves to higher frequencies (Figures 7, 8) and thus shortening of the fluorescence lifetime. Addition of 0 to 10 μM concentrations of biotin leads to a total change of 18° in phase angle. Present instrumentation allows the phase angle to be measured accurately to 0.1° and modulation with an accuracy of 0.005 (*30*).

Homogeneous immunoassays can be performed even in whole blood, because red and NIR dyes allow excitation beyond the absorptive bands of hemoglobin and tissue.

CONCLUSIONS

The hydrophilic, amine-reactive NIR fluorescent label Seta-633 exhibits favorable properties as a lifetime label for the measurement of small-molecular-weight analytes. The label is compatible with readily available light sources (635 nm or 640 nm diode lasers) and filter sets (as for Cy5 or Alexa Fluor 647). Seta-633 exhibits lower quantum yields and shorter fluorescence lifetimes when free in solution, but these values substantially increase upon interaction with proteins, which is contrary to fluorescent tracers like Cy5 or Alexa 647, which typically exhibit much smaller lifetime changes in particular upon binding to antibodies. Importantly, Seta-633 and its conjugates are also more photostable as compared to Cy5 and Alexa Fluor 647.

ACKNOWLEDGMENT

This work was supported by STCU grants no 3804 and P313.

Supporting Information Available: Mass spectrum of *N*-[2-(D-biotinylamino)ethyl]amine. This material is available free of charge via the Internet at http://pubs.acs.org.

LITERATURE CITED

(1) Daehne, S. , Resch-Genger, U., and Wolfbeis, O. S., Eds. (1998) *Near-Infrared Dyes for High Technology Applications, NATO ASI Ser. 3 (High Technology) 53*, Kluwer Academic Publishers, Dordrecht, The Netherlands.

(2) Van Dyke, K., Ed. (1990) *Luminescence lmmunoassay and Molecular Applications*, CRC Press, Boca Raton, FL.

(3) Lakowicz, J. R., Ed. (1992) Topics in Fluorescence Spectroscopy Volume 3, *Biochemical Applications*, Plenum Press, New York.

(4) Wolfbeis, O. S., Ed. (2008) Fluorescence Methods and Applications, *Spectroscopy, Imaging, and Probes*, Wiley-Blackwell, New York.

(5) Panchuk-Voloshina, N., Haugland, R. P., Bishop-Stewart, J., Bhalgat, M. K., Millard, P. J., Mao, F., Leung, W.-Y., and Haugland, R. P. (1999) Alexa dyes, a series of new fluorescent dyes that yield exceptionally bright, photostable conjugates. *J. Histochem. Cytochem. 47*, 1179–1188.

(6) Chen, F. T., and Evangelista, R. A. (1994) Feasibility studies for simultaneous immunochemical multianalyte drug assay by capillary electrophoresis with laser-induced fluorescence. *Clin. Chem. 40*, 1819–1822.

(7) Lay, M. J., and Wittwer, C. T. (1997) Real-time fluorescence genotyping of factor V Leiden during rapid-cycle PCR. *Clin. Chem. 43*, 2262–2267.

(8) Qin, Q.-P., Peltola, O., and Pettersson, K. (2003) Time-resolved fluorescence resonance energy transfer assay for point-of-care testing of urinary albumin. *Clin. Chem. 49*, 1105–1113.

(9) Mezzasoma, L., Bacarese-Hamilton, T., Di Cristina, M., Rossi, R., Bistoni, F., and Crisanti, A. (2002) Antigen microarrays for serodiagnosis of infectious diseases. *Clin. Chem. 48*, 121–130.

(10) Berlier, J. E., Rothe, A., Buller, G., Bradford, J., Gray, D. R., Filanoski, B. J., Telford, W. G., Yue, S., Liu, J., Cheung, C.-Y., Chang, W., Hirsch, J. D., Beechem, J. M., Haugland, R. P., and Haugland, R. P. (2003) Quantitative comparison of long-wavelength Alexa Fluor dyes to Cy dyes: Fluorescence of the dyes and their bioconjugates. *J. Histochem. Cytochem. 51*, 1699–1712.

(11) Huss, K. L., Blonigen, P. E., and Campbell, R. M. (2007) Development of a Transcreener kinase assay for protein kinase A and demonstration of concordance of data with a filter-binding assay format. *J. Biomol. Screen. 12*, 578–584.

(12) Miller, A. E., Fischer, A. J., Laurence, T., Hollars, C. W., Saykally, R. J., Lagarias, J. C., and Huser, T. (2006) Single-molecule dynamics of phytochrome-bound fluorophores probed by fluorescence correlation spectroscopy. *Proc. Natl. Acad. Sci. U.S.A. 103*, 11136–11141.

(13) Bruckbauer, A., James, P., Zhou, D., Yoon, J. W., Excell, J. D., Korchev, Y., Jones, R., and Klenerman, D. (2007) Nanopipette delivery of individual molecules to cellular compartments for single-molecule fluorescence tracking. *Biophys. J. 93*, 3120–3131.

(14) Terpetschnig, E., Szmacinski, H., Ozinskas, A., and Lakowicz, J. R. (1994) Synthesis of squaraine-N-hydroxysuccinimide esters and their biological application as long-wavelength fluorescent labels. *Anal. Biochem. 217*, 197–204.

(15) Terpetsehnig, E., Szmacinski, H., and Lakowicz, J. R. (1993) Synthesis, spectral properties and photostabilities of symmetrical and unsymmetrical squaraines; a new class of fluorophores with long-wavelength excitation and emission. *Anal. Chim. Acta 282*, 633–641.

(16) Oswald, B., Patsenker, L., Duschl, J., Szmacinski, H., Wolfbeis, O. S., and Terpetschnig, E. (1999) Synthesis, spectral properties, and detection limits of reactive squaraine dyes, a new class of diode laser compatible fluorescent protein labels. *Bioconjugate Chem. 10*, 925–931.

(17) Tatarets, A. L., Fedyunyayeva, I. A., Dyubko, T. S., Povrozin, Y. A., Doroshenko, A. O., Terpetschnig, E. A., and Patsenker, L. D. (2006) Synthesis of water-soluble, ring-substituted squaraine dyes and their evaluation as fluorescent probes and labels. *Anal. Chim. Acta 570*, 214–223.

(18) Patsenker, L., Tatarets, A., Kolosova, O., Obukhova, O., Povrozin, Y., Fedyunyayeva, I., Yermolenko, I., and Terpetschnig, E. (2008) Fluorescent probes and labels for biomedical applications. *Ann. N.Y. Acad. Sci. 1130*, 179–187.

(19) Yasui, S., Matsuaka, M., and Kitao, T. (1988) Synthesis and some properties of infrared-absorbing croconium and related dyes. *Dyes Pigm. 10*, 13–22.

(20) Turconi, S., Bingham, R. P., Haupts, U., and Pope, A. J. (2001) Developments in fluorescence lifetime-based analysis for ultra-HTS. *DDT 6*, 27–39.

(21) Lakowicz, J. R. (2006) *Principles of Fluorescence Spectroscopy*, 3rd ed., Springer, Berlin/Heidelberg.

(22) Mujumdar, S. R., Mujumdar, R. B., Grant, C. M., and Waggoner, A. S. (1996) Cyanine-labeling reagents: Sulfobenzindocyanine succinimidyl esters. *Bioconjugate Chem. 7*, 356–362.

(23) Povrozin, Y. A., Markova, L. I., Tatarets, A. L., Sidorov, V. I., Terpetschnig, E. A., and Patsenker, L. D. (2009) Near-infrared, dual-ratiometric fluorescent label for measurement of pH. *Anal. Biochem. 390* (2), 136–140.

(24) Schobel, U., Egelhaaf, H.-J., Brecht, A., Oelkrug, D., and Gauglitz, G. (1999) New donor-acceptor pair for fluorescent immunoassay by energy transfer. *Bioconjugate Chem. 10*, 1107–1114.

(25) Mujumdar, R. B., Ernst, L. A., Mujumdar, S. R., Lewis, C. J., and Waggoner, A. S. (1993) Cyanine dye labeling reagents: Sulfoindocyanine succinimidyl esters. *Bioconjugate Chem. 4*, 105–111.

(26) Parker, C. A. (1968) *Photoluminescence of Solutions*, Elsevier Publishing Company, Amsterdam.

(27) Law, C.-Y. (1987) Squaraine Chemistry. Effects of structural changes in the absorption and multiple fluorescence emission of bis[4-(dimethylamino)phenyl]squaraine and its derivatives. *J. Phys. Chem. 91*, 5184–5193.

(28) Patnaik, S., Swami, A., Sethi, D., Pathak, A., Garg, B. S., Gupta, K. C., and Kumar, P. (2007) .N-(Iodoacetyl)-N¢-(anthraquinon-2-oyl)-ethylenediamine (IAED): A new heterobifunctional reagent for the preparation of biochips. *Bioconjugate Chem. 18*, 8–12.

(29) Li, Z., Ortega-Vilain, A.-C., Patil, G. S., Chu, D.-L., Foreman, J. E., Eveleth, D. D., and Powers, J. C. (1996) Novel peptidyl r-keto amide inhibitors of calpains and other cysteine proteases. *J. Med. Chem. 39*, 4089–4098.

(30) Murtaza, Z., Chang, Q., Rao, G., Lin, H., and Lakowicz, J. R. (1997) Long-lifetime metal-ligand pH probe. *Anal. Biochem. 247*, 216–222.

BC9002458

Supporting information

Seta-633 – A NIR Fluorescence Lifetime Label for Low Molecular-Weight Analytes

Yevgen A. Povrozin,[†] Olga S. Kolosova,[†] Olena M. Obukhova,[†] Anatoliy L. Tatarets,[†] Vadim I. Sidorov,[†] Ewald A.Terpetschnig,*[,‡,§] and Leonid D. Patsenker[†,‡]

[†] SSI "Institute for Single Crystals" of the National Academy of Sciences of Ukraine, 60 Lenin Ave., Kharkov 61001, Ukraine

[‡] SETA BioMedicals, 2014 Silver Court East, Urbana IL 61802, USA

[§]ISS, Inc., 1602 Newton Drive, Champaign, IL 61822, USA

* Corresponding author: SETA BioMedicals, 2014 Silver Court East, Urbana IL 61802, USA, Phone: +1 217 417 2160, Fax: +1 217 689 4237. E-mail: ewaldte@juno.com.

Running Title: NIR Fluorescence Lifetime Label

Table 1. MS-EI spectrum data

Method Description: EI
Scan 1 Channel Description: 40.0:600.0> EI;Det 0;WI Q1 Cal;ST 0.010
Scan Information: cp = 1.0 mTorr
Precursor Mass Range: 40 - 600 m/z

Ion	Int	Norm	Ion	Int	Norm	Ion	Int	Norm	Ion	Int	Norm
61	2.293e+7	19	103	7.787e+7	63	139	1.374e+8	111	173	8.590e+7	70
67	1.389e+7	11	105	4.575e+7	37	140	5.412e+8	439	174	2.358e+7	19
69	1.470e+7	12	106	1.775e+7	14	141	1.181e+8	96	181	1.445e+7	12
70	1.345e+7	11	107	2.528e+7	20	142	1.086e+8	88	182	1.263e+7	10
71	1.366e+7	11	108	4.420e+7	36	143	1.009e+9	818	183	1.909e+7	15
72	1.691e+7	14	109	3.558e+7	29	144	2.020e+8	164	184	2.356e+7	19
73	7.791e+7	63	110	1.071e+8	87	145	3.253e+7	26	185	2.938e+7	24
74	1.252e+7	10	111	1.540e+8	125	148	1.585e+7	13	189	2.557e+7	21
79	2.301e+7	19	112	1.903e+8	154	149	1.400e+8	113	197	8.853e+7	72
80	1.998e+7	16	113	1.471e+8	119	150	7.842e+7	64	198	2.180e+7	18
81	5.549e+7	45	114	1.202e+8	97	151	1.772e+8	144	199	2.004e+7	16
82	9.476e+7	77	115	1.926e+8	156	152	1.137e+8	92	209	2.549e+7	21
83	4.439e+7	36	116	7.740e+7	63	153	7.574e+7	61	210	3.480e+7	28
84	8.054e+8	653	117	1.302e+7	11	154	9.270e+7	75	211	1.251e+7	10
85	4.491e+8	364	121	1.255e+7	10	155	1.261e+8	102	225	3.433e+7	28
86	3.186e+8	258	122	2.104e+7	17	156	6.351e+7	51	226	3.393e+7	28
87	2.011e+8	163	123	1.011e+8	82	157	6.513e+7	53	227	1.663e+8	135
88	8.974e+7	73	124	1.187e+8	96	158	5.050e+7	41	228	2.471e+7	20
89	7.056e+7	57	125	3.641e+8	295	159	1.370e+7	11	240	1.626e+7	13
91	2.726e+7	22	126	3.807e+8	309	160	8.396e+7	68	242	1.345e+7	11
93	3.425e+7	28	127	5.743e+7	47	161	1.377e+7	11	244	8.974e+7	73
94	4.782e+7	39	128	3.318e+7	27	164	1.887e+7	15	255	1.277e+7	10
95	1.347e+8	109	129	5.757e+7	47	165	3.095e+7	25	257	7.046e+7	57
96	1.376e+8	112	130	8.537e+7	69	166	6.102e+8	495	267	9.859e+7	80
97	1.232e+9	999	131	3.940e+7	32	167	1.490e+8	121	268	2.280e+7	18
98	8.565e+8	694	133	1.508e+7	12	168	5.915e+7	48	269	2.075e+7	17
99	3.282e+8	266	135	3.204e+7	26	169	5.700e+7	46	270	1.289e+7	10
100	4.083e+8	331	136	2.843e+7	23	170	2.038e+7	17	286	2.300e+7	19
101	1.090e+8	88	137	8.576e+7	70	171	2.350e+8	190	287	5.677e+7	46
102	9.686e+8	785	138	1.891e+8	153	172	2.880e+8	233			

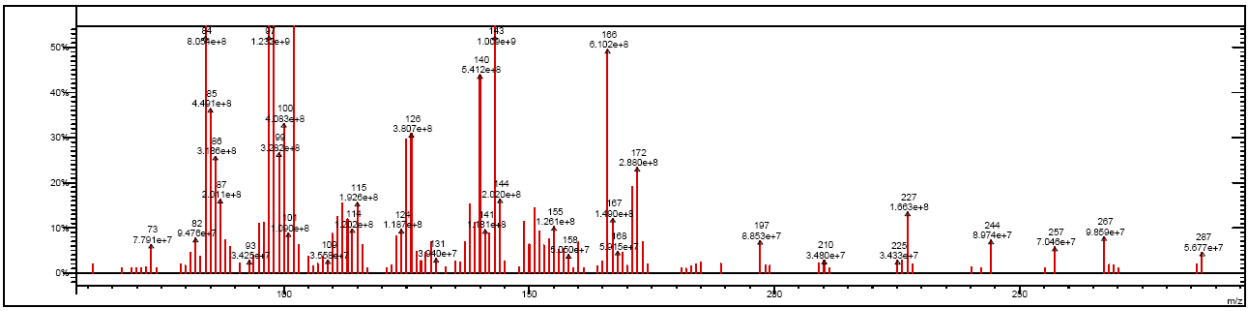

Figure 1. MS-EI spectrum (m/z [40-600]): Calcd. mass using formula $C_{12}H_{22}N_4O_2S$: 286.15; found m/z: $[M+H]^+$ = 287.

OCTOBER 2009
Volume 20, Number 10

© *Copyright 2009 by the American Chemical Society*

Bioconjugate Chemistry

COMMENT

Intelligent Drug Delivery Systems

Yu-Kyoung Oh

School of Pharmacy, Seoul National University, Sinlim-dong, Kwanak-gu, Seoul 151-742, South Korea

Peter D. Senter

Seattle Genetics, 21823 30th Drive SE, Bothell, Washington 98021

Soo-Chang Song

Division of Life Science, Korea Institute of Science and Technology, Seoul 130-650, South Korea. Received June 12, 2009; Revised Manuscript Received July 28, 2009

There has been a great deal of research in recent years toward improving drug delivery and selectivity through the use of macromolecular-based drug carriers such as monoclonal antibodies, liposomes, polymers, dendrimers, micelles, and hydrogels (*1*−*3*). These areas were featured at the 2009 International Symposium on Intelligent Drug Delivery Systems that was held at the Korea Institute of Science and Technology (KIST) in Seoul, South Korea on April 29−30, 2009. The meeting was sponsored by the Korean Ministry of Education, Science and Technology and the Korea Biotech R & D Group in an initiative to promote drug delivery research within the country. We felt that readers of *Bioconjugate Chemistry* would be interested in several of the presentations at the meeting, given the relevance to the scope of the journal.

Kinam Park from Purdue University provided a keynote address entitled "Practical nanotechnology and microfabrication for drug delivery" (*4*). The history of drug delivery systems was overviewed, beginning with examples of the first delayed and sustained release technologies in the 1950s and 1960s, through the development of nanotechnologies that are under active investigation. This has led to the approval of several macromolecular-based drugs such as Doxil, Abraxane, and Genexol for cancer therapy (*3*). "Smart polymers" and newer materials allow for controlled released of drugs under specific conditions (*5*). Advancements in material science has allowed for the production of solid supports for drug delivery in which imprinting technologies are used to produce novel scaffolds for drug attachment and controlled release (*6*). Several of the issues are being resolved including biocompatibility, scale-up, drug loading, and control of release kinetics. Some elegant examples of such technologies were provided by Ping Lee at the University of Toronto who described the development of osmotic tablets which are used in more than 20 approved drugs. Other delivery systems of great interest include osmotically driven miniaturized implants, hydrogel capsules, polymeric drug derivatives, and inhalable formulations (*7*). While these technologies may offer significant advantages over current formulations, the regulatory, cost, and compliance issues are significant.

Nanotechnology-based drug delivery systems were described that allow for both spatial and temporal control of drug release. Yongdoo Park from Korea University described biomimetic hydrogels that not only allowed for controlled drug release, but also could be devised to release mechanistically distinct drugs in a sequential manner (*8*). In a complementary approach, Keun-Hong Park from CHA University in Seoul described a dual drug delivery strategy involving a nanoparticle consisting of a drug-loaded poly(lactic acid)−poly(glycolic acid) copolymer (PLGA) with ionically associated drug−polyethyleneimine complexes (*9*). These

* scsong@kist.re.kr.

10.1021/bc900260x CCC: $40.75 © 2009 American Chemical Society
Published on Web 09/03/2009

novel carriers allowed for dual drug release in vivo over extended time periods. Kazuo Maruyama from Teikyo University in Japan described the preparation of liposomes containing perfluoropropane bubbles together with anticancer drugs, siRNA, or proteins of therapeutic interest (*10*). Upon exposure to ultrasonic radiation, the exploding bubbles disrupted liposomal structure, leading to drug release. The technology was applied to the delivery of antigens to dendritic cells for active tumor immunotherapy. Tatsuhiro Ishida from the University of Tokushima in Japan described how liposomal drug formulations can be used in combination with systemic drug therapy in metronomic therapeutic protocols. Low and frequent dosing regimens of various liposomal and free drug combinations resulted in pronounced intratumoral drug delivery and therapeutic efficacy (*11*).

The meeting featured talks on drug formulations that greatly extend the use and activities of clinically approved agents. Han-Gon Choi from Yeungnam University in Korea described how a solid dispersion system of poorly soluble drugs such as paclitaxel, valsartan, and tacrolimus improved drug solubility and pharmacologic properties such as AUC, C_{max}, and T_{max} values (*12*). Another example was provided by Han-Kwang Yang from Seoul National University who described the effects of biodegradable, thermosensitive hydrogels for drug encapsulation and release (*13*). Preparations were described that allowed for in vivo anticancer drug release over a period of 50 days, and these led to pronounced activity over systemic chemotherapy. It was possible to use such preparations for direct intratumoral injection. Doo Sung Lee from the Sungkyunkwan University in Suwon, South Korea, discussed pH-responsive micelles for therapy and diagnostics (*14*). Carboxylic acids were incorporated into the hydrophilic backbone of drug-loaded micelles, and upon acidification below pH 6.8, disruption of the micelle structure led to rapid and quantitative drug release. Pronounced therapeutic efficacy was obtained in tumor xenograft models. The technology was extended to include imaging agents, which were applied to both cancer and stroke indications.

While it is widely known that macromolecules penetrate slowly through solid tumors, little is known about low molecular weight anticancer drugs. Hyo-Jeong Kuh from the Catholic University in Korea utilized three-dimensional multicellular layer and spheroid models to track the penetration of doxorubicin, paclitaxel, and siRNA into tumors (*15, 16*). She found that penetration were functions of both the drug and the tumor model being tested. In some cases, penetration was uniform, but in other cases, it was biphasic. This type of work could provide insight into the development of synergistic drug combinations acting on tumor cells that are either near or distal to vascular beds. The power of attacking distinct cell populations was illustrated by Tae Woo Kim from Korea University, who demonstrated that large tumor masses could be eradicated using a multimodality approach that included anticancer drugs combined with agents that stimulate tumor-specific CD8 positive cells (*17*).

Claude Meares from the University of California at Davis provided the other keynote address in a presentation that overviewed radioimmunotherapy targeting technologies. An approach that has been clinically validated involves pretargeting, exemplified by antibody−streptavidin fusion protein administration, followed by a biotin-macrocyclic metal chelating agent, DOTA, radiometal chelate. This approach circumvents extensive radiation exposure to normal tissues, since the biotin−DOTA complex is rapidly cleared (*18*). The technology was extended to include genetically engineered antibodies with cysteine residues near the antigen binding sites that form covalent adducts with an electrophilic form of the DOTA hapten. These antibodies were referred to as antibodies with infinite affinity (*19, 20*). A variant of this technology included the imaging of tumors in vivo that were transfected with the cysteine-mutated antibodies. Felix Kratz from the Tumor Biology Center in Freiburg, Germany, described a novel form of anticancer drug delivery involving the administration of anticancer drugs that contain appended maleimides that form covalent bonds with cysteine-34 in albumin (*21, 22*). This leads to a macromolecule that has much longer circulating times than the free drug and has the ability to penetrate into tumors. The drug can be released from albumin through acid-mediated or enzymatic hydrolysis, depending on the linker system used. This is a versatile technology that allows for multidrug and targeted delivery approached. The lead agent, 6-maleimidocaproyl hydrazone derivative of doxorubicin (doxorubicin-EMCH), has provided evidence of response in early stage clinical testing. Peter Senter from Seattle Genetics utilized monoclonal antibodies for the delivery of highly potent drugs such as auristatins to tumors (*23*−*25*). The results from a phase I clinical trial demonstrated that 86% of patients with CD30 positive lymphomas experienced tumor reduction, which included complete and partial remissions. The results underscore the importance of drug potency, linker stability, and tumor selectivity in generating therapeutically effective drug conjugates for cancer therapy. This work was extended by Qiang Zhang from Peking University, China, to include the delivery of TNFα to tumors by administration of PEG-peptide-TNFα that could be cleaved by tumor-associated proteases. The conjugates with the cleavable linker were more active than those without.

One of the central aspects involved in drug delivery includes technologies for adhering drugs to the carriers of interest. Haeshin Lee from the Korea Advanced Institute of Science and Technology described adhesive molecules derived from those used by mussels for sticking to solid surfaces in water (*26, 27*). A series of catechol derivatives were able to form cross-links in water through either oxidative addition or through metal chelation chemistry. These agents were used to adhere proteins to surfaces for use in capturing cells through receptor-mediated interactions.

In summary, the 2009 International Symposium on Intelligent Drug Delivery Systems featured research in areas of great promise for new therapeutics. In particular, new micellar, liposomal, and hydrogel formulations allow for extended drug release, and new applications of water-insoluble drugs that are otherwise difficult to administer. Developments in nanotechnologies have produced materials that release drugs in a sequential manner or release complementary drugs under well-defined conditions. Specific targeting has advanced significantly, with clinically effective antibody−drug and radionuclide conjugates. Some of the challenges that lie ahead were illustrated by Hiroshi Kikuchi from Eisai Corporation in Japan and Kuchan Kimm of MSD Korea, the Korean branch of Merck & Co., both of whom discussed the difficulties in getting novel and expensive agents like those described in the meeting approved and widely utilized. However, as these agents progress through clinical trials and demonstrate activity beyond what is achievable with conventional agents, it is expected that they will comprise the drugs of the future. The next meeting will be held in May, 2010, at KIST in Seoul, South Korea.

LITERATURE CITED

(1) Belting, M., and Wittrup, A. (2009) Macromolecular drug delivery: basic principles and therapeutic applications. *Mol. Biotechnol*.

(2) Thierry, B. (2009) Drug nanocarriers and functional nanoparticles: applications in cancer therapy. *Curr. Drug Delivery*.

(3) Farokhzad, O. C., and Langer, R. (2006) Nanomedicine: Developing smarter therapeutic and diagnostic modalities. *Adv. Drug Delivery Rev. 58*, 1456–9.

(4) Kim, S., Kim, J. H., Jeon, O., Kwon, I. C., and Park, K. (2009) Engineered polymers for advanced drug delivery. *Eur. J. Pharm. Biopharm. 71*, 420–30.

(5) Traitel, T., Goldbart, R., and Kost, J. (2008) Smart polymers for responsive drug-delivery systems. *J. Biomater. Sci. Polym. Ed. 19*, 755–67.
(6) Gratton, S. E., Williams, S. S., Napier, M. E., Pohlhaus, P. D., Zhou, Z., Wiles, K. B., Maynor, B. W., Shen, C., Olafsen, T., Samulski, E. T., and Desimone, J. M. (2008) The pursuit of a scalable nanofabrication platform for use in material and life science applications. *Acc. Chem. Res. 41*, 1685–95.
(7) Zahedi, P., and Lee, P. I. (2007) Solid molecular dispersions of poorly water-soluble drugs in poly(2-hydroxyethyl methacrylate) hydrogels. *Eur. J. Pharm. Biopharm. 65*, 320–8.
(8) Kim, J., Park, Y., Tae, G., Lee, K. B., Hwang, S. J., Kim, I. S., Noh, I., and Sun, K. (2008) Synthesis and characterization of matrix metalloprotease sensitive-low molecular weight hyaluronic acid based hydrogels. *J. Mater. Sci. Mater. Med. 19*, 3311–8.
(9) Park, J. S., Park, K., Woo, D. G., Yang, H. N., Chung, H. M., and Park, K. H. (2008) PLGA microsphere construct coated with TGF-beta 3 loaded nanoparticles for neocartilage formation. *Biomacromolecules 9*, 2162–9.
(10) Suzuki, R., Oda, Y., Utoguchi, N., Namai, E., Taira, Y., Okada, N., Kadowaki, N., Kodama, T., Tachibana, K., and Maruyama, K. (2009) A novel strategy utilizing ultrasound for antigen delivery in dendritic cell-based cancer immunotherapy. *J. Controlled Release 133*, 198–205.
(11) Ishida, T., Shiraga, E., and Kiwada, H. (2009) Synergistic antitumor activity of metronomic dosing of cyclophosphamide in combination with doxorubicin-containing PEGylated liposomes in a murine solid tumor model. *J. Controlled Release 134*, 194–200.
(12) Park, Y. J., Kwon, R., Quan, Q. Z., Oh, D. H., Kim, J. O., Hwang, M. R., Koo, Y. B., Woo, J. S., Yong, C. S., and Choi, H. G. (2009) Development of novel ibuprofen-loaded solid dispersion with improved bioavailability using aqueous solution. *Arch. Pharm. Res. 32*, 767–72.
(13) Chun, C., Lee, S. M., Kim, S. Y., Yang, H. K., and Song, S. C. (2009) Thermosensitive poly(organophosphazene)-paclitaxel conjugate gels for antitumor applications. *Biomaterials 30*, 2349–60.
(14) Huynh, D. P., Nguyen, M. K., Pi, B. S., Kim, M. S., Chae, S. Y., Lee, K. C., Kim, B. S., Kim, S. W., and Lee, D. S. (2008) Functionalized injectable hydrogels for controlled insulin delivery. *Biomaterials 29*, 2527–34.
(15) Al-Abd, A. M., Lee, J. H., Kim, S. Y., Kun, N., and Kuh, H. J. (2008) Novel application of multicellular layers culture for in situ evaluation of cytotoxicity and penetration of paclitaxel. *Cancer Sci. 99*, 423–31.
(16) Al-Abd, A. M., Lee, S. H., Kim, S. H., Cha, J. H., Park, T. G., Lee, S. J., and Kuh, H. J. (2009) Penetration and efficacy of VEGF siRNA using polyelectrolyte complex micelles in a human solid tumor model in-vitro. *J. Controlled Release 137*, 130–5.
(17) Song, C. K., Han, H. D., Noh, K. H., Kang, T. H., Park, Y. S., Kim, J. H., Park, E. S., Shin, B. C., and Kim, T. W. (2007) Chemotherapy enhances CD8(+) T cell-mediated antitumor immunity induced by vaccination with vaccinia virus. *Mol. Ther. 15*, 1558–63.
(18) Goodwin, D. A., and Meares, C. F. (2001) Advances in pretargeting biotechnology. *Biotechnol. Adv. 19*, 435–50.
(19) Butlin, N. G., and Meares, C. F. (2006) Antibodies with infinite affinity: origins and applications. *Acc. Chem. Res. 39*, 780–7.
(20) Chmura, A. J., Orton, M. S., and Meares, C. F. (2001) Antibodies with infinite affinity. *Proc. Natl. Acad. Sci. U.S.A. 98*, 8480–4.
(21) Ajaj, K. A., Biniossek, M. L., and Kratz, F. (2009) Development of protein-binding bifunctional linkers for a new generation of dual-acting prodrugs. *Bioconjugate Chem. 20*, 390–6.
(22) Graeser, R., Esser, N., Unger, H., Fichtner, I., Zhu, A., Unger, C., and Kratz, F. (2009) INNO-206, the (6-maleimidocaproyl hydrazone derivative of doxorubicin), shows superior antitumor efficacy compared to doxorubicin in different tumor xenograft models and in an orthotopic pancreas carcinoma model, *Invest. New Drugs*.
(23) Alley, S. C., Zhang, X., Okeley, N. M., Anderson, M., Law, C. L., Senter, P. D., and Benjamin, D. R. (2009) The pharmacologic basis for antibody-auristatin conjugate activity, *J. Pharmacol. Exp. Ther*.
(24) Carter, P. J., and Senter, P. D. (2008) Antibody-drug conjugates for cancer therapy. *Cancer J. 14*, 154–69.
(25) Senter, P. D. (2009) Potent antibody drug conjugates for cancer therapy. *Curr. Opin. Chem. Biol*.
(26) Lee, H., Dellatore, S. M., Miller, W. M., and Messersmith, P. B. (2007) Mussel-inspired surface chemistry for multifunctional coatings. *Science 318*, 426–30.
(27) Lee, H., Lee, B. P., and Messersmith, P. B. (2007) A reversible wet/dry adhesive inspired by mussels and geckos. *Nature 448*, 338–41.

BC900260X

REVIEWS

Functionalized Congener Approach to the Design of Ligands for G Protein-Coupled Receptors (GPCRs)

Kenneth A. Jacobson*

Molecular Recognition Section, National Institute of Diabetes & Digestive & Kidney Diseases, National Institutes of Health, Bethesda, Maryland. Received February 4, 2009; Revised Manuscript Received March 22, 2009

Functionalized congeners, in which a chemically functionalized chain is incorporated at an insensitive site on a pharmacophore, have been designed from the agonist and antagonist ligands of various G protein-coupled receptors (GPCRs). These chain extensions enable a conjugation strategy for detecting and characterizing GPCR structure and function and pharmacological modulation. The focus in many studies of functionalized congeners has been on two families of GPCRs: those responding to extracellular purines and pyrimidines—i.e., adenosine receptors (ARs) and P2Y nucleotide receptors. Functionalized congeners of small molecule as ligands for other GPCRs and non-G protein coupled receptors have also been designed. For example, among biogenic amine neurotransmitter receptors, muscarinic acetylcholine receptor antagonists and adrenergic receptor ligands have been studied with a functionalized congener approach. Adenosine A_1, A_{2A}, and A_3 receptor functionalized congeners have yielded macromolecular conjugates, irreversibly binding AR ligands for receptor inactivation and cross-linking, radioactive probes that use prosthetic groups, immobilized ligands for affinity chromatography, and dual-acting ligands that function as binary drugs. Poly(amidoamine) dendrimers have served as nanocarriers for covalently conjugated AR functionalized congeners. Rational methods of ligand design derived from molecular modeling and templates have been included in these studies. Thus, the design of novel ligands, both small molecules and macromolecular conjugates, for studying the chemical and biological properties of GPCRs have been developed with this approach, has provided researchers with a strategy that is more versatile than the classical medicinal chemical approaches.

INTRODUCTION

G protein-coupled receptors (GPCRs[1]) serve as the mechanistic basis for a large fraction (roughly half) of the pharmaceuticals currently in clinical use. These receptors may serve as the direct target of an agonist or antagonist drug, or the activity of a given receptor induced by its naturally occurring extracellular transmitter may be modulated indirectly (through an allosteric mechanism or by alteration of uptake or metabolism) (*1*). GPCRs have an overall structural motif of seven transmembrane helical domains (TMs) that are embedded in and traverse the plasma membrane. Such heptahelical proteins constitute ~4% of the human genome.

The functionalized congener approach (Figure 1) is a widely applicable conceptual framework for the design of small, biologically active molecules that bind to biopolymers, such as receptor proteins on the cell surface. Beginning in the early 1980s, this approach was found to be particularly useful in the design of certain Family A GPCR ligands (*2*, *3*), and since that time, it has been applied to a wide range of GPCRs. This strategy allows the affinity or selectivity of a nonpeptide drug for its receptor to be greatly influenced by functions introduced at the terminus of an attached chain at a permissive site on the drug molecule. Ideally, the steric constraints of the pharmacophore-binding site are relaxed at the distal region of this chain. Figure 1A details this approach schematically, as it was conceived in 1987 (*4*) and applied to the adenosine receptors (ARs), long before knowledge of the structure of these receptors was available.

A further benefit of this approach is the ability to couple a biologically active ligand to a carrier such as a peptide and maintain or enhance its pharmacological profile (*5*, *6*). A distal moiety of an appended chemically functionalized chain may provide secondary favorable interactions with the receptor

* Correspondence to Dr. K. A. Jacobson, Acting Chief, Laboratory of Bioorganic Chemistry, Chief, Molecular Recognition Section, National Institute of Diabetes & Digestive & Kidney Diseases, National Institutes of Health, Bethesda, Maryland, USA 20892-0810. Tel. 301-496-9024; FAX 301-480-8422.

[1]Abbreviations: ADAC, adenosine amine congener (N^6-[4-[[[4-[[[(2-aminoethyl)amino]carbonyl]methyl]-anilino]carbonyl]methyl]phenyl]adenosine); APEC, 2-[[2-[4-[2-(2-aminoethyl)aminocarbonyl]ethyl]-phenyl]ethylamino]-5′-*N*-ethyl-carboxamidoadenosine; AR, adenosine receptor; BODIPY, 6-(((4,4-difluoro-5-(2-thienyl)-4-bora-3*a*,4*a*-diaza-*s*-indacene-3-yl)styryloxy)acetyl)aminohexanoic acid; FITC, fluorescein isothiocyanate; CCK, cholecystokinin; CGS21680, 2-[*p*-(2-carboxyethyl)phenyl-ethylamino]-5′-*N*-ethylcarboxamidoadenosine; CoMFA, Comparative Molecular Field Analysis; DHP, 1,4-dihydropyridine; DITC, phenylene diisothiocyanate; GPCR, G protein-coupled receptor; ICI-199,441, 2-(3,4-dichlorophenyl)-*N*-methyl-*N*-[(1*S*)-1-phenyl-2-(1-pyrrolidinyl)ethyl]acetamide hydrochloride; MRS2500, 2-iodo-N^6-methyl-(*N*)-methanocarba-2′-deoxyadenosine-3′,5′-bisphosphate; NECA, 5′-*N*-ethylcarboxamidoadenosine; NK, neurokinin; PAMAM, poly(amidoamine); PAPA, *p*-aminophenylacetyl group, SANPAH, *N*-succinimidyl 6-(4′-azido-2′-nitrophenylamino)hexanoate; SP, substance P; TAC, telenzepine amine congener (4,9-dihydro-3-methyl-4-[(4-(10-aminodecyl)-1-piperazinyl)-acetyl]-10*H*-thieno[3,4-*b*][1,5]benzodiazepin-10-one); TEMPO, 2,2,6,6-tetramethylpiperidine-1-oxyl; XAC, xanthine amine congener (8-[4-[[[[(2-aminoethyl)amino]-carbonyl]methyl]-oxy]phenyl]-l,3-dipropylxanthine).

10.1021/bc9000596 This article not subject to U.S. Copyright. Published 2009 by the American Chemical Society
Published on Web 04/30/2009

A

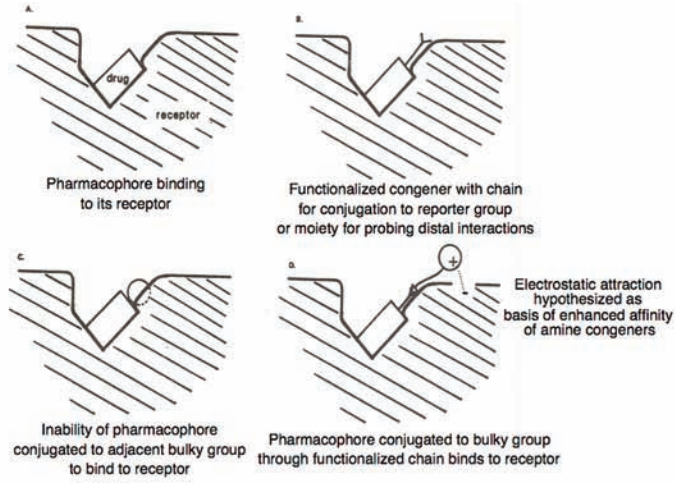

B

Functionalized congener of G protein-coupled receptor ligand (e.g. agonist or antagonist)

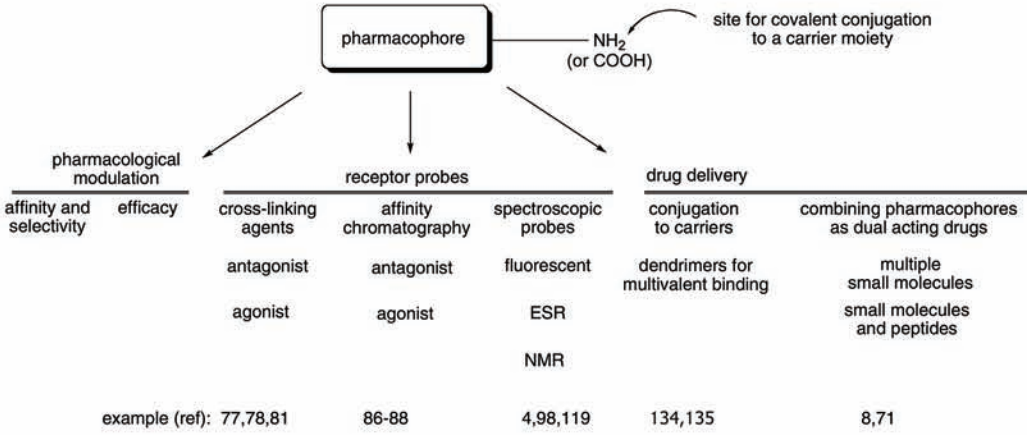

C

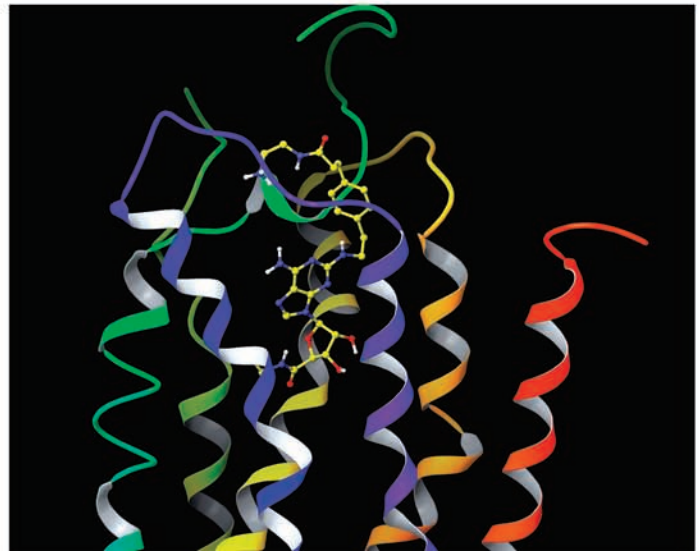

Figure 1. (A) Hypothetical interaction of adenosine functionalized congeners with the A_1 AR, as depicted in 1987. This figure is modified from ref 4, to illustrate the historical development of this conceptual approach prior to the structural elucidation of GPCRs. (B) Objectives and general considerations in functionalized congener approach to derivatizing ligands of GPCRs (applies to both small molecule agonists and antagonists). An amino group or carboxylic group is shown for conjugation, but those are only examples. The carrier moiety may be, for example, a prosthetic reporter group for radioactive or spectrospcopic detection, an electrophilic cross-linker for covalent receptor binding, or a macromolecular for targeting or immobilization. Many other approaches to conjugation chemistry are applicable. (C) A three-dimensional molecular model of APEC **39** bound to the human A_{2A} AR. The automatic docking of **39** to the recently published X-ray crystallographic structure (*22*) was carried out using the Schrodinger Glide XP program. The model shows that the functionalized chain of **39** protrudes into the extracellular regions of the receptor, as envisioned much earlier. The receptor helices are colored by residue position: N-terminus in red, TM 1 in orange, TM 2 in ochre, TM 3 in yellow, TM 4 in green, TM 5 in cyan, TM 6 in blue, TM 7 and C-terminus in purple.

(Figure 1A) to enhance ligand affinity and selectivity. This makes possible the design of spectroscopic probes of high receptor affinity, dual-acting drugs, carrier-bound drugs, and so forth (Figure 1B) (*4, 7*−*11*). Thus, prosthetic groups to provide various chemical or physical properties may be covalently coupled to these small molecules through an appropriately designed functionalized chain.

Beginning in 1984, a research group that later became the Molecular Recognition Section (MRS) of the National Institute of Diabetes and Digestive and Kidney Diseases sought to expand this design approach to a relatively unexplored GPCR as a test system and selected the ARs for this purpose. At the time, the newly discovered ARs were appealing because there were few potent ligands with which to probe these receptors pharmacologically (*12*). The widely used antiasthmatic drug theophylline (1,3-dimethylxanthine) had recently been identified as a prototypical adenosine antagonist (*13, 14*), and institute scientists delineated properties that distinguished an AR that stimulates adenylate cyclase from one that inhibits (*15*). Today, the ARs are considered one of the more advanced examples of GPCRs used in medicinal chemical development, with highly selective agonists and antagonists of nanomolar affinity at each of the four AR subtypes (*16*).

BACKGROUND: PROBING GPCR STRUCTURE AND FOCUS ON RECEPTORS FOR EXTRACELLULAR PURINES AND PYRIMIDINES

GPCRs sense chemical signals from the exofacial side of a cell membrane and transmit the activation signal via both signaling cascades that are G protein dependent and those that are not, such as arrestin (*17*). The ligand-binding function of Family A GPCRs occurs at the extracellular side and/or within the TM cleft of the GPCR, and signaling propagation depends on cytosolic regions of the receptors. Nonpeptide ligands tend to bind deeper in the TM domain than do peptide ligands, which typically associate largely with the extracellular domains of the receptor (*18*). The binding of an agonist ligand induces a conformational change of the receptor that enables the second and third intracellular loops to contact the G protein(s) (*19*).

The receptor concept remained a theoretical construct for decades, until the cloning of the β_2-adrenergic receptor by Lefkowitz and co-workers in 1986 (*20*). Because the drug-relevant GPCRs are membrane-bound proteins, directly determined structural information was unavailable until the recent X-ray structural determination of the adrenergic receptors (*21*). The X-ray structures of other GPCRs, including the A_{2A} AR (Figure 1C), followed closely on the heels of this initial breakthrough (*22*). Before this development, rhodopsin-based homology modeling was the only means of looking into the three-dimensional structure of the GPCRs, and this approach was used successfully in conjunction with site-directed mutagenesis and ligand docking (*23*−*25*). Often, it has been possible to correlate the structure−activity relationship (SAR) studies of ligands with structural insights gained from molecular modeling hypotheses. Hypotheses about ligand binding and receptor activation gleaned from molecular modeling have been supported by studies involving reengineered GPCRs and chemical cross-linking of strategically placed Cys residues in the TM regions (*19, 26*).

When our lab began medicinal chemical studies of GPCRs, we recognized the potential value for drug design of structural exploration of what were then elusive proteins. Knowledge of the three-dimensional structure of GPCRs (gained by indirect methods) could contribute to the design of novel agonists and antagonists. We began our testing with purine and pyrimidine receptors. With the synthesis of chemically related agonist and antagonist classes for a given GPCR, recognition elements that

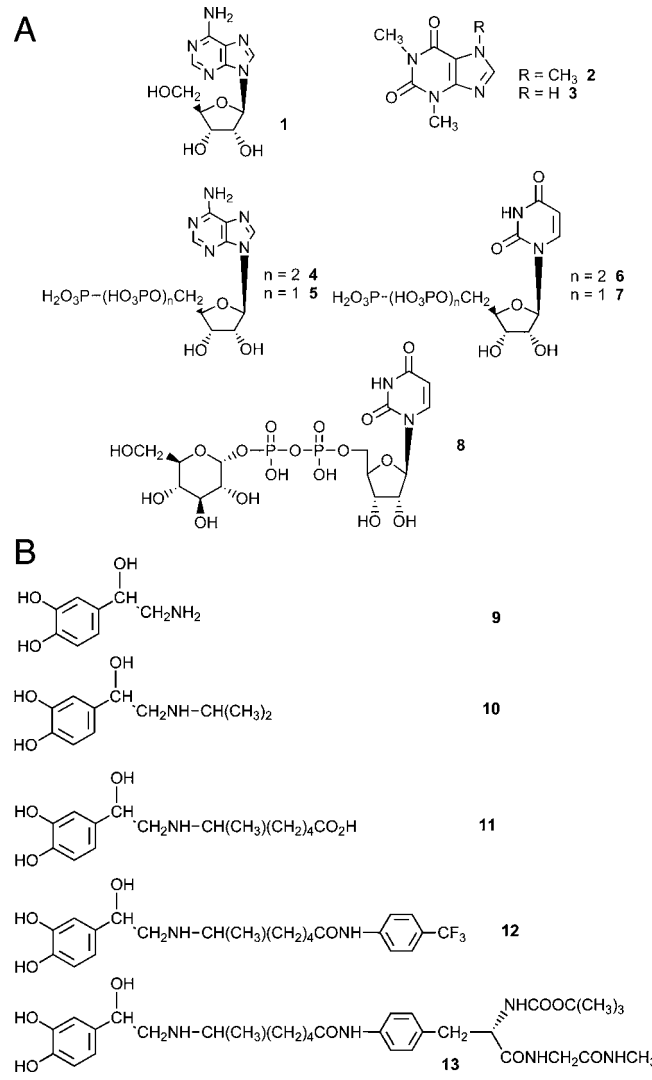

Figure 2. Structures of several classes of GPCR ligands: A) purines and pyrimidines as the native ligands of the adenosine and P2Y nucleotide receptors, and B) the naturally occurring catecholamine norepinephrine **9** and synthetic chain-elongated analogues of isoproterenol **10**.

distinguish these pharmacological actions can be pinpointed, thereby providing insights into the activation mechanisms (*27, 28*). Subtle structural differences within the same class of GPCR ligands for a given GPCR can alter the spectrum of activation of different signaling pathways. Elucidating how these GPCRs function in ligand recognition and activation as "nanomachines" is important because of the therapeutic potential of modulation of this large family of nucleoside and nucleotide receptors. If general phenomena can be identified, the analysis can be extended to other members of the GPCR superfamily.

Many studies of functionalized congeners have focused on GPCRs that respond to extracellular purines and pyrimidines, i.e., ARs for purine nucleosides and P2Y receptors for nucleotides. Extracellular adenosine **1** (Figure 2) acts as a depressant neuromodulator, and the alkylxanthine stimulants such as caffeine **2** and theophylline **3** competitively antagonize the actions of adenosine (*16*). Purine and pyrimidine nucleotides (such as ATP **4**, ADP **5**, UTP **6**, UDP **7**, and UDP-glucose **8**) act as neurotransmitter/neuromodulators at their own GPCRs (*29*). These ubiquitous signaling molecules modulate the function of diverse mammalian cell types and tissues under both normal and pathophysiological conditions. The receptors for extracellular nucleosides and nucleotides have been character-

ized through medicinal chemical, molecular biological, and pharmacological approaches. The nucleotide receptors (denoted P2) include both ligand-gated ion channels, termed P2X, and GPCRs, termed P2Y (*30*). The P2Y receptors are distinct from the ARs, for which four subtypes (A_1, A_{2A}, A_{2B}, and A_3, all GPCRs) have been defined (*16*).

In collaboration with Ad IJzerman, we initiated molecular modeling of the A_1 and A_{2A} ARs soon after their cloning in 1989 (*31*) and developed the first computer models of the putative binding sites of adenosine agonists and antagonists with the TM domain (*32*). The first model of a P2Y receptor (chick $P2Y_1$) was published in 1994 and was one of the first models based on rhodopsin (*33*). The initial purine receptor models, before 2000, were based on the structures of bacteriorhodopsin and earlier poorly resolved or incomplete structures of rhodopsin; yet even these early models suggested some features of ARs and the $P2Y_1$ receptor that were substantiated by more sophisticated modeling derived from the high-resolution rhodopsin structure. This computational probing of the architecture of both purine and pyrimidine receptors has been supported by our site-directed mutagenesis and SAR studies (*34, 35*).

These structural insights have successfully guided the design of new ligands for these GPCRs. In the course of the modeling studies, our laboratory discovered the importance of "meta" binding sites on the extracellular loops, particularly the EL2, in directing small-molecule ligands, such as ATP, to their principal binding sites in the transmembrane cleft (*36*). Later, when a high-resolution structure of rhodopsin was determined by Palczewski et al. (*37*), the conformation of the TM domains of a purine receptor almost exactly overlaid the X-ray structure.

Thus, these important GPCRs have been studied from the convergent perspectives of SARs of ligands and of structural probing of the receptor protein targets through mutagenesis and computational modeling. The protein structure of the first AR determined by X-ray crystallography also was closely estimated by the three-dimensional model predicted through homology modeling, including side chain orientations in the ligand-binding region (*38*).

BIOGENIC AMINE RECEPTOR LIGANDS AND ORIGINS OF THE FUNCTIONALIZED CONGENER APPROACH

In the late 1970s, Murray Goodman and co-workers at the University of California, San Diego, derivatized β-adrenergic receptor agonists and other biogenic amines for attachment to peptides as drug carriers (*3, 39*). Isoproterenol **10** (Figure 2) was the first analogue of a biogenic amine (norepinephrine **9**) successfully derivatized this way. A functionalized chain terminating in a carboxylic acid **11** was created as an extension of the *N*-isopropyl group of **10**. Unfortunately, the early experiments lacked a stereochemical control at the secondary carbon of the alkyl chain, which can have pharmacological consequences (*40*). These studies, a collaboration with Kenneth Melman at Stanford University, aimed to design drugs that could be attached to polypeptides for in vivo targeting (*40, 41*). The project grew out of a collaboration between Goodman and Nathan Kaplan at the University of California, San Diego, and his graduate student Craig Venter on immobilized drugs, which were later shown to be chemically heterogeneous (*41*).

While scrutinizing and modeling the chemistry of linkage of the catecholamines to peptides by means of small-molecule derivatives with elongated chains, Goodman and colleagues found β_2-adrenergic agonists that were superpotent. A *p*-trifluoromethylanilide derivative **12** (which was later resolved into four pure stereoisomers (*40*)) and a dipeptide conjugate **13** were significantly more potent than **10** at the β_2-adrenergic receptor. This potency enhancement was accomplished by manipulating the molecules at points distal from the pharmacophore (the business end). The pharmacological profile of the substances could be tuned without altering the pharmacophore moiety. The strategy of catecholamine derivatization depended on treating the hypothetical construct of β-adrenergic receptors as distinct molecular entities on the cell surface, which indeed they were shown to be, nearly a decade later (*20*).

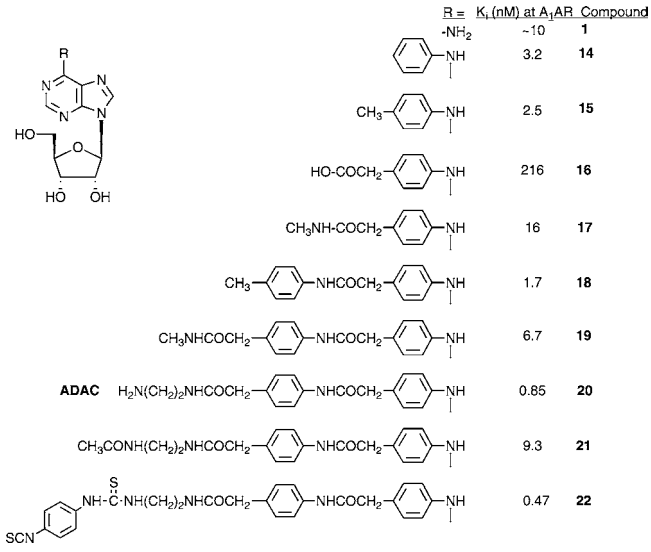

Figure 3. Stepwise derivatization of chain-functionalized adenosine derivatives designed to maintain and optimize rat A_1 AR receptor binding affinity. The N^6 position was most suitable as a derivatization site for functionalized congeners that selectively bound to and activated the A_1 AR. *N*-Aryl substitution at that site was favored over *N*-alkyl substitution. The structural elements of the chain were added in stepwise fashion, with affinity optimized at each step.

ADENOSINE AND P2Y RECEPTOR FUNCTIONALIZED CONGENERS

Extracellular adenosine **1** is involved in many of the body's cytoprotective functions through its actions at the four subtypes of ARs. For example, adenosine serves to precondition heart muscle against ischemia and toxicity by activation of the A_1 and A_3 ARs on the surface of cardiac myocytes (*42*). We showed that activation of the low-affinity A_{2B} AR by high concentrations of adenosine in the heart protects the muscle in the postreperfusion period (*43*). Adenosine counteracts the damaging effects of excitotoxicity and seizure activity in the central nervous system by activation of neuonal A_1 ARs, and it suppresses excessive immune and inflammatory responses by activation of the A_{2A} AR on immune cells. Selective agonist and antagonist ligands for all four of the AR subtypes are used as essential pharmacological probes. Selective ligands for the A_3 AR have therapeutic potential as anti-inflammatory (*44*), cardioprotective (*45, 46*), cerebroprotective (*47*), anticancer (*48*), and antiglaucoma (*49*) agents.

Functionalized congeners of ligands of the A_1 AR were first introduced in our laboratory in collaboration with John W. Daly (all of the National Institute of Diabetes & Digestive & Kidney Diseases), who was already exploring SAR at this receptor of simple derivatives of the agonist adenosine **1** and antagonist theophylline **3** (*2, 12*). In the agonist series, we hypothesized that the N^6-substituent had the greatest freedom of substitution; aryl and arylalkyl were the favored substitutions (*50*). Therefore, we incorporated functionalized chemical chains on an N^6-phenyl substituent in **14** and extended them in a stepwise fashion, optimizing affinity in binding to the rat brain A_1 AR at each stage (Figure 3).

It was evident that the substitution of the phenyl ring with electron-donating groups was conducive to high affinity.

However, it was not known whether the binding-site geometry within the receptor would accommodate a long extension of the chain. To answer this question, we expanded a *p*-methyl group in **15** into a carboxymethyl group to form **16** for attachment to larger moieties. Not only did amide derivatives at this position still bind to the A_1 AR, but aromatic amides (e.g., **18**) were clearly favored over aliphatic amides (e.g., **17**), suggesting that a distal region of the receptor-binding site was not sterically constrained and was hydrophobic and/or aromatic. The motif of p-substitution was continued with the attachment of an additional *p*-aminophenyl acetyl moiety, e.g., **19**.

The preferred terminal group at this stage of the chain extension was found to be a 2-aminoethylamido group in **20**, which was considerably more potent than a neutral amide in A_1 AR binding. This suggested that a distal negatively charged region exists on the receptor or in its vicinity. Thus, this prototypical adenosine amine congener **20** (ADAC) was used for additional derivatization, which indicated an essentially unlimited ability to elongate the carrier moiety (*2*). This suggested that the primary amino group of ADAC **20** protrudes out of the binding region for the adenosine pharmacophore, toward or into the extracellular medium, as shown in Figure 1A. Later, it was found that the charged residues in the extracellular regions of the ARs are predominantly anionic, which explained the observed affinity enhancement in positively charged functionalized congeners (*31, 32*). Acylation of **20** to form the neutral compound **21** somewhat reduced the potency of binding to the A_1 AR. Because an amino group in the chain enhances affinity at the ARs, we introduced a new functionalized congener **25**, which is related to ADAC but containing an extra amino group in the chain and also has favorable affinity at the human A_1 AR (Table 1). This secondary amine would remain free following coupling of the terminal primary amine to a carrier (*51*). Certain conjugates of ADAC with long chain fatty acids and other lipid derivatives displayed unusually high binding affinity at the A_1 AR, suggestive of distal anchoring of the hydrophobic chain in a lipid-rich environment surrounding the receptor (*137*).

Although the potency the rat A_1 AR was enhanced in this agonist series by the stepwise chain derivatization, the selectivity in comparison to the rat A_{2A} AR was not increased. The selectivities of N^6-phenyladenosine **14** and ADAC **20** were 200- and 250-fold, respectively.

A similar derivatization scheme was applied to xanthines, e.g., **26** and **27**, as AR antagonists (Table 1) (*52*). Curiously, as with adenosine, an attachment of a phenyl ring at the C8 position was highly favored in A_1 AR binding over aliphatic groups at that site. Chain extension with simple functionalized 8-alkyl chains greatly reduced AR-binding affinity. Thus, the 8-aryl ring is a specific recognition element for receptor binding and was therefore included in the functionalized congener series. The 1,3-dipropyl substitution of the methyl groups present in theophylline **3** was also included because it is known to enhance the A_1 AR affinity by 30- to 40-fold. Also, as in the N^6 position in the agonist series, the substitution of the 8-phenyl ring in the xanthine series with an electron-donating group was conducive to high affinity (*6, 53*). Thus, a methoxy substituent was elaborated into a carboxymethyloxy group for attachment to larger moieties through an amide linkage. This xanthine carboxylic congener **26** (XCC) and the elongated 2-aminoethylamide (xanthine amine congener, XAC **27**) overcame the biologically limiting low water solubility of the 8-arylxanthines noted previously (*12*).

As in the agonist series (Figure 3), the A_1 AR-preferred terminal group is an amine as in **27**, again suggesting that a distal negatively charged region exists on or near the receptor. As a systematic means of probing the effects of varied functionality at the distal end of the xanthine chain, amino acid conjugates of XAC such as **34** were prepared and analyzed in binding and functional assays (*6*). In general, a free amino group on a wide variety of amino acid conjugates, such as the diamine **34**, favored higher binding affinity at the A_1 AR, suggesting an electrostatic cause. The D-Lys conjugate **34** was intended for enhanced in vivo stability toward in the presence of peptidases through the pendant unnatural D-amino acid.

After the successes with the A_1 AR, we explored functionalized congeners of ligands of the A_{2A} AR, in collaboration with Gary L. Stiles (Figure 4) (*54*). In 1989, Michael Jarvis, Michael Williams, and co-workers reported the first potent A_{2A} AR-selective agonists (*55*). This group, which first reported CGS21680 **37** as an A_{2A} AR agonist, partnered with our lab to see if the functionalized congener approach could be extended to the A_{2A} AR. This resulted in a series of long-chain functionalized congeners of adenosine (more precisely, of its 5′-ethyluronamide derivative, NECA **36**) derivatized at the C2 position instead of the N^6 position. As with the A_1 AR, the chain was optimized in receptor binding at each stage of elongation. Consistent with the previous pattern, an amino terminal group was found to be beneficial for affinity at this receptor subtype.

The potent A_{2A} AR agonist CGS21680 **37** was condensed with an ethylenediamine unit to form APEC **39** (2-[[2-[4-[2-(2-aminoethyl)aminocarbonyl]ethyl]-phenyl]ethylamino]-5′-*N*-ethyl-carboxamidoadenosine), which became a prototypical amine functionalized congener with selectivity and higher affinity for the rat A_{2A} AR than for the rat A_1 AR. In Figure 1C, APEC is shown in its docked complex with the human A_{2A} AR, and its functionalized chain reaches the extracellular regions of the receptor. The A_{2A} AR, which induces vasodilitation to lower blood pressure, has been the subject of numerous biological investigations over several decades. It was not until a photoaffinity label selective for the A_{2A} AR derived from APEC was introduced that the molecular form of this receptor was proven to be distinct from the A_1 subtype (*56*). Compound **40**, which contains a *p*-aminophenylacetyl (PAPA) prosthetic group, could be radioiodinated on the aryl amine and then cross-linked to the receptor, either by conversion to the 4-azide or by chemical cross-linking with *N*-succinimidyl 6-(4′-azido-2′-nitrophenylamino)hexanoate (SANPAH). APEC itself is also useful for the study of behavioral effects, because it penetrates into brain better than its precursor carboxylic acid derivative (*57*).

8-Styrylxanthine derivatives that act as selective antagonists for the A_{2A} AR were also designed as functionalized congeners, e.g., the carboxylic acid derivative **44** (*58*). These 8-styrylxanthine derivatives include a 7-methyl group and could therefore be considered analogues of caffeine. Chain extension at the 7-alkyl position was not tolerated in receptor binding. Careful probing of the SAR identified the aryl ring of the styryl group as the most insenstitive site for functionalization in this series.

Selective ligands of the A_{2B} AR derived from functionalized congeners were recently reported. The same group that was used for xanthine antagonists of the A_{2B} AR (C8 substituted chain containing a 4-carbonylmethyloxy phenyl group) was introduced at the N^6 position in the agonist series (*59, 60*) resulting in A_{2B} AR selectivity.

Functionalized congeners of selective A_3 AR agonists were first studied in the ribose series, in which a functionalized chain extended from the 3 position of an N^6-benzyl group, e.g., **45**, where tolerance for steric bulk was discovered and quantified in a CoMFA (comparative molecular field analysis) model (*61*). Simple amino acid moieties could be coupled through a 3-aminobenzyl group with retention of moderate affinity. However, even at this position, which was somewhat removed from the nucleoside pharmacophore, we observed constraints

Table 1. Functionalized Congeners for ARs and P2Y Purine Receptors and Representative Conjugates

Structure	Conjugated to:	Name	Target Receptor and Function	Affinity K_i, nM (species)[a]	Ref.
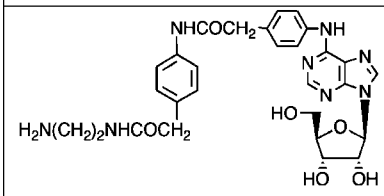 **20**	-	ADAC	A_1 AR agonist	0.85 (r)	2
	p-phenyl-enediiso-thiocyanate	*p*-DITC-ADAC **22**	A_1 AR agonist	0.47 (r)	76
	m-phenyl-enediiso-thiocyanate	*m*-DITC-ADAC **23**	A_1 AR agonist	0.87 (r)	76
	fluorescein isothio-cyanate	FITC-ADAC **24**	A_1 AR agonist	7.1 (r)	4
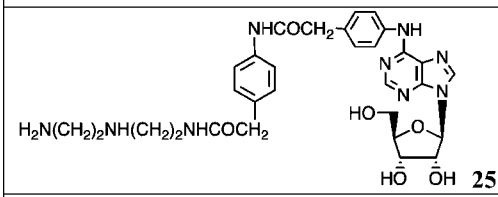 **25**	-	MRS5169	A_1 AR agonist	43 (h); Found to be potent at hA_3 AR(9.5)	51
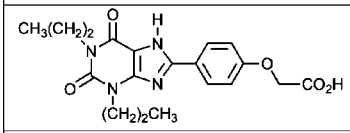 **26**	-	XCC	A_1 AR antagonist	58 (r)	52
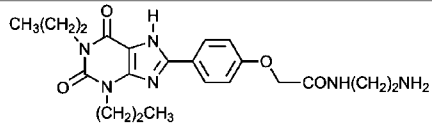 **27**	-	XAC	A_1 AR antagonist	1.2 (r)	52
	p-phenyl-enediiso-thiocyanate	*p*-DITC-XAC **28**	A_1 AR antagonist	6.6 (r)	76, 77
	m-phenyl-enediiso-thiocyanate	*m*-DITC-XAC **29**	A_1 AR antagonist	2.39 (r)	76, 77
	p-amino-phenylacetic acid	PAPA-XAC **30**	A_1 AR antagonist	40 (r)	4
	TEMPO-iso-thiocyanate	TEMPO-XAC **31**	A_1 AR antagonist	4.9 (b)	4
	Perfluoro-butyric acid	Heptafluoro-butyryl-XAC **32**	A_1 AR antagonist	0.83 (b)	4
	DTPA	DPTA-XAC **33**	A_1 AR antagonist	3.25 (b)	4
	D-lysine	D-Lys-XAC **34**	A_1 AR antagonist	1.74 (r)	6
	Bodipy-ε-amino-caproyl	XAC-BY630 **35**	A_1 AR antagonist	200 (h)	98
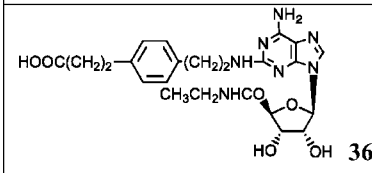 **36**	-	CGS21680	A_{2A} AR agonist	14.1 (b)	55
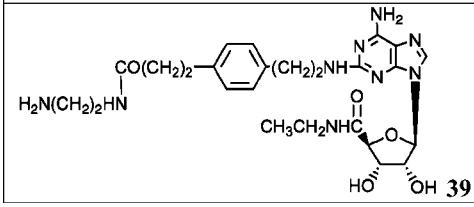 **39**	-	APEC	A_{2A} AR agonist	6.1 (b)	54
	p-amino-phenylacetic acid	PAPA-APEC **40**	A_{2A} AR agonist	43 (b), 23 (r)	56

Table 1. Continued

Structure	Conjugated to:	Name	Target Receptor and Function	Affinity K_i, nM (species)[a]	Ref.
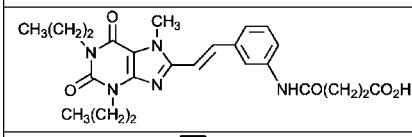 **44**	-		A_{2A} AR antagonist	143 (r)	58
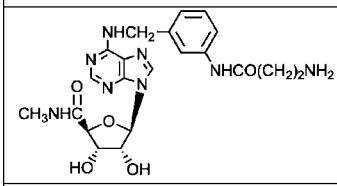 **45**	-		A_3 AR agonist	23 (r)	61
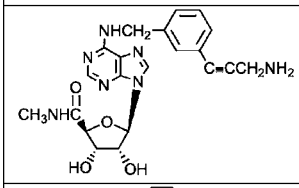 **46**	-		A_3 AR agonist	7.32 (h) (*N*-acetyl deriv.)	46
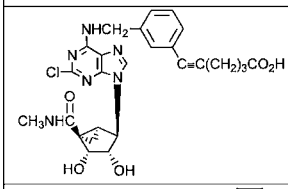 **47a**	-	MRS5168	A_3 AR agonist	17.1 (h)	62
	Amide with ethylene diamine	MRS5164 **47b**	A_3 AR agonist	5.21 (h)	62
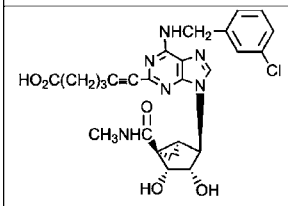 **48a**	-	MRS5151	A_3 AR agonist	2.38 (h)	62
	Amide with ethylene diamine	MRS5166 **48b**	A_3 AR agonist	2.17 (h)	62
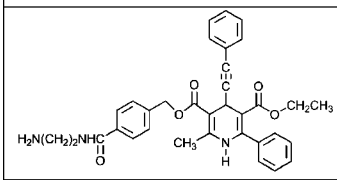 **49**	-		A_3 AR antagonist	128 (h)	63
	Biotin conjugate	**50**	A_3 AR antagonist	599 (h)	63
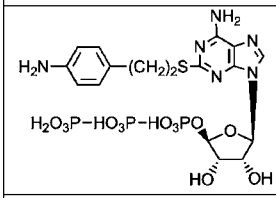 **51**	-		$P2Y_1$ agonist	1.53 (EC_{50}, t)	108
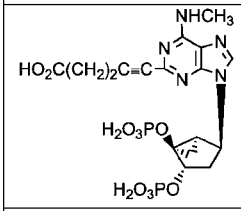 **52**	-	MRS2816	$P2Y_1$ antagonist	23 (h)	112
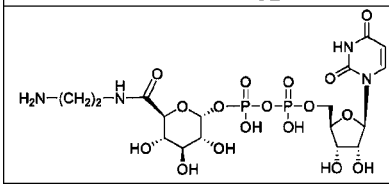 **53**	-		$P2Y_{14}$ agonist	496 (EC_{50}, h) (*N*-acetyl deriv.)	113

[a] r (rat); h (human); b (bovine); t turkey. Expressed as K_i, unless noted. ND, not determined.

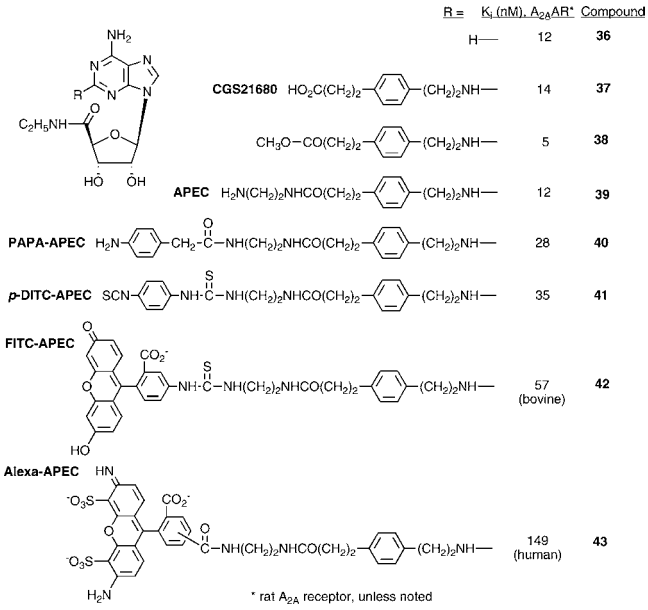

Figure 4. Stepwise derivatization of chain-functionalized adenosine derivatives that were designed to maintain and optimize A_{2A} AR receptor binding affinity. The adenine C2 position was most suitable as a derivatization site for functionalized congeners that selectively bound to and activated the A_{2A} AR. 2-Alkylamino substitution was selected as a favorable linkage based on previous SAR and further structural probing.

on the amount of steric bulk tolerated in A_3 receptor binding. Only a β-alanyl conjugate **45** was relatively unimpaired in binding. Later, we modified the linking chemistry for similar A_3 AR agonists to include a 3-alkynylbenzyl group of linear geometry, e.g., **46**, which better preserved nanomolar affinity (*46*).

Functionalized congeners were also reported for a series of selective A_3 AR agonists consisting of 5′-*N*-methylcarboxamidoadenosine analogues containing the (*N*)-methanocarba (bicyclo[3.1.0]hexane) ring system as a ribose substitute, e.g., **47** amd **48** (*62*). The rigid bicyclic ring system in this class of agonists provided a steric constraint of the riboselike moiety to enhance A_3 AR selectivity. Functionalized ethynyl chains terminating in amino or carboxylate groups were incorporated at both the N^6 and C2 positions and effects on affinity compared. Substitution at the C2 position of the purine moiety in the (*N*)-methanocarba series, e.g., **48**, preserved A_3 AR selectivity more effectively than similar chains attached at the 3 position of the N^6-benzyl group, e.g., **47**.

We also applied the functionalized congener approach to antagonists of the A_3 AR (*63*). 1,4-Dihydropyridine (DHP) derivatives containing 4-phenylethynyl and 6-phenyl groups are high-affinity antagonists at this receptor. We probed various sites of chain substitution on these DHPs to identify the least-sensitive position in receptor binding. Such functionalization of the 4-arylalkynyl moiety was not tolerated in A_3 AR binding. A para-substituted *O*-benzyl ester group at either the 3 or 5 position of the DHP was suitable for the attachment of a functionalized chain, which could then be linked to prosthetic groups. An amine derivative of a 3-benzyl ester **49** was conjugated to biotin to provide **50**.

MACROMOLECULAR CONJUGATES OF AR LIGANDS

At the time ADAC **20** and XAC **27** were first reported, little was known of the physical or chemical nature of the A_1 AR or of any GPCR. The structural similarity to rhodopsin was not yet evident. Thus, the functionalized congener approach served as a means of "blindly" exploring the solvent accessibility and environment of the hypothesized binding site for the pharmacophore. An early study by Ray Olsson and co-workers, in which adenosine agonists were coupled to polymeric carbohydrates (oxidized stachyose) with the retention of vasodilatory activity, led to the conclusion that the AR was located on the cell surface (*64*). More chemically well-defined, biologically active macromolecular conjugates were needed, and the functionalized congener approach proved useful for this purpose. The types of conjugates used in this effort are now more sophisticated. For example, dendrimers have recently been used as macromolecular carriers of AR functionalized congeners.

The ability to substitute ADAC **20** with a macromolecular carrier was first demonstrated through the biotin−avidin system (*65*−*67*). Acylation of **20** with biotin or with various chain-elongated derivatives of biotin provided conjugates **54** and **55**, which retained a relatively high affinity at the A_1 AR (Figure 5). Precomplexation of these ADAC−biotin conjugates with the tetrameric protein avidin of molecular weight ~68 000 Da only slightly reduced the receptor affinity. This clearly indicated that the steric constraints of the pharmacophore-binding site were entirely overcome. Thus, this functionalized chain must protrude toward the exofacial side of the receptor. The sequential elongation of the chain connecting biotin to the adenosine moiety allowed a crude estimation of the depth of the binding site, i.e., a "dipstick" approach to exploring the binding site. This calculation was based on the extended conformation of the shortest chain to be unimpaired in its ability to bridge the pharmacophore and the macromolecular carrier, i.e., avidin. By this method, the depth of the binding site of adenosine was estimated to be $\leq$12 Å. Later, molecular modeling of the receptor confirmed that this was a reasonable approximation. We used a similar method to conjugate the A_{2A} AR agonist APEC to biotin to provide **56**. Xanthine biotin conjugates **57**−**60**, when complexed to avidin, required a longer chain length to achieve moderate A_1 AR-binding affinity.

DUAL-ACTING LIGANDS: BINARY DRUGS

We designed ligands to interact equipotently with multiple subtypes of GPCRs, whether by tethering two components or by either fusing or merging favorable structures to create a dual selectivity in a single functional unit (*68*). Successes in the design of multiple ligands were recently reviewed by Morphy and Rankovic (*9*). One of the first examples of tethering two pharmacophoric units was reported by Portoghese and co-workers; this was achieved with the opioid system, in which ligands for either the same or different GPCRs were covalently coupled through flexible chains (*8*). The objective of tethering two GPCR ligands is to achieve a synergistic, net biological effect of activation or antagonism of multiple pathways (*46*) and potentially to bridge GPCR dimers (Figure 2C) (*8*, *69*, *70*). An approach to designing dual-acting ligands (termed binary drugs) derived from functionalized congeners was reported in 1987 (Figure 6) (*71*).

A functionalized congener antagonist of the A_1 AR, the 1,3-dialkylxanthine derivative XAC **27** (Table 1), was attached through an L-Lys linker to a segment derived from the neurotransmitter peptide substance P (SP) to form binary drug **61** (Figure 6A). The Lys linker preserved a free amino group in the spacer chain, which increased A_1 AR affinity and solubility. This binary conjugate bound to the rat A_1 receptor with a K_i value of 35 nM and to the NK1 (neurokinin type 1) receptor with a K_i value of 300 nM (*71*). Coupling of the functionalized adenosine agonist N^6-[4-(carboxymethyl)phenyl]-adenosine **16** (Figure 2A) to an SP C-terminal peptide also resulted in a binary drug **62** that bound to both receptors. The

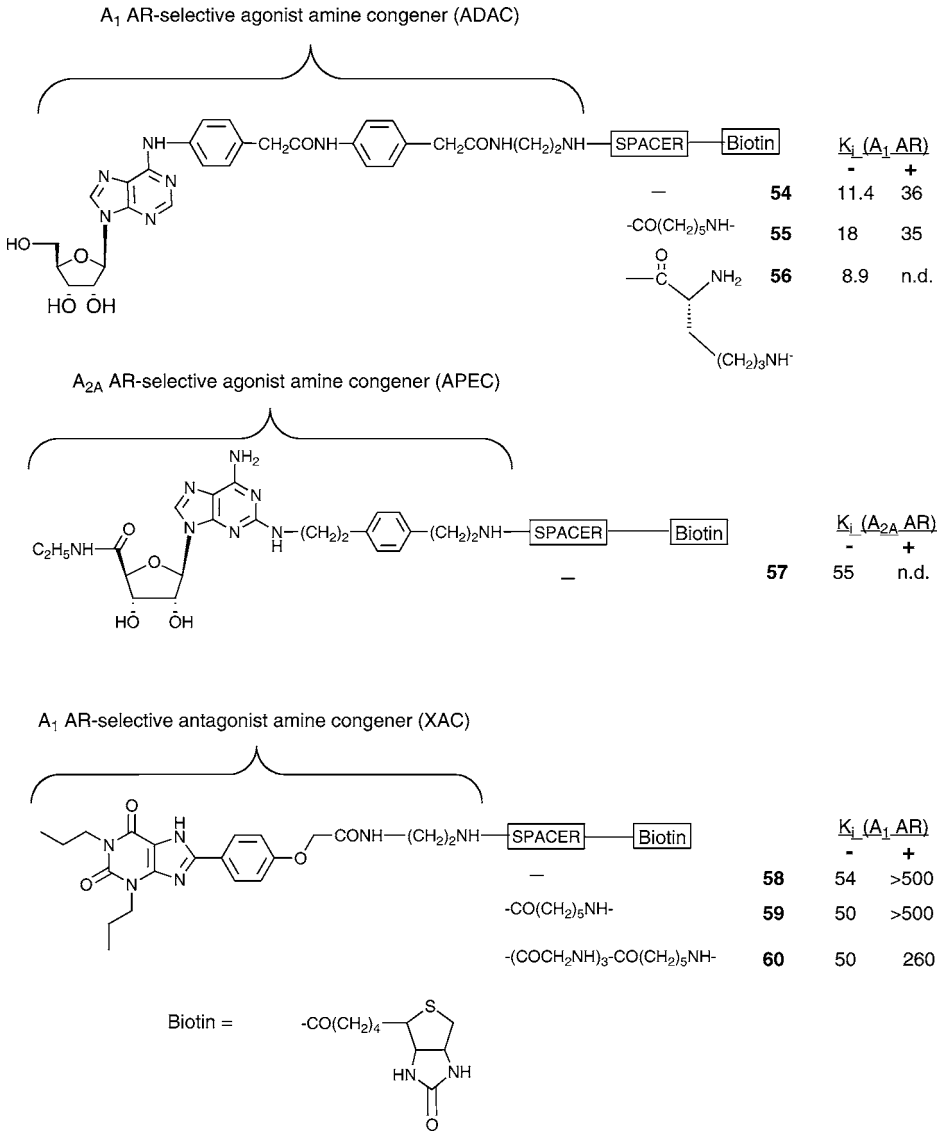

Figure 5. Use of biotin−avidin methodology to detect and characterize the A_1 AR (using agonist ADAC and antagonist XAC) and the A_{2A} AR (using agonist APEC). In several cases, the length and chemical fiunctionality of the spacer chain were varied to find the optimal receptor affinity of the biotin conjugate, both alone and as its avidin complex. K_i values (nM) at one of the rat ARs in the absence (−) and presence (+) of excess avidin are given. N.D. − not determined.

demonstration that the biochemical properties of two unrelated drugs, both of which act through binding at extracellular receptors, may be combined in the same molecule suggested a novel strategy for drug design. In principle, two different substances that produce the same final effect (e.g., hypotension by adenosine agonists and by SP analogues) should produce a combined effect. Adenosine analogues have analgesic properties, and the binary drugs derived from SP and adenosine agonists or antagonists were intended to serve as ligand tools for probing interrelationships of NK pathways and sites for the antinociceptive action of adenosine.

Considering the antinociceptive properties of AR ligands, we also sought to combine such ligands with opioid receptor agonists. Thus, nonpeptide ligands of the opioid receptors were conjugated to AR ligands, resulting in conjugates that retain affinity for both the A_1 AR and the μ-opioid receptor (Figure 6B) (*72*). We probed three structural classes of opioids, derivatives of tetrahydrooripavine, etonitazine, and fentanyl, for sites of functionalization for chain attachment. An amino group on the 7-*a* position of 6,14-endoethenotetrahydrooripavine was suitable for derivatization with long-chain substituents, such as Cbz-glycyl-glycine, without loss of affinity for the μ-opioid receptor. A binary conjugate of this tetrahydrooripavine with an alkylxanthine moiety **63** had morphinelike activity in the paraphenylquinone in vivo assay. Thiourea-linked conjugates of a benzimidazole derivative that was a potent opioid ligand and an AR functionalized congener, either ADAC **20** or XAC **27**, bound effectively to both receptors. For example, the ADAC conjugate **64** bound to the rat A_1 receptor with a K_i value of 31 nM and to the rat μ-opioid receptor with a K_i value of 150 nM.

Binary drugs that activate two subtypes of ARs have been proposed for cardioprotection (Figure 6C) (*73*). Adenosine released during cardiac ischemia exerts a potent, protective effect in the heart via activation of A_1 and A_3 receptors (*42, 45, 74*), which activate separate protective signaling cascades. To explore the interaction between these two cardioprotective ARs and the question of which receptor is the more important anti-ischemic receptor, we designed specialized binary ligands by tethering functionalized congeners. One objective was to use this ligand tool to test the hypothesis that activation of both receptors exerts a cardioprotective effect significantly greater than activation of either receptor individually. We used a novel design in which new binary conjugates of adenosine functionalized congeners that were pharmacologically complementary were synthesized

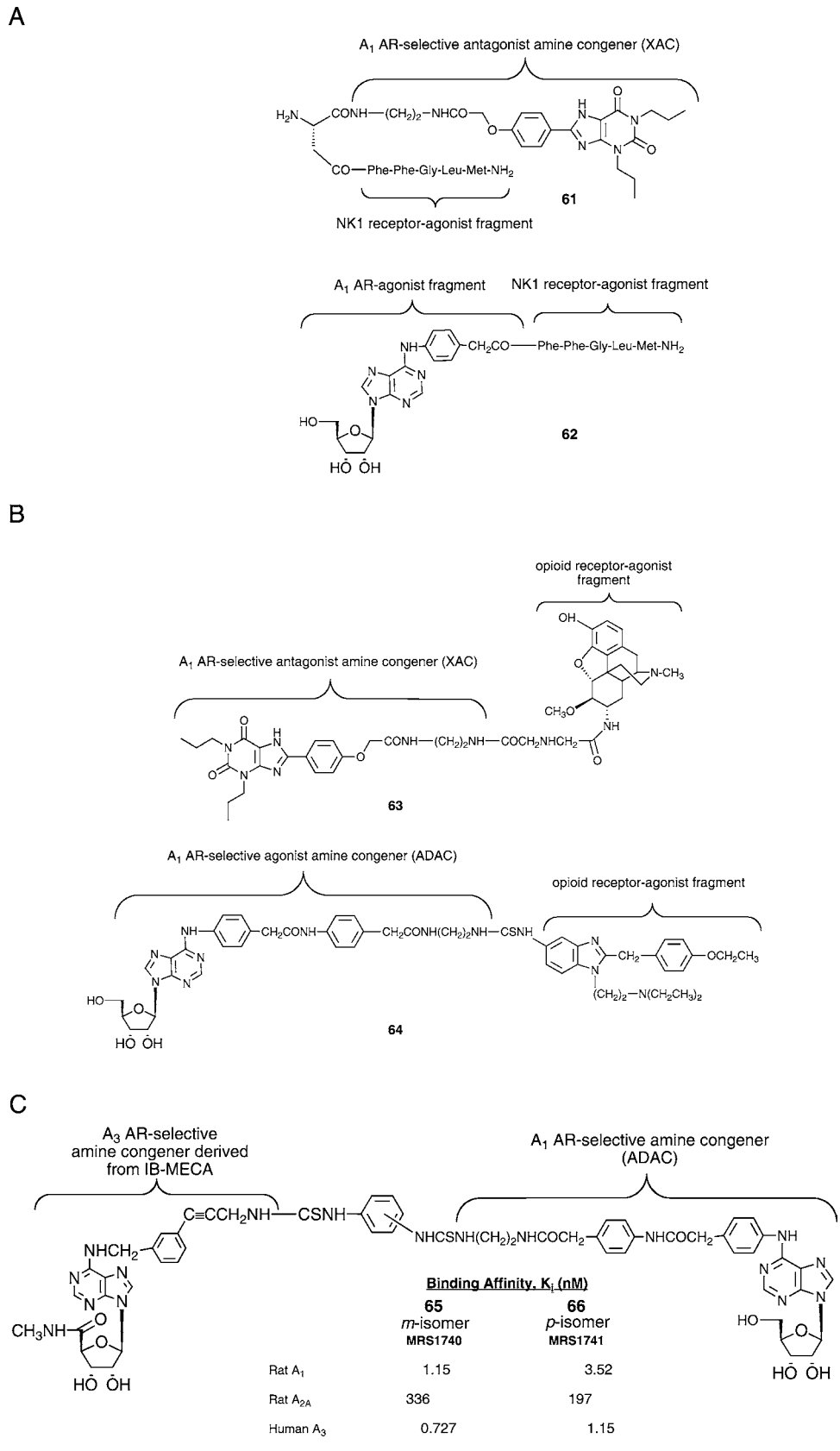

Figure 6. Binary drugs for a given AR in covalent combination with ligands for another GPCR. (A) Combination of A_1 AR-binding purines and substance P peptides as NK1 receptor ligands; (B) Combination of A_1 AR-binding purines and nonpeptide opioid receptor ligands; (C) Combination of agonist ligands for A_1 and A_3 ARs, which have cardioprotective properties. High-affinity binding to the A_{2A} AR remains excluded by this linking approach.

and tested in a novel cardiac myocyte model of adenosine-elicited cardioprotection.

Binary drugs with mixed selectivity for both A_1 and A_3 ARs were created through the covalent linking of functionalized

congeners of adenosine agonists, each of which is selective for either the A_1 or the A_3 AR subtype. MRS 1740 **65** and MRS 1741 **66**, thiourea-linked regioisomers of a binary conjugate, were highly potent and selective in radioligand-binding assays for the A_1 and A_3 ARs (K_i values of 0.7−3.5 nM) compared with the A_{2A} AR. The myocyte models used cultured myocardial muscle cells from chick embryo, either ventricular cells expressing native adenosine A_1 and A_3 ARs or engineered atrial cells, expressing either human A_3 receptors alone or both human A_1 and A_3 receptors. The binary agonist **66** activated both A_1 and A_3 receptors simultaneously, with full cardioprotection (EC_{50} ~0.1 nM) dependent on the expression of both receptors. Thus, coactivation of both adenosine A_1 and A_3 receptors by the binary A_1/A_3 agonists represents a novel general cardioprotective approach for the treatment of myocardial ischemia.

Scammells et al. recently reported bivalent conjugates of ligands of β2-adrenergic and adenosine A_1 receptors that activated both receptors and exploited crosstalk between these receptors (*75*). The N^6 position of adenosine was used as the site for chain derivatization. Hexyl and butyl-linked variations in the connecting chain were compared. The hexyl-linked conjugate displayed K_i values of 436 and 311 nM at A_1 and β2 receptors, respectively, and was even more potent in activation of the β2-adrenergic receptor with an EC_{50} of 6 nM.

IRREVERSIBLY BINDING AR LIGANDS FOR RECEPTOR INACTIVATION AND CROSS-LINKING

In collaboration with Gary Stiles and Mark Olah, then at Duke University, we coupled AR functionalized congeners in both the A_1 agonist and A_1 antagonist series to a variety of bifunctional cross-linking reagents present in excess to achieve a 1:1 stoichiometry in the product, thus leaving one chemically reactive group (*76*, *83*). These cross-linking reagents were typically symmetrical amine-reactive electrophiles. For example, 1,3- and 1,4-phenylene diisothiocyanates were conjugated to amine congeners that were potent and selective A_1 AR ligands. The resulting reactive conjugates, i.e., the A_1 AR agonist *p*-DITC-ADAC **22** (Figure 2) and the A_1 AR antagonist *p*-DITC-XAC **28** (Table 1), effectively and irreversibly bound to the A_1 AR at very low concentrations (10 nM to 1 μM) (*77*).

We coupled radiolabeled bifunctional reagents designed for photoaffinity labeling to the same amine congeners. One example of such a cross-linking group is the PAPA moiety, as in **30** and **40**, which was readily iodinated and then converted to the photoactivatable *p*-azide (*78*). Thus, XAC (available in its [^{3}H] form) served as the first high-affinity radiolabeled adenosine antagonist suitable for chemical or photochemical affinity cross-linking to the A_1 AR protein. This photoaffinity probe labeled the same receptor protein to which A_1 selective agonists bind, as indicated by molecular weight determined by gel electrophoresis. A comparison of proteolytic digests of agonist- and antagonist-occupied receptor proteins identified fragments formed at cleavage sites, which differ in accessibility. In addition to the electrophilic isothiocyanate group, the sulfonyl fluoride group was also effective for ligand cross-linking to the ARs because of its reactivity with nucleophiles on proteins with a sufficient aqueous stability (*79, 80*).

We also used chemically reactive bifunctional cross-linkers to prepare affinity labels from amine functionalized congeners for A_{2A} AR agonists. We found that *p*-DITC-APEC (2-[[2-[4-[2-[2-[(4-isothiocyanatophenyl)aminothiocarbonylamino]ethyl]-aminocarbonyl]-ethyl]phenyl]ethylamino]-5′-*N*-ethyl-carboxamidoadenosine) **41** effectively and irreversibly bound to the A_{2A} AR at very low concentrations (~10 nM) (*81*). Curiously, when this derivative was infused into the coronary artery of guinea pigs, there was a prolonged A_{2A} AR activation that could not be reversed by washing, leading to sustained vasodilitation.

We introduced trifunctional probes by simultaneously cross-linking a GPCR functionalized congener with a reporter group and a chemically reactive group, through a central symmetrically trisubstituted aryl unit (Figure 7) (*82, 83*). To further extend the use of isothiocyanates to covalently cross-link high-affinity ligands to the ARs, we prepared a series of analogues of *m*-DITC-XAC containing a third substituent in the phenyl isothiocyanate ring. Thus, the central aryl linker could consist of 1,3,5-triisothiocyanatobenzene (**67**, R = 5-NCS), although we also prepared some variants of conjugates containing 1,3,5-trichlorotriazine as a central aryl linker. This third substituent (R of **67**), when appropriately derivatized, modifed the physiochemical or spectroscopic properties of the conjugate. Thus, an amine congener reacted with a symmetrical trifunctional cross-linking intermediate bearing two isothiocyanate groups, which already contained a third substituent. We were thus able to synthesize derivatives of XAC containing hydrophilic, fluorescent, or reactive substituents, linked via an amide, thiourea, or methylene group in the 5 position of the central aryl ring, and found them to be irreversible inhibitors of the A_1 AR.

We examined the effects of modifying the 5-substituent on water solubility and on affinity. A conjugate of XAC and 1,3,5-triisothiocyanato-benzene, i.e., a trifunctional ligand intermediate (**68**, R = NCS), was 894-fold selective in binding to the rat A_1 AR. Reporter groups, such as fluorescent dyes and a spin label, were included as substituents in the third position of irreversibly binding analogues, which were designed for spectroscopic assays, histochemical characterization, and biochemical characterization of the receptor protein. We also designed and synthesized trifunctional ligands for the A_1 AR that contain a cleavable disulfide linkage in the chain, for chemically induced regeneration of the receptor-binding site for the purine by reduction of the disulfide (*82*).

RADIOACTIVE PROBES

Because functionalized congeners are used as a modular approach to ligand design, it is feasible to couple these derivatized pharmacophores to prosthetic groups for radiolabeling. For example, we used the active ester intermediate for the Bolton-Hunter reagent, *N*-succinimidyl-3-(4-hydroxy-phenyl)propionate, to incorporate a group for radioiodination both in simple functionalized congeners and in our trifunctional A_1 AR antagonists (Figure 7B) (*83*). The resulting conjugate covalently labeled the receptor protein, which was readily detectable on a Western blot.

We also introduced other novel prosthetic groups for radiolabeling. We selected a prosthetic group for radiofluorination by the ease of replacement of benzyl bromides with nucleophilic ^{18}F-fluoride and applied it to derivatization of insulin for imaging of insulin receptors (*84*). Other groups are now used for incorporating ^{18}F into peptides because of the in vivo lability of benzyl fluorides (*85*). Chelating groups capable of complexing radioactive metal ions were coupled to amine-functionalized congeners, e.g., **33**, with the retention of moderate affinity at the A_1 AR (Table 1) (*4*).

IMMOBILIZED AR LIGANDS FOR AFFINITY CHROMATOGRAPHY TO ISOLATE THE RECEPTOR PROTEIN

Amine functionalized congeners of AR agonists and antagonists have been used as immobilized high-affinity ligands for both A_1 and A_{2A} receptors, for the purpose of affinity chromatography leading to the isolation of the receptors and purification to homogeneity (*86*−*88*). For example, XAC was immobilized on a Sephadex column for isolation of the bovine A_1 receptor and for the isolation of the recombinant human A_{2A} receptor

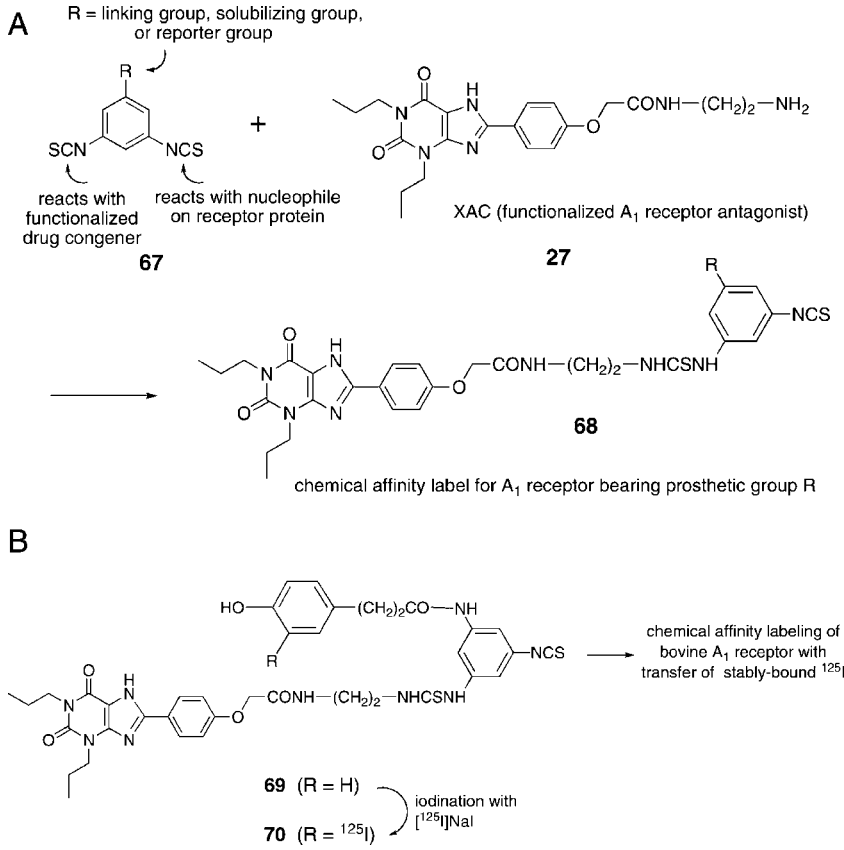

Figure 7. Trifunctional reagents for covalent binding to ARs. (A) General scheme for using a high affinity antagonist (XAC) to target a prosthetic group to the A_1 AR, at which it will bind covalently by virtues of the electrophilic isothiocyanate group, and (B) Application of this scheme to a prosthetic reporter group for radioiodination.

expressed in *E. coli*. The use of the agonist N^6-(4-aminobenzyl)adenosine for affinity chromatography allowed the isolation of the A_1 AR along with its associated G protein (*89*).

FUNCTIONALIZED AR LIGANDS AS SPECTROSCOPIC PROBES

Fluorescent probes of high affinity for GPCRs are being explored as an alternative to the use of radioligands in binding assays and histochemical studies (*90*). Fluorescent conjugates of both small-molecule ligands (*91*, *92*) and peptide ligands (*93*) of GPCRs have been used. A fluorescent-labeled naloxone has been used in confocal scanning laser microscopy to demonstrate specific binding to the μ-opioid receptor (*92*). Moreover, more detailed information about the binding site and its microenvironment can be obtained from fluorescent ligands than from radioisotopes. For example, flow cytometry analysis and confocal laser-scanning microscopy of living cells showed that a fluorescent BODIPY (6-(((4,4-difluoro-5-(2-thienyl)-4-bora-3*a*,4*a*-diaza-*s*-indacene-3-yl)styryloxy)acetyl)aminohexanoic acid) derivative of prazosin labels not only α1-adrenergic receptors on the cell surface, but also those localized inside the cell (*94*).

A conjugate of fluorescein isothiocyanate (FITC) with the amine functionalized congener APEC, which was a A_{2A} AR-selective agonist, has proven useful as an alternative to radioligands in receptor assays (*95*). FITC-APEC **42** was of suitably high affinity for use in the quantitative characterization of ligand binding to the bovine A_{2A} AR. Fluorescence measurements provided a B_{max} value of 2.3 $\pm$ 0.3 pmol/mg protein and K_D value of 57 $\pm$ 2 nM. This observed specific binding was saturable and rapid in its rates of association and dissociation, and the parameters were comparable to those obtained in competition studies that used a tritiated agonist radioligand at the same receptor. The potencies of chemically diverse A_{2A} AR ligands (and control compounds of low AR affinity), estimated by inhibition of FITC-APEC binding, were also in good agreement with their potencies determined by radioligand-binding techniques. Schulte and co-workers characterized another fluorescent conjugate **43** of APEC, in which the fluorescent moiety consisted of Alexafluor488; they were able to follow internalization into cells (Table 1) (*96*). Various other fluorescent derivatives have been prepared for the ARs through derivatization at sites on known ligands that are insensitive in receptor binding and are used for fluorescence correlation spectroscopy and other detection techniques (*4*, *7*, *51*, *97*−*99*). Hill and colleagues have prepared and characterized such fluorescent probes of the ARs, including a fluorescent derivative of XAC **35** (*7*).

We and others have reported spin label probes and highly fluorinated analogues derived from ADAC and XAC and other purine AR ligands obtained by a similar attachment method (*4*, *100*). For example, XAC was conjugated to the TEMPO moiety to yield **31**, which contains a nitroxyl radical, with the retention of high A_1 AR affinity (*4*). Compound **32** contained a perfluorinated acyl prosthetic group. The intended use of these analogues was receptor characterization by electron spin resonance (ESR) spectroscopy and fluorine-NMR, respectively (*101*, *102*).

FUNCTIONALIZED CONGENERS OF P2Y NUCLEOTIDE RECEPTOR LIGANDS

Although ARs constitute a mature field of medicinal chemistry, the P2Y nucleotide receptors are in the early stages of ligand development (*29*). The currently defined eight subtypes of P2Y receptors fall into two structural and functional clusters

of sequences (in general, low homology among subtypes), ligand preference, second messengers, and receptor sequence analysis (*103*). The distribution of P2Y receptors is broad, and the therapeutic interests include antithrombotic therapy, modulation of the immune system, cardiac ischemia, neurodegeneration, diabetes, and treatment of cystic fibrosis and other pulmonary diseases (*29, 104*−*107*).

$P2Y_1$, $P2Y_2$, $P2Y_4$, $P2Y_6$, and $P2Y_{11}$ receptor subtypes belong to a structurally distinct cluster of P2Y receptor sequences and couple through $G\alpha_q$ to activate phospholipase C. The remaining three subtypes, $P2Y_{12}$, $P2Y_{13}$, and $P2Y_{14}$ receptors, couple via $G\alpha_i$ to inhibit adenylate cyclase. $P2Y_{12}$ receptors stimulate an important proaggregatory signal in platelets, $P2Y_{13}$ receptors occur in immunocytes and neuronal cells, and the $P2Y_{14}$ receptor that is found in dendritic cells is activated by UDP-glucose **8**. $P2Y_1$, $P2Y_2$, and $P2Y_{11}$−$P2Y_{13}$ receptors are activated by adenine nucleotides, and $P2Y_2$, $P2Y_4$, $P2Y_6$, and $P2Y_{14}$ receptors are activated by uracil nucleotides. Pharmacological antagonism of the $P2Y_{12}$ receptor is widely used for antiplatelet therapy. We showed that a $P2Y_1$ antagonist can serve as an antithrombotic agent (*104*). Other potential therapeutic approaches, involving other P2Y subtypes, have been aided by the availability of recently introduced pharmacological probes.

A variety of factors have tended to confound the pharmacological characterization of both native and recombinant P2Y receptors. These include the dependence of P2Y receptor classification on the use of unstable nucleotides as agonists and a lack of potent, selective, and bioavailable antagonists. In addition to a lack of selectivity for the different P2Y receptors, commonly used P2Y receptor agonists (and their metabolite nucleosides) and antagonists often have the potential to interact with other biological targets. Thus, new P2Y receptor ligands of clearly defined selectivity, chemical and biological stability, and bioavailability are needed. P2Y receptor ligands that would pass the blood−brain barrier when administered peripherally are desperately needed by neuroscientists to study the role of these receptors in the central nervous system.

We have explored functionalized congeners of $P2Y_1$ receptor agonists (*108*). A functionalized chain was attached at the adenine C2 position of ATP derivatives. This design feature was based on the SAR of $P2Y_1$ receptor agonists, which indicates high potency of 2-thioethers compared with 2-amino or 2-oxo derivatives (*109, 110*). A tolerance for long extensions of this chain was found, by contrast to chain extension at the N^6 position of ATP, which eliminates $P2Y_1$ receptor recognition. Thus, in the putative binding site of the $P2Y_1$ receptor, only small hydrophobic groups in the N^6-region are tolerated; the C2 region has much less restricted tolerance of steric bulk. For example, N^6-(2-phenylethyl)-ATP was inactive at the $P2Y_1$ receptor; 2-(2-phenylethyl)thio ethers of ATP, such as **51**, were highly potent (*33, 108*). A biotinylated nucleotide analogue potentially suitable for specific $P2Y_1$ receptor isolation was reported (*111*). A functionalized chain was attached as a 2-thioether in this agonist series.

We employed $P2Y_1$ receptor nucleotide antagonists that display similar SAR to the agonist series in a functionalized congener approach. The high-affinity $P2Y_1$ receptor antagonist MRS2500, a 3′,5′-bisphosphate derivative that contains an (*N*)-methanocarba ring system as a 2′-deoxyribose substitute, was subjected to the functionalized congener approach. MRS2500 was effective in reducing thrombus formation in vivo, and it is more resistant to degradation than the related 9-riboside derivatives (*104*). Although the substitution in this family at other positions decreases antagonist potency at the $P2Y_1$ receptor, a 2-alkynyl substitution of the adenine ring maintains antagonist potency. We have extended our search for antagonists of the $P2Y_1$ receptor by modifying the adenine 2 position with various long-chain alkynyl subtituents that retain receptor affinity (*112*). Congener **52** was one such carboxylic acid derivative that was a potent $P2Y_1$ receptor antagonist (Table 1).

We prepared functionalized congeners of $P2Y_{14}$ receptor agonists that retain biological activity (*113*). The most insensitive site for derivatization on the native ligand **8** is through the glucose moiety. In fact, the 6-carboxylate of UDP-glucuronic acid was found to be suitable for chain derivatization, e.g., by amide coupling to an *N*-acetyl-ethylenediamino group to form **53**.

FUNCTIONALIZED CONGENERS OF LIGANDS FOR OTHER GPCRs AND NON-G PROTEIN COUPLED RECEPTORS

Functionalized congeners of ligands for other GPCRs and non-G protein coupled receptors have been reported. This review includes a few representative studies on chain attachment and tethering of GPCR and non-GPCR ligands.

Portoghese and colleagues reported novel bivalent ligands for opioid and other receptors. Separate pharmacophores representing a δ-antagonist and a κ-agonist were tethered and found to bridge δ 2 and κ1 opioid receptors (*114*). These heterodimeric conjugates contained the δ-antagonist naltrindole and the κ-agonist ICI-199,441 tethered by oligoglycine linkers of variable length. Novel tethered bivalent ligands for two different classes of GPCRs were found to induce the direct association of μ-opioid and CCK_2 (cholecystokinin) receptors (*115*). These bivalent ligands appear to induce the association of these two divergent GPCR subtypes.

In our studies of biogenic amine neurotransmitter receptors, we explored muscarinic acetylcholine receptor agonists (Figure 8A) and antagonists with a functionalized congener approach (*116*−*118*). We first used a chain extension method for muscarinic antagonists with the known antagonist pirenzepine **71** (*117*) and then extended our investigation to the more potent and selective M1 receptor antagonist telenzepine **73** (Figure 8B) (*118*). Sites for chain derivatization were compared, and the attachment of a spacer chain to a distal piperazinyl nitrogen, common to both antagonists, was the generally insensitive site. We varied the chain at this position in the pirenzepine series **72** was varied and compared the binding affinities. We observed a progressive increase in affinity in the longer members of the series (6 or more methylenes). We applied the findings to the telenzepine series, and a derivative containing a 10-aminodecyl group (TAC, telenzepine amine congener, analogous to **72e** but in the telenzepine series) was highly potent in receptor-binding affinity and provided a nucleophilic functionality for further derivatization. The K_i value of TAC was 2.39 nM at the recombinant m1 receptor and 15.8 nM for the corresponding pirenzepine derivative.

We synthesized conjugates of TAC to contain prosthetic groups for radioiodination, protein cross-linking, photoaffinity labeling, and fluorescent labeling and biotin for avidin complexation. A *p*-aminophenyacetyl derivative for radioiodination and photoaffinity labeling had a K_i value of 0.29 nM at rat forebrain M1 muscarinic receptors; by contrast, the K_i value for telenzepine was 4.7 nM). A biotin conjugate displayed a K_i value of 0.60 nM at cardiac M2-receptors and a 5-fold selectivity for M2 compared with the M1 receptor. The high affinity of these derivatives makes them suitable for the characterization of muscarinic receptors in pharmacological and spectroscopic studies, for peptide mapping, and for histochemical studies.

The telenzepine amine congener TAC has been used as the functionalized pharmacophore in other fluorescent probes of

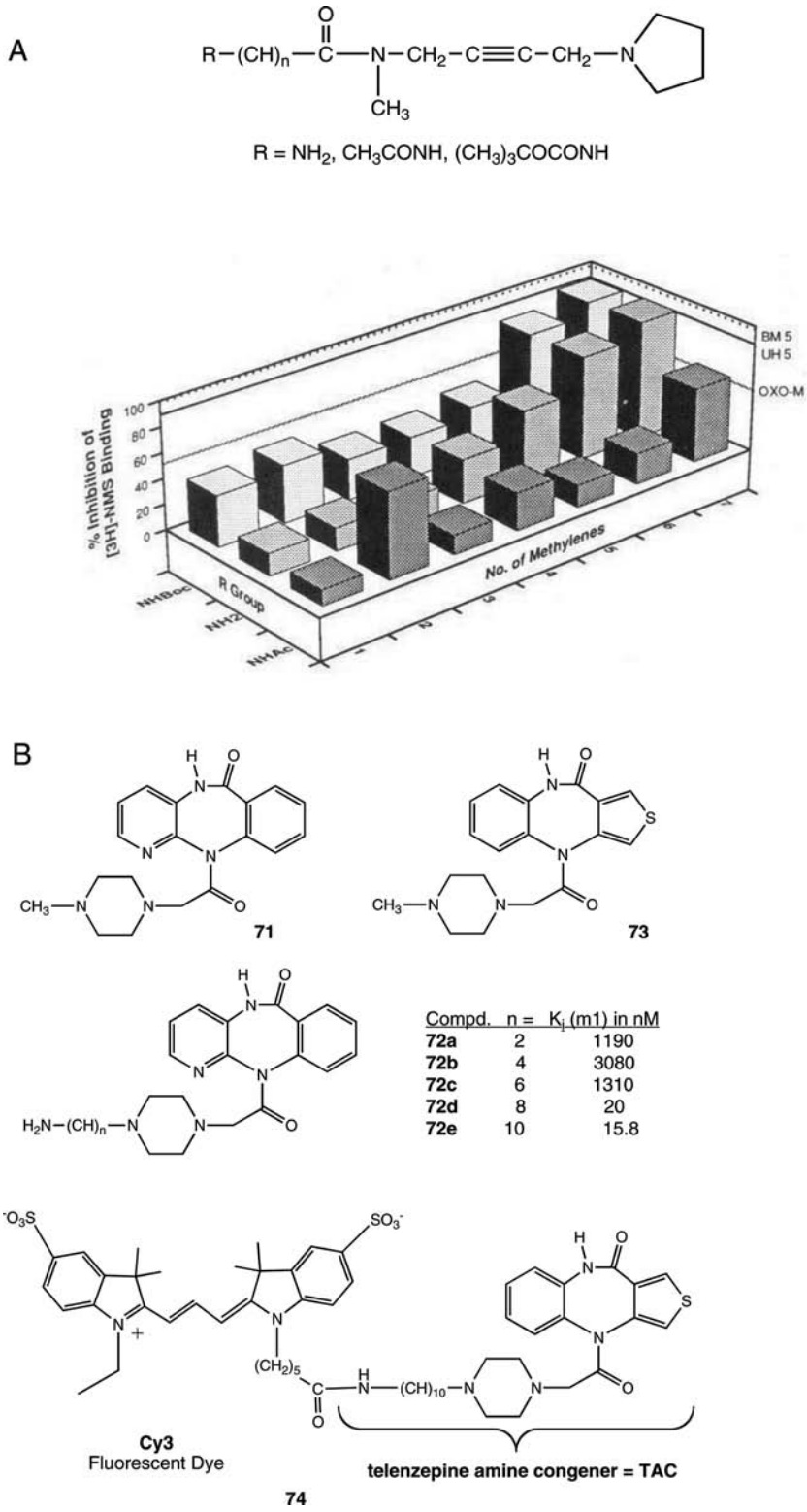

Figure 8. Functionalized congeners of ligands of the muscarinic acetylcholine receptors. (A) Dependence of the inhibition of radioligand binding at the m3 receptor (SK-N-SH cell membranes) on the chain length and terminal chemical functionality in the agonist series of butynyl amides (*116*). The levels corresponding to inhibition by the pharmacological standards oxotremorine-M, *N*-methyl-*N*-[4-[1-(pyrrolidinyl)]-2-butynyl]acetamide (UH5), and *N*-methyl-*N*-(1-methyl-4-pyrrolidino-2-butynyl)-acetamide (BM5) are shown (reproduced from ref (*138*), copyright 1990 Springer Science and Business Media). (B) Muscarinic antagonists and their amine fucntionalized congeners (affinity of **72** shown at the recombinant rat m1 receptor expressed in A9L cells). Use of a functionalized congener of the muscarinic antagonist telenzepine to provide a high affinity fluorescent tracer (*119*).

muscarinic receptors. For example, this approach recently resulted in a high-throughput screening method that uses live cells, made possible by the high-affinity fluorescent conjugate **74** of TAC with the cyanine dye Cy3B (*119*). The same fluorescent ligand was used recently by Birdsall et al. for single-molecule fluorescent imaging of muscarinic receptors (*120*).

Fluorescent pirenzepine analogues labeled with BODIPY were synthesized for studying fluorescence resonance energy transfer between the antagonist ligand and muscarinic M1 receptors that were fused to enhanced green fluorescent protein (*121*). Attachment of the fluorophore in these pirenzepine derivatives occurred through a functionalized chain at the

4-piperazine position. It appears that these analogues bridge the putative binding sites of the agonist acetylcholine and an allosteric modulator brucine.

A variety of other GPCRs have been studied using chain functionalization of small molecular ligands. For example, naltrexamine and 5′-guanidinonaltrindole have been linked through a polyamide spacer to form KDN-21, which is designed for interaction with heterodimeric delta-kappa opioid receptors (*122*). Numerous other examples of linkage of GPCR pharmacophores for the simultaneous activation of heteromeric receptors (*123, 124*) or homomeric receptors (*125, 126*) have been described. Symmetric bivalent ligands have been described for serotonin and for dopamine receptors (*125*), muscarinic acetylcholine receptors (*126*), and for melatoninergic receptors (*127*). Dual-acting drugs for activation of multiple receptors, even if not targeting GPCR dimers, have become important in drug development, for example, the antipsychotic agent ziprasidone was designed with separate pharmacophores to antagonize both the D2 dopamine receptor and the 5-HT_2 serotonin receptors (*128*). Combined ligands for the H1 histamine receptor and the 5-HT_2 serotonin receptors have been studied (*129*).

Although GPCRs are a major focus of studies of functionalized congeners, application to other classes of cell surface receptors and even nuclear hormone receptors is feasible (*130*). One of the earliest applications of a chain attachment approach to the study of receptors was carried out by Kosower and colleagues (*131*). Biologically active barbital and amphetamine derivatives were appended with an alkyl chain that terminated in a chemically reactive moiety, such as a thiol-reactive maleimide, designed for covalent bonding to the biopolymer with which these drugs interacted. The main mechanism of action of barbiturates is now known to be through the $GABA_A$ receptor chloride channel complex.

Antagonists of the $P2X_7$ receptor, an ATP-gated ion channel, have also been reported. We functionalized modified tyrosyl derivatives that block the action of adenine nucleotides at the $P2X_7$ receptor with extended chains at various positions (*132*). We observed only moderate antagonistic potency for these derivatives.

MULTIVALENT NANOCARRIERS FOR AR FUNCTIONALIZED CONGENERS

We are using the multivalency of dendrimer conjugates to test for interaction with dimeric and higher-order multimeric GPCR assemblies, as have been detected (*133*). Kim et al. recently reported the first poly(amidoamine) (PAMAM) dendrimer to which a functionalized congeners of a GPCR ligand was covalently attached (*134*). Specifically, 31 moieties of the A_{2A} AR agonist CGS21680 **37** were coupled to a G3 (3rd generation) PAMAM polyamine. This conjugate acted as a potent A_{2A} AR agonist and displayed characteristic antithrombotic activity. With multivalency of ligand substitution—e.g., 31 out of 32 possible substitutions on a G3 PAMAM dendrimer, of varying relative orientation—there could be a greater likelihood of bridging GPCR dimers than by tethering only two pharmacophores. We are expanding the application of nanotechnology to the study of GPCRs, for example, in dendrimer conjugation to a wide variety of ligands for ARs (*51, 135*) and other receptors. These dendrimer conjugates will be studied in diverse biological models.

We also employed the chemically reactive nucleoside A_{2A} AR agonist DITC-APEC (**41**, Figure 4) to derivatize the surface of G3 PAMAM dendrimers (*126*). The resulting conjugates carried multiple copies of the agonist attached through a thiourea linkage, and they differed in the number of attachments and in the presence of a fluorophore or additional surface modification. In vitro radioligand competition experiments showed effective binding of these PAMAM-DITC-APEC dendrimer conjugates at the human A_{2A} and A_3 ARs with submicromolar K_i values and in their weak activity at the human A_1 AR. Furthermore, these nucleoside-loaded dendrimers exhibited an A_{2A} AR-mediated inhibitory effect on ADP-induced aggregation of human platelets.

To target the human A_1 AR with dendrimer derivatives, we selected the amine functionalized congener ADAC **20** for covalent coupling (*51*). We used two variations on the linking chain: one was created by acylation of the terminal amine of **20**, and the other maintained an affinity favoring a free amino group (secondary) within the chain (i.e., **25** as an amine functionalized congener). The AR-binding profile of the latter derivative (MRS5183) unexpectedly indicated a shift toward A_3 AR selectivity, both in binding affinity and in functional potency. The key to this selectivity of >100-fold in both binding at the human A_3 AR (K_i app = 2.4 nM) and functional assays (EC_{50} = 1.6 nM in human A_3 AR-mediated inhibition of adenylate cyclase) was maintaining a free amino group (secondary) in an amide-linked chain.

We explored the interaction of dendrimer conjugates of GPCR ligands with their receptors through molecular modeling (*136*). The theoretical possibility was investigated for bivalent binding to a homodimer of a GPCR of a dendrimer, covalently appended with multiple copies of a small ligand (*25*). We constructed a molecular model of a G3 PAMAM dendrimer condensed with multiple copies of the potent A_{2A} AR agonist CGS21680 (Figure 2C). The dendrimer was bound to an A_{2A} AR homodimer. Two units of the nucleoside CGS21680 occupied the A_{2A} receptor homodimer simultaneously. The binding mode of CGS21680 moieties linked to the PAMAM dendrimer and docked to the A_{2A} receptor was similar to the binding mode of a monomeric CGS21680 ligand.

CONCLUSIONS

The development of functionalized congeners as selective ligands for ARs, P2Y nucleotide receptors, and other receptors has provided valuable new research tools and candidates for therapeutics. In general, medicinal chemistry has made possible and driven the biological exploration of the study of GPCRs that respond to purines and pyrimidines. Molecular modeling based on a rhodopsin template has provided structural insights into both binding and activation steps of the receptors, which have been adapted to structure-based design of ligands.

The functionalized congener approach, as introduced for GPCR drug design, involves structural variation at the distal unit of a preexisting ligand to improve the drug's pharmacological effects. The key pharmacophore unit of a small molecular ligand for a GPCR, especially Family A, generally binds within its heptahelical TM domain. In the case of functionalized congeners, the distal moiety of an appended chemically functionalized chain may reside and potentially interact at or near the extracellular domain of the GPCR. Indeed, providing a secondary interaction by this approach can significantly enhance the affinity and selectivity of certain ligands. Such modulation of the pharmacological profile can be achieved at the distal unit through a variation of the linker length, functional group manipulation, or a combination of both techniques.

A_1, A_{2A}, and A_3 AR functionalized congeners have thus far yielded macromolecular conjugates, irreversibly binding AR ligands for receptor inactivation and cross-linking, radioactive probes that use prosthetic groups, immobilized ligands for affinity chromatography, and dual-acting ligands as binary drugs. PAMAM dendrimers act as nanocarriers for covalently conjugated AR functionalized congeners. These studies employ rational methods of ligand design derived from molecular modeling and templates. Thus, the design of novel ligands, both

small molecules and macromolecular conjugates, for studying the chemical and biological properties of GPCRs has provided researchers with a strategy that is more versatile than the classical medicinal chemical approaches.

The review provides the historical background to functionalized congeners, as well as a summary of recent advances. In spite of the lack of that no drugs have yet evolved out of this approach, now several decades old, this field is now reenergized due to recent developments, such as the emerging concept of functional GPCR dimers. One possible reason for the lack of pharmaceuticals designed by this approach is that the molecular weight and H bonding character are increased, which is usually considered a disadvantage in conventional drug development. However, with the advent of biological therapeutic agents and other large molecular weight molecules in clinical use, the functionalized congener approach seems to have a new appeal. In fact, the full potential of such approaches as binary drugs and macromolecular conjugates has not been fully realized.

ACKNOWLEDGMENT

This work was supported by the NIDDK/NIH Intramural Research Program. We also thank Can-Fite Biopharma for funding. We thank Dr. Andrei A. Ivanov (NIDDK) for providing Figure 1C.

LITERATURE CITED

(1) Bridges, T. M., and Lindsley, C. W. (2008) G-protein-coupled receptors: from classical modes of modulation to allosteric mechanisms. *ACS Chem. Biol. 3*, 530–541.

(2) Jacobson, K. A., Kirk, K. L., Padgett, W. L., and Daly, J. W. (1985) Functionalized congeners of adenosine: preparation of analogues with high affinity for A_1-adenosine receptors. *J. Med. Chem. 28*, 1341–1346.

(3) Jacobson, K. A., Marr-Leisy, D., Rosenkranz, R. P., Verlander, M. S., Melmon, K. L., and Goodman, M. (1983) Conjugates of catecholamines. 1. N-alkyl-functionalized carboxylic acid congeners and amides related to isoproterenol. *J. Med. Chem. 26*, 492–499.

(4) Jacobson, K. A., Ukena, D., Padgett, W., Kirk, K. L., and Daly, J. W. (1987) Molecular probes for extracellular adenosine receptors. *Biochem. Pharmacol. 36*, 1697–1707.

(5) Rosenkranz, R. P., Jacobson, K. A., Verlander, M. S., Klevans, L., O'Donnell, M., Goodman, M., and Melmon, K. L. (1983) Conjugates of catecholamines. IV. In vitro and in vivo pharmacological activity of monodisperse oligopeptide conjugates. *J. Pharmacol. Exp. Ther. 227*, 267–273.

(6) Jacobson, K. A., Kirk, K. L., Padgett, W. L., and Daly, J. W. (1986) A functionalized congener approach to adenosine receptor antagonists: amino acid conjugates of 1,3-dipropylxanthine. *Mol. Pharmacol. 29*, 126–133.

(7) Briddon, S. J., Middleton, R. J., Cordeaux, Y., Flavin, F. M., Weinstein, J. A., George, M. W., Kellam, B., and Hill, S. J. (2004) Quantitative analysis of the formation and diffusion of A_1-adenosine receptor-antagonist complexes in single living cells. *Proc. Natl. Acad. Sci. U.S.A. 101*, 4673–4678.

(8) Portoghese, P. S. (2001) From models to molecules: opioid receptor dimers, bivalent ligands, and selective opioid receptor probes. *J. Med. Chem. 44*, 2259–2269.

(9) Morphy, R., and Rankovic, Z. (2005) Designed multiple ligands. An emerging drug discovery paradigm. *J. Med. Chem. 48*, 6523–6543.

(10) Balcells, E., Suarez, J., and Rubio, R. (1993) Implications of the coronary vascular endothelium as mediator of the vasodilatory and dromotropic actions of adenosine. *J. Mol. Cell Cardiol. 25*, 693–706.

(11) Zheng, J., Hashimoto, A., Putnam, M., Miller, K., and Koh, J. T. (2008) Development of a thyroid hormone receptor targeting conjugate. *Bioconjugate Chem. 19*, 1227–1234.

(12) Daly, J. W. (1982) Adenosine receptors: targets for future drugs. *J. Med. Chem. 25*, 197–207.

(13) Sattin, A., and Rall, T. W. (1970) The effect of adenosine and adenine nucleotides on the cyclic adenosine 3′,5′-phosphate content of guinea pig cerebral cortex slices. *Mol. Pharmacol. 6*, 13–23.

(14) Shimizu, H., Creveling, C. R., and Daly, J. W. (1970) Cyclic adenosine, 3′,5′-monophosphate formation in brain slices: Stimulation by batrachotoxin, ouabain, veratridine, and potassium ions. *Mol. Pharm. 6*, 184–188.

(15) Londos, C., Cooper, D. M., and Wolff, J. (1980) Subclasses of external adenosine receptors. *Proc. Natl. Acad. Sci. U.S.A. 77*, 2551–2554.

(16) Jacobson, K. A., and Gao, Z. G. (2006) Adenosine receptors as therapeutic targets. *Nat. Rev. Drug Discovery 5*, 247–264.

(17) Tobin, A. B., Butcher, A. J., and Kong, K. C. (2008) Location, location, location. . site-specific GPCR phosphorylation offers a mechanism for cell-type-specific signalling. *Trends Pharmacol. Sci. 29*, 413–420.

(18) Schwartz, T. W., Frimurer, T. M., Holst, B., Rosenkilde, M. M., and Elling, C. E. (2006) Molecular mechanism of 7TM receptor activation--a global toggle switch model. *Annu. Rev. Pharmacol. Toxicol. 46*, 481–519.

(19) Wess, J., Han, S.-J., Kim, S. K., Jacobson, K. A., and Li, J. H. (2008) Conformational changes involved in G-protein-coupled receptor activation. *Trends Pharmacol. Sci. 29*, 616–625.

(20) Dixon, R. A., Kobilka, B. K., Strader, D. J., Benovic, J. L., Dohlman, H. G., Frielle, T., Bolanowski, M. A., Bennett, C. D., Rands, E., Diehl, R. E., Mumford, R. A., Slater, E. E., Sigal, I. S., Caron, M. G., Lefkowitz, R. J., and Strader, C. D. (1986) Cloning of the gene and cDNA for mammalian beta-adrenergic receptor and homology with rhodopsin. *Nature 321*, 75–79.

(21) Rusmussen, S. G. F., Choi, H.-J., Rosenbaum, D. M., Kobilka, T. S., Thian, F. S., Edwards, P. C., Burghummer, M., Ratnala, V. R. P., Sanishvili, R., Fischetti, R. F., Schertler, G. F. X., Weis, W. I., and Kobilka, B. K. (2007) Crystal structure of the human β_2-adrenergic G-protein-coupled receptor. *Nature 450*, 383–388.

(22) Jaakola, V.-P., Griffith, M. T., Hanson, M. A., Cherezov, V., Chien, E. Y. T., Lane, J. R., IJzerman, A. P., and Stevens, R. C. (2008) The 2.6 ångstrom crystal structure of a human A_{2A} adenosine receptor bound to an antagonist. *Science 322*, 1211–1217.

(23) MRS/NIDDK created the first online mutational database of G protein-coupled receptors, which was the first website for chemical information to be featured in Chemical and Engineering News (1995).

(24) Cavasotto, C. N., Orry, A. J., Murgolo, N. J., Czarniecki, M. F., Kocsi, S. A., Hawes, B. E., O'Neill, K. A., Hine, H., Burton, M. S., Voigt, J. H., Abagyan, R. A., Bayne, M. L., and Monsma, F.J. Jr. (2008) Discovery of novel chemotypes to a G-protein-coupled receptor through ligand-steered homology modeling and structure-based virtual screening. *J. Med. Chem. 51*, 581–588.

(25) Filizola, M., and Weinstein, H. (2005) The study of G-protein coupled receptor oligomerization with computational modeling and bioinformatics. *FEBS J. 272*, 2926–2938.

(26) Jacobson, K. A., Gao, Z. G., and Liang, B. T. (2007) Neoceptors: Reengineering GPCRs to recognize tailored ligands. *Trends Pharmacol. Sci. 28*, 111–116.

(27) Gao, Z. G., Kim, S. K., Biadatti, T., Chen, W., Lee, K., Barak, D., Kim, S. G., Johnson, C. R., and Jacobson, K. A. (2002) Structural determinants of A_3 adenosine receptor activation: Nucleoside ligands at the agonist/antagonist boundary. *J. Med. Chem. 45*, 4471–4484.

(28) Zaveri, N., Jiang, F., Olsen, C., Polgar, W., and Toll, L. (2005) Small-molecule agonists and antagonists of the opioid receptor-like receptor (ORL1, NOP): ligand-based analysis of structural

factors influencing intrinsic activity at NOP. *AAPS J. 7*, E345−E352.

(29) Abbracchio, M. P., Burnstock, G., Boeynaems, J. M., Barnard, E. A., Boyer, J. L., Kennedy, C., Fumagalli, M., King, B. F., Gachet, C., Jacobson, K. A., and Weisman, G. A. (2006) International union of pharmacology LVIII. Update on the P2Y G protein-coupled nucleotide receptors: From molecular mechanisms and pathophysiology to therapy. *Pharmacol. Rev. 58*, 281–341.

(30) Abbracchio, M. P., and Burnstock, G. (1994) Purinoceptors: are there families of P2X and P2Y purinoceptors? *Pharmacol Ther. 64*, 445–475.

(31) Libert, F., Parmentier, M., Lefort, A., Dinsart, C., van Sande, J., Maenhaut, C., Simons, M. J., Dumont, J. E., and Vassart, G. (1989) Selective amplification and cloning of four new members of the G protein-coupled receptor family. *Science 244*, 569–572.

(32) IJzerman, A. P., van Galen, P. J. M., and Jacobson, K. A. (1992) Molecular modeling of adenosine receptors. I. The ligand binding site on the A_1 receptor. *Drug Des. Discovery 9*, 49–67.

(33) van Rhee, A. M., Fischer, B., van Galen, P. J. M., and Jacobson, K. A. (1995) Modelling the P_{2Y} purinoceptor using rhodopsin as template. *Drug Des. Discovery 13*, 133–154.

(34) Kim, J., Wess, J., van Rhee, A. M., Shöneberg, T., and Jacobson, K. A. (1995) Site-directed mutagenesis identifies residues involved in ligand recognition in the human A_{2a} adenosine receptor. *J. Biol. Chem. 270*, 13987–13997.

(35) Jiang, Q., Guo, D., Lee, B. X., van Rhee, A. M., Kim, Y. C., Nicholas, R. A., Schachter, J., Harden, T. K., and Jacobson, K. A. (1997) A mutational analysis of residues essential for ligand recognition at the human $P2Y_1$ receptor. *Mol. Pharmacol. 52*, 499–507.

(36) Moro, S., Hoffmann, C., and Jacobson, K. A. (1999) Role of the extracellular loops of G protein-coupled receptors in ligand recognition: A molecular modeling study of the human $P2Y_1$ receptor. *Biochemistry 38*, 3498–3507.

(37) Palczewski, K., Kumasaka, T., Hori, T., Behnke, C. A., Motoshima, H., Fox, B. A., Le Trong, I., Teller, D. C., Okada, T., Stenkamp, T. E., Yamamoto, M., and Miyano, M. (2000) Crystal structure of rhodopsin: A G protein-coupled receptor. *Science 289*, 739–745.

(38) Ivanov A., Barak, D., and Jacobson, K. A. (2009) Evaluation of homology modeling of GPCRs in light of the A_{2A} adenosine receptor crystallographic structure. *J. Med. Chem.*, in press, doi: 10.1021/jm801533x.

(39) Khan, M. M., Marr-Leisy, D., Rosenkranz, R., Hoffman, B. B., Verlander, M. S., Goodman, M., and Melmon, K. L. (1987) In vitro pharmacologic activity of congener derivatives and model conjugates of propranolol and practolol. *Biochem. Pharmacol. 36*, 2175–2182.

(40) Eigenmann, R., Burkard, W. P., Holck, M., Märki, H. P., Osterrieder, W., Goodman, M., and Melmon, K. L. (1989) In vitro pharmacological properties of a series of isoprenaline derivatives. *Arzneimittelforschung 39*, 842–847.

(41) Goodman, M., Verlander, M. S., Rosenkranz, R. P., Melmon, K. L., Jacobson, K. A., Reitz, A., Taulane, J. P., Avery, M. A., and Kaplan, N. O. (1983) Characterization of catecholamine-polypeptide conjugates. *Eur. Polym. J. 19*, 997–1004.

(42) Downey, J. M., Davis, A. M., and Cohen, M. V. (2007) Signaling pathways in ischemic preconditioning. *Heart Fail. Rev. 12*, 181–188.

(43) Eckle, T., Krahn, T., Grenz, A., Köhler, D., Mittelbronn, M., Ledent, C., Jacobson, M. A., Osswald, H., Thompson, L. F., Unertl, K., and Eltzschig, H. K. (2007) Cardioprotection by ecto-5′-nucleotidase (CD73) and A_{2B} adenosine receptors. *Circulation 15*, 1581–1590.

(44) Bar-Yehuda, S., Silverman, M. H., Kerns, W. D., Ochaion, A., Cohen, S., and Fishman, P. (2007) The anti-inflammatory effect of A_3 adenosine receptor agonists: a novel targeted therapy for rheumatoid arthritis. *Expert Opin. Investig. Drugs 16*, 1601–1613.

(45) Ge, Z. D., Peart, J. N., Kreckler, L. M., Wan, T. C., Jacobson, M. A., Gross, G. J., and Auchampach, J. A. (2006) Cl-IB-MECA [2-chloro-N6-(3-iodobenzyl)adenosine-5′-N methylcarboxamide] reduces ischemia/reperfusion injury in mice by activating the A_3 adenosine receptor. *J. Pharmacol. Exp. Ther. 319*, 1200–1210.

(46) Jacobson, K. A., Xie, R., Young, L., Chang, L., and Liang, B. T. (2000) A novel pharmacological approach to treating cardiac ischemia: binary conjugates of A_1 and A_3 adenosine receptor agonists. *J. Biol. Chem. 275*, 30272–30279.

(47) von Lubitz, D. K. J. E., Lin, R. C.-S., Popik, P., Carter, M. F., and Jacobson, K. A. (1994) Adenosine A_3 receptor stimulation and cerebral ischemia. *Eur. J. Pharmacol. 263*, 59–67.

(48) Madi, L., Ochaion, A., Rath-Wolfson, L., Bar-Yehuda, S., Erlanger, A., Ohana, G., Harish, A., Merimski, O., Barer, F., and Fishman, P. (2004) The A3 adenosine receptor is highly expressed in tumor vs. normal cells: Potential target for tumor growth inhibition. *Clin. Cancer Res. 10*, 4472–4479.

(49) Mitchell, C. H., Peterson-Yantorno, K., Carré, D. A., McGlinn, A. M., Coca-Prados, M., Stone, R. A., and Civan, M. M. (1999) A_3 adenosine receptors regulate Cl- channels of nonpigmented ciliary epithelial cells. *Am. J. Physiol. 276*, C659−C666.

(50) Daly, J. W., Padgett, W. L., Thompson, R. D., Kusachi, S., Bugni, W. J., and Olsson, R. A. (1986) Structure-activity relationships for N^6-substituted adenosines at a brain A_1-adenosine receptor with a comparison to an A_2-adenosine receptor regulating coronary blood flow. *Biochem. Pharmacol. 35*, 2467–2481.

(51) Klutz, A. M., Gao, Z. G., Lloyd, J., Shainberg, A., and Jacobson, K. A. (2008) Enhanced A_3 adenosine receptor selectivity of multivalent nucleoside-dendrimer conjugates. *J. Nanobiotechnol. 6*, 12.

(52) Jacobson, K. A., Kirk, K. L., Padgett, W. L., and Daly, J. W. (1985) Functionalized congeners of 1,3-dialkylxanthines: preparation of analogues with high affinity for adenosine receptors. *J. Med. Chem. 28*, 1334–1340.

(53) Shamim, M. T., Ukena, D., Padgett, W. L., Hong, O., and Daly, J. W. (1988) 8-Aryl- and 8 cycloalkyl-1, 3-dipropylxanthines: Further potent and selective antagonists for A_1-adenosine receptors. *J. Med. Chem. 31*, 613–617.

(54) Jacobson, K. A., Barrington, W. W., Pannell, L. K., Jarvis, M. F., Ji, X.-D., Williams, M., Hutchison, A. J., and Stiles, G. L. (1989) Agonist-derived molecular probes for A_2-adenosine receptors. *J. Mol. Recognition 2*, 170–178.

(55) Jarvis, M. F., Schulz, R., Hutchison, A. J., Do, U. H., Sills, M. A., and Williams, M. (1989) [^{3}H]CGS 21680, a selective A2 adenosine receptor agonist directly labels A2 receptors in rat brain. *J. Pharmacol. Exp. Ther 251*, 888–893.

(56) Barrington, W. W., Jacobson, K. A., Hutchison, A. J., Williams, M., and Stiles, G. L. (1989) Identification of the A_2 adenosine receptor binding subunit by photoaffinity crosslinking. *Proc. Natl. Acad. Sci. U.S.A. 86*, 6572–6576.

(57) Nikodijevic, O., Sarges, R., Daly, J. W., and Jacobson, K. A. (1991) Behavioral effects of A_1- and A_2-selective adenosine agonists and antagonists: Evidence for synergism and antagonism. *J. Pharm. Exp. Ther. 259*, 286–294.

(58) Jacobson, K. A., Gallo-Rodriguez, C., Melman, N., Fischer, B., Maillard, M., van Bergen, A., van Galen, P. J. M., and Karton, Y. (1993) Structure-activity relationships of 8-styrylxanthines as A_2-selective adenosine antagonists. *J. Med. Chem. 36*, 1333–1342.

(59) Kim, Y. C., Ji, X.-d., Melman, N., Linden, J., and Jacobson, K. A. (2000) Anilide derivatives of an 8-phenylxanthine carboxylic congener are highly potent and selective antagonists at human A_{2B} adenosine receptors. *J. Med. Chem. 43*, 1165–1172.

(60) Baraldi, P. G., Tabrizi, M. A., Fruttarolo, F., Romagnoli, R., and Preti, D. (2009) Recent improvements in the development of A_{2B} adenosine receptor agonists. *Purinergic Signalling 5*, 3–19.

(61) Siddiqi, S. M., Pearlstein, R. A., Sanders, L. H., and Jacobson, K. A. (1995) Comparative molecular field analysis of selective A_3 adenosine agonists. *Bioorg. Med. Chem. 3*, 1331–1343.

(62) Melman, A., Gao, Z. G., Kumar, D., Wan, T. C., Gizewski, E., Auchampach, J. A., and Jacobson, K. A. (2008) Design of (N)-methanocarba adenosine 5′-uronamides as species-independent A_3 receptor-selective agonists. *Bioorg. Med. Chem. Lett. 18*, 2813–2819.

(63) Li, A.-H., Chang, L., Ji, X.-d., Melman, N., and Jacobson, K. A. (1999) Functionalized congeners of 1,4-dihydropyridines as antagonist molecular probes for A_3 adenosine receptors. *Bioconjugate Chem. 10*, 667–677.

(64) Olsson, R. A., Davis, C. J., Khouri, E. M., and Patterson, R. E. (1976) Evidence for an adenosine receptor on the surface of dog coronary myocytes. *Circ. Res. 39*, 93–98.

(65) Jacobson, K. A., Kirk, K. L., Padgett, W., and Daly, J. W. (1985) Probing the adenosine receptor with adenosine and xanthine biotin conjugates. *FEBS Lett. 84*, 30–35.

(66) Wilchek, M., Bayer, E. A., and Livnah, O. (2006) Essentials of biorecognition: the (strept)avidin-biotin system as a model for protein-protein and protein-ligand interaction. *Immunol. Lett. 103*, 27–32.

(67) Jacobson, K. A. Probing adenosine receptors using biotinylated purine conjugates, In *Methods in Enzymology* (Wilchek, M., Bayer, E., Eds.) pp 668−671, Vol 184; 1990.

(68) Murugesan, N., Gu, Z., Fadnis, L., Tellew, J., Baska, R., Yang, Y., Beyer, S., Monshizadegan, H., Dickinson, K., Valentine, M., Humphreys, W., Lan, S., Ewing, W., Carlson, K., Kowala, M., Zahler, R., and Macor, J. (2005) Dual angiotensin II and endothelin A receptor antagonists: Synthesis of 2′-substituted *N*-3-isoxazolyl biphenylsulfonamides with improved potency and pharmacokinetics. *J. Med. Chem. 48*, 171–179.

(69) Ferre, S., Ciruela, F., Borycz, J., Solinas, M., Quarta, D., Antoniou, K., Quiroz, C., Justinova, Z., Lluis, C., Franco, R., and Goldberg, S. R. (2008) Adenosine A_1-A_{2A} receptor heteromers: new targets for caffeine in the brain. *Front Biosci. 13*, 2391–2399.

(70) Berque-Bestel, I., Lezoualc'h, F., and Jockers, R. (2008) Bivalent ligands as specific pharmacological tools for g protein-coupled receptor dimers. *Curr. Drug Discovery Technol. 5*, 312–318.

(71) Jacobson, K. A., Lipkowski, A. W., Moody, T. W., Padgett, W., Pijl, E., Kirk, K. L., and Daly, J. W. (1987) Binary drugs: conjugates of purines and a peptide that bind to both adenosine and substance P receptors. *J. Med. Chem. 30*, 1529–1532.

(72) Jacobson, K. A., Kirk, K. L., Daly, J. W., Lipkowski, A. W., Rice, K. C., and Jacobson, A. A. (1987) Preparation of binary drugs derived from a functionalized congener of 1,3 dipropyl-8-phenylxanthine and 6-[p-(carboxymethyl)phenyl]adenosine as adenosine receptor agonists and antagonists. *U. S. Pat. Appl.* (1987), US 30526 A0 19871015. CAN 110:108209.

(73) Jacobson, K. A., Xie, R., Young, L., Chang, L., and Liang, B. T. (2000) A novel pharmacological approach to treating cardiac ischemia: binary conjugates of A_1 and A_3 adenosine receptor agonists. *J. Biol. Chem. 275*, 30272–30279.

(74) Xu, Z., Jang, Y., Mueller, R. A., and Norfleet, E. A. (2006) IB-MECA and cardioprotection. *Cardiovasc. Drug Rev. 24*, 227–238.

(75) Karellas, P., McNaughton, M., Baker, S. P., and Scammells, P. J. (2008) Synthesis of bivalent beta2-adrenergic and adenosine A_1 receptor ligands. *J. Med. Chem. 51*, 6128–637.

(76) Jacobson, K. A., Barone, S., Kammula, U., and Stiles, G. L. (1989) Electrophilic derivatives of purines as irreversible inhibitors of A_1-adenosine receptors. *J. Med. Chem. 32*, 1043–1051.

(77) Stiles, G. L., and Jacobson, K. A. (1988) High affinity acylating antagonists for the A_1 adenosine receptor: identification of binding subunit. *Mol. Pharmacol. 34*, 724–728.

(78) Stiles, G. L., and Jacobson, K. A. (1987) A new high affinity, iodinated adenosine receptor antagonist as a radioligand/photoaffinity crosslinking probe. *Mol. Pharmacol. 32*, 184–188.

(79) Scammells, P. J., Baker, S. P., Belardinelli, L., and Olsson, R. A. (1994) Substituted 1,3-dipropylxanthines as irreversible antagonists of A_1 adenosine receptors. *J. Med. Chem. 37*, 2704–2012.

(80) Shryock, J. C., Snowdy, S., Baraldi, P. G., Cacciari, B., Spalluto, G., Monopoli, A., Ongini, E., Baker, S. P., and Belardinelli, L. (1998) A_{2A}-adenosine receptor reserve for coronary vasodilation. *Circulation 98*, 711–718.

(81) Niiya, K., Jacobson, K. A., Silvia, S. K., and Olsson, R. A. (1993) Covalent binding of a selective agonist irreversibly activates guinea pig coronary artery A_2 adenosine receptors. *Naunyn-Schmeideberg's Arch. Pharamacol. 347*, 521–526.

(82) Jacobson, K. A., Fischer, B., and Ji, X.-D. (1995) A "cleavable trifunctional" approach to receptor affinity labeling: regeneration of binding to A_1-adenosine receptors. *Bioconjugate Chem. 6*, 255–263.

(83) Jacobson, K. A., Olah, M. E., and Stiles, G. L. (1992) Trifunctional ligands: A radioiodinated high affinity acylating antagonist for the A_1 adenosine receptor. *Pharmacol. Comm. 1*, 145–154.

(84) Shai, Y., Kirk, K. L., Channing, M. A., Dunn, B. B., Lesniak, M. A., Eastman, R. C., Finn, R. D., Roth, J., and Jacobson, K. A. (1989) ^{18}F-labeled insulin: a prosthetic group methodology for incorporation of a positron emitter into peptides and proteins. *Biochemistry 28*, 4801–4806.

(85) de Bruin, B., Kuhnast, B., Hinnen, F., Yaouancq, L., Amessou, M., Johannes, L., Samson, A., Boisgard, R., Tavitian, B., and Dollé, F. (2005) 1-[3-(2-[^{18}F]fluoropyridin-3-yloxy)propyl]pyrrole-2,5-dione: design, synthesis, and radiosynthesis of a new [^{18}F]fluoropyridine-based maleimide reagent for the labeling of peptides and proteins. *Bioconjugate Chem. 6*, 406–420.

(86) Olah, M. E., Jacobson, K. A., and Stiles, G. L. (1991) Purification and characterization of bovine cerebral cortex A_1 adenosine receptor. *Arch. Biochem. Biophys. 283*, 440–446.

(87) Mahan, L. C., McVittie, L. D., Smyk-Randall, E. M., Nakata, H., Jr, Gerfen, C. R., and Sibley, D. R. (1991) Cloning and expression of an A_1 adenosine receptor from rat brain. *Mol. Pharmacol. 40*, 1–7.

(88) Weiss, H. M., and Grisshammer, R. (2002) Purification and characterization of the human adenosine A_{2A} receptor functionally expressed in Escherichia coli. *Eur. J. Biochem. 269*, 82–92.

(89) Munshi, R., and Linden, J. (1989) Co-purification of A1 adenosine receptors and guanine nucleotide-binding proteins from bovine brain. *J. Biol. Chem. 264*, 14853–14859.

(90) Kuder, K., and Kieć-Kononowicz, K. (2008) Fluorescent GPCR ligands as new tools in pharmacology. *Curr. Med. Chem. 15*, 2132–2143.

(91) Wang, Y., Gu, Q., Mao, F., Haugland, R. P., and Cynader, M. S. (1994) Activity-dependent expression and distribution of M1 muscarinic ACh receptors in visual cortex neuronal cultures. *J. Neurosci. 14*, 4147–4158.

(92) Madsen, B. W., Beglan, C. L., and Spivak, C. E. (2000) Fluorescein-labeled naloxone binding to mu opioid receptors on live Chinese hamster ovary cells using confocal fluorescent microscopy. *J. Neurosci. Methods 97*, 123–131.

(93) Tota, M. R., Daniel, S., Sirotina, A., Mazina, K. E., Fong, T. M., Longmore, J., and Strader, C. D. (1994) Characterization of a fluorescent substance P analog. *Biochemistry 33*, 13079–13086.

(94) Sugawara, T., Hirasawa, A., Hashimoto, K., and Tsujimoto, G. (2002) Differences in the subcellular localization of alpha1-adrenoceptor subtypes can affect the subtype selectivity of drugs in a study with the fluorescent ligand BODIPY FL-prazosin. *Life Sci. 70*, 2113–2124.

(95) McCabe, R. T., Skolnick, P., and Jacobson, K. A. (1992) FITC-APEC: A fluorescent ligand for A_2-adenosine receptors. *J. Fluoresc. 2*, 217–223.

(96) Brand, F., Klutz, A., Jacobson, K. A., Fredholm, B. B., and Schulte, G. (2008) Adenosine A_{2A} receptor dynamics studied with the novel fluorescent agonist Alexa488-APEC. *Eur. J. Pharmacol. 590*, 36–42.

(97) Briddon, S. J., and Hill, S. J. (2007) Pharmacology under the microscope: the use of fluorescence correlation spectroscopy to determine the properties of ligand-receptor complexes. *Trends Pharmacol. Sci. 28*, 637–645.

(98) Cordeaux, Y., Briddon, S. J., Alexander, S. P., Kellam, B., and Hill, S. J. (2008) Agonist-occupied A_3 adenosine receptors exist within heterogeneous complexes in membrane microdomains of individual living cells. *FASEB J. 22*, 850–860.

(99) Macchia, M., Bertini, S., Di Bussolo, V., Manera, C., Martini, C., Minutolo, F., Mori, C., Saccomanni, G., Tuscano, D., and Ferrarini, P. L. (2002) 4-[6-(Dansylamino)hexylamino]-7-methyl-2-phenyl-1,8-naphthyridine as a new potential fluorescent probe for studying A_1-adenosine receptor. *Farmaco 57*, 783–786.

(100) Ilas, J., Pecar, S., Hockemeyer, J., Euler, H., Kirfel, A., and Müller, C. E. (2005) Development of spin-labeled probes for adenosine receptors. *J. Med. Chem. 48*, 2108–2014.

(101) Chollet, A., and Turcatti, G. (1999) Biophysical approaches to G protein-coupled receptors: structure, function and dynamics. *J. Comput.-Aided Mol. Des. 13*, 209–219.

(102) Peng, J. W. (2001) Cross-correlated ^{19}F relaxation measurements for the study of fluorinated ligand-receptor interactions. *J. Magn. Reson. 153*, 32–47.

(103) The numbering system for P2Y subtypes is currently discontinuous; i.e., $P2Y_{1-14}$ receptors have been defined, but six of the intermediate-numbered cloned receptor sequences (e. g., $P2y_3$, $P2y_5$, $P2y_{7-10}$) do not correspond to distinct, functional mammalian nucleotide receptors [see ref 29].

(104) Hechler, B., Nonne, C., Roh, E. J., Cattaneo, M., Cazenave, J. P., Lanza, F., Jacobson, K. A., and Gachet, C. (2006) MRS2500 [2-iodo-N^6-methyl-(N)-methanocarba-2′-deoxyadenosine-3′,5′-bisphosphate], a potent, selective and stable antagonist of the $P2Y_1$ receptor, with strong antithrombotic activity in mice. *J. Pharm. Exp. Therap. 316*, 556–563.

(105) Koizumi, S., Shigemoto-Mogam, Y., Nasu-Tada, K., Shinozaki, Y., Ohsawa, K., Tsuda, M., Joshi, B. V., Jacobson, K. A., Kohsaka, S., and Inoue, K. (2007) UDP acting at $P2Y_6$ receptors is a novel mediator of microglial phagocytosis. *Nature 446*, 1091–1095.

(106) Yerxa, B. R., Sabater, J. R., Davis, C. W., Stutts, M. J., Lang-Furr, M., Picher, M., Jones, A. C., Cowlen, M., Dougherty, R., Boyer, J., Abraham, W. M., and Boucher, R. C. (2002) Pharmacology of INS37217 [P(1)-(uridine 5′)-P(4)- (2′-deoxycytidine 5′)tetraphosphate, tetrasodium salt], a next-generation $P2Y_2$ receptor agonist for the treatment of cystic fibrosis. *J. Pharmacol. Exp. Ther. 302*, 871–880.

(107) Solini, A., Chiozzi, P., Morelli, A., Passaro, A., Fellin, R., and Di Virgilio, F. (2003) Defective P2Y purinergic receptor function: A possible novel mechanism for impaired glucose transport. *J. Cell Physiol. 197*, 435–444.

(108) Fischer, B., Boyer, J. L., Hoyle, C. H. V., Ziganshin, A. U., Brizzolara, A. L., Knight, G. E., Zimmet, J., Burnstock, G., Harden, T. K., and Jacobson, K. A. (1993) Identification of potent, selective P_{2Y}-purinoceptor agonists: Structure activity relationships for 2-thioether derivatives of adenosine-5′-triphosphate. *J. Med. Chem. 36*, 3937–3946.

(109) Burnstock, G., Cusack, N. J., Hills, J. M., MacKenzie, I., and Meghji, P. (1983) Studies on the stereoselectivity of the P2-purinoceptor. *Br. J. Pharmacol. 79*, 907–913.

(110) Halbfinger, E., Major, D. T., Ritzmann, M., Ubl, J., Reiser, G., Boyer, J. L., Harden, K. T., and Fischer, B. (1999) Molecular recognition of modified adenine nucleotides by the $P2Y_1$-receptor. 1. A synthetic, biochemical, and NMR approach. *J. Med. Chem. 42*, 5325–5337.

(111) Zündorf, G., Schäfer, R., Vöhringer, C., Halbfinger, E., Fischer, B., and Reiser, G. (2001) Novel modified adenosine 5′-triphosphate analogues pharmacologically characterized in human embryonic kidney 293 cells highly expressing rat brain $P2Y_1$ receptor: Biotinylated analogue potentially suitable for specific $P2Y_1$ receptor isolation. *Biochem. Pharmacol. 61*, 1259–1269.

(112) de Castro, S., Costanzi, S., and Jacobson, K. A. (2008) Novel MRS2500 derivatives as $P2Y_1$ Receptor Antagonists, 31st National Medicinal Chemistry Symposium, Pittsburgh, PA.

(113) Das, A., Zhou, Y., Carter, R. L., Harden, T. K., and Jacobson, K. A. Enhanced potency of nucleotide-dendrimer conjugates as agonists of the $P2Y_{14}$ receptor: Multivalent effect in G protein-coupled receptor recognition, MEDI Abstract, American Chemical Society National Meeting, Washington, DC, Aug. 16−20, 2009.

(114) Daniels, D. J., Kulkarni, A., Xie, Z., Bhushan, R. G., and Portoghese, P. S. (2005) A bivalent ligand (KDAN-18) containing δ-antagonist and κ-agonist pharmacophores bridges $\delta 2$ and $\kappa 1$ opioid receptor phenotypes. *J. Med. Chem. 48*, 1713–1716.

(115) Zheng, Y., Akgün, E., Harikumar, K. G., Hopson, J., Powers, M. D., Lunzer, M. M., Miller, L. J., and Portoghese, P. S. (2009) Induced association of mu opioid (MOP) and type 2 cholecystokinin (CCK(2)) receptors by novel bivalent ligands. *J. Med. Chem. 52*, 247–258.

(116) Bradbury, B. J., Baumgold, J., and Jacobson, K. A. (1990) Functionalized congener approach for the design of novel muscarinic agents. Synthesis and pharmacological evaluation of N-methyl-N-[4-(1-pyrrolidinyl)-2-butynyl amides. *J. Med. Chem. 33*, 741–748.

(117) Karton, Y., Bradbury, B. J., Baumgold, J., Paek, R., and Jacobson, K. A. (1991) Functionalized congener approach to muscarinic antagonists: Analogues of pirenzepine. *J. Med. Chem. 34*, 2133–2145.

(118) Karton, Y., Baumgold, J., Handen, J. S., and Jacobson, K. A. (1992) Molecular probes for muscarinic receptors: Derivatives of the M_1-antagonist telenzepine. *Bioconjugate Chem. 3*, 234–240.

(119) Lee, P. H., Miller, S. C., van Staden, C., and Cromwell, E. F. (2008) Development of a homogeneous high-throughput live-cell G-protein-coupled receptor binding assay. *J. Biomolecular Screening 13*, 748–754.

(120) Birdsall, N. Single molecules of GPCRs, Abstract in *G Protein-Coupled Receptors in Drug Discovery*, 2008.

(121) Tahtaoui, C., Parrot, I., Klotz, P., Guillier, F., Galzi, J. L., Hibert, M., and Ilien, B. (2004) Fluorescent pirenzepine derivatives as potential bitopic ligands of the human M1 muscarinic receptor. *J. Med. Chem. 47*, 4300–4315.

(122) Xie, Z., Bhushan, R. G., Daniels, D. J., and Portoghese, P. S. (2005) Interaction of bivalent ligand KDN21 with heterodimeric delta-kappa opioid receptors in human embryonic kidney 293 cells. *Mol. Pharmacol. 68*, 1079–1086.

(123) Messer, W.S., Jr. (2004) Bivalent ligands for G protein-coupled receptors. *Curr. Pharm. Des. 10*, 2015–2020.

(124) Liu, Z., Zhang, J., and Zhang, A. (2009) Design of multivalent ligand targeting G protein-coupled receptors. *Curr. Pharm. Des. 15*, 682–718.

(125) Decker, M., and Lehmann, J. (2007) Agonistic and antagonistic bivalent ligands for serotonin and dopamine receptors including their transporters. *Curr. Top. Med. Chem. 7*, 347–353.

(126) Christopoulos, A., Grant, M. K., Ayoubzadeh, N., Kim, O. N., Sauerberg, P., Jeppesen, L., and El-Fakahany, E. E. (2001) Synthesis and pharmacological evaluation of dimeric muscarinic acetylcholine receptor agonists. *J. Pharmacol. Exp. Ther. 298*, 1260–1268.

(127) Descamps-Francois, C., Yous, S., Chavatte, P., Audinot, V., Bonnaud, A., Boutin, J. A., Delagrange, P., Bennejean, C., Renard, P., and Lesieur, D. (2003) Design and synthesis of naphthalenic dimers as selective MT_1 melatoninergic ligands. *J. Med. Chem. 46*, 1127–1129.

(128) Howard, H., Lowe, J., Seeger, T., Seymour, P., Zorn, S., Maloney, P., Ewing, F., Newman, M., Schmidt, A., Furman, J., Robinson, G., Jackson, E., Johnson, C., and Morrone, J. (1996) 3-Benzisothiazolylpiperazine derivatives as potential atypical antipsychotic agents. *J. Med. Chem. 39*, 143–148.

(129) Maynard, G., Bratton, L., Kane, J., Burkholder, T., Santiago, B., Stewart, K., Kudlacz, E., Shatzer, S., Knippenberg, R., Farrell, A., and Logan, D. (1997) Synthesis and SAR of 4-(1H-benzimidazole-2-carbonyl)piperidines with dual histamine H1/tachykinin NK1 receptor antagonist activity. *Bioorg. Med. Chem. Lett. 7*, 2819–2824.

(130) Zheng, J., Hashimoto, A., Putnam, M., Miller, K., and Koh, J. T. (2008) Development of a thyroid hormone receptor targeting conjugate. *Bioconjugate Chem. 19*, 1227–1234.

(131) Kosower, E. M., Miyadera, T., and Kosower, N. S. (1971) Receptor site labeling through functional groups. Barbital and amphetamine derivatives. *J. Med. Chem. 14*, 873–878.

(132) Chen, W., Ravi, R. G., Kertesy, S. B., Dubyak, G. R., and Jacobson, K. A. (2002) Functionalized congeners of tyrosine-based $P2X_7$ receptor antagonists: Probing multiple sites for linking and dimerization. *Bioconjugate Chem. 13*, 1100–1111.

(133) Gandia, J., Galino, J., Amaral, O. B., Soriano, A., Lluís, C., Franco, R., and Ciruela, F. (2008) Detection of higher-order G protein-coupled receptor oligomers by a combined BRET-BiFC technique. *FEBS Lett. 582*, 2979–2984.

(134) Kim, Y., Hechler, B., Klutz, A., Gachet, C., and Jacobson, K. A. (2008) Toward multivalent signaling across G protein-coupled receptors from poly(amidoamine) dendrimers. *Bioconjugate Chem. 19*, 406–411.

(135) Kim, Y., Klutz, A. M., Hechler, B., Gao, Z. G., Gachet, C., and Jacobson, K. A. (2009) Application of the functionalized congener approach to dendrimer-based signaling agents acting through A_{2A} adenosine receptors. *Purinergic Signalling 5*, 39–50.

(136) Ivanov, A. A., and Jacobson, K. A. (2008) Molecular modeling of a PAMAM-CGS21680 dendrimer bound to an A_{2A} adenosine receptor homodimer. *Bioorg. Med. Chem. Lett. 18*, 4312–4315.

(137) Jacobson, K. A., Zimmet, J., Schulick, R., Barone, S., Daly, J. W., and Kirk, K. L. (1987) Adenosine analogs with covalently attached lipids have enhanced potency at A_1-adenosine receptors. *FEBS Lett. 225*, 97–102.

(138) Jacobson, K. A., Bradbury, B. J., and Baumgold, J. (1990) A functionalized congener approach to muscarinic ligands, in Novel Treatments and Models for Alzheimer's Disease, Meyer, E., Simpkins, J., Yamamoto, J., Eds.; Plenum Press: New York, pp 1−10.

BC9000596

COMMUNICATIONS

"Zipper" Molecular Beacons: A Generalized Strategy to Optimize the Performance of Activatable Protease Probes

Juan Chen, Tracy W. B. Liu,† Pui-Chi Lo, Brian C. Wilson, and Gang Zheng*

Department of Medical Biophysics, Ontario Cancer Institute, University of Toronto, Toronto, Ontario M5G 1L7, Canada.
Received May 7, 2009; Revised Manuscript Received August 31, 2009

We report the proof-of-principle concept for zipper molecular beacons (ZMB) comprising an asymmetrical polyarginine/polyglutamate electrostatic "zipper" hairpin-linked fluorophore−quencher pair. The objective is to balance maximal quenching efficiency and optimal two-step activation (protease cleavage/zipper dissociation), while enhancing target cell uptake. This strategy also eliminates the peptide sequence dependence of conventional protease beacons. This ZMB concept is a generalizable approach to improve the functionality of a wide range of diagnostic/therapeutic probes through a simple switching of substrate sequences.

INTRODUCTION

Optical molecular imaging has become a powerful tool for biochemical and cellular studies (*1*). With the continual development of peptide-based "smart probes", the *in vivo* optical imaging of specific molecular targets, biological pathways, and disease progression is gaining momentum. Many of the initial fluorescent probes had limited image contrast due to poor target specificity. Hence, activatable optical probes (*2*−*9*) that require enzyme-triggered separation of an inhibitory moiety from an active partner were developed. More recently, we and others have extended this concept to photodynamic molecular beacons (*10*−*14*) for increased specificity in photodynamic therapy. These activatable protease probes comprise an enzyme-specific linker with a fluorophore (or photosensitizer) and quencher conjugated at its opposite ends. The probes are inactive until the linker is cleaved by a target-specific enzyme. Although such activatable imaging and therapeutic beacons have shown great promise, several challenges have arisen.

First, the quenching depends on the natural peptide folding of the enzyme-specific linker. Thus, the probes are limited to sequences with natural conformations that bring the quencher and active moiety in close proximity in order for effective silencing to occur. In other words, different peptide sequences have different background fluorescence. A second concern is most protease-specific probes are activated extracellularly, so that the activated probes may diffuse to nontarget cells/tissues before target cell uptake occurs. Third, probes that target soluble proteases may be activated at sites distant from the target due to leakage of the enzyme from the target cells into the general circulation (*15*−*17*), thereby contributing to background signal and reduced contrast. Lastly, the probes use nonspecific/passive delivery to the target cells/tissues, which is suboptimal.

Recently, the concept of activatable cell-penetrating peptides (ACPP) was introduced to address the passive delivery of first-generation activatable optical probes. These are based on the electrostatic formation of a polycation/polyanion "zipper", whose linker can be selectively cleaved by a protease to locally unleash the delivery function of cell-penetrating peptides (CPP) (*15*−*17*). The underlying mechanism is functionally reminiscent of molecular beacons themselves that require enzyme-triggered separation of an inhibitory moiety from an active partner: here, the separation is between a polyanionic peptide (polyanion) and a polycationic peptide (polycation). Inclusion of a quencher may improve imaging contrast by suppressing the active partner before cleavage of the linker (*15*). The concept is illustrated in Scheme 1.

MATERIALS AND METHODS

All amino acid derivatives and the Sieber amide resin were purchased from Novabiochem (San Diego, CA, USA). The black hole quencher3 carboxylic acid succinimdyl ester (BHQ3-NHS) was obtained from Biosearch Technologies (Novato CA, USA). The pyropheophorbide carboxylic acid succinimidyl ester (Pyro-NHS) was prepared according to a published procedure (*18*). Other chemicals were obtained from Aldrich (Oakville, ON) and were used as received. Reverse-phase HPLC was preformed on a XBridgeTM-C8 column (2.5 μm, 4.6 × 150 mm) using a Waters 2695 controller with a 2996 photodiode array detector and a Waters ZQTM mass detector (Waters Limited, Mississauga, ON).

Synthesis of ZMB. The peptide sequence Fmoc-[D-Glu(Ot-Bu)]$_x$-protected activatable peptide linker-[D-Arg(Pbf)]$_y$Lys(Mtt) was synthesized on the Sieber resin according to a solid-phase peptide synthesis (SPPS) protocol using a PS3 peptide synthesizer (Protein Technologies) with commercially available *N*-α-Fmoc-protected amino acids. After the last Fmoc group had been removed from the peptide resin with 20% piperidine in *N*,*N*-dimethylformamide (DMF), the resin was washed with DMF. BHQ3-NHS was then coupled to the N-terminal of the peptide in DMF with *N*,*N*-diisopropylethylamine (DIPEA) (BHQ3/peptide = 3:1 molar ratio). The mixtures were shaken under argon overnight at room temperature. The acquired dark-blue resin was washed with DMF and then treated with 95%

* Correspondence to G. Zheng, TMDT 5-363, 101 College St, Toronto, ON M5G 1L7, Canada. Fax: 416-581-7666, gang.zheng@uhnres.utoronto.ca.
† First two authors contributed equally to this work.

10.1021/bc900207k CCC: $40.75 © 2009 American Chemical Society
Published on Web 09/14/2009

Scheme 1. Universal Zipper Molecular Beacon Design[a]

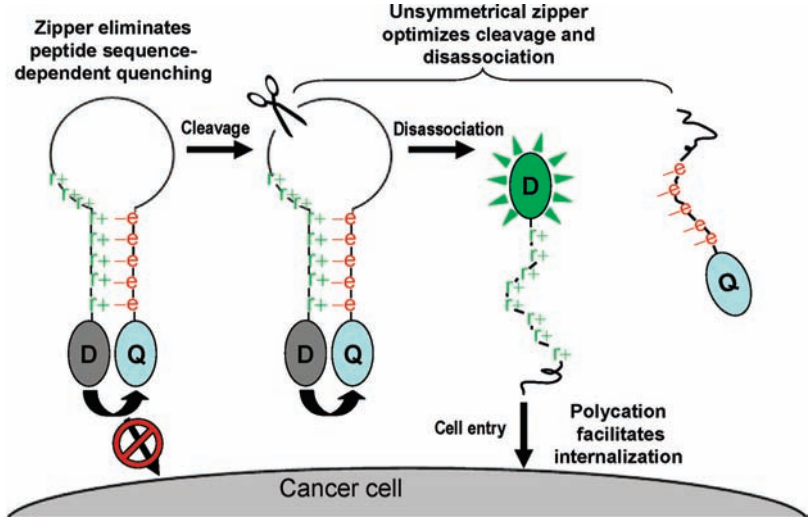

[a] The "zipper" is composed of a pair of polycation and polyanion arms holding the dye (D) and quencher (Q) in close proximity due to electrostatic attraction. This results in silenced dye activity independent of peptide linker variations. Upon specific enzymatic cleavage of the linker, the dye and quencher dissociate, resulting in dye photoactivity and unleashing the polycation, which increases cellular uptake.

trifluoroacetic acid (TFA) with 5% triisopropylsilane (Tis) to remove the protected groups on the peptide and cleave the peptide from the resin. After removing the solid support by filtration, the filtrates were concentrated and precipitated by diethyl ether to give the BHQ3-conjugated peptide, BHQ3-$_D$(e)x-activatable peptide linker-$_D$(r)yK(NH_2). The peptide was then reacted with Pyro-NHS in anhydrous DMSO with 1% DIPEA at ambient temperature for 6 h. The reaction mixture were then purified by HPLC to give pure BHQ3-$_D$(e)x-activatable peptide linker (r)yK(Pyro), which were characterized using UV−vis and ESI mass spectroscopy.

Synthesis of Controls. The synthesis of nonquencher control, Pyro-GPLGLARK (PP), and nonzipper control, Pyro-GPLGLARK-(BHQ3) (nonzip1), were reported previously (*12*). Nonzip2, Pyro-RPLALWRSK(BHQ3), was synthesized using the similar procedure as nonzip1. FITC-labeled polycation control, Fmoc-$_D$(r)x-K(FITC), was synthesized as follows: Fmoc-[D-Arg-(Pbf)]x-K(Mtt) was synthesized on the Sieber resin. The resin was then treated with 95% TFA with 5% Tis to remove the protected groups on the sequence and cleave the sequence from the resin. The acquired Fmoc-$_D$(r)x-K(ε-NH_2) was then reacted with fluorescein isothiocyanate (FITC) in anhydrous DMSO with 1% DIPEA at ambient temperature for 6 h. The reaction mixture were then purified by HPLC to give pure Fmoc-$_D$(r)x-K(FITC). Nonquencher ACPP control, Fmoc-$_D$(e)$_5$GPLGLA$_D$(r)$_8$K(Pyro) (Pyro-ACPP), was synthesized using a similar protocol to Fmoc-$_D$(r)x-K(FITC). The differences are in (1) replacing the peptide sequence and (2) conjugating Pyro-NHS on the C-terminal rather than FITC.

pH Dissociation Assay of ZMB. 0.5 μM of ZMB samples were prepared in adjusted PBS solutions with different pH (pH = 2, 3, 4, 5, 6, 7, 8, 9, 10, 11, 13). Their fluorescence emission was measured on a HORIBA FluoroMax-4 spectrofluorometer (excitation 650 nm, emission 675 ± 5 nm). Using the sample of pH = 7 as reference, the fluorescence increase in different pH conditions was calculated to evaluate the structure stability of ZMB.

Activation Studies. ZMB or nonzipper probes (1 nmol) were first dissolved in 2.5 μL of DMSO and 0.5 μL of Tween 80. The solution was diluted with 1 mL of phosphate-buffered saline (PBS) or minimum essential medium (MEM) Eagle cell media, and then incubated with 10 μL of human Proteinase K (2 μg) (ZMB/Proteinase K ∼ 50:1 molar ratio). The activation was monitored by the fluorescence increase, which was calculated by normalizing the sample's fluorescence emission on real-time to its initial fluorescence. $FI_{protease}$ and FI_{TFA} were used to define the fluorescence increase at 2 h post-Proteinase K cleavage and following fluorescence increase after adding 1% TFA to the cleavage solution.

Evaluation of Polycation Delivery Capability. MT1 cells were grown to 60% confluence in Nunc Lab-TekII-CC2 chambered slides. Eagle's minimum essential medium (MEM) medium with 10% fetal bovine serum containing 5 μM of Fmoc-$_D$(rrrrr)-K(FITC) and Fmoc-$_D$(rrrrrrr)-K(FITC) were added and incubated for 10 min at 37 °C. The cells were washed 3 times with PBS. The chamber slides were then imaged on an Olympus FluoView 1000 laser scanning confocal microscope equipped with a 488 nm argon laser.

Evaluation of Cell Uptake of ZMB before and after Activation. (1) Preparing nonactivation sample: Fresh MEM medium with 10% fetal bovine serum (without proteases) was used to prepare a 10 μM concentration of the probes. (2) Preparing postactivation samples: MT1 cells were grown in Nunc Lab-TekII-CC2 chambered slides for 3 days. A 10 μM concentration of the probes were prepared in this 3-day-old cell incubation medium (contains secreted proteases including MMP7) and incubated until the peptide linkers of probes were cleaved (monitored by HPLC). (3) Confocal study: 200 μL of these samples were incubated with MT1 cells in the chamber slides for 30 min. The chamber slides were washed with PBS 3 times and then imaged by a confocal microscope equipped with a 633 nm He−Ne laser.

RESULTS AND DISCUSSION

To test this concept, we designed a ZMB with four functional modules: (1) a protease cleavable peptide as the linker, (2) a polycation and a polyanion attached to each end of the linker, forming a "zipper" structure via electrostatic attraction, (3) pyropheophorbide as a fluorescent dye (D), and (4) a Black Hole Quencher 3 as a quencher (Q), conjugated to the end of the polycation and polyanion, respectively. As shown in Scheme 1, the zipper provides several potential advantages: (1) the formation of the polycation/polyanion "zipper" through electrostatic attraction improves the silencing of the beacon by bringing D and Q into closer contact, (2) a "hairpin" conformation of the substrate sequence occurs as a result of the zipper,

Table 1. Abbreviations of Protease Probes

probe	sequence
nonzip1	Pyro-GPLGLARK(BHQ3)
nonzip2	Pyro-RPLALWRSK(BHQ3)
zipXe	BHQ3-$_D$(e)$_X$GPLGLA$_D$(r)$_X$K(Pyro)
zip8e2	BHQ3-$_D$(e)$_8$ RPLALWRS$_D$(r)$_8$K(Pyro)
zip5e8r	BHQ3-$_D$(e)$_5$ GPLGLA$_D$(r)$_8$K(Pyro)
PP	Pyro-GPLGLARK

improving the cleavage rate of the enzyme-specific linker, (3) the polyanionic arm of the zipper prevents the probe from entering cells, by blocking the cell-penetrating function of the polycation, (4) the polycationic arm enhances cellular uptake of the dye after linker cleavage, and (5) quenching is no longer dependent upon the natural folding of the peptide linker, since the zipper is solely responsible for the "dormant" state. In the presence of a target protease, the peptide linker is first specifically cleaved; the Q-attached polyanion then dissociates from the D-attached polycation, becoming photoactive, and unleashes the polycation, which enhances the delivery of the activated dye locally into the target cells.

In order to examine the effect of the zipper conformation on the photophysical properties, two matrix metalloproteinase 7 (MMP7)-specific peptide sequences, GPLGLARK (*19*) and RPLALWRSK (*20*), were used to synthesize two ZMBs, zip8e and zip8e2, and their corresponding nonzipper controls, nonzip1 and nonzip2 (see Table 1). Eight consecutive D-arginines, $_D$(rrrrrrrr), and D-glutamates, $_D$(eeeeeeee), were selected as the polycation and polyanion, respectively, as these can assemble into a stable zipper hairpin structure (*15*). D-Amino acids were used for the zipper arms, since they are stable against proteolysis (*21*). Also, D-amino acid-based polycationic peptides present similar cell penetrating capabilities to the natural L-amino acids (*22*).

The fluorescence emission of these probes was evaluated, normalized to that of the nonquencher probe, PP. As shown in Figure 1C, a marked difference in the fluorescence of nonzip1 and nonzip2 was observed (<2% and 27.2%, respectively). There was only a slight difference in the length and solubility of the peptide linkers in nonzip1 and nonzip2, indicating that the fluorescence quenching efficiency in the nonzipper probes does depend on the natural folding of the linkers (Supporting Information Figure S1 and Table S1, HPLC retention time). However, with the inclusion of the zipper, the quenching efficiencies were enhanced, with the fluorescence of zip8e and zip8e2 being reduced to 0.4% and 0.9%, respectively. This comparable quenching in zip8e and zip8e2 indicates that the quenching dependence on the natural folding of the peptide linker has been eliminated. Moreover, in aqueous solution, the specific absorption peaks of Pyro (414 nm) and BHQ3 (676 nm) in zip8e were shifted relative to their corresponding nonzipper probes (nonzip1) (Figure 1A). By adjusting the solution to a low pH condition (pH = 2) to neutralize the polyanion sequence and unfold the peptide sequence, the fluorescence of zip8e was increased 4-fold and its specific absorption was restored (Figure 1B), while nonzip1 did not show any obvious changes. Therefore, the enhanced quenching efficiency in the ZMB is presumably the result of both the improved fluorescence resonance energy transfer (FRET) effect and the ground-state complex quenching (contact quenching) caused by annealing D and Q through the electrostatic attraction of the zipper arms.

We next verified the electrostatic nature of the zipper conformation using a pH dissociation assay. As shown in Figure 1D, the fluorescence values of both zip8e and nonzip1 were very stable at pH ~ 5−9. At pH < 5, the fluorescence of zip8e increased continually with decreasing pH, while that of nonzip1 was unchanged. This suggests that the zipper conformation disassociates at pH around 4, coinciding with the isoelectric point of the glutamic acid, and so confirming the electrostatic nature of the zipper conformation. The fluorescence increase at pH ≥ 10 observed in zip8e and nonzip1 is due to decomposition of BHQ3.

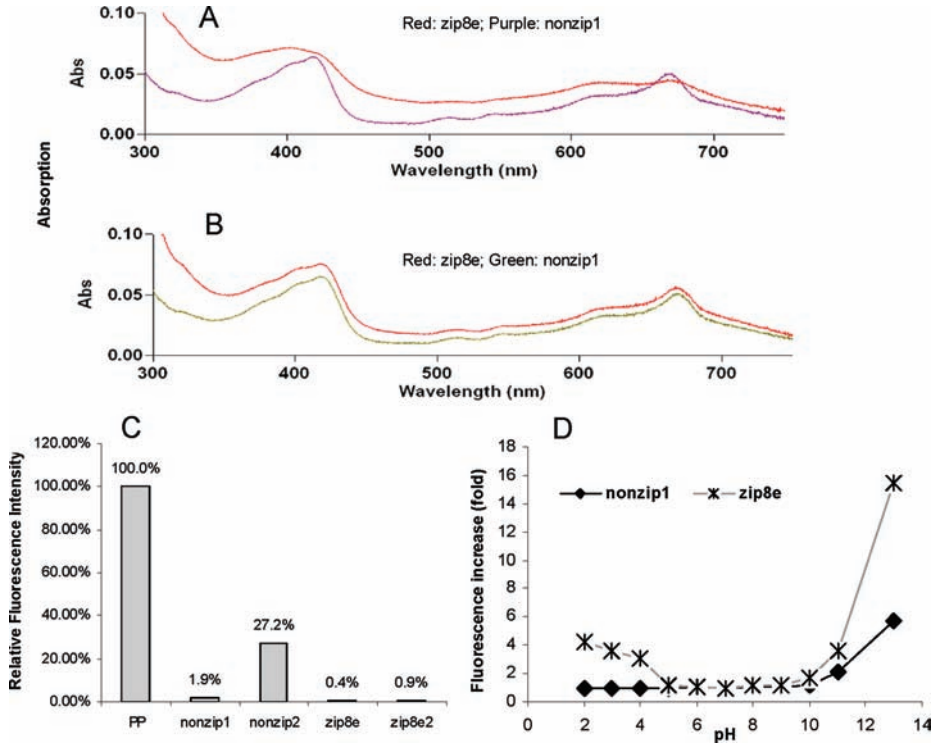

Figure 1. (A) Absorption spectra of zip8e and nonzip1 in (A) PBS buffer and (B) low-pH solution (pH = 2). (C) Relative fluorescence intensity of protease activatable probes (normalized to the fluorescence emission of PP). (D) The fluorescence stability of zip8e and nonzip1 in PBS buffer in the pH range 2−13.

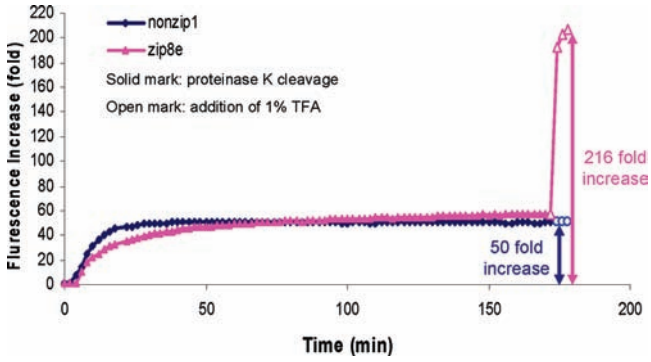

Figure 2. Comparison of the protease-mediated activation of ZMB and nonzipper probes: Cleavage kinetic profiles of probes depict increase in fluorescence after 3 h protease incubation and post TFA-induced disassociation.

Examining the protease-triggered activation of ZMB (Figure 2), we determined that the activation of ZMB is a two-step process. The first step is cleavage of the peptide linker and the second is dissociation of the zipper arms. Kinetic cleavage profiles of zip8e and nonzip1 were evaluated using Protease K to ensure complete proteolysis of the linker, and upon achieving stable fluorescence intensity, trifluoroacetic acid (TFA) was added. This decreased the pH to 2, neutralizing the polyanion arm and consequently causing dissociation of the zipper to produce maximum fluorescence. Both the nonzip1 and zip8e constructs were completely cleaved by Protease K in 3 h and produced similar maximum fluorescence. However, the fluorescence increases of these two probes were significantly different due to the enhanced quenching efficiency afforded by the zipper mechanism. As shown in Figure 2, nonzip1 resulted in a 50-fold fluorescence increase due to proteolysis with no further fluorescence increase after the addition of 1% TFA. In contrast, zip8e produced an overall 216-fold fluorescence increase. However, only a 57-fold fluorescence increase was observed 3 h after proteolysis and a 159-fold increase was contributed by forced dissociation of the zipper arms after the addition of 1% TFA. These results demonstrate that ZMB activation is a two-step process. When compared with the nonzip1 construct, ZMB offers much higher signal/background ratio after activation (216-fold vs 50-fold) due to a lower fluorescence background of intact ZMB, generated by zipper-enhanced fluorescence quenching.

This two-step activation creates a dilemma that is also observed in activatable cell-penetrating peptide probes in which the liberation of the peptide has a different mechanism on a much slower time scale (*15*). On one hand, a stable zipper conformation is necessary to achieve maximum quenching efficiency, which is critical for improving the probe sensitivity (by reducing the background fluorescence) and for creating the sequence-independent universal probe. On the other hand, if the zipper structure is too stable, it prevents or slows the prompt dissociation of the D- and Q-zipper arms upon target activation. This results in nonspecific diffusion of D from the target cells and diminishes the gain in probe selectivity. Hence, the optimal ZMB should have a high quenching efficiency balanced by rapid dissociation of the zipper arms after proteolysis.

Although zip8e provides near-maximum quenching efficiency (99.6%), its activation only produces a partial fluorescence increase (26%) from general proteolysis. In order to balance the quenching efficiency and activation, a collection of ZMBs with different zipper arm lengths (zip3e, zip4e, zip5e, zip6e) were synthesized (Supporting Information Figure S1 and Table S1). By comparing their fluorescence emission in PBS buffer, we found that the longer the zipper arm (polycation/ polyanion pair), the greater the quenching efficiency (Figure 3A). Upon

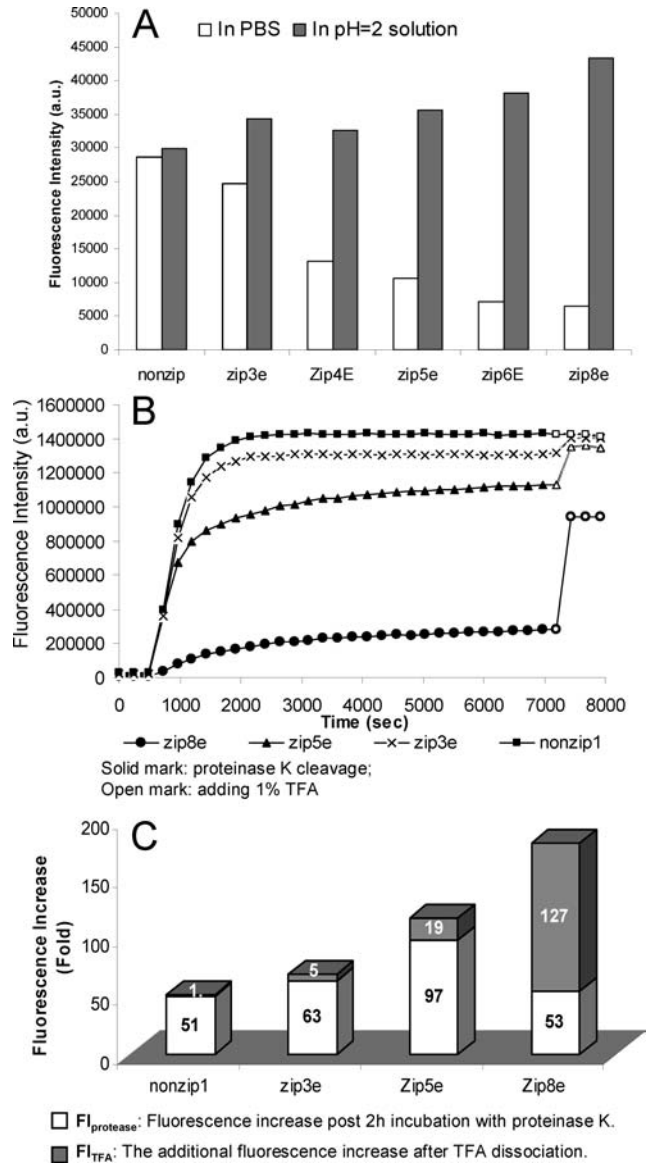

Figure 3. (A) Fluorescence emission of intact ZMBs in PBS and low pH condition (pH = 2). (B) Protease cleavage monitored by real time fluorescence. (C) $FI_{protease}$ and FI_{TFA} values for ZMBs and nonzipper controls.

adjusting the pH to 2, little to no fluorescence increase was observed in zip3e, suggesting that a zipper structure was not formed in this molecule, while a significant fluorescence increase, due to the low pH condition, was observed in zip4e, zip5e, zip6e, and zip8e, indicating that a zipper structure was formed in these molecules. The low pH conditions neutralize the polyanionic arm eliminating the electrostatic attraction between the zipper arms causing dissociation. This results in fluorescence release, as the D and Q are no longer electrostatically held together in close proximity.

As seen in Figure 3B, the activation of zip3e and zip5e was compared with that of nonzip1 and zip8e upon Proteinase K cleavage. Zip3e showed similar activation kinetics as nonzip1, further indicating that a 3-amino acid zipper arm length does not form a stable zipper. It had been previously observed that the 4-glutamate motif does not effectively attenuate the translocation of CPPs prior to proteolytic cleavage (*17*). Thus, these characteristics suggest that a stable zipper is formed when the ZMB is composed of more than 4 consecutive polycations and polyanions, resulting in enhanced fluorescence quenching efficiency and the two-step activation process. In Figure 3C, a

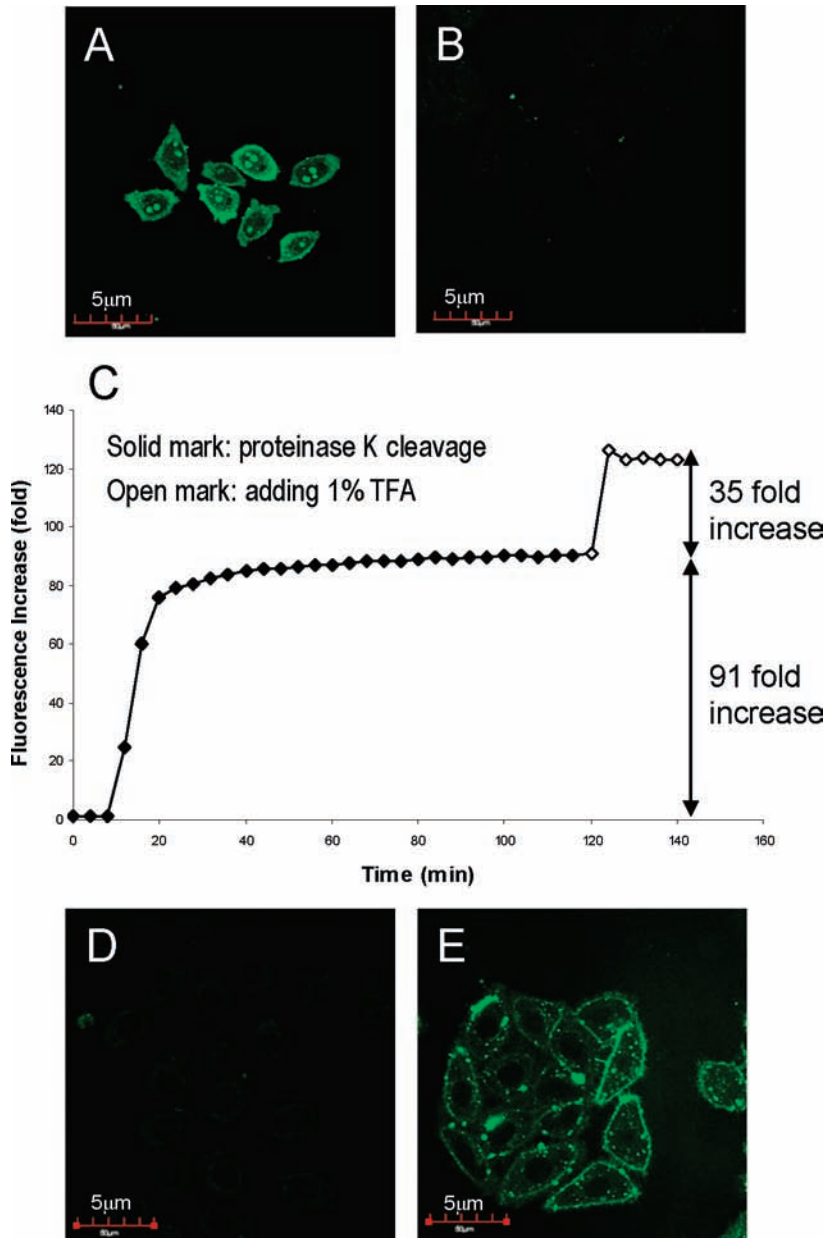

Figure 4. Confocal images of 5 μM (A) Fmoc-$_D$(rrrrrrrr)-K(FITC) and (B) Fmoc-$_D$(rrrrr)-K(FITC) in MT1 cells showing fluorescence in each case. (C) Activation kinetics of zip5e8r by Proteinase K in PBS. Confocal images of cell uptake of (D) nonzip1 and (E) zip5e8r at 30 min after cleavage by 3-day-old MT1 cell culture media.

97-fold fluorescence increase was seen in zip5e after proteolysis of the peptide linker ($FI_{protease}$), while only a 19-fold increase occurred after addition of TFA (FI_{TFA}). Thus, the dissociation of the zipper arms in zip5e is a much more efficient process than that of zip8e.

As all of the above fundamental studies were performed in PBS solution, we further evaluated the stability of the zipper arms in cell culture MEM media. Although the dissociation of the zipper arms is slightly increased in different buffered conditions, a 3−5% increase in fluorescence occurred; we assume that this buffer change will not greatly influence the kinetic profile of the zip PMBs (Supporting Information Figure S3).

Although zip5e has optimal cleavage and zipper arm dissociation rates, the practicality of a 5-amino acid polycation arm assisting in the internalization of the fluorophore is questionable. It has been reported that effective cell penetration requires at least 6 consecutive cationic amino acids (*23*). To validate this, *in vitro* confocal fluorescence microscopy was performed on Fmoc-$_D$(rrrrr)-K(FITC) and Fmoc-$_D$(rrrrrrrr)-K(FITC). As shown in Figure 4A,B, the 5-consecutive arginine cannot deliver the FITC into cells, whereas the 8-consecutive arginine showed a rapid uptake, within both the cytoplasm and nucleus after only 10 min incubation. This should address the limitation of nonspecific diffusion of the probe upon extracellular activation. Thus, by combining the optimal activation (cleavage and dissociation) of zip5e with the strong cell penetrating ability of 8-consecutive arginines, we designed an asymmetric ZMB with 8-consecutive arginines and 5-consecutive glutamates (zip5e8r): BHQ3-$_D$(eeeee)GPLGLA$_D$(rrrrrrrr)K(Pyro). This produces almost identical fluorescence quenching efficiency as zip5e (99.4% vs 99.3%), a similar rate of cleavage (2 h to completion) (Figure 4C) and comparable overall activation (72% vs 84%).

On the basis of these positive findings, zip5e8r was further evaluated in MT1 breast carcinoma cells *in vitro*, comparing the cell delivery of nonzip1 and zip5e8r after activation by 3-day-old cell incubated media. Although the peptide linker sequence is considered MMP7-specific (*12*), the old cell media

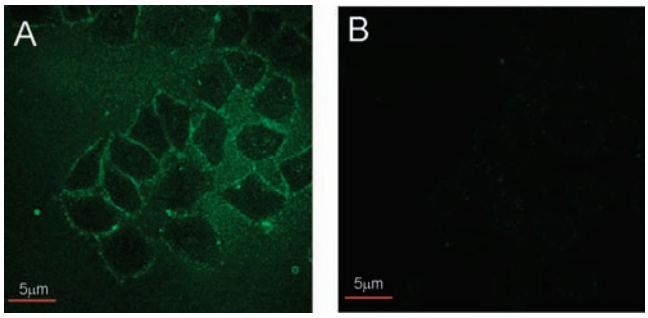

Figure 5. Confocal images comparing the background fluorescence in Pyro-ACPP (A) and zip5e8r (B).

contains a variety of different proteases, which might also lead to beacon activation. As shown in Figure 4D,E, the cleaved moiety of 8-consecutive arginine with Pyro (8r-Pyro) after zip5e8r activation accumulated inside the cells within 30 min, while the nonzip1 showed very weak uptake after activation. The improvement of zip5e8r ZMB over the corresponding nonquencher ACPP control, Pyro-ACPP, is shown in Figure 5 and Supporting Information Figure S5. By confocal imaging of the uptake of zip5e8r and Pyro-ACPP in fresh cell culture media and 3-day-old cell incubation media, we observed that the addition of a quencher significantly decreased the background signal, both before and after probe cleavage. Thus, ZMBs increased the resolution of activated probes and the contrast between the intact and activated beacon.

In summary, encoding a suitable zipper structure into protease-activatable probes significantly improves their functionality. First, by forming a stable zipper conformation, protease probes with different quenching efficiency can reach comparable maximum values (99.6% for zip8e and 99.1% for zip8e2). This effectively eliminates the peptide substrate sequence dependence of the quenching. Second, an optimal balance between high quenching efficiency and rapid activation (protease cleavage + zipper dissociation) can be achieved with 5-consecutive arginine paired with 5-consecutive glutamate (for both zip5e and zip5e8r). However, only the asymmetric zip5e8r with the extended polyarginine arm can facilitate rapid cell internalization. Thus, by incorporating an asymmetric zipper control, the quenching efficiency, activation, and delivery can all be optimized simultaneously, and the probe is no longer dependent on the specific peptide substrate sequence. Consequently, by simply switching the substrate sequences, the ZMB design can potentially be applied to a wide range of protease probe applications, with predictably similar functional performance.

This ZMB design has universal applications in targeted cancer fluorescence imaging/diagnostics, since in principle, any tumor biomarker can be targeted. Future advances may rely upon ZMBs targeted to novel early and reliable tumor markers that can discriminate malignant from benign lesions and detect micrometastases at distant sites. The application of ZMBs in cancer therapeutics is achievable by simply switching D to a fluorescent photosensitizer, such as pyropheophorbide. The ZMBs will then possess novel targeting capabilities for photodynamic therapy (PDT). With the activatable nature of ZMBs, another level of PDT selectivity should be achievable, improving the accuracy and reliability of this noninvasive therapeutic technique. Furthermore, with the fluorescent production upon activation of ZMBs, a "see and treat" approach in cancer therapeutics is also possible. The novelty of the ZMB construct is that it provides a universal design for any combination of Q and D or photosensitizer and any disease biomarker target. Thus, the applications of activatable molecular beacons in cancer diagnosis and therapy can be expanded with the incorporation of the "zipper" mechanism.

ACKNOWLEDGMENT

This work was supported by the Canadian Institute of Health Research, the Ontario Institute for Cancer Research through funding provided by the Government of Ontario, the Canadian Cancer Society Research Institute, and the Joey and Toby Tanenbaum/Brazilian Ball Chair in Prostate Cancer Research.

Supporting Information Available: Characterization of ZMB constructs, confirmation of protease K cleavage fragments of ZMBs, comparison of the fluorescence emission and kinetic profile of zip5e and zip8e in buffer solutions, comparison of ACPP vs ZMB in vitro after cleavage. This material is available free of charge via the Internet at http://pubs.acs.org.

LITERATURE CITED

(1) Weissleder, R., and Ntziachristos, V. (2003) Shedding light onto live molecular targets. *Nat. Med. 9*, 123–8.
(2) Weissleder, R., Tung, C. H., Mahmood, U., and Bogdanov, A. (1999) In vivo imaging of tumors with protease-activated near-infrared fluorescent probes. *Nat. Biotechnol. 17*, 375–8.
(3) McIntyre, J. O., Fingleton, B., Wells, K. S., Piston, D. W., Lynch, C. C., Gautam, S., and Matrisian, L. M. (2004) Development of a novel fluorogenic proteolytic beacon for in vivo detection and imaging of tumour-associated matrix metalloproteinase-7 activity. *Biochem. J. 377*, 617–628.
(4) Bullok, K., and Piwnica-Worms, D. (2005) Synthesis and characterization of a small, membrane-permeant, caspase-activatable far-red fluorescent peptide for imaging apoptosis. *J. Med. Chem. 48*, 5404–5407.
(5) Blum, G., von Degenfeld, G., Merchant, M. J., Blau, H. M., and Bogyo, M. (2007) Noninvasive optical imaging of cysteine protease activity using fluorescently quenched activity-based probes. *Nat. Chem. Biol. 3*, 668–677.
(6) Jaffer, F. A., Kim, D., Quinti, L., Tung, C., Aikawa, E., Pande, A. N., Kohler, R. H., Shi, G., Libby, P., and Weissleder, R. (2007) Optical visualization of cathepsin K activity in atherosclerosis with a novel, protease-activatable fluorescence sensor. *Circulation 115*, 2292–2298.
(7) Melancon, M. P., Wang, W., Wang, Y., Shao, R., Ji, X., Gelovani, J. G., and Li, C. (2007) A novel method for imaging in vivo degradation of poly(L-glutamic acid), a biodegradable drug carrier. *Pharm. Res. 24*, 1217–1224.
(8) Zhang, Z., Yang, J., Lu, J., Lin, J., Zeng, S., and Luo, Q. (2008) Fluorescence imaging to assess the matrix metalloproteinase activity and its inhibitor in vivo. *J. Biomed. Opt. 13*, 011006.
(9) Stefflova, K., Chen, J., Marotta, D., Li, H., and Zheng, G. (2006) Photodynamic therapy agent with a built-in apoptosis sensor for evaluating its own therapeutic outcome in situ. *J. Med. Chem. 49*, 3850–6.
(10) Chen, J., Stefflova, K., Niedre, M. J., Wilson, B. C., Chance, B., Glickson, J. D., and Zheng, G. (2004) Protease-triggered photosensitizing beacon based on singlet oxygen quenching and activation. *J. Am. Chem. Soc. 126*, 11450–1.
(11) Choi, Y., Weissleder, R., and Tung, C. (2006) Selective antitumor effect of novel protease-mediated photodynamic agent. *Cancer Res. 66*, 7225–7229.
(12) Zheng, G., Chen, J., Stefflova, K., Jarvi, M., Li, H., and Wilson, B. C. (2007) Photodynamic molecular beacon as an activatable photosensitizer based on protease-controlled singlet oxygen quenching and activation. *Proc. Natl. Acad. Sci. U.S.A. 104*, 8989–94.
(13) Gabriel, D., Campo, M. A., Gurny, R., and Lange, N. (2007) Tailoring protease-sensitive photodynamic agents to specific disease-associated enzymes. *Bioconjugate Chem. 18*, 1070–1077.
(14) Lo, P., Chen, J., Stefflova, K., Warren, M. S., Navab, R., Bandarchi, B., Mullins, S., Tsao, M., Cheng, J. D., and Zheng,

G. (2009) Photodynamic molecular beacon triggered by fibroblast activation protein on cancer-associated fibroblasts for diagnosis and treatment of epithelial cancers. *J. Med. Chem. 52*, 358–368.

(15) Jiang, T., Olson, E. S., Nguyen, Q. T., Roy, M., Jennings, P. A., and Tsien, R. Y. (2004) Tumor imaging by means of proteolytic activation of cell-penetrating peptides. *Proc. Natl. Acad. Sci. U.S.A. 101*, 17867–72.

(16) Goun, E. A., Shinde, R., Dehnert, K. W., Adams-Bond, A., Wender, P. A., Contag, C. H., and Franc, B. L. (2006) Intracellular cargo delivery by an octaarginine transporter adapted to target prostate cancer cells through cell surface protease activation. *Bioconjugate Chem. 17*, 787–96.

(17) Watkins, G. A., Jones, E. F., Scott Shell, M., VanBrocklin, H. F., Pan, M., Hanrahan, S. M., Feng, J. J., He, J., Sounni, N. E., Dill, K. A., Contag, C. H., Coussens, L. M., and Franc, B. L. (2009) Development of an optimized activatable MMP-14 targeted SPECT imaging probe. *Bioorg. Med. Chem. 17*, 653–9.

(18) Zhang, M., Zhang, Z., Blessington, D., Li, H., Busch, T. M., Madrak, V., Miles, J., Chance, B., Glickson, J. D., and Zheng, G. (2003) Pyropheophorbide 2-deoxyglucosamide: a new photosensitizer targeting glucose transporters. *Bioconjugate Chem. 14*, 709–14.

(19) Knight, C. G., Willenbrock, F., and Murphy, G. (1992) A novel coumarin-labelled peptide for sensitive continuous assays of the matrix metalloproteinases. *FEBS Lett. 296*, 263–6.

(20) Welch, A. R., Holman, C. M., Browner, M. F., Gehring, M. R., Kan, C. C., and Van Wart, H. E. (1995) Purification of human matrilysin produced in *Escherichia coli* and characterization using a new optimized fluorogenic peptide substrate. *Arch. Biochem. Biophys. 324*, 59–64.

(21) Hamamoto, K., Kida, Y., Zhang, Y., Shimizu, T., and Kuwano, K. (2002) Antimicrobial activity and stability to proteolysis of small linear cationic peptides with D-amino acid substitutions. *Microbiol. Immunol. 46*, 741–9.

(22) Gammon, S. T., Villalobos, V. M., Prior, J. L., Sharma, V., and Piwnica-Worms, D. (2003) Quantitative analysis of permeation peptide complexes labeled with Technetium-99m: chiral and sequence-specific effects on net cell uptake. *Bioconjugate Chem. 14*, 368–76.

(23) Mitchell, D. J., Kim, D. T., Steinman, L., Fathman, C. G., and Rothbard, J. B. (2000) Polyarginine enters cells more efficiently than other polycationic homopolymers. *J. Pept. Res. 56*, 318–25.

BC900207K

Supporting information for:

'Zipper' molecular beacons: A generalized strategy to optimize the performance of activatable protease probes

Juan Chen, Tracy W.B. Liu , Pui-Chi Lo, Brian C. Wilson, Gang Zheng*

Contents: ***Page***

Table S1. Description of ZMB protease probes constructs S2
Figure S1. Characterization of ZMB protease probes constructs S3
Figure S2. Proteinase K cleavage of nonzip, zip3e, zip5e and zip8e S11
Figure S3. Stability of ZMBs in buffer solution S13
Figure S4. Proteinase K Cleavage of optimized zip5e8r S13
Figure S5. Confocal imaging of activated ACPP vs zip5e8r S14

Table S1. Characterization of ZMB protease probe construcs.

Probe	Sequence	MW (Calc.)	MW (found)	HPLC (min) [a]
nonzip1	Pyro-GPLGLARK-BHQ3	1856.3	1855.8	31.8
nonzip2	Pyro-RPLALWRSK-BHQ3	2171.7	2171.0	30.4
zip8e	BHQ3-$(e)_8$GPLGLA$(r)_8$K-Pyro	3981.5	3981.7	23.8
zip8e2	BHQ3-$(e)_8$RPLALWRS$(r)_8$K-Pyro	4454.1	4453.6	23.6
PP	Pyro-GPLGLARK	1326.6	1327.2	29.5
zip3e	BHQ3-$(e)_3$GPLGLA$(r)_3$K-Pyro	2556.0	2556.3	26.5
zip5e	BHQ3-$(e)_5$GPLGLA$(r)_5$K-Pyro	3126.6	3126.8	24.8
zip5e8r	BHQ3-$(e)_5$GPLGLAR$(r)_8$K-Pyro	3753.2	3754.2	23.7

[a] HPLC from 20% A (acetonitrile) + 80% B [0.1% trifluoroacetic acid (TFA)] to 100% A in 40 min at a flow rate of 0.4 $mL.min^{-1}$.

Figure S1. Characterization of ZMB constructs. Providing (i) HPLC chromatography (416nm and 665nm), (ii) UV-Vis spectrum, and (iii) ESI mass spectrum of A) nonzip 1, B) nonzip 2, C) zip8e, D) zip8e2, E) PP, F) zip3e, G) zip5e, and H) zip5e8r

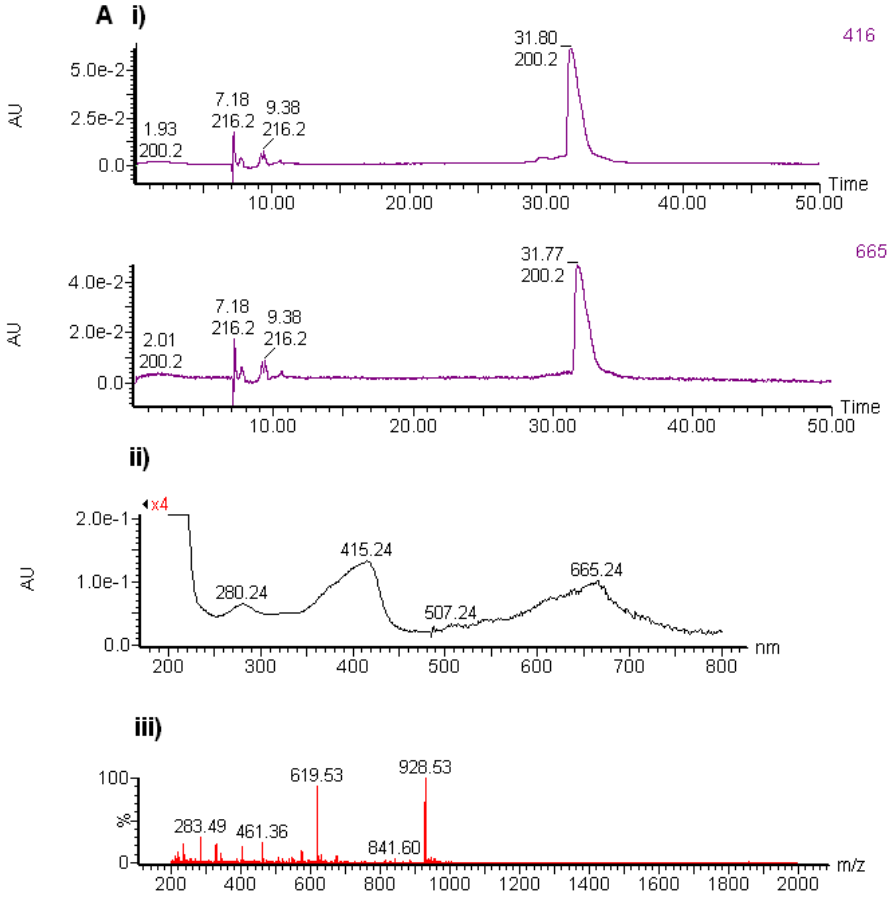

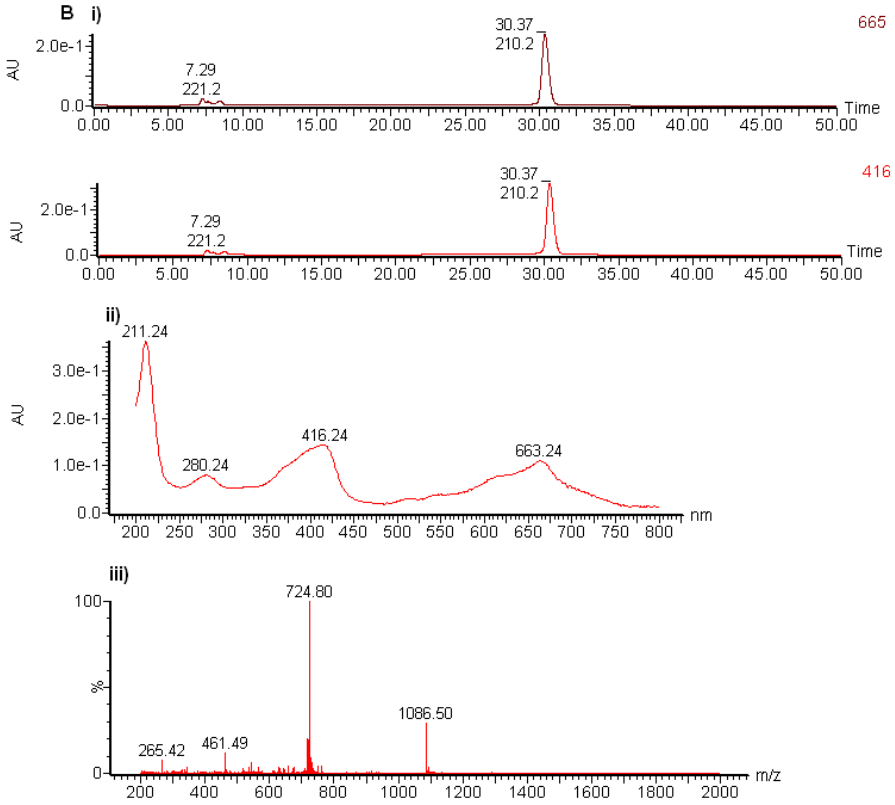
B i)
665
30.37
210.2
7.29
221.2
AU
Time
416
ii)
211.24
280.24
416.24
663.24
nm
iii)
724.80
1086.50
265.42
461.49
%
m/z

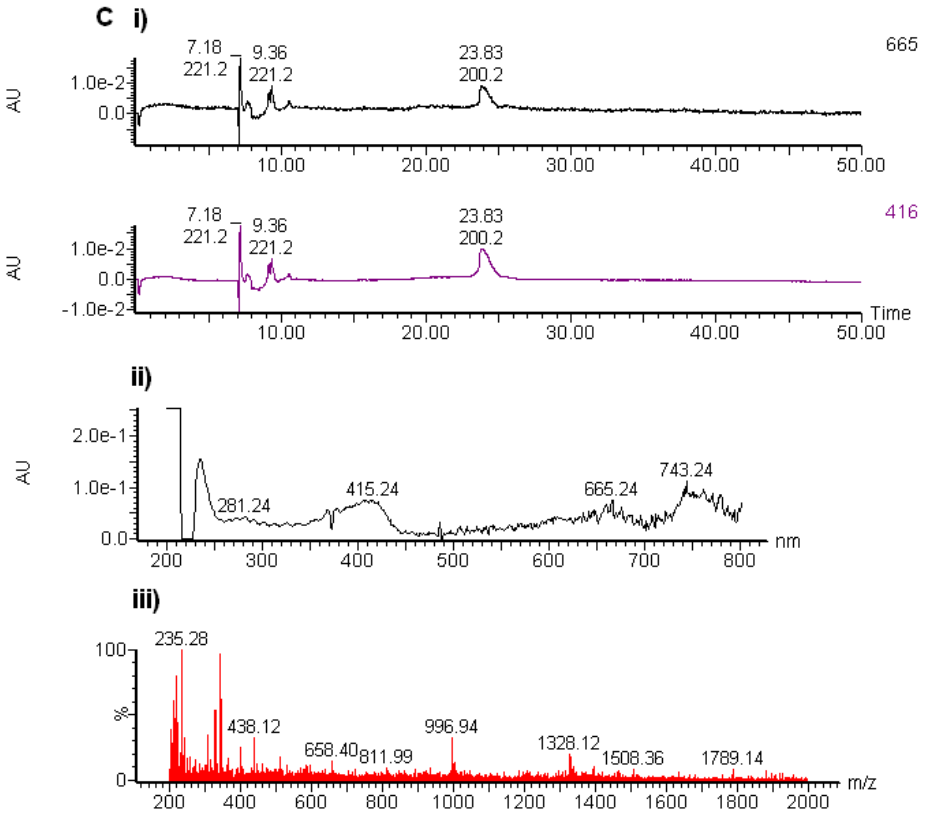
C i)
665
7.18
221.2
9.36
221.2
23.83
200.2
AU
1.0e-2
0.0
10.00
20.00
30.00
40.00
50.00
416
-1.0e-2
Time
ii)
2.0e-1
1.0e-1
281.24
415.24
665.24
743.24
nm
200
300
400
500
600
700
800
iii)
100
%
235.28
438.12
658.40
811.99
996.94
1328.12
1508.36
1789.14
m/z
0
200
400
600
800
1000
1200
1400
1600
1800
2000

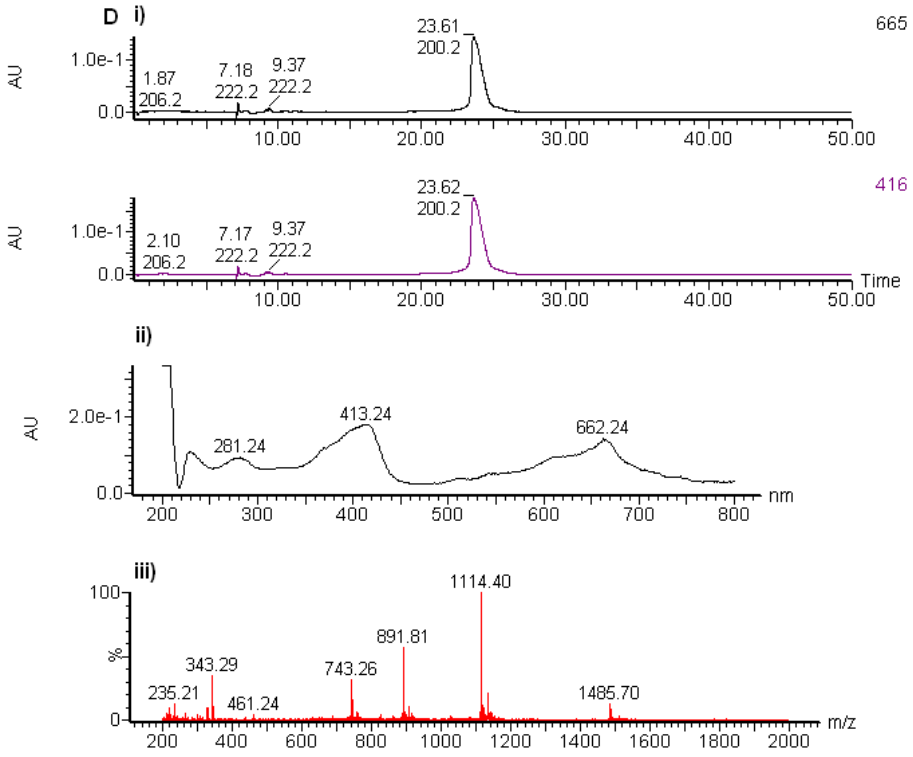
D i)
665
23.61
200.2
1.87
206.2
7.18
222.2
9.37
222.2
AU
1.0e-1
0.0
10.00
20.00
30.00
40.00
50.00
416
23.62
200.2
2.10
206.2
7.17
222.2
9.37
222.2
Time
ii)
2.0e-1
281.24
413.24
662.24
nm
200
300
400
500
600
700
800
iii)
100
%
0
1114.40
891.81
343.29
743.26
235.21
461.24
1485.70
m/z
200
400
600
800
1000
1200
1400
1600
1800
2000

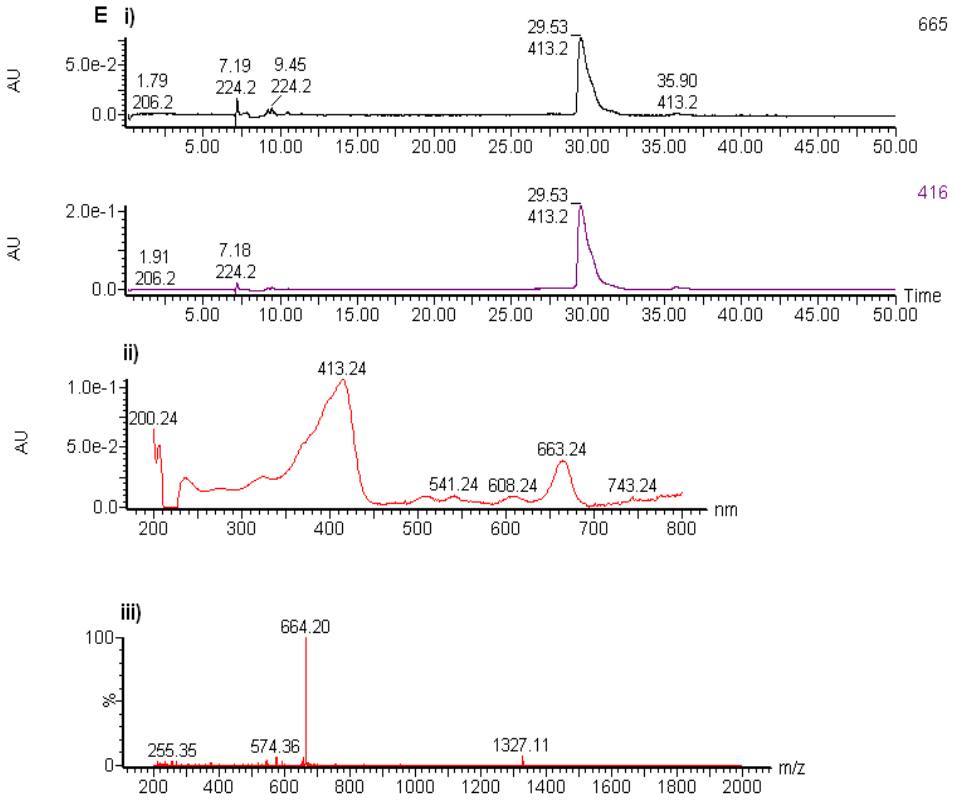
E i)
665
29.53
413.2
5.0e-2
0.0
AU
1.79
206.2
7.19
224.2
9.45
224.2
35.90
413.2
5.00
10.00
15.00
20.00
25.00
30.00
35.00
40.00
45.00
50.00
416
29.53
413.2
2.0e-1
0.0
AU
1.91
206.2
7.18
224.2
Time
ii)
413.24
1.0e-1
5.0e-2
0.0
AU
200.24
663.24
541.24
608.24
743.24
200
300
400
500
600
700
800
nm
iii)
664.20
100
%
0
255.35
574.36
1327.11
200
400
600
800
1000
1200
1400
1600
1800
2000
m/z

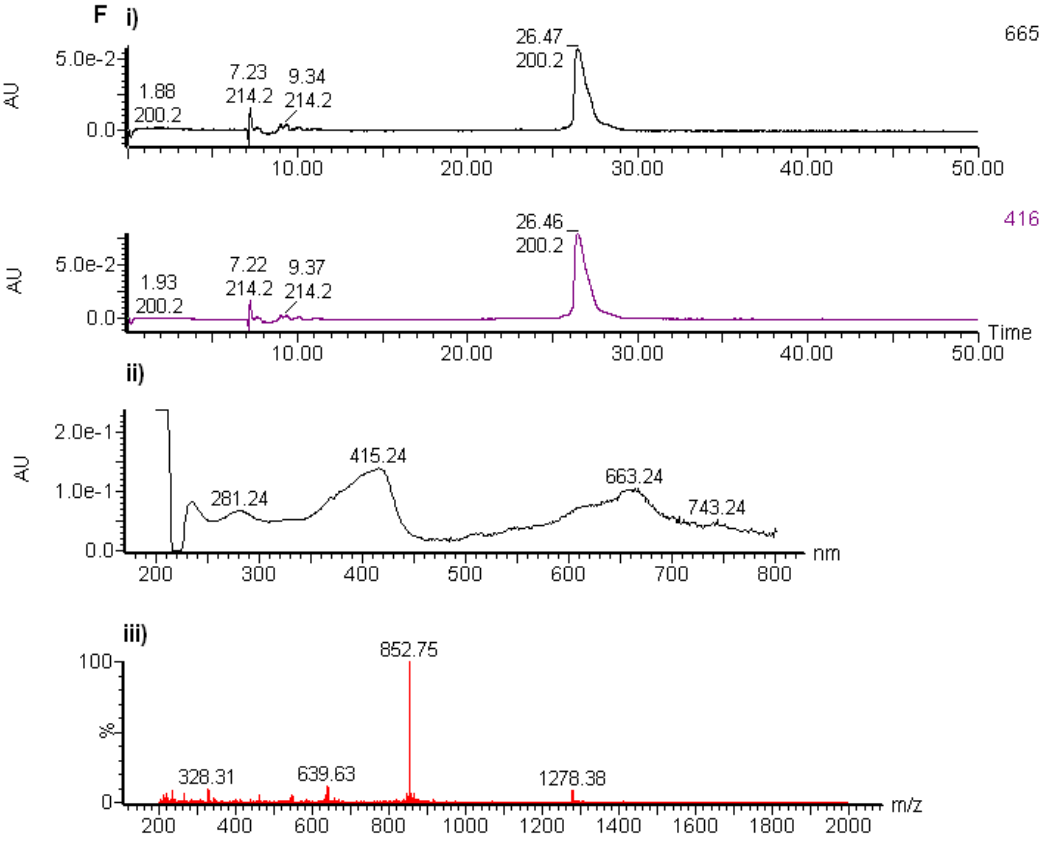
F i)
665
26.47
200.2
7.23
214.2
9.34
214.2
1.88
200.2
5.0e-2
0.0
AU
10.00
20.00
30.00
40.00
50.00
416
26.46
200.2
7.22
214.2
9.37
214.2
1.93
200.2
Time
ii)
2.0e-1
1.0e-1
415.24
281.24
663.24
743.24
nm
200
300
400
500
600
700
800
iii)
100
%
852.75
328.31
639.63
1278.38
m/z
0
200
400
600
800
1000
1200
1400
1600
1800
2000

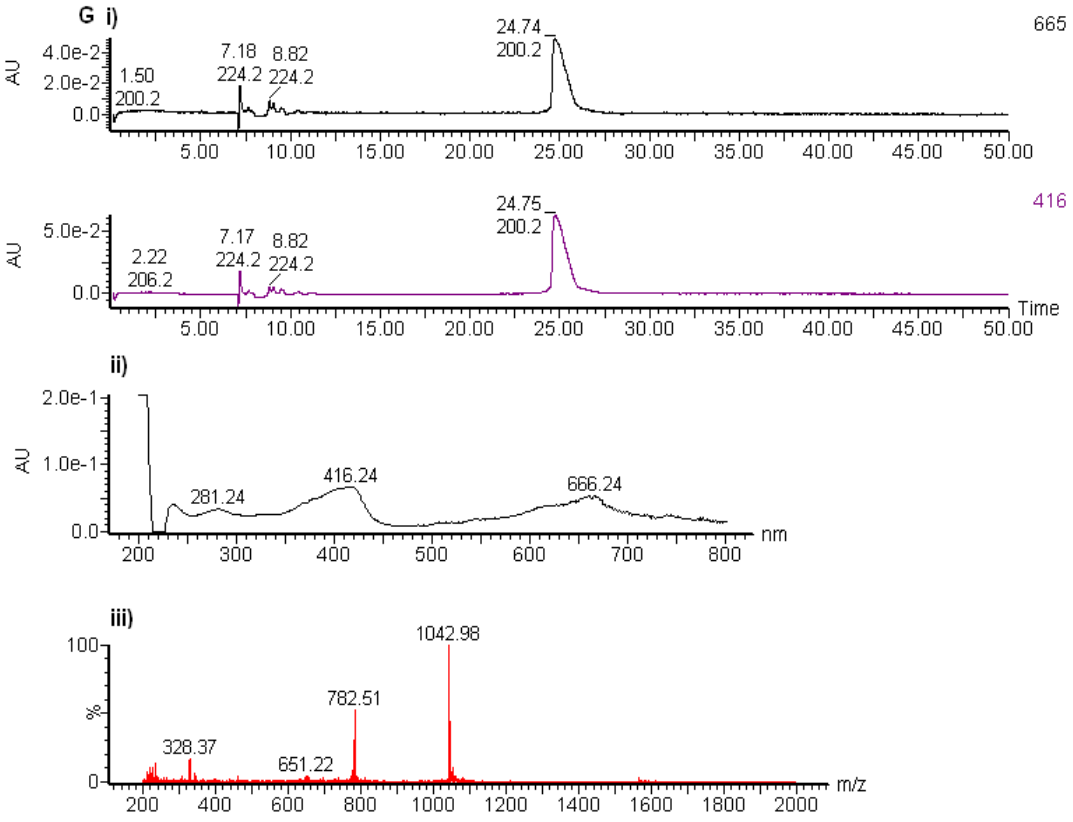
G i)
665
AU
4.0e-2
2.0e-2
0.0
1.50
200.2
7.18
224.2
8.82
224.2
24.74
200.2
5.00
10.00
15.00
20.00
25.00
30.00
35.00
40.00
45.00
50.00
416
5.0e-2
2.22
206.2
7.17
224.2
8.82
224.2
24.75
200.2
Time
ii)
2.0e-1
1.0e-1
281.24
416.24
666.24
nm
200
300
400
500
600
700
800
iii)
100
%
0
328.37
651.22
782.51
1042.98
m/z
200
400
600
800
1000
1200
1400
1600
1800
2000

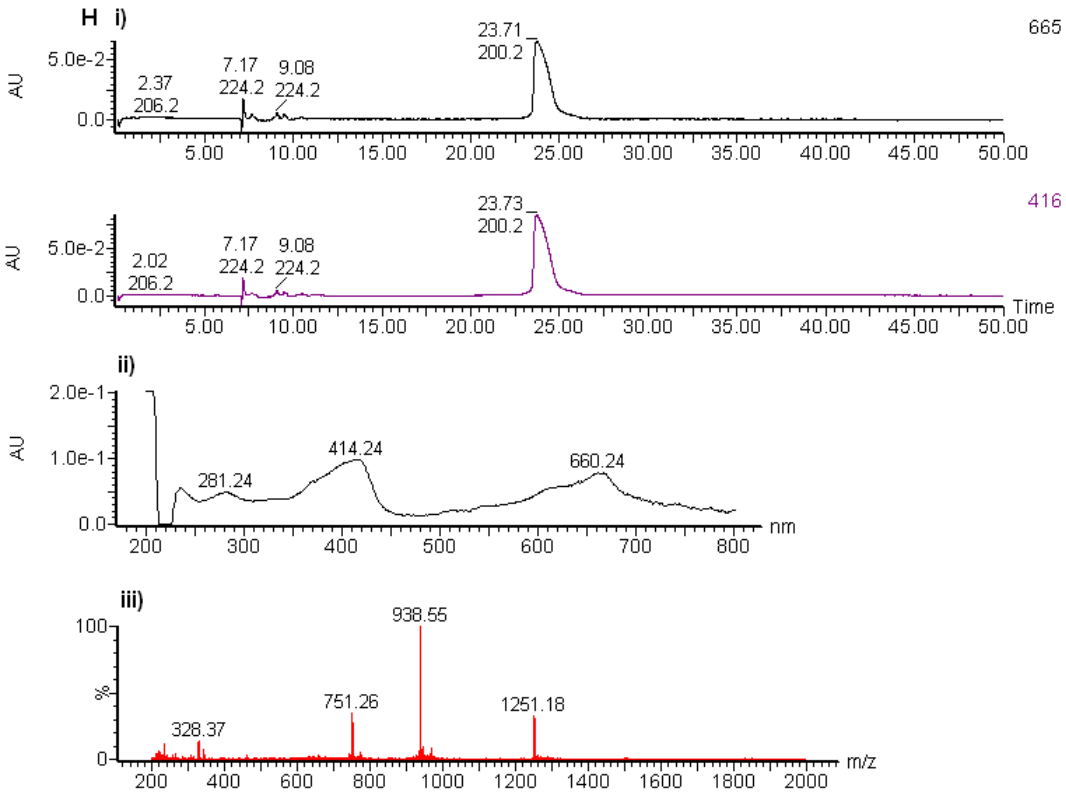
H i)
665
23.71
200.2
2.37
206.2
7.17
224.2
9.08
224.2
AU
5.0e-2
0.0
5.00
10.00
15.00
20.00
25.00
30.00
35.00
40.00
45.00
50.00
416
23.73
200.2
2.02
206.2
7.17
224.2
9.08
224.2
Time
ii)
2.0e-1
1.0e-1
281.24
414.24
660.24
nm
200
300
400
500
600
700
800
iii)
100
%
0
938.55
751.26
1251.18
328.37
m/z
200
400
600
800
1000
1200
1400
1600
1800
2000

Figure S2. Proteinase K cleavage of A) nonzip1, B) zip3e, C) zip5e and D) zip8e monitored by (i) HPLC chromatography (416nm and 665nm) and (ii) UV-Vis spectrum.

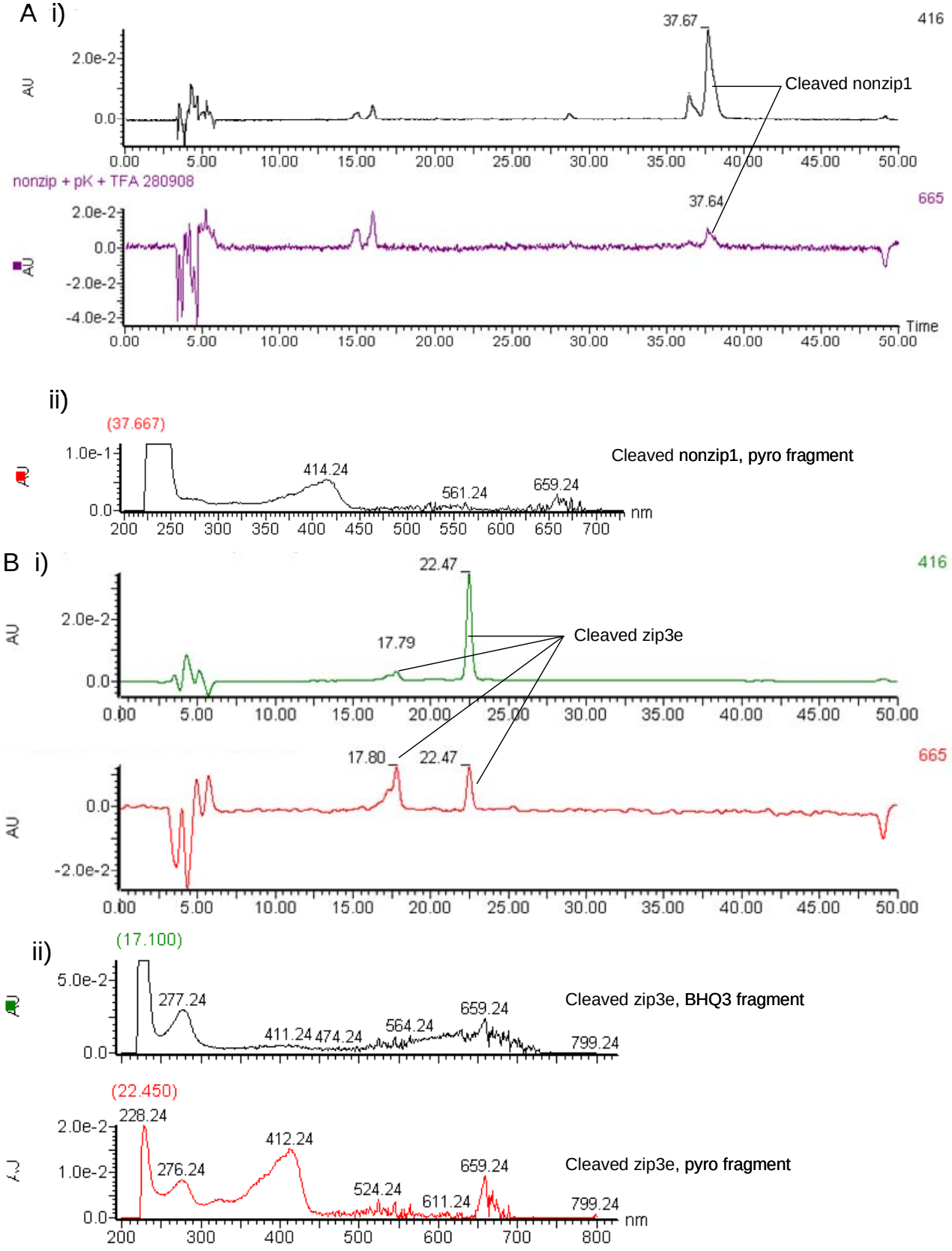

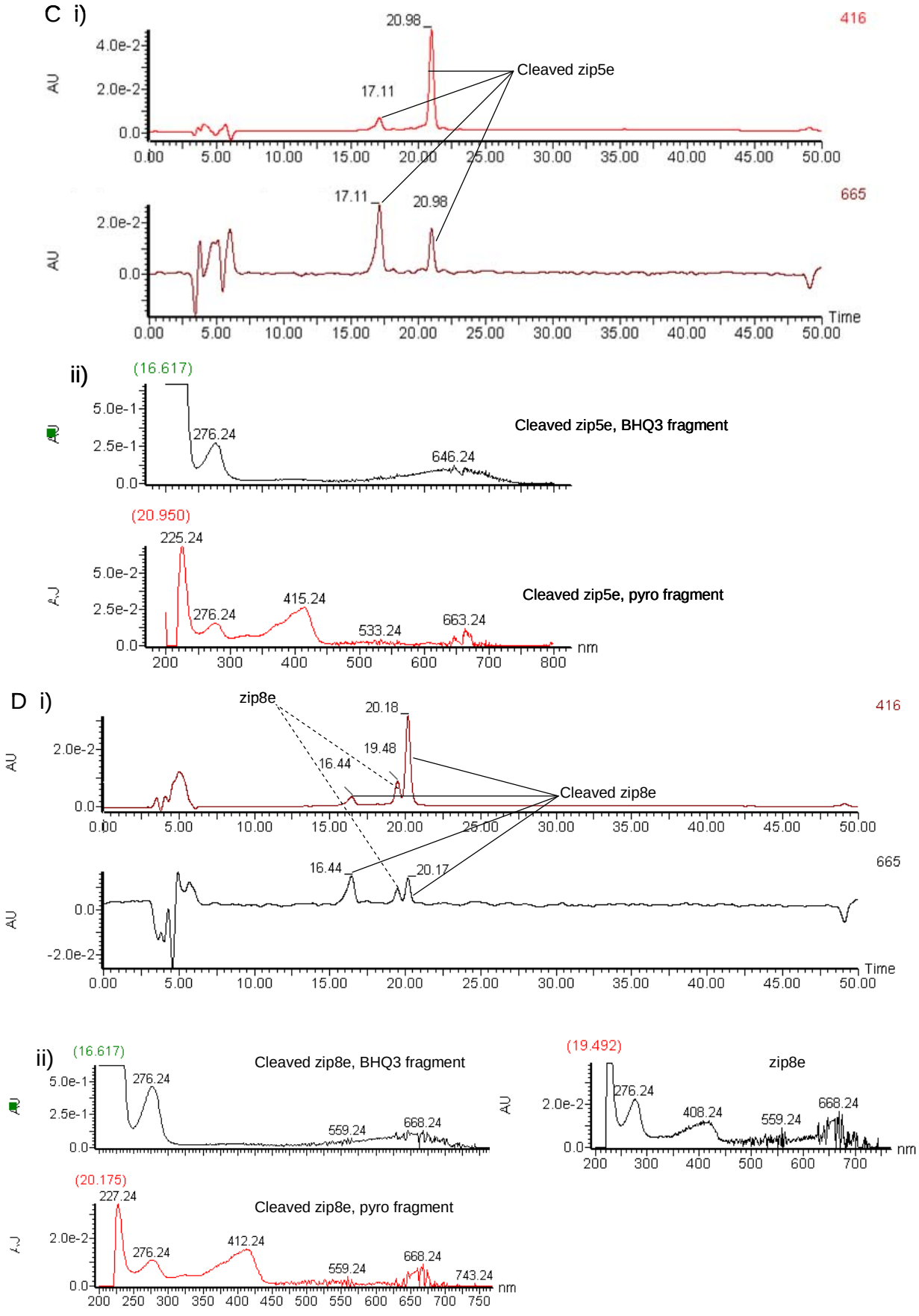
C i)
416
20.98
17.11
Cleaved zip5e
665
17.11
20.98
AU
Time
ii)
(16.617)
276.24
646.24
Cleaved zip5e, BHQ3 fragment
(20.950)
225.24
276.24
415.24
533.24
663.24
Cleaved zip5e, pyro fragment
nm
D i)
zip8e
20.18
19.48
16.44
Cleaved zip8e
416
665
16.44
20.17
Time
ii)
(16.617)
276.24
559.24
668.24
Cleaved zip8e, BHQ3 fragment
(19.492)
276.24
408.24
559.24
668.24
zip8e
(20.175)
227.24
276.24
412.24
559.24
668.24
743.24
Cleaved zip8e, pyro fragment

Figure S3. A) Fluorescence emission of ZMBs in buffered solution B) Protease cleavage monitored by real time fluorescence in buffered solution.

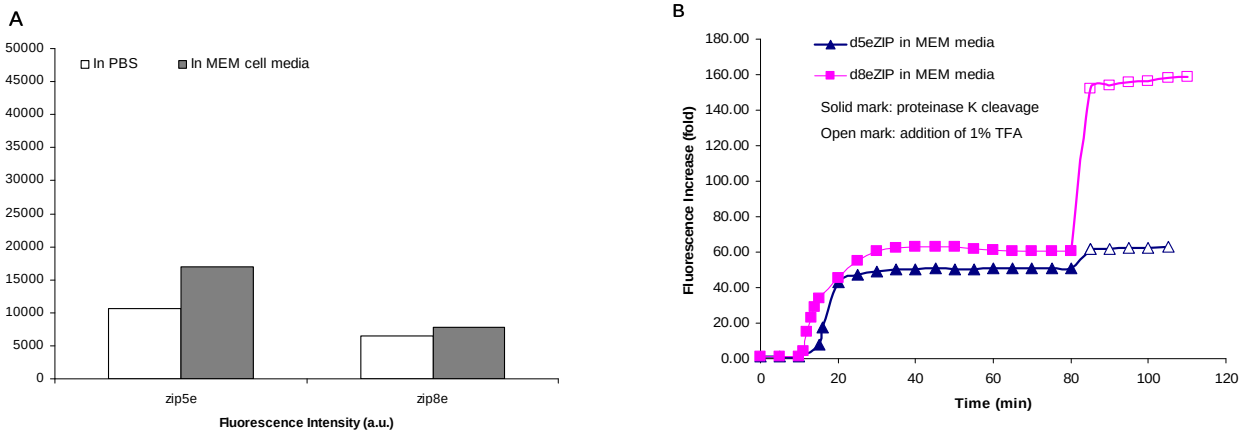

Figure S4. Proteinase K cleavage of zip5e8r monitored by (i) HPLC chromatography (416nm and 665nm) and (ii) UV-Vis spectrum

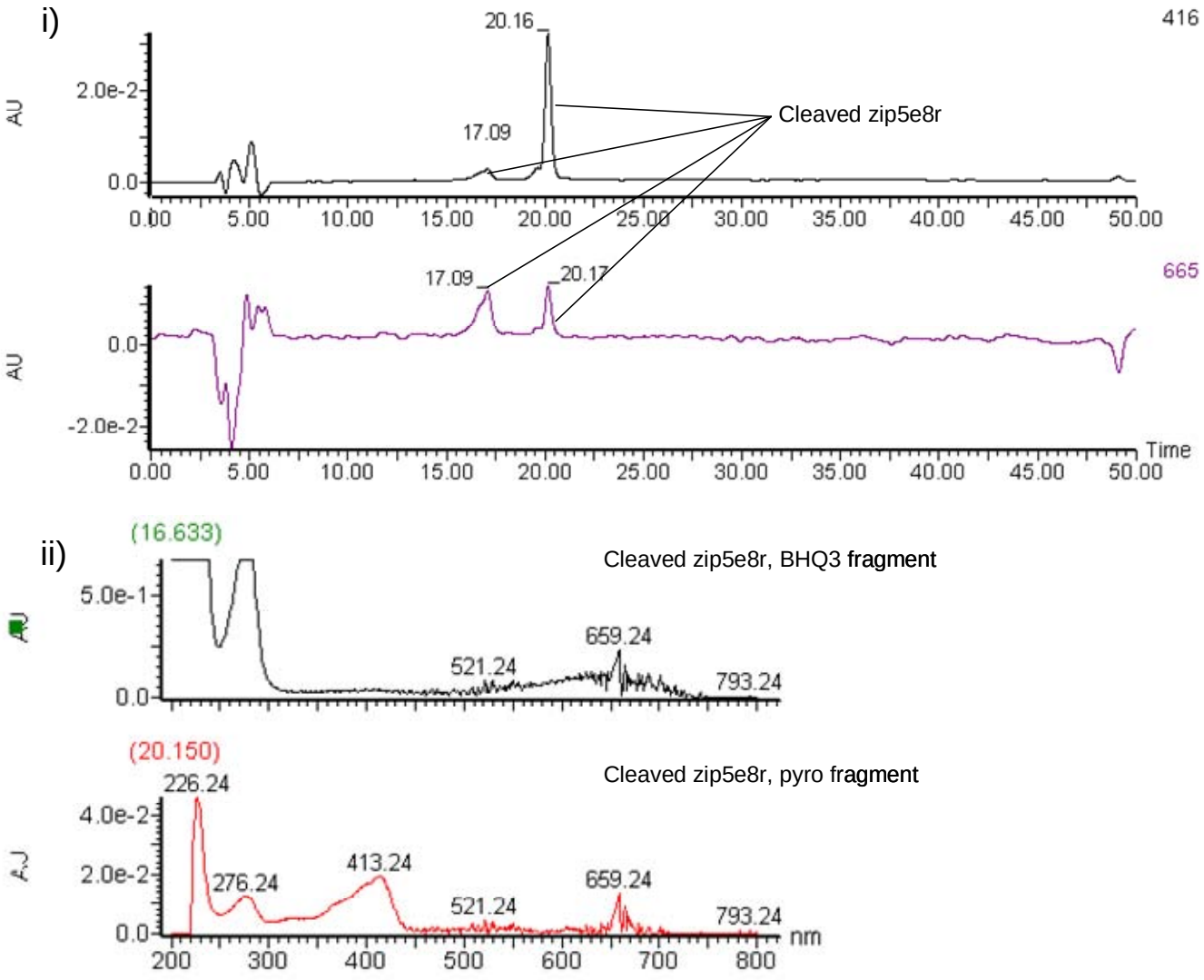

Figure S5. Confocal images comparing background fluorescence in A) Pyro-ACPP 10 min after cleavage and B) zip5e8r 10 min after cleavage.

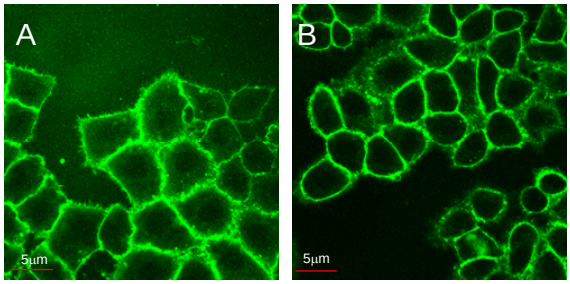

STED Nanoscopy in Living Cells Using Fluorogen Activating Proteins

James A. J. Fitzpatrick,[†,§] Qi Yan,[†,§] Jochen J. Sieber,[†,‡] Marcus Dyba,[‡] Ulf Schwarz,[‡] Chris Szent-Gyorgyi, Carol A. Woolford,[§] Peter B. Berget,[§] Alan S. Waggoner,[§] and Marcel P. Bruchez*[,||]

Molecular Biosensor and Imaging Center, Carnegie Mellon University, 4400 Fifth Avenue, Pittsburgh Pennsylvania 15213.
Received June 5, 2009; Revised Manuscript Received August 18, 2009

We demonstrate the effectiveness of a genetically encoded malachite green (MG) binding fluorogen activating protein (FAP) for live cell stimulated emission depletion nanoscopy (STED). Both extracellular and intracellular FAPs were tested in living cells using fluorogens with either membrane expressed FAP or as an intracellular FAP-actin fusion. Structures with widths of 110−122 nm were observed. Depletion data, however, suggest a resolution of 70 nm with the given instrument.

Fluorescence microscopy has experienced explosive growth of use over the past three decades, transforming from a disparate set of optical techniques to a cohesive tool set of imaging methodologies for biological research. This transformation has been greatly facilitated by the development of bright photostable fluorescent probes ranging from organic dyes (*1, 2*) to genetically expressible fluorescent proteins (*3*) as targeted fusions at the molecular level. This, in conjunction with the development of new lasers and low-noise photodetectors, has enabled the observation of many aspects of cell structure that were previously unseen. However, despite these incredible advances, conventional optical microscopy is inherently mismatched with biological length scales due to the far-field diffraction limit of light ($\sim\lambda$/2NA); i.e., one cannot resolve objects that are separated by less than half the wavelength of light. This is particularly restrictive when the spatial location of multiple interacting objects is desired, especially when the size of most protein complexes are on the order of 10−50 nm, and even subcellular organelles have dimensions on the order of 100 nm. To overcome this fundamental obstacle, the past decade has seen the birth of the completely new field of far-field super-resolution optical microscopy, which has revealed many aspects of cellular ultrastructure previously only discernible in electron microscopy. Currently, there are two distinct methodologies, one of which is based on single-molecule localization approaches, PALM (photoactivation localization microscopy) (*4, 5*) and STORM (stochasic optical reconstruction microscopy) (*6*), and the other on ensemble imaging employing either point-spread function engineering or low-frequency structured illumination (*7, 8*).

The latter methods rely on the manipulation of the point-spread function (PSF) of the microscope while imaging a complete ensemble of molecules. One very successful approach is stimulated emission depletion (STED) nanoscopy (*9*). In this method, an excitation laser beam is overlaid with a depletion laser that has an optically engineered point-spread function, resulting in a much smaller effective fluorescing spot. Currently, the best attained STED resolution is 6 nm, obtained for photonic crystal centers (*10*).

Compared to localization, such ensemble methods do not routinely yield the same spatial resolution enhancements (especially in biological samples), but do provide much higher temporal resolution. In the case of STED, video rate imaging of 28 frames/s has been achieved allowing the observation of synaptic vesicle movement in living neurons (*11*). This is almost 3 orders of magnitude faster than the fastest PALM-based dynamic imaging reported to date at 0.04 frames/s (*12*). Further live cell STED with fluorescent proteins has been successfully demonstrated in imaging both dendritic spines (*13*) and the endoplasmic recticulum (*14*), both making use of yellow fluorescent proteins (YFP). To minimize potential phototoxic effects in long-term live cell imaging experiments, especially with the high laser powers required for effective depletion, it is highly desirable to operate at wavelengths far to the red.

The far-red organic dye Atto647N has been applied in the case of video-rate STED of synaptic vesicle movement in living neurons (*11*) and to explore the nanoscale dynamics of lipid membranes using FCS-STED methodology (*15*). In addition, Atto655 has been used in conjunction with the Halo-Tag labeling technology to visualize β1-integrin in nonliving HeLa cell filiapodia (*16*). Both of these dyes are compatible with the commercial Leica TCS STED system. Unfortunately, these live cell approaches are inherently restrictive, as they require either the uptake of a dye-labeled lipid or antibody or internalization of an impermeant dye prebound to a genetic tag, which is not always biologically convenient. At present, no fluorescent protein has been reported to work with the commercial STED system in the same spectral range. As such, STED imaging of living cells in the far red has been limited to specific applications compatible with these labeling approaches. In order for the STED method to become generally useful for live cell imaging in the far red, it is highly desirable to have genetically targetable far-red fluorescent probes with quantum yields and spectral characteristics similar to those of the Atto Dyes. In this brief communication, we describe the first use of genetically expressed fluorogen activating proteins (FAPs) that bind and activate the far-red fluorogenic dye malachite green for live-cell STED nanoscopy. These results using extra and intracellular compatible FAPs have widespread implications in the development of live cell STED nanoscopy for high-speed dynamic super-resolution imaging.

Malachite green is a far-red nonfluorescent organic dye that has been used to generate fluorescent signal when bound specifically to selected proteins (such as FAPs (*17*)) and nucleic acid aptamers (*18*). Because the dye exists in a nonfluorescent

* Corresponding author: bruchez@andrew.cmu.edu.
[†] All authors contributed equally to this work.
[‡] Leica Microsystems, Am Friedensplatz 3, 68165 Mannheim, Germany.
[§] Department of Biological Sciences, Carnegie Mellon University.
[||] Department of Chemistry, Carnegie Mellon University.

10.1021/bc900249e CCC: $40.75 © 2009 American Chemical Society
Published on Web 09/08/2009

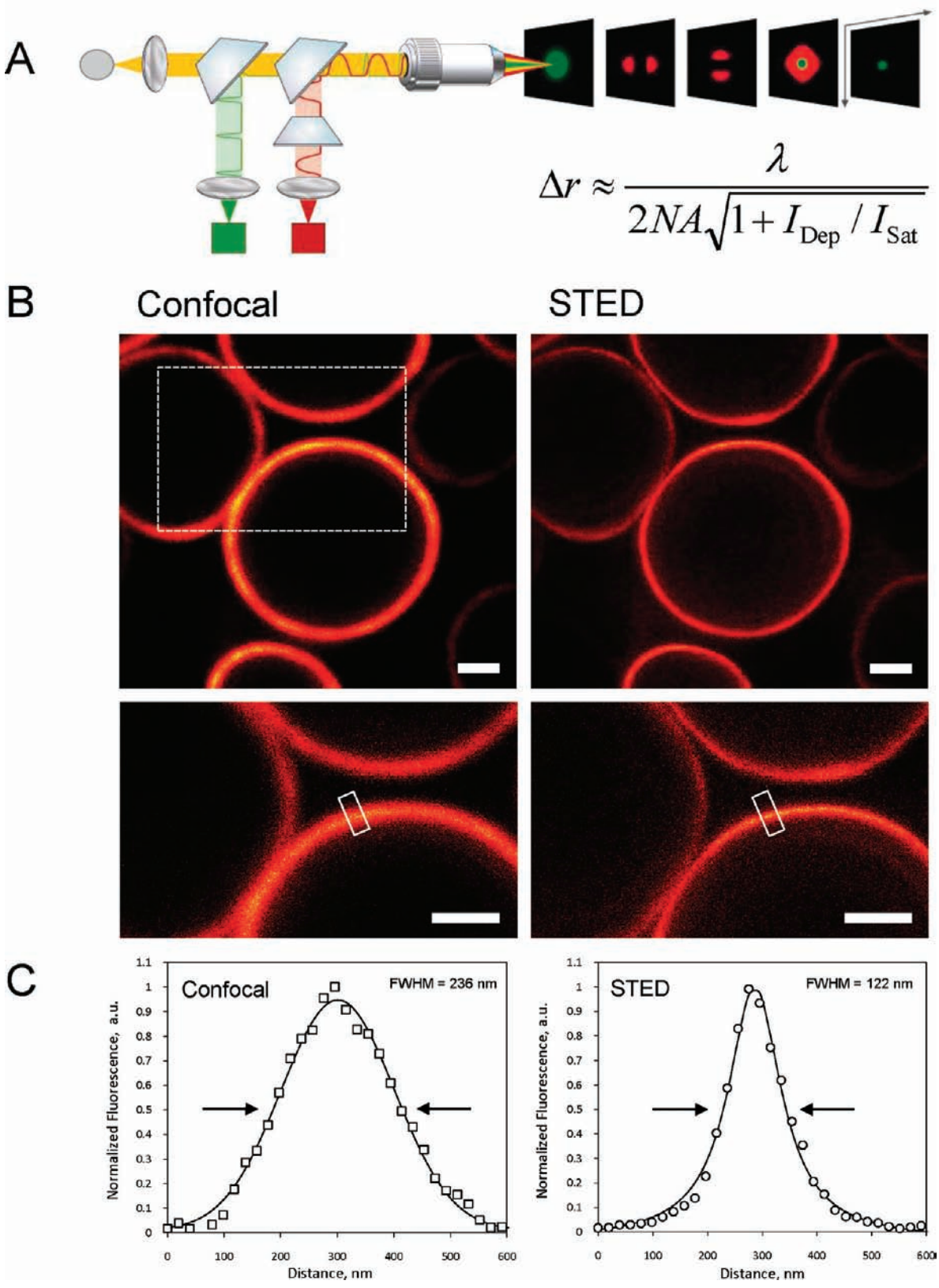

Figure 1. STED nanoscopy in living yeast cells. (A) Schematic of commercial Leica TCS STED optical setup. A pulsed 635 nm excitation diode laser is overlapped with the "donut"-shaped pulsed depletion infrared laser beam to produce a subdiffraction limited fluorescing spot whose diameter is approximated by $\Delta r \approx \lambda/2\mathrm{NA}(1 + I_{\mathrm{Dep}}/I_{\mathrm{Sat}})^{1/2}$ (*22*) where NA is the objective numerical aperture, I_{Dep} is the depletion intensity and I_{Sat} is the intensity of saturation which is fluorophore dependent. (B) Confocal and STED images of living yeast cells surface expressing the extracellular L5-MG-L90S FAP module labeled with MG-2p fluorogen. Hollow white bar denotes a 10-pixel-wide region of interest. (C) Line profiles generated from the averaged fluorescence intensity within the region of interest plotted as a function of distance. Solid lines indicate a fit to one-dimensional Gaussian (confocal) or Lorentzian (STED) functions. FWHM are 236 nm (confocal) and 122 nm (STED). Solid white lines indicate 1 μm scale bars.

form, it can be added to cells in media and/or buffer with no appreciable background signal. When the dye interacts specifically with its target, the fluorescence is activated up to ~20 000-fold resulting in genetically targetable, bright far-red emission.

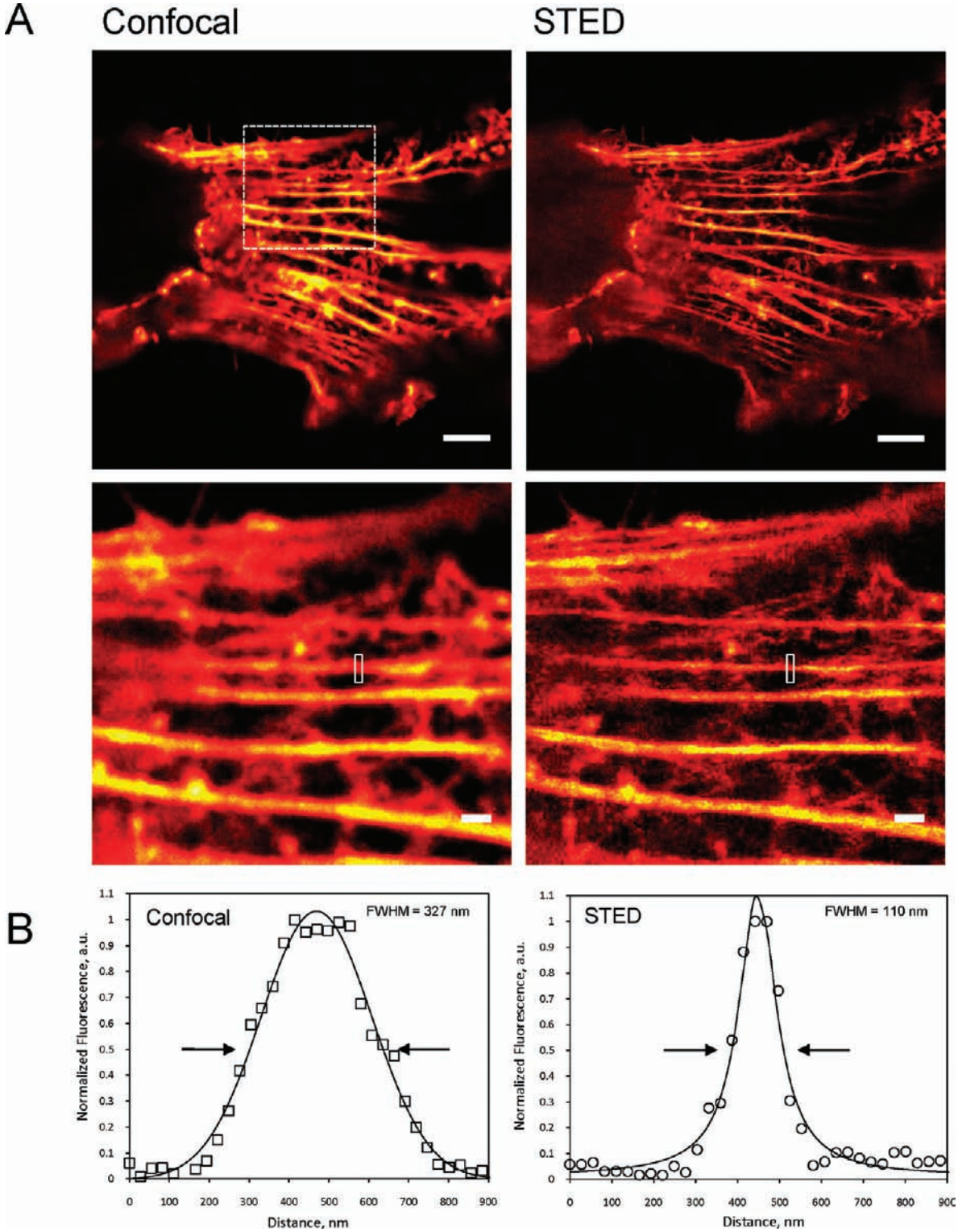

Figure 2. STED nanoscopy in living HeLa cells. (A) Living HeLa cells expressing the H6.2-MG disulfide free FAP module expressed as an N-terminal fusion to actin labeled using the MG-ester fluorogen (upper left panel confocal, upper right panel STED, with an enlarged region denoted by the dashed line box below each image). Hollow white bar denotes a 5-pixel-wide region of interest. (B) Line profiles generated from the averaged fluorescence intensity within the region of interest plotted as a function of distance. Solid lines indicate a fit to a one-dimensional Gaussian (confocal) or Lorentzian (STED) functions. The fitted FWHM are 327 nm (confocal) and 110 nm (STED). Solid white lines indicate 5 μm scale bars in the upper images and 1 μm scale bars in the cropped images.

The photophysical properties of malachite green are well-suited to excitation and depletion in the red and near-infrared spectral range as is available on the Leica TCS STED system.

The STED potential for different malachite green binding extracellular FAP modules was evaluated using yeast cells displaying the FAP on the cell surface. Yeast cells were grown and induced as described in Szent-Gyorgyi et al. (*17*) and imaged as described in the Supporting Information. Figure 1A illustrates the implementation of the STED microscope in a commercial apparatus. Briefly, a visible red excitation spot is overlapped with a "donut"-shaped engineered PSF of the infrared laser to enable shrinkage of the effective fluorescing spot size by stimulated emission. A variety of MG binding FAPs with 100nM of the MG-2p

Table 1. Comparison of the Photophysical Characteristics of Malachite Green Binding Fluorogen Activating Proteins, MG FAPs (obtained from Szent-Gyorgyi et al. (*17*)) and the Atto-Tec Organic Dyes (obtained from http://www.atto-tec.com/) Used in Far-Red STED Nanoscopy

dye/fluorogen	fluorogen activating protein	excitation maximum (nm)	emission maximum (nm)	extinction coefficient ($M^{-1}cm^{-1}$)	quantum yield (Φ)	brightness $\varepsilon \times \Phi$
MG-2p	HL4-MG	629	649	133 000	0.16	21
	H6-MG	635	656	105 000	0.25	26
	L5-MG (wt)	640	668	103 000	0.048	5
	L5-MG-L90S	632	664	128 000	0.38*	49
Atto647N	−	644	669	150 000	0.65	97
Atto655	−	663	684	125 000	0.30	37

* QY determined relative to native L5-MG.

fluorogen were tested throughout a range of wavelengths (730−750 nm) to elucidate which gave the most efficient depletion of fluorescence. The most promising module was L5-MG-L90S, which is a single-point mutation of the native single-chain FAP (L5-MG). Figure 1B illustrates both confocal and STED images with the extracellular L5-MG-L90S expressed on the surface of yeast (average image acquisition times were 5 s at a 100 Hz scan speed, and images were averaged 4 times to improve the signal-to-noise ratio). This FAP has a quantum yield of 0.23 and excitation and emission characteristics comparable to the organic dye Atto647N, which makes it amenable to commercial STED nanoscopy (see Table 1 for the characteristics of different FAP modules and Atto dyes). In order to quantify the gain in lateral resolution, a 10-pixel-wide region of interest was designated in the enlarged confocal and STED images (denoted by hollow white bars) and the fluorescence intensity was averaged using NIH *ImageJ* to generate the line profiles depicted in Figure 1C. The line profiles were fitted to one-dimensional Gaussian (confocal) or Lorentzian (STED) functions, which yielded full-width half-maximum (FWHM) values of 236 nm and 122 nm, respectively. This measured fwhm is somewhat higher than the expected subdiffraction limited STED resolution from the measured depletion curves, which is expected to be ∼70 nm for the given system and dye (see Supporting Information) but is consistent with current estimates of the yeast cell wall thickness (*19*).

As stated previously, the major benefit of using MG FAPs for STED nanoscopy is the unique ability to produce genetically targeted fusions in living cells. However, despite this advantage, to make the most use of STED as a high-speed super-resolution imaging technology for cellular applications it is necessary to have a fluorescent probe that functions within the cytoplasm of living cells. Given the noted folding problems of scFvs in reducing environments due to the loss of the stabilizing disulfide bridges (*20*), the H6-MG FAP has been modified via site-directed mutagenesis to remove the cysteine residues and subsequent affinity maturation to regain fluorogenic activation (H6.2-MG; manuscript submitted to Protein Engineering Design and Selection). This FAP has been expressed transiently as an N-terminal fusion to actin in living HeLa cells. Figure 2A illustrates visible stress fibers after labeling with 300nM of the permeant MG-ester fluorogen (average image acquisition times were 4 s at a 400 Hz scan speed, and images were averaged 8−10 times to improve the signal-to-noise ratio). The optically enlarged panels show the increase in the lateral resolution with many features obscured in the confocal image becoming distinct in the STED image. To determine structure size, a 5-pixel-wide region of interest was designated (denoted by the hollow white bar) and the fluorescence intensity averaged in NIH *ImageJ* to generate the line profiles depicted in Figure 2B. As before, the profiles were fitted to one-dimensional Gaussian and Lorentzian functions, yielding the fwhm of each peak. In the confocal image, the fitted fwhm was 327 nm, and in the STED image, it was 110 nm. This resolution is consistent with previous measures of actin stress fiber diameter via transmission electron microscopy (TEM) (*21*). In addition, living NIH 3T3 fibroblast cells also expressing the H6.2-MG FAP fused to actin, which were fixed and permeabilized and then labeled with 100nM MG-2p, still showed visible stress fibers despite the fixation process (see Supporting Information). Hence, these probes can be used for live cell STED and combined with conventional immunofluorescence assays in fixed cells.

We have demonstrated the first use of fluorogen activating proteins for STED nanoscopy in living cells. The biological structures imaged exhibited FWHMs in STED that were reduced by up to a factor of 3 over confocal microscopy. In this case, the measured fwhm is likely due to the sizes of the actual biological structures measured (*21*) and does not reflect the true subdiffraction limit of the probe and instrument. The ultimate achievable resolution as indicated by the depletion curves is equivalent to that of Atto647N which was determined to be ∼70 nm for the system used (see Supporting Information). These new genetically targetable far-red probes coupled with STED nanoscopy have the potential for making long-term dynamic measurements of living cells at near video rate and high resolution with reduced phototoxicity relative to conventional fluorescent proteins.

ACKNOWLEDGMENT

We would like to acknowledge the NIH National Technology Center for Networks and Pathways for financial support under grant number 5U54RR022241 and Dr. Erik Snapp for his kind assistance with cell culture and transfection experiments in HeLa cells. M.B. also wishes to acknowledge Carnegie Mellon University for faculty start-up funds.

Supporting Information Available: (1) Materials and methods for the growth, transfection and imaging of yeast and mammalian cells; (2) depletion efficiency of various different malachite green binding FAP modules; (3) survival of the intracellular FAP module through fixation and permeabilization; (4) methods used to fit Gaussian and Lorentzian functions to extracted line profiles; (5) estimating the maximum achievable resolution using the Leica TCS-STED system. This material is available free of charge via the Internet at http://pubs.acs.org.

LITERATURE CITED

(1) Berlier, J. E., Rothe, A., Buller, G., Bradford, J., Gray, D. R., Filanoski, B. J., Telford, W. G., Yue, S., Liu, J., Cheung, C. Y., Chang, W., Hirsch, J. D., Beechem, J. M., and Haugland, R. P. (2003) Quantitative comparison of long-wavelength Alexa Fluor dyes to Cy dyes: fluorescence of the dyes and their bioconjugates. *J. Histochem. Cytochem. 51*, 1699–712.

(2) Mujumdar, R. B., Ernst, L. A., Mujumdar, S. R., Lewis, C. J., and Waggoner, A. S. (1993) Cyanine dye labeling reagents: sulfoindocyanine succinimidyl esters. *Bioconjugate Chem. 4*, 105–11.

(3) Shaner, N. C., Steinbach, P. A., and Tsien, R. Y. (2005) A guide to choosing fluorescent proteins. *Nat. Methods 2*, 905–9.
(4) Betzig, E., Patterson, G. H., Sougrat, R., Lindwasser, O. W., Olenych, S., Bonifacino, J. S., Davidson, M. W., Lippincott-Schwartz, J., and Hess, H. F. (2006) Imaging intracellular fluorescent proteins at nanometer resolution. *Science 313*, 1642–5.
(5) Hess, S. T., Girirajan, T. P., and Mason, M. D. (2006) Ultra-high resolution imaging by fluorescence photoactivation localization microscopy. *Biophys. J. 91*, 4258–72.
(6) Rust, M. J., Bates, M., and Zhuang, X. (2006) Sub-diffraction-limit imaging by stochastic optical reconstruction microscopy (STORM). *Nat. Methods 3*, 793–5.
(7) Gustafsson, M. G. (2000) Surpassing the lateral resolution limit by a factor of two using structured illumination microscopy. *J. Microsc. 198*, 82–7.
(8) Gustafsson, M. G. (2005) Nonlinear structured-illumination microscopy: wide-field fluorescence imaging with theoretically unlimited resolution. *Proc. Natl. Acad. Sci. U.S.A. 102*, 13081–6.
(9) Hell, S. W., and Wichmann, J. (1994) Breaking the diffraction resolution limit by stimulated-emission - stimulated-emission-depletion fluorescence microscopy. *Opt. Lett. 19*, 780–782.
(10) Rittweger, E., Han, K. Y., Irvine, S. E., Eggeling, C., and Hell, S. W. (2009) STED microscopy reveals crystal colour centres with nanometric resolution. *Nat. Photonics 3*, 144–147.
(11) Westphal, V., Rizzoli, S. O., Lauterbach, M. A., Kamin, D., Jahn, R., and Hell, S. W. (2008) Video-rate far-field optical nanoscopy dissects synaptic vesicle movement. *Science 320*, 246–9.
(12) Shroff, H., Galbraith, C. G., Galbraith, J. A., and Betzig, E. (2008) Live-cell photoactivated localization microscopy of nanoscale adhesion dynamics. *Nat. Methods 5*, 417–23.
(13) Nagerl, U. V., Willig, K. I., Hein, B., Hell, S. W., and Bonhoeffer, T. (2008) Live-cell imaging of dendritic spines by STED microscopy. *Proc. Natl. Acad. Sci. U.S.A. 105*, 18982–7.
(14) Hein, B., Willig, K. I., and Hell, S. W. (2008) Stimulated emission depletion (STED) nanoscopy of a fluorescent protein-labeled organelle inside a living cell. *Proc. Natl. Acad. Sci. U.S.A. 105*, 14271–6.
(15) Eggeling, C., Ringemann, C., Medda, R., Schwarzmann, G., Sandhoff, K., Polyakova, S., Belov, V. N., Hein, B., von Middendorff, C., Schonle, A., and Hell, S. W. (2009) Direct observation of the nanoscale dynamics of membrane lipids in a living cell. *Nature 457*, 1159–62.
(16) Schroder, J., Benink, H., Dyba, M., and Los, G. V. (2009) In vivo labeling method using a genetic construct for nanoscale resolution microscopy. *Biophys. J. 96*, L1–3.
(17) Szent-Gyorgyi, C., Schmidt, B. F., Creeger, Y., Fisher, G. W., Zakel, K. L., Adler, S., Fitzpatrick, J. A., Woolford, C. A., Yan, Q., Vasilev, K. V., Berget, P. B., Bruchez, M. P., Jarvik, J. W., and Waggoner, A. (2008) Fluorogen-activating single-chain antibodies for imaging cell surface proteins. *Nat. Biotechnol. 26*, 235–40.
(18) Babendure, J. R., Adams, S. R., and Tsien, R. Y. (2003) Aptamers switch on fluorescence of triphenylmethane dyes. *J. Am. Chem. Soc. 125*, 14716–7.
(19) Klis, F. M., Boorsma, A., and De Groot, P. W. (2006) Cell wall construction in *Saccharomyces cerevisiae*. *Yeast 23*, 185–202.
(20) Worn, A., and Pluckthun, A. (2001) Stability engineering of antibody single-chain Fv fragments. *J. Mol. Biol. 305*, 989–1010.
(21) Okabe, S., and Hirokawa, N. (1989) Incorporation and turnover of biotin-labeled actin microinjected into fibroblastic cells: an immunoelectron microscopic study. *J. Cell Biol. 109*, 1581–95.
(22) Hell, S. W. (2007) Far-field optical nanoscopy. *Science 316*, 1153–8.

BC900249E

STED nanoscopy in living cells using Fluorogen Activating Proteins

Supplementary Data

James A.J. Fitzpatrick, Qi Yan, Jochen J. Sieber, Marcus Dyba, Ulf Schwarz, Chris Szent-Gyorgyi, Carol A. Woolford, Peter B. Berget, Alan S. Waggoner and Marcel P. Bruchez

Molecular Biosensor and Imaging Center, Carnegie Mellon University,

4400 Fifth Avenue, Pittsburgh PA 15213

1. Materials and Methods

Yeast cells were grown and expression of surface displayed scFvs induced as described in Szent-Gyorgyi *et al.*(*1*). Cells were washed in modified PBS containing 2 mM EDTA and 0.1% Pluronic F127(*1*) resuspended in modified PBS before plating onto 35mm petri dishes with 14mm optical microwells (MatTek Corporation, Ashland, MA) pre-treated with concanavalin-A to ensure immobilization of yeast cells. After cells had bound to optical microwell surface (typically 5-10 minutes) either MG-2p (impermeant) or MG-Ester (permeant) fluorogens were incubated at a resultant dye concentration of 100nM for 5 minutes prior to imaging.

NIH 3T3 and HeLa cells expressing the H6-AFM-MG FAP as an N-terminal fusion to actin were generated by transient transfection using Lipofectamine 2000 (Invitrogen, Eugene OR) and were grown in base DMEM with 10% bovine calf serum and 1% penicillin/streptomycin. Cells were plated and imaged under identical conditions to yeast described above. Positive transfectants were identified via confocal fluorescence microscopy (5-10% efficiency) with visible stress fibers after labeling with the MG-ester at 300nM concentration. In the NIH 3T3 cells actin stress fibers were only partially visible due to the large volume of monomeric actin. To counter this, dishes containing another subsequent round of transients were fixed in 4% para-formaldehyde and permeabilized and washed in 0.5% and 0.1% Triton-X respectively. Addition of MG-2p at 100nM concentration resulted in strong labeling of stress fibers without the diffuse background of monomeric actin.

The confocal and STED images shown in Figure 1, 2 and S3 were recorded with a commercially available system equipped with a specially corrected Oil objective (HCX Pl APO 100x 1.4NA STED): the Leica TCS STED. Excitation and depletion were provided by a 635nm pulsed diode laser (PicoQuant, Germany) and a tunable Spectra Phyics Mai Tai HP, respectively. For the chosen intensity settings 1.4 – 69µW were measured for the 635nm excitation in the back aperture of the objective. The spectral range of the fluorescence to be detected by the avalanche photodiode was selected applying 2 Semrock Brightline filters (FF01-685/40-25).The pinhole was set to values between 0.5 and 1 Airy to allow optical sectioning. Pixel sizes were kept between 19.2nm x 19.2nm and 27.7nm x 27.7nm to avoid undersampling. Shrinking the effective excitation spot results not only in increased resolution but also in less total signal in STED compared to confocal microscopy. In some cases this loss in signal intensity was compensated by raising the excitation power when recording the STED image, but to allow a fair comparison all other imaging parameters were always kept the same between the confocal and the according STED image. STED images for the MG-FAPs were recorded with the wavelength of the depletion laser set to 740nm. Depletion power at 740nm was up to 165mW measured at the back aperture of the objective.

All images were post-processed with a 1 pixel median filter within ImageJ. Confocal images were displayed at the full range of intensities (0-255) with the equivalent STED images displayed at three-quarters of that (0-192).

2. Depletion curves

To compare depletion efficiencies normalized fluorescence intensities are plotted against STED power. To generate these so called depletion curves for a given fluorogen/FAP combination two line sequential series of images of yeast were recorded with an Airy function used as depletion PSF overlaid with the excitation PSF. 50.5µW of excitation laser (635nm) were measured at the back aperture of the objective. The pinhole was set to Airy 0.5. The fluorescence collected on an internal PMT of the Leica TCS STED was selected with a Semrock Brightline filter (FF01-685/40-25). The power applied to the sample by the depletion laser was controlled via an AOM and varied for the individual images of a given series. For the first and second series 0, 5, 10, 15, 20, 25, 30, 35% and 0, 40, 50, 60, 70, 80, 90, 100% were chosen, respectively. The power of the STED laser was measured at the back aperture of the objective.

Typical images contained several yeast cells. The fluorescent regions to analyze (i.e. the cell wall) were identified applying a mask obtained by thresholding and median filtering For both image series background subtracted fluorescence intensity values obtained were normalized to the according 0% AOM frame and plotted against the STED power at the back aperture for the corresponding AOM setting. For a given fluorogen/FAP combination at least three depletion curves were recorded from different fields of views and averaged for a given wavelength. Figure S1 shows the depletion curves for L5-MG-L90S at three different depletion wavelengths (730, 740, 750nm). Figure S2 shows three different FAP clones depleted at 740nm compared to the organic dye Att647N used in indirect immunofluorescence and depleted at 750nm. Data for Atto647N were recorded with 39µW measured at the back aperture of the objective for the excitation laser. The areas to analyze were selected defining regions of interest on Atto647N stained Vero cells.

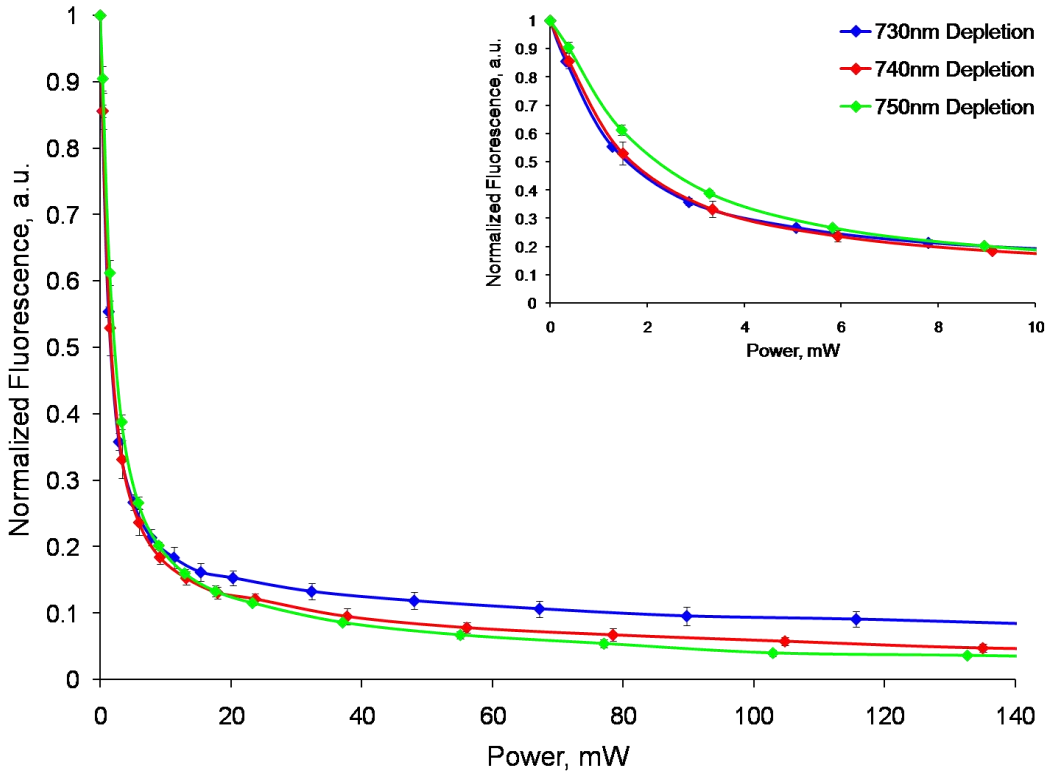

Figure S1. Depletion curves for L5-MG-L90S. Averaged curves (n=3) with standard deviation shown. Inset graph shows same depletion data for power range 0-10mW.

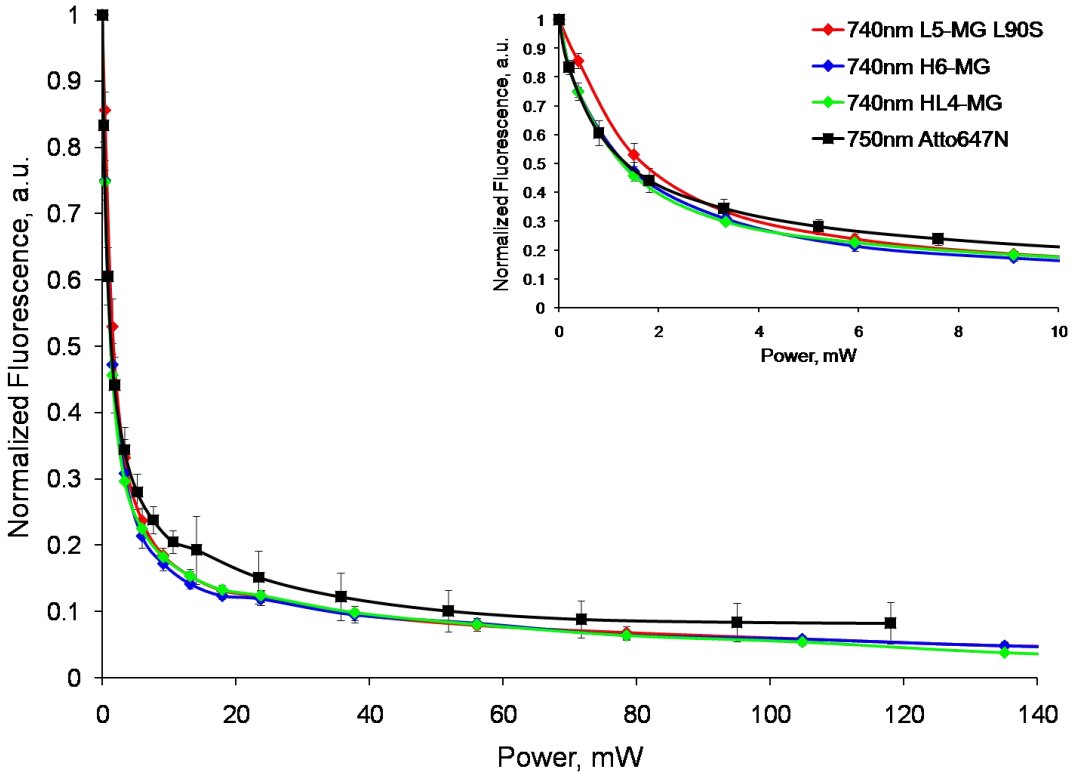

Figure S2. Depletion curves for L5-MG-L90S FAP depleted at 740nm and Atto647N organic dye depleted at 750nm. Note the similar depletion behavior of the probes which indicates that the same resolution increase can be expected. With the given commercial system a FWHM of ~70nm was measured for single fluorescent point sources for Atto647N (compare Figure S4). Averaged curves (n=3) with standard deviation shown.

3. Fixation of NIH 3T3 H6-AFM-MG-actin cells

Due to the presence of a diffuse background of fluorescence from monomeric actin in the H6-AFM-MG-actin construct expressed in living NIH 3T3 cells. These transfectants were fixed and permeabilized as described above to washout the monomeric actin and showed visible stress fibers upon labeling with 100nM of MG-2p. Figure S3 shows both confocal and STED images of fixed cells.

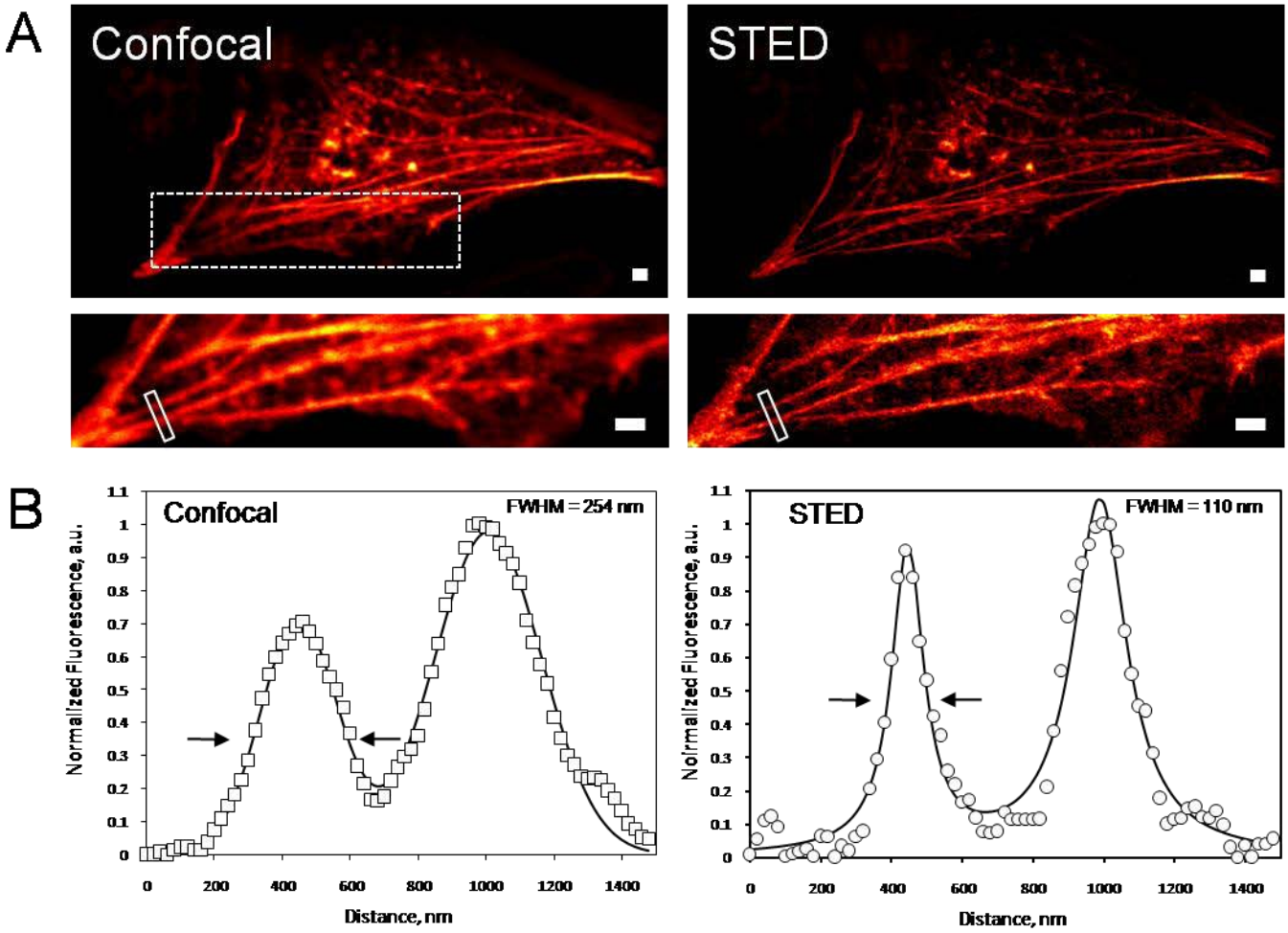

Figure S3. A. Fixed and permeabilized NIH 3T3 cells expressing the H6-MG-AFM disulfide free FAP module expressed as an N-terminal fusion to actin labeled using the MG-ester fluorogen (upper left panel confocal, upper right panel STED, with a zoomed in region denoted by the dashed line box below each image). Hollow white bar denotes a 10 pixel wide region of interest. **B.** Line profiles generated from the averaged fluorescence intensity within the region of interest plotted as a function of distance. Solid lines indicate a fit to a linear sum of one-dimensional Gaussian (confocal) or Lorentzian (STED) functions. The upper fiber in the image represents the first peak in the line profile whose FWHM are 254nm (confocal) and 110nm (STED). Solid white lines indicate 1μm scale bars.

4. Fitting confocal and STED line profiles

Line profiles were generated by taking a 10 pixel wide region of interest and averaging the fluorescence intensity over those 10 pixels as a function of lateral distance. Confocal line profiles were fitted to a one-dimensional Gaussian function of the form:

$$f(x) = ae^{-\frac{(x-x_0)^2}{\sigma^2}}$$

where *a* represents the peak intensity, x_0 the peak position and σ is related to the full-width at half maximum (FWHM) by the following equation: $\mathrm{FWHM} = 2\sqrt{2\ln 2}\,\sigma$. STED line profiles were instead fitted to a one-dimensional Lorentzian function of the form:

$$f(x) = a\left[\frac{\gamma}{(x-x_0)^2 + \gamma^2}\right]$$

where *a* represents the peak intensity, x_0 peak position and γ represents the true half-width at half maximum.

5. Estimating the resolution achievable for Atto647N with the given Leica TCS STED

The point spread function was experimentally determined on fluorescent point sources. For this purpose glass-adsorbed primary antibodies stained by Atto647N-labeled secondary antibodies mounted in Mowiol were imaged (as described in(*2*) with a depletion wavelength of 750nm). 183 objects were fitted with a 2D Lorentzian function. The obtained FWHM in x and y yielded an average of 71nm and 72nm, respectively.

For illustration, signals obtained for 183 single fluorescent point sources were overlaid (see **Figure S4**).

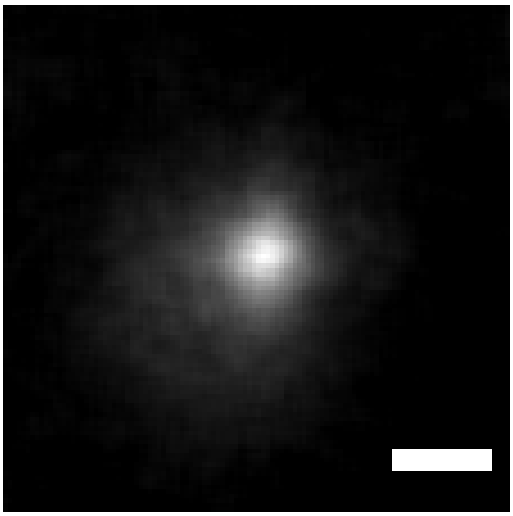

Figure S4. Overlaid signals from 183 single fluorescent point sources. Image is 112x112 pixels with pixel dimensions of 4.46nm (scale bar is 100nm).

Given the almost identical nature of the Atto647N and L5-MG-L90S depletion curves and I_{50} values, it is reasonable to project that the maximum resolution attainable with the L5-MG-L90S FAP module and the given system (Leica TCS-STED) will also be similar ~70nm.

References cited

(1) Szent-Gyorgyi, C., Schmidt, B. F., Creeger, Y., Fisher, G. W., Zakel, K. L., Adler, S., Fitzpatrick, J. A., Woolford, C. A., Yan, Q., Vasilev, K. V., Berget, P. B., Bruchez, M. P., Jarvik, J. W., and Waggoner, A. (2008) Fluorogen-activating single-chain antibodies for imaging cell surface proteins. *Nat Biotechnol 26*, 235-40.

(2) Sieber, J. J., Willig, K. I., Heintzmann, R., Hell, S. W., and Lang, T. (2006) The SNARE motif is essential for the formation of syntaxin clusters in the plasma membrane. *Biophys J 90*, 2843-51.

Gold Nanoparticle Arrangement on Viral Particles through Carbohydrate Recognition: A Non-Cross-Linking Approach to Optical Virus Detection

Kenichi Niikura,*[,‡] Keita Nagakawa,[†] Noriko Ohtake,[†] Tadaki Suzuki,[§] Yasutaka Matsuo,[‡] Hirofumi Sawa,[§,||] and Kuniharu Ijiro[‡]

Graduate School of Science and Research Institute for Electronic Science, Hokkaido University, N21W10, Sapporo 001-0021, Japan, Research Center for Zoonosis Control and Global COE program, Hokkaido University, N20W10, Sapporo 001-0020, Japan. Received June 9, 2009; Revised Manuscript Received August 8, 2009

We propose a new approach to optical virus detection based on the spatial assembly of gold nanoparticles on the surface of viruses. Since JC virus-like particles (VLPs) comprise a repeating viral capsid protein that binds to sialic acid, the conjugation of sialic acid-linked Au particles with VLPs enables the spatial arrangement of Au particles on the VLP surface. This structure produced a red shift in the absorption spectrum due to plasmon coupling between adjacent Au particles, leading to the construction of an optical virus detection system. Our system depends not on the simple cross-linking of VLPs and Au particles, but on an ordered Au structure covering the entire surface of the VLPs and can be applied to various virus detection systems using the inherent ligand recognition of animal viruses.

Plasmonic nanostructures have received increasing attention due to their potential application to the optical sensing of biological and chemical analytes. A metal nanoparticle sensor is based on the analyte-induced assembly of metal nanoparticles (*1*−*4*). The assembly of nanoparticles leads to a red shift in the peak wavelength of the surface plasmon resonance frequency. This principle has been applied to various sensing systems, including DNA (*5*), lectin (*6*), protein A (*7*), potassium ion (*8*), heavy metal ion (*9*), and nitrate detection (*10*). These methods require the cross-linking of nanoparticles by an analyte to form aggregations, in which the gap between nanoparticles is small enough to allow interparticle plasmon coupling. However, the analytes are much larger in size than the metallic nanoparticle, such as with viruses and bacteria; the nanoparticles cannot easily aggregate within the plasmon coupling distance.

In this paper, we propose a novel approach to the optical detection of viruses using gold nanoparticles. Recently, inorganic nanostructures prepared with viruses as templates have been often reported (*11*−*16*). However, there have been no reports on the use of their inherent molecular recognitions for the spatially ordered arrangement of metal nanoparticles, which can be applied to virus detection. Since the virus has multiple recognition sites for ligands on its surface, the ligand-displaying nanoparticles could be specifically arranged on the viral surface (Figure 1A). In this case, viruses can be detected from the plasmon shift derived from the assembled gold nanoparticles on the virus surface rather than the analyte-induced aggregation of metallic nanoparticles. The surface plasmon resonance shift strongly depends on both the interparticle distance and the number of coupled particles (*17*). The plasmon shift for multiple (more than two) nanoparticles in linear arrangement is larger than that for two nanoparticles; thus, the multiple coupling of nanoparticles on the virus is expected to cause a large shift of the plasmon band. In addition, the assembly of metallic nanoparticles into a shell-shaped structure is expected to lead to a large plasmon shift. Metallic clusters formed on a spherical body, such as silica particles (diameter∼100 nm) (*18*) or liposomes (diameter∼50 nm) (*19*), show a large red shift (∼200 nm) of the plasmon band. The virus-templated assembly of metallic nanoparticles in a shell-shaped structure is thought to contribute to this large plasmon shift.

To test our approach to the detection of viruses, we used JC virus, which belongs to the Polyomavirus family. This animal virus is a non-enveloped virus that infects humans through an *N*-glycoprotein with α2,6-linked sialic acid on the cell surface (*20*). The capsids contain 360 copies of viral protein 1 (VP1), arranged in 72 VP1 pentamers in an icosahedral lattice (*21*), and each VP1 monomer can bind to the α2,6-linked sialic acid. Since, without the inner DNA genome, the VP1s self-assemble to form virus-like particles (VLPs) *in vitro*, we used the VLPs as a model of native viruses. Using the binding affinity of VP1 to sialic acid, it is expected that the nanoparticles can be arranged on the virus surface corresponding to the spatial pattern of the VP1s (Figure 1A). Herein, using scanning transmission electron microscopy (STEM), we demonstrate that sialic acid-linked gold nanoparticles (sialyl-Au particles) can be assembled on the surface of VLPs. With the aid of a macromolecular crowding reagent, which promotes the association between VLPs and sialyl-Au particles, the interparticle plasmon coupling of the sialyl-Au particles on the viral surface could be detected in a solution as a red shift of the surface plasmon resonance band.

On the basis of previous literature (*22*, *23*), we synthesized a sialic acid-linked lipid (Figure 1B). Synthetic details are shown in the Supporting Information. On the surface of commercially available gold nanoparticles, a ligand-exchange reaction was carried out in the presence of the sialic acid-linked lipid (10 μM) in water. We prepared three sizes of sialyl-Au particles with diameters of 5, 10, and 15 nm, respectively. The binding of the sialic acid-linked lipid to the Au nanoparticles was qualitatively confirmed by FT-IR spectrometry (see Supporting Information Figure S1).

JC capsid protein VP1s recombinantly expressed in *Escherichia coli* spontaneously self-assemble into virus-like particles (VLPs) as described in our previous report (*24*). The conjugation

* Corresponding author. Tel/Fax: +81-11-706-9370. E-mail: kniikura@poly.es.hokudai.ac.jp.
‡ Research Institute for Electronic Science.
† Graduate School of Science.
§ Research Center for Zoonosis Control.
|| Global COE program.

10.1021/bc900255x CCC: $40.75 © 2009 American Chemical Society
Published on Web 09/11/2009

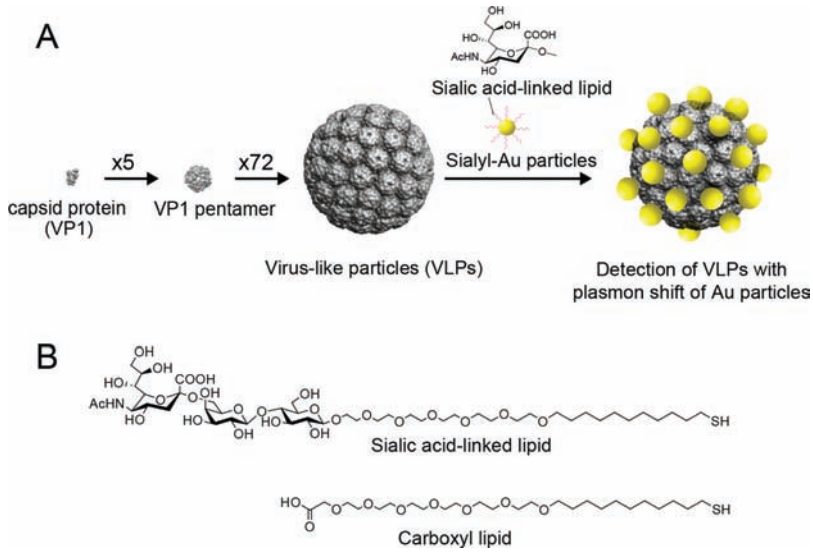

Figure 1. Schematic representation of the detection of virus particles. (A) The formation of the sialyl-Au particle array based on virus-like particles (VLPs) through viral ligand recognition. (B) Structures of the sialic acid-linked and carboxyl lipids used in the preparation of sialyl-Au and carboxyl-Au particles.

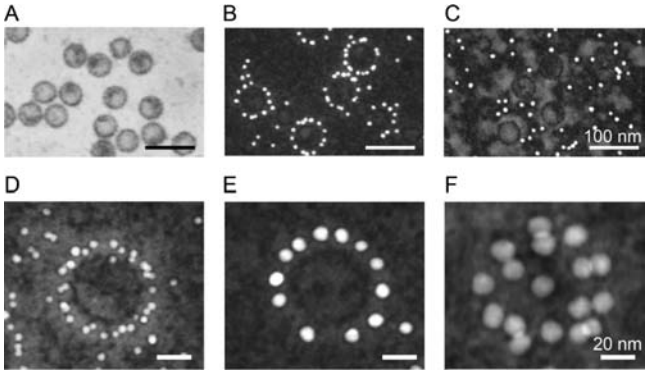

Figure 2. STEM images of (A) VLPs alone, (B) VLPs incubated with 10-nm sialyl-Au particles, and (C) VLPs with 10 nm carboxyl-Au particles. The scale bars represent 100 nm. Sialyl-Au particles were arranged on VLPs, and the diameters of the sialyl-Au particles were (D) 5 nm, (E) 10 nm, and (F) 15 nm, respectively. The scale bar represents 20 nm. The samples were stained with 2% phosphotungstic acid.

of sialyl-Au particles with VLPs was confirmed by STEM. VLP solutions were mounted and immobilized on a carbon-coated TEM grid. After bovine serum albumin (BSA) blocking, a solution of sialyl-Au particles was placed on the VLP-immobilized grid. It is important to note that, for effective binding, this solution was gradually concentrated by evaporation of the solvent on the TEM grid. After washing the grid surface with pure water to remove unbound nanoparticles, the samples were stained with 2% phosphotungstic acid. We observed a homogeneous population of VLPs of around 40 nm in diameter by STEM (Figure 2A). After incubation of the sialyl-Au particles (10 nm) with VLPs for 90 min, binding was confirmed by visualization (Figure 2B). In a control experiment, Au nanoparticles covered with carboxyl lipids were found not to bind onto the VLPs (Figure 2C), indicating that the binding is based on specific recognition between the sialyl-Au particles and the VLPs. The dark background observed in Figure 2B,C is due to BSA blocking.

Figure 2D,E,F shows the typical binding behavior between VLPs and sialyl-Au particles of 5 nm, 10 nm, and 15 nm, respectively. Using 5 and 10 nm sialyl-Au particles, the only observable nanoparticle assembly is in the form of a "ring" structure surrounding the VLPs. These "ring" TEM images have often been observed in noncovalent DNA interaction-driven nanoparticle assemblies (*25*, *26*). In the case of the 15 nm sialyl-Au particles, however, the particles were observed over the entire VLP surface (Figure 2F). We believe that the larger contact area of the 15 nm particles produces an increased number of sialic acid-VP1 interactions affording a stronger affinity between the VLPs and Au particles than that of 5 nm and 10 nm particles.

When Au nanoparticles are assembled, their surface plasmons combine, and the aggregate can be considered a single large particle. This causes a red shift and a broadening of the surface plasmon band. However, the dissociation constant of the native sialic acid-containing glycoprotein and VLPs is on the order of 10^{-7} M (*24*); thus, the concentration used in this study (nM order) was too low for the conjugation of Au nanoparticles with VLPs in solution. Thus, we added dextran as a macromolecular crowding reagent. Molecular crowding enhances the equilibrium association of dilute macromolecules (*27*−*29*). We expected the addition of dextran to induce complex formation, leading to a clear red shift in the plasmon spectra. Figure 3A shows the effect of the molecular crowding reagent on the red shift of the surface plasmon band. At above 30 wt %, dextran induced effective association between the 15 nm sialyl-Au particles and VLPs. As a control, without VLPs, no such shifts were observed, supporting the notion that the red shift can be attributed to the specific interaction between sialyl-Au particles and VLPs. The color of the sialyl-Au particle solution was changed from red to purple after the addition of VLPs (Supporting Information Figure S2). The surface plasmon spectrum of the 15 nm sialyl-Au particles in the presence of VLPs and 40 wt % dextran is shown together with the control spectra in Figure 3B. A 22 nm red shift was observed when 15 nm sialyl-Au particles were incubated with VLPs. To exclude the possibility of nonspecific binding driven by electrostatic interaction, we prepared other negatively charged gold nanoparticles coated with a carboxyl lipid (carboxyl-Au particles). The zeta potential of the sialyl-Au and carboxyl-Au particles were almost the same (-31 ± 1.9 mV and -29 ± 3.8 mV, respectively), indicating that the carboxyl-Au particles afford a suitable control for the negatively charged sialyl-Au particles. The addition of carboxyl-Au particles to a solution of VLPs did not cause a plasmon shift.

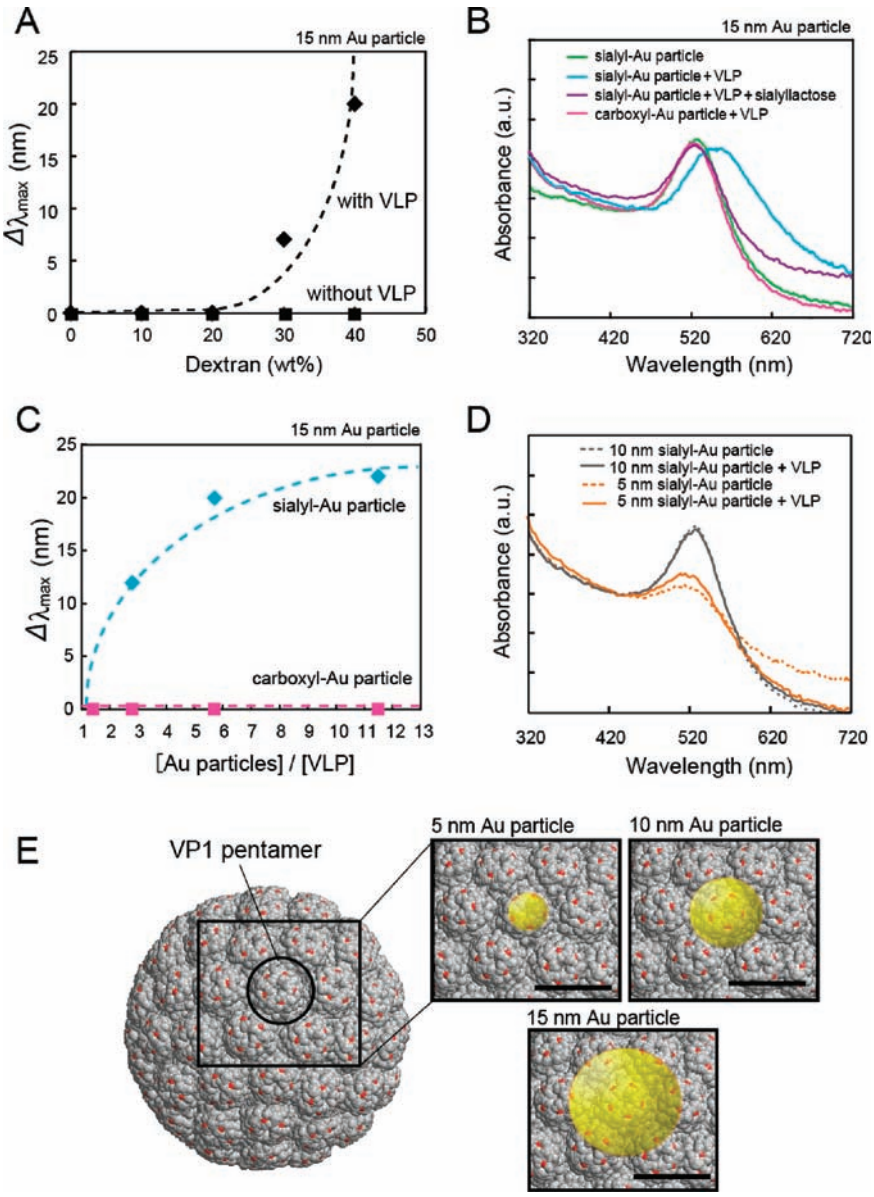

Figure 3. (A) The effect of dextran on the red shift of the surface plasmon band of sialyl-Au particles with or without VLPs ([sialyl-Au particles] = 4 nM, [VLPs] = 0.8 nM). (B) UV−vis spectra for sialyl-Au and carboxyl-Au particles with VLPs in the presence of 40 wt % dextran. As negative controls, 15 nm sialyl-Au particle solutions without VLPs in the presence of 40 wt % dextran and 15 nm sialyl-Au particle solutions containing 5.5 mM sialyllactose as an inhibitor were measured. (C) The red shift of the surface plasmon band of 15 nm sialyl-Au and carboxyl-Au particles in 40 wt % dextran-containing buffered solution as a function of the ratio of Au particles to VLPs. VLP concentration remained at 0.8 nM. (D) UV−vis spectra of solutions of 5 nm and 10 nm sialyl-Au particles containing 40 wt % dextran, with or without VLPs. (E) Schematic representations of the binding of each size of Au nanoparticle to the VLP structure (*35*). Red dots on VLP represent sialic acid binding sites, with each single VP1 pentamer having five binding sites in total. The yellow areas represent the area occupied by each size of Au nanoparticles. The 15 nm Au nanoparticle can be seen to overlap with the adjacent VP1 pentamers. The scale bar represents 10 nm.

Moreover, no red shift of the sialyl-Au particles was observed in the presence of VLPs and an excess amount of sialyllactose (Figure 3B).

This indicates that the red shift in Figure 3B is due to specific binding between the sialyl-Au particles and VLPs. Keating et al. have demonstrated the effect of macromolecular crowding reagents, such as dextran and poly(ethylene glycol) (PEG) solutions, on the thermodynamics of DNA-linked nanoparticle assembly (*30*). They reported that the macromolecular reagents induced not only DNA hybridization-driven nanoparticle assembly, but also undesired nonspecific nanoparticle aggregation. In our experiment on carbohydrate−virus interaction, we clearly demonstrate that the macromolecular crowding reagent is effective in enhancing the specific association of the nanoparticle−biomolecule conjugation. The degree of the red shift was increased in a dose-dependent manner as a function of sialyl-Au particle concentration (Figure 3C), indicating that the interparticle distances were gradually shortened and collective surface plasmon resonance (SPR) changed through modulation of dipole coupling. As an important control, the addition of carboxyl-Au particles to VLPs did not affect the wavelength of the plasmon peak.

On the other hand, the addition of dextran to solutions of 5 nm and 10 nm sialyl-Au particles in the presence of VLPs had no observable effect on the red shift (Figure 3D). Figure 3E shows the difference in size between each Au-particle and a VLP. Each VLP is composed of 72 VP1 pentamers, the diameter of which is approximately 8 nm. A single 5 nm Au particle is able to cover five binding sites of a single VLP pentamer. A 10 nm Au particle is larger than a VP1

pentamer, but it is not large enough to reach the binding sites located on adjacent VP1 pentamers. A 15 nm Au particle disposed on a particular VP1 pentamer, however, can reach six adjacent VP1 pentamers. The number of linkages between the single sialyl-Au particle and the recognition sites of the VLP proportionally influences the binding enthalpy due to cooperative interaction. The larger Au nanoparticles, which have a larger contact area, form a larger number of sialic acid-VLP linkages. Therefore, we can attribute the large plasmon shift of the 15 nm sialyl-Au particles in solution to the increased affinity.

The main factors controlling plasmon coupling are interparticle gap and particle size, and the relationship between these which can be quantitatively expressed as $D/(2r)$, where D is the distance between the centers of adjacent particles, and $2r$ is the diameter of the metal nanoparticle (*31*). It is known that strong interparticle coupling between a pair of adjacent nanoparticles occurs when $D/(2r)$ is smaller than 1.2. In the case of sialyl-Au particles, since the molecular length of the sialic acid lipid is approximately 4.5 nm, the minimum gap when two particles are attached to each other between the metal cores of two sialyl-Au particles is calculated to be 9 nm ($D/(2r) = 1.6$ for the 15 nm Au particles) (Supporting Information Figure S3). According to previous theoretical and experimental data (*17*, *32*), a plasmonic-coupled pair of Au particles having a $D/(2r)$ value of 1.6 cannot explain the pronounced shift (22 nm) observed in this study. Arrayed colloidal nanoparticles, however, have been reported to demonstrate near-field coupling, although the $D/(2r)$ value was larger than 1.2, leading to coherent interactions between multiple adjacent colloidal nanoparticles (*33*, *34*). Therefore, the shift observed here might be caused not by the interparticle coupling from a single pair of metal particles, but by multiple particle arrays.

In summary, we found that the 15 nm sialyl-Au particles are suitable to the optical detection of JC virus VLPs through sialic acid recognition with the aid of a crowding reagent. STEM images supported the notion of multiple Au particle interactions on the surface of a single VLP, leading to a red plasmon shift. Since animal viruses often show inherent molecular recognition, for example, recognizing carbohydrate molecules, the use of ligand-specific interactions could provide a versatile approach to virus detection. Furthermore, we propose that this method is not only applicable to virus detection but also as a simple approach to the investigation of the optical properties of a nanospace surrounded by multiple metal nanoparticles.

ACKNOWLEDGMENT

This study was supported in part by grants from the Ministry of Education, Culture, Sports, Science and Technology; the Ministry of Health, Labor and Welfare, Japan; and the Program of Founding Research Centers for Emerging and Reemerging Infectious Diseases, MEXT, Japan. Nagakawa and Ohtake appreciate the financial support provided by JSPS. The analysis of STEM was carried out at the OPEN FACILITY, Hokkaido University Sousei Hall and HINTS.

Supporting Information Available: Experimental details for the synthesis of sialic acid-linked lipid. Sample preparations for Au-nanoparticles-VLP conjugation. This material is available free of charge via the Internet at http://pubs.acs.org.

LITERATURE CITED

(1) Rosi, N. L., and Mirkin, C. A. (2005) Nanostructures in biodiagnostics. *Chem. Rev. 105*, 1547–1562.

(2) Hong, S., Choi, I., Lee, I., Yang, Y. I., Kang, T., and Yi, J. (2009) Sensitive and colorimetric detection of the structural evolution of superoxide dismutase with gold nanoparticles. *Anal. Chem. 81*, 1378–1382.

(3) Storhoff, J. J., Elaghantan, R., Mucic, R. C., Mirkin, C. A., and Letsinger, R. L. (1998) One-pot colorimetric differentiation of polynucleotides with single base imperfections using gold nanoparticle probes. *J. Am. Chem. Soc. 120*, 1959–1964.

(4) Aili, D., Enander, K., Baltzer, L., and Liedberg, B. (2008) Assembly of polypeptide-functionalized gold nanoparticles through a heteroassociation- and folding-dependent bridging. *Nano Lett. 8*, 2473–2478.

(5) Mirkin, C. A., Lestinger, R. L., and Mucic, R. C. (1996) A DNA-based method for rationally assembling nanoparticles into macroscopic materials. *Nature 382*, 607–609.

(6) Otsuka, H., Akiyama, Y., Nagasaki, Y., and Kataoka, K. (2001) Quantitative and reversible lectin-induced association of gold nanoparticles modified with α-lactosyl-ω-mercapto-poly(ethyleneglycol). *J. Am. Chem. Soc. 123*, 8226–8230.

(7) Thanh, N. T. K., and Rosenzweig, Z. (2002) Development of an aggregation-based immunoassay for anti-protein a using gold nanoparticles. *Anal. Chem. 74*, 1624–1628.

(8) Lin, S., Liu, S., Lin, C., and Chen, C. (2002) Recognition of potassium ion in water by 15-crown-5 functionalized gold nanoparticles. *Anal. Chem. 74*, 330–335.

(9) Kim, Y., Johnson, R. C., and Hupp, J. T. (2001) Gold nanoparticle-based sensing of "spectroscopically silent" heavy metal ions. *Nano Lett. 1*, 165–167.

(10) Daniel, W. L., Han, M. S., Lee, J., and Mirkin, C. A. (2009) Colorimetric nitrite and nitrate detection with gold nanoparticle probes and kinetic end points. *J. Am. Chem. Soc. 131*, 6362–6363.

(11) Blum, A. S., Soto, C. M., Wilson, C. D., Cole, J. D., Kim, M., Gnade, B., Chatterji, A., Ochoa, W. F., Lin, T., Johnson, J. E., and Ratna, B. R. (2004) Cowpea mosaic virus as a scaffold for 3-D patterning of gold nanoparticles. *Nano Lett. 4*, 867–870.

(12) Tseng, R. J., Tsai, C., Ma, L., Ouyang, J., Ozkan, C. S., and Yang, Y. (2006) Digital memory device based on tobacco mosaic virus conjugated with nanoparticles. *Nat. Nanotechnol. 1*, 72–77.

(13) Radloff, C., Vaia, R. A., Brunton, J., Bouwer, G. T., and Ward, V. K. (2005) Metal nanoshell assembly on a virus bioscaffold. *Nano Lett. 5*, 1187–1191.

(14) Slocik, J. M., Naik, R. R., Stone, M. O., and Wright, D. W. (2005) Viral templates for gold nanoparticle synthesis. *J. Mater. Chem. 15*, 749–753.

(15) Dujardin, E., Peet, C., Stubbs, G., Culver, J. N., and Mann, S. (2003) Organization of metallic nanoparticles using tobacco mosaic virus templates. *Nano Lett. 3*, 413–417.

(16) Liu, A., Abbineni, G., and Mao, C. (2009) Nanocomposite films assembled from genetically engineered filamentous viruses and gold nanoparticles: nanoarchitecture- and humidity-tunable surface plasmon resonance spectra. *Adv. Mater. 21*, 1001–1005.

(17) Zhong, Z., Patskovskyy, S., Bouvrette, P., Luong, J. H. T., and Gedanken, A. (2004) The surface chemistry of Au colloids and their interactions with functional amino acids. *J. Phys. Chem. B 108*, 4046–4052.

(18) Oldenburg, S. J., Averitt, R. D., Westcott, S. L., and Halas, N. J. (1998) Nanoengineering of optical resonances. *Chem. Phys. Lett. 288*, 243–247.

(19) Troutman, T. S., Barton, J. K., and Romanowski, M. (2009) Biodegradable plasmon resonant nanoshells. *Adv. Mater. 20*, 2604–2608.

(20) Gee, G. V., Tsomaia, N., Mierke, D. F., and Atwood, W. J. (2004) Modeling a sialic acid binding pocket in the external loops of JC virus VP1. *J. Biol. Chem. 279*, 49172–49176.

(21) Griffith, J. P., Griffith, D. L., Rayment, I., Murakami, W. T., and Casper, D. L. D. (1992) Inside polyomavirus at 25-Å resolution. *Nature 355*, 652–654.

(22) Barrientos, A. G., de la Fuente, J. M., Rojas, T. C., Fernández, A., and Penadés, S. (2003) Gold glyconanoparticles: Synthetic polyvalent ligands mimicking glycocalyx-like surfaces as tools for glycobiological studies. *Chem.—Eur. J. 9*, 1909–1921.

(23) Niikura, K., Nishio, T., Akita, H., Matsuo, Y., Kamitani, R., Kogure, K., Harashima, H., and Ijiro, K. (2007) Accumulation of *O*-GlcNAc-displaying CdTe quantum dots in cells in the presence of ATP. *ChemBioChem 8*, 379–384.

(24) Ohtake, N., Niikura, K., Suzuki, T., Nagakawa, K., Sawa, H., and Ijiro, K. (2008) Enhanced cellular uptake of virus-like particles through immobilization on a sialic acid-displaying solid surface. *Bioconjugate Chem. 19*, 507–515.

(25) Mucic, R. C., Storhoff, J. J., Mirkin, C. A., and Lestinger, R. L. (1998) DNA-directed synthesis of binary nanoparticle network materials. *J. Am. Chem. Soc. 120*, 12674–12675.

(26) Sebba, D. S., Mock, J. J., Smith, D. R., LaBean, T. H., and Lazarides, A. A. (2008) Reconfigurable core-satellite nanoassemblies as molecularly-driven plasmonic switches. *Nano Lett. 8*, 1803–1808.

(27) Minton, A. P. (2006) How can biochemical reactions within cells differ from those in test tubes? *J. Cell Sci. 119*, 2863–2869.

(28) Minton, A. P. (2001) The influence of macromolecular crowding and macromolecular confinement on biochemical reactions in physiological media. *J. Biol. Chem. 276*, 10577–10580.

(29) Ellis, R. J. (2001) Macromolecular crowding: obvious but underappreciated. *Trends Biochem. Sci. 26*, 597–604.

(30) Goodrich, G. P., Helfrich, M. R., Overberg, J. J., and Keating, C. D. (2004) Effect of macromolecular crowding on DNA: Au nanoparticle bioconjugate assembly. *Langmuir 20*, 10246–10251.

(31) Zhao, L., Kelly, K. L., and Schatz, G. C. (2003) The extinction spectra of silver nanoparticle arrays: influence of array structure on plasmon resonance wavelength and width. *J. Phys. Chem. B 107*, 7343–7350.

(32) Jain, P. K., Huang, W., and El-sayed, M. A. (2007) On the universal scaling behavior of the distance decay of plasmon coupling in metal nanoparticle pairs: a plasmon ruler equation. *Nano Lett. 7*, 2080–2088.

(33) Kang, Y., Erickson, K. J., and Taton, T. A. (2005) Plasmonic nanoparticle chains via a morphological, sphere-to-string transition. *J. Am. Chem. Soc. 127*, 13800–13801.

(34) Yockell-Lelièvre, H., Desbiens, J., and Ritcey, A. M. (2007) Two-dimensional self-organization of polystyrene-capped gold nanoparticles. *Langmuir 23*, 2843–2850.

(35) Carrillo-Tripp, M., Shepherd, C. M., Borelli, I. A., Venkataraman, S., Lander, G., Natarajan, P., Johnson, J. E., Brooks III, C. L., and Reddy, V. S. (2009) VIPERdb2: an enhanced and web API enabled relational database for structural virology. *Nucleic Acids Res. 37*, D436–D442.

BC900255X

Supporting Information

for

Gold Nanoparticle Arrangement on Viral Particles through Carbohydrate Recognition: A Non-crosslinking Approach to Optical Virus Detection

Kenichi Niikura*, Keita Nagakawa, Noriko Ohtake, Tadaki Suzuki, Yasutaka Matsuo, Hirofumi Sawa,and Kuniharu Ijiro

Experimental Section

General Methods.

Carboxyl-lipid was purchased from TOYOBO (Japan). CMP-*N*-acetylneuraminic acid disodium salt (CMP-NANA, 2Na) and α2, 6-Sialyltransferase was obtained from Nacalai Tesque, Inc. (Japan), and Japan Tobacco, Inc. (Japan), respectively. Gold nanoparticles (Diameter = 5, 10, or 15 nm) were purchased from BB International (UK). All commercial reagents were purchased from Wako Pure Chemical Industries (Japan) and used as received. MALDI-TOF MS spectra were measured with a Voyager-DE STR-H spectrometer (Applied Biosystems, USA) using 2, 5-dihydroxybenzoic acid (Bluker, Germany) as the matrix. NMR spectra were measured with a JEOL 400 spectrometer.

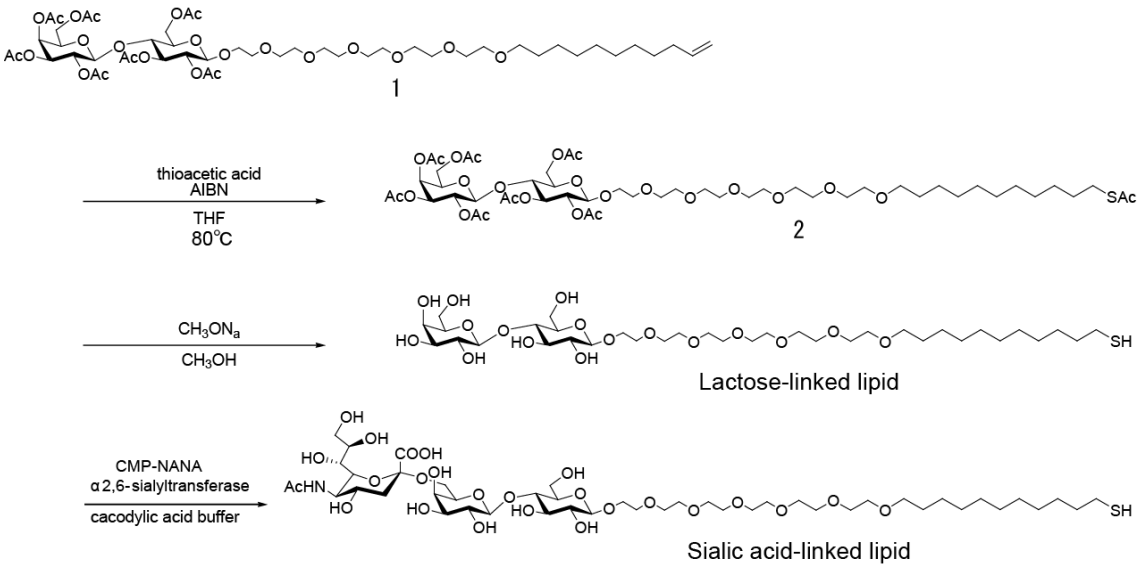

Scheme S1. Synthesis of sialic acid-linked lipid.

Synthesis of Compound 2

Compound **1** was synthesized according to Penadés' method.[1,2] To solutions of compound **1** (500 mg, 0.47 mmol) in THF (20 ml) was added thioacetic acid (50 µl, 0.7 mmol) and azobis(isobutyronitrile) (AIBN, 70 mg, 0.43 mmol). The mixture was refluxed for 16 h at 70-80 ˚C under illumination with UV light. The crude of reaction mixture was concentrated and purified by chromatography on silica gel using mixture solvents (AcOEt:CH_2Cl_2= 1:1). Compound **2** was obtained as a colorless syrup (400 mg, 0.35 mmol, 75 %).

^{1}H-NMR(400MHz, $CDCl_3$): δ = 5.34 (d, 1H, *J*= 3.2 Hz), 5.19 (t, 1H, *J*= 9.2Hz), 5.10 (dd, 1H, *J*= 11 and 7.8 Hz), 4.95 (dd, 1H, *J*= 3.6 and 11 Hz), 4.89 (t, 1H, *J*= 8.2 Hz), 4.56 (d, 1H, *J*= 7.9 Hz), 4.50-4.47 (m, 2H, *J*= 7.9 and 4.1 Hz), 4.10 (m, 3H), 3.89 (m, 2H), 3.79 (t, 1H, *J*= 9.4 Hz), 3.7 (m, 1H), 3.64 (m, 23H), 3.44 (t, 2H, *J*= 6.8 Hz), 2.86 (t, 2H, *J*= 7.4 Hz), 2.32-1.97 (s, 24H), 1.56 (m, 4H), 1.26 (m, 14H); MALDI-TOF MS (m/z) calcd. for $C_{51}H_{84}O_{25}SNa$: 1152.26 $[M+Na]^+$, found 1151.42.

Synthesis of Lactose-linked lipid

A solution of compound **2** (400 mg, 0.35 mmol) in dry MeOH (20 ml) was treated with a 28% methanolic solution of NaOMe (10 µl, 0.72 mmol). The reaction mixture was left for 1 h to complete the oxidation of the thiol group. The reaction was then neutralized with Dowex ion-exchange resin (Dowex 50WX8-200). Purification by reverse phase chromatography (Wakogel 50C18, water:methanol = 1:0.1-1) gave the lactose-linked lipid as a white powder (190 mg, 0.25 mmol, 70 %).

^{1}H NMR(400MHz, CD_3OD) : δ = 4.35 (t, 2H, *J*= 7.3 and 7.6 Hz), 3.4-4 (m, 37H), 3.26 (t, 1H, *J*= 8.3 Hz), 2.68 (t, 1H, *J*= 7.2 Hz), 2.49 (t, 1H, *J*= 7.2 Hz), 1.68 (qn, 1H, *J*= 7.4 Hz), 1.57 (qn, 3H, *J*= 7.0 Hz), 1.45-1.3 (m, 14H); MALDI-TOF MS (m/z) calcd. for $C_{35}H_{67}O_{17}SNa$: 814.97 $[M+Na]^+$, found 815.01.

Synthesis of Sialic acid-linked lipid

Sialylation of the lactose-lipid (5.0 mg, 6.6 µmol) was performed using recombinant α2,6-sialyltransferase (40 µl, 50 mU/ml) in 20 mM cacodylate buffer (1 ml, pH 7.5) containing CMP-NANA (15 mg, 23 µmol) at 30 ºC for 24 h. α2,6-sialyltransferase was used to enzymatically add *N*-acetylneuraminic acid (sialic acid) to the lactose-linked lipid. Purification by size exclusion chromatography (Sephadex G-25 Fine,GE Healthcare UK Ltd., England) gave the sialic acid-linked lipid as a white powder (3.4 mg, 47 %).

^{1}H NMR (400MHz, CD_3OD): δ = 4.30 (dd, 2H, *J*= 10Hz and 9.2 Hz), 3-4.23 (m, 45H), 2.79 (q, 1H, *J*= 12 Hz), 2.68 (t, 1H, *J*= 7.1 Hz), 2.49 (t, 1H, *J*= 6.6 Hz), 1.99 (s, 3H), 1.65 (t, 1H, *J*= 12 Hz), 1.6-1.2 (m, 18H); MALDI-TOF MS (m/z) calcd. for $C_{46}H_{84}NO_{25}S$: 1083.22 $[M-H]^-$, found 1082.05.

Synthesis of carboxyl-Au and sialyl-Au particles

Au nanoparticles (OD_{520nm}=1.0, 2 nM for 15-nm diameter Au particles) were stirred with 10 μM carboxyl-lipid or sialic acid-linked lipid in 5 ml of water for 16 h. The solution was passed through a spin filter (Microcon YM-30, Millipore, USA) to remove excess lipids. The Au nanoparticles remaining on the filter were washed with water several times, and then redispersed in HEPES buffer (pH 7.4, 20 mM HEPES-NaOH, 150 mM NaCl, 1 mM $CaCl_2$). The zeta potential of the carboxyl- and sialyl-Au particles was measured using a zetasizer nano ZS (Malvern, UK).

Scanning transmission electron microscopy (STEM) analysis

A VLP solution (2 μl) was mounted onto a carbon-coated TEM grid (400-mesh with a collodion film, Nisshin EM, Japan) for 5 min and the grid was washed with buffered solution. A BSA (40 mg/ml)-dissolved aqueous solution (2 μl) was dropped onto the VLP-immobilized grid and incubated for 5 min. After removal of the BSA solution by absorption using filter paper, a solution of sialyl-Au particles (5 nM) was dropped onto the grid. The gold nanoparticle solutions were concentrated for 90 min in a N_2 desiccator, and then negatively stained with 2 % phosphotungstic acid (pH 7.4). After desiccation overnight, VLP morphology was confirmed by scanning transmission electron microscopy (STEM) (HD-2000, Hitachi, Japan).

UV-vis spectroscopy analysis

To a 20 μl solution of VLPs (0.8 nM) in HEPES buffer (pH 7.4, 20 mM HEPES-NaOH, 150 mM NaCl, 1 mM $CaCl_2$) was added dextran (Mw 60,000, final concentration = 0~40 wt%) and gold nanoparticles. After incubation for 3 h at room temperature, the plasmon band of the gold nanoparticles was monitored using UV-vis spectroscopy (Nanodrop ND-1000, THERMO, USA).

Inhibition of sialyl-Au particle binding to VLP

To a 20 μl solution of VLPs (0.8 nM) containing sialyl-Au particles (9 nM) and dextran (40 wt%) was added an excess amount of sialyllactose (73 μg, 110 nmol, final concentration = 5.5 mM). After incubation for 3 h at room temperature, the plasmon band of the gold nanoparticles was monitored using UV-vis spectroscopy (Nanodrop ND-1000, THERMO, USA).

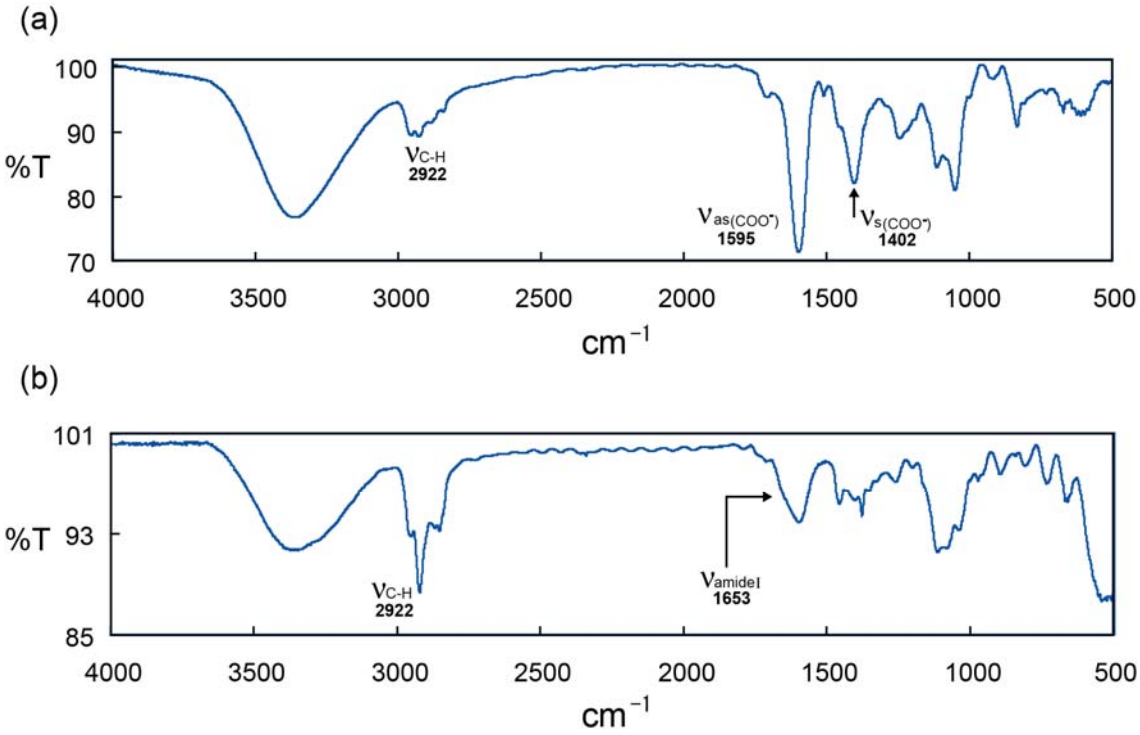

Figure S1. FT-IR spectrum of the Au nanoparticles a) before and b) after the ligand-exchange reaction. a) Before the ligand-exchange reactions, there were large peaks at 1595 cm^{-1} and 1402 cm^{-1}, corresponding to the asymmetric v_{as} (COO^-) and symmetric v_s (COO^-) stretching peaks of the carboxylate (citric acid)[3] on the surface of the Au nanoparticles. b) After ligand exchange to the sialic acid-linked lipid, the peak at 2922 cm^{-1}, corresponding to the C-H stretching vibration, was increased, indicating the presence of the alkyl chains in the sialic acid-linked lipid.[4] The characteristic peak of amide I derived from sialic acid [3] also appeared as a shoulder region peak at 1653 cm^{-1}.

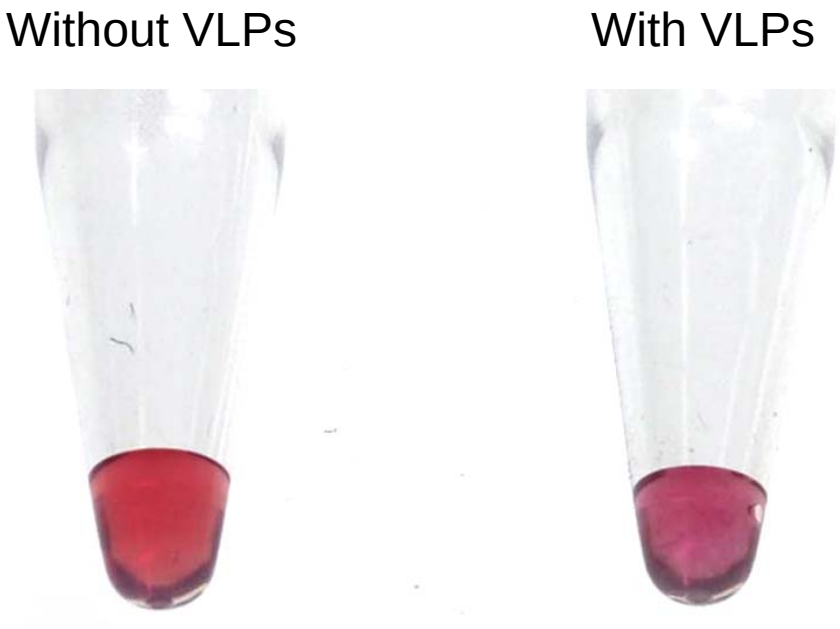

Figure S2. Photographs of particle solutions containing 15-nm sialyl-Au particles and 40 wt% dextran after incubation with or without VLPs. The solution with VLPs shows a red-shift of 20 nm.

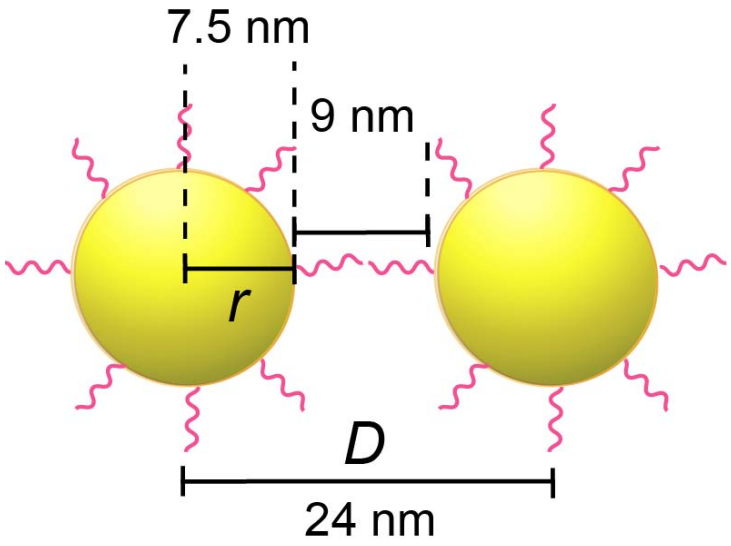

Figure S3. A scematic representation of the direct attachment of two sialyl-Au particles. The extended length of the sialic acid-linked lipid was determined to be 4.5 nm by Chem3D. The minimum gap between two Au-particles and the value of *D/(2r)* were calculated to be 9 nm and 1.6 nm, respectively.

References

(1) A. G. Barrientos, J. M. de la Fuente, T. C. Rojas, A. Fernández, S. Penadés, *Chem. Eur. J.* **2003**, *9*, 1909.

(2) K. Niikura, T. Nishio, Y. Matsuo, H. Akita, R. Kamitani, K. Kogure, H. Harashima, K. Ijiro, *ChemBioChem* **2007**, *8*, 379.

(3) P. Wulandari, T. Nagahiro, K. Michioka, K. Tamada, K. Ishibashi, Y. Kimura, M. Niwano, *Chem. Lett*. **2008**, *8*, 888.

(4) R. Stine, M. V. Pishko, C. Schengrund, *Anal. Chem.* **2005**, *77*, 2882.

ARTICLES

RGD Dendron Bodies; Synthetic Avidity Agents with Defined and Potentially Interchangeable Effector Sites That Can Substitute for Antibodies

Daniel Q. McNerny,[†,‡] Jolanta F. Kukowska-Latallo,[†] Douglas G. Mullen,[†,§] Joseph M. Wallace,[†,||] Ankur M. Desai,[†] Rameshwer Shukla,[†] Baohua Huang,[†] Mark M. Banaszak Holl,[†,§,||] and James R. Baker, Jr.*[,†,⊥]

Michigan Nanotechnology Institute for Medicine and Biological Sciences, Department of Chemical Engineering, Program in Macromolecular Science and Engineering, Department of Chemistry, and Department of Internal Medicine, University of Michigan, Ann Arbor, Michigan 48109 University of Michigan. Received January 13, 2009; Revised Manuscript Received August 17, 2009

Poly(amidoamine) (PAMAM) dendrons were synthesized with c(RGDyK) peptide on the surface to create a scaffold for cellular targeting and multivalent binding. Binary dendron-RGD conjugates were synthesized with a single Alexa Fluor 488, biotin, methotrexate drug molecule, or additional functionalized dendron at the focal point. The targeted dendron platform was shown to specifically target $\alpha_V\beta_3$ integrin expressing human umbilical vein endothelial cells (HUVEC) and human glioblastoma cells (U87MG) *in vitro* via flow cytometry. Specific targeting of the dendron−RGD platform was further confirmed by confocal microscopy. Biological activity of the targeted drug conjugate was confirmed via XTT assay. The orthogonal reaction chemistry used at the dendron focal point gives a precise 1:1 ratio of the attachment of multiple functionalities to a small-molecular-weight, chemically stable, high avidity molecule. These studies serve as a framework to selectively combine biologically relevant functions with enhanced specific binding activity to substitute for antibodies in many diagnostic and therapeutic applications.

INTRODUCTION

The development of specific targeting molecules for diagnostic and therapeutic applications is an important goal being pursued by the biomedical community. Precise targeting of molecules, cellular compartments, or tissues has the potential to positively affect a broad range of disciplines including diagnostic and imaging technologies, and could enhance the treatment of a wide range of conditions such as inflammation, infectious diseases, and cancer. The most common molecules currently employed for numerous applications are monoclonal antibodies (*1, 2*) or immunoconjugates of these antibodies, which take advantage of their high specific binding affinities for antigens. Almost all specific diagnostics are now based on some form of immunoconjugate (*3*−*7*), and numerous monoclonal antibody-based therapeutics are FDA-approved to meet clinical needs (*8, 9*).

Despite these successes, immunoconjugates suffer from significant disadvantages. There are many small molecules that are not immunogenic, and therefore cannot be identified by antibodies. In addition, antibodies are proteins that denature under many chemical and thermal conditions, and therefore necessitate strict refrigeration requirements for diagnostic kits or therapeutics based on immunoconjugates. The large size (approximately 150 kDa) of immunoconjugates limits blood clearance and potentially causes slow tumor penetration (*10, 11*). Being foreign proteins, antibodies elicit immunogenic responses in patients that limit their therapeutic utility (*12, 13*). Finally, biological molecules are difficult and costly to produce in bulk (*14*). Thus, alternative molecules to antibodies are needed.

Poly(amidoamine) (PAMAM) dendritic macromolecules are controllable in size and have defined, monodisperse (PDI = 1.02) structures. The macromolecule is significantly smaller than antibodies, which allows the device to enter the cell to potentially treat multiple proliferation pathways. In addition, the polyamide backbone helps the macromolecule maintain water solubility and minimizes immunogenicity (*15, 16*). The dendritic macromolecules also have large numbers of surface primary amines created by a branched architecture that allow for the attachment of multiple molecules with various functions. This has been demonstrated with targeting ligands, imaging agents, and therapeutics (*17, 18*). The ability to conjugate multiple targeting moieties provides the opportunity to create a platform with increased binding avidity through polyvalent cell interactions (*19*). Targeted dendrimer delivery platforms have been successfully tested in *in vitro* and *in vivo* model tumor systems (*20*−*29*).

To increase the utility of the dendritic scaffold, orthogonal and modular pathways can be used to construct binary devices with a greater degree of specificity and flexibility. However, current research pursuing such pathways to create functional

* Corresponding author. E-mail: jbakerjr@med.umich.edu, Michigan Nanotechnology Institute for Medicine and Biological Sciences, 9220 MSRB III, Box 5648, University of Michigan, Ann Arbor, MI 48109.
[†] Michigan Nanotechnology Institute for Medicine and Biological Sciences.
[‡] Department of Chemical Engineering.
[§] Program in Macromolecular Science and Engineering.
[||] Department of Chemistry.
[⊥] Department of Internal Medicine.

10.1021/bc900217h CCC: $40.75 © 2009 American Chemical Society
Published on Web 09/14/2009

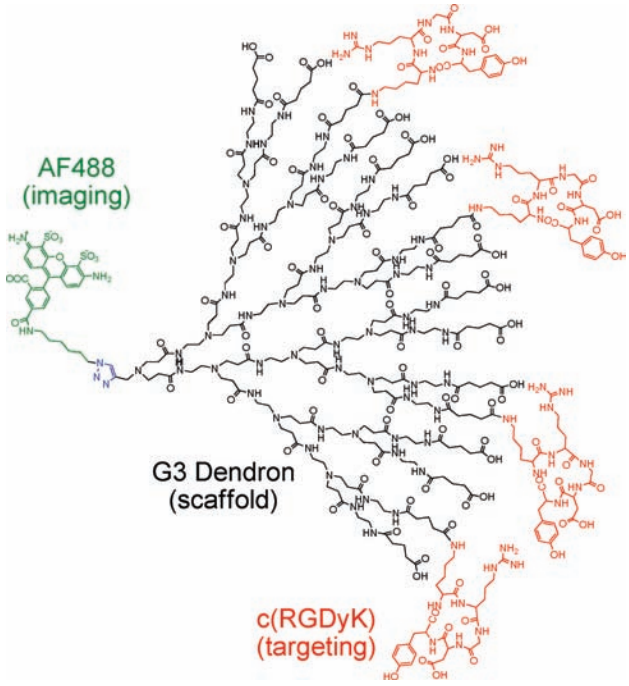

Figure 1. Dendron conjugate AF-G3$(COOH)_{11.9}(RGD)_{4.1}$ (**4**) where Alexa Fluor 488 is conjugated to the dendron focal point via a 1,3-dipolar cycloaddition. The targeting moiety, c(RGDyK) peptide, is conjugated to the carboxylated surface of the dendron.

dendritic devices has been sparse. PAMAM dendrimers have been developed with unique surface groups for modular synthesis via click chemistry (*30*), complementary oligonucleotide hybridization (*31*), or orthogonal functionalization (*32*). Dendrons with a bis-MPA backbone have been utilized by exploiting the unique reactive site at the focal point to create bifunctional materials (*33*). These approaches offer the potential to construct individual combinations for a specific targeting application from a common library of functionalized devices in a versatile manner and overcome the inefficiencies of stepwise conjugations on a single dendritic macromolecule. However, the central advantage of these techniques is that they provide increased homogeneity products by reducing the complexity of ligand distributions created by multifunctional platforms.

Herein, we present the synthesis and evaluation of *in vitro* biological activity for a targeted, PAMAM dendron avidity platform (Figure 1). The functionalized PAMAM dendron can maintain the binding specificity and multivalency of previous dendritic models (*25, 34*) while creating an orthogonally coupled scaffold more suitable for personalized medicine and applications. Binary devices were synthesized through a unique alkyne group at the dendron focal point. The alkyne is reacted with an azide-functionalized dye, biotin, therapeutic molecule or a second dye-conjugated dendron in a copper-catalyzed 1,3-dipolar cycloaddition, commonly referred to as "click chemistry" (*35*). This strategy is attractive because it provides high versatility and yields, mild reaction conditions, and no alteration to neighboring functional groups that eliminates the need for protecting groups. The platform itself gives a precise 1:1 ratio of the attachment of multiple functionalities, preventing aggregate formation. A dendron with multiple Arg-Gly-Asp (RGD) adhesion ligands on the surface and an additional function at the focal point can specifically target $\alpha_V\beta_3$ integrin expressing human umbilical vein endothelial cells (HUVEC) and human glioblastoma cells (U87MG), displaying the biological utility of the platform. The dendron−RGD platform also successfully inhibits tumor growth when conjugated to a therapeutic drug, such as methotrexate (MTX). Thus, the ability to conjugate specific and varied effector sites to the dendron periphery to generate a high avidity binding agent and use orthogonal reaction chemistry at the focal point to add additional functionalities makes these "dendro-bodies" an attractive alternative to antibodies for targeting applications.

EXPERIMENTAL PROCEDURES

General. Alexa Fluor 488 azide and Prolong Gold mounting agent were obtained from Invitrogen. c(RGDyK) peptide was obtained from Peptide International. Biotin-$dPEG_{3+4}$-azide was obtained from Quanta Biodesign. Sephadex G15 and G25 were obtained from GE Life Sciences. Spectra/Por 7 dialysis membrane (MWCO 1000) was obtained from Spectrum Laboratories. NeutrAvidin-Dylight 405 was obtained from Pierce. All other chemicals were obtained from Sigma. All purified reaction products were characterized by ^1H NMR, HPLC, and matrix-assisted laser desorption-ionization time-of-flight (MALDI-TOF) mass spectrometry.

Synthesis of Alkyne-G3-PAMAM Dendron (1). Alkyne-G3-PAMAM dendron was prepared as previously reported (*36*) and analyzed by ^1H and ^{13}C NMR and MALDI-TOF. MS (MALDI), 3479 Da; calculated for $C_{153}H_{305}N_{61}O_{30}$, 3479.45 Da.

Synthesis of Alkyne-G3$(COOH)_{16}$ (2). Glutaric anhydride (0.0164 g, 0.144 mmol) dissolved in anhydrous MeOH (0.8 mL) was added dropwise to a solution of **1** (0.0200 g, 0.00575 mmol) and triethylamine (Et_3N) (0.0186 g, 0.184 mol) in anhydrous MeOH (0.2 mL) while stirring, and the reaction mixture was allowed to stir for 24 h at room temperature. All solvent was removed in vacuo, and the reaction material was dissolved in H_2O, purified on a G-15 Sephadex column and lyophilized. MS (MALDI), 5305 Da; calculated for $C_{233}H_{401}N_{61}O_{78}$, 5305.04 Da.

Synthesis of Alkyne-G3$(COOH)_{11.9}(RGD)_{4.1}$ (3). 1-(3-(Dimethylamino)propyl)-3-ethylcarbodiimide HCl (EDC) (0.0838 g, 0.437 mmol) was allowed to react with **2** (0.0145 g, 0.00273 mmol) in 1:1 H_2O/DMSO (2 mL) for 2 h to form an active ester. c(RGDyK) (0.0169 g, 0.0273 mmol) in 4:1 H_2O/DMSO (1.25 mL) was added dropwise to the EDC and dendron solution and stirred for 2 days at room temperature. The DMSO was removed via dialysis in H_2O for 1 h. The resulting solution was lyophilized, redissolved in H_2O, purified on a G-15 Sephadex column, and again lyophilized. MS (MALDI): 5300−12 000 Da (broad).

Synthesis of AF-G3$(COOH)_{11.9}(RGD)_{4.1}$ (4). A mixture of azide-functionalized Alexa Fluor 488 (0.00022 g, 0.00026 mmol) and **3** (0.0015 g, 0.00019 mmol) in H_2O (1 mL) in the presence of copper(II) sulfate (2.5×10^{-5} g, 0.00010 mmol) and sodium ascorbate (4.0×10^{-5} g, 0.00020 mmol) was stirred for 36 h at room temperature. The solution was purified on a G-25 Sephadex column and lyophilized. MS (MALDI): 5300−12 600 Da (broad).

Synthesis of MTX-azide (5). Methotrexate (0.0238 g, 0.0524 mmol) was dissolved in DMF (1 mL) and cooled in a water/ice bath. *N*-Hydroxysuccinimide (0.0067 g, 0.057 mmol) and EDC (0.0110 g, 0.0576 mmol) were added, and the resulting mixture was stirred in the ice bath for 30 min to give a white precipitate. A solution of 11-azido-3,6,9-trioxaundecan-1-amine (0.0120 g, 0.0550 mmol) in DMF (0.5 mL) was added, and the resulting mixture was allowed to warm to room temperature and stirred for 24 h. The mixture was poured into water (50 mL) and washed with chloroform (50 mL × 3). The aqueous layer was lyophilized and further purified on a G-25 Sephadex column. MS, 654.7 Da; calculated for $C_{28}H_{38}N_{12}O_7$, 654.68 Da.

Synthesis of MTX-G3$(COOH)_{11.9}(RGD)_{4.1}$ (6). A mixture of **5** (0.0019 g, 0.0029 mmol) and **3** (0.0025 g, 0.00032 mmol) in H_2O (1 mL) in the presence of copper(II) sulfate (2.5×10^{-5} g, 0.00010 mmol) and sodium ascorbate (4.0×10^{-5} g, 0.00020 mmol) was stirred for 36 h at room temperature. The solution

was purified on a G-25 Sephadex column and lyophilized. MS (MALDI): 5300−12 600 Da (broad).

Synthesis of Biotin-G3(COOH)$_{11.9}$(RGD)$_{4.1}$ (7). A mixture of biotin-dPEG$_{3\ +\ 4}$-azide (0.0045 g, 0.0063 mmol) and **3** (0.0080 g, 0.00010 mmol) in 1:1 DMSO/H_2O (1 mL) in the presence of copper(II) sulfate (2.5×10^5 g, 0.0010 mmol) and sodium ascorbate (4.0×10^5 g, 0.00020 mmol) was stirred for 36 h at room temperature. The solution was purified on a G-25 Sephadex column and lyophilized. MS (MALDI): 5300−12 700 Da (broad).

Synthesis of Azide-G2-PAMAM Dendron (8). Azide-G2-PAMAM dendron was prepared as previously reported (*37*) and analyzed by ^{1}H and MALDI-TOF. MS (MALDI), 1698.1 Da; calculated for $C_{73}H_{148}N_{32}O_{14}$, 1698.16 Da.

Synthesis of Azide-G2(AF)$_2$(OH)$_{24}$ (9). Alexa Fluor 488 sulfodichlorophenol ester (0.0050 g, 0.0061 mmol) dissolved in 0.5 mL DMF was added dropwise to **8** (0.0028 g, 0.0016 mmol) in 0.5 mL 0.1 M sodium bicarbonate buffer while stirring, and the reaction mixture was allowed to stir for 24 h at room temperature. Solvent was removed in vacuo, and the resulting product was dissolved in 2 mL H_2O. Glycidol (0.0112 g, 0.1511 mmol) was added to the solution, and the mixture was allowed to stir for 24 h at room temperature. The solution was purified on a G-25 Sephadex column and lyophilized. MS (MALDI): 3000−7000 Da (broad).

Synthesis of (OH)$_{24}$(AF)$_2$G2-G3(COOH)$_{11.9}$(RGD)$_{4.1}$ Co-Dendron (10). A mixture of **9** (0.0030 g, 0.00067 mmol) and **3** (0.0044 g, 0.00056 mmol) in H_2O (1 mL) in the presence of copper(II) sulfate (2.5×10^5 g, 0.00010 mmol) and sodium ascorbate (4.0×10^5 g, 0.00020 mmol) was stirred for 36 h at room temperature. The solution was first purified on a G-25 Sephadex column and lyophilized. The product was further purified via HPLC to remove excess azide-G2(AF)(OH). MS (MALDI): 5000−29 000 Da (broad), 17 500 Da maximum.

Cell Culture and Incubation with the Dendron. HUVEC cells were obtained from Invitrogen (Cascade Biologics). U87MG and KB cells were obtained from American type Tissue Collection (Manasass, VA). HUVEC (cat. # C-015−10C), U87MG, and KB cells were grown and maintained according to the supplier's protocol. Compounds were prepared in non-supplemented cell culture medium (Medium 200) and incubated in cell suspensions for 2 h at 37 °C in a 5% CO_2 incubator. Blocking experiments were run by preincubating the cells with a 200 equiv excess of c(RGDyK) for 10 min at room temperature prior to incubation.

Flow Cytometry. Cells were washed with 5 mL of PBS, spun at 150 G for 7 min, and resuspended in 1 mL of PBS prior to being examined. Cells were examined quantitatively for dendron uptake via a flow cytometer (Beckman Coulter Epics XL-MCL). The FL1 fluorescence of 10 000 cells was measured, and the mean fluorescence of cells was quantified.

Confocal Microscopy. HUVEC cells were seeded and grown on 35 mm glass-bottomed culture dishes (MatTek Corp., Ashland, MA). After 2 days, cells were treated with 0.5 μM co-dendron **10** or biotin-conjugated dendron **7**. Blocked samples were run by preincubating the cells with a 200 equiv excess of c(RGDyK) for 10 min at room temperature prior to incubation. After the 2 h incubation period, biotin-conjugated dendron **7** treated cells were treated with 4 mg/mL BSA for 30 min to limit nonspecific binding followed by treatment with 0.5 μM NeutrAvidin-Dylight 405 for 30 min. Media was aspirated from the cells, washed 3 times with PBS, and fixed with 2% paraformaldehyde. The samples were again aspirated, washed 3 times, and aspirated before mounting with Prolong Gold, and a coverslip was added. Samples were imaged using an Olympus FluoView 500 Laser Scanning confocal microscope using 60×, 1.5 NA oil immersion objective. Fluorescence and differential interference contrast (DIC) images were collected simultaneously using either an argon laser with 488 nm excitation or a solid state diode laser with 405 nm excitation and *FluoView* software.

Cytotoxicity Assay. For cytotoxicity experiments, cells were seeded in 96-well microtiter plates (2500 cells/well) in Medium 200. The cells were treated in triplicate with different concentrations of free MTX or dendron conjugates for 72 h with a replenishing of 100 μL medium and the conjugates after 48 h. A colorimetric XTT assay (Invitrogen) was performed following the vendor's protocol. An aliquot of 30 μL of XTT working solution prepared according to manufacturer instructions was added to each well using a multichannel pipet followed by the addition of 20 μL of PBS. After 1 h incubation in the dark at 37 °C, the absorbance at 490 nm was recorded using a plate reader. 690 nm was selected as a reference wavelength. Cell viability was calculated on the basis of optical density (OD) from untreated cells. Statistical significance was assessed using two-way ANOVA with posthoc Bonferroni tests checking for main effects of conjugate and concentration. *P*-values less than 0.05 were considered significant.

RESULTS AND DISCUSSION

The surface amines of the G3 PAMAM dendron **1** were allowed to react with excess glutaric anhydride in MeOH, in the presence of Et_3N as base, to form carboxylic acids (Figure 2 i). The reaction yielded carboxyl terminal groups and eliminates potential nonspecific charge interactions with the cell

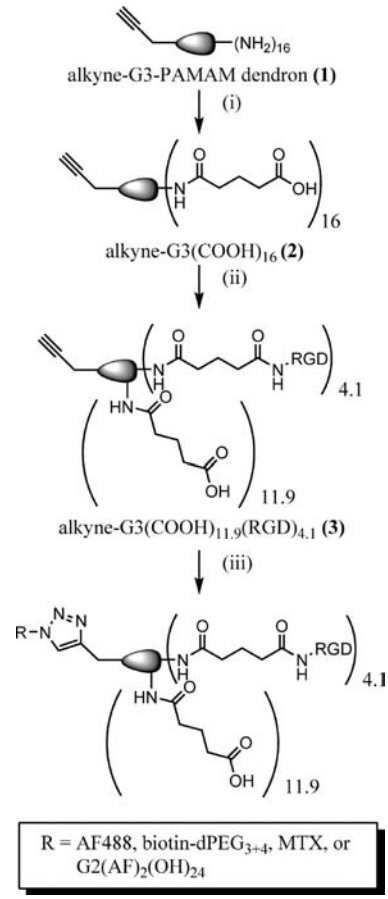

Figure 2. Reaction scheme for creating click-conjugated dendrons employed in the *in vitro* studies: (i) glutaric anhydride, MeOH, 24 h, r.t. (ii) EDC, c(RGDyK), H_2O/DMSO, 2 days, r.t. (iii) Alexa Fluor 488 azide OR biotin-dPEG$_{3+4}$-azide OR MTX-azide (**5**) OR azide-G2(AF)$_2$(OH)$_{24}$ (**9**), sodium ascorbate, copper(II) sulfate, H_2O, 36 h, r.t.

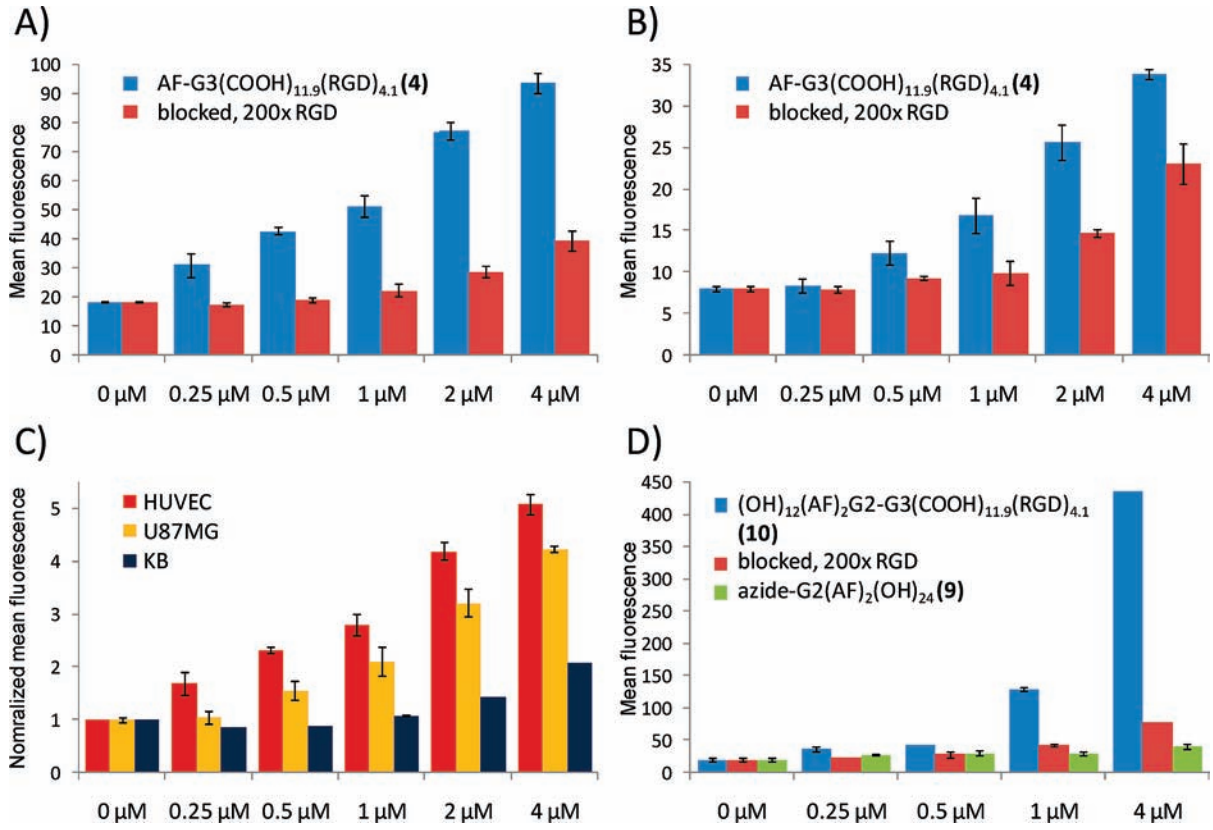

Figure 3. Dose-dependent uptake and specific targeting of binary dendrons determined via flow cytometry, with mean fluorescence plotted against the concentration of the dendron conjugate. Specific targeting of AF-G3$(COOH)_{11.9}(RGD)_{4.1}$ (**4**) was displayed in human umbilical vein endothelial cells (HUVEC) (A), and U87MG human glioblastoma cells (B). Blocking of **4** at all tested concentrations with a 200-fold molar excess of c(RGDyK) confirms specific targeting of the $\alpha_V\beta_3$ integrin by the dendron. A cell-line comparison among HUVEC, U87MG, and $\alpha_V\beta_3$ integrin deficient KB cells (C) shows that dendron uptake is greater in cell lines with increased $\alpha_V\beta_3$ integrin expression, demonstrating the active targeting capability of the binary dendron. A significant increase in mean fluorescence was displayed for a co-dendron structure capable of carrying additional dye, $(OH)_{24}(AF)_2$G2-G3$(COOH)_{11.9}(RGD)_{4.1}$ (**10**), in HUVEC (D). The specific uptake of the co-dendron was confirmed by inhibition with free RGD as well as from a nontargeted control, azide-G2$(AF)_2(OH)_{24}$ (**9**). Error bars indicate standard deviation as computed from the half-peak coefficient of variation.

plasma membrane caused by primary amines. ^{1}H NMR spectroscopy confirmed complete conversion of the primary amines and formation of dendron **2** by the loss of methylene peaks ($-CH_2CH_2NH_2$) at δ 2.80 and 3.30 ppm and the formation of new methylene peaks ($-NHCO(CH_2)_3COOH$) at δ 1.84, 2.21, and 2.27 ppm.

The targeting moiety, RGD peptide, was conjugated to the carboxylated surface of the PAMAM dendron (Figure 2(ii)). RGD binds to the $\alpha_V\beta_3$ integrin found on the luminal surface of endothelial cells during angiogenesis (*38*, *39*). This makes the $\alpha_V\beta_3$ integrin a unique marker that differentiates newly formed capillaries in the tumor vasculature from their mature counterparts (*40*−*42*). Antiangiogenic therapies, such as those that employ RGD targeting, prevent neovascularization by inhibiting differentiation, migration, and proliferation of endothelial cells (*43*).

The surface carboxyl groups were activated with EDC, followed by the addition of 12 equiv of c(RGDyK) to give dendron **3**. The product was purified by size exclusion chromatography and lyophilized. The ^{1}H NMR spectrum of the dendron−RGD body shows some of the aliphatic signals of the peptide overlap with the aliphatic signals of the dendron; however, using the peak integration values in the aromatic region from the phenyl ring of the peptide, an average of 4.1 attached RGD per dendron was calculated.

The dendron AF-G3$(COOH)_{11.9}(RGD)_{4.1}$ **4** (Figure 2(iii)) was synthesized by the reaction of azide-functionalized Alexa Fluor 488 with **3** in a copper-catalyzed 1,3-dipolar cycloaddition. Alexa Fluor 488 was chosen as the fluorescent label for detection

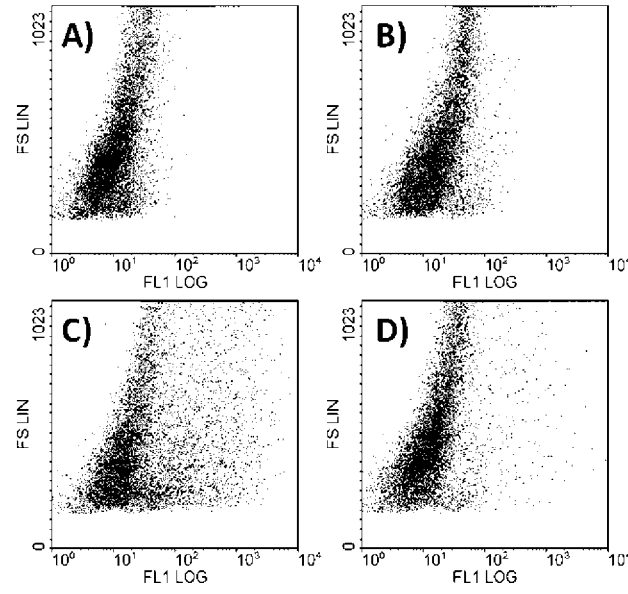

Figure 4. Flow cytometry plot of fluorescence versus forward scatter for $(OH)_{24}(AF)_2$G2-G3$(COOH)_{11.9}(RGD)_{4.1}$ (**10**) at 4 μM. The co-dendron conjugate (C) shows a significant broading in cell population compared to the untreated control (A). When preincubated with a 200-fold molar excess of free RGD (D), **10** is partially blocked, but outcompetes the excess monomeric RGD. The nontargeted control (B), azide-G2$(AF)_2(OH)_{24}$ (**9**), shows no significant change in cell population when compared to the control.

of conjugates by flow cytometry because it is brighter than fluorescein conjugates and more resistant to photobleaching. The products were purified via size exclusion chromatography and lyophilized. The characteristic triazole proton peak of a successful click reaction (δ 8.10 ppm) partially overlaps with the peaks for Alexa Fluor 488.

The specific binding of **4** to $\alpha_V\beta_3$ integrin expressing HUVEC and U87MG cells was examined via flow cytometry (Figure 3). KB cells, which express lower levels of $\alpha_V\beta_3$ integrin, were also evaluated. Cells were treated with dendron−RGD conjugates at final concentrations of 0.25, 0.50, 1, 2, and 4 μM, either with or without preincubation with 200-fold molar equivalents of free RGD peptide. Specific binding and dose dependence of dendron bodies to integrin expressing cells were evaluated after the 2 h incubation at 37 °C. The addition of excess free peptide to inhibit the uptake of the binary dendron by HUVEC and U87MG cells significantly blocked uptake. The inability to completely inhibit binding of the dendron may be due to a higher avidity of the dendron conjugate when compared to free RGD.

A co-dendron structure, $(OH)_{24}(AF)_2$G2-G3$(COOH)_{11.9}(RGD)_{4.1}$ **10** was created by reacting an Alexa Fluor 488 conjugated dendron **9** with an azide focal point with **3**. The product was purified via HPLC to remove excess **9**. The co-dendron structure offers an increased carrying capacity for conjugates, including the Alexa Fluor 488 used in this study. NMR of **9** showed an average of two Alexa Fluor 488 molecules attached per dendron; thus, it was expected to emit a stronger signal when conjugated to **3** compared to a single dye at the focal point.

The specific binding of co-dendron **10** to $\alpha_V\beta_3$ integrin-expressing HUVEC cells was determined via flow cytometry (Figure 3D). The co-dendron-treated samples see the expected increase in mean fluorescence compared to monodye conjugated **4**. Specific binding could be significantly blocked (Figure 4), but again, the higher avidity dendron conjugate out-competed free RGD. Nontargeted control **9** showed minimal nonspecific uptake.

The specific binding evaluated by flow cytometry was confirmed by confocal microscopy. HUVEC cells were treated with 0.5 μM **10** or biotin-conjugated **7** and incubated for 2 h. The biotin conjugate was detected by the addition of an avidin-functionalized dye. Confocal images confirm the uptake of the dendrons (Figure 5 B,D), as seen from the punctuate pattern within the cytoplasm. Partial inhibition of the dendron conjugates by preincubation with free RGD was also established (Figure 5C,E).

A drug conjugate, **6**, was synthesized to show the therapeutic potential of the platform. MTX was reacted with 11-azido-3,6,9-trioxaundecan-1-amine to yield an azide-functional drug. The resulting MTX-azide was then attached to the dendron at the focal point via click chemistry. The inhibition of cell growth induced by the dendron conjugates was tested by XTT colorimetric assay. **6** and free MTX showed comparable cytotoxicity to HUVEC cells after 3 days (Figure 6). Cell numbers were between 55% and 80% for all **6** and free MTX-treated samples at concentrations greater than 0.125 μM. The effects of **6** and MTX were not significantly different at these concentrations. **6** had a significantly greater effect on cell viability vs **3** for concentrations greater than 0.125 μM. **6** has an approximately equivalent concentration of MTX compared to free drug; the drug-conjugated dendron **6** treatments may have slightly lower drug concentration due to any remaining uncoupled dendron. The similar toxicities of **6** and free MTX show that the dendron scaffold is effective at delivering a therapeutic to cells.

We have shown that by exploiting the initiation point as a unique binding site in PAMAM dendrons, selective coupling

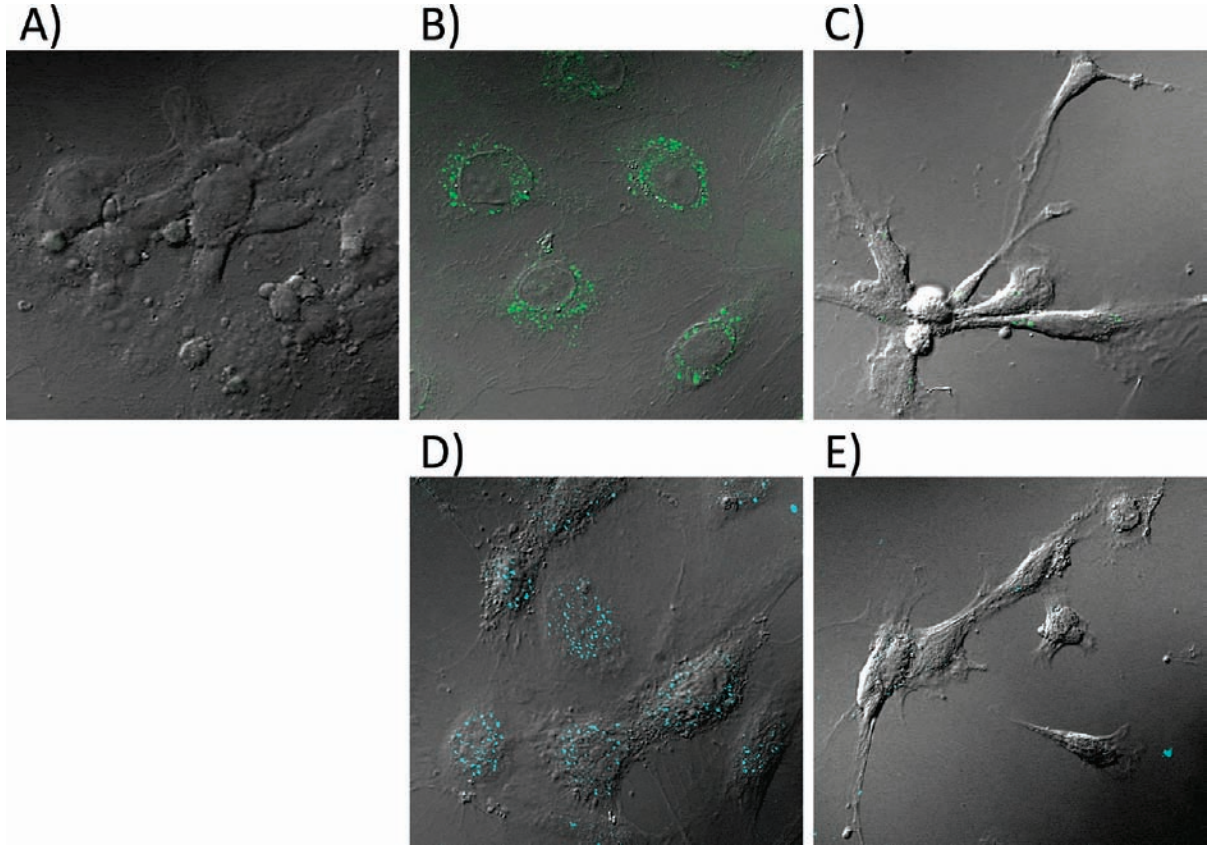

Figure 5. Confocal images of HUVEC cells either untreated (A) or treated with 0.5 μM $(OH)_{24}(AF)_2$G2-G3$(COOH)_{11.9}(RGD)_{4.1}$ (**10**) (B,C) or biotin-G3$(COOH)_{11.9}(RGD)_{4.1}$ (**7**) (D,E) dendron for 2 h. Samples C and E were preincubated with 100 μM c(RGDyK). Biotin-conjugated dendrons were detected by the addition of NeutrAvidin-Dylight 405.

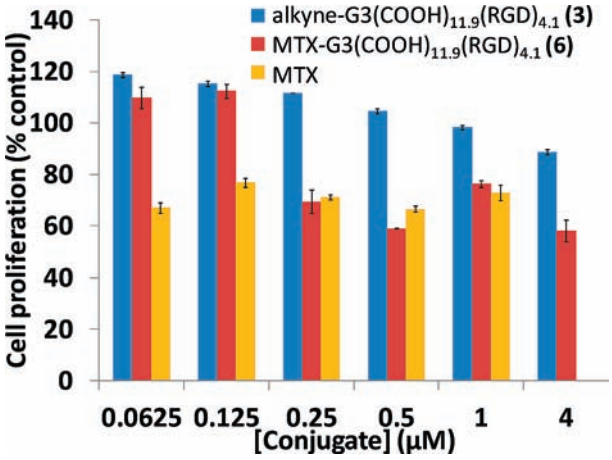

Figure 6. The antiproliferative effect of MTX-G3$(COOH)_{11.9}(RGD)_{4.1}$ (**6**). The dose-dependent inhibition of cell growth of **6** was compared to free MTX and alkyne-G3$(COOH)_{11.9}(RGD)_{4.1}$ control (**3**) using a XTT assay. The cells were treated with different concentrations of free MTX or dendron conjugates for 72 h with a replenishing of 100 μL medium and the conjugates after 48 h. **6** and MTX were determined to not be significantly different for concentrations greater than or equal to 0.25 μM. The effects of **6** and MTX were not significantly different for concentrations greater than 0.125 μM. **6** had a significantly greater effect on cell viability vs **3** for concentrations greater than 0.125 μM.

reactions can yield highly defined binary devices that exhibit the ability to bind to specific cells. Employing a 1,3-dipolar cycloaddition to the focal point of the dendron allows for additional functional moieties to be added in a precise manner without altering other molecules on the dendron. The prototype molecule, synthesized **4**, successfully displayed specific targeting to $\alpha_V\beta_3$ integrin, behaving similarly to RGD conjugates on previously studied multifunctional G5 PAMAM dendrimers (*25*,*34*) that lack the same degree of synthetic control. Detection can be enhanced by attaching an additional dendron with an increased carrying capacity, shown with **10**. The dendron can be combined with biotin, allowing it to interact with a variety of avidin-functionalized molecules. **6** was shown to successfully inhibit the growth of HUVEC cells similarly to free drug. The PAMAM dendron platform has potential to be important in targeted delivery chemistry, as our binary device can serve as a framework to selectively attach diagnostic and imaging agents, therapeutics, or other biologically relevant moieties and surfaces. In addition, coupling a second functionalized dendron or dendrimer to the dendron could address other applications requiring the delivery of multiple drugs or imaging agents.

ACKNOWLEDGMENT

This project was supported with Federal funds from the National Cancer Institute, National Institutes of Health, under award 1 R01 CA119409.

Supporting Information Available: ^{1}H NMR and UPLC/HPLC characterization of dendron conjugates. This material is available free of charge via the Internet at http://pubs.acs.org.

LITERATURE CITED

(1) Imai, K., and Takaoka, A. (2006) Comparing antibody and small-molecule therapies for cancer. *Nat. Rev. Cancer. 6*, 714–727.

(2) Wu, A. M., and Senter, P. D. (2005) Arming antibodies: Prospects and challenges for immunoconjugates. *Nat. Biotechnol. 23*, 1137–1146.

(3) Lequin, R. M. (2005) Enzyme immunoassay (EIA)/enzyme-linked immunosorbent assay (ELISA). *Clin. Chem. 51*, 2415–2418.

(4) Engvall, E., and Perlmann, P. (1971) Enzyme-linked immunosorbent assay (ELISA). quantitative assay of immunoglobulin G. *Immunochemistry 8*, 871–874.

(5) Van Weemen, B. K., and Schuurs, A. H. (1971) Immunoassay using antigen-enzyme conjugates. *FEBS Lett. 15*, 232–236.

(6) Renart, J., Reiser, J., and Stark, G. R. (1979) Transfer of proteins from gels to diazobenzyloxymethyl-paper and detection with antisera: A method for studying antibody specificity and antigen structure. *Proc. Natl. Acad. Sci. U.S.A. 76*, 3116–3120.

(7) Towbin, H., Staehelin, T., and Gordon, J. (1979) Electrophoretic transfer of proteins from polyacrylamide gels to nitrocellulose sheets: Procedure and some applications. *Proc. Natl. Acad. Sci. U.S.A. 76*, 4350–4354.

(8) Maloney, D. G., Grillo-Lopez, A. J., White, C. A., Bodkin, D., Schilder, R. J., Neidhart, J. A., Janakiraman, N., Foon, K. A., Liles, T. M., Dallaire, B. K., Wey, K., Royston, I., Davis, T., and Levy, R. (1997) IDEC-C2B8 (rituximab) anti-CD20 monoclonal antibody therapy in patients with relapsed low-grade non-hodgkin's lymphoma. *Blood 90*, 2188–2195.

(9) Carter, P., Presta, L., Gorman, C. M., Ridgway, J. B., Henner, D., Wong, W. L., Rowland, A. M., Kotts, C., Carver, M. E., and Shepard, H. M. (1992) Humanization of an anti-p185HER2 antibody for human cancer therapy. *Proc. Natl. Acad. Sci. U.S.A. 89*, 4285–4289.

(10) Carter, P. J. (2006) Potent antibody therapeutics by design. *Nat. Rev. Immunol. 6*, 343–357.

(11) Payne, G. (2003) Progress in immunoconjugate cancer therapeutics. *Cancer Cell 3*, 207–212.

(12) Huang, S., Armstrong, E. A., Benavente, S., Chinnaiyan, P., and Harari, P. M. (2004) Dual-agent molecular targeting of the epidermal growth factor receptor (EGFR): Combining anti-EGFR antibody with tyrosine kinase inhibitor. *Cancer Res. 64*, 5355–5362.

(13) Mukohara, T., Engelman, J. A., Hanna, N. H., Yeap, B. Y., Kobayashi, S., Lindeman, N., Halmos, B., Pearlberg, J., Tsuchihashi, Z., Cantley, L. C., Tenen, D. G., Johnson, B. E., and Janne, P. A. (2005) Differential effects of gefitinib and cetuximab on non-small-cell lung cancers bearing epidermal growth factor receptor mutations. *J. Natl. Cancer Inst. 97*, 1185–1194.

(14) Weiner, L. M. (2007) Building better magic bullets--improving unconjugated monoclonal antibody therapy for cancer. *Nat. Rev. Cancer 7*, 701–706.

(15) Kukowska-Latallo, J. F., Bielinska, A. U., Johnson, J., Spindler, R., Tomalia, D. A., and Baker, J. R., Jr. (1996) Efficient transfer of genetic material into mammalian cells using starburst polyamidoamine dendrimers. *Proc. Natl. Acad. Sci. U.S.A. 93*, 4897–4902.

(16) Wiener, E. C., Konda, S., Shadron, A., Brechbiel, M., and Gansow, O. (1997) Targeting dendrimer-chelates to tumors and tumor cells expressing the high-affinity folate receptor. *Invest. Radiol. 32*, 748–754.

(17) Majoros, I. J., Thomas, T. P., Mehta, C. B., and Baker, J. R., Jr. (2005) Poly(amidoamine) dendrimer-based multifunctional engineered nanodevice for cancer therapy. *J. Med. Chem. 48*, 5892–5899.

(18) Majoros, I. J., Myc, A., Thomas, T., Mehta, C. B., and Baker, J. R., Jr. (2006) PAMAM dendrimer-based multifunctional conjugate for cancer therapy: Synthesis, characterization, and functionality. *Biomacromolecules 7*, 572–579.

(19) Hong, S., Leroueil, P. R., Majoros, I. J., Orr, B. G., Baker, J. R., Jr., and and Banaszak Holl, M. M. (2007) The binding avidity of a nanoparticle-based multivalent targeted drug delivery platform. *Chem. Biol. 14*, 107–115.

(20) Kukowska-Latallo, J. F., Candido, K. A., Cao, Z., Nigavekar, S. S., Majoros, I. J., Thomas, T. P., Balogh, L. P., Khan, M. K., and Baker, J. R., Jr. (2005) Nanoparticle targeting of anticancer drug improves therapeutic response in animal model of human epithelial cancer. *Cancer Res. 65*, 5317–5324.

(21) Quintana, A., Raczka, E., Piehler, L., Lee, I., Myc, A., Majoros, I., Patri, A. K., Thomas, T., Mule, J., and Baker, J. R., Jr. (2002) Design and function of a dendrimer-based therapeutic nanodevice targeted to tumor cells through the folate receptor. *Pharm. Res. 19*, 1310–1316.

(22) Thomas, T. P., Patri, A. K., Myc, A., Myaing, M. T., Ye, J. Y., Norris, T. B., and Baker, J. R., Jr. (2004) In vitro targeting of synthesized antibody-conjugated dendrimer nanoparticles. *Biomacromolecules 5*, 2269–2274.

(23) Thomas, T. P., Majoros, I. J., Kotlyar, A., Kukowska-Latallo, J. F., Bielinska, A., Myc, A., and Baker, J. R., Jr. (2005) Targeting and inhibition of cell growth by an engineered dendritic nanodevice. *J. Med. Chem. 48*, 3729–3735.

(24) Wiener, E. C., Brechbiel, M. W., Brothers, H., Magin, R. L., Gansow, O. A., Tomalia, D. A., and Lauterbur, P. C. (1994) Dendrimer-based metal chelates: A new class of magnetic resonance imaging contrast agents. *Magn. Reson. Med. 31*, 1–8.

(25) Shukla, R., Thomas, T. P., Peters, J., Kotlyar, A., Myc, A., and Baker, J. R., Jr. (2005) Tumor angiogenic vasculature targeting with PAMAM dendrimer-RGD conjugates. *Chem. Commun. (Camb.) 46*, 5739–5741;.

(26) Shukla, R., Thomas, T. P., Peters, J. L., Desai, A. M., Kukowska-Latallo, J., Patri, A. K., Kotlyar, A., and Baker, J. R., Jr. (2006) HER2 specific tumor targeting with dendrimer conjugated anti-HER2 mAb. *Bioconjugate Chem. 17*, 1109–1115.

(27) Barth, R. F., Soloway, A. H., Adams, D. M. Alam, F. (1992) Delivery of boron-10 for neutron capture therapy by means of monoclonal antibody-starburst dendrimer immunoconjugates. In *Progress in neutron capture therapy for cancer* (Allen, B. J., Ed.) pp 265−268, Plenum Press, New York.

(28) Malik, N., Evagorou, E. G., and Duncan, R. (1999) Dendrimer-platinate: A novel approach to cancer chemotherapy. *Anticancer Drugs 10*, 767–776.

(29) Malik, N., Wiwattanapatapee, R., Klopsch, R., Lorenz, K., Frey, H., Weener, J. W., Meijer, E. W., Paulus, W., and Duncan, R. (2000) Dendrimers: Relationship between structure and biocompatibility in vitro, and preliminary studies on the biodistribution of ^{125}I-labelled polyamidoamine dendrimers in vivo. *J. Controlled Release 65*, 133–148.

(30) Mullen, D. G. Unpublished.

(31) Choi, Y., Thomas, T., Kotlyar, A., Islam, M. T., and Baker, J. R., Jr. (2005) Synthesis and functional evaluation of DNA-assembled polyamidoamine dendrimer clusters for cancer cell-specific targeting. *Chem. Biol. 12*, 35–43.

(32) Goyal, P., Yoon, K., and Weck, M. (2007) Multifunctionalization of dendrimers through orthogonal transformations. *Chemistry 13*, 8801–8810.

(33) Wu, P., Malkoch, M., Hunt, J. N., Vestberg, R., Kaltgrad, E., Finn, M. G., Fokin, V. V., Sharpless, K. B., and Hawker, C. J. (2005) Multivalent, bifunctional dendrimers prepared by click chemistry. *Chem. Commun. (Camb.) 46*, 5775–5777.

(34) Hill, E., Shukla, R., Park, S. S., and Baker, J. R., Jr. (2007) Synthetic PAMAM-RGD conjugates target and bind to odontoblast-like MDPC 23 cells and the predentin in tooth organ cultures. *Bioconjugate Chem. 18*, 1756–1762.

(35) Binder, W. H., and Kluger, C. (2006) Azide/alkyne-"With click" reactions: Applications in material science and organic synthesis. *Curr. Org. Chem. 10*, 1791.

(36) Lee, J. W., Kim, J. H., Kim, H. J., Han, S. C., Kim, J. H., Shin, W. S., and Jin, S. H. (2007) Synthesis of symmetrical and unsymmetrical PAMAM dendrimers by fusion between azide- and alkyne-functionalized PAMAM dendrons. *Bioconjugate Chem. 18*, 579–584.

(37) Lee, J. W., Kim, J. H., and Kim, B. K. (2006) Synthesis of azide-functionalized PAMAM dendrons at the focal point and their application for synthesis of PAMAM-like dendrimers. *Tetrahedron Lett. 47*, 2683–2686.

(38) Brooks, P. C., Clark, R. A., and Cheresh, D. A. (1994) Requirement of vascular integrin alpha v beta 3 for angiogenesis. *Science 264*, 569–571.

(39) Cleaver, O., and Melton, D. A. (2003) Endothelial signaling during development. *Nat. Med. 9*, 661–668.

(40) Baillie, C. T., Winslet, M. C., and Bradley, N. J. (1995) Tumour vasculature--a potential therapeutic target. *Br. J. Cancer 72*, 257–267.

(41) Ruoslahti, E. (2002) Specialization of tumour vasculature. *Nat. Rev. Cancer 2*, 83–90.

(42) Arap, W., Pasqualini, R., and Ruoslahti, E. (1998) Cancer treatment by targeted drug delivery to tumor vasculature in a mouse model. *Science 279*, 377–380.

(43) Los, M., and Voest, E. E. (2001) The potential role of antivascular therapy in the adjuvant and neoadjuvant treatment of cancer. *Semin. Oncol. 28*, 93–105.

BC900217H

SUPPORTING INFORMATION:

RGD Dendron bodies; synthetic avidity agents with defined and potentially interchangeable effector sites that can substitute for antibodies

Daniel Q. McNerny[†,‖], Jolanta F. Kukowska-Latallo[†], Douglas G. Mullen[†,‡], Joseph M. Wallace[†,§], Ankur M. Desai[†], Rameshwer Shukla[†], Baohua Huang[†], Mark M. Banaszak Holl[†,‡,§], James R. Baker Jr.[†,^,*]

Michigan Nanotechology Institute for Medicine and Biological Sciences, Department of Chemical Engineering, Program in Macromolecular Science and Engineering, Department of Chemistry, Department of Internal Medicine, University of Michigan, Ann Arbor, MI 48109

* Corresponding author. E-mail: jbakerjr@med.umich.edu, Mighigan Nanotechnology Institute for Medicine and Biological Sciences, 9220 MSRB III, Box 5648, University of Michigan, Ann Arbor, MI 48109

† Michigan Nanotechnology Institute for Medicine and Biological Sciences, University of Michigan

|| Department of Chemical Engineering, University of Michigan

‡ Program in Macromolecular Science and Engineering, University of Michigan.

§ Department of Chemistry, University of Michigan

^ Department of Internal Medicine, University of Michigan

CONTENTS PAGE

Figure S1: ^{1}H NMR spectrum of alkyne-G3-PAMAM dendron **(1)** 3

Figure S2: ^{1}H NMR spectrum of alkyne-G3$(COOH)_{16}$ dendron **(2)** 4

Figure S3: ^{1}H NMR spectrum of alkyne-G3$(COOH)_{11.9}(RGD)_{4.1}$ dendron **(3)** 5

Figure S4: ^{1}H NMR spectrum of AF- G3$(COOH)_{11.9}(RGD)_{4.1}$ dendron **(4)** 7

Figure S5: ^{1}H NMR spectrum of MTX-azide **(5)** 8

Figure S6: ^{1}H NMR spectrum of MTX-G3$(COOH)_{11.9}(RGD)_{4.1}$ dendron **(6)** 9

Figure S7: ^{1}H NMR spectrum of Biotin-G3$(COOH)_{11.9}(RGD)_{4.1}$ dendron **(7)** 10

Figure S8: ^{1}H NMR spectrum of azide-G2-PAMAM dendron **(8)** 11

Figure S9: ^{1}H NMR spectrum of azide-G2-$(AF)_2(OH)_{24}$ dendron **(9)** 12

Figure S10: ^{1}H NMR spectrum of $(OH)_{24}(AF)_2$G2- G3$(COOH)_{11.9}(RGD)_{4.1}$ **(10)** 13

Figure S11: HPLC Profile of alkyne-G3$(COOH)_{16}$ dendron **(2)** 14

Figure S12: HPLC Profile of alkyne-G3$(COOH)_{11.9}(RGD)_{4.1}$ dendron **(3)** 14

Figure S13: HPLC Profile of AF-G3$(COOH)_{11.9}(RGD)_{4.1}$ dendron **(4)** 15

Figure S14: UPLC Profile of MTX–azide **(5)** 15

Figure S15: UPLC Profile of MTX-G3$(COOH)_{11.9}(RGD)_{4.1}$ dendron **(6)** 16

Figure S16: UPLC Profile of Biotin-G3$(COOH)_{11.9}(RGD)_{4.1}$ dendron **(7)** 16

Figure S17: HPLC Profile of azide-G2-PAMAM dendron **(8)** 17

Figure S18: UPLC Profile of azide-G2$(AF)_2(OH)_{24}$ dendron **(9)** 17

Figure S19: UPLC and HPLC Profiles of

$(OH)_{24}(AF)_2$G2- G3$(COOH)_{11.9}(RGD)_{4.1}$ **(10)** 18

Figure S1: ^{1}H NMR spectrum of alkyne-G3-PAMAM dendron (1)

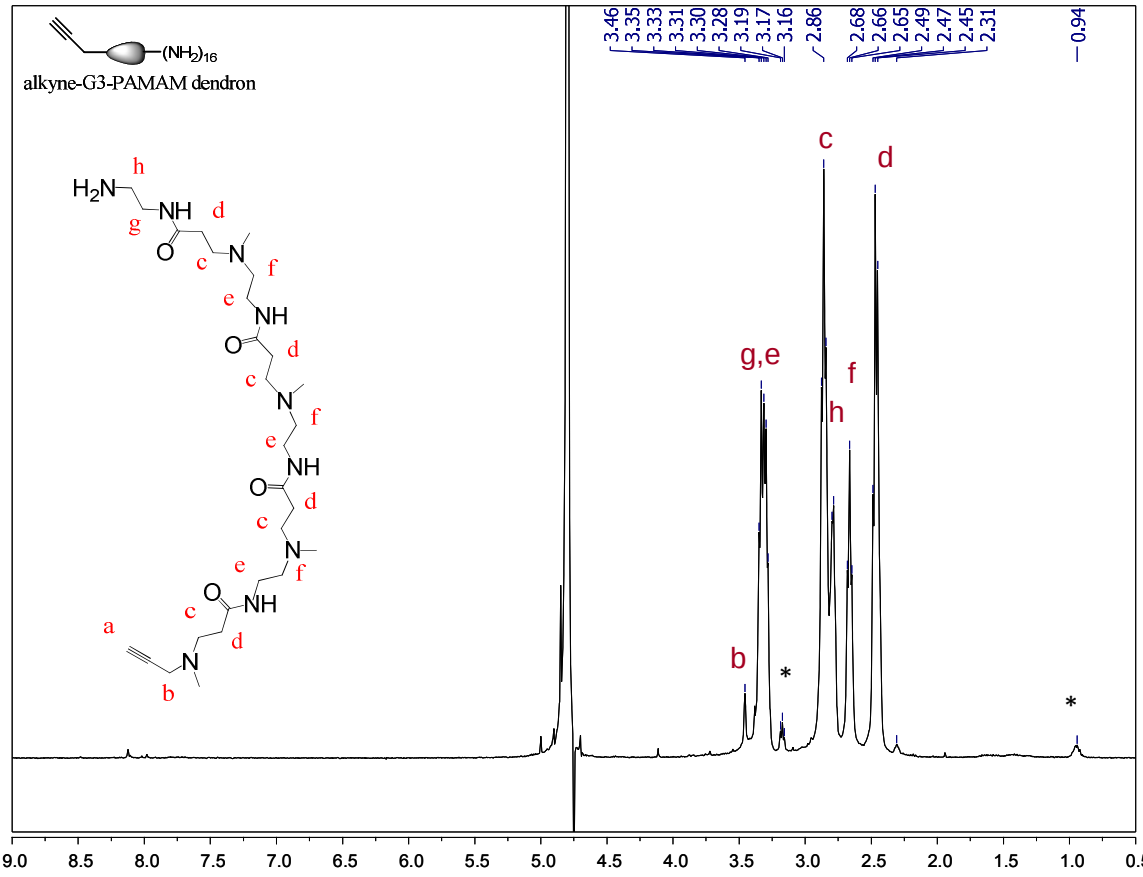

^{1}H NMR (400 MHz, D_2O): δ = 3.46 (s, 2H, N-C*H*$_2$-CH, “b”), 3.43-3.20 (m, 64H, NH-C*H*$_2$-CH$_2$-NH$_2$, NH-C*H*$_2$-CH$_2$-N, “g and e”), 2.86 (m, 60H, N-C*H*$_2$-CH$_2$-CO, “c”), 2.78 (m, 28H, NH-CH$_2$-C*H*$_2$-NH$_2$, “h”), 2.66 (t, 28H, NH-CH$_2$-C*H*$_2$-N, “f”), 2.47 (m, 60H, N-CH$_2$-C*H*$_2$-CO, “d”).

* denotes residual 1-butanol used in azeotropic removal of excess ethylenediamine.

Proton “a”, found at 2.61 ppm for smaller generation dendrons, is likely buried within peaks assigned “f”, or “d”.

Figure S2: ^{1}H NMR spectrum of alkyne-G3(COOH)$_{16}$ dendron (2)

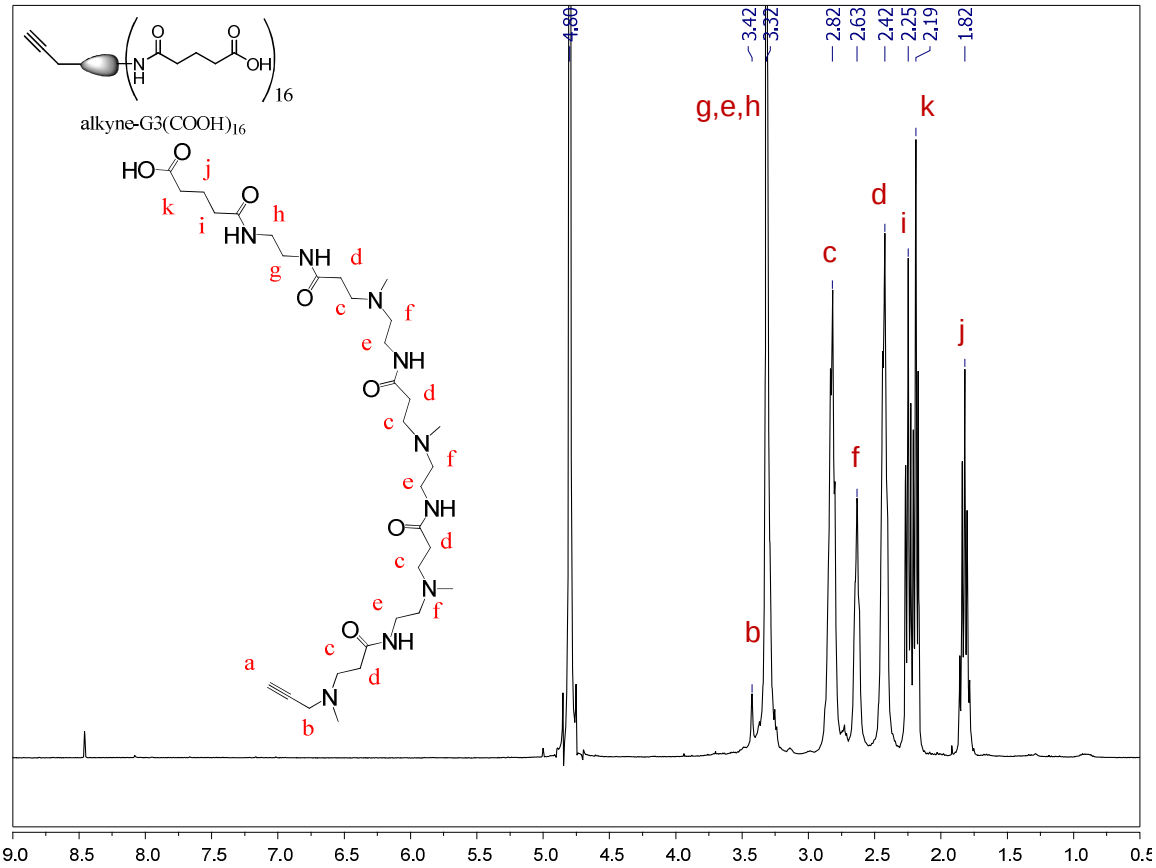

^{1}H NMR (400 MHz, D_2O): δ = 3.42 (s, 2H, N-C*H*$_2$-CH, “b”), 3.32 (m, 92H, NH-C*H*$_2$-CH$_2$-NH$_2$, NH-C*H*$_2$-CH$_2$-N, NH-CH$_2$-C*H*$_2$-NH$_2$, “g, e, and h”), 2.82 (m, 60H, N-C*H*$_2$-CH$_2$-CO, “c”), 2.62 (t, 28H, NH-CH$_2$-C*H*$_2$-N, “f”), 2.42 (m, 60H, N-CH$_2$-C*H*$_2$-CO, “d”), 2.25 (t, 32H, CO-C*H*$_2$-CH$_2$-CH$_2$-CO-OH, “i”), 2.19 (t, 32H, CO-CH$_2$-CH$_2$-C*H*$_2$-CO-OH), “k”, 1.84 (qt, 32H, CO-CH$_2$-C*H*$_2$-CH$_2$-CO-OH, “j”).

Proton “a” is overlapping with dendron peaks in the 2.75-2.50 ppm range.

Figure S3: ^{1}H NMR spectrum of alkyne-G3(COOH)$_{11.9}$(RGD)$_{4.1}$ dendron (3)

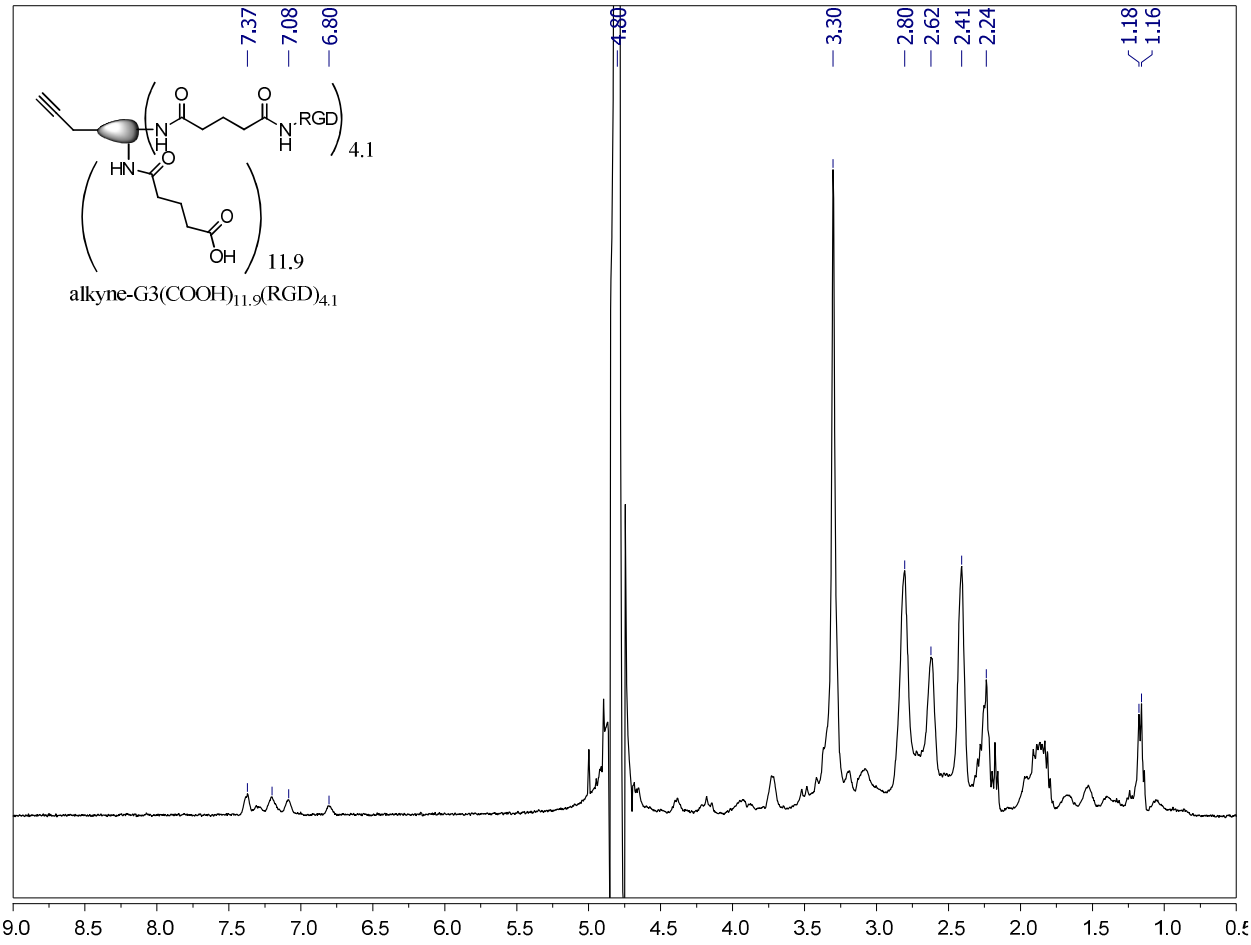

^{1}H NMR (400 MHz, D_2O): δ =

Dendron backbone: 3.42 (s, 2H, N-C*H*$_2$-CH), 3.30 (m, 92H, NH-C*H*$_2$-CH$_2$-NH$_2$, NH-C*H*$_2$-CH$_2$-N, NH-CH$_2$-C*H*$_2$-NH$_2$), 2.80 (m, 60H, N-C*H*$_2$-CH$_2$-CO,), 2.62 (b, 28H, NH-CH$_2$-C*H*$_2$-N), 2.41 (b, 60H, N-CH$_2$-C*H*$_2$-CO), 2.24 (b, 48H, CO-C*H*$_2$-CH$_2$-CH$_2$-CO-OH, CO-CH$_2$-CH$_2$-C*H*$_2$-CO-OH, from unreacted glutarate terminal groups “i an k”), 2.10-1.75 (m, 48H, “j” and “i’, j’, and k’” from conjugated glutarate terminal groups).

Conjugated RGD: 7.40-6.80 (16.4 H, aromatic RGD protons), 4.40 (8.2H), 4.20 (8.2H), 3.72 (8.2H), 3.10, 1.70 (8.2H), 1.53 (8.2H), 1.35 (8.2H) 1.17 (16.4H). Additional peaks are overlapping with peaks from the dendron backbone.

Figure S4: ^{1}H NMR spectrum of AF-G3(COOH)$_{11.9}$(RGD)$_{4.1}$ dendron (4)

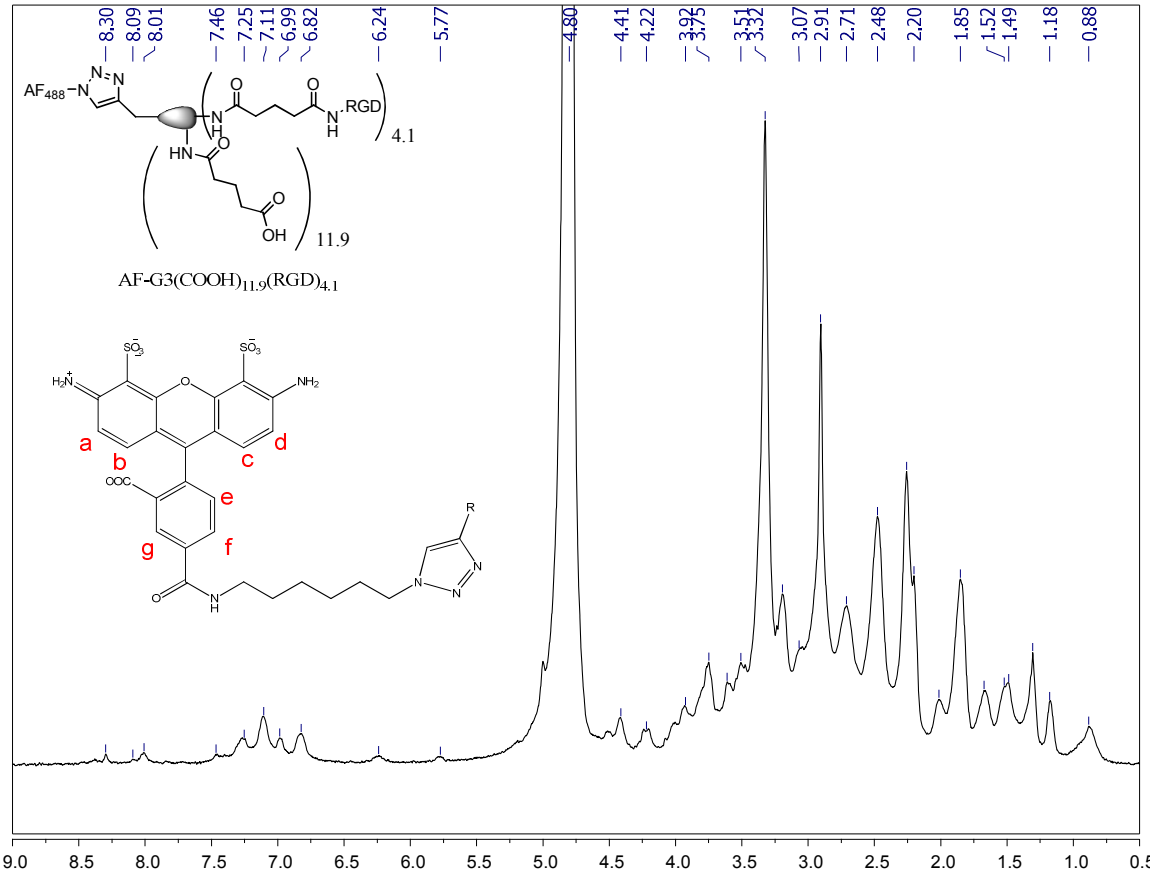

R = G3(COOH)$_{11.9}$(RGD)$_{4.1}$

^{1}H NMR (500 MHz, D_2O):

Aromatic Alexa Fluor 488 peaks at 8.30 (~0.65H, “g”), 8.09 (~0.65H, “f”), and 7.46 (~0.65H, “e”) can be resolved. Peaks “b” and “c” (expected at 7.17) and “a” and “d” (expected at 6.94) are overlapped by the aromatic RGD peaks.

Peaks from the $(CH_2)_6$ spacer are overlapped with the aliphatic dendron and RGD peaks.

Figure S5: ^{1}H NMR spectrum of MTX-azide (5)

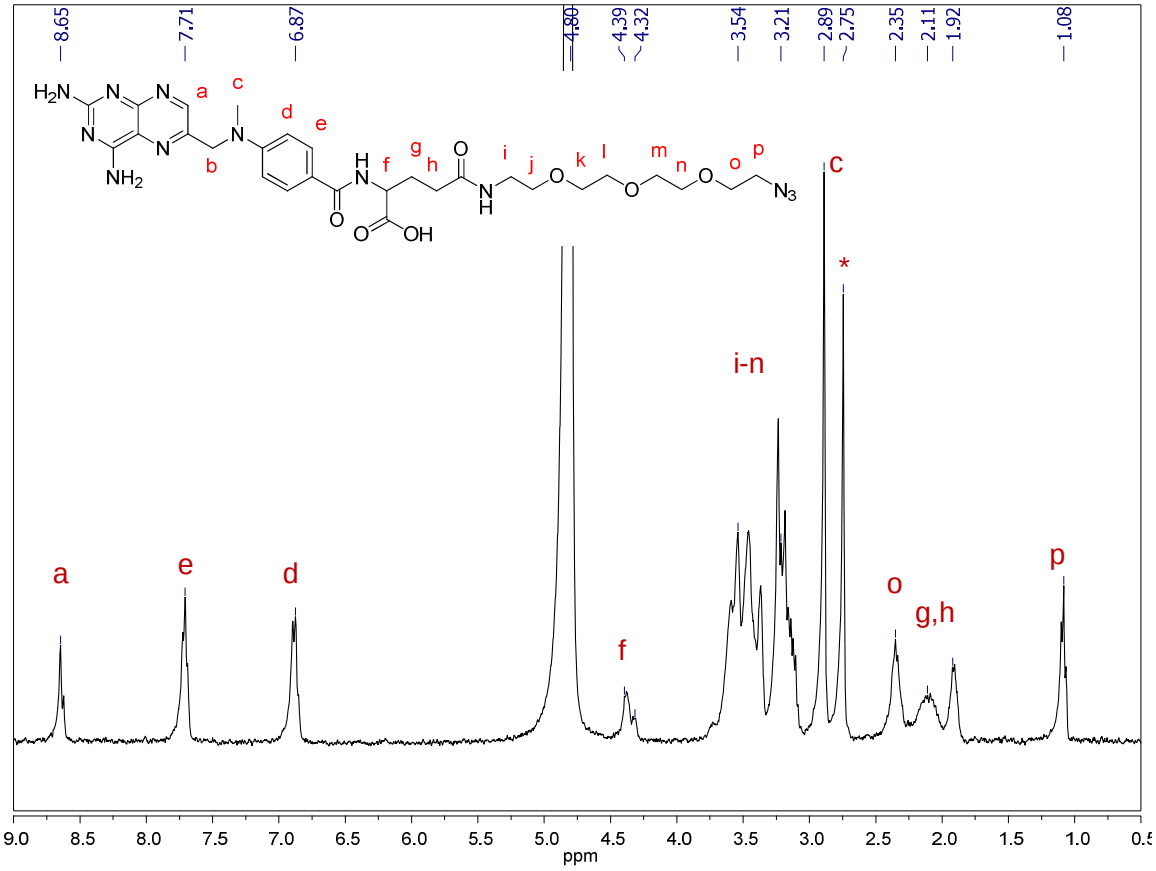

^{1}H NMR (500 MHz, D_2O): δ = 8.65 (1H, N-CH-C, “a”), 7.71 (d, 2H, C-C-CH-CH-C-CO, “e”), 6.87 (d, 2H, C-C-CH-CH-C-CO, “d”), 4.40-4.30 (b, 1H, NH-C*H*C-CH2, “f”), 3.7-3.05 (m, O-CH2-CH2-O, “i-n”), 2.89 (s, N-CH_3, “c”), 2.35 (b, 2H, O-CH_2-CH_2-N_3, “o”), 2.11 (b, 2H, CH-CH_2-CH_2-CO, “g”), 1.92 (b, 2H, CH-CH_2-CH_2-CO, “h”), 1.08 (t, 2H, O-CH_2-CH_2-N_3, “p”).

* denotes *N*-Hydroxysuccinimide impurity (3.4H)

Figure S6: ^{1}H NMR spectrum of MTX-G3(COOH)$_{11.9}$(RGD)$_{4.1}$ dendron (6)

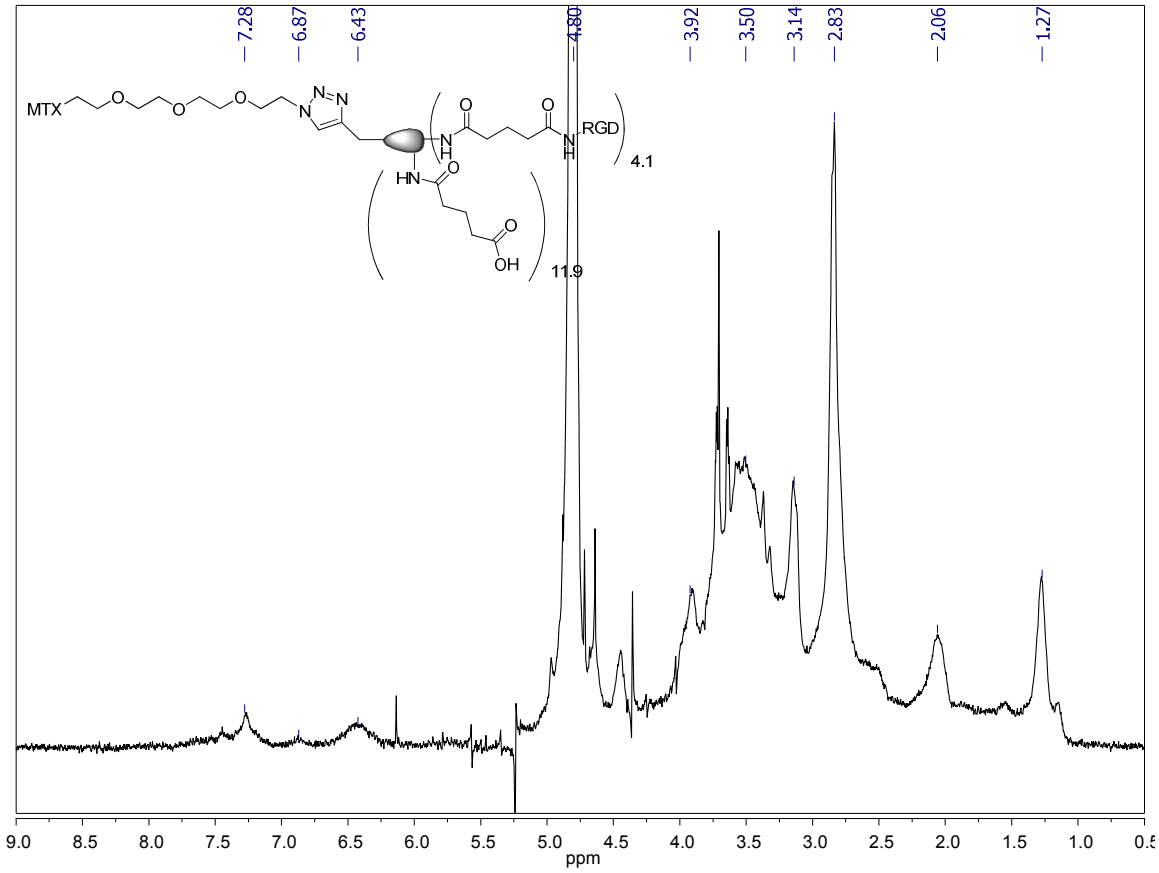

^{1}H NMR (500 MHz, D_2O)

Peaks were not resolved for this sample. MALDI, UPLC and *in vitro* functional assays were used to confirm the successful formation of the product.

Figure S7: ^{1}H NMR spectrum of Biotin-G3(COOH)$_{11.9}$(RGD)$_{4.1}$ dendron (7)

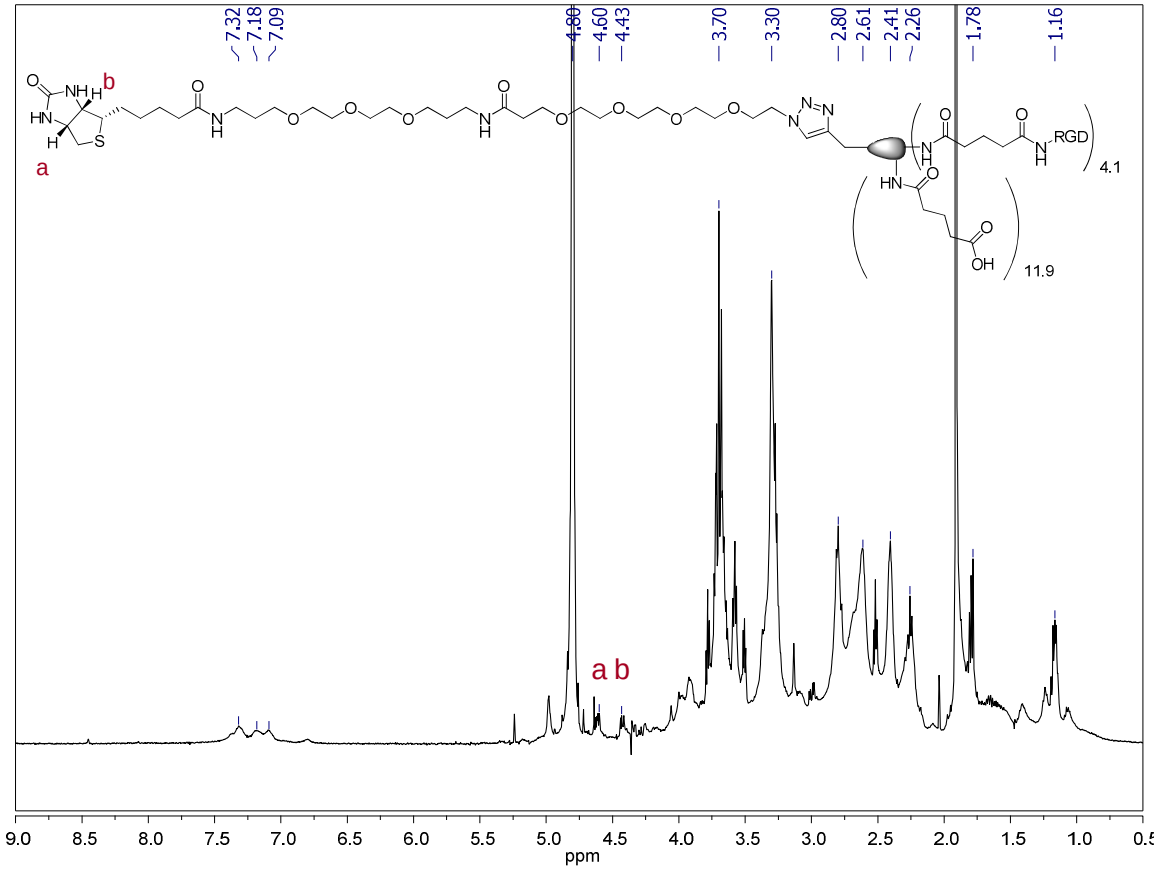

^{1}H NMR (400 MHz, D_2O): δ = 4.60 (1H, "a"), 4.43 (1H, "b"). The unassigned biotin peaks are overlapping with the aliphatic conjugated dendron peaks. The d-PEG spacer is overlapping in the dendron region (expected at 3.75-3.0)

An unknown impurity is present at 1.91.

Figure S8: ^{1}H NMR spectrum of azide-G2-PAMAM dendron (8)

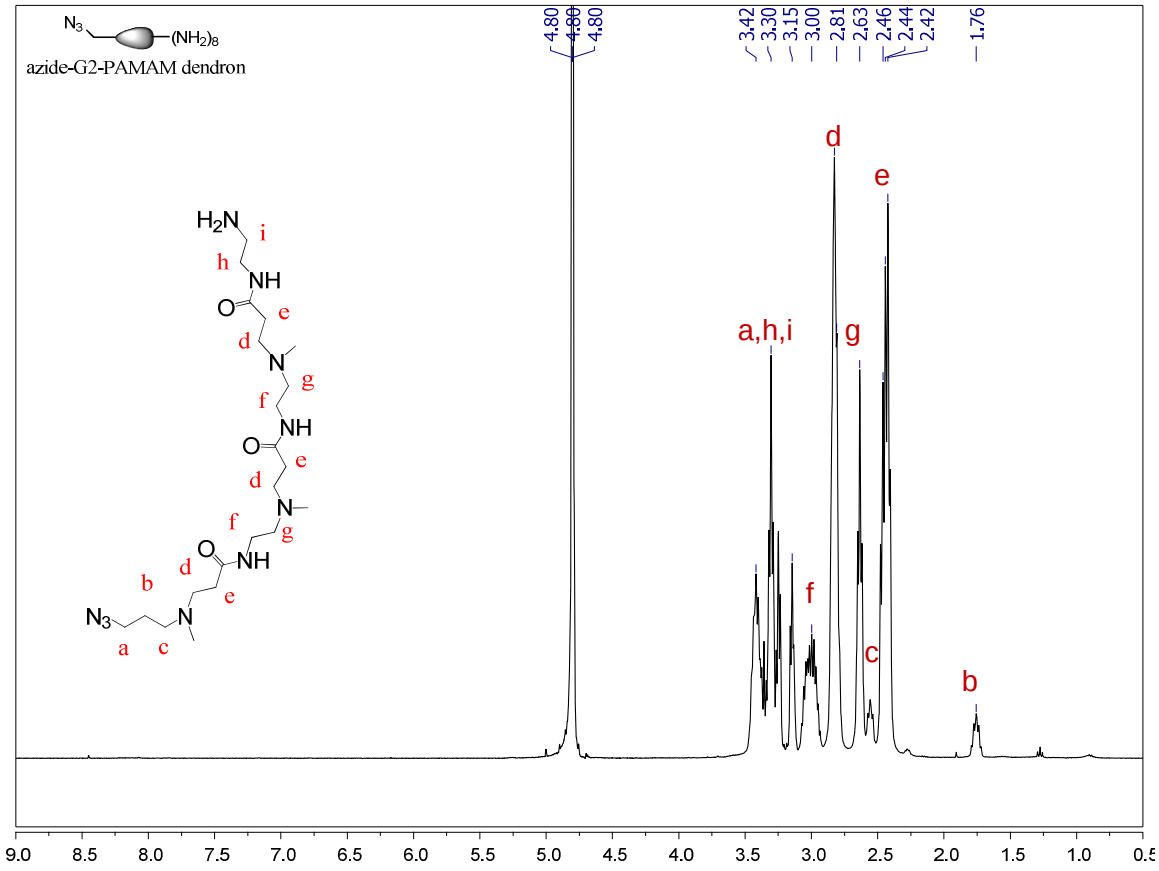

^{1}H NMR (400 MHz, D_2O): δ = 3.50-3.10 (34H, “a, h, and i”), 3.00 (12H, NH-C*H*$_2$-CH$_2$-N, “f”), 2.81 (28H, N-C*H*$_2$-CH$_2$-CO, “d”), 2.63 (12H, NH-CH$_2$-C*H*$_2$-N, “g”), 2.55 (2H, N$_3$-CH$_2$-CH$_2$-C*H*$_2$-N, “c”), 2.44 (28H, N-CH$_2$-C*H*$_2$-CO, “e”), 1.76 (2H, N$_3$-CH$_2$-C*H*$_2$-CH$_2$-N, “b”).

Figure S9: ^{1}H NMR spectrum of azide-G2(AF)$_2$(OH)$_{24}$ dendron (9)

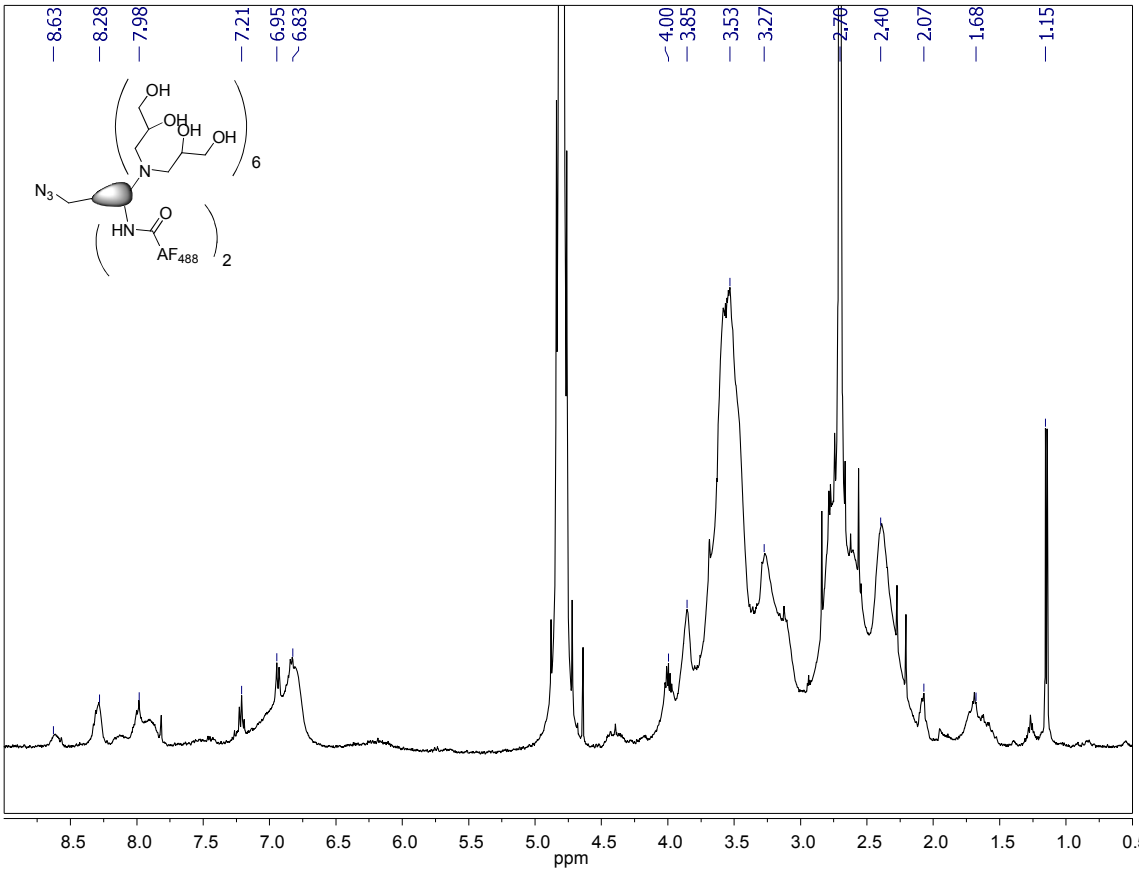

^{1}H NMR (500 MHz, D_2O)

Dendron peaks are indistinguishable between 4.0 and 1.0 ppm.

Sharp aromatic Alexa Fluor 488 peaks suggest that small free dye impurities were still present in this sample. The removal of detectable free dye after the attachment of this dendron to alkyne-G3(COOH)$_{11.9}$(RGD)$_{4.1}$ was confirmed via HPLC.

Figure S10: ^{1}H NMR spectrum of $(OH)_{24}(AF)_2G2\text{-}G3(COOH)_{11.9}(RGD)_{4.1}$ (10)

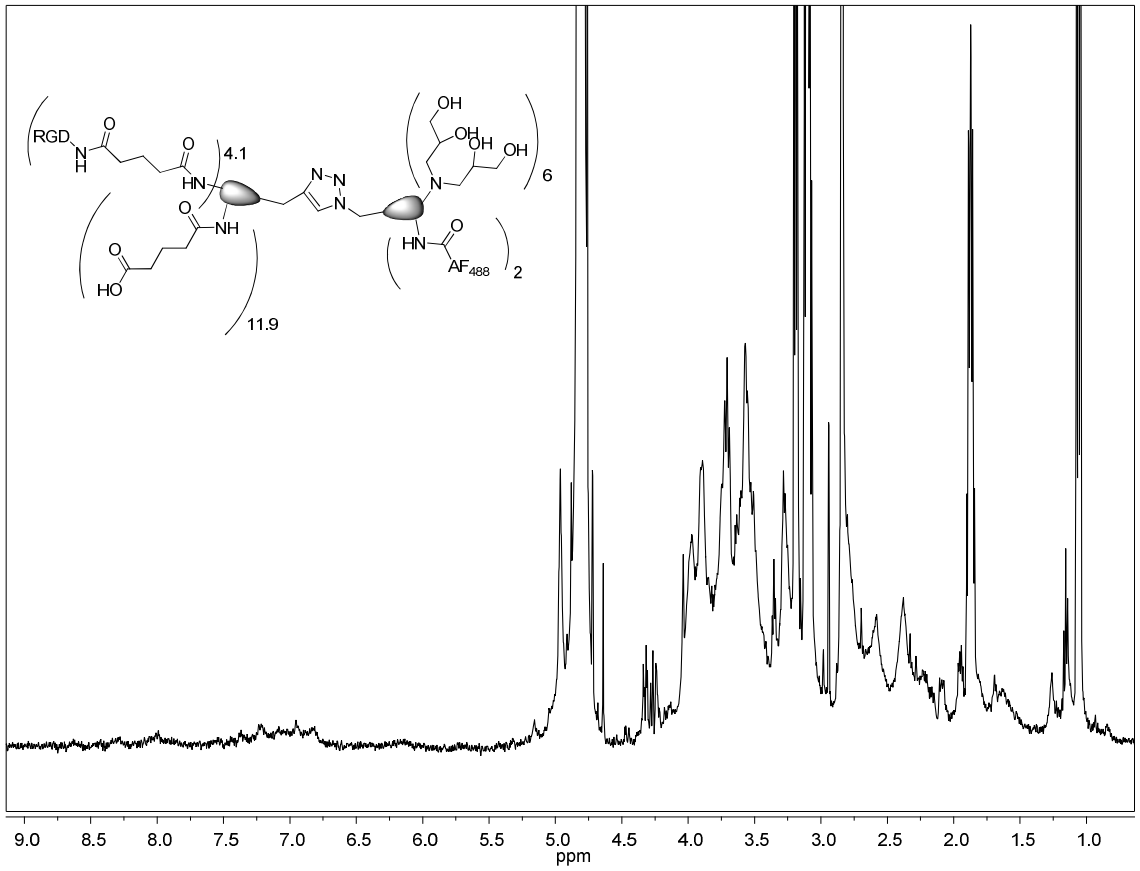

^{1}H NMR (500 MHz, D_2O)

The complexity and low concentration of the isolated co-dendron sample does not allow for proper assignments to be made. Aromatic RGD and Alexa Fluor 488 peaks are identifiable. MALDI, UPLC and *in vitro* experiments were used to confirm the successful formation of the product.

Figure S11: HPLC Profile of alkyne-G3(COOH)$_{16}$ dendron (2)

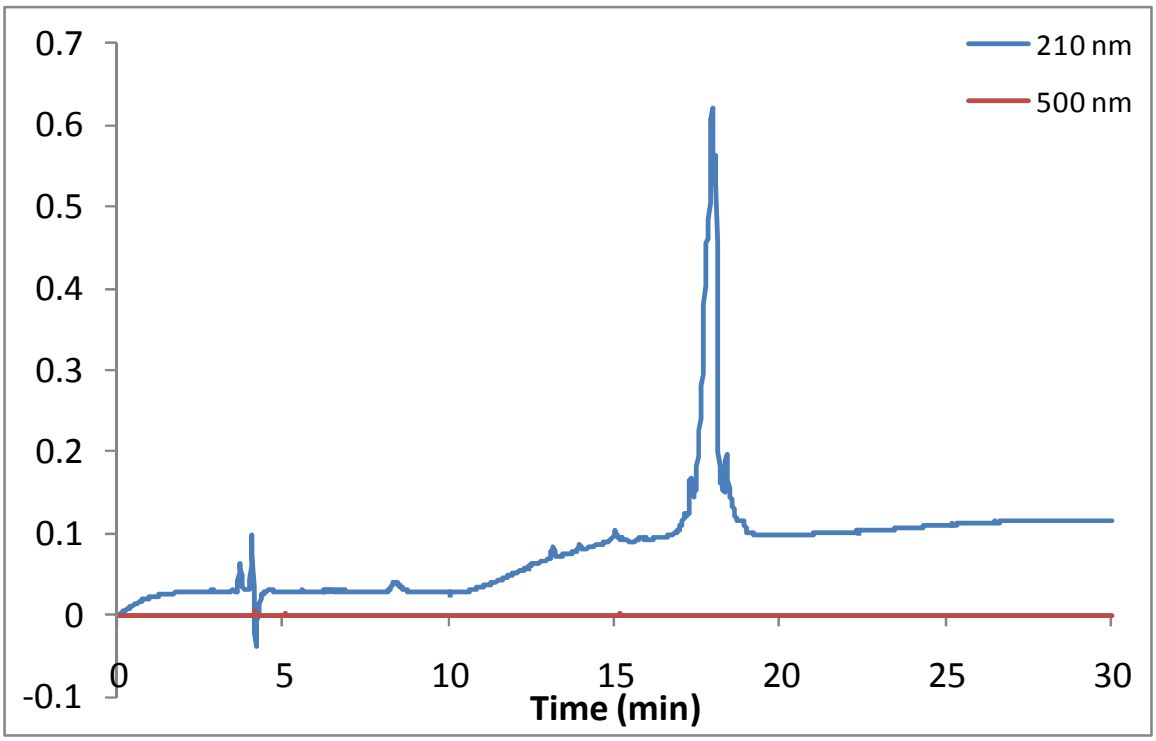

Figure S12: HPLC Profile of alkyne-G3(COOH)$_{11.9}$(RGD)$_{4.1}$ (3)

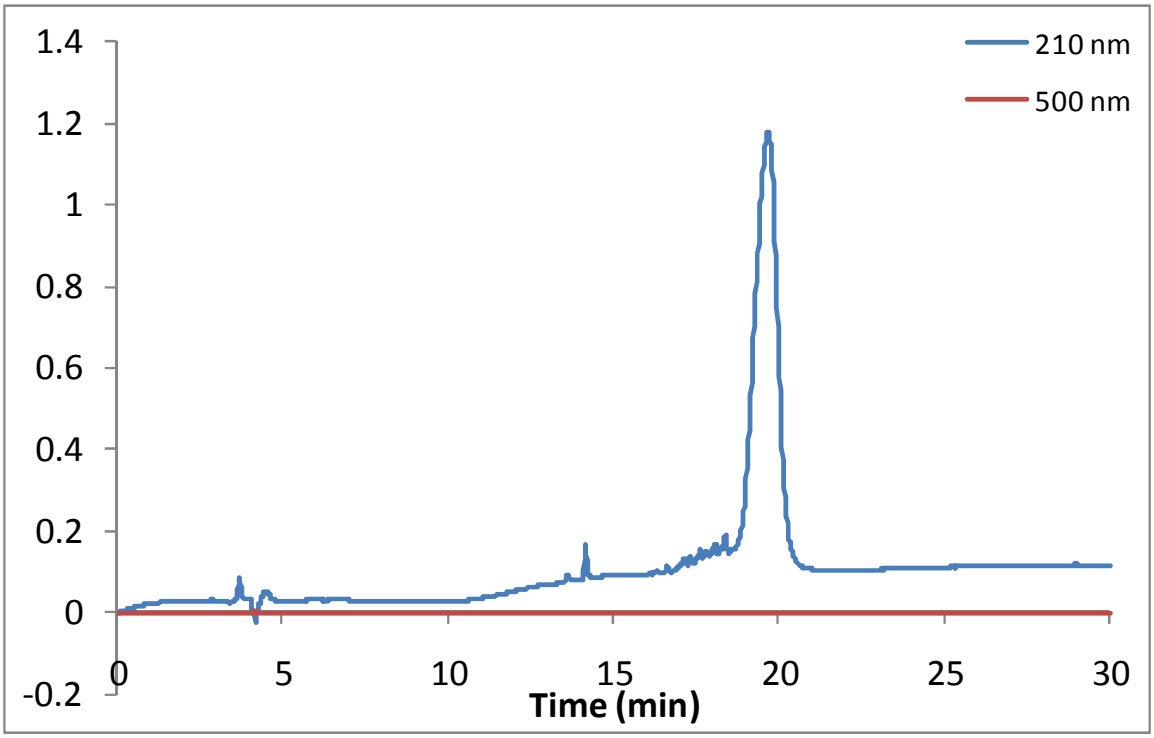

Figure S13: HPLC Profile of AF-G3(COOH)$_{11.9}$(RGD)$_{4.1}$ dendron (4)

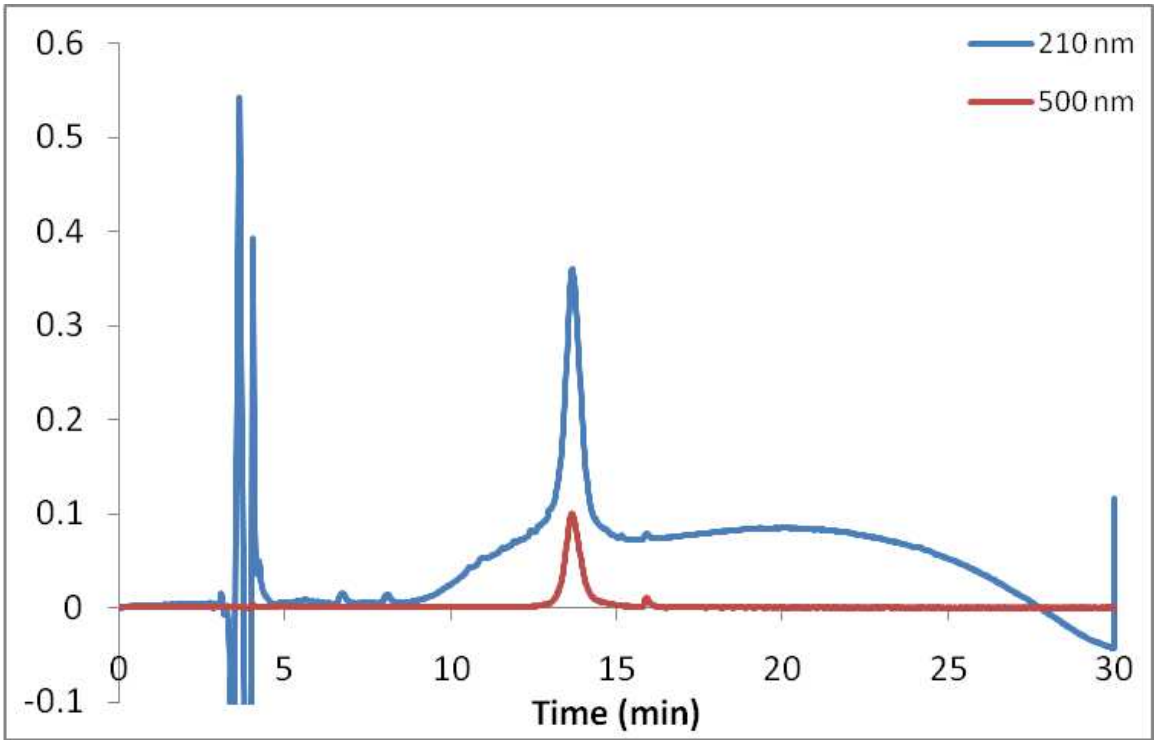

Figure S14: UPLC Profile of MTX–azide (5)

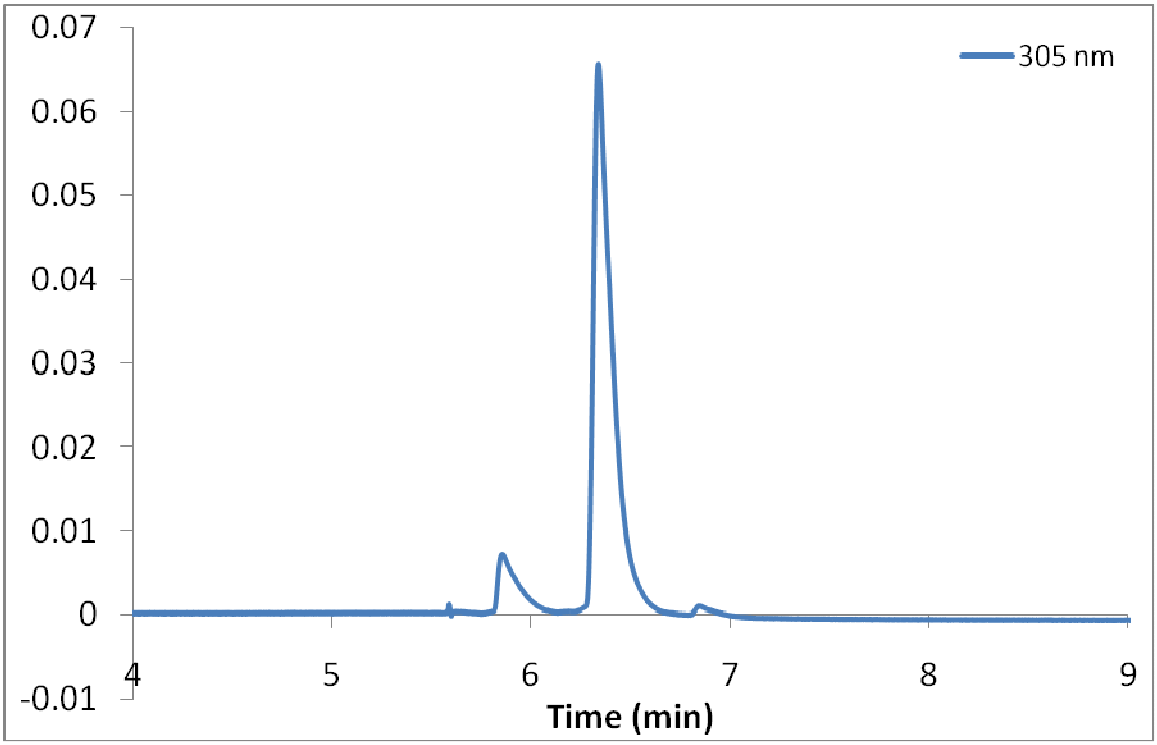

Figure S15: UPLC Profile of MTX-G3(COOH)$_{11.9}$(RGD)$_{4.1}$ dendron (6)

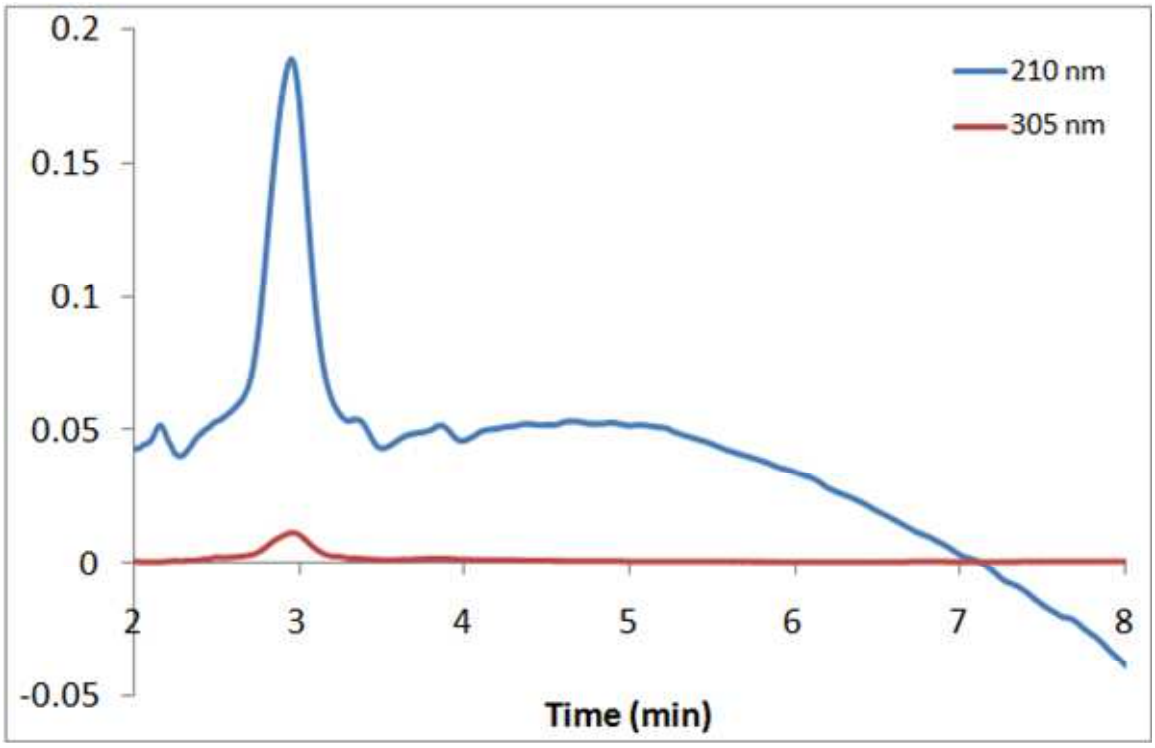

Figure S16: UPLC Profile of Biotin-G3(COOH)$_{11.9}$(RGD)$_{4.1}$ dendron (7)

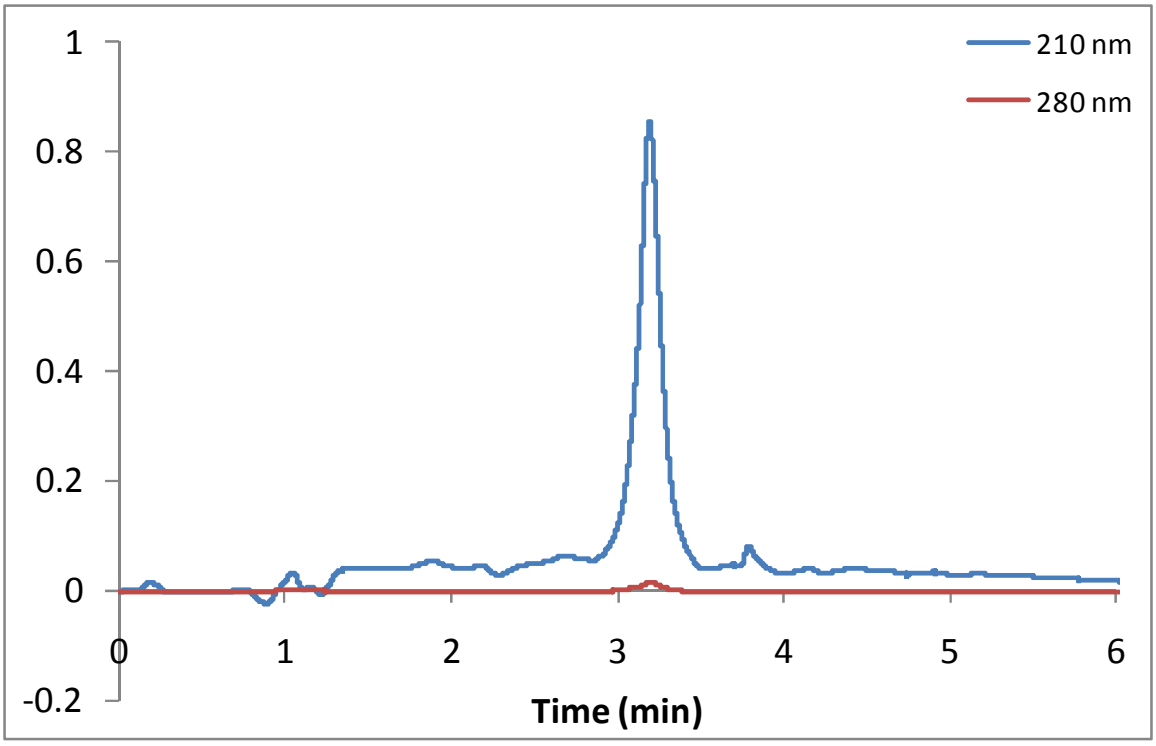

Figure S17: HPLC Profile of azide-G2-PAMAM dendron (8)

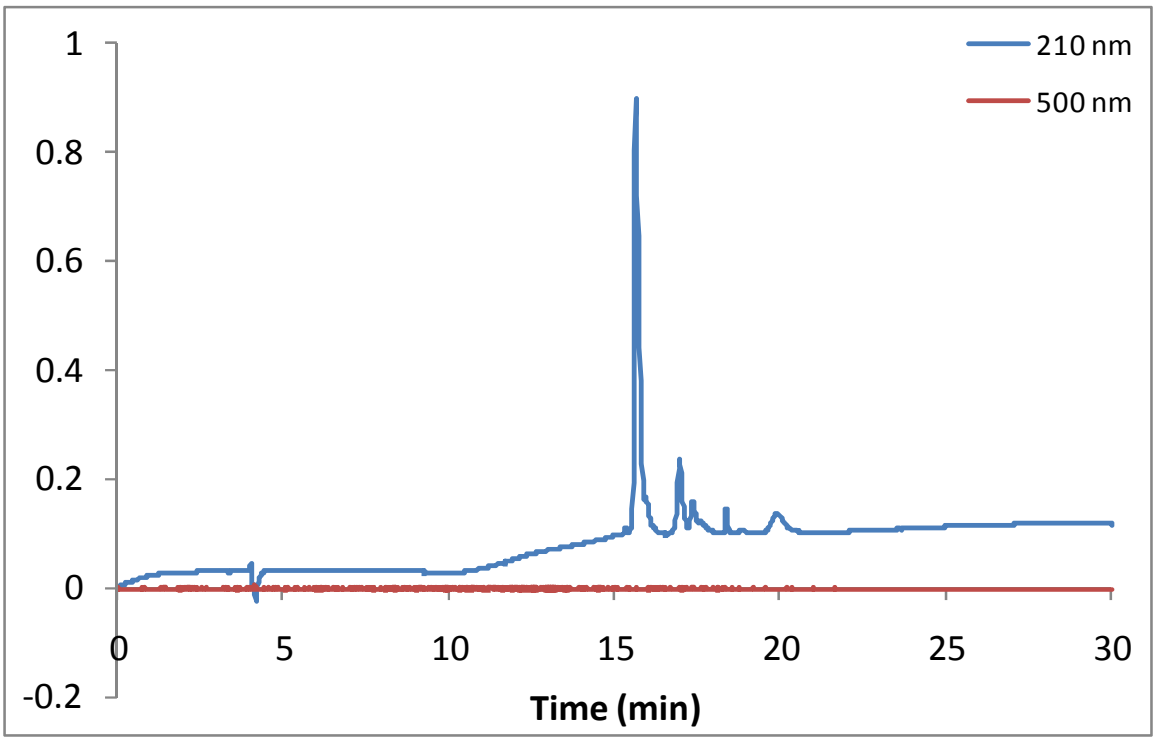

Figure S18: UPLC Profile of azide-G2-$(AF)_2(OH)_{24}$ dendron (9)

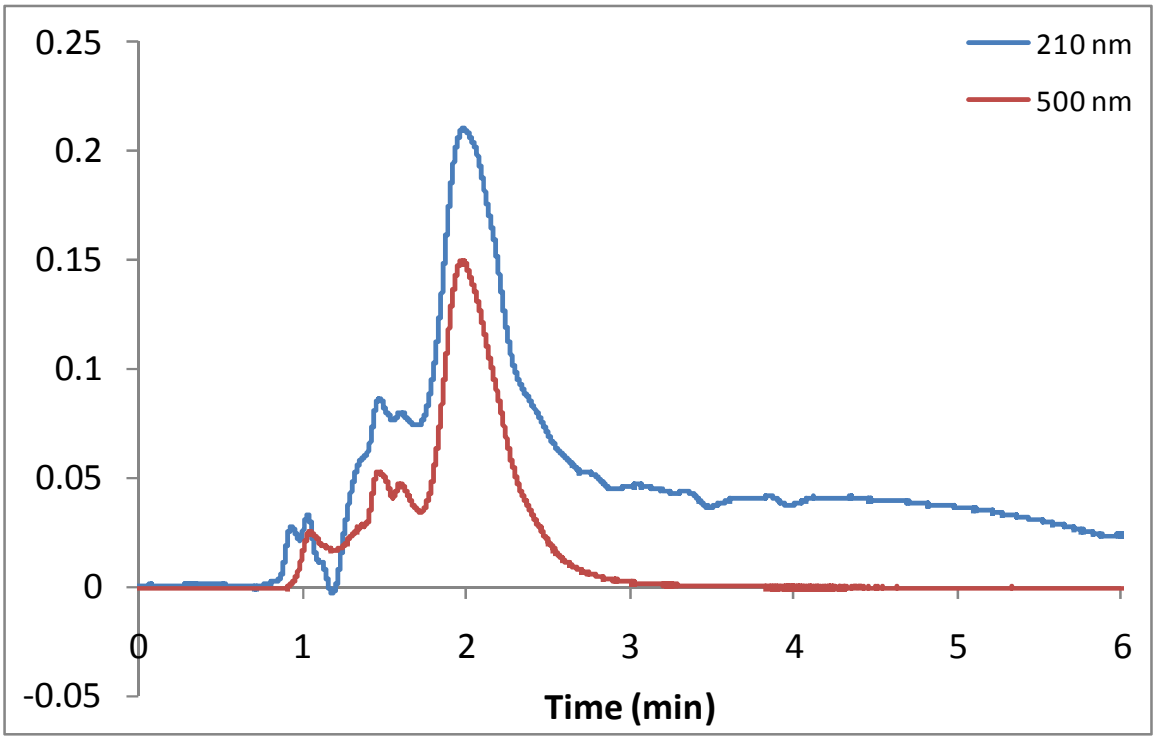

Figure S19: UPLC and HPLC Profiles of $(OH)_{24}(AF)_2G2\text{-}G3(COOH)_{11.9}(RGD)_{4.1}$ (10)

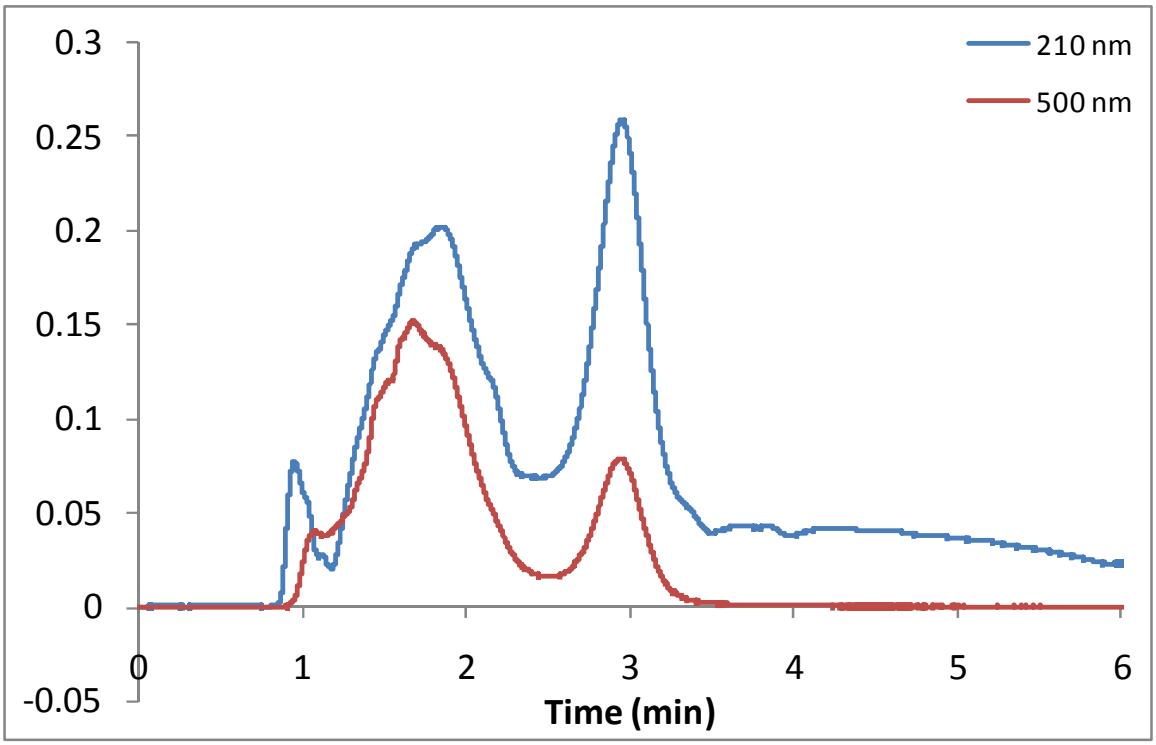

HPLC (dotted lines show collected fraction)

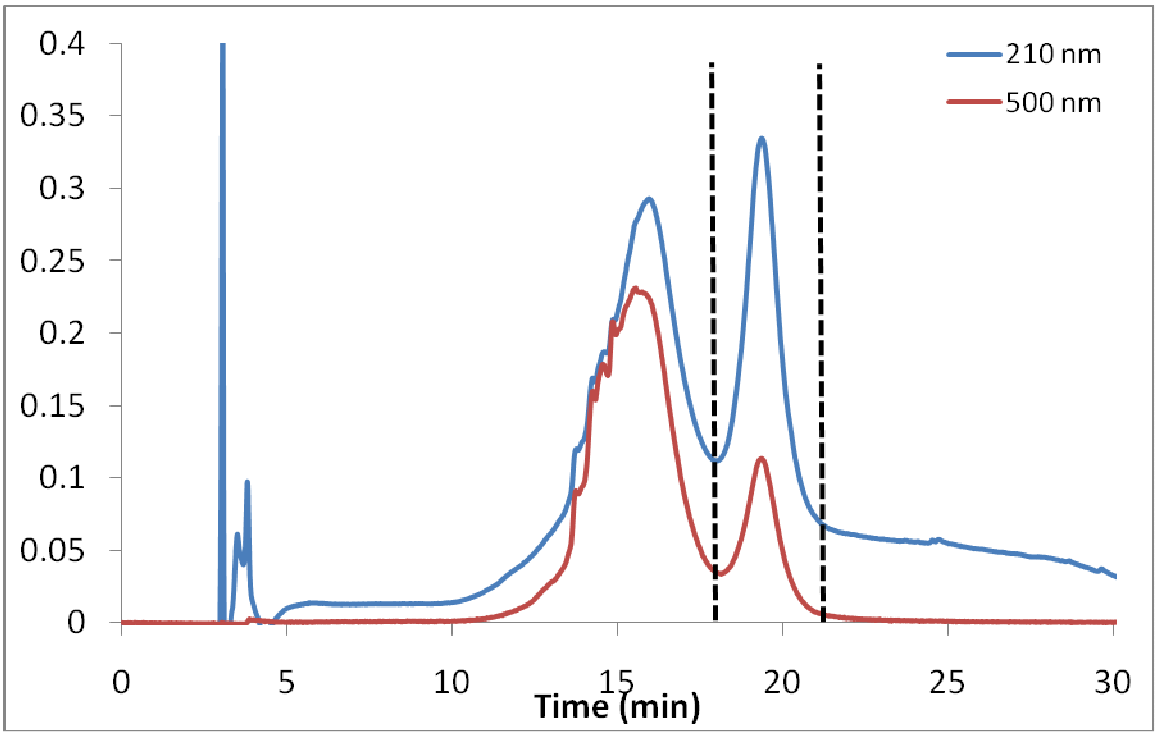

Cell-Penetrating Peptides and Peptide Nucleic Acid-Coupled MRI Contrast Agents: Evaluation of Cellular Delivery and Target Binding

Ritu Mishra,[†] Wu Su,[†,#] Rolf Pohmann,[†] Josef Pfeuffer,[†,§] Martin G. Sauer,[‡] Kamil Ugurbil,[†,⊥] and Jörn Engelmann*[,†]

High-Field Magnetic Resonance Center, Max Planck Institute for Biological Cybernetics, Spemannstrasse 41, Tübingen, 72076, Germany, and Pediatric Hematology and Oncology, Hannover Medical School, Hannover, 30625, Germany.
Received February 2, 2009; Revised Manuscript Received July 24, 2009

Molecular imaging of cells and cellular processes can be achieved by tagging intracellular targets such as receptors, enzymes, or mRNA. Seeking to visualize the presence of specific mRNAs by magnetic resonance (MR) imaging, we coupled peptide nucleic acids (PNA) with gadolinium-based MR contrast agents using cell-penetrating peptides for intracellular delivery. Antisense to mRNA of DsRed2 protein was used as proof of principle. The conjugates were produced by continuous solid-phase synthesis followed by chelation with gadolinium. Their cellular uptake was confirmed by fluorescence microscopy and spectroscopy as well as by MR imaging of labeled cells. The cell-penetrating peptide D-Tat$_{57-49}$ was selected over two other derivatives of HIV-1 Tat peptide, based on its superior intracellular delivery of the gadolinium-based contrast agents. Further improved delivery of conjugates was achieved upon coupling peptide nucleic acids (antisense to mRNA of DsRed2 protein and nonsense with no natural counterpart). Significant enhancement in MR contrast was obtained in cells labeled with concentrations as low as 2.5 μM of these agents. Specific binding of the targeting PNA containing conjugate to its complementary oligonucleotide sequence was proven by *in vitro* cell-free assay. In contrast, a lack of specific enrichment was observed in transgenic cells containing the target due to nonspecific vesicular entrapment of contrast agents. Preliminary biodistribution studies showed conjugate-related fluorescence in several organs, especially the liver and bladder, indicating high mobility of the agent in spite of its high molecular weight. No conjugate related toxicity was observed. These results are encouraging, as they warrant further molecular optimization and consecutive specificity studies *in vivo* of this new generation of contrast agents.

INTRODUCTION

Recently, remarkable progress in the understanding of cellular processes, at both the molecular and genetic levels, has been made by the development of molecular-biological assays. Despite this, a myriad of questions about biological processes under normal as well as diseased conditions remain. Of late, the new field of molecular imaging has evolved with the intent of translating knowledge gained from *in vitro* systems into studies of complete biological systems. Molecular imaging aims at noninvasive visualization of biological processes amid the complex networks and interactions in the intact individual (*1*−*3*). Imaging modalities being extensively used for this purpose are positron emission tomography (PET), single-photon emission computed tomography (SPECT), optical imaging using fluorescence or bioluminescence, and magnetic resonance imaging (MRI) (*4, 5*).

* To whom correspondence should be addressed: Jörn Engelmann. High-Field Magnetic Resonance Center, Max Planck Institute for Biological Cybernetics, Spemannstrasse 41, Tübingen, 72076, Germany. E-mail: joern.engelmann@tuebingen.mpg.de; Tel: +49-7071-601704; Fax: +49-7071-601702.

[†] Max Planck Institute for Biological Cybernetics.

[‡] Hannover Medical School.

[#] Present address: Department of Chemistry, University of Leicester, Leicester, LE17RH, U.K.

[§] Present address: Siemens Medical Solutions USA, Inc., Charlestown, MA 02129, USA.

[⊥] Present address Center for Magnetic Resonance Research, University of Minnesota, Department of Radiology, Minneapolis, MN 55455, USA.

MRI is a powerful tool in clinical diagnostics as well as for understanding developmental and biological processes. It visualizes the differences in tissues and organs, as well as between normal and pathological changes, as a function of water concentration and relaxation times, T_1 and T_2, in a given volume element (*6*). The main advantages of MRI over other imaging techniques are its high spatial and temporal resolution, the absence of harmful ionizing radiation, and the ability to noninvasively scan entire organisms in one, two, or three dimensions. The intrinsic contrast of MR images can be augmented by the use of contrast agents (CAs). Chelated paramagnetic metal ions, in particular gadolinium, have been primarily used as T_1-based CAs to increase the contrast in MR images (*7*). An assortment of gadolinium-based CAs are commercially available, and these agents are frequently employed for clinical diagnosis. However, their utility is based on enhancement of anatomical information due to differential biodistribution in the body (*8, 9*). For example, in the brain, these agents do not cross the blood−brain barrier (BBB) except when the BBB is broken because of pathology; as such, they lack specificity. Advancing from these agents toward extracellular targeting by conjugation of CAs to certain proteins and especially to monoclonal antibodies or antibody fragments has been explored. Most of the investigations were related to the development of tumor-specific agents (*10*−*14*).

Numerous intracellular imaging targets are available, however, and these can be tagged to provide molecular information. Regardless of the low number of targets at DNA level, molecules at RNA (overexpressed) or protein level could serve as potential targets (*1*). A possibility for monitoring gene expression by targeting a tumor-specific mRNA was evaluated by Heckl et

10.1021/bc9000454 CCC: $40.75 © 2009 American Chemical Society
Published on Web 09/29/2009

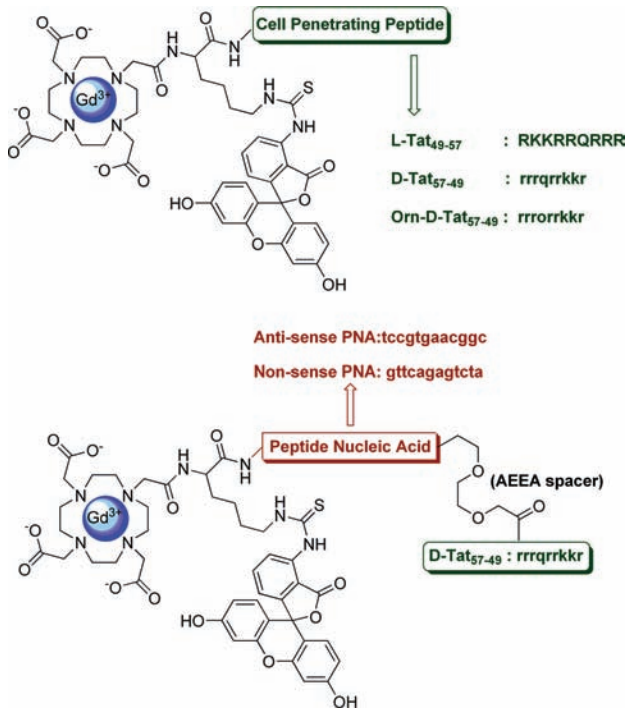

Figure 1. Schematic structures of CPP and PNA conjugated Gd(DOTA) based intracellular contrast agents. All amino acids are represented in a single letter code: R, arginine; K, lysine; Q, glutamine; and O, ornithine. D-Amino acids are represented in lower case. The PNA building blocks are represented as follows: a, adenine; t, thymine; g, guanine; c, cytosine.

al. (*15*). Our group has also reported the development of a gadolinium-based CA coupled to peptide nucleic acids (PNA) to target mRNA (*16*). Both studies utilized peptide-based delivery of their constructs to penetrate through the cell membrane. Such cell-penetrating peptides (CPPs) emerged as an extremely efficient way to overcome the most challenging delivery barrier. CPPs are a class of short peptides that have been reported to import a wide range of cell-membrane impermeable cargos into cells (*17*−*20*). Thus far, there is no consensus on the mechanism of uptake of CPPs and the maintenance of functionality of cargos after delivery. This is reflected by differences in reported labeling techniques, non-standardized protocols regarding uptake evaluation, and discrepancies caused by the use of different cellular model systems (*21*−*23*).

Keeping these issues in mind, we began by evaluating the most appropriate CPP, selected from three derivatives of the well-established CPP HIV-1 Tat peptide, to deliver CA into cells. The cargo attached to the CPP was a gadolinium-loaded chelator, 1,4,7,10-tetraazacyclododecane-*N*,*N*′,*N*″,*N*‴-tetraacetic acid (Gd-DOTA), for MR imaging, and fluorescein isothiocyanate (FITC) for optical imaging (Figure 1). Using the selected CPP, a targeting PNA (either targeting DsRed2 mRNA or a nonsense sequence) was introduced into the above-mentioned conjugate (Figure 1). DsRed2 protein, a variant of the DsRed protein, was used as a model system for proof-of-principle in a transgenic DsRed2-expressing cell line (*24*). The aim was to assess the intracellular delivery and distribution of these larger molecules in the presence or absence of target mRNA in the cells. The ability of the agents to bind with targets in a cell-free *in vitro* system, as well as by labeling cells, was also evaluated. The biodistribution of the CA containing the antisense PNA will also be briefly presented here using fluorescence for detection.

EXPERIMENTAL PROCEDURES

General. All chemicals were purchased at HPLC or peptide synthesis grade from commercial sources. Trifluoroacetic acid (TFA), dimethylformamide (DMF), dichloromethane (DCM), *N*,*N*-diisopropylethylamine (DIEA), triisopropylsilane (TIPS), methyl tertiary butyl ether (MTBE), and FITC were obtained from Acros Organics (Germany). All standard, protected Fmoc amino acid derivatives (the side chains of lysine and ornithine were protected by Boc and arginine by Pbf), 2-(1-*H*-benzotriazol-1-yl)-1,1,3,3-tetramethyluronium hexafluorophosphate (HBTU), preloaded Wang resin, and 1-hydroxybenzotriazole (HOBt) were purchased from Novabiochem, United Kingdom. For PNA synthesis, all Fmoc/Bhoc protected monomers and 2-(1-*H*-7-azabenzotriazole-1-yl)-1,1,3,3-tetramethyluronium hexafluorophosphate (HATU) were purchased from Applied Biosystems, Germany. 1,4,7,10-Tetraazacyclododecane (cyclen) was purchased from Strem Chemicals, France.

Analytical and semipreparative RP-HPLC was performed at room temperature on a Varian PrepStar Instrument (Australia) equipped with PrepStar SD-1 pump heads. UV absorbance was measured using a ProStar 335 photodiode array detector at 260 nm. A Varian Polaris C18-Ether column (4.6 × 250 mm, particle size 5 μm, particle pore diameter 100 Å) was used for analytical RP-HPLC. For semipreparative HPLC, a Varian Polaris C18-Ether column (21.2 × 250 mm, 5 μm, 100 Å) was used.

Gd-DOTA-conjugated CPPs and PNAs were analyzed and purified using one of the following two methods. Method A: A linear gradient was used starting from 90% solvent A (0.1% TFA in water) and 10% of solvent B (0.1% TFA in acetonitrile) to 90% B in 30 min. Method B: A linear gradient was used starting from 90% solvent A (0.05% TFA in water) and 10% of solvent B (0.05% TFA in acetonitrile) to 90% B in 30 min (flow rate of 1 mL/min for analytical and 3 mL/min for semipreparative HPLC).

ESI-MS was performed on Agilent SL 1100 Series LC/MSD Trap system (Agilent, Germany): nebulizer, 20.0 psi; dry gas, 5.0 L/min; dry temperature, 250 °C.

General Synthesis of Gd-DOTA-CPP(FITC) Conjugates. All the CPPs used in this work were chemically synthesized by solid-phase peptide synthesis with Fmoc/*t*Bu-strategy on a Heidolph Synthesis 1 synthesizer (Germany). As shown in Scheme 1, polystyrene-based Wang resin (substitution level of 0.50−0.60 mmol/g) was swollen in DCM for 30 min and washed four times with DMF. The resin was treated twice with a solution of 20% piperidine (3 mL) in DMF for 10 min, and subsequently washed four times with DMF. In a separate vial, Fmoc-protected amino acid (4 equiv), HBTU (3.6 equiv), and HOBt (3.6 equiv) were dissolved in DMF (2 mL), and DIEA (8 equiv) was added. The resulting solution was added to the resin and allowed to react under N_2 for 30 min. The resin was drained and rinsed four times with DMF. This procedure was repeated until Fmoc-protected CPPs (L-Tat$_{49-57}$, D-Tat$_{57-49}$, and Orn-D-Tat$_{57-49}$ peptides) bound to Wang resin were obtained. The resin-bound peptides were deprotected with 20% piperidine (3 mL) in DMF for 10 min, and coupled with one Fmoc-Lys(Dde)−OH residue by using HBTU and HOBt coupling agents. After deprotection with 20% piperidine (3 mL) in DMF for 10 min, in-house synthesized DOTA (*tert*-butyl)$_3$ ester was coupled to the α-NH_2 group of Lys (coupling condition: DOTA (*tert*-butyl)$_3$/HATU/DIEA = 4:3.6:8) (*16*). The resin was drained and rinsed four times with DMF. The resin-bound DOTA-conjugated L-Tat$_{49-57}$, D-Tat$_{57-49}$, and Orn-D-Tat$_{57-49}$ peptides were treated twice with hydrazine hydrate (2% in DMF, 2 min) to remove the Dde group. The ε-amino group of N-terminal

Scheme 1. Synthesis of CPP Conjugated MR Contrast Agents by Continuous Solid-Phase Synthesis

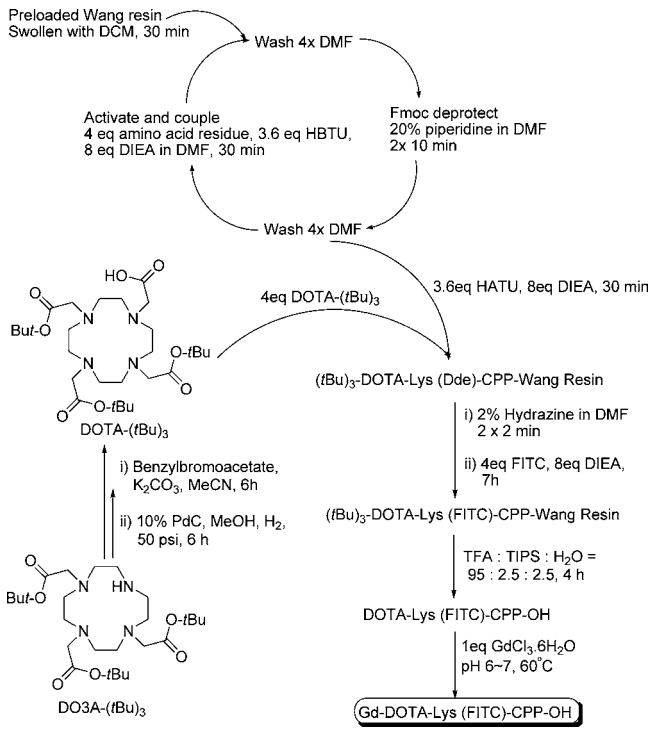

lysine was manually labeled with FITC (4-fold excess) mixed with triethylamine (1:2) in DMF overnight. The solvent was removed and the resin was washed with DMF, DCM, and MeOH subsequently four times. After drying under vacuum, DOTA-Lys(FITC)-conjugated peptides (L-Tat_{49-57}, D-Tat_{57-49}, and Orn-D-Tat_{57-49}) were cleaved off the resin using TFA/TIPS/H_2O (95:2.5:2.5, v/v/v). In the entire procedure described above, completion of Fmoc deprotection, coupling and thiourea formation were monitored by Kaiser Test (*25*).

Purification. All peptide conjugates were precipitated with cold MTBE. The precipitates were collected by centrifugation and resuspended in cold MTBE two times. Pellet was dissolved in water and *tert*-butyl alcohol (1:4) with 2% acetic acid, and lyophilized. All crude samples were purified by semipreparative RP-HPLC using linear gradients as described in the General Experimental Procedures before. The product-containing fractions were defined by analytical RP-HPLC.

Preparation of Gd Complexes. The ligands (DOTA-conjugated FITC-labeled CPPs) were dissolved in 5 mL water; a solution of $GdCl_3 \cdot 6H_2O$ (1 equiv) in water was added and the pH was periodically adjusted to 6.0−7.0 using a solution of 1 N NaOH or 1 N HCl as needed. The residues were purified by semipreparative RP-HPLC using method B to separate unstably bound Gd^{3+}. Afterward, the product was dialyzed (Float-ALyzer, cellulose ester membranes, MWCO 1000; Spectrum Laboratories Inc., Germany) to remove inorganic impurities. The solutions were lyophilized, and yellowish orange solids were obtained. The absence of free Gd^{3+} was checked with xylenol orange indicator (*26*).

Gd-DOTA-Lys(FITC)-L-Tat_{49-57}-OH. ESI-MS (+): calcd *m*/*z* 2397.08; found 800.2[$(M + 3H)^{3+}$], 600.2 [$(M + 4H)^{4+}$], 480.4 [$(M + 5H)^{5+}$], and 400.5 [$(M + 6H)^{6+}$].

Gd-DOTA-Lys(FITC)-D-Tat_{57-49}-OH. ESI-MS (+): calcd *m*/*z* 2397.08; found 799.7 [$(M + 3H)^{3+}$], 600.2 [$(M + 4H)^{4+}$], 480.3 [$(M + 5H)^{5+}$], and 400.7 [$(M + 6H)^{6+}$].

Gd-DOTA-Lys(FITC)-Orn-D-Tat_{57-49}-OH. ESI-MS (+): calcd *m*/*z* 2383.10; found 796.2 [$(M + 3H)^{3+}$], 596.5 [$(M + 4H)^{4+}$], 477.7 [$(M + 5H)^{5+}$], and 398.4 [$(M + 6H)^{6+}$].

Two PNA-containing conjugates, anti-dsred CA and nonsense CA were synthesized using the same synthetic scheme as reported before (*16*). In brief, PNA building blocks were coupled through an AEEA spacer to D-$Tat_{(57-49)}$ by a continuous solid-phase synthesis scheme. On completion of the PNA sequence, a Fmoc and Dde protected Lys residue was conjugated. DOTA tris(*tert*-butyl) ester was synthesized in-house (*27*) and coupled to the Lys on its α-NH_2 group after deprotection of Fmoc. Next, FITC was conjugated with the ε-NH_2 group of the Lys. The conjugates were cleaved off the resin and loaded with gadolinium under mild conditions. After purification by HPLC and dialysis, the products were characterized by ESI-MS.

Concentration Estimation. Peptide conjugates were dissolved in Milli-Q water to obtain a 10 mM solution by weight. For the determination of the real concentration, these stock solutions were diluted 1:100 in Dulbecco's Modified Eagle's Medium (DMEM; Biochrom AG, Germany). The absorbance of the solutions was measured in a multiplate reader (BMG Labtech, Germany) at 485 nm with ratiometric correction of turbidity at 690 nm. The concentrations of the stock solutions were calculated assuming $\varepsilon_{\text{carboxyfluorescein 485 nm}} = 81\,000$ L/(mol·cm), and all further dilutions were done according to this calculated concentration.

Cell Culture. NIH 3T3 cells were obtained from DSMZ, Germany, CCL-11 fibrosarcoma cells from ATCC, USA, and the DsRed2 protein-expressing fibrosarcoma CCL-11 cell line (DsRed cells) was a kind gift of Dr. Marna Ericsson, University of Minnesota, USA. NIH 3T3 mouse fibroblasts were cultured as a monolayer at 37 °C with 10% CO_2 in DMEM supplemented with 10% fetal bovine serum (FBS), 4 mM L-glutamine, 100 μg/mL streptomycin, and 100 U/mL penicillin (all purchased from Biochrom AG, Germany). Cultures of DsRed cells and the parent cell line CCL-11 were maintained at 37 °C with 5% CO_2 in NCTC 135 medium (Sigma, Germany) supplemented with 10% heat-inactivated fetal horse serum, 2.2 g/L sodium bicarbonate, and pH adjusted to 7.2. All cells were passaged by trypsinization with trypsin/EDTA 0.05/0.02% (w/v) in phosphate-buffered saline (PBS; Biochrom AG, Germany) every second to third day.

***In Vitro* Binding Assay.** The *in vitro* proof of specific binding of anti-dsred CA was obtained in a cell-free FITC immunoassay with slight modifications (*28*). A synthetic 45-mer single-stranded deoxynucleotide sequence containing the complementary target site of anti-dsred CA was obtained commercially (Eurofins MWG, Germany). The target oligodeoxynucleotide sequence extended by a 12-mer C linker was immobilized on DNA binding plates (Corning, Germany) in DNA binding buffer (50 mM sodium phosphate, 1 mM EDTA, pH 8.5) at 4 °C for 24 h. After washing off excess oligodeoxynucleotide with PBS, the plates were incubated with blocking buffer (DNA binding buffer containing 10% FBS and 3% bovine serum albumin (BSA)) for 2 h at 37 °C. Following a PBS wash, incubation with 16 nM of either anti-dsred CA or nonsense CA in 10 mM sodium phosphate, pH 6.5 was performed. For hybridization, the binding temperature was maintained at 60 °C for 1 h and then slowly decreased to 37 °C for another 1 h. The plates were left overnight at room temperature. The following day, plates were washed 3 times for 5 min each with wash buffer (PBS containing 0.01% Tween). Incubation with an anti-FITC-horseradish peroxidase (HRP)-conjugated antibody (Invitrogen, Germany) was carried out. Subsequent to thorough PBS washing to remove unbound antibody, the signal was developed with tetramethyl benzidine for 30 min at room temperature and absorbance was measured at 650 nm in a multiplate reader (BMG Labtech, Germany). Experiments were run at least three

times for each CA with two replicates. Statistical analysis was performed by Student's *t*-test. *P* values < 0.05 were considered significant.

Cellular Uptake Assay. Internalization experiments on cells were performed in 96 well microplates. At 70−80% confluency, cells were incubated with different concentrations of peptide-coupled CAs in complete culture medium for additional 18 h at routine culture conditions. After incubation, the labeling CAs were removed and cells were incubated with Bisbenzimid 33342 (Hoechst 33342), a nuclear stain, in order to assess the DNA content per well (correlates to the number of cells) (*29, 30*). Cells were washed with HBSS (Biochrom AG, Germany) and extracellular fluorescence was quenched by incubation with cold trypan blue (0.05% (w/v) in PBS) for 3 min followed by repeated washes with HBSS (*31*). Cell-related FITC fluorescence (Ex 485 nm/Em 530 nm) and cell number (Ex 346 nm/Em 460 nm) was evaluated in the multiplate reader. Experiments were run at least three times for each CA with six replicates. Statistical analysis was performed by ANOVA with Tukey's post test. *P* values < 0.05 were considered significant.

Microscopy. The cells in plates processed for fluorescence spectroscopic measurement, as mentioned above, were used for complementary fluorescence microscopy. Microscopy was performed without fixation using a Zeiss Axiovert 200 M microscope (Germany) with an LD Plan NeoFluor 40× objective. For high-resolution microscopy, 5×10^5 cells/mL were cultured on channel slides (Ibidi, Germany) for 24 h. Then, cells were incubated with CA in culture medium for another 18 h under normal culture conditions. These cells were subjected to nuclear staining and trypan blue quenching followed by extensive washing with HBSS. Images were made using a Zeiss Plan APOCHROMAT 63×/1.4 oil DIC objective. OptiGrid (Improvision, England), a structured light device, was used for acquiring images of confocal quality, and Volocity Acquisition and Visualization software (Improvision, England) was used for high-speed image capture and high-resolution rendering of data sets as images or movies. The imaging conditions were kept constant for the observation of all the different samples. Cellular localization and distribution of the peptide was observed by irradiating with blue light (Ex 470/40 nm) and observing at Em 525/50 nm. Apart from FITC fluorescence, the nuclear labeling by Hoechst was observed by Ex 365/15 nm and Em 460/50 nm and trypan blue fluorescence viewed by Ex 535/50 and Em 645/75 nm. Also, phase contrast images with differential interference contrast (DIC) microscopy of the same area were made to observe whether the cells maintain their normal morphology in the presence of CAs.

MR Measurement in Cells. For MR imaging of cells, exponentially growing cells were labeled with different concentrations of CAs in 175 cm^2 tissue culture flasks for 18 h. After repeated washes with HBSS, cells were trypsinized, centrifuged, and resuspended in 1.5 mL Eppendorf tubes at 2×10^7 cells for DsRed and CCL-11 in 500 μL complete medium. Cells were allowed to settle before MR measurements. Tubes with medium only and cells without CA were used as controls.

MR imaging of the cell pellets at room temperature (~21 °C) was performed in a 3 T (123 MHz) human MR scanner (MAGNETOM Tim Trio, Siemens Healthcare, Germany), using a 12-channel RF head coil and slice-selective measurements from a slice with a thickness of 1 mm positioned through the cell pellet.

T_1 was measured using an inversion−recovery sequence, with an adiabatic inversion pulse followed by a turbo−spin−echo readout. Between 10 and 15 images were taken, with the time between inversion and readout varying from 23 to 3000 ms. With a repetition time of 10 s, 15 echoes were acquired per scan and averaged six times. For T_2, a homewritten spin−echo sequence was used with echo times varying from 19 to 1000 ms in about 10 steps and a repetition time of 8 s. Diffusion sensitivity was reduced by minimizing the crusher gradients surrounding the refocusing pulse. All experiments scanned 256^2 voxels in a field-of-view of 110 mm in both directions resulting in a voxel volume of $0.43 \times 0.43 \times 1$ mm^3.

Data analysis was performed by fitting to relaxation curves with self-written routines under *MATLAB 7.1 R14* (The Mathworks Inc., United States). The series of T_1 and T_2 relaxation data were fitted to the following equations:

$$T_1 \text{ series with varying } t = T_I\text{: } S = S_0(1 - \exp(-t/T_1)) + S(T_I = 0)\exp(-t/T_1) \quad \text{(a)}$$

$$T_2 \text{ series with varying } t = TE\text{: } S = S_0 \exp(-t/T_2) \quad \text{(b)}$$

Nonlinear least-squares fitting of three parameters S_0, $S_{(TI = 0)}$, and T_1/T_2 was done for manually selected regions of interest with the Trust Region Reflective Newton algorithm implemented in *MATLAB*. The quality of the fit was controlled by visual inspection and by calculating the mean errors and residuals.

Biodistribution Study. C57BL/6 mice were used to study the *in vivo* distribution of anti-dsred CA. The CA was injected intravenously via the tail vein at a dose of 10 μmol/kg in 100 μL saline. An equivalent volume of saline was injected into the control animal. After 20 min, animals were sacrificed and biodistribution was assessed. Tissues harvested included lungs, liver, spleen, kidney, heart, bladder, and brain. All tissues were rinsed with PBS to remove blood or hair, and a slice of arbitrary thickness from each tissue was placed on a glass slide for microscopic observation. Microscopy was performed using a Zeiss EC Plan-NEOFLUOR 20×/0.5 objective. Fluorescence and bright field images of the tissues were obtained and observed for CA-related FITC fluorescence.

RESULTS AND DISCUSSION

Evaluation of Optimal CPP. Among the increasing number of transduction peptides that are being characterized, HIV-1 Tat and polyarginines represent two of the particularly well studied. Over the years, more efficient sequences have been derived by modifications of Tat CPP (*32, 33*). Although polyarginines were the foremost to be used for intracellular delivery of CAs (*34*), of late a higher toxicity of polyarginines has been suggested in comparison to Tat (*35*). Therefore, we decided to evaluate the efficiency of three HIV-1 Tat derivatives to translocate MR CAs together with FITC into cells. Thus far, there are only a few publications about the use of HIV-1 Tat to transport CAs for MRI (*36*−*38*). Large amounts of CA need to be transported into cells to obtain maximum MR contrast enhancement because of the low sensitivity of MRI. Therefore, we chose long incubation times. On the other hand, labeling protocols more close to *in vivo* conditions were applied using incubation in the presence of culture medium containing serum instead of serum-free buffer formulations and an incubation temperature of 37 °C. We observed that in the presence of serum the rate of uptake was slowed down (data not shown). This might be due to an interaction of the conjugates with serum components. A routine laboratory embryonic mouse fibroblasts cell line NIH 3T3 was selected for comparison of uptake efficiency.

We synthesized the Gd-DOTA-Lys(FITC) conjugates of L-$Tat_{(49-57)}$ (L-Tat CA), D-$Tat_{(57-49)}$ (D-Tat_{inv} CA), and Orn-D-$Tat_{(57-49)}$ (substitution of the glutamine residue with ornithine) (Orn-D-Tat_{inv} CA) in-house (*32*) (Figure 1). Peptide segments were synthesized by an online solid-phase synthesis scheme. Using an additional lysine as linker, DOTA tris(*tert*-butyl) ester was coupled on its α-NH_2 group and FITC on the ε-NH_2 group.

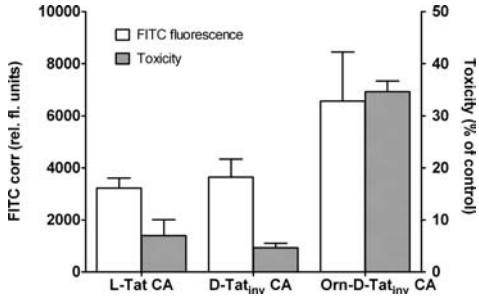

Figure 2. CA related fluorescence measured by fluorescence spectroscopy in NIH 3T3 embryonic mouse fibroblast cells. Cells were incubated with contrast agents at a concentration of 20 μM in complete medium for 18 h. External fluorescence was quenched with trypan blue and subsequent washes with HBSS. Values are means ± SEM; $n = 3$ with six replicates each.

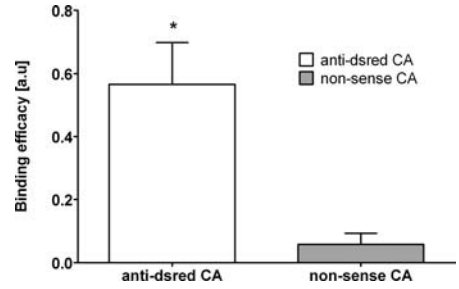

Figure 3. Binding efficacy of anti-dsred and nonsense CA in an *in vitro* binding assay. Synthetic single-stranded target DNA was immobilized on DNA binding plates, and nonspecific binding sites were blocked with BSA/FBS. Hybridization was performed with anti-dsred and nonsense CA, followed by extensive washing to eliminate nonspecific binding. Detection by anti-FITC-HRP-conjugated antibody. Values are means ± SEM, $n = 3$ with two replicates each. *: $p < 0.05$ statistically significantly different between contrast agents, Student's *t*-test.

The final gadolinium-loaded compounds were used to label cells. Fluorescence spectroscopy was applied to assess cellular uptake by FITC fluorescence and toxicity by nuclear DNA content estimation after staining with Hoechst 33342 (*29, 30*).

Of the three sequences tested, Orn-D-Tat$_{(57-49)}$ was the most efficient in delivering the conjugates across the cell membrane (Figure 2). However, its uptake was accompanied by a significant reduction of DNA content (directly correlated to the number of cells), thus limiting its exploitation. Our results did not reveal much difference in the uptake of conjugates with L-Tat$_{(49-57)}$ or D-Tat$_{(57-49)}$, both of which had negligible toxicity (although D-Tat$_{(57-49)}$ has been reported to be a more efficient transporter for other cargos (*39*)). This difference could be attributed to the influence of the Gd-loaded chelate on the molecular charge or three-dimensional conformation of the conjugate. Furthermore, it is well-established that D-isomers of amino acids are resistant to enzymatic cleavage and remain longer in the circulation (*39*). Thus, we chose D-Tat$_{(57-49)}$ as the CPP for experiments on further coupling of PNA sequences together with Gd-DOTA and FITC to obtain bimodal targeting agents.

Design and Synthesis of mRNA-Targeted CA. PNA was selected to target unique mRNA sequences. These polyamide nucleic acids are reported to be resistant to enzymatic cleavage in biological fluids and hybridize with DNA or RNA with high specificity and affinity (*40*). As per the base pairing rule, these PNA could bind sequences in cellular mRNA and, therefore, serve as high-affinity probes for molecular imaging. Although most mRNAs are expressed at low copy numbers under normal conditions (50−1000 per cell at any particular time point), these numbers increase manyfold in certain situations like disease or stress (*1*). The use of PNA for imaging specific mRNA could potentially serve for early detection of anomalies by monitoring molecular processes. Because PNAs have poor cellular uptake, they need to be coupled to delivery agents such as CPPs in order to pass through the biological membrane and interact with the intracellular target (*41*).

The intention of our study was to design a multimodal probe by the use of a facile building block approach. The blocks could easily be altered according to the target requirement without significant modification in the synthetic scheme. The molecule eventually designed contained MR and optical imaging moieties linked to PNA for targeting and CPP for intracellular transport. In order to establish proof of principle, mRNA from a variant of the red fluorescent protein, DsRed2, was chosen as the target. Through a BLAST database search, a 12mer antisense sequence (tcc gtg aac ggc, anti-dsred) specific to the DsRed2 mRNA was identified (*16*). Another sequence (gtt cag agt cta) that did not correspond to any known mammalian gene was selected as the nonsense control sequence (*16*).

Two PNA-containing conjugates, anti-dsred CA and nonsense CA, were synthesized using the same synthetic scheme as reported before (*16*) (Figure 1). The chelation of gadolinium in the macrocyclic chelator was confirmed by relaxivity measurements of CA in aqueous solutions. The relaxivity values for both the CAs (2.8 ± 0.3 $mM^{-1}s^{-1}$ for antisense CA and 4.3 ± 0.2 $mM^{-1}s^{-1}$ for nonsense CA) corresponded with values for compounds with one DOTA complexed gadolinium.

***In Vitro* Proof for Binding Specificity of Antisense CA.** The hybridization properties of PNA are crucial for specific antisense targeting. It is established that oligonucleotides of 12 or more bases are adequate for targeting unique genomic sequences (*42*). The targeting specificity of anti-dsred CA in comparison to nonsense CA was determined *in vitro* using a synthetic single-stranded oligodeoxynucleotide sequence (45-mer) as described in Experimental Procedures. Significant specific binding of the antisense CA to the synthetic target was observed (Figure 3). The nonsense counterpart almost completely failed to bind, such that the hybridization signal obtained can be mainly ascribed to specific binding. Thus, *in vitro* studies clearly demonstrated the applicability of the selected antisense PNA sequence for mRNA targeting. Gel retardation studies further verified the specific binding affinity of the antisense CA compared to the nonsense CA (data shown in Supporting Information). A retarded mobility of only the synthetic single-stranded DNA hybridized with the antisense PNA was observed, while the unhybridized DNA and DNA incubated with nonsense PNA showed no change in mobility.

Cellular Uptake and Internalization Studies. CPPs have been used for the delivery of a vast variety of biomolecules. The ability of D-Tat$_{(57-49)}$ to transport our covalently conjugated PNAs along with the imaging moieties was next investigated in whole cells. Murine fibrosarcoma cells transfected with the DsRed2 gene, referred to as DsRed cells (*24*), and their parent cell line CCL-11 were used for internalization assessment by fluorescence spectroscopy and microscopy.

The antisense CA as well as the nonsense CA very efficiently labeled DsRed cells (Figure 4a). Both CAs showed a concentration-dependent transfer into cells up to a labeling concentration of 5 μM. Saturation in internalization was observed at labeling concentrations of >2.5 μM, and a further dose increase was accompanied by increased toxicity but only a marginal improvement in cellular delivery. Thus, for subsequent studies a labeling concentration of 2.5 μM of the PNA-containing CA was used. A comparable uptake profile for both CAs was observed in the nontarget containing CCL-11 cells (data not shown).

Additionally, observations of DsRed and CCL-11 cells by fluorescence microscopy revealed similar uptake and distribution for both the PNA-containing CAs (Figure 4b). These agents

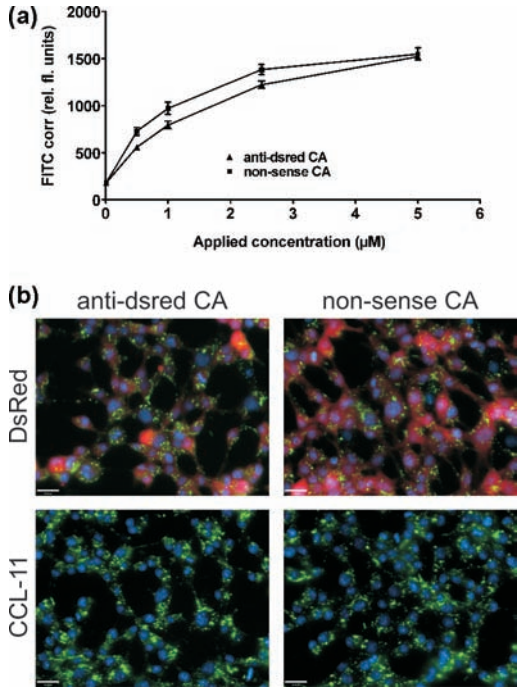

Figure 4. Internalization of anti-dsred and nonsense CA in DsRed and CCL-11 mouse fibrosarcoma cells. Fluorescence spectroscopy (a) and microscopy (b) were performed on cells incubated with 2.5 μM of either anti-dsred or nonsense CA for 18 h. External fluorescence was quenched with trypan blue and subsequent washes with HBSS; values are means $\pm$ SEM, $n = 3$ with six replicates each. The bar represents 20 μm.

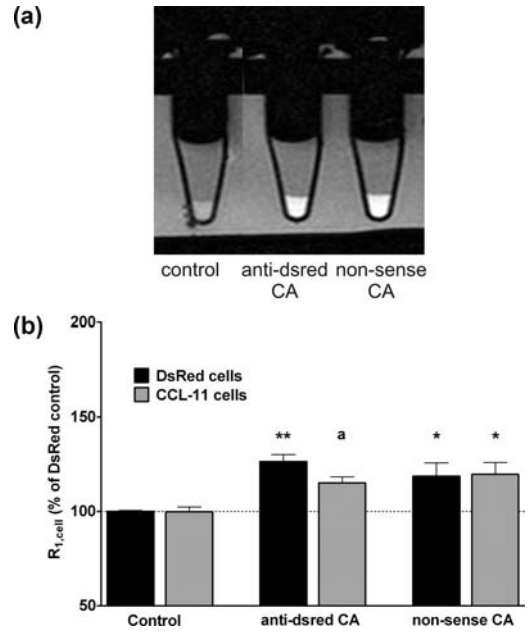

Figure 5. T_1-weighted MR images of DsRed cells after loading with 2.5 μM of anti-dsred and nonsense CA for 18 h (a). Cellular relaxation rate $R_{1,cell}$ in DsRed and CCL-11 cells after labeling with anti-dsred or nonsense CA (b). After treatment with DsRed CA for 18 h, cells were trypsinized, centrifuged, and resuspended in 1.5 mL Eppendorf tubes at 2×10^7 cells/500 μL in complete medium for MR studies. The measured relaxation rates were plotted vs the applied extracellular labeling concentration. Control: cells incubated with culture medium without CA. Values are means $\pm$ SEM; $n = 3$ with two replicates each. *: $p < 0.05$, **: $p < 0.01$ statistically significantly different to control. a: $p < 0.05$ statistically significantly different between cell lines, ANOVA with Tukey's post test.

were distributed in the perinuclear area as bright punctuate dots in both cell lines. This indicates that, despite the difference in the base composition of the two PNA sequences, both antisense and nonsense CA have similar cellular internalization efficacy and properties.

In our study, therefore, the feasibility of using D-Tat$_{(57-49)}$ as a transport vector for large-sized cargos has again been demonstrated. In fact, efficiency similar to that of the D-Tat$_{inv}$ CA was observed when an almost 10 times lower labeling concentration of the PNA-containing CAs was used. Attaching PNA to D-Tat$_{inv}$ largely increased the molecular weight and also raised the hydrophobic nature of the conjugates. We hypothesize that the CPP-PNA CAs might interact better with the cell membrane and hence enhance uptake. The high hydrophobicity of the conjugates containing PNA also reduced their solubility in water. Therefore, the PNA-containing conjugates could be used only at low micromolar concentrations for labeling cells.

Enhancement of MR Contrast in Cells. Previously, we reported that CPP-PNA CAs were highly efficient intracellular CAs yielding contrast enhancement in NIH 3T3 cells at concentrations as low as 0.5 μM (*16*). The possibility to utilize these PNA-containing conjugates as MR contrast-enhancing agents in target-containing cells has now been assessed. Cells producing target mRNA as well as nontarget expressing cells were labeled with 2.5 μM of either the antisense CA or nonsense CA. Cells were labeled for 18 h followed by repeated washings with Hank's buffered saline solution (HBSS, Biochrom AG, Germany). After trypsinization, an average of 2×10^7 cells were transferred into Eppendorf tubes for T_1 and T_2 measurements. Cells were also treated in a similar way but in the absence of any contrast agent to establish background control values.

In agreement with our earlier observations, both conjugates showed significant contrast enhancement in cells (*16*). The T_1 relaxation times in DsRed cells were substantially altered by the nonsense as well as antisense CA at concentrations as low as 2.5 μM (Figure 5a). Remarkably, this labeling concentration was 20−1000 times lower than the amount of CPP linked Gd-based chelators used for delivery into cells (*14, 15, 34, 36, 43*). T_1-weighted images of CCL-11 cells showed similar contrast changes at these low concentrations. The extended incubation times used for CA delivery into cells could be the reason this low concentration is sufficient for significant contrast enhancement.

The target-containing DsRed cells demonstrated a slightly higher cellular relaxation rate $R_{1,cell}$ for the antisense CA compared to the parent CCL-11 cells (Figure 5b). Whether a specific interaction between our anti-dsred CA and the cellular target mRNA was responsible for this observed effect remained unclear and is still under investigation. A decreased rotational correlation time and thus a greater τ_r effect was expected upon binding of antisense CA with DsRed2 mRNA (*44*). However, no such effect was observed even in the target-containing cells. In addition, no specific accumulation of the antisense CA in comparison to the nonsense CA could be detected in DsRed cells. Due to the predominantly endosomal uptake, a mainly unspecific accumulation could be observed. Additionally, the efflux from nontargeted cells would be disturbed and at least slowed down. These findings suggest that, although the CPP-PNA CAs efficiently permeate cells, their interaction with the target mRNA appears limited. This could arise due to the localization of the conjugates and the target in different cellular compartments.

Fluorescence Microscopy Studies. High-resolution microscopy was performed to elucidate the intracellular distribution of the FITC-containing CPP-PNA conjugates. DsRed cells were cultured in channel slides and labeled with antisense CA. After removal of surface-bound fluorescence by trypan blue and nuclear staining with Hoechst, cells were examined under the microscope. Confocal-like 3D image data were acquired using

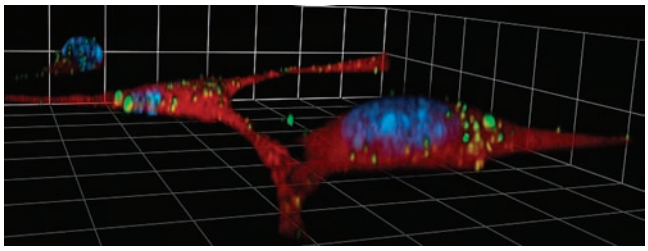

Figure 6. Endosomal localization of anti-dsred CA in DsRed cells. Cells were incubated with anti-dsred CA and cell nuclei were counterstained by Hoechst 33342. External fluorescence was quenched by trypan blue and subsequently washed with HBSS; DsRed CA, green (FITC fluorescence); nuclei, blue (Hoechst 33342). The 3D image was rendered from obtained 2D slices. A single unit represents 13.3 μm.

the OptiGrid Structured Illumination device that eliminates all out-of-focus information from the image (*45*). A high-speed Micro-Shutter was also integrated into the Zeiss microscope to control the exposure times and reduce sample photobleaching. Z-stacks were collected for a single time point using a multiple channel acquisition protocol. The combination of hardware and software used for microscopic evaluation was optimal for rapid and high-resolution observation of living cells with minimized damage to samples. 3D images were reconstructed from the 2D slice images thus obtained.

Examination of DsRed cells labeled with antisense CA in 3D clearly revealed encapsulation of green fluorescent CA in intracellular vesicles around the nucleus (Figure 6). Although the target mRNA cannot be visualized by microscopy, it is expected to be distributed mainly throughout the cytosol, as is the case with the red fluorescent DsRed2 protein itself. On the other hand, the CA seemed to be entering cells by endocytosis and subsequently entrapped in endosomal/lysosomal vesicles with little or no release into the cytosol. Hence, the absence of target binding in cells can be explained by the localization of both the antisense PNA and target mRNA in segregated compartments within the same cell.

As more information is obtained about the mechanism of cellular delivery by CPPs, it is becoming evident, as also reported by other groups, that endocytosis is the main route of trans-membrane movement (*46*−*48*). However, there is a lack of definitive evidence on the maintenance of functionality of the CPP-associated cargo once it is conveyed into cells. Some studies indicate successful PNA interaction with the target after being delivered by membrane-transducing peptides (*49*−*51*). Other studies indicate limited PNA binding with the target due to entrapment of PNA conjugates in endosomes (*52, 53*).

Another interesting observation was that subsequent to quenching with trypan blue no traces of green fluorescence binding to the cellular membrane were noticed (*31*). Trypan blue interacts with the aromatic groups on FITC, and therefore, the fluorophore in the extracellular environment as well as the FITC in cells with compromized cell membrane integrity becomes quenched. This justifies the use of this stain to efficiently eliminate extracellular and membrane-bound fluorescence. Microscopic examination also indicates that, because of the quenching step in our washing protocol, only the internalized probe signal is quantified by fluorescence spectroscopy.

Biodistribution Properties. Coupling of PNA with Gd-DOTA-CPP(FITC) more than doubles the size of the conjugate. Thus, it was important to investigate the mobility of this large molecule *in vivo*. Fluorescence studies performed 20 min after i.v. injection showed that within minutes the compound entered various organs via the bloodstream, and was by no means limited to the injection site (Table 1). The fluorescence observed in the liver and bladder was very high, and the exposure time for fluorescence images was reduced almost 3.5 times in comparison

Table 1. Biodistribution of the Antisense CA in Various Tissues Represented Qualitatively[a]

tissue	fluorescence intensity
liver	+++
urinary bladder	+++
kidney	++
spleen	++
lungs	+
heart	±
brain	−
blood	−

[a] Tissues from C57/BL6 mice were extracted 20 min after CA administration and tissue slices were assessed for antisense CA-related green fluorescence. Tissues from animals injected with saline alone served as control.

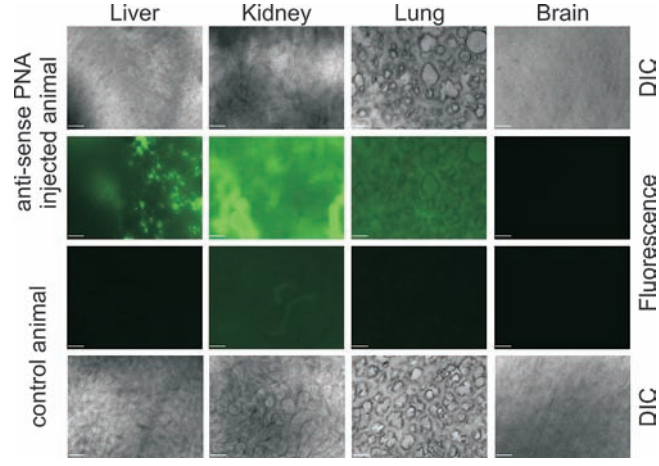

Figure 7. Distribution of anti-dsred CA in different tissues after *in vivo* labeling. Tissues were extracted 20 min after intravenous administration of anti-dsred CA to C57/BL6 mice. Fluorescence and bright field images of the tissues were obtained. For fluorescence images of liver, an exposure time of 175 ms was used, while for all other tissues, it was adjusted to 600 ms. The bar represents 160 μm.

to the rest of the tissues (Figure 7). The lipophilic nature of the PNA-containing CA explains the affinity of the conjugate for liver tissues. Kidneys and spleen were moderately labeled, whereas heart and lungs were only faintly fluorescent. Absolutely no penetration of the CA into the brain was detected, thus indicating a lack of penetration of the blood−brain barrier. Although these biodistribution studies are preliminary, they clearly indicate that the bulky PNA-containing antisense CA spontaneously disperses in the organism after injection and also rapidly enters the excretory system.

In conclusion, we report here the synthesis of a couple of cell-penetrating gadolinium-based conjugates, the most efficient of which was selected for coupling with PNA sequences. Both the PNA-CPP CAs labeled cells very well, regardless of whether they contained the specific target. mRNA targeting could not be realized; nevertheless, we have succeeded in generating highly efficient and nontoxic cell-internalizing and contrast-enhancing MR agents. Future studies need to be focused on the improvement of vesicular release after endocytosis or finding methods for direct cytosolic uptake and developing targeted contrast agents for better understanding of the mechanism of contrast enhancement at the cellular level.

ACKNOWLEDGMENT

The authors thank Dr. Marna Ericsson, University of Minnesota, for the generous gift of the DsRed2-transfected CCL-11 cell line. The authors especially acknowledge the help of Ms. Hildegard Schulz, High Field Magnetic Resonance Center,

Max Planck Institute for Biological Cybernetics, in carrying out these studies. This work was supported by the Max-Planck Society and was performed in the frame of COST action D38.

Supporting Information Available: Characterization data for the conjugates and gel retardation assay described. This material is available free of charge via the Internet at http://pubs.acs.org.

LITERATURE CITED

(1) Weissleder, R., and Mahmood, U. (2001) Molecular imaging. *Radiology 219*, 316–33.
(2) Doubrovin, M., Serganova, I., Mayer-Kuckuk, P., Ponomarev, V., and Blasberg, R. G. (2004) Multimodality in vivo molecular-genetic imaging. *Bioconjugate Chem. 15*, 1376–88.
(3) Willmann, J. K., van Bruggen, N., Dinkelborg, L. M., and Gambhir, S. S. (2008) Molecular imaging in drug development. *Nat. Rev. Drug Discovery 7*, 591–607.
(4) Massoud, T. F., and Gambhir, S. S. (2003) Molecular imaging in living subjects: seeing fundamental biological processes in a new light. *Genes Dev. 17*, 545–80.
(5) Min, J. J., and Gambhir, S. S. (2004) Gene therapy progress and prospects: noninvasive imaging of gene therapy in living subjects. *Gene Ther. 11*, 115–25.
(6) Merbach, A. E., and Toth, E. (2001) *The Chemistry of Contrast Agents in Medical Magnetic Resonance Imaging*, John Wiley and Sons, New York.
(7) Aime, S., Cabella, C., Colombatto, S., Geninatti Crich, S., Gianolio, E., and Maggioni, F. (2002) Insights into the use of paramagnetic Gd(III) complexes in MR-molecular imaging investigations. *J. Magn. Reson. Imaging 16*, 394–406.
(8) Weinmann, H. J., Ebert, W., Misselwitz, B., and Schmitt-Willich, H. (2003) Tissue-specific MR contrast agents. *Eur. J. Radiol. 46*, 33–44.
(9) Karabulut, N., and Elmas, N. (2006) Contrast agents used in MR imaging of the liver. *Diagn. Interv. Radiol. 12*, 22–30.
(10) Artemov, D., Mori, N., Okollie, B., and Bhujwalla, Z. M. (2003) MR molecular imaging of the Her-2/neu receptor in breast cancer cells using targeted iron oxide nanoparticles. *Magn. Reson. Med. 49*, 403–8.
(11) Artemov, D., Mori, N., Ravi, R., and Bhujwalla, Z. M. (2003) Magnetic resonance molecular imaging of the HER-2/neu receptor. *Cancer Res. 63*, 2723–7.
(12) Towner, R. A., Smith, N., Doblas, S., Tesiram, Y., Garteiser, P., Saunders, D., Cranford, R., Silasi-Mansat, R., Herlea, O., Ivanciu, L., Wu, D., and Lupu, F. (2008) In vivo detection of c-Met expression in a rat C6 glioma model. *J. Cell Mol. Med. 12*, 174–86.
(13) Wang, Z. J., Boddington, S., Wendland, M., Meier, R., Corot, C., and Daldrup-Link, H. (2008) MR imaging of ovarian tumors using folate-receptor-targeted contrast agents. *Pediatr. Radiol. 38*, 529–37.
(14) Lee, J., Burdette, J. E., MacRenaris, K. W., Mustafi, D., Woodruff, T. K., and Meade, T. J. (2007) Rational design, synthesis, and biological evaluation of progesterone-modified MRI contrast agents. *Chem. Biol. 14*, 824–34.
(15) Heckl, S., Pipkorn, R., Waldeck, W., Spring, H., Jenne, J., von der Lieth, C. W., Corban-Wilhelm, H., Debus, J., and Braun, K. (2003) Intracellular visualization of prostate cancer using magnetic resonance imaging. *Cancer Res. 63*, 4766–72.
(16) Su, W., Mishra, R., Pfeuffer, J., Wiesmuller, K. H., Ugurbil, K., and Engelmann, J. (2007) Synthesis and cellular uptake of a MR contrast agent coupled to an antisense peptide nucleic acid--cell- penetrating peptide conjugate. *Contrast Media Mol. Imaging 2*, 42–9.
(17) Lindgren, M., Hallbrink, M., Prochiantz, A., and Langel, U. (2000) Cell-penetrating peptides. *Trends Pharmacol. Sci. 21*, 99–103.
(18) Kersemans, V., Kersemans, K., and Cornelissen, B. (2008) Cell penetrating peptides for in vivo molecular imaging applications. *Curr. Pharm. Des. 14*, 2415–47.
(19) Derossi, D., Chassaing, G., and Prochiantz, A. (1998) Trojan peptides: the penetratin system for intracellular delivery. *Trends Cell Biol. 8*, 84–7.
(20) Mae, M., and Langel, U. (2006) Cell-penetrating peptides as vectors for peptide, protein and oligonucleotide delivery. *Curr. Opin. Pharmacol. 6*, 509–14.
(21) Howl, J., Nicholl, I. D., and Jones, S. (2007) The many futures for cell-penetrating peptides: how soon is now? *Biochem. Soc. Trans. 35*, 767–9.
(22) Zorko, M., and Langel, U. (2005) Cell-penetrating peptides: mechanism and kinetics of cargo delivery. *Adv. Drug Delivery Rev. 57*, 529–45.
(23) El-Andaloussi, S., Jarver, P., Johansson, H. J., and Langel, U. (2007) Cargo-dependent cytotoxicity and delivery efficacy of cell-penetrating peptides: a comparative study. *Biochem. J. 407*, 285–92.
(24) Wacnik, P. W., Baker, C. M., Herron, M. J., Kren, B. T., Blazar, B. R., Wilcox, G. L., Hordinsky, M. K., Beitz, A. J., and Ericson, M. E. (2005) Tumor-induced mechanical hyperalgesia involves CGRP receptors and altered innervation and vascularization of DsRed2 fluorescent hindpaw tumors. *Pain 115*, 95–106.
(25) Sarin, V. K., Kent, S. B., Tam, J. P., and Merrifield, R. B. (1981) Quantitative monitoring of solid-phase peptide synthesis by the ninhydrin reaction. *Anal. Biochem. 117*, 147–57.
(26) Paull, B., and Haddaad, P. R. (1999) Chelation ion chromatography of trace metal ions using metallochromic ligands. *Trends Anal. Chem. 18*, 107–114.
(27) Aarons, R. J., Notta, J. K., Meloni, M. M., Feng, J., Vidyasagar, R., Narvainen, J., Allan, S., Spencer, N., Kauppinen, R. A., Snaith, J. S., and Faulkner, S. (2006) A luminescent probe containing a tuftsin targeting vector coupled to a terbium complex. *Chem. Commun. (Camb.)* 909–11.
(28) Kelly, K. A., Reynolds, F., Weissleder, R., and Josephson, L. (2004) Fluorescein isothiocyanate-hapten immunoassay for determination of peptide-cell interactions. *Anal. Biochem. 330*, 181–5.
(29) Richards, W. L., Song, M. K., Krutzsch, H., Evarts, R. P., Marsden, E., and Thorgeirsson, S. S. (1985) Measurement of cell proliferation in microculture using Hoechst 33342 for the rapid semiautomated microfluorimetric determination of chromatin DNA. *Exp. Cell Res. 159*, 235–46.
(30) Blaheta, R. A., Franz, M., Auth, M. K., Wenisch, H. J., and Markus, B. H. (1991) A rapid non-radioactive fluorescence assay for the measurement of both cell number and proliferation. *J. Immunol. Methods 142*, 199–206.
(31) Rennert, R., Wespe, C., Beck-Sickinger, A. G., and Neundorf, I. (2006) Developing novel hCT derived cell-penetrating peptides with improved metabolic stability. *Biochim. Biophys. Acta 1758*, 347–54.
(32) Gammon, S. T., Villalobos, V. M., Prior, J. L., Sharma, V., and Piwnica-Worms, D. (2003) Quantitative analysis of permeation peptide complexes labeled with Technetium-99m: chiral and sequence-specific effects on net cell uptake. *Bioconjugate Chem. 14*, 368–76.
(33) Wender, P. A., Mitchell, D. J., Pattabiraman, K., Pelkey, E. T., Steinman, L., and Rothbard, J. B. (2000) The design, synthesis, and evaluation of molecules that enable or enhance cellular uptake: peptoid molecular transporters. *Proc. Natl. Acad. Sci. U.S.A. 97*, 13003–8.
(34) Allen, M. J., MacRenaris, K. W., Venkatasubramanian, P. N., and Meade, T. J. (2004) Cellular delivery of MRI contrast agents. *Chem. Biol. 11*, 301–7.
(35) Jones, S. W., Christison, R., Bundell, K., Voyce, C. J., Brockbank, S. M., Newham, P., and Lindsay, M. A. (2005) Characterisation of cell-penetrating peptide-mediated peptide delivery. *Br. J. Pharmacol. 145*, 1093–102.
(36) Bhorade, R., Weissleder, R., Nakakoshi, T., Moore, A., and Tung, C. H. (2000) Macrocyclic chelators with paramagnetic cations are internalized into mammalian cells via a HIV-tat

derived membrane translocation peptide. *Bioconjugate Chem. 11*, 301–5.
(37) Prantner, A. M., Sharma, V., Garbow, J. R., and Piwnica-Worms, D. (2003) Synthesis and characterization of a Gd-DOTA-D-permeation peptide for magnetic resonance relaxation enhancement of intracellular targets. *Mol. Imaging 2*, 333–41.
(38) Bullok, K. E., Dyszlewski, M., Prior, J. L., Pica, C. M., Sharma, V., and Piwnica-Worms, D. (2002) Characterization of novel histidine-tagged Tat-peptide complexes dual-labeled with (99m)Tc-tricarbonyl and fluorescein for scintigraphy and fluorescence microscopy. *Bioconjugate Chem. 13*, 1226–37.
(39) Wright, L. R., Rothbard, J. B., and Wender, P. A. (2003) Guanidinium rich peptide transporters and drug delivery. *Curr. Protein Pept. Sci. 4*, 105–24.
(40) Shakeel, S., Karim, S., and Ali, A. (2006) Peptide Nucleic Acids (PNA) - a review. *J. Chem. Technol. Biotechnol. 81*, 892–899.
(41) Oehlke, J., Wallukat, G., Wolf, Y., Ehrlich, A., Wiesner, B., Berger, H., and Bienert, M. (2004) Enhancement of intracellular concentration and biological activity of PNA after conjugation with a cell-penetrating synthetic model peptide. *Eur. J. Biochem. 271*, 3043–9.
(42) Woolf, T. M., Melton, D. A., and Jennings, C. G. (1992) Specificity of antisense oligonucleotides in vivo. *Proc. Natl. Acad. Sci. U.S. A. 89*, 7305–9.
(43) Endres, P. J., Macrenaris, K. W., Vogt, S., and Meade, T. J. (2008) Cell-permeable MR contrast agents with increased intracellular retention. *Bioconjugate Chem*.
(44) Zech, S. G., Eldredge, H. B., Lowe, M. P., and Caravan, P. (2007) Protein binding to lanthanide(III) complexes can reduce the water exchange rate at the lanthanide. *Inorg. Chem. 46*, 3576–84.
(45) Neil, M. A., Juskaitis, R., and Wilson, T. (1997) Method of obtaining optical sectioning by using structured light in a conventional microscope. *Opt. Lett. 22*, 1905–7.
(46) Chauhan, A., Tikoo, A., Kapur, A. K., and Singh, M. (2007) The taming of the cell penetrating domain of the HIV Tat: myths and realities. *J. Controlled Release 117*, 148–62.
(47) Gump, J. M., and Dowdy, S. F. (2007) TAT transduction: the molecular mechanism and therapeutic prospects. *Trends Mol. Med. 13*, 443–8.
(48) Futaki, S., Nakase, I., Tadokoro, A., Takeuchi, T., and Jones, A. T. (2007) Arginine-rich peptides and their internalization mechanisms. *Biochem. Soc. Trans. 35*, 784–7.
(49) Jia, F., Figueroa, S. D., Gallazzi, F., Balaji, B. S., Hannink, M., Lever, S. Z., Hoffman, T. J., and Lewis, M. R. (2008) Molecular imaging of bcl-2 expression in small lymphocytic lymphoma using ^{111}In-labeled PNA-peptide conjugates. *J. Nucl. Med. 49*, 430–8.
(50) Tripathi, S., Chaubey, B., Ganguly, S., Harris, D., Casale, R. A., and Pandey, V. N. (2005) Anti-HIV-1 activity of anti-TAR polyamide nucleic acid conjugated with various membrane transducing peptides. *Nucleic Acids Res. 33*, 4345–56.
(51) Morris, M. C., Chaloin, L., Choob, M., Archdeacon, J., Heitz, F., and Divita, G. (2004) Combination of a new generation of PNAs with a peptide-based carrier enables efficient targeting of cell cycle progression. *Gene Ther. 11*, 757–64.
(52) Abes, S., Williams, D., Prevot, P., Thierry, A., Gait, M. J., and Lebleu, B. (2006) Endosome trapping limits the efficiency of splicing correction by PNA-oligolysine conjugates. *J. Controlled Release 110*, 595–604.
(53) Turner, J. J., Ivanova, G. D., Verbeure, B., Williams, D., Arzumanov, A. A., Abes, S., Lebleu, B., and Gait, M. J. (2005) Cell-penetrating peptide conjugates of peptide nucleic acids (PNA) as inhibitors of HIV-1 Tat-dependent trans-activation in cells. *Nucleic Acids Res. 33*, 6837–49.

BC9000454

Supporting Information

Cell-Penetrating Peptides and Peptide Nucleic Acid-Coupled MRI Contrast Agents: Evaluation of Cellular Delivery and Target Binding

Ritu Mishra,[†] Wu Su,[†,#] Rolf Pohmann,[†] Josef Pfeuffer,[†,§] Martin G. Sauer,[‡] Kamil Ugurbil,[†,⊥] and Jörn Engelmann[†,*]

[†]High-Field Magnetic Resonance Center, Max Planck Institute for Biological Cybernetics, Spemannstrasse 41, Tübingen, 72076, Germany

[‡]Pediatric Hematology & Oncology, Hannover Medical School, Hannover, 30625, Germany

[#]Present address: Department of Chemistry, University of Leicester, Leicester, LE17RH, UK

[§]Present address: Siemens Medical Solutions USA, Inc., Charlestown, MA 02129, USA

[⊥]Present address Center for Magnetic Resonance Research, University of Minnesota, Department of Radiology, Minneapolis, MN 55455, USA

[*]To whom correspondence should be addressed:

Joern Engelmann

High-Field Magnetic Resonance Center,

Max Planck Institute for Biological Cybernetics,

Spemannstrasse 41,

Tübingen, 72076, Germany.

E-mail: joern.engelmann@tuebingen.mpg.de

Tel: +49-7071-601704

Fax: +49-7071-601702

Running title: Evaluation of CPP-PNA coupled MR contrast agents

ESI-MS.

ESI-MS spectra obtained for the conjugates were as follows:

Gd-DOTA-Lys(FITC)-L-Tat$_{49-57}$-OH. (MW=2397.08)

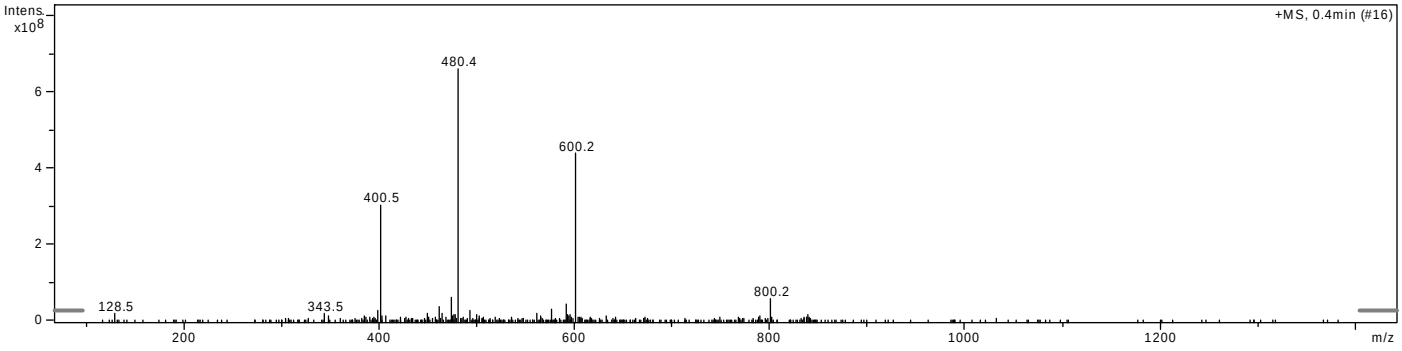

Gd-DOTA-Lys(FITC)-D-Tat$_{57-49}$-OH. (MW=2397.08)

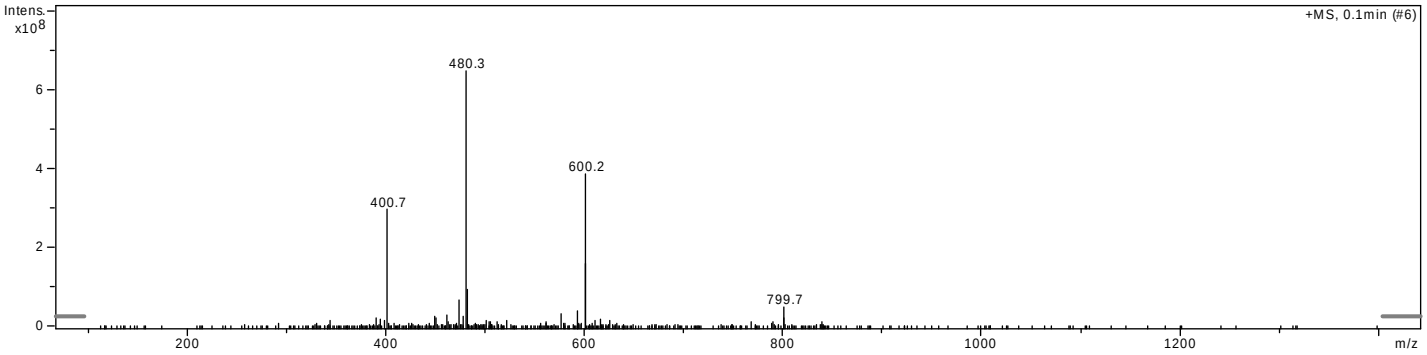

Gd-DOTA-Lys(FITC)-Orn-D-Tat$_{57-49}$-OH. (MW=2383.10)

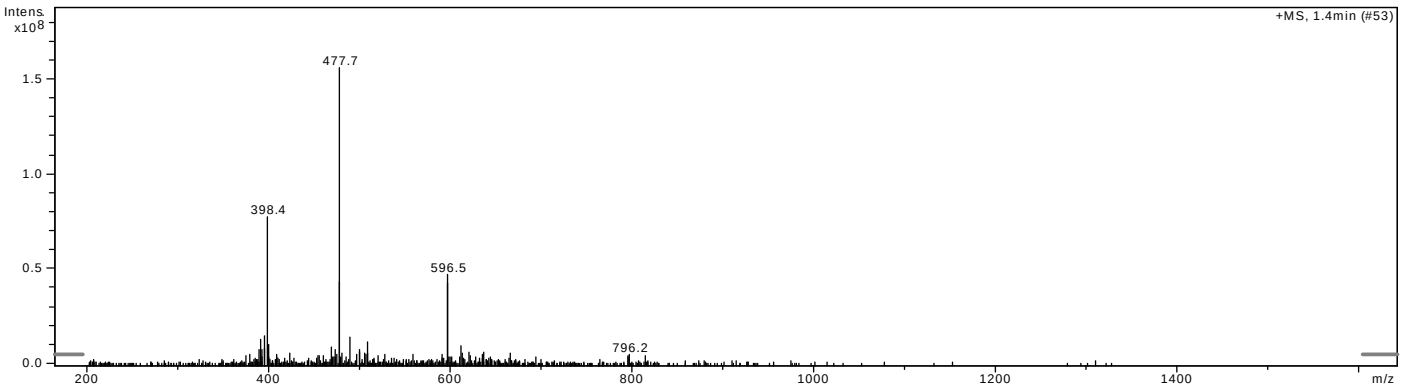

GELRETARDATION ASSAY.

The specificity of interaction between the anti-sense PNA and target sequence after pre-gel hybridization was verified by gel retardation assay (*1*). A 45-mer single-stranded deoxynucleotide sequence (5'-CTC GAA CTC GTG GCC GTT CAC GGA GCC CTC CAT GCG CAC CTT GAA GCG CAT GAA CTC CTT GAT-3'), selected from the DsRed2 cDNA was obtained commercially (Eurofins MWG, Germany). This sequence contained a stretch of bases complementary to the anti-sense sequence used in the anti-sense CA. The anti-sense CA or non-sense CA (10 pmol) were incubated with the synthetic 45-mer single-stranded deoxynucleotide (12.5 pmol) in hybridization buffer (12.5 mM Tris buffer, pH 8 containing 2.5 mM sodium chloride, 0.5 mM magnesium chloride and 0.05 mM dithiothritol (DTT)). This pre-loading hybridization was performed at 60°C for 1 h followed by a gradual reduction to room temperature. The samples were then run on 8% native acrylamide gel and subjected to electrophoresis in running buffer (200 mM Tris-acetate buffer, pH 8.3, 1 mM EDTA). Silver staining was used to detect the mobility of the DNA on the gel.

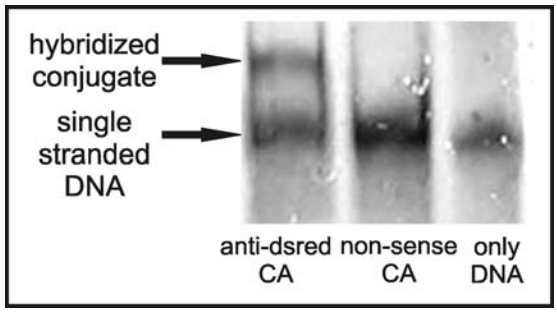

Figure S-1. Retardation of the mobility of the target oligodeoxynucleotide after hybridization with anti-sense CA. The hybridized synthetic DNA with anti-sense CA

shows a gel shift. The DNA does not interact with the non-sense CA and the excess of anti-sense CA and thus the unhybridized DNA has the same mobility on the gel as the control DNA. Since these PNA-CPP conjugated CAs have a positive charge, they tend to run out of the gel if they are unhybridized and cannot be visualized under the gel running conditions used.

REFERENCES

(1) Perry-O'Keefe, H., Yao, X. W., Coull, J. M., Fuchs, M., and Egholm, M. (1996) Peptide nucleic acid pre-gel hybridization: an alternative to southern hybridization. *Proc Natl Acad Sci U S A 93*, 14670-5.

Peptide Targeting of Platinum Anti-Cancer Drugs

Margaret W. Ndinguri,[†] Rajasree Solipuram,[‡] Robert P. Gambrell,[§] Sita Aggarwal,*[,‡] and Robert P. Hammer*[,†,||]

Department of Chemistry, Louisiana State University, Baton Rouge, Louisiana 70803, William Hansel Cancer Prevention Laboratory, Pennington Biomedical Research Center, Baton Rouge, Louisiana 70808, Department of Oceanography and Coastal Sciences, Louisiana State University, Baton Rouge, Louisiana 70803, and New England Peptide, Gardner, Massachusetts 01440.
Received February 11, 2009; Revised Manuscript Received August 24, 2009

Besides various side effects caused by platinum anticancer drugs, they are not efficiently absorbed by the tumor cells. Two Pt−peptide conjugates; cyclic mPeg-CNGRC-Pt (**7**) and cyclic mPeg-CNGRC-Pten (**8**) bearing the Asn-Gly-Arg (NGR) targeting sequence, a malonoyl linker, and low molecular weight miniPEG groups have been synthesized. The platinum ligand was attached to the peptide via the carboxylic end of the malonate group at the end of the peptide. The pegylated peptide is nontoxic and highly soluble in water. Platinum conjugates synthesized using the pegylated peptides are also water-soluble with reduced or eliminated peptide immunogenicity. The choice of carboplatin as our untargeted platinum complex was due to the fact that the malonate linker chelates platinum in a manner similar to that of carboplatin. Cell toxicity assay and competition assay on the PC-3 cells (CD13 positive receptors) revealed selective delivery and destruction of PC-3 cells using targeted Pt−peptide conjugates **7** and **8** significantly more than untargeted carboplatin. Platinum uptake on PC-3 cells was 12-fold more for conjugate **7** and 3-fold more for conjugate **8** compared to that of the untargeted carboplatin, indicating selective activation of the CD13 receptors and delivery of the conjugates to CD13 positive cells. Further analysis on effects of conjugates **7** and **8** on PC-3 cells using caspase-3/7, fluorescence microscopy, and DNA fragmentation confirmed that the cells were dying by apoptosis.

INTRODUCTION

Platinum compounds are widely used in cancer chemotherapy (*1, 2*). Cisplatin is an FDA-approved drug that is widely used for treatment of many types of cancers including lung, ovarian, as well as head and neck cancer (*3, 4*). Carboplatin, an analogue of cisplatin, is being used more often because it has decreased nonspecific toxicity and is active against cisplatin-resistant tumors (*2, 5*−*7*). Both carboplatin and cisplatin have been shown to form similar adducts with DNA by the formation of covalent bonds with the N7 of purine bases. This results in interference with normal transcription and DNA replication mechanisms leading to eventual cell death. While these drugs are effective, they have very serious side effects that include nephrotoxicity, myelotoxicity, neurotoxicity, vomiting, and nausea (*8*). Certain cancers can also develop resistance to drugs such as cisplatin via efflux pumps as reported by Katano et al. (*9, 10*).

One method to make toxic drugs more effective is by incorporation of a cell-specific targeting group. A number of peptide sequences are capable of mediating the delivery of therapeutic or imaging drugs (*11, 12*). Using phage display libraries, several peptide sequences that have the ability to target tumors have been discovered (*13, 14*). The Asn-Gly-Arg (NGR) motif was identified as a peptide that uniquely homed specifically to solid tumors in murine breast carcinoma models and that bound strictly to the endothelium of angiogenic blood vessels (*15*). Besides the NGR motif, other peptide sequences such as Arg-Gly-Asp (RGD) and luteinizing hormone releasing hormone (LHRH) have been used to target specific receptors found mainly in certain tumor cells (*16*−*20*). The NGR motif may be superior to the RGD-related motif for targeting because of the many types of cells that express the $\alpha V\beta_3$ and $\alpha V\beta_5$ integrins that bind the RGD-type sequence, which may lead to nonspecific targeting and toxicity (*14*). Recently, doxorubicin (DOX) and 5-fluoro-2′-deoxyuridine (5-FdUrd) conjugates have successfully been targeted using the NGR motif (*21, 22*). Specifically, the DOX−peptide conjugate treated animals had increased life expectancies relative to that of animals treated with DOX alone (*23*), and a 5-FdUrd−NGR conjugate produced selective accumulation of 5-FdUrd in tumor cells having CD 13 receptors (*24*). Haubner et al. revealed that radiolabeled RGD peptide was found to concentrate rapidly in the liver, which can lead to liver toxicity in drugs that are based on RGD targeting, hence limiting the usefulness of these drugs (*14*).

New blood vessels are required for tumor growth (*15, 25*). Thus, around solid tumors, angiogenesis is stimulated, and endothelial cells proliferate to form new blood sources to support the growing tumor. Modulating the growth of blood vessels is one of the effective ways to control the growth and spread of tumors. Therefore, the search for targets that can regulate angiogenesis is important. Aminopeptidase N (APN), also referred to as CD13, is a cell-surface antigen that binds specifically to NGR peptides (*26, 27*). CD13/APN is expressed selectively on the endothelial cells of angiogenic tissues and the vasculature of various carcinomas including kidney, colon, pancreas, prostate, and lung (*28*−*31*). It is not expressed in normal vasculature, which explains the tumor-specific destination of the NGR peptide (*3, 32*).

By conjugating the water-soluble cyclic peptide CNGRC to the conventional drugs cisplatin and dichloro(ethylenediamine)-platinum(II) ($PtenCl_2$), we hypothesized that we could increase specificity for CD13-expressing cancerous tissues and reduced toxicity to normal tissues. In this work, we describe the preparation of several malonoyl CNGRC peptides and their

* To whom correspondence should be addressed. (S.A.) E-mail: Sita.Aggarwal@pbrc.edu. (R.P.H.) E-mail: robert.hammer@newenglandpeptide.com.

[†] Department of Chemistry, Louisiana State University.

[‡] Pennington Biomedical Research Center.

[§] Department of Oceanography and Coastal Sciences, Louisiana State University.

[||] New England Peptide.

10.1021/bc900065r CCC: $40.75 © 2009 American Chemical Society
Published on Web 09/23/2009

platinum conjugates and evaluate their specific targeting on tumor cells with CD13 receptors.

EXPERIMENTAL SECTION

All starting reagents listed below were obtained from commercial sources and used without further purification: di-*tert*-butyl malonate, dry solvents, $AgNO_3$, 3-bromopropylphthalimide, dichloro(ethylenediamine)platinum(II), cis-diammineplatinum(II) dichloride, and glutaric anhydride were obtained from Aldrich (Milwaukee WI); Fmoc-11-amino-3,6,9-trioxaundecanoic acid (miniPEG, $mPEG_3$) was obtained from Peptides International (Louisville, KY), and all amino acids were from Novabiochem (Gibbstown, NJ).

NMR Spectroscopy. ^1H NMR spectra were recorded on either 300 or 400 MHz spectrometers. Peak positions are referenced to TMS. All NMR data were processed with *XWINNMR* and *Mestre-C* software.

HPLC. HPLC was performed using a Water 600E multisolvent delivery system with a model 486 tunable detector controlled by Empower software and a Water Deltaprep system, with detection at 220 nm. Different columns were used for analysis and purification of the peptides. Analytical and semipreparative chromatography was performed on a Delta-Pak C_4 (5 μm; 100 Å) reverse phase column (8 × 100 mm) at 1 mL/min (Column 1). Preparative HPLC was performed on Waters Delta-Pak C_4 (15 μm; 100 Å) reverse phase column (25 × 100 mm) at 15 mL/min (Column 2). Linear gradients of 0.1% TFA[1] in H_2O (Eluent A) and 0.1% TFA in MeCN (Eluent B) in all HPLC were used.

Mass Spectrometry. Compounds were analyzed using ESI on an Agilent Technologies instrument processed with Analyst QS1.1 (Applied Biosystems) or Mass Hunter (Agilent).

Inductive Coupled Plasma−Optical Emission Spectroscopy. Platinum uptake was analyzed using a Varian, Vista MPX CCD simultaneous spectrometer. PlasmaCal Pt (1000 μg/mL) from SCP Science was used for calibration by diluting it to standard solutions of known concentration.

Synthesis. *Peptide Synthesis.* All peptides were synthesized using standard Fmoc solid phase chemistry. Fmoc-PAL-PEG-PS (Peptide Amide Linker resin: 0.2 mmol, 0.24 mmol/g loading) was placed in a normal resin column and washed with DMF in continuous flow mode using a Pioneer Peptide Synthesizer. The side chain-protected amino acid derivatives used in the sequence were Fmoc-Cys(Acm)-OH, Fmoc-Arg-(Pbf)-OH, Fmoc-Gly-OH, Fmoc-Asn(Trt)-OH, and Fmoc-Cys(Acm)-OH. Fmoc-mini-peg-3 and the derivatized malonate linker di-*tert*-butyl 2-(3-glutaricaminopropyl)malonate were also used, depending on the peptide sequence. All couplings utilized four equivalents each of amino acids, malonate, and PyAOP (*33*) dissolved in 0.5 M DIEA in DMF (final concentration, 0.25 M) for 1 h at room temperature; minimal preactivation time was used in coupling. DMF was used for washing between coupling and deprotection cycles. The Fmoc group was removed using 20% piperidine in DMF for 5 min. Final washing was with DMF and dichloromethane.

*Synthesis of CNGRC-Mal (***1***).* In an attempt to synthesize CNGRC-Mal, we synthesized cyclic CNGRC using the method described by Anizon et al. using NovaSyn TGT alcohol resin (0.20 mmol, 0.20 mmol/g loading) (*23*). Conjugation of CNGRC with di-*tert*-butyl 2-(3-aminopropyl)malonate was unsuccessful (Scheme 1).

Scheme 1. Coupling of CNGRC with Di-*tert*-butyl 2-(3-aminopropyl)malonate

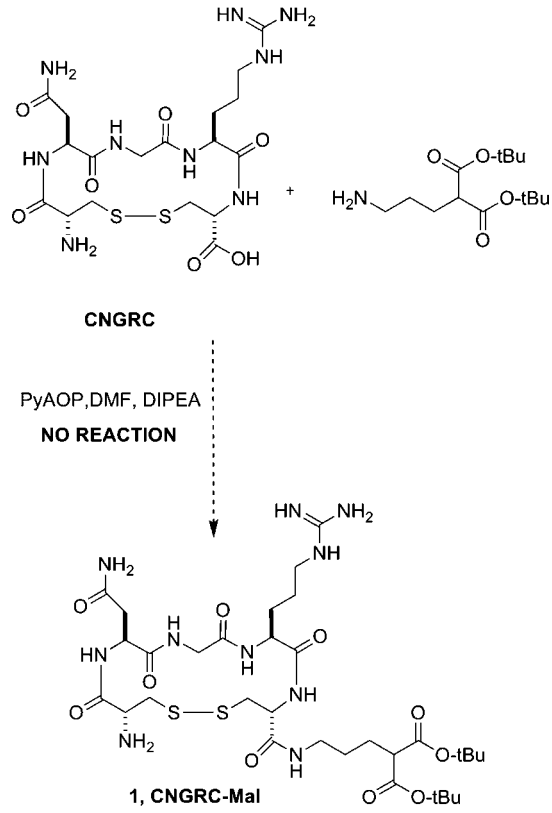

*Synthesis of Mal-Glut-CNGRC (***2***).* Using standard Fmoc chemistry, we synthesized Mal-Glut-CNGRC using the procedure described in the peptide synthesis section, using PAL-PEG-PS resin without the Fmoc-mini-peg-3 solubilizing group. Coupling the peptide with di-*tert*-butyl 2-(3-glutaricaminopropyl)malonate gave crude Mal-Glut-CNGRC peptide, which was purified by reverse phase HPLC on column 1 using a linear gradient from 5% to 70% B eluent in 60 min, t_R 11 min. The adduct gave the expected $(M + H)^+$ peak at 807.2893, calculated for $C_{29}H_{48}N_{11}O_{12}S_2$ 807.2925 (see Supporting Information). Using the procedure described for the preparation of cyclic mPeg-CNGRC-Pt, the peptide was reacted with cis-$[Pt(NH_3)_2(H_2O)_2]^{2+}(NO_3)_2$ to give an insoluble yellow solid (Scheme 2) which was not suitable for further characterization.

*Synthesis of Di-tert-butyl 2-(3-phthalimidopropyl)malonate (***3***).* Di-*tert*-butyl 2-(3-phthalimidopropyl)malonate was synthesized by a known method (Scheme 3) with slight modifications (*34*). NaH (0.38 g, 16 mmol) was suspended in dry THF (100 mL), and dry di-*tert*-butyl malonate (4.4 mL, 20 mmol) was added to the reaction mixture (with stirring) until gas evolution ceased. A solution of 3-bromopropylphthalimide (2.68 g, 10 mmol) was added dropwise to the reaction mixture, followed by stirring overnight. The THF was removed by evaporation, and the product was redissolved in CH_2Cl_2 and washed with 5% aqueous acetic acid. The organic fractions were combined, dried over $MgSO_4$, and concentrated. The final product was isolated using silica column chromatography (95% hexane; 5% ethyl acetate). Di-*tert*-butyl 2-(3-phthalimidopropyl)malonate was crystallized using a mixture of CH_2Cl_2 and hexane to give colorless plates (see Supporting Information). The yield was 80% (3.22 g). Spectroscopic data obtained for this compound were in agreement with literature values (*34*).

[1]Abbreviations. PyAOP, (7-azabenzotriazol-1-yloxy)tripyrrolidinophosphonium hexafluorophosphate; DMF, *N*,*N*-dimethylformamide; TFA, trifluoroacetic acid; DIEA, *N*,*N*-diisopropylethylamine; TIPS, triisopropylsilane; DMSO, dimethyl sulfoxide; Fmoc, fluorenylmethoxy carbonyl; PBS, phosphate-buffered saline; FBS, fetal bovine serum; ESI-MS, electrospray ionization mass spectrometry; TOF, time-of-flight; KOt-Bu, potassium *tert*-butoxide; PAL, 5-(4-aminomethyl-3,5-dimethoxyphenoxy)valeric acid (Peptide Amide Linker); PEG-PS, poly(ethylene glycol)-polystyrene; Pten, ethylenediamine platinum(II).

Scheme 2. Platination Reaction Using Mal-Glut-CNGRC

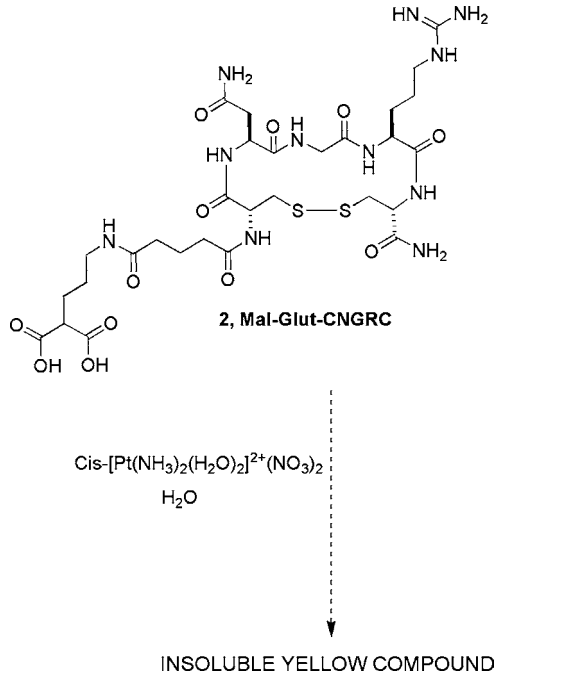

Scheme 3. Synthesis of Di-*tert*-butyl 2-(3-glutaricaminopropyl)-malonate

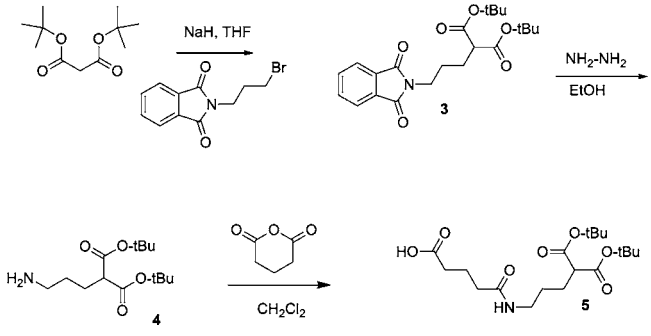

*Synthesis of Di-tert-butyl 2-(3-aminopropyl)malonate (***4***).* Compound **4** was prepared by a known method as described by Aronov et al. (*34*). Di-*tert*-butyl 2-(3-phthalimidopropyl)-malonate was deprotected using absolute hydrazine to give di-*tert*-butyl 2-(3-aminopropyl)malonate. The ^{1}H NMR spectrum of compound **4** (Scheme 3) in $CDCl_3$ matched the reported values.

*Synthesis of Di-tert-butyl 2-(3-(4-Carboxybutanamido)propyl)-malonate (***5***).* Compound **5** was synthesized as previously described in the literature (*34*). Glutaric anhydride was used for acylation in this reaction, yielding the glutaroyl(aminopropyl)malonic ester **5** (Scheme 3). The yield was 92%.^{1}H NMR ($CDCl_3$) (ppm): 3.27 (q, 2H), 3.14 (t, 1H), 2.41 (t, 2H), 2.28 (t, 2H), 1.98 (m, 2H), 1.81(m, 2H), 1.56 (m, 2H), 1.45(s, 18H).

*Synthesis of Cyclic mPeg-CNGRC-mal (***6***).* After synthesizing the linear mPeg-CNGRC-mal peptide and confirming its purity, the resin was suspended in DMF (60 mL) and the reaction mixture cooled to 0 °C in an ice bath before the addition of I_2 (10 equiv). The mixture was stirred at 0 °C for 2 h, filtered, and washed with DMF (10 × 10 mL) and CH_2Cl_2 (10 × 10 mL). Using a cocktail of TFA/phenol/water/TIPS (88:5:5:2) (15 mL), the peptide was cleaved from the resin, precipitated with ether, and dried under vacuum to give crude peptide **6**. The crude peptide was purified using reverse phase HPLC on column 1 with a linear gradient from 5% to 70% B eluent in 60 min; t_R 28 min. This yielded cyclic mPeg-CNGRC-mal (**6**) in 35% yield. ESI-MS (TOF) gave a signal at 1184.4764 $(M + H)^+$, calculated for $C_{45}H_{77}N_{13}O_{20}S_2$ 1184.4849 (see Supporting Information).

*Synthesis of Cyclic mPeg-CNGRC-Pt (***7***).* Cyclic mPeg-CNGRC-mal was dissolved in water, and the pH of the solution was adjusted to 7, by titration with 1 M NaOH (See Supporting Information). A solution of cis-$[Pt(NH_3)_2(H_2O)_2]^{2+}(NO_3)_2$ was made by stirring cis-$PtCl_2(NH_3)_2$ and $AgNO_3$ vigorously overnight in water in the dark. A precipitate was formed (AgCl) and then filtered to give cis-$[Pt(NH_3)_2(H_2O)_2]^{2+}(NO_3)_2$ (*35, 36*). A 2-fold excess of cis-$[Pt(NH_3)_2(H_2O)_2]^{2+}(NO_3)_2$ (10 mmol) was reacted with compound **6** (30 mg, 5 mmol) to form the crude cyclic mPeg-CNGRC-Pt conjugate (**7**), which was then purified by gel filtration on a Sephadex-G10 column to give the final product in 15% yield. ESI-MS (TOF) gave a signal at 1412.4913 $(M + H)^+$, calculated for $C_{45}H_{81}N_{15}O_{20}PtS_2$ 1412.4955 (see Supporting Information).

*Synthesis of Cyclic mPeg-CNGRC-Pten (***8***).* Cyclic mPeg-CNGRC-mal was dissolved in water, and the pH of the solution was adjusted to 7, by titration with 1 M NaOH. cis-$[Pten(H_2O)_2]^{2+}(NO_3)_2$ was synthesized by stirring $PtenCl_2$ and $AgNO_3$ vigorously overnight, in water in the dark. A precipitate was formed (AgCl) and then filtered to yield cis-$[Pten(H_2O)_2]^{2+}$-$(NO_3)_2$ (*37*−*39*). A 2-fold excess of cis-$[Pten(H_2O)_2]^{2+}(NO_3)_2$ (10 mmol) was reacted with compound **6** (30 mg, 5 mmol) to give the crude cyclic mPeg-CNGRC-Pten conjugate, which was then purified by gel filtration on a Sephadex-G10 column to give cyclic mPeg-CNGRC-Pten (**8**) in 10−12% yield. ESI-MS (TOF) gave a signal at 719.7571 $(M + H)^{2+}$, calculated for $C_{47}H_{83}N_{15}O_{20}PtS_2$ 719.7593 (see Supporting Information).

*Synthesis of Cyclic mPeg-CNGRC (***9***).* Free peptide (**9**) was assembled as described in the Peptide Synthesis section, without the malonate linker **5**. The crude peptide was purified by reverse phase HPLC on column 1 with a linear gradient from 5% to 70% B eluent in 60 min and t_R 10 min to give cyclic mPeg-CNGRC (**9**) in 38% yield. ESI-MS (TOF) gave a signal at 927.4032 $(M + H)^+$, calculated for $C_{34}H_{62}N_{12}O_{14}S_2$ 927.4023 (see Supporting Information).

Cell Culture. The prostate cancer cell line PC-3 (CRL-1435) was obtained from the American type Culture Collection (Manassas, VA). Penicillin, streptomycin, RPMI 1640, and fetal bovine serum (FBS) were obtained from Invitrogen (Grand Island, NY). The cell line was cultured in RPMI 1640 supplemented with 10% FBS, 100 units/mL penicillin, and 100 μg/mL streptomycin.

Fluorescence Microscopy. PC-3 cells were seeded on 6-well plates (500,000 cells/well) and incubated for 24 h in RPMI 1640 media. The cells were treated with 200 μM carboplatin, a mixture of carboplatin and free peptide **9**, or Pt−peptide conjugates **7** or **8** for 48 h. After incubation, the cells were washed once with RPMI and stained with JC-1 dye for 30 min. The stained cells were analyzed using a Leica DM RXA fluorescent microscope with Xenon lamp illumination, using a 40 × dip objective with an N.A. of 0.80. The filter cube for the green channel had the following characteristics: a 480/40 excitation filter, a 527/30 emission filter, and a 505 nm dichroic mirror. The filter cube used for the red channel had the following characteristics: a 537/45 excitation filter, an LP 590 emission filter, and a 580 nm dichroic mirror.

Cytotoxicity Assay. The cytotoxicity of the free carboplatin, free peptide cyclic mPeg-CNGRC-mal (**6**), the mixture of carboplatin, and mPeg-CNGRC (**9**) as well as the two platinum conjugates (cyclic mPeg-CNGRC-Pt (**7**) and cyclic mPeg-CNGRC-Pten (**8**)) was assayed using the MTT (3-(4,5-dimethylthiazol-2-yl)-2,5-diphenyltetrazolium bromide) assay as described (*40*). Briefly, 2000 cells/well were incubated in 96-well plates in triplicate, using different concentrations of platinum complexes in a cell growth medium. Three wells were used as

controls, receiving an equivalent volume of RPMI medium alone. The cells were treated with different concentrations (0, 50, 150, 200, and 300 μM) of carboplatin, free peptide **6**, the mixture of carboplatin and mPeg-CNGRC (**9**), and the Pt−peptide conjugates **7** and **8** for 48 h. After 48 h, a solution of MTT (5 mg/mL in PBS) was added to each well, and the cells were incubated for 2 h at 37 °C. The cells were then lysed using a lysis buffer (20% SDS and 50% DMSO). The lysed cells were incubated for 3 h at 37 °C, before the absorbance of the cell suspension was measured at 590 nm using an MRX Revelation 96-well multiscanner (Dynex Technologies, Chantilly, VA).

Drug Competition Assay. Using various concentrations of mPeg-CNGRC (**9**), a cell competition assay for carboplatin and conjugate **8** was carried out using the MTT assay. Two thousand cells/well were incubated in 96-well plates one day prior to the treatment to allow the cells to adhere to the plate in triplicate. On the next day, the cells were treated using various concentrations of the free peptide mPeg-CNGRC (**9**) (1, 2, 4, 8, and 10 mM) with simultaneous addition of 200 mM carboplatin and conjugate **8** for 48 h, respectively. The plate was analyzed as described in the cell cytotoxicity assay.

Drug Uptake Measurements. One million PC-3 cells were plated in a 6-well plate a day before for adherence. On the next day, the cells were treated with fresh medium containing 200 μM carboplatin, and Pt−peptide conjugates **7** and **8** for 24 h. After incubation, the cells were washed with PBS once and collected in a tube for further analysis. The collected samples were dissolved in 0.25 mL nitric acid (trace metal grade) and heated for 2 h at 60 °C for digestion. Upon cooling, approximately 5 mL of deionized water was added to dilute the samples to the minimum volume required for the ICP spectrometer.

Apo-ONE Homogeneous Caspase-3/7 Assay. The homogeneous caspase-3/7 assay kit (Promega, Madison, WI), which provides a profluorescent substrate with an optimized bifunctional cell lysis/activity buffer for caspase-3/7 activity assays, was used. PC-3 cells were treated with free peptide **9** or a mixture of free peptide **9** and carboplatin, conjugate **7**, or conjugate **8** at 100 μM concentration. After 24 h of incubation, the apo-ONE homogeneous caspase-3/7 assay was performed according to the manufacturer's protocol. The buffer and substrate were mixed and added to the samples. Upon sequential cleavage and removal of the DEVD (Asp-Glu-Val-Asp) peptides by caspase-3/7 activity and excitation at 499 nm, the rhodamine 110 leaving group became intensely fluorescent with an emission maximum at 512 nm (*41*). The excitation/emission was recorded on FlexStation from Molecular Devices (Sunnyvale, CA) with softMax Pro, version 4.8 software. This experiment was performed in duplicate, and the statistical analysis was done.

DNA Fragmentation Assay. The evaluation of nuclear morphological events such as internucleosomal DNA fragmentation was performed by standard agarose gel electrophoresis as described previously (*42*). Briefly, treated cells (one million cells) were washed in ice-cold PBS, resuspended in 0.2 mL of PBS in 1.5 mL Eppendorf tubes. Next, 0.2 mL of lysis buffer (20 mM Tris-HCl, pH 7.4, 1% triton x-100.10 mM EDTA, and 0.1 mg/mL proteinase K) was added, and the mixture was incubated at 55 °C for 2 h. Proteinase K was then heat inactivated at 70 °C for 10 min, and the sample was cooled to room temperature. RNase was added (10 μL of 20 mM Tris-HCl, pH 7.4, containing 0.5 mg/mL RNase) to the sample, which was further incubated for 2 h at 37 °C. Extraction of DNA was achieved with a 1:1 mixture of phenol/chloroform and precipitated with two volumes of cold ethanol and one-tenth volume of sodium acetate. The sample was centrifuged, and the pellet was resuspended in 50 μL of deinonized water. Samples were loaded on a 1.5% agarose gel and electrophoresed at 60 V for 2 h in TBE. The gel was stained with EtBr and visualized by UV trans-illumination using a Bio-Rad Versa Doc Imaging system (Model 3000).

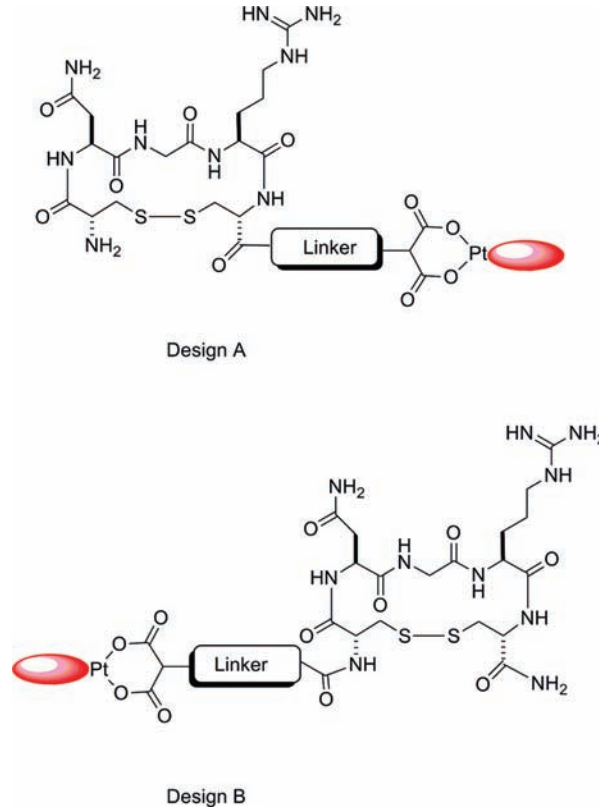

Figure 1. CNGRC model conjugate with platinum pro-drug.

RESULTS AND DISCUSSION

In order to evaluate the optimal construct for delivering a platinum−peptide conjugate, several CNGRC-chelator constructs were evaluated. Figure 1 shows the two designs that we tested for the formation of Pt−peptide complexes, with design B being the more successful of the two. Design A was based on attaching the chelator to the C-terminus of the peptide acid as had been done for the DOX−NGR conjugate (*23*). Design B has the linker attached to the N-terminus, which has potential advantages for incorporation by solid-phase synthesis.

Following design A, our initial attempt was to couple the cyclic CNGRC peptide with di-*tert*-butyl 2-(3-aminopropyl)-malonate using solution phase chemistry by conjugating the free carboxylic end of the cysteine with the free amine end of di-*tert*-butyl 2-(3-aminopropyl)malonate (Scheme 1). The cyclic CNGRC peptide was prepared as described by Anizon et al. (*23*), where the trityl alcohol resin was converted to the trityl chloride derivative with acetyl chloride. This was followed by loading of the Fmoc-Cys(Acm)-OH onto resin resulting in a 0.14 mmol/g (70%) loading yield. The resin was treated with Fmoc-Arg(Pbf)-OH, Fmoc-Gly−OH, Fmoc-Asn(Trt)-OH, and Fmoc-Cys(Acm)-OH to give crude CNGRC. The HPLC chromatogram and the mass spectrum revealed the expected $(M + H)^+$ peak at 550.76, which was in agreement with the reported values. Di-*tert*-butyl 2-(3-aminopropyl)malonate was prepared as described in the Experimental Section using a slight modification of the Aronov method (*34*). The malonate was alkylated using a strong base to give product in 80% yield. A similar synthesis was achieved by the Aronov group using KOt-Bu as a base; however, using a stronger base (NaH) in the reaction improved the yields from 60% to 80% yield. A 2-fold excess of di-*tert*-butyl malonate was used to ensure monoalky-

lation and the ease of separation between the malonate and di-*tert*-butyl 2-(3-phthalimidopropyl)malonate. The excess of the di-*tert*-butyl malonate that was used was easily removed by column chromatography (*34*). Attempts to couple the cyclic peptide CNGRC and di-*tert*-butyl 2-(3-aminopropyl)malonate (Scheme 3) using various coupling reagents were unsuccessful (Scheme 1). We do not understand why the reaction failed as similar reactions between CNGRC and DOX with similar functional groups have been successful (*23*). Analysis of the crude product revealed high amounts of the starting materials, including CNGRC, di-*tert*-butyl 2-(3-aminopropyl)malonate, and coupling reagents.

In order to overcome the above problem, we explored design B. This enabled us to conjugate the linker on the N-terminus of peptide resin, thereby avoiding solution phase chemistry in the conjugation of the linker−chelator group to the peptide CNGRC, as shown in Scheme 2. To achieve this synthesis, malonate linker with a carboxylic acid end (**5**) was synthesized using glutaric anhydride and di-*tert*-butyl 2-(3-aminopropyl)-malonate (**4**), as shown in Scheme 3. Starting from an amide-based resin and using Fmoc chemistry, the peptide was assembled, then conjugated to di-*tert*-butyl 2-(3-glutaricamino-propyl)malonate, and cyclized on the solid support to yield Mal-Glut-CNGRC. After purification, HPLC and mass spectral analysis confirmed the purity and identity of the cyclic Mal-Glut-CNGRC. Platination of the purified Mal-Glut-CNGRC using cis-$[Pt(NH_3)_2(H_2O)_2]^{2+}(NO_3)_2$ gave an insoluble yellow compound in most solvents, including water, DMSO, DMF, MeOH, acetone, MeCN, CH_3Cl, and CH_2Cl_2. The compound could not be characterized by mass spectra to confirm the formation of the platinum complex.

Our third and final approach was to increase the solubility of the CNGRC sequence by adding short oligomeric PEG-based residues to both the N- and C-termini of the peptide. Additionally, the PEG linker would provide additional spacing of the Pt ligand from the targeting peptide. Various studies have shown that pegylation does not affect targeting and may have other positive effects such as an increase in stability that reduces the chance of the drug efflux (*34*), and it reduces or eliminates immunogenicity (*43*−*45*). We chose the $mPEG_3$ derivative as the spacer as it is conveniently available as an Fmoc-protected amino acid derivative. The peptide was prepared as before, adding on these residues at each terminus. The glutaric anhydride and linker-malonate were added at the N-terminus, and the linear peptide was cyclized on solid support and cleaved to give target compound **6** (Scheme 4), which was purified by HPLC, and its identity was confirmed by mass spectroscopy (see Supporting Information).

Peptide−Platinum Complexes. Platination with a 2-fold excess of activated cis-$[Pt(NH_3)_2(H_2O)_2]^{2+}(NO_3)_2$ and cis-$[Pten(H_2O)_2]^{2+}(NO_3)_2$ using a standard procedure gave Pt−peptide conjugates **7** and **8** as shown in Scheme 4. The platinum complexes could not be purified by HPLC using either an acidic or a neutral buffer system because the platinum complexes dissociated. The products were, therefore, purified by gel filtration to remove the excess platinum. Fractions containing the Pt−peptide complex in water were identified by ESI-MS and then combined and lyophilized to give pure platinum complexes for cyclic mPeg-CNGRC-Pt (**7**) and cyclic mPeg-CNGRC-Pten (**8**) in a 10−15% yield. Mass spectra revealed the expected $(M + H)^+$ peak at 1412.4913 for conjugate **7** and the $(M + 2H)^{2+}$ peak at 719.7571 for conjugate **8**. During the study, we noticed that platinum conjugate **7** was not very stable in PBS at −20 °C and formed precipitates after a day of storage. Any experiment with conjugate **7** had to use freshly dissolved conjugate. The ethylene diamine Pt conjugate **8** was stable at −20 °C, and the stock solutions could be used in later

Scheme 4. Formation of Cyclic mPeg-CNGRC-Pt (7) and Cyclic mPeg-CNGRC-Pten (8)

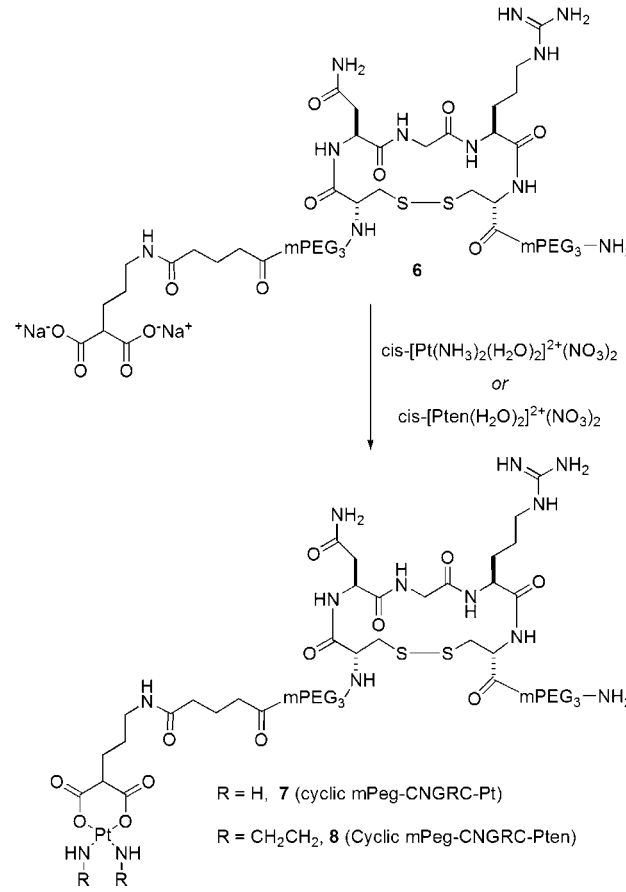

experiments. Both Pt conjugates were stable as lyophilized powders at −20 °C, and fresh samples were made by reconstituting the dry samples to the desired concentration. The integrity of redissolved Pt−peptide conjugates was confirmed by ESI mass spectrometry before use.

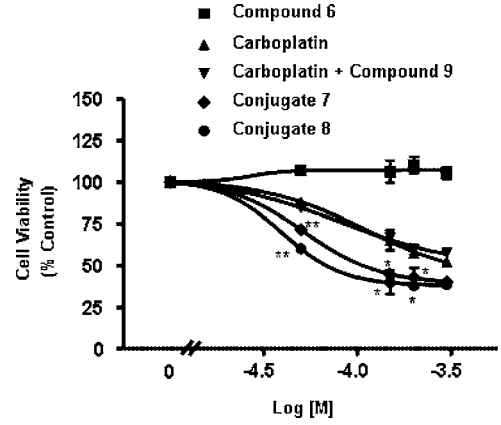

Figure 2. Cytotoxic effects of Pt complexes on PC-3 cells. Cyclic mPeg-CNGRC-mal (**6**), carboplatin, mixture of carboplatin and free peptide **9** (carboplatin + compound **9**), and Pt−peptide conjugates; cyclic mPeg-CNGRC-Pt (**7**) and cyclic mPeg-CNGRC-Pten (**8**) on the proliferation of prostate cancer PC-3 (CD13 positive) cells. PC-3 cells were exposed to the compounds listed above and incubated for 48 h at different concentrations. All points are a representative of the mean ± SD of triplicate readings of three independent experiments. $*P = 0.0190$ (carboplatin and conjugate **7**); $P = 0.0126$ (carboplatin and conjugate **8**); $*P = 0.0407$ (conjugates **7** and **8**). The difference is statistically significant as $P < 0.05$ at 150 μM concentration. Statistical difference was determined by Student's *t*-test; one tailed by using Graph Pad Prism software, version 5.0.

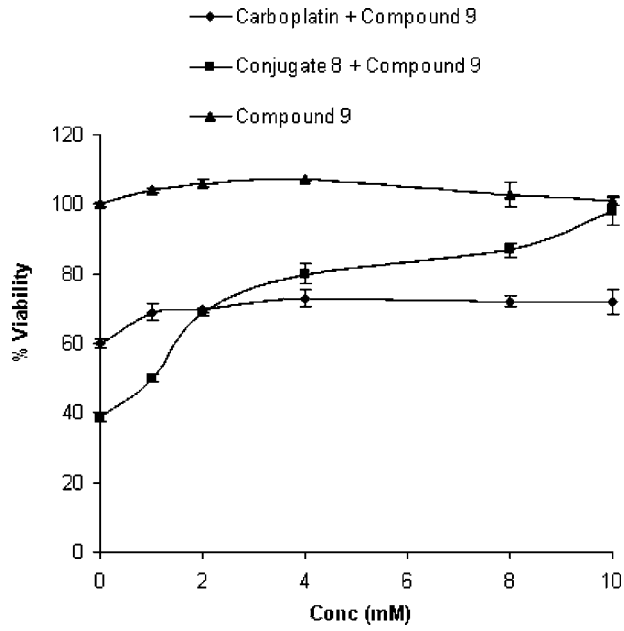

Figure 3. Role of the NRG peptide in cytoxicity. The effect of various concentrations of the free peptide **9** on 200 μM carboplatin and conjugate **8**. Two thousand PC-3 cells were incubated with various concentrations of the free peptide mPeg-CNGRC (**9**), 200 μM carboplatin, and conjugate **8** for 48 h. All points are representative of the mean ± SD of triplicate readings of three independent experiments.

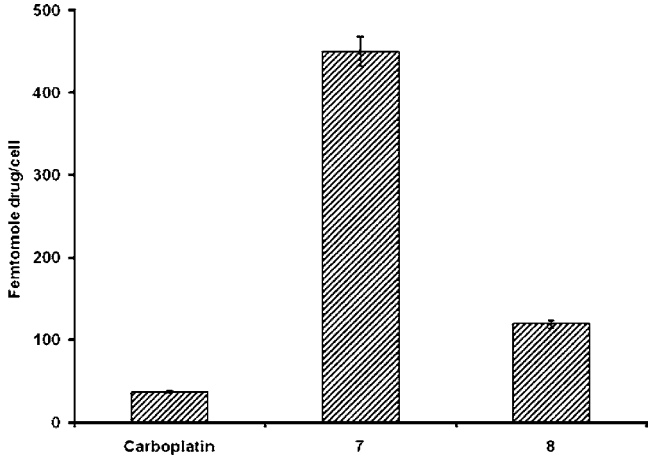

Figure 4. Platinum uptake of PC-3 (CD13 positive) cancer cells. One million cells were incubated with 200 μM carboplatin or Pt−peptide conjugates **7** or **8** for 24 h. Pt levels in the washed cells were measured by atomic absorption spectroscopy as described in the Experimental Section. All points are representative of the mean ± SD of triplicate readings of three independent experiments.

In Vitro Studies on Pt Conjugates: Their Toxicity and Uptake. It has been shown that the NGR motif binds specifically to the CD13 receptors that are expressed on some tumor cells. We examined the effect of the free peptide as a control experiment to determine the effect of the peptide. As shown in Figure 2, the free peptide (**6**) was not toxic to the PC-3 cells and caused a slight increase in the MTT assay, suggesting that the PC-3 receptors were activated by the NGR ligand. Two CNGRC platinum conjugates were prepared to test our hypothesis. As expected, the targeted Pt−peptide conjugates **7** and **8** were more toxic to the PC-3 cells at all concentrations tested compared to the untargeted carboplatin (even at concentrations as low as 50 μM). Pt conjugate **8** shows the highest effect on the suppression of cell proliferation, followed by Pt conjugate **7** and carboplatin. Carboplatin was the least toxic to PC-3 cells of this series of platinum compounds, indicating that the

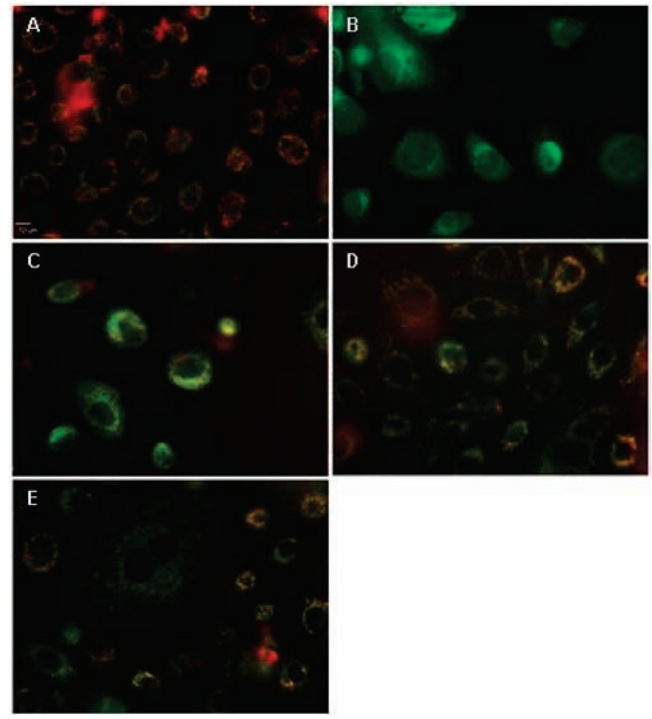

Figure 5. JC-1 dye staining of cells treated with Pt compounds. Fluorescence microscopy of cells that have been treated with various compounds, incubated for 48 h at 37 °C and then imaged by JC-1 staining after a further 30 min of incubation. Image A shows PC-3 cells, treated with RPMI media only. Image B shows PC-3 cells, treated with 50% DMSO. Image C shows PC-3 cells, treated with 200 μM of Pt−peptide conjugate **8** in RPMI media. Images D and E show PC-3 cells incubated with a mixture of carboplatin/free peptide **9** (1:50) and carboplatin only (200 μM), respectively. Scale bar: 10 μm.

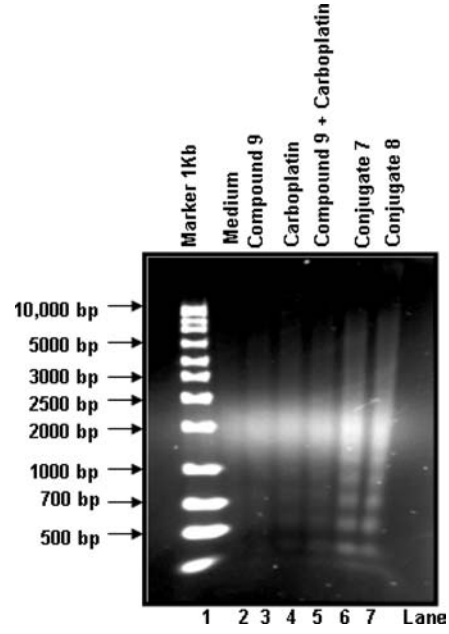

Figure 6. DNA fragmentation assay. PC-3 cells were treated with 5 μL of 1 kb DNA marker (lane 1), medium only (lane 2), and 100 μM each of compound **9** alone (lane 3), carboplatin alone (lane 4), compound **9** + carboplatin (lane 5), conjugate **7** (lane 6), and conjugate **8** (lane 7) for 48 h. DNA was extracted and internucleosomal cleavage visualized on a 1.5% agarose gel. Image is representative of three independent experiments.

platinum complexes bearing the CNGRC sequence are more effective at suppressing tumor cell proliferation. The % growth inhibition on PC-3 cells caused by the mixture of mPeg-CNGRC

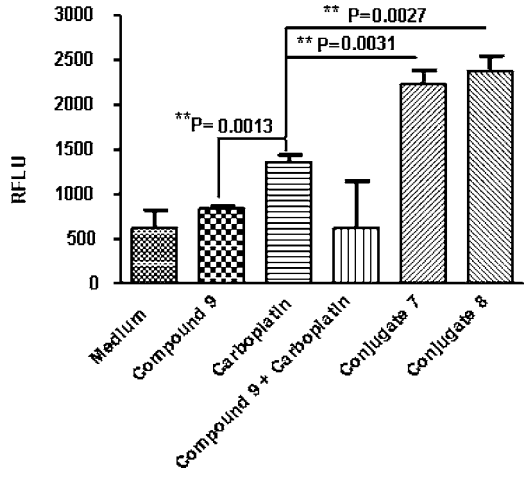

Figure 7. Caspase activation as a result of Pt drug treatment. The apo-ONE homogeneous caspase-3/7 assay where PC-3 cells (10,000 cells/well) in triplicate were treated with medium only and 100 μM concentration of the compound **9**, carboplatin alone, mixture of compound **9** and carboplatin, conjugate **7**, and conjugate **8** for 24 h. After 24 h, the caspase activity was measured in the wells by adding 100 μL of the apo-ONE caspase-3/7 assay reagent. The cells were incubated for an additional hour at ambient temperature prior to recording fluorescence (485 Ex/527Em). The *P* values are statistically significant and calculated by Student's *t*-test; one tailed.

(**9**); (peptide not bearing a Pt chelating group) and carboplatin was similar to that caused by carboplatin alone, suggesting that there was no effect of the peptide on the toxicity of carboplatin. At 150 μM, less than 50% of the PC-3 cells were viable when exposed to the targeted Pt−peptide conjugates, compared to greater than 60% for the untargeted carboplatin drug. A concentration of 200 μM showed the most substantial effect on cell proliferation (Figure 2). These results suggest that higher uptake of Pt leads to greater suppression of the proliferation of PC-3 cells. Our results are in agreement with those of the other groups, who have shown that the CNGRC motif contributes to the increased intracellular concentration of drugs that are attached to this motif because of targeting to CD13 positive cells. A 5-FdUrd conjugate bearing the homing peptide CNGRC was found to penetrate into the CD13 positive cells (HT-1080) but not in CD13 negative cells (MDA-MB-231). This enhanced the selective accumulation of 5-FdUrd, resulting in a more effective immunotherapy (*24*). IC_{50} values for conjugates **7** and **8** are 149 mM and 115 μM, respectively.

Competition Assay. Figure 3 demonstrates that the free peptide **9** had no cytotoxic effect on the PC-3 cells and can effectively compete off the NGR−Pt conjugate toxicity by simultaneous incubation of the free peptide **9** and conjugate **8**. A slight increase in the % viability with peptide **9** suggests the activation and nourishment of the PC-3 cells. The use of free peptide **9** instead of free peptide **6** was to ensure that carboplatin was not chelated by free peptide **6**, which has a free malonate group that is capable of reacting with the hydrolyzed carboplatin to give ambiguous results. Carboplatin and conjugate **8** were incubated with various concentrations of free peptide **9**. Incubation of carboplatin with various concentrations of free peptide **9** had the same effect on the % viability irrespective of the amount of free peptide **9** used. Incubation of conjugate **8** with various concentrations of free peptide **9** showed that the free peptide was competing with conjugate **8** in targeting the CD13 receptors. With an initial 5-fold excess of free peptide **9**, conjugate **8** was more cytotoxic than free carboplatin, but with a 10-fold excess, the free peptide **9** was able to compete away the effect of conjugate **8** in comparison to carboplatin. A further 50-fold increase in the free peptide concentration resulted in the elimination of the cytotoxic effect from conjugate **8**. The results also demonstrate that the CNGRC motif contributes to the accumulation of platinum in tumor cells, causing a significant difference in the suppression of the proliferation of PC-3 tumor cells.

High uptake seems related to the toxicity of Pt−peptide conjugates **7** and **8**, supporting the hypothesis that high uptake of platinum drugs results in high cytotoxicity. When other targeting ligands have been used, platinum uptake in some cell lines show comparable values and trends closely related to our results, where targeted drugs had a higher uptake than untargeted platinum drugs (*46*−*49*). To confirm the cell toxicity results obtained above, the uptake of platinum by PC-3 cells was determined by exposing the cells to 200 μM carboplatin, Pt−peptide conjugate **7**, and Pt−peptide conjugate **8** for 24 h. The greatest Pt uptake occurred with Pt−peptide conjugate **7** followed by conjugate **8**, and the lowest uptake occurred with carboplatin, in PC-3 cells. The uptake of untargeted carboplatin was determined to evaluate the difference with the targeted complexes. From the data in Figure 4, platinum uptake by the PC-3 cells was 12-fold greater when using conjugate **7** and 3-fold greater when using conjugate **8** compared to that of untargeted carboplatin. These results clearly suggest that the PC-3 cells more readily take up Pt when it is conjugated with the CNGRC-containing ligands, most likely mediated by the CD13 receptors. However, there is no direct correlation between the amount of Pt that is taken in and how toxic the compounds are. For example, Pten complex **8** has a lower IC_{50} but shows less uptake of platinum. Thus, the form of the Pt complex may make a difference in the ultimate effectiveness of the drug. This may explain why Pten complex **8** still is more toxic to the PC-3 cells than the more readily taken up Pt−amine complex **7**. Clinical trials of ethylenediamine platinum complexes were suspended, as previous animal studies have shown high nephrotoxicity relative to cisplatin (*50*, *51*). Our findings suggest that targeting of the Pten conjugate **8** may be a mechanism to reduce the nonspecific toxicity of this extremely potent compound. This shows that care should be taken when interpreting whether high platinum uptake has a direct relationship with cell death and that more studies need to be done in this area. Our major concern during this experiment was to ensure that the cisplatin/carboplatin moiety detaches from the carrier at the right place at the right time. With this in mind, we chose carboplatin as our control drug in the experiment because we expected that our targeted compound would release the drug in a manner similar to that of carboplatin.

Mechanism of Action of Pt Complex Toxicity. The putative mechanism of action of Pt drugs is cross-linking of nuclear DNA through reaction with the N7 of purines, and there are several competing hypotheses that suggest that Pt compounds may react with effector molecules in the mitochondria that lead to apoptosis (*52*). We have investigated the mechanism of action of the Pt−peptide conjugates relative to carboplatin. Since it was established that both the diamino-Pt conjugate **7** and the ethylenediamino-Pt complex **8** have cellular toxicity mediated by binding to the CD13 receptor and that Pt was getting into the cells, we wanted to further establish the mechanism of action of these complexes. It is known that Pt drugs act by a variety mechanisms on cells including interaction with the mitochondria resulting in apoptosis (*52*, *53*). To determine whether Pt−peptide conjugates **7** and **8** can induce apoptosis, we used a series of experiments to further elucidate their mechanism of toxicity relative to that of carboplatin. We investigated various steps of the apoptotic pathway that are in response to Pt compounds. Decrease in mitochondrial membrane potential during apoptosis, leads to the loss of outer mitochondrial membrane integrity and release of cytochrome *c* from the mitochondria. The released cytochrome *c* binds APAF1, forming an apoptosome that

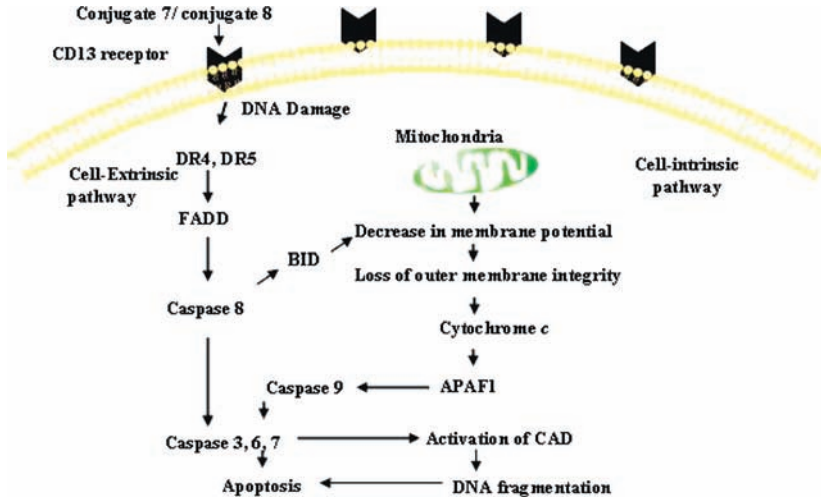

Figure 8. Predicted pathways of apoptosis by conjugate **7** or **8**. Cell-extrinsic apoptosis is engaged through death receptors (DR4 and DR5), and cell-intrinsic apoptosis is triggered through mitochondrial receptors.

activates the apoptotic protease caspase 9, which, in turn activates downstream caspases, such as caspase 3, 6, and 7 (*54*), leading to the final stages of apoptosis, which is typified by DNA fragmentation.

Using the JC-1 dye that is sensitive to mitochondrial membrane potential, we qualitatively examined the action of Pt−peptide conjugates on PC-3 cells (Figure 5) by fluorescence microscopy. Image A shows untreated, healthy cells grown in media which have aggregated JC-1 dye concentrated in their mitochondrial membranes that give a predominantly red fluorescence. Apoptotic cells have a low membrane potential resulting in a green fluorescence, which is evident in image B. Fifty percent DMSO was used to induce 100% cell cytotoxicity. The results shown in Figure 5C confirmed that targeted Pt−peptide conjugate **8** (see Supporting Information for data on compound **7**) causes a decrease in the membrane potential, suggesting death by apoptosis in the PC-3 cell line. Images D and E show PC-3 cells treated with a mixture of carboplatin/free peptide **9** (1:50) and carboplatin alone, respectively. The images show more cells with normal membrane potentials when compared to PC-3 cells treated with targeted conjugate **7** (*55*).

DNA Fragmentation Assay. The microscopy results suggest that the Pt−peptide conjugates may be acting by an apoptotic mechanism. To confirm that conjugates **7** and **8** induce internucleosomal DNA fragmentation, we incubated PC-3 cells with 100 μM each of conjugates **7** and **8** for 48 h along with appropriate controls. Results from Figure 6 clearly indicate that conjugates **7** and **8** displayed increased DNA fragmentation relative to that of carboplatin alone.

An intermediate step in apoptosis is the activation of caspase 9 and eventual activation of caspase 3. Figure 7 shows the results of the apo-ONE caspase assay of cells treated with Pt−peptide conjugates and carboplatin relative to that of controls. Treatment of the cells with carboplatin alone induces the caspase-3/7 activity significantly relative to treatment with medium alone or a non-Pt-containing peptide **9**. This result is consistent with literature reports that anticancer Pt drugs act at least in part through an apoptotic pathway (*56*). Incubation of PC-3 cells with 100 μM conjugate **7** and conjugate **8** results in significantly higher activation of caspase-3/7 relative to carboplatin treatment, which suggests stronger induction of apoptosis in PC-3 cells with the Pt−peptide conjugates. This is consistent with the DNA fragmentation assay as well as the microscopy results with JC-1 that supports targeted conjugates being much more efficient at entering and activating apoptosis than the nontargeted carboplatin alone.

Besides the interaction of the Pt(II) compound with DNA, other effectors in the cell including mitochondrial RNA and sulfur-containing enzymes such as metallothionein and glutathione also bind to platinum (*1, 2*). Although, much attention has been focused on various Pt-DNA adduct formation (*57*−*59*), their role in cytotoxicity and antitumor activity is still unclear (*60*−*62*). There are many studies that have described the depolarization of the mitochondrial membrane as an important characteristic of the mitochondrial or intrinsic pathway leading to apoptosis (*63, 64*). However, data with reduction in mitochondrial membrane potential argues for and against apoptosis and therefore remains controversial (*65*). From fluorescence microscopy and caspase-3/7 and DNA fragmentation data, it is clear that the intrinsic pathway is engaged through mitochondria, leading to cell death, but we cannot exclude the extrinsic pathway. However, more studies need to be done to delineate the exact pathway leading to apoptosis. Figure 8 shows the suggested pathway that is leading to the apoptotic death of the PC-3 cells incubated with conjugates **7** and **8.**

CONCLUSIONS

Our work focused on synthesizing novel targeted Pt−peptide conjugates using the NGR motif and a malonoyl linker. The advantage of the targeted platinum analogues that we synthesized and studied in this work is that they increase the selectivity and specificity of the cancer cells and are less toxic to normal tissues. This study reveals two new low molecular weight Pt−peptide conjugates that effectively deliver the cisplatin and $PtenCl_2$ to the tumor cells, thereby increasing the toxicity toward PC-3 tumor cells. Pegylation of the peptide CNGRC allowed us to study the carrier at physiological conditions; however, the solubility problem did not allow us to compare the difference in cytotoxicity of the nonpegylated peptides. The presence of the bidentate dicarboxylate ligand in carboplatin has been shown to slow the degradation of carboplatin into potentially damaging derivatives, thereby reducing nonspecific toxicity and increasing the potency relative to cisplatin (*66, 67*). With the aid of the miniPEG and the bidentate ligand, we show that Pt−peptide conjugates **7** and **8**, which are analogues of carboplatin, were able to target tumor cells that had CD13 receptors.

ACKNOWLEDGMENT

We thank Dr. Azeem Hasan for mass spectra analysis, Martha Juban for expert technical support with peptide synthesis and purification, and Dr. Matthew Brown for assistance with

fluorescence microscopy. Cell Biology and Bioimaging Core at Pennington Biomedical Research Center are supported in part by COBRE (NIH P20-RR021945) and CNRU (NIH 1P30-DK072476).

Supporting Information Available: ^{1}H NMR, crystal structure, HPLC analysis spectra and fluorescence microscopy images. This material is available free of charge via the Internet at http://pubs.acs.org.

LITERATURE CITED

(1) Wang, D., and Lippard, S. J. (2005) Cellular processing of platinum anticancer drugs. *Nat. Rev. Drug Discovery 4*, 307–320.

(2) Reedijk, J. (1996) Improved understanding in platinum antitumor chemistry. *Chem. Commun. (Cambridge)* 801–806.

(3) Shipp, M., and Look, T. (1993) Hematopoietic differentiation antigens that are membrane-associated enzymes: Cutting is the key! *Blood 82*, 1052–1070.

(4) Jamieson, E., and Lippard, S. (1999) Structure, recognition, and processing of cisplatin-DNA adducts. *Chem. Rev. 99*, 2467–2498.

(5) Hamelers, I. H. L., Van Loenen, E., Staffhorst, R. W. H. M., De Kruijff, B., and De Kroon, A. I. P. M. (2006) Carboplatin nanocapsules: a highly cytotoxic, phospholipid-based formulation of carboplatin. *Mol. Cancer Ther. 5*, 2007–2012.

(6) Sood, P., Thurmond, K. B., II, Jacob, J. E., Waller, L. K., Silva, G. O., Stewart, D. R., and Nowotnik, D. P. (2006) Synthesis and characterization of AP5346, a novel polymer-linked diaminocyclohexyl platinum chemotherapeutic agent. *Bioconjugate Chem. 17*, 1270–1279.

(7) Kelland, L. R., Murrer, B. A., Abel, G., Giandomenico, C. M., Mistry, P., and Harrap, K. R. (1992) Ammine/amine platinum(IV) dicarboxylates: a novel class of platinum complex exhibiting selective cytotoxicity to intrinsically cisplatin-resistant human ovarian carcinoma cell lines. *Cancer Res. 52*, 822–828.

(8) Cubeddu, L. X., Hoffmann, I. S., Fuenmayor, N. T., and Finn, A. L. (1990) Efficacy of ondansetron (GR 38032F) and the role of serotonin in cisplatin-induced nausea and vomiting. *N. Engl. J.Med. 322*, 810–816.

(9) Ghezzi, A., Aceto, M., Cassino, C., Gabano, E., and Osella, D. (2004) Uptake of antitumor platinum(II) complexes by cancer cells, assayed by inductively coupled plasma mass spectrometry (ICP-MS). *J. Inorg. Biochem. 98*, 73–78.

(10) Katano, K., Kondo, A., Safaei, R., Holzer, A., Samimi, G., Mishima, M., Kuo, Y.-M., Rochdi, M., and Howell, S. B. (2002) Acquisition of resistance to cisplatin is accompanied by changes in the cellular pharmacology of copper. *Cancer Res. 62*, 6559–6565.

(11) van Zutphen, S., and Reedijk, J. (2005) Targeting platinum anti-tumour drugs: Overview of strategies employed to reduce systemic toxicity. *Coord. Chem. Rev. 249*, 2845–2853.

(12) Galanski, M., and Keppler, B. K. (2007) Searching for the magic bullet: anticancer platinum drugs which can be accumulated or activated in the tumor tissue. *Anti-Cancer Agents Med. Chem. 7*, 55–73.

(13) Pasqualini, R., Koivunen, E., and Ruoslahti, E. (1995) A peptide isolated from phage display libraries is a structural and functional mimic of an RGD-binding site on integrins. *J. Cell Biol. 130*, 1189–1196.

(14) Haubner, R., Wester, H.-J., Burkhart, F., Senekowitsch-Schmidtke, R., Weber, W., Goodman, S., Kessler, H., and Schwaiger, M. (2001) Glycosylated RGD-containing peptides: Tracer for tumor targeting and angiogenesis imaging with improved biokinetics. *J. Nucl. Med. 42*, 326–336.

(15) Bhagwat, S., Lahdenranta, J., Giordano, R., Arap, W., Pasqualini, R., and Shapiro, L. (2001) CD13/APN is activated by angiogenic signals and is essential for capillary tube formation. *Blood 97*, 652–659.

(16) Hansel, W., Enright, F., and Leuschner, C. (2007) Destruction of breast cancers and their metastases by lytic peptide conjugates in vitro and in vivo. *Mol. Cell. Endocrinol. 260*−*262*, 183–189.

(17) Leuschner, C., Kumar, C. S. S. R., Hansel, W., and Hormes, J. (2005) Targeting breast cancer cells and their metastases through luteinizing hormone releasing hormone (LHRH) receptors using magnetic nanoparticles. *J. Biomed. Nanotechnol. 1*, 229–233.

(18) Nagy, A., and Schally, A. V. (2002) Cytotoxic analogs of luteinizing hormone-releasing hormone (LHRH): a new approach to targeted chemotherapy. *Drugs Future 27*, 359–370.

(19) Schally, A. V., and Nagy, A. (1999) Cancer chemotherapy based on targeting of cytotoxic peptide conjugates to their receptors on tumors. *Eur. J. Endocrinol. 141*, 1–14.

(20) Schally, A. V., and Nagy, A. (2003) New approaches to treatment of various cancers based on cytotoxic analogs of LHRH, somatostatin and bombesin. *Life Sci. 72*, 2305–2320.

(21) Pasqualini, R., Koivunen, E., Kain, R., Lahdenranta, J., Sakamoto, M., Stryhn, A., Ashmun, R., Shapiro, L., Arap, W., and Ruoslahti, E. (2000) Aminopeptidase N is a receptor for tumor-homing peptides and a target for inhibiting angiogenesis. *Cancer Res. 60*, 722–727.

(22) Arap, W., Pasqualini, R., and Ruoslahti, E. (1998) Cancer treatment by targeted drug delivery to tumor vasculature in a mouse. *Science 279*, 377–380.

(23) Anizon, F., Boyle, T., Fisher, J., and Kocienski, P. (2002) Synthesis and characterisation of a doxorubicin-CNGRC peptide conjugate that target tumor vasculature. *Synthesis 18*, 2733–2736.

(24) Zhang, Z., Hatta, H., Tanabe, K., and Nishimoto, S.-i. (2005) A new class of 5-fluoro-2-deoxyuridine prodrugs conjugated with atumor-homing cyclic peptide CNGRC by ester linkers: Synthesis, reactivity, and tumor-cell-selective cytotoxicity. *Pharm. Res. 22*, 381–389.

(25) Hanahan, D., and Folkman, J. (1996) Patterns and emerging mechanisms review of the angiogenic switch during tumorigenesis. *Cell 86*, 353–364.

(26) Bhagwat, S., Petrovic, N., Okamoto, Y., and Shapiro, L. (2003) The angiogenic regulator CD13/APN is a transcriptional target of Ras signaling pathways in endothelial morphogenesis. *Blood 101*, 1818–1826.

(27) Birkenkamp-Demtroder, K., Christensen, L. L., Olesen, S. H., Frederiksen, C. M., Laiho, P., Aaltonen, L. A., Laurberg, S., Sorensen, F. B., Hagemann, R., and Orntoft, T. F. (2002) Gene expression in colorectal cancer. *Cancer Res. 62*, 4352–4363.

(28) Curnis, F., Arrigoni, G., Sacchi, A., Fischetti, L., Arap, W., Pasqualini, R., and Corti, A. (2002) Differential binding of drugs containing the NGR motif to CD13 isoforms in tumor vessels, epithelia, and myeloid cells. *Cancer Res. 62*, 867–874.

(29) Ikeda, N., Nakajima, Y., Tokuhara, T., Hattori, N., Sho, M., Kanehiro, H., and Miyake, M. (2003) Clinical significance of aminopeptidase N/CD13 expression in human pancreatic carcinoma. *Cancer Res. 9*, 1503–1508.

(30) Shepherd, F., and Sridhar, S. (2003) Angiogenesis inhibitors under study for the treatment of lung cancer. *Lung Cancer 41*, 63–72.

(31) Giguere, C. M., Bauman, N. M., and Smith, R., J. H. (2002) New treatment options for lymphangioma in infants and children. *Ann. Otol. Rhinol. Laryngol. 111*, 1066–1075.

(32) Hashida, H., Takabayashi, A., Kanai, M., Adachi, M., Kondo, K., Kohno, N., Yamaoka, Y., and Miyake, M. (2002) Aminopeptidase N is involved in cell motility and angiogenesis: its clinical significance in human colon cancer. *Gastroenterology 122*, 376–386.

(33) Albericio, F., Cases, M., Alsina, J., Triolo, S. A., Carpino, L. A., and Kates, S. A. (1997) On the use of PyAOP, a phosphonium salt derived from HOAt, in solid-phase peptide synthesis. *Tetrahedron Lett. 38*, 4853–4856.

(34) Aronov, O., Horowitz, A., Gabizon, A., and Gibson, D. (2003) Folate-targeted PEG as a potential carrier for carboplatin analogs. Synthesis and in vitro studies. *Bioconjugate Chem. 14*, 563–574.

(35) Berners-Price, S. J., Frenkiel, T. A., Frey, U., Ranford, J. D., and Sadler, P. J. (1992) Hydrolysis products of cisplatin: pKa determinations via [1H, 15N] NMR spectroscopy. *J. Chem. Soc., Chem. Commun* 789–791.

(36) Appleton, T. G., Hall, J. R., Ralph, S. F., and Thompson, C. S. M. (1989) NMR study of acid-base equilibria and other reactions of ammineplatinum complexes with aqua and hydroxo ligands. *Inorg. Chem. 28*, 1989–1993.

(37) Appleton, T. G., Berry, R. D., Davis, C. A., Hall, J. R., and Kimlin, H. A. (1984) Reactions of platinum(II) aqua complexes. 1. Multinuclear (platinum-195, nitrogen-15, and phosphorus-31) NMR study of reactions between the cis-diamminediaquaplatinum(II) cation and the oxygen-donor ligands hydroxide, perchlorate, nitrate, sulfate, phosphate, and acetate. *Inorg. Chem. 23*, 3514–3521.

(38) Palocsay, F. A., and Rund, J. V. (1969) Reaction between 1,10-phenanthroline and platinum(II) compounds. I. Reaction in aqueous solution. *Inorg. Chem. 8*, 524–528.

(39) Basolo, F., Bailar, J. C., Jr., and Tarr, B. R. (1950) The stereochemistry of complex inorganic compounds. X. The stereoisomers of dichlorobis(ethylenediamine)platinum(IV) chloride. *J. Am. Chem. Soc. 72*, 2433–2438.

(40) Aggarwal, S., Takada, Y., Singh, S., Myers, J. N., and Aggarwal, B. B. (2004) Inhibition of growth and survival of human head and neck squamous cell carcinoma cells by curcumin via modulation of nuclear factor-kB signaling. *Int. J. Cancer 111*, 679–692.

(41) Alnemri, E. S., Livingston, D. J., Nicholson, D. W., Salvesen, G., Thornberry, N. A., Wong, W. W., and Yuan, J. (1996) Human ICE/CED-3 protease nomenclature. *Cell 87*, 171.

(42) Dupere-Minier, G., Hamelin, C., Desharnais, P., and Bernier, J. (2004) Apoptotic volume decrease, pH acidification and chloride channel activation during apoptosis requires CD45 expression in HPB-ALL T cells. *Apoptosis 9*, 543–551.

(43) Roberts, M. J., Bentley, M. D., and Harris, J. M. (2002) Chemistry for peptide and protein PEGylation. *Adv. Drug Delivery Rev. 54*, 459–476.

(44) Veronese, F. M., and Pasut, G. (2005) PEGylation, successful approach to drug delivery. *Drug Discovery Today 10*, 1451–1458.

(45) Esposito, P., Barbero, L., Caccia, P., Caliceti, P., D'Antonio, M., Piquet, G., and Veronese, F. M. (2003) PEGylation of growth hormone-releasing hormone (GRF) analogs. *Adv. Drug Delivery Rev. 55*, 1279–1291.

(46) Milanesio, M., Monti, E., Gariboldi, M. B., Gabano, E., Ravera, M., and Osella, D. (2008) Trend in cytotoxic activity of a series of cis-[APtCl2] (*A*=ethylenediamine methylated at different positions) complexes. *Inorg. Chim. Acta 361*, 2803–2814.

(47) Gabano, E., Colangelo, D., Ghezzi, A. R., and Osella, D. (2008) The influence of temperature on antiproliferative effects, cellular uptake and DNA platination of the clinically employed Pt(II)-drugs. *J. Inorg. Biochem. 102*, 629–635.

(48) Bonetti, A., Apostoli, P., Zaninelli, M., Pavanel, F., Colombatti, M., Cetto, G. L., Franceschi, T., Sperotto, L., and Leone, R. (1996) Inductively coupled plasma mass spectroscopy quantitation of platinum-DNA adducts in peripheral blood leukocytes of patients receiving cisplatin- or carboplatin-based chemotherapy. *Clin. Cancer Res. 2*, 1829–1835.

(49) Harris, A., Yang, X., Hegmans, A., Povirk, L., Ryan, J., Kelland, L., and Farrell, N. (2005) Synthesis, characterization, and cytotoxicity of a novel highly charged trinuclear platinum compound. Enhancement of cellular uptake with charge. *Inorg. Chem. 44*, 9598–9600.

(50) Elferink, F., van der Vijgh, W. J., ten Bokkel Huinink, W. W., Vermorken, J. B., Klein, I., Winograd, B., Knobf, M. K., Simonetti, G., Gall, H. E., and McVie, J. G. (1987) Pharmacokinetics of ethylenediaminemalonatoplatinum(II) (JM-40) during phase I trial. *Br. J. Cancer 56*, 479–483.

(51) Hydes, P. C., and Russell, M. J. H. (1988) Advances in platinum cancer chemotherapy. Advances in the design of cisplatin analogs. *Cancer Metastasis Rev. 7*, 67–89.

(52) Cullen, K. J., Yang, Z., Schumaker, L., and Guo, Z. (2007) Mitochondria as a critical target of the chemotheraputic agent cisplatin in head and neck cancer. *J. Bioenerg. Biomembr. 39*, 43–50.

(53) Singh, S., Chhipa, R. R., Vijayakumar, M. V., and Bhat, M. K. (2006) DNA damaging drugs-induced down-regulation of Bcl-2 is essential for induction of apoptosis in high-risk HPV-positive HEp-2 and KB cells. *Cancer Lett. 236*, 213–221.

(54) Kumar, s., and Lavin, M. F. (1996) The ICE family of cysteine proteases as effectors of cell death. *Cell Death Differ. 3*, 255–267.

(55) Chaoui, D., Faussat, A.-M., Majdak, P., Tang, R., Perrot, J.-Y., Pasco, S., Klein, C., Marie, J.-P., and Legrand, O. (2006) JC-1, a sensitive probe for a simultaneous detection of P-glycoprotein activity and apoptosis in leukemic cells. *Cytometry, Part B 70*, 189–196.

(56) Cepeda, V., Fuertes, M. A., Castilla, J., Alonso, C., Quevedo, C., and Pérez, J. M. (2007) Biochemical mechanisms of cisplatin cytotoxicity. *Anti-Cancer Agents Med. Chem. 7*, 3–18.

(57) Fichtinger-Schepman, A. M. J., Van der Veer, J. L., Den Hartog, J. H. J., Lohman, P. H. M., and Reedijk, J. (1985) Adducts of the antitumor drug cis-diamminedichloroplatinum(II) with DNA: formation, identification, and quantitation. *Biochemistry 24*, 707–713.

(58) Eastman, A. (1986) Reevaluation of interaction of cis-dichloro(ethylenediamine)platinum(II) with DNA. *Biochemistry 25*, 3912–3915.

(59) Johnson, N. P., Mazard, A. M., Escalier, J., and Macquet, J. P. (1985) Mechanism of the reaction between cis-$[PtCl_2(NH_3)_2]$ and DNA in vitro. *J. Am. Chem. Soc. 107*, 6376–6380.

(60) Erickson, L. C., Zwelling, L. A., Ducore, J. M., Sharkey, N. A., and Kohn, K. W. (1981) Differential cytotoxicity and DNA crosslinking in normal and transformed human fibroblasts treated with cis-diamminedichloroplatinum(II). *Cancer Res. 41*, 2791–2794.

(61) Strandberg, M. C., Bresnick, E., and Eastman, A. (1982) The significance of DNA crosslinking to cis-diamminedichloroplatinum(II)-induced cytotoxicity in sensitive and resistant lines of murine leukemia L1210 cells. *Chem.-Biol. Interact. 39*, 169–180.

(62) Dijt, F. J., Fichtinger-Schepman, A. M. J., Berends, F., and Reedijk, J. (1988) Formation and repair of cisplatin-induced adducts to DNA in cultured normal and repair-deficient human fibroblasts. *Cancer Res. 48*, 6058–6062.

(63) Kroemer, G., Zamzami, N., and Susin, S. A. (1997) Mitochondrial control of apoptosis. *Immunol. Today 18*, 44–51.

(64) Shimizu, S., Eguchi, Y., Kamiike, W., Waguri, S., Uchiyama, Y., Matsuda, H., and Tsujimoto, Y. (1996) Bcl-2 blocks loss of mitochondrial membrane potential while ICE inhibitors act at a different step during inhibition of death induced by respiratory chain inhibitors. *Oncogene 13*, 21–29.

(65) Ly, J. D., Grubb, D. R., and Lawen, A. (2003) The mitochondrial membrane potential (Delta ym) in apoptosis; an update. *Apoptosis 8*, 115–128.

(66) Pasini, A., and Zunino, F. (1987) New cisplatin analogs: on the way to better carcinostatics. *Angew. Chem. 99*, 632–641.

(67) Reedijk, J., Fichtinger-Schepman, A. M. J., Van Oosterom, A. T., and Van de Putte, P. (1987) Platinum amine coordination compounds as anti-tumor drugs. Molecular aspects of the mechanism of action. *Struct. Bonding (Berlin, Ger.) 67*, 53–89.

BC900065R

Supporting Information

PEPTIDE TARGETING OF PLATINUM ANTI-CANCER DRUG

Margaret W. Ndinguri,[†] Rajasree, Solipuram,[‡] Robert P. Gambrell,[§] Sita, Aggarwal,[‡] William Hansel,[‡] and Robert P. Hammer[*,†,||]

[†]Department of Chemistry, Louisiana State University, Baton Rouge, LA 70803

[‡]Cancer Prevention Laboratory, Pennington Biomedical Research Center, Baton Rouge, LA 70808

[§]Department of Oceanography and Coastal Sciences, Louisiana State University, Baton Rouge, LA 70803

[||]Chemical Development, New England Peptide, Gardner, MA 01440

[*]Author to whom all the correspondence, proof, and request for reprints should be addressed.

E-mail: robert.hammer@newenglandpeptide.com

Scheme on synthesis of free peptide **6** and Conjugates **7** and **8**……....S1

Structure of cyclic mPeg-CNGRC **(9)**……..S2

Fluorescence microscopy image of conjugate **7**……S3

Crystal structure of ligand **3**……..S4

^{1}H NMR of ligand **5**……..S5

HPLC trace and mass spectra ……S6-S13

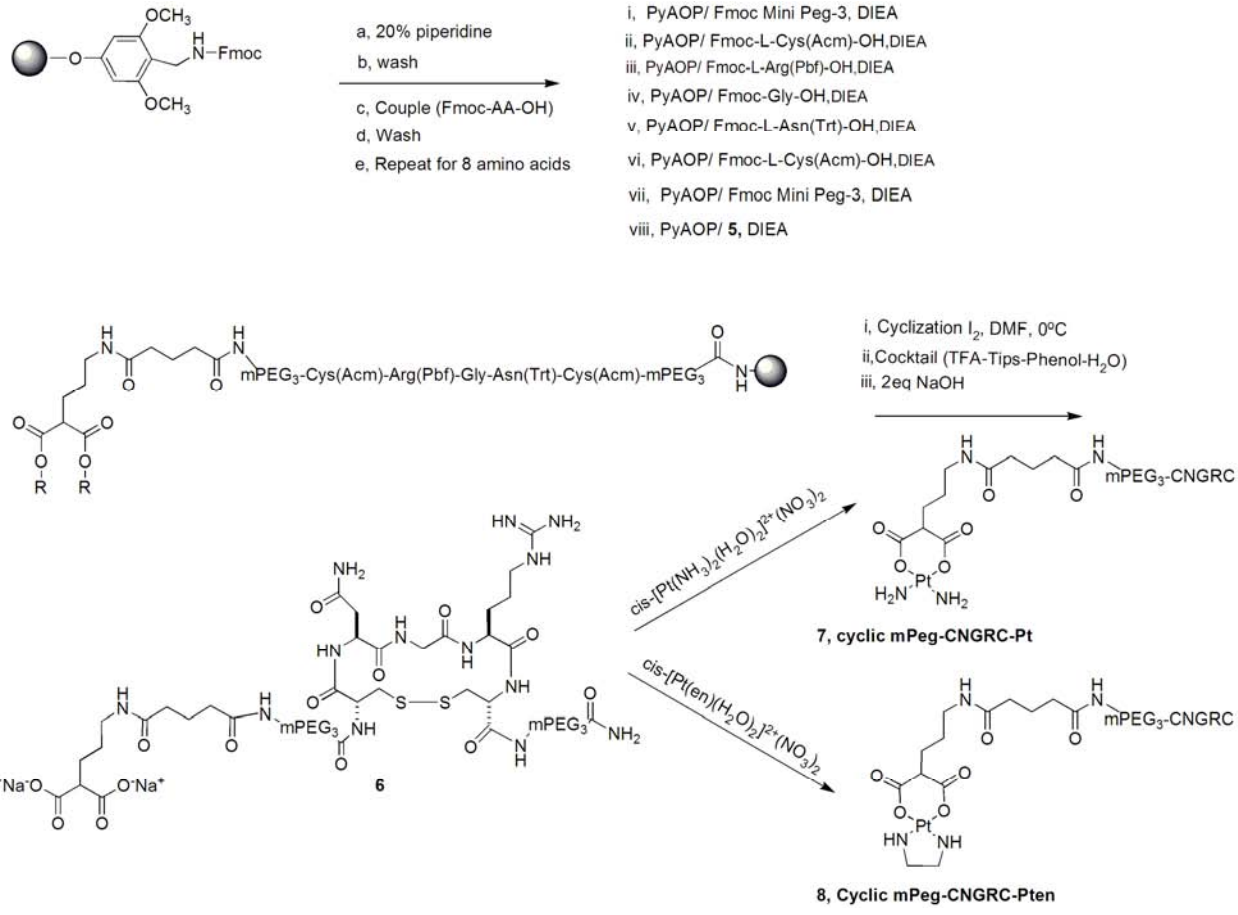

Figure S1. Scheme on **s**ynthesis of cyclic mPeg-CNGRC-Pt **(7)** and cyclic mPeg-CNGRC-Pten **(8),** where Fmoc mini peg-3^{TM} is 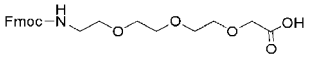

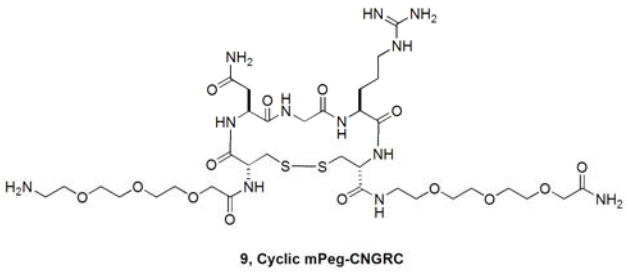

Figure S2. Structure of cyclic mPeg-CNGRC **(9)**

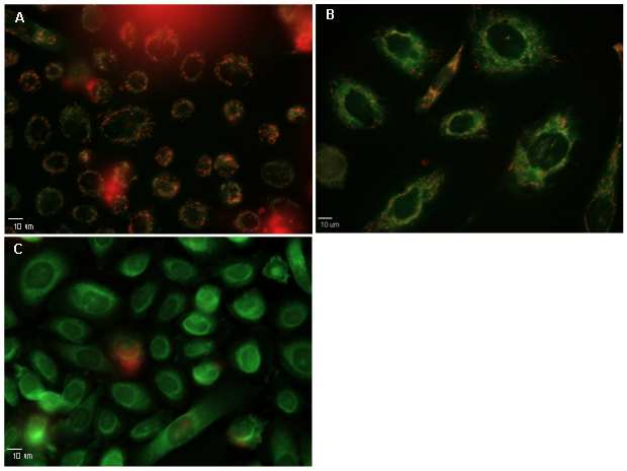

Figure S3. Fluorescence microscopy of cells that have been treated with various compounds, incubated for 48 h at 37 °C and then imaged by JC-1 staining after a further 30 min of incubation. Image **A** shows PC-3 cells treated with RPMI media only. Image **B** shows PC-3 cells treated with 200 µM of Pt-peptide conjugate **7** in RPMI media. Image **C** shows PC-3 cells respectively treated with 50% DMSO.

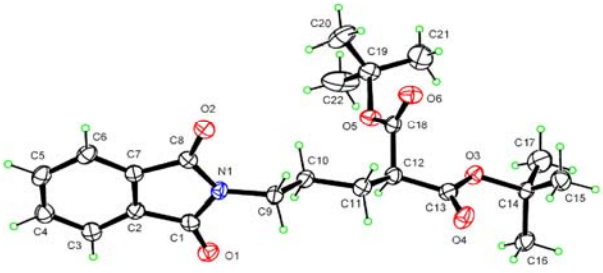

Figure S4. Ortep rendering of the structure of di-tert-butyl 2-(3-phthalimidopropyl)malonate (50% probability)

Experimental

Crystal data

$C_{22}H_{29}NO_6$	Mo $K\alpha$ radiation
$M_r = 403.46$	$\lambda = 0.71073$ Å
Orthorhombic	Cell parameters from 4240 reflections
$Pca2_1$	$\theta = 2.5$–$25.0°$
$a = 16.373$ (6) Å	$\mu = 0.090$ mm^{-1}
$b = 8.350$ (2) Å	$T = 110$ K
$c = 31.743$ (10) Å	Plate
$V = 4340$ (2) Å^3	Colorless
$Z = 8$	0.35 × 0.30 × 0.05 mm
$D_x = 1.235$ Mg m^{-3}	Crystal source: local laboratory
D_m not measured	

Data collection

KappaCCD (with Oxford Cryostream) diffractometer	3025 reflections with $I > 2\sigma(I)$
ω scans with κ offsets	$R_{int} = 0.038$
Absorption correction: none	$\theta_{max} = 25.0°$
18711 measured reflections	$h = -19 \rightarrow 19$
3880 independent reflections	$k = -9 \rightarrow 9$
	$l = -37 \rightarrow 37$
	Intensity decay: <2%

Refinement

Refinement on F^2	$w=1/[\sigma^2(F_o^2) + (0.0762P)^2]$ where $P = (F_o^2 + 2F_c^2)/3$
$R[F^2 > 2\sigma(F^2)] = 0.044$	$(\Delta/\sigma)_{max} = 0.000$
$wR(F^2) = 0.117$	$\Delta\rho_{max} = 0.34$ e Å^{-3}
$S = 1.027$	$\Delta\rho_{min} = -0.18$ e Å^{-3}
3880 reflections	Extinction correction: none
523 parameters	Scattering factors from *International Tables for Crystallography* (Vol. C)
H-atom parameters constrained	

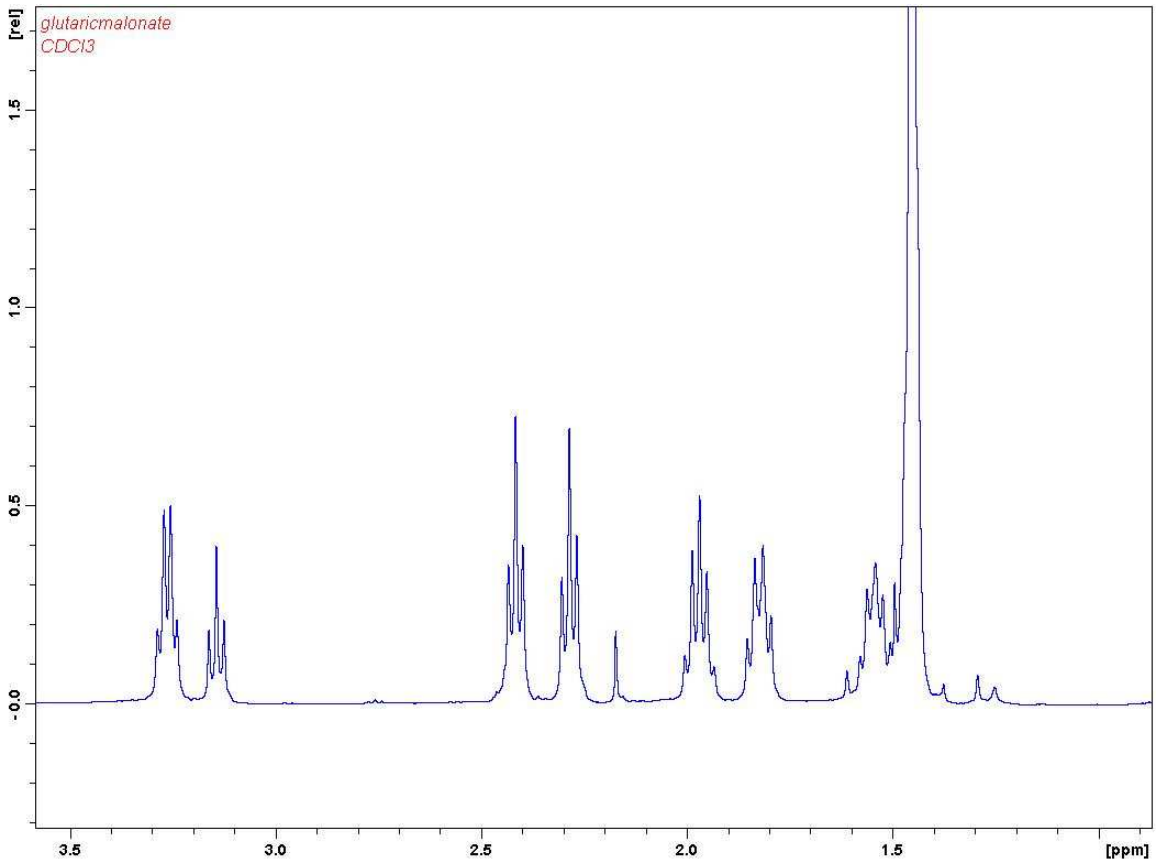

Figure S5. 1H NMR of di-tert-butyl 2-(3-glutaricaminopropyl)malonate

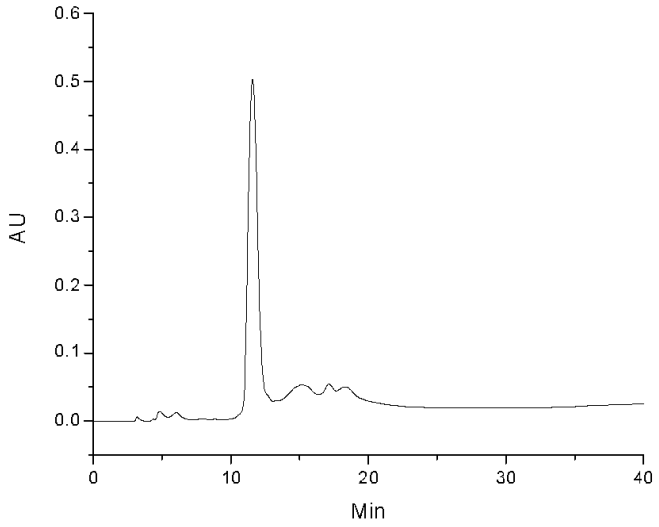

Figure S6. HPLC chromatogram of conjugate **2** (Mal-Glut-CNGRC) Column: Delta-Pak C4 (5 µm 100 Å) reverse phase column (8× 100 mm) Waters USA. Eluent: (A) 0.1% TFA in H_2O; (B) 0.1% TFA in MeCN. Linear gradient from 5% to 70% B in 60 min, t_R 11 min. Flow rate: 1 mL/min.

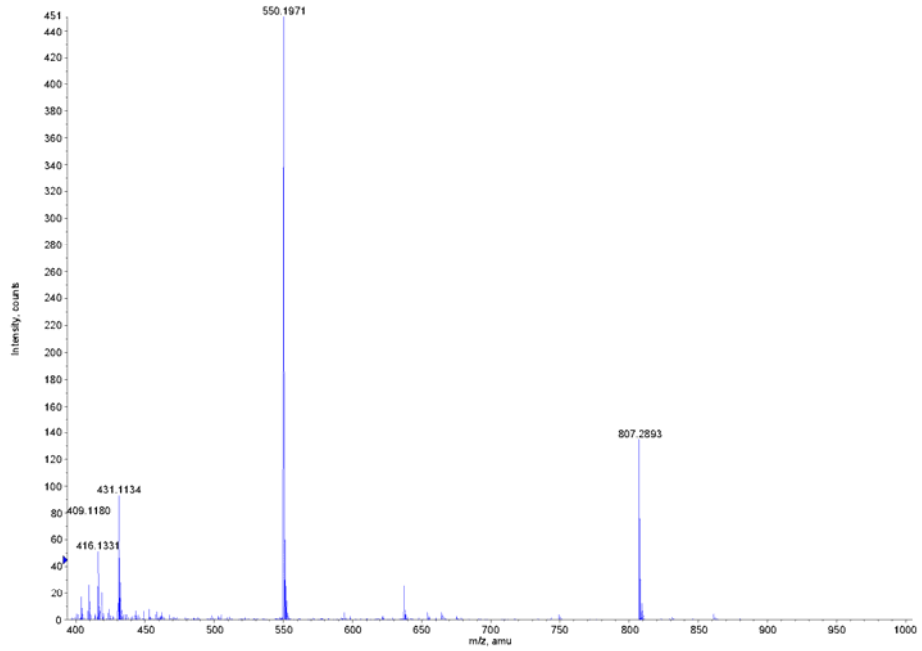

Figure S7. Mass spectrum of conjugate **2** (Mal-Glut-CNGRC).

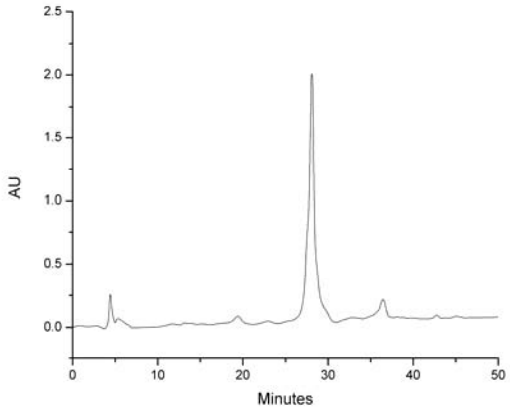

Figure S8. HPLC chromatogram of free peptide **6** (cyclic mPeg-CNGRC-mal) Column: Delta-Pak C_4 (5 µm 100 Å) reverse phase column (8× 100 mm) Waters USA. Eluent: (A) 0.1% TFA in H_2O; (B) 0.1% TFA in MeCN. Linear gradient from 5% to 70% B in 60 min, t_R 28 min. Flow rate: 1 mL/min.

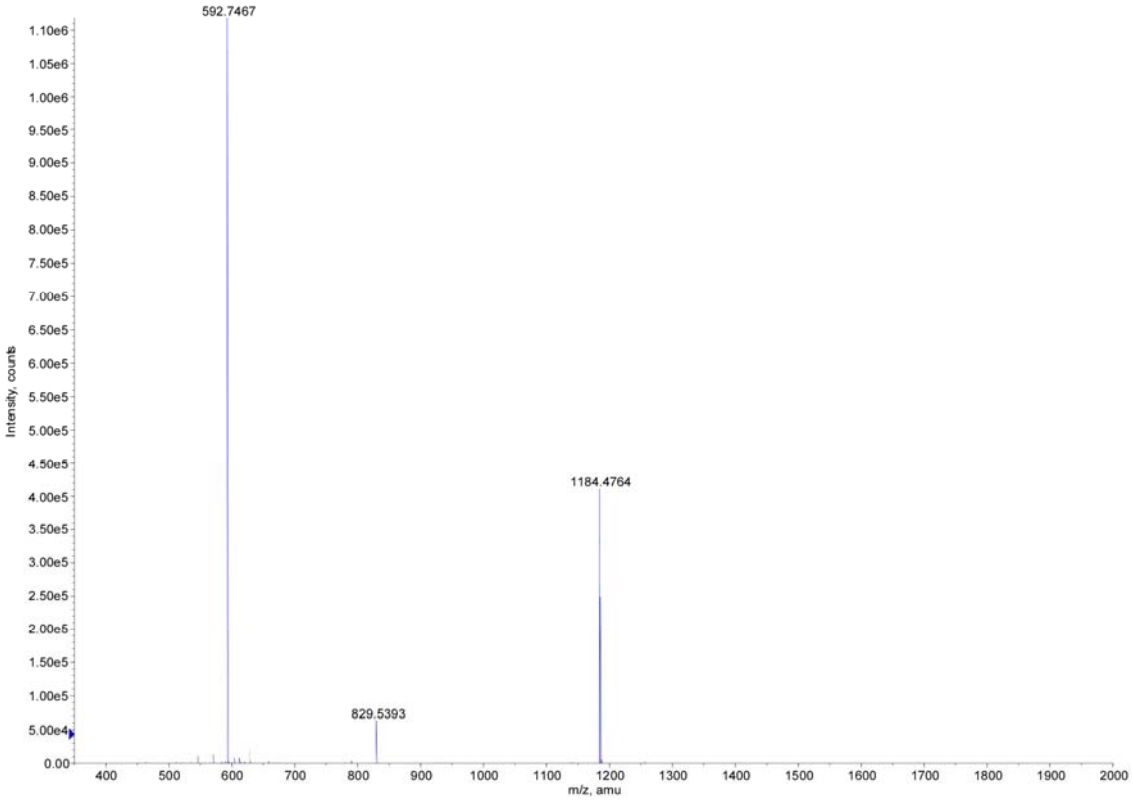

Figure S9. Mass spectrum of free peptide **6** (cyclic mPeg-CNGRC-mal).

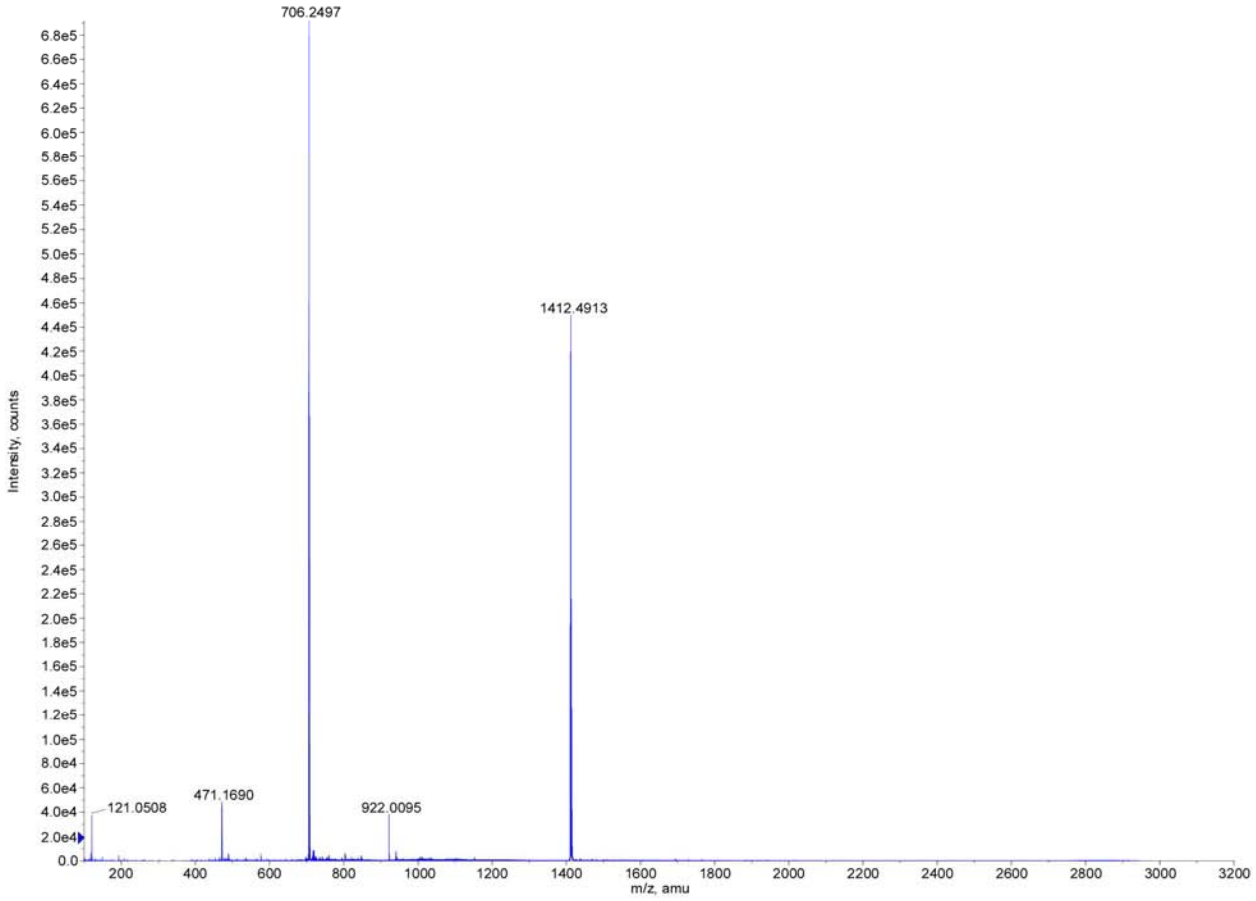

Figure S10. Mass spectrum of conjugate **7** (cyclic mPeg-CNGRC-Pt).

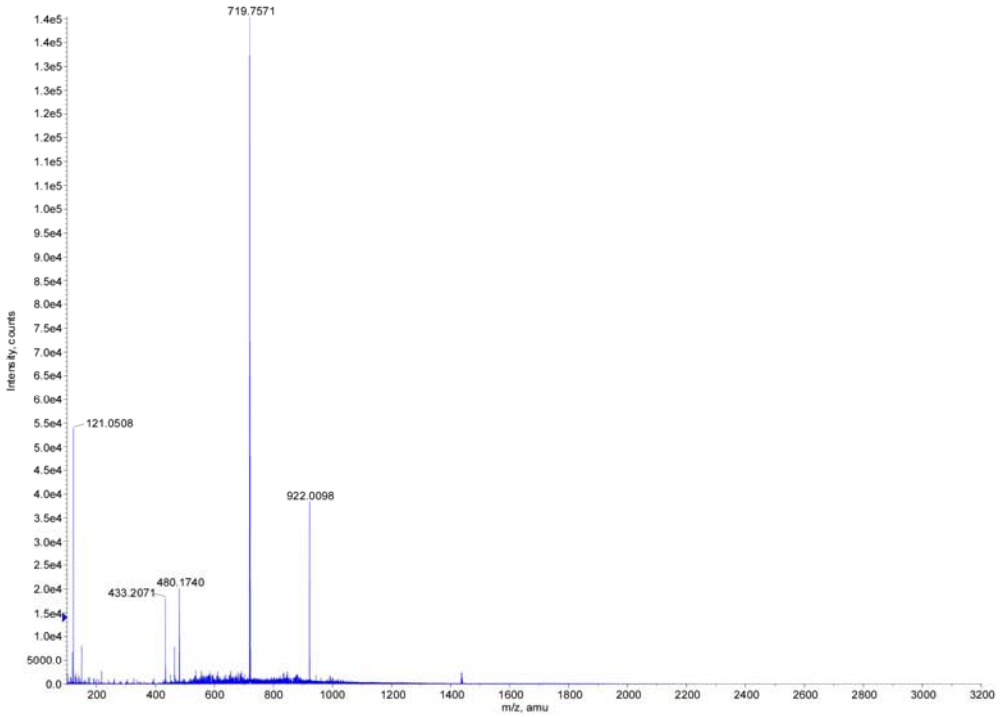

Figure S11. Mass spectrum of conjugate **8** (cyclic mPeg-CNGRC-Pten).

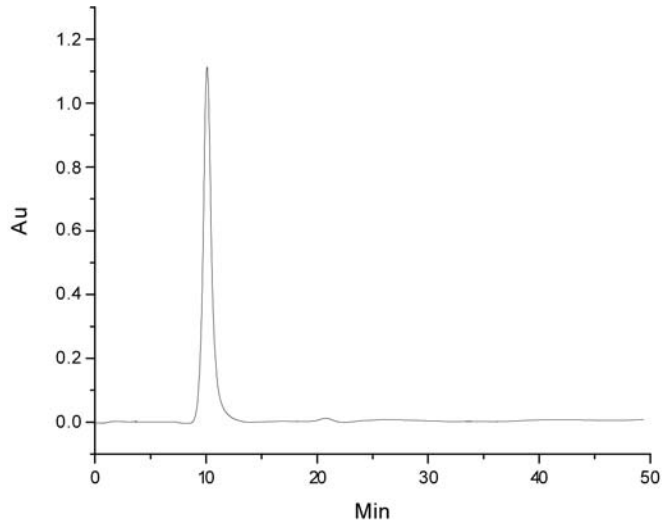

Figure S12. HPLC chromatogram of free peptide **9** (cyclic mPeg-CNGRC) Column: Delta-Pak C_4 (5 µm 100 Å) reverse phase column (8× 100 mm) Waters USA. Eluent: (A) 0.1% TFA in H_2O; (B) 0.1% TFA in MeCN. Linear gradient from 5% to 70% B in 60 min, t_R 10 min. Flow rate: 1 mL/min.

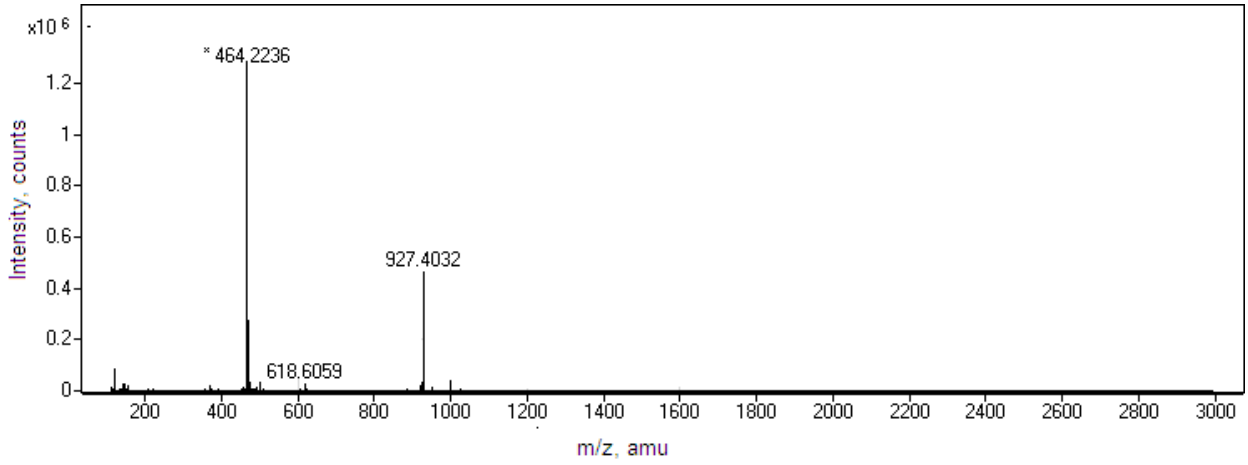

Figure S13. Mass spectrum of cyclic mPeg-CNGRC (**9**).

Self-Assembly and Cellular Uptake of Degradable and Water-Soluble Polyperoxides

Tamami Fujioka, Shuji Taketani, Takeshi Nagasaki,* and Akikazu Matsumoto*

Department of Applied Chemistry and Bioengineering, Graduate School of Engineering, Osaka City University, 3-3-138, Sugimoto, Sumiyoshi-ku, Osaka 558-8585, Japan. Received April 10, 2009; Revised Manuscript Received August 7, 2009

Water-soluble polyperoxides (**PP**s) as a new type of degradable and polymeric material were synthesized by the radical alternating copolymerization of sorbic derivatives containing a tetra(ethylene oxide) unit in the ester group using molecular oxygen. The obtained **PP**s showed a lower critical solution temperature (LCST)-type phase separation, and the transition temperature decreased according to the content of the hydrophobic ester group in the **PP**s. The **PP**s formed nanoaggregates with a diameter of 250−370 nm in water under the LCST. These **PP** aggregates were revealed to include 1-anilinonaphthalene-8-sulfonic acid as the fluorescence probe and epirubicin as the anticancer drug in their hydrophobic compartment. We evaluated the cytotoxicity and cellular uptake of the **PP**s in order to test their ability as a carrier used for the delivery of anticancer drugs. The cell viability in the presence of the **PP**s was comparable to those for the other biodegradable polymers, and epirubicin was taken up into the A549 efficiently with the **PP**s via an endocytosis mechanism.

INTRODUCTION

Polymeric micelles are spontaneously formed by the self-assembly of amphiphilic polymers containing hydrophobic and hydrophilic segments. Nonpolar molecules are incorporated into the core part of the micelles formed in an aqueous medium. Such polymeric micelles have attracted significant attention in the fields of cosmetics, agrichemicals, and medicines, because of their many advantages such as greater solubility of included compounds, stability of the formed micelles, narrow size distribution, and reduced toxicity in the human body (*1*−*8*). Drug delivery systems (DDS) are useful for the controlled release of drugs in humans and the effective delivery of drugs to target tissues and cell in order to increase drug bioavailability (*9*−*16*). For example, more prolonged circulation of carriers allows them to be preferentially accumulated at a certain site by enhanced permeation and retention (EPR) effects (*17*). Controlled release using various types of stimuli, such as biological molecules (*18*), pH change (*19*−*21*), irradiation (*22*−*24*), and heating (*25*−*27*), have also been investigated. The success of DDS depends on the availability of a suitable carrier. There is a significant need for biocompatible and biodegradable delivery polymers, because of reducing toxicity, avoiding accumulation, and enhancing the drug release. Poly(ethylene oxide), poly(lactic acid), poly(ε-caprolactone), poly(aspartic acid), and several other polymers with an excellent biocompatibility and biodegradability (*28*−*30*) have been intensively investigated as pharmaceutical carriers in various forms, e.g., dendrimers (*31*−*33*), microcapsules (*34*−*36*), liposomes (*37*), and micelles (*38*−*40*). Recently, polyperoxides (**PP**s) containing peroxy repeating units in the main chain were developed as new types of degradable polymers (*41*−*47*). The **PP**s are readily synthesized by the radical copolymerization process using sorbic derivatives and molecular oxygen as the starting materials (Scheme 1). The degradation of the **PP**s is induced by the action of any stimulus, for example, heating, photoirradiation, reducing agents, and enzymes, and the degradation reaction

Scheme 1

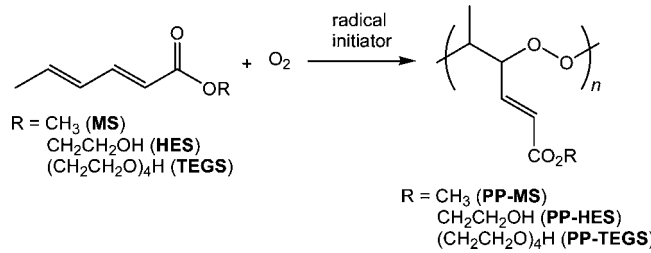

proceeds via a radical chain reaction mechanism to yield well-defined and low-molecular-weight products (*48*, *49*). We prepared water-soluble **PP**s by the introduction of the tetra(ethylene oxide) units in the ester group of the side chain, and preliminary experiments revealed the formation of aggregates of the amphiphilic **PP**s in water by self-assembly and their LCST (lower critical solution temperature)-type phase separation behavior (*50*). The water-soluble **PP**s are expected to be used as degradable drug carriers. In the present study, we characterized the features of the water-soluble **PP**s and evaluated the cytotoxicity and cellular uptake of the **PP**s as a fundamental research study for DDS.

EXPERIMENTAL SECTION

General Procedures. The number- and weight-average molecular weights (M_n and M_w) were determined by gel permeation chromatography (GPC) at 30 °C in tetrahydrofuran (THF) using a Tosoh GPC-8000 series system and calibrated with standard polystyrenes. The NMR spectra were recorded using a JEOL JMN A-400 spectrometer. Dynamic light scattering (DLS) measurements were carried out using a Zetasizer Nano Series Nano-ZS (Malvern Instruments, Ltd.) photometer. The UV−vis spectra were recorded using a JASCO V-550 photometer with an ETC-505T temperature controller. In order to determine the cloud point (T_{cp}), the transmittance was monitored at 500 nm in the UV−vis spectrum. The turbidity was determined after the solution was kept at each temperature for 5−10 min. A fresh solution was prepared for each measure-

* Corresponding authors. Fax: +81-6-6605-2981. E-mail: nagasaki@bioa.eng.osaka-cu.ac.jp and matsumoto@a-chem.eng.osaka-cu.ac.jp.

10.1021/bc9001618 CCC: $40.75 © 2009 American Chemical Society
Published on Web 09/23/2009

ment in order to avoid the effect of any degradation. When the transmittance value was not constant at a high temperature due to the occurrence of degradation, an initial value was used. The fluorescence spectra were recorded using a JASCO FP-6600 photometer at room temperature. In the WST assay, an absorbances at 450 and 620 nm were determined using a Multiskan Ascent microplate reader (Thermo Labsystems). The fluorescence emitted from the cells was analyzed by a FACS Calibur flow cytometer (BD Biosciences) with excitation at 488 nm using an emission filter of 585 ± 21 nm. The microscopic images were obtained using an Olympus IX-71 fluorescence microscope with a Yokogawa CSU-10 confocal scan unit and a Hamamatsu Photonics ORCA-ER CCD camera.

Materials. 2,2′-Azobis-(4-methoxy-2,4-dimethylvaleronitrile) (AMVN) (Wako Pure Chemical Industries, Ltd., Japan) was used after recrystallization from methanol. Commercially available methyl sorbate (Tokyo Kasei Kogyo Co., Ltd., Japan) was used after distillation under reduced pressure. The solvents were used after distillation. Other reagents were used without any further purification. Epirubicin was purchased from Pfizer Japan, Inc. The A549 cells were supplied from the American type Culture Collection and grown in Dulbecco's modified Eagle's medium (DMEM) containing 10% fetal bovine serum (FBS), 100 U/mL penicillin, 100 mg/mL streptomycin, and 0.1 mmol/L nonessential amino acid at 37 °C under a 5% CO_2 atmosphere.

Synthesis of Tetraethylene Glycol Monosorbic Ester (TEGS). Sorbic acid (5.6 g, 50 mmol), tetraethylene glycol (9.7 g, 50 mmol), and 4-(dimethylamino)pyridine (0.56 g, 4.6 mmol) were dissolved in 40 mL of 1,2-dichloroethane. To the solution, *N*,*N*′-dicyclohexylcarbodiimide (11 g, 53.4 mmol) in 5 mL of 1,2-dichloroethane was dropwise added over 15 min with stirring at 0 °C. After the addition, the reaction mixture was further stirred at room temperature overnight. The reaction mixture was filtered, washed with a 1 mol/L HCl aqueous solution, the $NaHCO_3$ aqueous solution, and brine, and then the solvent was evaporated. The obtained crude product was purified by silica gel column chromatography with *tert*-butyl methyl ether. The TEGS monomer was obtained in 41% yield.

TEGS. Viscous and colorless liquid; ^{1}H NMR ($CDCl_3$, 400 MHz) δ 7.28 (dd, J = 15.6 and 9.2 Hz, C*H*═CHCO, 1H), 6.11−6.23 (m, CH_3CH═C*H*, 2H), 5.79 (d, J = 15.6 Hz, CH═C*H*CO, 1H), 4.31 (t, CO_2CH_2, 2H), 3.73−3.75 (m, $CH_2O(CH_2CH_2O)_2CH_2CH_2OH$, 4H), 3.66 (s, $(CH_2CH_2O)_2CH_2CH_2OH$, 8H), 3.60−3.63 (t, CH_2CH_2OH, 2H), 2.53 (broad, CH_2CH_2OH, 1H), 1.85 (d, J = 5.6 Hz, CH_3CH═CH, 3H); ^{13}C NMR ($CDCl_3$, 100 MHz) δ 167.09 (C═O), 145.30 (*C*H═CHCO), 139.51 (CH_3CH═*C*H), 129.60 (CH_3CH═CH), 118.42 (CH═*C*HCO), 72.38 (CH_2CH_2OH), 70.19, 70.38, 70.41, 70.49 ($(CH_2CH_2O)_2CH_2CH_2OH$), 69.12 ($CO_2CH_2CH_2$), 63.22 (CO_2CH_2), 61.53 (CH_2OH), 18.54 (CH_3CH═CH).

Synthesis of Tetraethylene Glycol Disorbic Ester (TDS). To the mixture of sorbic acid (5.6 g, 50 mmol), tetraethylene glycol (4.85 g, 25 mmol), and 4-(dimethylamino)pyridine (0.56 g, 4.6 mmol) in 40 mL of 1,2-dichloroethane, *N*,*N*′-dicyclohexylcarbodiimide (11 g, 53.4 mmol) in 5 mL of 1,2-dichloroethane was dropwise added over 15 min with stirring at 0 °C. The reaction mixture was further stirred at room temperature overnight. The solution was filtered, washed, and the solvent evaporated, followed by purification using silica gel column chromatography (chloroform/*tert*-butyl methyl ether = 6/1). The TDS monomer was obtained in 52% yield.

TDS. Viscous and colorless liquid; ^{1}H NMR ($CDCl_3$, 400 MHz) δ 7.28 (dd, J = 15.6 and 10.0 Hz, C*H*═CHCO, 2H), 6.11−6.23 (m, CH_3CH═C*H*, 4H), 5.79 (d, J = 15.6 Hz, CH═C*H*CO, 2H), 4.30 (t, $CO_2CH_2CH_2$, 4H), 3.73 (t, $CO_2CH_2CH_2$, 4H), 3.67 (s, $CO_2CH_2CH_2(OCH_2CH_2)_2$, 8H), 1.85 (d, J = 5.6 Hz, CH_3CH═CH, 6H); ^{13}C NMR ($CDCl_3$, 100 MHz) δ 167.20 (C═O), 145.37 (*C*H═CHCO), 139.57 (CH_3CH═*C*H), 129.76 (CH_3CH═CH), 118.63 (CH═*C*HCO), 70.62 ($CO_2CH_2CH_2O(CH_2CH_2O)_3H$), 69.27 ($CO_2CH_2CH_2$), 63.38 ($CO_2CH_2$), 18.65 ($CH_3CH$═CH).

Synthesis of 1-Pyrenylmethyl Sorbate (PyMS). Sorbic acid (0.5 g, 4.4 mmol), 1-pyrenylmethanol (1.02 g, 4.4 mmol), and 4-(dimethylamino)pyridine (0.5 g, 4.1 mmol) were dissolved in 5 mL of 1,2-dichloroethane, and then *N*,*N*′-dicyclohexylcarbodiimide (1.0 g, 4.8 mmol) in 5 mL of 1,2-dichloroethane was dropwise added with stirring at 0 °C. After stirring at room temperature overnight, **PyMS** was isolated by a procedure similar to those for the synthesis of the other sorbates, and purified by recrystallization from 1,2-dichloroethane/*n*-hexane. Yield 42.3%.

PyMS. Colorless solid; mp 113−114 °C; ^{1}H NMR ($CDCl_3$, 400 MHz) δ 8.39−8.01 (m, Ar, 9H), 7.31 (dd, J = 10.0 and 15.6 Hz, C*H*═CHCO, 1H), 6.13 (m, CH_3CH═C*H*, 2H), 5.91 (s, CH_2, 2H), 5.84 (d, J = 15.6 Hz, CH═C*H*CO, 1H), 1.82 (d, J = 6.0 Hz, CH_3CH═CH, 3H); ($CDCl_3$, 100 MHz) δ 167.5 (C═O), 145.9 (*C*H═CHCO), 140.1 (CH_3CH═*C*H), 132.0, 131.5, 131.0, 130.0, 129.8, 129.4, 128.4, 128.0, 127.9, 127.6, 126.2. 125.7, 125.6, 125.1, 124.9, and 123.3 (Ar), 130.1 (CH_3CH═CH), 118.9 (CH═*C*HCO), 64.8 (CH_2), 19.0 (CH_3CH═CH).

Polymerization. The polymerization was carried out in a two-necked flask with bubbling oxygen at 30 °C in the presence of AMVN (monomer/initiator = 50/1 by weight). 1,2-Dichloroethane was used as the solvent (monomer/solvent = 1/1 by weight). After the polymerization, the contents of the flask were poured into a large amount of *n*-hexane to precipitate the resulting **PP**s. The solvent was removed by decantation and the precipitated **PP**s were dried in a vacuum overnight at room temperature. In the case of **PP-TEGS/TDS**, to remove a gel fraction, the polymerization product was soaked in THF at room temperature for 6 h and filtered. The filtrate was concentrated and the **PP** was precipitated into a large amount of *n*-hexane.

Cytotoxicity of PPs by WST Assay. The cytotoxicity of **PP-TEGS** and **PP-TEGS/TDS**−70/30 was determined by the WST assay method. The A549 cells were seeded onto a 96-well plate at a density of 1×10^4 cells/well in 100 μL of a cell culture medium, and incubated for 1 day at 37 °C, under atmospheric conditions controlled at 5% CO_2. The culture medium of each well was then replaced by 100 μL of a fresh medium containing various concentrations of the **PP**s. After the cells were further incubated for 1 day, the medium was aspirated and 100 μL of a fresh medium was added, followed by the addition of 10 μL of the WST-8 solution (cell counting kit-8, Dojindo Laboratory). After the cells were incubated for additional 2 h at 37 °C, the absorbance of each well was measured at 450 and 620 nm using a microplate reader.

Confocal Microscopic Observation of Internalized Fluorophore. The A549 cells were seeded onto a 35 mm dish containing a cover glass treated with 2 mmol/L HCl aqueous solution at a density of 2×10^5 cells in 2 mL of the cell culture medium and incubated for 1 day (37 °C, 5% CO_2). The culture medium was replaced with 2 mL of fresh medium containing the fluorescent samples. After incubation for a certain period, the cells were washed with a phosphate buffer solution (PBS), fixed with 3.7% HCHO, and used for the fluorescence microscopic observations.

Internalization Efficiency of Epirubicin in the Presence of PPs. The A549 cells (1×10^5 cells/well) were grown to just before confluence in a 12-well culture plate in an atmosphere of 5% CO_2 at 37 °C. The culture medium of each well was replaced with 0.5 mL of fresh medium containing 0.49 mg/mL of the polymers and 0.37 mg/mL of epirubicin. After the cells were further incubated for 3 h, the medium was aspirated and the cells were treated with 0.25% trypsin solution. The cell

Table 1. Results of the Characterization of PPs Obtained by the Radical Copolymerization of Various Sorbates with Oxygen[a]

PPs	yield, %	$M_n \times 10^{-3}$	$M_w \times 10^{-3}$	M_w/M_n	T_{cp}, °C	solubility[b]			
						$CHCl_3$	THF	CH_3OH	H_2O
PP-TEGS	29.1	3.9	6.6	1.7	[c]	s	s	s	s
PP-HES	23.0	4.1	6.6	1.6	−	s	s	s	i
PP-MS	49.3	3.2	5.1	1.6	−	s	s	s	i
PP-TEGS/MS−80/20	38.3	3.3	5.3	1.6	78	s	s	s	[d]
PP-TEGS/MS−75/25	41.9	3.8	6.5	1.7	55	s	s	s	[d]
PP-TEGS/MS−70/30	32.0	[e]	[e]	[e]	37	s	s	s	[d]
PP-TEGS/MS−60/40	36.5	[e]	[e]	[e]	18	s	s	s	[d]
PP-TEGS/MS−50/50	44.7	4.1	7.4	1.8	−	s	s	s	i
PP-TEGS/TDS−95/5	25.1(20.3)[f]	1.9[g]	4.6[g]	2.5[g]					
PP-TEGS/TDS−90/10	29.9(22.7)[f]	2.0[g]	6.1[g]	3.1[g]					
PP-TEGS/TDS−80/20	28.0(13.4)[f]	1.7[g]	4.1[g]	2.5[g]					
PP-TEGS/TDS−70/30	29.0(10.7)[f]	1.8[g]	5.6[g]	3.0[g]					

[a] Copolymerization was carried out with bubbling oxygen in 1,2-dichloroethane for 6 h at 30 °C. Monomer/solvent = 1/1 by weight. Monomer/AMVN = 50/1 by weight. [b] Determined at room temperature. s: soluble, i: insoluble. [c] Not determined because of thermal degradation. [d] Apparently soluble at a temperature below the T_{cp}. [e] Not determined. [f] The values in parentheses are the yield of a soluble part. [g] Determined for the soluble fraction.

suspension was washed twice with PBS. The intracellular fluorescence of epirubicin (λ_{ex} = 480 nm, λ_{em} = 580 nm) was measured by flow cytometry. A minimum of 2×10^4 events were analyzed for each histogram.

RESULTS AND DISCUSSION

Self-Assembly of Water-Soluble PP. The **PP**s were produced by the radical copolymerization of the sorbates and molecular oxygen. Table 1 summarizes the yield, M_n, M_w, and M_w/M_n values, and the solubility of the produced **PP**s. The M_n values were $(3-4) \times 10^3$ and independent of the structure of the ester group in the side chain. The low-molecular-weight **PP**s, which are classified as an oligomer rather than a high polymer, were formed as a result of the slow addition of a peroxy radical as the propagating chain end to a sorbate monomer and the frequent occurrence of a chain transfer reaction during the copolymerization (*44*, *51*). The formation of the 5,4-structure of the sorbates as the predominant repeating unit (Scheme 1) was confirmed on the basis of the peaks due to the methine (CH−CH in the main chain) and vinylene (CH═CH in the side chain) hydrogens observed at 4.2−5.2 and 6.1−7.0 ppm, respectively, in the NMR spectra of the **PP**s (*44*, *45*). The water-soluble **PP** was obtained by the introduction of a tetra(ethylene oxide) unit into the ester group in the side chain, while the **PP**s with the methyl and 2-hydroxyethyl esters were insoluble in water due to the presence of the hydrophobic main chain.

The **PP-TEGS** aqueous solution was transparent at room temperature, while the solution readily became turbid upon heating. This phenomenon is called LCST-type phase separation, which is typically observed for the aqueous solutions of poly(*N*-isopropylacrylamide) (*52*) and poly(vinyl ether)s (*53*). The intermolecular interaction between the polymer chains is enhanced by the dehydration upon heating, which results in macroscopic aggregation of the polymers. For the **PP-TEGS** solution in the present study, an accurate cloud point (T_{cp}) was not determined because the **PP**s readily degraded upon heating. Therefore, we fabricated **PP-TEGS/MS**-m/n as copolymers of **TEGS** with **MS** with a different ratio in the feed in order to increase the hydrophobicity of the produced polymers (Scheme 2). Here, *m*/*n* is the molar ratio of **TEGS** and **MS** monomers in the feed. The results of the copolymerization are shown in Table 1. The **PP-TEGS/MS**s were apparently soluble in water at room temperature when the **TEGS** concentration was greater than 60 mol % in the feed.

The phase diagrams of the **PP-TEGS/MS**s with different compositions are shown in Figure 1a. Here, the T_{cp} was defined as the temperature corresponding to a 50% decrease in the transmittance. The T_{cp} value decreased from 78 to 18 °C with

Scheme 2

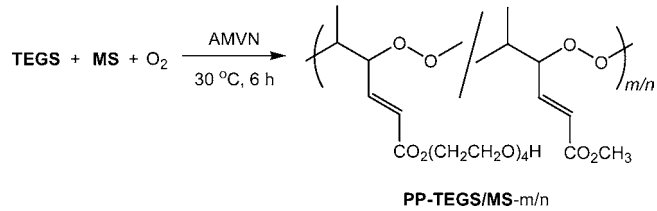

PP-TEGS/MS-m/n

an increase in the concentration of the hydrophobic **MS** in the feed. In order to confirm reversibility in the LCST-type phase separation behavior, the transmittance of **PP-TEGS/MS**−60/40 was repeatedly traced during the heating and cooling processes. In this experiment, the temperature was stepwise changed every 10 min using the same sample. As shown in Figure 1b, similar curves during the first and second heating processes were obtained. Hysteresis observed during the cooling process was very small due to the low molecular weight of the **PP**.

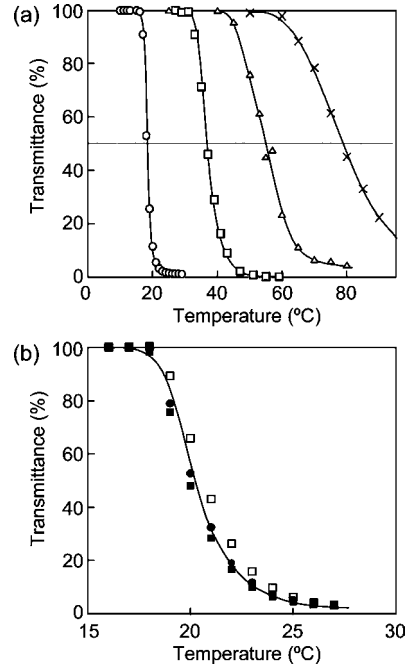

Figure 1. (a) Phase diagrams for the 0.5 wt % aqueous solution traced by transmittance at 500 nm. (○) **PP-TEGS/MS**−60/40, (□) **PP-TEGS/MS**−70/30, (Δ) **PP-TEGS/MS**−75/25, (×) **PP-TEGS/MS**−80/20. (b) Traces for **PP-TEGS/MS**−60/40 on (■) the first heating, (□) the cooling, and (●) the second heating.

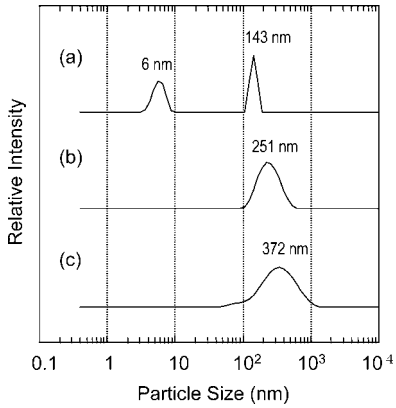

Figure 2. Particle size distribution of the **PP**s determined by DLS at 25 °C. (a) **PP-TEGS** in water, (b) **PP-TEGS/TDS**−80/20 in water, and (c) **PP-TEGS/TDS**−70/30 in water. The polymer concentration is 0.24 mg/mL.

Scheme 3

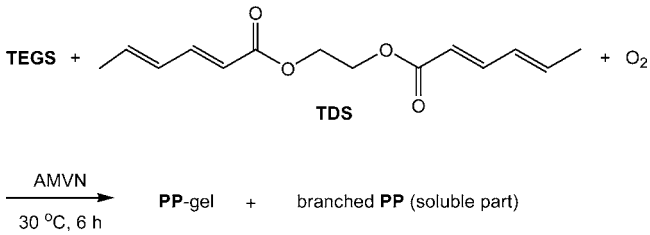

The **PP-TEGS** molecules are self-assembled in water and form an aggregate with a size smaller than the wavelength of visual light. The aggregates can be dispersed in water at a temperature lower than the LCST, resulting in a transparent solution. The DLS analysis confirmed the formation of the **PP-TEGS** assembly, which consists of a bimodal distribution with average diameters of 6 and 143 nm (Figure 2). The assembly with a diameter of 143 nm is probably produced by the secondary aggregation of the small particles of less than a 10 nm size. The peak intensity of the distribution curves in Figure 2 is based on the relative intensity of the observed scattering light, but not based on the number and weight fractions of the particles. Therefore, the number of the smaller particles with an average diameter of 6 nm is much greater than that of the larger one with a 143 nm diameter. In a 20 mol % aqueous solution of glycerin, no assembly with a particle size larger than 1 nm was observed. This is due to fragmentation of the assemblies into free polymer chains by the addition of glycerin, which decreases the hydrophobic interaction between the **PP-TEGS** molecules.

As an attempt to synthesize a high-molecular-weight **PP**, we carried out the copolymerization of **TEGS** and **TDS**, which is a difunctional sorbate monomer (Scheme 3). The results of the copolymerization are already shown in Table 1. The **PP** recovered after copolymerization was fractionated into the soluble and insoluble parts, which consist of the branched **PP** and **PP**-gel, respectively, by extraction with THF. The amount of the soluble fraction decreased with an increase in the ratio of **TDS** in the feed. The M_n values of the soluble **PP-TEGS/TDS** were only (1.7−2.0) × 10^3, smaller than those for **PP-TEGS**. This result was opposite from the expected one. Fortunately, however, we found that the aggregates of the **PP-TEGS/TDS** in water provided a monomodal distribution with a diameter of 250 and 370 nm when the **TDS** content was 20 and 30 mol %, respectively, in the feed (Figure 2b,c). This suggests that the **PP-TEGS/TDS**s are favorable for the fabrication of a large-sized molecular assembly, although the reason is still unclear.

Scheme 4

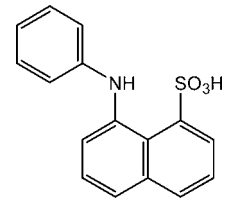

ANS

These **PP** assemblies can include many molecules. For example, the wavelength and intensity of the fluorescent emission of 1-anilinonaphthalene-8-sulfonic acid (ANS) as a fluorescence probe (Scheme 4) changed depending on the concentration of the **PP**s. With an increase in the amount of the **PP-TEGS**, the wavelength of the emission peak shifted to a shorter wavelength region and the intensity increased. From a plot of the wavelength of the emission peak ($\lambda_{em,max}$) versus the ANS concentration (Figure 3a), the critical micelle-formation concentration (cmc) of **PP-TEGS** was evaluated to be 5 × 10 μg/mL at room temperature. The formed assembly was stable, and no change was observed in the emission spectrum over 7 days. It was also revealed that the **PP-TEGS/TDS** with a greater TDS content more effectively included ANS and afforded a more hydrophobic environment (Figure 3b). This is due to the formation of the aggregates with a larger size from the **PP-TEGS/TDS** containing a high TDS content, as shown in Figure 2.

Cytotoxicity and Cellular Uptake of PP. The in vitro cytotoxicity of **PP-TEGS** was investigated using the A549 cells (human lung carcinoma) by the WST assay at 37 °C. The change in the cell viability is shown in Figure 4. The A549 cells showed excellent cell viability during the short incubation time (within 3 h) even in the presence of a high concentration of **PP-TEGS** up to 1 mg/mL. No toxicity of **PP-TEGS** was simultaneously confirmed at a low concentration of less than 10^2 μg/mL similar to the conditions for use as a drug carrier, irrespective of the incubation period. The viability decreased at a high **PP-TEGS**

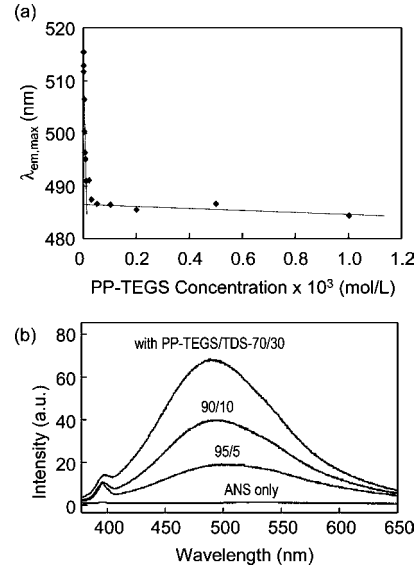

Figure 3. (a) Shift in the peak wavelength for the emission of ANS versus the **PP-TEGS** concentration at room temperature. (b) Fluorescence spectrum of ANS in the presence and absence of the **PP-TEGS/TDS**s at room temperature.

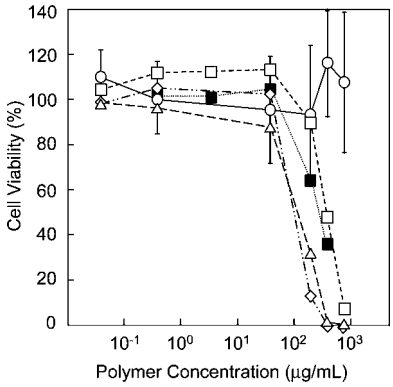

Figure 4. Cytotoxicity of **PP**s using the A549 cell lines after incubation for different times at 37 °C. (○) **PP-TEGS** for 3 h, (□) 24 h, (Δ) 48 h, (◊) 96 h, and (■) **PP-TEGS/TDS**−70/30 for 24 h. Determined by the WST assay. Error bars are shown for only the 3 h incubation data for clarity.

Scheme 5

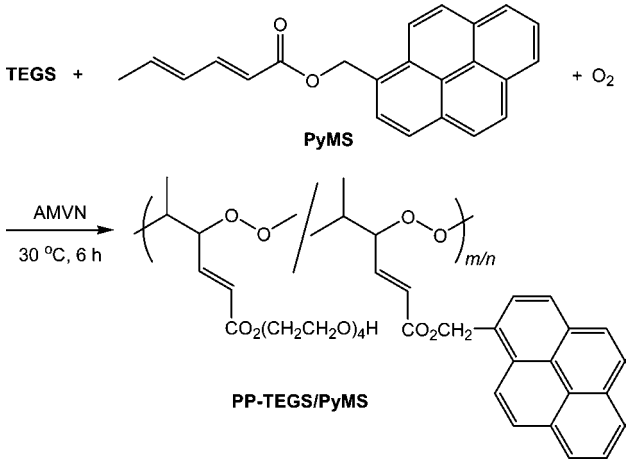

concentration (>10^2 μg/mL) and a long incubation time (>24 h). The effect of the degradation of the **PP**s is not negligible under the conditions at a concentration and for a log time, as described later. It was also revealed that the branched structure of the **PP**s had no effect on the cell viability, as shown in the results of the experiments using **PP-TEGS** and **PP-TEGS/TDS**−70/30. It is concluded that the cell viability in the presence of the **PP**s is comparable to those for the other biodegradable polymers such as poly(D,L-lactide-*co*-glycolide) and poly(aspartic acid)-*block*-polylactide in the literature (*21*, *35*, *54*−*56*).

To directly monitor the cellular uptake of the **PP**s, we synthesized a fluorescence-labeled **PP** by the copolymerization of **TEGS** with oxygen in the presence of 1 mol % of **PyMS** (Scheme 5). The solubility of **PP-TEGS/PyMS** was similar to that of **PP-TEGS**, because of the low content of the **PyMS** unit (1 mol % in the feed). In this experiment, the exact composition of the repeating units in the **PP-TEGS/PyMS** was not determined. The average number of the **PyMS** unit internalized into the **PP-TEGS** is calculated to be ca. 0.05−0.1 per a **PP** chain on the basis of the M_n values for the **PP-TEGS**. The fluorescence spectra of the **PyMS** monomer and **PP-TEGS/PyMS** are shown in Figure 5. A fluorescent emission due to the eximer of the pyrene moieties (λ_{max} = 470 nm) was observed from the ethanol solution containing 1% of **PyMS**. In contrast, the aqueous solution of **PP-TEGS/PyMS** mainly provided a monomer emission. This indicates that the **PyMS** repeating unit as the fluorophore is isolated in a hydrophobic compartment of the **PP-TEGS/PyMS** aggregates, because the average number of the **PyMS** repeating unit per a **PP-TEGS/PyMS** chain is

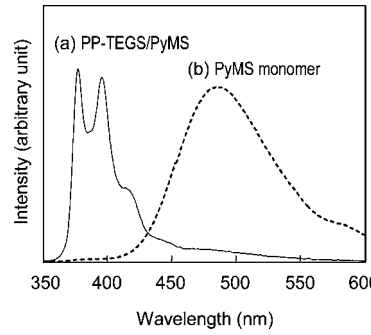

Figure 5. Fluorescence spectra of (a) **PP-TEGS/PyMS** at 0.195 mg/mL in water and (b) **PyMS** monomer at 2 μg/mL in ethanol at room temperature.

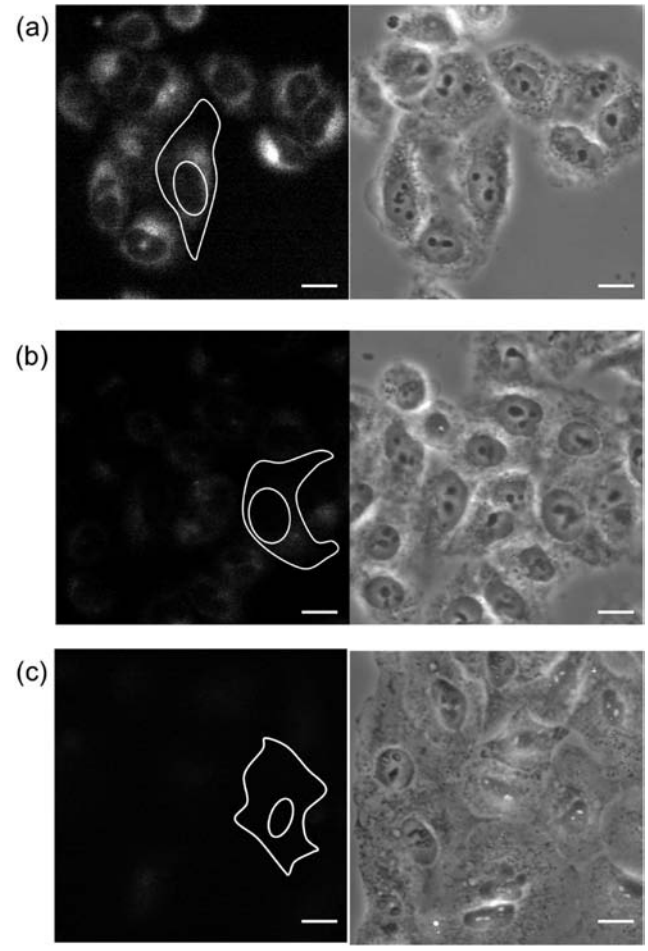

Figure 6. Fluorescence microscopic images of the A549 cells in the presence of **PP-TEGS/PyMS** after incubation for 3 h at (a) 37 and (b) 4 °C. (c) Control (in the absence of **PP-TEGS/PyMS**). Left: fluororescence images. Right: transmittance photomicrographs. Scale bar, 10 μm. Fluorescent images were observed using a band path filter (420−460 nm) by excitation at 365 nm.

much lower than unity and the nonpolar pyrene moiety is surrounded by the **PP-TEGS** segments, while the pyrenyl group of **PyMS** tends to aggregate even in a dilute solution in ethanol.

The cellular uptake and intracellular distribution of **PP-TEGS/PyMS** are confirmed by confocal fluorescence microscopy (Figure 6). The microscopic images revealed that the **PP-TEGS/PyMS** was distributed in the cytoplasm rather than in the nucleus of the cell. The **PP-TEGS/TDS-70/30-PyMS** showed a similar fluorescence microscopic image (data not shown). In the literature, many polymer micelles may involve the mechanism of energy-dependent endocytosis during a

Scheme 6

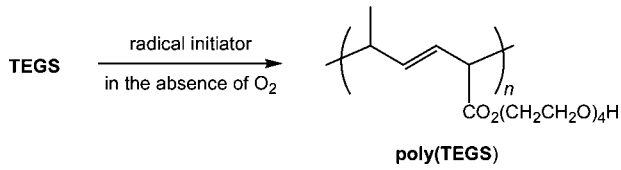

cellular uptake process (*57*). For example, large-sized substances, such as proteins, DNA, enzymes, and polymers, favorably enter the inside of the cells via an endocytosis mechanism. Polar and ionic substances generally inhibit their membrane penetration due to the presence of a hydrophobic area in the cell membranes. The fluorescence intensity of internalized **PP-TEGS/PyMS** at 37 °C is obviously stronger than that at 4 °C (Figure 6a,b). The temperature dependence of the uptake of the **PP**s has supported the fact that PPs are energy-dependently internalized by the endocytic pathway. However, the energy-dependent uptake of **PP-TEGS/PyMS** was not completely inhibited at 4 °C. The **PP-TEGS** with tetra(ethylene glycol) units in the side chain may have a fusogenic activity, similar to water-soluble polymers, such as poly(ethylene glycol) (*58*).

The **PP**s were stable in organic solvents, such as chloroform and THF, and in pure water, as already shown in the results of the NMR, GPC, and LCST experiments, but the degradation rate of the **PP**s may be accelerated in the cell conditions, because the degradation of the **PP**s is induced by the biochemical and redox systems (*49, 59*). The biochemical decomposition of the **PP**s by horseradish peroxidase (HRP) was already reported in a previous paper (*49*). The conversion of the **PP**s was 46% during the degradation in the presence of HRP for 3 days at 30 °C. We also reported that the **PP**s readily degraded by the addition of base and the weight loss of the **PP**s increased with an increase in the basicity of the additives (*59*). A small amount of triethylamine induced the immediate degradation of the **PP**s within a few minutes, while the addition of a weaker base, such as *N*,*N*-dimethylformamide and aniline, resulted in degradation at a moderate rate. In fact, we confirmed the slow degradation of the **PP**s in a phosphate saline buffer solution (pH = 7.4). In the present study, however, we could not directly evaluate the degradation rate of the **PP**s under the cell conditions because of the difficulty of the isolation of the unreacted **PP**s and the degradation products from the incubation mixture.

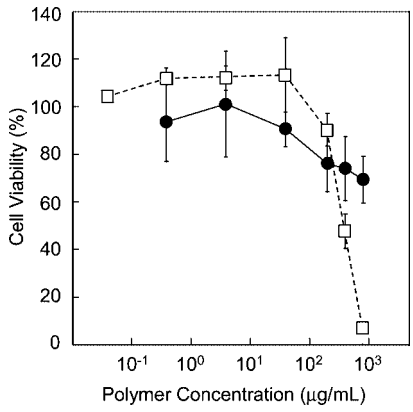

Figure 7. Comparison of the cytotoxicity of poly(TEGS) and **PP-TEGS** using the A549 cell lines after incubation at 37 °C for 24 h. (●) Poly(TEGS) and (□) **PP-TEGS**. Determined by the WST assay. Data for **PP-TEGS** are the same as those in Figure 4.

Scheme 7

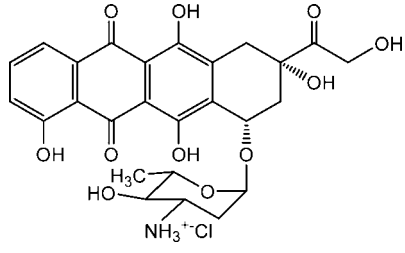

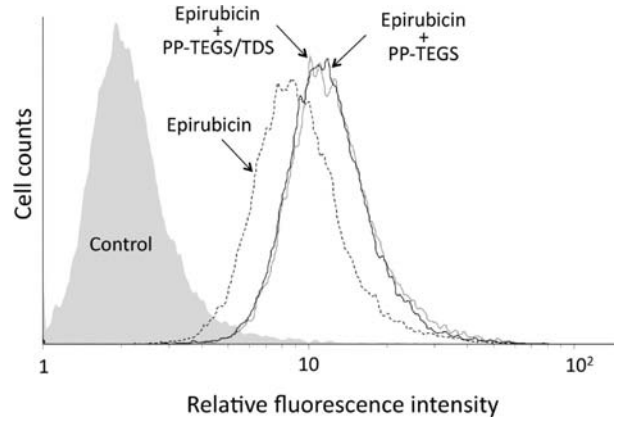

Figure 8. Flow cytometry analysis of the uptake of epirubicin in the A549 cells after incubation for 3 h at 37 °C. Black curve: with **PP-TEGS**. Gray curve: with **PP-TEGS/TDS**−70/30. Dotted curve: without **PP**. Monitored by emission from epirubicin at 585 nm. Control experiment was incubated in the absence of **PP** and epirubicin.

Table 2. Epirubicin Uptake into the A549 Cells in the Presence and Absence of the PPs

sample	temperature, °C	average fluorescence intensity[a]
PP-TEGS	37	1.59
	4	0.65
PP-TEGS/TDS−70/30	37	1.70
	4	0.68
none (only epirubicin)	37	1.00 (standard)
	4	0.42
control (without epirubicin)	37	0.23

[a] Relative values versus the fluorescence intensity obtained using only epirubicin in the absence of the **PP**s at 37 °C.

In order to further investigate the effects of the peroxy repeating structure in the main chain of the **PP**s on the cellular uptake behavior and cytotoxicity, the homopolymer of **TEGS** [poly(TEGS)] was synthesized as the reference material. The radical polymerization was carried out in the absence of oxygen using di-*tert*-butyl peroxide as a radical initiator (Scheme 6) in toluene for 6 h at 120 °C (**TEGS**/initiator = 50/1 and **TEGS**/toluene =1/1 by weight) to obtain poly(TEGS) (*60*). As a result for the polymerization under these conditions, the poly(TEGS) with the M_n and M_w/M_n values of 2.0×10^3 and 1.5, respectively, were obtained in 13.7% yield, and it was soluble in chloroform, THF, methanol, and water at room temperature. The NMR spectrum of poly(TEGS) confirmed its 5,2-trans repeating structure; that is, the peaks due to the CH═CH units in the main chain were observed at 5.4 ppm and those for the CH−CH unit were at 1.7−2.9 ppm as the broad and split signals, similar to the spectra previously reported for the polymers obtained from the other sorbates (*60*). The chemical shifts for poly(TEGS) differed from those of **PP-TEGS** observed at 6.1−7.0 and 4.2−5.2 ppm for the CH═CH and CH−CH units, respectively.

We revealed that poly(TEGS) also formed self-assembly with the average diameters of 160 nm in water and carried out the in vitro cytotoxicity experiments using poly(TEGS) under the conditions identical to that for the experiments using **PP-TEGS** (Figure 4). Figure 7 shows the comparison of the cytotoxicity of poly(TEGS) and **PP-TEGS**. As a result, no decrease in the

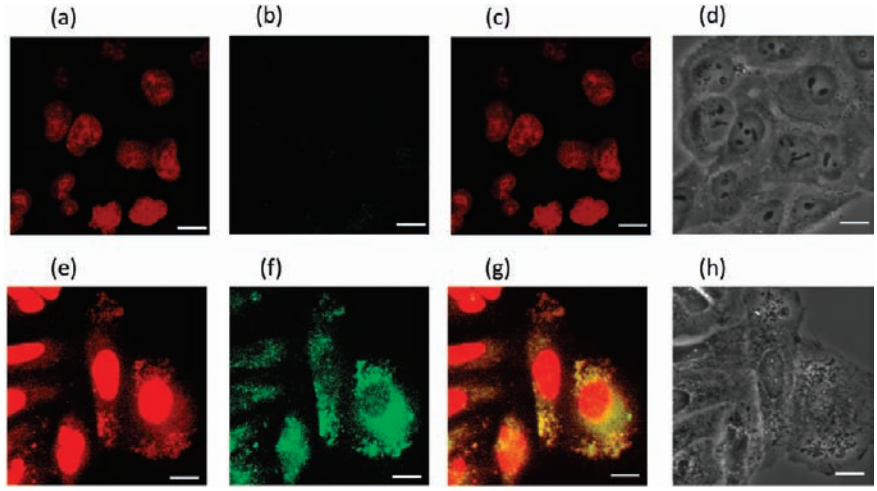

Figure 9. Cellular distribution of epirubicin (red, a and e, monitored at 585 nm) and **PP-TEGS/TDS/PyMS** (green, b and f, monitored at 420−460 nm) in the A549 cells after incubation in the presence of 0.37 mg/mL epirubicin without (a−d) and with (e−h) 0.49 mg/mL **PP-TEGS/TDS/PyMS** for 1 h at 37 °C. The images shown in c and g are the overlay of the red and green images (a+b and e+f) and in d and h are the phase contrast images. Scale bar, 10 μm.

viability was observed even at a concentration around 10^3 μg/mL in the presence of poly(TEGS), while the viability decreased in the presence of **PP-TEGS** under the same concentration conditions. This result suggests that the cell viability is influenced by the slow decomposition of **PP-TEGS** at 37 °C. It is expected that the oxy radicals and aldehydes produced from **PP-TEGS** by the decomposition induce the death of the A549 cells.

Cellular Uptake of Epirubicin in the Presence of PP. A flow cytometric analysis was carried out in order to quantitatively estimate the uptake of epirubicin (*61*), which is an anticancer drug (Scheme 7) and the stereoisomer of doxorubicin, into A549 cells in the presence and absence of **PP**s after incubation at 37 and 4 °C for 3 h. The fluorescence emission from the epirubicin molecules was monitored at 585 nm to count the number of cells containing epirubicin. Figure 8 shows the typical results for counting the number of cells with different fluorescence intensities, that is, including different amounts of epirubicin in the A549 cells. These results are summarized in Table 2. The amount of epirubicin internalized into the cells was enhanced in the presence of **PP-TEGS** and **PP-TEGS/TDS**−70/30 compared to the case using the free epirubicin. No difference was observed between the results for the experiments using **PP-TEGS** and those using **PP-TEGS/TDS**. The uptake of epirubicin depended on the temperature. In contrast to the facile uptake at 37 °C, only a small amount of epirubicin was incorporated into the cells at 4 °C, irrespective of the presence and absence of the **PP**s (Table 2). These results suggest that the epirubicin and the epirubicin/**PP** complex mainly enter the cells via an endocytosis mechanism.

We used confocal fluorescence microscopy and the emissions of different colors from the epirubicin molecules and the **PyMS** unit in the **PP**s in order to analyze the intracellular distribution of epirubicin and the **PP**s in the A549 cells. Figure 9a indicates that epirubicin was accumulated in the nucleus after a 1 h incubation. When the A549 cells were incubated in the presence of both epirubicin and **PP-TEGS/TDS/PyMS** (Figure 9e), some epirubicin molecules are still present in the cytoplasm. The migration of the free epirubicin into the nucleus of the cell has readily occurred, but epirubicin has remained in the cytoplasm for a certain time in the presence of the **PP**. The distribution of the **PP** in the cytoplasm was also confirmed by an experiment using fluorescent **PP-TEGS/TDS/PyMS** (Figure 9f). The overlay of the red and green images (Figure 9g) indicates that epirubicin as the free form is imported into the nucleus (red part in Figure 9g) and the epirubicin incorporated into the cell with the **PP** is localized in the cytoplasm, especially endocytic vesicles such as endosomes (yellow part in Figure 9g). Thus, some epirubicin molecules remain in a hydrophobic compartment in the **PP** aggregates in the cytoplasm during the short incubation period such as 1 h, but the epirubicin molecules gradually migrated into the nucleus after a longer incubation period. The free epirubicin molecules, which entered the cells, immediately migrated and accumulated in the nucleus due to its cationic charge. On the other hand, the epirubicin molecules incorporated into the **PP-TEGS** assembly are slowly released. Therefore, the epirubicin molecules combined with the **PP** are slowly imported into the nucleus. Finally, the stronger fluorescence emission of epirubicin in the presence of **PP-TEGS** than that of the absence of **PP-TEGS** (Figure 9) also supported the increased efficiency of cellular uptake with **PP-TEGS** (Figure 8) followed by the nuclear import of the epirubicin molecules. Figure 10 shows a schematic illustration for the process of the formation of self-assemblies of the **PP**s in the presence of an anticancer drug, uptake into the cell by endocytosis, and the release of the drug in the cell, followed by the import of the drug into a nucleus.

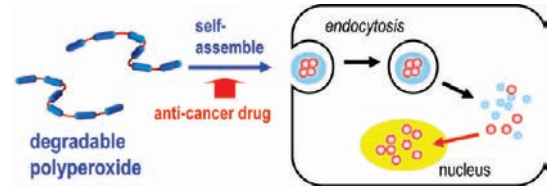

Figure 10. Schematic illustration for the formation of self-assembly of the PPs and an anticancer drug, uptake into the cell by endocytosis, and the release of the drug.

In conclusion, the water-soluble **PP**s were prepared by the radical copolymerization of a sorbic ester containing a tetra(ethylene oxide) unit with molecular oxygen. The obtained **PP**s showed an amphiphilic property and formed assemblies in water. We further evaluated the cytotoxicity and cellular uptake of the **PP**s in order to test the ability as a carrier used for drug delivery systems. It was also revealed that epirubicin as an anticancer drug is taken up into cells more efficiently in the presence of the **PP**s than in the absence of the **PP**s via an endocytosis mechanism. Such a water-soluble and degradable polymer assembly bearing a hydrophobic domain could be one of the candidates of a carrier for drugs. Any synergy effect as an

anticancer drug by the degradation of the **PP** is also expected because the **PP**s are readily degraded by various stimuli. Further investigation of the use of the **PP**s as drug carriers is now underway.

LITERATURE CITED

(1) Kwon, G. S., and Kataoka, K. (1995) Block copolymer micelles as long-circulating drug vehicles. *Adv. Drug Delivery Rev. 16*, 295–309.

(2) Kwon, G. S., and Okano, T. (1996) Polymeric micelles as new drug carriers. *Adv. Drug Delivery Rev. 21*, 107–116.

(3) Torchilin, V. P. (2001) Structure and design of polymeric surfactant-based drug delivery systems. *J. Controlled Release 73*, 137–172.

(4) Kakizawa, Y., and Kataoka, K. (2002) Block copolymer micelles for delivery of gene and related compounds. *Adv. Drug Delivery Rev. 54*, 203–222.

(5) Ladmiral, V., Melia, E., and Haddleton, D. M. (2004) Synthetic glycopolymers: an overview. *Eur. Polym. J. 40*, 431–449.

(6) Hawker, C. J., and Wooley, K. L. (2005) The convergence of synthetic organic and polymer chemistries. *Science 309*, 1200–1205.

(7) Harada, A., and Kataoka, K. (2006) Supramolecular assemblies of block copolymers in aqueous media as nanocontainers relevant to biological applications. *Prog. Polym. Sci. 31*, 949–982.

(8) Rapoport, N. (2007) Physical stimuli-responsive polymeric micelles for anti-cancer drug delivery. *Prog. Polym. Sci. 32*, 962–990.

(9) Park, K., Shalaby, W. S. W., Park, H. (1993) *Biodegradable Hydrogels for Drug Delivery*, Technomic, Lancaster.

(10) Uhrich, K. E., Cannizzaro, S. M., Langer, R. S., and Shakesheff, K. M. (1999) Polymeric systems for controlled drug release. *Chem. Rev. 99*, 3181–3191.

(11) Miyata, T., Uragami, T., and Nakamae, K. (2002) Biomolecule-sensitive hydrogels. *Adv. Drug Delivery Rev. 54*, 79–98.

(12) Langer, R., and Tirrell, D. A. (2004) Designing materials for biology and medicine. *Nature 428*, 487–492.

(13) Schmaljohann, D. (2006) Thermo- and pH-responsive polymers in drug delivery. *Adv. Drug Delivery Rev. 58*, 1655–1670.

(14) Nagasaki, T., and Shinkai, S. (2007) The concept of molecular machinery is useful for design of stimuli-responsive gene delivery systems in the mammalian cell. *J. Inclusion Phenom. Macrocyclic Chem. 58*, 205–219.

(15) Oh, J. K., Drumright, R., Siegwert, D. J., and Matyjaszewski, K. (2008) The development of microgels/nanogels for drug delivery applications. *Prog. Polym. Sci. 33*, 448–477.

(16) Ganta, S., Devalapally, H., and Amiji, M. (2008) A review of stimuli-responsive nanocarriers for drug and gene delivery. *J. Controlled Release 126*, 187–204.

(17) Maeda, H. (2001) SMANCS and polymer-conjugated macromolecular drugs: advantages in cancer chemotherapy. *Adv. Drug Delivery Rev. 46*, 169–185.

(18) Katayama, Y., Fujii, K., Ito, E., Sakakihara, S., Sonoda, T., Murata, M., and Maeda, M. (2002) Intracellular signal-responsive artificial gene regulation for novel gene delivery. *Biomacromolecules 3*, 905–909.

(19) Murthy, N., Campbell, J., Fausto, N., and Hoffman, A. S. (2003) Bioinspired pH-responsive polymers for the intracellular delivery of biomolecular drugs. *Bioconjugate Chem. 14*, 412–419.

(20) You, J., Hu, F., Du, Y., and Yuan, H. (2007) Polymeric micelles with glycolipid-like structure and multiple hydrophobic domains for mediating molecular target delivery of paclitaxel. *Biomacromolecules 8*, 2450–2456.

(21) Jung, J., Lee, I. H., Park, J., and Jon, S. (2007) pH-sensitive polymer nanospheres for use as a potential drug delivery vehicle. *Biomacromolecules 8*, 3401–3407.

(22) Irie, M., and Kunwatchakun, D. (1986) Photoresponsive polymers. 8 Reversible photostimulated dilation of polyacrylamide gels having triphenylmethane leuco derivatives. *Macromolecules 19*, 2476–2480.

(23) Patnaik, S., Sharma, A. K., Garg, B. S., Gandhi, R. P., and Gupta, K. C. (2007) Photoregulation of drug release in azo-dextran nanogels. *Int. J. Pharm. 342*, 184–193.

(24) Vivero-Escoto, J. L., Slowing, I. I., Wu, C. W., and Lin, V. S. (2009) Photoinduced intracellular controlled release drug delivery in human cells by gold-capped mesoporous silica nanosphere. *J. Am. Chem. Soc. 131*, 3462–3463.

(25) Kono, K., Murakami, T., Yoshida, T., Haba, Y., Kanaoka, S., Takagishi, T., and Aoshima, S. (2005) Temperature sensitization of liposomes by use of thermosensitive block copolymers synthesized by living cationic polymerization: Effect of copolymer chain length. *Bioconjugate Chem. 16*, 1367–1374.

(26) Lo, C., Huang, C., Lin, K., and Hsiue, G. (2007) Mixed micelles formed from graft and diblock copolymers for application in intracellular drug delivery. *Biomaterials 28*, 1225–1235.

(27) Jeong, B., Bae, Y. H., and Kim, S. W. (1999) Thermoreversible gelation of PEG-PLGA-PEG triblock copolymer aqueous solutions. *Macromolecules 32*, 7064–7069.

(28) Dumitriu, S., Ed. (2002) *Polymeric Biomaterials*, 2nd ed, Marcel Dekker, New York.

(29) Domb, A. J., Kost, J., Wiseman, D. M. (1997) *Handbook of Biodegradable Polymers*, Harwood Academic, Amsterdam.

(30) Kumar, N., Ravikumar, M. N. V., and Domb, A. J. (2001) Biodegradable block copolymers. *Adv. Drug Delivery Rev. 53*, 23–44.

(31) Li, Y., and Kissel, T. (1998) Synthesis, characteristics and in vitro degradation of star-block copolymers consisting of L-lactide, glycolide and branched multi-arm poly(ethylene oxide). *Polymer 39*, 4421–4427.

(32) Liu, M., Kono, K., and Fréchet, M. J. (2000) Water-soluble dendritic unimolecular micelles: Their potential as drug delivery agents. *J. Controlled Release 65*, 121–131.

(33) Goodwin, A. P., Lam, S. S., and Fréchet, M. J. (2007) Rapid, efficient synthesis of heterobifunctional biodegradable dendrimers. *J. Am. Chem. Soc. 129*, 6994–6995.

(34) Ozalp, Y., Ozdemir, N., Kocagöz, S., and Hasirci, V. (2001) Controlled release of vancomycin from biodegradable microcapsules. *J. Microencapsul. 18*, 89–110.

(35) Zhang, Z., and Feng, S. S. (2006) The drug encapsulation efficiency, in vitro drug release, cellular uptake and cytotoxicity of paclitaxel-loaded poly(lactide)-tocopheryl polyethylene glycol succinate nanoparticles. *Biomaterials 27*, 4025–4033.

(36) Zhao, Q., and Li, B. (2008) pH-controlled drug loading and release from biodegradable microcapsules. *Nanomedicine 4*, 302–310.

(37) Stenekes, R. J. H., Loebis, A. E., Fernandes, C. M., Crommelin, D. J. A., and Hennink, W. E. (2001) Degradable dextran microspheres for the controlled release of liposomes. *Int. J. Pharm. 214*, 17–30.

(38) Yokoyama, M., Miyauchi, M., Yamada, N., Okano, T., Sakurai, Y., Kataoka, K., and Inoue, S. (1990) Characterization and anticancer activity of the micelle-forming polymeric anticancer drug adriamycin-conjugated poly(ethylene glycol)-poly(aspartic acid) block copolymer. *Cancer Res. 50*, 1963–1700.

(39) Hagan, S. A., Coombes, A. G. A., Garnett, M. C., Dunn, S. E., Davies, M. C., Illum, L. L., and Davis, S. S. (1996) Polylactide-poly(ethylene glycol) copolymers as drug delivery systems. 1. Characterization of water dispersible micelle-forming systems. *Langmuir 12*, 2153–2161.

(40) Allen, C., Yu, Y., Myasinger, D., and Eisenberg, A. (1998) Polycaprolactone-*b*−poly(ethylene oxide) block copolymer micelles as a novel drug delivery vehicle for neurotrophic agents FK506 and L-685, 818. *Bioconjugate Chem. 9*, 564–572.

(41) Bovey, F. A., and Kolthoff, I. M. (1948) Inhibition and retardation of vinyl polymerization. *Chem. Rev. 42*, 491–525.

(42) Mukundan, T., and Kishore, K. (1990) Synthesis, characterization and reactivity of polymeric peroxides. *Prog. Polym. Sci. 15*, 475–505.

(43) Matsumoto, A., Ishizu, Y., and Yokoi, K. (1998) Solid-state photopolymerization of octadecyl sorbate to yield an alternating copolymer with oxygen. *Macromol. Chem. Phys. 199*, 2511–2516.

(44) Matsumoto, A., and Higashi, H. (2000) Convenient synthesis of polymers containing labile bonds in the main chain by radical alternating copolymerization of alkyl sorbates with oxygen. *Macromolecules 33*, 1651–1655.

(45) Sugimoto, Y., Taketani, S., Kitamura, T., Uda, D., and Matsumoto, A. (2006) Regiospecific structure, degradation, and functionalization of polyperoxides prepared from sorbic acid derivatives with oxygen. *Macromolecules 39*, 9112–9119.

(46) Kitamura, T., and Matsumoto, A. (2007) Synthesis of poly(lactic acid) with branched and network structures containing thermally degradable junctions. *Macromolecules 40*, 509–517.

(47) Sato, E., Kitamura, T., and Matsumoto, A. (2008) In-situ collapse of phase-separated structure by covalent bond cleavage at a branching point upon heating. *Macromol. Rapid Commun. 29*, 1950–1953.

(48) Matsumoto, A., and Taketani, S. (2006) Regiospecific radical polymerization of a tetra-substituted ethylene monomer with molecular oxygen for the synthesis of a new degradable polymer. *J. Am. Chem. Soc. 128*, 4566–4567.

(49) Matsumoto, A., and Taketani, S. (2004) Fabrication and degradation of polyperoxides by a radical chain process under mild conditions. *Chem. Lett. 33*, 732–733.

(50) Taketani, S., and Matsumoto, A. (2006) Synthesis of degradable polymer exhibiting LCST-type phase separation by radical copolymerization of sorbic esters and molecular oxygen. *Chem. Lett. 35*, 104–105.

(51) Nanda, A. K., Ganesh, K., Kishore, K., and Surinaranyanan, M. (2000) End-group analysis of vinyl polyperoxides by MALDI-TOF-MS, FT-IR technique and thermochemical calculations. *Polymer 41*, 9063–9072.

(52) Schild, H. G. (1992) Poly(*N*-isopropylacrylamide): experiment, theory and application. *Prog. Polym. Sci. 17*, 163–249.

(53) Aoshima, S., and Kanaoka, S. (2008) Synthesis of stimuli-responsive polymers by living polymerization: Poly(*N*-isopropylacrylamide) and poly(vinyl ether)s. *Adv. Polym. Sci. 210*, 169–208.

(54) Kim, S. C., Kim, D. W., Shim, Y. H., Bang, J. S., Oh, H. S., Kim, S. W., and Seo, M. H. (2001) In vivo evaluation of polymeric micellar paclitaxel formulation: toxicity and efficacy. *J. Controlled Release 72*, 191–202.

(55) Akimura, H., Ohya, Y., and Ouchi, T. (2005) Formation of core-shell type biodegradable polymeric micelles from amphiphilic poly(aspartic acid)-*block*-polylactide diblock copolymer. *Biomacromolecules 6*, 720–725.

(56) Huhtala, A., Pohjonen, T., Saiminen, L., Saiminen, A., Kaarniranta, K., and Uusitalo, H. (2007) In vitro biocompatibility of degradable biopolymers in cell line cultures from various ocular tissues: Direct contact studies. *J. Biomed. Mater. Res. A 83A*, 407–413.

(57) Rejman, J., Bragonzi, A., and Conese, M. (2005) Role of clathrin- and caveolae-mediated endocytosis in gene transfer mediated by lipo- and polyplexes. *Mol. Ther. 12*, 468–474.

(58) Karinaga, R., Koumoto, K., Mizu, M., Anada, T., Shinkai, S., and Sakurai, K. (2005) PEG-appended $\beta-(1\rightarrow3)$-D-glucan schizophyllan to deliver antisense-oligonucleotides with avoiding lysosomal degradation. *Biomaterials 26*, 4866–4873.

(59) Taketani, S., and Matsumoto, A. (2004) Facile synthesis of a degradable gel by radical copolymerization of vinyl sorbate and molecular oxygen. *Macromol. Chem. Phys. 205*, 2451–2456.

(60) Matsumoto, A., Horie, A., and Otsu, T. (1991) Synthesis and thermal properties of poly(adamantyl sorbate). *Makromol. Chem., Rapid Commun. 12*, 681–685.

(61) Goldin, A., Venditti, J. M., and Geran, R. (1985) The effectiveness of the anthhracycline analog 4′-epidoxorubicin in the treatment of experimental-tumors: A review. *Invest. New Drugs 3*, 3–21.

BC9001618

PEGylated Dendritic Unimolecular Micelles as Versatile Carriers for Ligands of G Protein-Coupled Receptors

Yoonkyung Kim,[†,§] Béatrice Hechler,[‡] Zhan-Guo Gao,[†] Christian Gachet,[‡] and Kenneth A. Jacobson*[,†]

Molecular Recognition Section, Laboratory of Bioorganic Chemistry, National Institute of Diabetes and Digestive and Kidney Diseases, National Institutes of Health, Bethesda, Maryland 20892, and UMR 5949 INSERM, Université de Strasbourg, Etablissement Français du Sang-Alsace, Strasbourg, France. Received April 13, 2009; Revised Manuscript Received August 12, 2009

Despite its widespread application in nanomedicine, poly(ethylene glycol) (PEG) is seldom used for covalent modification of ligands for G protein-coupled receptors (GPCRs) due to potential steric complications. In order to study the influence of PEG chains on the biological activity of GPCR ligands bound to a common macromolecular carrier, we prepared a series of G3 polyamidoamine (PAMAM) dendrimers derivatized with Alexa Fluor 488, varying numbers of PEG_{550}/PEG_{750}/PEG_{2000}, and nucleoside moieties derived from the A_{2A} adenosine receptor (AR) agonist CGS21680 (2-[4-(2-carboxylethyl)phenylethylamino]-5′-*N*-ethylcarboxamidoadenosine). These dendrimer conjugates were purified by size exclusion chromatography and characterized by ^{1}H NMR and MALDI MS. In radioligand binding assays, some PAMAM-PEG conjugates showed enhanced subtype-selectivity at the human A_{2A} AR compared to monomeric ligands of comparable affinity. The functional potency was measured in the A_{2A} AR-mediated activation of adenylate cyclase and inhibition of ADP-induced platelet aggregation. Interestingly, the dendrimer conjugate **10c** bearing 11 PEG_{750} chains (out of theoretical 32 amino end groups) and 14 nucleoside moieties was 5-fold more potent in A_{2A} AR-mediated stimulation of cyclic AMP formation than **10d** with 4 PEG_{2000} chains and 21 nucleosides, although the binding affinities of these 2 compounds were similar. Thus, a relatively small (≤10 nm) multivalent ligand **10c** modified for water solubility maintained high potency and displayed increased A_{2A} AR binding selectivity over the monomeric nucleosides. The current study demonstrates the feasibility of using short PEG chains in the design of carriers that target ligand−receptor interactions.

INTRODUCTION

Nanocarriers such as polymeric/inorganic nanoparticles, liposomes, micelles, dendrimers, and nanotubes present a superior means to tackle various challenging issues in biomedical research, such as *in vivo* lability and insolubility of pharmaceutical substances (*1*). Despite the excellent functional improvements over small molecules as shown in numerous examples, the ultimate success of recruiting these unnatural nanostructures for therapy/diagnosis will depend on meeting the rigorous safety standards that apply to humans.

Dendritic scaffolds (*2*) offer a robust spatial control, particularly valuable when the imparted multivalency (*3*) can significantly enhance the desired effects. Previously, we employed polyamidoamine (PAMAM) dendrimers (*4*) to conjugate multiple copies of a nucleoside-based agonist CGS21680 (2-[4-(2-carboxylethyl)phenylethylamino]-5′-*N*-ethylcarboxamidoadenosine, **1**, Figure 1 (*5*)) of the A_{2A} adenosine receptor (AR) (*6*), a member of the G protein-coupled receptor (GPCR) family, in an effort to enhance the therapeutic potential through a multivalent effect (*3*). Generally, small-molecule agonists of GPCRs bind primarily at their heptahelical transmembrane domains (*7*), to trigger various intracellular signaling pathways. Diseases related to the actions of extracellular adenosine include cancer, arthritis, thrombosis, ischemia, and sleep disorders. Here, we report a simple PEGylation (*8*) strategy to improve the bioavailability (*9*) of dendritic carriers for GPCR ligands, which did not impose significant sterics and manifested potent biological activities in comparison to the monovalent species, using a third generation (G3) PAMAM dendrimer as an example.

* E-mail: kajacobs@helix.nih.gov.
† National Institutes of Health.
‡ UMR 5949 INSERM.
§ Current Address: BioNanotechnology Research Center, Korea Research Institute of Bioscience and Biotechnology, Daejeon, 305-806, Korea.

EXPERIMENTAL PROCEDURES

Materials and Methods. Glassware was oven-dried and cooled in a desiccator before use. All reactions were carried out under a dry nitrogen atmosphere at room temperature. Solvents were purchased as anhydrous grade and used without further purification. Suppliers of the commercial compounds are listed as follows: amine-terminated G3 PAMAM dendrimer with an ethylenediamine core, poly(ethylene glycol) methyl ether (PEG, M_n = 550, 750, and 2000), acetic anhydride (Ac_2O), and triethylamine were purchased from Aldrich; (benzotriazol-1-yloxy)tripyrrolidinophosphonium hexafluorophosphate (PyBOP) was purchased from NovaBiochem; CGS21680 (**1**) hydrochloride hemihydrate was purchased from Tocris; Alexa Fluor 488 (AF_{488}) 5-carboxylic acid 2,3,5,6-tetrafluorophenyl (TFP) ester (AF_{488}−OTFP) was purchased from Invitrogen; dimethyl sulfoxide (DMSO)-d_6 and D_2O were purchased from Cambridge Isotope Laboratories. 2-[4-(2-Aminoethylaminocarbonylethyl)phenylethylamino]-5′-*N*-ethylcarboxamidoadenosine (APEC, **2**) bistrifluoroacetic acid was provided by NIMH Chemical Synthesis and Drug Supply Program. Compound **3** (*11*) and PEGylated PAMAM dendrimer conjugates (**4a**, **4b**, **4c**, and **4d** (*17*)) were prepared as described before.

Preparative size exclusion chromatography (SEC) was performed on Bio-Beads S-X1 beads (BIO-RAD, molecular weight (MW) operating range 600−14 000 Da), 200−400 mesh, with DMF (Aldrich 99.8%, anhydrous) as an eluent at ambient pressure.

10.1021/bc9001689 CCC: $40.75 © 2009 American Chemical Society
Published on Web 09/28/2009

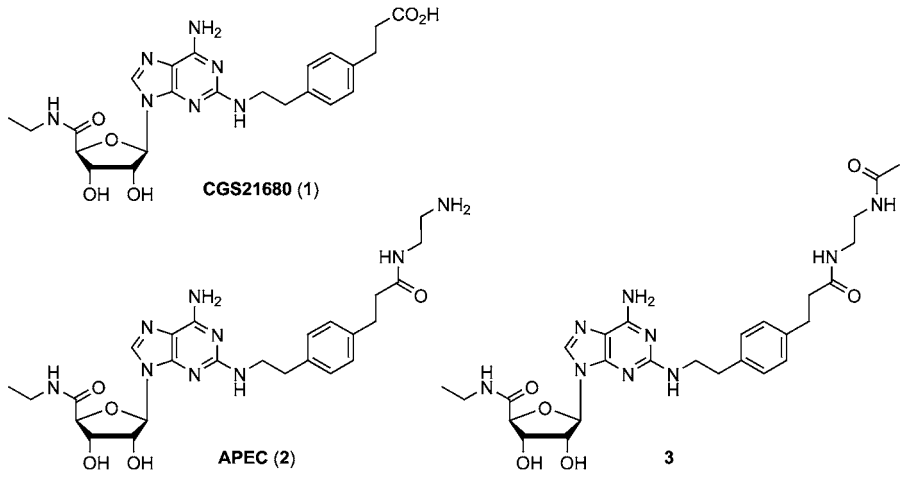

Figure 1. Structures of small molecule GPCR ligands (A_{2A} AR agonists) **1**−**3** used as monomeric controls.

Table 1. Structural Analysis of PAMAM Dendrimer Conjugates by ^{1}H NMR and MALDI MS

		NMR[b]						MALDI							
								DHB matrix				THAP matrix			
cmpd	PEG[a]	*m*	*n*	*x*	*y*[c]	*z*	MW[d]	M_n[e]	M_w[f]	PDI[g]	*z*[h]	M_n[e]	M_w[f]	PDI[g]	*z*[h]
7a	550	12.31	7.99	14.19	1	0	13021	10565	10974	1.04	0	n.d.[i]	n.d.[i]	n.d.[i]	0
7b	550	12.64	14.34	7.45	1	0	16758	13472	13922	1.03	0	13520	13930	1.03	0
7d	2000	43.89	4.61	19.32	1	0	17621	11844[j]	12809[j]	1.08[j]	0	11875[j]	12800[j]	1.08[j]	0
8c	750	15.40	11.81	0	1	0	16325	11620	12033	1.04	0	11238	11637	1.04	0
8d	2000	45.21	5.29	0	1	0	18470	n.d.[i]	n.d.[i]	n.d.[i]	0	9617[j]	10444[j]	1.09[j]	0
9a	550	12.34	8.17	14.28	1	1.20	13721	10800	11127	1.03	0.32	10911	11262	1.03	N/A
9b	550	12.48	15.00	7.57	1	2.00	18026	14702	15457	1.05	3.19	15331	15831	1.03	3.95
9d	2000	43.25	4.74	19.30	1	1.14	18294	12843[j]	13329[j]	1.04[j]	1.08	n.d.[i]	n.d.[i]	n.d.[i]	N/A
10c	750	15.75	11.32	0	1	14.05	22904	18575	19180	1.03	14.84	18848	19561	1.04	16.46
10d	2000	41.16	5.60	0	1	20.51	27982	21607	22824	1.06	N/A	22493	23518	1.05	27.15

[a] M_n of the commercial PEG monomethyl ether (Aldrich) originally used to prepare compound **4**. [b] Based on ^{1}H NMR integration determined in DMSO-d_6. *m* = number of PEG repeat unit, *n* = number of PEG, *x* = number of acetamide, *y* = number of AF_{488}, *z* = number of CGS21680 (see Scheme 1). [c] Based on the stoichiometry of addition. [d] Dendrimer conjugates were assumed to be made from the commercial PAMAM dendrimer with 32 peripheral amino groups and no structural defects. Counterions of sulfonate for AF_{488} were assumed to be triethylammonium groups. [e] Number-average molar mass. [f] Weight-average molar mass. [g] Polydispersity index. [h] Based on MALDI MS results. No matrix adduct was considered for the estimation. ΔM_w between **9**/**10** and its precursor **7**/**8** was divided by the MW increase upon the covalent attachment of a CGS21680 ligand (481.5 Da) to the PAMAM amino group. Purification by SEC was assumed not to affect the MW distribution. [i] n.d. = not determined. [j] Mass range selected for the average MW calculations contained a part of the peak region corresponding to the half-size of each desired compound.

NMR spectra were recorded on a Bruker DRX-600 spectrometer at 25.0 °C under an optimized parameter setting for each sample, unless otherwise mentioned. ^{1}H NMR chemical shifts were measured relative to the residual solvent peak at 2.50 ppm in DMSO-d_6 and at 4.80 ppm in D_2O. Complete NMR peak assignments were made possible with 2D COSY and NOESY experiments. Each PAMAM dendrimer conjugate was not unimolecular, and thus, the characterization by NMR represented the average value from its polymeric distribution. The integration values were reported only for the peaks clearly resolved (i.e., with a relatively good baseline-separation) in the ^{1}H NMR spectra and in two decimal places. Assignments of peaks for the PEGylated PAMAM dendrimer conjugates were based on the labeling method shown in Supporting Information Figure S2. A methylene peak of the G3 PAMAM dendrimer at 2.18 ppm in DMSO-d_6 ("c"; see Supporting Information Figure S2) was used as an internal standard (set at 120 H) for the integration, assuming 32 peripheral groups without any defects in the structure. Detailed methods used for the structural analysis of dendrimers by NMR in DMSO-d_6 were described before (as Supporting Information *10, 17*). The stoichiometry and the average MWs of the PAMAM dendrimer conjugates determined as such are summarized in Table 1 and Supporting Information Figures S1 and S2.

MALDI-TOF MS experiments were performed on an Applied Biosystems Voyager-DE STR spectrometer at the Mass Spectrometry Laboratory, University of Illinois. 2,5-Dihydroxybenzoic acid (DHB) or 2,4,6-trihydroxyacetophenone (THAP) was used as the matrix for the MALDI samples. Average MWs determined by MALDI are listed in Table 1 and the spectra are shown in Supporting Information Figures S7 and S8.

General Procedure for Acetylation of G3 PAMAM-PEG Dendrimer Conjugates. PEGylated G3 PAMAM dendrimer **4a**, **4b**, or **4d** was dried *in vacuo* extensively and then was dissolved in DMSO-d_6. To this stirred dendrimer solution was added triethylamine, followed by a 0.317 M solution of Ac_2O in DMSO-d_6 (30.0 μL/1.00 mL, total volume). The final concentration of the dendrimer solution was ca. 0.5−1.1 mM. The reaction was stirred at room temperature for 21 h, then purified by SEC in DMF, and dried *in vacuo* to give dendrimer **5** as a colorless glassy solid.

Acetylated PAMAM-PEG Dendrimer 5a. PAMAM-PEG dendrimer **4a** (*17*) (12.1 mg, 1.10 μmol) in DMSO-d_6 (944 μL) was treated with triethylamine (8.10 μL, 58.1 μmol) and 0.317 M Ac_2O solution in DMSO-d_6 (48.5 μL, 15.4 μmol). The crude mixture was loaded on a SEC column (H 47 cm × O.D. 4.5 cm) to isolate the dendrimer conjugate **5a** (9.28 mg). ^{1}H NMR (600 MHz, DMSO-d_6) δ 8.06−7.82 (m, NH_{G3}, NH_{Ac}, NH_{G2}, NH_{G1}, and NH_{G0}), 7.23 (br s, 7.44H, NH_{PEG} of major isomer), 6.81 (br s, 0.61H, NH_{PEG} of minor isomer), 4.03 (t, 16.25H, J = 4.2 Hz, H_{hPEG}), 3.62−3.38 (m, 389.27H, satellites J = 69.0 Hz, H_i, H_j, and H_k), 3.23 (s, 30.11H, H_l), 3.12−2.99 (m, H_d,

Scheme 1. Synthetic Route to PAMAM-PEG-CGS21680 Dendrimer Conjugates

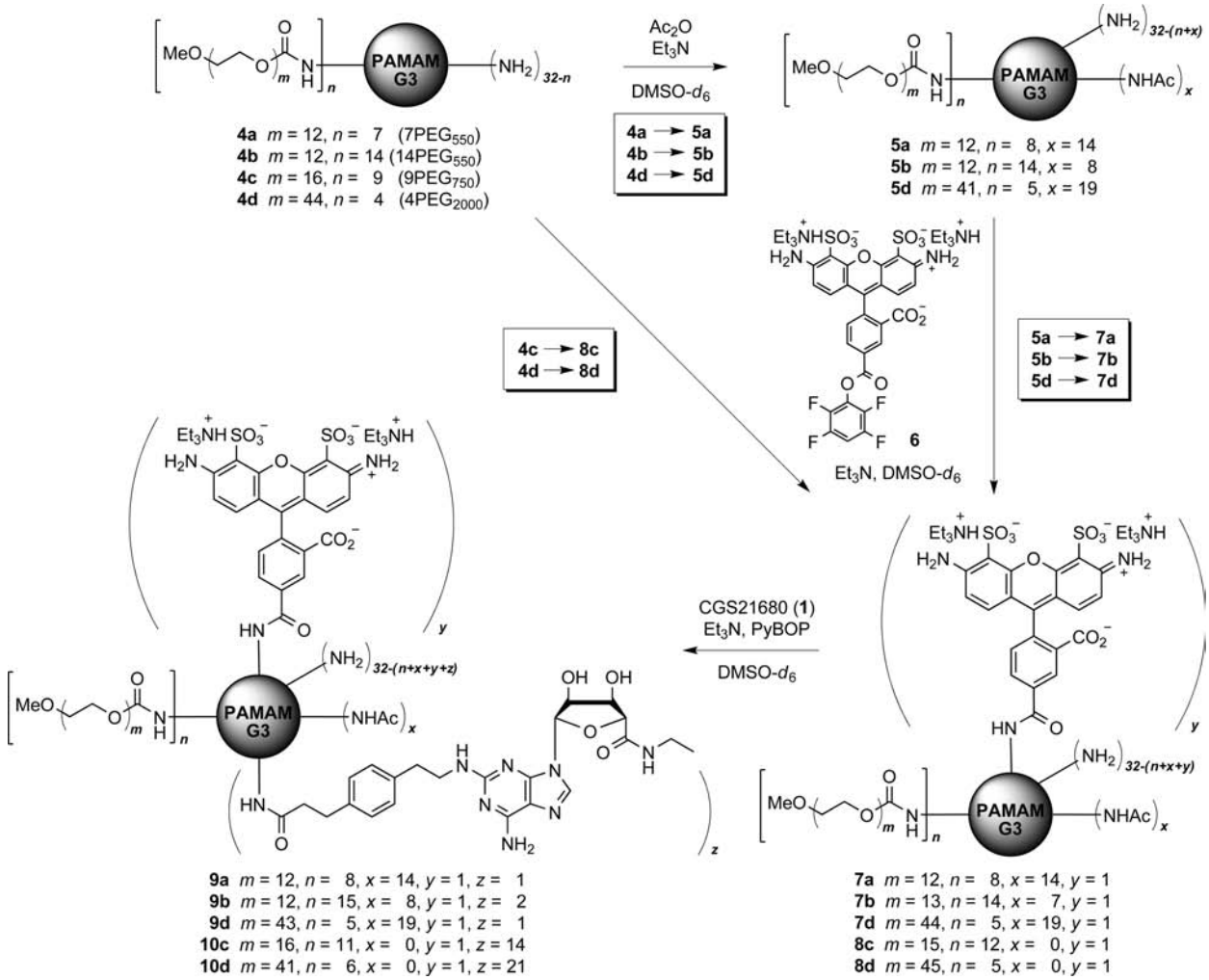

H_f, H_{fAc}, H_{gAc}, H_{fPEG}, and H_{gPEG}), 2.64 (m, 118.64H, H_b and H_g), 2.42 (m, 60.10H, H_e and H_a), 2.18 (m, 120.00H, H_c), 1.79 (s, 41.73H, H_{hAc}).

Acetylated PAMAM-PEG Dendrimer 5b. PAMAM-PEG dendrimer **4b** (*17*) (11.3 mg, 0.746 μmol) in DMSO-d_6 (1.28 mL) was treated with triethylamine (3.30 μL, 23.7 μmol) and 0.317 M Ac_2O solution in DMSO-d_6 (16.5 μL, 5.24 μmol). The crude mixture was loaded on a SEC column (H 40 cm × O.D. 3.0 cm) to isolate the dendrimer conjugate **5b** (11.44 mg). ^{1}H NMR (600 MHz, DMSO-d_6) δ 8.04−7.81 (m, NH_{G3}, NH_{Ac}, NH_{G2}, NH_{G1}, and NH_{G0}), 7.23 (br s, 12.70H, NH_{PEG} of major isomer), 6.81 (br s, 1.14H, NH_{PEG} of minor isomer), 4.03 (t, 27.47H, J = 4.1 Hz, H_{hPEG}), 3.62−3.38 (m, 659.19H, satellites J = 70.7 Hz, H_i, H_j, and H_k), 3.23 (s, 47.25H, H_l), 3.12−2.99 (m, H_d, H_f, H_{fAc}, H_{gAc}, H_{fPEG}, and H_{gPEG}), 2.64 (m, 117.00H, H_b and H_g), 2.42 (m, 57.69H, H_e and H_a), 2.18 (m, 120.00H, H_c), 1.79 (s, 21.64H, H_{hAc}).

Acetylated PAMAM-PEG Dendrimer 5d. PAMAM-PEG dendrimer **4d** (*17*) (13.3 mg, 0.895 μmol) in DMSO-d_6 (944 μL) was treated with triethylamine (7.70 μL, 55.2 μmol) and 0.317 M Ac_2O solution in DMSO-d_6 (48.0 μL, 15.2 μmol). The crude mixture was loaded on a SEC column (H 45 cm × O.D. 4.5 cm) to isolate the dendrimer conjugate **5d** (13.28 mg). ^{1}H NMR (600 MHz, DMSO-d_6) δ 8.07−7.83 (m, NH_{G3}, NH_{Ac}, NH_{G2}, NH_{G1}, and NH_{G0}), 7.24 (br s, 4.45H, NH_{PEG} of major isomer), 6.82 (br s, 0.43H, NH_{PEG} of minor isomer), 4.03 (t, 9.77H, J = 4.1 Hz, H_{hPEG}), 3.62−3.38 (m, 795.81H, satellites J = 70.7 Hz, H_i, H_j, and H_k), 3.23 (s, 17.88H, H_l), 3.12−2.99 (m, H_d, H_f, H_{fAc}, H_{gAc}, H_{fPEG}, and H_{gPEG}), 2.64 (m, 114.51H, H_b and H_g), 2.42 (m, 58.04H, H_e and H_a), 2.18 (m, 120.00H, H_c), 1.79 (s, 57.24H, H_{hAc}).

General Procedure for Conjugation of AF_{488}. PEGylated G3 PAMAM dendrimer **5a**, **5b**, **5d**, **4c**, or **4d** was dried *in vacuo* extensively, and then was dissolved in DMSO-d_6. To this stirred dendrimer solution was added triethylamine, followed by a freshly prepared 11.3 mM solution of AF_{488}−OTFP in DMSO-d_6 (1.00 mg/100 μL). The final concentration of the dendrimer solution was ca. 0.4−1.0 mM. The reaction was stirred for 22 h protected from light, and then a portion of crude product **7**/**8** was transferred into another flask for the next step without any purification. The remaining reaction mixture was subjected to purification by SEC in DMF, and the column fractions corresponding to the first major fluorescent band were combined and dried *in vacuo* to give dendrimer **7**/**8** as a colored glassy solid.

PAMAM-PEG-AF_{488} Dendrimer 7a. PAMAM-PEG dendrimer **5a** (9.77 mg, 0.804 μmol) in DMSO-d_6 (1.53 mL) was treated with triethylamine (1.50 μL, 10.8 μmol) and 11.3 mM AF_{488}−OTFP solution in DMSO-d_6 (71.0 μL, 0.802 μmol). 1.10 mL of the crude reaction mixture was taken for the next step and the remainder was purified by SEC (H 23 cm × O.D. 2.5 cm) to isolate the dendrimer conjugate **7a** (3.78 mg). The color of a 1.0 mM solution of **7a** in water (HPLC grade, Aldrich) prepared for the biological assay was light yellow. ^{1}H NMR (600 MHz, DMSO-d_6) δ 8.04−7.81 (m, 76.71H, NH_{G3}, NH_{Ac}, NH_{G2}, NH_{G1}, and NH_{G0}), 7.21 (br s, 8.38H, NH_{PEG} of major isomer), 6.79 (br s, 0.85H, NH_{PEG} of minor isomer), 4.03 (t, 15.98H, J = 4.2 Hz, H_{hPEG}), 3.62−3.38 (m, 377.45H, satellites J = 70.0 Hz, H_i, H_j, and H_k), 3.23 (s, 30.54H, H_l), 3.13−2.99

(m, 182.37H, H_d, H_f, H_{fAc}, H_{gAc}, H_{fPEG}, and H_{gPEG}), 2.64 (m, 118.15H, H_b and H_g), 2.42 (m, 57.66H, H_e and H_a), 2.18 (m, 120.00H, H_c), 1.79 (s, 42.58H, H_{hAc}).

PAMAM-PEG-AF$_{488}$ Dendrimer 7b. PAMAM-PEG dendrimer **5b** (11.2 mg, 0.702 μmol) in DMSO-d_6 (1.44 mL) was treated with triethylamine (1.10 μL, 7.89 μmol) and 11.3 mM AF_{488}−OTFP solution in DMSO-d_6 (62.0 μL, 0.701 μmol). 1.00 mL of the crude reaction mixture was taken for the next step, and the remainder was purified by SEC (H 38 cm × O.D. 3.0 cm) to isolate the dendrimer conjugate **7b** (4.29 mg). The color of a 1.0 mM solution of **7b** in water (HPLC grade, Aldrich) prepared for the biological assay was yellowish orange. ^{1}H NMR (600 MHz, DMSO-d_6) δ 8.42 (br s, 0.37H, H_F), 8.22 (br s, 0.65H, H_E), 8.04−7.79 (m, 69.52H, NH_{G3}, NH_{Ac}, NH_{G2}, NH_{G1}, and NH_{G0}), 7.30 (br s, 0.68H, H_D), 7.20 (br s, 14.83H, NH_{PEG} of major isomer), 6.79 (br s, 1.32H, NH_{PEG} of minor isomer), 6.45 (br s, 0.64H, H_B/H_C), 6.35 (br s, 0.55H, H_B/H_C), 4.03 (t, 28.68H, J = 4.2 Hz, H_{hPEG}), 3.62−3.38 (m, 696.24H, satellites J = 70.2 Hz, H_i, H_j, and H_k), 3.23 (s, 48.74H, H_l), 3.11−2.99 (m, 188.79H, H_d, H_f, H_{fAc}, H_{gAc}, H_{fPEG}, and H_{gPEG}), 2.64 (m, 120.55H, H_b and H_g), 2.42 (m, 56.57H, H_e and H_a), 2.18 (m, 120.00H, H_c), 1.79 (s, 22.34H, H_{hAc}).

PAMAM-PEG-AF$_{488}$ Dendrimer 7d. PAMAM-PEG dendrimer **5d** (12.9 mg, 0.788 μmol) in DMSO-d_6 (1.63 mL) was treated with triethylamine (1.20 μL, 8.61 μmol) and 11.3 mM AF_{488}−OTFP solution in DMSO-d_6 (70.0 μL, 0.791 μmol). 1.16 mL of the crude reaction mixture was taken for the next step and the remainder was purified by SEC (H 38 cm × O.D. 3.0 cm) to isolate the dendrimer conjugate **7d** (4.52 mg). The color of a 1.0 mM solution of **7d** in water (HPLC grade, Aldrich) prepared for the biological assay was light yellow. ^{1}H NMR (600 MHz, DMSO-d_6) δ 8.05−7.82 (m, 83.64H, NH_{G3}, NH_{Ac}, NH_{G2}, NH_{G1}, and NH_{G0}), 7.22 (br s, 5.69H, NH_{PEG} of major isomer), 6.80 (br s, 0.68H, NH_{PEG} of minor isomer), 4.03 (t, 9.22H, J = 4.2 Hz, H_{hPEG}), 3.62−3.38 (m, 800.08H, satellites J = 70.9 Hz, H_i, H_j, and H_k), 3.24 (s, 21.04H, H_l), 3.12−2.99 (m, 198.41H, H_d, H_f, H_{fAc}, H_{gAc}, H_{fPEG}, and H_{gPEG}), 2.64 (m, 120.33H, H_b and H_g), 2.42 (m, 59.43H, H_e and H_a), 2.18 (m, 120.00H, H_c), 1.79 (s, 57.95H, H_{hAc}).

PAMAM-PEG-AF$_{488}$ Dendrimer 8c. PAMAM-PEG dendrimer **4c** (*17*) (12.2 mg, 0.888 μmol) in DMSO-d_6 (809 μL) was treated with triethylamine (2.85 μL, 20.5 μmol) and 11.3 mM AF_{488}−OTFP solution in DMSO-d_6 (78.7 μL, 0.889 μmol). 592 μL of the crude reaction mixture was taken for the next step and the remainder was purified by SEC (H 38 cm × O.D. 3.0 cm) to isolate the dendrimer conjugate **8c** (3.37 mg). The color of a ca. 0.5 mM solution (not fully homogeneous) of **8c** in water (HPLC grade, Aldrich) prepared for the biological assay was yellowish orange. ^{1}H NMR (600 MHz, DMSO-d_6) δ 8.17−7.80 (m, 71.97H, NH_{G3}, NH_{G2}, NH_{G1}, and NH_{G0}), 7.21 (br s, 11.31H, NH_{PEG} of major isomer), 6.79 (br s, 1.68H, NH_{PEG} of minor isomer), 4.03 (t, 23.61H, J = 4.1 Hz, H_{hPEG}), 3.62−3.38 (m, 703.42H, satellites J = 70.4 Hz, H_i, H_j, and H_k), 3.23 (s, 44.08H, H_l), 3.11−2.99 (m, 182.07H, H_d, H_f, H_{fPEG}, and H_{gPEG}), 2.64 (m, 136.23H, H_b and H_g), 2.42 (m, 58.27H, H_e and H_a), 2.18 (m, 120.00H, H_c).

PAMAM-PEG-AF$_{488}$ Dendrimer 8d. PAMAM-PEG dendrimer **4d** (*17*) (7.63 mg, 0.512 μmol) in DMSO-d_6 (1.15 mL) was treated with triethylamine (2.30 μL, 16.5 μmol) and 11.3 mM AF_{488}−OTFP solution in DMSO-d_6 (46.0 μL, 0.520 μmol). 850 μL of the crude reaction mixture was taken for the next step, and the remainder was purified by SEC (H 23 cm × O.D. 2.5 cm) to isolate the dendrimer conjugate **8d** (3.44 mg). The color of a ca. 0.5 mM solution (not fully homogeneous) of **8d** in water (HPLC grade, Aldrich) prepared for the biological assay was yellowish orange. ^{1}H NMR (600 MHz, DMSO-d_6) δ 8.13−7.80 (m, 69.31H, NH_{G3}, NH_{G2}, NH_{G1}, and NH_{G0}), 7.23 (br s, 7.21H, NH_{PEG} of major isomer), 4.03 (t, 10.57H, J = 4.1 Hz, H_{hPEG}), 3.62−3.38 (m, 945.12H, satellites J = 71.1 Hz, H_i, H_j, and H_k), 3.24 (s, H_l), 3.12−2.99 (m, 161.83H, H_d, H_f, H_{fPEG}, and H_{gPEG}), 2.64 (m, 132.91H, H_b and H_g), 2.42 (m, 56.76H, H_e and H_a), 2.19 (m, 120.00H, H_c).

PAMAM-PEG$_{550}$-Ac-AF$_{488}$−CGS21680 Dendrimer 9a. To a crude reaction mixture of fluorescent dendrimer **7a** in DMSO-d_6 (1.10 mL), was added triethylamine (3.50 μL, 25.1 μmol) and CGS21680 (**1**, as a hydrochloride hemihydrate form, 4.95 mg, 9.08 μmol). Subsequently, a freshly prepared 42.2 mM solution of PyBOP in DMSO-d_6 (180 μL, 7.60 μmol) was added slowly to the stirred mixture of **7a**. The reaction was stirred for 20 h, and the reaction mixture was loaded directly on a SEC column (H 43 cm × O.D. 4.5 cm) in DMF for purification, and the fractions containing the desired product were identified by ^{1}H NMR. The first and last SEC fractions that were confirmed by NMR to contain minor amounts of the desired dendrimer were eliminated deliberately to reduce the polydispersity of the dendrimer conjugates. The SEC fractions selected as such were combined and dried *in vacuo* to give 5.55 mg of **9a′** (structure not shown). Unfortunately, the analysis of **9a′** by ^{1}H NMR in DMSO-d_6 indicated only ca. 0.38 CGS21680 groups were attached out of ca. nine available PAMAM amino groups. In an attempt to bring the CGS21680 attachment to completion, dendrimer **9a′**, the isolated derivative of **7a**, underwent another round of conjugation reaction, but this time under an exhaustive coupling condition. In a separate flask, CGS21680 (**1**, as a hydrochloride hemihydrate form, 23.3 mg, 42.8 μmol) in DMSO-d_6 (978 μL) was treated with triethylamine (21.8 μL, 156 μmol) and PyBOP (20.3 mg, 39.1 μmol) [Solution A], and stirred for 15 min. Subsequently, dendrimer **9a′** (5.55 mg) in DMSO-d_6 (190 μL) was treated with 220 μL (8.59 μmol) of Solution A, and the reaction mixture was stirred for 72 h protected from light. Another batch of preactivated ester of CGS21680 (**1**, as a hydrochloride hemihydrate form, 19.6 mg, 36.0 μmol) was freshly prepared in DMSO-d_6 (985 μL) by treating with triethylamine (14.8 μL, 106 μmol) and PyBOP (17.4 mg, 33.5 μmol) [Solution B], which was stirred for 12 min. The dendrimer mixture was treated with 120 μL (4.02 μmol) of Solution B and stirring continued for 39 h. The crude mixture was loaded on a SEC column (H 38 cm × O.D. 3.0 cm) for purification in DMF, and the fractions containing the desired compound were determined similarly by ^{1}H NMR. The selected SEC fractions were combined and dried *in vacuo* to give dendrimer **9a** (6.20 mg) as a glassy solid. The color of a 1.0 mM solution of **9a** in water (HPLC grade, Aldrich) prepared for the biological assay was light yellow. ^{1}H NMR (600 MHz, DMSO-d_6) δ 8.04−7.80 (m, 80.15H, H_8, H_{8Ad} NH_{G3}, NH_{Ac}, NH_{CGS}, NH_{G2}, NH_{G1}, and NH_{G0}), 7.22 (br s, 8.54H, NH_{PEG} of major isomer), 7.15, 7.10 (d (each), 5.42H, H_4 and H_5), 6.79 (br s, 2.75H, H_{6Ad}, NH_{PEG} of minor isomer), 6.19 (s, 0.91H, H_1), 5.84 (d, 0.86H, J = 6.5 Hz, $H_{1'}$), 5.63, 5.56 (br s (each), 1.70H, $H_{3'\text{-}OH}$ and $H_{2'\text{-}OH}$), 4.72 (m, 0.86H, $H_{2'}$), 4.25 (s, $H_{4'}$), 4.19 (s, 1.03H, $H_{3'}$), 4.03 (t, 16.34H, J = 4.4 Hz, H_{hPEG}), 3.62−3.38 (m, 388.25H, satellites J = 70.1 Hz, H_i, H_j, and H_k, one of H_2), 3.23 (s, 30.93H, H_l), 3.13−2.99 (m, 190.69H, H_d, H_f, H_{fAc}, H_{gAc}, H_{fCGS}, H_{gCGS}, H_{fPEG}, H_{gPEG}, and H_9), 2.76 (m, H_3 and H_6), 2.64 (m, 110.80H, H_b and H_g), 2.42 (m, 58.01H, H_e and H_a), 2.34 (t, H_7), 2.18 (m, 120.00H, H_c), 1.79 (s, 42.84H, H_{hAc}), 0.97 (t, 3.60H, J = 7.1 Hz, H_{10}).

PAMAM-PEG$_{550}$-Ac-AF$_{488}$−CGS21680 Dendrimer 9b. The conjugation reaction was performed following a procedure similar to that described for **9a**. To a crude reaction mixture of fluorescent dendrimer **7b** in DMSO-d_6 (1.00 mL), was added triethylamine (2.50 μL, 17.9 μmol) and CGS21680 (**1**, as a hydrochloride hemihydrate form, 3.50 mg, 6.42 μmol). Subsequently, a freshly prepared 42.2 mM solution of PyBOP in

DMSO-d_6 (129 μL, 5.45 μmol) was added slowly to the stirred mixture of **7b**. The reaction was stirred for 20 h, and then the reaction mixture was loaded directly on a SEC column (H 38 cm × O.D. 3.0 cm) in DMF and purified to give 8.82 mg of **9b′** (structure not shown). Unfortunately, the analysis of **9b′** by ^{1}H NMR in DMSO-d_6 indicated only ca. 1.24 CGS21680 groups were attached out of ca. nine available PAMAM amino groups. Next, dendrimer **9b′** (8.82 mg) in DMSO-d_6 (148 μL) was treated with 170 μL (6.64 μmol) of Solution A (*vide supra*, stirred for 12 min), and the reaction mixture was stirred for 72 h protected from light. Then, the dendrimer mixture was treated with 100 μL (3.35 μmol) of Solution B (*vide supra*, stirred for 11 min), and stirring continued for 39 h. The crude mixture was loaded on a SEC column (H 43 cm × O.D. 4.5 cm) for purification in DMF, and the fractions containing the desired compound were determined similarly by ^{1}H NMR. The selected SEC fractions were combined and dried *in vacuo* to give dendrimer **9b** (7.87 mg) as a glassy solid. The color of a 1.0 mM solution of **9b** in water (HPLC grade, Aldrich) prepared for the biological assay was orange. ^{1}H NMR (600 MHz, DMSO-d_6) δ 8.86 (br s, 0.45H, NH_{AF}), 8.43 (br s, 0.98H, H_F), 8.21 (br s, H_E), 8.04−7.80 (m, 74.60H, H_8, H_{8Ad} NH_{G3}, NH_{Ac}, NH_{CGS}, NH_{G2}, NH_{G1}, and NH_{G0}), 7.30 (br s, 0.72H, H_D), 7.21 (br s, 14.06H, NH_{PEG} of major isomer), 7.14, 7.10 (d (each), 10.14H, H_4 and H_5), 6.79 (br s, 5.23H, H_{6Ad}, NH_{PEG} of minor isomer), 6.45 (br s, 0.69H, H_B/H_C), 6.35 (br s, 0.66H, H_B/H_C), 6.19 (s, 1.73H, H_1), 5.84 (d, 1.72H, J = 5.9 Hz, $H_{1'}$), 5.63, 5.56 (br s (each), 2.57H, $H_{3'\text{-}OH}$ and $H_{2'\text{-}OH}$), 4.71 (m, 1.62H, $H_{2'}$), 4.26 (s, 2.29H, $H_{4'}$), 4.19 (s, 1.97H, $H_{3'}$), 4.03 (br s, 29.99H, H_{hPEG}), 3.62−3.38 (m, 720.52H, satellites J = 70.6 Hz, H_i, H_j, and H_k, one of H_2), 3.23 (s, 51.65H, H_l), 3.19−2.99 (m, 189.36H, H_d, H_f, H_{fAc}, H_{gAc}, H_{fCGS}, H_{gCGS}, H_{fPEG}, H_{gPEG}, and H_9), 2.76 (m, 18.44H, H_3 and H_6), 2.64 (m, 111.40H, H_b and H_g), 2.42 (m, 54.30H, H_e and H_a), 2.34 (t, 8.37H, H_7), 2.18 (m, 120.00H, H_c), 1.79 (s, 22.70H, H_{hAc}), 0.97 (t, 6.01H, J = 6.9 Hz, H_{10}).

PAMAM-PEG$_{2000}$-Ac-AF$_{488}$−CGS21680 Dendrimer 9d. The conjugation reaction was performed following a procedure similar to that described for **9a**. To a crude reaction mixture of fluorescent dendrimer **7d** in DMSO-d_6 (1.16 mL), was added triethylamine (2.70 μL, 19.4 μmol) and CGS21680 (**1**, as a hydrochloride hemihydrate form, 3.83 mg, 7.03 μmol). Subsequently, a freshly prepared 42.2 mM solution of PyBOP in DMSO-d_6 (138 μL, 5.81 μmol) was added slowly to the stirred mixture of **7d**. The reaction was stirred for 20 h, and then the reaction mixture was loaded directly on a SEC column (H 41 cm × O.D. 4.5 cm) in DMF and purified to give 8.81 mg of **9d′** (structure not shown). Unfortunately, the analysis of **9d′** by ^{1}H NMR in DMSO-d_6 indicated only ca. 0.65 CGS21680 groups were attached out of ca. seven available PAMAM amino groups. Next, dendrimer **9d′** (8.81 mg) in DMSO-d_6 (300 μL) was treated with 180 μL (7.03 μmol) of Solution A (*vide supra*, stirred for 8 min), and the reaction mixture was stirred for 72 h protected from light. Then, the dendrimer mixture was treated with 100 μL (3.35 μmol) of Solution B (*vide supra*, stirred for 10 min) and stirring continued for 39 h. The crude mixture was loaded on a SEC column (H 38 cm × O.D. 4.5 cm) for purification in DMF, and the fractions containing the desired compound were determined similarly by ^{1}H NMR. The selected SEC fractions were combined and dried *in vacuo* to give dendrimer **9d** (8.82 mg) as a glassy solid. The color of a 1.0 mM solution of **9d** in water (HPLC grade, Aldrich) prepared for the biological assay was light orange. ^{1}H NMR (600 MHz, DMSO-d_6) δ 8.87 (br s, NH_{AF}), 8.43 (br s, H_F), 8.05−7.81 (m, 83.00H, H_8, H_{8Ad} NH_{G3}, NH_{Ac}, NH_{CGS}, NH_{G2}, NH_{G1}, and NH_{G0}), 7.22 (br s, 4.43H, NH_{PEG} of major isomer), 7.14, 7.10 (d (each), 5.22H, H_4 and H_5), 6.80 (br s, 1.95H, H_{6Ad}, NH_{PEG} of minor isomer), 6.47 (br s, H_B/H_C), 6.36 (br s, H_B/H_C), 6.19 (s, 0.67H, H_1), 5.84 (d, 0.68H, J = 6.7 Hz, $H_{1'}$), 5.65, 5.58 (br s (each), 0.61H, $H_{3'\text{-}OH}$ and $H_{2'\text{-}OH}$), 4.72 (m, 0.78H, $H_{2'}$), 4.26 (s, 1.71H, $H_{4'}$), 4.19 (s, 0.90H, $H_{3'}$), 4.03 (t, 9.47H, J = 4.0 Hz, H_{hPEG}), 3.62−3.39 (m, 810.85H, satellites J = 70.7 Hz, H_i, H_j, and H_k, one of H_2), 3.24 (s, 20.59H, H_l), 3.14−2.99 (m, 190.63H, H_d, H_f, H_{fAc}, H_{gAc}, H_{fCGS}, H_{gCGS}, H_{fPEG}, H_{gPEG}, and H_9), 2.76 (m, H_3 and H_6), 2.64 (m, 115.71H, H_b and H_g), 2.42 (m, 55.85H, H_e and H_a), 2.34 (t, H_7), 2.18 (m, 120.00H, H_c), 1.79 (s, 57.89H, H_{hAc}), 0.97 (t, 3.42H, J = 7.0 Hz, H_{10}).

PAMAM-PEG$_{750}$-AF$_{488}$−CGS21680 Dendrimer 10c. CGS21680 (**1**, as a hydrochloride hemihydrate form, 14.7 mg, 27.0 μmol) in DMSO-d_6 (242 μL) was treated with triethylamine (10.4 μL, 74.6 μmol) and PyBOP (12.9 mg, 24.9 μmol) [Solution C] and stirred for 8 min. Subsequently, in a separate flask, a crude reaction mixture of fluorescent dendrimer **8c** in DMSO-d_6 (592 μL) was treated with 150 μL (14.8 μmol) of Solution C, and the reaction mixture was stirred for 50 h protected from light. Then, the dendrimer mixture was treated with 220 μL (7.37 μmol) of Solution B (*vide supra*, stirred for 7 min) and stirring continued for 14 h. The crude mixture was loaded on a SEC column (H 38 cm × O.D. 4.5 cm) for purification in DMF, and the fractions containing the desired compound were determined similarly by ^{1}H NMR. The selected SEC fractions were combined and dried *in vacuo* to give dendrimer **10c** (9.98 mg) as a glassy solid. The color of a 1.0 mM solution of **10c** in water (HPLC grade, Aldrich) prepared for the biological assay was intense orange. ^{1}H NMR (600 MHz, DMSO-d_6) δ 8.85 (br s, NH_{AF}), 8.44 (br s, H_F), 8.05, 8.02 (s (each), 36.49H, H_8 and H_{8Ad}), 7.93, 7.89 (br s, 47.73H, NH_{G3}, NH_{CGS}), 7.80 (br s, 25.82H, NH_{G2}, NH_{G1}, and NH_{G0}), 7.20 (br s, 12.52H, NH_{PEG} of major isomer), 7.13, 7.09 (d (each), 60.79H, H_4 and H_5), 6.80 (br s, 25.16H, H_{6Ad}, NH_{PEG} of minor isomer), 6.19 (s, 12.19H, H_1), 5.85 (d, 13.94H, J = 6.1 Hz, $H_{1'}$), 5.62, 5.56 (br s (each), 21.91H, $H_{3'\text{-}OH}$ and $H_{2'\text{-}OH}$), 4.72 (m, 13.13H, $H_{2'}$), 4.26 (s, 14.50H, $H_{4'}$), 4.19 (s, 13.88H, $H_{3'}$), 4.03 (br s, 22.64H, H_{hPEG}), 3.61−3.38 (m, 704.59H, satellites J = 67.0 Hz, H_i, H_j, and H_k, one of H_2), 3.23 (s, 63.37H, H_l), 3.17−2.99 (m, 209.06H, H_d, H_f, H_{fCGS}, H_{gCGS}, H_{fPEG}, H_{gPEG}, and H_9), 2.76 (m, 76.79H, H_3 and H_6), 2.64 (m, 115.47H, H_b and H_g), 2.42 (m, 54.39H, H_e and H_a), 2.33 (t, 39.56H, J = 7.3 Hz, H_7), 2.18 (m, 120.00H, H_c), 0.96 (br s, 42.16H, H_{10}).

PAMAM-PEG$_{2000}$-AF$_{488}$−CGS21680 Dendrimer 10d. The conjugation reaction was performed following a procedure similar to that described for **9a**. To a crude reaction mixture of fluorescent dendrimer **8d** in DMSO-d_6 (850 μL), was added triethylamine (5.10 μL, 36.6 μmol) and CGS21680 (**1**, as a hydrochloride hemihydrate form, 6.96 mg, 12.8 μmol). Subsequently, a freshly prepared 42.2 mM solution of PyBOP in DMSO-d_6 (280 μL, 11.8 μmol) was added slowly to the stirred mixture of **7d**. The reaction was stirred for 43 h, and the reaction mixture was loaded directly on a SEC column (H 43 cm × O.D. 4.5 cm) in DMF and purified to give 9.44 mg of **10d′** (structure not shown). Unfortunately, the analysis of **10d′** by ^{1}H NMR in DMSO-d_6 indicated only ca. 18.49 CGS21680 groups were attached out of ca. 26 available PAMAM amino groups. Next, dendrimer **10d′** (9.44 mg) in DMSO-d_6 (300 μL) was treated with 170 μL (6.64 μmol) of Solution A (*vide supra*, stirred for 6 min), and the reaction mixture was stirred for 72 h protected from light. Then, the dendrimer mixture was treated with 100 μL (3.35 μmol) of Solution B (*vide supra*, stirred for 8 min) and stirring continued for 14 h. The crude mixture was loaded on a SEC column (H 38 cm × O.D. 3.0 cm) for purification in DMF, and the fractions containing the desired compound were determined similarly by ^{1}H NMR. The selected SEC fractions were combined and dried *in vacuo* to give dendrimer **10d** (8.39 mg) as a glassy solid. The color of a 1.0

mM solution of **10d** in water (HPLC grade, Aldrich) prepared for the biological assay was intense red. ^{1}H NMR (600 MHz, DMSO-d_6) δ 8.05, 8.02 (s (each), 47.63H, H_8 and H_{8Ad}), 7.93, 7.89 (br s, 54.71H, NH_{G3}, NH_{CGS}), 7.80 (br s, 25.60H, NH_{G2}, NH_{G1}, and NH_{G0}), 7.21 (br s, 7.03H, NH_{PEG} of major isomer), 7.13, 7.09 (d (each), 85.97H, H_4 and H_5), 6.81 (br s, 36.71H, H_{6Ad}, NH_{PEG} of minor isomer), 6.19 (s, 19.05H, H_1), 5.85 (d, 20.03H, J = 6.5 Hz, $H_{1'}$), 5.62, 5.56 (br s (each), 35.34H, $H_{3'\text{-OH}}$ and $H_{2'\text{-OH}}$), 4.72 (m, 18.36H, $H_{2'}$), 4.26 (s, 20.93H, $H_{4'}$), 4.19 (s, 18.93H, $H_{3'}$), 4.02 (br s, 11.19H, H_{hPEG}), 3.62−3.37 (m, 930.57H, satellites J = 73.3 Hz, H_i, H_j, and H_k, one of H_2), 3.23 (s, 23.17H, H_l), 3.19−2.99 (m, 240.33H, H_d, H_f, H_{fCGS}, H_{gCGS}, H_{fPEG}, H_{gPEG}, and H_9), 2.76 (m, 99.23H, H_3 and H_6), 2.64 (m, 110.31H, H_b and H_g), 2.41 (m, 55.64H, H_e and H_a), 2.33 (t, 54.85H, J = 7.7 Hz, H_7), 2.18 (m, 120.00H, H_c), 0.96 (br s, 61.52H, H_{10}).

Receptor Binding and Functional Assays[1]. *Materials.* [^{125}I]N^6-(4-Amino-3-iodobenzyl)adenosine-5′-*N*-methyluronamide (I-AB-MECA; 2000 Ci/mmol) and other radioligands were purchased from Perkin-Elmer Life and Analytical Science (Boston, MA). [^{3}H]2-chloro-N^6-cyclopentyladenosine (CCPA) was a custom synthesis product (Perkin-Elmer). Samples for binding and functional assays were prepared as follows: compounds **1**, **2**, and **3** as 5.0 mM stock solutions in DMSO (ACS spectroscopic grade, >99.9%, Aldrich); dendrimers **7a**, **7b**, **7d**, **9a**, **9b**, **9d**, **10c**, and **10d** as 1.0 mM stock solutions in water (HPLC grade, Aldrich). Achieving a complete dissolution of dendrimer **8c** or **8d** in water (1.0 mM) was difficult, and thus, experiments were not performed for these compounds. Stock solutions were stored frozen at −80 °C.

Cell Culture and Membrane Preparation (18). Chinese hamster ovary (CHO) cells stably expressing the recombinant human (*h*) A_1, hA_{2B}, or hA_3 AR or human embryonic kidney (HEK)-293 cells stably expressing the recombinant hA_{2A} AR were cultured in DMEM (Dulbecco's modified Eagle's medium) and F12 (1:1, v/v) supplemented with 10% fetal bovine serum, 100 units/mL penicillin, 100 μg/mL streptomycin, 2 μmol/mL glutamine, and 800 μg/mL Geneticin. After harvest, homogenization, and suspension, cell membranes were centrifuged at 500 × *g* for 10 min, and the pellet was resuspended in 50 mM Tris-HCl buffer (pH 7.4) containing 10 mM $MgCl_2$ and 1 mM EDTA. The suspension was homogenized with an electric homogenizer for 10 s and was then re-centrifuged at 20 000 × *g* for 20 min at 4 °C. The resultant pellets were resuspended in buffer in the presence of 3 U/mL adenosine deaminase, and the suspension was stored at −80 °C until the binding experiments. The protein concentration was measured using the Bradford assay (*19*).

Binding Assays at the hA_1 and hA_{2A} ARs. For binding to hA_1 ARs (*20, 21*), membranes (40 μg/tube) from CHO cells stably expressing the receptor were incubated with [^{3}H]N^6-[(*R*)-phenylisopropyl]adenosine (R-PIA; 2 nM) or [^{3}H]CCPA (0.5 nM) at 25 °C for 60 min in 50 mM Tris-HCl buffer (pH 7.4, 10 mM $MgCl_2$) and increasing concentrations of the test ligands in a total assay volume of 200 μL. Nonspecific binding was determined using 10 μM of N^6-cyclopentyladenosine (CPA).

For hA_{2A} AR binding (*22*), membranes (20 μg/tube) from HEK-293 cells stably expressing the receptor were incubated with [^{3}H]CGS21680 (15 nM) at 25 °C for 60 min in 50 mM Tris-HCl buffer (pH 7.4, 10 mM $MgCl_2$) and increasing concentrations of the test ligands in a total assay volume of 200 μL. Nonspecific binding was determined using 10 μM of 5′-*N*-ethylcarboxamidoadenosine (NECA).

For hA_3 AR binding (*22*), membranes (20 μg/tube) from CHO cells stably expressing the receptor were incubated with [^{125}I]I-AB-MECA (0.2 nM) (*23*) at 37 °C for 60 min in 50 mM Tris-HCl buffer (pH 7.4, 10 mM $MgCl_2$) in a total assay volume of 200 μL. Nonspecific binding was determined using 10 μM of Cl-IB-MECA.

Binding reactions were terminated by filtration through Whatman GF/B filters under reduced pressure using an MT-24 cell harvester (Brandell, Gaithersburg, MD). Filters were washed three times with 9 mL ice-cold buffer. Radioactivity was determined in a Beckman 5500B γ-counter. IC_{50} values were converted to K_i values as described (*24*).

Cyclic AMP Accumulation Assay. CHO cells expressing the A_{2A} or A_{2B} AR were seeded in 24-well plates and incubated at 37 °C overnight. The following day the medium was removed and replaced with DMEM containing 50 mM HEPES, 10 μM rolipram, 3 U/mL adenosine deaminase, and increasing concentrations of agonists. The medium was removed, and the cells were lysed with 200 μL of 0.1 M HCl. 100 μL of the HCl solution was used in the Sigma Direct cAMP Enzyme Immunoassay following the instructions provided with the kit. The results were interpreted using a Bio-Tek ELx808 Ultra Microplate reader at 405 nm.

Statistical Analysis. Binding and functional parameters were calculated using *Prism 4.0* software (GraphPAD, San Diego, CA). IC_{50} values obtained from competition curves were converted to K_i values using the Cheng-Prusoff equation (*24*). Data were expressed as the mean ± standard error. Statistical analysis was performed using analysis of variance (ANOVA) with post hoc test or Student's *t*-test where appropriate with *p* values less than 0.05 being considered significant.

Studies of Human Washed Platelets. *Preparation.* Human washed platelets were prepared as previously described (*25*). Briefly, fresh blood obtained from healthy donors was centrifuged at 175 × *g* for 15 min at 37 °C, platelet-rich plasma was removed, and centrifuged at 1570 × *g* for 15 min at 37 °C. The platelet pellet was washed twice in Tyrode's buffer (137 mM NaCl, 2 mM KCl, 12 mM $NaHCO_3$, 0.3 mM NaH_2PO_4, 1 mM $MgCl_2$, 2 mM $CaCl_2$, 5.5 mM glucose, 5 mM Hepes, pH 7.3) containing 0.35% human serum albumin, and finally resuspended at a density of 3 × 10^5 platelets/μL in the same buffer in the presence of 0.02 U/mL of the adenosine 5′-diphosphate (ADP) scavenger apyrase (adenosine 5′-triphosphate diphosphohydrolase, EC 3.6.1.5), a concentration sufficient to prevent desensitization of platelet ADP receptors during storage. Platelets were kept at 37 °C throughout all experiments.

Platelet Aggregation Studies[1]. Aggregation was measured at 37 °C by a turbidimetric method in a dual-channel Payton aggregometer (Payton Associates, Scarborough, Ontario, Canada). The stock solutions for platelet aggregation and internalization studies were prepared as follows: compounds **1**, **2**, and **3** as 5.0 mM solutions in DMSO (ACS spectroscopic grade, >99.9%, Aldrich); dendrimers **7a**, **7b**, **7d**, **9a**, **9b**, **9d**, **10c**, and **10d** as 1.5 mM solutions in water (HPLC grade, Aldrich); dendrimers **8c** and **8d** as 750 μM solutions in water (HPLC grade, Aldrich). A small amount of DMSO in monomer was previously demonstrated not to affect the platelet aggregation (*10*). A 450 μL aliquot of platelet suspension was stirred at 1100 rpm and activated by addition of ADP (5 μM), in the presence or absence of various monomers/dendrimers and in the presence of human fibrinogen (0.8 mg/mL), in a final volume of 500 μL. The extent of aggregation was estimated quantitatively by measuring the maximum curve height above the baseline level.

[1]All of our *in vitro* assay results (including platelet studies) are reported in dendrimer concentrations, not in ligand concentrations. This was intended because of potential limitations in simultaneously achieving full accessibility to receptors of all ligands covalently bound to a single carrier such as in our dendrimer conjugates. We maintain that our system is different from those carriers loaded with drugs as either physically entrapped or covalently bound through cleavable linkers for their release for activation as monomeric forms.

Flow Cytometry Analysis[1]. Human washed platelets (3×10^5 platelets/μL) were incubated with various dendrimers for 30 min at 37 °C. The platelet suspension was then centrifuged at 1900 $\times$ *g* for 8 min at 37 °C and platelets were resuspended in Tyrode's buffer containing 0.35% human serum albumin and fixed with paraformaldehyde 2% for 15 min. A 5 μL aliquot of sample was then diluted with 500 μL PBS for flow cytometry analysis. Samples were analyzed using a Becton Dickinson FACScalibur flow cytometer and *Cell Quest* software (Becton Dickinson, San Jose, CA). All parameters were acquired on a logarithmic scale, and 20 000 events were recorded in the platelet population.

RESULTS AND DISCUSSION

Molecular Design. Our recent investigation showed that a relatively low degree of surface modification (ca. $\leq$25%) by short poly(ethylene glycol) monomethyl ether (PEG) chains (M_n = 550/750) sufficiently increased water solubility and reduced the cytotoxicity of G3 PAMAM dendrimers (*17*). Here, our goal was to examine whether this PEGylation principle could be effectively applied to our earlier dendrimer constructs bearing GPCR ligands that interact within the transmembrane domain of the receptor to induce biological effects. Accordingly, three G3 PAMAM dendrimers (theoretical 32 end groups) containing relatively small weight portions of PEG that differ in number and size ($7PEG_{550}$ (**4a**), $14PEG_{550}$ (**4b**), and $4PEG_{2000}$ (**4d**); Scheme 1) were initially selected for a comparative study. We planned partial substitution of the dendrimer with a fixed number of agonist ligands (CGS21680) and with all remaining free amino groups concealed by prior acetylation in order to precisely evaluate the influence of different PEG groups on receptor-mediated activity. A fluorophore was also attached to the dendrimers for detection in biological systems. In addition, preparation of an unacetylated fluorescent PAMAM-$4PEG_{2000}$ derivative with an increased number of CGS21680 ligands was intended to determine whether any multivalent effect is discernible with this PEGylated system. The stoichiometry in the substitution reactions of the amine-terminated G3 PAMAM dendrimers has been well-controlled (*10, 11, 17*). To summarize, our original molecular design considered the following: (1) partial acetylation of three G3 PAMAM-PEG dendrimers to leave similar numbers of free amino groups; (2) attachment of 1 equiv of Alexa Fluor 488 (AF_{488}) for fluorescent imaging; (3) conjugation of CGS21680 at all remaining amino groups.

Synthesis. Acetylation of **4a**, **4b**, and **4d** was achieved with a relatively efficient stoichiometric control to leave a similar fraction of free amino groups (31% for **5a**; 35% for **5b**; 25% for **5d**) (Scheme 1). Purification by SEC in DMF after each step slightly shifted the composition (*m* and *n*) of each dendrimer mixture and its MW distribution as determined by ^{1}H NMR integration (see Supporting Information) (*17*). Subsequently, each acetylated PAMAM-PEG dendrimer **5** was treated with an equimolar amount of AF_{488} as an activated ester (**6**). Some unreacted dye **6** was recovered during the SEC purification from all three reactions (**5**$\rightarrow$**7**). In contrast, no free dye **6** was found when unacetylated dendrimer **4d** was reacted similarly.

Next, the fluorescent dendrimers **7a**, **7b**, **7d**, and **8d** were treated with CGS21680 in slight excess for its conjugation to the PAMAM periphery via PyBOP-mediated coupling. Unfortunately, the conversion fraction in these reactions determined after SEC purification turned out to be low, being more prominent for the acetylated dendrimers **7** (0.38 CGS21680 attachments for **7a** out of approximately nine remaining peripheral amino groups, 1.24 for **7b**, 0.65 for **7d**, and 18.5 for **8d** by ^{1}H NMR integration). The low coupling yield was in contrast to the full substitution of the G3 PAMAM amino ends with CGS21680 under the same reaction conditions (*10*). Obviously, the presence of an adjacent PEG chain, irrespective of its number and size, interfered sterically with the coupling reaction. Furthermore, we speculate that applying the partial acetylation at the PEGylated PAMAM surface may further phase-separate these unimolecular micelles intramolecularly (into microphase domains of hydrophobic core and hydrophilic PEG corona) to shrink the PAMAM surface and lower the reactivity of the remaining amino groups considerably. To overcome the low reactivity, the SEC-purified dendrimer mixture was further treated with two separate additions of the excess preactivated ester of CGS21680 and was allowed to react for several additional days. Nevertheless, application of this exhaustive coupling condition did not substantially improve the total conversion for all cases. Among the three acetylated dendrimers, **7b** with a lower proportion of acetamide groups showed a slightly better coupling efficiency. Since our goal was to systematically study the influence of adjacent PEG chains in eliciting biological activity through ligand-receptor interactions, attachment of CGS21680 earlier in the synthetic sequence was avoided in order to facilitate the stoichiometric control in PEG derivatization. Moreover, the activated form of PEG (as a *p*-nitrophenyl carbonate) potentially reacts with the hydroxy and the adenine amino groups of CGS21680. Another unacetylated fluorescent dendrimer analogue **10c** with shorter PEG chains was prepared similarly from **4c** ($9PEG_{750}$), in order to compare the influence of PEG on the chemical reactivity and the biological effects between unacetylated dendrimer conjugates. Again, a complete conjugation of CGS21680 to **8c** was not achieved.

Characterization by ^{1}H NMR and MALDI-TOF MS. The final dendrimer conjugates **7**$-$**10** used for biological assays were characterized by analysis of ^{1}H NMR integrals in DMSO-d_6 (Table 1). NMR analysis of **9a**, **9b**, and **9d** in D_2O gave similar results; however, analysis of **10c** and **10d** in D_2O was not feasible due to the significant peak broadening. This may have resulted from poor desolvation in D_2O (*26*) of the relatively hydrophobic interior$-$CGS21680 moieties and the PAMAM domain. The average MW of each dendrimer was also determined by MALDI MS in two different matrices (DHB and THAP) to give somewhat underestimated values compared to those obtained by NMR (Table 1). Underestimation of MWs of similar PAMAM conjugates by MALDI was previously noted (*10, 17*). The number of CGS21680 groups (*z*) attached to each dendrimer calculated by MALDI was similar to (or slightly higher for **9b** and **10d**) NMR-estimated values.

Solution Conformation of Dendrimer Conjugates by NOESY. To predict the solution conformation of PAMAM-PEG-CGS21680 dendrimer conjugates (Figure 2) in the aqueous phase, 2D NOESY experiments were carried out for selected dendrimers **9b**, **10c**, and **10d** in D_2O (see Supporting Information Figures S4$-$S6). Our previous investigation on various PAMAM-PEG conjugates (without ligands) suggested no backfolding of the PEG chains into the interior of the PAMAM domain (*17*). Intense NOE cross-peaks were found between the peaks from PAMAM and CGS21680 segments of dendrimers **10c** and **10d** with high loading of CGS21680, but much weaker (or no) signals were detected from the corresponding cross-peaks (if any) of **9b**. Related to this observation, it may be important to note the small difference in the chemical shift ($\Delta\delta \approx 0.15$ ppm) of the methyl group of the 5′-uronamide moiety of CGS21680 in 1D NMR in D_2O, between the dendrimers with low loading (0.97$-$0.98 ppm for **9a**, **9b**, and **9d**) and high loading (0.85 ppm for **10c**; 0.82 ppm for **10d**) of ligands. Hardly any NOE cross-peaks were observed between the peaks from CGS21680 and PEG regions in all three spectra. Detection of the NOE cross-peaks between those from PAMAM and PEG regions was difficult due to the severe overlapping of peaks. However, weak NOE cross-peaks between PAMAM and PEG peaks were indicated, particularly with dendrimer **10c**, which were more vivid for the isolated PEG peaks (h_{PEG}, i; see Supporting

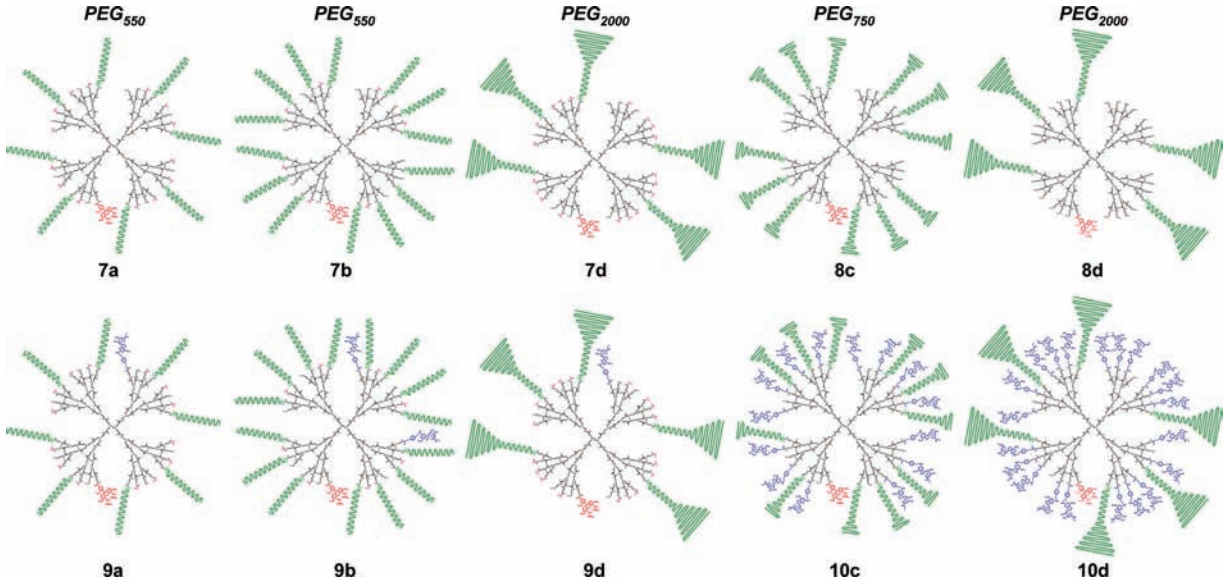

Figure 2. Structures of PEGylated PAMAM dendrimer conjugates **7**−**10** (black, PAMAM; green, PEG; pink, acetyl; red, AF_{488}; blue, CGS21680). The illustration of dendrimer conjugates shows the average number of attached pendant groups in each statistical mixture as determined by ^{1}H NMR integrals and reflects the approximate PEG length (550/750/2000) relative to the size of the CGS21680 ligand. The geometry of each component as drawn, particularly of the PEG chains, does not represent the actual solution conformation.

Table 2. Binding and Functional Assay Results of Monomers and Dendrimers at Four Subtypes of *h*ARs[a]

	binding[b] at ARs						activation[c] at ARs		
	hA_1		hA_{2A}		hA_3		hA_{2A}		hA_{2B}
cmpd	K_i [nM]	% inhibition	K_i [nM]	% inhibition	K_i [nM]	% inhibition	EC_{50} [nM]	% activation	% activation
1	5780 ± 590	24.9 ± 4.6	67 ± 19	84.7 ± 0.9	247 ± 79	59.8 ± 4.4	53.0 ± 16.0	100 ± 10	3.6 ± 6.3
2	168 ± 36	56.9 ± 9.1	12 ± 6	101 ± 1	38 ± 11	85.3 ± 3.2	8.2 ± 1.7	96.0 ± 6.0	5.5 ± 4.7
3	984 ± 223	36.9 ± 7.5	210 ± 19	82.1 ± 0.3	58 ± 24	85.2 ± 11.4	51.0 ± 8.0	103 ± 5	−1.7 ± 5.0
7a	n.d.[d]	5.5 ± 8.8	n.d.[d]	1.6 ± 7.4	n.d.[d]	−13.4 ± 2.7	n.d.[d]	2.4 ± 1.7	5.3 ± 8.9
7b	n.d.[d]	13.8 ± 4.5	n.d.[d]	−11.6 ± 2.5	n.d.[d]	−17.2 ± 5.2	n.d.[d]	n.a.[d]	1.6 ± 7.3
7d	n.d.[d]	7.1 ± 4.5	n.d.[d]	3.2 ± 4.9	n.d.[d]	−7.5 ± 2.2	n.d.[d]	n.a.[d]	−4.4 ± 3.8
9a	n.d.[d]	12.2 ± 1.6	488 ± 59	61.4 ± 2.0	n.d.[d]	24.4 ± 6.5	n.d.[d]	92.6 ± 5.4	1.4 ± 5.5
9b	n.d.[d]	19.3 ± 3.6	496 ± 18	62.7 ± 1.2	n.d.[d]	27.6 ± 3.2	n.d.[d]	101 ± 5	16.6 ± 3.7
9d	n.d.[d]	13.3 ± 3.1	752 ± 34	55.8 ± 1.8	n.d.[d]	25.4 ± 4.0	n.d.[d]	91.0 ± 8.3	9.4 ± 5.4
10c	4870 ± 1360	19.9 ± 4.8	151 ± 36	81.2 ± 1.5	1130 ± 310	29.0 ± 12.0	11.2 ± 4.9	90.0 ± 6.7	2.8 ± 1.4
10d	4230 ± 1310	19.8 ± 2.6	215 ± 12	75.5 ± 3.1	1320[e]	24.4 ± 8.0	60.6 ± 12.8	97.0 ± 7.1	3.3 ± 3.0

[a] Values are presented as the mean ± standard error of three or more independent experiments. The hA_1, hA_{2B}, and hA_3 ARs were expressed in CHO cells and the hA_{2A} AR in HEK-293 cells for binding and in CHO cells for the functional assay. [b] K_i values were determined through the radioligand binding, and the percent inhibition refers to the inhibition of binding at 1 μM. [c] EC_{50} values were determined by measuring the degree of stimulation of adenylate cyclase in cells stably expressing hA_{2A} or hA_{2B} AR. Percent activation refers to the activation of adenylate cyclase in comparison to the effects exerted by the full agonist NECA (100%) at 10 μM. [d] n.d. = not determined, i.e., binding/functional experiment was not conducted, or n.a. = no binding/activation was detected under the given assay conditions. [e] Performed only once.

Information Figure S5) close to the PAMAM region. Taken together, NOESY analysis suggests that CGS21680 ligands attached to the PEGylated PAMAM are more likely positioned in proximity to the PAMAM domain—by adhering to its surface or by partially backfolding into its interior void—rather than in the outer hydrophilic PEG layer in contact with the water molecules.

***In Vitro* Binding Assay at *h*ARs.** Next, the biological activities of these PEGylated PAMAM-CGS21680 conjugates **9** and **10** were examined by binding and functional assays in cell membranes (CHO or HEK-293 cells) expressing each *h*AR (Table 2) (*11*). Each of the four subtypes of ARs (A_1, A_{2A}, A_{2B}, and A_3) is associated with characteristic pathways of signaling, typically in a species-dependent manner (*12*). Recent evidence indicates the importance of secondary binding near the extracellular domain of a GPCR in enhancing selectivity and affinity of GPCR ligands (*27, 28*). Here, we compared the binding and activity profiles of these five dendrimers (**9** and **10**, Figure 2) with dendritic controls (precursors without the ligand, **7**, Figure 2) and three monomeric controls (**1**−**3**, Figure 1). APEC (**2**) is an analogue of CGS21680 (**1**) with an ethylenediamine extension at the distal unit (*28*) that exhibits a higher binding affinity at the hA_{2A} AR compared to **1**, but only threefold selectivity in comparison to the hA_3 AR. We also envisioned that **2**, particularly with a free amino group, may serve as a rough topological mimic for some of the dendrimer-attached CGS21680 moieties that are adjacent to the unreacted PAMAM amino groups. Compound **3** (*11*) was intended as a monomeric mimic of the dendrimer-attached form of **1**, because its terminal portion was identical to the linking segment in the dendrimer conjugates.

Overall, the inhibition constants (K_i) of the dendritic ligands at all tested AR subtypes (hA_1, hA_{2A}, and hA_3) were higher than those of the monovalent ligands **1**−**3**. Interestingly, this reduced affinity of dendritic ligands was more prominent at hA_1 and hA_3 compared to hA_{2A} AR. The selectivity for hA_{2A} compared to hA_3 AR was nearly an order of magnitude for the dendritic ligand **10c** ($hA_{2A,Ki}/hA_{3,Ki}$ = 0.13; 0.16 for **10d**), whereas the monomeric mimic of the dendrimer-attached nucleoside **3** showed selectivity (3.62-fold) for the hA_3. Indeed, high-loaded dendrimer conjugates **10** successfully achieved similar K_i values at hA_{2A} AR to that of **3**. In contrast, dendrimers **9** with low-loading of CGS21680 showed a reduction in binding

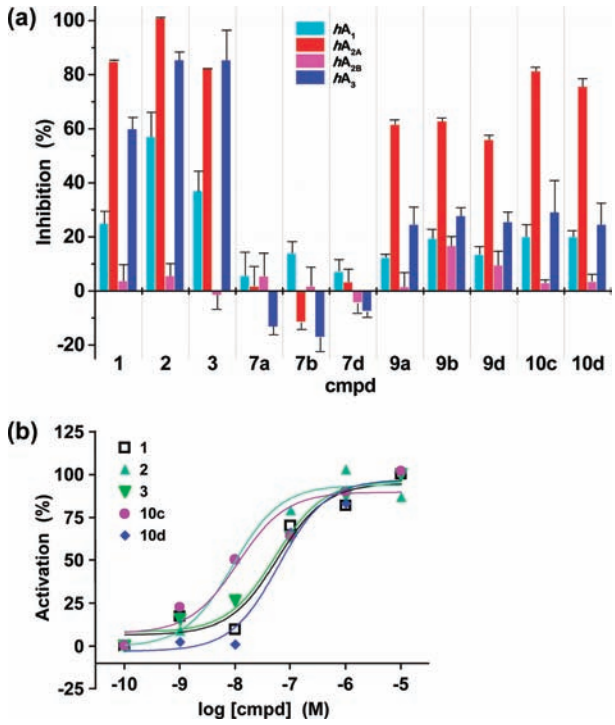

Figure 3. In vitro assay results of monomers (**1**−**3**) and selected dendrimers (**7**−**10**). (a) Interaction with four subtypes of *h*ARs (percent inhibition of specific radioligand binding at hA_1, hA_{2A}, and hA_3 ARs at a fixed concentration of 1 μM, and percent activation of adenylate cyclase at hA_{2B} AR at 10 μM); (b) agonistic effect at hA_{2A} AR as determined by measuring the degree of stimulation of adenylate cyclase in cells stably expressing the hA_{2A} AR. The hA_1, hA_{2B}, and hA_3 ARs were expressed in CHO cells and the hA_{2A} AR in HEK-293 cells for binding and in CHO cells for the functional assay.

affinity compared to monovalent ligand **3**, where **9d** bearing longer PEG_{2000} chains was the weakest. This may suggest an increased degree of steric inhibition (by neighboring PEG chains or the PAMAM backbone) experienced by a single ligand moiety in a macromolecular carrier with fewer ligands, significantly impairing ligand accessibility.

A similar trend was observed when comparing the inhibition at a fixed concentration of 1 μM (Figure 3a, Table 2). The dendritic controls **7** displayed essentially no inhibitory effect (<15%) at all subtypes of ARs. Inhibition of radioligand binding at the hA_{2A} AR was more pronounced for dendrimers **10** with high loading of CGS21680 compared to **9** with low loading, and similar to the effects by CGS21680 (**1**) and monomeric control **3**, but somewhat lower than inhibition by APEC (**2**). The differences in K_i values at hA_{2A} AR between dendrimers **9** and dendrimers **10** are statistically significant ($p < 0.01$). The relative inhibitory effect at the hA_{2A} vs the hA_3 AR was more than twice as high ($hA_{2A,\%inhibition}/hA_{3,\%inhibition} = 2.20-3.09$) for all PAMAM-PEG-CGS21680 dendrimer conjugates and nearly three times as high for dendrimers **10** with high loading of CGS21680. This represented an improvement in hA_{2A} selectivity in comparison to the hA_3 AR (0.96−1.42), considering the low selectivity of monomers **1**−**3**. Furthermore, selectivity for hA_{2A} compared to hA_1 has also increased (3.25−5.03 by **9** and **10**; 1.77−3.40 by **1**−**3**).

Cyclic AMP Accumulation Assay. The potency (i.e., agonistic effects) of monomers and dendrimers at hA_{2A} AR was determined by measuring the stimulation of adenylate cyclase—to produce intracellular adenosine 3′,5′-cyclic monophosphate (cAMP)—in CHO cells (Figure 3b, Table 2) (*12*). Dendrimer **10c** ($EC_{50} = 11.2 \pm 4.9$ nM, with PEG_{750}) was more potent than dendrimer **10d** ($EC_{50} = 60.6 \pm 12.8$ nM, with PEG_{2000}) in activating the hA_{2A} AR ($p < 0.05$). Considering the numbers of CGS21680 ligands (ca. 14 for **10c**; ca. 21 for **10d**) and PEG chains attached to these dendrimers, the longer PEG_{2000} chains appeared to significantly impede the ligand-receptor interaction, whereas the shorter PEG_{750} chains negligibly affected receptor binding and activation.

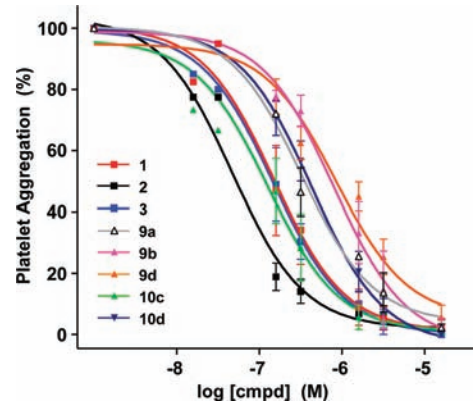

Figure 4. Platelet aggregation induced by ADP (5 μM) in the presence of various monomeric or dendritic A_{2A} agonists at 37 °C. The degree of platelet aggregation was normalized against that induced by ADP at 5 μM (100%). The extent of aggregation was estimated quantitatively by measuring the maximum curve height (i.e., percent light transmission) above the baseline level.

The EC_{50} values at the hA_{2A} AR of dendrimer **10c** (11.2 ± 4.9 nM, with PEG_{750}) and its corresponding monomer **3** (51.0 ± 8.0 nM) are significantly different ($p < 0.05$), although the hA_{2A} AR binding affinity of **10c** ($K_i = 151 \pm 36$ nM) was not significantly different from that of monomer **3** (210 ± 19 nM). Unlike the potency determined by measuring cAMP concentration that is directly associated with the intracellular signaling cascade initiated through AR activation, binding affinity was measured in isolated membranes of mammalian cells heterologously expressing specific ARs (see Experimental Section).

Recent reports described the dynamic behavior of GPCRs including receptor reorganization and oligomerization (*7, 29, 30*), which can be potentially regulated allosterically upon binding of a ligand. In such case, usage of clustered multivalent ligands would be particularly advantageous to amplify the desired cellular response. Therefore, this substantial enhancement in EC_{50} of a high-loaded dendrimer **10c** might reflect the involvement of more than one receptor-ligand interaction simultaneously. Indeed, a recent computer modeling study showed the possibility to bridge both primary binding sites at the transmembrane domain of a GPCR homodimer by two separate CGS21680 units covalently attached to a single G3 PAMAM dendrimer (*31*). Nevertheless, although enhancement of potency and/or selectivity was observed here, it was not sufficient to prove receptor clustering or oligomerization in this system.

Platelet Aggregation Studies. The effective inhibition of ADP-induced platelet aggregation was previously demonstrated using PAMAM dendrimers with multiple copies of an A_{2A} AR agonist (added as a DMSO solution) (*10, 11*). Here, the anti-aggregatory effect of *water-soluble* PAMAM-PEG-CGS21680 dendrimer conjugates **9** and **10** was measured (Figure 4, Supporting Information Table S1). A submicromolar inhibitory effect on platelet aggregation of **10c** ($IC_{50} = 151 \pm 53$ nM) was validated, which was better than that of another high-loaded dendrimer **10d** (495 ± 145 nM) with longer PEG chains. Unlike the cAMP assay, here the potency of **10c** was similar to those of CGS21680 **1** (192 ± 90 nM) and the dendrimer-attached mimic **3** (173 ± 72 nM), but lower than that of APEC **2** (35.9 ± 17.0 nM). Dendrimer **9a** bearing eight units of short PEG chains but with only one ligand on average ($8PEG_{550}$-1CGS21680), exhibited a similar or slightly lower IC_{50}

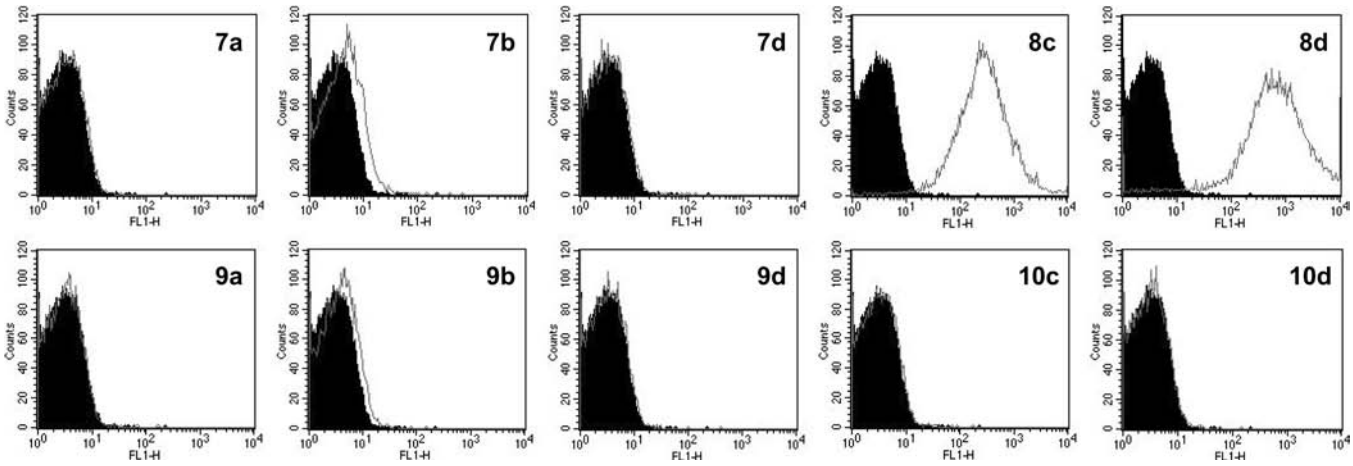

Figure 5. Flow cytometry histograms (AF_{488}, control: black area) obtained from human washed platelets incubated with 3 μM of each G3 PAMAM dendrimer conjugate for 30 min at 37 °C.

value (337 ± 77 nM) than **10d** carrying ca. 21 CGS21680 units. Accordingly, it seems apparent that the intracellular activity triggered by ligand-receptor interactions is more influenced by the length of the PEG chains (i.e., sterics) than the total number of ligands available on the dendrimer surface for a potential multivalent binding. Obviously, when the PEG size and the number of ligands were similar ($8PEG_{550}$-1CGS21680 (**9a**) vs $15PEG_{550}$-2CGS21680 (**9b**)), the dendrimer with a smaller number of PEG chains showed higher activity. Likewise, when the PEG size and its number were more or less the same ($6PEG_{2000}$-21CGS21680 (**10d**) vs $5PEG_{2000}$-1CGS21680 (**9d**); $11PEG_{750}$-14CGS21680 (**10c**) vs $8PEG_{550}$-1CGS21680 (**9a**)), the dendrimer carrying more ligands exhibited higher agonistic potency. The weakest activity was shown by **9b** and **9d**, either highly substituted with PEG or carrying long PEG chains, and both having only ca. 1−2 ligand attachments. Also, APEC **2** was found most potent in this study as in the cAMP assay, suggesting the importance of the terminal amino group in enhancing the agonistic effect. In fact, the number of unreacted amines in PAMAM-PEG-CGS21680 conjugates **9** and **10** estimated from the ^{1}H NMR integration (Table 1) was in a similar range (ca. 5−7), and thus, the modulation of the agonistic effects among dendrimers by the PAMAM amino groups is somewhat unlikely. It is important to note the moderate inhibitory effects in platelet aggregation exerted by two of the dendrimers without any ligands, **7d** (71% at 15 μM) and **8d** (40% at 7.5 μM) (Supporting Information Figure S9), suggesting the involvement of longer PEG_{2000} chains in inhibiting platelet aggregation possibly through a mechanism unrelated to the A_{2A} AR.

Flow Cytometry Analysis. Our earlier platelet uptake studies using PAMAM-CGS21680 conjugates (no PEG) showed a sustained anti-aggregatory effect, which might have resulted from the slow release of internalized conjugates as monitored by fluorescent confocal microscopy (*10*). Despite its known benefits, the presence of PEG groups on the surface of nanocarriers generally hampers the internalization process (*4*). Here, we investigated by flow cytometry[2] the potential for internalization of the PEGylated PAMAM dendrimers into human washed platelets (Figure 5; Supporting Information Figures S10 and S11). The best internalization efficiency at 3 μM (30 min incubation) was achieved by dendrimers **8c** and **8d**, which did not carry any ligand and had relatively poor water solubility. Interestingly, the water solubility of **4c** and **4d** dropped significantly upon conjugation of 1 equiv of AF_{488}, whereas that of partially acetylated **5a**, **5b**, and **5d** was not affected. A minor degree of uptake was detected from **9b** ($15PEG_{550}$-2CGS21680) and its precursor **7b**. Neither of the high-loaded dendrimers **10c** and **10d** showed any indication of internalization at 3 μM. When the dendrimer concentration was increased to 50 μM (30 min incubation), some internalization was detected from **10c** and **10d** (Supporting Information Figure S10), with **10c** being slightly higher in its efficiency. Similar observations were made in the fluorescent confocal microscopy studies (data not shown) to confirm these results. It is difficult to conclude whether the low water solubility (as demonstrated by the fully conjugated water-insoluble PAMAM-CGS21680 dendrimer (*10*)) or the presence of many cationic amino groups (*11*)—or the combination of both—aided in the effective internalization of PEGylated PAMAM dendrimers **8c** and **8d**. In any case, the internalization of dendritic controls **8c** and **8d** conceivably did not involve ligand interactions with the A_{2A} AR. This suggests the involvement of uptake pathways other than GPCR-mediated endocytosis (*16, 32, 33*) for PEGylated dendrimers into the platelets.

In conclusion, an approach to the design and synthesis of potent and water-soluble macromolecular ligands of GPCRs was demonstrated through our systematic studies on dendritic carriers. A PAMAM dendrimer conjugate bearing multiple copies of a nucleoside ligand and relatively short PEG chains manifested enhanced receptor subtype-selectivity and highly potent agonistic effects, without experiencing any disadvantageous steric effects. Longer PEG chains reduced affinity at the A_{2A} AR. With growing evidence to support the oligomerization of GPCRs and the potential intervention of ligands in GPCR clustering (*7, 29, 30*), acquiring synergistic cooperativity among ligands through multivalent binding may be desirable for GPCR therapeutics based on ligand-receptor interactions. Dendrimers of higher generations are envisioned for use in exploring multiple interactions with higher-order GPCR aggregates. In addition, the potential of PEGylated PAMAM dendrimers as carriers to deliver genes across the blood-brain barrier by derivatizing their periphery with the brain-targeting ligands has been demonstrated recently (*34, 35*). Consequently, our PEGylation strategy described in this communication may find versatile utility in various nanomedical applications aimed at multivalent ligand-receptor interactions.

[2]Strictly, fluorescent confocal microscopy analysis detects fluorescence only from the internalized dendrimers, while flow cytometry measures fluorescence from both internalized and surface-bound dendrimers. Accordingly, the estimation of internalization efficiency by flow cytometry analysis may be limited.

ACKNOWLEDGMENT

This research was supported in part by the Intramural Research Program of the NIH, NIDDK. We thank Dr. Haijun Yao at the Mass Spectrometry Laboratory of the University of Illinois for collecting MALDI spectra of our dendrimer samples,

and Dr. Herman Yeh at the NIDDK for the helpful advice on the NMR experiments. Y.K. thanks the Can-Fite Biopharma for financial support.

Supporting Information Available: Experimental procedures and characterization, ^{1}H NMR, NOESY, and MALDI MS spectra, results of platelet aggregation assays and flow cytometry histograms. This material is available free of charge via the Internet at http://pubs.acs.org.

LITERATURE CITED

(1) Peer, D., Karp, J. M., Hong, S., Farokhzad, O. C., Margalit, R., and Langer, R. (2007) Nanocarriers as an emerging platform for cancer therapy. *Nat. Nanotechnol. 2*, 751–760.

(2) Torchilin, V. P. (2006) Multifunctional nanocarriers. *Adv. Drug Delivery Rev. 58*, 1532–1555.

(3) Duncan, R. (2003) The dawning era of polymer therapeutics. *Nat. Rev. Drug Discov. 2*, 347–360.

(4) Tomalia, D. A., Reyna, L. A., and Svenson, S. (2007) Dendrimers as multi-purpose nanodevices for oncology drug delivery and diagnostic imaging. *Biochem. Soc. Trans. 35*, 61–67.

(5) Boas, U., Christensen, J. B., Heegaard, P. M. H. (2006) *Dendrimers in medicine and biotechnology*, The Royal Society of Chemistry, Cambridge.

(6) Lee, C. C., MacKay, J. A., Fréchet, J. M. J., and Szoka, F. C. (2005) Designing dendrimers for biological applications. *Nat. Biotechnol. 23*, 1517–1526.

(7) Kiessling, L. A., Gestwicki, J. E., and Strong, L. E. (2006) Synthetic multivalent ligands as probes of signal transduction. *Angew. Chem., Int. Ed. 45*, 2348–2368.

(8) Badjić, J. D., Nelson, A., Cantrill, S. J., Turnbull, W. B., and Stoddart, J. F. (2005) Multivalency and cooperativity in supramolecular chemistry. *Acc. Chem. Res. 38*, 723–732.

(9) Mammen, M., Choi, S.-K., and Whitesides, G. M. (1998) Polyvalent interactions in biological systems: implications for design and use of multivalent ligands and inhibitors. *Angew. Chem., Int. Ed. 37*, 2754–2794.

(10) Kim, Y., Hechler, B., Klutz, A. M., Gachet, C., and Jacobson, K. A. (2008) Toward multivalent signaling across G protein-coupled receptors from poly(amidoamine) dendrimers. *Bioconjugate Chem. 19*, 406–411.

(11) Kim, Y., Klutz, A. M., Hechler, B., Gao, Z.-G., Gachet, C., and Jacobson, K. A. (2009) Application of the functionalized congener approach to dendrimer-based signaling agents acting through A_{2A} adenosine receptors. *Purinergic Signalling 5*, 39–50.

(12) Jacobson, K. A., and Gao, Z.-G. (2006) Adenosine receptors as therapeutic targets. *Nat. Rev. Drug Discovery 5*, 247–264.

(13) Jaakola, V.-P., Griffith, M. T., Hanson, M. A., Cherezov, V., Chien, E. Y. T., Lane, J. R., IJzerman, A. P., and Stevens, R. C. (2008) The 2.6 angstrom crystal structure of a human A_{2A} adenosine receptor bound to an antagonist. *Science 322*, 1211–1217.

(14) Landry, Y., Niederhoffer, N., Sick, E., and Gies, J. P. (2006) Heptahelical and other G-protein-coupled receptors (GPCRs) signaling. *Curr. Med. Chem. 13*, 51–63.

(15) Harris, J. M., and Chess, R. B. (2003) Effect of pegylation on pharmaceuticals. *Nat. Rev. Drug Discov. 2*, 214–221.

(16) Duncan, R., and Izzo, L. (2005) Dendrimer biocompatibility and toxicity. *Adv. Drug Delivery Rev. 57*, 2215–2237.

(17) Kim, Y., Klutz, A. M., and Jacobson, K. A. (2008) Systematic investigation of polyamidoamine dendrimers surface-modified with poly(ethylene glycol) for drug delivery applications: synthesis, characterization, and evaluation of cytotoxicity. *Bioconjugate Chem. 19*, 1660–1672.

(18) Gao, Z.-G., Mamedova, L. K., Chen, P., and Jacobson, K. A. (2004) 2-Substituted adenosine derivatives: affinity and efficacy at four subtypes of human adenosine receptors. *Biochem. Pharmacol. 68*, 1985–1993.

(19) Bradford, M. M. (1976) A rapid and sensitive method for the quantitation of microgram quantities of protein utilizing the principle of protein-dye binding. *Anal. Biochem. 72*, 248–254.

(20) Schwabe, U., and Trost, T. (1980) Characterization of adenosine receptors in rat brain by (-)[^{3}H]N^6-phenylisopropyladenosine. *Naunyn-Schmiedeberg's Arch. Pharmacol. 313*, 179–187.

(21) Perreira, M., Jiang, J. K., Klutz, A. M., Gao, Z.-G., Shainberg, A., Lu, C., Thomas, C. J., and Jacobson, K. A. (2005) "Reversine" and its 2-substituted adenine derivatives as potent and selective A3 adenosine receptor antagonists. *J. Med. Chem. 48*, 4910–4918.

(22) Jarvis, M. F., Schutz, R., Hutchison, A. J., Do, E., Sills, M. A., and Williams, M. (1989) [^{3}H]CGS 21680, a selective A_2 adenosine receptor agonist directly labels A_2 receptors in rat brain. *J. Pharmacol. Exp. Ther. 251*, 888–893.

(23) Olah, M. E., Gallo-Rodriguez, C., Jacobson, K. A., and Stiles, G. L. (1994) ^{125}I-4-Aminobenzyl-5′-*N*-methylcarboxamidoadenosine, a high affinity radioligand for the rat A_3 adenosine receptor. *Mol. Pharmacol. 45*, 978–982.

(24) Cheng, Y.-C., and Prusoff, W. H. (1973) Relationship between the inhibition constant (K_I) and the concentration of inhibitor which causes 50% inhibition (I_{50}) of an enzymatic reaction. *Biochem. Pharmacol. 22*, 3099–3108.

(25) Cazenave, J. P., Ohlmann, P., Cassel, D., Eckly, A., Hechler, B., and Gachet, C. (2004) Preparation of washed platelet suspensions from human and rodent blood. *Methods Mol. Biol. 272*, 13–28.

(26) Hunter, C. A. (2004) Quantifying intermolecular interactions: guidelines for the molecular recognition toolbox. *Angew. Chem., Int. Ed. 43*, 5310–5324.

(27) Avlani, V. A., Gregory, K. J., Morton, C. J., Parker, M. W., Sexton, P. M., and Christopoulos, A. (2007) Critical role for the second extracellular loop in the binding of both orthosteric and allosteric G protein-coupled receptor ligands. *J. Biol. Chem. 282*, 25677–25686.

(28) Jacobson, K. A. (2009) Functionalized congener approach to the design of ligands for G protein-coupled receptors (GPCRs). *Bioconjugate Chem.* DOI: 10.1021/bc900059.

(29) Gandia, J., Galino, J., Amaral, O. B., Soriano, A., Lluís, C., Franco, R., and Ciruela, F. (2008) Detection of higher-order G protein-coupled receptor oligomers by a combined BRET-BiFC technique. *FEBS Lett. 582*, 2979–2984.

(30) Szidonya, L., Cserzö, M., and Hunyady, L. (2008) Dimerization and oligomerization of G-protein-coupled receptors: debated structures with established and emerging functions. *J. Endocrinol. 196*, 435–453.

(31) Ivanov, A. A., and Jacobson, K. A. (2008) Molecular modeling of a PAMAM-CGS21680 dendrimer bound to an A_{2A} adenosine receptor homodimer. *Bioorg. Med. Chem. Lett. 18*, 4312–4315.

(32) Conner, S. D., and Schmid, S. L. (2003) Regulated portals of entry into the cell. *Nature 422*, 37–44.

(33) Watson, P., Jones, A. T., and Stephens, D. J. (2005) Intracellular trafficking pathways and drug delivery: fluorescence imaging of fixed and living cells. *Adv. Drug Delivery Rev. 57*, 43–61.

(34) Huang, R.-Q., Qu, Y.-H., Ke, W.-L., Zhu, J.-H., Pei, Y.-Y., and Jiang, C. (2007) Efficient gene delivery targeted to the brain using a transferring-conjugated polyethyleneglycol-modified polyamidoamine dendrimer. *FASEB J. 21*, 1117–1125.

(35) Huang, R., Ke, W., Liu, Y., Jiang, C., and Pei, Y. (2008) The use of lactoferrin as a ligand for targeting the polyamidoamine-based gene delivery system to the brain. *Biomaterials 29*, 238–246.

BC9001689

Supporting Information for *Bioconjugate Chemistry*

PEGylated Dendritic Unimolecular Micelles as Versatile Carriers for G Protein-Coupled Receptor Ligands

Yoonkyung Kim,[†,§] Béatrice Hechler,[‡] Zhan-Guo Gao,[†] Christian Gachet,[‡] and Kenneth A. Jacobson[*,†]

† Molecular Recognition Section, Laboratory of Bioorganic Chemistry, National Institute of Diabetes and Digestive and Kidney Diseases, National Institutes of Health, Bethesda, Maryland 20892.
‡ INSERM U.311, EFS-Alsace, and Université Louis Pasteur, Strasbourg, France.
§ Current Address: Biomedical Research Center, Korea Institute of Science and Technology, 39-1 Hawolgok-dong, Seongbuk-gu, Seoul, 136-791, Korea.
** E-mail: kajacobs@helix.nih.gov.*

Table of Contents

Table S1	Inhibitory effects (IC_{50}) of monomers and dendrimers on platelet aggregation.	p. 2
Figure S1	^{1}H NMR spectra of PAMAM-PEG dendrimers **7a**, **7b**, **7d**, **8c**, and **8d** in DMSO-d_6.	p. 3
Figure S2	^{1}H NMR spectra of PAMAM-PEG-CGS21680 dendrimers **9a**, **9b**, **9d**, **10c**, and **10d** in DMSO-d_6.	p. 4
Figure S3	^{1}H NMR spectra of PAMAM-PEG-CGS21680 dendrimers **9a**, **9b**, **9d**, **10c**, and **10d** in D_2O.	p. 5
Figures S4–S6	NOESY spectra of PAMAM-PEG-CGS21680 dendrimer **9b**, **10c**, and **10d** in D_2O.	pp. 6–8
Figure S7	MALDI-TOF MS spectra of PAMAM-PEG dendrimers **7a**, **7b**, **7d**, **8c**, and **8d**.	p. 9
Figure S8	MALDI-TOF MS spectra of PAMAM-PEG-CGS21680 dendrimers **9a**, **9b**, **9d**, **10c**, and **10d**.	p. 10
Figure S9	Platelet aggregation studies for dendrimer controls **7** and **8**.	p. 11
Figures S10–S11	Flow cytometry results of PAMAM dendrimer conjugates at 50 μM and monomers **1**–**3**.	pp. 12–13

Table S1. Inhibitory effects (IC_{50}) of monomers and dendrimers on platelet aggregation induced by ADP (5 μM).[a]

cmpd	IC_{50} [nM]
1	192 ± 90
2	35.9 ± 17.0
3	173 ± 72
9a	337 ± 77
9b	1180 ± 570
9d	914 ± 305
10c	151 ± 53
10d	495 ± 145

[a] Values are presented as the mean ± standard error of three independent experiments. Aggregation was measured at 37 °C by a turbidimetric method in a dual-channel Payton aggregometer (Payton Associates, Scarborough, Ontario, Canada). A 450 μL aliquot of human washed platelet suspension was stirred at 1100 rpm and activated by addition of ADP (5 μM), in the presence or absence of various monomers/dendrimers and in the presence of human fibrinogen (0.8 mg/mL), in a final volume of 500 μL. The extent of aggregation was estimated quantitatively by measuring the maximum curve height above the baseline level.

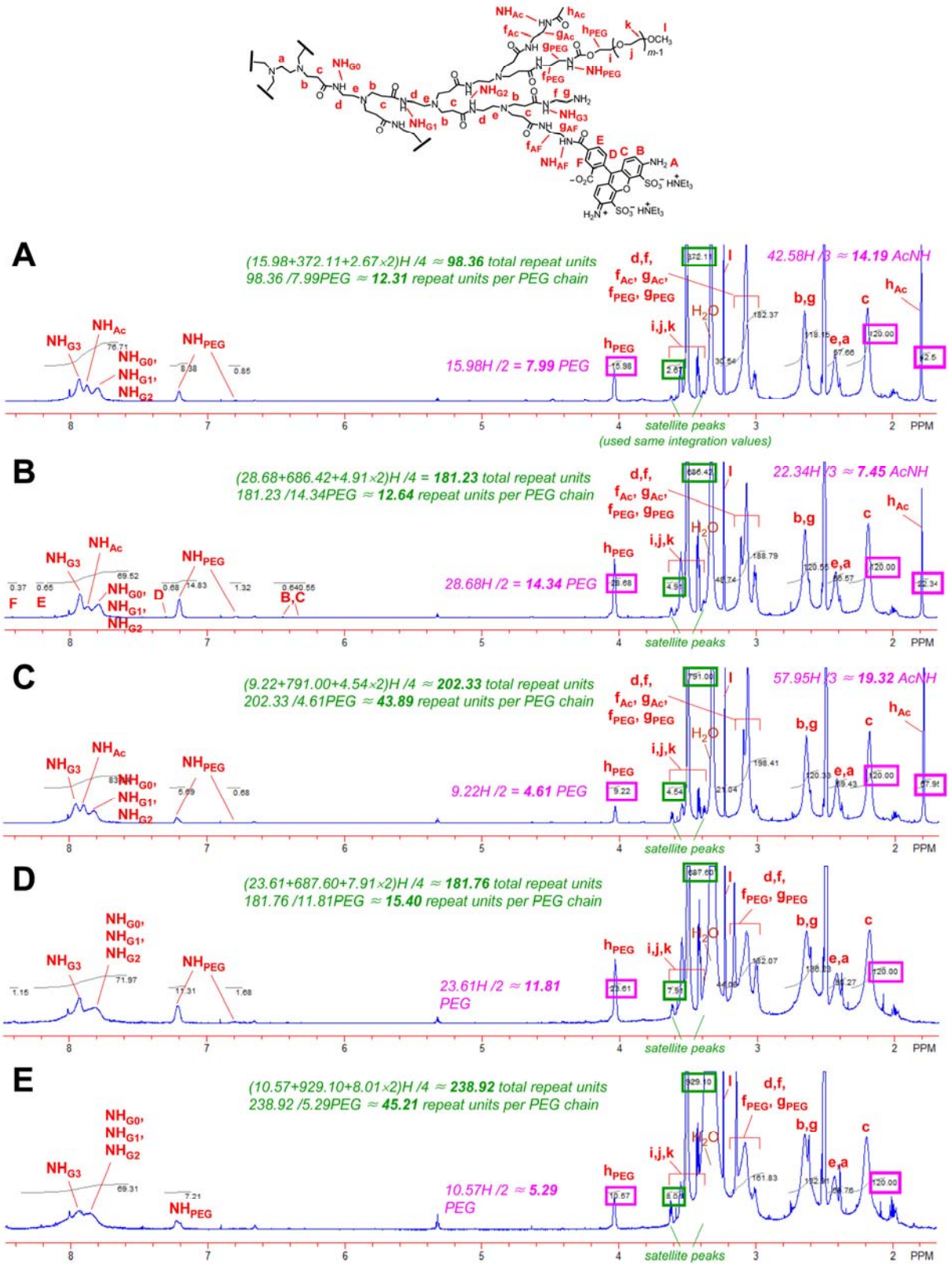

Figure S1. ^{1}H NMR spectra of PAMAM-PEG dendrimer conjugates (A) **7a**, (B) **7b**, (C) **7d**, (D) **8c**, and (E) **8d** in DMSO-d_6.

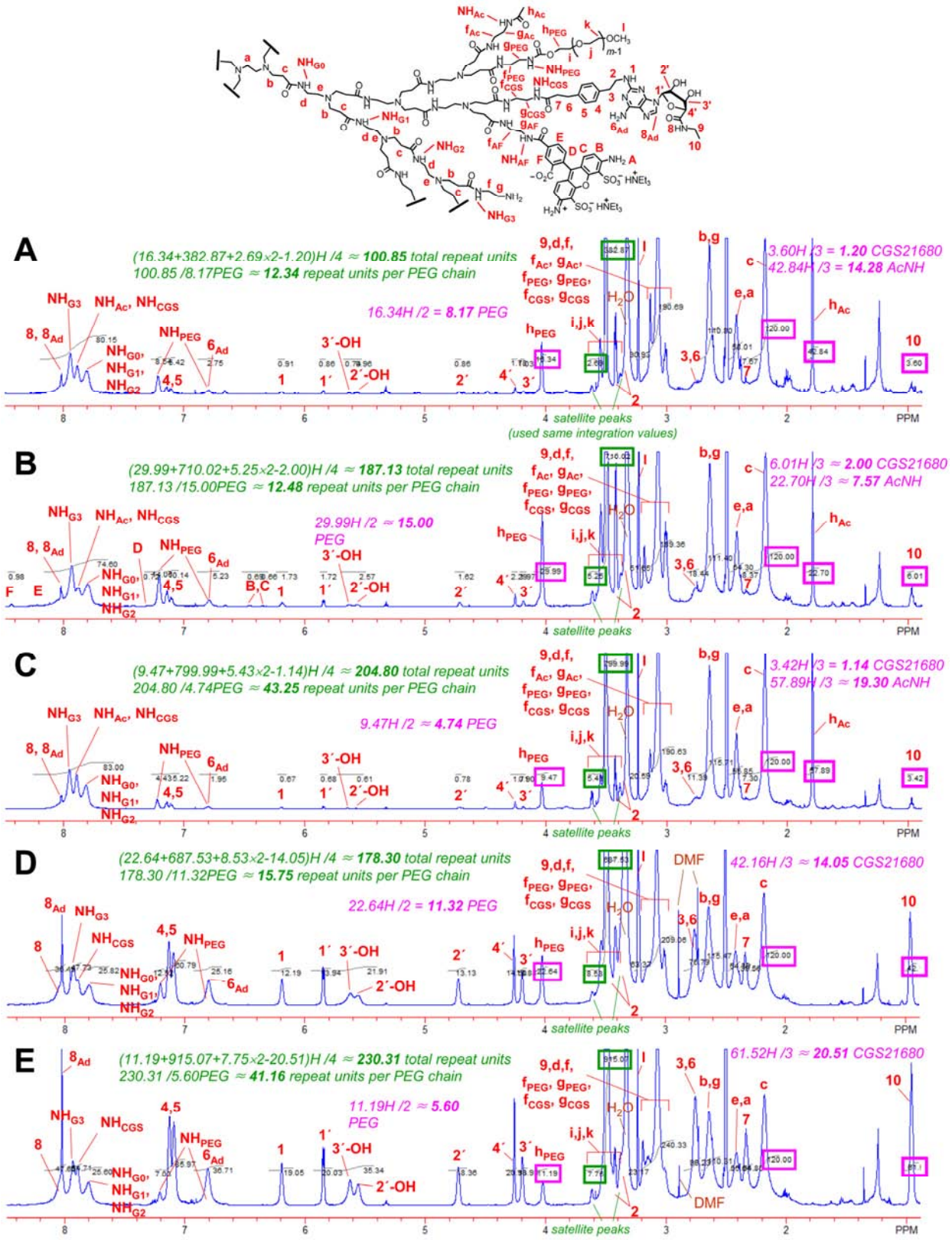

Figure S2. ^{1}H NMR spectra of PAMAM-PEG-CGS21680 dendrimer conjugates (A) **9a**, (B) **9b**, (C) **9d**, (D) **10c**, and (E) **10d** in DMSO-d_6.

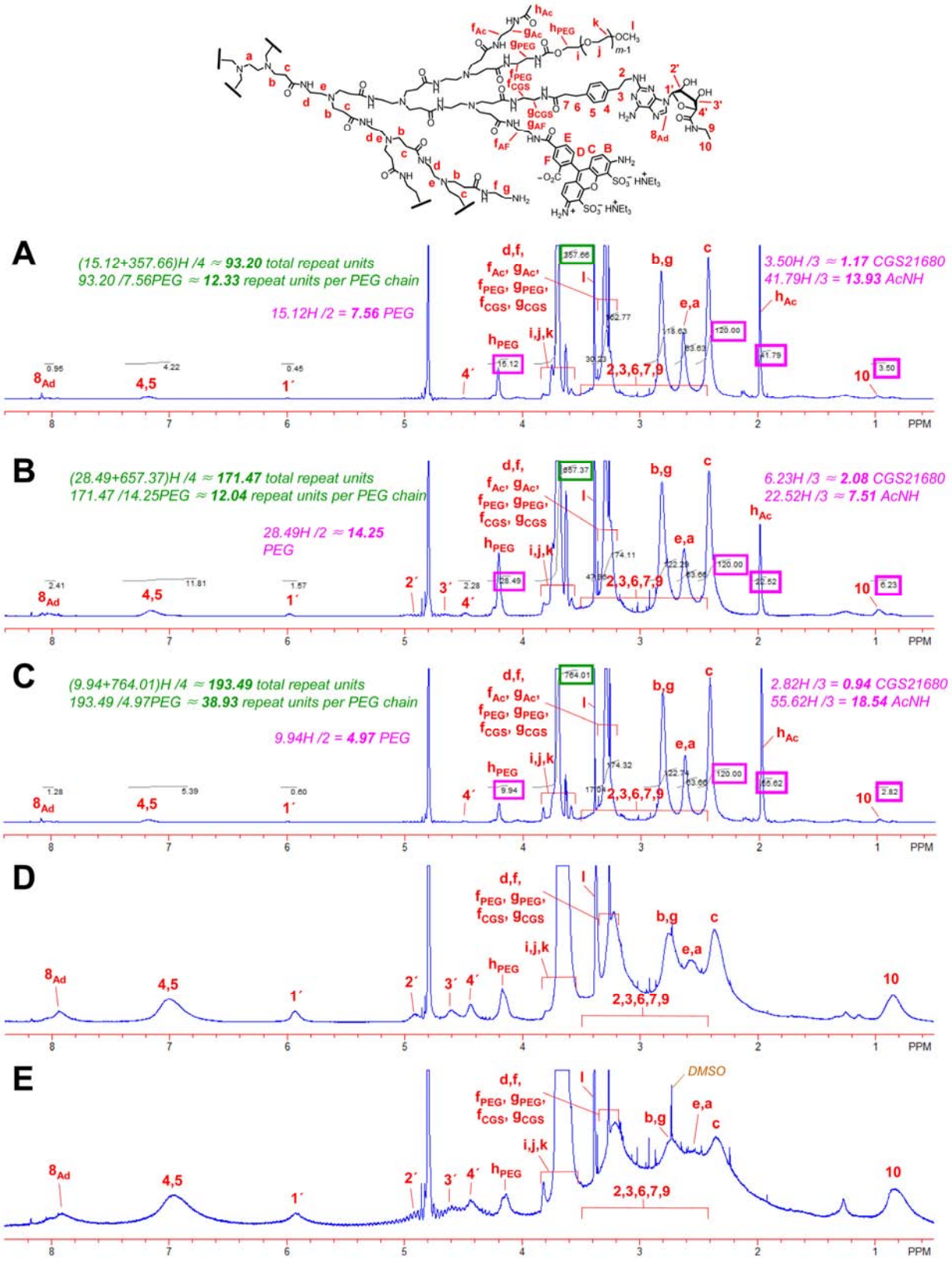

Figure S3. ^{1}H NMR spectra of PAMAM-PEG-CGS21680 dendrimer conjugates (A) **9a**, (B) **9b**, (C) **9d**, (D) **10c**, and (E) **10d** in D_2O.

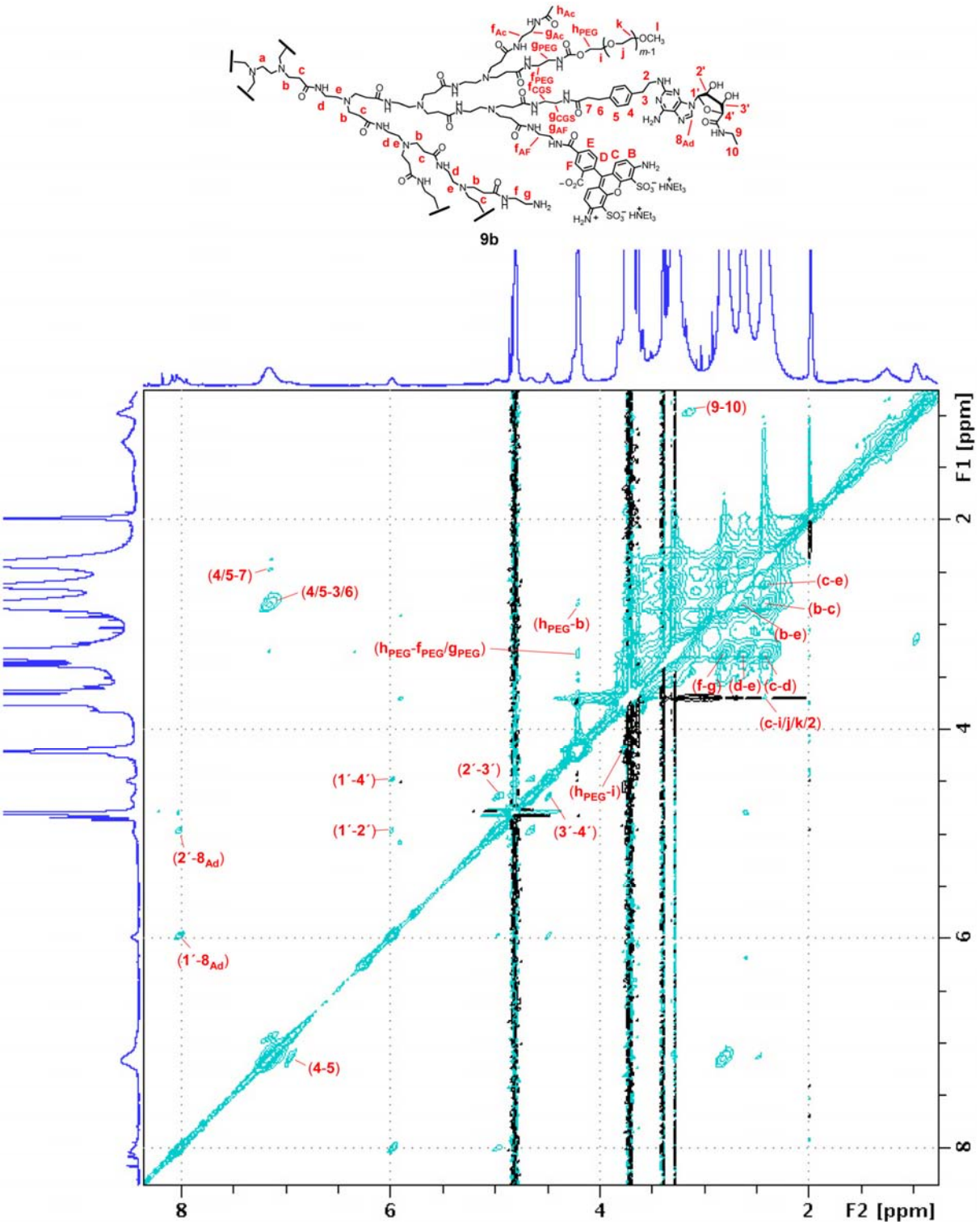

Figure S4. NOESY spectrum of PAMAM-PEG-CGS21680 dendrimer conjugate **9b** in D_2O.

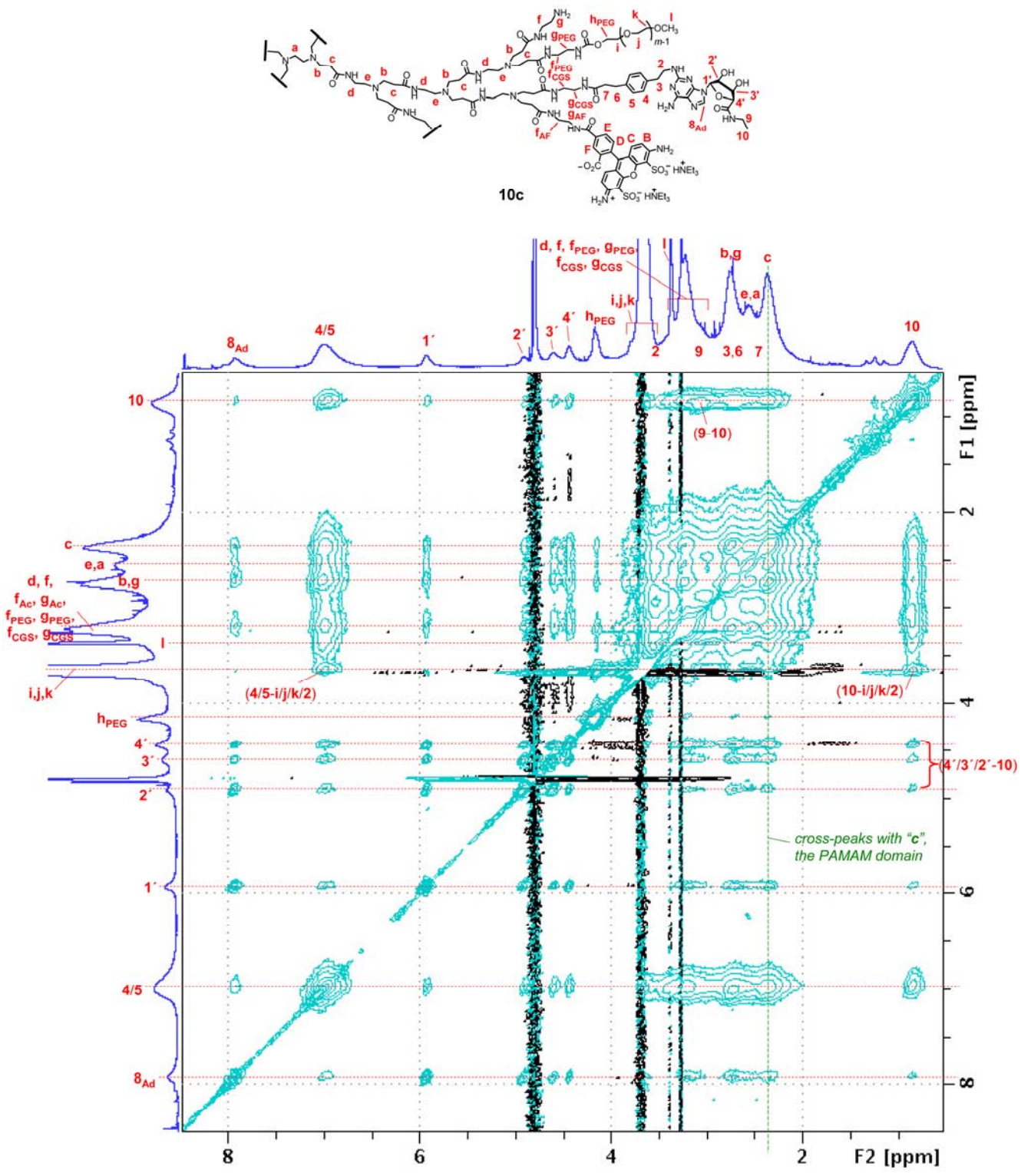

Figure S5. NOESY spectrum of PAMAM-PEG-CGS21680 dendrimer conjugate **10c** in D_2O.

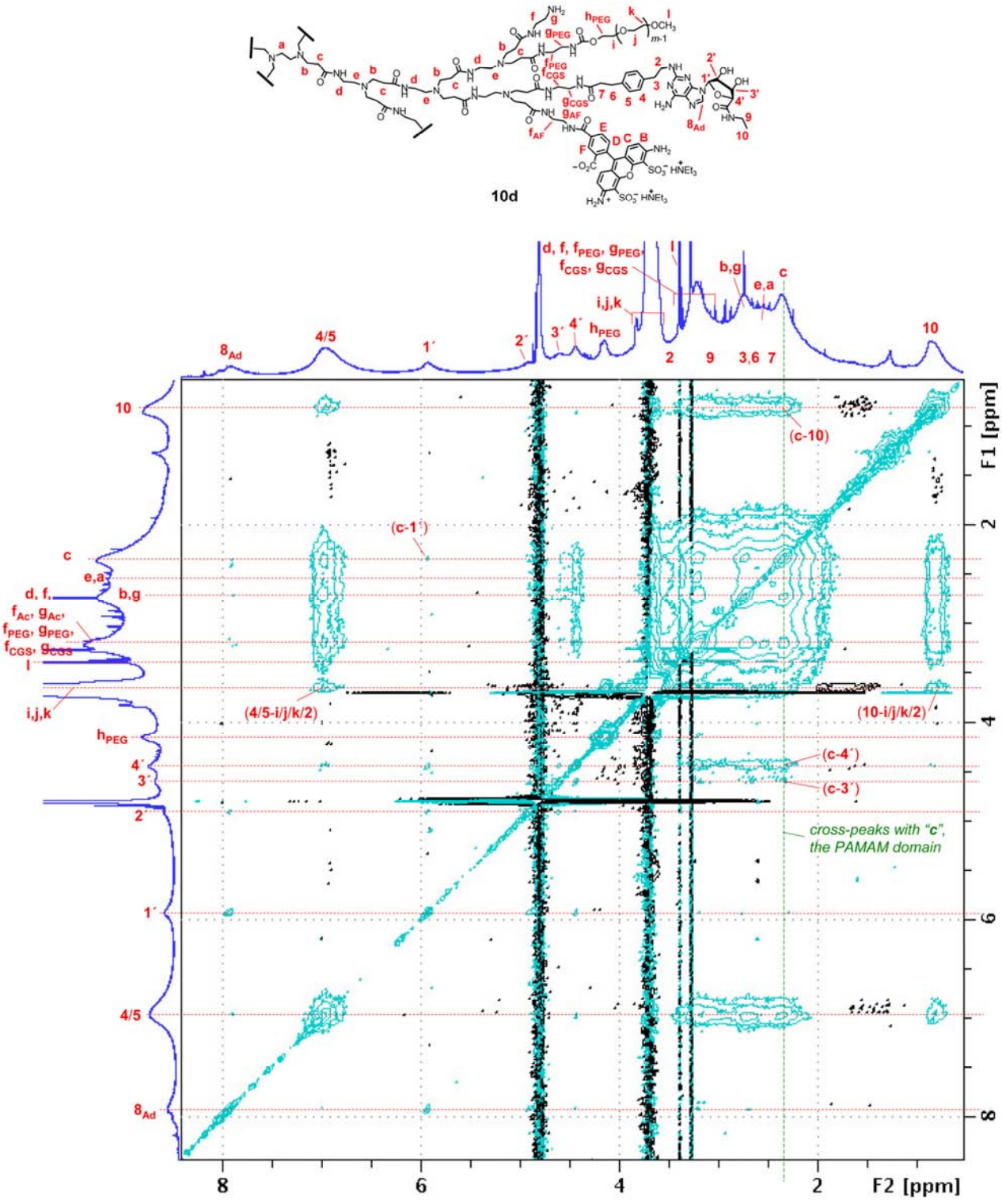

Figure S6. NOESY spectrum of PAMAM-PEG-CGS21680 dendrimer conjugate **10d** in D_2O.

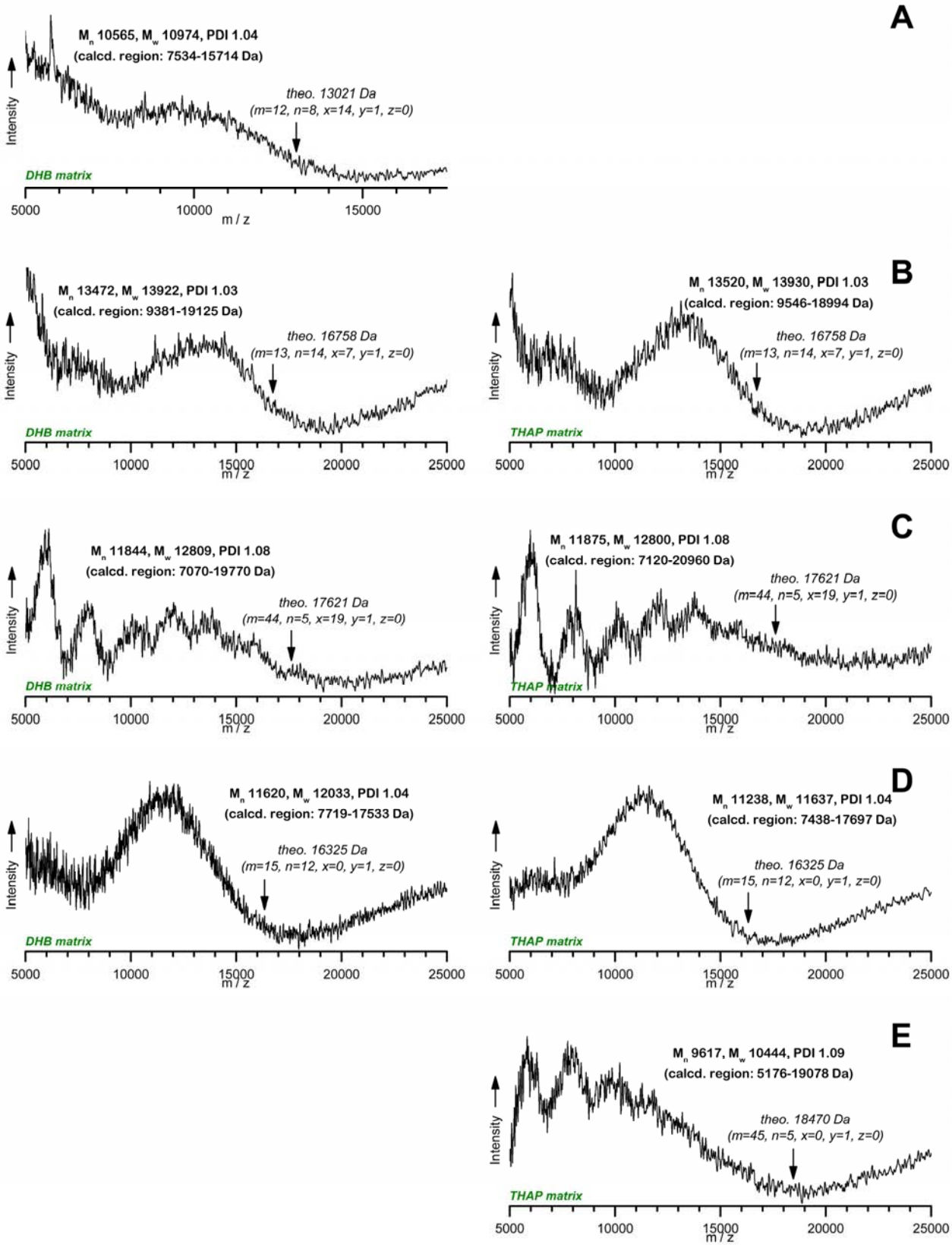

Figure S7. MALDI-TOF MS spectra of PAMAM-PEG dendrimers (A) **7a**, (B) **7b**, (C) **7d**, (D) **8c**, and (E) **8d**.

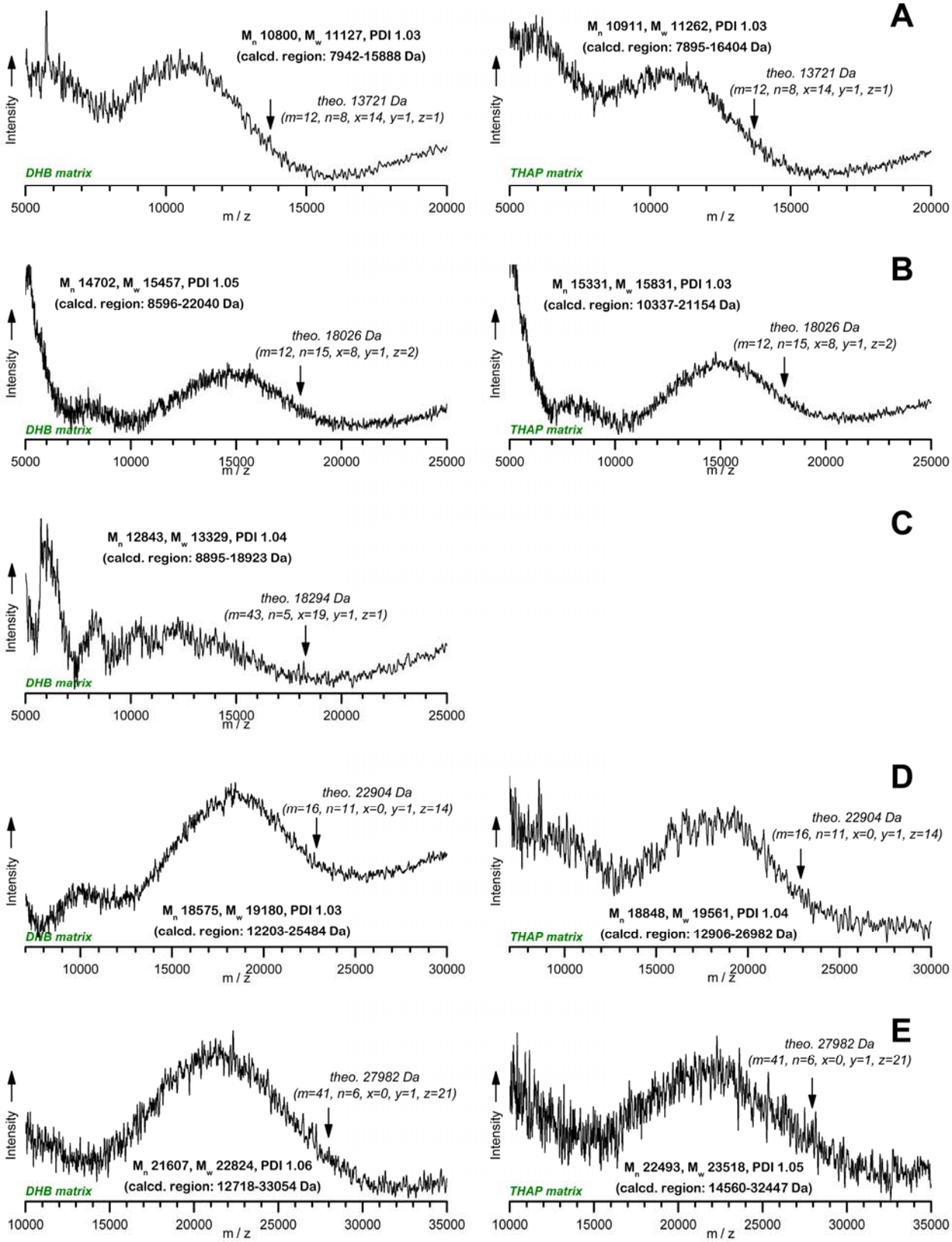

Figure S8. MALDI-TOF MS spectra of PAMAM-PEG-CGS21680 dendrimers (A) **9a**, (B) **9b**, (C) **9d**, (D) **10c**, and (E) **10d**.

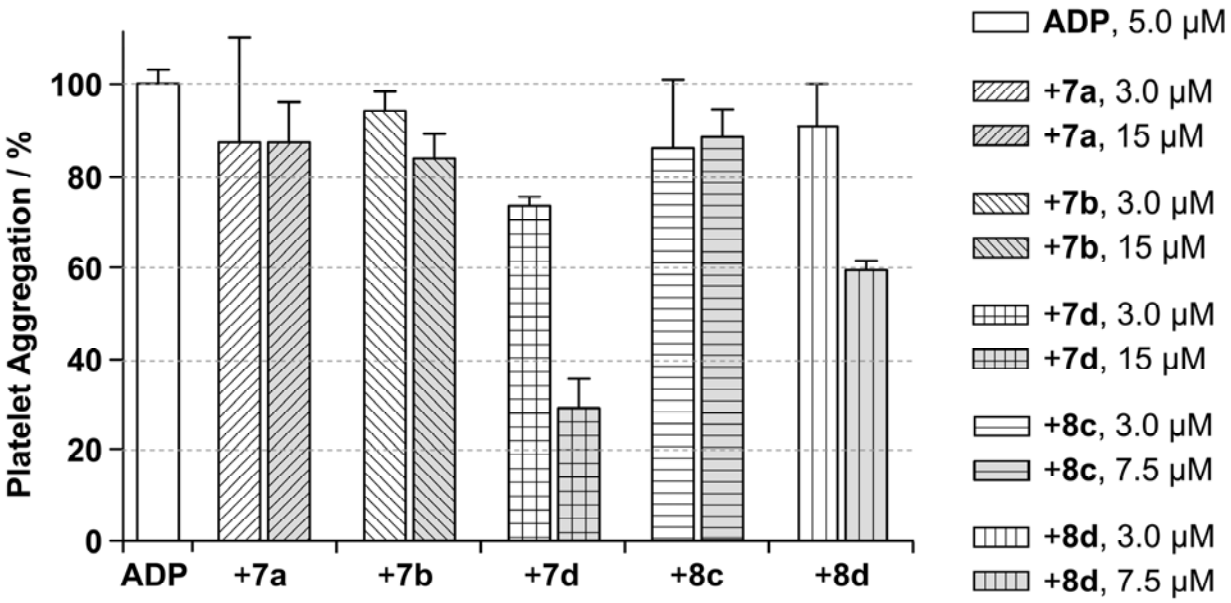

Figure S9. Platelet aggregation studies at 37 °C for dendrimer controls **7**/**8**, which did not bear any CGS21680 ligands. The degree of platelet aggregation was normalized against that induced by ADP at 5 μM (100%). A suspension of human washed platelets was incubated in the presence or absence of dendrimers, to which ADP was added 30 s later to induce the platelet aggregation. Dendrimers were added as aqueous solutions and the final concentration of each dendrimer in the media is shown (final volume: 500 μL). Each experiment was repeated three times (n = 3).

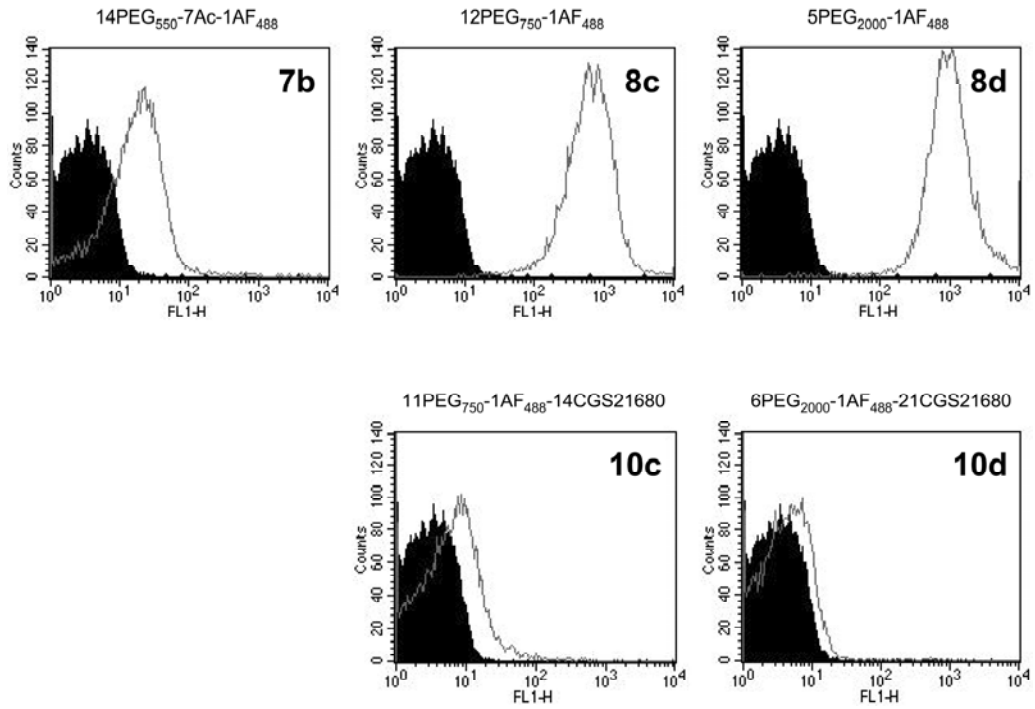

Figure S10. Flow cytometry histograms (AF_{488}, control: black area) obtained from human washed platelets incubated with 50 μM of each selected G3 PAMAM dendrimer conjugate for 30 min at 37 °C.

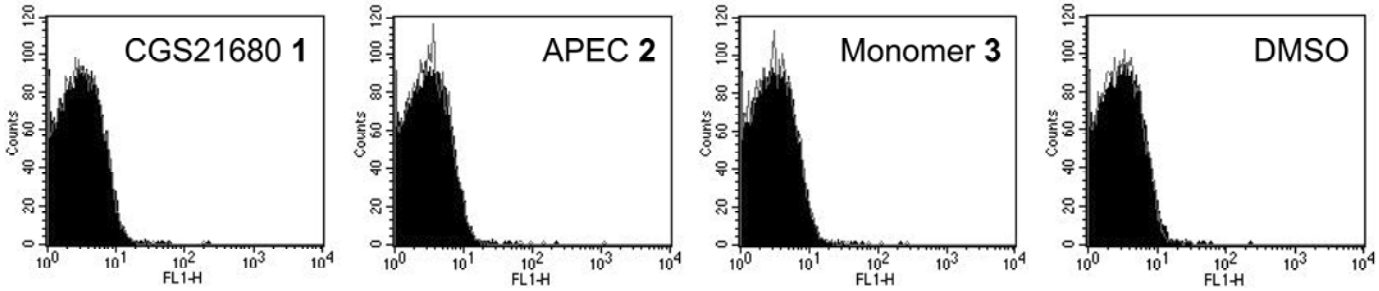

Figure S11. Flow cytometry histograms (AF_{488}, control: black area) obtained from human washed platelets incubated with 3 μM of monomeric ligands **1**–**3** or DMSO (control, same volume) for 30 min at 37 °C. Unlike dendrimer samples, stock solutions of monomeric ligands **1**–**3** were prepared in DMSO (see Experimental Section).

A New Method to Produce MonoPEGylated Dimeric Cytokines Shown with Human Interferon-α2b

Chien-Hsing Chang,*[,†,‡] Edmund A. Rossi,[†] Thomas M. Cardillo,[‡] Diane L. Nordstrom,[‡] William J. McBride,[‡] and David M. Goldenberg[§]

IBC Pharmaceuticals, Inc., Morris Plains, New Jersey 07950, Immunomedics, Inc., 300 American Road, Morris Plains, New Jersey 07950, and Garden State Cancer Center, Center for Molecular Medicine and Immunology, Belleville, New Jersey 07109. Received April 17, 2009; Revised Manuscript Received June 24, 2009

We have adapted the dock-and-lock (DNL) method into a novel PEGylation technology using human interferon-α2b (IFN-α2b) as an example. Central to DNL is a pair of distinct protein domains involved in the natural association between cAMP-dependent protein kinase (PKA) and A-kinase anchoring proteins (AKAPs). These domains serve as linkers for site-specific conjugation of poly(ethylene glycol) (PEG) to a dimeric form of IFN-α2b. The combination of a fusion protein comprising IFN-α2b and the dimerization-and-docking domain (DDD) of PKA with a PEG-derivatized anchoring domain (AD) of an interactive AKAP results in facile formation of a trimeric complex containing two copies of IFN-α2b and a single site-specifically linked PEG chain. Three such monoPEGylated dimers of IFN-α2b have been generated, the first with a 20 kDa linear PEG, referred to as α2b-362, the second with a 30 kDa linear PEG (α2b-413), and the third with a 40 kDa branched PEG (α2b-457). All three retained antiviral and antitumor activity *in vitro* and showed improved pharmacokinetic properties in mice, which translated into potent and prolonged therapeutic efficacy in the Daudi human lymphoma xenograft model. We anticipate wide applicability of the DNL method for developing long-acting therapeutics that are dimeric and monoPEGylated with the increased bioavailability allowing for less frequent dosing.

INTRODUCTION

Interferons (IFNs[1]), in the half-century since their discovery, have been found to regulate infections with RNA and DNA viruses, enhance innate and acquired immunity, and affect normal and tumor cell growth and death (*1*). The therapeutic effectiveness of IFNs has also been validated to date by the approval of IFN-α2 for treating hairy cell leukemia, chronic myelogenous leukemia, malignant melanoma, follicular lymphoma, condylomata acuminata, AIDS-related Kaposi sarcoma, and chronic hepatitis B and C; IFN-β for treating multiple sclerosis; and IFN-γ for treating chronic granulomatous disease and malignant osteopetrosis. Despite a vast body of literature on this group of autocrine and paracrine cytokines, their functions in health and disease are still being elucidated, including more effective and novel forms being introduced clinically (*2, 3*).

As demonstrated by PEGINTRON (*4*) and PEGASYS (*5*), the efficacy of IFNs can be enhanced by improving the bioavailability with PEGylation, a process of chemically linking PEG to the therapeutic agent of interest, with the resulting conjugate exhibiting an increased serum half-life (*6*). Additional advantages of PEGylation in general include reduced immunogenicity, decreased dosing frequency, increased solubility, enhanced resistance to proteolysis, and exclusion of renal clearance. For example, a popular approach for improving the therapeutic efficacy of an enzyme has been to prepare conjugates containing multiple PEGs of small size, as known for methioninase (*7*), L-methione γ-lyase (*8*), arginine deiminase (*9*), adenosine deaminase (*10*), L-asparaginase (*11*), and liver catalase (*12*). PEGylations of nonenzyme proteins, such as bovine serum albumin (*13*); small molecules, such as inhibitors of integrin α4β1 (*14*); anti-VEGF aptamer (*15*), and oligodeoxynucleotides (*16*), have also been described.

Because the most common reactive sites on proteins (including peptides) for attaching PEG are the ε-amino groups of lysine and the α-amino group of the N-terminal residue, most methods of PEGylation result in modification of multiple sites, yielding not only monoPEGylated conjugates consisting of mixtures of positional isomers (*4, 5*), but also adducts comprising more than one PEG chain. Nevertheless, site-specific attachment of a single PEG to the α-amino group of the N-terminal residue was reported to be the predominant product upon reacting PEG-aldehyde at low pH with IFN-β1b (*17*) or IFN-β1a (*18*). Similar strategies were applied to prepare N-terminally linked PEG to G-CSF (*19*) or type I soluble necrosis factor receptor (*20*). Site-directed PEGylation of an endogenous or engineered free cysteine residue in a target protein has also been demonstrated with PEG-maleimide for G-CSF (*21*), hemoglobin (*22*), IL-2 (*23*), IFN-α2 (*24*), GM-CSF (*25*), EPO (*26*), scFv (*27*), Fab (*28*), and miniantibodies (*29*). Moreover, the feasibility of reversible or releasable PEGylation, wherein covalently attached

* To whom correspondence should be addressed. Tel: (973) 605-1330. Fax: (973)-605-1103. E-mail: kchang@immunomedics.com.

† IBC Pharmaceuticals, Inc.

‡ Immunomedics, Inc.

§ Garden State Cancer Center.

[1]Abbreviations: AD, anchoring domain; AKAPs, A-kinase anchoring proteins; AUC, area under curve; BCN3, bicin3; DDD, dimerization and docking domain; DNL, dock and lock; EDANS, 5-(2′-aminoethyl)-aminonaphthalene-1-sulfonic acid; EPO, erythropoietin; G-CSF, granulocyte colony-stimulating factor; GM-CSF, granulocyte-macrophage colony-stimulating factor; IFNs, interferons; IL-2, interleukin-2; mPEG, monomethoxyPEG; mPEG2-MAL-40K, a 40 kDa branched PEG with a maleimide; MST, median survival time; MTS, [3-(4,5-dimethylthiazol-2-yl)-5-(3-carboxymethoxyphenyl)-2-(4-sulfophenyl)-2*H*-tetrazolium]; OPTE, *ortho*-pyridylthioester; PBST, phosphate-buffered saline containing Tween; PEG, poly(ethylene glycol); PEGINTRON, Peginterferon alfa-2b; PEGASYS, Peginterferon alfa-2a; PKA, cAMP-dependent protein kinase; TCEP, Tris [2-carboxyethyl] phosphine hydrochloride.

10.1021/bc9001773 CCC: $40.75 © 2009 American Chemical Society
Published on Web 09/08/2009

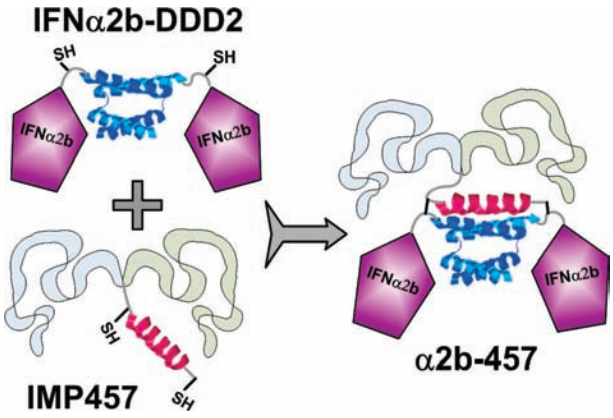

Figure 1. Schematics of IMP457, α2b-DDD2, and α2b-457. Ribbons indicate 40 kDa branched PEG; red helix, AD2; blue helix, DDD2; SH, free sulfhydryl groups of engineered cysteine residues.

PEG can be cleaved *in vivo*, has been achieved with a variety of degradable linkages as exemplified by linking a 40-kDa PEG-SH to IFN-α2 with a 2-sulfo-9-fluorenylmethoxycarbonyl-containing bifunctional reagent (*30*), by attaching linear or branched PEG-BCN3 to lyzosome or IFN-*β*1b (*31*), or by conjugating PEG to lysozyme via a dithiobenzyl urethane linkage (*32*). Recently, an innovative strategy for site-specific PEGylation of disulfide bonds has been reported (*33*), but its use may be limited to only those proteins with native disulfide bonds that are suitably oriented for such modification.

The dock-and-lock (DNL) method developed by us (*34*, *35*) provides a unique approach to build multivalent, multifunctional complexes of defined composition and retained bioactivity. The key to the DNL method is the exploitation of the specific protein−protein interactions occurring in nature between the regulatory (R) subunits of cAMP-dependent protein kinase (PKA) and the anchoring domain (AD) of A-kinase anchoring proteins (AKAPs) (*36*, *37*). Isozymes of PKA are found with two types of R subunits (RI and RII), and each type has α and *β* isoforms (*38*). The R subunits have been isolated only as stable dimers and the dimerization domain has been shown to consist of the first 44 amino-terminal residues (*39*). The AD of AKAPs for PKA is an amphipathic helix of 14−18 residues (*40*). Interestingly, AKAPs will only bind to dimeric R subunits. For human RIIα, the AD binds to a hydrophobic surface formed by the 23 amino-terminal residues (*41*). Thus, the dimerization domain and AKAP binding domain of human RIIα are both located within the same N-terminal 44 amino acid sequence (*39,42*), which is termed the dimerization and docking domain (DDD) herein.

Because an entity derivatized with the DDD (termed the DDD-module) is expected to self-associate to form a dimer, thereby creating a docking site for an entity derivatized with the AD (termed the AD-module), combining a DDD-module with an AD-module results in the formation of a noncovalent complex containing three entities, which can be stably tethered by introducing cysteine residues into the DDD and AD at strategic positions, as demonstrated with the DDD2 and AD2 (*34*).

Here, with a DDD2-module of IFN-α2b expressed as a fusion protein and three synthetic AD2-modules of different mPEG, we describe the successful adaptation of the DNL method into a novel PEGylation technology, which has the salient feature of monoPEGylating a dimeric form of IFN-α2b at a specific site that is outside the sequence of native IFN-α2b (Figure 1).

EXPERIMENTAL PROCEDURES

Generation of IMP360. The AD2-peptide with an EDANS at its carboxyl terminus to provide a fluorescent tag was termed IMP360 and made at 0.1 mmol scale with EDANS resin (Novabiochem, EMD Biosciences, Inc., San Diego, CA) on a PS3 peptide synthesizer (Protein Technologies, Tucson, Az) using Fmoc methodology. Starting from the C-terminus, the protected amino acids used were Fmoc-Cys(t-Buthio)-OH, Fmoc-Gly-OH, Fmoc-Ala-OH, Fmoc-Gln(Trt)-OH, Fmoc-Gln-(Trt)-OH, Fmoc-Ile-OH, Fmoc-Ala-OH, Fmoc-Asn(Trt)-OH, Fmoc-Asp(OBut)-OH, Fmoc-Val-OH, Fmoc-Ile-OH, Fmoc-Gln(Trt)-OH, Fmoc-Lys(Boc)-OH, Fmoc-Ala-OH, Fmoc-Leu-OH, Fmoc-Tyr(But)-OH, Fmoc-Glu(OBut)-OH, Fmoc-Ile-OH, Fmoc-Gln(Trt)-OH, Fmoc-Gly-OH, and Fmoc-Cys(Trt)-OH. The peptide was cleaved from the resin, purified by RP-HPLC, and determined to have a molecular mass of 2660 Da. The sequence of IMP360 is CGQIEYLAKQIVDNAIQQAGC(SS-tbu)-EDANS.

Generation of IMP362 and IMP413. The two linear PEG-AD2 modules were prepared by coupling IMP360 to mPEG-OPTE (Nectar Therapeutics, San Carlos, CA) of 20 kDa or 30 kDa, resulting in IMP362 or IMP413, respectively. The sulfhydryl group of the N-terminal cysteine of IMP360 displaces pyridine-2-thiol from mPEG-OPTE and forms a thioester bond to mPEG. A subsequent reaction of the adjacent amino group with the carbonyl group of the thioester leads to the formation of a more stable amide bond and the regeneration of the sulfhydryl group. To prepare IMP362, IMP360 (11.5 mg) was mixed with 20 kDa mPEG-OPTE (127 mg) in 7 mL of 1 M Tris-HCL, pH 7.8. Acetonitrile (1 mL) was added to dissolve some suspended material. The reaction was stirred at room temperature for 4 h to effect the attachment of mPEG to the amino-terminal cysteine via an amide bond. Subsequently, 41 mg of Tris [2-carboxyethyl] phosphine hydrochloride (TCEP) and 43 mg of cysteine were added to deprotect the remaining cysteine. The reaction mixtures were stirred for 1 h and desalted using PD-10 columns, which had been equilibrated with 20% methanol in water. The samples were lyophilized to obtain approximately 150 mg of IMP362 (MH^+ 23 713). IMP413 (MH^+ 34 499) was made similarly using 30 kDa mPEG-OPTE (190 mg).

Generation of IMP421 and IMP457. The AD2-containing peptide (IMP421, MH^+ 2891, Figure 2) was made for derivatizing mPEG2-MAL-40K (Nectar Therapeutics) to obtain the branched PEG-AD2 module (IMP457). IMP421 was synthesized on NovaSyn TGR resin (487.6 mg, 0.112 mmol) by adding the following amino acids to the resin in the order shown: Fmoc-Gly−OH, Fmoc-Cys(t-Buthio)-OH, Fmoc-Gly-OH, Fmoc-Ala-OH, Fmoc-Gln(Trt)-OH, Fmoc-Gln(Trt)-OH, Fmoc-Ile-OH, Fmoc-Ala-OH, Fmoc-Asn(Trt)-OH, Fmoc-Asp(OBut)-OH, Fmoc-Val-OH, Fmoc-Ile-OH, Fmoc-Gln(Trt)-OH, Fmoc-Lys(Boc)-OH, Fmoc-Ala-OH, Fmoc-Leu-OH, Fmoc-Tyr(But)-OH, Fmoc-Glu(OBut)-OH, Fmoc-Ile-OH, Fmoc-Gln(Trt)-OH, Fmoc-Gly-OH, Fmoc-Cys(t-Buthio)-OH, Fmoc-NH-PEG_3-COOH, Fmoc-Cys(Trt)-OH. The peptide was then cleaved from the resin and purified by RP-HPLC to yield 32.7 mg of a white solid. The N-terminal cysteine of IMP421 has its amino group protected as an acetyl derivative and provides a sulfhydryl group to react with the maleimide of mPEG2-MAL-40K.

IMP457 was made as follows. To a solution of IMP421 (15.2 mg, 5.26 *μ*mol) and mPEG2-MAL-40K (274.5 mg, 6.86 *μ*mol) in 1 mL of acetonitrile was added 7 mL of 1 M Tris pH 7.8. After 3 h at room temperature, the excess mPEG2-MAL-40K was quenched with L-cysteine (49.4 mg), followed by S-S-*t*Bu deprotection over 1 h with TCEP (59.1 mg). The resulting solution was dispensed into two 10K Slide-A-Lyzer dialysis cassettes (4 mL in each) and dialyzed overnight at 2−8 °C against 5 L of 5 mM ammonium acetate, pH 5.0. Following three additional 5 L buffer changes, the dialyzed solution (19.4 mL) was transferred into two 20 mL scintillation vials, frozen,

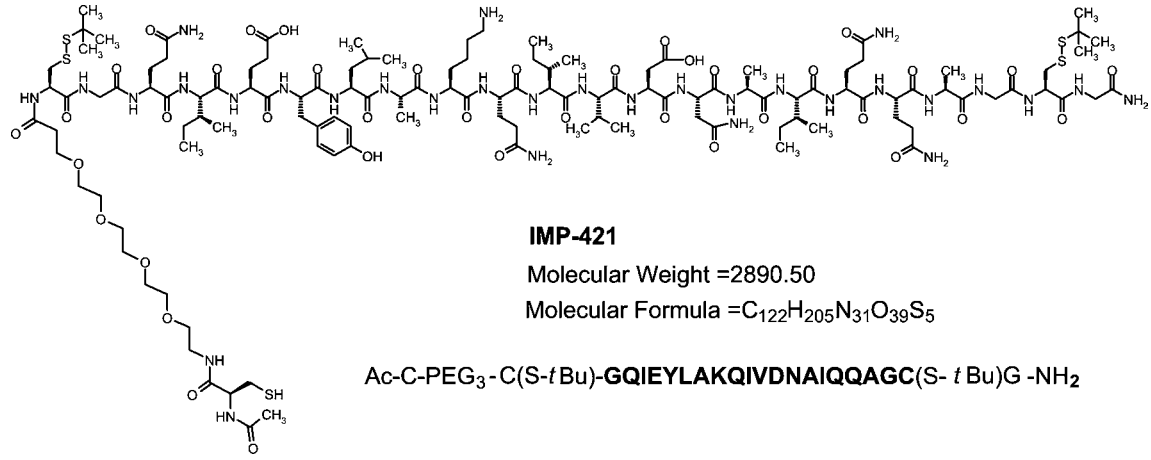

Figure 2. Schematic structure of IMP421.

and lyophilized to yield a white solid (246.7 mg). The molecular mass as determined by MALDI-TOF was 42 982 for mPEG2-MAL-40K (Supporting Information Figure S1A) and 45 500 for IMP457 (Supporting Information Figure S1B).

Generation of α2b-DDD2. All restriction enzymes were purchased from New England Biolabs (Beverly, MA). A full-length human IFN-α2b cDNA clone (Invitrogen Ultimate ORF human clone cat# HORF01Clone ID IOH35221) was used as a template for amplification by PCR to generate a sequence comprising XbaI—SP—IFN-α2b—6 His—*Bam*HI, where XbaI/*Bam*HI, SP, and 6 His are restriction sites, the signal peptide native to IFN-α2b, and a hexahistidine tag, respectively. The following oligonucleotides were synthesized by Sigma Genosys (Haverhill, UK) and used as primers.

IFNA2 XbaI left

5′-TCTAGACACAGGACCTCATCATGGCCT-TGACCTTTGCTTTACTGG-3′

IFNA2 *Bam*HI right

5′-GGATCCATGATGGTGATGATGGTGT-GACTTTTCCTTACTTCTTAAACTTTCTTGC-3′

PCR reactions were performed using Amplitaq polymerase (Applied Biosystems, Foster City, CA) and a Perkin-Elmer (Wellesley, MA) GeneAmp PCR system 9600. The PCR amplimer was cloned into the pGemT vector (Promega) from which the IFN-α2b amplimer was excised with XbaI and *Bam*HI and ligated to a DDD2-pdHL2 mammalian expression vector (*34*) previously digested with XbaI and *Bam*HI to generate *IFNα2b-DDD2-pdHL2*, the expression vector for α2b-DDD2.

IFNα2b-DDD2-pdHL2 (30 μg) was linearized by digestion with *Sal*I and stably transfected by electroporation (450 V, 25 μF) into Sp/ESF myeloma cells (2.8×10^6 cells), an engineered derivative of Sp2/0 that can be grown and transfected in serum-free medium. Transfectants were cultured in Hybridoma SFM (Invitrogen, Carlsbad, CA) supplemented with 0.2 μM methotrexate (Calbiochem, La Jolla, CA) in 96-well plates, and screened for IFN-α2b expression with a human interferon alpha ELISA kit (PBL Interferon Source, Piscataway, NJ) following the manufacturers' instructions.

α2b-DDD2 was purified from terminal batch cultures of a select clone grown in roller bottles. Briefly, the supernatant fluid was clarified by centrifugation, filtered through 0.2 μm membranes, diafiltered into 1× binding buffer (10 mM imidazole, 0.5 M NaCl, 50 mM NaH_2PO_4, pH 7.5), concentrated 20-fold, and loaded onto a Ni-NTA column (Qiagen). After washing with 0.02% Tween 20 in 1× binding buffer and then 30 mM imidazole, 0.02% Tween 20, 0.5 M NaCl, 50 mM NaH_2PO_4, pH 7.5, α2b-DDD2 was eluted with 250 mM imidazole, 0.02% Tween 20, 150 mM NaCl, 50 mM NaH_2PO_4, pH 7.5, and stored in the same buffer at 2−8 °C until needed. The mass of α2b-DDD2 was determined by MALDI-TOF to be 52 185, indicating a dimer. The monomeric form of α2b-DDD2 consists of IFN-α2b fused at its carboxyl-terminus to a 63-residue peptide of K S H H H H H H G S G G G G S G G G C G H I Q I P P G L-TELLQGYTVEVLRQQPPDLVEFAVEYFTRLREARA.

Preparation and Purification of α2b-362, α2b-413, and α2b-457. Conjugations of α2b-DDD2 with IMP362, IMP413, and IMP457 were performed to generate PEGylated α2b-362, α2b-413, and α2b-457, respectively. In general, a 10-fold molar excess of reduced and lyophilized IMP362, IMP413, or IMP457 was added to 2.25 mg of α2b-DDD2 in 3.5 mL of 250 mM imidazole, 0.02% Tween 20, 150 mM NaCl, 1 mM EDTA, 50 mM NaH_2PO_4, pH 7.5. After 6 h at room temperature in the dark, the reaction mixture was dialyzed against CM loading buffer (150 mM NaCl, 20 mM NaAc, pH 4.5) at 4 °C in the dark. The PEGylated product was purified by cation exchange chromatography using a 1 mL Hi-Trap CM-FF column (Amersham), which was equilibrated with CM loading buffer. After sample loading, the column was washed with CM loading buffer to baseline, followed by washing with 15 mL of 0.25 M NaCl, 20 mM NaAc, pH 4.5. The PEGylated product was eluted with 12.5 mL of 0.5 M NaCl, 20 mM NaAc, pH 4.5.

SDS-PAGE, Fluorescence Imaging, and Immunoblot. SDS-PAGE analyses were performed using 4−20% gradient Tris-glycine gels (Cambrex Bio Science Rockland, Rockland, ME). To normalize the samples for direct protein mass comparison, each fraction eluted from the CM-FF column was concentrated to 3.5 mL to match the reaction volume. Samples were diluted with an equal volume of 2× sample buffer (2% SDS, 5% glycerol, 62.5 mM Tris-HCl, pH 6.8) and heated to 95 °C before loading 10 μL per lane. For reducing gels, 5% of β-2-mercaptoethanol was included in the sample buffer. Gels were imaged by direct fluorescence to visualize bands containing the EDANS tag using a Kodak Image Station 4000R before staining with Coomassie blue to visualize the protein bands. Duplicate gels were transferred to PVDF membranes for immunoblot analysis. Blots were probed with rabbit anti-interferon alpha polyclonal antibody (AB1434, Chemicon International) diluted 1:1000 in 1% BSA-PBST. Signal was detected with HRP-conjugated goat antirabbit IgG (Jackson Immunoresearch) and Pierce ECL Western Blotting Substrate (Pierce Biotechnology, Rockford, IL).

Antiviral Assay. The reduction of viral cytopathic effect (CPE) was determined by an independent laboratory (PBL Interferon Source, Piscataway, NJ) using encephalomyocarditis virus (EMCV) to infect human lung epithelial A549 cells. Plates were stained with crystal violet and the OD was measured by spectrophotometry on a 96-well plate reader following solubilization of the dye. The data were analyzed with GraphPad *Prism*

software (Advanced Graphics Software, Encinitas, CA) using a sigmoidal fit (variable slope) nonlinear regression. The antiviral titer was determined by comparison of EC_{50} values with that of an IFNα standard.

Antiproliferative Assay. Each test article was diluted to 500 pM in RPMI 1640 media supplemented with 10% FBS, from which triplicate, 3-fold serial dilutions were made in 96-well tissue culture plates (50 μL/well). Daudi cells were diluted to 4 × 10^5 cells/mL and 50 μL was added to each well (20K/well). After 4 days at 37 °C, viable cell densities were determined by MTS using a CellTiter 96 Cell Proliferation Assay (Promega, Madison, WI). Dose−response curves were generated and EC_{50} values were obtained by sigmoidal fit nonlinear regression using GraphPad *Prism* software. Specific activities were determined by comparison of EC_{50} values with PEGINTRON using the specific activity provided with the product insert.

Reporter Gene Assay. The iLite Human Interferon Alpha Cell-Based Assay Kit (PBL Interferon Source) was used to determine specific activities following the manufacturers' suggested protocol. Briefly, samples were diluted in 1% BSA-PBS to 5, 1.25, and 0.3125 ng/mL for α2b-362 and α2b-413; to 10, 2.5, and 0.625 ng/mL for α2b-457 and PEGASYS; and to 1, 0.25, and 0.0625 ng/mL for PEGINTRON. Each dilution was assayed in triplicate and incubated overnight with the supplied cells. Specific activities were extrapolated from a standard curve generated with the supplied standard.

Pharmacokinetics in Mice. The initial study evaluating α2b-362, α2b-413, PEGINTRON, and rhIFN-α2a (Chemicon IF007, lot 06008039084) was performed in 4 groups of adult female Swiss-Webster mice (∼35 g) with 2 animals in each group. Each test article was administered as a single bolus i.v. injection at mole-equivalent dose: rhIFN-α2a, 3 μg; PEGINTRON, 5 μg; α2b-362, 11 μg; and α2b-413, 13 μg. Mice were bled via the retro-orbital method at various time points (predose, 5 min, and 2, 8, 24, 48, 72, 96, and 168 h postinjection). The subsequent study evaluating α2b-457, α2b-413, PEGINTRON, and PEGASYS was performed in 4 groups of adult male Swiss-Webster mice (∼40 g) with 4 animals in each group. Each test article was administered as a single s.c. injection at mole-equivalent dose (100 pmol) in equal volumes (250 μL). Mice were bled via the retro-orbital method at various time points (30 min, and 2, 8, 24, 48, 72, and 96 h postinjection). For each study, the blood was allowed to clot, centrifuged, and the serum removed for storage at −70 °C until analysis. Concentrations of IFN-α in the serum samples were determined using a human interferon alpha ELISA kit (PBL Interferon Source) following the manufacturers' instructions. Briefly, the serum samples were diluted appropriately according to the human IFN-α standard provided in the kit. The antibody immobilized to the microtiter plate wells captures interferon. A second antibody is then used to reveal the bound interferon, which is quantified by antisecondary antibody conjugated to horseradish peroxidase (HRP) following the addition of tetramethyl benzidine. The plates were read at 450 nm. The amount of IFN in the serum for each animal was used to determine the various PK parameters. These data were analyzed with *WinNonLin PK* software (v 5.1; Pharsight Corp.; Mountain View, CA) using noncompartmental analysis (representing the best-fit model for the data).

***In Vivo* Antitumor Efficacy.** All four studies were performed with the approval of the local animal care and use committee in eight-week-old female SCID mice injected i.v. with 1.5 × 10^7 Daudi cells per animal. Therapy commenced 1 day after the Daudi transplantation. Mice were observed daily for signs of distress and paralysis. They were weighed weekly. In the event a mouse lost greater than 15% of its body weight (but <20%), it was weighed every 2 days until it either gained back its weight to <15% loss or was sacrificed due to >20% loss.

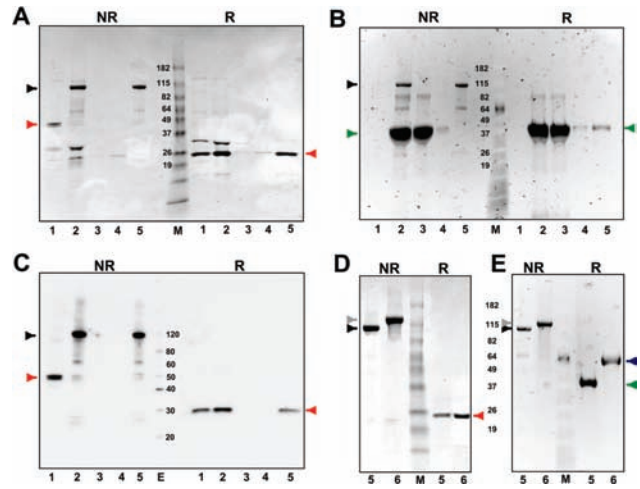

Figure 3. Reducing (R) and nonreducing (NR) SDS-PAGE analysis of the conjugation and purification of α2b-362 and α2b-413. Gels were stained with Coomassie blue (A,D), imaged with direct fluorescence (B,E), or transferred to PVDF membranes and probed by immunoblotting with anti-IFN-α (C). Arrowheads show the positions of α2b-362 (black), α2b-413 (gray), IFNα2b-DDD2 (red), IMP362 (green), and IMP413 (blue). Lane 1, IFNα2b-DDD2; Lane 2, the reaction mixture of α2b-362 before purification; Lane 3, unbound fraction of α2b-362; Lane 4, wash fraction of α2b-362 (0.25 M NaCl elution); Lane 5, purified α2b-362 (0.5 M NaCl elution); Lane 6, purified α2b-413; Lane M, prestained molecular weight markers; Lane E, ECL molecular weight markers.

Mice were also terminated when hindlimb paralysis developed or if they became otherwise moribund.

For the first study, there were 10 different treatment groups of 5 mice each. Equivalent units of activity of PEGINTRON, α2b-362, and α2b-413 were administered once every 7 days via s.c. injection in either the left or right flank at 3 different doses (3500, 7000, and 14 000 IU). In the second study, 14 000 IU of PEGINTRON or α2b-413 was administered s.c. with varied dosing schedules: once weekly for 4 weeks (q7d×4), once every other week over 8 weeks (q2wk×4), and once every 3 weeks over 12 weeks (q3wk×4). There were 7 different treatment groups of 6−7 mice each. All mice received a total of 4 injections. The third study was performed in 4 treatment groups of 10 each, evaluating 14 000 IU of α2b-413, PEGASYS, or PEGINTRON given s.c. once every 4 weeks vs once weekly. In the fourth study, α2b-457 was compared with α2b-413, PEGINTRON, and PEGASYS in 2 different doses (20 and 10 pmol) given 4 weeks apart.

RESULTS AND DISCUSSION

Design and Characterization of α2b-362 and α2b-413. We produced a DDD2 module of IFN-α2b with a hexahistidine tag in myeloma cells and synthesized two AD2 modules of linear PEG, one with a 20 kDa PEG, designated IMP362, and the other with a 30 kDa PEG, designated IMP413. In addition, each PEG-AD2 module also contains EDANS as a fluorescent tag. The fusion protein (α2b-DDD2) was reacted with IMP362 and IMP413 in excess to yield the two PEGylated conjugates, α2b-362 and α2b-413, respectively, which were purified by cation exchange chromatography at pH 4.5. The DNL process for generating α2b-362 was analyzed by nonreducing (NR) and reducing (R) SDS-PAGE with three visualization methods: Coomassie blue staining (Figure 3A,D), fluorescence imaging (Figure 3B,E), and immunoblotting (Figure 3C). The Coomassie blue-stained gel shown in Figure 3A revealed the presence of a major band of ∼110 kDa in the reaction mixture (lane 2, NR), which was absent in the unbound (lane 3, NR) or 0.25 M NaCl wash (lane 4, NR), but evident in the 0.5 M NaCl fraction (lane

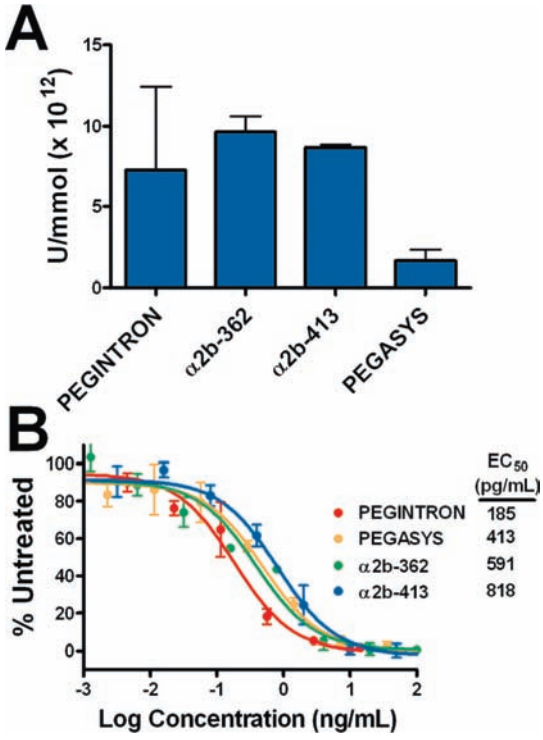

Figure 4. *In vitro* bioactivity assays. (A) Reduction of CPE was performed with EMCV challenge of A549 cells to determine the antiviral specific activity of each test article. The antiviral titer was determined by comparison of EC_{50} values with that of an IFNα standard. (B) Antitumor activity was determined be measuring the inhibition of Daudi proliferation *in vitro*. Dose−response curves were generated from a 4 day MTS assay. The percent of the signal obtained from untreated cells was plotted vs the log of the concentration in ng/mL. EC_{50} values were obtained with GraphPad *Prism* software. Data shown are representative of multiple repeated experiments.

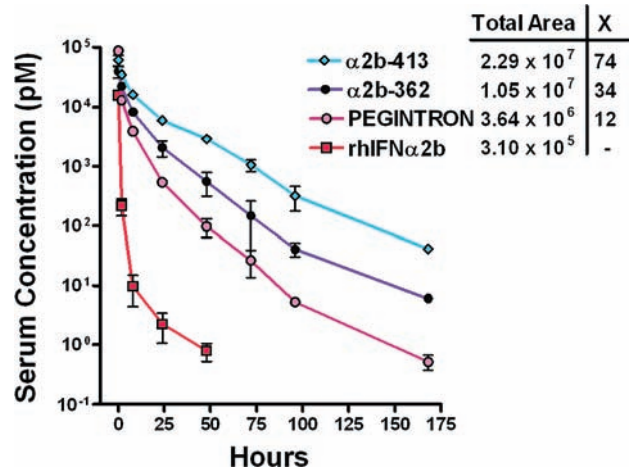

Figure 5. Blood clearance in Swiss-Webster mice following a single i.v. injection of each agent at equimolar protein dose, with concentrations in serum at various time points determined by ELISA. The data shown were the mean values from two animals. X denotes the fold-increase of total area over that of rhIFNα2b.

5, NR). Fluorescence imaging was used to detect the EDANS tag on IMP362, and the results shown in Figure 3B indicate the presence of covalently attached IMP362 in the 110 kDa band (lanes 2 and 5, NR) as well as the presence of excess IMP362, which does not stain with Coomassie blue. Immunoblotting with anti-IFN-α confirmed the inclusion of IFN-α2b in the 110 kDa band (Figure 3C, lanes 2 and 5, NR and R). The average mass of α2b-326 was determined by MALDI-TOF to be 76 728 Da, which is close to the sum (75 898 Da) of the mass of one dimeric IFN-α2b-DDD2 (52 185 Da) and one IMP362 (23 713 Da). The observed discrepancy between the measured mass (∼77 kDa) by MALDI- TOF and the estimated molecular weight (∼110 kDa) by SDS-PAGE is due to PEG, which is known to increase the apparent molecular weight of PEGgylated products as determined by SDS-PAGE or SE-HPLC (*43*, *44*). In all reducing gels, the components of α2b-362 (lane 5) are dissociated into IMP362 and the monomeric form of α2b-DDD2, as expected. For α2b-413, which was generated and purified similarly, both Coomassie blue staining (Figure 3D) and fluorescence imaging (Figure 3E) show a major band of ∼125 kDa (lane 6, NR) migrating behind α2b-362 (lane 5, NR). Moreover, reducing SDS-PAGE shows only the presence of a single band corresponding to the monomeric form of α2b-DDD2 for both α2b-362 (lane 5, R) and α2b-413 (lane 6, R) by Coomassie blue staining, and the two distinct bands corresponding to IMP362 (Figure 3E, lane 5, R) and IMP413 (Figure 3E, lane 6, R) by fluorescence imaging. These results demonstrate that α2b-362 and α2b-413 were generated as designed and substantially pure.

The biological activities of α2b-362 and α2b-413 were compared with PEGINTRON and PEGASYS by measuring the cytopathic effect (CPE) of encephalomyocarditis virus (EMCV) on human lung epithelial A549 cells, and the resulting EC_{50} values were calculated to determine the antiviral specific activities based on a validated IFN-α2b standard. As shown in

Table 1. PK Analysis of rhIFNα2b, PEGINTRON, α2b-362, and α2b-413 Administered as Intravenous Injections to Naive Swiss-Webster Mice

animal number	injected dose (pmol)	C_{max} (pM)	$T_{1/2\alpha}$ (h)	$T_{1/2\beta}$ (h)	$AUC_{0.08\rightarrow\infty}$ (h × pM)	elimination rate (1/h)	$MRT_{0.08\rightarrow\infty}$ (h)
				rhIFNα2b			
1	160	16 411	0.29	10.53	7011	2.34	0.63
2	160	21 835	0.31	7.14	10 147	2.15	0.78
mean	160	19 123	0.30	8.84	8579	2.25	0.71
				PEGINTRON			
1	160	87 090	0.53	6.29	137 790	0.63	5.42
2	160	105 774	0.43	5.11	150 905	0.70	4.79
mean	160	96 432	0.48	5.70	144 348	0.67	5.11
				α2b-362			
1	320	60 833	1.72	7.54	379 462	0.16	9.03
2	320	97 089	1.43	10.14	570 336	0.17	11.56
mean	320	78 961	1.58	8.84	474 899	0.17	10.30
				α2b-413			
1	320	152 923	0.69	12.85	1,012 470	0.15	16.75
2	320	100 495	4.03	28.53	1,179 056	0.09	26.56
mean	320	126 709	2.36	20.69	1,095 763	0.12	21.66

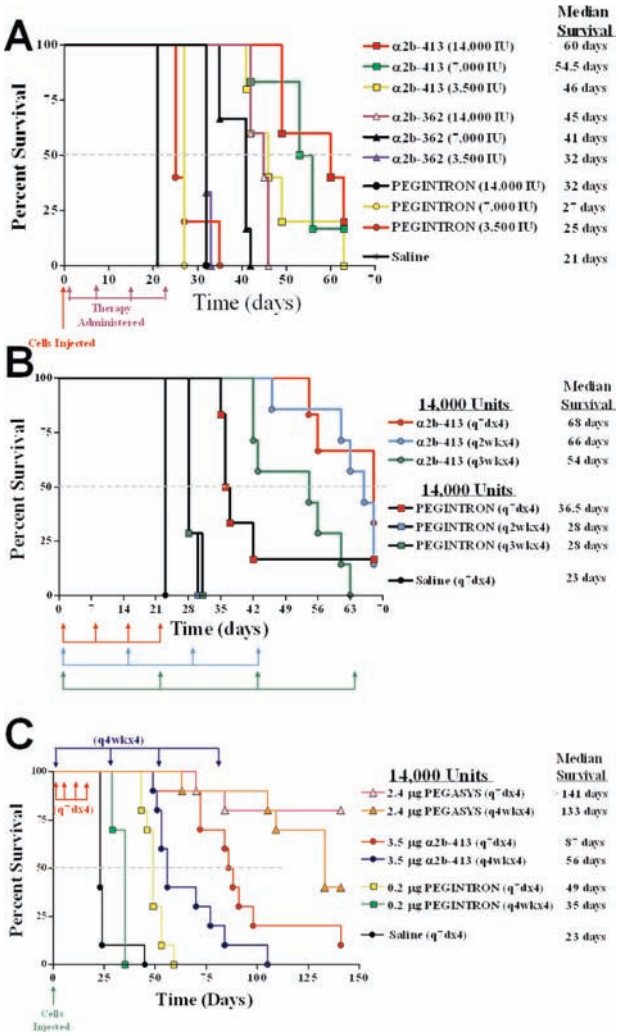

Figure 6. Antitumor efficacy in Daudi models. Units of activity were based on *in vitro* antiproliferation assay. Injection times are indicated with arrows, and median survival is shown for each treatment regimen. (A) Three different doses of each test article were given s.c. weekly for 4 weeks one day after inoculating Daudi cells. (B) Three different dosing schedules (q7d×4, q2wk×4, and q3wk×4) were evaluated in groups of 6−7 mice administered 4 × 14 000 IU s.c. of PEGINTRON or α2b-413. (C) Two different dosing schedules (q7d×4 and q4wk×4) were evaluated in groups of 10 mice administered 14 000 IU s.c. of PEGASYS, PEGINTRON, or α2b-413.

Figure 4A, on a molar basis, α2b-362, α2b-413, and PEGINTRON all have similar specific activities (averaging 7×10^{12} to 9×10^{12} U/mmol) and are about 5-fold more potent than PEGASYS. These data indicate that site-specific PEGylation by DNL may preserve biological activity better, particularly when using large PEG molecules. In addition, a cell-based kit, which utilizes a transgenic human pro-monocyte cell line carrying a reporter gene fused to an interferon-stimulated response element, was used to determine the specific activities of α2b-362 and α2b-413 to be 2940 IU/pmol and 816 IU/pmol, respectively, both of which were higher than PEGASYS (170 IU/pmol) but lower than PEGINTRON (3400 IU/pmol).

We also compared the antiproliferative activity of α2b-362 and α2b-413 with PEGINTRON and PEGASYS in Daudi lymphoma, with the finding (Figure 4B) that α2b-362 and α2b-413 had 2−3-fold lower EC_{50} values than PEGINTRON (~1×10^{12} U/mmol vs 2.2×10^{12} U/mmol), but comparable to PEGASYS.

We next determined the pharmacokinetics (PK) of α2b-362 and α2b-413 in mice following a single i.v. injection and compared to those of PEGINTRON and recombinant human

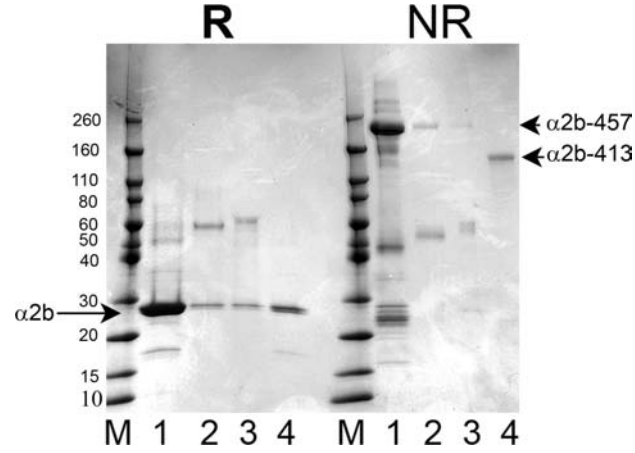

Figure 7. Purity of α2b-457 examined by reducing (R) and nonreducing (NR) SDS-PAGE. Lane 1, CM-purified α2b-457; lane 2, CM-column fraction −250 mM wash; lane 3, CM-column fraction-unbound; lane 4, α2b-413; lane M, molecular weight markers.

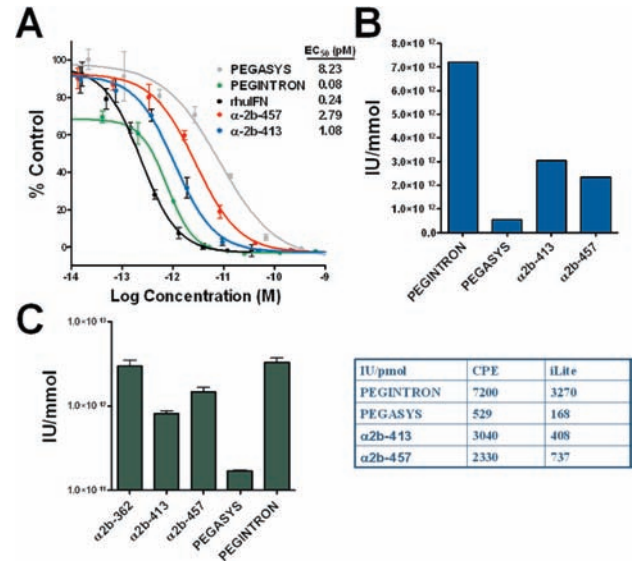

Figure 8. *In vitro* bioactivities of α2b-457. (A) Antiproliferative activity determined by inhibiting Daudi growth. (B) Antiviral activity determined by CPE. (C) Specific activity determined by reporter gene assay.

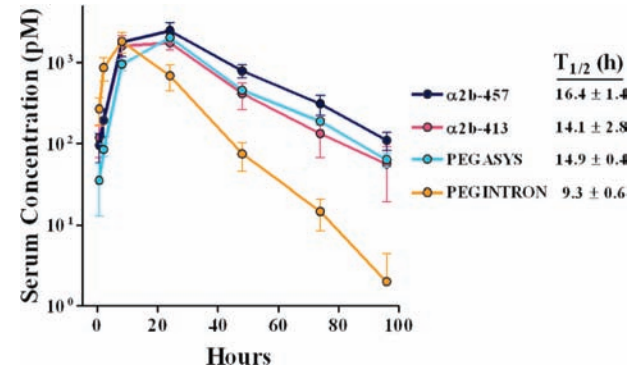

Figure 9. Blood clearance of α2b-413 and α2b-457 after a single s.c. injection in male Swiss-Webster mice.

IFN-α2b (rhIFN-α2b). The PK properties of each agent are summarized in Table 1 and the elimination curves are plotted in Figure 5. As expected, rhIFN-α2b cleared most rapidly from the blood of injected mice, approximately 3-fold faster than PEGINTRON and more than 13-fold faster than 2b-362 or 2b-413, either of which clears about 4-fold more slowly than

Table 2. Comparison of PK Data Obtained for α2b-457, α2b-413, PEGASYS and PEGINTRON after a Single Subcutaneous Injection to Naive Swiss-Webster Mice

injected material	animal number	C_{max} (pM)	T_{max} (h)	$T_{1/2}$ (h)	$AUC_{0\to\infty}$ (h × pM)	Cl (L/h)	$MRT_{0\to\infty}$ (h)
α2b-457	1	4326	24	16.9	169 119	0.0012	34.7
	2	6538	24	16.6	249 852	0.0008	33.4
	3	5424	24	16.3	192 651	0.0010	29.9
	4	5052	8	15.9	194 122	0.0010	31.6
		5335 ± 923	20 ± 8	16.4 ± 0.4	201 436 ± 34 250	0.0010 ± 0.0002	32.4 ± 2.1
α2b-413	1	3014	24	15.5	123 440	0.0016	30.1
	2	4104	8	20.5	170 183	0.0012	30.1
	3	2888	24	11.3	92 415	0.0022	24.1
	4	4122	8	14.9	166 127	0.0012	27.0
		3532 ± 673	16 ± 9.2	15.6 ± 3.8	138 041 ± 37 044	0.0016 ± 0.0005	27.8 ± 2.9
PEGASYS	1	1948	24	14.5	64 294	0.0016	33.1
	2	1887	24	14.6	58 596	0.0017	33.3
	3	1902	24	15.0	59 147	0.0017	34.1
	4	2377	24	15.3	47 116	0.0013	33.5
		2029 ± 234	24	14.9 ± 0.4	64 038 ± 7192	0.0016 ± 0.0002	33.5 ± 0.4
PEGINTRON	1	1885	8	9.4	34 063	0.0029	17.1
	2	1301	8	8.4	24 667	0.0041	15.5
	3	1609	8	9.8	32 833	0.0030	18.5
	4	2521	8	9.6	50 129	0.0020	17.3
		1829 ± 519	8	9.3 ± 0.6	35 423 ± 10 654	0.0030 ± 0.0008	17.1 ± 1.3

PEGINTRON, with little difference in the elimination rates between α2b-362 and α2b-413. As for mean residence time (MRT), a clear correlation with size is apparent among the various agents: the larger the molecular size, the longer the MRT. Finally, a test for bioequivalence showed that none of the agents tested were the same in terms of PK.

We then investigated the antitumor therapeutic efficacy of α2b-362 and α2b-413 in a Daudi mouse xenograft model. In the initial study, PEGINTRON, α2b-362, and α2b-413, at equivalent units of activity based on the *in vitro* growth inhibition assay, were each administered once weekly at three different doses (3500, 7000, and 14 000 IU), commencing 1 day after tumor inoculation. Survival curves and median survival time (MST) are provided in Figure 6A, which shows that PEGINTRON, α2b-362, and α2b-413 all demonstrate significant improvement in survival when compared to saline control ($P < 0.0016$), and the efficacy of α2b-362 or α2b-413 at the lowest dose (3500 IU) was similar to or better than that of PEGINTRON at the highest dose (14 000 IU). Both α2b-362 and α2b-413 at the two higher doses (7000 and 14 000 IU) were significantly superior to PEGINTRON ($P < 0.0027$). Moreover, α2b-413 was significantly more active than α2b-362 ($P < 0.0025$) when administered at equivalent doses. Although the MST of mice treated with the 14 000 IU dose was 60 days compared to 46 days of those treated with the 3500 IU dose, there were no statistically significant differences in survival benefit among the three doses of α2b-413 ($P = 0.1255$). These *in vivo* efficacy results correlate well with the PK data and demonstrate that the two monoPEGylated dimers of IFN-α2b made by the DNL method are more potent and longer-lasting than PEGINTRON, which prompted us to test whether less frequent dosing would be feasible with α2b-413.

We performed a second study in which PEGINTRON and α2b-413 at equal units of activity were administered with varied dosing schedules (Figure 6B). All animals that received either form of IFN at any of the various schedules had significantly improved survival in comparison to saline control mice ($P < 0.0009$). For biweekly (q2wk×4) therapy, mice treated with α2b-413 had significantly improved survival compared to those treated with PEGINTRON (MST = 66 days vs 28 days; $P = 0.0002$). Importantly, mice treated on a three-week schedule with α2b-413 (q3wk×4) not only had significantly improved survival in comparison to those treated with PEGINTRON at the same schedule (MST = 54 days vs 28 days; $P = 0.0002$), but also showed longer MST than those treated with PEGINTRON biweekly (MST = 28 days; $P = 0.0002$). However, when compared with mice treated with PEGINTRON weekly (MST = 36.5 days), the *P* value (0.3901) is statistically insignificant, as one mouse survived in this group.

In a third study (Figure 6C), we found that administering α2b-413 at 14 000 IU on a four-week schedule increased the MST to 56 days from 23 days of the saline control and was more potent than PEGINTRON given 14 000 IU every week. However, the group of mice treated with PEGASYS on a four-week schedule at 14 000 IU had a median survival of 133 days, which was considerably longer than that observed with α2b-413.

***In Vitro* and *In Vivo* Characterization of α2b-457.** For a better comparison with PEGASYS, we also conjugated IFNα2b-DDD2 to IMP457, an AD2-module of 40 kDa branched PEG, and obtained the resulting α2b-457 of substantial purity in the 0.5 M NaCl fraction off the CM column, as shown in Figure 7 (lane 1, NR and R). The average mass of α2b-457 was determined by MALDI-TOF to be 97 831 Da (Supporting Information Figure S1C), which is close to the sum (97 685 Da) of the mass of one dimeric α2b-DDD2 (52 185 Da) and one IMP457 (45 500 Da). The *in vitro* biological activities of α2b-457 were determined by three different assays (Figure 8A−C) to be lower than that of PEGINTRON, comparable to that of α2b-413, and considerably higher than that of PEGASYS. The PK data obtained in mice with a single s.c. injection are shown in Figure 9, which indicates a longer circulating half-life of α2b-457 than either α2b-413 or PEGASYS, with all three clearing much more slowly than PEGINTRON. Table 2 summarizes the key PK parameters calculated; the observed differences in AUC or C_{max} between α2b-457 and each of α2b-413, PEGASYS, and PEGINTRON, or between α2b-413 and PEGASYS or PEGINTRON, are significant by statistical analysis (data not shown). When given on a four-week schedule at a low dose of 20 pmol, α2b-457 extended the median survival of Daudi-bearing mice to 47 days from 23 days of the saline group (Figure 10) and was significantly better than either α2b-413 or PEGINTRON at 20 pmol (MST = 47 days vs 41 and 37 days, respectively; $P < 0.0151$) but was inferior to PEGASYS given either at 10 or 20 pmol. The 20 pmol dose of α2b-413 also improved survival in comparison to PEGINTRON ($P = 0.002$). At 10 pmol, there was no difference between α2b-457

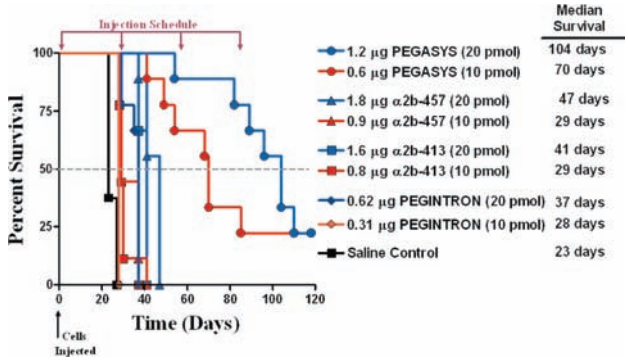

Figure 10. Antitumor efficacy of α2b-457, α2b-413, PEGINTRON, and PEGASYS in a Daudi xenograft model. Two different doses of each agent were given s.c. once every 4 weeks. Not all groups received all four injections. Treatment started one day after inoculating Daudi cells.

and α2b-413, but both significantly improved survival over PEGINTRON-treated mice ($P < 0.001$).

CONCLUSIONS

These studies show that the *in vitro* antiviral and antiproliferative activities of α2b-362, α2b-413, and α2b-457 are higher than PEGASYS but lower than or similar to PEGINTRON. The PK data obtained in mice indicate superiority of all three DNL complexes over PEGINTRON and comparability of α2b-413 and a2b-457 to PEGASYS. Both α2b-413 and α2b-457 display potent antitumor activity in Daudi human Burkitt lymphoma models superior to PEGINTRON. Intriguingly, α2b-457, despite its more favorable PK, is not as effective as PEGASYS in the Daudi model. Noting that the antiproliferative and antiviral activities of IFN-α are separate (*45*), such suboptimal antitumor response may be an attractive property of α2b-457, since it could suggest less toxicity of α2b-457 than PEGASYS to hematological and other normal cells *in vivo*. The generation of antibodies to IFN in patients during IFN therapy is well-known (*46*). For example, the incidence of neutralizing antibodies to various IFN preparations was found to be 20−38% for rhIFN-α2a, 3−10% for rhIFN-α2b, and less than 2% for natural IFN-α (*47*). For PEGASYS, 2% (8/409) of patients developed low-titer neutralizing antibodies and 6% (24/409) of patients developed binding antibodies to IFN-α2a (*48*). In mice, recombinant human IFN-α2a was reported to induce neutralizing antibodies, whereas its 40 kDa branched PEGylated form (PEGASYS) appeared to be little or not immunogenic (*5*). Because α2b-457 also comprises the 40 kDa branched PEG as PEGASYS, we would expect similarly reduced immunogenicity of α2b-457 in mice and even more so in humans. Thus, although the immunogenicity of α2b-457 is still a valid concern, these encouraging preliminary results provoke clinical evaluation of α2b-457 as well as the anticipation of a broader use of the DNL method for developing other PEGylated cytokines.

ACKNOWLEDGMENT

We thank Meiyu Loo and Eric Chan for producing α2b-DDD2 in cell culture, John Kopinski for preparing α2b-362, α2b-413, and α2b-457, Christopher D'Souza for providing IMP421 and IMP457, Diana Pilas and Preeti Trisal for processing PK data, and Anju Nair and Maria Zalath for performing animal studies.

Supporting Information Available: Figure S1. This material is available free of charge via the Internet at http://pubs.acs.org.

LITERATURE CITED

(1) Borden, E. C., Sen, G. C., Uze, G., Silverman, R. H., Ransohoff, R. M., Foster, G. R., and Stark, G. R. (2007) Interferons at age 50: past, current and future impact on biomedicine. *Nat. Rev. Drug Discovery 6*, 975–990.

(2) Pestka, S. (2007) The interferons: 50 years after their discovery, there is much more to learn. *J. Biol. Chem. 282*, 20047–20051.

(3) Vilcek, J. (2006) Fifty years of interferon research: aiming at a moving target. *Immunity 25*, 343–348.

(4) Grace, M., Youngster, S., Gitlin, G., Sydor, W., Xie, L., Westreich, L., Lacobs, S., Brassard, D., Bausch, J., and Bordens, R. (2001) Structural and biologic characterization of pegylated recombinant IFN-α2b. *J. Interferon Cytokine Res. 21*, 1103–1115.

(5) Bailon, P., Palleroni, A., Schaffer, C. A., Spence, C. L., Fung, W.-J., Porter, J. E., Ehrlich, G. K., Pan, W., Xu, Z.-X., Modi, M. W., Farid, A., and Berthold, W. (2001) Rational design of a potent, long-lasting form of interferon: a 40 kDa branched polyethylene glycol-conjugated interferon α2a for the treatment of hepatitis C. *Bioconjugate Chem. 12*, 195–202.

(6) Harris, J. M., and Chess, R. B. (2003) Effect of pegylation on pharmaceuticals. *Nat. Rev. Drug. Discovery 2*, 214–221.

(7) Yang, Z., Wang, J., Lu, Q., Xu, J., Kobayashi, Y., Takakura, T., Takimoto, A., Yoshioka, T., Lian, C., Chen, C., Zhang, D., Zhang, Y., Li, S., Sun, X., Tan, Y., Yagi, S., Frenkel, E. P., and Hoffman, R. M. (2004) PEGylation confers greatly extended half-life and attenuated immunogenicity to recombinant methioinase in primates. *Cancer Res. 64*, 6673–6678.

(8) Takakura, T., Takimoto, A., Notsu, Y., Yoshida, H., Ito, T., Nagatome, H., Ohno, M., Kobayashi, Y., Yoshioka, T., Inagaki, K., Yagi, S., Hoffman, R. M., and Esaki, N. (2006) Physicochemical and pharmacokinetic characterization of highly potent recombinant $_L$-methionine γ-lyase conjugated with polyethylene glycol as an antitumor agent. *Cancer Res. 66*, 2807–2814.

(9) Wang, M., Basu, A., Palm, T., Hua, J., Youngster, S., Hwang, L., Liu, H.-S., Li, X., Peng, P., Zhang, Y., Zhao, H., Zhang, Z., Longley, C., Mehlig, M., Borowski, V., Sai, P., Viswanathan, M., Jang, E., Petti, G., Liu, S., Yang, K., and Filpula, D. (2006) Engineering an arginine catabolizing bioconjugate: biochemical and pharmacological characterization of pegylated derivatives of arginine deiminase from *Mycoplasma arthritidis*. *Bioconjugate Chem. 17*, 1447–1459.

(10) Davis, S., Abuchowski, A., Park, Y. K., and Davis, F. F. (1981) Alteration of the circulating life and antigenic properties of bovine adenosine deaminase in mice by attachment of polyethylene glycol. *Clin. Exp. Immunol. 46*, 649–652.

(11) Bendich, A., Kafkewitz, D., Abuchowski, A., and Davis, F. F. (1982) Immunological effects of native and polyethylene glycol-modified asparaginases from *Vibrio succinogenes* and *Escherichia coli* in normal and tumor-bearing mice. *Clin. Exp. Immunol. 48*, 273–278.

(12) Abuchowski, A., McCoy, J. R., Palczuk, N. C., van Es, T., and Davis, F. F. (1977) Effect of covalent attachment of polyethylene glycol on immunogenicity and circulating life of bovine liver catalase. *J. Biol. Chem. 252*, 3582–3586.

(13) Abuchowski, A., van Es, T., Palczuk, N. C., and Davis, F. F. (1977) Alteration of immunological properties of bovine serum albumin by covalent attachment of polyethylene glycol. *J. Biol. Chem. 252*, 3578–3581.

(14) Pepinsky, R. B., Lee, W.-C., Cornebise, M., Gill, A., Wortham, K., Chen, L. L., Leone, D. R., Giza, K., Dolinski, B. M., Perper, S., Nickerson-Nutter, C., Lepage, D., Chakrabort, A., Whalley, E. T., Petter, R. C., Adams, S. P., Lobb, R. R., and Scott, D. M. (2005) Design, synthesis, and analysis of a polyethylene glycol-modified (PEGylated) small molecule inhibitor of integrin α4β1 with improved pharmaceutical properties. *J. Pharmacol. Exp. Ther. 312*, 742–750.

(15) Ng, E. W. M., Shima, D. T., Calias, P., Jr., Guyer, D. R., and Adamis, A. P. (2006) Pegaptanib, a targeted anti-VEGF aptamer for ocular vascular disease. *Nat. Rev. Drug Discovery 5*, 123–132.

(16) Fisher, D., Osburg, B., Petersen, H., Kissel, T., and Bickel, U. (2004) Effect of poly(ethylene imine) molecular weight and pegylation on organ distribution and pharmacokinetics of poly-

plexes with oligodeoxynuclotides in mice. *Drug Metab. Dispos. 32*, 983–992.
(17) Basu, A., Yang, K., Wang, M., Liu, S., Chintala, R., Palm, T., Zhao, H., Peng, P., Wu, D., Zhang, Z., Hua, J., Hsieh, M.-C., Zhou, J., Petti, G., Li, X., Janjua, A., Viswanathan, M., and Filpula, D. (2006) Structure-function engineering of interferon-β-1b for improving stability, solubility, potency, immunogenicity, and pharmacokinetic properties by site-selective mono-PEGylation. *Bioconjugate Chem. 17*, 618–630.
(18) Pepinsky, R. B., Lepage, D. J., Gill, A., Chakraborty, A., Vaidyanathan, S., Green, M., Baker, D. P., Whalley, E., Hochman, P. S., and Martin, P. (2001) Improved pharmacokinetic properties of a polyethylene glycol-modified form of interferon-β-1a with preserved *in vitro* bioactivity. *J. Pharmacol. Exp. Ther. 297*, 1059–1066.
(19) Molineux, G. (2004) The design and development of pegfilgrastim (PEG-rmetHuG-CSF, NeulastaÒ). *Curr. Phar. Des. 10*, 1235–1244.
(20) Kerwin, B. A., Chang, B. S., Gegg, C. V., Gonnelli, M., Li, T., and Strambini, G. B. (2002) Interactions between PEG and type I soluble tumor necrosis factor receptor: modulation by pH and by PEGylation at the N terminus. *Protein Sci. 11*, 1825–1833.
(21) Veronese, F. M., Mero, A., Caboi, F., Sergi, M., Marongiu, C., and Pasut, G. (2007) Site-specific PEGylation of G-CSF by reversible denaturation. *Bioconjugate Chem. 18*, 1824–1830.
(22) Manjula, B. N., Tsai, A., Upadhya, R., Perumalsamy, K., Smith, P. K., Malavalli, A., Vandegriff, K., Winslow, R. M., Intaglietta, M., Prabhakaran, M., Friedman, J. M., and Acharya, A. S. (2003) Site-specific PEGylation of hemoglobin at cys-93 (β): correlation between the colligative properties of the PEGylated protein and the length of the conjugated PEG chain. *Bioconjugate Chem. 14*, 464–472.
(23) Goodson, R. J., and Katre, N. V. (1990) Site-directed PEGylation of recombinant interleukin-2 at its glycosylation site. *Biotechnology 8*, 343–346.
(24) Rosendahl, M. S., Doherty, D. H., Smith, D. J., Carlson, S. J., Chlipala, E. A., and Cox, G. N. (2005) A long-acting, highly potent interferon $\alpha-2$ conjugate created using site-specific PEGylation. *Bioconjugate Chem. 16*, 200–207.
(25) Doherty, D. H., Rosendahl, M. S., Smith, D. J., Hughes, J. M., Chlipala, E. A., and Cox, G. N. (2005) Site-specific PEGylation of engineered cysteine analogs of recombinant human granulocyte-macrophage colony-stimulating factor. *Bioconjugate Chem. 16*, 1291–1298.
(26) Long, D. L., Doherty, D. H., Eisenberg, S. P., Smith, D. J., Rosendahl, M. S., Christensen, K. R., Edwards, D. P., Chlipala, E. A., and Cox, G. N. (2006) Design of homogeneous, monoPEGylated erythropoietin analogs with preserved in vitro bioactivity. *Exp. Hematol. 34*, 697–704.
(27) Yang, K., Basu, A., Wang, M., Chintala, R., Hsieh, M.-C., Liu, S., Hua, J., Zhang, Z., Zhou, J., Li, M., Phyu, H., Petti, G., Mendez, M., Janjua, H., Peng, P., Longley, C., Borowski, V., Mehlig, M., and Filpula, D. (2003) Tailoring structure-function and pharmacokinetic properties of single-chain Fv proteins by site-specific PEGylation. *Protein Eng. 16*, 761–770.
(28) Humphreys, D. P., Heywood, S. P., Henry, A., Ait-Lhsdj, L., Antoniw, P., Palframan, R., Greenslade, K. J., Carrington, B., Reeks, D. G., Bowering, L. C., West, S., and Brand, H. A. (2007) Alternative antibody Fab' fragment PEGylation strategies: combination of strong reducing agents, disruption of the interchain disulphide bond and disulphide engineering. *Protein Eng. Des. Sel. 2*, 227–234.
(29) Kubetzko, S., Balic, E., Waibel, R., Zangemeister-Wittke, U., and Pluckthun, A. (2006) PEGylation and multimerization of the anti-p185^{HER-2} single chain Fv fragment 4D5. *J. Biol. Chem. 201*, 35186–35201.
(30) Peleg-Shulman, T., Tsubery, H., Mironchik, M., Fridkin, M., Schreiber, G., and Shechter, Y. (2004) Reversible PEGylation: a novel technology to release native interferon $\alpha2$ over a prolonged time period. *J. Med. Chem. 47*, 4897–4904.
(31) Zhao, H., Yang, K., Martinez, A., Basu, A., Chintala, R., Liu, H.-C., Janjua, A., Wang, M., and Filpula, D. (2006) Linear and branched bicin linkers for releasable PEGylation of macromolecules: controlled release *in vivo* and *in vitro* from mono- and multi-PEGylated proteins. *Bioconjugate Chem. 17*, 341–351.
(32) Zalipsky, S., Mullah, N., Engbers, C., Hutchins, M. U., and Kiwan, R. (2007) Thiolytically cleavable dithiobenzyl urethane-linked polymer-protein conjugates as macromolecular prodrugs: reversible PEGylation of proteins. *Bioconjugate Chem. 18*, 1869–1878.
(33) Shaunak, S., Godwin, A., Choi, J.-W., Balan, S., Pedone, E., Vijayarangam, D., Heidelberger, S., Teo, I., Zlob, M., and Brocchini, S. (2006) Site-specific PEGylation of native disulfide bonds in therapeutic proteins. *Nat. Chem. Biol. 2*, 312–313.
(34) Rossi, E. A., Goldenberg, D. M., Cardillo, T. M., McBride, W. J., Sharkey, R. M., and Chang, C.-H. (2006) Stably tethered multifunctional structures of defined composition made by the dock and lock method for use in cancer targeting. *Proc. Natl. Acad. Sci. U.S.A. 103*, 6841–6846.
(35) Chang, C.-H., Rossi, E. A., and Goldenberg, D. M. (2007) The dock and lock method: a novel platform technology for building multivalent, multifunctional structures of defined composition with retained bioactivity. *Clin. Cancer Res. 13* (19 Suppl), 5586s–5591s.
(36) Baillie, G. S., Scott, J. D., and Houslay, M. D. (2005) Compartmentalisation of phosphodiesterases and protein kinase A: opposites attract. *FEBS Lett. 579*, 3264–3270.
(37) Wong, W., and Scott, J. D. (2004) AKAP signaling complexes: focal points in space and time. *Nat. Rev. Mol. Cell Biol. 5*, 959–970.
(38) Scott, J. D. (1991) Cyclic nucleotide-dependent protein kinases. *Pharmacol. Ther. 50*, 123–145.
(39) Newlon, M. G., Roy, M., Morikis, D., Hausken, Z. E., Coghlan, V., Scott, J. D., and Jennings, P. A. (1999) The molecular basis for protein kinase A anchoring revealed by solution NMR. *Nat. Struct. Biol. 6*, 222–227.
(40) Carr, D. W., Stofko-Hahn, R. E., Fraser, I. D. C., Bishop, S. M., Acott, T. S., Brennan, R. G., and Scott, J. D. (1991) Interaction of the regulatory subunit (RII) of cAMP-dependent protein kinase with RII-anchoring proteins occurs through an amphipathic helix binding motif. *J. Biol. Chem. 266*, 14188–14192.
(41) Colledge, M., and Scott, J. D. (1999) AKAPs: from structure to function. *Trends Cell Biol. 6*, 216–222.
(42) Newlon, M. G., Roy, M., Morikis, D., Carr, D. W., Westphal, R., Scott, J. D., and Jennings, P. A. (2001) A novel mechanism of PKA anchoring revealed by solution structures of anchoring complexes. *EMBO J. 20*, 1651–1662.
(43) Dhalluin, C., Ross, A., Leuthold, L.-A., Foser, S., Gsell, B., Muller, F., and Senn, H. (2005) Structural and biophysical characterization of the 40 kDa PEG-interferon-α2a and its individual positional isomers. *Bioconjugate Chem. 16*, 504–517.
(44) Grace, M. J., Lee, S., Bradshaw, S., Chapman, J., Spond, J., Cox, S., DeLorenzo, M., Brassard, D., Wylie, D., Cannon-Carlson, S., Cullen, C., Indelicato, S., Voloch, M., and Bordens, R. (2005) Site of pegylation and polyethylene glycol moleculae size attenuate interferon-α antiviral and antiproliferative activities through the JAK/STAT signaling pathway. *J. Biol. Chem. 280*, 6327–6336.
(45) Pfeffer, L. M., Wabg, C., Constantinescu, S. N., Croze, E., Blatt, L. M., Albino, A. P., and Nanus, D. M. (1996) Human renal cancers resistant to IFN's antiproliferative action exhibits sensitivity to IFN's gene-inducing and antiviral actions. *J. Urol. 155*, 1867–1871.
(46) Antonelli, G. (1997) In vivo development of antibodies to interferons: an update to 1996. *J. Interferon Cytokine Res. 17*, S39–S46.
(47) Einhorn, S., and Grander, D. (1996) Why do so many cancer patients fail to respond to interferon therapy? *J. Interferon Cytokine Res. 16*, 275–281.
(48) http://www.rocheusa.com/programs/pegasysmono.pdf.

BC9001773

A New Method to Produce MonoPEGylated Dimeric Cytokines Shown with Human Interferon-α2b

Chien-Hsing Chang, [†, ‡, *] Edmund A. Rossi, [†] Thomas M. Cardillo, [‡] Diane L. Nordstrom, [‡] William J. McBride, [‡] and David M. Goldenberg [‼]

Figure S1

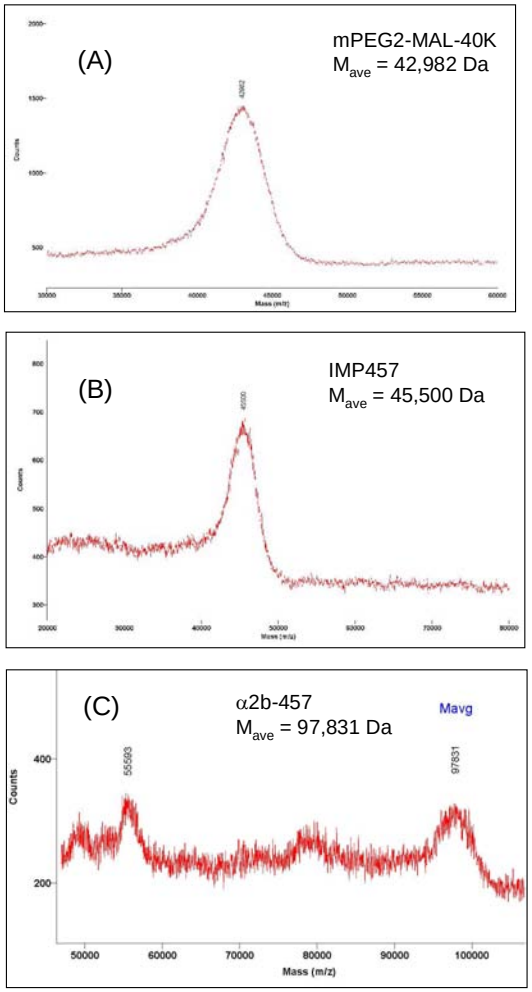

Figure S1. MALTI-TOF spectra of (A) mPEG2-MAL-40K; (B) IMP457; and (C) α2b-457.

PAMAM-RGD Conjugates Enhance siRNA Delivery Through a Multicellular Spheroid Model of Malignant Glioma

Carolyn L. Waite[†] and Charles M. Roth*[,†,‡]

Department of Chemical and Biochemical Engineering and Department of Biomedical Engineering, Rutgers University, 599 Taylor Road, Piscataway, New Jersey 08854. Received June 1, 2009; Revised Manuscript Received August 14, 2009

Generation 5 poly(amidoamine) (PAMAM) dendrimers were modified by the addition of cyclic RGD targeting peptides and were evaluated for their ability to associate with siRNA and mediate siRNA delivery to U87 malignant glioma cells. PAMAM-RGD conjugates were able to complex with siRNA to form complexes of approximately 200 nm in size. Modest siRNA delivery was observed in U87 cells using either PAMAM or PAMAM-RGD conjugates. PAMAM-RGD conjugates prevented the adhesion of U87 cells to fibrinogen-coated plates, in a manner that depends on the number of RGD ligands per dendrimer. The delivery of siRNA through three-dimensional multicellular spheroids of U87 cells was enhanced using PAMAM-RGD conjugates compared to the native PAMAM dendrimers, presumably by interfering with integrin-ECM contacts present in a three-dimensional tumor model.

INTRODUCTION

Gene silencing using RNA interference (RNAi) is a powerful platform technology being developed clinically for a variety of diseases including cancer, where it is typically considered as part of a multipronged approach (*1, 2*). While RNAi holds promise as an anticancer therapeutic modality, the ability to efficiently and safely deliver siRNA molecules to cells is the main barrier limiting its widespread clinical use (*3*). The use of synthetic, nonviral delivery vectors such as polymers and liposomes has shown promise in mediating cellular delivery of siRNA molecules (*4*). Benefits of synthetic delivery vectors include their ability to be manufactured on a large-scale, low immunogenic response compared to their viral counterparts and the ability to chemically tailor their structure for a particular application.

Poly(amidoamine) (PAMAM) dendrimers are a family of highly branched, synthetic polymers that have garnered interest as potential delivery vectors for nucleic acids, recently including siRNA. Several studies have demonstrated successful delivery of siRNA using PAMAM dendrimers or their derivatives (*5*−*10*). The branched architecture of dendrimers makes them particularly attractive for targeted delivery applications, as they can present targeting ligands in a manner favorable to promote multivalent binding to target cellular receptors. Multivalent ligand presentation from PAMAM dendrimers has been demonstrated for various targeted systems including folic acid (*11*), mannose, and glucose (*12, 13*).

Integrin proteins are a family of cell-surface receptors, several of which are known to be overexpressed on the surface of cancer cells. The $\alpha_v\beta_3$ integrin is particularly known for its role in cancer progression and is overexpressed in melanomas, glioblastoma, ovarian, breast, and prostate cancers (*14*). The high-affinity interaction between RGD peptides and cancer-related integrins has led to the widespread use of RGD peptide sequences as ligands for integrin-targeted drug and gene delivery applications (*15*). Several examples of PAMAM dendrimer-RGD conjugates have been reported to enhance the delivery of imaging agents to target carcinoma cells (*16, 17*). PAMAM-RGD conjugates have also been found to mediate cellular binding and adhesion (*18, 19*).

As significant promise has been shown for PAMAM-RGD conjugates in drug delivery and imaging applications, the goal of this study was to evaluate this bioconjugate for use as a siRNA delivery vector. Specifically, we sought to investigate the effects of extent of ligand functionalization (multivalency) on cellular delivery. To this end, the ability of dendrimers to deliver siRNA to malignant glioma cells with varying extents of RGD conjugation was evaluated. Furthermore, we hypothesized that the ligand presentation would have a greater impact on delivery in a three-dimensional tumor, where the interactions among the delivery vector, extracellular matrix, and cells are more pronounced. To evaluate this hypothesis, the ability of PAMAM-RGD conjugates to interfere with cell−ECM interactions and to mediate siRNA delivery in a three-dimensional cell-culture model of malignant glioma was studied.

EXPERIMENTAL PROCEDURES

Materials. A 22 nt siRNA sequence previously identified as an effective inhibitor of pd1EGFP expression (*20*) (sense strand 5′-UUG UGG CCG UUU ACG UCG CCG U-3′, antisense strand 3′-UGA ACA CCG GCA AAU GCA GCG G-5′) and an irrelevant siRNA sequence (targeted against firefly luciferase; sense strand 5′-CUU ACG CUG AGU ACU UCG A dTdT-3′, antisense strand 5′-UCG AAG UAC UCA GCG UAA G dTdT-3′) were purchased from Dharmacon (Chicago, IL). A fluorescently labeled anti-GFP siRNA sequence (5′ Cy3 end modified on the sense strand) was purchased from Integrated DNA Technologies (Coralville, IA, USA). A 20 nt phosphorothioated antisense oligonucleotide targeted against pd1EGFP with a fluorescent label was also purchased from Integrated DNA Technologies (5′-Cy5-TTG TGG CCG TTT ACG TCG CC-3′). The lyophilized powder was resuspended according to the manufacturer's protocol before use. Generation 5 PAMAM dendrimers with an ethylenediamine core and amine terminal groups were purchased as a 5 wt % solution in methanol from Dendritech (Midland, MI). Unless otherwise stated, all chemicals

* To whom correspondence should be addressed. Tel: +732-445-4500; Fax: +732-445-3753, E-mail: cmroth@rci.rutgers.edu.
[†] Department of Chemical and Biochemical Engineering.
[‡] Department of Biomedical Engineering.

10.1021/bc900228m CCC: $40.75 © 2009 American Chemical Society
Published on Web 09/23/2009

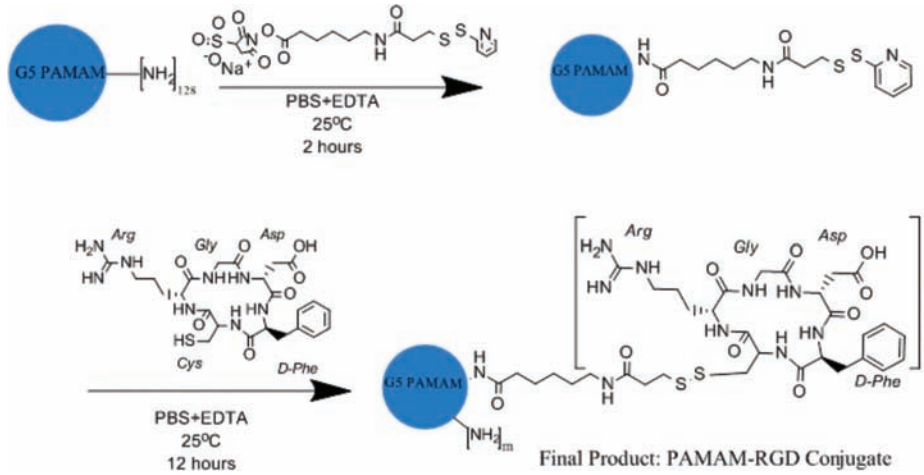

Figure 1. PAMAM dendrimers are reacted with Sulfo-LC-SPDP to yield SPDP-activated PAMAM intermediates. SPDP-activated PAMAM was reacted with cyclic RGD peptides to obtain final PAMAM-RGD conjugates.

were purchased from Sigma, and all cell culture products were obtained from Invitrogen (Carlsbad, CA).

Conjugation of PAMAM Dendrimers with RGD Peptides. Approximately 6 mg of dry generation 5 PAMAM dendrimers was obtained after the removal of methanol from the storage solution using rotary evaporation. The polymer residue was dissolved in ~2 mL of phosphate buffered saline (PBS) with 1 mM EDTA (reaction buffer). Various molar equivalents (6, 9, 12, or 15) of a Sulfo-LC-SPDP cross-linker (Pierce, Rockford, IL) were added to the polymer solution to yield SPDP-activated PAMAM after a 2 h reaction at room temperature. Dialysis with a 10 000 MWCO Slide-A-Lyzer dialysis cassette (Pierce, Rockford, IL) was performed against 1 L of reaction buffer overnight to remove any unreacted SPDP cross-linker. Following dialysis, 1.5 mol equiv (to SPDP groups added) of cyclic RGDfC peptide (Peptides International, Louisville, KY) were added to the SPDP-activated PAMAM dendrimers to yield PAMAM-RGD conjugates after an overnight reaction (Figure 1). Following conjugation, 10 000 MWCO dialysis was performed against reaction buffer followed by water to remove any unreacted RGD peptide. Purified PAMAM-RGD conjugates were lyophilized overnight to obtain a white powder.

UV Spectrophotometry of PAMAM-RGD Conjugates. A series of PAMAM-RGD conjugates were characterized using UV spectrophotometry to determine the number of RGD peptides conjugated to each dendrimer. A disulfide reducing agent, DTT, was used to cleave the disulfide bond present in the SPDP cross-linker to release pyridine-2-thione (P2T), which has a UV absorbance at 343 nm. This analysis of pyridine-2-thione release was first performed on the intermediate product, PAMAM-SPDP, and used to quantify the average number of SPDP groups added to each dendrimer. After removal of excess SPDP by dialysis, 50 μL of the PAMAM-SPDP solution was added to 450 μL of reaction buffer, and the absorbance of the solution at 343 nm was read using a Unicam UV 300 model UV spectrophotometer (Thermo Spectronics, Rockford, IL) (this reading indicated background absorbance). To the same sample, 5 μL of DTT (Pierce, Rockford, IL) (15 mg/mL) was added, and the absorbance at 343 nm was recorded after a 15 min incubation at room temperature. The increase in UV absorbance observed after the addition of DTT corresponded to the addition of LC-SPDP groups to dendrimers. The average molar ratio of SPDP:PAMAM was calculated according to the manufacturer's protocol (Pierce, Rockford, IL). The same analysis was performed on the final PAMAM-RGD conjugate to confirm replacement of all SPDP groups with RGD peptides. After the replacement of P2T groups by RGD peptides, an increase in UV absorbance at 343 nm was not observed.

MALDI-TOF Mass Spectrometry. PAMAM-RGD conjugates were dissolved in water at a concentration of 1 mg/mL prior to MALDI-TOF MS analysis. A matrix solution of 2′-4′-6′-trihydroxyacetophenone monohydrate (THAP) (10 mg/mL THAP in 50%ACN/(50% H_2O with 0.1% trifluoroacetic acid)) was used. The matrix solution and PAMAM dendrimers were mixed 1:1 by volume and spotted on a 100-well stainless steel sample plate. MALDI-TOF MS analysis was performed in linear positive mode of a Voyager DE Pro instrument (Applied Biosystems) using 25 kV accelerating voltage, 95% grid voltage, 0.3% guide wire voltage, and a delay time of 700 ns. For each spectrum, 75 shots were taken, and a minimum of 3 spectra were accumulated for each sample.

PicoGreen Assay for PAMAM/siRNA Complexation. Complexes were prepared at various charge ratios by mixing equal volumes of PAMAM with siRNA in PBS. Charge ratios (N/P) were calculated as a ratio of the number of primary amines in the polymer to the number of anionic phosphate groups in the siRNA. The samples were then vortexed and incubated at room temperature for 15 min to ensure complex formation. The complexes were prepared at a final siRNA concentration of 0.2 μg of siRNA/100 μL of solution and varying polymer concentrations to reach the desired charge ratio. One hundred microliter aliquots of each complex were transferred to a 96-well (black-walled, clear-bottom, nonadsorbing) plate (Corning, NY, USA). A total of 100 μL of diluted PicoGreen dye (Molecular Probes, Eugene, OR) (1:200 dilution in Tris-EDTA (TE) buffer) was added to each sample. Fluorescence measurements were made after a 30 min incubation at room temperature using a DTX800 Multimode Detector (Beckman Coulter, CA), at exitation and emission wavelengths of 485 and 535 nm, respectively. All measurements were corrected for background fluorescence from a solution containing only buffer and PicoGreen dye.

Dynamic Light Scattering. Dynamic light scattering (DLS) analysis was performed using a Malvern Instruments Zetasizer Nano ZS-90 instrument (Southboro, MA) with reproducibility verified by collection and comparison of sequential measurements. Polymer/siRNA complexes (siRNA concentration = 100 nM, N/P = 15) were prepared using purified water (resistivity = 18.5 MΩ cm). DLS measurements were performed at a 90° scattering angle at 37 °C. *Z*-average sizes of three sequential measurements were collected and analyzed approximately 30 min after the polymer/siRNA complexes were formed.

Cell Culture. U-87 MG cells (ATCC HTB-14) were maintained in D-MEM medium supplemented with 10% fetal bovine serum (FBS), L-glutamine, and penicillin−streptomycin solution. A U87 cell line containing a stably integrated destabilized EGFP (d1EGFP) transgene (U87-d1EGFP) was generated as described

previously (*10*) and was maintained under constant selective pressure by G418 (500 ug/mL), and the growth medium was supplemented with sodium pyruvate and nonessential amino acids. All cell lines were cultivated in a humidified atmosphere of 5% CO_2 at 37 °C.

Multicellular Spheroid Formation. Multicellular tumor spheroids (MCTS) were formed from the U87 or U87-d1EGFP malignant glioma cell lines using the hanging drop method as described previously (*21*). Cells from a confluent T-25 flask were detached using trypsin-EDTA and resuspended in 5 mL of culture medium to a concentration of $\sim 10^6$ cells/mL. Twenty microliter droplets of this concentrated cell suspension were deposited into the lid of a Petri dish. The bottom of the Petri dish was filled with 2 mL of cell culture medium to facilitate moisture transfer. The lid containing the drops was inverted over the Petri dish to form hanging drops. The Petri dish was placed in the incubator for a period of 3 days, after which visible cell aggregates were formed in the hanging drops. The cell aggregates were harvested from the hanging drop suspension by adding ~2 mL of culture medium to suspend the aggregates. The cell aggregates were individually transferred in 100 μL of culture medium to wells of a 96-well tissue culture plate that was base-coated with 2% agarose. After 24 h on agarose, cell aggregates formed MCTS of diameters ranging from ~600 to 800 μm and were subjected to siRNA transfection and confocal imaging analysis.

SiRNA Delivery Assay. U87-d1EGFP cells were plated at a density of 1.5×10^5 cells/well in 12-well plates ~18 h prior to transfection. Prior to treatment of cells, PAMAM/siRNA complexes were prepared as described above in 200 μL of PBS (N/P = 15). PolyFect (Qiagen, Valencia, CA), a commercially available dendrimer transfection reagent, was used as a positive control. Eight hundred microliter aliquots of OptiMEM medium were mixed with each sample to obtain a final siRNA concentration of 100 nM. The serum-containing culture medium was aspirated from the cells, and each well was treated with 1 mL of the PAMAM/siRNA complexes in OptiMEM medium. After a 4 h incubation period, the transfection mixture was replaced with serum-containing culture medium and maintained under normal growth conditions until the cells were assayed for fluorescence by flow cytometry at various time points after initial treatment. For cells being analyzed for GFP fluorescence, unlabeled siRNA was utilized. To determine intracellular siRNA uptake, non-transformed U87 cells were treated with a Cy-3 labeled siRNA.

To analyze siRNA delivery in multicellular tumor spheroids, a similar transfection protocol was performed as with cells on 12-well tissue culture plates. MCTS transfections were performed in 96-well plates that had been base-coated with 2% agarose. Transfections were performed in a total volume of 150 μL in OptiMEM medium. MCTS were exposed to a Cy3-labeled siRNA sequence to enable confocal imaging of siRNA localization throughout the spheroids at both 4 and 24 h post-transfection. Spheroids generated from the U87-d1EGFP cell line were treated with a Cy5-labeled (red) antisense oligonucleotide (AON) targeted against d1EGFP so that the label and transgene fluorescence spectra would not overlap. U87-d1EGFP spheroids were imaged at 24, 48, and 72 h after the initial treatment to evaluate both GFP silencing and localization of the AON with the various dendrimer/ODN formulation conjugates.

Flow Cytometry. Cells were washed with PBS, detached with trypsin-EDTA, and collected in growth medium, before they were pelleted by centrifugation for 3.5 min at 200 *g* and resuspended in 150 μL PBS. Samples were maintained on ice before being subjected to flow cytometry analysis. Ten thousand cells were analyzed on a FACSCalibur two-laser, four-color flow cytometer (BD Biosciences) for GFP fluorescence (FL-1) or Cy3 fluorescence (FL-2). *CellQuest* software was used to acquire and analyze the results. Viable cells were gated according to their typical forward/side scatter characteristics.

Competitive Cell Adhesion Assay. High-binding 96-well plates (Nunc Maxi SORP) were coated with fibrinogen protein by adding 100 μL/well of fibrinogen solution (100 μg/mL in PBS) overnight at 4 °C. The next day, the plate was blocked with 150 μL/well of bovine serum albumin (BSA) solution (10 mg/mL in PBS) for 1 h at 37 °C. The plate was washed in triplicate with cold PBS. Ten microliter aliquots of test compounds (RGD-conjugated polymers) at various concentrations were added to wells of the fibrinogen-coated plate on ice in triplicate. Following the addition of test compounds, 90 μL of U87 cells in culture medium (330 000 cells/mL) were added to the plate and mixed thoroughly with a multichannel pipet. The plate was incubated at 37 °C for 3 h until the cells attached to the plate. Nonadherent cells were washed from the plate with PBS, and adherent cells were fixed by the addition of 100 μL of 70% ethanol for 30 min at room temperature. Following one wash with PBS, 100 μL of PicoGreen dye in TE buffer were added to the plate for 30 min to detect adherent cells. PicoGreen fluorescence was measured using a DTX800 Multimode Detector (Beckman Coulter, CA) at excitation and emission wavelengths of 485 and 535 nm, respectively. PicoGreen fluorescence values of wells treated with a RGD-containing competitor was normalized to wells that received no competitor (maximum cells adhering). Data analysis and calculation of IC_{50} values was performed using *GraphPad Prism 4* software (GraphPad Software, La Jolla, CA).

Confocal Microscopy of Multicellular Spheroids. Uptake and distribution of Cy3-labeled siRNA or Cy5-labeled AS ODN in U87 MCTS or U87-d1EGFP MCTS, respectively, were analyzed using confocal microscopy. Imaging was performed at various time points after siRNA transfection of spheroids using an Olympus IX81 model confocal microscope (Olympus, Center Valley, PA). Images of MCTS were performed directly on agarose-coated 96-well plates at 10× magnification. *Z*-stack imaging was performed to take image slices through spheroids at 20 μm intervals for a total depth of 100 μm. The following excitation and emission wavelengths were used to detect the fluorophores used in this study: GFP fluorescence (excitation = 482 nm, emission = 536 nm), Cy3 siRNA (excitation = 543 nm, emission = 593 nm), and Cy5 AS ODN (excitation = 628 nm, emission = 692 nm).

Image Analysis of Multicellular Spheroid Fluorescence. The fluorescence intensities of both the Cy5 and GFP channels of the confocal images of the U87-d1EGFP spheroids were quantified using *ImageJ* software (*22*).

Statistics. All statistical comparisons among treatment groups were performed using a one-way ANOVA test with Fisher's all-pairs post hoc comparison test. To compare among IC_{50} fits in the cell adhesion assay, a Monte Carlo procedure was employed. The standard error of measurement was used to randomly perturb individual experimental values around their means. Fits were then applied to the perturbed data and compared across groups. This procedure was repeated 10 000 times. If a particular group had a lower IC_{50} in at least 95% of the Monte Carlo trials, then the fitted IC_{50} value was considered significant at the $p < 0.05$ level.

RESULTS

Reaction and Characterization of PAMAM-RGD Conjugates. Generation 5 PAMAM dendrimers were conjugated with various amounts of a cyclic RGD targeting peptide, RGDfC, using a Sulfo-LC-SPDP cross-linker in a scheme depicted in Figure 1. The PAMAM-RGD conjugates were characterized

A

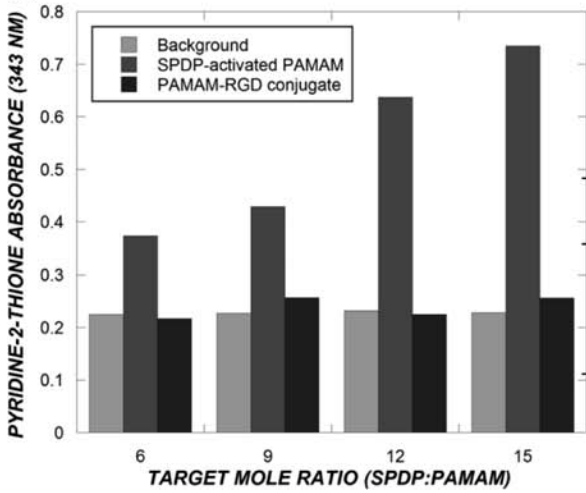

B

Theoretical Molar Ratios	Actual Ratios by DTT Release	Sample Name
6	2.12	G5-2RGD
9	3.21	G5-3RGD
12	7.07	G5-7RGD
15	9.65	G5-10RGD

Figure 2. UV detection of pyridine-2-thione release from SPDP-activated PAMAM and PAMAM-RGD conjugates after the addition of DTT (A). Experimentally determined extents of RGD conjugation and sample names (B).

using UV spectrophotometry at various stages during the cross-linking process. For this purpose, a disulfide reducing agent, DTT, was added to the conjugates to break the disulfide bond present in the SPDP cross-linker, enabling the release of pyridine-2-thione, a molecule that is UV active at 343 nm. PAMAM dendrimers were first reacted with various molar equivalents (6, 9, 12, or 15) of Sulfo-LC-SPDP to attain SPDP-activated PAMAM. After the addition of DTT, increasing amounts of pyridine-2-thione absorbance were detected with increasing SPDP/PAMAM ratios, as expected (Figure 2A). This information was used to calculate the average molar ratios of SPDP/PAMAM yielded in this reaction, ranging from approximately 2 to 10 SPDP/PAMAM. Following reaction with cyclic RGD peptides, the pyridine-2-thione absorbance decreased back to baseline, indicating complete replacement of pyridine-2-thione groups from the cross-linker with RGD peptides. The resulting PAMAM-RGD conjugates are denoted by their experimentally determined extents of RGD conjugation (rounded to whole numbers) as G5−2RGD, G5−3RGD, G5−7RGD, and G5−10RGD.

PAMAM-RGD conjugates were further characterized using MALDI-TOF mass spectrometry to confirm conjugation of RGD peptides to the dendrimers. Several previous studies have successfully utilized MALDI-TOF MS to characterize PAMAM bioconjugates by observing an increase in molecular weight of dendrimers upon conjugation to other molecules (*23, 24*). As expected, a shift to the right of MALDI MS curves correlated to increased extents of RGD conjugation, indicating an increase in the molecular weight of the conjugates (Supporting Information). As MALDI MS has been shown to underestimate the actual molecular weight of high-generation dendrimers (*23*), it was not used to estimate the molecular weight of PAMAM-RGD conjugates, but as a tool to confirm successful cross-linking of RGD to PAMAM dendrimers. The molecular weight of the PAMAM-RGD conjugates was calculated instead from the RGD cross-linking extent determined using UV spectrophotometry as described above.

Characterization of Dendrimer/siRNA Complexes. To facilitate siRNA delivery, cationic polymers such as PAMAM dendrimers should form electrostatic complexes with anionic siRNA molecules. The ability of PAMAM-RGD conjugates to complex with siRNA was evaluated using a dye exclusion assay. The amount of unbound siRNA in solutions of PAMAM/siRNA was determined by measuring the fluorescence of a commercially available dye, PicoGreen, that fluoresces upon binding

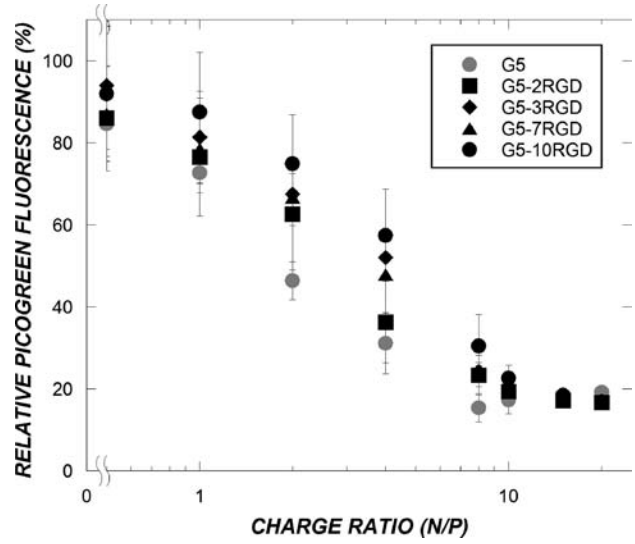

Figure 3. PAMAM/siRNA complexes were formed in PBS (final siRNA concentration = 2 μg/mL) and allowed to incubate for 15 min before measurement. Relative PicoGreen fluorescence corresponds to unbound siRNA present in solution. The data represent mean ± SEM ($n \geq 3$).

to double-stranded DNA or RNA. The fluorescence intensity of PicoGreen decreased following incubation of increasing amounts of polymer with added to a fixed amount of siRNA, indicating association of siRNA with the polymer (Figure 3). For all dendrimer conjugates tested, most of the PicoGreen fluorescence was quenched by N/P = 10, indicating that the dendrimers had formed complexes with siRNA. At lower charge ratios, however, it is possible to discern trends in siRNA complexation as a function of RGD cross-linking extent, with higher extents of RGD conjugation corresponding to somewhat less siRNA complexation. To ensure the presence of stable complexes, N/P = 15 was chosen for subsequent experiments.

Having demonstrated the ability of PAMAM-RGD conjugates to complex with anionic siRNA, the characteristics of the siRNA/PAMAM complexes formed at N/P = 15 were evaluated further by dynamic light scattering (DLS) measurements. Particle size analysis by DLS showed the formation of ~200 nm complexes between dendrimers and siRNA, regardless of extent of RGD conjugation (Table 1).

Table 1. Particle Diameter of Dendrimer/siRNA Complexes As Determined by Dynamic Light Scattering[a]

sample	particle diameter (nm)
G5	192 ± 3
G5−2RGD	166 ± 36
G5−3RGD	187 ± 14
G5−7RGD	193 ± 14
G5−10RGD	182 ± 5

[a] The data represent mean ± standard deviation ($n = 3$).

siRNA Delivery and GFP Silencing in U87 Cells. The ability of PAMAM-RGD conjugates to deliver siRNA to U87 cells and elicit a gene silencing response was evaluated. A fluorescently labeled siRNA sequence was delivered to U87 cells with PAMAM-RGD conjugates to evaluate siRNA uptake into cells, which was assayed using flow cytometry. Separately, but under the same conditions, a siRNA sequence targeted against the short half-life green fluorescent protein, d1EGFP, was delivered to U87-d1EGFP cells, and relative GFP expression was assayed using flow cytometry.

Significant intracellular siRNA levels were observed 24 h after exposure of U87 cells to PAMAM-RGD/Cy3-siRNA complexes (Figure 4A). If cell binding is a limiting step in dendrimer-mediated siRNA delivery, intracellular siRNA levels would be expected to increase with increasing extent of RGD conjugation onto PAMAM dendrimers, as U87 cells express $\alpha_v\beta_3$ receptors for which cyclic RGD peptides have high binding affinities (*25*). In this system, a statistically significant increase in siRNA delivery was not observed upon conjugation of dendrimers with RGD peptides ($p > 0.05$).

Having observed intracellular siRNA delivery by PAMAM-RGD conjugates, the ability of the system to deliver siRNA to elicit a GFP silencing response was evaluated by flow cytometry. Modest silencing (approximately 40%) of the GFP transgene was observed in U87-d1EGFP cells using unmodified G5 PAMAM dendrimers compared to control cells receiving no siRNA treatment. The extent of GFP silencing achieved was not significantly altered after the conjugation of RGD peptides to PAMAM dendrimers ($p > 0.05$) (Figure 4B). An irrelevant siRNA sequence not targeted against d1EGFP was used as a control and resulted in ~20% silencing relative to no siRNA treatment. As these values are rather low and not statistically different from each other ($p > 0.05$), it appears that, even with RGD modification, uptake of G5 PAMAM dendrimers is nonspecific and does not result in intracellular trafficking sufficient for robust gene silencing (*10*). A commercially available dendrimer-based transfection reagent, PolyFect, was used as a positive control in this experiment and elicited ~60% GFP knockdown, which was statistically greater than that induced when the irrelevant sequence was delivered with PolyFect (Figure 4B).

Competitive Binding Cell Adhesion Assay. Having observed that the addition of RGD peptides to PAMAM did not significantly alter the ability of PAMAM to deliver siRNA to U87 cells, probably due to significant nonspecific cellular uptake of PAMAM/siRNA complexes, we sought to study whether active integrin targeting was occurring to any extent by the use of a cell adhesion assay. Here, the ability of PAMAM-RGD bioconjugates to bind specifically to $\alpha_v\beta_3$ integrin receptors on cells and prevent their adhesion to a fibrinogen-coated plate was evaluated. Polymers functionalized with various numbers of RGD peptides inhibited adhesion of U87 cells to fibrinogen protein in a concentration-dependent manner (Figure 5A). In contrast, unmodified G5 PAMAM dendrimer did not prevent the adhesion of U87 cells to fibrinogen, demonstrating the specificity of this assay to integrin-RGD binding, and the lack of nonspecific effects by PAMAM. This result indicated that, in all PAMAM-RGD constructs, RGD was presented to the cells in a manner such that it binds to $\alpha_v\beta_3$ integrin receptor proteins and is sufficient to prevent adhesion of U87 cells to the extracellular matrix protein, fibrinogen.

To discern trends in adhesion as a function of RGD conjugation extent, binding curves were fit to a competitive binding model to determine a concentration of RGD at which each dendrimer inhibited 50% of cells from adhering to the plate (IC_{50}) (Figure 5B). Fitted IC_{50} values were compared statistically using a Monte Carlo procedure described in the Experimental Procedures section. When a low number of RGD peptides were conjugated to the dendrimers (2 or 3), a significantly lower IC_{50} concentration (or a higher binding avidity) was achieved than with free RGD peptide ($p < 0.05$). However, by increasing the number of peptides per dendrimer (7 or 10), a sharp increase in the IC_{50} value was observed, corresponding to a decreased net avidity of these PAMAM-RGD conjugates to the integrin protein compared to those conjugates containing just 2 or 3 RGD peptides ($p < 0.05$). Further, a significant difference was observed between the IC_{50} values of dendrimers containing 7 or 10 RGDs ($p < 0.05$). Using this assay, we found that three RGD peptides per dendrimer were optimal for preventing U87 adhesion to fibrinogen protein on a flat plate.

siRNA Delivery through Multicellular Glioma Spheroids. The strong effect of PAMAM-RGD on U87 cell adhesion suggests that these bioconjugates can interfere with integrin−ECM interactions, which would likely influence delivery in a three-dimensional tumor. To investigate this hypothesis, the ability of PAMAM-RGD to deliver siRNA through a three-dimensional multicellular tumor spheroid (MCTS) model of U87 cells was evaluated. As carcinoma cells cultured as 3D spheroids are known to secrete ECM proteins and feature active integrin−ECM interactions (*26*), we expected that PAMAM-RGD conjugates would be able to facilitate siRNA delivery through MCTS by interfering with integrin−ECM interactions formed by cells in three dimensions. To this end, cellular aggregates of U87 cells were formed using the hanging drop method, and aggregates were then transferred to agarose-coated tissue-culture plates to promote the formation of spheroids. U87 spheroids on agarose were treated with PAMAM-RGD/Cy3-siRNA complexes in a similar manner as for cells cultured on standard 12-well tissue culture plates. PAMAM-RGD polymers containing either 3 or 10 RGDs were used for this study, as G5−3RGD was found to be optimal in the cell adhesion assay and G5−10RGD represents the highest extent of RGD conjugation used in this work. Confocal imaging was performed at 4 and 24 h after transfection to evaluate the delivery and localization of Cy3-siRNA within U87 spheroids.

When delivered by G5 PAMAM dendrimers not containing RGD targeting ligands, siRNA fluorescence was observed primarily on the periphery of U87 spheroids (Figure 6). This result is consistent with previous studies on DNA delivery to MCTS using polyethylenimine (PEI), where poor tissue penetration using PEI/DNA complexes was observed (*27*). However, when PAMAM-RGD conjugates were used, siRNA was delivered successfully throughout the spheroid volume, suggesting that tissue penetration was enhanced by the presence of RGD targeting ligands (Figure 6). Significant siRNA delivery to the center of spheroids was observed when using PAMAM-RGD conjugates containing either 3 or 10 RGD ligands.

Having observed the ability of PAMAM-RGD conjugates to enhance siRNA delivery through U87 MCTS, spheroids generated from U87-d1EGFP cells were used to study simultaneously the delivery of a fluorescently labeled antisense oligonucleotide (AON) and its target GFP silencing. Consistent with the Cy3-siRNA localization observed in U87 spheroids, AON fluorescence was observed primarily on the spheroid periphery, at a

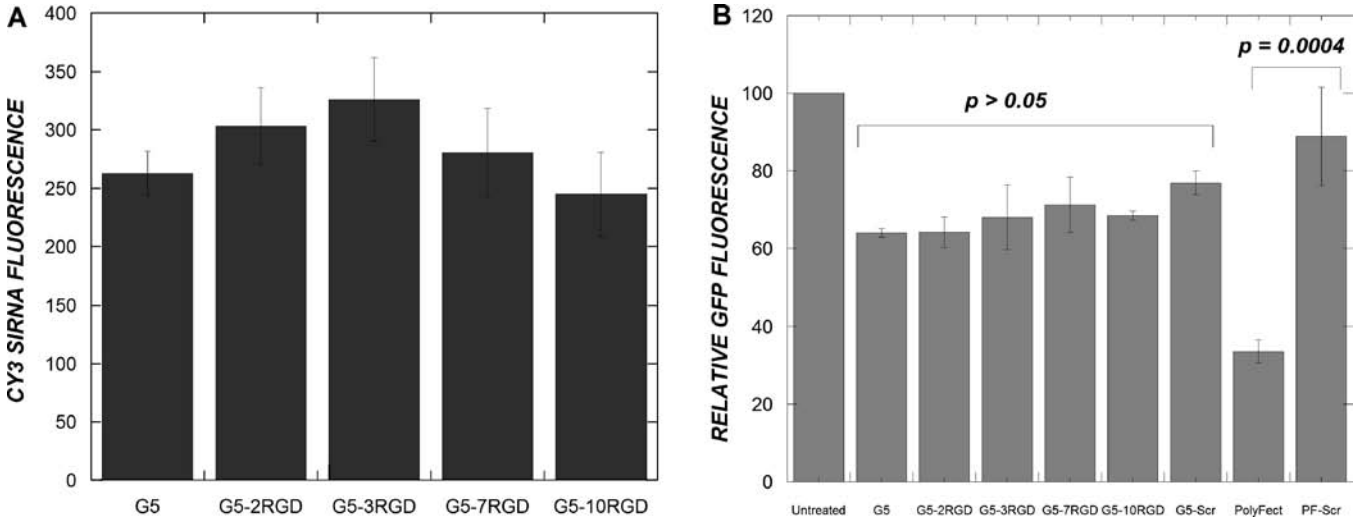

Figure 4. U87 cells (A) or U87-d1EGFP cells (B) were treated with PAMAM-RGD/siRNA complexes at a final siRNA concentration of 100 nM for 4 h under serum-free conditions. Cells were analyzed using flow cytometry for Cy3 fluorescence (A) or GFP fluorescence (B) 24 h after the initial treatment. A 5:1 wt ratio of PolyFect/siRNA was used (B). A scrambled siRNA sequence was delivered with PolyFect and G5 PAMAM dendrimer denoted by PF-Scr and G5-Scr, respectively. Data represent mean ± SEM.

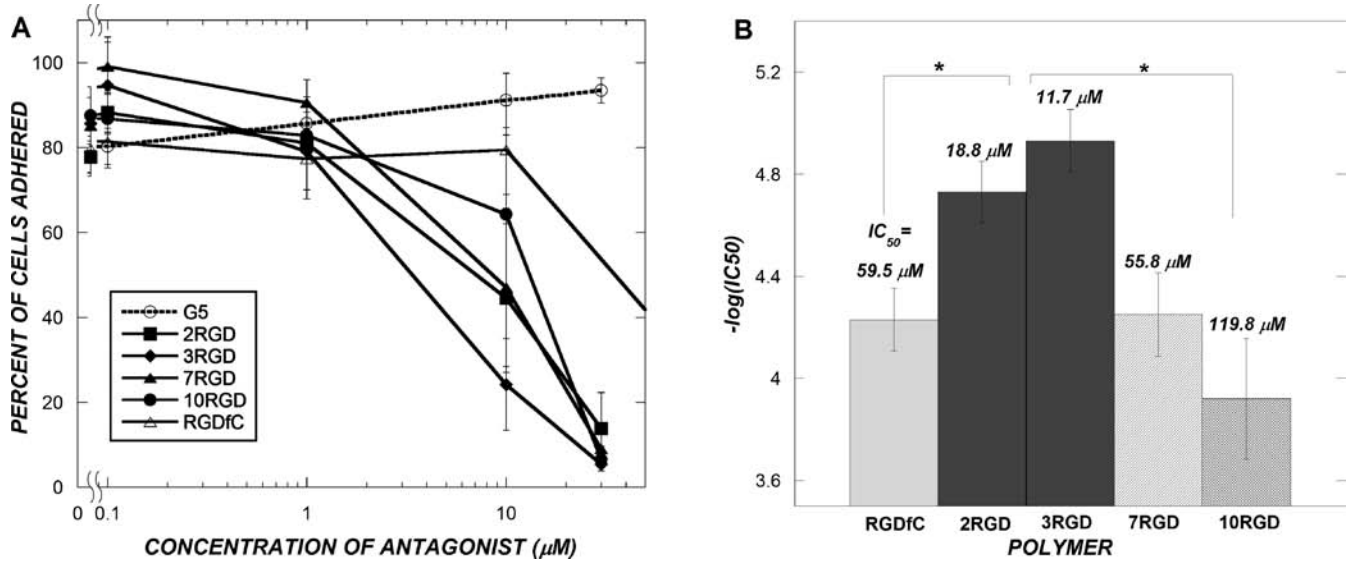

Figure 5. Competitive binding curves for U87 cells binding to fibrinogen-coated plates in the presence of RGD-containing antagonists (A). Results of IC_{50} values obtained from binding curves for each antagonist used (B). Differently colored bars represent statistically different IC_{50} values ($p < 0.05$) as determined using a Monte Carlo curve fitting algorithm (B). Data represent mean ± SEM ($n \geq 3$) (A) or mean IC_{50} ± standard deviation (B).

depth of 80 μm into the MCTS, when delivered by unmodified G5 PAMAM (Figure 7A). When delivered by PAMAM-RGD conjugates, however, AON fluorescence was observed throughout the spheroid volume. A statistically significant increase in Cy5 AON fluorescence was observed in the interior of the spheroids when AON was delivered by dendrimers containing RGD peptides compared to the native dendrimers at both 48 ($p < 0.002$) and 72 h ($p < 0.0001$) after treatment (Figure 7B). Despite the accumulation of AON within the MCTS, quantification of the GFP levels did not reveal significant gene silencing, consistent with the two-dimensional cell culture results (Figure 4B).

DISCUSSION

Integrins have proven to be promising targets for macromolecular drug and nucleic acid delivery systems for cancer. Several bioconjugate molecules containing RGD motifs have been successfully targeted to integrins to promote enhanced uptake and bioactivity in carcinoma cells. However, few studies have systematically evaluated how the number of RGD targeting ligands affects the bioactivity of targeted delivery systems. Hence, in this work, we conjugated cationic PAMAM dendrimers with various amounts of cyclic RGD targeting peptides to evaluate the ability of these bioconjugates to deliver siRNA to U87 glioma cells.

PAMAM dendrimers functionalized with varying levels of RGD peptides (2−10 RGDs/PAMAM) were able to deliver siRNA to U87 glioma cells, which express the $\alpha_v\beta_3$ integrin receptor, to elicit modest GFP silencing. However, contrary to our initial hypothesis, the attachment of RGD to PAMAM dendrimers did not enhance their ability to deliver siRNA to U87 glioma cells. This is likely due to the fact that nonspecific uptake of PAMAM dendrimers, mediated by their high cationic charge density, was more considerable than integrin-mediated

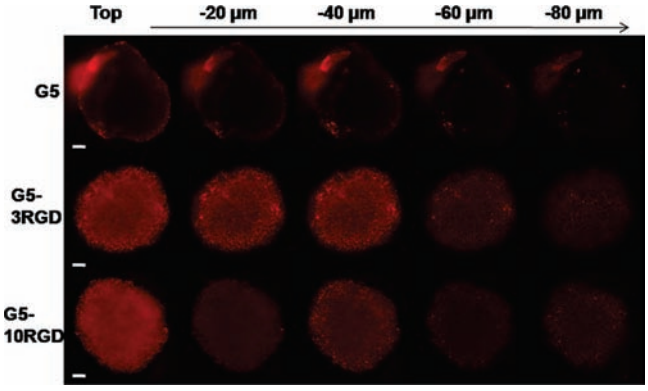

Figure 6. Confocal images of U87 spheroids 24 h after treatment with dendrimer/siRNA complexes. Cy3 siRNA fluorescence is shown in red. *Z*-stack images were obtained starting at the top of the spheroid in 20 μm intervals for a total of 100 μm into the spheroids. Images of each treatment were taken from three independent experiments with representative images shown here. The scale bar represents 100 μm.

uptake mediated by the presence of RGD ligands. This result is consistent with other literature reports that have found poor active tumor cell targeting from cationic polymers such as PEI and PAMAM when a short cross-linker was used to conjugate a targeting peptide (*5*, *28*, *29*). However, in addition to enhancing uptake of macromolecules into integrin-expressing cells, RGD targeting strategies can serve other purposes, such as interfering with integrin-mediated tumor cell adhesion to ECM proteins (*30*). This in turn may affect delivery of cargo in a tissue as opposed to a two-dimensional cell culture.

The integrin $\alpha_v\beta_3$ is intimately involved in tumor cell growth, proliferation, and angiogenesis. Thus, the ability to interfere specifically with the activity of this integrin could help to slow tumorigenesis in malignant glioma, and indeed a cyclic RGD peptide, Cilengitide, is undergoing clinical trials for glioma therapy (*31*, *32*). The PAMAM-RGD conjugates developed in this study inhibited the adhesion of U87 cells to the extracellular matrix protein, fibrinogen. A trend in inhibition of adhesion was observed as a function of RGD conjugation extent, with a maximum inhibition of cell adhesion observed with 3 RGD/PAMAM. Thus, a pronounced effect of RGD conjugation was observed in this cell adhesion model, contrasting the results obtained for siRNA delivery in which a trend was not observed as a function of RGD conjugation. Hence, the results of this assay support the ability of the PAMAM-RGD conjugates to perform active integrin binding.

MCTS models for cancer are garnering significant attention for anticancer drug screening as they mimic the microenvironment of tumors found in vivo more accurately than standard two-dimensional culture models (*33*, *34*), and they have recently been shown to display angiogenic phenotypes akin to those observed in vivo (*35*). Previous studies using spheroid cell culture models to evaluate nucleic acid delivery by synthetic polymers such as PEI or lipids have found that gene delivery using these carriers was confined to the outer layers of cells in spheroids due to poor penetration through the cell-matrix network (*27*). However, one study reported that conjugating lactose targeting moieties onto a polymeric micelle delivery system enabled deeper penetration of siRNA into a spheroid model of human hepatocarcinoma (*36*). Further, the presence of ECM proteins was found to inhibit the transport of nanoparticles through tumor spheroids (*37*). Since PAMAM-RGD conjugates were found to interfere with cell adhesion mediated by ECM, we hypothesized that using PAMAM-RGD conjugates would facilitate deeper penetration into a spheroid model of malignant glioma than unmodified PAMAM dendrimers via RGD modulation of cell−ECM interactions present in three-dimensional culture. As expected, PAMAM dendrimers conjugated with either 3 or 10 RGD peptides significantly improved the PAMAM-mediated delivery of siRNA to the spheroid interior compared to the native G5 dendrimer, suggesting that the addition of RGD peptides was able to overcome the poor tissue penetration of PAMAM dendrimers through spheroids. Notably, the PAMAM-RGD conjugates, in contrast to the G5 dendrimer, continued to penetrate into the MCTS throughout the 72 h time course of the experiment, suggesting a dynamic interaction among bioconjugate, ECM, and cell. However, despite the significant increases in tumor penetration, silencing levels of GFP remained insignificant. This outcome highlights the fact that cellular accumulation is not sufficient for efficient gene silencing. The siRNA must also be internalized by the cell and trafficked efficiently intracellularly, particularly with regards to endosomal escape. Modification of the dendrimers

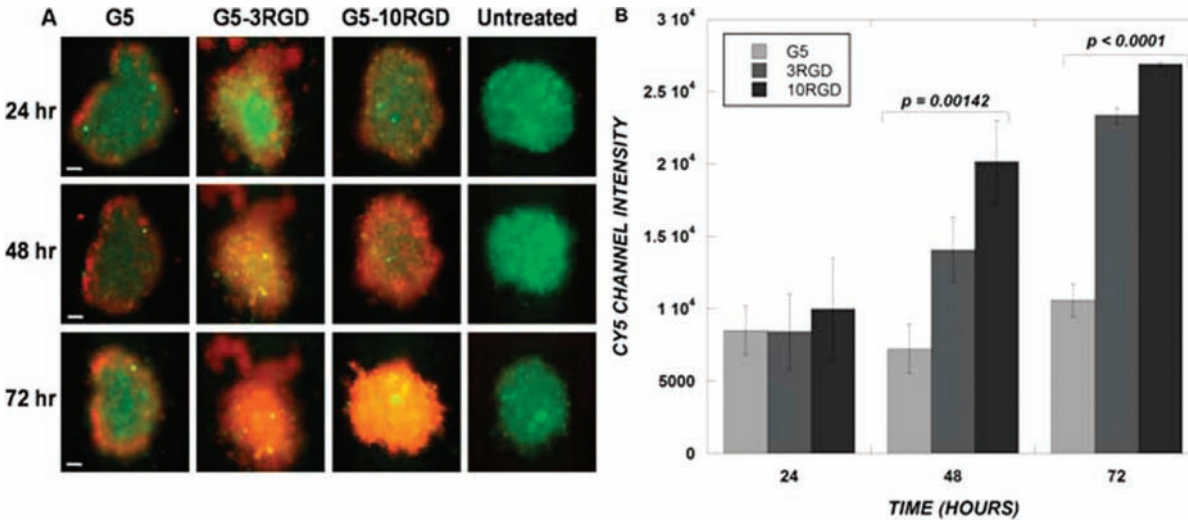

Figure 7. (A) Confocal images of U87 GFP spheroids treated with dendrimer/Cy5-ODN complexes. GFP fluorescence of U87 GFP cells is shown in green, and Cy5 ODN fluorescence is shown in red. All images shown are from a depth of 80 μm into each spheroid. The time points shown indicate the time post-transfection. The scale bar represents 100 μm. (B) Quantified intensities of Cy5 fluorescence. Data represent mean channel intensities of five cross-sectional slices for each spheroid with three spheroids for each condition. Error bars represent mean $\pm$ standard deviation.

to enhance these steps is necessary for ultimate application to tumor oncogene silencing.

A major goal of this work was to study how the number of RGD peptides on a PAMAM dendrimer affects its ability to interfere with important cell−ECM interactions. Previous studies have found that controlling RGD ligand presentation from a nanoparticle platform can significantly impact the extent of integrin-targeting that is achieved (*38*, *39*). Here, three RGDs per dendrimer were found to exhibit the strongest integrin-binding response using a competitive binding cell adhesion assay, and a greater number of peptides per dendrimer did not provide any additional benefit. However, in contrast to the trend observed in the competitive binding cell adhesion assay, dendrimers displaying 10 RGD peptides yielded significantly greater delivery of oligonucleotides to U87 spheroids than did dendrimers containing 3 RGD peptides. The three-dimensional architecture of the spheroids likely confers a greater advantage to dendrimers with a greater RGD multivalency, allowing for multiple contacts with ECM molecules within the MCTS. The results of this study highlight the importance of screening novel chemical entities and drug delivery systems in three dimensions.

Taken together, these results suggest that RGD-conjugated dendrimers hold promise for siRNA delivery to solid tumors. Their ability to interfere with integrin−ECM interactions can potentially enable penetration into malignant tumors to improve siRNA delivery, and they may also interfere directly with tumor angiogenesis and integrin-mediated growth signaling by malignant cells. Such multifunctional delivery systems that can modify the biological processes of cancer cells and deliver a therapeutic cargo in concert represent a new venue for cancer therapy. Due to the architecture of dendrimers with many exterior functional groups, the concept can be extended easily to incorporation of conventional drugs and/or imaging agents. Such developments will amplify the impact of siRNA on human disease.

ACKNOWLEDGMENT

We are grateful for financial support from the NIH (R01 GM65913), Charles and Johanna Busch Memorial Fund, and an NSF IGERT Fellowship (DGE-0504497) to CW. The authors thank the following people for access to and assistance with various instruments: Dr. Sobin Kim and Daniel Duffield (MALDI-ToF MS), Dr. Rene Schloss and Jeffrey Barminko (confocal microscope), and Dr. Kathryn Uhrich and Sarah Sparks (dynamic light scattering). We also thank Dr. Kathryn Uhrich, Dr. Prabhas Moghe, and Lavanya Peddada for helpful discussions and Paul Gianella for technical assistance.

Supporting Information Available: MALDI-ToF mass spectra of native G5 PAMAM and PAMAM-RGD conjugates. This material is available free of charge via the Internet at http://pubs.acs.org.

LITERATURE CITED

(1) Aagaard, L., and Rossi, J. J. (2007) RNAi therapeutics: principles, prospects and challenges. *Adv. Drug Delivery Rev. 59*, 75–86.

(2) Gartel, A. L., and Kandel, E. S. (2006) RNA interference in cancer. *Biomol. Eng. 23*, 17–34.

(3) Morille, M., Passirani, C., Vonarbourg, A., Clavreul, A., and Benoit, J. P. (2008) Progress in developing cationic vectors for non-viral systemic gene therapy against cancer. *Biomaterials 29*, 3477–96.

(4) Zhang, S., Zhao, B., Jiang, H., Wang, B., and Ma, B. (2007) Cationic lipids and polymers mediated vectors for delivery of siRNA. *J. Controlled Release 123*, 1–10.

(5) Kang, H., DeLong, R., Fisher, M. H., and Juliano, R. L. (2005) Tat-conjugated PAMAM dendrimers as delivery agents for antisense and siRNA oligonucleotides. *Pharm. Res. 22*, 2099–106.

(6) Patil, M. L., Zhang, M., Betigeri, S., Taratula, O., He, H., and Minko, T. (2008) Surface-modified and internally cationic polyamidoamine dendrimers for efficient siRNA delivery. *Bioconjugate Chem. 19*, 1396–403.

(7) Tsutsumi, T., Hirayama, F., Uekama, K., and Arima, H. (2007) Evaluation of polyamidoamine dendrimer/alpha-cyclodextrin conjugate (generation 3, G3) as a novel carrier for small interfering RNA (siRNA). *J. Controlled Release 119*, 349–59.

(8) Zhou, J., Wu, J., Hafdi, N., Behr, J. P., Erbacher, P., and Peng, L. (2006) PAMAM dendrimers for efficient siRNA delivery and potent gene silencing. *Chem. Commun. (Camb.)* 2362–4.

(9) Patil, M. L., Zhang, M., Taratula, O., Garbuzenko, O. B., He, H., and Minko, T. (2009) Internally cationic polyamidoamine PAMAM-OH dendrimers for siRNA delivery: effect of the degree of quaternization and cancer targeting. *Biomacromolecules 10*, 258–66.

(10) Waite, C. L., Sparks, S. M., Uhrich, K. E., and Roth, C. M. (2009) Acetylation of PAMAM dendrimers for cellular delivery of siRNA. *BMC Biotechnol. 9*, 38.

(11) Hong, S., Leroueil, P. R., Majoros, I. J., Orr, B. G., Baker, J. R., Jr., and Banaszak Holl, M. M. (2007) The binding avidity of a nanoparticle-based multivalent targeted drug delivery platform. *Chem. Biol. 14*, 107–15.

(12) Wolfenden, M. L., and Cloninger, M. J. (2005) Mannose/glucose-functionalized dendrimers to investigate the predictable tunability of multivalent interactions. *J. Am. Chem. Soc. 127*, 12168–9.

(13) Woller, E. K., Walter, E. D., Morgan, J. R., Singel, D. J., and Cloninger, M. J. (2003) Altering the strength of lectin binding interactions and controlling the amount of lectin clustering using mannose/hydroxyl-functionalized dendrimers. *J. Am. Chem. Soc. 125*, 8820–6.

(14) Cai, W., and Chen, X. (2006) Anti-angiogenic cancer therapy based on integrin alphavbeta3 antagonism. *Anticancer Agents Med. Chem. 6*, 407–28.

(15) Dunehoo, A. L., Anderson, M., Majumdar, S., Kobayashi, N., Berkland, C., and Siahaan, T. J. (2006) Cell adhesion molecules for targeted drug delivery. *J. Pharm. Sci. 95*, 1856–72.

(16) Boswell, C. A., Eck, P. K., Regino, C. A., Bernardo, M., Wong, K. J., Milenic, D. E., Choyke, P. L., and Brechbiel, M. W. (2008) Synthesis, characterization, and biological evaluation of integrin alphavbeta3-targeted PAMAM dendrimers. *Mol. Pharm. 5*, 527–39.

(17) Shukla, R., Thomas, T. P., Peters, J., Kotlyar, A., Myc, A., and Baker, J. R., Jr. (2005) Tumor angiogenic vasculature targeting with PAMAM dendrimer-RGD conjugates. *Chem. Commun. (Camb.)* 5739–41.

(18) Hill, E., Shukla, R., Park, S. S., and Baker, J. R., Jr. (2007) Synthetic PAMAM-RGD conjugates target and bind to odontoblast-like MDPC 23 cells and the predentin in tooth organ cultures. *Bioconjugate Chem. 18*, 1756–62.

(19) Yang, H., and Kao, W. J. (2007) Synthesis and characterization of nanoscale dendritic RGD clusters for potential applications in tissue engineering and drug delivery. *Int. J. Nanomed. 2*, 89–99.

(20) Lee, L. K., Dunham, B. M., Li, Z., and Roth, C. M. (2006) Cellular dynamics of antisense oligonucleotides and short interfering RNAs. *Ann. N. Y. Acad. Sci. 1082*, 47–51.

(21) Del Duca, D., Werbowetski, T., and Del Maestro, R. F. (2004) Spheroid preparation from hanging drops: characterization of a model of brain tumor invasion. *J. Neurooncol. 67*, 295–303.

(22) Rasband, W. S. (1997−2009), http://rsb.info.nih.gov/ij/, National Institues of Health, Bethesda, MD, USA.

(23) Muller, R., Laschober, C., Szymanski, W. W., and Allmaier, G. (2007) Determination of molecular weight, particle size, and density of high number generation PAMAM dendrimers using

MALDI-TOF-MS and nES-GEMMA. *Macromolecules 40*, 5599–5605.
(24) Shi, X. Y., Lesniak, W., Islam, M. T., Muniz, M. C., Balogh, L. P., and Baker, J. R. (2006) Comprehensive characterization of surface-functionalized poly (amidoamine) dendrimers with acetamide, hydroxyl, and carboxyl groups. *Colloids Surf., A 272*, 139–150.
(25) Marinelli, L., Lavecchia, A., Gottschalk, K. E., Novellino, E., and Kessler, H. (2003) Docking studies on alphavbeta3 integrin ligands: pharmacophore refinement and implications for drug design. *J. Med. Chem. 46*, 4393–404.
(26) Sutherland, R. M. (1988) Cell and environment interactions in tumor microregions: the multicell spheroid model. *Science 240*, 177–84.
(27) Mellor, H. R., Davies, L. A., Caspar, H., Pringle, C. R., Hyde, S. C., Gill, D. R., and Callaghan, R. (2006) Optimising non-viral gene delivery in a tumour spheroid model. *J. Gene Med. 8*, 1160–70.
(28) Sun, Y. X., Zeng, X., Meng, Q. F., Zhang, X. Z., Cheng, S. X., and Zhuo, R. X. (2008) The influence of RGD addition on the gene transfer characteristics of disulfide-containing polyethyleneimine/DNA complexes. *Biomaterials 29*, 4356–65.
(29) Clements, B. A., Bai, J., Kucharski, C., Farrell, L. L., Lavasanifar, A., Ritchie, B., Ghahary, A., and Uludag, H. (2006) RGD conjugation to polyethyleneimine does not improve DNA delivery to bone marrow stromal cells. *Biomacromolecules 7*, 1481–8.
(30) Mitra, A., Mulholland, J., Nan, A., McNeill, E., Ghandehari, H., and Line, B. R. (2005) Targeting tumor angiogenic vasculature using polymer-RGD conjugates. *J. Controlled Release 102*, 191–201.
(31) Eskens, F. A., Dumez, H., Hoekstra, R., Perschl, A., Brindley, C., Bottcher, S., Wynendaele, W., Drevs, J., Verweij, J., and van Oosterom, A. T. (2003) Phase I and pharmacokinetic study of continuous twice weekly intravenous administration of Cilengitide (EMD 121974), a novel inhibitor of the integrins alphavbeta3 and alphavbeta5 in patients with advanced solid tumours. *Eur. J. Cancer 39*, 917–26.
(32) Nabors, L. B., Mikkelsen, T., Rosenfeld, S. S., Hochberg, F., Akella, N. S., Fisher, J. D., Cloud, G. A., Zhang, Y., Carson, K., Wittemer, S. M., Colevas, A. D., and Grossman, S. A. (2007) Phase I and correlative biology study of cilengitide in patients with recurrent malignant glioma. *J. Clin. Oncol. 25*, 1651–7.
(33) Friedrich, J., Seidel, C., Ebner, R., and Kunz-Schughart, L. A. (2009) Spheroid-based drug screen: considerations and practical approach. *Nat. Protoc. 4*, 309–24.
(34) Goodman, T. T., Ng, C. P., and Pun, S. H. (2008) 3-D tissue culture systems for the evaluation and optimization of nanoparticle-based drug carriers. *Bioconjugate Chem. 19*, 1951–9.
(35) Fischbach, C., Kong, H. J., Hsiong, S. X., Evangelista, M. B., Yuen, W., and Mooney, D. J. (2009) Cancer cell angiogenic capability is regulated by 3D culture and integrin engagement. *Proc. Natl. Acad. Sci. U.S.A. 106*, 399–404.
(36) Oishi, M., Nagasaki, Y., Nishiyama, N., Itaka, K., Takagi, M., Shimamoto, A., Furuichi, Y., and Kataoka, K. (2007) Enhanced growth inhibition of hepatic multicellular tumor spheroids by lactosylated poly(ethylene glycol)-siRNA conjugate formulated in PEGylated polyplexes. *ChemMedChem 2*, 1290–7.
(37) Goodman, T. T., Chen, J., Matveev, K., and Pun, S. H. (2008) Spatio-temporal modeling of nanoparticle delivery to multicellular tumor spheroids. *Biotechnol. Bioeng. 101*, 388–99.
(38) Montet, X., Funovics, M., Montet-Abou, K., Weissleder, R., and Josephson, L. (2006) Multivalent effects of RGD peptides obtained by nanoparticle display. *J. Med. Chem. 49*, 6087–93.
(39) Ng, Q. K., Sutton, M. K., Soonsawad, P., Xing, L., Cheng, H., and Segura, T. (2009) Engineering clustered ligand binding into nonviral vectors: alphavbeta3 targeting as an example. *Mol. Ther. 17*, 828–36.

BC900228M

Supplementary Data

PAMAM-RGD Conjugates Enhance siRNA Delivery Through a Multicellular Spheroid Model of Malignant Glioma

Carolyn L. Waite and Charles M. Roth

The following are the MALDI TOF mass spectra obtained for the PAMAM-RGD conjugates formulated in this work:

G5 PAMAM

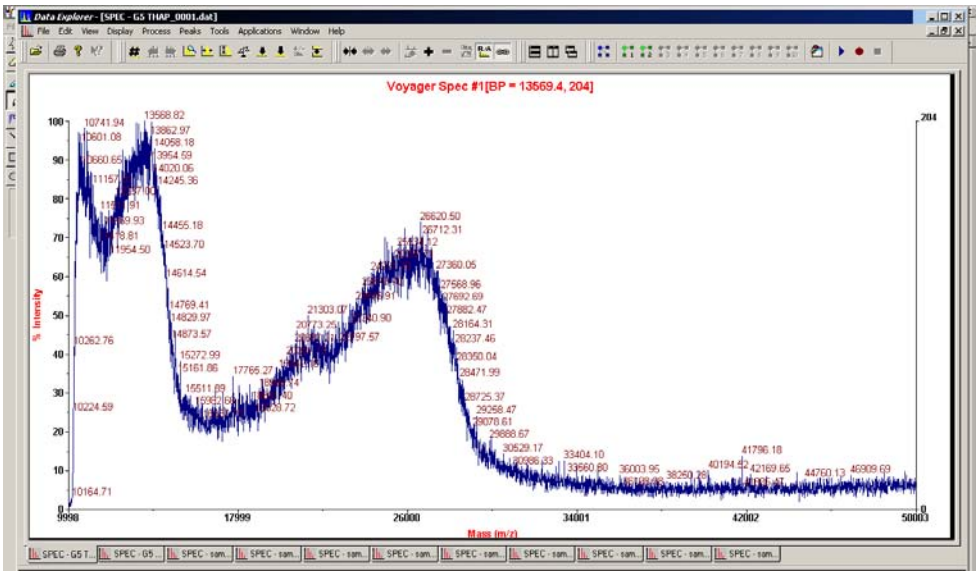

G5-2RGD

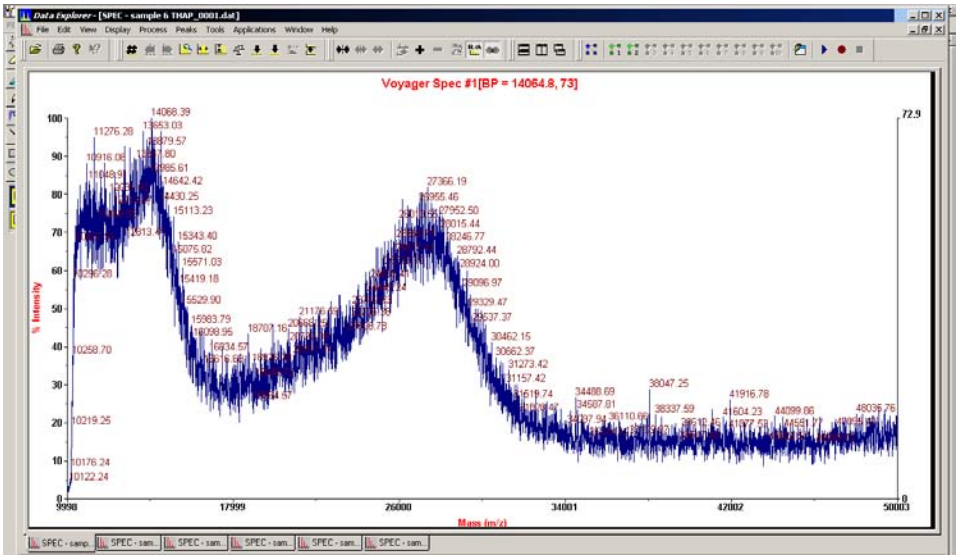

G5-3RGD

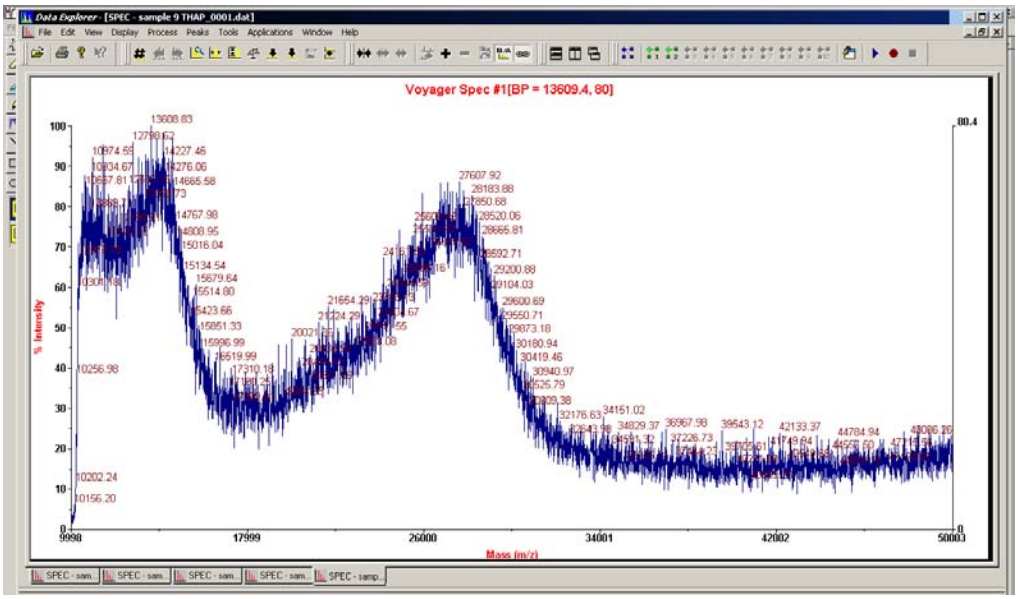

G5-7RGD

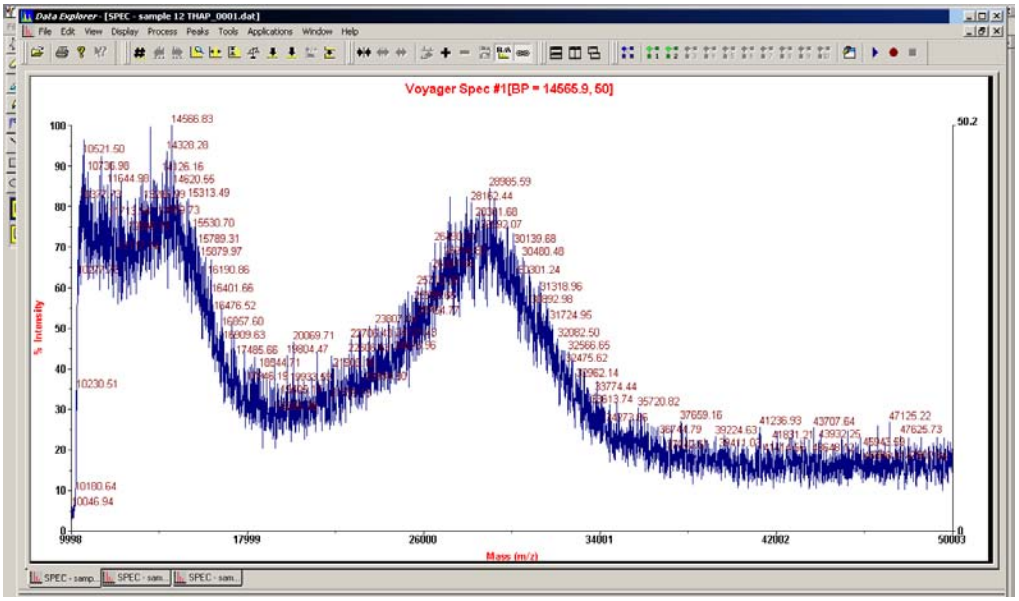

G5-10RGD

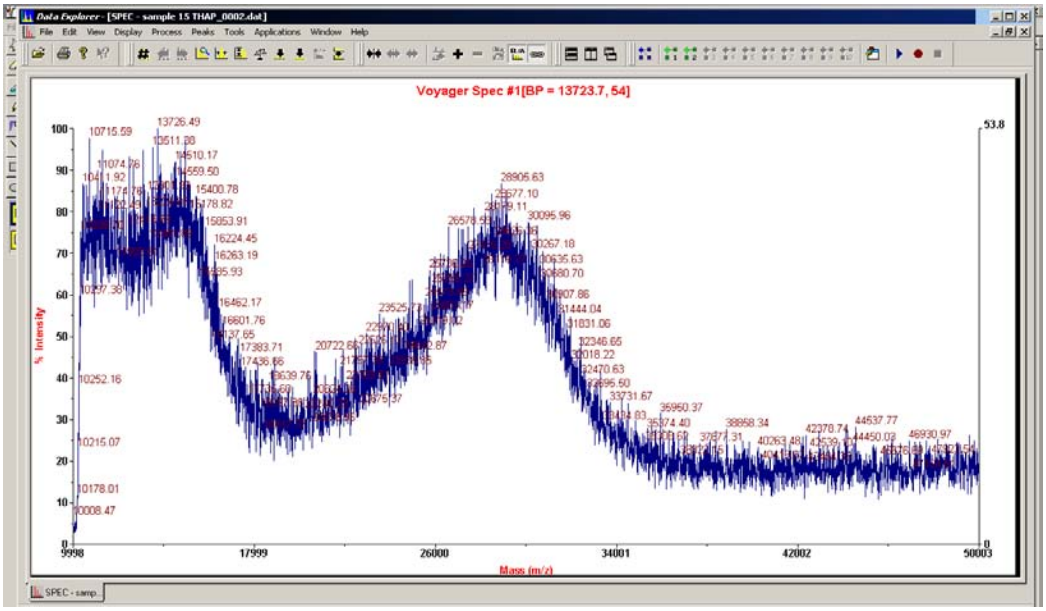
Data Explorer - [SPEC - sample 15 THAP_0002.dat]
File Edit View Display Process Peaks Tools Applications Window Help
Voyager Spec #1[BP = 13723.7, 54]
% Intensity
Mass (m/z)
9998
17999
26000
34001
42002
50003
53.8
SPEC - samp

Photo-Cross-Linking Induces Size Change and Stealth Properties of Water-Dispersible Cinnamic Acid Derivative Nanoparticles

Dongjian Shi, Michiya Matsusaki, and Mitsuru Akashi*

Department of Applied Chemistry, Graduate School of Engineering, Osaka University, 2-1 Yamada-oka, Suita 565-0871, Japan. Received June 3, 2009; Revised Manuscript Received August 4, 2009

Hydrophilic poly(ethylene glycol) (PEG) was grafted onto poly(4-cinnamic acid)-*co*-poly(3,4-cinnamic acid) (PCA) by Michael addition. The chemical structures of the PCA-*graft*-PEG (PCA-PEG) copolymers were confirmed by FT-IR and ^{1}H NMR measurements. The PCA-PEG nanoparticles were self-assembled by the solvent mixing method, in which additional water was dropped into a DMSO solution of the copolymer. The diameter of the PCA-PEG nanoparticles was below 100 nm, and decreased to about 30 nm upon increasing the composition ratio and molecular weight of PEG. The PCA-PEG nanoparticles showed [2 + 2] cyclobutane formation (cross-linking) following UV irradiation at $\lambda > 280$ nm. Moreover, the photo-cross-linking induced size decrement of the nanoparticles depending on the grafting degree and molecular weight of PEG. The amount of protein adsorption onto the surface of the nanoparticles was less than 30 ng/cm^2, due to the high density of PEG chains on their corona layers. Furthermore, photo-cross-linking induced a significant decrement in protein adsorption, due to an increase in PEG chain density triggered by the size decrement of the nanoparticles. These water-dispersible and photoresponsive nanoparticles would be useful as novel, functional carriers for drug delivery systems and biological diagnosis.

INTRODUCTION

Polymeric nanoparticles are typically useful as carriers for drugs and proteins and as catalyst molecules in biomedical and environmental applications because of their high surface area compared to nanofibers and films (*1*−*3*). Many studies have focused on nanoparticles composed of biodegradable polymers, such as poly(lactic acid) (PLA), poly(ε-caprolactone) (PCL), and polysaccharides, for drug delivery systems (DDS) (*4*−*6*). We have also reported various self-assembling synthetic (*7, 8*) and biodegradable (*9*−*12*) nanoparticles and hollow capsules (*13, 14*) as controlled release carriers and nanosphere-based vaccines. In using the nanoparticles as carriers for biomedical applications, there is a serious problem with nonspecific protein adsorption onto the surface of the nanoparticle, which affects the stable dispersity of the nanoparticle and targeted delivery of a drug or protein. To solve this problem, it is necessary to prepare a bioinert surface, which can inhibit the nonspecific adsorption of serum proteins and hemocytes, for maintaining their stable circulation and property in the blood without being scavenged nonselectively (*15, 16*). Therefore, introduction of hydrophilic groups onto the material surface for protein resistance had been reported to develop a bioinert surface on the nanoparticles. By increasing the density of hydrophilic groups on the material surface, the resistance against protein adsorption onto the nanoparticles was improved (*17*−*19*). However, there was no report on improving the resistance of the protein adsorption by external stimuli such as light stimuli. Light-induced responses have been attracted much attention, since it is one of the most desirable methods for the easy, rapid, and efficient control of material properties by tuning the light wavelength or energy (*20*). Photoresponsive materials have great potential applications in DDS, RNA/DNA recognition, and shape-memory systems and as recording and switching sensors (*21*−*23*). Therefore, photoresponsive, nanoscaled materials such as nanoparticles, nanofibers, and nanofilms are expected to have applications not only in nanotechnologies, but also in biomedical fields.

Cinnamic acid and its derivates exist in plant cell walls as an intermediate metabolite in the biosynthetic pathway of lignin and other biological materials, and show photoreactions such as [2 + 2] cycloaddition and trans/cis isomerization, which lead to the transformation of the photoactive yellow protein in photosynthetic bacteria (*24*). We have reported a series of cinnamic acid derivative homopolymers and copolymers possessing liquid crystal phases, photoreactivities, degradabilities, and cell compatibilities (*25*−*29*). Moreover, wholly aromatic polyester, poly(3,4-dihydroxycinnamic acid-*co*-4-hydroxycinnamic acid) (PCA), was synthesized from the phenolic phytomonomers 3,4-dihydroxycinnamic acid (3,4DHCA) and 4-hydroxycinnamic acid (4HCA) (*30*). The PCA copolymer has high photosensitivity and degradability, as well as strong mechanical properties. Zhao's group also reported polymer micelles with coumarin moieties as side chains for cross-linking and de-cross-linking of micelles with UV irradiation, and controlled the release rate of the encapsulated component with a tunable photo-cross-linking density (*31*). Therefore, nanoparticles containing cinnamate groups are useful for developing photoresponsive nanoscaled materials for biomedical and environmental applications. However, conventional photosensitive nanoparticles cannot induce a significant size change because they contain only a few chromophoric groups.

In previous studies, we reported that the self-assembled PCA nanoparticles underwent a significant diameter change property following photo-cross-linking and photocleavage of cinnamate groups with UV irradiation (*32, 33*). Furthermore, the size change phenomena of these nanoparticles depending on the photo-cross-linking degree during hydrolysis were also observed (*34*). However, the nanoparticles could not disperse in aqueous

* To whom correspondence should be addressed. Mitsuru Akashi, Professor, Department of Applied Chemistry, Graduate School of Engineering, Osaka University, 2-1 Yamada-oka, Suita 565-0871, Japan. Tel: +81-6-6879-7356, Fax: +81-6-6879-7359, E-mail: akashi@chem.eng.osaka-u.ac.jp.

10.1021/bc900239j CCC: $40.75 © 2009 American Chemical Society
Published on Web 09/18/2009

Scheme 1. (a) Synthesis of the PCA-PEG Copolymer Composed of Hydrophobic Poly(cinnamic acid) and Hydrophilic Poly(ethylene glycol) Segments. (b) Schematic Representation of the Self-Assembling PCA-PEG Nanoparticles and a Typical Photoimage of the PCA-PEG2k-0.5 Nanoparticles in Aqueous Solution

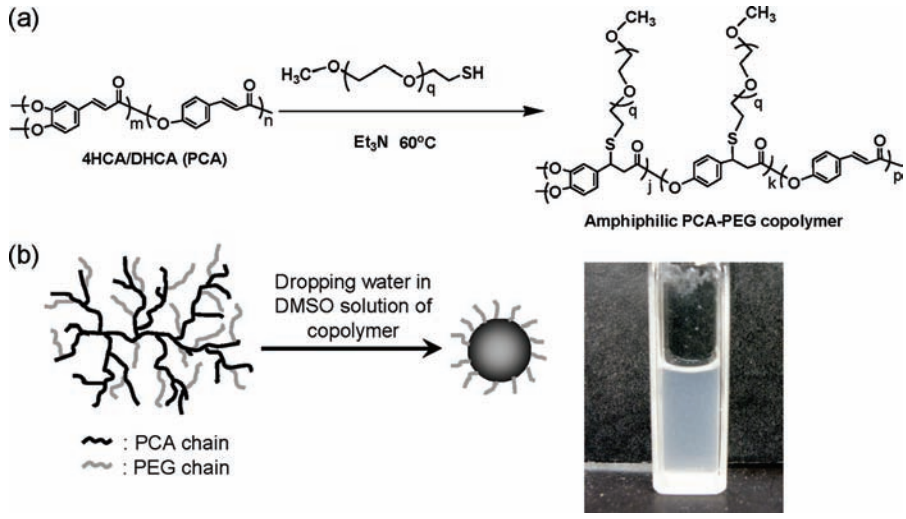

solution, which limited their applications in biomedical fields. If water-dispersible PCA nanoparticles were developed, the photoresponsive nanoparticles might be useful for drug delivery systems.

Poly(ethylene glycol) (PEG) is well-known as a water-soluble and nontoxic polymer, which is useful for obtaining the water-dispersibility and biocompatibility, especially resistance against the nonspecific adsorption of serum proteins and hemocytes for material and particle surfaces (*35*−*37*). Herein, we used α-mercaptoethyl-*ω*-methoxy poly(ethylene glycol) (SH-PEG-OCH_3) to prepare biocompatible and photoresponsive PCA-*graft*-PEG (PCA-PEG) nanoparticles by Michael addition (Scheme 1). The nonspecific protein adsorption onto the surfaces of the nanoparticles was evaluated, and the effects of photo-cross-linking on the nanoparticle size and nonspecific protein adsorption related to the PEG density on the surface of the nanoparticles were investigated in detail.

EXPERIMENTAL PROCEDURES

Materials. 4-Hydroxycinnamic acid (4HCA) and 3,4-dihydroxycinnamic acid (3,4DHCA) were purchased from Tokyo Chemical Industry (TCI, Japan) and Wako Pure Chemical Industries, Ltd., Japan, respectively, and used as received. α-Mercaptoethyl-*ω*-methoxy poly(ethylene glycol) (SH-PEG-OCH_3; M_n: 2, 10, and 20 kDa) were purchased from NOF Corp. Japan. *N*,*N*-Dimethylformamide (DMF), dimethyl sulfoxide (DMSO), and trifluoroacetic acid (TFA) were purchased from Wako Pure Chemical Industries Ltd., Japan, and used without further purification. Bovine serum albumin (BSA) was purchased from Sigma (St. Louis, MO, USA).

Synthesis of PCA-PEG Copolymers. The PCA copolymer was prepared from 3,4DHCA and 4HCA monomers at the same molar ratio by thermal polycondensation at 200 °C for 6 h, according to a previous report (*30*). The PEG grafted PCA copolymers (PCA-PEG) were synthesized by Michael addition (*38*,*39*) in the presence of a few drops of triethylamine as a catalyst at 60 °C for 12 h. After a predetermined time, the reacted solutions were precipitated from methanol. The obtained precipitates were dissolved in DMSO and filtered to remove any unsubstituted PCA, and then reprecipitated in methanol to remove any unreacted PEG twice. The products were then dried under vacuum at room temperature overnight. The average molecular weights of the PCA-PEG copolymers were determined by gel permeation chromatography (GPC) using a HLC-8220 GPC (Tosoh co. Ltd., Japan) with TSK-GEL super H2000 and H4000 columns in DMF containing 10 mM lithium chloride (LiCl) and calibrated with monodispersed polystyrene standards (Shodex, Japan) at a flow rate of 0.6 mL/min at 40 °C. The structures of the copolymers were confirmed by Fourier transform infrared spectroscopy (FT-IR) on a FT-IR spectrometer (Spectrum 100, Perkin-Elmer, Japan) using an attenuated total reflection (ATR) method. ^{1}H NMR spectrum was measured using a JNM-GSX400 spectrometer (JEOL, 400 MHz, Japan) in dichloromethane (CD_2Cl_2). The grafting degrees of PEG were calculated from the ^{1}H NMR spectrum by comparing the peak areas of the cinnamate and methylene groups and UV−vis spectrum (U3010 spectrometer, Hitachi, Japan) by comparing the absorbance of the cinnamate groups using a calibration curve of the copolymer solution.

Preparation and Photo-Cross-Linking of Water-Dispersible PCA-PEG Nanoparticles. The obtained PCA-PEG copolymers were dissolved in DMSO to a concentration of 1 mg/mL, and additional water was dropped into the copolymer solution until formation of a turbid solution. The nanoparticles were purified by dialysis in distilled water for 4 days and then collected by lyophilization for 3 days. The obtained nanoparticles were redispersed in pure water at a concentration of 0.5 mg/mL, and then the aqueous solution was filled in a quartz cell and irradiated with focused UV light at $\lambda > 280$ nm (80 mW/cm^2) by a 350 W high-pressure mercury lamp (Supercuere-352S UV light source, SAN-EI electric co. Ltd., Japan). The distance between the solution and the lamp was approximately 5 cm. The photo-cross-linking of the cinnamate groups was confirmed by UV−vis and ^{1}H NMR spectra. Dynamic light scattering (DLS, Malvern Zeta-sizer Nano ZS Instruments, Japan) was used to measure the diameter of the nanoparticles in water at a concentration of 0.5 mg/mL at room temperature. Scanning electron microscopy (SEM, JEOL JSM-6701F, Japan) was used to observe the size and surface morphology of the PCA-PEG nanoparticles after casting the sample solutions onto a stage and subsequent drying in vacuo overnight. Transmission electron microscopy (TEM, JEM-100CS-S1, JEOL, Japan) images were obtained after dropping the nanoparticle solutions onto a collodion-coated copper mesh grid, drying at ambient condition, and then carbon sputtering.

Protein Adsorption onto the Surface of the PCA-PEG Nanoparticles. The PCA-PEG nanoparticles were dispersed in phosphate buffered saline (PBS, pH 7.4) at 10 mg/mL and

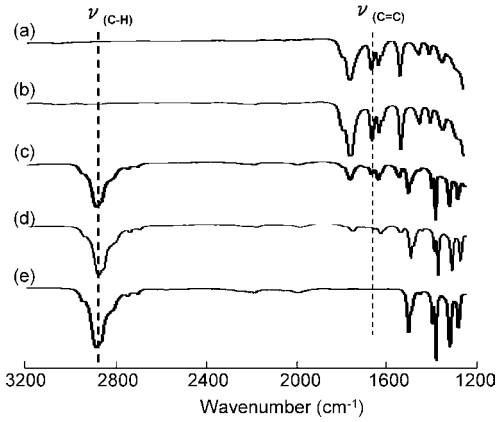

Figure 1. FT-IR spectra of the copolymers: PCA (a), PCA-PEG2k-0.5 (b), PCA-PEG2k-10 (c), PCA-PEG2k-100 (d), and PEG2k (e).

incubated with equivalent of a 4 mg/mL protein (BSA) solution in PBS at 4 °C for 24 h. The nanoparticles were collected by centrifugation, washed twice with PBS, and resuspended at 5 mg/mL in PBS. The amount of protein adsorbed onto the nanoparticles was determined by the Lowry method (*40*). Briefly, the obtained nanoparticle solution was added to the same volume of 4% sodium dodecyl sulfate solution (SDS) to dissolve the nanoparticles, and then the amount of adsorbed BSA was determined on a microplate reader (BIO-RAD, model 680, Japan) by a reduction in Folin-phenol to molybdenum blue using the copper ion-catalyzed oxidation of aromatic acids under alkaline conditions.

RESULTS AND DISCUSSION

Synthesis of the PCA-PEG Copolymers. PCA copolymers were synthesized from phytomonomers 3,4DHCA and 4HCA at the same molar ratio by thermal polycondensation based on our previous report (*32*). The molecular weight and structure of the PCA copolymer were confirmed by GPC measurements and the ^{1}H NMR spectra. Amphiphilic PEG grafted PCA (PCA-PEG) copolymers were synthesized by Michael addition (Scheme 1a).

Figure 1 shows FT-IR spectra of the PCA-PEG2k copolymers with different grafting degrees of PEG2k (PCA-PEG2k as examples). The peak at 1630 cm^{-1} was assigned to the double carbon bond ($\nu_{C=C}$) of the cinnamate groups in the PCA segments (Figure 1a−d). The peak area of the double carbon decreased upon increasing the PEG grafting degree (Figure 1b,c), and the peak disappeared when the PEG grafting degree reached almost 100% (Figure 1d), indicating successful substitution of the double carbon bond (CH═CH) to S−CH bond by Michael addition. The peak at 2860 cm^{-1} was assigned to stretching vibration of the C−H group in the PEG chains (Figure 1c−e), and the peak area for the PCA-PEG copolymers increased with increasing grafting degree of PEG (Figure 1b−d). Figure 2 shows ^{1}H NMR spectra of PCA, PEG2k, and PCA-PEG2k copolymers with different grafting degrees. Peaks at 6.8 and 8.2 ppm were assigned to the double carbon bonds of the cinnamate groups in PCA (Figure 2a−d). The peak appearing at ∼3.8 ppm was assigned to the PEG methylene groups (Figure 2b−e). When the grafting degree of PEG was above 10%, a new peak at approximately 3.0 ppm appeared, which was assigned to the S-CH group (Figure 2c,d), indicating the PEG chain was successfully introduced into PCA. When the grafting degree was 100%, the peaks at 6.8 and 8.2 ppm disappeared, suggesting the complete introduction of the PEG chains into the double carbon bonds of PCA (Figure 2d). The degree of grafting of the PCA-PEG copolymers was calculated from ^{1}H NMR spectrum by comparing the peak area between cinnamate groups at 6.8 ppm and methylene groups of the PEG repeat units at 3.8 ppm, as summarized in Table 1. Moreover, the results from UV−vis spectra also revealed a decrement of double carbon bond depending on the PEG grafting degree (data not shown), supporting the formation of the PCA-PEG copolymers. By calculating the absorbance of the cinnamate groups using a calibration curve derived from the PCA-PEG copolymer solution, the grafting degrees were obtained from UV−vis spectra as summarized in Table 1, and the values agreed well with the grafting degrees estimated from ^{1}H NMR measurements.

These results suggested that the PEG chains were successfully introduced into PCA by Michael addition. By controlling the molecular weight of PEG and the molar ratio between the cinnamate groups in PCA and the thiol groups in PEG, PCA-

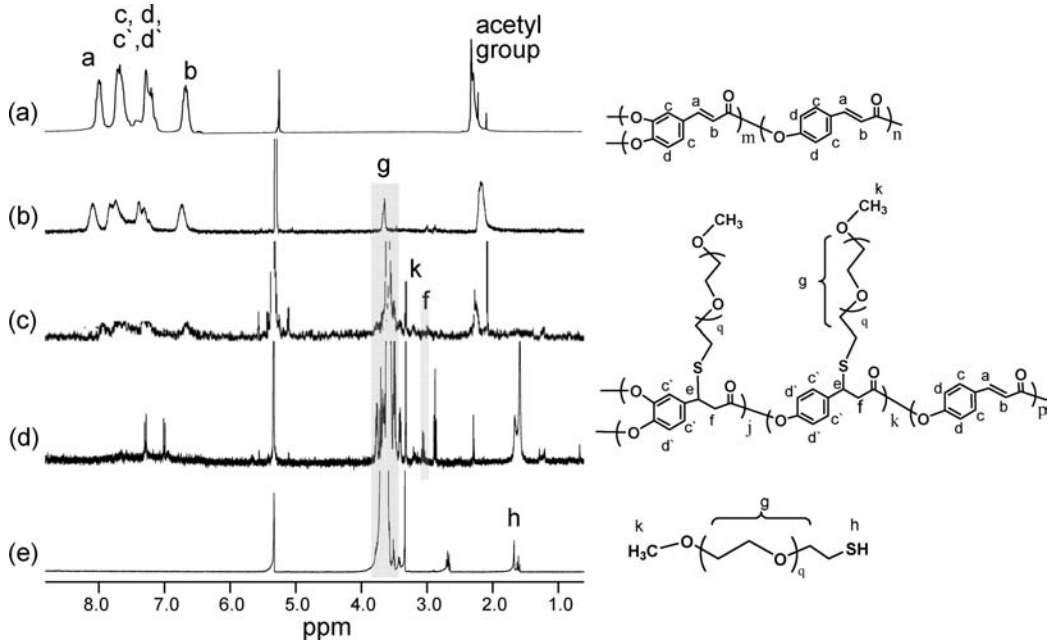

Figure 2. ^{1}H NMR spectra of the PCA and PEG2k polymers and their copolymers: PCA (a), PCA-PEG2k-0.5 (b), PCA-PEG2k-10 (c), PCA-PEG2k-100 (d), and PEG2k (e).

Table 1. Synthesis and Characterization of the PCA-PEG Copolymers with Different Molecular Weights and Grafting Degrees of PEG

					grafting degree (%)[c]				
sample[a]	PCA (mg)	PEG (mg)	yield (%)	molecular weight[b] ($M_n \times 10^3$)	(1)	(2)	(3)	diameter[d] (nm)	CV[e] (%)
PCA				3.4					
PCA-PEG2k-0.5	417	25	70	1.5	0.5	0.3	0.2	102	20.8
PCA-PEG2k-1	625	74	69	3.3	1	0.6	2.0	90	20.2
PCA-PEG2k-5	125	74	28	4.1	5	2.0	3.0	51	21.3
PCA-PEG2k-10	63	74	73	3.8	10	12.0	7.0	46	30.0
PCA-PEG2k-50	13	74	69	3.1	50	61.0	46.0	33	43.6
PCA-PEG2k-100	5	74	75	3.2	100	n.d.[f]	97.0	-[g]	-
PCA-PEG10k-0.5	250	74	61	4.8	0.5	0.4	0.2	93	25.3
PCA-PEG10k-1	125	74	69	3.8	1	0.6	1.0	56	21.0
PCA-PEG10k-5	25	74	84	17.3	5	16.0	5.0	53	38.0
PCA-PEG10k-10	25	147	91	13.4	10	27.0	6.0	49	36.0
PCA-PEG10k-50	3	74	76	14.1	50	30.0	48.0	-	-
PCA-PEG10k-100	1	74	80	16.9	100	n.d.	98.0	-	-
PCA-PEG20k-0.5	250	39	74	3.9	0.5	0.3	0.1	69	43.0
PCA-PEG20k-1	100	118	71	3.4	1	0.4	0.7	50	40.2
PCA-PEG20k-5	20	118	65	20.0	5	7.0	4.0	43	23.6
PCA-PEG20k-10	10	118	70	21.5	10	14.0	7.5	37	27.5
PCA-PEG20k-50	2	118	73	30.0	50	n.d.	60.0	-	-
PCA-PEG20k-100	0.4	118	79	35.7	100	n.d.	95.0	-	-

[a] 2k, 10k, and 20k mean the molecular weight of PEG as 2, 10, and 20 kDa, and 0.5, to 100 mean grafting degree of PEG against double bond of cinnamic acid, respectively. [b] GPC measurement in DMF with monodispersed polystyrene standards. [c] (1) in feed of molar ratio of PEG. [c] (2) the grafting degree calculated from ^{1}H NMR spectrum. [c] (3) the grafting degree calculated from UV−vis spectrum. [d] The diameter by DLS measurement. [e] CV (coefficient of variation, %) = standard deviation/mean diameter. [f] Not detected. [g] No particle formation.

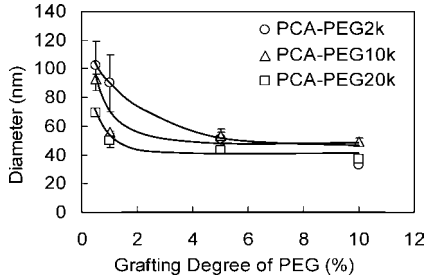

Figure 3. Diameters of PCA-PEG nanoparticles with different molecular weights and grafting degrees of PEG chains by DLS measurements ($n = 3$).

PEG copolymers with different composition ratios were obtained (Table 1). The molecular weights of the PCA-PEG copolymers obtained from the GPC measurements are also listed in Table 1, and the results showed that the molecular weights of the copolymers increased upon increasing the composition and molecular weight of PEG.

Preparation of the PCA-PEG Nanoparticles. A turbid solution appeared by adding water into the copolymer solution in DMSO (Scheme 1b), suggesting the formation of PCA-PEG nanoparticles. We observed the formation of the regular and monodispersed nanoparticles at DMSO/water = 1:2 (v/v). Thus, all of the nanoparticles were prepared at 1:2 volume ratios of DMSO and water. The nanoparticle size was detected by DLS measurements, and is shown in Table 1 and Figure 3. The diameter of the PCA-PEG 2k, 10k, and 20k nanoparticles was approximately 100, 90, and 70 nm, respectively. When the grafting degree of PEG was increased, the diameters gradually decreased to about 30 to 50 nm (Figure 3). The increase in the hydrophilic chains induced the formation of a smaller nanoparticle size due to a decrement in the hydrophobic interactions. However, when the grafting degree was over ca. 50%, particle formation was not observed even after adjusting the volume ratio of DMSO and water or the concentration of the copolymers, maybe due to a disruption of the hydrophilic−hydrophobic balance between hydrophilic PEG and hydrophobic PCA chains. The obtained PCA-PEG nanoparticles showed a unimodal distribution by DLS measurements.

Figure 4 shows SEM and TEM observations of the nanoparticles (PCA-PEG with 1% grafting degree as examples). Both

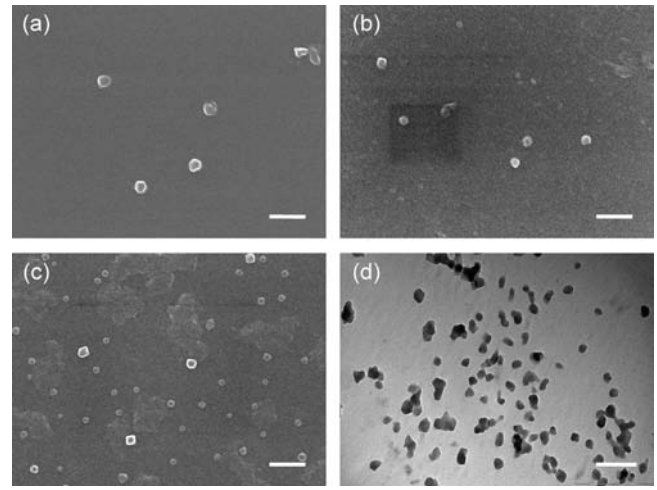

Figure 4. SEM images of the PCA-PEG2k-1 (a), PCA-PEG10k-1 (b), and PCA-PEG20k-1 (c) nanoparticles and a TEM image of the PCA-PEG20k-1 nanoparticle (d). The scale bars are 250 nm.

SEM (Figure 4a−c) and TEM (Figure 4d) images revealed the spherical morphology of the PCA-PEG nanoparticles, suggesting the successful preparation of monodispersed nanoparticles. The average diameters calculated from SEM images were 90, 60, and 50 nm for PCA-PEG2k-1, PCA-PEG10k-1, and PCA-PEG20k-1 nanoparticles, respectively, indicating good agreement with the results from DLS measurements (Table 1 and Figure 3).

These results demonstrated that the homogeneous nanoparticles were self-assembled from PCA-PEG copolymers by hydrophilic−hydrophobic balance and the grafting degrees and molecular weights of PEG strongly affected the nanoparticles size.

Effect of Photo-Cross-Linking on the PCA-PEG Nanoparticle Size. Cinnamic acid and its derivates show well-known [2 + 2] cycloaddition (cross-linking) formation with UV irradiation at $\lambda > 280$ nm (Figure 5a) (*20*−*22*). To evaluate the photoreactivities of the PCA-PEG nanoparticle, PCA-PEG10k-2 nanoparticles in aqueous solution were irradiated with UV light at $\lambda > 280$ nm for 10 min, and then the UV−vis spectra were measured to assay the cross-linking formation as shown in

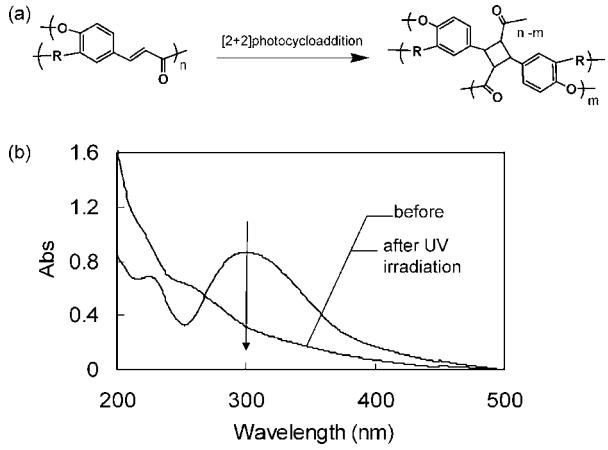

Figure 5. (a) Chemical structure of UV irradiation at $\lambda > 280$ nm induced [2 + 2] cycloaddition (cross-linking) formation of the cinnamate groups. (b) UV−vis spectra of PCA-PEG10k-2 in aqueous solution before and after photo-cross-linking with UV irradiation at $\lambda > 280$ nm for 10 min.

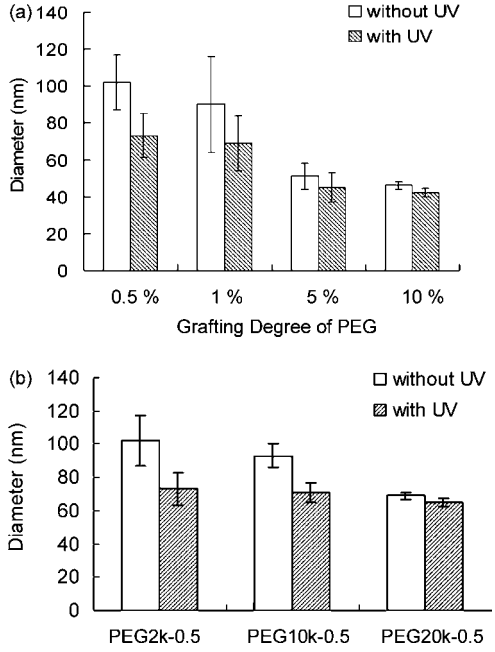

Figure 6. Diameter and size change ratio of PCA-PEG2k nanoparticles with different grafting degrees (a) and molecular weights (b) of PEG-0.5 before and after photo-cross-linking with UV irradiation at $\lambda > 280$ nm to reach 90% cross-linking degree as determined by DLS measurements ($n = 3$).

Figure 5b. The absorbance of the cinnamate groups at 300 nm strongly decreased with UV irradiation, demonstrating cross-linking formation. The cross-linking degree calculated from the change of the cinnamate group in absorbance at 300 nm was about 90%. These results indicated the formation of cross-linking in the core part of the nanoparticles.

The effects of photo-cross-linking on nanoparticle size were investigated by DLS measurements. Figure 6a shows the diameter change of the PCA-PEG2k nanoparticles with different grafting degrees of PEG before and after photo-cross-linking (90% cross-linking degree). The diameter of the nanoparticles decreased after cross-linking, and the size change ratio varied depending on the PEG composition. The size change ratio was about 28% for the PCA-PEG2k nanoparticles with 0.5% grafting degree, and decreased to 8% at a 10% grafting degree (Figure 6a). The higher PEG compositions (over 5%) had a lower amount of the cinnamate groups in the nanoparticles, resulting in a smaller size change property of the nanoparticles after photo-cross-linking. The size change ratio of the nanoparticles decreased upon increasing the molecular weight of PEG (Figure 6b), possibly due to the hydrophobic−hydrophilic balance. In the case of PCA-PEG20k nanoparticles, the occupied volume of the hydrophilic PEG (corona layer) should be larger than that of hydrophobic PCA (core part); accordingly, the size change phenomena might not be observed well. Moreover, a longer hydrophilic chain stretching well into the aqueous solution would maintain the size even after photo-cross-linking. The size distribution of the PCA-PEG nanoparticles was a unimodal peak after photo-cross-linking.

From these results, the driving force for the diameter decrement after UV irradiation should be the photo-cross-linking of the cinnamate groups in the nanoparticles, and the obtained particle size was strongly influenced by the character of the PEG chains.

Surface PEG Density of the Nanoparticles and Protein Adsorption onto the Surface with and without Photo-Cross-Linking. The number of PEG chains on a single nanoparticle was determined by per unit mass of the PEG methylene peak in the region 3.5−3.8 ppm as compared with the methyl proton peak of DSS at 0 ppm from the ^{1}H NMR spectrum in D_2O (*18*). The number of PEG chains on a single nanoparticle ($N(\mathrm{PEG})_{\mathrm{surface}}$) and the surface density of the PEG chains (σ_{PEG}) were calculated from the size (as determined by DLS measurements) and density (generally assumed to be 1.05 g/cm^3) of the nanoparticles, and the results are summarized in Table 2. These results showed that a large amount of PEG chains were on the nanoparticles and that the $N(\mathrm{PEG})_{\mathrm{surface}}$ increased with an increasing composition ratio and molecular weight of PEG, suggesting a brush conformation for the PEG chains on the surface of the PCA-PEG nanoparticles. The PEG densities of the nanoparticles were estimated to be 0.11 (PCA-PEG2k-0.5), 0.19 (PCA-PEG2k-1), 0.4 (PCA-PEG2k-5), 0.29 (PCA-PEG10k-0.5), and 0.59 (PCA-PEG10k-1) chains/nm^2, respectively. Upon photo-cross-linking formation of the cinnamate groups, the $N(\mathrm{PEG})_{\mathrm{surface}}$ showed almost no change (Table 2), indicating that it was not effective for the number of the surface PEG chains. Interestingly, the σ_{PEG} for the PCA-PEG2k-0.5 and PCA-PEG2k-1 nanoparticles increased to about twice after photo-cross-linking, due to a size decrement of the nanoparticles

Table 2. Structure of PEG Chains on the PCA-PEG Nanoparticles and BSA Adsorption onto the Surface of the PCA-PEG Nanoparticles

	$N(\mathrm{PEG})_{\mathrm{surface}}$[a]		σ_{PEG} (chains/nm^2)[b]		diameter (nm)[c]		BSA adsorption (ng/cm^2)[d]	
Sample	before[e]	after[f]	before[e]	after[f]	before[e]	after[f]	before[e]	after[f]
PCA-PEG2k-0.5	1.6×10^5	2.1×10^5	0.11	0.21	102 ± 15	75 ± 12	29.3 ± 9	15.1 ± 8
PCA-PEG2k-1	2.4×10^5	2.3×10^5	0.19	0.24	90 ± 26	70 ± 15	16.6 ± 4	11.7 ± 3
PCA-PEG2k-5	2.9×10^5	2.9×10^5	0.40	0.45	50 ± 7	45 ± 9	12.8 ± 2	4.2 ± 3
PCA-PEG2k-10	1.5×10^5	1.4×10^5	0.23	0.24	46 ± 2	42 ± 3	17.9 ± 5	3.5 ± 2
PCA-PEG10k-0.5	2.3×10^5	2.3×10^5	0.29	0.33	93 ± 7	72 ± 8	15.3 ± 1	7.4 ± 1
PCA-PEG10k-1	4.5×10^5	4.5×10^5	0.59	0.63	56 ± 10	50 ± 7	11.5 ± 2	2.5 ± 1

[a] $N(\mathrm{PEG})_{\mathrm{Surface}}$ means the number of PEG chain on a single nanoparticle surface, and was estimated by ^{1}H NMR spectrum in D_2O using DSS as reference. [b] σ_{PEG} means the surface density of PEG chains on the nanoparticles. [c] Diameter was measured by DLS. [d] BSA adsorption of the nanoparticles was calculated by Lowry method. [e] Before photo-cross-linking of the cinnamate groups. [f] After photo-cross-linking of the cinnamate groups.

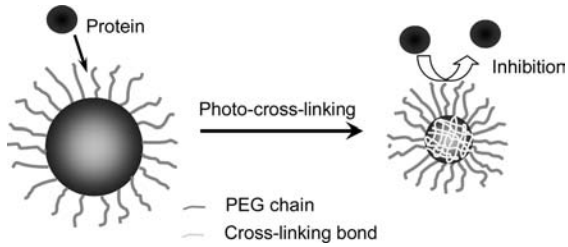

Figure 7. Schematic illustration of protein adsorption onto the nanoparticle surface before and after photo-cross-linking of the cinnamate groups with UV irradiation at $\lambda > 280$ nm.

(Figure 6). However, in the case of nanoparticles with higher grafting degrees and molecular weights of PEG, the σ_{PEG} showed a negligible change after photo-cross-linking. To the best of our knowledge, this is the first report on controlling PEG chain density on the nanoparticles by controlling the size of the nanoparticle with UV irradiation.

To evaluate the stealth properties against nonspecific protein adsorption onto the nanoparticles, bovine serum albumin (BSA) was used because albumin is one of the major proteins in serum. Table 2 shows the BSA adsorption against the surface area of the nanoparticles. The amount of adsorbed BSA onto the PCA-PEG2k-0.5 nanoparticles was about 30 ng/cm^2, and the amount of BSA decreased with increasing PEG grafting degree and molecular weight. However, the amount of adsorbed BSA was not detected when the grafting degree of PEG10k was over 5% and the molecular weight of PEG was 20k. These results suggested that PEG chains in the coronal layers can inhibit nonspecific protein adsorption. Interestingly, after photo-cross-linking of the cinnamate groups in the PCA-PEG nanoparticles with UV irradiation, the BSA adsorption significantly decreased to almost one-half as compared to the un-cross-linked one. From the results, the decrement in BSA adsorption after cross-linking seemed to contribute to the high density of the PEG brush on the coronal layer of the nanoparticles (Figure 7). Interestingly, PCA-PEG2k-5, 2k-10, 10k-0.5, and 10k-1 also showed a significant decrement in BSA adsorption, although the diameter change was not observed even after photo-cross-linking. The reason of the decrement in BSA adsorption of these samples after photo-cross-linking is still unclear. One of the possibilities for the phenomena might be a fraction of conformational and morphological change of the PEG chains in the corona layer triggered by cross-linking of PCA chains in core part. The detailed experiments to clarify these phenomena are now in progress. Although many researchers have reported controlling stealth properties by the introduction of a high density of hydrophilic groups (*17*−*19*), there is no report on improving the stealth properties by only UV irradiation. This is the first example of a significant improvement of the stealth properties of a hydrolyzable nanoparticle by controlling its photo-cross-linking-induced size change.

CONCLUSIONS

Amphiphilic PCA-PEG copolymers were prepared by Michael addition of PEG, and the copolymers were self-assembled into nanoparticles by the solvent mixing method. The nanoparticle size could be altered by the composition ratio and molecular weight of PEG. Photo-cross-linking formation of the cinnamate groups induced a size decrement of the nanoparticles depending on the grafting degree and molecular weight of PEG. Protein adsorption onto the surface of the nanoparticles was very low due to the high density of PEG chains (brush conformation). Moreover, photo-cross-linking induced a significant decrement in protein adsorption, due to an increase in the PEG chain density triggered by the size decrement of the nanoparticles. The water-dispersible and photoresponsive nanoparticles would be useful as novel functional carriers for drug delivery systems and biological diagnosis.

ACKNOWLEDGMENT

This research was supported by 21st Century COE Program "Center for Integrated Cell and Tissue Regulation", Osaka University, Japan. Authors thank N. Hasegawa (the Research Center in Osaka University) for helping transmission electron microscopy observation.

LITERATURE CITED

(1) Santos, C. A., Freedman, B. D., Leach, K. J., Press, D. L., Scarpulla, M., and Mathiowitz, E. (1999) Poly(fumaric-*co*-sebacic anhydride): a degradation study as evaluated by FTIR, DSC, GPC and X-ray diffraction. *J. Controlled Release 60*, 11–22.

(2) Matsusaki, M., Waku, T., Kaneko, T., Kida, T., and Akashi, M. (2006) One-step advanced preparation of surface-functional peptide nanospheres by the polymerization of L-phenylalanine *N*-carboxyanhydride with dual initiators. *Langmuir 22*, 1396–1399.

(3) Harada, A., and Kataoka, K. (1999) Chain length recognition: core-shell supramolecular assembly from oppositely charged block copolymers. *Science 283*, 65–67.

(4) Park, T. G. (1995) Degradation of poly(lactic-*co*-glycolic acid) microspheres: effect of copolymer composition. *Biomaterials 16*, 1123–1130.

(5) Wiltshire, J. T., and Qiao, G. G. (2006) Selectively degradable core cross-linked star polymers. *Macromolecules 39*, 9018–9027.

(6) Lee, W. C., and Chu, I. M. (2008) Preparation and degradation behavior of polyanhydrides nanoparticles. *J. Biomed. Mater. Res. Part B: App. Biomater. 84B*, 138–146.

(7) Akashi, M., Kirikihira, I., and Miyauchi, N. (1985) Synthesis and polymerization of a styryl terminated oligovinylpyrrolidone macromonomer. *Angew. Makromol. Chem. 132*, 81–89.

(8) Serizawa, T., Takehara, S., and Akashi, M. (2000) Transmission electron microscopic study of cross-sectional morphologies of core-corona polymeric nanospheres. *Macromolecules 33*, 1759–1764.

(9) Matsusaki, M., Hiwatari, K., Higashi, M., Kaneko, T., and Akashi, M. (2004) Stably-dispersed and surface-functional bionanoparticles prepared by self-assembling amphipathic polymers of hydrophilic poly(g-glutamic acid) bearing hydrophobic amino acids. *Chem. Lett. 33*, 398–399.

(10) Matsusaki, M., Fuchida, T., Kaneko, T., and Akashi, M. (2005) Self-assembling bionanoparticles of poly(ε-lysine) bearing cholesterol as a biomesogen. *Biomacromolecules 6*, 2374–2379.

(11) Akagi, T., Higashi, M., Kaneko, T., Kida, T., and Akashi, M. (2006) Hydrolytic and enzymatic degradation of nanoparticles based on amphiphilic poly(γ-glutamic acid)-*graft*-L-phenylalanine copolymers. *Biomacromolecules 7*, 297–303.

(12) Akagi, T., Wang, X., Uto, T., Baba, M., and Akashi, M. (2007) Protein direct delivery to dendritic cells using nanoparticles based on amphiphilic poly(amino acid) derivatives. *Biomaterials 28*, 3427–3436.

(13) Itoh, Y., Matsusaki, M., Kida, T., and Akashi, M. (2004) Preparation of biodegradable hollow nanocapsules by silica template method. *Chem. Lett. 33*, 1552–1553.

(14) Itoh, Y., Matsusaki, M., Kida, T., and Akashi, M. (2006) Enzyme-responsive release of encapsulated proteins from biodegradable hollow capsules. *Biomacromolecules 7*, 2715–2718.

(15) Kataoka, K., Harada, A., and Nagasaki, Y. (2001) Block copolymer micelles for drug delivery: design, characterization and biological significance. *Adv. Drug Delivery Rev. 47*, 113–131.

(16) Katre, N. V. (1993) The conjugation of proteins with polyethylene glycol and other polymers: altering properties of proteins to enhance their therapeutic potential. *Adv. Drug Delivery Rev. 10*, 91–114.

(17) Yokoyama, M., Kwon, S. G., Okano, T., Sakurai, Y., Seto, T., and Kataoka, K. (1992) Preparation of micelle-forming polymer-drug conjugates. *Bioconjugate Chem. 3*, 295–301.
(18) Waku, T., Matsusaki, M., Kaneko, T., and Akashi, M. (2007) PEG brush peptide nanospheres with stealth properties and chemical functionality. *Macromolecules 40*, 6385–6392.
(19) Yamamoto, S., Ejaz, M., Tujii, Y., Matsumoto, M., and Fukuda, T. (2000) Surface interaction forces of well-defined, high-density polymer brushes studied by atomic force microscopy. 1. effect of chain length. *Macromolecules 33*, 5602–5607.
(20) Schreier, W. J., Schrader, T. E., Koller, F. O., Gilch, P., Crespo-Hernández, C. E., Swaminathan, V. N., Carell, T., Zinth, W., and Kohler, B. (2007) Thymine dimerization in DNA is an ultrafast photoreaction. *Science 315*, 625–629.
(21) Yuan, X., Fischer, K., and Schartl, W. (2005) Photocleavable microcapsules built from photoreactive nanospheres. *Langmuir 21*, 9374–9380.
(22) Lendlein, A., Jiang, H., Junger, O., and Langer, R. (2005) Light-induced shape-memory polymers. *Nature 434*, 879–882.
(23) Hayashi, G., Hagihara, M., Dohno, C., and Nakataniko., K. (2007) Photoregulation of a peptide-RNA interaction on a gold surface. *J. Am. Chem. Soc. 129*, 8678–8679.
(24) Hoff, W. D., Dux, P., Hard, K., Devreese, B., Nugteren-Roodzant, I. M., Crielaard, W., Boelens, R., Kaptein, R., Beeumen, J., and Hellingwerf, K. J. (1994) Thiol ester-linked *p*-coumaric acid as a new photoactive prosthetic group in a protein with rhodopsin-like photochemistry. *Biochemistry 33*, 13959–13962.
(25) Kaneko, T., Matsusaki, M., Tran, H. T., and Akashi, M. (2004) Thermotropic liquid crystalline biopolymer derived from natural cinnamoyl monomers. *Macromol. Rapid Commun. 25*, 673–677.
(26) Matsusaki, M., Tran, H. T., Kaneko, T., and Akashi, M. (2005) Enhanced effects of lithocholic acid incorporation into liquid-crystalline biopolymer poly(coumaric acid) on structural ordering and cell adhesion. *Biomaterials 26*, 6263–6270.
(27) Tran, H. T., Matsusaki, M., Shi, D. J., Kaneko, T., and Akashi, M. (2008) Synthesis and properties of coumaric acid derivative homo-polymers. *J. Biomater. Sci. Polym. Ed. 19*, 75–85.
(28) Kaneko, T., Tran, H. T., Matsusaki, M., and Akashi, M. (2006) Biodegradable LC oligomers with cranked branching points form highly oriented fibrous scaffold for cytoskeletal orientation. *Chem. Mater. 18*, 6220–6226.
(29) Tran, H. T., Matsusaki, M., and Akashi, M. (2009) Development of photoreactive degradable branched polyesters with high thermal and mechanical properties. *Biomacromolecules 10*, 766–772.
(30) Kaneko, T., Tran, H. T., Shi, D. J., and Akashi, M. (2006) Environmentally degradable, high-performance thermoplastics from phenolic phytomonomers. *Nat. Mater. 5*, 966–970.
(31) Jiang, J., Qi, B., Lepage, M., and Zhao, Y. (2007) Polymer micelles stabilization on demand through reversible photo-cross-linking. *Macromolecules 40*, 790–792.
(32) Shi, D. J., Kaneko, T., and Akashi, M. (2007) Particulation of hyperbranched aromatic biopolyesters self-organized by solvent transformation in ionic liquids. *Langmuir 23*, 3485–3488.
(33) Shi, D. J., Matsusaki, M., Kaneko, T., and Akashi, M. (2008) Photo-cross-linking and cleavage induced reversible size change of bio-based nanoparticles. *Macromolecules 41*, 8167–8172.
(34) Shi, D. J., Matsusaki, M., and Akashi, M. (2009) Unique size-change behavior of photo-crosslinked cinnamic acid derivative nanoparticles during hydrolytic degradation. *Macromol. Biosci. 9*, 248–255.
(35) Zalipsky, S. (1995) Functionalized poly(ethylene glycols) for preparation of biologically relevant conjugates. *Bioconjugate Chem. 6*, 150–165.
(36) Benhabbour, S. R., Sheardown, H., and Adronov, A. (2008) Protein resistance of PEG-functionalized dendronized surfaces: effect of PEG molecular weight and dendron generation. *Macromolecules 41*, 4817–4823.
(37) Hamada, K., Kaneko, T., Chen, M. Q., and Akashi, M. (2007) Size-selective material adsorption property of polymeric nanoparticles with projection coronas. *Chem. Mater. 19*, 1044–1052.
(38) Sundararajan, G., and Prabagaran, N. (2001) A new polymer-anchored chiral catalyst for asymmetric Michael addition reactions. *Org. Lett. 3*, 389–392.
(39) Vanderhooft, J., Mann, B. K., and Preswich, G. D. (2007) Synthesis and characterization of novel thiol-reactive poly(ethylene glycol) cross-linkers for extracellular-matrix-mimetic biomaterials. *Biomacromolecules 8*, 2883–2889.
(40) Peterson, G. L. (1977) A simplification of the protein assay method of Lowry *et al.* which is more generally applicable. *Anal. Biochem. 83*, 346–356.

BC900239J

Precise Site-Selective Termination of DNA Replication by Caging The 3-Position of Thymidine and Its Application to Polymerase Chain Reaction

Akinori Kuzuya,* Fuminori Okada, and Makoto Komiyama*

Research Center for Advanced Science and Technology, The University of Tokyo, 4-6-1 Komaba, Meguro-ku, Tokyo 153-8904, Japan. Received June 9, 2009

A new caged thymidine, 3-*N*-(2-(2-nitrophenyl)propyloxymethyl)thymidine (T^{NPPOM}) was synthesized and used as a site-selective terminator of DNA-polymerase reaction in light-assisted cohesive-ending PCR (LACE-PCR), which directly gives sticky-ended PCR products after brief UVA irradiation. Primer-extension experiments using a template involving T^{NPPOM} have shown that this caged nucleotide efficiently and site-selectively blocks reactions of a variety of polymerases commonly used in PCR. Misincorporation of nucleobases, observed with the use of other previously reported caged thymidines, scarcely occurred. It has turned out that a slight structural difference of caging groups can significantly improve the termination yield of polymerase reactions. A LACE-PCR product coding GFP gene was prepared by using primers containing T^{NPPOM} and was ligated with a vector fragment prepared using restriction enzymes. The resulting recombinant vector successfully transformed *E. coli*.

INTRODUCTION

Photocaging of oligonucleotides has become an attractive topic because of its potential to control genetic events simply by irradiating light without changing either chemical nor physical conditions (*1, 2*). Various oligonucleotides protected with photocleavable groups (caged oligonucleotides) have been reported. Recently, we have developed a quite simple and effective new PCR system for easily preparing sticky-ended products utilizing caged nucleotides (*3, 4*).

In current molecular biology and biotechnology, vectors are usually constructed by digesting plasmid DNA with restriction enzymes, followed by connection of this vector with predetermined gene fragment using ligase (*5*). In many cases, those gene fragments are prepared by PCR from various sources, and the blunt ends of the PCR products are converted to cohesive ends by the restriction enzymes for ligation with the vector. Although this technology has been mostly successful, two problems still remain unsolved for further developments of the field. First, recognition sites of commonly used restriction enzymes are mostly limited to some palindromic sequences, and it is sometimes difficult to find appropriate enzyme to digest DNA at (or near) the target manipulation site. Second, most of these enzymes recognize only 4 to 8 DNA-base sequences; thus, precise manipulation of large vectors such as adenovirus (30−38 kbp) with restriction enzymes is not very practical since their digestion occurs at too many sites in such large DNA. In light-assisted cohesive-ending (LACE) PCR (*4*), however, products with desired sticky ends on both ends are directly prepared after standard PCR procedures following a brief UVA irradiation, and thus no restriction enzyme treatment is necessary (Scheme 1). In order to terminate the polymerase reaction at a desired position, a caged nucleotide is incorporated into PCR primers. Within PCR cycles, elongation of the nascent strand (5′→3′ direction) is site-selectively terminated at the 3′ side of the caged nucleotide. Accordingly, the 5′ portion in the primer from the caged nucleotide remains single-stranded throughout the cycles, and predetermined sticky ends are obtained after the removal of the protecting group by brief UVA irradiation. In the previous studies, we have used a caged nucleotide 4-*O*-(2-(2-nitrophenyl)propyl)thymidine developed by Heckel et al. (T^{NPP} in Figure 1) as the site-selective terminator (*6*). We found that T^{NPP} is stable enough to survive repetitive thermal cycles for PCR and indeed terminates polymerase reaction site-selectively. The LACE-PCR products coding green fluorescent protein (GFP) gene was successfully prepared, directly ligated to vectors, and used to transform *E. coli*.

Scheme 1. Outline of the Light-Assisted-Cohesive-Ending PCR (LACE-PCR) Using a Caged Nucleotide

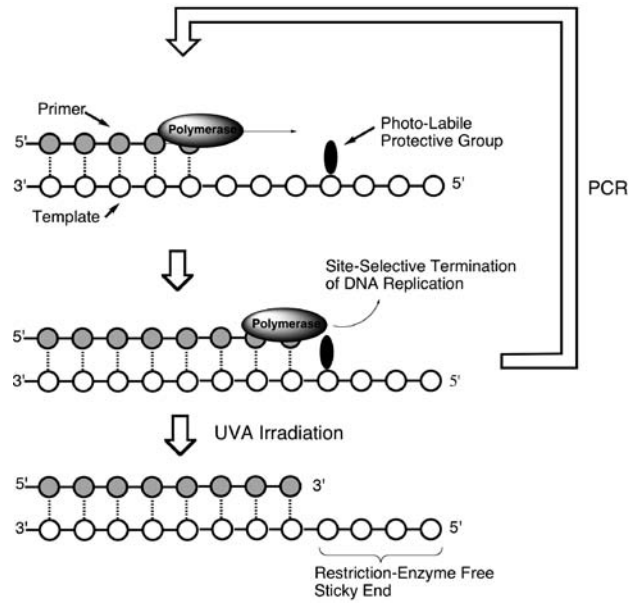

Although it was successful for an initial trial, some difficulties in using T^{NPP} as the terminator have come to light. Particularly, some of the polymerases misincorporate dG in front of T^{NPP} almost quantitatively, probably because the hydrogen-bonding property of T^{NPP} is similar to that of dC. Ligase is known to be a very strict enzyme; thus, such mismatches at the ends of a PCR product are unfavorable for making recombinant plasmids for standard cloning. Another difficulty of T^{NPP} is the necessity

* (+81) 3 5452 5200; FAX: (+81) 3 5452 5209; E-mail: kuzu@mkomi.rcast.u-tokyo.ac.jp, komiyama@mkomi.rcast.u-tokyo.ac.jp.

10.1021/bc900254e CCC: $40.75 © 2009 American Chemical Society
Published on Web 09/25/2009

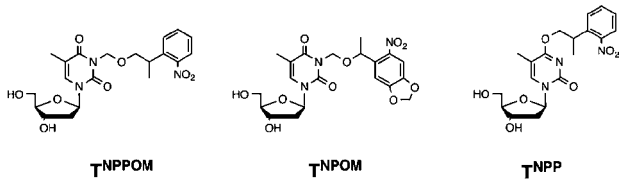

10 5'- TT**T**^{NPPOM}TT -3'
5'- AGC**X**GTCCGGCGTAGAGGATCGAG -3'
X = T^{NPP} : **11**
T^{NPPOM} : **12**
T^{NPOM} : **13**
14 5'- FAM-CTCGATCCTCTACGCCG -3'
15 5'- AAT**T**^{NPPOM}CACCGTCACCCTGGATGCTG -3'

Figure 1. Structures of the caged thymidines (T^{NPPOM}, T^{NPOM}, and T^{NPP}) and oligonucleotides (**10**−**15**) used in the present work.

of using special phosphoramidite monomers in automated DNA synthesis. Chemically synthesized DNA is usually treated with conc aqueous ammonia at elevated temperatures (typically 55 °C for 8 h) to deprotect nucleobases. However, T^{NPP} under such vigorous condition is easily transformed to dC via ammonolysis of the substituted 4-*O*. Thus, in combination with T^{NPP}, it is essential to use ultramild dG and dA phosphoramidite monomers that can be deprotected under much milder conditions. This is not a very convenient situation for wider use of LACE-PCR.

To solve these problems, we decided to introduce an NPP group to the 3-*N* position of the thymine base instead of 4-*O*, and have designed a new caged thymidine in this study. The 3-*N*-(2-(2-nitrophenyl)propyloxymethyl)thymidine (T^{NPPOM}, Figure 1) bears a 2-(2-nitrophenyl)propyloxymethyl (NPPOM) group on the 3-*N* position. This group was stable enough to survive vigorous deprotection conditions in standard DNA synthesis, and thus can be used with normal phosphoramidite monomers. Primer-extension experiments using a template involving T^{NPPOM} have shown that this caged nucleotide in fact efficiently and site-selectively blocks the reaction of a variety of polymerases commonly used in PCR. An application of LACE-PCR using T^{NPPOM} as the site-selective terminator for constructing recombinant plasmid was also examined.

While we were preparing this paper, Young et al. proposed the usage of 3-(6-nitropiperonyloxymethyl)thymidine (T^{NPOM}) residues, which also possess a caging group on the 3-*N*, in light regulating mutagenesis (*7*). We have examined the detailed termination efficiency of T^{NPOM} as well.

EXPERIMENTAL PROCEDURES

Syntheses of Oligonucleotides Containing Caged Thymines. The phosphoramidite monomer of T^{NPPOM} was synthesized from thymidine as shown in Scheme 2 (see Supporting Information for the details). Phosphoramidite monomers of T^{NPP} and T^{NPOM} were synthesized according to the literature (*6, 8*). The oligonucleotides containing T^{NPPOM} (**10**, **12**, and **15**) or T^{NPOM} (**13**) were prepared using standard phosphoramidite monomers on an automated DNA synthesizer. An extended 10 min coupling step was employed for T^{NPPOM} incorporation. After deprotection with conc aqueous ammonia at 55 °C for 8 h, they were purified using denaturing PAGE (except for **10**) and reverse-phase (RP) HPLC, and characterized by ESI (for **10**, Hitachi M-8000) and MALDI-TOF/MS (Bruker AutoFLEX). The oligonucleotide containing T^{NPP} (**11**) was prepared using a set of ultramild cyanoethyl phosphoramidites (phenoxyacetyl protected dA and 4-isopropyl-phenoxyacetyl protected dG monomers from Glen Research), and the deprotection was performed with conc aqueous ammonia at room temperature for 24 h. Their sequences are shown in Figure 1.

Analyses of Uncaging Oligonucleotides. UVA irradiation ($300 < \lambda < 400$ nm) on a mixture containing the caged oligonucleotide substrate **10** (1 mM) was performed by using UV Spot Light Source (Hamamatsu Photonics; 200 W) through a UTVAF-50S-36U filter (Sigma Koki) at 2.5 mW/cm^2. After predetermined times, 10 μL aliquots were analyzed on RP-HPLC with a linear gradient of acetonitrile from 5% to 50% in 45 min in the presence of ammonium formate (50 mM). The peaks at 12.8, 17.0, and 17.3 min in Figure 2A were collected and further analyzed by ESI-MS in negative ion mode for identification.

Primer Extension Reaction Using Caged Oligonucleotides as the Template. A mixture containing the caged oligonucleotide substrate **14** (2 μM), the primer oligo **11**−**13** (1 μM), and dNTPs (1.35 mM for each) was prepared. Unintended light exposure was carefully avoided throughout the process. After ExTaq polymerase (Takara) was added to the solution (0.1 U/μL), the following cycles were repeated 30 times on a thermal cycler: denaturation, 94 °C (15 s); annealing, 50 °C (30 s); elongation, 60 °C (70 s). The product was then analyzed on 20% denaturing PAGE. Extension with other polymerases were also examined under the following concentration without UV irradiation: [KOD -Plus- polymerase (Toyobo)] = 0.02 U/μL, [KOD Dash polymerase (Toyobo)] = 0.05 U/μL, and [*Pfu* DNA polymerase (Stratagene)] = 0.05 U/μL. The thermal cycles for KOD -Plus- and KOD Dash were the same as for ExTaq. For *Pfu*: denaturation, 94 °C (30 s); annealing, 55 °C (30 s); elongation, 72 °C (70 s). Imaging and quantification of gel electrophoresis were carried out on a FLA-3000G fluorescent imaging analyzer (Fujifilm, Japan).

Light-Assisted Cohesive-Ending PCR (LACE-PCR). Using pQBI T7-GFP (Wako, 0.96 ng/μL) as the template, PCR was performed under the following conditions: [**12** and **15**] = 300 nM, [dNTPs] = 200 μM, and [*Pfu* Ultra polymerase] = 0.05 U/μL. Thermal cycles are the same as described in the primer extension experiments.

After purification with a QIAquick PCR Purification kit (Qiagen), the product in TE buffer (pH 8.5) was irradiated with UVA for 30 min at room temperature.

Construction of a Recombinant Plasmid (Scheme 3). The vector for the LACE-PCR product was prepared by cutting pUC18 with *Eco*RI and *Hind*III. The product was then dephosphorylated with alkaline phosphatase. To a 1:3 mixture of this vector and LACE-PCR product, the same volume of DNA Ligation Kit (Mighty Mix) solution was added. After incubation overnight at 16 °C, JM109 (Toyobo) was transformed with the ligation product and cultured on LB-agar media containing ampicillin (50 μg/mL) and X-gal (40 μg/mL). White colonies were subjected to colony direct PCR, and a positive colony was picked up and cultured in LB media. The recombinant vector was purified with a QIAprep spin Miniprep Kit (Qiagen), and its sequence starting 150 bp away from each conjunction was determined on a 3130× Genetic Analyzer (Applied Biosystems). For both the colony direct PCR and sequencing, 5′-TCGCCATTCAGGCTGCGCAAC-3′ (243−263 bp region of pUC18 plasmid) and 5′-TGGAAAGCGGGCAGTGAGC-3′ (590−608 bp region of pUC18 plasmid) were used as the primers. In order to observe the fluorescence from expressed GFP, the purified vector was introduced into BL21-Gold (DE3) (Stratagene). The picture of the culture was taken on a Safe Imager blue-light transilluminator equipped with a Safe Imager amber filter unit (Invitrogen).

RESULTS AND DISCUSSION

Synthesis of Phosphoramidite Monomer of T^{NPPOM} and the Caged Oligonucleotides. The structures of the caged thymidines and oligonucleotides used in this study are shown

Scheme 2. Synthetic Route of the Phosphoramidite Monomer of T^{NPPOM}

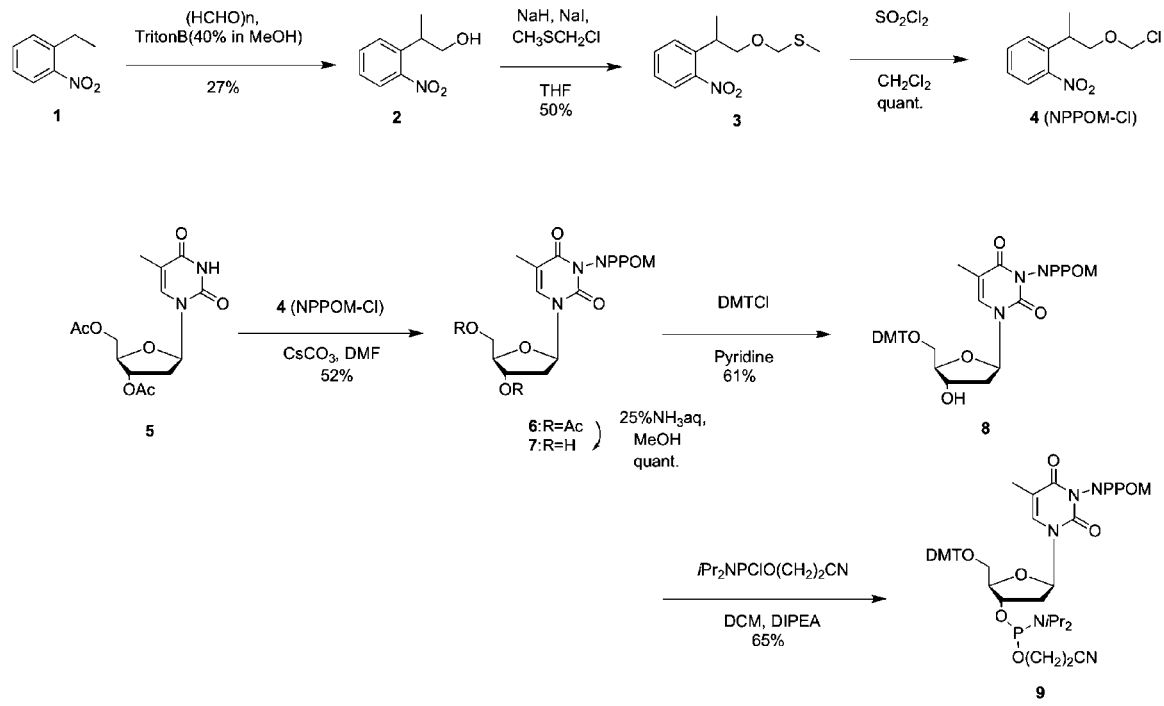

in Figure 1. T^{NPP} is the caged thymidine we used in our previous studies, and bears an NPP group on the 4-*O* position. T^{NPPOM} is the newly designed caged thymidine that bears an NPP group on the 3-*N* position via a methoxy group. T^{NPOM} is another caged thymidine that bears a caging group on the 3-*N* position. All of the oligonucleotides were synthesized on an automated DNA synthesizer using standard phosphoramidite chemistry. The phosphoramidite monomer of T^{NPPOM} was synthesized from thymidine and 2-ethylnitrobenzene as shown in Scheme 2 (see Supporting Information for the details). Phosphoramidite monomers for T^{NPOM} and T^{NPP} were prepared according to the literature (*6*, *8*). For the synthesis of **11** containing T^{NPP}, a set of ultramild cyanoethyl phosphoramidite monomers were used for dA and dG, and the deprotection was done with conc aqueous ammonia at room temperature for 24 h. Other oligonucleotides bearing T^{NPPOM} or T^{NPOM} were synthesized with standard monomers and protocols. The short oligonucleotide **10** was purified using reversed-phase (RP) HPLC and characterized by ESI and MALDI-TOF/MS analyses. Oligonucleotides **11**−**15** were purified using denaturing polyacrylamide gel electrophoresis (PAGE) and RP-HPLC, and characterized by MALDI-TOF/MS analyses (see Supporting Information).

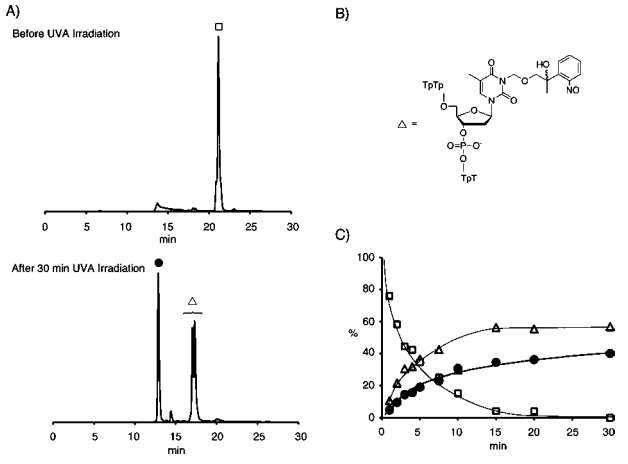

Figure 2. Uncaging of T^{NPPOM}. (A) RP-HPLC analyses of **10** before (upper) and after (lower) 30 min UVA irradiation. The peak indicated by the hollow square is **10**, the filled circle is the desired T_5, and those indicated by the hollow triangle are the byproduct bearing nitroso-species. (B) Proposed structure of the byproduct. (C) Time-course of the uncaging.

Photoremoval of NPPOM Group. Photoremoval of NPPOM group from thymine ring was examined by irradiating UVA light of $300 < \lambda < 400$ nm on a buffered solution of **10** and analyzing it on RP-HPLC. Figure 2A shows RP-HPLC charts of the mixture before and after 30 min UVA irradiation. Before UVA irradiation, a sharp peak of the caged **10** was observed at 22 min. After UVA irradiation, on the other hand, the peak at 21 min completely disappeared, and three new peaks were observed at 12.8, 17.0, and 17.3 min. MALDI-TOF/MS analyses of the isolated peak at 12.8 min showed that this is the desired product, T_5. The two peaks around 17 min, the areas of which are always equivalent to each other, were also separately isolated and subjected to ESI-MS analyses. The observed masses for them are the same in relation to each other (824.19 $[M-2H]^{2-}$, 549.85 $[M-3H]^{3-}$, 412.05 or 412.25 $[M-4H]^{4-}$), showing that these species are the diastereomers bearing a nitrosobenzene formed via the side reaction of photoremoval pathway of NPP group (Figure 2B) (*9*).

Figure 2C shows the time dependence of the yield of each species. Photoremoval of NPPOM (and also the side reaction) rapidly proceeds, and almost saturates after 15 min UVA irradiation. The average yield of the desired T_5 was around 34% in five independent reactions. Considering the mechanism of NPP photoremoval that proceeds via an ionic nitronic acid intermediate (*9*), the low yield of the desired T_5 may be caused by pH dependence of NPP removal. However, the yield did not improve much even when the pH was raised up to 9.0 or an Mg^{2+} ion was added to the solution. Higher pH is not favorable for the present system, since it elevates the risk of oxidative base damages (*10*), so we decided to fix the pH at 8.5 for UVA irradiation.

Site-Selective Termination of Polymerase Reaction by the Three Caged Thymines in the Template under PCR Conditions. Although the yield of photoremoval is unexpectedly low for T^{NPPOM}, its ability to terminate site-selective replication

Scheme 3. Construction of a Recombinant Plasmid Coding GFP Gene Using LACE-PCR

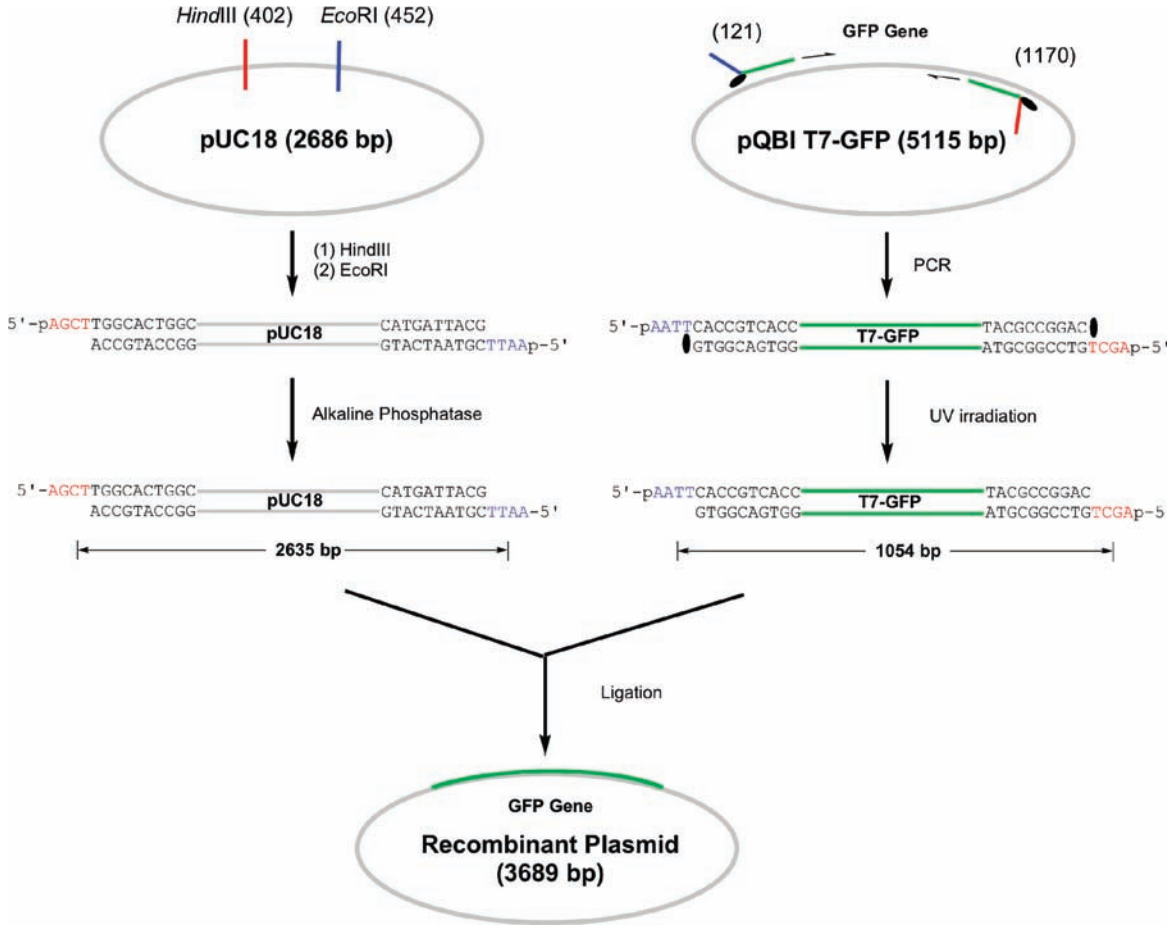

turned out to be significantly superior compared to the other two caged thymidines. Site-selective termination of polymerase reaction by the three caged thymines was first examined by primer-extension experiments under PCR thermal cycle conditions in Figure 3A. By using various polymerases commonly used for PCR, FAM-labeled primer **14** (17 nt, FAM = 6-fluoresceinamide) was extended on the modified oligonucleotide template **11**−**13** (24 nt), which contains one T^{NPP}, T^{NPPOM}, or T^{NPOM} at the fourth position from the 5′-end. When **11** was used as the template and Ex Taq was used as the polymerase, the longest product formed after predetermined thermal cycles was 20 nt, showing that primer extension was efficiently terminated at the 3′-side of T^{NPP} (lane 2 in Figure 3B). This result is completely consistent with our previous report (*4*). Similar efficient termination was observed for another template **12**, in which T^{NPPOM} is introduced in place of T^{NPP} (lane 3). The yields of the 20-mer product for the systems employing **11** and **12** was 94% and 94%, respectively. MALDI-TOF/MS analysis of the reaction mixture also confirmed that d(GAC) was correctly added to the 3′-end of **12** (Figure 4A). When T^{NPOM} was introduced in place of T^{NPPOM}, on the other hand, significant amounts of further elongated products were obtained (lane 4). The yields of the 20-mer, 21-mer, and 23-mer products in lane 4 were 65%, 25%, and 10%, respectively. No undesired removal of NPPOM (or NPOM) was observed in the control HPLC analysis of the template **12** (or **13**) even after the corresponding PCR thermal cycles (Supporting Figure 1 in Supporting Information). Thus, the difference between T^{NPPOM} and T^{NPOM} cannot be ascribed to the difference in the thermal stability of the caging group, but may be related to their structural aspects.

Similar differences in termination ability were observed for other polymerases such as KOD and *Pfu*. Figure 3C,D shows primer-extension experiments using *Pfu* polymerases. Two commercially available cocktails of this polymerase, which are optimized to the amplification of different length of the templates, were examined. Both of the cocktails showed fairly good termination for all of the three caged thymidines. Particularly, the yield of the 20-mer product for both of the NPPOM systems was around 92−94%, which is one of the best numbers we have observed so far. For NPP and NPOM systems, on the other hand, ca. 30% formation of 21-mer product was observed. Primer-extension experiments were performed with KOD polymerase and its related cocktails, as well. In our previous study, this proofreading polymerase was found to introduce dG in front of T^{NPP} almost quantitatively as in lane 3 in Figure 3E. As a result, the major product using KOD polymerase in combination with T^{NPP} is 21-mer (the yield is 43%), and significant amount (up to 40%) of longer products was also produced. In contrast, introduction of T^{NPPOM} in the template resulted in fairly good termination of the KOD reaction in front of T^{NPPOM} as in lane 4. The yield of the desired 20-mer product was 77%, and that of the longer byproduct was only 20%. Quite interestingly, the desired 20-mer product was obtained only with 16% yield by use of the template bearing T^{NPOM} (**13**) even if the hydrogen bonding face of thymine is completely blocked by T^{NPOM}. The major product was the 21-mer (58% yield). MALDI-TOF/MS analysis of the reaction mixture revealed that both 20- and 21-mer products are a mixture of two or more species with different sequences around the end (Figure 4D). The mass difference between the smaller peaks corresponding to 21-mer and 20-mer is 200−230, which

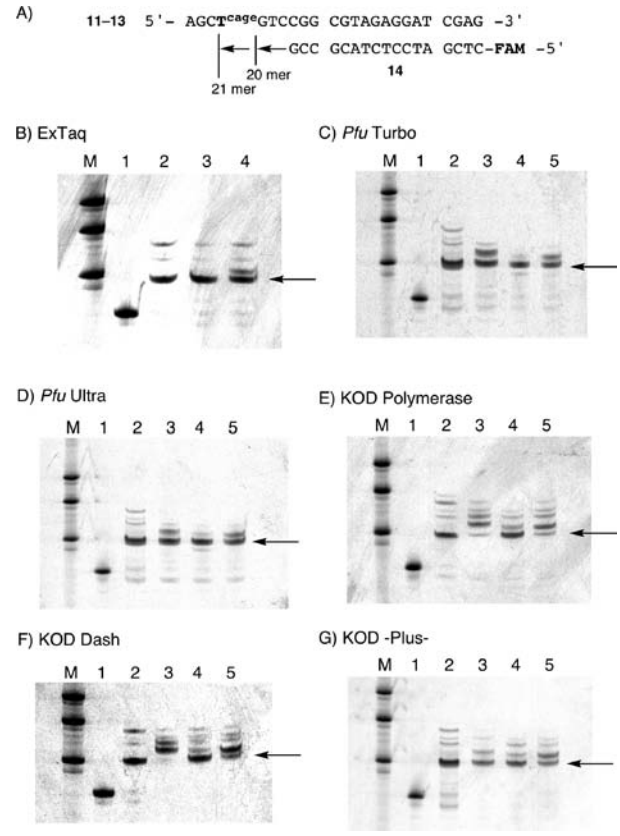

Figure 3. 20% denaturing PAGE patterns for primer extension reaction using caged oligonucleotides **11**−**13** as a template. (A) Structures of the oligonucleotides. (B) Lane 1, unreacted **14**; lane 2, **11** + **14**; lane 3, **12** + **14**; lane 4, **13** + **14**. (C−G) Lane 1, unreacted **14**; lane 2, **11** + **14** with ExTaq (the same as (B) lane 2); lane 3, **11** + **14**; lane 4, **12** + **14**; lane 5, **13** + **14**; M, size markers (20-, 25-, and 30-mer single-stranded DNA). The 20-mer products are indicated by the arrows.

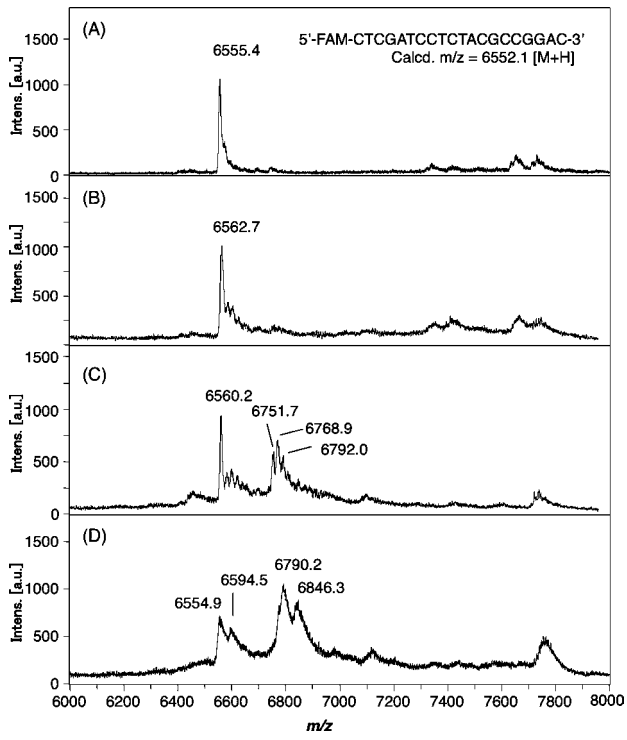

Figure 4. MALDI-TOF/MS spectra of the reaction mixture of (A) **12** + **14** with ExTaq, (B) **12** + **14** with *Pfu* Turbo, (C) **12** + **14** with KOD polymerase, (D) **13** + **14** with KOD polymerase.

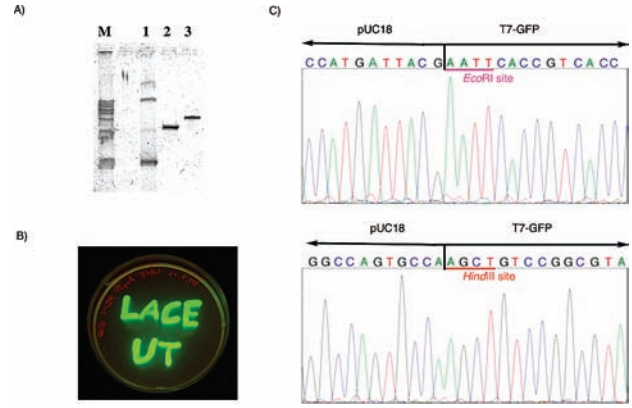

Figure 5. Analyses of the recombinant vector. (A) Agarose gel electrophoresis patterns for the LACE-PCR product and the recombinant vector. Lane 1, LACE-PCR product; lane 2, pUC18 plasmid treated with *Eco*RI and *Hind*III; lane 3, the recombinant plasmid extracted from JM109 and linearized with *Eco*RI; lane M, 1 kbp ladder. (B) The fluorescence of GFP expressed from the recombinant vector in BL21-Gold (DE3) cells. (C) Sequencing of the cloned recombinant vector extracted from JM109 around the *Eco*RI conjunction and the *Hind*III site conjunction.

is significantly smaller than the minimum mass increase of native DNA elongation (addition of one dC is +289). Considering that multiple peaks were observed even for the 20-mer products, it is presumed that KOD polymerase misincorporates the wrong nucleotide also in front of the adjacent residues in the 3′ side of T^{NPOM} (marginally for T^{NPPOM} as well), which is upstream of elongation. It is possible that the present finding is related to the mutation mechanism induced by 3-Me-thymidine lesion in cells (*11*). KOD Dash, which is a cocktail of KOD polymerase and KOD exo(-) variant gave very similar PAGE patterns to KOD polymerase (Figure 3F). The yields of the 20-mer product with T^{NPP}, T^{NPPOM}, and T^{NPOM} were 8%, 65%, and 26%, and the yields of the 21-mer were 54%, 17%, and 52%, respectively. Undesired additional incorporation of the 21st nucleotide in front of T^{NPP} and T^{NPOM} was rather marginal for KOD -Plus-, another cocktail of KOD polymerase with customized buffer contents (Figure 3G). The yield of the desired 20-mer product using T^{NPP} improved to 73% (lane 3), which is almost the same as 74% yield with the use of T^{NPPOM} (lane 4). However, the major product for the reaction using T^{NPOM} was still the 21-mer (47%), and only 42% of the product was the desired 20-mer.

Construction of a Recombinant Vector Coding GFP Gene with LACE-PCR Using Primers Containing T^{NPPOM}. To check whether the site-selective termination practically occurs and desired sticky ends can be obtained after LACE-PCR using T^{NPPOM} as the site-selective terminator, PCR products bearing sticky ends complementary to *Eco*RI and *Hind*III termini were prepared. By using **12** and **15** as the primers, the 121−1170 bp region of pQBI T7-GFP plasmid was amplified. This portion of the plasmid involves GFP gene with T7 promoter. For this experiment, *Pfu* Ultra was used as the polymerase for its high fidelity and excellent termination by T^{NPPOM} observed above. Deprotection of NPPOM groups in the PCR product was performed with UVA irradiation for 30 min on the purified product solution. Considering the yield of NPP removal (ca. 40% for each NPP), approximately 16% of the product is expected to have fully deprotected, desired sticky ends at both ends. As shown in Figure 5A, a product of desired length (1 kbp) was successfully amplified (lane 1).

The insert obtained above was ligated to a vector fragment, which was prepared by digesting pUC18 with *Eco*RI, *Hind*III, and was dephosphorylated with alkaline phosphatase. Then, JM109 competent cells were transformed with the ligation

product. After overnight incubation on a culture plate containing ampicillin and X-gal, ca. 500 white colonies were obtained (only one blue colony was observed). A total of eight colonies were subjected to direct PCR using primers complementary to pUC18 plasmid 150 bp away from each of the digestion site, and one colony gave the expected amplicon of 1.4 kbp from the designed recombinant. The size of the extracted plasmid from this colony (linearized with *Eco*RI, lane 3 in Figure 5A) was significantly larger than the parent pUC18 fragment and consistent with the expected 3689 bp. The other seven colonies gave no apparent amplicon. Taking into account that all of these colonies are white, the latter seven colonies are presumed to have pQBI T7-GFP, which was the template for LACE-PCR.

When the extracted plasmid was introduced into BL21-Gold (DE3) competent cells, in which T7 polymerase is expressed, emission of green fluorescence from the expressed GFP was clearly observed (Figure 5B), showing that no undesired and critical DNA mutation was induced in the gene in this clone by UVA irradiation. Precise construction of the recombinant vector was directly confirmed by sequencing the extracted plasmid (Figure 5C). The sequences near the *Eco*RI site and the *Hind*III site were both completely consistent with the expected ones. Successful formation of both of the sticky ends by LACE-PCR using T^{NPPOM} as the site-selective replication terminator, and its practical use has been evidenced.

Recent studies have shown that UVA radiation as well as UVB causes various oxidative damages on DNA, which result in DNA degradation or mutation (*12*). According to the calculation in the previous study, ca. 4% of the population can contain one damage bases such as cyclobutane pyrimidine dimer (CPD) formation, purine oxidative damage, pyrimidine oxidative damage, and abasic damage in total, and the other 96% are expected to be intact after the UVA irradiation. However, the competent cells commonly used today lack the RecA system, which is mainly responsible for repairing such damage. Thus, the cells transformed with plasmids containing such damaged bases cannot multiply themselves, and consequently, only the intact ones will be selected. We have not yet found any mutation in more than twenty kinds of recombinant plasmids we have obtained with LACE-PCR so far (data not shown). Similarly, it is strongly expected that the byproduct formed after UVA irradiation is not ligated to the vector fragment because of the strict selectivity of the ligase, and nothing to do with the recombinants.

CONCLUSIONS

The newly synthesized T^{NPPOM} residue site-selectively and efficiently blocks polymerase reaction under PCR conditions, and the selectivity was the best among the three caging group examined in this study. The caged primers involving T^{NPPOM} can be synthesized in combination with conventional phosphoramidite monomers on an automated DNA synthesizer, and no change in deprotection conditions is necessary. Although the yield of light triggered deprotection is not very high under the conditions employed in this study, the 1-kbp LACE-PCR products using the caged primers involving T^{NPPOM} were successfully ligated with a vector fragment prepared by restriction-enzyme treatments, and the GFP coded in the resulting recombinant plasmid was efficiently expressed in the transformed bacteria.

The present findings in primer-extension reactions using three kinds of caged thymidines have shown that the blocking of hydrogen bonding between nucleobases is not the only requirement to achieve efficient and selective termination of the polymerase reaction. A significant difference in termination efficiency and selectivity was observed between T^{NPPOM} and T^{NPOM}. A noticeable difference between these two caging groups is the position of just one methylene: in the main chain or on the benzene ring. Structural aspects of the caging group may play an important role here in a close connection with the enzymatic mechanisms of substrate recognition for each of the polymerases. Future detailed study on this topic may be relevant to understanding the mechanism of mutation in vivo as well.

ACKNOWLEDGMENT

This work was partially supported by a Grant-in-Aid for Specially Promoted Scientific Research (18001001) and Grant-in-Aid for Young Scientists (B) (20750126) from the Ministry of Education, Science, Sports, Culture and Technology, Japan. The support from the Global COE Program for Chemistry Innovation is also acknowledged.

Supporting Information Available: Detailed synthetic procedures, MALDI-TOF/MS analyses of the caged oligonucleotides (Supporting Table 1) and RP-HPLC analyses on the thermostability of T^{NPPOM} and T^{NPOM} in the oligonucleotides (Supporting Figure 1). This material is available free of charge via the Internet at http://pubs.acs.org.

LITERATURE CITED

(1) Mayer, G., and Heckel, A. (2006) Biologically active molecules with a light switch. *Angew. Chem., Int. Ed. 45*, 4900–4921.
(2) Tang, X. J., and Dmochowski, I. J. (2007) Regulating gene expression with light-activated oligonucleotides. *Mol. Biosyst. 3*, 100–110.
(3) Tanaka, K., Kuzuya, A., and Komiyama, M. (2008) Site-selective termination of DNA replication by using a caged template. *Chem. Lett. 37*, 584–585.
(4) Tanaka, K., Katada, H., Shigi, N., Kuzuya, A., and Komiyama, M. (2008) Site-selective blocking of PCR by a caged nucleotide leading to direct creation of desired sticky ends in the products. *ChemBioChem 9*, 2120–2126.
(5) Sambrook, J., and Russell, D. (2001) *Molecular Cloning: A Laboratory Manual*, 3rd ed., Cold Spring Harbor Laboratory Press, Cold Spring Harbor.
(6) Krock, L., and Heckel, A. (2005) Photoinduced transcription by using temporarily mismatched caged oligonucleotides. *Angew. Chem., Int. Ed. 44*, 471–473.
(7) Young, D. D., Lusic, H., Lively, M. O., and Deiters, A. (2009) Restriction enzyme-free mutagenesis via the light regulation of DNA polymerization. *Nucleic Acids Res. 37*, e58.
(8) Lusic, H., Young, D. D., Lively, M. O., and Deiters, A. (2007) Photochemical DNA activation. *Org. Lett. 9*, 1903–1906.
(9) Pelliccioli, A. P., and Wirz, J. (2002) Photoremovable protecting groups: reaction mechanisms and applications. *Photochem. Photobiol. Sci. 1*, 441–458.
(10) Faraggi, M., Broitman, F., Trent, J. B., and Klapper, M. H. (1996) One-electron oxidation reactions of some purine and pyrimidine bases in aqueous solutions. Electrochemical and pulse radiolysis studies. *J. Phys. Chem. 100*, 14751–14761.
(11) Delaney, J. C., and Essigmann, J. M. (2004) Mutagenesis, genotoxicity, and repair of 1-methyladenine, 3-alkylcytosines, 1-methylguanine and 3-methylthymine, in alkB Escherichia coli. *Proc. Natl. Acad. Sci. U.S.A. 101*, 14051–14056.
(12) Pfeifer, G. P., You, Y. H., and Besaratinia, A. (2005) Mutations induced by ultraviolet light. *Mutat. Res. 571*, 19–31.

BC900254E

Supporting Information for

"**Precise Site-Selective Termination of DNA Replication by Caging The 3-Position of Thymidine and Its Application to Polymerase Chain Reaction**"

Akinori Kuzuya, Fuminori Okada, and Makoto Komiyama

Detailed synthetic procedures.

Supporting Table 1, MALDI-TOF/MS analyses of the caged oligonucleotides.

Supporting Figure 1, RP-HPLC analyses on the thermostability of T^{NPPOM} and T^{NPOM} in the oligonucleotides.

Synthesis of 3-*N*-(2-(2-nitrophenyl)propyloxymethyl)thymidine phosphoramidite 9.

2-(2-nitrophenyl)propanol (2)

2-Ethylnitrobenzene **1**(6.0 g, 40 mmol) and $(HCHO)_n$ (1.5 g, 40 mmol) were added to TritonB (40% in MeOH) (17 g) and the mixture was refluxed for 7 h. The solvent was evaporated, and the residue was dissolved in EtOAc. The organic layer was washed with 5% HCl, dried over Na_2SO_4, filtered and evaporated. The product was purified by silica gel column chromatography using hexane/EtOAc (3:1) as eluent affording **2** as reddish purple oil in 27% yield (1.95 g 10.7 mmol).
^{1}H NMR ($CDCl_3$) δ 1.34 (3H, d, CH_3), 3.50–3.58 (1H, m, CH), 3.77–3.86 (2H, m, CH_2), 7.36 (1H, t, Ar-H), 7.50 (1H, d, Ar-H), 7.58 (1H, t, Ar-H), 7.76 (1H, d, Ar-H).

2- (2-nitrophenyl) methylthiomethoxypropane (3)

Compound **2**(1.95 g 10.7 mmol) was added in 20 mL of THF and stirred at 0 ˚C under nitrogen. Sodium hydride (60% assay) (0.6 g) was added to the solution and stirred at 0 ˚C. After 45min sodium iodide (1.62 g, 10.7 mmol) was added to the reaction mixture and then chloromethyl methyl sulfide (1.29 g, 13.35 mmol) was added. After 4h the reaction mixture was warmed to room temperature and the solvent was evaporated. The residue was poured into 30 mL of water and extracted with ether. The organic layer was dried over Na_2SO_4, filtered and evaporated. The product was purified by silica gel column chromatography using CH_2Cl_2 as eluent affording **3** as brown oil in 50% yield (1.32 g, 5.43 mmol).
^{1}H NMR ($CDCl_3$) δ 1.36 (3H, d, CH_3), 2.00 (3H, s, CH_3), 3.63–3.76 (3H, m, CH, CH_2), 4.58 (2H, d, CH_2), 7.34 (1H, t, Ar-H), 7.52 (2H, m, Ar-H), 7.75 (1H, d, Ar-H).

2-(2-nitrophenyl)chloromethoxypropane (4)

Compound **3**(1.32 g, 5.43 mmol) was added in 20 mL of CH_2Cl_2 and stirred at 0 ˚C under nitrogen. SO_2Cl_2 (0.94 g, 6.96 mmol) was added to the solution and stirred for 4 h. The reaction mixture was warmed to room temperature and the solvent and excess SO_2Cl_2 was evaporated in vacuo. This procedure afforded **4** as brown oil (quantitative conversion) which was directly used without purification.
^{1}H NMR ($CDCl_3$) δ 1.37 (3H, d, CH_3), 3.66 (1H, m, CH), 3.81 (2H, m, CH_2), 5.43 (2H, q, CH_2), 7.36 (1H, t, Ar-H), 7.48 (1H, d, Ar-H), 7.57 (1H, t, Ar-H), 7.76 (1H,d, Ar-H).

Thymidine diacetate (5)

Thymidine (2.93 g, 12.1 mmol) and DMAP (40 mg, 0.327 mmol) were added in 60 mL of Ac_2O under nitrogen. Pyridine (30 mL) was added to the solution and stirred at room temperature over night. The solvent and excess Ac_2O was evaporated in vacuo and the residue was poured into 100 mL of $CHCl_3$. The organic layer was washed with 100 mL of water, dried over Na_2SO_4, filtered and evaporated. The product was purified by silica gel column chromatography using EtOAc/hexane (3:1) as eluent affording **5** as white solid foam in 71% yield (2.82 g, 8.64 mmol).

^{1}H NMR ($CDCl_3$) δ 1.94 (3H, s, CH_3), 2.10-2.22 (8H, m, $2CH_3$, CH_2), 2.46 (1H, m, CH), 4.36 (2H, dd, CH_2), 5.22 (1H, d, CH), 6.32 (1H, q, CH), 7.29 (1H, s, CH), 8.65 (1H, s, NH).

3-*N*-(2-(2-nitrophenyl)propyloxymethyl)thymidine diacetate (6)

Compound **5** was dissolved in 20 mL of DMF. Cs_2CO_3 was added to the solution and stirred for 1 h at room temperature. The reaction mixture was then cooled to 0 ˚C. Compound **4** (1.26 g, 5.47 mmol, dissolved in 10 mL of DMF) was added dropwise to the reaction mixture and stirred at room temperature over night. The solvent was evaporated in vacuo and the residue was poured into EtOAc. The organic layer was washed with 2 × 30 mL of water and 30 mL of a sat. $NaHCO_3$ solution. Then the organic layer was dried over Na_2SO_4, filtered and evaporated. The product was purified by silica gel column chromatography using EtOAc/hexane (2:1) as eluent affording **6** as yellow foam in 52% yield (1.50 g, 2.89 mmol).

^{1}H NMR ($CDCl_3$) δ 1.31 (3H, dd, CH_3), 1.93 (3H, d, CH_3), 2.11 (8H, m, $2CH_3$, CH_2), 3.57 (1H, m, CH), 3.74–3.88 (2H, m, CH_2), 4.25 (1H, s, CH), 4.34 (2H, m, CH_2), 5.21 (1H, d, CH), 5.36 (2H, m, CH_2), 7.28 (1H, s, CH), 7.31 (1H, t, Ar-H), 7.46 (1H, d, Ar-H), 7.51 (1H, t, Ar-H), 7.71 (1H, t, Ar-H).

3-*N*-(2-(2-nitrophenyl)propyloxymethyl)thymidine (7)

Compound **6**(1.50 g, 2.89 mmol) was dissolved in 20 mL of MeOH. Concentrated aqueous ammonia (8 mL) was added to the solution and stirred for 1 h at room temperature. The solvent was evaporated in vacuo. This procedure afforded **7** as yellow foam (quantitative conversion) which was directly used without purification.

^{1}H NMR ($CDCl_3$) δ 1.31 (3H,d, CH_3), 1.90 (3H, d, CH_3), 2.31–2.42 (2H, m, CH_2), 3.55–3.65 (1H, m, CH), 3.75–3.95 (4H, m, $2CH_2$), 3.97 (1H,q, CH), 4.55 (1H, m, CH), 5.34 (2H, m, CH_2), 7.31 (1H, t, CH), 7.43 (2H, t, 2Ar-H), 7.52 (1H, t, Ar-H), 7.70 (1H, dd, Ar-H).

3-*N*-(2-(2-nitrophenyl)propyloxymethyl)thymidine dimethoxytrityl ether (8)

Compound **7** (1.26 g, 2.89 mmol) and dimethoxytrityl chloride (1.19 g, 3.51 mmol) were dissolved in 20 mL of Pyridine under nitrogen and stirred at room temperature over night. The solvent was evaporated in vacuo and the residue was poured into 30 mL of EtOAc. The organic layer was washed with brine, dried over Na_2SO_4, filtered and evaporated. The product was purified by silica gel column chromatography using hexane/EtOAc (1:1) and 3% TEA as eluent affording **8** as yellow foam in 61% yield (1.31 g, 1.77 mmol).

^{1}H NMR ($CDCl_3$) δ 1.31 (3H, d, CH_3), 1.92 (3H,d, CH_3), 2.28–2.50 (2H, m, CH_2), 3.56 (1H, m, CH), 3.76–3.90 (10H, m, $2CH_2$, $2CH_3$), 3.92 (1H, m, CH), 4.56 (1H, m, CH), 5.37 (2H, m, CH_2), 6.16 (1H, d, CH), 6.84 (4H, d, 4Ar-H), 7.17 (3H, d, 3Ar-H), 7.27–7.36 (7H, m, 6Ar-H, CH), 7.36 (1H, d, Ar-H), 7.47 (1H, d, Ar-H), 7.51 (1H, q, Ar-H), 7.71 (1H, d, Ar-H).

ESI-MS: *m/z* 760.8 $[M+Na]^+$.

3-*N*-(2-(2-nitrophenyl)propyloxymethyl)thymidine phosphoramidite (9)

Compound **8** (0.30 g, 0.406 mmol) was dissolved in 2 mL of AN under nitrogen. DIPEA and

2-cyanoethyl-diisopropyl-chloro phosphoramide (200 µL, 0.912 mmol) were added to the solution and stirred for 1.5 h at room temperature. The solvent was evaporated. The residue was poured into sat. $NaHCO_3$ solution and extracted with EtOAc. The organic layer was washed with brine. The organic layer was dried over Na_2SO_4, filtered and evaporated. The product was purified by silica gel column chromatography using $CHCl_3$/MeOH (20:1) with 3% TEA as eluent affording **9** as yellow foam in 65% yield (0.25 g, 0.26 mmol).

ESI-MS: *m/z* 961.7 $[M+Na]^+$.

Supporting Table 1. MALDI-TOF/MS analyses of the caged oligonucleotides.

	calcd. *m/z* $[M+H]^+$	found
10	1651.4	1653.9
11	7618.5	7625.9
12	7711.4	7738.2
13	7741.4	7742.5
15	7541.4	7558.7

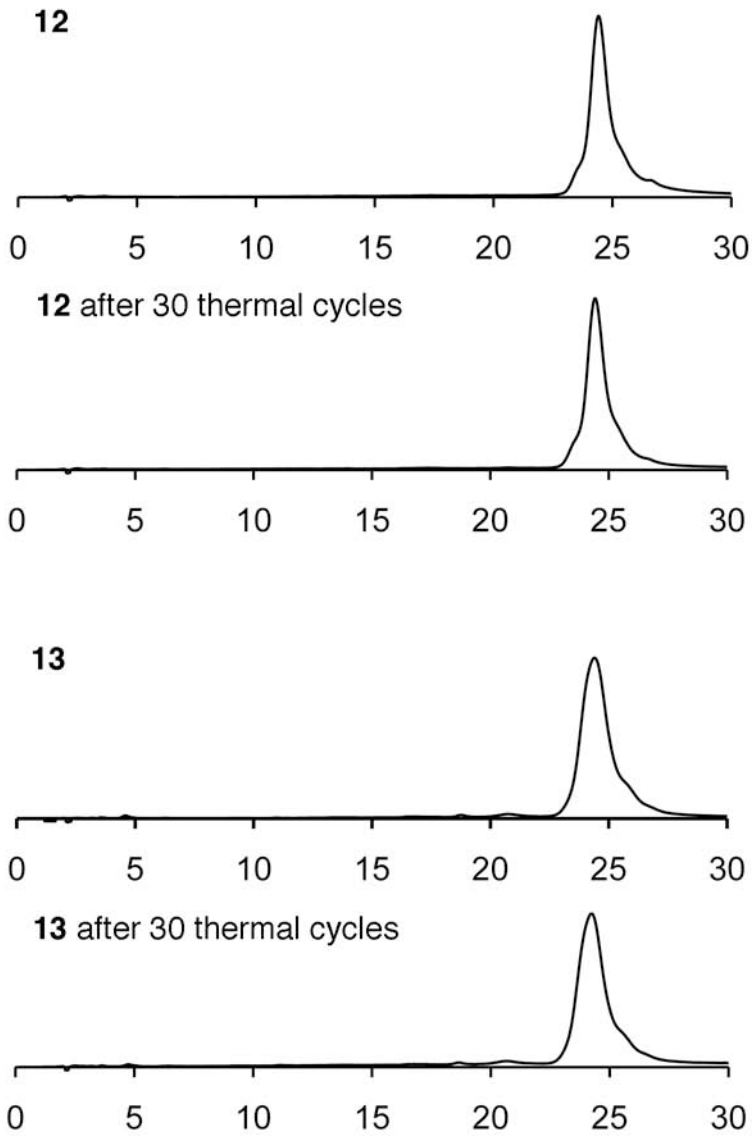

Supporting Figure 1. RP-HPLC analyses of **12** and **13** before (upper) and after 30 thermal cycles for ExTaq (lower). Linear gradient: 5% – 45% acetonitrile (40 min) in the presence of ammonium formate (50 mM).

Protein Binding and the Electronic Properties of Iron(II) Complexes: An Electrochemical and Optical Investigation of Outer Sphere Effects

Kylie D. Barker,[‡] Amanda L. Eckermann,[‡] Matthew H. Sazinsky,[‡,⊥] Matthew R. Hartings,[‡] Carnie Abajian,[‡] Dimitra Georganopoulou,[†] Mark A. Ratner,[‡] Amy C. Rosenzweig,[‡,§] and Thomas J. Meade*[,‡,§,∥]

Departments of Chemistry, Biochemistry and Molecular and Cell Biology, Neurobiology and Physiology, and Radiology, Northwestern University, 2145 Sheridan Road, Evanston, Illinois 60208. Received June 17, 2009; Revised Manuscript Received September 1, 2009

Metalloenzymes and electron transfer proteins influence the electrochemical properties of metal cofactors by controlling the second-sphere environment of the protein active site. Properties that tune this environment include the dielectric constant, templated charge structure, van der Waals interactions, and hydrogen bonds. By systematically varying the binding of a redox-active ligand with a protein, we can evaluate how these noncovalent interactions alter the electronic structure of the bound metal complex. For this study, we employ the well-characterized avidin−biotin conjugate as the protein−ligand system, and have synthesized solvatochromic biotinylated and desthiobiotinylated iron(II) bipyridine tetracyano complexes ($[Fe(BMB)(CN)_4]^{2-}$ (**1**) and $[Fe(DMB)(CN)_4]^{2-}$ (**2**)). The binding affinities of **1** and **2** with avidin are 3.5×10^7 M^{-1} and 1.5×10^6 M^{-1}, respectively. The redox potentials of **1** and **2** (333 mV and 330 mV) shift to 193 mV and 203 mV vs Ag/AgCl when the complex is bound to avidin and adsorbed to a monolayer-coated gold electrode. Upon binding to avidin, the **MLCT1** band red-shifts 20 nm for **1** and 10 nm for **2**. Similarly, the **MLCT2** band for **1** red-shifts 7 nm and the band for **2** red-shifts 6 nm. For comparison, the electronic properties of **1** and **2** were investigated in organic solvents, and similar shifts in the MLCT bands and redox potentials were observed. An X-ray crystal structure of **1** bound to avidin was obtained, and molecular dynamics simulations were performed to analyze the protein environment of the protein-bound transition metal complexes. Our studies demonstrate that changes in the binding affinity of a ligand-receptor pair influence the outer-sphere coordination of the ligand, which in turn affects the electronic properties of the bound complex.

INTRODUCTION

The properties of coordinatively saturated transition metal complexes can be profoundly influenced by their environment (*1*−*7*). The ligands of a transition metal complex can interact with surrounding solvent molecules, macromolecular species, or proteins to affect the electronic state of the metal complex. These noncovalent interactions (known as outer-sphere or second-sphere coordination) include hydrogen bonding, $\pi-\pi$ stacking, electrostatic, hydrophobic, and van der Waas interactions (*8*−*11*).

The concept of outer-sphere coordination was introduced by Werner to explain phenomena such as solvents of crystallization and the formation of adducts between amines and coordinatively saturated complexes (*12, 13*). In 1981, Stoddart and co-workers presented the first crystallographic evidence of this type of interaction, in which a crown ether is associated with a Pt-ammine complex through noncovalent interactions (*14*). In recent years, it has been shown that interactions with the second sphere of coordination complexes affect the physical properties. For example, interaction of 18-crown-6-ether with the second sphere of a series of ruthenium-ammine complexes results in changes in the spectroscopic and electrochemical properties of the complexes (*6, 7*).

Second-sphere coordination is important in biological processes such as iron siderophore recognition, and is currently being investigated as a means to mimic the diverse functionality of metalloenzymes (*9, 15, 16*). The ability to modulate the properties of transition metal complexes through second-sphere ligand design is of interest for the development of artificial metalloenzymes that combine the features of both heterogeneous and enzyme catalysis (*17, 18*). Ward and co-workers use chemogenetic protein engineering to optimize artificial metalloenzymes comprising a catalyst anchored to a biological macromolecule (*19*−*21*). Second-sphere coordination is known to play an important role in activity and enantioselectivity in these catalytic reactions (*17, 19*−*22*).

Previously, we reported a series of redox active transition metal-modified biotin complexes designed to probe the effects of protein binding on the electrochemical response (Figure 1) (*23*). The biotin−avidin system was chosen as a model due to its strong binding interaction ($K_a = 10^{15}$ M^{-1}) and extensive structural characterization (*24*−*26*). Electrochemical studies demonstrated that the avidin-bound complexes are shielded and unable to effectively interact with the electrode. However, the bound complexes can be accessed via electrochemical mediators, suggesting that the complex is only partially shielded in the binding pocket of the protein (*23*). Quantitative results could not be obtained for the electrochemical potential of the protein-bound complex. Therefore, to investigate the effects of the protein binding on the electronic properties of the bound complex, we chose to use $[Fe(bpy)(CN)_4]^{2-}$ complexes (Figure 1). $[Fe(bpy)(CN)_4]^{2-}$ complexes possess electrochemical and optical properties that are highly sensitive to the local environment (*4, 27*−*29*).

To investigate how differences in ligand-receptor binding energetics influence the second-sphere coordination environment

* E-mail: tmeade@northwestern.edu.
[‡] Department of Chemistry.
[⊥] Current Address: Department of Chemistry, Pomona College.
[†] Ohmx Corporation, 1801 Maple Avenue, Suite 6143, Evanston, Illinois 60201.
[§] Departments of Biochemistry and Molecular and Cell Biology.
[∥] Departments of Neurobiology and Physiology and Radiology.

10.1021/bc900270a CCC: $40.75 © 2009 American Chemical Society
Published on Web 09/29/2009

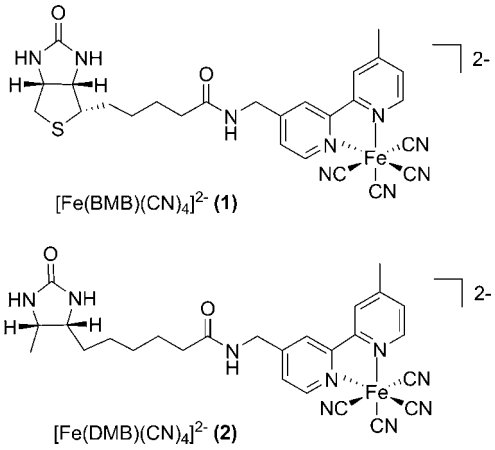

Figure 1. Structures of $[Fe(BMB)(CN)_4]^{2-}$ and $[Fe(DMB)(CN)_4]^{2-}$. Solvatochromic $[Fe(bpy)(CN)_4]^{2-}$ complexes are targeted to bind avidin by modification with biotin (**1**) or desthiobiotin (**2**) through amide derivatization of 4-aminomethyl-methyl-2,2′-bipyridine.

of a small molecule when bound to a protein, we designed two redox-active, solvatochromic transition metal complexes that bind to avidin with different affinities. Herein, we directly correlate systematic modifications of the complex environment to observed changes in electrochemical and spectroscopic signals. The influence of avidin binding on the electrochemical and spectroscopic properties of $[Fe(BMB)(CN)_4]^{2-}$ (**1**) and $[Fe(DMB)(CN)_4]^{2-}$ (**2**) is discussed in light of X-ray crystallographic, electrochemical, optical, computational, and thermodynamic studies.

EXPERIMENTAL SECTION

Materials and Methods. Deglycosylated avidin was used for crystallization studies and obtained from Belovo, Inc. Egg white avidin, used for thermodynamic studies, was obtained from Molecular Probes. Poly(ethylene glycol) was obtained from Fisher Scientific. All other chemicals were obtained from Aldrich. $K_2[Fe(BMB)(CN)_4]$ (**1**) and $K_2[Fe(DMB)(CN)_4]$ (**2**) were prepared according to previously reported methods (*23*).

Electrochemistry. Cyclic voltammetry experiments were carried out in a conventional three-electrode cell using a CH Instruments 660A workstation (Austin, TX), glassy carbon working electrode (3 mm dia, CH Instruments), Pt wire counter electrode, and Ag/AgCl reference electrode. The reference electrode was calibrated to Fc/Fc^+. The electrode was polished with alumina on a polishing cloth and the sample purged with N_2 before each experiment. All electrochemical potentials ($E_{1/2}$) are reported vs Ag/AgCl [where $E_{1/2}$ is defined as $(E_{pa} + E_{pc})/2$].

Cyclic voltammograms of **1** were collected in solvents of varying acceptor number (AN). A 200 μL aliquot of a 50 mM aqueous solution of **1** was added to 3 mL of a 50/50 solvent/100 mM PBS buffer (pH 7.2) mixture where the solvents were water (AN = 55), methanol (AN = 41), DMSO (AN = 19), or DMF (AN = 16) (*30*). Cyclic voltammograms of **1** and **2** in 0%, 10%, 20%, 30%, 40%, and 50% DMF in PBS buffer were collected. Samples were prepared by adding appropriate amounts of solvent and water to 1.5 mL 100 mM PBS buffer (pH 7.2) to make a 3 mL sample with a constant electrolyte concentration of 50 mM. A 200 μL aliquot of a 50 mM aqueous solution of **1** or **2** was added to the solution. For example, the 10% DMF sample was prepared by adding 0.3 mL DMF and 1.2 mL water to 1.5 mL 100 mM PBS buffer.

In order to obtain cyclic voltammograms of **1** and **2** bound to avidin, a gold ball electrode was prepared by melting the end of a 0.127-mm-diameter gold wire into a ball approximately 0.75 mm in diameter. The electrode was cleaned electrochemically by immersing it in 2 N H_2SO_4 and cycling the potential between 0 and 1.6 V at a scan rate of 500 mV/s. The electrode was rinsed with water followed by ethanol and immediately immersed in a 5 mM ethanolic solution of 11-mercaptoundecanoic acid for 16 h. The electrode was washed with ethanol followed by water and 10% $NH_4OH_{(aq)}$. It was then immersed in an aqueous solution consisting of 0.1 mM **1** or **2** and 4 mg/mL avidin for 2 h. The electrode was washed with water, and cyclic voltammograms were obtained in 100 mM PBS buffer (pH 7.2).

Absorption Spectroscopy. UV−vis absorption studies were performed using an Agilent 8453 spectrophotometer (Foster City, CA). Samples were prepared as described for electrochemical experiments. UV−vis spectra of **1** and **2** bound to avidin were obtained by preparing a solution of each in 100 mM PBS buffer and adding a 1.5-fold excess of avidin.

Isothermal Titration Calorimetry. Thermodynamic studies of **1** and **2** were carried out using a VP-ITC microcalorimeter from MicroCal, Inc. (Northampton, MA). In a typical experiment, the reference cell was filled with pure distilled water. The reaction cell was filled with 1.8 mL of a 6 μM solution of avidin (24 μM avidin protomer) in pH 7.0 phosphate buffer. The injection syringe was filled with a 300 μM solution of **1**. After thermal equilibration to 25 °C, **1** was injected into the reaction cell in 5 μL aliquots every 200 s until saturation was achieved (18 injections). A reference offset of 25% was used. The experiment was repeated injecting **1** into pH 7.0 phosphate buffer. The data were subtracted from the binding data to correct for heats of dilution. The data were fit using the *Origin 7.0* OneSites model to determine binding constants (K_a) and heats of binding (ΔH). The above procedure was repeated for compound **2**.

Crystallization and Data Collection. The $K_2[Fe(BMB)(CN)_4]$ complex was incubated with avidin for 1 h at room temperature. The avidin-$[Fe(BMB)(CN)_4]^{2-}$ complex was crystallized at 18 °C by using the sitting drop vapor diffusion method. A protein solution containing 3.0 mg/mL avidin bound by $[Fe(BMB)(CN)_4]^{2-}$ in phosphate buffer pH 7.0 was combined with an equal volume of precipitant solution comprising 100 mM sodium acetate (pH 4.6) and 25% PEG 3000. The resulting crystals were harvested after six weeks. The crystals were hexagonal, space group $P3_221$, with unit cell dimensions $a = b = 74.20$, $c = 85.82$.

X-ray data were collected at 100 K at the Advanced Photon Source on beamline 5-ID from crystals flash-frozen in liquid nitrogen after soaking in a cryo-protectant composed of the well solution plus 20% ethylene glycol. The diffraction data were integrated with MOSFLM (*31*) and scaled by using SCALA (*32*). The statistics are presented in Table 5.

Structure Determination and Refinement. Phases were determined by molecular replacement using the program PHASER (*33*) and avidin from the pdb file 1LDO as the search model. The ligand-bound form of avidin was modeled with XtalView (*34*), refined with CNS (*35*), and validated with PROCHECK (*36*).

Molecular Modeling. Force field parameters were derived for $[Fe(BMB)(CN)_4]^{2-}$ and $[Fe(BMB)(CN)_4]^{2-}$. Atomic partial charges were taken from the Mulliken population analysis of ab initio geometry minimizations. These calculations were carried out at the Hartree−Fock (HF) level in the program Gamess (*37*). A Hay−Watt effective core potential was used to describe the iron atoms (*38*). The carbon and nitrogen atoms in the bipyridyl and cyano ligands were described by 6-31+G* basis set (*39*). All other atoms were described by the 6-31 G* basis set (*40*). Geometries and charges were calculated for both 2+ and 3+ metal ionization states.

Table 1. Variation of MLCT Wavelengths and Electrochemical Potential of K_2[Fe(BMB)$(CN)_4$] with Acceptor Number (AN)

solvent	AN	**MLCT1** (nm)	**MLCT2** (nm)	$E_{1/2}$ (mV)
water	55	480	341	333
MeOH	41	496	348	257
DMSO	19	512	356	195
DMF	16	519	357	181
avidin	−	500	348	193

Iron-ligand bonds were modeled using the points-on-a-sphere methodology (*41*). In this method, iron−nitrogen and iron−carbon bond lengths are held constant (acquired from crystal structures of similar compounds) (*42*) and the atom−iron−atom bond angles are determined by the electrostatic interaction of the atoms around the metal center.

The crystal structure of the biotin−avidin complex (obtained from the Protein Data Bank) was used as the starting geometry for the molecular dynamics simulation (*26*). Hydrogen atoms and other atoms missing from the crystal structure were added referencing standard amino acid residues from AMBER. The ab initio optimized geometry coordinates for the [Fe(bpy)-$(CN)_4]^{2-}$ complex were appended to the coordinates of the crystal structure of avidin bound biotin for each of the four binding avidin protomers. The energy of the avidin/{[Fe(BMB)-$(CN)_4]^{2-}\}_4$ tetrameric complex was minimized using a combined steepest descent and conjugate gradient minimization technique. The minimized structure was solvated with a 75 Å × 75 Å × 75 Å box of water of approximately 13 800 TIP3P water molecules. The solvated protein structure was minimized using the method described above.

Molecular dynamics (MD) simulations were carried out for the avidin/$\{[Fe(BMB)(CN)_4]^{2-}\}_4$ tetrameric complex using the *Amber 94* force field (*43*). Constant volume periodic boundary conditions were employed; the simulation boundary box constructed was slightly larger than the extent of the water buffer used to solvate the protein. A dielectric constant of 4 was assigned to the boundary box to dampen the effects of electrostatics on the system. MD simulations were run for 1 ns recording energy and trajectory information every picosecond.

The isopotential surfaces were rendered with HARLEM from a calculation of the electrostatic potential by solving the Poisson−Boltzmann equation using the method of finite differences (*44*). Electrostatic calculations were carried out using the partial charges on the avidin/$\{[Fe(BMB)(CN)_4]^{2-}\}_4$ complex to represent the charge distribution. The static dielectric constant as a function of position, also used in the Poisson equation, was mapped by defining the low dielectric volume of the protein by a solvent-accessible surface (SAS). A solvent probe radius of 1.4 Å was used to define the SAS. Atoms contained inside the boundary of the surface are assigned a low dielectric constant of 4, outside the surface the dielectric is assigned value of 80 for water. These calculations yield the isopotential surface surrounding the modified ligands. Calculations were made for atoms within a 10 Å shell around the binding ligand. This calculation provides an estimate of the electric field immediately surrounding the ligand and indicates portions of the protein with net positive or net negative charge.

RESULTS

Electrochemistry. The $E_{1/2}$ of **1** and **2** in PBS pH 7.2 are 333 mV and 330 mV, respectively. These values are in agreement with previously reported values and comparable to that of [Fe(4,4′-dimethyl-2,2′-bipyridine)$(CN)_4]^{2-}$ (312 mV) (*23*, *45*). The $E_{1/2}$ of **1** increases with increasing solvent acceptor number (AN) where AN describes the Lewis acidity of the solvent (Table 1, Figure 2) (*30*, *46*). When DMF is introduced incrementally to an aqueous solution of **1** or **2**, the $E_{1/2}$ decreases linearly (Tables 2 and 3, Figure 3). The plot of current (*i*) vs

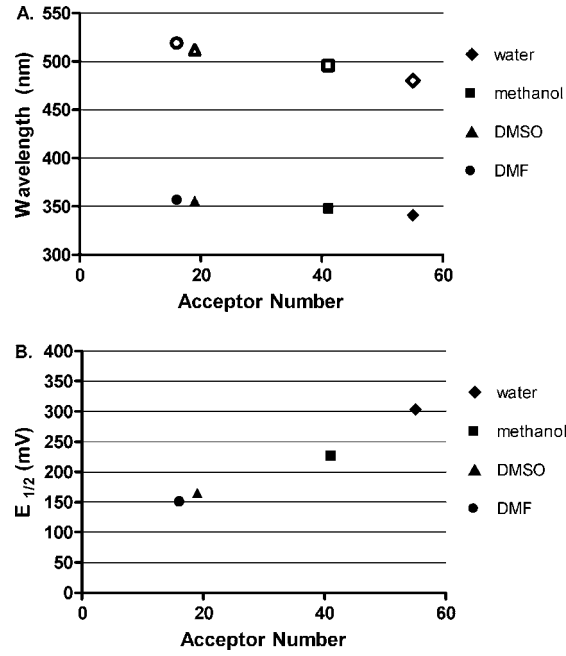

Figure 2. (A) Correlation of the K_2[Fe(BMB)$(CN)_4$] MLCT bands with solvent acceptor number. Closed (•) symbols represent **MLCT2**; open symbols (○) represent the **MLCT1**. (B) Correlation of the K_2[Fe(BMB)$(CN)_4$] $E_{1/2}$ with solvent acceptor number. Cyclic voltammograms were collected at 100 mV/s using a glassy carbon electrode and Ag/AgCl reference. Values are reported vs Ag/AgCl.

Table 2. Variation of MLCT Wavelengths and Electrochemical Potential of K_2[Fe(BMB)$(CN)_4$] with Increasing DMF

% DMF	**MLCT1** (nm)	**MLCT2** (nm)	$E_{1/2}$ (mV)
0	480	341	333
10	490	345	301
20	496	347	270
30	510	349	246
40	514	352	221
50	519	357	211
avidin	500	348	193

Table 3. Variation of MLCT Wavelengths and Electrochemical Potential of K_2[Fe(DMB)$(CN)_4$] with Increasing DMF

% DMF	**MLCT1** (nm)	**MLCT2** (nm)	$E_{1/2}$ (mV)
0	486	345	330
10	494	351	302
20	501	357	269
30	510	360	238
40	519	363	212
50	529	368	184
avidin	496	351	203

square root of scan rate (υ) is linear for **1** and **2** in all solvent systems. The average ΔE_p (difference of the peak potentials) for **1** and **2** is 64 mV and is consistent for all solvent systems. The i_a/i_c ratio is 0.8 for **1** and 1.0 for **2** in all solvent systems.

An electrochemical signal is not observed for **1** or **2** bound to avidin in solution (*23*). When adsorbed to a mercaptoundecanoic acid (MUA) SAM-coated gold electrode, **1** has an $E_{1/2}$ of 193 mV and **2** has an $E_{1/2}$ of 203 mV. At 100 mV/s, the ΔE_p for **1** in this experiment is 85 mV with an i_a/i_c ratio of 1.1 (Supporting Information Figure S1). The ΔE_p for **2** is 75 mV with an i_a/i_c ratio of 1.1 (Figure 4).

Absorption Spectroscopy. For an aqueous solution of **1**, a charge transfer (CT) band is observed at 293 nm and two MLCT bands are observed at 341 nm [metal dπ → bipyridine π^* (2) (**MLCT2**)] and 480 nm (metal dπ → bipyridine π^* (1) (**MLCT1**)) (*47*). The λ_{max} of the MLCT peaks are red-shifted

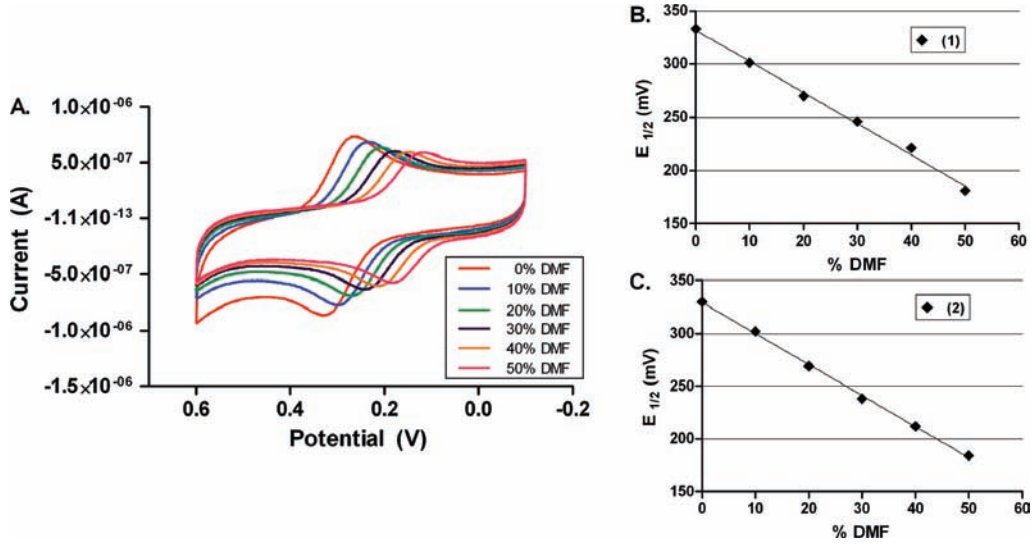

Figure 3. Electrochemistry of $K_2[Fe(BMB)(CN)_4]$ and $K_2[Fe(DMB)(CN)_4]$ in increasing concentrations of DMF in PBS buffer at pH 7.2. (A) Representative cyclic voltammograms of $K_2[Fe(DMB)(CN)_4]$ (B) Correlation of the $E_{1/2}$ of $K_2[Fe(BMB)(CN)_4]$ with increasing amounts of DMF (C) Correlation of the $E_{1/2}$ of $K_2[Fe(DMB)(CN)_4]$ with increasing amounts of DMF. Cyclic voltammograms were collected at 100 mV/s using a glassy carbon electrode and Ag/AgCl reference. Values are reported vs Ag/AgCl.

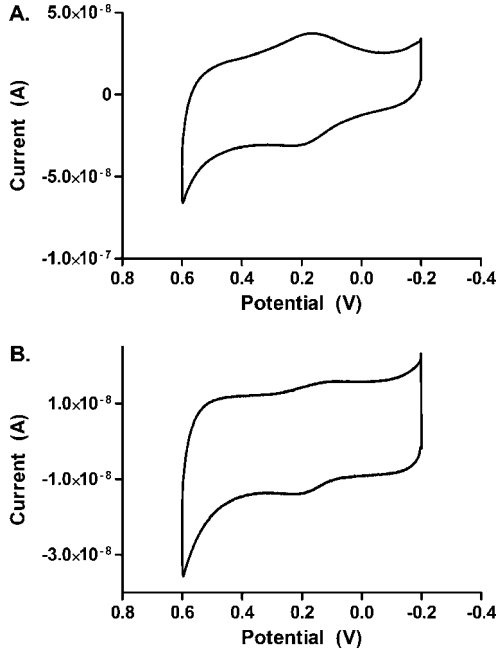

Figure 4. Cyclic voltammogram of (A) $K_2[Fe(DMB)(CN)_4]$ and (B) $K_2[Fe(BMB)(CN)_4]$ adsorbed to a mercaptoundecanoic acid SAM on a gold ball electrode. The cyclic voltammograms were collected at 100 mV/s in 100 mM PBS at pH 7.2 with Ag/AgCl as a reference.

linearly with decreasing solvent acceptor number (Table 1, Figure 2). When DMF is introduced incrementally to an aqueous solution of **1**, the λ_{max} values of the MLCT peaks are red-shifted proportionally (Table 2, Figure 5). Upon addition of avidin to **1** in PBS buffer, the **MLCT1** band shifts 20 nm (833 cm^{-1}) and the **MLCT2** band shifts 7 nm (590 cm^{-1}) (Table 2). When an excess of biotin is added to the solution of **1**-avidin, the λ_{max} values of the MLCT peaks are shifted back to the original values.

For an aqueous solution of **2**, a CT band is observed at 293 nm and two MLCT bands are observed at 345 nm (**MLCT2**) and 486 nm (**MLCT1**). When DMF is introduced incrementally to an aqueous solution of **2**, the λ_{max} values of the MLCT peaks are red-shifted proportionally (Table 3, Figure 5). Upon addition of avidin to **2** in buffer, the **MLCT1** band shifts 10 nm (415 cm^{-1}) and the **MLCT2** band shifts 6 nm (495 cm^{-1}) (Table 3). When an excess of biotin is added to the solution of **2**-avidin, the λ_{max} values of the MLCT peaks are shifted back to the original values.

Isothermal Titration Calorimetry. For **1** and **2**, the amount of energy released per mole of complex titrated was plotted versus the molar ratio of complex to protein. The curve was best fit using the Origin OneSites model to give the binding constant (Supporting Information Figure S1). The reduced χ^2 value was 1.3 and 1.1 for **1** and **2**, respectively. Binding constants and heats of binding for **1** and **2** binding to avidin are summarized in Table 4.

Structure of the $[Fe(BMB)(CN)_4]^{2-}$-Avidin Complex. Complex **1** bound to both protomers in the 3.1 Å resolution crystal structure of the avidin complex is shown in Figure 6. As expected, the biotin group binds to a site identical to one previously characterized (*26*). In one protomer, electron density for the $[Fe(BMB)(CN)_4]^{2-}$ group is observed on the surface of the protein, sandwiched among three loops: L3,4; L5,6; and L7,8 (Figure 6B). This configuration appears stabilized by several hydrogen bonding pairs including interactions of N12, S16, Y33, T35, T77, and N118 with the ureido portion of the complex, S73 and S75 with the carbonyl of the amide bond, and S31 and S102 with the transition metal portion of the complex. In the second protomer, electron density for the $[Fe(BMB)(CN)_4]^{2-}$ group and residues 41−44 on the L3,4 loop were not observed.

Molecular Modeling. In the course of the molecular dynamics simulation, several conformations were found to be accessible to **1** when bound to avidin (Supporting Information Figure S2). The conformation in closest agreement with the crystal structure was chosen to compare the second-sphere environment of **1** and **2** when bound to avidin. In this conformation, the distances from the α carbon of Ser 41 and the metal atom of **1** and **2** are 5.76 and 5.92 Å, respectively. The distance between Ser 101 and the metal atom was found to be approximately 10 Å for both **1** and **2**. The distance between Ser 102 and the metal atom was found to be approximately 5 Å for both **1** and **2**. Loss of β architecture in strands 3 and 4 is observed and loops 7,8 and 5,6 are disordered for **2** bound to avidin. The models of **1** and **2** bound to avidin are compared in Figure 7. The isopotential surface of the portion of the protein that surrounds avidin (Figure

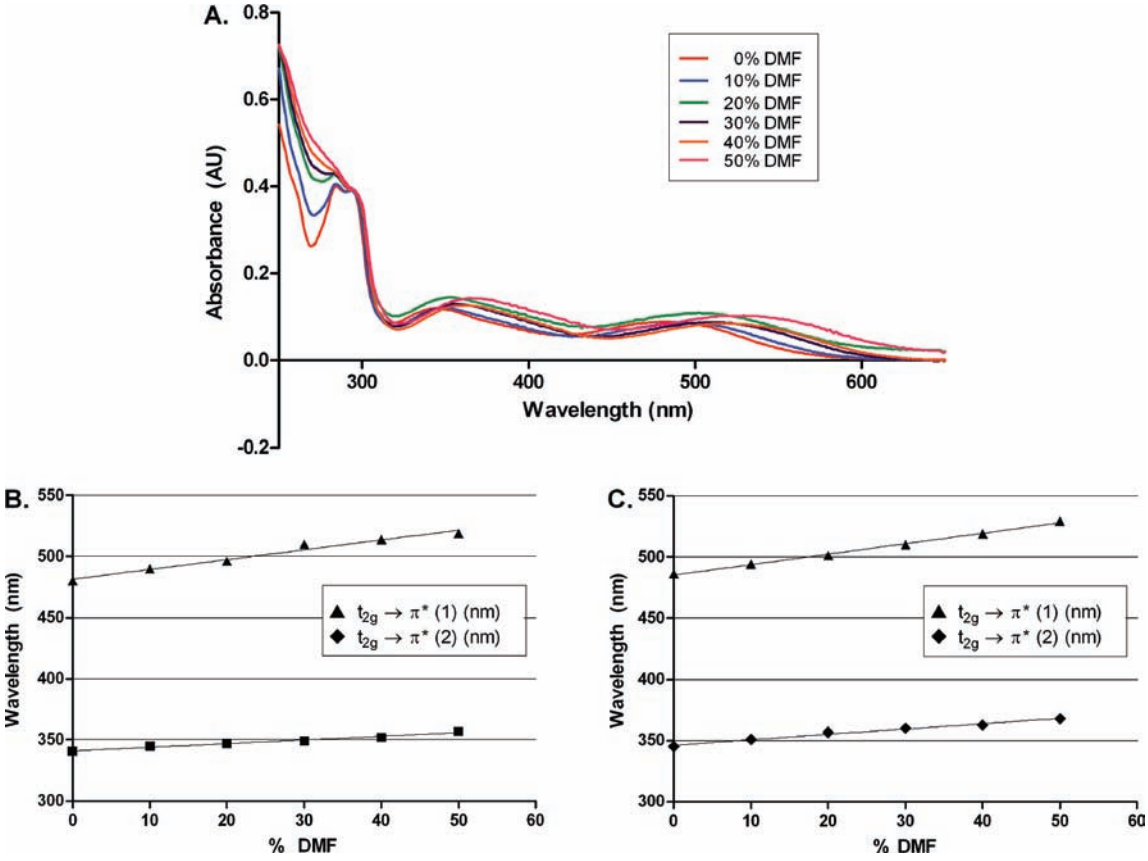

Figure 5. Absoprtion spectroscopy of $K_2[Fe(BMB)(CN)_4]$ and $K_2[Fe(DMB)(CN)_4]$ in increasing concentrations of DMF in PBS buffer at pH 7.2. (A) Representative UV−vis spectra of $K_2[Fe(DMB)(CN)_4]$. (B) Correlation of the $K_2[Fe(BMB)(CN)_4]$ MLCT bands. (C) Correlation of the $K_2[Fe(DMB)(CN)_4]$ MLCT bands with increasing amounts of DMF. The wavelengths of the MLCT bands are linearly correlated to the solvent fraction indicating that no preferential solvation of the complexes occurs.

Table 4. Binding Constants and Enthalpy of Binding for Iron(II) Complexes

ligand	K (M^{-1})	ΔH (kcal/mol)
$K_2[Fe(BMB)(CN)_4]$	3.5×10^7	−104
$K_2[Fe(DMB)(CN)_4]$	1.5×10^6	−80

8) is mainly positive in nature. This portion of the protein should have favorable interactions with the net negative charge of **1** and **2**.

DISCUSSION

The redox properties of metal complexes in proteins are influenced by changes in the surrounding protein environment (e.g., cytochrome c and blue copper proteins) (*48*−*50*). Metal cofactors bound to proteins experience a solvation environment with a lower local dielectric constant than that of aqueous buffer. The dielectric constant (ε) of water is 80, whereas ε is estimated to be between 4 and 20 inside a protein (*51*−*53*). Changes in the dielectric constant affect the energetics for electronic transitions of metal redox centers. Further, the protein imparts a structured charge environment around the metal complex due to the partial charges of each atom. This charge structure, with its partial positive or negative properties, stabilizes more strongly either the reduced or oxidized state of the metal. Finally, the protein can be viewed as a scaffold containing electrophilic or nucleophilic residues capable of multiple interactions with the metal cofactor.

In order to probe changes in outer-sphere coordination induced by changes in ligand-receptor binding, we have synthesized a biotinylated iron(II) complex (**1**) and a desthiobiotinylated iron(II) complex (**2**). These redox-active, solvatochromic transition metal complexes are designed to bind to the protein avidin. Biotin and desthiobiotin bind to avidin with K_a's of 10^{15} M^{-1} and 10^{13} M^{-1}, respectively (*54*). Therefore, weaker ligand-receptor binding is expected to give the $[Fe(DMB)(CN)_4]^{2-}$ complex slightly more flexibility within the binding pocket as compared to $[Fe(BMB)(CN)_4]^{2-}$. Therefore, the dielectric constant, charge structure, van der Waals, and

Table 5. Data Collection, Phasing, and Refinement Statistics

data collection	
beamline	DND-CAT (Sector 5)
wavelength (Å)	1.279
resolution range (Å)[a]	30−3.1 (3.27−3.10)
total observations	64 647 (9347)
unique observations	9587 (742)
completeness (%)	99.9 (100)
redundancy	12.3 (12.6)
I/σ	28.0 (5.7)
R_{sym}[b] (%)	9.9 (40.6)
Refinement	
no. of reflections, working/test	8292/975
R_{work} (%)[c]	25.5
R_{free} (%)[d]	33.0
Protein atoms	1856
ligand atoms	61
water molecules	22
r.m.s.d. bond length (Å)	0.009
r.m.s.d. bond angle (°)	1.4
average *B*-value (Å^2)	65.5

[a] Values in parentheses are for the highest-resolution shell. [b] $R_{sym} = \Sigma_i \Sigma_{hkl} |I_i(hkl) - \langle I(hkl)\rangle| / \Sigma_{hkl} \langle I(hkl)\rangle$, where $I_i(hkl)$ is the ith measured diffraction intensity and $\langle I(hkl)\rangle$ is the mean of the intensity for the Miller index (hkl). [c] $R_{work} = \Sigma_{hkl} |F_o(hkl)| - |F_c(hkl)| / \Sigma_{hkl} |F_o(hkl)|$. [d] $R_{free} = R_{work}$ for a test set of reflections (5%).

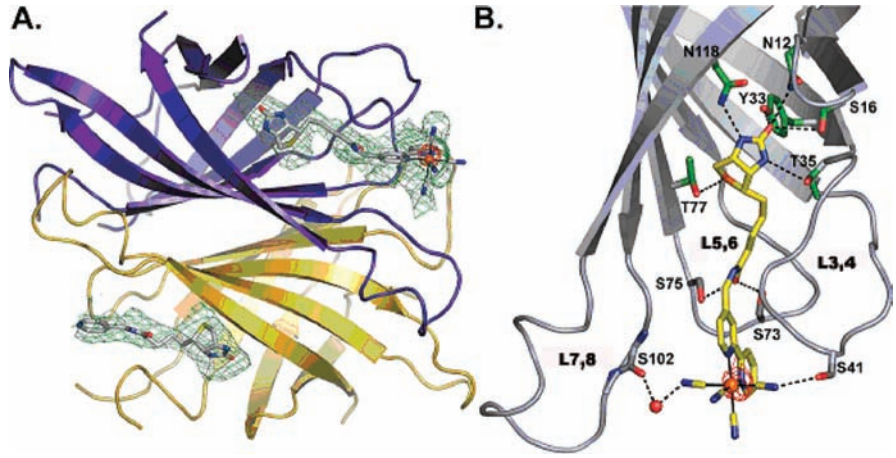

Figure 6. Structure of $[Fe(BMB)(CN)_4]^{2-}$ bound to avidin. (A) The asymmetric unit shows $[Fe(BMB)(CN)_4]^{2-}$ bound to two avidin protomers. The other two protomers are related by crystallographic symmetry. $2|F_o| - |F_c|$ omit maps are depicted around the modeled ligand at 1σ (green) and 4σ (red). (B) View of ligand−protein interactions. Amino acids in green interact with biotin as observed in crystal structures of native D-biotin bound to avidin (*26*). Residues in gray hydrogen bond to the $[Fe(bpy)(CN)_4]$ portion of the complex. The $2|F_o| - |F_c|$ omit density is superposed at 4σ.

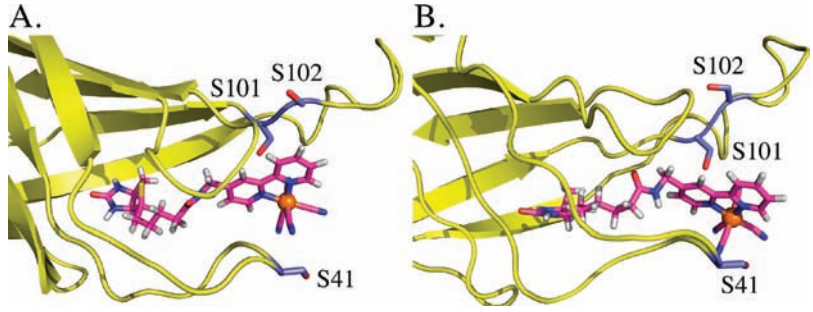

Figure 7. A view of the final structure of the molecular dynamics simulation of avidin bound by (A) $[Fe(BMB)(CN)_4]^{2-}$ and (B) $[Fe(DMB)(CN)_4]^{2-}$. One monomer of the tetramer avidin is shown.

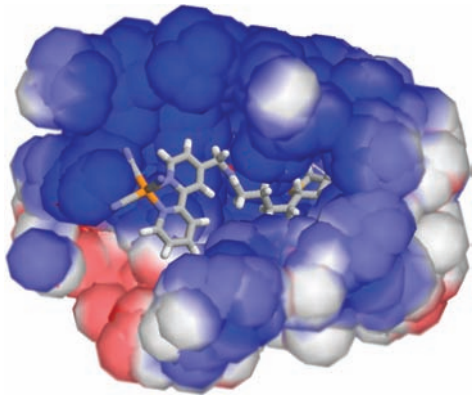

Figure 8. Isopotential surfaces of the avidin binding pocket (shown in space filling mode) as calculated by the program HARLEM. Blue corresponds to positive charges, and red corresponds to negative charges. This representation indicates that there are favorable interactions between the binding pocket and the negatively charged **1** (shown) and **2**.

hydrogen bonding contacts near the metal will differ for **1** and **2**. We have used a variety of techniques to observe differences in the electronic structure of these complexes as imparted by the protein.

Electronic Structure, Solvatochromism, and Acceptor Number. Iron(II) tetracyano complexes are known to be highly sensitive to changes in environment (*4, 27, 29, 55, 56*). $[Fe(bpy)CN)_4]^{2-}$ is a paramagnetic complex with C_{2v} symmetry that has completely filled $d\pi$ orbitals (d_{xy}, d_{xz}, d_{yz}), and these orbitals act as the HOMO set for the molecule. Oxidation of the iron(II) to iron(III) species requires removal of an electron from one of these metal-centered orbitals.

The environmental sensitivity of these complexes is largely due to noncovalent interactions with the lone pair electrons on the cyano ligands. Solvent molecules interact noncovalently with these lone pairs. Strong electron acceptors such as water decrease the electron density at the CN and therefore increase π backbonding with the metal ion. This interaction stabilizes the iron(II) state with respect to the iron(III) state. Depending on solvent, the LUMO in $[Fe(bpy)(CN)_4]^{2-}$ might be either the unfilled metal d-orbitals (d_{z2} and d_{x2-y2}) or the π^* levels of the bipyridine ligands (*28*). The first optically allowed transitions from the $d\pi$ orbitals, however, are to the π^* orbitals of the bipyridine ligand (*47*). Weak acceptors such as DMF decrease the π backbonding as compared to water. Therefore, as DMF is added to the system, water molecules are displaced and the iron(II) state becomes destabilized. A solvent with a high acceptor number such as water will result in a higher-energy metal to ligand charge transfer (MLCT) as compared to weak acceptors such as DMF. These changes in MLCT energy are significant enough to be observed spectroscopically. Likewise, stabilization of the iron(II) complex will result in higher oxidation potentials that can be observed by electrochemical methods such as cyclic voltammetry.

The absorbance of **1** in various solvents was measured to investigate the sensitivity of the physical properties of **1** to second-sphere effects. The solvents were chosen to represent a range of ANs. We observed a larger shift of the low-energy **MLCT1** band compared to the **MLCT2** band. This result indicates that the solvent is interacting with both the cyano and bipyridine ligands to stabilize the π^* orbitals of the bipyridine

ligand to varying degrees. This phenomenon has been described for cyanoiron(II) complexes by Toma and co-workers and demonstrates that changes in the second-sphere environment around any part of the molecule, whether it is the bipyridine or the cyano ligands, result in spectroscopic changes (*56*).

As increasing amounts of DMF are added to an aqueous solution of **1** or **2**, the energy of MLCT bands decreases linearly (Table 2, Figures 3 and 5). This linear correlation in a binary solvent system demonstrates the effect of an increasingly nonpolar environment and indicates that no preferential solvation of the complexes occurs (*56*). DMF displaces water molecules from the second sphere of the metal complex, and the complexes do not have a tendency to maintain a solvation shell of water when a nonpolar solvent is introduced.

To investigate the sensitivity of the redox potentials of **1** and **2** to second-sphere coordination, the electrochemical potential $E_{1/2}$ of **1** and **2** was determined in a variety of solvents. As the AN is decreased, the $E_{1/2}$ decreases (Table 1, Figure 2). Further, as increasing amounts of DMF are added to an aqueous solution of **1** or **2**, the $E_{1/2}$ decreases linearly (Table 2, Figures 3 and 5).

These solvent experiments provide a basis for rough comparison with avidin-binding results. Upon addition to an aqueous solution of **1** or **2**, DMF replaces water in the vicinity of the metal complex; when **1** or **2** binds to avidin, water will be displaced from the metal center in a similar way.

X-ray Crystal Structure and Binding Properties. Isothermal titration calorimetry was used to measure the binding constants of **1** and **2** to avidin. The binding affinities of **1** and **2** for avidin are $3.5 \times 10^7\ M^{-1}$ and $1.5 \times 10^6\ M^{-1}$, respectively. These values demonstrate a significant decrease in binding affinity compared to that of native D-biotin ($K = 1 \times 10^{15}\ M^{-1}$) and D-desthiobiotin ($K = 1 \times 10^{13}\ M^{-1}$). The data fit best to the case where all four binding sites are identical, and binding is independent. Previous studies by Livnah and co-workers demonstrate that when bound to avidin, modification of biotin at the carboxyl terminus by a caproic acid results in disruption of the hydrogen bonding of Thr 38, Ala 39, and Thr 40 with the carboxyl terminus of biotin. This disruption results in a decrease in binding affinity (7 to 8 orders of magnitude) for biotin analogues that have an amide at the carboxylic acid (*57*).

The crystal structure shows two unique protomers (Figure 6). Avidin is a tetramer; the other two protomers are related by crystallographic symmetry. It is apparent that **1** is in a relatively hydrophobic (low dielectric) environment and interacts directly with the protein via electrostatic and hydrogen bonding interactions. While several biotinylated-transition metal complexes have been synthesized, only one other has been structurally characterized bound to avidin (*20, 23, 58*−*61*). Similar to the observations of Ward et al., there are short contacts between the metal center of **1** and amino acid residues. Importantly, there is no major reorganization of the host protein.

The three-dimensional structure of **1** bound to avidin shows that the cyano ligands of the iron complex interact with specific residues in the avidin binding pocket. In one protomer, the Ser 41 residue of the L3,4 loop interacts directly with a CN group on the iron(II) complex, and Ser 102 of the L5,6 loop interacts with a CN group through a water molecule. We expect these interactions with the cyano groups to have an observable effect on the electrochemical properties of **1** and **2** bound to avidin. The stabilizing, attractive interaction of the protein with the cyano groups prevents the loops from opening as they do in the cases where the carboxyl terminus is derivatized by caproic acid (*40, 57, 62*).

In the second protomer, electron densities for the $[Fe(bpy)CN)_4]^{2-}$ moiety of **1** and residues 41−44 on the L3,4 loop were not observed. These differences are most likely due to disorder imposed by crystal packing. This conclusion is supported by ITC data that are best fit for a system with four identical binding events.

We have used the program HARLEM to calculate the isopotential surface of avidin and show that the binding pocket of avidin is positive in nature (Figure 8). **1** and **2** are negatively charged and have small polar ligands that should promote interactions with the protein. This portion of the protein should have favorable interactions with the net negative charges of **1** and **2**.

Molecular Dynamics Simulations. Molecular dynamics simulations were carried out with **1** and **2** bound to avidin to compare the local environments of the transition metal complexes when bound to avidin. Several similar conformations were found to be accessible to **1** and **2** when bound to avidin in the course of the molecular dynamics simulation (conformations of **1** shown in Supporting Information Figure S2). The conformation in closest agreement with the crystal structure of **1** bound to avidin was chosen to compare the second-sphere environment of **1** and **2** when bound to avidin. For comparison, the distance between the apex of loop 3,4 (Ser 41) and the metal center was measured. This distance is specifically of interest because the crystal structure shows that Ser 41 has a direct interaction with **1**. The distance from the α-carbon of Ser 41 to the iron center in **1** is 5.76 Å, whereas in **2**, the distance is 5.92 Å. We did not observe a water molecule between Ser 102 and the cyano group in the molecular dynamics simulation, as was observed in the crystal structure of avidin with **1**. The MD simulations show that Ser 101 has a stronger interaction with the binding ligand than does Ser 102. The distance between Ser 101 and the iron center is ∼5 Å, while the distance between Ser 102 and the iron atom is ∼10 Å. These observations are slightly different than values determined from the crystal structure; however, they are reasonable due to the fluxional nature of the protein in the molecular dynamics simulations. While the location of the ligand within the protein in the crystal structure is very informative, it is only a snapshot of the ensemble of configurations that the metal complex samples during a spectral or electrochemical measurement. The MD simulations further show that, when **2** is bound, the protein structure is more disordered. Figure 7 shows the disorder in strands 3 and 4 and loops 7,8 and 5,6 for **2** as compared to **1** bound to avidin. The environment of **2** is slightly more open and water-accessible than the environment that **1** experiences.

Electronic Affects of Avidin Binding. UV−vis spectroscopy was used to measure roughly the HOMO−LUMO gaps of **1** and **2** while bound to the protein. The optical spectra in aqueous solution show two MLCT bands, one to each of the first two π^* levels of the bipyridine ligands (**MLCT1** at lower energies, 480 nm for **1** and 486 nm for **2**; and **MLCT2** at higher energies, 341 nm for **1** and 345 nm for **2**). Upon binding of avidin to **1**, the **MLCT1** band red-shifts 20 nm and the **MLCT2** band red-shifts 7 nm. Upon binding of avidin to **2**, the **MLCT1** band red-shifts 10 nm and the **MLCT2** band red-shifts 6 nm. When an excess of biotin is added to displace **1** or **2** from avidin, the λ_{max} of the MLCT bands shifts back to the original values reported for the compounds in aqueous solution. These results demonstrate that the outer-sphere coordination of the molecule changes with the ligand receptor binding. The UV−vis studies show that the molecule with the lower binding constant (**2**) has smaller changes in MLCT bands compared to that of **1**, consistent with a higher acceptor number environment.

The spectroscopic shifts upon avidin binding to **1** and **2** are similar to the shifts observed when increasing amounts of DMF are added to aqueous solutions of **1** or **2**. The protein binding event displaces water molecules from the metal center just as DMF replaces water molecules that are interacting with the metal center. This solvent system provides a convenient model

for systematically varying the environment to crudely mimic protein binding.

Electrochemistry. The redox potentials of **1** and **2** while bound to avidin were found to shift by −140 and −127 mV, respectively. These potentials were measured by electrostatically adsorbing the protein to a monolayer of mercaptoundecanoic acid (MUA). These dramatic shifts are most likely due to the interaction of the complex with the monolayer as well as the protein. Being sandwiched between the protein and the monolayer minimizes any interaction with bulk water and places the complexes in an even lower dielectric environment compared to avidin in solution. The protein/monolayer combination destabilizes the iron(II) state with respect to the iron(III) state, compared with the complex in aqueous solution, raising the energy level of the orbitals that comprise the HOMO. The HOMO is destabilized by 1130 cm^{-1} and 1050 cm^{-1} for **1** and **2**, respectively.

Immobilization techniques are commonly used to study electroactive proteins (*61*, *63*−*70*). In our case, a monolayer of MUA was formed and then washed with $NH_4OH_{(aq)}$ in order to leave a number of negatively charged acids on the surface (the pI of avidin is ∼10, and therefore the protein should be positively charged at pH 7). Figure 8 shows the charge distribution at the binding pocket of avidin at pH 7. There is a significant area with a positive charge near the binding site. This positive charge ensures that a portion of the avidin on the monolayer will be oriented so that the bound iron complexes will make effective contact. The observed electrochemical signal is likely from these bound complexes (*61*). Since avidin is a tetramer, it is likely that a maximum of two of the binding sites are in contact with the monolayer at any given time.

CONCLUSION

We have established that the electronic structures of $[Fe(BMB)(CN)_4]^{2-}$ and $[Fe(DMB)(CN)_4]^{2-}$ are highly sensitive to noncovalent interactions. The optical spectrum shifts up to 20 nm in organic solvents with lower acceptor numbers than water. The shift is linearly dependent on the solvent acceptor number indicating there are specific interactions between the solvent and the CN and bpy ligands. Similarly, the electrochemical response of **1** and **2** in various organic solvents shows a shift that is linearly dependent on solvent AN; shifts of up to 150 mV are observed. These data suggest that the electronic structure of **1** and **2** is sensitive to second-sphere coordination changes and solvation.

The results from solvent studies confirm that the complexes can be used as sensitive probes to investigate the electronic properties of protein binding sites. Binding of **1** and **2** to avidin results in visible changes in the electronic spectra. The shifts are similar to those observed in the solvent studies. We expect the binding event to exclude water from the metal complex, resulting in a lower AN environment. For example, binding of **1** to avidin can be compared to a solution of **1** in 23% DMF in water.

Our data show that the environments of **1** and **2** in avidin are observably different. ITC measurements show that the binding of **2** is weaker than that of **1** by a factor of ∼20. Therefore, we expect **1** and **2** to sample slightly different environments in the binding pocket. Indeed, small differences are observed in both the optical and electrochemical data. Upon binding to avidin, the optical spectrum shifts 20 and 7 nm for **1**, while the same transitions shift 10 and 6 nm for **2**. The binding of **2** can be compared to 12% DMF in water. The difference in redox potential shifts is small (10 mV), yet well above the error for such a measurement.

The three-dimensional X-ray structure of **1** bound to avidin shows **1** partially buried in a hydrophobic pocket with a direct interaction between the protein and the transition metal complex. An open-loop conformation, expected from the presence of the amide, would prevent the avidin from shielding the complex from bulk water and minimize the observable change in electrochemical potential and absorbance properties. Isopotential calculations, however, show a patch of positive charge near the binding site that should favor binding of the negatively charged **1** and **2**. These interactions may partially counteract the effects of having the amide in place of the carboxylic acid. Finally, molecular dynamics simulations show that, when **2** is bound to avidin, the protein structure is slightly more disordered. However, for the MD snapshot most resembling the crystal structure, the distances between the metal center and select residues are nearly the same as when **1** is bound.

Together, these results demonstrate that even small changes in the binding of a ligand (**1** or **2**) result in small yet experimentally observable changes in second-sphere coordination imposed by the protein. Specifically, these changes include the partial charge structure, van der Waals interactions, and hydrogen bonds. Small changes in these weak interactions are powerful enough to induce changes in the electrochemical and optical properties of the metal cofactors.

The synthetic versatility and the sensitivity of $[Fe(bpy)(CN)_4]^{2-}$ complexes to local environmental changes makes these complexes candidates for use in electronic and optical protein detection devices for any number of ligand-receptor pairs. For example, by systematic change of the protein binding ligand (e.g., adding or removing hydrogen bond donors) and observing the effect of protein binding on the spectroscopic properties, the nature of an unknown binding pocket can be evaluated. Further, the shift in the electrochemical potential indicates whether solvent is being excluded from the metal center and therefore can be used to evaluate the hydrophobicity of the binding site.

Sensitivity to small changes in binding affinities indicates that these species can be used as probes for remotely evaluating the noncovalent factors that affect ligand-receptor binding. Our future studies will translate this approach to self-assembled monolayer systems for investigating the effects of protein binding on the electrochemical properties of the metal complex.

ACKNOWLEDGMENT

We thank Belovo, Inc. for providing deglycosylated avidin. We thank Harry Gray, Igor Kurnikov, Baudilio Tejerina, and Alec Durrell for helpful discussions. This work was funded by the Nanoscale Science and Engineering Initiative of the National Science Foundation under NSF Award Number EEC-0647560 and Ohmx Corporation. MR thanks the MURI program of the DoD for support.

Supporting Information Available: Molecular modeling overlay with crystal structure, isothermal titration calorimetry data, cyclic voltammograms of 1 in 0−50% DMF/water. This material is available free of charge via the Internet at http://pubs.acs.org.

LITERATURE CITED

(1) Lever, A. B. P. (1984) *Inorganic Electronic Spectroscopy*, 2nd ed., Vol 33, Elsevier, Amsterdam.
(2) Nigam, S., and Rutan, S. (2001) Principles and applications of solvatochromism. *Appl. Spectrosc. 55*, 362a–370a.
(3) Dodsworth, E. S., Hasegawa, M., Bridge, M., and Linert, W. (2004) Solvatochromism. *Compr. Coord. Chem. II 2*, 351–365.
(4) Alousy, A., Blundell, N. J., Burgess, J., Hubbard, C. D., and Van Eldik, R. (2002) Solvatochromism and piezochromism of dicyano-, tricyano-, and tetracyano-diimine-iron(II) complexes. *Transition Met. Chem. (Dordrecht, Neth.) 27*, 244–252.

(5) Gritzner, G., Danksagmuller, K., and Gutmann, V. (1976) Outer-sphere coordination effects on redox behavior of $Fe(CN)_6^{3-}$-$Fe(CN)_6^{4-}$ couple in non-aqueous solvents. *J. Electroanal. Chem. 72*, 177–185.

(6) Ando, I. (2004) Hydrogen bonding of 18-crown-6 ether to ruthenium-ammine complexes at second sphere. *Coord. Chem. Rev. 248*, 185–203.

(7) Todd, M. D., Dong, Y., and Hupp, J. T. (1991) Crown ether encapsulation effects upon optical electron-transfer energetics in a symmetrical mixed-valence system. *Inorg. Chem. 30*, 4685–4687.

(8) Beck, M. T. (1968) Chemistry of outer-sphere complexes. *Coord. Chem. Rev. 3*, 91–115.

(9) Harwani, S., and Telford, J. R. (2005) Outer-sphere coordination of metal complexes in biological and cyclodextrin-based systems. *Chemtracts: Inorg. Chem. 18*, 437–448.

(10) Raymo, F. M., and Stoddart, J. F. (1996) Second-sphere coordination. *Chem. Ber. 129*, 981–990.

(11) Colquhoun, H. M., Stoddart, J. F., and Williams, D. J. (1983) Second-sphere coordination -- a novel role for molecular receptors. *Angew. Chem., Int. Ed. 25*, 487–582.

(12) Werner, A. (1913) *Neuere Anschauungen auf dem Gebiete der anorganischen Chemie*, 3rd ed, Vieweg, Braunschweig.

(13) Werner, A. (1912) *Ber. Dtsch. Chem. Ges. 64*, 121.

(14) Colquhoun, H. M., Stoddart, J. F., and Williams, D. J. (1981) Formation and X-ray crystal structure of $[Pt(H_2NCH_2CH_2NH_2)_2.18\text{-crown-}6]_n^{2+}[PF_6]_{2n}^{-}$. A hydrogen bonded stepped-chain copolymer. *Chem. Commun.* 847–849.

(15) Shook, R. L., and Borovik, A. S. (2008) The effects of hydrogen bonds on metal-mediated O_2 activation and related processes. *Chem. Commun.* 6095–6107.

(16) Bjerre, J., Rousseau, C., Marinescu, L., and Bols, M. (2008) Artificial enzymes, "chemzymes": current state and perspectives. *Appl. Microbiol. Biotechnol. 81*, 1–11.

(17) Steinreiber, J., and Ward, T. R. (2008) Artificial metalloenzymes as selective catalysts in aqueous media. *Coord. Chem. Rev. 252*, 751–766.

(18) Ward, T. R. (2008) Artificial enzymes made to order: combination of computational design and directed evolution. *Angew. Chem., Int. Ed. 47*, 7802–7803.

(19) Pordea, A., and Ward, T. R. (2008) Chemogenetic protein engineering: an efficient tool for the optimization of artificial metalloenzymes. *Chem. Commun.* 4239–4249.

(20) Creus, M., Pordea, A., Rossel, T., Sardo, A., Letondor, C., Ivanova, A., Le Trong, I., Stenkamp, R. E., and Ward, T. R. (2008) X-ray structure and designed evolution of an artificial transfer hydrogenase. *Angew. Chem., Int. Ed. 47*, 1400–1404.

(21) Loosli, A., Rusbandi, U. E., Gradinaru, J., Bernauer, K., Schlaepfer, C. W., Meyer, M., Mazurek, S., Novic, M., and Ward, T. R. (2006) (Strept)avidin as host for biotinylated coordination complexes: Stability, chiral discrimination, and cooperativity. *Inorg. Chem. 45*, 660–668.

(22) Pordea, A., Creus, M., Panek, J., Duboc, C., Mathis, D., Novic, M., and Ward, T. R. (2008) Artificial metalloenzyme for enantioselective sulfoxidation based on vanadyl-loaded streptavidin. *J. Am. Chem. Soc. 130*, 8085–8088.

(23) Eckermann, A. L., Barker, K. D., Hartings, M. R., Ratner, M. A., and Meade, T. J. (2005) Synthesis and electrochemical characterization of a transition-metal-modified ligand-receptor pair. *J. Am. Chem. Soc. 127*, 11880–11881.

(24) Green, N. M. (1990) Avidin and streptavidin. *Methods Enzymol. 184*, 51–67.

(25) Livnah, O., Bayer, E. A., Wilchek, M., and Sussman, J. L. (1993) Three-dimensional structures of avidin and the avidin-biotin complex. *Proc. Natl. Acad. Sci. U.S.A. 90*, 5076–80.

(26) Livnah, O., and Sussman, J. L. (1990) Crystal forms of avidin. *Methods Enzymol. 184*, 90–93.

(27) Gritzner, G., Danksagmuller, K., and Gutmann, V. (1976) Outer-sphere coordination effects on the redox behaviour of the $Fe(CN)_6^{3-}/Fe(CN)_6^{4-}$ couple in non-aqueous solvents. *J. Electroanal. Chem. 72*, 177–185.

(28) Winkler, J. R., Creutz, C., and Sutin, N. (1987) Solvent tuning of the excited-state properties of (2,2′-bipyridine)tetracyanoferrate(II): direct observation of a metal-to-ligand charge-transfer excited state of iron(II). *J. Am. Chem. Soc. 109*, 3470–3471.

(29) Burgess, J., Chambers, J. G., and Haines, R. I. (1981) Solvatochromic behavior of intramolecular charge-transfer spectra of inorganic diimine complexes. *Transition Met. Chem. (Dordrecht, Neth.) 6*, 145–151.

(30) Mayer, U., Gutmann, V., and Gerger, W. (1975) Acceptor number - quantitative empirical parameter for electrophilic properties of solvents. *Monatsh. Chem. 106*, 1235–1257.

(31) Leslie, A. G. W. (1992) Recent changes to the MOSFLM package for processing film and image plate data. *Joint CCP4+ESF-EAMCB Newsletter on Protein Crystallography* 26.

(32) (1995) Collaborative Computational Project, The CCP4 suite: Programs for protein crystallography. *Acta Crystallogr., Sect. D D50*, 760−763.

(33) McCoy, A. J., Grosse-Kunstleve, R. W., Storoni, L. C., and Read, R. J. (2005) Likelihood-enhanced fast translation functions. *Acta Crystallogr., Sect. D D61*, 458–464.

(34) McRee, D. E. (1999) XtalView/Xfit - A versatile program for manipulating atomic coordinates and electron density. *J. Struct. Biol. 125*, 156–165.

(35) Brünger, A. T., Adams, P. D., Clore, G. M., Delano, W. L., Gros, P., Grosse-Kunstleve, R. W., Jiang, J.-S., Kuszewski, J., Nilges, N., Pannu, N. S., Read, R. J., Rice, L. M., Simonson, T., and Warren, G. L. (1998) Crystallography and NMR system (CNS): A new sofware system for macromolecular structure determination. *Acta Crystallogr., Sect. D 54*, 905–921.

(36) Laskowski, R. A., MacArthur, M. W., Moss, D. S., and Thorton, J. M. (1993) PROCHECK: A program to check the stereochemical quality of protein structures. *J. Appl. Crystallogr. 26*, 283–291.

(37) Schmidt, M. W., Baldridge, K. K., Boatz, J. A., Elbert, S. T., Gordon, M. S., Jensen, J. H., Koseki, S., Matsunaga, N., Nguyen, K. A., et al. (1993) General atomic and molecular electronic structure system. *J. Comput. Chem. 14*, 1347–1363.

(38) Hay, P. J., and Wadt, W. R. (1985) Ab initio effective core potentials for molecular calculations. Potentials for the transition metal atoms scandium to mercury. *J. Chem. Phys. 82*, 270–283.

(39) Hehre, W. J., Radom, L., and Pople, J. A. (1972) Molecular orbital theory of the electronic structure of organic compounds. XII. Conformations, stabilities, and charge distributions in monosubstituted benzenes. *J. Am. Chem. Soc. 94*, 1496–1504.

(40) Huberman, T., Eisenberg-Domovich, Y., Gitlin, G., Kulik, T., Bayer, E. A., Wilchek, M., and Livnah, O. (2001) Chicken avidin exhibits pseudo-catalytic properties: biochemical, structural, and electrostatic consequences. *J. Biol. Chem. 276*, 32031–32039.

(41) Hay, B. P. (1993) Methods for molecular mechanics modeling of coordination compounds. *Coord. Chem. Rev. 126*, 177–236.

(42) Lescoueezec, R., Lloret, F., Julve, M., Vaissermann, J., and Verdaguer, M. (2002) $[Fe(bipy)(CN)_4]^{-}$ as a versatile building block for the design of heterometallic systems: synthesis, crystal structure, and magnetic properties of $PPh_4[FeIII(bipy)(CN)_4]\cdot H_2O$, $[\{FeIII(bipy)(CN)_4\}2MII(H_2O)_4]\cdot 4H_2O$, and $[\{FeIII(bipy)(CN)_4\}2ZnII]\cdot 2H_2O$ [bipy = 2,2′-Bipyridine; M = Mn and Zn]. *Inorg. Chem. 41*, 818–826.

(43) Cornell, W. D., Cieplak, P., Bayly, C. I., Gould, I. R., Merz, K. M., Jr., Ferguson, D. M., Spellmeyer, D. C., Fox, T., Caldwell, J. W., and Kollman, P. A. (1995) A second generation force field for the simulation of proteins, nucleic acids, and organic molecules. *J. Am. Chem. Soc. 117*, 5179–5197.

(44) Kurnikov, I. personal communication.

(45) Terrettaz, S., Becka, A. M., Traub, M. J., Fettinger, J. C., and Miller, C. J. (1995) ω-Hydroxythiol monolayers at Au electrodes. 5. Insulated electrode voltammetric studies of cyano/bipyridyl iron complexes. *J. Phys. Chem. 99*, 11216–11224.

(46) Gutmann, V. (1976) Empirical parameters for donor and acceptor properties of solvents. *Electrochim. Acta 21*, 661–670.

(47) Bryant, G. M., Fergusson, J. E., and Powell, H. K. J. (1971) Charge-transfer and intraligand electronic spectra of bipyridyl complexes of iron, ruthenium, and osmium. I. Bivalent complexes. *Aust. J. Chem. 24*, 257–73.

(48) Machczynski, M. C., Gray, H. B., and Richards, J. H. (2002) An outer-sphere hydrogen-bond network constrains copper coordination in blue proteins. *J. Inorg. Biochem. 88*, 375–380.

(49) Worrall, J. A. R., Schlarb-Ridley, B. G., Reda, T., Marcaida, M. J., Moorlen, R. J., Wastl, J., Hirst, J., Bendall, D. S., Luisi, B. F., and Howe, C. J. (2007) Modulation of heme redox potential in the cytochrome c6 family. *J. Am. Chem. Soc. 129*, 9468–9475.

(50) Shifman, J. M., Gibney, B. R., Sharp, R. E., and Dutton, P. L. (2000) Heme redox potential control in de novo designed four-α-helix bundle proteins. *Biochemistry 39*, 14813–14821.

(51) Schutz, C. N., and Warshel, A. (2001) What are the dielectric \"constants\" of proteins and how to validate electrostatic models? *Proteins: Struct., Funct., Genet. 44*, 400–417.

(52) Simonson, T., and Perahia, D. (1995) Internal and interfacial dielectric properties of cytochrome c from molecular dynamics in aqueous solution. *Proc. Natl. Acad. Sci. U.S.A. 92*, 1082–1086.

(53) Rodgers, K. K., and Sligar, S. G. (1991) Surface electrostatics, reduction potentials, and the internal dielectric constant of proteins. *J. Am. Chem. Soc. 113*, 9419–9421.

(54) Green, N. M. (1975) Avidin. *Adv. Protein Chem. 29*, 85–133.

(55) Shraydeh, B. F., and Zatar, N. (1994) Donor and acceptor number effects on the solvatochromic behavior of bis(2,2′-bipyridyl)biscyanoiron(II) in binary aqueous mixtures. *Monatsh. Chem. 125*, 655–659.

(56) Toma, H. E., and Takasugi, M. S. (1983) Spectroscopic studies of preferential and asymmetric solvation in substituted cyanoiron(II) complexes. *J. Solution Chem. 12*, 547–561.

(57) (a) Eisenberg-Domovich, Y., Pazy, Y., Nir, O., Raboy, B., Bayer, E. A., Wilchek, M., and Livnah, O. (2004) Structural elements responsible for conversion of streptavidin to a pseudoenzyme. *Proc. Natl. Acad. Sci. U.S.A. 101*, 5916–5921. (b) Pazy, Y., Kulik, T., Bayer, E. A., Wilcheck, M., and Livnah, O. (2002) Ligand exchange between proteins. *J. Biol. Chem. 277 (34)*, 20892–30900.

(58) Lo, K. K.-W., and Hui, W.-K. (2005) Design of rhenium(I) polypyridine biotin complexes as a new class of luminescent probes for avidin. *Inorg. Chem. 44*, 1992–2002.

(59) Lo, K. K.-W., Hui, W.-K., and Ng, D. C.-M. (2002) Novel rhenium(I) polypyridine biotin complexes that show luminescence enhancement and lifetime elongation upon binding to avidin. *J. Am. Chem. Soc. 124*, 9344–9345.

(60) Collot, J., Gradinaru, J., Humbert, N., Skander, M., Zocchi, A., and Ward, T. R. (2003) Artificial metalloenzymes for enantioselective catalysis based on biotin-avidin. *J. Am. Chem. Soc. 125*, 9030–9031.

(61) Jhaveri, S. D., Trammell, S. A., Lowy, D. A., and Tender, L. M. (2004) Electron conduction across electrode-immobilized neutravidin bound with biotin-labeled ruthenium pentaamine. *J. Am. Chem. Soc. 126*, 6540–6541.

(62) Pazy, Y., Raboy, B., Matto, M., Bayer, E. A., Wilchek, M., and Livnah, O. (2003) Structure-based rational design of streptavidin mutants with pseudo-catalytic activity. *J. Biol. Chem. 278*, 7131–7134.

(63) Yokoyama, K., Leigh, B. S., Sheng, Y., Niki, K., Nakamura, N., Ohno, H., Winkler, J. R., Gray, H. B., and Richards, J. H. (2008) Electron tunneling through *Pseudomonas aeruginosa* azurins on SAM gold electrodes. *Inorg. Chim. Acta 361*, 1095–1099.

(64) Yue, H., and Waldeck, D. H. (2006) Understanding interfacial electron transfer to monolayer protein assemblies. *Curr. Opin. Solid State Mater. Sci. 9*, 28–36.

(65) Tarlov, M. J., and Bowden, E. F. (1991) Electron-transfer reaction of cytochrome c adsorbed on carboxylic acid terminated alkanethiol monolayer electrodes. *J. Am. Chem. Soc. 113*, 1847–1849.

(66) Feng, Z. Q., Imabayashi, S., Kakiuchi, T., and Niki, K. (1997) Long-range electron-transfer reaction rates to cytochrome c across long- and short-chain alkanethiol self-assembled monolayers: Electroreflectance studies. *J. Chem. Soc., Faraday Trans. 93*, 1367–1370.

(67) Clark, R. A., and Bowden, E. F. (1997) Voltammetric peak broadening for cytochrome c/alkanethiolate monolayer structures: dispersion of formal potentials. *Langmuir 13*, 559–565.

(68) Chobot, S. E., Hernandez, H. H., Drennan, C. L., and Elliott, S. J. (2007) Direct electrochemical characterization of archaeal thioredoxins. *Angew. Chem., Int. Ed. 46*, 4145–4147.

(69) Ye, T., Kaur, R., Wen, X., Bren, K. L., and Elliott, S. J. (2005) Redox properties of wild-type and heme-binding loop mutants of bacterial cytochromes c measured by direct electrochemistry. *Inorg. Chem. 44*, 8999–9006.

(70) Armstrong, F. A., Hill, H. A. O., and Walton, N. J. (1988) Direct electrochemistry of redox proteins. *Acc. Chem. Res. 21*, 407–413.

BC900270A

Outer-Sphere Effects of Protein Binding on the Electronic Properties of Iron (II) Complexes: An Electrochemical and Optical Investigation

*Kylie D. Barker,[‡] Amanda L. Eckermann,[‡] Matthew H. Sazinsky, [‡,⊥] Matthew R. Hartings,[‡] Carnie Abajian,[‡] Dimitra G. Georganopoulou,† Mark A. Ratner [‡] Amy C. Rosenzweig,[‡, §] Thomas J. Meade[‡,§,||]**

Departments of Chemistry, Biochemistry and Molecular and Cell Biology, Neurobiology and Physiology, and Radiology, Northwestern University, 2145 Sheridan Road, Evanston, IL 60208

Supporting Information

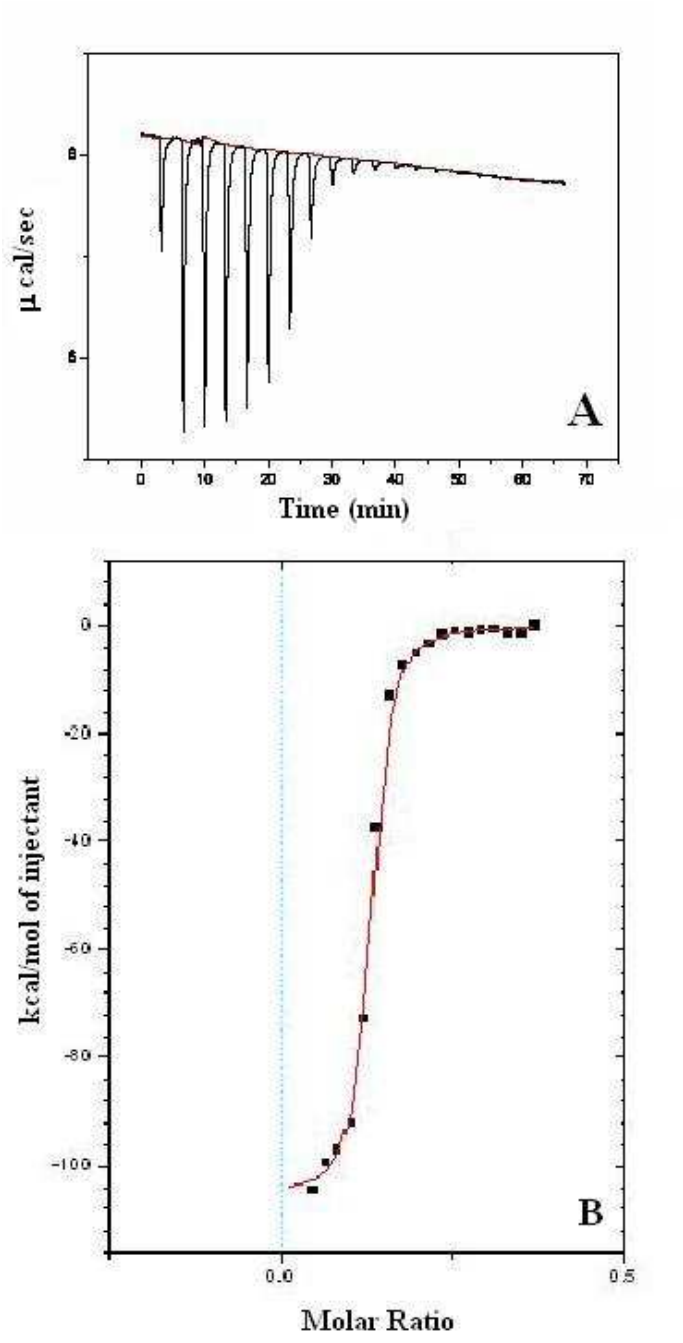

Figure S1: Calorimetric titration of avidin (24 µM in protomer) with $K_2[Fe(BMB)(CN)_4]$ (300 µM) at 25 ºC. (A) Raw data obtained for 18 injections of 4 µL each plus an initial injection of 2 µL; (B) Heat of reaction plotted versus molar ratio of metal complex to protein at each injection point. This plot is fit using Origin 7.0 OneSites model to obtain thermodynamic information and a reduced χ^2 value of 1.3 was obtained for the fit.

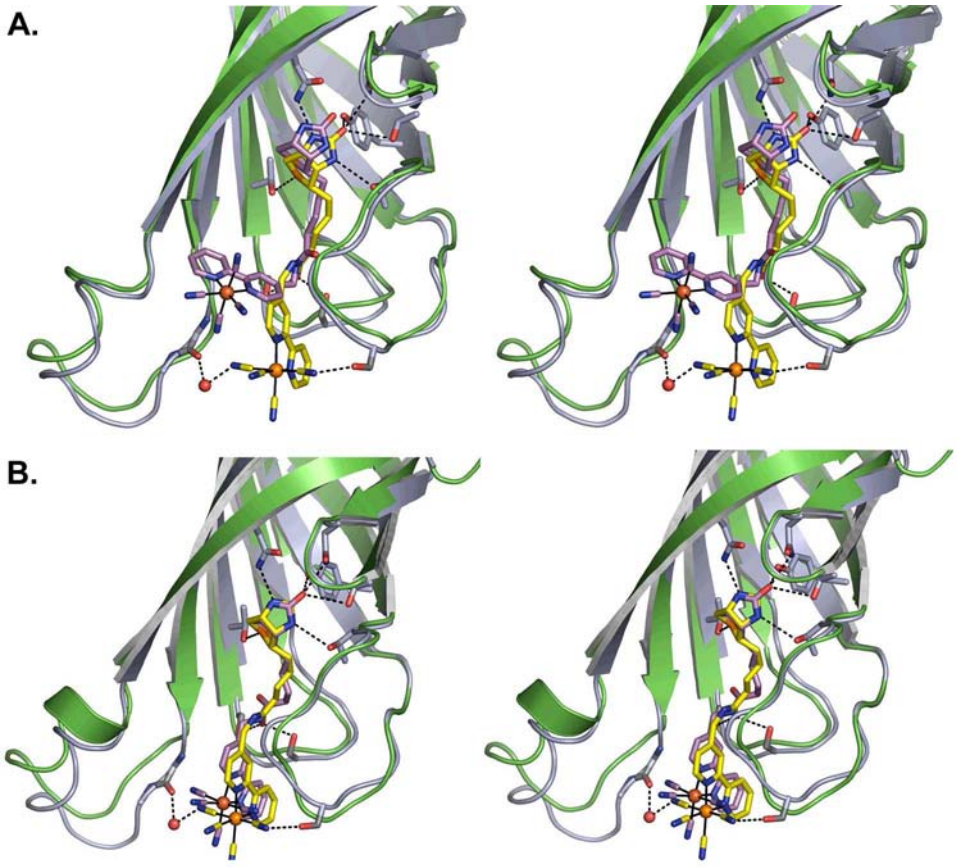

Figure S2: The crystal structure of $[Fe(BMB)(CN)_4]^{2-}$ (white) bound to avidin (gray) overlayed by molecular models of $[Fe(BMB)(CN)_4]^{2-}$ (pink) bound to avidin (yellow). Molecular modeling predicts four thermodynamically stable conformations at room temperature. (A) The structure of the molecular model is in agreement with that of the crystal structure. (B) The model shows the probe in a similar conformation as in the crystal structure however, the avidin pocket is in a more open configuration. This conformation is similar to the open loop conformation observed by Livnah and coworkers for avidin bound by amide derivatized biotin ligands (*9*). (C) The iron complex is rotated about the methylene between the biotin and the redox portion of the probe situating the redox portion about 180º from that in the crystal structure. (D) The iron complex is rotated about the methylene between the biotin and the redox portion of the probe in a slightly different conformation from that of (C).

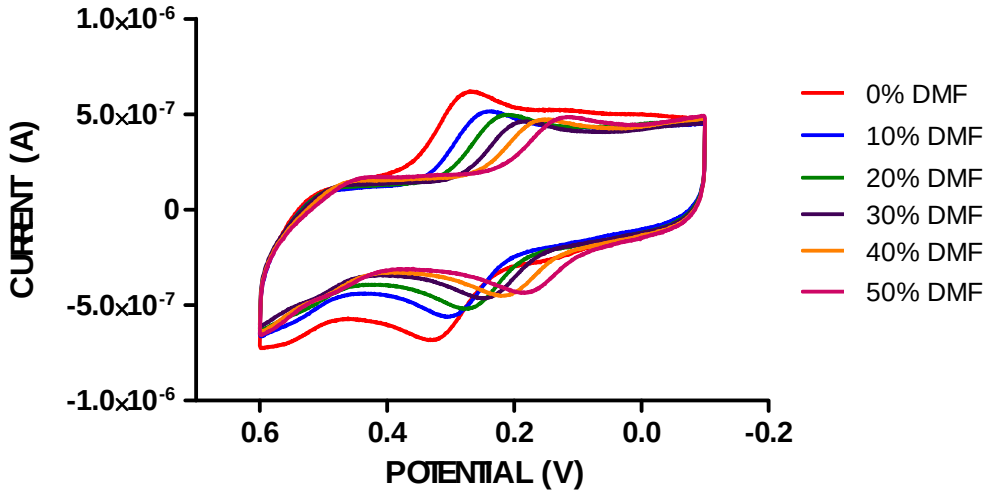

Figure S3: Cyclic voltammograms of $K_2[Fe(BMB)(CN)_4]$ in increasing concentrations of DMF in PBS buffer pH 7.2. Cyclic voltammograms we collected at 100 mV/s using a glassy carbon electrode with a Ag/AgCl reference.

A "Click Chemistry" Approach to the Efficient Synthesis of Multiple Imaging Probes Derived from a Single Precursor

Thomas L. Mindt,*[,†,§] Cristina Müller,[||] Florian Stuker,[⊥] Jean-Frédéric Salazar,[‡,§] Alexander Hohn,[||] Thomas Mueggler,[⊥] Markus Rudin,[⊥,#] and Roger Schibli*[,§,||]

Department of Chemistry and Applied Biosciences, ETH Zurich, Center for Radiopharmaceutical Science ETH-PSI-USZ, Paul Scherrer Institute, Villigen, Institute for Biomedical Engineering and Institute of Pharmacology and Toxicology, University and ETH Zurich, Switzerland. Received June 24, 2009; Revised Manuscript Received September 3, 2009

Different imaging modalities can provide complementary information on biological processes at the cellular or molecular level *in vitro* and *in vivo*. However, specific molecular probes suitable for a comparison of different imaging modalities are often not readily accessible because their preparation is usually accomplished by individually developed and optimized syntheses. Herein, we present a general, modular synthetic approach that provides access to multiple probes derived from a single precursor by application of the same, efficient functionalization strategy, the Cu(I)-catalyzed cycloaddition of terminal alkynes and azides (click chemistry). To demonstrate the viability and efficiency of this approach, folic acid (FA) was selected as a targeting vector because the preparation of FA-based imaging probes used for SPECT, PET, MRI, and NIRF by reported synthetic strategies is usually difficult to achieve and often results in low overall yields. We prepared a versatile γ-azido-FA precursor as well as a set of alkyne functionalized probes and precursors including ligand systems suitable for the chelation of various (radio)metals, an NIR dye and ^{18}F- and ^{19}F-derivatives, which enabled the parallel development of new FA-imaging probes. The Cu(I)-mediated coupling of the alkynes with the γ-azido-FA precursor was accomplished in high yields and with minimal use of protective groups. The various probes were fully characterized spectroscopically as well as *in vitro* and *in vivo*. *In vitro*, all new FA-derivatives exhibited high affinity toward the folic acid receptor (FR) and/or were specifically internalized into FR-overexpressing KB cells. *In vivo* experiments with nude mice showed that all probes (except the MRI probes which have not been tested yet) accumulated specifically in FR-positive organs and human KB-cell xenografts. However, *in vivo* imaging revealed significant differences between the various FA-derivatives with respect to unspecific, off-target localization. In general, the comparison of different probes proved the superiority of the more hydrophilic, radiometal-based imaging agents, a result which will guide future efforts for the development of FA-based imaging probes and therapeutic agents. In addition, the strategy presented herein should be readily applicable to other molecules of interest for imaging and therapeutic purposes and thus represents a valuable alternative to other synthetic approaches.

INTRODUCTION

Molecular imaging can be defined as the noninvasive visualization of biological processes at the cellular or molecular level *in vivo* (*1*). To this end, different imaging modalities can be applied (e.g., single photon emission computed tomography (SPECT), positron emission tomography (PET), magnetic resonance imaging (MRI), and near-infrared fluorescence imaging (NIRF)), each of which has certain advantages as well as limitations (*2, 3*). Regardless the modality employed, targeted imaging approaches require the use of specific molecular probes. These are usually composed of a suitable imaging entity which is covalently linked to a targeting (bio)molecule (vector). The multifunctional character of both components can complicate the preparation of such conjugates, in particular, because of potential side reactions or the lack of specificity of the coupling step. As a consequence, multistep syntheses including the use of protective groups are often employed that can lower significantly the overall efficiency of the preparation procedure. In addition, the syntheses of related imaging probes (e.g., for a comparison of different imaging modalities) are usually developed and optimized individually, which reflects the lack of general synthetic transformations for the connection of structurally diverse precursors and building blocks. Therefore, new, efficient, and universally applicable synthetic strategies are needed.

The discovery of the Cu(I)-catalyzed version of Huisgen's dipolar [2 + 3] cycloaddition of terminal alkynes and azides by the groups of Sharpless (*4*) and Meldal (*5*) has had a great impact on the scientific community as demonstrated by countless reports describing its application in different areas of research (*6*). In general, the formation of 1,4-disubstituted 1,2,3-triazoles by the cycloaddition proceeds efficiently and selectively under benign (aqueous) reaction conditions and in the presence of various other functionalities (*7*). Termed a "click reaction" (*8*), this transformation has also found application in the development of targeted or nontargeted imaging agents (*9, 10*). The majority of reported applications of the click cycloaddition

* Thomas L. Mindt, Department of Medical Radiology, Division of Radiological Chemistry, University Hospital Basel, Telephone: +41-61-556-53-80, Fax: +41-61-265-55-59, E-mail mindtt@uhbs.ch; Roger Schibli, Department of Chemistry and Applied Biosciences, ETH Zurich, Telephone: +41-56-310-28-37, Fax: +41-56-310-2849, E-mail roger.schibli@pharma.ethz.ch.

† Current address: Department of Medical Radiology, Division of Radiological Chemistry, University Hospital Basel, Basel (Switzerland).

‡ Current address: GlaxoSmithKline R&D, Clinical Imaging Centre, Hammersmith Hospital, London (UK).

§ Department of Chemistry and Applied Biosciences, ETH Zurich.

|| Paul Scherrer Institute.

⊥ Institute for Biomedical Engineering, University and ETH Zurich.

Institute of Pharmacology and Toxicology, University and ETH Zurich.

10.1021/bc900276b CCC: $40.75 © 2009 American Chemical Society
Published on Web 10/05/2009

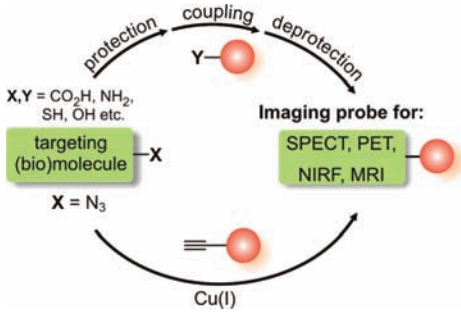

Figure 1. Sequential synthesis of imaging probes via "classical" synthetic strategies (top) in comparison to a parallel approach by which reaction of a common azide precursor with various alkyne-functionalized probes gives directly imaging agents suitable for different modalities (bottom). Spheres represent various probes or precursor thereof to be attached to the targeting (bio)molecule.

employ the 1,2,3-triazole formed as a stable linker to connect two chemical/biochemical entities. This conjugate design has been successfully applied to the preparation of optical (*11*, *12*) and MR imaging agents (*13*) and radioactive tracers suitable for SPECT (*14*) and PET (*15*−*17*). More recently, applications which make use of the 1,2,3-triazole heterocycle as a part of a probe (integrated design) have also been described (*18*−*20*).

We recognized that, once a "clickable" derivative of a targeting (bio)molecule has been prepared, a number of imaging probes would become readily available in a parallel fashion rather than by sequential synthesis (Figure 1). Such a parallel approach can significantly reduce the number of precursors and intermediates required for the synthesis of different imaging agents based on the same vector. Folic acid (FA) was chosen as a tumor-targeting molecule to demonstrate that multiple imaging probes can be derived from a single precursor using the same functionalization strategy. FA is an essential nutrient (vitamin B_9) required by eukaryotic cells for the biosynthesis of nucleotide bases. As a consequence, acquirement of the vitamin is essential for cell survival and proliferation. A number of cancer cell lines exhibit high levels of the cell surface folate receptor (FR), while its expression is highly restricted in most normal tissues and organs (*21*). These circumstances allow the specific delivery of conjugated diagnostic probes and therapeutic agents to FR overexpressing tumors (*22*, *23*). Herein, we wish to report a modular, general click chemistry approach for the short and efficient synthesis of FA-based probes suitable for SPECT, PET, NIRF, and MRI and their assessment *in vitro* and *in vivo*.

EXPERIMENTAL PROCEDURES

Compounds **1** and **10** (*24*), **9** (*16*), **15** and **16** (*25*), as well as **20** (*26*) have been previously published. For details on the synthesis and characterization of intermediates and final products, please see the references.

Syntheses. *General Methods.* Melting points were taken on a Büchi-535 apparatus and are uncorrected. Infrared spectra were recorded on a Jasco FT/IR-6200 ATR-IR and UV-spectra on a Cary 300 (Varian). Nuclear magnetic resonance spectra were recorded with a Bruker 400 or 500 MHz spectrometer with the corresponding solvent signals as an internal standard. Chemical shifts are reported in parts per million (ppm) relative to tetramethylsilane (0.00 ppm). Values of the coupling constant, *J*, are given in Hertz (Hz); the following abbreviations are used in the experimental section for the description of ^{1}H-NMR spectra: singlet (s), doublet (d), triplet (t), quartet (q), multiplet (m), doublet of doublets (dd), and bs (broad singlet). The chemical shifts of complex multiplets are given as the range of their occurrence. High-resolution mass spectra (HRMS-ESI) were recorded with a Bruker FTMS 4.7T BioAPEXII (ESI) using either the positive or negative ionization mode.

Reactions were monitored by thin layer chromatography (TLC, performed on EM Science 0.25-mm-thick, precoated silica gel 60 F-254 glass supported plates) or HPLC. HPLC was performed on a Merck-Hitachi L-7000 system equipped with an L-7400 tunable absorption detector and a Berthold LB 506 radiometric detector. The following systems were used for HPLC: Analytical HPLC: XBridge column (C18, 5 μm, 4.6 × 150 mm, Waters); 0.1% aq TFA (solvent A), acetonitrile (solvent B); 0−1 min, 95% A; 1−15 min, 95→5% A; 15−20 min, 5% A; 20→22 min, 5→95% A; 22→25 min, 95% A; flow rate: 1 mL/min. Semipreparative HPLC was performed with an XBridge column (C18, 5 μm, 10 × 150 mm, Waters) using the solvent system and gradient as indicated in the description of the individual experiments. Flow rate: 3 mL/min.

[In-111] $InCl_3$ and [Ga-67] $GaCl_3$ were purchased from Mallinckrodt, Petten (The Netherlands), CY5.5-$(CH_2)_5CO_2H$ was provided by M. Rudin and ^{3}H-folic acid was purchased from Moravek Biochemicals Inc. (USA). All other commercially available reagents and solvents were purchased from Sigma-Aldrich and used as supplied unless stated otherwise.

CY5.5-Alkyne Derivative ***4.*** CY5.5-$(CH_2)_5$COOH (tripotassium salt; 4.5 mg, 4.4 μmol) was dissolved in dry DMF (400 μL) and DIPEA (50 mg, 0.5 mmol) and HBTU (9.5 mg, 25 μmol) were added. The solution was stirred at rt in the dark for 30 min, propargyl amine (16 mg, 0.3 mmol) was added, and stirring was continued for 30 min. The mixture was diluted with water (400 μL) and purified by semipreparative HPLC (CH_3CN (A)/aq NH_4HCO_3 10 mM (B), gradient 5→50% (A) within 13 min). Concentration of the collected material and lyophilization provided compound **4** as a blue solid (4 mg, 80% yield as determined by UV/vis: $\lambda_{(max)} = 675$ nm, $d = 1$ cm, $\varepsilon = 250\,000$ M^{-1} cm^{-1}; purity according to HPLC >95%): HRMS-ESI *m*/*z* $[M]^+ = 954.2071$ (calcd. for $C_{44}H_{48}N_3O_{13}S_4$: 954.2064).

DOTA-Alkyne Derivative ***5.*** DOTA-NHS (82 mg, 0.1 mmol) was dissolved in CH_2Cl_2 (1.5 mL) and a solution of propargyl amine (11 mg, 0.2 mmol) and DIPEA (50 μL, 0.3 mmol) in CH_2Cl_2 (0.5 mL) was added. The solution was stirred at rt for 1 h and then diluted with CH_2Cl_2 (5 mL) and washed with aq citric acid (0.1 M) and water. The aqueous phases were extracted twice with CH_2Cl_2. The organic extracts were then combined, dried over Na_2SO_4, and concentrated under reduced pressure yielding compound **5** as a solidified white foam (60 mg, 98%): IR (neat) ν 2979, 2840, 1727, 1680, 1369, 1156, 823 cm^{-1}. ^{1}H NMR ($CDCl_3$) δ 7.19 (bs, 1H), 3.98 (dd, 2H, $J = 5.5$ and 2.2 Hz), 3.66 and 3.60 (each s, each 2H), 3.42 (s, 4H), 3.06, 3.01, 2.95, and 2.91 (each s, each 4H), 2.18 (t, 1H, $J = 2.2$ Hz), 1.46 (s, 9H), 1.44 (s, 18H) ppm. ^{13}C NMR ($CDCl_3$) δ 169.7, 169.4, 168.4, 83.0, 82.7, 79.6, 71.6, 56.5, 55.9, 52.3, 52.2, 50.4, 50.3, 29.3, 28.4, 28.3 ppm. HRMS-ESI *m*/*z* $[M+Na]^+ = 632.3994$ (calcd for $C_{31}H_{55}N_5O_7Na$: 632.3999).

Deprotected DOTA-Alkyne Derivative ***6.*** DOTA(^{t}Bu)$_3$-propargyl amide **5** (12 mg, 0.02 mmol) was dissolved in CH_2Cl_2/TFA (4:1, 1 mL) and stirred at rt for 18 h, after which time tlc (CH_2Cl_2/MeOH 9:1) indicated complete conversion of the substrate. Removal of the volatile components under reduced pressure yielded compound **6** as a yellow oil (15 mg; multiple TFA salt): HRMS-ESI *m*/*z* $[M+Na]^+ = 464.2118$ (calcd for $C_{19}H_{31}N_5O_7Na$: 464.2121).

DTPA-Alkyne Derivative ***7.*** *p*-NH_2-Bn-DTPA(^{t}Bu)$_5$ (97 mg, 0.13 mmol) was dissolved in THF (2.0 mL) and propargyl bromide (80% in toluene; 42 μL, 0.39 mmol) and pyridine (31 μL, 0.39 mmol) were added. The solution was stirred at reflux for 16 h, after which time the volatile components were removed under reduced pressure. Purification of the crude product by flash chromatography on silica gel with mixtures of ethyl acetate

and hexane containing 0.5% Et_3N yielded compound **7** as a yellow oil (56 mg, 55%): IR (neat) ν 2977, 2927, 1731, 1519, 1365, 1252, 1216, 1148, 843 cm^{-1}; ^1H NMR ($CDCl_3$) δ 7.04 and 6.57 (each d, 2H, $J = 8.4$ Hz), 3.88 (d, 2H, $J = 2.5$ Hz), 3.43 and 3.42 (each s, 2H), 3.38 (s, 4H), 3.34 (s, 2H), 3.05−2.98 (m, 1H), 2.82−2.65 (m, 7H), 2.54−2.45 (m, 2H), 2.18 (t, 1H, $J = 2.5$ Hz), 1.43 and 1.42 (each s, each 18H), 1.38 (s, 9H) ppm. ^{13}C NMR ($CDCl_3$) δ 171.6, 171.5, 170.9, 145.1, 130.9, 130.2, 113.8, 81.4, 80.9, 80.6, 71.4, 63.4, 56.4, 56.2, 55.9, 53.8, 53.1, 52.8, 36.5, 34.1, 28.4, 28.3 ppm. HRMS-ESI *m/z* $[M+H]^+ = 817.5322$ (calcd for $C_{44}H_{73}N_4O_{10}$: 817.5327).

Deprotected DTPA-Alkyne Derivative ***8.*** Propargyl-*p*NH-BnDTPA(^{t}Bu)$_5$ **7** (8 mg, 0.01 mmol) was dissolved in CH_2Cl_2/TFA (4:1, 1 mL) and stirred at rt for 18 h, after which time tlc (EtOAc/hexane 1:2, containing 0.1% Et_3N) indicated complete conversion of the substrate. Removal of the volatile components under reduced pressure yielded compound **8** as a yellow oil (11 mg; multiple TFA salt): purity according to HPLC >98% (retention time: 4.95 min); HRMS-ESI *m/z* $[M+Na]^+ = 559.2009$ (calcd for $C_{24}H_{32}N_4O_{10}Na$: 559.2016).

F-19 Folate Derivative ***11.*** Folate-γ-(4-azido)-butane amide **1** (pentahydrochloride, 29 mg, 40 μmol) was dissolved in ^{t}BuOH/aq NH_4HCO_3 10 mM (1:1; 6 mL) and $Cu(OAc)_2$ (1.5 mg, 20 mol %), sodium ascorbate (3 mg, 40 mol %), and 3,3,3-tris(trifluoromethyl)-1-propyne (**3**; 49 mg, 0.2 mmol) were added. The reaction flask was sealed and the mixture was stirred at rt for 18 h. Centrifugation (5 min, 13 000 rpm) and decantation of the solution gave a brown solid. The crude product was dissolved in warm MeOH (2 mL) and precipitated by addition to dilute aq HCl (buffered to pH 3−4 by addition of dilute NaOH; 6 mL). The solid was isolated by centrifugation and dried under reduced pressure to give compound **11** as an orange solid (5 mg; purity according to HPLC >92%): mp: >200 °C (decomposition); IR (neat) ν 3356, 2914, 1593, 1406, 1340, 1252, 1016, 972 cm^{-1}; ^{1}H-NMR (DMSO-d_6) δ 8.82 (s, 1H), 8.67 (bs, 1H), 8.18 (bs, 1H), 7.85 (s, 1H), 7.65 (d, 2H, $J = 8.4$ Hz), 7.09−6.73 (m, 3H), 6.64 (d, 2H, $J = 8.4$ Hz), 4.54−4.42 (m, 4H), 4.28 (bs, 1H), 3.11−3.00 (m, 2H), 2.23−2.11 (m, 2H), 2.10−1.78 (m, 4H), 1.37−1.27 (m, 2H), 1.22 (bs, 1H) ppm; ^{19}F-NMR (DMSO-d_6) δ −64.71 ppm; ^{13}C-NMR (DMSO-d_6) δ 173.9, 171.5, 166.3, 160.8, 156.5, 153.7, 150.7, 148.7, 148.5, 129.9, 128.9, 127.2, 121.4, 120.8 (q, $J = 290$ Hz), 111.2, 58.9 (q, $J = 30$ Hz), 52.1, 49.8, 46.0, 37.7, 32.0, 27.1, 26.6, 26.0 ppm (one aromatic carbon is not observed presumably because of overlapping signals); HRMS-ESI *m/z* $[M-H]^- = 780.2063$ (calcd for $C_{29}H_{27}F_9N_{11}O_5$: 780.2053).

NIRF Folate Derivative ***12.*** CY5.5-propargylamide (**4**; 4 mg; approximately 3.5 μmol) was dissolved in water (1.5 mL), and a solution of folate-γ-butylazide (**1**; pentahydrochloride salt; 2.9 mg, 4.0 μmol) in aq NH_4HCO_3 (10 mM, 100 μL) and $Cu(OAc)_2$ (0.7 mg, 10 mol %) and sodium ascorbate (1.5 mg, 20 mol %) were added. The mixture was stirred at rt in the dark for 18 h and purified by semipreparative HPLC (CH_3CN (A)/aq NH_4HCO_3 10 mM (B), gradient: 5→28% (A) within 13 min). Concentration of the collected solutions of product under reduced pressure, dissolving of the residue in water (2.0 mL), and lyophilization provided compound **12** as a blue fluffy solid (3.3 mg; 60% yield as determined by UV/vis: $\lambda_{(max)} = 675$ nm, $d = 1$ cm, $\varepsilon = 250\,000$ M^{-1} cm^{-1}; purity according to HPLC >95%): HRMS-ESI *m/z* $[M]^+ = 1491.4284$ (calcd for $C_{67}H_{75}N_{14}O_{18}S_4$: 1491.4261).

DOTA-Folate Derivative ***13.*** To a solution of folate-γ-(4-azido)-butane amide **1** (pentahydrochloride, 30 mg, 0.04 mmol) and DOTA(^{t}Bu)$_3$-propargyl amide **5** (25 mg, 0.04 mmol) in ^{t}BuOH/DMF/H_2O (2 mL, 1:1:1) containing DIPEA (70 μL, 0.4 mmol) at 85 °C was added dropwise over 30 min a solution of $Cu(OAc)_2$ (0.4 mg, 0.05 equiv) and sodium ascorbate (0.8 mg, 0.2 equiv) in water (0.6 mL). For the removal of the ^{t}Bu protective groups, aq HCl (1 M, 3 mL) was added and stirring was continued at 85 °C for 30 min. Complete conversion of azido folate **1** and the ^{t}Bu-protected intermediate, respectively, was confirmed by HPLC for each step. The mixture was filtered through Celite and purified by semipreparative HPLC (isochratic MeOH (18%) and aq 0.1% TFA (82%)). The product obtained was dissolved in water and lyophilized to yield FA-(γ)-DOTA **13** as a yellow solid (18 mg, 45% (2 steps); purity according to HPLC: >98%): mp 169−171 °C; IR (neat) ν 3282, 3097, 2953, 2861, 1677, 1636, 1611, 1511, 1406, 1198, 1129, 832, 720 cm^{-1}. ^{1}H NMR (DMSO-d_6) δ 8.96 (bs, 1H), 8.68 (s, 1H), 8.20 (d, 1H, $J = 7.5$ Hz), 7.95 (s, 1H), 7.88 (bs, 1H), 8.0−7.3 (broad signal, ca. 4H, exchange with MeOD), 7.66 and 6.65 (each d, each 2H, $J = 8.2$ Hz), 4.52 (s, 2H), 4.35 (d, 2H, $J = 5.2$ Hz), 4.32−4.25 (m, 3H), 4.06 and 3.92 (each bs, each 2H), 3.62 (bs, 4H), 3.37 (bs, 6H), 3.14 (bs, 10H) 3.06−3.00 (m, 2H), 2.18 (t, 2H, $J = 7.5$ Hz), 2.08−2.01 (m, 1H), 1.93−1.85 (m, 1H), 1.79−1.73 (m, 2H), 1.35−1.30 (m, 2H) ppm; ^{13}C NMR (DMSO-d_6) δ 174.0, 171.6, 168.9, 166.5, 165.8, 160.5, 158.7, 158.4, 158.2, 153.5, 150.7, 149.6, 148.3, 143.6, 129.0, 128.0, 123.0, 121.4, 120.2, 117.8, 155.5, 113.1, 111.2, 54.6, 53.9, 52.7, 52.1, 50.5, 50.5, 50.4, 49.0, 48.5, 48.2, 45.9, 37.8, 34.6, 32.0, 27.2, 26.6, 26.1 ppm; HRMS-ESI *m/z* $[M+Na]^+ = 1001.4308$ (calcd for $C_{42}H_{58}N_{16}O_{12}Na$: 1001.4318).

Preparation of ^{67}Ga-DOTA-Folate ***14*** *[^{67}Ga(**13**)].* Radiolabeling of FA-(γ)-DOTA **13** (20 μL, 10^{-3} M in water) was performed in sodium acetate buffer pH 5.0 (200 μL). A solution of $^{67}GaCl_3$ was added (50 MBq, 20 μL), and the reaction solution was incubated for 30 min at 85 °C. Then, Na-DTPA (10 μL, 5 mM, pH 5.0) was added to the solution for chelation of potential traces of free radionuclides. HPLC analysis of SPECT tracer **14** was performed to determine radiochemical yield (>90%).

Cold Gallium Standard of Compound ***14.*** The cold analogue of complex **14** ([Ga(**13**)]) was prepared by the reaction of FA-(γ)-DOTA **13** (5 mg, ca. 5 μmol) and $GaCl_3$ (0.9 mg, 1.5 equiv) in water (0.3 mL) at 75 °C for 30 min. The crude reaction mixture was purified by semipreparative HPLC (5%→90% CH_3CN within 14 min; rest: 0.1% aq TFA) to yield the cold analogue of complex **14** ([Ga(**11**)]) as a yellow solid after lyophilization (3 mg, 58%; purity according to HPLC >95%): mp >200 °C (decomposition). IR (neat) ν 3342, 2937, 1680, 1605, 1401, 1206, 1180, 1130, 1010, 721 cm^{-1}; HRMS-ESI *m/z* $[M+H]^+ = 1045.3521$ (calcd for $C_{42}H_{56}GaN_{16}O_{12}$: 1045.3519).

Preparation of Gd-DOTA-Folate ***17:*** *[Gd(**13**)].* FA-(γ)-DOTA **13** (5 mg, ca. 5 μmol) and $GdCl_3$ (hexahydrate; 2.8 mg, 1.5 equiv) were dissolved in water (0.5 mL) and stirred at reflux for 10 min. The crude reaction mixture was purified by semipreparative HPLC (5%→90% CH_3CN within 14 min; rest 0.1% aq TFA) to yield Gd complex **17** ([Gd(**13**)]) as a yellow solid after lyophilization (4 mg, 71%; purity according to HPLC >95%): mp >240 °C (decomposition). IR (neat) ν 3339, 2933, 1688, 1607, 1407, 1206, 1187, 1136, 723 cm^{-1}; HRMS-ESI *m/z* $[M+H]^+ = 1156.3320$ (calcd for $C_{42}H_{55}GdN_{16}NaO_{12}$: 1156.3324).

DTPA-Folate Derivative ***18.*** Propargyl-*p*-NH_2-Bn-DTPA-(^{t}Bu)$_5$ (**7**; 38 mg, 46 μmol) and folate-γ-(4-azido)-butane amide **1** (pentahydrochloride, 33 mg, 46 μmol) were dissolved in water (1.25 mL), and $Cu(OAc)_2$ (0.6 mg, 10 mol %) and sodium ascorbate (1.2 mg, 20 mol %) were added. The resulting mixture was stirred at 85 °C for 25 min. After cooling to rt, the precipitated product was isolated by centrifugation (3 min, 13 000 rpm). The crude product was dissolved in MeOH/ethyl acetate (1:1, 4.0 mL) and precipitated by slow addition of hexane (20 mL) yielding the protected intermediate FA-(γ)-*p*-Bn-DTPA(^{t}Bu)$_5$ as a brown solid (23 mg, 41%; purity according to HPLC >95%): mp >200 °C; IR (neat) ν 3280, 2977, 2932,

1724, 1699, 1607, 1519, 1367, 1248, 1148, 843 cm^{-1}; HRMS-ESI *m/z* $[M+Na]^+$ = 1354.7529 (calcd for $C_{67}H_{100}N_{15}O_{15}$: 1354.7523). (NMR analysis was inconclusive presumably because of micelle formation.)

The intermediate FA-(γ)-*p*-Bn-DTPA(^{t}Bu)$_5$ (15 mg, 11 μmol) was dissolved in CH_2Cl_2/TFA (2:1, 3.0 mL) and kept at rt for 18 h. The mixture was concentrated under reduced pressure, and the residue was dissolved in aq NaOH (0.1 M; 2 mL). The turbid solution was centrifuged (5 min, 13 000 rpm), and the yellow solution was decanted. Acidification of the solution by addition of dilute aq HCl (0.1 M) to a final pH ~3 resulted in precipitation of the product, which was isolated by centrifugation. Drying under reduced pressure yielded DTPA-folate derivative **18** as an orange solid (11 mg; multiple hydrochloride salt; purity according to HPLC >93%; retention time = 6.84 min): mp >200 °C (decomposition); IR (neat) ν 3353, 2918, 1596, 1507, 1403, 1333, 1178, 1053, 1024, 834 cm^{-1}; ^{1}H NMR (D_2O with one drop of NaOD 5% in D_2O) δ 8.34 (s, 1H), 7.47 (d, 2H, J = 8.0 Hz), 7.40 (s, 1H), 6.86 (d, 2H, J = 9.3 Hz), 6.61 (d, 2H, J = 8.0 Hz), 6.50 (d, 2H, J = 9.3 Hz), 4.33 (s, 2H), 4.22 (dd, 1H, J = 9.6 and 3.6 Hz), 4.08 (s, 2H), 3.85 (t, 2H, J = 7.3 Hz), 3.53−3.12 (m, 7H), 3.46 (s, 4H), 3.10−2.67 (m, 8H), 2.39−1.88 (m, 6H), 1.41−1.28 (m, 1.5H), 1.22−1.06 (m, 0.5H), 1.04−0.89 (m, 2H) ppm (^{13}C NMR was not conclusive due to overlapping signals); HRMS-ESI *m/z* $[M+H]^+$ = 1074.4372 (calcd for $C_{47}H_{60}N_{15}O_{15}$: 1074.4393).

*Preparation of ^{111}In-DTPA-Folate **19**: [^{111}In(**18**)]*. A stock solution (50 μL) of DTPA-folate derivative **18** (10^{-3} M) was mixed with 200 μL PBS pH 6.5. Then, $^{111}InCl_3$ was added (40 MBq, 50 μL) and the reaction solution was incubated for 1 h at room temperature. Then, Na-DTPA (10 μL, 5 mM, pH 5.0) was added to the solution for chelation of potential traces of free radionuclides. HPLC analyses was performed to determine the radiochemical yield of **19** (>95%).

*Cold Indium Standard of Compound **19**.* The cold In-analogue of complex **19** ([In(**18**)]) was prepared by to the following procedure: DTPA-folate derivative **18** (multiple hydrochloride salt; 5 mg, ca. 4 μmol) was dissolved in water (3 mL), and $InCl_3$ (1 mg, ca. 4 μmol) was added (resulting pH ~2). The mixture was heated for 1 min with a heat gun (~reflux), and the pH was adjusted to pH 4 by addition of dilute NaOH (0.05 M). The precipitated product was isolated by centrifugation and dried under reduced pressure: (3 mg yellow powder; multiple hydrochloride; quantitative conversion according to HPLC; purity according to HPLC > 95%): mp >220 °C (decomposition); IR (neat) ν 3326, 2927, 1602, 1512, 1392, 1329, 916 cm^{-1}; HRMS-ESI *m/z* $[M+H]^+$ = 1186.3181 (calcd for $C_{47}H_{57}InN_{15}O_{15}$: 1186.3197).

***In Vitro* Experiments.** *In vitro* binding assays (competition binding assays of cold FA derivatives with ^{3}H-folic acid) and internalization studies (including blocking experiments with excess folic acid) were performed with FR overexpressing KB cells according to previously reported procedures (*24*−*26*). For details, see the Supporting Information.

In order to image the internalization of NIRF probe **12** into KB cells *in vitro*, monolayers were generated on Falcon PET-insert (polyethylene terephthalate) after 3 days of growth and incubated with the test compound (**12**) at a final concentration of 11 nM. The specificity of this uptake was challenged by the presence of folic acid at high concentration (1.1 μM). Cells were mounted with fixation and scanned using a Zeiss CLSM 410 inverted microscope. 3D multichannel image processing was performed using the *IMARIS* software (Bitplane AG, Switzerland).

***In Vivo* Experiments.** All animal experiments were performed in accordance to the Swiss law of animal protection. A human nasopharyngeal epidermoid carcinoma (KB) cell line (American type Culture Collection, ATCC, Manassas, VA) with folate receptor (FR) overexpression was cultured at 37 °C in a humidified atmosphere containing 5% CO_2 in folate-deficient medium RPMI 1640 (Cell Culture Technologies, Gravesano, Switzerland) with 10% fetal calf serum (Gibco BRL/Life Technologies, Rockville, MD). To induce solid tumors for optical imaging studies, 10^6 KB cells were injected subcutaneously into the left shoulder of male nude Balb/c mice at day 0. Within 7−10 days after inoculation, mice developed tumors with mean diameter of 8 mm. For SPECT/CT scans, the female Balb/c mice were used bearing KB tumor xenografts on each shoulder. Mice were kept on folic acid free diet (*25*) prior to administration of the folic acid tracers in order to minimize interference with dietary folate. For all imaging studies, animals were anesthetized using 1.8% isoflurane delivered in air/oxygen (4:1). Body temperature of the animals was maintained at 36.5 ± 0.5 °C for both SPECT and NIRF experiments.

SPECT/CT Imaging Studies. SPECT/CT experiments were performed approximately 18 h after injection of the radiofolates with a small-animal SPECT/CT device (X-SPECT, Gamma Medica Inc. Northridge, CA, USA). ^{111}In-DTPA-folate **19** (20 MBq) or ^{67}Ga-DOTA-folate **14** (15 MBq) were diluted in 0.9% NaCl and administered via a lateral tail vein. SPECT data were acquired and reconstructed by software *LumaGEM* (version 5.407 lum 10). CT data were acquired by the manufacturer's software and reconstructed with the software *COBRA* (version 4.5.1). Fusion of SPECT and CT data was performed by software *IDL Virtual Machine* (version 6.0). Images were generated by the software *Amira* (version 4.0.1).

NIRF Imaging Studies. NIRF imaging was performed using a time-domain *in vivo* small animal fluorescence imager, eXplore Optix (ART Advanced Research Technologies, Montreal, Canada) composed of a pulsed laser diode at 666 nm as light source and a photomultiplier tube (PMT) coupled with a time-correlated single-photon-counting system for detection. A combination of filters was installed for optimal Cy5.5 fluorescence measurement. KB tumor bearing Balb/c mice were measured approximately 24 h after intravenous injection of the NIRF probe FA-(γ)-CY5.5 **12** at a dose of 2 nmol. Images were analyzed using a program written in *MATLAB* (MathWorks, Natick, US).

RESULTS AND DISCUSSION

In the past, a number of FA derivatives conjugated to various diagnostic probes suitable for different imaging techniques and their (pre)clinical evaluations have been reported. For example, FA-based radiotracers for SPECT (*24*, *27*−*32*) and PET (*26*, *33*, *34*) as well as FA conjugates suitable for optical imaging (*35*, *36*) and potentially MRI (*37*) have been described. However, the synthesis of FA derivatives functionalized via the glutamic acid moiety (but not the pteroic acid pharmacophore) is not a trivial task, especially because of the poor solubility of FA and/or intermediates. In general, two synthetic approaches have been described for the preparation of FA conjugates in solution: (1) The direct modification of FA by amide coupling protocols. This approach yields mixtures of products functionalized via either the α- or γ-carboxylate of the glutamic acid moiety (see Figure 2) and requires the laborious separation of the isomers obtained (*38*). (2) A fragment coupling approach by which FA derivatives are obtained by the coupling of pteroic acid precursors with glutamates (*39*). This strategy entails the individual synthesis of glutamic acid derivatives which are functionalized specifically via the α- or γ-carboxylate. Even under optimized reaction conditions as reported in some cases, both solution-phase syntheses tend to provide the final FA conjugate in low yields (often <10–30%), a potential issue for the future development of FA-based imaging probes and therapeutic agents.

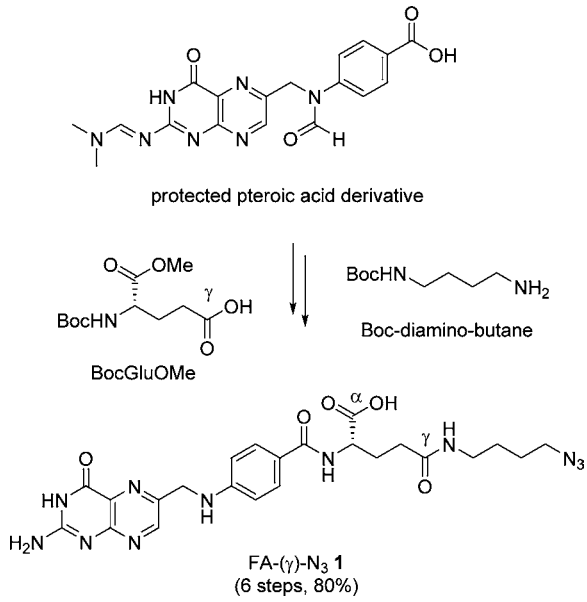

Figure 2. Synthesis of common azido-folic acid precursor FA-(γ)-N_3 **1** from a protected pteroic acid derivative and commercial building blocks BocGluOMe and Boc-diamino-butane (see ref 24).

Syntheses. Folic acid-γ-(4-azido)-butylamide **1** (FA-(γ)-N_3) was prepared selectively as previously described (Figure 2) (*24*). In brief, amide coupling of a protected pteroic acid derivative (N_2-*N*,*N*-dimethylaminomethylene-10-formyl-pteroic acid) with glutamic acid γ-(4-azido)-butylamide (derived from Boc-diaminobutane and BocGluOMe) followed by removal of protective groups provided the desired azido-FA precursor in a total of 6 steps and 80% yield.

Alkyne substrates described in the following were either commercially available (L-propargyl glycine **2** and 3,3,3-tris(trifluoromethyl)-1-propyne **3**) or prepared in 1−2 steps and high yields (Scheme 1). Thus, coupling of the near-infrared (NIR) dye derivative CY5.5-$(CH_2)_5CO_2H$ with propargyl amine under standard amide coupling conditions provided alkyne **4**. Similarly, reaction of DOTA(^{t}Bu)$_3$-NHS with propargyl amine yielded DOTA(^{t}Bu)$_3$-propargyl amide **5**. DTPA derivative **7** was synthesized by alkylation of *p*-NH_2-Bn-DTPA(^{t}Bu)$_5$ with propargyl bromide. For the experiments described below, samples of alkyne derivatives **5** and **7** were deprotected under acidic conditions to yield the free carboxylic acids **6** and **8**, respectively. Finally, [^{18}F]-6-fluorohex-1-yne (**9**) was prepared from 6-tosyl-hex-1-yne according to a literature procedure (*16*).

With the precursor FA-(γ)-N_3 **1** and a set of alkyne derivatives of imaging probes or precursors thereof, respectively, in hand, we next investigated their coupling via a 1,4-disubstituted 1,2,3-triazole by click chemistry (Scheme 2). Near-infrared fluorescence (NIRF) probe FA-CY5.5 **12** and F-19 MRI probe **11** were prepared efficiently according to the procedure initially described by the Sharpless group (*4*). Thus, reaction of FA-(γ)-N_3 **1** with the alkyne derivative of CY5.5 **4** or 3,3,3-tris(trifluoromethyl)-1-propyne (**3**) was performed at rt in aqueous media (H_2O/^{t}BuOH, 1:1) at room temperature in the presence of catalytic amounts of *in situ* generated Cu(I) catalyst ($Cu(OAc)_2$/sodium ascorbate). Notably, starting from the valuable precursor CY5.5.-$(CH_2)_5CO_2H$, application of click chemistry provided NIRF probe **12** in only 2 steps and good yield, an improved procedure compared to reported syntheses of FA-based optical probes (*35*,*36*), which employ the direct modification strategy (see above) and thus, require the separation of FA isomers. Similarly, unprotected L-propargyl glycine (**2**) (*7*) was reacted with FA-(γ)-N_3 **1** resulting in the simultaneous formation of a 1,2,3-triazole-containing, tridentate chelating system and its attachment to FA. The intermediate obtained could be used directly for the *in situ* complex formation with $[^{99m}Tc(CO)_3(H_2O)_3]^+$ (*40*), thus providing SPECT probe **10** in quantitative yields by a convenient one-pot procedure (*24*). F-18 PET tracer **20** was prepared under optimized conditions in good radiochemical yields and high specific activity by the reaction of FA-(γ)-N_3 **1** with [^{18}F]-6-fluorohex-1-yne (**9**) at 60 °C in a mixture of CH_3CN/DMF/water and in the presence of amine bases (DIPEA and 2,6-lutidine) (*26*).

While the synthesis of metal ligand systems of low denticity (*19*) can readily be achieved by the click cycloaddition (*41*), employment of multidentate chelators such as DTPA (diethylene triamine pentaacetic acid) or DOTA (1,4,7,10-tetraazacyclododecane-1,4,7,10-tetraacetic acid) in this context can pose additional challenges. Particularly, in unprotected form, these ligand systems are excellent chelators for copper which could lead to the sequestering of copper ions required for the formation of the catalyst. Indeed, attempted click reaction of FA-(γ)-N_3 **1** using unprotected alkynes **6** or **8** and catalytic amounts of Cu(I) did not yield detectable amounts of the corresponding 1,2,3-triazole conjugates (data not shown). Furthermore, it is important to remove carefully all copper species because they could impact with the subsequent radiolabeling step (*42*). It has been reported that the Cu-catalyst can be removed efficiently from click reaction mixtures even if the formed 1,2,3-triazole products represent potentially potent chelating agents for the metal catalyst itself. Examples of separation procedures described in the literature include extraction steps with aqueous solutions of EDTA (ethylenediaminetetraacetic acid) (*43*−*45*) or ammonium salts (*19*, *45*) and precipitation procedures with sodium sulfide (*15*). In addition, we have reported that commercial metal scavenger resins can be applied in this context (*18*). Alternatively, separation of 1,2,3-triazole derivatives of DTPA or DOTA from copper species can be accomplished by HPLC purification (*14*, *18*). We were pleased to find that reaction of protected DTPA derivative **7** with FA-(γ)-N_3 **1** in aqueous media and in the presence of catalytic amounts of Cu(I) (10 mol %) at 85 °C for 25 min cleanly provided the desired coupling product in good yields. These results are in agreement with reports of other groups describing the use of protected DTPA derivatives or related ligand systems for click chemistry applications (*43*−*45*). Subsequent removal of the *tert*-butyl protective groups of intermediate FA-(γ)-DTPA(^{t}Bu)$_5$ by treatment with TFA gave the desired FA-(γ)-*p*NHBnDTPA **18**. Radiolabeling of compound **18** with $^{111}InCl_3$ was performed in PBS (pH 6.5) at rt for 1 h yielding efficiently SPECT probe **19** ([^{111}In(**18**)]). In contrast, attempted click reaction of FA-(γ)-N_3 **1** with the alkyne derivative of protected DOTA **5** by simple mixing of the substrates with catalytic amounts of Cu(I) at different temperatures yielded only a mixture of unreacted alkyne **5** along with the Cu complex of the desired coupling product FA-(γ)-DOTA(^{t}Bu)$_3$ in yields that corresponded approximately to the amount of copper catalyst employed (HPLC, MS). Employment of excess Cu(I) catalyst as reported by Knör et al. (*15*) followed by removal of the copper metal by any of the extraction/precipitation procedures described above did not give satisfying results in our hands. After some experimentation, we found that slow addition of a solution of Cu(I) (0.05 mol % $Cu(OAc)_2$/sodium ascorbate) to a mixture of FA-(γ)-N_3 **1** and DOTA(^{t}Bu)$_3$-propargylamide **5** at elevated temperature (85 °C) gave the desired compound FA-(γ)-DOTA(^{t}Bu)$_3$ in high yields. We speculate that the slow addition of the copper catalyst enables the cycloaddition to take place before the metal is complexed by the DOTA ligand present. The intermediate FA-(γ)-DOTA(^{t}Bu)$_3$ was deprotected *in situ* under acidic conditions (aq HCl, 1 M), and the final product FA-(γ)-DOTA **13** was separated by HPLC from small amounts (∼5%) of the corre-

Scheme 1. Alkyne Derivatives Employed in This Study and Their Syntheses[a]

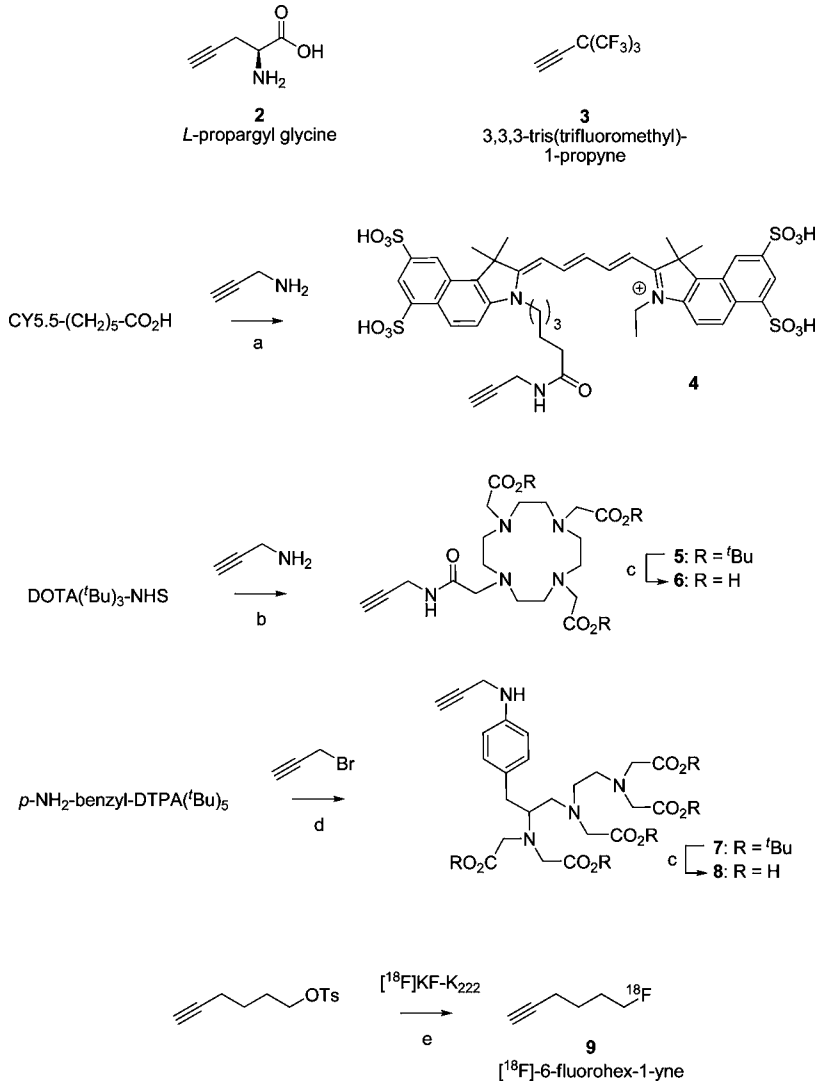

[a] (a) HBTU, DIPEA, DMF, rt; (b) CH_2Cl_2, DIPEA, rt; (c) CH_2Cl_2/TFA, rt; (d) pyridine, THF, reflux; (e) see ref 26.

sponding Cu-complex (MS) inevitably formed under the conditions applied. Unlike other ligand systems described herein, application of DTPA and DOTA required the employment of protective groups for the click cycloaddition conjugation step, however, the desired compounds specifically in a short reaction sequence and with high efficiency.

The macrocyclic chelating system DOTA has the advantage that it can be used for the complexation of different radiometals providing stable metal complexes suitable for *in vivo* applications (*46*). Thus, radiolabeling of FA-(γ)-DOTA **13** with $^{67}GaCl_3$ performed in sodium acetate buffer (pH 5.0) at 85 °C provided SPECT probe **14** in high radiochemical yield. On the other hand, complex formation of FA-(γ)-DOTA **13** with $GdCl_3$ in water at reflux gave MRI probe **17** in excellent yield and purity. In addition, we have previously reported that FA-(γ)-DOTA **13** can be labeled with ^{111}In and ^{177}Lu, giving rise to SPECT probes **15** and **16**, the latter of which also represents a potential therapeutic agent (*25*). It is likely that other radiometals known to form well-defined and stable complexes with the DOTA chelator (e.g., ^{64}Cu, ^{67}Cu, ^{68}Ga, ^{90}Y) could also be employed for the preparation of a set of additional FA-based imaging probes and therapeutic agents.

***In Vitro* Experiments.** Folic acid derivatives functionalized via the γ-carboxylate of the glutamic acid moiety have been shown to retain high specific affinity to the FR *in vitro* and *in vivo*. Nevertheless, the folic acid probes (or derivatives thereof) presented in this work were evaluated *in vitro* prior to *in vivo* experiments (see Supporting Information for details). In brief, NIRF probe **12**, the cold gallium analogue of **14** and the F-19 analogue of PET probe **20** (*26*) were assessed regarding their receptor affinity with FR overexpressing KB cells by competition studies using ^{3}H-FA according to a protocol previously described (*24*−*26*). Experimentally determined IC_{50} values were higher compared to that of folic acid ($IC_{50} = \sim 1$ nM) but still in the low nanomolar range (~2−20 nM). Thus, the compounds were considered to be well-suited for *in vivo* investigations. FA derivatives **19** and the **14** were characterized by internalization experiments with FR-overexpressing KB cells by published procedures (in analogy to compounds **15** and **16**) (*25*). For both SPECT probes, a cell uptake of approximately 50% of total added radioactivity was observed of which roughly one-third was found internalized. Experiments performed with excess folic acid resulted in an almost complete blockade of the internalization, thus proving FR-specific uptake. In the case of the NIR optical probe **12**, confocal microscopy was also employed to demonstrate specific cell uptake *in vitro* (Figure 3). Again, blocking experiments with excess folic acid proved FR-specific internalization of the optical probe.

***In Vivo* Experiments.** In order to assess the novel FA probes *in vivo* and compare different imaging modalities, experiments

Scheme 2. Synthesis of Multiple Imaging Probes from a Single Precursor by Click Chemistry[a]

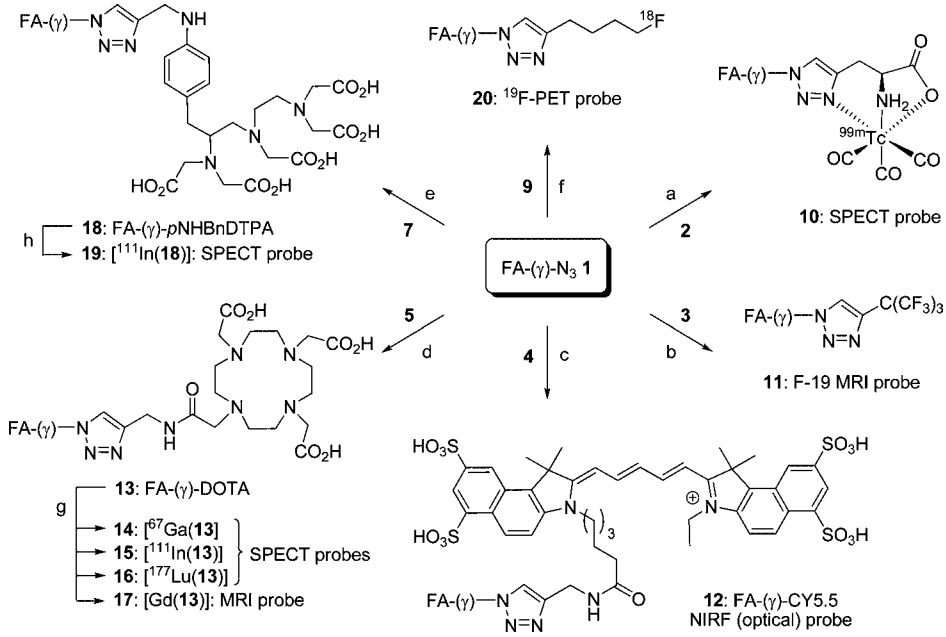

[a] (a) see ref 24; (b and c) 0.2 mol % $Cu(OAc)_2$/sodium ascorbate, (H_2O/^{t}BuOH, 1:1), rt; (d) (i) 0.05 mol % $Cu(OAc)_2$/sodium ascorbate, ^{t}BuOH/DMF/H_2O (1:1:1), DIPEA, 85 °C; (ii) aq HCl 1 M, 85 °C; (e) (i) 0.2 mol % $Cu(OAc)_2$/sodium ascorbate water, 85 °C; (ii) CH_2Cl_2/TFA (2:1), rt; (f) see ref 26; (g) For **14**: $^{67}GaCl_3$, sodium acetate buffer (pH 5.0), 85 °C; for **15** and **16**: see ref 25; for **17**: $GdCl_3$, H_2O, reflux; (h) $^{111}InCl_3$, PBS pH 6.5, rt.

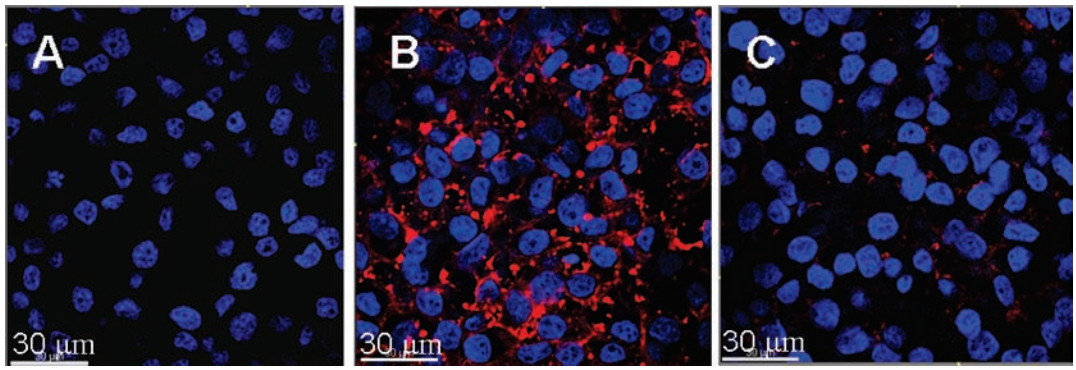

Figure 3. Convocal microscopy scanning studies of the internalization of NIRF probe **12** (red color) into FR-overexpressing KB cells. (A) control (without **12**); (B) incubation of the cells with 10 nM of **12**; (C) blocking experiments in the presence of 1.1 μM folic acid. Cell nuclei (blue) were stained with DAPI for visualization.

with nude mice bearing KB tumor xenografts were performed. SPECT and NIRF images were acquired approximately 18 and 24 h p.i., respectively. PET scans were performed 15−45 min p.i. All FA imaging probes accumulated specifically in the tumors (white arrows) which could clearly be visualized by either modality SPECT, NIRF, and PET (Figure 4). Besides in the tumor xenografts, substantial amounts of radiotracers **10**, **14**, **19**, and **20** were found in the FR-positive kidneys (orange arrows). High renal retention of folate-based probes is a known phenomenon due to reabsorption after filtration via FRs that are highly expressed at the luminal side of the proximal tubule cells (*47*). The apparent attenuated accumulation of the NIRF probe **12** in the kidneys does not necessarily reflect a significant difference of the pharmacokinetic profile of the NIRF probe compared to that of the radiotracers, but is likely to be the result of the limited tissue penetration depth of current optical imaging techniques operating in the reflectance mode. For this reason, it cannot be estimated reliably to what extent NIRF probe **12** is present in other organs such as the liver and the intestines.

Of the metallic SPECT tracers investigated, the Ga-67 and In-111 probes **14** and **19**, respectively, exhibited favorable characteristics in comparison to the Tc-99m tracer **10**, which accumulated to a higher extent in the liver and also in the intestines (yellow arrow). This is presumably a consequence of the increased lipophilicity of the Tc-99m derivative in comparison to the DTPA or DOTA derivative as previous studies have shown (*48*). Thus, a pre-selection of the most promising SPECT probe(s) for future investigations could be made on the basis of images obtained. F-18 PET probe **20** also showed high accumulation in the bile and intestines. This indicates strong hepatobiliary elimination as the result of its lipophilic character (*26*). Imaging at later time points p.i. of the ^{18}F-tracer, after clearance of the tracer and/or metabolites thereof, was not possible because of the short half-live of F-18. Overall, the direct comparison of different FA-based SPECT, PET, and NIRF probes revealed the superiority of hydrophilic tracers, a result which will guide future efforts for the development of FA-based radiotracers and other imaging probes.

Two MRI probes **11** (F-19) and **17** (Gd) were synthesized of which, in particular, the F-19 probe is a promising candidate for FR imaging applications, because unlike ^{1}H MRI, ^{19}F MRI measurements do not suffer from interference or low contrast

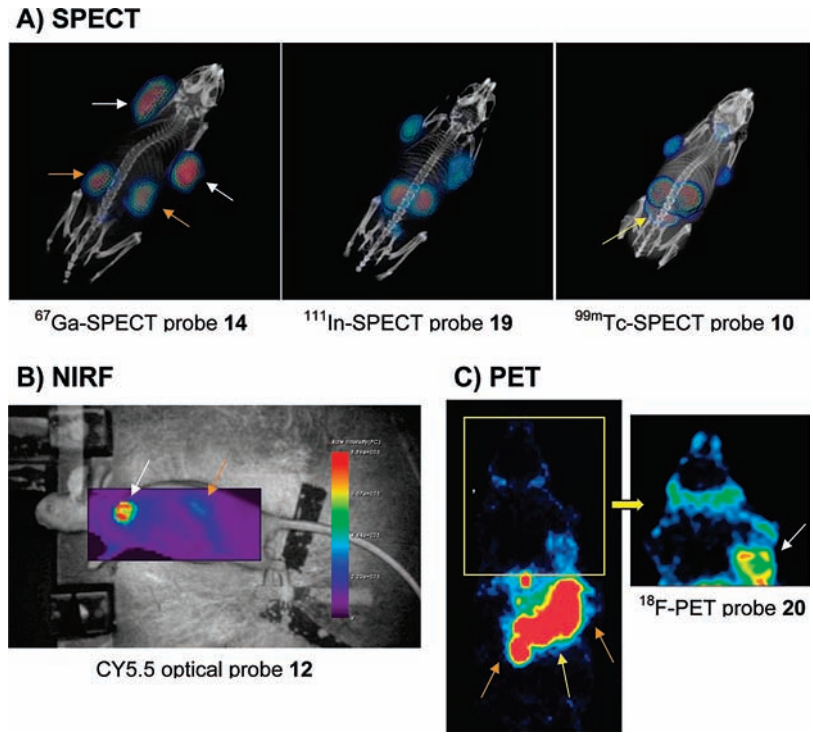

Figure 4. *In vivo* evaluation of novel folate-based imaging probes by SPECT (A), NIRF (B), and PET (C). Imaging of the xenografted FR-positive tumors (white arrows) was achieved with all probes. Accumulation of the probes in FR-positive kidneys (orange arrows) was also observed in each case. Unfavorable enrichment in the intestines and bile (yellow arrows) was detected only with the more lipophilic probes **10** and **20**. Figure 3C was adapted from ref 26.

due to background signals (*49*). In addition, compound **11** contains nine chemically and magnetically identical fluorine atoms (introduced in 1 step) which, in comparison to mono-fluorinated compounds, increases the apparent concentration of F-19 by almost 1 order of magnitude. Thus, this class of compounds could provide a useful tool for improving the sensitivity limitations of MR-based molecular imaging applications. Studies investigating the applicability of the MRI probes for *in vivo* experiments are currently ongoing.

CONCLUSIONS

We have demonstrated that multiple imaging probes for different imaging modalities can be obtained from a single precursor by application of the same general conjugation strategy, the Cu(I)-promoted click cycloaddition of alkynes and azides. Starting from a readily available azido-folic acid derivative, targeted imaging probes suitable for SPECT, PET, NIRF, and potentially MRI were prepared in few synthetic steps and high yields.

The modular synthetic approach facilitates not only the assessment of different probes for a given technique (e.g., SPECT probes based on different radiometals or metallic (Gd) vs organic (^{19}F) MRI probes) but also a comparison of different imaging modalities, the latter of which may find future applications for the collection of complementary data by taking advantage of the strengths of individual imaging techniques. *In vivo* evaluation using SPECT, PET, and NIRF showed that the novel folate probes presented are all suitable for the imaging of FR-positive tumors however, differed significantly in terms of their overall pharmacokinetics and rate and route of excretion. We were able to correlate the observed differences of metallic SPECT tracers to their physical properties (hydrophilicity), a result important for the future development of folic acid-based diagnostics and therapeutic agents.

In summary, the presented "click chemistry" approach will expedite the parallel development of new imaging probes and facilitate a comparison of different imaging modalities and, thus, the selection of the optimal probe and technique for *in vitro* and *in vivo* studies.

ACKNOWLEDGMENT

We thank Merck Eprova AG, Switzerland for providing the precursor *N2*−*N*,*N*-dimethyl-aminomethylene-10-formyl-pteroic acid, Dr. Bernhard Pfeiffer (ETH) for assistance with NMR spectroscopic measurements, Christine DePasquale (PSI) for assistance with animal experiments, and Maja Günthert (ETH) for confocal microscopy.

Supporting Information Available: Additional information as described in the text. This material is available free of charge via the Internet at http://pubs.acs.org.

LITERATURE CITED

(1) Ametamey, S. M., Honer, M., and Schubiger, P. A. (2008) Molecular imaging with PET. *Chem. Rev. 108*, 1501–1516.
(2) Rudin, M., and Weissleder, R. (2003) Molecular imaging in drug discovery and development. *Nat. Rev. Drug Discovery 2*, 123–131.
(3) Willmann Jurgen, K., van Bruggen, N., Dinkelborg Ludger, M., and Gambhir Sanjiv, S. (2008) Molecular imaging in drug development. *Nat. Rev. Drug Discovery 7*, 591–607.
(4) Rostovtsev, V. V., Green, L. G., Fokin, V. V., and Sharpless, K. B. (2002) A stepwise Huisgen cycloaddition process: copper(I)-catalyzed regioselective "ligation" of azides and terminal alkynes. *Ang. Chem., Int. Ed. 41,* 2596–2599.
(5) Tornoe, C. W., Christensen, C., and Meldal, M. (2002) Peptidotriazoles on solid phase: [1,2,3]-triazoles by regiospecific copper(i)-catalyzed 1,3-dipolar cycloadditions of terminal alkynes to azides. *J. Org. Chem. 67*, 3057–3064.
(6) Meldal, M., and Tornoe, C. W. (2008) Cu-catalyzed azide-alkyne cycloaddition. *Chem. Rev. 108*, 2952–3015.

(7) Few side reactions of the Cu(I)-catalyzed cycloaddition of azides and terminal alkynes have been reported. See, e.g.,: Mindt, T. L., and Schibli, R. (2007) Cu(I)-catalyzed intramolecular cyclization of alkynoic acids in aqueous media: a "click side reaction". *J. Org. Chem. 72*, 10247–10250, and ref 6 and literature cited therein.

(8) Kolb Hartmuth, C., and Sharpless, K. B. (2003) The growing impact of click chemistry on drug discovery. *Drug Discovery Today 8*, 1128–37.

(9) Numerous reports on click applications for the functionalization of materials (e.g., nanoparticles or surface modifications), macromolecules (polymers, proteins, DNA) and small molecules (e.g., peptides and carbohydrates) with various probes and tags have been published in the past few years. A review of this material is beyond the scope of this manuscript and only selected examples are included. For a more comprehensive collection of data, it is referred to various general and specific review articles (e.g. ref 6. and reviews cited therein).

(10) Mamat, C., Ramenda, T., and Wuest, F. R. (2009) Recent applications of click chemistry for the synthesis of radiotracers for molecular imaging. *Mini-Rev. Org. Chem. 6*, 21–34.

(11) von Maltzahn, G., Ren, Y., Park, J.-H., Min, D.-H., Kotamraju, V. R., Jayakumar, J., Fogal, V., Sailor, M. J., Ruoslahti, E., and Bhatia, S. N. (2008) In vivo tumor cell targeting with "click" nanoparticles. *Bioconjugate Chem. 19*, 1570–1578.

(12) Shimokawa, K., Ohno, O., Yamada, K., Oba, Y., and Uemura, D. (2009) Application of FITC-labeled ternatin on its cellular localization in 3T3-L1 murine preadipocytes. *Chem. Lett. 38*, 150–151.

(13) Bryson, J. M., Chu, W.-J., Lee, J.-H., and Reineke, T. M. (2008) A beta -cyclodextrin "Click cluster" decorated with seven paramagnetic chelates containing two water exchange sites. *Bioconjugate Chem. 19*, 1505–1509.

(14) Dijkgraaf, I., Rijnders, A. Y., Soede, A., Dechesne, A. C., Van Esse, G. W., Brouwer, A. J., Corstens, F. H. M., Boerman, O. C., Rijkers, D. T. S., and Liskamp, R. M. J. (2007) Synthesis of DOTA-conjugated multivalent cyclic-RGD peptide dendrimers via 1,3-dipolar cycloaddition and their biological evaluation: implications for tumor targeting and tumor imaging purposes. *Org. Biomol. Chem. 5*, 935–944.

(15) Knör, S., Modlinger, A., Poethko, T., Schottelius, M., Wester, H.-J., and Kessler, H. (2007) Synthesis of novel 1,4,7,10-tetraazacyclodecane-1,4,7,10-tetraacetic acid (DOTA) derivatives for chemoselective attachment to unprotected polyfunctionalized compounds. *Chem.—Eur. J. 13*, 6082–6090.

(16) Marik, J., and Sutcliffe, J. L. (2006) Click for PET: rapid preparation of [^{18}F]fluoropeptides using CuI catalyzed 1,3-dipolar cycloaddition. *Tetrahedron Lett. 47*, 6681–6684.

(17) Schirrmacher, R., Lakhrissi, Y., Jolly, D., Goodstein, J., Lucas, P., and Schirrmacher, E. (2008) Rapid in situ synthesis of [^{11}C]methyl azide and its application in ^{11}C click-chemistry. *Tetrahedron Lett. 49*, 4824–4827.

(18) Mindt, T. L., Struthers, H., Brans, L., Anguelov, T., Schweinsberg, C., Maes, V., Tourwe, D., and Schibli, R. (2006) "Click to chelate": synthesis and installation of metal chelates into biomolecules in a single step. *J. Am. Chem. Soc. 128*, 15096–15097.

(19) Mindt, T. L., Schweinsberg, C., Brans, L., Hagenbach, A., Abram, U., Tourwé, D., Garcia-Garayoa, E., and Schibli, R. (2009) A click approach to structurally diverse conjugates containing a central di-1,2,3-triazole metal chelate. *ChemMedChem 4*, 529–539, and references cited therein.

(20) Struthers, H., Spingler, B., Mindt, T. L., and Schibli, R. (2008) "Click-to-chelate": design and incorporation of triazole-containing metal-chelating systems into biomolecules of diagnostic and therapeutic interest. *Chem.—Eur. J. 14*, 6173–6183.

(21) Garin-Chesa, P., Campbell, I., Saigo, P. E., Lewis, J. L., Jr., Old, L. J., and Rettig, W. J. (1993) Trophoblast and ovarian cancer antigen LK26: sensitivity and specificity in immunopathology and molecular identification as a folate-binding protein. *Am. J. Pathol. 142*, 557–67.

(22) Hilgenbrink, A. R., and Low, P. S. (2005) Folate receptor-mediated drug targeting: From therapeutics to diagnostics. *J. Pharm. Sci. 94*, 2135–2146.

(23) Low, P. S., Henne, W. A., and Doorneweerd, D. D. (2008) Discovery and development of folic-acid-based receptor targeting for imaging and therapy of cancer and inflammatory diseases. *Acc. Chem. Res. 41*, 120–129.

(24) Mindt, T. L., Müller, C., Melis, M., de Jong, M., and Schibli, R. (2008) "Click-to-chelate": in vitro and in vivo comparison of a ^{99m}Tc(CO)$_3$-labeled N(τ)-histidine folate derivative with its isostructural, clicked 1,2,3-triazole analogue. *Bioconjugate Chem. 19*, 1689–1695.

(25) Müller, C., Mindt, T. L., Jong, M. d., and Schibli, R. (2009) Evaluation of a novel radiofolate in tumour-bearing mice: promising prospects for folate-based radionuclide therapy. *Eur. J. Nucl. Med. Mol. Imaging 36*, 938–946.

(26) Ross, T. L., Honer, M., Lam, P. Y. H., Mindt, T. L., Groehn, V., Schibli, R., Schubiger, P. A., and Ametamey, S. M. (2008) Fluorine-18 click radiosynthesis and preclinical evaluation of a new ^{18}F-labeled folic acid derivative. *Bioconjugate Chem. 19*, 2462–2470.

(27) Müller, C., Schubiger, P. A., and Schibli, R. (2006) Synthesis and in vitro/in vivo evaluation of novel ^{99m}Tc(CO)$_3$-folates. *Bioconjugate Chem. 17*, 797–806.

(28) Leamon, C. P., Parker, M. A., Vlahov, I. R., Xu, L.-C., Reddy, J. A., Vetzel, M., and Douglas, N. (2002) Synthesis and biological evaluation of EC20: a new folate-derived, ^{99m}Tc-based radiopharmaceutical. *Bioconjugate Chem. 13*, 1200–1210.

(29) Ilgan, S., Yang, D. J., Higuchi, T., Zareneyrizi, F., Bayhan, H., Yu, D., Kim, E. E., and Podoloff, D. A. (1998) ^{99m}Tc-ethylenedicysteine-folate: a new tumor imaging agent. Synthesis, labeling and evaluation in animals. *Cancer Biother. Radio. 13*, 427–35.

(30) Guo, W., Hinkle, G. H., and Lee, R. J. (1999) ^{99m}Tc-HYNIC-folate: a novel receptor-based targeted radiopharmaceutical for tumor imaging. *J. Nucl. Med. 40*, 1563–1569.

(31) Wang, S., Luo, J., Lantrip, D. A., Waters, D. J., Mathias, C. J., Green, M. A., Fuchs, P. L., and Low, P. S. (1997) Design and synthesis of [^{111}In]DTPA-folate for use as a tumor-targeted radiopharmaceutical. *Bioconjugate Chem. 8*, 673–679.

(32) Wang, S., Lee, R. J., Mathias, C. J., Green, M. A., and Low, P. S. (1996) Synthesis, purification, and tumor cell uptake of ^{67}Ga-deferoxamine-folate, a potential radiopharmaceutical for tumor imaging. *Bioconjugate Chem. 7*, 56–62.

(33) Bettio, A., Honer, M., Müller, C., Bruehlmeier, M., Mueller, U., Schibli, R., Groehn, V., Schubiger, A. P., and Ametamey, S. M. (2006) Synthesis and preclinical evaluation of a folic acid derivative labeled with ^{18}F for PET imaging of folate receptor-positive tumors. *J. Nucl. Med. 47*, 1153–1160.

(34) Mathias, C. J., Lewis, M. R., Reichert, D. E., Laforest, R., Sharp, T. L., Lewis, J. S., Yang, Z.-F., Waters, D. J., Snyder, P. W., Low, P. S., Welch, M. J., and Green, M. A. (2003) Preparation of ^{66}Ga- and ^{68}Ga-labeled Ga(III)-deferoxamine-folate as potential folate-receptor-targeted PET radiopharmaceuticals. *Nucl. Med. Biol. 30*, 725–731.

(35) Moon Woo, K., Lin, Y., O'Loughlin, T., Tang, Y., Kim, D.-E., Weissleder, R., and Tung, C.-H. (2003) Enhanced tumor detection using a folate receptor-targeted near-infrared fluorochrome conjugate. *Bioconjugate Chem. 14*, 539–45.

(36) Kennedy Michael, D., Jallad Karim, N., Lu, J., Low Philip, S., and Ben-Amotz, D. (2003) Evaluation of folate conjugate uptake and transport by the choroid plexus of mice. *Pharm. Res. 20*, 714–9.

(37) Wedeking, P. W., Wager, R. E., Arunachalam, T., Ramalingam, K., Linder, K. E., Ranganathan, R. S., Nunn, A. D., Raju, N., Tweedle, M. F. (1999) pp US 6221334 (B1) (Bracco International B.V., Neth.).

(38) Most folate derivatives reported for diagnostic or therapeutic applications are functionalized via the gamma-caboxylate of the glutamic acid moiety, which is the major product obtained by direct modifications of FA. However, employment of the alpha-

analogue, mixtures of the two isomers and pteroic acid derivatives lacking the entire glutamic acid moiety have also been reported in this context (see, e.g., Müller, C., Hohn, A., Schibiger, P. A., and Schibli, R. (2006) Preclinical evaluation of novel organometallic ^{99m}Tc folate and ^{99m}Tc-pteroate radiotracers for folate receptor-positive tumour targeting. *Eur. J. Nucl. Med. 33*, 1007–1016.

(39) The fragment coupling approach has also been successfully developed in the context of solid phase synthesis (see, e.g., ref 28.).

(40) Alberto, R., Schibli, R., Egli, A., Schubiger, A. P., Abram, U., and Kaden, T. A. (1998) A novel organometallic aqua complex of technetium for the labeling of biomolecules: synthesis of $[^{99m}Tc(OH_2)_3(CO)_3]^+$ from $[^{99m}TcO_4]^-$ in aqueous solution and its reaction with a bifunctional ligand. *J. Am. Chem. Soc. 120*, 7987–7988.

(41) In fact, poly-1,2,3-triazole containing chelators are used as Cu(I)-stabilizer for the same click reaction that has enabled their syntheses (see, e.g., Chan, T. R., Hilfgraf, R., Sharpless, K. B., and Fokin, V. V. (2004) Polytriazoles as copper(I)-stabilizing ligands in catalysis. *Org. Lett. 6*, 2853–2855.

(42) In this context, it has been reported that click cycloaddition can be carried out with pre-formed, non-radioactive metal complexes of DOTA derivatives (see, e.g., (i) Viguier, R. F. H., and Hulme, A. N. (2006) A sensitized europium complex generated by micromolar concentrations of copper(I): Towards the detection of copper(I) in biology. *J. Am. Chem. Soc. 128*, 11370−11371 and (ii) Bryson, J. M., and Reinecke, T. M. (2007) Gadolinium-containing glycopolymers for MRI. *PMSE Prepr. 96*, 658).

(43) Ketola, J., Katajisto, J., Hakala, H., and Hovinen, J. (2007) Synthesis of lanthanide(III) chelates by using 'click' chemistry. *Helv. Chim. Acta 90*, 607–615.

(44) Antoni, P., Malkoch, M., Vamvounis, G., Nystroem, D., Nystroem, A., Lindgren, M., and Hult, A. (2008) Europium confined cyclen dendrimers with photophysically active triazoles. *J. Mater. Chem. 18*, 2545–2554.

(45) Camp, C., Dorbes, S., Picard, C., and Benoist, E. (2008) Efficient and tunable synthesis of new polydentate bifunctional chelating agents using click chemistry. *Tetrahedron Lett. 49*, 1979–1983.

(46) De Leon-Rodriguez, L. M., and Kovacs, Z. (2008) The synthesis and chelation chemistry of DOTA-peptide conjugates. *Bioconjugate Chem. 19*, 391–402.

(47) Birn, H., Spiegelstein, O., Christensen, E. I., and Finnell, R. H. (2005) Renal tubular reabsorption of folate mediated by folate binding protein 1. *J. Am. Soc. Nephrol. 16*, 608–615.

(48) The log D value of Tc-99m probe **10** is -3.41 ± 0.06, whereas that of the In-111 derivative **15** is -4.21 ± 0.11 (partition between octanol and PBS pH 7.4; see refs 24 and 25). On the basis of the retention factor (κ'-value) determined by reversed phase HPLC, probes **14**, **15**, **17**, and **19** are of similar lipophilicity ($\kappa' = 0.38-0.42$) and clearly more hydrophilic than the Tc-99m probe **10** ($\kappa' = 0.62$) (data not shown).

(49) Reid, D. G., and Murphy, P. S. (2008) Fluorine magnetic resonance in vivo: A powerful tool in the study of drug distribution and metabolism. *Drug Discovery Today 13*, 473–480.

BC900276B

A "Click Chemistry" Approach to the Efficient Synthesis of Multiple Imaging Probes Derived from a Single Precursor

Thomas L. Mindt,[*1, †] Cristina Müller,[2] Florian Stuker,[3] Jean-Frédéric Salazar,[1, ‡] Alexander Hohn,[2] Thomas Müggler,[3] Markus Rudin,[3, 4] Roger Schibli[1, 2]

[1] Department of Chemistry and Applied Biosciences, ETH Zurich, Zurich (Switzerland)

[2] Center for Radiopharmaceutical Science ETH-PSI-USZ, Paul Scherrer Institute, Villigen (Switzerland)

[3] Institute for Biomedical Engineering, University and ETH Zurich, Zurich (Switzerland)

[4] Institute of Pharmacology and Toxicology, University and ETH Zurich (Switzerland)

[†] *Current address: Department of Medical Radiology, Division of Radiological Chemistry, University Hospital Basel, Basel (Switzerland)*

[‡] *Current address: GlaxoSmithKline, Clinical Imaging Centre, Hammersmith Hospital, London (UK)*

* Corresponding author:

Thomas L. Mindt, Department of Medical Radiology, Division of Radiological Chemistry, University Hospital Basel, Telephone: +41-61-556-53-80, Fax: +41-61-265-55-99; Roger Schibli, Center for Radiopharmaceutical Science ETH-PSI-USZ, Telephone: +41-56-310-28-37, Fax: +41-56-310-2849

1. TABLE OF CONTENT

1. Table of Content 2

2. NMR spectra 3

2.1. DOTA-Alkyne 5 3

2.2. DTPA-Alkyne 7 4

2.3. F-19 probe 11 5

2.4. Folate-DOTA 13 7

2.5. Folate-DTPA 18 8

3. HPLC Chromatograms 9

3.1. NIRF probe 12 9

3.2. Cold Ga^{III} analogue of probe 14 9

3.3. Gd^{IIII} complex 17 10

3.4. Cold Indium(III) analogue of probe 19 10

4. In Vitro Experiments 11

4.1. IC50 Determination of NIRF Probe 12, cold Gallium Analogue of Derivative of 14 and F-19 Analogue of PET Probe 20 11

4.2. Cell Internalization Studies of SPECT Probes 15 and 19 13

5. Time-Dependant In Vivo Experiments with NIRF Probe 12 14

2. NMR SPECTRA

DOTA-Alkyne 5

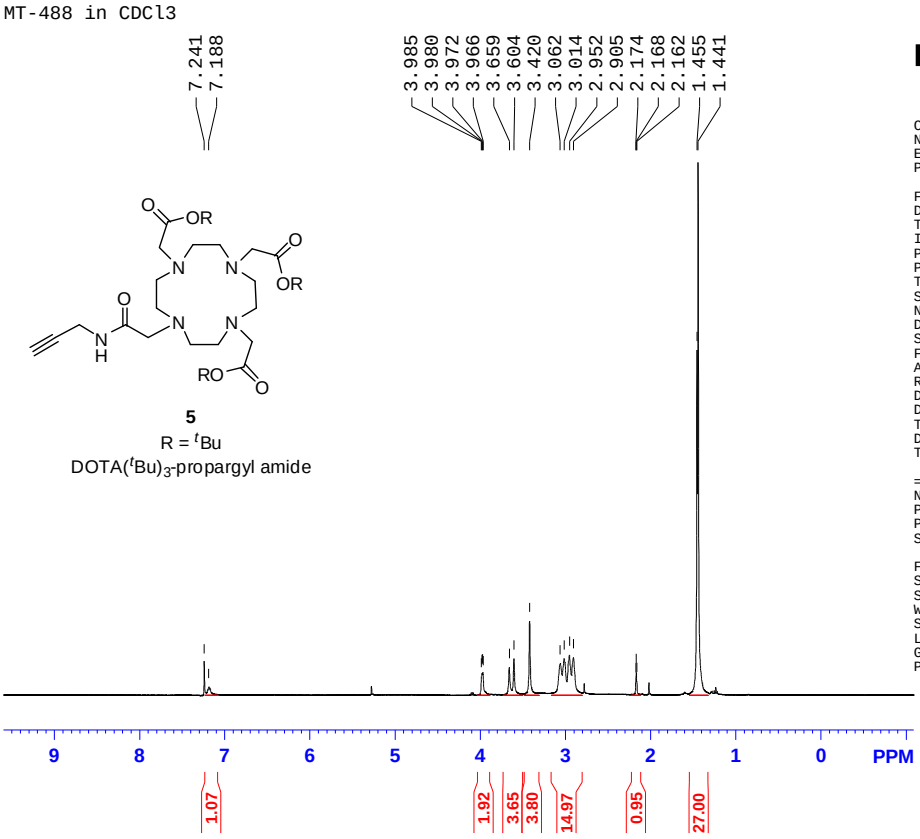

5

R = ^{t}Bu

DOTA(^{t}Bu)$_3$-propargyl amide

```
Current Data Parameters
NAME            R10MT488
EXPNO                  1
PROCNO                 1

F2 - Acquisition Parameters
Date_           20070313
Time               16.29
INSTRUM            av400
PROBHD   5 mm PABBO BB-
PULPROG             zg30
TD                 65536
SOLVENT            CDCl3
NS                    16
DS                     2
SWH             8278.146 Hz
FIDRES          0.126314 Hz
AQ              3.9584243 sec
RG                 203.2
DW                60.400 usec
DE                 6.00 usec
TE                299.9 K
D1             1.00000000 sec
TD0                    1

======== CHANNEL f1 ========
NUC1                  1H
P1                 14.00 usec
PL1                -1.00 dB
SFO1         400.1324710 MHz

F2 - Processing parameters
SI                 32768
SF           400.1300171 MHz
WDW                   EM
SSB                    0
LB                 0.30 Hz
GB                     0
PC                 1.00
```

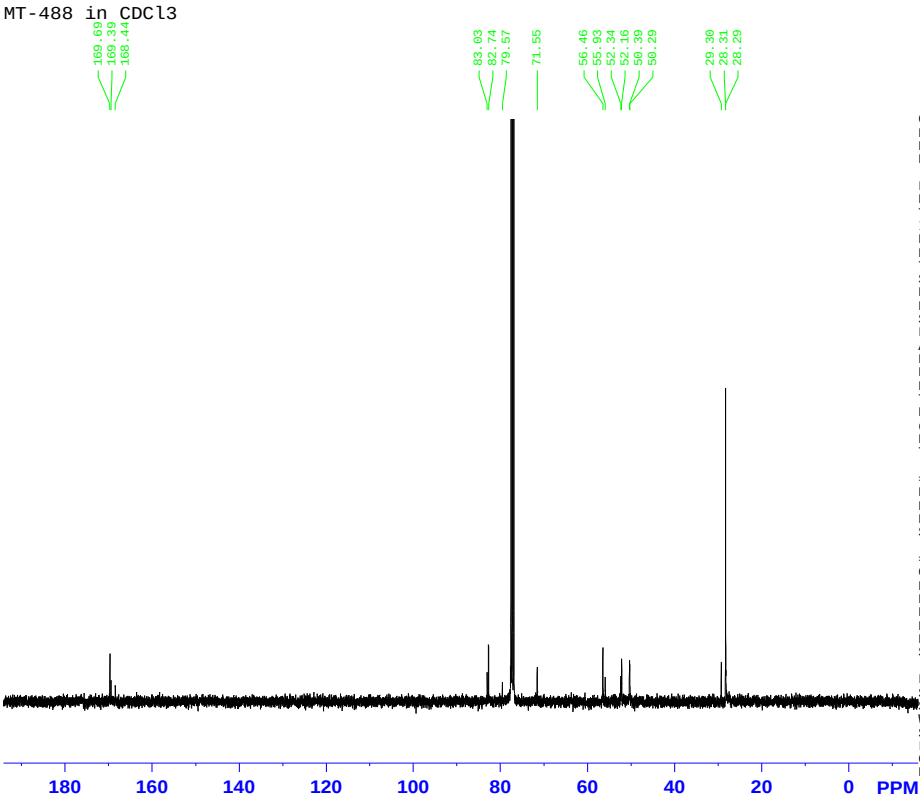


```
Current Data Parameters
NAME            R10MT488
EXPNO                  4
PROCNO                 1

F2 - Acquisition Parameters
Date_           20070313
Time               20.03
INSTRUM            av400
PROBHD   5 mm PABBO BB-
PULPROG           zgpg30
TD                 65536
SOLVENT            CDCl3
NS                  1024
DS                     4
SWH            23980.814 Hz
FIDRES          0.365918 Hz
AQ              1.3664756 sec
RG                 161.3
DW                20.850 usec
DE                 6.00 usec
TE                300.5 K
D1             2.00000000 sec
d11            0.03000000 sec
DELTA          1.89999998 sec
TD0                    1

======== CHANNEL f1 ========
NUC1                 13C
P1                  5.40 usec
PL1                -5.00 dB
SFO1         100.6228298 MHz

======== CHANNEL f2 ========
CPDPRG2          waltz16
NUC2                  1H
PCPD2              80.00 usec
PL2                -1.00 dB
PL12               15.50 dB
PL13               21.50 dB
SFO2         400.1316005 MHz

F2 - Processing parameters
SI                 32768
SF           100.6127472 MHz
WDW                   EM
SSB                    0
LB                 1.00 Hz
GB                     0
PC                 1.40
```

DTPA-Alkyne 7

MT-668/F2 in CDCl3

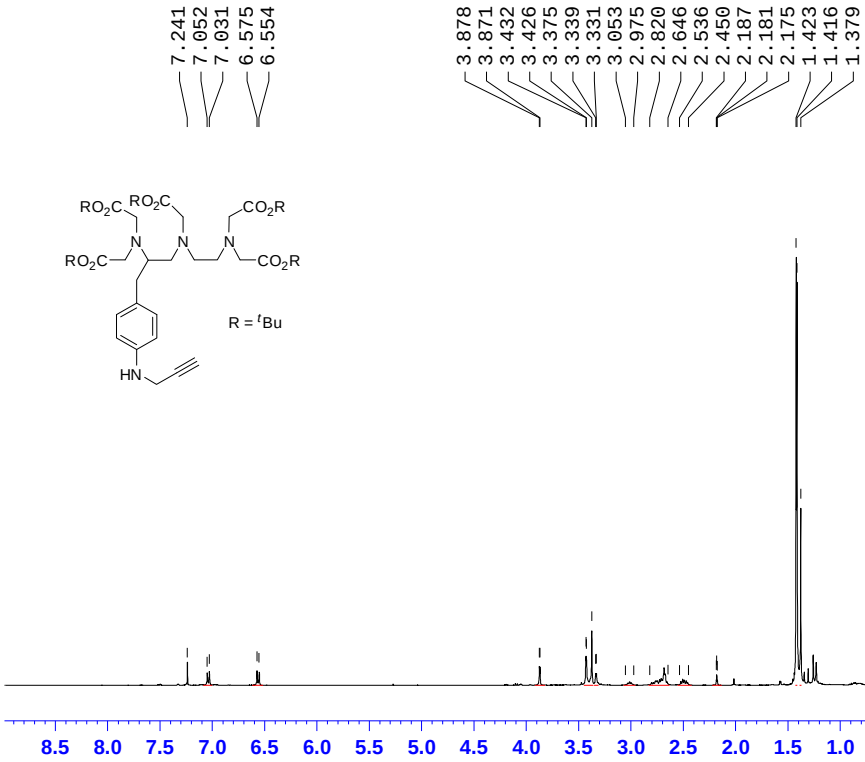


```
Current Data Parameters
NAME          R05MT668F2
EXPNO                  1
PROCNO                 1

F2 - Acquisition Parameters
Date_           20080205
Time               16.12
INSTRUM            av400
PROBHD   5 mm PABBO BB-
PULPROG             zg30
TD                 65536
SOLVENT            CDCl3
NS                    16
DS                     2
SWH             8278.146 Hz
FIDRES         0.126314 Hz
AQ             3.9584243 sec
RG                   128
DW                60.400 usec
DE                 6.00 usec
TE                299.3 K
D1           1.00000000 sec
TD0                    1

======== CHANNEL f1 ========
NUC1                  1H
P1                14.00 usec
PL1               -1.00 dB
SFO1        400.1324710 MHz

F2 - Processing parameters
SI                 32768
SF          400.1300173 MHz
WDW                   EM
SSB                    0
LB                0.30 Hz
GB                     0
PC                1.00
```

MT-668/F2 in CDCl3

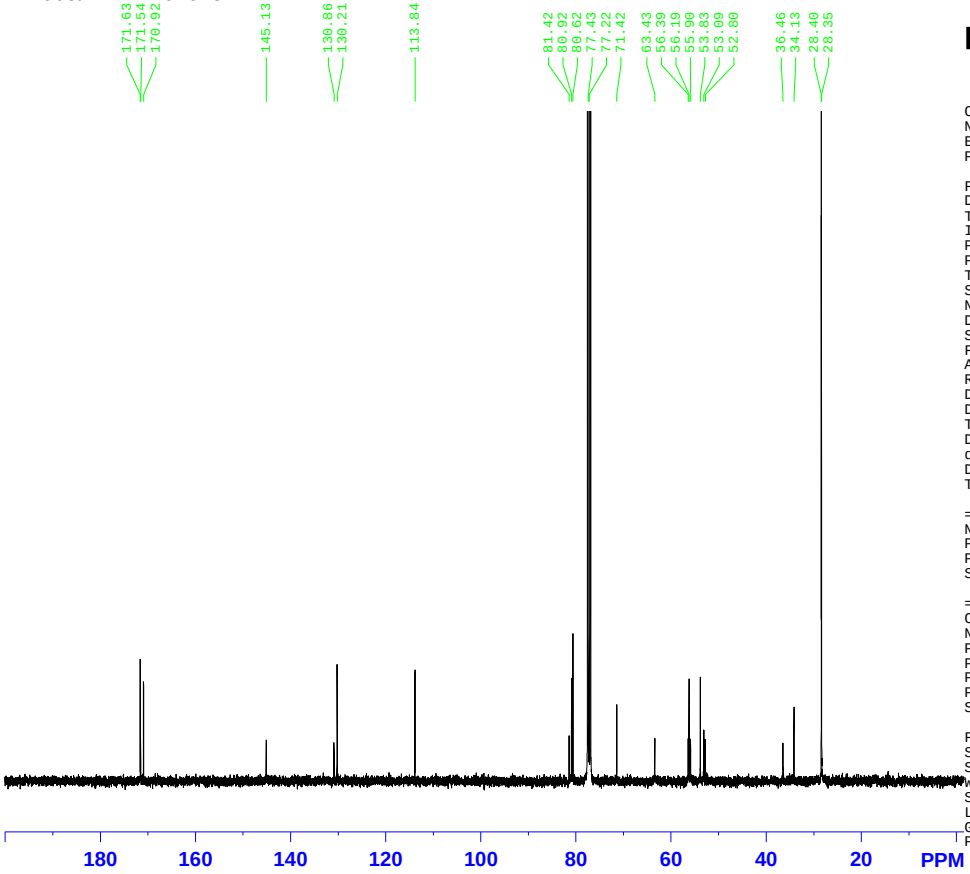


```
Current Data Parameters
NAME          R05MT668F2
EXPNO                  2
PROCNO                 1

F2 - Acquisition Parameters
Date_           20080205
Time               20.39
INSTRUM            av400
PROBHD   5 mm PABBO BB-
PULPROG           zgpg30
TD                 65536
SOLVENT            CDCl3
NS                  1024
DS                     4
SWH            23980.814 Hz
FIDRES         0.365918 Hz
AQ             1.3664756 sec
RG                   114
DW                20.850 usec
DE                 6.00 usec
TE                299.9 K
D1           4.00000000 sec
d11          0.03000000 sec
DELTA        3.90000010 sec
TD0                    1

======== CHANNEL f1 ========
NUC1                 13C
P1                 5.40 usec
PL1               -5.00 dB
SFO1        100.6228298 MHz

======== CHANNEL f2 ========
CPDPRG2          waltz16
NUC2                  1H
PCPD2             80.00 usec
PL2               -1.00 dB
PL12              15.50 dB
PL13              21.50 dB
SFO2        400.1316005 MHz

F2 - Processing parameters
SI                 32768
SF          100.6127482 MHz
WDW                   EM
SSB                    0
LB                1.00 Hz
GB                     0
PC                1.40
```

F-19 probe 11

DRX-500: 1H of MT-632B_500 in DMSO-d6 at 298K

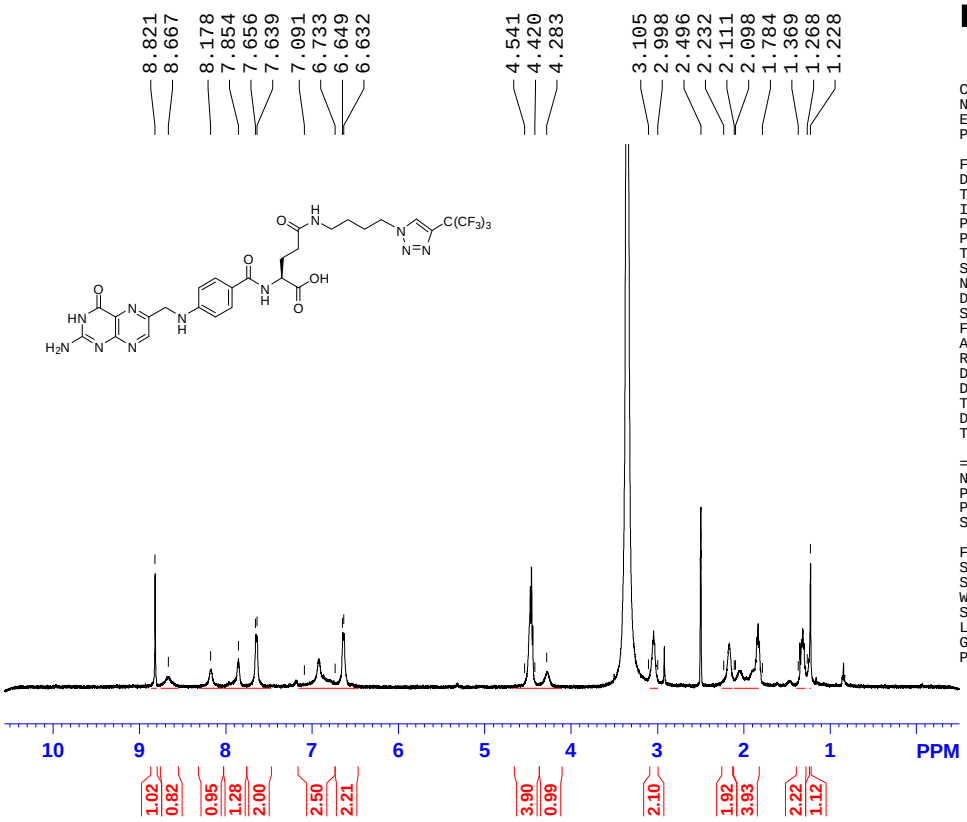


```
Current Data Parameters
NAME      R44MT-632_500
EXPNO                 1
PROCNO                1

F2 - Acquisition Parameters
Date_           20071108
Time               19.20
INSTRUM          drx500
PROBHD   5 mm BBO BB-1H
PULPROG             zg30
TD                 32768
SOLVENT             DMSO
NS                  2048
DS                     4
SWH            5530.974 Hz
FIDRES         0.168792 Hz
AQ            2.9623675 sec
RG                   181
DW                90.400 usec
DE                 6.00 usec
TE                298.0 K
D1           0.10000000 sec
TD0                    1

======== CHANNEL f1 ========
NUC1                  1H
P1                 9.30 usec
PL1               -4.00 dB
SFO1        500.1325219 MHz

F2 - Processing parameters
SI                 16384
SF          500.1300052 MHz
WDW                   no
SSB                    0
LB                 0.00 Hz
GB                     0
PC                 1.00
```

Av400: 19F of MT-632/B in DMSO-d6 at 298K

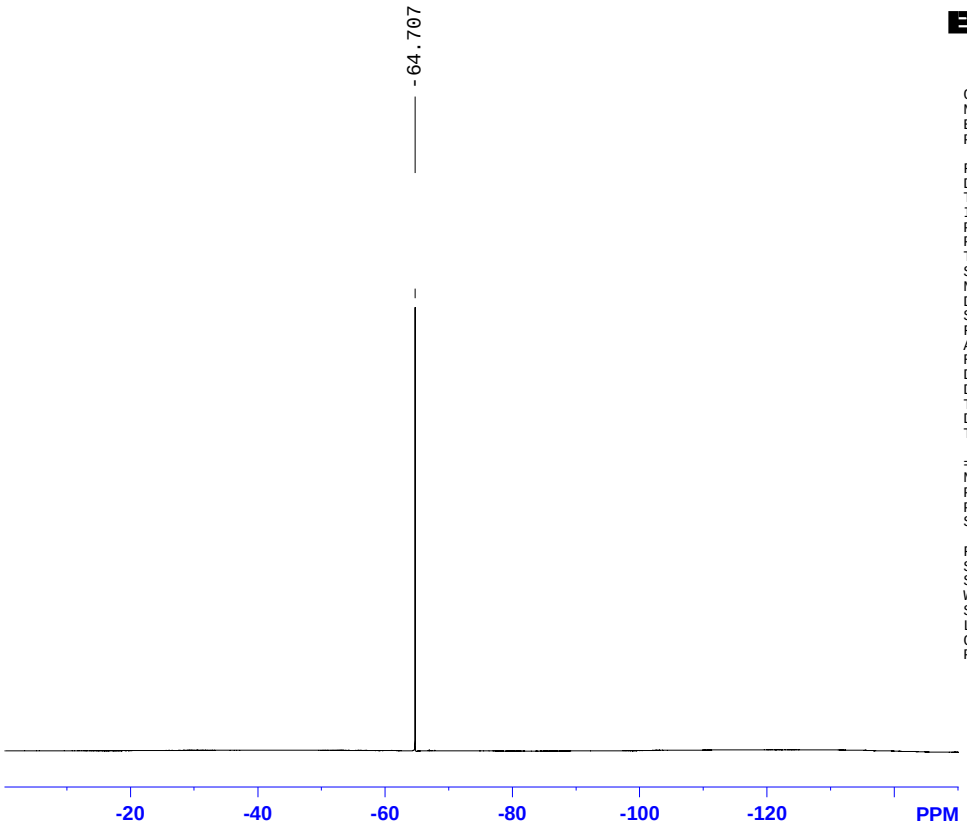


```
Current Data Parameters
NAME      R45 MT-632B 19F
EXPNO                 100
PROCNO                  1

F2 - Acquisition Parameters
Date_           20071108
Time               9.48
INSTRUM          av400
PROBHD   5 mm PABBO BB-
PULPROG               zg
TD                 32768
SOLVENT             DMSO
NS                    64
DS                     2
SWH           75187.969 Hz
FIDRES         2.294555 Hz
AQ            0.2179572 sec
RG                 322.5
DW                6.650 usec
DE                 6.00 usec
TE                297.9 K
D1           5.00000000 sec
TD0                    1

======== CHANNEL f1 ========
NUC1                 19F
P1                14.90 usec
PL1               -2.00 dB
SFO1        376.4607162 MHz

F2 - Processing parameters
SI                 16384
SF          376.4983660 MHz
WDW                   no
SSB                    0
LB                 0.00 Hz
GB                     0
PC                 1.00
```

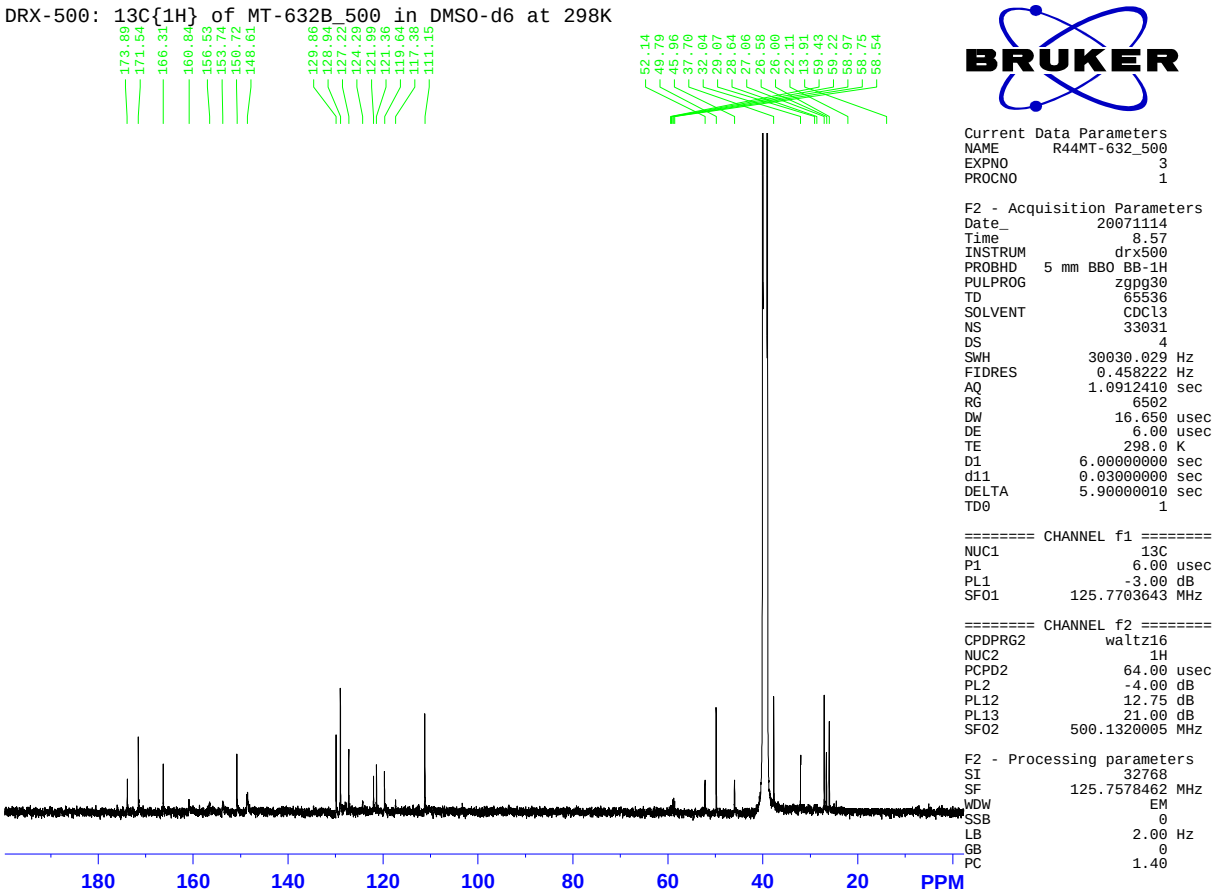
DRX-500: 13C{1H} of MT-632B_500 in DMSO-d6 at 298K
173.89
171.54
166.31
160.84
156.53
153.74
150.72
148.61
129.86
128.94
127.22
124.29
121.99
121.36
119.64
117.38
111.15
52.14
49.79
45.96
37.70
32.04
29.07
28.64
27.06
26.58
26.00
22.11
13.91
59.43
59.22
58.97
58.75
58.54
BRUKER
Current Data Parameters
NAME R44MT-632_500
EXPNO 3
PROCNO 1
F2 - Acquisition Parameters
Date_ 20071114
Time 8.57
INSTRUM drx500
PROBHD 5 mm BBO BB-1H
PULPROG zgpg30
TD 65536
SOLVENT CDCl3
NS 33031
DS 4
SWH 30030.029 Hz
FIDRES 0.458222 Hz
AQ 1.0912410 sec
RG 6502
DW 16.650 usec
DE 6.00 usec
TE 298.0 K
D1 6.00000000 sec
d11 0.03000000 sec
DELTA 5.90000010 sec
TD0 1
======== CHANNEL f1 ========
NUC1 13C
P1 6.00 usec
PL1 -3.00 dB
SFO1 125.7703643 MHz
======== CHANNEL f2 ========
CPDPRG2 waltz16
NUC2 1H
PCPD2 64.00 usec
PL2 -4.00 dB
PL12 12.75 dB
PL13 21.00 dB
SFO2 500.1320005 MHz
F2 - Processing parameters
SI 32768
SF 125.7578462 MHz
WDW EM
SSB 0
LB 2.00 Hz
GB 0
PC 1.40
180
160
140
120
100
80
60
40
20
PPM

Folate-DOTA 13

DRX-500: 1H of in DMSO-d6 at 298K

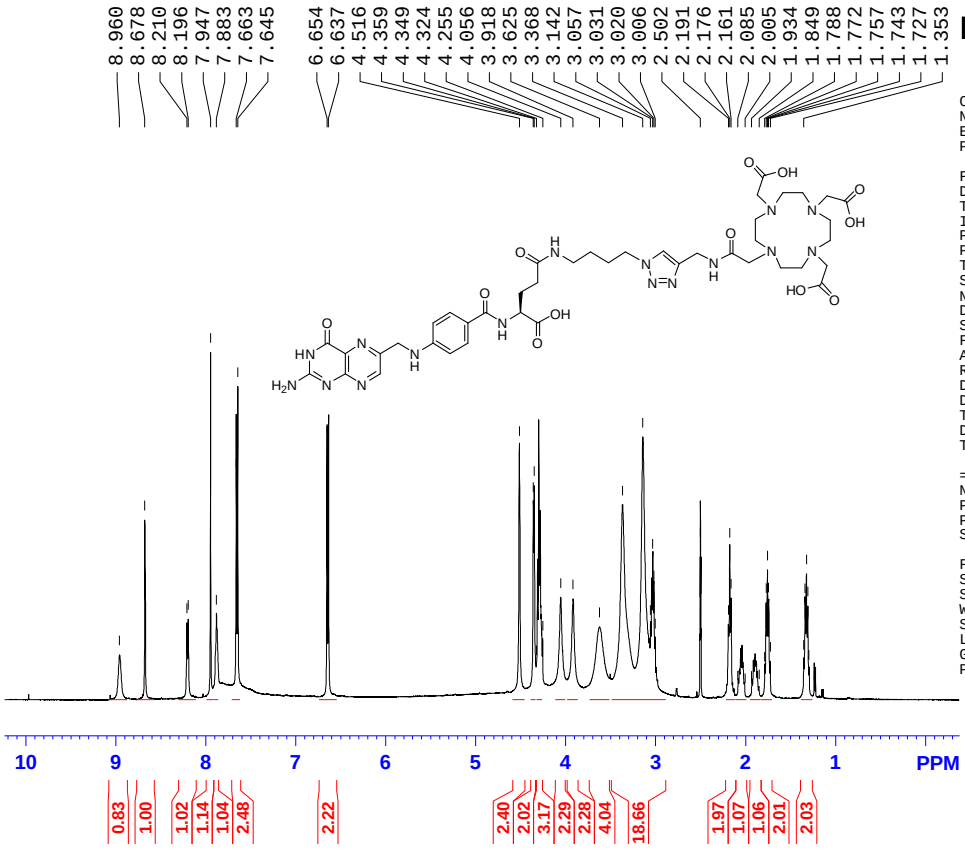


```
Current Data Parameters
NAME      R48MT-650-C_500
EXPNO                  1
PROCNO                 1

F2 - Acquisition Parameters
Date_           20071203
Time              16.47
INSTRUM         drx500
PROBHD   5 mm BBO BB-1H
PULPROG           zg30
TD               32768
SOLVENT           DMSO
NS                  256
DS                    4
SWH            5530.974 Hz
FIDRES         0.168792 Hz
AQ             2.9623675 sec
RG                  181
DW                90.400 usec
DE                 6.00 usec
TE                298.0 K
D1           0.10000000 sec
TD0                    1

======== CHANNEL f1 ========
NUC1                  1H
P1                 9.30 usec
PL1                -4.00 dB
SFO1        500.1325219 MHz

F2 - Processing parameters
SI                 16384
SF          500.1300049 MHz
WDW                   no
SSB                    0
LB                  0.00 Hz
GB                     0
PC                  1.00
```

DRX-500: 13C{1H} of in CDCl3 at 298K

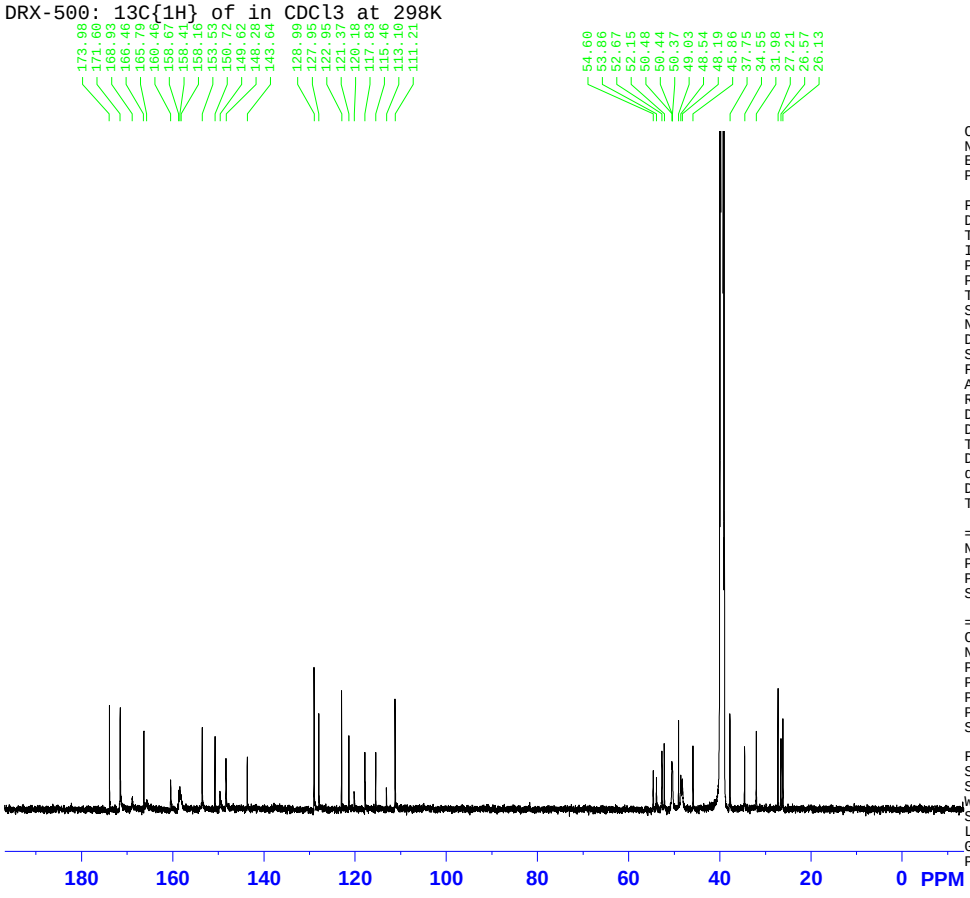


```
Current Data Parameters
NAME      R48MT-650-C_500
EXPNO                  2
PROCNO                 1

F2 - Acquisition Parameters
Date_           20071204
Time               9.31
INSTRUM         drx500
PROBHD   5 mm BBO BB-1H
PULPROG         zgpg30
TD               65536
SOLVENT           CDCl3
NS                16860
DS                    4
SWH           32679.738 Hz
FIDRES         0.498653 Hz
AQ             1.0027661 sec
RG               23170.5
DW                15.300 usec
DE                 6.00 usec
TE                298.0 K
D1           4.00000000 sec
d11          0.03000000 sec
DELTA        3.90000010 sec
TD0                    1

======== CHANNEL f1 ========
NUC1                 13C
P1                 6.00 usec
PL1                -3.00 dB
SFO1        125.7703643 MHz

======== CHANNEL f2 ========
CPDPRG2          waltz16
NUC2                  1H
PCPD2              64.00 usec
PL2                -4.00 dB
PL12               12.75 dB
PL13               21.00 dB
SFO2        500.1320005 MHz

F2 - Processing parameters
SI                 32768
SF          125.7578459 MHz
WDW                   EM
SSB                    0
LB                  2.00 Hz
GB                     0
PC                  1.00
```

Folate-DTPA 18

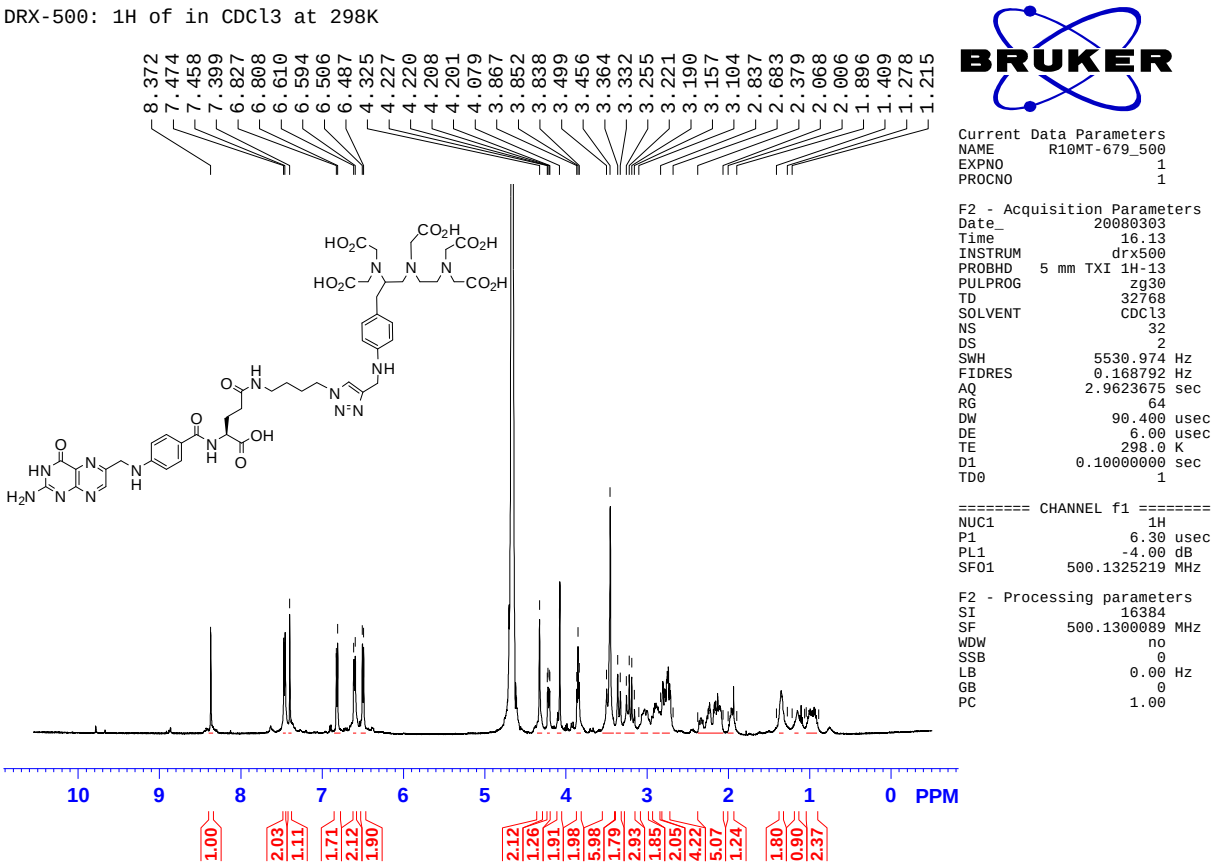


```
Current Data Parameters
NAME       R10MT-679_500
EXPNO                  1
PROCNO                 1

F2 - Acquisition Parameters
Date_           20080303
Time               16.13
INSTRUM          drx500
PROBHD   5 mm TXI 1H-13
PULPROG             zg30
TD                 32768
SOLVENT            CDCl3
NS                    32
DS                     2
SWH             5530.974 Hz
FIDRES          0.168792 Hz
AQ             2.9623675 sec
RG                    64
DW                90.400 usec
DE                 6.00 usec
TE                298.0 K
D1            0.10000000 sec
TD0                    1

======== CHANNEL f1 ========
NUC1                  1H
P1                 6.30 usec
PL1                -4.00 dB
SFO1         500.1325219 MHz

F2 - Processing parameters
SI                 16384
SF           500.1300089 MHz
WDW                   no
SSB                    0
LB                  0.00 Hz
GB                     0
PC                  1.00
```

3. HPLC CHROMATOGRAMS

NIRF probe 12

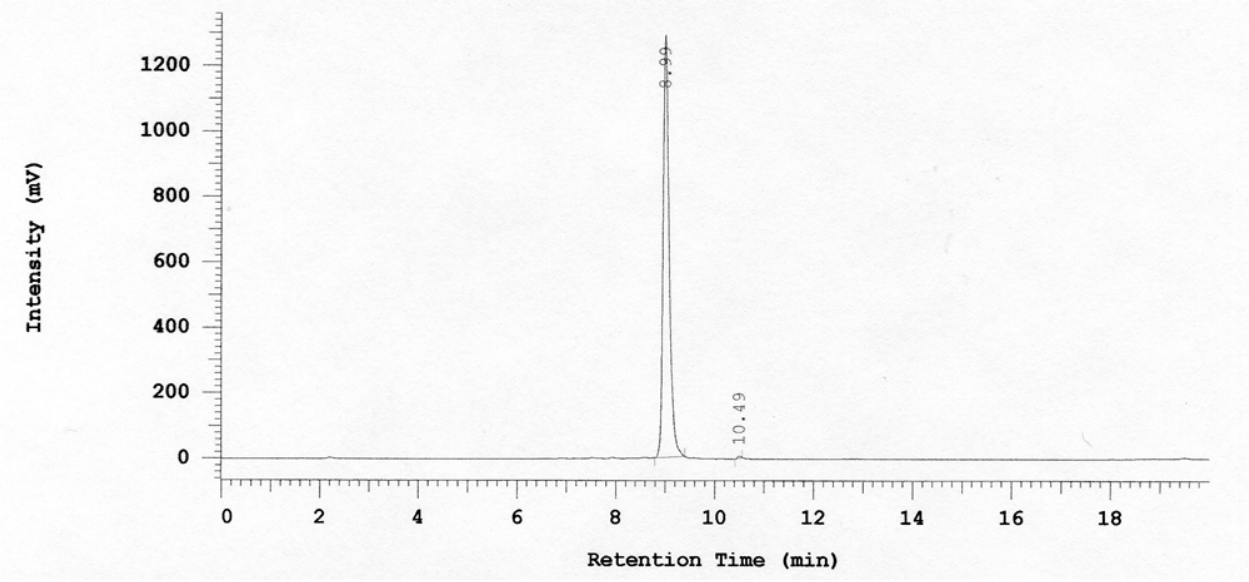

Cold Ga^{III} analogue of probe 14

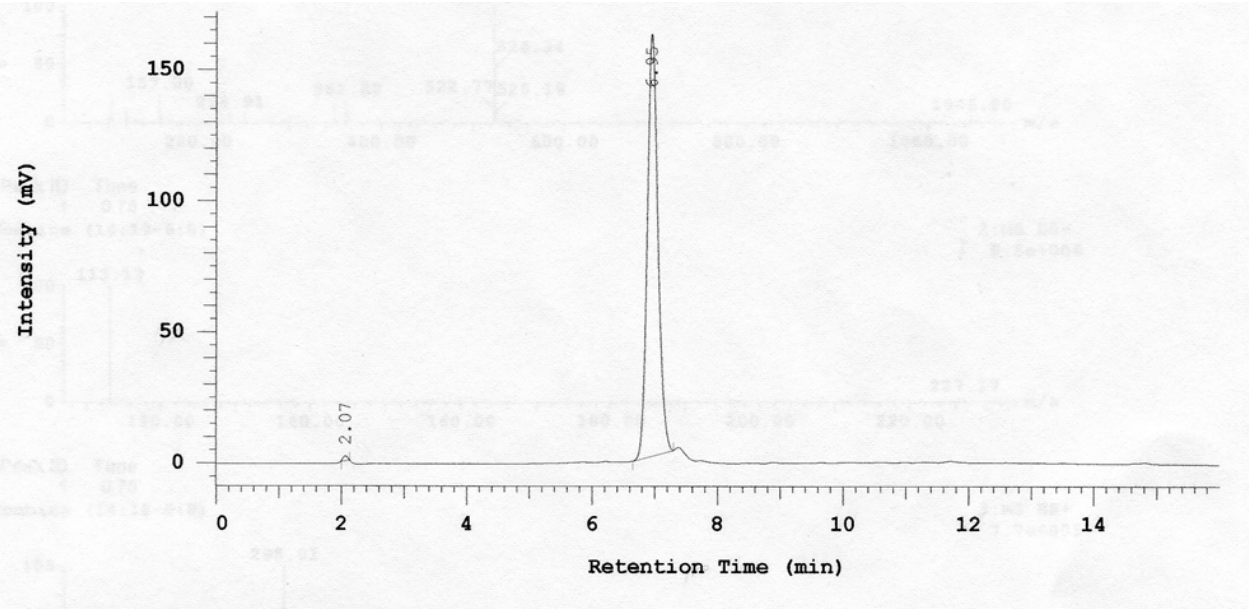

Gd^{III} complex 17

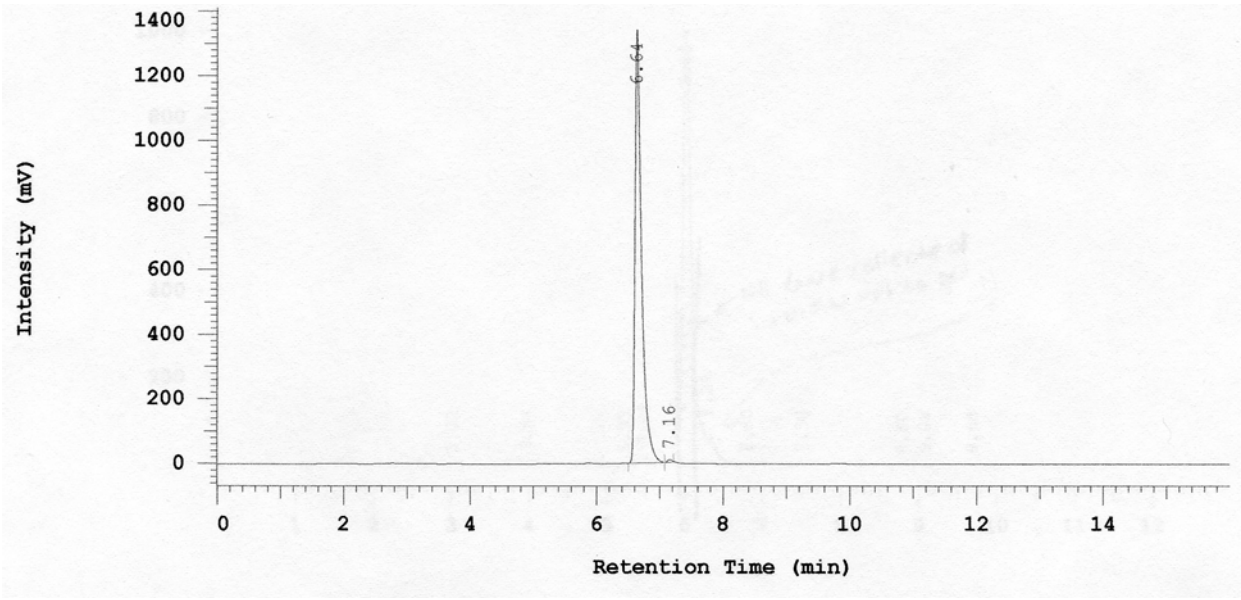

Cold Indium(III) analogue of probe 19

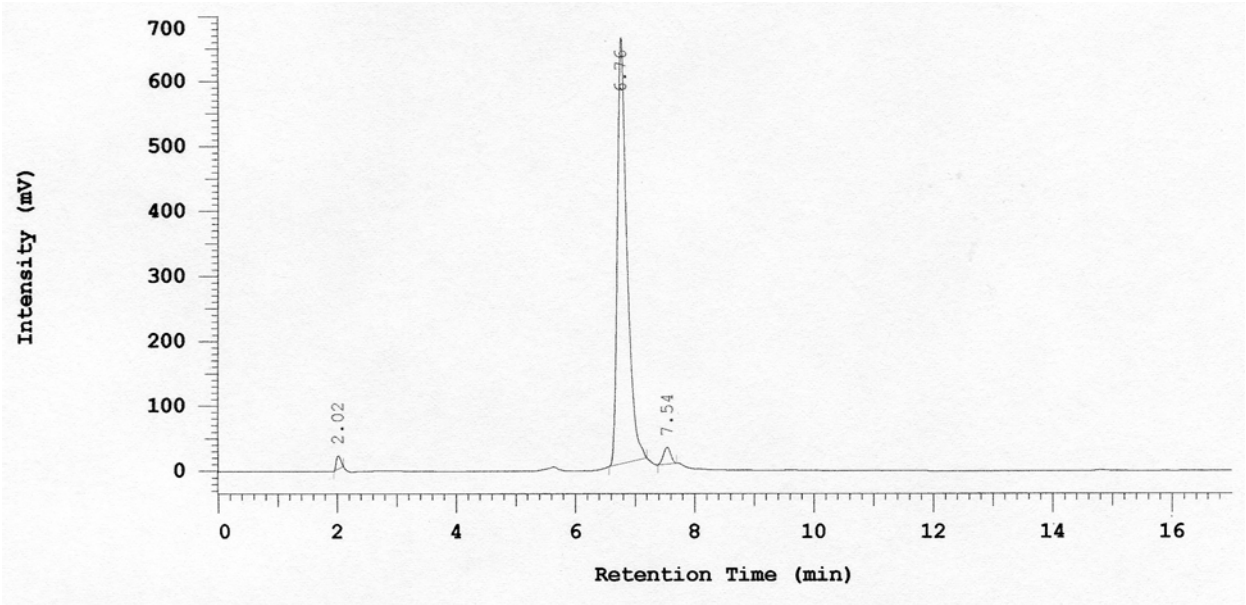

4. IN VITRO EXPERIMENTS

4.1. IC50 Determination of NIRF Probe 12, cold Gallium Analogue of Derivative of 14 and F-19 Analogue of PET Probe 20

The IC50 of NIRF probe **12** and cold Gallium analogue of derivative of **14** as well as the F-19 analogue of PET probe **20** were determined according to the method described by Westerhof et al.[1,2] with slight modifications.[3] Briefly, FR–positive KB cells were gently trypsinized in 0.25% trypsin in phosphate-buffered saline (PBS) at 37°C for 3 min and then diluted in FFRPMI containing 10% heat-inactivated fetal calf serum. After a 3-min 300 *g* spin and one PBS wash, the final cell pellet was suspended in FFRPMI 1640 (no serum). Cells were incubated for 15 min on ice with 20 nM of 3H-folic acid in the absence and presence of increasing concentrations [5E-6 to 5E-12 M final] of the test compounds. Samples were centrifuged at 800 *g* for 10 min; cell pellets were suspended in PBS, transferred to individual vials containing 4 mL of scintillation cocktail, and then counted for radioactivity. Negative control tubes contained only the ^{3}H-folic acid in FFRPMI (no competitor). Positive control tubes contained a final concentration of 1 mM folic acid, and counts per minute (cpm) measured in these samples (representing nonspecific binding of label) were subtracted from all samples. All measurements were performed in triplicates. Notably, IC50 values were defined as the concentration of competing ligand which displaces 50% of the specific binding of the radioligand, ^{3}H-folic acid bound to the FR on KB cells.

[1] G. R. Westerhof et al.*Cancer Res.* **1995,** *55*, 3795-3802.
[2] G. R. Westerhof et al. *Mol. Pharmacol.* **1995,** *48*, 459-471.
[3] For details see also : T. Ross et al *Bioconj. Chem.* **2008**, *19*, 2462.

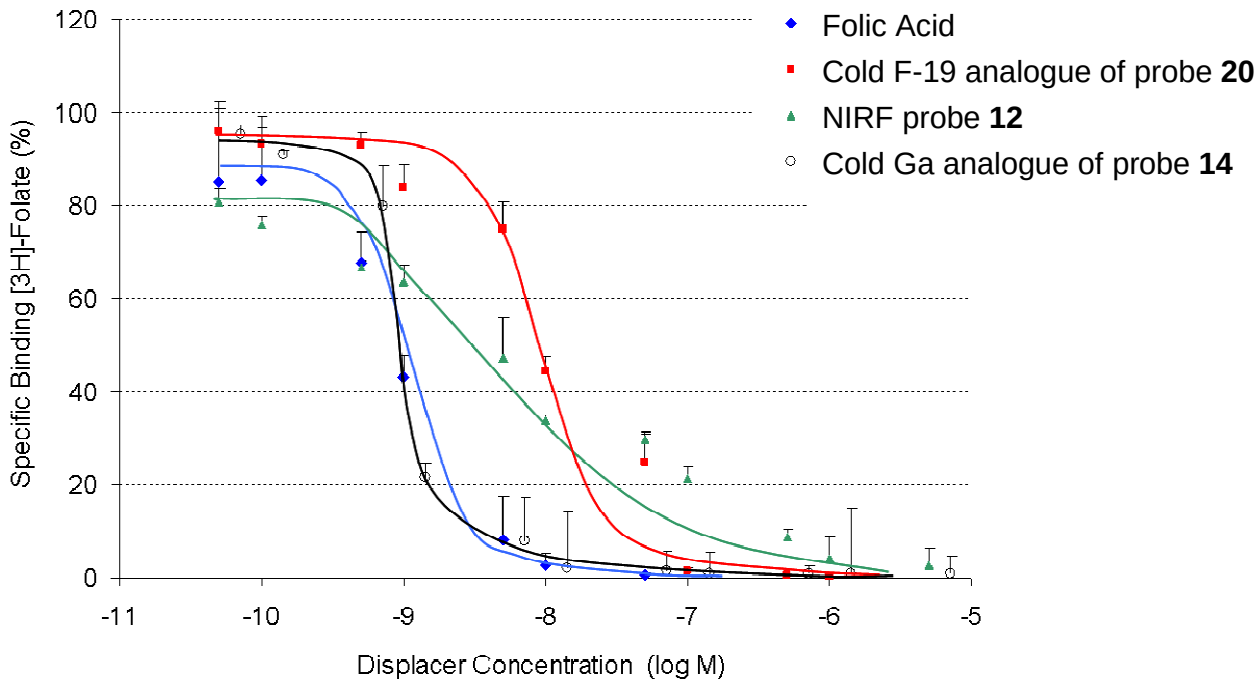

Figure S1. Competitive blocking of ^{3}H-folic acid binding to KB cells with test compounds and native folic acid (reference). KB cells were incubated for 15 min on ice with 20 nmol/L ^{3}H-folic acid in the presence and absence of increasing concentrations of the test compounds. Error bars represent 1 SD (*n* =3).

Folate conjugates are typically analyzed using an in vitro relative affinity assay that measures a ligand's ability to directly compete with folic acid for binding to cell surface FRs. Thus, ^{3}H-folic acid is used as the radioligand, whereas unlabeled folic acid serves as the reference compound. We have previously reported that the cold F-19 analogue of PET probe **20** has an IC50 value of 18.0 ± 7.1 nM.[3] As shown in Figure S1, NIRF probe **12** and the cold Gallium analogue of derivative **14**, were determined to have an IC50 value of 12.3 nM and 1.6 nM, respectively. Although binding affinity of the cold F-19 analogue of PET probe **20** and NIRF probe **12** for the FR is lower compared to that of folic acid (IC50 = 1.12 ± 0.44 nM), all new agents are considered to be a high-binding ligand for the FR (consistent with in vivo findings).

4.2. Cell Internalization Studies of SPECT Probes 15 and 19

Eighteen hours prior to the experiment, the KB cells were seeded in 12-well plates (7.5×10^5 cells/well) to form confluent monolayers overnight. The experiments were performed in triplicate. Cell binding experiments of the radiofolates **15**[4] and **19** were performed according to the following procedure: Cell monolayers were rinsed twice with PBS (pH 7.4). Pure FFRPMI medium (without FCS/L-glutamine/antibiotics, 975 μL) was added into each well. Blocking studies were performed with FFRPMI medium (475 mL) and a folic acid solution (200 μM, 500 μL). The well plates were pre-incubated at 37°C for 40 min. A solution of the corresponding radiotracer (25 μL, 1.5 MBq/mL) was added, and the well plates were incubated for 1 h at 37°C. Then, the monolayers were washed several times: radioactivity counted in samples washed with only PBS (pH 7.4) could be ascribed to the sum of FR-bound radiotracer on the cell surface and the internalized fraction. Cell samples washed with stripping buffer (an aqueous solution of 0.1 M acetic acid and 0.15 M NaCl, pH 3) in order to release radiotracers from FRs on the cell surface enabled determination of the internalized fraction of radioactivity. The monolayers were lysed in 1 N NaOH (1 mL), transferred into 4 mL-tubes, and homogenized by vortex. The radioactivity of each sample was measured with a γ-counter. The concentration of proteins was determined for each sample in order to normalize measured radioactivity of the samples with respect to the averaged sample protein content. The raw data were converted from counts per minute (cpm) into percentage of total radioactivity added.

In vitro cell binding experiments were performed with ^{111}In labelled compounds **15** and **19**. For both SPECT probes, a cell uptake of approximately 50% of total added radioactivity was observed of which roughly one third was found internalized. FR-specific binding of the radiofolates was proved by an experiment with excess cold folic acid that resulted in an almost

[4] C. Müller et al. *Eur. J. Nucl. Med. Mol. Im.* **2009**, on-line.

complete blockade of radiofolate uptake (<0.5% cell binding of total added radioactivity). The time-dependent experiment showed a constantly increasing cellular uptake of radiofolate 1 until steady state was reached after 2 h at 37°C. The time course of the cellular uptake of the two ^{111}In-labelled compounds was largely comparable to the results found with organometallic ^{99m}Tc radiofolates as previously reported by our group.[5]

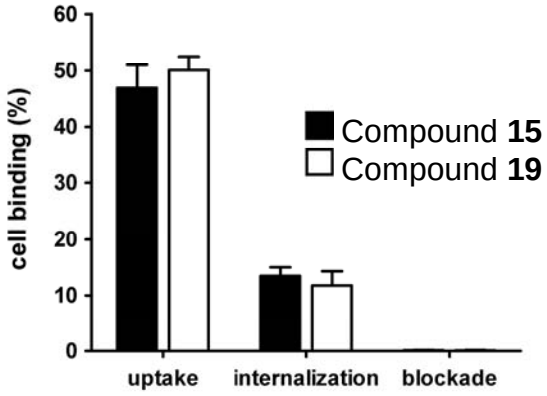

Figure S2. FR-specific internalization of radioactive probes **15** and **19** into FR-over expressing KB cells.

5. TIME-DEPENDANT IN VIVO EXPERIMENTS WITH NIRF PROBE 12

KB tumor bearing Balb/c mice were divided in 3 groups. Animals of group 1 received 2 nmol of the NIRF tracer **12**, group 2 received 2 nmol Cy5.5-CO_2H (Scheme S3) and group 3 was co-injected with the NIRF tracer **12** (2 nmol) and free folic acid (600nmol) to test for competitive inhibition. For all groups NIRF imaging was performed 10-12 days after tumor inoculation and prior (-1h) and 1, 5, 24, 48 h after intravenous injection of the respective dye. Additionally animals from group 1 and 2 were measured 120 h after tracer administration.

[5] C. Müller et al. *Eur. J. Nucl. Med. Mol. Im.* **2006**, *33*, 1007.

NIRF imaging was carried out on a time-domain in vivo small animal fluorescence imager, eXplore Optix (ART Advanced Research Technologies, Montreal, Canada) equipped with a pulsed laser diode at 666 nm as light source. The fluorescent light emitted from the sample (mouse) was detected by photomultiplier tube (PMT) coupled with a time correlated single-photon-counting system. A combination of filters was installed for optimal Cy5.5 fluorescence measurement. Exposure time was set to 0.5-2 s per scanned image point, and the rectangular region of interest (ROI) was manually placed within the visible tumor margins. The maximum excitation power (10-35μW) was set at 80% of the PMT saturation limit which was measured within the ROI. Images were analyzed using a program written in MATLAB (MathWorks, Natick, US) where the ROI within the tumor region is placed manually. The mean fluorescence intensity of the tumor area above a certain threshold (applied to all images) was calculated for each animal. The fluorescence intensity data are presented as mean and standard error of the mean (SEM). Statictical analysis was performed using OriginPro 8.0 (Origin Lab corporation, Northampton, US).

In mice bearing KB tumors fluorescence intensity can be detected at the first measurement time-point 1h after administration of the NIRF tracer **12** at a dose of 2 nmol. Time-course analysis shows that signal intensity peaked at 1h post injection and decreased over the duration of the experiment. A similar time course can be observed in mice which were injected with the control dye Cy5.5-CO_2H (Figure S3). However a clear difference is observed between NIRF tracer **12** and the control tracer Cy5.5-CO_2H at time point 1h as demonstrated for representative animals of the two groups (Figure S4). Signal intensity in group 1 was significantly higher ($p<0.05$, two-sample t-test) compared to group 2. Albeit not significant a clear reduction in signal intensity can be measured after co-injection of NIRF tracer **12** with excessive folic acid indicating competitive uptake and hence specificity of the synthetic NIRF tracer **12**. Both Cy5.5-CO_2H and NIRF tracer

12 show a transient pattern reaching signal intensity values at around 20% of maximum peak intensity after 120 h.

The data obtained is in good agreement with results published by Moon et al investigating a structurally different folate-based NIRF probe.[6]

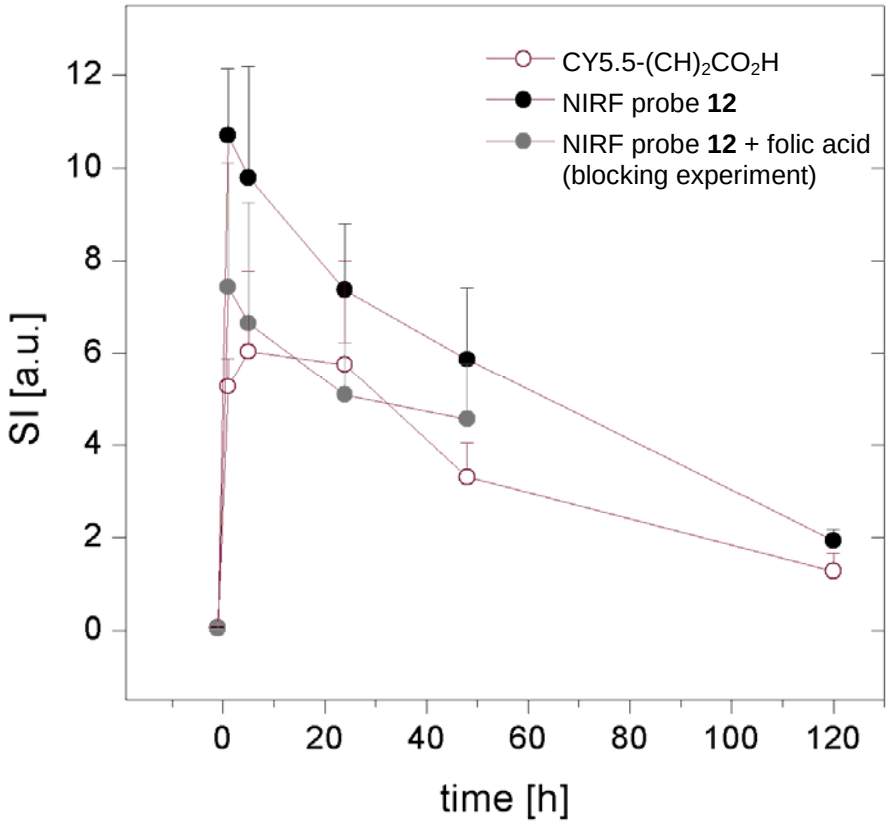

Figure S3. Time course of fluorescent signal intensities derived from ROI in KB tumors prior and after systemic administration of various probes. Signal intensities are given in arbitrary units (a.u.) plotted as mean±SEM for all three groups: NIRF tracer **12**, Cy5.5-CO_2H as control dye and the NIRF tracer **12** co-injected with folic acid (blocking experiment).

[6] W. K. Moon et al. *Bioconjugate Chem* **2003**, *14*, 539.

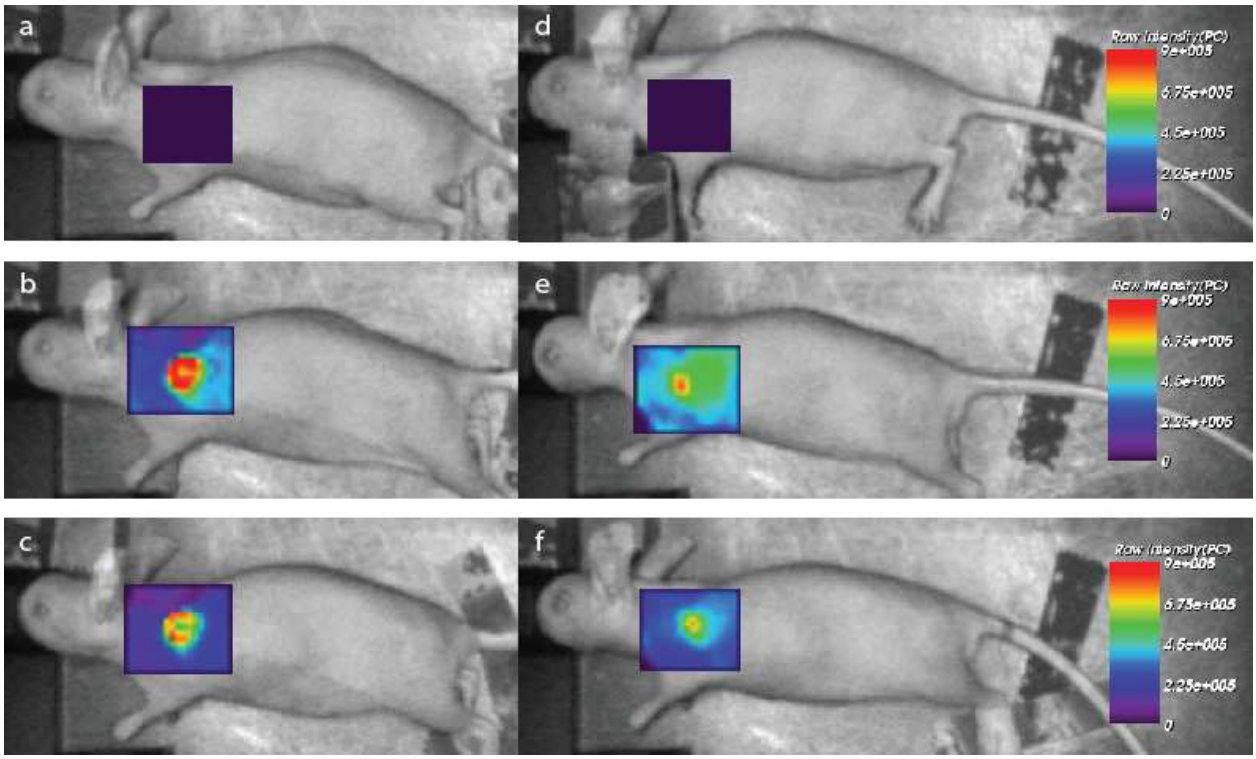

Figure S4. Representative images from KB tumor bearing mice obtained at 1 h prior (a, d) and the two first time points 1 h (b, e) and 5 h (c, f) post-injection of equal amounts of NIRF tracer **12** (left panel a-c) and Cy5.5-CO_2H (right panel d-f). Images are composed of color-coded NIRF images superimposed on white-light images.

Single-Step Conjugation of Bioactive Peptides to Proteins via a Self-Contained Succinimidyl Bis-Arylhydrazone

Joy A. Phillips,[†] Edward L. Morgan,[†] Yuxiang Dong,[‡] Garry T. Cole,[§] Cody McMahan,[§] Chiung-Yu Hung,[§] and Sam D. Sanderson*,[||]

Biosciences Center, San Diego State University, 5500 Campanile Drive, San Diego, California 92182, Department of Pharmaceutical Sciences, University of Nebraska Medical Center, 986025 Nebraska Medical Center, Omaha, Nebraska 68198-6025, Department of Biology and South Texas Center for Emerging Diseases, University of Texas at San Antonio, One UTSA Circle, San Antonio, Texas 78249-0662, and School of Allied Health Professions, University of Nebraska Medical Center, 984000 Nebraska Medical Center, Omaha, Nebraska 68190-4000. Received June 27, 2009; Revised Manuscript Received August 18, 2009

This paper describes a method for a single-step, site-specific conjugation of bioactive peptides to proteins that exploits the monitoring advantages provided by the unique UV signature absorbance of a bis-arylhydrazone. The utility of this method is demonstrated by the conjugation of a decapeptide molecular adjuvant, YSFKDMP(MeL)aR (EP67), to two test proteins, ovalbumin (OVA) and bovine serum albumin (BSA), and to proteins expressed on intact influenza virons and fungal arthroconidia (spores) of *Coccidioides*. Conjugation is accomplished with a version of EP67 in which its N-terminus is modified with succinimidyl-4-benzoylhydrazino-nicotinamide (S4BHyNic) (peptide **7**), thus enabling conjugation to these large entities via formation of amide bonds with surface-exposed amino groups. The presence of the strongly absorbing bis-arylhydrazone S4BHyNic ($\varepsilon_{354\ nm}$ = 29 000 L mol^{-1} cm^{-1}) allows for determination of EP67-to-protein molar substitution ratios (MSR), which are in good agreement with the MSRs determined by amino acid analysis. Conjugation to OVA does not compromise the ability of EP67 to engage C5a receptor bearing antigen presenting cells (APC) as measured by the EP67-mediated release of interleukin-6 (IL-6) from APCs. Mice immunized with the resulting OVA-EP67 vaccine conjugate produce high serum titers of OVA-specific IgG antibodies relative to OVA alone. Also, the conjugation of EP67 does not affect the surface integrity of influenza virons or the biological viability of *Coccidioides* spores. This method of conjugating bioactive peptides to proteins and other large biological entities may represent a convenient and effective way of generating various bioconjugates for use in mechanistic studies or novel therapeutic entities such as EP67-containing vaccines.

INTRODUCTION

Conjugation of bioactive peptides to proteins with retention of biological activity requires a method of chemoselective ligation that does not interfere with or obscure the essential topochemical features that impart biological activity to the peptide. Typically, this is achieved by first modifying the protein with a functional group that possesses reactive specificity for a complementary functional group introduced on a specific site on the peptide.

An innovative example of such chemoselective ligation is the formation of a bis-arylhydrazone linkage between a protein modified with an aromatic aldehyde (4-formyl benzoic acid) and a peptide modified with a hydrazinonicotinamide (HyNic) moiety (*1*, *2*). This method has the advantage that the resulting bis-arylhydrazone conjugate possesses a strong signature absorbance at 354 nm (ε = 29 000 L mol^{-1} cm^{-1}), which can be used to follow the course of the conjugation reaction and to determine the final peptide-to-protein molar substitution ratio (MSR). However, this conjugation method requires multiple steps, the first being modification of the protein with an excess of the OSu ester of 4-formylbenzoic (S4FB) at high pH (7.5−8.0). Unreacted S4FB is removed via dialysis and the high pH buffer is replaced with low pH buffer (4.5−6.0) for the formation of the bis-arylhydrazone linkage with the HyNic-modified peptide. Unreacted peptide is removed via dialysis and the low pH reaction buffer replaced with a more physiologically compatible buffer. The principal encumbrance of this multistep conjugation is that it presents opportunities for inadvertent loss of protein at each modification, conjugation, and buffer exchange step. Another drawback is that not all 4SFB moieties on the protein will react with the HyNic-containing peptide, leaving behind 4SFB-modified sites that could unnecessarily alter certain biological attributes of the protein such as immunogenicity.

In this paper, we describe a method of conjugating bioactive peptides to proteins that retains the chemoselective and monitoring advantages of the bis-arylhydrazone conjugation, but is accomplished in a single step. This is achieved by conjugating the intact protein with a peptide modified with a self-contained bis-arylhydrazone in the form of succinimidyl-4-benzoylhydrazino-nicotinamide (S4BHyNic). Conjugation occurs efficiently in a single step through the formation of stable amide bonds via the OSu ester on the peptide. This single-step method does not require prior modification of the protein and retains the same monitoring advantages provided by the bis-arylhydrazone in the multistep conjugation method described above.

* Corresponding author. Dr. Sam D. Sanderson, School of Allied Health Professions, 984000 Nebraska Medical Center, Omaha, NE 68198-4000, e-mail: sdsander@unmc.edu.

[†] San Diego State University.

[‡] Department of Pharmaceutical Sciences, University of Nebraska Medical Center.

[§] University of Texas at San Antonio.

[||] School of Allied Health Professions, University of Nebraska Medical Center.

10.1021/bc9002794 CCC: $40.75 © 2009 American Chemical Society
Published on Web 09/29/2009

Scheme 1

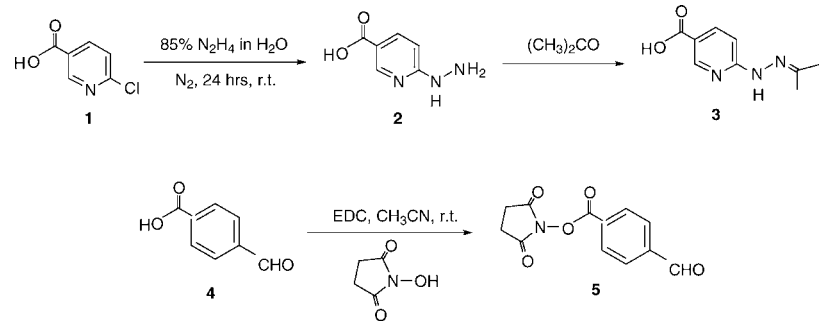

Scheme 2

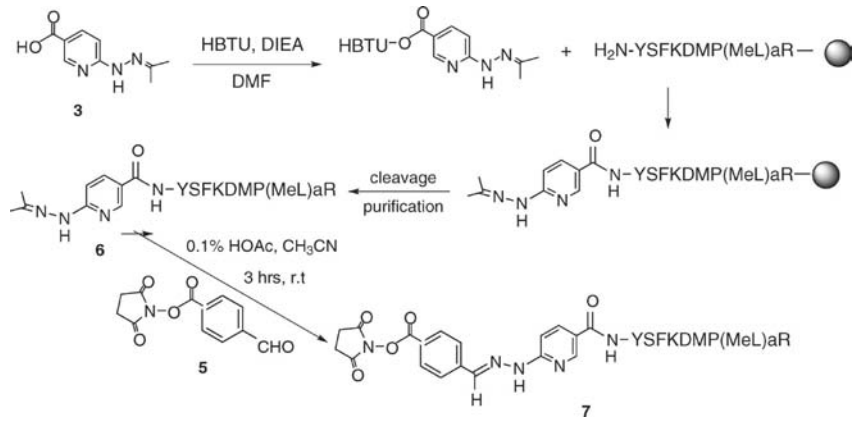

The utility of this single-step process is demonstrated by the conjugation of our molecular adjuvant EP67 (Tyr-Ser-Phe-Lys-Asp-Met-Pro-N-methylLeu-D-Ala-Arg or YSFKDMP(MeL)aR) to two test proteins ovalbumin (OVA) and bovine serum albumin (BSA) as well as with intact influenza virons and live *Coccidioides* spores. EP67 is a conformationally biased, response-selective agonist of human C5a and operates as a molecular adjuvant by targeting covalently attached antigens (Ag) to and stimulating the Ag processing and presentation capacity of antigen presenting cells (APC) via interaction with C5a receptors (C5aR) expressed on the surface of these cells (*3*−*6*).

Conjugation of EP67 to these larger molecular and biological entities is accomplished by modifying the N-terminus of EP67 with S4BHyNic, which in the presence of the selected proteins, virons, and live fungal spores, forms stable amide linkages with ε-amino groups of Lys residues on the exposed proteins. This single-step conjugation method exploits the bis-aryhydrazone signature absorbance as a convenient method of following the course of the conjugation reaction and determination of the peptide-to-protein MSR. A key feature of this method is that it allows conjugation at a specific site on EP67, the N-terminus, which leaves the biologically important C-terminal region of EP67 free to interact withC5aRs expressed on APCs.

The results presented in this paper are discussed against the backdrop of a new generation of EP67-containing vaccines in which whole intact proteins and biological entities such as viruses and live attenuated fungal spores can be used as target Ags. This not only expands the repertoire of Ags that can be used in such vaccines, but enables the EP67-activated APCs to process and present multiple epitopes within the protein(s) in the context of MHC classes I and II.

EXPERIMENTAL PROCEDURES

Reagents and General Methods. Chemicals and reagents for peptide synthesis were purchased from Sigma-Aldrich (St. Louis, MO), AAPPTEC (Louisville, KY), Creosalus (Louisville, KY), and AnaSpec (San Jose, CA). All reagents were used as supplied by the manufacturer without further purification. UV-inactivated influenza virus (A/Puerto Rico/8/34) was obtained from Charles River Laboratory. Conjugation of EP67 to live spores of *Coccidioides posadasii,* which has been designated as a select agent by the Centers for Disease Control and Prevention (http://www.selectagents.gov/agentToxinlist.htm), was performed in a certified biological safety level 3 (BSL3) laboratory at the University of Texas at San Antonio.

For protein conjugate analyses, single-wavelength absorbance measurements were obtained with a Shimadzu BioSpec-1601 spectrometer in 1.5 mL quartz cuvettes (1 cm path length). Scanning spectra for proteins, viral, and fungal conjugates were obtained using a Molecular Devices Spectra Max M2 spectrometer in 1.5 mL quartz cuvettes (1 cm path length) against a water standard.

Mice. Female C57BL/6 mice (2−3 months old) were purchased from Harlan−Sprague−Dawley and housed in the Sidney Kimmel Cancer Center (SKCC) vivarium under specific pathogen free conditions. All animal experiments were approved by the SKCC Institutional Animal Care and Use Committee (IACUC) and performed in compliance with the institute's guidelines.

Synthesis. Compounds **3** and **5** were synthesized by the reactions shown in Scheme 1 and the bis-arylhydrazone-containing peptide, S4BHyNic-YSFKDMP(MeL)aR (**7**), as shown in Scheme 2.

6-Hydrazinonicotinic Acid Acetone Hydrazone (3). 6-Chloronicotinic acid (**1**) (2.1 g, 13.3 mmol) was dissolved in 10 mL of 85% hydrazine in water and stirred overnight under a N_2 atmosphere to generate the hydrazine **2** (*7*). The reaction solution was placed on ice and cooled for several minutes and the hydrazone (**3**) precipitated by the slow addition of acetone (ca. 150 mL) with stirring. The precipitate was collected by filtration

and washed three times with dichloromethane (DCM) to remove the acetone hydrazone impurity. Yield 81%. mp 260−262 °C. ^{1}H NMR (500 MHz, DMSO-d_6) δ 1.94 (s, 3H), 1.97 (s, 3H), 7.07 (d, J = 8.8 Hz, 1H), 7.99 (d, J = 8.8 Hz, 1H), 8.60 (s, 1H), 9.89 (s, 1H) 12.55 (brs, 1H). ^{13}C NMR (125.7 MHz, DMSO-d_6) δ 17.36, 25.41, 105.62, 116.81, 138.82, 149.96, 150.49, 160.33, 166.76. $C_9H_{11}N_3O_2$, M_{calc} = 193, MH^+ = 194.08.

Succinimidyl 4-Formylbenzoate (5). 4-Formyl benzoic acid (**4**) (2.0 g, 13.3 mmol) was dissolved in acetonitrile (CH_3CN) (ca. 50 mL) along with 1.1 equiv each of *N*-hydroxysuccinimide and *N*-(3-dimethylaminopropyl)-*N*′-ethylcarbodiimide HCl (EDC) and stirred overnight at room temperature. CH_3CN was removed in vacuo and replaced by DCM (ca. 100 mL) and washed three times with water. The solution was dried over $MgSO_4$ and DCM removed in vacuo to yield **5** as a white powder. Yield 91%. mp 173−175 °C. ^{1}H NMR (500 MHz, $CDCl_3$) δ 2.94 (s, 4H), 8.03 (d, J = 7.8 Hz, 2H), 8.31 (d, J = 7.8 Hz, 2H), 10.14 (s, 1H). ^{13}C NMR (125.7 MHz, $CDCl_3$) δ 25.64, 129.70, 129.92, 131.15, 140.28, 161.02, 168.95, 191.18.

EP67 and HyNic-EP67 (6). EP67 was synthesized by standard solid-phase methods (AAPPTEC Apex 396 synthesizer) on a preloaded Arg Wang resin using the Fmoc (9-fluorenylmethoxycarbonyl) method of orthogonal synthesis with HBTU [2-(1*H*-benzotriazol-1-yl)-1,1,3,3-tetra-methyluronium hexafluorophospate]-activated esters of the amino acids. HyNic-EP67 (**6**) was generated by coupling the HBTU-activated ester of **5** to the Fmoc-deprotected and exposed N-terminus of EP67 while still attached to the Wang resin. The course of this HyNic coupling reaction was monitored by the loss of the free amine using the ninhydrin reaction.

EP67 was cleaved from the resin and side-chain protecting groups removed by stirring the peptide resin for 1.5 h at room temperature in a cleavage cocktail made of TFA (87.5%), phenol (5%), water (5%), and triisopropylsilane (2.5%). NyNic-EP67 was cleaved under identical conditions but with a cocktail made of TFA (92.5%), water (2.5%), triisopropylsilance (2.5%), and acetone (2.5%), which was added in order to generate the acetone hydrazone **6**.

EP67 and HyNic-EP67 were precipitated by the addition of cold ether (ca. 50 mL) to the cleavage cocktails and were collected by centrifugation. Peptides were purified by analytical and preparative reverse-phase HPLC on C18-bonded silica columns with a running buffer of 0.1% TFA (solvent A) and 60% CH_3CN in 0.1% TFA (solvent B) as the eluant. Peptides were characterized by confirmation of molecular mass using MALDI mass spectrometry. EP67: M_{calc} = 1240, MH^+ = 1241.3. HyNic-EP67: M_{calc} = 1604, MH^+ = 1605.2.

Succinimidyl-4-benzoylhydrazinonicotinamide-EP67 (S4B-HyNic-EP67) (7). HyNic-EP67 (**6**) (20 mg, 0.015 mmol), 1.1 equiv of S4FB (**5**), and 1.0 μL of anisole were dissolved in 15 mL of 0.1% acetic acid and CH_3CN (70:30) and stirred at room temperature for 3 h. The solution was frozen and lyophilized to yield **7** as a dry yellow powder, which was purified using the HPLC conditions described above and characterized by MALDI mass spectrometry, M_{calc} = 1603, MH^+ = 1604.4.

Conjugation of EP67 to Proteins. Conjugation of **7** to proteins was accomplished via the reaction shown in Scheme 3. BSA and OVA (ca. 5 mg) were dissolved in 1.0 mL of 0.1 M phosphate buffer pH 8.0. To these solutions was added 100 μL of a stock solution of **7** dissolved in dimethylsulfoxide (DMSO) such that at least a10-fold molar excess of **7** was introduced. The protein−peptide reaction solutions were mixed at room temperature for 2 h, after which unreacted peptide removed and buffer replaced with water by centrifugation dialysis (MW cutoff 10K).

Scheme 3

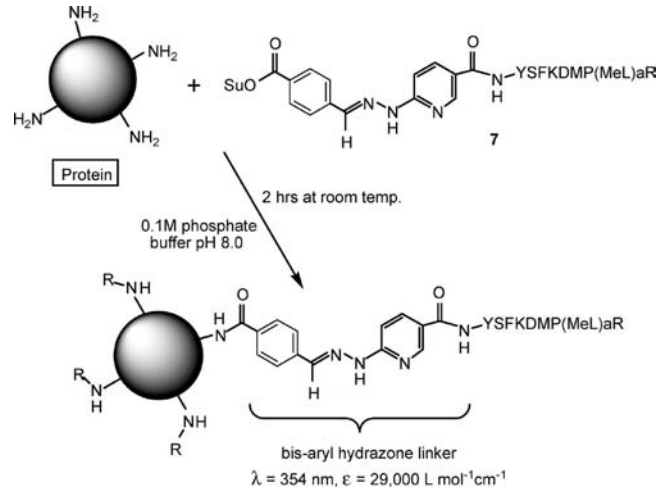

Conjugation of EP67 to Influenza. Conjugation of **7** to UV-inactivated influenza was performed under identical conditions with the 10-fold molar excess of **7** estimated from the known total protein content and composition of the virus. Unreacted peptide was removed and buffer replaced with water by centrifugation dialysis (MW cutoff 100K).

Conjugation of EP67 to Fungal Spores. Conjugation of **7** to live spores of *C. posadasii* isolated from a genetically engineered, attenuated vaccine strain (*8*) was performed by a modification of the above method. Spores were harvested from Petri plate cultures of *C. posadasii* grown on GYE medium (1% glucose, 0.5% yeast extract, 1.5% agar) after 4 weeks of incubation at 30 °C. The plates were washed and spores suspended in 0.1 M phosphate buffer, pH 8.0. The concentration of viable spores in the buffer suspension was calculated by hemocytometer counts compared to serial dilutions of the suspension to determine plate counts of colony-forming units grown on GYE medium. A stock solution of **7** dissolved in DMSO was prepared as above. Aliquots of the spore suspension, each containing 1.0×10^7 viable cells, were mixed with **7** at different concentrations (10 μg to 1000 μg) in a final volume of 1.0 mL of phosphate buffer pH 8.0. The spore suspensions were incubated for 2 h at room temperature with mild agitation and then washed twice with PBS to remove unreacted **7** and resuspended in 1.0 mL of PBS.

Determination of Molar Substitution Ratios (MSR). At the end of the 2 h conjugation reaction of **7** with OVA or BSA, 20 μL of the reaction solution was diluted with water to 1.0 mL in a quartz cuvette (1 cm path length). The concentration of the protein−**7** conjugate was determined by measuring the absorbance (A) of the bis-arylhydrazone linker at 354 nm and using Beer's law to determine final concentration: $A = \varepsilon lc$, where ε = 29 000 L mol^{-1} cm^{-1}, l = cuvette path length, and c = concentration in mol/L. MSR was determined by dividing the concentration of the bis-arylhydrazone-containing protein−peptide conjugate by the known concentration of the protein used in the conjugation reaction. MWs for OVA and BSA used in these calculations were 45 000 and 66 400, respectively.

MSR also was determined by amino acid compositional analysis, which was performed by the Protein Structure Core Facility at the University of Nebraska Medical Center using a Hitachi L-8800A amino acid analyzer. Conjugate samples were hydrolyzed for 20 h at 110 °C in 6 N HCl vapor under an argon atmosphere with 1% phenol and 0.5% sodium sulfite in the hydrolysis mix. After hydrolysis, the samples were dissolved in 200 μL of 0.02 N HCl and 50 μL was injected automatically onto the amino acid analyzer. Norleucine was added to a

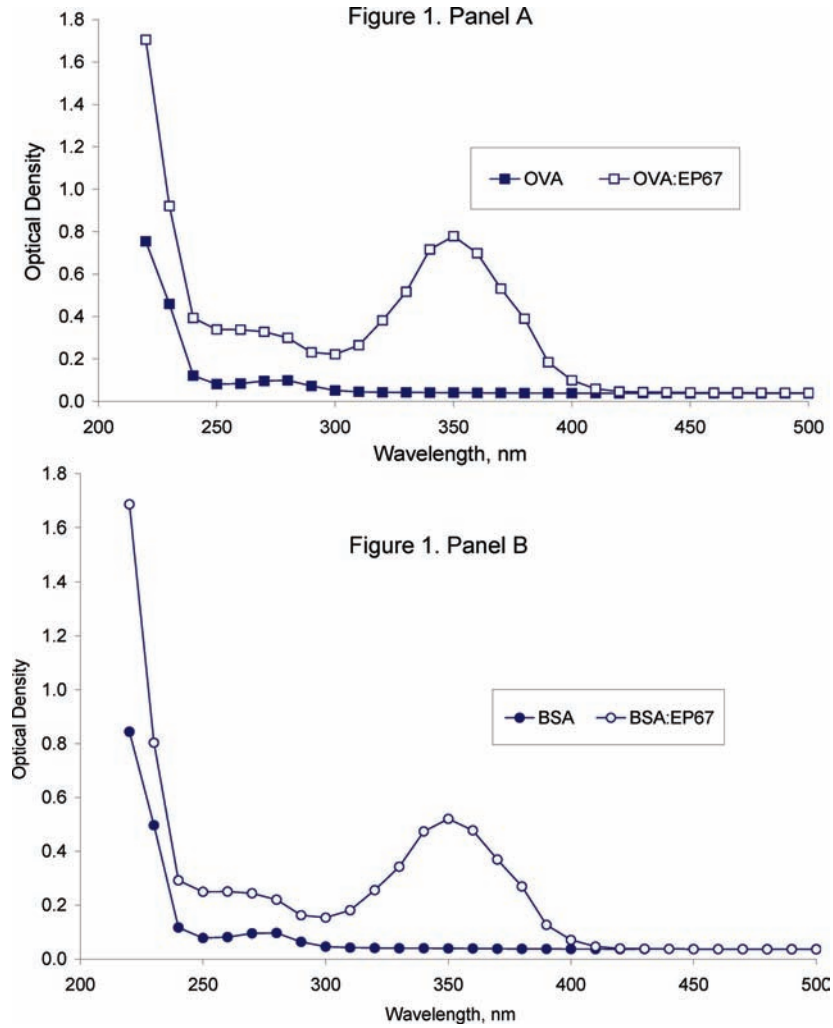

Figure 1. Panel A. Absorbance spectra of 4.3 mg OVA and OVA reacted in the presence of a 20-fold molar excess of **7** in 1.0 mL of phosphate buffer pH 8.0 for 2 h at room temperature. Spectra were generated from 20 μL of the solutions (after dialysis) diluted to 1.0 mL with water. Panel B. Absorbance spectra of 4.0 mg BSA and BSA reacted in the presence of a 20-fold molar excess of **7** in 1.0 mL of phosphate buffer pH 8.0 for 2 h at room temperature. Spectra were generated from 20 μL of the solutions (after dialysis) diluted to 1.0 mL with water.

measured amount of sample as an internal standard. Chromatographic runs were monitored at 570 and 440 nm. In data analysis, a correction was made to the amount of the internal standard, thus minimizing dilutional errors.

Post-Conjugation Determination of EP67 Biologic Activity. Prior to assaying for biological activity in vitro or in vivo, the OVA-EP67 conjugates were depleted of any potentially interfering endotoxin by utilizing an AffinityPak Detoxi-Gel endotoxin removal kit (ThermoScientific, Rockford, IL) according to the manufacturer's instructions. Retention of biologic activity of EP67 after its conjugation to OVA was assessed by measurement of the EP67-medated release of interleukin-6 (IL-6) from C5aR-bearing APCs derived from the spleens of C57BL/6 mice. Spleen cells were cultured for 48 h in the presence of EP67 or OVA-EP67, supernatants collected, and assayed for the presence IL-6 by a sandwich ELISA as described previously (*9*).

Immunologic activity of the OVA-EP67 conjugate vaccine was assessed by measuring the titers of OVA-specific antibodies (Ab) in the sera of C57BL/6 mice immunized with the OVA-EP67 construct. Mice were immunized by intraperitoneal injection of 100 μg (100 μL) of OVA-EP67 on day 0 and bled on day 21. Anti-OVA Ab titers (total IgG) were measured by a direct ELISA as previously described (*10*).

Electron Microscopy. Viral particles were negatively stained with a mixture of uranyl acetate and methyl cellulose (25 cPs, Sigma M-6385) in water at a final concentration of 1.3% each for 10 min at room temperature. Images were obtained with a Morgagni 268D electron microscope equipped with a MegaView III digital camera at 100 kV.

Viability and Immunofluorescence. Serial dilutions of known number of spores incubated with different initial concentrations of **7** as described above, or spores incubated in buffer alone, were plated on GYE medium and the numbers of CFUs were determined. The percent spore viability was calculated as CFUs of EP67-conjugated spores/CFUs of non-conjugated spores X 100.

For immunofluorescence studies, the EP67-conjugated spores (reacted with 1000 μg of **7**/mL in phosphate buffer) and nonconjugated spores incubated as described above. The cells were subsequently fixed with 1% paraformaldehyde for 15 min at room temperature, washed with PBS, blocked with10% fetal bovine serum at 4 °C overnight, and then incubated with rabbit anti-EP67 Ab followed by fluorescein isothiocyanate (FITC)-labeled goat antirabbit IgG. The cells were examined with a Leica DM6000 fluorescence microscope equipped with a DFC 300FX digital camera.

RESULTS

EP67 Conjugates to OVA and BSA. A 10-fold molar excess of S4BHyNic-modified EP67 (**7**) effectively conjugates to the proteins OVA (Figure 1, panel A) and BSA (Figure 1, panel

Table 1. MSR Determination of OVA-EP67 and BSA-EP67 Conjugates

method	MSR(OVA-EP67)	MSR(BSA-EP67)
Beer's law[a]	10	13
amino acid analysis[b]	14	19

[a] Average of 3 measurements. [b] Average of 2 measurements.

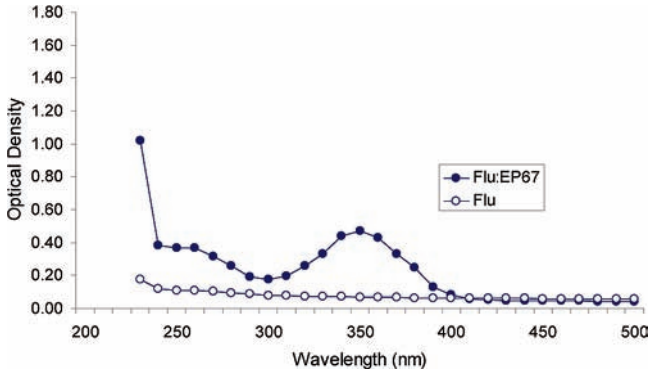

Figure 2. Absorbance spectra of intact, UV-inactivated influenza virons equivalent to 1.7 mg of protein in the presence of an approximate 20-fold molar excess of **7** in 1.5 mL phosphate buffer pH 8.0 for 3 h at room temperature. The spectrum was generated from 50 μL of the reaction solution (after dialysis) diluted to 1.0 mL with water.

B) in 0.1 M phosphate buffer pH 8.0 after a 2 h reaction as indicated by the increased absorbance at 354 nm from the bis-arylhydrazone on the peptide. MSRs determined by Beer's law are in good agreement with those determined by amino acid analysis of the conjugates (Table 1). Neither total absorbance at 354 nm nor MSR (as determined by Beer's law) were changed significantly by reaction with a 20-fold molar excess of **7** or increased reaction time up to 16 h (data not shown). Conjugation of **7** to protein appears to go to completion, since eluents obtained from dialysis of the reaction mixtures were free of **7** as indicated by a lack of ninhydrin-detectable amino groups from the available Lys in EP67.

EP67 Conjugates to Intact Influenza. An absorbance peak at 354 nm is observed after reaction of **7** with intact UV-inactivated influenza for 2 h in 0.1 M phosphate buffer pH 8.0 (Figure 2). Electron micrographs of the influenza virus are shown in Figure 3 prior to (Panel A) and after (Panel B) conjugation of **7**. A comparison of these electron micrographs shows that the conjugation process does not appear to alter overall viral structure.

EP67 Conjugates to Live Spores of Coccidioides. Figure 4 shows an absorbance peak at 354 nm after reaction of 10^7 viable spores of *C. posadasii* with 1000 μg/mL of **7** in 0.1 M phosphate buffer pH 8.0 for 2 h at room temperature, stored at 4 °C for 24 h, and followed by incubation at room temperature for an additional period of 4 h. The absorbance peak at 354 nm increased with higher concentrations of **7** added to equal numbers of spores of *C. posadasii* with a maximum being obtained at 1000 μg/mL of **7**. Determination of the CFUs of spore suspensions incubated with different concentrations of **7** revealed no statistically significant difference between the viability of EP67-conjugated and nonconjugated cells (Figure 5, Student's t test, $P < 0.05$).

Immunofluorescence microscopy of EP67-conjugated spores (Figure 6, Panel A) and EP67-conjugated spores incubated with primary rabbit anti-EP67 antiserum followed by secondary FITC-labeled goat antirabbit IgG clearly show the presence of EP67 on the surface of the live fungal cells (Figure 6, Panel B). The spores were universally labeled, although they displayed variable levels of fluorescence intensity. Spores that were not conjugated with EP67 but were incubated with both the primary and secondary FITC-conjugated Ab, showed an absence of the fluorescent label (Figure 6, Panels C and D).

S4B-HyNic-EP67 (*7*) is not Self-Reactive. Conjugation of **7** to proteins is accomplished via amide bond formation between the activated OSu ester of **7** with ε-amino groups on the side chains of Lys residues on the protein surface. Because a potentially reactive ε-amino group is also available from the lone Lys residue in EP67, the possibilities of self-reactivity cannot be ignored. Thus, to determine whether the OSu-activated ester of the bis-arylhydrozone moiety of one EP67 peptide can react with the free ε-amino group on the Lys side chain of another EP67, 2.1 mg of **7** was dissolved in 1 mL of 0.1 M phosphate buffer pH 8.0 and mixed at room temperature for 2.5 h. The concentration of the ε-amino group contributed by EP67 was determined with a quantitative ninhydrin reaction as previously described (*11*). The concentration of free ε-NH_2 was 1.13×10^{-6} M after 5 min and 1.10×10^{-6} M after 2.5 h, indicating negligible self-reactivity under the conditions used in the conjugation reactions described above.

Conjugation of EP67 to OVA Does Not Interfere with EP67 Activity. Conjugation of the small decapeptide, EP67, to a whole protein raises the possibilities that the bulk introduced by the protein may sterically hinder the biologically important C-terminal region of EP67 from interacting with C5aRs on APCs. To assess for this possibility, OVA-EP67 constructs were evaluated for the EP67-mediated release of IL-6 from C5aR-bearing splenic APCs obtained from C57BL/6 mice. The OVA-EP67 conjugate effectively engages C5aR-bearing APCs to induce the release of IL-6 relative to OVA alone (Table 2).

To further demonstrate that EP67 activity is unaffected by conjugation to a large protein, C57BL/6 mice were immunized once either with OVA alone or with an OVA-EP67 conjugate vaccine, and the postinjection Ab titers were measured 21 days later by direct ELISA. As shown in Table 3, mice immunized with OVA-EP67 showed a significantly greater anti-OVA Ab response than mice immunized with OVA alone. These results indicate that the EP67 moiety of these conjugates retains biological activity in vivo.

DISCUSSION

This paper describes a convenient method for the single-step conjugation of bioactive peptides to proteins, viruses, and live fungal cells via formation of stable amide bonds with a peptide modified at a specific site with S4BHyNic. The presence of the bis-arylhydrazone moiety in the conjugation linkage provides a unique UV signature for monitoring/verifying the conjugation reaction and determining the final peptide-to-protein molar substitution ratio. An important benefit of this method is that it enables conjugation via a site chosen on the peptide that will not interfere with topochemical features required for biological activity. This is readily accomplished by first modifying a specific amino group on the peptide with the HBTU-activated ester of HyNic (**3**) while attached to the solid-phase resin. The HyNic-modified peptide is cleaved from the resin, purified, and then used in the solution-phase formation of the bis-arylhydrazone by reaction with OSu4FB (**5**). The resulting S4BHyNic-modified peptide (**7**) now can be conjugated to intact proteins in a single step via formation of amide linkages with ε-amino groups on the protein surface.

An important advantage of this single-step method is that it does not require the prior modification of the protein in order to achieve the chemoselective ligation with the peptide. Thus, there are fewer chances for the inadvertent and irreversible modification of important biologic or immunologic features on the protein. Also, since conjugation is accomplished in a single step, there are fewer chances of protein loss.

The applicability of this single-step chemoselective ligation is demonstrated by the successful conjugation of the im-

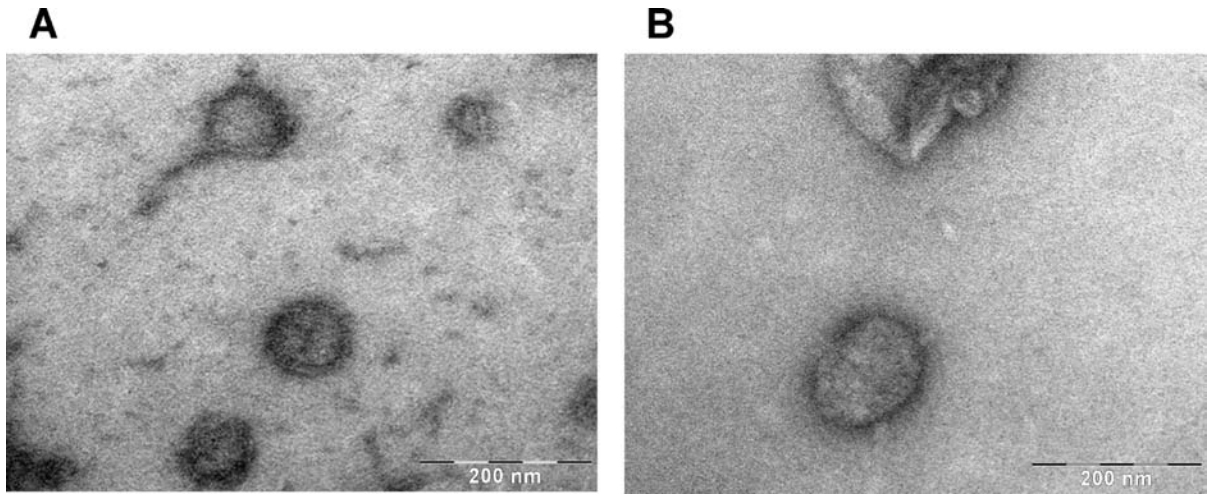

Figure 3. Scanning electron micrograph of intact, UV-inactivated influenza virons before (Panel A) and after (Panel B) conjugation with **7**.

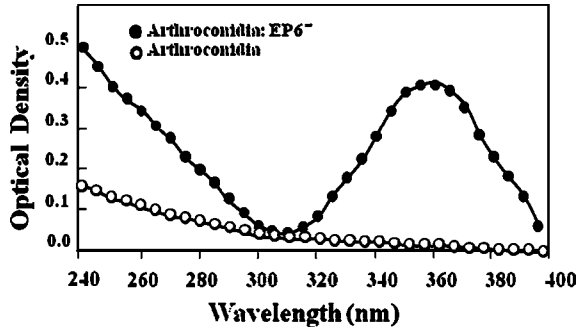

Figure 4. Absorbance spectra of arthroconidia (10^7 viable cells) incubated with **7** (1000 μg/mL) in 0.1 M phosphate buffer pH 8.0 for 2 h at room temperature (closed circles) and arthroconidia (10^7 viable cells) only (open circles).

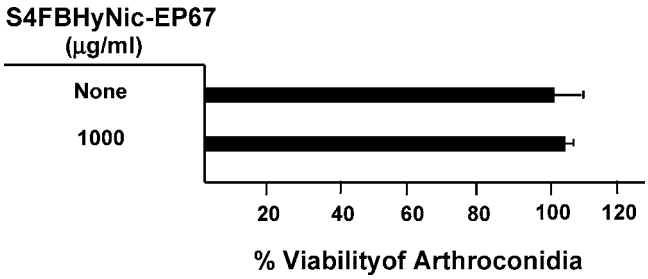

Figure 5. Arthroconidia of *C. posadasii* (isolate C735) grown on GYE plate cultures for 4 weeks at 30 °C, harvested in PBS (ca. 10^7 cells), incubated for 2 h with and without 1000 μg/mL of **7** at room temperature, and assessed for viability.

munologically active decapeptide EP67 to proteins, influenza virons, and *Coccidioides* spores. EP67 is a conformationally biased, response-selective agonist of complement component C5a. The unique conformational features biased in EP67 are well-accommodated by C5aRs expressed on APCs, but not on inflammatory neutrophils (*3*−*5*). Thus, EP67 has the ability to induce C5a-like immune stimulatory responses via engagement of C5aR-bearing APCs at the expense of C5a-like inflammatory responses via engagement of C5aR-bearing neutrophils.

We have used EP67 (YSFKDMP(MeL)aR) and an earlier sister analogue EP54 (YSFKPMPLaR) as molecular adjuvants in peptide-based vaccines made by the covalent attachment of well-characterized peptide epitopes to their N-termini. The EP67/EP54 moiety targets the attached epitope to and simultaneously activates C5aR-bearing APCs such that the Ag processing and presentation capacity of the APC is enhanced (*6*). Immunization with these EP67/EP54-containing vaccines in the absence of added adjuvants results in robust Ag-specific humoral and/or cell-mediated immune outcomes with no discernible inflammatory side effects (*10, 12*−*16*). However, these adjuvant activities of EP67/EP54 are abrogated if the C-terminal carboxyl group is blocked (*10, 12*), which underscores the necessity of chemoselective ligation via the N-terminus of EP67 if proteins are to be used as the target Ags in protein−EP67 conjugate vaccine constructs.

The ability to effectively conjugate EP67 to proteins is significant, because until now such EP67/EP54-containing vaccines have been restricted to the use of well-characterized peptide epitopes as the target Ags. This was because the only effective way of covalently attaching the epitope to the N-terminus of EP67 was by the solid-phase synthesis of the entire eptiope-EP67 peptide. While such EP67/EP54-containing vaccines are easy to generate, their effectiveness is dependent upon an intimate knowledge of the specific immunogenic epitope(s) within a particular disease-associated protein. Typically, this information is difficult to come by and, consequently, has imposed severe limitations the broad applicability of EP67/EP54-containing vaccines.

The results presented in this paper show that EP67 retains its adjuvant activities following single-step conjugation to large immunogenic entities. The ability to conjugate EP67 to intact proteins, viruses, or live fungal spores greatly expands the repertoire of Ags that can now be used in such molecular adjuvant-containing vaccines. The entire immunogenic entity can now be used as the target Ag with *all* potential immunoreactive epitopes contained therein available for processing and presentation by the EP67-activated APCs.

Results presented in this study indicate that the bulk contributed by the protein (OVA) does not interfere with the ability of EP67 to engage C5aR-bearing APCs. It is not know whether this will hold true for all possible EP67-containing vaccine conjugates. However, should the bulk contributed by other large target Ag entites interfere with the ability of EP67 to engage C5aR-bearing APCs, it is a straightforward synthetic process to introduce a variety of spacers between the bis-arylhydrazone moiety and EP67 to more effectively expose the C-terminal region of EP67 for C5aR interactions.

Also encouraging was the observation of negligible self-reactivity between S4BHyNic-modified EP67 peptides. This can be explained by a general inaccessibility of the ε-amino group on the Lys side chain of one EP67 to the reactive S4HyNic moiety on the N-terminus of another. Such inaccessibility may be due to the conformational constraints imposed on the EP67

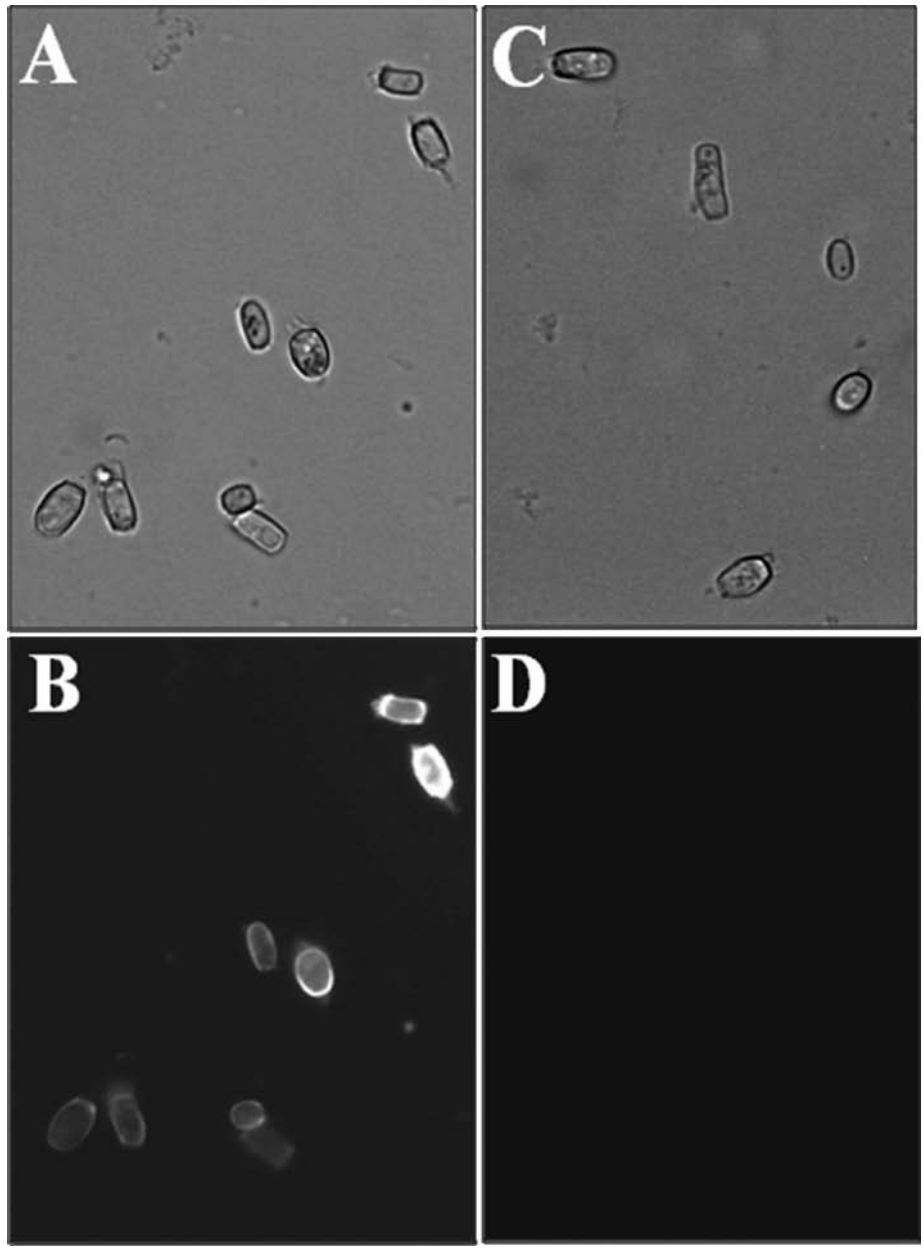

Figure 6. Arthroconidia of *C. posadasii* (isolate C735) grown on GYE plate cultures for 4 weeks at 30 °C. Panel A: Cells (ca. 10^7) incubated with **7** (1000 μg/mL) for 2 h at room temperature in 0.1 M phosphate buffer pH 8.0, washed with PBS, fixed with 1% paraformaldehyde, washed with PBS, and blocked with 10% FBS overnight at 4 °C. Panel B: Cells from Panel A incubated with rabbit anti-EP67 followed by incubation with FITC-labeled goat antirabbit IgG and examined by fluorescence microscopy. Control cells (Panels C and D) were not incubated with **7**, but were otherwise prepared and examined as in Panels A and B.

Table 2. EP67-Induced IL-6 Production

activator	μg/mL	IL-6 (pg/mL ± S.D.)
none	0	125 ± 7
OVA-EP67	500	420 ± 11
OVA	500	200 ± 3

Table 3. EP67-Induced Enhancement of Anti-OVA IgG Responses in C57BL/6 Mice

activator	IgG (OD ± SEM)[a]
OVA	0.064 ± 0.002
OVA-EP67	0.306 ± 0.013[b]

[a] 1:1000 dilution. [b] $p < 0.05$, using a single-tailed *t*-test.

backbone and resulting topographic masking of this side chain along with the likelihood of a salt bridge between the side-chain carboxyl moiety of the adjacent Asp residue (*3, 5*).

Finally, it is worth noting that the immunogenicity of the target Ag does not appear to be affected by the conjugation of EP67. This is supported by the robust humoral response seen in mice vaccinated with OVA-EP67. Serum titers of anti-OVA Abs were significantly higher in mice immunized with OVA-EP67 than mice immunized with OVA alone. Immune outcomes of the influenza virus-EP67 vaccine and the live attenuated fungal spore-EP67 vaccine are currently being evaluated in our laboratories.

ACKNOWLEDGMENT

This project was supported in part by NIH grants AI065712 and AG031496 (JP), AI071118 (GTC), and pilot project funding form the School of Allied Health Professions at the University of Nebraska Medical Center. We would like to thank Halina Witkiewicz and Elisabeth Stein of the Sidney Kimmel Cancer Center for their expert assistance in electron microscopy and

cytokine-specific ELISA analysis, respectively. We also acknowledge the assistance of the Protein Structure Core Laboratory at the University of Nebraska Medical Center for mass spectrometry and amino acid analyses.

LITERATURE CITED

(1) Schwartz, D. A., Abrams, M. J., Hauser, M. M., Gaul, F. E., Larsen, S. K., Rauh, D., and Zubieta, J. A. (1991) Preparation of hydrazino-modified proteins and their use for the synthesis of technietium-99m protein conjugates. *Bioconjugate Chem. 2*, 333–338.

(2) Miranda-Olvera, A. D., Ferro-Flores, G., Pedraza-Lopez, M., Arteaga de Murphy, C., and De Leon-Rodriguez, L. M. (2007) Synthesis of oxytocin HYNIC derivatives as potential diagnostic agents for breast cancer. *Bioconjugate Chem. 18*, 1560–1567.

(3) Taylor, S. M., Sherman, S. A., Kirnarsky, L., and Sanderson, S. D. (2001) Development of response-selective agonists of human C5a anaphylatoxin: conformational, biological, and therapeutic considerations. *Curr. Med. Chem. 8*, 675–684.

(4) Short, A. J., Paczkowski, N. J., Vogen, S. M., Sanderson, S. D., and Taylor, S. M. (1999) Response-selective C5a agonists: differential effects on neutropenia and hypertension in the rat. *Br. J. Pharmacol. 128*, 511–514.

(5) Vogen, S. M., Paczkowski, N. J., Kirnarsky, L., Short, A., Whitmore, J. B., Sherman, S. A., Taylor, S. M., and Sanderson, S. D. (2001) Differential activities of decapeptide agonists of human C5a: the conformational effects of backbone N-methylation. *Int. Immunopharmacol. 1*, 2151–2162.

(6) Hegde, G. V., Meyers-Clark, E., Joshi, S. S., and Sanderson, S. D. (2008) A conformationally-biased, response-selective agonist of C5a acts as a molecular adjuvant by modulating antigen processing and presentation activities of human dendritic cells. *Int. Immunopharmacol. 8*, 819–827.

(7) Bao, T., Bai, Y., Chang, Y., Chen, S., and Li, Z. (2007) Technetium-99m-labeling and synthesis of thydmidine analogs: potential candidates for tumor imaging. *Bioorg. Med. Chem. Lett. 17*, 3440–3444.

(8) Xue, J., Chen, X., Selby, D., Hung, C.-Y., Yu, J.-J., and Cole, G. T. (2009) A genetically engineered live attenuated vaccine of *Coccidioides posadasii* protects BALB/c mice against coccidioidomycosis. *Infect. Immun. 77*, in press.

(9) Morgan, E. L., Sanderson, S. D., Scholz, W., Noonan, D. J., Weigle, W. O., and Hugli, T. E. (1992) Identification and characterization of the effector region within human C5a responsible for stimulation of IL-6 synthesis. *J. Immunol. 148*, 3937–3942.

(10) Tempero, R. M., Hollingsworth, M. A., Burdick, M. D., Finch, A. M., Taylor, S. M., Vogen, S. M., Morgan, E. L., and Sanderson, S. D. (1997) Molecular adjuvant effects of a conformationaly biased agonist of human C5a anaphylatoxin. *J. Immunol. 158*, 1377–1382.

(11) Sarin, V. K., Kent, S. B. H., Tam, J. P., and Merrifield, R. B. (1981) Quantitative monitoring of solid phase peptide synthesis by the ninhydrin reaction. *Anal. Biochem. 117*, 147–157.

(12) Ulrich, J. T., Cieplak, W., Paczkowski, N. J., Taylor, S. M., and Sanderson, S. D. (2000) Induction of an antigen-specific CTL response by a conformationally biased agonist of human C5a anaphylatoxin as a molecular adjuvant. *J. Immunol. 164*, 5492–5498.

(13) Buchner, R., Vogen, S. M., Sanderson, S. D., Ye, R. D., and Morgan, E. L. (1997) Anti-human kappa opioid receptor antibodies: characterization of site-directed neutralizing antibodies specific for a peptide κR(33−52) derived from the predicted amino-terminal region of the human kappa receptor. *J. Immunol. 158*, 1670–1680.

(14) Sanderson, S. D., Cheruku, S. R., Padmanilayam, M. P., Vennerstrom, J. L., Thiele, G. M., Palmatier, M. I., and Bevins, R, A. (2003) Immunization to nicotine with a peptide-based vaccine composed of a conformationally biased agonist of C5a as a molecular adjuvant. *Int. Immunopharmacol. 3*, 137–146.

(15) Floreani, A. A., Gunselman, S. J., Heires, A. J., Hauke, R. J., Tarantolo, S., and Jackson, J. D. (2007) Novel C5a agonist-based dendritic cell vaccine in a murine model of melanoma. *Cell Cycle 6*, 2835–2839.

(16) Duryee, M. J., Bevins, R. A., Reichel, R. M., Murray, J. E., Dong, T., Thiele, G. M., and Sanderson, S. D. (2009) Immune responses to methamphetamine by active immunization with peptide-based, molecular adjuvant-containing vaccines. *Vaccine 27*, 2981–2988.

BC9002794

Novel Platelet Substitutes: Disk-Shaped Biodegradable Nanosheets and their Enhanced Effects on Platelet Aggregation

Yosuke Okamura,[†] Yoshihito Fukui,[†] Koki Kabata,[†] Hidenori Suzuki,[‡] Makoto Handa,[§] Yasuo Ikeda,[†] and Shinji Takeoka*[,†]

Department of Life Science and Medical Bioscience, Graduate School of Advanced Science and Engineering, Waseda University, TWIns, Tokyo, 162-8480, Japan, Center for Electron Microscopy, Tokyo Metropolitan Institute of Medical Science, Tokyo, 113-8613, Japan, and Department of Transfusion Medicine and Cell Therapy, Keio University, Tokyo, 160-8582, Japan.
Received July 23, 2009

We have studied biocompatible spherical carriers carrying a dodecapeptide, HHLGGAKQAGDV (H12), on their surface as platelet substitutes. This peptide is a fibrinogen γ-chain carboxy-terminal sequence (γ400−411) and specifically recognizes the active form of glycoprotein IIb/IIIa on activated platelets. Our purpose is to assess the possibility of making a novel platelet substitute consisting of disk-shaped nanosheets having a large contact area for the targeting site, rather than conventional small contact area spherical carriers. The H12 peptide was conjugated to the surface of the free-standing nanosheets made of biodegradable poly(D,L-lactide-*co*-glycolide) (PLGA). These H12-PLGA nanosheets were fabricated onto 3 μm disk-shaped patterned hydrophobic octadecyl regions on a SiO_2 substrate. By way of comparison, spherical H12-PLGA microparticles with the same surface area and conjugation number of H12 were also prepared. The resulting H12-PLGA nanosheets specifically interacted with the activated platelets adhered on the collagen surface at twice the rate of the H12-PLGA microparticles under flow conditions, and showed platelet thrombus formation in a two-dimensional spreading manner. Thus, H12-PLGA nanosheets might be a suitable candidate novel platelet alternative substitute for infused human platelet concentrates for the treatment of bleeding in patients with severe thrombocytopenia.

INTRODUCTION

Transfusion of platelet concentrates by blood donation is currently the only means of efficiently treating or preventing bleeding caused by quantitative platelet disorders. Particularly, the supply of platelet concentrates is always in a critical situation because of the short shelf life (4 days in Japan, 5−7 days in the United States and Europe) under stringent storage conditions. Moreover, the risk of blood-borne infections such as bacterial sepsis and acute immune reactions remains a major concern for allogeneic platelet transfusion (*1, 2*). For these reasons, a number of trials have been conducted to develop platelet substitutes (artificial platelets) reproducing platelet functions such as infusible platelet membranes (IPMs) (*3*), fibrinogen-bonded red blood cells (*4*), fibrinogen-bearing liposomes (*5*), fibrinogen-coated albumin microcapsules (Synthocyte) (*6*), and arginine-glycine-asparaginic acid (RGD) peptide-bound red blood cells (Thromboerythrocytes) (*7*). All platelet substitutes proposed so far consist of materials derived from blood components and are micrometer sized.

Glycoprotein (GP) IIb/IIIa exists on the membrane of distinctive disk-shaped platelets at the dimensions of 2.5−3.0 by 0.2−0.5 μm and changes its shape from inactive to active when platelets adhere to collagen exposed on the sites of vascular injury (*8, 9*). The activated GPIIb/IIIa acts as a receptor for bifunctional fibrinogen, which leads to platelet aggregation. Several sequences in fibrinogen have been designated as GPIIb/IIIa recognition sites: the RGD-based sequences ^{95}RGDF^{98} and ^{572}RGDS^{575} in the Aα chains and ^{400}HHLGGAKQAGDV^{411} (H12, the fibrinogen γ-chain dodecapeptide) in the carboxyl-terminal of the γ-chain (*10, 11*). We selected H12 for this study from general observations that H12 interacts with GPIIb/IIIa specifically, whereas RGD-related peptides are promiscuous for many integrins from various cell types (*12*).

Our strategy for the development of platelet substitutes has been straightforward: biocompatible spherical carriers such as phospholipid vesicles (liposomes) (*13*−*15*) and polymerized albumin particles (*16, 17*) are specifically accumulated at sites of vascular injury, and fill up the injury sites by virtue of their own mass. In order to construct carriers having a specific accumulation ability for the activated GPIIb/IIIa on the platelet, we conjugated an H12 sequence to these carriers and succeeded in the preparation of H12-conjugates, which dose-dependently reduced the bleeding time in rats or rabbits with thrombocytopenia *in vivo* (*14, 15, 18*−*20*).

Sheet-shaped carriers, having a large contact area for a targeting site, would have an ultimate advantage over spherical carriers, which have an extremely small contact area. Recently, several approaches have been implemented for fabrication of free-standing nanosheets (often called nanofilms and nanomembranes), including the use of polymers and/or inorganic materials such as cast films (*21*), layer-by-layer films of polyelectolytes (*22*−*24*), cross-linked amphiphilic Langmuir−Blodgett films (*25*), and self-assembled monolayers (SAMs) (*26*). They have been developed as applications in a variety of fields such as nanoseparation membranes, nanosensors, and functional nanofilms for electrochemical and photochemical applications. However, there have been no reports on the fabrication of free-standing nanosheets with suitable biocompatibility and biodegradability for biomedical application.

Organosilane SAMs have been widely used in applications designed to change the physical and chemical properties of the surfaces of glass, quartz, and SiO_2/Si wafers (*27*). It is generally

* To whom correspondence should be addressed. E-mail: takeoka@waseda.jp, Tel: +813-5369-7324, Fax: +813-5369-7324.
[†] Waseda University.
[‡] Tokyo Metropolitan Institute of Medical Science.
[§] Keio University.

10.1021/bc900325w CCC: $40.75 © 2009 American Chemical Society
Published on Web 09/29/2009

easy to construct patterned SAMs with uniform size and shape on SiO_2 using conventional photolithography processes (*28*). They are excellent tools for immobilization of proteins (redox proteins (*29*) and enzymes (*30*)) via covalent or noncovalent bonding with various terminal groups of the SAMs, and for two-dimensional close-packed particle array via a micromold method and lateral capillary force (*31*). Recently, we proposed a novel method for the preparation of free-standing 100 nm thick, uniformly shaped microsized nanosheets derived from polystylene nanoparticles using patterned hydrophobic SAMs on the SiO_2 substrate (*32*).

Our main purpose here was to assess the possibility of constructing disk-shaped nanosheets as a novel platelet substitute. In this study, H12 was conjugated to the surface of free-standing biodegradable poly(D,L-lactide-*co*-glycolide) (PLGA) platelet-like nanosheets (H12-PLGA nanosheets), which had been attached to a SiO_2 substrate patterned with 3 μm disk-shaped hydrophobic regions of octadecyltrimethoxysilane-SAM (ODS-SAM). Furthermore, we explore the enhanced effects on platelet thrombus formation of the H12-PLGA nanosheets in comparison with that of the H12-PLGA microparticles under flow conditions.

MATERIALS AND METHODS

Reagents. P-type Si (100) wafers (below 0.02 Ω cm) covered with thermally grown silicon oxide (approximately 200 nm) were purchased from KST World Co. (Fukui, Japan). *n*-Octadecyltrimethoxysilane (ODS, 97%) and 2-methyl[(polyethyleneoxy)propyl] trichlorosilane (Cl_3Si-mPEO, M_w: 422−558, >97%) were purchased from Gelest Inc. (Morrisville, PA). Poly(D,L-lactide-*co*-glycolide) (PLGA) (lactide/glycolide = 85:15, M_w 20 kDa) was purchased from Polysciences Inc. (Warrington, PA). Chitosan (M_w 88 kDa) and poly(vinyl alcohol) (PVA, M_w 22 kDa (99% hydrolyzed), 20 kDa (87−89% hydrolyzed)) were obtained from Nacalai Tesque, Inc. (Kyoto, Japan) and Sigma-Aldrich Co. (Saint Louis, MO), respectively. Poly(ethylene glycol), α-(3-[3-maleimido-1-oxopropyl]amino) propyl-ω-succinimidyl carboxypentyloxy poly(ethylene glycol) (MALPEG-NHS, M_w 5.0 kDa) was purchased from NOF Co. (Tokyo, Japan). Fibrinogen γ-chain dodecapeptide (C-HHLGGAKQAGDV, Cys-H12) was synthesized with a solid-phase synthesizer by BEX Co. (Tokyo). The platelet fluorescent dye 3,3′-dihexyloxacarbocyanine iodide ($DiOC_6$) and dioctadecyloxacarbocyanine perchlorate ($DiOC_{18}$), a fluorescent dye for PLGA particles, were purchased from Invitrogen Co. (Eugene, OR). Fluorescamine was purchased from Sigma-Aldrich Co.

SAM Preparation. Silicon wafers (size 3 cm × 3 cm) were treated with a piranha solution (96% H_2SO_4/30% H_2O_2 = 4:1 (v/v)) at 120 °C followed by rinsing with distilled water. The resulting wafers were placed in a 100 mL Teflon vial containing a glass cup filled with 200 μL ODS liquid. The vials were sealed with a cap and then heated for 8 h at a constant temperature of 110 °C in a glovebox to prepare a hydrophobic ODS-SAM on the silicon oxide (*33*).

Patterning Processes. The ODS/mPEO-SAM patterned with hydrophobic octadecyl regions and hydrophilic poly(ethylene oxide) regions on the substrate was prepared by conventional photolithography and chemical conjugation processes. The ODS-SAM on the silicon oxide (size 3 cm × 3 cm) was covered with photoresist (OFPR-800 500 cP, Tokyo Ohka Kogyo, Co. Ltd., Kanagawa, Japan), and was irradiated with a UV lamp (350 nm, MA-10, Mikasa Ltd., Tokyo) using a photomask (size 5 cm × 5 cm, patterning 3 μm disk, Topic Co., Ltd., Saitama, Japan). After developing (NMD-3), the substrate was exposed to an oxygen plasma (Plasma Reactor PR301, Yamato Scientific Co. Ltd., Tokyo) at an input power of 200 W and an oxygen flow rate of 80 sccm for removal of the ODS. The photoresist was removed by acetone washing, and then the patterned ODS-SAM substrate was immersed in a 2 mM solution of Cl_3Si-mPEO in toluene at r.t. for 24 h in a glovebox in order to reduce the nonspecific adsorption of the PLGA nanoparticles, as suggested in an original report by Cecchet et al. (*34*).

Preparation of PLGA Nano- and Microparticles. PLGA nanoparticles were prepared by a very successful emulsion diffusion−evaporation technique, as reported previously (*35*). The methodology in brief is described as follows. First, 200 mg of PLGA was dissolved in 10 mL ethyl acetate at r.t. The organic phase was then added to an aqueous solution (10 mL) containing 200 mg PVA (87−89% hydrolyzed) as a stabilizer and 30 mg chitosan with stirring. The emulsion was stirred at r.t. for 3 h before homogenizing at 30 000 rpm for 10−70 min (Physcotron NS-51, Microtec, Co. Ltd., Chiba, Japan). Distilled water (50 mL) was gradually added to the emulsion with stirring, and then stirring was continued in a water bath maintained at 40 °C to remove the organic solvent. The uncoated polymer reagents such as PVA and chitosan were removed by repeated centrifugation (35 000*g*, 10 min, 4 °C) and washing with phosphate buffer (PB, pH 7.4) to obtain the purified PLGA nanoparticles. The particle diameter was analyzed by a dynamic light-scattering (DLS) method (N4 PLUS; Beckman-Coulter, Fullerton, FL).

In addition, PLGA microparticles were prepared by the same technique. Two hundred milligrams of PLGA was dissolved in 10 mL methylene chloride at r.t. The organic phase was then added to an aqueous solution (10 mL) containing 200 mg PVA (87−89% hydrolyzed) and 30 mg chitosan at r.t. under 1000 rpm stirring without homogenization. Distilled water (50 mL) was gradually added to the emulsion under stirring, and then stirred at 40 °C to remove the organic solvent. The uncoated polymer reagents such as PVA and chitosan were removed by repeated centrifugation (2200*g*, 5 min, 4 °C) and washing with PB (pH 7.4) to obtain the purified PLGA microparticles.

The particle concentration was calculated from the volume ratio of the PLGA particles in the suspension as follows: the suspension was mixed with a PEG solution (M_w = 100 kDa, final concentration 25 mg/mL), inserted into a hematocrit capillary tube, and then precipitated by centrifugation (15 000*g*, 10 min, r.t.) to measure the volume ratio of PLGA particles. The particle concentration (N, particles/mL) was calculated by eq 1:

$$N = 3B/(A - B) \times 4\pi r^3 \times 10^3 \quad (1)$$

where $A(m)$, $B(m)$, and $r(m)$ were the height of the suspension surface from the bottom of the capillary tube, the height of the particle precipitate, and the particle radius, respectively.

The amino groups in the surface of the PLGA nano- and microparticles, which were derived from chitosan, were calculated from the fluorescent intensity after a fluorescamine reaction as follows: fluorescamine in acetone (0.1 M, 10 μL) was added to the PLGA particle suspension in a boracic acid buffer (pH 8.0) at a concentration of 2.0×10^{11} /mL. The same experiment was performed for the control PLGA particles (not modified with chitosan). The fluorescent intensities after incubation at r.t. for 10 min were measured (E_x = 390 nm, E_m = 475 nm) with a spectrofluorometer (FP-750, JASCO, Tokyo), and the amino groups par PLGA particle were calculated from the difference in intensities between particles before and after chitosan modification and the extrapolation of calibration was performed using a glycine solution of which concentration was varied from 0.1 to 2 μM.

The glass transition temperature (T_g) of the PLGA particles was measured by differential scanning calorimetry (DSC, Thermo plus DSC 8230, Rigaku Co., Osaka, Japan). The analysis was performed with an approximately 10 mg freeze−dried

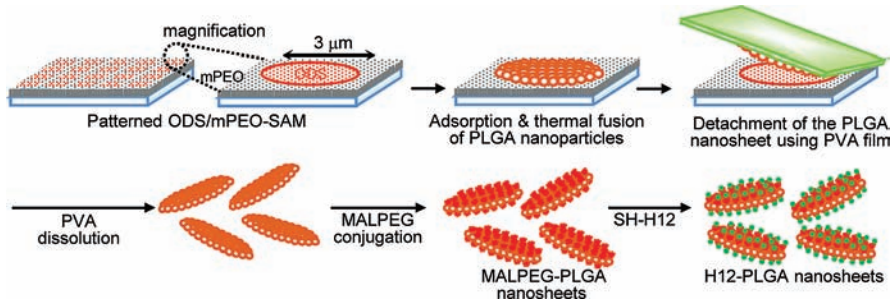

Figure 1. Preparative scheme of free-standing PLGA nanosheets carrying H12 using a patterned ODS/mPEO-SAM on a SiO_2 substrate.

sample under a dynamic nitrogen atmosphere at a heating rate of 10 °C/min.

Preparation of the Free-Standing PLGA Nanosheets Carrying H12. As shown in Figure 1, the substrate having the patterned ODS/mPEO-SAM on the surface was immersed into a PB suspension (pH 7.0) of the PLGA nanoparticles at a concentration of 1.0×10^{12} /mL. After withdrawing the substrate from the suspension, the suspension remaining on the substrate was slowly blown off with a horizontal N_2 flow in order to adsorb the PLGA nanoparticles onto the hydrophobic octadecyl patterned region, and then the substrate was immediately washed with distilled water. The operations of adsorption and washing of PLGA nanoparticles on the substrate was repeated ten times to obtain a closely packed pattern of PLGA nanoparticles. After drying the substrate under N_2 flow, it was heated at 70 °C for 2 min to initiate thermal fusion of the adsorbed PLGA nanoparticles. A PVA solution (50 mg/mL, 0.5 mL) was cast on the substrate and dried at r.t. for 15 h to make a supporting film. After peeling off the resulting PVA film, it was dissolved in a PB solution at pH 7.0, and PVA was removed by centrifugation (8000*g*, 5 min, 4 °C) to obtain a suspension of free-standing PLGA nanosheets. A solution of MALPEG in DMSO (1 mM, 100 μL) was added to the suspension and incubated at r.t. for 20 min. The unreacted MALPEG was removed by centrifugation (8000*g*, 5 min, 4 °C). Finally, the nanosheet suspension was reacted with H12 in PB (1 mM, 70 μL) at r.t. for 12 h, and the unreacted reagents were removed by repeated centrifugation (8000*g*, 5 min, 4 °C) to obtain the purified (MALPEG)PLGA nanosheets carrying H12 (H12-PLGA nanosheets).

The densities of MALPEG and H12 conjugated to the surface of the PLGA nanosheet were determined by quantifying each unreacted reagent in the supernatant of the nanosheets using high-pressure liquid chromatography (HPLC) on a TSK-GEL G3000PW_{XL} column (7.8 mm o.d. × 300 mm h using a mobile phase of 36% acetonitrile and 0.1% trifluoroacetic acid at 1 mL/min). The unreacted reagents were detected using a refractive index (RI) detector and the absorbance at 220 nm.

The concentration of PLGA nanosheets was calculated as follows. First, $DiOC_{18}$ (1 mM, 300 μL) in DMSO was added to the solution of PLGA in ethyl acetate before addition to an aqueous stabilizer as described above. After preparation of the free-standing PLGA nanosheets using $DiOC_{18}$-labeled PLGA nanoparticles, the nanosheets were dissolved in DMSO and the fluorescent intensity was measured (E_x = 485 nm, E_m = 500 nm, ARVO SX, LKB-Wallac, Bromma, Sweden). The PLGA nanosheet concentration was calculated from an extrapolation of the calibration curve of the $DiOC_{18}$-labeled PLGA nanoparticles at a concentration of 1.2×10^9 to 1.5×10^{11} /mL, assuming that the PLGA nanoparticles were arranged and closely packed as a monolayer.

The resulting nanosheets were observed with a Hitachi S-4500 field emission scanning electron microscope (SEM) as follows: the nanosheets adsorbed on a silicon substrate and the free-standing nanosheets collected on glass plate (diameter 24 mm, thickness 0.12−0.17 mm) coated with a poly(L-lysine) were coated with osmium tetroxide (thickness: ca. 20 nm) using an osmium plasma coater (NL-OPC80, Nippon Laser & Electronics Lab., Nagoya, Japan), and were observed with an SEM at an accelerating voltage of 10 kV.

Interaction of Platelets or H12-PLGA Nanosheets with the Collagen Surface Using Imitation Thrombocytopenia Blood under Flow Conditions. Imitation thrombocytopenia blood was prepared as follows. Whole blood treated with a thrombin inhibitor, D-Phe-Pro-Arg-chloromethylketone (PPACK, 40 μM), was filtered with a leukocyte removal filter (NEO1J, Nihon Poll Co., Ltd., Tokyo), which removed platelets as well as leukocytes. The residual platelet count of the filtered blood was determined to be $(6.0 \pm 2.0) \times 10^3$ /μL, and the final platelet count was adjusted to 2.0×10^4 /μL by PRP addition. This blood preparation was termed imitation thrombocytopenia blood.

Collagen I-A (3.0 mg/mL) was suspended in PBS at 4 °C (30 μg/mL), and a glass plate (diameter 24 mm, thickness 0.5 mm) was immersed into the collagen suspension at 4 °C for 8 h. The glass plate was carefully rinsed with PBS and immersed in a bovine serum albumin solution (20 mg/mL) at r.t. for 2 h before a perfusion study was performed as described below.

In the perfusion study, either platelets or H12-PLGA nanosheets were labeled with a fluorescent marker (platelets, $DiOC_6$; nanosheets, $DiOC_{18}$). The imitation thrombocytopenia blood ($2.0 \times 10^4/\mu$L) in the absence or presence of the H12-PLGA nanosheets ($2.0 \times 10^5/\mu$L) were placed in a recirculating flow chamber mounted on an epifluorescent microscope (ECLIPS TE300, Nikon, Tokyo) equipped with a CCD camera, and the interaction of the nanosheets with the collagen immobilized on the surface was observed. All perfusion studies were performed at 37 °C. Calculation of the surface coverage of platelets or the H12-PLGA nanosheets on the plates was carried out with an image processor, Argus-20 (Hamamatsu Photonics, Hamamatsu, Japan). The interaction of nanosheets with platelets was observed with an SEM as described above.

RESULTS AND DISCUSSION

Fabrication of the Free-Standing H12-PLGA Nanosheets. Fabrication of the free-standing PLGA nanosheets carrying H12 involved several sets of procedures. This section summarizes the results at each stage. The nanosheets themselves were prepared starting from unimodal PLGA nanoparticles prepared, as described above, by a combination of emulsion−diffusion−evaporation and homogenization, following the original report of Ravi-Kumar et al. (*35*). We used a blend of PVA and chitosan as a stabilizer for the PLGA nanoparticles. A recent paper indicates that PVA will remain on the surface of the nanoparticles despite repeated washing of the stabilizer because PVA forms an interconnected network with the polymer at the interface (*36*). Chitosan on the surface of the nanoparticles is

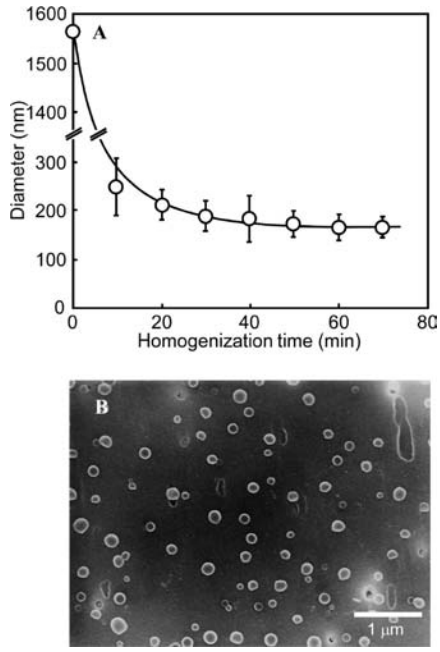

Figure 2. PLGA nanoparticles prepared by a combination of emulsion−diffusion−evaporation plus homogenization techniques. (A) Control of the diameter of the PLGA nanoparticles by the homogenization time. (B) SEM image of the resulting nanoparticles after homogenization for 60 min collected on a membrane filter (pore size: 0.05 μm).

used to conjugate various molecules to its amino groups. The concentration of the stabilizers (PVA and chitosan) has also been optimized for the smallest particle size (*35*). According to the optimum procedure, the emulsion of PLGA in the PVA−chitosan solution was stirred for 3 h at r.t. to produce particles with a diameter of 1563 ± 768 nm (Figure 2A). When the emulsion was homogenized at 30 000 rpm, the diameter decreased with increasing homogenization time and plateaued at 164 ± 26 nm at 60 min after homogenization (Figure 2A). We also confirmed that the diameter of the resulting PLGA nanoparticles was approximately 160 nm by SEM observation (Figure 2B). The amount of the amino groups introduced on the surface of the PLGA nanoparticle was quantified to be approximately 3.8×10^3 molecules, indicating that the surface of the PLGA nanoparticles was fully coated with chitosan to be conjugated H12 molecules.

Using the PLGA nanoparticles, we prepared free-standing PLGA nanosheets carrying H12 by a combination of the four processes shown in Figure 1:

1. Specific adsorption of the PLGA nanoparticles onto the disk-patterned hydrophobic ODS regions of ODS/mPEO-SAM.

2. Fabrication of PLGA nanosheets via thermal fusion of the adsorbed nanoparticles.

3. Preparation of the free-standing nanosheets by detachment from the disk-patterns using a water-soluble PVA as a sacrificial supporting film.

4. Conjugation of H12 to the surface of the nanosheets.

In the first step, a conventional dry patterning process was adopted for the specific adsorption of the PLGA nanoparticles onto the disk-patterned ODS/mPEO-SAM. When the dispersion of the nanoparticles was dropped on the substrate and the dispersion remaining on the substrate was then slowly blown off with a horizontal stream of N_2 gas, the nanoparticles were arranged as a monolayer on the entire substrate, regardless of hydrophobic or hydrophilic regions (data not shown). It is possible that assembly of the PLGA nanoparticles leads to nucleation initiated by capillary forces and growth driven by a laminar flow to evaporate water, thereby forcing the particles to arrange in a monolayer (*37*). The following immediate and repeated washings of the substrate with PB (pH 7.0) detached the PLGA nanoparticles from the hydrophilic mPEO region, leaving nanoparticles firmly adsorbed on the hydrophobic disk patterns of ODS (3 μm) via a hydrophobic interaction. In fact, the net charge of the PLGA nanoparticles at pH 7.0 was nearly zero from the ζ-potential analysis. After repeating the adsorption of the PLGA nanoparticles and washing cycle ten times, the PLGA nanoparticles were closely packed in a monolayer pattern, as shown in Figure 3A,B.

Furthermore, the substrate could be reused at least ten times by sonication in acetone and distilled water (Supporting Information Figure S1). In the case of substrates having bare SiO_2 regions (not modified with mPEO), the nanoparticles were nonspecifically adsorbed to the SiO_2 region as well as the ODS region, and the substrate could not be reused even after heavy sonication (Supporting Information Figure S2A). Using PLGA nanoparticles at 1/10th of the usual concentration (1.0×10^{11}/mL) could prevent the nonspecific adsorption. However, repeated adsorption plus washing over 60 times were required for closely packing of the PLGA nanoparticles in this case (Supporting Information Figure S2B). These results indicated that mPEO modification to the SiO_2 region contributes not only to the inhibition of nonspecific adsorption of the nanoparticles, but also to drastic shortens the preparation time.

Next, the T_g of freeze−dried PLGA nanoparticles was found to be 58.8 °C by a DSC measurement in order to set the temperature required for thermal fusion of the nanoparticles adsorbed on the disk patterns. When the nanoparticle-covered substrate was heated at 60 °C for 2 min with a hotplate, the neighboring PLGA nanoparticles were sufficiently fused to form nanosheets. Heating at 60 °C for 1 min or less was insufficient to properly fuse the particles into nanosheets. On the other hand, heating over 5 min resulted in melting and spreading of the PLGA outward from the disk patterns.

In the second step, the transference of the nanosheets to a supporting PVA film is a convenient method to obtain an aqueous dispersion of the nanosheets (*32*). In practice, the PVA solution was cast on the patterned substrate on which the nanosheets had been fabricated, and dried at r.t. for 15 h. The PVA film peeled off from the substrate was tough and transparent as shown in Figure 3C. SEM observation of the PVA film confirmed that the PLGA nanosheets were completely transferred to the PVA film, and no nanosheets were remained on the substrate (data not shown). Such complete transfer is possible because the hydrogen bonding between the PVA film and the PLGA nanosheets is stronger than the van der Waals interaction of the dried nanosheets with the CH_3-terminal ODS. These results are in agreement with the report by Stroock et al. (*38*), describing the exquisite transfer of an LbL film prepared on hydrophobic SAM patterns to a poly(acrylic acid) (PAA) film. They obtained a suspension by dispersing the PAA film in an aqueous solution. We also used this latter technique for our nanosheets, using PVA as a supporting film. In this case, we could obtain free-standing PLGA nanosheets by dissolution of the PVA film, which is readily soluble in PB at pH 7.4. The nanosheets were collected on a glass plate coated with poly(L-lysine). Thanks to efficient adsorption as a result of the electrostatic interaction, abundant nanosheets with a disk-shaped structure were observed on the plate by SEM, as shown in Figure 3D. This result confirmed that the neighboring PLGA nanoparticles had fused effectively and were sufficiently connected to retain a two-dimensional shape. Fluorescence measurements gave an estimate of approximately 1.2×10^7 nanosheets/mL for the concentration of the resulting disk-shaped nanosheets.

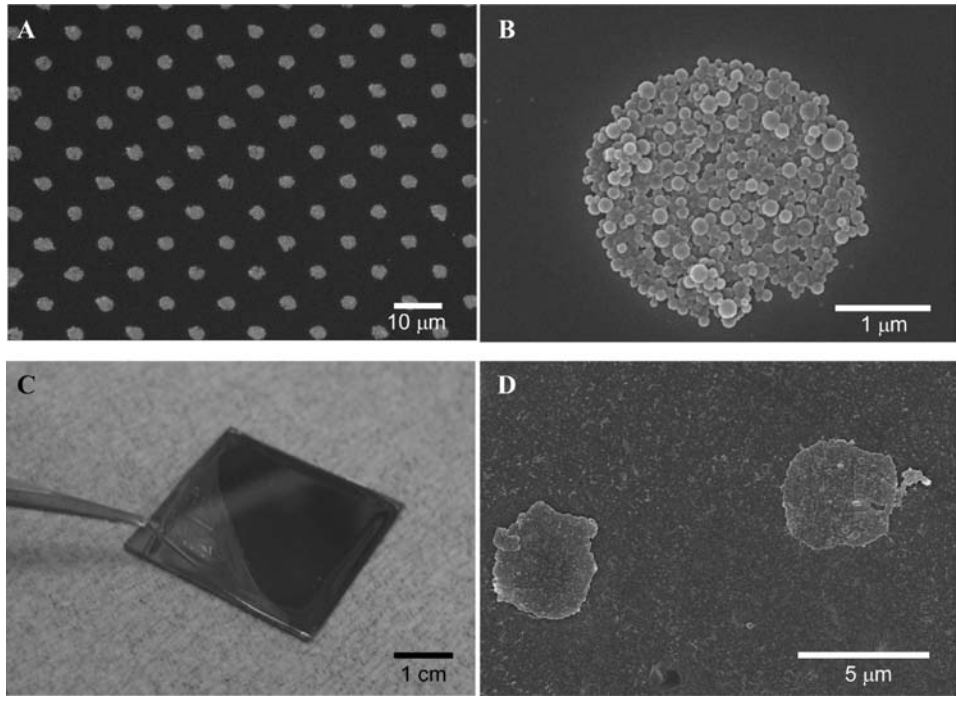

Figure 3. (A) SEM image of the PLGA nanoparticles adsorbed specifically onto the disk-patterned ODS/mPEO-SAM. (B) Magnified SEM image of (A). (C) Photo of the PLGA nanosheets transferred from the ODS/mPEO-SAM to the PVA film. (D) SEM image of the free-standing PLGA nanosheets after dissolution of the resulting PVA film.

In the final step, H12 molecules were conjugated to the surface of the PLGA nanosheets via the maleimide group of MALPEG-NHS as a cross-linker, which targeted the amino groups derived from chitosan. The number of H12 molecules on one nanosheet was indirectly estimated to be approximately 6.1×10^5 molecules from the quantification of free H12 molecules. For an average surface area per nanosheet of 14.9 μm^2, the resulting conjugation density on the nanosheet surface was approximately 4.1×10^4 molecules/μm^2. The density seems to be sufficient for our purposes for the following reasons: In our previous studies on H12-nanoparticles (liposomes and albumin nanoparticles), a conjugation density of H12 over 4.0×10^4 molecules/μm^2 was necessary to maintain the binding ability toward activated platelets, based on flow cytometric analyses and the hemostatic evaluation of the nanoparticles using thrombocytopenic rats *in vivo* (*18*−*20*).

Fabrication of H12-PLGA Microparticles. In order to reveal the differences in hemostatic abilities of disk-shaped and spherical carriers, we also tried to fabricate H12-PLGA microparticles having the same surface area and conjugation number of H12 as those of disk-shaped nanosheets. Using conventional emulsion−diffusion−evaporation methodology with PVA/chitosan as a stabilizer, we obtained PLGA microparticles with an average diameter of 2.2 ± 0.5 μm, corresponding to a surface area per microparticle (15.2 μm^2) that is almost the same as that of the nanosheet. After H12 molecules were bonded to the surface of the particles via MALPEG-NHS, the number of H12 molecules on one microparticle were indirectly estimated to be approximately 6.5×10^5 molecules, corresponding to a conjugation density of approximately 4.2×10^4 molecules/μm^2, a value very close to that of H12-PLGA nanosheets.

Enhanced Effects of H12-PLGA Nanosheets on Platelet Aggregation under Flow Conditions. In order to explore whether the H12-PLGA nanosheets have a specific binding ability toward activated platelets under flow conditions, we prepared imitation thrombocytopenia blood, adjusting the platelet count to 2.0×10^4 /μL (corresponding to one-tenth of that of normal blood). In comparison, we also performed the same experiment using the H12-PLGA microparticles having the same surface area and H12 conjugation number as the nanosheets. When the blood containing the H12-PLGA nanosheets or H12-PLGA microparticles, which were labeled with the fluorescent marker $DiOC_{18}$, was allowed to flow over the collagen surface at a shear rate of 150 s^{-1}, both carriers gradually adhered and accumulated significantly on the surface in a time-dependent manner (Supporting Information movie S1). It was interesting to note that the H12-PLGA nanosheets adhered on the surface at twice the rate of the H12-PLGA microparticles; the adhesive rates of the H12-PLGA nanosheets and H12-PLGA microparticles were calculated to be 14.5 ± 2.3 and 7.7 ± 1.3 /mm^2/s, respectively (Figure 4). A simulation by Mortensen et al. suggests that ellipsoidal particles tend to align in the near-wall region of the turbulent shear flow, and that their alignment increases with an increase in the particle aspect ratio between the semiminor and semimajor axis of ellipsoid from 10 to 50

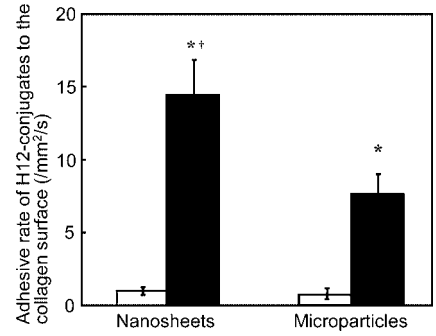

Figure 4. Adhesive rates of the H12-PLGA nanosheets and H12-PLGA microparticles in the thrombocytopenic blood toward the collagen-immobilized surface at a shear rate of 150 s^{-1}. Solid or open columns show H12-conjugates or nonconjugates, respectively. Count of platelets and the H12-PLGA nanosheets or H12-PLGA microparticles was $2.0 \times 10^4/\mu$L. *$P < 0.05$ for H12-PLGA nanosheets or H12-PLGA microparticles group vs PBS group, and †$P < 0.05$ for H12-PLGA nanosheets group vs H12-PLGA microparticles group. Data are expressed as the mean ± SD of three independent experiments.

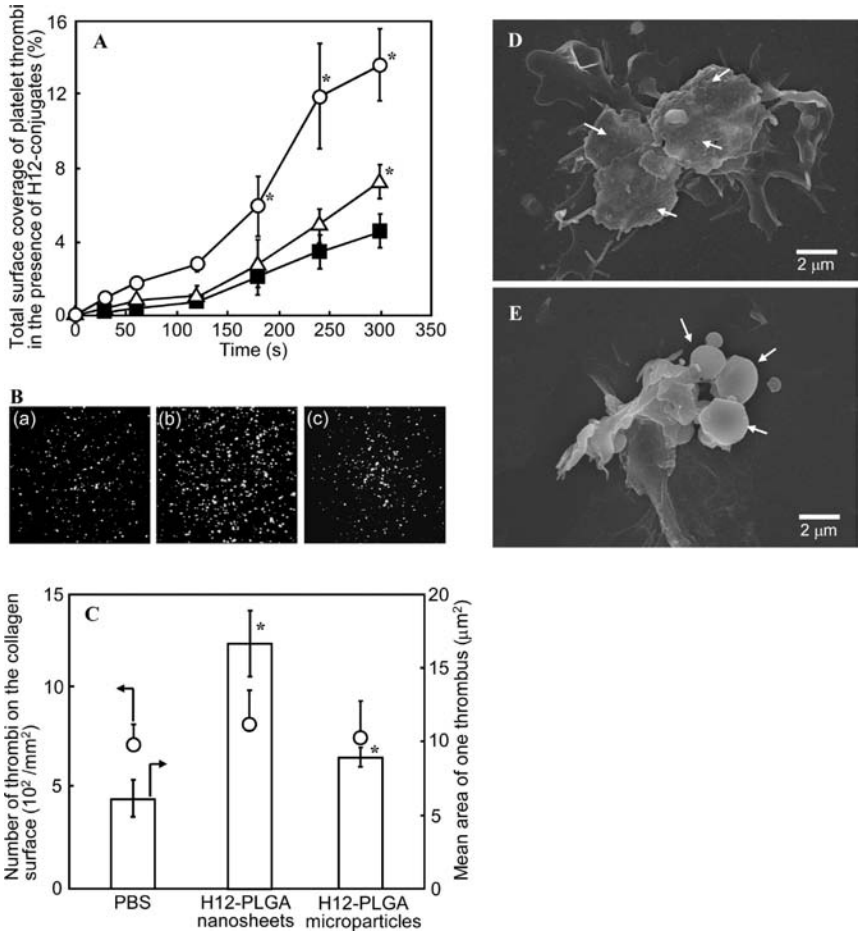

Figure 5. Enhancement of platelet aggregation by H12-PLGA nanosheets under flow conditions. Data are expressed as the mean ± SD of three independent experiments. (A) Time course of the surface coverage of platelet thrombi in the imitation thrombocytopenia blood on the collagen surface after addition of (○) H12-PLGA nanosheets, (Δ) H12-PLGA microparticles, and (■) PBS at a shear rate of 150 s^{-1}. Platelet count was 2.0 × $10^4/\mu$L, and the count of the nanosheets or microparticles was 2.0 × $10^4/\mu$L. *$P < 0.05$ for H12-PLGA nanosheets or H12-PLGA microparticles group vs PBS group. (B) Images of platelet thrombi on a collagen surface after 300 s flow of the imitation thrombocytopenia blood in the presence of (a) PBS, (b) H12-PLGA nanosheets, and (c) H12-PLGA microparticles. (C) Number of platelet thrombi on the collagen surface and mean area of one thrombus based on images of (B). (D,E) SEM images of platelet thrombi involving H12-PLGA nanosheets and H12-PLGA microparticles, respectively. Arrows in the SEM images indicate nanosheets and microparticles.

(*39*). Decuzzi et al. reported on the adhesive strength of ellipsoidal particles toward endothelial cells under a linear shear flow (*40*). They found that ellipsoidal particles adhered more effectively to the cells than classical spherical particles with the same volume because of multivalent bonding of ellipsoidal particles to the cells, and that the adhesive strength was significantly increased by increasing the particle aspect ratio from 1 to 10. On the basis of these studies, we estimate that the high adhesive rate of the H12-PLGA nanosheets is due to an aspect ratio of approximately 20 for the nanosheet. Such a thin sheet can easily flow in the near-wall region (collagen surface) of the flow chamber. The asymmetric shape of the sheets also produces a higher adhesive strength than the spherical microparticles. These experiments clearly demonstrate that the adhesive rate of the carriers on the collagen surface could be controlled solely by changing their shape.

On the other hand, neither carrier adhered to the surface when the platelet count in the blood was below (5.0 ± 1.0) × $10^3/\mu$L (data not shown). Furthermore, both control carriers (without the H12 modification) failed to adhere to the surface (Figure 4). This indicated that the adhesion of the both H12-conjugated carriers was triggered by a specific interaction with the activated platelets, which had already adhered on the surface of the collagen plate. Additionally, we also tried to perform the same flow experiment using 5 by 10 μm rectangular H12-PLGA nanosheets having a very high aspect ratio of over 60 (Supporting Information Figure S3). However, these nanosheets did not adhere to the collagen surface even when H12 was well-conjugated and the shear rate was low (10 s^{-1}) (Supporting Information movie S2). We speculate that this failure to adhere was because it was difficult for these larger nanosheets, together with erythrocytes, to flow in the near-wall region of the flow chamber, and hence they, then did not attach to the activated platelets on the collagen surface. At present, we can say that the platelet-like disk-shaped PLGA-nanosheets with a size of 3 μm have an optimal size and aspect ratio.

Next, in order to know whether the H12-PLGA nanosheets actually have the ability to reinforce platelet thrombus formation under flow conditions, we employed platelets, with an adjusted platelet count of 2.0 × $10^4/\mu$L, were labeled with the fluorescent marker, $DiOC_6$. With the addition of PBS as a control, the flowing platelets gradually adhered to and aggregated on the collagen surface; the surface coverage of platelets after flowing for 300 s increased to 4.7 ± 1.6% as shown in Figure 5A (■) and B (a). When the H12-PLGA nanosheets were added instead of PBS to the thrombocytopenic blood, the surface coverage after 300 s flow was significantly higher at 14.6 ± 1.9% (Figure 5A (○) and B (b)). Furthermore, we confirmed that H12-PLGA nanosheets labeled with rhodamine were involved in the platelet thrombi labeled with $DiOC_6$ by a double-staining method (data not shown). These data indicate that the H12-PLGA nanosheets were specifically bound on the activated platelets adhered on

the collagen surface, and that the number of the H12 peptides on the nanosheets would be sufficient to act as binding sites for the flowing platelets. In case of the H12-PLGA microparticles, their surface coverage was also significantly higher (6.6 ± 1.3%) than that of PBS; however, their effect was lower than that of H12-PLGA nanosheets (Figure 5A (Δ) and B (c)).

In order to clarify the reason the H12-PLGA nanosheets had a more pronounced effect on platelet aggregation than did H12-PLGA microparticles, we calculated the mean area of one platelet thrombus. The numbers of platelet thrombi formed on the collagen surface after 300 s flow were almost comparable in each experiment (PBS, $(7.2 \pm 1.1) \times 10^2/mm^2$; H12-PLGA nanosheets, $(8.1 \pm 1.7) \times 10^2/mm^2$; and H12-PLGA microparticles, $(7.5 \pm 2.1) \times 10^2/mm^2$) (Figure 5C (○)). On the basis of the total area of platelet thrombi, the mean area of one platelet thrombus with the addition of PBS as a negative control was calculated to be $6.1 \pm 1.2\ \mu m^2$. In the presence of the nanosheets, it was interestingly to note that the mean area was significantly increased to $16.6 \pm 2.3\ \mu m^2$ (Figure 5C). The mean area in the presence of the H12-PLGA microparticles was also significantly higher than that of the PBS control at $8.9 \pm 0.7\ \mu m^2$, although this value was significantly lower than that of H12-PLGA nanosheets. This indicates that the H12-PLGA nanosheets make the platelet thrombi spread in a two-dimensional manner.

We also observed with an SEM the surface of the collagen plate after the flow experiments. There were abundant platelet thrombi containing nanosheets or microparticles, where the platelets had adhered first on the collagen surface (Figure 5D,E, respectively). In particular, the H12-PLGA nanosheets two-dimensionally spread the platelet thrombi on the collagen surface, producing a low contrast over the entire SEM image (Figure 5D). On the other hand, the H12-PLGA microparticles made the platelet thrombi pile up dramatically, and the SEM image showed relatively high contrast (Figure 5E). We suggest that the difference may arise from one of the following mechanisms: (1) the adhesion of the both carriers (H12-PLGA nanosheets and H12-PLGA microparticles) could be initiated by the activated platelets, which had already adhered on the surface of the collagen plate, (2) the flat nanosheets adhering to the activated platelets could act as broader scaffolds for binding of the flowing platelets than spherical microparticles, which can only effect point contact with the flowing platelets, or (3) the nanosheets could accelerate two-dimensional platelet thrombus formation because of their ultrathin disk structure, whereas the spherical microparticles would naturally tend to lead to the formation of piled up thrombi. From the viewpoint of hemostasis, the H12-PLGA nanosheets should be more effectively occluded in the thrombi on the collagen exposed at the bleeding site in comparison with H12-PLGA microparticles. Moreover, the biological implications of platelets that have a distinctive disk-shape may be following: the platelets find it easy to adhere to the collagen at the vascular injury, and then their aggregation is two-dimensionally accelerated.

In conclusion, we have successfully prepared biocompatible and biodegradable free-standing, disk-shaped, PLGA nanosheets using patterned ODS/mPEO-SAM, and modified their surfaces with fibrinogen-derived dodecapeptide (H12). The resulting H12-PLGA nanosheets specifically interacted under flow conditions with activated platelets on a collagen surface faster than did H12-PLGA microparticles. Furthermore, the nanosheets, but not the microparticles, induced two-dimensional spreading of platelet thrombi on collagen-immobilized plates. Therefore, H12-PLGA nanosheets might be a suitable candidate as novel platelet substitutes and an alternative to human platelet concentrates infused to treat bleeding in patients with severe thrombocytopenia. We are assessing the *in vivo* hemostatic ability of the H12-PLGA nanosheets to treat animals with severe thrombocytopenia. Moreover, this experimental strategy can be applied to other situation than platelet substitutes, such as other drug delivery carriers like antihemostatic reagents and wound dressings for burn injury, and others.

ACKNOWLEDGMENT

This work was supported as a "Consolidated Research Institute for Advanced Science and Medical Care" and "High-tech Research Center" project by MEXT, Japan (S.T.), and by the Futaba Electronics Memorial Foundation (Y.O.). This work was also supported in part by a Health and Labor Sciences Research Grant (Research on Pharmaceutical and Medical Safety, M.H., Y.I., and S.T.), Ministry of Health, Labor and Welfare, Japan. Y.O. was the recipient of a Research Fellowship from the Japan Health Science Foundation.

Supporting Information Available: Additional figures and movie files as described in the text. This material is available free of charge via the Internet at http://pubs.acs.org.

LITERATURE CITED

(1) Slichter, S. J. (2007) Platelet transfusion therapy. *Hematol. Oncol. Clin. North Am. 21*, 697–729.
(2) Stroncek, D. F., and Rebulla, P. (2007) Platelet transfusions. *Lancet 370*, 427–438.
(3) Graham, S. S., Gonchoroff, N. J., and Miller, J L. (2001) Infusible platelet membranes retain partial functionality of the platelet GPIb/IX/V receptor complex. *Am. J. Clin. Pathol. 115*, 144–147.
(4) Agam, G., and Livine, A. A. (1992) Erythrocytes with covalently bound fibrinogen as a cellular replacement for the treatment of thrombocytopenia. *Eur. J. Clin. Invest. 22*, 105–112.
(5) Casals, E., Verdaguer, A., Tonda, R., Galan, A., Escolar, G., and Estelrich, J. (2003) Atomic force microscopy of liposomes bearing fibrinogen. *Bioconjugate Chem. 14*, 593–600.
(6) Levi, M., Friedrich, P. W., Middleton, S., De Groot, P. G., Wu, Y. P., Harris, R., Biemond, B. J., Heijien, F. G., Levin, J., and Ten Cate, J. W. (1999) Fibrinogen-coated albumin microcapsules reduce bleeding in severely thrombocytopenic rabbits. *Nat. Med. 5*, 107–111.
(7) Coller, B. S., Springer, K. T., Beer, J. H., Mohandas, N., Scudder, L. E., Norton, K. J., and West, S. M. (1992) Thromboerythrocytes. In vitro studies of a potential autologous, semi-artificial alternative to platelet transfusion. *J. Clin. Invest. 89*, 546–555.
(8) Takagi, J., Petre, B. M., Walz, T., and Springer, T. A. (2002) Global comformational rearrangemrents in integrin extracellular domains in outside-in and inside-out signaling. *Cell 110*, 599–611.
(9) Xiao, T., Takagi, J., Coller, B. S., Wang, J. H., and Springer, T. A. (2004) Structual basis for allostery in integrins and binding to fibrinogen-mimetic therapeutics. *Nature 432*, 59–67.
(10) Lam, S. C., Plow, E. F., Smith, M. A., Andrieux, A., Ryckwaert, J. J., Marguerie, G., and Ginsberg, M. H. (1987) Evidence that arginyl-glycyl-aspartate peptides and fibrinogen γ chain peptides share a common binding site on platelets. *J. Biol. Chem. 262*, 947–950.
(11) Andrieux, A., Hudry-Clergeon, G., Ryckewaert, J. J., Chapel, A., Ginsberg, M. H., Plow, E. F., and Marguerie, G. (1989) Amino acid sequences in fibrinogen mediating its interaction with its platelet receptor, GPIIbIIIa. *J. Biol. Chem. 264*, 9258–9265.
(12) Ruoslahti, E. (1996) RGD and other recognition sequences for integrins. *Annu. Rev. Cell Dev. Biol. 12*, 697–715.
(13) Takeoka, S., Teramura, Y., Okamura, Y., Tsuchida, E., Handa, M., and Ikeda, Y. (2002) Rolling properties of rGPIbα-conjugated phospholipid vesicles with different membrane flex-

ibilities on vWf surface under flow conditions. *Biochem. Biophys. Res. Commun. 296*, 765–770.
(14) Okamura, Y., Maekawa, I., Teramura, Y., Maruyama, H., Handa, M., Ikeda, Y., and Takeoka, S. (2005) Hemostatic effects of phospholipid vesicles carrying fibrinogen-γ chain dodecapeptide in vitro and in vivo. *Bioconjugate Chem. 16*, 1589–1596.
(15) Okamura, Y., Takeoka, S., Eto, K., Maekawa, I., Fujie, T., Maruyama, H., Ikeda, Y., and Handa, M. (2009) Development of fibrinogen γ-chain peptide-coated, adenosine diphosphate-encapsulated liposomes as a synthetic platelet substitute. *J. Thromb. Haemost. 7*, 470–477.
(16) Takeoka, S., Teramura, Y., Okamura, Y., Handa, M., Ikeda, Y., and Tsuchida, E. (2001) Fibrinogen-conjugated albumin polymers and their interaction with platelets under flow conditions. *Biomacromolecules 2*, 1192–1197.
(17) Teramura, Y., Okamura, Y., Takeoka, S., Kainoh, M., Narumi, H., Tsuchiyama, H., Handa, M., Ikeda, Y., and Tsuchida, E. (2003) Hemostatic effects of polymerized albumin particles bearing rGPIa/IIa in thrombocytopenic mice. *Biochem. Biophys. Res. Commun. 306*, 256–260.
(18) Okamura, Y., Takeoka, S., Teramura, Y., Maruyama, H., Tsuchida, E., Handa, M., and Ikeda, Y. (2005) Hemostatic effects of fibrinogen γ-chain dodecapeptide-conjugated polymerized albumin particles in vitro and in vivo. *Transfusion 45*, 1221–1228.
(19) Okamura, Y., Fujie, T., Maruyama, H., Handa, M., Ikeda, Y., and Takeoka, S. (2007) Prolonged hemostatic ability of poly(ethylene glycol)-modified polymerized albumin particles carrying fibrinogen γ-chain dodecapeptide. *Transfusion 47*, 1254–1262.
(20) Okamura, Y., Fujie, T., Nogawa, M., Maruyama, H., Handa, M., Ikeda, Y., and Takeoka, S. (2008) Hemostatic effects of polymerized albumin particles carrying fibrinogen γ-chain dodecapeptide as platelet substitutes in severely thrombocytopenic rabbits. *Transf. Med. 18*, 158–166.
(21) Mattson, J., Forrest, J. A., and Borjesson, L. (2000) Quantifying glass transition behaviour in ultrathin free-standing polymer films. *Phys. Rev. E 62*, 5187–5200.
(22) Tang, Z., Kotov, N. A., Magonov, S., and Ozturkk, B. (2003) Nanostructured artificial nacre. *Nat. Mater. 2*, 413–418.
(23) Mallwitz, F., and Laschewsky, A. (2005) Direct access to stable, freestanding polymer membranes by layer-by-layer assembly of polyelectrolytes. *Adv. Mater. 17*, 1296–1299.
(24) Fujie, T., Okamura, Y., and Takeoka, S. (2007) Ubiquitous transference of free-standing polysaccharide nanosheet in the development of a nano-adhesive plaster. *Adv. Mater. 19*, 3549–3553.
(25) Mallwitz, F., and Goedel, W. A. (2001) Physically cross-linked ultrathin elastomeric membranes. *Angew. Chem., Int. Ed. 40*, 2645–2647.
(26) Eck, W., Küller, A., Grunze, M., Völkel, B., and Gölzhäuser, A. (2005) Freestanding nanosheets from crosslinked biphenyl self-assembled monolayers. *Adv. Mater. 17*, 2583–2587.
(27) Ulman, A. (1991) *An introduction to ultrathin organic films from langmuir-blodgett to self-assembly*, Academic Press, San Diego, CA.
(28) Niwa, D., Yamada, Y., Homma, T., and Osaka, T. (2004) Formation of molecular templates for fabricating on-chip biosensing devices. *J. Phys. Chem. B 108*, 3240–3245.
(29) Khoshtariya, D. E., Wei, J., Liu, H., Yue, H., and Waldeck, D. H. (2003) Charge-transfer mechanism for cytochrome *c* adsorbed on nanometer thick films. Distinguishing frictional control from conformational gating. *J. Am. Chem. Soc. 125*, 7704–7714.
(30) Ferapontova, E. E., Shipovskov, S., and Gorton, L. (2007) Bioelectrocatalytic detection of theophylline at theophylline oxidase electrodes. *Biosens. Bioelectron. 22*, 2508–2511.
(31) Sun, Y., and Walker, G. C. (2002) Two-dimensional self-assembly of latex particles in wetting films on patterned polymer. *J. Phys. Chem. B 106*, 2217–2223.
(32) Okamura, Y., Utsunomiya, S., Suzuki, H., Niwa, D., Osaka, T., and Takeoka, S. (2008) Fabrication of freestanding nanoparticle-fused sheets and their hetero-modification using sacrificial film. *Colloids Surf., A 318*, 184–190.
(33) Sugimura, H., Ushiyama, H., Hozumi, A., and Takai, O. (2000) Micropatterning of alkyl- and fluoroalkylsilane self-assembled monolayers using vacuum ultraviolet light. *Langmuir 16*, 885–888.
(34) Cecchet, F., Meersman, B. D., Demoustier-Champagne, S., Nysten, B., and Jonas, A. M. (2006) One step growth of protein antifouling surface: monolayers of poly(ethylene oxide) (PEO) derivatives on oxdized and hydrogen-passivated silicon surfaces. *Langmuir 22*, 1173–1181.
(35) Ravi Kumar, M. N. V., Bakowsky, U., and Lehr, C. M. (2004) Preparation and characterization of cationic PLGA nanospheres as DNA carriers. *Biomaterials 25*, 1771–1777.
(36) Sahoo, S. K., Panyam, J., Prabha, S., and Labhasetwar, V. (2002) Residual polyvinyl alcohol associated with poly(d,l-lactide-co-glycolide) nanoparticles affects their physical properties and cellular uptake. *J. Controlled Release 82*, 105–14.
(37) Denkov, N. D., Velev, O. D., Kralchevsky, P. A., Ivanov, I. B., Yoshimura, H., and Nagayama, K. (1992) Mechanism of formation of two-dimensional crystals from latex particles on substrates. *Langmuir 8*, 3183–3190.
(38) Stroock, A. D., Kane, R. S., Weck, M., Metallo, S. J., and Whitesides, G. M. (2003) Synthesis of free-standing quasi-two-dimensional polymers. *Langmuir 19*, 2466–2472.
(39) Mortensen, P. H., Andersson, H. I., Gillissen, J. J. J., and Boersma, B. J. (2008) On the orientation of ellipsoidal particles in a turbulent shear flow. *Int. J. Multiphase Flow 34*, 678–683.
(40) Decuzzi, P., and Ferrari, M. (2006) The adhesive strength of non-spherical particles mediated by specific interactions. *Biomaterials 27*, 5307–5314.

BC900325W

Supporting Information Available

Novel Platelet Substitutes: Disk-Shaped Biodegradable Nanosheets and their Enhanced Effects on Platelet Aggregation

Yosuke Okamura[†§], Yoshihito Fukui[†], Hidenori Suzuki[‡], Koki Kabata[†], Makoto Handa[§], Yasuo Ikeda[†] and Shinji Takeoka[†*]

[†]Department of Life Science and Medical Bioscience, Graduate School of Advanced Science and Engineering, Waseda University, TWIns, Tokyo, 162-8480, Japan. [‡]Center for Electron Microscopy, the Tokyo Metropolitan Institute of Medical Science, Tokyo, 113-8613, Japan. [§]Department of Transfusion Medicine & Cell Therapy, Keio University, Tokyo, 160-8582, Japan.

Content:

1. Three Supporting Figures (Figure S1-S3)

2. Two Supporting Movies (Movie S1, S2)

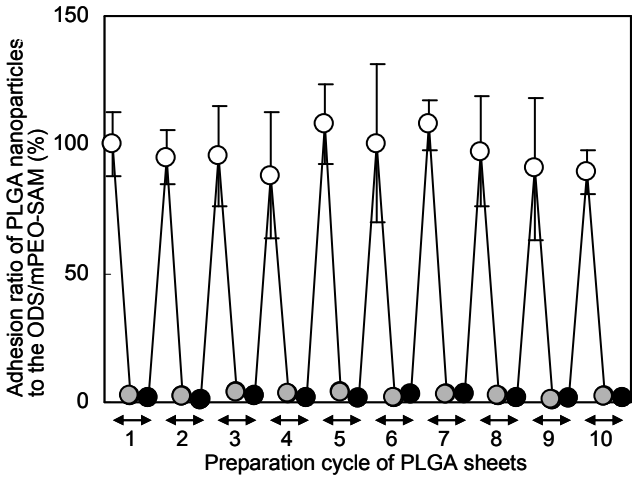

Figure S1 Recycle-tests of ODS/mPEO-SAM on the substrate before and after adsorption & detachment of PLGA particles. Percent of Adhesion ratio of PLGA nanoparticles to the ODS/mPEO-SAM were calculated as follows; the same magnified images of ODS/mPEO-SAM after (○) adsorption & thermal fusion of PLGA particles, (◎) detachment of nanosheets by the PVA film, and (●) Washing of sonication into acetone and distilled water were taken. Pixel number of the PLGA nanoparticles on the ODS region was calculated by Adobe softwere Photoshop 6.0. The pixel number after the first adsorption of the PLGA nanoparticles was calculated as 100%.

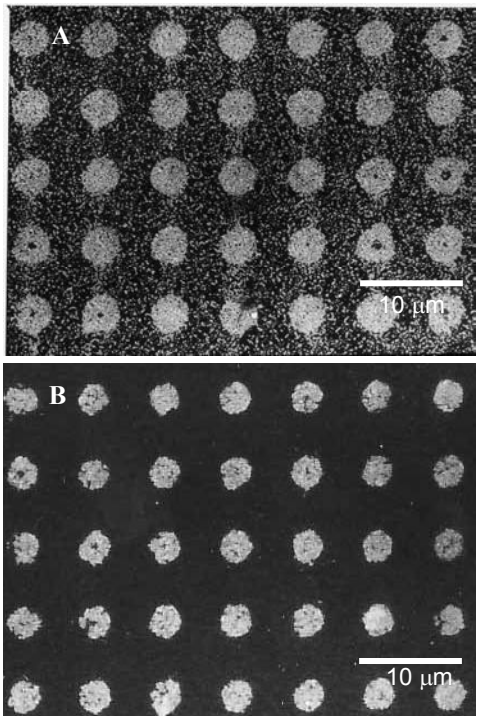

Figure S2 SEM images of patterned ODS-SAM without mPEO modification after adsorption of the PLGA nanoparticles at a concentration of **(A)** 1.0 x 10^{12} /mL and **(B)** 1.0 x 10^{11} /mL.

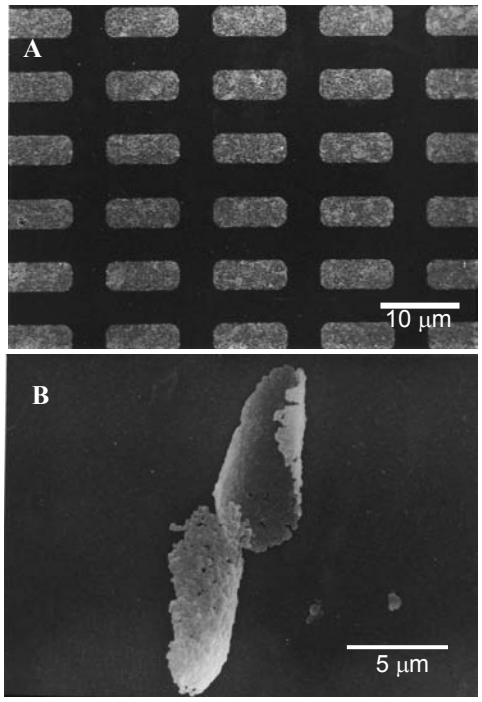

Figure S3 (A) SEM image of PLGA nanoparticles specifically adsorbed onto the 5 x 10 μm rectangle patterned ODS/mPEO-SAM. **(B)** SEM image of free-standing PLGA nanosheets peeled by PVA film on the glass plate. The rectangle patterned ODS/mPEO-SAM substrate was prepared as follows. The ODS-SAM on the silicon oxide (size: 4 cm x 4 cm) was covered with photoresist, and was irradiated with a 350 nm UV lamp using a photomask (size: 5 cm x 5 cm, patterning; 5 x 10 μm rectangle, Topic Co., Ltd., Saitama, Japan). After developing (NMD-3), the substrate was exposed to oxygen plasma at an input power of 200 W and an oxygen flow rate of 80 sccm for removal of ODS. The photoresist was removed by acetone washing, and then a patterned ODS-SAM substrate was immersed in a 2 mM solution of Cl_3Si-mPEO in toluene at r.t. for 24 hrs in a glovebox.

The resulting nanosheets were observed with a Hitachi S-4500 field emission scanning electron microscope (SEM) as follows: the nanosheets adsorbed on a silicon substrate and the free-standing nanosheets collected on glass plate (diameter 24 mm, thickness 0.12-0.17 mm) coated a poly-L-lysine were coated with osmium tetroxide (ca. 20 nm thick) using an osmium plasma coater (NL-OPC80, Nippon Laser & Electronics Lab., Nagoya, Japan), and were observed at an accelerating voltage of 10 kV.

Movie S1 Adhesion of H12-PLGA nanosheets at a size of 3 μm in imitation thrombocytopenia blood (platelet counts: 2.0 x 10^4 /μL) to a collagen surface under flow condition at a shear rate of 150 s^{-1} (H12-PLGA nanosheets: 2.0 x 10^4 /μL).

Movie S2 Adhesion of H12-PLGA nanosheets at a rectangular size of 5 x 10 μm in imitation thrombocytopenia blood (platelet counts: 2.0 x 10^4 /μL) to a collagen surface under flow condition at a shear rate of 10 s^{-1} (H12-PLGA nanosheets: 2.0 x 10^4 /μL).

Single-Domain Antibody-Nanoparticles: Promising Architectures for Increased *Staphylococcus aureus* Detection Specificity and Sensitivity

Shannon Ryan,[†,‡] Arnold J. Kell,[†,§] Henk van Faassen,[‡] Li-Lin Tay,[||] Benoit Simard,[§] Roger MacKenzie,[‡,⊥] Michel Gilbert,[‡] and Jamshid Tanha*[,‡,⊥,#]

Institute for Biological Sciences, Steacie Institute for Molecular Sciences, and Institute for Microstructural Sciences, National Research Council Canada, Ottawa, Ontario, Canada K1A 0R6, Department of Environmental Biology, Ontario Agricultural College, University of Guelph, Guelph, Ontario, Canada N1G 2W1, Department of Biochemistry, Microbiology and Immunology, University of Ottawa, Ottawa, Ontario, Canada K1N 6N5. Received July 27, 2009

Because antibodies are highly target-specific and nanoparticles possess diverse, material-dependent properties that can be exploited in order to label and potentially identify biomolecules, the development of antibody−nanoparticle conjugates (nanoconjugates) has huge potential in biodiagnostics. Here, we describe a novel superparamagnetic nanoconjugate, one whose recognition component is a single-domain antibody. It is highly active toward its target *Staphylococcus aureus*, displays long shelf life, lacks cross-reactivity inherent to traditional homologue whole antibodies, and captures a few dozen *S. aureus* cells in a mixed cell population with ∼100% efficiency and specificity. We ascribe the excellent performance of our nanoconjugate to its single-domain antibody component and recommend it as a general purpose recognition element.

INTRODUCTION

An area where antibody−nanoparticle conjugates (nanoconjugates) would be of great benefit is in the field of bacteria detection such as for identifying the presence of potentially harmful bacterial pathogens in food and water and in hospitals and elderly care facilities (*1*−*6*). Effective and timely preventive measures against such bacteria require that they be detected in trace amounts, thus calling for a detection system which is highly specific, sensitive, and fast. Superparamagnetic nanoconjugates are an attractive option for bacterial detection. By virtue of their magnetic property, they can magnetically confine/preconcentrate bacterial samples, leading to an increase in detection sensitivity. Though whole antibodies (e.g., IgGs, Figure 1) have been previously employed in a number of biodiagnostic applications to interface superparamagnetic nanoparticles (SPNs) to bacteria, antibodies have an inherent cross-reactivity associated with them because the Fc region is common to different antibodies and can interact with multiple targets despite the fact that their variable region (F_V) is unique. For example, Ho et al. recently demonstrated that IgG-based nanoparticles interact with protein A (a surface protein unique to *Staphylococcus aureus*) as well as other surface markers such as protein M present on the surface of other bacteria (*3, 7, 8*). To avoid the cross-reactivity problems associated with traditional antibodies, smaller, single-chain variable fragments (scFv) lacking the Fc region can be utilized (Figure 1), but these fragments are frequently unstable and prone to aggregation. For many scFvs, the two binding domains can dissociate and then reassociate intermolecularly; on the surface of nanoparticles, this would lead to nanoparticle agglutination. A more attractive approach is to employ single-domain antibodies (sdAbs) (*9*). sdAbs (e.g., V_H, Figure 1) can be readily cloned, resulting in small, chemically/thermally stable, and highly selective targeting moieties (*10, 11*). Nanoparticle agglutination is not an issue with V_Hs because of their single domain nature. Additionally, V_Hs display a lower number of reactive sites, and as a result, unlike larger IgGs or scFvs, very few V_Hs become linked to more than one nanoparticle during conjugation reactions, greatly reducing conjugation-induced nanoparticle aggregation. Smaller size also translates to higher binding density on the surface of nanoparticles.

In this article, we demonstrate that a sdAb-SPN nanoconjugate can interact strongly and selectively with protein A expressed on the surface of *S. aureus*, leading to its sensitive magnetic confinement even in competition with other bacterial species (*12*). The nanoconjugate captures a few dozen *S. aureus* cells in a mixed-cell population with ∼100% efficiency and specificity.

EXPERIMENTAL PROCEDURES

Materials. *Salmonella typhimurium* (ATCC19585), *S. aureus* (ATCC12598), *Streptococcus pyogenes* (ATCC12385), and *Staphylococcus saprophyticus* (ATCC15305) were obtained from American type Culture Collection (Manassas, VA). *Streptococcus pneumoniae* 35C was from an in-house stock (NRCC 4758). Xylose lysine desoxycholate (XLD), Baird-Parker (BP) agar, and chocolate agar plates were purchased from Oxoid (Nepean, ON, Canada). (By titration studies, it was shown that the XLD plate only supported the growth of *S. typhimurium* and not *S. aureus* and the BP plate only the growth of *S. aureus* and not *S. typhimurium*. The titers obtained when *S. typhimurium* and *S. aureus* were grown on nutrient broth (NB) and brain heart infusion (BHI, EMD Chemicals Inc., Darmstadt, Germany) media plates, respectively, were the same as those on selective media.) Protein A R-PE conjugate (1 mg/mL) was purchased from Innova Biosciences Ltd. (Babraham, Cambridge, UK).

Methods. *Synthesis of the Carboxylic Acid-Modified Superparamagnetic Nanoparticle,* **SPN**, *and Its Conjugate Derivative,* **1-SPN.** The synthesis of the silica encapsulated iron oxide

* To whom correspondence should be addressed. Phone: 613-990-7206. Fax: 613-952-9092. E-mail: jamshid.tanha@nrc-cnrc.gc.ca.

† S. Ryan and A. J. Kell contributed equally to this work.

‡ Institute for Biological Sciences, National Research Council Canada.

§ Steacie Institute for Molecular Sciences, National Research Council Canada.

|| Institute for Microstructural Sciences, National Research Council Canada.

⊥ University of Guelph.

University of Ottawa.

10.1021/bc900332r CCC: $40.75 © 2009 American Chemical Society
Published on Web 09/14/2009

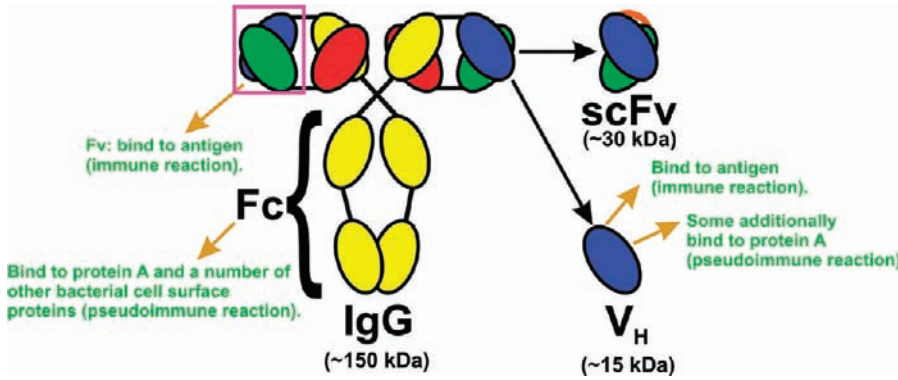

Figure 1. Cartoon representation of an antibody and antibody fragments. The antibody domains are shown as ovals. An antibody, e.g., an IgG, comprises two identical heavy chains (yellow and blue) and two identical light chains (red and green). The Fc region of the IgG can interact indiscriminantly with several different bacterial targets, decreasing specificity. Alternatives to whole antibodies include scFv (a light chain binding domain (V_L) plus a heavy chain binding domain (V_H) covalently joined by a linker (orange)) and, most simply, V_H domain.

nanoparticles has been previously described by us (*13*). Specifically, a commercially available ferrofluid (0.4 mL, ferrotec EMG304) was diluted to 400 mL with 18 Ω Millipore water. The resulting stock solution was further diluted (12 mL diluted to 45 mL) in Millipore water, and the solution was sonicated for 30 min. Following sonication, the ferrofluid solution was transferred to a 500 mL flask containing 400 mL isopropanol and mechanically stirred. Tetraethoxyorthosilane (0.140 mL) was added to the flask and stirred for ~1 min at which time 6 mL of concentrated ammonium hydroxide was added. The nanoparticles were then stirred overnight. The resulting nanoparticles were ~49 ± 7 nm in diameter consisting of a 10 nm iron oxide core and a smooth silicon dioxide shell with a thickness of 20−25 nm.

Surface Modification of the Silica Encapsulated Iron Oxide Nanoparticles. Six 45-mL samples of the crude nanoparticle solution described above were transferred to 50 mL Falcon tubes, and 1.0 mL of aminopropyldiethoxymethylsilane (APDEMS) was added to each tube in order to modify the surface with a functional amine group. The mixture was shaken for 24 h and centrifuged at 5300 *g* for 20 min in order to precipitate the amine-modified nanoparticles. The contents of all of the tubes were combined and washed with ethanol (15 mL) and dimethylformamide (DMF, 15 mL) through repeated centrifugations. Following purification, the amine-modified nanoparticles were dispersed in a 1% solution of succinic anhydride and shaken overnight. The resulting carboxylic acid modified nanoparticles (SPN) were washed with fresh DMF several times to ensure all succinic anhydride had been removed. The nanoparticles were then dispersed in MES buffer (30 mM MES, 70 mM NaCl, pH 6.0) and centrifuged and redispersed in fresh MES buffer. The conversion efficiency for the reaction between the amine and the succinic anhydride was determined by reacting the resulting nanoparticle with fluorescamine, which did not result in a fluorescence response, suggesting that all of the accessible amine moieties had reacted with the succinic anhydride.

The resulting **SPN** were surface modified with HVHP428 V_H (**1**) (*12*) by first activating **SPN** (10 mL in MES buffer, 1×10^{14} nanoparticles) with *N*-(3-dimethylaminopropyl)-*N*′-ethylcarbodiimide hydrochloride (EDC, 5 mg) and *N*-hydroxysuccinimiude (NHS, 5 mg) to yield the NHS-ester modified **SPN**. Following purification to remove any unreacted EDC and NHS, the nanoparticles were mixed with **1** (100 μL of a 1.8 mg/mL solution in phosphate-buffered saline (PBS)) and gently vortexed for at least 5 h. It is believed that **1** is covalently bound to the nanoparticle surface through primary amines, of which there are 7 on each antibody. Following modification with **1**, the resulting **1-SPN** particles were purified via repeated centrifugation cycles and redispersion in MES buffer to remove any unbound **1**. Finally, the nanoparticles were redispersed in 10 mL of MES buffer.

In order to elucidate the number of HVHP428 (**1**) anchored to the surface of each **SPN**, **1-SPN** was reacted with tetramethylrhodamine isothiocyanate (TRITC). The reaction was carried out in MES buffer with **1-SPN** (6×10^{12} nanoparticles) and TRITC (50 μg, 1.2×10^{-7} mol) and the resulting TMR-modified **1-SPN** was purified and analyzed by UV−visible spectroscopy in order to elucidate the number of sdAbs (**1**) on the surface of the nanoparticle. The UV−visible absorption spectra of freshly prepared, day-old **1-SPN** and one-year-old **1-SPN** (6×10^{12} nanoparticles/mL) and the original **1-SPN** are presented in the Supporting Information (Figure S1). Analysis of these spectra suggests that TMR has reacted with the sdAb on **1-SPN**, where there is an increase in absorption centered at 550 nm in comparison to the unmodified **1-SPN**. When the number of TMR molecules was known, the number of sdAb (**1**) per nanoparticle could be elucidated by assuming that only one of the seven amine groups on **1** is responsible for anchoring it to the surface of the **SPN**. Construction of a calibration curve for TRITC in MES-buffered water and the comparison of the absorption intensity for the **1-SPN** samples suggest that there are 12 and 4 sdAbs per **1-SPN** for one-day-old nanoparticles and nanoparticles sitting in MES buffer at pH 6 for 1 year, respectively. This data are also presented in the Supporting Information (Figure S2). The slow loss of **1** over several months is consistent with the slow hydrolysis of silica surface ligands in aqueous solution.

Construction and Binding Analysis of Pentamers. Standard cloning techniques were used to construct V_H and V_L (Figure 1) pentamers, $\mathbf{1}^{\mathbf{P}}$ and $\mathbf{2}^{\mathbf{P}}$, respectively (*14*). $\mathbf{2}^{\mathbf{P}}$ serves as the control pentamer. Pentamers were expressed, purified, and quantified as described (*14*, *15*). The binding kinetics for the interaction of $\mathbf{1}^{\mathbf{P}}$ with protein A and $\mathbf{2}^{\mathbf{P}}$ with protein L were determined from surface plasmon resonance (SPR) data collected with BIACORE 3000 biosensor system (GE Healthcare, Baie d'Urfé, QC, Canada). For the $\mathbf{1}^{\mathbf{P}}$ analysis, 520 resonance units (RUs) of protein A or a Fab reference were immobilized on research grade CM5 sensor chips (GE Healthcare). For the $\mathbf{2}^{\mathbf{P}}$ analysis, 680 RUs of protein L or 870 RUs of the Fab reference were immobilized. Immobilizations were carried out at protein concentrations of 25 μg/mL (protein A) or 50 μg/mL (protein L and Fab) in 10 mM sodium acetate buffer pH 4.5, using the amine coupling kit provided by the manufacturer. In all instances, analyses were carried out at 25 °C in 10 mM HEPES, pH 7.4, containing 150 mM NaCl, 3 mM EDTA, and 0.005% P20 at a flow rate of 20 μL/min, and surfaces were regenerated by washing with 50 mM HCl for 3 s. Data were evaluated using *BIAevaluation 4.1* software (GE Healthcare).

Association rate constants, k_as, were independently calculated from plots of k_{obs} vs concentration. More than one dissociation rate constant, k_d, could be calculated due to the heterogeneity in multivalent binding among the pentamer population. Therefore, more than one affinity (K_A) could be obtained (see Figure 4 legend).

Growth of Cells. A single *S. aureus* colony from a plate of BHI media was used to inoculate 15 mL of BHI media. The bacteria were grown overnight at 37 °C and 200 rpm. In the morning, the culture was spun down in a fixed rotor, Sorval RT6000B refrigerated centrifuge at 4000 rpm for 10 min, the supernatant was removed, and the cell pellet was resuspended in an appropriate buffer. The cells were respun, the supernatant was removed, and the cell pellet was resuspended followed by measuring cell density at OD_{600}. Serial dilutions of the cells were spread on BHI plates at 37 °C for overnight growth. The cell titer was determined in the morning. An OD_{600} of 1.0 corresponded to 1×10^8 cells/mL. *S. typhimurium* was grown as described for *S. aureus* but with NB media (5 g peptone and 3 g meat extract in 1 L water, pH 7.0) (*16*). For *S. typhimurium*, an OD_{600} of 1 corresponded to 3×10^8 cells/mL. *S. saprophyticus* was prepared as outlined for *S. aureus*. An OD_{600} of 1 corresponded to 1×10^8 cells/mL. *S. pyogenes* was streaked onto chocolate agar plates from frozen stock and grown at 37 °C overnight. Plate contents were scraped into sterile PBS and adjusted to an OD_{600} of 1 which corresponded to 1×10^8 cells/mL. *S. pneumoniae* was grown in media (Columbia broth 17.5 g, Todd Hewitt broth 15 g, 1% glucose in 1 L water, pH 7.0) at 37 °C, 5% CO_2, without shaking. The cells were spun down as stated for *S. aureus*. An OD_{600} of 1 corresponded to 1×10^8 cells/mL. Cells were used in microagglutination assays, transmission electron microscopy (TEM), and scanning electron microscopy (SEM) experiments and capture studies.

Binding Analysis by Flow Cytometry. Samples of 100 μL **1-SPN** or **SPN** (10^{12} particles) were blocked in PBS/0.1% (v/v) Tween-20 overnight at 4 °C. To these, 1 μL aliquots of various concentrations of fluorescently active protein A (protein A R-PE conjugate) were added and the reaction volumes were increased by adding 200 μL of PBS/0.75% Tween-20. The samples were incubated for 1 h at 4 °C and were directly used for flow cytometry analysis with a FACSCanto Analyzer (BD Biosciences, Mississauga, ON, Canada). The R-PE fluorescence of 100 000 events per sample was analyzed, and data were generated using *BD FACSDiva* software (BD Biosciences).

Binding Analysis by Cell Microagglutination. Cell microagglutination assay was performed to find out if $\mathbf{1^P}$ and **1-SPN** bind multivalently to *S. aureus*, in other words, find out if the apparent K_A values of $\mathbf{1^P}$ and **1-SPN** are increased compared to that of monomeric **1**. If multivalent—and functional—$\mathbf{1^P}$ and **1-SPN** would be expected to cross-link and agglutinate cells. In the absence of agglutination, the cells settle out over time and form a circular dot at the center of the well. If there is agglutination, the cells settle out as a sheet (diffused pattern). Cell microagglutinations were performed essentially as described by Saito et al. (*17*). Twofold dilutions of pentamers or nanoparticles were performed in MES buffer from wells 1 to 11 of a microtiter plate. Well 12 had only buffer, and the total volume in each well was 50 μL. Subsequently, 1 OD_{600} unit of cells (see *Growth of Cells*) in 50 μL buffer was added to all wells, and the plate was incubated overnight at 4 °C. In the morning, photos of the plates were taken for further analysis. Minimum agglutination concentration (MAC), the minimum concentration of nanoparticles or pentamers that promoted bacterial agglutination, was used to express the agglutination activity of nanoparticles and pentamers.

Binding Analysis by TEM Experiments. In general, we found that the most effective TEM images of the **1-SPN** or **SPN** interacting with the variety of bacteria could be obtained by extracting ~1 μL of the solution in the microagglutination plates described above. That is, where the nanoparticles agglutinate effectively, 1 μL of the solution was extracted and expelled directly onto the TEM grid, dried, and analyzed via TEM. In the case where poor or no microagglutination is observed, the 1 μL of solution is extracted from the precipitate that has settled to the bottom of the microtiter plate. Here, because both **1-SPN** and **SPN** are colloidally stable, there are significantly fewer nanoparticles interacting with the bacteria than in the case where agglutination is effective. The TEM images of the nanoparticle—cell conjugates were acquired using a Philips CM20 FEG microscope operating at 200 keV.

Capture Studies. **1-SPN** and **SPN** were first blocked with 0.1% (v/v) Tween 20 in MES buffer overnight at 4 °C in an Eppendorf tube. One hundred microliters of the blocked nanoparticles (1×10^{12} **1-SPN**) were mixed with 1 μL of cells in MES buffer. The mixture was incubated at room temperature for 2 h with gentle rocking followed by a 1-h-long capture with a neodynium-based rare earth magnet ($Nd_{0.23}Fe_{0.74}B_{0.03}$, Lee Valley, Ottawa, ON, Canada). The magnetic is rated at 5000 gauss. Fixing the sample on a homemade magnet stand, the supernatant was removed and plated on BHI media at various dilutions to determine the number of noncaptured cells. The nanoparticles were separated from the magnet, resuspended in 100 μL of MES buffer, and used to determine the number of captured cells. Capture efficiency was calculated as follows:

$$\text{capture efficiency} = (\text{no. of captured cells}/[\text{no. of captured cells} + \text{no. of non-captured cells}]) \times 100$$

In specificity capture studies, 1 μL of each of *S. aureus* and *S. typhimurium* cells was added to 99 μL of overnight blocked conjugated or unconjugated nanoparticles (1×10^{12} **1-SPN**) in MES buffer/1% Tween 20. Incubation, nanoparticle capture, and fractionation of mixtures into captured and noncaptured cells were performed as above. Cell titration was performed as above except that the fractionated cells were plated on both XLD (selective for *S. typhimurium*) and BP (selective for *S. aureus*) media. Capture specificity was calculated on the basis relative number of *S. aureus* and *S. typhimurium* in the captured fraction, after normalizing for the total number of cells:

$$\text{capture specificity} = \text{no. of } \textit{S. aureus} \text{ in the captured fraction}/\text{no. of } \textit{S. typhimurium} \text{ in the captured fraction}$$

Alternatively, capture specificity was determined by direct comparison of the number of captured *S. aureus* vs the number of captured *S. typhimurium* in the mixed cell captured fraction. In some instances, a single wash step between the binding step and the fractionation step was included. The wash step comprised (i) resuspending the nanoparticles in 100 μL MES buffer/1% Tween 20, (ii) capturing the nanoparticles for 30 min, and (iii) removing the wash solution, which was subsequently titrated. Control experiments in which cells (*S. aureus* alone, *S. typhimurium* alone, or a mixture of both cells) were incubated with the MES buffer had the same total titer as the nanoparticle-treated cells.

Binding Analysis by Capture/SEM Experiments. Cell were grown as described above, centrifuged in a benchtop centrifuge (800 *g*, 5 min), resuspended in 1/2 MES buffer, and pelleted again. Cells were resuspended in 10^{12} **1-SPN** in MES buffer/0.1% Tween 20 (v/v) and incubated for binding for 30 min. The solutions were magnetically confined for 3 min and the supernatant removed—leaving the last 20 μL behind to ensure the confined materials are not disturbed and lost. The captured materials were resuspended in 200 μL MES buffer. This step was repeated, but the captured materials were resuspended in

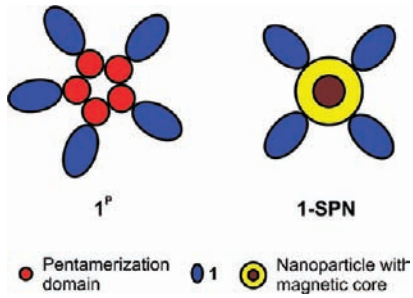

Figure 2. Cartoon representations of the pentameric sdAbs (**1**^{P}), comprising five identical monomeric V_H units (blue) assembled on a pentamerization domain, and the multivalent nanoparticles comprising a superparpamagnetic nanoparticle covalently modified with sdAbs (**1-SPN**). The average valency of the year-old **1-SPN** preparation used in this study was 4 sdAb.

200 μL sterile double-distilled H_2O (ddH_2O). The magnetic confinement was performed once more and the captured materials were resuspended in 50 μL ddH_2O. One microliter suspensions were used for SEM imaging. SEM was performed on cells plated on Si substrate with a Hitachi S-4700 field-emission scanning electron microscope. Samples were imaged with an acceleration voltage of 3 KV and at a working distance of 6 mm. Identical experiments were carried out with **SNP**.

RESULTS

Synthesis of 1-SPN Nanoconjugate and Its Binding Activity Assessment by Flow Cytometry. In this investigation, we utilize a silica encapsulated iron oxide nanoparticle (**SPN**) that can be readily modified with a V_H sdAb (HVHP428) (*12*) previously demonstrated to selectively interact with protein A (**1**), a surface marker unique to *S. aureus* bacteria, to generate **1-SPN** (Figure 2). Details of the synthesis and modification of the **SPN** and the conjugation chemistry employed in this investigation are provided in the Methods section. To assess the functionality of **1-SPN**, nanoparticles were incubated with fluorophore-conjugated protein A (protein A R-PE) and analyzed in a series of flow cytometry experiments. As highlighted in Figure 3, there is a gradual shift in the population of fluorescently active nanoconjugate for **1-SPN** as a function of protein A R-PE concentration, whereas the nanoparticle without the V_H on its surface (**SPN**) does not show any binding activity (i.e., there is no significant shift in the fluorescence, suggesting the protein A does not interact with the nanoparticles). This demonstrates that **1-SPN** effectively interacts with protein A through its sdAb moiety.

Construction of 1^{P}, the Pentameric Version of HVHP428 V_H. An attractive feature of sdAbs—a consequence of their stability—is the flexibility they allow for in terms of choosing optimal conjugation chemistry conditions and nanoparticle purification protocols (*10, 11*). Though the interactions between sdAbs and their ligand are quite selective, monomeric sdAbs may exhibit low affinities for target ligands. For example, the sdAb utilized in this investigation (**1**) has an affinity (K_A) of 5.6×10^5 M^{-1} with protein A (*12*), the surface marker that will allow the modified SPN to interact selectively with *S. aureus*. Interestingly, the apparent K_A, determined by SPR experiments, is increased by at least 1000-fold following the generation of a pentameric version of **1** (**1**^{P}, Figures 2 and 4) (*18*). The increase of apparent K_A is rationalized through the increased avidity brought on by the multivalent interactions between protein A and **1**^{P}. Because **1** is quite small (more than 10× smaller than IgGs), it can be conjugated to the surface of **SPN**s with a high binding density (>5-fold compared to IgGs and 2-fold compared to scFvs) (Figure 1) and will not promote nanoparticle aggregation as expected with scFvs and IgGs. The resulting **1-SPN** is also expected to improve the apparent K_A between the **SPN**-bound **1** and protein A simply because of increased avidity inherent to the now multimeric interactions (i.e., multiple **1** per **SPN**). To elucidate how the incorporation of the sdAb onto the nanoparticle surface affects the apparent K_A between **1** and protein A, the binding of the **1-SPN** was benchmarked against **1**^{P} by means of a cell microagglutination assay. (Attempts to obtain an apparent K_A for the interaction of **1-SPN** with protein A by SPR were not successful, presumably because the relatively large size of the nanoparticles prevented

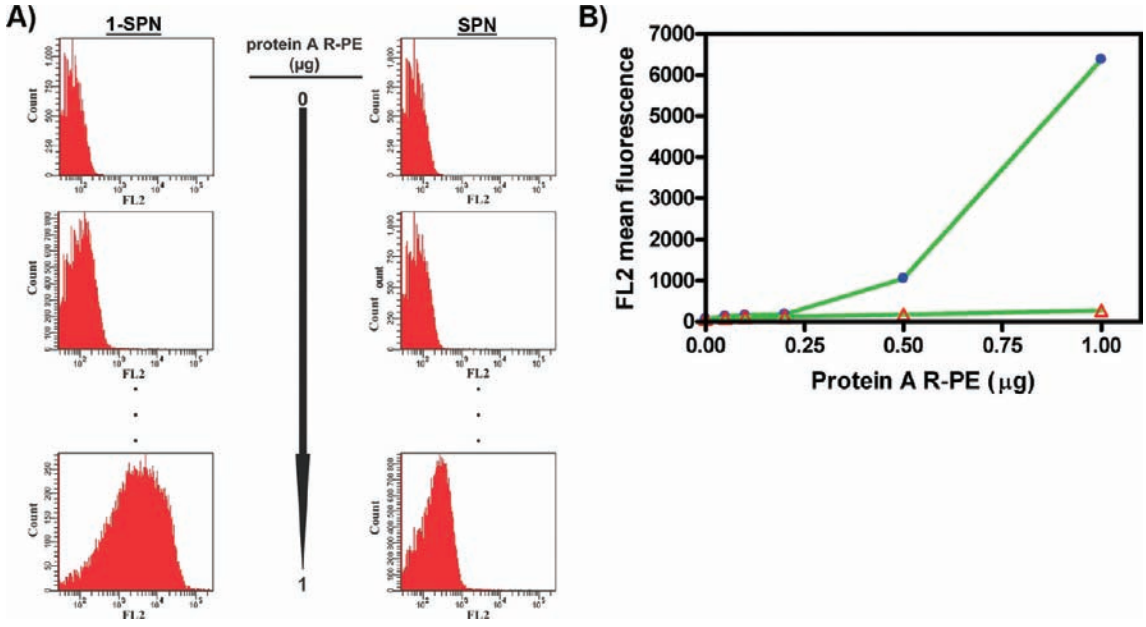

Figure 3. Assessing the functionality of **1-SPN** by flow cytometry. Nanoparticles were incubated with 0, 0.05, 0.1, 0.2, 0.5, and 1 μg of fluorescently active protein A (protein A R-PE) and assessed directly for binding by flow cytometry. (A) Binding, indicated as the rightward fluorescence shifts of nanoparticle populations, can be seen with the increase in protein A R-PE concentration. (B) Binding is shown as the mean fluorescence, extracted from data in (A), vs protein A R-PE concentration. Blue circles, **1-SPN**; red triangles, **SPN**.

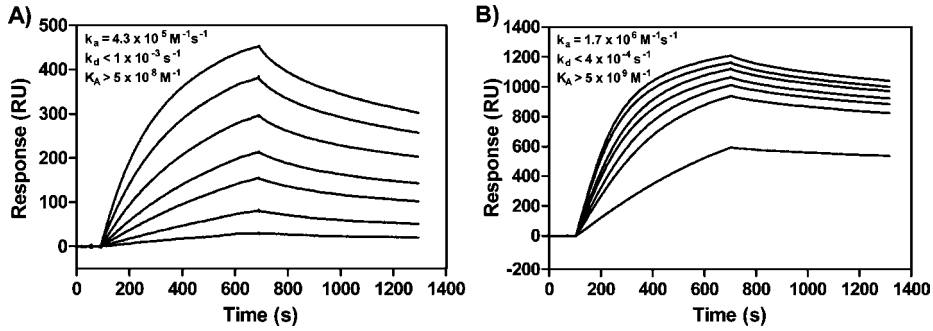

Figure 4. Assessing the binding activity of V_H and V_L pentamers by surface plasmon resonance. Sensorgram overlays showing the binding of $\mathbf{1^P}$ to immobilized protein A at 1, 2, 3, 4, 6, 8, and 10 nM concentrations (A) and of $\mathbf{2^P}$ to immobilized protein L at 1, 2, 2.5, 3, 3.5, 4, and 4.5 nM concentrations (B). Association and dissociation rate constants, k_a and k_d, respectively, and equilibrium constants, K_A, for the bindings of $\mathbf{1^P}$ and $\mathbf{2^P}$ to proteins A and L, respectively, are shown on the graphs. $\mathbf{1^P}$ and $\mathbf{2^P}$ had minimum K_As of $5 \times 10^8\ M^{-1}$ and $5 \times 10^9\ M^{-1}$, respectively. With slower k_ds, $\mathbf{1^P}$ and $\mathbf{2^P}$ had K_As as high as $1.1 \times 10^9\ M^{-1}$ and $1.1 \times 10^{10}\ M^{-1}$, respectively. RU, resonance units.

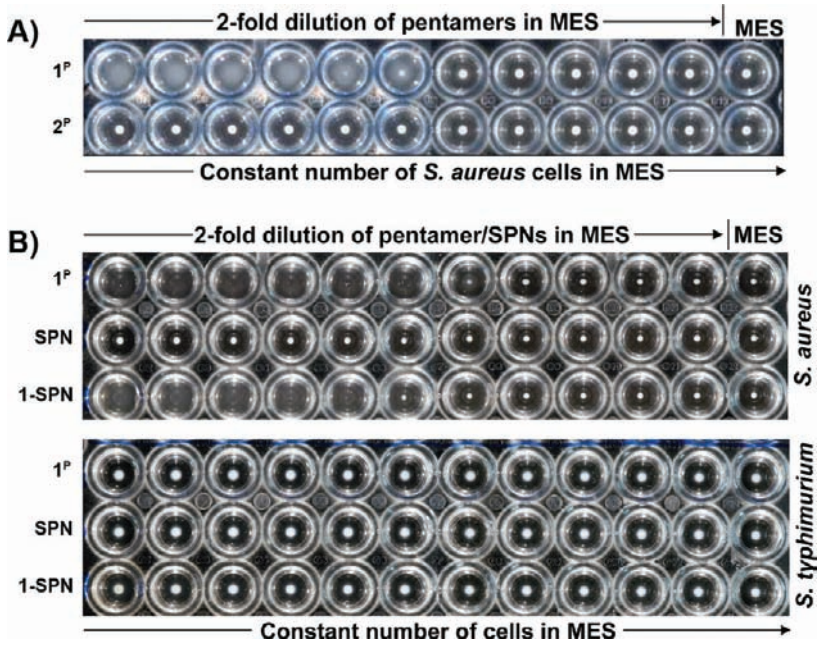

Figure 5. Representative microagglutination assays, where the concentrations of pentamers and SPNs decrease 2-fold from well 1 to well 11 with well 12 having only MES buffer.

their penetration into the dextran matrix on the sensor chip, making them inaccessible to essentially all of the immobilized protein A).

Assessing the Binding Activity of 1-SPN Against $\mathbf{1^P}$ by Microagglutination Assays. Microagglutination assays are typically performed by incubating a constant number of target cells (in this case, *S. aureus*) with decreasing concentrations of an antibody (in this case, either $\mathbf{1^P}$ or **1-SPN**) along a row of wells in a microtiter plate. In the absence of interactions between $\mathbf{1^P}$ (or **1-SPN**) and *S. aureus*, the bacteria simply precipitate into a circular pellet in the bottom of the well (Figure 5, column 12 contains only bacteria cells). However, when $\mathbf{1^P}$ or **1-SPN** are present and interact with the *S. aureus* there is a clumping or agglutination characterized by the absence of the circular pellet and the presence of a diffuse pattern in the well. As highlighted in Figure 5A, $\mathbf{1^P}$ is capable of agglutinating *S. aureus* cells up to well 6 (evidenced by the diffuse cell morphology), and beyond well 6, the concentration of $\mathbf{1^P}$ is too low for agglutination and the cells sediment as round dots. A control pentamer ($\mathbf{2^P}$), whose pentameric nature was confirmed by SPR (Figure 4), does not show any agglutination (Figure 5A), demonstrating that the activity of the $\mathbf{1^P}$ is due to its V_H binding component and not the pentamerization domains (Figure 2). Interestingly **1-SPN** is also capable of strongly interacting with the *S. aureus* cells in the agglutination assay, where agglutination occurs up to well 5 (Figure 5B). Note that the starting concentrations of $\mathbf{1^P}$ and **1-SPN** are 1.0×10^{15} pentamers/mL and 2.5×10^{12} nanoparticles/mL, respectively. There is a 2-fold dilution across the rows, translating to a MAC value of 3×10^{13} pentamers/mL and 1.5×10^{11} particles/mL for $\mathbf{1^P}$ and **1-SPN**, respectively. That is, **1-SPN** binds to protein A expressed on the surface of *S. aureus* 200 times more strongly than $\mathbf{1^P}$. Importantly, in the absence of **1**, **SPN** itself does not agglutinate with *S. aureus* under identical conditions. It is also noteworthy that **1-SPN** is specific to *S. aureus* exclusively. As highlighted in Figure 5B, neither **1-SPN** nor $\mathbf{1^P}$ agglutinate with *S. typhimurium* under identical conditions to that for the aforementioned *S. aureus* (only the circular pellet appears in these wells). Finally, the long-term stability of **1-SPN** is impressive; the MAC values do not significantly decrease even following a year of storage in a pH 6 MES buffer at 4 °C, presumably due to the multivalency inherent to the four remaining sdAb on the surface of the **1-SPN**.

Assessing Capture Efficiency and Specificity of 1-SPN. In this series of experiments, **1-SPN** is first incubated with *S. aureus* cells. If effectively and strongly labeled with **1-SPN**, the resulting bacteria will be magnetically responsive, making it possible to isolate the cells from bulk solution with a simple

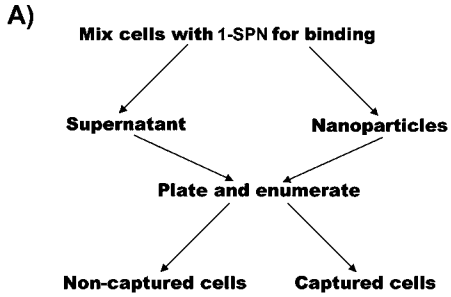

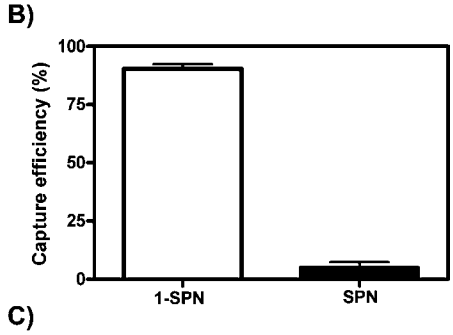

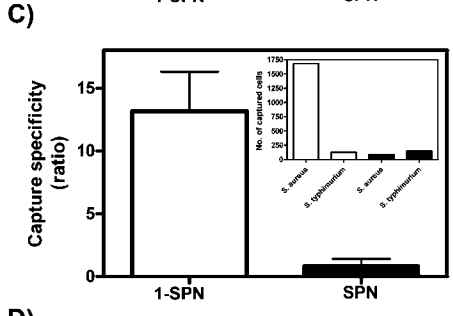

D)

Capture efficiency	
1-SPN	**SPN**
90.4%	5%

Capture specificity (*S. aureus* : *S. typhimurium*)	
1-SPN	**SPN**
13.2	0.85

Figure 6. (A) Scheme representing the steps involved in the magnetic capture studies. Capture efficiency and specificity were calculated as described in the Methods section. (B) Capture efficiency of **1-SPN** nanoconjugate toward *S. aureus*. The data are an average of five trials. (C) Capture specificity of **1-SPN** in terms of the ratio of the number of *S. aureus* to *S. typhimurium* in the captured fraction. This is the average of two trials. *S. aureus* and *S. typhimurium* data were normalized for the total number of cells. The inset shows the number of cells (average of the two trials) captured with **1-SPN** (white bars) and **SPN** (black bars). (D) Tabular presentation of results.

rare earth magnet (Figure 6A). In agreement with the microagglutination results, *S. aureus* cells are readily labeled with **1-SPN** and can be magnetically confined. Nonspecific capture could be completely suppressed by coating nanoparticles overnight with 0.1% Tween 20 and performing the binding in the presence of 1% Tween 20. It is noteworthy that such conditions may denature other antibody fragments, but the chemical stability inherent to sdAbs allows them to maintain activity under these conditions. As can be seen in Figure 6 (B,D), **1-SPN** is able to label and capture *S. aureus* with a capture efficiency of over 90% with as few as 180 cells (the number of cells subjected to capture studies ranged from 180−4000). As expected, the capture is mediated by **1**, as evidenced by the poor capture efficiency exhibited by **SPN** (5%). Finally, a competition assay was performed involving several samples containing both *S. aureus* and *S. typhimurium* cells.

In these competition assays, mixtures of both bacteria were incubated with **1-SPN** and subsequently magnetically confined. The capture selectivity was determined through the enumeration of the captured cells onto selective culture plates (BP plates for *S. aureus*, XLD plates for *S. typhimurium*), where the ratio of the *S .aureus* to *S. typhimurium* in the captured fraction was used to determine capture specificity. The total numbers of cells in the **1-SPN** mixtures were 1170 *S. aureus* and 525 *S. typhimurium* cells in one trial and 2780 *S. aureus* and 2420 *S. typhimurium* in the second trial. As can be seen in Figure 6C,D, **1-SPN** discriminately captures *S. aureus* over *S. typhimurium* with a ratio of 13:1. The number of *S. typhimurium* cells captured by **1-SPN** is at the background level and is essentially the same as the numbers captured by **SPN** in the case of both bacteria (Figure 6C, inset).

The capture selectivity could be further improved simply by including a wash step immediately following the binding step. As highlighted in Figure 7A,C, the capture efficiency was as high as 98% for **1-SPN** vs only 0.8% for the **SPN**. (The total number of *S. aureus* cells was 338 in the **1-SPN** mixture and 278 in the **SPN** mixture; the wash step removed 6 *S. aureus* from the **1-SPN** mixture and 24 from the **SPN** mixture.) Without the wash step, **1-SPN** capture efficiency would have remained at exactly the same level, but that of **SPN** would have been as high as 9%. This demonstrates that there is very little nonspecific absorption contributing to the interaction between **1-SPN** and the *S. aureus* cells. In the case of specificity capture studies, we used a mixture of cells with as few as 80 *S. aureus* cells and 56 *S. typhimurium* cells (Figure 7B,C). The capture specificity was adequate (80 *S. aureus*/4 *S. typhimurium*) immediately following incubation and magnetic confinement and extremely high following the washing step after confinement (78 *S. aureus* and no *S. typhimurium*; the wash step removed 2 *S. aureus* and 4 *S. typhimurium*). Thus, without the wash step the capture specificity ratio would have been significantly lower.

Assessing the Binding Specificity of 1-SPN by Capture Studies and Electron Microscopy. The binding (or lack of interaction) of both **1-SPN** and **SPN** to *S. aureus* cells could also be qualitatively assessed by means of TEM analysis. Examples of these TEM binding experiments are provided in Figure 8. From these images, two factors are clear. First, **1-SPN** interacts much more effectively over the entire surface of the *S. aureus* cells (Figure 8A) as opposed to **SPN** (Figure 8B), indicating that the sdAb mediates the specific interaction between the nanoparticles and the *S. aureus* cells. Second, in agreement with the microagglutination and capture specificity investigations highlighted above, the TEM analysis suggests that there is very little interaction between **1-SPN** and the *S. typhimurium* cells (Figure 8C). Also as expected, there was essentially no interaction between **SPN** and *S. typhimurium* (data not shown).

Previously an IgG-modified SPN conjugate was reported to interact with *S. aureus*, *S. saprophyticus*, and *S. pyogenes* (group A *Streptococcus*) through the Fc-region of the antibody (Figure 1) and surface ligands on the various bacteria (*3*). It is expected that such constructs may also cross-react with group C and G *Streptococci* through interaction with bacterial protein G (*19*). Because specificity/selectivity is an important characteristic that is required for most biodiagnostic applications, we also assessed the specificity of **1-SPN** through capture/SEM experiments with *S. saprophyticus*, *S. pyogenes*, *and S. pneumoniae* (a protein G-containing *Streptococcus* species of bacteria). Mixtures of nanoparticles (10^{12}) and cells (10^{8}) were incubated for binding and were subsequently subjected to magnetic confinement. While in the case of **1-SPN**/*S. aureus*, the solution became clear in a couple of minutes following the magnetic confinement with cells clumped against the vessel wall, indicating a very strong

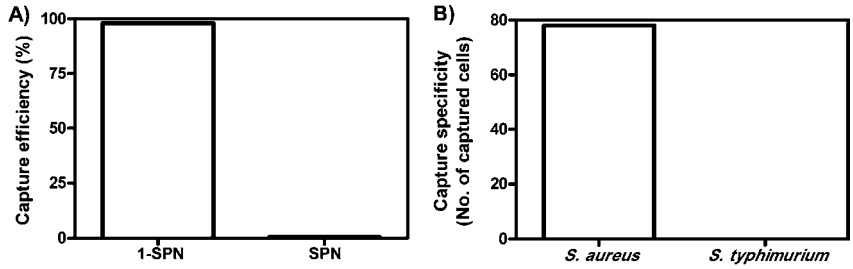

C)

	Capture efficiency		Capture specificity
	1-SPN	**SPN**	**No. *S. aureus*/No. *S. typhimurium***
With wash	98%	0.8%	78/0
Without wash	98%	9%	80/4

Figure 7. Cell capture efficiency and specificity of **1-SPN** nanoconjugate when a single wash step is included after the binding step. Capture specificity is shown by comparing the number of *S. aureus* vs *S. typhimurium* in the mixed capture fraction. (C) Tabular presentation of results.

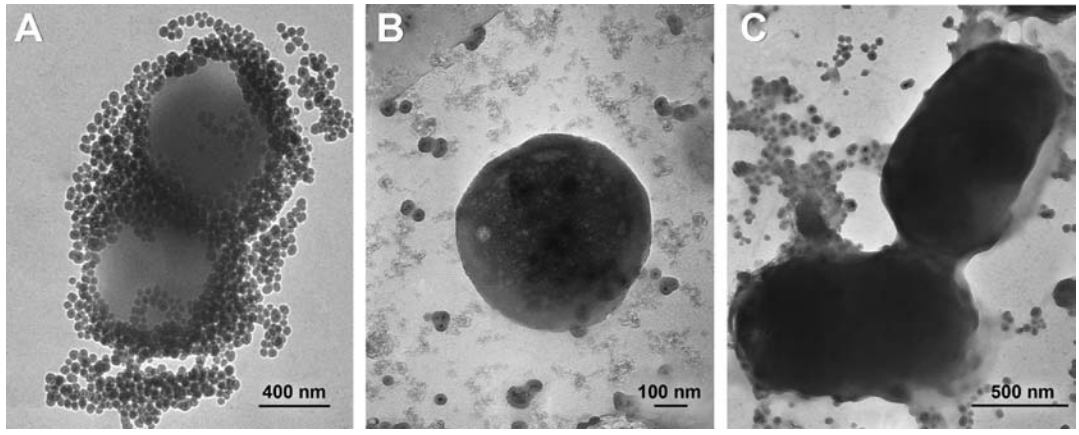

Figure 8. Representative TEM images of the **1-SPN**−bacteria conjugates where there is a strong interaction between **1-SPN** and *S. aureus* cells (A) in contrast to the inefficient labeling of *S. typhimurium* by the same nanoparticles (C). Control TEM images were also acquired confirming that **SPN** does not interact effectively with *S. aureus* cells in the absence of **1** (B).

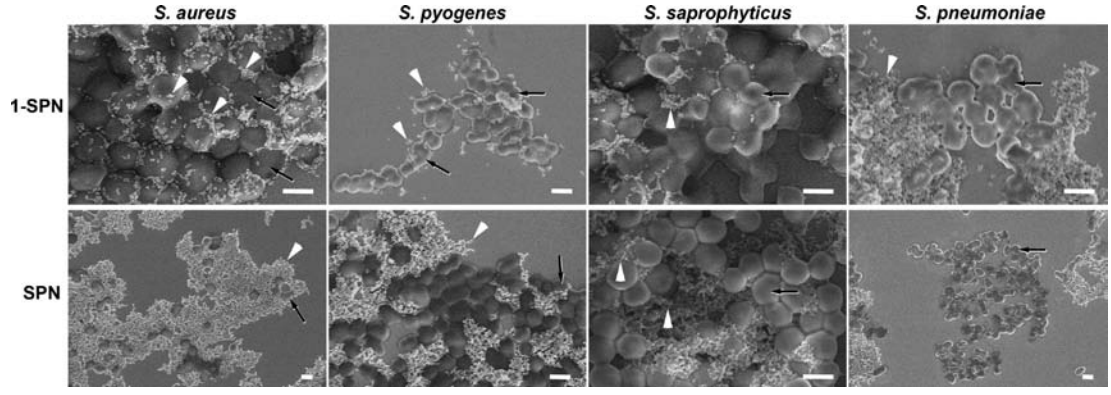

Figure 9. Assessing the cross-reactivity of **1-SPN** toward *S. saprophyticus*, *S. pneumoniae*, and *S. pyogenes* by SEM experiments. Cells and nanoparticles are shown by black and white arrows, respectively. The scale bar corresponds to 1 μm.

binding interaction between **1-SPN** and *S. aureus*, in the case of **SPN**/*S. aureus*, the solution stayed cloudy over the course of the confinement and there was no visible captured cells. With *S. pyogenes* and *S. pneumoniae*, both **1-SPN** and **SPN** hardly gave any captured cells, and by the end of the two washes (cycles of resuspension and confinement), there was no visible pack of confined cells. Only in the case of *S. saprophyticus* was some capture observed, albeit with a significant amount of cells still in the supernatant fraction. However, the capture was the same for both **1-SPN** and **SPN**, indicating some nonspecific interactions between **SPN** and *S. saprophyticus*. An aliquot of the confined materials following the last wash was used for SEM imaging.

Figure 9 summarizes results of the capture studies in a series of SEM images. The top panels of Figure 9 depict the interaction of cells with **1-SPN**, while bottom panels are the control experiments performed with **SPN**. In the *S. aureus* interaction with **1-SPN** capture study, SEM images showed each of the captured cells (dark sphere, ~1 μm) are flanked with **1-SPN** with most cells partially covered by the NP aggregates, which indicates positive binding response between cells and **1-SPN**. On the contrary, in the control experiment (*S. aureus* vs **SPN**), very large aggregates of **SPN** were observed with a few cells embedded in the **SPN** aggregates. Unlike the *S. aureus* vs **1-SPN** interaction, the captured cells in the control experiment have no **SPN** on their surface, nor were they flanked by the

nanoparticles. This suggests the lack of interaction between the control nanoparticles and *S. aureus*. It is possible that the few cells trapped in the control experiment were from the remaining 20 μL of the solution left after the capture step rather than magnetically confined. SEM images of the interaction between **1-SPN** with *S. pyogenes* and *S. pneumoniae* showed very similar patterns. Both images showed clusters of cells without any nanoparticles binding to their surfaces nor flanked in between the cells, which suggests the non-interactive nature of the **1-SPN** to both *S. pyogenes* and *S. pneumoniae*. Control experiments of both species exposed to **SPN** also showed a similar noninteraction pattern. Despite the observation of very large aggregates of **SPN** in the images of the control study, there were no nanoparticles binding to the surface of the cells as observed in the case of *S. aureus* vs **1-SPN** image. Since, in the case of both *S. pyogenes* and *S. pneumoniae*, there is no binding seen in the images as well as during the earlier confinement step, it is very likely that the cells seen in the images are carryover from the nonbinding fraction (see above and Experimental Procedures). We did, however, observe some interaction between both **1-SPN** and **SPN** with *S. saprophyticus* as suggested by Figure 9. In both *S. saprophyticus* vs **1-SPN** and *S. saprophyticus* vs **SPN** images, cells are flanked and partially covered by the nanoparticles, indicating a positive interaction between the nanoparticles and the cell. Because this is observed in both experiments, it is likely that the interactions are nonspecific, a conclusion that is also supported by the results of the capture step above. It is possible that such nonspecific interaction can be further reduced by passivating the nanoparticles surfaces with agents that suppress nonspecific interactions such as serum albumins. It is also very likely that the interaction between **1-SPN** and *S. saprophyticus* could be distinguished from the interaction between **1-SPN** and *S. aureus* in a real detection situation simply by looking at all of these interactions together.

DISCUSSION

Protein A is (i) highly characteristic of *S. aureus* with some 99% of *S. aureus* strains having protein A on their surface (*20, 21*) and (ii) highly abundant on the surface of *S. aureus* (*22*). These characteristics make protein A an attractive marker for effective and specific detection of *S. aureus* (*3, 21, 23*−*25*). In fact, the commercially available latex agglutination test, which is a standard method for *S. aureus* detection, is based on protein A−antibody interaction (*23, 25*). Recently, a gold nanoparticle-based immunochromatographic test developed for *S. aureus* detection and based on IgG−protein A interaction gave an impressive sensitivity of 100% for 130 *S. aureus* strains and specificities of 94.7% and 100% for *S. aureus* when also tested against 19 and 17 *Staphylococus* spp. (non-*S. aureus*) and non-*Staphylococci* strains, respectively (*25*). The latex agglutination test, which operates on the same recognition principle as the immunochromatographic test, gave identical results (*25*). The one false positive seen in the case of *S. xylosus* in the *Staphylococus* spp. group was presumably due to the presence of protein G on the surface of *S. xylosus*, which can cross-react with antibodies. This protein G-based cross-reactivity should not exist in the case of our nanconjugate, a conclusion supported by the lack of interaction between **1-SPN** and the protein G-displaying *S. pneumoniae* (Figure 9). Thus, on the basis of the above facts, the highly selective nature of the antibody−protein A pseudoimmune interaction (see Figure 1) and our own specificity/cross-reactivity studies, we expect **1-SPN** architecture to be *at least* as specific as the previously described detection systems, which rely on whole antibody−protein A interactions.

A potential advantage to the approach presented here involves the logical extension to dye or quantum dot-labeled superparamagnetic nanoparticles, which in addition to target preconcentration would provide detection signals. Alternatively, the detecting signals can be provided with SERS (surface enhanced Raman scattering)-active sdAb nanoconjugates (*10*) when used in combination with the present superparamagnetic nanoconjugates. Standard clinical detection methods, e.g., latex agglutination test for *S. aureus*, are time-consuming (takes a few days to obtain results) and laborious, as they involve steps such as plating and bacterial enrichment (*21, 26*). Detection platforms based on the present concept, besides offering better specificity (see above), would be fast and simple to perform. We have shown that it takes as little as 10 min to capture *S. aureus* with **1-SPN** (unpublished results) and no more than 10 min to detect the captured *S. aureus* by SERS-active sdAb conjugates, with single cell sensitivity (*28*). Additional advantages inherent to nanoparticle-based targeting agents include superior labeling efficiencies owing to large surface area to volume ratios and the fact that the nanoparticles are colloidally stable and are small, so binding kinetics should be significantly improved in comparison to micrometer-sized analogues (*27*).

On the basis of the performance of the present nanoconjugates and previously described SERS-active sdAb-silver nanoparticles (*10*) and the aforementioned properties of sdAbs, we strongly recommend sdAbs over other antibody formats as the recognition moiety of nanoparticles and nanowires.

CONCLUSION

In summary, sdAbs are highly stable, active, and specific agents capable of mediating interactions between superparamagnetic nanoparticles and a few tens of pathogenic bacteria in mixed cell populations with exceptionally high specificity and efficiency. The use of sdAb eliminates much of the cross-reactivity previously reported for nanoconjugates utilizing whole antibodies to interface the nanoparticles with the bacteria (*3*). These superparamagnetic nanoconjugates owe their excellent performance to a combination of multivalency and the unique properties of its sdAb component. A previously reported *S. aureus*-specific silver nanoconjugate which also relied on a sdAb for its recognition also performed very well (*10*), and it is expected that a combination of such nanoparticles could lead to very effective magnetic confinement and optical detection scaffolds for sensitive pathogen detection.

ACKNOWLEDGMENT

This is National Research Council of Canada Publication 50005. We acknowledge Rebecca To for constructing pentameric single-domain antibodies, Tomoko Hirama for performing surface plasmon resonance experiments, and Tom Devecseri for preparing publication quality figures. We are indebted to Catherine Bibby for acquiring the TEM images. We also thank NRC-NSC-ITRI for funding.

Supporting Information Available: Description of experimental procedures for quantifying the number of sdAbs on the nanoparticles and representative TEM images of the **1-SPN** nanoparticles. This material is available free of charge via the Internet at http://pubs.acs.org.

LITERATURE CITED

(1) Gu, H., Xu, K., Xu, C., and Xu, B. (2006) Biofunctional magnetic nanoparticles for protein separation and pathogen detection. *Chem. Commun. (Camb.)* 941–949.

(2) Kalele, S. A., Kundu, A. A., Gosavi, S. W., Deobagkar, D. N., Deobagkar, D. D., and Kulkarni, S. K. (2006) Rapid detection of *Escherichia coli* by using antibody-conjugated silver nanoshells. *Small 2*, 335–338.

(3) Ho, K. C., Tsai, P. J., Lin, Y. S., and Chen, Y. C. (2004) Using biofunctionalized nanoparticles to probe pathogenic bacteria. *Anal. Chem. 76*, 7162–7168.

(4) Su, X. L., and Li, Y. (2004) Quantum dot biolabeling coupled with immunomagnetic separation for detection of *Escherichia coli* O157:H7. *Anal. Chem. 76*, 4806–4810.

(5) Tu, S.-I., Uknalis, J., Gore, M., Irwin, P., and Feder, I. (2003) Factors affecting the bacterial capture efficiency of immuno beads: A comparison between beads with different size and density. *J. Rapid Methods Autom. Microbiol. 11*, 35–46.

(6) Tu, S.-I., Uknalis, J., Gore, M., and Irwin, P. (2002) The capture of *Escherichia coli* O157:H7 for light addressable potentiometric sensor (LAPS) using two different types of magnetic beads. *J. Rapid Methods Autom. Microbiol. 10*, 185–195.

(7) Sjoquist, J., Movitz, J., Johansson, I. B., and Hjelm, H. (1972) Localization of protein A in the bacteria. *Eur. J. Biochem. 30*, 190–194.

(8) Burova, L. A., Nagornev, V. A., Pigarevskii, P. V., Gladilina, M. M., Molchanova, I. V., Selivestrova, V. G., Tern, A., Lindahl, G., and Totolian, A. A. (1999) Streptococcal IgG Fc-binding proteins - initiation factors of experimental glomerulonephritis. *Biull. Eksp. Biol. Med. 128*, 548–552.

(9) Holliger, P., and Hudson, P. J. (2005) Engineered antibody fragments and the rise of single domains. *Nat. Biotechnol. 23*, 1126–1136.

(10) Tay, L., Tanha, J., Ryan, S., Veres, T. (2007) Detection of *Staphylococci aureus* cells with single domain antibody functionalized Raman nanoparobes. Photonics North (Armitage, J., Ed.) Proceedings of the SPIE, 6796: 67960C.

(11) Arbabi-Ghahroudi, M., Tanha, J., and MacKenzie, R. (2005) Prokaryotic expression of antibodies. *Cancer Metastasis Rev. 24*, 501–519.

(12) To, R., Hirama, T., Arbabi-Ghahroudi, M., MacKenzie, R., Wang, P., Xu, P., Ni, F., and Tanha, J. (2005) Isolation of monomeric human V_HS by a phage selection. *J. Biol. Chem. 280*, 41395–41403.

(13) Kell, A. J., and Simard, B. (2007) Vancomycin architecture dependence on the capture efficiency of antibody-modified microbeads by magnetic nanoparticles. *Chem. Commun.* 1227–1229.

(14) Zhang, J., Li, Q., Nguyen, T.-D., Tremblay, T. T. L., Stone, E., To, R., Kelly, J., and MacKenzie, C. R. (2004) A pentavalent single-domain antibody approach to tumor antigen discovery and the development of novel proteomics reagents. *J. Mol. Biol. 341*, 161–169.

(15) Pace, C. N., Vajdos, F., Fee, L., Grimsley, G., and Gray, T. (1995) How to measure and predict the molar absorption coefficient of a protein. *Protein Sci. 4*, 2411–2423.

(16) Sambrook, J., Fritsch, E. F., Maniatis, T. *Molecular Cloning: A Laboratory Manual*, 2nd ed., Cold Spring Harbor Laboratory: Cold Spring Harbor, NY, 1989.

(17) Saito, T., Kawabata, S., Hirata, M., and Iwanaga, S. (1995) A novel type of limulus lectin-L6. Purification, primary structure, and antibacterial activity. *J. Biol. Chem. 270*, 14493–14499.

(18) Zhang, J., Tanha, J., Hirama, T., Khieu, N. H., To, R., Tong-Sevinc, H., Stone, E., Brisson, J. R., and MacKenzie, C. R. (2004) Pentamerization of single-domain antibodies from phage libraries: A novel strategy for the rapid generation of high-avidity antibody reagents. *J. Mol. Biol. 335*, 49–56.

(19) Tashiro, M., and Montelione, G. T. (1995) Structures of bacterial immunoglobulin-binding domains and their complexes with immunoglobulins. *Curr. Opin. Struct. Biol. 5*, 471–481.

(20) Forsgren, A. (1970) Significance of protein A production by *Staphylococci*. *Infect. Immun. 2*, 672–673.

(21) Chang, Y. H., Chang, T. C., Kao, E. F., and Chou, C. (1996) Detection of protein A produced by *Staphylococcus aureus* with a fiber-optic-based biosensor. *Biosci. Biotechnol. Biochem. 60*, 1571–1574.

(22) Kronvall, G., Quie, P. G., and Williams, R. C., Jr. (1970) Quantitation of Staphylococcal protein A: Determination of equilibrium constant and number of protein A residues on bacteria. *J. Immunol. 104*, 273–278.

(23) Fukuda, S., Tatsumi, H., Igarashi, H., and Igimi, S. (2000) Rapid detection of *Staphylococcus aureus* using bioluminescent enzyme immunoassay. *Lett. Appl. Microbiol. 31*, 134–138.

(24) Mongodin, E., Bajolet, O., Hinnrasky, J., Puchelle, E., and de Bentzmann, S. (2000) Cell wall-associated protein A as a tool for immunolocalization of *Staphylococcus aureus* in infected human airway epithelium. *J. Histochem. Cytochem. 48*, 523–534.

(25) Huang, S. H. (2006) Gold nanoparticle-based immunochromatographic test for identification of *Staphylococcus aureus* from clinical specimens. *Clin. Chim. Acta 373*, 139–143.

(26) Zhao, X., Hilliard, L. R., Mechery, S. J., Wang, Y., Bagwe, R. P., Jin, S., and Tan, W. (2004) A rapid bioassay for single bacterial cell quantitation using bioconjugated nanoparticles. *Proc. Natl. Acad. Sci. U.S.A. 101*, 15027–15032.

(27) Gu, H. W., Xu, K. M., Xu, C. J., and Xu, B. (2006) Biofunctional magnetic nanoparticles for protein separation and pathogen detection. *Chem. Commun.* 941–949.

(28) Huang, P.-J., Tay, L.-L., Tanha, J., Ryan, S., Chau, L.-K. (2009) Single-domain antibody-conjugated nanoaggregate-embedded beads for targeted detection of pathogenic bacteria. *Chemistry* DOI: 10.1002/chem.200901397.

BC900332R

Supporting Information

Contents

1. Title
2. Authors
3. Experimental Procedures

Single-Domain Antibody-Nanoparticles: Promising Architectures for Increased *Staphylococcus aureus* Detection Specificity and Sensitivity

Shannon Ryan, Arnold J. Kell, Henk van Faassen, Li-Lin Tay, Benoit Simard, Roger MacKenzie, Michel Gilbert, and Jamshid Tanha

EXPERIMENTAL PROCEDURES

In order to elucidate the number of single-domain antibodies (sdAbs) anchored to the surface of each SPN, **1-SPN** was reacted with tetramethylrhodamine isothiocyanate (TRITC). The reaction was carried out in MES buffer with **1-SPN** (6×10^{12} nanoparticles) and TRITC (50 µg, 1.2×10^{-7} moles) and the resulting TMR-modified **1-SPN** was purified and analyzed by UV-visible spectroscopy in order to elucidate the number of sdAbs (**1**) on the surface of the nanoparticle. The UV-visible absorption spectra of freshly prepared, day-old **1-SPN** and one-year-old **1-SPN** (6×10^{12} nanoparticles/mL) and the original **1-SPN** are presented in Figure S1. Analysis of these spectra suggests that TMR has reacted with the sdAb on **1-SPN**, where there is an increase in absorption centered at 550 nm in comparison to the unmodified **1-SPN**. Note that an accurate absorption spectrum of the TMR can be obtained by subtracting the unmodified **1-SPN** from the **1-SPN(TMR)** (Figure S1). When the number of TMR molecules was known, the number of sdAb (**1**) per nanoparticle could be elucidated by assuming that only one of the six amine groups on **1** is responsible for anchoring it to the surface of the SPN. Construction of a calibration curve for TRITC in MES-buffered water and the comparison of the absorption intensity for the **1-SPN** samples suggest that there are 12 and 4 sdAbs per **1-SPN** for one-day-old nanoparticles and nanoparticles sitting in MES buffer at pH 6 for 1 year, respectively. This data is presented in Figure S2.

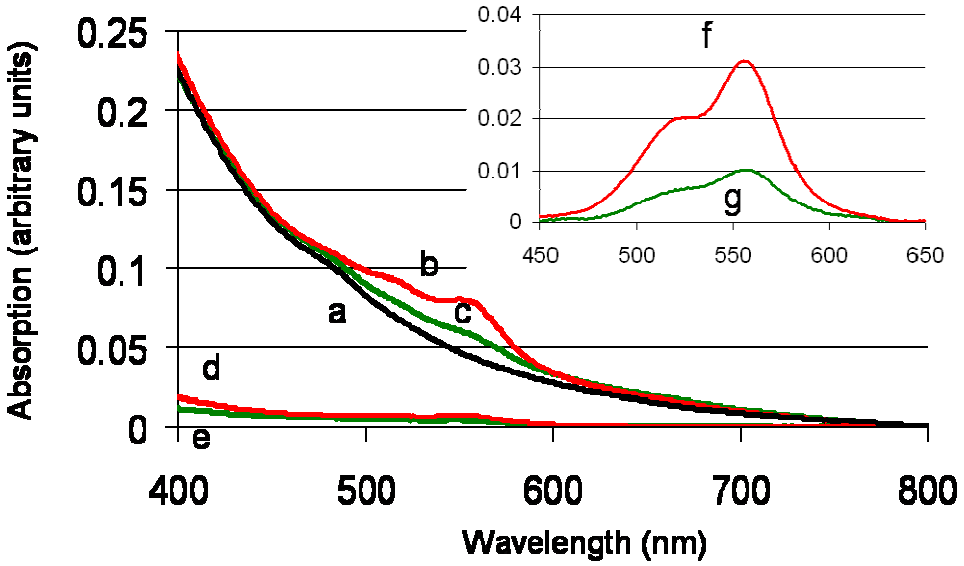

a) 1-SPN ($6x10^{12}$ particles)

b) One-day-old 1-SPN modified with TMR ($6x10^{12}$ particles)

c) Year-old 1-SPN modified with TMR ($6x10^{12}$ particles)

d) Magnetically confined one-day-old 1-SPN modified with TMR ($6x10^{12}$ particles)

e) Magnetically confined year-old 1-SPN modified with TMR ($6x10^{12}$ particles)

f) Corrected absorption spectra for one-day-old 1-SPN modified with TMR ($6x10^{12}$ particles) (i.e., b – a)

g) Corrected absorption spectra for year old 1-SPN modified with TMR ($6x10^{12}$ particles) (i.e., c – a)

Figure S1. The UV-visible absorption spectra of **1-SPN** (black), one-day-old **1-SPN** reacted with TRITC (red) and a year-old **1-SPN** reacted with TRITC (green). Note that when the nanoparticle absorption is subtracted, there is a clear absorption consistent with TMR (inset). Upon magnetic confinement, the absorption intensity of both the nanoparticle and TMR have decreased (bottom two spectra) suggesting that the TMR is covalently linked to the **1-SPN** in both cases.

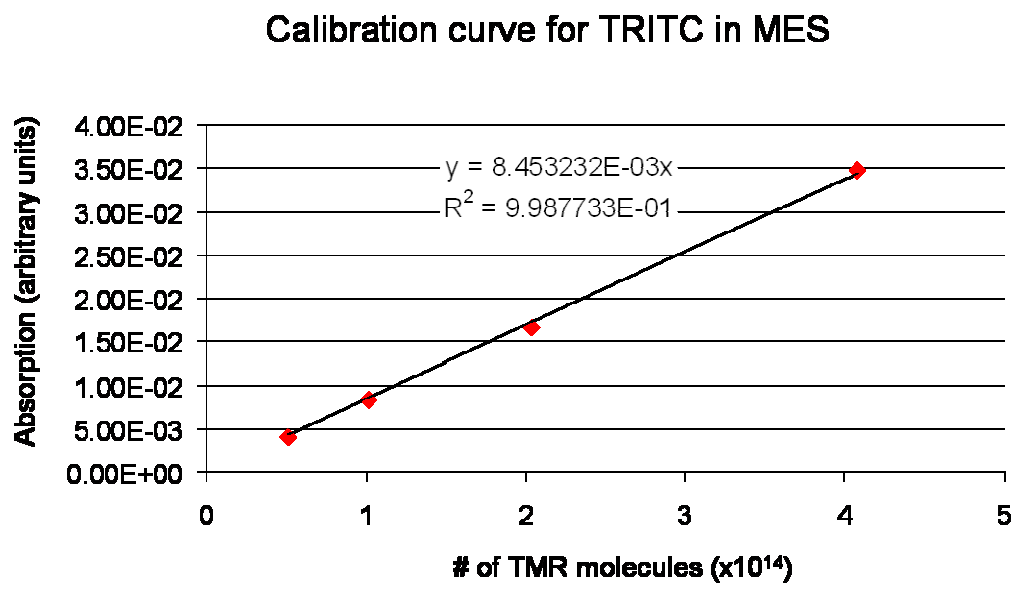

One-day-old 1-SPN modified with TMR (6×10^{12} particles)

Absorption = 0.031
# of TMR molecules = 3.7×10^{14}
# TMR molecules per SPN = 61
# TMR molecules per sdAb = 5
# sdAb per SPN = ~12

Year-old 1-SPN modified with TMR (6×10^{12} particles)

Absorption = 0.010
# of TMR molecules = 1.2×10^{14}
# TMR molecules per SPN = 19.7
# TMR molecules per sdAb = 5
# sdAb per SPN = ~4

Figure S2. The calibration curve for TRITC in MES buffer and the calculations used to determine the average number of sdAb (**1**) on each nanoparticle. The calculations are based on the UV-visible absorption data shown in Figure S1.

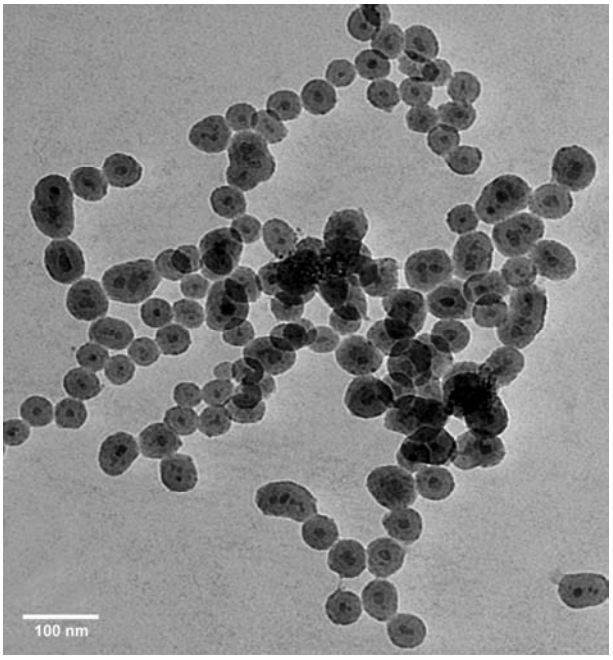

Figure S3. A representative TEM image of the nanoparticles employed in this investigation (**1-SPN**).

The average size of **1-SPN** was determined to be 49 ± 7 nm.

Antibody Internalization after Cell Surface Antigen Binding is Critical for Immunotoxin Development

Shu-Ru Kuo, Randall W. Alfano, Arthur E. Frankel, and Jen-Sing Liu*

Cancer Research Institute of Scott & White Hospital; Department of Internal Medicine, Health Science Center, College of Medicine, Texas A&M University, 5701 South Airport Road, Temple, Texas 76502. Received July 27, 2009; Revised Manuscript Received September 3, 2009

Immunotoxin potency is dependent on cell surface binding specificity as well as internalization efficiency. Current approaches for immunotoxin development are dependent on existing antibodies that were selected for high affinity and/or high production yield. However, these antibodies may demonstrate low internalization efficiency upon cell surface binding and thus are not necessarily the best candidates for immunotoxin design. Here, we have developed an assay with a novel protein, DTG3, to compare and evaluate the internalization efficiency of monoclonal antibodies in order to circumvent the possibility of low internalization. DTG3 is a fusion protein containing the N-terminus of diphtheria toxin (DT) and three copies of streptococci Protein G immunoglobulin binding domains. We show that antibody-DTG3 complexes formed in the test tube are able to bind their antigen on the target cell surface, resulting in cell internalization, DT-mediated protein synthesis inhibition, and host cell apoptosis. We tested this system with two well-studied antibodies, antihuman CD3ε, and anti-PSMA antibodies and were able to show efficiency of this assay. We further examined commercially available anti-CD123 antibodies for potential leukemia-targeting immunotoxin development. Finally, we applied this system in the early-stage screening of newly generated anti-CD123 hybridomas. Our data showed that this internalization assay system is sensitive, time efficient, and reproducible, and has provided a tool to compare monoclonal antibodies for the clinical development of effective immunotoxins for the treatment of a variety of neoplasms.

INTRODUCTION

Attempts to explicitly target proliferating tumor cells, and thus enhance therapeutic efficacy, have led to the development of targeted immunotoxins (*1*). These agents direct the powerful lethal action of recombinant bacterial or plant toxins to tumor cells through the fusion to growth factors, monoclonal antibodies, or antibody fragments that recognize tumor cell-specific epitopes. Toxins typically utilized for this application are referred to AB-toxins due to their structural organization. The A moiety consists of an enzymatic domain that modifies a specific intracellular target, causing the disruption of cell functions that are critical for cell survival. The B moiety, which is often modified for tumor cell targeting, comprises one or multiple subunits that bind cell surface receptors and permit the translocation of the A moiety into the host cytosol. Rapid progress in the understanding of toxin structure and function has fueled the development of numerous novel immunotoxins for use in hematological cancer therapy (*2*).

The selection of cell-binding peptides that have high specificity to the intended target cell as well as high internalization efficiency upon cell surface binding is critical in immunotoxin design. Traditional methods used to study internalization efficiency of cell surface targeting peptides were dependent on the use of isotopes such as ^{125}I or microscopy techniques (*3*−*6*). However, these methods proved to have inadequate sensitivity. More sensitive techniques included chemically conjugating the cell-targeting antibody to a toxin to measure cell killing directly (*7*). Since catalytic toxins are able to kill cells with as few as one molecule per cell, this assay can have much higher sensitivity than isotope or fluorescent-based techniques. However, chemical conjugation is time-consuming, costly, and has poor reproducibility. Recently, Mazor et al. (*8*) reported the development of a novel IgG binding toxin fusion protein (ZZ-PE38) for antibody internalization assays. The ZZ-PE38 fusion protein contains two copies of IgG-binding motif from Streptococcal protein A and a truncated *Pseudomonas* exotoxin A (PE38). The strong binding of protein A to the IgG Fc domain generated a bridge between the IgG and the catalytic toxin and, therefore, conveniently eliminated the need for chemical conjugation. Purified ZZ-PE38 and antibody complexes were shown to be homogeneous with antigen-binding domain exposed. This method has proved to be an invaluable tool to be further developed for antibody internalization studies.

Our laboratory has been studying the therapeutic potential of several diphtheria toxin based immunotoxins for treatment in leukemia (*9*). Efforts have been focused on targeting the interleukin-3 (IL3)[1] receptor via a fusion protein composed of the catalytic and translocation domains of diphtheria toxin (DT_{388}) linked to the IL3 cytokine (*10*−*13*). This fusion protein, known as DT_{388}IL3, is currently under evaluation for efficacy and safety in phase I clinical trials (*9*). Although still ongoing, alternative approaches for IL3R targeting are already underway. The α subunit of IL3R (CD123) has been shown to be up-regulated in acute myeloid leukemias, acute lymphoblastic leukemias, plasmacytoid dendritic cell leukemias, and some chronic myeloid leukemias (*3*, *14*−*17*). In contrast, the IL3R common β subunit (CDw131) is not always coexpressed in those leukemias (*18*). Thus, therapeutic agents targeting CD123 alone have potential for broader applications.

* To whom correspondence should be addressed. Dr. Jen-Sing Liu, Cancer Research Institute of Scott & White, 5701 South Airport Road, Temple, Texas 76502, USA. Tel: (254) 724-1839; Fax: (254) 724-2324; Email: jliu@swmail.sw.org.

[1]Abbreviations: IL3, interleukin-3; IL3R, interleukin-3 receptor; IgG, immunoglobulin G; DT, diphtheria toxin; PE, *Pseudomonas* exotoxin; AML, acute myeloid leukemia; PSMA, prostate specific membrane antigen; DMP, dimethyl pimelimidate; PBS, phosphate buffer saline.

10.1021/bc900333j CCC: $40.75 © 2009 American Chemical Society
Published on Web 09/28/2009

These findings prompted the development of immunotoxins targeting CD123. Du et al. (*19*) produced constructs consisting of *Pseudomonas* exotoxin PE38 and single-chain Fv of anti-CD123 antibodies. *In vitro* potency assays showed that an optimized construct, 26292(Fv)-PE38KDEL, had an IC_{50} in leukemia cells at around 500 pM. Although encouraging, this construct exhibited lower cytotoxicity than that of $DT_{388}IL3$ (IC_{50} at ~10 pM) (*12*, *20*). Since 26292(Fv)-PE38KDEL showed strong cell-surface binding to the targeted cells, the observed 50-fold lower potency might have been a result of low internalization efficiency.

In order to address these preliminary findings, we have developed a new antibody internalization assay with a novel recombinant protein, DTG3. This protein consists of the truncated diphtheria toxin (DT_{388}) fused to 3 copies of IgG biding motif from group G streptococci Protein G (*21*). Here, we describe the efficiency of this method using the well-studied antihuman CD3ε and PSMA antibodies in order to demonstrate biological activity and thus provide proof of principle. Our results indicate that the DTG3 coupling system described here provides a rapid method with high sensitivity to compare and evaluate antibody internalization efficiencies. We further prove that this method can be used in the early stage of hybridoma screening to identify new anti-CD123 antibodies with high internalization efficiency.

EXPERIMENTAL PROCEDURES

Plasmids. (1) pDTG1-His, pDTG2-His, and pDTG3-His: The plasmids expressing DT-proteinG fusion proteins were made of 2 parts: the sequence of the N-terminal 388 amino acids of diphtheria toxin (DT) was derived from pRKDTIL3 (*22*); and the DNA fragment containing the codon-maximized sequence for IgG binding proteins and linkers was synthesized by GenScript (Piscataway, NJ). To construct IgG binding protein, the sequence of the second IgG binding domain of wild-type group G streptococci Protein G (GBII) (*21*) was used. Seven and 8 amino acids immediately adjacent to the N-terminus and C-terminus, respectively, of the 55-amino-acid GBII core domain were also added to provide spacers when multiple copies were cloned. This amino acid sequence was reverse translated into the DNA sequence following preferred codon usage in *E. coli*. Six-nucleotide linkers recognized by restriction enzyme *Bam*H 1 and *Bgl*II were added to the 5′ and 3′ ends, respectively. To the 3′ end, DNA sequence of 6 histidines, a termination codon (TGA) and a *Hind* III recognition site were then added. The entire sequence was synthesized by GenScript and delivered within pUC57 plasmid (pUC57-G1-His). The *Bam*H 1-*Hind* III fragment of pUC57-G1-His was inserted to pET-EE plasmid (*23*) to generate pET-EE-G1-His. The *Bam*H 1-*Bgl*II fragment from pUC57-G1-His was then inserted to *Bam*H1 site of pET-EE-G1-His to produce pET-EE-G2-His. The same strategy was used to generate pET-EE-G3-His. The *Nde* I-*Hind* III fragments from pET-EE-G1-His, pET-EE-G2-His, and pET-EE-G3-His were inserted into pRKDTIL3 to create pDTG1-His, pDTG2-His, and pDTG3-His expression plasmids. (2) pcDNA-CD123: The cDNA of human CD123 was reverse-transcribed and amplified from leukemia cell line TF1 using Qiagen RNeasy mini and onestep RT-PCR kits. The PCR primers used are 5′-CCGGAGCTAGCGTTCCCGATGGTCC-3′ with one underlined *Nhe* I recognition site and 5′-TGGCCCGGCCGGG-GAGATTGAGGCA-3′. The 1.2 kb PCR product was first cloned into the pDrive vector using Qiagen PCR cloning kit and followed by subcloning into the *Kpn*I and *Nhe* I sites of a eukaryotic expression vector pcDNA3.1/Zeo (Invitrogen, Carlsbad, CA) to generate pcDNA-CD123.

Cell Lines and Antibodies. Jurkat cells, kindly provided by Dr. David M. Neville, and TF1/H-ras (*24*) cells were maintained in RPMI medium containing 10% FBS. PSMA-stably transfected NIH3T3 cells, a kind gift from Dr. Michel Sadelain, were maintained in DMEM medium containing 10% FBS. CHO-K1 cells (ATCC, Manassas, VA) were maintained in ATCC-formulated F-12K medium containing 10% FBS. pcDNA-CD123-stably transfected CHO-K1 cells expressing high copy number of CD123 were cultured in F-12K medium supplemented with 10% FBS and 0.4 mg/mL zeocin (Invitrogen, Carlsbad, CA).

Antihuman CD3ε antibody UCHT1 and antihuman PSMA antibody J591 were kindly provided by Drs. Jung Hee Woo and Neil H. Bander. Anti-CD123 antibodies 7G3 and 6H6 were purchased from BD Biosciences (San Jose, CA) and Abcam (Cambridge, MA), respectively. Anti-CDw131 antibody 1C1 was purchased from eBioscience (San Diego, CA).

Expression and Purification of DTG1, DTG2, and DTG3. Bacteria BL21(DE3) transformed with pDTG1-His, pDTG2-His, or pDTG3-His were cultured in SuperBroth containing 1.6 mM $MgCl_2$, 0.5% glucose, and 100 μg/mL ampicillin. A 4 mL overnight culture was added to 200 mL fresh medium at 37 °C until OD^{600} reached 0.6. The culture was cooled down to 18 °C (~1 h) before addition of IPTG to a final concentration of 0.2 mM. The induction was continued at 18 °C for 18 h. The cells were harvested and treated with 100 μg/mL lysozyme on ice for 30 min. The cell pellet was then resuspended in 20 mL of ice-cold hypotonic buffer (20 mM HEPES-K^+ pH 7.5, 5 mM KCl, 1 mM $MgCl_2$) on ice for 5 min. Cells were lysed by sonication once at 35 W for 30 s, followed by the addition of 5 mL 5 M NaCl, and three more sonications at 35 W for 30 s on ice. After centrifugation at 15 000 × *g* for 10 min, clear supernatant was mixed with 1 mL of $NiCl_2$-charged Chelator Sepharose beads (GE Healthcare, Piscataway, NJ) at 4 °C for 2 h. Beads were spun down and washed with 20 mM HEPES-K^+ pH 7.5 with 1 M NaCl followed by 5 mL each of Buffer A (20 mM HEPES-K^+ pH 7.5 with 100 mM NaCl), Buffer A with 2 mM imidazole, and Buffer A with 20 mM imidazole. The bound proteins were eluted with Buffer A with 200 mM imidazole. The collected protein peak fraction (about 1 mL) was loaded immediately into a 10/30 Superose 200 column (GE Healthcare, Piscataway, NJ) pre-equilibrated with Buffer A using a Purifier system (GE Healthcare, Piscataway, NJ). The fractions containing DT-proteinG fusion proteins (about 1.5 mL) was pooled, aliquoted, and stored at −20 °C.

Protein Gel Analysis. In a 10 μL reaction, 1 μg of DTG1, DTG2, or DTG3 was mixed with 0, 2, or 4 μg of antibody in phosphate buffer saline (PBS) pH 7.4 at room temperature. Control reactions had only 4 μg of antibody. For native gel analysis, the mixture was incubated at room temperature for 60 min. Two microliter aliquots of loading buffer (20 mM Tris-HCl pH 8.0, 50% glycerol) were added to each reaction before loading to a 5% native polyacrylamide gel. Electrophoresis was carried out at 60 V for 4 h on ice. The gel was then fixed with 35% methanol and 15% acetic acid for 10 min followed by Coomassie blue staining (BioRad, Hercules, CA) for 30 min. After destaining, images were taken by a gel documentation system and labeled by Photoshop.

For denatured gel analysis, the same reactions as described above were incubated at room temperature for 45 min before the addition of 1 μL 200 mM freshly prepared dimethyl pimelimidate (DMP; Sigma-Aldrich, St. Louis, MO) in PBS. The reactions were incubated for another 15 min before the addition of 1 μL of 1 M Tris−HCl pH 8.0 to neutralize unused DMP. Four microliters of 4× SDS sample buffer (Invitrogen, Carlsbad, CA) were added into each reaction and analyzed by an 8% SDS polyacrylamide gel running at 120 V for 90 min.

The gel was stained and destained as described above. Images were taken by a gel documentation system and labeled by Photoshop.

Chemical Conjugation. Antibodies were conjugated to CRM9 (a mutated DT) following the protocol of Zangemeister-Wittke (*7*). Ten milligrams of nicked CRM9 was prepared at 5 mg/mL in 50 mM sodium borate pH 8.0 with 1 mM EDTA. A fresh solution of SMCC (Pierce, Rockford, IL) was prepared at a concentration of 10 mM in dry DMF (Sigma-Aldrich, St. Louis, MO). A 20-fold molar excess of SMCC (Pierce, Rockford, IL) over CRM9 was added and mixed for 1 h at room temperature. This would add maleimide groups to CRM9 proteins. The filtered mixture was then added to a PD-10 desalting column (GE Healthcare, Piscataway, NJ) equilibrated with nitrogen flushed 10 mM sodium phosphate pH 7.0. The first peak was collected according to Bradford reading (BioRad, Hercules, CA), which corresponds to the derivitized toxin. The derivitized CRM9 was kept at 4 °C until use.

Two milligrams of antibodies was prepared in 50 mM sodium borate pH 8.0 and 1 mM EDTA. They were derivitized by adding a 20-fold molar excess of fresh 10 mM 2-IT (iminothiolane) solution (Pierce, Rockford, IL) in borate buffer, pH 8.3. This would add terminal sulfhydryl groups to antibodies. The mixture was allowed to react at room temperature for 1 h before it was applied to a PD-10 column (GE Healthcare, Piscataway, NJ) equilibrated with nitrogen-flushed 10 mM sodium phosphate pH 7.0. The first protein peak was collected and added to the derivitized CRM9 in a 15 mL conical tube. The mixture was allowed to react for 20 h at room temperature. Conjugates were purified through a Superdex 200 column (GE Healthcare, Piscataway, NJ) equilibrated by 10 mM sodium phosphate pH 8.0, 90 mM sodium sulfate, and 1 mM EDTA. The peak corresponding to the monoconjugated antibody was subsequently collected and concentrated using the centrifugal filter (Millipore, Billerica, MA). Concentration was determined via Bradford assay (BioRad, Hercules, CA).

Complex Formation. In a 10 μL reaction, 4 μg of monoclonal antibody was mixed with 2.5 μg of DTG3 at room temperature for 45 min. One microliter of 200 mM freshly prepared DMP in PBS was then added into each reaction and incubated for another 15 min before the addition of 1 μL 1 M Tris-HCl pH 8.0 to neutralize unused DMP. For the control, either antibody or DTG3 was omitted from the reactions.

Potency Assays. Potency of antibodies complexed with DT-proteinG fusion proteins or antibody−CRM9 conjugates was evaluated by their ability to suppress 50% of H^3-thymidine incorporation in treated cells (IC_{50}). The reactions were first diluted with fresh culture medium to the highest testing concentration (from 3 to 100 nM) based on antibody contents into the first column of 96-well round-bottom plates. Each sample was either triplicated or quadruplicated in the same plate. The first column was then diluted 1:3 to the second column and 3-fold dilution continued all the way to the 12th column. 50 μL aliquots of the diluted complexes were added to 96-well cell plates containing 1×10^4 cells in 100 μL per well. The cells were incubated at 37 °C in CO_2 incubator for 48 h before the addition of 1 μCi of H^3-thymidine to each well. After additional 18 h incubation at 37 °C in CO_2 incubator, the cells were harvested and counted in a β-counter. The potency curves were graphed using Prism fitted with sigmoid dose response curve with variable slopes.

Hybridoma Cell Line Production. All experiments involving animals were preapproved by IACUC of Scott & White Hospital (2008-049-R). Briefly, groups of 3 Balb/c mice were intraperitoneally injected with 5 million CD123-transfected CHO-K1 cells at day 1, day 15, and day 29. Blood samples were collected at day 36 to evaluate antibody titer induced in each animal by C-ELISA (see below) with parental or CD123-transfected CHO-K1 cells. The mouse with higher antibody titer was given a final boost at day 57 with intravenous injection of 2 million CD123-transfected CHO-K1 cells. Splenocytes were harvested at day 60 and fused with P3 × 63Ag8.653 myeloma cells (ATCC, Manassas, VA) following the published protocol (*25, 26*). Hybridoma cells were mixed in HAT selection medium containing methylcellulose and Hybridoma Fusion and Cloning Supplement (HFCS; Roche, Basel, Switzerland) and plated in ten 100-mm Petri dish (*26*). Ten days later, single colonies were picked and expanded in 96-well flat bottom plates with 200 μL of hybridoma culture medium. Culture supernatant from each well was diluted 1:10 and tested in C-ELISA with parental or CD123-transfected CHO-K1 cells to select clones that produced anti-CD123 antibodies. The initial culture supernatant from positive clones was used for iso-type identification with an Iso-Gold kit (BioAssay Works, Ijamsville, MD) and for IgG quantification with a mouse-IgG ELISA kit (Roche, Basel, Switzerland). The identified anti-CD123 antibody-producing hybridomas cell lines were expanded for further antibody purification.

Cell-Based ELISA (C-ELISA). One day prior to the experiment, 5×10^4 parental or CD123-transfeced CHO-K1 cells were seeded in each well of a flat-bottom 96-well plate. The next day, cells were washed with PBS and fixed with 3% formaldehyde in PBS at room temperature for 10 min. Fixed cells were washed thrice with PBS with 0.5% Tween 20 and incubated in Blocking Solution (PBS with 10% goat serum) for 30 min. Primary antibodies were then added at room temperature for 60 min followed by HRP-conjugated secondary antibodies (Jackson Lab, West Grove, PA) at room temperature for 45 min. The HRP activity was detected by HRP substrate (R&D, Minneapolis, MN) for 10 min and stopped by 0.5 M H_2SO_4. The plates were read by a plate reader set at 450 nm.

Antibody Purification. Hybridoma culture supernatant (200 mL) was mixed with 400 mL of 20 mM Tris-HCl pH8.0 at room temperature and applied to a 5 mL Q-Sepharose column (GE Healthcare, Piscataway, NJ). Total bound proteins were eluted with 20 mM Tris-HCl pH 8.0 with 1 M NaCl, adjusted to a final NaCl concentration of 3 M, and applied to a 2 mL Protein G Sepharose column (Pierce, Rockford, IL). Antibodies were eluted with 100 mM glycine pH 3.0 and neutralized immediately with 1/10 volume of 1.5 M Tris-HCl pH 8.8. Desalting column PD-10 (GE Healthcare, Piscataway, NJ) was used to exchange the buffer of purified antibodies to PBS with 20% glycerol. Protein concentrations were measured by Bradford assays (BioRad, Hercules, CA) with BSA (Pierce, Rockford, IL) as standards and verified by reduced SDS-PAGE.

RESULTS

Construction, Expression, and Production of DTG1, DTG2, and DTG3. DT-proteinG fusion proteins carrying one to three copies of the protein G IgG binding domains were expressed and purified from bacteria transformed with overexpression plasmids. These DT-ProteinG fusion proteins carry the N-terminus of diphtheria toxin (DT_{388}) that contains the catalytic and translocation domains but not the cell surface-binding domain (Figure 1A). The purified proteins with expected sizes were ≥95% pure (Figure 1B).

Complex Formation and Stabilization. The ability of the DT-ProteinG fusion proteins to form complexes with monoclonal antibodies was examined by native protein gel electrophoresis. Increasing amounts of anti-PSMA antibody J591 were titrated to fixed amounts of DT-proteinG fusion proteins. While both DTG2 and DTG3 formed stable complexes with J591 and appeared as a more slowly migrating band (compare lanes 6 and 9 to lane 10), DTG3 had a higher complex-forming

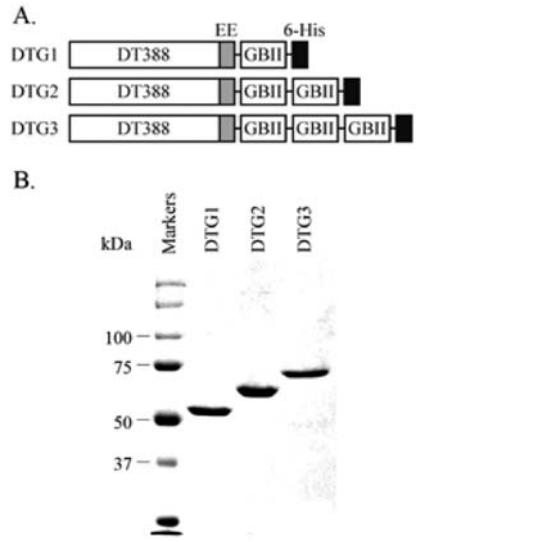

Figure 1. Construction and production of DTG1, DTG2, and DTG3. (A) N-terminal 388 amino acids of diphtheria toxin (DT388) was fused to a 9-amino-acid EE spacer (*32*) and 1−3 copies of the second copy of protein G IgG binding domain (GBII). The C-terminal histidine tag (6-His) allows easy purification. (B) Purified DTG1, DTG2, and DTG3 migrated in a 10% SDS-PAGE between markers of 50 and 75 kDa.

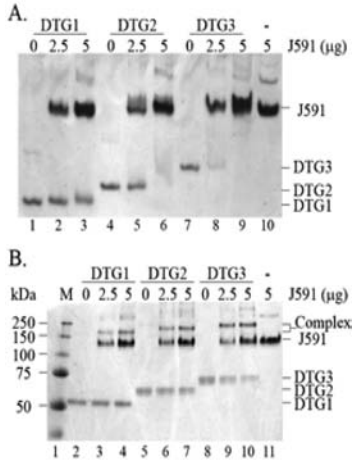

Figure 2. J591 and DT-proteinG fusion protein complex formation. (A) Native gel analysis. One microgram of DTG1, DTG2, or DTG3 was mixed with 0, 2.5, or 5 μg of J591 in PBS pH 7.4 at room temperature for 1 h. Protein mixtures were then loaded to a 5% native polyacrylamide gel and run on ice at 60 V for 4 h. (B) SDS-PAGE analysis. The same reactions as in (A) were added with 20 mM DMP to stabilize the complexes and loaded to a nonreduced 8% SDS-PAGE. Migration of each protein monomer, complexes, and the sizes of protein markers are labeled on the sides of each diagram. The faster migration of J591 at ~130 kDa (lane 10) was caused by DMP cross-linking.

efficiency (Figure 2A). The complete shift of 1 μg of DTG3 appeared at lane 8 where the antibody to DTG3 molar ratio was at about 1:1. Unfortunately, the protein complexes migrated only slightly more slowly than J591 alone, and J591-DTG1 complexes, if present, were not distinguishable from J591 (lanes 1−3).

In order to separate J591 from the complexes, a bifunctional cross-linker dimethyl pimelimidate (DMP) was added to stabilize these complexes and then analyzed in SDS-PAGE (Figure 2B). While DMP cross-linked only ~70% of the complexes (compare Figure 2A, lanes 8 and 9 to Figure 2B, lanes 9 and 10), this reagent does help to maintain the complex stability between J591 and DTG1 (Figure 2B, lanes 2 and 3). On the basis of the migration of the complexes to calculate their molecular weights,

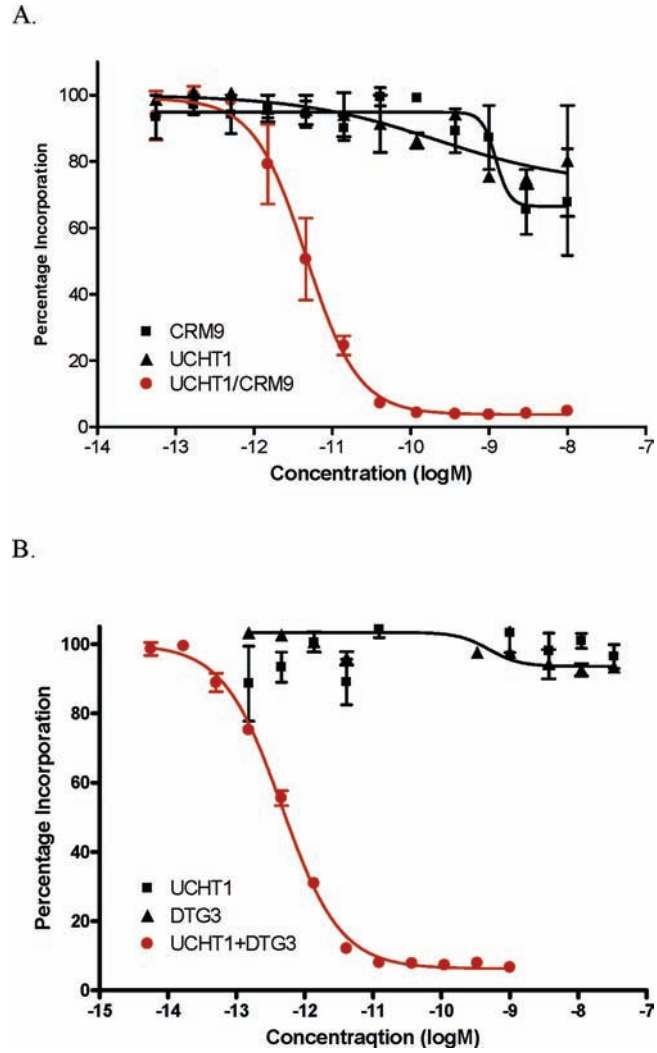

Figure 3. Potency of (A) UCHT1-CRM9 conjugates and (B) UCHT1-DTG3 complexes in Jurkat cells.

J591 and DT-proteinG fusion proteins formed complexes at 1:1 ratio. We concluded that a single copy of GBII has the ability to form complex with antibodies while multiple copies of GBII can help to increase stability of the complexes. On the basis of these results, we chose DTG3 to further evaluate the system.

Potency of UCHT1 and DTG3 Complexes. We subsequently determined the potency of DTG3/monoclonal antibody complexes. In order to do this, we chose the well-characterized immunotoxin A-dmDT390-bisFv(UCHT1) (*27*). This construct consists of diphtheria toxin fused to bivalent antihuman CD3ε antibody. The parental monoclonal antihuman CD3ε antibody UCHT1 was chemically conjugated to a cell surface binding-deficient diphtheria toxin mutant CRM9 using a set of cross-linkers and subsequently purified (Materials and Methods). Potency of UCHT1-CRM9 was tested in Jurkat cells. The IC_{50} of two separated batches of UCHT1-CRM9 conjugates were at 4 pM and 13 pM (Figure 3A and data not shown).

The DTG3 was then used to replace CRM9 in the same tests. UCHT1 was mixed with DTG3 in PBS in 10 μL reactions at room temperature. The complexes were stabilized by DMP. Without further purification, potency of these complexes was tested directly on Jurkat cells. While UCHT1 or DTG3 alone had no toxicity to treated cells, UCHT1 coupled with DTG3 had IC_{50} at 0.32 pM (Figure 3B).

Potency of J591 and DT-Protein G Fusion Protein Complexes. The potential of using DTG3 to study antibody internalization was further evaluated in another ongoing project

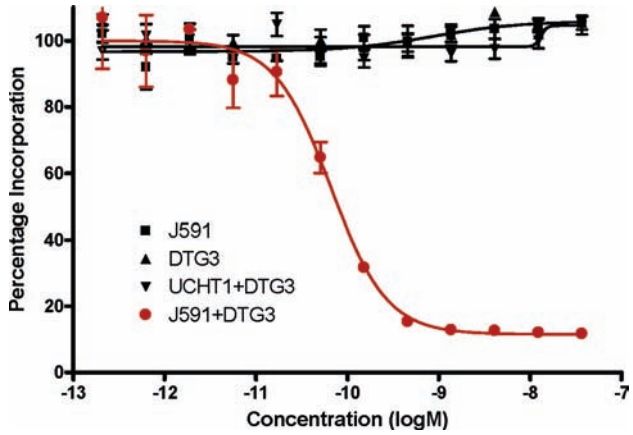

Figure 4. Potency of J591-DTG3 complexes in PSMA-transfected NIH3T3 cells.

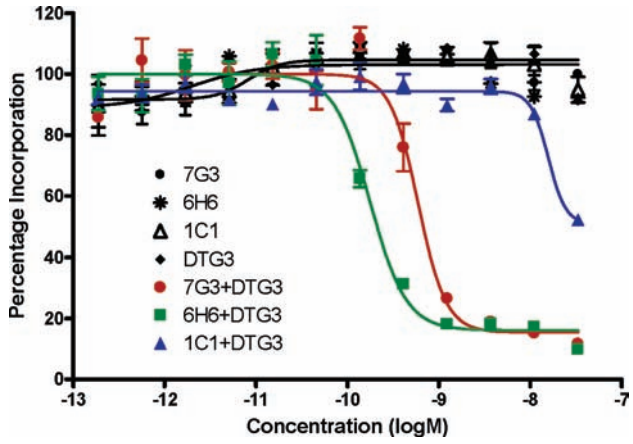

Figure 5. Potency of anti-IL3R antibodies-DTG3 complexes in CD123-transfected CHO-K1 cells.

in our group. Anti-PSMA antibody J591 was shown to have a high internalization rate upon binding to cell-surface PSMA proteins (*28*). When J591 was mixed with DTG3 at room temperature and stabilized by DMP, the potency of the complexes was tested in PSMA-transfected NIH3T3 cells. As shown in Figure 4, while J591 or DTG3 alone and UCHT1-DTG3 complexes had no toxicity to treated cells, J591-DTG3 complexes had an IC_{50} at 36 pM.

Potency of αIL3R Antibodies and DT Fusion Protein Complexes. Our optimal goal is to evaluate the possibility of generating an anti-IL3R immunotoxin for leukemia treatment. Two most commonly used anti-IL3Rα (CD123) antibodies 7G3 and 6H6 and anti-IL3Rβ (CDw131) antibody 1C1 were obtained commercially and mixed with DTG3 at room temperature. The complexes were stabilized by DMP. The potency of these complexes was then tested in CD123-transfected CHO-K1 cells. The IC_{50} for two different lots of 7G3 coupled with DTG3 was at 423 ± 66 pM (Figures 5 and 8, Table 1, and data not shown). Conversely, in repeated experiments, two different lots of 6H6 showed inconsistent results from 180 pM to 1.2 nM (Figures 5 and 8, Table 1, and data not shown) for unclear reasons. Regardless of their moderate potency as efficient immunotoxin candidates, they clearly showed that different clones of antibodies can have different internalization efficiency. Since there is no cell surface CDw131 (IL3Rβ) on CHO-K1 cells, 1C1 coupled with DTG3 showed only low toxicity at a very high immunotoxin concentration (Figure 5).

Production of New Anti-CD123 Antibodies. To produce anti-CD123 antibodies that have higher internalization efficiencies, Balb/c mice were immunized with CD123-transfected CHO-K1 cells. Hybridoma cells were generated by fusing splenocytes from the immunized mice and myeloma cells. To identify the antibody producing hybridoma, the culture supernatants from individual clones were screened for their ability to bind CD123-transfected CHO-K1 cells but not parental CHO-K1 cells in C-ELISA. These CHO-K1 cells were seeded in 96-well plates and fixed with formaldehyde before the addition of antibodies to prevent potential internalization. Among ~600 selected hybridoma clones from 1 immunized mouse, 5 clones (12F1, 12E8, 12H12, 12E7, 16G7) showed positive response. The specific binding was further confirmed by flow cytometry analysis. The cytometry graph showed that all five clones bind CD123-transfected CHO-K1 and leukemia cells TF1/H-ras but not parental CHO-K1 or lymphocyte Jurkat cells (data not shown).

Table 1. Antibodies Qualification and Quantification

		culture supernatant			purified antibody	
clones	subtype	μg/mL	nM	IC_{50} (pM)	K_d	IC_{50} (pM)
12F1	$IgG_{2b}\kappa$	4.7	29	34	50 ± 1	42 ± 7
12E8	$IgG_{2a}\kappa$	5.3	33	76	65 ± 20	175 ± 11
12H12	$IgG_{2b}\kappa$	4.8	30	30	57 ± 17	42 ± 5
12E7	$IgG_{2a}\kappa$	0.8	5	217	63 ± 15	117 ± 2
16G7	$IgG_{2a}\kappa$	5.2	33	77	75 ± 29	120 ± 7
7G3[a]	$IgG_{2a}\kappa$				131 ± 29	423 ± 66
6H6[a]	$IgG_{1}\kappa$				175 ± 43	620 ± 500

[a] 7G3 and 6H6 are commercial antibodies and the iso-type information was provided by venders.

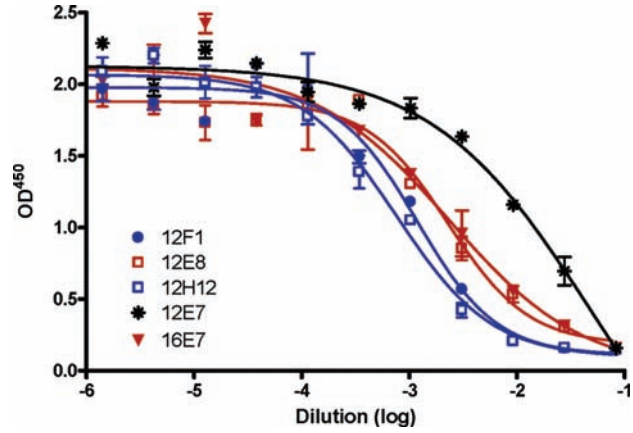

Figure 6. Cytotoxicity assay. Hybridoma culture supernatant coupled with DTG3 was tested in CD123-transfected CHO-K1 cells.

One hundred microliters of initial culture supernatant from these five positive clones were saved from the 96-well plates to be used in several assays. The first one is an immunoglobulin iso-typing assay. 12F1 and 12H12 were identified to be $IgG_{2b}\kappa$; and 12E7, 12E8 and 16G7 were $IgG_{2a}\kappa$ (data not shown; Table 1). Mouse IgG ELISA quantification assays were then used to measure antibody concentrations in these crude culture supernatants. Four of the five clones had very similar antibody concentrations at 4−5 μg/mL or ~30 nM, but slower-growing 12E7 had a much lower concentration (0.8 μg/mL; ~5 nM) than the others (Table 1).

Twenty microliters of each culture supernatant (80−100 ng, or 16 ng of 12E7) were mixed with an excess amount of DTG3 (200 ng) at room temperature for 1 h and stabilized with DMP. DTG3 alone at this dose range does not have any nonspecific cytotoxic effect (data not shown, but see Figure 8). Serial dilutions of these antibody-DTG3 mixtures were tested in potency assays with CD123-transfected CHO-K1 cells. As shown in Figure 6, different internalization rates were observed among these five clones. On the basis of the titration curve and

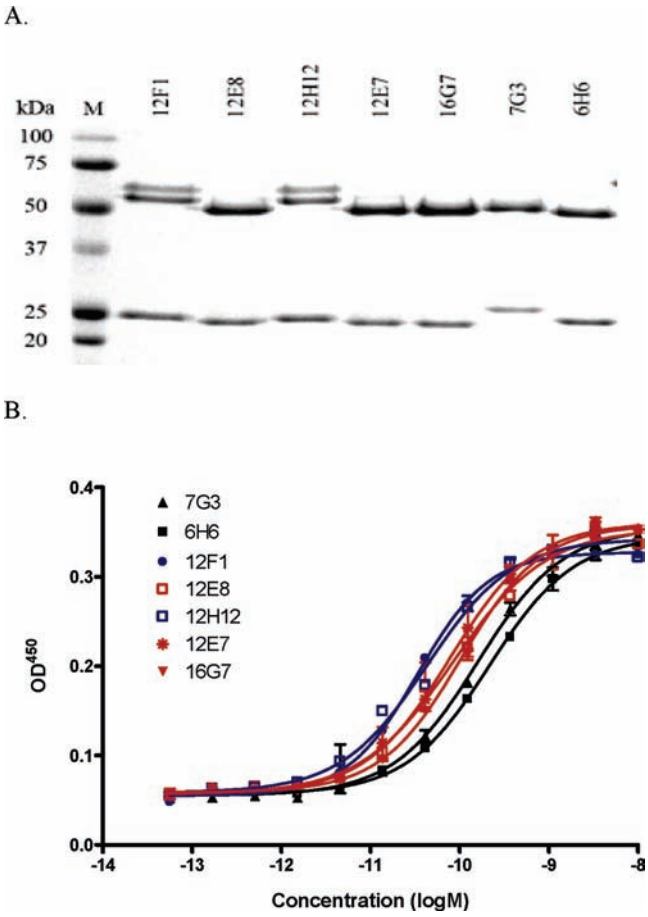

Figure 7. Protein quantification and qualification. (A) 2 μg of purified antibodies and commercial available 7G3 and 6H6 were analyzed by a reduced 12.5% SDS-PAGE. (B) Cell binding affinity of purified antibodies was tested in C-ELISA with CD123-transfected CHO-K1 cells.

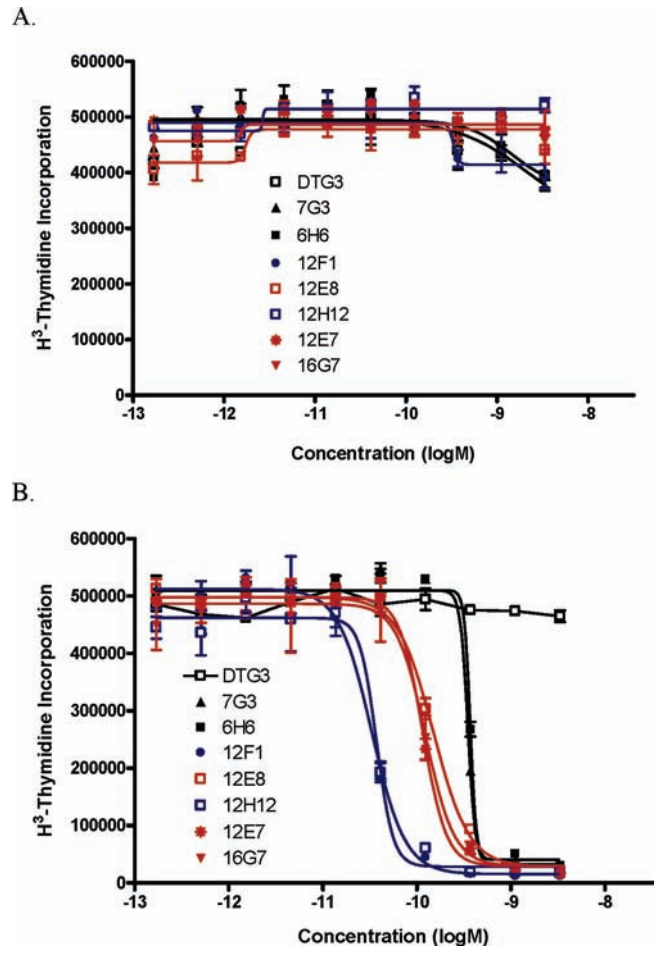

Figure 8. Cytotoxicity assays. Anti-CD123 antibodies-DTG3 complexes were tested in (A) parental CHO-K1 cells and (B) CD123-transfected CHO-K1 cells for their potencies.

individual concentration, DTG3-coupled 12F1 and 12H12 showed higher potency in CD123-transfected CHO-K1 cells with IC_{50} calculated to be at around 30−35 pM (Table 1).

To further confirm our findings, these hybridoma cell lines were expanded for antibody production. Monoclonal antibodies were purified via protein-G chromatography (Figure 7A). Both 12F1 and 12H12 had higher levels of modifications, possibly glycosylation, on the heavy chains. C-ELISA was used again to examine their binding affinity (Figure 7B; Table 1). All five new anti-CD123 antibodies showed higher CD123 binding affinity than the commercially available 7G3 or 6H6. The same amounts of purified antibodies were then mixed with DTG3, stabilized by DMP and tested for their cytotoxicity with parental CHO-K1 cells or CD123-transfected CHO-K1 cells. The dilutions of 7G3 and 6H6 were also used as a comparison. As shown in Figure 8A,B, when coupled with DTG3, 12F1 and 12H12 had an IC_{50} of approximately 42 pM, very similar to what was found with initial culture supernatants from 96-well plates (Table 1). These antibodies alone had no effect on cell growth (data not shown). 12F1 and 12H12 had ∼2−10-fold higher internalization activities than existing antibodies and appeared to be the best candidates for immunotoxin production.

DISCUSSION

Current monoclonal antibody production utilized in immunotoxin design is based on the selection of hybridoma cell lines that are able to produce large quantities of antibodies that have high affinity for the intended target. However, this approach may not be adequate for the design of successful conjugates, as immunotoxin efficacy is critically dependent on antibody internalization after cell surface antigen binding. We have reported here the development of DTG3, a novel protein conjugate specifically for the quantification of antibody internalization.

Conventional chemical conjugation of monoclonal antibodies to the cell-surface binding deficient mutant diphtheria toxin CRM9 was previously used to determine antibody internalization efficiency. However, this method has proven too costly, inefficient, and time-consuming. In order to minimize wasted reagents, the reaction was scaled down by our laboratory. Regardless, 10 mg CRM9 and 2 mg antibody were still required for the acquisition of adequate amounts of immunoconjugates for cytotoxicity analysis. Purification of the conjugate from free toxin and unconjugated antibody also proved to be time-consuming and tedious. After product purification and concentration determination, enough pure products remained for 1−2 cytotoxicity assays. Further, since chemical linkers are randomly conjugated to nonspecific sites on the proteins, activity of functional groups has the potential to be reduced, causing false negative results and low reproducibility between batches.

Conversely, DTG3 fusion proteins require only 2 to 3 μg of antibody per duplicate cytotoxicity assay. The preferential binding of Protein G to the immunoglobulin F_c region permits full exposure of the antigen binding domains. In addition, this system has proven to be extremely time efficient. Coupling reactions can be performed in about 1 h without any additional purification or concentration of the final product. Therefore,

these results indicate that the utilization of DTG3 facilitates the investigation of the internalization efficiency of monoclonal antibodies, and thus eases the cost and labor of immunotoxin development. As shown in Figure 6 and Table 1, we are able to use culture supernatant at the earliest stage of screening to examine their ability to be internalized upon binding to the cell surface antigens.

Inspiration for the generation of this novel DTG3 fusion protein was achieved from earlier work by Mazor et al. (*8*). This group demonstrated that a fusion protein consisting of the *Pseudomonas* exotoxin (PE) and two copies of Protein A IgG binding domain, known as ZZ-PE38, was useful to determine antibody internalization efficiency. However, several considerations resulted in numerous modifications in order to optimize this system for the application in our laboratory. Primarily, a specific cellular trafficking mechanism is required for PE to reach the cytosol, inhibit ribosome function, and thus kill the target cells. It is known that many cell types, including myeloid cells, have an inefficient translocation mechanism and are more resistant to PE (*29*). Our primary interests in myeloid cell malignancies prompted the substitution of PE to DT in order to circumvent this faulty trafficking mechanism, since the catalytic subunit of diphtheria toxin (DT) can be released from endosome to cytosol directly (*30*, *31*).

Additionally, Protein A demonstrates a differential affinity for immunoglobulins based on the species of origin and immunoglobulin iso-types. It has been shown that murine monoclonal antibody iso-type IgG_2 has the highest affinity for Protein A, causing a limited usefulness of ZZ-PE38. However, Protein G has a much broader spectrum of immunoglobulin binding ability. Protein G is therefore chosen in order to enhance the convenience of this assay.

Finally, our studies indicate that DTG3 was able to bind all antibodies tested within 60 min at a 1:1 ratio. In contrast to the published data (*8*), further purification of antibody-DTG3 complexes is not necessary. However, titration of the antibody-DTG3 complexes into cell culture medium without prestabilization by DMP will result in the dissociation of these complexes via exchange reactions with immunoglobulins in the media serum (data not shown). In order to eliminate the competition effects, we adapted Jurkat cells to serum free AIM-V medium (Invitrogen) and used them in UCHT1-DTG3 potency assays. Indeed, under serum free condition, UCHT1-DTG3 without pretreated with DMP had an IC_{50} in Jurkat cells at ~40 pM (data not shown). However, this number is still about 2 orders higher than DMP-stabilized UCHT1-DTG3 complexes (Figure 3). After consulting with technical service at Invitrogen, they indicated that the BSA added in the AIM-V medium could contain a low amount of immunoglobulin. When UCHT1-DTG3 was titrated down to ~10 pM or 1 ng/mL, a small amount of immunoglobulin contaminant could have a big effect. These findings indicate that the inclusion of DMP to stabilize antibody-DTG3 complexes is essential for the success of this assay.

In conclusion, antibody internalization by the target cell is critical in immunotoxin development. We have described a rapid protocol to quantify antibody internalization via potency on the target cell. The development and validation of this user-friendly system has potential to facilitate the design of viable immunotoxins and thus reduce the time and cost needed for clinical development.

ACKNOWLEDGMENT

We would like to thank Drs. JH Woo, NH Bander, DM Neville, and M Sadelain for providing antibodies and cell lines, Johnny Lee for assisting in the operation of flow cytometer, and Kent Claypool (Institute for Regenerative Medicine, TAMU) for performing cell sorting to isolate transfected CHO-K1 cells with high copy number of cell surface CD123. This project is supported by Scott & White setup fund to JSL.

LITERATURE CITED

(1) Pastan, I., Hassan, R., FitzGerald, D. J., and Kreitman, R. J. (2007) Immunotoxin treatment of cancer. *Annu. Rev. Med. 58*, 221–37.

(2) Reichert, J. M., and Valge-Archer, V. E. (2007) Development trends for monoclonal antibody cancer therapeutics. *Nat. Rev. Drug Discovery 6*, 349–56.

(3) Jordan, C. T., Upchurch, D., Szilvassy, S. J., Guzman, M. L., Howard, D. S., Pettigrew, A. L., Meyerrose, T., Rossi, R., Grimes, B., Rizzieri, D. A., Luger, S. M., and Phillips, G. L. (2000) The interleukin-3 receptor alpha chain is a unique marker for human acute myelogenous leukemia stem cells. *Leukemia 14*, 1777–84.

(4) Sun, Q., Woodcock, J. M., Rapoport, A., Stomski, F. C., Korpelainen, E. I., Bagley, C. J., Goodall, G. J., Smith, W. B., Gamble, J. R., Vadas, M. A., and Lopez, A. F. (1996) Monoclonal antibody 7G3 recognizes the N-terminal domain of the human interleukin-3 (IL-3) receptor alpha-chain and functions as a specific IL-3 receptor antagonist. *Blood 87*, 83–92.

(5) Rappoport, J. Z. (2008) Focusing on clathrin-mediated endocytosis. *Biochem. J. 412*, 415–23.

(6) Rapoport, A. P., Luhowskyj, S., Doshi, P., and DiPersio, J. F. (1996) Mutational analysis of the alpha subunit of the human interleukin-3 receptor. *Blood 87*, 112–22.

(7) Zangemeister-Wittke, U. (2005) Antibodies for targeted cancer therapy -- technical aspects and clinical perspectives. *Pathobiology 72*, 279–86.

(8) Mazor, Y., Barnea, I., Keydar, I., and Benhar, I. (2007) Antibody internalization studied using a novel IgG binding toxin fusion. *J. Immunol. Methods 321*, 41–59.

(9) Frankel, A., Liu, J. S., Rizzieri, D., and Hogge, D. (2008) Phase I clinical study of diphtheria toxin-interleukin 3 fusion protein in patients with acute myeloid leukemia and myelodysplasia. *Leuk. Lymphoma 49*, 543–53.

(10) Black, J. H., McCubrey, J. A., Willingham, M. C., Ramage, J., Hogge, D. E., and Frankel, A. E. (2003) Diphtheria toxin-interleukin-3 fusion protein (DT_{388}IL3) prolongs disease-free survival of leukemic immunocompromised mice. *Leukemia 17*, 155–9.

(11) Cohen, K. A., Liu, T. F., Cline, J. M., Wagner, J. D., Hall, P. D., and Frankel, A. E. (2004) Toxicology and pharmacokinetics of DT388IL3, a fusion toxin consisting of a truncated diphtheria toxin (DT388) linked to human interleukin 3 (IL3), in cynomolgus monkeys. *Leuk. Lymphoma 45*, 1647–56.

(12) Urieto, J. O., Liu, T., Black, J. H., Cohen, K. A., Hall, P. D., Willingham, M. C., Pennell, L. K., Hogge, D. E., Kreitman, R. J., and Frankel, A. E. (2004) Expression and purification of the recombinant diphtheria fusion toxin DT388IL3 for phase I clinical trials. *Protein Expr. Purif. 33*, 123–33.

(13) Cohen, K. A., Liu, T. F., Cline, J. M., Wagner, J. D., Hall, P. D., and Frankel, A. E. (2005) Safety evaluation of DT388IL3, a diphtheria toxin/interleukin 3 fusion protein, in the cynomolgus monkey. *Cancer Immunol. Immunother. 54*, 799–806.

(14) Garnache-Ottou, F., Feuillard, J., and Saas, P. (2007) Plasmacytoid dendritic cell leukaemia/lymphoma: towards a well defined entity? *Br. J. Hamaetol. 136*, 539–48.

(15) Djokic, M., Bjorklund, E., Blennow, E., Mazur, J., Soderhall, S., and Porwit, A. (2009) Overexpression of CD123 correlates with the hyperdiploid genotype in acute lymphoblastic leukemia. *Haematologica 94*, 1016–9.

(16) Orazi, A., Chiu, R., O'Malley, D. P., Czader, M., Allen, S. L., An, C., and Vance, G. H. (2006) Chronic myelomonocytic leukemia: The role of bone marrow biopsy immunohistology. *Mod. Pathol. 19*, 1536–45.

(17) Florian, S., Sonneck, K., Hauswirth, A. W., Krauth, M. T., Schernthaner, G. H., Sperr, W. R., and Valent, P. (2006) Detection of molecular targets on the surface of CD34+/CD38--

stem cells in various myeloid malignancies. *Leuk. Lymphoma 47*, 207–22.

(18) Riccioni, R., Diverio, D., Riti, V., Buffolino, S., Mariani, G., Boe, A., Cedrone, M., Ottone, T., Foa, R., and Testa, U. (2009) Interleukin (IL)-3/granulocyte macrophage-colony stimulating factor/IL-5 receptor alpha and beta chains are preferentially expressed in acute myeloid leukaemias with mutated FMS-related tyrosine kinase 3 receptor. *Br. J. Hamaetol. 144*, 376–87.

(19) Du, X., Ho, M., and Pastan, I. (2007) New immunotoxins targeting CD123, a stem cell antigen on acute myeloid leukemia cells. *J. Immunother. 30*, 607–13.

(20) Liu, T. F., Urieto, J. O., Moore, J. E., Miller, M. S., Lowe, A. C., Thorburn, A., and Frankel, A. E. (2004) Diphtheria toxin fused to variant interleukin-3 provides enhanced binding to the interleukin-3 receptor and more potent leukemia cell cytotoxicity. *Exp. Hematol. 32*, 277–81.

(21) Sjobring, U., Bjorck, L., and Kastern, W. (1991) Streptococcal protein G. Gene structure and protein binding properties. *J. Biol. Chem. 266*, 399–405.

(22) Frankel, A. E., Ramage, J., Kiser, M., Alexander, R., Kucera, G., and Miller, M. S. (2000) Characterization of diphtheria fusion proteins targeted to the human interleukin-3 receptor. *Protein Eng. 13*, 575–81.

(23) Kuo, S. R., Liu, J. S., Broker, T. R., and Chow, L. T. (1994) Cell-free replication of the human papillomavirus DNA with homologous viral E1 and E2 proteins and human cell extracts. *J. Biol. Chem. 269*, 24058–65.

(24) Kiser, M., McCubrey, J. A., Steelman, L. S., Shelton, J. G., Ramage, J., Alexander, R. L., Kucera, G. L., Pettenati, M., Willingham, M. C., Miller, M. S., and Frankel, A. E. (2001) Oncogene-dependent engraftment of human myeloid leukemia cells in immunosuppressed mice. *Leukemia 15*, 814–8.

(25) Yokoyama, W. M. Christensen, M., Santos, G. D., and Miller, D. (2006) Production of monoclonal antibodies, In *Current Protocols in Immunology*, Chapter 2, Unit 2.5, John Wiley & Sons, New Jersey.

(26) Davis, J. M. (1986) A single-step technique for selecting and cloning hybridomas for monoclonal antibody production. *Methods Enzymol. 121*, 307–22.

(27) Woo, J. H., Liu, J.-S., Kang, S. H., Singh, R., Park, S. K., Su, Y., Ortiz, J., Neville, D. M., Jr., Willingham, M. C., and Frankel, A. E. (2008) GMP production and characterization of the bivalent anti-human T cell immunotoxin, A-dmDT390-bisFv(UCHT1) for phase I/II clinical trials. *Protein Expr. Purif. 58*, 1–11.

(28) Liu, H., Rajasekaran, A. K., Moy, P., Xia, Y., Kim, S., Navarro, V., Rahmati, R., and Bander, N. H. (1998) Constitutive and antibody-induced internalization of prostate-specific membrane antigen. *Cancer Res. 58*, 4055–60.

(29) Frankel, A. E., Hall, P. D., Burbage, C., Vesely, J., Willingham, M., Bhalla, K., and Kreitman, R. J. (1997) Modulation of the apoptotic response of human myeloid leukemia cells to a diphtheria toxin granulocyte-macrophage colony-stimulating factor fusion protein. *Blood 90*, 3654–61.

(30) Falnes, P. O., and Sandvig, K. (2000) Penetration of protein toxins into cells. *Curr. Opin. Cell Biol. 12*, 407–13.

(31) Collier, R. J. (2001) Understanding the mode of action of diphtheria toxin: a perspective on progress during the 20th century. *Toxicon 39*, 1793–803.

(32) Grussenmeyer, T., Scheidtmann, K. H., Hutchinson, M. A., Eckhart, W., and Walter, G. (1985) Complexes of polyoma virus medium T antigen and cellular proteins. *Proc. Natl. Acad. Sci. U.S.A. 82*, 7952–4.

BC900333J

TECHNICAL NOTES

Reagents for Astatination of Biomolecules. 4. Comparison of Maleimido-*closo*-Decaborate(2-) and *meta*-[^{211}At]Astatobenzoate Conjugates for Labeling anti-CD45 Antibodies with [^{211}At]Astatine

D. Scott Wilbur,*[,†] Monica S. Thakar,[||,⊥] Donald K. Hamlin,[†] Erlinda B. Santos,[⊥] Ming-Kuan Chyan,[†] Hirohisa Nakamae,[⊥] John M. Pagel,[‡,⊥] Oliver W. Press,[‡,§,⊥] and Brenda M. Sandmaier[‡,⊥]

Departments of Radiation Oncology, Medicine, Biological Structure, and Pediatrics, University of Washington, Seattle, Washington, and Clinical Research Division, Fred Hutchinson Cancer Research Center, Seattle, Washington. Received February 19, 2009; Revised Manuscript Received August 8, 2009

An investigation was conducted to compare the in vivo tissue distribution of a rat antimurine CD45 monoclonal antibody (30F11) and an irrelevant mAbs (CA12.10C12) labeled with ^{211}At using two different labeling methods. In the investigation, the mAbs were also labeled with ^{125}I to assess the in vivo stability of the labeling methods toward deastatination. One labeling method employed *N*-hydroxysuccinimidyl *meta*-[^{211}At]astatobenzoate, [^{211}At]**1c**, and *N*-hydroxysuccinimidyl *meta*-[^{125}I]iodobenzoate, [^{125}I]**1b**, in conjugation reactions to obtain the radiolabeled mAbs. The other labeling method involved conjugation of a maleimido-*closo*-decaborate(2-) derivative, **2**, with sulfhydryl groups on the mAbs, followed by labeling of the mAb-**2** conjugates using Na[^{211}At]At or Na[^{125}I]I and chloramine-T. Concentrations of the ^{211}At/^{125}I pair of radiolabeled mAbs in selected tissues were examined in BALB/c mice at 1, 4, and 24 h post injection (pi). The co-injected anti-CD45 mAb, 30F11, labeled with [^{125}I]**1b** and [^{211}At]**1c** targeted the CD45-bearing cells in the spleen with the percent injected dose (%ID) of ^{125}I in that tissue being 13.31 ± 0.78; 17.43 ± 2.56; 5.23 ± 0.50; and ^{211}At being 6.56 ± 0.40; 10.14 ± 1.49; 7.52 ± 0.79 at 1, 4, and 24 h pi (respectively). However, better targeting (or retention) of the ^{125}I and ^{211}At was obtained for 30F11 conjugated with the *closo*-decaborate(2-), **2**. The %ID in the spleen of ^{125}I (i.e., [^{125}I]30F11-**2**) being 21.15 ± 1.33; 22.22 ± 1.95; 12.41 ± 0.75; and ^{211}At (i.e., [^{211}At]30F11-**2**) being 22.78 ± 1.29; 25.05 ± 2.35; 17.30 ± 1.20 at 1, 4, and 24 h pi (respectively). In contrast, the irrelevant mAb, CA12.10C12, labeled with ^{125}I or ^{211}At by either method had less than 0.8% ID in the spleen at any time point, except for [^{211}At]CA12.10C12-**1c**, which had 1.62 ± 0.14%ID and 1.21 ± 0.08%ID at 1 and 4 h pi. The higher spleen concentrations in that conjugate appear to be due to in vivo deastatination. Differences in ^{125}I and ^{211}At concentrations in lung, neck, and stomach indicate that the *meta*-[^{211}At]benzoyl conjugates underwent deastatination, whereas the ^{211}At-labeled *closo*-decaborate(2-) conjugates were very stable to in vivo deastatination. In summary, using the *closo*-decaborate(2-) ^{211}At labeling approach resulted in higher concentrations of ^{211}At in target tissue (spleen) and higher stability to in vivo deastatination in this model. These findings, along with the simpler and higher-yielding ^{211}At-labeling method, provide the basis for using the *closo*-decaborate(2-) labeling reagent, **2**, in our continued studies of the application of ^{211}At-labeled mAbs for conditioning in hematopoietic cell transplantation.

INTRODUCTION

Our laboratory is investigating the application of antibody-targeted α-particle emitting radionuclides as a replacement to total body irradiation (TBI) in conditioning for hematopoietic cell transplantation (*1*). In prior studies, we demonstrated that anti-CD45 and anti-TCR$\alpha\beta$ monoclonal antibodies (mAbs) labeled with the α-emitting radionuclide [^{213}Bi]bismuth could replace TBI in a conditioning regimen to obtain stable hematopoietic cell engraftment in a dog model (*2*−*4*). Although the studies successfully demonstrated that stable chimera could be obtained by combining the targeted alpha therapy with immunosuppression, the cost and availability of the parent radionuclide [^{225}Ac]actinium required to generate the ^{213}Bi precluded translation into a clinical study.

The ability to produce the α-emitting radionuclide [^{211}At]-astatine at our institution led us to consider that radionuclide as an alternative to ^{213}Bi in the conditioning regimen. In planning the transition to ^{211}At, we deliberated about the best method for coupling ^{211}At to the mAb. It has been well-established that direct coupling of ^{211}At to mAbs through electrophilic astatination results in proteins that are rapidly deastatinated in vivo (*5*). To circumvent the in vivo deastatination, our research group (*6*) and other research groups (*7*−*11*) have developed reagents for astatination using ^{211}At-labeled aryl-containing pendant groups for conjugation with proteins. The ^{211}At-labeled aryl

* Corresponding author. D. Scott Wilbur, Department of Radiation Oncology, University of Washington, Box 355016, 616 N. E. Northlake Place, Seattle, WA 98105. Phone: 206-616-9246. Fax: 206-616-8798. dswilbur@u.washington.edu.

† Department of Radiation Oncology, University of Washington.

‡ Department of Medicine, University of Washington.

§ Department of Biological Structure, University of Washington.

|| Department of Pediatrics, University of Washington.

⊥ Fred Hutchinson Cancer Research Center.

10.1021/bc9000799 CCC: $40.75 © 2009 American Chemical Society
Published on Web 09/04/2009

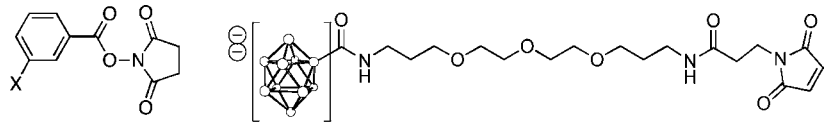

1a: X = $SnBu_3$
1b: X = ^{125}I
1c: X = ^{211}At

2

Figure 1. Conjugation reagents used to radiolabel mAbs with ^{211}At. The stannylbenzoate ester **1a** is reacted with ^{211}At or ^{125}I to prepare [^{211}At]**1c** or [^{125}I]**1b** prior to conjugation with the mAb. The maleimide-*closo*-decaborate(2-) reagent, **2**, is conjugated with the mAb, and that conjugate is subsequently labeled with ^{211}At or ^{125}I. (Note: the open circles in the *closo*-decaborate(2-) cage structure in compound **2** represent B or B−H atoms.)

conjugates are now widely used to radiolabel mAbs with ^{211}At for preclinical studies. Importantly, one of the astatination reagents, *N*-hydroxysuccinimidyl *meta*-[^{211}At]astatobenzoate, [^{211}At]**1c**, has been used for labeling mAbs in a clinical trial for therapy of malignant brain tumors (*12*).

Our studies have shown that ^{211}At-labeled benzoates can be relatively stable to in vivo deastatination on intact mAbs, but are quite unstable when used with more rapidly metabolized mAb Fab′ fragments (*6*, *13*) or smaller biomolecules such as biotin derivatives (*14*). To improve in vivo stability, we have evaluated protein conjugates that contain boron cage moieties as ^{211}At-labeling functionalities. From those studies, it was found that ^{211}At-labeled conjugates containing *closo*-decaborate(2-) are stable to in vivo deastatination (*15*). One conjugate in particular, a maleimido-*closo*-decaborate(2-) derivative, **2** (Figure 1), was found to have high stability to deastatination while having minimal effect on the conjugated protein.

Both of the ^{211}At labeling reagents, [^{211}At]**1c** and **2**, have features that make them attractive for use in labeling mAbs for conditioning regimens. The fact that the astatinated benzoate [^{211}At]**1c** had previously been used in a clinical trial made that reagent particularly attractive. However, that fact did not override the issues of the potential for (a) radiolysis in the preparation of [^{211}At]**1c** (*16*−*18*), (b) hydrolysis of the active ester during mAb conjugation of [^{211}At]**1c**, and (c) in vivo instability to deastatination on the ^{211}At-labeled mAb. The simplicity of direct labeling of proteins conjugated with the maleimide-*closo*-decaborate(2-) derivative, **2**, and the high in vivo stability observed for the ^{211}At-labeled proteins when using the reagent made this novel reagent attractive for our studies. To choose between the two reagents, we conducted an investigation to compare the ^{211}At-labeling efficiency and in vivo stability of a rat antimurine-CD45 mAb (30F11) and an irrelevant mAb (CA12.10C12) in mice. The results of that investigation are described herein.

MATERIALS AND METHODS

Reagents. All reagents obtained from commercial sources were used without further purification. Bismuth metal used as the target for preparation of ^{211}At was obtained from Alpha Aesar (Ward Hill, MA) as Puratronic 99.999%. Solvents for HPLC analysis were obtained as HPLC grade and were filtered (0.2 μm) prior to use. Chloramine-T (ChT) and phosphate buffered saline (PBS) were obtained from Sigma (St. Louis, MO). Sephadex G-25 desalting columns (PD-10 and NAP-10) were obtained from Amersham Biosciences (Piscataway, NJ). Vivaspin 20 ultrafiltration concentrators were obtained from Sartorius Stedim North America, Inc. (Edgewood, NY). The reagents, **1a** and **2**, used in labeling the antibodies, 30F11 and CA12.10C12, were prepared prior to the study. The *N*-hydroxysuccinimidyl *meta*-(tri-*n*-butylstannyl)benzoate, **1a**, was prepared as previously described (*19*). The protein modification reagent, *N*-(15-(aminoacyl-*closo*-decaborate)-4,7,10-trioxatridecanyl)-3-maleimidopropionamide, **2**, was prepared as previously described (*15*).

Antibodies. The rat antimurine CD45 mAb, 30F11, employed in the study is a rat IgG2b antibody that recognizes all murine CD45 isoforms (*20*). A 30F11 hybridoma cell line expressing the rat antimurine CD45 mAb was a gift from Dr. Irv Bernstein (FHCRC). The 30F11 was produced by injecting the hybridoma into pristane-primed mice to generate ascites. The 30F11 was purified from ascitic fluid by protein G immunoabsorption column chromatography. The irrelevant mAb, CA12.10C12, is an IgG1 anti-CD45 canine-specific antibody (*21*). A hybridoma producing monoclonal antibodies against canine CD45 was provided by Dr. Peter Moore (School of Veterinary Medicine, University of California, Davis). This mAb was produced and purified at the Biologics Production Facilities of the Fred Hutchinson Cancer Research Center (Seattle, WA) as described previously (*22*). A fluorescein isothiocyanate (FITC) labeled goat $F(ab')_2$ antirat antibody was obtained from Biosource International (Camarillo, CA) for murine hematopoietic cell binding (serum) using flow cytometry. The 30F11 mAbs, both native and conjugated with **2**, were conjugated with fluorescein isothiocyanate according to manufacturer's standard protocols, and were also used in flow cytometry studies.

Radioactivity. All radioactive materials were handled according to approved protocols at the University of Washington. Na[^{125}I]I was purchased from Perkin-Elmer Life and Analytical Sciences, Inc. (Waltham, MA) as a high concentration solution in 0.1 N NaOH. ^{211}At was produced by irradiation of a thin layer of bismuth metal with a 28 MeV α-particle beam on a Scandatronix MC-50 cyclotron (University of Washington). Isolation of Na[^{211}At]At was conducted in a charcoal-filtered glovebox (Innovative Technologies, Inc., radioisotope glovebox) by distillation from the irradiated target using the conditions previously described (*13*, *15*). Radiohalogenations were conducted within a charcoal-filtered Plexiglas enclosure (Biodex Medical Systems Inc., Shirley, NY) housed in a radiochemical fume hood. Radiohalogenation reactions were carried out in vials capped with Teflon-coated septa vented through a 10 mL charcoal-filled syringe.

Measurement of ^{125}I and ^{211}At quantities was accomplished on the Capintec CRC-15R Radioisotope Calibrator using the manufacturer's settings for those radionuclides. Tissue samples were counted in a γ-counter (PACKARD COBRA GMI, Inc., Minnesota, USA), using the open window setting: channels 20−2000. In experiments, $^{211}At/^{125}I$ counting was conducted twice, soon after animal sacrifice to obtain total counts and after samples had decayed for 3−5 days to obtain the ^{125}I counts. ^{211}At counts were obtained by subtracting ^{125}I counts from the total counts. All ^{211}At counts were corrected for decay during the counting process using 1 μL of injectate as standards.

Analytical Chromatography. HPLC separations of the nonradioactive compounds, **1a** and **2** (and their precursors), were obtained using a system that contained a Hewlett-Packard quaternary 1050 gradient pump, a variable wavelength UV detector (254 nm), and an ELSD 2000 evaporative light-scattering detector (Alltech, Deerfield, IL). Analyses of the HPLC data were conducted on Hewlett-Packard HPLC Chem-

Station software. Reversed-phase HPLC chromatography was carried out on an Alltech Altima C-18 column (5 μm, 250 × 4.5 mm) using a gradient solvent system at a flow rate of 1 mL/min. The gradient mixture was composed of MeOH (eluant A) and 0.05 M, pH 5.5, aqueous triethylammonium acetate (eluant B). The gradient started with 40% MeOH and 60% eluant B for two minutes; then, the % MeOH was increased linearly to 100% over a 13 min period; following this, the elution continued with 100% MeOH for an additional 5 min.

Radio-HPLC. The product mixtures from the preparation of [^{125}I]**1b** and [^{211}At]**1c** were analyzed by HPLC using a 5 μm C-18 column (PartiSphere C-18, Whatman) eluting at a flow rate of 1 mL/min with a gradient beginning with 40% MeOH/60% of an aqueous Et_3NHOAc solution. The HPLC equipment used in the analyses consisted of a HP 1050 quaternary pump, a Waters 481 UV detector (254 nm), a 1050 A/D converter, and a Beckman model 170 radioisotope detector.

Isoelectric Focusing. IEF were obtained on a Novex PowerEase 500 instrument with the XCell II chamber using Invitrogen (Novex) precast gels, pH 3−10 (1.0 mm, 12 well) or pH 3−7 (1.0 mm, 12 well) running under the standard IEF Program. The protein was stained with GelCode Blue Stain (Pierce). IEF standards used were from Serva Electrophoresis GmbH (Heidelberg, Germany): (pI) 10.7, cytochrome C; 9.5, ribonuclease A; 8.3, 8.0, 7.8, lectin; 7.4, 6.9, myoglobin; 6.0, carbonic anhydrase; 5.3, 5.2, β-lactoglobulin; 4.5, trypsin inhibitor; 4.2, glucose oxidase; 3.5, amyloglucosidase.

Fluorescein Isothiocyanate (FITC) Conjugation. One milligram of fluorescein isothiocyanate (Sigma-Aldrich, Wisconsin, MI) was dissolved in 0.05 mL of DMSO and further diluted to a concentration of 1 mg/mL with 1 M sodium bicarbonate, pH 9.4. Then, 0.25 mL of this solution is added to 1 mg/mL of the antibody in 1× phosphate buffered saline (PBS). After incubation at 37 °C, CO_2 humidified incubator, the antibody was transferred to a dialysis cassette, 10 MW cutoff (Pierce Biotechnology, Rockford, IL) and dialyzed against 1× PBS to remove unbound FITC. Antibody concentration was measured using a BioMate spectrophotometer (Thermo Electron Corporation, Madison, WI).

Flow Cytometry. Flow cytometry was used to assess antigen binding after modification of the anti-CD45 mAb, 30F11, with the maleimido-*closo*-decaborate(2-) reagent, **2**. SL2 cells, a mouse cell line expressing the CD45 antigen, was grown in 10% fetal bovine serum−RPMI until ready for use. Two hundred thousand SL2 cells in 50 μL of 15% horse serum (HS)−1× PBS were incubated with 50 μg/mL of the 30F11 or 30F11−**2** conjugate on ice for 20 min. After washing, cells were resuspended in 50 μL of 15% HS-PBS and added 10 μg/mL of the secondary antibody, goat F(ab′)$_2$ antirat FITC (Biosource, Camarillo, CA), and incubated on ice for 20 min. To test the blocking ability of the antibody, FITC conjugated 30F11 was added to cells incubated with 30F11 or 30F11-**2**, respectively. After incubation, cells were washed once with 2% HS-PBS, then once with 1× PBS, and resuspended in 200 μL of 1% paraformaldehyde. Cells were analyzed on a FACScan Flow cytometer (Becton Dickinson, San Jose, CA).

Radioiodination of 30F11 using [^{125}I]1b. To 100 μL of a solution of **1a** (1 mg/mL in MeOH/5% HOAc) was added 3.5 μL (1.2 mCi) of Na[^{125}I]I in 0.1 N NaOH followed by 20 μL of a *N*-chlorosuccinimide solution (1 mg/mL in MeOH). After 10 min at room temperature, 20 μL of a sodium metabisulfite solution (1 mg/mL in H_2O) was added to quench the reaction. A small amount of the mixture was injected on the HPLC to check the reaction yield (require at least 90%). The mixture was then reduced to dryness under a stream of argon and a mixture containing 500 μL of a 0.5 M sodium borate solution, pH 8.0, and 100 μL of 30F11 solution (6.7 mg/mL in PBS) was added. The conjugation reaction was allowed to run for 15 min at room temperature before eluting on a PD-10 column with PBS, pH 7.2. The protein fractions were pooled to give [^{125}I]30F11-**1b** with a specific activity of 0.8 mCi/mg and a radiochemical yield of 61%.

Radioiodination of CA12.10C12 with [^{125}I]1b. This reaction was conducted using the same conditions as described for preparation of [^{125}I]30F11-**1b** with the following differences. 1.5 μL of Na[^{125}I]I (920 μCi) in 0.1 N NaOH and 147 μL of 2.7 mg/mL CA12.10C12 were used. [^{125}I]CA12.10C12-**1b** was obtained with a specific activity of 0.92 mCi/mg and a radiochemical yield of 63%.

Astatination of 30F11 with [^{211}At]1c. To a 200 μL solution of **1a** (1 mg/mL in MeOH/5% HOAc) was added 20 μL (780 μCi) of Na[^{211}At]At (in 0.05 N NaOH) followed by 20 μL of a *N*-chlorosuccinimide solution (1 mg/mL in MeOH). After 10 min at room temperature, 20 μL of a sodium metabisulfite solution (1 mg/mL in H_2O) was added to quench the reaction. A small amount of the mixture was injected on the HPLC to check the reaction yield (90% [^{211}At]**1c** required). The mixture was then reduced to dryness under a stream of argon and a mixture containing 500 μL of a 0.5 M sodium borate solution, pH 8.0, and 90 μL of 30F11 solution (6.7 mg/mL in PBS). The conjugation reaction was allowed to run for 15 min at room temperature before eluting on a PD-10 column with PBS. The protein fractions were pooled to give [^{211}At]30F11-**1c** with a specific activity of 0.03 mCi/mg and a radiochemical yield of 4.4%.

Astatination of CA12.10C12 with [^{211}At]1c. This reaction was conducted under the same conditions as those used to prepare [^{211}At]30F11-**1c**, with the following changes. A 100 μL quantity of **1c**, 150 μL of Na[^{211}At]At (1.2 mCi), 30 μL of 1 mg/mL *N*-chlorosuccinimide, and 147 μL of a CA12.10C12 solution (2.7 mg/mL in PBS) were used. [^{211}At]CA12.10C12-**1c** was obtained with a specific activity of 0.03 mCi/mg and a radiochemical yield of 4.8%.

Conjugation of 30F11 with 2. To a 2 mL solution containing 5.3 mg/mL 30F11 in PBS, pH 7.2, was added 270 μL of 100 mM dithiothreitol. After 1 h of gentle mixing at room temperature, the reduced protein was eluted over a PD-10 column with PBS (pH 6.5 containing 1 mM EDTA). The protein-containing fractions were pooled to give 7 mL at a concentration of 1.5 mg/mL (UV 280 nm). To that solution was added 49.3 μL (10 equiv) of a 10 mg/mL solution of **2** in DMF. The reaction solution was gently mixed for 30 min at room temperature before quenching with 2.4 mg of sodium tetrathionate. The protein was concentrated in a Vivaspin 30K MWCO concentrator and washed 5× with 10 mL each of PBS pH 7.2, concentrating between each wash. The isolated 30F11-**2** was obtained in 4 mL solution at a concentration of 2.4 mg/mL (90% protein recovery).

Conjugation of CA12.10C12 with 2. The same procedure as described for conjugation with 30F11 (above) was used, with the following difference in reagent quantities. To 1.5 mL solution containing 6.1 mg/mL CA12.10C12 in PBS was added 200 μL of 100 mM dithiothreitol. The CA12.10C12-**2** was obtained in 6.5 mL at a concentration of 1.2 mg/mL (85% protein recovery).

Radioiodination of 30F11-2. To 25 μL of a 0.5 M solution of sodium phosphate, pH 7.4, was added 1.5 μL (274 μCi) of Na[^{125}I]I solution (0.1 N NaOH), followed by 163 μL (400 μg) 30F11-**2** and 20 μL of a chloramine-T solution (1 mg/mL in H_2O). The reaction was allowed to run for 30 s at room temperature before quenching with 20 μL of a sodium metabisulfite solution (1 mg/mL in H_2O). The mixture was eluted over a NAP-10 column using PBS, pH 7.2. The protein fractions

were pooled to give [^{125}I]30F11-**2** with a specific activity of 0.63 mCi/mg and a radiochemical yield of 81%.

Radioiodination of CA12.10C12-2. The radioiodination was conducted using the same conditions as used for preparation of [^{125}I]30F11-**2**, with the following changes. One microliter (484 μCi) of Na[^{125}I]I in 0.1 N NaOH was added, followed by 250 μL (300 μg) CA12.10C12-**2** and 30 μL of chloramine-T solution (1 mg/mL in H_2O). [^{125}I]CA12.10C12-**2** was obtained with a specific activity of 1.5 mCi/mg and a radiochemical yield of 62%.

Astatination of 30F11-2. To 100 μL of a 0.5 M aqueous sodium phosphate solution, pH 7.4, was added 400 μL (580 μCi) of Na[^{211}At]At solution (0.05 N NaOH) followed by 163 μL (400 μg) 30F11-**2** and 80 μL of a chloramine-T solution (1 mg/mL in H_2O). The reaction was allowed to run for 30 s at room temperature before quenching with 80 μL of sodium metabisulfite solution (1 mg/mL). The mixture was eluted over a NAP-10 column using PBS. The protein fractions were pooled to give [^{211}At]30F11-**2** with a specific activity of 0.9 mCi/mg and a radiochemical yield of 65%.

Astatination of CA12.10C12-2. The astatination was conducted using the same conditions as described for preparation of [^{211}At]30F11-**2**, with the following changes. One hundred microliters (577 μCi) of Na[^{211}At]At in ~0.05 N NaOH, followed by 250 μL (300 μg) CA12.10C12-**2** and 50 μL of a chloramine-T solution (1 mg/mL in H_2O). [^{211}At]CA12.10C12-**2** was obtained with a specific activity of 1.6 mCi/mg and a radiochemical yield of 81%.

Biodistribution Studies. Biodistribution studies were conducted under a protocol approved by the Institutional Animal Care and Use Committee (IACUC) at the Fred Hutchinson Cancer Research Center. Female BALB/c mice were obtained from the Jackson Laboratory (Bar Harbor, Maine, USA). In each biodistribution experiment, the radioactive mAbs isolated from size-exclusion columns (Sephadex G25; PD-10) were mixed to prepare an admixture. The admixture was diluted with phosphate buffered saline (PBS) to prepare injection quantities of ~200 μL. This quantity was injected into each of 15 mice via the lateral tail vein. The actual amount of injectate each animal received was determined by weighing the administering syringe before and after injection. Groups of 5 mice were sacrificed at 1, 4, and 24 h post injection. Selected tissues were excised, blotted free of blood, weighed, and counted. Blood weight was estimated to be 6% of the total body weight (*23*). Calculation of the percent injected dose per gram (%ID/g) and percent injected dose (%ID) in the tissues was accomplished using internal standards for the ^{211}At and ^{125}I counts. The tissues examined, quantities injected, and biodistribution data obtained in the studies are provided in Tables S1−S4 (Supporting Information).

RESULTS

mAb Modification and Labeling. The rat antimurine CD45 mAb, 30F11, and canine-specific (irrelevant) mAb, CA12.10C12, were each radiolabeled with ^{211}At and ^{125}I by two different methods. One labeling method involved preparation of *N*-hydroxysuccinimidyl *meta*-[^{211}At]astatobenzoate, [^{211}At]**1c**, and *N*-hydroxysuccinimidyl *meta*-[^{125}I]iodobenzoate, [^{125}I]**1b** from *N*-hydroxysuccinimidyl *meta*-tri-*n*-butylstannylbenzoate **1a** (Figure 1). Radioiodination and astatination of **1a** was accomplished by reaction with *N*-chlorosuccinimide (NCS) in MeOH/5% HOAc at room temperature for 10 min. Preparation of the radiolabeled intermediates [^{125}I]**1b** and [^{211}At]**1c** was accomplished in >90% purity by HPLC analyses (see Figures S1−S4 in Supporting Information). Once prepared, [^{125}I]**1b** was reacted with 670 μg of 30F11 or 397 μg of CA12.10C12 in borate buffer, pH 8.0, for 15 min at room temperature to give

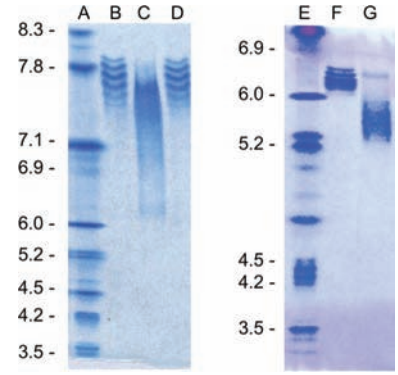

Figure 2. Isoelectric focusing gels showing protein bands of 30F11 (left gel, Novex 3−10) and CA12.10C12 (right gel, Novex 3−7) before and after the proteins were conjugated with maleimide-*closo*-decaborate(2-), **2**. Lanes are as follows: (A) IEF markers, (B) unmodified 30F11, (C) 30F11-**2**, (D) unmodified 30F11, (E) IEF markers, (F) unmodified CA12.10C12, and (G) CA12.10C12-**2**. IEF markers (Serva) are as follows: (pI) 10.7, cytochrome C; 9.5, ribonuclease A; 8.3, 8.0, 7.8, lectin; 7.4, 6.9, myoglobin; 6.0, carbonic anhydrase; 5.3, 5.2, β-lactoglobulin; 4.5, trypsin inhibitor; 4.2, glucose oxidase; 3.5, amyloglucosidase.

conjugation yields of 61% and 63%, respectively. In contrast to the radioiodinations using [^{125}I]**b**, astatinations under the same conditions using [^{211}At]**1c** produced very low yields, providing only 4.4% of [^{211}At]30F11-**1c** and 4.8% of [^{211}At]CA12.10C12-**1c**. The reason for the difference in radiochemical (conjugation) yields between the astatinated benzoates, [^{211}At]**1c**, and the radioiodinated benzoates, [^{125}I]**1b**, is unknown. Since the quantities of mAb employed (603 μg 30F11 and 397 μg CA12.10C12) in the conjugation reactions using [^{211}At]**1c** were similar to those used in the conjugations of [^{125}I]**1b**, differences in protein concentrations does not appear to be the reason for the lower yields. Although the radiolabeled intermediates in each reaction were >90% pure by HPLC analyses prior to removal of the solvents, it is possible that impurities or differences in pH of the astatinated preparations led to a more rapid hydrolysis of [^{211}At]**1c** upon removal of the solvents. The volumes of aqueous Na[^{125}I]I solution used (1.5 or 3.5 μL) in the radiolabeling reactions were considerably lower than the volumes of aqueous Na[^{211}At]At solution used (i.e., 20 and 150 μL), making this possibility plausible. Irrespective of the low conjugation yields for the astatinated proteins, enough labeled protein was obtained after purification in each case to conduct the animal studies.

The second method of labeling mAbs involved conjugation of the maleimide-*closo*-decaborate(2-) reagent, **2** (Figure 1), followed by direct radiolabeling of the mAb conjugates. In the conjugation, 30F11 or CA12.10C12 was treated with dithiothreitol (DTT) for 1 h at room temperature, then 10 mol equiv of **2** in DMF was added and the reaction mixture was stirred for 30 min at room temperature. After that time, sodium tetrathionate was added to stop the reaction by reformation of disulfide bonds (*24*). The resulting mAb conjugates, 30F11-**2** and CA12.10C12-**2**, were purified by Sephadex G-25 size exclusion chromatography (PD-10). Although the number of *closo*-decaborate(2-) conjugates per modified mAb was not readily obtained, the extent of modification was assessed by the change in protein isoelectric point (pI) observed with isoelectric focusing (IEF) gel electrophoresis. Each conjugation of **2** changes the overall protein charge by −2. Scanned IEF gels are shown as Figure 2. In Figure 2, it is apparent that the two unmodified IgG have very different pI values (30F11, ~7.5−7.9; CA12.10C12, ~6.2−6.6) and that the proteins are modified in the conjugation reaction. While not quantifiable, it appears that at least one *closo*-decaborate derivative, **2**, was conjugated to each protein molecule, as all of the bands (lanes

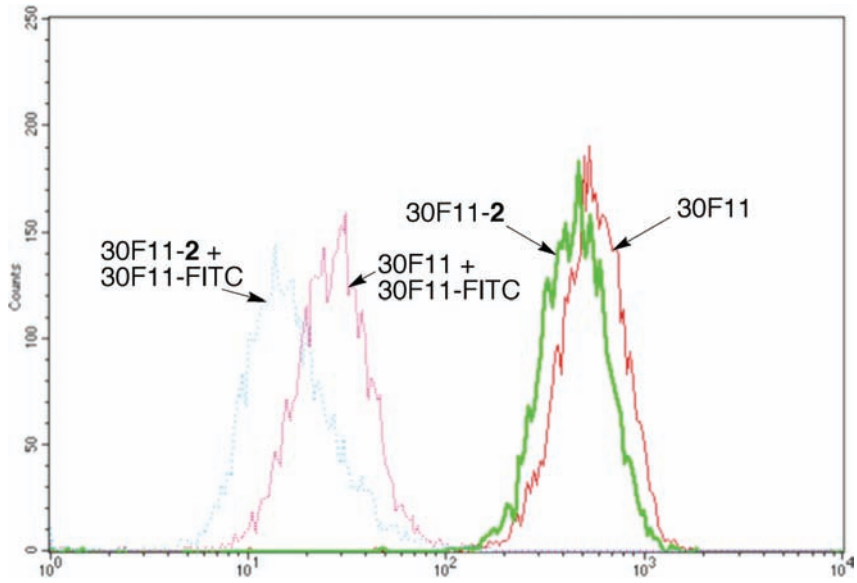

Figure 3. Histograms from flow cytometry showing cell binding of unmodified 30F11 (red) and *closo*-decaborate(2-) modified 30F11 (green). Competitive binding of 30F11-FITC with 30F11 (purple) and 30F11-**2** (blue) is also shown.

C and G) of the native protein are shifted to a more negative pI in the conjugation reaction. Further characterization was conducted to determine if the CD45 cell binding was affected in the 30F11. Cell binding for the 30F11-**2** and nonmodified 30F11 as measured by a FITC-labeled goat antirat $F(ab')_2$ mAb are shown in Figure 3. The graphed data indicate that there is similar binding of 30F11-**2** relative to the nonmodified 30F11. Running the samples in the presence of excess FITC-labeled 30F11 shows that the cell-bound 30F11-**2** (and 30F11) is CD45 specific binding, as it can be displaced.

Direct labeling of 30F11-**2** and CA12.10C12-**2** was accomplished by reaction of Na[^{211}At]At or Na[^{125}I]I with chloramine-T in sodium phosphate buffer. The reactions were quenched after 30 s to provide high yields of the labeled anti-CD45 mAb, [^{211}At]30F11-**2** or [^{125}I]30F11-**2** (65% and 81%, respectively), and the labeled irrelevant mAb, [^{211}At]CA12.10C12-**2** or [^{125}I]CA12.10C12-**2** (81% and 62%, respectively), after purification by size exclusion chromatography.

Biodistribution Studies. Four biodistribution studies were conducted in this investigation. Two biodistributions were conducted with the rat antimurine CD45 mAb, 30F11, and two biodistributions were conducted with a canine-specific irrelevant mAb, CA12.10C12. In all biodistribution studies, 10 μg quantities of ^{125}I-labeled (1−5 μCi) and ^{211}At-labeled (1−10 μCi) mAbs were mixed (20 μg total protein) and were injected into 15 BALB/c mice. Sacrifices of groups of 5 mice were conducted at 1, 4, and 24 h post injection (pi). The data obtained are shown graphically as panels A−D in Figure 4 and are provided in Tables S1−S4 (Supporting Information). Note that the concentrations in spleen shown in Figure 4, which can be very high (as high as 546%ID/g in panel A; 1409%ID/g in panel B), are graphed off-scale so that the concentrations in the other tissues can be compared visually. There was a large animal-to-animal variance in the concentration of radionuclides in the groups. The %ID/g variation in spleen from individual mice appeared to correlate with the spleen size. Indeed, the variance was much smaller when the size of spleen was not factored in; thus, the percent total injected dose (%ID) of each radionuclide in the spleen was used for comparison of CD45 targeting. Presumably, some of the spleen size variance was due to a decreased weight after ^{211}At was localized to the spleen. Because of the large variation in radionuclide concentrations in spleens of mice from the same group, discussions of localization or retention in that organ in the following paragraphs are limited to the percent of injected dose rather than injected dose per gram. The %ID in spleens for the ^{211}At and ^{125}I-labeled mAbs in the four biodistributions is shown graphically in Figure 5 and is provided in Table S5 (Supporting Information).

In an initial biodistribution study, [^{125}I]30F11-**1b** and [^{211}At]30F11-**1c** were coinjected and their tissue concentrations were evaluated. The concentrations (%ID/g) of ^{125}I and ^{211}At in selected tissues is shown graphically as Figure 4, panel A (Table S1, Supporting Information). Specific targeting of the CD45-containing cells in spleen can be seen in the average (±std dev) percent injected dose (%ID) of [^{125}I]30F11-**1b** in that tissue, which was 13.31 ± 0.78; 17.43 ± 2.56; 5.23 ± 0.50; and for [^{211}At]30F11-**1c** was 6.56 ± 0.40; 10.14 ± 1.49; 7.52 ± 0.79 at 1, 4, and 24 h sacrifice times (respectively). The concentrations of ^{211}At and ^{125}I in blood taken from mice at 1 h pi were found to be significantly different (Student's *t* test, $P < 0.05$), as were their concentrations in lung, liver, neck, and stomach. The fact that the concentrations of ^{211}At are higher than ^{125}I in lung, neck, and stomach is an indication that deastatination has occurred (*5*).

In a second biodistribution study, [^{125}I]30F11-**2** and [^{211}At]30F11-**2** were coinjected and their tissue concentrations were evaluated. The concentrations (%ID/g) of ^{125}I and ^{211}At in selected tissues are shown graphically as Figure 4, panel B (Table S2, Supporting Information). Specific targeting of the CD45-containing cells in spleen can be seen in the average (±std dev) of %ID in spleens of mice injected with [^{125}I]30F11-**2**, which was 21.15 ± 1.33; 22.22 ± 1.95; 12.41 ± 0.75; and [^{211}At]30F11-**2**, which was 22.78 ± 1.29; 25.05 ± 2.35; 17.30 ± 1.20 at 1, 4, and 24 h pi (respectively). It should be noted that the %ID values found in spleen for the radiolabeled 30F11 modified with a *closo*-decaborate(2-), **2**, is higher than that obtained for the same mAb modified using the *meta*-halobenzoate, **1b**/**1c**, labeling approach. This difference may be due to retention of the dianionic radiolabeled *closo*-decaborate(2-) mAb or metabolites rather than a difference in the labeled mAb targeting. Indeed, the fact that the liver and kidney concentrations of the radiolabeled *closo*-decaborate(2-) conjugate, 30F11-**2**, do not appear to decrease as quickly as the blood or lung concentrations seems to support retention in the metabolizing/excretory tissue. It is important to note that the only significant differences in distributions at 1 and 4 h pi of the two radionuclides, when using 30F11-**2**, was noted in the neck (1 h) and liver (4 h).

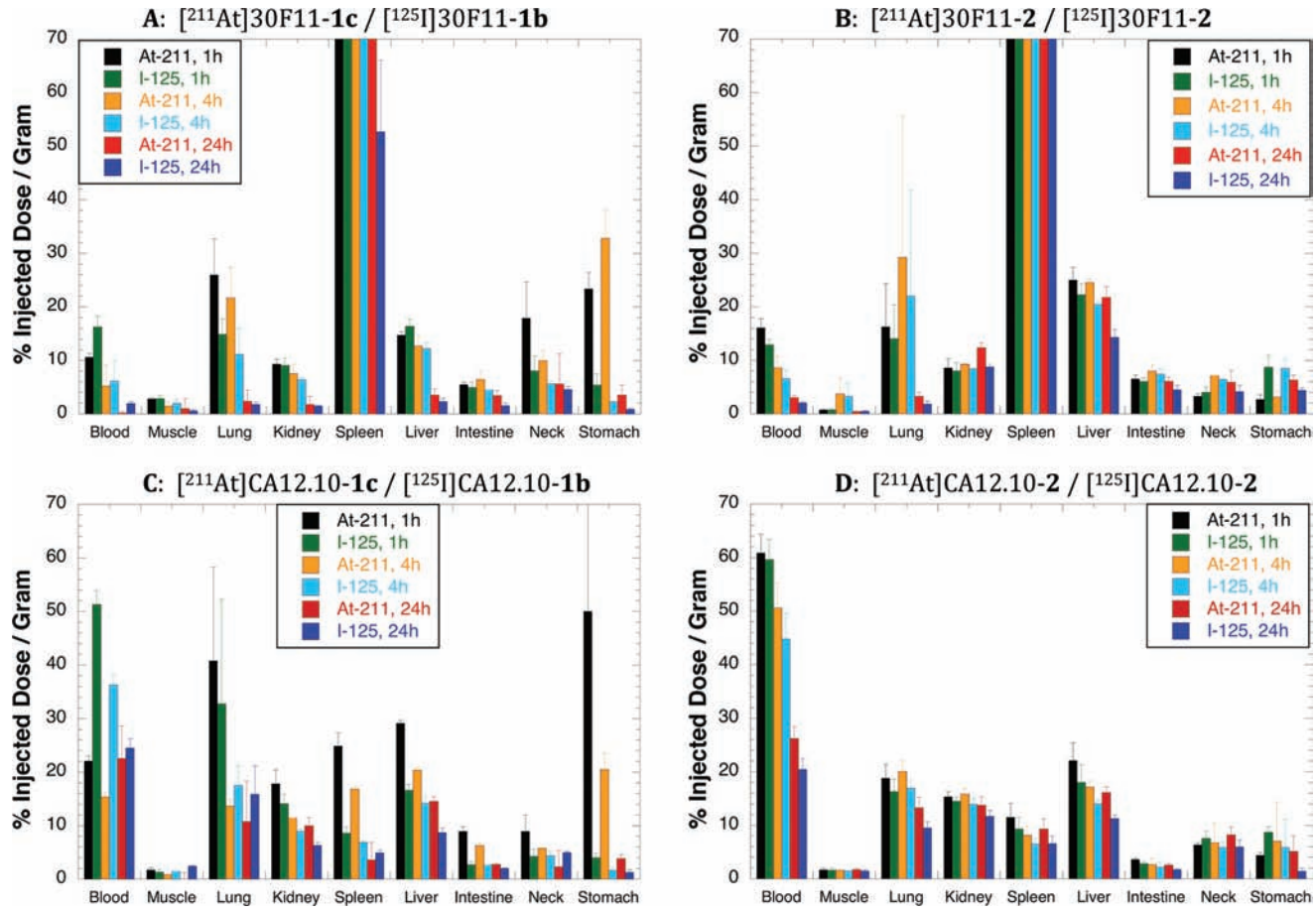

Figure 4. Graphs in panels A−D show concentrations of ^{211}At and ^{125}I in selected tissues of BALB/c mice. The four graphs are plots of data for the two mAbs labeled using two different methods. Black, brown, and red bars represent ^{211}At concentrations (%ID/g) at 1, 4, and 24 h pi (respectively), and green, light blue, and dark blue bars represent ^{125}I concentrations at 1, 4, and 24 h pi (respectively). The graphed data are from 5 mice per time point ± standard deviation (error bars). The highest concentration value has been limited to 70% ID/g so that the tissues with lower concentrations than spleen can be compared (see Tables S1−S4 in Supporting Information for complete data, including spleen values).

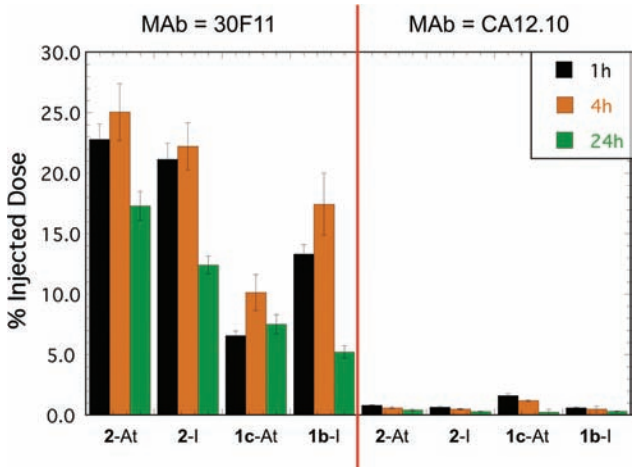

Figure 5. Graphed percent injected dose (%ID) of radiolabeled mAb conjugates in spleens of BALB/c mice. Each set of 3 bars represents the amount of ^{211}At- or ^{125}I-labeled mAb in spleen at 1 h (black), 4 h (brown), and 24 h (green) post injection. The conjugate on the antibody and radionuclide attached (At = ^{211}At; I = ^{125}I) are listed below each set of bars. The antibodies used are shown above the graph, with a red line separating the CD45 specific mAb (30F11) and the irrelevant mAb (CA12.10C12). Data were obtained from 5 mice per time period (per bar) and are plotted as the average %ID/g ± standard deviation (error bars).

The significant difference in neck concentrations at 1 h was not brought about by release of ^{211}At (it is lower), but rather by release of ^{125}I. Our studies have shown that the ^{211}At only reacts with the *closo*-decaborate(2-) (*15*). However, the ^{125}I appears to react with the *closo*-decaborate(2-) moiety (primarily), but also with tyrosine residues. Reaction with tyrosine residues permits release of [^{125}I]iodide after degradation of the protein (*25*). The low ^{211}At quantities in lung, stomach, and neck support our belief that there is a high stability of ^{211}At toward deastatination when attached to the *closo*-decaborate(2-) moiety.

In a third biodistribution, [^{125}I]CA12.10C12-**1b** and [^{211}At]CA12.10C12-**1c** were coinjected and their tissue concentrations were evaluated. The concentrations (%ID/g) of ^{125}I and ^{211}At in selected tissues is shown graphically as Figure 4, panel C (Table S3, Supporting Information). As expected, the canine-specific irrelevant antibody did not target the spleen. Significant differences (Student's *t* test; $P < 0.05$) between the ^{125}I and ^{211}At were seen in most tissues at all three time points. The differences in radionuclide concentrations in lung, spleen, neck, and stomach are visible on the graph. The higher concentrations of ^{211}At in those tissues indicate that deastatination has occurred.

In a fourth biodistribution, [^{125}I]CA12.10C12-**2** and [^{211}At]CA12.10C12-**2** were coinjected and their tissue concentrations were evaluated. The concentrations (%ID/g) of ^{125}I and ^{211}At in selected tissues is shown graphically as Figure 4, panel D (Table S4, Supporting Information). Interestingly, the blood concentrations for the irrelevant mAb are what might be expected for an intact mAb that does not localize in any tissue and does not release the ^{211}At. There were no significant differences (Student's *t*; $P < 0.05$) in ^{211}At or ^{125}I concentrations for most tissues. Although there are significant differences in intestine and stomach at 1 h pi, and

lung, kidney, and liver at 4 h pi, the differences are quite small. Deastatination does not appear to occur, and again, the significant difference between the radionuclides at 1 h pi appears to be due to deiodination rather than deastatination.

DISCUSSION

Our interest in switching from ^{213}Bi-labeled anti-CD45 mAb to ^{211}At-labeled anti-CD45 mAb as a replacement for TBI in a conditioning regimen required additional preclinical studies to be conducted. Prior to evaluation of ^{211}At-labeled anti-CD45 mAb in the dog model, we felt it was important to gain a better understanding of the differences between ^{211}At- and ^{213}Bi-labeled anti-CD45 mAbs in the mouse model. The mouse represents a better model to observe the differences that were expected as larger numbers of animals could be assessed to gain statistical significance in the data (*26*). Before initiating that study, a decision on the method to be used for labeling the mAb with ^{211}At was required.

Labeling of proteins with ^{211}At is very different from labeling with its nearest halogen neighbor, radioiodine, as directly astatinated proteins are readily deastatinated in vivo (*5*). To circumvent this inherent instability, indirect (two-step) protein labeling approaches employing protein reactive reagents that have ^{211}At-aryl bonds were developed (*27, 28*). One of those reagents, *N*-hydroxysuccinimidyl *meta*-[^{211}At]astatobenzoate, [^{211}At]**1c**, has been used in preparation of an astatinated antibody for clinical evaluation (*12*). That fact made the [^{211}At]**1c** labeling reagent of particular interest, as its prior use in a clinical study may make it easier to conduct another clinical study employing that labeling approach from a regulatory standpoint. Further, literature examples demonstrating that intact mAbs labeled with aryl conjugates can be relatively stable to in vivo deastatination (*6,29,30*) offered hope that would be the case for our anti-CD45 mAbs. However, the two-step procedure for labeling with the benzoate NHS ester can be quite problematic. While labeling the stannylbenzoate, **1a**, provides high yields, issues with hydrolysis of the active ester in the second step often decrease the yields substantially (maximum yields 40−60% being obtained). Recent reports indicate that this is particularly true when scaling up to clinical levels of ^{211}At. Although the initial report on using the [^{211}At]**1c** in clinical preparations indicated that radiolysis was not a factor in labeling (*31*), subsequent studies indicated that there was a problem with radiolysis in higher-level clinical preparations (*16*−*18*). This difficulty in obtaining high labeling yields, along with the fact that aryl-^{211}At conjugates are not always stable toward in vivo deastatination, made it prudent to evaluate another labeling approach as well.

Results from our studies of boron cage moieties as reactive groups for labeling with ^{211}At also made that approach to labeling of interest for astatination of the anti-CD45 mAb. In prior studies, it was demonstrated that mAb Fab′ fragments conjugated with a halogen-reactive *closo*-decaborate(2-), **2**, then astatinated had a high in vivo stability toward deastatination (*15*). The same mAb Fab′ labeled with *N*-hydroxysuccinimidyl *para*-[^{211}At]benzoate was quite unstable to in vivo deastatination, making it apparent that ^{211}At-labeled mAb conjugates containing the *closo*-decaborate(2-) moiety had higher in vivo stability to deastatination. In addition to the high stability, the simplicity of direct labeling of the protein (same as radioiodination reactions) and high yields obtained (70−80%) in the prior studies made this new labeling approach very attractive for the anti-CD45 study. Further, direct labeling of mAb-decaborate(2-) conjugates with ^{211}At eliminates the issues of hydrolysis and/or radiolysis of the labeling reagents used in the two-step approach. The direct labeling approach should also minimize radiolysis of the labeled protein as the reactions are conducted in aqueous medium and the fast labeling kinetics (i.e., 30 s) allows rapid introduction of a radioprotective reagent such as citrate or ascorbate.

The differences in ^{211}At labeling yields for the two approaches were surprising. While the high labeling yields for the mAbs conjugated with the *closo*-decaborate(2-) were expected, the low yields obtained with [^{211}At]**1c** were unexpected. Our prior experiences with labeling mAbs using the astatinated benzoate esters suggest that the conjugation yields should be in the range 40−60%. On the basis of the purity of the ^{211}At-labeled benzoate NHS ester (see Figures S1 and S3, Supporting Information), it seems likely that hydrolysis of the NHS ester occurred during isolation or conjugation, resulting in the low yields. Importantly, the results point out the potential for difficulties in labeling using the ^{211}At-labeled benzoate approach.

The in vivo distribution might be considered the most important measure of the value of each ^{211}At-labeling approach. Specific targeting of radiolabeled 30F11 to CD45-containing cells within the spleen was achieved irrespective of the method of labeling; however, higher quantities appeared to be attained with radiolabeled 30F11-**2** (Figure 5). The difference seen may be reflective of a higher retention of the radiohalogenated *closo*-decaborate(2-) metabolites rather than lower amounts accumulated with the radiohalogenated benzoate conjugates. While the amounts of ^{125}I and ^{211}At in spleen are similar for radiolabeled 30F11-**2**, they are very different for 30F11-[^{211}At]**1c** and 30F11-[^{125}I]**1b**. That difference is likely due to deastatination of the benzoate, but that does not occur unless the protein is metabolized. We did not expect to observe deastatination of mAbs labeled with [^{211}At]**1c** in these studies, as the CD45 antigen is not internalized. However, this example is consistent with other examples in the literature that suggest stability toward in vivo deastatination may be dependent on the antibody/cell targeting system involved (*9, 10, 32*).

The deastatination decreases the amount of ^{211}At in the target organ (spleen) and increases it in the nontarget tissues, e.g., lung. On the other hand, the ^{211}At-labeled *closo*-decaborate(2-) conjugate, [^{211}At]30F11-**2**, has a higher uptake in liver than the *meta*-benzoate conjugate, [^{211}At]30F11-**1c**. This might be perceived as a problem of nonspecific localization (or retention) in the liver. However, after comparison of the liver ^{211}At concentrations in Figure 4, panels B, C, and D, it appears that the higher concentrations in liver may be due to specific binding with CD45 antigens in that tissue. This statement is based on the fact that the amount of radioiodinated irrelevant mAb, CA12.10C12, in the liver is the same irrespective the method of the labeling.

CONCLUSIONS

This investigation was conducted to compare ^{211}At labeling of an anti-CD45 mAb, 30F11, and an irrelevant mAb, CA12.10C12, using a conventional astatination approach, i.e., conjugation of *N*-hydroxysuccinimidyl *meta*-[^{211}At]astatobenzoate, and a new labeling approach where the mAbs were labeled after conjugation with a *closo*-decaborate(2-) derivative. The studies demonstrated the utility of *closo*-decaborate(2-) mAb conjugates over the *meta*-[^{211}At]benzoate conjugates for labeling with ^{211}At. The studies further confirmed that the ^{211}At-labeled mAb conjugates had a high in vivo stability to deastatination. Additionally, it was demonstrated that CD45 specific targeting was not adversely affected by the protein modification step. These factors, along with the simplicity of labeling using this method and the potential benefit for scale-up to clinical levels of ^{211}At labeled mAbs, make the mAb-*closo*-decaborate(2-) conjugates our preferred choice for continuing studies with ^{211}At-

labeled anti-CD45 mAbs as a replacement of TBI in conditioning for hematopoietic cell transplantation.

ACKNOWLEDGMENT

We are appreciative for the funds provided by NCI, NIH (CA118940, CA113431, CA76287 and CA109663), for this research.

Supporting Information Available: Tables (S1−S5) containing biodistribution data, either %ID/g or %ID, in selected tissues, and copies of UV- and radiochromatograms (Figures S1−S4) for [^{211}At]**1c** and [^{125}I]**1b**. This material is available free of charge via the Internet at http://pubs.acs.org.

LITERATURE CITED

(1) Bethge, W. A., Wilbur, D. S., and Sandmaier, B. M. (2006) Radioimmunotherapy as non-myeloablative conditioning for allogeneic marrow transplantation. *Leuk. Lymphoma 47*, 1205–14.

(2) Sandmaier, B. M., Bethge, W. A., Wilbur, D. S., Hamlin, D. K., Santos, E. B., Brechbiel, M. W., Fisher, D. R., and Storb, R. (2002) Bismuth-213-labeled anti-CD45 radioimmunoconjugate to condition dogs for nonmyeloablative allogeneic marrow grafts. *Blood 100*, 318–26.

(3) Bethge, W. A., Wilbur, D. S., Storb, R., Hamlin, D. K., Santos, E. B., Brechbiel, M. W., Fisher, D. R., and Sandmaier, B. M. (2003) Selective T-cell ablation with bismuth-213-labeled anti-TCR$\alpha\beta$ as nonmyeloablative conditioning for allogeneic canine marrow transplantation. *Blood 101*, 5068–75.

(4) Bethge, W. A., Wilbur, D. S., Storb, R., Hamlin, D. K., Santos, E. B., Brechbiel, M. W., and Sandmaier, B. M. (2004) Radioimmunotherapy with bismuth-213 as conditioning for nonmyeloablative allogeneic hematopoietic cell transplantation in dogs: a dose deescalation study. *Transplantation 78*, 352–359.

(5) Wilbur, D. S. (2008) [^{211}At]astatine-labeled compound stability: issues with released [^{211}At]astatide and development of labeling reagents to increase stability. *Curr. Radiopharm. 1*, 144–176.

(6) Hadley, S. W., Wilbur, D. S., Gray, M. A., and Atcher, R. W. (1991) Astatine-211 labeling of an antimelanoma antibody and its Fab fragment using N-succinimidyl p-[^{211}At]astatobenzoate: comparisons in vivo with the *p*-[^{125}I]iodobenzoyl conjugate. *Bioconjugate Chem. 2*, 171–9.

(7) Zalutsky, M. R., and Narula, A. S. (1988) Astatination of proteins using an N-succinimidyl tri-*n*-butylstannyl benzoate intermediate. *Appl. Radiat. Isot. 39*, 227–232.

(8) Zalutsky, M. R., Garg, P. K., Friedman, H. S., and Bigner, D. D. (1989) Labeling monoclonal antibodies and F(ab')$_2$ fragments with the α-particle-emitting nuclide astatine-211: Preservation of Immunoreactivity and in vivo localizing capacity. *Proc. Natl. Acad. Sci. U.S.A. 86*, 7149–7153.

(9) Yordanov, A. T., Garmestani, K., Zhang, M., Zhang, Z., Yao, Z., Phillips, K. E., Herring, B., Horak, E., Beitzel, M. P., Schwarz, U. P., Gansow, O. A., Plascjak, P. S., Eckelman, W. C., Waldmann, T. A., and Brechbiel, M. W. (2001) Preparation and in vivo evaluation of linkers for ^{211}At labeling of humanized anti-Tac. *Nucl. Med. Biol. 28*, 845–856.

(10) Persson, M. I., Gedda, L., Jensen, H. J., Lundqvist, H., Malmstrom, P. U., and Tolmachev, V. (2006) Astatinated trastuzumab, a putative agent for radionuclide immunotherapy of ErbB2-expressing tumours. *Oncol. Rep. 15*, 673–80.

(11) Talanov, V. S., Yordanov, A. T., Garmestani, K., Milenic, D. E., Arora, H. C., Plascjak, P. S., Eckelman, W. C., Waldmann, T. A., and Brechbiel, M. W. (2004) Preparation and in vivo evaluation of novel linkers for ^{211}At labeling of proteins. *Nucl. Med. Biol. 31*, 1061–1071.

(12) Zalutsky, M. R., Reardon, D. A., Akabani, G., Coleman, R. E., Friedman, A. H., Friedman, H. S., McLendon, R. E., Wong, T. Z., and Bigner, D. D. (2008) Clinical experience with alpha-particle emitting ^{211}At: treatment of recurrent brain tumor patients with ^{211}At-labeled chimeric antitenascin monoclonal antibody 81C6. *J. Nucl. Med. 49*, 30–8.

(13) Wilbur, D. S., Vessella, R. L., Stray, J. E., Goffe, D. K., Blouke, K. A., and Atcher, R. W. (1993) Preparation and evaluation of *para*-[^{211}At]astatobenzoyl labeled anti-renal cell carcinoma antibody A6H F(ab')$_2$. In vivo distribution comparison with *para*-[^{125}I]iodobenzoyl labeled A6H F(ab')$_2$. *Nucl. Med. Biol. 20*, 917–27.

(14) Wilbur, D. S., Hamlin, D. K., Chyan, M. K., Kegley, B. B., Quinn, J., and Vessella, R. L. (2004) Biotin reagents in antibody pretargeting. 6. Synthesis and in vivo evaluation of astatinated and radioiodinated aryl- and *nido*-carboranyl-biotin derivatives. *Bioconjugate Chem. 15*, 601–16.

(15) Wilbur, D. S., Chyan, M. K., Hamlin, D. K., Vessella, R. L., Wedge, T. J., and Hawthorne, M. F. (2007) Reagents for astatination of biomolecules. 2. Conjugation of anionic boron cage pendant groups to a protein provides a method for direct labeling that is stable to in vivo deastatination. *Bioconjugate Chem. 18*, 1226–40.

(16) Pozzi, O. R., and Zalutsky, M. R. (2005) Radiopharmaceutical chemistry of targeted radiotherapeutics, part 1: effects of solvent on the degradation of radiohalogenation precursors by ^{211}At alpha-particles. *J. Nucl. Med. 46*, 700–6.

(17) Pozzi, O. R., and Zalutsky, M. R. (2005) Radiopharmaceutical chemistry of targeted radiotherapeutics, Part 2: radiolytic effects of ^{211}At alpha-particles influence N-succinimidyl 3-^{211}At-astatobenzoate synthesis. *J. Nucl. Med. 46*, 1393–400.

(18) Pozzi, O. R., and Zalutsky, M. R. (2007) Radiopharmaceutical chemistry of targeted radiotherapeutics, Part 3: alpha-particle-induced radiolytic effects on the chemical behavior of ^{211}At. *J. Nucl. Med. 48*, 1190–6.

(19) Garg, P. K., Archer, G. E., Jr., Bigner, D. D., and Zalutsky, M. R. (1989) Synthesis of radioiodinated N-succinimidyl iodobenzoate: optimization for use in antibody labelling. *Int. J. Rad. Appl. Instrum. [A] 40*, 485–90.

(20) Matthews, D. C., Martin, P. J., Nourigat, C., Appelbaum, F. R., Fisher, D. R., and Bernstein, I. D. (1999) Marrow ablative and immunosuppressive effects of ^{131}I-anti-CD45 antibody in congenic and H2-mismatched murine transplant models. *Blood 93*, 737–45.

(21) Caniatti, M., Roccabianca, P., Scanziani, E., Paltrinieri, S., and Moore, P. F. (1996) Canine lymphoma: immunocytochemical analysis of fine-needle aspiration biopsy. *Vet. Pathol. 33*, 204–12.

(22) Barsoukov, A. A., Moore, P. F., Storb, R., Santos, E. B., and Sandmaier, B. M. (1999) The use of an anti-TCR$\alpha\beta$ monoclonal antibody to control host-versus-graft reactions in canine marrow allograft recipients conditioned with low dose total body irradiation. *Transplantation 67*, 1329–35.

(23) Kaplan, H. M., Brewer, N. R., Blair, W. H. (1983) Physiology, In *The Mouse in Biomedical Research* (Foster, H. L., Small, J. D., and Fox, J. G., Eds.) pp 248−292, Academic Press, New York.

(24) Hylarides, M. D., Mallett, R. W., and Meyer, D. L. (2001) A robust method for the preparation and purification of antibody/streptavidin conjugates. *Bioconjugate Chem. 12*, 421–427.

(25) Wilbur, D. S., Hadley, S. W., Grant, L. M., and Hylarides, M. D. (1991) Radioiodinated iodobenzoyl conjugates of a monoclonal antibody Fab fragment. In vivo comparisons with chloramine-T-labeled Fab. *Bioconjugate Chem. 2*, 111–16.

(26) Nakamae, H., Wilbur, D. S., Hamlin, D. K., Thakar, M. S., Santos, E. B., Fisher, D. R., A. L., K., Pagel, J. M., Press, O. W., Storb, R., and Sandmaier, B. M. (2009) Biodistributions, myelosuppression and toxicities in mice treated with an anti-CD45 antibody labeled with the α-emitting radionuclides bismuth-213 or astatine-211. *Cancer Res. 69*, 2408–2415.

(27) Zalutsky, M. R., and Vaidyanathan, G. (2000) Astatine-211-labeled radiotherapeutics: an emerging approach to targeted alpha-particle radiotherapy. *Curr. Pharm. Des. 6*, 1433–55.

(28) Wilbur, D. S. (1992) Radiohalogenation of proteins: an overview of radionuclides, labeling methods, and reagents for conjugate labeling. *Bioconjugate Chem. 3*, 433–70.

(29) Garg, P. K., Harrison, C. L., and Zalutsky, M. R. (1990) Comparative tissue distribution in mice of the alpha-emitter ^{211}At and ^{131}I as labels of a monoclonal antibody and F(ab′)$_2$ fragment. *Cancer Res. 50*, 3514–20.

(30) Zalutsky, M. R., Stabin, M. G., Larsen, R. H., and Bigner, D. D. (1997) Tissue distribution and radiation dosimetry of astatine-211-labeled chimeric 81C6, an alpha-particle-emitting immunoconjugate. *Nucl. Med. Biol. 24*, 255–61.

(31) Zalutsky, M. R., Zhao, X. G., Alston, K. L., and Bigner, D. (2001) High-level production of alpha-particle-emitting ^{211}At and preparation of ^{211}At-labeled antibodies for clinical use. *J. Nucl. Med. 42*, 1508–15.

(32) Larsen, R. H., Hoff, P., Alstad, J., and BrulandØ. S. (1994) Preparation and quality control of ^{211}At-labelled and ^{125}I-Labelled monoclonal antibodies. Biodistribution in mice carrying human osteosarcoma xenografts. *J. Labelled. Compd. Radiopharm. 34*, 773–785.

BC9000799

Supporting Information For:

Reagents for Astatination of Biomolecules. 4. Comparison of Maleimido-*closo*-Decaborate(2-) and *meta*-[^{211}At]Astatobenzoate Conjugates for Labeling anti-CD45 Antibodies with [^{211}At]Astatine.

D. Scott Wilbur[1]*, Monica S. Thakar[4,5], Donald K. Hamlin[1], Erlinda B. Santos[5], Ming-Kuan Chyan[1], Hirohisa Nakamae[5], Aimee L. Kenoyer[5], John M. Pagel[2,5], Oliver W. Press[2,3,5], and Brenda M. Sandmaier[2,5]

Departments of [1]Radiation Oncology, [2]Medicine, [3]Biological Structure and [4]Pediatrics, Univ. of Washington, Seattle, WA; [5]Clinical Research Division, Fred Hutchinson Cancer Research Center, Seattle, WA

Table S1: **Concentration (%ID/g) of Radioactivity for Co-injected [^{125}I]- and [^{211}At]-Labeled 30F11-2 in selected tissues of BALB/c mice.**

Table S2: **Concentration (%ID/g) of Radioactivity for Co-injected [^{125}I]- and [^{211}At]-Labeled 30F11-1a/b in selected tissues of BALB/c mice.**

Table S3: **Concentration (%ID/g) of Radioactivity for Co-injected [^{125}I]- and [^{211}At]-Labeled CA12.10C12-2 in selected tissues of BALB/c mice.**

Table S4: **Concentration (%ID/g) of Radioactivity for Co-injected [^{125}I]- and [^{211}At]-Labeled CA12.10C12-1a/b in selected tissues of BALB/c mice.**

Table S5: **Percent of injected dose (%ID) of radioactivity that localized in spleens of BALB/c mice.**

Figure S1: **HPLC Chromatograms (UV & radioactivity) of reaction of 1a to prepare [^{211}At]1c for reaction with CA12.10C12.**

Figure S2: **HPLC Chromatograms (UV & radioactivity) of reaction of 1a to prepare [^{125}I]1b for reaction with CA12.10C12.**

Figure S3: **HPLC Chromatograms (UV & radioactivity) of reaction of 1a to prepare [^{211}At]1c for reaction with 30F11.**

Figure S4: **HPLC Chromatograms (UV & radioactivity) of reaction of 1a to prepare [^{125}I]1b for reaction with 30F11**

Table S1: Concentration (%ID/g) of Radioactivity for Co-injected [^{125}I]- and [^{211}At]-Labeled 30F11-2 in selected tissues of BALB/c mice.[a]

Tissues	1 h[b,c]		4 h		24h	
	I-125	At-211	I-125	At-211	I-125	At-211
blood	12.88 ± 1.13	16.03 ± 1.69	6.60 ± 1.60	8.66 ± 2.14	2.09 ± 0.23*	3.07 ± 0.35*
muscle	0.77 ± 0.08	0.77 ± 0.09	3.30 ± 2.53	3.78 ± 2.91	0.47 ± 0.13	0.45 ± 0.16
lung	14.04 ± 6.30	16.24 ± 8.11	22.00 ± 19.82	29.27 ± 26.35	2.09 ± 0.23*	3.07 ± 0.35*
kidney	8.03 ± 1.53	8.61 ± 1.73	8.41 ± 0.13	9.29 ± 0.11	8.75 ± 0.56*	12.32 ± 0.93*
spleen	498.24 ± 162.40	540.52 ± 176.9	1239.0 ± 1256.1	1409.0 ± 1429.8	195.81 ± 36.13*	274.00 ± 59.91*
liver	22.26 ± 2.04	24.99 ± 2.39	20.47 ± 1.60*	24.53 ± 2.14*	2.09 ± 0.23*	3.07 ± 0.35*
intestine	12.88 ± 1.13	16.03 ± 1.69	6.60 ± 0.67	8.66 ± 0.66	14.31 ± 1.44*	21.74 ± 2.03*
neck	4.04 ±0.93*	3.32 ± 0.48*	6.40 ± 0.14	7.15 ± 0.01	4.18 ± 1.13*	5.90 ± 2.19*
stomach	8.67 ± 2.27	2.71 ± 0.88	8.56 ± 1.67	3.20 ± 1.05	4.36 ± 0.44*	6.33 ± 0.90*

[a]Values shown are % injected dose / gram ± standard deviation. [b]Time of sacrifice from injection of radiolabeled antibodies, [^{125}I]30F11-**2** and [^{211}At]30F11-**2**. [c]Data were obtained for n = 5 mice at each time point; average animal weight, 16.34 ± 0.99 g; Radiolabeled antibodies were isolated (purified) from PD-10 columns and diluted with saline for injection; Injectate for each animal had 5 μCi of [^{125}I]30F11-**2** and 10 μCi of [^{211}At]30F11-**2** in approximately 100 μL of 0.9% sterile saline. *Significant difference found in values by paired Student's t test, $P<0.05$.

Table S2: Concentration (%ID/g) of Radioactivity for Co-injected [^{125}I]- and [^{211}At]-Labeled 30F11-1a/b in selected tissues of BALB/c mice.[a]

Tissues	1 h[b,c]		4 h		24h**	
	I-125	At-211	I-125	At-211	I-125	At-211
blood	16.22 ± 2.09*	10.58 ± 0.71*	6.16 ± 3.71	5.24 ± 3.91	1.93 ± 0.39	0.20 ± 0.27
muscle	2.86 ± 0.61	2.79 ± 0.27	1.98 ± 0.71	1.46 ± 0.86	0.64 ± 0.24	0.95 ± 1.90
lung	14.86 ± 2.93*	25.96 ± 6.77*	11.15 ± 4.92*	21.72 ± 5.72*	1.78 ± 0.47	2.38 ± 2.05
kidney	9.10 ± 1.28	9.34 ± 0.85	6.38 ± 0.48	7.51 ± 1.81	1.45 ± 0.08	1.80 ± 1.52
spleen	206.90 ± 36.69	100.65 ± 16.08	546.36 ± 552.28	318.26 ± 320.59	52.71 ± 13.30	75.76 ± 19.36
liver	16.36 ± 1.31*	14.72 ± 0.68*	12.19 ± 1.22*	12.70 ± 1.78*	2.31 ± 0.61	3.56 ± 1.13
intestine	4.93 ± 1.04	5.50 ± 0.43	4.44 ± 0.04	6.48 ± 1.51	1.56 ± 0.47	3.40 ± 0.95
neck	8.00 ± 2.82*	17.89 ± 6.78*	5.59 ± 0.41*	9.97 ± 1.86*	4.54 ± 0.56	5.64 ± 5.62
stomach	5.40 ± 2.09*	23.37 ± 3.06*	2.26 ± 0.10*	32.85 ± 5.27*	0.89 ± 0.19	3.52 ± 1.93

[a]Values shown are % injected dose / gram ± standard deviation. [b]Time of sacrifice from injection of radiolabeled antibodies, [^{125}I]30F11-**1b** and [^{211}At]30F11-**1c**. [c]Data were obtained for *n* = 5 mice at each time point; average animal weight, 29.28 ± 2.68 g; Radiolabeled antibodies were isolated (purified) from PD-10 columns and diluted with saline for injection; Injectate for each animal had 1 μCi of [^{125}I]**1b** and 1 μCi of [^{211}At]**1c** in approximately 100 μL of 0.9% sterile saline. *Significant difference found in values by paired Student's *t* test, P<0.05. **Significance of difference between radionuclides not determined due to low counts of ^{211}At.

Table S3: Concentration (%ID/g) of Radioactivity for Co-injected [^{125}I]- and [^{211}At]-Labeled CA12.10C12-2 in selected tissues of BALB/c mice.[a]

Tissues	1 h[b,c]		4 h		24h	
	I-125	At-211	I-125	At-211	I-125	At-211
blood	59.64 ± 3.73	60.85 ± 3.48	44.81 ± 4.76	50.66 ± 4.60	20.40 ± 2.02*	26.17 ± 2.20*
muscle	1.62 ± 0.35	1.65 ± 0.36	1.38 ± 0.21	1.59 ± 0.25	1.44 ± 0.29	1.69 ± 0.35
lung	16.29 ± 2.30	18.82 ± 2.60	16.88 ± 1.69*	20.05 ± 1.99*	9.47 ± 1.17*	13.24 ± 2.00*
kidney	14.48 ± 0.78	15.32 ± 1.00	13.94 ± 1.03*	15.90 ± 0.99*	11.64 ± 1.14*	13.72 ± 1.57*
spleen	9.34 ± 2.15	11.52 ± 2.63	6.53 ± 0.96	8.13 ± 1.72	6.58 ± 1.36*	9.30 ± 1.95*
liver	17.96 ± 3.38	22.05 ± 3.38	14.00 ± 0.70*	17.14 ± 1.10*	11.24 ± 0.72*	16.13 ± 1.09*
intestine	2.79 ± 0.35*	3.59 ± 0.29*	2.18 ± 0.95	2.65 ± 1.20	1.68 ± 0.22*	2.57 ± 0.39*
neck	7.58 ± 1.38	6.37 ± 0.36	5.84 ± 0.99	6.74 ± 3.58	5.98 ± 1.25*	8.23 ± 1.48*
stomach	8.69 ± 1.02*	4.42 ± 0.54*	5.87 ± 5.19	7.06 ± 7.29	1.40 ± 0.60*	5.15 ± 2.86*

[a]Values shown are % injected dose / gram ± standard deviation. [b]Time of sacrifice from injection of radiolabeled antibodies, [^{125}I]CA12.10C12-**1b** and [^{211}At]CA12.10C12-**1c**. [c]Data were obtained for n = 5 mice at each time point; average animal weight, 29.28 ± 2.68 g; Radiolabeled antibodies were isolated (purified) from PD-10 columns and diluted with saline for injection; Injectate for each animal had 5 μCi of [^{125}I]CA12.10C12-**2** and 10 μCi of [^{211}At]CA12.10C12-**2** in approximately 100 μL of 0.9% sterile saline. *Significant difference found in values by paired Student's t test, $P<0.05$.

Table S4: Concentration (%ID/g) of Radioactivity for Co-injected [^{125}I]- and [^{211}At]-Labeled CA12.10C12-1a/b in selected tissues of BALB/c mice.[a]

Tissues	1 h[b,c]		4 h		24h	
	I-125	At-211	I-125	At-211	I-125	At-211
blood	51.28 ± 2.60*	22.06 ± 1.00*	36.28 ± 1.87*	15.39 ± 0.77*	24.49 ± 1.77	22.55 ± 6.08
muscle	1.36 ± 0.47	1.74 ± 0.39	1.44 ± 0.05*	0.89 ± 0.07*	2.43 ± 0.17*	0.00 ± 1.37*
lung	32.78 ± 19.52	40.78 ± 17.52	17.50 ± 3.72	13.70 ± 1.23	15.87 ± 5.25	10.78 ± 7.52
kidney	14.10 ± 1.78	17.85 ± 2.61	8.95 ± 0.35*	11.45 ± 0.02*	6.34 ± 0.55*	9.94 ± 1.61*
spleen	8.60 ± 1.11*	24.87 ± 2.49*	6.91 ± 0.24*	16.84 ± 0.45*	4.92 ± 0.54	3.58 ± 3.32
liver	16.60 ± 1.13*	29.12 ± 0.53*	14.19 ± 1.36*	20.36 ± 0.57*	8.70 ± 0.93*	14.54 ± 0.90*
intestine	2.68 ± 0.62*	8.96 ± 0.92*	2.62 ± 0.00*	6.33 ± 0.43*	2.04 ± 0.12*	2.78 ± 0.15*
neck	4.27 ± 1.36	8.95 ± 3.06	4.38 ± 0.92*	5.79 ± 0.14*	4.99 ± 0.19*	2.33 ± 3.01*
stomach	4.05 ± 0.82*	49.99 ± 26.40*	1.65 ± 0.55*	20.49 ± 3.04*	1.27 ± 0.53*	3.84 ± 0.74*

[a]Values shown are % injected dose / gram ± standard deviation. [b]Time of sacrifice from injection of radiolabeled antibodies, [^{125}I]CA12.10C12-**1b** and [^{211}At]CA12.10C12-**1c**. [c]Data were obtained for n = 5 mice at each time point; average animal weight, 18.39 ± 0.71 g; Radiolabeled antibodies were isolated (purified) from PD-10 columns and diluted with saline for injection; Injectate for each animal had 1 μCi of [^{125}I]CA12.10C12-**1b** and 1 μCi of [^{211}At]CA12.10C12-**1c** in approximately 100 μL of 0.9% sterile saline. *Significant difference found in values by paired Student's t test, $P<0.05$.

Table S5: Percent of injected dose (%ID) of radioactivity that localized in spleens of BALB/c mice.[a]

Tissues	1 h[b,c]		4 h		24h	
	I-125	At-211	I-125	At-211	I-125	At-211
30F11-**2**	21.15 ± 1.33	22.78 ± 1.29	22.22 ± 1.95	25.05 ± 2.35	12.41 ± 0.75	17.30 ± 1.20
30F11-**1b/c**	13.31 ± 0.78	6.56 ± 0.40	17.43 ± 2.56	10.14 ± 1.49	5.23 ± 0.50	7.52 ± 0.79
CA12.10C12-**2**	0.65 ± 0.05	0.80 ± 0.05	0.49 ± 0.03	0.61 ± 0.07	0.30 ± 0.02	0.42 ± 0.07
CA12.10C12-**1b/c**	0.60 ± 0.04	1.62 ± 0.14	0.49 ± 0.24	1.21 ± 0.08	0.33 ± 0.02	0.24 ± 0.23

[a]Values shown are % injected dose ± standard deviation. [b]Time of sacrifice from injection of radiolabeled antibodies. [c]Data were obtained for $n = 5$ mice at each time point.

Figure S1

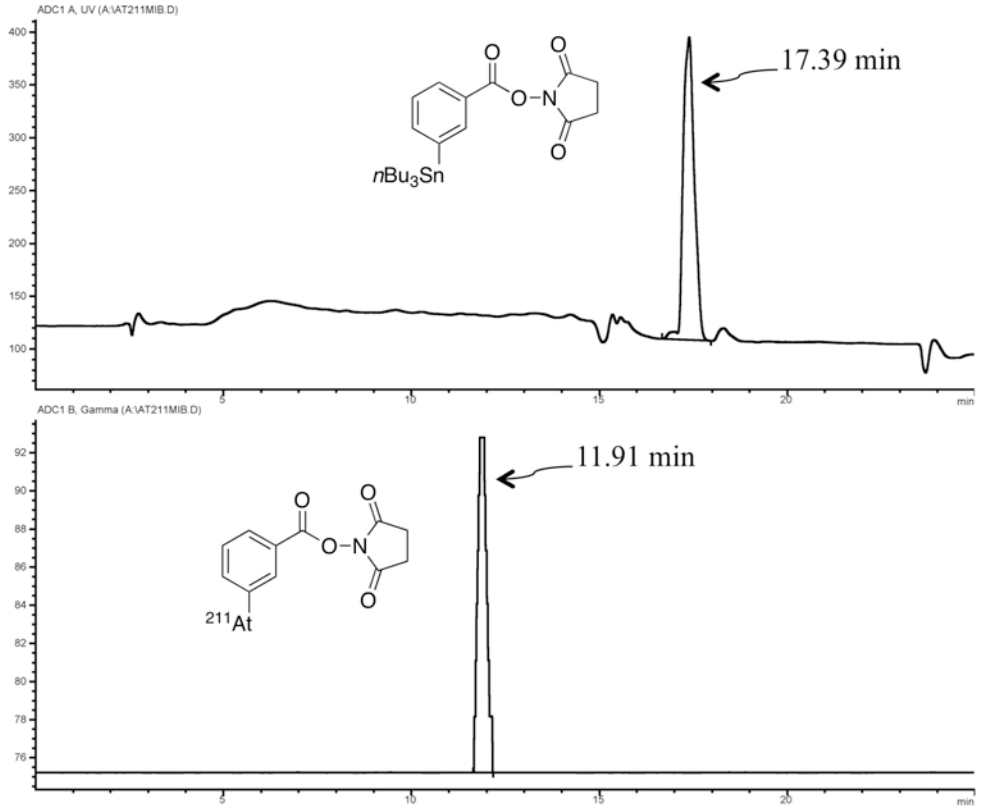
ADC1 A, UV (A:\AT211MIB.D)
17.39 min
nBu3Sn
ADC1 B, Gamma (A:\AT211MIB.D)
11.91 min
211At
min

Figure S2

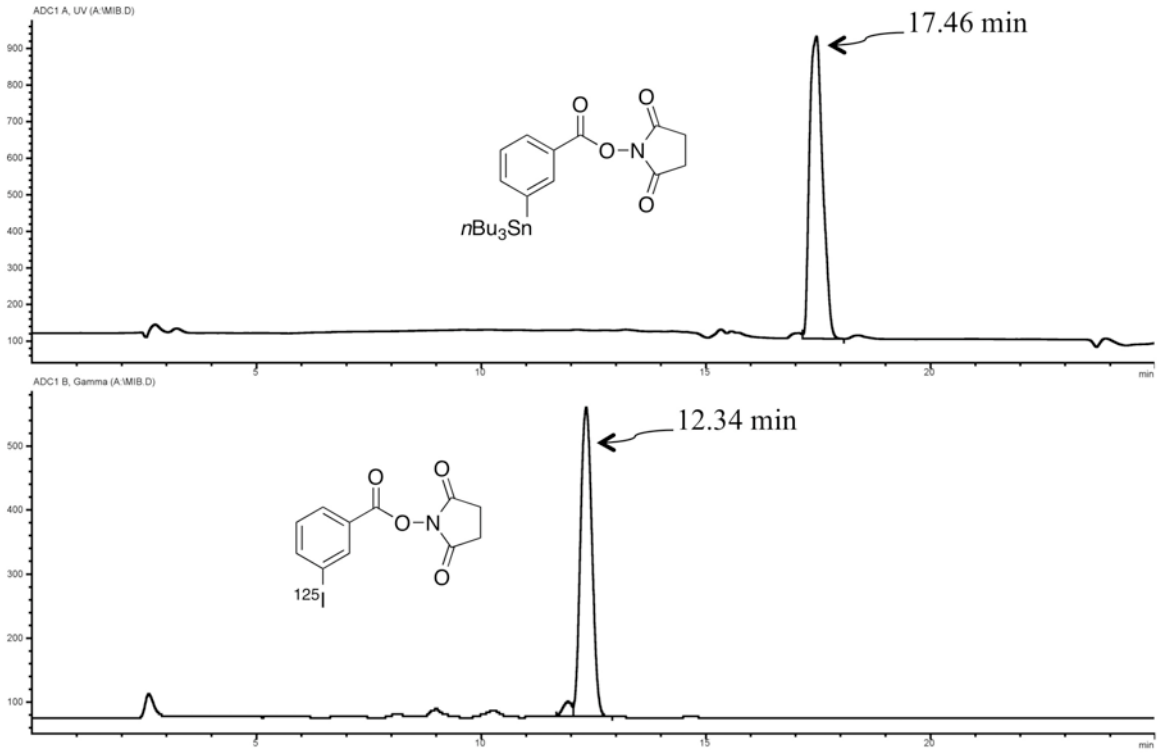
ADC1 A, UV (A:\MIB.D)
17.46 min
nBu3Sn
ADC1 B, Gamma (A:\MIB.D)
12.34 min
125I
min

Figure S3

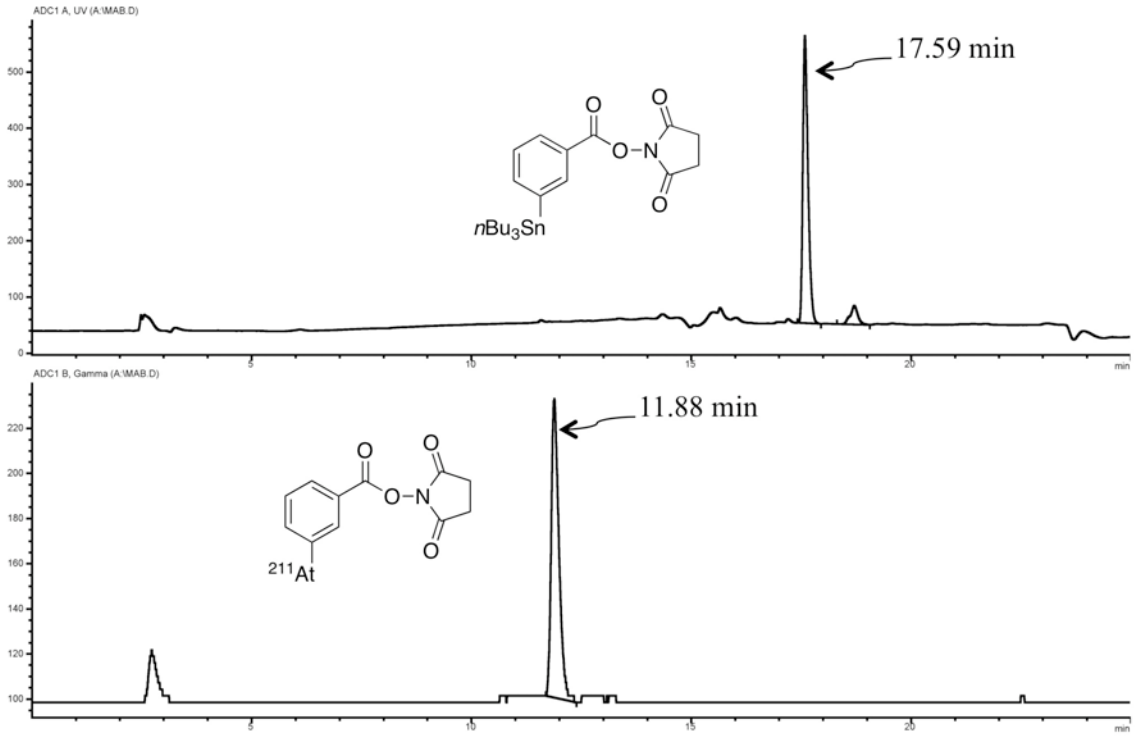
ADC1 A, UV (A:\MAB.D)
17.59 min
nBu3Sn
ADC1 B, Gamma (A:\MAB.D)
11.88 min
211At
min

Figure S4

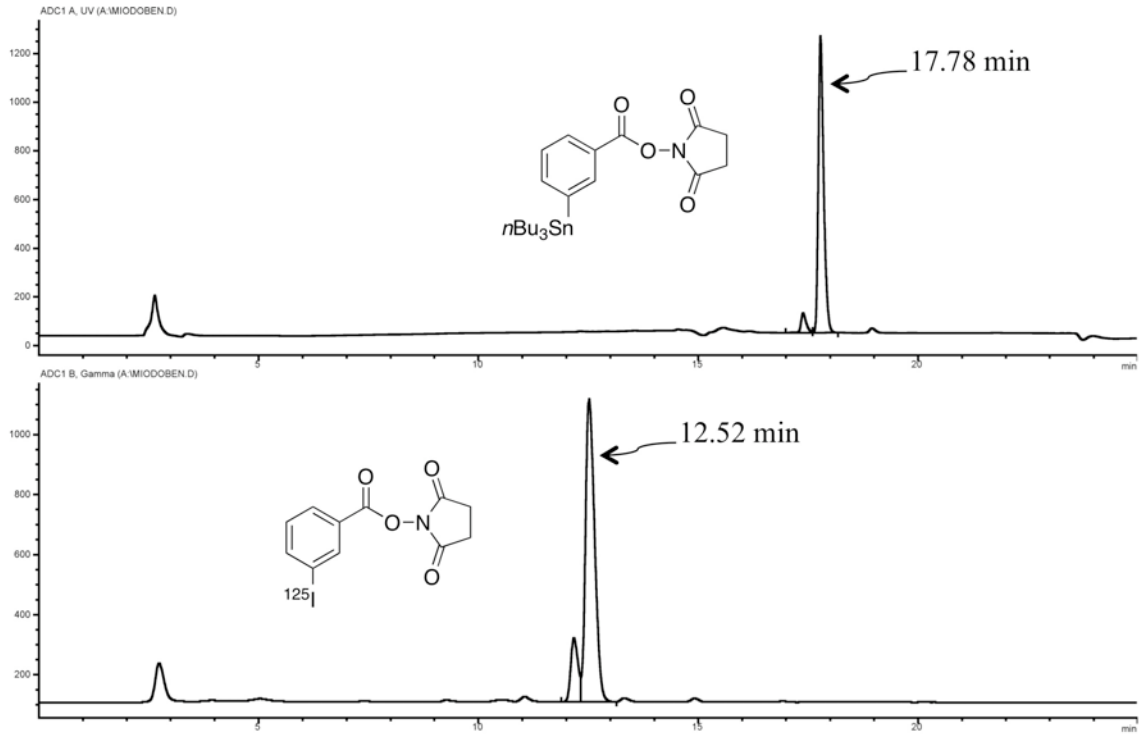
ADC1 A, UV (A:\MIODOBEN.D)
17.78 min
nBu3Sn
ADC1 B, Gamma (A:\MIODOBEN.D)
12.52 min
125I
min

Biomolecule Labeling and Imaging with a New Fluorenyl Two-Photon Fluorescent Probe

Alma R. Morales,[†] Ciceron O. Yanez,[†] Katherine J. Schafer-Hales,[§] Adam I. Marcus,[§] and Kevin D. Belfield*[,†,‡]

Department of Chemistry, CREOL, The College of Optics and Photonics, University of Central Florida, P.O. Box 162366, Orlando, Florida 32816-2366, and Winship Cancer Institute, Emory University School of Medicine, Atlanta, Georgia 30322. Received July 8, 2009; Revised Manuscript Received September 8, 2009

Closely involved in the progression of nonlinear bioimaging is the development of optical probes for investigating biological function and activity. Introduction of new fluorescent compounds possessing enhanced nonlinearities is essential for advancing the utility of two-photon absorption (2PA) processes in the biological sciences. Herein, we report the synthesis of fluorene-based fluorophores tailored for multiphoton imaging, incorporating the succinimidyl ester and thioester functionality as reactive linkers for further coupling with a wide variety of biologically relevant molecules. The succinimidyl ester amine reactive probe was conjugated with the cyclic peptide RGDfK and polyclonal antirat IgG protein. Upon conjugation, the basic molecular architecture and photophysical properties of the active 2PA chromophore remain unchanged. Conventional and two-photon fluorescence microscopy (2PFM) imaging of COS-7 and HeLa cells, incubated with either the fluorene−RGD peptide conjugate or the fluorene−IgG conjugate, was demonstrated. The fluorene−IgG conjugate was used to image cell spindles at early mitotic developmental stages.

INTRODUCTION

In recent years, enormous interest in the design, synthesis, and characterization of fluorescent compounds with high two-photon absorption (2PA) cross sections has been increasing because of their recognized application in a number of multidisciplinary areas, particularly in the rapidly developing fields of multiphoton fluorescence imaging, optical data storage and switching, optical sensor protection, laser dyes, three-dimensional (3D) microfabrication, and photodynamic therapy (*1*−*6*). Multiphoton fluorescence bioimaging is one of the most promising among these applications, using fluorescent markers or intrinsic fluorescence in biological samples to gain insight into 3D cell structure.

Compared to conventional optical microscopy, two-photon excited fluorescence (2PEF) microscopy has a number of advantages, with the first being the inherent 3D localization of excitation and fluorescence arising from the quadratic dependence on the input intensity. This quadratic or nonlinear dependence limits excitation to a tiny focal volume, which restricts both out-of-focus background excitation and provides intrinsic confocality, since only fluorophores in the plane of the focused beam will be excited. This prevents the need for a confocal aperture in front of the detector, thus maximizing the amount of light detected (*7*). Second, 2PEF microscopy utilizes the near-infrared (NIR) spectral window, so the imaging depth is much greater and scattering is reduced, resulting in less photodamage and photobleaching than that caused by one-photon excited fluorescence techniques (*8*−*10*). In addition, higher signal-to-background ratios for fluorescence detection are possible resulting from well-separated excitation and emission wavelengths and reduced attenuation of NIR light in biological specimens relative to UV and visible wavelengths (*7*). To overcome depth of light penetration challenges, recently, progress has been reported in the use of luminescence upconversion using lanthanide ion-doped nanoscrystals (*11*). The lanthanide ion-doped nanocrystals exhibit good photostability and show reduced auotfluorescence, though spatial resolution is still an issue, since the excitation relies on sequential linear absorption of two photons.

The potential of two-photon excitation (2PE) as a tool in fluorescence microscopy of biological samples cannot be realized without fluorescent probes or dyes possessing high 2PA cross sections for labeling nonfluorescent molecules, such as proteins, nucleic acids (NA), and peptides. Fluorescent dyes such as Alexa Fluor 405, ethidium bromide, 4′,6-diamidine-2-phenylindole (DAPI), and Hoechst, which are widely used in fluorescence studies, have been shown to undergo 2PE fluorescence when complexed with NAs (*12*, *13*) though their 2PA cross sections are low.

Fluorescent probes with reactive groups are highly desirable since they can be conjugated with a vast number of biomolecules (*14*−*21*). Fluorene derivatives typically exhibit high fluorescence quantum yields and excellent photostability (*22*, *23*). Recently, fluorene-based bioconjugates have been reported as excellent 2PF materials, possessing high 2PA cross sections (*24*−*28*). As part of our efforts to develop high-efficiency 2PA fluorene derivatives as novel fluorescent biomarkers, we found that A-$\pi-\pi-\pi$-A type compounds (where A is an electron withdrawing moiety and π represents a conjugated system of π bonds), such as 2,7-bis[4-(9,9-didecylfluoren-2-yl)vinyl]phenylbenzothiazole, exhibited reasonably high 2PA cross sections in the NIR, e.g., ∼1185 GM at 800 nm (1 GM = 10^{-50} cm^4 s photon^{-1}) (*25*, *28*) with near-unity fluorescence quantum yield. However, this compound is rather hydrophobic, thereby limiting its applications in biological imaging.

By introducing one or two ethylene glycol moieties at the 9-position of the fluorene, the water solubility of the fluorene-based fluorescent probes can be greatly improved, facilitating

* To whom all correspondence should be addressed. Department of Chemistry, University of Central Florida, P.O. Box 162366, 4000 Central Florida Blvd., Orlando, FL 32816-2366, USA, Ph: 407-823-1028, Fax: 407-823-2252, E-mail: belfield@mail.ucf.edu.

[†] Department of Chemistry, University of Central Florida.

[‡] The College of Optics and Photonics, University of Central Florida.

[§] Emory University School of Medicine.

10.1021/bc900302t CCC: $40.75 © 2009 American Chemical Society
Published on Web 10/02/2009

the use of these dyes for cellular imaging. In addition, substitution at the fluorenyl 9-position with a succinimidyl-containing moiety provides a reactive linker for further biomolecule conjugation. Herein, we report the synthesis and comprehensive characterization of a new fluorescent probe and a simple protocol of attaching this fluorescent label on an antibody to increase immunoassay sensitivity. In this work, goat antirat IgG antibody labeled with fluorene-NHS (**1**) was used to stain microtubules and mitotic cells.

EXPERIMENTAL SECTION

Materials and Methods. 2-(4-Vinylphenyl)benzothiazole **E** was synthesized as previously reported (*25*). The cyclic peptide (Ar-Gly-Asp-D-Phe-Lys) c(RGDfK) was purchased from Peptides International, Inc. Polyclonal antirat IgG (whole molecule) was purchased from Aldrich. All other chemicals and reagents were purchased from Aldrich or Acros Organics, and used as received unless otherwise noted. ^{1}H and ^{13}C NMR spectroscopic measurements were performed using Varian 500 or 300 NMR spectrometers at 500 or 300 MHz for ^{1}H (referenced to TMS at $\delta = 0.0$ ppm) and 125 or 75 MHz for ^{13}C (referenced to $CDCl_3$ at $\delta = 77.0$ ppm). Elemental analyses were performed at Atlantic Microlab, Inc., Norcross GA. High-resolution mass spectrometry (HR-MS) analysis was performed in the Department of Chemistry, University of Florida, Gainesville, FL.

Synthesis of 9-(2-(2-Methoxyethoxy)ethyl)-fluorene (A). A solution of fluorene (6 g, 36.09 mmol) in dry THF (120 mL) was treated under nitrogen at −78 °C with *n*-BuLi (1.6 M in hexanes, 24 mL) over a 25 min period. After addition, the temperature was allowed to rise to room temperature and stirring continued for 1 h. The mixture was then cooled to −78 °C and treated with a solution of bromo-2-(methoxyethoxy)ethane (4.9 mL, 36.1 mmol) in THF (30 mL). The temperature was then allowed to rise to room temperature, and the mixture was stirred overnight. The yellow solution was neutralized with 5% HCl, and the THF was evaporated in vacuo. Extraction of the aqueous phase with CH_2Cl_2 yielded yellow oil. Purification was carried out by column chromatography using hexane/ethyl acetate (4:2) to give 7.45 g of colorless oil (77% yield). ^{1}H NMR (500 MHz, $CDCl_3$) δ: 7.75 (d, 2H, Ph-H), 7.53 (d, 2H, Ph-H), 7.37 (m, 4H, Ph-H), 4.11 (t, 1H, CH), 3.5 (m, 10H, CH_2O, CH_3), 2.31 (q, 2H, CH_2). ^{13}C NMR (125 MHz, $CDCl_3$) δ: 147.01, 140.94, 127.03, 126.92, 124.55, 119.86, 71.94, 70.15, 68.42, 59.13 (CH_3), 44.52 (C9), 32.85 (CH_2). Anal. Calc. for $C_{18}H_{20}O_2$ (MW: 268.35): C, 80.56; H, 7.51; O, 11.92. Found: C, 80.55; H, 7.56.

Synthesis of 3-(9-(2-(2-Methoxyethoxy)ethyl)-fluoren-9-yl)-propanenitrile (B). 9-(2-(2-Methoxyethoxy)ethyl)-fluorene (4.44 g, 16.54 mmol) was dissolved in *p*-dioxane (28 mL) at room temperature. The solution was degassed under vacuum and nitrogen, after which it was treated with 40% aqueous solution of Triton B (0.25 mL). After addition, the mixture turned from light yellow to reddish brown color. The resulting solution was then treated with acrylonitrile over a 10 min period. The reaction temperature was maintained between 30 and 40 °C by occasional cooling with ice−water throughout the addition period. The red solution thus obtained was then stirred at room temperature for 16 h. The reaction was neutralized with 10% HCl, followed by addition of distilled water. Extraction with CH_2Cl_2 afforded orange oil. The crude product was purified by column chromatography using hexane/ethyl acetate (3:2) as eluent to afford 4.43 g of colorless oil (83% yield). ^{1}H NMR (500 MHz, $CDCl_3$) δ: 7.72 (d, 2H, Ph-H), 7.41 (m, 6H, Ph-H), 3.29 (bd, 7H), 2.81 (t, 2H, CH_2), 2.45 (q, 4H, CH_2), 1.49 (t, 2H, CH_2). ^{13}C NMR (125 MHz, $CDCl_3$) δ: 146.74, 140.80, 128.07, 127.90, 122.93, 120.23, 119.60 (CN), 71.71, 69.95, 67.08, 59.01, 52.31, 39.04 (C9), 35.94, 11.76 (CH_2). Anal. Calc. for $C_{21}H_{23}NO_2$ (MW: 321.41): C, 78.47; H, 7.21; N, 4.36. Found: C, 78.37; H, 7.19; N, 4.44.

Synthesis of 3-(9-(2-(2-Methoxyethoxy)ethyl)-2,7-dibromo-fluoren-9-yl)propanenitrile (C). To a solution of 3-(9-(2-(2-methoxyethoxy)ethyl)-fluoren-9-yl)propanenitrile (4.71 g, 14.66 mmol) in propylene carbonate (31 mL) at 60 °C, *N*-bromosuccinimide (NBS, 7.38 g, 44.02 mmol) was added in one portion and the mixture was kept at 60 °C for 24 h. The reaction was diluted with water and extracted with CH_2Cl_2. The organic phase was washed several times with water, dried over $MgSO_4$, filtered, and concentrated under reduced pressure to give viscous brown oil. Purification was carried out by silica gel column chromatography using hexanes/ethyl acetate (3.5:1.5) as eluent to afford 4.5 g of a white solid (64% yield) mp = 92.5−93.5 °C. ^{1}H NMR (500 MHz, $CDCl_3$) δ: 7.54 (m, 6H, Ph-H), 3.31 (s, 5H), 3.22 (t, 2H), 2.87 (t, 2H), 2.43 (t, 2H), 2.36 (t, 2H), 1.53 (t, 2H). ^{13}C NMR (125 MHz, $CDCl_3$) δ: 148.77, 138.75, 131.54, 126.54, 122.23, 121.66, 118.94 (CN), 71.70, 70.06, 66.79, 59.07, 52.93, 38.93 (C9), 35.53, 11.90 (CH_2). Anal. Calc. for $C_{21}H_{21}Br_2NO_2$ (MW: 479.2): C, 52.63; H, 4.42; Br, 33.35; N, 2.92; O, 6.68. Found: C, 52.50; H, 4.43; N, 2.93.

Synthesis of 3-(9-(2-(2-Methoxyethoxy)ethyl)-2,7-dibromo-fluoren-9-yl)propanoic Acid (D). A mixture of 3-(9-(2-(2-methoxyethoxy)ethyl)-2,7-dibromo-fluoren-9-yl)propanenitrile (2.1 g, 4.38 mmol), ethylene glycol (100 mL), and aqueous NaOH (3M, 14 mL) was heated to reflux for 24 h. Ethylene glycol was removed under vacuum distillation producing yellow oil that was then neutralized with 10% HCl (aq) and extracted with CH_2Cl_2. The crude product was purified via column chromatography using hexanes/ethyl acetate (1:1) as eluent to afford 1.65 g of a white solid (76% yield) mp = 96−97 °C. ^{1}H NMR (500 MHz, $CDCl_3$) δ: 7.44 (m, 6H, Ph-H), 3.23 (bm, 7H, CH_2O, CH_3), 2.73 (t, 2H, CH_2), 2.31 (m, 4H, CH_2), 1.51 (t, 2H, CH_2). ^{13}C NMR (125 MHz, $CDCl_3$) δ: 178.10 (COOH), 149.94, 138.81, 131.04, 126.55, 121.90, 121.43, 71.69, 69.96, 66.92, 59.04, 52.85, 39.08 (C9), 34.50, 28.21. Anal. Calc. for $C_{21}H_{22}Br_2O_4$ (MW: 498.2): C, 50.63; H, 4.45; Br, 32.08; O, 12.85. Found: C, 50.68; H, 4.56.

Synthesis of 3-(9-(2-(2-Methoxyethoxy)ethyl)-2,7-bis(4-(benzothiazol-2-yl)styryl)-fluoren-9-yl)propanoic Acid (F). 3-(9-(2-(2-Methoxyethoxy)ethyl)-2,7-dibromo-fluoren-9-yl)propanoic acid (0.25 g, 0.50 mmol), 2-(4-vinylphenyl)benzothiazole (0.26 g, 1.51 mmol), $Pd(OAc)_2$ (0.04 g, 0.19 mmol), and P(*o*-tolyl)$_3$ (0.10 g, 0.34 mmol) were transferred to a high-pressure Schlenk tube. To this, 8 mL of DMF/Et_3N (5:1) mixture was added. The Schlenk tube was then sealed and stirred at 90 °C for 90 h. The mixture was cooled to room temperature and filtered. The solvent was removed under reduced pressure. The crude product was purified by column chromatography on silica gel, eluting first with hexane/THF (1:1), then hexane/ethyl acetate (1:1) as eluent to afford a yellow solid 0.28 g (70% yield) mp = 179−180 °C. ^{1}H NMR (500 MHz, DMSO) δ: 11.95 (s, 1H, COOH), 8.08−8.04 (m, 6H, Ph-H), 7.98 (d, 2H, Ph-H), 7.84 (s, 2H, Ph-H), 7.79−7.74 (m, 6H, Ph-H), 7.59 (d, 2H, Ph-H), 7.50−7.37 (m, 4H, CH═CH, and 4H, Ph-H), 3.27 (q, 2H, CH_2O), 3.04−3.017(m, 5H, CH_2O, CH_3), 2.64 (t, 2H, CH_2O), 2.39−2.30 (m, 4H, CH_2), 1.33 (t, 2H, CH_2). ^{13}C NMR (125 MHz, $CDCl_3$) δ: 174.46 (COOH), 167.42 (Ar−C═N), 154.12, 149.95, 140.79, 140.52, 136.78, 134.90, 132.10, 128.21, 128.05, 127.78, 127.62, 127.18, 126.86, 123.35, 123.18, 122.93, 122.73, 121.61, 121.46, 121.09, 71.55, 69.62, 67.07, 58.18, 52.39, 38.86 (C9), 34.20, 28.99. HR-MS-ESI theoretical *m*/*z* $[M+H]^+$ = 811.26, found 811.26.

Synthesis of Fluorene−NHS (1). 3-(9-(2-(2-Methoxyethoxy)-ethyl)-2,7-bis(4-(benzothiazol-2-yl)styryl)-fluoren-9-yl)propanoic acid (0.2 g, 0.246 mmol) was dissolved in dimethylformamide

(DMF) (3.5 mL) under N_2; then, *N*-hydroxysuccinimide (0.031 g, 0.27 mmol) was added to the mixture at room temperature. *N*,*N*′-Dicyclohexylcarbodiimide (DCC) (0.057 g) was added via syringe and the mixture was stirred at room temperature for 36 h. The mixture was then filtered and diluted with 3−4 volumes of ether to precipitate the dye. The solid was collected by filtration, redissolved in a minimum volume of DMF, and then reprecipitated by addition of ether. The solid was collected and dried to afford 0.2 g of a yellow solid (90% yield) mp = 217−218 °C. ^{1}H NMR (500 MHz, $CDCl_3$) δ: 8.13 (dd, 6H, Ph-H), 7.93 (d, 2H, Ph-H), 7.72 (t, 6H, 4H, CH═CH, and 4H, Ph-H), 7.61 (s, 2H, Ph-H), 7.58 (d, 2H, Ph-H), 7.52 (t, 2H, Ph-H), 7.41 (t, 2H, Ph-H), 7.33 (m, 4H, Ph-H), 3.23 (m, 7H, OCH_2, CH_3), 2.88 (t, 2H, OCH_2), 2.76 (s, 4H, CH_2), 2.58 (m, 4H, CH_2), 1.95 (m, 2H, CH_2). ^{13}C NMR (125 MHz, $CDCl_3$) δ: 170.54 (C═O), 167.41 (Ar−C═N), 157.10, 154.17, 149.36, 140.85, 140.51, 137.07, 135.01, 132.23, 131.35, 128.26, 127.85, 127.31, 123.42, 122.97, 121.77, 71.85, 69.92, 58.76, 55.73, 52.60, 48.34, 34.23, 26.22, 25.38. HR-MS-ESI theoretical *m*/*z* $[M+H]^+$ = 908.27, found 908.28, theoretical *m*/*z* $[M+Na]^+$ = 930.26, found 930.26.

Synthesis of Fluorene−RGD Conjugate (2). Cyclic peptide (Ar-Gly-Asp-D-Phe-Lys) c(RGDfK) (15 mg, 0.024 mmol) was dissolved in DMSO (1.5 mL) and the pH was adjusted to 9 by adding aqueous $NaHCO_3$ (0.1 M). Fluorene−NHS (24 mg, 0.027 mmol) was added to the reaction mixture and stirred for 22 h. The mixture was then diluted with 4 volumes of ether to precipitate the dye. The solid was collected by filtration, redissolved in a minimum volume of DMSO, and then reprecipitated by addition of ether. The solid was collected and dried to afford 32 mg of a yellow solid (94% yield) mp = 236−236.5 °C. HR-MS-ESI theoretical *m*/*z* $[M+H]^+$ = 1396.56, found 1396.54, theoretical *m*/*z* $[M+Na]^+$ = 1418.55, found 1418.52. ^{13}C NMR (125 MHz, $CDCl_3$) δ:172.63, 172.10, 171.75, 171.48, 171.10, 167.66 (Ar−C═N), 157.37, 154.37, 150.50, 141.04, 140.80, 138.98, 136.97, 135.14, 132.33, 131.60, 129.62, 128.66, 128.37, 127.92, 127.60, 127.42, 126.66, 126.21, 123.50, 123.08, 121.87, 121.20, 107.66, 71.79, 69.84, 67.30, 58.65, 55.53, 53.44, 52.81, 51.48, 49.27, 43.77, 38.94, 33.84, 31.42, 29.58, 29.01, 25.82, 25.12, 24.26, 23.69.

Synthesis of *S*-Benzyl 3-(9-(2-(2-methoxyethoxy)ethyl)-2,7-bis(4-(benzo[d]thiazol-2-yl)styryl)-9*H*-fluoren-9-yl)propanethioate (3). The reaction was performed under dry N_2 atmosphere. Benzylmercaptan (140 μL, 1.2 mmol) was slowly added to a mixture of 0.6 mL of 2.0 M $Al(CH_3)_3$ (1.2 mmol) in hexane and 2.5 mL of anhydrous CH_2Cl_2 cooled to 0 °C. The reaction mixture was allowed to warm to room temperature over 30−40 min. A 2.5 mL solution of fluorene−NHS (50 mg, 0.05 mmol) in DMF was added slowly to the reaction mixture and stirred under nitrogen for 16 h. The reaction mixture was then poured into distilled water and extracted with CH_2Cl_2. The organic phase was dried over $MgSO_4$ and concentrated by vacuum. The mixture was then filtered and diluted with 4 volumes of ether to precipitate the dye. The solid was collected by filtration, redissolved in a minimum volume of DMF, and reprecipitated by addition of ether. The solid was collected and dried to afford 28 mg of a yellow solid (70% yield) mp = 164−165 °C. ^{1}H NMR (500 MHz, $CDCl_3$) δ: 8.04 (t, 6H, Ph-H), 7.84 (d, 2H, Ph-H), 7.61 (q, 6H, Ph-H), 7.49 (m, 6H, Ph-H), 7.33 (t, 2H, Ph-H), 7.16 (m, 10H, Ph-H), 3.88 (s, 2H, CH_2), 3.23 (m, 7H, OCH_2, CH_3), 2.78 (t, 2H, OCH_2), 2.47(q, 4H, CH_2), 1.82 (t, 2H, CH_2). ^{13}C NMR (125 MHz, $CDCl_3$) δ: 198.72 (C═O), 167.94 (Ar−C═N), 156.94, 154.47, 149.25, 140.77, 140.26, 137.67, 136.85, 135.27, 132.84, 130.62, 139.66, 129.37, 128.99, 128.80, 128.79, 128.73, 128.21, 127.93, 127.52, 127.45, 127.30, 127.27, 127.20, 126.63, 125.44, 123.40, 121.88, 121.27, 120.65, 71.97, 70.24, 67.48, 59.27, 52.48, 49.39, 39.75, 38.51, 34.20. HR-MS-ESI theoretical *m*/*z* $[M+H]^+$ = 917.28, found 917.28, theoretical *m*/*z* $[M+Na]^+$ = 939.27, found 939.26.

Preparation of Fluorene−IgG Conjugate (4). A solution of IgG (1 mg/mL) in freshly prepared $NaHCO_3$ (0.1 M, pH 9) solution was used. A stock solution of the amine-reactive probe **1** dissolved in anhydrous DMF (1.43×10^{-3} M) was freshly prepared and aliquots added dropwise into the IgG solution (0.3 mL) with gentle stirring. The concentration of the probe solution was varied such that a 1:15, 1:10, and a 1:5 mol ratio of protein to probe was prepared to obtain the desired dye to protein molar ratios. The reaction was kept in the dark and allowed to stir at room temperature for 2 h. The reaction mixtures were purified from the unreacted dye by size exclusion chromatography column (12 cm length, Bio-Rad Econo-Pac 10DG) equilibrated in and eluted with phosphate buffered saline (PBS, pH 7.2; Fisher). Fractions containing the IgG−fluorene bioconjugate were identified spectrophotometrically by monitoring both the protein fraction at 280 nm and the dye at 418 nm. The degree of labeling (DOL) was determinated as the ratio of moles of fluorophore to moles of protein (F/P) as previously described (*30*).

COS-7 Cells Incubated with Fluorene−RGD Peptide Conjugate (2). COS-7 cells were plated onto 4-well glass chamber slides. Stock solutions of fluorene−RGD peptide conjugate **2** dissolved in DMSO were prepared at concentrations of either 1 or 10 μM. Diluted solutions in complete growth medium were then freshly prepared and placed over the cells for either a 1 or 2 h period. All cells were washed with PBS buffer (3×) and fixed using 3.7% formaldehyde solution for 5 min at room temperature.

Immunofluorescence Analysis. HeLa Cells were fixed in PHEMO buffer (68 mmol/L PIPES, 25 mmol/L HEPES, 15 mmol/L EGTA, 3 mmol/L $MgCl_2$, 10% DMSO) with 3.7% formaldehyde, 0.05% glutaraldehyde, and 0.5% Triton X-100. Cells were washed in PBS buffer thrice for 5 min then blocked in 10% goat serum for 15 min. Microtubule staining was performed by incubating the cells with a primary antibody against tubulin from mouse, followed by incubating with the secondary antibody directed against mouse conjugated with amine reactive tag **1**.

One-Photon Spectral Measurements. Linear photophysical properties of new fluorescent probes were investigated in spectroscopic-grade solvents at room temperature. The steady-state absorption spectra were obtained with Agilent 8453 UV−visible spectrophotometer using 10 mm path length quartz cuvettes with dye concentrations of 1×10^{-5} M. The steady-state fluorescence spectra were measured with a PTI QuantaMaster spectrofluorimeter in 10 mm spectrofluorometric quartz cuvettes with dye concentrations of 1×10^{-6} M. All fluorescence spectra were corrected for the spectral responsivity of PTI detection system. Fluorescence quantum yields, *Q*, were measured for all compounds by a standard method (*31*), relative to Rhodamine 6G in ethanol ($Q = 0.94$) (*32*).

Conventional single-photon fluorescence images were obtained using an inverted microscope (Olympus IX70) equipped with a QImaging cooled CCD (Model Retiga EXi) and excitation mercury lamp 100 W. In order to improve the fluorescence background-to-image ratios, a customized filter cube (Ex 377/50, DM 409, Em 460/50) was used for the one-photon fluorescence images. The specifications of the filter cube were tailored to match the excitation wavelength of compounds **2** and **4**, and to capture most of its emission profile.

Two-Photon Absorption and Imaging Measurements. 2PA spectra of **1** were determined over a broad spectral region via a typical two-photon induced fluorescence (2PF) method relative to Rhodamine B in methanol and Fluorescein in water (pH = 11) as a standards (*33*, *34*). A PTI QuantaMaster spectrofluo-

Scheme 1. Preparation of the Succinimidyl Amine-Reactive Tag 1

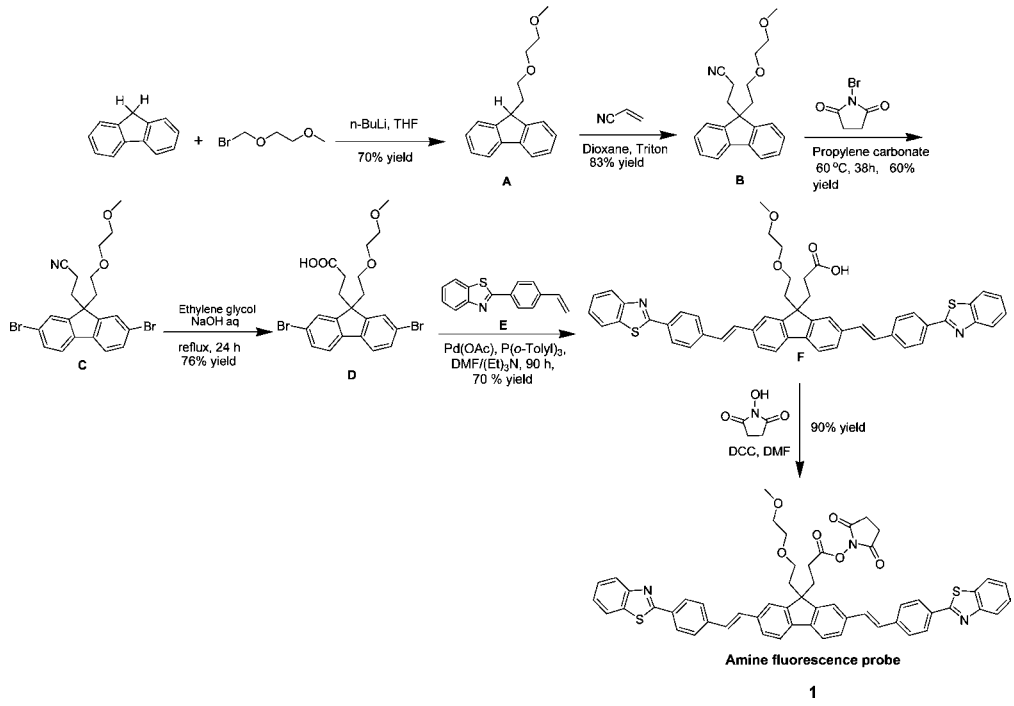

rimeter and femtosecond Clark-MXR CPA-2010 laser that pumped an optical parametric generator/amplifier (TOPAS, Light Conversion), with pulse duration, ~140 fs, (fwhm), tuning range 580−940 nm, pulse energies ≤0.15 μJ, and 1 kHz repetition rate were used. Two-photon fluorescence measurements were performed in 10 mm fluorometric quartz cuvettes with dye concentrations of 3×10^{-5} M in DMSO. The quadratic dependence of two-photon induced fluorescence intensity on the excitation power was confirmed for each excitation wavelength.

Two-photon fluorescence microscopic images were obtained with a modified Olympus Fluoview FV300 microscope system combined with a tunable Coherent Mira 900F Ti:sapphire laser. The femtosecond NIR laser beam (with 220 fs pulse width and 76 MHz repetition rate) was tuned to 730 nm and used as a two-photon excitation source. The two-photon induced fluorescence intensity was collected by a 60× microscopic objective (UPlanSApo 60×, NA = 1.35, Olympus). A high-transmittance (>95%) short-pass filter (cutoff 685 nm, Semrock) was placed in front of the PMT detector of the FV300 scan head in order to filter off background radiation from the laser source (730 nm).

RESULTS AND DISCUSSION

Synthesis and Characterization of the Fluorenyl Probes. Our previous results with 2PA fluorene-based dyes (*22*−*28*), encouraged us to further investigate this class of chromophores as two-photon excitable labels. Herein, we report the synthesis of novel two-photon excitable fluorescent labeling reagents, specifically designed to be used for molecular labeling. The symmetric hydrophobic compound 2,7-bis[4-(9,9-didecylfluoren-2-yl)vinyl]phenylbenzothiazole, an A-$\pi-\pi-\pi$-A archetype, comprises a rather promising chromophore and exhibited a 2PA cross section of ca. 1185 GM at 800 nm. Thus, we decided to design an amine reactive probe based on the same chemical structure of this chromophore.

Scheme 1. depicts the design of the amine reactive probe (**1**) and shows our straightforward strategy to incorporate the succinimidyl functionality as a reactive linker on the fluorenyl 9-position for further linkage with peptides or antibody or label a wide variety of biologically significant molecules. Synthesis of the reactive probe began with the monoalkylation of fluorene upon treatment with *n*-butyl lithium and 1-bromo-2-(2-methoxyethoxy)ethane in dry THF at −78 °C under nitrogen atmosphere. The product was purified via silica gel column chromatography to afford 9-[2-(2-methoxyethoxy)-ethyl]-fluorene (**A**) in 70% yield. The condensation of acrylonitrile in the presence of benzyltrimethylammonium hydroxide ("Triton B") as a catalyst with intermediate **A** via Michael addition reaction provided 3-{9-[2-(2-methoxyethoxy)-ethyl]-fluoren-9-yl}-propionitrile (**B**). Bromination of (**B**) with NBS in propylene carbonate produced intermediate (**C**) in 60% yield. The nitrile intermediate (**C**) was hydrolyzed with NaOH in ethylene glycol to afford 3-{2,7-dibromo-9-[2-(2-methoxyethoxy)-ethyl]-fluoren-9-yl}-propionic acid (**D**). 3-{2,7-Bis-[2-(4-benzothiazol-2-yl-phenyl)-vinyl]-9-[2-(2-methoxyethoxy)-ethyl]-fluoren-9-yl}-propionicacid (**F**) was prepared via efficient Pd-catalyzed Heck coupling reaction of **D** with 2-(4-vinylphenyl)benzothiazole (**E**) in 70% yield. Esterification reaction of intermediate **G** with *N*-hydroxysuccinimide was carried out in the presence of 1,3-dicyclohexylcarbodiimide (DCC), affording the succinimidyl amine reactive probe **1** in high yield (90%) as shown in Scheme 1.

The utility of the activated ester was demonstrated by coupling chromophore **1** with RGDfK. Conjugation reaction of amine reactive probe **1** with commercial cyclopeptide (Ar-Gly-Asp-D-Phe-Lys) c(RGDfK) was carried out in DMSO at room temperature for 22 h, affording fluorene−RGD peptide conjugate (**2**) in high yield (Scheme 2). A similar protocol to the one described by Schuler et al. (*35*) was followed for the synthesis of the fluorene thioester probe (**3**), with slight modifications for the isolation and purification due to the specific properties of our probe (Scheme 3). This further demonstrates the versatility of amine-reactive probe **1**, as it can readily be converted to the thiol-reactive probe (**3**). All compounds were fully characterized by NMR and elemental)analysis or HR-MS.

Labeling of IgG. The use of specific antibodies labeled with fluorescent dyes to localize substances in tissues was first

Scheme 2. Preparation of the Fluorene-RGD Peptide Conjugate 2 with the Amine-Reactive Tag 1

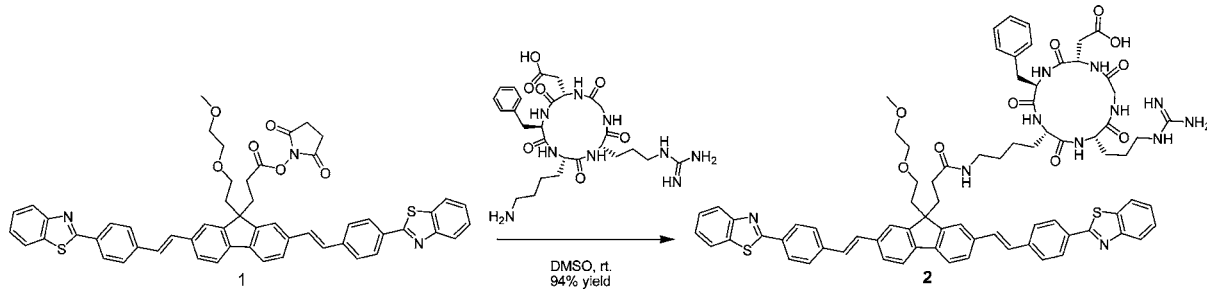

Scheme 3. Preparation of the Thioester Probe 3 with the Amine-Reactive Tag 1

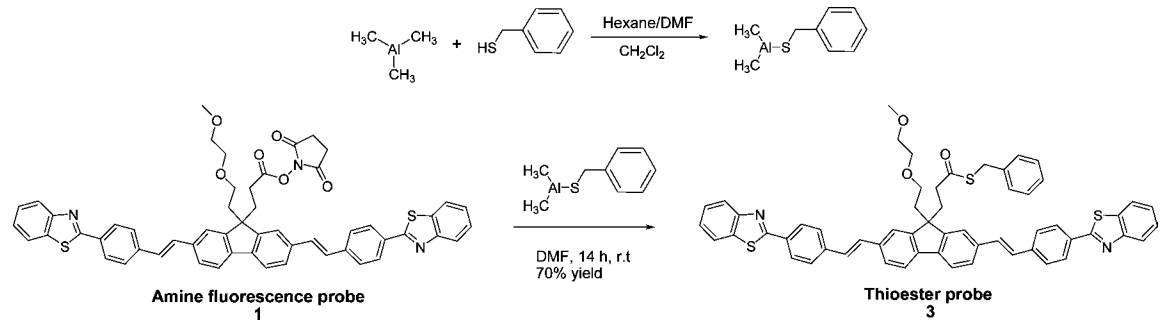

devised by A. H. Coons and associates (*36*). At first, the specific antibody itself was labeled and applied to the tissue section to identify the antigenic sites. Later, a more sensitive and versatile indirect method (*37*) was introduced. The primary, unlabeled antibody is applied to the tissue section, and the excess is washed off with buffer. A second, labeled antibody from another species, raised against the IgG of the animal donating the first antibody, is then applied. The primary antigenic site is thus revealed.

A major advantage of the indirect method is enhanced sensitivity. In addition, a labeled secondary antibody can be used to locate any number of primary antibodies raised in the same animal species without the necessity of labeling each primary antibody. There are many fluorophores used in labeling, including coumarin derivatives, phycobiliproteins, fluorescein, and rhodamine. The isothiocyanate derivatives of fluorescein and rhodamine are widely used to label antibodies. In addition, the newly introduced Alexa fluorochromes are a series of fluorescent dyes with excitation/emission spectra similar to that of commonly used probes under single-photon excitation (*38, 39*).

We previously reported the results of the conjugation of certain fluorene-based fluorophores with bovine serum albumin (BSA, fraction V) and Reelin (*40, 41*). BSA is an inexpensive commercially available protein, while Reelin is a large extracellular matrix glycoprotein, important in guiding neural stem cells in the central nervous system in normal development (*42, 43*).

Performance of the amine reactive probe **1** was studied by labeling of polyclonal antirat IgG. The conjugation of succidimidyl ester probe **1** with IgG was carried out according to standard methods (*30*). The fluorene−IgG conjugates were separated from unbound succidimidyl ester by gel filtration chromatography in saline phosphate buffer solution (PBS, pH 7.2). The conjugation did not lead to the quenching of the fluorescence signal of the succidimidyl ester. Thus, a series of experiments were carried out in order to evaluate (1) the maximum succinimidyl dye to protein molar ratio that can be attained without protein precipitation; (2) the optimum reaction time; and (3) the optical stability of the bioconjugate. The labeling degrees were determined spectrophotometrically. With

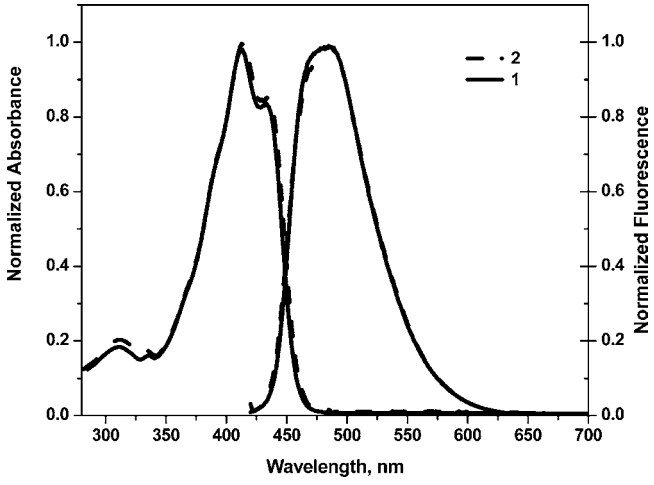

Figure 1. Normalized UV−visible absorbance and fluorescence emission spectra of amine-reactive tag **1** (—) $Qy = 0.68$, and fluorene−RGD peptide conjugate**2** (---) in DMSO $\lambda_{max}^{abs} = 413$ nm; $\lambda_{max}^{em} = 485$ nm; $Qy = 0.69$.

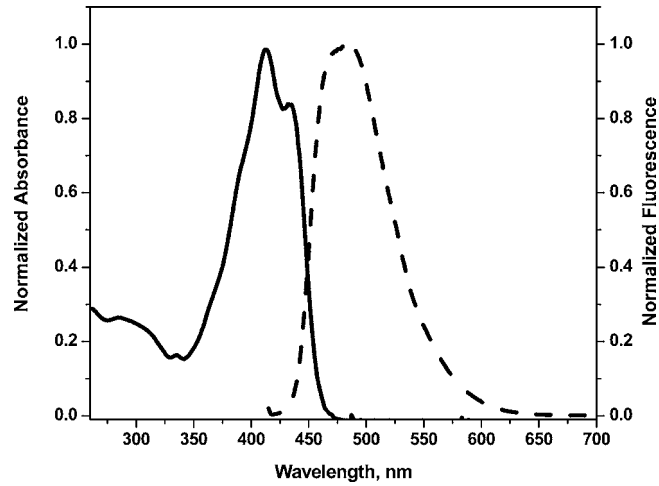

Figure 2. Normalized UV−visible absorbance (—) and fluorescence emission (---) spectra of thioester probe **3** in DMSO $\lambda_{max}^{abs} = 413$ nm; $\lambda_{max}^{em} = 485$ nm; $Qy = 0.67$.

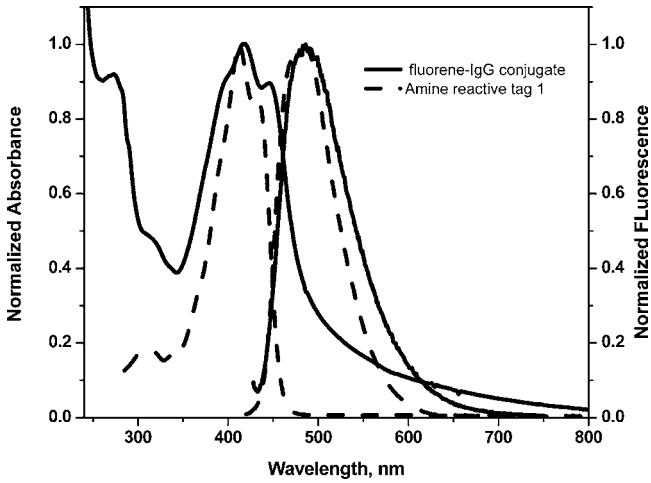

Figure 3. Normalized absorption spectra and steady-state fluorescence emission spectrum of amine-reactive tag **1** (—) and fluorene−IgG conjugate (---) in PBS buffer.

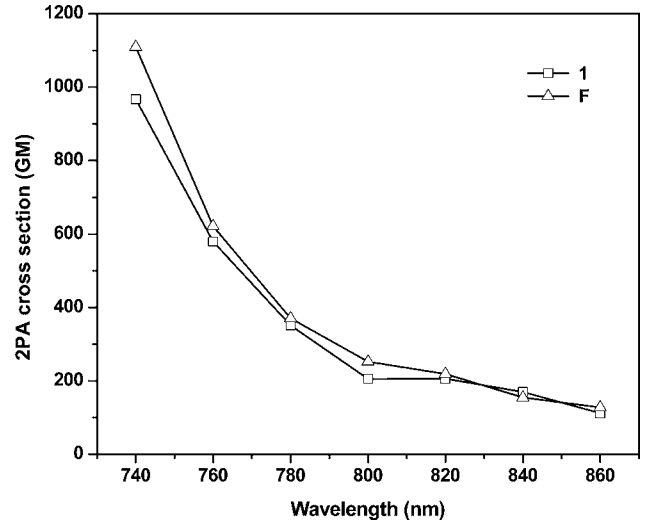

Figure 4. 2PA cross section values of carboxylic acid **F** and amine reactive tag **1** in DMSO, measured by the 2PF method using fluorescein at pH = 11 as reference.

succinimidyl derivative **1**, a degree of labeling of 3 and 6 fluorophores per IgG was obtained after a few hours of mixing the solutions containing the succinimidyl dye and the IgG, without precipitation of the conjugate. The intensities of the emission spectrum of the conjugates indicated that the signal intensity increased as the succinimidyl dye/protein molar ratio increased.

The normalized UV−visible absorption and steady-state fluorescence emission spectra of amine-reactive probe **1** and fluorene−IgG conjugate **4** in PBS (buffer pH 7.2) are shown in Figure 3. The fluorene−IgG conjugate exhibited absorption peaks corresponding to that of the IgG protein in the shorter-wavelength range (λ_{max} = 280 nm) as well as that of the fluorescent dye in the longer absorption range (λ_{max} = 416 and 447 nm), and exhibited an emission maximum at 445 nm (characteristic of the fluorenyl moiety). The absorption spectrum of the fluorene−IgG conjugate **4** showed only slight broadening compared to the absorption spectrum of the unbound fluorophore **1**.

Optical Properties of Fluorescent Markers. The RGD peptide substituent on the 9-position is not part of the chromophore's π-conjugated system of **1**; thus, there is no significant alteration of the photophysical properties of fluorene−RGD

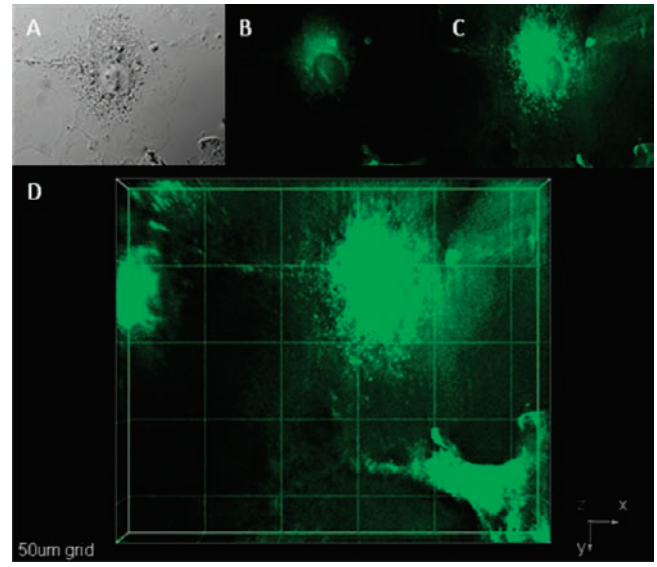

Figure 5. COS-7 cells in PBS media, incubated for 1 h with the fluorene−RGD peptide conjugate **2** from a 10 μM solution in DMSO; UPlanSApo, NA = 1.35, 60× oil immersion. (A) DIC, 34 ms; (B) one-photon fluorescence (Ex: 377/50-DM:409-Em: 525/40), 755 ms; (C) two-photon upconverted fluorescence, overlay of all planes, 730 nm; (D) 3D reconstruction from overlaid upconverted fluorescence images from complete field, 50 μm grid.

peptide conjugate **2** relative to succinimidyl amine reactive probe **1**. The absorbance maximum was observed at 413 nm for both derivatives with an emission maximum at 485 nm in DMSO. The fluorescence quantum yield (0.68) was nearly unaltered in fluorene−RGD peptide conjugate **2** (Figure 1). Additionally, no significant differences of the fluorene thioester **3** compared to the succinimidyl ester **1** were detected. The absorbance maximum was at 413 nm for both derivatives, and the fluorescence quantum yield (0.69) remained practically unaltered for the thioester (Figure 2).

2PA cross sections (δ) were obtained by the up-conversion fluorescence method using a femtosecond Ti:sapphire laser as excitation source (*33*, *34*). The uncertainty in the experimental δ values is estimated to be ±15%. The 2PA cross section measurements of symmetrical amine-reactive probe **1** and carboxylic intermediate **F** were performed in DMSO (1.6×10^{-3} M). Although, the symmetric fluorene derivatives **1** and **F** are not strictly centrosymmetric systems, they exhibit the same parity selection rules associated with centrosymmetric systems. As indicated in Figure 4, amine-reactive probe **1** and intermediate **F** show small 2PA in the first excited state, identified by the peak in the linear absorption spectrum located approximately at 415 nm (250 GM at 830 nm). This is expected given the symmetric structure of the A-$\pi-\pi-\pi$-A molecules **1** and **F**. The second 2PA peak at ~370 nm is a two-photon allowed state and exhibited a substantially higher 2PA cross section of ~1000−1100 GM at 740 nm (Figure 4).

Single- and Two-Photon Fluorescence and Cell Imaging. The ability of fluorene−RGD peptide conjugate **2** to be taken up into cells was examined using COS-7 cells (Figure 5a−d). Cells were incubated with a solution of 10 μM DMSO solution of chromophore **2**, and after 1 and 5 h incubation times, images were taken with a modified Olympus Fluoview FV300 microscope system. Strong fluorescence was observed after 5 h of incubation, with a homogeneous coloration of the cytoplasmic region. Differential interference contrast (DIC) and conventional (one-photon) fluorescence microscopic images of the stained cells are shown in Figure 5a,b. Two-photon fluorescence microscopy (2PFM) images of the fluorene−RGD peptide conjugate **2** containing cells were collected using a modified

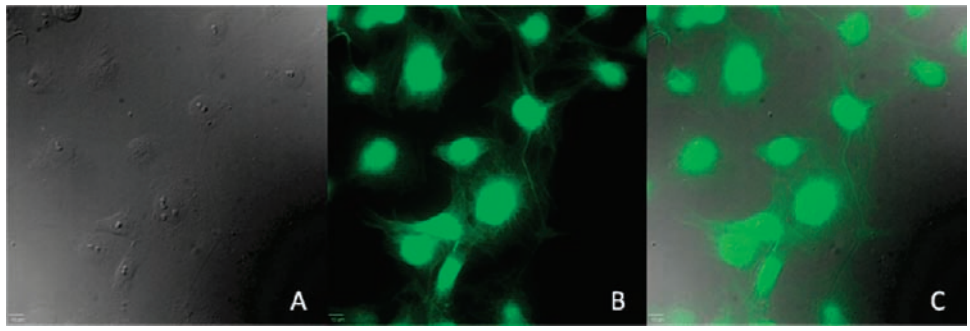

Figure 6. HeLa cells in PBS media, incubated for 1 h with fluorene−IgG conjugate from a 40 μM solution in PBS buffer; UPlanSApo, NA = 1.35, 60× oil immersion. (A) DIC, 350 ms; (B) one-photon fluorescence (Ex: 377/50-DM:409-Em: 525/40), 400 ms; (C) overlay of A and B. Scale bar 10 μm.

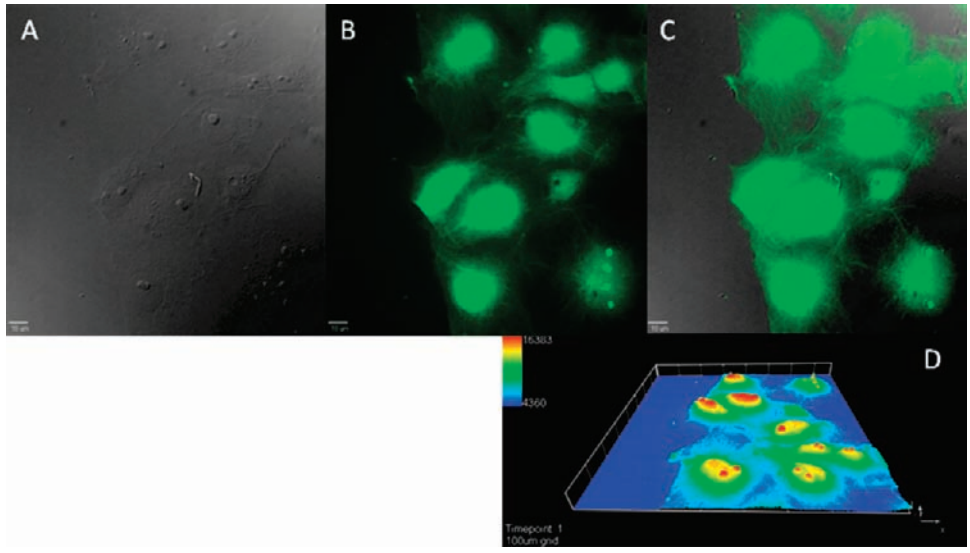

Figure 7. HeLa cells in PBS media, incubated for 5 h with fluorene−IgG conjugate from a 40 μM solution in PBS buffer; UPlanSApo, NA = 1.35, 60× oil immersion. (A) DIC, 350 ms; (B) one-photon fluorescence (Ex: 377/50-DM:409-Em: 525/40) 450 ms; (C) overlay of A and B; (D) one-photon fluorescence intensity plot, 450 ms. Scale bar 10 μm.

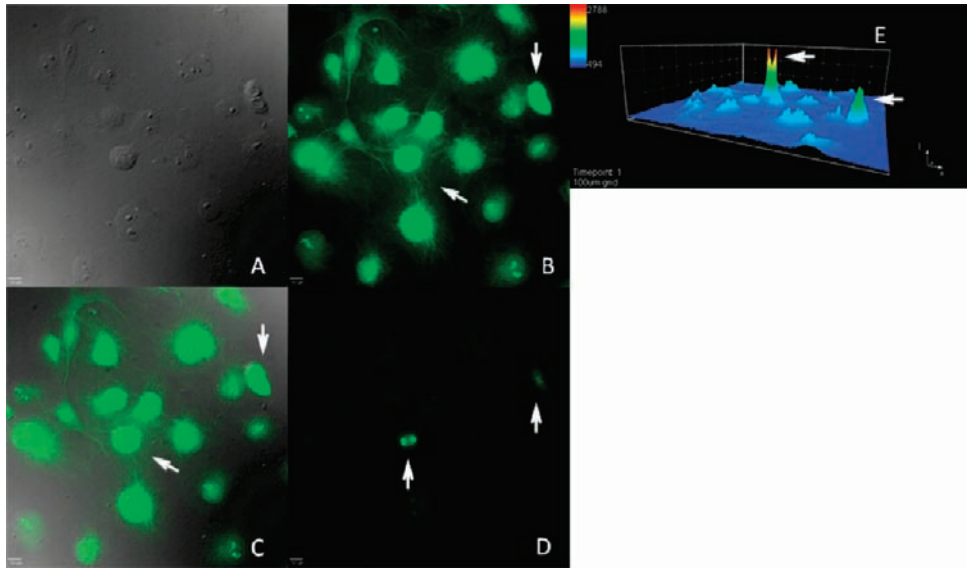

Figure 8. HeLa cell lines in PBS media, incubated for 5 h with fluorene−IgG conjugate from a 40 μM solution in PBS buffer; UPlanSApo, NA = 1.35, 60× oil immersion. (A) DIC, 350 ms; (B) one-photon fluorescence (Ex: 377/50-DM:409-Em: 525/40), 350 ms; (C) overlay of A and B; (D) one-photon fluorescence (Ex: 377/50-DM:409-Em: 525/40), 25 ms; (E) one-photon fluorescence intensity graphs, 25 ms. Arrows in B, D, and E show mitotic cells. Scale bar 10 μm.

Olympus Fluoview FV300 microscope system coupled to a tunable Coherent Mira 900F Ti:sapphire laser. Two-photon induced fluorescence was observed predominantly from the cytoplasmic region, consistent with the images collected via one-

photon fluorescence imaging (Figure 5c). 3D reconstruction from overlaid upconverted fluorescence images from the complete field is shown in Figure 5d.

Having confirmed the cellular uptake of the fluorescent probes, the fluorene−IgG conjugate was investigated and compared with the analogous Alexa 488 conjugate, known for its efficiency in microtubule staining. Amine-reactive dye **1** was conjugated on a secondary antibody (Antirat IgG). The images were acquired via confocal microscopy and shown in Figure 6, panels a−c. Imaging results with the fluorene−IgG conjugate were reproducible and in accordance with images using the Alexa Fluor 488 conjugate. Figure 6b visibly shows the localization of microtubules labeled with the bioconjugate. The fluorescence intensity of microtubules labeled with fluorene−IgG conjugate was comparable to that of Alexa Fluor 488, with the fluorene-based probe possessing both higher two-photon absorptivity and increased photostability.

Mitosis, the process by which identical copies of the replicated genome are distributed to the daughter cells at each cell division, depends on the action of a bipolar protein machine—the mitotic spindle. The action of mitotic spindles is crucial for the formation, maintenance, and reproduction of healthy organisms. Consequently, the morphology and dynamics of zygote spindles during the mitotic process contains abundant biological information (*44*, *45*). Here, labeling microtubules with amine reactive probe **1**, conjugated with the antirat IgG antibody, facilitated acquisition of images of spindles by confocal fluorescence microscopy at different stages of mitosis (Figure 7). Application of fluorene−IgG conjugate for investigating the ultrastructure of cells and tissues by one-photon and two-photon fluorescence microscopy greatly expands the possibilities for localization of antigens. In addition, a wide variety of fluorene conjugates of immunoglobulins of different specificities or a variety of other proteins can be prepared. Further, this method offers new possibilities to perform double labeling experiments with two antibodies at the ultrastructural level.

The high selectivity that this fluorene−IgG conjugate exhibited for microtubules may lead to interesting applications, e.g., cytometric assays for mitosis where co-staining would not be necessary. Simply recording the image with different exposure times may allow calculation of the average number of cells that are undergoing mitosis. In the case of Figure 8, a cell count can easily be made (Figure 8b,e) using longer exposure times (350 ms) and an intermediate fluorescence intensity threshold (shown in Figure 8e in light blue) to account for the overall number of cells by the fluorescence signal of their nuclei. Subsequently, a higher fluorescence intensity threshold can be set, and after recording the image with a shorter exposure time (25 ms, Figure 8d), mitotic cells can be accounted for based on this threshold (shown in green). In this particular example, if this picture represented the entirety of the cell population, 2 of the 20 cells (10%) would be undergoing mitosis. In addition, a higher fluorescence intensity signal for different stages of the mitotic process (anaphase, metaphase, and cytokinesis) was observed, and comparable relative fluorescence intensity signals were observed.

CONCLUSIONS

Probe **1** is a promising new candidate as a contrast agent for multiphoton fluorescence imaging, partciularly considering its high fluorescence quantum yield, high photostability, and suitably high two-photon absoprtivity in the NIR. An immunolabeling procedure employing this amine reactive probe demonstrated sensitivity and versatility of amine reactive probe **1**. In combination with efficient synthesis and availability of antibodies, this protocol represents a widely applicable procedure that offers a good alternative to traditionally used methods. Experimental results demonstrated the validity of the fluorene−IgG conjugate as an effective probe to image cell spindles at early mitotic developmental stages. The intrinsically less invasive physical character of two-photon excitation for biological imaging, coupled with stable, efficient 2PA probes, provides a powerful tool for studying such sensitive systems.

ACKNOWLEDGMENT

The authors wish to acknowledge support from the National Institutes of Health (1 R15 EB008858-01), the U.S. Civilian Research and Development Foundation (UKB2-2923-KV-07), and the National Science Foundation (CHE-0832622).

LITERATURE CITED

(1) Bhawalkar, J. D., He, G. S., and Prasad, P. N. (1996) Nonlinear multiphoton processes in organic and polymeric materials. *Rep. Prog. Phys. 59*, 1041–1070.

(2) Reinhardt, B. A., Brott, L. L., Clarson, S. J., Dillard, A. G., Bhatt, J. C., Kannan, R., Yuan, L., He, G. S., and Prasad, P. N. (1998) Highly active two photon dyes: design, synthesis, and characterization toward application. *Chem. Mater. 10*, 1863–1874.

(3) Wu, L.-Z., Tang, X.-J., Jiang, M.-H., and Tung, C.-H. (1999) Two-photon induced fluorescence of novel dyes. *Chem. Phys. Lett. 315*, 379–382.

(4) Fakis, M., Polyzos, J., Tsigaridas, G., Parthenios, J., Fragos, A., Giannetas, V., Persephonis, P., and Mikroyannidis, J. (2000) Novel class of pyrylium dyes with high efficiency in lasing and two-photon absorption fluorescence. *Chem. Phys. Lett. 323*, 111–116.

(5) Wang, H. Z., Lei, H., Wei, Z. C., Zhao, F. L., Zheng, X. G., Hu, N. S., Wang, X. M., Ren, Y., Tian, Y. P., Fang, Q., and Jiang, M. H. (2000) Spectral properties and effective upconverted lasing of new organic molecules. *Chem. Phys. Lett. 324*, 349–353.

(6) Ehrlich, J. E., Wu, X. L., Lee, L. Y. S., Hu, Z. Y., Rockel, H., Marder, S. R., and Perry, J. W. (1997) Two-photon absorption and broadband optical limiting with bis-donor stilbenes. *Opt. Lett. 22*, 1843–1845.

(7) So, P. T. C., Dong, C. Y., Master, B. R., and Berland, K. M. (2000) Two photon excitation fluorescence microscopy. *Annu. Rev. Biomed. Eng. 2*, 399–429.

(8) Helmchen, F., and Denk, W. (2005) Deep tissue two-photon microscopy. *Nat. Methods 2*, 932–940.

(9) Zipfel, W. R., Williams, R. M., and Webb, W. W. (2003) Nonlinear magic: multiphoton microscopy in the biosciences. *Nat. Biotechnol. 21*, 1369–1377.

(10) Diaspro, A., and Shepard, C. J. R. (2002) *Two-Photon Microscopy: Basic Principles and Architectures*, Wiley & Sons, New York.

(11) Wang, F., and Liu, X. (2009) Recent advances in the chemistry of lanthanide-doped upconversion nanocrystals. *Chem. Soc. Rev. 38*, 976–989.

(12) Gryczynski, I., Malak, H., and Lakowicz, J. R. (1996) Multiphoton excitation of the DNA stains DAPI and Hoechst. *Bioimaging 4*, 138–148.

(13) Malak, H., Castellano, F. N., Gryczynski, I., and Lakowicz, J. R. (1997) Two-photon excitation of ethidium bromide labeled DNA. *Biophys. Chem. 67*, 35–41.

(14) Hayek, A., Bolze, F. E., Nicoud, J.-F., Duperray, A., Grichine, A., Baldeck, P. L., and Vial, J.-C. (2006) Two-photon water-soluble dyes and their amine-reactive derivative for two-photon bio-imaging applications. *Nonlinear Opt. Quant. Opt. 35*, 155–164.

(15) Konecsni, T., and Kilar, F. (2004) Monitoring of the conjugation reaction between human serum transferrin and fluorescein isothiocyanate by capillary electrophoresis. *J. Chromatogr., A 1051*, 135–139.

(16) Barbarella, G. (2002) Oligothiophene isothiocyanates as fluorescent markers. *Chem.—Eur. J. 8*, 5072–5077.
(17) Meltola, N. J., Wahlroos, R., and Soini, A. E. (2004) Hydrophilic labeling reagents of dipyrrylmethene-BF2 dyes for two-photon excited fluorometry: syntheses and photophysical characterization. *J. Fluoresc. 14*, 635–647.
(18) Meltola, N. J., Soini, A. E., and Hanninen, P. E. (2004) Syntheses of novel dipyrrylmethene-BF2 dyes and their performance as labels in two-photon excited fluoroimmunoassay. *J. Fluoresc. 14*, 129–138.
(19) Hayek, A., Ercelen, S., Zhang, X., Bolze, F., Nicoud, J.-F., Schaub, E., Baldeck, P. L., and Mély, Y. (2007) Conjugation of a new two-photon fluorophore to poly(ethylenimine) for gene delivery imaging. *Bioconjugate Chem. 18*, 844–851.
(20) Hayek, A., Bolze, F. E., Nicoud, J.-F., Duperray, A., Grichine, A., Baldeck, P. L., and Vial, J.-C. (2006) Two-photon water-soluble dyes and their amine-reactive derivative for two-photon bio-imaging applications. *Nonlinear Opt. Quant. Opt. 25*, 155–164.
(21) Lartia, R., Allain, C., Bordeau, G., Schmidt, F., Fiorini-Debuisschert, C., Charra, F., and Teulade-Fichou, M.-P. (2008) Synthetic Strategies to Derivatizable Triphenylamines Displaying High Two-Photon Absorption. *J. Org. Chem. 5*, 1732–1744.
(22) Belfield, K. D., Bondar, M. V., Przhonska, O. V., and Schafer, K. J. (2004) Photostability of a series of two-photon absorbing fluorene derivatives. *J. Photochem. Photobiol. A: Chem. 162*, 489–496.
(23) Belfield, K. D., Bondar, M. V., Przhonska, O. V., and Schafer, K. J. (2004) Photochemical properties of (7-benzothiazol-2-yl-9,9-didecylfluoren-2-yl)diphenylamine under one- and two-photon excitation. *J. Photochem. Photobiol. A: Chem. 162*, 569–574.
(24) Belfield, K. D., Schafer, K. J., Mourad, W., and Reinhardt, B. A. (2000) Synthesis of new two-photon absorbing fluorene derivatives via Cu-mediated Ullmann condensations. *J. Org. Chem. 65*, 4475–4481.
(25) Belfield, K. D., Morales, A. R., Hales, J. M., Hagan, D. J., Van Stryland, E. W., Chapela, V. M., and Percino, J. (2004) Linear and two-photon photophysical properties of a series of symmetrical diphenylaminofluorenes. *Chem. Mater. 16*, 2267–2273.
(26) Belfield, K. D., Morales, A. R., Kang, B.-S., Hales, J. M., Hagan, D. J., Van Stryland, E. W., Chapela, V. M., and Percino, J. (2004) Synthesis, characterization, and optical properties of new two-photon-absorbing fluorene derivatives. *Chem. Mater. 16*, 4634–4641.
(27) Morales, A. R., Belfield, K. D., Hales, J. M., Hagan, D. J., and Van Stryland, E. W. (2006) Synthesis of two-photon absorbing unsymmetrical fluorenyl-based chromophores. *Chem. Mater. 18*, 4972–4980.
(28) Yao, S., and Belfield, K. D. (2005) Synthesis of two-photon absorbing unsymmetrical branched chromophores through direct tris-(bromomethylation) of fluorene. *J. Org. Chem. 70*, 5126–5132.
(29) Corredor, C. C., Huang, Z.-L., and Belfield, K. D. (2006) Two-photon 3D optical data storage via fluorescence modulation of an efficient fluorene dye by a photochromic diarylethene. *Adv. Mater. 18*, 2910–2914.
(30) Haugland, R. P. (1995) *Methods in Molecular Biology: Monoclonal Antibody Protocols* (Davis, W. C., Ed.) pp 205−215, Chapter 22, Humana Press, Totowa, NJ.
(31) Lakowicz, J. R. (1999) *Principles of Fluorescence Spectroscopy*, pp 52−53, 298−300, and 648, Kluwer Academic/Plenum, New York.
(32) Fischer, M., and Georges, J. (1996) Fluorescence quantum yield of Rhodamine 6G in ethanol as a function of concentration using thermal lens spectrometry. *Chem. Phys. Lett. 260*, 115–118.
(33) Xu, C., and Webb, W. W. (1996) Measurement of two-photon excitation cross sections of molecular fluorophores with data from 690 to 1050 nm. *J. Opt. Soc. Am. B 13*, 481–491.
(34) Albota, M. A., Xu, C., and Webb, W. W. (1998) Two-photon fluorescence excitation cross section of biomolecular probes from 690 to 960 nm. *Appl. Opt. 37*, 7352–7356.
(35) Schuler, B., and Pannell, L. K. (2002) Specific labeling of polypeptides at amino-terminal cysteine residues using Cy5-benzyl thioester. *Bioconjugate Chem. 13*, 1039–1043.
(36) Coons, A. H., Creech, H. J., and Jones, R. N. (1941) Immunological properties of an antibody containing a fluorescent group. *Proc. Soc. Exp. Biol. Med. 47*, 200–202.
(37) Coons, A. H., Leduc, E. H., and Connolly, J. M. (1955) Studies on antibody production I. A method for the histochemical demonstration of specific antibody and its application to a study of the hyperimmune rabbit. *J. Exp. Med. 102*, 49–60.
(38) Panchuk-Voloshina, N., Haugland, R. P., Bishop-Stewart, J., Bhalgat, M. K., Millard, P. J., Mao, F., Leung, W. Y., and Haugland, R. P. (1999) Alexa dyes, a series of new fluorescent dyes that yield exceptionally bright, photostable conjugates. *J. Histochem. Cytochem. 47*, 1179–1188.
(39) Waterman-Storer, C., Duey, D. Y., Weber, K. L., Keech, J., Cheney, R. E., Salmon, E. D., and Bement, W. M. (2000) Microtubules remodel actomyosin networks in Xenopus egg extracts via two mechanisms of F-actin transport. *J. Cell Biol. 150*, 361–376.
(40) Schafer-Hales, K. J., Belfield, K. D., Yao, S., Frederiksen, P. K., Hales, J. M., and Kolattukudy, P. E. (2005) Fluorene-based fluorescent probes with high two-photon action cross-sections for biological multiphoton imaging applications. *J. Biomed. Opt. 10*, 051402/1–051402/8.
(41) Morales, A. R., Schafer-Hales, K. J., Marcus, A. I., and Belfield, K. D. (2008) Amine-reactive fluorene probes: synthesis, optical characterization, bioconjugation, and two-photon fluorescence imaging. *Bioconjugate Chem. 19*, 2559–2567.
(42) Dulabon, L., Olson, E. C., Taglienti, M. G., Eisenhuth, S., McGrath, B., Walsh, C. A., Kreidberg, J. A., and Anton, E. S. (2000) Reelin binds alpha$_3$beta$_1$ integrin and inhibits neuronal migration. *Neuron 27*, 33–44.
(43) Costa, E., Davis, J., Grayson, D. R., Guidotti, A., Pappas, G. D., and Pesold, C. (2001) Dendritic spine hypoplasticity and down regulation of reelin and GABAergic tone in schizophrenia vulnerability. *Neurobiol. Dis. 8*, 723–742.
(44) Kwon, M., and Scholey, J. M. (2004) Spindle mechanics and dynamics during mitosis in Drosophila. *Trends Cell Biol. 14*, 194–205.
(45) Kline-Smith, S. L., and Walczak, C. E. (2004) Mitotic spindle assembly and chromosome segregation: Refocusing on microtubule dynamics. *Mol. Cell 15*, 317–327.

BC900302T

Bioconjugate Chemistry

NOVEMBER 2009
Volume 20, Number 11

© *Copyright 2009 by the American Chemical Society*

REVIEWS

Synthesis and Applications of Biomedical and Pharmaceutical Polymers via Click Chemistry Methodologies

Maarten van Dijk,[†,‡] Dirk T. S. Rijkers,[‡] Rob M. J. Liskamp,[‡] Cornelus F. van Nostrum,[†] and Wim E. Hennink*[,†]

Department of Pharmaceutics and Department of Medicinal Chemistry and Chemical Biology, Utrecht Institute for Pharmaceutical Sciences, Utrecht University, P.O. Box 80082, 3508 TB Utrecht, The Netherlands. Received February 26, 2009; Revised Manuscript Received June 19, 2009

In this review, the synthesis and application of biomedical and pharmaceutical polymers synthesized via the copper(I)-catalyzed alkyne-azide cycloaddition, the thiol−ene reaction, or a combination of both click reactions are discussed. Since the introduction of both "click" methods, numerous articles have disclosed new approaches for the synthesis of polymers with different architectures, e.g., block and graft copolymers, dendrimers, and hydrogels, for pharmaceutical and biomedical applications. By describing selected examples, an overview is given of the possibilities and limitations that these two "click" methods may offer.

INTRODUCTION

The use of polymers for biomedical and pharmaceutical applications has gained an enormous impact during the past decades. Polymers can be applied in drug delivery systems, as scaffolds for tissue-engineering and -repair, and as novel biomaterials (*1*). These applications have led to an increasing demand of well-defined polymers with tailorable properties. The emergence of the "click chemistry" concept greatly facilitated the synthesis of these polymers. Click chemistry provides very attractive possibilities for (bio)conjugation reactions, because it can be performed at ambient conditions with readily available starting materials. In recent years, click chemistry has also been applied for the synthesis of polymers with different architectures (such as block and graft copolymers), including polymers with pharmaceutical and biomedical applications. This review will focus on the different click chemistry strategies to synthesize this class of polymers and will describe some selected examples in more detail to highlight their applications in the biomedical and pharmaceutical field.

In 2001, Sharpless and co-workers coined the concept of "click chemistry" (*2*) to classify a particular set of nearly perfect reactions, among others, the Cu(I)-catalyzed 1,3-dipolar cycloaddition, vide infra. By means of the "click reaction" concept, large (bio)macromolecules can be synthesized by coupling small building blocks via heteroatom-containing linkages. Such a coupling reaction should meet several criteria: it should be modular, high-yielding, and generate only harmless side products, and it should be carried out under mild reaction conditions, preferentially in the presence of many other functional groups using readily available starting materials and reagents.

There are several well-known reactions that comply with the "click chemistry" concept, including the hetero-Diels−Alder reaction (*3*), the thiol−ene coupling (*4*), the Staudinger ligation (*5*−*7*), native chemical ligation (*8, 9*), the amidation reaction between thio acids and sulfonyl azides (sulfo-click) (*10*−

* Author to whom correspondence should be addressed. Tel.: +31 302536964, fax: +31 302517839. E-mail: W.E.Hennink@uu.nl.
[†] Department of Pharmaceutics.
[‡] Department of Medicinal Chemistry and Chemical Biology.

10.1021/bc900087a CCC: $40.75 © 2009 American Chemical Society
Published on Web 07/17/2009

Table 1. List of Reviews Dealing with the Synthesis of Large (Multivalent) Systems and Macromolecules by the CuAAC

An overview of polymer synthesis and modification via the CuAAC.	Binder et al. (*19, 20*)
Review about click polymerization reactions as well as ligation and functionalization of polymers.	Meldal (*21*)
Reviews dealing with the CuAAC in material science.	Nandivada et al. (*22*), Lutz (*23*), and Johnson et al. (*24*)
Review about synthesis of peptidomimetics via CuAAC.	Angell et al. (*25*)
Overview of carbohydrates and peptide-based dendrimers/polymers.	Pieters et al. (*26*)
Reviews about the construction of biohybrid materials.	Dirks et al. (*27*) Le Droumaguet et al. (*28*) and Lutz (*29*)
Review with emphasis on the synthesis of well-defined polymer architectures.	Fournier et al. (*30*)
Review about various cross-linking methods of micelles including CuAAC.	Read et al. (*31*)
An overview of the synthesis of biodegradable polyesters by ring-opening polymerization and CuAAC.	Lecomte et al. (*32*)
A review about copper-free azide−alkyne cycloaddition reactions.	Lutz (*33*)
Other important reviews dealing with CuAAC.	Meldal and Tornøe. (*34*), Bock et al. (*35*), Moses et al. (*36*), Moorhouse et al. (*37*)

15), and presently the most popular and already mentioned copper(I)-catalyzed alkyne−azide cycloaddition (CuAAC) (*16*−*18*).

Since a large number of recent original publications and (specialized) reviews have been published during the past years on CuAAC (for a detailed list, see Table 1), we will focus in this review on the synthesis of polymers and/or their postsynthetic modification/functionalization by the CuAAC and the thiol−ene reaction. In addition, we will describe some selected examples of biomedically and pharmaceutically relevant polymers that have been synthesized by these two click reactions. This review covers the literature until April, 2009.

GENERAL CONSIDERATIONS

The Cu(I) catalysis of the well-known 1,3-dipolar cycloaddition reaction (CuAAC) between an azide and an alkyne (*38*) was discovered in 2002 independently by the groups of Meldal (*16, 17*) and Sharpless (*18*). In this cycloaddition reaction, an organic azide reacts with an alkyne to form a triazole ring, similar to the classical Huisgen cycloaddition reaction (*38*). However, in the presence of copper(I) the reaction proceeds faster even under ambient reaction conditions (Scheme 1A). Moreover, in the presence of copper(I) only the 1,4-disubstituted triazole ring is formed in contrast to the classical Huisgen cycloaddition reaction in which both 1,4- and 1,5-disubstituted triazole regioisomers are formed (*39*). Since this Cu(I)-catalyzed 1,3-dipolar cycloaddition reaction is very selective, it is highly compatible with almost all other functional groups present in biological macromolecules such as proteins, polysaccharides, and DNA/RNA. Additionally, the CuAAC can be performed in aqueous media with a high reaction rate and generally leads to good product yields. Moreover, recent studies showed that the 1,2,3-triazole moiety, which is formed during the Cu(I)-catalyzed 1,3-dipolar cycloaddition, is similar to the peptide-amide bond in terms of geometry. Therefore, the triazole moiety has been suggested as a mimic of a peptide amide bond and has been used for example as a dipeptide isostere in β-strands and α-helical coiled coils (*40*−*42*).

A potential drawback of the Cu(I)-catalyzed cycloaddition reaction for the synthesis of polymers aimed for biomedical and pharmaceutical applications is the cytotoxicity of Cu(I). This can be especially troublesome when it is difficult to remove the copper catalyst from the synthesized polymers. Therefore, the use of ring strain has been investigated as an alternative for Cu(I) as catalyst to activate acetylenes. Wittig and Krebs (*43*) had already reported in 1961 that the reaction between a cyclooctyne and phenyl azide resulted in the formation of a triazole functionality (Scheme 1C), and in 2004, Bertozzi and co-workers (*44*) demonstrated that the [3 + 2] cycloaddition of azides and cyclooctyne derivatives occurs under physiological conditions. However, the first generation of cyclooctynes was hampered with a relatively low reactivity toward azides, as compared to the CuAAC, resulting in long reaction times and lower coupling efficiencies. To improve their reactivity, Boons and co-workers (*45*) synthesized several 4-dibenzocyclooctynols (Scheme 1D). By introducing aromatic moieties to the cyclooctyne, additional ring strain was created, and also, better conjugation was achieved as an additional factor to increase the reactivity of the alkyne. However, the first generation of these cyclooctynes and 4-dibenzocyclooctynols was rather insoluble in water, and in an attempt to improve the reactivity and water solubility, Bertozzi and co-workers designed and synthesized a second generation of difluorinated cyclooctynes (*46, 47*) (Scheme 1E). These difluorinated cyclooctynes possess similar reaction kinetics as the Cu(I)-catalyzed cycloaddition reaction. Unfortunately, these difluorinated cyclooctynes are rather difficult to synthesize (*48*). A slightly different approach toward Cu-free click reactions was explored by Rutjes and co-workers (*49*). They used a tandem [3 + 2] cycloaddition-retro-Diels−Alder ligation method in which trifluoromethyl-substituted oxanorbornadiene derivatives react with an azide to form a triazole linkage (Scheme 1F). This approach was successfully applied for labeling proteins and to the synthesis of pegylated oligopeptides in various media at ambient temperature. Although the trifluoromethyl-substituted oxanorbornadiene derivatives are much easier to synthesize than difluorinated cyclooctynes, they have a lower reactivity toward azides compared to the difluorinated cyclooctynes. Recently, an overview of the development and perspective of copper-free azide−alkyne cycloadditions was given by Lutz (*33*).

While the CuAAC generally yields a 1,4-disubstituted 1,2,3-triazole, in some cases, however, (e.g., for the synthesis of certain enzyme inhibitors) the 1,5-disubstituted triazole is preferred (*50*). In order to obtain exclusively the 1,5-disubstituted 1,2,3-triazoles from organic azides and alkynes, the groups of Fokin and Jia (*51*) used a ruthenium(II) catalyst (Scheme 1B). This Ru-catalyzed process, RuAAC, exhibits a good scope with respect to both azides and terminal or internal alkynes (*52*) and functional group tolerance. In contrast to CuAAC, RuAAC requires more stringent reaction conditions with respect to temperature and solvent (*53, 54*), which hampers a broad application as a bioconjugation reaction for biologically relevant molecules.

Another reaction that is becoming increasingly popular as an attractive click reaction is the Michael addition between thiols and acrylates (*55*), acrylamides (*56*), vinyl sulfones (*57, 58*), or maleimides (*59*) to form thioethers (Scheme 2). This Michael addition reaction, which is also called thiol−ene coupling (TEC) or "thio-click" (*60, 61*), is highly efficient and orthogonal to a wide variety of functional groups. The thiol−ene coupling makes use of the high nucleophilicity of the sulfhydryl moiety and proceeds under physiological conditions. The formed thioether linkage is very stable under physiological conditions and resists a strong basic or acidic environment and is also stable toward reducing agents; however, it is susceptible toward oxidizing agents.

A drawback of the thiol−ene coupling reaction is the sensitivity of the free thiol functionality toward oxidation into

Scheme 1. Cycloaddition Reactions between Azides and Alkynes[a]

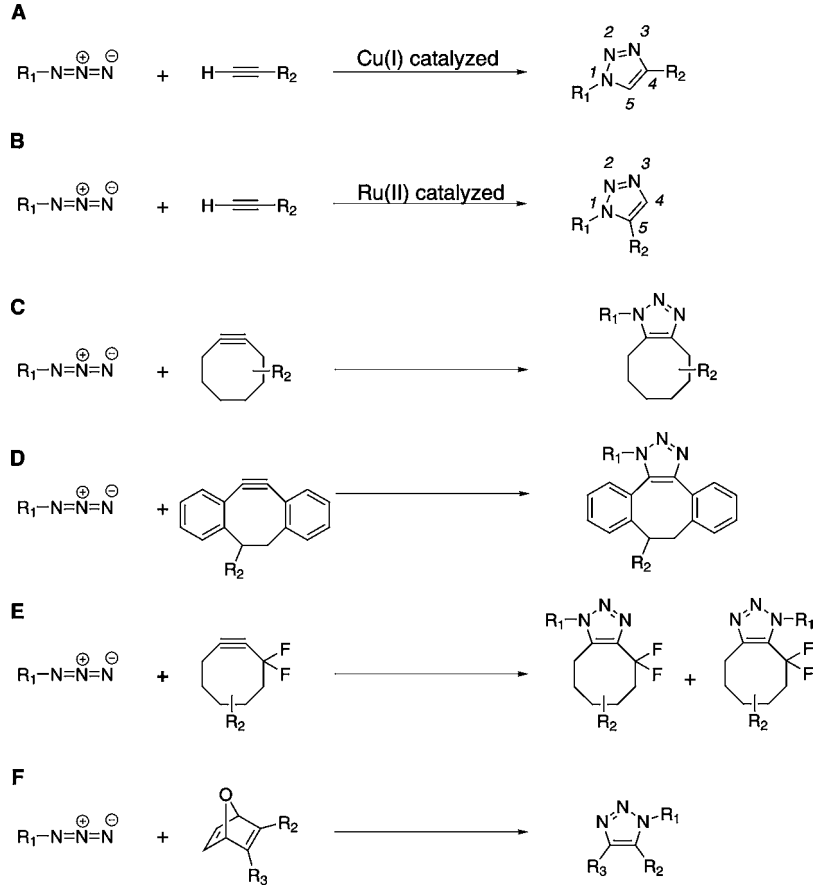

[a] (A) Cu(I)-catalyzed 1,3-dipolar cycloaddition reaction (*16*−*18*), (B) ruthenium(II)-catalyzed cycloaddition (*51*), (C) ring strain promoted cycloaddition (*44*), (D) ring strain promoted cycloaddition with 4-dibenzocyclooctynol (*45*), (E) second generation of ring strain promoted cycloaddition (*46*, *47*), (F) the tandem [3 + 2] cycloaddition-retro-Diels−Alder ligation method (*49*).

Scheme 2. Variations of the Thiol−Ene Reaction[a]

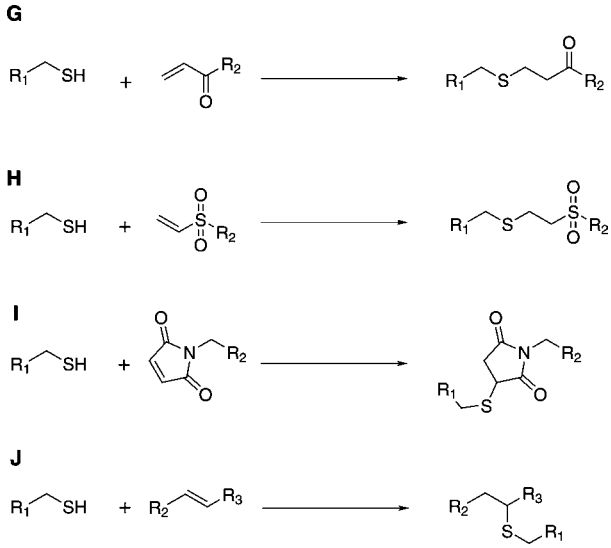

[a] (G) Michael addition between thiols and acrylates (*55*), (H) thiols and vinyl sulfones (*57*, *58*), (I) thiols and maleimides (*59*), (J) thiols and alkenes (R_2 and R_3 have to be electron withdrawing groups) (*62*−*64*).

a disulfide. This unwanted side reaction can be overcome by excluding oxygen from the reaction medium or by adding reducing agents, such as TCEP, or by using protected thiol derivatives. Such protecting groups must meet several requirements: they have to be removed quantitatively under mild conditions and the byproduct should be nontoxic. Goessl and co-workers successfully protected the thiol functionality as a thio acetate (*65*, *66*). Thio esters are highly sensitive toward mild base and can be cleaved at pH 8.

A detailed discussion on the reaction rate of the thiol−ene coupling reaction was provided by Hoyle et al. (*67*). On the basis of extensive studies by Morgan et al. (*68*), the influence of both thiol and ene structure on the thiol−ene free radical reaction rate is directly related to the electron density on the ene moiety. Electron-rich enes react more rapidly than electron-poor enes, e.g., alkene ≈ vinyl ester > allyl ether > acrylate > N-substituted maleimide > methacrylate (*67*).

POLYPEPTIDE-BASED POLYMERS

There is great interest in the use of functional peptides as building blocks for the synthesis of peptide-based polymers, since these polymers can be applied for the design of drug delivery systems, scaffolds for tissue engineering and repair, and as novel biomaterials (*1*, *69*). However, the synthesis of peptide-based polymers imposes several major synthetic challenges. Current methods to synthesize such polymers require the elaborated use of protection groups and/or unstable preactivated building blocks (*70*−*72*), or the polymers have to be synthesized via protein engineering, which can be very challenging (*73*). Recently, new methods have been developed to synthesize peptide-based polymers by chemoselective ligation, where *unprotected* functional peptides are coupled by an orthogonal conjugation method to form polypeptide products. In particular, the CuAAC is very suitable, because the formed 1,2,3-triazole moiety is a mimic of a native peptide bond (*40*, *41*). In view of the scope of this review, native chemical ligation

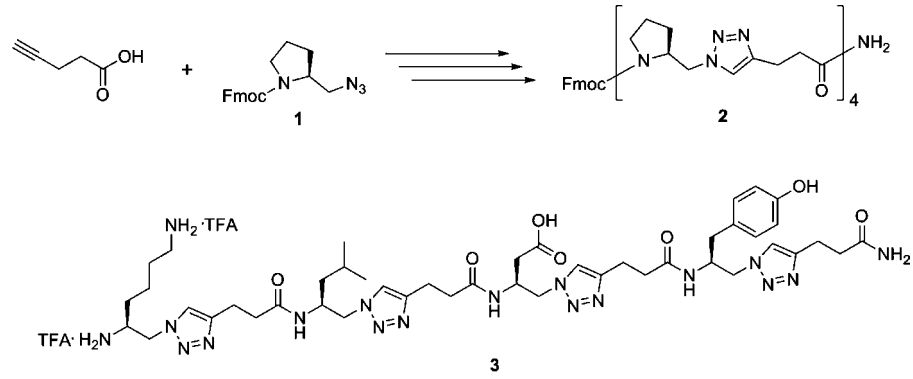

Figure 1. Examples of peptidetriazole sequences synthesized by Fan and co-workers (*75*).

Scheme 3. Synthesis of Ditriazole via "Click−Click" Strategy (*76*)

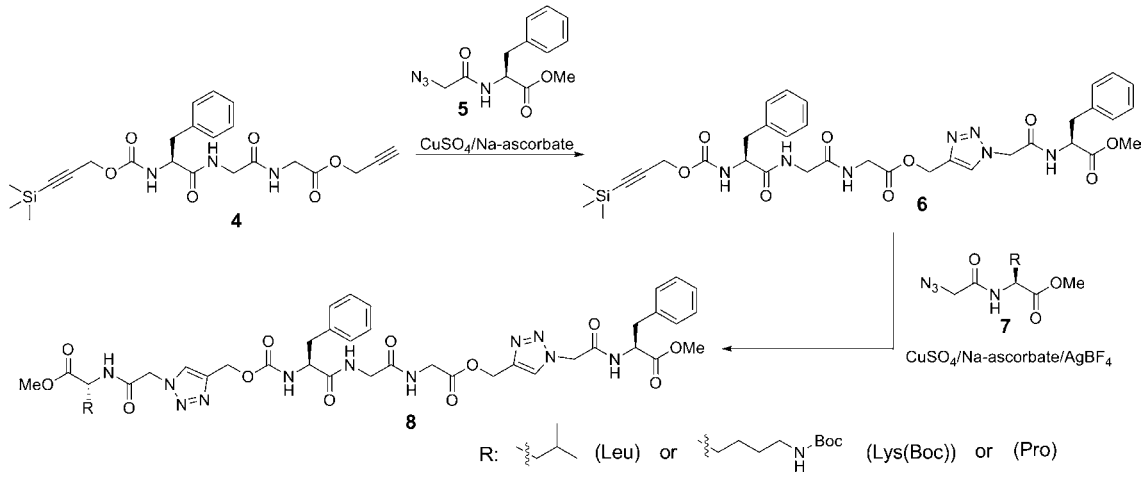

Scheme 4. Schematic Representation of the Synthesis of Peptide-Based Polymers as Described in Ref *79*[a]

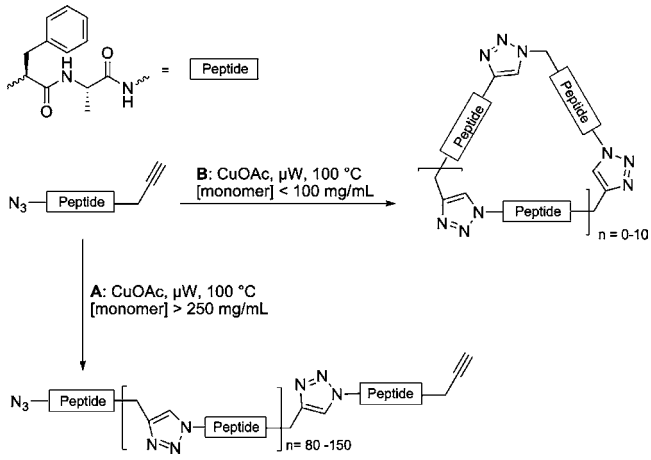

[a] Approach A: using CuOAc and high concentration of monomer led to predominantly linear polymers. Approach B: using CuOAc and low monomer concentration led to predominantly cyclic oligomers.

(NCL) for the synthesis of peptide-based polymers is not discussed. A recent review on protein synthesis by NCL is given by Kent (*74*).

In 2005, Fan and co-workers (*75*) developed a protocol for the solid-phase synthesis of peptidotriazoles with alternating triazole and amide linkages in the backbone. The first peptidotriazole they synthesized consisted of four repeating units of 4-pentynoic acid and Fmoc-proline azide **1** (Figure 1). First, 4-pentynoic acid was grafted onto the resin with PyBOP/HOBt as coupling reagents. Next, Fmoc-proline azide was clicked in the presence of CuI/ascorbic acid/DIPEA/30% 2,6-lutidine/DMF, followed by the removal of the Fmoc group with 20% piperidine/DMF, and the cycle was repeated. After four cycles, the peptidotriazole was cleaved from the resin to yield the desired product **2** in high purity. To demonstrate the versatility of this approach and its compatibility with the common protecting groups used in peptide chemistry, the synthesis was repeated, replacing Fmoc-proline azide by side chain-protected tyrosine, aspartic acid, and lysine building blocks (Figure 1). Also, in this case the desired product **3** was obtained in high yield and purity.

Leigh and co-workers (*76*) developed synthetic methodologies in which the copper(I)-mediated alkyne−azide cycloaddition reaction was combined with a silver(I)-catalyzed TMS-alkyne deprotection (*77*, *78*), and this so-called "click−click" strategy was used to synthesize step-by-step oligomers of peptide triazoles (Scheme 3). The authors started with the tripeptide phenylalanyl-glycyl-glycinate hydrochloride and functionalized the C-terminus of this peptide with an alkyne and the N-terminus with a TMS-protected alkyne (compound **4**, Scheme 3). In the first reaction, they performed a click reaction with azide-containing pseudodipeptides, based on the amino acids phenylalanine **5**, leucine, proline, or N^{ϵ}-Boc-protected lysine. In the presence of $CuSO_4$/Na-ascorbate, an almost quantitative yield of monoclicked product was obtained after 18 h. After the first click reaction, the TMS group was removed by treatment with $AgBF_4$. The addition of the second azido pseudodipeptide **7** resulted in the formation of the ditriazole **8** (Scheme 3). Additional $CuSO_4$/Na-ascorbate was needed to drive the reaction to completion. This one-pot method can be a promising tool for peptide ligation reactions and the synthesis of peptide-based polymers.

Scheme 5. Synthesis of Diblock Copolymers Containing Poly(γ-benzyl-L-glutamate) and Poly(N^{ε}-trifluoroacetyl-L-lysine) (*82*)

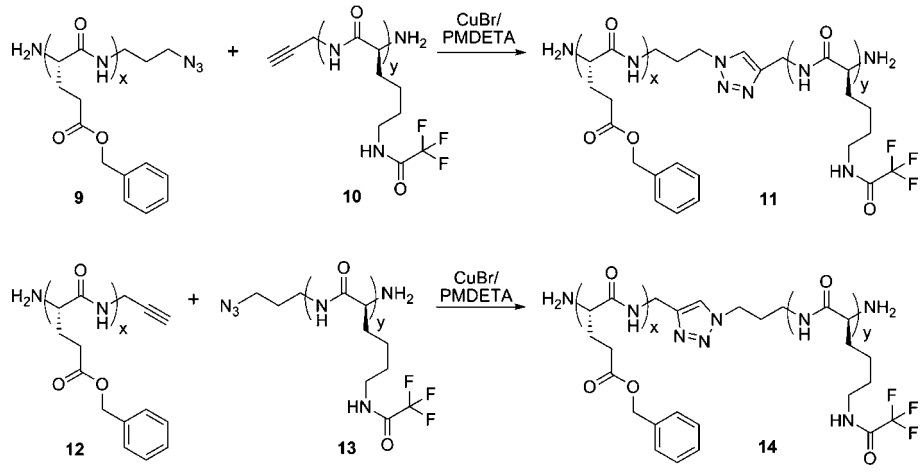

Scheme 6. Synthesis of Alkyne Functionalized Polyesters (*83*)

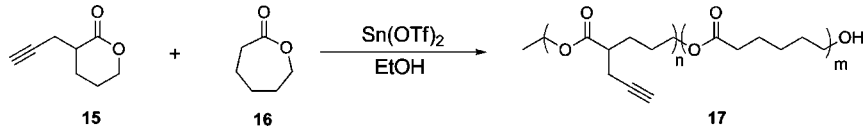

Scheme 7. Synthesis of Glycopolymers via Click Reactions[a]

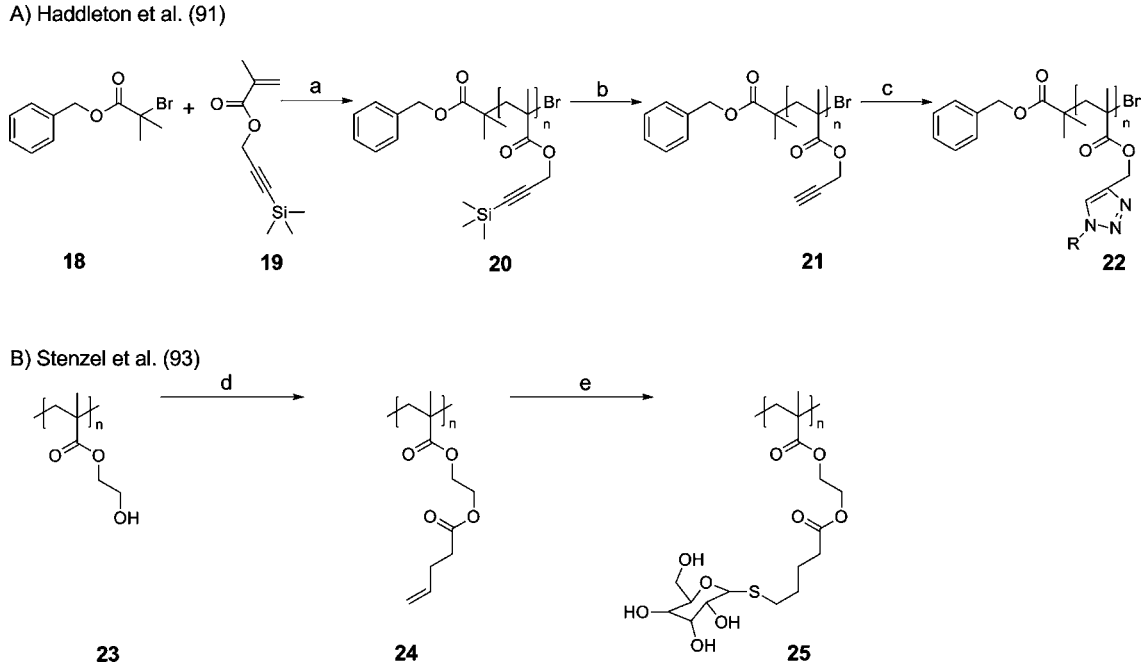

[a] (A) Reagents and conditions: (a) *N*-(ethyl)-2-pyridylmethanimide/CuBr, toluene, 70 °C; (b) TBAF, acetic acid, THF, −20 to +25 °C; (c) RN_3, [$CuBr(Ph_3P)_2$], DIPEA. (B) (d) 4-Pentenoic anhydride, DMP, pyridine, DMF; (e) UV, glucothiose, DMPA, DMF.

Rather than a step-by-step method, Liskamp and co-workers. explored the one-step polymerization of azido-phenylalanyl-alanyl-propargyl amide as a model peptide under different reaction conditions (Scheme 4) (*79*), aiming to develop an efficient method for the synthesis of mimics of natural biopolymers with repetitive peptide sequences. It was demonstrated that the degree of polymerization was strongly dependent on the polymerization conditions (e.g., type of catalyst, monomer concentration, and reaction temperature). When the monomer was polymerized at room temperature with $CuSO_4$/Na-ascorbate as the catalyst, only relatively low molecular weight (M_n: 6.9 kDa) and mostly linear polypeptides were formed. When the same monomer was polymerized in the presence of CuOAc as

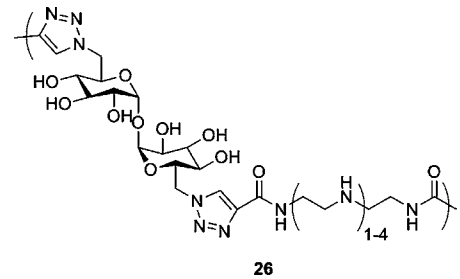

Figure 2. Structure of trehalose polymers synthesized by Reineke and co-workers (*89, 90*).

Scheme 8. Synthesis of Degradable-Brushed pHEMA-pDMAEMA (*102*)

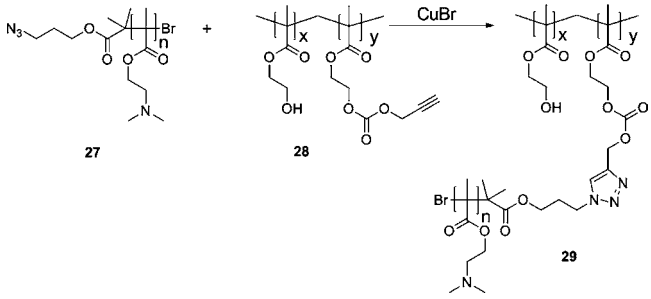

catalyst using microwave irradiation at 100 °C, long linear dipeptide-based polymers were formed with an M_n up to 45 kDa (300 amino acid residues) as shown in Scheme 4 (approach A). Interestingly, when the monomer was polymerized at low monomer concentration, using CuOAc as catalyst and under microwave irradiation at 100 °C, cyclic oligomeric structures were formed (approach B, Scheme 4). In a followup study, these optimized polymerization conditions were used to synthesize biodegradable peptide-based polymers with functional groups, such as the ε-NH_2 group of lysine (*80*). The polymers based on the monomers azido-phenylalanyl-alanyl-lysyl-propargyl amide or azido-phenylalanyl-alanyl-glycoloyl-lysyl-propargyl amide were designed to contain recognition sites for proteases like trypsin and chymotrypsin. Moreover, the latter polymer also contains ester bonds that can be cleaved by chemical hydrolysis. It was shown that the number average molecular weight (M_n) of the polymers could be tailored between 4500 and 14 000 Da (33 to 100 amino acid residues) depending on the monomer concentration used during the polymerization. As anticipated, the synthesized polymers were cleaved by both proteases yielding low molecular weight degradation products. The polymer with the ester bond (polymers based on azido-phenylalanyl-alanyl-glycoloyl-lysyl-propargyl) was also degraded under physiological conditions ($t_{1/2}$ = 5 h) due to hydrolysis of the ester bond. In a similar approach, Guan and co-workers (*81*) recently reported on the synthesis of peptide-based polymers that can fold into well-defined β-sheets followed by a self-assembly into hierarchical nanostructures.

Taton and co-workers (*82*) developed a methodology for the synthesis of diblock copolypeptides by combining ring-opening polymerization (ROP) of N-carboxyanhydrides (NCA) combined with CuAAC-catalyzed click-chemistry. In their approach, azide- and alkyne-terminated poly(γ-benzyl-L-glutamate) (**9** and **12**, Scheme 5) and poly(N^{ε}-trifluoroacetyl-L-lysine) (**10** and **13**, Scheme 5) were synthesized by ROP of the corresponding NCA with an azide- or alkyne-containing initiator. The azide and alkyne polymers were subsequently conjugated in DMF at 50 °C with CuBr complexed by *N*,*N*,*N*′,*N*″,*N*″-pentamethyldiethylenetriamine (PMDETA) as catalyst. After 36 h, the block copolymers (**11** and **14**) were obtained in almost quantitative yield (Scheme 5).

Emrick and co-workers (*83*) developed a method for the synthesis of biocompatible amphiphilic graft polyesters. In their approach, aliphatic polyesters with pendant acetylene groups were synthesized by ROP of α-propargyl-δ-valerolactone **15** with ε-caprolactone **16** (Scheme 6). These acetylene-functionalized polymers **17** were subsequently grafted with PEG and oligopeptides, using CuAAC and azide-terminated PEG or oligopeptides in the presence of $CuSO_4$/Na-ascorbate for 16 h at 80 °C. The amphiphilic graft polyesters were shown to be biocompatible by *in vitro* cytotoxicity evaluation, suggesting their suitability for a range of biomaterial applications.

GLYCOPOLYMERS

Carbohydrates are involved in a number of important biological processes such as cell−cell recognition and cell−protein interactions and play a role in the targeting of hormones. Moreover, antibodies and toxins make use of carbohydrates for selective recognition of their antigens and target receptors (*84*−*86*). However, individual protein−carbohydrate interactions are generally weak; therefore, protein-binding carbohydrates exist in higher-order oligomeric structures, presenting multiple bind-

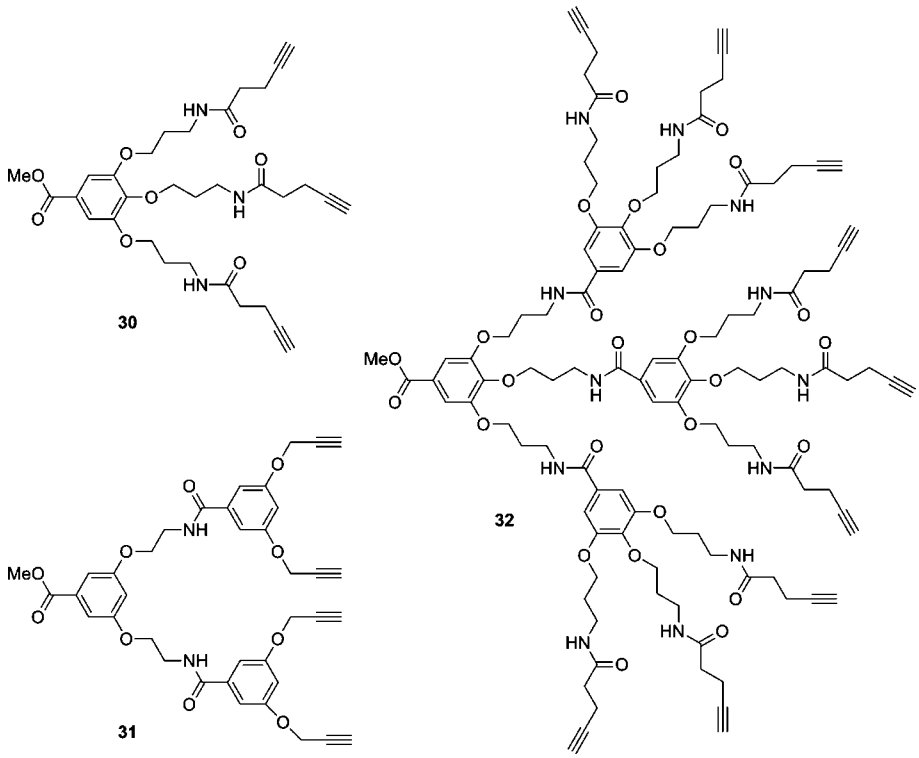

Figure 3. Structures of alkyne-bearing dendrimers used by Pieters, Liskamp, and co-workers (*106, 107*).

Scheme 9. Synthesis of Dendrimers via Thiol−Ene Reaction (*109*)[a]

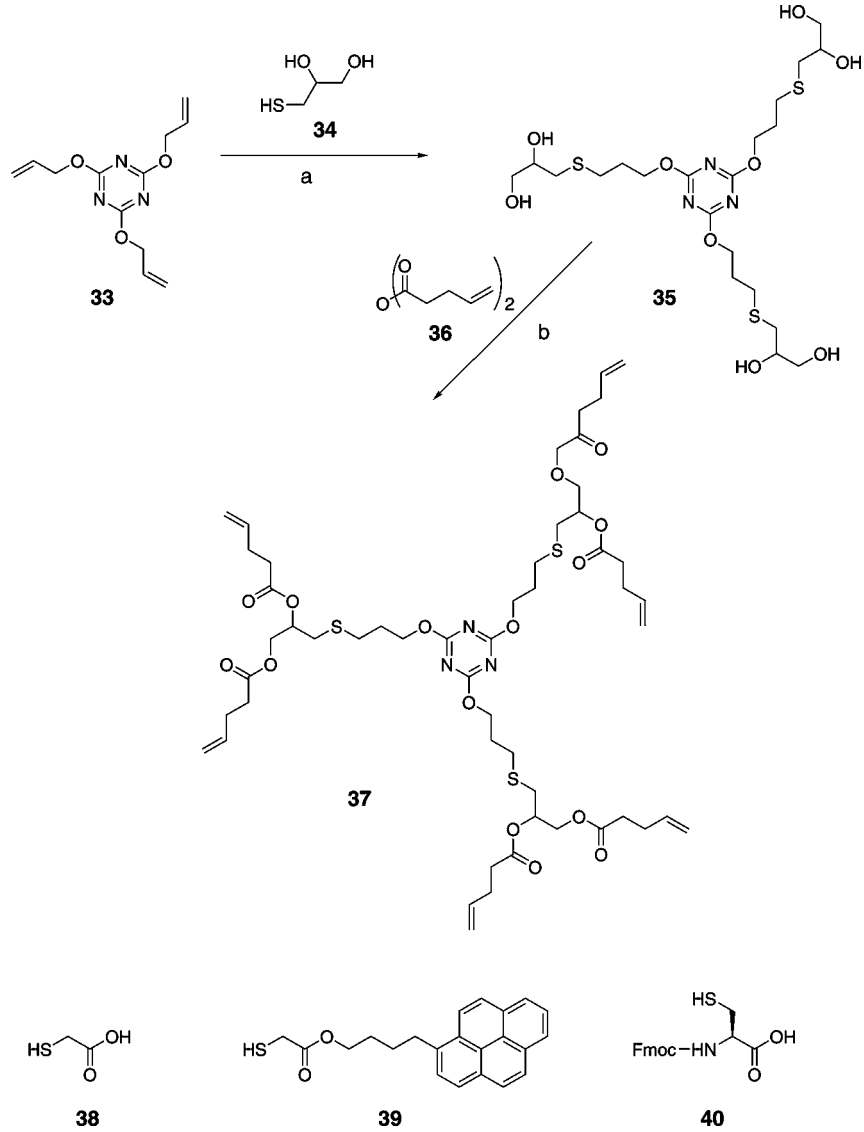

[a] Reaction conditions: (a) 2,2-dimethoxy-2-phenylacetophenone, *hν* (30 min), solvent free; (b) DMAP, pyridine.

ing sites, known as the "cluster glycoside effect" (*87, 88*). These multiple binding sites help to improve the weak individual interactions to achieve strong and selective interactions. Scientists have attempted to mimic this "cluster glycoside effect" by synthesizing various well-defined synthetic glycopolymers.

Depending on the method applied, such glycopolymers can be divided into two different classes. They can be synthesized either by polymerization of carbohydrate containing monomers (vide infra, Reineke et al. *89, 90*) or by postfunctionalization of polymers with carbohydrates. Especially for the latter approach, click chemistry turned out to be a valuable tool.

Several examples to obtain glycopolymers employing both CuAAC and the thiol−ene coupling reaction have been mentioned in the literature. Haddleton and co-workers have synthesized various glycopolymers from alkyne backbone-functionalized polymers and azide-functionalized carbohydrates via the CuAAC as shown in Scheme 7A (*91, 92*), such as various mannose- and galactose-containing multidentate ligands for studying lectin binding (*91*). In this approach, the alkyne-functionalized polymers were synthesized by transition-metal-mediated living radical polymerization (TMM-LRP) of methacrylate **19**. After polymerization, the TMS group was removed with TBAF and acetic acid, followed by the coupling of various protected and unprotected azide-functionalized carbohydrates via CuAAC in the presence of $[CuBr(Ph_3P)_2]$ and DIPEA (Scheme 7A).

Alternatively, Stenzel and co-workers (*93*) used the thiol−ene coupling reaction for the postsynthesis modification of glycopolymers. First, a block copolymer containing di(ethylene glycol) methyl ether methacrylate (DEGMA) and 2-hydroxyethyl methacrylate (HEMA) was synthesized via RAFT polymerization. Then, the blockcopolymer and a commercially available HEMA polymer were grafted with glucothiose in the presence of the photoinitiator 2,2-dimethoxy-2-phenyl-acetophenone (DMPA) under UV irradiation for 2 h (shown for homopolymer **24** in Scheme 7B). The resulting block copolymer was used to form thermo-responsive micelles that can be used as a potential drug carrier.

In a recent article by Diehl and Schlaad (*94*), the thiol−ene coupling reaction has been used to functionalize poly[2-(isopropyl/3-butenyl)-2-oxazoline] copolymers with various thiols (e.g., octanethiol, 3-mercaptopropionic acid, and 2-mercaptoethanol). Via this approach, these authors synthesized a series of thermosensitive glycopolymers with cloud points tunable over a wide temperature range.

In a recent article by Haddleton and co-workers (*95*), the synthesis of alkyne-functionalized polymers via chain transfer polymerization (CCTP) is described. The polymers obtained by

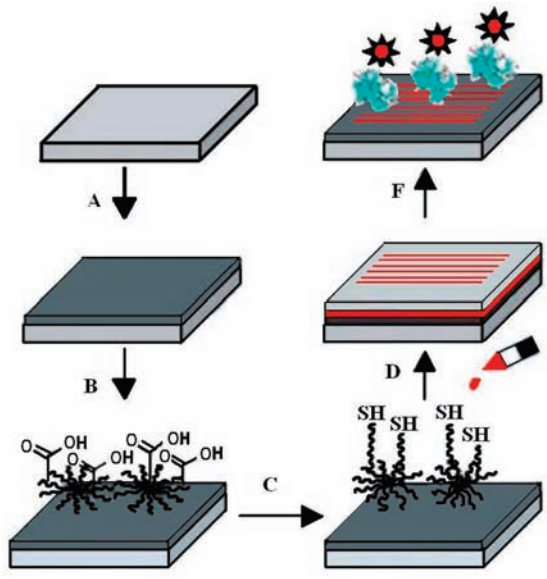

Figure 4. Schematic representation of the approach to immobilize proteins on a solid support (*110*). (A) activation of the surface; (B) attachment of dendrimers (aminocaproic acid linker, dendrimers); (C) functionalization with thiols; (D) drop casting of terminal-olefin-functionalized proteins and immediate coverage with a photomask; (E) removal of the mask. (Copyright Wiley-VCH Verlag GmbH & Co. KGaA. Reproduced with permission (*110*).)

this approach can be end-functionalized via the thiol−ene coupling reaction as well as the CuAAC reaction. In this article, several azide-functionalized carbohydrates were grafted via the CuAAC reaction onto the alkyne side chain of the polymers. The grafted polymers on their turn were end-functionalized using the thiol−ene coupling reaction with different thiols. The synthesized mannose-and galactose-containing glycopolymers were able to function as multivalent ligands for the recognition of lectins. The CCTP in combination with the thiol−ene coupling reaction and the CuAAC reaction is a powerful tool for the convenient synthesis of many different types of functional polymers and conjugates.

POLYMERS FOR NONVIRAL GENE DELIVERY

Gene therapy holds a great promise for the treatment of diseases with a genetic origin that are currently incurable. The success of gene therapy largely depends on the availability of suitable delivery vehicles. Although viral vectors display rather good transfection properties, both *in vitro* and *in vivo*, there are a large number of problems associated with the use of these vectors (*96*, *97*). Therefore, there is an increasing interest in the development of so-called nonviral gene delivery systems (*98*). Two major classes of nonviral systems can be distinguished, namely, those based on cationic lipids or those based on cationic polymers. However, generally speaking, the cationic polymers developed to date often display cytotoxicity effects likely due to interactions with proteins and phospholipid membranes. Therefore, new polymers with a significantly reduced cytotoxicity have to be developed. The click reaction can be a valuable tool to synthesize these new polymers for nonviral drug delivery systems.

Reineke and co-workers (*89*) exploited the CuAAC to synthesize a family of trehalose-based glycopolymers, e.g., **26** (Figure 2). They were inspired by the work of Dervan et al., who showed that macromolecules that contain various heterocyclic residues, such as derivatives of pyrrole and imidazole, are able to bind nucleic acids (*99*). Three polymers with different amine stoichiometry were synthesized from diazide functionalized trehalose monomers and dialkyne-amide comonomers in the presence of $CuSO_4$/Na-ascorbate. The polymers contained a trehalose unit for increased biocompatibility, an oligoamine unit for electrostatic interactions with DNA, and a triazole functionality for hydrophobic, van der Waals, and hydrogen-bonding interactions with nucleic acids (Figure 2).

All three newly synthesized polymers were effective as nucleic acid carriers in the absence as well as in the presence of serum. The polymer with the highest secondary amine density gave polyplexes with low toxicity and high cellular delivery. The transfection efficiency of the trehalose polymers was an order of magnitude higher than Jet-PEI, one of the most efficient *in vitro* gene delivery polymers, in serum-free conditions. In a second study (*90*), the same group investigated the influence of the molecular weight of the trehalose click polymer on polyplex stability and pDNA cellular delivery efficiency. In this study, it was shown that a higher degree of polymerization resulted in a higher polyplex stability, although no effect was observed in pDNA binding affinity, cellular uptake, and DNase protection in relation to the M_w.

Ideally, suitable polymeric transfectants should be nontoxic, nonimmunogenic, and preferably biodegradable in a controlled manner. Furthermore, biodegradable polymers should yield degradation products with a molecular weight lower than 30 kDa, because these degradation products can be excreted by the kidneys (*100*, *101*). To reduce the cytotoxicity of cationic polymers, Hennink and co-workers (*102*) designed a high-molecular-weight polymer composed of a low-molecular-weight cationic poly(2-dimetylamino)ethyl methacrylate) (pDMAEMA) that was grafted onto a polymer backbone of an uncharged hydrophilic polymer, poly(hydroxyethyl methacrylate) (pHEMA), via biodegradable linkages. Both pDMAEMA and pHEMA were synthesized by atom transfer radical polymerization (ATRP). For this goal, pDMAEMA was end-functionalized with an azide (**27**), while pHEMA was randomly functionalized with acetylene moieties (**28**, Scheme 8). The polymers were "clicked" together via the CuAAC in DMF at 50 °C with CuBr as catalyst (Scheme 8). The molecular weight of the polymer as well as the number of grafts could easily be varied. Upon incubation at physiological conditions (pH 7.4, 37 °C), the carbonate ester bonds were readily hydrolyzed ($t_{1/2}$: 96 h). The molecular weight of the final main degradation product was very close to that of the starting pDMAEMA, indicating that the carbonate esters were quantitatively hydrolyzed. Furthermore, the synthesized polymers were able to condense DNA into small particles, which were able to transfect cells efficiently in the presence of endosome-disruptive INF/7 peptide. Finally, the polymers had a lower toxicity compared to high molecular weight pDMAEMA, making this an effective approach to reduce the toxicity of high-molecular-weight cationic polymers (*102*).

DENDRIMERS

Dendrimers are highly branched well-defined polymers and among others used for the simultaneous presentation of biologically relevant but individually weakly interacting ligands (*103*). Multivalent ligands often bind much more strongly to the interacting protein than their monovalent counterparts (*103*−*105*). Pieters and co-workers (*106*) developed a versatile microwave-assisted CuAAC approach that allowed the conjugation of azido carbohydrates with different kinds of alkyne-bearing dendrimers (Figure 3). With this procedure, they were able to synthesize triazole glycodendrimers in high yields, up to the nonavalent level. These glycodendrimers can be used to increase affinities in various applications such as the binding with bacteria, bacterial toxins, and lectins.

In a similar approach, Liskamp and co-workers (*107*) used the microwave-assisted 1,3-dipolar cycloaddition reaction to

Scheme 10. Schematic Representation of the Approach Described by Caruso and Co-Workers for the Synthesis of Ultrathin pH-Responsive Polymer Films (*115, 116*)

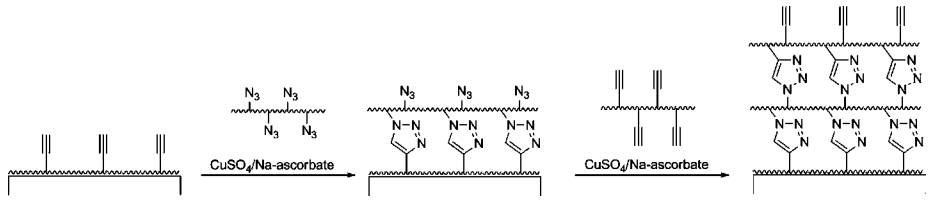

Scheme 11. Synthesis and Hydrolysis of Dextran-Based Multilayers (*118*)

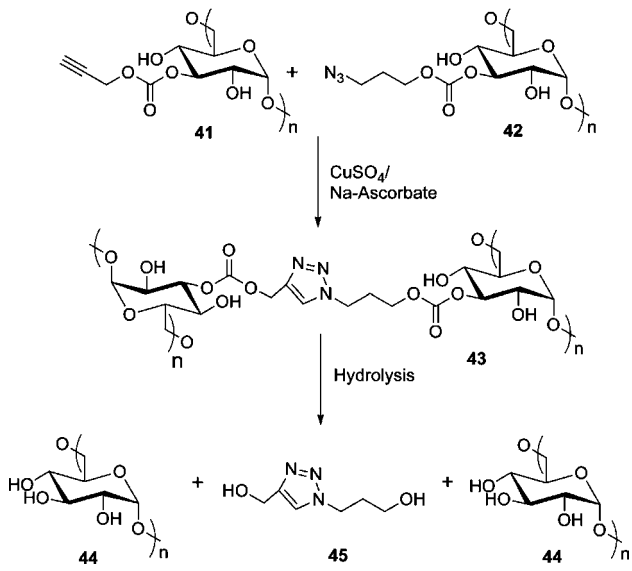

synthesize peptide-presenting multivalent dendrimers. The azido-peptides were mixed with the acetylene-functionalized dendrimers (e.g., **31**, Figure 3) in the presence of $CuSO_4$/Na-ascorbate in aqueous DMF and heated at 100 °C in a microwave reactor. The products were obtained in nearly quantitative yield in a relatively short reaction time (5−10 min). With this method, di-, tetra-, octa-, and hexadecavalent dendrimeric peptides were successfully synthesized. In a recent study, Liskamp and co-workers (*108*) used the same strategy as described above to synthesize ^{111}In-labeled DOTA-conjugated dendrimers with multivalent cyclic RGD peptides. The tetravalent ^{111}In-labeled RGD dendrimers had increased affinity toward the $\alpha_v\beta_3$ integrin receptor and had better tumor targeting properties than their monovalent congeners.

Recently, Hawker and co-workers (*109*) developed a facile and efficient method for the synthesis and end-functionalization of poly(thioether) dendrimers using the thio−ene coupling reaction. The synthesis of the dendrimers was started from the tris-alkene core 2,4,6-triallyloxy-1,3,5-triazine (**33**, Scheme 9). To this core, 1-thioglycerol (**34**) in the presence of catalytic amounts of photoinitiator 2,2-dimethoxy-2-phenylacetophenone was coupled by means of UV irradiation for 30 min at room temperature to yield the first-generation dendrimer **35**. Subsequent esterification of the hexa-hydroxy dendrimers with 4-pentenoic anhydride **36** yielded the ene-functionalized dendrimers **37**. Repeating the final two reaction steps resulted in the synthesis of dendrimers functionalized with 48 alkene functionalities. End-functionalization was also performed with the thiol−ene coupling reaction with suitable thiol-containing reagents, e.g., thioglycolic acid **38**, 4-(pyren-1-yl)butyl 2-mercaptoacetate **39**, and Fmoc-Cys-OH (**40**) as shown in Scheme 9.

Waldmann and co-workers (*110*) used dendrimers and the thiol−ene coupling reaction to immobilize proteins and other biomolecules onto solid surfaces in a patterned way. In detail, they first attached polyamidoamine dendrimers covalently to silicon oxide surfaces (Figure 4B). The dendrimers were extended with an aminocaproic acid spacer, and cystamine was coupled to this spacer and subsequently reduced to obtain a free thiol functionality (Figure 4C). Next, the silicon oxide wafers were incubated with terminal-olefin-functionalized proteins dissolved in ethylene glycol and covered with a photomask (Figure 4D). Subsequent irradiation led to patterning with protein adducts covalently attached via a thioether moiety. The amount of protein that was immobilized could be tailored by varying the irradiation time. With this approach, various biomolecules, like biotin, calf-intestine-alkaline phosphatase, the small GTPase Ras, and a phosphopeptide, were photochemically attached to the dendrimer-coated wafers. All biomolecules were successfully attached and retained their structure and activity. The authors anticipate that this method can be used for the controlled fabrication of structured assemblies of proteins on artificial surfaces.

PREPARATION AND MODIFICATION OF MICRO- AND NANOPARTICLES

Nanoparticles have great potential in the biomedical and pharmaceutical field (*111*). Nanoparticles can, for example, serve as delivery vehicles for drugs (*112, 113*). However, current methods to encapsulate drugs in polymeric nanoparticles require the use of organic solvents or harsh conditions, which may result in significant loss of activity, especially if complex biomolecules are used as the active compound. Consequently, novel and mild approaches to obtain nanoparticles are highly desirable.

With the aim to prepare functionalized polymersomes from amphiphilic polystyrene-*block*-poly(acrylic acid), van Hest and co-workers (*114*) used ATRP to synthesize the block copolymers followed by the substitution of the bromine functional end group of the hydrophilic block by an azide. Upon slow addition of water to a solution of block copolymers in dioxane, the amphiphilic block copolymers self-assemble into polymersomes with surface-exposed azide functionalities. These azide-functionalized vesicles were used as scaffold for further conjugation with alkyne-functionalized dansyl, biotin, and enhanced green fluorescent protein using $CuSO_4$/Na-ascorbate in the presence of the ligand tris-(benzyltriazolylmethyl)amine (TBTA).

Caruso and co-workers developed a general approach for the layer-by-layer assembly of ultrathin polymer films on planar substrates (*115*) and particles (*116*) for the preparation of pH-responsive nanocapsules. In their approach, poly(acrylic acid) with either alkyne or azide functionalities were synthesized by living radical polymerization. Subsequently, the azide and alkyne functionalized poly(acrylic acid)s were alternately assembled on alkyne-functionalized silica particles, with $CuSO_4$/Na-ascorbate as catalyst (Scheme 10). The silica template was removed by treatment with NH_4F-buffered HF at pH 5. The "click capsules" showed pH reversible responsive behavior in a reversible manner, i.e., the capsule diameter varied between about 5 μm in acidic and 8 μm in basic conditions. This pH-responsiveness could be exploited to load and concentrate drugs inside the capsules. Moreover, the presence of azide or alkyne

Scheme 12. The Two Different Approaches to Synthesize PVA Hydrogels (*123*)

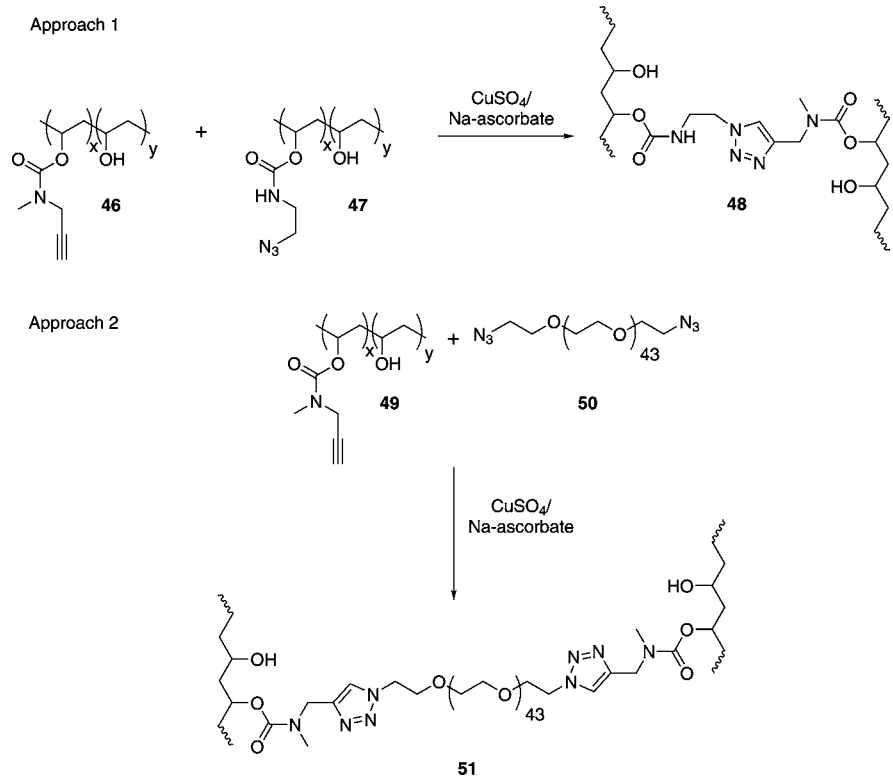

Scheme 13. Formation of Hyaluronic Acid Based Click Gels (*125*)

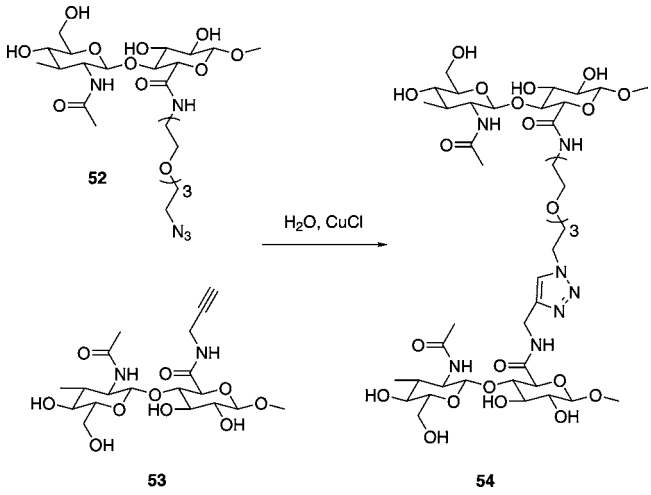

moieties on the outer shell of the capsules allows for the chemoselective postfunctionalization of the nanoparticles.

In a similar approach, De Geest and co-workers (*117*) synthesized dextran-based multilayer films and hollow capsules. By introducing carbonate ester bonds in the azide and alkyne linkages, the multilayers can be degraded by chemical hydrolysis (Scheme 11). In a subsequent article (*118*), the potential of the biodegradable dextran multilayers for drug delivery was examined. The microcapsules were loaded with fluorescein isothiocyanate-labeled dextran as a model drug compound and incubated at physiological conditions. It was shown that the drug release rate could be tailored by the cross-linking density of the dextran multilayers.

In a recent paper by Caruso and co-workers (*119*), the development of a thiol−ene version of the layer-by-layer assembly of polymer films on silica particles is described. In this approach, poly(methacrylic acid), containing either thiol groups or ene functionalities, was alternatively deposited with poly(vinylpyrrolidone) on silica particles under UV irradiation.

Schlaad and co-workers (*62*) used a thiol−ene coupling reaction for the synthesis of self-assembling peptide hybrid amphiphiles. They grafted cysteine and cysteine-containing dipeptides onto the hydrophobic block of polybutadiene-*block*-poly(ethylene oxide) polymer. The grafting of cysteine had little effect on micelle formation. However, when the dipeptide cysteinyl-phenylalanine was coupled to the amphiphilic polymer, vesicles and worm-like micelles were formed. More recently, Schlaad and co-workers (*63*, *64*) used the same method to synthesize polybutadienes modified with hydrophilic functionalities. The thiol−ene coupling reaction was used to incorporate thiol-containing molecules, in which the carboxylic acid or amine functional groups and amino acid residues were unprotected. With the incorporation of such titratable groups, the polymers were able to self-assemble into pH-responsive unilamellar or multilamellar vesicles.

Riguera and co-workers (*120*) reported an efficient method to synthesize polyion complex (PIC) micelles with the CuAAC catalyzed click reaction that are stable under physiological conditions. In their approach, azide-functionalized gallic acid-triethylene glycoside (GATG) dendrimers and PEG-GATG block copolymers were coupled to different alkynes functionalized with sulfate, sulfonate, or carboxylate groups in the presence of $CuSO_4$/Na-ascorbate. When the sulfated PEG-

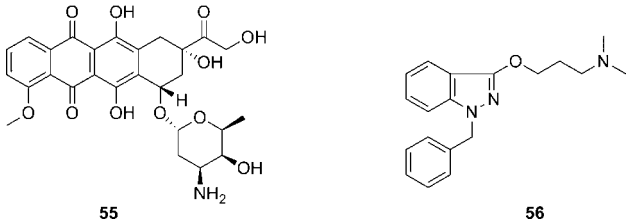

Figure 5. Structures of doxorubicin **55** and benzidamine **56**.

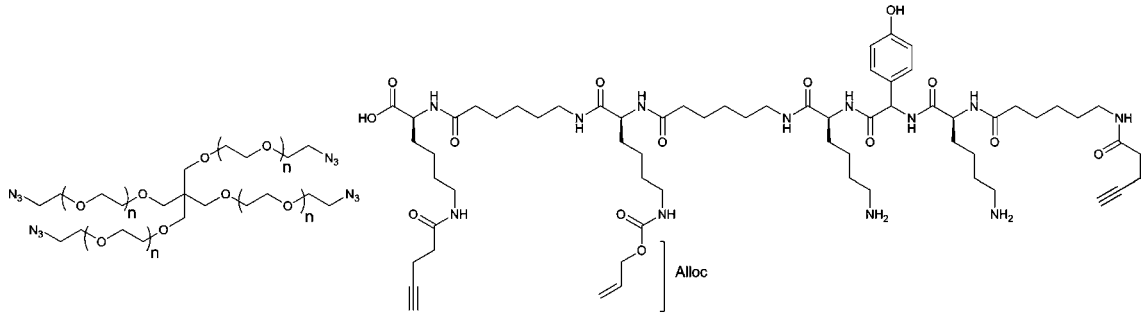

Figure 6. Structure of tetraazide-functionalized four-armed star-shaped PEG **57** and diacetylene-functionalized peptide **58** (*126*).

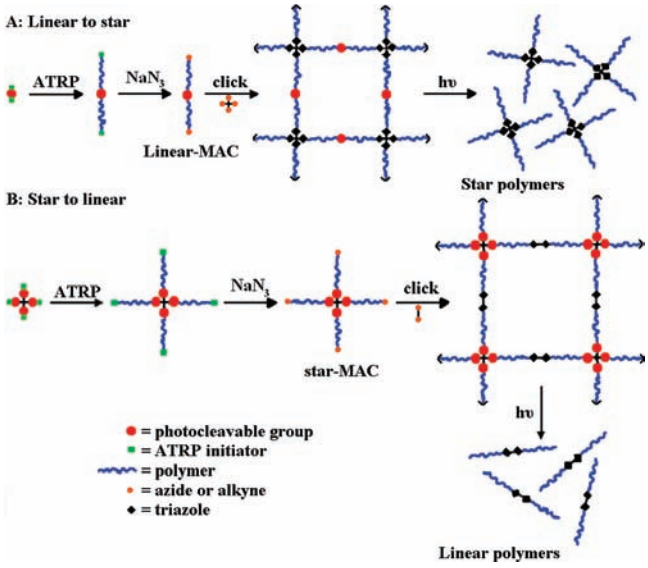

Figure 7. Two different approaches to synthesize photocleavable hydrogels (reproduced with permission from ref *128*).

GATG block copolymer was mixed in a stoichiometric ratio with poly(L-lysine), spherical micelles with a narrow size distribution were obtained.

In a recent article authored by Pine and co-workers (*121*), a new generic method for the covalent linkage of a wide variety of molecules to the surface of colloidal polymer microspheres via the CuAAC reaction has been described. In their approach, polystyrene particles containing 4-vinylbenzyl chloride moieties were converted into the corresponding azides and subsequently reacted with various alkynes to obtain triazole-functionalized microparticles. As a typical example, the authors functionalized polystyrene microspheres with two polyethylene oxide-based polymers. However, it has been stated that this approach is sufficiently general since it can readily be adapted to colloids that consist of other (polymeric) materials.

HYDROGELS

Hydrogels are three-dimensional, hydrophilic polymeric networks capable of absorbing large amounts of water (*122*). Hydrogels have received great interest over the past decades, since they can be used for a wide range of applications including drug delivery systems and scaffolds for tissue engineering and repair. In 2006, Hilborn and co-workers were the first to apply click chemistry to synthesize hydrogels (*123*). They synthesized poly(vinyl alcohols) (PVA) functionalized with either acetylene or azide groups (**46** and **47**, Scheme 12). Upon addition of $CuSO_4$/Na-ascorbate, a hydrogel was formed within a few minutes (**48**, Scheme 12). However, in order to retain the water solubility of the azide- or alkyne-functionalized PVA, only low degrees (1−5%) of modification were possible. In a second approach to synthesize PVA-based hydrogels, acetylene-functionalized polyvinyl alcohol **49** was cross-linked with telechelic bifunctional poly(ethylene glycol) diazide **50** (Scheme 12). This approach was superior in gel formation and gave higher values of gel fraction.

Hawker and co-workers used PEG as the main structural component for model "click" hydrogels. In their approach, diacetylene-functionalized telechelic PEG derivatives and tetraazide-functionalized PEG were coupled by "click chemistry" at room temperature using 2 equiv of PEG diacetylene, 0.4 equiv $CuSO_4$, and 1 equiv of Na-ascorbate. Under these conditions, the hydrogels were formed within 30 min, and fluorescence analysis revealed the presence of maximal 0.2% unreacted azide/acetylene moieties. By varying the length of the diacetylene PEG chain, they showed that the properties (swelling degree and max true stress) of the hydrogels could be tailored (*124*).

Lamanna and co-workers (*125*) developed a procedure for the formation of hydrogels based on hyaluronan derivatives suitable for tissue engineering applications. They synthesized hyaluronic acid bearing either azide or alkyne groups (**52** and **53**, Scheme 13). Hydrogels were formed within a few minutes by dissolving both components in H_2O in the presence of 1% w/v of CuCl (Scheme 13). Residual copper entrapped in the hydrogel was removed by dialyzing the hydrogel against an aqueous buffer containing EDTA as metal chelator. The synthesized hydrogels were evaluated for drug-release capabilities with doxorubicin **55** and benzidamine **56** as model drugs (Figure 5). Benzidamine was quantitatively released within hours, whereas the release of doxorubicin was prolonged over several weeks. The release rate could be tailored by varying the degree of cross-linking. The slower release of doxorubicin was explained by strong electrostatic interactions between the protonated amino group of doxorubicin and carboxylate groups of the hydrogels. The authors also argued that $\pi-\pi$ stacking interactions between the triazole ring and the aromatic moiety likely contributed to the slower release of doxorubicin.

Lamanna and co-workers also examined the suitability of their hyaluronan hydrogels as scaffolds for tissue engineering. Therefore, a hydrogel was formed in a YPD (yeast peptone dextrose) cell suspension and the gels were stored for 2 days at 28 °C. Subsequently, the gels were mechanically broken and the number of cells was counted, and 24 h later, 80% of the cells exhibited proliferating activity.

Anseth and co-workers (*126*) developed a procedure to integrate multifunctional photoreactive polypeptides into a hydrogel network. In their approach, they combined both the CuAAC and thiol−ene coupling reaction. First, they synthesized hydrogels by clicking tetraazide-functionalized four-arm star-shaped PEG **57** with diacetylene-functionalized peptide **58** (Figure 6). The hydrogels were formed within a few minutes

Scheme 14. Dextran Hydrogel Formation by Thiol−Ene Coupling (*135, 136*)

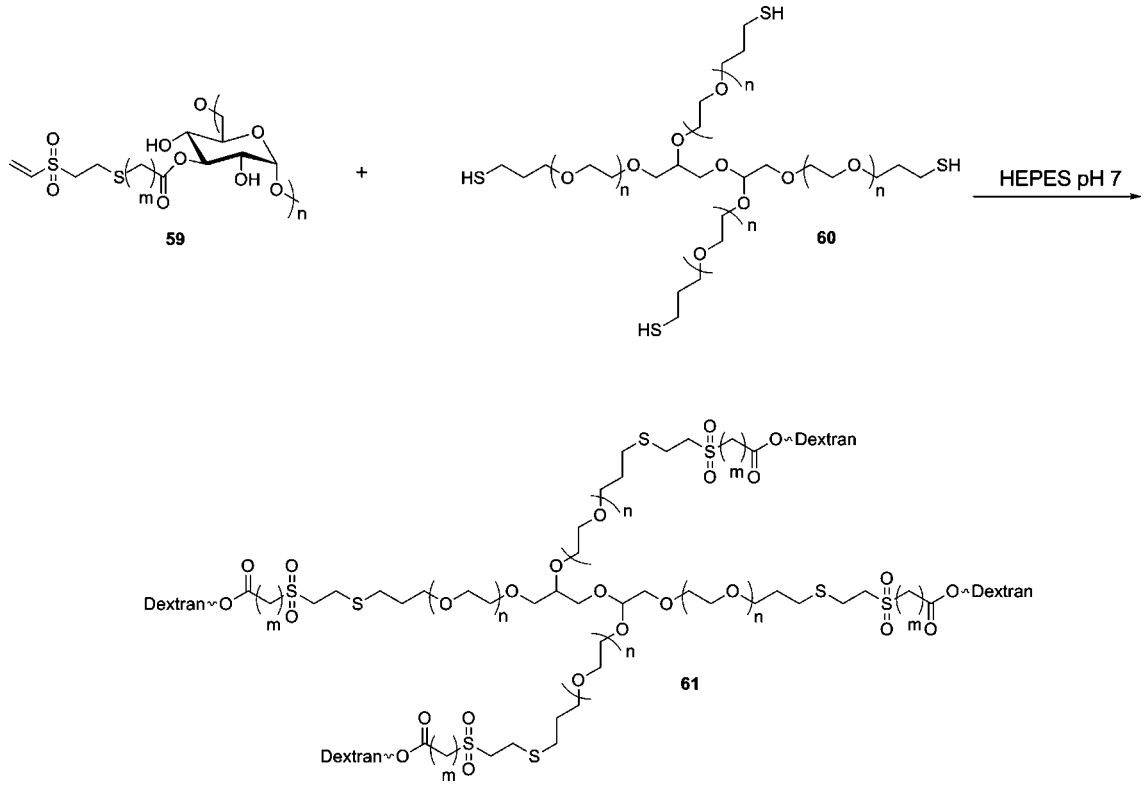

in the presence of 0.25 equiv $CuSO_4$ (based on azide functionality) and Na-ascorbate. Next, a cysteine containing fluorescently labeled peptide was incorporated by thiol−ene photocoupling to the Alloc protecting group present in the hydrogel.

Dubois and co-workers (*127*) synthesized adaptative and amphiphilic polymer conetworks based on hydrophilic poly(*N*,*N*-dimethylamino-2-ethyl methacrylate) (pDMAEMA) and hydrophobic poly(ε-caprolactone) (pCL) by a combination of ATRP, ROP, and CuAAC. In their approach, the azido-containing 2-(2-azidoethoxy)ethyl methacrylate (AEEMA) was copolymerized with DMAEMA by ATRP. The p(DMAEMA-*co*-AEEMA) copolymer was subsequently cross-linked with diacetylene-functionalized pCL, in the presence of CuBr complexed with 2,2′-bipyridine as a ligand at room temperature for 24 h to obtain a highly porous amphiphilic co-network.

Turro and co-workers (*128*) utilized ATRP and CuAAC for the synthesis of photodegradable polymeric model networks. For the synthesis of the networks, the authors employed two different approaches (Figure 7). In their first approach, linear azido-telechelic macromonomers (MAC) possessing a photocleavable group (nitrobenzyloxycarbonyl) at the center were synthesized by ATRP. Subsequently, both end groups of the linear polymers were reacted with NaN_3. The obtained azide-functionalized macromonomers were cross-linked with a small tetrafunctional alkyne in the presence of CuBr as catalyst and *N*,*N*,*N*′,*N*″,*N*″-pentamethyldiethylenetriamine (PMDETA) as ligand. In a second approach, the authors started from a tetrafunctional ATRP initiator containing four photocleavable groups to yield four-armed star-shaped poly(*tert*-butyl acrylate) polymers. Next, the four end groups were converted into azide functionalities, and the star-shaped polymers were cross-linked with a linear bifunctional alkyne. Both model networks were degraded upon exposure to UV light of 350 nm to yield soluble well-defined polymer fragments. In a second paper, Turro and co-workers (*129*) optimized this procedure by substituting the CuAAC cross-linking with a strain-promoted azide−alkyne cycloaddition, thereby abolishing the need of a (cytotoxic) copper catalyst.

Zhou and co-workers (*130*) developed a strategy for the in situ gelation of poly(*N*-isopropylacrylamide-*co*-hydroxyethyl methacrylate) (p(NIPAAm-co-HEMA))-based polymers by the CuAAC. Two p(NIPAAm-co-HEMA)-based polymers, with either pendant azide or alkyne groups, were synthesized. Hydrogels were formed by dissolving the two polymers and incubating them with $CuSO_4$/Na-ascorbate as catalyst and PMDETA as ligand for 24 h at room temperature. The obtained CuAAC hydrogels had faster shrinking/swelling kinetics compared with traditionally synthesized p(NIPAAm) hydrogels.

Yang et al. (*131*) synthesized PEG-RGD peptide hydrogels for cell entrapment using the CuAAC. PEG is an ideal polymer for hydrogel formation, because the formed gels generally have a high water absorbing capacity and are resistant to protein adsorption. However, the viability of encapsulated cells in PEG hydrogels is generally low due to the nonadherent properties for the cells. By virtue of introducing RGD peptides into the PEG hydrogels, cell adhesion properties were increased, resulting in higher cell viability. For the PEG precursor of the hydrogel, the authors prepared tetra-acetylene PEG by esterification of tetra-hydroxy-terminated four-armed PEG with 4-pentynoic acid. As a cross-linking agent, they synthesized a series of diazide-functionalized RGD peptides by reacting RGD peptides with 6-azidohexanoic acid. Hydrogels were prepared by combining the acetylene-functionalized PEG and diazide-functionalized RGD peptides in the presence of $CuSO_4$/Na-ascorbate at ambient temperatures. The gelation time could be tailored between 2 and 30 min by variation of the catalyst or precursor concentration and by variation of the temperature. To investigate if the hydrogels could be used as cell delivery vehicle, the hydrogels were seeded with primary human dermal fibroblasts cells. The hydrogels without or at low RGD peptide loading were unable to adhere cells after 18 h. When the RGD peptide loading in the precursor solution was increased, the

attachment and proliferation of cells was also enhanced. These data hold promise to use these types of hydrogels as carriers for cell entrapment and tissue engineering.

In 2003, Stein and co-workers (*132*) reported a method, based on the thiol−ene coupling, to synthesize PEG-based hydrogels in situ. They used PEG-based copolymers containing multiple thiol groups synthesized from diamino-PEG and 2-mercapto-succinic acid. As cross-linking agent, PEG functionalized with vinylsulfone groups was used. Upon combining both PEG polymers, hydrogels with a water content higher than 90% were rapidly formed under mild conditions (pH 6.0−8.0 at room temperature). Furthermore, it has been shown that increasing the pH gave rapid gel formation, which is in line with the increasing nucleophilicity of the thiol functionality at higher pH values. The authors have demonstrated that the reaction between thiol and vinylsulfone is compatible with other functional groups present in, e.g., proteins, by carrying out a release study of fluorescein-labeled BSA, which showed quantitative release after 25 days.

Hubbell and co-workers (*133*) examined the formation of hydrolytically degradable PEG hydrogels via thiol−ene coupling. They used a four-armed and eight-armed PEG spacer functionalized with acrylate end groups and either dithiothreitol or PEG-dithiol as cross-linking agents. The hydrogels were prepared by mixing the acrylate-functionalized star-shaped PEG and dithiol in 1:1 stoichiometric ratio in PBS (pH 7.8) and incubated overnight at 37 °C to ensure complete conversion. The PEG-acrylate contains an ester bond that can be cleaved by chemical hydrolysis. The presence of the thioether group in the proximity of the PEG-acrylate ester greatly increases the sensitivity of the ester toward hydrolysis by several orders of magnitude (*134*). By altering the molecular weight of the PEG derivative, or by varying the concentration of either the cross-linker or the PEG-acrylate molecules, resulted in hydrogels with swelling ratios. The different swelling ratios also resulted in different degradation kinetics.

Feijen and co-workers (*135, 136*) synthesized biodegradable dextran hydrogels by thiol−ene coupling. The dextran hydrogels were formed in situ by mixing solutions of vinylsulfone dextran **59** (Scheme 14) and tetramercapto four-armed star poly(ethylene glycol) **60**. The degradation time of hydrogels **61** could be tailored by varying the length of the spacer of the dextran polymers and the degree of vinylsulfone substitution. To study the versatility of these gels as a drug delivery system, four model proteins (immunoglobulin, bovine serum albumin, lysozyme, and fibroblast growth factor) were entrapped inside the gel. The release of the proteins did not show a burst effect and depended on the degree of vinylsulfone substitution and dextran molecular weight.

Hoffman and co-workers (*137*) used the thiol−ene coupling method to synthesize heparin-based hydrogels. In their approach, heparin was first reacted with EDC/HOBt and an excess of cysteamine to obtain thiol-functionalized heparin. PEG-diacrylate was used as the cross-linking agent. The mechanical properties and gelation kinetics of the hydrogels could be tailored by the degree of thiol group substitution of heparin. The heparin-based hydrogels were degraded at physiological pH by chemical hydrolysis of the ester bond present in the PEG diacrylate cross-linker. To prove that the hydrogels are compatible with cells, the hydrogels were gelated in the presence of fibroblasts. After gelation, most of the cells (95%) retained their viability.

CONCLUSIONS

The CuAAC reaction as well as thiol−ene coupling reaction as discussed in this review allow the synthesis of well-defined polymers with tailored properties and provide very attractive possibilities for (bio)conjugation reactions. Several examples of the synthesis and applications of biomedical and pharmaceutical polymers synthesized by the CuAAC, the thiol−ene reaction, or a combination of both reactions were highlighted. In recent years, the CuAAC and thiol−ene reactions have been used to synthesize polymers with different architectures. e.g., block and graft polymers, dendrimers, and hydrogels, for pharmaceutical and biomedical polymers. Although the CuAAC and thiol−ene reactions have many advantages, they also have some drawbacks. The CuAAC reaction requires the need of a cytotoxic copper catalyst, which is sometimes difficult to remove, while the free thiol needed for the thiol−ene reaction is susceptible to oxidation. The development of new variations of these "click reactions", such as the strain-promoted click reaction, can address the problem of cytotoxic copper catalyst. Nevertheless, both the CuAAC and thiol−ene reactions have acquired central positions in the synthesis of polymers for biomedical and pharmaceutical applications, and it is expected that their importance for the design and synthesis of such polymers will increase rapidly in the coming years.

LITERATURE CITED

(1) Deming, T. J. (1997) Polypeptide materials: New synthetic methods and applications. *Adv. Mater. 9*, 299–311.
(2) Kolb, H. C., Finn, M. G., and Sharpless, K. B. (2001) Click chemistry: diverse chemical function from a few good reactions. *Angew. Chem., Int. Ed. 40*, 2004–21.
(3) Gacal, B., Durmaz, H., Tasdeln, M. A., Hizal, G., Tunca, U., Yagci, Y., and Demirel, A. L. (2006) Anthracene-maleimide-based Diels-Alder "click chemistry" as a novel route to graft copolymers. *Macromolecules 39*, 5330–6.
(4) Posner, T. (1905) Beiträge zur Kenntniss der ungesättigten Verbindungen. II. Ueber die Addition von Mercaptanen an ungesättigte Kohlenwasserstoffe. *Chem. Ber. 38*, 646–57.
(5) Saxon, E., Armstrong, J. I., and Bertozzi, C. R. (2000) A "traceless" Staudinger ligation for the chemoselective synthesis of amide bonds. *Org. Lett. 2*, 2141–3.
(6) Nilsson, B. L., Kiessling, L. L., and Raines, R. T. (2000) Staudinger ligation: A peptide from a thioester and azide. *Org. Lett. 2*, 1939–41.
(7) Saxon, E., and Bertozzi, C. R. (2000) Cell surface engineering by a modified Staudinger reaction. *Science 287*, 2007–10.
(8) Dawson, P. E., Muir, T. W., Clark-Lewis, I., and Kent, S. B. H. (1994) Synthesis of proteins by native chemical ligation. *Science 266*, 776–9.
(9) Ruttekolk, I. R., Duchardt, F., Fischer, R., Wiesmuller, K. H., Rademann, J., and Brock, R. (2008) HPMA as a scaffold for the modular assembly of functional peptide polymers by native chemical ligation. *Bioconjugate Chem. 19*, 2081–7.
(10) Shangguan, N., Katukojvala, S., Greenburg, R., and Williams, L. J. (2003) The reaction of thio acids with azides: A new mechanism and new synthetic applications. *J. Am. Chem. Soc. 125*, 7754–5.
(11) Merkx, R., Brouwer, A. J., Rijkers, D. T. S., and Liskamp, R. M. J. (2005) Highly efficient coupling of beta-substituted aminoethane sulfonyl azides with thio acids, toward a new chemical ligation reaction. *Org. Lett. 7*, 1125–8.
(12) Kolakowski, R. V., Shangguan, N., Sauers, R. R., and Williams, L. J. (2006) Mechanism of thio acid/azide amidation. *J. Am. Chem. Soc. 128*, 5695–702.
(13) Barlett, K. N., Kolakowski, R. V., Katukojvala, S., and Williams, L. J. (2006) Thio acid/azide amidation: An improved route to N-acyl sulfonamides. *Org. Lett. 8*, 823–6.
(14) Merkx, R., van Haren, M. J., Rijkers, D. T. S., and Liskamp, R. M. (2007) Resin-bound sulfonyl azides: efficient loading and activation strategy for the preparation of the N-acyl sulfonamide linker. *J. Org. Chem. 72*, 4574–7.
(15) Zhang, X., Li, F., Lu, X. W., and Liu, C. F. (2009) Protein C-terminal modification through thioacid/azide amidation. *Bioconjugate Chem. 20*, 197–200.

(16) Tornøe, C. W., Meldal, M. (2001) Peptidotriazoles: Copper(I)-catalyzed 1,3-dipolar cycloadditions on solid phase. In *Peptides: The Wave of the Future: Proceedings of the 2nd International and the 17th American Peptide Symposium*; Lebl, M., and Houghten, R. A. Eds.; American Peptide Society and Kluwer Academic Publishers: San Diego, 263−4.
(17) Tornøe, C. W., Christensen, C., and Meldal, M. (2002) Peptidotriazoles on solid phase: [1,2,3]-triazoles by regiospecific copper(I)-catalyzed 1,3-dipolar cycloadditions of terminal alkynes to azides. *J. Org. Chem. 67*, 3057–64.
(18) Rostovtsev, V. V., Green, L. G., Fokin, V. V., and Sharpless, K. B. (2002) A stepwise Huisgen cycloaddition process: Copper(I)-catalyzed regioselective "ligation" of azides and terminal alkynes. *Angew. Chem., Int. Ed. 41*, 2596–9.
(19) Binder, W. H., and Sachsenhofer, R. (2007) 'Click' chemistry in polymer and materials science. *Macromol. Rapid Commun. 28*, 15–54.
(20) Binder, W. H., and Sachsenhofer, R. (2008) 'Click' chemistry in polymer and material science: An update. *Macromol. Rapid Commun. 29*, 952–81.
(21) Meldal, M. (2008) Polymer "Clicking" by CuAAC reactions. *Macromol. Rapid Commun. 29*, 1016–51.
(22) Nandivada, H., Jiang, X. W., and Lahann, J. (2007) Click chemistry: Versatility and control in the hands of materials scientists. *Adv. Mater. 19*, 2197–208.
(23) Lutz, J. F. (2007) 1,3-dipolar cycloadditions of azides and alkynes: A universal ligation tool in polymer and materials science. *Angew. Chem., Int. Ed. 46*, 1018–25.
(24) Johnson, J. A., Finn, M. G., Koberstein, J. T., and Turro, N. J. (2008) Construction of linear polymers, dendrimers, networks, and other polymeric architectures by copper-catalyzed azide-alkyne cycloaddition "Click" chemistry. *Macromol. Rapid Commun. 29*, 1052–72.
(25) Angell, Y. L., and Burgess, K. (2007) Peptidomimetics via copper-catalyzed azide-alkyne cycloadditions. *Chem. Soc. Rev. 36*, 1674–89.
(26) Pieters, R. J., Rijkers, D. T. S., and Liskamp, R. M. J. (2007) Application of the 1,3-dipolar cycloaddition reaction in chemical biology: Approaches toward multivalent carbohydrates and peptides and peptide-based polymers. *QSAR Comb. Sci. 26*, 1181–90.
(27) Dirks, A. J., Cornelissen, J. J. L. M., van Delft, F. L., van Hest, J. C. M., Nolte, R. J. M., Rowan, A. E., and Rutjes, F. P. J. T. (2007) From (bio)molecules to biohybrid materials with the click chemistry approach. *QSAR Comb. Sci. 26*, 1200–10.
(28) Le Droumaguet, B., and Velonia, K. (2008) Click chemistry: A powerful tool to create polymer-based macromolecular chimeras. *Macromol. Rapid Commun. 29*, 1073–89.
(29) Lutz, J. F., and Zarafshani, Z. (2008) Efficient construction of therapeutics, bioconjugates, biomaterials and bioactive surfaces using azide-alkyne "click" chemistry. *Adv. Drug Delivery Rev. 60*, 958–70.
(30) Fournier, D., Hoogenboom, R., and Schubert, U. S. (2007) Clicking polymers: a straightforward approach to novel macromolecular architectures. *Chem. Soc. Rev. 36*, 1369–80.
(31) Read, E. S., and Armes, S. P. (2007) Recent advances in shell cross-linked micelles. *Chem. Commun.* 3021–35.
(32) Lecomte, P., Riva, R., Jerome, C., and Jerome, R. (2008) Macromolecular engineering of biodegradable polyesters by ring-opening polymerization and 'Click' chemistry. *Macromol. Rapid Commun. 29*, 982–97.
(33) Lutz, J. F. (2008) Copper-free azide-alkyne cycloadditions: New insights and perspectives. *Angew. Chem., Int. Ed. 47*, 2182–4.
(34) Meldal, M., and Tornøe, C. W. (2008) Cu-catalyzed azide-alkyne cycloaddition. *Chem. Rev. 108*, 2952–3015.
(35) Bock, V. D., Hiemstra, H., and van Maarseveen, J. H. (2005) Cu(I)-catalyzed alkyne-azide "click" cycloadditions from a mechanistic and synthetic perspective. *Eur. J. Org. Chem.* 51–68.
(36) Moses, J. E., and Moorhouse, A. D. (2007) The growing applications of click chemistry. *Chem. Soc. Rev. 36*, 1249–62.
(37) Moorhouse, A. D., and Moses, J. E. (2008) Click chemistry and medicinal chemistry: a case of "cyclo-addiction". *ChemMedChem 3*, 715–23.
(38) Huisgen, R. (1968) Cycloadditions - definition, classification, and characterization. *Angew. Chem., Int. Ed. Engl. 7*, 321–8.
(39) Huisgen, R., Szeimies, G., and Mobius, L. (1967) 1.3-Dipolare Cycloadditionen, XXXII. Kinetik der Additionen organischer Azide an CC-Mehrfachbindungen. *Chem. Ber. 100*, 2494–507.
(40) Horne, W. S., Yadav, M. K., Stout, C. D., and Ghadiri, M. R. (2004) Heterocyclic peptide backbone modifications in an alpha-helical coiled coil. *J. Am. Chem. Soc. 126*, 15366–7.
(41) Angelo, N. G., and Arora, P. S. (2005) Nonpeptidic foldamers from amino acids: Synthesis and characterization of 1,3-substituted triazole oligomers. *J. Am. Chem. Soc. 127*, 17134–5.
(42) van Maarseveen, J. H., Horne, W. S., and Ghadiri, M. R. (2005) Efficient route to C2 symmetric heterocyclic backbone modified cyclic peptides. *Org. Lett. 7*, 4503–6.
(43) Wittig, G., and Krebs, A. (1961) Zur Existenz niedergliedriger Cycloalkine, I. *Chem. Ber. 94*, 3260–75.
(44) Agard, N. J., Prescher, J. A., and Bertozzi, C. R. (2004) A strain-promoted [3 + 2] azide-alkyne cycloaddition for covalent modification of biomolecules in living systems. *J. Am. Chem. Soc. 126*, 15046–7.
(45) Ning, X. H., Guo, J., Wolfert, M. A., and Boons, G. J. (2008) Visualizing metabolically labeled glycoconjugates of living cells by copper-free and fast Huisgen cycloadditions. *Angew. Chem., Int. Ed. 47*, 2253–5.
(46) Codelli, J. A., Baskin, J. M., Agard, N. J., and Bertozzi, C. R. (2008) Second-generation difluorinated cyclooctynes for copper-free click chemistry. *J. Am. Chem. Soc. 130*, 11486–93.
(47) Sletten, E. M., and Bertozzi, C. R. (2008) A hydrophilic azacyclooctyne for Cu-free click chemistry. *Org. Lett. 10*, 3097–9.
(48) Baskin, J. M., Prescher, J. A., Laughlin, S. T., Agard, N. J., Chang, P. V., Miller, I. A., Lo, A., Codelli, J. A., and Bertozzi, C. R. (2007) Copper-free click chemistry for dynamic in vivo imaging. *Proc. Natl. Acad. Sci. U.S.A. 104*, 16793–7.
(49) van Berkel, S. S., Dirks, A. T., Debets, M. F., van Delft, F. L., Cornelissen, J. J. L. M., Nolte, R. J. M., and Rutjes, F. P. J. T. (2007) Metal-free triazole formation as a tool for bioconjugation. *ChemBioChem 8*, 1504–8.
(50) Mocharla, V. P., Colasson, B., Lee, L. V., Roper, S., Sharpless, K. B., Wong, C. H., and Kolb, H. C. (2004) In situ click chemistry: enzyme-generated inhibitors of carbonic anhydrase II. *Angew. Chem., Int. Ed. 44*, 116–20.
(51) Zhang, L., Chen, X. G., Xue, P., Sun, H. H. Y., Williams, I. D., Sharpless, K. B., Fokin, V. V., and Jia, G. C. (2005) Ruthenium-catalyzed cycloaddition of alkynes and organic azides. *J. Am. Chem. Soc. 127*, 15998–9.
(52) Majireck, M. M., and Weinreb, S. M. (2006) A study of the scope and regioselectivity of the ruthenium-catalyzed [3 + 2]-cycloaddition of azides with internal alkynes. *J. Org. Chem. 71*, 8680–3.
(53) Rasmussen, L. K., Boren, B. C., and Fokin, V. V. (2007) Ruthenium-catalyzed cycloaddition of aryl azides and alkynes. *Org. Lett. 9*, 5337–9.
(54) Boren, B. C., Narayan, S., Rasmussen, L. K., Zhang, L., Zhao, H. T., Lin, Z. Y., Jia, G. C., and Fokin, V. V. (2008) Ruthenium-catalyzed azide-alkyne cycloaddition: Scope and mechanism. *J. Am. Chem. Soc. 130*, 8923–30 (correction: *J. Am. Chem. Soc.*, 14900).
(55) Jemal, M., and Hawthorne, D. J. (1997) Quantitative determination of BMS186716, a thiol compound, in dog plasma by high-performance liquid chromatography-positive ion electrospray mass spectrometry after formation of the methyl acrylate adduct. *J. Chromatogr., B: Biomed. Sci. Appl. 693*, 109–16.
(56) Romanowska, A., Meunier, S. J., Tropper, F. D., Laferriere, C. A., and Roy, R. (1994) Michael additions for syntheses of neoglycoproteins. *Methods Enzymol. 242*, 90–101.
(57) Masri, M. S., and Friedman, M. (1988) Protein reactions with methyl and ethyl vinyl sulfones. *J. Protein Chem. 7*, 49–54.
(58) Morpurgo, M., Veronese, F. M., Kachensky, D., and Harris, J. M. (1996) Preparation of characterization of poly(ethylene glycol) vinyl sulfone. *Bioconjugate Chem. 7*, 363–8.

(59) Pounder, R. J., Stanford, M. J., Brooks, P., Richards, S. P., and Dove, A. P. (2008) Metal free thiol-maleimide 'Click' reaction as a mild functionalisation strategy for degradable polymers. *Chem. Commun.* 5158–60.
(60) Gress, A., Volkel, A., and Schlaad, H. (2007) Thio-click modification of poly[2-(3-butenyl)-2-oxazoline]. *Macromolecules 40*, 7928–33.
(61) Dondoni, A. (2008) The emergence of thiol-ene coupling as a click process for materials and bioorganic chemistry. *Angew. Chem., Int. Ed. 47*, 8995–7.
(62) Geng, Y., Discher, D. E., Justynska, J., and Schlaad, H. (2006) Grafting short peptides onto polybutadiene-block-poly(ethylene oxide): A platform for self-assembling hybrid amphiphiles. *Angew. Chem., Int. Ed. 45*, 7578–81.
(63) Hordyjewicz-Baran, Z., You, L. C., Smarsly, B., Sigel, R., and Schlaad, H. (2007) Bioinspired polymer vesicles based on hydrophilically modified polybutadienes. *Macromolecules 40*, 3901–3.
(64) Justynska, J., Hordyjewicz, Z., and Schlaad, H. (2005) Toward a toolbox of functional block copolymers via free-radical addition of mercaptans. *Polymer 46*, 12057–64.
(65) Woghiren, C., Sharma, B., and Stein, S. (1993) Protected thiol-polyethylene glycol: a new activated polymer for reversible protein modification. *Bioconjugate Chem. 4*, 314–8.
(66) Goessl, A., Tirelli, N., and Hubbell, J. A. (2004) A hydrogel system for stimulus-responsive, oxygen-sensitive in situ gelation. *J. Biomater. Sci. Polym. Ed. 15*, 895–904.
(67) Hoyle, C. E., Lee, T. Y., and Roper, T. (2004) Thiol-enes: Chemistry of the past with promise for the future. *J. Polym. Sci., Part A: Polym. Chem. 42*, 5301–38.
(68) Morgan, C. R., Magnotta, F., and Ketley, A. D. (1977) Thiol/ene photocurable polymers. *J. Polym. Sci., Polym. Chem. Ed. 15*, 627–45.
(69) van Hest, J. C. M., and Tirrell, D. A. (2001) Protein-based materials, toward a new level of structural control. *Chem. Commun.* 1897–904.
(70) Kricheldorf, H. R. (1987) *Alpha-Aminoacid-N-Carboxyanhydrides and Related Heterocycles*, Springer, Berlin.
(71) Chiu, H. C., Kopeckova, P., Deshmane, S. S., and Kopecek, J. (1997) Lysosomal degradability of poly(alpha-amino acids). *J. Biomed. Mater. Res. 34*, 381–92.
(72) Metzke, M., O'Connor, N., Maiti, S., Nelson, E., and Guan, Z. B. (2005) Saccharide-peptide hybrid copolymers as biomaterials. *Angew. Chem., Int. Ed. 44*, 6529–33.
(73) Haider, M., Megeed, Z., and Ghandehari, H. (2004) Genetically engineered polymers: status and prospects for controlled release. *J. Controlled Release 95*, 1–26.
(74) Kent, S. B. H. (2009) Total chemical synthesis of proteins. *Chem. Soc. Rev. 38*, 338–51.
(75) Zhang, Z. S., and Fan, E. (2006) Solid phase synthesis of peptidotriazoles with multiple cycles of triazole formation. *Tetrahedron Lett. 47*, 665–9.
(76) Aucagne, V., and Leigh, D. A. (2006) Chemoselective formation of successive triazole linkages in one pot: " Click-click" chemistry. *Org. Lett. 8*, 4505–7.
(77) Orsini, A., Viterisi, A., Bodlenner, A., Weibel, J.-M., and Pale, P. (2005) A chemoselective deprotection of trimethylsilyl acetylenes catalyzed by silver salts. *Tetrahedron Lett. 46*, 2259–62.
(78) Carpita, A., Mannocci, L., and, and Rossi, R. (2005) Silver(I)-catalysed protiodesilylation of 1-(trimethylsilyl)-1-alkynes. *Eur. J. Org. Chem.* 1859–64.
(79) van Dijk, M., Mustafa, K., Dechesne, A. C., van Nostrum, C. F., Hennink, W. E., Rijkers, D. T. S., and Liskamp, R. M. J. (2007) Synthesis of peptide-based polymers by microwave-assisted cycloaddition backbone polymerization. *Biomacromolecules 8*, 327–30.
(80) van Dijk, M., Nollet, M. L., Weijers, P., Dechesne, A. C., van Nostrum, C. F., Hennink, W. E., Rijkers, D. T. S., and Liskamp, R. M. J. (2008) Synthesis and characterization of biodegradable peptide-based polymers prepared by microwave-assisted click chemistry. *Biomacromolecules 9*, 2834–43.
(81) Yu, T.-B., Bai, J. Z., and Guan, Z. (2009) Cycloaddition-promoted self-assembly of a polymer into well-defined β sheets and hierarchical nanofibrils. *Angew. Chem., Int. Ed. 48*, 1097–101.
(82) Agut, W., Agnaou, R., Lecommandoux, S., and Taton, D. (2008) Synthesis of block copolypeptides by click chemistry. *Macromol. Rapid Commun. 29*, 1147–55.
(83) Parrish, B., Breitenkamp, R. B., and Emrick, T. (2005) PEG- and peptide-grafted aliphatic polyesters by click chemistry. *J. Am. Chem. Soc. 127*, 7404–10.
(84) Tirrell, D. A. (2004) Chemical biology - Hitting the sweet spot. *Nature 430*, 837.
(85) Dwek, R. A. (1996) Glycobiology: Toward understanding the function of sugars. *Chem. Rev. 96*, 683–720.
(86) Kiessling, L. L., and Cairo, C. W. (2002) Hitting the sweet spot. *Nat. Biotechnol. 20*, 234–5.
(87) Ambrosi, M., Cameron, N. R., and Davis, B. G. (2005) Lectins: tools for the molecular understanding of the glycocode. *Org. Biomol. Chem. 3*, 1593–608.
(88) Lundquist, J. J., and Toone, E. J. (2002) The cluster glycoside effect. *Chem. Rev. 102*, 555–78.
(89) Srinivasachari, S., Liu, Y. M., Zhang, G. D., Prevette, L., and Reineke, T. M. (2006) Trehalose click polymers inhibit nanoparticle aggregation and promote pDNA delivery in serum. *J. Am. Chem. Soc. 128*, 8176–84.
(90) Srinivasachari, S., Liu, Y. M., Prevette, L. E., and Reineke, T. M. (2007) Effects of trehalose click polymer length on pDNA complex stability and delivery efficacy. *Biomaterials 28*, 2885–98.
(91) Ladmiral, V., Mantovani, G., Clarkson, G. J., Cauet, S., Irwin, J. L., and Haddleton, D. M. (2006) Synthesis of neoglycopolymers by a combination of "click chemistry" and living radical polymerization. *J. Am. Chem. Soc. 128*, 4823–30.
(92) Geng, J., Mantovani, G., Tao, L., Nicolas, J., Chen, G., Wallis, R., Mitchell, D. A., Johnson, B. R., Evans, S. D., and Haddleton, D. M. (2007) Site-directed conjugation of "clicked" glycopolymers to form glycoprotein mimics: binding to mammalian lectin and induction of immunological function. *J. Am. Chem. Soc. 129*, 15156–63.
(93) Chen, G. J., Amajjahe, S., and Stenzel, M. H. (2009) Synthesis of thiol-linked neoglycopolymers and thermo-responsive glycomicelles as potential drug carrier. *Chem. Commun.* 1198–200.
(94) Diehl, C., and Schlaad, H. (2009) Thermo-responsive polyoxazolines with widely tuneable LCST. *Macromol. Biosci. 9*, 157–61.
(95) Nurmi, L., Lindqvist, J., Randev, R., Syrett, J., and Haddleton, D. M. (2009) Glycopolymers via ctalytic chain transfer polymerisation (CCTP), huisgens cycloaddition and thiol-ene double click reactions. *Chem. Commun.* 2727–9.
(96) El-Aneed, A. (2004) Current strategies in cancer gene therapy. *Eur. J. Pharmacol. 498*, 1–8.
(97) Zhou, H. S., Liu, D. P., and Liang, C. C. (2004) Challenges and strategies: the immune responses in gene therapy. *Med. Res. Rev. 24*, 748–61.
(98) Mintzer, M. A., and Simanek, E. E. (2009) Nonviral vectors for gene delivery. *Chem. Rev. 109*, 259–302.
(99) White, S., Szewczyk, J. W., Turner, J. M., Baird, E. E., and Dervan, P. B. (1998) Recognition of the four Watson-Crick base pairs in the DNA minor groove by synthetic ligands. *Nature 391*, 468–71.
(100) Petersen, H., Merdan, T., Kunath, K., Fischer, D., and Kissel, T. (2002) Poly(ethylenimine-co-L-lactamide-co-succinamide): a biodegradable polyethylenimine derivative with an advantageous pH-dependent hydrolytic degradation for gene delivery. *Bioconjugate Chem. 13*, 812–21.
(101) Luten, J., van Nostrum, C. F., De Smedt, S. C., and Hennink, W. E. (2008) Biodegradable polymers as non-viral carriers for plasmid DNA delivery. *J. Controlled Release 126*, 97–110.
(102) Jiang, X., Lok, M. C., and Hennink, W. E. (2007) Degradable-brushed pHEMA-pDMAEMA synthesized via ATRP and click chemistry for gene delivery. *Bioconjugate Chem. 18*, 2077–84.
(103) Varki, A. (1993) Biological roles of oligosaccharides: all of the theories are correct. *Glycobiology 3*, 97–130.

(104) Kramer, R. H., and Karpen, J. W. (1998) Spanning binding sites on allosteric proteins with polymer-linked ligand dimers. *Nature 395*, 710–3.

(105) Mammen, M., Choi, S.-K., and Whitesides, G. M. (1998) Polyvalent interactions in biological systems: implications for design and use of multivalent ligands and inhibitors. *Angew. Chem., Int. Ed. 37*, 2754–94.

(106) Joosten, J. A. F., Tholen, N. T. H., El Maate, F. A., Brouwer, A. J., van Esse, G. W., Rijkers, D. T. S., Liskamp, R. M. J., and Pieters, R. J. (2005) High-yielding microwave-assisted synthesis of triazole-linked glycodendrimers by copper-catalyzed [3 + 2] cycloaddition. *Eur. J. Org. Chem.* 3182–5.

(107) Rijkers, D. T. S., van Esse, G. W., Merkx, R., Brouwer, A. J., Jacobs, H. J. J., Pieters, R. J., and Liskamp, R. M. J. (2005) Efficient microwave-assisted synthesis of multivalent dendrimeric peptides using cycloaddition reaction (click) chemistry. *Chem. Commun.* 4581–3.

(108) Dijkgraaf, I., Rijnders, A. Y., Soede, A., Dechesne, A. C., van Esse, G. W., Brouwer, A. J., Corstens, F. H., Boerman, O. C., Rijkers, D. T. S., and Liskamp, R. M. J. (2007) Synthesis of DOTA-conjugated multivalent cyclic-RGD peptide dendrimers via 1,3-dipolar cycloaddition and their biological evaluation: implications for tumor targeting and tumor imaging purposes. *Org. Biomol. Chem. 5*, 935–44.

(109) Killops, K. L., Campos, L. M., and Hawker, C. J. (2008) Robust, efficient, and orthogonal synthesis of dendrimers via thiol-ene "click" chemistry. *J. Am. Chem. Soc. 130*, 5062–4.

(110) Jonkheijm, P., Weinrich, D., Kohn, M., Engelkamp, H., Christianen, P. C., Kuhlmann, J., Maan, J. C., Nusse, D., Schroeder, H., Wacker, R., Breinbauer, R., Niemeyer, C. M., and Waldmann, H. (2008) Photochemical surface patterning by the thiol-ene reaction. *Angew. Chem., Int. Ed. 47*, 4421–4.

(111) Xia, Y. N. (2008) Nanomaterials at work in biomedical research. *Nat. Mater. 7*, 758–60.

(112) Schiffelers, R. M., Ansari, A., Xu, J., Zhou, Q., Tang, Q., Storm, G., Molema, G., Lu, P. Y., Scaria, P. V., and Woodle, M. C. (2004) Cancer siRNA therapy by tumor selective delivery with ligand-targeted sterically stabilized nanoparticle. *Nucleic Acids Res. 32*, e149.

(113) Panyam, J., and Labhasetwar, V. (2003) Biodegradable nanoparticles for drug and gene delivery to cells and tissue. *Adv. Drug Delivery Rev. 55*, 329–47.

(114) Opsteen, J. A., Brinkhuis, R. P., Teeuwen, R. L. M., Löwik, D. W. P. M., and van Hest, J. C. M. (2007) "Clickable" polymersomes. *Chem. Commun.* 3136–8.

(115) Such, G. K., Quinn, J. F., Quinn, A., Tjipto, E., and Caruso, F. (2006) Assembly of ultrathin polymer multilayer films by click chemistry. *J. Am. Chem. Soc. 128*, 9318–9.

(116) Such, G. K., Tjipto, E., Postma, A., Johnston, A. P., and Caruso, F. (2007) Ultrathin, responsive polymer click capsules. *Nano Lett. 7*, 1706–10.

(117) De Geest, B. G., Van Camp, W., Du Prez, F. E., De Smedt, S. C., Demeester, J., and Hennink, W. E. (2008) Degradable multilayer films and hollow capsules via a 'click' strategy. *Macromol. Rapid Commun. 29*, 1111–8.

(118) De Geest, B. G., Van Camp, W., Du Prez, F. E., De Smedt, S. C., Demeester, J., and Hennink, W. E. (2008) Biodegradable microcapsules designed via 'click' chemistry. *Chem. Commun.* 190–2.

(119) Connal, L. A., Kinnane, C. R., Zelikin, A. N., and Caruso, F. (2009) Stabilization and functionalization of polymer multilayers and capsules via thiol-ene click chemistry. *Chem. Mater. 21*, 576–8.

(120) Sousa-Herves, A., Fernandez-Megia, E., and Riguera, R. (2008) Synthesis and supramolecular assembly of clicked anionic dendritic polymers into polyion complex micelles. *Chem. Commun.* 3136–8.

(121) Breed, D. R., Thibault, R., Xie, F., Wang, Q., Hawker, C. J., and Pine, D. J. (2009) Functionalization of polymer microspheres using click chemistry. *Langmuir 25*, 4370–6.

(122) Peppas, N. A., Bures, P., Leobandung, W., and Ichikawa, H. (2000) Hydrogels in pharmaceutical formulations. *Eur. J. Pharm. Biopharm. 50*, 27–46.

(123) Ossipov, D. A., and Hilborn, J. (2006) Poly(vinyl alcohol)-based hydrogels formed by "click chemistry". *Macromolecules 39*, 1709–18.

(124) Malkoch, M., Vestberg, R., Gupta, N., Mespouille, L., Dubois, P., Mason, A. F., Hedrick, J. L., Liao, Q., Frank, C. W., Kingsbury, K., and Hawker, C. J. (2006) Synthesis of well-defined hydrogel networks using Click chemistry. *Chem. Commun.* 2774–6.

(125) Crescenzi, V., Cornelio, L., Di Meo, C., Nardecchia, S., and Lamanna, R. (2007) Novel hydrogels via click chemistry: Synthesis and potential biomedical applications. *Biomacromolecules 8*, 1844–50.

(126) Polizzotti, B. D., Fairbanks, B. D., and Anseth, K. S. (2008) Three-dimensional biochemical patterning of click-based composite hydrogels via thiolene photopolymerization. *Biomacromolecules 9*, 1084–7.

(127) Mespouille, L., Coulembier, O., Paneva, D., Degée, E., Rashkov, I., and Dubois, P. (2008) Synthesis of adaptative and amphiphilic polymer model conetworks by versatile combination of ATRP, ROP and "click chemistry". *J. Polym. Sci., Part A: Polym. Chem. 46*, 4997–5013.

(128) Johnson, J. A., Finn, M. G., Koberstein, J. T., and Turro, N. J. (2007) Synthesis of photocleavable linear macromonomers by ATRP and star macromonomers by a tandem ATRP-click reaction: precursors to photodegradable model networks. *Macromolecules 40*, 3589–98.

(129) Johnson, J. A., Baskin, J. M., Bertozzi, C. R., Koberstein, J. T., and Turro, N. J. (2008) Copper-free click chemistry for the in situ crosslinking of photodegradable star polymers. *Chem. Commun.* 3064–6.

(130) Xu, X., Chen, C., Wang, Z., Wang, G., Cheng, S., Zhang, X., and Zhou, R. (2008) "Click" chemistry for in situ formation of thermoresponsive p(NIPAAm-co-HEMA)-based hydrogels. *J. Polym. Sci., Part A: Polym. Chem. 46*, 5263–77.

(131) Lui, S. Q., Ee, P. L. R., Ke, C. Y., Hendrick, J. L., and Yang, Y. Y. (2009) Biodegradable poly(ethylene glycol)-peptide hydrogels with well-defined structure and properties for cell delivery. *Biomaterials 30*, 1453–61.

(132) Qiu, B., Stefanos, S., Ma, J., Lalloo, A., Perry, B. A., Leibowitz, M. J., Sinko, P. J., and Stein, S. (2003) A hydrogel prepared by in situ cross-linking of a thiol-containing poly(ethylene glycol)-based copolymer: a new biomaterial for protein drug delivery. *Biomaterials 24*, 11–8.

(133) Metters, A., and Hubbell, J. (2005) Network formation and degradation behavior of hydrogels formed by Michael-type addition reactions. *Biomacromolecules 6*, 290–301.

(134) Schoenmakers, R. G., van de Wetering, P., Elbert, D. L., and Hubbell, J. A. (2004) The effect of the linker on the hydrolysis rate of drug-linked ester bonds. *J. Controlled Release 95*, 291–300.

(135) Hiemstra, C., Zhong, Z., Van Tomme, S. R., van Steenbergen, M. J., Jacobs, J. J. L., Den Otter, W., Hennink, W. E., and Feijen, J. (2007) In vitro and in vivo protein delivery from in situ forming poly(ethylene glycol)-poly(lactide) hydrogels. *J. Controlled Release 119*, 320–7.

(136) Hiemstra, C., van der Aa, L. J., Zhong, Z. Y., Dijkstra, P. J., and Feijen, J. (2007) Novel in situ forming, degradable dextran hydrogels by Michael addition chemistry: Synthesis, rheology, and degradation. *Macromolecules 40*, 1165–73.

(137) Tae, G., Kim, Y. J., Choi, W. I., Kim, M., Stayton, P. S., and Hoffman, A. S. (2007) Formation of a novel heparin-based hydrogel in the presence of heparin-binding biomolecules. *Biomacromolecules 8*, 1979–86.

BC900087A

COMMUNICATIONS

Cationic Glyco-Functionalized Single-Walled Carbon Nanotubes as Efficient Gene Delivery Vehicles

Marya Ahmed, Xiaoze Jiang, Zhicheng Deng, and Ravin Narain*

Department of Chemical and Materials Engineering, ECERF, University of Alberta, Edmonton, Alberta T6G 2G6, Canada, and Department of Chemistry and Biochemistry, Biomolecular Sciences Program, Laurentian University, 935 Ramsey Lake Road, Sudbury, Ontario P3E 2C6, Canada. Received May 29, 2009; Revised Manuscript Received September 16, 2009

Carbon nanotubes are an emerging class of nanomaterials that are receiving enormous attention in the field of biomedicines due to their biocompatibility, degradability, cell penetrating abilities, and, more specifically, their remarkable ability to localize in the nucleus of the cell without the need of nuclear localizing signals. They are used as drug and gene delivery agent for *in vitro* studies; however, their transfection efficiencies *in vitro* are still questionable. We report here the surface functionalization of single-walled carbon nanotubes (SWNTs) with cationic glycopolymers and their use as an *in vitro* gene transfer agent. The copolymer modified SWNTs are found to be biocompatible and exhibit transfection efficiencies that are comparable to the commercially available agent lipofectamine 2000.

The research efforts focused on the improvement of synthetic gene delivery vectors have led to the exploration of a variety of nanomaterials. The carbon nanotubes, although comparatively recent in the race, present important characteristics desirable for gene delivery purposes (*1*). They are reported to be non-cytotoxic, can mediate endocytosis, and are biodegradable. All these properties make them ideal for a gene delivery scaffold (*2*−*6*). Although a handful of reports mention the nucleic acid delivery to the cells with the help of carbon nanotubes, their transfection efficiency and cytotoxicity issues are still not fully explored (*4, 7*−*10*). The transfection efficiencies of modified carbon nanotubes were found to be low, and very few reports present cytotoxicity data of these modified nanomaterials (*8, 11*). The extensive use of carbon nanotubes in biomedical applications is highly dependent upon their surface chemistry, biocompatibility, and water solubility. The noncovalent approaches to anchor the nucleic acids on the surfaces of nanotubes are desirable to prevent the denaturation of DNA and to enhance its release from the gene delivery scaffold inside the cell (*4, 7, 8*). Another dominating factor in designing the ideal gene delivery vehicle is its compatibility toward living tissues. The cationic polymer grafted carbon nanotubes have been produced and are shown to mediate some degree of gene transfer, but their biocompatibility towards living systems is not known (*4, 8*). An ideal approach is to fabricate the surface of carbon nanotubes with biocompatible cationic ligands to yield gene delivery systems that simultaneously render low toxicity and high gene transfer ability to living cells. Herein, we report the facile synthesis of biocompatible cationic glycopolymer functionalized single-walled carbon nanotubes (SWNTs). The SWNTs produced are then used as potential gene delivery vehicles and are found to contain the transfection efficiencies that mimic widely used commercial standard, Lipofectamine 2000, with considerably low toxicity. To the best of our knowledge, facile functionalization of carbon nanotubes with cationic glycopolymer, their long-term stability, and their use as biocompatible gene delivery agents has not yet been reported.

A variety of reports discuss the fabrication of carbon nanotubes with water-soluble polymers or biomolecules to improve their water solubility and biocompatibility (*3, 12*−*14*). The surface functionalization of nanotubes with polymers is typically obtained by two covalent approaches, namely, "grafting from" and "grafting to" techniques (*15, 16*). The comparison of the "grafting from" method with "grafting to" reveals the significance of the latter and has been used to covalently attach the biocompatible moieties such as the carbohydrate and phosphorylcholine to the surface of SWNTs with high grafting density (*13, 17*). However, the reported functionalized carbon nanotubes were prepared via the atom transfer radical polymerization (ATRP) technique, which has questions about the toxicity of the residual copper (*13*). To obtain biocompatible water-dispersible carbon nanotubes for the *in vitro* uses, the need is to fabricate the surface of carbon nanotubes with biocompatible polymers by covalent bonding. The ideal candidate for this purpose is glycopolymers, which can be grafted on the carboxylic groups present on the surface of nanotubes via "grafting to" approach. The glycopolymers bearing pendant amino groups were prepared by using monomers, 3-aminopropyl methacrylamide (APMA), 3-gluconamidopropyl methacrylamide (GAPMA), and 2-lactobionamidoethyl methacrylamide (LAEMA) by the reversible addition−fragmentation chain transfer (RAFT) method, yielding diblock copolymers, while eliminating the possible toxic effects of residual metals. The cationic block polymers thus synthesized were P($APMA_{31}$-*b*-$LAEMA_{32}$) and P($APMA_{38}$-*b*-$GAPMA_{20}$) (Supporting Information Figure S1).

* Corresponding author. narain@ualberta.ca or rnarain@laurentian.ca, Tel: 1 780 492 1736 or 1 705 675 1151 (2186), Fax: 1 780 492 2881 or 1 705 675 4844.

10.1021/bc900229v CCC: $40.75 © 2009 American Chemical Society
Published on Web 10/13/2009

Scheme 1. Carboxyl Functionalized SWNTs Are Surface Functionalized with RAFT Prepared Block Copolymers[a]

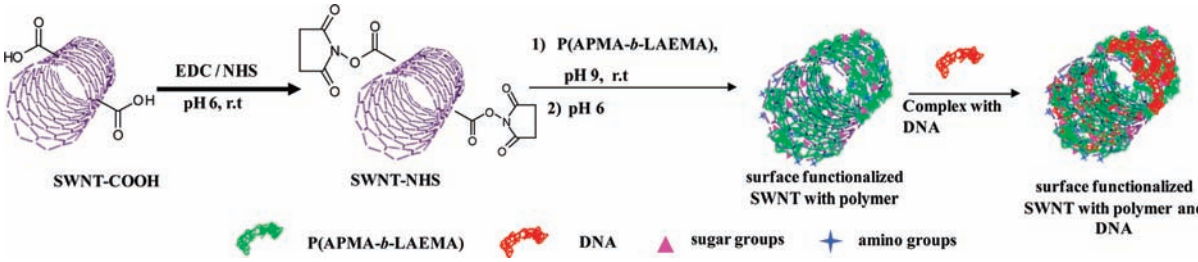

[a] The cationic glycopolymer-functionalized SWNTs are further complexed with plasmid (pEGFP).

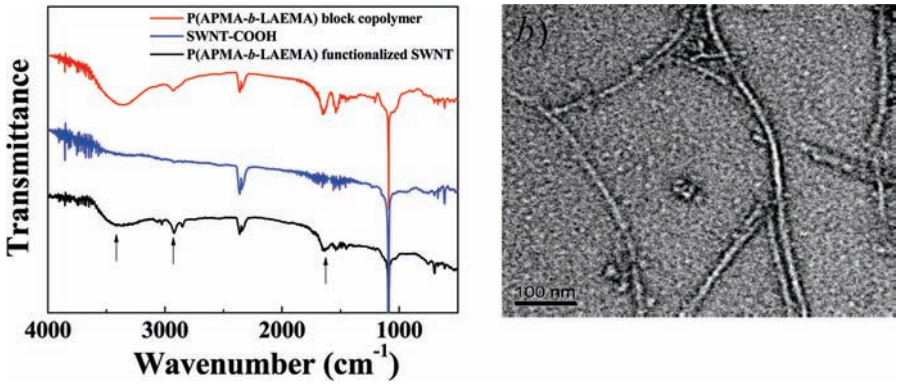

Figure 1. (a) IR absorption spectra showing the functionalization of SWNTs with P($APMA_{31}$-*b*-$LAEMA_{32}$) block copolymer (b) HRTEM image confirms the diameter of surface functionalized P($APMA_{31}$-*b*-$LAEMA_{32}$)-SWNTs.

The detailed synthesis and characterization of diblock copolymers P($APMA_{38}$-*b*-$GAPMA_{20}$) used for the functionalization of SWNTs have been reported in our group (*18*). The carboxyl groups present on the surface of SWNTs were conjugated to the amino groups of PAPMA by the 1-ethyl-3(3-dimethylaminopropyl)carbodiimide (EDC)-*N*-hydroxysuccinimide (NHS) coupling. In our experiments, the SWNTs were first sonicated for 3 h to disperse them into water. The presence of carboxyl groups on the surface increased their dispersion. The carboxyl groups on the surface were converted to succinimide-terminated surface by the addition of EDC/NHS reagents at pH 6 (Scheme 1). The cationic glycopolymers were then conjugated to the surface of SWNTs at pH 9, thus leading to the formation of surface glycopolymer functionalized SWNTs, which had high water solubility and showed no precipitation of SWNTs, even after months at room temperature. In contrast, unfunctionalized SWNTs were found to precipitate in 12 h under the same conditions. The cationic glycopolymer functionalized SWNTs were then centrifuged at 20 000 rpm for 2 h to remove the excess polymer, a technique that has largely been used in our group to purify the nanomaterials from their corresponding polymers.

The purified SWNTs were then characterized by IR spectroscopy. The comparison among original SWNTs, glycopolymers, and glycopolymer functionalized SWNTs is shown (Figure 1a). The spectrum of the original SWNTs reveals an absorbance at 1716 cm^{-1}, which is a characteristic of the carbonyl stretch of the carboxylic acid group. The subsequent functionalization of the carbon nanotubes with P($APMA_{31}$-*b*-$LAEMA_{32}$) block copolymer shows the characteristic and pronounced absorbance signals from the respective polymers. The acrylamide groups of the P(APMA-*b*-PLAEMA) block show IR absorptions bands at 3409, 2915, and 1642 cm^{-1}, and these peaks can be detected on the IR spectrum of the glycopolymer functionalized SWNTs. To further confirm the functionalization of SWNTs, UV−visible spectra were also recorded (see Supporting Information Figure S2). The spectra showed only a very small absorbance by original SWNTs solution for the presence of carboxyl groups on the surface of SWNTs. A sharp increase in the absorbance was noted for glycopolymer-functionalized SWNT in the range 200−350 nm, due to an increase in the solubility of functionalized SWNTs after the modification with water-soluble polymer chains. To determine the extent of functionalization or polymer content, the functionalized carbon nanotubes were further analyzed by thermogravimetric analysis. The polymer content was determined to be in the range 30−35% (see Supporting Information Figure 12). The functionalized SWNTs produced were assessed with high-resolution transmission electron microscopy (HRTEM), to determine the size of nanotubes after the functionalization (shown in Figure 1b). The samples were prepared by the immersion of a carbon-coated copper grid in the functionalized SWNTs aqueous solution followed by drying in vacuum. The images of functionalized SWNTs revealed an average diameter of around 20 nm.

To further explore the possible applications of glycopolymer-functionalized SWNTs for biomedical applications, the glycopolymer-functionalized SWNTs were conjugated to biotin to yield cationic glycopolymer-functionalized biotin labeled carbon nanotubes. For this purpose, the biotin-NHS was added into the glycopolymer-functionalized SWNTs solution at basic condition and stirred overnight. The purified mixture was then tested using HABA/avidin binding assay to detect the presence of biotin on the surface of functionalized SWNTs. The decrease in absorbance at 500 nm after the addition of biotinylated glycopolymer-functionalized SWNTs confirms the presence of biotin groups on the surface of functionalized SWNTs (Supporting Information Figure S3). The presence of amino groups on the surface of biocompatible cationic polymer functionalized nanotubes assures their further successful functionalization with the molecule of choice, as demonstrated with biotin. The novel synthesis of cationic glycopolymer-functionalized biotin labeled SWNTs introduces other possibilities for their use in various applications including targeted drug and gene delivery.

The extensive study of uptake mechanism of carbon nanotubes by human cells reveals the endogenous nature of this material to be endocytosed (*17, 19*). However, Jin et al. have shown that, like other nanomaterials, uptake of SWNTs by

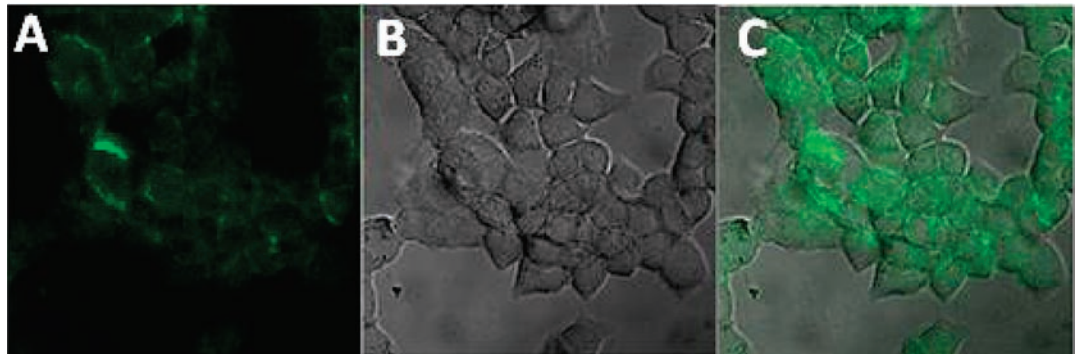

Figure 2. Confocal microscopic images of Hela cells, showing the uptake and localization of FITC-labeled-P($APMA_{31}$-*b*-$LAEMA_{32}$)-*f*-SWNTs at 37 °C. (A) Fluorescence images, (B) bright field images, (C) fluorescent image overlaid on bright field image.

human cells is also a size-dependent process (*20, 21*). The nanotubes with effective radius of 26.4 nm are found to be the most efficient in crossing the cell membrane barrier by receptor-mediated endocytosis (*20*). The glycopolymer-functionalized SWNTs prepared were studied for their cell penetrating abilities. For this purpose, 0.15 mg/mL of cationic SWNTs was first complexed with 4 μM fluorescein isothiocyanate (FITC)-labeled oligonucleotides, thus assuring the excess of the latter in the experiment. Hela cells grown on glass coverslips were incubated with FITC-oligonucleotide labeled SWNTs for 48 h, and the confocal microscopic images were obtained after extensive washing of coverslips with DPBS buffer. The images revealed the successful uptake of nanotubes by Hela cells, showing the disperse ability of nanotubes inside the cells. Although some nanotubes can be found attached to the surface of cells, most are either dispersed in the cytosol or can be traced in perinuclear regions (Figure 2). In contrast, FITC labeled oligonucleotides without SWNTs used as a control showed no fluorescent signal, when excited by laser at 490 nm to detect the presence of FITC dye.

The cytotoxicity assay was performed at different concentrations of cationic glycopolymer-functionalized SWNTs, and the results were expressed in terms of both concentration and mass of SWNTs used, for the purpose of comparison with both transfection studies and other literature (Supporting Information Figures S4 and S5). The functionalization of SWNTs with glycopolymer and glycoproteins has been reported previously (*4, 22*). The glycoprotein stabilized SWNTs are found to be involved in glycan−receptor interactions, thus binding to the surface of cell membrane, with no significant toxicity at the concentration of 0.1 mg/mL (*22*). We report the use of glycopolymer-functionalized SWNTs as gene delivery scaffolds, where the glycopolymer segment of the block copolymer not only participates in cell mediated interactions, but also masks the cationic component of the polymer to provide biocompatibility, thus eliminating the need of stealth barriers. The cytotoxicity assay of glycopolymer stabilized SWNTs reveals that, at very low concentrations of copolymer-functionalized SWNTs (4 μg/mL), the cell growth is promoted, owing to the glycopolymer segment of the functionalized nanotubes. The increase in concentration leads to the decrease in cell viability, and the cell viability is found to be ∼75% for up to 0.2 mg/mL of copolymer-functionalized SWNTs alone (Supporting Information Figures S4 and S5). Thus, it can be concluded that the carbohydrate component successfully masks the cationic character of the copolymer present on the surface of nanotubes.

As discussed earlier, the uptake of carbon nanotubes by receptor mediated endocytosis, their ability to protect DNA strands from denaturation, their ability to localize inside the nucleus, and their reported biocompatibility make them ideal vehicles for gene delivery purposes, and yet only a handful of reports discuss the gene delivery by carbon nanotubes (*4, 7−9, 23*). The comparison of efficiency of transfection is done by their corresponding polymers; for example, PEI is compared to PEI-grafted MWNTs and the latter is found to transfect at higher levels in 293 cells (*4*). It has already been well-understood that polymer stabilized nanomaterials tend to deliver genes more efficiently, compared to their corresponding polymers, due to the stability issues with the latter (*24−26*). Singh et al. compared the transfection efficiencies of single- and multiwalled carbon nanotubes, proving better transfection ability of SWNTs over MWNTs; however, no cytotoxicity studies are provided by them, while others report the cytotoxicity of nanotubes by assays that are now debatable (*4, 8, 11*). We present a novel type of functionalized SWNTs that show the transfection efficiencies that mimic that of Lipofectamine, with enhanced cell viability. The varying masses of glycopolymer-functionalized SWNTs were complexed with green fluorescence protein encoded plasmid (pEGFP), and the process of complexation was studied by agarose gel electrophoresis. The calculation of mass ratios was done by incubating the various volumes of SWNTs with 340 ng of pEGFP plasmid. The stock solution of initial concentration of 1 mg/mL of functionalized SWNT was used and 5, 10, 15, and 20 μL of SWNTs were incubated with 340 ng of plasmid separately. It was found that complete complexation of plasmid is obtained at w/w DNA to SWNTs ratio of 1:14.5, and the complexes were found to be retained in the wells of agarose gel (Supporting Information Figure S6). The transfection efficiencies were then obtained by incubating Hela cells at varying w/w ratios of SWNTs to DNA. The transfected cells were excited at $\lambda_{ex} = 490$ nm and the emission spectrum was collected at $\lambda_{em} = 520$ nm. The glowing cells detected under the microscope confirmed the expression of GFP proteins, which were then divided by total number of cells in the field of view, to obtain the percent cells transfected in the given treatment. Each experiment was performed in triplicate to calculate the random error between samples, and the experiments were repeated twice to confirm the reproducibility of the data. The values of transfection efficiencies obtained were normalized compared to plasmid alone treated cells to determine the percent value of transfection efficiency. It was found that the transfection efficiency was highest at w/w DNA to SWNT ratio of 1:58, due to the increase in net cationic component of the vehicle. As reported earlier, the higher transfection efficiencies obtained are attributed to strong noncovalent immobilization of DNA on the surface of SWNTs (*8*). The presence of net positive charge of the complex produces a "proton sponge" effect thus leading to the release of DNA in cytosol. The increase in net positive charge of the complex further increases the transfection ability of the vehicle, regardless of the type of cationic glycopoymer used for the surface functionalization of SWNTs (Figure 3).

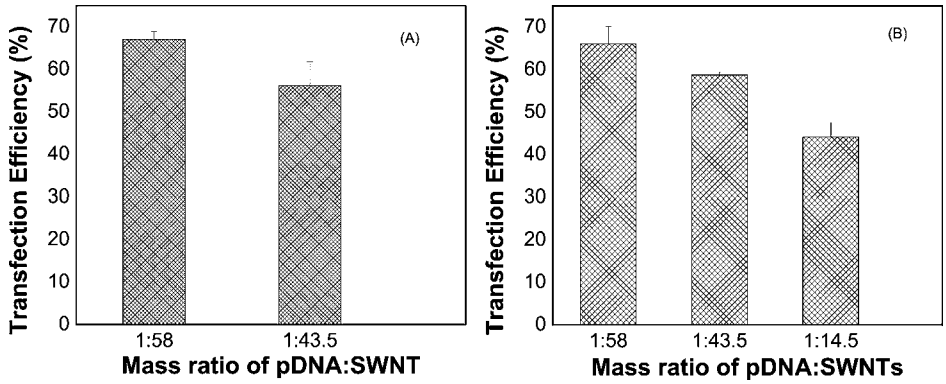

Figure 3. Transfection efficiencies of P($APMA_{31}$-*b*-$LAEMA_{32}$)-*f*-SWNTs after modification with pEGFP plasmid (A) and transfection efficiencies of P($APMA_{38}$-*b*-$GAPMA_{20}$)-*f*-SWNTs upon complexation with pEGFP-plasmid (B).

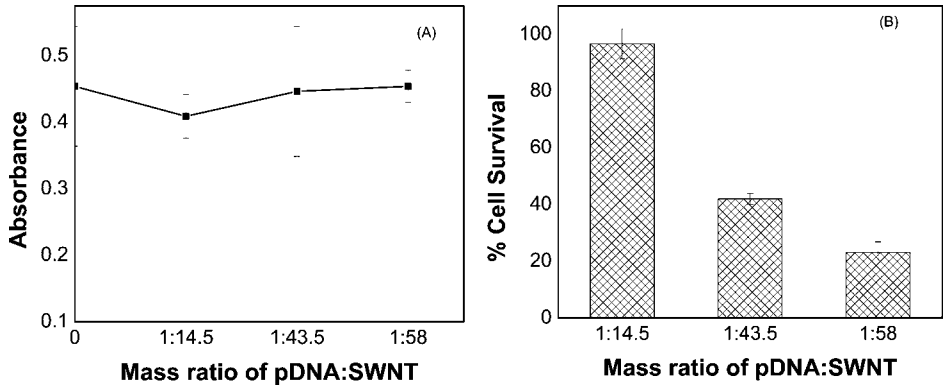

Figure 4. The comparison of cell viability assays after the treatment of Hela cells with P($APMA_{38}$-*b*-$GAPMA_{20}$)-*f*-SWNTs plasmid complex. (A) MTT assay of cell viability. (B) Trypan blue assay for cell viability.

The use of two types of surface-functionalized SWNTs, containing same cationic moiety but different glycopolymer segments, confirms that the transfection abilities of nanotubes is a function of the presence of cationic component (PAPMA) on the surface of the nanotubes, thus leading to the same DNA condensation abilities of nanotubes. The role of glycopolymer moieties (PLAEMA and PGAPMA) is limited to providing the biocompatibility and cell-mediated interactions to the vehicles. The cytotoxicity of carbon nanotubes was then assessed after transfection using two different assays, Trypan blue assay and MTT assay. (Figure 4 and Supporting Information Figure S6).

The cytotoxicity of carbon nanotubes is an uncertain but important parameter for their use in biomedical applications. The toxicity of carbon nanotubes is found to be dependent upon the type of cell line used, type and degree of surface functionalization of nanotubes, and type of test used to study the toxicity (*11*, *27*, *28*). Wrle-Knirsch et al. has demonstrated the need to use more than one independent viability tests to determine the accurate cell viability of SWNTs treated cells (*11*). We further confirm that the use of more than one cell viability tests is crucial, when dealing with new nanomaterials like CNTs, as their exact mechanism of interaction with viability tests is unclear. The cell viability results of cells treated under the same conditions as used for transfection experiments were compared by using MTT and trypan blue assay. The media alone and untreated cells were used as negative and positive controls, respectively, to calculate the percent cell viability after the treatments (Figure 4).

Liu et al. and other researchers have reported that MTT assay shows no net loss in cell viability before and after the treatment of cells with carbon nanotubes during the transfection process (*4*, *10*). We, hereby, report the same results, showing no loss in cell viability after the treatment of cells with gene delivery vehicle using MTT assay. In contrast, a concentration-dependent loss in cell viability of the transfected cells was found with trypan blue assay. The trypan blue assay also called the dye exclusion method involves a manual count of live and dead cells and is tedious but is more reliable than other photometric assays available. The comparison among photometric assays of cell viability after their treatment with carbon nanotubes has already been studied, and it has been reported that, compared to other assays, MTT shows a reduction in cell viability due to the possible interactions of nanotubes with formazan crystals. We suggest the need to compare the photometric tests with manual counting of cells after the treatment with carbon nanotubes, as the exact mechanism of interaction of carbon nanotubes with other photometric assays is not known.

It should also be noted that the viability of the transfected cells was improved in comparison to the cells treated with functionalized SWNTs in the absence of DNA for 12 h. The DNA complexation of nanotubes leads to a considerable decrease in the toxicity of the material, even after 24 h of exposure, possibly due to the decrease in the net cationic character of the nanotube complex. The toxicity results of transfected cells are also compared to those where cells are incubated with functionalized SWNTs alone. It can be seen that in the case of transfected cells 15 μg of SWNTs complexed with plasmid yield about 60 $\pm$ 12% cell viability, and the same cytotoxicity values are obtained when 7 μg of SWNTs (in the absence of plasmid) is incubated with cells for 12 h (Supporting Information Figures S4, S5, and S6). The results are similar to the other studies, where complexation of DNA to nanomaterials is found to decrease the toxicity and increase the solubility of material, causing an enhancement in their cellular uptake (*29*).The transfection

efficiencies of glycopolymer-functionalized SWNTs were compared to their cytotoxicity profiles. The increase in transfection efficiency is proportionally associated with an increase in toxicity of the material, due to an increase in the cationic component of the vehicle. However, a desirable contrast of cell viability and transfection efficiency is achieved at DNA/P($APMA_{31}$-*b*-$LAEMA_{32}$)-*f*-SWNT w/w ratio of 1:43.5. The cell viability is found to be 60 ± 12% accompanied by ~60% transfection efficiency (Figure 3a and Supporting Information Figure S6). A further increase in cationic component of the vehicle to DNA/SWNT w/w ratio of 1:58 noticeably decreases the cell viability, yielding ~25% viable cells, associated with less than 10% increase in transfection efficiency (Figure 3a and Supporting Information Figure S6). The DNA/SWNT w/w ratio of 1:43.5 showed the combination of transfection efficiency and cell viability that resembles commercially available standard Lipofectamine 2000 (Figures 3, 4, and Supporting Information Figures S6 and S8−S10). It was found that lipofectamine yields the transfection efficiency of 55 ± 5% with high toxicity values (~25%, measured by MTT assay) under the same conditions (Supporting Information Figure S10). Although two types of cationic glycopolymer-functionalized SWNTs show similar transfection efficiencies, owing to their similar cationic component, their toxicity profiles are quite different from each other. The toxicity profiles of the two types of nanotubes are found to be associated with their glycopolymer segments; the nanotubes with higher glycopolymer segment are less toxic and vice versa. As indicated by our results, although the cationic component of two types of functionalized nanotubes is the same P(APMA-*b*-LAEMA)-*f*-SWNTs are found to be less toxic than P(APMA-*b*-GAPMA)-*f*-SWNTs mainly due to the difference in their glycopolymer segment (Figure 4 and Supporting Information Figure S6). This further demonstrates the role of the glycopolymer segment in masking the cationic component of the gene delivery agent, thus contributing toward the successful synthesis of gene delivery vehicle with improved properties.

To summarize, we report here the facile synthesis, characterization, and *in vitro* studies of biocompatible cationic single-walled carbon nanotubes. The glycopolymer functionalized carbon nanotubes are found to have the potential to replace other commercially available gene delivery vehicles due to their high transfection efficiency and relatively low toxicity. Future studies will focus upon the functionalization of SWNTs with block copolymers of different compositions, with the idea to explore a wide range of block copolymer to find an appropriate composition of glycopolymer segment that can yield considerable transfection values with relatively low toxicity.

ACKNOWLEDGMENT

This work is supported jointly by Natural Sciences and Engineering Research Council of Canada (NSERC) and Ontario Centres of Excellence, Emerging Materials and Knowledge (OCE-EMK). The authors thank Dr. R. Lafrenie (Sudbury Regional Hospital) for his help in obtaining confocal images of cells and use of instruments.

Note Added after ASAP Publication: This paper was published ASAP with missed corrections on October 13, 2009. The revised version was published on October 20, 2009.

Supporting Information Available: Details of experimental procedures, GPC and ^{1}H NMR data of block copolymer synthesis, toxicity results, agarose gel electrophoresis for the complexation of DNA to carbon nanotubes, and transfection images. This material is available free of charge via the Internet at http://pubs.acs.org.

LITERATURE CITED

(1) Prato, M., Kostarelos, K., and Bianco, A. (2008) Functionalized carbon nanotubes in drug design and discovery. *Acc. Chem. Res. 41*, 60–68.

(2) Allen, L. B., Kichambare, D. P., Gou, P., Vlasova, I. I., Kapralov, A. A., Kondru, N., Kaga, E. V., and Star, A. (2008) Biodegradation of single walled carbon nanotubes through enzymatic catalysis. *Nano Lett. 8*, 3899–3903.

(3) Kam, S. W. N., Jessop, C. T., Wender, A. P., and Dai, H. (2004) Nanotube molecular transporters: internalization of carbon nanotube-protein conjugates into mammalian cells. *J. Am. Chem. Soc. 126*, 6850–6851.

(4) Liu, Y., Wu, C.-D., Jiang, X., He, C.-B., Chung, S. T., Goh, H. S., and Leong, W. K. (2005) Polyethylenimine-grafted multiwalled carbon nanotubes for secure noncovalent immobilization and efficient delivery of DNA. *Angew. Chem., Int. Ed. 44*, 4782–4785.

(5) Cheng, J., Fernando, S. A. K., Veca, M. L., Sun, Y.-P., Lamond, I. A., Lam, W. Y., and Cheng, S. H. (2008) Reversible accumulation of PEGylated single-walled carbon nanotubes in the mammalian nucleus. *ACS Nano 2*, 2085–2094.

(6) Dumortier, H., Lactte, S., Pastorin, G., Marega, R., Davide, W. W., Bonifazi, D., Briand, J.-P., Prato, M., Muller, S., and Bianco, A. (2006) Functionalized carbon nanotubes are noncytotoxic and preserve the functionality of primary immune cells. *Nano Lett. 6*, 1522–1528.

(7) Delogu, G. L., Magrini, A., Bergamaschi, A., Rosato, N., Dawson, I. M., Bottini, N., and Bottini, M. (2009) Conjugation of antisense oligonucleotides to PEGylated carbon nanotubes enables efficient knockdown of PTPN22 in T lymphocytes. *Bioconjugate Chem. 3*, 427–431.

(8) Singh, R., Pantarotto, D., McCarthy, D., Chalion, O., Hoebeke, J., Partidos, D. C., Briand, J.-P., Prato, M., Bianco, A., and Kostarelos, K. (2005) Binding and condensation of plasmid DNA onto functionalized carbon nanotubes: toward the construction of nanotube-based gene delivery vectors. *J. Am. Chem. Soc. 127*, 4388–4396.

(9) Kam, S. W. N., Liu, Z., and Dai, H. (2005) Functionalization of carbon nanotubes via cleavable disulfide bonds for efficient intracellular delivery of siRNA and potent gene silencing. *J. Am. Chem. Soc. 127*, 12492–12493.

(10) Lu, Q., Moore, M. J., Huang, G., Mount, S. A., Rao, M. A., Larcom, L. L., and Ke, C. P. (2004) RNA polymer translocation with single walled carbon nanotubes. *Nano Lett. 4*, 2473–2477.

(11) Wrle-Knirsch, M. J., Pulskamp, K., and Krug, F. H. (2006) Oops they did it again! Carbon nanotubes hoax scientists in viability assay. *Nano Lett. 6*, 1261–1268.

(12) Crouzier, T., Nimmagadda, A., Nollert, U. M., and McFetridge, S. P. (2008) Modification of single walled carbon nanotube surface chemistry to improve aqueous solubility and enhance cellular interactions. *Langmuir 24*, 13173–13181.

(13) Narain, R., Housni, A., and Lane, L. (2006) Modification of carboxyl-functionalized single-walled carbon nanotubes with biocompatible, water-soluble phosphorylcholine and sugar-based polymers: bioinspired nanorods. *J. Polym. Sci, Part A: Polym. Chem. 44*, 6558–6568.

(14) Chen, J. R., Zhang, Y., Wang, D., and Dai, H. (2001) Noncovalent sidewall functionalization of single-walled carbon nanotubes for protein immobilization. *J. Am. Chem. Soc. 123*, 3838–3839.

(15) Matyjaszewski, K., Miller, P. J., Shukla, N., Immaraporn, B., Gelman, A., Luokala, B. B., Siclovan, T. M., Kickelbick, G., Vallant, T., Hoffmann, H., and Pakula, T. (1999) Polymers at interfaces: using atom transfer radical polymerization in the controlled growth of homopolymers and block copolymers from silicon surfaces in the absence of untethered sacrificial initiator. *Macromolecules 32*, 8716–8724.

(16) Shen, M. W., Wang, S. H., Shi, X. Y., Chen, X. S., Huang, Q. G., Petersen, E. J., Pinto, R. A., Baker, J. R., and Weber, W. J., Jr. (2009) Polyethyleneimine-mediated functionalization of multiwalled carbon nanotubes: synthesis, characterization, and in vitro toxicity assay. *J. Phys. Chem. C 113*, 3150–3156.

(17) Gao, C., Muthukrishnan, S., Li, W. W., Yuan, J. Y., Xu, Y. Y., and Müller, A. H. E. (2007) Linear and hyperbranched glycopolymer-functionalized carbon nanotubes: synthesis, kinetics, and characterization. *Macromolecules 40*, 1803–1815.

(18) Deng, Z., Ahmed, M., and Narain, R. (2009) Novel well-defined glycopolymers synthesized via the reversible addition fragmentation chain transfer process in aqueous media. *J. Polym. Sci., Part A: Polym. Chem. 47*, 614–627.

(19) Kam, S. W. N., Liu, Z., and Dai, H. (2006) Carbon nanotubes as intracellular transporters for proteins and DNA: an investigation of the uptake mechanism and pathway. *Angew. Chem., Int. Ed. 45*, 577–581.

(20) Jin, H., Heller, A. D., Sharma, R., and Strano, S. M. (2009) Size-dependent cellular uptake and expulsion of single-walled carbon nanotubes: single particle tracking and a generic uptake model for nanoparticles. *ACS Nano 3*, 149–158.

(21) Chithrani, D. B., and Chan, W. C. W. (2007) Elucidating the mechanism of cellular uptake and removal of protein-coated gold nanoparticles of different sizes and shapes. *Nano Lett. 7*, 1542–1550.

(22) Chen, X., Tam, C. U., Czlapinski, L. J., Lee, S. G., Rabuka, D., Zetti, A., and Bertozzi, R. C. (2006) Interfacing carbon nanotubes with living cells. *J. Am. Chem. Soc. 128*, 6292−6293.

(23) Wu, Y., Phillips, A. J., Liu, H., Yang, R., and Tan, W. (2008) Carbon nanotubes protect DNA strands during cellular delivery. *ACS Nano 2*, 2023–2028.

(24) Ghosh, S. P., Kim, C. K., Han, G., Forbes, S. N., and Rotello, M. V. (2008) Efficient gene delivery vectors by tuning the surface charge density of amino acid-functionalized gold nanoparticles. *ACS Nano 2*, 2213–2218.

(25) Li, P., Li, D., Zhang, L., Li, G., and Wang, E. (2008) Cationic lipid bilayer coated gold nanoparticles-mediated transfection of mammalian cells. *Biomaterials 29*, 3617–3624.

(26) Zhou, X., Zhang, X., Yu, X., Zha, X., Fu, Q., Liu, B., Wang, X., Chen, Y., Chen, Y., Shan, Y., Jin, Y., Wu, Y., Liu, J., Kong, W., and Shen, J. (2008) The effect of conjugation to gold nanoparticles on the ability of low molecular weight chitosan to transfer DNA vaccine. *Biomaterials 29*, 111–117.

(27) Manna, K. S., Sarkar, S., Barr, J., Wise, K., Barrera, V. E., Jejelowo, O., Rise-Ficht, C. A., and Ramesh, T. G. (2005) Single-walled carbon nanotube induces oxidative stress and activates nuclear transcription factor-κB in human keratinocytes. *Nano Lett. 5*, 1676–1684.

(28) Magrez, A., Kasas, S., Salicio, V., Pasquier, N., Seo, W. J., Celio, M., Catsicas, S., Schwaller, B., and Forro, L. (2006) Cellular toxicity of carbon-based nanomaterials. *Nano Lett. 6*, 1121–1125.

(29) Gijohann, A. D., Seferos, S. D., Patel, C. P., Millstone, E. J., Rosi, L. N., and Mirkin, C. A. (2007) Oligonucleotide loading determines cellular uptake of DNA-modified gold nanoparticles. *Nano Lett. 7*, 3818–3821.

BC900229V

Supporting Information for "**Cationic Glyco-Functionalized Single-Walled Carbon Nanotubes as Efficient Gene Delivery Vehicles**"

Marya Ahmed, Xiaoze Jiang, Zhicheng Deng, and Ravin Narain[*]

University of Alberta, Department of Chemical and Materials Engineering, ECERF, Edmonton, AB, T6G 2G6, Canada and Department of Chemistry and Biochemistry, Biomolecular Sciences Program, Laurentian University, 935, Ramsey Lake Rd, Sudbury, ON, P3E 2C6, Canada

[*]Corresponding author: narain@ualberta.ca or rnarain@laurentian.ca

Materials and Methods

Materials

All chemicals were purchased from Sigma–Aldrich, Acros, or Pierce Chemicals and were used without further purification. High-purity single walled carbon nanotubes (SWNTs) (80–90%) were obtained from Carbon Solutions, Inc. The SWNTs had an average bundle length of 1–5 μm and an average bundle diameter of 2–10 nm and were used without further purification. The carboxylic acid content in the SWNTs was determined by Carbon Solutions and was estimated to be around 4–6 atom%. The biotinyl-*N*-hydroxysuccinimide ester (Biotin-NHS) and p(LAEMA$_{32}$-*b*- APMA$_{31}$) diblock copolymer were synthesized as previously described, and the degrees polymerization (DPs) of PAPMA and PLAEMA are 31 and 32, respectively, calculated from the ^{1}H NMR spectra. GPC trace of P(LAEMA-*b*-APMA) shows the copolymer has the molecular weight of 20,500 and a narrow polydispersity (1.21).

Characterization. ^{1}H NMR spectra of the monomers and polymers were recorded on a Varian 200 MHz instrument. Aqueous gel permeation chromatography analysis was performed on a Viscotek Instrument using a 0.5 M sodium acetate/acetic acid buffer as eluent, two Waters WAT011545 columns and a flow rate of 1.0 mL/min. Six near-monodisperse PEO standards (Mp = 1,010 - 101,200 g mol^{-1}) were used for calibration.

Infrared (IR) spectra were recorded on a Bomem MB series spectrometer. The analyses were performed with Win-Bomem Easy software. Thermogravimetric analysis (TGA) was performed on a TA 500 instrument at a heating rate of 5 ^{o}C/min for a temperature range of 25–900 ^{o}C.

Ultraviolet–visible (UV–vis) spectra of the functionalized SWNTs were recorded on a Biochrom Ultro- Spec 2100 instrument. Transmission electron microscopy (TEM) images were recorded using a Philips CM120 electron microscope at an accelerating voltage of 200 kV.

Confocal Microscopy

The fluorescent images were obtained using Zeiss LSM 510 Meta confocal microscope with 63x objective. The wavelengths of excitation and emission used were 490 nm and 520 nm, respectively.d

The preparation of glycopolymer Surface-functionalized SWNTs. The glycopolymer functionalized SWNTs were prepared from the P($LAEMA_{32}$-*b*-$APMA_{31}$) diblock copolymer and carboxyl functionalized SWNTs. A typical protocol was as follows. The SWNTs (20 mg) was added into aqueous solution (pH 6, 20 mL) of EDC (19.2 mg) and NHS (11.5 mg). The reaction mixture was sonicated for 3 h at room temperature. Then 5 mL aqueous solution of diblock copolymer (198.4 mg) was added into above active SWNT solution and changed the solution pH to 9. The mixture was sonicated for 4 h and stirred the reaction mixture overnight at room temperature. The solution was placed for 2 days for the precipitation of un-functionalized SWNT in water without any disturbance. The above solution was carefully decanted, and removed the solvent under vacuum. The obtained black solid was then dispersed into water. A dark solution was obtained with a tiny amount of a black, insoluble precipitate. The solution was filtered, and the dark solution was centrifuged to remove the free polymer chains under 20,000 rpm for 30 min and repeated three times. The final product (38 mg) was freeze-dried under vacuum for 2 days.

The preparation of biotinylated glyco-functionalized SWNTs.

Glyco-functionalized SWNT solutions were dispersed into water at pH 9 and sonicated for 30 min, 1 mL of DMF and Biotin-NHS was added into above aqueous solution. This mixture was sonicated for 2 h and stirred overnight at room temperature; the solvents were evaporated under reduced pressure. The residue was washed with acetone to remove free biotin molecules repeated three times. The black powder was dried overnight under vacuum.

Plasmid Preparation and Purification. pEGFP-N1, enhanced green fluorescent plasmid driven by cytomegalovirus (CMV) promoter, was transformed in supercompetent E. Coli cells and was amplified in 30 μg/mL Kanmycin containing LB broth media at 37 °C overnight with 225 rpm. After sufficient bacterial growth, the cells were pelleted by centrifugation at 2000*g* and 20 °C for 5 min followed by plasmid extraction using QIAGEN mini plasmid purification kit as per vendor's protocol. Plasmid purity was assessed by UV spectrophotometry ($A_{260/280}$ > 1.75), and by agarose gel electrophoresis.

DNA Complexation

DNA complexation of p($APMA_{38}$-*b*-$GAPMA_{20}$)-functionalized-CNTs and p($APMA_{31}$-b-$LAEMA_{32}$)-functionalized carbon nanotubes was studied using agarose gel electrophoresis. The varying concentrations of carbon nanotubes (0.05, 0.1, 0.15 & 0.20 mg/mL) were incubated with 340 ng of pEGFP-N1 plasmid and the complexes were loaded into 0.7% agarose gel. The gel was run for one hour at 70 V and the complexes were characterized after staining the gel with 0.5μg/mL of ethidium bromide. The images were obtained on an ultraviolet transilluminator.

Confocal Microscopy

Hela cells were grown in Dubelcco's modified eagle medium, DMEM containing 10% fetal bovine serum and 1% penicillin/streptomycin, in a humidified atmosphere with 5% CO_2 at 37 °C. Upon 80% confluency, cells were trypsinized and neutralized with the equal amount of

medium. The cells were then reseeded in a 6 well plate, in which each well contained sterile glass cover slips. The plate was incubated in humidified atmosphere at 37 °C and upon 80% confluency, 0.15 mg/mL p($APMA_{31}$-*b*-$LAEMA_{32}$) and p($APMA_{38}$-*b*-$GAPMA_{20}$) functionalized carbon nanotubes complexed with 4 μM FITC-labeled oligonucleotides containing medium was introduced in separate chambered cover glass. The other two wells served as controls, containing no treatment, and 4 μM FITC-labeled oligonucleotides in the medium, respectively. The cells were further incubated for 48 hours at 37 ˚C. The growth medium was then removed, and cells were washed several times with phosphate buffer saline. The cells were fixed with 4% paraformaldehyde solution at room temperature for 5 minutes, followed by washing with PBS. The cover glass was then mounted on microscopic glass slide and was studied under the microscope.

Transfection

Hela cells were maintained in Dulbecco's modified Eagles' medium, supplemented with 10% Fetal bovine serum at 37 ˚C, in a humidified 5% CO_2 atmosphere, as described above. Before the experiment, 10,000 Hela cells were seeded on a 96 well tissue culture plate and allowed to adhere over night. The test samples were prepared for each well by mixing 340 ng of pEGFP-plasmid with varying amounts of carbon nanotubes. The mixture was incubated for 15 minutes and was added to the cells, and the plate was incubated for 24 hours at 37 ˚C, in serum free medium. The cells were washed three times with Dulbecco's Phosphate Buffer (DPBS) and were allowed to grow for another 24 hours in fresh culture medium supplemented with 10% FBS. The gene expression was evaluated using fluorescent microscopy. The presence of GFP protein was confirmed using the emission spectrum of green fluorescence protein at 520 nm.

The transfection studies with Lipofectamine were done as described by standard protocol. The lipofectamine was incubated with pEGFP plasmid and complexes were transferred in 96 well plates containing 10,000 Hela cells. The media was changed after six hours and was replaced with fresh serum containing medium. The cells were allowed to grow for further 48 hours, and the gene expression was evaluated as described above.

Toxicity assay on Transfected cells using MTT Assay: Hela cells maintained at 80% confluency were seeded at 10,000 cells/well in 96 well plate and were allowed to adhere overnight. The varying concentrations of carbon nanotube-plasmid complex in serum free medium were added to each well and each experiment was done in triplicate, as describes above. After six hours the medium was changed to serum containing medium and cells were allowed to grow for another 48 hours. The cell viability was tested using MTT assay. The 25 µL MTT dye was added to each well and plate was incubated for 2 hours. Next 100 µL of MTT lysis solution was added to each well and cells were incubated overnight. Absorbance was measured at 570 nm with Power wave instrument. Survival percentage was calculated by comparison to untreated cells (100% survival).

Toxicity assay on Transfected cells using Trypan Blue Assay: Hela cells were seeded at 10,000 cells/well in 96 well plate and were allowed to adhere overnight. The varying concentrations of carbon nanotube-plasmid complex in serum free medium were added to each well and each experiment was done in triplicate, as describes above. After 24 hours the medium was changed to serum containing medium and cells were allowed to grow for another 24 hours. The cells were then trypsinized, neutralized and stained with trypan blue solution. The stained cells were then counted using hematocytometer and percent cell viability was determined by dividing the number viable transfected cells with the number of untreated cells.

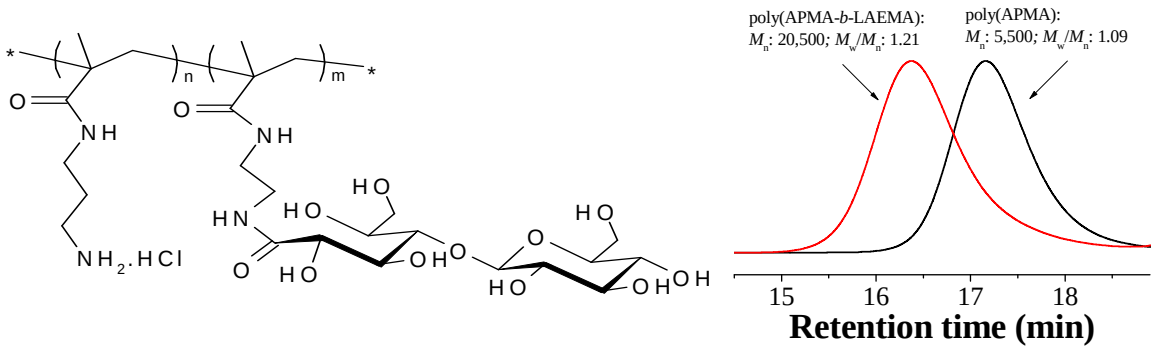

Figure 1: The chemical structure (left) and GPC data (right) showing the molecular weight distribution of the block co-polymer p($APMA_{31}$-*b*- $LAEMA_{32}$).

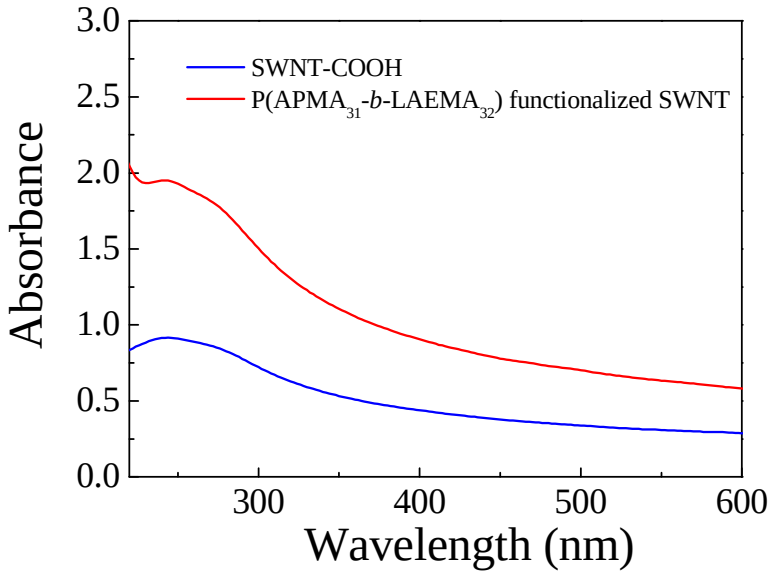

Figure 2: UV-visible spectra recorded for the original nanotubes and compared to the functionalized SWNTs.

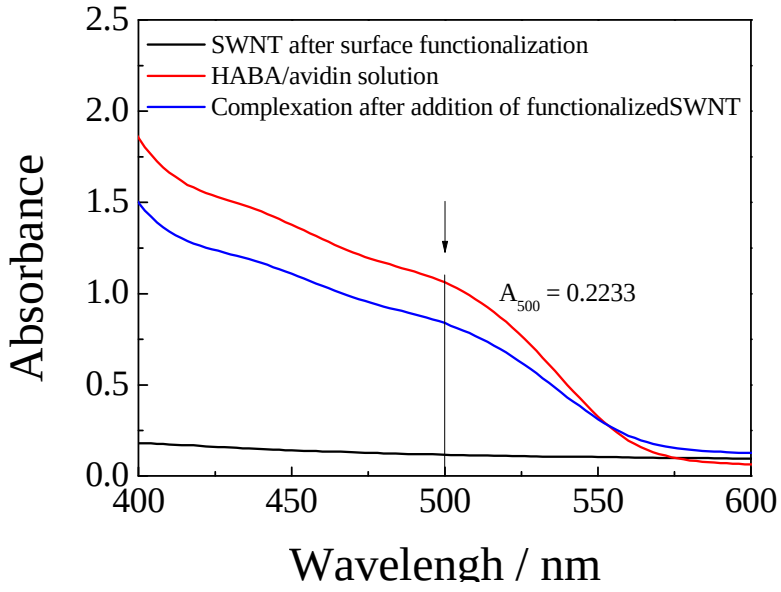

Figure 3: HABA/Avidin assay detects the presence of biotin of the surface of functionalized carbon nanotubes.

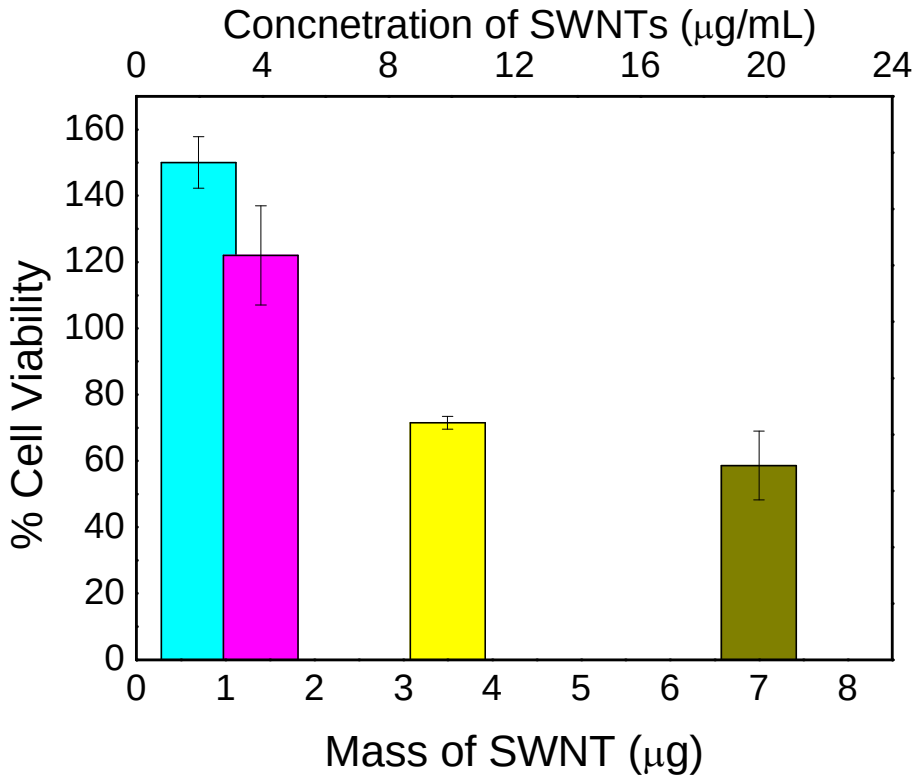

Figure 4: The toxicity of p(GAPMA$_{20}$-*b*-APMA$_{38}$) functionalized SWNTs after incubation for 12 hours with Hela cells using different concentration of SWNTs, using Trypan blue assay.

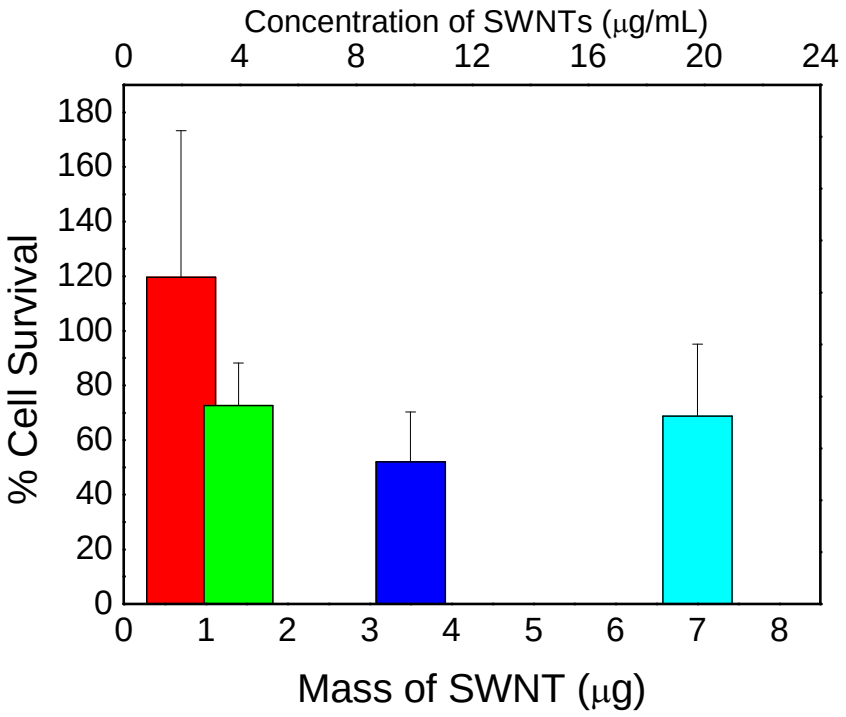

Figure 5: Toxicity of p(LAEMA$_{32}$-*b*-APMA$_{31}$) functionalized SWNT of Hela cells after treatment with different concentration of SWNTs for 12 hours, using Trypan blue assay.

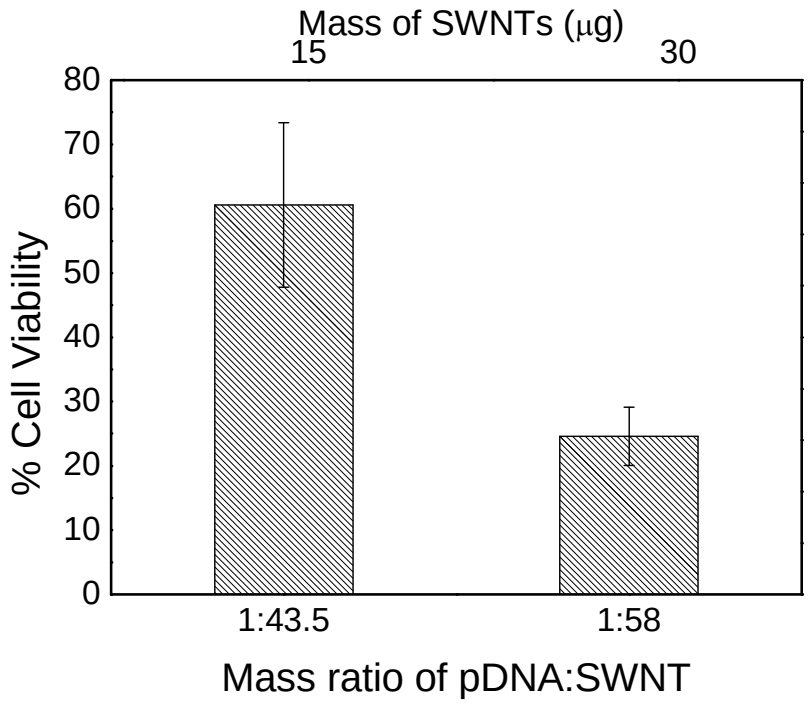

Figure 6: Toxicity of p(LAEMA$_{32}$-*b*-APMA$_{31}$) functionalized SWNTs after transfection of Hela cells with SWNT-plasmid complex for 24 hours, using Trypan blue assay.

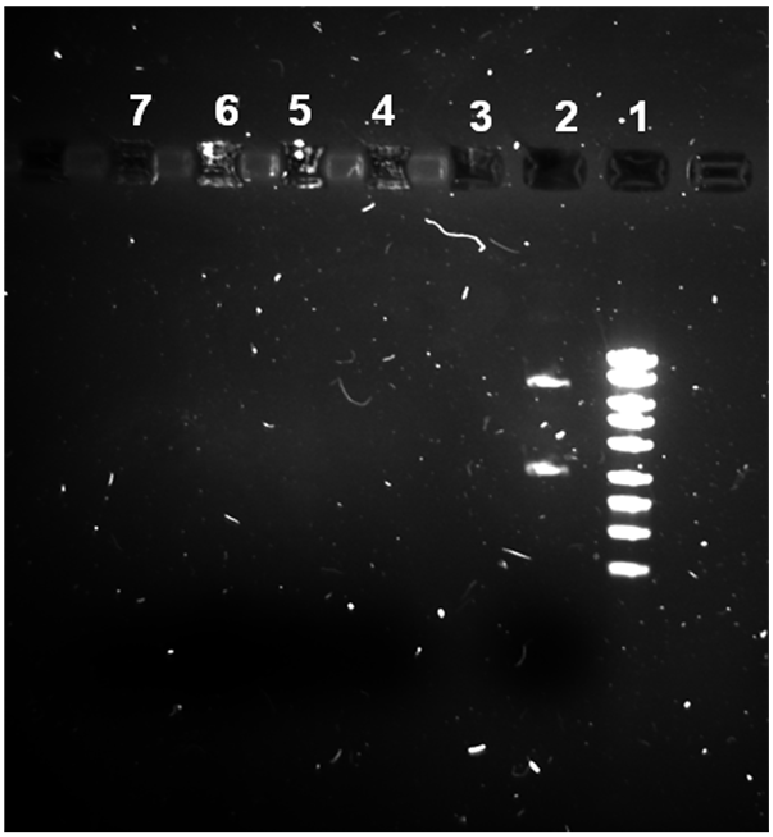

Figure 7: Agarose Gel Electrophoresis showing the complexation of GFP with p(GAPMA$_{20}$-*b*-APMA$_{38}$)-*f*-SWNTs: 1. Ladder, 2. GFP plasmid only, 3. SWNTs only 4. 0.05 mg/mL of SWNTs +340ng of GFP (mass ratio of pDNA:CNTs is 1: 14.5) 5. 0.1mg/mL of SWNT + 340ng of plasmid (mass ratio of pDNA:CNTs is 1:29) 6. 0.15mg/mL of SWNTs + 340 ng of plasmid (mass ratio of pDNA:CNTs is 1: 43.5) 7. 0.20 mg/mL of SWNT + 340 ng of plasmid (mass ratio of pDNA:CNTs is 1: 58).

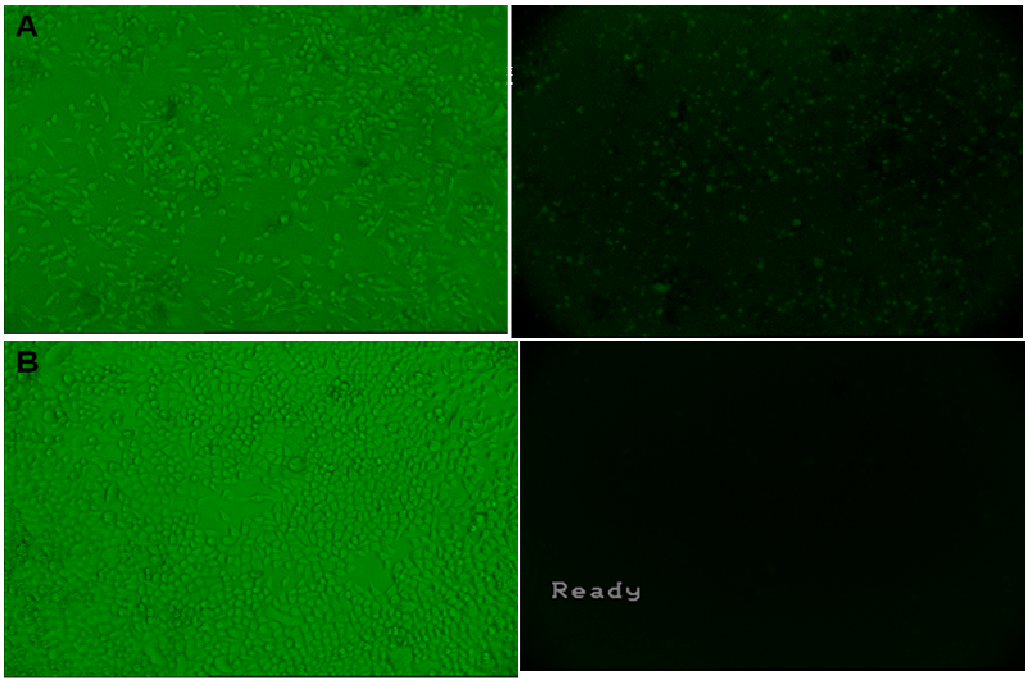

Figure 8: Transfection Studies of A) p(GAPMA$_{20}$-b-APMA$_{38}$)-functionalized-SWNTs complexed with GFP plasmid. B) plasmid only (control)

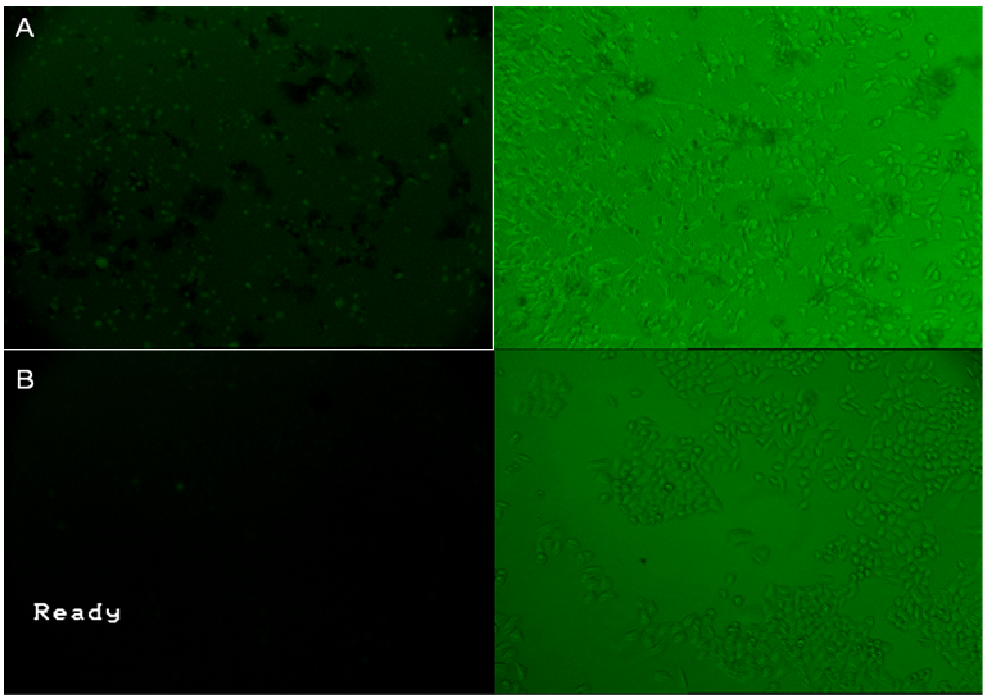

Figure 9: Transfection Studies of A) p(LAEMA$_{32}$-*b*-APMA$_{31}$)-functionalized-CNTs complexed with GFP plasmid, B) Plasmid only (control)

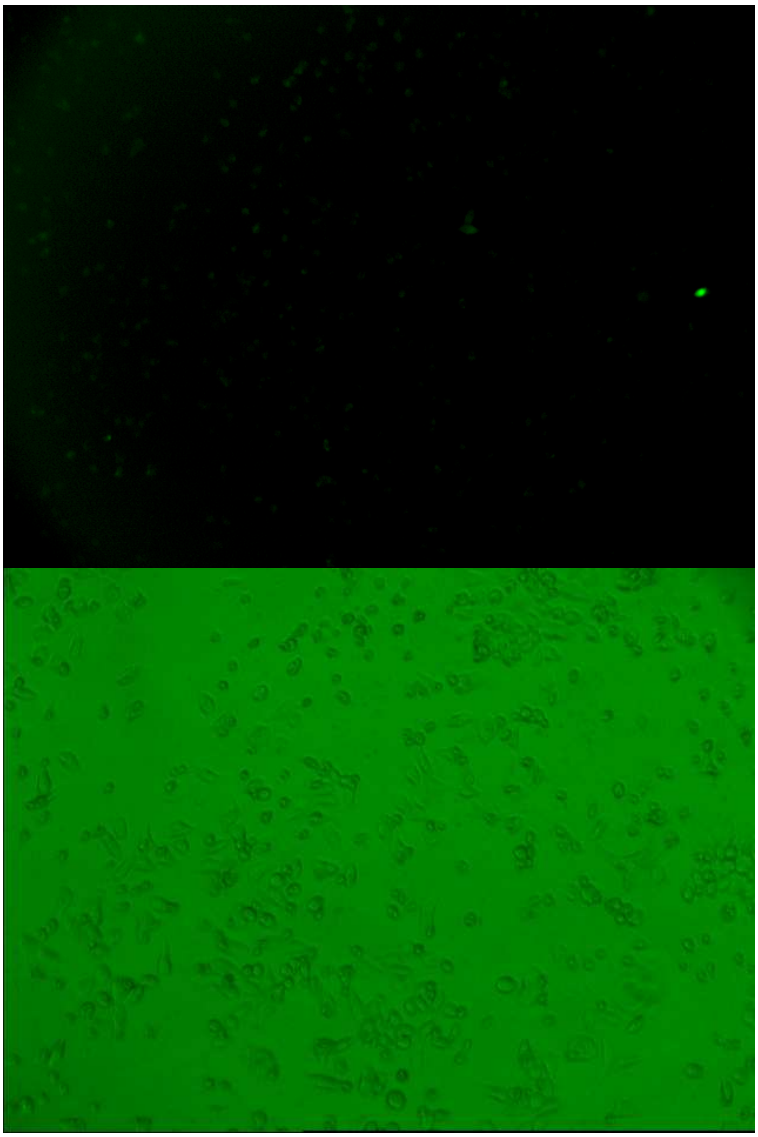

Total number of cells calculated in white light after treatment with lipofectamine = 456

Total number of fluorescent cells after treatment with lipofectamine = 316 cells

Figure 10: Transfection Efficiencies of lipofectamine 2000 with pEGFP plasmid.

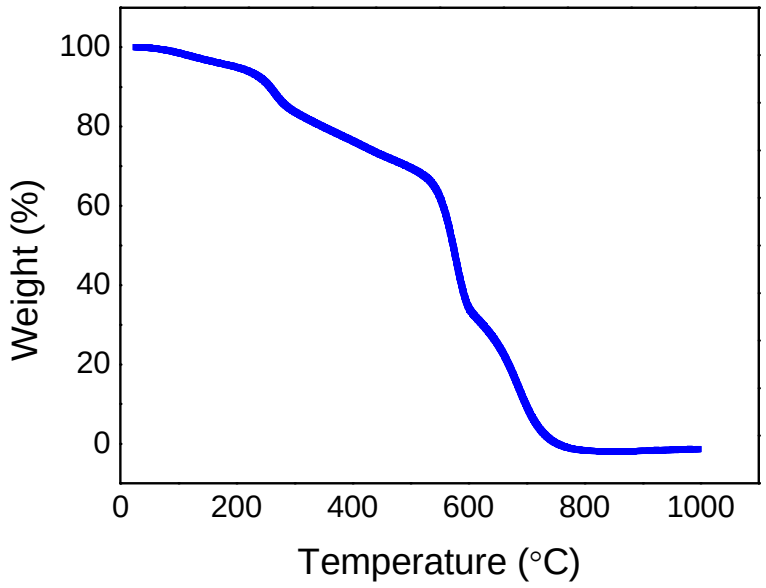

Figure 11: Thermogravimetric analysis (TGA) data of p(APMA$_{31}$-*b*-LAEMA$_{32}$)-*f*-CNTs in air.

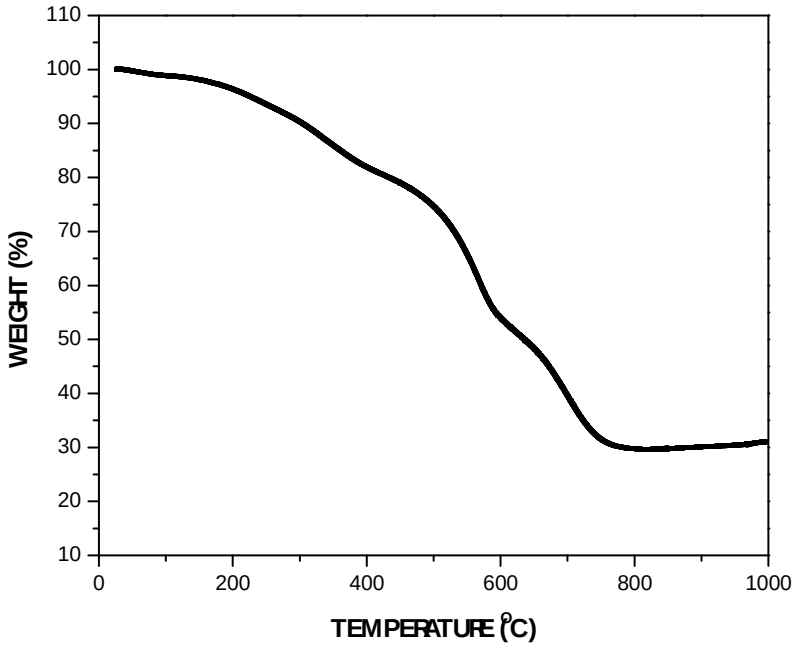

Figure 12: Thermogravimetric analysis (TGA) data of p(APMA$_{38}$-*b*-GAPMA$_{29}$)-*f*-CNTs in air.

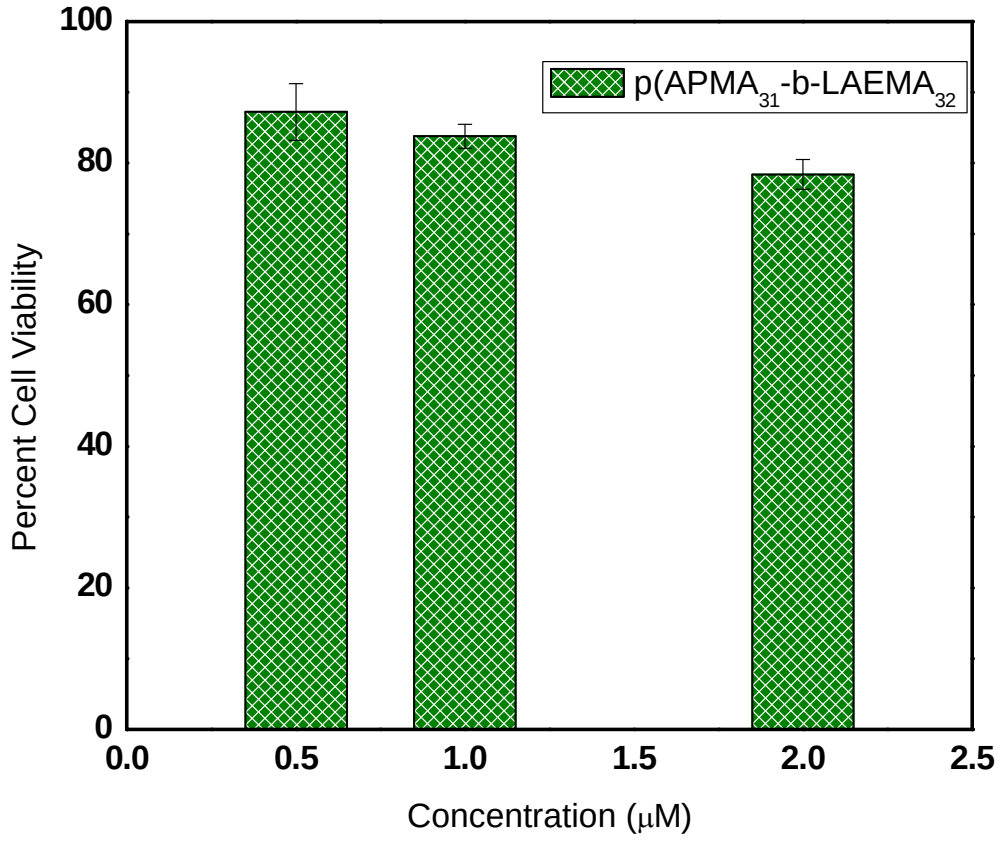

Figure 13: MTT assay of Hela cells incubated with different concentrations of cationic glycopolymer.

Synthesis and Evaluation of a Stable Bacteriochlorophyll-Analog and Its Incorporation into High-Density Lipoprotein Nanoparticles for Tumor Imaging

Weiguo Cao,[†,§,⊥] Kenneth K. Ng,[‡,⊥] Ian Corbin,[†] Zhihong Zhang,[†,||] Lili Ding,[†] Juan Chen,[†] and Gang Zheng*[,†,‡]

Department of Medical Biophysics, Ontario Cancer Institute, Institute of Biomaterials and Biomedical Engineering, University of Toronto, Canada, Department of Chemistry, Shanghai University, China, and Britton Chance Center for Biomedical Photonics, Huazhong University of Science and Technology, Wuhan, China. Received September 14, 2009

The syntheses of novel near-infrared (NIR) dyes with excellent optical properties in biological tissues have driven the continued improvement of fluorescence imaging of deeply seated tumors. Bacteriochlorophyll *a* (Bchl), a dye synthesized by the phototrophic bacteria, *R. sphaeroids*, is particularly suited for deep tissue imaging due to its high absorbance coefficient and good fluorescence quantum yield in the NIR spectrum. However, obstacles that impede the development of this fluorophore are its poor stability and lack of tumor specificity. These issues ultimately limit its utility for tumor detection. Herein we describe a robust synthesis of a novel Bchl analog, bacteriochlorin e_6 bisoleate (BchlBOA), which is chemically stable, has excellent photophysical properties (ex, 752 nm; em, 762 nm) and is tailored for the incorporation into a tumor targetable high-density lipoprotein (HDL)-like nanoparticle (NP). Incorporating BchlBOA into HDL (HDL−BchlBOA) yielded 12 nm sized particles, corresponding well with the diameter of native HDL. Functional cell uptake studies showed that HDL−BchlBOA was taken up by cells expressing the HDL receptor, scavenger receptor B type I (SR-BI), and was inhibited by 25-fold excess native HDL. Furthermore, the NP was successfully detected in KB cancer cells both in vitro and in tumor xenografts. Taken together, these results demonstrate that we successfully synthesized and formulated a stable analog of Bchl that is capable of being incorporated within HDL-like NPs for tumor-targeted imaging.

INTRODUCTION

Near-infrared (NIR) fluorescence imaging of cancerous tumors offers several advantages over other imaging modalities. These advantageous include its noninvasive detection, good sensitivity, and utilization of nonionizing radiation. Since the absorbance coefficients of endogenous absorbers including water and hemoglobin are at a minimum within the NIR window (650−900 nm) (*1*), NIR fluorescent probes offer optimal spectral properties and can theoretically be used to visualize tissues as deep as 10 cm depending on tissue type and the imaging modality (*2*). Polymethine cyanine-based dyes are the most commonly used NIR probes. These dyes are very useful in designing probes with adjustable wavelengths because they can be tuned to desired wavelengths by altering the heterocyclic nucleus (indolenine or benzindolenine) and the number of double bonds ($n = 1-3$) in the polymethine chain. For example, the water-soluble and bioconjugatable CyDyes (*3*) such as Cy5 ($n = 2$, indolenine nucleus, Ex_{max}, 649 nm; Em_{max}, 670 nm), Cy5.5 ($n = 2$, benzindolenine nucleus, Ex_{max}, 676 nm; Em_{max}, 694 nm), and Cy7 ($n = 3$, indolenine nucleus, Ex_{max}, 743 nm; Em_{max}, 767 nm) are NIR active and proven to be useful in a wide range of in vivo imaging applications (*4*−*6*). Furthermore, the only FDA approved NIR dye, indocyanine green (ICG), also belongs to this family ($n = 3$, benzindolenine nucleus, Ex_{max}, 805 nm; Em_{max}, 830 nm, $\xi > 150\,000$ $M^{-1}\cdot cm^{-1}$ with a quantum efficiency ∼4−5%) and is approved for imaging of retinal vasculature (*7*) and monitoring hepatic function (*8*).

Another important class of exogenous probes are the porphyrin-based or porphyrin-like fluorophores (phthalocyanines, expanded porphyrins, porphycenes, etc.). Porphyrins are 18 π-electron aromatic macrocycles, where two of its peripheral double bonds are not required to maintain aromaticity. Thus, reduction of one or both of these bonds respectively leads to chlorins and bacteriochlorins with bathochromically shifted bands with higher extinction coefficients. Generally, the longest wavelength absorptions (and extinction coefficients) for porphyrin, chlorin, and bacteriochlorin are at 630 nm (ε ∼5 000 $M^{-1}\cdot cm^{-1}$), 660 nm (ε ∼45 000 $M^{-1}\cdot cm^{-1}$) and 760 nm (ε ∼75 000 $M^{-1}\cdot cm^{-1}$), respectively (*9*). Nature uses the optical properties of the reduced porphyrins to harvest solar energy for photosynthesis with chlorophylls and Bchls acting as both antenna and photochemical reaction center pigments. The NIR absorption and fluorescence of these natural dyes clearly make them potential candidates as contrast agents for NIR optical imaging, although they are better known for their applications as photodynamic therapy (PDT) agents due to their high triplet state and singlet oxygen quantum yields. Nevertheless, there are already some reports using NIR-active porphyrin-based fluorophores for cancer imaging (*10*−*13*) and the fact they are both NIR fluorophores and photosensitizers make them ideal candidates for image-guided therapy (*14*−*17*).

Bchl extracted from *R. sphaeroids* is a NIR fluorophore with excitation and emission profile (750−850 nm) highly suited for imaging deeply seated tumors. However, two issues which hinder the utilization of this agent for tumor imaging include (i) poor stability caused by rapid oxidation and (ii) lack of specificity for cancer tissue. Various investigators have attempted to address the poor stability of the Bchl molecule. These include replacing the central magnesium with other metal ions (e.g., palladium) to form more stable complexes (*18*), modifying

* To whom correspondence should be addressed. Address: TMDT 5-363, 101 College St, Toronto, ON M5G 1L7, Canada. Fax: 416-581-7666. E-mail: gang.zheng@uhnres.utoronto.ca.

† Department of Medical Biophysics, Ontario Cancer Institute, University of Toronto.

‡ Institute of Biomaterials and Biomedical Engineering, University of Toronto.

§ Shanghai University.

|| Huazhong University of Science and Technology.

⊥ These authors contributed equally to this research article.

10.1021/bc900404y CCC: $40.75 © 2009 American Chemical Society
Published on Web 10/19/2009

the isocyclic ring (*19*), and replacing the phytyl group at the propionyl residue either through transesterification or by conversion to an amide derivative (*20*). In particular, Pandey et al. have shown that naturally occurring unstable Bchl *a* can be converted to stable bacteriochlorins, bacteriopurpurin-18, and bacteriopurpurinimide (*19*). In this approach, converting the fused isocyclic ring to a cyclic imide moiety enhanced the stability and solubility of the Bchl analogs, while attachment of a variable alkyl substituent to the imide moiety allowed the lipophilicity of the molecule to be fine-tuned (*21*). In another elegant demonstration, Fiedor et al. found that inserting palladium into the Bchl ring significantly improves the stability of this molecule, however fluorescence properties of this complex is compromised (*22*). Nevertheless, this Bchl analog led to the development of the promising PDT agent Tookad, which is currently in clinical trials (*23*, *24*). So far there have been minimal efforts in developing target-specific Bchls and even fewer attempts in exploring the utility of stable Bchl analogs as NIR fluorescent probes.

High-density lipoproteins (HDL) are endogenous carriers used to transport hydrophobic compounds throughout the body. The structural/functional properties of these particles, ultrasmall size (7−12 nm) (*25*), long circulation time (*26*, *27*), nonimmunogenic, and biodegradable, also make them attractive as delivery vehicles for exogenous compounds. HDL's hydrophobic core facilitates the incorporation of hydrophobic compounds into this carrier, while the small size and favorable surface properties enable these particles to remain undetected by the reticular endothelial system as well as rendering them accessible to most tissues. Furthermore, some cancer cell lines have been shown to have a high expression of the HDL receptor, formally known as scavenger receptor type B1 receptor (SR-BI). Since HDL's core lipid transfer is mediated through the SR-BI pathway, targeting this receptor represents a novel way to deliver imaging agents to cancer tumors which overexpress this receptor. This paper outlines (1) a simple and high yield synthesis of a stable Bchl analog; (2) methods of actively incorporating this Bchl analog into HDL-like NPs (HDL BchlBOA); and (3) the utility of HDL−BchlBOA as a novel diagnostic agent for cancer imaging. The overall goal of this work is to combine the advances of both technologies to generate a new tool for the diagnostic imaging of cancers in vivo.

EXPERIMENTAL PROCEDURES

Reagents. All chemicals were of reagent grade and used as such. Reactions were carried out under nitrogen atmosphere and were monitored by precoated (0.20 mm) silica TLC plastic sheet (20 × 20 cm) strips (POLYGRAM SIL N-HR) and/or UV−visible spectroscopy. Silica gel 60 (70−230 mesh, Merck) was used for column chromatography. UV−visible spectra were recorded on a Varian (Cary-50 Bio) spectrophotometer. Fluorescence spectra were collected using a FluoroMax-4 (HORIBA Scientific, Kyoto, Japan) spectrofluorometer. Bacteriopheophorbide *a* (**1**) was synthesized from *R. sphaeroids* (Frontier Sciences, Utah). Proton NMR spectra were recorded on a Bruker AMX 400 MHz NMR spectrometer operating at 303 K. Proton chemical shifts (δ) are reported in parts per million (ppm) relative to $CDCl_3$ (7.26 ppm), or TMS (0.00 ppm). MS and purity data were obtained by a Waters Analytical HPLC equipped with a Waters 600 Controller, a Delta 600 pump, and a 996 Photodiode Array Detector and a Waters ZQTM mass detector (Waters Limited, Mississauga, ON). A reverse phase, Symmetry C18, 5 μm, 4.6 × 150 mm column (Waters, Made in Ireland) was used under an isocratic setting of $MeCN/H_2O$ for all compounds. The solvent flow rate was kept constant at 1.00 mL/min. All final products were found to be >95% pure.

Synthesis of BchlBOA. *Synthesis of Bacteriopheophorbide a (Bchl-acid 1).* Bacteriopheophorbide *a* (Bchl-acid **1**) was synthesized from Bchl which was extracted from *R. sphaeroids* in an inert atmosphere using 1-propanol following literature methods (*28*).

Synthesis of Bacteriochlorin e_6 Di-N-Boc-aminopropylamide (Bchl-2BOC 2). Bchl-acid **1** (330 mg, 0.54 mmol) was first dissolved in 20 mL of dichloromethane. To this solution, 160 mg of 4-*N*,*N*-dimethylaminopyridine (DMAP, 1.31 mmol) and 400 mg of *N*-Boc-1,3-diaminopropane (2.30 mmol) were added. This mixture was stirred under argon for 30 min at room temperature. Subsequently, 260 mg of dicyclohexylcarbodiimide (DCC, 1.26 mmol) was added, and the mixture was stirred for 40 h. The solvent was then removed by vacuum. The crude product was purified by silica gel column chromatography with 8% acetone in dichloromethane, and then with 4% methanol in dichloromethane. The desired product Bchl-2BOC **2** (368.3 mg) and a side-product Bchl-BOC-DCC **3** (140.8 mg) were obtained in 72% (0.39 mmol) yield and 26% yield (0.14 mmol), respectively.

Bchl-2BOC **2**: Mass calculated for $C_{51}H_{72}N_8O_9$: 941.17. Found by ESI-MS: 941.8 (M^+). ^{1}H NMR ($CDCl_3$, δ ppm): 9.31, 8.65, and 8.56 (each, s, 3H for 5, 10, 20-H), 7.30, 6.42, 6.07, and 5.98 (each, brs, 4H for 4 × NH), 5.21 (s, 2H, 15^1-CH_2), 4.32 (br, 1H for 18-H), 4.25 (brs, 1H, for 7-H), 4.23 (d, 1H, for 17-H), 4.14 (brs, 1H, for 8-H), 3.72 (s, 3H, for 15^2-CO_2CH_3), 3.69 (m, 2H, for 13^3-NCH_2), 3.39 (s, 3H, for 12-CH_3), 3.38 (m, 2H, 17^5-NCH_2), 3.32 (s, 3H, for 2-CH_3), 3.17 (s, 3H, for 3-$COCH_3$), 2.84−2.59 (m, 4H, for 13^5-CH_2N, 17^7-CH_2N), 2.36 (m, 1H, for 17^1-H), 2.22 (m, 1H, for 17^1-H), 2.04 (m, 2H, for 17^2-CH_2), 1.94 (m, 2H, for 8^1-CH_2), 1.82 (d, 3H, for 18-CH_3), 1.63 (m, 5H, for 7-CH_3, 13^4-CH_2), 1.40−1.23 (brs, 20H, for 17^6-CH_2, 13^9-$C(CH_3)_3$, 17^{11}-$C(CH_3)_3$), 1.08 (t, 3H, for 8^2-CH_3), −1.21 and −1.25 (each, s, 2H, for 2 × NH).

Bchl-BOC-DCC **3**: Mass calculated for $C_{56}H_{78}N_8O_8$: 991.27. Found by ESI-MS: 991.8 (M^+). ^{1}H NMR ($CDCl_3$, δ ppm): 9.29, 8.67, and 8.57 (each, s, 3H for 5, 10, 20-H), 7.14 and 5.16 (each, brs, 2H for 2 × NH), 5.16−5.35 (m, 3H, 15^1-CH_2 + NH), 4.20−4.33 (m, 4H for 18-H, 7-H, 17-H and 8-H), 3.72 (m, 2H, for 13^3-NCH_2), 3.70 (s, 3H, for 15^2-CO_2CH_3), 3.58 (s, 3H, for 12-CH_3), 3.35 (s, 3H, for 2-CH_3), 3.18 (s, 3H, for 3-$COCH_3$), 2.36 (m, 1H, for 17^1-H), 2.25−2.29 (m, 2H, for 13^5-CH_2N), 1.82−2.08 (m, 7H, for 17^1-H, 17^2-CH_2, 8^1-CH_2 and 2 × N−CH in cyclohexyl), 1.59 (d, 3H, for 18-CH_3), 1.52 (m, 2H, 13^4-CH_2), 1.39 (s, 9H, 13^9-$C(CH_3)_3$), 1.32 (m, 3H, for 7-CH_3), 0.83−1.25 (m, 23H, for cyclohexyl-H and 8^2-CH_3), −1.23 and −1.27 (each, s, 2H, for 2 × NH).

Synthesis of Bacteriochlorin e_6 Diaminopropylamide (Bchl-2NH$_2$ 4) and Bacteriochlorin e_6 Bisoleate (BchlBOA 5). Bchl-2BOC **2** 40 mg (0.043 mmol) was dissolved in 1.5 mL of trifluoroacetic acid (TFA). The solution was stirred first in an ice−water bath under argon atmosphere for 1 h, and then at room temperature for 1 h. The TFA was removed under vacuum, the crude product Bchl-2NH$_2$ **4** did not require further purification and was used directly for the next reaction.

The crude product Bchl-2NH$_2$ **4** was dissolved in 5 mL dichloromethane upon which 0.15 mL of diisopropylethylamine (DIPEA) was added to the solution. The mixture was then stirred under argon atmosphere at room temperature for 0.5 h, oleoyl chloride 0.15 mL was added into the mixture and stirred for an additional 4 h at room temperature. The solution was poured into 50 mL of ice water and washed with ice water three times (3 × 20 mL). The organic layer was dried over anhydrous Na_2SO_4 (100 mg) for 1 h. After the solvent was removed by vacuum, the crude product was purified by silica gel column chromatography with 5% methanol in dichloromethane. The desired product BchlBOA **5** (30 mg, 0.024 mmol) was obtained in 63% yield from two steps.

Bchl-2NH$_2$ **4**: Mass calculated for $C_{41}H_{56}N_8O_5$: 740.93. Found by ESI-MS: 741.5 (M^+).

BchlBOA **5**: UV−vis in $CHCl_3$ λ_{max}: 357 nm (ε, 8.6 × 10^4), 386 nm (6.5 × 10^4), 522 nm (2.4 × 10^4), and 752 nm (8.4 × 10^4).

Mass calculated for $C_{77}H_{120}N_8O_7$: 1269.83. Found by ESI-MS: 1270.2 (M^+). ^{1}H NMR ($CDCl_3$, δ ppm): 9.31, 8.67, and 8.57 (each s, 3H for 5-H, 10-H, and 20-H), 7.16, 6.36, 5.98, and 5.82 (each brs, 4H for 4 × NH), 5.31−5.15 (m, 6H, for 2 × CH═CH in oleoyl and 15^1-CH_2), 4.32 (brs, 1H, for 18-H), 4.25 (brs, 1H, for 7-H), 4.22 (brs, 1H, for 17-H), 4.13 (brs, 1H, for 8-H), 3.68 (s, 3H, 15-CO_2CH_3), 3.66 (m, 2H, for 13^3-NCH_2), 3.55 (s, 3H, 12-CH_3), 3.47 (m, 2H, 17^5-NCH_2), 3.30 (s, 3H, for 2-CH_3), 3.15 (s, 3H, for 3-$COCH_3$), 2.91−2.83 (m, 4H, for 13^5-CH_2N, 17^7-CH_2N), 2.37 (m, 1H, 17^1-H), 1.94−2.08 (m, 25H, 17^1-H, 13^{14}-CH_2−CH═, 17^{16}-CH_2−CH═, 13^{17}-═CH−CH_2, 13^{19}- ═CH−CH_2, 13^8-$COCH_2$, 17^{10} $COCH_2$, 17^2-CH_2, 13^{12}-CH_2, 13^{13}-CH_2, 17^{14}-CH_2, 17^{15}-CH_2, and 8^1-CH_2), 1.82 (d, 3H, 18-CH_3), 1.61 (d, 3H, 7-CH_3), 1.51 (m, 2H, 13^4-CH_2), 1.43 (m, 2H, 17^6-CH_2), 1.23−1.17 (brs, 34H, other H in oleoyl), 1.08 (t, 3H, 8^2-CH_3), 0.85 (m, 6H, 13^{24}-CH_3, 17^{26}-CH_3), −1.24 and −1.27 (each s, 1H, 2 × NH).

Apolipoprotein Preparation. Lipoproteins were isolated by sequential ultracentrifugation of human plasma using standard methods (*29*). Expired human plasma was obtained from the local blood transfusion services and was approved by the University Health Network's research ethics board.

Apolipoprotein A-1 (ApoA-1) was isolated from HDL by delipidation with organic solvents as reported by Scanu and colleagues (*30*). All incubation steps were conducted at −20 °C. Briefly, 1 mL of HDL in 0.1 M sodium phosphate buffer (pH 7.5) was pipetted into a 50 mL Falcon tube containing 50 mL of a precooled 3:2 ethanol/diethyl ether mixture. This solution was mixed in a rotating mixer for 6 h. The precipitate was pelleted by centrifugation at 2000 rpm for 10 min and the supernatant was decanted. After this step, the pellet was resuspended in 50 mL of fresh diethyl ether and mixed in a rotating mixer for an additional 18 h. Subsequently, the delipidated protein was subjected to 3 washes of diethyl ether. After the last step, each tube of delipidated ApoA-1 protein was resuspended in 1 mL of fresh diethyl ether, aliquoted and dried using a centrifuge under high vacuum.

Formulation of HDL−BchlBOA. HDL−BchlBOA was formulated by combining BchlBOA (0.35 mg), dimyristoylphosphatidylcholine (DMPC) (2.16 mg) and cholesterol oleate (CO) (0.08 mg) in a 5 mL glass tube. The mixture was dried by vortexing the sample under N_2 for 5 min. Once the solvent was evaporated, the sample was dried under vacuum for 1 h. The dried film was resuspended with 1 mL Tris buffered saline (10 mM Tris, 0.1 M KCl, 1 mM EDTA; pH 8.0; degassed) and transferred to a sonicator bath (Bransonic Model 5510, Branson, Danbury, CT) where it was sonicated for 1.5 h at 50 °C. The sample was diluted to 8 mL with Tris buffer and returned to the sonication bath at 40 °C. ApoA-1 (4 mg) dissolved in 1 mL of urea (4 M) was added dropwise to the lipid-dye complex over a period of 10 min. The formulation was then sonicated for an additional 50 min. Subsequently, the sample was removed from the bath and allowed to cool to room temperature before storing overnight (approximately 15 h) at 4 °C. The next day, the sample was passed through a 0.22 μm filter and concentrated to 2 mL using a 10 000 MW cutoff Amicon centrifugal filter device (Millipore, Billerica, MA) (980 g for 30 min). The sample was then purified by fast protein liquid chromatography (FPLC) using a Superdex 200pg 26/60 column (GE Healthcare, Piscataway, NJ) and stored at 4 °C until use.

Characterization of Formulation. *Chemical Composition.* The total protein content of the formulation was measured using a modified Lowry Protein Assay (Sigma-Aldrich, St. Louis, MO). BchlBOA concentration was measured by extracting the dye twice using a $CHCl_3$/MeOH mixture (2:1). The organic layer was dried by vacuum and redissolved in 1 mL $CHCl_3$. The concentration of BchlBOA in the sample was calculated from the molar extinction coefficient by measuring the absorbance at 752 nm.

Dynamic Light Scattering (DLS). The volume size distribution of the HDL−BchlBOA particles was obtained by DLS (Nanosizer ZS90, Malvern, Worcestershire, UK).

Transmission Electron Microscopy (TEM). TEM (Hitachi 7000, Japan) in combination with negative staining was used to visualize the morphology of the HDL-like NPs. Briefly, carbon film 400 mesh copper grids (Lakefield, QC, Canada) were glow discharged prior to addition of the sample. Ten microliters of purified HDL formulations diluted 1000−2000 times using distilled and deionized H_2O was pipetted onto the copper grid such that a droplet was formed. The droplet was allowed to stand on the copper grid for 1 min. Subsequently, 6 μL of 1% uranyl acetate was added to the droplet and allowed to stand for 1 min. All liquid was then removed by whisking the droplet away using filter paper. The sample was allowed to dry for 1 min before mounting into the apparatus. The acceleration voltage of the TEM was set to 75 kV. Samples were viewed at 100 000−150 000 times magnification.

Cell Culture. All cells were cultured in 5% CO_2/95% air at 37 °C. KB cells were grown as a monolayer in a 125 cm^2 culture flask using modified Eagle's medium (ATCC 30−2003), supplemented with 10% fetal bovine serum (FBS). SR-BI positive ldlA[mSR-BI] cells were cultured in RPMI 1640 medium supplemented with 10% FBS. SR-BI negative ldlA7 cells were cultured in Ham's F-12 medium, supplemented with 2 mM L-glutamine, 1% penicillin/streptomycin, and 25% FBS.

Western Blot Analysis. ldlA[mSR-BI], ldlA7, and KB cells were cultured in a 6-wellplate. After confluence, protein was extracted from the cells using lysis buffer (20 mmol/L Tris, pH 7.5, 150 mmol/L NaCl, 1 mmol/L EDTA, 1 mmol/L EGTA, 1% Triton X-100, 2.5 mmol/L sodium pyrophosphate, 1 mmol/L β-glycerolphosphate) with a protease inhibitor cocktail (Sigma-Aldrich, St. Louis, MO) on ice for 10 min and centrifuged (11 000 g for 15 min, 4 °C). Supernatant protein levels were assayed using the Bradford method (Biorad Laboratories Inc., Hercules, CA). Twenty micrograms of each sample was separated on a 10% SDS-polyacrylamide gel and then transferred onto polyvinylidene difluoride membranes for standard Western blot analysis using monoclonal antibodies specific for SR-BI receptor (1:2000× dilution; AbCam, Cambridge, MA).

Cell Uptake Studies. ldlA[mSR-BI], KB, ldlA7 cells were seeded into 8-well Lab-tek chamber slides (0.8 cm^2/well) at a density of 3.0 × 10^4 cells per well. After 24 h, cells were washed with PBS followed by the addition of either cell media alone, cell media containing HDL−BchlBOA (8 μM), or cell media containing HDL−BchlBOA with 25-fold excess of HDL. The cells were allowed to incubate at 37 °C for 4 h after which the cells were washed twice with PBS and reincubated with 300 μL of incubation medium for imaging. Cell uptake was visualized using the Olympus FluoView 1000 laser scanning confocal microscope equipped with a Multiline Argon Laser and a 60× objective lens (oil; NA, 1.4). Fluorescence in the near-infrared was monitored from 700−800 nm using a tunable filter with a 515 nm excitation laser source.

Animal Studies. All animal experiments were conducted in accordance to the animal use protocol approved by University Health Network's animal care committee. Female athymic nude mice (7−8 weeks; 25 g) were purchased from Harlan Laboratories (Mississauga, ON). Tumor xenografts were generated in the right flank by inoculating mice subcutaneously with KB cells (3 × 10^6

Scheme 1. Synthesis of BchlBOA

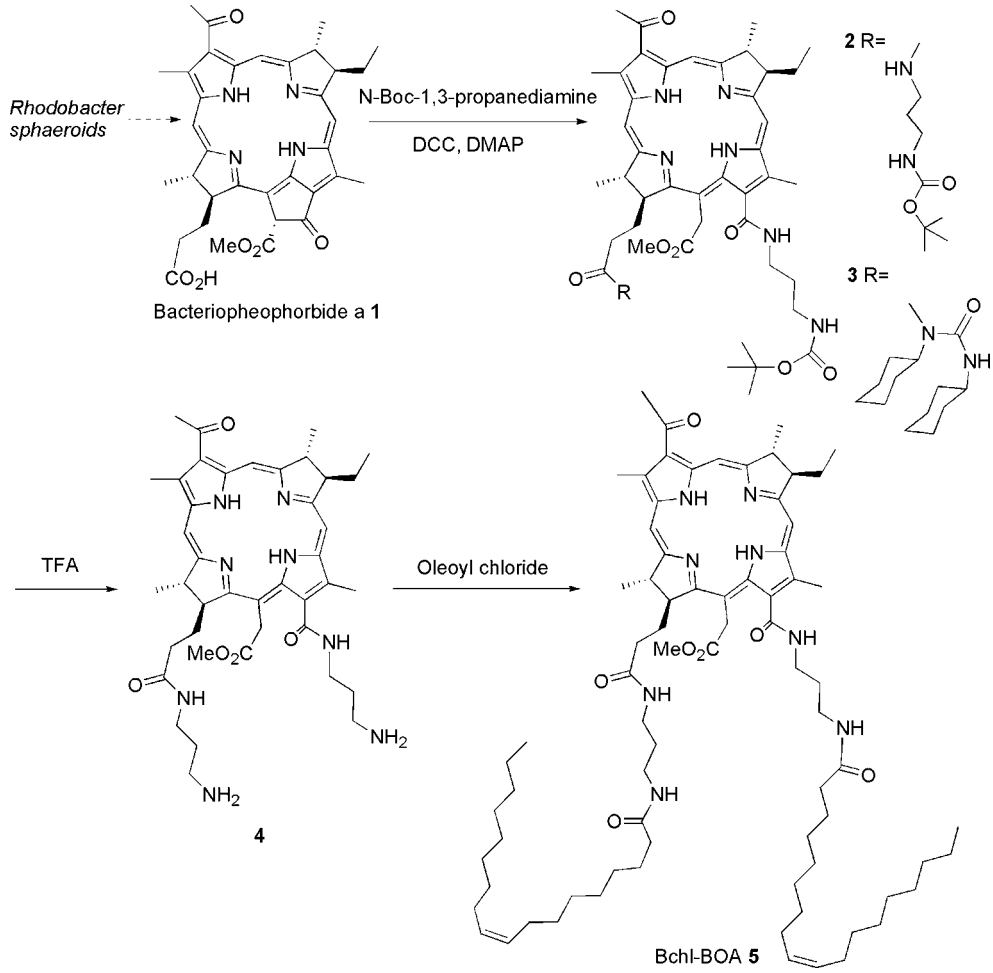

cells) three weeks prior to the study. In order to decrease the background signal during fluorescence imaging, animals were fed a chlorophyll-free diet (TD.97184, Harlan Laboratories) 2 days before the imaging study.

In Vivo Fluorescence Imaging. Spectral reflectance fluorescence imaging was conducted on KB tumor-bearing mice using the Maestro in vivo imaging system (Cambridge Research and Imaging Inc., Woburn, MA). The NIR fluorescence reflectance system is comprised of a halogen light source with an excitation bandpass filter in the range of 641−681 nm and a 700 nm long-pass emission filter connected to a CCD camera. The image cube was taken from 700−800 nm in 10 nm steps, while the exposure time was set to 2000 ms.

Animals were prescanned to determine background autofluorescence. After prescanning, animals received an intravenous tail vein injection of 37 μM HDL−BchlBOA (dye concentration;

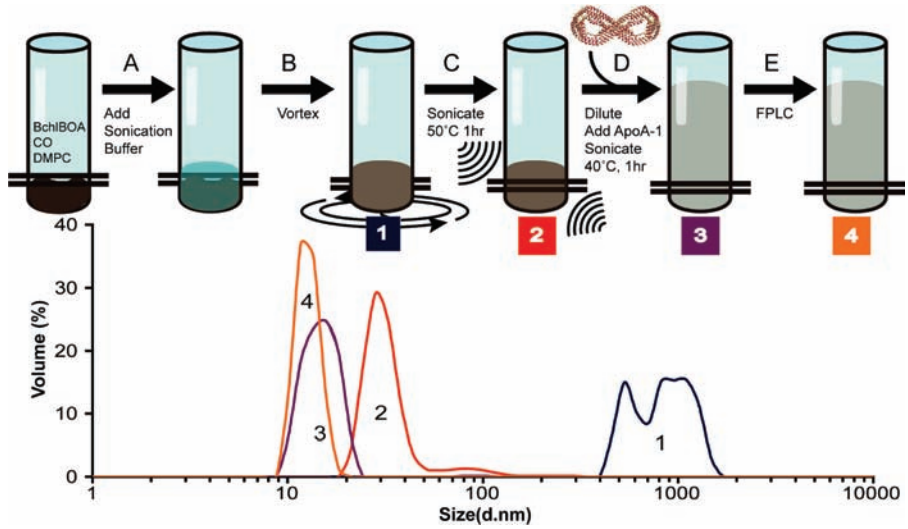

Figure 1. Schematic illustration of the formulation process for the incorporation of BchlBOA within HDL-like NPs. The size change of the particles in each step of the formulation is shown by DLS.

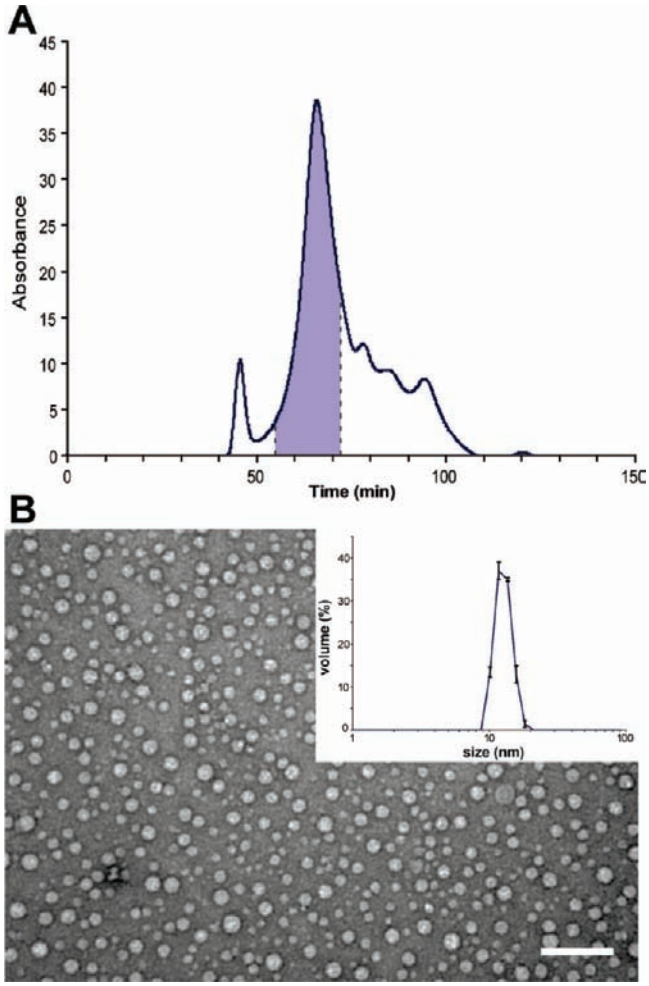

Figure 2. Purification and characterization of HDL−BchlBOA. (A) Purification of the formulated sample by size exclusion FPLC yielded three major size populations. The largest peak was collected as it corresponded with the size of native HDL (filled in blue). (B) The purified HDL−BchlBOA was sized for DLS (inset) and imaged by TEM at 100 000× magnification with 75 kV acceleration voltage. Scale bar equals 100 nm.

200 μL) and imaged at 1, 3, 6, and 48 h. After 48 h, animals were sacrificed and tissues were removed for tissue biodistribution characterization. Fifteen to 55 mg of tissue were weighed and homogenized in 1.5 mL phosphate-buffered saline. This homogenate then underwent organic extraction using $CHCl_3$:MeOH (2:1). The organic layer was removed and measured by fluorescence (excitation, 742 nm; emission, 762 nm; slit size, 5 nm).

RESULTS AND DISCUSSION

The synthesis of BchlBOA is outlined in Scheme 1. The final product, BchlBOA **5** was synthesized via the following 4-step procedure: (1) Bchl was extracted from *R. sphaeroids* (*15*), which was further hydrolyzed in dilute HCl to generate the key starting material, Bchl-acid **1**. (2) Bchl-acid was then reacted with *N*-Boc-1,3-diaminopropane in the presence of DMAP and DCC to yield the desired product Bchl-2BOC **2** in 72% yield as well as a minor side product, Bchl-BOC-DCC **3** in 26% yield. These products were obtained via (i) *N*-Boc-1,3-diaminopropane attack at the 13-C position of the β-keto ester, resulting in ring-opening to form an amide bond and (ii) a DCC-activated amidation reaction of the carboxylic acid located on the 17-C side chain. (3) Deprotection of the BOC group was carried out in TFA, and the product Bchl-2NH_2 **4** was used directly in the next step. (4) The desired final product, BchlBOA **5**, was synthesized through the reaction of Bchl-2NH_2 with oleoyl chloride in the presence of DIPEA in dichloromethane. The purity of the product was confirmed to be 96% by analytical HPLC and the overall yield for deprotection and acylation from Bchl-2BOC was 63%.

Native HDL particles transport lipophilic molecules such as triacylglycerides and cholesterol esters throughout the body by incorporating these molecules into its hydrophobic core. Introducing exogenous compounds to HDL particles can be challenging as the right conditions must be met to successfully incorporate compounds into the core of the particle. In general, the HDL core-loading works best with compounds containing a long unsaturated hydrocarbon chain (e.g., oleic or linoleic acid) or branched side chains (e.g., polyisoprenes such as phytol). Our strategy of incorporating the Bchl derivative into HDL was to attach dual unsaturated lipid "anchors" to the molecule. This strategy has been used in our lab and others to incorporate

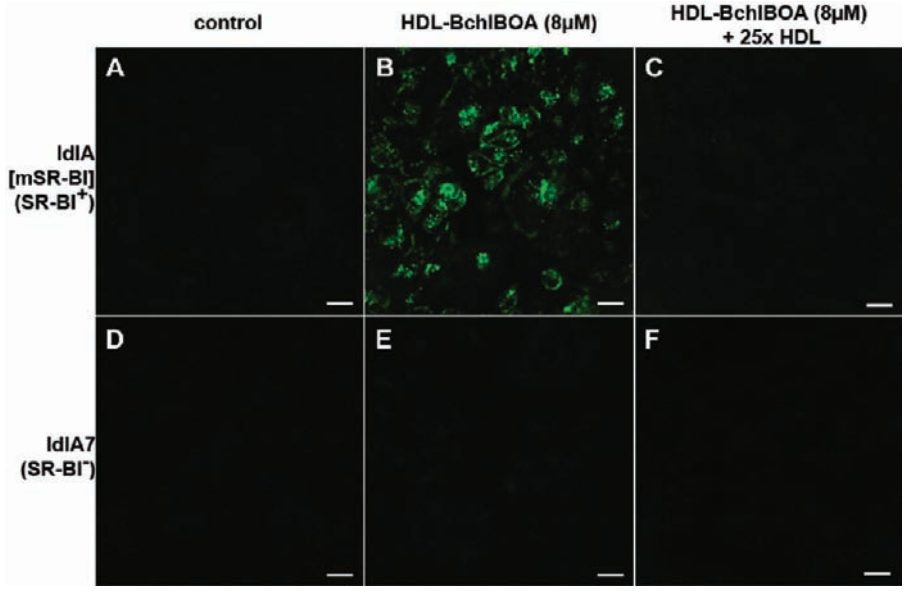

Figure 3. Representative fluorescence microscope images of cells treated with HDL−BchlBOA. Wells were seeded with ldlA[mSR-BI] (A−C) or ldlA7 (D−F) cells 24 h before imaging at a density of 3×10^4 cells per well. Final well volume was 200 μL. Cells either had no treatment (A,D), 8 μM HDL−BchlBOA (dye concentration) (B,E), or 8 μM HDL−BchlBOA (dye concentration) with 25-fold molar excess of HDL protein (C,F). Cells were excited at 515 nm and emission was captured from 700−800 nm. Scale bars correspond to 20 μm.

compounds such as bisoleoyl fluorescein (*31*), oleoyl-conjugated 5-fluorodeoxyuridine (*32*), bisoleoyl derivatives of silicon phthalocyanine, (*33*) and naphthalocyanine (*34*) into low density lipoproteins. Furthermore, attempts to incorporate oleoyl conjugated molecules into HDL have also been successful (*35*). By utilizing this strategy in the development of a novel HDL compatible fluorophore, we synthesized Bchl with bisoleate chains at the 13 and 17-C positions and successfully incorporated it into the HDL−BchlBOA.

The formulation of HDL−BchlBOA first involved preparing a thin film comprised of BchlBOA, CO, and DMPC. We found that a molar ratio of 22:1:2:1 (DMPC/CO/BchlBOA/ApoA-1) generated the desired HDL-sized NPs. In the initial steps, the addition of TRIS buffer and vortexing created a suspension of large emulsion particles, this is observed by the large and broad size distribution in DLS measurements (Figure 1). In order to prepare the sample for the addition of ApoA-1, we subsequently sonicated the formulation in a temperature-controlled bath sonicator at 50 °C for 1 h. Mechanical disruption of the lipid emulsion at this elevated temperature allowed for the generation of emulsion particles approximately 35 nm in diameter. At this point, the solution changed from an opaque appearance to a clear brown color. In the next step, ApoA-1 dissolved in 4 M urea, which served to maintain the protein in an unfolded state, was added over a period of 10 min to the diluted 8 mL emulsion. The concentration of urea decreased to 0.4 M upon addition to the sample, which allowed the protein to renature and interact with the lipid emulsion (*36*). Confirmation of this interaction and the formation of the desired HDL particles were validated by DLS size measurements as the diameter of the particle dropped to an average of 12 nm. This result corresponded well with the size of native HDL which ranges from 7−12 nm (*25*, *37*). Lastly, purification by FPLC allowed us to isolate a narrow size distribution of NPs and remove any remaining unbound ApoA-1 (Figure 2A). We next calculated the payload of BchlBOA within the HDL and found that there were on average 3 dyes per ApoA-1 protein, while the incorporation efficiency was calculated to be 40%. With the assumption that each HDL particle had between 2 to 3 molecules of ApoA-1 (*37*), this results in 6−9 molecules of dye per particle and represents a significant improvement on previous HDL-like NP formulations (*35*).

We next visualized our formulations by TEM to observe the morphology of our NP. Negative stain showed HDL−BchlBOA overwhelming possessed a spherical shape (Figure 2B). This shape was expected as neutral lipids (i.e., cholesterol oleate, BchlBOA) loaded into HDL particles will partition to the core and transform it into a spherical particle under favorable conditions (*38*).

To validate that HDL−BchlBOA retained similar functional properties as the native particle, cell uptake studies were performed. ApoA-1, the major protein found in HDL, is responsible for both the structural and functional properties of the native particle. Functionally, ApoA-1 is able to bind to the SR-BI receptor, which mediates the transfer of its cholesterol content into the host cell (*39*). Two Chinese hamster ovary (CHO) mutant clones, ldlA[mSR-BI] (ldlA7 with stably transfected mSR-BI receptor) and ldlA7 were used to delineate the high and low SR-BI receptor expression groups, respectively (*39*). In this study, we monitored the uptake of HDL−BchlBOA in these two cell lines. Under identical treatment conditions, HDL−BchlBOA was taken up exclusively by ldlA[mSR-BI] cells (Figure 3B) but was not taken up by ldlA7 cells (Figure 3E). Furthermore, the degree of uptake of HDL−BchlBOA by ldlA[mSR-BI] cells was successfully inhibited by a 25-fold excess native HDL (Figure 3C). These results indicate that the SR-BI mediated lipid transfer activity of HDL−BchlBOA was retained.

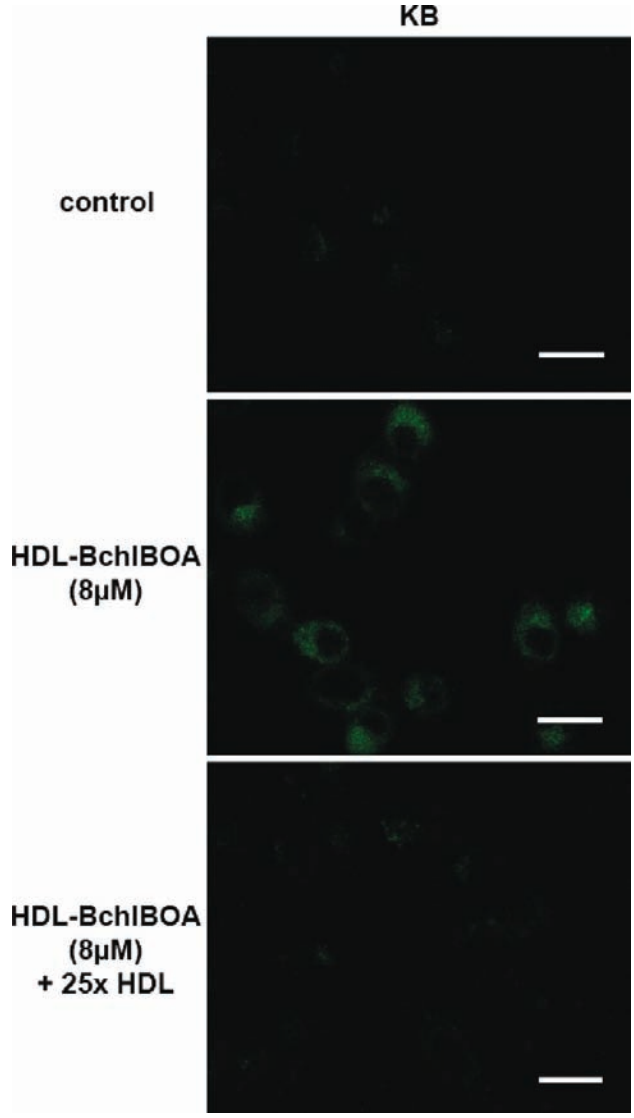

Figure 4. Fluorescence microscopic images of cells treated with HDL−BchlBOA. Cells were seeded with KB cells at a density of 3×10^4 cells per well 24 h before imaging. Final well volume was 200 μL. Cells either received no treatment (top), 8 μM HDL−BchlBOA (dye concentration) (middle), or 8 μM HDL−BchlBOA (dye concentration) with 25-fold molar excess of HDL protein (bottom). Cells were excited at 515 nm and fluorescence was captured from 700−800 nm. Scale bar corresponds to 20 μm.

The next question that needed to be addressed was whether HDL−BchlBOA can be taken up by cancer cells. Since KB cells express the SR-BI receptor, evidenced by the Western blot analysis of SR-BI expression (Supporting Information Figure S1), it was expected that HDL−BchlBOA should bind and transfer lipids to KB cells. KB cells were cultured and treated with the same conditions as the ldlA[mSR-BI] and ldlA7 cells. As expected, we observed a weaker but similar pattern of uptake as ldlA[mSR-BI] (Figure 4B). Furthermore, this uptake was also successfully inhibited by a 25-fold excess of HDL (Figure 4C). These results demonstrate that KB cancer cells are able to bind and take up lipids from HDL-like NPs through the SR-BI receptor.

To assess the tumor targeting capacity of HDL−BchlBOA, we employed a mouse tumor xenograft model. Athymic nude mice bearing KB tumors in the right flank were injected

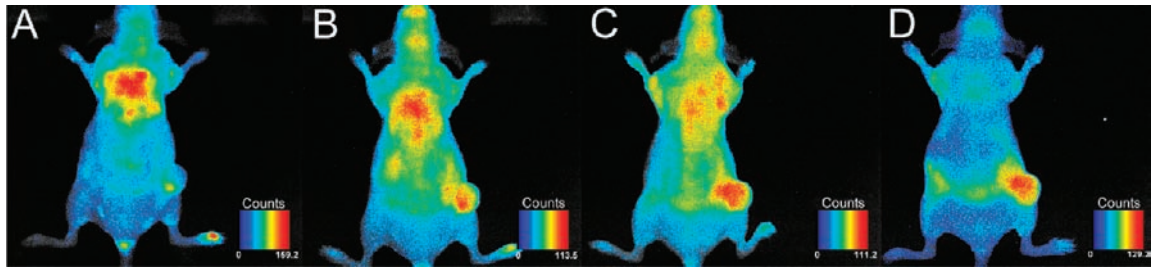

Figure 5. Spectral reflectance fluorescence images of tumor-bearing mice dosed with HDL−BchlBOA. Mice were dosed with 7.4 nmoles (200 uL) HDL−BchlBOA (dye concentration) and imaged at 1 h (A), 3 h (B), 6 h (C), and 48 h (D). Pseudo color images were captured with 2000 ms exposure.

intravenously with HDL−BchlBOA. Whole body distribution of the dye was monitored over 48 h by multispectral reflectance fluorescence imaging (Figure 5). We observed rapid accumulation of the probe in the chest area as early as 1 h. This fluorescence decreased over time, with a concomitant increase in signal intensity in the tumor vicinity. After 6 h, the signal was visualized intensely at the tumor site. Extraction of BchlBOA from various tissues after 48 h revealed that the liver and adrenal glands had the greatest accumulation of BchlBOA, followed by the spleen and tumor (data not shown). This pattern of fluorescence accumulation in the liver and adrenal glands was consistent with immunoblot studies conducted by Acton et al. which showed that the greatest SR-BI receptor expression in mice was found to be in these tissues (*39*). The fact that the HDL−BchlBOA signal remained visible in the tumor after 48 h can be explained by the long plasma circulation half-life of HDL (approximately 12 h) (*26*) as well as the enhanced permeability and retention (EPR) effect (*40*). The EPR effect allows NPs of a given size (10−100 nm) to penetrate through fenestrated vasculature into the tumor microenvironment (*41*). Furthermore, since the tumors generally do not have an effective lymphatic drainage system, NPs will tend to penetrate and accumulate around the tumor (*42*). Both of these effects enhance the probability of interactions between the particles and surface SR-BI receptors found on the KB cells.

Taken together, these results demonstrate that we successfully synthesized an imaging agent derived from Bchl that is stable and has excellent NIR fluorescence properties. We have also shown that this dye can be inserted into HDL-like NPs that retained its endogenous structure and function. More importantly, these NPs were delivered and visualized in cancer cells and implanted tumors. While the ability of the particle to distribute to cancer cells and tumor tissues are mediated by the SR-BI pathway, it is conceivable that a wide range of tumor-specific targets can be applied to HDL-like NPs such as the folate receptor or the prostate-specific membrane antigen. This will largely be dependent on the types of targeting ligands as well as the conjugation strategies. Examples of targeting ligands that may be conjugated to HDL-like NPs include folate (*43*, *44*), peptides, (*45*) and aptamer-based (*46*) moieties. Further work will be required to validate whether these targeting strategies can improve the tumor specificity of HDL−BchlBOA.

In addition to its NIR fluorescence properties, BchlBOA also has important implication for PDT. Currently, TOOKAD, a derivative of Bchl with similarities to BchlBOA is being investigated in phase II/III clinical trials as a PS for PDT in patients with recurrent prostate cancer (*24*). However, BchlBOA differs from TOOKAD in that (i) it is stabilized through modifications to the isocyclic ring, (ii) it is fluorescent, and (iii) can be incorporated into HDL-like NPs. These differences may be significant as we predict that HDL−BchlBOA may also potentially be used for NIR fluorescence-guided PDT of prostate cancer.

In conclusion, the present study outlines the synthesis of a novel Bchl-analog that is stable, fluorescent, and has dual lipid anchors for its efficient incorporation into HDL-like NPs. The resulting HDL−BchlBOA has similar characteristics to HDL in size and morphology. Furthermore, these particles can interact specifically with SR-BI receptors on both ldlA[mSR-BI] and KB cancer cell lines. This uptake was also observed in KB tumor xenografts. Our results demonstrate HDL−BchlBOA is a useful tool for in vivo molecular imaging. With this knowledge in hand, future work will continue investigating the applicability of this NP for cancer imaging and therapy. Emphasis will be placed on functionalizing the NP surface with ligands for specific targeting to tumor cells and tissues. The PDT efficiency of BchlBOA delivered in HDL will also be examined to determine the suitability of HDL−BchlBOA for image-guided therapy.

ACKNOWLEDGMENT

This work was supported by the Canadian Institutes for Health Research, the Ontario Institute for Cancer Research through funding provided by the Government of Ontario, the Canadian Cancer Society Research Institute, and the Joey and Toby Tanenbaum/Brazilian Ball Chair in Prostate Cancer Research.

Supporting Information Available: Western blot analysis of SR-BI receptor expression in various cancer cell lines versus SR-BI control cell lines. This material is available free of charge via the Internet at http://pubs.acs.org.

LITERATURE CITED

(1) Klohs, J., Wunder, A., and Licha, K. (2008) Near-infrared fluorescent probes for imaging vascular pathophysiology. *Basic Res Cardiol 103*, 144–51.
(2) Weissleder, R. (2001) A clearer vision for in vivo imaging. *Nat. Biotechnol. 19*, 316–7.
(3) Ernst, L. A., Gupta, R. K., Mujumdar, R. B., and Waggoner, A. S. (1989) Cyanine dye labeling reagents for sulfhydryl groups. *Cytometry 10*, 3–10.
(4) Achilefu, S., Jimenez, H. N., Dorshow, R. B., Bugaj, J. E., Webb, E. G., Wilhelm, R. R., Rajagopalan, R., Johler, J., and Erion, J. L. (2002) Synthesis, in vitro receptor binding, and in vivo evaluation of fluorescein and carbocyanine peptide-based optical contrast agents. *J. Med. Chem. 45*, 2003–15.
(5) Licha, K., Riefke, B., Ntziachristos, V., Becker, A., Chance, B., and Semmler, W. (2000) Hydrophilic cyanine dyes as contrast agents for near-infrared tumor imaging: synthesis, photophysical

properties and spectroscopic in vivo characterization. *Photochem. Photobiol. 72*, 392–8.

(6) Becker, A., Hessenius, C., Licha, K., Ebert, B., Sukowski, U., Semmler, W., Wiedenmann, B., and Grotzinger, C. (2001) Receptor-targeted optical imaging of tumors with near-infrared fluorescent ligands. *Nat. Biotechnol. 19*, 327–31.

(7) Wei, X., Runnels, J. M., and Lin, C. P. (2003) Selective uptake of indocyanine green by reticulocytes in circulation. *Invest. Ophthalmol. Visual Sci. 44*, 4489–96.

(8) Caesar, J., Shaldon, S., Chiandussi, L., Guevara, L., and Sherlock, S. (1961) The use of indocyanine green in the measurement of hepatic blood flow and as a test of hepatic function. *Clin. Sci. 21*, 43–57.

(9) Stefflova, K., Chen, J., and Zheng, G. (2007) Killer beacons for combined cancer imaging and therapy. *Curr. Med. Chem. 14*, 2110–25.

(10) Ghoroghchian, P. P., Frail, P. R., Susumu, K., Blessington, D., Brannan, A. K., Bates, F. S., Chance, B., Hammer, D. A., and Therien, M. J. (2005) Near-infrared-emissive polymersomes: self-assembled soft matter for in vivo optical imaging. *Proc. Natl. Acad. Sci. U.S.A. 102*, 2922–7.

(11) Koyama, T., Tsubota, A., Nariai, K., Mitsunaga, M., Yanaga, K., and Takahashi, H. (2007) Novel biomedical imaging approach for detection of sentinel nodes in an experimental model of gastric cancer. *Br. J. Surg. 94*, 996–1001.

(12) Akers, W., Lesage, F., Holten, D., and Achilefu, S. (2007) In vivo resolution of multiexponential decays of multiple near-infrared molecular probes by fluorescence lifetime-gated whole-body time-resolved diffuse optical imaging. *Mol. Imaging 6*, 237–46.

(13) Zhang, Z., Li, H., Liu, Q., Zhou, L., Zhang, M., Luo, Q., Glickson, J., Chance, B., and Zheng, G. (2004) Metabolic imaging of tumors using intrinsic and extrinsic fluorescent markers. *Biosens. Bioelectron. 20*, 643–50.

(14) Pichlmeier, U., Bink, A., Schackert, G., and Stummer, W. (2008) Resection and survival in glioblastoma multiforme: an RTOG recursive partitioning analysis of ALA study patients. *Neuro-Oncology 10*, 1025–34.

(15) Pandey, S. K., Gryshuk, A. L., Sajjad, M., Zheng, X., Chen, Y., Abouzeid, M. M., Morgan, J., Charamisinau, I., Nabi, H. A., Oseroff, A., and Pandey, R. K. (2005) Multimodality agents for tumor imaging (PET, fluorescence) and photodynamic therapy. A possible "see and treat" approach. *J. Med. Chem. 48*, 6286–95.

(16) Stefflova, K., Chen, J., Li, H., and Zheng, G. (2006) Targeted photodynamic therapy agent with a built-in apoptosis sensor for in vivo near-infrared imaging of tumor apoptosis triggered by its photosensitization in situ. *Mol. Imaging 5*, 520–32.

(17) Stefflova, K., Li, H., Chen, J., and Zheng, G. (2007) Peptide-based pharmacomodulation of a cancer-targeted optical imaging and photodynamic therapy agent. *Bioconjug. Chem. 18*, 379–88.

(18) Fiedor, J., Fiedor, L., Kammhuber, N., Scherz, A., and Scheer, H. (2002) Photodynamics of the bacteriochlorophyll-carotenoid system. 2. Influence of central metal, solvent and beta-carotene on photobleaching of bacteriochlorophyll derivatives. *Photochem. Photobiol. 76*, 145–52.

(19) Chen, Y., Graham, A., Potter, W., Morgan, J., Vaughan, L., Bellnier, D. A., Henderson, B. W., Oseroff, A., Dougherty, T. J., and Pandey, R. K. (2002) Bacteriopurpurinimides: highly stable and potent photosensitizers for photodynamic therapy. *J. Med. Chem. 45*, 255–8.

(20) Rosenbach-Belkin, V., Chen, L., Fiedor, L., Tregub, I., Pavlotsky, F., Brumfeld, V., Salomon, Y., and Scherz, A. (1996) Serine conjugates of chlorophyll and bacteriochlorophyll: photocytotoxicity in vitro and tissue distribution in mice bearing melanoma tumors. *Photochem. Photobiol. 64*, 174–81.

(21) Chen, Y., Potter, W. R., Missert, J. R., Morgan, J., and Pandey, R. K. (2007) Comparative in vitro and in vivo studies on long-wavelength photosensitizers derived from bacteriopurpurinimide and Bacteriochlorin p6: fused imide ring enhances the in vivo PDT efficacy. *Bioconjug. Chem. 18*, 1460–73.

(22) Drzewiecka-Matuszek, A., Skalna, A., Karocki, A., Stochel, G., and Fiedor, L. (2005) Effects of heavy central metal on the ground and excited states of chlorophyll. *J. Biol. Inorg. Chem. 10*, 453–62.

(23) Trachtenberg, J., Bogaards, A., Weersink, R. A., Haider, M. A., Evans, A., McCluskey, S. A., Scherz, A., Gertner, M. R., Yue, C., Appu, S., Aprikian, A., Savard, J., Wilson, B. C., and Elhilali, M. (2007) Vascular targeted photodynamic therapy with palladium-bacteriopheophorbide photosensitizer for recurrent prostate cancer following definitive radiation therapy: assessment of safety and treatment response. *J. Urol. 178*, 1974–9; discussion 1979.

(24) Trachtenberg, J., Weersink, R. A., Davidson, S. R., Haider, M. A., Bogaards, A., Gertner, M. R., Evans, A., Scherz, A., Savard, J., Chin, J. L., Wilson, B. C., and Elhilali, M. (2008) Vascular-targeted photodynamic therapy (padoporfin, WST09) for recurrent prostate cancer after failure of external beam radiotherapy: a study of escalating light doses. *BJU Int. 102*, 556–62.

(25) Lund-Katz, S., Liu, L., Thuahnai, S. T., and Phillips, M. C. (2003) High density lipoprotein structure. *Front Biosci. 8*, d1044–54.

(26) Eisenberg, S., Windmueller, H. G., and Levy, R. I. (1973) Metabolic fate of rat and human lipoprotein apoproteins in the rat. *J. Lipid Res. 14*, 446–58.

(27) Daerr, W. H., Pethke, W., Windler, E. T., and Greten, H. (1990) Biotinyl-high-density lipoproteins as a probe for the determination of high-density lipoprotein turnover in humans. *Biochim. Biophys. Acta 1043*, 311–7.

(28) Kozyrev, A. N., Chen, Y., Goswami, L. N., Tabaczynski, W. A., and Pandey, R. K. (2006) Characterization of porphyrins, chlorins, and bacteriochlorins formed via allomerization of bacteriochlorophyll a. Synthesis of highly stable bacteriopurpurinimides and their metal complexes. *J. Org. Chem. 71*, 1949–60.

(29) Havel, R. J., Eder, H. A., and Bragdon, J. H. (1955) The distribution and chemical composition of ultracentrifugally separated lipoproteins in human serum. *J. Clin. Invest. 34*, 1345–53.

(30) Scanu, A. (1966) Forms of human serum high density lipoprotein protein. *J. Lipid Res. 7*, 295–306.

(31) Krieger, M., Smith, L. C., Anderson, R. G., Goldstein, J. L., Kao, Y. J., Pownall, H. J., Gotto, A. M., Jr., and Brown, M. S. (1979) Reconstituted low density lipoprotein: a vehicle for the delivery of hydrophobic fluorescent probes to cells. *J. Supramol. Struct. 10*, 467–78.

(32) Rensen, P. C., de Vrueh, R. L., Kuiper, J., Bijsterbosch, M. K., Biessen, E. A., and van Berkel, T. J. (2001) Recombinant lipoproteins: lipoprotein-like lipid particles for drug targeting. *Adv. Drug Deliv. Rev. 47*, 251–76.

(33) Li, H., Marotta, D. E., Kim, S., Busch, T. M., Wileyto, E. P., and Zheng, G. (2005) High payload delivery of optical imaging and photodynamic therapy agents to tumors using phthalocyanine-reconstituted low-density lipoprotein nanoparticles. *J. Biomed. Opt. 10*, 41203.

(34) Song, L., Li, H., Sunar, U., Chen, J., Corbin, I., Yodh, A. G., and Zheng, G. (2007) Naphthalocyanine-reconstituted LDL nanoparticles for in vivo cancer imaging and treatment. *Int. J. Nanomed. 2*, 767–74.

(35) Corbin, I. R., Chen, J., Cao, W., Li, H., Lund-Katz, S., and Zheng, G. (2007) Enhanced Cancer-Targeted Delivery Using Engineered High-Density Lipoprotein-Based Nanocarriers. *J. Biomed. Nanotechnol. 3*, 367–376.

(36) Pittman, R. C., Glass, C. K., Atkinson, D., and Small, D. M. (1987) Synthetic high density lipoprotein particles. Application to studies of the apoprotein specificity for selective uptake of cholesterol esters. *J. Biol. Chem. 262*, 2435–42.

(37) Silva, R. A., Huang, R., Morris, J., Fang, J., Gracheva, E. O., Ren, G., Kontush, A., Jerome, W. G., Rye, K. A., and Davidson, W. S. (2008) Structure of apolipoprotein A-I in spherical high density lipoproteins of different sizes. *Proc. Natl. Acad. Sci. U.S.A. 105*, 12176–81.

(38) Sparks, D. L., Davidson, W. S., Lund-Katz, S., and Phillips, M. C. (1995) Effects of the neutral lipid content of high density lipoprotein on apolipoprotein A-I structure and particle stability. *J. Biol. Chem. 270*, 26910–7.

(39) Acton, S., Rigotti, A., Landschulz, K. T., Xu, S., Hobbs, H. H., and Krieger, M. (1996) Identification of scavenger receptor SR-BI as a high density lipoprotein receptor. *Science 271*, 518–20.

(40) Maeda, H., Sawa, T., and Konno, T. (2001) Mechanism of tumor-targeted delivery of macromolecular drugs, including the EPR effect in solid tumor and clinical overview of the prototype polymeric drug SMANCS. *J. Controlled Release 74*, 47–61.

(41) Roberts, W. G., and Palade, G. E. (1997) Neovasculature induced by vascular endothelial growth factor is fenestrated. *Cancer Res. 57*, 765–72.

(42) Haag, R. (2004) Supramolecular drug-delivery systems based on polymeric core-shell architectures. *Angew. Chem., Int. Ed. 43*, 278–82.

(43) Zheng, G., Chen, J., Li, H., and Glickson, J. D. (2005) Rerouting lipoprotein nanoparticles to selected alternate receptors for the targeted delivery of cancer diagnostic and therapeutic agents. *Proc. Natl. Acad. Sci. U.S.A. 102*, 17757–62.

(44) Chen, J., Corbin, I. R., Li, H., Cao, W., Glickson, J. D., and Zheng, G. (2007) Ligand conjugated low-density lipoprotein nanoparticles for enhanced optical cancer imaging in vivo. *J. Am. Chem. Soc. 129*, 5798–9.

(45) von Maltzahn, G., Ren, Y., Park, J. H., Min, D. H., Kotamraju, V. R., Jayakumar, J., Fogal, V., Sailor, M. J., Ruoslahti, E., and Bhatia, S. N. (2008) In vivo tumor cell targeting with "click" nanoparticles. *Bioconjug. Chem. 19*, 1570–8.

(46) Lupold, S. E., Hicke, B. J., Lin, Y., and Coffey, D. S. (2002) Identification and characterization of nuclease-stabilized RNA molecules that bind human prostate cancer cells via the prostate-specific membrane antigen. *Cancer Res. 62*, 4029–33.

BC900404Y

Supporting Information for:

Synthesis and evaluation of a stable bacteriochlorophyll-analog and its incorporation into high-density lipoprotein nanoparticles for tumor imaging

Weiguo Cao, Kenneth K. Ng, Ian Corbin, Zhihong Zhang, Lili Ding, Juan Chen, and Gang Zheng*

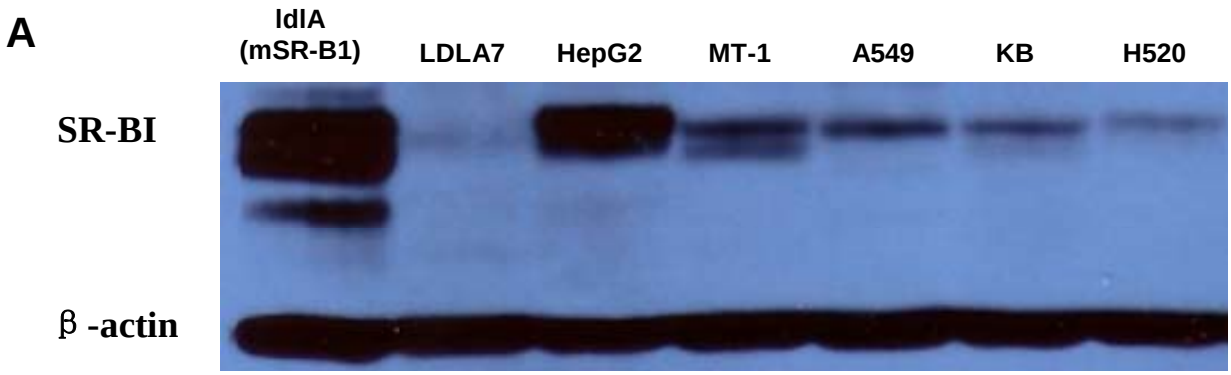

Figure S1 Western blot of SR-BI receptor expression in various cancer cell lines vs control cell lines ($SR\text{-}BI^+$ and $SR\text{-}BI^-$).

ARTICLES

Synthesis and Transfection Properties of a Series of Lipidic Neamine Derivatives

Tony Le Gall,[†] Isabelle Baussanne,[‡] Somnath Halder,[‡] Nathalie Carmoy,[†] Tristan Montier,[†] Pierre Lehn,*[,†] and Jean-Luc Décout*[,‡]

INSERM U613, IFR 148 ScInBIoS, Université de Bretagne Occidentale, C.S. 2653, F-29275 Brest Cedex, France, and Université de Grenoble/CNRS, UMR 5063, Département de Pharmacochimie Moléculaire, ICMG FR 2607, BP 53 F-38041 Grenoble Cedex 9, France. Received February 11, 2009; Revised Manuscript Received September 22, 2009

With the view to develop novel bioinspired nonviral vectors for gene delivery, we synthesized a series of cationic lipids with a neamine headgroup, which incorporates rings I and II of the natural antibiotic aminoglycoside neomycin B. Indeed, we reasoned that neamine might constitute a straightforward and versatile building block for synthesizing a variety of lipophilic aminoglycosides and modulating their characteristics such as size, topology, lipophilicity, number of charges, and charge density. Neamine derivatives bearing long dialkyl chains, one or two neamine headgroups, and four to ten protonatable amine functions were prepared through the selective alkylation of the 4′- or 5-hydroxyl function in ring I and ring II of neamine, respectively. The transfection activity of the twelve derivatives synthesized was investigated *in vitro* in gene transfection experiments using several mammalian cell lines. The results allowed us to unveil interesting structure−activity relationships and to identify a formulation incorporating a small neamine derivative as a highly efficient gene delivery system.

INTRODUCTION

The natural aminoglycosides are antibiotics broadly used in medicine for their antibacterial activity due to their ability to bind the bacterial rRNA and thus interfere with protein synthesis (*1*). Aminoglycosides were also reported to selectively bind *in vitro* to viral RNAs such as HIV DIS, RRE, and TAR RNA (*2, 3*). Recently, aminoglycosides were also found to allow, via binding to rRNA, the read-through of disease-causing nonsense mutations by the translation complex and therefore the synthesis of full-length active proteins; this read-through activity is presently being evaluated for the treatment of genetic diseases such as cystic fibrosis (*4*−*7*).

It was recently demonstrated that lipophilic derivatives of natural aminoglycosides, including tobramycin, kanamycin A (compound **1** in Chart 1), paromomycin (**2**), and neomycin B (**3**), were able to mediate transfections of either plasmid DNA (*8*−*12*) or siRNA (*13*).

A main feature of these lipophilic pseudo-oligosaccharides (bearing lipidic chains or cholesteryl groups) was their multivalent character due to the presence of four to six protonatable amine functions and thus allowing strong binding of the phosphodiester groups of DNA or RNA. It is noteworthy that these lipidic aminoglycoside derivatives, which carried up to six amine groups distributed over three or four rings, were synthesized from their natural aminoglycoside counterparts mainly through acylation of the most accessible and reactive amine function.

With regard to the development of gene delivery agents, it is widely recognized that the affinity of the vector for the DNA to be transferred as well as the size and the supramolecular organization of the complexes formed with DNA are key parameters for their transfection activity (*14*−*16*). The delineation of structure−activity relationships, which implies evaluating variations of many parameters such as the positive charge density and the lipophilicity balance, is thus highly important.

With the view of developing novel antiviral and antibiotic agents, we have previously reported a synthetic route for preparing 4′-, 5-, and 4′,5-neamine derivatives (*17*). Here, the neamine core was conjugated to peptide nucleic acids (PNA) targeting the HIV TAR RNA (*18, 19*). One of the PNA conjugates prepared was able to cleave TAR and inhibit viral replication (*18, 19*). A study of fluorescent PNA conjugates demonstrated that the presence of the neamine core in the PNA conjugates permitted their cellular uptake, whereas the PNA alone was not taken up by the cells (*19*).

Taking into account this last work and the previously reported transfection properties of lipidic derivatives of natural aminoglycosides (see above), we reasoned that it may be interesting to develop transfection agents based on the small aminoglycoside neamine (**4** in Chart 1) through its conjugation to lipophilic alkyl chains. Indeed, neamine, incorporating rings I and II of neomycin B, presents a higher charge density and is easier to modify on the hydroxyl groups than the natural aminoglycosides, thereby enabling the continued presence of all protonatable amine functions for DNA binding.

We herein report the synthesis and the gene transfection activity of a series of lipidic neamine derivatives. Indeed, neamine appeared to be a straightforward and versatile building block for synthesizing lipidic aminoglycosides and modifying their characteristics such as size, topology, number of charges,

* To whom correspondence should be addressed. E-mail: Pierre.Lehn@univ-brest.fr; Jean-Luc.Decout@ujf-grenoble.fr.
[†] INSERM U613.
[‡] UMR Université de Grenoble/CNRS 5063.

10.1021/bc900062z CCC: $40.75 © 2009 American Chemical Society
Published on Web 10/22/2009

Chart 1. Structure of the Natural Aminoglycosides Kanamycin A, Paromomycin, and Neomycin B and of Neamine Prepared by Methanolysis of Neomycin B[a]

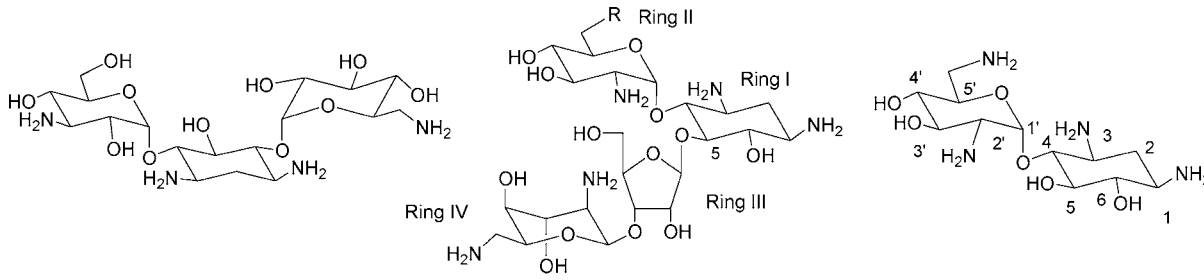

1: Kanamycin A: *Mw* = 484; 4 NH_2 **2**: Paromomycin: R= OH; *Mw* = 616; 5 NH_2 **4**: Neamine: *Mw* = 322; 4 NH_2
3: Neomycin B: R= NH_2; *Mw* = 615; 6 NH_2

[a] For each compound, the molecular weight (M_w, g/mol) and the number of amino groups (NH_2) are indicated. Neamine displays a higher positive charge as illustrated by the ratio value between the number of amino groups and the molecular weight: Ratio [NH_2/M_w] = 0.0083, 0.0081, 0.0098, and 0.0124 for kanamycin A, paromomycin, neomycin B, and neamine, respectively.

Scheme 1[a]

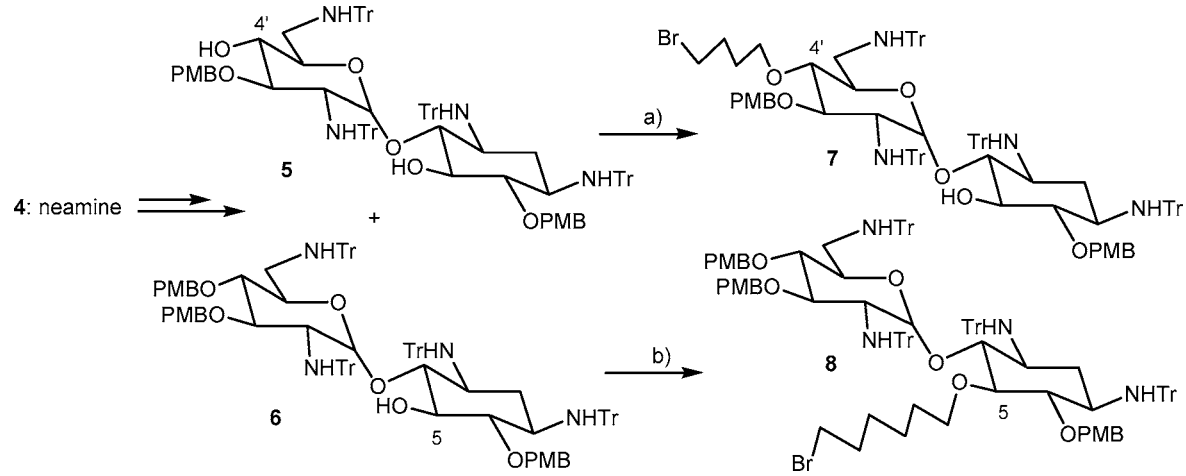

[a] (a) NaH, DMF, 1-bromobutane, 60−70 °C. (b) NaH, DMF, 1-bromohexane, 60−70 °C.

and charge density. In the present work, in contrast to the previously reported aminoglycosides derivatives (see above), a series of twelve compounds incorporating one or two neamine cores with four to ten protonatable (at pH 7) amine functions were prepared through the selective alkylation of the 4′- or 5-hydroxyl functions in rings I and II, respectively. The gene transfection experiments revealed interesting structure−activity relationships and allowed us to identify a highly efficient formulation based on a small neamine derivative with a single neamine core.

EXPERIMENTAL PROCEDURES

Materials. Dulbecco's Modified Eagle Medium (DMEM), Eagle's Minimum Essential Medium (EMEM), fetal bovine serum (FBS), OptiMEM, penicillin, streptomycin, and Lipofectamine (LFM; liposome formulation of DOSPA/DOPE 3/1, w/w) were purchased from Invitrogen (UK). The 1,2-dioleoyl-*sn*-glycero-3-phosphoethanolamine (DOPE) was purchased from Sigma (Saint Quentin Fallavier, France). Two reporter plasmids were used: pEGFP-Luc (6.4 kb) and pTG11033 (9.6 kb), obtained from Clontech (UK) and Transgene (France), respectively. In all *in vitro* assays, we used the pEGFP-Luc which encodes a fusion of an enhanced green fluorescent protein (EGFP; excitation maximum at 488 nm, emission maximum at 507 nm) and the luciferase from the firefly *Photinus pyralis*. For the *in vivo* experiments, in order to facilitate the detection of the luciferase reporter activity, we used the plasmid pTG11033, which contains not only the firefly luciferase reporter gene under the control of the strong viral CMV promoter, but also the HMG-1 intron, which allows enhanced transgene protein synthesis (via increased mRNA export from the nucleus to the cytosol); this plasmid was used with highly purified synthetic D-luciferin (Interchim, Montluçon, France). All other chemicals were of cell culture and molecular biology quality.

Synthesis of the Most Transfection Efficient 4′-Neamine Derivatives 12b and 13b. For clarity purposes, we describe here only the synthesis of the neamine derivatives **12b** and **13b**, which were the most efficient for gene transfection. The synthesis and the characteristics of the other neamine derivatives studied herein (i.e., **11**, **12a**, **14b**, **15a**, **18**, **22**, **24**, **27**, **30**, and **32**) are available as Supporting Information. It should also be noted that the schemes presented here actually deal with the synthesis of all the different neamine derivatives investigated.

4′-*O*-(4-Bromobutyl) Protected Neamine Derivative 7 (Scheme 1). To a solution of **5** (2.9 g, 1.89 mmol) in DMF (58 mL) under argon atmosphere were added successively NaH (60% suspension, 761 mg, 19.0 mmol) and 1,4-dibromobutane (8.7 mL, 72.5 mmol). The mixture was stirred for 4 h at 70 °C. After cooling, CH_2Cl_2 and a saturated aqueous NH_4Cl solution were added. The organic layer was washed with water, dried over $MgSO_4$, filtered, and concentrated under reduced pressure. The residue obtained was chromatographed on alumina gel with a mixture of pentane/CH_2Cl_2 (70/30, v/v) to lead to the dialkylated product (6%) and the monoalkylated product **7**

Scheme 2[a]

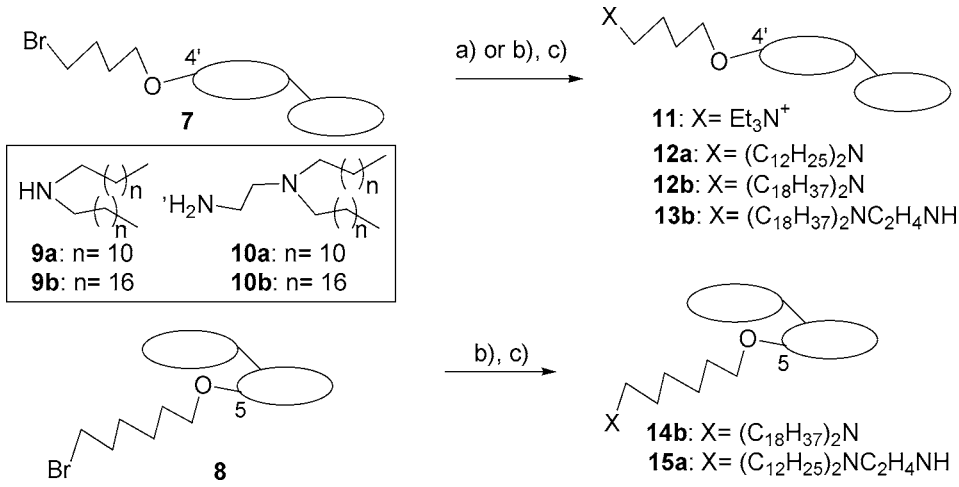

[a] (a) DMF, NEt_3, 60−70 °C; (b) DMF, K_2CO_3, 60−70 °C; amine: **9a**, **9b**, **10a**, or **10b**. (c) TFA, CH_2Cl_2, anisole, rt.

(white powder, 54%, mp 132−133 °C). ^{13}C NMR ($CDCl_3$) δ 159.1, 159.0 ($COCH_3$) 147.0−146.0 (*C* arom.), 125.7−130.9 (*CH* arom.), 113.7−113.8 (*CH o*-OCH_3), 95.0 (C1′), 81.8, 81.6, 77.3, 73.8, 72.8, 71.9, 71.0, 70.8, 70.5, (C4, C5, C6, C3′, C4′, C5′, $OCH_2(CH_2)_3Br$, $2CH_2Ph$), 58.1, 53.0, 52.6 (C2′, C1, C3), 55.2 (OCH_3), 45.4 (C6′), 33.8 ($O(CH_2)_3CH_2Br$), 29.6, 29.2, 28.9(C2, $OCH_2(CH_2)_2CH_2Br$). LRMS (FAB$^+$, NBA) *m*/*z*: 1689 $[M+Na]^+$, 1665 $[M+H]^+$, 1423. HRMS (ESI$^+$) *m*/*z*: $[M+H]^+$ calculated 1665.7194, found 1665.7186.

4′-*O*-[4-(*N*,*N*-di-*n*-Octadecylamino)butyl] Neamine Derivative 12b (Scheme 2). Step b. To a solution of compound **7** (190 mg, 0.11 mmol) in DMF (5 mL) under argon atmosphere was added successively K_2CO_3 (110 mg, 0.79 mmol) and di-*n*-octadecylamine **9b** (60 mg, 0.11 mmol). The reaction mixture was stirred for 24 h at 70 °C. After cooling, the reaction mixture was filtered, then concentrated under reduced pressure. The residue was chromatographed on alumina gel with cyclohexane/CH_2Cl_2 (70/30, v/v) to lead to the protected derivative of **12b** in 30% yield. HRMS (ESI$^+$) *m*/*z*: $[M+H]^+$ calculated 2107.3832, found 2107.3847, $[M+Na]^+$ calculated 2129.3651, found 2129.3665.

Step c. The protected compound was dissolved in CH_2Cl_2/TFA (1/1, v/v, 4 mL) with anisole (0.1 mL). After 2 h stirring at room temperature (rt), solvents were removed under reduced pressure. H_2O and Et_2O were added and the aqueous layer washed twice with Et_2O before being concentrated and poured on a C18 reversed-phase column. After elution with a gradient of H_2O/MeOH, **12b** was obtained as the TFA salt with 67% yield. ^{1}H NMR (D_2O) δ 5.85 (d, $J_{1'-2'} = 4.0$ Hz, 1H, H1′), 4.04 (m, 2H, H3′, H5′), 3.89 (m, 1H, $OCH_2(CH_2)_3N$), 3.80 (dd, $J_{4-5} = J_{4-3} = 8.5$ Hz, 1H, H4), 3.67 (m, 2H, H5, $OCH_2(CH_2)_3N$), 3.55 (dd, $J_{6-5} = J_{6-1} = 9.5$ Hz, 1H, H6), 3.08−3.37 (m, 6H, H1, H3, H2′, H4′, 2H6′), 2.82−3.08 (m, 6H, $3NCH_2$), 2.41 (ddd, $J_{2eq-1} = J_{2eq-3} = 4.0$ Hz, $J_{2eq-2ax} = 12.0$ Hz, 1H, $H2_{eq}$), 1.40−1.75 (m, 9H, $H2_{ax}$, $OCH_2(CH_2)_2CH_2N$, $N[CH_2CH_2(CH_2)_{15}CH_3]_2$), 1.00−1.40 (m, 60H, $N[CH_2CH_2(CH_2)_{15}CH_3]_2$), 0.87 (t, $J = 6.7$ Hz, 6H, $2CH_3$). ^{13}C NMR (D_2O) δ 95.8 (C1′), 79.3 (C4′, C4), 75.2 (C5), 72.8 (C6), 72.4 ($OCH_2(CH_2)_3N$), 69.1, 68.4 (C3′, C5′), 53.8 (C2′), 51.2 ($3NCH_2$), 50.0 (C1), 48.4 (C3), 40.2 (C6′), 32.1, 30.2, 29.7, 29.2, 28.7, 26.5, 25.9, 22.7, 22.3, 20.5 (C2, $OCH_2(CH_2)_2CH_2N$, $[NCH_2(CH_2)_{16}CH_3]_2$), 13.8 ($2CH_3$). HRMS (ESI$^+$) *m*/*z*: $[M+H]^+$ calculated 898.8299, found 898.8297, $[M+Na]^+$ calculated 920.8119, found 920.8112.

4′-*O*-[4-(*N*-2-aminoethyl-*N*,*N*-di-*n*-octadecylamino)butyl] Neamine Derivative 13b (Scheme 2). The same procedure as described for the synthesis of **12b** (steps b and c) was applied to compound **7** (300 mg, 0.18 mmol) with *N*-2-aminoethyl-*N*,*N*-di-*n*-octadecylamine **10b** (114 mg, 0.20 mmol). **13b** was obtained in 42% yield in two steps. ^{1}H NMR (CD_3OD) δ 5.94 (d, $J_{1'-2'} = 4.0$ Hz, 1H, H1′), 4.07−4.17 (m, 2H, H3′, H5′), 4.01 (dd, $J_{4-5} = J_{4-3} = 9.6$ Hz, 1H, H4), 3.97 (m, 1H, $OCH_2(CH_2)_3N$), 3.66 (m, 1H, $OCH_2(CH_2)_3N$), 3.62 (dd, $J_{4-5} = J_{5-6} = 9.2$ Hz, 1H, H5), 3.40−3.70 (m, 7H, H3, H6, H6′b, $2NCH_2$), 3.31 (m, 1H, H2′), 2.99−3.24 (m, 9H, H1, H4, H6′a, $3NCH_2$), 2.47 (ddd, $J_{2eq-1} = J_{2eq-3} = 4.4$ Hz, $J_{2eq-2ax} = 12.0$ Hz, 1H, $H2_{eq}$), 2.01 (ddd, $J_{2ax-1} = J_{2ax-3} = J_{2eq-2ax} = 12.4$ Hz, 1H, $H2_{ax}$), 1.65−1.90 (m, 8H, $OCH_2(CH_2)_2CH_2N$, $N[CH_2CH_2(CH_2)_{15}CH_3]_2$), 1.20−1.50 (m, 60H, $N[CH_2CH_2(CH_2)_{15}CH_3]_2$), 0.90 (t, $J = 6.7$ Hz, 6H, $2CH_3$). ^{13}C NMR (CD_3OD) δ 95.7 (C1′), 79.7 (C4′), 78.1 (C4), 75.8 (C5), 72.9 (C6), 71.8 ($OCH_2(CH_2)_5N$), 70.0, 68.6 (C3′, C5′), 54.2 (C2′), 53.4 ($2NCH_2$), 50.1, 48.7 (C3, C1), 48.3, 48.0 ($2NCH_2$), 41.8 (NCH_2), 40.5 (C6′), 31.7, 29.4, 29.2, 29.1, 28.8, 28.5, 26.7, 26.1, 23.5, 22.7, 22.3 (C2, $OCH_2(CH_2)_2CH_2N$, $[NCH_2(CH_2)_{16}CH_3]_2$), 13.0 ($2CH_3$). HRMS (ESI$^+$) *m*/*z*: $[M+H]^+$ calculated 941.8722, found 941.8754.

Chemical Descriptions. MarvinSketch software [Marvin 5.0.2.1, 2008, ChemAxon (http://www.chemaxon.com)] was used for drawing, displaying, and characterizing chemical structures and substructures. The log *P* plug-in in this software calculates the octanol/water partition coefficient, which is used in QSAR analysis and rational drug design as a measure of molecular hydrophobicity. The calculation method used here is based on a modification of the method published by Viswanadhan et al. (*20*).

Cell Cultures. Three different cell lines were used. Two of them were obtained from the American Type Culture Collection (USA): A549, bronchial alveolar type II epithelial cells derived from a human pulmonary carcinoma (ATCC No. CCL-185); HeLa, epithelial cells derived from a human epithelioid cervical carcinoma (ATCC No. CCL-2). The third cell line used was 16HBE, human bronchial epithelial cells, kindly provided by D. Gruenert, University of Vermont, Burlington, VT, USA (*21*). These cells were grown in DMEM (A549 and HeLa) or EMEM (16HBE), supplemented with 100 units/mL penicillin, 100 μg/mL streptomycin, and 10% heat-inactivated fetal bovine serum (FBS), and maintained at 37 °C, 5% CO_2, in a humidified atmosphere.

Formulations and Preparation of Complexes. Each of the original neamine compounds synthesized in this study was formulated alone or in combination with the neutral lipid DOPE at a 1/1 molar ratio. All neamine derivatives were not miscible in chloroform but were highly soluble in water. So, for neamine formulations without DOPE, these molecules were directly

dissolved in sterile water. For neamine formulations with DOPE, a volume of DOPE dissolved in chloroform was first introduced into the glass vial, then chloroform was evaporated under vacuum to obtain a dry lipid film. Neamine compounds dissolved in an appropriate volume of sterile water were next added. All formulations were subsequently stored overnight at 4 °C. Before use, solutions were subjected to several cycles of sonication in a sonicator bath (Prolabo, France) and to vortex mixing, in order to obtain small vesicles. To prepare the cationic reagent/DNA complexes, plasmid DNA was first diluted in OptiMEM (except when otherwise stated) and then added to vector solutions, the mixtures being kept at room temperature for at least 30 min before use in order to allow the formation of the DNA complexes. Complexes characterized by different charge ratios were prepared, the charge ratio being defined as the ratio of the vector positive charges (assuming that all amine functions of the neamine headgroup were protonated) to the negative DNA phosphate charges.

DNA Condensation and Relaxation. The condensation of plasmid DNA by the cationic agents studied was investigated using ethidium bromide (EtB) intercalation into the DNA. Upon condensation, EtB is expelled from DNA and, thus, the fluorescence signal is decreased. Next, the effects of serum or dextran sulfate, as counteranions, were also studied, as these molecules can induce a relaxation of the preformed complexes, which results in recovery of fluorescence (*22*). These assays were performed in 96 well plates in OptiMEM (pH 7.4), in 0.9% NaCl (pH ~5.0), in 0.9% NaCl 20 mM HEPES (pH 7.3), or in 5% glucose (pH ~5.0). The maximum fluorescence signal was obtained when ethidium bromide (1.5 μg/mL final) was bound to plasmid DNA (1.0 μg/well). DNA was added to the wells containing reagents at different amounts in order to obtain different charge ratios (positive charges of the carrier divided by the negative charges of DNA). The fluorescence signals were measured using a Fluoroskan Ascent FL plate reader (Thermo-Electron Instruments, France) at excitation wavelength 530 nm and emission wavelength 590 nm. Thereafter, increasing amounts of serum or dextran sulfate were added to the complexes, and the effect on DNA relaxation was followed by measuring the fluorescence recovery.

***In Vitro* Transfections.** Transfections were performed as previously described (*23*), with the following modifications. Twenty-four hours before transfection, cells were seeded in 96 well plates at a density of 12 500 cells per well in a final volume of 200 μL (i.e., at about 70% confluency). Immediately prior to transfection, the growth medium was removed and replaced with 140 μL of OptiMEM per well. The transfection mixtures (60 μL, corresponding to 0.25 μg DNA, per well) were then added dropwise to the cell cultures, and cells were exposed to transfection reagents for 4 h. At the end of this incubation time, and before replacing the medium containing the transfection mixtures with complete growth medium, an aliquot of supernatant in each well was taken apart in order to conduct a cytotoxicity assay using the Toxilight kit (Cambrex, Belgium). Thereafter, cultures were maintained 48 h at 37 °C until reporter gene activity measurements. In order to estimate the effect of serum on gene delivery, some transfections were also performed in the presence of serum, i.e., in complete growth medium with no medium change before the addition of complexes onto the cell cultures.

***In Vitro* Reporter Gene Measurements: Luciferase and FACS-GFP Assays.** As all *in vitro* transfections were performed using a GFP-Luc plasmid, positively transfected cells expressed both the luciferase enzyme and the green fluorescent protein. Therefore, these cells can be detected either by luminescence or by fluorescence. For luciferase assays, cells were first lysed using the Passive Lysis Buffer (Promega, France), then centrifuged, and the luciferase activity in each supernatant was measured using a microtiter plate luminometer (Dynatech Laboratories, France). The total protein content of each supernatant was also quantified using the BC Assay kit (Interchim, France). Results were thus expressed as RLU (relative light units) per milligram of total protein. For FACS-GFP assays, cells were harvested and analyzed with a FACScan (Becton Dickinson, USA) by measuring the GFP emission considering the signals measured on two channels, FL1-channel (emission wavelength 520 nm) versus FL2-channel (emission wavelength 575 nm), as previously reported (*24*). Positive cells were those for which a FL1 signal greater than or equal to twice the FL2 signal was measured.

Cytotoxicity Evaluation. Cytotoxicity was evaluated by two different methods. (1) The Toxilight Assay is a chemiluminescent test (Cambrex, Belgium) used to quantitatively measure the release into the growth medium from damaged cells of a normally cytoplasmic enzyme (adenylate kinase). The toxicity assay was carried out as specified by the manufacturer, a few hours after addition of complexes onto the cells (in order to estimate early cytotoxicity). The relative light units measured here were proportional to the number of viable cells. Untreated cells were used as a reference (*2*). The total amount of extractable cell proteins, at 48 h after addition of the complexes onto the cells, was used as an index of the cell number present in each well. The cell density is indeed the result of (i) the number of cells initially plated, (ii) the normal or induced mortality depending on the treatment(s) applied, and (iii) the cell growth, normal or delayed. In this case, cytotoxicity data were expressed as the percentage of missing proteins compared to the total protein content of untreated cells. The deficit in total protein content was considered as an estimation of the final, cumulated, toxicities.

***In Vivo* Transfection.** Female Swiss OF1 mice of six to nine weeks old (Elevage Janvier, France) were housed and maintained at the university animal facility; they were processed in accordance with the Laboratory Animal Care Guidelines of the University. Complexes were prepared at room temperature in 5% glucose, 0.9% NaCl, or OptiMEM before administration to mice via intravenous injection. Mice were placed in a restrainer and 200 μL of complexes incorporating 50 μg of pDNA per mouse were injected into the tail vein within 5 to 10 s, using a 1/2 in 26-gauge needle and a 1 mL syringe. Twenty-four hours after transfection, mice were killed by cervical elongation and their lungs were removed for analysis. Luciferase expression *in vivo* was evaluated as previously described (*25*). Briefly, tissue pieces were washed in 1× PBS and rapidly frozen in liquid nitrogen, then disrupted and finally collected in 1× PLB (Promega, France). Complete lysis was achieved by vigorous shaking at 4 °C for 45 min, and the supernatant was obtained by centrifugation. Luciferase activity and total protein content were then evaluated as indicated above. Results were expressed as RLU per milligram of total proteins.

Statistical Analyses. Data are presented as means and standard deviations. Comparisons among groups were done by using the Student's *t* test assuming two-tailed distributions and unequal variances.

RESULTS AND DISCUSSION

Synthesis of the Lipophilic Derivatives of Neamine. We have previously reported a synthetic route for preparing 4′-, 5-,

[1]Abbreviations: LFM, Lipofectamine; CR, charge ratio; EtB, ethidium bromide; RLU, relative light unit; TFA, trifluoroacetic acid; EDC, 1-[3-(dimethylamino)propyl]-3-ethylcarbodiimide; HOBT, 1-hydroxybenzotriazole; rt, room temperature; Δ, heating; Tr, trityl; PMB, *p*-methoxybenzyl.

Scheme 3[a]

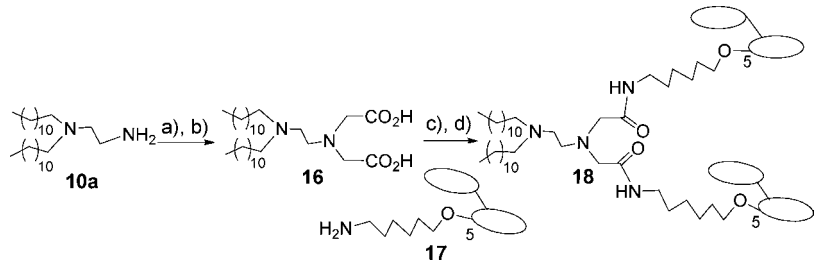

[a] (a) K_2CO_3, TBAI, CH_3CN, $BrCH_2CO_2Bn$, Δ; (b) Pd/C, cyclohexadiene, EtOH, rt; (c) HOBT, EDC, **17**, DMF, Δ; (d) TFA, CH_2Cl_2, anisole, rt.

Scheme 4[a]

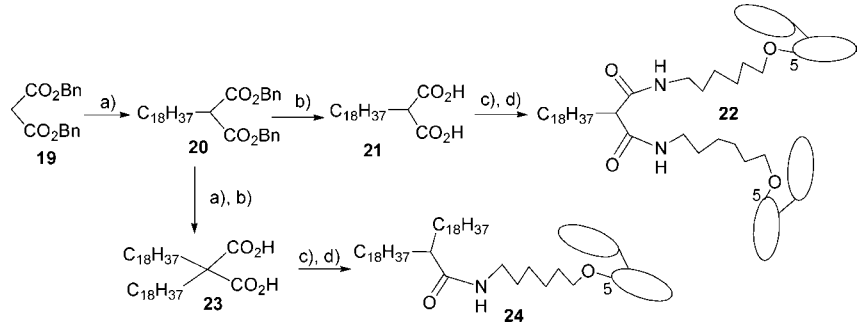

[a] (a) 1-Bromo-octadecane, NaH, THF, rt; (b) Pd/C, cyclohexadiene, EtOH, rt; (c) HOBT, EDC, **17**, DMF, rt; (d) TFA, CH_2Cl_2, anisole, rt.

and 4′,5-neamine derivatives using trityl (Tr^1) and *p*-methoxybenzyl (PMB) groups for protecting the amine and hydroxyl functions, respectively (*17*). From some of the neamine derivatives described previously, a series of twelve 4′- and 5-neamine derivatives carrying long alkyl chains were synthesized: (i) seven lipidic neamine derivatives incorporating one neamine core (three derivatives bearing lipidic chains attached to the 5-oxygen atom and four with the lipid chains linked to the 4′-oxygen) and (ii) five lipidic derivatives characterized by neamine 5,5-dimers.

Derivatives Incorporating One Neamine Ring. The protected neamine derivative **8** (Scheme 1) previously prepared, which carries at the 5-position a hexamethylenic arm and a terminal bromine atom, was a main intermediate in the synthesis of the 5-neamine derivatives studied here.

As previously reported, it was obtained from the protected neamine derivative **6**, in which only the 5-hydroxyl function is free, by alkylation with 1,6-dibromohexane in the presence of NaH. Unfortunately, it was not possible to introduce at this position, in good yield, shorter alkyl arms from 6-halogenoalkanes in order to decrease the length of the linking chain in the transfecting agents prepared. Therefore, all 5-neamine derivatives prepared carry a first hexamethylenic arm attached to the 5-oxygen atom. The lipidic moiety (like bis-dodecyl or bis-octadecyl chains) of the molecules was linked to the end of the hexyl arm through a nitrogen atom as a conjugation center.

In contrast, selective alkylation of the 4′-hydroxyl function in the previously described compound **5** was feasible with 1,4-dibromobutane in the presence of NaH and allowed to prepare the novel 4′-bromobutyl derivative **7**, which has not previously been reported (Scheme 1). Starting from the 4′-bromobutyl (**7**) and the 5-bromohexyl (**8**) derivatives, two sets of derivatives incorporating only one neamine core were prepared. Through reaction of the 4′-bromo intermediate with triethylamine at 65 °C, it was easy to substitute the bromine atom for a triethylammonium group to obtain the derivative **11** (Scheme 2). The reaction of the 4′-bromo derivative **7** with didodecylamine **9a** and dioctadecylamine **9b** led in good yields to the potential transfection agents **12a** and **12b**, respectively (Scheme 2).

With the view to add to the lipidic chains a second nitrogen atom and an additional spacer, the two lipidic reagents **10a** and **10b** (Scheme 2) were prepared. The reaction of the 4′-bromo derivative **7** with reagent **10b** led to the dioctadecyl neamine derivative **13b** (Scheme 2). The corresponding 5-derivative **15a** and its didodecyl 5-analogue **14b** were also prepared from the 5-bromo neamine derivative **8** and the reagents **9b** and **10a**, respectively (Scheme 2).

5,5-Neamine Dimers. The five 5,5-dimers were synthesized using coupling reactions between prepared bifunctional reagents carrying lipidic chains and possessing either two carboxylic functions (**16**, **21**, **23**, and **26**) or two primary amine functions (**29**). These compounds were conjugated to the previously described neamine derivatives incorporating an aminohexyl arm (**17**), carrying a carboxylic acid function (**31**) or a bromine atom (**8**).

A first 5,5-dimer **18** carrying two dodecyl chains was obtained from the neamine derivative **17** and the dicarboxylic acid **16**. Compound **16** was prepared through reaction of the 1,2-diaminoethane derivative **10a**, in which one of the amine function carries two dodecyl groups, with benzyl bromoacetate (Scheme 3).

Two other coupling reagents possessing two carboxylic acid functions and carrying one (**21**) or two (**23**) octadecyl chains also were prepared from dibenzyl malonate **19** (Scheme 4).

Mono- and bis-alkylation of compound **19** with 1-bromooctadecane and, then, debenzylation led to the dicarboxylic acids **21** and **23**, respectively. The reaction of the monooctadecyl derivative **21** with the 5-aminohexyl neamine derivative **17** afforded the 5,5-neamine dimer **22**. It was not possible to obtain the corresponding dioctadecyl 5,5-dimer from the dioctadecyl dicarboxylic acid derivative **23**. During the coupling reaction, a decarboxylation of the reagent **23** occurred leading to the dioctadecyl derivative incorporating one neamine core **24** in good yield (Scheme 4). This compound is an interesting analogue of the derivative **14b** which was evaluated as a potential transfection vector.

Another dicarboxylic acid coupling reagent **26** was prepared from diethyl aminomalonate **25** through acylation of the amino

Scheme 5[a]

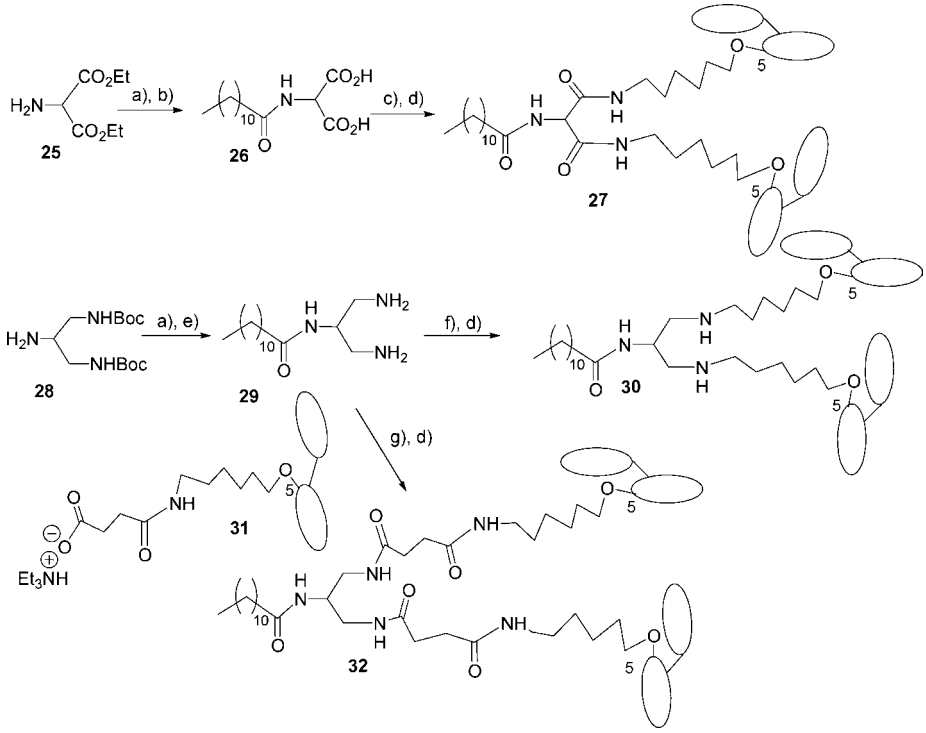

[a] (a) EDC, HOBT, dodecanoic acid, CH_2Cl_2, rt; (b) 2 M aq. NaOH, EtOH, Δ; (c) EDC, HOBT, **17**, DMF, rt; (d) TFA, CH_2Cl_2, anisole, rt; (e) TFA, CH_2Cl_2, rt; (f) **8**, K_2CO_3, DMF, Δ; (g) EDC, HOBT, **31**, DMF, rt.

function with dodecyl carboxylic acid and saponification (Scheme 5). Reaction of the prepared reagent **26** with the 5-aminohexyl neamine derivative **17** afforded the dimer **27**.

Two other dimers **30** and **32** incorporating one dodecyl chain were obtained by condensation of the prepared 1,2,3-triaminopropyl derivative **29** with the 5-bromohexyl neamine **8** and the succinylated derivative **31**, respectively.

Transfection Properties of the Neamine Derivatives: Structure−Activity Relationships. The twelve neamine derivatives prepared, which constitute amphiphilic compounds, were evaluated as DNA transfection reagents. As gene transfection involves the formation of DNA complexes in which the DNA is condensed by the cationic amphiphiles, we first characterized the lipohilicity of the neamine derivatives and evaluated their DNA condensation ability by ethidium bromide exclusion and by DNA retardation on agarose gel electrophoresis.

Log P Values. The lipophilic character of the neamine derivatives prepared was estimated through the calculation of log *P* values (octanol/water partition coefficients) using the MarvinSketch software (http://www.chemaxon.com). For our twelve neamine derivatives, the log *P* values were scattered over a wide range, from −3.8 (**24**, most lipophilic compound) to −39.9 (**30**, most hydrophilic compound) (Supporting Information Table S1).

DNA Condensation Assays. DNA condensation can adequately be evaluated by ethidium bromide (EtB) exclusion, the increase in the amount of lipid added (thus in charge ratio) leading to a decrease in observed fluorescence. The EtB exclusion assay thus allowed us to classify the various neamine derivatives according to their efficiency to condense DNA (Figure 1). The ranking order, from the most efficient to the least, was as follows: **18** (5,5-dinea), **12a** (4′-mononea), **13b** (4′-mononea), **15a** (5-mononea), **12b** (4′-mononea), **24** (5-mononea), **14b** (5-mononea), and **22** (5,5-dinea). The other derivatives did not significantly condense the plasmid DNA, the fluorescence signal always remaining higher than 90% of the signal of DNA alone. DNA gel retardation assays were also performed (data not shown) and yielded results in good agreement with the EtB exclusion assays ($R^2 > 0.90$).

It is noteworthy here that the DNA condensing ability of the most efficient neamine derivatives was higher than that of the lipidic derivative of paromomycin (DOSP) (*13*). However, it was lower than that of the commercial multivalent Lipofectamine (LFM) and the monovalent arsonium-based lipophosphoramidate KLN47 (*26*) (Figure 1). Interestingly, the 5,5-dimer **18** carrying two dodecyl chains showed a stronger DNA condensation ability than the 5,5-dimers **30**, **27**, and **22**, which bear only a single fatty acid chain. This emphasizes the requirement of two close lipidic chains in a cationic lipid for efficient DNA condensation.

In Vitro Gene Transfection Experiments. In initial *in vitro* transfection experiments, ten neamine derivatives were evaluated for their ability to transfect a GFP-Luc plasmid into two types of mammalian cells (the HeLa and A549 cell lines). As cationic lipids are often formulated with DOPE (a neutral colipid, which is believed to enhance their activity via its fusogenic property), we also tested the effects of the addition of DOPE on the transfection activity of our neamine derivatives. Lipofectamine (LFM) and the lipidic derivative of paromomycin DOSP [DOSP/DOPE (*13*)] were used as positive controls. Flow cytometry assays were conducted, and observed percentages of transfected A549 cells (GFP positive cells) are shown in Figure 2. Supporting Information Figure S1 depicts the results obtained using HeLa cells.

First, the results obtained indicated that the different neamine derivatives studied, when used alone (i.e., without DOPE), displayed broad range abilities to transfect cell lines *in vitro*. Some compounds appeared as completely inefficient (**11**, **27**, **30**, and **32**). On the contrary, others produced highly significant GFP transgene expressions (e.g., **13b** and **15a**) which reached, depending on the cell lines evaluated, levels either comparable to or even higher than the ones obtained when using reference cationic lipids. Regardless of the two cell lines considered (HeLa and A549), the two best transfectionally effective derivatives

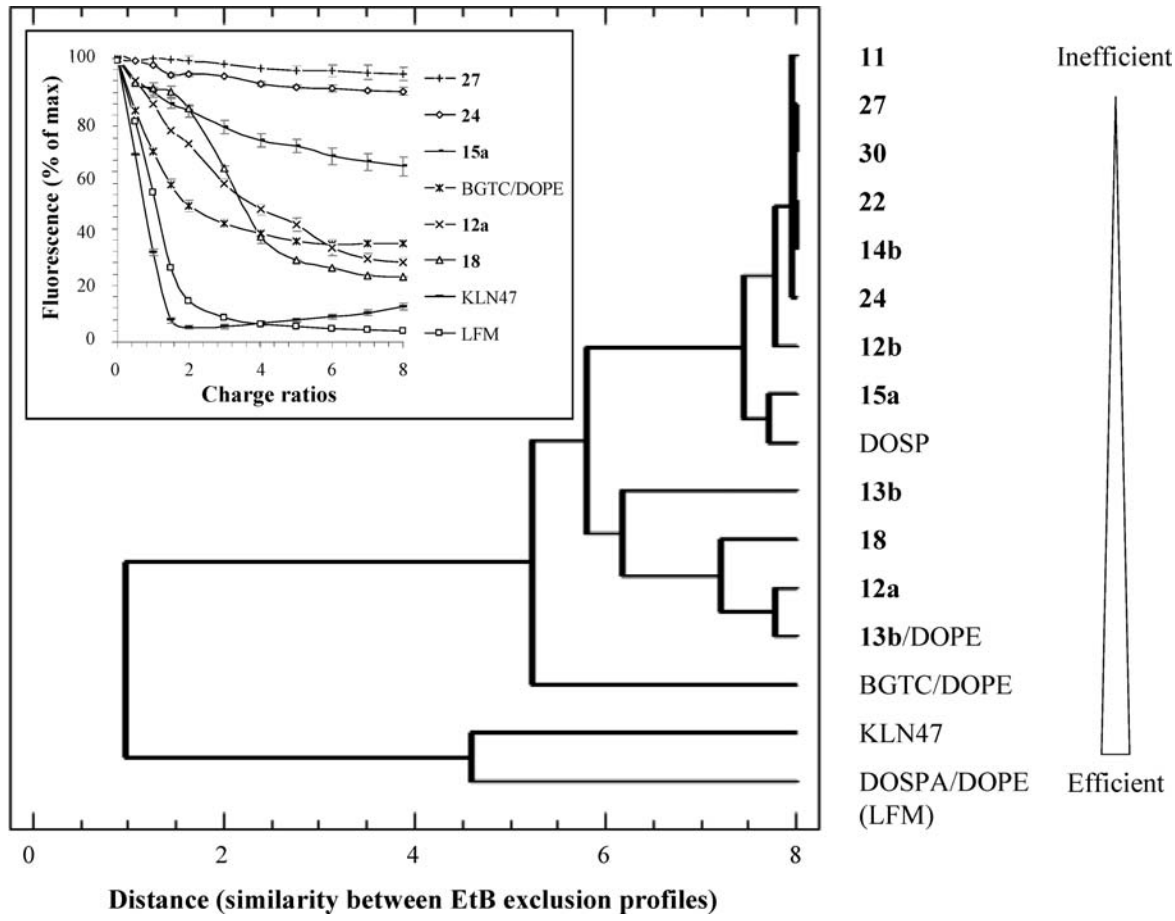

Figure 1. DNA condensation ability of neamine derivatives and some more standard cationic lipids as a function of the lipoplex charge ratio. Complexes were obtained by mixing in OptiMEM cationic liposomes at the required concentrations with plasmid DNA incubated first with ethidium bromide (EtB). The fluorescence decrease allowed the evaluation of nucleic acid entrapment within complexes (see Experimental Procedures section). Each test was performed in triplicate, and fluorescence measurements were obtained at several time points, from 30 min up to 1 h after mixing. The dendrogram summarizes the overall results obtained for all reagents tested, assuming that the more similar the EtB exclusion profiles between 2 reagents, the closer these 2 molecules in the tree. The reagents tested are clustered from the most efficient to complex DNA (i.e., LFM) to the least (i.e., **11**). **32**, not tested. Inset: profiles obtained with some neamine derivatives and other cationic lipids. Data are expressed as a percentage of the EtB fluorescence intercalated into DNA in the absence of carrier (mean ± SD with $n = 3$). See Supporting Information Scheme S1 for the chemical structure of neamine derivatives; **13b**/DOPE is **13b**/DOPE 1/1; BGTC/DOPE is BGTC/DOPE 3/2 (*27*); KLN47 (*26*); LFM (Lipofectamine, Invitrogen).

were **13b** then **15a**. Other derivatives showing weak (<1% positive cells) or undetectable efficiencies on both cell lines were **22**, **24**, **18**, **12a**, **11**, **27**, **30**, and **32**. Considering the sensitivity of this method (GFP reporter), it was not easy to further classify those reagents according to their transfection efficiencies.

Regarding the comparative efficiencies of formulations incorporating DOPE, we observed in general that the transfection reagents for which a detectable positive signal was measured when used alone became more efficient when they were combined with this helper lipid (Figure 2 and Supporting Information Figure S1). As an example, for **13b**/DOPE (1/1 molar ratio) compared with **13b** used alone, highly significant increases (from 2- to 10-fold) were measured with the A549 and HeLa cell lines (Figure 2 and Supporting Information Figure S1). Such a clear increase in the transfection efficiencies of the formulation with DOPE was also observed with other derivatives, especially with compounds **15a**, **24** (Figure 2), or **22** (Supporting Information Figure S1). The beneficial effect observed when formulating with DOPE may have several explanations. First, there may be a structuring effect of DOPE on the cationic liposomes formed by the neamine derivatives, as the latter contain only saturated lipid chains while DOPE contains two monounsaturated lipid chains. Of interest here, the **13b** derivative formulated with DOPE appears to complex DNA better than **13b** alone (Figure 1). Such a structuring effect may also be proposed for compound **22**, which contains only one long lipid chain (C18:0). Second, the fusogenic properties of DOPE may allow a better escape of the DNA from the endosome into the cytosol. Third, another beneficial effect of DOPE could be an increase of the global lipophylicity as reflected by the estimation of the log *P* values of equimolar cationic lipid/colipid formulations. Indeed, when formulated with DOPE, all derivatives undergo an increase in their log *P* value, and for some of them, e.g., **13b**, their log *P* values become close to that of monocationic lipids such as KLN47 and DOTAP (Supporting Information Table S1). Furthermore, it has been reported that the combination of cationic lipids characterized by different lipidic parts can lead to a significant increase in transfection efficiency (*28*, *29*). We have ourselves observed such a synergistic effect when associating two different cationic lipids, one with aliphatic chains and the other one with a cholesterol moiety (T. Le Gall, unpublished results). From this point of view, the formation of unstable lipid structures, with increased disassembling properties permitting a better release of the DNA, may be proposed here for DOPE-containing formulations of neamine derivatives with dodecyl chains such as **15a**.

As DOPE incorporating formulations enhanced transfection efficiencies, it allowed to more precisely classify the efficient neamine derivatives. Using A549 cells, the ranking order of

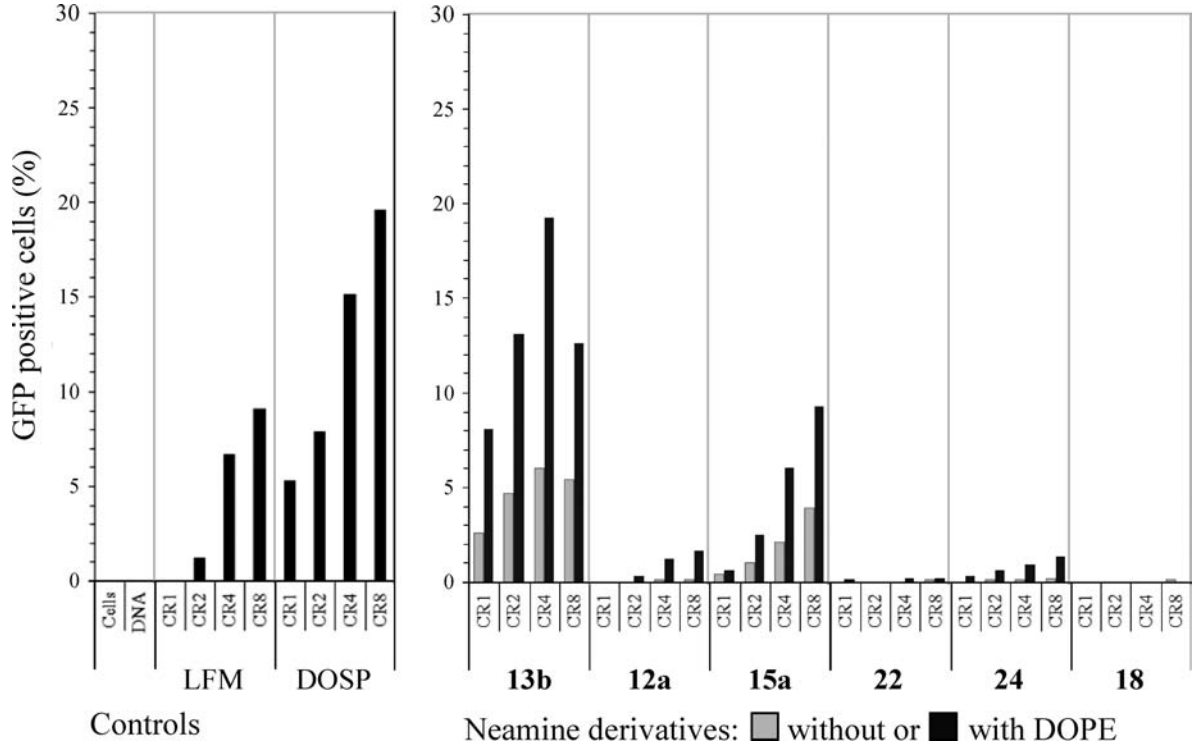

Figure 2. Flow cytometry measurements (GFP assays): transfection efficiencies of lipidic derivatives of neamine used alone or formulated with the colipid DOPE (molar ratio 1/1). The reagents indicated were complexed with DNA (pEGFP-Luc; see Experimental Procedures section) in order to obtain increasing charge ratios (CR), from CR1.0 up to CR8.0. The commercial Lipofectamine (LFM, DOSPA/DOPE, Invitrogen) and the paromomycin derivative [DOSP, DOSP/DOPE (*13*)] were used as cationic lipid references. Cell samples were analyzed by flow cytometry in order to estimate the gene delivery efficiency as a percentage of positive cells (GFP positive cells). Other derivatives (**11**, **27**, **30**, and **32**) were found to be completely inefficient, and thus, they are not indicated here. These results were obtained with A549 cells. The data obtained using HeLa cells provided similar observations.

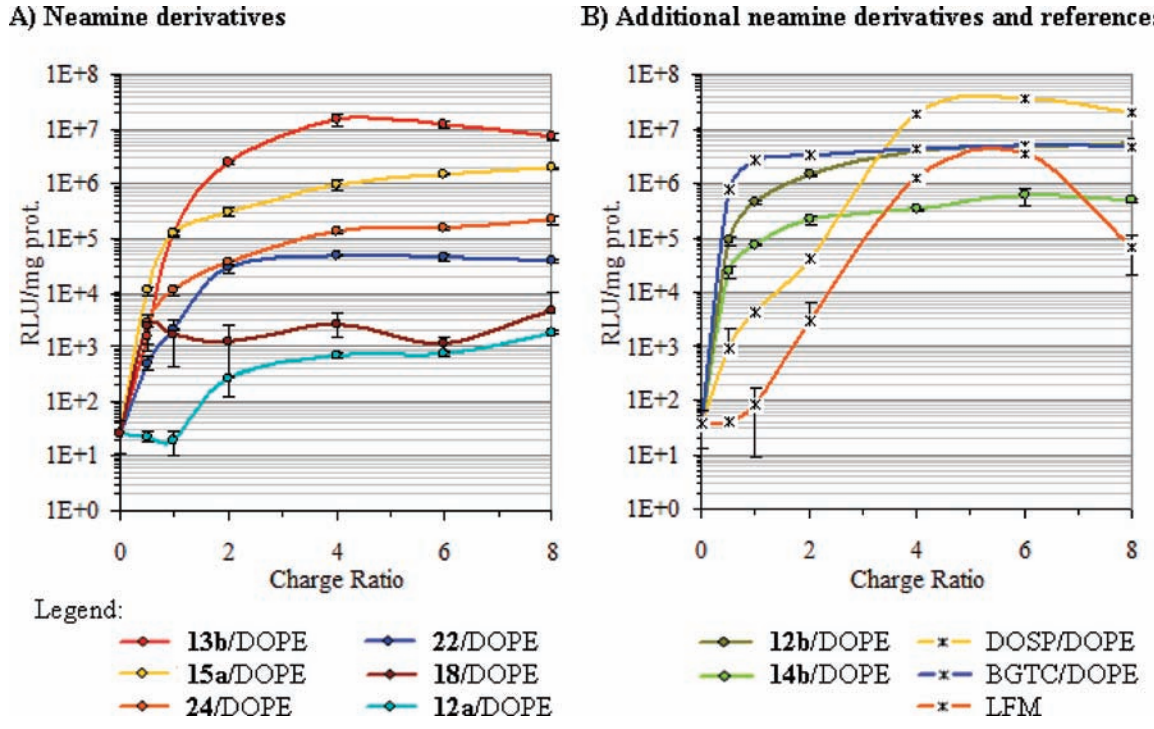

Figure 3. Luminometry measurements (luciferase assays): dose responses of the *in vitro* transfection activity of lipidic neamine derivatives formulated with the colipid DOPE (molar ratio 1/1). Luciferase reporter gene expression is indicated as a function of the charge ratio (CR) of lipoplexes, from CR0.5 up to CR8.0. The commercial Lipofectamine (LFM, Invitrogen), the paromomycin derivative [DOSP (*13*)] and the bisguanidinium tren-cholesterol BGTC [BGTC/DOPE 3/2 (*27*)] derivative were used as cationic lipid references. Cells were transfected as described in the Experimental Procedures section, using lipoplexes prepared by mixing DNA (pEGFP-Luc) with the required amounts of lipids. Data are expressed as relative light units (RLU) per milligram of total proteins (mean ± SD with $n = 3$). These results were obtained using A549 cells; experiments using HeLa and 16HBE cells provided similar observations (see Supporting Information Figure S2).

Chart 2. Structure of the Most Efficient Neamine-Based Vectors for Gene Transfection

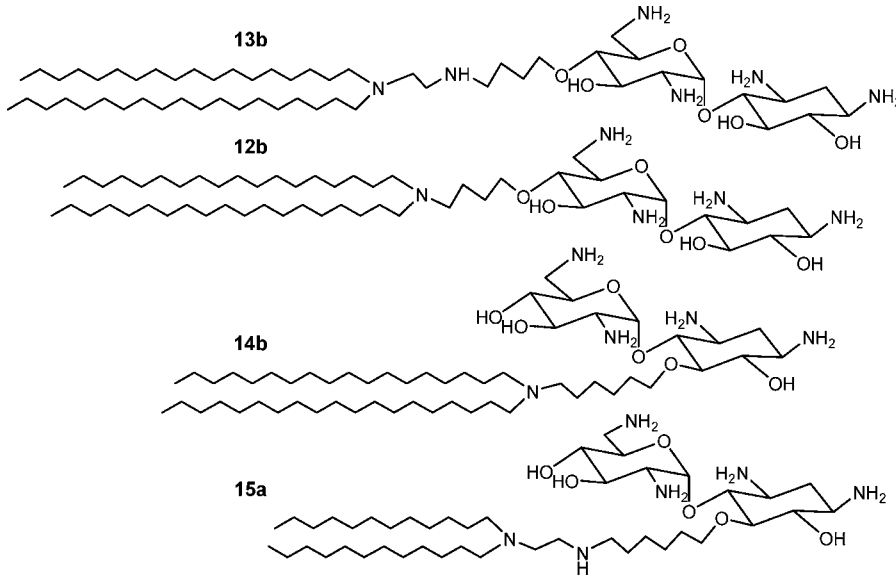

compounds, from the most efficient to the least, was thus **13b**, **15a**, **12a**, **24**, and **22** (Figure 3). Of note, this order was the same using HeLa cells (Supporting Information Figure S1), except for compound **22**, which became more efficient than **12a**.

Following those measurements, additional experiments were performed in an attempt to confirm and further detail the results previously obtained. Three cell lines were used here (A549, HeLa, and 16HBE). Thus, the series of ten neamine derivatives plus two additional compounds (**12b** and **14b**) were evaluated, when formulated with DOPE (as it was found to significantly enhance the transfection efficiencies of neamine derivatives; see above) and using luminometry assays (as this is a more sensitive method allowing us to better distinguish between active and nonactive transfection compounds). These evaluations aimed at more precise characterization of the transfection efficiency of each compound in order to facilitate the delineation of structure−activity relationships. Lipofectamine (LFM), the lipidic derivative of paromomycin DOSP [DOSP/DOPE (*13*)], and the bisguanidinium tren-cholesterol BGTC [BGTC/DOPE 3/2 (*27*)] were used as positive controls. Observed levels of luciferase expression using A549 cells are shown in Figure 3. Data obtained using two other cell lines (HeLa and 16HBE) provided similar observations (Supporting Information Figure S2).

First, as previously reported, luminometry is indeed more sensitive than cytometry, as some derivatives found to be inefficient by cytometry yielded low but not null luminometry signals. Accordingly, it was possible to estimate here the minimal luciferase level required to detect GFP positive cells by cytometry (threshold at about 1×10^5 RLU/mg protein). Using A549 cells, neamine derivative efficiencies ranged from 2×10^3 (**12a**) up to 2×10^7 (**13b**) RLU/mg proteins (Figure 3).

Second, the results obtained by cytometry and luminometry were found to be consistent, as these two methods yielded similar ranking orders when classifying neamine derivatives according to their highest transfection efficiency (comparison between Figures 2 and 3A). Of note, the addition of DOPE enhanced the transfection efficiencies, as already mentionned above, but it did not affect the ranking order of the various derivatives according to their efficiencies (except for compound **22** used to transfect HeLa cells; Supporting Information Figure S1). Moreover, mostly identical trends were obtained using the three different cell lines, thereby allowing us to unveil general structure−activity relationships (see below). Globally, neamine/DOPE formulations could thus be classified from the most to the least efficient. In all experiments conducted, **13b** was the most efficient transfection reagent among all neamine derivatives tested. For example, using A549 cells, a **13b**/DOPE formulation was able to mediate transgene expression (GFP reporter, Figure 2, or Luc reporter, Figure 3) at levels either higher than LFM or of the same order of magnitude as DOSP/DOPE (comparison of maximum efficiencies of **13b**/DOPE, LFM, and DOSP/DOPE: 19.2%, 9.1%, 19.6% GFP and 1×10^7, 3×10^6, 4×10^7 RLU/mg protein, respectively). The next efficient compounds identified were **12b**, **14b**, and **15a**. Slightly efficient derivatives were **24**, **18**, and **12a**. Finally, **11**, **27**, **30**, and **32** were always found to be inefficient, regardless of the cell lines and the assays used. It is noteworthy here that compound **22** represented an exception. Depending on the cell lines used, this derivative (characterized by a headgroup with two neamine cores) displayed, when formulated with DOPE, very different efficiencies; for instance, it was able to reach high transfection levels (up to 1×10^6 RLU/mg protein) with 16HBE cells (Supporting Information Figure S2).

Delineation of Structure−Activity Relationships. By combining the data obtained for the different neamine derivatives and related to their chemical structures (Supporting Information Chart S1 and Table S1) with data from (i) DNA condensation assays (Figure 1) and (ii) *in vitro* gene transfection experiments (Figures 2, 3, and Supporting Information Figure S1, S2), it was possible to unveil interesting structure−activity relationships. First, a quite clear association was observed between the DNA condensing ability and the *in vitro* transfection efficiency, as the molecules inefficient for DNA condensation did not transfect cells *in vitro*. However, the reverse was not true, i.e., a high ability to condense DNA is not obligatorily associated with a high transfection activity. In fact, the most efficient compound identified in our DNA condensation assays (i.e., **18**) showed only weak activity in the transfection experiments.

Four compounds (**13b**, **12b**, **14b**, and **15a**) were actually identified as the most efficient neamine-based vectors. Their structures are shown in Chart 2. They are characterized by a headgroup bearing only one neamine core, which is linked to a lipid moiety consisting of two fatty acid chains. These vectors were more efficient than the more polar 5,5-dimers, whereas the derivatives with only one fatty acid chain were ineffective. Of note, an additional compound consisting of three neamine

cores linked together without any lipidic moiety was also totally ineffective (not shown), a finding highlighting the requirement of a sufficient hydrophobic part for transfection. Indeed, all the most efficient derivatives have a calculated log *P* in the range −7.9 to −12.8; i.e., they exhibit a lipophilic character equivalent to that of the previously reported lipidic aminoglycosides. These relatively slightly hydrophilic molecules do in fact condense DNA with different efficiencies. It is also noteworthy that the very polar derivative **11** which incorporates one neamine ring (log $P = -21.9$) was found to be inefficient for transfection, like the more polar 5,5-dimers (log $P = -29.7$ to -39.9). The 4′-derivative **24** was also less efficient for transfection, because it may be too lipophilic (log $P = -3.8$). However, it should be mentioned here that compounds **18** and **22** (log $P = -32.5$ and -22.7, respectively), characterized by headgroups incorporating two neamine cores, yielded significant gene transfection abilities. This was clearly observed with **22**/DOPE formulation used to transfect HeLa and 16HBE cells (Supporting Information Figures S1 and S2). It is also interesting to note here that the best transfection results were obtained with derivatives carrying two octadecyl chains (**13b**, **12b**, and **14b**, with log *P* values of −8.8, −8.7, and −7.9, respectively) in comparison to compounds incorporating two dodecyl chains (**15a**, **12a**, with log *P* = −12.8 and −14.4, respectively). Altogether, these data indicate that efficient gene transfection can be achieved with lipidic aminoglycoside derivatives incorporating only two rings carrying four positive charges, whereas the previously described aminoglycoside derivatives contained three to four rings bearing three to six positive charges (Figure 2). These results also emphasize the importance of parameters such as (i) the hydrophylicity/lipophilicity balance (amphiphilic character), (ii) the headgroup size and the resulting charge density, and (iii) the presence of two fatty acid chains (formation of lipidic bilayers).

Compound **13b** was the most efficient among these four best neamine derivatives. When compared to the other ones (Chart 2), **13b** is characterized by the fact that it combines the following features: (1) the attachment of the lipidic moiety at the 4′-position of the neamine headgroup and (2) the incorporation of a diaminoethyl group in the spacer linking the neamine core to the fatty acid chains. (1) On one hand, the 4′-neamine derivative **12b** appeared to be clearly more efficient than the corresponding 5-derivative analogue **14b** (Figure 3). Thus, attachment of the lipidic chains at the 4′-position, i.e., at an end of the neamine core, may allow "better" interactions in the DNA complexes (and hence a more efficient transfection) than attachment at the 5-position, in the middle of the neamine core. (2) On the other hand, incorporation of an additional diaminoethyl group, between the neamine headgroup and the lipidic chains, clearly improved the transfection activity of **13b**, in comparison with derivatives of similar lipophily, especially its analogue **12b**, which also carries two octadecyl chains but in which only this diaminoethyl group is absent. The importance of such an additional spacer for obtaining a more efficient transfection was confirmed with the 5-neamine derivative **15a** carrying two dodecyl chains; this derivative appeared indeed more efficient than the 4′-derivative **12a** also characterized by two dodecyl chains but without the diaminoethyl group. It may be hypothesized here that the beneficial effect on gene transfection of the incorporation of a diaminoethyl group in **13b** could be related to the fact that it provides the linker between the neamine headgroup and the octadecyl chains with a favorable length; in addition, as for other cationic lipids such as BGTC (*27*), the introduction of an additional protonable amine function may provide the vector with some endosomal buffering capacity, which could favor the endosomal escape of the DNA complexes. Indeed, at physiological pH, only one amine function in the diaminoethyl spacer should be protonated due to the electron-withdrawing effect of the first protonated nitrogen atom. Thus, at pH 7, compounds **12b** and **13b** should not differ in their number of positive charges. However, their charge near the lipidic moiety is probably differently located, as in **13b**, it is the secondary amine function that should be protonated (Supporting Information Scheme S1). Altogether, the diaminoethyl group in **13b** may provide (i) its linker with a favorable length, (ii) some endosomal buffering capacity, and (iii) some additional flexibility (between the polar headgroup and the lipidic moiety), a series of features which, when combined, could explain the better transfection activity measured with this derivative in our experiments. Finally, these considerations also invite the introduction of such a diaminoethyl group into more lipophilic dimers, especially into 4′,4′-dimers.

13b/DOPE Formulations: Further Characterization of Their Transfection Properties. *Cytotoxicity Evaluations and Comparison with Reference Cationic Lipid Systems.* In order to further characterize the transfection activity of the **13b** derivative, this compound formulated with DOPE (at molar ratio 1/1) was compared with other commercial or original cationic lipid formulations: (i) the commercially available Lipofectamine (LFM), (ii) the dioleyl-succinyl-paromomycin DOSP [DOSP/DOPE 1/1 (*13*)], and (iii) the bisguanidium-tren-cholesterol BGTC [BGTC/DOPE 3/2 (*27*)]. All these reagents were tested simultaneously under the same experimental conditions in order to compare both their transfection activity and their cytotoxicity. Regarding transfection efficiency, we measured luciferase expressions similar to those reported in Figure 3 and Supporting Information Figure S2. This indicated that **13b**/DOPE was generally as efficient as these control vectors for transfection of the different cell lines tested, in particular, as efficient as the recently reported aminoglycoside derivative DOSP (*13*).

Interestingly, among the four vectors evaluated here, the **13b**/DOPE was also characterized by a relatively low cytotoxicity (Figure 4), both (i) at the early time point of 4 h after transfection (toxicity assessed by measurement of the release into the culture medium of an enzyme normally located in the cytoplasm) and (ii) at the late time point of 48 h (toxicity assessed by measurement of the total amount of extractable proteins as an index of the number of cells). In addition, **13b**/DOPE formulations never produced the highest toxicity levels in these evaluations. Taken together, these findings indicate that a high transfection efficiency is not obligatorily associated with an increased cytotoxicity. This also validates the choice of **13b**/DOPE formulations for further evaluations (see below).

Storage Stability of Neamine Derivative Formulations. Another interesting feature of the **13b**/DOPE formulation was the finding that its transfection activity was conserved over time. Indeed, this is an important point to consider as lipid-based transfection reagents do not always meet this requirement; thus, instability of formulations can correspond to a major drawback (reproducibility) for the successful and wide use of a given cationic lipid.

The results obtained (Figure 5) clearly indicated that **13b**/DOPE was still able to transfect various cells lines, with high efficiency levels, even 3 years after its formulation in water. The observed efficiencies were indeed very close to those measured before (comparison of **13b**/DOPE levels in Figure 3 and Figure 5); they were still higher than or at least of the same order of magnitude as those observed with LFM. In addition, LFM dose responses were characterized by a "bell-shaped" curve, with a maximum efficiency at CR4, whereas **13b**/DOPE rapidly reached a high transfection level at CR1 and retained high levels at CR above. Of note, these storage stability properties were also observed with other neamine derivatives (**24** and **15a**; data not shown).

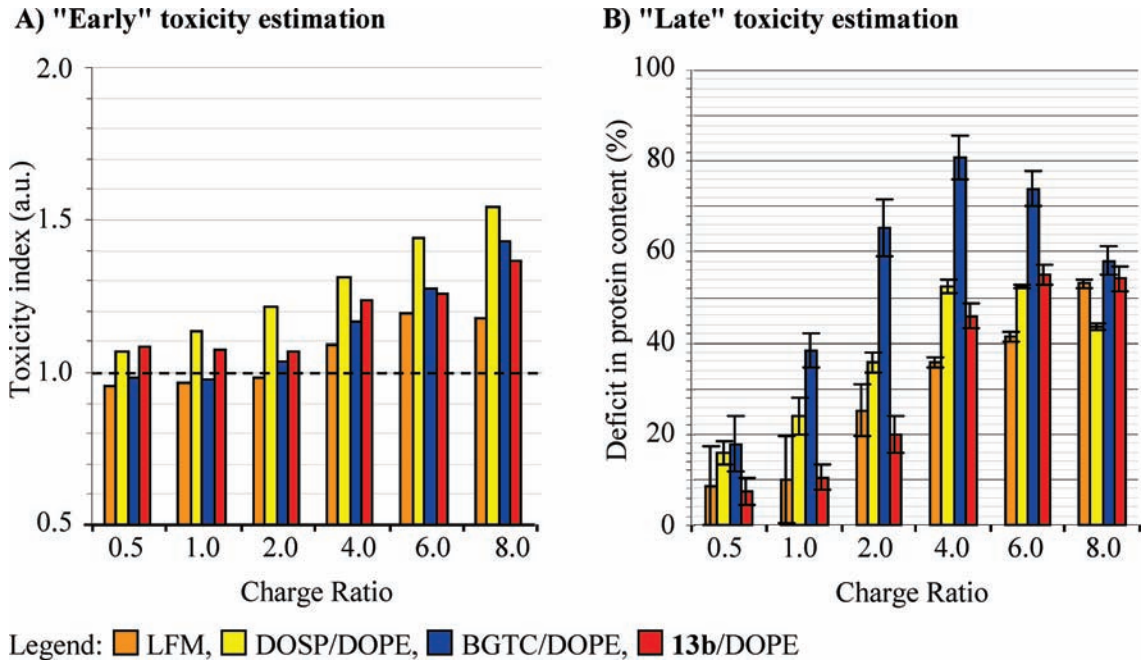

Figure 4. Cytotoxicity of **13b**/DOPE and some other reference gene transfer agents. The induced toxicity of **13b** formulated with DOPE (at molar ratio 1/1) was compared with other commercial or original cationic vectors: Lipofectamine (LFM, Invitrogen), the lipidic derivative of paromomycin DOSP [DOSP/DOPE 1/1 (*13*)], and the bisguanidium tren-cholesterol BGTC [BGTC/DOPE 3/2 (*27*)]. Estimations of cytotoxicities considered either the membrane integrity of cells through measurement of the level of cytoplamic enzyme adenylate kinase released into the growth medium (A; Toxilight, Cambrex; the minimum value is 1, it indicates an absence of cytotoxicity) or the content in total extractable proteins (B; the deficit in protein content corresponds to the percentage of missing proteins compared to the total protein content measured for untreated cells), as described in the Experimental Procedures section. These results were obtained using A549 cells; experiments using HeLa and 16HBE cells yielded similar observations.

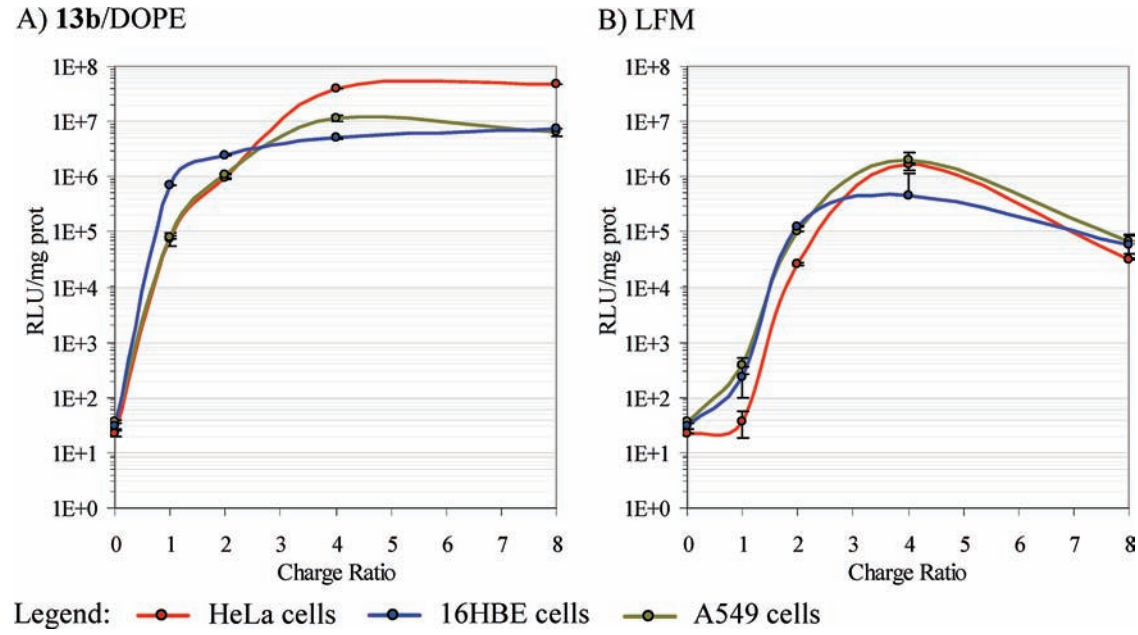

Figure 5. Transfection efficiency of **13b**/DOPE formulation after long-term storage as liposomes in water. A formulation of **13b**/DOPE prepared in water three years ago was here evaluated and compared with the commercial cationic lipid Lipofectamine (LFM, Invitrogen). Efficiencies were estimated using three different cell lines. Data are expressed as relative light units (RLU) per mg of total extractable proteins (mean ± SD with $n = 3$).

Toward the in Vivo Use of **13b***/DOPE: in Vitro Transfection Properties under Various Experimental Conditions.* Here, we first compared the transfection efficiency of the **13b**/DOPE lipoplexes prepared either in conventional OptiMEM or in isotonic saline or glucose, as these two latter media are suitable for *in vivo* administration.

The results showed that, although the use of isotonic sodium chloride or glucose allowed a significant improvement of DNA complexation compared to OptiMEM (data not shown), the transfection efficiency of the resulting complexes was lower than that of complexes prepared in OptiMEM; indeed, we observed in general a clear transfection activity decrease when using

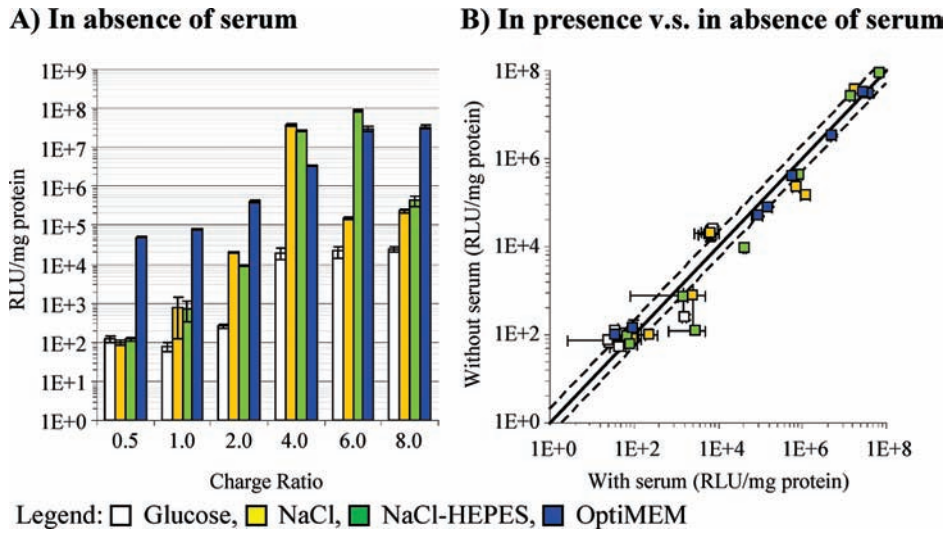

Figure 6. Effects of the complexation medium and of the presence of serum on the *in vitro* transfection efficiency of **13b**/DOPE. Luciferase reporter gene expression is indicated as a function of the charge ratio (CR) of lipoplexes, from CR0.5 up to CR8.0. Cells were transfected as described in the Experimental Procedures section using lipoplexes prepared by mixing DNA (pEGFP-Luc) with the required amounts of lipids, in 4 different solutions: (i) glucose (5%), (ii) NaCl (0.9%), (iii) NaCl-HEPES (0.9% NaCl, 20 mM HEPES), and (iv) OptiMEM. The complexes were then used to transfect cells either in the absence of serum (A; cells in OptiMEM) or in the presence of serum (cells in complete growth medium including 10% fetal bovine serum). The graph in B compares the transfection efficiencies obtained in those two conditions (transfection in presence versus in absence of serum). Data are expressed as relative light units (RLU) per milligram of total proteins (mean ± SD with $n = 3$). These results were obtained using A549 cells. The data obtained using HeLa and 16HBE cells provided similar observations.

complexes made in NaCl or NaCl-HEPES 1× (except at CR4 and 6) and only a very low efficiency when using complexes formed in glucose (Figure 6A). Here, the differences in DNA condensing abilities may be explained by differences in parameters such as ionic strength or pH of the media. Indeed, the pH may impact the complexation ability of reagents with ionizable amines such as **13b**. At pH 7.4, the electric charge *Z* of **13b** should be 4 or 5 (due to partial protonation with probably a mixture of differently protonated species), whereas at pH 5.0, this compound charge may be 6 (i.e., with all amines being fully protonated, as estimated with the MarvinSketch software). Of note, when complexation was performed in NaCl (at pH 5.0 or 7.0), the association with DNA was improved and, as well, DNA relaxation was much more difficult, as reflected by the higher amount of dextran sulfate required to completely recover the free DNA (Supporting Information Figure S3). Altogether, these results suggest that the best transfection conditions may be those leading to a complexation that is not too strong between the neamine vector and the DNA. Indeed, a very strong interaction between the vector and the DNA may be deleterious for transfection, as it may hamper the dismantling of the complexes during their cellular trafficking toward the cell nucleus. This is also supported by the results obtained with **18** showing that it was one of the best neamine compounds in DNA condensation assays (Figure 1) but a very inefficient neamine reagent to deliver DNA (Figure 2).

Next, we took into account that, when compared with *in vitro* transfection conditions, one major hurdle for *in vivo* transfection via intravascular administration is the presence of serum. Indeed, the anionic compounds present in the serum may interact with the cationic vectors, resulting in decreased transfection efficiency (*30*−*32*). Thus, investigation of the sensitivity to serum of a given transfection reagent may be of great help to predict its *in vivo* transfection efficiency, in particular, after systemic administration. Here, the transfection experiments performed in the presence or in the absence of serum did not reveal any significant difference regardless of the medium (OptiMEM, NaCl, or Glucose) used for the preparation of the **13b**/DOPE complexes ($p > 0.1$; Figure 6, comparison of panels A and B). These data indicate that the insensitivity to serum is a very general feature of **13b**/DOPE lipoplexes, which is of great interest when considering their *in vivo* use.

Combining **13b***/DOPE with Small PEI.* Additional experiments were performed in order to determine if neamine derivatives could be advantageously combined with other cationic reagents in strategies aiming at developing multimodular gene delivery systems. For instance, considering our neamine vectors as polyamines, we combined **13b**/DOPE and PEI 2 kDa (Sigma, France). In transfection experiments performed with 3 different cell lines, very different effects were measured: with increasing quantities of PEI polymer, there was a progressive increase for $1 \leq CR \leq 2$, then a progressive decrease for $4 \leq CR \leq 8$ (Figure 7 and Supporting Information Figure S4). These results extended the observations previously made by Lampela et al. for combinations of PEI 2 kDa with DOSPER, Lipofectamine, or DOTAP (*33, 34*). We confirmed that the synergy between PEI 2 kDa and cationic lipids might be, in a certain range (i.e., at low charge ratios), a general rule. However, the higher levels measured for whatever combinations does not exceed the higher level reached when using **13b**/DOPE alone, at CR4. Furthermore, antagonistic effects were also observed indicating that an optimization is required in each case. Concerning the cytotoxicity of such combinations, it was found that the synergy measured between PEI 2 kDa and **13b**/DOPE was not obligatorily associated with a higher cytotoxicity. Indeed, when compared with **13b**/DOPE, it was even possible to identify **13b**/DOPE/PEI 2 kDa combinations which were able to reach increased transfection efficiencies while displaying reduced cytotoxicities (data not shown). In addition, we also found that **13b**/DOPE may be part of the efficient formulations involving other lipidic neamine derivatives, other lipidic aminoglycoside derivatives (such as DOSK or DOSP), or even LFM, a fact thus highlighting its versatility (data not shown). Altogether, these data indicate that **13b**/DOPE can be advantageously used in the design of multimodular gene delivery systems in order to obtain higher transfection efficiencies with reduced toxicities.

In Vivo Administration of **13b***/DOPE Formulations.* Finally, following these various *in vitro* investigations, we recently also undertook *in vivo* transfection experiments with the aim of

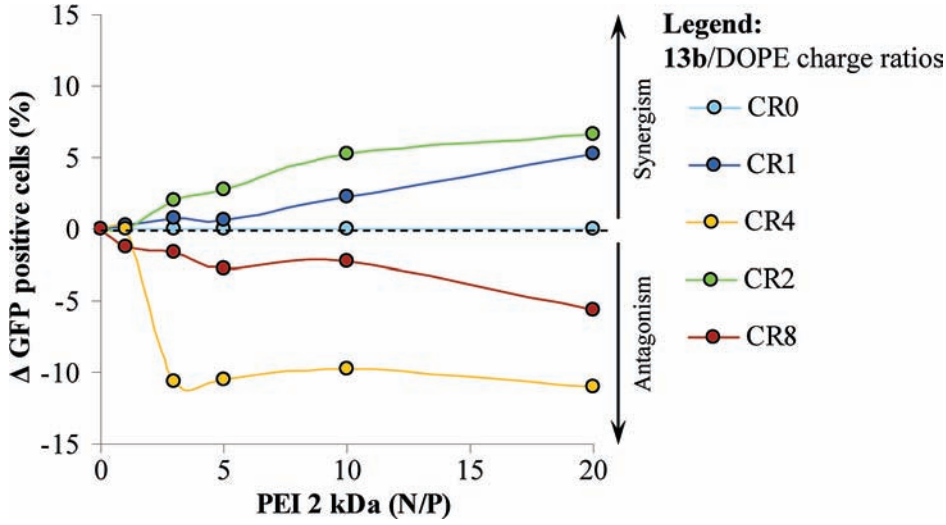

Figure 7. *In vitro* transfection activity for combinations of PEI 2 kDa and **13b**/DOPE 1/1. Lipoplexes (**13b**/DOPE mixed with DNA, from CR1.0 up to CR8.0), polyplexes (PEI 2 kDa with DNA, from N/P1 up to N/P20), and lipopolyplexes (combinations of PEI 2 kDa with DNA, from N/P 1 up to 20, + **13b**/DOPE, from CR1.0 up to CR8.0) were used to transfect cell lines as described in the Experimental Procedures section. For each CR, the variation of %GFP positive cells (Δ = % lipopolyplex − % lipoplex) is indicated [polyplexes alone (CR0) are ineffective, regardless of the N/P tested]. Thus, compared with a lipoplex at a given CR, a lipopolyplex is more efficient if a Δ value higher than 0 is measured, whereas it is less if a Δ value lower than 0 is obtained. These results were obtained using A549 cells. The data obtained using HeLa and 16HBE cells provided similar observations (see Supporting Information Figure S4).

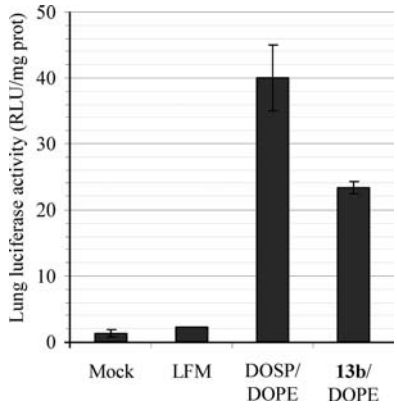

Figure 8. *In vivo* transfection efficiency of **13b**/DOPE lipoplexes. Lipoplexes were prepared at CR6, then administrated i.v. in mice. LFM and DOSP/DOPE were evaluated under same experimental conditions (except that these lipoplexes were prepared at CR4). Lung luciferase activity was measured 24 h later, on complete lung extracts. Mock corresponded to measurements on mice which have received the same amount of naked DNA (not associated with any reagents; $n = 2$, with 4 repeated measurement per animal sample).

transfecting the mouse lung. Preliminary results have indicated that, after intravenous injection, **13b**/DOPE formulations may be able to transfect the lungs *in vivo*. However, in spite of the *in vitro* insensitivity to serum (Figure 8), the luciferase signals measured *in vivo* were relatively weak; they were in fact much higher than those obtained with LFM and similar to those observed with the aminoglycoside derivative DOSP/DOPE formulation (Figure 8). Of note, these signals were, however, significantly lower than those obtained when using the cationic polymer PEI22 kDa (data not shown).

Interestingly, no lethality was observed in mice, regardless of the amount of **13b**/DOPE injected through the tail vein (with 50 μg pDNA per dose and at charge ratios up to 6). On the contrary, the PEI22 kDa is a transfection reagent well-known for its efficiency as well as toxicity. Thus, these data confirm that, as is widely recognized, *in vitro* results do not enable us to perfectly predict the *in vivo* behavior of a given gene delivery system. They also invite us to work out **13b**-based formulations for improved *in vivo* transfection. Accordingly, in ongoing work, we are attempting to design **13b**-based formulations optimized for different routes of *in vivo* administration. Here, it is of great interest to note that **13b**/DOPE could be beneficially incorporated into formulations with the cationic polymer PEI, as efficient *in vivo* transfection might require the development of sophisticated lipopolyplexes.

CONCLUSION

In conclusion, our results demonstrate that efficient gene transfection can be achieved with cationic lipids bearing a headgroup consisting of neamine, a compound which, in comparison to the natural aminoglycosides, incorporates only two rings and has an increased charge density. The most efficient derivative studied herein, **13b**, carries two octadecyl chains linked to a diaminoethyl spacer attached at the 4′-position of a neamine core. As discussed above, both the presence of that spacer and such an attachment position, i.e., at an extremity of the neamine core, appear to play a role in the increase of the gene transfection efficiency. Thus, our present work validates the interest of the neamine core as a straightforward and versatile cationic building block for the development of novel nonviral vectors for gene transfection.

With a view to future developments, the results obtained herein first invite us to perform some chemical modifications of the **13b** structure. For example, it might be interesting to introduce double bonds into the lipidic chains in order to modify their mobility. The replacement of aliphatic chains by a cholesterol moiety could also be envisaged in order to further modulate the fluidity/rigidity balance. Finally, another proposition originating from our study is the use of neamine in several copies associated inside a single molecule. Despite the fact that the most effective neamine derivatives identified herein contained only one neamine moiety, it has to be noted that two derivatives bearing a double neamine headgroup (i.e., compounds **18** and **22**) showed a (weak but not null) transfection efficiency. It is noteworthy that those two derivatives did not display all the beneficial characteristics this study has pointed out, in particular, the attachment of

the linker onto the neamine core as in **13b**. Thus, the synthesis of lipophilic neamine oligomers may constitute an interesting approach for the development of novel nonviral vectors for gene transfection, which can be investigated by taking into account all the critical parameters identified in the present work.

ACKNOWLEDGMENT

The authors thank the "Conseil Régional de Bretagne", the "Association de Transfusion Sanguine et de Biogénétique Gaétan Saleün", and the association "Vaincre La Mucoviscidose" (Paris, France) for financial support.

Supporting Information Available: Synthesis and characteristics of the neamine derivatives **11**, **12a**, **14b**, **15a**, **18**, **22**, **24**, **27**, **30**, and **32**. Chemical structures of the 12 neamine derivatives evaluated in this study and a comparison of some of their chemical features. More detailed evaluation of the *in vitro* transfection efficiencies of the neamine derivatives. For compound **13b**, supplementary data related to DNA condensation and relaxation as well as transfection activity when combined with small polyethylenimine (PEI 2 kDa, Sigma, France). This material is available free of charge via the Internet at http://pubs.acs.org.

LITERATURE CITED

(1) Magnet, S., and Blanchard, J. S. (2005) Molecular insights into aminoglycoside action and resistance. *Chem. Rev. 105*, 477–498.

(2) Mei, H. Y., Galan, A. A., Halim, N. S., Mack, D. P., Moreland, D. W., Sanders, K. B., Truong, H. N., and Czarnik, A. W. (1995) Inhibition of an HIV-1 Tat-derived peptide binding to TAR RNA by aminoglycoside antibiotics. *Bioorg. Med. Chem. Lett. 5*, 2755–2760.

(3) Ennifar, E., Paillart, J. C., Marquet, R., Ehresmann, B., Ehresmann, C., Dumas, P., and Walter, P. (2003) HIV-1 RNA dimerization initiation site is structurally similar to the ribosomal A site and binds aminoglycoside antibiotics. *J. Biol. Chem. 278*, 2723–2730.

(4) Wilschanski, M., Yahav, Y., Yaacov, Y., Blau, H., Bentur, L., Rivlin, J., Aviram, M., Bdolah-Abram, T., Bebok, Z., Shushi, L., Kerem, B., and Kerem, E. (2003) Gentamicin-induced correction of CFTR function in patients with cystic fibrosis and CFTR stop mutations. *N. Engl. J. Med. 349*, 1433–1441.

(5) Bedwell, D. M., Kaenjak, A., Benos, D. J., Bebok, Z., Bubien, J. K., Hong, J., Tousson, A., Clancy, J. P., and Sorscher, E. J. (1997) Suppression of a CFTR premature stop mutation in a bronchial epithelial cell line. *Nat. Med. 3*, 1280–1284.

(6) Stephenson, J. (2001) Antibiotics show promise as therapy for genetic disorders. *JAMA 285*, 2067–2068.

(7) Luft, F. C. (2002) Gentamicin as gene therapy. *J. Mol. Med. 80*, 543–544.

(8) Aissaoui, A., Oudrhiri, N., Petit, L., Hauchecorne, M., Kan, E., Sainlos, M., Julia, S., Navarro, J., Vigneron, J. P., Lehn, J. M., and Lehn, P. (2002) Progress in gene delivery by cationic lipids: guanidinium-cholesterol-based systems as an example. *Curr. Drug Targets 3*, 1–16.

(9) Belmont, P., Aissaoui, A., Hauchecorne, M., Oudrhiri, N., Petit, L., Vigneron, J. P., Lehn, J. M., and Lehn, P. (2002) Aminoglycoside-derived cationic lipids as efficient vectors for gene transfection *in vitro* and *in vivo*. *J. Gene Med. 4*, 517–526.

(10) Sainlos, M., Belmont, P., Vigneron, J. P., Lehn, P., and Lehn, J. M. (2003) Aminoglycoside-derived cationic lipids for gene transfection: synthesis of kanamycin A derivatives. *Eur. J. Org. Chem.* 2764–2774.

(11) Martin, B., Sainlos, M., Aissaoui, A., Oudrhiri, N., Hauchecorne, M., Vigneron, J. P., Lehn, J. M., and Lehn, P. (2005) The design of cationic lipids for gene delivery. *Curr. Pharm. Des. 11*, 375–394.

(12) Sainlos, M., Hauchecorne, M., Oudrhiri, N., Zertal-Zidani, S., Aissaoui, A., Vigneron, J. P., Lehn, J. M., and Lehn, P. (2005) Kanamycin A-derived cationic lipids as vectors for gene transfection. *ChemBioChem 6*, 1023–1033.

(13) Desigaux, L., Sainlos, M., Lambert, O., Chèvre, R., Letrou-Bonneval, E., Vigneron, J. P., Lehn, P., Lehn, J. M., and Pitard, B. (2007) Self-assembled lamellar complexes of siRNA with lipidic aminoglycoside derivatives promote efficient siRNA delivery and interference. *Proc. Natl. Acad. Sci. U.S.A. 104*, 16534–16539.

(14) Gao, X., and Huang, L. (1995) Cationic liposome-mediated gene transfer. *Gene Ther. 2*, 710–722.

(15) Horobin, R. W., and Weissig, V. (2005) A QSAR-modeling perspective on cationic transfection lipids. 1. Predicting efficiency and understanding mechanisms. *J. Gene Med. 7*, 1023–1034.

(16) Gruneich, J. A., and Diamond, S. L. (2007) Synthesis and structure-activity relationships of a series of increasingly hydrophobic cationic steroid lipofection reagents. *J. Gene Med. 9*, 381–391.

(17) Riguet, E., Désiré, J., Bailly, C., and Décout, J. L. (2004) A route for preparing new neamine derivatives targeting HIV-1 TAR RNA. *Tetrahedron 60*, 8053–8064.

(18) Riguet, E., Tripathi, S., Chaubey, B., Désiré, J., Pandey, V. N., and Décout, J. L. (2004) A peptide nucleic acid-neamine conjugate that targets and cleaves HIV-1 TAR RNA inhibits viral replication. *J. Med. Chem. 47*, 4806–4809.

(19) Chaubey, B., Tripathi, S., Désiré, J., Baussanne, I., Décout, J. L., and Pandey, V. N. (2007) Mechanism of RNA cleavage catalyzed by sequence specific polyamide nucleic acid-neamine conjugate. *Oligonucleotides 17*, 302–313.

(20) Viswanadhan, V. N., Ghose, A. K., Revankar, G. R., and Robins, R. K. (1989) Atomic physicochemical parameters for three dimensional structure directed quantitative structure-activity relationships. 4. Additional parameters for hydrophobic and dispersive interactions and their application for an automated superposition of certain naturally occurring nucleoside antibiotics. *J. Chem. Inf. Comput. Sci. 29*, 163–172.

(21) Cozens, A. L., Yezzi, M. J., Kunzelmann, K., Ohrui, T., Chin, L., Eng, K., Finkbeiner, W. E., Widdicombe, J. H., and Gruenert, D. C. (1994) CFTR expression and chloride secretion in polarized immortal human bronchial epithelial cells. *Am. J. Respir. Cell Mol. Biol. 10*, 38–47.

(22) Ruponen, M., Yla-Herttuala, S., and Urtti, A. (1999) Interactions of polymeric and liposomal gene delivery systems with extracellular glycosaminoglycans: physicochemical and transfection studies. *Biochim. Biophys. Acta 1415*, 331–341.

(23) Felgner, P. L., Gadek, T. R., Holm, M., Roman, R., Chan, H. W., Wenz, M., Northrop, J. P., Ringold, G. M., and Danielsen, M. (1987) Lipofection: a highly efficient, lipid-mediated DNA-transfection procedure. *Proc. Natl. Acad. Sci. U.S.A. 84*, 7413–7417.

(24) Blaauw, M., Linskens, M. H., and van Haastert, P. J. (2000) Efficient control of gene expression by a tetracycline-dependent transactivator in single *Dictyostelium discoideum* cells. *Gene 252*, 71–82.

(25) Delépine, P., Guillaume, C., Floch, V., Loisel, S., Yaouanc, J., Clément, J., Des Abbayes, H., and Férec, C. (2000) Cationic phosphonolipids as nonviral vectors: *in vitro* and *in vivo* applications. *J. Pharm. Sci. 89*, 629–638.

(26) Picquet, E., Le Ny, K., Delépine, P., Montier, T., Yaouanc, J. J., Cartier, D., des Abbayes, H., Férec, C., and Clément, J. C. (2005) Cationic lipophosphoramidates and lipophosphoguanidines are very efficient for *in vivo* DNA delivery. *Bioconjugate Chem. 16*, 1051–1053.

(27) Vigneron, J. P., Oudrhiri, N., Fauquet, M., Vergely, L., Bradley, J. C., Basseville, M., Lehn, P., and Lehn, J. M. (1996) Guanidinium-cholesterol cationic lipids: efficient vectors for the transfection of eukaryotic cells. *Proc. Natl. Acad. Sci. U.S.A. 93*, 9682–9686.

(28) Koynova, R., Tarahovsky, Y. S., Wang, L., and MacDonald, R. C. (2007) Lipoplex formulation of superior efficacy exhibits high surface activity and fusogenicity, and readily releases DNA. *Biochim. Biophys. Acta 1768*, 375–386.

(29) Koynova, R., Wang, L., and MacDonald, R. C. (2007) Synergy in lipofection by cationic lipid mixtures: superior activity at the gel-liquid crystalline phase transition. *J. Phys. Chem. B 111*, 7786–7795.

(30) Dodds, E., Dunckley, M. G., Naujoks, K., Michaelis, U., and Dickson, G. (1998) Lipofection of cultured mouse muscle cells: a direct comparison of Lipofectamine and DOSPER. *Gene Ther. 5*, 542–551.

(31) Ghosh, Y. K., Visweswariah, S. S., and Bhattacharya, S. (2000) Nature of linkage between the cationic headgroup and cholesteryl skeleton controls gene transfection efficiency. *FEBS Lett. 473*, 341–344.

(32) Faneca, H., Simoes, S., and de Lima, M. C. (2002) Evaluation of lipid-based reagents to mediate intracellular gene delivery. *Biochim. Biophys. Acta 1567*, 23–33.

(33) Lampela, P., Raisanen, J., Mannisto, P. T., Yla-Herttuala, S., and Raasmaja, A. (2002) The use of low-molecular-weight PEIs as gene carriers in the monkey fibroblastoma and rabbit smooth muscle cell cultures. *J. Gene Med. 4*, 205–214.

(34) Lampela, P., Soininen, P., Urtti, A., Mannisto, P. T., and Raasmaja, A. (2004) Synergism in gene delivery by small PEIs and three different nonviral vectors. *Int. J. Pharm. 270*, 175–184.

BC900062Z

ms ID: bc-2009-00062z.R3

SUPPORTING INFORMATION

Synthesis and transfection properties of a series of lipidic neamine derivatives

Tony Le Gall, Isabelle Baussanne, Somnath Halder, Nathalie Carmoy, Tristan Montier, Pierre Lehn and Jean-Luc Décout

This material first provides more details about the synthesis and characteristics of the neamine derivatives **11**, **12a**, **14b**, **15a**, **18**, **22**, **24**, **27**, **30** and **32**. Next, the chemical structures of the 12 neamine derivatives evaluated in this study are indicated in Chart S1 and a comparison between some of their chemical features is shown in Table S1. In addition, the evaluation of the *in vitro* transfection efficiencies of the neamine derivatives is also more detailed: Figure S1 indicates the observed percentages of transfected HeLa cells (GFP-positive cells as estimated by flow cytometry) whereas Figure S2 shows the luciferase activities (luminometry assays) obtained when using the HeLa and 16HBE cell lines. For compound **13b**, supplementary data related to DNA condensation and relaxation as well as transfection activity when combined with small polyethylenimine (PEI 2 kDa, Sigma, France) are given in Figures S3 and S4, respectively. The literature cited here is detailed at the end of the document.

Synthesis and characteristics of neamine derivatives 11, 12a, 14b, 15a, 18, 22, 24, 27, 30 and 32.

General experimental and analytical conditions: ^{1}H NMR (400 MHz) and ^{13}C NMR (100 MHz) spectra were recorded with a BRUKER ADVANCE 400 spectrometer using the residual solvent signal as internal standard. LRMS were achieved with NERMAG spectrometer for the FAB, DCI and EI techniques, with an AUTOFLEX BRUKER spectrometer for the MALDI and with a ZQ WATERS for the ESI. HRMS were obtained from the Mass Spectrometry Service, CRMPO, at the University of Rennes I, France, using a MICROMASS ZABSPEC-TOF spectrometer and a VARIAN MAT311 spectrometer. Melting points were determined with a BUCHI 510 apparatus. Thin layer chromatographies were performed on silica gel (Alugram Sil G/UV_{254}) or alumina gel (Alugram Alox N/UV_{254}) from Macherey-Nagel and spots were detected either by UV-absorption, by charring with ninhydrin or with cerium molybdate. Preparative chromatographies were performed on alumina gel (MP Ecochrom Biomedicals, Act II-III acc. to Brockman), silica gel (Acros Organic, 0.060-0.200 mm, 60 Å) or on C_{18} reversed phase (Macherey-Nagel polygoprep 60-50 C_{18}). All starting materials were obtained from suppliers and used without further purification unless otherwise noted. DMF was distilled in the presence of CaH_2, THF over sodium with benzophenone, CH_2Cl_2 and CH_3CN over P_2O_5 then stored under argon atmosphere prior to use.

The neamine derivatives **5**, **6**, **8**, **17** and **31** have been previously described (*1, 2*) and the amines **10a, 10b** (*3, 4*) and **28** (*5*) were synthesized according to the literature.

Synthesis of neamine derivatives 11, 12a, 14b, 15a, 18, 22, 24, 27, 30 and 32.

4'-*O*-[4-(triethylammonium)butyl] neamine derivative 11 (Scheme 2). Step a: A solution of compound **7** (450 mg, 0.27 mmol) and triethylamine (4 mL) in DMF (10 mL) under argon

atmosphere was stirred for 24 h at 70°C. After cooling, the reaction mixture was concentrated under reduced pressure. The residue was chromatographed on alumina gel with 6% MeOH in CH_2Cl_2 to lead to the protected derivative of compound **11** in 53% yield. LRMS (MALDI, DHB) *m/z*: 1687.8 $[M+H]^+$, 1445.7 $[M-Tr+H]^+$, 1202.5 $[M-2Tr+H]^+$, 960.4 $[M-3Tr+H]^+$, 718.3 $[M-4Tr+H]^+$. HRMS (ESI^+) *m/z*: $[M+H]^+$ calculated 1686.9137, found 1686.9140.

Step c: The protected compound was dissolved in CH_2Cl_2/TFA (1/1, v/v, 4 mL) with anisole (0.1 mL). After 2 h stirring at rt, solvents were removed under reduced pressure. H_2O and Et_2O were added and the aqueous layer was washed twice with Et_2O before being concentrated and poured on a C18 reversed phase column. **11** was eluted with a gradient of H_2O/MeOH. The pure compound was obtained as the TFA salt with 90% yield. ^1H NMR (CD_3OD) 5.88 (d, $J_{1'-2'}$= 4.0 Hz, 1H, H1'), 4.06 (m, 2H, H3', H5'), 3.97 (dd, 1H, J_{4-5}= J_{4-3}= 9.6 Hz, H4), 3.90 (m, 1H, OCH_2(CH_2)$_3$N), 3.62 (m, 1H, OCH_2(CH_2)$_3$N), 3.57 (dd, 1H, J_{4-5}= J_{5-6}= 9.2 Hz, H5), 3.05-3.48 (m, 15H, O(CH_2)$_3$$CH_2$N, N($CH_2$$CH_3$)$_3$, H1, H3, H6, H2', H4', 2H6'), 2.40 (ddd, J_{2eq-1}= J_{2eq-3}= 4.0 Hz, $J_{2eq-2ax}$= 12.8 Hz, 1H, $H2_{eq}$), 1.93 (ddd, J_{2ax-1}= J_{2ax-3}= $J_{2eq-2ax}$= 12.8 Hz, 1H, $H2_{ax}$), 1.55-1.78 (m, 4H, OCH_2(CH_2)$_2$$CH_2$N), 1.23 (t, *J*= 6.8 Hz, 9H, 3CH_3). ^{13}C NMR (CD_3OD) δ 97.1 (C1'), 81.1 (C4'), 79.3 (C4), 77.2 (C5), 74.4 (C6), 73.3 (OCH_2(CH_2)$_3$N), 70.4, 70.1 (C3', C5'), 58.0 (3NCH_2), 55.8 (C2'), 51.6 (C1), 50.2 (C3), 42.0 (C6'), 29.9 (C2), 28.1, 19.9 (OCH_2(CH_2)$_2$$CH_2$N), 7.8 (3$CH_3$). LRMS ($ESI^+$) *m/z*: 478.18 $[M+H]^+$. HRMS (ESI^+) m/z: $[M+H]^+$ calculated 478.3605, found 478.3602.

4'-*O*-[4-(*N*,*N*-di-*n*-dodecylamino)butyl] neamine derivative 12a (Scheme 2). Step b: To a solution of compound **7** (300 mg, 0.18 mmol) in DMF (10 mL) under argon atmosphere was added successively K_2CO_3 (180 mg, 1.3 mmol) and di-*n*-dodecylamine **9a** (64 mg, 0.18 mmol). The reaction mixture was stirred for 24 h at 70°C. After cooling, the reaction mixture was filtered then concentrated under reduced pressure. The residue was chromatographed on

alumina gel with cyclohexane/CH_2Cl_2 (65/35, v/v) to lead to the protected derivative of **12a** with 48% yield. **Step c:** The protected compound was dissolved in CH_2Cl_2/TFA (1/1, v/v, 4 mL) with anisole (0.1 mL). After 2 h stirring at rt, solvents were removed under reduced pressure. H_2O and Et_2O were added and the aqueous layer washed twice with Et_2O before being concentrated and poured on a C18 reversed phase column. After elution with a gradient of H_2O/MeOH, **12a** was obtained as the TFA salt with 89% yield. ^{1}H NMR (CD_3OD) 5.92 (d, $J_{1'\text{-}2'}$= 3.8 Hz, 1H, H1'), 4.04-4.15 (m, 2H, H3', H5'), 4.00 (dd, $J_{4\text{-}5}$= $J_{4\text{-}3}$= 9.7 Hz, 1H, H4), 3.94 (m, 1H, OCH_2(CH_2)$_3$N), 3.65 (m, 1H, OCH_2(CH_2)$_3$N), 3.60 (dd, $J_{4\text{-}5}$= $J_{5\text{-}6}$= 9.2 Hz, 1H, H5), 3.27-3.49 (m, 4H, H3, H6, H2', H6'b), 3.09-3.23 (m, 9H, H1, H4', H6'a, 3NCH_2), 2.45 (ddd, $J_{2eq\text{-}1}$= $J_{2eq\text{-}3}$= 4.1 Hz, $J_{2eq\text{-}2ax}$= 12.4 Hz, 1H, H2$_{eq}$), 2.00 (ddd, $J_{2ax\text{-}1}$= $J_{2ax\text{-}3}$= $J_{2eq\text{-}2ax}$= 12.5 Hz, 1H, H2$_{ax}$), 1.60-1.85 (m, 8H, OCH$_2$(CH_2)$_2$CH$_2$N, N[CH$_2$$CH_2$($CH_2$)$_9CH_3$]$_2$), 1.24-1.42 (m, 36H, N[CH$_2$CH$_2$(CH_2)$_9$CH$_3$]$_2$), 0.90 (t, J= 6.7 Hz, 6H, 2CH_3). ^{13}C NMR (CD_3OD) δ 97.3 (C1'), 81.3 (C4'), 79.6 (C4), 77.3 (C5), 74.5 (C6), 73.4 (OCH_2(CH_2)$_3$N), 70.4, 70.1 (C3', C5'), 55.8 (C2'), 54.3 (3NCH_2), 51.6 (C1), 50.2 (C3), 42.0 (C6'), 30.0 (C2), 33.2, 30.9, 30.8, 30.7, 30.6, 30.4, 28.5, 27.7, 25.0, 23.9, 21.9 (OCH$_2$(CH_2)$_2$CH$_2$N, N[CH$_2$(CH_2)$_{10}$CH$_3$]$_2$), 14.6 (2CH_3). LRMS (ESI$^+$) *m/z*: 730.4 [M+H]$^+$, 426.4, 408.4, 240.3. HRMS (ESI$^+$) *m/z*: [M+H]$^+$ calculated 730.6422, found 730.6425.

5-*O*-[6-(*N,N*-di-*n*-octadecylamine)hexyl] neamine derivative 14b (Scheme 2). The same procedure as described for the synthesis of **12a** (steps b and c) was applied to compound **8** with di-*n*-octadecylamine **9b**. **14b** was obtained with 32% yield for two steps. ^{1}H NMR (CD_3OD) 5.85 (d, $J_{1'\text{-}2'}$= 4.0 Hz, 1H, H1'), 4.00-4.18 (m, 4H, H4, H3', H5', OCH_2(CH_2)$_5$N), 3.77 (m, 1H, OCH_2(CH_2)$_5$N), 3.49-3.66 (m, 3H, H3, H5, H6), 3.37-3.48 (m, 3H, H2', H4', H6'b), 3.20-3.32 (m, 2H, H1, H6'a), 3.08-3.20 (m, 6H, O(CH_2)$_5$$CH_2$N, N[CH$_2$$CH_2$($CH_2$)$_9CH_3$]$_2$), 2.43 (ddd, $J_{2eq\text{-}1}$= J$_{2eq\text{-}3}$= 4.0 Hz, $J_{2eq\text{-}2ax}$= 12.8 Hz 1H, H2$_{eq}$), 1.98

(ddd, J_{2ax-1}= J_{2ax-3}= $J_{2eq-2ax}$= 12.8 Hz, 1H, $H2_{ax}$), 1.62-1.78 (m, 8H, $OCH_2CH_2(CH_2)_2$, CH_2CH_2N, $N[CH_2CH_2(CH_2)_{15}CH_3]_2$), 1.22-1.50 (m, 64H, $OCH_2CH_2(CH_2)_2CH_2CH_2N$, $N[CH_2CH_2(CH_2)_{15}CH_3]_2$), 0.90 (t, *J*= 6.8 Hz, 9H, $3CH_3$). ^{13}C NMR (CD_3OD) δ 93.0 (C1'), 83.2 (C5), 74.3 (C4), 73.4 (C6), 72.1 ($OCH_2(CH_2)_5N$), 71.4 (C5'), 70.8 (C4'), 68.2 (C3'), 53.4 (C2'), 52.7 ($2NCH_2$), 50.2, 49.2 (C1, C3), 40.1 (C6'), 33.9, 31.7, 29.7, 29.4, 29.2, 29.1, 28.8, 28.1, 26.2, 25.1, 23.6, 23.4, 22.3 (C2, $OCH_2(CH_2)_4CH_2N$, $[NCH_2(CH_2)_{16}CH_3]_2$), 13.0 ($2CH_3$). HRMS (ESI^+) *m/z*: $[M+H]^+$ calculated 926.8613, found 926.8634.

5-*O*-[6-(*N*-2-aminoethyl-*N*,*N*-di-*n*-dodecylamine)hexyl] neamine derivative 15a (Scheme 2). The same procedure as described for the synthesis of **12a** (steps b and c) was applied to compound **8** with *N*-2-aminoethyl-*N*,*N*-di-*n*-dodecylamine **10a**. **15a** was obtained with 39% yield for two steps. ^{1}H NMR (D_2O) 5.70 (d, $J_{1'-2'}$= 4.0 Hz, 1H, H1'), 3.75-3.95 (m, 4H, H4, H3', H5', $OCH_2(CH_2)_5N$), 3.51-3.65 (m, 4H, H3, H5, H6, $OCH_2(CH_2)_5N$), 3.36-3.48 (H2', H4', $3NCH_2$), 3.15-3.21 (m, 5H, H6'b, $2NCH_2$), 2.90-3.03 (m, 2H, H1, H6'a), 2.32 (ddd, J_{2eq-1}= J_{2eq-3}= 4.0 Hz, $J_{2eq-2ax}$= 12.8 Hz, 1H, $H2_{eq}$), 1.70 (ddd, J_{2ax-1}= J_{2ax-3}= $J_{2eq-2ax}$= 12.8 Hz, 1H, $H2_{ax}$), 1.35-1.57 (m, 8H, $OCH_2CH_2(CH_2)_2$ CH_2CH_2N, $N[CH_2CH_2(CH_2)_{15}CH_3]_2$), 1.03-1.27 (m, 64H, $OCH_2CH_2(CH_2)_2CH_2CH_2N$, $N[CH_2CH_2(CH_2)_{15}CH_3]_2$), 0.74 (t, *J*= 6.8 Hz, 9H, $3CH_3$). ^{13}C NMR (D_2O) δ 93.0 (C1'), 82.6 (C5), 73.6 (C4), 72.7 (C6), 72.2 ($OCH_2(CH_2)_5N$), 70.1 (C5'), 69.9 (C4'), 68.4 (C3'), 61.6 ($3NCH_2$), 53.2 (C2'), 49.7, 48.8 (C1, C3), 39.9 (C6'), 32.0, 31.1, 29.7, 29.2, 28.0, 24.9, 24.8, 22.6 (C2, $OCH_2(CH_2)_4CH_2N$, $[NCH_2(CH_2)_{16}CH_3]_2$), 13.8 ($2CH_3$). LRMS (ESI^+) *m/z*: 845.6 $[M+K]^+$, 801.7 $[M+H]^+$, 685.5, 633.4, 423.3, 380.5.

2-(*N*-(*N'*,*N'*-di-*n*-dodecyl)ethylamino)aminodiethanoic acid 16 (Scheme 3). Step a: To a solution of amine **10a** (209 mg, 0.52 mmol) in dry CH_3CN (5 mL) under argon atmosphere were added K_2CO_3 (218 mg, 1.6 mmol) and TBAI (194 mg, 0.5 mmol). The mixture was stirred under reflux 15 min before the addition of bromoethylbenzoate (362 mg, 1.58 mmol)

then 3 days. After cooling, the mixture was filtrated and concentrated under reduced pressure. The crude product was dissolved in CH_2Cl_2 and washed with water, an aqueous saturated $NaHCO_3$ solution then brine. The organic solution was dried over $MgSO_4$, filtrated and concentrated under reduced pressure. The residue obtained was chromatographed on alumina gel with a mixture of CH_2Cl_2/MeOH (98/2, v/v) to lead to the benzylic ester of **16** with 98% yield. ^{1}H NMR ($CDCl_3$) 7.32-7.40 (m, 10H, H arom.), 5.13 (s, 4H 2CO*CH*$_2$Ph), 4.14 (m, 2H, N*CH*$_2$CH$_2$N), 3.80 (td, *J*= 4.8 and 12.8 Hz, 2H, N[*CH*$_2$(CH$_2$)$_{10}$CH$_3$]$_2$), 3.57 (td, *J*= 4.4 and 12.8 Hz, 2H, N[*CH*$_2$(CH$_2$)$_{10}$CH$_3$]$_2$), 3.46 (s, 4H, 2CO*CH*$_2$*N*), 3.24 (m, 2H, N*CH*$_2$CH$_2$N), 1.72 (m, 4H, 2NCH$_2$*CH*$_2$(CH$_2$)$_9$CH$_3$), 1.23-1.36 (m, 36H, 2NCH$_2$CH$_2$(*CH*$_2$)$_9$CH$_3$), 0.89 (t, *J*= 6.4 Hz, 6H, 2*CH*$_3$). ^{13}C NMR ($CDCl_3$) δ 170.6 (*C*OOBn), 135.13 (*C* arom.), 128.8-128.4 (*CH* arom.), 68.1 (N*CH*$_2$CO), 66.9 (*CH*$_2$Ph), 60.9, 55.2, 48.2 (4N*CH*$_2$), 31.9, 29.6, 29.5, 29.4, 29.3, 29.0, 26.3, 22.7 (20*CH*$_2$), 15.3 (2*CH*$_3$). LRMS (DCI$^+$) *m/z*: 693 [M+H]$^+$, 366, 294, 250. **Step b:** The benzylic ester of **16** (130 mg, 0.19 mmol) was stirred in EtOH (2 mL) at rt with Pd/C (10%, 130 mg) and cyclohexadiene (177 L, 1.87 mmol) for 1 h. The mixture was filtrated on kieselguhr and concentrated under reduce pressure. The diacid **16** was obtained as a white solid with 86% yield and enough pure for doing the next step without purification. ^{1}H NMR ($CDCl_3$) 4.28 (m, 2H, N*CH*$_2$CH$_2$N), 3.77 (m, 2H, N[*CH*$_2$(CH$_2$)$_{10}$CH$_3$]$_2$), 3.48-3.67 (m, 6H, 2CO*CH*$_2$*N*, N[*CH*$_2$(CH$_2$)$_{10}$CH$_3$]$_2$), 3.26 (m, 2H, N*CH*$_2$CH$_2$N), 1.63 (m, 4H, 2NCH$_2$*CH*$_2$(CH$_2$)$_9$CH$_3$), 1.22-1.35 (m, 36H, 2NCH$_2$CH$_2$(*CH*$_2$)$_9$CH$_3$), 0.89 (t, *J*= 6.4 Hz, 6H, 2*CH*$_3$). ^{13}C NMR ($CDCl_3$) δ 173.5 (*C*OOH), 59.5 (N*CH*$_2$CO), 58.4, 55.5, 47.8 (4N*CH*$_2$), 31.9, 29.7, 29.6, 29.5, 29.4, 29.2, 26.4, 22.7 (20*CH*$_2$), 14.1 (2*CH*$_3$). LRMS (FAB$^+$, NBA) *m/z*: 513 [M+H]$^+$, 496, 468, 412, 366.

5,5-Dineamine derivative 18 (Scheme 3). Step c: Compound **16** (19.5 mg, 0.04 mmol) was dissolved in dry DMF (3 mL) under argon atmosphere. To the solution were added HOBT

(15.4 mg, 0.11 mmol) and EDC (21.7 mg, 0.11 mmol), then the mixture was stirred at rt for 30 min before the addition of a solution of **17** (200 mg, 0.11 mmol) in DMF (2 mL). The mixture was stirred at 60°C for 12 h. After cooling and concentration of the solution under reduced pressure, the crude product was dissolved in CH_2Cl_2 and washed successively with water, an aqueous saturated $NaHCO_3$ solution then brine. The organic layer was dried over $MgSO_4$, filtrated and concentrated under reduced pressure. The residue obtained was chromatographed on alumina gel with a mixture of CH_2Cl_2/MeOH (99/1, v/v) to lead to the protected dineamine compound with 55% yield. **Step d:** This compound dissolved in CH_2Cl_2 (2 mL) was treated with TFA (2 mL) and anisole (0.1 mL). After 12 h stirring at rt, the solvents were removed under reduced pressure. H_2O and Et_2O were added and the aqueous layer washed twice with Et_2O before being concentrated and poured on a C18 reversed phase column. **18** was eluted with a gradient of H_2O/MeOH and obtained as the TFA salt with 91% yield. ^{1}H NMR (CD_3OD) 5.85 (d, $J_{1'-2'}$= 3.8 Hz, 2H, H1'), 4.20 (m, 2H), 4.00-4.16 (m, 6H), 3.71-3.84 (m, 4H), 3.3-3.65 (m, 20H), 3.18-3.29 (m, 8H), 3.02-3.11 (m, 2H), 2.41-2.51 (m, 2H, $H2_{eq}$), 1.88-2.05 (m, 2H, $H2_{ax}$), 1.49-1.82 (m, 8H), 1.24-1.48 (m, 36H), 0.92 (t, *J*= 6.8 Hz, 6H, 2CH_3). ^{13}C NMR (CD_3OD) δ 171.2 (2*C*ONH), 162.0, 161.7 (*C*OCF_3), 121.1, 118.2, 115.3, 112.4 (CO*C*F_3), 92.7 (2C1'), 83.2 (2C5), 74.2 (2C4), 73.5 (2C6), 72.3 (2OCH_2(CH_2)$_5$N), 71.4 (2C4'), 70.8 (2C5'), 68.3 (2C3'), 60.3, 57.9, 57.5, 56.5 (6 NCH_2), 53.5 (2C2'), 50.2 (2C1), 49.2 (2C3), 40.2 (2C6'), 38.9 (2 N*CH2*CONH), 31.7, 29.8, 29.3, 29.2, 29.1, 29.0, 28.7, 28.0, 26.6, 25.8, 25.1, 22.3, 21.6 (2C2, 2OCH_2(CH_2)$_4$$CH_2$N, N[$CH_2$($CH_2$)$_{10}$$CH_3$]$_2$), 14.6 (2$CH_3$). LRMS (MALDI, DHB) *m/z*: 1782.6 $[M+4TFA]^+$, 1320.2 $[M+H]^+$, 966.8.

Dibenzyl 2-(octadecyl)malonate 20 (Scheme 4). Step a: To a THF solution of dibenzyl malonate **19** (0.5 mL, 2 mmol, 20 mL) under argon atmosphere at 0°C, were added NaH (60%

suspension, 96 mg, 2.4 mmol) and after 30 min stirring at rt, bromooctadecane (667 mg, 2 mmol). The mixture was stirred for 24 h, then, an aqueous saturated NH_4Cl solution was added. After separation of the organic and aqueous layers, the latter was washed 3 times with Et_2O. The organic layers were dried over $MgSO_4$, filtrated and concentrated under reduced pressure. The crude product was purified by chromatography on silica gel with a mixture of cyclohexane/CH_2Cl_2 (40/60, v/v) to lead to the alkylated product **20** with 64% yield. ^{1}H NMR ($CDCl_3$) 7.28-7.35 (m, 10H, *CH* arom.), 5.19 (s, 4H 2CH_2Ph), 3.46 (t, *J*= 7.6 Hz, 1H, $CH_2CH(CO_2Bn)_2$), 1.95 (m, 2H, $CH_3(CH_2)_{16}CH_2CH(CO_2Bn)_2$), 1.23-1.36 (m, 32H, $CH_3(CH_2)_{16}CH_2CH(CO_2Bn)_2$), 0.89 (t, *J*= 6.8 Hz, 3H, CH_3). LRMS (FAB$^+$,NBA) *m/z*: 559 $[M+Na]^+$, 538 $[M+H]^+$, 427.

2-(Octadecyl)malonic acid 21 (Scheme 4). Step b: The dibenzylic ester **20** (320 mg, 0.59 mmol) was stirred in EtOH/THF (4 mL, 1/1, v/v) at rt with Pd/C (10%, 320 mg) and cyclohexadiene (570 L, 5.96 mmol) for 3 h. The mixture was filtrated on kieselguhr and concentrated under reduce pressure. The diacid **21** was obtained as a white solid with 95% yield and enough pure for doing the next step without purification. ^{1}H NMR (DMSO-d_6) δ 3.14 (t, *J*= 7.6 Hz, 1H, $CH_2CH(CO_2H)_2$), 1.69 (m, 2H, $CH_3(CH_2)_{16}CH_2CH(CO_2H)_2$), 1.17-1.30 (m, 32H, $CH_3(CH_2)_{16}CH_2CH(CO_2H)_2$), 0.86 (t, *J*= 6.8 Hz, 3H, CH_3). ^{13}C NMR (DMSO-d_6) δ 171.6 (CO_2H), 51.9 ($CH_2CH(CO_2H)_2$), 31.2 ($CH_3(CH_2)_{16}CH_2CH(CO_2H)_2$), 29.5, 29.2, 28.9, 27.3, 22.6 ($CH_3(CH_2)_{16}CH_2CH(CO_2H)_2$), 14.4 ($CH_3$). LRMS (FAB$^+$, NBA) *m/z*: 396 $[M+K]^+$, 357 $[M+H]^+$.

5,5-Dineamine derivative 22 (Scheme 4). Step c: Compound **21** (14.3 mg, 0.04 mmol) was dissolved in dry DMF (3 mL) under argon atmosphere. To the solution were added HOBT (13.6 mg, 0.1 mmol) and EDC (19.2 mg, 0.1 mmol). The mixture was stirred at rt for 40 min before the addition of a solution of neamine derivative **17** (180 mg, 0.1 mmol) in DMF (3

mL). After 12 h stirring, the mixture was concentrated under reduced pressure. The crude product was dissolved in CH_2Cl_2 and washed successively with water, an aqueous saturated $NaHCO_3$ solution then brine. The organic layer was dried over $MgSO_4$, filtrated and concentrated under reduced pressure. The residue obtained was chromatographed on alumina gel with a mixture of CH_2Cl_2/cyclohexane (50/50, v/v) to lead to the dineamine protected compound with 37% yield. **Step d:** This compound dissolved in CH_2Cl_2 (2 mL) was treated with TFA (2 mL) and anisole (0.1 mL). After 12 h stirring at rt, solvents were removed under reduced pressure. H_2O and Et_2O were added and the aqueous phase washed twice with Et_2O before being concentrated and poured on a C18 reversed phase column. **22** was eluted with a gradient of H_2O/MeOH and obtained as the TFA salt with 35% yield. ^{1}H NMR (CD_3OD) 5.83 (d, $J_{1'-2'}$= 3.6 Hz, 2H, H1'), 4.01-4.16 (m, 8H, H4, H3', H5', OCH_2(CH_2)$_5$N), 3.74 (m, 2H, OCH_2(CH_2)$_5$N), 3.45-3.62 (m, 4H, H5, H6), 3.46-3.35 (m, 6H, H3, H4', H6'b), 3.32-3.15 (m, 6H, H1, H2', H6'a), 2.43 (ddd, J_{2eq-1}= J_{2eq-3}= 4.4 Hz, $J_{2eq-2ax}$ = 12.4 Hz, 2H, $H2_{eq}$), 2.19 (m, 1H, *CH*CONH), 1.98 (ddd, J_{2ax-1}= J_{2ax-3}= $J_{2eq-2ax}$= 12.4 Hz, 2H, $H2_{ax}$), 1.57-1.69 (m, 4H, O(CH_2)$_5$$CH_2$N), 1.48-1.55 (m, 2H), 1.25-1.45 (m, 48H), 0.92 (t, *J*= 6.8 Hz, 3H, CH_3). ^{13}C NMR (CD_3OD) δ 174.9 (2*C*ONH), 98.2 (2C1'), 83.3 (2C5), 74.4 (2C4), 73.4 (2C6), 72.3 (2OCH_2(CH_2)$_5$N), 71.6 (2C4'), 70.6 (2C5'), 68.2 (2C3'), 53.4 (2C2'), 50.1 (2C1), 49.2 (2C3), 47.9 (2*CH*CONH), 40.9 (2C6'), 38.7 (2O(CH_2)$_5$$CH_2$N), 35.8, 31.7, 29.8, 29.4, 29.1, 28.9, 26.3, 25.8, 25.0, 22.3 (2C2, 25CH_2), 13.0 (CH_3). LRMS (MALDI, DHB) *m/z*: 1185.7 $[M+Na]^+$, 1163.8 $[M+H]^+$, 716.5.

2-(Dioctadecyl)malonic acid 23 (Scheme 4). Step a: To a solution of the dibenzyl monoalkylmalonate **20** (300 mg, 0.56 mmol) in THF (20 mL) under argon atmosphere at 0°C, were added NaH (60% suspension, 50 mg, 1.25 mmol), and after 30 min stirring at rt, bromooctadecane (667 mg, 2 mmol). The mixture was stirred for 24 h at reflux. After cooling

at rt, an aqueous saturated NH_4Cl solution was added. After separation of the organic and aqueous layers, the latter was washed 3 times with Et_2O. The organic layers were dried over $MgSO_4$, filtrated and concentrated under reduced pressure. The crude product was purified by chromatography on silica gel with a mixture of cyclohexane/CH_2Cl_2 (70/30, v/v) to lead to the dibenzyl dialkylmalonate with 30% yield. ^{1}H NMR ($CDCl_3$) 7.27-7.35 (m, 10H, *CH* arom.), 5.13 (s, 4H 2CH_2Ph), 1.91 (m, 4H, $(CH_3(CH_2)_{16}CH_2)_2C(CO_2Bn)_2$), 1.20-1.36 (m, 30H, $(CH_3CH_2(CH_2)_{15}CH_2)_2C(CO_2Bn)_2$), 1.08 (m, 4H, $(CH_3CH_2(CH_2)_{15}CH_2)_2C(CO_2Bn)_2$), 0.92 (t, *J*= 6.8 Hz, 6H, 2CH_3). ^{13}C NMR ($CDCl_3$) δ 171.7 (2*C*ONH), 135.7 (2*C* arom.), 128.2, 128.5 (10*CH* arom.), 66.7 (2*CH*Ph), 57.8 ($(CH_3(CH_2)_{17})_2C(CO_2Bn)_2$), 32.2, 32.0, 29.8, 29.7, 29.6, 29.4, 29.3, 23.9, 22.7 ($(CH_3(CH_2)_{17})_2C(CO_2Bn)_2$), 14.2 (2$CH_3$). LRMS ($FAB^+$, NBA) *m/z*: 812 $[M+Na]^+$, 790 $[M+H]^+$, 613. **Step b:** The dialkylated product was debenzylated (124 mg, 0.16 mmol) following the same procedure as for the dibenzyl monoalkylmalonate **20**. The diacid **23** was obtained as a white solid with 91% yield and enough pure for doing the next step without purification. ^{1}H NMR ($CDCl_3$) 1.94 (m, 4H, $(CH_3(CH_2)_{16}CH_2)_2C(CO_2H)_2$), 1.18-1.45 (m, 64H, $(CH_3(CH_2)_{16}CH_2)_2C(CO_2H)_2$), 0.90 (t, *J*= 6.8 Hz, 6H, 2CH_3). ^{13}C NMR ($CDCl_3$) δ 57.9 ($(CH_3(CH_2)_{17})_2C(CO_2H)_2$), 32.0, 29.7, 29.4, 29.3, 24.9, 22.7 ($(CH_3(CH_2)_{17})_2C(CO_2H)_2$), 14.1 (2$CH_3$). LRMS ($FAB^+$, NBA) *m/z*: 632 $[M+Na]^+$, 610 $[M+H]^+$, 564, 546.

5-Neamine derivative 24 (Scheme 4). Step c: Compound **23** (15.8 mg, 0.026 mmol) was dissolved in dry DMF (3 mL) under argon atmosphere. To the solution were added HOBT (10.8 mg, 0.08 mmol) and EDC (15.2 mg, 0.08 mmol). The mixture was stirred at rt for 40 min before the addition of a solution of neamine derivative **17** (120 mg, 0.068 mmol) in DMF (3 mL). After 12 h stirring, the mixture was concentrated under reduced pressure. The crude product was dissolved in CH_2Cl_2 and washed successively with water, an aqueous saturated

$NaHCO_3$ solution then brine. The organic layer was dried over $MgSO_4$, filtrated and concentrated under reduced pressure. The residue obtained was chromatographed on alumina gel with a mixture of CH_2Cl_2/cyclohexane (40/60, v/v) to lead to the mononeamine protected compound with 35% yield. **Step d:** This compound dissolved in CH_2Cl_2 (2 mL) was treated with TFA (2 mL) and anisole (0.1 mL). After 12 h stirring at rt, the solvents were removed under reduced pressure. H_2O and Et_2O were added and the aqueous layer was washed twice with Et_2O before being concentrated and poured on a C18 reversed phase column. After elution with a gradient of H_2O/MeOH, **24** was obtained as the TFA salt with a quantitative yield. ^{1}H NMR (CD_3OD) 5.82 (d, $J_{1'-2'}$= 3.6 Hz, 1H, H1'), 3.99-4.08 (m, 4H, H4, H3', H5', OCH_2(CH_2)$_5$N), 3.76 (m, 1H, OCH_2(CH_2)$_5$N), 3.49-3.61 (m, 2H, H5, H6), 3.32-3.45 (m, 3H, H3, H4', H6'b), 3.15-3.27 (m, 3H, H1, H2', H6'a), 2.40 (ddd, J_{2eq-1}= J_{2eq-3}= 4.0 Hz, $J_{2eq-2ax}$ = 12.8 Hz, 1H, $H2_{eq}$), 2.18 (m, 1H, *CH*CONH), 1.89 (ddd, J_{2ax-1}= J_{2ax-3}= $J_{2eq-2ax}$= 12.8 Hz, 1H, $H2_{ax}$), 1.64 (m, 2H, O(CH_2)$_5$$CH_2$N), 1.49-1.60 (m, 4H), 1.20-1.50 (m, 72H), 0.92 (t, *J*= 6.8 Hz, 6H, 2CH_3). ^{13}C NMR (CD3OD) δ 177.6 (*C*ONH), 162.1, 161.7 (*C*OCF_3), 121.1, 118.2, 115.2, 112.4 (CO*C*F_3), 93.2 (C1'), 83.3 (C5), 75.0 (C4), 73.5 (C6), 72.2 (OCH_2(CH_2)$_5$N), 71.2 (C4'), 71.0 (C5'), 68.5 (C3'), 53.6 (C2'), 50.3 (C1), 49.2 (C3), 46.8 (*CH*CONH), 40.2 (C6'), 38.6 O(CH_2)$_5$$CH_2$N, 32.7, 31.7, 29.8, 29.4, 29.3, 29.2, 29.1, 28.7, 27.2, 26.4, 25.0, 22.3 (C2, 38CH_2), 13.1 (2CH_3). LRMS (MALDI, DHB) *m/z*: 990.9 $[M+Na]^+$, 968.9 $[M+H]^+$. HRMS (ESI^+) *m/z*: $[M+H]^+$ calculated 968.8718, found 968.8718.

2-(Dodecylamido)malonic acid 26 (Scheme 5). Step a: To a solution of dodecanoic acid (254 mg, 1 mmol) in CH_2Cl_2 (14 mL) at rt were added EDC (288 mg, 1.5 mmol) and HOBT (203 mg, 1.5 mmol) then, after 45 min stirring, the chlorhydrate **25** (254 mg, 1.2 mmol) and Et_3N (1 mL). 12 h later, the mixture was washed successively with water, HCl 1M, an aqueous saturated $NaHCO_3$ solution then brine. The organic layer was dried over $MgSO_4$,

filtrated and concentrated under reduced pressure. The residue obtained was chromatographed on silica gel with a mixture of CH_2Cl_2/MeOH (99:1, v/v) to lead to diethyl 2-(dodecylamido)malonate with 95% yield. ^{1}H NMR ($CDCl_3$) 6.45 (d, *J*= 6.8 Hz, 1H, *NH*), 5.18 (d, *J*= 6.8 Hz, 1H, NH*CH*$(CO_2)_2$), 4.29 (m, 4H, 2CH_3*CH_2*OCO), 2.30 (t, *J*= 7.6 Hz, 2H, *CH_2*CONH), 1.66 (m, 2H, *CH_2*), 1.32 (t, *J*= 7.2 Hz, 6H, 2*CH_3*), 1.27 (m, 16H, 8*CH_2*), 0.86 (t, *J*= 6.8 Hz, 3H, *CH_3*). ^{13}C NMR ($CDCl_3$) δ 172.9 (*C*ONH), 166.5 (2*C*OOEt), 62.6 (2CH_3*CH_2*OCO), 56.4 (NH*CH*$(CO_2)_2$), 36.1 (*CH_2*CONH), 31.9, 29.6, 29.5, 29.3, 29.2, 25.4, 22.7 (9*CH_2*), 14.1, 14.0 (3*CH_3*). LRMS (FAB^+, NBA) *m/z*: 358 $[M+H]^+$, 342, 328, 316, 297, 284, 277, 256, 228. **Step b:** This compound in EtOH (9 mL) was treated with NaOH aq. 2M at 70°C for 2 h. After cooling, the solution was neutralized with HCl aq. 1M. The solution was filtrated and concentrated under reduced pressure to give the diacid **26** with 90% yield, enough pure for doing the next step without purification. ^{1}H NMR (CD_3OD) 4.87 (m, 1H, NH*CH*$(CO_2)_2$), 2.25 (t, *J*= 7.2 Hz, 2H, *CH_2*CONH), 1.55 (m, 2H, *CH_2*), 1.24 (m, 16H, 8*CH_2*), 0.84 (t, *J*= 6.8 Hz, 3H, *CH_3*). ^{13}C NMR (CD3OD) δ 174.8 (*C*ONH), 168.1 (2*C*OOH), 48.2 (NH*CH*$(CO_2H)_2$), 35.0 (*CH_2*CONH), 31.7, 29.4, 29.2, 29.1, 28.2, 25.4, 22.4 (9*CH_2*), 13.0 (*CH_3*). LRMS (FAB^+, NBA) *m/z*: 302 $[M+H]^+$, 284, 256, 228, 200.

5,5-Dineamine derivative 27 (Scheme 5). Step c: The diacid **26** (13 mg, 0.043 mmol) was dissolved in dry DMF (3 mL) under argon atmosphere. To the solution were added HOBT (17.4 mg, 0.13 mmol) and EDC (24.7 mg, 0.13 mmol). The mixture was stirred at rt for 40 min before the addition of a solution of neamine derivative **17** (230 mg, 0.12 mmol) in DMF (2 mL). After 12 h stirring, the mixture was concentrated under reduced pressure. The crude product was dissolved in CH_2Cl_2 and washed successively with water, an aqueous saturated $NaHCO_3$ solution then brine. The organic layer was dried over $MgSO_4$, filtrated and concentrated under reduced pressure. The residue obtained was chromatographed on alumina

gel with a mixture of CH_2Cl_2/MeOH (99/1, v/v) to lead to the protected compound with 30% yield. **Step d:** This compound dissolved in CH_2Cl_2 (2 mL) was treated with TFA (2 mL) and anisole (0.1 mL). After 12 h stirring at rt, the solvents were removed under reduced pressure. H_2O and Et_2O were added then the aqueous layer was washed twice with Et_2O before being concentrated. The crude product was eluted on a C18 reversed phase column with a gradient of H_2O/MeOH. Pure compound **27** was obtained as the TFA salt with a quantitative yield. ^{1}H NMR (D_2O) 5.69 (d, $J_{1'-2'}$= 3.6 Hz, 2H, H1'), 3.71-3.94 (m, 8H, H4, H3', H5', OCH_2(CH_2)$_5$N), 3.68 (s, 1H, NCH(CONH)$_2$), 3.51-3.65 (m, 6H, OCH_2(CH_2)$_5$N, H5, H6), 3.30-3.49 (m, 6H, H4', O(CH_2)$_5$$CH_2$N), 3.10-3.27 (m, 6H, H3, H2', H6'b), 2.97-3.08 (m, 2H, H1, H6'a), 2.32 (ddd, J_{2eq-1}= J_{2eq-3}= 4.0 Hz, $J_{2eq-2ax}$= 12.8 Hz, 1H, H2$_{eq}$), 2.13 (t, J= 7.6 Hz, 4H, CH_3(CH_2)$_9$$CH_2$CO), 1.72 (ddd, J_{2ax-1}= J_{2ax-3}= $J_{2eq-2ax}$= 12.4 Hz, 1H, H2$_{ax}$), 1.28-1.50 (m, 10H), 1.01-1.22 (m, 20H), 0.71 (t, J= 7.2 Hz, 6H, 2CH_3). ^{13}C NMR (D_2O) δ 176.9 (CONH), 171.1 (2NHCO(CH_2)$_2$$C$ONH), 163.3, 163.0, 162.6, 162.3 (COCF_3), 120.7, 117.7, 114.9, 112.0 (COCF$_3$), 92.81 (2C1'), 82.6 (2C5), 73.3, 72.8 (2C4, 2C6, NCH(CONH)$_2$), 72.2 (2OCH_2(CH_2)$_5$N), 70.1 (2C4', 2C5'), 68.3 (2C3'), 53.2 (2C2'), 49.7 (2C1), 48.8 (2C3), 42.6, 40.0, 39.2, 35.6, 31.6, 29.3, 29.2, 29.0, 28.7, 28.3, 27.8, 25.8, 25.4, 24.6, 22.3 (2C2, 2C6', 20CH_2), 13.6 (CH_3). LRMS (MALDI, DHB) *m/z*: 1316.9 $[M+K]^+$, 1300.9 $[M+Na]^+$, 1278.9 $[M+H]^+$.

***N*-2-(1,3-diaminopropane)dodecylamide 29 (Scheme 5). Step a:** To a solution of dodecanoic acid (101.1 mg, 0.5 mmol) in CH_2Cl_2 (7 mL) were added at rt EDC (144 mg, 0.75 mmol) and HOBT (101.5 mg, 0.75 mmol) then, after 45 min stirring, the amine **28** (175.3 mg, 0.6 mmol). 2 h later, the mixture was washed successively with water, an aqueous saturated $NaHCO_3$ solution and brine. The organic layer was dried over $MgSO_4$, filtrated and concentrated under reduced pressure. The residue obtained was chromatographed on silica gel

with a mixture of CH_2Cl_2/MeOH (96/4, v/v) to lead to *N*-2-(*N*^{1},*N*^{3}-di-t-boc-1,3-diaminopropane)dodecylamide with 90% yield. ^{1}H NMR ($CDCl_3$) 7.0 (s, 1H, CH_2CONH), 5.40 (m, 2H, 2N*H*COOtBu), 3.76 (m, 1H, NH*CH*(*CH*$_2$NHBoc)$_2$), 3.36 (m, 2H, NHCH(*CH*$_2$NHBoc)$_2$), 3.19 (m, 2H, NHCH(*CH*$_2$NHBoc)$_2$), 2.17 (t, *J*= 8.0 Hz, 2H, *CH*$_2$CONH), 1.60 (m, 2H, *CH*$_2$), 1.46 (s, 18H, 6*CH*$_3$ tBu), 1.27 (m, 16H, 8*CH*$_2$), 0.89 (t, *J*= 6.8 Hz, 3H, *CH*$_3$). ^{13}C NMR ($CDCl_3$) δ 174.0 (CH_2*C*ONH), 157.5 (2*C*OOtBu), 79.8 (2*C* tBu), 52.7 (NH*CH*(CH_2NHBoc)$_2$), 40.8 (NHCH(*CH*$_2$NHBoc)$_2$), 36.9 (*CH*$_2$CONH), 31.9, 29.6, 29.5, 29.3, 29.2 (7*CH*$_2$), 28.3 (6*CH*$_3$ tBu), 25.6, 22.7 (2*CH*$_2$), 14.1 (*CH*$_3$). LRMS (FAB$^+$, NBA) *m/z*: 472 [M+H]$^+$, 416, 372, 360. **Step e:** This compound was treated in a solution of CH_2Cl_2/TFA (4 mL, 1/1, v/v) at rt for 1 h. After concentration of the mixture under reduce pressure, the diamine **29** was obtained with a quantitative yield enough pure for doing the next step without purification. ^{1}H NMR (CD_3OD) 7.0 (s, 1H, CH_2CONH), 5.40 (m, 2H, 2N*H*COOtBu), 3.76 (m, 1H, NH*CH*(*CH*$_2$NHBoc)$_2$), 3.36 (m, 2H, NHCH(*CH*$_2$NHBoc)$_2$), 3.19 (m, 2H, NHCH(*CH*$_2$NHBoc)$_2$), 2.17 (t, J = 8.0 Hz, 2H, *CH*$_2$CONH), 1.60 (m, 2H, *CH*$_2$), 1.46 (s, 18H, 6*CH*$_3$ tBu), 1.27 (m, 16H, 8*CH*$_2$), 0.89 (t, *J*= 6.8 Hz, 3H, *CH*$_3$). ^{13}C NMR (CD_3OD) δ 178.0 (CH_2*C*ONH), 47.6 (NH*CH*(CH_2NHBoc)$_2$), 42.1 (NHCH(*CH*$_2$NH$_2$), 37.1 (*CH*$_2$CONH), 33.2, 30.9, 30.8, 30.7, 30.6, 26.3, 23.9 (9*CH*$_2$), 14.6 (*CH*$_3$). LRMS (FAB$^+$, NBA) *m/z*: 272 [M+H]$^+$, 254, 225.

5,5-Dineamine derivative 30 (Scheme 5). Step f: The diamine **29** (24 mg, 0.047 mmol) was dissolved in dry DMF (4 mL) under argon atmosphere. To the solution were added successively K_2CO_3 (32 mg, 0.23 mmol) and neamine derivative **8** (200 mg, 0.12 mmol). After 24 h stirring under reflux, the mixture was cooled to rt and concentrated under reduced pressure. The crude product was dissolved in CH_2Cl_2 and washed successively with water and brine. The organic layer was dried over $MgSO_4$, filtrated and concentrated under reduced

pressure. The residue obtained was chromatographed on alumina gel with a mixture of cyclohexane/CH_2Cl_2 (50/50, v/v) then CH_2Cl_2 to lead to the protected compound with 50% yield. **Step d:** This compound dissolved in CH_2Cl_2 (2 mL) was treated with TFA (2 mL) and anisole (0.1 mL). After 24 h stirring at rt, the solvents were removed under reduced pressure. H_2O and Et_2O were added. The aqueous layer was washed twice with Et_2O before being concentrated. The crude product was eluted on a C18 reversed phase column with a gradient of H_2O/MeOH. The pure compound **30** was obtained as the TFA salt with 80% yield. ^{1}H NMR (D_2O) 5.69 (d, $J_{1'-2'}$= 3.6 Hz, 2H, H1'), 3.73-3.92 (m, 9H, H4, H3', H5', OCH_2(CH_2)$_5$N, NCH(CH_2NHCO)$_2$), 3.49-3.68 (m, 6H, OCH_2(CH_2)$_5$N, H5, H6), 3.31-3.43 (m, 12H, H3, H2', H4', H6'b, NCH(CH_2NHCO)$_2$), 3.12-3.25, (m, 8H, H1, H6'a, O(CH_2)$_5$$CH_2$N), 2.32 (ddd, 2H, J_{2eq-1}= J_{2eq-3}= 4.0 Hz, $J_{2eq-2ax}$= 12.4 Hz, 1H, H2$_{eq}$), 1.71 (ddd, J_{2ax-1}= J_{2ax-3}= $J_{2eq-2ax}$= 12.4 Hz, 1H, H2$_{ax}$), 1.32-1.51 (m, 12H), 1.05-1.29 (m, 24H), 0.76 (t, J= 7.2 Hz, 6H, 2CH_3). ^{13}C NMR (D_2O) δ 173.6 (CONH), 163.1, 162.7 (COCF_3), 120.6, 117.7, 114.8, 111.9 (COCF$_3$), 92.9 (2C1'), 82.6 (2C5), 73.3 (2C4), 72.7 (2C6), 72.2 (2OCH_2(CH_2)$_5$N), 70.0 (2C4', 2C5'), 68.3 (2C3'), 61.6 (NCH(CH_2NH)$_2$), 53.1 (2C2'), 49.7 (2C1), 48.8 (2C3), 39.9 (2C6'), 31.0, 29.2, 27.9, 24.8, 24.7 (2C2, CH_2), 13.5 (CH_3). LRMS (MALDI, DHB) *m/z*: 1102.9 $[M+Na]^+$, 1080.9 $[M+H]^+$, 800.6.

5,5-Dineamine derivative 32 (Scheme 5). Step g: The neamine derivative **31** (102 mg, 0.055 mmol) was dissolved in dry DMF (3 mL) under argon atmosphere. To the solution were added HOBT (15 mg, 0.11 mmol) and EDC (21.3 mg, 0.11 mmol). The mixture was stirred at rt for 40 min before the addition of a solution of diamine **29** (11.1 mg, 0.022 mmol) in DMF (2 mL). After 24 h stirring, the mixture was concentrated under reduced pressure. The crude product was dissolved in CH_2Cl_2 and washed successively with water, an aqueous saturated $NaHCO_3$ solution and brine. The organic layer was dried over $MgSO_4$, filtrated and

concentrated under reduced pressure. The residue obtained was chromatographed on alumina gel with a mixture of CH_2Cl_2/MeOH (98/2, v/v) to lead to the protected compound with 20% yield. **Step d:** This compound dissolved in CH_2Cl_2 (2 mL) was treated with TFA (2 mL) and anisole (0.1 mL). After 12 h stirring at rt, the solvents were removed under reduced pressure. H_2O and Et_2O were added. The aqueous layer was washed twice with Et_2O before being concentrated. The compound **32** was eluted on a C18 reversed phase column with a gradient of H_2O/MeOH. The pure compound **32** was obtained as the TFA salt with 80% yield. ^{1}H NMR (D_2O) 5.67 (d, $J_{1'-2'}$= 3.6 Hz, 2H, H1'), 3.96 (m, 1H, N*CH*$(CH_2NHCO)_2$), 3.76-3.90 (m, 8H, H4, H3', H5', O*CH*$_2(CH_2)_5$N), 3.48-3.63 (m, 6H, O*CH*$_2(CH_2)_5$N, H5, H6), 3.18-3.39 (m, 20H, H1, H3, H2', H4', H6'a, H6'b, O$(CH_2)_5$*CH*$_2$N, NCH(*CH*$_2$NHCO)$_2$), 2.34 (s, 8H, NHCO(*CH*$_2$)$_2$CONH), 2.28 (ddd, J_{2eq-1}= J_{2eq-3}= 4.0 Hz, $J_{2eq-2ax}$ = 12.4 Hz, 1H, H2$_{eq}$), 2.07 (t, *J*= 7.2 Hz, 2H, $CH_3(CH_2)_9$*CH*$_2$CO), 1.71 (ddd, J_{2ax-1}= J_{2ax-3}= $J_{2eq-2ax}$= 12.4 Hz, 1H, H2$_{ax}$), 1.28-1.52 (m, 10H), 1.04-1.25 (m, 24H), 0.92 (t, *J*= 7.2 Hz, 6H, 2*CH*$_3$). ^{13}C NMR (D_2O) δ 177.4 (*C*ONH), 174.9, 174.2 (2NH*C*O$(CH_2)_2$*C*ONH), 163.1, 162.8 (*C*OCF_3), 120.6, 117.7, 114.8, 111.9 (CO*C*F$_3$), 93.1 (2C1'), 82.8 (2C5), 73.9 (2C4), 72.9 (2C6), 72.2 (2O*CH*$_2(CH_2)_5$N), 70.4 (2C4'), 69.7 (2C5'), 68.6 (2C3'), 53.3 (2C2'), 49.8 (2C1), 48.8 (2C3), 40.4, 40.2, 39.2 (2C6', 2O$(CH_2)_5$*CH*$_2$N, NCH(*CH*$_2$NHCO)$_2$), 35.9 (N*CH*$(CH_2NHCO)_2$), 31.2, 29.3, 28.7, 28.6, 28.4, 28.2, 25.9, 25.3, 24.7, 22.0 (2C2, 22*CH*$_2$), 13.4 (*CH*$_3$). LRMS (MALDI, DHB) *m/z*: 1300.9 $[M+Na]^+$, 1278.9 $[M+H]^+$, 871.

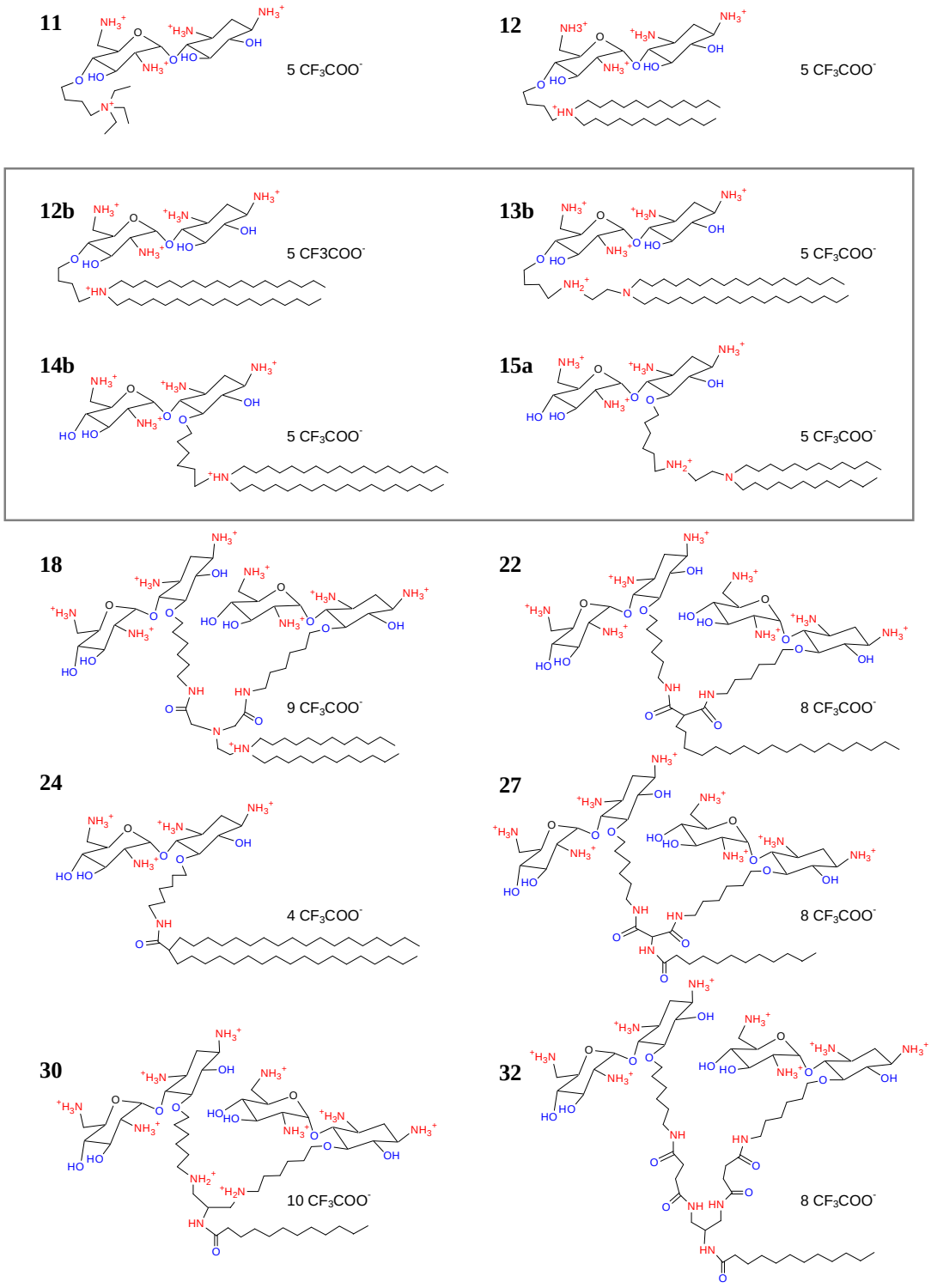

Chart S1. Chemical structure of the twelve neamine derivatives studied. For each derivative, the most likely charged species at physiological pH 7.4 is indicated, as determined with the MarvinSketch software [Marvin 5.0.2.1, 2008, ChemAxon (http://www.chemaxon.com)]. The four derivatives, which displayed the highest transfection activity, are here boxed.

Table S1. Comparison of some chemical features of lipidic derivatives of neamine and some others published cationic lipids.

	Cationic lipid	Mw (g/mol)	Z+ pH 7.4	Z+ pH 5.0	HG type	SP size (g/mol)	LD type	LogP	LogP+	References
Lipidic Neamine Derivatives	**30**, 10 TFA^-	2220	10	10	5,5-dinea	257	12C (1)	-39.9	1.0	This study
	32, 8 TFA^-	1964	8	8	5,5-dinea	455	12C (1)	-35.5	-1.0	This study
	27, 8 TFA^-	2020	8	8	5,5-dinea	285	12C (1)	-33.7	1.0	This study
	18, 9 TFA^-	2345	9	9	5,5-dinea	374	12C (2)	-32.5	5.5	This study
	22, 8 TFA^-	2075	8	8	5,5-dinea	270	18C (1)	-29.7	5.0	This study
	11, 5 TFA^-	1047	5	5	4'-mononea	73	2C (3)	-21.9	3.5	This study
	12a, 5 TFA^-	1300	5	5	4'-mononea	73	12C (2)	-14.4	12.0	This study
	15a, 5 TFA^-	1371	5	6	5-mononea	145	12C (2)	-12.8	12.5	This study
	13b, 5 TFA^-	1511	5	6	4'-mononea	117	18C (2)	-8.8	16.5	This study
	12b, 5 TFA^-	1468	5	5	4'-mononea	74	18C (2)	-8.7	17.0	This study
	14b, 5 TFA^-	1496	5	5	5-mononea	102	18C (2)	-7.9	17.5	This study
	24, 4 TFA^-	1424	4	4	5-mononea	143	18C (2)	-3.8	18.3	This study
Reference cationic lipids	DOSN, 6 TFA^-	1957	6	6	Neomycin B	176	18C (2)	-17.3	-6.5	Desigaux et al., 2007
	DOSP, 4 TFA^-	1671	4	4	Paromomycin	101	18C (2)	-10.8	11.5	Desigaux et al., 2007
	DOST, 4 TFA^-	1523	4	4	Tobramycin	101	18C (2)	-8.6	14.0	Desigaux et al., 2007
	DOSK, 3 TFA^-	1426	3	3	Kanamycin	101	18C (2)	-5.8	5.0	Desigaux et al., 2007
	BGTC, 2 Cl^-	719	2	3	Guanidinium	89	Chol (1)	-1.9	14.0	Vigneron et al., 1996
	DOTAP, $CH_3SO_4^-$	774	1	1	Ammonium	76	18C (2)	7.7	18.5	Leventis et al., 1990
	KLN47, I^-	871	1	1	Arsonium	125	18C (2)	14.2	24.0	Picquet et al., 2005

Mw, molecular weight; Z+ pH 7.4 or pH 5.0, most likely positive charge number at physiological pH 7.4 or pH 5.0, respectively; HG type, headgroup structure distinguishing, for neamine derivatives, between compounds containing one or two neamines and the attachment position of the spacer onto the neamine core (4'-mononea, 5-mononea or 5,5-dinea); LD type, lipid domain structure indicating the length and the number of aliphatic chains (except for BGTC which is a cholesteryl derivative); SP size, sum of atomic masses in the spacer (SP) domain; LogP, partitioning value of ionic species (average value of octanol-water portioning coefficient); LogP+, partitioning value estimation for a formulation combining one molecule of cationic lipid + one molecule of neutral colipid DOPE (molar ratio 1/1). All those values were calculated using the MarvinSketch software [Marvin 5.0.2.1, 2008, ChemAxon (http://www.chemaxon.com)]. Cationic lipids are listed according to their logP values. Lipidic derivatives of neamine (see Scheme S1); DOST, DOSP, DOSK, DOSN [lipidic derivatives of tobramycin, paromomycin, kanamycin and neomycin, respectively (*6*)]; BGTC (*7*); KLN47 (*8*).

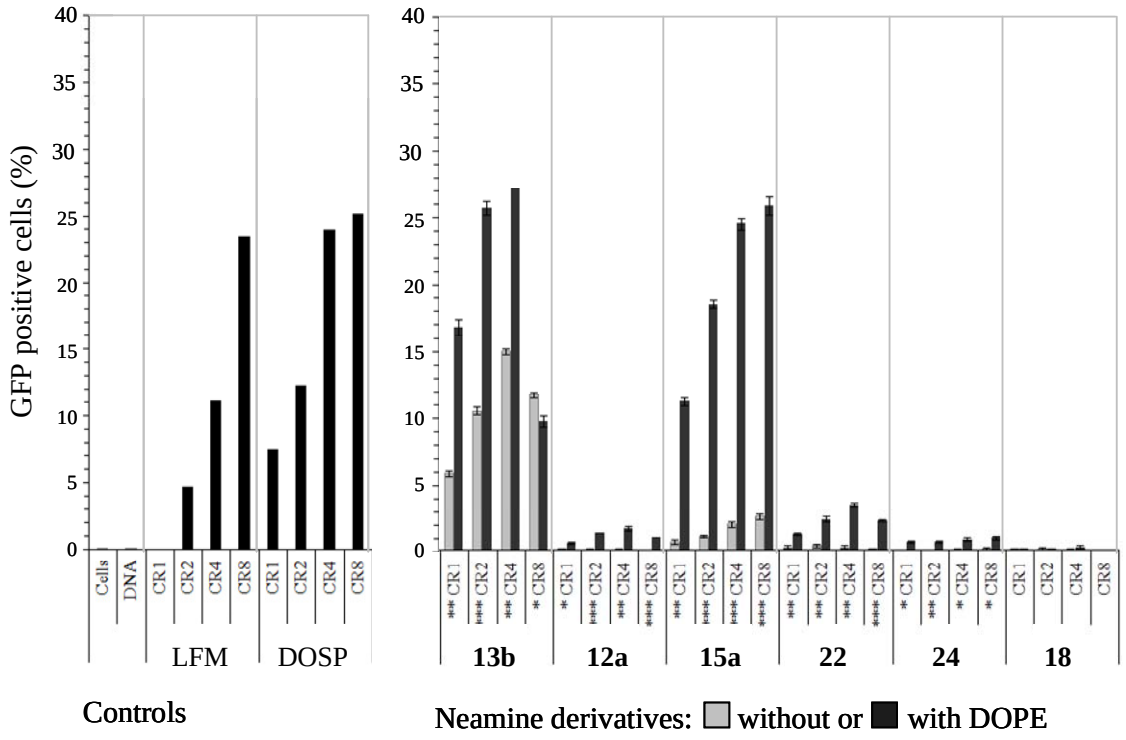

Figure S1. Flow cytometry measurements (GFP assays): transfection efficiencies of lipidic derivatives of neamine used alone or formulated with the colipid DOPE (molar ratio 1/1). The reagents indicated were complexed with DNA (pEGFP-Luc, see "Experimental Procedure" section) in order to obtain increasing charge ratios (CR), from CR1.0 up to CR8.0. The commercial Lipofectamine (LFM, DOSPA/DOPE, Invitrogen) and the paromomycin derivative [DOSP, DOSP/DOPE (*6*)] were used as cationic lipid references. Cell samples were analysed by flow cytometry in order to estimate the gene delivery efficiency as a percentage of positive cells (GFP positive cells). Other derivatives (**11**, **27**, **30**, and **32**) were found completely inefficient and, thus, they are not indicated here. These results were obtained with HeLa cells. Tests were performed in triplicates so efficiencies of formulations of neamine derivatives with or without DOPE can be compared (student t-test: *, $p < 0.05$; **, $p < 0.005$; ***, $p < 0.0005$).

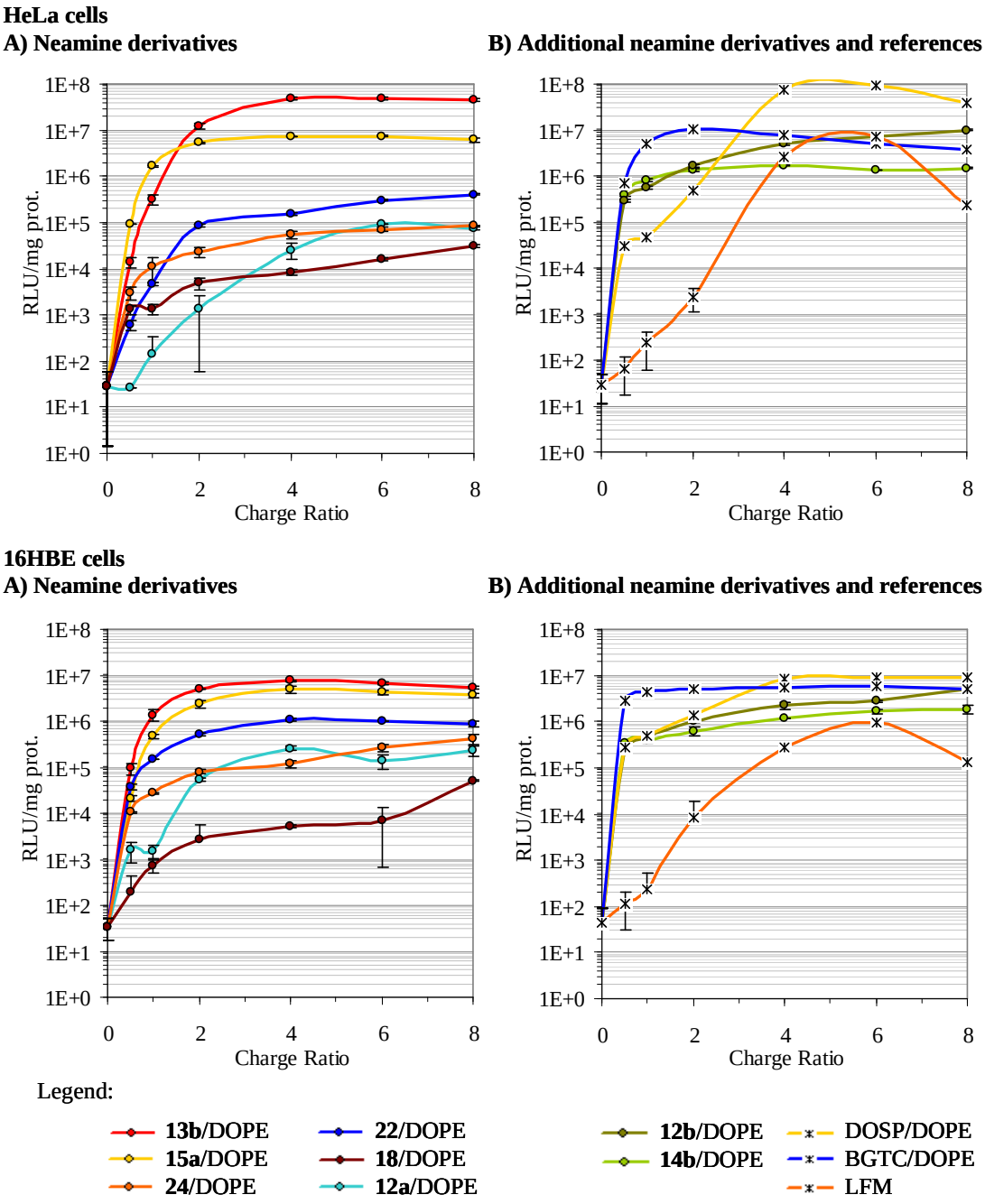

Figure S2. Luminometry measurements (luciferase assays): dose responses of the *in vitro* transfection activity of lipidic neamine derivatives formulated with the colipid DOPE (molar ratio 1/1). Luciferase reporter gene expression is indicated as a function of the charge ratio (CR) of lipoplexes, from CR0.5 up to CR8.0. The commercial Lipofectamine (LFM, Invitrogen), the paromomycin derivative [DOSP, (*6*)] and the bisguanidinium tren-cholesterol BGTC [BGTC/DOPE 3/2, (*7*)] derivative were used as cationic lipid references in those tests. Cells were transfected as described in "Experimental Procedure" section, using lipoplexes prepared by mixing DNA (pEGFP-Luc) with the required amounts of lipids. Data are expressed as relative light units (RLU) per mg of total proteins (mean +/- SD with n=3). These results were obtained using HeLa and 16HBE cells.

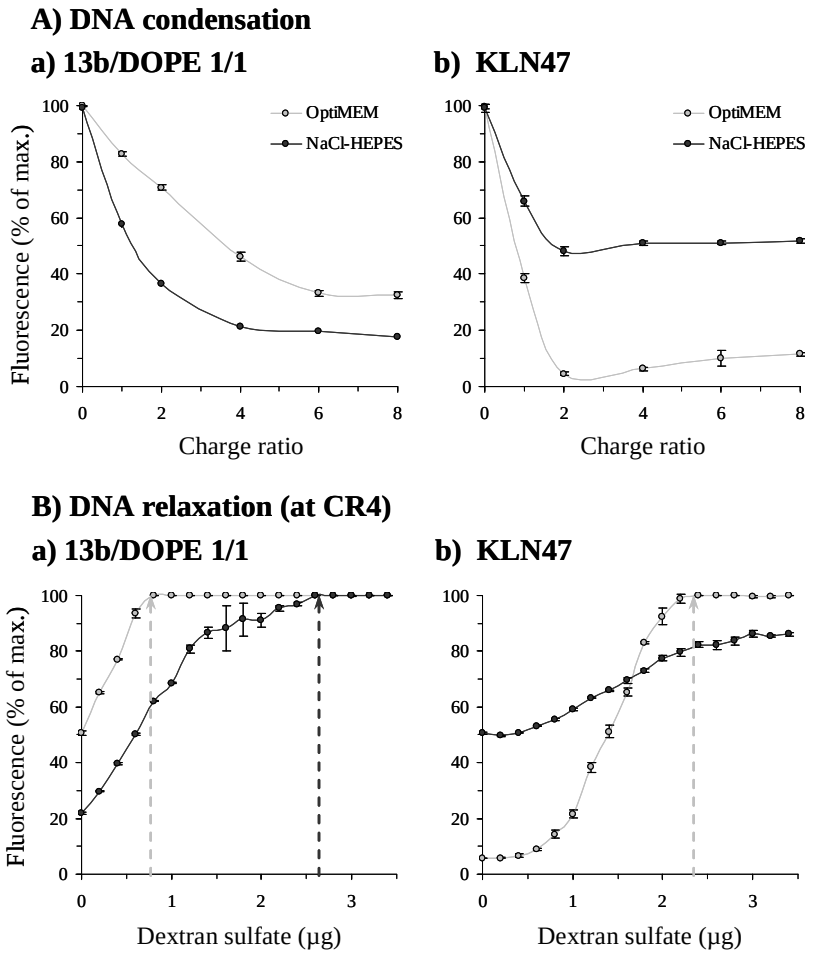

Figure S3. DNA condensation and relaxation assays with cationic liposomes 13b/DOPE 1/1 and KLN47. Complexes were obtained by mixing cationic liposomes at the required concentrations with plasmid DNA incubated first with ethidium bromide (EtB). The fluorescence decrease allowed the evaluation of nucleic acid entrapment within complexes (A; see "Experimental Procedure" section). Complexes at charge ratio 4 were then mixed with increasing quantities of dextran sulfate as a counter-anion. The recovery of fluorescence enabled to follow the DNA relaxation (B). The minimal quantity of counter-anion required to recover maximum fluorescence intensity can then be estimated (arrows). Assays were performed either in OptiMEM or in NaCl-HEPES (0.9% NaCl, 20 mM HEPES). Data are expressed as a percentage of the EtB fluorescence intercalated into DNA in absence of carrier (mean +/- SD with $n \geq 3$).

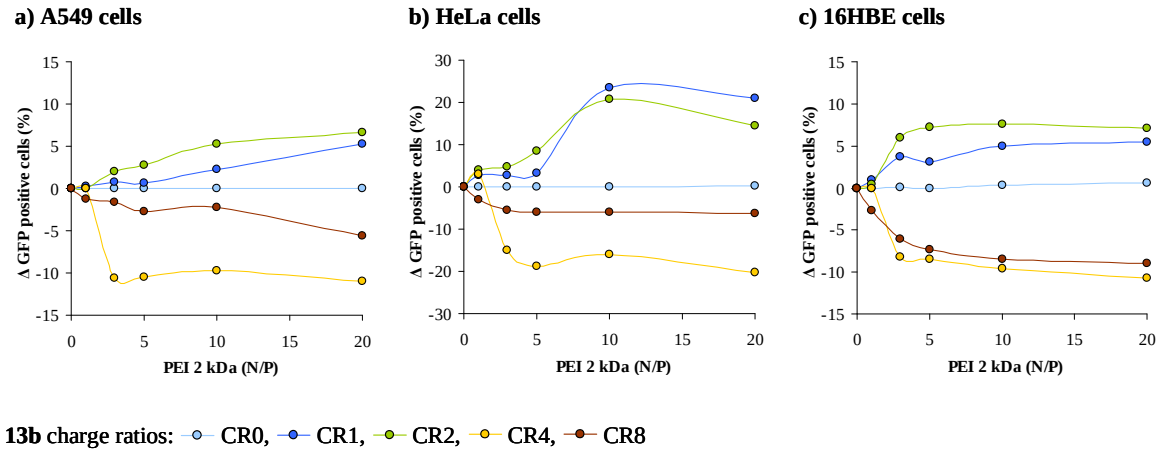

Figure S4. *In vitro* transfection activity for combinations of PEI 2 kDa and 13b/DOPE 1/1 with three different cell lines. Lipoplexes (**13b**/DOPE mixed with DNA, from CR1.0 up to CR8.0), polyplexes (PEI 2 kDa with DNA, from N/P1 up to N/P20) and lipopolyplexes (combinations of PEI 2 kDa with DNA, from N/P 1 up to 20, + **13b**/DOPE, from CR1.0 up to CR8.0) were used to transfect cell lines as described in "Experimental Procedure" section. For each CR, the variation of %GFP positive cells (Δ = % lipopolyplex - % lipoplex) is indicated [polyplexes alone (CR0) are ineffective, whatever the N/P tested]. Thus, compared with a lipoplex at a given CR, a lipopolyplex is more efficient if a Δ value higher than 0 is measured whereas it is less if a Δ value lower than 0 is obtained.

LITERATURE CITED

(1) Riguet, E., Désiré, J., Bailly, C., and Décout, J. L. (2004) A route for preparing new neamine derivatives targeting HIV-1 TAR RNA. *Tetrahedron 60*, 8053-8064.

(2) Riguet, E., Tripathi, S., Chaubey, B., Désiré, J., Pandey, V. N., and Décout, J. L. (2004) A peptide nucleic acid-neamine conjugate that targets and cleaves HIV-1 TAR RNA inhibits viral replication. *J Med Chem 47*, 4806-4809.

(3) Cameron, F. H., Moghaddam, M. J., Bender, V. J., Whittaker, R. G., Mott, M., and Lockett, T. J. (1999) A transfection compound series based on a versatile Tris linkage. *Biochim Biophys Acta 1417*, 37-50.

(4) Kumar, V. V., Pichon, C., Refregiers, M., Guerin, B., Midoux, P., and Chaudhuri, A. (2003) Single histidine residue in head-group region is sufficient to impart remarkable gene transfection properties to cationic lipids: evidence for histidine-mediated membrane fusion at acidic pH. *Gene Ther 10*, 1206-1215.

(5) Jones, D. S., Srinivasan, A., Kasina, S., Fritzberg, A. R., and Wilkening, D. W. (1989) Convenient and simplified approaches to N-monoprotected triaminopropane derivatives: key intermediates for bifunctional chelating agent synthesis. *J Org Chem 54*, 1940-1943.

(6) Desigaux, L., Sainlos, M., Lambert, O., Chèvre, R., Letrou-Bonneval, E., Vigneron, J. P., Lehn, P., Lehn, J. M., and Pitard, B. (2007) Self-assembled lamellar complexes of siRNA with lipidic aminoglycoside derivatives promote efficient siRNA delivery and interference. *Proc Natl Acad Sci U S A 104*, 16534-16539.

(7) Vigneron, J. P., Oudrhiri, N., Fauquet, M., Vergely, L., Bradley, J. C., Basseville, M., Lehn, P., and Lehn, J. M. (1996) Guanidinium-cholesterol cationic lipids: efficient vectors for the transfection of eukaryotic cells. *Proc Natl Acad Sci U S A 93*, 9682-9686.

(8) Picquet, E., Le Ny, K., Delépine, P., Montier, T., Yaouanc, J. J., Cartier, D., des Abbayes, H., Férec, C., and Clément, J. C. (2005) Cationic lipophosphoramidates and lipophosphoguanidines are very efficient for *in vivo* DNA delivery. *Bioconjug Chem 16*, 1051-1053.

FOOTNOTES

LFM, Lipofectamine; CR, charge ratio; EtB, ethidium bromide; RLU, relative light unit; TFA, trifluoroacetic acid; EDC, 1-[3-(dimethylamino)propyl]-3-ethylcarbodiimide; HOBT, 1-hydroxybenzotriazole; rt, room temperature; Δ, heating; Tr, trityl; PMB, *p*-methoxybenzyl.

Physico-Chemical Characterization of Polylipid Nanoparticles for Gene Delivery to the Liver

Maung T. Nyunt,[†] Christopher W. Dicus,[‡] Yi-Yao Cui,[§] M. Cecilia Yappert,[||] Thomas R. Huser,[†] Michael H. Nantz,[||] and Jian Wu*[,§]

NSF Center for Biophotonics Science and Technology, and Department of Internal Medicine, Transplant Research Program, University of California, Davis Medical Center, Sacramento, California 95817, Department of Chemistry, University of California, Davis, California 95616, and Department of Chemistry, University of Louisville, Louisville, Kentucky 40292.
Received April 3, 2009; Revised Manuscript Received October 1, 2009

Polylipid nanoparticles (PLNP) have been shown to be very effective in delivering antioxidative genes in the treatment of liver injury in mice. To build on our previous studies and to further characterize PLNP formulated from polycationic lipid (PCL) and cholesterol, we report here the synthesis of multigram quantities of PCL and employ analytical tools, such as Raman spectroscopy of single PLNP and live-cell imaging of lipofection, for the physicochemical characterization of PCL, PLNP, and the transfection process. Mass spectrometry demonstrates the characteristics of polymeric lipids. Raman spectrum of PCL reveals the polymeric structure of the polymers. The presence of cholesterol in PLNP formulation did not markedly change the Raman spectrum. PLNP-derived polyplexes exhibit Raman spectra very similar to PLNP except that the C−H out-of-plane deformation mode of the polymeric lipid is significantly suppressed, indicating the interaction with plasmid DNA. Zeta potential measurement indicates a large DNA-carrying capacity of PLNP and their stability for *in vivo* gene delivery. The live-cell fluorescent imaging dynamically shows that PLNP exerts transfection efficiency similar to lipofectamine in leading to early reporter gene expression in live hepatic cells. In conclusion, polylipid nanoparticles possess a high DNA carrying capacity and lipofection efficiency, rendering them suitable for testing in large animals. The employment of novel state-of-the-art technologies in the study of lipofection represents the level of physicochemical and biological characterization that is needed to best understand the key elements involved in the lipofection process.

INTRODUCTION

Lipid nanoparticles (LNP) have been used widely for *in vitro* gene delivery; however, their potential for *in vivo* gene delivery has been hampered by stability issues in the bloodstream, poor targeting efficiency, and transient transfection efficacy (*1*). Polylipid nanoparticles (PLNP), formulated from polycationic lipid (PCL) and cholesterol, on the other hand, have been documented to be more stable than DOTAP-DOPE[1]or DOTAP-cholesterol formulations in the bloodstream (*2*). We have also shown that PLNP-derived polyplexes were effective in delivering reporter genes, human antioxidative genes (extracellular superoxide dismutase (EC-SOD) or catalase) to the liver for the treatment of acute liver injury caused by hepatotoxins, or an ischemia/reperfusion procedure in two separate preclinical model systems (*3*, *4*). These studies suggest that PLNP are a very effective gene transfer agent for liver-based delivery and have great potential to move from small animals to large animal trials as a step toward clinical applications (*5*). To develop an even more biocompatible gene delivery agent and to move this antioxidative gene approach from "bench to bedside", in-depth characterization of PCL, PLNP, and polyplexes, as well as feasible technologies for larger-scale synthesis of PCL, are needed. In this study, we employ state-of-the-art technologies, such as Raman microspectroscopy, mass spectrometry, and DeltaVision deconvolution microscopy (DVDM) for live cell imaging together with zeta potential measurements to further characterize PCL, PLNP, and PLNP-derived polyplexes. These novel technologies enable us to characterize the physicochemical features of PCL, PLNP, and PLNP-derived polyplexes, as well as the lipofection process, and further determine the stability of the polyplexes. We also describe modifications to our original method of PCL synthesis that enable multigram preparations of PCL sufficient for large animal experiments.

EXPERIMENTAL PROCEDURES

Synthesis of PCL. *Synthetic Procedures and Validation.* PCL (**1**) was prepared according to the synthetic route outlined in Figure 1. Prior to use, CH_2Cl_2 was immediately distilled from CaH_2. After reaction workup, solutions were dried using Na_2SO_4, and solvents were subsequently removed by rotary evaporation. Nuclear magnetic resonance (NMR) spectra were recorded with a General Electric QE-300 spectrometer (^{1}H at 300 MHz, ^{13}C at 75 MHz). Infrared spectra were recorded on a Mattson Genesis II FTIR 3000 spectrometer. Melting points are uncor-

* All correspondence should be addressed to Jian Wu, MD, PhD, Department of Internal Medicine, Transplant Research Program, UC Davis Medical Center, 4635 2nd Ave. Suite 1001, Sacramento, CA 95817, Tel. (916) 734-8044, Fax: (916) 734-8097, E-mail: jdwu@ucdavis.edu. Michael H. Nantz, PhD, Department of Chemistry, University of Louisville, Louisville, KY 40292, Tel. (502) 852-8069, Fax: (502) 852-8149, E-mail: mhnant01@louisville.edu.

[†] NSF Center for Biophotonics Science and Technology, University of California, Davis Medical Center.

[‡] Department of Chemistry, University of California, Davis.

[§] Department of Internal Medicine, Transplant Research Program, University of California, Davis Medical Center.

[||] Department of Chemistry, University of Louisville.

[1]Abbreviations: DOPE, L-α dioleoyl phosphatidylethanolamine; DOTAP, 1,2-bis(dioleoyloxy)-3-(trimethylammonio)propane; LNP, lipid nanoparticle; PCL, poly(cationic lipid); NMR, nuclear magnetic resonance; PLNP, polylipid nanoparticles; DVDM, DeltaVision deconvolution microscope.

10.1021/bc900150v CCC: $40.75 © 2009 American Chemical Society
Published on Web 10/27/2009

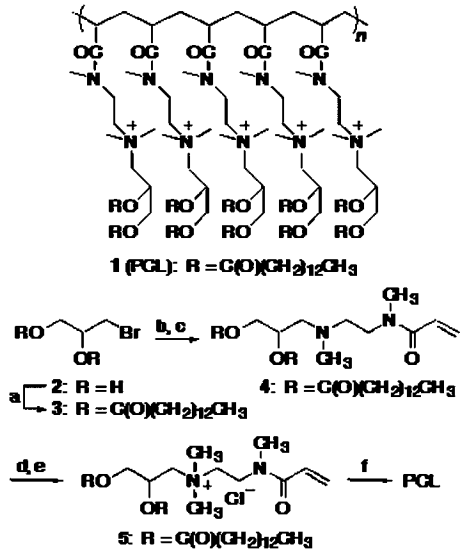

Figure 1. PCL synthetic route: (a) myristoyl chloride (2.5 equiv), Et_3N, cat. DMAP, CH_2Cl_2, 0 °C to rt, 3 h, 92%; (b) *N*,*N*′-dimethylethylenediamine (8 equiv), DMF, 70 °C, 45 min; (c) acryloyl chloride (1.5 equiv), Et_3N, CH_2Cl_2, 0 °C - rt, 2 h, 32% (2 steps); (d) CH_3I, rt, 18 h; (e) DOWEX 1 × 8−400, CH_2Cl_2/MeOH (9:1), 92% (2 steps); (f) *n*-dodecyl mercaptan (0.34 equiv), AAPH (0.1 equiv), H_2O, 80 °C, 15 h, 97%.

rected. Elemental analyses were performed by Midwest Microlabs (Indianapolis, IN). All sonications were performed in a bath sonicator (Laboratory Supplies Inc., Hicksville, NY).

*3-Bromo-1,2-bis(tetradecanoyloxy)propane (**3**).* To a solution of 3-bromo-1,2-propane-diol (**2**) (9.20 g, 59.4 mmol) in CH_2Cl_2 (50 mL) were added triethylamine (16.5 mL, 119 mmol) and 4-(*N*,*N*-dimethylamino)pyridine (400 mg). The reaction mixture was cooled to 0 °C, and then myristoyl chloride (40.4 mL, 149 mmol) was added dropwise. The reaction was warmed to room temperature and quenched after 4 h by pouring over saturated aqueous $NaHCO_3$ (100 mL). The aqueous layer was separated and the organic layer was washed successively with saturated aqueous $NaHCO_3$, water, and brine, and then dried (Na_2SO_4). The solvents were concentrated in vacuum, the crude residue was dissolved in ethanol, and minimal water was added to provide a cloudy suspension. The solution was placed in the freezer overnight causing bromodiester **3** to precipitate as a white solid (31.4 g, 54.6 mmol, 92%); mp 40−41.5 °C; IR (neat) 2913, 2848, 1731 cm^{-1}; ^1H NMR ($CDCl_3$) δ 0.85 (t, J = 6.6 Hz, 6H), 1.23 (m, 40H), 1.59 (m, 4H), 2.29 (m, 4H), 3.48 (m, 2H), 4.21 (dd, J = 11.9, 5.6 Hz, 1H), 4.30 (dd, J = 11.9, 4.4 Hz, 1H), 5.18 (m, 1H); ^{13}C NMR ($CDCl_3$) δ 14.0, 22.6, 24.8, 29.0−29.8 (6 signals), 31.9, 33.9−34.1 (3 signals), 62.9, 69.9, 172.6, 173.0; Anal. Calcd for $C_{31}H_{59}O_4Br$: C, 64.68; H, 10.33. Found: C, 64.75; H, 10.32.

*3-(N-Methyl-N-(2-N′-acrylamide-N′-methylamino)ethyl)amino)-1,2-bis(tetradecanoyl-oxy)propane (**4**).* To a solution of bromo diester **3** (23.9 g, 42.8 mmol) in *N*,*N*-dimethylformamide (200 mL) was added *N*,*N*′-dimethylethylenediamine (DMF) (36.8 mL, 342 mmol) via a syringe. The reaction was stirred under an argon atmosphere at 70 °C. After stirring 45 min, DMF and the unreacted diamine were removed by vacuum distillation. The residue was suspended in CH_2Cl_2 (250 mL) and washed successively with saturated aqueous $NaHCO_3$, water, and brine, and then dried (Na_2SO_4). The solvent was removed, and the crude product was passed through a short column of silica gel, eluting with 15% MeOH/CH_2Cl_2, to afford the crude diamino diester as yellow oil (9.6 g).

To a solution of the crude diamino diester (9.6 g, 16.5 mmol) in CH_2Cl_2 (100 mL) at 0 °C were added triethylamine (2.3 mL, 16 mmol) and 4-(*N*,*N*-dimethylamino)pyridine (200 mg). Acryloyl chloride (1.6 mL, 25 mmol) was added dropwise to the resulting solution, and the reaction mixture was warmed to room temperature. After stirring 3 h, the reaction was quenched by pouring over saturated aqueous $NaHCO_3$. The layers were separated, and the organic layer was washed with water and brine, dried (Na_2SO_4), and then concentrated by rotary evaporation. The residue was purified by column chromatography (SiO_2), eluting with a 3:2 mixture of EtOAc/hexane, to give the diester acrylamide **4** as a light yellow oil (8.72 g, 13.7 mmol, 32%); IR (neat) 2921 2852, 1737, 1654, 1614 cm^{-1}; ^1H NMR ($CDCl_3$) δ 0.87 (t, J = 6.6 Hz, 6H), 1.25 (m, 40H), 1.59 (m, 4H), 2.30 (m, 7H), 2.57 (m, 4H), 3.00 (s, 1.5H)*, 3.09 (s, 1.5H)*, 3.41 (m, 1H)*, 3.50 (m, 1H)*, 4.06 (m, 1H), 4.30 (m, 1H), 5.15 (m, 1H), 5.67 (dd, J = 10.2, 2.10 Hz, 1 H), 6.30 (dd, J = 2.1, 16.8 Hz, 0.5 H)*, 6.32 (dd, J = 2.0, 16.7 Hz, 0.5 H)*, 6.60 (dd, J = 10.2, 16.8 Hz, 1H); ^{13}C NMR ($CDCl_3$) δ 13.9, 22.5, 24.7, 28.9−29.4 (5 signals), 31.7, 34.0, 34.2, 36.0, 42.7, 43.0, 45.8, 48.2, 55.3, 56.3, 57.6, 58.0, 63.4, 63.6, 69.0, 69.2, 127.4, 127.6, 166.0*, 166.3*, 172.9, 173.1. Anal. Calcd for $C_{38}H_{72}O_5N_2$: C, 71.65; H, 11.39; N 4.40. Found: C, 71.32; H, 11.47; N 4.35. (*signals arising from amide stereoisomers).

N-(2-(*N*′-Acryloyl-*N*′-methylamino)ethyl)-*N*,*N*-dimethyl-*N*-[2,3-bis(tetradecanoyloxy)] propanammonium chloride (**5**). Acrylamide **4** (8.68 g, 13.6 mmol) was dissolved in methyl iodide (25 mL) and stirred at room temperature. After stirring for 18 h, methyl iodide was removed using a stream of argon. The crude residue was purified by column chromatography (SiO_2), eluting with a 9:1 mixture of CH_2Cl_2/MeOH. The product then was passed through a column of Dowex 1 × 8−400 ion-exchange resin (∼70 g), eluting with MeOH, to give **5** as a white solid (8.63 g, 12.6 mmol, 92%); IR (neat) 3564, 3358, 2954, 2916, 2848, 1743 cm^{-1}; ^1H NMR ($CDCl_3$) δ 0.84 (t, J = 6.2 Hz, 6H), 1.22 (m, 40H), 1.54 (m, 4H), 2.28 (m, 4H), 3.27 (s, 3H), 3.38 (s, 3H), 3.41 (s, 3H), 3.88 (m 2H), 4.04 (m, 4H), 4.29 (d, J = 13.8 Hz, 1H), 4.47 (dd, J = 2.6, 11.6 Hz, 1H), 5.59 (m, 1H), 5.73 (dd, J = 1.5, 10.5 Hz, 1H), 6.29 (dd, J = 1.5, 16.5 Hz, 1 H), 6.57 (dd, J = 10.4, 16.7 Hz, 1H); ^{13}C NMR ($CDCl_3$) δ 13.9, 22.5, 24.6, 24.7, 29.0−29.5 (4 signals), 31.8, 33.8, 34.1, 36.1, 42.3, 51.9, 62.5, 63.3, 64.2, 66.0, 127.2, 128.5, 167.3, 172.5, 172.9.

*The Final Product, PCL (**1**).* Monomer **5** (4.32 g, 6.28 mmol) was suspended in nanopure water (400 mL) by sonication at 50 °C for 45 min. The resultant homogeneous suspension was degassed by bubbling a stream of nitrogen through the suspension for 20 min. The suspension then was heated to 80 °C and stirred vigorously while adding *n*-dodecyl mercaptan (432 mg, 2.13 mmol), followed by a solution of 2,2′-azobis(2-methylpropionamidine) dihydrochloride (AAPH) (175 mg in 45 mL H_2O, 0.645 mmol). The resulting mixture was stirred at 80 °C for 15 h, after which the reaction vessel was placed in a freezer overnight (−10 °C). After thawing at room temperature, the precipitated solids were filtered and washed successively with cold diethyl ether to remove trace mercaptan and then dried under vacuum to afford PCL (4.21 g, 97%) as a white solid with spectral characterization identical to that previously reported (*6*).

Mass Spectral Analysis of PCL. PCL (5 mg) was dissolved in 1 mL of isopropanol. Both a 0.17 M solution of *para*-nitroaniline (PNA) and a 0.5 M solution of 2,5-dihydroxybenzoic acid (DHB) were prepared in isopropanol and used as matrices. PNA has been used previously for the detection of phospholipids in positive- and negative-ion spectra (*7*). A 1 μL aliquot of the analytical solution was spotted in each of five different sample wells of a 100-spot stainless steel MALDI plate (Applied Biosystems, Foster City, CA). The matrix (1 μL) was then added on top of each sample spot (dried droplet method). After

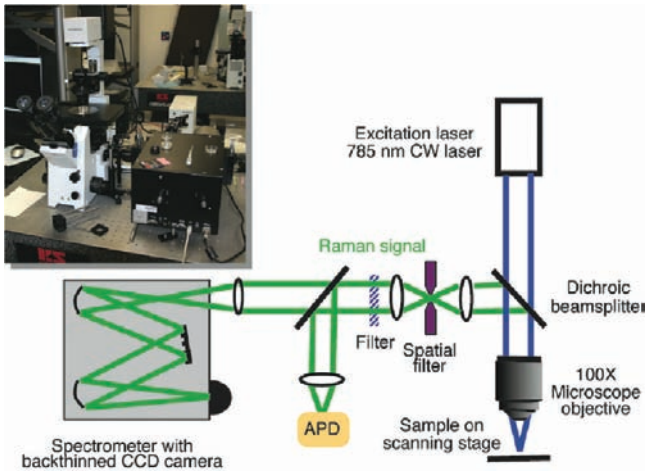

Figure 2. Schematic diagram of the Raman system combining a microscope, confocal detection system, and various laser sources. See the Methods and Materials part for details.

crystallization at ambient conditions, mass spectra were recorded on a Voyager Biospectrometry DE workstation (Applied Biosystems, Foster City, CA) equipped with a Nitrogen laser (λ = 337 nm). The extraction voltage was set to 20 kV. Mass spectra were acquired in both positive and negative modes.

Raman Micromicroscopy Analysis of PCL, PLNP, and PLNP-Derived Polyplexes. The Raman spectra of various LNP formulations were acquired using a Laser-Tweezers Raman microspectroscopy system, which is custom-built around a commercial inverted microscope platform (*8*). The main microscope frame consists of an Olympus IX-71 microscope, utilizing a 60×, NA 1.2, water immersion objective optimized for near-infrared operation. The laser source is an 80 mW, 785 nm diode-pumped solid-state laser, resulting in ~30 mW laser power in the microscope focus after passing multiple mirrors, a bandpass filter, and the microscope objective. The laser beam is focused to a diffraction-limited laser spot of ~500 nm diameter. The microscope is equipped with a mercury arc lamp for white-light fluorescence excitation through appropriate filters, as well as differential interference contrast for visualizing cells. Laser trapping and fluorescence excitation can be performed simultaneously. Spectroscopy is performed through an attached SP2300i spectrograph (Acton Research Corporation) and a back-illuminated thermoelectrically cooled deep-depletion CCD camera with 1340 × 1000 pixels (Figure 2).

The Use of a Fluorescence Deconvolution Microscopy System to Monitor the Lipofection Process. The automated fluorescence deconvolution microscopy system (*9*) (Personal DV, Applied Precision, LLC., Issaquah, WA) makes use of an Olympus IX-71 inverted optical microscope with a 250 W xenon illumination source, a 60× oil-immersion objective lens with a numerical aperture (NA) of 1.4 and a precision stepper-motor driven XYZ stage. The microscope is equipped with DAPI, FITC, TRITC, CY3, and CY5 filter sets, as well as 5 neutral density filters for the excitation source. It is capable of exciting fluorophores from the UV to the far-red and also collects transmitted light (bright field, differential interference contrast (DIC)) images. Image capture is achieved with a CoolSnap ES2 (Photometrics, Tucson, AZ)—a fast, high-resolution, high quantum efficiency, thermoelectrically cooled CCD camera. It can be used for both slow scan, high-resolution imaging of fixed samples or fast, high-sensitivity image capture of live cell samples.

The DeltaVision acquisition, image processing, and analysis software (*softWoRx 3.7.0*) run on a dual-processor personal computer running Cent OS Linux. The microscope is capable of separating up to 4 dyes and displaying triply labeled samples in a single image window through false colors. The DeltaVision software package automates the deconvolution computations, generates 3D reconstructions, and enables autofocusing, cell tracking, and live-cell imaging.

In our experiment, Hep G_2 cells were seeded on 35-mm-diameter round glass bottom culture dishes (MatTek Corp., Ashland, MA). The next day, cells were transfected with plasmid pEGFP-C1 by either PLNP or Lipofectamine, and then incubated at 37 °C. At specified time points, the culture dishes were mounted on the DeltaVision Deconvolution microscope. The temperature of the microscope stage was kept constant at 37 °C using an air-stream incubator (ASI-400, NevTek, Williamsburg, VA). GFP fluorescence of Hep G_2 cells was detected using a standard FITC filter set and corresponding bright field images were also collected. A series of images at different vertical focus positions resulting in optical sections (step size 0.1 μm) were captured with an image size of 512 by 512 pixels and setting binning to 2 × 2. The exposure time of between 0.1 to 0.3 s was sufficient to obtain images suitable for the dynamic range of the cooled CCD camera. Images were saved and processed using the DeltaVision software package (*softWoRx 3.7.0*) and Adobe Photoshop CS3.

Zeta Potential of PCL, PLNP, and Polyplexes. PLNPs were generated as reported previously and complexed with plasmid DNA at different charge ratios. The size distribution was determined by laser light scattering as reported previously (*10*). PLNPs or polyplexes in 2 μL were suspended in 2.5 mL water, and their zeta potentials were determined at room temperature in a Zeta Potential/Particle Sizer Nicomp 280 ZCS PSS-Nicomp Particle Sizing System (Santa Barbara, CA).

Statistical Analysis. The data of zeta potential in different charge ratios were analyzed by one-way variance test followed by multiple comparisons between groups with Newman-Keuls test. A *p*-value of less than 0.05 was considered as statistically significant.

RESULTS

Synthesis of PCL in a Multigram Quantity. The PCL synthesis proceeded from commercially available diol **2** by bisesterification using myristoyl chloride. Subsequent bromide displacement by *N*,*N*′-dimethylethylenediamine followed by reaction of the crude adduct with acryloyl chloride gave acrylamide **4**. Amine quaternization followed by counterion exchange using an established procedure (*11*) afforded acrylamide **5** as the chloride salt. The polymerization of **5** was accomplished by heating a suspension of **5** in water (ca. 15 mM) to 80 °C and then adding *n*-dodecyl mercaptan (*12*) and the water-soluble free radical initiator 2,2′-azobis(2-methylpropionamidine) dihydrochloride (AAPH) (*13*). The delay in addition of *n*-dodecyl mercaptan until the formulation of lipid nanoparticle with **5** differs from our previous protocol (*6*) and helps minimize conjugate addition of the thiol to the acrylamide. All intermediate products were validated by NMR spectral analysis, and the final polymeric product was determined in both negative and positive modes by mass spectral analysis (MALDI-TOF MS). The strongest MALDI-TOF MS signals were obtained with the use of *para*-nitroaniline (PNA) as the matrix. Although no detectable peaks were obtained in the negative mode, strong signals with maximal intensity at m/z = 651.6 were observed in positive-ion spectra, consistent with a polymeric product derived from monomer **5** (Figure 3). The product arising from conjugate addition of dodecyl mercaptan to the acrylamide moiety of **5** was observed at m/z = 853.6. Thus, our modified synthetic method produced PCL in multigram quantities, which is essential for generating enough PLNP for experiments in large animals.

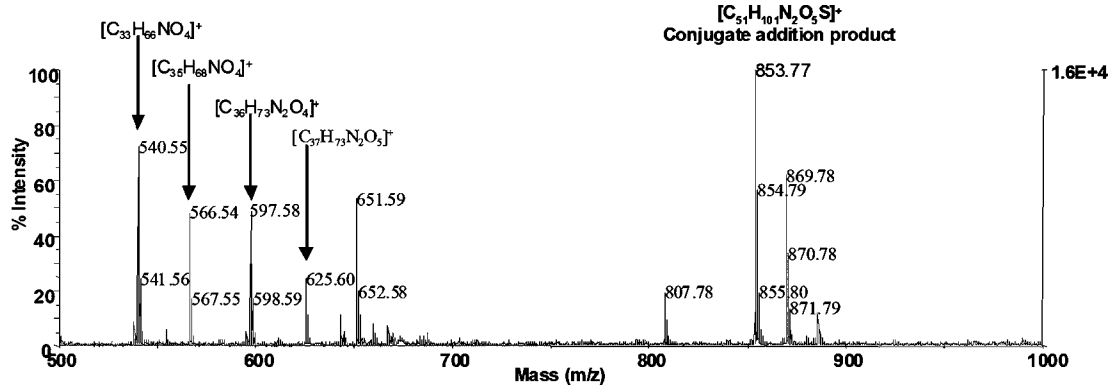

Figure 3. Mass spectral analysis of polycationic lipids. MALDI mass spectrum of PCL was obtained with the use of *para*-nitroaniline as the matrix. Mass spectra were recorded on a Voyager Biospectrometry DE workstation in both positive and negative modes. Strong signals with maximal intensity at $m/z = 651.6$ were observed in positive-ion spectra, indicating the product of polymerized cationic lipids (PCL).

Raman Spectroscopic Analysis of PCL, PLNP, and PLNP-Derived Polyplexes. We have obtained Raman spectra of the various starting materials at high concentration, such as plasmid DNA (3.6 μg/μL), pure lipofectamine, and pure cholesterol as received from the manufacturer, as well as unformulated PCL as synthesized (Figure 4A). For comparison, spectra of lipofectamine complexes with plasmid DNA (Figure 4B), as well as those of PCL vesicles, PLNP, and PLNP-derived polyplexes, were taken (Figure 4C). The Raman data from unformulated PCL are due to Raman scattering on carbon bonds, i.e., C−C, C═C, C−H, CH_2, and clearly show the polymeric nature of PCL (*14*, *15*). The most prominent peaks are C−C stretch modes in the 1100−1200 cm^{-1} and the 1300 cm^{-1} range, and the 1445 cm^{-1} methylene bending vibration in the polymer. Similar features with less pronounced peaks besides the 1445 cm^{-1} methylene deformation mode were found for lipofectamine and cholesterol. Cholesterol contains an additional strong C═C vibration at ~1670 cm^{-1}. The spectrum of plasmid DNA (Figure 4A) is dominated by DNA marker modes such as the 785 cm^{-1} cytosine ring breathing vibration, the 1090 cm^{-1} vibration from the phosphate backbone, the abundant 1442 cm^{-1} CH mode, and the 1575 cm^{-1} adenine vibration (*16*). In addition, this spectrum contains contributions from the solvent (Tris-EDTA buffer) at 1060 cm^{-1}, as well as from polysaccharides from bacterial lysate at 860 cm^{-1} (*15*, *17*). These endotoxins are, however, only present in this highly concentrated form of plasmid DNA, which was required to obtain its Raman spectrum. The DNA used for forming lipoplexes or polyplexes is free of endotoxins. The spectrum of lipofectamine remains unaltered upon dilution (data not shown). Lipofectamine-derived lipoplexes exhibit combined Raman peaks due to lipofectamine as well as DNA. Most noticeable are a weak 785 cm^{-1} cytosine breathing mode, the 1090 cm^{-1} vibration from the phosphate backbone, and the 1660 cm^{-1} amide I mode (Figure 4B). Raman spectra were acquired from individual optically trapped PCL, PLNPs, and PLNP polyplex vesicles within a 30 s signal integration time. Interestingly, PCL changes its spectrum between unformulated PCL and formulated PCL nanoparticles. Most notable is the addition of a strong 1001 cm^{-1} C−H out-of-plane deformation mode. C−H and C−C modes in this spectral range are known to be sensitive markers of acyl chain disorder (*8*, *14*). This has been widely observed in lipid vesicles. On the basis of these observations, we attribute this strong peak to the increased chain disorder in formulated PCL when compared to unformulated PCL powder. Interestingly, the addition of cholesterol to PCL nanoparticles to form PLNP does not noticeably change the Raman spectrum of these particles, i.e., the disordered state of the polymer chains is retained in the presence of cholesterol. PLNP-derived polyplexes undergo a marked change in their Raman spectrum when compared to PLNP. Here, the 1001 cm^{-1} C−H out-of-plane deformation mode is significantly suppressed due to interaction with plasmid DNA. We attribute this to strong interactions of the charged DNA backbone with the charged polymer chains, which apparently leads to strong ordering in the vesicle chain structure (Figure 4C). The presence of DNA in polyplexes is further confirmed by the presence of weak DNA markers, such as the 785 cm^{-1} cytosine breathing mode, the 1090 cm^{-1} phosphate vibration, and the 1660 cm^{-1} amide I mode.

Use of Fluorescence Deconvolution Microscopy to Dynamically Monitor Reporter Gene Expression. To dynamically determine the earliest expression of a reporter gene, enhanced green fluorescent protein (GFP), we employed a fluorescence microscopy imaging system for time-elapsed live cell imaging to compare the transfection efficiency of PLNP with lipofectamine. As shown in Figure 5, the earliest GFP expression in Hep G_2 cells was seen 60 min after PLNP-mediated transfection with a pEGFP-C1-EGFP plasmid at the charge ratio of 5:1 (Figure 5A,D), while focal and faint GFP expression was also seen in Hep G_2 cells 70 min after lipofectamine transfection (Figure 5G,J), indicating that lipid nanoparticle-mediated plasmid DNA entering a cell and the nucleus, i.e., the transcription of the reporter gene, is a rather fast process. GFP expression then became more intense and spread throughout Hep G_2 cells transfected either with PLNP (Figure 5B,C,E,F) or lipofectamine (Figure 5H,I,K,L). This observation indicates that the transfection efficiency of PLNP is at least as good as lipofectamine in Hep G_2 cells.

Zeta Potential, Charge Ratios, Size, and Visualization of PLNP and Polyplexes. In order to further determine the relationship of charge ratios and zeta potential of PLNP and PLNP-derived polyplexes, we mixed PLNP with plasmid DNA at various charge ratios, and measured the zeta potential and size of PLNP and PLNP-derived polyplexes at the same time. It is clear from Figure 6 that, for *in vitro* transfection at a charge ratio of 5:1, the zeta potential of polyplexes was slightly lower than PLNP without DNA ($p > 0.05$). For *in vivo* gene delivery at the charge ratio of 1.25:1, the zeta potential of the polyplexes was negative (-6.46 ± 0.97 mV), which is consistent with them being less reactive to serum proteins as reported previously (*2*). We also noticed that the size of polyplexes increased when PLNP were complexed with plasmid DNA. The polyplex size was within the range 200−400 nm, which are similar to many other lipid formulations reported (*18, 19*). The stability of our PLNP was further confirmed *in vitro* when PCL and PLNP vesicles were prepared by sonication to result in nanoparticles with a diameter of 149 ± 62 nm. Under the microscope, we were able to visualize the vesicles of both PCL and PLNP by their absorption of transmitted light (highlighted by a circle) (Figure 7A). The vesicles appear homogeneous in size and

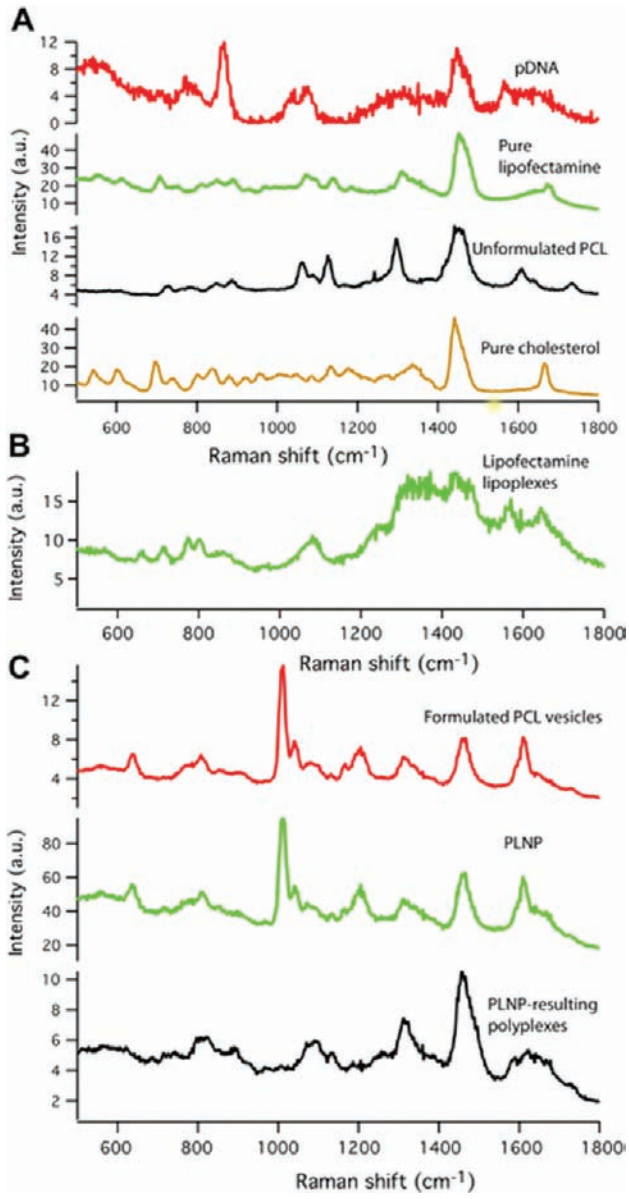

Figure 4. Representative Raman spectrum of pure compounds, nanoparticles, and lipoplexes or polyplexes. (A) Plasmid DNA (red), pure lipofectamine (green), unformulated PCL (black), and pure cholesterol (orange). (B) Lipofectamine-derived lipoplexes (green) in 30s signal integration time. (C) PCL vesicles (red), PLNP (green), and PLNP-derived polyplexes (black). The Raman spectrum was obtained in a Laser-Tweezers Raman microspectroscopy system, and representative spectrum is shown from each condition.

shape. The morphology of these particles did not change significantly after complexation with plasmid DNA (Figure 7B), whereas lipofectamine formed large aggregates in the presence of plasmid DNA (4 μL liposomes/2 μg DNA) (Figure 7C). These data indicate that our PLNP formulation is superior to lipofectamine in DNA binding capacity and particle stability when forming complexes with plasmid DNA.

DISCUSSION

In our previous study, a cationic acrylamide lipid was polymerized to form PCL (*6*). Our PLNP formulated from PCL and cholesterol have been considered as one of a few nonviral lipid nanoparticle formulations (*20, 21*) useful for *in vivo* gene transfer due to their nontoxic feature, high stability in the bloodstream, and superior transfection efficacy in mouse liver (*2, 6*). The preclinical proof-of-concept experiments in two separate model systems demonstrated that the delivery of antioxidative genes, either EC-SOD or catalase, or in combination, protected mouse from acute liver injury induced by hepatotoxins or hepatic ischemia/reperfusion procedures (*3, 4*). These studies were highlighted as "the basis for studies with larger animals and may help bridge the gap between the basic understanding of pathophysiologic processes in animal models towards a practical clinical application in liver transplantation" (*5*). In order to perform large animal experimentation, such as in pigs or nonhuman primates, or for clinical use, we developed a feasible synthetic route for synthesizing PCL on a relatively large scale. The purity of the final product with the polymeric features was verified by mass spectrometry; and PLNP were formulated with the final product and used in the experiments of this study.

Raman spectroscopy is a laser-based analytical technique that enables chemical characterization of molecules in microscopically small samples (*8*). Raman microspectroscopy is based on the inelastic scattering of photons by molecular bond vibrations and is a useful tool for the chemical analysis of lipids, lipoplexes, or polyplexes due to its ability to provide chemical group identification (*22*). A particular advantage of micro-Raman spectroscopy is its unrivaled sensitivity and its relative noninvasiveness, which enables the nondestructive analysis of nanoscopic compounds as small as 50 nm diameter (*8, 14*). We have employed Raman microspectral analysis in a number of studies (*23, 24*), including analyzing the chemical composition of individual triglyceride-rich lipoproteins (*25*). A Raman spectrum appears when a small portion of the photons from a monochromatic light source is scattered by interaction with the bonds resulting in a shift toward higher or lower frequencies. The energy difference between the incident and scattered photons corresponds to the vibrational energy of the specific molecular bond interrogated. A Raman spectrum obtained from lipids, DNA, or their complexes provides an intrinsic molecular fingerprint of these samples, and reveals characteristic information about macromolecular conformations (*8*). In order to further characterize the chemical features of PCL, PLNP, and PLNP-derived polyplexes, we employed a laser-tweezers Raman microspectroscopy system to observe morphologic changes in these particles after complexation with plasmid DNA and to acquire Raman spectra of polyplexes and compare them with lipofectamine lipoplexes. After carefully comparing with pure reagents for PLNP formulation and polyplex formation, we found that the Raman spectra of PCL exhibits polymeric characteristics of the synthetic polymer and that the spectra of PLNP indicate that they readily interacted with plasmid DNA and formed complexes without aggregation. Lipofectamine, on the other hand, was observed to form large aggregates devoid of specific interactions with DNA after complexation with plasmid DNA. These findings, which have not been reported, imply the feasibility of *in vivo* application of PLNP.

The appearance and extent of reporter gene expression in transfected cells are generally determined either by measuring activity of luciferase after lysing cells or by observing the onset of fluorescence from GFP expression at certain time points with a regular fluorescent microscope. It is generally believed that the lipofection process usually takes at least 6 h in transfected cells (*26*). In our previous experiments, we compared transfection efficiency in Hep G_2 cells between PLNP and lipofectamine by luciferase activity and cytotoxicity, and found that PLNP is less toxic than lipofectamine in primary hepatocytes and displayed transfection efficiency in Hep G_2 cells similar to lipofectamine (*6*). The automated fluorescence microscopy imaging system offers the possibility to dynamically monitor the transfection process in live cells, and we noticed that the earliest GFP appearance was within 1 h in Hep G_2 cells

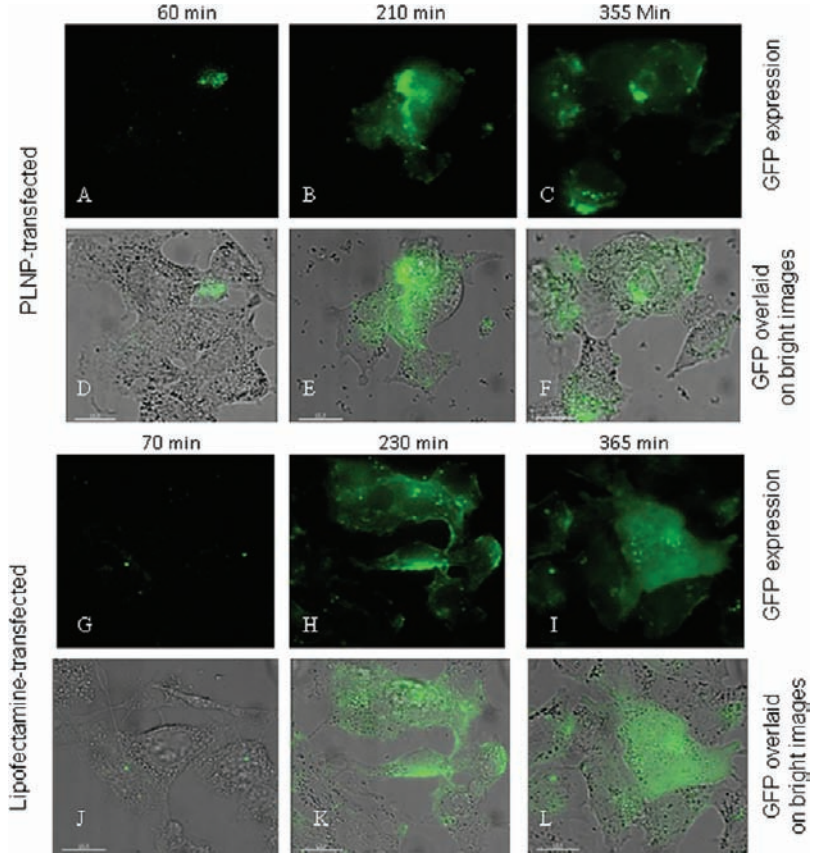

Figure 5. Representative vertical section images of automated fluorescence deconvolution microscopy examination of GFP expression in Hep G2 cells. After transfection, the culture well was mounted in the temperature-controlled platform. Image capture is achieved with a fast, high-resolution, high quantum efficiency, thermoelectrically cooled CCD camera at various time points as indicated. A, B, C and G, H, I representative images are selected from a stack of vertical section images of individual cells at indicated time points. C, D, E, and J, K, L are the overlaid images of A, B, C and G, H, I with their bright field images.

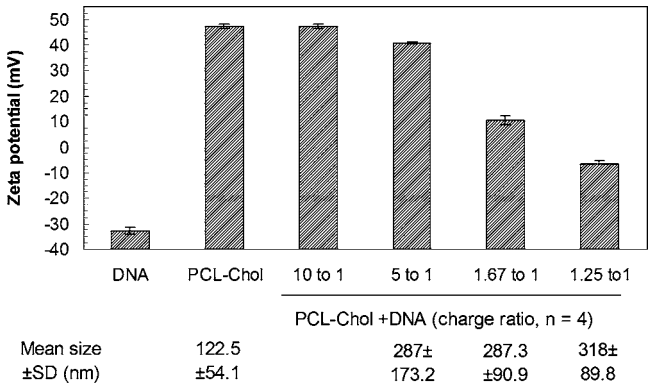

Figure 6. Zeta potential and size changes of PLNP formulation (PCL-Chol). The zeta potential and size were measured by a zeta potential/particle sizer at the charge ratios used for both *in vitro* and *in vivo* experiments ($n = 3$). It is found that the zeta potential was reduced to be neutral or even negative when the charge ratio was decreased to a range from 1.25 to 1, and that lipoplex size increased, but stayed within the 200−400 nm range.

transfected with PLNP, and a relatively faint GFP image was also seen in Hep G_2 cells transfected with lipofectamine 20 min later. Thereafter, the intensity and spread of GFP were similar in cells transfected by either PLNP or lipofectamine. Thus, we were able to dynamically monitor an early lipofection process in live cells over time. The time-lapsed imaging mode of the automated fluorescence deconvolution microscope minimizes long-term photobleaching by rapidly shuttering the excitation source on and off. The detection is based on a digital thermoelectrically cooled CCD camera, which enables us to quantitatively and dynamically determine GFP fluorescence (i.e., expression) levels in the cytoplasm over time. When specific dyes are used to indicate subcellular organelles, the DVDM system also allows detection of multiple, different-colored fluorescence signals simultaneously from cells with high sensitivity together with their morphology in three dimensions without damaging cells (*9*). The figure in Supporting Information is an example of this application. With this system, it is possible to investigate at a specific time point which subcellular organelles are involved in the lipofection process and critical events, such as intracellular trafficking of plasmid DNA, interaction, or synchronization of multiple subcellular organelles.

One of the critical features of cationic lipid, polymers, lipid nanoparticles, lipoplexes, or polyplexes is the zeta potential, which reflects charge force for nucleotide binding. Both size distribution and zeta potential may change after the formation of complexes with plasmid DNA. These two are important parameters of polyplex stability, and are even more critical when polyplexes are used for *in vivo* gene transfer. When forming polyplexes, the charge ratio will be a key factor affecting both zeta potential and transfection efficiency (*27*). A high zeta potential often benefits *in vitro* transfection, whereas neutral or negative zeta potential of lipoplexes or polyplexes may have less serum reactivity and is beneficial for complex stability in the bloodstream (*27, 28*). When similar transfection efficiency is reached, a lower charge ratio (positive charge from cationic lipid over negative charge in DNA) indicates that less cationic lipid is needed for maximal plasmid DNA binding, which indicates the carrying capacity of specific lipids. We have previously shown that our PLNP formulation exhibited similar transfection efficiency when the charge ratio was changed from

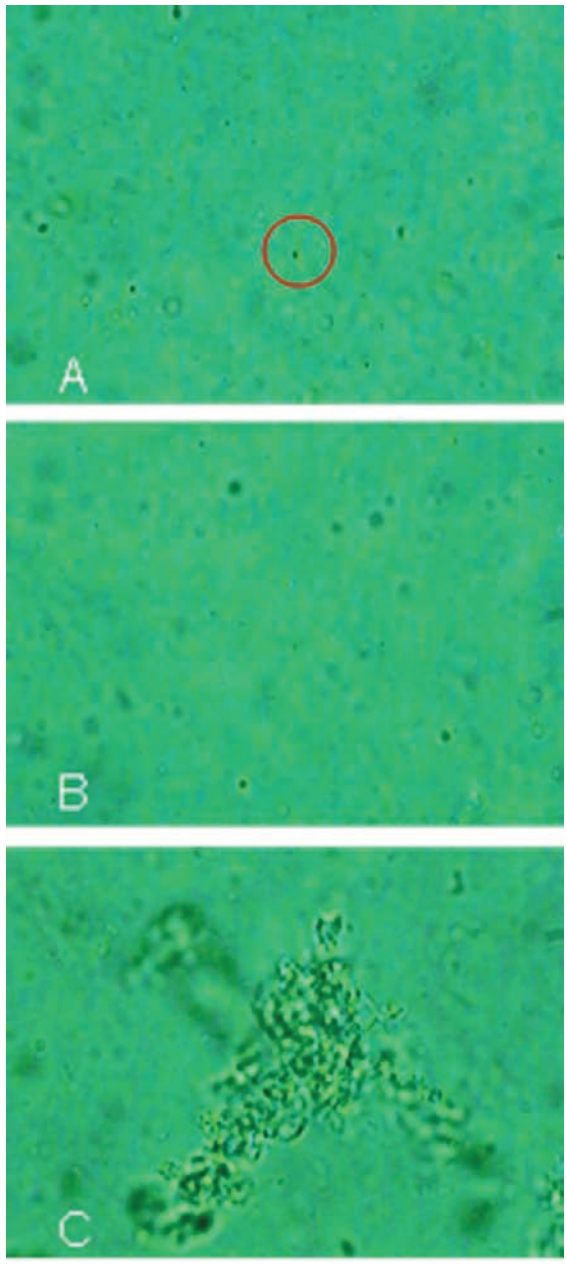

Figure 7. Visualization of lipid vesicles under a light microscope. (A) A PLNP vesicle was visualized under the microscope used for Raman spectromicroscopy analysis (600×), and it is marked with a circle. (B) Polyplexes derived from PLNP and plasmid DNA. (C) Lipoplexes derived from lipofectamine with plasmid DNA. The PLNP morphology of these particles did not change after complexation with plasmid DNA; however, lipofectamine formed large aggregates in the presence of plasmid DNA.

1:3 to 1:5, indicating higher DNA binding and carrying capacity of this formulation (*6*). In the present study, we found that the zeta potential was reduced to be neutral or even negative when the charge ratio was decreased to a range from 1.25 to 1, and the data indicate that this charge ratio is beneficial for *in vivo* delivery through intravenous administration because it may have less reactivity to negatively charged serum proteins. This is a key issue that is under-addressed in the field of lipofection. The net positive charge of polyplexes or lipoplexes is the principal reason for the formation of large aggregates after intravenous administration of lipoplexes or polyplexes and may affect tissue distribution and gene transfer efficacy in specific organs, such as livers when nonviral lipid nanoparticles are used as gene transfer vectors (*29*). The microscopic morphology of PLNP and polyplexes, as shown in Figure 7, further confirmed the stability after complexation with plasmid DNA, and there is a striking contrast to the formation of large aggregates of lipofectamine-derived lipoplexes. Therefore, our PLNP are useful for both *in vitro* and *in vivo* gene transfer as demonstrated in our previous studies and may also be useful in delivering siRNA, similar to other cationic lipid nanoparticles (*30*).

In summary, the employment of novel state-of-the-art technologies in the study of lipofection represents the level of physicochemical and biological characterization that is needed to best understand the key elements involved in the lipofection process. In the present study, we have described a refined method of PCL synthesis on a multigram scale. The data demonstrate that the morphology of PLNP derived from PCL did not change significantly after interaction with plasmid DNA, which is in striking contrast to the formation of large aggregates when using lipofectamine. The large DNA carrying capacity allows PLNP to be saturated with negatively charged plasmid DNA, and the negative zeta potential of PLNP-derived polyplexes is beneficial for *in vivo* stability. The Raman spectral signatures of PCL, PLNP, and polyplexes reflect the polymeric nature of PLNP and the close interaction of PLNP with plasmid DNA. These data are in concordance with the good stability observed for PLNP in the bloodstream and the higher transfection efficiency *in vivo* compared to other formulations of lipid nanoparticles.

ACKNOWLEDGMENT

We thank Mr. Souvik Biswas for his assistance in preparing samples for analysis. C.W.D. is grateful for the award of an R. Bryan Miller Fellowship from the UCD Department of Chemistry during the course of this study. This work was supported by grants from the NIH (DK069939) and the UCD Medical Center (Technology Transfer Grant to J.W.), from the National Science Foundation (to T.R.H.). The Center for Biophotonics, an NSF Science and Technology Center, is managed by the University of California, Davis, under Cooperative Agreement No. PHY 0120999. Part of the data was presented in the 11th Annual meeting of the American Society for Gene Therapy (ASGT), May 28−June 1, 2008, Boston, MA. Mr. Maung Nyunt received a travel award from the ASGT for the presentation.

Supporting Information Available: The use of the DVDM system enables us to section cells at 0.1 μm thicknesses, and a three-dimensional structure of a cell can be built from the sections at the *Z* axis. This material is available free of charge via the Internet at http://pubs.acs.org.

LITERATURE CITED

(1) Li, S. D., and Huang, L. (2006) Gene therapy progress and prospects: non-viral gene therapy by systemic delivery. *Gene Ther. 13*, 1313–9.
(2) Liu, L., Zern, M. A., Lizarzaburu, M. E., Nantz, M. H., and Wu, J. (2003) Poly(cationic lipid)-mediated in vivo gene delivery to mouse liver. *Gene Ther. 10*, 180–7.
(3) He, S. Q., Zhang, Y. H., Venugopal, S. K., Dicus, C. W., Perez, R. V., Ramsamooj, R., Nantz, M. H., Zern, M. A., and Wu, J. (2006) Delivery of antioxidative enzyme genes protects against ischemia/reperfusion-induced liver injury in mice. *Liver Transpl. 12*, 1869–79.
(4) Wu, J., Liu, L., Yen, R. D., Catana, A., Nantz, M. H., and Zern, M. A. (2004) Liposome-mediated extracellular superoxide dismutase gene delivery protects against acute liver injury in mice. *Hepatology 40*, 195–204.
(5) Luedde, T., and Trautwein, C. (2006) The role of oxidative stress and antioxidant treatment in liver surgery and transplantation. *Liver Transpl. 12*, 1733–5.

(6) Wu, J., Lizarzaburu, M. E., Kurth, M. J., Liu, L., Wege, H., Zern, M. A., and Nantz, M. H. (2001) Cationic lipid polymerization as a novel approach for constructing new DNA delivery agents. *Bioconjugate Chem. 12*, 251–7.

(7) Estrada, R., and Yappert, M. C. (2004) Alternative approaches for the detection of various phospholipid classes by matrix-assisted laser desorption/ionization time-of-flight mass spectrometry. *J Mass Spectrom. 39*, 412–22.

(8) Chan, J. W., Motton, D., Rutledge, J. C., Keim, N. L., and Huser, T. (2005) Raman spectroscopic analysis of biochemical changes in individual triglyceride-rich lipoproteins in the pre- and postprandial state. *Anal. Chem. 77*, 5870–6.

(9) Falk, M. M. (2000) Connexin-specific distribution within gap junctions revealed in living cells. *J. Cell Sci. 113*, 4109–20 (Pt 22).

(10) Wu, J., Liu, P., Zhu, J. L., Maddukuri, S., and Zern, M. A. (1998) Increased liver uptake of liposomes and improved targeting efficacy by labeling with asialofetuin in rodents. *Hepatology 27*, 772–8.

(11) Aberle, A. M., Bennett, M. J., Malone, R. W., and Nantz, M. H. (1996) The counterion influence on cationic lipid-mediated transfection of plasmid DNA. *Biochim. Biophys. Acta 1299*, 281–3.

(12) Madruga, E. L., San Roman, J., and Benedi, P. (1990) High conversion polymerization of methyl methacrylate in the presence of n-dodecylmercaptan. *J. Appl. Polym. Sci. 41*, 1133–1140.

(13) Dorn, K., Klingbiel, R. T., Specht, D. P., Tyminski, P. N., Ringsdorf, H., and O'Brien, D. F. (1984) Permeability characteristics of polymeric bilayer membranes from methacryloyl and butadiene lipids. *J. Am. Chem. Soc. 106*, 1627–1633.

(14) Chan, J., Fore, S., Wachsmann-Hogiu, S., and Huser, T. (2008) Raman spectroscopy and microscopy of individual cells and cellular components. *Laser Photon Rev. 2*, 325–334.

(15) Manoharan, R., Wang, Y., and Feld, M. S. (1996) Histochemical analysis of biological tissues using Raman spectroscopy. *Spectrochim. Acta, Part A 52*, 215–249.

(16) Huser, T., Orme, C., Hollars, C., Corzett, M., and Balhorn, R. (2009) Raman spectroscopy of DNA packaging in individual human sperm cells distinguishes normal from abnormal cells. *J. Biophotonics 2*, 322–332.

(17) Serban, D., Benevides, J. M., and Thomas, G. J. (2002) DNA secondary structure and Raman markers of supercoiling in Escherichia coli plasmid pUC19. *Biochemistry 41*, 847–853.

(18) Pelisek, J., Gaedtke, L., DeRouchey, J., Walker, G. F., Nikol, S., and Wagner, E. (2006) Optimized lipopolyplex formulations for gene transfer to human colon carcinoma cells under in vitro conditions. *J. Gene Med. 8*, 186–97.

(19) Almofti, M. R., Harashima, H., Shinohara, Y., Almofti, A., Baba, Y., and Kiwada, H. (2003) Cationic liposome-mediated gene delivery: biophysical study and mechanism of internalization. *Arch. Biochem. Biophys. 410*, 246–53.

(20) Elfinger, M., Uzgun, S., and Rudolph, C. (2008) Nanocarriers for gene delivery - polymer structure, targeting ligands and controlled-release devices. *Curr. Nanosci. 4*, 322–353.

(21) Ambegia, E., Ansell, S., Cullis, P., Heyes, J., Palmer, L., and MacLachlan, I. (2005) Stabilized plasmid-lipid particles containing PEG-diacylglycerols exhibit extended circulation lifetimes and tumor selective gene expression. *Biochim. Biophys. Acta 1669*, 155–63.

(22) Braun, C. S., Jas, G. S., Choosakoonkriang, S., Koe, G. S., Smith, J. G., and Middaugh, C. R. (2003) The structure of DNA within cationic lipid/DNA complexes. *Biophys. J. 84*, 1114–23.

(23) Wachsmann-Hogiu, S., Weeks, T., and Huser, T. (2009) Chemical analysis in vivo and in vitro by Raman spectroscopy-from single cells to humans. *Curr. Opin. Biotechnol. 20*, 1–11.

(24) Chan, J., Fore, S., Wachsmann-Hogiu, S., and Huser, T. (2008) Raman spectroscopy and microscopy of individual cells and cellular components. *Laser Photon Rev. 2*, 325–334.

(25) Chan, J. W., Motton, D., Rutledge, J. C., Keim, N. L., and Huser, T. (2005) Raman spectroscopic analysis of biochemical changes in individual triglyceride-rich lipoproteins in the pre- and postprandial state. *Anal. Chem. 77*, 5870–6.

(26) Lang, I., Scholz, M., and Peters, R. (1986) Molecular mobility and nucleocytoplasmic flux in hepatoma cells. *J. Cell Biol. 102*, 1183–90.

(27) Eliyahu, H., Joseph, A., Schillemans, J. P., Azzam, T., Domb, A. J., and Barenholz, Y. (2007) Characterization and in vivo performance of dextran-spermine polyplexes and DOTAP/cholesterol lipoplexes administered locally and systemically. *Biomaterials 28*, 2339–49.

(28) Fumoto, S., Kawakami, S., Shigeta, K., Higuchi, Y., Yamashita, F., and Hashida, M. (2005) Interaction with blood components plays a crucial role in asialoglycoprotein receptor-mediated in vivo gene transfer by galactosylated lipoplex. *J. Pharmacol. Exp. Ther. 315*, 484–93.

(29) Wu, J., Nantz, M. H., and Zern, M. A. (2002) Targeting hepatocytes for drug and gene delivery: emerging novel approaches and applications. *Front. Biosci. 7*, d717–25.

(30) Kim, H. R., Kim, I. K., Bae, K. H., Lee, S. H., Lee, Y., and Park, T. G. (2008) Cationic solid lipid nanoparticles reconstituted from low density lipoprotein components for delivery of siRNA. *Mol. Pharm. 5*, 622–31.

BC900150V

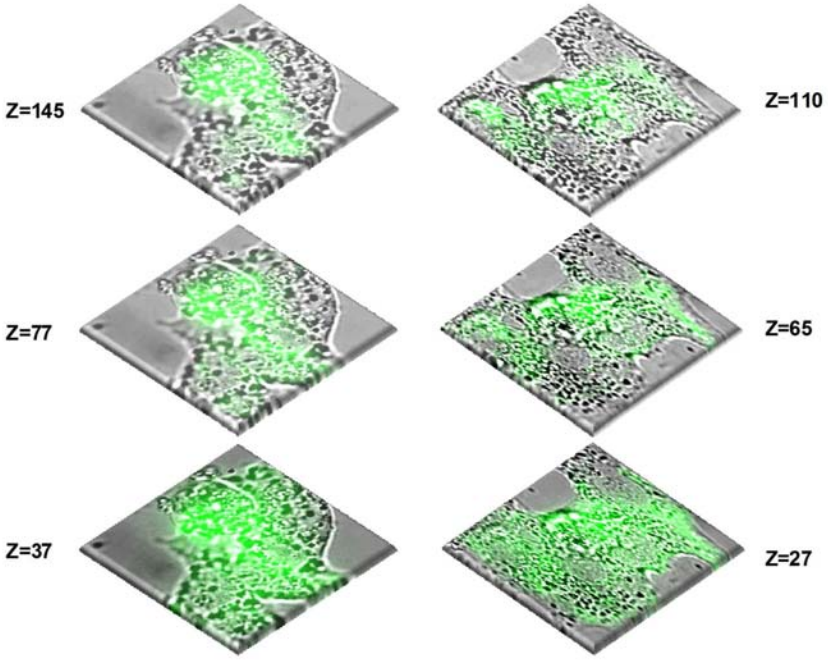

Supplemental Fig. 1 3-dimentional images of Hep G2 cells in vertical sections at different Z-axis levels. The images are obtained in cells transfected with pEGFP-C1 plasmid by either PLNP at 210 min or Lipofectamine at 230 min. This image demonstrates the capability of the DVDM system in investigating which subcellular organelles of a live cell are involved in lipofection when specific fluorescent dyes are used to label these organelles.

169x191mm (300 x 300 DPI)

Hydrophobically Modified Oligoethylenimines as Highly Efficient Transfection Agents for siRNA Delivery

Alexander Philipp,[‡] Xiaobin Zhao,[§] Peter Tarcha,[§] Ernst Wagner,[‡] and Arkadi Zintchenko*[,†,‡]

Center for Drug Research, Department of Pharmacy, Pharmaceutical Biology-Biotechnology, and Center for NanoScience (CeNS), Ludwig-Maximilians-University, Butenandstr. 5-13, D-81377 Munich, Germany, and Department of Advanced Drug Delivery, Abbott Laboratories, D-R43D, AP31-2, 200 Abbott Park Road, Abbott Park, North Chicago, Illinois 60064. Received April 7, 2009; Revised Manuscript Received August 19, 2009

RNA interference is a promising therapeutic strategy for treatment of diseases, in particular, cancer. Despite a huge number of targets identified for different cancer types, there are no effective delivery strategies available so far. Polymeric delivery vehicles are often based on large macromolecules. Such approaches often lead to accumulation of toxicity and narrow therapeutic windows. In the current paper, an alternative approach is presented. Low molecular weight oligoethylenimine (OEI) 800 Da was hydrophobically modified through the Michael addition of different alkyl acrylates. An optimal structure containing ten hexyl acrylate residues per one OEI chain (OEI-HA-10) was found to be a promising candidate for siRNA delivery. Hydrophobic modification stabilized the siRNA polyplex structure, increased the colloidal stability of the nanoparticles, and provided lytic properties to OEI required for crossing cellular membranes in the delivery process. In addition, the acrylate ester bond enables fast degradation of OEI-HA-10 into far less toxic components. Further improvement of biological properties of the OEI-HA-10 polyplexes by different formulation strategies was demonstrated. In particular, a remarkable increase of biocompatibility without loss of efficiency could be achieved by coformulation of OEI-HA-10 with lauryl acrylate modified OEI-LA-5.

INTRODUCTION

Small interfering RNA (siRNA)[1]is a promising tool for both basic and applied biology. The ability to knock down essentially any gene of interest has led to an increased interest in identifying important therapeutic genes and develop siRNA-based treatment. This is particularly interesting for cancer, where a large number of disease-related genes have been understood (*1, 2*). However, the successful application of siRNA-based therapy still represents a great challenge. The in vivo application of siRNAs, in reality, poses many hurdles, especially in humans. One of the main hurdles is the optimization of the delivery strategy, especially the carrier systems. Generally, the carrier must be effectively bound to siRNA, ensuring high stability against dissociation of nucleic acid in physiological fluids. It must provide effective transport of siRNA to the cytosol of the target cells and show low toxicity. Accumulation of the carrier in the body leads normally to accumulation of the toxicity (*3*), which narrows the therapeutic window and limits the dosing frequency of the therapeutics. Therefore, relatively fast biodegradation of the carrier is a desired property for the application of transfection vectors in vivo.

Recently, several strategies for the development of polymeric carriers were introduced, which are mainly based on optimization of the conventional vectors for DNA delivery. Different polyethylenimines (PEIs), which are known to be powerful agents for DNA delivery, are far less effective for siRNA. Different approaches were utilized for the enhancement of their efficiency. In the case of linear PEI, the activity can be enhanced with "sticky" siRNA (ssiRNA) applied for polyplex formation (*4*). Acetylation of the amines of branched PEI or introduction of negatively charged carboxylic groups into structure remarkably increased the knockdown efficiency of the carrier (*5*). Large PEI macromolecules (>5 kDa) are generally nondegradable and cannot be cleared from the body. Thus, they are characterized by only limited potential for therapeutic applications. Low molecular weight PEIs are far less toxic, but also rather inefficient and require high excess of oligoamine in the formulation (*6, 7*). The polyplex stability of such formulations, especially in vivo, is a big concern. Covalent cross-linking of oligoamines by biodegradable linkers provides to the formulation the stability and efficiency of polyamines, and can be degraded in the body to excretable degradation products. Polyamidoamine approaches for cross-linking of oligoamines often lead to rather effective carriers (*8, 9*). However, slow degradation of amide bonds generally limits the therapeutic window of the formulation. Introduction of secondary break points into bifunctional diacrylate structures (i.e., disulfide) can provide much higher degradation rates (*10*). Degradable synthetic polypeptides (i.e., PLL) are rather inefficient in both DNA and siRNA delivery. Conjugation with endosomolytic agents enhanced efficiency of the carrier (*11*). "Dynamic polyconjugates" introduced by Rozema et al. (*12*) are based on biocompatible poly(vinyl alcohol) backbones modified by amine and hydrophobic alkyl groups. Such structures showed a pronounced lytic activity (*13*), which could be reversibly switched off by modification of amines with maleic anhydride-based reagent (*14*). These "dynamic polyconjugates" were rather nontoxic in vivo and showed good efficiency for delivery of siRNA to liver hepatocytes (*12*). Other hydrophobic pH-responsive polymer-based carriers were described by Convertine et al. (*15*). Copolymers

* Correspondence to Arkadi Zintchenko, tel +31 53 489 3272, fax +31 53 489 2155, e-mail A.Zinchenko@tnw.utwente.nl.

† Current address: University of Twente, Faculty of Science and Technology, Institute for BioMedical Technology (BMTI), Zuidhorst, NL-7500 AE Enschede, The Netherlands.

‡ Ludwig-Maximilians-University.

§ Abbott Laboratories.

[1]Abbreviations: OEI 800, oligoethylenimine 800 Da; EA, ethyl acrylate; BA, butyl acrylate; HA, hexyl acrylate; LA, lauryl acrylate; EtBr, ethidium bromide; siRNA, short interfering RNA.

10.1021/bc9001536 CCC: $40.75 © 2009 American Chemical Society
Published on Web 10/19/2009

containing cationic binding block and pH-responsive hydrophobic block based on propylacrylic acid and butyl methacylate showed remarkable knockdown of the target genes with relatively low toxicity.

In the current paper, an alternative approach is presented. Instead of cross-linking, OEI 800 was hydrophobically modified by Michael addition of alkyl acrylates. As expected, such structures formed polyplexes with siRNA and demonstrated increased stability against dissociation. Structures with enhanced endosomolytic properties (in particular, hexyl acrylate modified OEI) were efficient in siRNA delivery. Furthermore, coformulation with different agents could significantly improve the parameters of toxicity and efficiency of the carrier. The optimized formulation could represent a promising carrier for delivery to cancer cells.

EXPERIMENTAL PROCEDURES

Materials. Ethyl, butyl, hexyl, and lauryl acrylate (EA, BA, HA, or LA respectively), were obtained from Sigma-Aldrich (Munich, Germany). The plasmid pEGFPLuc (Clontech Laboratories, Heidelberg, Germany) containing a CMV promoter driven fusion of the genes encoding for enhanced green fluorescent protein and luciferase was used for generation of stably transfected cells. Oligoethylenimine with an average molecular weight of 800 Da and all other chemicals were purchased by Sigma-Aldrich (Munich, Germany). Lipofectamine 2000 (LF2000), cell culture media, antibiotics, and fetal calf serum (FCS) were purchased from Invitrogen (Karlsruhe, Germany). Ready to use siRNA duplexes were purchased from Dharmacon (Lafayette, CO), namely, luciferase-siRNA: GL3 luciferase duplex: 5′-CUUACGCUGAGUACUUCGAdTdT-3′ (sense); control-siRNA: nontargeting control duplex: 5′-AUGUAUUGGCCUGUAUUAGUU-3′ (sense).

Modification of OEI by Ethyl, Butyl, and Hexyl Acrylate (EA, BA, and HA). PEI (1 g) was dissolved in chloroform. The solution was heated to 40 °C. The desired amount of acrylate was added to the solution under stirring. The reaction proceeded at 40 °C. After 4 h, the chloroform was removed by rotor evaporator. The waxy product was dissolved in 15 mL water and neutralized by HCl to pH 4−5 and freeze−dried. The gravimetric yields were generally between 80% and 140%. Some yields above 100% were due to additional mass of chloride as a counterion in the lyophilized sample. The modification degree was analyzed by ^{1}H NMR in D_2O on a Jeol JNMR-GX400 (400 MHz) or a Jeol JNMR-GX500 (500 MHz) spectrometer from the ratio between the peaks of OEI (δ 2.4−3.3 ppm) and methyl of acrylates ($\delta = 0.8$ for HA, $\delta = 0.9$ for BA, and $\delta = 1.3$ for EA). The modification degree was expressed as the number of modifications per OEI molecule. According to FTIR spectra recorded on a Jasco FT/IR-410 spectrometer (Jasco Labor and Datentechnik GmbH, Germany), a pronounced ester peak (1730 cm^{-1}) was detected. No significant amide band (1652 cm^{-1}) was found.

Modification of OEI by Lauryl Acrylate (LA). One gram of OEI was dissolved in chloroform and heated to 40 °C. After this, the calculated amount of lauryl acrylate (LA) was added dropwise to the OEI solution. The ratios of OEI to LA were 2.5, 5, and 7.5. The mixture was incubated for 4 h. The resulting solution was evaporated on a rotovap to 1/3 of the initial volume. An excess of diethyl ether was added resulting in a clear solution. After this, an excess of concentrated HCl (37% vol) was added, which resulted in precipitation of the product. The precipitate was filtered, washed with diethyl ether, frozen in liquid nitrogen, and dried under vacuum.

The composition of the products was determined by NMR as a ratio between methyl protons of LA (0.8 ppm) and a broad peak of OEI (2.4−3.3 ppm). The peak at 4.1 ppm represents the CH_2−O proton of the ester bond. It was found to be stable over time and show good proportionality to the weights of all other peaks of LA (2:3 if compared to methyl).

Preparation of Liposomes. Lipid mixtures were prepared as a film by chloroform evaporation method. Dioleoyl phosphatidylethanolamine (DOPE, Sigma-Aldrich, Germany), dioleoylphosphatidylcholine (DOPC, Sigma-Aldrich, Germany), and dipalmitoylphosphatidylcholine (DPPC, Sigma-Aldrich, Germany) were used.

For the preparation of liposomes, about 10 mg of lipid (DOPE, DOPC, DPPC or mixtures) was dissolved in 0.1 mL of ethanol under mild heating (50 °C). The solution containing 0.5, 1.0, 2.0, or 5.0 mg of lipid was added to Eppendorf tubes and flash-mixed with 1 mL of OEI-HA-10 solution (1 mg/mL in water pH ∼3). The turbid suspension of nanoparticles was formed in all cases. Mixing of lipid (1 mg in 100 μL ethanol) with 1 mL of HBG buffer (without OEI-HA-10) resulted in precipitation of the lipid. The final suspensions were sonicated for 1−2 min resulting in nearly clear solutions in the case of DOPE/OEI-HA10 (weight ratios 0.5, 1, and 2) and slightly opalescent solution in the case of DOPE/OEI-HA10 with a weight ratio of 5. The size of the nanoparticles was analyzed using photon correlation (Zetasizer Nano ZS, Malvern Instruments, Herrenberg, Germany). All nanoparticles were around 80−110 nm in diameter.

Preparation of Polymer Mixtures. For the preparation of OEI-HA-10/OEI mixtures, the amounts of OEI-HA-10 and OEI stock solutions were calculated according to the desired ratio in a final mixture (2/1, 1/1, or 1/2 w/w). The resulting solutions (1 mg/mL total OEI) were used as a stock for preparation of the polyplexes.

Polyplex Formation. In all studies, the composition of polyplexes was characterized by the w/w ratio of the polymer to nucleic acid in the mixture. The weight of modified OEIs represents the weight of lyophilized product, which was previously neutralized and, therefore, includes the mass of counterions (chloride). Formulations for siRNA delivery were prepared in HBG (20 μL) as follows: First, different concentrations of the nucleic acid and oligoamine formulations were diluted at various polymer/nucleic acid ratios in separate tubes in HBG (HEPES buffered glucose solution; 20 mM HEPES, 5% glucose, pH 7). Then, the HBG solution of oligoamine was added to the HBG solution of the nucleic acid, mixed and incubated for 30−40 min at room temperature to form stable complexes. In the case of LF2000, formulations with siRNA were prepared according to the manufacturer's standard protocol (Invitrogen).

Agarose Gel Retardation Assay. Polyplexes were prepared as indicated in the corresponding experimental settings containing 500 ng siRNA in 10 μL. Then complexes were mixed with loading buffer (6 mL glycerine, 1.2 mL 0.5 M EDTA, 2.8 mL H_2O, 0.02 g xylenecyanole) and placed into a 2.5% agarose gel in TBE buffer (trizma base 10.8 g, boric acid 5.5 g, disodium EDTA 0.75 g, and 1 L water) containing ethidium bromide (EtBr). Electrophoresis was performed at 80 V for 40 min and evaluated under UV-light.

Ethidium Bromide Exclusion Assay. siRNA condensation ability was evaluated in HBG (20 mM HEPES, 5% glucose, pH 7) using an ethidium bromide exclusion assay. Aliquots of the respective polymer were added stepwise to a siRNA solution (10 μg/mL) in HBG containing 400 ng/mL EtBr, and the decrease of fluorescence was measured in a Cary Eclipse fluorescence spectrophotometer (Varian Deutschland GmbH, Darmstadt, Germany). EtBr/siRNA fluorescence (λ_{ex} 510 nm and λ_{em} 590 nm) was set to 100% prior to addition of polycation, and results are given as relative fluorescence intensities to plain siRNA. Values are given as mean of triplicates ± SD.

Particle Size and Zeta-Potential Measurement. Particle size and zeta-potential of polyplexes were determined by laser light scattering using a Zetasizer Nano ZS (Malvern Instruments, Herrenberg, Germany). For measurement of zeta potentials, the polyplexes (prepared in HBG) were diluted with 1 mM NaCl to a final siRNA concentration of 10 μg/mL (total volume 1 mL). Values are given as mean of triplicates ± SD.

Degradation of Hydrophobically Modified Polyamines. Degradation of conjugates was investigated in an aqueous solution (1 mL, D_2O) at pH 7 at 37 °C. Resulting products were characterized by ^{1}H NMR spectroscopy. Degradation results in formation of alcohol with a peak at δ 3.6 different from those of ester at δ 4.1 (Supporting Information Figure 1). The percentage of degraded ester bond was expressed as the ratio δ 3.6/(δ 3.6 + δ 4.1).

Cell Culture. All cultured cells were grown at 37 °C in 5% CO_2 humidified atmosphere. For siRNA delivery experiments, murine neuroblastoma cells Neuro2A/EGFPLuc, human hepatoma cells HUH7/EGFPLuc stably transfected with the EGFPLuc gene, or human lung carcinoma cells H1299/Luc stably transfected with the luciferase gene (kindly provided by Abbott Laboratories, Chicago) were used. Neuro2A/EGFPLuc cells were grown in Dulbecco's modified Eagle's medium (DMEM, 1 g/L glucose), HUH7/EGFPLuc were grown in DMEM/Ham's F-12 medium, and H1299/Luc cells were grown in RPMI 1640 medium (4.5 g/L glucose), whereby all media were supplemented with 10% FCS, 4 mM stable glutamine, 100 U/mL penicillin, and 100 μg/mL streptomycin. All cells were seeded 24 h prior to transfection using 5000 cells per well in 96-well plates for analysis of protein expression. For the generation of stably transfected cells, the same protocol was used as previously reported (*5*).

Cytotoxicity of Polymers. Neuro2A/EGFPLuc cells (5000/well) were seeded into a 96-well plate in 100 μL medium. After 24 h, medium was replaced with 100 μL/well of serial dilutions of polymer stock solutions in serum containing (10% FCS) growth medium. After incubation at 37 °C for 48 h without medium change, the cell viability was analyzed using a MTT-assay. MTT (3-(4,5-dimethylthiazol-2-yl)-2,5-diphenyltetrazoliumbromide) (Sigma-Aldrich, Germany) was dissolved in phosphate buffered saline at 5 mg/mL, and 10 μL aliquots were added to each well reaching a final concentration of 0.5 mg MTT/mL. After incubation for 1 h, unreacted dye with medium was removed. The purple formazan product was dissolved in 100 μL/well dimethyl sulfoxide and quantified by a plate reader (Tecan Spectrafluor Plus, Grödig, Austria) at 590 nm with background correction at 630 nm. The relative metabolic activity (%) related to untreated control cells was calculated by [A] test/[A] control × 100. Values are given as mean of triplicates ± SD.

Erythrocyte Lysis Assay. Freshly collected citrate buffered murine blood was washed several times with PBS, and erythrocytes were resuspended in HBG/10% FCS at a concentration of 4% (v/v). 75 μL of a polymer solution was mixed with 75 μL erythrocyte suspension in a 96-well plate (NUNC, V-bottom, Denmark). After incubation for 45 min at 37 °C under constant shaking, blood cells were removed by centrifugation and 80 μL of the supernatant was transferred to a new 96-well plate. Hemoglobin absorption was determined at 405 nm using a microplate reader (Tecan Spectrafluor Plus, Grödig, Austria). HBG/10% FCS and 1% Triton X-100 solution in PBS were used as negative and positive controls, respectively. Hemolysis is defined as percentage ($OD_{polymer} - OD_{buffer}$) × 100/($OD_{TritonX-100} - OD_{buffer}$). Values are given as mean of triplicates ± SD.

In Vitro Gene Silencing with siRNA. In vitro gene silencing experiments were performed in stably transfected Neuro2A/EGFPLuc, HUH7/EGFPLuc, and H1299/Luc cells using Luc-siRNA. siCONTROL was used as an unspecific control siRNA. In all experiments, siRNA delivery was performed in 96-well plates with 5000 cells per well in triplicates. Cells were seeded 24 h prior to transfection, and then, medium was replaced with 80 μL fresh growth medium containing 10% FCS or 50% FCS where indicated. Transfection complexes for siRNA delivery (20 μL in HBG) at different w/w ratios were added to each well and incubated at 37 °C without medium change for 48 h. In case of the 50% FCS experiments and H1299/Luc cells, a medium change was performed after 24 h with fresh serum containing (10% FCS) growth medium. Cells were washed with phosphate-buffered saline (PBS) and treated with 50 μL cell lysis buffer (25 mM Tris, pH 7.8, 2 mM EDTA, 2 mM DTT, 10% glycerol, 1% Triton X-100) 48 h following siRNA transfection. Luciferase activity in cell lysate (20 μL) was measured using a luciferase assay kit (100 μL luciferase assay buffer, Promega, Mannheim, Germany) on a luminometer for 10 s (Lumat LB9507 instrument, Berthold, Bad Wildbad, Germany). The relative light units (RLU) were related to untreated control cells.

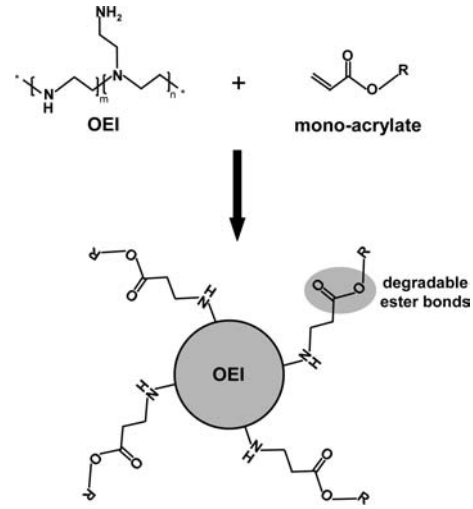

Figure 1. Structure of hydrophobically modified OEIs, which mediate steric stabilization of the polyplexes and cause cell membrane destabilization.

Statistical Analysis. Results are presented as mean ± s.d., and statistical significance of differences was evaluated by variance analysis (one-way ANOVA): p values smaller than 0.05 were considered to be significant, * $p < 0.05$.

RESULTS

Synthesis of the Polymers. All polymer products were synthesized by Michael addition of acrylate to the amines of OEI at 40 °C for 4 h (Figure 1). Higher temperature or longer reaction times are known to cause the aminolysis of the pendant ester bond resulting in cross-linking of the OEI units. Isolation was performed either by evaporation of residual acrylate at high vacuum (<100 mbar) or by precipitation of the product in diethyl ether. No unsaturation could be detected by proton NMR, which indicated effective isolation of the products from unreacted acrylate. Neutralization of the reactive amines before product isolation was essential to prevent slow cross-linking, even during storage at −20 °C (Zintchenko, unpublished observation). According to the FTIR spectra, no amide bond formation and consequently cross-linking could be detected in neutralized samples even after two years' storage at −20 °C. In addition, no peak of corresponding alcohol could be observed on ^{1}H NMR spectra during the storage period, indicating high stability of the products. The compositions of the products were close to

Table 1. Compositions of Hydrophobically Modified OEIs

acrylate	OEI/acrylate, feed mol/mol	OEI/acrylate, product mol/mol
OEI-EA-5	5	4.75
OEI-EA-10	10	9.03
OEI-BA-5	5	4.81
OEI-BA-10	10	9.44
OEI-HA-5	5	5.34
OEI-HA-10	10	10.5
OEI-LA-2.5	2.5	2.37
OEI-LA-5	5	5.4

the reaction feed (Table 1), indicating nearly quantitative reaction of the acrylate with OEI.

Biophysical Characterization of Polyplexes. The binding stability of the oligoamines to siRNA was studied by EtBr and gel shift assay. The EtBr assay was performed in low-salt HBG buffer. OEI and practically all modified oligoamines were effective in binding with siRNA. Only in the case of OEI-EA-10 was the binding significantly suppressed, presumably due to a steric barrier between the charges of siRNA and oligoamine introduced by the bulky acrylate group (data not shown).

Gel shift assay (in salt-containing TBE buffer) showed differences in polyplex stability (Supporting Information Figure 2). Unmodified OEI is quite ineffective in electrophoretic retention of siRNA. Modification by EA did not lead to any improvement of this property. Polyplexes of OEI-BA-5 showed much higher stability, whereas siRNA binding was slightly reduced again by higher BA modification (OEI-BA-10). Both modifications of higher hydrophobicity (HA, LA) were characterized by good binding affinity to siRNA.

Polyplexes with OEI were relatively small immediately after mixing in HBG. However, due to extremely low colloidal stability, rapid aggregation within several minutes was observed. No particles were found 30 min after mixing, probably due to fast sedimentation of aggregates. The same behavior was found in the case of EA and BA modified OEI. Only the in case of HA and LA modifications were polyplexes small and showed good colloidal stability at least 4 h after mixing (Supporting Information Tables 1 and 2). The short chains of OEI (even in excess) are not able to overcharge the polyplex particles and provide colloidal stability. The same was found also for EA and BA modified oligoamines. It seems to be that the hydrophobic interactions between oligoamines with long hydrophobic alkyl chains (HA and LA) could provide additional binding of excess oligoamine to the surface of the particle and, thus, provide improved stability of the polyplexes.

Similar to several endosomolytic peptides, the combination of hydrophobicity in oligoamine structure could increase the ability of the synthesized structures to lyse the lipid membranes and, thus, facilitate the delivery of siRNA into cytoplasm. Therefore, this property was studied by an erythrocyte lysis assay. The modifications with acrylate of low hydrophobicity (EA) were not able to lyse the erythrocytes (data not shown). The same corresponds to the oligoamines with the longest hydrophobic tail (LA). Only in the case of BA and HA modifications were significant lytic properties of the polymers observed (Supporting Information Figure 3).

Bioactivity of siRNA Formulations. Bioactivity of hydrophobically modified oligoamines with siRNA was evaluated by transfection of Neuro2A/EGFPLuc cells at different mixing ratios (w/w). Only OEI-HA-10 formulations containing around 10 HA residues per one OEI unit were able to induce efficient knockdown (Figure 2). Neither the formulations with short hydrophobic tails on oligoamine (EA and BA series) nor those with long (LA series) showed any reduction of luciferase activity (Supporting Information Figure 4). In addition, the formulations with lower degree of HA modification (OEI-HA-5) were

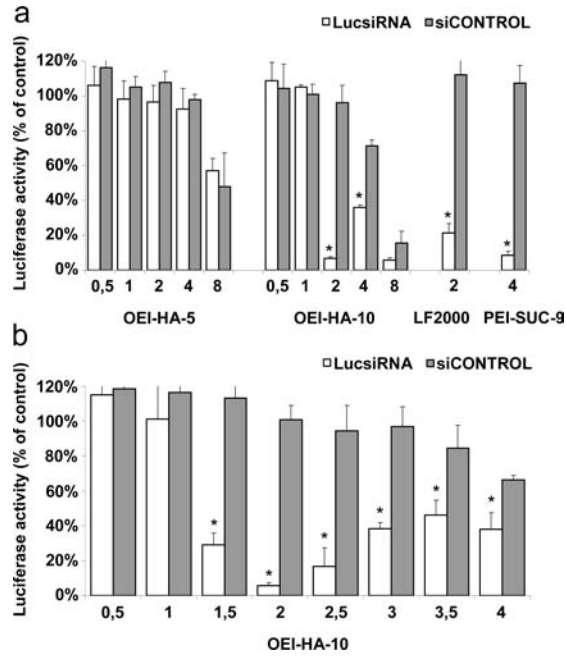

Figure 2. Induction of luciferase knockdown by siRNA formulations in Neuro2A/EGFPLuc cells with (a) OEI-HA-5 or OEI-HA-10 and (b) OEI-HA-10 tested in more detail at several w/w ratios. LF2000 and PEI-SUC-9 were used as reference formulations. White bars, LucsiRNA; black bars, siCONTROL. The numbers on the *x*-axis represent the mixing ratio oligoamine/siRNA (w/w) and LF2000/siRNA (w/w), respectively, in the formulations. Asterisks indicate statistical significance compared to control treated cells (* $p < 0.05$; ANOVA).

ineffective as well (Figure 2). The optimal knockdown efficiency of OEI-HA-10 formulations was observed at oligoamine/siRNA ratio of 2 (w/w) and was comparable to Lipofectamine 2000 and PEI-SUC-9 (*5*) formulations. Further increase of OEI-HA-10 content in the formulation led to a decrease of knockdown efficiency. The similar efficiency profile was found also on H1299/Luc and HUH7/EGFPLuc cell lines (Supporting Information Figure 5). Such unusual bell-shaped behavior cannot be explained by formation of polyplex aggregates, which (in the case of standard PEI) may mediate more efficient delivery of nucleic acid in comparison to small particles (*16*). Polyplex particles at all ratios under investigation were relatively small (Supporting Information Table 1). In addition, cytotoxicity of the formulations could not be the explanation, since the luciferase expression levels at the optimal ratio remain unaffected after transfection with a formulation of a control siRNA sequence. Importantly, the formulations caused significant knockdown even in the medium with high content of serum (50%) (Supporting Information Figure 6).

The toxicity of OEI-HA-10 is relatively high, which could lead to a high acute toxicity during in vivo applications and, thus, represent a problem (Figure 3a). The incubation of oligoamines OEI-HA-10 and OEI-LA-5 for 7 days at 37 °C in HBG buffer led to a remarkable decrease of the toxicity (Figure 3b), presumably due to degradation of the ester bonds. NMR studies revealed that up to 30% of ester bonds were degraded after 3 days of incubation at 37 °C and pH 7 (Supporting Information Figure 1). Thus, long-term toxicity does not seem to be problematic.

Improvement of OEI-HA-10 Formulation. Incorporation of active transfection agents into an appropriative formulation could often improve the physicochemical (solubility, stability, particle size, etc.) and biological parameters (efficiency and biocompatibility) of the final formulation. Helper lipids (*17*−*21*) or helper polymers (*22, 23*) could be utilized for this purpose. In order to improve the efficiency and toxicity profiles of OEI-

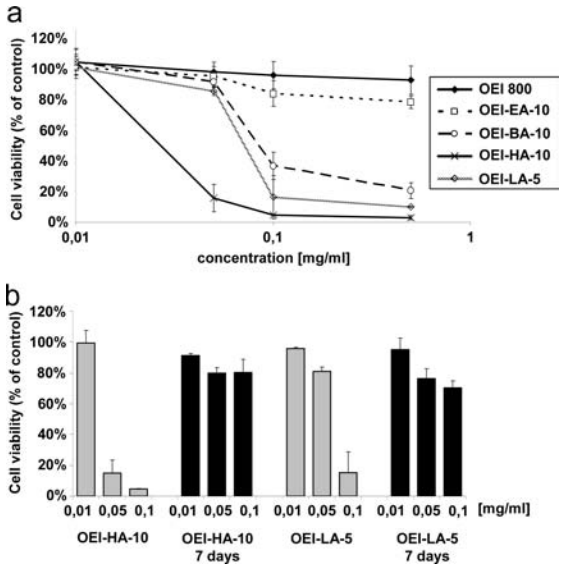

Figure 3. (a) Cell viability of Neuro2A/EGFPLuc cells as a function of concentration of modified oligoamines. (b) Cell viabilities before and after degradation of oligoamines. The black bars represent oligoamines which were incubated for 7 days in HBG buffer at 37 °C prior to application to the cell culture; the gray bars show oligoamines without preincubation.

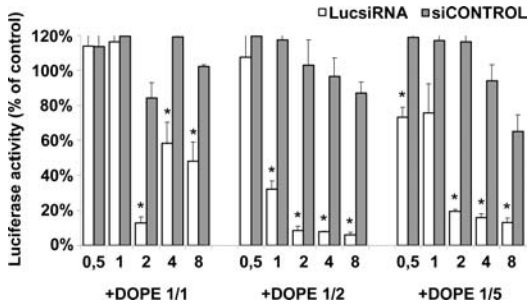

Figure 4. Induction of luciferase knockdown by DOPE/OEI-HA-10/siRNA formulations in Neuro2A/EGFPLuc cells. White bars, LucsiRNA; black bars, siCONTROL. The numbers on the *x*-axis represent the mixing ratio OEI-HA-10/siRNA (w/w) in the formulation. The OEI-HA-10/DOPE ratios were 1/1, 1/2, and 1/5 w/w as indicated under the *x*-axis. Asterisks indicate statistical significance compared to control treated cells (* $p < 0.05$; ANOVA).

HA-10/siRNA formulations, both approaches were utilized. First, OEI-HA-10 was combined with different helper lipids (DOPC, DPPC, and DOPE). Due to hydrophobic groups on OEI-HA-10, it could integrate into the lipid bilayer and improve the toxicity profile of the formulations. Second, the OEI-HA-10 formulation was diluted by nonmodified OEI or OEI-LA-5 as helper polymers, which were far less toxic in comparison to OEI-HA-10.

Combinations of OEI-HA-10 with DOPE led to some decrease of toxicity with a great improvement of the efficiency profile (Figure 4). In the case of the formulation with low content of DOPE (OEI-HA-10/DOPE 1/1 w/w), the efficiency profile was very similar to those of OEI-HA-10 alone, with a rather sharp optimum at polymer/siRNA w/w ratio of 2. The formulations with higher contents of DOPE behaved differently. The knockdown effect was persistent for a wide range of C/P mixing ratios. The optimal composition (OEI-HA-10/DOPE 1/2 w/w) induced the best knockdown, whereas a further increase of DOPE (1/5 w/w) in the formulation resulted in a decrease of the efficiency.

Formulations with DPPC and DOPC could also decrease the toxicity but also dramatically decreased the efficiency (Supporting Information Figure 7). Substitution of a certain amount of DPPC or DOPC with DOPE could not improve the efficiency of the formulations (data not shown).

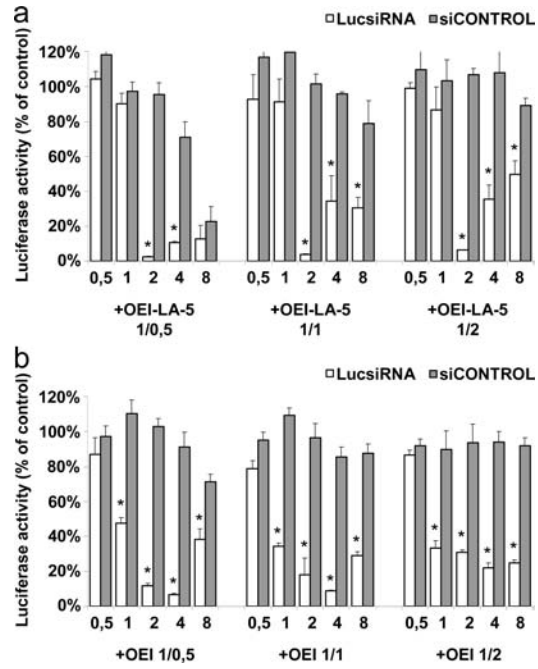

Figure 5. Induction of luciferase knockdown by (a) OEI-HA-10/OEI-LA-5/siRNA and (b) OEI-HA-10/OEI/siRNA formulations in Neuro2A/EGFPLuc cells. White bars, LucsiRNA; black bars, siCONTROL. The numbers on the *x*-axis represent the mixing ratio of total oligoamine/siRNA (w/w) in the formulation. The OEI-HA-10/OEI-LA-5 or OEI-HA-10/OEI ratios were 2/1, 1/1, and 1/2 w/w as indicated under the *x*-axis. Asterisks indicate statistical significance compared to control treated cells (* $p < 0.05$; ANOVA).

Substitution of a certain amount of OEI-HA-10 by relatively nontoxic low molecular weight OEI or OEI-LA-5 oligoamines in the formulation led to a remarkable decrease of the toxicity (Figure 5). A gradual increase of the ratio between OEI (or OEI-LA-5) and OEI-HA-10 in the formulation resulted in a gradual decrease in the toxicity of the formulations. Additionally, the efficiency profile was improved. For example, the OEI-HA-10/OEI 1/2 formulations induced efficient knockdown at lower mixing ratios in comparison to pure OEI-HA-10; the efficiency profile was less dependent on the mixing ratio. Importantly, unmodified OEI alone was not active at all studied mixing ratios and serves only as a helper reagent in the formulation.

DISCUSSION

The development of polymeric vectors for siRNA delivery is mainly attributed to the high molecular weight polyamines. Several classes of such carriers, which were previously proven to be effective in DNA delivery, were found to be effective in transfer of siRNA and knockdown of target genes. The application of high molecular weight structures for in vivo delivery often represents a problem due to relatively narrow therapeutic window. Being either nondegradable (e.g., PEI) or showing relatively slow degradation kinetics, such structures lead to accumulation of the toxicity after repeated application. Short oligoamines are far less toxic (*24*, *25*) and could be rapidly excreted from the body. However, the formulations show low stability in blood and low knockdown efficiency, mainly due to poor endosomolytic properties.

In the current paper, an alternative approach was evaluated. Instead of covalent cross-linking into high molecular weight structures, oligoamines were hydrophobically modified. Such a concept has several advantages. First, they are supposed to

have low half-life times in the organism, presumably due to low molecular weight, which is favorable for excretion and metabolism. Second, the hydrophobic interactions stabilize polyplexes during storage and after administration. Third, similarly to endosomolytic peptides, certain modifications could enhance the interaction with a cell membrane and promote transfer across the cell membrane barrier, for example, by lysis of the endosomes.

Most recently, in a parallel study the similar structures were derived for siRNA delivery as a result of chemical screening of a wide class of products of combinatorial synthesis (*19*). Their formulations showed high efficiency in knockdown of target genes in the hepatocytes and nasal epithelium (*19, 26*). Combining low molecular weight branched PEI with lipid moiety has been reported by Kim's group. Conjugates of cholesterol and short polyethylenimine (1.8 kDa) formulated with VEGF siRNA showed a moderate knockdown in vitro and significant reduction of tumor growth in vivo after intratumoral application (*27*).

In our study, oligoethyleneimine 800 Da was taken as an oligoamine and modified via Michael addition of different alkyl acrylates. An advantage of such structure (in comparison to modification by alkyl acrylamides) could be relatively rapid enzymatic degradation of ester bond in the body and renal clearance of the metabolite. Even in pH neutral buffer (without enzymes), the degradation of ester bond proceeds relatively quickly (Figure 3b).

OEI shows relatively poor condensation of siRNA in salt buffers. The incorporation of short alkyl chains of low hydrophobicity (EA modification) leads to a decrease of binding affinity to siRNA. In the case of BA modifications, OEI-BA-5 was quite effective in complexation, whereas at higher modification degree (OEI-BA-10) led to loss of condensation ability of oligoamine. Most probably, such an effect is due to steric barrier between the charges of siRNA and OEI introduced by a bulky alkyl-β-propionate group. A similar trend could also be seen in the case of HA modified OEI. Nevertheless, due to stronger hydrophobic interactions this effect is generally suppressed for longer alkyl chains (HA and LA) and the stability of the polyplex structure increases remarkably.

Among all oligoamines, only BA and HA modifications could effectively induce the erythrocyte lysis. The formulations with BA modified OEI as well as OEI-HA-5 were, however, quite unstable against aggregation even in salt-free HBG buffer. On the basis of combination of these two parameters, OEI-HA-10 was the only effective oligoamine for siRNA delivery. All other potentially active formulations either precipitated during the preparation step or were not able to be internalized due to the large size of the polyplex particles. Surprisingly, oligoamines with long hydrophobic tails (LA) did not show any ability to lyse the cell membranes. Even OEI-LA-5, despite similar hydrophilic/hydrophobic balance as OEI-HA-10, was rather ineffective in erythrocyte lysis.

Due to strong lytic activity, OEI-HA-10 formulations were relatively toxic in vitro, which led to enhanced acute toxicity and lethality during in vivo applications (Nicole Tietze, EW, AZ; our unpublished observations). Co-formulation with different lipophilic agents (DOPC, DPPC, DOPE liposomes) was able to decrease the toxicity of the formulations in vitro. However, in most cases (except DOPE) these led to inactivation of the formulations. Additionally, the strongest decrease of the toxicity corresponded to the strongest inactivation of the formulations. The DOPE/OEI-HA-10 formulations were only slightly less toxic in comparison to OEI-HA-10 alone, which set certain restrictions for application of such formulations in vivo. The efficiency was, however, greatly improved. Due to inverse head−tail symmetry of DOPE lipid, it is known to destabilize the bilayer structure after incorporation into lipid membranes. The endosomolytic character of the DOPE lipid seems to be the reason for improved efficiency of DOPE/OEI-HA-10 formulations.

The most promising optimization procedure was a dilution of OEI-HA-10 in the formulation by far less toxic but ineffective oligoamines, OEI and OEI-LA-5. Gradual decrease of the OEI-HA-10 content in the formulations led to a strong decrease of cytotoxicity. Importantly, no decrease of the efficiency was observed even for formulations containing as low as 33% (weight % to total oligoamine content) of OEI-HA-10. The combination with OEI-LA-5 (as compared with unmodified OEI) shows the advantage of colloidal stabilization, which could be potentially important during translation of the system to in vivo. Incorporation of OEI to the polyplexes decreases both colloid stability and stability against dissociation, whereas OEI-LA-5 significantly increases colloidal stability (Supporting Information Figure 8; Supporting Information Table 2). Such an optimized formulation, if stable in the bloodstream, could potentially serve as an effective system for siRNA delivery in vivo with low toxicity.

CONCLUSION

Hydrophobic modification of low molecular weight OEI by alkyl acrylates could lead to efficient carriers for siRNA delivery. In particular, OEI modified by ten hexyl acrylates was the most promising delivery vector. Such a structure underwent fast degradation even in pH neutral buffer. The polyplex stability against dissociation and colloidal stability of the polyplex particles was remarkably improved through hydrophobic interactions between OEI chains. The lytic properties of such an oligoamine ensure effective intracellular transport across cellular membranes, presumably by promoting escape from the endosomes. In addition, different formulation strategies, including helper lipid-based and polymer-based modification, could greatly improve the biocompatibility and efficiency of the carrier. Overall, hydrophobically modified oligoamines and their co-formulations represent a promising siRNA delivery approach that warrants further investigation.

ACKNOWLEDGMENT

The financial support of the project by a grant from Abbott Laboratories, the German Research Foundation (DFG) SFB486 and Excellence Cluster Nanosystems Initiative Munich (NIM) is gratefully acknowledged.

Supporting Information Available: Figures: Determination of degradation rate of ester bonds (1); gel shift for the polyplexes of siRNA with different modified oligoamines (2); lysis of erythrocytes by different modified oligoamines (3); induction of luciferase knockdown (4−7); gel shift for the formulations of siRNA with the mixtures of oligoamines (8). Tables: particle sizes and zeta-potentials of polyplex particles. This material is available free of charge via the Internet at http://pubs.acs.org.

LITERATURE CITED

(1) Dykxhoorn, D. M., Novina, C. D., and Sharp, P. A. (2003) Killing the messenger: short RNAs that silence gene expression. *Nat. Rev. Mol. Cell Biol. 4*, 457–467.

(2) Novina, C. D., and Sharp, P. A. (2004) The RNAi revolution. *Nature 430*, 161–164.

(3) Tietze, N., Pelisek, J., Philipp, A., Roedl, W., Merdan, T., Tarcha, P., Ogris, M., and Wagner, E. (2008) Induction of apoptosis in murine neuroblastoma by systemic delivery of transferrin-shielded siRNA polyplexes for downregulation of Ran. *Oligonucleotides 18*, 161–174.

(4) Bolcato-Bellemin, A. L., Bonnet, M. E., Creusat, G., Erbacher, P., and Behr, J. P. (2007) Sticky overhangs enhance siRNA-mediated gene silencing. *Proc. Natl. Acad. Sci. U.S.A. 104*, 16050–16055.

(5) Zintchenko, A., Philipp, A., Dehshahri, A., and Wagner, E. (2008) Simple modifications of branched PEI lead to highly efficient siRNA carriers with low toxicity. *Bioconjugate Chem. 19*, 1448–1455.

(6) Werth, S., Urban-Klein, B., Dai, L., Hobel, S., Grzelinski, M., Bakowsky, U., Czubayko, F., and Aigner, A. (2006) A low molecular weight fraction of polyethylenimine (PEI) displays increased transfection efficiency of DNA and siRNA in fresh or lyophilized complexes. *J. Controlled Release 112*, 257–270.

(7) Urban-Klein, B., Werth, S., Abuharbeid, S., Czubayko, F., and Aigner, A. (2005) RNAi-mediated gene-targeting through systemic application of polyethylenimine (PEI)-complexed siRNA in vivo. *Gene Ther. 12*, 461–466.

(8) Tarcha, P. J., Pelisek, J., Merdan, T., Waters, J., Cheung, K., von Gersdorff, K., Culmsee, C., and Wagner, E. (2007) Synthesis and characterization of chemically condensed oligoethylenimine containing beta-aminopropionamide linkages for siRNA delivery. *Biomaterials 28*, 3731–3740.

(9) Hoon, J. J., Christensen, L. V., Yockman, J. W., Zhong, Z., Engbersen, J. F., Jong, K. W., Feijen, J., and Wan, K. S. (2007) Reducible poly(amido ethylenimine) directed to enhance RNA interference. *Biomaterials 28*, 1912–1917.

(10) Christensen, L. V., Chang, C. W., Kim, W. J., Kim, S. W., Zhong, Z., Lin, C., Engbersen, J. F., and Feijen, J. (2006) Reducible poly(amido ethylenimine)s designed for triggered intracellular gene delivery. *Bioconjugate Chem. 17*, 1233–1240.

(11) Meyer, M., Philipp, A., Oskuee, R., Schmidt, C., and Wagner, E. (2008) Breathing life into polycations: functionalization with pH-responsive endosomolytic peptides and polyethylene glycol enables siRNA delivery. *J. Am. Chem. Soc. 130*, 3272–3273.

(12) Rozema, D. B., Lewis, D. L., Wakefield, D. H., Wong, S. C., Klein, J. J., Roesch, P. L., Bertin, S. L., Reppen, T. W., Chu, Q., Blokhin, A. V., Hagstrom, J. E., and Wolff, J. A. (2007) Dynamic PolyConjugates for targeted in vivo delivery of siRNA to hepatocytes. *Proc. Natl. Acad. Sci. U.S.A. 104*, 12982–12987.

(13) Wakefield, D. H., Klein, J. J., Wolff, J. A., and Rozema, D. B. (2005) Membrane activity and transfection ability of amphipathic polycations as a function of alkyl group size. *Bioconjugate Chem. 16*, 1204–1208.

(14) Rozema, D. B., Ekena, K., Lewis, D. L., Loomis, A. G., and Wolff, J. A. (2003) Endosomolysis by masking of a membrane-active agent (EMMA) for cytoplasmic release of macromolecules. *Bioconjugate Chem. 14*, 51–57.

(15) Convertine, A. J., Benoit, D. S., Duvall, C. L., Hoffman, A. S., and Stayton, P. S. (2009) Development of a novel endosomolytic diblock copolymer for siRNA delivery. *J. Controlled Release 133*, 221–229.

(16) Ogris, M., Steinlein, P., Kursa, M., Mechtler, K., Kircheis, R., and Wagner, E. (1998) The size of DNA/transferrin-PEI complexes is an important factor for gene expression in cultured cells. *Gene Ther. 5*, 1425–1433.

(17) Oku, N., Yamazaki, Y., Matsuura, M., Sugiyama, M., Hasegawa, M., and Nango, M. (2001) A novel non-viral gene transfer system, polycation liposomes. *Adv. Drug Delivery Rev. 52*, 209–218.

(18) Matsuura, M., Yamazaki, Y., Sugiyama, M., Kondo, M., Ori, H., Nango, M., and Oku, N. (2003) Polycation liposome-mediated gene transfer in vivo. *Biochim. Biophys. Acta 1612*, 136–143.

(19) Akinc, A., Zumbuehl, A., Goldberg, M., Leshchiner, E. S., Busini, V., Hossain, N., Bacallado, S. A., Nguyen, D. N., Fuller, J., Alvarez, R., Borodovsky, A., Borland, T., Constien, R., de Fougerolles, A., Dorkin, J. R., Narayanannair, J. K., Jayaraman, M., John, M., Koteliansky, V., Manoharan, M., Nechev, L., Qin, J., Racie, T., Raitcheva, D., Rajeev, K. G., Sah, D. W., Soutschek, J., Toudjarska, I., Vornlocher, H. P., Zimmermann, T. S., Langer, R., and Anderson, D. G. (2008) A combinatorial library of lipid-like materials for delivery of RNAi therapeutics. *Nat. Biotechnol. 26*, 561–569.

(20) Li, S., and Huang, L. (1997) In vivo gene transfer via intravenous administration of cationic lipid-protamine-DNA (LPD) complexes. *Gene Ther. 4*, 891–900.

(21) Chono, S., Li, S. D., Conwell, C. C., and Huang, L. (2008) An efficient and low immunostimulatory nanoparticle formulation for systemic siRNA delivery to the tumor. *J. Controlled Release 131*, 64–69.

(22) Saul, J. M., Wang, C. K., Ng, C. P., and Pun, S. H. (2008) Multilayer nanocomplexes of polymer and DNA exhibit enhanced gene delivery. *Adv. Mater. 20*, 19–25.

(23) Kabanov, A., Zhu, J., and Alakhov, V. (2005) Pluronic block copolymers for gene delivery. *Adv. Genet. 53*, 231–261.

(24) Fischer, D., Bieber, T., Li, Y., Elsasser, H. P., and Kissel, T. (1999) A novel non-viral vector for DNA delivery based on low molecular weight, branched polyethylenimine: effect of molecular weight on transfection efficiency and cytotoxicity. *Pharm. Res. 16*, 1273–1279.

(25) Ahn, C. H., Chae, S. Y., Bae, Y. H., and Kim, S. W. (2002) Biodegradable poly(ethylenimine) for plasmid DNA delivery. *J. Controlled Release 80*, 273–282.

(26) Frank-Kamenetsky, M., Grefhorst, A., Anderson, N. N., Racie, T. S., Bramlage, B., Akinc, A., Butler, D., Charisse, K., Dorkin, R., Fan, Y., Gamba-Vitalo, C., Hadwiger, P., Jayaraman, M., John, M., Jayaprakash, K. N., Maier, M., Nechev, L., Rajeev, K. G., Read, T., Rohl, I., Soutschek, J., Tan, P., Wong, J., Wang, G., Zimmermann, T., de Fougerolles, A., Vornlocher, H. P., Langer, R., Anderson, D. G., Manoharan, M., Koteliansky, V., Horton, J. D., and Fitzgerald, K. (2008) Therapeutic RNAi targeting PCSK9 acutely lowers plasma cholesterol in rodents and LDL cholesterol in nonhuman primates. *Proc. Natl. Acad. Sci. U.S.A. 105*, 11915–11920.

(27) Kim, W. J., Chang, C. W., Lee, M., and Kim, S. W. (2007) Efficient siRNA delivery using water soluble lipopolymer for anti-angiogenic gene therapy. *J. Controlled Release 118*, 357–363.

BC9001536

Hydrophobically Modified Oligoethylenimines as Highly Efficient Transfection Agents for siRNA Delivery

Alexander Philipp[1], Xiaobin Zhao[2], Peter Tarcha[2], Ernst Wagner[1], Arkadi Zintchenko[1†]

[1]Center for Drug Research, Department of Pharmacy, Pharmaceutical Biology-Biotechnology, and Center for NanoScience (CeNS), Ludwig-Maximilians-University, Butenandstr. 5-13, D-81377 Munich, Germany

[2]Department of Advanced Drug Delivery, Abbott Laboratories, D-R43D, AP31-2, 200 Abbott Park Rd, Abbott Park, North Chicago, IL 60064, USA

Supporting Information

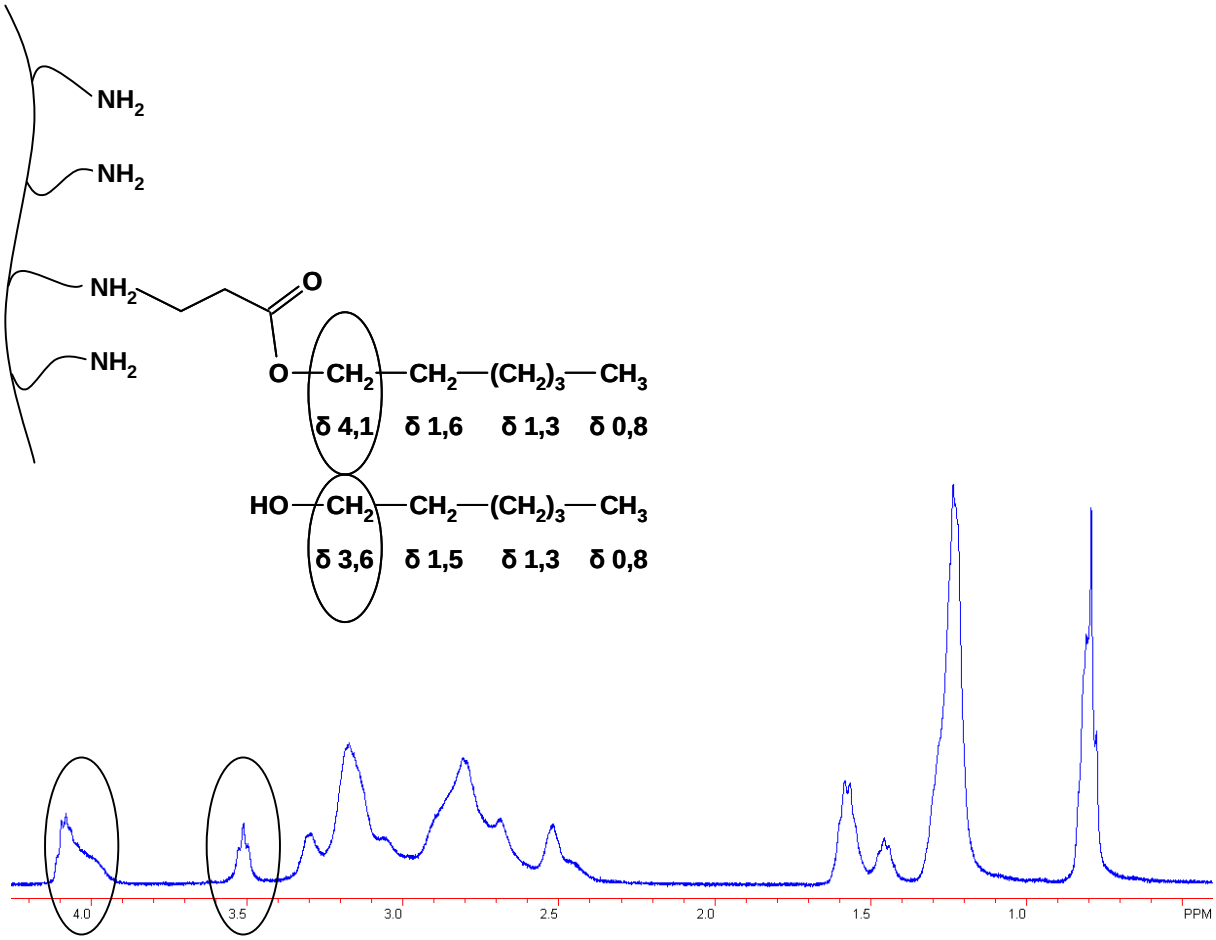

SI-Fig.1 ^{1}H-NMR of degradation product of OEI-HA-10 after 3 days incubation at 37 °C in aqueous medium at pH 7.

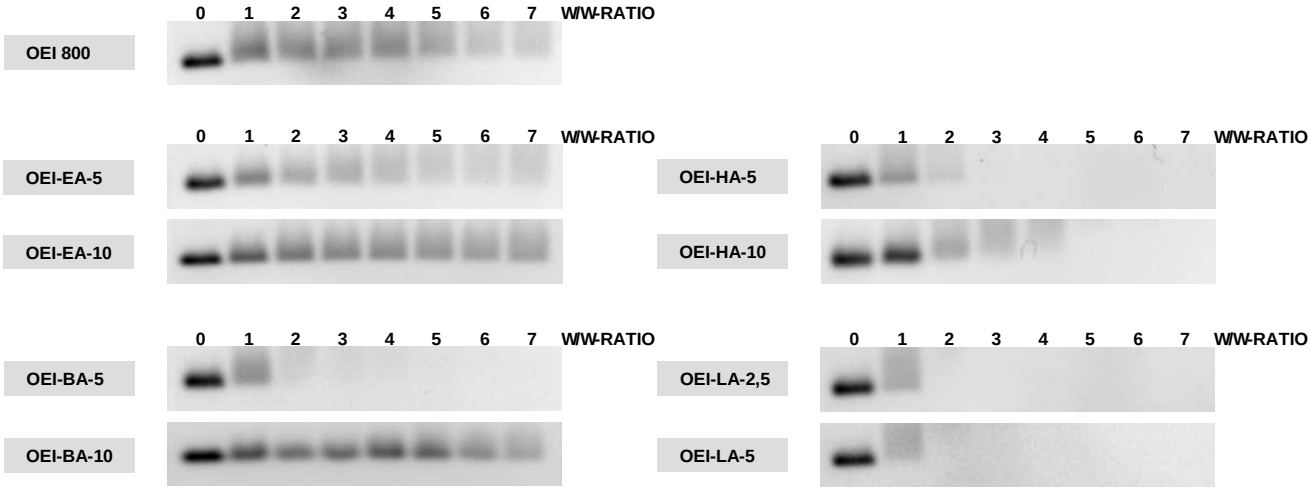

SI-Fig.2 Gel shift for the polyplexes of siRNA with different modified oligoamines. The numbers represent oligoamine/siRNA mixing ratio w/w.

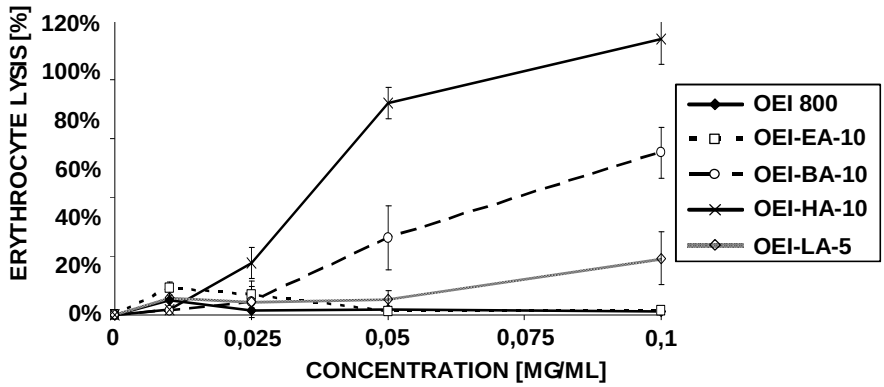

SI-Fig.3 Lysis of erythrocytes by different modified oligoamines. Freshly collected murine erythrocytes were incubated with increasing concentrations of polymer and haemolysis was determined by UV measurement (λ = 405 nm) relative to Triton X (100 % lysis).

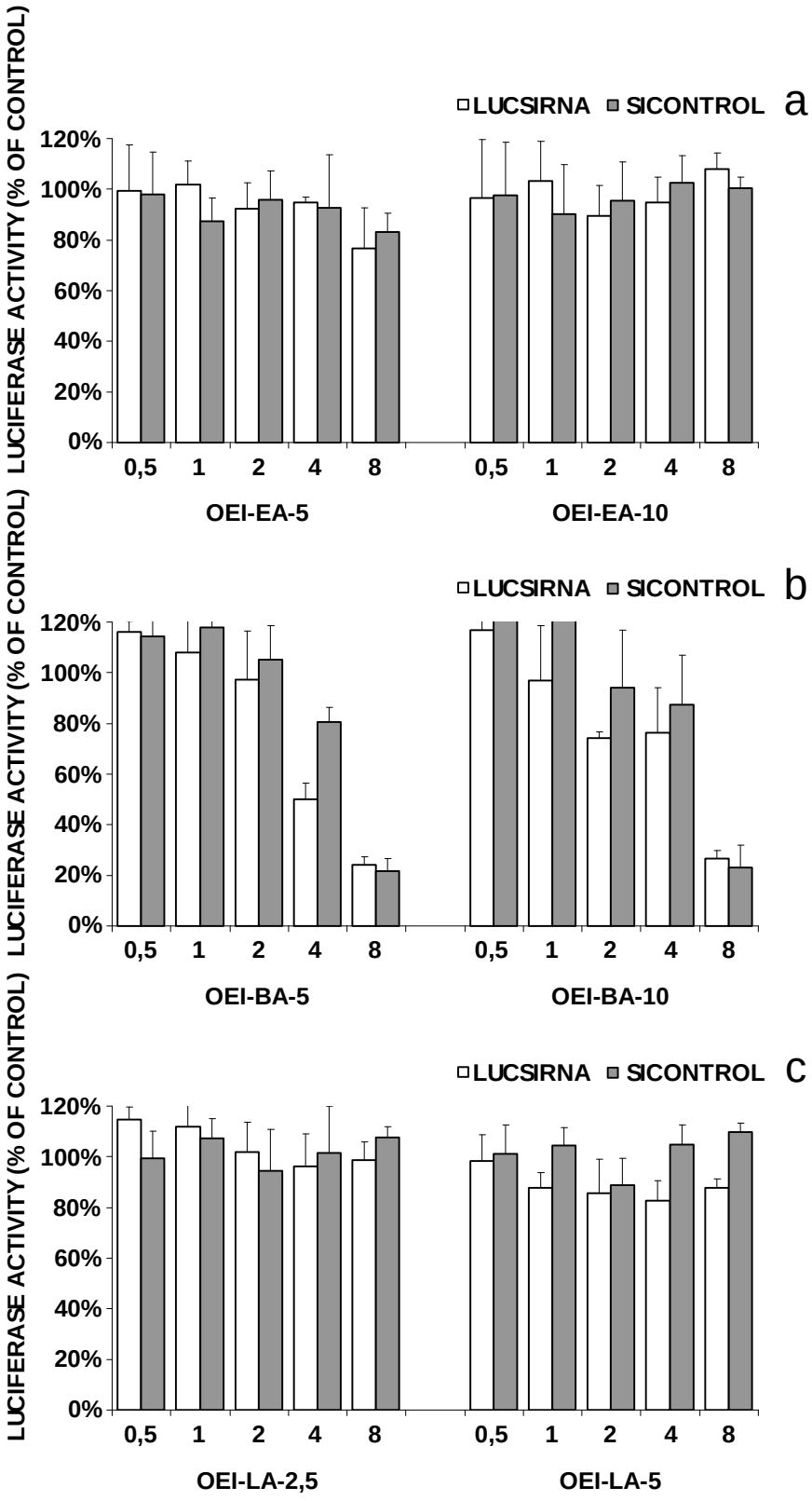

SI-Fig.4 Induction of luciferase knockdown by siRNA formulations with different modified oligoamines in Neuro2A/EGFPLuc cells. a) EA-modifications, b) BA-modifications, c) LA-modifications. White bars - LucsiRNA, Black bars - siCONTROL. The numbers on the x-axis represent the mixing ratio oligoamine/siRNA (w/w) in the formulation.

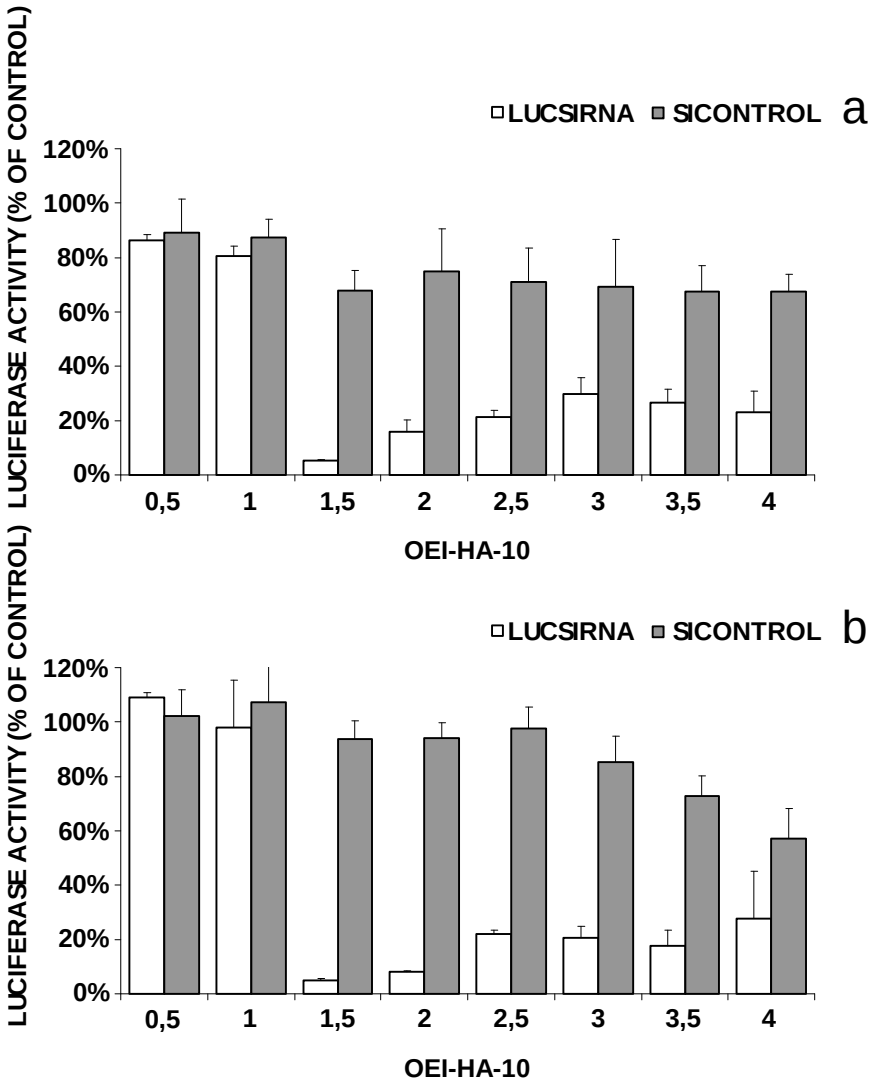

SI-Fig.5 Induction of luciferase knockdown by OEI-HA-10/siRNA formulations in a) H1299/Luc and b) HUH7/EGFPLuc cells. White bars - LucsiRNA, Black bars - siCONTROL. The numbers on the x-axis represent the mixing ratio OEI-HA-10/siRNA (w/w) in the formulation.

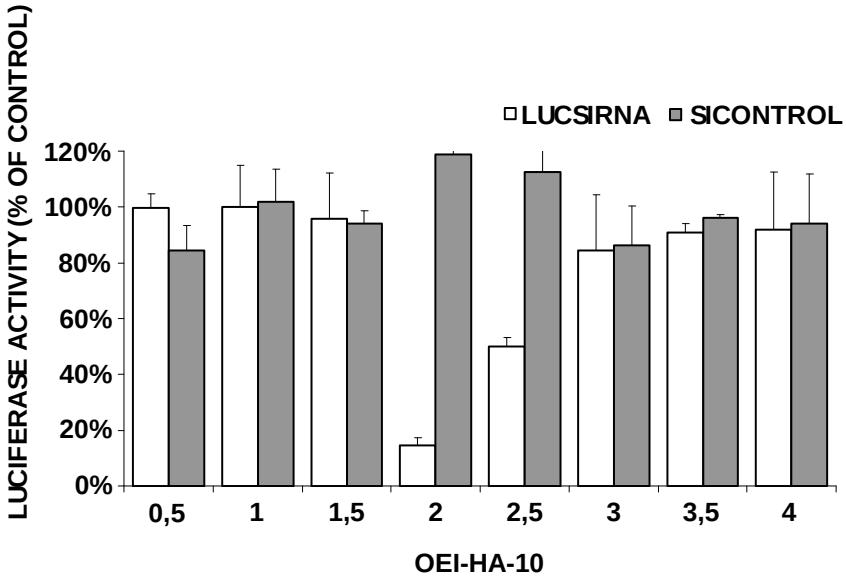

SI-Fig.6 Induction of luciferase knockdown by OEI-HA-10/siRNA formulations in Neuro2A/EGFPLuc cells in the presence of 50 % serum in the medium. White bars - LucsiRNA, Black bars - siCONTROL. The numbers on the x-axis represent the mixing ratio OEI-HA-10/siRNA (w/w) in the formulation.

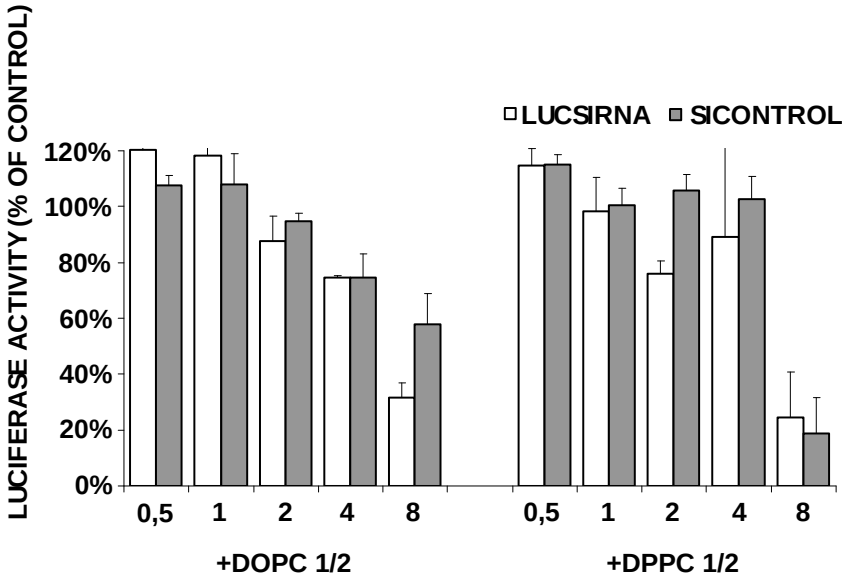

SI-Fig.7 Induction of luciferase knockdown by DOPC/OEI-HA-10/siRNA or DPPC/OEI-HA-10/siRNA formulations in Neuro2A/EGFPLuc cells. White bars - LucsiRNA, Black bars - siCONTROL. The numbers on the x-axis represent the mixing ratio OEI-HA-10/siRNA (w/w) in the formulation. The OEI-HA-10/lipid ratio was 1/2 as indicated under x-axis.

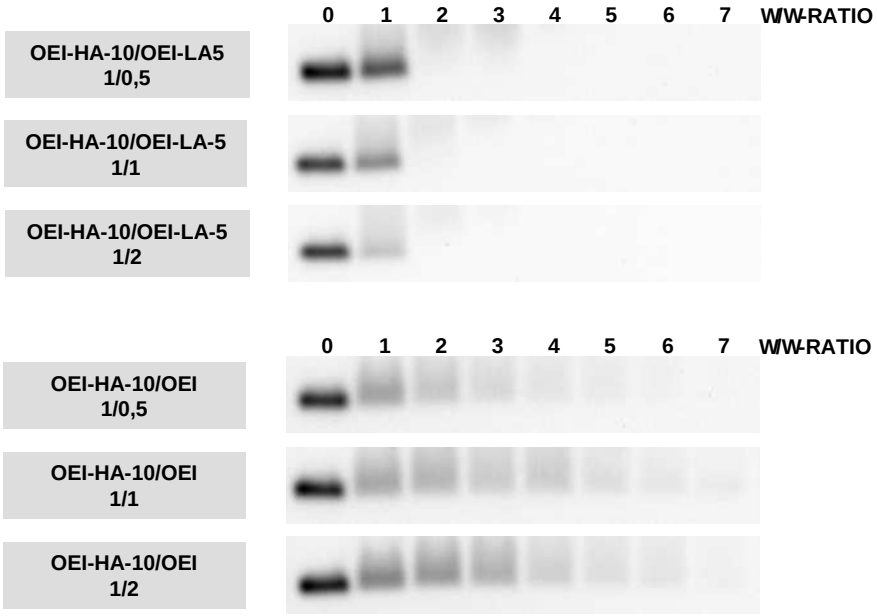

SI-Fig.8 Gel shift for the formulations of siRNA with the mixtures of oligoamines: OEI-HA-10/OEI-LA-5 (upper panel), and OEI-HA-10/OEI (lower panel). The numbers represent oligoamine/siRNA mixing ratio w/w.

SI-Table1 Particle sizes and zeta-potentials of polyplex particles for the formulations with modified OEI.

FORMULATION	W/W	MEAN DIAMETER [NM]	ZETA-POTENTIAL [MV]
OEI-EA-5	2/1	n.a.	7,2 ± 0,7
	4/1	n.a.	10,6 ± 1,0
OEI-EA-10	2/1	n.a.	-4,4 ± 0,6
	4/1	n.a.	-1,0 ± 0,3
OEI-BA-5	2/1	902 ± 15	16,5 ± 0,2
	4/1	n.a.	7,9 ± 1,7
OEI-BA-10	2/1	n.a.	-30,6 ± 3,7
	4/1	n.a.	-29,1 ± 0,8
OEI-HA-5	2/1	580 ± 10	12,9 ± 0,2
	4/1	208 ± 2	22,9 ± 0,4
OEI-HA-10	2/1	171 ± 2	21,0 ± 0,3
	4/1	194 ± 3	25,0 ± 1,8
OEI-LA-2,5	2/1	238 ± 4	8,4 ± 0,8
	4/1	136 ± 4	29,2 ± 1,0
OEI-LA-5	2/1	137 ± 2	40,9 ± 1,2
	4/1	119 ± 2	42,3 ± 1,6

n.a. not available due to low count rate

SI-Table2 Colloidal stability of polyplex particles for OEI-HA-10, OEI-LA-5 and OEI-HA-10/OEI-LA-5 formulations.

FORMULATION	W/W	MEAN DIAMETER [NM]				ZETA-POTENTIAL [MV]			
		T = 0	T = 2H	T = 4H	T = 24H	T = 0	T = 2H	T = 4H	T = 24H
OEI-HA-10	2/1	223 ± 4	292 ± 14	272 ± 9	638 ± 17	18,0 ± 0,6	18,1 ± 0,9	17,9 ± 0,5	12,3 ± 0,2
	4/1	119 ± 1	116 ± 1	152 ± 1	229 ± 7	24,2 ± 1,2	26,4 ± 3,4	28,0 ± 0,4	20,5 ± 1,1
OEI-LA-5	2/1	122 ± 1	243 ± 4	168 ± 3	139 ± 2	36,7 ± 1,0	38,5 ± 2,4	42,1 ± 1,2	26,4 ± 1,9
	4/1	125 ± 4	197 ± 2	129 ± 1	148 ± 1	40,8 ± 0,8	40,6 ± 0,8	35,9 ± 1,2	31,0 ± 0,8
OEI-HA-10/OEI-LA-5 1/0,5	2/1	162 ± 2	215 ± 3	157 ± 2	183 ± 3	33,6 ± 1,3	29,3 ± 0,5	28,4 ± 2,5	25,6 ± 1,0
	4/1	137 ± 1	125 ± 1	108 ± 3	174 ± 2	34,6 ± 1,5	30,8 ± 3,0	31,4 ± 1,2	33,2 ± 1,5
OEI-HA-10/OEI-LA-5 1/1	2/1	154 ± 5	132 ± 2	185 ± 4	145 ± 2	30,6 ± 1,2	26,2 ± 1,6	34,4 ± 0,6	28,9 ± 0,9
	4/1	128 ± 3	133 ± 1	176 ± 3	139 ± 1	41,1 ± 0,2	39,1 ± 1,9	35,8 ± 2,0	34,0 ± 3,7
OEI-HA-10/OEI-LA-5 1/2	2/1	131 ± 1	129 ± 1	137 ± 1	151 ± 1	38,5 ± 0,6	34,8 ± 2,2	38,0 ± 3,3	37,3 ± 1,4
	4/1	145 ± 4	134 ± 1	194 ± 3	145 ± 4	40,6 ± 2,1	36,5 ± 1,6	39,6 ± 0,6	39,1 ± 1,6

Extension Arm Facilitated Pegylation of αα-Hemoglobin with Modifications Targeted Exclusively to Amino Groups: Functional and Structural Advantages of Free Cys-93(*β*) in the PEG-Hb Adduct

Dongxia Li,[†,‡] Tao Hu,[†,‡] Belur N. Manjula,[‡] and Seetharama A. Acharya*[,‡,§]

Departments of Physiology and Biophysics, and of Medicine, Albert Einstein College of Medicine, Bronx, New York 10461.
Received April 14, 2009; Revised Manuscript Received August 30, 2009

Cys-93(*β*) of hemoglobin (Hb) was reversibly protected as a mixed disulfide with thiopyridine during extension arm facilitated (EAF) PEGylation and its influence on the structural and functional properties of the EAF-PEG-Hb has been investigated. Avoiding PEGylation of Cys-93(*β*) in the EAF-PEG-Hb lowers the level of perturbation of heme pocket, α1*β*2 interface, autoxidation, heme loss, and the O_2 affinity, as compared to the EAF-PEG-Hb with PEGylation of Cys-93(*β*).The structural and functional advantages of reversible protection of Cys-93(*β*) during EAF PEGylation of oxy-Hb has been compared with Euro PEG-Hb generated by EAF PEGylation of deoxy Hb where Cys-93(*β*) is free in the final product. The αα-fumaryl cross-linking and EAF PEGylation targeted exclusively to Lys residues has been combined together for generation of second-generation EAF-PEG-Hb with lower oxygen affinity. The PEG chains engineered on Lys as well as PEGylation of Cys-93(*β*) independently contribute to the stabilization of oxy conformation of Hb and hence increase the oxygen affinity of Hb. However, oxygen affinity of the EAF-PEG-αα-Hb is more sensitive to the presence of PEGylation on Cys-93(*β*) than that of the EAF-PEG-Hb. The present modified EAF PEGylation platform is expected to facilitate the design of novel versions of the EAF-PEG-Hbs that can now integrate the advantages of avoiding PEGylation of Cys-93(*β*).

INTRODUCTION

PEGylation, conjugation with polyethylene glycol (PEG[1]) chains, can improve the therapeutic potentials of peptides and proteins by camouflaging the immune system and diminishing the *in vivo* glomerular filtration (*1*−*3*). Recently, PEGylation of hemoglobin (Hb) has emerged as a novel chemical approach to neutralize the vasoactivity of acellular Hb, a major obstacle for its therapeutic application as Hb based oxygen carriers (HBOC) (*4, 5*). The PEGylated bovine Hb developed by Enzon Inc. (*6*) is one of the early PEG-Hbs and carries ten copies of PEG-5K chain per tetramer on amino groups (*7*). Another PEGylation protocol, extension arm facilitated (EAF) PEGylation (*8*−*11*), has been developed by us recently. The 2-iminothiolane (IT), an internally cyclized form of *δ*-mercapto butyrimidate, is used to introduce *δ*-mercapto butirimidyl chain on the *ε*-amino groups of Hb. The newly engineered thiol group is then PEGylated using PEG maleimide.

The hexaPEGylated Hb, $(SP\text{-}PEG5K)_6$-Hb generated by the EAF PEGylation, has served as the model molecule to develop MP4 (a hexa-PEG-Hb at 4 g/dL) that is in phase III clinical trial. $(SP\text{-}PEG5K)_6$-Hb carries four PEG-5K chains on the extrinsic thiol groups engineered on the *ε*-amino groups and two on the intrinsic thiols of two Cys-93(*β*) residues of Hb. Thus, EAF PEGylation of oxy Hb introduces two PEG-5K chains by direct PEGylation of Cys-93(*β*) (i.e., without an extension arm). Cys-93(*β*) is located ∼1.4 nm from the heme and is adjacent to proximal His-92(*β*) that coordinates to the center iron of a heme (*12*). Proton NMR spectra has shown that chemical modification of Cys-93(*β*) significantly influences the heme pocket of the *β* chain (*13*). $(SP\text{-}PEG5K)_2$-Hb, a Hb derivative with PEGylation exclusively on Cys-93(*β*), shows a change in the Fe-proximal His residue stretching frequency (*14*). Manjula et al. (*15*) reported that $(SP\text{-}PEG5K)_2$-Hb exhibits a higher oxygen affinity and a lower Hill coefficient than Hb. PEGylation of Cys-93(*β*) also enhanced the autoxidation rate and the rate of heme loss from metHb (*16*). Thus, PEGylation of Cys-93(*β*) unfavorably influences the structural and functional properties of Hb. These unfavorable structural and functional changes could be minimized or eliminated in the EAF-PEG-Hb by avoiding PEGylation of Cys-93(*β*).

The high oxygen affinity of $(SP\text{-}PEG5K)_6$-Hb was one of the attractive features for Sangart in developing MP4. The high oxygen affinity is expected to achieve a targeted O_2 delivery *in vivo* to the hypoxic regions (*7*). The high O_2 affinity is also expected to minimize the O_2 unloading on the arterial side of circulation and thus reduce the possible vasoactivity that is induced through antoregulatory mechanism. Though high O_2 affinity of the EAF-PEG-Hb has been attributed to the PEGylation of Cys-93(*β*) initially (*15*), the EAF PEGylation of rHb[Cys-93(*β*)→Ala] suggested that the high O_2 affinity of the

* Address correspondence to Seetharama A. Acharya, Albert Einstein College of Medicine, 1300 Morris Park Avenue, Bronx, NY 10461, Tel: 1-718-430-2133; Fax: 1-718-430-8819; E-mail: acharya@aecom.yu.edu.

† The authors make same contribution on the work.

‡ Department of Physiology and Biophysics.

§ Department of Medicine.

[1]ABBREVIATIONS: Hb, hemoglobin; PEG, polyethylene glycol; PEGylation, conjugation with polyethylene glycol; EAF, extension arm facilitated; PEG-Hb, the PEGylated hemoglobin; αα-Hb, αα-fumaryl cross-linked hemoglobin; PEG-αα-Hb, the PEGylated αα-Hb; PBS, phosphate buffered saline; TFA, trifluoroacetic acid; K_d, the dissociation constant; HBOC, hemoglobin based oxygen carrier; P_{50}, partial oxygen pressure at half saturation; SEC, size exclusion chromatography; RP-HPLC, reverse phase high performance liquid chromatography; CD, circular dichroism; *n*, Hill coefficient; 2,3-DPG, 2,3-diphosphoglycerate; 4-PDS, 4,4′-dithiopyridine; IT, 2-iminothiolane; TCEP, Tris(2-carboxyethyl) phosphine; NEM, *N*-ethyl maleimide; k_{ox}, the first-order autoxidation rate constant; HSA, human serum albumin; k_{fast}, the rate constant for the fast phase of heme loss.

10.1021/bc900170e CCC: $40.75 © 2009 American Chemical Society
Published on Web 10/20/2009

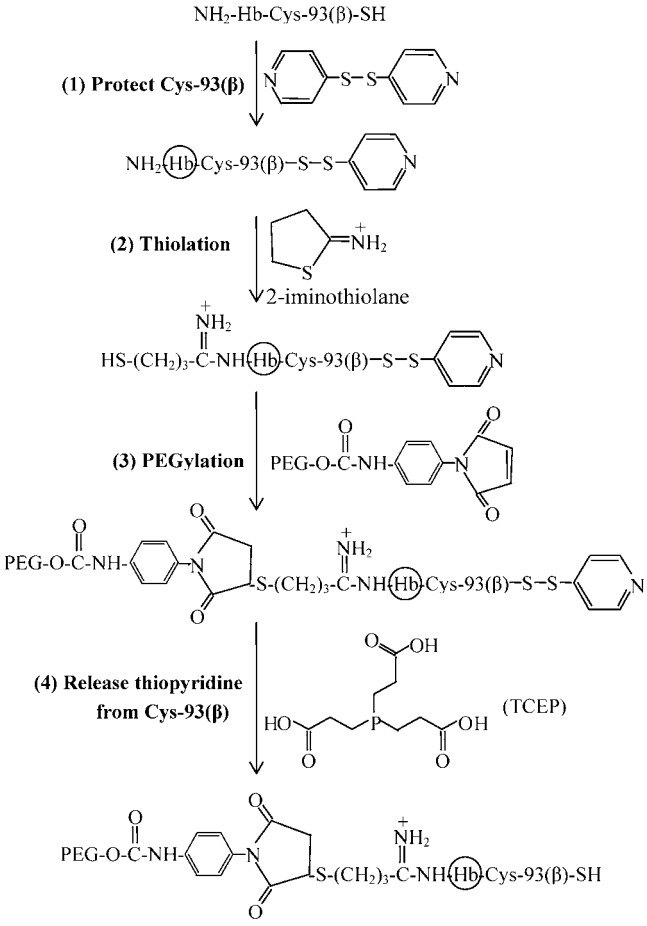

Figure 1. Schematic representation of the extension arm facilitated PEGylation of Hb with reversible protection of Cys-93(β).

EAF-PEG-Hb is an intrinsic aspect of the PEG-Hb and is presumably a consequence of the hydrated PEG-shell around Hb (*10*).

Recent studies have suggested that the O_2 affinity of the PEG-Hb may have to be lower than that of MP4 to achieve an efficient tissue oxygenation (*17*). The high oxygen affinity of the EAF-PEG-Hb represents the synergistic effects of EAF PEGylation at the amino groups and the direct PEGylation at Cys-93(β). Avoiding the direct PEGylation of Cys-93(β) may be necessary to generate the PEG-Hb with an O_2 affinity lower than the ones in the current version of the EAF-PEG-Hb. EAF PEGylation of deoxy Hb is an approach that can protect Cys-93(β) from PEGylation (*9, 36*). Reversible protection of Cys-93(β) during EAF PEGylation of oxy-Hb is an alternative approach developed in the present study.

EAF PEGylation platform has been modified here by designing reversible protection of Cys-93(β). Briefly, the thiol group of Cys-93(β) of oxy-Hb is converted to a mixed disulfide form by reaction with 4,4′-dithiopyridine (4-PDS), followed by EAF PEGylation of the modified Hb and the release of the thiopyridyl group using Tris(2-carboxy-ethyl) phosphine (TCEP) (Figure 1). A low oxygen affinity Hb, $\alpha\alpha$-fumaryl cross-linked Hb ($\alpha\alpha$-Hb), was also EAF PEGylated with protection of Cys-93(β) in order to generate a PEG-Hb with lower oxygen affinity. The influence of avoiding the PEGylation of Cys-93(β) on the generation of a doubly modified Hb ($\alpha\alpha$-cross-linking and EAF-PEGylation) has also been investigated. This modified EAF PEGylation platform is expected to integrate the structural and functional advantages of protection of Cys-93(β) in the EAF-PEG-Hbs.

EXPERIMENTAL PROCEDURES

Preparation of the PEG-Hbs. Human adult hemoglobin (HbA) was purified from human erythrocytes as previously described (*18*). $\alpha\alpha$-Hb was prepared as previously described (*19*). The conditions for EAF PEGylation were slightly modified from Manjula et al. (*9*). Briefly, HbA or $\alpha\alpha$-Hb at 1.0 mM (tetramer) was reacted with 10 mM maleimide phenyl-PEG5K (Malphe-PEG5K, Bioaffinity Inc., Rockford, IL) or 10 mM *N*-ethyl maleimide (NEM) in the presence of 5 mM IT in PBS buffer (pH 7.4) at 4 °C for 4 h. The resultant products are dialyzed extensively against PBS buffer (pH 7.4). For removal of free PEG, the sample was centrifuged at 6000 *g* using Centricon with 50 K cutoff membrane (Millipore) five times. The retentate was stored at −80 °C.

Preparation of the PEG-Hbs with Reversible Protection of Cys-93(β). HbA or $\alpha\alpha$-Hb at 0.25 mM (tetramer) was reacted with 5 mM 4-PDS in PBS buffer (pH 7.4) at 4 °C for 1 h. The resultant samples were dialyzed extensively against PBS buffer (pH 7.4). The absence of 4-PDS was confirmed by adding excess TCEP that did not change the absorbance at 324 nm as compared to the control. The concentrated modified Hb (1 mM as tetramer) was reacted with 10 mM Malphe-PEG5K or 10 mM NEM in the presence of 5 mM IT in PBS buffer (pH 7.4) at 4 °C for 4 h. NEM was added to terminate the reaction. The resultant samples were centrifuged at 6000 *g* using Centricon with 50 K cutoff membrane five times to remove excess free PEG. A large excess of TCEP is added to release the thiopyridyl moiety from the disulfide moiety. For removal of TCEP, the sample was centrifuged at 6000 *g* using Centricon with 50 K cutoff membrane five times. The retentate was stored at −80 °C.

Analytical Methods. Size exclusion chromatography (SEC) analysis was carried out on two Superose 12 columns (GE Healthcare, 1 × 31 cm^2) in series at room temperature. The columns were equilibrated and eluted with PBS buffer (pH 7.4) at a flow rate of 0.5 mL/min. Reverse-phase HPLC analysis was carried out on a Vydac C4 column (4.6 × 250 mm^2). The sample was eluted using a linear gradient of 35−50% acetonitrile containing 0.1% TFA in 100 min and then 50−70% acetonitrile containing 0.1% trifluoroacetic acid (TFA) in 30 min at a flow rate of 1.0 mL/min. SDS-PAGE analysis was carried out on a precast 14% tris-glycine gel (Invitrogen Inc.). Molecular radius of the Hb samples (1 mg/mL) was measured using a dynamic light scattering instrument (DynaPro, Protein Solutions, Lakewood, NJ).

Autoxidation Experiments. Autoxidation studies of the PEG-Hb are carried out by incubating the Hb samples at 25 μM (1.6 mg/mL in tetramers) in PBS buffer (pH 7.4) plus 0.3 mM EDTA in sealed tubes at 37 °C. Aliquots of the sample were taken out at various time intervals. The first-order autoxidation rate constant (k_{ox}) of the Hb sample was measured and calculated as in the method by Hu et al. (*16*). The PEG-Hbs (40 mg/mL) in PBS (pH 7.4) were mixed with the bovine plasma (Sigma) at a volume ratio of 1:1. These diluted samples were used to simulate 50% exchange transfusion of the blood volume. The percentage of plasma metHb was measured as previously described (*16*).

Heme Exchange Experiment. Heme exchange rate between metHb and human serum albumin (HSA) (Sigma) was measured as previously described (*20, 21*). MetHb was formed by reaction of oxyHb with potassium ferricyanide (*22*). The ferro- and ferricyanide were removed by passing the reaction mixture through a Sephadex G-25 column in 50 mM BisTris-Ac buffer (pH 7.5) containing 0.1 M NaCl. The heme exchange reaction was measured as in the method of Hu et al. (*16*).

Tetramer−Dimer Dissociation Constant. Tetramer−dimer dissociation constant (K_d) of the PEG-Hbs was measured essentially as Manning et al. (*23*). Briefly, Hb samples in PBS

buffer (pH 7.4) were diluted to a series of Hb concentrations and subjected to two Superose 12 columns (1 × 31 cm^2) in series. The columns were equilibrated and eluted with PBS buffer (pH 7.4) at the flow rate of 0.5 mL/min. αα-Hb was set as the tetramers for HbA. The PEG-αα-Hbs were set as the tetramers for the PEG-Hbs. The Hb samples in the presence of PBS buffer containing 0.9 M $MgCl_2$ were set as the dimers.

Circular Dichroism Spectroscopy. Circular dichroism (CD) spectra of the Hb samples were recorded on a JASCO-J815 spectropolarimeter (JASCO, Tokyo, Japan) at 25 °C with a 0.2 cm light path cuvette (310 μL). For the CD spectra from 250 to 200 nm, the Hb concentration was 1.3 μM as tetramer. For the CD spectra from 480 to 250 nm, the Hb concentration was 26.0 μM as tetramer. All the Hb samples were in PBS buffer, pH 7.4. The molar ellipticity (θ) is expressed in deg.cm^2/dmol on a heme basis.

Front-Face Fluorescence Measurements. Intrinsic front-face fluorescence measurements of the Hb samples were performed using a Shimadzu RF-5301 spectrofluorimeter at room temperature. The emission spectra were recorded from 300 to 350 nm using an excitation wavelength of 280 nm. Excitation and emission slit widths were both 5 nm. All the samples used were at Hb concentration of 6.0 mg/mL in PBS, pH 7.4. Cuvette with 1 cm path-length was used.

Oxygen Affinity Measurements. Oxygen equilibrium measurements of the Hb samples were carried out using Hem-O-Scan (Aminco) at 37 °C in PBS buffer (pH 7.4). Triplicate measurements for each sample were performed to obtain the averaged values of P_{50} (oxygen affinity) and Hill coefficient (n). The Hb samples were at Hb concentration of 0.5 mM as tetramer in the presence and the absence of 2.5 mM 2,3-DPG.

RESULTS

EAF PEGylation of Un-Cross-Linked Hb with Protection of Cys-93(β). *Size Exclusion Chromatographic Analysis of the PEG-Hbs.* The SEC pattern of the PEG-Hbs is presented in Figure 2A. The elution position of the PEG-Hb (curve c) is earlier than that of HbA (curve a). The elution pattern of the PEGylated bisthiopyridyl Hb (curve d) is slightly right-shifted and exhibits some asymmetry on the descending side of the peak. This is presumably due to the absence of PEGylation on Cys-93(β). Moreover, the elution pattern shows a small peak at the position of Hb, reflecting the presence of minor unPEGylated thiopyridyl Hb. The elution pattern shows no noticeable changes upon releasing the thiopyridyl group from Cys-93(β) (curve e).

Characterization of the PEG-Hb with Protection of Cys-93(β). *RP-HPLC Analysis of the PEG-Hbs.* RP-HPLC analysis of the PEG-Hbs is shown in Figure 3A. The HPLC pattern of Hb shows two peaks corresponding to β and α globin chains (curve a). Upon EAF PEGylation, the two globin chains decrease significantly, along with generation of one major and two minor elution peaks (curve b). These new peaks were estimated to correspond to the mono-, di-, and tri-PEGylated globin chains, according to the procedure by Hu et al. (*24*). The preferential PEGylation at β chain is apparently due to the efficient PEGylation at Cys-93(β). Since the absorbance of the PEG chains at 210 nm is very weak, the absorbance at 210 nm essentially detects the globin chains. Accordingly, the EAF-PEG-Hb has been calculated to carry ~5.7 PEG-5K chains per tetramer. The pattern of the PEGylated bisthiopyridyl Hb (curve c) shows minor thiopyridyl β-globin and unmodified α-globin, along with three new peaks. The peak for the monoPEGylated globin is asymmetrical and becomes symmetrical upon releasing the thiopyridyl moiety (curve d). This PEG-Hb was calculated to carry ~5.0 PEG-5K chains per tetramer. It should be mentioned that the sum of peak areas in the HPLC pattern of the individual samples are taken as 100% for calculating the level of PEGylation in the respective PEG-Hbs.

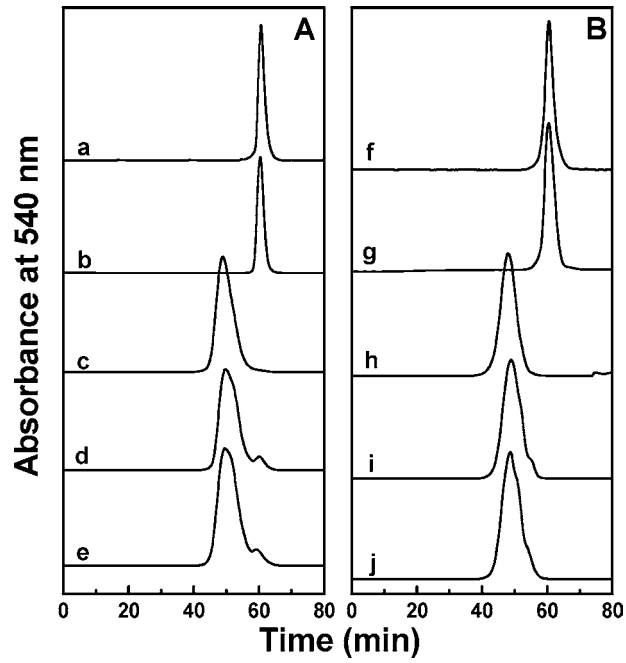

Figure 2. Size exclusion chromatography analysis of the PEG-Hb (A) and the PEG-αα-Hb (B). (a) HbA; (b) the bisthiopyridyl Hb; (c) the PEG-Hb without protection of Cys-93(β); (d) the PEGylated bisthiopyridyl Hb; (e) the PEG-Hb with free Cys-93(β); (f) αα-Hb; (g) the bisthiopyridyl αα-Hb; (h) the PEG-αα-Hb; (i) the PEGylated bisthiopyridyl αα-Hb; (j) the PEG-αα-Hb with free Cys-93(β). All samples were loaded on two HR10/30 Superose 12 columns at room temperature. The column was eluted with PBS, pH 7.4, at 0.5 mL/min.

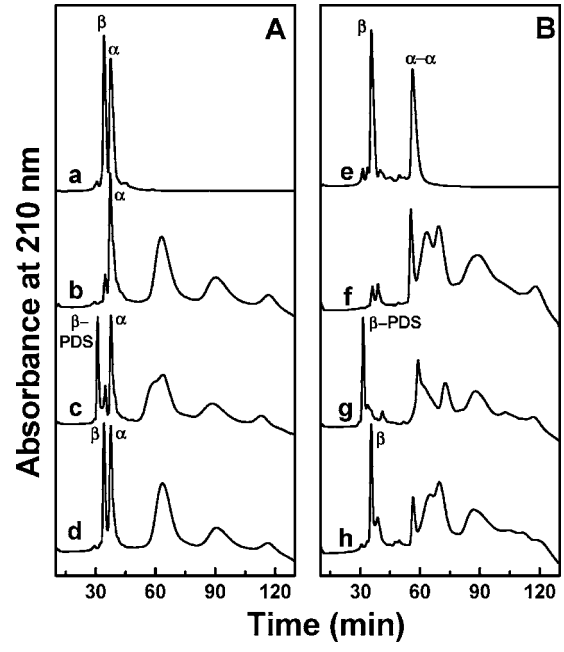

Figure 3. RP-HPLC analysis of the PEG-Hb (A) and the PEG-αα-Hb (B). (a) HbA; (b) the PEG-Hb; (c) the PEGylated bisthiopyridyl Hb; (d) the PEG-Hb with free Cys-93(β); (e) αα-Hb; (f) the PEG-αα-Hb; (g) the PEGylated bisthiopyridyl αα-Hb; (h) the PEG-αα-Hb with free Cys-93(β). The samples were loaded on a Vydac C4 column (0.46 × 25 cm^2). The column was eluted with a linear gradient of 35−50% acetonitrile containing 0.1% TFA in 100 min, followed by 50−70% acetonitrile containing 0.1% TFA in 30 min at 1.0 mL/min.

SDS-PAGE Analysis of the PEG-Hbs. The SDS-PAGE pattern of HbA shows a doublet band corresponding to α and β globin

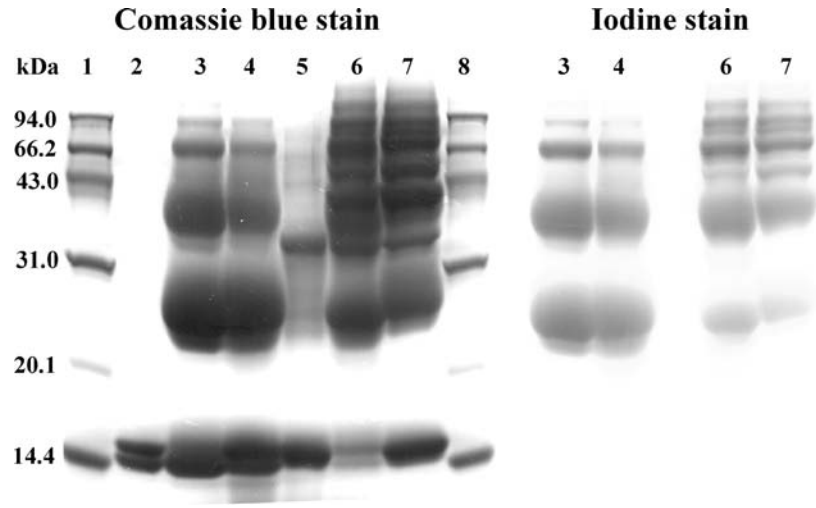

Figure 4. SDS-PAGE analysis of the PEG-Hbs and the PEG-αα-Hb. SDS-PAGE was carried out on a precast 14% Tris-glycine gel from the Invitrogen Corporation. Lanes 1 and 8, the molecular weight markers; lane 2, HbA; lane 3, the PEG-Hb; lane 4, the PEG-Hb with free Cys-93(β); lane 5, αα-Hb; lane 6, the PEG-αα-Hb; lane 7, the PEG-αα-Hb with free Cys-93(β). Proteins were identified by Coomassie blue staining. The PEG chain was detected by iodine staining.

Table 1. Molecular Radius of the PEG-Hb Samples

sample	radius (nm)	molecular volume (nm^3)
HbA	3.04	117.6
EAF-PEG-Hb without free Cys-93(β)	5.23	598.9
EAF PEG-Hb with free Cys-93(β)	4.94	504.7
αα-Hb	3.10	124.8
EAF-PEG-αα-Hb without free Cys-93(β)	5.52	704.2
EAF-PEG-αα-Hb with free Cys-93(β)	5.15	571.9

(~16 kDa) (lane 2, Figure 4). EAF PEGylation of HbA resulted in the appearance of four bands. Iodine staining confirms that these bands (lane 3) correspond to one globin conjugated with 1, 2, 3, and 4 PEG-5K chains. When Cys-93(β) is reversibly protected, these bands are essentially unchanged (lane 4) except that the band corresponding to the tetraPEGylated globin is noticeably reduced.

Molecular Radius of the PEG-Hbs by Dynamic Light Scattering. The molecular radius of Hb increased from 3.04 to 5.23 nm upon EAF PEGylation (Table 1). The molecular radius of the PEG-Hb decreased to 4.94 nm upon reversible protection of Cys-93(β), consistent with the results from the SEC and HPLC analysis.

Reactivity of Cys-93(β) of the PEG-Hbs. As reflected by the titration with 4-PDS (*25*), the PEG-Hb with protection of Cys-93(β) has two free thiols per tetramer (curve b, Figure 5) and its reactivity to 4-PDS is comparable to that of HbA (curve a). Since the change in the reactivity of Cys-93(β) in the oxy state can be considered as an indicator of a change at the $\alpha_1\beta_2$ interface in a chemically modified Hb, EAF PEGylation of Hb with protection of Cys-93(β) did not induce any perturbation at the $\alpha_1\beta_2$ interface of Hb. In contrast, the reactivity of Cys-93(β) of two other hexaPEG-Hbs, (Propyl-PEG5K)$_6$-Hb (curve c), and (Propionyl-PEG5K)$_6$-Hb (curve d) is significantly increased, indicating the structural perturbation at the $\alpha_1\beta_2$ interface of the two PEG-Hbs. It should be mentioned that (Propyl-PEG5K)$_6$-Hb and (Propionyl-PEG5K)$_6$-Hb are prepared using reductive alkylation and acylation chemistry, respectively, where the PEG chains are directly conjugated to the amine groups of Hb (*26, 27*).

Tetramer Stability of the PEG-Hbs. The K_d of HbA increased slightly upon EAF PEGylation with reversible protection of Cys-93(β) (Figure 6). In contrast, the K_d of the EAF-PEG-Hb increased significantly. However, the K_d of HbA increased slightly upon NEM modification and further marginally decreased upon reversible protection of Cys-93(β). This indicated that the NEM modification at Cys-93(β) has little effect on the K_d of Hb. Accordingly, the PEG chains conjugated at Cys-93(β) play a predominant role in the tetramer stability of the EAF-PEG-Hb. In contrast, the reductive alkylation and acylation chemistry based PEG-Hbs exist essentially as Hb dimers (*26, 27*).

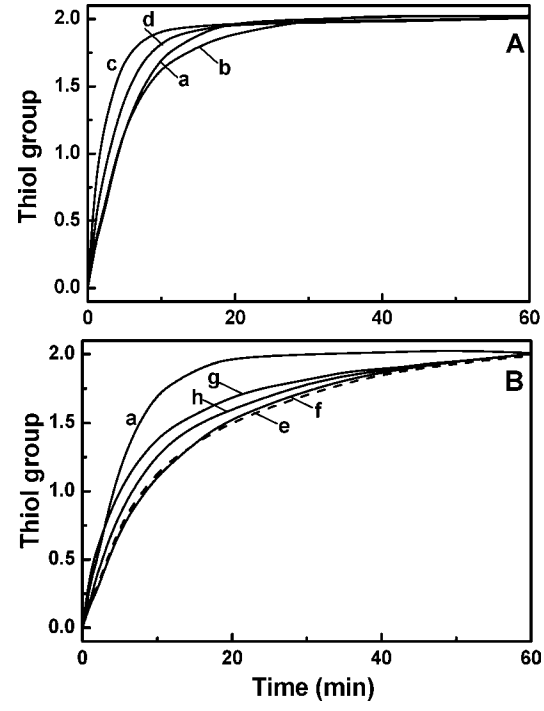

Figure 5. The reactivity of Cys-93(β) of the PEG-Hb (A) and the PEG-αα-Hb (B). HbA (a), the PEG-Hb with free Cys-93(β) (b), (Propyl-PEG5K)$_6$-Hb (c), (Propionyl-PEG5K)$_6$-Hb (d), αα-Hb (e), the PEG-αα-Hb with free Cys-93(β) (f), (Propyl-PEG5K)$_6$-αα-Hb (g), and (Propionyl-PEG5K)$_6$-αα-Hb (h) at the Hb concentration of 5 μM were incubated with 50 μM 4-PDS at room temperature in PBS, pH 7.4. The SH groups were estimated by measuring the conversion of 4-PDS to 4-thiopyridine at 324 nm as a function of time.

Structure and Function of the PEG-Hbs. *Circular Dichroism Study of the PEG-Hbs.* The L band (centered around 260 nm) is considered to be sensitive to the interactions between the heme and the surrounding globin, being influenced by the ligand interactions (*28*). As shown in the near-UV CD region,

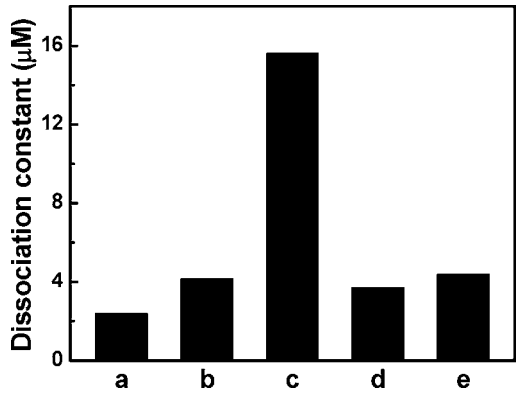

Figure 6. The tetramer−dimer dissociation constant of the PEG-Hb. HbA (a), the PEG-Hb with free Cys-93(β) (b), the PEG-Hb without free Cys-93(β) (c), the NEM modified thiolated Hb with free Cys-93(β) (d), and the NEM modified thiolated Hb without free Cys-93(β) (e) were loaded on the Superose 12 column for the dissociation constant measurement.

NEM modification of Hb did not alter the L band of Hb (Figure 7B). However, EAF PEGylation of Hb (Figure 7A) markedly decreased the L band of the proteins. Interestingly, reversible protection of Cys-93(β) restores the ellipticity of the L band of the EAF-PEG-Hb to the level of the unmodified Hb. Because the EAF-PEG-Hb can be taken as NEM conjugated with the PEG chains, it follows that the PEG chains conjugated at Cys-93(β) unfavorably alter the interactions between the heme and the surrounding globin chain.

The Soret band of Hb is informative of the interactions of the heme prosthetic group with the surrounding aromatic residues (*29*). It should be mentioned that all the Hb samples in the present study were in the oxy form and in the ferrous state. In the Soret region, the ellipticity with the maximal at 421 nm of HbA increased upon EAF PEGylation (Figure 7A) and NEM mediated modification (Figure 7B). However, the ellipticity of the EAF-PEG-Hb is slightly lower than that of the NEM modified Hb. In contrast, the ellipticity of the EAF-PEG-Hb decreased upon reversible protection of Cys-93(β). Thus, the reversible protection of Cys-93(β) reduced the perturbation of the heme environment of the EAF-PEG-Hb.

Intrinsic Front-Face Fluorescence of the PEG-Hb. Front-face fluorescence spectroscopy of Hb has been used to monitor the quaternary changes of Hb upon chemical modification of the protein. The fluorescence sensitivity has been assigned mostly to Trp-37(β) and reflects the conformational changes at the $\alpha_1\beta_2$ interface of Hb. When excited at 280 nm (Figure 8A), the fluorescence intensity of HbA (curve a) decreased upon EAF PEGylation (curve b) and the NEM modification (curve d). In contrast, reversible protection of Cys-93(β) increases the fluorescence intensity of the PEG-Hb (curve c) and the NEM modified Hb (curve e). Thus, the quaternary changes of the EAF-PEG-Hb around the $\alpha_1\beta_2$ interface is primarily a consequence of maleimide modification at Cys-93(β) and not a result of the PEG chains.

O_2 Affinity of the PEG-Hb. The P_{50} of HbA decreases from 14.4 to 6.9 mmHg upon EAF PEGylation, along with a decrease in the Hill coefficient (Table 2). The NEM modified thiolated Hb control showed a P_{50} (oxygen affinity) comparable to the EAF-PEG-Hb. This suggests that the PEG chains play a limited role in dictating the oxygen affinity of the EAF-PEG-Hb. However, the P_{50} of the PEG-Hb and the NEM modified Hb increased upon reversible protection of Cys-93(β), along with a slight decrease in the Hill coefficient. The PEG-Hb and the NEM modified Hb are essentially insensitive to the allosteric effector, 2,3-DPG. On the other hand, the adducts with reversible protection of Cys-93(β) exhibit a small but noticeable sensitivity to 2,3-DPG.

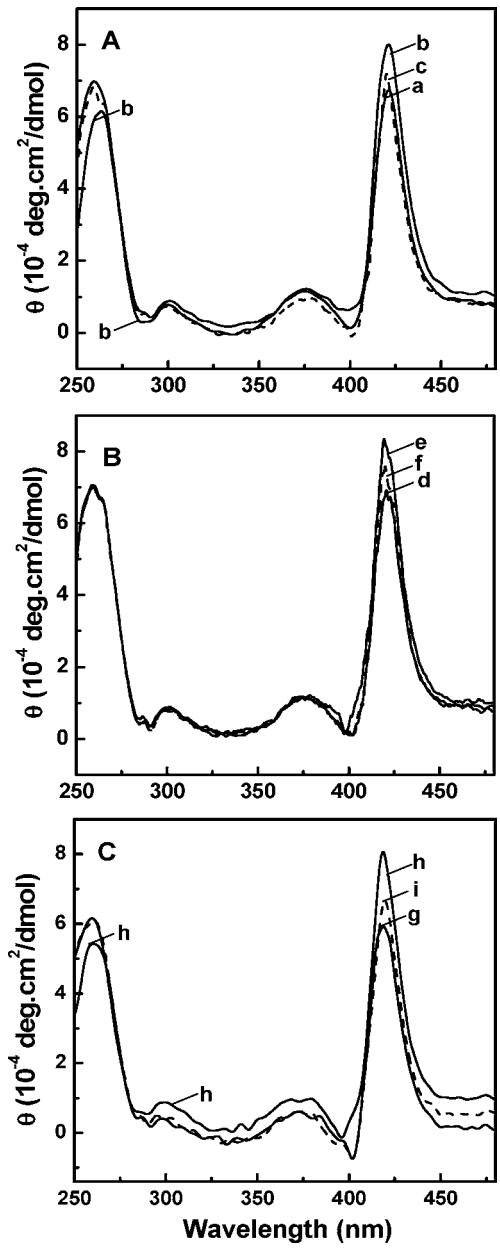

Figure 7. Circular dichroism spectra of the PEG-Hb (A), the NEM modified thiolated Hb (B), and the PEG-αα-Hb (C). Circular dichroic spectra of HbA (a), the PEG-Hb (b), the PEG-Hb with free Cys-93(β) (c), HbA (d), the NEM modified thiolated Hb (e), the NEM modified thiolated Hb with free Cys-93(β) (f), αα-Hb (g), the PEG-αα-Hb (h), and the PEG-αα-Hb with free Cys-93(β) (i). The Hb samples were recorded at 25 °C with a 0.2 cm light path cuvette (310 μL).

Autoxidation and Heme Loss of the PEG-Hbs. The autoxidation rate of PEG-Hb is an integrated result of the maleimide modification of the thiolated Hb and the conjugated PEG chains (*16*). Therefore, the NEM modified thiolated Hb was used as a control to investigate the autoxidation and the heme loss of the PEG-Hb.

Autoxidation of the PEG-Hb in PBS Buffer. As shown in Table 3, the autoxidation rate constant (k_{ox}) of HbA increased upon NEM modification and further increased upon conjugation of the PEG chains. The k_{ox} of the hexaPEG-Hb is marginally higher than that of the diPEG-Hb site-specifically modified at Cys-93(β) (*16*). The k_{ox} for the PEG-Hb and the NEM modified Hb decreased significantly upon reversible protection of Cys-93(β). Accordingly, PEGylation of Cys-93(β) makes a significant contribution to increasing the autoxidation of the PEG-Hb.

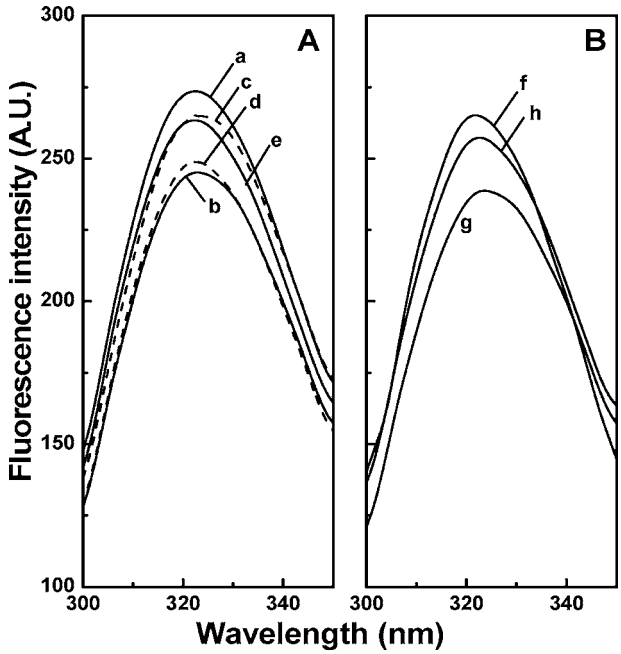

Figure 8. Intrinsic fluorescence emission spectra of the PEG-Hbs. (a) Hb; (b) the PEG-Hb without free Cys-93(β); (c) the PEG-Hb with free Cys-93(β); (d) the NEM modified Hb without free Cys-93(β); (e) the NEM modified Hb with free Cys-93(β); (f) αα-Hb; (g) the PEG-αα-Hb without free Cys-93(β); (h) the PEG-αα-Hb with free Cys-93(β). The excitation wavelength for the fluorescence emission was 280 nm. The measurements were performed using a Shimadzu spectrofluorimeter at room temperature at Hb concentration of 6.0 mg/mL in PBS, pH 7.4.

Table 2. Functional Properties of the PEG-Hbs[a]

sample	P_{50} (mmHg)/n	
	no effector	2.5 mM DPG
HbA	14.4/2.8	22.0/2.6
EAF-PEG-Hb without free Cys-93(β)	6.9/2.1	7.0/2.2
EAF-PEG-Hb with free Cys-93(β)	8.5/2.0	11.6/1.7
EAF-NEM-Hb without free Cys-93(β)	7.0/2.0	7.3/2.0
EAF-NEM-Hb with free Cys-93(β)	8.5/2.1	10.0/1.9
αα-Hb	30.5/2.4	36.4/2.0
EAF-PEG-αα-Hb without free Cys-93(β)	9.9/1.7	10.5/1.7
EAF-PEG-αα-Hb with free Cys-93(β)	18.5/1.7	21.5/1.5

[a] Oxygen equilibrium curves of the samples were measured at 37 °C in PBS (pH 7.4) at Hb tetramer concentration of 0.5 mM. The Hill coefficient is given in the parentheses. P_{50} is the partial oxygen pressure at 50% saturation and is expressed in mmHg on the left of the Hill coefficient.

Table 3. Autoxidation of the PEG-Hb at 37 °C[a]

sample	k_{ox} (h^{-1})
HbA	0.012
$(SP\text{-}PEG5K)_2$-Hb[b]	0.027
EAF-PEG-Hb without free Cys-93(β)	0.036
EAF-PEG-Hb with free Cys-93(β)	0.024
$(SE)_2$-Hb[b]	0.019
EAF-NEM-Hb without free Cys-93(β)	0.027
EAF-NEM-Hb with free Cys-93(β)	0.017
αα-Hb	0.018
$(SP\text{-}PEG5K)_2$-αα-Hb[b]	0.031
EAF-PEG-αα-Hb without free Cys-93(β)	0.042
EAF-PEG-αα-Hb with free Cys-93(β)	0.029

[a] The initial pO_2 of the Hb samples is around 150 mmHg before the autoxidation experiment and decreases during the process of the autoxidation. [b] Data obtained from Hu et al. (*16*).

Heme Loss of the PEG-Hb. Oxidation of ferrous heme iron to the ferric state weakens its fifth coordinate bond to proximal His residue and thereby increases the probability of the heme loss (*30*). The heme loss rate (Figure 9A) and the fast-phase heme loss rate

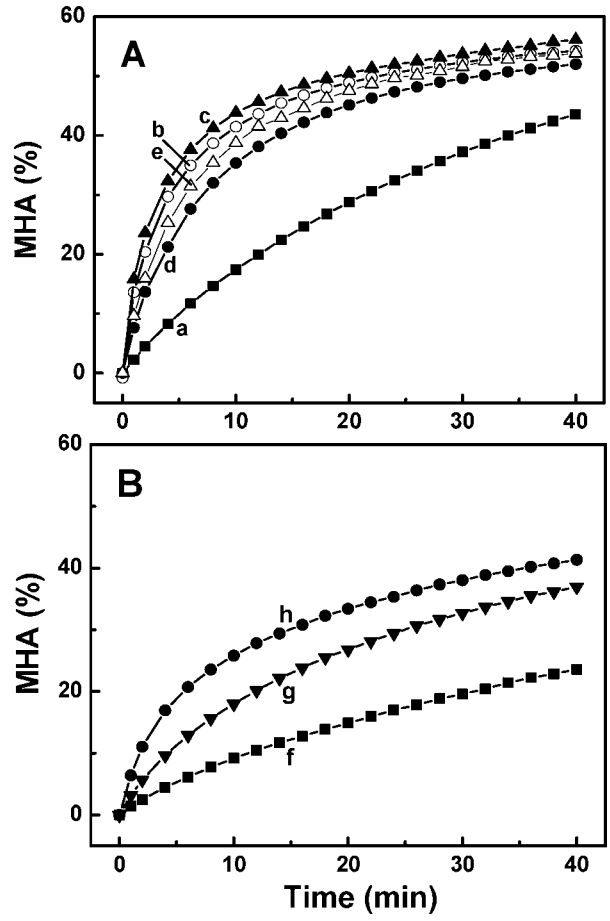

Figure 9. Kinetics of the heme transfer from the oxidized Hb samples to albumin. (A) PEG-Hb. HbA (a), the PEG-Hb (b), the NEM modified thiolated Hb (c), the PEG-Hb with free Cys-93(β) (d), and the NEM modified thiolated Hb with free Cys-93(β) (e). (B) PEG-αα-Hb. αα-Hb (f), the PEG-αα-Hb (g), and the PEG-αα-Hb with reversible protection of Cys-93(β) (h). Percent metheme−albumin (MHA) = [MHA]/([metHb] + [MHA]) × 100%.

Table 4. Fast Heme Loss Rate Constant of the PEG-Hbs

sample	k_{fast}[a] (min^{-1})
HbA	0.043
$(SP\text{-}PEG5K)_2$-Hb[b]	0.100
EAF-PEG-Hb without free Cys-93(β)	0.160
EAF-PEG-Hb with free Cys-93(β)	0.118
$(SE)_2$-Hb[b]	0.161
EAF-NEM-Hb without free Cys-93(β)	0.187
EAF-NEM-Hb with free Cys-93(β)	0.141
αα-Hb	0.020
$(SP\text{-}PEG5K)_2$-αα-Hb[b]	0.036
EAF-PEG-αα-Hb without free Cys-93(β)	0.064
EAF-PEG-αα-Hb with free Cys-93(β)	0.042

[a] Fast heme loss rate constant. [b] Data obtained from Hu et al. (*16*).

constant (k_{fast}) of Hb (Table 4) increased significantly upon EAF PEGylation. Reversible protection of Cys-93(β) significantly decreased the heme loss rate and the k_{fast} of the PEG-Hb. Accordingly, PEGylation of Cys-93(β) significantly increased the heme loss of the PEG-Hb. Moreover, the NEM modified Hb showed a slightly higher heme loss rate and k_{fast} than its corresponding PEG-Hb. Therefore, the conjugated PEG chains can increase the heme stability of the PEG-Hb.

Autoxidation of the PEG-Hb in the Plasma. The PEG-Hb (40 mg/mL) is mixed with the plasma at equal volume to mimic the *in vivo* 50% exchange transfusion. As seen earlier with PEG-Hb (*16*), k_{ox} of the PEG-Hb is attenuated in the plasma as compared to that in PBS buffer (Table 5). The reversible

Table 5. Autoxidation of the PEG-Hb in Plasma at 37 °C

sample	k_{ox}[a] (h^{-1}) in PBS buffer[b]	k_{ox}[a] (h^{-1}) in plasma[c]
HbA	0.019	0.009
EAF-PEG-Hb without free Cys-93(β)	0.047	0.023
EAF-PEG-Hb with free Cys-93(β)	0.025	0.016
αα-Hb	0.029	0.015
EAF-PEG-αα-Hb without free Cys-93(β)	0.070	0.040
EAF PEG-αα-Hb with free Cys-93(β)	0.042	0.025

[a] Autoxidation rate constant measured at 37 °C. [b] Hb concentration is at 20 mg/mL in PBS buffer, pH 7.4 [c] Hb concentration is at 20 mg/mL in the mixture of equal volumes of PBS buffer (pH 7.4) and bovine plasma.

protection of Cys-93(β) further reduces the k_{ox} of the EAF-PEG-Hb in the plasma.

Design of the Second-Generation EAF-PEG-Hb, the EAF-PEG-αα-Hb. *Characterization of the EAF-PEG-αα-Hb with Reversible Protection of Cys-93(β).* The PEG-αα-Hb (curve h, Figure 2B) shows a higher hydrodynamic volume than αα-Hb (curve f). Besides, the PEG-αα-Hb shows a more symmetrical elution pattern than the PEG-Hb (curve c). The EAF PEGylated bis-thiopridyl αα-Hb (curve i) exhibits a slightly smaller hydrodynamic volume than the PEG-αα-Hb (curve h) and no essential change upon releasing the thiopyridyl groups from Cys-93(β) (curve j).

RP-HPLC patterns of the EAF-PEG-αα-Hb are presented in Figure 3B. The α-globin of Hb was right-shifted upon αα-fumaryl cross-link (curve e). The EAF-PEG-αα-Hb (curve f) has essentially no unmodified β-globin and small amount of αα-globin, along with the presence of mono-, di-, and tri-PEGylated globins. For the PEGylated bisthiopyridyl αα-Hb, the unPEGylated β-globin increased with the peak left-shifted, whereas the αα-globin decreased (curve g). Upon releasing the thiopyridyl moiety from Cys-93(β), the peak corresponding to the unPEGylated β-globin is right-shifted (curve h).

SDS-PAGE pattern of αα-Hb shows a new band with an apparent molecular weight of 32 kDa (lane 5, Figure 4). Some smaller additional bands are observed, possibly due to the presence of a small amount of impurity that is not well-separated from αα-Hb. It may be noted that the sample was not heated at 60 °C after chromatographic purification as done by Baxter to increase the purity of the αα-Hb. EAF PEGylation of αα-Hb generated several new bands (about six to eight) (lane 6). Reversible protection of Cys-93(β) did not essentially alter the pattern of the EAF-PEG-αα-Hb (lane 7), except for the intensity of the mono- and diPEGylated β-globin.

The molecular radius of the EAF-PEG-αα-Hb is slightly higher than that of the EAF-PEG-Hb and further slightly decreased upon reversible protection of Cys-93(β) (Table 1).

Structure of the EAF-PEG-αα-Hb. The reactivity of Cys-93(β) of αα-Hb is lower than that of HbA (Figure 5B). The EAF-PEG-αα-Hb with reversible protection of Cys-93(β) carries two thiols per tetramer (curve f). EAF PEGylation targeted exclusively to the amino groups has little influence on the reactivity of Cys-93(β) of αα-Hb (curve e). The PEG-αα-Hbs generated by reductive alkylation (curve g) and acylation chemistry (curve h) based PEGylation exhibit higher reactivity of Cys-93(β) than αα-Hb and the EAF-PEG-αα-Hb.

The presence of the αα-intramolecular cross-link slightly lowers the ellipticity of Hb in the Soret CD region (Figure 7C). EAF PEGylation of αα-Hb increases its ellipticity in the Soret region, reflecting the structural perturbation of the heme pocket upon PEGylation. However, reversible protection of Cys-93(β) can reduce this structural perturbation of the EAF-PEG-αα-Hb. The fluorescence studies (Figure 8B) further confirm that reversible protection of Cys-93(β) could stabilize the quaternary structure of the EAF-PEG-αα-Hb.

Autoxidation, Heme Loss, and Oxygen Affinity of the EAF-PEG-αα-Hb. Both αα-intramolecular cross-linking and EAF PEGylation significantly influence the k_{ox} of Hb (Table 3). When the two modifications are introduced into Hb simultaneously, the increase in k_{ox} is not additive. Presumably, the PEGylation induced increase in the k_{ox} of Hb is partly due to the destabilization of Hb tetramers. However, this destabilization is counteracted by the αα-intramolecular cross-link. On the other hand, the reversible protection of Cys-93(β) reduces the k_{ox} of the EAF-PEG-αα-Hb. The presence of αα-fumaryl cross-link in Hb and the PEG-Hb reduces the k_{fast} by 53% and 60%, respectively (Table 4). Reversible protection of Cys-93(β) further increases the heme stability of the EAF-PEG-αα-Hb (Figure 9B and Table 4).

The EAF-PEG-αα-Hb shows lower oxygen affinity than the EAF-PEG-Hb (Table 2). The oxygen affinity of the EAF-PEG-αα-Hb exhibits little sensitivity to the presence of 2,3-DPG. In contrast, it shows some sensitivity to the presence of 2,3-DPG upon protection of Cys-93(β). Thus, the quaternary structural features of Hb are conserved better in the EAF-PEG-αα-Hb upon protection of Cys-93(β). The high O_2 affinity of the EAF-PEG-Hb comes from the site-specific PEGylation of Cys-93(β) and EAF PEGylation of the amino groups. Introduction of αα-fumaryl cross-bridge and protection of Cys-93(β) could partially lower the O_2 affinity of the EAF-PEG-Hb.

DISCUSSION

EAF PEGylation of Hb was developed to simplify the surface decoration of Hb with the PEG chains and develop a non-vasoactive Hb derivative (*9*). This new PEGylation platform is a cost-effective protocol as exemplified in the development of MP4 by Sangart (*31*). Subsequent studies have established that the extension arm sandwiched between the amino groups and the PEG chains affords a unique structural advantage with Hb over the direct PEGylation platforms. EAF PEGylation has little impact on the tetramer stability of the PEG-Hb. In contrast, direct PEGylation destabilizes the quaternary structure of the PEG-Hb. We have now generated the hexaPEG-Hbs using the four PEGylation platforms, namely, EAF PEGylation (*9*), reductive alkylation (*26*), active ester chemistry (*27*), and thiocarbamoylation chemistry based PEGylation (*32*). The hexaPEG-Hbs generated by direct PEGylation exist essentially as Hb dimers (*26, 27*). On the other hand, the EAF-PEG-Hb is present predominantly as tetrameric species (Figure 5). The preclinical and clinical studies of MP4 have established that it does not induce any undesirable toxicity (*31*). Accordingly, the absence of toxicity in MP4 and the reported toxicity in Enzon PEG-bovine-Hb implicated by Baldwin et al. (*33*) may be related to the anticipated low tetramer stability of the Enzon product.

Recently, Kluger and his associates (*34*) have shown that EAF PEGylation increased the nitrite reductase activity of Hb, predominantly due to PEGylation of Cys-93(β). They suggested that this activity is responsible for the vasoinactivity of the PEG-Hb. Accordingly, avoiding PEGylation of Cys-93(β) may result in the vasoactivity of PEG-Hb. However, Cys-93(β) is free in the vasoinactive PEG-bovine-Hb (Enzon product) that was prepared using acylation chemistry based PEGylation. Besides, the Euro PEG-Hb, a product prepared using EAF PEGylation under deoxy condition to avoid PEGylation of Cys-93(β), was also vasoinactive (*35, 36*). Thus, the vasoinactivity of the PEG-Hb does not correlate to the presence of PEGylation of Cys-93(β).

Avoiding PEGylation of Cys-93(β) has a limited influence on the oxygen affinity of the EAF-PEG-Hb. This further confirms that the high oxygen affinity of the EAF-PEG-Hb is an intrinsic consequence of PEGylation and not a direct result of PEGylation of Cys-93(β). The same conclusion has been

Table 6. Site Selectivity of EAF PEGylation in Three Preparations

modified residue	MP4[a]	Euro PEG-Hb[b]	$(SP\text{-}PEG5K)_6$-Hb[c]
Cys-93∉(β)	+	−	+
Lys-40 (α)	+	−	+
Lys-120 (β)	−	−	+
Lys-61 (α)	−	−	+
Lys-7 (α)	+	+	−
Lys-8 (β)	+	+	+
Val-1 (β)	−	−	+
Lys-11 (α)	−	+	+
Lys-16 (α)	+	+	+
Lys-56 (α)	−	+	+
Lys-60 (α)	−	+	−
Lys-90 (α)	−	+	+
Lys-99(α)	−	+	−
Lys-139 (α)	−	+	−
Lys-17 (β)	+	+	+
Lys-59 (β)	+	+	−
Lys-61 (β)	−	+	−
Lys-65 (β)	−	+	−
Lys-66 (β)	+	+	−
Lys-95 (β)	+	+	−
Lys-132 (β)	+	−	−
Lys-144 (β)	−	+	+

[a] The data obtained from Vandegriff et al. (*37*). [b] The data obtained from Iafelice et al. (*36*). [c] The data obtained from Manjula et al. (*9*).

drawn previously based on EAF PEGylation of rHb[Cys-93(β)→Ala] (*10*). We have also carried out the EAF PEGylation of bis thiopyridyl Hb under deoxy condition, isolated the PEGylated product, and released the thiopyridyl moiety. This EAF-PEG-Hb prepared under deoxy conditions exhibited an O_2 affinity comparable to the product generated under oxy condition.

The site selectivity of $(SP\text{-}PEG5K)_6$-Hb (*9*), MP4 (*37*), and Euro PEG-Hb (*36*) has been compared in Table 6. This confirms that EAF PEGylation of the amino groups is not quantitative except for PEGylation of Cys-93(β) in $(SP\text{-}PEG5K)_6$-Hb and MP4. Even though Euro PEG-Hb was generated under deoxy conditions, the pattern of PEGylation is generally comparable to those of $(SP\text{-}PEG5K)_6$-Hb and MP4. Moreover, Lys-40(α) is modified under the oxy condition, but not under the deoxy condition. Thus, PEGylation of Lys-40(α) may marginally influence the oxygen affinity of Hb. In addition, the amino groups of Hb accessible for EAF PEGylation are overlapping irrespective of the oxy or deoxy conditions used for PEGylation. Accordingly, we speculate that the hydrated PEG shell of the EAF-PEG-Hb with free Cys-93(β) leads to a preferential stabilization of the R state over the T state of Hb. This is the primary molecular aspect that increases the O_2 affinity of Hb on PEGylation. The site-specific PEGylation of Cys-93(β) increases the O_2 affinity of Hb (*15*), predominantly due to maleimide modification of Cys-93(β). These two molecular aspects are not additive and appear to significantly overlap each other.

The high O_2 affinity of MP4 is considered a desirable feature for HBOC, in terms of achieving a targeted O_2 delivery to the hypoxic areas and reducing the vasoactivity with the autoregulatory mechanism. Our present data establish that the reversible protection of Cys-93(β) of un-cross-linked Hb does not significantly decrease the oxygen affinity of the PEG-Hb (Table 2). Accordingly, design of new versions of MP4 with free Cys-93(β) essentially does not have an impact on the concepts of the new paradigms for the design of the HBOCs. This will provide an opportunity to evaluate the potential merits of avoiding PEGylation of Cys-93(β) in terms of the efficacy of the EAF-PEG-Hb. Besides, the new version of the EAF-PEG-Hbs with free thiols may also have an impact on counteracting the reperfusion injury during transfusion.

The optimum level of O_2 affinity of a PEG-Hb to achieve adequate tissue oxygenation without activating the autoregulatory principles has been the subject of intense study in recent years (*17, 35, 38, 39*). The Ajinomoto PEG-Hb (PHP) exhibits an O_2 affinity lower than that of unmodified Hb. However, the vasoinactivity of PHP is not comparable to that seen with Enzon PEG-bovine-Hb (*40*). The PEG-Hb with an oxygen affinity close to that of unmodified Hb (P50 around 15 mmHg) is being considered as a better choice for achieving adequate tissue oxygenation. The O_2 affinity of the PEG-$\alpha\alpha$-Hb with free Cys-93(β) is higher than that of $\alpha\alpha$-Hb but slightly lower than that of HbA. EAF PEGylation of $\alpha\alpha$-Hb is less efficient in increasing the O_2 affinity of $\alpha\alpha$-Hb. Presumably, the low oxygen affinity of $\alpha\alpha$-Hb is partially counteracted by the PEG shell to stabilize the oxy state of Hb.

The $\alpha\alpha$-Hb has been PEGylated by us using three PEGylation platforms, reductive alkylation chemistry, acylation chemistry, and the present modified EAF PEGylation. Comparison of the reactivity of Cys-93(β) suggests that the oxy conformation of Hb is stabilized to a maximum level by the propyl-PEG chains of $(Propyl\text{-}PEG5K)_6$-Hb, whereas to a minimal level by the EAF PEGylation. In the reductive alkylation based PEGylation, four of the six PEG chains are targeted to the four α-amino groups of Hb, while in the other two protocols, the PEG chains are targeted exclusively to the ε-amino groups. PEGylation on the α-amino groups is most effective in stabilizing the oxy conformation, while PEGylation of ε-amino by propionyl PEG chains reduces this propensity of the PEG shell. The oxygen affinity of the three PEG-$\alpha\alpha$-Hbs can reflect the stabilization of the oxy conformation by the PEG chains and correlates well with the reactivity of Cys-93(β). Engineering the extension arm between the ε-amino groups and the PEG chains further reduces this efficiency of the PEG shell to stabilize the R state of Hb.

Many intramolecularly cross-linked and/or oligomerized Hbs have been designed as potential HBOC. However, their application as oxygen therapeutics has been impeded due to their vasoactivity and/or autoxidation mediated toxicities. PEGylation of Hb has emerged as a new chemical approach to overcome the vasoactivity of acellular Hb. EAF PEGylation is a new cost-effective approach to neutralize their vasoactivity. Reversible protection of Cys-93(β) during EAF PEGylation has many beneficial effects on the EAF-PEG-Hbs. In the present study, EAF PEGylation of $\alpha\alpha$-Hb has been investigated as a second generation of the EAF-PEG-Hb with lower oxygen affinity. This modified EAF PEGylation approach is expected to integrate the structural and functional advantages of avoiding the PEGylation of Cys-93(β). On the other hand, it is expected to conserve the potential of PEGylation to neutralize the vasoactivity of Hb and have minimal perturbation of the quaternary structural aspects of Hb.

ACKNOWLEDGMENT

This work was supported by a grant-in-aid from the American Heart Association Heritage Affiliate 9951021T, the National Institutes of Health grants HL58247 and HL71064, and the U.S. Army grant PR023085.

LITERATURE CITED

(1) Harris, J. M., and Chess, R. B. (2003) Effect of PEGylation on pharmaceuticals. *Nat. Rev. Drug Discovery 2*, 214–221.
(2) Pasut, G., Guiotto, A., and Veronese, F. M. (2004) Protein, peptide and non-peptide drug PEGylation for therapeutic application. *Expert Opin. Ther. Pat. 14*, 859–894.
(3) Roberts, M. J., Bentley, M. D., and Harris, J. M. (2002) Chemistry for peptide and protein PEGylation. *Adv. Drug Delivery Rev. 54*, 459–476.
(4) Chang, T. M. (1999) Future prospects for artificial blood. *Trends Biotechnol. 17*, 61–67.
(5) Klein, H. G. (2000) The prospects for red-cell substitutes. *New Engl. J. Med. 342*, 1666–1668.

(6) Conover, C. D., Linberg, R., Shum, K. L., and Shorr, R. G. (1999) The ability of polyethylene glycol conjugated bovine hemoglobin (PEG-Hb) to adequately deliver oxygen in both exchange transfusion and top-loaded rat models. *Artif. Cells, Blood Substitutes, Immobilization Biotechnol. 27*, 93–107.

(7) Winslow, R. M., Gonzales, A., Gonzales, M. L., Magde, M. D., McCarthy, M., Rohlfs, R. J., and Vandegriff, K. D. (1998) Vascular resistance and efficacy of red cell substitutes in a rat hemorrhage model. *J. Appl. Physiol. 85*, 993–1003.

(8) Acharya, A. S., Intaglietta, M., Tsai, A. G., Malavalli, A., Vandegriff, K., Winslow, R. M., Smith, P. K., Friedman, J. M., and Manjula, B. N. (2005) Enhanced molecular volume of conservatively PEGylated Hb: $(SP\text{-}PEG5K)_6$-Hb is non-hypertensive. *Artif. Cells, Blood Substitutes, Immobilization Biotechnol. 33*, 239–255.

(9) Manjula, B. N., Tsai, A. G., Intaglietta, M., Tsai, C. H., Ho, C., Smith, P. K., Perumalsamy, K., Kanika, N. D., Friedman, J. M., and Acharya, A. S. (2005) Conjugation of multiple copies of polyethylene glycol to hemoglobin facilitated through thiolation: Influence on hemoglobin structure and function. *Protein J. 42*, 133–146.

(10) Li, D., Ho, N. T., Simplaceanu, V., Ho, C., Acharya, S. A., and Manjula, B. N. (2007) Molecular aspects of the high oxygen affinity of non-hypertensive hexaPEGylated Hb, $(SP\text{-}PEG5K)_6$-Hb. *Artif. Cells, Blood Substitutes, Immobilization Biotechnol. 35*, 107–118.

(11) Li, D., Manjula, B. N., and Acharya, S. A. (2006) Extension arm facilitated PEGylation of proteins: correlation of the structure of PEGylated Hemoglobin with the extent of PEGylation. *Protein J. 25*, 263–274.

(12) Muirhead, H., Cox, J. M., Mazzarella, L., and Perutz, M. F. (1967) Structure and function of haemoglobin. 3. A three-dimensional fourier synthesis of human deoxyhaemoglobin at 5.5 Angstrom resolution. *J. Mol. Biol. 28*, 117–156.

(13) Cheng, Y., Shen, T. J., Simplaceanu, V., and Ho, C. (2002) Ligand binding properties and structural studies of recombinant and chemically modified hemoglobins altered at beta 93 cysteine. *Biochemistry 41*, 11901–11913.

(14) Juszczak, L. J., Manjula, B. N., Bonaventura, C., Acharya, S. A., and Friedman, J. M. (2002) UV resonance Raman study of β-93 modified hemoglobin A: chemical modifier-specific effects and added influence of attached poly(ethylene glycol) chains. *Biochemistry 41*, 376–385.

(15) Manjula, B. N., Tsai, A., Upadhya, R., Perumalsamy, K., Smith, P. K., Malavalli, A., Vandegriff, K. D., Winslow, R. M., Intaglietta, M., Prabhakaran, M., Friedman, J. M., and Acharya, A. S. (2003) Site-specific PEGylation of hemoglobin at cys-93(β): correlation between the colligative properties of the PEGylated protein and the length of the conjugated PEG chain. *Bioconjugate Chem. 14*, 464–472.

(16) Hu, T., Li, D., Manjula, B. N., and Acharya, S. A. (2008) Autoxidation of the site-specifically PEGylated hemoglobins: role of the PEG chains and the sits of PEGylation in the autoxidation. *Biochemistry 47*, 10981–10990.

(17) Acharya, S. A., Intaglietta, M., and Tsai, A. G. (2007) Modulation of the polyethylene glycol-hemoglobin structure to increase the efficiency of plasma expansion and O_2 carrying capacity. *Trans. Altern. Trans. Med. 9*, 254–264.

(18) Manjula, B. N., and Acharya, A. S. (2003) Purification and molecular analysis of hemoglobin by high-performance liquid chromatography. *Methods Mol. Med. 82*, 31–47.

(19) Chatterjee, R., Welty, E. V., Walder, R. Y., Pruitt, S. L., Rogers, P. L., Arnone, A., and Walder, J. A. (1986) Isolation and characterization of a new hemoglobin derivative cross-linked between the α chains (lysine 99α1-lysine 99α2). *J. Biol. Chem. 261*, 9929–9937.

(20) Benesch, R. E., and Kwong, S. (1990) The stability of the heme-globin linkage in some normal, mutant, and chemically modified hemoglobins. *J. Biol. Chem. 265*, 14881–14885.

(21) Benesch, R. E. (1994) The stability of the heme-globin linkage: measurement of heme exchange. *Methods Enzymol. 231*, 496–502.

(22) Di Iorio, E. E. (1981) Preparation of derivatives of ferrous and ferric hemoglobin. *Methods Enzymol. 75*, 57–72.

(23) Manning, L. R., Jenkins, W. T., Hess, J. R., Vandegriff, K., Winslow, T. M., and Manning, J. M. (1996) Subunit dissociations in natural and recombinant hemoglobins. *Protein Sci. 5*, 775–781.

(24) Hu, T., Prabhakaran, M., Acharya, S. A., and Manjula, B. N. (2005) Influence of the chemistry of conjugation of poly(ethylene glycol) to Hb on the oxygen-binding and solution properties of the PEG-Hb conjugate. *Biochem. J. 392*, 555–564.

(25) Ampulski, R. S., Ayers, V. E., and Morell, S. A. (1969) Determination of the reactive sulfhydryl groups in heme proteins with 4,4′-dipyridine disulfide. *Anal. Biochem. 32*, 136–169.

(26) Hu, T., Manjula, B. N., Li, D., Brenowitz, M., and Acharya, A. S. (2007) Influence of intramolecular cross-links on the molecular, structural and functional properties of PEGylated hemoglobin. *Biochem. J. 402*, 143–151.

(27) Li, D., Hu, T., Manjula, B. N., and Acharya, S. A. (2008) Non-conservative surface decoration of hemoglobin. *Biochim. Biophys. Acta 1784*, 1395–1401.

(28) Zentz, C., Pin, S., and Alpert, B. (1994) Stationary and time-resolved circular dichroism of hemoglobins. *Methods Enzymol. 232*, 247–266.

(29) Hsu, M. C., and Woody, R. W. (1971) The origin of the heme Cotton effects in myoglobin and hemoglobin. *J. Am. Chem. Soc. 93*, 3515–3525.

(30) Bunn, H. F., and Jandl, J. H. (1968) The renal handling of hemoglobin. *J. Biol. Chem. 243*, 465–475.

(31) Young, M. A., Malavalli, A., Winslow, N., Vandegriff, K. D., and Winslow, R. M. (2007) Toxicity and hemodynamic effects after single dose administration of malPEG-hemoglobin (MP4) in rhesus monkeys. *Transl. Res. 149*, 333–342.

(32) Acharya, S. A, Smith, P. K., and Manjula, B. N. (2006) PEGylated non-hypertensive hemoglobins, methods of preparing same and used there off, U. S. Patent 7,144,989.

(33) Baldwin, A. L., Wilson, L. M., and Valeski, J. E. (1998) Ultrastructural effects of intravascularly injected polyethylene glycol-hemoglobin in intes-tinal mucosa. *Am. J. Physiol. 275*, H615–H625.

(34) Lui, F. E., Dong, P., and Kluger, R. (2008) Polyethylene glycol conjugation enhances the nitrite reductase activity of native and cross-linked hemoglobin. *Biochemistry 47*, 10773–10780.

(35) Portoro, I., Kocsis, L., Herman, P., Caccia, D., Perrella, M., Ronda, L., Bruno, S., Bettati, S., Micalella, C., Mozzarelli, A., Varga, A., Vas, M., Lowe, K. C., and Eke, A. (2008) Towards a novel haemoglobin-based oxygen carrier: Euro-PEG-Hb, physico-chemical properties, vasoactivity and renal filtration. *Biochim. Biophys. Acta 1784*, 1402–1409.

(36) Iafelice, R., Cristoni, S., Caccia, D., Russo, R., Rossi-Bernardi, L., Lowe, K. C., and Perrella, M. (2007) Identification of the sites of deoxyhaemoglobin PEGylation. *Biochem. J. 403*, 189–196.

(37) Vandegriff, K. D., Malavalli, A., Mkrtchyan, G. M., Spann, S. N., Baker, D. A., and Winslow, R. M. (2008) Sites of modification of Hemospan, a poly(ethylene glycol)-modified human hemoglobin for use as an oxygen therapeutic. *Bioconjugate Chem. 19*, 2163–2170.

(38) Cabrales, P., and Friedman, J. M. (2007) PEGylated hemoglobins: mechanisms to avoid vasoconstriction and maintain perfusion. *Trans. Altern. Trans. Med. 9*, 281–293.

(39) Acharya, S. A., Acharya, V. N., Kanika, N. D., Tsai, A. G., Intaglietta, M., and Manjula, B. N. (2007) Non-hypertensive tetraPEGylated canine heamoglobin: correlation between PEGylation, O_2 affinity and tissue oxygenation. *Biochem. J. 405*, 503–511.

(40) Rohlfs, R. J., Bruner, E., Chiu, A., Gonzales, A., Gonzales, M. L., Magde, D., Jr., Vandegriff, K. D., and Winslow, R. M. (1998) Arterial blood pressure responses to cell-free hemoglobin solutions and the reaction with nitric oxide. *J. Biol. Chem. 273*, 12128–12134.

BC900170E

Efficient Site-Specific Radiolabeling of a Modified C2A Domain of Synaptotagmin I with $[^{99m}Tc(CO)_3]^+$: A New Radiopharmaceutical for Imaging Cell Death

Richard Tavaré, Rafael Torres Martin De Rosales, Philip J. Blower, and Gregory E. D. Mullen*

Division of Imaging Sciences, King's College London, St. Thomas' Hospital, London, SE1 7EH, United Kingdom. Received April 23, 2009; Revised Manuscript Received September 22, 2009

We describe the design and synthesis of a new Tc-99m labeled bioconjugate for cell-death imaging, based on C2A, the phosphatidylserine (PS)-binding domain of rat synaptotagmin I. Since several lysine residues in this protein are critical for PS binding, we engineered a new protein, C2AcH, to include the C-terminal sequence CKLAAALEHHHHHH, incorporating a free cysteine (for site-specific covalent modification) and a hexahistidine tag (for site-specific radiolabeling with $[^{99m}Tc(CO)_3(OH_2)_3]^+$). We also engineered a second derivative, C2Ac, in which the C-terminal sequence included only the C-terminal cysteine. These proteins were characterized by electrospray mass spectrometry, SDS/PAGE, and size exclusion chromatography and radiolabeled with $[^{99m}Tc(CO)_3(OH_2)_3]^+$. Conjugates of the proteins with the rhenium analogue $[Re(CO)_3(OH_2)_3]^+$ were also synthesized. Site-specific labeling was confirmed by performing a tryptic digest of rhenium tricarbonyl-labeled C2AcH, and only peptides containing the His-tag contained the $[Re(CO)_3]^+$. The labeled proteins were tested for binding to red blood cells (RBC) with exposed PS in a calcium dependent manner. Labeling 100 μg of C2AcH with $[^{99m}Tc(CO)_3(OH_2)_3]^+$ at 37 °C for 30 min gave a radiochemical yield of >96%. However, C2AcH that had first been conjugated with fluorescein maleimide or iodoacetamide via the Cys residue gave only 50% and 83% radiochemical yield, respectively, after incubation for 30 min at 37 °C. Serum stability results indicated that >95% of radiolabeled C2AcH remained stable for at least 18 h at 37 °C. Site-specifically labeled C2AcH exhibited calcium-dependent binding to the PS on the RBC, whereas a nonspecifically modified derivative, C2AcH-B, in which lysines had been modified with benzyloxycarbonyloxy, did not. We conclude that (i) the combination of Cys and a His-tag greatly enhances the rate and efficiency of labeling with $[^{99m}Tc(CO)_3(OH_2)_3]^+$ compared to either the His-tag or the Cys alone, and this sequence deserves further evaluation as a radiolabeling tag; (ii) non-site-specific modification of C2A via lysine residues impairs target binding affinity; (iii) ^{99m}Tc-C2AcH has excellent radiolabeling, stability and PS binding characteristics and warrants *in vivo* evaluation as a cell-death imaging agent.

INTRODUCTION

Apoptosis is an energy-dependent, genetically controlled process by which cell death is activated through an internally regulated suicide program (*1*). It results in the exposure of specific components of the inner leaflet of the plasma membrane, such as phosphatidylserine (PS), on the surface of the cell. In contrast to necrotic cell death, which occurs following exposure to high concentrations of endogenous or exogenous toxins, heat treatment, freeze−thawing, or other immediately disruptive insults, apoptosis tends to occur during less intense, chronic tissue insult. The ability to investigate and image apoptosis/necrosis, or "cell death", noninvasively in diseases such as cancer, heart disease, or immune rejection, is an important goal in monitoring response to treatment or assessment of tissue injury, and may also be of value in acquiring a deeper understanding of the pathophysiology of disease. In particular, the use of imaging techniques such as single photon emission computed tomography (SPECT) and positron emission tomography (PET) is assuming an important role in cell death imaging (*2*).

A common method of detecting externalized PS is the use of PS-binding proteins such as Annexin V or the C2A domain of synaptotagmin I. These are amphipathic molecules that bind to PS in a Ca^{2+}-dependent manner (*3, 4*). Neither Annexin V nor C2A can discriminate between PS on the outer or inner leaflet of lysed cells, and hence, neither can distinguish between apoptosis and necrosis (*5, 6*). Nevertheless, using a variety of radiolabeling strategies, labeled Annexin V and C2A have been evaluated in several preclinical cell death imaging studies, and Annexin V has also progressed to several clinical trials (*7*).

When radiolabeling small proteins such as these, it is often important to exert maximum control over the number and site of modifications to the molecule. This is starkly illustrated by the example of In-111-DTPA-N-TIMP-2, a radiolabeled recombinant protein designed for imaging of matrix metalloprotein (MMP) expression. The attachment of the first DTPA occurred at a single location and was accompanied by full retention of MMP binding; whereas attachment of a second led to complete loss of function (*8*). In the case of Annexin V, Tait et al. elegantly showed that nonspecific "amine-directed" labeling of Annexin V led to reduction or abolition of PS affinity and poor *in vivo* performance (*9*). Until recently, nearly all molecular imaging studies with Annexin V and C2A had been done using amine-reactive bifunctional agents (*10, 11*). In most cases, the extent and statistical distribution of modification have not been measured, and it has not been quantitatively demonstrated that the bioconjugates retain full bioactivity compared with unmodified protein. In cases such as these, the detrimental effects are compounded because the lowest affinity (most heavily modified)

* Corresponding author. Division of Imaging Sciences, King's College London, Lambeth Wing, St. Thomas' Hospital, London, SE1 7EH, UK, Tel: +44 (0) 207 1888371, Fax: + 44 (0) 20 7188 5442, Email: greg.mullen@kcl.ac.uk.

10.1021/bc900160j CCC: $40.75 © 2009 American Chemical Society
Published on Web 10/29/2009

Scheme 1. Labeling of C2A Domain of Synaptotagmin I with $[M(CO)_3]^+$ (M = ^{99m}Tc or Re) and/or a Fluorescein

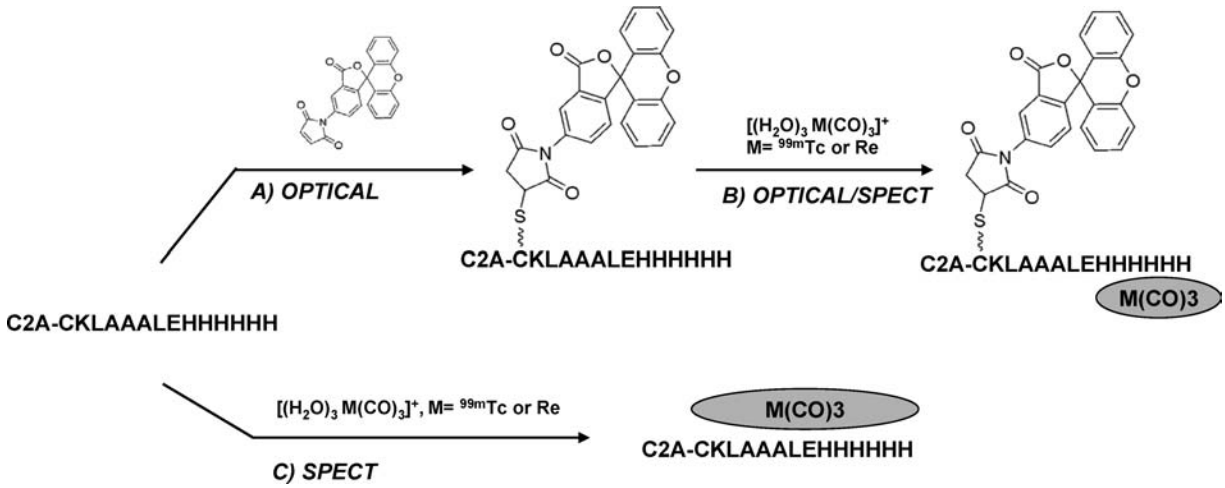

protein molecules carry a disproportionately high radiolabel signal. The biodistributions of Annexin V derivatives were improved to some extent by refining the non-site-specific labeling methods, leading eventually to ^{99m}Tc-HYNIC-Annexin V (*12*).

Like Annexin V, C2A (~16 kDa) is vulnerable to inactivation by inappropriate modification. The Ca^{2+} binding sites within C2A-domain are surrounded by positively charged amino acids, among them several Lys residues, that were shown by mutagenesis to also be involved in phospholipid binding (*13, 14*). Since Lys residues are the usual site of modification for radiolabeling, great caution in bioconjugate synthesis and careful characterization of the products are required. C2A was first used as an MR cancer imaging agent in the form of a glutathione-S-transferase (GST) fusion protein which forms a noncovalent dimer of ~85 kDa. The GST-C2A protein was nonspecifically modified and covalently linked via Lys residues to either superparamagnetic iron oxide particles or the gadolinium complex of *S*-2-(4-isothiocyanatobenzyl)-DTPA (*p*-SCN-Bn-DTPA) (*15, 16*). This nonspecific labeling method resulted in a decreased affinity for PS (*17*). For SPECT imaging, ^{99m}Tc-labeled GST-C2A has been used in preclinical cardiac and cancer applications (*18, 19*). In these studies too, a non-site-specific method was employed: the fusion protein GST-C2A was treated with 2-iminothiolane to modify GST-C2A Lys amines to thiols then labeled with ^{99m}Tc-glucoheptonate.

Given these problems, producing recombinant protein conjugates to current good manufacturing practice (cGMP) standards with consistent batch-to-batch quality using non-site-specific modification for clinical imaging is problematic. Removal of any inactive or low-affinity protein prior to injection, if achievable at all, requires additional affinity chromatography purification steps (*16*). A cGMP cell death imaging agent developed for clinical application should be labeled site-specifically, reproducibly, efficiently, and at room temperature. Preferably, it should be a simple kit-based method providing a well-characterized, homogeneous, fully functional and stable product. Tait et al. approached this objective by genetically engineering a derivative with an N-terminal amino acid AG-GCGH tag, which can be labeled with ^{99m}Tc (*12, 20*). Others have recently genetically engineered a free Cys for the site-specific modification and radiolabeling of Annexin V (*21*). However, no derivative of C2A for site-specific labeling has yet been reported.

With this in mind, we have genetically engineered and recombinantly expressed C2A with a C-terminal domain designed for site-specific modification with maximum versatility, incorporating both a HexaHistidine tag (His-tag) and an additional cysteine residue. Here, the term site-specific refers to the ability to radiolabel a radiopharmaceutical via His-tag without interfering with its function. The His-tag can be used not only for immobilized metal affinity chromatography (IMAC) purification, but also in principle for site-specifically labeling with ^{99m}Tc using $[^{99m}Tc(CO)_3(OH_2)_3]^+$ (*22*), while the Cys can be used for site-specific covalent modification with prosthetic groups for optical or radiolabeling. The His-tag is nonimmunogenic and does not hinder the clinical development of His-tag -containing recombinant proteins (*23*−*27*). We have also engineered C2A with a single C-terminal Cys residue but no His-tag. This strategy should facilitate concomitant fluorescent histological evaluation of a SPECT signal for preclinical validation (see Scheme 1). In this paper, we report the use of this strategy to develop a site-specifically radiolabeled radiopharmaceutical for the imaging of cell death. We describe the labeling and modification properties of the new appended C-terminal amino acid sequence and the effect of modification on PS binding.

EXPERIMENTAL PROCEDURES

Molecular Biology. The pET-29b vector containing amino acid residues 140−267 of rat Synaptotagmin I, the C2A domain, (provided by Bazbek Davletov, University of Cambridge, UK) was used as a template for the polymerase chain reaction (PCR) and subsequent subcloning to create two variants, both without the inherent S-Tag domain in the vector: C2Ac (C2A with a single cysteine residue on the C-terminus) and C2AcH (C2A with a single cysteine residue on the C-terminus, a linker (KLAAALE), and a hexahistidine tag). The two constructs used the same forward primer: 5′-CAC ACA CAT ATG GAG AAA CTG GGA AAG CTC CAA with the reverse primer for C2Ac: 5′-CAC ACA AAG CTT TCA GCA TTT CTC AGC GCT CTG GAG ATC GCG and for C2AcH: 5′-CAC ACA AAG CTT GCA TTT CTC AGC GCT CTG GAG ATC GCG. The resulting PCR fragments were subcloned back into the pET-29b vector using the restriction enzymes NdeI and *Hin*dIII and sequenced (King's College London, Molecular Biology Unit, UK). After sequence confirmation, DNA constructs for C2Ac and C2AcH were transformed into the BL21 (DE3) strain of *Escherichia coli*. For both constructs, cultures in 10 mL of L-broth containing 50 μg/mL kanamycin (Sigma, Gillingham, UK) were grown overnight at 37 °C with agitation, and then added to 1000 mL L-Broth and grown at 37 °C with agitation until the OD_{600} reached 0.8. Expression was then induced by adding 1 mM isopropyl β-D-1-thiogalactopyranoside (IPTG) (Merck Chemicals, Nottingham, UK) followed by further

incubation at 37 °C with agitation for 4 h. Cells were then pelleted by centrifugation at 4100 relative centrifugal force (RCF) for 10 min at 4 °C and then frozen at −80 °C. Pellets were resuspended in 50 mL resuspension buffer (RB, 20 mM Tris-HCl pH 7.5, 150 mM NaCl, 1 mM EDTA, 0.1% Triton X-100, and Complete Protease Inhibitors (Roche Diagnostic, Burgess Hill, UK)). Suspensions were then sonicated four times for 15 s with 1 min intervals on ice and allowed to recover for 30 min on ice. The suspension was then centrifuged at 4 °C for 20 min at 35 000 RCF. For C2AcH purification, the supernatant was added to a 1 mL nickel column (GE Healthcare, Amersham, UK) at 1 mL/min using an AKTA FPLC (GE Healthcare, Amersham, UK), which had previously been equilibrated with nickel binding buffer (NBB, 20 mM Tris-HCl pH 7.5, 150 mM NaCl). The column was then flushed with 10 column volumes (CV) of NBB and washed with 20 CV of nickel wash buffer (NWB, 20 mM Tris-HCl pH 7.5, 150 mM NaCl, 50 mM imidazole). The protein was then eluted with 20 CV of nickel elution buffer (NEB, 20 mM Tris-HCl pH 7.5, 150 mM NaCl, 500 mM imidazole). Elution fractions containing protein were dialyzed overnight against 3 L NBB using a 7 kDa molecular weight cutoff dialysis tubing at 4 °C with gentle stirring. Four millimolar $CaCl_2$ was then added to dialyzed protein before addition to a 5 mL Heparin Column (GE Healthcare, Amersham, UK), which had previously been equilibrated with Heparin Binding Buffer (HBB, 20 mM Tris-HCl, 150 mM NaCl, 2 mM $CaCl_2$, pH 7.5) at 1 mL/min. The column was washed with 10 CV of HBB, and the protein was then eluted with 10 CV of Heparin Elution Buffer (HEB, 20 mM Tris-HCl, 200 mM NaCl, 10 mM EDTA, pH 7.5). To elute any dimer that may have formed, the column was eluted with 10 CV of Heparin Clean Buffer (HCB, 20 mM Tris-HCl, 1.5 M NaCl, 100 mM EDTA, pH 7.5). Any dimer present in this eluate was reduced with 10 mM dithiothreitol (DTT) for 4 h at RT and then loaded on a Sephacryl 100 size exclusion column (60 cm height, GE Healthcare, Amersham, UK) equilibrated with PBS such that the load volume did not exceed 5% of a column volume. C2Ac was purified using the heparin procedure and the elution pool was loaded on a Sephacryl 100 size-exclusion column as described above. The gel permeation elution peak was collected and the concentration was determined by absorbance at 280 nm using a calculated extinction coefficient of 12 210 M^{-1} cm^{-1}. Purified proteins were analyzed by SDS-PAGE, analytical HPLC-SEC, and LC-MS (University of Kent, UK). C2AcH was purified at 20 mg per liter culture and C2Ac was purified at 40 mg per liter culture.

Fluorescein-5-maleimide, *N*-(benzyloxycarbonyloxy) Succinimide and Iodoacetamide Conjugates of C2Ac and C2AcH. C2Ac and C2AcH were conjugated to fluorescein-5-maleimide (Sigma-Aldrich, Poole, UK). One millilitre of C2AcH or C2Ac (2 mg/mL in PBS) were mixed with a 5-fold molar excess of fluorescein-5-maleimide dissolved in 50 μL of dimethylsulfoxide (DMSO) and incubated at room temperature for 4 h. Unreacted fluorescein-5-maleimide was removed using a PD-10 column which had been pre-equilibrated with PBS. PD-10 fractions were monitored by UV absorbance at 280 nm and analyzed by SDS-PAGE and LC-MS. The fluorescein conjugates of C2Ac and C2AcH are referred to as C2Ac-F and C2AcH-F, respectively.

To generate a non-Cys-like "mutant", the thiol was modified with iodoacetamide. C2AcH was incubated at 2 mg/mL with a 1.5 molar excess of iodoacetamide (Sigma-Aldrich, Poole, UK) overnight at 4 °C. Unreacted iodoacetamide was removed using a PD-10 column and protein fractions were analyzed by SDS-PAGE and LC-MS. The iodoacetamide conjugate of C2AcH is referred to as C2AcH-A. The free thiol content of C2AcH and C2AcH-A was determined by Ellman's Reagent as described by the manufacturer (Pierce Biotechnology, Rockford, US) (*28*).

To generate a nonspecifically modified C2A protein for radiolabeling, C2AcH was derivatized with *N*-(benzyloxycarbonyloxy)succinimide (Sigma-Aldrich, Poole, UK) as described above except a 20 to 1 molar ratio of *N*-(benzyloxycarbonyloxy)succinimide to C2AcH was used with incubation for only 1 h, giving rise to C2AcH-B, and samples were analyzed by SDS-PAGE.

Flow Cytometry and Immunofluorescence. J774.2 murine macrophage cell line (ECACC, Porton Down, UK) were grown in DMEM (Invitrogen, UK) supplemented with penicillin (100 units/mL), streptomycin (100 μg/mL), L-glutamate (5 mM), fetal bovine serum (10%, Sigma), sodium pyruvate (1 mM), and HEPES (10 mM). To test the binding capability of C2Ac and C2AcH-F to necrotic and apoptotic cells, the fluorescein conjugates were incubated with control or etoposide (MBL International, Woburn, US) treated (15 μM, overnight at 1×10^6 cells/mL) murine macrophages and compared to Annexin V-FITC (Invitrogen, Vybrant Apoptosis Kit) using a FACS-calibur (Becton, Dickinson, Oxford UK) flow cytometry. Acquisition was performed according to commercial kit instructions.

For confocal microscopy, macrophages were plated at 5×10^5 cells per well in a 6-well cell culture plate on sterile glass coverslips. On day 2, cells were treated overnight with 15 μM etoposide or PBS control. Cells were washed 3 times in PBS and then 3 times in either cell binding buffer (CBB, 10 mM HEPES, 140 mM NaCl, 2 mM $CaCl_2$, pH 7.4) or cell nonbinding buffer (CNBB, 10 mM HEPES, 140 mM NaCl, 10 mM EDTA, pH 7.4). Coverslips were then incubated for 15 min in 200 μL of CBB or CNBB containing 2 μL propidium iodide (PI) and 3 μL of 0.6 μM C2AcH-F, washed 3 times with CBB or CNBB then 3 times in PBS, fixed with 4% paraformaldehyde (PFA) for 10 min at room temperature (RT), and washed a further 3 times in PBS. For immunostaining, cells were permeabilized in 0.1% Triton X-100 in 10% FBS for 10 min at RT. Anti-cleaved caspase-3 antibody (Cell Signaling Technology) was diluted 1:200 in 2% FBS and incubated with cells for 1 h at RT. Coverslips were washed 3 times in PBS and then incubated with Alexa Fluor 546 goat-anti-rabbit (Invitrogen) diluted 1:200 in 2% FBS for 1 h at RT. Coverslips were again washed 3 times in PBS, then 3 times in water before being mounted on a slide with fluorescent mounting medium (Dako). Slides where analyzed by confocal microscopy in the microscope core facility (University College London, UK).

Rhenium Labeling of C2AcH and C2AcH-A. Rhenium tricarbonyl (*fac*-$[Re(CO)_3(OH_2)_3]Br$) was prepared and characterized as previously reported (*29*). Briefly, $[Re(CO)_5]Br$ was refluxed in distilled H_2O for 24 h. The crude mixture was filtered, and the solution concentrated under vacuum to give *fac*-$[Re(CO)_3(OH_2)_3]Br$ as a light green powder in nearly quantitative yield. The final product was characterized by IR and ES-MS. C2AcH or C2AcH-A was labeled with rhenium by incubating 100 μg of C2AcH or C2AcH-A in 100 μL of PBS with a 10-fold molar excess of $[Re(CO)_3(OH_2)_3]Br$. This mixture was left to incubate at 37 °C for 30 min before being passed through a PD-10 column (Sephadex G-25, GE Healthcare). The protein was analyzed by SDS-PAGE and LC-MS.

To investigate whether rhenium tricarbonyl bound to the Cys, C2AcH was incubated with or without $[Re(CO)_3(OH_2)_3]Br$ as described above. After reacting, a 100 μL of PBS pH 8.0 was added to each of the C2AcH solutions and left overnight at 37 °C. The formation of a dimer was monitored by running equal amounts (as determined by A_{280}) of C2AcH with and without $[Re(CO)_3(OH_2)_3]Br$ on a nonreduced SDS/PAGE gel. Monomeric (~16 kDa) and dimeric (~32 kDa) of C2AcH bands were quantified using *ImageJ* analysis software (NIH, Bethesda, US).

In order to map the specific binding of rhenium tricarbonyl to the C-terminal CKLAAALEHHHHHH sequence, a tryptic digest was performed on rhenium tricarbonyl labeled and unlabeled C2AcH using a method previously described (*8*). Briefly, 100 μg of C2AcH in 100 μL was dissolved in 25 μL of 8 M urea and 100 mM ammonium carbonate. The urea was then diluted by the addition of water (75 μL) and modified sequence-grade trypsin (Promega) was added (10 μL of a 0.5 mg/mL solution) and incubated for 4 h at RT. Analysis was by rapid in-line reverse-phase HPLC/electrospray mass spectrometry (University of Kent, UK).

^{99m}Tc Labeling of C2Ac, C2AcH, C2Ac-F, C2AcH-F, C2AcH-A, and C2AcH-B. ^{99m}Tc pertechnetate eluted with saline from a Drytec generator (GE Healthcare, Amersham, UK) was converted to $[^{99m}Tc(CO)_3(OH_2)_3]^+$ using the Isolink kit (generously provided by Covidien, Petten, The Netherlands). Quality control was carried out according to manufacturer's instructions using instant thin layer chromatography (ITLC) and analysis with a gamma-ray TLC scanner (Lablogic, UK) and high-performance liquid chromatography (HPLC series 1200, Agilent, UK) equipped with an in-line gamma detector (Lablogic, UK). C2A proteins were labeled with ^{99m}Tc by incubating 100 μg of C2Ac, C2Ac-F, C2AcH, C2AcH-F, C2AcH-A, or C2AcH-B in 100 μL of PBS with up to 700 MBq of $[^{99m}Tc(CO)_3(OH_2)_3]^+$ in 100 μL. Unless otherwise stated, the labeling of all species was performed at a specific activity of 4 MBq/μg. However, to reproduce a high (clinically relevant) specific activity, C2AcH was also labeled at 7 MBq/μg. This mixture was left to incubate at either 10 or 37 °C for up to 120 min before radiolabeling efficiency was determined by ITLC. The same ITLC conditions were used as described above, and the radiolabeling efficiency was calculated as a ratio of the radiolabeled protein peak integral ($R_f = 0$) to the unincorporated $[^{99m}Tc(CO)_3(OH_2)_3]^+$ peak integral ($R_f = 1.0$). We also determined the labeling efficiency by passing the protein through a PD-10 column (Sephadex G-25, GE Healthcare). Labeling efficiency was calculated by comparing the amount of radioactivity associated with the eluted protein fraction versus unincorporated eluted (low molecular weight) radioactivity using a gamma counter (LKB Wallac, 1282 COMPUGAMMA) or dose calibrator (CRC-25R, Capintec, US). It should be noted that up to ~5% of activity remains bound to the PD-10 column. Binding of radioactivity to protein was also confirmed by SDS-PAGE of the protein fraction followed by electronic autoradiography of the gel (Cyclone phosphorimager, Perkin-Elmer, UK).

Binding of ^{99m}Tc Labeled C2AcH and C2AcH-B to PS on Red Blood Cells. The binding of radiolabeled C2AcH to PS on red blood cells (RBC) was performed according to a literature method (*30*). A commercial preparation of preserved human RBC was obtained from Beckman-Coulter (High Wycombe, UK). Calcium titrations of RBC were performed in a buffer of 50 mM HEPES-sodium, pH 7.4, 100 mM NaCl, 3 mM NaN_3, with 1 mg/mL BSA as carrier protein. Reactions were prepared with 1 nM ^{99m}Tc labeled C2AcH and calcium; RBC were then added, and the reaction (1 mL) was incubated for 8 min at RT. The cells were then centrifuged (3 min at 7500 RCF), the supernatant was removed, and the cells were resuspended in 1 mL assay buffer containing the same concentration of calcium used during the incubation step. The cells were centrifuged again, the supernatant was removed, and the pellet was resuspended in 0.7 mL assay buffer plus 10 mM ethylenediaminetetraacetic acid (EDTA) to release ^{99m}Tc labeled C2AcH bound in a calcium-dependent manner. After centrifugation to remove the RBC, the released ^{99m}Tc labeled C2AcH in the supernatant was measured using a gamma counter. The EC_{50} was calculated as described in the literature using the equation $Y = [Ca]^N/([Ca]^N + EC_{50}{}^N)$ (*30*) where $Y = B/B_{max}$, B is the observed amount of radiolabeled protein bound at a given calcium concentration, and B_{max} is the concentration of radiolabeled protein bound at saturating calcium concentrations. Curve fitting was performed using a nonlinear curve fit by a routine based on the Levenberg−Marquardt algorithm using *Kaleidagraph* (Synergy Software, Reading, US).

Serum Stability. C2AcH and C2AcH-F were labeled with 400 MBq $[^{99m}Tc(CO)_3(OH_2)_3]^+$ in 100 μL for 30 min or 1 h at 37 °C. After purification on a PD-10 column, 100 μL of labeled C2AcH or C2AcH-F was added to 400 μL human serum (Sigma, Poole, UK). As a control, 100 μL of labeled C2AcH or C2AcH-F was also added to PBS. The samples were then incubated at 37 °C. At 0, 3, 6, and 18 h, samples were taken and analyzed by ITLC using a mobile phase of methanol and 1% concentrated HCl. As a control, a separate ITLC of $[^{99m}Tc(CO)_3(OH_2)_3]^+$ and $[TcO_4]^-$ was performed in the same mobile phase. ITLC were then monitored using a radio TLC scanner (LabLogic, UK). Serum stability was calculated as the area under the protein peak ($R_f = 0$) versus the area under the curve of the remainder of the chromatogram $[^{99m}Tc(CO)_3(OH_2)_3]^+$ or $[TcO_4]^-$ $R_f = 1.0$).

RESULTS

Cloning, Preparation, and Characterization of C2Ac, C2AcH, C2AcH-F, C2AcH-A, and C2AcH-B. C2A was cloned into the pET-29d bacterial expression vector with the addition of a C-terminal site-specific Cys with and without a His-tag, forming two constructs C2AcH (with His-tag) and C2Ac (without His-tag), respectively (Scheme 1). After induced expression in *E. coli*, C2Ac and C2AcH were isolated from the soluble fraction. C2AcH was purified first via IMAC and further purified by heparin affinity chromatography in the presence of Ca^{2+}, while C2Ac was purified directly using heparin affinity chromatography. C2Ac and C2AcH were buffer-exchanged and purified by size exclusion chromatography (Figure 1a). C2AcH eluted as a single discrete peak with a retention time expected for a protein of ~16 kDa, with no evidence of significant aggregation or dimerization. C2AcH was analyzed by reduced and nonreduced SDS-PAGE, giving rise to a single monomeric band at the expected molecular weight (Figure 1b). The final protein products were analyzed by electrospray mass spectrometry (ES-MS) and were of the expected molecular weights (Table 1). C2AcH and C2Ac were modified with fluorescein maleimide, iodoacetamide, or *N*-(benzyloxycarbonyloxy)succinimide to give conjugates C2AcH-F, C2AcH-A, and C2AcH-B. These were analyzed by ES-MS. C2AcH-F was of the expected molecular weights for the addition of one fluorescein but also exhibited a second minor peak in the liquid chromatography, which by ES-MS is due to the addition of a second fluorescein molecule. For C2AcH-A, the addition of only one acetamide group, with no unconjugated C2AcH, was observed in the LC-MS (Table 1). The modification at the Cys residue was confirmed by Ellmans' Reagent, which showed no detectable free thiol in C2AcH-A, while the expected amount of free thiol was observed in C2AcH.

On forming C2AcH-B, the benzyloxycarbonyloxy conjugate of C2AcH, a minor fraction of the protein precipitated from solution. The soluble fraction did not give rise to any peaks in ES-MS and was therefore analyzed by nonreducing and reducing SDS/PAGE, giving rise to a single band at a lower molecular weight than C2AcH, indicating that the C2AcH-B had an altered conformation (data not shown).

C2AcH-F Binds to Apoptotic Cells in a Calcium Dependent Manner. The ability of C2AcH-F to bind apoptotic cells was monitored by the incubation of C2AcH-F with live murine macrophages in culture that had been treated with

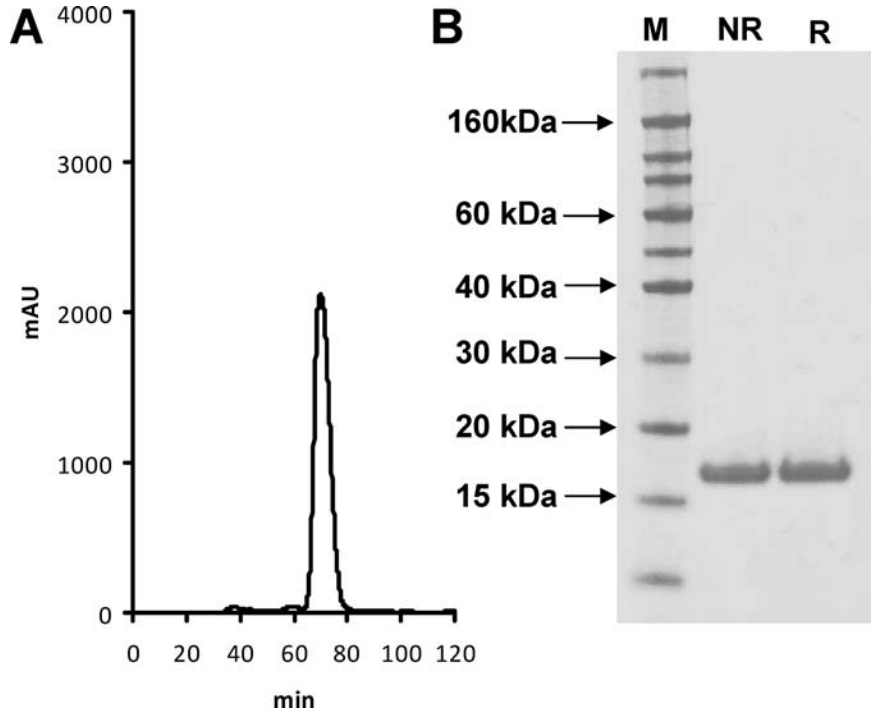

Figure 1. Size exclusion, SDS/PAGE, and ES-MS characterization of C2AcH. (A) After expression and purification by IMAC and heparin affinity chromatography, C2AcH was further purified by preparative size exclusion chromatography. In fast protein liquid chromatography (FPLC) size exclusion chromatogram shown, a discrete single peak with a retention time of 71 min as expected for a globular ~16 kDa protein compared to molecular weight standards (data not shown). (B) The single peak obtained from the preparative size exclusion chromatography was analyzed by reduced (R) and nonreduced (NR) SDS/PAGE electrophoresis. In the SDS/PAGE gel shown, a single band under both the nonreduced and reduced conditions of ~16 kDa was observed as compared to molecular weight markers (M). This indicates that C2AcH exists as a single species and no dimer is present.

Table 1. Summary of ES-MS Data of C2Ac and C2AcH Protein Conjugates and Peptides Post Tryptic Digest

protein (M)/peptide (P)	expected (Da)	found (Da)
C2Ac	14997	14998 $[M + H]^+$
C2AcH	16517	16518 $[M + H]^+$
C2AcH-A	16574	16575 $[M + H]^+$
C2Ac-F	15542	15542 $[M + H]^+$, 15524 $[M - H_2O]^+$; 15869 $[M + 2xF + H_2O]^+$
C2AcH-F	16944	16944 $[M + H]^+$, 16962 $[M + H_2O]^+$ 17389 $[M + 2xF]^+$; 17407 $[M + 2xF + H_2O]^+$
C2AcH-$^{187/185}$Re(CO)$_3$	16787	16787 $[M]^+$
LAAALEHHHHHH	705	705 $[P + 2H]^{2+}$
LAAALEHHHHHH-$^{187/185}$Re(CO)$_3$	840	840 $[P + Re(CO)_3 + H]^{2+}$
CKLAAALEHHHHHH	820	not observed
CKLAAALEHHHHHH-$^{187/185}$Re(CO)$_3$	956	956 $[P + Re(CO)_3 + H]^{2+}$

etoposide (Figure 2). After fixation, permeabilization, and staining with anti-cleaved caspase-3 confocal microscopy confirmed that, in the presence of calcium, C2AcH-F binds to the extracellular membrane of caspase 3 positive cells, while in the absence of calcium, there is no binding of C2AcH-F to the cell membrane. Therefore, after the labeling of C2AcH with fluorescein via the cysteine thiol, it retained its calcium-dependent function. Cells were also analyzed by flow cytometry by incubating live macrophages with C2AcH-F or Annexin V-FITC, and similar results were observed (data not shown).

Labeling of C2Ac, C2AcH, C2Ac-F, C2AcH-F, C2AcH-B, and C2AcH-A with $[^{99m}Tc(CO)_3]^+$ or $[Re(CO)_3]^+$. To compare the labeling efficiency of the proteins with $[M(CO)_3]^+$ (where M = ^{99m}Tc or Re), C2Ac, C2AcH, C2Ac-F, C2AcH-F, and C2AcH-A were labeled by incubating either $[^{99m}Tc(CO)_3(OH_2)_3]^+$ or 10-fold excess of $[Re(CO)_3(OH_2)_3]^+$ with the proteins (100 μg) at 10 or 37 °C for up to 120 min (Scheme 1). Radiolabeled proteins were purified on a PD-10 column and analyzed by SDS/PAGE and autoradiography (Figure 3). A radiochemical yield of >95% (as analyzed by ITLC) was achieved with 1 μg/μL of C2AcH (which possesses both a free Cys and His-tag) at 37 °C within 30 min (Figure 4). The radiochemical purity was 100%. Longer incubation times did not improve the radiochemical yield. However, when a 10-fold lower protein concentration of C2AcH (0.1 μg/μL) was used at 37 °C a radiolabeling yield of only 25% was achieved, which increased over time to reach 98% after 24 h (data not shown). When C2AcH was radiolabeled at the lower temperature of 10 °C for 30 min, radiochemical yields of 65% and 10% were achieved at protein concentrations of 1 and 0.1 μg/μL, respectively. In order to assess the contribution of the free Cys to the excellent radiolabeling efficiency of C2AcH, the Cys thiol was "blocked" using iodoacetamide. At a C2AcH-A concentration of 1 μg/μL, radiochemical yields of only ~83% at 37 °C and ~40% at 10 °C at 30 min were achieved. At a C2AcH-A concentration of 0.1 μg/μg, a radiochemical yield of 16% was achieved at 37 °C, which increased over time to reach 88% after 24 h (data not shown). When C2AcH-A was radiolabeled at the lower temperature of 10 °C for 30 min, radiochemical yields of 40% and 7% were achieved at protein concentrations of 1 and 0.1 μg/μL, respectively. When C2Ac (no His-tag) was radiolabeled, a maximum radiochemical yield did not exceed 15%, and did not improve upon further incubation or increase in temperature (data not shown). When C2AcH and C2AcH-A

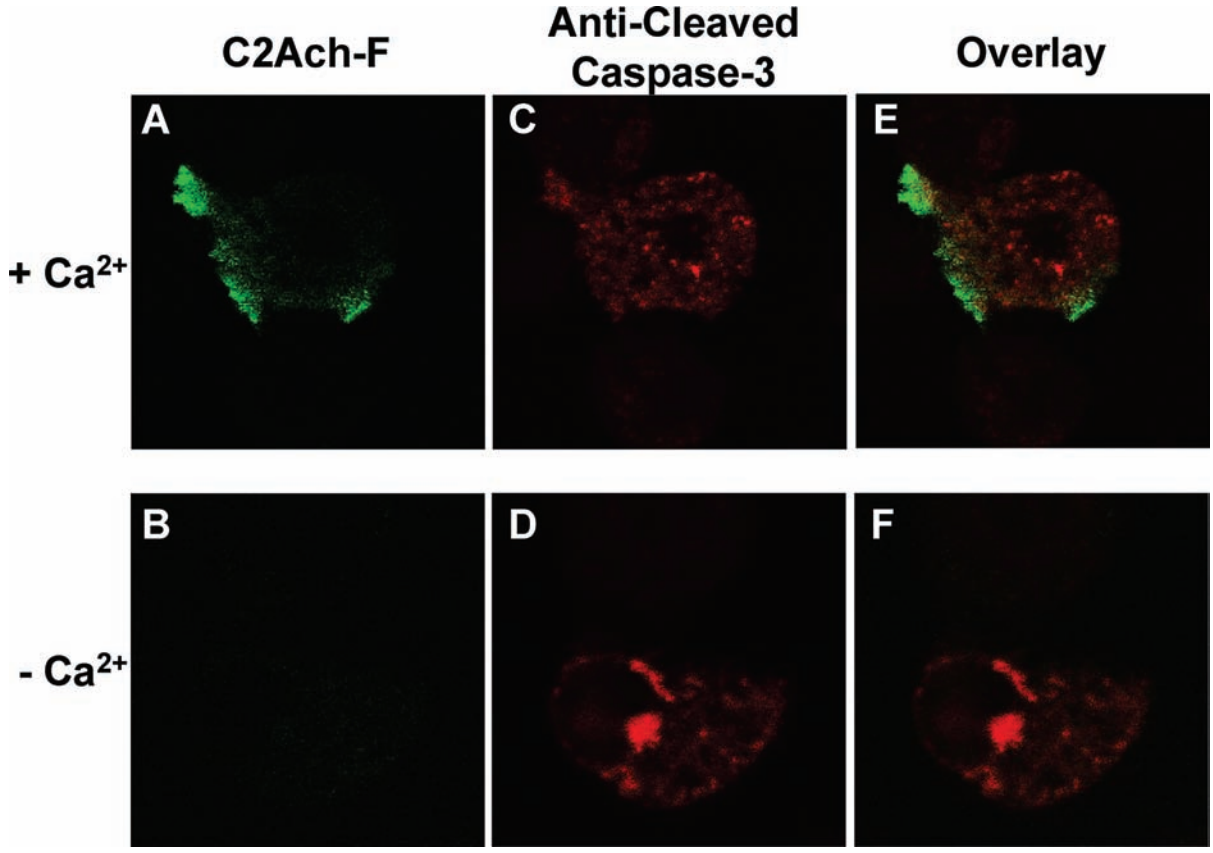

Figure 2. Confocal microscopy of apoptotic mouse macrophages stained with C2AcH-F and/or anti-cleaved caspase-3. C2AcH was site specifically modified at the Cys with fluorescein-maleimide. To show that C2AcH-F was functional and recognized apoptotic cells, C2AcH-F (panels A and B) was incubated with etoposide-treated macrophages in the presence (panels A, C, and E) and absence (panels B, D, and F) of 4 mM calcium. Cells were then permeabilized and stained for a specific intracellular marker of apoptosis, using rabbit anti-cleaved caspase-3 followed by an Alexa Fluor 546 goat-anti-rabbit secondary antibody (panels C and D). The C2acH-F (green) images and anti-cleaved caspase-3 (red) images were overlaid (panels E and F). C2Ac-F and anti-cleaved caspase-3 did not bind to live (non-apoptotic) cells (data not shown).

were radiolabeled at higher and more clinically relevant specific activities (i.e., 7 MBq/μg) at 37 °C for 30 min, radiolabeling efficiencies of 94% and 88%, respectively, were achieved.

Labeling of C2AcH and C2AcH-A with $[Re(CO)_3]^+$ was confirmed by ES-MS showing the correct molecular weight assuming that $[Re(CO)_3]^+$ replaces a proton (Table 1). Despite the presence of a 10-fold excess of $[Re(CO)_3(OH_2)_3]^+$ over protein, no evidence of proteins with more than one $[Re(CO)_3]^+$ attached to a protein was seen in the ES-MS data, suggesting that only one modification occurs per protein molecule. Furthermore, when a tryptic digest was performed on rhenium tricarbonyl labeled and unlabeled C2AcH, only peptides containing the amino acid sequence CKLAAALEHHHHHH or LAAALEHHHHHH contained only one $[Re(CO)_3]^+$ group (Table 1). The reaction of C2Ac with $[Re(CO)_3]^+$ under these conditions did not give rise to a detectable rhenium conjugate, and only unmodified C2Ac was detected by ES-MS. These results suggest that only the C-terminal domain is modified and that the Cys and His-tag act synergistically to improve significantly the rate and efficiency of labeling with $[^{99m}Tc(CO)_3]^+$ and $[Re(CO)_3]^+$, compared to protein with either the His-tag alone or the Cys alone.

To investigate whether $[Re(CO)_3]^+$ remained bound to the Cys, the dimerization of the protein by aerial oxidation of the Cys thiol group was used as a probe(Figure 5). Unmodified C2AcH undergoes extensive dimerization (approximately 67% of protein) after exposure to air at room temperature at pH 8.0 for 16 h, as detected by nonreducing SDS/PAGE analysis. On the other hand, C2AcH that had been incubated at 37 °C with an 10-fold excess of $[Re(CO)_3(OH_2)_3]^+$ overnight, resulting in a preparation in which only the C2AcH-$Re(CO)_3$ conjugate and no free C2AcH could be detected by ES-MS, dimerization was partially inhibited (30% of protein) but not completely blocked. One explanation of this is that the $Re(CO)_3$ fragment is engaged in binding with the Cys thiolate group, although not irreversibly, such that it can be made available for oxidation over time.

Site-Specifically ^{99m}Tc Labeled C2AcH Binds to Apoptotic Cells in a Calcium Dependent Manner. To determine whether or not radiolabeled C2AcH was still functional after radiolabeling, the protein was incubated with preserved red blood cells at varying concentrations of calcium from 0 to 10 mM (Figure 6). Binding of ^{99m}Tc labeled C2AcH to red blood cells can be detected with as little as 0.25 mM $CaCl_2$ with maximal binding observed at 4 mM $CaCl_2$. After nonlinear curve fitting ($R = 0.9996$), the EC_{50} of labeled C2AcH was calculated to be 0.76 mM of calcium, which is comparable to that observed for Annexin V (*30*), while for C2AcH-F, the EC_{50} was 1.03 mM (determined similarly, data not shown). To determine the comparative effect of non-site-specific lysine modification, C2AcH was incubated with a 20-fold excess of the NHS derivative *N*-(benzyloxycarbonyloxy)succinimide and the resultant modified protein, C2AcH-B, was radiolabeled with ^{99m}Tc tricarbonyl, giving radiochemical purity of >95%, and subjected to the same PS-binding assay. No C2AcH-B calcium dependent binding to cells was observed even at the highest concentration of Ca^{2+} of 10 mM (Figure 6).

Serum Stability of Radiolabeled C2AcH and C2AcH-F. The stabilities of C2AcH-$[^{99m}Tc(CO)_3]$ and C2AcH-F-$[^{99m}Tc(CO)_3]$ during incubation in PBS or serum over 18 h were determined (Table 2) using ITLC with gamma detection.

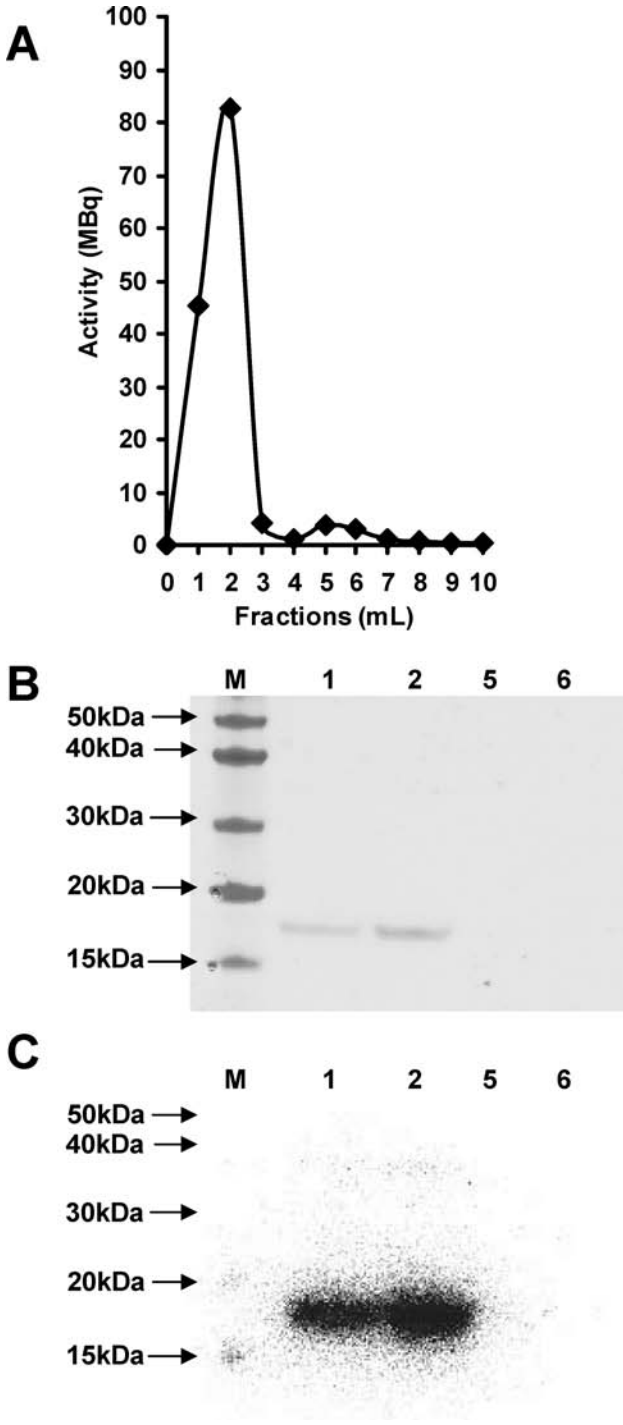

Figure 3. Radiolabeling, size exclusion purification, SDS/PAGE, and phosphor image analysis of C2AcH-[^{99m}Tc(CO)$_3$]. (A) C2AcH was radiolabeled with [^{99m}Tc(CO)$_3$ (OH$_2$)$_3$]$^+$ and purified on a PD 10 size exclusion column to remove any unincorporated radiolabel. In the graph shown, the eluted fractions (1 mL) were collected and the activity (MBq) per fraction was determined. (B) The labeled protein fractions 1 and 2 and unincorporated radiolabel fractions 5 and 6 from the PD-10 size exclusion column were then analyzed by SDS/PAGE electrophoresis under nonreducing conditions with molecular weight markers (M). In the SDS/PAGE gel shown, no activity was observed in lanes corresponding to fraction 5 and 6 presumably because the lower molecular weight radioactive species runs off the gel. (C) ^{99m}Tc radioactive markers were placed at the 15 and 20 kDa molecular weight protein markers on the SDS/PAGE gel and the image shown was acquired using a medium MultiSensitive phosphor screen for 30 s and analyzed using a phosphor imager (PerkinElmer Cyclone).

C2AcH-[^{99m}Tc(CO)$_3$], C2AcH-F-[^{99m}Tc(CO)$_3$], [^{99m}TcO$_4$]$^-$, and [^{99m}Tc(CO)$_3$(OH$_2$)$_3$]$^+$ were analyzed before in order to determine their migration on ITLC plates (data not shown). For C2AcH-[^{99m}Tc(CO)$_3$], only one radioactive peak, with $R_f = 0$, was observed for the duration of the stability study, both in PBS and in serum. However, C2AcH-F-[^{99m}Tc(CO)$_3$] after 18 h in serum gave rise to a second minor peak with $R_f = 1.0$ with approximately 5% of the radioactivity, while the PBS control showed little degradation.

DISCUSSION

To the best of our knowledge, the addition of the sequence CKLAAALEHHHHHH to the C-terminus of C2AcH represents the first use of a combination of a His-tag and a free cysteine residue as a tag for incorporation of imaging probes into recombinant proteins. Although it was designed for versatility, to allow the incorporation of both a ^{99m}Tc radiolabel via the His-tag and other imaging probes via covalent modification of the Cys, an unexpected benefit was that the efficiency of labeling with [^{99m}Tc(CO)$_3$]$^+$ dramatically increased, giving higher labeling yield and specific activity under mild conditions (37 °C, 30 min) than the His-tag alone (C2AcH-A, ~83%, C2AcH-F, ~60%) or Cys alone (C2Ac, ~15%). Radiochemical yields as measured by ITLC always exceeded 96% at a concentration of 1 μg/μL of C2AcH. This suggests that, with little further optimization, a simple kit-based labeling method could be developed without need for postlabeling purification. The present data indicate that, with the His-tag alone, a purification step would be required, adding unwanted complexity. Earlier reported ^{99m}Tc labeling conditions for model His-tagged proteins described conditions involving 15 to 30 min at 37 °C to achieve a 95% radiochemical yield (*22*). However, we have been unable to achieve this efficiency with C2AcH-A or C2AcH-F in which the Cys is blocked by acetamide or maleimide conjugation, respectively. Other groups also have reported that higher temperatures and/or longer incubation times maybe required to achieve adequate radiochemical yields with some His-tagged proteins (*31*).

The C2Ac construct without a His-tag was labeled with 15% radiochemical yield, which is comparable to reports in the literature for non-His-tagged proteins (*32*). This nonzero labeling efficiency raises the possibility that [Tc(CO)$_3$]$^+$-labeling may not be fully site specific for His-tags. However, in the mass spectrum of the [Re(CO)$_3$]$^+$ adducts, despite the presence of a 10-fold excess of [Re(CO)$_3$(OH$_2$)$_3$]$^+$ over protein, there is no evidence that more than one [Re(CO)$_3$]$^+$ binds to C2AcH and no evidence of any binding to C2Ac. This site specificity was confirmed by tryptic digest of C2AcH, which indicated that only peptide sequences containing the His-tag sequence contained the addition of only one [Re(CO)$_3$]$^+$. All other peptides from the tryptic digest were the same as unmodified C2AcH and did not show the addition of [Re(CO)$_3$]$^+$. However, it should be noted that, when [Re(CO)$_3$]$^+$ binds to the His-tag there are multiple potential regio- and steroisomers that can be formed upon complexation. Site specificity is also consistent with the excellent PS-binding affinity observed for C2AcH-[^{99m}Tc(CO)$_3$]. The calcium EC$_{50}$ data suggest that the PS-affinity of C2AcH-[^{99m}Tc(CO)$_3$] is slightly better than that of C2Ac-F. This is not unexpected, since the latter contains some non-site-specifically fluorescein-modified protein, as evidenced by the detection of some doubly modified protein in its mass spectrum.

The observation that conjugation with [Re(CO)$_3$]$^+$ markedly reduces dimer formation by thiol oxidation in air suggests that the thiol group is protected. One possible explanation for this observation is that the thiol binds to the metal. If this is the case, however, the Re−S interaction must be labile to some extent, because aerial oxidation is merely slowed and not completely blocked (Figure 5). In addition, if the thiol group plays a major part in maintaining the protein−metal bond one

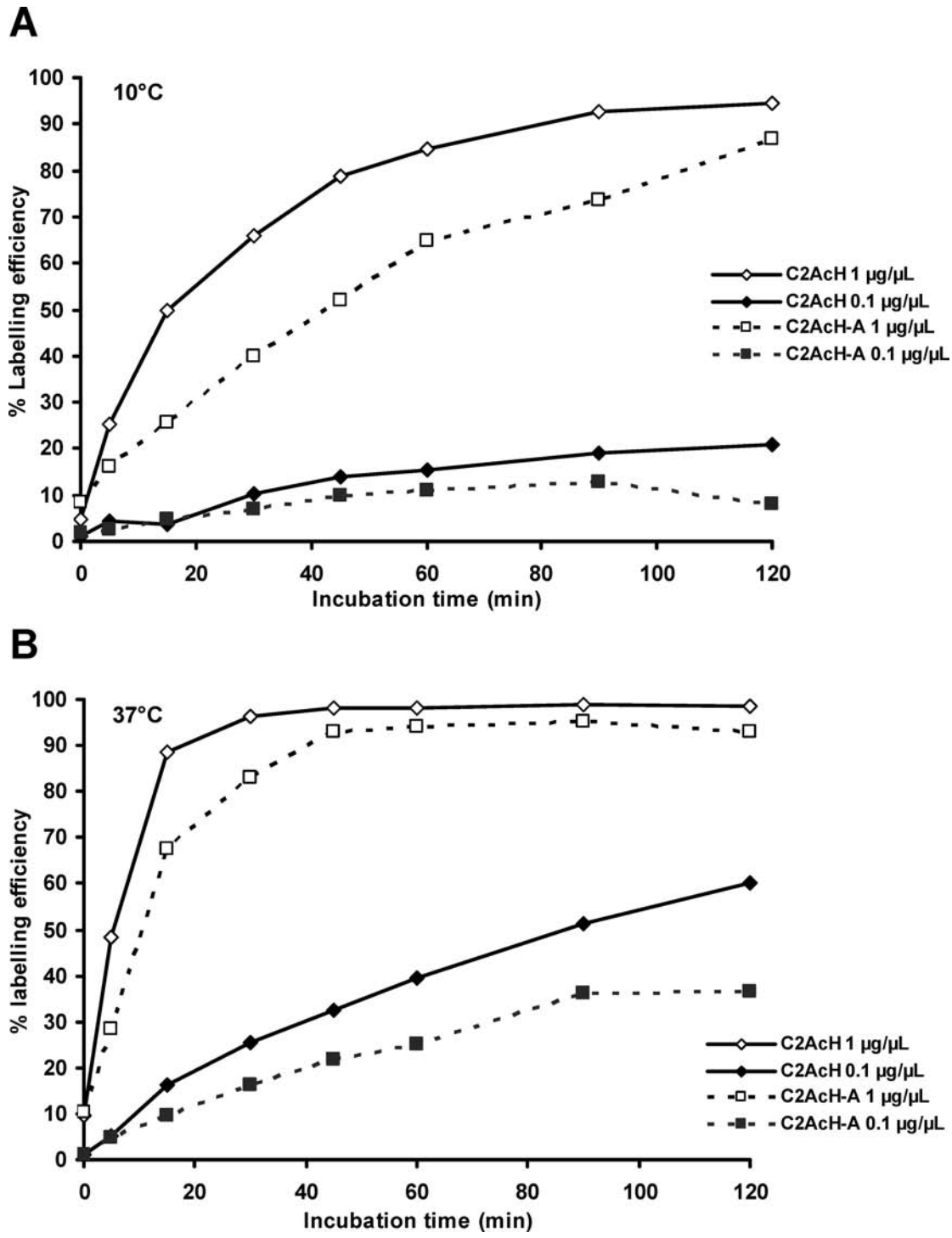

Figure 4. Radiolabeling efficiencies of C2AcH and C2AcH-A. (A) The C2AcH (solid line) and C2AcH-A (dashed line) were incubated with $[^{99m}Tc(CO)_3(OH_2)_3]^+$ at 10 °C for 120 min at a protein concentration of 1 μg/μL (open symbol) and 0.1 μg/μL (closed symbol). (B) The C2AcH (solid line) and C2AcH-A (dashed line) were incubated with $[^{99m}Tc(CO)_3(OH_2)_3]^+$ at 37 °C for 120 min at a protein concentration of 1 μg/μL (open symbol) and 0.1 μg/μL (closed symbol).

might expect C2Ac to undergo labeling more efficiently than is observed. An alternative model to account for the dimerization behavior is that the proximity of the $[M(CO)_3]^+$ (M = Tc, Re) group bound to the His-tag may induce a structural change or cause steric hindrance that inhibits disulfide bond formation without the need to invoke an M−S bond. In this model, the role of the Cys thiol may be important in the initial formation of the protein−metal complex, but not in the final structure. This is consistent with the serum stability results, which show only a marginal (possibly insignificant) loss in stability by blocking the Cys thiol group with fluorescein-maleimide. Given the well-established role of cysteine thiol groups as powerful nucleophilic catalysts in many enzymes, it is conceivable that the thiol or thiolate group acts as a local catalyst by performing the initial nucleophilic attack on the positively charged rhenium tricarbonyl complex, to form an intermediate containing a M−S bond, followed by displacement of the thiolate from the metal coordination sphere by histidine.

The results we described suggest that the combination of Cys and His-tag is an excellent efficient sequence for $[^{99m}Tc(CO)_3]^+$

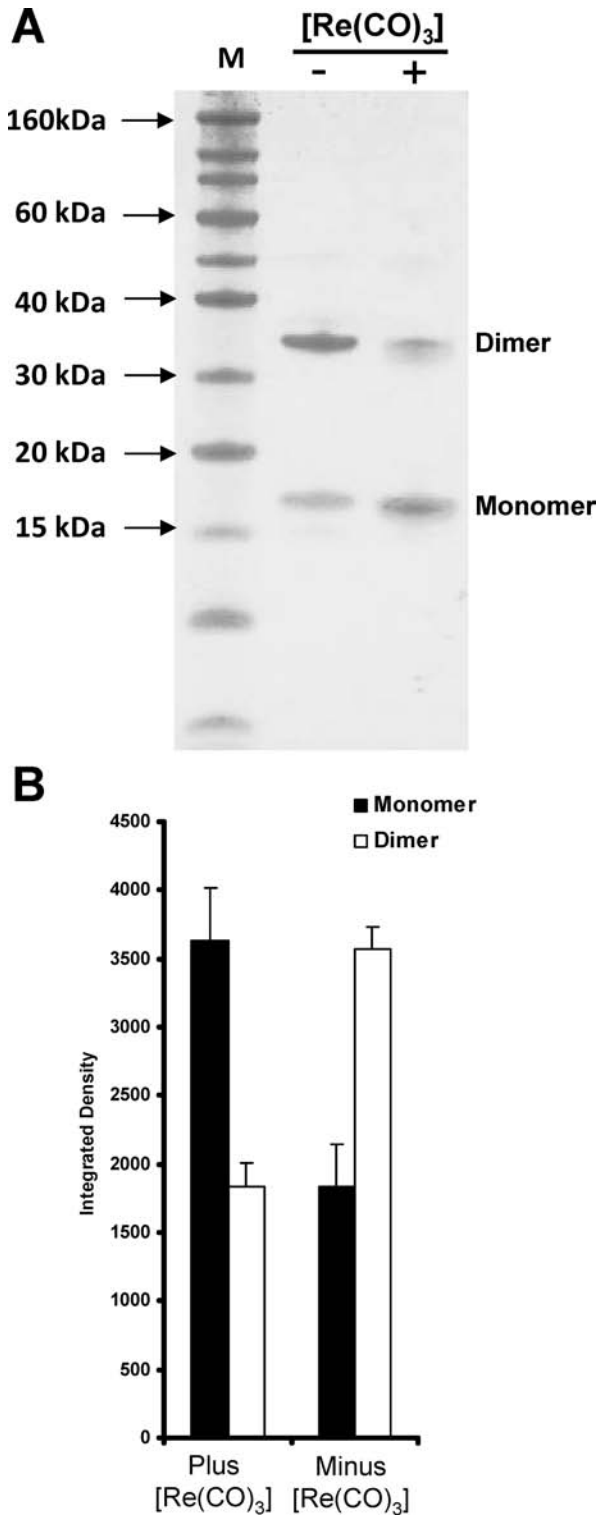

Figure 5. $[Re(CO)_3(OH_2)_3]^+$ reduces formation of dimeric C2AcH by binding to Cys. (A) C2AcH was incubated with and without $[Re(CO)_3(OH_2)_3]^+$ and shown is a nonreducing SDS/PAGE gel of samples after overnight incubation. M indicates molecular weight markers, and monomeric and dimeric C2AcH protein bands are indicated. (B) The monomer and dimer protein bands of C2AcH with and without $[Re(CO)_3(OH_2)_3]^+$ incubation were quantified using the *ImageJ* image analysis software. The data represent the mean of three samples with standard error bars.

labeling, with improved properties compared to the His-tag alone. The sequence deserves further investigation both in its own right and as a guide to further sequence optimization to

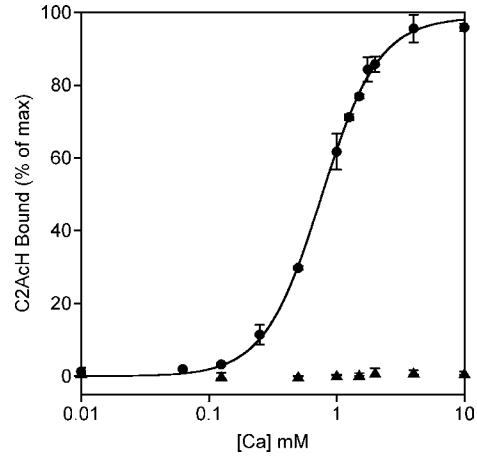

Figure 6. Site-specifically radiolabeled C2AcH binds to PS in a calcium dependent manner on RBC. Radiolabeled C2AcH (circles) or C2AcH-B (triangles) were incubated with preserved RBC in increasing calcium concentrations up to 10 mM. The cells were then washed and treated with 10 mM EDTA, and the activity eluted was counted using a gamma counter. The data are shown as the mean of three replicates with standard deviation error bars.

Table 2. Serum Stability of Technetium-Labeled C2AcH and C2AcH-F Proteins

		incubation time (hrs)			
		0	3	6	18
C2AcH	PBS control	99.54	99.34	98.81	99.22
	serum	99.15	98.58	98.23	97.88
C2AcH-F	PBS control	99.75	99.68	99.57	98.82
	serum	99.38	97.24	96.31	94.39

improve limits of specific activity/amount of protein that can be labeled, with greater specificity, under milder conditions for shorter labeling times.

The PS-binding assay results with these proteins further highlight the value of a site-specific approach to labeling. The site-specifically labeled conjugates C2AcH-$[^{99m}Tc(CO)_3]$ and C2AcH-F bound to PS on RBCs in a calcium-dependent manner, while nonspecifically modified C2AcH-B, formed by incubation with an excess of N-(benzyloxycarbonyloxy) succinimide before radiolabeling, did not bind to PS on RBCs even at the highest concentrations of calcium.

In conclusion, we have developed and characterized a new radiopharmaceutical for imaging cell death, based on C2A, the phosphatidylserine-binding domain of synaptotagmin I. It incorporates a novel $[^{99m}Tc(CO)_3]^+$- and $[Re(CO)_3]^+$-binding amino acid sequence that labels with excellent efficiency and site-specificity, with excellent serum stability, and is suitable for evaluation with other recombinant proteins for molecular imaging. The new site-specifically labeled C2AcH-$[^{99m}Tc(CO)_3]$ has excellent affinity for phosphatidylserine and warrants in vivo evaluation for cell death imaging in oncological, cardiovascular, and graft rejection preclinical models.

ACKNOWLEDGMENT

We thank Kevin Howland (University of Kent) and EPSRC Mass Spectrometry Service (University of Swansea) for performing the ES-MS, Bazbek Davletov (University of Cambridge) for supplying the original C2A plasmid, Chris Thrasivoulou (Univesrity College London) for help with confocal microscopy, Hector Knight (Covidien) for providing the Isolink kits, and Jim Ballinger and the Nuclear Medicine Department of Guy's and St Thomas' NHS Foundation Trust for supplying ^{99m}Tc pertechnetate. The authors acknowledge

financial support from King's College London, Division of Imaging Sciences, BHF Centre of Excellence, the Department of Health via the National Institute for Health Research (NIHR) comprehensive Biomedical Research Centre award to Guy's & St Thomas' NHS Foundation Trust in partnership with King's College London and King's College Hospital NHS Foundation Trust and CRUK/EPSRC Comprehensive Cancer Imaging Centre at King's College London in partnership with UCL.

LITERATURE CITED

(1) Kerr, J. F., Wyllie, A. H., and Currie, A. R. (1972) Apoptosis: a basic biological phenomenon with wide-ranging implications in tissue kinetics. *Br. J. Cancer 26*, 239–257.

(2) Boersma, H. H., Kietselaer, B. L., Stolk, L. M., Bennaghmouch, A., Hofstra, L., Narula, J., Heidendal, G. A., and Reutelingsperger, C. P. (2005) Past, present, and future of annexin A5: from protein discovery to clinical applications. *J. Nucl. Med. 46*, 2035–2050.

(3) Blankenberg, F. G., Katsikis, P. D., Tait, J. F., Davis, R. E., Naumovski, L., Ohtsuki, K., Kopiwoda, S., Abrams, M. J., Darkes, M., Robbins, R. C., Maecker, H. T., and Strauss, H. W. (1998) In vivo detection and imaging of phosphatidylserine expression during programmed cell death. *Proc. Natl. Acad. Sci. U.S.A. 95*, 6349–6354.

(4) Fukuda, M., Kojima, T., and Mikoshiba, K. (1996) Phospholipid composition dependence of Ca^{2+}-dependent phospholipid binding to the C2A domain of synaptotagmin IV. *J. Biol. Chem. 271*, 8430–8434.

(5) Zhao, M., Zhu, X., Ji, S., Zhou, J., Ozker, K. S., Fang, W., Molthen, R. C., and Hellman, R. S. (2006) 99mTc-labeled C2A domain of synaptotagmin I as a target-specific molecular probe for noninvasive imaging of acute myocardial infarction. *J. Nucl. Med. 47*, 1367–1374.

(6) Hirt, U. A., and Leist, M. (2003) Rapid, noninflammatory and PS-dependent phagocytic clearance of necrotic cells. *Cell Death Differ. 10*, 1156–1164.

(7) Blankenberg, F. G. (2008) Monitoring of treatment-induced apoptosis in oncology with PET and SPECT. *Curr. Pharm. Des. 14*, 2974–2982.

(8) Giersing, B. K., Rae, M. T., CarballidoBrea, M., Williamson, R. A., and Blower, P. J. (2001) Synthesis and characterization of 111In-DTPA-N-TIMP-2: a radiopharmaceutical for imaging matrix metalloproteinase expression. *Bioconjugate Chem. 12*, 964–971.

(9) Tait, J. F., Smith, C., Levashova, Z., Patel, B., Blankenberg, F. G., and Vanderheyden, J. L. (2006) Improved detection of cell death in vivo with annexin V radiolabeled by site-specific methods. *J. Nucl. Med. 47*, 1546–1553.

(10) Vriens, P. W., Blankenberg, F. G., Stoot, J. H., Ohtsuki, K., Berry, G. J., Tait, J. F., Strauss, H. W., and Robbins, R. C. (1998) The use of technetium Tc 99m annexin V for in vivo imaging of apoptosis during cardiac allograft rejection. *J. Thorac. Cardiovasc. Surg. 116*, 844–853.

(11) Zhu, X., Migrino, R. Q., Hellman, R. S., Brahmbhatt, T., and Zhao, M. (2008) Early uptake of 99mTc-C2A in the acute phase of myocardial infarction as a prognostic indicator for follow-up cardiac dysfunction. *Nucl. Med. Commun. 29*, 764–769.

(12) Tait, J. F., Smith, C., and Blankenberg, F. G. (2005) Structural requirements for in vivo detection of cell death with 99mTc-annexin V. *J. Nucl. Med. 46*, 807–815.

(13) Zhang, X., Rizo, J., and Sudhof, T. C. (1998) Mechanism of phospholipid binding by the C2A-domain of synaptotagmin I. *Biochemistry 37*, 12395–12403.

(14) Sugita, S., and Sudhof, T. C. (2000) Specificity of Ca^{2+}-dependent protein interactions mediated by the C2A domains of synaptotagmins. *Biochemistry 39*, 2940–2949.

(15) Zhao, M., Beauregard, D. A., Loizou, L., Davletov, B., and Brindle, K. M. (2001) Non-invasive detection of apoptosis using magnetic resonance imaging and a targeted contrast agent. *Nat. Med. 7*, 1241–1244.

(16) Jung, H. I., Kettunen, M. I., Davletov, B., and Brindle, K. M. (2004) Detection of apoptosis using the C2A domain of synaptotagmin I. *Bioconjugate Chem. 15*, 983–987.

(17) Krishnan, A. S., Neves, A. A., de Backer, M. M., Hu, D. E., Davletov, B., Kettunen, M. I., and Brindle, K. M. (2008) Detection of cell death in tumors by using MR imaging and a gadolinium-based targeted contrast agent. *Radiology 246*, 854–862.

(18) Wang, F., Fang, W., Zhao, M., Wang, Z., Ji, S., Li, Y., and Zheng, Y. (2008) Imaging paclitaxel (chemotherapy)-induced tumor apoptosis with 99mTc C2A, a domain of synaptotagmin I: a preliminary study. *Nucl. Med. Biol. 35*, 359–364.

(19) Audi, S., Poellmann, M., Zhu, X., Li, Z., and Zhao, M. (2007) Quantitative analysis of [99mTc]C2A-GST distribution in the area at risk after myocardial ischemia and reperfusion using a compartmental model. *Nucl. Med. Biol. 34*, 897–905.

(20) Tait, J. F., Smith, C., and Gibson, D. F. (2002) Development of annexin V mutants suitable for labeling with Tc(I)-carbonyl complex. *Bioconjugate Chem. 13*, 1119–1123.

(21) Fonge, H., de Saint Hubert, M., Vunckx, K., Rattat, D., Nuyts, J., Bormans, G., Ni, Y., Reutelingsperger, C., and Verbruggen, A. (2008) Preliminary in vivo evaluation of a novel 99mTc-labeled HYNIC-cys-annexin A5 as an apoptosis imaging agent. *Bioorg. Med. Chem. Lett. 18*, 3794–3798.

(22) Waibel, R., Alberto, R., Willuda, J., Finnern, R., Schibli, R., Stichelberger, A., Egli, A., Abram, U., Mach, J. P., Pluckthun, A., and Schubiger, P. A. (1999) Stable one-step technetium-99m labeling of His-tagged recombinant proteins with a novel Tc(I)-carbonyl complex. *Nat. Biotechnol. 17*, 897–901.

(23) Dicko, A., Diemert, D. J., Sagara, I., Sogoba, M., Niambele, M. B., Assadou, M. H., Guindo, O., Kamate, B., Baby, M., Sissoko, M., Malkin, E. M., Fay, M. P., Thera, M. A., Miura, K., Dolo, A., Diallo, D. A., Mullen, G. E., Long, C. A., Saul, A., Doumbo, O., and Miller, L. H. (2007) Impact of a Plasmodium falciparum AMA1 vaccine on antibody responses in adult Malians. *PLoS ONE 2*, e1045.

(24) Dicko, A., Sagara, I., Ellis, R. D., Miura, K., Guindo, O., Kamate, B., Sogoba, M., Niambele, M. B., Sissoko, M., Baby, M., Dolo, A., Mullen, G. E., Fay, M. P., Pierce, M., Diallo, D. A., Saul, A., Miller, L. H., and Doumbo, O. K. (2008) Phase 1 study of a combination AMA1 blood stage malaria vaccine in Malian children. *PLoS ONE 3*, e1563.

(25) Malkin, E. M., Diemert, D. J., McArthur, J. H., Perreault, J. R., Miles, A. P., Giersing, B. K., Mullen, G. E., Orcutt, A., Muratova, O., Awkal, M., Zhou, H., Wang, J., Stowers, A., Long, C. A., Mahanty, S., Miller, L. H., Saul, A., and Durbin, A. P. (2005) Phase 1 clinical trial of apical membrane antigen 1: an asexual blood-stage vaccine for Plasmodium falciparum malaria. *Infect. Immunun. 73*, 3677–3685.

(26) Mullen, G. E., Ellis, R. D., Miura, K., Malkin, E., Nolan, C., Hay, M., Fay, M. P., Saul, A., Zhu, D., Rausch, K., Moretz, S., Zhou, H., Long, C. A., Miller, L. H., and Treanor, J. (2008) Phase 1 trial of AMA1-C1/Alhydrogel plus CPG 7909: an asexual blood-stage vaccine for Plasmodium falciparum malaria. *PLoS ONE 3*, e2940.

(27) Sagaraa, I., Dicko, A., Ellis, R. D., Fay, M. P., Diawaraa, S. I., Assadoua, M. H., Sissokoa, M. S., Konea, M., Dialloa, A. I., Sayea, R., Guindoa, M. A., Ousmane Kantea, Niambelea, M. B., Miura, K., Mullen, G. E. D., Pierce, M., Martin, L. B., Doloa, A., Dialloa, D. A., Doumboa, O. K., Miller, L. H., Saul, A. (2009) A randomized controlled phase 2 trial of the blood stage AMA1-C1/Alhydrogel malaria vaccine in children in Mali. Vaccine In Press.

(28) Ellman, G. L. (1959) Tissue sulfhydryl groups. *Arch. Biochem. Biophys. 82*, 70–77.

(29) Lazarova, N., James, S., Babich, J., and Zubieta, J. (2004) A convenient synthesis, chemical characterization and reactivity of [Re(CO)3(H2O)3]Br: the crystal and molecular structure

of [Re(CO)3(CH3CN)2Br]. *Inorg. Chem. Commun. 7*, 1023–1026.

(30) Tait, J. F., Gibson, D. F., and Smith, C. (2004) Measurement of the affinity and cooperativity of annexin V-membrane binding under conditions of low membrane occupancy. *Anal. Biochem. 329*, 112–119.

(31) Orlova, A., Nilsson, F. Y., Wikman, M., Widstrom, C., Stahl, S., Carlsson, J., and Tolmachev, V. (2006) Comparative in vivo evaluation of technetium and iodine labels on an anti-HER2 affibody for single-photon imaging of HER2 expression in tumors. *J. Nucl. Med. 47*, 512–519.

(32) Schibli, R., and Schubiger, P. A. (2002) Current use and future potential of organometallic radiopharmaceuticals. *Eur. J. Nucl. Med. Mol. Imaging 29*, 1529–1542.

BC900160J

TSPO Targeted Dendrimer Imaging Agent: Synthesis, Characterization, and Cellular Internalization

Lynn E. Samuelson, Madeline J. Dukes, Colette R. Hunt, Jonathan D. Casey, and Darryl J. Bornhop*

Department of Chemistry, The Vanderbilt Institute for Chemical Biology and Vanderbilt-Ingram Cancer Center, Vanderbilt University, VU Station B 351822 Nashville, Tennessee 37235-1822. Received May 11, 2009; Revised Manuscript Received September 25, 2009

While it has become common practice for dendrimers to deliver imaging and therapeutic agents, there are few reported examples of cellular internalization of dendrimers. Moreover, targeting of dendrimers to the mitochondria in cells has not yet been reported. Previously, we have delivered small molecule imaging agents into glioma and breast cancer cells by targeting the translocator protein (TSPO; formerly known as the peripheral benzodiazepine receptor or PBR) with a family of high-affinity conjugable ligands. The 18 kDa multimeric TSPO is expressed in steroid-producing cells, primarily on the outer mitochondrial membrane. This protein is a prime candidate for molecular targeting because tumors and other disease-related cells contain high densities of TSPO. Here, we present the synthesis, characterization, and cellular internalization into C6 rat glioma cells of a TSPO targeted dendrimer imaging agent.

INTRODUCTION

Developments of clinically relevant molecular probes to image diseases or biological processes are essential for the advancement of personalized medicine. A variety of biomarkers specific to cancer and other diseases have been identified and used for therapeutic and/or imaging agent specific site delivery (*1*) (*2, 3*). For example, targeting proteins has been accomplished using antibodies (*4*), proteins (*5*), small molecules (*6*−*8*), nanoparticles (*9*−*11*), and dendrimers (*1, 12, 13*). Attachment of multiple different species to a single dendrimer has produced a single molecule which targets, images, and/or delivers a therapeutic dose to the site of disease (*14, 15*). The advantages of using dendrimers include (a) multiple moieties or multiple copies of the targeting agent on a single particle, (b) biocompatibility, (c) size solubility, and (d) tunability. However, the challenges of using dendermers include (a) the difficulty in characterization of functionalized molecule, (b) nonuniform distribution of the adduct(s), (c) complexity in determining the optimum size, and (d) ensuring that the targeting moiety retains activity after attachment to the dendrimer. It is clear that macromolecules will play an important role in personalized medicine; however, the current synthetic scaffolds are particularly ineffective in targeting intracellular receptors.

The translocator protein (TSPO, previously known as the peripheral-type benzodiazepine receptor or PBR) spans the mitochondrial membrane and has become an attractive receptor for therapeutics and targeted imaging (*16*). TSPO is associated with a number of biological processes including cell proliferation, apoptosis, steroidogenesis, and immunomodulation; yet, its exact physiological role is still not fully defined (*16*−*18*). Overexpression of TSPO has been shown in numerous types of cancer including brain, breast, colorectal, prostate, and ovarian cancers, as well as astrocytomas, hepatocellular, and endometrial carcinomas (*17*). Two well-characterized cell lines with high TSPO expression are C6 Rat Glioma cells (*19*) and MDA-MB-231 human breast cancer cells (*20*). Several small, high binding, selective molecules have been developed for TSPO and made into positron emission tomography (PET), magnetic resonance (MR), and optical imaging agents (*621*−*24*). While attractive, prior to this report macromolecules targeting TSPO have not been reported, possibly due to difficulty in internalizing synthetic molecules.

Dendrimers have been studied as potential delivery systems to target, image, and/or deliver a therapeutic specifically to diseased tissue because of their globular shape, multiple surface attachment sites, biocompatibility, tunable size, monodispersity, and low production cost (*25*). The multiple surface end groups available on a dendrimer allow for attachment of several moieties and or copies of each drug, ligand, or imaging agent. Furthermore, dendrimers can be adapted for advancements in coupling technology allowing them to be used with emerging targets, therapeutics, and imaging strategies. Multiple attachment points can provide increased therapeutic efficacy, reduced drug side effects, and increased signal-to-noise for improved imaging detection limits. Methods of targeting include attaching several copies of a binding molecule (small molecules, peptides, proteins, or antibodies) to the surface of the dendrimer to capitalize on polyvalency or the enhanced permeability and retention (EPR) effect where tumor accumulation occurs due to the particle size and the increased vasculature of the tumor (*26, 27*). Imaging with dendrimers is possible through the attachment of small molecule fluorophores (for optical), metal chelates (for fluorescence, MRI, PET and SPECT), or with a switch activated by a physiological process for enhanced tissue characterization (*28, 29*). Dendrimers can serve as effective prodrug scaffolds with the drug molecules being attached through a linkage which activates the drug in vivo once they reach the delivery site. Cleavage from the scaffold can occur through a change in pH, enzyme reaction, or slow degradation of the macromolecule (*29*). While internalization of large nanoparticles through the cellular membrane has been shown, targeting of specific organelles has scarcely been reported (*30, 31*). In this paper, we present the synthesis, characterization, cellular internalization, and mitochondria labeling of a dendrimer nanoparticle. Here, we demonstrate that a

* To whom correspondence should be addressed. Darryl Bornhop, Ph.D., Department of Chemistry, Vanderbilt University, VU Station B 351822, Nashville, TN 37235-1822, Tel: 615.322.4226, Fax: 615.343.1234, e-mail: darryl.j.bornhop@vanderbilt.edu.

10.1021/bc9002053 CCC: $40.75 © 2009 American Chemical Society
Published on Web 10/28/2009

functionalized fourth generation (G(4)-PAMAM) dendrimer particle, which targets an internal cellular receptor and binds that target by passing through the cellular membrane under normal physiological conditions and without the external perturbation of the cellular membrane, can be prepared, characterized, and imaged.

EXPERIMENTAL PROCEDURES

Materials. G(4)-PAMAM dendrimer in a 10% w/w solution of methanol was purchased from Fischer Scientific and pipetted into a preweighed vial immediately before use. The methanol was evaporated under a stream of $Ar_{(g)}$, and the resulting viscous oil was dissolved in water, frozen, and lyophilized to give a fluffy white powder. The mass of the dendrimer was determined by reweighing the vial and calculating the mass difference. 1-(2-Chlorophenyl)isoquinoline-3-carboxylic acid (ClPhIQ Acid) was synthesized in our laboratory as previously reported (*6*, *32*). All 1,4,7,10-tetraazacyclododecane-1,4,7,10-tetraacetic acid (DOTA) and DOTA derivatives were purchased form Macrocyclics and used as received. All other chemicals were purchased from Fischer Scientific and used as is unless otherwise indicated.

MALDI-TOF MS were obtained on a PerSeptive Biosystems Voyager-DE STR mass spectrometer. Freshly recrystallized trans-indole acrylic acid (IAA) was used as the matrix in a 10 mg/mL solution of DMSO. The plate was spotted with 1 μL of a 10:1 solution of matrix to analyte. NMR spectra were obtained on a 400 MHz Bruker AV-400 instrument with a 5 mm *Z*-gradient broadband inverse probe. NMR spectra were obtained in d_6-dimethyl sulfoxide. UV−vis spectra were obtained on a Shimadzu 1700 UV−vis spectrophotometer. Fluorescence spectra were obtained using a ISS PCI spectrofluorometer at room temperature.

ClPhIQ-G(4)-PAMAM (1). First, ClPhIQ Acid (152.9 mg, 540 μmol) and benzotriazol-1-yloxytris(dimethylamino)-phosphonium hexafluorophosphate (BOPCl, 288.1 mg, 651 μmol) were dissolved in 2 mL of DMSO each. Triethyl amine (Et_3N, 100 μL) was added to the ClPhIQ Acid solution. The BOPCl solution was added to the ClPhIQ Acid solution. The mixture was stirred for 5−10 min (sometimes a change from clear to bright orange would occur) and was then added to a stirred solution of G(4)-PAMAM dendrimer (252.2 mg, 18 nmol) in DMSO (5 mL). The reaction was stirred at room temperature overnight. Unreacted ClPhIQ Acid was removed by diluting the solution 4-fold with water and placing the solution in an Amicon centrifugation molecular weight filter (molecular weight cutoff = 5 kDa) and concentrating the solution to approximately 500 μL via centrifuging at 3000 rpm (1419 × *g*) for 1 h. The solution was diluted and reconcentrated three times with water to wash any unreacted materials away. Finally, the solution was lyophilized to give 441.2 mg (100% yield) of a slightly yellow powder. The same procedure was followed for synthesizing the (ClPhIQ)12-PAMAM using fewer equivalents of ClPhIQ Acid and BOPCl. ClPhIQ30-G(4)-PAMAM: MALDI-TOF MS 19 500 amu ^{1}H NMR (300 MHz, $CDCl_3$) 8.8 (1H, s), 8.6 (1H, s), 8.2−8.5 (5H, m), 7.5−8.0 (9H, multi), 2.9 (3H, bs), and 3.1−3.5 (28H, m) ppm.

ClPhIQ-G(4)-PAMAM-Lissamine (2). G(4)-PAMAM (9 mg, 400 nmol) with or without ClPhIQ Acid was dissolved in 2 mL of dimethylformamide (DMF). Next, 23 μL of a 17.3 mM solution of Lissamine sulfonyl chloride was added to the stirred dendrimer solution. The reaction was stirred overnight followed by purification in Amicon centrifugation filters as described above and lyophilized to give 5.6 mg (61% yield) of a pink fluffy solid. The presence of the fluorophor was confirmed with UV−vis (max absorbance at 551 nm) and fluorescence (ex 551 nm, em 586 nm) spectroscopies. Specific conditions and yields provided above were for ClPhIQ23-G(4)-PAMAM, but UV−vis and fluorescence spectra were identical for ClPhIQ12-PAMAM and PAMAM-Liss.

Scheme 1. Synthesis of ClPhIQ-PAMAM

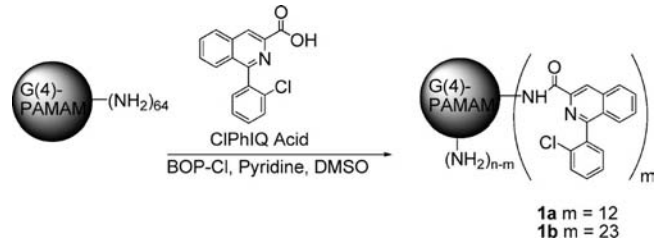

Cell Internalization Experiments. with G(4)-PAMAM-Lissamine derivatives: Either 20 000 C6 rat glioma or 40 000 MDA-MB-231 breast cancer cells were plated into collagen coated glass-bottomed microscopy (MatTeck) dishes and allowed to grow for two days in cell media. After two days, the cells had normal morphology and were attached, and approximately 20% confluent. G(4)-PAMAM-Lissamine compounds (with or without other moieties) were diluted to 1 μM (in ClPhIQ) with media from a 10 mg/mL (12 μM in ClPhIQ) stock solution in DMSO. The media over the cells was replaced with the media containing the fluorophor (either ClPhIQ-PAMAM-Liss or PAMAM-Liss) diluted as noted above and incubated for 6−12 h. The media was then poured off, and the cells were carefully rinsed 3−4 times with Dulbecco's Phosphate Buffered Saline (DPBS). The cells were imaged live. Both white light and fluorescence pictures were obtained.

For fixed cells, the rinsed cells were incubated at room temperature for 30 min with a 4% *para*-formaldehyde solution. The cells were carefully washed 4 times with DPBS and stored under DPBS at 4 °C until imaged (not longer than 1 week, typically overnight). Immediately before imaging, the fixed cells were incubated with a 25 nM solution of mitotracker green (MTG) for 10 min. Excess MTG was removed by four washings with DPBS and the cells were imaged. Cellular images were obtained using a A Nikon Eclipse TE2000-U fluorescence microscope (Lewisville, TX) equipped with a Nikon FITC-Texas Red filter sets employed for the in vitro imaging. The Texas Red filter (ex, 560−580 nm; polychromatic mirror, 585−665 nm; barrier filter, 600−650 nm) set was used to image Lissamine, and the FITC filter was used to image MTG (ex, 450−505 nm; polychromatic mirror, 510−555 nm; barrier filter, 515−545 nm). Fluorescence integration times ranged 100−5000 ms, but were typically 100−500 ms. All controls were integrated for at least 5000 ms. Sample homogeneity was maintained by keeping the samples under DPBS the entire time of imaging. For live cells, images were taken within 20 min after replacing media with DPBS and were discontinued if the cellular morphology changed in any way from the media containing morphology.

RESULTS AND DISCUSSION

The TSPO targeted dendrimer was synthesized using 1-(2-chlorophenyl)isoquinoline-3-carboxylic acid (ClPhIQ Acid), a precursor of the conjugable TSPO binding molecule previously reported (*6*). ClPhIQ Acid (Scheme 1) was activated with benzotriazol-1-yloxytris(dimethylamino)-phosphonium hexafluorophosphate (BOPCl), in pyridine and dimethyl sulfoxide (DMSO), and added to a solution of G(4)-PAMAM dendrimer in DMSO. An average of 12 and 23 ClPhIQ Acids were attached by reacting G(4)-PAMAM dendrimer with 15 and 30 mol equiv of the activated TSPO ligand, respectively, to obtain two ClPhIQ-PAMAM compounds, **1a** and **1b** (Scheme 1). Excess ClPhIQ Acid and coupling agent were removed by diafiltration with a molecular weight cutoff (MWCO) of 5 kDa. Both

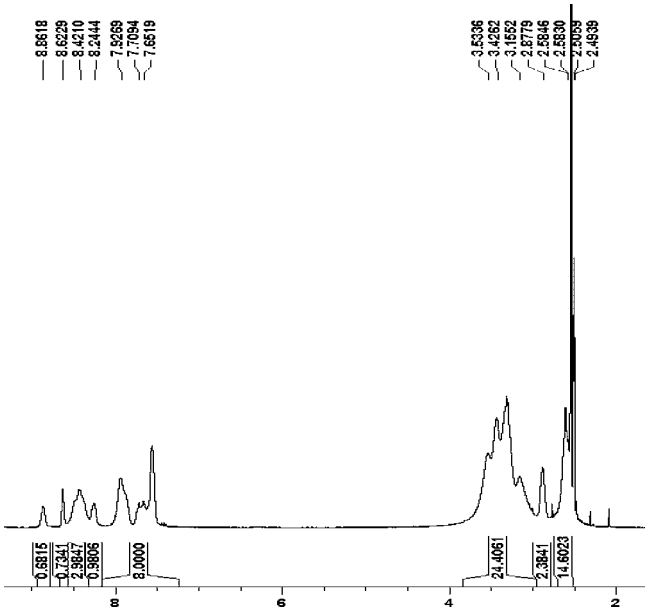

Figure 1. NMR of 23 ClPhIQ Acids attached to G(4)-PAMAM (ClPhIQ23-PAMAM).

ClPhIQ-PAMAM molecules were characterized with nuclear magnetic resonance (NMR) and matrix assisted laser desorption ionization time-of-flight mass spectrometry (MALDI-TOF-MS).

The average number of TSPO ligands per dendrimer was estimated using NMR integrations. It was shown from proton NMR spectra of the PAMAM and ClPhIQ pieces individually that the aromatic proton signals are exclusively from the ClPhIQ Acids attached (7.0−7.9 ppm) to the particle, while the interior PAMAM methylenes are the only signal observed from 2 to 4 ppm and the amides are found from 8.4 to 9 ppm (Figure 1). By calculation, there are approximately 930 methylene protons in a G(4)-PAMAM dendrimer and 9 protons (all aromatic) per ClPhIQ Acid molecule. To determine the average number of ClPhIQ Acids per dendrimer, the integral from 7.0 to 8.2 was calibrated to 9 and the resulting integral from 2 to 4 ppm was divided into 930. As shown in Figure 1, we find 23 ClPhIQ Acids attached to the dendrimer when the dendrimer was reacted with 30 equiv of ClPhIQ Acid. NMR spectra indicate that 12 ClPhIQ acids are attached when 15 equiv of ligand are reacted with the dendrimer (data not shown). Interestingly, the amount of ClPhIQ that binds to the dendrimer nearly doubles (from 12 to 23) when doubling the amount of ClPhIQ in the reaction (from 15 to 30).

MALDI-TOF MS was also utilized to confirm the average number of ClPhIQ Acids attached to the dendrimer (Figure 2). First, a MALDI-TOF MS was acquired of the G(4)-PAMAM with the average molecular weight (MW) found to be 13 244 Da, significantly lower than the 14 215 Da of a G(4)-PAMAM without any of the widely reported structural defects (*33*). These defects include incomplete reactions, making one arm of the dendrimer consistently a generation behind, and side reactions that stop the expansion of that branch of dendrimer altogether. The ClPhIQ-PAMAM (**1a**) has an average MW of 16 513, and thus, by calculation has 12 ClPhIQ Acid molecules per PAMAM. This result is consistent with the NMR data, as was the number of ClPhIQ Acids per PAMAM for ClPhIQ-PAMAM (**1b**) with 23 ClPhIQ ligands attached. Additionally, it was calculated that ClPhIQ-PAMAM, **1b**, had approximately 24 ClPhIQ Acids per PAMAM, consistent with NMR data.

Following characterization of the ClPhIQ-PAMAM molecules with NMR and MALDI-TOF-MS, the dendrimer was further functionalized by reacting it with Lissamine rhodamine B sulfonyl chloride (Lissamine) in dimethyl formamide (DMF) overnight to give 1 or 2 Lissamine dyes per dendrimer (Scheme 2). The DMF was removed in vacuo and excess dye was removed by diafiltration (MWCO = 5000) in water. UV−vis and fluorescence were employed to characterize the optical imaging agent. Attaching the dye to the dendrimer produced a compound with an absorbance maximum at 571 nm (versus 563 nm for free dye) and a slightly red-shifted emission at 586 nm (versus 583 nm for free dye). A control compound (PAMAM-Liss), the agent absent of the targeting moiety, was synthesized similarly to the targeting agent by reacting G(4)-PAMAM dendrimer with Lissamine (Scheme 2). The PAMAM-Liss conjugate was also purified by diafiltration in which the first low molecular weight fraction was slightly pink (from dye) and subsequent washing resulted in lighter color until no color was present. A minimum of three colorless washings in the low molecular weight fraction were completed to provide pure ClPhIQ-PAMAM-Liss with no unreacted Lissamine dye. A molecular weight difference for the PAMAM and PAMAM-Liss of 500−600 amu was observed in the MALDI-TOF MS spectrum, consistent with an average of 1 dye per dendrimer. The small spectral shift in absorbance and emission was similar to the targeted moiety.

Finally, the solubility extraction coefficients between octanol and water were determined for both the PAMAM compounds by using the shake method. Briefly, the shake method for finding log *P* is determined by mixing an aqueous solution of the PAMAM-dye with a solution PAMAM-dye in octanol and allowing the two solvents to equilibrate. The absorbances of each layer (octanol and water) were then recorded and used to determine the concentration of dye in each layer. The log P for ClPhIQ-PAMAM-Liss is estimated to be 2.9, while that for PAMAM-Liss (no ClPhIQ) is 1.0. These log *P* values indicate that the ClPhIQ-PAMAM-Liss is more lipophilic than the PAMAM-Liss and therefore is more likely to interact favorably with the cellular membrane.

To evaluate the biological activity of the imaging agent, C6 rat glioma cells, shown to express a high concentration of TSPO (*34, 35*), were incubated with the dendrimer compounds **2b** and **3** for 12 h in collagen coated MatTek dishes and visualized by fluorescence microscopy. Live cell imaging was preformed immediately after rinsing the cells with PBS or saline to remove media and unbound or uninternalized imaging agent. A Nikon Eclipse TE2000-U fluorescence microscope (Lewisville, TX) equipped with Texas Red and FITC filter sets was employed for the in vitro imaging. As shown in Figure 3, the ClPhIQ-PAMAM-Liss labels the cell, while the control (PAMAM-Liss) does not produce fluorescence. As another control, cells were incubated with Lissamine rhodamine B sulfonyl chloride and again no fluorescence was observed (data not shown). The imaging experiments were performed in triplicate with observations being consistent with respect to absorbance and fluorescence intensity and the absence of fluorescence in the controls. We hypothesize that the dendrimer with the TSPO binding ligand (ClPhIQ-PAMAM-Liss, **2b**) produced bright, localized cellular fluorescence due to its ability to pass through the cellular membrane and bind to the target protein TSPO (Figure 3). Since ClPhIQ Acid conjugated dye is known to bind TSPO, glioma cells overexpress TSPO, and it is an organellular protein, we believe that the dendrimer labels the mitochondria by binding to TSPO. In the labeling experiment where the dendrimer without the targeting ligand (compound **3**) was used, no fluorescence was found in the cell (either intracellularly or at the membrane) at exposure times as long as 5 s. Taken together, these results indicate that the ClPhIQ moiety is necessary for cellular uptake of the dendrimer at labeling concentrations of 1 μM and equilibration times of 6−12 h.

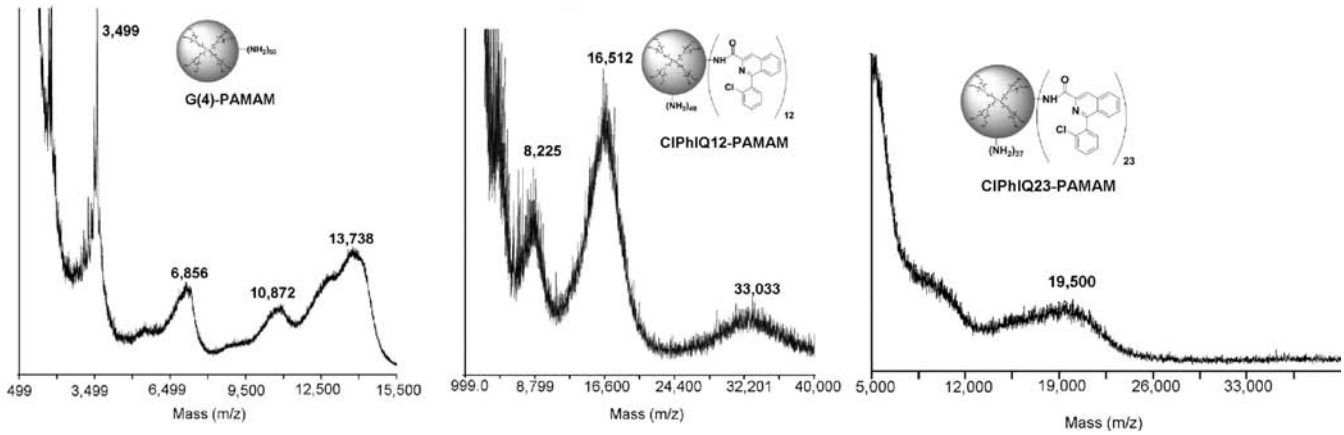

Figure 2. Characterization and determination of the average number of ClPhIQ per dendrimer by MALDI-TOF MS. Left: MALDI-TOF spectrum of G(4)-PAMAM. Middle: MALDI-TOF spectrum of ClPhIQ(12)-PAMAM. Right: MALDI-TOF spectrum of ClPhIQ(23)-PAMAM.

Scheme 2. Attachment of Lissamine Dye to PAMAM

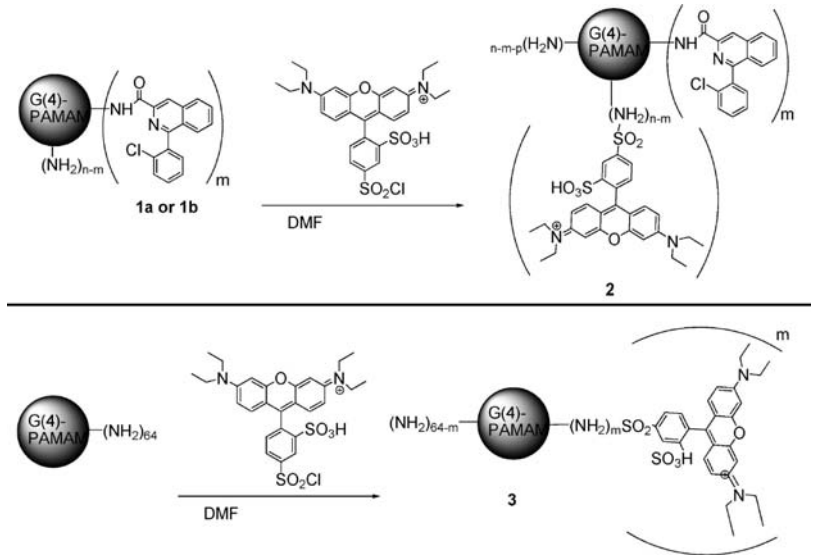

To further confirm that the agent was intracellular, a series of *z*-stacked images (pseudoconfocal) were obtained allowing different regions of the cells to be viewed (Figure 4). These *z*-stacked images were accomplished by changing the lens position incrementally, moving the focal planes of the microscope through cells, and collecting the images by viewing fluorescence. In the center focal planes, there is a dark hole, consistent with the nucleus as shown in the fluorescence-DIC overlay (Figure 4). This observation suggests that the agent undergoes internalization, passive or active, and does not just label the membrane due to the lipophilic nature of the ClPhIQ moiety. Since only a small amount of out-of-focus light is observed in the membrane slices of the *z* stack (data not shown), labeling of the membrane appears to be negligible. Furthermore, fluorescence signal is observed through the cell to the entire nuclear membrane, but not in the nucleus, indicating uptake of the dendrimer by the cells but not the nucleus. Previously reported small molecule agents have not labeled the nucleus, although low concentrations of TSPO are present there (*24*). The reported macromolecular agent behaved as expected and targeted the mitochondria and was not taken up into the nucleus as indicated in Figure 4.

To further explore whether ClPhIQ-PAMAM-Liss was targeting the mitochondria, a co-incubation experiment was preformed. This was accomplished by first incubating C6 rat glioma cells with ClPhIQ-PAMAM-Liss as described above for the live cellular imaging, followed by fixation using paraformaldehyde, and then treating the cells with Mitotracker Green (MTG) according to the manufacturer's guidelines. The cells were then imaged using a Texas Red filter set to detect the Lissamine (red) fluorescence and a FITC filter set to detect the MTG (green) fluorescence. Figure 5 shows C6 rat glioma cells incubated with either ClPhIQ-PAMAM-Liss or the control, PAMAM-Liss. The DIC images in Figure 5A and G are present to indicate the location of the cells relative to fluorescence signal of ClPhIQ-PAMAM-Liss (Figure 5A) and PAMAM-Liss dosed cells (Figure 5G). Fluorescence from the imaging agent is displayed in red (Figure 5B) and fluorescence from the MTG as green (Figure 5C). As demonstrated above with live cell imaging, the ClPhIQ-PAMAM-Liss agent labels the fixed cells principally perinuclearly (Figure 5B). MTG was used in low concentration (25 nM) to ensure that it primarily labeled mitochondria in the cell. The MTG labels the mitochondria of cells, as shown by numerous investigators (*36*, *37*), particularly when used in low concentrations as those employed here (25nM). More careful investigation of the fluorescence signals allow insight into where the species are within the cell. Figure 5 panels D and E display co-registration of ClPhIQ-PAMAM-Liss and MTG with yellow indicating areas of overlap while red and green indicate areas where ClPhIQ-PAMAM-Liss (red) and MTG (green) are not coincident. It is encouraging to see that most of the red and green converge to yellow, indicating

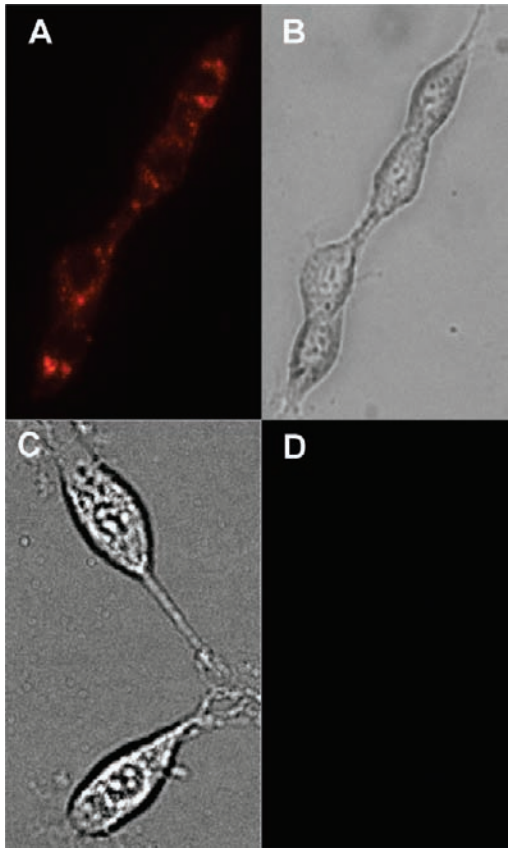

Figure 3. Live cell images of C6 rat glioma cells. Panel A: Red fluorescence of ClPhIQ-PAMAM-Liss dosed cells. Panel B: DIC image of ClPhIQ-PAMAM-Liss dosed cells. Panel C: DIC image of PAMAM-Liss dosed cells. Panel D: Red fluorescence image of PAMAM-Liss dosed cells.

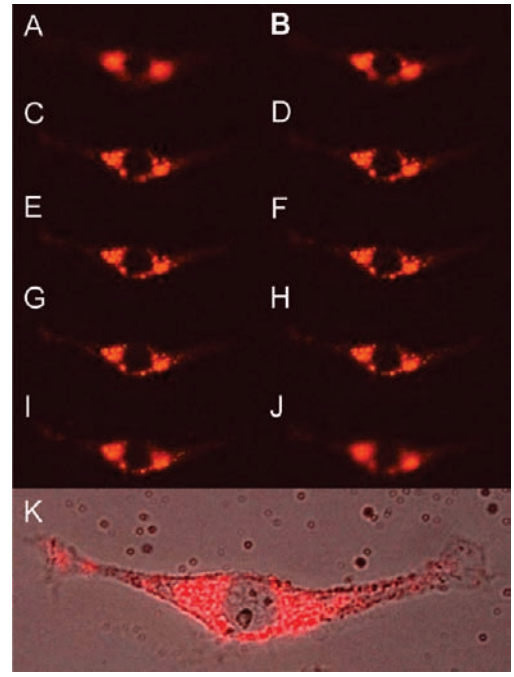

Figure 4. Selected montage of red fluorescence images of ClPhIQ-PAMAM-Liss dosed cells from the *z* series. Panel A: slice 10, Panel B: slice 15. Panel C: slice 20, Panel D: slice 21. Panel E slice 22. Panel F: slice 23. Panel G: slice 24. Panel H: slice 325. Panel I: slice 30. Panel J: slice 35. Panel K: DIC Fluorescence overlay.

that the majority of ClPhIQ-PAMAM-Liss is in the same location of the cell as the MTG. This good colocalization is further evidence that ClPhIQ-PAMAM-Liss is labeling the mitochondria and not other parts of the cell. As demonstrated in Figure 5 panels F—I and in the live cell imaging (Figures 3 and 4), fluorescence from the dendrimer is only detected if ClPhIQ Acid is incorporated into the dendrimer. In other words, images from cells inoculated with the control agent (PAMAM-Liss) exhibit no fluorescence (Figure 5I). MTG fluorescence was not affected (Figure 5C,F,H) by the presence or absence of dendrimer agent, and the cellular membrane was not perturbed by nonphysiological chemical or physical processes prior to or during the incubation with ClPhIQ-PAMAM-Liss. Of course, excess imaging agent was removed prior to fixation in all experiments. Taken together, the fluorescence images in Figure 5 indicate that the ClPhIQ-PAMAM-Liss is targeting the mitochondria and that the ClPhIQ ligand is necessary for this mitochondrial labeling to occur. The *z*-stacked images and coincubation experimental results indicate that the imaging agent is internalized into the cell through normal cellular functions.

Although no quantitative binding studies were completed, the agent binds with high enough affinity to remain in the cell after fixation, washing, and treatment with MTG. Studies beyond the scope of this report are necessary to determine the exact mechanism of cellular transport and binding; however, insight is shown into some initial experiments performed using shorter incubation times with the fluorescent agents (ClPhIQ-PAMAM-Liss and PAMAM-Liss). In these trials, no fluorescence was observed for either compound (with and without ClPhIQ ligand) after incubation for as long as 3 h (data not shown). It was only after a minimum of 6 h of incubation that fluorescence was found in the dosed cells. One possible explanation for this observation is that the dendrimeric compound is slowly taken up into the cell and the ClPhIQ is absolutely necessary for uptake. Another possibility is that the molecule freely enters and exits the cell and eventually binds the target (TSPO), that dye is completely removed (both inter- and intracellular) when the cells are rinsed immediately after incubating.

Imaging with IEC-6 cells was completed as an initial estimate as to whether the ClPhIQ-PAMAM-Liss would be taken up and bind mitochondria in cells that express low levels of TSPO. Since TSPO is necessary for cellular function, there are no cell lines that do not express TSPO. No fluorescence was seen when imaging the IEC-6 cells with ClPhIQ-PAMAM-Liss at dosing concentrations as high as 1 μM in dye (data not shown). The indication is that the ClPhIQ-PAMAM-Liss imaging agent is TSPO protein specific. Again, the mechanism of cellular uptake into the cell needs further investigation in order to pinpoint the exact mechanism of cellular uptake.

Further evidence of the utility of ClPhIQ-PAMAM-Liss was demonstrated by labeling MDA-MB-231 human breast cancer cells, an aggressive human cancer cell line. Like the C6 rat glioma cells, the MDA-MB-231 human breast cancer cells have been shown to overexpress TSPO (*20*). The cells were incubated with ClPhIQ-PAMAM-Liss following the same procedures as with the C6 rat glioma cells, fixed, and treated with MTG for coregistration investigations. The individual red and green fluorescence of ClPhIQ-PAMAM-Liss and MTG, respectively, in fixed MDA-MB-231 cells is demonstrated in panels A and C of Figure 6, while panels E and F show the lack of red fluorescence in the PAMAM-Liss treated cells. Association between the red and green (shown in yellow) is evident in the overlays of panels B and D indicating colocalization of the ClPhIQ-PAMAM-Liss and MTG. These additional results represent further evidence that ClPhIQ-PAMAM-Liss is able to label TSPO rich mitochondria in cancer cells.

The observations made in the cellular imaging experiments show that the ClPhIQ labeled dendrimers enter the cell and bind

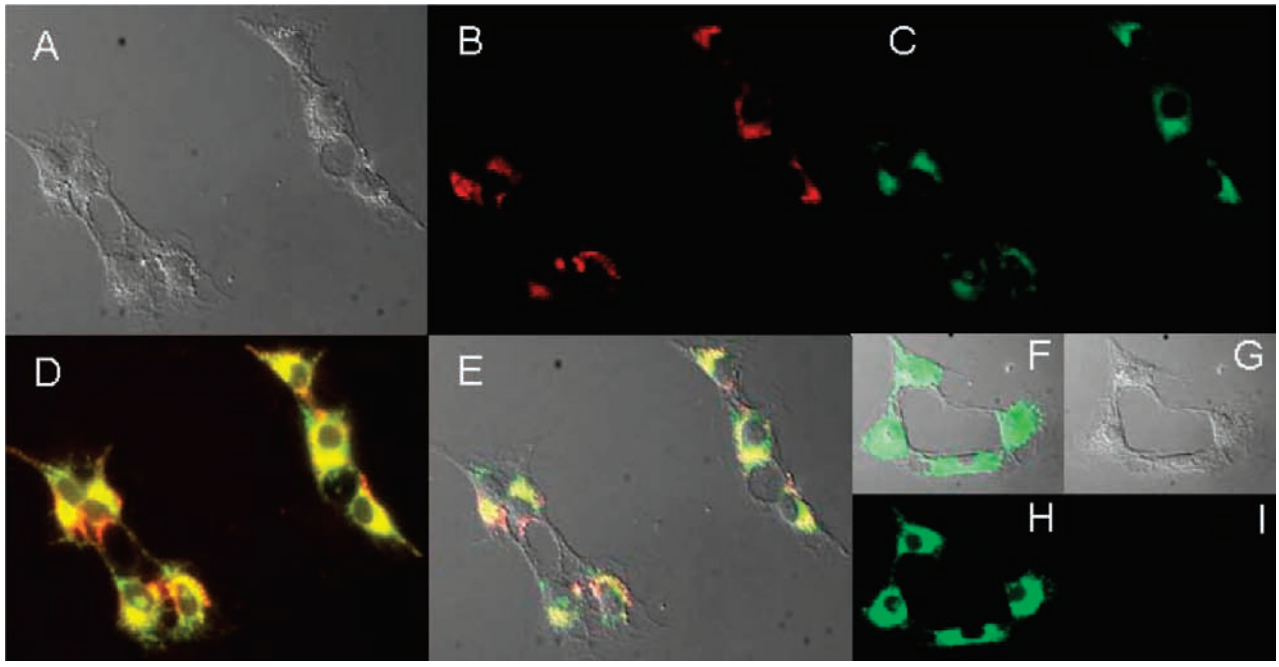

Figure 5. Fluorescence images of fixed C6 rat glioma cells. Panel A: DIC of ClPhIQ(23)-PAMAM-Liss and MTG dosed cells. Panel B: Red fluorescence of ClPhIQ(23)-PAMAM-Liss and MTG dosed cells. Panel C: Green fluorescence of ClPhIQ(23)-PAMAM-Liss and MTG dosed cells. Panel D: Red and Green fluorescence overlay of ClPhIQ(23)-PAMAM-Liss and MTG dosed cells. Panel E: DIC, Red, and Green fluorescence overlay of ClPhIQ(23)-PAMAM-Liss and MTG dosed cells. Panel F: DIC, Red and, Green Fluorescence overlay of PAMAM-Liss and MTG dosed cells. Panel G: DIC of PAMAM-Liss and MTG dosed cells. Panel H: Green fluorescence of PAMAM-Liss and MTG dosed cells. Panel I: Red fluorescence of PAMAM-Liss and MTG dosed cells.

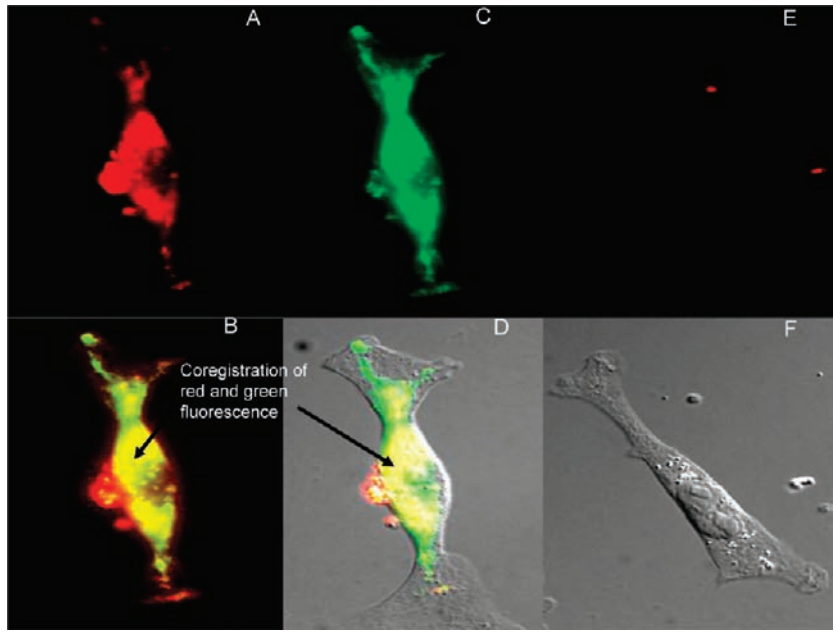

Figure 6. Microscope images of MDA-MB-231 cells. Panel A: Red fluorescence of ClPhIQ(23)-PAMAM-Liss and MTG dosed cells. Panel B: Red and Green Fluorescence overlay of ClPhIQ(23)-PAMAM-Liss and MTG dosed cells. Panel C: Green fluorescence of ClPhIQ(23)-PAMAM-Liss and MTG dosed cells. Panel D: Red and Green Fluorescence and DIC overlay of ClPhIQ(23)-PAMAM-Liss and MTG dosed cells. Panel E: Red fluorescence of PAMAM-Liss dosed cells. Panel F: DIC image of PAMAM-Liss dosed cells.

the mitochondria, but do not appear in the nucleus or cellular membrane. The dendrimers without the ClPhIQ do not label the cell in any significant way. Although the molecules are small enough to enter through the cellular and nuclear membranes, as shown previously the literature suggests that it is not as trivial as size (*38*). First, dendrimers are structurally different than biological molecules such as proteins and antibodies. Biological molecules are typically well-defined, folded structures, while dendrimers are floppier, not well-defined structures. Second, the end functional groups dictate the interactions with the membranes, which may block or enhance the uptake of the compound, depending on the chemical interactions. In amine-terminated dendrimers, the amines can be protonated and do not pass through the lipophilic cellular membrane. Our observations in the cellular imaging experiments, along with the log *P* data, indicated that the lipophilicity of the ClPhIQ ligand allows for the dendrimeric molecule to pass into the cell.

In conclusion, a TSPO targeted imaging agent was synthesized using a G(4)-PAMAM backbone, ClPhIQ Acid, and Lissamine (ClPhIQ-PAMAM-Liss). The imaging agent was

characterized with MALDI-TOF-MS and NMR and imaged in C6 rat glioma and MDA-MB-231 human breast cancer cells. To our knowledge, this is the first example of a TSPO-targeted dendrimer and among the few dendrimeric compounds that are internalized into the cell under normal physiological conditions. Co-localization of the ClPhIQ-PAMAM-Liss and MTG indicates that the compound binds to the mitochondria. The ability for synthetic dendrimers to be internalized into the cell and target a specific protein is a step closer to understanding biological events at the molecular level and ultimately enabling personalized medicine; however, further investigation is required to determine the exact mechanism by which this agent enters the cell.

ACKNOWLEDGMENT

This work was supported by grants from the National Science Foundation (Bes-0323281), Department of Defense (W81XWH-04-1-0432), and the National Institute of Health (5P20 GM072048-4).

LITERATURE CITED

(1) Tomalia, D. A., Reyna, L. A., and Svenson, S. (2007) Dendrimers as multi-purpose nanodevices for oncology drug delivery and diagnostic imaging. *Biochem. Soc. Trans. 35*, 61–67.

(2) Portney, N. G., and Ozkan, M. (2006) Nano-oncology: drug delivery, imaging, and sensing. *Anal. Bioanal. Chem. 384*, 620–630.

(3) Bremer, C., Ntziachristos, V., and Weissleder, R. (2003) Optical-based molecular imaging: contrast agents and potential medical applications. *Eur. Radiol. 13*, 231–243.

(4) Sharkey, R. M., Cardillo, T. M., Rossi, E. A., Chang, C. H., Karacay, H., McBride, W. J., Hansen, H. J., Horak, I. D., and Goldenberg, D. M. (2005) Signal amplification in molecular imaging by pretargeting a multivalent, bispecific antibody. *Nat. Med. 11*, 1250–1255.

(5) Lee, L. A., and Wang, Q. (2006) Adaptations of nanoscale viruses and other protein cages for medical applications. *Nanomedicine 2*, 137–49.

(6) Manning, H. C., Goebel, T., Marx, J. N., and Bornhop, D. J. (2002) Facile, efficient conjugation of a trifunctional lanthanide chelate to a peripheral benzodiazepine receptor ligand. *Org. Lett. 4*, 1075–1078.

(7) Bai, M., Wyatt, S. K., Han, Z., Papadopoulos, V., and Bornhop, D. J. (2007) A novel conjugable translocator protein ligand labeled with a fluorescence dye for in vitro imaging. *Bioconjugate Chem. 18*, 1118–22.

(8) Bai, M. F., Sexton, M., Stella, N., and Bornhop, D. J. (2008) MBC94, a conjugable ligand for cannabinoid CB2 receptor imaging. *Bioconjugate Chem. 19*, 988–992.

(9) Mulder, W. J. M., Strijkers, G. J., van Tilborg, G. A. F., Griffioen, A. W., and Nicolay, K. (2006) Lipid-based nanoparticles for contrast-enhanced MRI and molecular imaging. *NMR Biomed. 19*, 142–164.

(10) Morawski, A. M., Winter, P. M., Crowder, K. C., Caruthers, S. D., Fuhrhop, R. W., Scott, M. J., Robertson, J. D., Abendschein, D. R., Lanza, G. M., and Wickline, S. A. (2004) Targeted nanoparticles for quantitative imaging of sparse molecular epitopes with MRI. *Magn. Reson. Med. 51*, 480–486.

(11) Li, K. C. P., and Bednarski, M. D. (2002) Vascular-targeted molecular imaging using functionalized polymerized vesicles. *J. Magn. Reson. Imaging 16*, 388–393.

(12) Gillies, E. R., and Frechet, J. M. J. (2005) Dendrimers and dendritic polymers in drug delivery. *Drug Discovery Today 10*, 35–43.

(13) Lee, C. C., Yoshida, M., Frechet, J. M. J., Dy, E. E., and Szoka, F. C. (2005) In vitro and in vivo evaluation of hydrophilic dendronized linear polymers. *Bioconjugate Chem. 16*, 535–541.

(14) Wickline, S. A., Neubauer, A. M., Winter, P., Caruthers, S., and Lanza, G. (2006) Applications of nanotechnology to atherosclerosis, thrombosis, and vascular biology. *Arterioscler. Thromb. Vasc. Biol. 26*, 435–441.

(15) Sinha, R., Kim, G. J., Nie, S. M., and Shin, D. M. (2006) Nanotechnology in cancer therapeutics: bioconjugated nanoparticles for drug delivery. *Mol. Cancer Ther. 5*, 1909–1917.

(16) Papadopoulos, V., Baraldi, M., Guilarte, T. R., Knudsen, T. B., Lacapere, J. J., Lindemann, P., Norenberg, M. D., Nutt, D., Weizman, A., Zhang, M. R., and Gavish, M. (2006) Translocator protein (18 kDa): new nomenclature for the peripheral-type benzodiazepine receptor based on its structure and molecular function. *Trends Pharmacol. Sci. 27*, 402–409.

(17) Decaudin, D., Castedo, M., Nemati, F., Beurdeley-Thomas, A., De Pinieux, G., Caron, A., Pouillart, P., Wijdenes, J., Rouillard, D., Kroemer, G., and Poupon, M. F. (2002) Peripheral benzodiazepine receptor ligands reverse apoptosis resistance of cancer cells in vitro and in vivo. *Cancer Res. 62*, 1388–1393.

(18) Casellas, P., Galiegue, S., and Basile, A. S. (2002) Peripheral benzodiazepine receptors and mitochondrial function. *Neurochem. Int. 40*, 475–486.

(19) Hardwick, M., Fertikh, D., Culty, M., Li, H., Vidic, B., and Papadopoulos, V. (1999) Peripheral-type benzodiazepine receptor (PBR) in human breast cancer: Correlation of breast cancer cell aggressive phenotype with PBR expression, nuclear localization, and PBR-mediated cell proliferation and nuclear transport of cholesterol. *Cancer Res. 59*, 831–842.

(20) Olson, J. M., Mcneel, W., Young, A. B., and Mancini, W. R. (1992) Localization of the peripheral-type benzodiazepine binding-site to mitochondria of human glioma-cells. *J. Neuro-Oncol. 13*, 35–42.

(21) Chen, J. W., Breckwoldt, M. O., Aikawa, E., Chiang, G., and Weissleder, R. (2008) Myeloperoxidase-targeted imaging of active inflammatory lesions in murine experimental autoimmune encephalomyelitis. *Brain 131*, 1123–33.

(22) Nahrendorf, M., Sosnovik, D., Chen, J. W., Panizzi, P., Figueiredo, J. L., Aikawa, E., Libby, P., Swirski, F. K., and Weissleder, R. (2008) Activatable magnetic resonance imaging agent reports myeloperoxidase activity in healing infarcts and noninvasively detects the antiinflammatory effects of atorvastatin on ischemia-reperfusion injury. *Circulation 117*, 1153–60.

(23) Hammoud, D. A., Endres, C. J., Chander, A. R., Guilarte, T. R., Wong, D. F., Sacktor, N. C., McArthur, J. C., and Pomper, M. G. (2005) Imaging glial cell activation with [C-11]-R-PK11195 in patients with AIDS. *J. Neurovirol. 11*, 346–355.

(24) Manning, H. C., Goebel, T., Thompson, R. C., Price, R. R., Lee, H., and Bornhop, D. J. (2004) Targeted molecular imaging agents for cellular-scale bimodal imaging. *Bioconjugate Chem. 15*, 1488–1495.

(25) Svenson, S., and Tomalia, D. A. (2005) Dendrimers in biomedical applications--reflections on the field. *Adv. Drug Delivery Rev. 57*, 2106–29.

(26) Khandare, J., and Minko, T. (2006) Polymer-drug conjugates: Progress in polymeric prodrugs. *Prog. Polym. Sci. 31*, 359–397.

(27) Satchi-Fainaro, R., Duncan, R., and Barnes, C. M. (2006) Polymer therapeutics for cancer: Current status and future challenges. *Polymer Therapeutics II: Polymers as Drugs, Conjugates and Gene Delivery Systems 193*, 1–65.

(28) Winter, P. M., Cai, K. J., Chen, J., Adair, C. R., Kiefer, G. E., Athey, P. S., Gaffney, P. J., Buff, C. E., Robertson, J. D., Caruthers, S. D., Wickline, S. A., and Lanza, G. M. (2006) Targeted PARACEST nanoparticle contrast agent for the detection of fibrin. *Magn. Reson. Med. 56*, 1384–1388.

(29) Pham, W., Choi, Y. D., Weissleder, R., and Tung, C. H. (2004) Developing a peptide-based near-infrared molecular probe for protease sensing. *Bioconjugate Chem. 15*, 1403–1407.

(30) Kolonko, E. M., and Kiessling, L. L. (2008) A polymeric domain that promotes cellular internalization. *J. Am. Chem. Soc. 130*, 5626+.

(31) Kitchens, K. M., Foraker, A. B., Kolhatkar, R. B., Swaan, P. W., and Ghandehari, H. (2007) Endocytosis and interaction

of poly (amidoamine) dendrimers with Caco-2 cells. *Pharm. Res. 24,* 2138–2145.

(32) Newman, A. H., Lueddens, H. W. M., Skolnick, P., and Rice, K. C. (1987) Novel irreversible ligands specific for peripheral type benzodiazepine receptors - (±) (+) and (-)-1-(2-chlorophenyl)-N-(1-methylpropyl)-N-(2-isothiocyanatoethyl)-3-isoquinolinecarboxamide and 1-(2-isothiocyanatoethyl)-7-chloro-1,3-dihydro-5-(4-chlorophenyl)-H-2-1,4-benzodiazepin-2-one. *J. Med. Chem. 30,* 1901–1905.

(33) Hummelen, J. C., vanDongen, J. L. J., and Meijer, E. W. (1997) Electrospray mass spectrometry of poly(propylene imine) dendrimers - The issue of dendritic purity or polydispersity. *Chem.—Eur. J. 3,* 1489–1493.

(34) Kozikowski, A. P., Kotoula, M., Ma, D. W., Boujrad, N., Tuckmantel, W., and Papadopoulos, V. (1997) Synthesis and biology of a 7-nitro-2,1,3-benzoxadiazol-4-yl derivative of 2-phenylindole-3-acetamide: A fluorescent probe for the peripheral-type benzodiazepine receptor. *J. Med. Chem. 40,* 2435–2439.

(35) Starostarubinstein, S., Ciliax, B. J., Penney, J. B., Mckeever, P., and Young, A. B. (1987) Imaging of a glioma using peripheral benzodiazepine receptor ligands. *Proc. Natl. Acad. Sci. U.S.A. 84,* 891–895.

(36) Sehgal, I., Sibrian-Vazquez, M., and Vicente, M. G. H. (2008) Photoinduced cytotoxicity and biodistribution of prostate cancer cell-targeted porphyrins. *J. Med. Chem. 51,* 6014–6020.

(37) Sacchi, S., Bernasconi, M., Martineau, M., Mothet, J. P., Ruzzene, M., Pilone, M. S., Pollegioni, L., and Molla, G. (2008) pLG72 modulates intracellular D-serine levels through its interaction with D-amino acid oxidase - Effect on schizophrenia susceptibility. *J. Biol. Chem. 283,* 22244–22256.

(38) Najlah, M., Freeman, S., Attwood, D., and D'Emanuele, A. (2006) Synthesis, characterization and stability of dendrimer prodrugs. *Int. J. Pharm. 308,* 175–182.

BC9002053

Biological Evaluation of Polymeric Micelles with Covalently Bound Doxorubicin

David Vetvicka,*[,†] Martin Hruby,[‡] Ondrej Hovorka,[†] Tomas Etrych,[‡] Miroslav Vetrik,[§] Lubomir Kovar,[†] Marek Kovar,[†] Karel Ulbrich,[‡] and Blanka Rihova[†]

Institute of Microbiology AS CR, v.v.i., Videnska 1083, 142 20 Prague 4, Czech Republic, Institute of Macromolecular Chemistry AS CR, v.v.i., Heyrovsky Sq. 2, 162 06 Prague 6, Czech Republic, and Nuclear Physics Institute AS CR, v.v.i., 250 68 Rez, Czech Republic. Received May 11, 2009; Revised Manuscript Received September 8, 2009

The main limitation of contemporary anticancer chemotherapy remains to be the insufficient specifity of the drugs for tumor tissue, which decreases the maximum tolerated dose due to severe side effects. Micellar drug delivery systems based on amphiphilic block copolymers with a very narrow size distribution (10 to 100 nm in diameter) is a novel innovative approach. Here, we report biological and pharmacological properties of polymeric micellar conjugate containing doxorubicin (DOX) covalently bound via hydrolytically cleavable hydrazone bonds to the micelle core. The system had a very low systemic toxicity (almost 20 times lower than free DOX) and long circulation in the bloodstream (with half of the dose after 24 h). Significant accumulation of tested micelles within the tumor was confirmed by fluorescent whole body imaging. Our new micellar system showed promising therapeutic activity against established murine EL-4 T-cell lymphoma; it was found that it is able to completely cure about 75% of tumor-bearing mice (with doses of either 1×150 mg DOX kg^{-1} or 2×75 mg DOX kg^{-1}, administered i.v.). Moreover, treatment with micelles in cured mice induced tumor-specific resistance. Up to 80% of these mice survived rechallenge with original but not with distinct tumor cells.

INTRODUCTION

The main handicap of classical chemotherapeutics is still their low specificity (*1*). The other limitations include poor water solubility of cytostatic drugs, their unfavorable pharmacokinetic profile, and induction of multidrug resistance.

One possible approach to overcome the disadvantages of the classical low-molecular-weight drug is its binding to a polymeric carrier (*2*−*4*). Conjugation to water-soluble polymers, such as poly[*N*-(2-hydroxypropyl)methacrylamide] (*5*, *6*) or poly(ethylene oxide) (*7*) increases the solubility in aqueous environment and significantly prolongs the plasma half-life. The half-life of free doxorubicin (DOX) in the blood circulation in a murine model is measured in tens of minutes, while polymeric derivatives are detectable in the blood even after tens of hours (*8*). The longer period in circulation and the high molecular weight of polymeric drug delivery systems (DDSs) improve passive accumulation in solid tumors due to the enhanced permeation and retention (EPR) effect (*9*, *10*).

Contemporary drug delivery research is focused on nanoscale delivery systems, such as liposomes, polymeric nanoparticles, or micelles (*11*). Among these, micellar drug delivery systems (MDDS) assembled from amphiphilic block copolymers with a very narrow size distribution (10 to 100 nm in diameter) might be a promising modality (*12*, *13*). They are characterized by a unique core−shell architecture, where hydrophilic blocks form a shell, which separates the core of hydrophobic polymer chains from the aqueous exterior. The hydrophobic core serves as the loading space for various therapeutic agents. The hydrophilic shell, which is the outer part, stabilizes the micellar particle in aqueous solutions. Poly(ethylene oxide) (PEO) is known to be nontoxic, nonimmunogenic, and soluble and therefore is often used as the micellar shell-forming block (*7*). PEO chains also avoid opsonization and interactions with other serum proteins, and successfully prevent recognition of such particles by the cells of the reticuloendothelial system (RES) (*14*). Micellar particles are passively accumulated in the tumor via an EPR effect (*15*).

In most studied polymeric micellar drug delivery systems are molecules of drug physically entrapped in the inner core by the use of hydrophobic interactions. However, additional selectivity may be achieved by binding the drug to the polymeric carrier by a bond preferentially cleavable in neoplastic tissues (*16*−*18*). For instance, the tissue of solid tumors has, due to hypoxia, a lower pH value than blood plasma (*19*). As a result, the use of bonds, which release the active drug from the inactive conjugate in a mildly acidic environment, such as the hydrazone bond (*6*, *20*, *21*), may be one of such improvements over the systems with physically entrapped drug. This is why we decided to use it in our system described in this paper.

One of the most promising anticancer drugs conjugated with the polymeric micelles is doxorubicin, which has been incorporated into the micelle core in both a hydrophobic and covalent manner (*18*, *22*−*24*). We have recently synthesized a polymeric micellar drug delivery system with anthracycline antibiotic doxorubicin bound in the micelle core via a hydrolytically labile hydrazone bond (see Scheme 1 for structure) (*21*), where the cleavage of bonds between DOX and polymer leads to hydrophilization of the micelle core, which triggers the destabilization and consequent disruption of the micelles. Free diblock unimers are quite small ($M_w = 10\,000$ Da) and will undergo renal elimination from the organism. The system design using poly(allyl glycidyl ether) as starting material of the core-forming block also brings some additional benefits in comparison with systems that use poly(amino acid) as the core-forming block (*18*); in particular, the synthesis of the polymeric conjugate is

* Corresponding author. Videnska 1083, 142 20 Prague 4, Czech Republic. E-mail: vetvicka@biomed.cas.cz, phone: +420 241 062 365, fax: +420 241 721 143.

† Institute of Microbiology AS CR.

‡ Institute of Macromolecular Chemistry AS CR.

§ Nuclear Physics Institute AS CR.

10.1021/bc900212k CCC: $40.75 © 2009 American Chemical Society
Published on Web 10/16/2009

Scheme 1. Synthesis of the Polymeric Micellar Conjugate of Doxorubicin

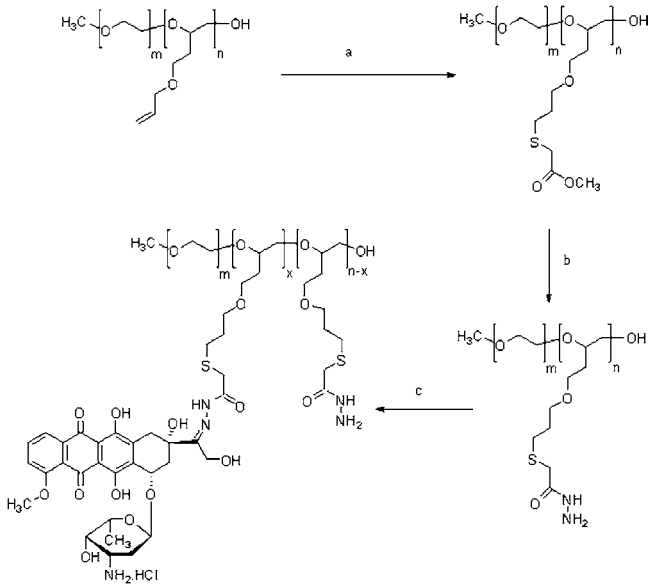

Scheme 2. Scheme of Labeling of the Polymeric Micellar Conjugate with Diethylenetriamminepentaacetic Acid (DTPA) Isotopically Labeled Moiety and with Fluorescent Dye Dyomics 615

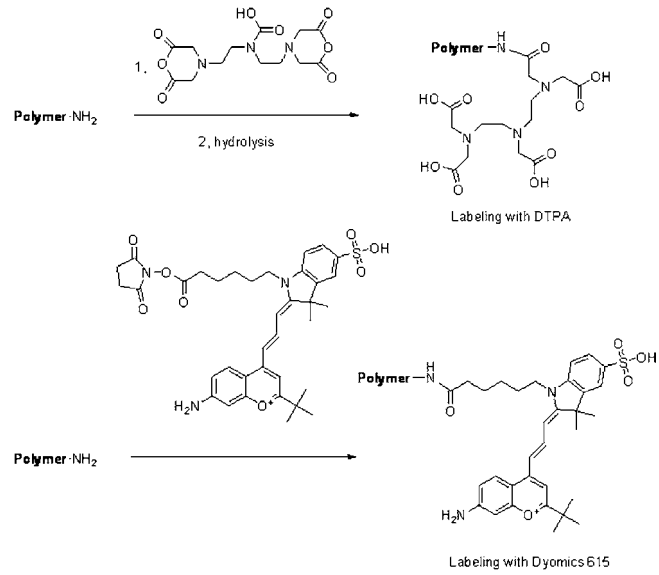

significantly less complicated, e.g., it does not require synthesis monomers that are not commercially available. The poly(ethylene oxide)-*block*-poly(allyl glycidyl ether) may also be after polymerization effectively purified from homopolymers and other impurities by a method described in (Hruby et al. 25), so a very well-defined system may subsequently be prepared.

EXPERIMENTAL PROCEDURES

Materials. Allyl glycidyl ether (AGE, Sigma-Aldrich, USA) was dried with anhydrous magnesium sulfate and distilled under reduced pressure (bp 51 °C at 2 kPa), benzene (Lach-Ner Ltd., Czech Republic) was dried with sodium and distilled, tetrahydrofuran (THF; Lach-Ner Ltd., Czech Republic) was kept over sodium and distilled before use, and cyclohexane (Lach-Ner Ltd., Czech Republic) was dried with sodium metal and distilled before use. Poly(ethylene oxide) monomethyl ether (PEO, M_w = 5000), dimethyl sulfoxide (DMSO), hydrazine hydrate, DOX hydrochloride, and methyl sulfanylacetate were purchased from Sigma-Aldrich (USA) and were used without additional purification. Other chemicals were purchased from Lach-Ner Ltd. (Czech Republic) and were used without additional purification.

Dialysis tubing Spectra/Por 3 (molecular weight cutoff 3500 Da) was purchased from Serva Electrophoresis (Germany); Sephadex LH-60 and Sephadex G-25 gel permeation chromatography media as well as PD-10 desalting column were purchased from Amersham Pharmacia Biotech (Sweden). $^{111}InCl_3$ solution was purchased from Lacomed Ltd. (Czech Republic).

Synthesis of Micellar Conjugate. The micellar conjugate was prepared as described in using the poly(ethylene oxide)-*block*-poly(allyl glycidyl ether) with $M_{w[PEO)]}$ = 5000 Da and M_w = 1600 Da (PAGE, poly(allyl glycidyl ether)) as starting material synthesized according to Hruby et al. (*25*) (see Scheme 1). We have improved the DOX conjugation procedure (*21*); DOX was conjugated to the polymer carrier as follows: The hydrazide precursor α-methyl-poly(oxirane)-*block*-poly(3-{[({[hydrazinocarbonyl]methyl}sulfanyl)propoxy]methyl}oxirane) (1.28 g, 1.85 mmol hydrazide according to the N analysis), acetic acid (960 μL, 16.8 mmol), DOX hydrochloride (320 mg, 552 μmol), and anhydrous sodium acetate (1.44 g, 17.6 mmol) were dissolved in this order in the mixture of dry DMSO (24 mL)−dry methanol (24 mL), and then anhydrous sodium sulfate (960 mg, 6.76 mmol) was added. The mixture was stirred in the dark at room temperature for 48 h and centrifuged. The polymer was isolated from the supernatant according to procedure described in (*21*). To obtain a stabilized dry preparative D-lactose, the aqueous solution of the polymer containing D-lactose (5 mg D-lactose/1 mg polymer) was freeze−dried. The conjugate containing 17 wt % of DOX in polymer forms micelles in aqueous solutions with *z*-average hydrodynamic diameter D_H = 75 nm as determined by dynamic light scattering (DLS) at room temperature ($c_{polymer}$ = 1 mg mL^{-1}) on a Nano-ZS (Malvern, UK) zetasizer at the scattering angle ϕ = 173°. The DTS (Nano) program was used for the evaluation of the data.

To label the micelles with Dyomics 615 and diethylenetriamine pentaacetic acid (DTPA), respectively (see Scheme 2), the dry micellar formulation with D-lactose (420 mg, i.e., 70 mg polymer) was dissolved in *N*,*N*-dimethylacetamide (3.0 mL) and reacted with Dyomics 615 NHS ester (Exbio Ltd., Czech Republic, 1.4 mg) or, after removal of D-lactose by filtration, with DTPA dianhydride (1.4 mg), at room temperature for 1 h. The solution was then purified from unreacted label and solvent by gel permeation chromatography on Sephadex G-25 in water and freeze−dried with D-lactose as described above to form the dry formulation. The Dyomics 615 content, assayed spectrophotometrically in methanol (λ_{max} = 621 nm, ε = 200 000 L mol^{-1} cm^{-1}), was 1.1 wt % in polymer. The content of DTPA groups was sufficient to allow >90% labeling yield (see below) with ^{111}In even at 10× higher ^{111}In/polymer ratio than used for biological experiments.

Isotopic labeling of the micellar conjugate containing DTPA chelating groups with ^{111}In was done in ammonium acetate buffer according to Jalilian et al. (*26*). Briefly, the freeze−dried D-lactose stabilized micellar formulation (82.8 mg, 13.7 mg polymer) was dissolved in aqueous ammonium acetate (500 μL, 0.1 mol L^{-1}), and the aqueous $^{111}InCl_3$ solution (100 Bq mL^{-1}; 250 μL, 25 MBq) was added. The mixture was incubated at room temperature for 10 min, and then, the polymer fraction was separated by gel filtration on a PD-10 column using phosphate buffered saline (PBS) as a mobile phase. The solution of micelles (1800 μL) was immediately frozen and kept at −78 °C. It was melted and applied just before injection (see below).

Atomic Force Microscopy. AFM was used to determine the size and shape of the micelles after binding DOX into the hydrophobic part of the amphiphilic copolymer. The solution of micellar conjugate in distilled water (30 mg L^{-1} polymer) was deposited on mica substrate and after suction of redundant liquid was immediately evaporated under vacuum atmosphere (13 Pa). All measurements were performed under ambient conditions using a commercial atomic force microscope (Nano-Scope Dimension IIIa, MultiMode Digital Instruments, USA) equipped with a PPP-NCLR tapping-mode probe with reflex aluminum coating (force constant 41 nm^{-1}, drive frequency 161 kHz). The tapping mode AFM technique was used for all the images. The final analysis of obtained data was driven by *WSxN* 4.0 software (Nanotec Electronica, Spain). The results from AFM were compared with the results obtained from dynamic light scattering; for the method, see ref *21*.

In Vitro Experiments. *Cancer Cell Lines.* Six different cell lines of either human (metastazing colorectal carcinoma SW620; lymphoblastic leukemia CEM) or murine (fibroblasts 3T3; B cell lymphoma 38C13; monocyte-macrophage lymphoma P388; T-cell lymphoma EL-4) origin were used for in vitro studies. P388 cell line was a kind gift from Prof. Lefkovits from the University of Basel, Switzerland. All other cell lines were purchased from American type Culture Collection (ATCC, Rockville, MD, USA). For fluorescent whole body imaging, the EL-4 cell line (stably expressing Enhanced Green Fluorescent Protein; EL-4-$EGFP^+$) was used. Subline was established by our group (*27*). SW620 and CEM cells were cultivated in RPMI 1640 medium with extra L-glutamine (4 mM), penicillin (100 U mL^{-1}), streptomycin (100 U mL^{-1}), and 10% v/v fetal bovine serum. P388 cell line was cultivated in RPMI 1640 with extra L-glutamine (4 mM), nonessential amino acids (75 mg L^{-1}), sodium pyruvate (1.0 mM), penicillin (100 U $mL)^{-1}$, streptomycin (100 U mL^{-1}), and 10% v/v fetal bovine serum. 38C13 cell line was cultivated in RPMI 1640 with extra L-glutamine (4 mM), 2-mercaptoethanol (5×10^{-5} M), HEPES (10 mM), sodium pyruvate (1.0 mM), penicillin (100 U mL^{-1}), streptomycin (100 U mL^{-1}), and 10% v/v fetal bovine serum. EL-4 and EL-4-$EGFP^+$ T-cell lymphomas were cultivated in RPMI 1640 medium with extra L-glutamine (4 mM), sodium pyruvate (1.0 mM), 4.5 g L^{-1} glucose, penicillin (100 U mL^{-1}), streptomycin (100 U mL^{-1}), and 10% v/v fetal bovine serum. 3T3 fibroblasts were cultivated in D-MEM medium with extra L-glutamine (4 mM), HEPES (10 mM), 4.5 g L^{-1} glucose, penicillin (100 U mL^{-1}), streptomycin (100 U mL^{-1}), and 10% v/v fetal bovine serum.

Hemolytic Assay. Human blood was collected in 5 mL Heparin coated vacutainers (Greiner Bio-One, Austria) and centrifuged for 5 min at 3000 rpm. Blood was twice washed in fresh PBS (pH 7.4), and 4% human red blood cell (RBC) suspension was prepared. Micellar delivery system or Saponin from *Quillaja* bark (Sigma-Aldrich, USA) were added to RBC suspensions to achieve desired final concentrations (range for micelles 0.01−150 μg DOX equiv mL^{-1} and range for Saponin 0.01−10 μg mL^{-1}). All samples were incubated at 37 °C in a humidified 5% CO_2/95% air atmosphere for either 30 min or 24 h and then centrifuged for 5 min at 3000 rpm. As a positive control the absorbance in distilled water and as a negative control absorbance in PBS were used. The supernatants were spectrophotometricaly analyzed at 550 nm (Spectra Rainbow, Tecan, Austria). A value of hemolytic activity was calculated by considering absorbance of positive control as 100% hemolysis. Absorbance was determined using background absorbance in PBS (for Saponin samples) or, to overcome an effect of DOX absorbing light also at wavelength of the measurement, doxorubicin of the same concentration (for micellar samples).

In Vitro Cytostatic Activity. Cytostatic potential of micellar conjugate was assesed using a [^{3}H]thymidine incorporation assay on a panel of human as well as murine cancer cell lines. 96-well flat-bottomed microplates (NUNC, Denmark) were seeded with 200 μL of cancer cells: EL-4 - murine T-cell lymphoma (5×10^3 cells/well); 38C13 - murine B cell lymphoma (2×10^3 cells/well); 3T3 - murine fibroblastoma (2×10^4 cells/well); P388 - murine monocyte−macrophage lymphoma (2×10^4 cells/well); SW620 - human colorectal carcinoma (1×10^4 cells/well); CEM - human lymphoblastic leukemia (3×10^4 cells/well). Tested samples (in triplicate) were then added (50 μL) to the wells to achieve the desired DOX concentrations (range 0.0003−33 μg mL^{-1}). Plates were incubated at 37 °C in a humidified 5% CO_2/95% air atmosphere for 72 h (EL-4 cells for 48 h). 18.5 kBq (0.5 μCi) of [^{3}H]thymidine was added per well for the last 6 h of incubation. The cells were then collected onto glass fiber filters (Filtermat, Wallac, Finland) using a cell harvester (Tomtec, USA), and the radioactivity of the samples was measured in a scintilation counter (1450 MicroBeta TriLux, Wallac, Finland). Cells cultivated in fresh medium were used as controls. All IC_{50} values are the mean of four independent experiments.

In Vivo Experiments. *Maximum Tolerated Dose (MTD).* All animal studies described hereinafter were performed in accordance with the Act on Experimental Work with Animals (decrees no. 311/97, 117/87; and act no. 246/96) of the Czech Republic, which is fully compatible with the corresponding European Union directives. Tumor free C57BL/6 male mice were used for the determination of single dose MTD (i.v.) of the DDS. The doses applied in slow intravenous injection were in the range 200−400 mg DOX equivalent to 1 kg of body weight, six animals per group. Survival and changes of body weight of each animal were recorded every other day after administration.

Noninvasive In Vivo Whole Body Imaging. For in vivo experiments, murine T cell lymphoma EL-4 stably expressing enhanced green fluorescent protein (EL-4-$EGFP^+$) was used. Male C57BL/6 mice were inoculated subcutaneously with 2×10^5 EL-4-$EGFP^+$ lymphoma cells on the shaved right flank on day 0. The tumor volume at the time of the drug administration (day 7−8) was 200−400 mm^3. For better observing conditions, conjugate containing Dy-615 was used and mice were shaved with Opilca (GlaxoSmithKline, USA) at every monitoring point. Noninvasive visualizations of DDS accumulation in tumor site and treatment efficiency were performed on OV100 Whole Mouse System (Olympus Corp., Tokyo, Japan) containing an MT-20 light source and an Orca II ERG (Hamamatsu, Japan) CCD camera. Animals were anaesthetized by intraperitoneal injection of Narkamon Spofa 1% (Spofa, Czech Republic). EGFP of tumor was visualized with U-MWIB3 cube (Ex 460−495, Em 510IF), and Dy-615 labeled micelles were visualized with U-DM-CY5 cube (Ex 600−650, Em 660−740). Images were taken separately for each fluorescent channel and also transmitted light, and merged, and colorized in *AnalySIS* software 3.2.822 (SIS systems Germany).

Blood Levels and Tumor Accumulation via ^{111}In. Six C57BL/6 mice were injected i.v. (tail vein) with micellar DDS labeled with ^{111}In. The injected dose was 2 MBq ^{111}In (in 1.5 mg polymer dissolved in 200 μL PBS) per mouse at the time of application. The radioactivity levels in blood samples and tumor tissue samples were measured by gamma counter Minaxi 5000 (Canberra Packard, Austria) at selected time points (4, 24, 48, and 72 h) after injection. The measured radioactivities were corrected on the radioisotope decay ($T_{1/2}$ = 67.31 h).

In Vivo Antitumor Activity. Murine T cell lymphoma EL-4 was used for in vivo evaluation of antitumor activity of micellar formulation of DOX. Mice of inbred strain C57BL/6, obtained

from Animal Facility of the Institute of Physiology, Academy of Sciences of the Czech Republic, v. v. i., were inoculated subcutaneously with 1×10^5 EL-4 T-cell lymphoma cells on the right flank on day 0. Micellar conjugate was administered into the tail vein when the tumors were well-established, i.e., when the tumor volume reached 200−400 mm^3 (day 7−8). The animals were divided into 5 groups of 8 animals each. The animals were observed every second day for signs of tumor progression; measurements of tumor size were done using calipers. Tumor volume was calculated as $V = ab^2/2$ (a = longer diameter, b = shorter perpendicular diameter). Survival time and body weight of experimental animals were checked. All cured animals were observed for an additional 100 days after complete remission, and then they were challenged by subcutaneous re-transplantation by a lethal dose of EL-4 (1×10^5) cells. After re-transplantation, mice were checked and tumor growth was observed three times a week.

RESULTS

Preparation of Micellar DDS. An improved version of our previously described (*21*) doxorubicin (DOX)-containing micelles was used. The system is based on an amphiphilic diblock copolymer consisting of a poly(ethylene oxide) hydrophilic block, and a hydrophobic block containing doxorubicin bound via a pH-labile hydrazone bond (Scheme 1). The improvement consists of an increase of the DOX loading from the original 3% (w/w polymer) to 17% without the loss of stability of the micelles. This was achieved by modification of the method of DOX attachment; the conjugation was carried on using the pH-buffering system acetic acid−sodium acetate under anhydrous conditions (dimethyl sulfoxide−methanol mixture due to solubility of all components). The reaction is catalyzed by acid, but the conjugation using acetic acid alone or without catalysis always gave significantly lower yields of conjugation. For the buffering system used in this study, the conjugation yield was 85% (17 wt % DOX in polymer compared to theoretical 20 wt % in conjugation mixture), while for acid only or noncatalyzed reaction, it was never above 34% and yields drop significantly at higher DOX loadings (Hruby et al. (*21*)). D-Lactose was added as a cryoprotective to prepare the stable dry micellar formulation. It prevents aggregation of the micelles during freeze−drying and resolubilization.

The initial in vitro DOX release rate (hydrolysis at pH 7.4 and 5.5) was not significantly influenced in comparison to the previous system with lower drug loading (*21*); however, a plateau in the release curve (DOX release versus time) plausibly caused by equilibration due to reversible nature of the hydrazone bond formation−hydrolysis was somehow shifted to lower DOX release. AFM proved the shape and size distribution of the micelles. The micelles are of spherical shape, however, with somehow broader size distribution with average diameter (D) according to AFM 97 nm (Figure 1).

Hemolysis Assay. We found no hemolytic activity of the micellar conjugate of DOX in concentration ranging from 0.01 μg DOX equiv mL^{-1} to 150 μg DOX equiv mL^{-1}. Because of the absence of hemolytic activity, we do not expect any membrane related toxicity in vivo (Figure 2).

Proliferation Assay. The in vitro antiproliferative activity of the micellar conjugate was tested on six cell lines of different origin and sensitivity to free DOX (EL-4, 38C13, 3T3, SW620, P388, and CEM; Table 1). Micelle-conjugated DOX was 1 order of magnitude less potent than free drug for human cancer cell lines (SW620 and CEM) and for murine fibroblasts (3T3). Detected IC_{50} values of micellar DOX for 38C13, EL-4, and P388 cells were even higher by 2 orders of magnitude. The IC_{50} values were in the range 0.09−1.23 μg DOX equiv mL^{-1} depending on the cell line (Table 1).

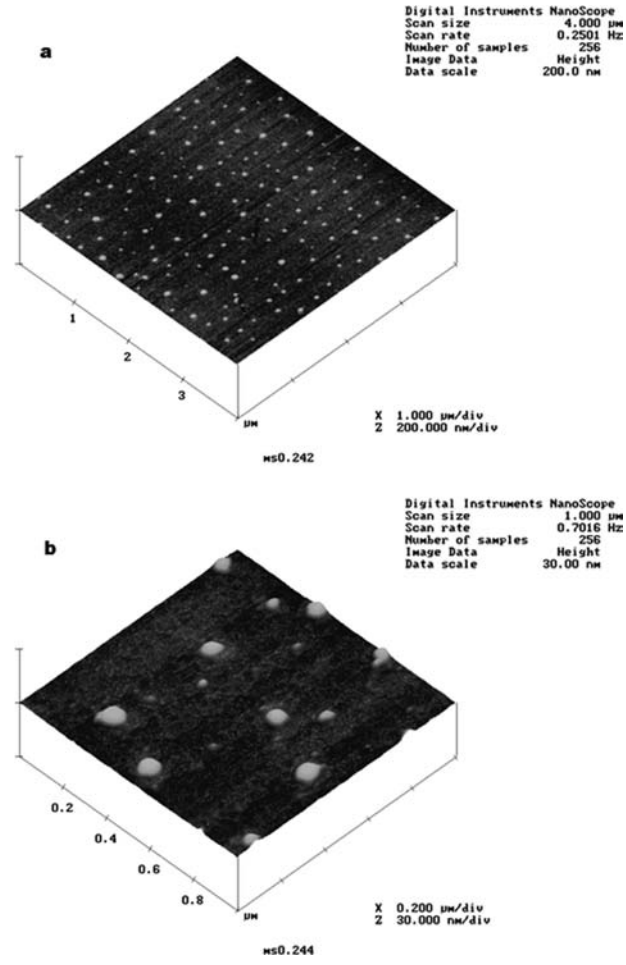

Figure 1. Atomic force microscopy image of the micelles on mica surface. (A) segment 4×4 μm^2, (B) detail 1×1 μm^2.

Maximum Tolerated Dose (MTD). The determination of maximum tolerated dose revealed extremely low systemic toxicity of the micellar conjugate. Up to dose 320 mg DOX equiv kg^{-1}, no body weight loss or other obvious symptoms of systemic toxicity were recorded. Significant loss of body weight (in the range 10−21%) was observed after application of 360 mg DOX equiv kg^{-1}, but all animals recovered and henceforth stayed without any obvious evidence of serious side effects. Dose 380 mg DOX equiv kg^{-1} killed one-third of the animals, while the dose 400 mg DOX equiv kg^{-1} was lethal for all animals (Figure 3). The MTD of the micelles 360 mg DOX equiv kg^{-1} is thus more than 1 order of magnitude higher compared to MTD of free DOX hydrochloride (15 mg/kg (*32*)).

Blood Levels and Tumor Accumulation. To analyze blood levels, micelles were labeled with ^{111}In. The chelating groups were introduced in the polymeric DOX conjugate by reaction with DTPA dianhydride, and the resulting conjugate was labeled with ^{111}In. For the first 24 h, we have seen a stabile concentration plateau. Then, the concentration of ^{111}In-labeled micelles in the blood slowly decreased. The half-life of the dose was determined in circulation after 24 h (Figure 4A), which is sufficiently long to ensure both prolonged exposure of the tumor cells to DOX and effective EPR effect.

In the tumor tissue, the indium-111 radioactivity increased for the first 24 h up to 8%, and then continuously decreased again after this peak (Figure 4B). In vivo tumor accumulation followed via Dyomics 615 fluorescence (Figure 4C) using OV100 Whole Mouse System corresponds well with the radioactivity measurements. Strong fluorescence signal was

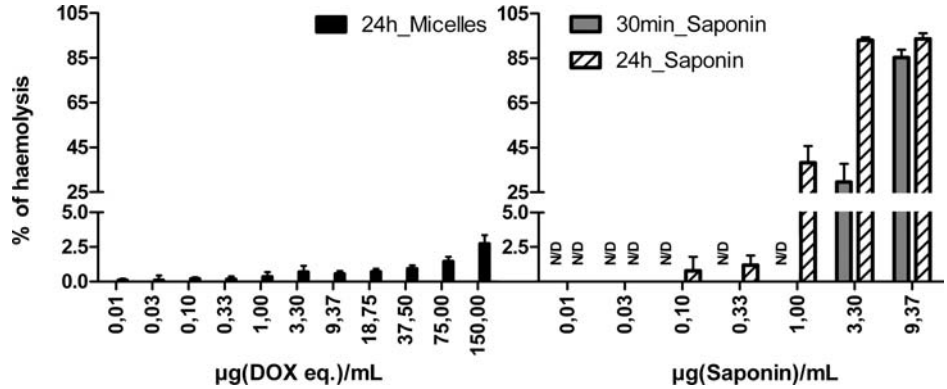

Figure 2. Percentage of hemolysis compared to values of distilled water (100% hemolysis) of human red blood cells caused by micellar drug delivery system or free Saponin (from Quillaja bark) with the SD values.

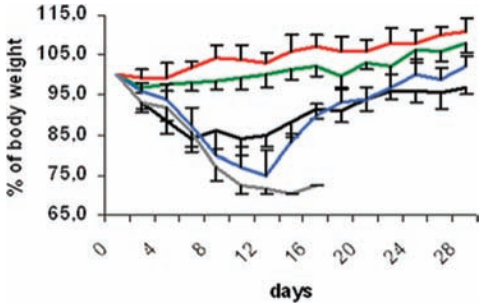

Figure 3. Micellar conjugate was intravenously administered to C57BL/6 mice, and changes in body weight as a sign of systemic toxicity were regularly recorded (red line, controls; green line,1 × 320 mg (DOX equiv) kg^{-1}; black line, 1 × 360 mg (DOX equiv) kg^{-1}; blue line, 1 × 380 mg (DOX equiv) kg^{-1}; gray line, 1 × 400 mg (DOX equiv) kg^{-1}).

Table 1. Cytostatic Activity Expressed as IC_{50} Values

	micellar DOX IC_{50} μg (DOX equiv)/mL	free DOX IC_{50} μg/mL	micellar DOX IC_{50}/free DOX IC_{50}
38C13	0.235 ± 0.066	0.005 ± 0.001	47
SW620	0.476 ± 0.237	0.011 ± 0.004	43.3
EL-4	1.113 ± 0.283	0.032 ± 0.018	34.8
P388	1.233 ± 0.521	0.058 ± 0.020	21.3
CEM	0.865 ± 0.238	0.068 ± 0.033	12.7
3T3	0.089 ± 0.026	0.009 ± 0.006	9.9

detectable only up to 24 h after micelle administration, and no evincible signal was obtained after 48 h or later.

In Vivo Antitumor Activity. The in vivo therapeutic efficiency of micellar DDS with DOX was tested both with single dose and with two subsequent doses (three days delay between the doses). The dose 1 × 75 mg DOX equiv kg^{-1} significantly prolonged the survival of the mice (Figure 5A), but no mice were completely cured, while the doses 2 × 75 mg DOX equiv kg^{-1} and 1 × 150 mg DOX equiv kg^{-1} completely cured 75% and 62.5% of mice, respectively (Figure 5A).

The cured mice were re-inoculated with the lethal dose of EL-4 cells (1×10^5 cells per mouse, i.e., the same dose as the first transplantation) 100−105 days after the original tumor was cured and left without treatment. Eighty percent of re-inoculated mice were able to destroy transplanted cells (Figure 5B), showing the establishment of very significant immunological memory against the EL-4 T-cell line, similar to the soluble HPMA-based derivative (*28*).

DISCUSSION

Formerly described synthesis of micellar system based on poly(allyl glycidyl ether)-*block*-poly(ethylene oxide) (*21, 25*) showed only very low loading efficiency (3% of DOX content). We have achieved significantly higher DOX loading (17%) by using acetic acid−sodium acetate pH-buffering system under anhydrous conditions. The most plausible explanation to why this environment gives high conjugation yields is that the buffering system maintains mildly acidic conditions required for the reaction and hinders electrostatic repulsive forces among the polymer and DOX molecules in solution by its ionic strength. Since the original system would become sensitive to aggregation in aqueous solution while increasing the DOX loading, here we have used a longer poly(ethylene oxide) block for stabilization (M_w = 5000 Da instead of 2000 Da).

When comparing the rate of in vitro DOX release (hydrolysis at pH 7.4 and 5.5), between previous system (*21*) and the one reported here (with higher drug loading), we have not seen any significant variations. This is the difference from micellar systems with a more hydrophobic core and a drug bound by an irreversibly cleavable bond, e.g., methotrexate bound to poly(ethylene oxide)-*block*-poly(2-hydroxyethyl-L-aspartamide) (*17*), where the drug release rate is significantly lowered by the increasing drug loading and does not reach equilibration plateau during in vitro release experiments. If the core is sufficiently hydrophobic, water activity in the core is significantly lower than in surrounding aqueous milieu, so the higher the drug loading is, the more hydrophobic the micelle core is, and the lower is water activity in it; due to this, the drug release rate slows down (in fact, in the extreme cases it is expected that drug is hydrolyzed predominantly from unimers). In the case of the DOX-containing micelles described in this study, the micelle core is probably sufficiently swollen with water even at higher DOX loadings, so the hydrolysis rate is not heavily influenced by lower water content in the micelle core. This is also supported by lower particle density (~0.1 g mL^{-1} polymer) calculated from light scattering.

Amphiphilic block copolymers are commonly used as micellar drug delivery systems (MDDS), as they allow preparation of colloid solution with a very narrow size distribution. The size of polymeric micelles may be set from 10 to 100 nm in diameter, which is a size suitable for passive accumulation via the EPR effect (*23*). The size of particles tested here obtained using AFM (D = 97 nm; Figure 1) was slightly higher than that determined by dynamic light scattering (hydrodynamic diameter D_H = 75 nm), which was interpreted to be an artifact of spreading and drying on the mica surface.

Due to their detergent properties, many amphiphilic molecules possess membrane disruptive properties (*29, 30*). Although amphiphilic diblock polymers are generally less toxic than low-molecular-weight surfactants due to lower critical micellar concentration and thus lower equilibrium concentration of the surface active unimer, their membrane toxicity may still be

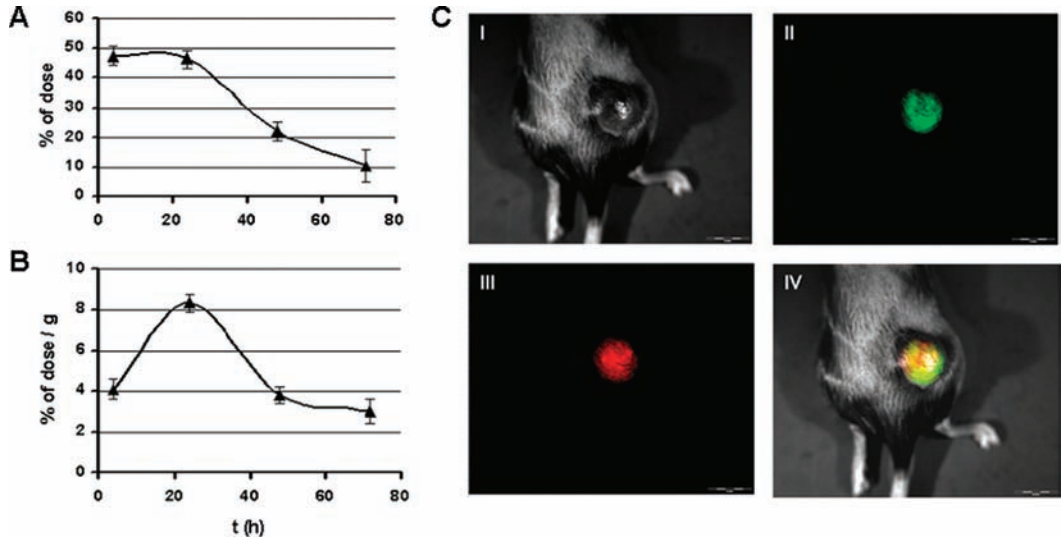

Figure 4. Pharmacokinetics of micellar conjugate in C57BL/6 mice. (A) Blood level of ^{111}In labeled micelles. (B) Tumor accumulation of ^{111}In labeled micelles. (C) EGFP expressing tumor cells were subcutaneously transplanted and tumor accumulation of the micellar conjugate (conjugated with fluorescent dye Dyomics 615) was followed by fluorescence imaging: I, bright-field; II, EGFP fluorescence; III, Dyomics 615 fluorescence; IV, merged (I + II + III).

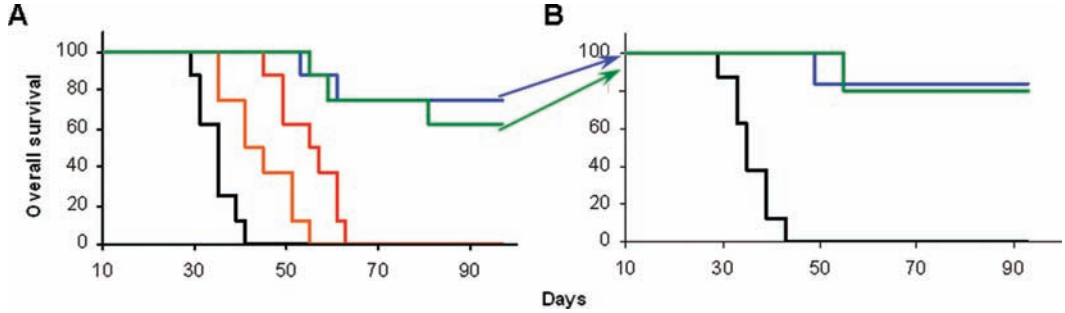

Figure 5. (A) Survival of mice bearing EL-4 T-cell lymphoma and treated with micellar DOX (black line, controls; orange line, 2 × 5 mg (DOX) kg^{-1}; red line, 1 × 75 mg (DOX equiv) kg^{-1}; blue line, 2 × 75 mg (DOX equiv) kg^{-1}; green line, 1 × 150 mg (DOX equiv) kg^{-1}). (B) Cured mice were re-transplanted with a lethal dose of the same cancer cells and left without treatment (black line, controls; blue line, mice previously cured with 2 × 75 mg (DOX equiv) kg^{-1}; green line, mice previously cured with 1 × 150 mg (DOX equiv) kg^{-1}). Displayed data represent a typical result of independent experiments ($P < 0.05$).

unacceptable. Our micellar DDS was designed to prolong the blood circulation period and maximize the efficiency of the EPR effect. Once within the tumor site, lower pH leads to DOX release, and consequently to the destabilization of the micelles. When the micellar architecture is broken down, the free diblock unimers can undergo the renal excretion and DOX acts at the site of micellar disruption as a free drug. There is a low risk that these nonassembled diblock unimers with their hydrophobic PAGE blocks could anchor and disrupt plasma membrane. However, neither micelles with attached DOX nor free diblock unimers of PAGE-block-PEO showed significant membrane toxicity to human red blood cells (Figure 2).

Most delivery systems based on polymer carriers usually exhibit decreased antiproliferative activity in in vitro system compared to free drug (*6, 31*). We assume that the lower in vitro antiproliferative activity of described MDDS is caused by slower cellular uptake and intracellular drug release due to their high molecular weight.

However, the increase in MTD compared to the free drug is convincing. Soluble polymers with bound drug exhibit an increase in MTD because the drug is inactive while bound to the polymer. Tested polymeric micelles showed a massive increase in MTD not only when compared with free DOX (*32*), but also when compared with other water-soluble copolymers with DOX bound via hydrazon bond (MTD ∼ 130 mg/kg (*28*)). This is probably caused by slow, gradual release of DOX from the micellar carrier (see our previous work (*21*)) for the in vitro release study showing the half-life 198 h at pH 7.4 and 8.62 h at pH 5.0), which allows the organism to detoxify/eliminate the DOX released within the organism.

Higher MTD, prolonged continuance in blood circulation, and efficient EPR effect together cured murine T-cell lymphoma (EL-4) bearing mice with a single dose of 150 mg DOX equiv kg^{-1} without any signs of side toxicity (loss of weight of animals) (Figure 3). This is a significant improvement compared with the effect of treatment with free DOX (2 × 5 mg kg^{-1}). Moreover, the fact that only one-third of the detected MTD (for micellar DOX) is efficient opens a wide therapeutical window for further improvement of therapeutic schedule. Such a possibility should be examined for more resistant tumors, where recently available polymeric derivatives of DOX are less effective. This MDDS is a new approach to those already described (*28, 33, 34*). Of course, it is clear that broad variability in tumor diseases would also require a broad range of structures of polymer drug carriers, thus opening space for development of various drug delivery systems differing in their physico-chemical and biological behavior. Importantly, except for the cytotoxic effect, the treatment with MDDS described here triggers long-lasting systemic anticancer resistance, similarly to what was reported for other HPMA-based polymeric systems bearing DOX (*35*) (Figure 5). This finding is extremely important as it potentially protects tumor-bearing host against

second (metastatic) cancer attack. Experiments with various types of polymer drug carriers are in progress to understand the involved immunological mechanisms and influence of the carrier structure on it.

Biological properties of the micellar drug carrier system containing DOX covalently bound via hydrazone bonds to the micelle core were investigated. The system has a very low systemic toxicity (almost 2 orders of magnitude higher maximum tolerated dose than free DOX on the DOX equivalent basis) and long circulation time (tens of hours). Promising therapeutical efficiency against the EL-4 T-cell lymphoma was found completely curing up to 75% of tumor-bearing mice. Moreover, treatment with micellar conjugate of DOX activated the immune system and established an effective antitumor immunological memory. Significant accumulation of the polymeric micellar system within the tumor site was found by noninvasive fluorescent whole body imaging.

ACKNOWLEDGMENT

This work was supported in parts by grant of Academy of the Sciences of the Czech Republic no. KAN 200200651, by grant no. 310/08/H077 awarded by Czech Science Foundation, by grant of the Grant Agency of the Academy of Sciences of the Czech Republic no. IAA400480616, and by the Institutional Research Concept AV 0Z 502 00 510. We would like to acknowledge excellent technical assistance of Helena Misurcova and Pavlina Jungrova (Institute of Microbiology AS CR, v.v.i.), and Dr. Milena Spirkova (Institute of Macromolecular Chemistry AS CR, v.v.i.) for measuring the AFM images.

LITERATURE CITED

(1) Avendano, C. M., and Menendez, J. C. (2008) *Medicinal Chemistry of Anticancer Drugs*, Elsevier, Amsterdam.

(2) Greco, F., and Vicent, M. J. (2008) Polymer-drug conjugates: current status and future trends. *Front. Biosci. 13*, 2744–2756.

(3) Kratz, F., Müller, I. A., Ryppa, C., and Warnecke, A. (2008) Prodrug startegies in anticancer chemotherapy. *ChemMedChem 3*, 20–53.

(4) Pasut, G., and Veronese, F. M. (2007) Polymer-drug conjugation, recent achievements and general strategies. *Prog. Polym. Sci. 32*, 933–961.

(5) Rihova, B. (2007) Biocompatibility and immunocompatibility of water-soluble polymers based on HPMA. *Composites 38*, 386–397.

(6) Kopecek, J., Kopeckova, P., Minko, T., and Lu, Z. (2000) HPMA copolymer-anticancer drug conjugates: design, activity, and mechanism of action. *Eur. J. Pharm. Biopharm. 50*, 61–81.

(7) Howard, M. D., Jay, M., Dziublal, T. D., and Lu, X. L. (2008) PEGylation of nanocarrier drug delivery systems: State of the art. *J. Biomed. Nanotechnol. 4*, 133–148.

(8) Chytil, P., Etrych, T., Konak, C., Sirova, M., Mrkvan, T., Boucek, J., Rihova, B., and Ulbrich, K. (2008) New HPMA copolymer-based drug carriers with covalently bound hydrophobic substituents for solid tumour targeting. *J. Controlled Release 127*, 121–130.

(9) Seymour, L. W., Miyamoto, Y., Maeda, H., Brereton, M., Strohalm, J., Ulbrich, K., and Duncan, R. (1995) Influence of molecular weight on passive tumour accumulation of a soluble macromolecular drug carrier. *Eur. J. Cancer 31*, 766–70.

(10) Maeda, H. (2001) The enhanced permeability and retention (EPR) effect in tumor vasculature: the key role of tumor-selective macromolecular drug targeting. *Adv. Enzyme Regul. 41*, 189–207.

(11) Sawant, R. M., Hurley, J. P., Salmaso, S., Kale, A., Tolcheva, E., Levchenko, T. S., and Torchilin, V. P. (2006) "SMART" drug delivery systems: double-targeted pH-responsive pharmaceutical nanocarriers. *Bioconjugate Chem. 17*, 943–949.

(12) Mahmud, A., Xiong, X. B., Aliabadi, H. M., and Lavasanifar, A. (2007) Polymeric micelles for drug targeting. *J. Drug Targeting 15*, 553–584.

(13) Qiu, L. Y., Zheng, C., Jin, Y., and Zhu, K. J. E. (2007) Polymeric micelles as nanocarriers for drug delivery. *Exp. Opin. Therapeut. Pat. 17*, 819–830.

(14) Owens 3rd, D. E., and Peppas, N. A. (2006) Opsonization, biodistribution, and pharmacokinetics of polymeric nanoparticles. *Int. J. Pharm. 307*, 93–102.

(15) Iyer, A. K., Greish, K., Seki, T., Okazaki, S., Fang, J., Takeshita, K., and Maeda, H. (2007) Polymeric micelles of zinc protoporphyrin for tumor targeted delivery based on EPR effect and singlet oxygen generation. *J. Drug Targeting 15*, 496–506.

(16) Bader, H., Ringsdorf, H., and Schmidt, B. (1984) Watersoluble polymers in medicine. *Angew. Chem. 123/124*, 457–485.

(17) Li, Y., and Kwon, G. S. (2000) Methotrexate ester of poly(ethylene oxide)-block-poly(2-hydroxyethyl-L-aspartamide). Part 1: Effects of the level of methotrexate conjugation on the stability of micelles and on drug release. *Pharm. Res. 157*, 607–611.

(18) Bae, Y., Nishiyama, N., Fukushima, S., Koyama, H., Yasuhiro, M., and Kataoka, K. (2005) Preparation and biological characterization of polymeric micelle drug carriers with intracellular pH-triggered drug release property: tumor permeability, controlled subcellular drug distribution, and enhanced in vivo antitumor efficacy. *Bioconjugate Chem. 16*, 122–30.

(19) Gerweck, L. E., and Seetharaman, K. (1996) Cellular pH gradient in tumor versus normal tissue: potential exploitation for the treatment of cancer. *Cancer Res. 56*, 1194–1198.

(20) Etrych, T., Mrkvan, T., Chytil, P., Konak, C., Rihova, B., and Ulbrich, K. (2008) N-(2-hyroxypropyl)methacrylamide-based polymer conjugates with pH-controlled activation of doxorubicin. I. New synthesis, physicochemical characterization and preliminary biological evaluation. *J. Appl. Polym. Sci. 109*, 3050–3061.

(21) Hruby, M., Konak, C., and Ulbrich, K. (2005) Polymeric micellar pH-sensitive drug delivery system for doxorubicin. *J. Controlled Release 103*, 137–148.

(22) Kataoka, K., Matsumoto, T., Yokoyama, M., Okano, T., Sakurai, Y., Fukushima, S., Okamoto, K., and Kwon, G. S. (2000) Doxorubicin-loaded poly(ethylene glycol)-poly(beta-benzyl-l-aspartate) copolymer micelles: their pharmaceutical characteristics and biological significance. *J. Controlled Release 64*, 143–153.

(23) Greish, K., Sawa, T., Fang, J., Akaike, T., and Maeda, H. (2004) SMA-doxorubicin, a new polymeric micellar drug for effective targeting to solid tumours. *J. Controlled Release 97*, 219–230.

(24) Nakanishi, T., Fukushima, S., Okamoto, K., Suzuki, M., Matsumura, Y., Yokoyama, M., Okano, T., Sakurai, Y., and Kataoka, K. (2001) Development of the polymer micelle carrier system for doxorubicin. *J. Controlled Release 74*, 295–302.

(25) Hruby, M., Konak, C., and Ulbrich, K. (2005) Poly(allyl glycidyl ether)-block-poly(ethylene oxide): A novel promising polymeric intermediate for the preparation of micellar drug delivery systems. *J. Appl. Polym. Sci. 95*, 201–211.

(26) Jalilian, A. R., Rowshanfarzad, P., Shafaii, K., Kamali-Dehghan, M., Moafian, J., Akhlaghi, M., Babaii, M., Rajabifar, S., and Mirzaii, M. (2005) Development of In-III-DTPA-human polyclonal antibody complex for long-term inflammation/infection detection. *Nukleonika 50*, 91–96.

(27) Vetvicka, D., Hovorka, O., Kovar, L., and Rihova, B. (2009) Establishment of imageable murine model of T-cell lymphoma growing in syngenic mice, *Anticancer Res.*, in press.

(28) Mrkvan, T., Sirova, M., Etrych, T., Chytil, P., Strohalm, J., Plocova, D., Ulbrich, K., and Rihova, B. (2005) Chemotherapy based on HPMA copolymer conjugates with pH-controlled release of doxorubicin triggers anti-tumor immunity. *J. Controlled Release 110*, 119–29.

(29) Yessine, M. A., Lafleur, M., Meier, C., Petereit, H. U., and Leroux, J. C. (2003) Characterization of the membrane-destabilizing properties of different pH-sensitive methacrylic acid copolymers. *Biochim. Biophys. Acta 1613*, 28–38.

(30) Wang, X. L., Ramusovic, S., Nguyen, T., and Lu, Z. R. (2007) Novel polymerizable surfactants with pH-sensitive amphiphilicity and cell membrane disruption for efficient siRNA delivery. *Bioconjugate Chem. 18*, 2169–2177.

(31) Kovar, L., Strohalm, J., Chytil, P., Mrkvan, T., Kovar, M., Hovorka, O., Ulbrich, K., and Rihova, B. (2007) The same drug but a different mechanism of action: Comparison of free doxorubicin with two different N-(2-hydroxypropyl)methacrylamide copolymer-bound doxorubicin conjugates in EL-4 cancer cell line. *Bioconjugate Chem. 18*, 894–902.

(32) Colbern, G. T., Hiller, A. J., Musterer, E. P., Pegg, E., Hendersonand, I. C., and Working, P. K. (1999) Significant increase in antitumor potency of doxorubicin Hc1 by its encapsulation in pegylated liposomes. *J. Liposome Res. 9*, 523–538.

(33) Etrych, T., Chytil, P., Mrkvan, T., Sirova, M., Rihova, B., and Ulbrich, K. (2008) Conjugates of doxorubicin with graft HPMA copolymers for passive tumor targeting. *J. Controlled Release 132*, 184–192.

(34) Etrych, T., Mrkvan, T., Rihova, B., and Ulbrich, K. (2007) Star-shaped immunoglobulin-containing HPMA-based conjugates with doxorubicin for cancer therapy. *J. Controlled Release 122*, 31–38.

(35) Rihova, B., Kovar, L., Kovar, M., and Hovorka, O. (2009) Cytotoxicity and immunostimulation: double attack on cancer cells with polymeric therapeutics. *Trends Biotechnol. 27*, 11−17.

BC900212K

Expedited Solid-Phase Synthesis of Fluorescently Labeled and Biotinylated Aminoalkane Diphenyl Phosphonate Affinity Probes for Chymotrypsin- and Elastase-Like Serine Proteases

Brendan F. Gilmore, Derek J. Quinn, Thomas Duff, George R. Cathcart, Christopher J. Scott, and Brian Walker*

School of Pharmacy, Queens University Belfast, Medical Biology Centre, 97 Lisburn Road, Belfast BT9 7BL, United Kingdom.
Received May 14, 2009; Revised Manuscript Received August 24, 2009

In this study, we report on a novel, expedited solid-phase approach for the synthesis of biotinylated and fluorescently tagged irreversible affinity based probes for the chymotrypsin and elastase-like serine proteases. The novel solid-phase biotinylation or fluorescent labeling of the aminoalkane diphenyl phosphonate warhead using commercially available Biotin-PEG-NovaTag or EDANS NovaTag resin permits rapid, facile synthesis of these reagents. We demonstrate the kinetic evaluation and utilization of a number of these irreversible inactivators for chymotrypsin-like (chymotrypsin/human cathepsin G) and elastase-like serine proteases. Encouragingly, these compounds display comparable potency against their target proteases as their *N*-benzyloxycarbonyl (Cbz)-protected parent compounds, from which they were derived, and function as efficient active site-directed inactivators of their target proteases. We subsequently applied the biotinylated reagents for the sensitive detection of protease species via Western blot, showing that the inactivation of the protease was specifically mediated through the active site serine. Furthermore, we also demonstrate the successful detection of serine protease species with the fluorescently labeled derivatives "in-gel", thus avoiding the need for downstream Western blotting. Finally, we also show the utility of biotinylated and pegylated affinity probes for the isolation/enrichment of serine protease species, via capture with immobilized streptavidin, and their subsequent identification via de novo sequencing. Given their selectivity of action against the serine proteases, we believe that these reagents can be exploited for the direct, rapid, and selective identification of these enzymes from biological milieu containing multiple protease subclasses.

INTRODUCTION

The completion of the human genome sequencing project (*1*) has facilitated a comprehensive analysis of known and potential gene products which may represent novel targets for pharmacological intervention/modulation. Original estimates of the "druggable genome" (i.e., those genes that encode protein products predicted to possess structural domains or motifs which are likely to favor interactions with drug-like molecules) indicated that approximately 3000 genes belonged to this unique group (*2*). More recent functional genomic analysis of the druggable genome has been in close agreement with these earlier estimates, although, significantly, the proportion of the predicted major target families of proteins appears to have changed somewhat. For example, these latter studies indicate a reduction in the numbers of putative protein kinases and rhodopsin-like G-protein coupled receptors (GPCRs) and an increased number of putative protease targets which are potentially "druggable" (*3*). Proteases have long been regarded as important therapeutic targets, in recognition of their multifarious roles in numerous diseases, and much focus has been directed toward protease inhibition in pathological conditions. However, it is significant that, although many proteases have recently been identified through genomic analysis, only a small proportion (~15%) have been characterized through functional studies (*4*). Thus, the application of specific and sensitive protease detection methodologies that can be utilized in high-throughput proteomic formats to facilitate the functional identification of poorly characterized species is urgently required. A number of substrate approaches have previously been developed for the detection of protease activities, following electrophoresis from a range of biological samples (*5, 6*).

We have previously reported on the synthesis and methodologies for the profiling of serine proteases by utilizing biotinylated aminoacylchloromethanes (*7*) and cysteine proteases, using biotinylated peptidyldiazomethanes (*8*−*10*). Powers and co-workers (*11*) pioneered the development of potent and exquisitely selective peptide derivatives of diphenyl [1-(*N*-peptidylamino)alkyl] phosphonate esters as irreversible inactivators of the serine proteases and utilized biotinylated and fluorescently labeled derivatives to detect a range of serine proteolytic activities including lymphocyte serine proteases (granzymes) (*12, 13*). We have also reported on the application of such phosphonate-based inhibitors for the detection of trypsin-like serine proteases (*14*) and, more recently, on the development of an active site directed probe for dipeptidyl peptidase IV-like serine proteases, based on a biotinylated dipeptide proline diphenylphosphonate (*15, 16*). In a related approach, Cravatt and co-workers have employed fluorophosphonate derivatives of long-chain fatty acids for visualization and characterization of catalytically active serine hydrolases including fatty acid esterases and serine proteases (*6, 17*). Development of such "activity profiling" approaches has been particularly useful in assigning function to proteolytic enzymes from diverse biological milieu. Indeed, such approaches may be of particular utility in validating protease targets in disease processes where analysis of levels of transcription and translation of a protease do not necessarily correlate well with enzyme activity (*18*).

We now report on a novel solid-phase synthesis approach for the generation of active site directed affinity probes based upon aminoalkyl diphenyl phosphonates and their application for the profiling and characterization of serine proteases obtained

* Author for correspondence. Prof. Brian Walker, School of Pharmacy, Queens University Belfast, Medical Biology Centre, 97 Lisburn Road, Belfast BT9 7BL, UK, Tel: +44 (0) 28 90 972 047, Fax: +44 (0) 28 90 247 794, Email: brian.walker@qub.ac.uk.

10.1021/bc9002162 CCC: $40.75 © 2009 American Chemical Society
Published on Web 10/07/2009

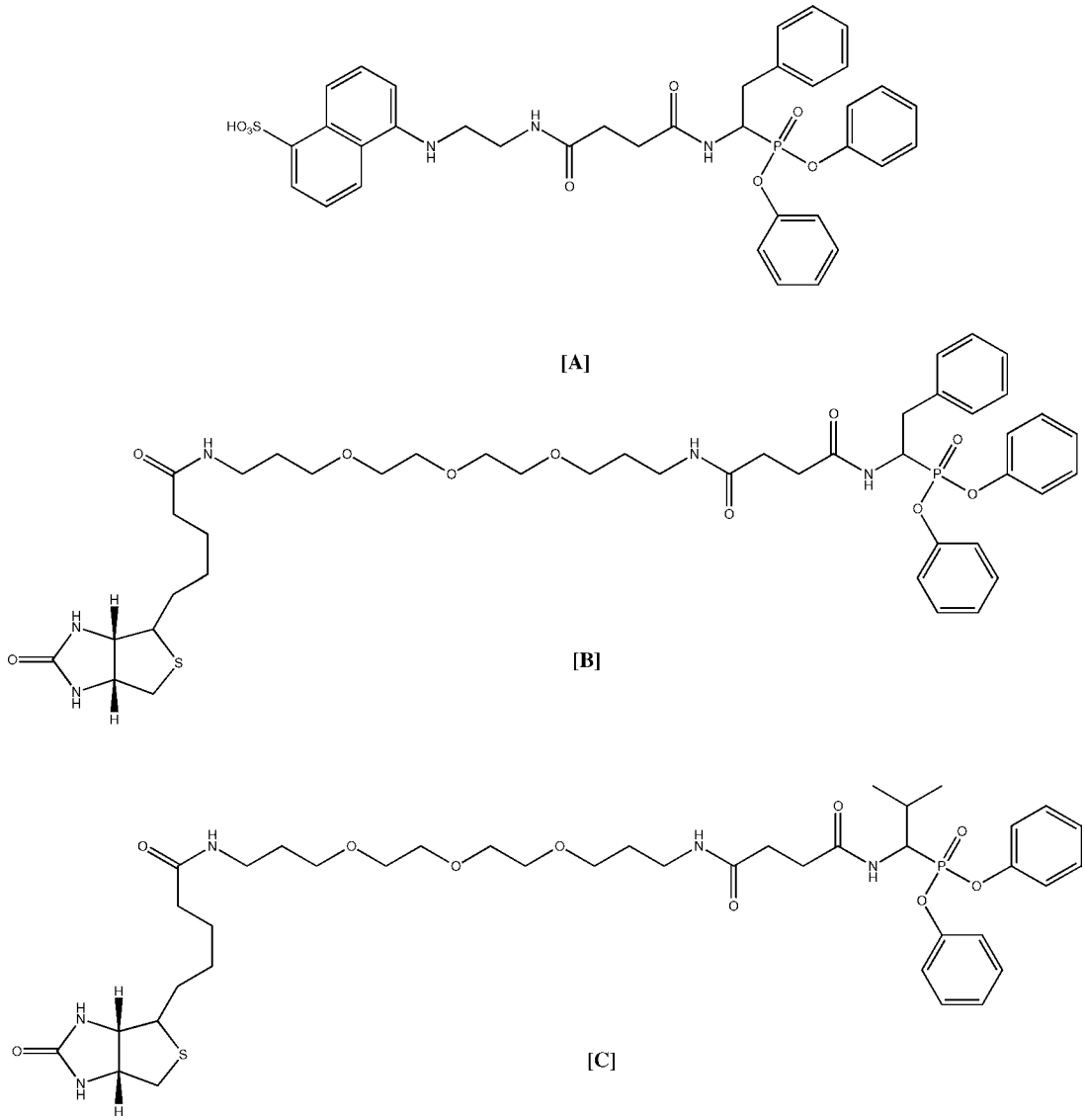

Figure 1. Affinity based probes synthesized for this study, according to Scheme 1. [A] EDANS-succinyl-Phe^{P}(OPh)$_2$. [B] Biotinyl-PEG-succinyl-Phe^{P}(OPh)$_2$. [C] Biotinyl-PEG-succinyl-Val^{P}(OPh)$_2$.

from a broad variety of biological sources. The synthetic scheme employs recently available NovaTag resin technology that enables the facile synthesis of activity probes bearing biotin or fluorescent tags and which can also incorporate pegylated spacer units, if desired. Using this approach, we have synthesized a number of affinity probes that target serine proteases with differing P1 specificities and demonstrate their detection by Western blot. Furthermore, the application of fluorescently tagged active site directed probes for "in-gel" detection is examined. We also demonstrate the utility of biotinylated and pegylated affinity probes for the isolation/enrichment of serine protease species, in this case, the *Pseudomonas aeruginosa* MucD peptidase (*19*), via exploitation of their interaction with immobilized streptavidin, and their subsequent *de novo* sequencing, using mass spectrometry.

EXPERIMENTAL PROCEDURES

Biotin-PEG NovaTag resin, EDANS NovaTag resin, and 2-(1*H*-benzotriazole-1-yl)-1,1,3,3-tetramethylaminium hexafluorophosphate (HBTU) were purchased from Novabiochem, Nottingham, U.K. *N*,*N*-Dimethylformamide (DMF) was supplied by BDH Chemicals Ltd. (Poole, England). *N*,*N*-Diisopropylethylamine (DIPEA) and piperidine/DMF (20% v/v) were supplied by PerSeptive Biosystems Ltd. (Warrington, England). Succinic anhydride and dimethylamino pyridine were purchased from Aldrich Chemical Co., Poole, Dorset (UK). All chemicals and solvents were of the highest purity and were subjected to no further purifications prior to use. Horseradish peroxidase streptavidin was obtained from Vector Laboratories Ltd., Burlingame, CA, USA. SuperSignal West Pico Chemiluminescent Substrate was supplied by Pierce Biotechnology Inc., Rockford, IL, USA.

Synthesis of Active Site Probes. The protected aminoalkane diphenylphosphonate derivatives diphenyl-1-[*N*-benzyloxycarbonyl]-amino phenylethane phosphonate (Cbz.Phe^{P}(OPh)$_2$)[1] and diphenyl-1-[*N*-benzyloxycarbonyl]-amino isobutane phosphonate (Cbz.Val^{P}(OPh)$_2$) were prepared by reacting triphenylphosphite, benzyl carbamate and the appropriate aldehyde corresponding to the desired amino acid side chain according to the method of Oleksyszen et al. (*11*, *20*). Each of the

[1]Abbreviations: Bio; Biotin, Cbz; benzyloxycarbonyl, EDANS; 5-[(2-aminoethyl)amino]naphthalene-1-sulfonic acid, HNE; Human Neutrophil Elastase, ITPG; isopropyl-β-D-1-thiogalactopyranoside, PEG; poly(ethylene glycol), PMSF; phenylmethanesulphonylfluoride, SDS; sodium dodecyl sulfate, Suc-; succinyl, TFA; trifluoroacetic acid, TIPS; tri-isopropylsilane, (Xaa)^{P}(OPh)$_2$; Xaa-diphenyl phosphonate.

Scheme 1. General Solid-Phase Synthetic Scheme for Biotinylated P1-Aminoalkane Diphenylphosphonate Affinity Probes for the Serine Proteases Utilizing Biotin PEG NovaTag Resin

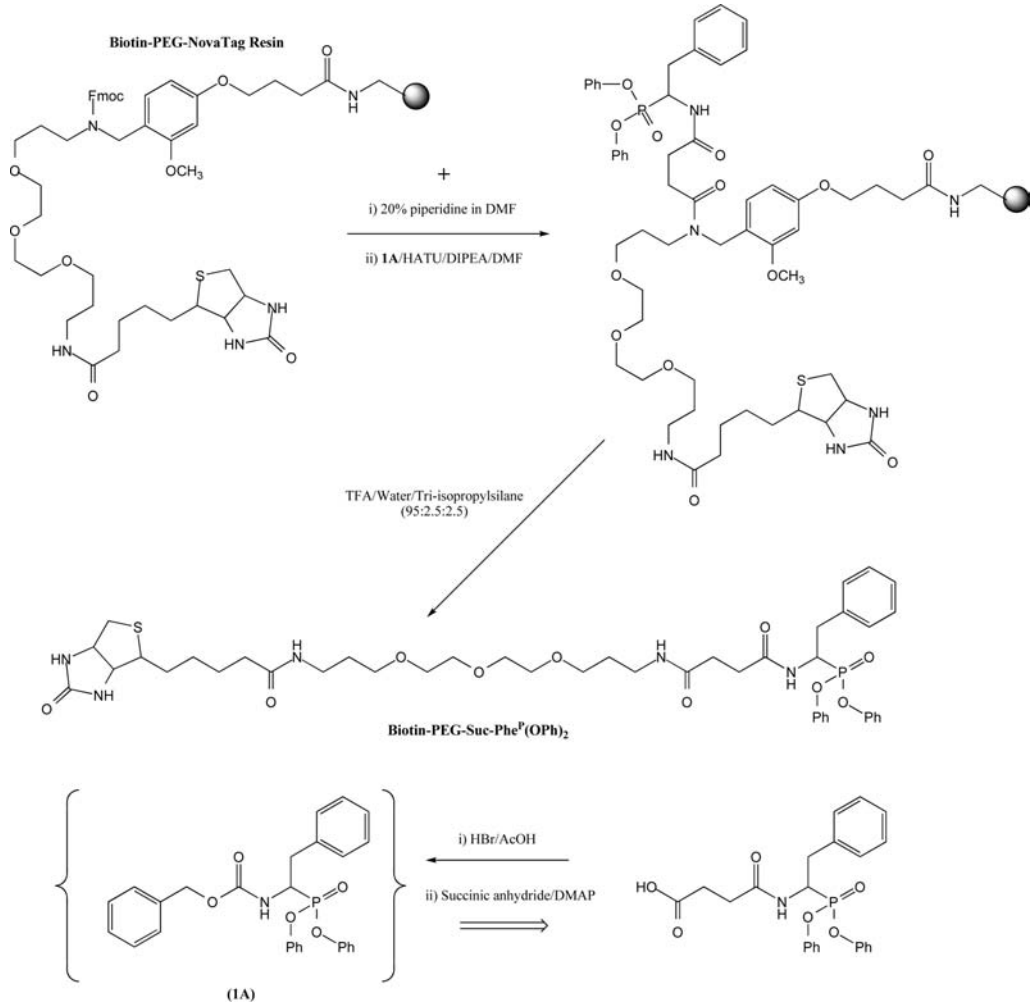

compounds was found to be correct by elemental analysis and ^{1}H NMR, and had melting points in close agreement with the literature values (*11, 20*). Each derivative was obtained as a 50/50 mix of the L and D enantiomers.

Removal of the Cbz-protecting group was achieved by treatment with HBr/acetic acid (~33% v/v) for 90 min at room temperature. The succinyl derivatives of each of the deprotected aminoalkyl diphenyl phosphonate were then prepared by reaction with succinic anhydride, in dry DMF, at room temperature, overnight, in the presence of 2.0 equiv of DIPEA. These succinyl derivatives were then used to acylate samples of Biotin-PEG NovaTag (Novabiochem: cat no 04−12−3908) or EDANS-NovaTag (Novabiochem: cat no 04−12−3904) resin. This was achieved by first removing the Fmoc-protecting group from the benzyl-linked amine of the resin, by treatment with piperidine/DMF (20%, v/v), for 15 min at room temperature. After standard washing procedures (*8*), the succinylated aminoalkyl diphenylphosophonates were then coupled to the newly exposed secondary amine grouping on the resin via HATU-mediated condensation. The labeled diphenyl phosphonate derivatives of phenylalanine and valine were then cleaved from the resin by treatment with TFA/H_2O/TIPS (95/2.5/2.5; v/v/v) for 90 min at room temperature.

Kinetic Evaluation of Affinity Based Probes. Stock solutions (10 mM) of each affinity based probe were diluted in the appropriate assay buffer to give final concentrations of 5 μM, 10 μM, 25 μM, 50 μM, and 100 μM, which are evaluated for inhibitory activity against each target proteinase using a standard microtiter plate assay. Fluorogenic substrate was added such that a final concentration of 50 μM in each well initiates the reaction. The inhibitory potency of each inhibitor was determined at five individual concentrations using a standard microtiter plate assay where the rate of substrate hydrolysis at 37 °C, in each instance, was monitored every 60 s over a period of 90 min by measuring the rate of increase of fluorescence at (excitation λ_{nm} 395 ± 45, emission λ_{nm} 460 ± 40) in a CYTOFLUOR Multiwell Plate Reader Series 4000 spectrofluorimeter. Each experiment is performed in triplicate. Typical progress curves are shown in Figure 2.

Labeling and Detection of Peptidases. *Electrophoresis.* Electrophoresis in the presence of sodium dodecyl sulfate (SDS) was performed by a modification of the method of Laemmli (*21*). Initially, SDS-PAGE was performed on NuPage Novex 4−12% Bis-Tris gels. Labeled proteins were denatured by boiling for 10 min in Laemmli treatment buffer. SeeBlue Plus2 prestained molecular weight standards were included in each gel.

Western Blotting. Electroblotting of the separated proteins was carried out using a modification of the methodology described first by Towbin et al. (*22*). Separated proteins were electroblotted onto Immobilon-P polyvinylidene difluoride (PVDF) membranes (Milipore) in NuPage Transfer Buffer (Invitrogen Ltd.). The running time was 2 h at 200 mA, at room temperature.

Detection of Labeled Peptidases. Labeled peptidases were detected using the methods previously described (*9, 16*).

Table 1. Mass Spectrum Analysis

reagent	predicted	observed
Bio-PEG-Suc-Val^P(OPh)$_2$	833.99	834.2/835.2
Bio-PEG-Suc-Phe^P(OPh)$_2$	882	882.2/883.2
EDANS-Suc-Phe^P(OPh)$_2$	635	636.3

Essentially, following protein transfer, unbound sites on the Immobilon-P PVDF membrane were blocked by incubation of the blot membrane in a 3% (w/v) solution of bovine serum albumin (BSA) in Tris-buffered saline (TBS; 0.05 M Tris/HCl, 0.1 M NaCl, pH 7.4) for at least 1 h at room temperature. After washing with TBS, the solution was discarded and replaced with streptavidin/horseradish peroxidase (Streptavidin-HRP) (Vector Laboratories) prepared at a dilution of 1 in 10 000 in blocking solution containing 0.3% BSA at room temperature for 45 min. The membrane was washed at least six times with TBS containing 0.1% Tween 20 and excess liquid removed. Horseradish peroxidase activity was detected by overlay with SuperSignal West Pico chemiluminescent substrate. After removal of the substrate, the blot was placed between acetate sheets and overlaid with photographic film in a film cassette. Films were exposed for ~30 s developed and fixed.

Direct Detection. For labeling studies employing EDANS-labeled probe, the method above was followed except that the electrophoresis unit was protected from light during each run. The gel was removed from the cassette, and labeled peptidases were viewed directly on a high-performance ultraviolet transilluminator (Ultraviolet Products Ltd., Cambridge, UK). Images were captured using a Syngene Gene-Genius Bioimaging system with on-board UV transilluminator or using standard photographic film.

Labeling of Recombinant MucD in Crude Cell Lysates. The MucD gene of *Pseudomonas aeruginosa* PA01 was amplified from genomic DNA by PCR and subsequently cloned into the *E. coli* expression vector pQE30 (Qiagen). Site-directed mutagenesis of the putative active site serine to an alanine at position 217 was carried out using site-directed mutagenesis kit (Stratagene) as per the manufacturers instructions. TOP10F' *E. coli* cells (Invitrogen) harboring empty pQE30 plasmid, wild-type MucD, and Ser-Ala active site mutant grown to early log phase (37 °C) were induced using isopropyl-β-D-1-thiogalactopyranoside (ITPG, 1 mM final concentration), prior to a further 3 h incubation. Cells were harvested and lysed by sonication in assay buffer (25 mM Hepes, 5 mM $CaCl_2$, pH 7.5). Biotinylated DPP probes (final concentration, 50 uM) were incubated with the freshly prepared lysates for 90 min at either 37 or 45 °C. Labeled peptidases were detected as described previously.

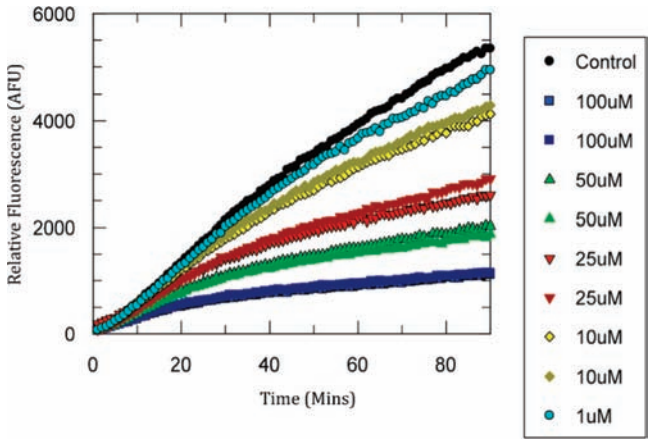

Figure 2. Typical progress curves for the generation of 7-amino-4-methylcoumarin from the chymotrypsin catalyzed hydrolysis of N-succinyl-Ala-Ala-Pro-Phe-NHMec in the presence of EDANS-succinyl-Phe^P(OPh)$_2$ The figures represent the best fit of data to the equation for irreversible inhibition (Walker and Elmore, 1984) of chymotrypsin by EDANS-succinyl-Phe^P(OPh)$_2$ in the presence of N-succinyl-Ala-Ala-Pro-Phe-NHMec. The inactivation studies were carried out at a fixed substrate concentration (50 μM) and varying concentrations of inactivator as indicated above.

Mechanism Based Affinity Capture of Recombinant MucD in Crude Cell Lysates. *Escherichia coli* TOP10F' cells harboring pQE30 plasmid expressing wild-type MucD and Ser-Ala active site mutant were grown to early log phase (37 °C) and induced using ITPG (1 mM final concentration), prior to a further 3 h incubation. Cells were harvested and lysed by sonication in MucD assay buffer (25 mM HEPES, 5 mM $CaCl_2$, pH 7.5). The Biotin-PEG-Suc-Val^P(OPh)$_2$ probe (final concentration, 50 μM) was incubated with the freshly prepared lysates for 90 min at 37 °C. Samples were subjected to affinity capture with strepavadin magnetic Dynabeads (dynal Biotech) and washed 6 times in PBS Tween 20 (0.1%). Samples were subjected to SDS-PAGE electrophoresis and stained with Brilliant Blue G - Colloidal Coomassie. Protein bands were excised from the Coomassie stained gel, treated with acetonitrile, and dried. Sequencing grade trypsin (Promega) was added, and samples were incubated at 30 °C overnight. Digested peptides were extracted from the gel pieces using 5% v/v trifluoroacetic acid and 50% v/v acetonitrile and dried. The samples were then rehydrated, desalted, and concentrated using in-tip reverse-phase resin (Zip Tip C18, Millipore). Using a Thermoquest LCQ Deca mass spectrometer, in nanospray mode, the samples were analyzed and MS/MS data collected by Xcalibur. Finally, MS/MS ion search was performed by Mascot (*23*), using the database NCBInr.

RESULTS

Synthesis of Affinity Probes. Our primary aim in this study was the development of a robust and broadly applicable solid-phase approach for the synthesis of diphenyl phosphonate activity probes for the serine proteinases. As an example, the synthetic scheme for the synthesis of the P_1-Phe containing inhibitor (Biotin-PEG-Phe^P(OPh)$_2$) is shown in Scheme 1. In essence, this inhibitor sequence was constructed from the succinyl-derivatized diphenyl phosphonate analogue of phenylalanine (**1A**), which in turn was prepared from the benzloxycarbonyl protected analogue (Cbz-Phe^P(OPh)$_2$). The synthesis of Biotin-PEG-Phe^P(OPh)$_2$ was expedited, using standard Fmoc solid-phase protocols, employing a CEM Liberty instrument, and using the recently developed Biotin-PEG NovaTag. We have found that the use of this solid-phase approach has eliminated the problems typically encountered with the solution-phase synthesis of biotin-containing derivatives, namely, poor solubility and sluggish coupling kinetics of biotin and its derivatives. We have incorporated the "PEG unit" into the inhibitor sequence to minimize steric hindrance limitations in the interaction between the biotin reporter group and streptavidin. This reporter moiety facilitates both the detection of labeled species using steptavidin horseradish peroxidase/alkaline phosphatase conjugated by Western blot and also the capture and purification inhibitor/protease complex for the purposes of sequencing by mass spectrometry (described below). The synthesis of EDANS-derived affinity probes follows exactly the same synthetic pathway as in Scheme 1, using the EDANS-NovaTag resin. The structures of the affinity-based probes synthesized in this study, according to Scheme 1, are shown in Figure 1. The identity of each compound was confirmed by electrospray mass spectroscopy, and the results shown in Table 1.

Kinetic Evaluation. The determined values for second-order rate constant, [A], for each inhibitor concentration were used

Table 2. Inhibitor Constants[a]

protease	inhibitor	k_i (min^{-1})	K_i (M)	$(k_i)/(K_i)$ (M^{-1} min^{-1})
chymotrypsin	Bio PEG-Suc-$Phe^P(OPh)_2$	0.119 ± 0.002	1.08×10^{-6}	1.11×10^5
cathepsin G	Bio PEG-Suc-$Phe^P(OPh)_2$	0.016 ± 0.003	2.59×10^{-6}	8.41×10^4
chymotrypsin	EDANS-Suc-$Phe^P(OPh)_2$	ND	ND	0.18×10^4
cathepsin G	EDANS-Suc-$Phe^P(OPh)_2$	0.029 ± 0.002	1.39×10^{-5}	0.22×10^4
HNE	Bio PEG-Suc-$Val^P(OPh)_2$	ND	ND	1.29×10^4

[a] ND - not determined.

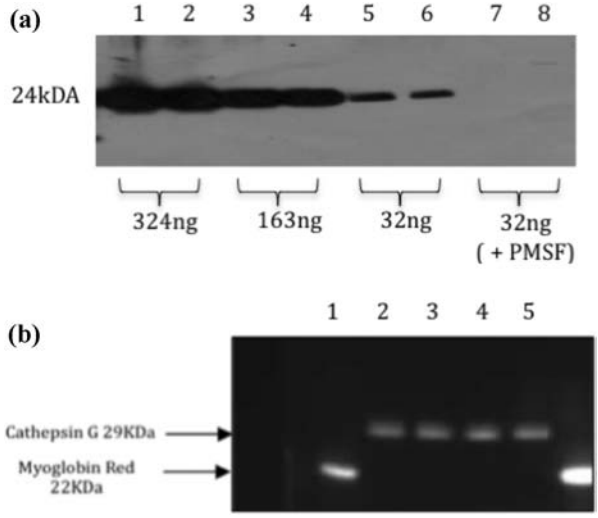

Figure 3. (a) Selective, active site directed labeling of recombinant human neutrophil elastase (HNE) by Biotin-PEG-succinyl-$Val^P(OPh)_2$ (20 μM). Lanes 1−2, 324 ng HNE; lanes 3−4, 162 ng HNE; lanes 5−6, 32 ng; lanes 7−8, 32 ng HNE preincubated with pretreated with Pefabloc (100 μM) for 15 min at 37 °C. (b) Direct visualization of purified cathepsin G protease affinity labeling using EDANS-succinyl-$Phe^P(OPh)_2$ (20 μM). Lane 1, SeeBlue prestained molecular weight markers; lanes 2−5 Cathepsin G (100 ng) incubated for 30 min with EDANS affinity based probe.

to determine the kinetic constants, K_i and k_i, for the kinetic scheme I, taken from Walker and Elmore (*25*). Progress curves were transformed using Grafit to give their linear transformations. Evaluation of the inhibitor constant K_i and the apparent first-order rate constant, k_i, for the irreversible inactivation was carried out using the methods of Tian and Tsou (*26*). A summary of determined overall second-order rate constants (k_i/K_i) for irreversible affinity-based probe inhibitors of each exemplar proteinase are shown in Table 2. In general, these compounds were found to be moderately potent irreversible inactivators of their target protease. The overall second-order rate constants are comparable to the corresponding Cbz-protected amino acid analogues Cbz-$Phe^P(OPh)_2$ (for Chymotrypsin; $k_i/K_i = (2.3 \pm 0.4) \times 10^4$ M^{-1} min^{-1}, Cathepsin G $k_i/K_i = (3.8 \pm 0.4) \times 10^3$ M^{-1} min^{-1}) and Cbz-$Val^P(OPh)_2$ (for human neutrophil elastase $k_i/K_i = (2.3 \pm 0.1) \times 10^3$ M^{-1} min^{-1}).

Proteinase Profiling. Initial profiling studies were performed on purified neutrophil elastase (HNE). Figure 3a illustrates the labeling of HNE using Bio-Peg-succinyl-$Val^P(OPh)_2$. In essence, samples of purified HNE were incubated with 20 μM biotinylated-inhibitor, for 30 min at 37 °C, prior to SDS-PAGE and Western blotting. Figure 3a shows a series of duplicates in which differing amounts of purified HNE are incubated with the fixed concentration of biotinylated inhibitor. From these results, it can be seen that, under these standard detection conditions, as little as 32 ng of protease can be detected, demonstrating the sensitivity of these irreversible probes. Crucially, the specificity of this probe was established by pre-inactivation of the protease using phenylmethanesulphonylfluoride (PMSF), which modifies the active site serine hydroxyl group, rendering the enzyme inactive. Preincubation of protease with PMSF prior to addition of the biotinylated probe completely blocked incorporation of the latter, indicating that it is active site directed.

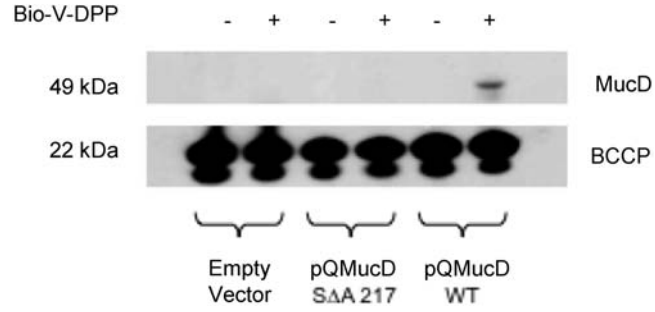

Figure 4. Bio-PEG-Succ-$Val^P(OPh)_2$ (Bio-V-DPP) specifically labels recombinant serine protease MucD in *E. coli* lysates. Bio-V-DPP (50 μM) was incubated (90 min, 37 °C) with sonicated pellets from *E. coli* cultures harboring pMucD and catalytically inactive SΔA217, with MucD expression induced with IPTG (1 mM) in all samples. Protein samples were then applied to SDS-PAGE and Western blotted; bands with incorporated biotin moieties were disclosed using streptavidin-HRP. Biotin carboxyl carrier protein (BCCP) is endogenously biotinylated and is used here as a loading control.

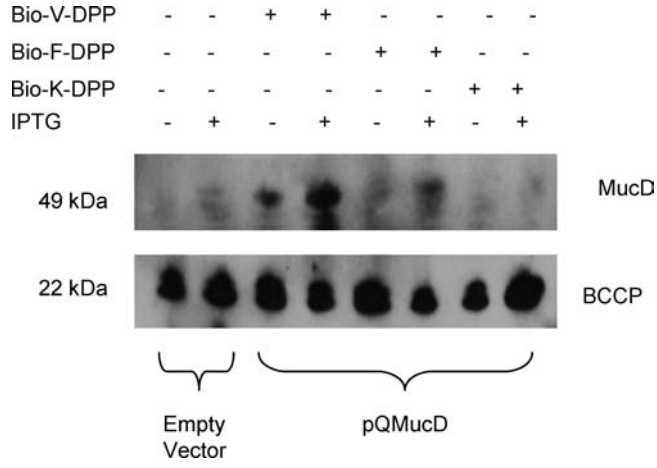

Figure 5. Biotinylated probes (50 μM) were incubated with sonicated cell pellets from cultures harboring pMucD, with MucD expression induced with IPTG (1 mM). Probes were incubated with sonicates for 90 min at 37 °C, prior to application to SDS-PAGE and Western blotting. Bands with incorporated biotin moieties are disclosed using streptavidin−HRP. Biotin carboxyl carrier protein (BCCP) is endogenously biotinylated and is used here a loading control.

The ability to detect protein species by Western blotting is a routinely used methodology, but it is not without its limitations. As it uses a number of steps beyond electrophoresis, including membrane transfer, blocking, and application of primary and/or secondary detection reagents, the process can frequently take a number of hours, if not overnight. Furthermore, the more steps involved, the more possibilities arise for human error in the visualization of the labeled proteins. Therefore, in an effort to circumvent these potential limitations, we have investigated the replacement of the biotin reporter with a fluorescent moiety to permit "in-gel" visualization. The direct labeling of cathepsin

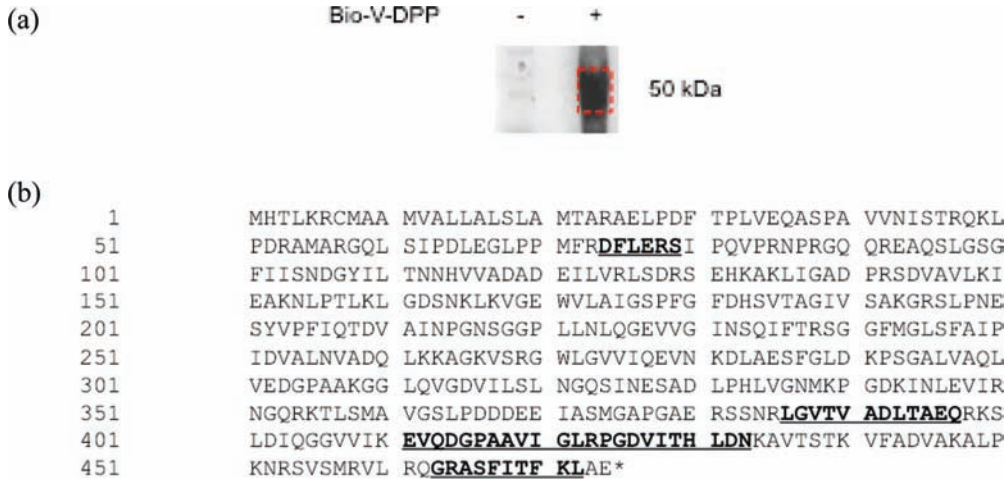

Figure 6. Capture and identification of MucD from *Pseudomonas aeruginosa* cell lysates. (a) Lysates probed with Bio-V-DPP were subsequently incubated with streptavidin agarose beads and captured proteins eluted, electrophoresed, and visualized by silver staining. A band at 50 kDa (see highlighted) was specifically captured in the presence of the probe and was subsequently excised and characterized by mass spectrometry. (b) Tryptic digestion of the protein in the band was performed and peptides subjected to MS/MS. MS/MS ion searches using MASCOT identified four peptides from *P. aeruginosa* MucD (Accession number NM_002516).

G (100 ng) using a fluorescently labeled affinity based probe (EDANS-succinyl-Phe^{P}(OPh)$_2$) is shown in Figure 3b.

Labeling, Capture, and Identification of Protease Species. Next, we wished to examine the application of these probes for the detection and identification of serine protease species in protein extracts. For these studies, we chose a model protease, MucD, from *P. aeruginosa.* MucD is an important mediator of virulence in *P. aeruginosa* infections (*26*) and is a negative regulator of alginate production (*27*). MucD mutants have been shown to exhibit reduced virulence in a number of different pathogen−host models (*26*). Furthermore, *P. aeruginosa* MucD inactivation results in decreased resistance to H_2O_2 and thermal kill (*28*). Therefore, selective inactivation of MucD may constitute a novel antivirulence approach in the treatment of *P. aeruginosa* infections.

To study the ability to label MucD using the diphenyl phosphonate probes, the open reading frame was cloned into an *Escherichia coli* expression vector (pQE30), from which the inducible expression of MucD could be stimulated using IPTG. The insertion of the open reading frame into pQE30 also facilitates the incorporation of an N-terminal hexahistidine tag, which allowed the visualization of the expressed recombinant protein at the anticipated 49 kDa in the presence of IPTG (data not shown). Next, lysates from IPTG-induced cultures expressing MucD were incubated with Bio-PEG-Suc-Val^{P}(OPh)$_2$, where we observed clear labeling of the recombinant enzyme (Figure 4, lane 6). A catalytically inactive mutant (SerΔAla217) was also prepared, and the probe failed to label this species, further demonstrating the need for the hydroxyl side chain in the Ser residue to which the diphenyl phosphonate probes react and bind.

On the basis of these findings, we then examined the P_1 specificity in the probes on the basis of their ability to label the recombinant MucD protein. Valine, phenylalanine, and lysine derived biotinylated diphenylphosphonates where incubated with MucD overexpressing bacterial lysates, and as anticipated, the Val probe showed labeling as before (Figure 5, lanes 3 and 4). Under the same conditions, labeling by the Phe-derived probe was also visualized, albeit at lower intensities than the Val probe (lanes 5 and 6). Conversely, under these conditions no binding of the Lys probe was observed. Collectively, these data suggest that the enzyme has a clear preference for hydrophobic residues in the P_1 position (Val > Phe) over the positively charged Lys derivative. Although no comprehensive substrate specificity profiling of *P. aeruginosa* MucD has yet been published, these results are perhaps unsurprising given that MucD is orthologous to the *Escherichia coli* periplasmic protease and chaperone HtrA (DegP) (*26*), which has a demonstrated P1 preference for valine (*29*).

As we could identify and visualize the labeling of recombinant MucD, we then examined the application of the biotinylated Bio-PEG-Suc-V-DPP (Bio-V-DPP) probe to facilitate the capture and isolation of MucD from *P. aeruginosa* cultures. Cultures were lysed and incubated with the Bio-V-DPP probe as described and then incubated with streptavidin beads. Eluted proteins were analyzed by SDS-PAGE allowing clear visualization of a 50 kDa band specific to probe-treated samples (Figure 6a). This band was subsequently excised and protein species analyzed by mass spectrometry where it was established that MucD was successfully identified (Figure 6b). Analysis of the corresponding gel fraction from samples purified in the absence of probe did not facilitate the identification of MucD (data not shown), demonstrating that its capture and identification were dependent on the preincubation with the biotinylated probe. Collectively, these results show that these biotinylated reagents have applicability in not only the visualization of protease species, but also their activity-based capture, purification, and downstream characterization.

DISCUSSION

We have described a novel facile synthesis route for substrate-derived diphenyl phosphonate probes for the detection of serine proteases. During these studies, we have demonstrated the ability of these probes to label proteases, simply on the basis of their catalytic activity, and facilitate their downstream visualization. Using biotin reporter groups, we have demonstrated the ability to visualize bound species by Western blot. Furthermore, replacement of biotin with a fluorescent tag facilitates the direct sensitive analysis of bound species by SDS-PAGE, which has the advantage of circumventing the need for downstream Western blotting. Finally, we also demonstrate that the compounds synthesized here can be used for the affinity capture and retrieval of protease species from biological lysates.

Although the affinity-based probes developed in this study have been utilized here primarily for the detection and identification of bacterial/prokaryotic proteases, the kinetic evaluation studies were performed against eukaryotic pro-

Scheme 2. Kinetic Scheme for Irreversible Inhibitors Acting via a Complexing Mechanism, Taken from Walker and Elmore (1984)

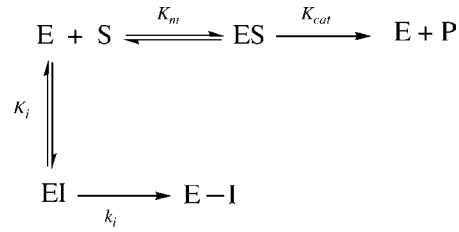

teases, namely, bovine chymotrypsin, cathepsin G (from human leukocytes), and human neutrophil elastase demonstrate the broad applicability of these probes. Indeed, we have shown in a previous study that biotinylated proline diphenyl phosphonate derived inhibitors were capable of inactivation and labeling of dipeptidyl peptidase IV purified from porcine kidney (*16*). These observations, taken together with the extensive characterization of diphenyl phosphonate derived inhibitors against a wide range of serine protease already published in the literature (*11*−*13*, *15*, *16*), indicate that the affinity based probes described here will have utility in the detection, profiling, and identification of a wide range of serine proteases from both prokaryotic and eukaryotic sources. The ability to capture, purify, and characterize protease species on the basis of their catalytic activity represents a powerful discovery methodology rather than merely revealing additional members of known proteinase families through homology screening approaches. Therefore, the large-scale screening of complex protein milieu for protease species could highlight proteins of novel sequences/conformations that have yet to be demonstrated to possess proteolytic activity.

ACKNOWLEDGMENT

This work was supported by a BBSRC Project grant (BB/D005957/1).

LITERATURE CITED

(1) International Human Genome Sequencing Consortium (2004) Finishing the euchromatic sequence of the human genome. *Nature 431*, 931−945.

(2) Hopkins, A. L., and Groom, C. R. (2002) The druggable genome. *Nat. Rev. Drug Discovery 1*, 727–730.

(3) Russ, A. P., and Lampel, S. (2005) The druggable genome: an update. *Drug Discovery Today 10*, 1607–1610.

(4) Southan, C. (2001) A genomic perspective on human proteases. *FEBS Lett. 498*, 214–218.

(5) Kleiner, D. E., and Stetler-Stevenson, W. G. (1994) Quantitative zymography: Detection of picogram quantities of gelatinases. *Anal. Biochem. 218*, 235–239.

(6) Liu, Y., Patricelli, M. P., and Cravatt, B. F. (1999) Activity based protein profiling: The serine hydrolases. *Proc. Natl. Acad. Sci. U.S.A. 96*, 14964–14699.

(7) Kay, G., Bailie, J. R., Halliday, I. M., Nelson, J., and Walker, B. (1992) The synthesis, kinetic characterization and application of biotinylated aminoacylchloromethanes for the detection of chymotrypsin and trypsin-like serine proteinases. *Biochem. J. 283*, 455–459.

(8) Walker, B., Cullen, B. M., Kay, G., Halliday, I. M., McGinty, A., and Nelson, J. (1992) The synthesis, kinetic characterisation and application of a novel biotinylated affinity label for cathepsin B. *Biochem. J. 283*, 449–453.

(9) Cullen, B. M., Halliday, I. M., Kay, G., Nelson, J., and Walker, B. (1992) The application of a novel biotinylated affinity label for the detection of a cathepsin B-like precursor produced by breast-tumour cells in culture. *Biochem. J. 283*, 461–465.

(10) Scott, C. J., McDowell, A., Martin, S. L., Lynas, J. F., Vandenbroeck, K., and Walker, B. (2002) Irreversible inhibition of the bacterial cysteine protease-transpeptidase sortase (SrtA) by substrate-derived affinity labels. *Biochem. J. 366*, 953–958.

(11) Oleksyszyn, J., and Powers, J. C. (1991) Irreversible inhibition of serine proteases by peptide derivatives of (alpha-aminoalkyl)phosphonate diphenyl esters. *Biochemistry 30*, 485–493.

(12) Abuelyaman, A. S., Hudig, D., Woodard, S. L., and Powers, J. C. (1994) Fluorescent derivatives of diphenyl [1-(N-peptidylamino)alkyl]phosphonate esters: synthesis and use in the inhibition and cellular localization of serine proteases. *Bioconjugate Chem. 5*, 400–405.

(13) Abuelyaman, A. S., Jackson, D. S., Hudig, D., Woodard, S. L., and Powers, J. C. (1997) Synthesis and kinetic studies of diphenyl 1-(N-peptidylamino)alkanephosphonate esters and their biotinylated derivatives as inhibitors of serine proteases and probes for lymphocyte granzymes. *Arch. Biochem. Biophys. 344*, 271–280.

(14) Hawthorne, S. J., Halton, D. W., and Walker, B. (1994) Identification and characterisation of the cysteine and serine proteinases of the trematode, *Haplometra cylindracea* and determination of their haemoglobinase activity. *Parasitology 108*, 595–601.

(15) Gilmore, B. F., Lynas, J. F., Scott, C. J., McGoohan, C., Martin, L., and Walker, B. (2006) Dipeptide proline diphenyl phosphonates are potent, irreversible inhibitors of seprase (FAPα). *Biochem. Biophys. Res. Commun. 346*, 436–446.

(16) Gilmore, B. F., Carson, L., McShane, L. L., Quinn, D., Coulter, W. A., and Walker, B. (2006) Synthesis, kinetic evaluation and utilisation of a biotinylated dipeptide proline diphenyl phosphonate for the disclosure of dipeptidyl peptidase IV-like serine proteases. *Biochem. Biophys. Res. Commun. 347*, 373–379.

(17) Kidd, D., Liu, Y., and Cravatt, B. F. (2001) Profiling serine hydrolase activities in complex proteomes. *Biochemistry 40*, 4005–4015.

(18) Bilello, J. A. (2005) The agony and ecstasy of 'OMIC' technologies in drug development. *Curr. Mol. Med. 5*, 39–52.

(19) Wood, L. F., and Ohman, D. E. (2006) Independent regulation of MucD, an HrtA-like protease in *Pseudomonas aeruginosa*, and the role of it's proteolytic motif in alginate gene regulation. *J. Bacteriol. 188*, 3134–3137.

(20) Oleksyszen, J., Subotkowska, L., and Mastalerz, P. (1979) Diphenyl 1-aminoalkanephosphonates. *Synthesis 12*, 985–986.

(21) Laemmli, U. K. (1970) Cleavage of structural proteins during the assembly of the head of bacteriophage T4. *Nature (London) 227*, 680–685.

(22) Towbin, H., Staehelin, T., and Gordon, J. (1979) Electrophoretic transfer of proteins from polyacrylamide gels to nitrocellulose sheets: Procedure and some applications. *Proc. Natl. Acad. Sci. U.S.A. 76*, 4350–4354.

(23) Perkins, D. N., Pappin, D. J., Creasy, D. M., and Cottrell, J. S. (1999) Probability-based protein identification by searching sequence databases using mass spectrometry data. *Electrophoresis 20*, 3551–67.

(24) Walker, B., and Elmore, D. T. (1984) The irreversible inhibition of urokinase, kidney-cell plasminogen activator, plasmin and beta-trypsin by 1-(N-6-amino-n-hexyl) carbamoylimidazole. *Biochem. J. 221*, 277–280.

(25) Tian, W.-X., and Tsou, C.-L. (1982) Determination of the rate constant of enzyme modification by measuring the substrate reaction in the presence of the modifier. *Biochemistry 21*, 1028–1032.

(26) Yorgey, P., Rahme, L. G., Tan, M.-W., and Ausubel, F. M. (2001) The roles of mucD and alginate in the virulence of *Pseudomonas aeruginosa* in plants, nematodes and mice. *Mol. Microbiol. 41*, 1063–1076.

(27) Gutsche, J., Remminghorst, U., and Rehm, B. H. A. (2005) Biochemical analysis of alginate biosynthesis protein AlgX from *Pseudomonas aeruginosa*: purification of an AlgX-MucD (AlgY) protein complex. *Biochimie 88*, 245–251.

(28) Boucher, J. C., Martinez-Salazar, J., Schurr, M. J., Mudd, M. H., Yu, H., and Deretic, V. (1996) Two distinct loci affecting conversion to mucoidy in *Pseudomonas aeruginosa* in cystic fibrosis encode homologs of the serine protease HtrA. *J. Bacteriol. 178*, 7369–7377.

(29) Hauske, P., Meltzer, M., Ottmann, C., Krojer, T., Clausen, T., Ehrmann, M., and Kaiser, M. (2009) Selectivity profiling of DegP substrates and inhibitors. *Bioorg. Med. Chem. 17*, 2920–2924.

BC9002162

Analysis of the Dynamics of Assembly and Structural Impact for a Histidine Tagged FGF1−1.5 nm Au Nanoparticle Bioconjugate

Joshua M. Kogot,[†] Alex M. Parker,[†] Jihun Lee,[‡] Michael Blaber,[‡] Geoffrey F. Strouse,*[,†] and Timothy M. Logan*[,†]

Department of Chemistry and Biochemistry and Kasha Laboratory Institute of Molecular Biophysics, and Department of Biomedical Sciences, College of Medicine, Florida State University, Tallahassee, Florida 32306. Received May 21, 2009; Revised Manuscript Received September 4, 2009

Whether assembling proteins onto nanoscale, mesoscopic, or macroscopic material surfaces, maintaining a protein's structure and function when conjugated to a surface is complicated by the high propensity for electrostatic or hydrophobic surface interactions and the possibility of direct metal coordination of protein functional groups. In this study, the assembly of a 1.5 nm CAAKA passivated gold nanoparticle (AuNP) onto FGF1 (human acidic fibroblast growth factor) using an amino terminal His_6 tag is analyzed. The impact of structure and time-dependent changes in the structural elements in FGF1and FGF1-heparin in the presence of the AuNP is probed by a molecular beacon fluorescence assay, circular dichroism, and NMR spectroscopy. Analysis of the results indicates that a time-dependent evolution of the protein structure without loss of FGF1 heparin binding occurs following the formation of the initial FGF1-AuNP complex. The time-dependent changes are believed to reflect protein sampling of the AuNP surface to minimize the free energy of the AuNP-FGF1 complex without impacting FGF1 function.

INTRODUCTION

With the use of nanomaterials for biological assays (*1*−*7*), the desire to develop robust linkages that possess adaptable chemistries to interface biological molecules with nanomaterials, yet have minimal structural impact on the protein, has become a rapidly growing area of interest. A plethora of assembly strategies exist, using cysteine or thiol modifications (*8*−*10*), botin−streptavidin interactions (*11, 12*), click chemistry (*13*), and transition metal mediated histidine binding (*14, 15*), to name a few of the typical approaches (*1, 16, 17*). Each of these strategies has advantages and disadvantages, but all of the strategies require engineering non-native sequences into the protein, a secondary metal ion mediator, or antibody−antigen recognition step to form the construct, thus limiting the ability to extrapolate the results to the broader recombinantly engineered proteins employed by the biological community. Many of the studies to date have assumed that the structural elements are marginally perturbed in the local site of binding correlating the structural changes to the effect of nanoparticle (NP) charge, NP structure, and the site of protein substitution (*9, 18, 19*). While studies have shown protein function (*18, 20*), there is a notable lack of studies that fully investigate the dynamic changes occurring to the protein construct during the nanomaterial−protein assembly. In analogy to formation of self-assembled monolayers of proteins onto a surface, engineering a linkage that does not perturb the protein structure is challenging since the profusion of interactions stemming from potential backbone and side chain interactions with the NP surface can lead to alteration of protein structure and thus to protein misfolding (*7, 21*−*25*) and a loss in protein function (*21, 24, 26*−*29*). As demonstrated in several phage display assays (*30, 31*) on metal and semiconductor surfaces, the surface-mediated exchange reactions are governed by the amino acid functional groups, as well as electrostatic and hydrophobic interactions with the side chain and backbone of the protein.

The hexa-histidine (His_6) modification is widely used by recombinant protein chemists because of its high affinity for metal chelation, thereby facilitating purification by Ni(II) chelation chromatography. Several groups, including our own, have explored the use of the His_6 tag for assembly onto NP surfaces (*15, 32*−*37*). Our earlier results on peptide assembly demonstrated that the His_6-tag allows for region-selective assembly of small peptides onto the surface of the 1.5 nm AuNP through formation of a Au−Nε imidazole bond (*37*). Here, we extend the use of the His_6 tag recombinantly engineered to the amino terminus of FGF1 (human acidic fibroblast growth factor) to form a AuNP-FGF1 construct in order to assess the structural and potential functional impact on the protein. FGF1 is an important protein that exhibits mitogenic (cell division) and angiogenic (wound healing) properties and has emerged as a candidate for revascularization strategies of cardiac muscle following ischemic events (*38*−*40*). FGF1 binds heparin on the surfaces of cells and can accommodate oligosaccharides of varying sizes in the positively charged heparin binding pocket (*41*), but requires at least an octasaccharide heparin for FGF receptor (FGFR) activation. In this study, we probe the time-dependent conformational changes of an FGF1 sym6ΔΔ mutant during the assembly of the protein onto a 1.5 nm AuNP passivated by CAAKA, a zwitterionic peptide passivant layer. The use of a zwitterionic passivant layer on the nanoparticle surface has been shown to decrease the likelihood of nonspecific interactions between the protein and AuNP (*9, 42*), which allows the passivating peptide to be displaced and the exchange of passivants to dominate the final assemblage. The FGF1 sym6ΔΔ mutant was used for this study rather than the native FGF1, since the mutant is more sensitive to competitive binding interactions due to a modest folding free energy ($\Delta G_f = -33.9$ kJ/mol, 8.1 kcal/mol) (*43*), yet exhibits increased thermal stability compared to wild-type FGF1. In addition, the lower

* Corresponding authors. G.F.S: strouse@chem.fsu.edu, 95 Chieftan Way, Dept. of Chemistry and Biochemistry, Tallahassee, FL 32306. T.M.L: tlogan@fsu.edu, 91 Chieftan Way, Institute of Molecular Biophysics, Tallahassee, FL 32306.

[†] Department of Chemistry and Biochemistry and Kasha Laboratory Institute of Molecular Biophysics.

[‡] Department of Biomedical Sciences, College of Medicine.

10.1021/bc900224d CCC: $40.75 © 2009 American Chemical Society
Published on Web 10/07/2009

heparin binding affinity for the mutant will allow the impact of AuNP interactions with the protein to be assessed (*44*).

Analysis of the time-dependent changes in structure and function of FGF1 sym6ΔΔ and the heparin-bound analogue in the presence of the 1.5 nm AuNP is examined through the use of a combination of biophysical techniques, including CD, NMR, and molecular beacon kinetic assays, to assess the formation of the FGF1-AuNP conjugate. Observation of a time-dependent evolution of the FGF1structural elements over 18 h is observed and attributed to initial binding of FGF1 to AuNP at multiple locations on the protein surface followed by the more energetically favorable binding of the His_6 tail selectively to the AuNP surface. The time-dependent evolution is consistent with earlier results for peptide assembly onto a AuNP (*37*). The maintenance of structure and heparin binding ability for the FGF1 mutant confirms that the His_6 metal affinity tag (His-tag) used to enhance purification of recombinant proteins can be routinely utilized for site-specific assembly of recombinant proteins onto AuNP surfaces. The development of more robust methods for site-specific attachment that minimize nonspecific interactions while maintaining the structural integrity and functionality of a protein when appended to the surface of a nanometal is critical if these systems are to be used in biomedical technologies (*9, 10, 13, 45, 46*). Although not pursued in this study, region-selective coupling of the FGF1 without perturbation of the protein function may allow tracking FGF1 activity in cells via optical or electron microscopy methods.

Experimental Procedures. *Expression and Purification of sym6ΔΔ Mutant of Human FGF-1.* The amino-terminal His_6-tag (*47*) form of the sym6ΔΔ mutant of FGF-1 (*44*) (for simplicity referred to here as FGF1) was expressed and purified according to published procedures (*47*−*49*). Briefly, clarified cell lysate was purified by nickel affinity chromatography (HisPrep FF 16/10 column, GE Biosciences) followed by size exclusion chromatography (Superdex75 10/300 GL column, GE Biosciences). U-^{15}N-FGF was grown in M9 media with $(^{15}NH_4)_2SO_4$ as the sole nitrogen source and purified as above. FGF1-heparin complexes were formed by incubating low molecular weight heparin sodium salt (Sigma) with an equimolar solution of FGF1 for 30 min prior to all experiments.

Preparation of Au-CAAKA and Au-CAAKA-FITC. Au nanoparticles (1.5 nm AuNP) were passivated initially with triphenylphosphine (TPP) in toluene (*50*) and then ligand-exchanged with a zwitterionic peptide (CAAKA) to yield a water-soluble CAAKA-AuNP. The Au particle size was confirmed by electron microscopy and by UV−vis, noting the absence of a plasmon resonance at 520 nm, typically observed for AuNPs greater than 2.5 nm in diameter. For molecular beacon studies, CAAKA was labeled with fluorescein 5-isothiocyanate (FITC) (Sigma) through the lysine amine according to manufacturer instructions and purified by HPLC (C_{18}-RP) before being exchanged onto the AuNP.

Molecular Beacon Assay of FGF1 Assembly onto AuNP Surface. FGF1 or FGF1−heparin were exchanged onto Au-CAAKA-FITC in 50 mM sodium phosphate, 10 mM $(NH_4)_2SO_4$, 100 mM NaCl, pH = 7.5 (Buffer A), at a 1:1 protein to AuNP (1 μM) ratio at 25 °C. Exchange was monitored at 7 min intervals over an 18 h period using a nanometal surface energy transfer (NSET) (*51*) based molecular beacon assay based on dequenching of CAAKA-FITC fluorescence upon release from AuNP. The fluorescence spectra were collected from 300 to 600 nm in triplicate on a Cary Eclipse (Varian) in 1 cm path length cell (100 μL total volume) at 25 °C in Buffer A.

Time-Dependent Structural Changes in FGF1 by CD Spectroscopy. Circular dichroism (CD) spectra were collected between 190 and 260 nm with 0.5 nm steps and 1 s signal averaging on an AVIV 202 CD spectrometer at 25 °C in Buffer A using a 1 cm path length cell. Each sample, including buffer, was measured in triplicate and averaged before buffer subtraction. Sample concentrations were typically 5 μM FGF1 and/or 5 μM Au-CAAKA. The secondary structure content of FGF1 sym6ΔΔ mutant was analyzed in the CD spectra using *CDPro* software (*52*).

2D HSQC NMR Analysis of Protein Structural Perturbations. 2D-^{1}H,^{15}N HSQC experiments were performed on U-^{15}N-FGF1 on a Varian Inova spectrometer operating at 11.74T (Varian Inc., Palo Alto, CA). Protein concentrations were typically 200 μM in 100 mM phosphate, 200 mM $(NH_4)_2SO_4$, 100 mM NaCl at pH = 6.0 (Buffer B). HSQC spectra were collected over 8333 Hz (1500 Hz) and digitized by 1024 (220) complex points in the ^{1}H (^{15}N) dimensions in 16 scans per t_1 increment for a total data collection time of ∼45 min. Data collection for each HSQC spectrum was initiated at 0, 5, and 18 h following addition of Au-CAAKA. Data were processed with zero-filling to yield a final digital resolution of 4 and 15.7 Hz in ^{1}H and ^{15}N dimensions, respectively. Data processing was performed using NMRPipe and analyzed using NMR-View (*53*). Changes in resonance position ($\Delta\delta$) upon addition of CAAKA-Au were quantified as $\Delta\delta = [(\delta H)^2 + (\delta N/6)^2]^{1/2}$ (*54*).

RESULTS

Following secretion from the cell, FGF1 binds to heparin and the FGF1-heparin complex is then recognized by the FGF receptor to initiate signaling (*55*). Heparin has a net negative charge, and electrostatic interactions between heparin and the protein binding pocket impact the binding affinity of heparin to FGF1. A structural model indicating residue location and the electrostatic potential at physiological pH of FGF1 sym6ΔΔ is presented in Figure 1. The amino-terminal His_6-tag should minimally perturb the protein structure and, more importantly, the heparin binding pocket, as the His_6-tag will position the AuNP on the side of FGF1 opposite the heparin binding pocket. The assembly of the FGF1 onto the AuNP is expected to occur via a surface-mediated ligand exchange reaction of the CAKKA peptide passivant shell appended to the AuNP by the formation of the Nε imidazole−Au interaction. The presence of the roughly 2 nm positively charged heparin binding pocket on FGF1 increases the potential for deleterious interactions between the protein and the 1.5 nm AuNP, and thus, the hypoactive form of FGF1 (sym6ΔΔ mutant) is the ideal test case for assessing potential loss of protein activity in the presence of the AuNP.

To minimize potential heparin binding pocket interactions, the 1.5 nm AuNP is passivated with the zwitterionic peptide sequence CAKKA (Cys-Ala-Lys-Lys-Ala) (*9, 42*). The CAAKA peptide is ligated to the AuNP via a Au-*S* interaction via the reduced Cys (C) amino acid. Fluorescent labeling of the CAAKA passivant by FITC (fluorescein) appended to the Lys (K) allows the recovery of FITC photoluminescence (PL) to be used as a probe of CAAKA displacement from the surface of the AuNP. When the CAAKA-FITC fluorogenic agent is appended to the AuNP, the FITC PL is quenched via energy transfer (*51, 56*).

In Figure 2, displacement of the CAAKA-FITC passivant from the AuNP surface by FGF1 binding is observed to result in the onset of FITC PL. The loss of the CAAKA-FITC passivant (onset of FITC PL) from the AuNP exhibits bimodal kinetics for both the addition of FGF1 and FGF1-heparin to the 1.5 nm Au-CAAKA-FITC construct (Figure 2). No time-dependent optical changes in the Au-CAAKA-FITC construct are observed in the absence of added protein (not shown). The bimodal trajectory in Figure 2 is verified by *F*-statistics through the analysis of χ^2 by fitting a series of functions with increasing number of exponentials. Fitting to a single exponential resulted in large χ^2 values which were significantly reduced in a

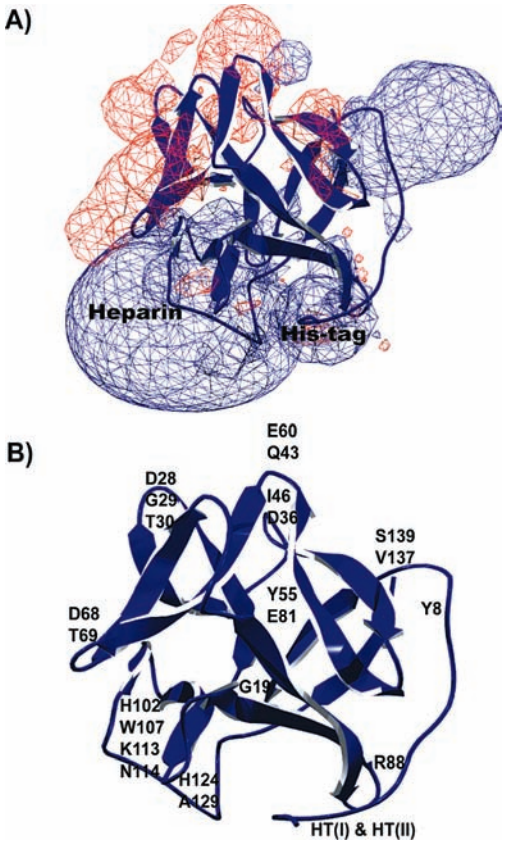

Figure 1. FGF1 crystallographic structure model (PDB ID: 1RG8) showing (A) an electrostatic surface potential model for FGF1 with the heparin binding region and His-tag region and (B) FGF1 structure with labeled key residues using the single letter code for the amino acids and the numbering for amino acid sequence.

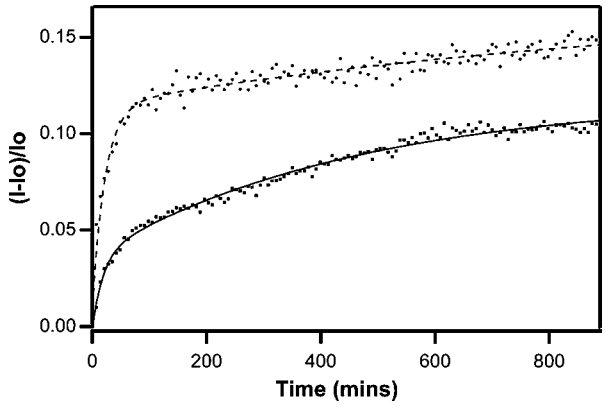

Figure 2. FGF1 and FGF1-heparin FITC PL intensity for the CAAKA-FITC displacement on the 1.5 nm AuNP surface byFGF1 (solid) and FGF1-heparin (dash). The PL intensity is monitored at 520 nm.

biexponential fit; fitting to a triexponential function did not significantly improve the quality of the fit according to the *F*-statistic.

Table 1 lists the experimentally fit rates and amplitudes for release of CAAKA-FITC upon addition of FGF1 or FGF1-heparin. The observed fast and slow rates are quite similar, within a factor of 2 for FGF1 and FGF1-heparin. However, the contribution to the total intensity recovery is reversed, with FGF1-heparin exhibiting higher amplitude for the fast phase, while FGF1 shows higher amplitude for the slow phase. The difference in rate and amplitude for CAAKA-FITC release between the FGF1 and the FGF1-heparin complex is intriguing and may reflect the fewer sampling configurations available for the heparin-bound FGF1 relative to FGF1 when interacting with the AuNP surface. The loss of conformational freedom arising from the binding of heparin to FGF1 eliminates the positive heparin binding pocket and reduces the conformational dynamics of the FGF1, which could lead to the observed differences in the rate of structural minimization for the two forms of FGF1.

Table 1. Calculated Rate and Amplitude Values for the Release of CAAKA-FITC from the Surface of a 1.5 nm AuNP when Treated withFGF1 or FGF1-Heparin

	fast phase		slow phase	
	rate (min^{-1})	amplitude (%)	rate (min^{-1})	amplitude (%)
FGFI	0.0532(0.0080)	23	0.0022(0.0002)	77
FGFI heparin	0.0446(0.0036)	67	0.0009(0.0005)	33

The FITC intensity trajectories in Figure 2 have not reached an asymptotic value within the time scale of the experiment, although extrapolation of the data to time infinity implies that both systems will achieve similar asymptotic values. The observed FITC PL recovery for FGF1 after 15 h is ~9% and ~14% for FGF1-heparin. Assuming a loading level of approximately 40 CAAKA-FITC based on the analysis of passivant exchange on AuNPs by Woehrle et al. (*57*), the displacement corresponds to between four and six CAAKA-FITC peptide passivants from the AuNP surface, four in the case of FGF and six in the case of FGF1-heparin. Assuming the peptide displacement results from one His residue interacting with the NP surface, this yields one protein per AuNP, which is consistent with our previous report of a single His_6 peptide binding to a AuNP (*37*).

Further evidence of a strong bonding interaction between the AuNP and the FGF1 is provided by chromatographic analysis using size exclusion and PAGE electrophoresis (Supporting Information Figures 1 and 2). Upon addition of FGF1 to a solution of AuNP in a 10:1 mol ratio, loss of the original sharp AuNP signal is observed by size exclusion analysis in Superdex75 after 1 h of mixing the AuNP and FGF1 (Supporting Information Figure 1). The signal loss in FGF1 is correlated with the appearance of a new broad feature at shorter retention time. The decrease in the FGF1 band is approximately 10% (~90% unchanged) for identical concentrations of FGF1, indicating approximately a 1:1 binding ratio. The broad feature for the AuNP-FGF1 assembly appears to have multiple components that could not be separated and is believed to reflect more than one binding motif at this short mixing time (1 h). The assumption from the optical assay for the FGF1-AuNP assembly having not fully evolved to the final structural conformation based on the biexponential rise time of the signal is consistent with the size-exclusion results. Further evidence of chromatographic stability is provided by Native-PAGE analysis of a 1: 1 ratio of FGF1 to AuNP (Supporting Information Figure 2). In the native PAGE, no free FGF1 is observed after treatment with the AuNP as evidenced by the lack of Coomassie blue stained FGF1 protein (lanes 4 and 7, Supporting Information Figure 2B). In addition, a slight mobility shift is observed for the AuNP due to the mobility difference of the FGF1-AuNP complex (lanes 4 and 7, Supporting Information Figure 2A). The small shift in the mobility between the AuNP and FGF1-AuNP and FGF1 (sane 3 vs 4) and the FGF1-heparin-AuNP (lane 3 vs 7) is consistent with the AuNP creating a strong assembly with the FGF1 protein.

Evidence of Structural Perturbation of FGF1 in the Presence of the AuNP. On the basis of the electrostatic map in Figure 1, the possibility that protein sampling gives rise to the observed dynamics is not surprising. The possibility for electrostatic and hydrophobic interactions can impact the secondary structure as well. In Figure 3, the CD spectrum of FGF1 prior to addition of the AuNP, 15 min, 6 h, and 24 h

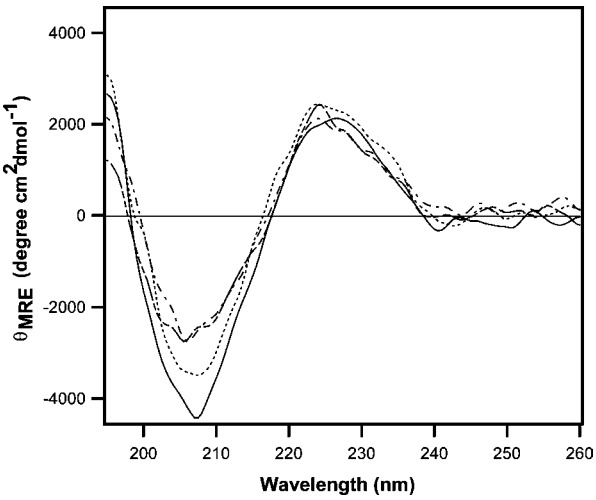

Figure 3. Circular dichroism spectra of FGF1 (—) and changes at 15 min (••••), 6 h (----), and 24 h (-•-) following the addition of Au-CAAKA to the FGF1 solution.

following addition of equimolar AuNP is shown. FGF1-heparin was not analyzed by CD spectroscopy.

The secondary structure of FGF1 are composed of β-sheet, β-turn, random coil, and α-helix character based upon crystallography and analysis by *CDPro* (*52*) fitting of the CD spectra. Using *CDPro* software, in the absence of the AuNP, FGF1 contains 35% β-sheet and 25% β-turn, with the remaining 40% attributed to random coil and α-helix character. Following addition of AuNP to FGF1, the 207 nm negative phase signal, which likely arises from a combination of α-helix and β-sheet signals, exhibits a loss of intensity during the first 6 h. The positive CD signal maximum at 230 nm, arising from β-turn, exhibits no substantial change over the entire experimental time domain. Analyzing the signal change in the presence of the AuNP indicates that a 10% increase in β-sheet and a 7% decrease in β-turn content occur for the FGF1−AuNP conjugate during the first 6 h, with minimal subsequent structural perturbations observed relative to the native FGF1 structure at longer experimental times.

A more detailed picture of the structural perturbations of FGF1 upon binding to the AuNP can be analyzed by 2D NMR when the experimental data for CAAKA-FITC release and the CD spectra suggest the FGF1-AuNP has approached a structural minimum. Inspection of the NMR data at 22 min (Supporting Information Figure 3) and 6 h (Supporting Information Figure 4) is intriguing but complicated by the fact that the structure is still evolving and thus exhibits more global changes in the protein; therefore, the discussion below is limited to the data obtained at 18 h exposure times (Figure 4) to simplify data interpretation.

Figure 4A shows the HSQC spectrum of FGF1 in the absence of the AuNP (cyan) and 18 h following addition of the AuNP (magenta). Comparison of the 2D NMR plots indicates that the vast majority of the residues of FGF1 are minimally impacted with the exception of the His_6-tag residues HT(I) and HT(II). The two resonances assigned, HT(I) and HT(II), are not observable immediately after exposure to the AuNP. Whether these changes in resonance intensity arise from altered conformational exchange or a true increase in transverse relaxation rates cannot be determined from these spectra. In addition, subtle changes are observable for the individual intensity and protein resonances following FGF1 interaction with the AuNP, particularly for protein residues in or near the His_6-tag region (Figure 1). S139 shows significantly lower resonance intensity 18 h after addition of AuNP (Figure 4B), whereas H124 and E60 show changes in resonance frequency with little affect on intensity. In general, the same residue changes for the 6 h time point are observed, but in addition, G19, V55, and I25 also show chemical shift changes (Supporting Information Figure 4). The intensity and resonance changes clearly indicate these residues are significantly impacted by addition of the AuNP.

Greater insight into the changes occurring at the individual protein residues in the presence of the AuNP can be deduced by plotting the change in chemical shift ($\Delta\delta$) in the HSQC experiment for individual protein residues relative to FGF1 in the absence of the AuNP (Figure 5) at 18 h and 6 h (Supporting Information Figure 5). Residues showing $\Delta\delta \geq 20$ Hz (digital resolution = 8.3 Hz on this scale) are considered significant and are labeled in the $\Delta\delta$ plot with their single letter abbreviation at position in the protein (Figure 1). A residue showing >100 Hz shift or a complete loss of intensity is artificially shown in the $\Delta\delta$ plot as a negative value.

The $\Delta\delta$ plots indicate that residues G19, E60, and H102, which are related structurally by the threefold symmetry of the FGF1 β-trefoil (*55*), along with Q43 and H124 show the largest chemical shift change between the protein in the presence and absence of the AuNP. The changes in the residue intensity and frequency are apparent at the earliest time point (22 min) and remain relatively constant through the 18 h time point (Figure 5). Residue G19 also shows a significant change, although a

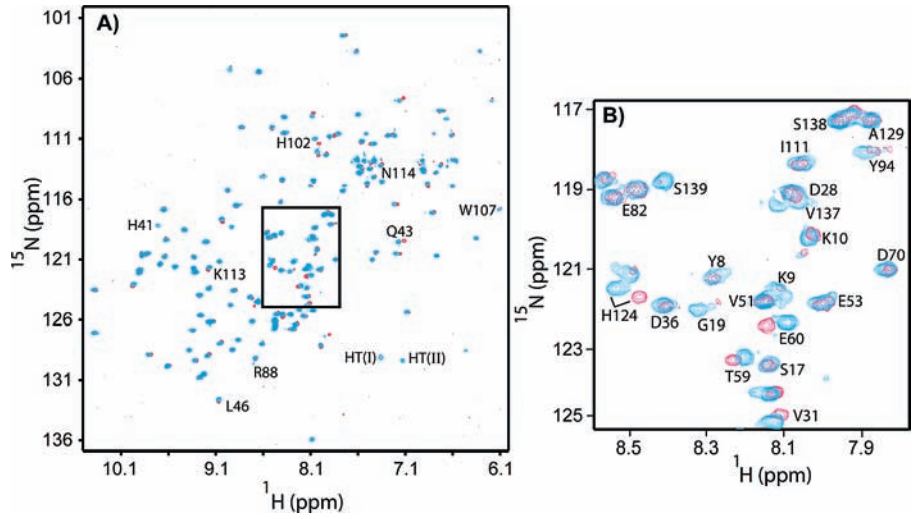

Figure 4. (A) $^1H-^{15}N$ HSQC NMR spectrum of FGF1 (cyan) and FGF1-AuNP (magenta) at 18 h. (B) Expanded representative region of HSQC spectra highlighting chemical shift changes, peak loss, and no change for FGF1-AuNP at 18 h postincubation.

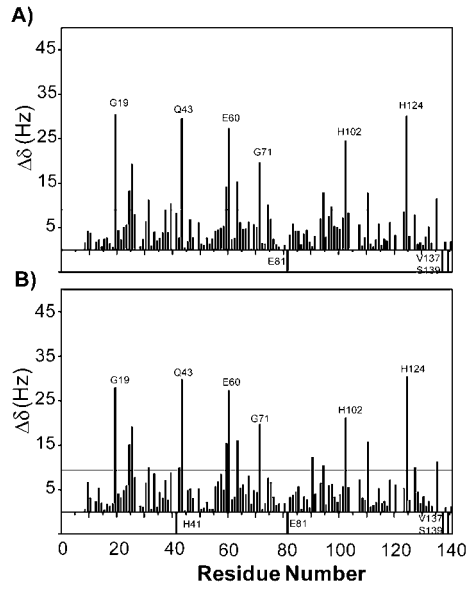

Figure 5. Δδ plot showing chemical shift differences and peak intensity loss (negative intensity) (A) 22 min and (B) 18 h incubation of FGF1 sym6ΔΔ with a 1.5 nm CAAKA passivated AuNP.

weak resonance G19 has a large shift in frequency implying that a structural perturbation may arise upon binding of the AuNP.

Residues H41, E81, V137, and S139 are not observed following the addition of AuNP and are represented as negative values in Figure 5. The signal loss for H41 may not be significant, as the loss of the resonance signal may reflect the weak native intensity observed for H41 in the FGF1 NMR spectra in the absence of the AuNP. However, the loss of E81, V137, and S139 is significant, as these are strong resonances in the FGF1 NMR spectra, implying that either a large frequency shift or a drastic change in dynamics for these residues occurs upon interaction of FGF1 with the AuNP. Residue E81 is located in close proximity to the His_6-tag region and changes in V137 and S139 are not surprising, since the C-terminal β-strand region is unstructured in both the His_6-tag (PDB accession 1JQZ or high-resolution 1RG8) and non-His_6-tag form of FGF1 (PDB accession 2AFG) and has a β-sheet interaction with the N-terminus β-strand. Changes in the N-terminal β-strand near the His_6-tag may indicate either ordering or disordering of the C-terminus β-strand upon AuNP binding.

Investigation of Heparin Binding in Presence of AuNP. NMR and crystallographic evidence for FGF1 binding with heparin suggest that heparin binding occurs through interactions with residues between G110-G120 and R122-A129, with large effects seen for residues K113 and K118 (*38, 40, 58*). On the basis of analysis of the NMR data for the FGF1-AuNP construct, the structural perturbations in FGF1 appear to be localized in the His_6-tag region and possibly the heparin binding pocket, which may potentially impact the heparin binding affinity. It is worth noting that changes in NMR resonances do occur in regions distal from the site of binding. For instance, it is well-known that heparin binding affects residues outside the heparin binding pocket (*40*).

A Δδ plot for heparin bound to FGF1 sym6ΔΔ in the absence of the AuNP calculated from the $^1H-^{15}N$ HSQC at 6 h (Supporting Information Figure 6) shows resonance and intensity perturbations for residues G19, D36, H42, R88, W107, K113, N114, and I130 (Figure 6B) in good agreement with previously reported NMR results on wild-type FGF1 (*38, 40, 58*). Comparison of the Δδ NMR plot derived from the $^1H-^{15}N$ HSQC spectra (Figure 6A) for adding heparin to FGF1 in the

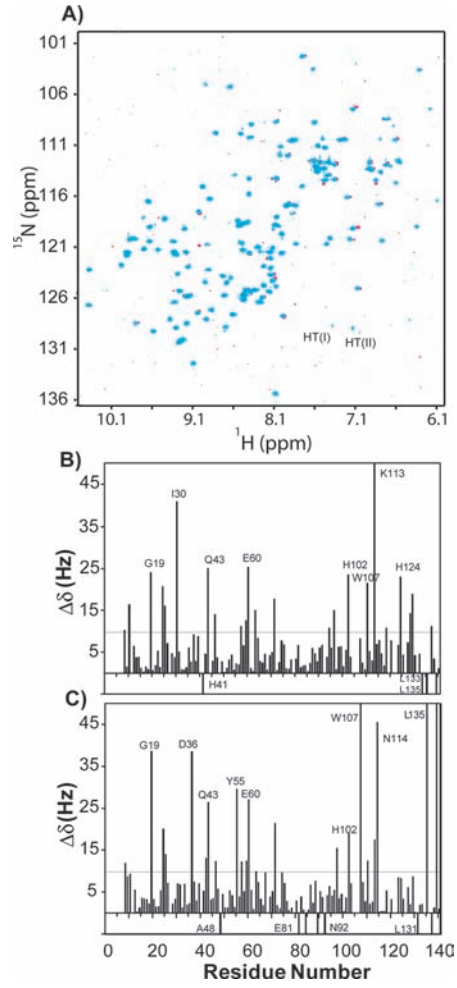

Figure 6. (A) $^1H-^{15}N$ HSQC NMR spectrum of FGF1 (cyan) and FGF1-heparin-AuNP (magenta) at 18 h. (B) Δδ plot showing chemical shift changes and loss of intensity (negative value) for (C) FGF1 with heparin and (B) FGF1 with heparin and AuNP after 18 h incubation.

presence and absence of AuNP (Figure 6C) shows similar perturbations as when AuNP is added to FGF1 in the presence and absence of heparin, indicating that the AuNP does not compete with heparin binding. Namely, residues W107, G110, K113, and N114 are impacted in the heparin−FGF1 alone and also show similar perturbations for the AuNP heparin−FGF1. In addition, residues A48, E81, L84, L89, and N92 show a complete intensity loss after 18 h with heparin and the AuNP (indicated as a negative value in Figure 4B), which is not observed in the absence of the AuNP. The loss of intensity of residues L89 and N92 is not surprising, since these residues are located in close proximity to the His_6-tag region in a flexible β-turn that has been shown to adopt significantly different structural conformations in FGF1/FGFR complexes (*59, 60*). The AuNP-specific changes are similar to those observed for FGF1 assembly onto the AuNP in the absence of heparin. Thus, the observation that a number of residues that are impacted only if the AuNP is present, including HT(I), HT(II), Y55, V137, and S139, and residues specific for experiments with heparin binding to FGF1 such as W107, G110, K113, and N114 also have chemical shift differences compared to FGF1 alone further confirms that both the AuNP and heparin remain bound after 18 h.

DISCUSSION

Our results show a strong time dependence for FGF1−AuNP complex formation. Correlating the changes observed in

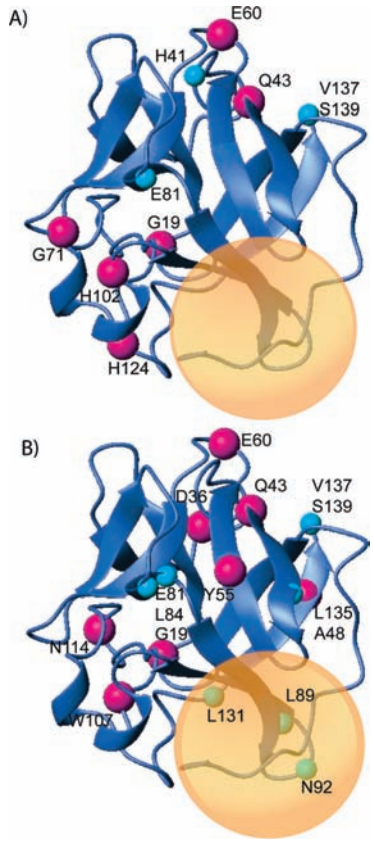

Figure 7. FGF1 crystallographic structure model (PDB ID: 1RG8) showing residues that exhibit chemical shift change (magenta), intensity differences (cyan), and His-tag (gold) affected by AuNP binding after 18 h for (A) FGF1 and (B) FGF1-heparin. The AuNP is overlaid in the His_6-tag region and does not represent a cocrystallized structure.

the NMR spectra for FGF1 and FGF1−heparin in the presence of the AuNP allows a model to be drawn indicating the regions of proposed AuNP interactions. Figure 7 shows the position of FGF1 residues that are most strongly affected by addition of AuNP after 18 h. Magenta balls indicate the position of backbone amides showing the largest $\Delta\delta$ values, and cyan indicates the positions of largest resonance intensity change. In addition to the residues of the His_6-tag, AuNP binding affects residues in β-turn regions, with little impact on β-sheet residues. A comparison of the affected residues (large or small) indicates that AuNP effects are noted in both positive and negative charge regions, and could be due to both nonspecific electrostatic interactions or motional dynamic changes, which are often seen with FGF1 flexibility changes upon heparin binding (*40*). The number and location of residues affected by AuNP binding in the NMR results are consistent with the relatively modest changes in secondary structure detected by CD. Importantly, the heparin binding pocket on the FGF1 remains largely unaffected by the AuNP binding, although the E81 residue (a surface residue in close spatial proximity to the His_6-tag region) is affected by AuNP binding. Comparison of the binding of FGF1-sym6ΔΔΔ in the absence of the His_6-tag could not be carried out due to the poor expression level and stability of FGF1 in the absence of the His_6 tag (*43*).

The bimodal kinetics for CAAKA release during the FGF1 assembly onto the AuNP can be attributed to one of two simple models, which may not be mutually exclusive. In one model, the bimodal nature of CAAKA-FITC release upon FGF binding reflects His_6-tag binding directly to readily accessible vertices and edges of the AuNP (*61, 62*) followed by slower release of CAAKA-FITC due to steric clash with the assembled FGF1. The zwitterionic CAAKA surface ligand is likely to minimize the nonspecific interactions, but given the degree of both positive and negative surface regions (Figure 1), electrostatic interactions between FGF1 and AuNP likely are inevitable. Alternatively, the bimodal kinetics may represent a rapid but nonspecific adsorption of FGF1 onto the AuNP followed by a slow rearrangement toward the more stable binding through the His_6-tag. The higher initial rate of assembly for FGF1−heparin would then reflect the fact that the His_6-tag is more favorable for binding than in FGF1 alone, or that the bound heparin eliminates some of the nonspecific adsorption by blocking the large positive charge region near the His_6-tag (Figure 1). Regardless of the mechanistic pathway for assembly, both models suggest an evolving interaction driven by protein sampling of the AuNP surface leading to a stable complex that minimally perturbs protein secondary structure or biological function by positioning the heparin binding pocket away from the His_6-tag-driven AuNP surface-mediated assemblage.

The correlation of the molecular beacon, gel electrophoresis, NMR, and CD spectroscopies supports a conclusion that the His_6-tag is the dominant interaction with the AuNP surfaces at long incubation times leading to small perturbations on the global FGF1 structure. The assembly arises from peptide displacement by the His residue leading to a His (Nε)-Au coordination. While it is surprising that the thiol (cys-) functionality is displaced by the His residue since thiols are strong coordinators of Au surfaces, the strong association of the His_6-tag reflects the enhanced thermodynamic stability for the His_6 residue arising from the multichelate effect, a common observation for metal−liagnd stabilization in metal coordination chemistry (*63*−*65*). The slow dynamics of assembly reflects minimization of the protein AuNP conjugate as the protein samples the AuNP surface. The ability to bind a AuNP to His_6-tag proteins opens another interfacial bridge between biology and nanoscience. This structure/function study of FGF1-AuNP binding provides evidence of stable, direct protein−Au conjugation without loss of normal function. The His_6-tag FGF1 sym6ΔΔ binding to the AuNP is stable in size-exclusion chromatography (Supporting Information Figure 1) and PAGE analysis (Supporting Information Figure 2) further confirming the suitability of the His_6-tag as a robust, stable linkage to a AuNP. This study enables further use of AuNP with recombinant His-tag proteins for intracellular delivery, biophysical studies, sensing, imaging, and other nanobiomedical applications.

ACKNOWLEDGMENT

The authors would like to thank Dr. Claudius Mundoma, Director of the Physical Biochemistry Facility in the Institute of Molecular Biophysics at Florida State, for help with circular dichroism measurements. The authors would also like to thank Dr. Tom Gedris and Steve Freitag in the NMR facility in the Department of Chemistry and Biochemistry at Florida State University. This work was supported by NIH NBIB-R0EB000832 (GFS) and NIH AI-R01021628 (TML).

Supporting Information Available: (SF1) Size-exclusion chromatography of FGF1:AuNP (10:1); (SF2) Native PAGE gel of FGF1:AuNP (1:1); (SF3) HSQC spectra for FGF1-FGF-AuNP (22 min); (SF4) HSQC spectra for FGF1-FGF1-AuNP (6 h); (SF5) FGF1 and FGF1-AuNP $\Delta\delta$ plot 6 h incubation time; (SF6) HSQC spectra for FGF1-FGF1-heparin at 18 h. This material is available free of charge via the Internet at http://pubs.acs.org.

LITERATURE CITED

(1) Medintz, I. L., Uyeda, H. T., Goldman, E. R., and Mattoussi, H. (2005) Quantum dot bioconjugates for imaging, labelling and sensing. *Nat. Mater. 4*, 435–446.

(2) Gao, X. H., Yang, L. L., Petros, J. A., Marshal, F. F., Simons, J. W., and Nie, S. M. (2005) In vivo molecular and cellular imaging with quantum dots. *Curr. Opin. Biotechnol. 16*, 63–72.

(3) Fritzsche, W., and Taton, T. A. (2003) Metal nanoparticles as labels for heterogeneous, chip-based DNA detection. *Nanotechnology 14*, R63–R73.

(4) Porta, F., Speranza, G., Krpetic, Z., Dal Santo, V., Francescato, P., and Scari, G. (2007) Gold nanoparticles capped by peptides. *Mater. Sci. Eng., B 140*, 187–194.

(5) You, C. C., De, M., and Rotello, V. M. (2005) Monolayer-protected nanoparticle-protein interactions. *Curr. Opin. Chem. Biol. 9*, 639–46.

(6) Chan, W. C., Maxwell, D. J., Gao, X., Bailey, R. E., Han, M., and Nie, S. (2002) Luminescent quantum dots for multiplexed biological detection and imaging. *Curr. Opin. Biotechnol. 13*, 40–6.

(7) Chah, S., Hammond, M. R., and Zare, R. N. (2005) Gold nanoparticles as a colorimetric sensor for protein conformational changes. *Chem. Biol. 12*, 323–328.

(8) Krpetic, Z., Nativo, P., Porta, F., and Brust, M. (2009) A Multidentate peptide for stabilization and facile bioconjugation of gold nanoparticles. *Bioconjugate Chem. 20*, 619–624.

(9) Aubin-Tam, M. E., and Hamad-Schifferli, K. (2005) Gold nanoparticle-cytochrome C complexes: the effect of nanoparticle ligand charge on protein structure. *Langmuir 21*, 12080–4.

(10) Becker, C. F. W., Marsac, Y., Hazarika, P., Moser, J., Goody, R. S., and Niemeyer, C. M. (2007) Functional immobilization of the small GTPase Rab6A on DNA-gold nanoparticles by using a site-specifically attached poly(ethylene glycol) linker and thiol place-exchange reaction. *ChemBioChem 8*, 32–36.

(11) Weiss, B., Schneider, M., Muys, L., Taetz, S., Neumann, D., Schaefer, U. F., and Lehr, C. M. (2007) Coupling of biotin-(poly(ethylene glycol))amine to poly(D,L-lactide-co-glycolide) nanoparticles for versatile surface modification. *Bioconjugate Chem. 18*, 1087–94.

(12) Ackerson, C. J., Jadzinsky, P. D., Jensen, G. J., and Kornberg, R. D. (2006) Rigid, specific, and discrete gold nanoparticle/antibody conjugates. *J. Am. Chem. Soc. 128*, 2635–2640.

(13) Brennan, J. L., Hatzakis, N. S., Tshikhudo, T. R., Dirvianskyte, N., Razumas, V., Patkar, S., Vind, J., Svendsen, A., Nolte, R. J. M., Rowan, A. E., and Brust, M. (2006) Bionanoconjugation via click chemistry: The creation of functional hybrids of lipases and gold nanoparticles. *Bioconjugate Chem. 17*, 1373–1375.

(14) Abad, J. M., Mertens, S. F., Pita, M., Fernandez, V. M., and Schiffrin, D. J. (2005) Functionalization of thioctic acid-capped gold nanoparticles for specific immobilization of histidine-tagged proteins. *J. Am. Chem. Soc. 127*, 5689–94.

(15) Medintz, I. L., Clapp, A. R., Mattoussi, H., Goldman, E. R., Fisher, B., and Mauro, J. M. (2003) Self-assembled nanoscale biosensors based on quantum dot FRET donors. *Nat. Mater. 2*, 630–8.

(16) Aubin-Tam, M. E., and Hamad-Schifferli, K. (2008) Structure and function of nanoparticle-protein conjugates. *Biomed. Mater. 3*, 034001.

(17) You, C. C., Verma, A., and Rotello, V. M. (2006) Engineering the nanoparticle-biomacromolecule interface. *Soft Matter 2*, 190–204.

(18) Aubin-Tam, M. E., Hwang, W., and Hamad-Schifferli, K. (2009) Site-directed nanoparticle labeling of cytochrome c. *Proc. Natl. Acad. Sci. U.S.A. 106*, 4095–100.

(19) Verma, A., Nakade, H., Simard, J. M., and Rotello, V. M. (2004) Recognition and stabilization of peptide alpha-helices using templatable nanoparticle receptors. *J. Am. Chem. Soc. 126*, 10806–7.

(20) Niemeyer, C. M. (2003) Functional hybrid devices of proteins and inorganic nanoparticles. *Angew. Chem., Int. Ed. Engl. 42*, 5796–800.

(21) Staii, C., Wood, D. W., and Scoles, G. (2008) Verification of biochemical activity for proteins nanografted on gold surfaces. *J. Am. Chem. Soc. 130*, 640–646.

(22) Blum, A. S., Soto, C. M., Wilson, C. D., Brower, T. L., Pollack, S. K., Schull, T. L., Chatterji, A., Lin, T. W., Johnson, J. E., Amsinck, C., Franzon, P., Shashidhar, R., and Ratna, B. R. (2005) An engineered virus as a scaffold for three-dimensional self-assembly on the nanoscale. *Small 1*, 702–706.

(23) Soto, C. M., Blum, A. S., Wilson, C. D., Lazorcik, J., Kim, M., Gnade, B., and Ratna, B. R. (2004) Separation and recovery of intact gold-virus complex by agarose electrophoresis and electroelution: Application to the purification of cowpea mosaic virus and colloidal gold complex. *Electrophoresis 25*, 2901–2906.

(24) Calabretta, M. K., Matthews, K. S., and Colvin, V. L. (2006) DNA binding to protein-gold nanocrystal conjugates. *Bioconjugate Chem. 17*, 1156–1161.

(25) Hu, Y., Das, A., Hecht, M. H., and Scoles, G. (2005) Nanografting de novo proteins onto gold surfaces. *Langmuir 21*, 9103–9109.

(26) Bayraktar, H., You, C. C., Rotello, V. M., and Knapp, M. J. (2007) Facial control of nanoparticle binding to cytochrome c. *J. Am. Chem. Soc. 129*, 2732−+.

(27) Ao, L. M., Gao, F., Pan, B. F., Cui, D. X., and Gu, H. C. (2006) Interaction between gold nanoparticles and bovine serum albumin or sheep antirabbit immunoglobulin G. *Chin. J. Chem. 24*, 253–256.

(28) Aubin, M. E., Morales, D. G., and Hamad-Schifferli, K. (2005) Labeling ribonuclease S with a 3 nm Au nanoparticle by two-step assembly. *Nano Lett. 5*, 519–22.

(29) Brewer, S. H., Glomm, W. R., Johnson, M. C., Knag, M. K., and Franzen, S. (2005) Probing BSA binding to citrate-coated gold nanoparticles and surfaces. *Langmuir 21*, 9303–9307.

(30) Whaley, S. R., English, D. S., Hu, E. L., Barbara, P. F., and Belcher, A. M. (2000) Selection of peptides with semiconductor binding specificity for directed nanocrystal assembly. *Nature 405*, 665–8.

(31) Peelle, B. R., Krauland, E. M., Wittrup, K. D., and Belcher, A. M. (2005) Design criteria for engineering inorganic material-specific peptides. *Langmuir 21*, 6929–33.

(32) Kroger, D., Liley, M., Schiweck, W., Skerra, A., and Vogel, H. (1999) Immobilization of histidine-tagged proteins on gold surfaces using chelator thioalkanes. *Biosens. Bioelectron. 14*, 155–61.

(33) Medintz, I. L., Konnert, J. H., Clapp, A. R., Stanish, I., Twigg, M. E., Mattoussi, H., Mauro, J. M., and Deschamps, J. R. (2004) A fluorescence resonance energy transfer-derived structure of a quantum dot-protein bioconjugate nanoassembly. *Proc. Natl. Acad. Sci. U.S.A. 101*, 9612–7.

(34) Goldman, E. R., Medintz, I. L., Hayhurst, A., Anderson, G. P., Mauro, J. M., Iverson, B. L., Georgiou, G., and Mattoussi, H. (2005) Self-assembled luminescent CdSe-ZnS quantum dot bioconjugates prepared using engineered poly-histidine terminated proteins. *Anal. Chim. Acta 534*, 63–67.

(35) Lee, I. S., Lee, N., Park, J., Kim, B. H., Yi, Y. W., Kim, T., Kim, T. K., Lee, I. H., Paik, S. R., and Hyeon, T. (2006) Ni/NiO core/shell nanoparticles for selective binding and magnetic separation of histidine-tagged proteins. *J. Am. Chem. Soc. 128*, 10658–10659.

(36) Lim, J. K., Kim, Y., Lee, S. Y., and Joo, S. W. (2008) Spectroscopic analysis of L-histidine adsorbed on gold and silver nanoparticle surfaces investigated by surface-enhanced Raman scattering. *Spectrochim. Acta, Part A 69*, 286–289.

(37) Kogot, J. M., England, H. J., Strouse, G. F., and Logan, T. M. (2008) Single peptide substitution onto a 1.5 nm Au surface via a histidine tag. *J. Am. Chem. Soc. 130*, 16156–16157.

(38) Ogura, K., Nagata, K., Hatanaka, H., Habuchi, H., Kimata, K., Tate, S., Ravera, M. W., Jaye, M., Schlessinger, J., and

Inagaki, F. (1999) Solution structure of human acidic fibroblast growth factor and interaction with heparin-derived hexasaccharide. *J. Biomol. NMR 13*, 11–24.
(39) Blaber, S. I., Culajay, J. F., Khurana, A., and Blaber, M. (1999) Reversible thermal denaturation of human FGF-1 induced by low concentrations of guanidine hydrochloride. *Biophys. J. 77*, 470–7.
(40) Canales, A., Lozano, R., Lopez-Mendez, B., Angulo, J., Ojeda, R., Nieto, P. M., Martin-Lomas, M., Gimenez-Gallego, G., and Jimenez-Barbero, J. (2006) Solution NMR structure of a human FGF-1 monomer, activated by a hexasaccharide heparin-analogue. *FEBS J. 273*, 4716–27.
(41) Ostrovsky, O., Berman, B., Gallagher, J., Mulloy, B., Fernig, D. G., Delehedde, M., and Ron, D. (2002) Differential effects of heparin saccharides on the formation of specific fibroblast growth factor (FGF) and FGF receptor complexes. *J. Biol. Chem. 277*, 2444–53.
(42) Otsuka, H., Nagasaki, Y., and Kataoka, K. (2003) PEGylated nanoparticles for biological and pharmaceutical applications. *Adv. Drug Delivery Rev. 55*, 403–419.
(43) Brych, S. R., Dubey, V. K., Bienkiewicz, E., Lee, J., Logan, T. M., and Blaber, M. (2004) Symmetric primary and tertiary structure mutations within a symmetric superfold: a solution, not a constraint, to achieve a foldable polypeptide. *J. Mol. Biol. 344*, 769–80.
(44) Brych, S. R., Kim, J. W., Logan, T. M., and Blaber, M. (2003) Accommodation of a highly symmetric core within a symmetric protein superfold. *Protein Sci. 12*, 2704–2718.
(45) Teichroeb, J. H., Forrest, J. A., Ngai, V., and Jones, L. W. (2006) Anomalous thermal denaturing of proteins adsorbed to nanoparticles. *Eur. Phys. J. E 21*, 19–24.
(46) You, C. C., De, M., Han, G., and Rotello, V. M. (2005) Tunable inhibition and denaturation of alpha-chymotrypsin with amino acid-functionalized gold nanoparticles. *J. Am. Chem. Soc. 127*, 12873–81.
(47) Brych, S. R., Blaber, S. I., Logan, T. M., and Blaber, M. (2001) Structure and stability effects of mutations designed to increase the primary sequence symmetry within the core region of a beta-trefoil. *Protein Sci. 10*, 2587–2599.
(48) Blaber, M., DiSalvo, J., and Thomas, K. A. (1996) X-ray crystal structure of human acidic fibroblast growth factor. *Biochemistry 35*, 2086–2094.
(49) Blaber, S. I., Culajay, J. F., Khurana, A., and Blaber, M. (1999) Reversible thermal denaturation of human FGF-1 induced by low concentrations of guanidine hydrochloride. *Biophys. J. 77*, 470–477.
(50) Weare, W. W., Reed, S. M., Warner, M. G., and Hutchison, J. E. (2000) Improved synthesis of small (d(CORE) approximate to 1.5 nm) phosphine-stabilized gold nanoparticles. *J. Am. Chem. Soc. 122*, 12890–12891.
(51) Yun, C. S., Javier, A., Jennings, T., Fisher, M., Hira, S., Peterson, S., Hopkins, B., Reich, N. O., and Strouse, G. F. (2005) Nanometal surface energy transfer in optical rulers, breaking the FRET barrier. *J. Am. Chem. Soc. 127*, 3115–9.
(52) Sreerama, N., and Woody, R. W. (2000) Estimation of protein secondary structure from circular dichroism spectra: comparison of CONTIN, SELCON, and CDSSTR methods with an expanded reference set. *Anal. Biochem. 287*, 252–60.
(53) Johnson, B. A., and Blevins, R. A. (1994) Nmr view - a computer-program for the visualization and analysis of nmr data. *J. Biomol. NMR 4*, 603–614.
(54) Mulder, F. A., Schipper, D., Bott, R., and Boelens, R. (1999) Altered flexibility in the substrate-binding site of related native and engineered high-alkaline Bacillus subtilisins. *J. Mol. Biol. 292*, 111–23.
(55) Blaber, M., DiSalvo, J., and Thomas, K. A. (1996) X-ray crystal structure of human acidic fibroblast growth factor. *Biochemistry 35*, 2086–2094.
(56) Jennings, T. L., Singh, M. P., and Strouse, G. F. (2006) Fluorescent lifetime quenching near $d = 1.5$ nm gold nanoparticles: probing NSET validity. *J. Am. Chem. Soc. 128*, 5462–7.
(57) Woehrle, G. H., Brown, L. O., and Hutchison, J. E. (2005) Thiol-functionalized, 1.5-nm gold nanoparticles through ligand exchange reactions: Scope and mechanism of ligand exchange. *J. Am. Chem. Soc. 127*, 2172–2183.
(58) Pellegrini, L., Burke, D. F., von Delft, F., Mulloy, B., and Blundell, T. L. (2000) Crystal structure of fibroblast growth factor receptor ectodomain bound to ligand and heparin. *Nature 407*, 1029–34.
(59) Stauber, D. J., DiGabriele, A. D., and Hendrickson, W. A. (2000) Structural interactions of fibroblast growth factor receptor with its ligands. *Proc. Natl. Acad. Sci. U.S.A. 97*, 49–54.
(60) Kim, J., Lee, J., Brych, S. R., Logan, T. M., and Blaber, M. (2005) Sequence swapping does not result in conformation swapping for the beta4/beta5 and beta8/beta9 beta-hairpin turns in human acidic fibroblast growth factor. *Protein Sci. 14*, 351–9.
(61) Hong, R., Fernandez, J. M., Nakade, H., Arvizo, R., Emrick, T., and Rotello, V. M. (2006) In situ observation of place exchange reactions of gold nanoparticles. Correlation of monolayer structure and stability. *Chem. Commun.* 2347–2349.
(62) Donkers, R. L., Song, Y., and Murray, R. W. (2004) Substituent effects on the exchange dynamics of ligands on 1.6 nm diameter gold nanoparticles. *Langmuir 20*, 4703–4707.
(63) Letsinger, R. L., Elghanian, R., Viswanadham, G., and Mirkin, C. A. (2000) Use of a steroid cyclic disulfide anchor in constructing gold nanoparticle-oligonucleotide conjugates. *Bioconjugate Chem. 11*, 289–291.
(64) Li, Z., Jin, R. C., Mirkin, C. A., and Letsinger, R. L. (2002) Multiple thiol-anchor capped DNA-gold nanoparticle conjugates. *Nucleic Acids Res. 30*, 1558–1562.
(65) Roux, S., Garcia, B., Bridot, J. L., Salome, M., Marquette, C., Lemelle, L., Gillet, P., Blum, L., Perriat, P., and Tillement, O. (2005) Synthesis, characterization of dihydrolipoic acid capped gold nanoparticles, and functionalization by the electroluminescent luminol. *Langmuir 21*, 2526–2536.

BC900224D

SUPPLEMENTAL INFORMATION:

Maintaining Structure and Function of a Recombinant Poly-Histidine Tagged Protein Covalently Attached to a 1.5 nm Au Nanoparticle.

Joshua M. Kogot, Alex M. Parker, Jihun Lee, Michael Blaber, Geoffrey F. Strouse, and Timothy M. Logan**

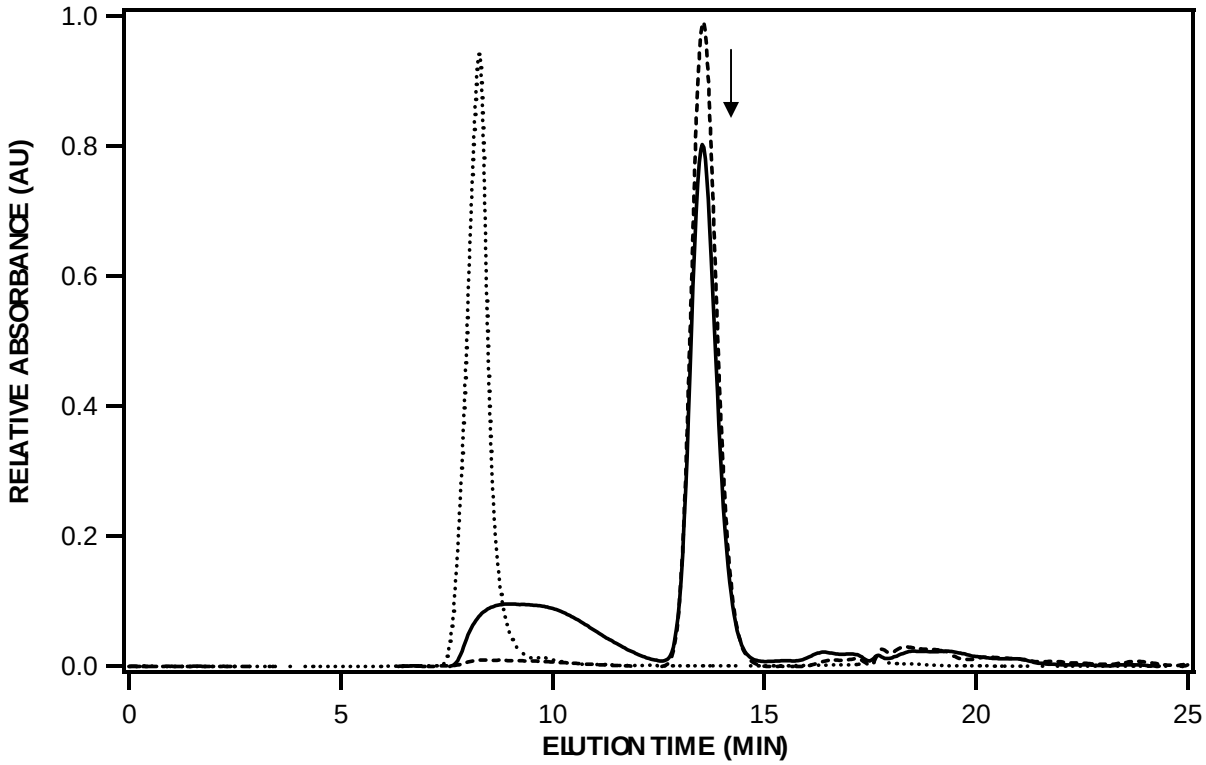

SUPPLEMENTAL FIGURE 1

Size-exclusion Chromatography (Superdex75) of FGF 10μM in Buffer A (----), concentrated Au-CAAKA in H_2O 1μM (••••), and FGF + Au-CAAKA at 10 μM : 1 μM (—) in Buffer A. The decreased absorbance at 13.5 mins (~10%) in the FGF + Au-CAAKA sample suggests that a 1 : 1 complex of FGF1 – Au-CAAKA forms without impacting the remaining FGF1 sample.

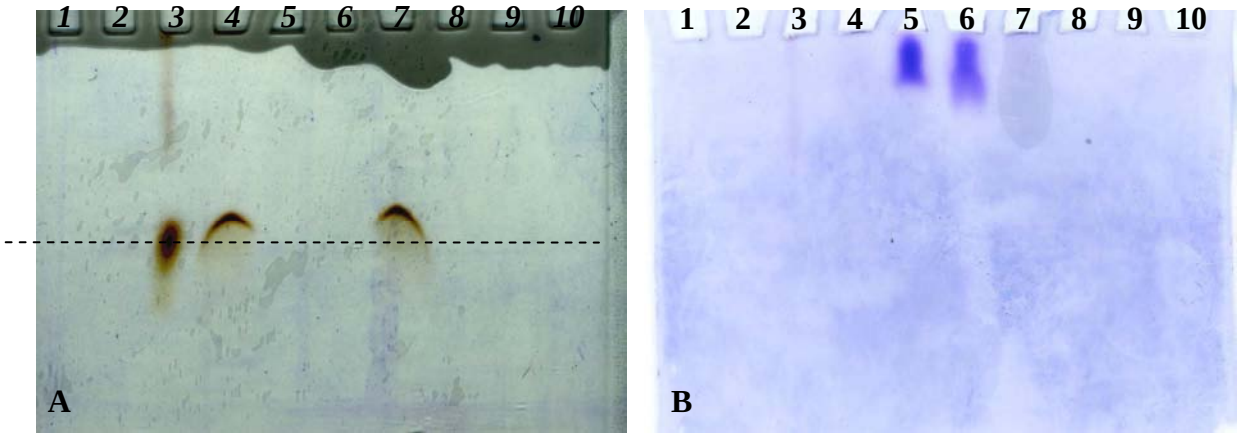

SUPPLEMENTAL FIGURE 2

10% TBE-PAGE (Native) pH = 8.8 electrophoresis gel representing an A) unstained and B) Coomassie Blue stained gel. The PAGE gel was run at 100 V for 90 mins. The lanes are identical in both gels such that (Lane 3) 25 μM Au-CAAKA; (Lane 4) 25 μM FGF + 25 μM Au-CAAKA; (Lane 5) 25 μM FGF; (Lane 6) 25 μM FGF + 25 μM heparin; and Lane 7) 25 μM FGF1-heparin + 25 μM Au-CAAKA . Lanes 1, 2, 8, 9, and 10 are empty.

The relative mobilities for each band in the unstained gel are 35.5 mm for Au-CAAKA, 31.0 mm for FGF1 + Au-CAAKA, and 30.4 mm for FGF1-heparin + Au-CAAKA. The mobility difference for FGF1 + Au-CAAKA and FGF1-heparin + Au-CAAKA compared to Au-CAAKA alone in the unstained gel, as well as the absence of protein bands in the Coomassie blue stained gel suggest that there is a 1 : 1 complex of FGF1 : Au-CAAKA.

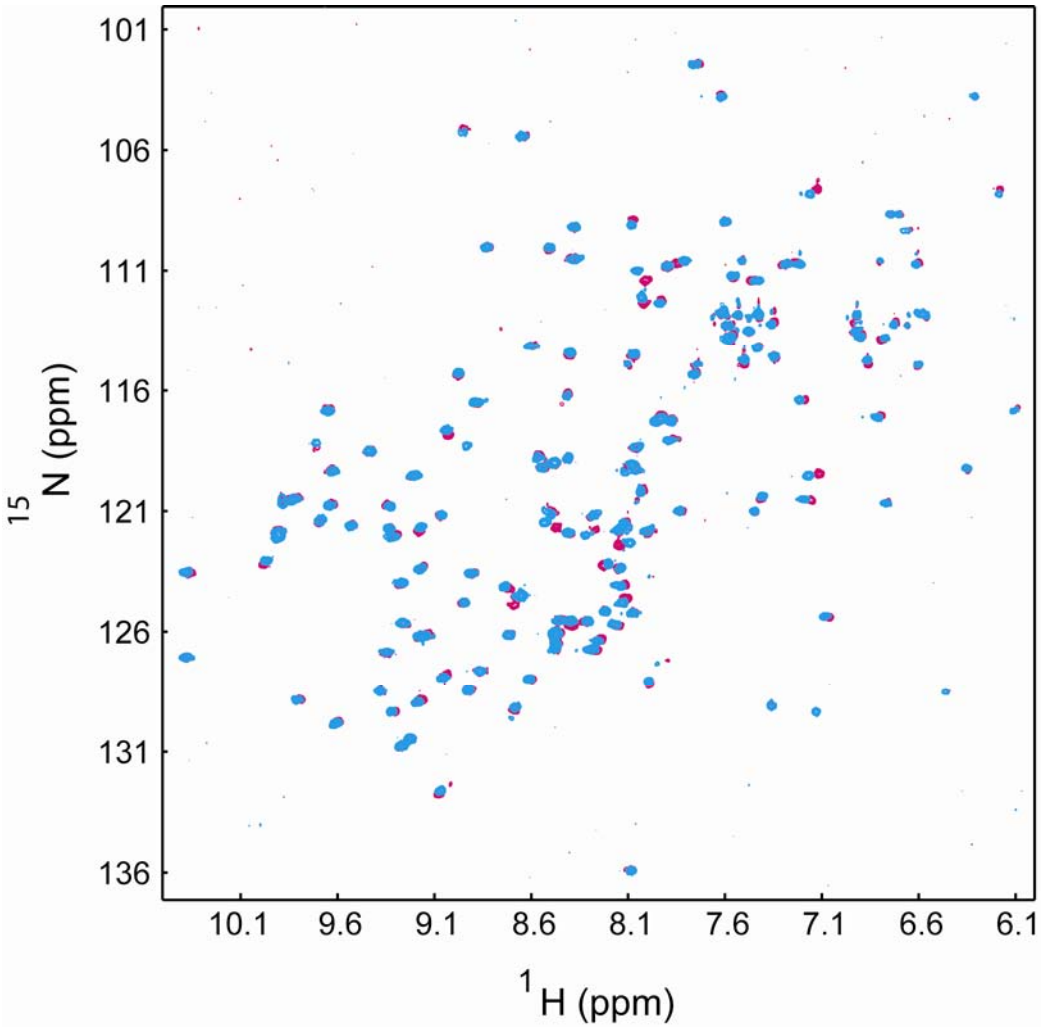

SUPPLEMENTAL FIGURE 3 HSQC overlay of FGF1(cyan) and FGF1-AuNP (magenta) after initial addition (0 h) of AuNP.

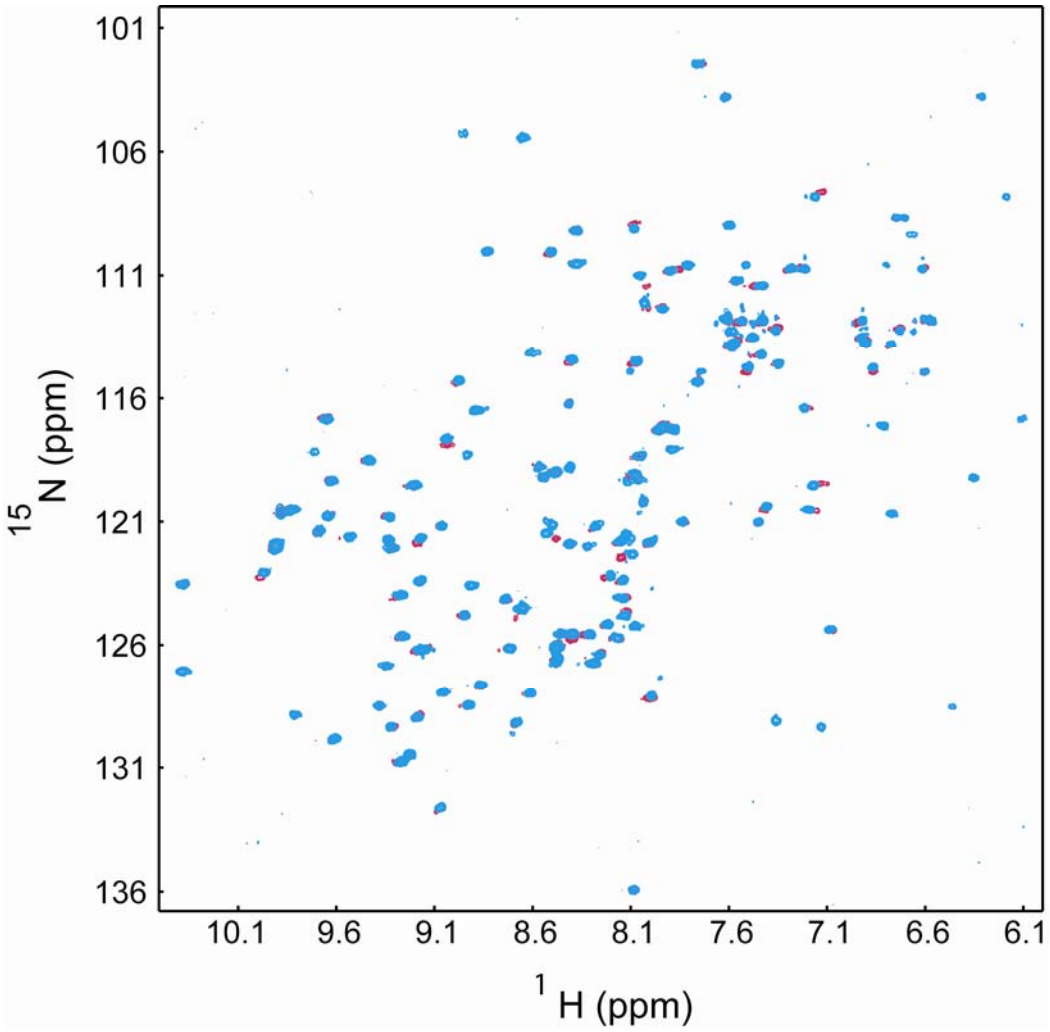

SUPPLEMENTAL FIGURE 4: HSQC overlay of FGF1(cyan) and FGF1-AuNP (magenta) after initial addition (6 h) of AuNP.

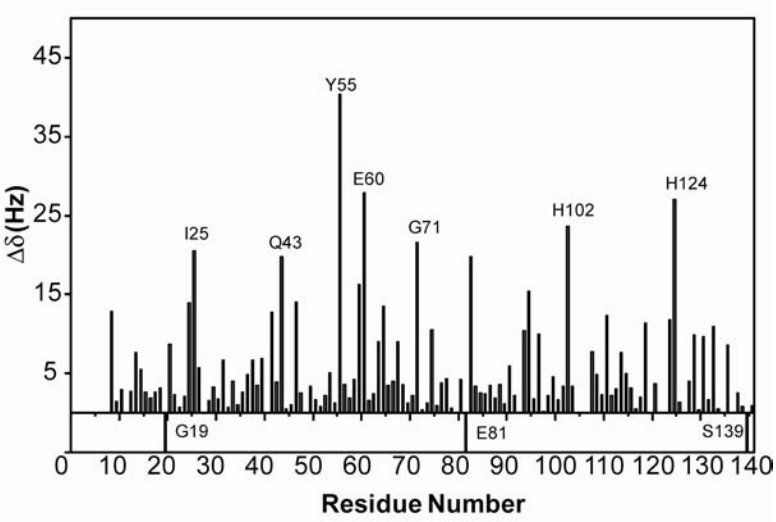

SUPPLEMENTAL FIGURE 5: Δδ plot of FGF1 and FGF1-AuNP at 6h after AuNP addition.

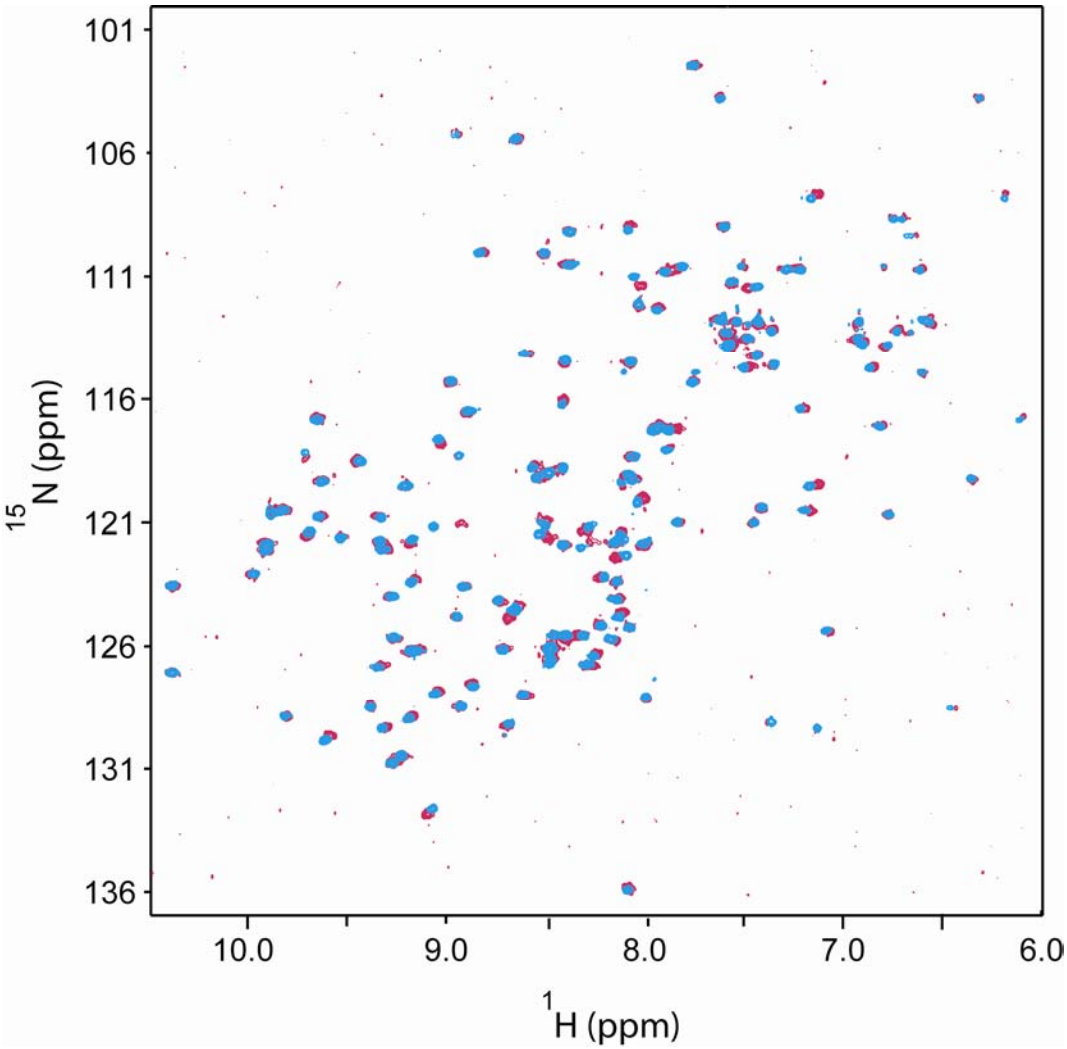

SUPPLEMENTAL FIGURE 6 HSQC overlay of FGF1(cyan) and FGF1-heparin (magenta) after 18 h.

Annexin A5-Functionalized Liposomes for Targeting Phosphatidylserine-Exposing Membranes

Boris Garnier,[†,‡] Anthony Bouter,[†] Céline Gounou,[†] Klaus G. Petry,[‡] and Alain R. Brisson*[,†]

Molecular Imaging and NanoBioTechnology, IECB, UMR-5248 CBMN CNRS-University Bordeaux1-ENITAB, Avenue des Facultés, F-33402 Talence, France, and INSERM EA-2966, University Bordeaux, 146 rue Léo Saignat, F-33076 Bordeaux, France. Received June 11, 2009; Revised Manuscript Received September 4, 2009

Long-circulating liposomes functionalized with cell-targeting elements and loaded with bioactive compounds present high interest as drug delivery nanosystems. We present here the synthesis and physicochemical characterization of liposomes containing PEGylated lipids covalently linked to oriented Annexin-A5 (Anx5) proteins, and we show that Anx5-functionalized liposomes are able to target phosphatidylserine (PS)-exposing membranes. The covalent coupling of Anx5 to liposomes is almost quantitative, which is mainly due to the high accessibility of the reacting groups. The influence of Anx5 functionalization on liposome aggregation was investigated by dynamic light scattering, showing that Anx5-functionalized liposomes are stable below a threshold density of 250 Anx5 molecules per liposome. Anx5-functionalized liposomes bind PS-containing membranes with very high efficacy, which is mainly due to the controlled orientation of the Anx5 at the liposome surface. A striking result, obtained by quartz crystal microbalance with dissipation monitoring, is that one single Anx5 molecule is able to anchor a liposome to a PS-containing supported membrane. Finally, we show by fluorescence microscopy that Anx5-functionalized liposomes bind PS-exposing apoptotic K562 cells with high specificity. This study demonstrates that Anx5-functionalized liposomes bind specifically to PS membranes and are thus potential candidates to deliver drug or imaging agents to sites of apoptosis or thrombosis.

INTRODUCTION

Liposomes are hollow lipid bilayer vesicles which have found practical applications as drug delivery systems, thanks to their intrinsic property of entrapping either hydrophilic compounds within their aqueous interior or hydrophobic compounds within their hydrophobic lipid boundary (*1*−*5*). Drug encapsulation provides several advantages over direct administration, such as preventing drug dilution, avoiding potential deleterious side effects, or reducing the volume of distribution of the drug (*6, 7*)}. Efforts have been developed to design liposomes that achieve long circulation times in the body in order to increase drug accumulation in the desired tissues and organs. Parameters have been identified which are important for increasing the circulation time of liposomes, in particular, a small (∼100 nm) size and the addition of a hydrophilic poly(ethylene glycol) (PEG) coat. Small size strongly reduces elimination of vesicles by body filters, while the attachment of a brush-like layer of PEG molecules helps them escape capture by cells from the reticuloendothelial system and prevents their accumulation in the liver or the spleen (*1*). The circulation half-life of PEGylated stealth liposomes extends to several hours, compared to a few minutes for uncoated vesicles (*8*).

The surface functionalization of liposomes with molecular recognition elements able to recognize and bind specific targets constitutes a major challenge in the field of drug delivery systems (*6, 9*−*12*). Liposomes exposing several types of cell recognition molecules, from small molecules like folic acid to large proteins like antibodies, have already been produced and used successfully as drug carriers *in vitro* as well as in mice (*13*).

Our aim is to develop long-circulating liposomal nanovectors functionalized with protein-based recognition elements. We present here our initial study which concerns the synthesis and characterization of PEGylated liposomes functionalized with the Annexin-A5 (Anx5) protein.

Anx5 is the prototype member of the annexin family, proteins which share the property of binding to membranes containing negatively charged phospholipids in a Ca^{2+}-dependent manner (*14*). Although the exact biological functions of annexins are still being debated, Anx5 has already found wide application both as a research tool and as a clinical tool for labeling cell membranes exposing phosphatidylserine (PS) molecules. It is indeed well-established that eukaryotic cell membranes present an asymmetric distribution of lipid molecules, with the majority of anionic phospholipids, particularly PS molecules, being located in the inner leaflet of the plasma membrane (*15*). The exposure of PS molecules on the cell membrane outer leaflet is a hallmark of several basic processes, such as apoptosis or programmed cell death (*16*) and blood platelet activation (*17*). The ability of Anx5 to bind PS-exposing membranes in a Ca^{2+}-dependent manner explains the use of labeled Anx5 proteins as research tools (*18*−*20*) and also as *in vivo* diagnostic agents to detect cell death in cancer chemotherapy, organ transplant rejection, or myocardial infarction (*21*−*23*). In addition, drug-targeting and drug-delivery strategies based on chimerical Anx5 entities coupled to various types of bioactive moieties have recently been proposed, e.g., for delivering thrombolytic enzymes to thrombotic sites or for delivering compounds intracellularly via Anx5-mediated endocytosis (*24, 25*).

Our first goal is to design liposomes functionalized with oriented Anx5 proteins in such a way that the Anx5 proteins maintain their property of binding to PS-exposing cells. The

* Corresponding author. Alain R. Brisson. Mailing address: Bat. B8, Avenue des Facultés, F-33402 Talence, France, E-mail: a.brisson@iecb.u-bordeaux.fr; Tel: +33 540003458; Fax: +33 540002200.

[†] Molecular Imaging and NanoBioTechnology.

[‡] INSERM EA-2966.

10.1021/bc9002579 CCC: $40.75 © 2009 American Chemical Society
Published on Web 10/19/2009

structures of the soluble form (*26, 27*) and membrane-bound form of Anx5 (*28*−*31*) indicate that this protein presents a slightly bent shape with a convex membrane-binding face and an opposite concave face. On the basis of this structural knowledge, we have designed an Anx5-SH mutant protein harboring a unique sulfhydryl group inserted in a highly accessible loop on the concave face of the protein (*32*). We present here the synthesis and characterization of Anx5-functionalized PEGylated liposomes. Conditions of covalent functionalization were monitored by SDS-PAGE, and the interaction of Anx5-liposomes with PS-exposing model membranes was characterized in a systematic manner by quartz crystal microbalance with dissipation monitoring method (QCM-D). The QCM-D method is particularly well adapted for studying the interaction of proteins or proteolipid complexes with model membranes (*33*−*35*). The encapsulation property and the ability of Anx5-liposomes to bind PS-exposing apoptotic cells were investigated by fluorescence spectroscopy and microscopy, respectively.

EXPERIMENTAL PROCEDURES

Materials. 1,2-dioleoyl-*sn*-glycero-3-phosphocholine (DOPC), cholesterol, 1,2-dipalmytoyl-*sn*-glycero-3-phosphoethanolamine-*N*-[methoxy(poly(ethylene glycol))-2000] (PEG_{2000}-DPPE), 1, 2-distearoyl-*sn*-glycero-3-phosphoethanolamine-*N*-[maleimide-(poly(ethylene glycol))2000] (Mal-PEG_{2000}-DSPE), and 1,2-dioleoyl-*sn*-glycero-3-[phospho-L-serine] (DOPS) were obtained from Avanti Polar Lipids (Alabaster, AL, USA). All other chemicals were of ultrapure grade. Water was purified with a RiOs system (Millipore, St Quentin en Yvelines, France). STI-571 (imatinib mesilate) was from Novartis (Basel, Switzerland).

Buffer Preparation. A HEPES buffered saline (HBS) solution made of 10 mM HEPES, 150 mM NaCl, and 2 mM NaN_3 was prepared in ultrapure water. The pH was set at 7.4, except for Anx5 and liposome solutions used in covalent coupling reactions where pH was set at 6.3. Buffer solutions were supplemented with either 2 mM $CaCl_2$ or 2 mM EGTA for QCM-D and cell experiments, as indicated in the text.

Liposome Preparation. Liposomes were prepared by lipid film hydration (*36*) followed by extrusion, as briefly described here. Lipids were dissolved in chloroform, mixed in desired amounts, and the solvent was evaporated to dryness using a rotary evaporator during 20 min. Lipids were hydrated in HBS, resulting in multilamellar vesicles (MLVs), and homogenized by three cycles of freezing−thawing and subsequent vortexing. Large unilamellar vesicles (LUVs) were obtained by hand extrusion of the resulting lipid dispersion, passing the mixture twenty times through 0.1 μm polycarbonate filters with a LiposoFast extruder (Avestin, Sodexim, France). LUVs were composed of DOPC/cholesterol/Mal-PEG_{2000}-DSPE/PEG_{2000}-DPPE in proportions specified in each experiment. Small unilamellar vesicles (SUVs), composed of DOPC/DOPS (weight ratio 4/1), were obtained by sonication of a MLV suspension with a tip sonicator (Misonix, Farmingdale, NY), operated in a pulsed mode at 20% duty cycle for 30 min with refrigeration. Phospholipid concentrations were determined by phosphate analysis according to Rouser (*37*).

Annexin Protein Preparation. Rat recombinant AnxA5-SH and AnxA5-S-S-Anx5 dimers were produced and purified as described (*32*). The AnxA5-SH protein is a double mutant (C314S, T163C) in which the only cysteine in wt-Anx5 has been replaced by a serine (C314S) and a single cysteine has been introduced, at position 163 (T163C), in a highly exposed region on the concave face of the protein.

Covalent Coupling of Anx5-SH to Liposomes. To produce Anx5-SH proteins, Anx5-S-S-Anx5 dimers were reduced by incubation with 10 mM DTT in HBS at pH 6.3 for 30 min. Reduced Anx5-SH was purified on a HiTrap desalting column (GE-Healthcare, Brabant, Belgique) equilibrated with HBS at pH 6.3. Anx5-SH was mixed with desired amounts of LUVs containing Mal-PEG_{2000}-DSPE lipids, in HBS at pH 6.3, and incubated at least for 4 h at room temperature. The number of maleimide groups available for covalent coupling was calculated assuming that lipids are equally distributed among the two membrane leaflets and that only maleimide groups located on the outer leaflet are accessible.

Characterization of Covalent Coupling of Anx5-SH to Liposomes. A given amount of liposomes composed of DOPC/cholesterol/Mal-PEG_{2000}-DSPE (74/25/1 mol %) was incubated with Anx5-SH solutions of increasing concentration. The extent of coupling was analyzed by SDS-PAGE (*38*) using a 10% resolving gel and visualization of protein bands by Coomassie blue staining. Since free maleimides from the inner leaflet are exposed upon solubilization of the liposomes by SDS, the remaining free thiol groups of the suspension were blocked by addition of 5 μM *N*-ethylmaleimide for 4 h before running the gels.

Dynamic Light Scattering (DLS). DLS measurements were performed using an ALV laser goniometer, equipped with a 22 mW HeNe linearly polarized laser operating at a wavelength of 632.8 nm and an ALV-5000/EPP multiple τ digital correlator with 125 ns initial sampling time. The liposome suspensions were maintained at a temperature of 25.0 ± 0.1 °C in all experiments. The counting time was 300 s for each sample. The liposome composition was DOPC/cholesterol/Mal-PEG_{2000}-DSPE (70/25/5 mol %). Samples contained 200 μg phospholipids in a total volume of 900 μL, pH 7.4. All measurements were performed at three scattering angles (50°, 90°, 120°); the presented results correspond to 90° scattering. Data were analyzed using ALV Correlator Control software.

Quartz Crystal Microbalance with Dissipation Monitoring (QCM-D). QCM-D measurements were performed with a Q-SENSE E4 system (Q-SENSE, Gothenburg, Sweden) (*39*). Briefly, upon interaction of matter with the surface of a sensor crystal, changes in the resonance frequency, *f*, related to adsorbed mass (including coupled water), and in the dissipation, *D*, related to viscous losses in the adlayer are measured.

Measurements were performed in flow mode; i.e., the solution was continuously delivered to the measurement chamber (flow speed 150 μL/min) by the aid of a peristaltic pump (ISM935C, Ismatec, Zürich, Switzerland). The working temperature was 24 °C. Variations in resonance frequency (Δf) and dissipation (ΔD) were measured at several harmonics (15, 25, 35 MHz) simultaneously. Adsorbed masses, Δm, are calculated according to the Sauerbrey equation, $\Delta m = -C\Delta f_{norm}$, with the mass sensitivity constant $C = 17.7\ ng \cdot cm^{-2} \cdot Hz^{1-}$ and $\Delta f_{norm} = \Delta f_n / n$, with n being the overtone number (*40*). The presented Δm and ΔD values correspond to the fifth harmonics ($n = 5$, i.e., 25 MHz). Prior to use, the QCM-D sensor crystals were cleaned by two cycles of exposure to a 2% SDS solution for 15 min, rinsing with ultrapure water, blow-drying with nitrogen, and exposure to UV/ozone for 10 min, as described in Richter et al. (*41*).

A supported lipid bilayer (SLB) was formed on silica-coated quartz sensor crystals by deposition of SUVs made of DOPC/DOPS (4:1, w:w), as described in *refs* 41−43. After rinsing the chamber with Ca^{2+}-containing HBS to remove the excess of SUVs, solutions of functionalized vesicles were introduced in the chamber. The vesicle composition was DOPC/cholesterol/Mal-PEG_{2000}-DSPE 74/25/1 mol % for all experiments, except for experiments dealing with the influence of the PEG layer on targeting efficiency. In this latter case, three kinds of formulation

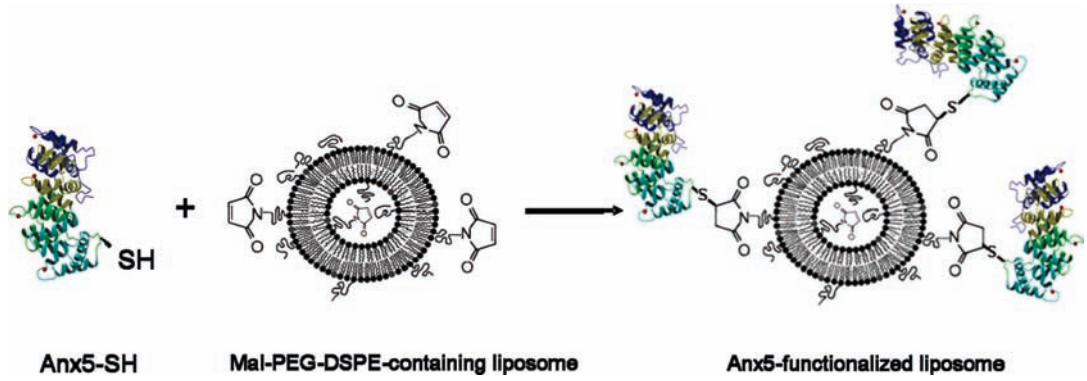

Figure 1. Scheme of covalent coupling of Anx5-SH to liposomes containing Mal-PEG_{2000}-DSPE.

were used: PEG_{2000}-DPPE × mol %/Mal-PEG_{2000}-DSPE 1 mol %/cholesterol 25 mol %/DOPC 74 − x mol %, with $x = 0$, 2, or 4 mol %.

Liposome Leakage Assay. The self-quenching property of the fluorescent dye sulforhodamine B was characterized by measuring the intensity of dye solutions of increasing concentrations.

The fluorophore was passively encapsulated into liposomes as follows. The dry lipid film was hydrated with a HBS solution containing 50 mM sulforhodamine B at pH 7.4. Vesicles were then prepared and covalently coupled to Anx5 as described above. Nonencapsulated dye molecules were discarded by gel filtration on a Sephacryl S-400 column (Amersham Bioscience, Buckinghamshire, UK). Leakage was followed by measuring the fluorescence intensity of the liposome solutions. Complete release of sulforhodamine B was achieved by addition of Triton X100 (100 μL at 0.5% v/v), and the proportion of fluorophore released was calculated as

$$\%\ \text{sulforhodamine}_{\text{free}} = \frac{I_t - I_0}{I_r - I_0}$$

where I_t is the fluorescence intensity after the desired period of time, I_0 is the fluorescence baseline, and I_r is the fluorescence after complete fluorophore release.

All measurements were realized with a Perkin Ellmer LS55 (Burckinghamshire, UK) at $\lambda_{exc} = 535$ nm and $\lambda_{em} = 595$ nm with emission and excitation slits of 2.5 nm. Two kinds of formulation were used: PEG_{2000}-DPPE 4 mol %/Mal-PEG_{2000}-DSPE 1 mol %/cholesterol 25 mol %/DOPC 70 mol %, and Mal-PEG_{2000}-DSPE 5 mol %/cholesterol 25 mol %/DOPC 70 mol %.

Cell Targeting *in Vitro*. A solution of 12.5 μM sulforhodamine B in HBS at pH 7.4 was passively encapsulated into liposomes, followed by covalent coupling of Anx5. Nonencapsulated dyes and excess Anx5 were discarded by filtration on an Amicon Ultra filter with a 100 kDa molecular weight cutoff (Millipore, Billerica, USA).

Bcr/Abl^+ K562 leukemic cells (*44*) were grown in RPMI 1640 medium (Gibco, Cergy Pontoise, France), supplemented with 30% fetal calf serum and a mixture of antibiotics (100 units mL^{-1} penicillin, 0.1 mg mL^{-1} streptomycin; Gibco). Cells were grown at 37 °C in humidified atmosphere and 5% CO_2. At J_0, K562 cells were resuspended at 3×10^5 cells/mL^{-1}. Twenty-four hrs later (J_1), 2 μM STI-571 was added to induce apoptosis (*45*). Twenty-four hrs later (J_2), 30 $\mu g_{phospholipids}$ of liposomes at a concentration of 300 $\mu g_{phospholipids}$/mL were added and incubated for 1 h at 37 °C before separation of the cells from unbound vesicles by centrifugation for 5 min at 200 g at 25 °C, followed by microscopy observations. The vesicles' composition was DOPC/cholesterol/Mal-PEG_{2000}-DSPE/PEG_{2000}-DPPE 70/25/1/4.

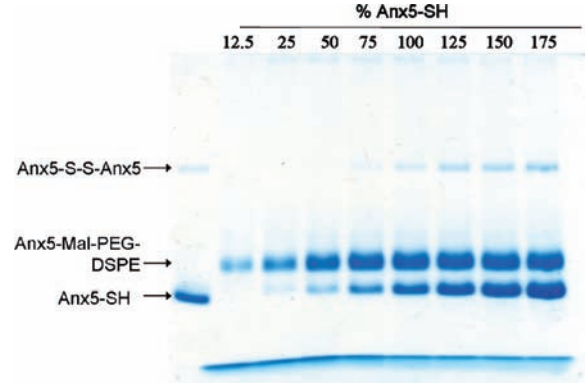

Figure 2. Quantitative analysis of the covalent coupling of Anx5-SH to liposomes containing Mal-PEG_{2000}-DSPE, by SDS-PAGE Fisrt lane: pure Anx5-SH. Following lanes: a fixed amount of liposomes, corresponding to 20 μg total phospholipid content, was incubated overnight with varying amounts of Anx5-SH. Prior to the SDS-PAGE analysis, a 5-fold excess of NEM was added to the samples to block unreacted thiol groups, and the mixture incubated for 4 h. The amounts of Anx5 are expressed both in micrograms and as the theoretical ratio of the (number of SH groups/number of accessible NEM groups) considering that half of the NEM groups are exposed on the outer lipid layer (from left to right: 0.825 μg to 11.55 μg or 12.5% to 175%).

Laser Scanning Confocal Microscopy. Live K562 cells (1.2×10^5 cells/cm^2) were mixed with liposomes containing sulforhodamine-B in 8-well Labteck plates (Nalc Nunc International). Image acquisition was performed with a Zeiss LSM510 laser scanning confocal microscope equipped with HeNe laser and with a Plan-Apochromat 63.0 × 1.40 oil objective lens (Carl Zeiss). Cells immerged in 0.5 mL of culture medium were excited with the 543 nm laser line (intensity set at 60% of maximal power) and their emission observed through a 560 nm long-pass filter. Photomultiplier detector voltage values (offset and gain) were adjusted on cells containing nonfluorescent samples for each set of experiments. The liposomes composition was DOPC/cholesterol/Mal-PEG_{2000}-DSPE/PEG_{2000}-DPPE 70/25/1/4.

RESULTS

Covalent Coupling of Anx5-SH to Liposomes. The covalent coupling of Anx5-SH proteins to liposomes containing lipid molecules exposing a maleimide group (referred to hereafter as Mal-liposomes) at their PEG distal end was achieved on preformed vesicles. The ligation reaction, represented schematically in Figure 1, was monitored by SDS-PAGE (Figure 2). For the protein alone, the major Anx5-SH band is accompanied by a minor band, of variable intensity, which corresponds to disulfide-bonded Anx5 dimers. After incubating Mal-liposomes with Anx5-SH, an additional band was observed, which is

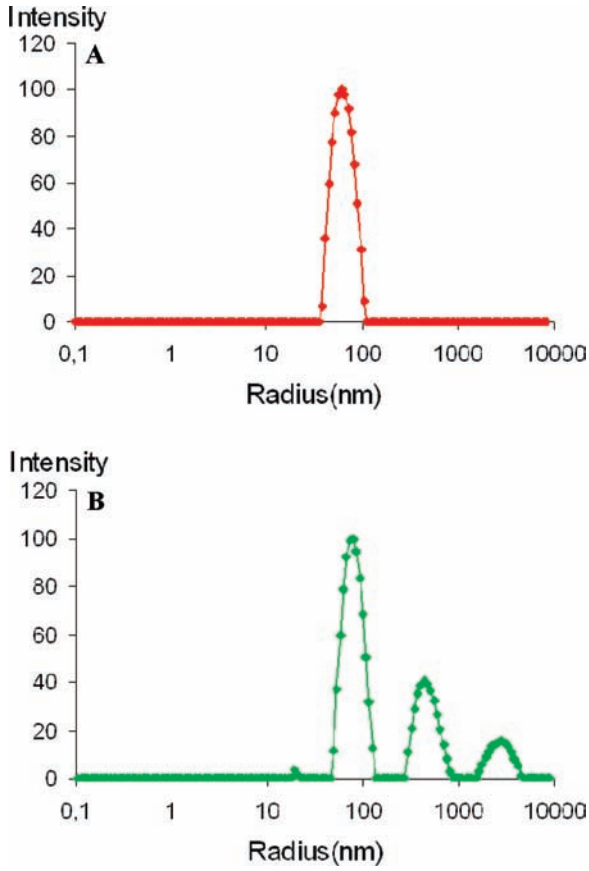

Figure 3. Dispersity of Anx5-functionalized liposome suspensions, by DLS size distribution profiles of Anx5-functionalized liposomes, determined by DLS at 90°. Densities of Anx5 per liposome: (A) 250; (B) 2000.

located slightly above the Anx5 monomer, as expected for covalent Anx5-PEG_{2000}-DSPE complexes. The molecular mass determined by MALDI-TOF mass spectrometry was 38 578 Da, in agreement with the theoretical value of 38 538 Da. Figure 2 shows that maximal coupling was obtained for a ratio between sulfhydryl groups and exposed maleimide groups close to a 1:1 stoichiometry. In these conditions, 80% of Anx5-SH was covalently coupled to Mal-liposomes. The fact that about 20% Anx5 remains uncoupled is attributed to partial hydrolysis of the maleimide group and to the spontaneous oxidation of Anx5-SH into Anx5 dimers, as indicated above. Complementary experiments indicated that maximal coupling was reached in 4 h at μM protein concentration and that the coupling efficiency was not influenced by the addition of nonmaleimidated PEG_{2000}-DPPE molecules (up to 4%) (data not shown).

Dispersity of Liposome Suspensions. The dispersity of liposome suspensions was monitored by DLS (Figure 3). Nonfunctionalized liposomes were uniform in size, with a mean radius of 60 ± 4 nm, as expected for 100 nm extruded liposomes (data not shown). We found that the liposome dispersity was highly dependent on the extent of Anx5 coupling. Up to 250 Anx5/vesicle, liposomes showed a homogeneous population with a radius of 62 ± 6 nm (Figure 3A). At higher values of Anx5/vesicle (≥250 Anx5/vesicle), aggregation occurred and precipitates were observed in the samples. The precipitates were found to be polydisperse with particle sizes ranging from hundreds of nanometers to several micrometers (Figure 3B).

Binding of Anx5-Functionalized Liposomes to Model Membranes, Monitored by QCM-D. In order to characterize the ability of Anx5-functionalized liposomes to bind to lipid membranes exposing PS molecules, we investigated the interaction of Anx5-liposomes with SLBs made of DOPC/DOPS (4:1, w:w), by the QCM-D method.

Figure 4A presents a reference experiment consisting of three steps: (1) the formation of a PS-containing SLB by adsorption and cooperative rupture of SUVs (arrow 1), followed by (2) the Ca^{2+}-dependent binding of Anx5 (arrow 2) and (3) the EGTA-induced desorption of Anx5 (arrow 3). The values obtained for the adsorbed mass and dissipation shift of a SLB, namely, 460 ng × cm^{-2} and ∼0 × 10^{-6}, respectively, and for a saturating Anx5 monolayer, namely, 275 ng × cm^{-2} and <0.1 × 10^{-6}, respectively, are in total agreement with reference values (*33, 41, 42*).

The injection of Anx5-functionalized liposomes over a PS-containing SLB was followed by a rapid and large increase of mass and dissipation, as illustrated in Figure 4B for liposomes grafted with a density of 8 Anx5/liposome. The values of adsorbed mass (2600 ng × cm^{-2}) and dissipation (43 × 10^{-6}) at saturation are characteristic of the extensive adsorption of flexible objects, as expected for liposomes linked via a PEG spacer (*35, 46*). The absence of liposome release upon rinsing with a Ca^{2+}-containing buffer (dashed arrow) indicates that functionalized liposomes are stably bound to the target SLB, in keeping with the known properties of Anx5 (*33*). As expected, vesicles were removed to a large extent from the SLB surface upon rinsing with an EGTA-containing buffer (arrow 3).

Control experiments showed that nonfunctionalized liposomes did not bind to PS-containing SLBs in the presence of Ca^{2+} and that Anx5-liposomes did not bind to PS-SLBs in the absence of Ca^{2+} (data not shown). Altogether, these results demonstrate that binding of Anx5-liposomes to PS-SLBs is mediated by Anx5 and reflects the specific formation of ternary Anx5-Ca^{2+}-PS complexes.

To assess the influence of Anx5 density on the efficiency of binding to PS-containing membranes, the mass of bound liposomes was monitored for various densities of Anx5-grafting (Figure 5). The binding of Anx5-liposomes increases with the density of Anx5 and reaches a maximum of about 3250 ng × cm^{-2} for a density of about 60 Anx5/liposome. Interestingly, liposome binding was observed at low Anx5 density, being detected down to an average density of 0.25 Anx5/liposome. The mass of adsorbed liposomes at an average density of 1 Anx5/liposome was 2045 ng × cm^{-2}. This indicates that one, or only a few, Anx5 molecules covalently linked to a liposome via a PEG spacer are sufficient to target a liposome to a membrane surface.

We used the system of Anx5-functionalized liposomes bound to a target membrane to address the following question: After formation of an elementary anchoring point to a target area, do lipid-bound ligands diffuse laterally within the liposome membrane and cluster at the target point? Anx5-functionalized liposomes containing various Anx5 densities were first immobilized on PS-containing SLBs, and then, the presence of Anx5 molecules accessible from the aqueous phase was assessed by measuring the Ca^{2+}-dependent binding of DOPC/DOPS (4:1) SUVs to SLB-bound liposomes (Figure 6). A signal of SUV binding was observed only when Anx5 density was higher than 125 Anx5/liposome. The absence of SUV binding at lower Anx5 density contrasts with the result presented before that one Anx5 is sufficient to immobilize one liposome on a SLB. We propose the following scenario: (i) as a first step, Anx5-functionalized liposomes bind to the PS-exposing SLB, which involves only one or a few Anx5 molecules; (ii) as the liposome membrane is fluid, Anx5-PEG-DSPE molecules diffuse laterally within the outer leaflet of the liposome; (iii) Anx5-PEG-DSPE molecules cluster at the target membrane; as a consequence, their density on the opposite liposome face is lower than the average density. SUV binding can only take place when Anx5 molecules are

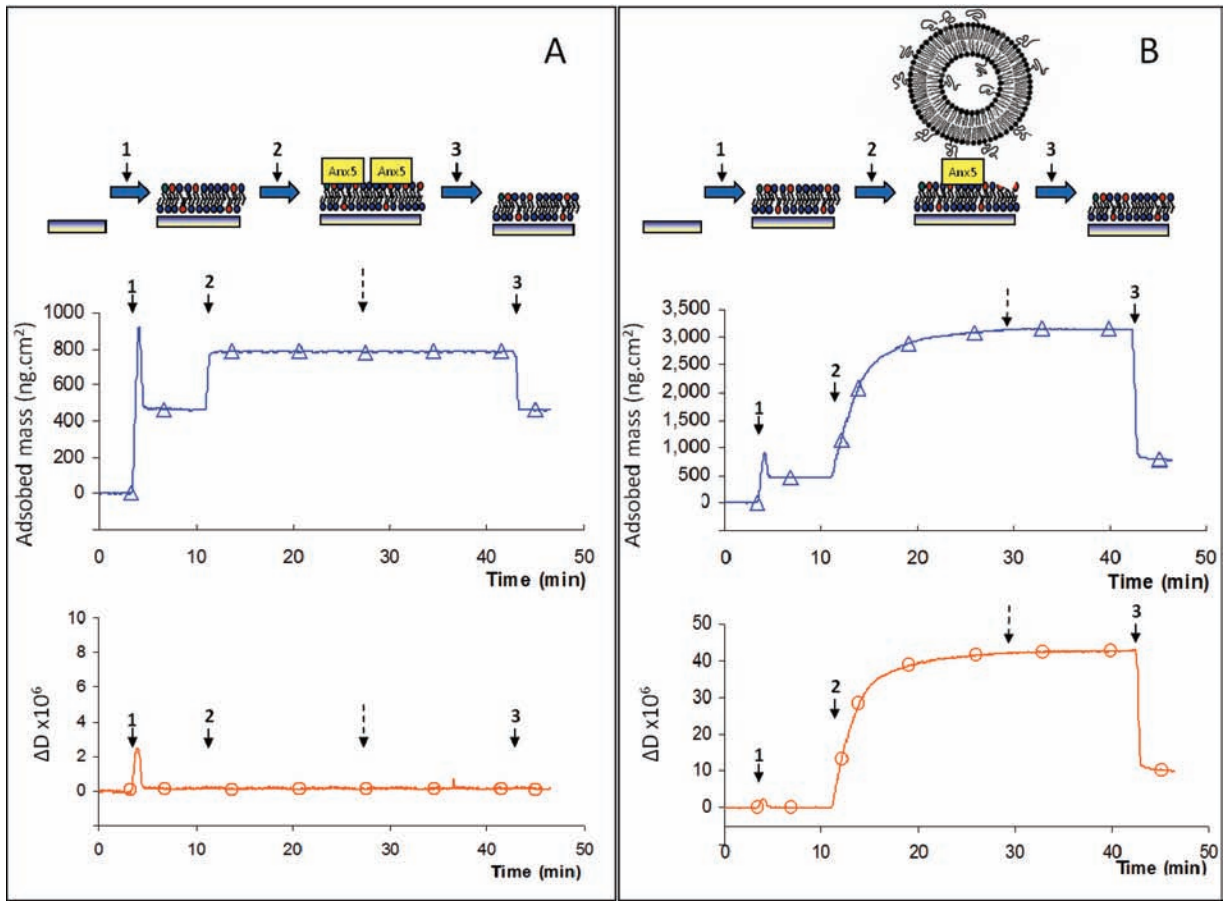

Figure 4. Binding of Anx5-functionalized liposomes to a solid supported lipid membrane, by QCM-D. Changes in adsorbed mass (Δ*m*, upper curves; open triangles) and dissipation (Δ*D*, lower curves; open circles) versus time upon successive injections of DOPC/DOPS (4:1, w:w) vesicles (arrow 1), Anx5 (arrow 2, A) or Anx5-functionalized liposomes (arrow 2, B), and EGTA-containing buffer (arrow 3). Rinses of the QCM-D chamber with a Ca^{2+}-containing buffer are indicated by a dashed arrow.

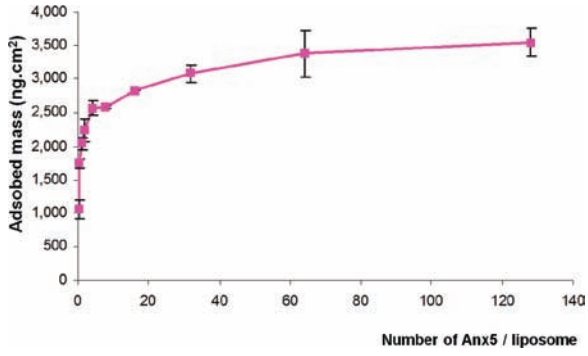

Figure 5. Influence of Anx5 density on the binding of Anx5-liposomes to DOPC/DOPS SLBs, by QCM-D. The adsorbed mass values correspond to plateau values from experiments similar to the one presented in Figure 4B.

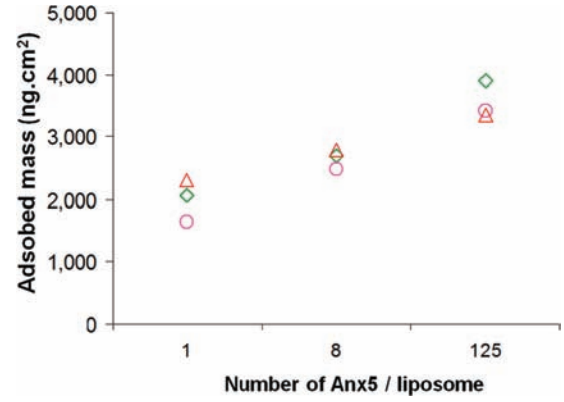

Figure 6. Influence of the PEG-layer density on binding of Anx5-functionalized liposomes to DOPC/DOPS SLBs. The adsorbed mass values correspond to plateau values from experiments similar to the one presented in Figure 4B. Open squares, 0% DPPE-PEG; open circles, 2% DPPE-PEG; open triangles, 4% DPPE-PEG.

present, in a sufficient number, at the liposome surface. This is achieved for an average threshold density of 125 Anx5/liposome.

We investigated also the influence of the PEG layer density on the targeting efficiency of Anx5-liposomes toward PS-exposing SLB. Figure 7 shows that the amount of PEG molecules present on the vesicle surface has a negligible influence on the amount of bound liposomes and thus on Anx5-mediated recognition of PS-SLBs.

Influence of Anx5 Conjugation on Liposome Membrane Stability. To investigate whether the conjugation of Anx5-SH affected the stability of liposomes, their membrane integrity was assessed by measuring the leakage of fluorescent dyes entrapped within the liposome interior.

First, we determined the self-quenching property of sulforhodamine-B solutions and found that fluorescence quenching takes place at dye concentration above 0.75 mM (Figure 8A). Sulforhodamine B was therefore encapsulated at 50 mM concentration. The leakage of fluorescent dyes was followed by measuring the fluorescence intensity of liposome solutions. Fluorescence intensity is expressed as a percentage of the maximal fluorescence intensity, which is obtained after solubilization of the liposomes with Triton X100, as shown in Figure 8B at 200 min.

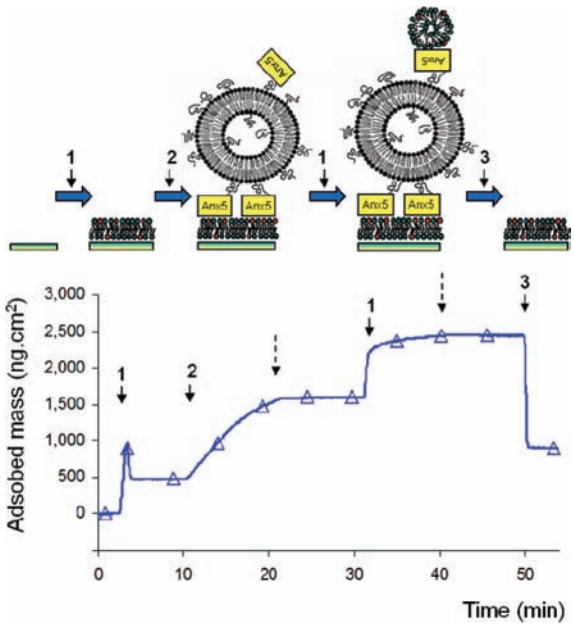

Figure 7. Binding of DOPC/DOPS vesicles to Anx5-functionalized liposomes anchored to a PS-SLB. Changes in adsorbed mass (Δm, open triangles) versus time, upon successive injections of DOPC/DOPS (4/1) vesicles (arrow 1), Anx5-functionalized vesicles (arrow 2), and EGTA-containing buffer (arrow 3). Rinses of the QCM-D chamber with a Ca^{2+}-containing buffer are indicated by dashed arrows.

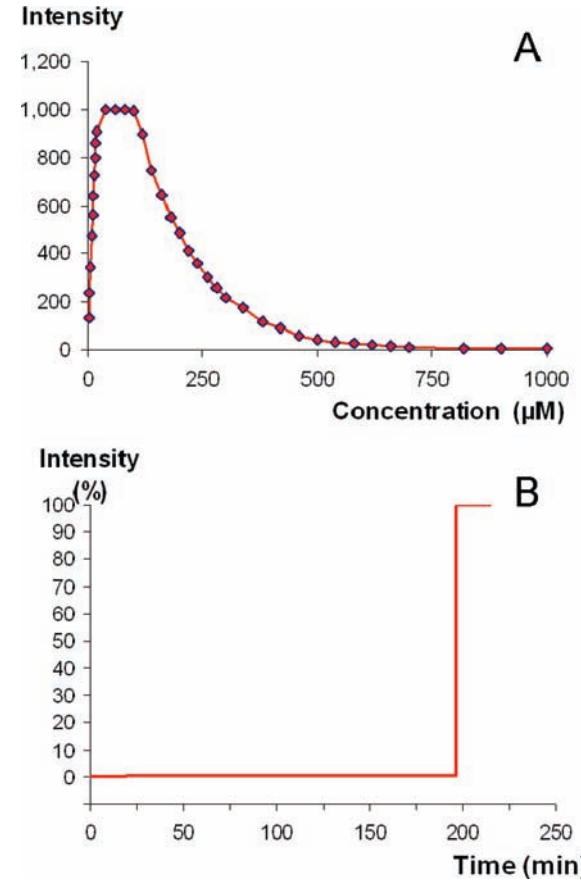

Figure 8. Analysis of the encapsulation properties of Anx5-functionalized liposomes, by fluorescence spectroscopy. (A) Self-quenching of sulforhodamine fluorescence. (B) Dequenching assay: leakage of entrapped sulforhodamine molecules was evaluated by measuring the increase of fluorescence intensity, in HBS at 23 °C. The liposomal formulation used for this experiment contained 1% Mal-PEG_{2000}-DSPE, and 80% of the accessible maleimide groups were conjugated to Anx5-SH. Complete release of fluorescent dyes from liposomes was induced by addition of 20% Triton X100. Extent of leakage was expressed as a percentage of the maximum fluorescence signal obtained after complete release.

No measurable leak of encapsulated dye was detected upon covalent coupling of Anx5-SH, nor after 10 h incubation of Anx5-liposomes in HBS buffer at 23 °C, for various formulations of Mal-liposomes (Figure 8B).

Targeting of Anx5-Grafted Liposomes to PS-Exposing Apoptotic Cells. The targeting of Anx5-grafted liposomes was then assessed on cellular systems, using Bcr/Abl^+ K562 leukemic cells (*44*) stimulated with 2 μM STI-571, an apoptosis-inducing compound in these cells (*45*). Apoptosis is accompanied by the exposure of PS molecules on the outer lipid layer of activated cells and derived cellular fragments (*16*). Anx5-grafted liposomes rendered fluorescent by encapsulation of 12.5 μM sulforhodamine B and fluorescence microscopy was used to follow the binding of liposomes to PS-exposing apoptotic cell membranes. About 30% of STI-stimulated K562 cells presented a homogeneous fluorescent labeling at their membrane surface (Figure 9A). Such a staining pattern is consistent with the fact that about 30% of the cells are induced in apoptosis. Control experiments showed that no binding of Anx5-grafted liposomes was observed on nonstimulated K562 cells (Figure 9D). Some parasite staining was visible, which is due to the presence of few necrotic cells or cell debris in cultured cells (Figure 9D).

DISCUSSION

Our aim is to develop long-circulating liposomal nanovectors functionalized with protein-based recognition elements for delivering imaging agents or drugs at specific cellular targets. The present study deals with the first step of this project, namely, the synthesis and characterization of liposomes functionalized with functional proteins and the analysis of their targeting efficiency. The choice of Anx5 as functionalizing agent had a twofold motivation. First, Anx5 binds with extremely high affinity to membranes exposing PS molecules, as evidenced by K_D values of 10^{-12} M or even lower, at millimolar Ca^{2+} concentrations (*47*), so that the targeting of Anx5-exposing vectors toward PS-exposing cells is expected to be highly efficient. Second, Anx5-liposomes have potential prognostic or therapeutic applications in *in vivo* imaging or drug delivery at sites of apoptosis in pathological association with atherosclerosis or ischemia (*21*, *48*, *49*).

This paper addresses the issues of covalent coupling of proteins to liposomes and of the correlation between the extent of functionalization and the efficiency of targeting.

The covalent grafting of Anx5-SH proteins to maleimide-exposing liposomes was found to be almost quantitative, as stoichiometric amounts of both species lead to an almost complete reaction in 4 h. In comparison, several studies have reported variable coupling yields (*50*−*53*), together with the need of excess lipid reactive groups to reach reasonable coupling rates. The high efficiency of the coupling reaction of Anx5-SH to Mal-PEG-liposomes is mainly due to the use of an engineered Anx5-SH with a unique and highly accessible sulfhydryl group (*32*), and to the high yield of the sulfhydryl-maleimide reaction. The efficiency of the coupling reaction of allowed us to analyze in detail the physicochemical and functional properties of Anx5-functionalized liposomes.

The size of Anx5-functionalized liposomes was investigated, because the size criterion is a determining parameter for the efficiency of drug delivery systems *in vivo*. The size of vesicles is known to affect both their circulation half-life and the volume available to load compounds. Large vectors would deliver high drug payload but would be retained by physical barriers playing

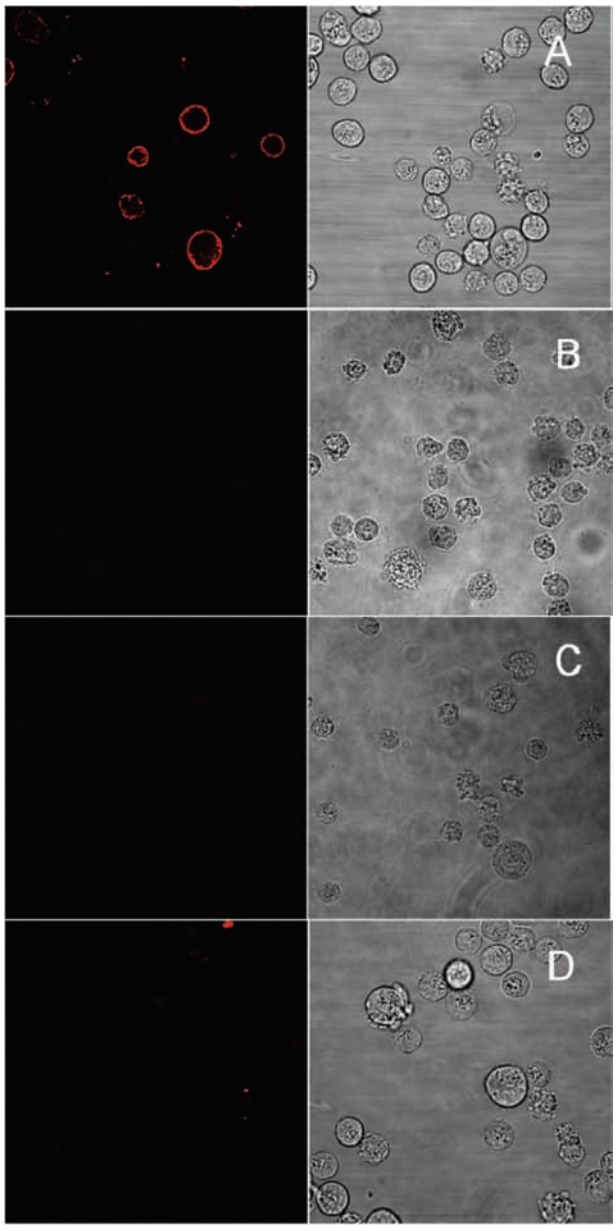

Figure 9. Interaction between K562 cells and liposomes, by laser scanning confocal microscopy. K562 cells, either untreated (B,D) or treated with 2 μM STI (A,C), were incubated for 1 h in a Ca^{2+}-containing RPMI 1640 medium with sulforhodamine-labeled liposomes, either nonfunctionalized (B,C) or Anx5-functionalized (A,D). A fluorescence image (left) and a bright-field image (right) of the same areas are presented for each condition. Image size: 145 μm × 145 μm. (A) untreated K562 cells incubated with nonfunctionalized liposomes; (B) STI-treated K562 cells incubated with nonfunctionalized liposomes; (C) untreated K562 cells incubated with Anx5-functionalized liposomes; (D) STI-treated K562 cells incubated with Anx5-functionalized liposomes.

the role of filters. On the other hand, small-sized liposomes would entrap a lower amount of drug and may present low circulation time, since below 70 nm, liposomes are removed from circulation by leaking out from blood vessels, mostly into liver cells (*1*). An optimal size accommodating both constraints of long circulation half-life and large volume for entrapping compounds is around 100 nm (*54*−*56*). We found that liposomal vesicles functionalized with low-to-moderate densities of Anx5, up to 250 Anx5/liposome, remain monodisperse and present a size, around 120 nm, in concordance with the use of 100 nm extrusion filters and compatible with their use *in vivo*. A density of 250 Anx5/liposome corresponds to coverage of about 1/4th of the liposome surface. We do not have a conclusive interpretation of the aggregation of Anx5-functionalized liposomes at higher Anx5 surface density, yet we speculate that this due to the change of the hydrophilic−hydrophobic balance of Mal-PEG-lipids after coupling of Anx5.

To determine the density of Anx5 providing optimal target binding efficiency, we used a model membrane system made of solid-supported lipid bilayers and measured the interaction of Anx5-functionalized liposomes to SLB in a systematic manner by QCM-D. SLBs with a PS content similar to PS-exposing apoptotic cells have been previously shown to be relevant models for studying the interaction of Anx5 or other PS-binding proteins (*33, 57*).The SLB/QCM-D assay is simple, fast, reproducible, and versatile and requires only a limited amount (few hundred micrograms) of functionalized liposomes.

Our results show that Anx5, once coupled to PEGylated lipids, maintains its ability to address liposomes toward PS-exposing membranes. As expected, the targeting efficiency depends on the number of Anx5-ligands per liposome. Increasing the Anx5 density increases both the total amount of bound liposomes at saturation (Figure 5) and the rate of liposome binding (data not shown). This result is in good agreement with studies carried out both *in vitro* (*52, 53, 58*−*60*) and *in vivo* (*61*). The value of about 60 Anx5/liposome corresponding to the plateau is in line with ligand densities of 30 to 80 ligands/liposome reported in other studies (*52, 53, 58*−*60*). Furthermore, as expected for ligands linked through a PEG spacer and regardless of the Anx5-SH density, the recognition efficiency is not impaired by the presence of a PEG coating, added to provide extended systemic circulation.

A major result of our study is that, statistically, one single Anx5 molecule is sufficient to target one liposome to a PS-exposing membrane. The estimation of the number of Anx5 is based on SDS-PAGE data and on a phospholipid determination assay (*37*). The main error in our calculations comes from the SDS-PAGE analysis, which we estimate to be less than a factor of 2. The fact that binding of liposomes is detected at a density of less than 1 Anx5 per liposome (namely, 0.25 Anx5/liposome) means that only 1/4th of the liposomes need to present one Anx5 in order for binding to be detected. This exceptional targeting efficiency must originate from the very high affinity of Anx5 for PS-membranes, the controlled orientation of Anx5, the use of a PEG spacer separating the Anx5 moiety from the liposome surface (*61, 62*), or a combination of these factors.

The combined results of DLS and QCM-D experiments allowed us to optimize the number of conjugated Anx5-SH/liposome. DLS measurements showed that less than 250 Anx5 molecules should be attached per liposome in order to avoid liposome aggregation. QCM-D experiments indicated that a density of 60 proteins/liposome ensures maximal targeting efficiency. As a consequence, for the rest of the study, we chose the following formulation: DOPC/cholesterol/Mal-PEG_{2000}-DSPE/PEG_{2000}-DPPE 70.75/25/0.25/4 mol % grafted with a density of 60 Anx5 per liposome. Liposomes with this formulation were also shown to be stable, retaining encapsulated fluorescent dyes.

The ability of Anx5-functionalized liposomes to deliver imaging agents to PS-exposing cells *in vitro* was further demonstrated by the specific labeling of PS-exposing apoptotic cells by Anx5-liposomes. Leukemic K562 cells were chosen for this study as a model system of PS-exposing cells. The staining pattern was limited to the periphery of the apoptotic cells, which indicates that Anx5-functionalized vesicles were not internalized. This result is in contrast with a recent study concluding to Anx5 internalization into apoptotic cells, which may be due to a difference in cells' properties (*25*).

As a side result of this study, the ability of Anx5-PEG-lipids to form ligand clusters at target sites was investigated. Anx5 is known to self-assemble into two-dimensional arrays of trimers on PS-containing membranes through two-dimensional diffusion in the membrane plane and protein−protein interaction (*30, 57*). We interpret the absence of binding of SUVs to SLB-bound Anx5-functionalized liposomes at Anx5 density lower than 125 Anx5 molecules/liposome as due to the clustering of Anx5-PEG-lipids at target sites.

In conclusion, these results demonstrate that Anx5-functionalized liposomes bind specifically to PS-exposing synthetic and natural membranes. These liposomal nanovectors are thus good candidates for delivering drugs or imaging agents to sites of apoptosis or thrombosis (*22*−*24, 63*).

ACKNOWLEDGMENT

We thank Nicolas Guidolin, Sébastien Lecommandoux, and Christophe Schatz for their help with DLS measurements. We are grateful to Emilie Bled for her experimental help and to Benoit Frisch for the gift of modified lipids at an early stage of this work. We thank Jean-Max Pasquet for introducing us to the K562 cells and his expert help and advices. We thank the members of the Consortium "Nanobioimaging" for helpful discussions. We acknowledge the financial support of the French National Research Agency programs ANR-Tecsan (grant 2006-15 "Nanobioimaging" to K.G.P.) and ANR-EMPB (grant 2007-021-01 "MP-NPAuA5 to AB) and the Conseil Régional d'Aquitaine to K.G.P. B.G. is recipient of a PhD fellowship from the ANR-Tecsan 2006-15.

LITERATURE CITED

(1) Lasic, D. D. (1993) *Liposome from Physic to application*, Vol. 575, Elsevier, Amsterdam.

(2) Torchilin, V. P. (2005) Recent advances with liposomes as pharmaceutical carriers. *Nat. Rev. Drug Discovery 4*, 145–60.

(3) Torchilin, V. P. (2006) Multifunctional nanocarriers. *Adv. Drug Delivery Rev. 58*, 1532–55.

(4) Pinto-Alphandary, H., Andremont, A., and Couvreur, P. (2000) Targeted delivery of antibiotics using liposomes and nanoparticles: research and applications. *Int. J. Antimicrob. Agents 13*, 155–68.

(5) Nishiyama, N., and Kataoka, K. (2009) Current status and prospects for development of nanodevices for advanced medicine. *Biotherapy 23*, 71–77.

(6) Allen, T. M., and Cullis, P. R. (2004) Drug delivery systems: entering the mainstream. *Science 303*, 1818–22.

(7) Puisieux, F., Fattal, E., Lahiani, M., Auger, J., Jouannet, P., Couvreur, P., and Delattre, J. (1994) Liposomes, an interesting tool to deliver a bioenergetic substrate (ATP). in vitro and in vivo studies. *J. Drug Targeting 2*, 443–8.

(8) Klibanov, A. L., Maruyama, K., Torchilin, V. P., and Huang, L. (1990) Amphipathic polyethyleneglycols effectively prolong the circulation time of liposomes. *FEBS Lett. 268*, 235–7.

(9) Allen, T. M. (2002) Ligand-targeted therapeutics in anticancer therapy. *Nat. Rev. Cancer 2*, 750–763.

(10) Beduneau, A., Saulnier, P., and Benoit, J. P. (2007) Active targeting of brain tumors using nanocarriers. *Biomaterials 28*, 4947–67.

(11) Schelte, P., Boeckler, C., Frisch, B., and Schuber, F. (2000) Differential reactivity of maleimide and bromoacetyl functions with thiols: application to the preparation of liposomal diepitope constructs. *Bioconjugate Chem. 11*, 118–23.

(12) Said Hassane, F., Frisch, B., and Schuber, F. (2006) Targeted liposomes: convenient coupling of ligands to preformed vesicles using "click chemistry". *Bioconjugate Chem. 17*, 849–54.

(13) Cheng, W. W., and Allen, T. M. (2008) Targeted delivery of anti-CD19 liposomal doxorubicin in B-cell lymphoma: a comparison of whole monoclonal antibody, Fab' fragments and single chain Fv. *J. Controlled Release 126*, 50–8.

(14) Gerke, V., Creutz, C. E., and Moss, S. E. (2005) Annexins: linking Ca2+ signalling to membrane dynamics. *Nat. Rev. Mol. Cell Biol. 6*, 449–61.

(15) Devaux, P. F. (1991) Static and dynamic lipid asymmetry in cell membranes. *Biochemistry 30*, 1163–73.

(16) Fadok, V. A., Voelker, D. R., Campbell, P. A., Cohen, J. J., Bratton, D. L., and Henson, P. M. (1992) Exposure of phosphatidylserine on the surface of apoptotic lymphocytes triggers specific recognition and removal by macrophages. *J. Immunol. 148*, 2207–16.

(17) Bevers, E. M., Comfurius, P., and Zwaal, R. F. (1983) Changes in membrane phospholipid distribution during platelet activation. *Biochim. Biophys. Acta 736*, 57–66.

(18) Dachary-Prigent, J., Freyssinet, J. M., Pasquet, J. M., Carron, J. C., and Nurden, A. T. (1993) Annexin V as a probe of aminophospholipid exposure and platelet membrane vesiculation: a flow cytometry study showing a role for free sulfhydryl groups. *Blood 81*, 2554–65.

(19) Koopman, G., Reutelingsperger, C. P., Kuijten, G. A., Keehnen, R. M., Pals, S. T., and van Oers, M. H. (1994) Annexin V for flow cytometric detection of phosphatidylserine expression on B cells undergoing apoptosis. *Blood 84*, 1415–20.

(20) van Tilborg, G. A., Mulder, W. J., Chin, P. T., Storm, G., Reutelingsperger, C. P., Nicolay, K., and Strijkers, G. J. (2006) Annexin A5-conjugated quantum dots with a paramagnetic lipidic coating for the multimodal detection of apoptotic cells. *Bioconjugate Chem. 17*, 865–8.

(21) Blankenberg, F. G., Katsikis, P. D., Tait, J. F., Davis, R. E., Naumovski, L., Ohtsuki, K., Kopiwoda, S., Abrams, M. J., Darkes, M., Robbins, R. C., Maecker, H. T., and Strauss, H. W. (1998) In vivo detection and imaging of phosphatidylserine expression during programmed cell death. *Proc. Natl. Acad. Sci. U.S.A. 95*, 6349–54.

(22) Narula, J., Acio, E. R., Narula, N., Samuels, L. E., Fyfe, B., Wood, D., Fitzpatrick, J. M., Raghunath, P. N., Tomaszewski, J. E., Kelly, C., Steinmetz, N., Green, A., Tait, J. F., Leppo, J., Blankenberg, F. G., Jain, D., and Strauss, H. W. (2001) Annexin-V imaging for noninvasive detection of cardiac allograft rejection. *Nat. Med. 7*, 1347–52.

(23) Thimister, P. W., Hofstra, L., Liem, I. H., Boersma, H. H., Kemerink, G., Reutelingsperger, C. P., and Heidendal, G. A. (2003) In vivo detection of cell death in the area at risk in acute myocardial infarction. *J. Nucl. Med. 44*, 391–6.

(24) Tanaka, K., Einaga, K., Tsuchiyama, H., Tait, J. F., and Fujikawa, K. (1996) Preparation and characterization of a disulfide-linked bioconjugate of annexin V with the B-chain of urokinase: an improved fibrinolytic agent targeted to phospholipid-containing thrombi. *Biochemistry 35*, 922–9.

(25) Kenis, H., van Genderen, H., Bennaghmouch, A., Rinia, H. A., Frederik, P., Narula, J., Hofstra, L., and Reutelingsperger, C. P. (2004) Cell surface-expressed phosphatidylserine and annexin A5 open a novel portal of cell entry. *J. Biol. Chem. 279*, 52623–9.

(26) Huber, R., Romisch, J., and Paques, E. P. (1990) The crystal and molecular structure of human annexin V, an anticoagulant protein that binds to calcium and membranes. *EMBO J. 9*, 3867–74.

(27) Concha, N. O., Head, J. F., Kaetzel, M. A., Dedman, J. R., and Seaton, B. A. (1993) Rat annexin V crystal structure: Ca(2+)-induced conformational changes. *Science 261*, 1321–4.

(28) Mosser, G., Ravanat, C., Freyssinet, J. M., and Brisson, A. (1991) Sub-domain structure of lipid-bound annexin-V resolved by electron image analysis. *J. Mol. Biol. 217*, 241–5.

(29) Voges, D., Berendes, R., Burger, A., Demange, P., Baumeister, W., and Huber, R. (1994) Three-dimensional structure of membrane-bound annexin V. A correlative electron microscopy-X-ray crystallography study. *J. Mol. Biol. 238*, 199–213.

(30) Oling, F., Bergsma-Schutter, W., and Brisson, A. (2001) Trimers, dimers of trimers, and trimers of trimers are common building blocks of annexin a5 two-dimensional crystals. *J. Struct. Biol. 133*, 55–63.
(31) Oling, F., Santos, J. S., Govorukhina, N., Mazeres-Dubut, C., Bergsma-Schutter, W., Oostergetel, G., Keegstra, W., Lambert, O., Lewit-Bentley, A., and Brisson, A. (2000) Structure of membrane-bound annexin A5 trimers: a hybrid cryo-EM - X-ray crystallography study. *J. Mol. Biol. 304*, 561–73.
(32) Bérat, R., Rémy-Zolghadry, M., Gounou, C., Manigand, C., Tan, S., Saltó, C., Arenas, E., Bordenave, L., and Brisson, A. (2007) Peptide-presenting two-dimensional protein matrix on supported lipid bilayers: an efficient platform for cell adhesion. *BioInterphases 2*, 165–172.
(33) Richter, R. P., Lai-Kee-Him, J., Tessier, B., Tessier, C., and Brisson, A. R. (2005) On the kinetics of adsorption and two-dimensional self-assembly of annexin A5 on supported lipid bilayers. *Biophys. J. 89*, 3372–85.
(34) Glasmastar, K., Larsson, C., Hook, F., and Kasemo, B. (2002) Protein adsorption on supported phospholipid bilayers. *J. Colloid Interface Sci. 246*, 40–7.
(35) Buzhynskyy, N., Golczak, M., Lai-Kee-Him, J., Lambert, O., Tessier, B., Gounou, C., Berat, R., Simon, A., Granier, T., Chevalier, J. M., Mazeres, S., Bandorowicz-Pikula, J., Pikula, S., and Brisson, A. R. (2009) Annexin-A6 presents two modes of association with phospholipid membranes. A combined QCM-D, AFM and cryo-TEM study. *J. Struct. Biol.* doi: 10 1016/j.jsb. 2009 03.007.
(36) Bangham, A. D., Standish, M. M., and Watkins, J. C. (1965) Diffusion of univalent ions across the lamellae of swollen phospholipids. *J. Mol. Biol. 13*, 238–52.
(37) Rouser, G., Fkeischer, S., and Yamamoto, A. (1970) Two dimensional then layer chromatographic separation of polar lipids and determination of phospholipids by phosphorus analysis of spots. *Lipids 5*, 494–6.
(38) Laemmli, U. K. (1970) Cleavage of structural proteins during the assembly of the head of bacteriophage T4. *Nature 227*, 680–5.
(39) Rodahl, M., Hook, F., Krozer, A., Brzezinski, P., and Kasemo, B. (1995) Quartz-crystal microbalance setup for frequency and q-factor measurements in gaseous and liquid environments. *Rev. Sci. Instrum. 66*, 3924–3930.
(40) Sauerbrey. (1959) Verwendung von schwingquarzen zur wägung dünner schichten und zur mikrowägung. *Z. Phys. A 155*, 206–222.
(41) Richter, R., Mukhopadhyay, A., and Brisson, A. (2003) Pathways of lipid vesicle deposition on solid surfaces: a combined QCM-D and AFM study. *Biophys. J. 85*, 3035–47.
(42) Keller, C. A., Glasmastar, K., Zhdanov, V. P., and Kasemo, B. (2000) Formation of supported membranes from vesicles. *Phys. Rev. Lett. 84*, 5443–6.
(43) Richter, R. P., Berat, R., and Brisson, A. R. (2006) Formation of solid-supported lipid bilayers: an integrated view. *Langmuir 22*, 3497–505.
(44) McGahon, A. J., Brown, D. G., Martin, S. J., Amarante-Mendes, G. P., Cotter, T. G., Cohen, G. M., and Green, D. R. (1997) Downregulation of Bcr-Abl in K562 cells restores susceptibility to apoptosis: characterization of the apoptotic death. *Cell Death Differ. 4*, 95–104.
(45) Gambacorti-Passerini, C., le Coutre, P., Mologni, L., Fanelli, M., Bertazzoli, C., Marchesi, E., Di Nicola, M., Biondi, A., Corneo, G. M., Belotti, D., Pogliani, E., and Lydon, N. B. (1997) Inhibition of the ABL kinase activity blocks the proliferation of BCR/ABL+ leukemic cells and induces apoptosis. *Blood Cells Mol. Dis. 23*, 380–94.
(46) Pignataro, B., Steinem, C., Galla, H. J., Fuchs, H., and Janshoff, A. (2000) Specific adhesion of vesicles monitored by scanning force microscopy and quartz crystal microbalance. *Biophys. J. 78*, 487–98.
(47) Tait, J. F., Gibson, D., and Fujikawa, K. (1989) Phospholipid binding properties of human placental anticoagulant protein-I, a member of the lipocortin family. *J. Biol. Chem. 264*, 7944–9.
(48) Tait, J. F., Engelhardt, S., Smith, C., and Fujikawa, K. (1995) Prourokinase-annexin V chimeras. Construction, expression, and characterization of recombinant proteins. *J. Biol. Chem. 270*, 21594–9.
(49) Zhao, Y., Kuge, Y., Zhao, S., Morita, K., Inubushi, M., Strauss, H. W., Blankenberg, F. G., and Tamaki, N. (2007) Comparison of ^{99m}Tc-annexin A5 with ^{18}F-FDG for the detection of atherosclerosis in ApoE−/−mice. *Eur. J. Nucl. Med. Mol. Imaging 34*, 1747–55.
(50) Allen, T. M., Brandeis, E., Hansen, C. B., Kao, G. Y., and Zalipsky, S. (1995) A new strategy for attachment of antibodies to sterically stabilized liposomes resulting in efficient targeting to cancer cells. *Biochim. Biophys. Acta 1237*, 99–108.
(51) Hansen, C. B., Kao, G. Y., Moase, E. H., Zalipsky, S., and Allen, T. M. (1995) Attachment of antibodies to sterically stabilized liposomes: evaluation, comparison and optimization of coupling procedures. *Biochim. Biophys. Acta 1239*, 133–44.
(52) Kirpotin, D., Park, J. W., Hong, K., Zalipsky, S., Li, W. L., Carter, P., Benz, C. C., and Papahadjopoulos, D. (1997) Sterically stabilized anti-HER2 immunoliposomes: design and targeting to human breast cancer cells in vitro. *Biochemistry 36*, 66–75.
(53) Mercadal, M., Domingo, J. C., Petriz, J., Garcia, J., and de Madariaga, M. A. (1999) A novel strategy affords high-yield coupling of antibody to extremities of liposomal surface-grafted PEG chains. *Biochim. Biophys. Acta 1418*, 232–8.
(54) Charrois, G. J., and Allen, T. M. (2003) Rate of biodistribution of STEALTH liposomes to tumor and skin: influence of liposome diameter and implications for toxicity and therapeutic activity. *Biochim. Biophys. Acta 1609*, 102–8.
(55) Awasthi, V. D., Garcia, D., Goins, B. A., and Phillips, W. T. (2003) Circulation and biodistribution profiles of long-circulating PEG-liposomes of various sizes in rabbits. *Int. J. Pharm. 253*, 121–32.
(56) Kawahara, K., Sekiguchi, A., Kiyoki, E., Ueda, T., Shimamura, K., Kurosaki, Y., Miyaoka, S., Okabe, H., Miyajima, M., and Kimura, J. (2003) Effect of TRX-liposomes size on their prolonged circulation in rats. *Chem. Pharm. Bull. (Tokyo) 51*, 336–8.
(57) Reviakine, I. I., Bergsma-Schutter, W., and Brisson, A. (1998) Growth of protein 2-D crystals on supported planar lipid bilayers imaged in situ by AFM. *J. Struct. Biol. 121*, 356–61.
(58) Mercadal, M., Carrion, C., Domingo, J. C., Petriz, J., Garcia, J., and de Madariaga, M. A. (1998) Preparation of immunoliposomes directed against CD34 antigen as target. *Biochim. Biophys. Acta 1371*, 17–23.
(59) Mercadal, M., Domingo, J. C., Petriz, J., Garcia, J., and de Madariaga, M. A. (2000) Preparation of immunoliposomes bearing poly(ethylene glycol)-coupled monoclonal antibody linked via a cleavable disulfide bond for ex vivo applications. *Biochim. Biophys. Acta 1509*, 299–310.
(60) Nielsen, U. B., Kirpotin, D. B., Pickering, E. M., Hong, K., Park, J. W., Refaat Shalaby, M., Shao, Y., Benz, C. C., and Marks, J. D. (2002) Therapeutic efficacy of anti-ErbB2 immunoliposomes targeted by a phage antibody selected for cellular endocytosis. *Biochim. Biophys. Acta 1591*, 109–118.
(61) Maruyama, K., Takizawa, T., Yuda, T., Kennel, S. J., Huang, L., and Iwatsuru, M. (1995) Targetability of novel immunoliposomes modified with amphipathic poly(ethylene glycol)s conjugated at their distal terminals to monoclonal antibodies. *Biochim. Biophys. Acta 1234*, 74–80.
(62) Blume, G., Cevc, G., Crommelin, M. D., Bakker-Woudenberg, I. A., Kluft, C., and Storm, G. (1993) Specific targeting with poly(ethylene glycol)-modified liposomes: coupling of homing devices to the ends of the polymeric chains combines effective target binding with long circulation times. *Biochim. Biophys. Acta 1149*, 180–4.
(63) van Tilborg, G. A., Mulder, W. J., Deckers, N., Storm, G., Reutelingsperger, C. P., Strijkers, G. J., and Nicolay, K. (2006) Annexin A5-functionalized bimodal lipid-based contrast agents for the detection of apoptosis. *Bioconjugate Chem. 17*, 741–9.

BC9002579

Synthesis and Biological Evaluation of Clicked Curcumin and Clicked KLVFFA Conjugates as Inhibitors of β-Amyloid Fibril Formation

Myriam Ouberai, Pascal Dumy, Sabine Chierici,* and Julian Garcia*

Département de Chimie Moléculaire (DCM), UMR 5250, ICMG-FR, Université Joseph Fourier, BP 53, 38041 Grenoble Cedex 9, France. Received June 29, 2009; Revised Manuscript Received August 11, 2009

Abnormal aggregation of β-amyloid (Aβ) peptides into toxic aggregates has been identified as a key event in Alzheimer's disease (AD). Inhibition of this process has thus emerged as a major therapeutic track against AD. The present work describes the synthesis and *in vitro* study of a novel class of inhibitors. Two copies of Aβ-binding motifs (either curcumin or the KLVFFA peptide) are clicked via copper(I)-mediated azide−alkyne cycloaddition on a constrained cyclopeptide scaffold designed to interfere with Aβ aggregation. Our conjugates strongly inhibit amyloid fibril formation from $A\beta_{40}$ at low inhibitor to Aβ molar ratios (e.g., 0.02:1 in the case of the KLVFFA conjugate) at which Aβ-binding motifs alone are fully inactive (thioflavin T assays and atomic force microscopy observation). This work highlights the value of combining Aβ-recognition domains with a steric hindrance-inducing scaffold for preventing amyloid fibril formation.

INTRODUCTION

In Alzheimer's disease (AD), abnormal aggregation of β-amyloid (Aβ) peptides into toxic aggregates is one of the key pathogenic events (*1*−*4*). However, the exact nature of the toxic Aβ species is still a topic of debate. Insoluble Aβ fibrils with characteristic β-sheet structures as well as soluble protofibrils and other intermediates on the pathway toward mature fibrils have each been shown to induce neurotoxicity in cell culture (*2, 5*−*8*). Nevertheless, the current consensus states that Aβ has to be in an aggregated form in order to be toxic. For this reason, major efforts have been achieved to find molecules that can interfere with Aβ aggregation. The identification of the residues 16−20, KLVFF, of the β-amyloid peptide as a self-recognition element during Aβ assembly (*9*) led to the development of a series of short peptides incorporating this $A\beta_{16-20}$ region, which bind to Aβ and prevent its autoassociation (*10*). Then by modifying the peptides containing the Aβ-recognition motif with proline residues, N-methylated, D-, or charged amino acids, or organic reagents, other β-sheet breaker peptides have been identified and showed, in some cases, an activity on mouse models (*11*−*17*). Small organic molecules (*18*−*22*) have also been reported as inhibitors of Aβ peptide aggregation *in vitro*. Most of them present aromatic parts interfering, through hydrophobic interactions, with hydrophobic and aromatic residues of the misfolding Aβ peptides that are critical to fibril formation (*23, 24*).

However, a majority of the above inhibitors showed only a moderate inhibition efficiency attributed to their poor ability to interact over the large interface of interaction of Aβ peptides during the aggregation process or to interact simultaneously with the multiple binding surfaces (*18, 25*). High levels of plasticity of Aβ to accommodate to small molecules may also be involved. Novel classes of molecules were thus designed to yield more potent AD inhibitors. For instance, high Aβ-affinity compounds featuring multiple copies of an Aβ-recognition domain were developed in the aim to interact simultaneously with several binding sites of Aβ or several Aβ peptides. Several copies of KLVFF or its retro-inverso analogue, ffvlk, have been thus displayed onto a poly(ethylene glycol) (PEG) (*26*) or a dendrimer-based scaffold (*27*). These compounds showed stronger ability to block fibril formation *in vitro* than the corresponding monomers. An alternative approach consists in linking an Aβ-binding domain and a bulky element, designed to block Aβ's surface. The efficiency *in vitro* of the cholyl-LVFFA, reported a few years ago, can be attributed to the steric effects of the cholyl group that prevent the interaction with other Aβ peptides (*13*). More recently, this approach was highlighted by an original study. A high Aβ-affinity compound (Congo Red) was covalently attached to a synthetic ligand of the FK-binding protein (*25*). The recruitment of the bulky protein via its ligand prevents any interaction within a large surface and blocks aggregation. This system has shown an increased efficiency as compared to Congo Red alone and is one of the most efficient inhibitors of fibril formation reported so far.

In a previous work (*28*), we contributed to the field of AD inhibitors by investigating a tetramer of acridine on a cyclopeptide scaffold. Despite its moderate inhibition activity, the latter still contrasted strongly with the nonactive monomer. These results encouraged us to prepare more potent assemblies by displaying higher Aβ-affinity ligands on this scaffold, which is developed in our group (*29*). We chose the amyloid peptide mimick KLVFFA (*13*) and curcumin (*23, 30*) as the well-known ligand of Aβ and inhibitor of amyloid aggregation (Figure 1). Our new inhibitors thus feature two copies of the KLVFFA peptide or two copies of the curcumin molecule on the upper face of the cyclopeptide scaffold and four arginine residues on the lower face (Figure 1, compounds **9** and **10** respectively). By presenting two copies of KLVFFA or of the polyphenolic compound onto the cyclopeptide, we aim to associate a dimeric Aβ-binding region with the steric hindrance-inducing effect of the scaffold. Arginine residues were chosen first to improve the solubility of the hydrophobic ligands, but they may interfere with Aβ aggregation. The effect of arginine on aggregation and protein folding has been reported in the literature (*31, 32*). Even if the mechanism by which arginine affects aggregation and protein folding is not well understood, guanidinium groups of our conjugates may act as aggregation disrupting elements.

* To whom correspondence should be addressed. Phone: +33 4 76 51 44 31. Fax: +33 4 76 51 49 46. E-mail: sabine.chierici@ujf-grenoble.fr (S.C.); julian.garcia@ujf-grenoble.fr (J.G.).

10.1021/bc900281b CCC: $40.75 © 2009 American Chemical Society
Published on Web 10/12/2009

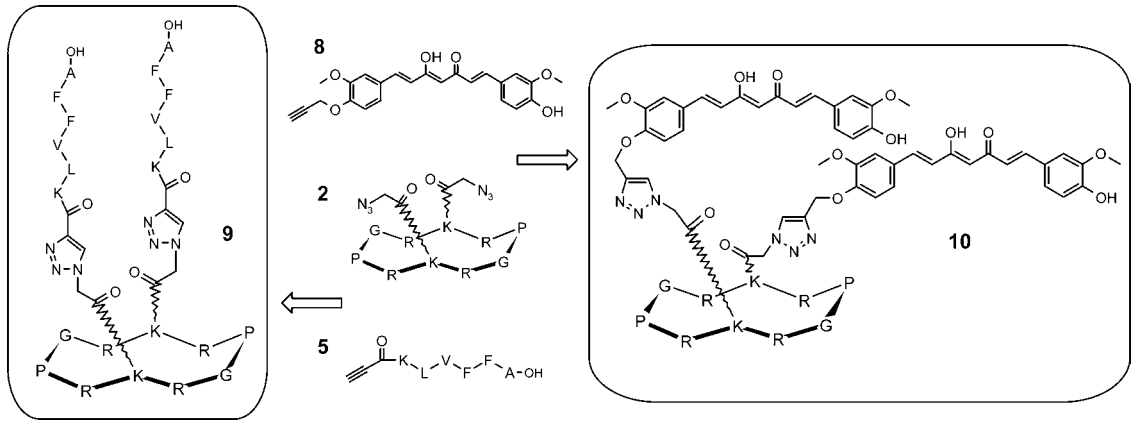

Figure 1. Design of conjugates **9** and **10**.

Scheme 1. Synthesis of the Azide-Functionalized Cyclodecapeptide 2 and Control Cyclodecapeptide 3[a]

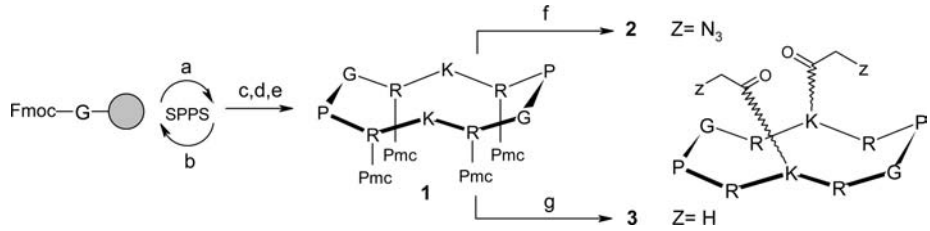

[a] (a) Piperidine/DMF (1:4); (b) Fmoc-Xaa-OH (2 equiv), PyBOP (2 equiv), DIPEA (3−4 equiv), DMF; (c) TFA/CH_2Cl_2 (1:99), 10 min (three times); (d) PyBOP (1.2 equiv), DIPEA (3−4 equiv), DMF (0.5 10^{-3} M), 1 h; (e) Hydrazine/DMF (2:98), 2 h, 76% from the linear form of **1**; (f) (i) Azidoacetic acid (2.2 equiv), PyBOP (2.2 equiv), DIPEA, DMF (10^{-2} M), 2 h; (ii) TFA/H_2O (9:1), 2 h, 18% for **2** (2 steps); (g) (i) Ac_2O/Pyridine/DMF (1:2:7), 30 min; (ii) TFA/H_2O (9:1), 2 h, 64% for **3** (2 steps).

To assemble the Aβ-binding motifs (curcumin or KLVFFA) onto the cyclopeptide, we favored the copper(I)-mediated alkyne−azide cycloaddition (CuAAC) over the oxime bond ligation method used in our previous work (*28*). Despite its high chemoselectivity, oximation occurs in aqueous salt medium (sodium phosphate buffer) impairing the ligation efficiency of hydrophobic molecules. In contrast, the high versatility of CuAAC in terms of solvents and conditions (*33*−*35*), makes it more suitable for the synthesis of our conjugates.

In the present work, we describe the synthesis of conjugates **9** and **10** using the so-called click chemistry as well as their evaluation as inhibitors of $A\beta_{40}$ fibril formation using thioflavin T (ThT) assays and atomic force microscopy (AFM).

MATERIALS AND METHODS

All protected peptides were prepared by solid phase synthesis using Fmoc/*t*Bu strategy on an Advanced ChemTech 348 Ω synthesizer. The alkyne curcumin derivative **8** was prepared as reported in the literature (*36*).

RP-HPLC analyses and purifications were performed on Waters equipment consisting of a Waters 600E controller, a Waters 2487 Dual absorbance detector, and a Waters In-Line Degasser. The analytical column (Nucleosil C18, particles size 3 μm, pore size 120 Å, 30 × 4 mm^2) was operated at 1.3 $mL \cdot min^{-1}$ using linear A−B gradients in 15 min run time (solvent A, H_2O containing 0.1% trifluoroacetic acid (TFA); solvent B, CH_3CN containing 9.9% H_2O and 0.1% TFA). For reversed-phase high performance liquid chromatography (RP-HPLC) purifications, three columns were used in 30 min run time with linear A−B gradients: a preparative Delta-Pak column (C18 particles size 15 μm, pore size 300 Å, 200 × 25 mm^2) at 22 $mL \cdot min^{-1}$; a semipreparative Nucleosil 100-7 column (C18 particles size 7 μm, pore size 100 Å, 250 × 10 mm^2) at 5 $mL \cdot min^{-1}$; and a semipreparative Discovery BIO Wide Pore column (C5 particles size 10 μm, pore size 300 Å, 250 × 10 mm^2) at 5 $mL \cdot min^{-1}$. UV monitoring was performed most of the time at 214 and 250 nm. Mass spectra were obtained by electrospray ionization (ESI-MS) on a VG Platform II in positive mode.

Synthesis of Cyclopeptide 2 and Control Cyclopeptide 3 (Scheme 1). The linear peptide R(Pmc)-K(Dde)-R(Pmc)-P-G-R(Pmc)-K(Dde)-R(Pmc)-P-G was built up automatically on Fmoc-Gly-Sasrin resin (500 mg, 0.69 $mmol \cdot g^{-1}$) and cyclized (415 mg, $1.59 \cdot 10^{-4}$ mol) in dimethylformamide (DMF) (0.5 $mmol \cdot L^{-1}$) under high dilution using (Benzotriazol-1-yloxy)-tripyrrolidinophosphonium hexafluorophosphate (PyBOP) (100 mg, $1.91 \cdot 10^{-4}$ mol) and N-ethyldiisopropylamine (DIPEA) to adjust the pH to 8−9. The white solid powder obtained after precipitation in diethyl ether was solubilized in a solution of 2% of hydrazine in DMF to remove Dde protecting groups. The cyclopeptidic intermediate **1** (272 mg, $1.21 \cdot 10^{-4}$ mol) was then obtained by precipitation in diethyl ether (76% yield from the linear peptide). HPLC t_R = 10.1 min. ESI-MS calcd for $C_{106}H_{164}N_{24}O_{22}S_4$ 2253.1; found, 2253.6.

To access compound **2**, azidoacetic acid (*37*) was first coupled (18 mg, $1.78 \cdot 10^{-4}$ mol) on the lysine side chains of **1** (182 mg, $8.07 \cdot 10^{-5}$ mol). The reaction was performed during 2 h at r.t. in DMF (0.01 $mol \cdot L^{-1}$), with PyBOP (93 mg, $1.78 \cdot 10^{-4}$ mol) and DIPEA (pH to 8−9). Then Pmc protecting groups were removed using a solution of TFA/H_2O (9:1) (0.01 M). After 2 h, the solvent was evaporated, and the crude compound **2** was obtained by precipitation in diethyl ether (74 mg, 51% yield). It was purified by RP-HPLC (C18 Nucleosil column, 5−100% B in 30 min) to get pure compound **2** (26 mg, $1.43 \cdot 10^{-5}$ mol) as a white powder with 18% yield. HPLC t_R = 6.5 min. ESI-MS calcd for $C_{54}H_{94}N_{30}O_{12}$ 1354.7; found, 1354.4.

To get the control cyclopeptide **3**, precursor **1** (20 mg, $8.87 \cdot 10^{-6}$ mol) was first acetylated during 30 min in a mixture (0.01 $mol \cdot L^{-1}$) of Ac_2O/Pyridine/DMF (1:2:7). After evaporation of solvents, the acetylated intermediate was precipitated in

Scheme 2. Synthesis of the Alkyne-Functionalized Aβ_{16-21} Intermediate 5 and Control Aβ_{16-21} Peptide 7[a]

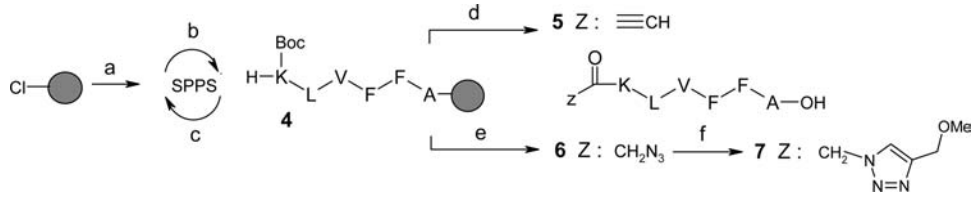

[a] (a) (i) Fmoc-Ala-OH (1.2 equiv), DIPEA (4 equiv), DCM, 30 min; (ii) wash 3 times with DCM/MeOH/DIPEA (17:2:1); (b) Piperidine/DMF (1:4); (c) Fmoc-Xaa-OH (2 equiv), PyBOP (2 equiv), DIPEA (3−4 equiv), DMF; (d) (i) Propiolic acid (3 equiv), PyBOP (3 equiv), DIPEA (3−4 equiv), DMF, 30 min (twice); (ii) TFA/H_2O (9:1), 10 min (three times), 21% for **5** from the resin; (e)(i) Azidoacetic acid (5 equiv), PyBOP (5 equiv), DIPEA (3−4 equiv), DMF, 30 min (twice); (ii) TFA/H_2O (9:1), 10 min (three times), 25% for **6** from the resin; (f) 3-methoxy-1-propyne (1.1 equiv), $CuSO_4$ (0.5 equiv), sodium ascorbate (1 equiv), H_2O/*t*BuOH/TFE (1:15:30), 40 °C, 20 h, 20% for **7**.

Table 1. Optimization of the Triazole-Forming Reaction

entry	product[a]	copper source	additive	solvent	temp (°C)	time	conversion rate[b]
1	**9**	$CuSO_4$ 0.1 equiv	NaAsc 0.2 equiv	*t*BuOH/H_2O 1:1	60 °C	20 h	gel
2		CuI 0.5 equiv	2,6-lutidine 2 equiv DIPEA 2 equiv	DMF	60 °C	24 h 76 h	0% 11%
3		Cu turning		*t*BuOH/H_2O/TFE 1:1:1	60 °C	4 h	16% gel
4		$CuSO_4$ 0.02 equiv	NaAsc 0.05 equiv	*t*BuOH/H_2O/TFE 1:1:1	MW	20 min	quantitative
5	**10**	$CuSO_4$ 0.1 equiv	NaAsc 0.1 equiv	*t*BuOH/H_2O/TFE 1:1:1	60 °C	24 h	5% precipitation
6		Cu turning		*t*BuOH/H_2O/TFE 1:1:2	60 °C	24 h	precipitation
7		Cu turning	NaAsc 0.1 equiv	DMSO/H_2O/TFE 2:1:1	60 °C	7 h	quantitative

[a] Products were identified by ESI-MS analysis. [b] Conversion rates were determined by HPLC.

diethyl ether. The Pmc protecting groups were then removed by adding a solution of TFA/H_2O (9:1) (0.01 mol·L^{-1}). After 2 h, the mixture was concentrated under reduced pressure, and the crude product was precipitated in diethyl ether. Its purification by RP-HPLC (C18 Delta-Pak column, 5−100% B in 30 min) afforded pure compound **3** (9.8 mg, $5.67\cdot10^{-6}$ mol) as a white powder (64% yield). HPLC $t_R = 5.4$ min. ESI-MS calcd for $C_{54}H_{96}N_{24}O_{12}$ 1272.7; found, 1272.7.

Synthesis of Alkyne Aβ_{16-21} Peptide 5 and Control Aβ_{16-21} Peptide 7 (Scheme 2). The peptide precursor K(Boc)-L-V-F-F-A **4** was automatically assembled on 2-chlorotrityl-chloride resin (450 mg, 1.4 mmol·g^{-1}). The coupling of propiolic acid (120 μL, $1.89\cdot10^{-3}$ mol) on the *N*-terminal position was then performed with PyBOP (982 mg, $1.89\cdot10^{-3}$ mol) in 10 mL of DMF adjusted with DIPEA to pH 8−9. The mixture was stirred for 30 min at r.t. The coupling reaction was realized once again. After removing the Boc protecting group and releasing from the resin with a solution of TFA/H_2O (9:1), **5** (115 mg, $1.29\cdot10^{-4}$ mol) was obtained with 21% overall yield after purification by RP-HPLC (C18 Nucleosil column, 5−100% B in 30 min). HPLC $t_R = 9.3$ min. ESI-MS calcd for $C_{41}H_{57}N_7O_8$ 775.4; found, 775.4.

The Aβ_{16-21} peptide derivative **7** (Scheme 2) was also prepared from **4**. The supported peptide **4** (135 mg, 1.4 mmol·g^{-1}) was swirled in 10 mL of DMF adjusted with DIPEA to pH 8−9. Azidoacetic acid (189 mg, $9.30\cdot10^{-4}$ mol) and PyBOP (483 mg, $9.30\cdot10^{-4}$ mol) were added, and the mixture was stirred for 30 min at r.t. This procedure was realized once more. After removing the Boc protecting group and releasing from the resin with a solution of TFA/H_2O (9:1), the azide peptide **6** (42 mg, $4.56\cdot10^{-5}$ mol) was obtained with 25% overall yield after purification by RP-HPLC (C18 Nucleosil column, 5−100% B in 30 min). It (5 mg, $5.43\cdot10^{-6}$ mol) was then condensed at 40 °C for 20 h with 3-methoxy-1-propyne (522 μL, $6.18\cdot10^{-6}$ mol) in 510 μL of TFE/*t*BuOH/H_2O (30:15:1) in the presence of (+)-sodium L-ascorbate (55 μL, 0.1 M, $5.50\cdot10^{-6}$ mol) and $CuSO_4$ (27 μL, 0.1 M, $2.70\cdot10^{-6}$ mol). Compound **7** was obtained with 20% yield (1.1 mg, $1.11\cdot10^{-6}$ mol) after purification by RP-HPLC (C18 Nucleosil column, 10−100% B in 30 min). HPLC $t_R = 8.4$ min. ESI-MS calcd for $C_{44}H_{64}N_{10}O_9$ 876.4; found, 876.4.

Optimization of Triazole Linkage. All of the assays of the cycloaddition reaction described in Table 1 were carried out in 110 μL of solvents with $1.1\cdot10^{-6}$ mol of the azide cyclodecapeptide **2** (1.99 mg) and $2.42\cdot10^{-6}$ mol of the complementary alkyne compounds, peptide **5** (2.15 mg) or curcumin derivative **8** (0.98 mg). Conversion into final material was determined by HPLC.

Synthesis of Compound 9. Peptide **5** (7.9 mg, $8.88\cdot10^{-6}$ mol) and cyclopeptide **2** (7.3 mg, $4.03\cdot10^{-6}$ mol) were dissolved in 750 μL of trifluoroethanol (TFE)/H_2O/*t*BuOH (1:1:1). (+)-Sodium L-ascorbate (22 μL, 0.01 M, $2.20\cdot10^{-7}$ mol) and $CuSO_4$ (11 μL, 0.01 M, $1.10\cdot10^{-7}$ mol) were added, and the mixture was heated with a domestic microwave for 20 min. The product was purified by RP-HPLC (C5 column, 25−100% B in 30 min) to afford pure compound **9** (5.6 mg, $1.56\cdot10^{-6}$ mol) in 39% yield. HPLC $t_R = 7.7$ min. ESI-MS calcd for $C_{136}H_{208}N_{44}O_{28}$ 2907.4; found, 2906.9.

Synthesis of Compound 10. Curcumin derivative **8** (1.8 mg, $4.42\cdot10^{-6}$ mol) and cyclopeptide **2** (3.9 mg, $2.15\cdot10^{-6}$ mol) were dissolved in 200 μL of TFE/H_2O/dimethyl sulfoxide (DMSO) (1:1:2). (+)-Sodium L-ascorbate (20 μL, 0.01 M, $2.15\cdot10^{-7}$ mol) and Cu turning (20 mg) were added, and the mixture was heated at 60 °C for 7 h. The product was purified by RP-HPLC (C5 column, 25−100% B in 30 min) to afford pure compound **10** (1.7 mg, $6.48\cdot10^{-7}$ mol) in 30% yield. HPLC $t_R = 10.4$ min. ESI-MS calcd for $C_{102}H_{138}N_{30}O_{24}$ 2167.0; found, 2166.9.

Preparation of Aβ_{40} Peptide Stock Solution. Synthetic Aβ_{40} was prepared as previously described (*38*). For aggregation assays, a stock solution of Aβ_{40} was prepared. Then 2.7 mg of Aβ_{40} was dissolved in 200 μL of 1,1,1,3,3,3-hexafluoro-2-propanol to disassemble preformed aggregates. After lyophiliza-

tion, 1 mL of pure water was added to the peptide, and the solution was centrifuged at 12000*g* to remove eventual aggregates. The stock solution was divided into portions and stored at −20 °C until use. The stock concentration of Aβ_{40} was 500 μM.

Preparation of Compound Stock Solutions. Compounds **3**, **7**, **9**, and **10**, and curcumin were dissolved in DMSO/H_2O (1:1). Stock solutions of 5 to 20 mM were first prepared and then diluted with DMSO/H_2O (1:1) to get solutions of 500 μM to 0.5 μM. Final concentrations of DMSO in inhibition studies were less than 2%.

Fibril Formation Measurement of Aβ_{40}. Aggregation of Aβ_{40} was performed in 96-well black polypropylene microplates (Greiner). The aggregation buffer consists of 100 mM sodium phosphate buffer at pH 7.4 to which 200 mM sodium chloride was added. To each well (final volume = 100 μL), an aliquot of the Aβ_{40} peptide stock solution (10 μL) was mixed into 50 μL of the aggregation buffer in the presence of 10 μL of a 100 μM ThT solution, giving a final concentration of 50 μM in Aβ_{40} and 10 μM in thioflavin T (ThT). Then, aliquots of 2 μL of compounds **3**, **7**, **9**, and **10** and curcumin were added along with 28 μL of water. Microplates were sealed with a plastic sheet and incubated in a Molecular Devices Spectra MAX Gemini XS microplate reader at 37 °C.

Fibril Formation Measurement of Aβ_{40} with Preformed Fibrils. The seeded experiment was similar to the experiment described above except that preformed fibrils (5 μM) were added to each well. Performed fibrils were obtained after the incubation of fresh Aβ_{40} (50 μM) in aggregation buffer at pH 7.4 at 37 °C for 8 days and were sonicated for 10 s immediately before use.

Fluorescence Spectroscopy. Microplates were analyzed in a Molecular Devices Spectra MAX Gemini XS microplate spectrophotometer at 37 °C. Measurements of ThT binding were recorded once or twice daily using bandpass filters of 445 nm for excitation and 485 nm for emission, and a cutoff filter of 475 nm.

Atomic Force Microscopy. Study was performed on the NanioBio platform in Grenoble, France. An aliquot, 3 μL, from each inhibition study was withdrawn after 12 days of incubation and deposited onto freshly cleaved mica sheets for AFM inspection. The sample was incubated on mica for 2 min followed by three washes with 5 μL of water to gently remove the material not adsorbed to the substrate. The mica was dried in air for 1 h. In-air AFM images were acquired in noncontact mode in a vibration insulated environment, using a PicoPlus microscope (Molecular Imaging), equipped with a PicoScan-3000 controller. For imaging, we used single beam aluminum-coated cantilevers (type NSC36/ALBS, μMasch) with *Rc* <10 nm, 110−130 μm lengths, and nominal spring constant 0.6 N/m. The drive frequency was between 200 and 400 kHz.

RESULTS

Synthesis. The synthesis of conjugates **9** and **10** through CuAAC is summarized in Figure 1. The azide-substituted cyclodecapeptide **2**, the acetylene curcumin **8**, and the alkyne-functionalized KLVFFA **5**, were first prepared as complementary building blocks for the ligation by click chemistry.

Cyclodecapeptide **2** was obtained from intermediate **1** by coupling azidoacetic acid to the amine side chain of its lysine residues (Scheme 1). The noncommercial azidoacetic acid was extemporaneously prepared from bromoacetic acid and sodium azide as reported (*37*). A total conversion of **1** was observed by HPLC after a 2 h reaction with azidoacetic acid. Compound **2** was, however, obtained in low yield after arginine protecting group (Pmc) removal. The stability of the azido group under acidic conditions tends to support the formation of aggregates of **2** rather than degradation products during Pmc removal.

KLVFFA derivative **5** containing the Aβ_{16-21} sequence was efficiently prepared by solid phase peptide synthesis in 21% overall yield (Scheme 2). Propiolic acid, selected as the alkyne precursor, was introduced at the *N*-terminal position of the supported peptide. Curcumin derivative **8** (Figure 1) was obtained from propargyl bromide and curcumin as described in the literature (*36*).

The coupling of the building blocks **2**, **5**, and **8** by CuAAC was then performed and optimized (Table 1). In all reactions, a slight excess of the alkyne partner (**5** or **8**) as compared to the azide-containing cyclodecapeptide **2** was used (1.1 equiv/per azide group). The propensity of **5** to form aggregates is highly dependent on experimental conditions such as high concentration in aqueous media and the presence of salts. By using $CuSO_4$ with sodium ascorbate (NaAsc) as the reducting agent in *t*BuOH/H_2O, we observed the formation of a gel and no occurrence of the reaction (entry 1, Table 1). CuI as catalyst was further used in the presence of organic bases in DMF (entry 2, Table 1) (*39*, *40*). By using an organic solvent, we expected to improve the solubility of the peptide and to avoid its aggregation. Unfortunately, no reaction occurred up to 24 h at 60 °C, and only 11% of compound **9** was detected by HPLC after 76 h. We suspect the low conversion rate to be due to the instability of the catalytic system despite the special care undertaken (inert atmosphere and anhydrous DMF). In order to overcome the solubility issue and to limit the quantity of salt in the reaction mixture, we also considered using copper turning rather than the copper sulfate/NaAsc system. Trifluoroethanol (TFE) was added as cosolvent to improve solubility. After 4 h, a modest 16% conversion rate was obtained and the reaction mixture turned into a gel (entry 3, Table 1). If TFE seemed to improve the solubility, the coupling reaction appeared nevertheless too slow down as compared to the formation of the gel. We finally opted for using microwaves (MWs) to activate the reaction. A combination of Cu(I) with MWs in CuAAC has shown to complete reactions in a few minutes and in clean conditions (*41*). Under MW activation and in the presence of TFE as cosolvent, a complete conversion of **2** into **9** was observed in only 20 min with no gel formation. Conjugate **9** was isolated as a pure compound in 39% yield after semipreparative RP-HPLC purification and was characterized by ESI mass spectrometry.

In the case of the curcumin derivative **8**, several attempts were also necessary to efficiently form conjugate **10** (entries 5−7, Table 1). Similar to the KLVFFA peptide, the major issue to deal with was the precipitation of **8** in the reaction mixture because of its strong hydrophobicity (entry 5, Table 1). Using copper turning instead of $CuSO_4$/NaAsc and increasing the ratio of TFE (entry 6, Table 1) failed to avoid precipitation. We managed to achieve complete conversion of **2** into **10** after 7 h by replacing *t*BuOH with DMSO, by increasing the amount of organic solvent, and by using copper turning in NaAsc (entry 7, Table 1). Purification by RP-HPLC provided conjugate **10** as a pure compound in 30% yield.

To assess the specificity of the inhibitory response of our conjugates **9** and **10**, control compounds were needed. Cyclopeptide **3** and peptide **7** (Schemes 1 and 2) were prepared with this aim. Cyclopeptide **3** presenting acetylated functions instead of the clicked Aβ-binding elements was obtained from intermediate **1** in 64% yield (Scheme 1). The Aβ_{16-21} peptide **7** featuring a *N*-terminal triazole was obtained from intermediate **4** on the solid support (Scheme 2). Azidoacetic acid was coupled to the *N*-terminal end of **4** to obtain the azide-functionalized peptide **6** after release from the resin. The click reaction of **6** with 3-methoxy-1-propyne in the presence of NaAsc/$CuSO_4$ afforded **7** in only 20% yield. Addition of TFE in *t*BuOH/H_2O and heating at 40 °C for more than 20 h were not sufficient to

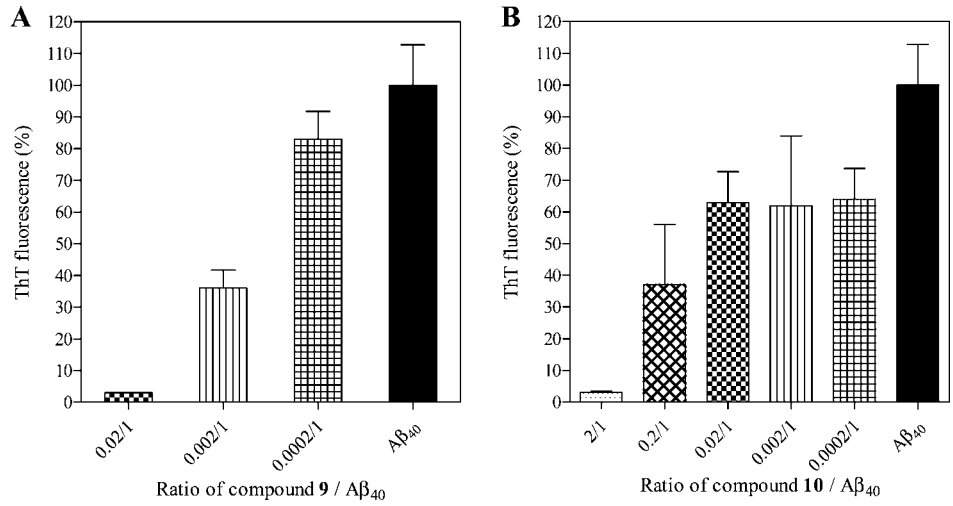

Figure 2. Aβ_{40} (50 μM) coincubated with compounds **9** and **10** in the indicated molar ratios (compound/Aβ_{40}) during 8 days. Values are the maximal fluorescence intensity at 485 nm compared to that of the control (Aβ_{40} with no inhibitor). Results are the mean ± standard deviation of 2−3 experiments.

prevent the precipitation of precursor **6**. Compound **7** was prepared prior to the use of MWs, in the synthesis of **9**, to efficiently activate the alkyne KLVFFA peptide **5** and avoid its precipitation (entry 4, Table 1). We presume that the activation by MWs of peptide **6**, whose solubility is similar to that of **5**, may improve the yield in compound **7**.

Thioflavin T Assay. Measurement of thioflavin T (ThT) fluorescence was used to evaluate the ability of conjugates **9** and **10** to inhibit Aβ_{40} fibril formation. We coincubated Aβ_{40} (50 μM) and ThT (10 μM) with a concentration range of each compound for a period of 8 days and studied the ThT fluorescence change at 485 nm. The relative change of ThT fluorescence (as compared to the condition of Aβ with no compound) was reported as a function of the molar ratio of tested compound to Aβ peptide (compound/Aβ_{40}). ThT was added directly to the fibril forming mixture as it has been shown to have little effect on the assembly process (*12, 42*). Control compounds were also studied in order to compare the activity of conjugates **9** and **10** with individual parts of their molecules: the single KLVFFA analogue **7**, curcumin, and cyclodecapeptide **3**. The results are presented in Figures 2 and 3. In order to check if the tested compounds can self-aggregate in the experimental conditions, we also performed ThT assays without Aβ_{40} (data not shown). At a 100 μM concentration which corresponds to the highest concentration of inhibitors used in the assays, neither compound **3** nor compound **10** showed ThT binding in the absence of Aβ_{40} after incubation for 8 days. On the contrary, we observed an immediate ThT fluorescence for compounds **7** and **9** at 100 μM and at a 10-fold lower concentration of 10 μM for **9**. These data indicate that, at these concentrations, compounds **7** and **9** bound ThT and formed structures with high β-sheet content by self-aggregation, whereas compounds **3** and **10** did not. Consequently, in the ThT assays in the presence of Aβ_{40}, compounds **7** and **9** were incubated at a maximum concentration of 10 μM and 1 μM, respectively.

Compound **9** with Aβ_{40} at a 0.02/1 ratio significantly reduced the ThT signal with an inhibition higher than 95% (Figure 2A). Even by reducing the ratio down to 0.002/1, more than 60% inhibition was still observed. Compound **10** required a higher 2/1 ratio to reduce 95% of ThT fluorescence (Figure 2B). At the 0.02/1 ratio, the ThT signal was still inhibited by 30%.

While compound **9** caused a strong reduction of ThT fluorescence at 0.02/1 and 0.002/1 ratios, the KLVFFA control **7** showed no inhibition on Aβ fibril formation (Figure 3A) at the same ratios. In the case of curcumin, significant reduction of the ThT signal was observed at 2/1 and 0.2/1 ratios, but no inhibition was observed at lower ratios (Figure 3B). Finally, no decrease in the ThT signal was observed for the scaffold alone, compound **3** (Figure 3C).

The capacity of compounds **9** and **10** in preventing fibril growth was also studied by ThT assay in the presence of preformed Aβ_{40} fibrils as seeds (Figure 4). The increase of ThT fluorescence at 485 nm was measured for 24 h after the addition of Aβ_{40} preformed fibrils (5 μM) on the mixture containing the compounds and fresh Aβ_{40} (50 μM). In comparison with unseeded experiments (Figure 2), compound **9** showed a more moderate activity in reducing fibril formation. At the 0.02/1 ratio, still 55% of ThT fluorescence remained (Figure 4). For compound **10**, a similar effect was observed in seeded and unseeded experiments with an inhibition around 85% at the 2/1 ratio.

AFM Observations. Samples were observed after 12 days of incubation of the compounds with Aβ_{40} in the same conditions as those used in the ThT assay (Figure 5). In the control sample of Aβ_{40} with no inhibitor, a number of long protofilaments of 1−4 μm in length and 5−10 nm in height were formed (Figure 5F). No fibril was observed for compound **9** at 0.02/1 ratio (Figure 5A). Compound **10** at 0.2/1 ratio showed much shorter fibrils than the control: 500 nm maximum length, 300 nm average, and 4 nm maximum height (Figure 5B). For compound **7**, the number of protofilaments observed at 0.2/1 ratio confirmed that the monomeric KLVFFA analogue alone is not able to inhibit fibril formation (Figure 5D). With curcumin at the 0.2/1 ratio with Aβ_{40}, long protofilaments (1−2 μm maximal length, 950 nm average) were detected (Figure 5E). With the scaffold alone, **3** at 2/1 ratio, shorter fibrils, compared to those of the control, were observed (0.3−1 μm), attesting an effect of **3** on fibril morphology (Figure 5C).

DISCUSSION

Synthesis. The azide−alkyne cycloaddition strategy required the synthesis of the cyclodecapeptide **2**, bearing two azido functionalities on the upper face, and of the KLVFFA and curcumin precursors **5** and **8**, displaying the suitable complementary alkyne functions (Figure 1). The alkyne monofunctional derivative **8** previously reported to prepare a clicked curcumin dimer (*36*) appeared to be well suited for our study. Consequently, we simply applied the described procedure from curcumin and propargylbromide. For the preparation of peptides

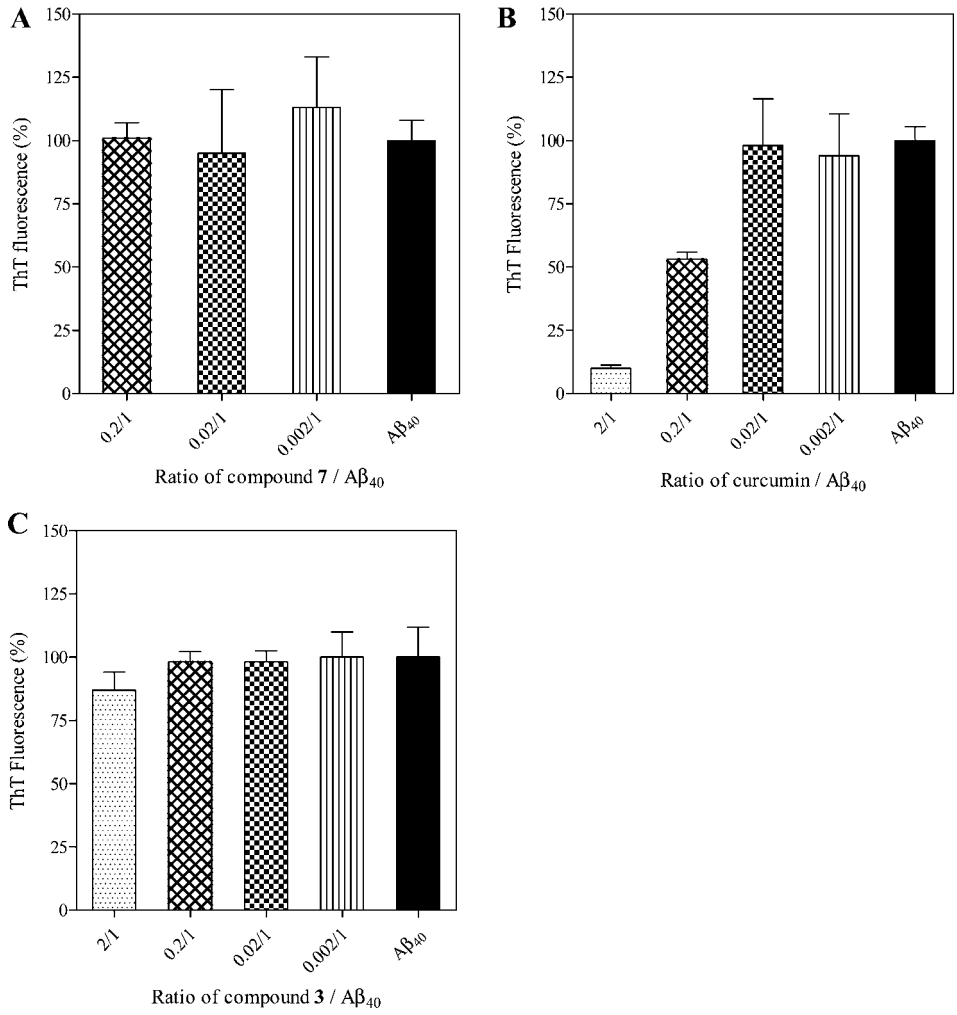

Figure 3. Aβ_{40} (50 μM) coincubated with control compounds **3**, **7**, and curcumin in the indicated molar ratios (compound/Aβ_{40}) during 8 days. Values are the maximal fluorescence intensity at 485 nm compared to that of the control (Aβ_{40} with no inhibitor). Results are the mean ± standard deviation of 2−3 experiments.

2 and **5**, a combination of solid and solution-phase syntheses was employed (Schemes 1 and 2). Azidoacetic and propiolic acids, selected as the azide and alkyne handles, respectively, have proven (*43*) to be convenient reactants to acylate peptides on their *N*-terminal end or amine side chains. They were efficiently tethered using PyBOP as coupling agent to the corresponding peptides in solution phase or on solid support in the case of **5**.

The ligation of the appropriate alkyne building block (**5** or **8**) to the azidocyclopeptide **2** was then considered. As we presumed, the major limitation to their ligation was their low hydrophilicity as well as the propensity of **5** to form aggregates. Indeed self-aggregation of amyloid sequence derivatives such as **5** are known to be highly promoted by certain experimental conditions such as manipulation at high concentration and the presence of salts (*44*, *45*). Concerning curcumin, its poor solubility in water is reported to be the major limitation to its biological use, justifying the development of more soluble derivatives (*36*). To address the solubility issue, we had to test several conditions of CuAAC (Table 1) in order to optimize the formation of the triazole linkage from our lipophilic derivatives. A wide number of CuAAC conditions have been reported in the literature that differ in Cu(I) sources, solvents, additives, or activation conditions (*33*). The catalyst can be introduced as a Cu(I) salt (CuI, CuBr, Cu(CH$_3$CN)$_4$PF$_6$...) with the use of base. It can also be generated *in situ* by oxidation of metal copper Cu(0) or by reduction of Cu(II) salts (CuSO$_4$) with

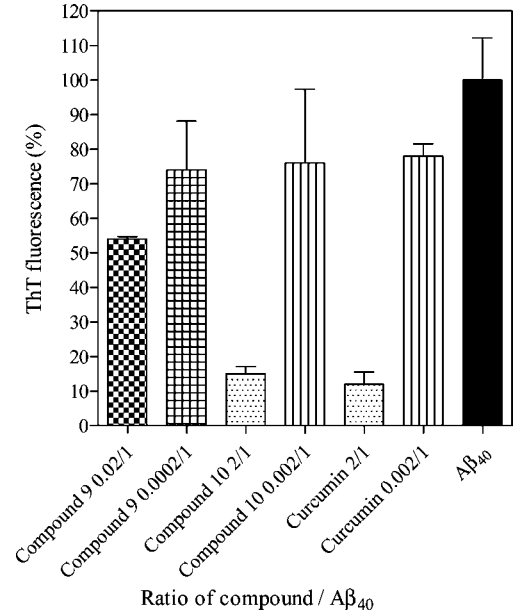

Figure 4. Fresh Aβ_{40} (50 μM) and preformed fibrils (5 μM) coincubated with compounds **9**, **10**, and curcumin in the indicated molar ratios (compound/Aβ_{40}) during 24 h. Values are the maximal fluorescence intensity at 485 nm compared to that of the control (Aβ_{40} with no inhibitor). Results are the mean ± standard deviation of 2−3 experiments.

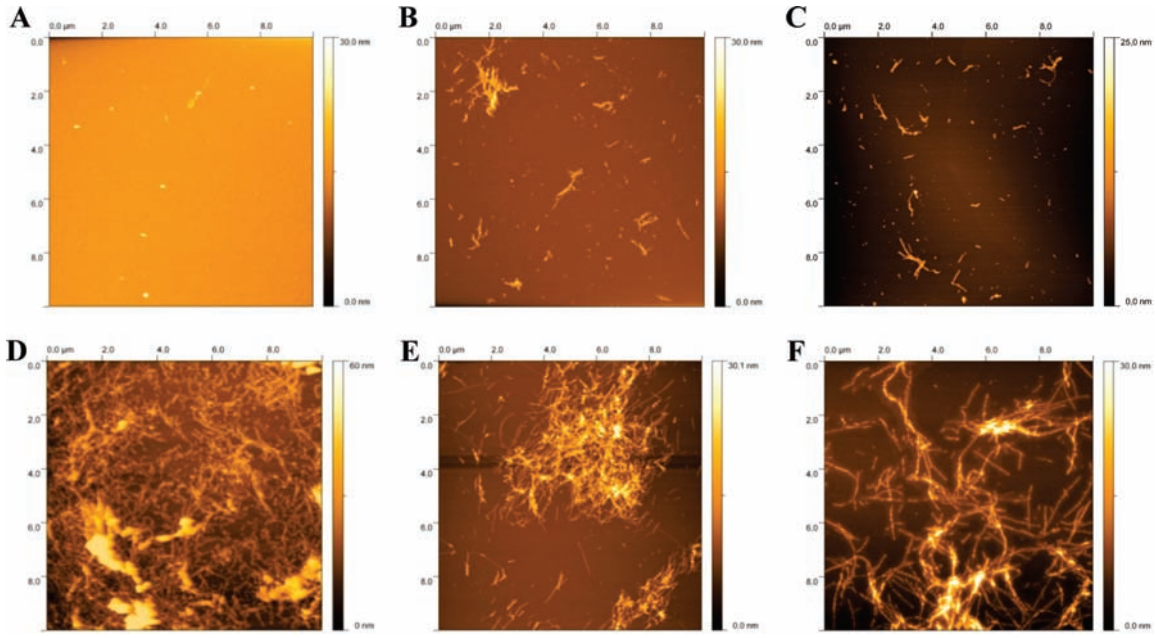

Figure 5. AFM images (height data) of protofilaments formed from Aβ_{40} (50 μM) after 12 days of incubation at 37 °C with the different compounds (scan size 10 μm). (A) compound **9**/Aβ_{40} 0.02/1, (B) compound **10**/Aβ_{40} 0.2/1, (C) compound **3**/Aβ_{40} 2/1, (D) compound **7**/Aβ_{40} 0.2/1, (E) curcumin/Aβ_{40} 0.2/1, and (F) Aβ_{40} with no inhibitor.

sodium ascorbate. The reaction can be performed in aqueous conditions, in various organic solvents (DMF, CH_3CN, THF, EtOH, DMSO...) or in organo-aqueous systems (*t*BuOH/H_2O, DMSO/H_2O...). Microwave irradiation has also be reported to shorten reaction times and to provide a selective conversion into the 1,4-substitued triazole similar to elevated temperature conditions.

The common procedure using copper(II) sulfate and sodium ascorbate as reducing agent in *t*butanol/water solution was first attempted. These conditions have indeed proved successful in conjugating azide-modified sugars or peptides onto alkyne-cyclopeptides (*46, 47*). This protocol, however, failed in the case of derivatives **5** and **8** because of their precipitation in the reaction medium.

Regarding the variety of reported CuAAC procedures, suitable conditions were finally found to access conjugates **9** and **10** from alkyne derivatives **5** and **8** (Table 1) in reasonable yields. To obtain the KLVFFA conjugate **9**, the addition of trifluoroethanol TFE as cosolvent and activation of the reaction by microwaves were found to give the best results (total conversion of **2** in only 20 min). A click reaction involving curcumin derivative **8** using the $CuSO_4$/NaAsc combination was reported in the literature to prepare the clicked curcumin dimer (*36*). In this study, the addition of chloroform in the *t*butanol/water solution was necessary to obtain the desired clicked product in a moderate 41% yield. In our case, the addition of TFE was not sufficient to avoid precipitation of **8**, and a combination of copper turning and NaAsc in a DMSO/water/TFE mixture was required to access conjugate **10**. It is worth noting that the use of a mixture of Cu(0) and sodium ascorbate is unusual. Indeed Cu(0), found as wire, turnings, powder, or nanoparticles, is usually employed alone or in combination with a Cu(II) source (*43, 48*). The active Cu(I) catalyst is then formed via comproportionation of the Cu(II)/Cu(0) complex. The success of this unusual combination can be explained by the presence of a significant amount of Cu(II) on the surface of the copper turning that was converted into Cu(I) with NaAsc.

***In Vitro* Inhibition Studies of Aβ_{40} Fibril Formation.** Synthetic fibrils made from Aβ_{40} monomers are commonly used *in vitro* for screening inhibitors. The formation of Aβ_{40} fibrils is monitored by fluorimetric assay using thioflavin T, a sensitive and highly specific dye to the characteristic cross-β-sheet structure of fibrils (*42, 49*). Even if the fluorescence in the ThT assay is well correlated with the highly ordered aggregation morphology, atomic force microscopy (AFM) observation is most of the time used in parallel to ensure that the observed effect is indeed due to fibril inhibition.

In this study, we performed both the ThT assay and AFM to evaluate our conjugates. In the ThT assay, we examined for each inhibitor candidate a range of concentrations and expressed the results in terms of inhibitor candidate to Aβ molar ratios. Using a constant concentration of Aβ_{40}, comparison of the relative potency of each inhibitor is facilitated. Compounds **9** and **10** showed a strong antiamyloidogenic effect since a significant inhibition of fibril formation from Aβ_{40} monomers was observed even at low molar ratios (Figure 2). Compound **9** displayed a high inhibitory activity as almost complete inhibition is observed at a 0.02/1 ratio of **9**/Aβ (Figure 2A). This is to compare with the control peptide KLVFFA **7**, which is totally inactive at up to 10-fold higher ratio (Figure 3A). Concerning compound **10**, an inhibition higher than 95% was observed at a 2/1 ratio. Compound **10** remained active at 0.02/1 and even at lower ratios where curcumin proved to be totally inactive (Figures 2B and 3B). These results demonstrate the benefit of the dimeric presentation of the Aβ-recognition motif in our assemblies to inhibit fibril formation. The synergistic effect is particularly impressive for compound **9**. With two copies of the KLVFFA peptide, this conjugate is at least 5-fold more active in blocking the formation of well ordered fibrils than the KLVFFA monomer **7** (considering the number of moles in KLVFFA subunits). This is in concordance with previously reported studies demonstrating the increased efficiency of multivalent KLVFF conjugates against Aβ peptide aggregation (*26, 27*). Moreover, conjugate **9** appeared 100 times more potent than conjugate **10**. The fact that the KLVFFA motif is not only a target recognition motif but also a part of the β-sheet breaker can explain this difference in activity.

The morphology of Aβ fibrils by AFM was consistent with the results of the ThT assays (Figure 5). No fibril was observed for conjugate **9** at the low 0.02/1 ratio, whereas fibrils were

detected with monomer **7**. AFM observation also confirmed that curcumin conjugate **10** is more active than curcumin in preventing Aβ_{40} aggregation at low concentrations. Indeed, at identical 0.2/1 ratio, long protofilaments similar to those observed in Aβ control were observed with curcumin, while much shorter fibrils were observed in the presence of **10**.

The possibility that the inhibitory effect of our conjugates is due to the nature of the cyclodecapeptide scaffold was also considered. The scaffold alone, compound **3**, showed no inhibition effect in the ThT assay (Figure 3C). However, AFM observation revealed that fibril morphology was affected. At high 2/1 ratio of **3**/Aβ, shorter fibrils than the Aβ control were observed. We suspect the arginine residues, previously shown to affect protein folding, to be involved (*31, 32, 50*). Guanidium groups of arginines were known to interact through hydrogen bonding interactions with the protein backbone or through π-electron−cation interactions with specific protein domains, such as aromatic amino acid side chains (*50*). Although there is insufficient evidence for drawing a firm explanation, interaction of arginines with aromatic side chains of Aβ peptides which are essential for aggregation could disturb the aggregation process leading to shorter protofilaments. Moreover, arginine residues may act by preventing the network of hydrogen bonds between the Aβ backbone amides, which is essential for the formation of an extended β-sheet fibril. The influence of arginine on Aβ-amyloid aggregate morphology has been reported using hybrid peptides (*51*). With an arginine hexamer R_6, fibrillar aggregates much shorter than Aβ alone were observed. With a KLVFF-R_6 hybrid, simultaneously featuring the KLVFF Aβ-recognition domain and the R_6 disrupting domain, no aggregate with fibrillar morphology was observed, but large globular-like clumps of material were observed. If arginine compounds may have very different effects depending on the context in which arginine was presented, this study confirms that arginine can have significant effects on the path of Aβ aggregation.

The Aβ fibril formation process is presumed to occur in two successive phases, precisely, nucleation followed by extension (*17*). During the nucleation phase, Aβ monomers self-assemble from a random coil structure into oligomers and aggregation-prone species that can aggregate once a critic concentration is reached. After the nucleus has formed, additional monomers rapidly form extended fibrils. This polymerization step starts when a shift to β-sheet structured protofibrils occurs. Inhibitors of fibril formation can thus act by binding to monomers or to aggregation-prone species during the nucleation phase or by binding to the nascent fibrils during the polymerization phase. Seeded experiments, where preformed fibrils are added to the Aβ aggregation mixture, enable one to follow only the exponential growth of fibrils and thus to identify specific inhibitors of Aβ polymerization (*13*). In such an experiment, both **9** and **10** decreased fibril growth, suggesting that they impair the Aβ polymerization process (Figure 4). However, in comparison with the corresponding unseeded experiments, the ThT fluorescence was higher at the same ratios, implying that they also disrupt the nucleation phase. Indeed, conjugate **9** proved to have an effect both on the initial nucleation phase and on Aβ polymerization (95% and 45% inhibition in unseeded and seeded experiments, respectively, at identical 0.02/1 ratios). Conversely, conjugate **10** mostly affects the polymerization phase since the difference between the two scenarios is less impressive (95% and 85% inhibition at 2/1 ratio).

Both conjugates **9** and **10** proved to be more effective than curcumin in preventing Aβ fibril formation. Indeed, at 0.02/1 molar ratio (i.e., 1 μM inhibitor concentration), conjugates **9** and **10** inhibit Aβ_{40} aggregation by 95% and 35%, respectively. At comparable ratios and by using the same experimental procedure, curcumin showed no inhibition at all. With our most potent inhibitor, conjugate **9**, inhibition occurs at 0.02/1 ratio, whereas most peptide inhibitors reported in the literature require much higher excess of Aβ. For instance, the small LPFFD peptide (*16*) and the cholyl-LVFFA (*13*), shown to significantly reduce Aβ_{40} amyloid formation, are active only at 10/1 and 1/1 ratios, respectively. In comparison with reported multimeric KLVFF conjugates, the activity of compound **9** is also very interesting. Maximum inhibition with PEG conjugates featuring either KLVFF or the retro-inverso peptide, ffvlk, (80% and 70%, respectively) were attained with 0.33/1 ratio for the hexamer and 1/1 for the dimer forms (*26*). Conjugate **9** is at least 8 times more active since 90% inhibition is obtained at 0.04/1 ratio (expressed as per mol of KLVFFA subunit). Our conjugate **9** also appears 100 times more active than a dendrimer, featuring four copies of KLVFF (90% inhibition of Aβ_{42} aggregation at 4/1 ratio) (*27*). Careful attention should, however, be paid when comparing to this dendrimer since it was tested against Aβ_{42} aggregation. It has indeed been shown with KLVFF analogues that some compounds could be more active on Aβ_{40} than on Aβ_{42} aggregation (*16*).

The potency of our conjugate **9** in preventing Aβ neurotoxicity remains to be evaluated. Concerning its potential use *in vivo* as a drug against AD, the ability to cross the blood−brain barrier (BBB) should be taken into account. Despite a recent study showing the efficiency of a non-BBB crossing anti-Aβ antibody in reducing amyloid deposits (*52*), this capability is a critical issue in drug development against AD. The high molecular weight of **9** is surely a limiting factor; however, the scaffold-based architecture of this conjugate allows facile modification with other components such BBB-crossing carriers (e.g., Tat peptide *53, 54*). Current progress in drug delivery materials across the BBB such as polymeric nanoparticles is also likely to promote in the near future the accessibility of drugs targeting AD (*55*).

CONCLUSIONS

This work confirms that the versatility of CuAAC is an indubitably powerful tool to assemble biomolecules. Aβ recognition domains have been efficiently clicked on a bulky cyclopeptidic scaffold to prepare inhibitors of Aβ amyloid fibril formation. In terms of inhibition, the arginine-rich scaffold covalently associated with two copies of the KLVFFA sequence has shown a potent effect on Aβ_{40} aggregation, whereas the curcumin conjugate exhibited a more modest effect. Although the exact mechanism is not fully understood yet, we assume that the dimeric presentation of KLVFFA favors interactions with Aβ peptides and that the scaffold acts as a disrupting element on Aβ aggregation. While previously reported inhibitors required equimolar ratio to Aβ or even higher, our most effective conjugate still induced 95% inhibition with a ratio as low as 0.02/1. Our strategy based on a modular assembly herein applied to conjugates targeting AD will likely be further exploited to develop inhibitors of others amyloid related disorders (*56*).

ACKNOWLEDGMENT

This work was supported by grants from the European FP6 EURAMY project "Systemic amyloidoses in Europe". We are grateful to the NanoBio program for the facilities of the Synthesis and Surface Characterization platforms. We also thank Dr. Martine Demeunynck for helpful discussions about synthesis.

Supporting Information Available: HPLC and ESI-MS data of all isolated compounds. HPLC and mass spectrometry analyses of conjugates **9** and **10**. This material is available free of charge via the Internet at http://pubs.acs.org.

LITERATURE CITED

(1) Dobson, C. M. (2004) Principles of protein folding, misfolding and aggregation. *Semin. Cell Dev. Biol. 15*, 3–16.

(2) Lansbury, P. T., Jr. (1999) Evolution of amyloid: what normal protein folding may tell us about fibrillogenesis and disease. *Proc. Natl. Acad. Sci. U.S.A. 96*, 3342–3344.

(3) Murphy, R. M. (2002) Peptide aggregation in neurodegenerative disease. *Annu. Rev. Biomed. Eng. 4*, 155–174.

(4) Jakob-Roetne, R., and Jacobsen, H. (2009) Alzheimer's disease: from pathology to therapeutic approaches. *Angew. Chem. Int. Ed. 48*, 3030–3059.

(5) Hartley, D. M., Walsh, D. M., Ye, C. P., Diehl, T., Vasquez, S., Vassilev, P. M., Teplow, D. B., and Selkoe, D. J. (1999) Protofibrillar intermediates of amyloid beta-protein induce acute electrophysiological changes and progressive neurotoxicity in cortical neurons. *J. Neurosci. 19*, 8876–8884.

(6) Kayed, R., Head, E., Thompson, J. L., McIntire, T. M., Milton, S. C., Cotman, C. W., and Glabe, C. G. (2003) Common structure of soluble amyloid oligomers implies common mechanism of pathogenesis. *Science 300*, 486–489.

(7) Lambert, M. P., Barlow, A. K., Chromy, B. A., Edwards, C., Freed, R., Liosatos, M., Morgan, T. E., Rozovsky, I., Trommer, B., Viola, K. L., Wals, P., Zhang, C., Finch, C. E., Krafft, G. A., and Klein, W. L. (1998) Diffusible, nonfibrillar ligands derived from Abeta1−42 are potent central nervous system neurotoxins. *Proc. Natl. Acad. Sci. U.S.A. 95*, 6448–6453.

(8) Mattson, M. P. (2004) Pathways towards and away from Alzheimer's disease. *Nature 430*, 631–639.

(9) Tjernberg, L. O., Naslund, J., Lindqvist, F., Johansson, J., Karlstrom, A. R., Thyberg, J., Terenius, L., and Nordstedt, C. (1996) Arrest of beta-amyloid fibril formation by a pentapeptide ligand. *J. Biol. Chem. 271*, 8545–8548.

(10) Tjernberg, L. O., Lilliehook, C., Callaway, D. J., Naslund, J., Hahne, S., Thyberg, J., Terenius, L., and Nordstedt, C. (1997) Controlling amyloid beta-peptide fibril formation with protease-stable ligands. *J. Biol. Chem. 272*, 12601–12605.

(11) Chacon, M. A., Barria, M. I., Soto, C., and Inestrosa, N. C. (2004) Beta-sheet breaker peptide prevents Abeta-induced spatial memory impairments with partial reduction of amyloid deposits. *Mol. Psychiatr. 9*, 953–961.

(12) Chalifour, R. J., McLaughlin, R. W., Lavoie, L., Morissette, C., Tremblay, N., Boule, M., Sarazin, P., Stea, D., Lacombe, D., Tremblay, P., and Gervais, F. (2003) Stereoselective interactions of peptide inhibitors with the beta-amyloid peptide. *J. Biol. Chem. 278*, 34874–34881.

(13) Findeis, M. A., Musso, G. M., Arico-Muendel, C. C., Benjamin, H. W., Hundal, A. M., Lee, J. J., Chin, J., Kelley, M., Wakefield, J., Hayward, N. J., and Molineaux, S. M. (1999) Modified-peptide inhibitors of amyloid beta-peptide polymerization. *Biochemistry 38*, 6791–6800.

(14) Gordon, D. J., Sciarretta, K. L., and Meredith, S. C. (2001) Inhibition of beta-amyloid(40) fibrillogenesis and disassembly of beta-amyloid(40) fibrils by short beta-amyloid congeners containing N-methyl amino acids at alternate residues. *Biochemistry 40*, 8237–8245.

(15) Permanne, B., Adessi, C., Saborio, G. P., Fraga, S., Frossard, M. J., Van Dorpe, J., Dewachter, I., Banks, W. A., Van Leuven, F., and Soto, C. (2002) Reduction of amyloid load and cerebral damage in a transgenic mouse model of Alzheimer's disease by treatment with a beta-sheet breaker peptide. *FASEB J. 16*, 860–862.

(16) Soto, C., Kindy, M. S., Baumann, M., and Frangione, B. (1996) Inhibition of Alzheimer's amyloidosis by peptides that prevent beta-sheet conformation. *Biochem. Biophys. Res. Commun. 226*, 672–680.

(17) Takahashi, T., and Mihara, H. (2008) Peptide and protein mimetics inhibiting amyloid beta-peptide aggregation. *Acc. Chem. Res. 41*, 1309–1318.

(18) Binder, W. H., and Smrzka, O. W. (2006) Self-assembly of fibers and fibrils. *Angew. Chem. Int. Ed. 45*, 7324–7328.

(19) LeVine, H. (2007) Small molecule inhibitors of Abeta assembly. *Amyloid 14*, 185–197.

(20) Ono, K., Hasegawa, K., Naiki, H., and Yamada, M. (2004) Curcumin has potent anti-amyloidogenic effects for Alzheimer's beta-amyloid fibrils in vitro. *J. Neurosci. Res. 75*, 742–750.

(21) Ono, K., Yoshiike, Y., Takashima, A., Hasegawa, K., Naiki, H., and Yamada, M. (2003) Potent anti-amyloidogenic and fibril-destabilizing effects of polyphenols in vitro: implications for the prevention and therapeutics of Alzheimer's disease. *J. Neurochem. 87*, 172–181.

(22) Taniguchi, S., Suzuki, N., Masuda, M., Hisanaga, S., Iwatsubo, T., Goedert, M., and Hasegawa, M. (2005) Inhibition of heparin-induced tau filament formation by phenothiazines, polyphenols, and porphyrins. *J. Biol. Chem. 280*, 7614–7623.

(23) Porat, Y., Abramowitz, A., and Gazit, E. (2006) Inhibition of amyloid fibril formation by polyphenols: structural similarity and aromatic interactions as a common inhibition mechanism. *Chem. Biol. Drug Des. 67*, 27–37.

(24) Talaga, P. (2001) Beta-amyloid aggregation inhibitors for the treatment of Alzheimer's disease: dream or reality? *Mini-Rev. Med. Chem. 1*, 175–186.

(25) Gestwicki, J. E., Crabtree, G. R., and Graef, I. A. (2004) Harnessing chaperones to generate small-molecule inhibitors of amyloid beta aggregation. *Science 306*, 865–869.

(26) Zhang, G., Leibowitz, M. J., Sinko, P. J., and Stein, S. (2003) Multiple-peptide conjugates for binding beta-amyloid plaques of Alzheimer's disease. *Bioconjugate Chem. 14*, 86–92.

(27) Chafekar, S. M., Malda, H., Merkx, M., Meijer, E. W., Viertl, D., Lashuel, H. A., Baas, F., and Scheper, W. (2007) Branched KLVFF tetramers strongly potentiate inhibition of beta-amyloid aggregation. *ChemBioChem 8*, 1857–1864.

(28) Dolphin, G. T., Chierici, S., Ouberai, M., Dumy, P., and Garcia, J. (2008) A multimeric quinacrine conjugate as a potential inhibitor of Alzheimer's beta-amyloid fibril formation. *ChemBioChem 9*, 952–963.

(29) Singh, Y., Dolphin, G. T., Razkin, J., and Dumy, P. (2006) Synthetic peptide templates for molecular recognition: recent advances and applications. *ChemBioChem 7*, 1298–1314.

(30) Yang, F., Lim, G. P., Begum, A. N., Ubeda, O. J., Simmons, M. R., Ambegaokar, S. S., Chen, P. P., Kayed, R., Glabe, C. G., Frautschy, S. A., and Cole, G. M. (2005) Curcumin inhibits formation of amyloid beta oligomers and fibrils, binds plaques, and reduces amyloid in vivo. *J. Biol. Chem. 280*, 5892–5901.

(31) Arakawa, T., and Tsumoto, K. (2003) The effects of arginine on refolding of aggregated proteins: not facilitate refolding, but suppress aggregation. *Biochem. Biophys. Res. Commun. 304*, 148–152.

(32) Xie, Q., Guo, T., Lu, J., and Zhou, H. M. (2004) The guanidine like effects of arginine on aminoacylase and salt-induced molten globule state. *Int. J. Biochem. Cell Biol. 36*, 296–306.

(33) Meldal, M., and Tornoe, C. W. (2008) Cu-catalyzed azide-alkyne cycloaddition. *Chem. Rev. 108*, 2952–3015.

(34) Rostovtsev, V. V., Green, L. G., Fokin, V. V., and Sharpless, K. B. (2002) A stepwise huisgen cycloaddition process: copper(I)-catalyzed regioselective "ligation" of azides and terminal alkynes. *Angew. Chem. Int. Ed. 41*, 2596–2599.

(35) Tornoe, C. W., Christensen, C., and Meldal, M. (2002) Peptidotriazoles on solid phase: [1,2,3]-triazoles by regiospecific copper(i)-catalyzed 1,3-dipolar cycloadditions of terminal alkynes to azides. *J. Org. Chem. 67*, 3057–3064.

(36) Shi, W., Dolai, S., Rizk, S., Hussain, A., Tariq, H., Averick, S., L'Amoreaux, W., El ldrissi, A., Banerjee, P., and Raja, K. (2007) Synthesis of monofunctional curcumin derivatives, clicked curcumin dimer, and a PAMAM dendrimer curcumin conjugate for therapeutic applications. *Org. Lett. 9*, 5461–5464.

(37) Khoukhi, N., Vaultier, M., and Carrie, R. (1987) Synthesis and reactivity of methyl γ-azidobutyrates and ethyl δ-azidovalerates and of the corresponding acid chlorides as useful reagents for the aminoalkylation. *Tetrahedron 43*, 1811–1822.

(38) Dolphin, G. T., Ouberai, M., Dumy, P., and Garcia, J. (2007) Designed amyloid beta peptide fibril: a tool for high-

throughput screening of fibril inhibitors. *ChemMedChem 2*, 1613–1623.
(39) Lee, L. V., Mitchell, M. L., Huang, S. J., Fokin, V. V., Sharpless, K. B., and Wong, C. H. (2003) A potent and highly selective inhibitor of human alpha-1,3-fucosyltransferase via click chemistry. *J. Am. Chem. Soc. 125*, 9588–9589.
(40) Franke, R., Doll, C., and Eichler, J. (2005) Peptide ligation through click chemistry for the generation of assembled and scaffolded peptides. *Tetrahedron Lett. 46*, 4479–4482.
(41) Guezguez, R., Bougrin, K., El Akria, K., and Benhidaa, R. (2006) A highly efficient microwave-assisted solvent-free synthesis of α- and *β*-2′-deoxy-1,2,3-triazolyl-nucleosides. *Tetrahedron Lett. 47*, 4807–4811.
(42) LeVine, H. (1993) Thioflavine T interaction with synthetic Alzheimer's disease beta-amyloid peptides: detection of amyloid aggregation in solution. *Protein Sci. 2*, 404–410.
(43) Meldal, M., and Tornoe, C. W. (2008) Cu-catalyzed azide-alkyne cycloaddition. *Chem. Rev. 108*, 2952–3015.
(44) Burdick, D., Soreghan, B., Kwon, M., Kosmoski, J., Knauer, M., Henschen, A., Yates, J., Cotman, C., and Glabe, C. (1992) Assembly and aggregation properties of synthetic Alzheimer's A4/beta amyloid peptide analogs. *J. Biol. Chem. 267*, 546–554.
(45) Gorevic, P. D., Castano, E. M., Sarma, R., and Frangione, B. (1987) Ten to fourteen residue peptides of Alzheimer's disease protein are sufficient for amyloid fibril formation and its characteristic x-ray diffraction pattern. *Biochem. Biophys. Res. Commun. 147*, 854–862.
(46) Galibert, M., Dumy, P., and Boturyn, D. (2009) One-pot approach to well-defined biomolecular assemblies by orthogonal chemoselective ligations. *Angew. Chem.-Int. Ed. 48*, 2576–2579.
(47) Wang, J., Li, H., Zou, G., and Wang, L. X. (2007) Novel template-assembled oligosaccharide clusters as epitope mimics for HIV-neutralizing antibody 2G12. Design, synthesis, and antibody binding study. *Org. Biomol. Chem. 5*, 1529–1540.
(48) Bock, V. D., Hiemstra, H., and van Maarseveen, J. H. (2006) CuI catalyzed alkyne-azide "click" cycloadditions from a mechanistic and synthetic perspective. *Eur. J. Org. Chem.* 51–68.
(49) LeVine, H. (1999) Quantification of beta-sheet amyloid fibril structures with thioflavin T. *Methods Enzymol. 309*, 274–284.
(50) Tsumoto, K., Umetsu, M., Kumagai, I., Ejima, D., Philo, J. S., and Arakawa, T. (2004) Role of arginine in protein refolding, solubilization, and purification. *Biotechnol. Prog. 20*, 1301–1308.
(51) Gibson, T. J., and Murphy, R. M. (2005) Design of peptidyl compounds that affect beta-amyloid aggregation: importance of surface tension and context. *Biochemistry 44*, 8898–8907.
(52) DeMattos, R. B., Bales, K. R., Cummins, D. J., Paul, S. M., and Holtzman, D. M. (2002) Brain to plasma amyloid-beta efflux: a measure of brain amyloid burden in a mouse model of Alzheimer's disease. *Science 295*, 2264–2267.
(53) Dietz, G. P., and Bahr, M. (2004) Delivery of bioactive molecules into the cell: the Trojan horse approach. *Mol. Cell. Neurosci. 27*, 85–131.
(54) Dietz, G. P., and Bahr, M. (2005) Peptide-enhanced cellular internalization of proteins in neuroscience. *Brain Res. Bull. 68*, 103–114.
(55) Roney, C., Kulkarni, P., Arora, V., Antich, P., Bonte, F., Wu, A., Mallikarjuana, N. N., Manohar, S., Liang, H. F., Kulkarni, A. R., Sung, H. W., Sairam, M., and Aminabhavi, T. M. (2005) Targeted nanoparticles for drug delivery through the blood-brain barrier for Alzheimer's disease. *J. Controlled Release 108*, 193–214.
(56) Chiti, F., and Dobson, C. M. (2006) Protein misfolding, functional amyloid, and human disease. *Annu. Rev. Biochem. 75*, 333–366.

BC900281B

Synthesis and Biological Evaluation of Clicked curcumin and Clicked KLVFFA Conjugates as Inhibitors of β-amyloid Fibril Formation

Myriam Ouberai,[†] Pascal Dumy,[†] Sabine Chierici,[,†] and Julian Garcia[*,†]*

* To whom correspondence should be addressed. Phone: +33 4 76 51 44 31. Fax: +33 4 76 51 49 46. E-mail: sabine.chierici@ujf-grenoble.fr, julian.garcia@ujf-grenoble.fr

[†] Département de Chimie Moléculaire (DCM), UMR 5250, ICMG-FR, Université Joseph Fourier, BP 53, 38041 Grenoble Cedex 9, France.

Supporting Information Available:

Table 1. RP-HPLC and ESI-MS data of isolated compounds
Figure 1. RP-HPLC profile of **9.**
Figure 2. ESI-MS analysis of **9**
Figure 3. RP-HPLC profile of **10.**
Figure 4: ESI-MS analysis of **10**

Table 1. RP-HPLC and ESI-MS data of isolated compounds.

Product	HPLC t_R (min)	ESI-MS
1	10.1	calc for $C_{106}H_{164}N_{24}O_{22}S_4$: 2253.1 found: 2253.6
2	6.5	calc for $C_{54}H_{94}N_{30}O_{12}$: 1354.7 found: 1354.4
3	5.4	calc for $C_{54}H_{96}N_{24}O_{12}$: 1272.7 found: 1272.7
5	9.3	calc for $C_{41}H_{57}N_7O_8$: 775.4 found: 775.4
6	9.3	calc for $C_{40}H_{58}N_{10}O_8$: 806.4 found: 806.4
7	8.4	calc for $C_{44}H_{64}N_{10}O_9$: 876.4 found: 876.4
8	11.9	calc for $C_{24}H_{22}O_6$: 406.4 found: 406.0
9	7.7	calc for $C_{136}H_{208}N_{44}O_{28}$: 2907.4 found: 2906.9
10	10.4	calc for $C_{102}H_{138}N_{30}O_{24}$: 2167.0 found: 2166.9

Figure 1. RP-HPLC profile of **9**.

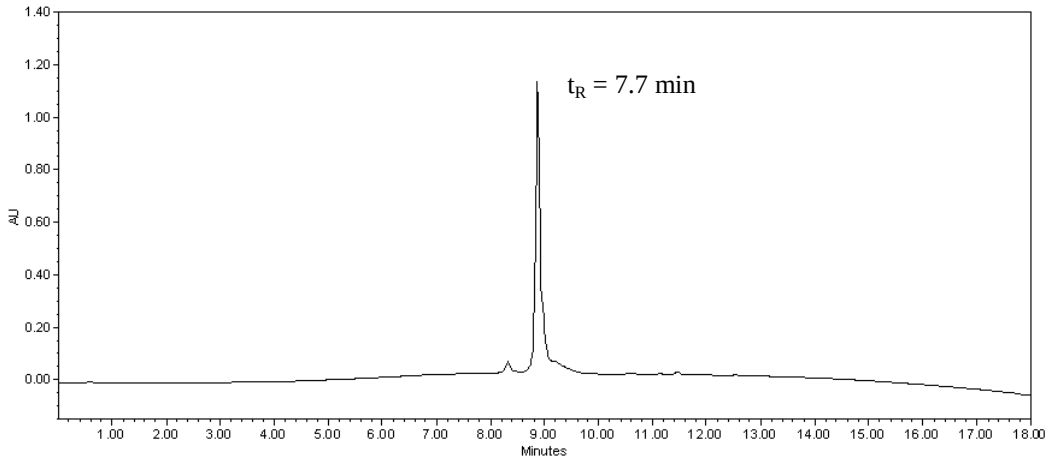

Figure 2. ESI-MS analysis of **9** (**9** was dissolved in acetonitrile containing 9.9% H_2O and 0.1% TFA).

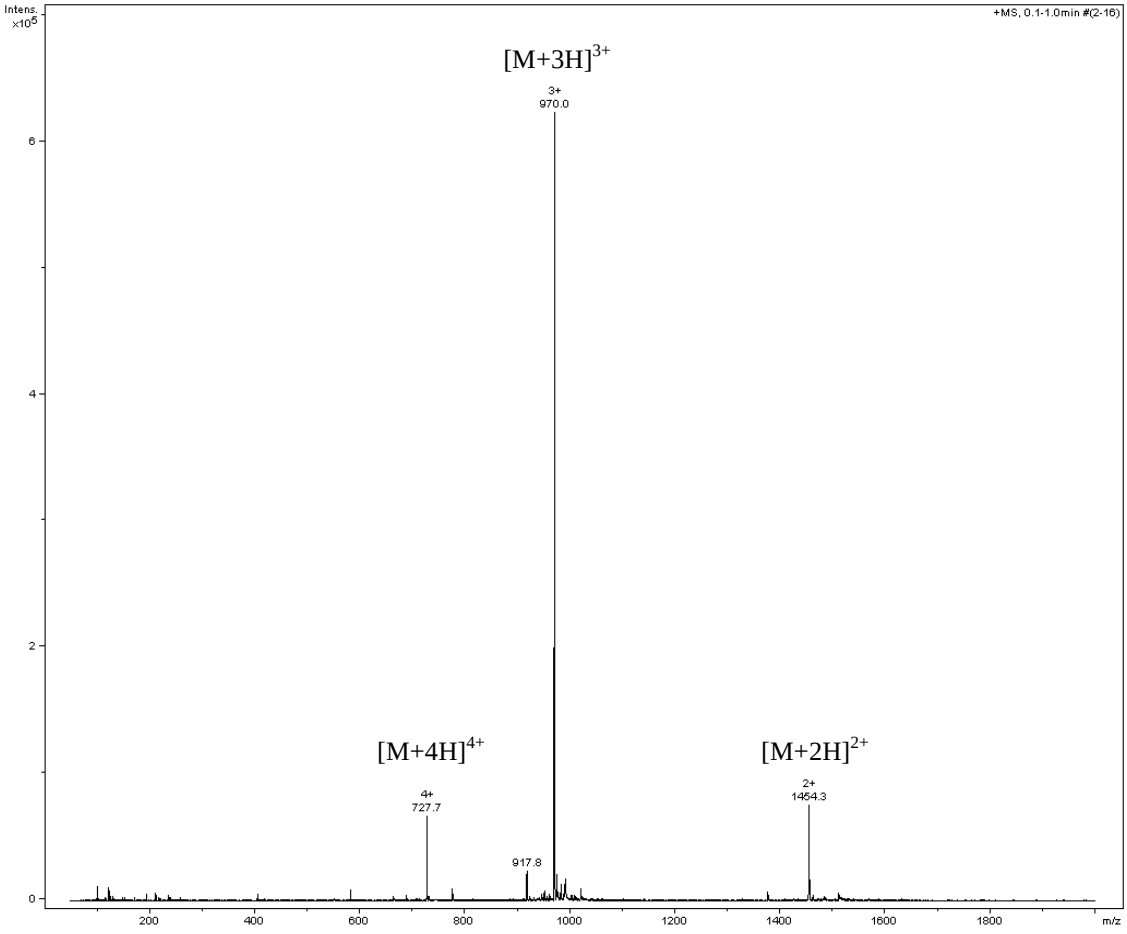

Figure 3. RP-HPLC profile of **10**.

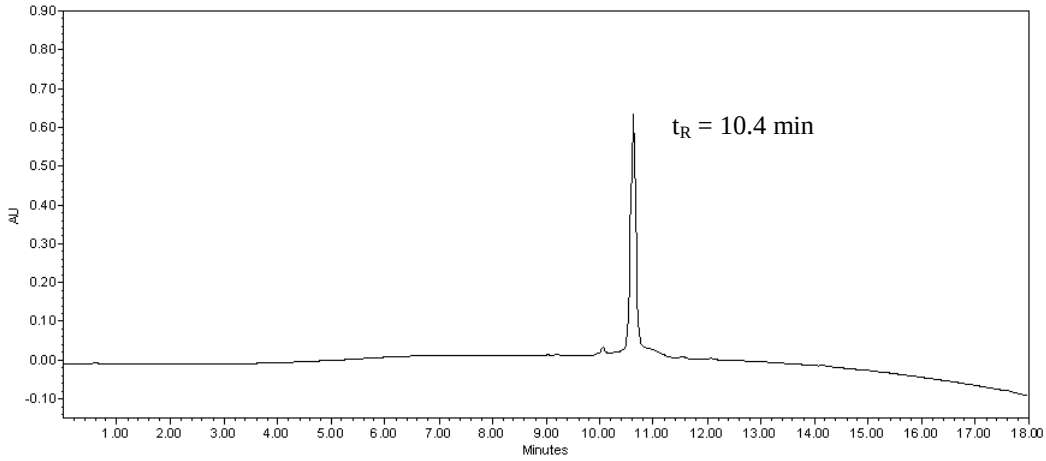

Figure 4: ESI-MS analysis of **10** (**10** was dissolved in acetonitrile containing 9.9% H_2O and 0.1% TFA).

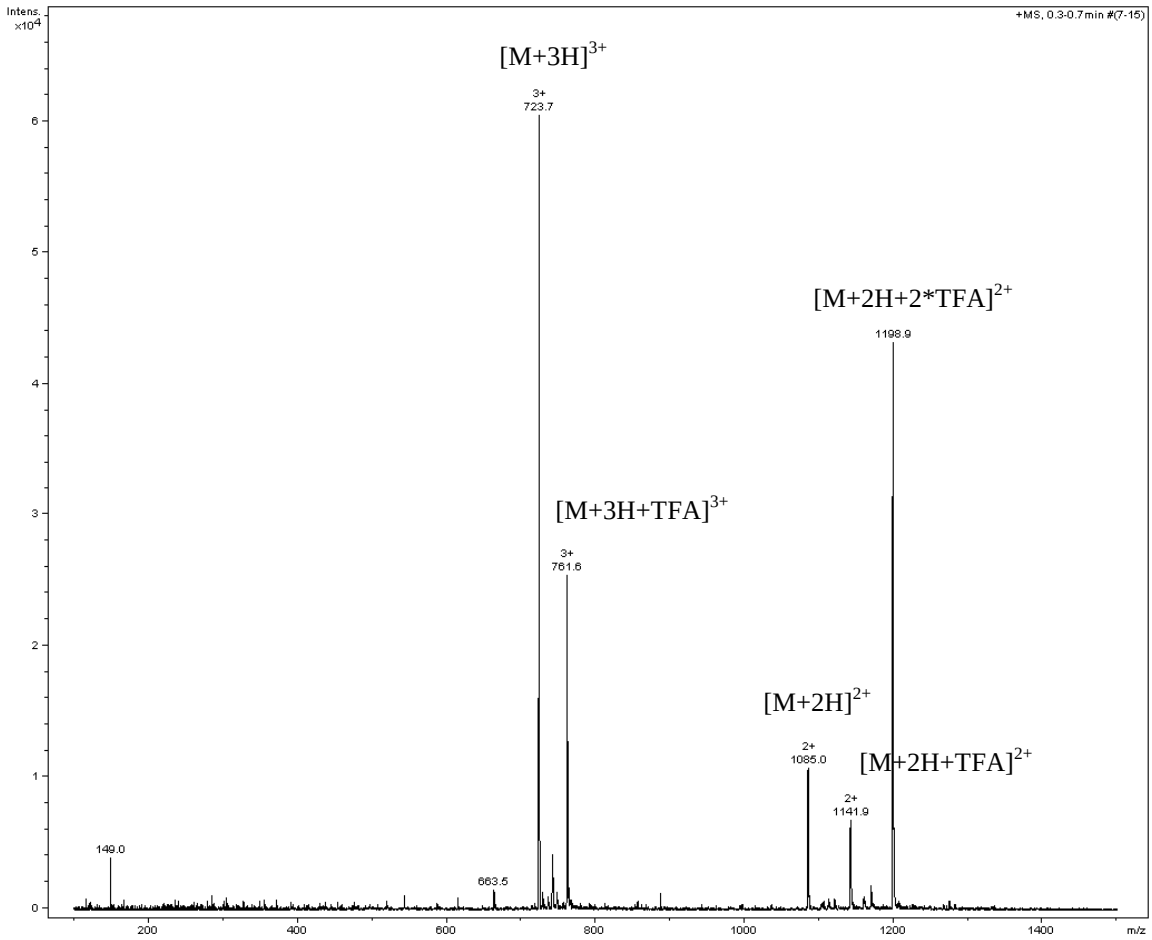

Thiol-Reactive Derivatives of the Solvatochromic 4-*N*,*N*-Dimethylamino-1,8-naphthalimide Fluorophore: A Highly Sensitive Toolset for the Detection of Biomolecular Interactions

Galen Loving and Barbara Imperiali*

Departments of Chemistry and Biology, Massachusetts Institute of Technology, 77 Massachusetts Avenue, Cambridge, Massachusetts 02139. Received July 17, 2009; Revised Manuscript Received September 18, 2009

The solvatochromic fluorophore 4-*N*,*N*-dimethylamino-1,8-naphthalimide (4-DMN) possesses extremely sensitive emission properties due largely to the low intrinsic fluorescence it exhibits in polar protic solvents such as water. This makes it well suited as a probe for the detection of a wide range of biomolecular interactions. Herein we report the development and evaluation of a new series of thiol-reactive agents derived from this fluorophore. The members of this series vary according to linker type and the electrophilic group required for the labeling of proteins and other biologically relevant molecules. Using the calcium-binding protein calmodulin as a model system, we compare the performance of the 4-DMN derivatives to that of several commercially available solvatochromic fluorophores identifying many key factors important to the successful application of such tools. This study also demonstrates the power of this new series of labeling agents by yielding a fluorescent calmodulin construct capable of producing a greater than 100-fold increase in emission intensity upon binding to calcium.

INTRODUCTION

The solvatochromic properties of many environment-sensitive fluorophores have been exploited in a wide range of biological applications such as detecting protein−peptide binding events (*1*−*6*), monitoring changes in protein allostery (*7*−*12*), and reporting various forms of post-translational modification (*13*, *14*). These fluorophores possess emission properties that are highly sensitive to the nature of the immediate solvent environment. If that environment is altered in a manner that impacts the degree of exposure to water, then such an event could produce a significant change in one or more of the emission properties of the fluorophore (i.e., fluorescence lifetime, emission wavelength, and fluorescence quantum yield) (*15*). Since both intra- and intermolecular interactions of many proteins often involve a dynamic veiling and unveiling of discrete hydrophobic clefts or pockets within the topology of these macromolecules, an appropriately placed solvatochromic fluorophore can provide a general and facile method of detecting protein function or activation. Because of the adaptable nature of these tools for addressing an array of problems in the biological sciences, many classes of solvatochromic fluorophores are now commercially available in reactive forms ready for direct conjugation to proteins and other relevant biomolecules (*16*). This diversity offers greater prospects of identifying fluorescent constructs with signaling characteristics suitable for study.

A common application of solvatochromic fluorophores is the development of constructs in which the measured fluorescence change is integrally coupled to a perturbation in a specific aspect of protein structure. Such an approach is particularly advantageous when structural changes are too subtle to be detected by other fluorescence-based methods such as Förster resonance energy transfer (FRET) (*17*) and fluorescence polarization (FP) (*18*). However, a practical limitation often encountered when using many of the commercially available solvatochromic probes is that the magnitude of the observed fluorescence change rarely approaches the maximum potential obtained in the context of a typical solvent comparison study (*6*). The reasons for this observation are varied but can frequently be attributed in part to the high degree of intrinsic fluorescence exhibited by these fluorophores in water as well as insufficient sensitivity to changes in the local environment.

Herein we report the development of a new series of cysteine modifying agents, **1**−**4**, derived from the solvatochromic fluorophore 4-*N*,*N*-dimethylamino-1,8-naphthalimide (4-DMN). The principle advantage of this fluorophore, along with other members of the dimethylaminophthalimide family, is that it exhibits extremely low fluorescence quantum yields when exposed to polar protic solvents such as water (*6*). This greatly reduces the background signal thereby creating the effect of on−off or switch-like changes in the observed emission intensity with the potential to exceed ratios of 1000-fold. Furthermore, as previously reported we have determined that this fluorophore possesses significantly greater chemical stability than the other dimethylaminophthalimide dyes we have investigated (*6*), making it particularly suitable for applications that require prolonged exposure to a wide range of aqueous conditions relevant for most biological applications.

Much of our former work with the dimethylaminophthalimide dyes focused on the development of fluorescent amino acids for incorporation into small peptide-based probes designed to recognize and report binding to discrete protein motifs such as 14−3−3 domains (*19*), SH2 domains (*3*), and PDZ domains (*20*). While these efforts have proved highly successful, our current aim has been to expand the scope of applications to include the integration of these tools into native proteins. However, several fundamental differences must be considered when applying these tools in proteins versus short peptides. With increasing peptide length, the polymer chain exhibits greater potential for adopting higher order structure (*21*), leading, in some instances, to significant changes in the local environment of the attached fluorophore.

* To whom correspondence should be addressed. Tel: 1-617-253-1838. Fax: 1-617-452-2419. E-mail: imper@mit.edu.

10.1021/bc900319z CCC: $40.75 © 2009 American Chemical Society
Published on Web 10/12/2009

Chart 1. 4-DMN-Based Cysteine Modifying Agents

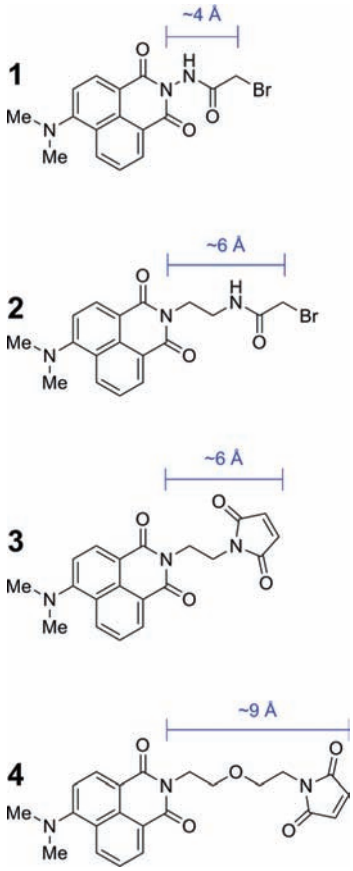

Such changes may include the degree of solvent exposure, the frequency of collisional quenching, and the emergence of local electrostatic fields. Additionally, the arrangement of the polymer chain around the dye could restrict certain vibrational modes responsible for nonradiative decay processes that compete with fluorescence. The influence of such structural elements and the effects they impart on the photophysical properties of the fluorophore are difficult to predict and can often complicate efforts toward developing useful fluorescent protein probes that utilize the full potential of the fluorescent tool. Hence, empirical screening approaches are typically required, leading us to focus on the development of a series of cysteine labeling agents. This offers a direct and facile method for the site-selective incorporation of these probes into proteins.

This study identifies key variables that influence the fluorescent response of labeled proteins to changes in protein structure, providing a general framework for understanding the ways in which solvatochromic tools may best be applied. Additionally, it reveals a systematic approach to developing future fluorescent protein probes for detecting various biomolecular interactions. The members of this new series of thiol-modifying agents vary according to the linker type and the nature of the electrophilic group necessary for cysteine labeling (Chart 1). Using the calcium-sensing protein calmodulin as a model system for our study, we demonstrate the power of this suite of solvatochromic tools to develop highly effective sensors of dynamic biomolecular interactions.

EXPERIMENTAL PROCEDURES

Synthesis of the 4-DMN Cysteine Modifying Agents (1−4). The 4-DMN derivatives **1**, **3**, and **4** were each prepared from a common precursor, **5**, which was synthesized according to the method described by Kollár et al. (*22*). The anhydride ring system of **5** offers a convenient point of attachment for introducing a diverse array of linker types with high yields. Compounds **6**, **7**, and **8** were obtained by refluxing a solution of **5** in anhydrous ethanol under an atmosphere of N_2 in the presence of hydrazine monohydrate, ethanolamine, and 2-(2-aminoethoxy)-ethanol, respectively. The intermediate **6** was then dissolved in dichloromethane with *N*,*N*-diisopropylethylamine and treated with bromoacetyl bromide to yield the labeling agent **1** (Scheme 1). Both compounds **7** and **8** were subjected to a modified Mitsunobu reaction developed by Walker (*23*) in order to install the maleimide group. The conditions of this reaction require dissolving triphenylphosphine in freshly distilled tetrahydrofuran under an atmosphere of N_2 before cooling to −78 °C. A solution of the diethyl azodicarboxylate was then added dropwise and stirred for several minutes to allow for the formation of the betaine. Solutions of either **7** or **8** were then transferred to the reaction vessel along with neopentyl alcohol. Again, the reaction was allowed to stir for several minutes to permit the formation of the reactive oxyphosphonium salt intermediate before adding solid maleimide. The reaction was run overnight at room temperature, producing compounds **3** and **4** (Scheme 1).

The preparation of compound **2** begins with commercially available 4-nitro-1,8-naphthalic anhydride, **9**. The anhydride, **9**, was dissolved in dimethylformamide with *N*,*N*-diisopropylethylamine and stirred as a solution of *N*-Boc-ethylenediamine was added via an addition funnel. The starting materials initially proceed to a ring-opened intermediate formed from the attack of the primary amine on the anhydride ring system. The free carboxylate of the intermediate was then activated using the coupling agents HOBt/HBTU to facilitate ring closure forming the naphthalimide, **10**. A suspension of compound **10** in isoamyl alcohol was refluxed under N_2 until fully dissolved, at which point 3-dimethylamino-propionitrile was added. The reaction was run overnight before isolating the product **11** in good yield. Finally, the Boc protecting group of **11** was removed using a solution of trifluoroacetic acid in dichloromethane to liberate the free amine, which was subsequently acetylated using bromoacetyl bromide under conditions similar to those used in generating compound **1**, giving the cysteine labeling agent **2** (Scheme 1).

Fluorescent Labeling and Isolation of Calmodulin Cysteine Mutants. The following procedure was performed on each of seven cysteine mutants of calmodulin (E11C, S38C, M76C, E87C, N111C, E114C, and M145C) as well as the wild-type, which served as a control to determine whether any of the labeling agents exhibited nonspecific labeling under the selected reaction conditions. All eight of the calmodulin constructs were labeled separately with one of the nine fluorophores (Charts 1 and 2) examined in this study [4-DMN derivatives **1**−**4**, 7-diethylamino-3-((((2-maleimidyl)ethyl)amino)carbonyl)-coumarin (MDCC), *N*,*N*′-dimethyl-*N*-(iodoacetyl)-*N*′-(7-nitrobenz-2-oxa-1,3-diazol-4-yl)ethylenediamine (IANBD), 6-bromoacetyl-2-dimethylaminonaphthalene (BADAN), 5-((((2-iodoacetyl)amino)ethyl)amino)naphthalene-1-sulfonic acid (IAEDANS), and 1-(2-maleimidylethyl)-4-(5-(4-methoxyphenyl)oxazol-2-yl)pyridinium methanesulfonate (PyMPO)] (*16*) to yield the 72 possible combinations. Following the expression and purification of each calmodulin mutant, the protein concentration was adjusted to 100 μM in Tris-buffered saline (TBS, pH 7.4) containing 1 mM of the reducing agent tris(2-carboxyethyl)phosphine (TCEP) and allowed to incubate at 4 °C overnight. The proteins were then analyzed by SDS−PAGE gel under nonreducing conditions to confirm that the cysteine mutants were in the fully reduced state. Aliquots of each protein (0.6 mL) were then transferred to

Scheme 1. Synthesis of 4-DMN Cysteine Modifying Agents (1−4)[a]

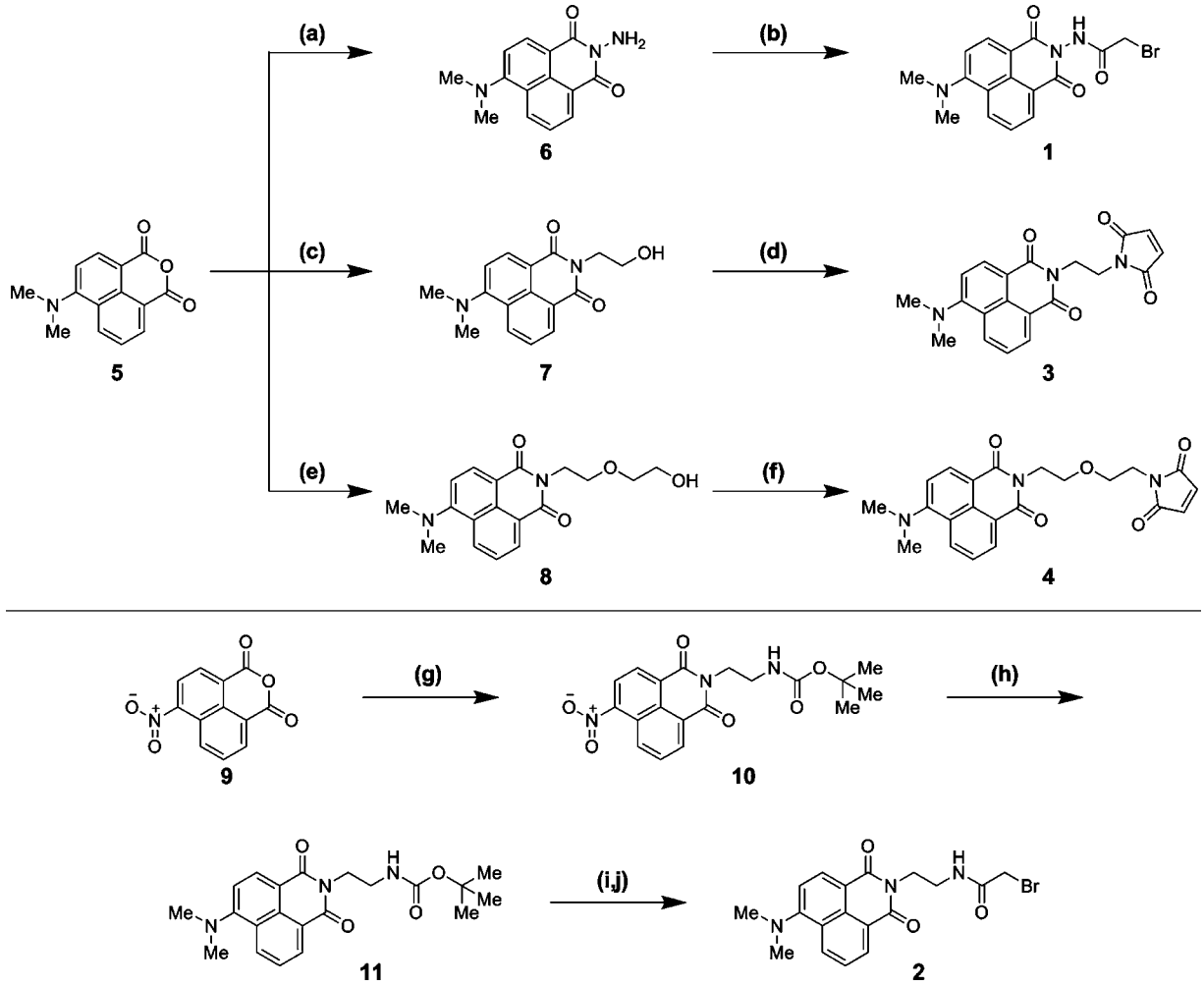

[a] Reagents and conditions: (a) hydrazine monohydrate, ethanol, Δ, N_2 (1 atm), 45 min, 87% yield; (b) bromoacetyl bromide, DIPEA, DCM (dry), −15 °C to room temperature, N_2 (1 atm), overnight, 48% yield; (c) ethanolamine, ethanol, Δ, N_2 (1 atm), 1.5 h, quantitative yield; (d) PPh_3, DEAD, neopentyl alcohol, maleimide, THF, −78 °C to room temp, N_2 (1 atm), overnight, 22% yield; (e) 2-(2-aminoethoxy)-ethanol, ethanol, Δ, N_2 (1 atm), 1.5 h, 98% yield; (f) PPh_3, DEAD, neopentyl alcohol, maleimide, THF, −78 °C to room temperature, N_2 (1 atm), overnight, 24% yield; (g) two steps, 1st *N*-Boc-ethylenediamine, DIPEA, DMF, room temperature, 1 h and 2nd HOBt/HBTU, overnight, 72% yield; (h) 3-dimethylamino-propionitrile, isoamyl alcohol, Δ, N_2 (1 atm), 22 h, 74% yield; (i) TFA/DCM (1:1), room temperature, 1.5 h; (j) bromoacetyl bromide, DIPEA, DCM (dry), −15 °C to room temperature, N_2 (1 atm), 1.5 h, 91% overall yield for steps i and j.

clear 1.7 mL microcentrifuge tubes to which 6 μL of the respective cysteine labeling agent was added from a 100 mM stock solution in DMSO. The final concentration of the labeling agent in each reaction was 1 mM. The reaction mixtures were inverted 4−6 times immediately following the addition of the labeling agent and allowed to react overnight in the dark at 4 °C. The following day, the microcentrifuge tubes containing the reaction mixtures were spun at 16,000*g* for 5 min at 4 °C to pellet any insoluble material before transferring the protein solutions to a 0.5 mL centrifugal filtering device (Millipore Ultrafree-MC, Durapore PVDF 0.22 μm). The samples were spun again at 16,000*g* for 5 min at 4 °C. The excess unreacted labeling agent in each reaction mixture was then removed using a 5 mL HiTrap desalting column obtained from GE Healthcare Life Sciences. The desalting columns were preequilibrated with TBS buffer (pH 7.4). The eluted fractions containing the labeled proteins were then quantified using the Bio-Rad protein assay where a stock solution of wild-type calmodulin of predetermined concentration was used to generate the standard curve. The labeling efficiency was determined by measuring the absorbance of the fluorophore for each construct at the corresponding wavelength of maximum absorption (λ_{max}). The calculated fluorophore concentration was then compared to the quantified protein concentration to establish the extent of protein labeling (see Supporting Information Table S1).

Fluorescence Studies of Calmodulin Mutants. Upon isolating the fluorescently labeled calmodulin constructs, stock solutions of each were prepared at 30 μM in TBS buffer (pH 7.4). Stock solutions of $CaCl_2$ (2 mM), EDTA (5 mM), guanidine hydrochloride (8 M), and the M13 peptide (*24*) (1 mM) were also prepared in TBS buffer (pH 7.4) and filtered through a 0.2 μm Nalgene cellulose acetate syringe filter prior to use. The fluorescence spectra of each construct were then measured in triplicate under five different conditions: (1) calmodulin construct only (5 μM); (2) calmodulin construct (5 μM) with $CaCl_2$ (200 μM); (3) calmodulin construct (5 μM) with $CaCl_2$ (200 μM) plus M13 peptide (10 μM); (4) calmodulin construct (5 μM) with M13 peptide (10 μM); and (5) calmodulin construct (5 μM) with guanidine hydrochloride (6.67 M). Additionally, each of these experimental conditions included 40 μM EDTA to ensure that no extraneous calcium, which may have been carried through the protein preparation, interfered with any of the fluorescence measurements. The samples were loaded in a 96 well black Polysorp Fluoronunc plate from NUNC, and the fluorescence spectra were measured for each

Chart 2. Commercially Available Solvatochromic Fluorophores

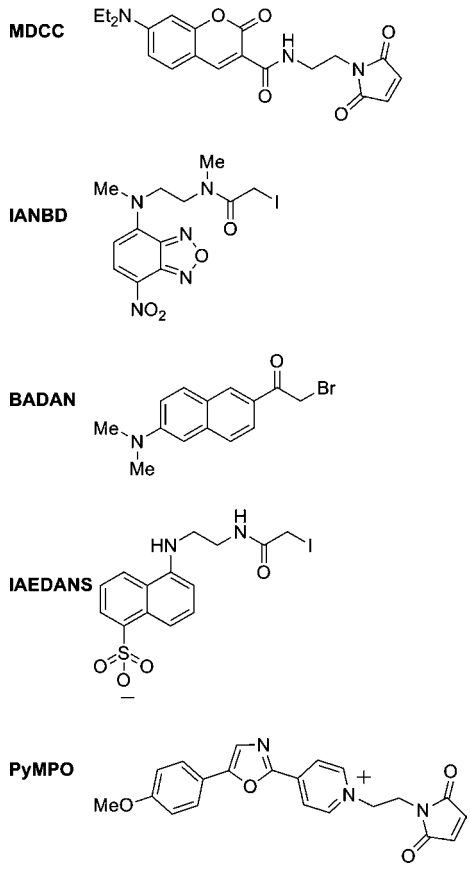

condition using a SPECTRAmax GEMINI XS plate reader from Molecular Devices. The total sample volume for each well was 200 μL. The excitation and emission settings selected for each construct are listed in Table S2 of the Supporting Information.

RESULTS

The calcium binding protein calmodulin (CaM) (Figure 1a), which has been extensively characterized by a number of research groups (*25*), was selected as the model system for a comparative study to evaluate the performance of the 4-DMN cysteine modifying agents **1**−**4**. CaM is a soluble protein that responds to sudden influxes of cytosolic Ca^{2+} levels (*26*) by rapidly chelating as many as four of these cations through specialized Ca^{2+}-binding motifs called EF-hands. The binding event induces an allosteric change in the N- and C-terminal domains of the protein resulting in the formation of two hydrophobic pockets, which can then bind critical hydrophobic residues of certain peptide motifs that are recognized by the protein (Figure 1b) (*25, 27*). One advantage to using calmodulin is that the wild-type protein is devoid of native cysteine residues. This characteristic affords considerable freedom in selecting discrete sites for cysteine mutagenesis and subsequent modification by a thiol-reactive agent. The exceptional attributes offered by this unique system provides a useful benchmark for our studies as numerous research groups (*12, 28*−*32*) over the last 30 years have attempted to develop CaM-based calcium sensors by labeling the protein at a variety of sites with various solvatochromic probes. However, despite extensive efforts, the reported changes in fluorescence emission are modest and typically encumbered by high background fluorescence, which strongly limits the utility of these constructs in certain applications such as fluorescence microscopy.

Based on careful examination of available X-ray and NMR structures of calmodulin in the apo-state (*33*), as well as the calcium-bound (*34*) and calcium-peptide-bound (*35*) states, seven sites were selected for cysteine mutagenesis (Figure 1a). The basis for the selection process was the identification of residues that are relatively solvent exposed when the protein exists in the apo-state and do not appear to play an important functional role that might be disrupted through mutagenesis and labeling. By exploring multiple sites spanning the breadth of the protein structure, it is possible to resolve trends that are site-dependent from those that are site-independent and better ascertain the robustness of those trends. Site-directed mutagenesis was performed on the wild-type template to introduce cysteine residues at two sites on the N-terminal domain (E11C

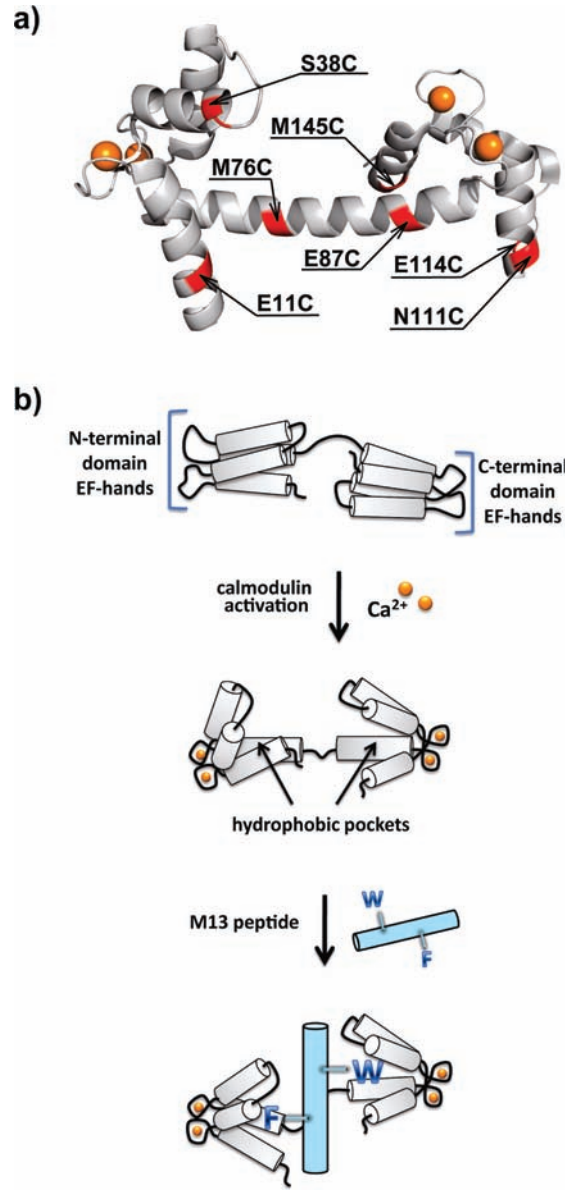

Figure 1. (a) Crystal structure of the Ca^{2+}−CaM complex deposited by Rupp et al. (PDB entry 1UP5) (*34*). The structure indicates the seven sites selected for cysteine mutagenesis (red). The bound calcium ions are indicated by spheres (yellow). (b) Ca^{2+} activation of a CaM mutant (gray) can result in the burying of an attached solvatochromic fluorophore within one of the newly formed hydrophobic pockets. In response, the fluorophore exhibits a change in one or more of the emission properties. Subsequent addition of the M13 peptide (cyan) can displace the fluorophore from the pocket through insertion of an aromatic side chain from the phenylalanine or tryptophan residue indicated here using the single-letter notation for amino acids.

and S38C), two sites within the linker region (M76C and E87C), and three sites in the C-terminal domain (N111C, E114C, and M145C).

In addition to the 4-DMN derivatives **1**−**4**, five commercially available solvatochromic fluorophores were also included in this study for comparison (Chart 2). These fluorophores provide a representative sampling of the major classes of solvatochromic probes that are currently available and commonly used at this time. The reagents vary fundamentally in size, shape, and hydrophobicity, and each exhibits distinct photophysical properties (*16*). For the comparison, we focused on common dyes that were available as thiol-reactive labeling agents possessing dimensions similar to that of the 4DMN derivatives. With a total of 9 fluorescent labeling agents and 7 cysteine mutants of calmodulin, the 63 possible fluorescent constructs were prepared for evaluation. The wild-type CaM construct was included as a control in the labeling experiments, although no significant background labeling was observed.

In order to gauge the capacity of each labeling agent to report a change in the structural state of the calmodulin mutants, fluorescence spectra were collected in the presence and absence of saturating calcium. Additionally, since the Ca^{2+}−CaM complex is capable of binding certain peptide motifs with high affinity, a known peptide binding partner commonly referred to as the M13 peptide (*24*) was also introduced to the fluorescent constructs, in the presence and absence of calcium, to observe whether further changes in the emission spectra occur. The constructs were compared by measuring the ratio of fluorescence intensity at the wavelength of maximum emission of the Ca^{2+}−CaM complex to that of the apo-state for the three examined conditions (saturating Ca^{2+}, saturating M13 peptide, and saturating Ca^{2+} with the M13 peptide).[1] The results of these studies are shown in Figure 2.

A common feature observed among most of the cysteine mutants of this study was the tendency to exhibit higher fluorescence intensity in the Ca^{2+}-bound state compared to that of the full Ca^{2+}−CaM−M13 peptide complex (Figure 2a-f). This propensity for the labeled constructs to display a diminished fluorescent signal in the presence of a native peptide-binding partner was general for all of the solvatochromic fluorophores, with the exception of the two charged species IAEDANS and PyMPO included in this study. The effect is attributed to a process of competitive displacement in which the fluorophore and ligand both compete for occupancy of the same hydrophobic binding site, thereby increasing the average exposure of the fluorophore to the surrounding solvent environment. However, this behavior was by no means a rule as many constructs included in this study, particularly those of the M145C mutant (Figure 2g), exhibited the greatest fluorescence intensity for the Ca^{2+}−CaM−M13 peptide complex.

A number of key trends emerged from the fluorescence screen. One among these was a pronounced dependence of the measured fluorescence change on the linker type for the 4-DMN series of compounds **1**−**4**. For instance, the E11C mutant exhibited a strong bias for the shortest linker of the series (4 Å), whereas the trend was the reverse for the S38C mutant, which yielded the best response with linkers of intermediate to longer length (6−9 Å). This result was largely site-dependent and yielded no clear pattern for determining the optimal linker type *a priori*. Hence, the process of identifying a construct with the desired fluorescence properties may best be accomplished through an empirical approach, utilizing the set of 4-DMN labeling agents as a combined suite.

The next revealed trend was the marked ability of the calmodulin cysteine mutants labeled with the 4-DMN derivatives, **1**−**4**, to produce greater signal increases in response to the presence of saturating calcium (or calcium plus the M13 peptide) over those modified by the other dyes considered in the study. Although in some cases these differences were modest, the overall trend demonstrated that this property was robust and relatively site-independent. This is particularly apparent for the S38C mutant (Figure 2b) labeled with compound **3**, which showed a greater than 100-fold increase in emission intensity upon binding calcium. Among the commercially available fluorophores, IANBD was the closest by comparison exhibiting only a 15-fold increase in intensity. Although the influence of linker type, which played a crucial role in obtaining optimal results with the 4-DMN fluorophore, was not examined when comparing the other commercial fluorophores, the limiting factor for those dyes was largely due to the high degree of intrinsic fluorescence that each exhibits in aqueous environments. This high background effectively reduces the maximum attainable signal-to-noise ratio despite these dyes being good fluorophores.

Results of the study also suggest that certain factors known to enhance hydrophilicity can negatively influence the capacity of a solvatochromic fluorophore to respond to perturbations within the local topology of the protein surface. This was particularly apparent among the two charged dyes included in the series (IAEDANS and PyMPO). Neither dye displayed significant changes in emission properties when the associated cysteine mutants were exposed to combinations of Ca^{2+} and the M13 peptide. By bearing a formal positive or negative charge, the energetic cost of desolvating these fluorescent species may negate any benefit gained by burying the aromatic ring systems deep within a hydrophobic pocket formed as the result of a conformational change to the protein structure. This would greatly impact the equilibrium of the buried versus solvated state, making these probes less sensitive to such structural dynamics despite otherwise exhibiting good solvatochromic properties. Although this trend was relatively site-independent for the mutants of the calmodulin protein, it is expected that these probes could be better suited for applications where the possibility of charge complementarity exists or where other molecular driving forces are responsible for the partitioning of the probes between two distinct environments (*36*).

DISCUSSION

In developing this series of 4-DMN cysteine labeling agents, an essential question we wished to address was whether there was value in utilizing an assortment of linker types or if this simply introduced an element of redundancy. The results of this study strongly indicate that the linker type does play a critical role in influencing the magnitude of the fluorescent response. For a solvatochromic probe to function optimally, it must directly interact with a feature of interest. If this feature happens to be a hydrophobic pocket located far from the point of attachment on the protein surface, then a longer linker would clearly be favored over one that is unable to span this distance (Figure 3a). However, a caveat of using a longer linker is that the greater range may inadvertently increase the probability that the fluorophore will encounter and bind a shallow hydrophobic patch that is unaltered by the structural state of the protein. Such a static interaction would produce an undesirable increase in the fluorescence background. In this instance, a shorter linker could prove better suited (Figure 3b). In fact, this appears to be the case for mutant E11C where compound **1** produced a much greater increase in fluorescence intensity than compound **4** upon

[1]For the fluorescent constructs of the M145C CaM mutant, all fluorescence measurements were made at the wavelength of maximum emission for the Ca^{2+}−CaM−M13 peptide complex instead of the of the Ca^{2+}−CaM complex since this state generally exhibited greater emission intensity.

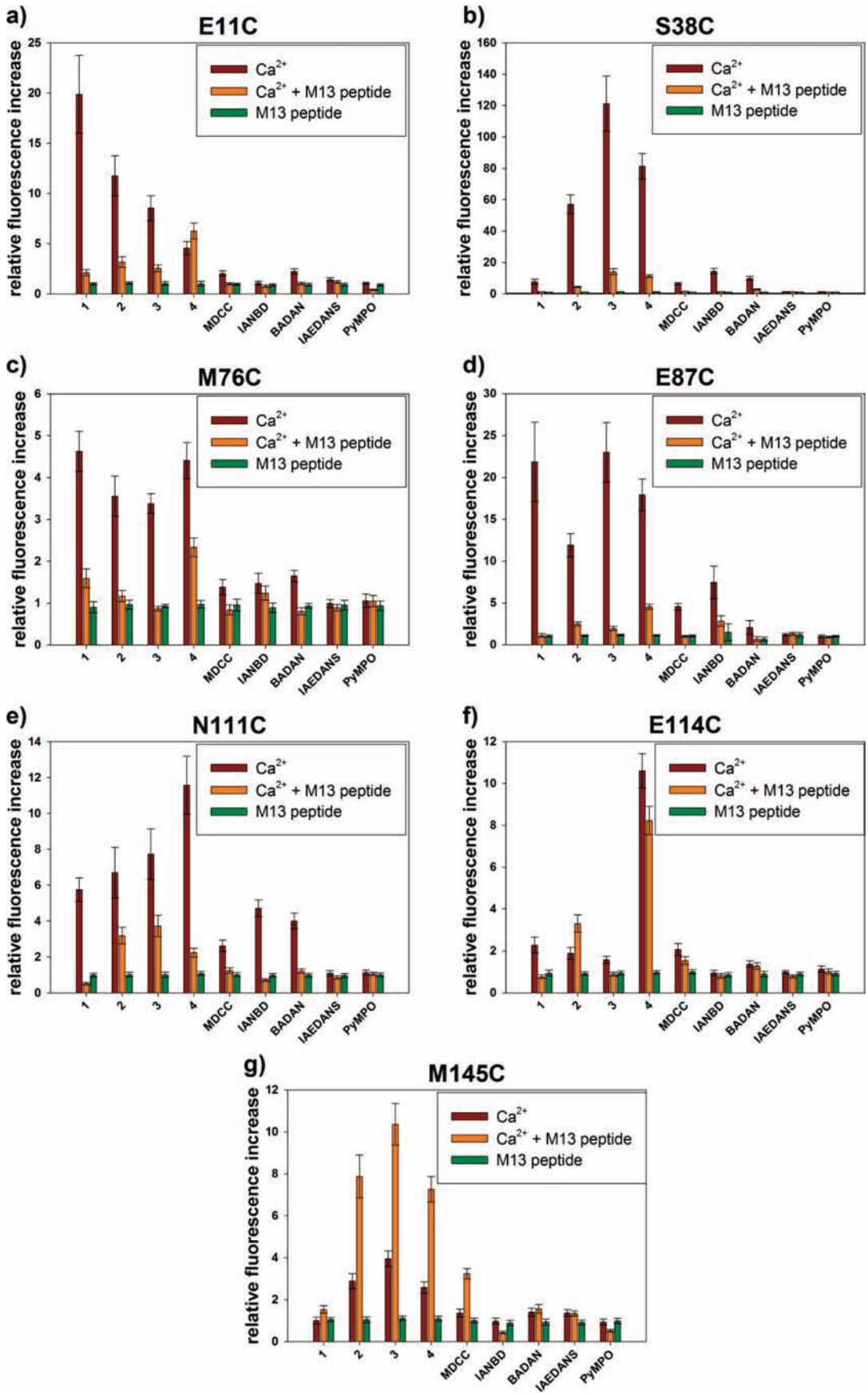

Figure 2. (a−g) Histograms indicating the fluorescence results obtained from the seven cysteine mutants examined in this study. The vertical bars represent the ratio of fluorescence intensity measured at the wavelength of maximum emission under the condition that yielded the brightest state for each construct with respect to that of the apo-state. The fluorophores are indicated along the horizontal axis below the associated results. For each condition, saturating levels of Ca^{2+} and/or the M13 peptide were used. The indicated errors represent the 90% confidence intervals determined from three trials.

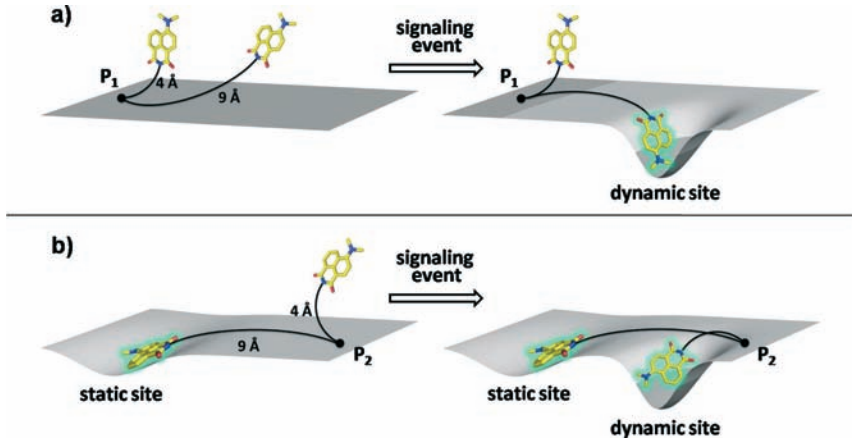

Figure 3. (a) Attachment point P_1 is located far from a hydrophobic pocket formed upon a structural change in the protein. Here, a longer linker is preferred to a shorter one. (b) Attachment point P_2 is located near the hydrophobic pocket formed in response to a structural change. Such sites may favor shorter linkers as longer linkers could tend to allow the fluorophore to encounter nonspecific hydrophobic patches that remain static with regard to the dynamics of protein topology. This would result in higher background fluorescence.

the addition of saturating Ca^{2+}. Both constructs displayed comparable emission intensities in the Ca^{2+} bound state. However, the apo-state of the construct labeled with **4** exhibited a fluorescence background that was roughly 5-fold greater than that of the construct with the shortest linker, resulting in the smaller observed increase.

Interference by background fluorescence is a phenomenon that affects all solvatochromic fluorophores and extends beyond the model system used in this study. Solvatochromic fluorophores often display somewhat different emission properties when appended to globular proteins such as calmodulin.[2] A bulky hydrophobic fluorophore protruding into the surrounding solvent environment demands a large enthalpic cost due to the disruption of the dense network of hydrogen-bonded water molecules. Consequently, the probe will exhibit a strong tendency to associate with any hydrophobic clefts or pockets formed by structural elements within the immediate vicinity to minimize this exposure. The degree of background fluorescence associated with these nonspecific interactions is largely site-dependent for a fluorophore of a given linker-type. This interference is further compounded by any intrinsic fluorescence already produced by the probe in water. A convenient method we have developed for measuring the background resulting from such effects involves comparing the emission spectra of the construct under both natured (TBS buffer at pH 7.4) and denatured conditions (TBS buffer at pH 7.4 with 6.67 M guanidine hydrochloride). This was performed with all 63 fluorescently labeled calmodulin constructs and the results summarized in Figure S2 of the Supporting Information. Although site-dependent background fluorescence appeared to be a critical limitation to many of the commercial dyes, this issue proved much less consequential for the 4-DMN derivatives because of the negligible degree of intrinsic fluorescence exhibited by these probes in water.

An ideal site for labeling would be one that precludes the solvatochromic fluorophore from forming any surface associations of this sort until a structural change in the protein has occurred. In practice, however, identifying an optimal labeling site is often challenging even when exceptional structural data for the protein is available. As a result, screening of a strategically selected series of cysteine mutants is typically required. When applied in combination with the series of 4-DMN labeling agents, this approach allowed us to readily identify a number of fluorescent mutants that respond sensitively and selectively to the formation of the $Ca^{2+}-$CaM complex. Additionally, although the 4-DMN labeled M145C mutants showed only a modest selectivity for the $Ca^{2+}-$CaM$-$M13 peptide complex over that of the $Ca^{2+}-$CaM complex, it is possible that a more extensive screen could yield a construct with greatly improved properties permitting access to a set powerful sensors of either state.

[2]We have observed similar effects in our work with SH2 domains, PDZ domains, and the regulatory light-chain of myosin.

CONCLUSIONS

In this study, the 4-DMN derivatives **1**$-$**4** were evaluated and compared with five other well-established solvatochromic fluorophores to address a number of critical factors pertaining to the successful application of such tools in detecting specific types of bimolecular interactions. These factors include the importance of linker type, the influence of hydrophobicity, and the deleterious effects of high intrinsic fluorescence.

Because of the rarity in which solvatochromic fluorophores exhibit the maximum potential fluorescence changes when used in many biological applications, the large intrinsic fluorescence exhibited by many of these probes in aqueous environments represents a critical issue that can ultimately be limiting. This matter is further compounded by the strong tendency for these probes to show a marked enhancement in fluorescent signal when appended to proteins as a result of nonspecific topological interactions. Because the 4-DMN derivatives possess such low intrinsic fluorescence in water, these effects are significantly less consequential.

Linker variety is a fundamental component to designing sensors that incorporate solvatochromic dyes and is a feature that is not typically examined systematically. Often, the linker is considered a passive component of fluorescent labeling agents, serving merely to connect the dye to the target molecule without interfering with native properties such as function or solubility. Here, we demonstrate that linkers play a more active role and can be a vital element in the optimization of the fluorescent response. When applied in combination with cysteine-scanning mutagenesis, the number of fluorescent constructs is greatly expanded, thereby increasing the potential for obtaining a sensor with the desired properties. We therefore present this series of labeling agents as a combined suite that offers the excellent properties of the 4-DMN dye in a format ready to meet the strict demands required by a wide spectrum of applications ranging from high-throughput screening assays to fluorescence microscopy.

ACKNOWLEDGMENT

This research was supported by NSF CHE-0414243 (BI), the NIH Cell Migration Consortium (GM064346), and the Biotechnology Training Program (T32-GM08334). We offer special thanks to Dr. M. A. Sainlos (MIT) and Dr. A. Aemissegger (MIT) for their helpful advice and insight. The Department of Chemistry Instrumentation Facility (NSF CHE-9808061, DBI-9729592, and CHE-0234877) and the Biophysical Instrumentation Facility for the Study of Complex Macromolecular Systems (NSF-0070319) are also gratefully acknowledged.

Supporting Information Available: Synthesis and characterization of the 4-*N*, *N*-dimethylamino-1,8-naphthalimide thiol-reactive agents **1**−**4**; synthesis and characterization of the M13 peptide; cysteine mutagenesis of the CaM construct; expression and purification of the CaM cysteine mutants; labeling efficiencies for each of the prepared fluorescent constructs; emission and excitation settings for the SPECTRAmax GEMINI XS plate reader; and background emission studies of denatured fluorescent CaM constructs. This material is available free of charge via the Internet at http://pubs.acs.org.

LITERATURE CITED

(1) Venkatraman, P., Nguyen, T. T., Sainlos, M., Bilsel, O., Chitta, S., Imperiali, B., and Stern, L. J. (2007) Fluorogenic probes for monitoring peptide binding to class II MHC proteins in living cells. *Nat. Chem. Biol 3*, 222–228.

(2) Vazquez, M. E., Nitz, M., Stehn, J., Yaffe, M. B., and Imperiali, B. (2003) Fluorescent caged phosphoserine peptides as probes to investigate phosphorylation-dependent protein associations. *J. Am. Chem. Soc. 125*, 10150–10151.

(3) Vazquez, M. E., Blanco, J. B., and Imperiali, B. (2005) Photophysics and biological applications of the environment-sensitive fluorophore 6-N,N-dimethylamino-2,3-naphthalimide. *J. Am. Chem. Soc. 127*, 1300–1306.

(4) Wang, Q. Z., and Lawrence, D. S. (2005) Phosphorylation-driven protein-protein interactions: A protein kinase sensing system. *J. Am. Chem. Soc. 127*, 7684–7685.

(5) Enander, K., Choulier, L., Olsson, A. L., Yushchenko, D. A., Kanmert, D., Klymchenko, A. S., Demchenko, A. P., Mely, Y., and Altschuh, D. (2008) A peptide-based, ratiometric biosensor construct for direct fluorescence detection of a protein analyte. *Bioconjugate Chem. 19* 1864–1870.

(6) Loving, G., and Imperiali, B. (2008) A versatile amino acid analogue of the solvatochromic fluorophore 4-N, N-dimethylamino-1,8-naphthalimide: A powerful tool for the study of dynamic protein interactions. *J. Am. Chem. Soc. 130*, 13630–13638.

(7) Zhu, J. G., and Pei, D. H. (2008) A LuxP-based fluorescent sensor for bacterial autoinducer II. *ACS Chem. Biol. 3*, 110–119.

(8) Hibbs, R. E., Talley, T. T., and Taylor, P. (2004) Acrylodan-conjugated cysteine side chains reveal conformational state and ligand site locations of the acetylcholine-binding protein. *J. Biol. Chem. 279*, 28483–28491.

(9) Cohen, B. E., Pralle, A., Yao, X. J., Swaminath, G., Gandhi, C. S., Jan, Y. N., Kobilka, B. K., Isacoff, E. Y., and Jan, L. Y. (2005) A fluorescent probe designed for studying protein conformational change. *Proc. Natl. Acad. Sci. U.S.A. 102*, 965–970.

(10) Hahn, K., Debiasio, R., and Taylor, D. L. (1992) Patterns of elevated free calcium and calmodulin activation in living cells. *Nature 359*, 736–738.

(11) Dattelbaum, J. D., Looger, L. L., Benson, D. E., Sali, K. M., Thompson, R. B., and Hellinga, H. W. (2005) Analysis of allosteric signal transduction mechanisms in an engineered fluorescent maltose biosensor. *Protein Sci. 14*, 284–291.

(12) SchauerVukasinovic, V., Cullen, L., and Daunert, S. (1997) Rational design of a calcium sensing system based on induced conformational changes of calmodulin. *J. Am. Chem. Soc. 119*, 11102–11103.

(13) Post, P. L., Trybus, K. M., and Taylor, D. L. (1994) A genetically-engineered, protein-based optical biosensor of myosin-II regulatory light-chain phosphorylation. *J. Biol. Chem. 269*, 12880–12887.

(14) Cassidy, P. B., Dolence, J. M., and Poulter, C. D. (1995) Continuous fluorescence assay for protein prenyltransferases. *Methods Enzymol. 250*, 30–43.

(15) Lakowicz, J. R. (2006) *Principles of Fluorescence Spectroscopy*, pp 205−235, Springer, New York.

(16) Haugland, R. P., Spence, M. T. Z., Johnson, I. D., and Basey, A. (2005) *The Handbook: A Guide to Fluorescent Probes and Labeling Technologies*, 10th ed., Molecular Probes, Eugene, OR.

(17) Vogel, S. S., Thaler, C., and Koushik, S. V. (2006) Fanciful FRET. *Sci. STKE 2006*, *re2*.

(18) Goulko, A. A., Zhao, Q., Guthrie, J. W., Zou, H., Le, X. C. (2008) Fluorescence Polarization: Recent Bioanalytical Applications, Pitfalls, and Future Trends, in *Springer Series on Fluorescence* (Wolfbeis, O. S. , Ed.) pp 303−322, Springer, New York.

(19) Vazquez, M. E., Rothman, D. M., and Imperiali, B. (2004) A new environment-sensitive fluorescent amino acid for Fmoc-based solid phase peptide synthesis. *Org. Biomol. Chem. 2*, 1965–1966.

(20) Sainlos, M., Iskenderian, W. S., and Imperiali, B. (2009) A general screening strategy for peptide-based fluorogenic ligands: probes for dynamic studies of PDZ domain-mediated interactions. *J. Am. Chem. Soc. 131*, 6680–6682.

(21) Hill, D. J., Mio, M. J., Prince, R. B., Hughes, T. S., and Moore, J. S. (2001) A field guide to foldamers. *Chem. Rev. 101*, 3893–4011.

(22) Kollar, J., Hrdlovic, P., Chmela, T., Sarakha, M., and Guyot, G. (2005) Spectral properties of probes based on pyrene and piperazine: the singlet and triplet route of deactivation. *J. Photochem. Photobiol., A 171*, 27–38.

(23) Walker, M. A. (1995) A high-yielding synthesis of N-alkyl maleimides using a novel modification of the Mitsunobu reaction. *J. Org. Chem. 60*, 5352–5355.

(24) Blumenthal, D. K., Takio, K., Edelman, A. M., Charbonneau, H., Titani, K., Walsh, K. A., and Krebs, E. G. (1985) Identification of the calmodulin-binding domain of skeletal muscle myosin light chain kinase. *Proc. Natl. Acad. Sci. U.S.A. 82*, 3187–3191.

(25) Crivici, A., and Ikura, M. (1995) Molecular and structural basis of target recognition by calmodulin. *Annu. Rev. Biophys. Biomol. Struct. 24*, 85–116.

(26) Berridge, M. J., Bootman, M. D., and Roderick, H. L. (2003) Calcium signalling: dynamics, homeostasis and remodelling. *Nat. Rev. Mol. Cell Biol. 4*, 517–529.

(27) Yap, K. L., Kim, J., Truong, K., Sherman, M., Yuan, T., and Ikura, M. (2000) Calmodulin target database. *J. Struct. Funct. Genomics 1*, 8–14.

(28) Torok, K., and Trentham, D. R. (1994) Mechanism of 2-chloro-(epsilon-amino-Lys75)-[6-[4-(N, N- diethylamino)phenyl]-1,3,5-triazin-4-yl]calmodulin interactions with smooth muscle myosin light chain kinase and derived peptides. *Biochemistry 33*, 12807–12820.

(29) Milikan, J. M., and Bolsover, S. R. (2000) Use of fluorescently labelled calmodulins as tools to measure subcellular calmodulin activation in living dorsal root ganglion cells. *Pflugers Arch. 439*, 394–400.

(30) Olwin, B. B., and Storm, D. R. (1983) Preparation of fluorescent labeled calmodulins. *Methods Enzymol. 102*, 148–157.

(31) Nakanishi, J., Nakajima, T., Sato, M., Ozawa, T., Tohda, K., and Umezawa, Y. (2001) Imaging of conformational changes of proteins with a new environment/sensitive fluorescent probe designed for site specific labeling of recombinant proteins in live cells. *Anal. Chem. 73*, 2920–2928.

(32) Hahn, K. M., Waggoner, A. S., and Taylor, D. L. (1990) A calcium-sensitive fluorescent analog of calmodulin based on a novel calmodulin-binding fluorophore. *J. Biol. Chem. 265*, 20335–20345.

(33) Zhang, M., Tanaka, T., and Ikura, M. (1995) Calcium-induced conformational transition revealed by the solution structure of apo calmodulin. *Nat. Struct. Biol. 2*, 758–767.

(34) Rupp, B., Marshak, D. R., and Parkin, S. (1996) Crystallization and preliminary X-ray analysis of two new crystal forms of calmodulin. *Acta Crystallogr., Sect. D 52*, 411–413.

(35) Ikura, M., Clore, G. M., Gronenborn, A. M., Zhu, G., Klee, C. B., and Bax, A. (1992) Solution structure of a calmodulin-target peptide complex by multidimensional NMR. *Science 256*, 632–638.

(36) Savalli, N., Kondratiev, A., Toro, L., and Olcese, R. (2006) Voltage-dependent conformational changes in human Ca(2+)- and voltage-activated K(+) channel, revealed by voltage-clamp fluorometry. *Proc. Natl. Acad. Sci. U.S.A 103*, 12619−12624.

BC900319Z

Supporting Information for:

Thiol-reactive Derivatives of the Solvatochromic 4-*N*,*N*-Dimethylamino-1,8-naphthalimide Fluorophore: A Highly Sensitive Toolset for the Detection of Biomolecular Interactions

*Galen Loving, Barbara Imperiali**

Departments of Chemistry and Biology, Massachusetts Institute of Technology,

77 Massachusetts Avenue, Cambridge, Massachusetts 02139, USA

Table of Contents

10× TBS Buffer **3**

Synthesis of 4-*N*,*N*-dimethyl-1,8-naphthalimide cysteine modifying reagents **3**

4-Nitro-*N*-(2-*tert*-butoxycarbonylamino-ethyl)-1,8-naphthalimide (**10**) 3

4-*N*,*N*-Dimethylamino-*N*-(2-*tert*-butoxycarbonylamino-ethyl)-1,8-naphthalimide (**11**) 4

4-*N*,*N*-Dimethylamino-*N*-[2-(2-bromo-acetylamino)-ethyl]-1,8-naphthalimide (**2**) 5

4-*N*,*N*-Dimethylamino-*N*-(2-hydroxy-ethyl)-1,8-naphthalimide (**7**) 6

4-*N*,*N*-Dimethylamino-*N*-(2-maleimidyl-ethyl)-1,8-naphthalimide (**3**) 7

4-*N*,*N*-Dimethylamino-*N*-[2-(2-hydroxy-ethoxy)-ethyl]-1,8-naphthalimide (**8**) 8

4-*N*,*N*-Dimethylamino-*N*-[2-(2-maleimidyl-ethoxy)-ethyl]-1,8-naphthalimide (**4**) 9

N-Amino-4-*N*,*N*-dimethylamino-1,8-naphthalimide (**6**) 10

4-*N*,*N*-Dimethylamino-*N*-[2-bromoacetamido]-1,8-naphthalimide (**1**) 11

NMR spectra of synthesized compounds **12**

Synthesis of the M13 peptide **21**

Subcloning of the synthetic CaM gene into the pET-14b vector **22**

Sequence of codon-optimized CaM gene 22

Translation of codon-optimized CaM gene 22

Subcloning of codon-optimized CaM gene 23

Cysteine mutagenesis of wild-type CaM gene **24**

Expression and purification of wild-type CaM and cysteine mutants **26**

ESI-MS of expressed CaM constructs **28**

Labeling efficiencies (Table S1) **29**

Emission and Excitation settings for SPECTRAmax GEMINI XS plate reader (Table S2) **29**

Denaturing of fluorescent CaM constructs to determine background emission (Figure S2) **31**

10× TBS Buffer:

60.6 g Tris-HCl
87.7 g NaCl

Dissolved salts in 800 mL of distilled H_2O and adjusted pH to 7.3 with concentrated HCl. The volume was then adjusted to 1 L. Upon diluting 10× TBS buffer ten-fold with distilled H_2O, the pH should be 7.4. The final 1× TBS concentrations are 50 mM Tris-HCl, 150 mM NaCl, and pH 7.4. All references to solutions prepared in TBS buffer pertain to this recipe.

Synthesis of 4-*N,N*-dimethyl-1,8-naphthalimide cysteine modifying reagents:

All reagents were procured from Sigma-Aldrich unless otherwise stated.

NMR and FT-MS of the following derivatives: ^{1}H and ^{13}C NMR spectra were recorded on a Varian Mercury 300 MHz NMR and Varian Inova 500 MHz NMR spectrometer. Chemical shifts (δ) for ^{1}H and ^{13}C NMR spectra are reported in parts per million (ppm) and are referenced to residual protium in the deuterated solvent. Coupling constants (*J*) are reported in Hertz (Hz) and multiplicities are abbreviated as singlet (s), doublet (d), triplet (t), and multiplet (m). High-resolution mass spectra were obtained using a Bruker Daltonics APEXIV 4.7 Tesla Fourier Transform Ion Cyclotron Resonance Mass Spectrometer (FT-ICR-MS).

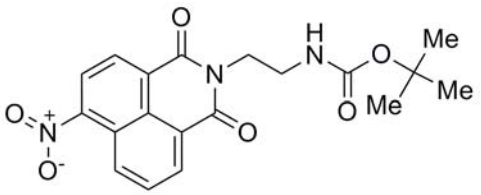

4-Nitro-*N*-(2-*tert*-butoxycarbonylamino-ethyl)-1,8-naphthalimide (10). Dissolved 4-nitro-1,8-naphthalic anhydride, **9** (9.2 g, 37.7 mmol), in 50 mL of DMF, then added DIPEA (17.9 mL, 102.9 mmol). In a separate flask, *N*-Boc-ethylenediamine was dissolved in another 50 mL DMF and added over 4 min to the solution containing the anhydride via an addition funnel. The reaction was allowed to

proceed for 1 hr at ambient temperature before adding the coupling reagents HOBt/HBTU (100 mL, 0.58 M each in DMF) to facilitate closure of the imide ring system. The reaction was allowed to proceed overnight. The next day, the reaction mixture was poured into a large separatory funnel containing 400 mL of diethyl ether and washed with brine (3 × 200 mL) to remove DMF (note- some precipitation of the product from the organic layer may be observed if left for extended periods of time). The organic layer was then dried with $MgSO_4$, filtered, and concentrated to dryness. The crude product was then purified by flash column chromatography using 3:1 hexanes/ethyl acetate to give a light cream colored solid (9.56 g, 24.8 mmol, 72.3% yield, R_f = 0.1 in 3:1 hexanes/EtOAc). ^{1}H NMR (300 MHz, $CDCl_3$, δ): 1.21 (s, 9H), 3.53 (m, 2H), 4.34 (t, 2H, J = 5.7 Hz), 4.97 (m, 1H), 7.94 (dd, 1H, J_1 = 8.7 Hz, J_2 = 7.5 Hz), 8.36 (d, 1H, J = 8.1 Hz), 8.65 (d, 1H, J = 8.1 Hz), 8.69 (dd, 1H, J_1 = 7.4 Hz, J_2 = 1.1 Hz), 8.77 (dd, 1H, J_1 = 8.7 Hz, J_2 = 0.9 Hz). ^{13}C NMR (300 MHz, $CDCl_3$, δ): 28.4, 39.3, 40.7, 79.5, 123.0, 123.7, 124.1, 127.0, 129.3, 129.5, 130.1, 130.1, 132.7, 149.7, 156.3, 163.0, 163.8. HRMS-ESI (*m/z*): $[M+Na]^+$ calcd for $C_{19}H_{19}N_3O_6$, 408.1166; found, 408.1188.

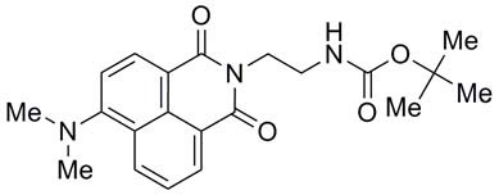

4-*N*,*N*-Dimethylamino-*N*-(2-*tert*-butoxycarbonylamino-ethyl)-1,8-naphthalimide (11). The 4-nitro-*N*-(2-*tert*-butoxycarbonylamino-ethyl)-1,8-naphthalimide, **10** (2.00 g, 5.19 mmol), was added to a 250 mL two-necked round-bottom flask equipped with a reflux condenser, rubber septum, and magnetic stir bar. The assembled reaction vessel was then charged with and inert atmosphere by evacuating the air under reduced pressure and purging with N_2 gas (3×). The flask then received 52 mL of isoamyl alcohol transferred by syringe through the rubber septum. The suspension was stirred as the temperature was raised to 132 ºC. Once the starting material dissolved, 3-dimethylamino-propionitrile (2.35 mL, 20.8 mmol) was added by syringe through the septum of the reaction vessel. The reaction

was refluxed for 22 hrs before stopping by concentrating the reaction mixture to dryness by rotary evaporation. The crude was then purified by flash chromatography using 7:3 hexanes/ethyl acetate to give an orange solid (1.47 g, 3.83 mmol, 74% yield, R_f = 0.25 in 1:1 hexanes/ethyl acetate). ^{1}H NMR (300 MHz, $CDCl_3$, δ): 1.31 (s, 9H), 3.10 (s, 6H), 3.51 (m, 2H), 4.34 (t, 2H, J = 5.6 Hz), 5.09 (br, 1H), 7.09 (d, 1H, J = 8.1 Hz), 7.64 (dd, 1H, J_1 = 8.6 Hz, J_2 = 7.4 Hz), 8.42 (dd, 1H, J_1 = 8.4 Hz, J_2 = 1.2 Hz), 8.46 (d, 1H, J = 8.1 Hz), 8.56 (dd, 1H, J_1 = 7.4 Hz, J_2 = 1.1 Hz). ^{13}C NMR (500 MHz, $CDCl_3$, δ): 28.2, 39.4, 39.8, 44.7, 78.9, 113.1, 114.5, 122.7, 124.7, 125.1, 130.2, 131.1, 131.2, 132.8, 156.0, 157.0, 164.3, 164.9. HRMS-ESI (*m/z*): $[M+H]^+$ calcd for $C_{21}H_{25}N_3O_4$, 384.1923; found, 384.1932.

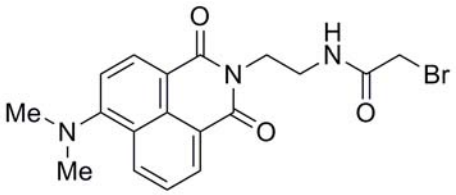

4-*N*,*N*-Dimethylamino-*N*-[2-(2-bromo-acetylamino)-ethyl]-1,8-naphthalimide (2). Dissolved **11** (0.50 g, 1.30 mmol) in dichloromethane (22.0 mL) in a 100 mL round-bottom flask. Cold trifluoroacetic acid (22.0 mL) was then added slowly over 5 min by addition funnel while stirring the reaction. The reaction was allowed to proceed at room temperature for 1.5 hrs before concentrating to dryness by rotary evaporation. The crude solid was redissolved in dichloromethane (100 mL) and washed with 2% $NaHCO_3$ aq. solution (100 mL). The aqueous layer was back-extracted with fresh dichloromethane (2 × 100 mL) and the organic layers were combined (total volume of 300 mL). The organic layer was dried with $MgSO_4$, filtered and concentrated to give the free amine as an orange solid. The free base was then transferred to a 250 mL Schlenk flask under an atmosphere of nitrogen and dissolved in dry dichloromethane (100 mL). The Schlenk flask was cooled to -15 °C in a 1:3 sodium chloride/ice bath. The bromoacetyl bromide (0.40 g, 1.96 mmol) was then added dropwise by syringe followed by *N,N*-diisopropylethylamine (0.25 mL, 1.43 mmol). The reaction was allowed to run for 5 min at -15 ºC before warming to room temperature. After 1.5 hrs, the reaction mixture was diluted to a total volume of 100 mL in dichloromethane and washed with 2% $NaHCO_3$ aq. solution (100 mL)

followed by a second wash with brine (100 mL). The organic layer was dried with $MgSO_4$, filtered, and concentrated by rotary evaporation. The product was purified by flash chromatography using 2:3 hexanes/ethyl acetate to give an orange solid (0.48 g, 1.19 mmol, 91% yield, R_f = 0.10 in 2:3 hexanes/ethyl acetate). The product was stored as solid at -20 ºC. ^{1}H NMR (300 MHz, $CDCl_3$, δ): 3.11 (s, 6H), 3.67 (m, 2H), 3.78 (s, 2H), 4.43 (t, 2H, J = 5.4 Hz), 7.09 (d, 1H, J = 8.1 Hz), 7.27 (br s, 1H), 7.64 (dd, 1H, J_1 = 8.6 Hz, J_2 = 7.4 Hz), 8.43 (dd, 1H, J_1 = 8.7 Hz, J_2 = 1.2 Hz), 8.46 (d, 1H, J = 8.4 Hz), 8.56 (dd, 1H, J_1 = 7.4 Hz, J_2 = 1.1 Hz). ^{13}C NMR (300 MHz, $CDCl_3$, δ): 28.9, 38.5, 40.4, 44.6, 113.1, 114.0, 122.4, 124.7, 124.9, 130.2, 131.2, 131.5, 133.0, 157.2, 164.4, 165.0, 166.0. HRMS-ESI (*m/z*): $[M+H]^+$ calcd for $C_{18}H_{18}BrN_3O_3$, 404.0610; found 404.0612.

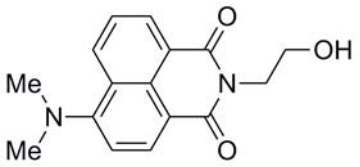

4-*N*,*N*-Dimethylamino-*N*-(2-hydroxy-ethyl)-1,8-naphthalimide (7). Added 4-*N,N*-dimethylamino-1,8-naphthalic anhydride, **5** (1.00 g, 4.15 mmol), to a 200 mL two-necked round-bottom flask equipped with a reflux condenser, magnetic stir bar, and rubber septum. The reaction vessel was then evacuated of air by applying vacuum and flushing with N_2 gas (3×). Anhydrous ethanol (42 mL) was then added to the flask by syringe. The suspension was stirred as the temperature was raised to reflux. The anhydride was still present as a solid as the suspension reached reflux until the addition of ethanolamine (0.28 mL, 4.56 mmol) by syringe. The slurry then turned to a clear deep orange solution. The reaction was allowed to proceed at reflux for 1.5 hrs then stopped by cooling to room temperature. The solvent was then removed using rotary evaporation and the crude placed under high vacuum overnight to remove excess ethanolamine. The product obtained was an orange solid requiring no further purification (1.18 g, 4.15 mmol, quantitative yield). ^{1}H NMR (300 MHz, $CDCl_3$, δ): 2.70 (br s, 1H), 3.10 (s, 6H), 3.95 (t, 2H, J = 5.3 Hz), 4.42 (t, 2H, J = 5.3 Hz), 7.06 (d, 1H, J = 8.1 Hz), 7.62 (dd, 1H, J_1

= 8.6 Hz, J_2 = 7.4 Hz), 8.40 (dd, 1H, J_1 = 8.4 Hz, J_2 = 1.2 Hz), 8.42 (d, 1H, J = 8.4 Hz), 8.52 (dd, 1H, J_1 = 7.5 Hz, J_2 = 1.2 Hz). ^{13}C NMR (300 MHz, $CDCl_3$, δ): 42.7, 44.7, 62.1, 113.1, 114.2, 122.6, 124.8, 124.9, 130.2, 131.3, 131.5, 132.9, 157.1, 164.9, 165.4. HRMS-ESI (*m/z*): $[M+Na]^+$ calcd for $C_{16}H_{16}N_2O_3$, 307.1053; found, 307.1059.

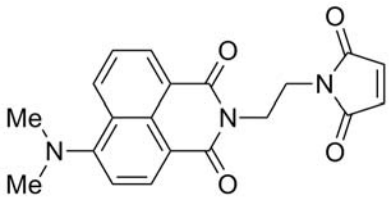

4-*N*,*N*-Dimethylamino-*N*-(2-maleimidyl-ethyl)-1,8-naphthalimide (3). Solid triphenylphosphine (0.42 g, 1.60 mmol) was added to an oven-dried 100 mL Kjeldahl-style Schlenk flask equipped with a magnetic stir bar and rubber septum. The flask was evacuated of air under high vacuum and charged with N_2 gas (3×). The triphenylphosphine was then dissolved in freshly distilled anhydrous THF. The reaction vessel was then cooled to -78 ºC by immersing the Schlenk flask in a dry ice/isopropanol bath. Next, diethyl azodicarboxylate (0.696 mL, 40% solution in toluene, 1.60 mmol) was added dropwise via syringe over 1.5 min. The mixture was allowed to stir for approximately 5 min to allow formation of the betaine. At this point, the reaction mixture was a pale yellow color. The alcohol, **7** (0.50 g, 1.8 mmol), was then added as a solid followed by neopentyl alcohol (0.07 g, 0.8 mmol) to form the oxyphosphonium ion intermediate. Once the two alcohols were fully dissolved, maleimide was added as a solid and the reacting mixture was allowed to warm to room temperature. The reaction was allowed to proceed at room temperature overnight before stopping by concentrating to dryness using a rotary evaporator. TLC indicated that the reaction only preceded 30-40%. The product was isolated by flash column chromatography using toluene with 5% methanol. The product was a bright yellow solid (0.13 g, 0.36 mmol, 22.4% yield, R_f = 0.24 in 1:1 hexanes/ethyl acetate) and was dissolved in DMSO for storage at -80 ºC in 100 mM aliquots. ^{1}H NMR (300 MHz, $CDCl_3$, δ): 3.06 (s, 6H), 3.94 (t, 2H, J = 5.1 Hz), 4.36 (t, 2H, J = 5.1 Hz), 6.58 (s, 2H), 7.04 (d, 1H, J = 8.4 Hz), 7.58 (dd, 1H, J_1 = 8.6 Hz, J_2 = 7.4 Hz), 8.36 (d, 1H, J = 8.1 Hz), 8.38 (dd, 1 H, J_1 = 8.7 Hz, J_2 = 1.2 Hz), 8.46 (dd, 1H, J_1 = 7.4 Hz, J_2 =

1.1 Hz). ^{13}C NMR (300 MHz, $CDCl_3$, δ): 36.2, 38.6, 44.6, 113.1, 114.3, 122.4, 124.7, 125.1, 130.2, 131.0, 131.3, 132.6, 133.9, 156.8, 164.0, 164.6, 170.7. HRMS-ESI (*m/z*): $[M+H]^+$ calcd for $C_{20}H_{17}N_3O_4$, 364.1292; found, 364.1308.

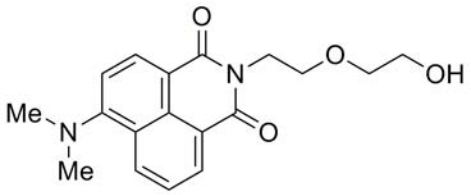

4-*N*,*N*-Dimethylamino-*N*-[2-(2-hydroxy-ethoxy)-ethyl]-1,8-naphthalimide (8). Added 4-*N,N*-dimethylamino-1,8-naphthalic anhydride, **5** (1.00 g, 4.15 mmol), to a 200 mL two-necked round-bottom flask equipped with a reflux condenser, magnetic stir bar, and rubber septum. The reaction vessel was then evacuated of air by applying vacuum and flushing with N_2 gas (3×). Anhydrous ethanol (42 mL) was then added to the flask by syringe. The suspension was stirred as the temperature was raised to reflux. The anhydride was still present as a solid as the suspension reached reflux until the addition of 2-(2-aminoethoxy)-ethanol (0.454 mL, 4.56 mmol) by syringe. The slurry then turned to a clear deep orange solution. The reaction was allowed to proceed at reflux for 1.5 hrs then stopped by cooling to room temperature. The solvent was removed by rotary evaporation and the crude placed under high vacuum overnight to remove excess 2-(2-aminoethoxy)-ethanol. The product was isolated by flash column chromatography using a gradient of 1:3 to 1:4 hexanes/ethyl acetate. The product was a dark orange oil (1.33 g, 4.05 mmol, 97.7% yield, R_f = 0.1 in 1:3 hexanes/ethyl acetate). ^{1}H NMR (300 MHz, $CDCl_3$, δ): 2.76 (br s, 1H), 3.07 (s, 6H), 3.66 (m, 4H), 3.82 (t, 2H, J = 5.6 Hz), 4.39 (t, 2H, J = 5.7 Hz), 7.05 (d, 1H, J = 8.4 Hz), 7.60 (dd, 1H, J_1 = 8.3 Hz, J_2 = 7.4 Hz), 8.38 (dd, 1H, J_1 = 8.6 Hz, J_2 = 1.1 Hz), 8.42 (d, 1H, J = 8.4 Hz), 8.51 (dd, 1H, J_1 = 7.4 Hz, J_2 = 1.1 Hz). ^{13}C NMR (300 MHz, $CDCl_3$, δ): 39.2, 44.6, 61.7, 68.4, 72.1, 113.1, 114.4, 122.7, 124.7, 125.0, 130.2, 131.1, 131.3, 132.8, 157.0, 164.2, 164.8. HRMS-ESI (*m/z*): $[M+H]^+$ calcd for $C_{18}H_{20}N_2O_4$, 329.1496; found, 329.1506.

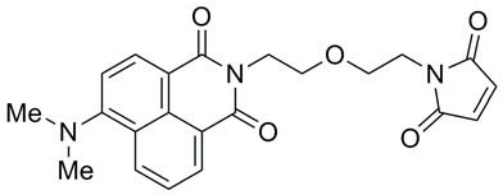

4-*N*,*N*-Dimethylamino-*N*-[2-(2-maleimidyl-ethoxy)-ethyl]-1,8-naphthalimide (4). Prior to assembling the Mitsunobu reaction, the alcohol, **8** (0.50 g, 1.51 mmol), was transferred to a 50 mL pear-shaped flask equipped with rubber stopper and placed under high vacuum overnight to remove trace water that may inhibit the reaction. An oven-dried 100 mL Kjeldahl-style Schlenk flask equipped with a magnetic stir bar and rubber septum was charged with solid triphenylphosphine (0.36 g, 1.37 mmol). The Schlenk flask was then evacuated of air by placing under high vacuum and charged with N_2 gas (3×). Freshly distilled dry THF (4 mL) was then transferred to the Schlenk flask by syringe and the triphenylphosphine stirred at ambient temperature until completely dissolved. This solution was then lowered to -78 ºC by immersing in a dry ice/isopropanol bath. Next, diethyl azodicarboxylate (0.597 mL, 40% solution in toluene, 1.37 mmol) was added dropwise via syringe over 2 min. The mixture was allowed to stir for approximately 5 min to allow formation of the betaine. At this point, the reaction mixture was a pale yellow color. Meanwhile, a solution of the alcohol, **8**, was prepared by dissolving in 6 mL of freshly distilled dry THF. This solution was then transferred very slowly to the reaction vessel by syringe to avoid raising the temperature. Once the transfer was complete, neopentyl alcohol (0.06 g, 0.69 mmol) was added as a solid. The reaction was allowed to stir approximately 5 min to allow formation of the oxyphosphonium ion intermediate. Solid maleimide (0.13 g, 1.37 mmol) was then added and the reaction was allowed to warm to room temperature and stirred overnight. The reaction was stopped by concentrating to dryness on the rotary evaporator and the product was isolated by flash column chromatography using 1:2 hexanes/ethyl acetate. The product was a bright yellow solid (0.15 g, 0.37 mmol, 24.4 % yield, R_f = 0.22 in 1:2 hexanes/ethyl acetate) and was dissolved in DMSO for storage at -80 ºC in 100 mM aliquots. ^{1}H NMR (300 MHz, $CDCl_3$, δ): 3.09 (s, 6H), 3.65 (m, 4H), 3.74 (t, 2H, J = 6.0 Hz), 4.34 (t, 2H, J = 5.9 Hz), 6.50 (s, 2H), 7.09 (d, 1H, J = 8.1 Hz), 7.63 (dd, 1H, J_1 = 8.4

Hz, J_2 = 7.2 Hz), 8.42 (apparent d, 2H, J = 8.1 Hz), 8.51 (dd, 1H, J_1 = 7.5 Hz, J_2 = 1.2 Hz). ^{13}C NMR (300 MHz, $CDCl_3$, δ): 37.2, 38.8, 44.7, 67.2, 67.6, 113.2, 114.9, 122.9, 124.8, 125.1, 130.2, 131.0, 131.1, 132.6, 133.8, 156.6, 163.9, 164.4, 170.5. HRMS-ESI (*m/z*): $[M+H]^+$ calcd for $C_{22}H_{21}N_3O_5$, 408.1554; found, 408.1567.

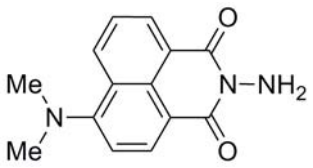

***N*-Amino-4-*N*,*N*-dimethylamino-1,8-naphthalimide (6)**. Added 4-*N,N*-dimethylamino-1,8-naphthalic anhydride, **5** (1.00 g, 4.14 mmol), to a 200 mL two-necked round-bottom flask equipped with a reflux condenser, magnetic stir bar, and rubber septum. The reaction vessel was then evacuated of air by applying vacuum and flushing with N_2 gas (3×). Anhydrous ethanol (42 mL) was then added to the flask by syringe. The suspension was stirred as the temperature was raised to reflux. The anhydride was still present as a solid as the suspension reached reflux until the addition of hydrazine monohydrate (0.402 mL, 8.29 mmol) by syringe. The slurry then turned to a clear deep orange solution. The reaction was allowed to proceed at reflux for 45 min then stopped by cooling to room temperature. The reaction mixture was diluted to a final volume of 200 mL with cold water to precipitate the product, which was then filtered and purified by flash chromatography using 1:3 hexanes/ethyl acetate. The product was a bright yellow solid (0.925 g, 3.624 mmol, 87.4 % yield, R_f = 0.23 in 1:3 hexanes/ethyl acetate). ^{1}H NMR (300 MHz, $CDCl_3$, δ): 3.09 (s, 6H), 5.26 (br s, 2H), 7.02 (d, 1H, J = 8.4 Hz), 7.58 (dd, 1H, J_1 = 8.4 Hz, J_2 = 7.5 Hz), 8.37 (dd, 1H, J_1 = 8.6 Hz, J_2 = 0.8 Hz), 8.38 (d, 1H, J = 8.4 Hz), 8.49 (dd, 1H, J_1 = 7.4 Hz, J_2 = 0.8 Hz). ^{13}C NMR (300 MHz, $CDCl_3$, δ): 44.8, 113.0, 113.4, 121.9, 124.6, 124.9, 128.7, 131.0, 131.5, 132.8, 157.3, 160.7, 161.0. HRMS-ESI (*m/z*): $[M+H]^+$ calcd for $C_{14}H_{13}N_3O_2$, 256.1081; found, 256.1083.

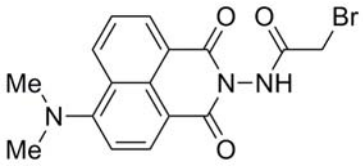

4-*N*,*N*-Dimethylamino-*N*-[2-bromoacetamido]-1,8-naphthalimide (1). The solid *N*-amino-4-*N,N*-dimethylamino-1,8-naphthalimide, **6** (0.50 g, 1.96 mmol), was transferred to an oven-dried 100 mL Schlenk flask along with a magnetic stir bar. The flask was then capped with a rubber septum and evacuated of air by placing under high vacuum followed by charging with N_2 gas (3×). The starting material was then partially dissolved in dry dichloromethane (39 mL) and stirred as *N,N*-diisopropylethylamine (0.357 mL, 2.15 mmol) was added through the septum via syringe. The Schlenk flask was then cooled to -15 ºC in an ice bath of 3:1 ice/NaCl. Once cooled, bromoacetyl bromide (0.255 mL, 2.94 mmol) was added to the suspension dropwise via syringe and stirred for 5 min before bringing the reaction vessel back to room temperature. A white solid, presumed to be a bromide salt, was observed precipitating from the reaction mixture over time. After allowing the reaction to run overnight, the mixture was diluted to a total volume of 100 mL in dichloromethane and washed with $NaHCO_3$ (3 × 50 mL). The organic layer was dried with $MgSO_4$, filtered, and concentrated on the rotary evaporator. The desired product was isolated by flash chromatography using 1:1 hexanes/ethyl acetate. The reaction yielded two products: the desired monoacylated product, **1** (0.24 g, 0.93 mmol, 47.6% yield, R_f = 0.10 in 1:1 hexanes/ethyl acetate), and a diacylated byproduct in nearly a 1:1 ratio. The desired product was stored as a solid at -20 ºC. ^{1}H NMR (300 MHz, $CDCl_3$, δ): 3.13 (s, 6H), 4.31 (s, 2H), 7.08 (d, 1H, J = 8.4Hz), 7.64 (dd, 1H, J_1 = 8.6 Hz, J_2 = 6.9 Hz), 8.44 (dd, 1H, J_1 = 8.4 Hz, J_2 = 1.2 Hz), 8.46 (d, 1H, J = 8.1 Hz), 8.57 (dd, 1H, J_1 = 7.5 Hz, J_2 = 1.2 Hz), 8.62 (br s, 1H). ^{13}C NMR (500 MHz, $CDCl_3$, δ): 26.5, 44.7, 113.2, 113.5, 122.3, 124.8, 125.1, 130.4, 132.0, 132.3, 133.7, 157.8, 161.6, 162.2, 164.5. HRMS-ESI (*m/z*): $[M+H]^+$ calcd for $C_{16}H_{14}BrN_3O_3$, 376.0291; found, 376.0304.

NMR spectra of synthesized derivatives:

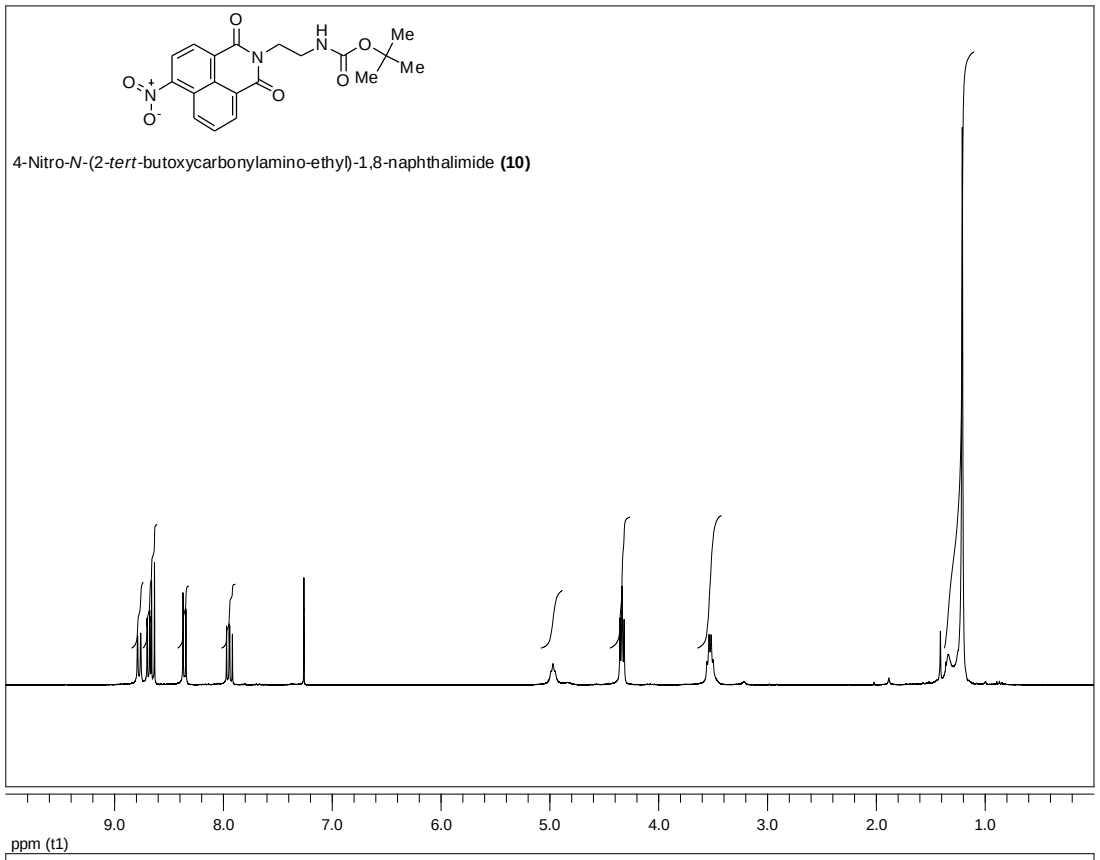

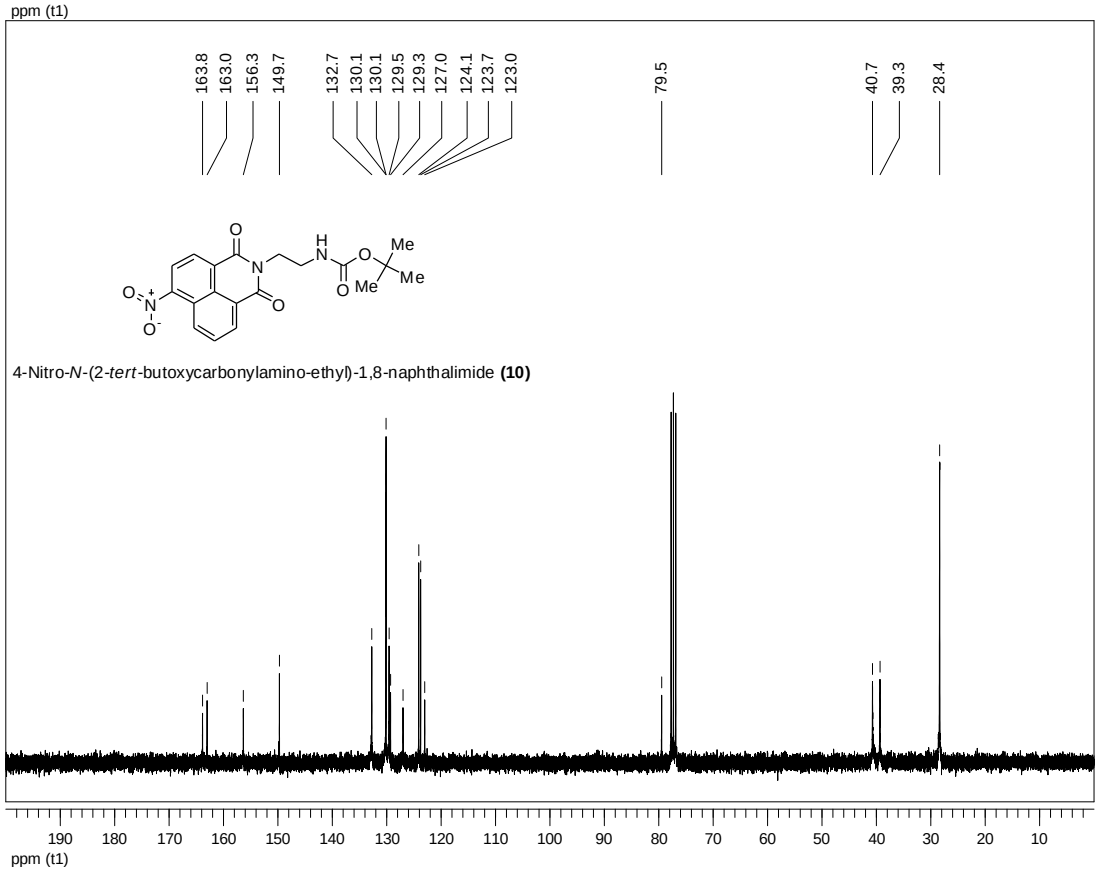

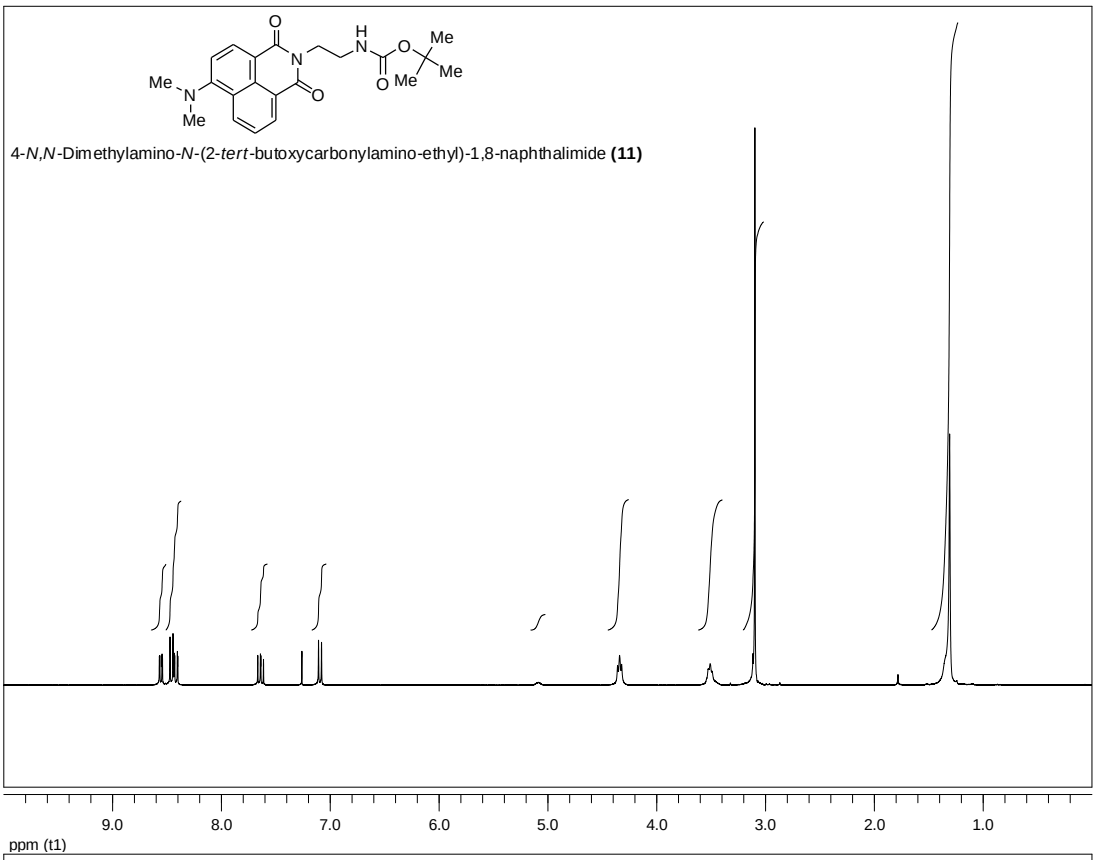
4-*N*,*N*-Dimethylamino-*N*-(2-*tert*-butoxycarbonylamino-ethyl)-1,8-naphthalimide **(11)**
9.0
8.0
7.0
6.0
5.0
4.0
3.0
2.0
1.0
ppm (t1)

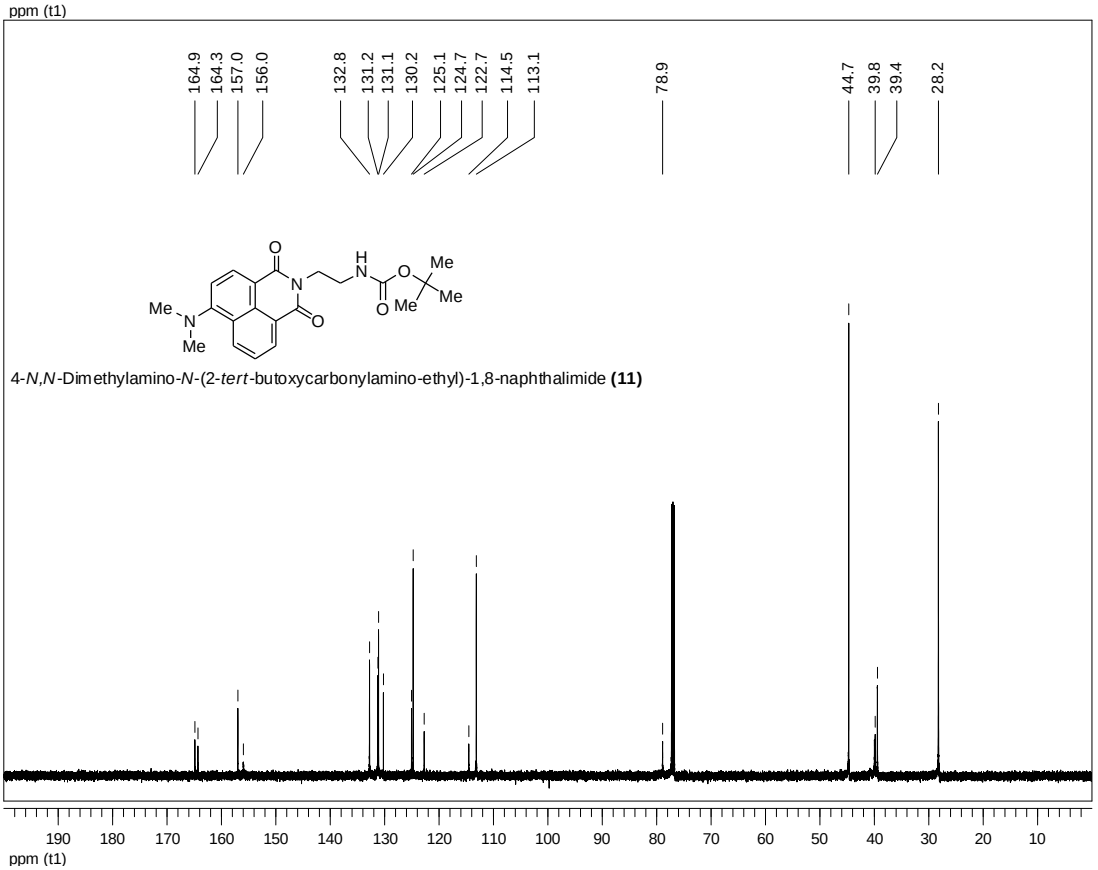
164.9
164.3
157.0
156.0
132.8
131.2
131.1
130.2
125.1
124.7
122.7
114.5
113.1
78.9
44.7
39.8
39.4
28.2
4-*N*,*N*-Dimethylamino-*N*-(2-*tert*-butoxycarbonylamino-ethyl)-1,8-naphthalimide **(11)**
190
180
170
160
150
140
130
120
110
100
90
80
70
60
50
40
30
20
10
ppm (t1)

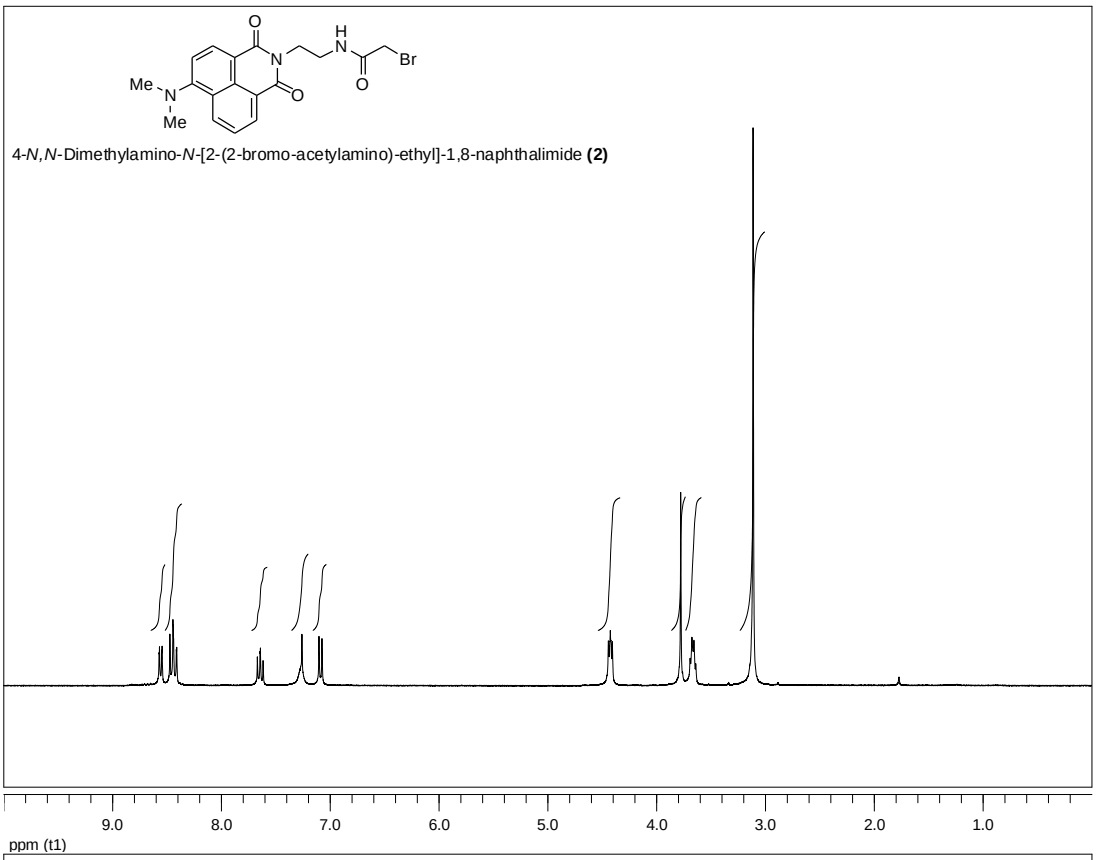
4-*N*,*N*-Dimethylamino-*N*-[2-(2-bromo-acetylamino)-ethyl]-1,8-naphthalimide **(2)**
9.0
8.0
7.0
6.0
5.0
4.0
3.0
2.0
1.0
ppm (t1)

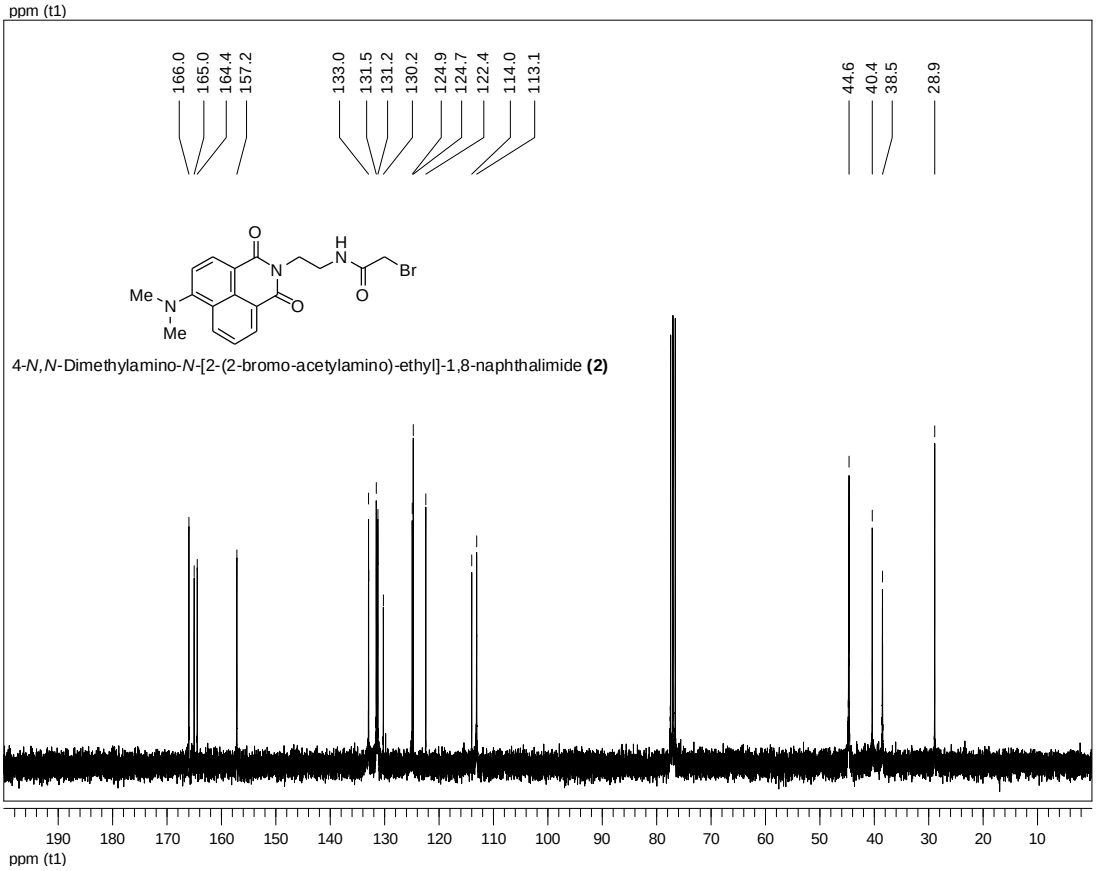
166.0
165.0
164.4
157.2
133.0
131.5
131.2
130.2
124.9
124.7
122.4
114.0
113.1
44.6
40.4
38.5
28.9
4-*N*,*N*-Dimethylamino-*N*-[2-(2-bromo-acetylamino)-ethyl]-1,8-naphthalimide **(2)**
190
180
170
160
150
140
130
120
110
100
90
80
70
60
50
40
30
20
10
ppm (t1)

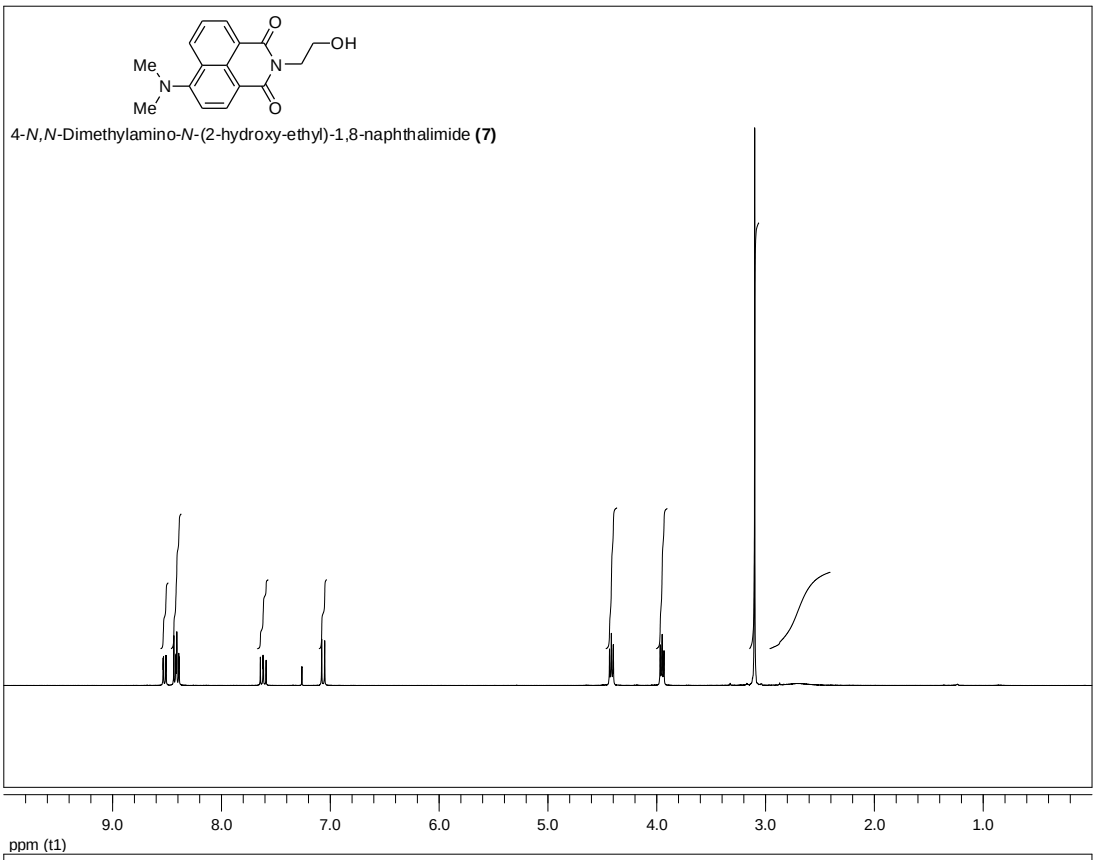
Me
N
Me
O
N
OH
O
4-*N*,*N*-Dimethylamino-*N*-(2-hydroxy-ethyl)-1,8-naphthalimide **(7)**
9.0
8.0
7.0
6.0
5.0
4.0
3.0
2.0
1.0
ppm (t1)

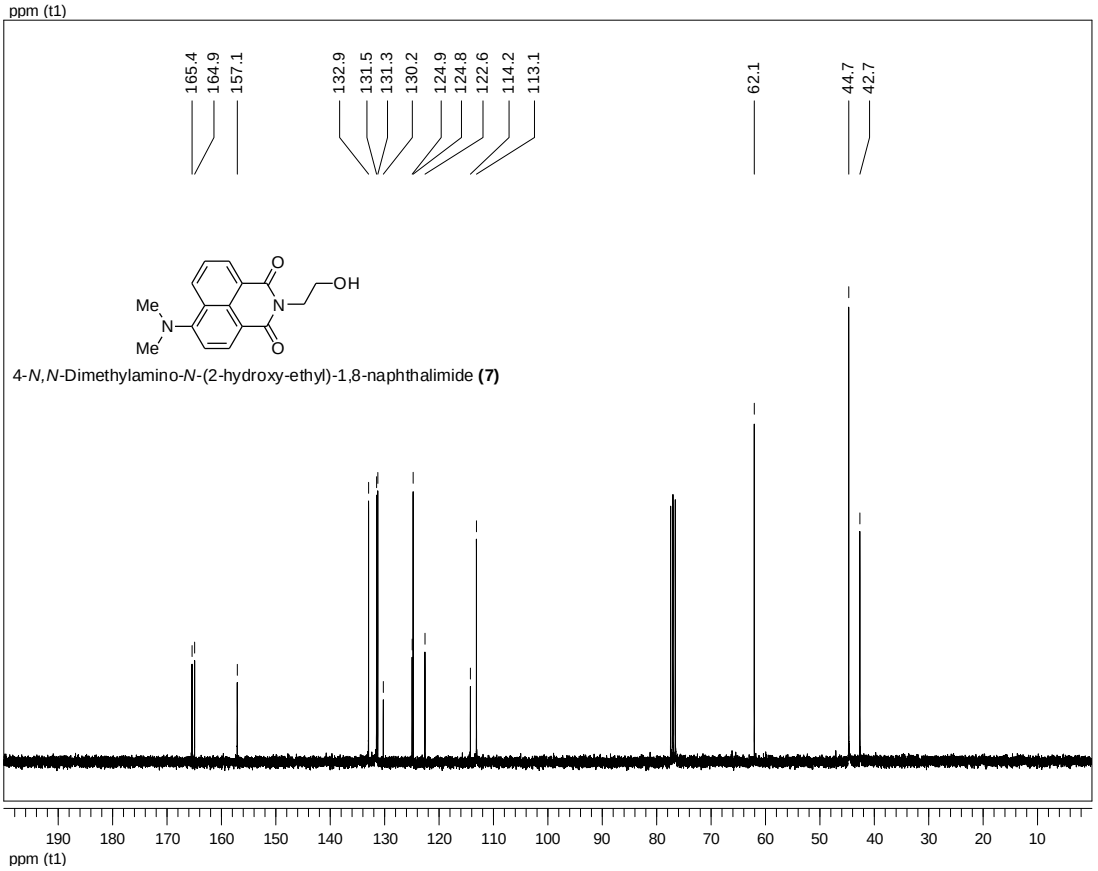
165.4
164.9
157.1
132.9
131.5
131.3
130.2
124.9
124.8
122.6
114.2
113.1
62.1
44.7
42.7
Me
N
Me
O
N
OH
O
4-*N*,*N*-Dimethylamino-*N*-(2-hydroxy-ethyl)-1,8-naphthalimide **(7)**
190
180
170
160
150
140
130
120
110
100
90
80
70
60
50
40
30
20
10
ppm (t1)

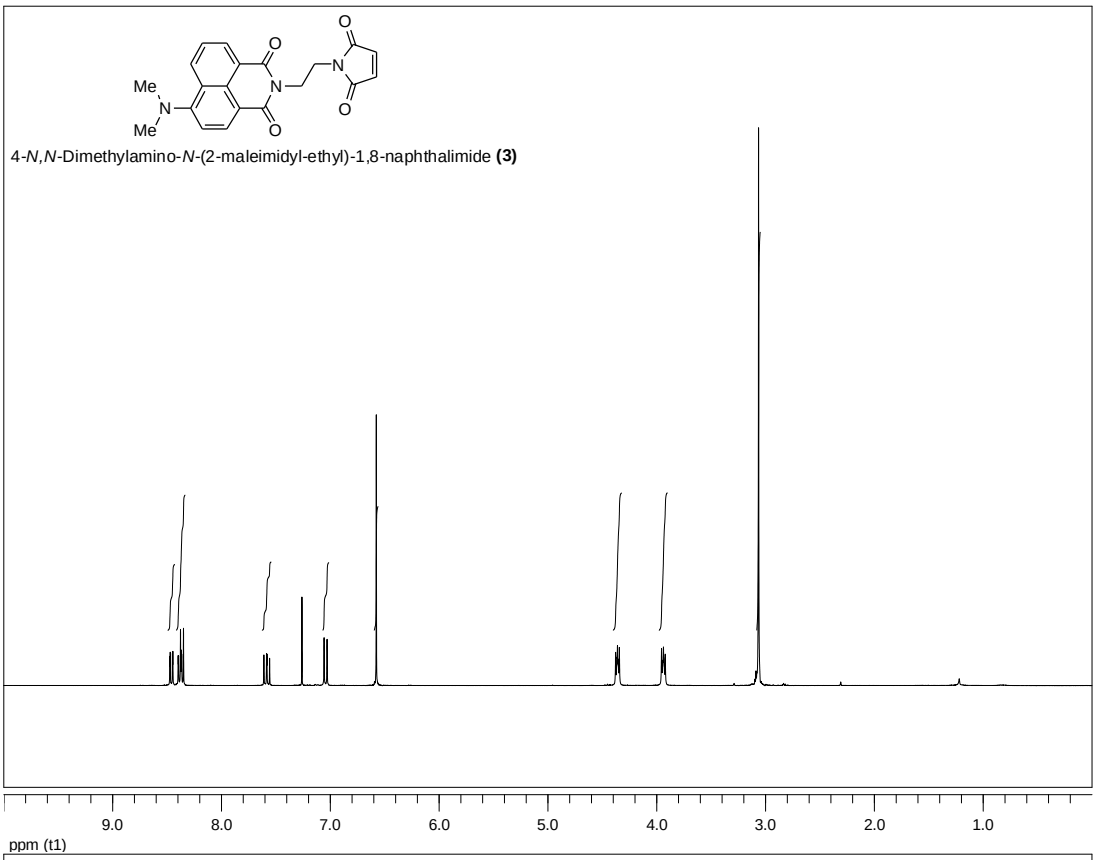
4-*N*,*N*-Dimethylamino-*N*-(2-maleimidyl-ethyl)-1,8-naphthalimide **(3)**
9.0
8.0
7.0
6.0
5.0
4.0
3.0
2.0
1.0
ppm (t1)

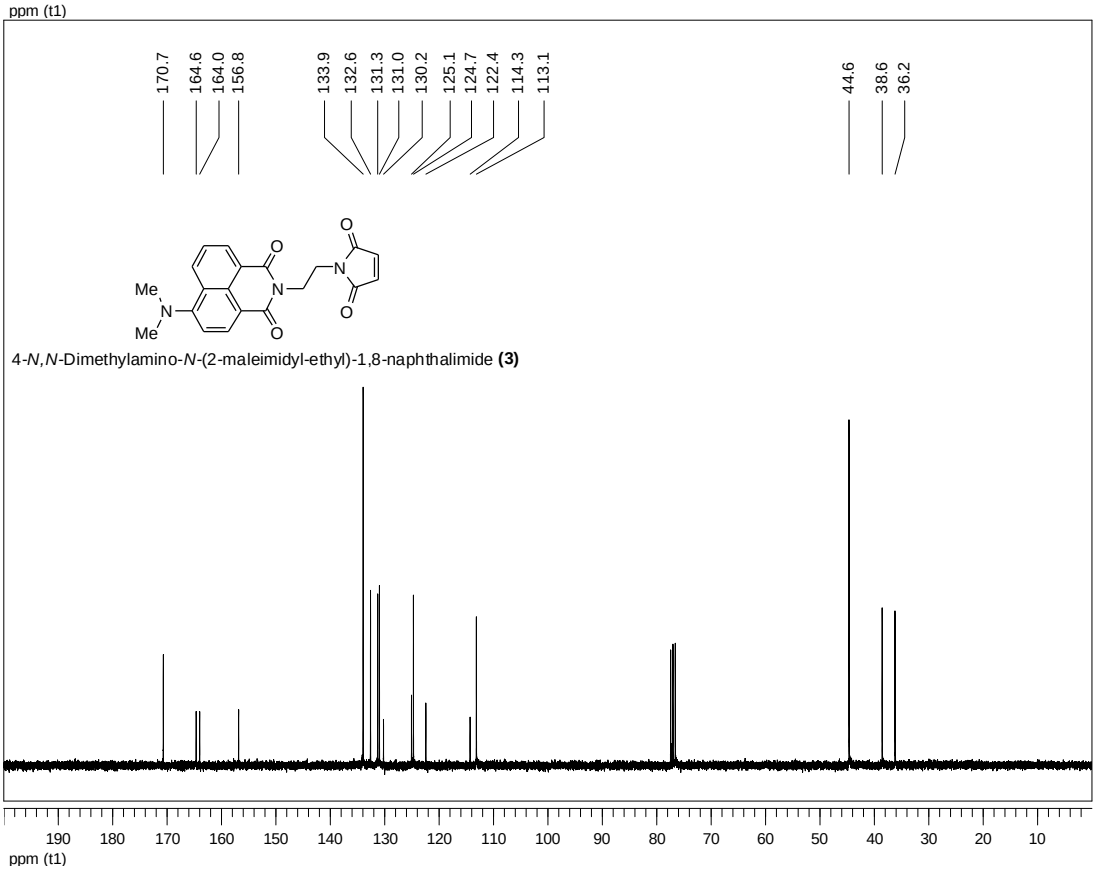
170.7
164.6
164.0
156.8
133.9
132.6
131.3
131.0
130.2
125.1
124.7
122.4
114.3
113.1
44.6
38.6
36.2
4-*N*,*N*-Dimethylamino-*N*-(2-maleimidyl-ethyl)-1,8-naphthalimide **(3)**
190
180
170
160
150
140
130
120
110
100
90
80
70
60
50
40
30
20
10
ppm (t1)

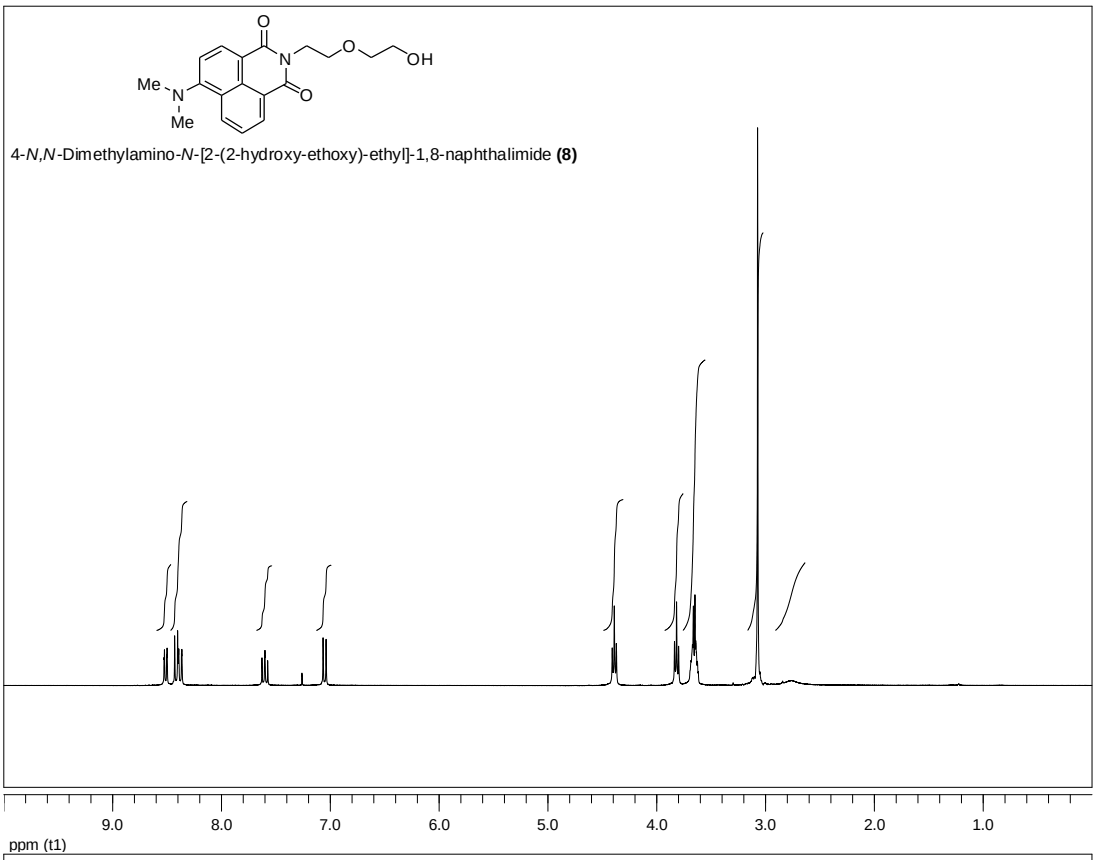
4-*N*,*N*-Dimethylamino-*N*-[2-(2-hydroxy-ethoxy)-ethyl]-1,8-naphthalimide **(8)**
9.0
8.0
7.0
6.0
5.0
4.0
3.0
2.0
1.0
ppm (t1)

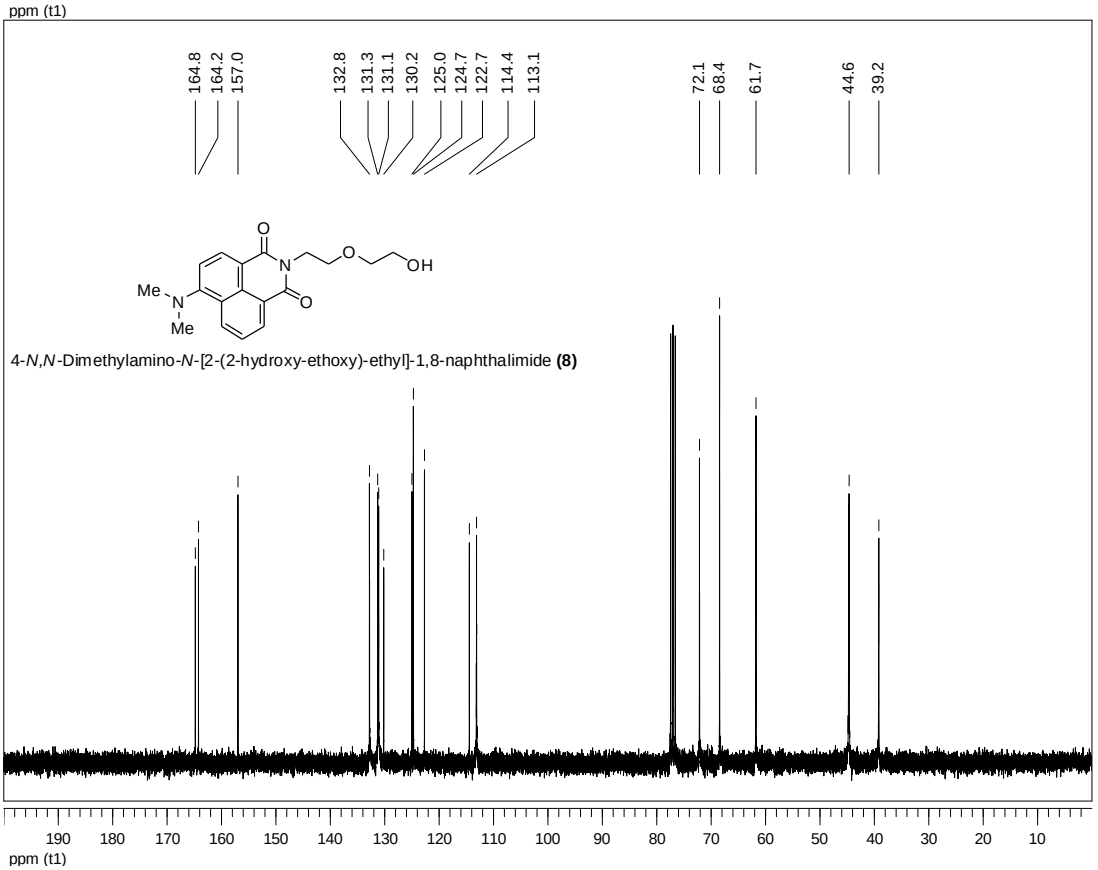
164.8
164.2
157.0
132.8
131.3
131.1
130.2
125.0
124.7
122.7
114.4
113.1
72.1
68.4
61.7
44.6
39.2
4-*N*,*N*-Dimethylamino-*N*-[2-(2-hydroxy-ethoxy)-ethyl]-1,8-naphthalimide **(8)**
190
180
170
160
150
140
130
120
110
100
90
80
70
60
50
40
30
20
10
ppm (t1)

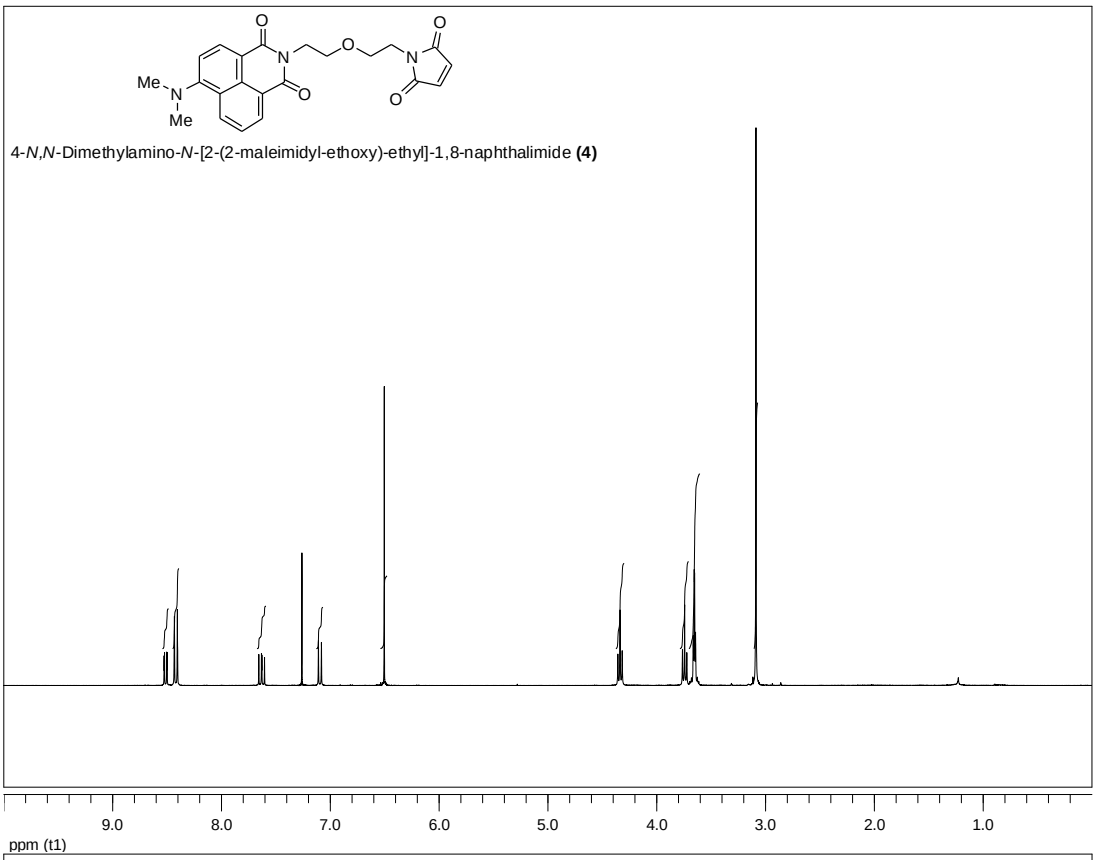
4-*N*,*N*-Dimethylamino-*N*-[2-(2-maleimidyl-ethoxy)-ethyl]-1,8-naphthalimide **(4)**
9.0
8.0
7.0
6.0
5.0
4.0
3.0
2.0
1.0
ppm (t1)

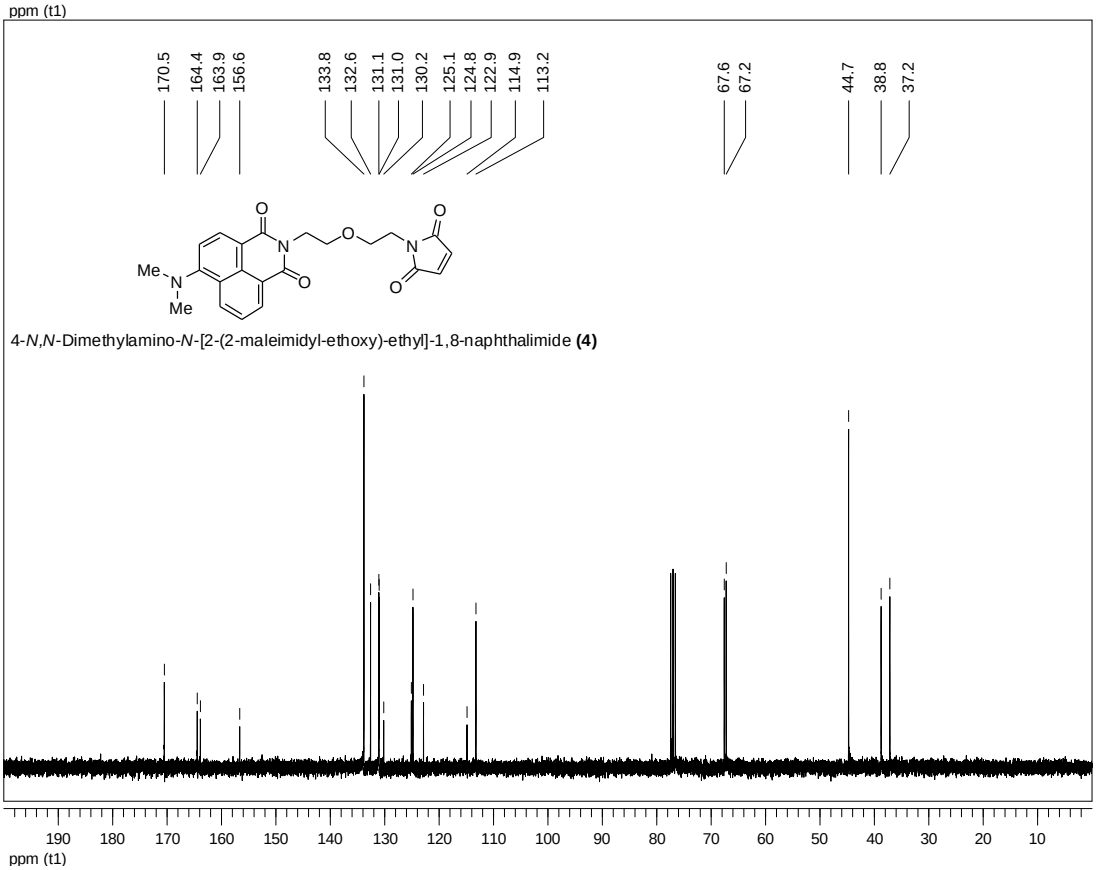
170.5
164.4
163.9
156.6
133.8
132.6
131.1
131.0
130.2
125.1
124.8
122.9
114.9
113.2
67.6
67.2
44.7
38.8
37.2
4-*N*,*N*-Dimethylamino-*N*-[2-(2-maleimidyl-ethoxy)-ethyl]-1,8-naphthalimide **(4)**
190
180
170
160
150
140
130
120
110
100
90
80
70
60
50
40
30
20
10
ppm (t1)

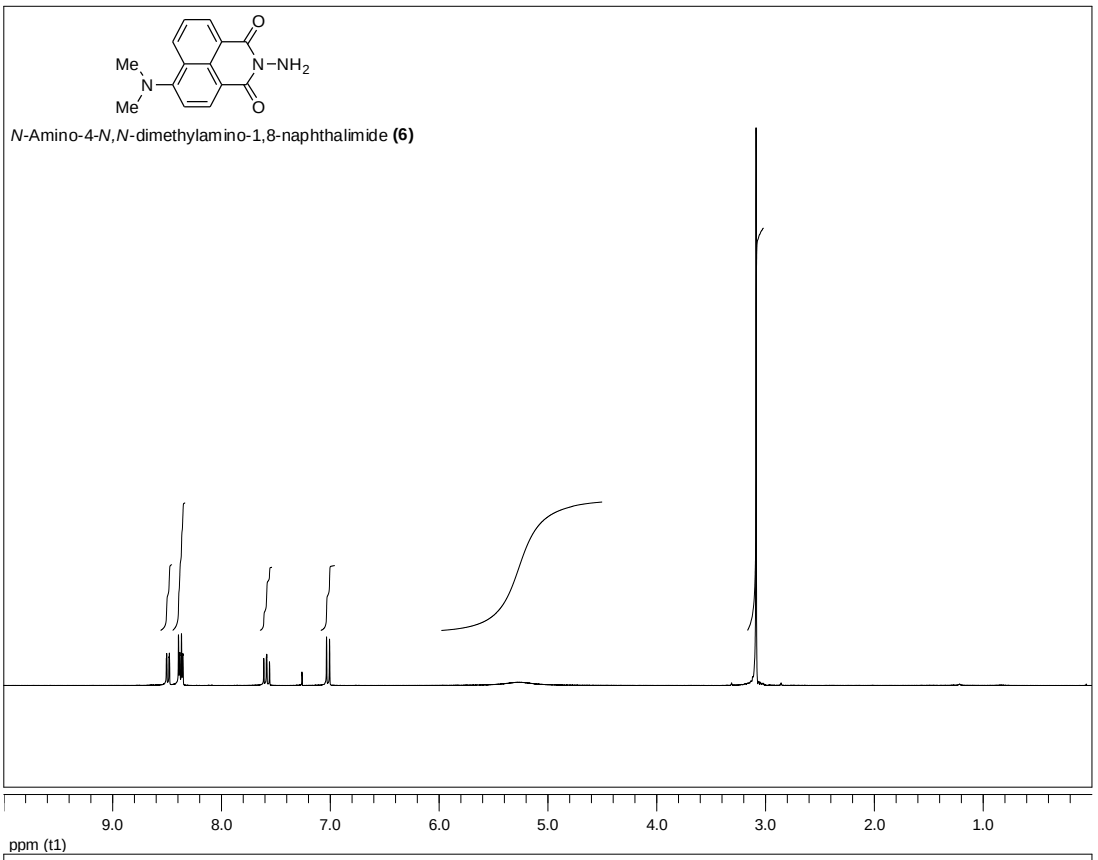
Me
N
Me
O
N–NH2
O
N-Amino-4-N,N-dimethylamino-1,8-naphthalimide (6)
9.0
8.0
7.0
6.0
5.0
4.0
3.0
2.0
1.0
ppm (t1)

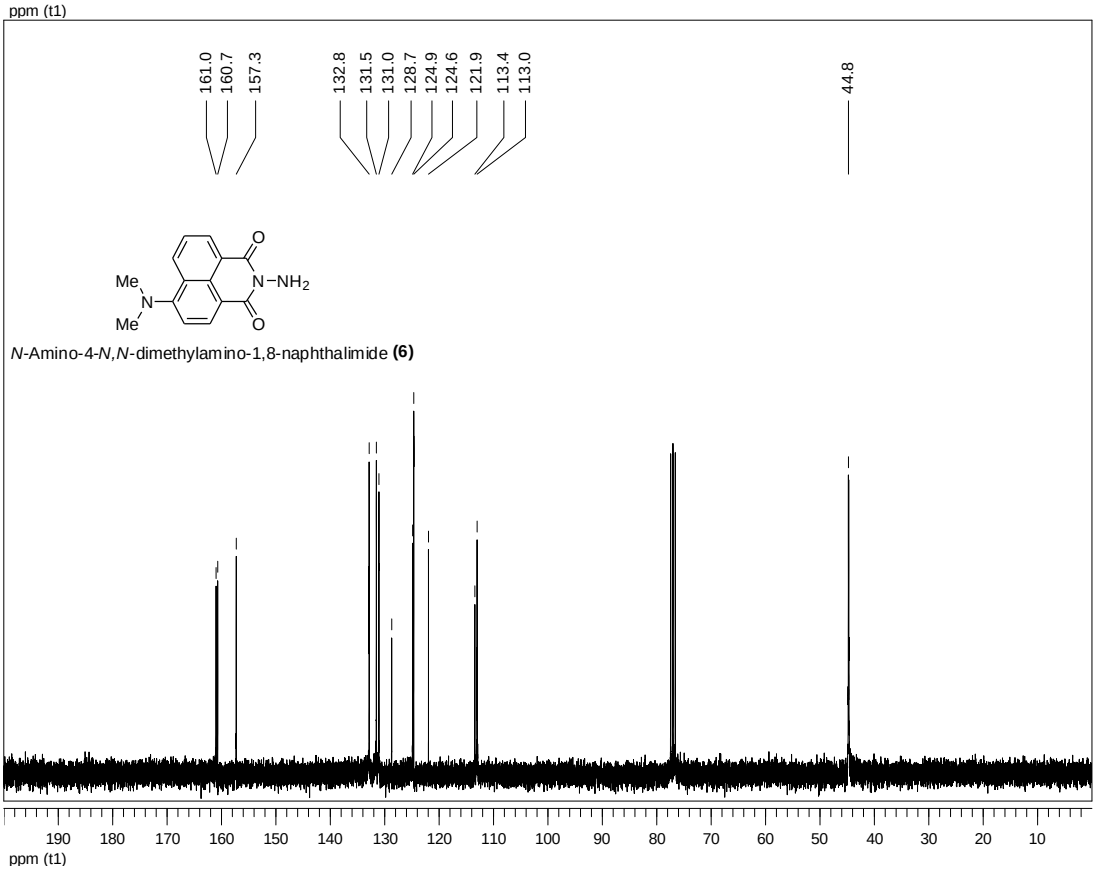
161.0
160.7
157.3
132.8
131.5
131.0
128.7
124.9
124.6
121.9
113.4
113.0
44.8
Me
N
Me
O
N–NH2
O
N-Amino-4-N,N-dimethylamino-1,8-naphthalimide (6)
190
180
170
160
150
140
130
120
110
100
90
80
70
60
50
40
30
20
10
ppm (t1)

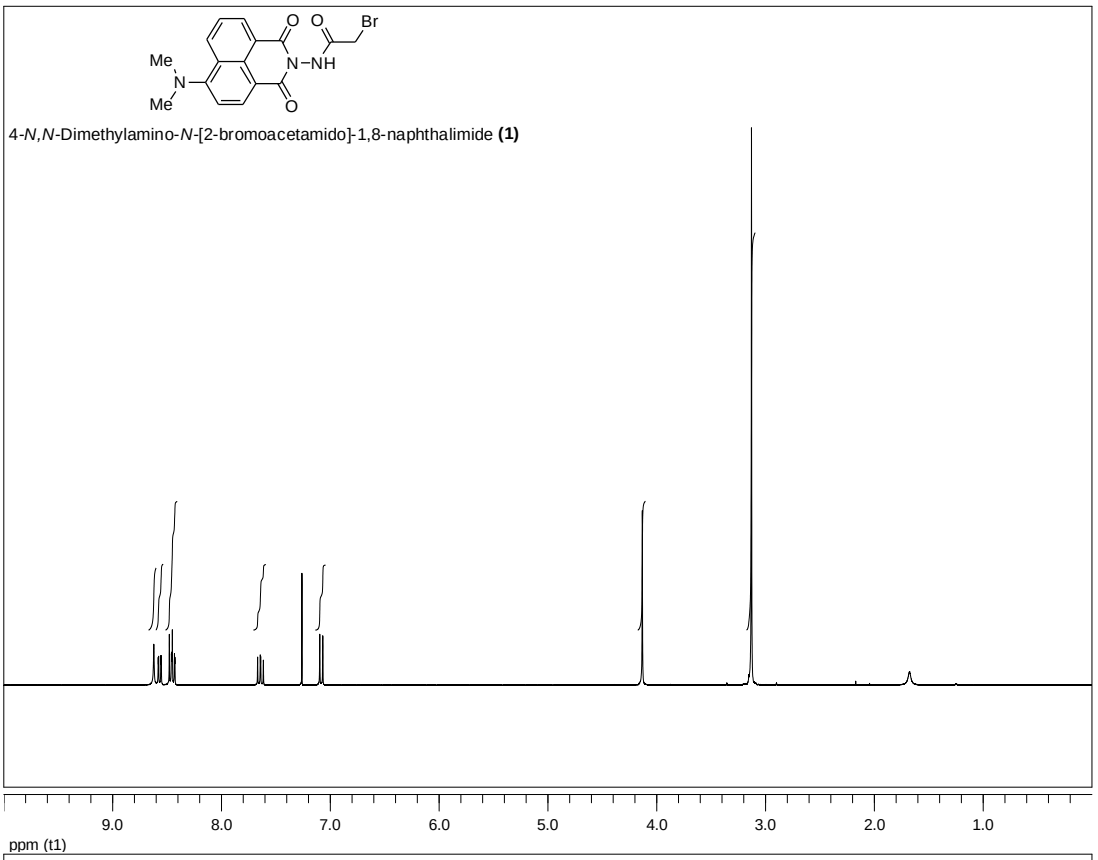
Me
N
Me
O
O
N–NH
O
O
Br
4-*N*,*N*-Dimethylamino-*N*-[2-bromoacetamido]-1,8-naphthalimide **(1)**
9.0
8.0
7.0
6.0
5.0
4.0
3.0
2.0
1.0
ppm (t1)

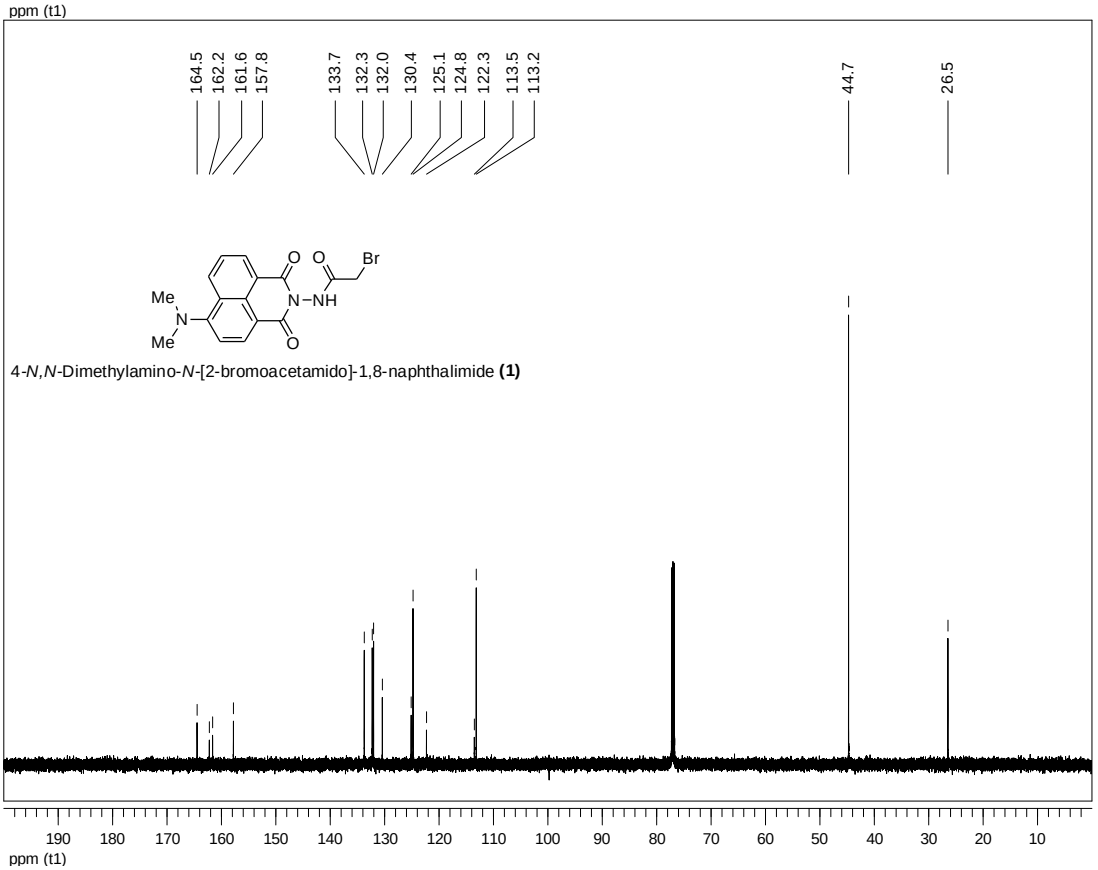
164.5
162.2
161.6
157.8
133.7
132.3
132.0
130.4
125.1
124.8
122.3
113.5
113.2
44.7
26.5
Me
N
Me
O
O
N–NH
O
O
Br
4-*N*,*N*-Dimethylamino-*N*-[2-bromoacetamido]-1,8-naphthalimide **(1)**
190
180
170
160
150
140
130
120
110
100
90
80
70
60
50
40
30
20
10
ppm (t1)

Synthesis of the M13 peptide:

The peptide used in this study represents a truncated form of the originally described M13 peptide discovered by Blumenthal et al. (1). The sequence encompasses only the minimum residues required to bind the Ca^{2+}-CaM activated complex. The residue numbering refers to that of the original fragment.

M13 Peptide

Residue #	N-term	2	3	4	5	6	7	8	9	10	11	12	13	14	15	16	17	18	19	C-term
Sequence	H_2N-	R	R	W	K	K	N	F	I	A	V	S	A	A	N	R	F	K	K	-$CONH_2$

The M13 peptide was prepared using standard Fmoc-based solid-phase peptide synthesis techniques (SPPS) (*2*) with 0.17 mmol/g loading Fmoc-NovaPEG Rink Amide resin LL (Cat. No. 01-64-0483, Novabiochem®). Fmoc-protected amino acids with the standard side-chain protecting groups were used: Fmoc-Ala-OH, Fmoc-Phe-OH, Fmoc-Ile-OH, Fmoc-Lys(Boc)-OH, Fmoc-Asn(Trt)-OH, Fmoc-Arg(Pbf)-OH, Fmoc-Ser(tBu)-OH, Fmoc-Val-OH, and Fmoc-Trp(Boc)-OH. Synthesis of the peptide began by coupling the first seven residues (positions 13-19) with an ABI 431A peptide synthesizer (Applied Biosystems). The synthesis was performed on the 40 μmol scale using 4 equiv of the Fmoc amino acids in each cycle. It had been discovered from earlier attempts at making the M13 peptide that the coupling efficiency was extremely low for residues incorporated after the alanine at position 10 in the sequence. This problem was overcome by using a pseudoproline dipeptide, Fmoc-Val-Ser($\Psi^{Me,Me}$pro)-OH (Cat. No. 05-20-1001, Novabiochem), for positions 11-12 in place of Fmoc-Val-OH and Fmoc-Ser(tBu)-OH. The remaining residues were coupled manually using 6 equiv of the Fmoc amino acids. The building blocks were dissolved to a final concentration of 50 mM in DMF containing a 1:1 mixture of HOBt/HBTU (50 mM each) with *N,N*-diisopropylethylamine (100 mM, 12 equiv). Each coupling reaction was allowed to proceed at room temperature for 30-45 min. The coupling efficiency was monitored using the TNBS test (*3*). Removal of the Fmoc group prior to each coupling step was performed using a 20% 4-methylpiperidine solution (4) in DMF (3 × 5 min). A Boc-Arg(Pbf)-OH residue was incorporated at the N-terminus of the peptide in order to yield the free α-amino group following cleavage from the solid support. The M13 mutant peptide was cleaved from the resin using a

solution of 96:2:2 TFA/H_2O/EDT for 3 hrs. The cleavage cocktail was then filtered and evaporated. The crude peptide was triturated with cold diethyl ether (3 × 10 mL) and purified by HPLC using a Waters 600E HPLC with a Waters 600 automated control module and Waters 2487 dual wavelength absorbance detector set at 228 and 280 nm. The separation was performed using a preparative YMC-pack, C_{18}, 20 × 250 mm reverse-phase column. A YMC-pack, C_{18}, 4.6 ×150 mm reverse-phase column was used for analytical HPLC. The following analytical HPLC method was used to characterize the peptide:

Time (min)	Flow Rate (mL/min)	H_20 % (with 0.1% TFA)	MeCN % (with 0.1% TFA)	Gradient
initial	1.00	93	7	linear
5.0	1.00	93	7	linear
40.0	1.00	0	100	linear

The peptide mass was determined by ESI-MS on a Mariner electrospray mass spectrometer (PerSeptive Biosystems).

Retention time (min)	ESI-MS (m/z) $[M+xH]^{x+}$ calcd	ESI-MS (m/z) $[M+xH]^{x+}$ found
21.6	740.9 [M+3]	740.6 [M+3]
	555.9 [M+4]	555.7 [M+4]
	444.9 [M+5]	444.8 [M+5]

Subcloning of the synthetic CaM gene into the pET-14b vector:

Sequence of codon-optimized CaM gene.

```
ATGGCAGATCAACTGACTGAAGAACAGATTGCGGAATTTAAAGAAGCATTCAGCCTGTTC
GACAAAGATGGCGATGGCACCATTACGACCAAGGAGCTGGGTACGGTGATGCGTTCTCTG
GGTCAGAACCCAACTGAGGCAGAACTGCAGGATATGATCAACGAGGTTGATGCTGACGGT
AATGGCACCATCGACTTCCCGGAATTCCTGACCATGATGGCCCGTAAAATGAAAGACACC
GATTCCGAAGAAGAAATCCGTGAGGCTTTCCGTGTATTCGACAAAGACGGTAACGGCTAC
ATTTCTGCGGCGGAACTGCGCCATGTGATGACCAACCTGGGCGAAAAACTGACCGACGAA
GAAGTTGACGAGATGATCCGCGAAGCTGATATCGACGGTGATGGTCAGGTCAACTATGAA
GAATTTGTTCAGATGATGACTGCGAAGCACCACCACCACCACCAC
```

Translation of codon-optimized CaM gene.

```
MADQLTEEQIAEFKEAFSLFDKDGDGTITTKELGTVMRSLGQNPTEAELQDMINEVDADG
NGTIDFPEFLTMMARKMKDTDSEEEIREAFRVFDKDGNGYISAAELRHVMTNLGEKLTDE
EVDEMIREADIDGDGQVNYEEFVQMMTAKHHHHHH
```

Subcloning of codon-optimized CaM gene. The synthetic CaM construct ordered from Bio Basic Inc. was designed for optimal expression in *E. coli.* The gene was inserted into a high-copy pUC-57 vector for ease of amplification. The product was delivered as a lyophilized powder and also as a stab of transformed DH5α cells in LB agar with carbenicillin. A sterile loop was dipped in the stab and swabbed over a fresh LB agar plate containing carbenicillin (50 μg/mL). The plate was incubated overnight at 37 ºC. The next day, a colony was selected and amplified in order to isolate the vector using a Qiagen Plasmid Miniprep kit. The DNA was then quantified by Abs at 260 nm (0.11 μg/μl).

A double digestion of the amplified pUC-57(CaM) vector was performed simultaneously with the double digestion of the pET-14b vector. The reaction conditions were as follows:

pET-14b vector:		pUC-57 vector:	
1.28 μL	pET-14b (2.34 μg/μL)	27.0 μL	pUC-57 (0.11 μg/μL)
41.2 μL	dH_2O (sterile)	15.5 μL	dH_2O (sterile)
5.0 μL	10× NEB buffer 2	5.0 μL	10× NEB buffer 2
0.5 μL	100× BSA	0.5 μL	100× BSA
1.0 μL	XhoI	1.0 μL	XhoI
1.0 μL	NcoI	1.0 μL	NcoI
50.0 μL	total volume	50.0 μL	total volume

The reactions were allowed to proceed for 1 hr at 37 ºC before stopping with the addition of 12.5 μL of 5× DNA loading buffer. The both reaction mixtures were then loaded onto a 1% agarose gel and resolved at 110 V. The desired restriction products (the CaM insert of the pUC-57 vector and the linearized pET-14b expression vector) were cut from the gel and isolated using a QIAquick™ Gel Extraction kit. The subcloning vector and insert were then quantified on 1% agarose gel by comparing band intensities to those of the NEB 2-Log DNA ladder.

Two ligation reactions were assembled: one containing both the CaM insert and the pET-14b vector, and the other with only the pET-14b vector as a negative control. The reaction conditions were as follows:

vector (control)		vector + insert	
0.3 µL	pET-14b (120 ng/µL)	0.3 µL	pET-14b (120 ng/µL)
3.2 µL	dH_2O (sterile)	1.0 µL	CaM insert (15 ng/µL)
1.0 µL	T4 DNA ligase	2.2 µL	dH_2O (sterile)
0.5 µL	10× T4 ligase buffer	1.0 µL	T4 DNA ligase
		0.5 µL	10× T4 ligase buffer
5.0 µL	total volume	5.0 µL	total volume

Note- There were 36 µg of pET-14b vector in each reaction and 15 µg of the insert in the ligation. The insert is 480 bp and the vector is 4500 bp. This corresponds to a 4:1 molar ratio of insert to vector.

The reactions were allowed to proceed for 16 hrs at 16 ºC. The reactions were then used to transform two 30 µL batches of DH5α cells plated on LB/agar with 50 µg/mL carbenicillin. The next day, no colonies were observed for the negative control. Three colonies from the non-control plate were selected and amplified for sequencing. All selected colonies were determined to be the desired construct. The new vector, pET-14b[CaM], was transformed into BL21-Gold(DE3) competent cells from Stratagene for protein expression.

Cysteine mutagenesis of wild-type CaM gene:

These seven cysteine mutants of the CaM construct were prepared by site-directed mutagenesis using the following set of PAGE-purified primers along with the corresponding reverse compliments ordered on the 50 nmole scale from Operon:

E11C-
CTGACTGAAGAACAGATTGCGTGCTTTAAAGAAGCATTCAGCCTG

S38C-
GGGTACGGTGATGCGTTGTCTGGGTCAGAACCC

M76C-
CCTGACCATGATGGCCCGTAAATGCAAAGACACCGATTCCG

E87C-
CCGATTCCGAAGAAGAAATCCGTTGCGCTTTCCGTGTATTCGAC

N111C-
CTGCGCCATGTGATGACCTGCCTGGGCGAAAAACTGACC

E114C-
GTGATGACCAACCTGGGCTGCAAACTGACCGACGAAGAAG

M145C-
CTATGAAGAATTTGTTCAGATGTGCACTGCGAAGCACCACCACC

Upon receiving the primers, stock solutions were prepared in sterile water (125 ng/µl). The reactions were assembled accordingly:

5.0 µL	10× Pfu Turbo rxn buffer.
0.5 µL	pET14b vector [CaM] (20 ng/µL)
1.0 µL	fwd primer (125 ng/µL)
1.0 µL	rev primer (125 ng/µL)
2.5 µL	dNTP's (10 mM each)
40.0 µL	dH_2O (sterile)
50.0 µL	total volume

A control reaction was also performed in which the primers were excluded from the reaction mixture. Next, 1 µL of Pfu Turbo (2.5 U/µL, Stratagene) was added to each reaction. The reaction solutions were mixed thoroughly by gentle pipetting, centrifuged briefly and loaded into an MJ-mini PCR machine from Bio-Rad. The PCR method employed was as follows:

PCR method:

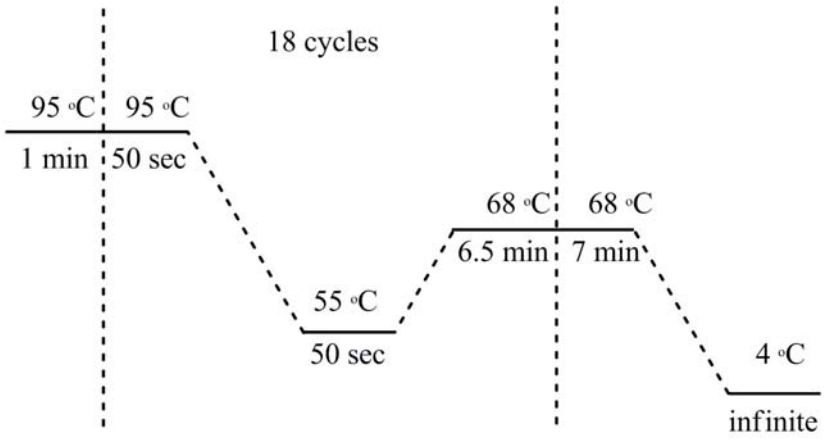

After the PCR reaction was complete the parent vector was digested by adding 1 μL of DpnI (20 U/μL) to each reaction mixture. The reactions were then mixed with gentle pipetting and incubated at 37 ºC for 1.5 hrs each. The reaction mixtures were then used to transform XL1-blue DH5α cells obtained from Stratagene. Colonies from each transformation were selected and submitted for sequencing to confirm the desired constructs were obtained. The DNA from each of the chosen colonies was isolated using a Qiagen Miniprep kit.

Expression and purification of wild-type CaM and cysteine mutants:

The calmodulin constructs were designed with a C-terminal hexahistidine tag for easy purification of the expressed product. The CaM-His_6 mutants were transformed in BL21-Gold(DE3) competent cells from which 20% glycerol stocks were prepared for subsequent protein expression. The stocks were used to inoculate 5 mL LB-broth starter cultures containing carbenicillin (50 μg/mL). The starter cultures were allowed to grow overnight in a 37 ºC shaker at 225 rpm. The next day, the starter cultures were used to inoculate 1 L LB-broth cultures containing carbenicillin (50 μg/mL) and grown at 37 ºC with agitation at 225 rpm. The cultures were allowed to grow to an $OD_{600nm} \approx 0.5$ after which the 1 L shaker flasks were transferred to a 25 ºC shaker (225 rpm) for induction. The cells were induced with 0.1 mM IPTG and shaken for 4 hrs before harvesting at 5000 × g (4 ºC). The pellets were then resuspended in a 0.9% NaCl aqueous solution (30 mL) and transferred to 50 mL conical tubes to be repelleted for storage at -80 ºC.

On the day of the protein preparation, the pellets were thawed at room temperature and resuspended in the following lysis buffer:

4 mL	10× TBS buffer
400 μL	NP-40 Alternative
4 mL	glycerol
40 mg	lysozyme
6 mg	dithiothreitol
40 μL	Protease Cocktail III (Calbiochem)
40 mL	final vol. after diluting with dH_2O

Once the pellets were fully resuspended, the cells were sonicated using a Branson Sonifier 450 at 50% power with a 30% duty cycle for 2 min at 4 ºC. The lysates were then transferred to 45 mL polycarbonate bottles and spun at 100,000 × g in a Type 28 rotor from Beckman Coulter to pellet DNA and other cellular debris. Meanwhile, a 5 mL bed of Ni-NTA agarose resin obtained from Qiagen was pre-equilibrated in TBS buffer for each construct. After the spin, the clarified supernatants were transferred to clean 50 mL conical tubes and mixed with the pre-equilibrated Ni-NTA agarose resin. The samples were tumbled gently on a rotisserie at 4 ºC for 1 hr to allow binding of the His-tagged proteins. The resin was then recovered by passing the lysates through 20 mL spin columns obtained from Bio-Rad. The resin was washed first with 4 mL of TBS buffer, then 4 mL of 10 mM imidazole in TBS buffer and then with 4 mL of 20 mM imidazole in TBS buffer at 4 ºC. The protein was then eluted in 6 × 1 mL fractions of 250 mM imidazole in TBS buffer at 4 ºC. The fractions were assayed for protein and combined appropriately. The imidazole was removed by dialysis using a 3.5 kDa MWCO Slide-A-Lyzer dialysis cassette from Pierce. The protein solutions were dialyzed against 3 × 2 L changes of TBS buffer. The protein concentrations were then quantified using the Bio-Rad protein assay solution. Protein yields were ~80 mg/L for the purified CaM mutants.

SDS PAGE (15% polyacrylamide) analysis was performed on the proteins to confirm purity by Coomassie staining. Western blotting of the gel also confirmed the presence of the poly-histidine tag when probed with the mouse anti-his IgG. After transferring to nitrocellulose for 1 hr at 4 ºC under 100 V, the nitrocellulose membrane was blocked with nonfat dry milk (3 g) in TBS buffer (30 mL) for approximately 4 hrs. The milk solution was then poured off and the membrane washed with TBST buffer (3 × 30 mL for 5 min each wash). Next, a 1:10,000 dilution in TBST (15 mL) of the mouse anti-his IgG was added to the nitrocellulose and incubated for 1 hr. The antibody solution was poured off and the nitrocellulose membrane was again washed with TBST buffer (3 × 30 mL) for 5 min each wash). A 1:10,000 dilution of the goat anti-mouse IgG(H+L) alkaline phosphatase conjugate in TBST (15 mL) was added to the nitrocellulose and incubated for 1 hr. The antibody solution was poured off and the nitrocellulose membrane was again washed with TBST buffer (3 × 30 mL) for 5 min each

wash). Last, 10 mL of 1-Step™ NBT/BCIP from Pierce was added and incubated with the nitrocellulose until the band was visible. The nitrocellulose was then washed with dH_2O and dried.

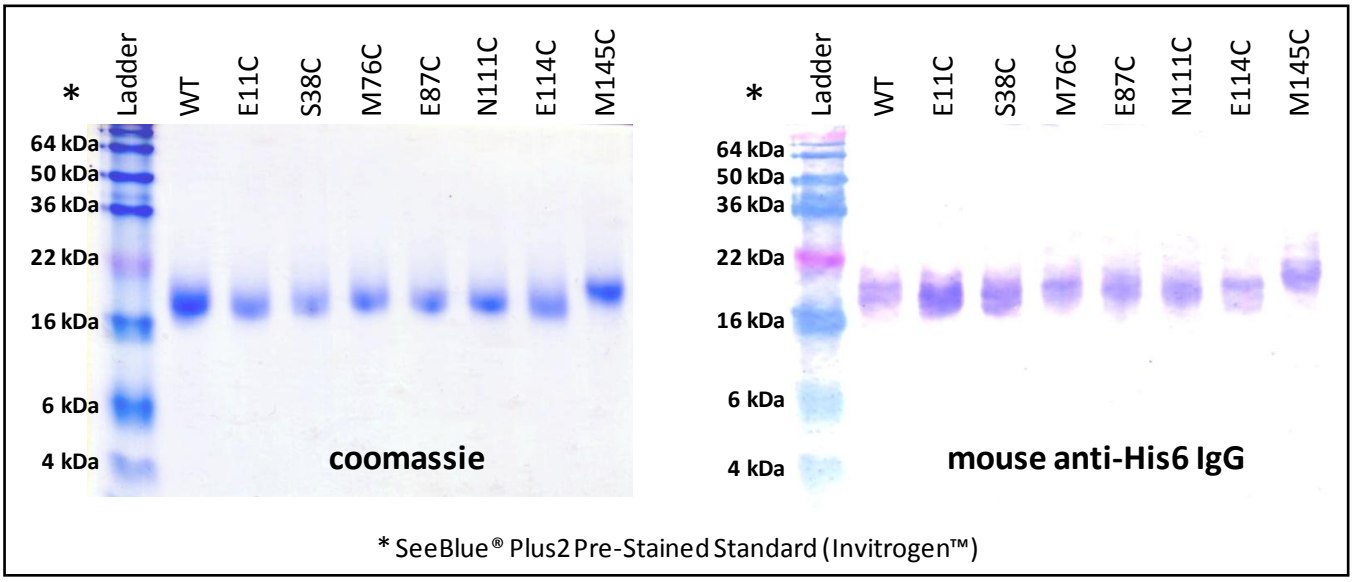

ESI-MS of expressed CaM constructs:

The cysteine mutants of the CaM-His_6 protein were also analyzed by mass spectrometry to confirm the identity of the isolated protein products. All eight of the expressed products matched the calculated molecular weights determine from the primary structures minus the N-terminal methionine due to methionine aminopeptidase activity in *E. coli*.

CaM-His6 construct	ESI-MS (m/z) $[M+xH]^{x+}$ calcd	ESI-MS (m/z) $[M+xH]^{x+}$ found
Wild-type	1948.7 [M+9]	1948.1 [M+9]
	1753.9 [M+10]	1755.2 [M+10]
	1594.6 [M+11]	1593.8 [M+11]
E11C	1945.8 [M+9]	1945.1 [M+9]
	1751.3 [M+10]	1750.5 [M+10]
	1592.2 [M+11]	1591.4 [M+11]
S38C	1950.5 [M+9]	1950.2 [M+9]
	1755.5 [M+10]	1754.7 [M+10]
	1596.0 [M+11]	1595.3 [M+11]
M76C	1945.6 [M+9]	1944.9 [M+9]
	1751.1 [M+10]	1750.3 [M+10]
	1592.0 [M+11]	1591.3 [M+11]

CaM-His6 construct	ESI-MS (m/z) $[M+xH]^{x+}$ calcd	ESI-MS (m/z) $[M+xH]^{x+}$ found
E87C	1945.8 [M+9]	1945.3 [M+9]
	1751.3 [M+10]	1750.6 [M+10]
	1592.2 [M+11]	1593.4 [M+11]
N111C	1947.5 [M+9]	1946.7[M+9]
	1752.8 [M+10]	1752.2 [M+10]
	1593.6 [M+11]	1592.9 [M+11]
E114C	1945.8 [M+9]	1944.9 [M+9]
	1751.3 [M+10]	1752.7 [M+10]
	1592.2 [M+11]	1591.2 [M+11]
M145C	1945.6 [M+9]	1945.1 [M+9]
	1751.1 [M+10]	1751.5 [M+10]
	1592.0 [M+11]	1591.4 [M+11]

The protein masses were determined by ESI-MS on a Mariner electrospray mass spectrometer (PerSeptive Biosystems).

Labeling efficiencies:

The extent of labeling of each construct was determined by measuring the absorbance of the attached dye and dividing that value by the known extinction coefficient to calculate the dye concentration (Table S1). This value was then compared to the predetermined concentration of the protein construct to yield the ratios shown below.

Table S1

			Labeling ratio of CaM Mutants:							
Fluorophore:	Abs_{max} (nm)	ε (cm^{-1} M^{-1})[a]	Wild-type	E11C	S38C	M76C	E87C	N111C	E114C	M145C
1	440	8800	0.01	0.64	0.16	0.47	0.62	0.62	0.84	0.55
2	440	8800	0.04	0.85	0.41	0.61	0.70	0.78	0.84	0.50
3	440	8800	0.00	0.81	0.63	0.60	0.62	0.69	0.84	0.53
4	440	8800	0.00	0.72	0.67	0.60	0.60	0.65	0.79	0.67
MDCC	419	50000	0.00	0.42	0.35	0.30	0.28	0.25	0.31	0.21
IANBD	478	25000	0.01	0.56	0.18	0.46	0.47	0.43	0.52	0.31
BADAN	387	21000	0.01	0.53	0.31	0.43	0.43	0.42	0.48	0.31
IAEDANS	336	5700	0.00	0.30	0.25	0.27	0.39	0.32	0.52	0.30
PyMPO	412	23000	0.02	0.60	0.52	0.45	0.47	0.43	0.50	0.41

[a]The extinction coefficients of the commercial dyes were obtained from the suppliers (AnaSpec, Inc. and Molecular Probes®).

Emission and Excitation settings for SPECTRAmax GEMINI XS plate reader:

Table S2

Fluorophore	exc (nm)	em (nm)
1-4	405	440-660
MDCC	400	430-650
IANBD	455	490-710
BADAN	365	400-620
IAEDANS	336	440-660
PyMPO	412	440-660

Denaturing of fluorescent CaM constructs to determine background emission:

There exist two primary sources of background fluorescence directly associated with a solvatochromic fluorophore when used to develop a fluorescent protein probe. The first involves the intrinsic

fluorescence exhibited by the fluorophore when fully solvated by water. The second is a ramification of appending the fluorophore to the surface of a globular protein. This frequently results in a change in the photophysical properties of the fluorophore that would be expected if it were participating in some type of non-specific interaction with the local topology of the attached protein. By denaturing the protein in a concentrated solution of guanidine hydrochloride, the secondary and tertiary structures that may contribute to this effect are disrupted permitting one to determine the degree of background emission generated (Figure S1).

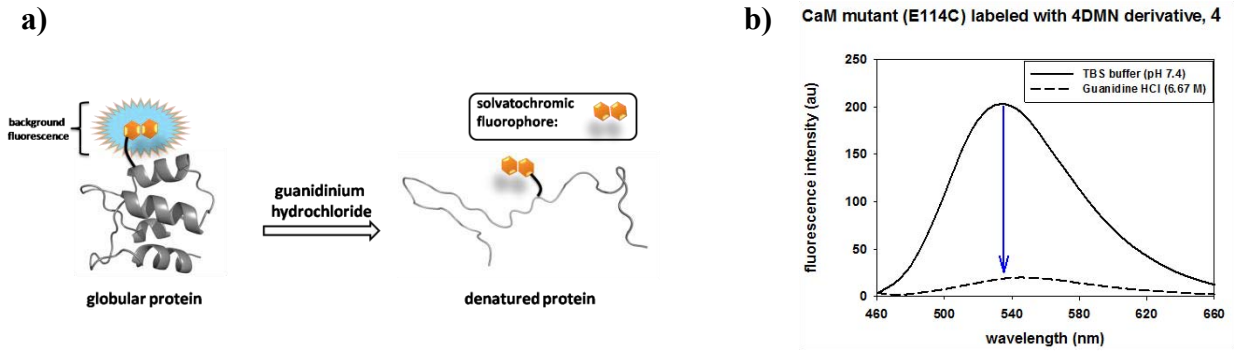

Figure S1. (a) Graphic depicting the tendency of solvatochromic fluorophore to exhibit background fluorescence when appended to a globular protein until denatured, thus fully exposing the fluorophore to the aqueous environment. (b) Example of a typical fluorescent response of a labeled CaM mutant under both natured and denatured conditions (TBS buffer versus guanidine hydrochloride solution at pH 7.4)

A series of experiments were conducted on each of the sixty-three fluorescent CaM constructs prepared in this study in which the degree of background fluorescence associated with the appending of the fluorophore to the protein was determine by measuring the emission spectra of the constructs in TBS buffer (pH 7.4) and guanidine hydrochloride (6.67 M, pH 7.4) and calculating the ratio of intensity at the wavelength of maximum emission in the natured state. The results of this work are displayed in Figure S2.

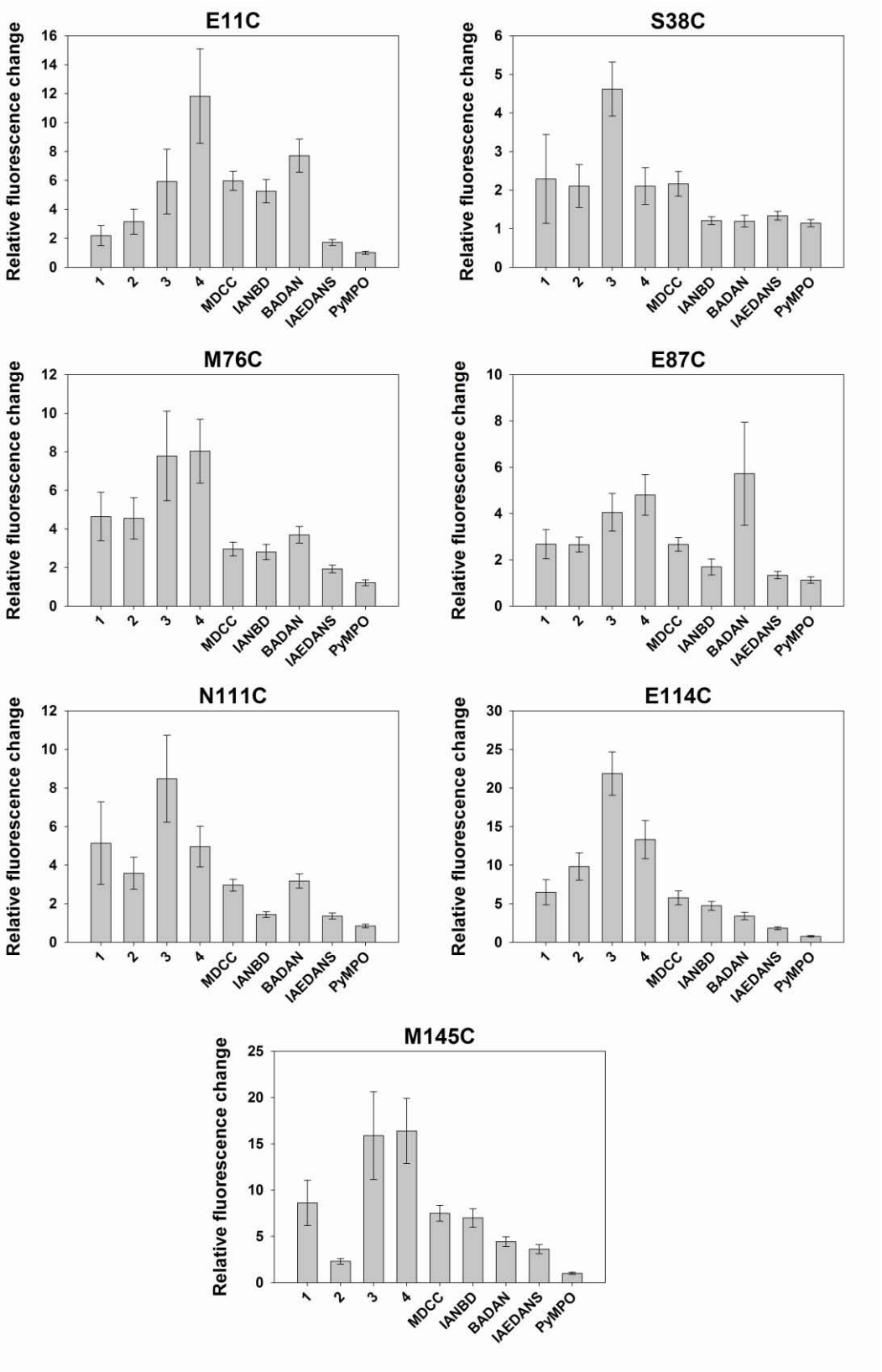

Figure S2. The fluorescent constructs were measured at a concentration of 5 μM in TBS buffer (pH 7.4) and guanidine hydrochloride (6.67 M, pH 7.4). The vertical bars represent the magnitude of the ratio of fluorescence in TBS buffer over that of the construct in the guanidine solution. A greater ratio indicates higher initial background fluorescence due to non-specific interactions of fluorophore with

local features of the attached protein. Indicated errors represent the 90% confidence interval for three trials.

---

(1) Blumenthal, D. K., Takio, K., Edelman, A. M., Charbonneau, H., Titani, K., Walsh, K. A., and Krebs, E. G. (1985) Identification of the Calmodulin-Binding Domain of Skeletal Muscle Myosin Light Chain Kinase. *Proc. Natl. Acad. Sci. U.S.A. 82*, 3187-3191.

(2) Chan, W. C., and White, P. D. (2000) *Fmoc solid phase peptide synthesis: a practical approach*, Oxford University Press, New York.

(3) Hancock, W. S., and Battersby, J. E. (1976) New Micro-Test for Detection of Incomplete Coupling Reactions in Solid-Phase Peptide-Synthesis Using 2,4,6-Trinitrobenzene-Sulphonic Acid. *Anal. Biochem. 71*, 260-264.

(4) Hachmann, J., and Lebl, M. (2006) Alternative to piperidine in Fmoc solid-phase synthesis. *J. Comb. Chem. 8*, 149-149.

PAMAM Dendrimers Conjugated with an Uncharged Gadolinium(III) Chelate with a Fast Water Exchange: The Influence of Chelate Charge on Rotational Dynamics

Miloslav Polášek,[†] Petr Hermann,*[,†] Joop A. Peters,[‡] Carlos F. G. C. Geraldes,[§] and Ivan Lukeš[†]

Department of Inorganic Chemistry, Faculty of Science, Universita Karlova (Charles University), Hlavova 2030, 128 40 Prague 2, Czech Republic, Biocatalysis and Organic Chemistry, Department of Biotechnology, Delft University of Technology, Julianalaan 136, 2628 BL Delft, The Netherlands, and Department of Biochemistry, Faculty of Science and Technology, Center of Neurosciences and Cell Biology, University of Coimbra, 3001-401 Coimbra, Portugal. Received July 20, 2009; Revised Manuscript Received October 9, 2009

A bifunctional ligand, DO3A-py^{NO-C} (DO3A-py^{NO-C} = 10-[(4-carboxy-1-oxidopyridin-2-yl)methyl]-1,4,7,10-tetraazacyclododecane-1,4,7-triacetic acid), was attached to different generations (G0, G1, G2, and G4) of ethylenediamine-cored PAMAM dendrimers (PAMAM = polyamidoamine). The gadolinium(III) complex of this ligand possesses one molecule of water in its first coordination sphere and has a unique combination of a short water residence lifetime (τ_M = 34 ns), a neutral overall charge, and a possibility for rigid attachment to molecules bearing primary amino groups. These favorable properties predestine the ligand for constructions of highly efficient nanosized contrast agents for magnetic resonance imaging (MRI). The coupling reaction between the carboxylic group on the pyridine-*N*-oxide moiety of the protected ligand molecule and primary amines in the dendrimers was achieved by an active ester method under nonaqueous conditions using the coupling agent TBTU. This reaction afforded conjugates with high loadings (80−100% of the theoretically available primary amines) and of high purity. The gadolinium(III) complexes of the conjugates were studied by variable-temperature ^{17}O NMR and ^{1}H NMRD measurements. The water residence lifetime (τ_M = 55 ns) found in the largest conjugate G4-[Gd(H_2O)(do3a-py^{NO-C})]$_{57}$, though somewhat longer compared to the "monomeric" complex, is still short enough not to limit the relaxivity. Surprisingly, compared with analogous conjugates with negatively charged chelates, the prepared uncharged compounds displayed much faster global rotational correlation times (τ_g) and lower relaxivities. This phenomenon can be explained on the basis of Coulomb interactions. The motion of the charged chelates is restrained due to interactions with their counterions and the chelates themselves, while the uncharged chelates are not affected. Comparison of the PAMAM-based conjugates bearing uncharged and (1−)-charged chelates based on relaxometric data, ^{1}H DOSY spectra, and SAXS measurements reveals that τ_g reflects the rotational motion of large segments (dendrons) of the conjugates rather than that of the whole macromolecule.

INTRODUCTION

Magnetic resonance imaging (MRI) is a powerful and rapidly developing diagnostic technique, which is indispensable for imaging of soft tissues. The basic MRI image reflects the concentration of ^{1}H nuclei in the 3D space; however, employing T_1 and T_2 relaxation times of protons helps to significantly improve the quality of the images. Though the use of contrast agents (CAs) is not essential to this technique, it is advantageous to use paramagnetic CAs to accelerate the relaxation of the ^{1}H nuclei.

Among the various available MRI contrast agents, the gadolinium(III) chelates with polydentate ligands, such as the macrocyclic DOTA and open-chain DTPA (Chart 1) and their various derivatives, are probably the most popular ones. These paramagnetic chelates act mainly as T_1-contrast agents. Since the discovery of these first-generation CAs, there has been a continuous effort to improve the properties of the chelates in order to obtain CAs with higher relaxivity (i.e., the efficiency expressed as relaxation rate enhancement per milimolar concentration of metal ion) and higher selectivity (*1*−*5*). The latest development moves toward targeted agents and the field of molecular imaging (*6*−*10*), which allows in vivo investigation of cellular molecular events involved in normal and pathological processes. However, the applicability of MRI contrast agents in molecular imaging encounters a tremendous obstacle in an unfavorable combination of low efficiency of the CAs and low concentration of the target receptors (*6, 7*).

There are, in principle, two basic strategies to overcome this limitation. (i) A high payload of paramagnetic metal ions can be delivered at the target by conjugating a large number of CA molecules with a macromolecule or a particle that is linked to a targeting vector. (ii) The efficiency of the individual CA molecules can be enhanced by rational design of the Gd(III) chelates. Preferably, both approaches should be combined in order to attain the maximum relaxivity. Important physicochemical parameters in this respect are the molecular tumbling (characterized by the rotational correlation time τ_R) and the mean residential time of the water molecule(s) in the coordination sphere of the Gd(III) ion (related to the water exchange by $\tau_M = 1/k_{ex}$). Both parameters should be optimized in order to attain the high relaxivity. Too fast or two slow water exchange can both limit the relaxivity; therefore, the values of τ_M should ideally be within the range 10−30 ns. The optimum of τ_R somewhat varies with the magnetic field and can be tuned by an attachment of the Gd(III) chelate to another molecule.

* E-mail: petrh@natur.cuni.cz. Tel: (+420) 22195-1263. Fax: (+420) 22195-1253.
[†] Universita Karlova.
[‡] Delft University of Technology.
[§] University of Coimbra.

10.1021/bc900288q CCC: $40.75 © 2009 American Chemical Society
Published on Web 11/02/2009

Chart 1. Structures of Ligands Discussed in This Work

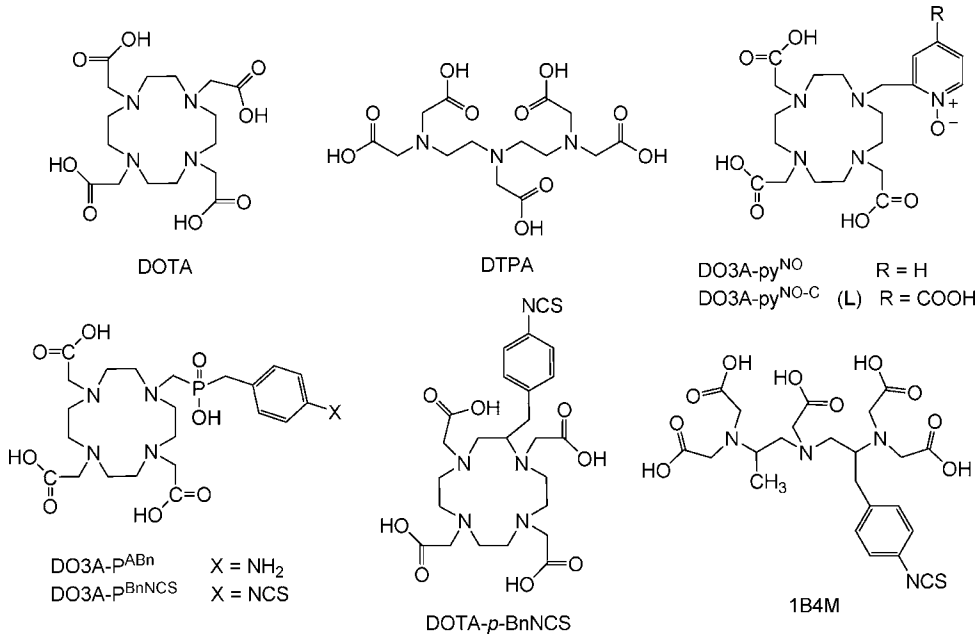

Chart 2. Selected Bifunctional Ligands and Modes of Their Attachment to PAMAM Dendrimers

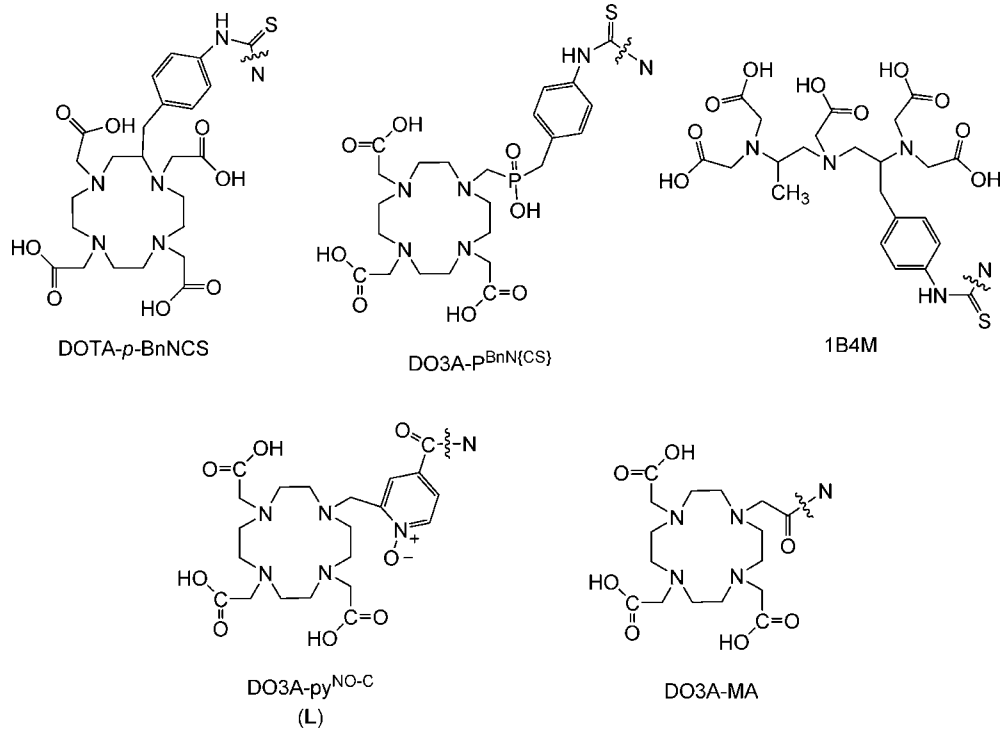

A number of different macromolecules have been explored as molecular scaffolds, spanning a vast range of sizes and chemical nature. Various Gd(III) chelates were covalently attached to dendrimers (*11*−*17*), modified polysaccharides (*18*−*21*), or linear polymers (*18*, *22*) or incorporated into micelles (*23*) and linear polymers (*24*−*28*). A widely used class of substrates for this purpose are the polyamidoamine (PAMAM) dendrimers (*11*−*16*) which provide well-defined, nearly spherical structures of tunable sizes and accordingly adjustable pharmacokinetic properties of the conjugates (*29*−*31*). PAMAM dendrimers have found applications in MRI visualizations of blood vessels (*32*, *33*), lymphatic system (*34*), or targeted imaging of tumors (*35*−*37*). In most of the reported cases, the relaxivity has been limited by a too-slow water exchange in the Gd(III) chelates. Only a few systems with fast water exchange have been presented until now (*14*, *15*). In all cases, it was found that the relaxivity can be additionally limited by a fast local motion of the attached chelates that cancels the effect of the slow overall motion of the conjugate (*14*, *15*, *38*).

The strategies to attach the Gd(III) chelates to macromolecules (Chart 2) include the most popular reaction between isothiocyanates and primary amino groups to form a thiourea bridge (e.g., in 1B4M (*9*, *10*, *29*, *31*, *32*, *34*, *39*), DOTA-*p*-BnNCS (*16*), DO3A-P^{BnNCS} (*15*) (see Chart 1), and others (*11*, *14*, *35*, *40*), the analogous reaction of isocyanates (*41*, *42*), and the formation of amide bonds either with (*12*) or without (*16*, *17*) the use of an additional spacer. The latter method is especially attractive,

as it can help to evade the problematic fast local motion by minimizing the number of atoms involved in the linking group.

Besides having optimal relaxivity (i.e., optimized values of τ_R and τ_M), the Gd(III) chelate should be sufficiently thermodynamically and kinetically stable in order to prevent complications arising from the recently discovered toxicity of some less stable contrast agents (*43*). In addition, the chelates of uncharged nature can be advantageous in several aspects: (i) there is lower osmolality of the intravenously injected solution; (ii) they might interfere less with the molecular recognition processes in molecular imaging applications; and (iii) uncharged chelates internalize into cells more easily than the charged ones, and therefore, they are more appropriate for cell labeling applications (*44*). Meeting all the requirements in one compound is an extremely challenging task, as some of the parameters cannot be changed without affecting the others.

Recently, we reported the synthesis and characterization of a new bifunctional derivative of DOTA bearing one pyridine-*N*-oxide pendant arm, ligand DO3A-py$^{NO\text{-}C}$ (**L**, Chart 1) (*45, 46*). The Gd(III) complex of this compound exhibits a water exchange rate that is optimal for MRI applications ($\tau_M = 34$ ns). The carboxylic group at the 4-position of the pyridine ring can be used for attachment of the ligand to any molecule bearing primary amino groups. Such an attachment minimizes the number of bonds that allow rotation and, therefore, should restrict the local motion. In addition, the attached Gd(III) chelates are electroneutral. This combination of properties makes the ligand **L** an interesting alternative to other existing bifunctional ligands for a variety of applications.

In this work, we describe the synthesis of G0 to G4 PAMAM conjugates of **L** that cover a vast range of molecular masses. The PAMAM dendrimers were chosen as good reference models, which allow a direct comparison of the properties with other conjugates. Unlike the aqueous conditions used in the preparations of the thiourea-bridged conjugates, our synthetic route required the combination of a nonaqueous chemistry, orthogonal protection of the acetate groups, activation and coupling of the pyridine-carboxylic group, and final deprotection. The properties of the gadolinium(III)-loaded conjugates were explored using ^{1}H and ^{17}O relaxometry, ^{1}H DOSY spectra, and SAXS measurements. For the first time, an uncharged gadolinium(III) complex endowed with a fast water exchange was attached to a macromolecule.

EXPERIMENTAL SECTION

Chemicals. D_2O (99.95% D) and CD_3OD (99.8% D) were purchased form Chemotrade. LiOH monohydrate was obtained from Lachema. Diisopropylethylamine (DIPEA) was received from Merck. 4-(Dimethylamino)pyridine (DMAP), *O*-(1*H*-benzotriazol-1-yl)-*N*,*N*,*N*′,*N*′-tetramethyluronium tetrafluoroborate (TBTU), HOBt, EDC, HOAt, TSTU, and dry DMSO were purchased from Fluka. The solutions of polyamidoamine (PAMAM) dendrimers with ethylenediamine core of generations 0, 1, 2 (all 20 wt % in methanol), and 4 (10 wt % in methanol) were obtained from Aldrich. Trifluoroacetic acid (TFA, extra pure) was received from Acros. Dry acetonitrile was prepared by distillation from P_2O_5. The following extra pure chemicals were used for buffer preparations: ammonium acetate and anhydrous sodium acetate (both Fractopur), acetic acid, and 25% aqueous NH_3 (both p.a.) were purchased from Merck; NaOH (puriss) and citric acid monohydrate (puriss) were obtained from Fluka. High-purity deionized water and supragradient-grade acetonitrile (Scharlau) were used for HPLC. Methanol ANASOLV-P (Analytika, Czech Republic) was used for ultrafiltration. The Dowex 50 ion-exchange resin was purchased from Fluka. Complexes of the DO3A-P$^{BnN\{SC\}}$-containing dendrimers were available from previous studies (*15*).

Methods. Elemental analyses were performed at the Institute of Macromolecular Chemistry of the Czech Academy of Science (Prague). NMR spectra were acquired on Varian UNITY INOVA 400 and Varian NMRS 300. The chemical shifts were referenced on the signal of CHD_2OD (= 3.31 ppm, in CD_3OD) or *t*-BuOH (= 1.20 ppm, in D_2O). ES/MS spectra were recorded on a Bruker ESQUIRE 3000 with ion-trap detection in the positive mode.

MALDI-TOF MS. Spectra were acquired on a 4800 Plus MALDI TOF/TOF analyzer (Applied Biosystems/MDS Sciex) equipped with a Nd:YAG laser (355 nm, firing rate 200 Hz) in the linear positive ion mode. Samples were spotted onto the MALDI target and left to dry. Dried droplets were covered by the matrix solution (10 mg/mL sinapinic acid in 50% (v/v) acetonitrile and 0.05% (v/v) trifluoroacetic acid) and left to dry.

Ultrafiltration. The device consisted of an ultrafiltration cell 8050 (50 mL), CDS10 selector valve, and an RC800 mini-reservoir (800 mL). The membranes were selected according to their cutoff with respect to the molecular weights of the conjugates: PLAC (1 kDa, for G0 and G1 conjugates), YM3 (3 kDa, for G2), and YM10 (10 kDa, for G4). All ultrafiltration equipment was purchased from Millipore.

RP-HPLC. The HPLC system was composed of a Beta 10 gradient pump (ECOM, Czech Republic) equipped with an active mixer Knauer A0285 and a Topaz dual-UV detector (ECOM, Czech Republic). Experiments were performed on an XTerra RP8, 5 μm, 150 × 4.6 mm column (Waters) equipped with a Security Guard system (Phenomenex) holding a C8 cartridge. The mobile phase was continuously vacuum-degassed in a DG 3014 degasser (ECOM, Czech Republic). The mobile phase was mixed in the gradient pump from three stock solvents and solutions: CH_3CN (solvent A), H_2O with 0.1 vol % of TFA (mixture B), and H_2O (solvent C). The detector wavelengths were set to 210 and 289 nm. Concentrations of the samples were ~0.5 mg/mL. Injection volumes were 20 μL. The flow rate was maintained at 1 mL/min. Collecting and processing of the data were performed using Clarity (DataApex, Czech Republic) software.

SEC. Size-exclusion chromatography was performed on the system described above, on a TSKgel G2000SW 300 × 7.5 mm column equipped with a TSKgel SW Guardcolumn 75 × 7.5 mm (TOSOH Bioscience). A differential refractometer RIDK-102 (ECOM, Czech Republic) detector was attached in series after the UV-absorbance detector. The UV-absorbance wavelengths were set to 230 and 289 nm. A premixed 0.1 M sodium citrate buffer pH = 2.77 was used as the mobile phase. The flow-rate was maintained at 0.5 mL/min. The concentration of the samples was 1−2 mg/mL; the injection volumes were 20 μL.

^{1}H NMRD Profiles. The ^{1}H longitudinal relaxation rates (defined as $1/T_1$) were measured with a Stelar Spinmaster Spectrometer FFC-2000 using the field-cycling method. The range of magnetic fields was 0.00024−0.24 T (corresponding to 0.01−10 MHz proton Larmor frequency). Additional data points at 0.47 T (20 MHz) and 1.41 T (60 MHz) were obtained with Bruker Minispec mq-20 and Bruker Minispec mq-60 relaxometers, respectively. The T_1 values were determined using the standard inversion recovery pulse sequence. The measurements were performed at 25 and 37 (±1) °C.

^{17}O NMR Variable-Temperature Measurements. The ^{17}O NMR measurements were performed on a Varian UNITY INOVA 400 spectrometer (9.4 T, 54.22 MHz). The temperature was controlled with L-900 VT-unit and calibrated on ^{1}H signals of methanol and ethylene glycol (*47*). The samples were enriched to ca. 0.1% of ^{17}O by addition of $H_2{}^{17}O$ (30%, IsoTrade) and approximately 0.5% of *t*-BuOH was added as internal standard. Longitudinal relaxation times were measured

using the inversion recovery pulse sequence and transversal relaxation times by the Carr-Purcell-Meiboom-Gill spin echo pulse sequence. No spinning of the samples and no frequency lock were used. The BMS contributions to chemical shifts in the paramagnetic samples were determined from the differences of ^{1}H signals of *t*-BuOH between the diamagnetic and paramagnetic sample and were subtracted. The samples were kept in the probe for at least 10 min prior to the measurement to ensure temperature equilibration.

Fitting of Data. The simultaneous analyses of ^{1}H NMRD and ^{17}O NMR variable-temperature T_1, T_2, and chemical shift data were performed with the Micromath Scientist computer program using a least-squares procedure (for complete set of used equations, see Supporting Information).

DOSY. DOSY experiments were performed on 500 MHz Avance Bruker Spectrometer with a BBI Bruker 5 mm probe. The sequence for diffusion measurements included a stimulated echo using bipolar gradients. Diffusion time = 200 ms; gradient duration = 2 × 1.750 ms. Spectra were generated with NMRnotebook software, DOSY kit (NMRTec).

Small-Angle X-ray Scattering (SAXS). The SAXS experiments were performed using a pinhole camera (Molecular Metrology SAXS System) attached to a microfocused X-ray beam generator (Osmic MicroMax 002) operating at 45 kV and 0.66 mA (30 W). The camera was equipped with a multiwire, gas-filled area detector with an active area diameter of 20 cm (Gabriel design). Two experimental setups were used to cover the q range of 0.005−1.1 Å^{-1} ($q = (4\pi/\lambda)\sin\Theta$, where λ is the wavelength and 2Θ is the scattering angle). The scattering intensities were put on absolute scale using a glassy carbon standard.

MR Imaging. The contrast agent (G4-[Gd(H_2O)(do3a-py$^{NO\text{-}C}$)]$_{57}$) was intravenously applied to a healthy Lewis rat (Charles River, Germany). The dose was 125 μL of solution in 0.9% NaCl that was 181 mM per Gd(III). MR images of rat kidney prior to and after the application of CA were obtained at a 4.7 T Bruker MR spectrometer by T_{1w} gradient echo and spin echo sequences. Parameters of the gradient echo sequence were as follows: repetition/echo time TR/TE, 60 ms/3.7 ms; flip angle 30°; slice thickness, 2 mm; number of acquisitions, 16; scan time, 4 min 6 s; in-plane resolution, 234 μm. Parameters of the spin echo sequence were as follows: repetition/echo time TR/TE, 215 ms/12 ms; slice thickness, 2 mm; number of acqusitions, 8; scan time, 11 min 27 s; turbo factor, 2; in-plane resolution, 234 μm. The protocol was approved by the Ethical Committee of the Institute for Clinical and Experimental Medicine and the experiments were carried out in accordance with the European Communities Council Directive of 24 November 1986 (86/609/EEC). Evaluation of MR images was done using the software *ImageJ* (copyright NIH, USA).

*Preparation of t-Bu$_3$***L**·*DIPEA Salt (***2***).* First, a column with Dowex 50 ion-exchange resin in H^+ cycle was prepared, and water in the column was exchanged for MeOH. A solution of DIPEA in MeOH was passed through until the ion-exchange resin was saturated with DIPEA. The excess of DIPEA was then flushed away with MeOH. A solution of 1.2 equiv of LiOH·H_2O (0.250 g, 5.96 mmol) in 5 mL of water was then added dropwise to a stirred solution of *t*-Bu$_3$Me**L** (**1**, 3.37 g, 4.96 mmol) (*45*) in 20 mL of MeOH at RT. After 10 min, RP-HPLC analysis confirmed complete hydrolysis of the methyl ester function (A/B/C: linear gradient from 20/40/40 to 40/40/20 in 10 min, 40/40/20 held for 5 min; retention times: *t*-Bu$_3$Me**L** 11.17 min, *t*-Bu$_3$**L** 9.50 min). The solution was then slowly passed through the column of Dowex 50. The yellow eluate was concentrated on a rotary evaporator, the residue was dissolved in benzene (100 mL), and the solution was freeze-dried. The product was obtained as a pale yellow solid foam (3.86 g, 97%). δ_H (300 MHz, CD_3OD) 1.38 (3 H, t, DIPEA $CH_2C\mathbf{H}_3$, J_{HH} = 7.5 Hz); 1.38 (12 H, d, DIPEA CH($C\mathbf{H}_3$)$_2$, J_{HH} = 6.6 Hz); 1.46 (18 H, s, *t*-Bu$_3$**L** −C(CH_3)$_3$); 1.47 (9 H, s, *t*-Bu$_3$**L** −C(CH_3)$_3$); 2.88−2.96 (8 H, m, *t*-Bu$_3$**L** ring CH_2); 3.08−3.14 (4 H, m, *t*-Bu$_3$**L** ring CH_2); 3.19−3.25 (4 H, m, *t*-Bu$_3$**L** ring CH_2); 3.23 (2 H, quartet, DIPEA C$\mathbf{H}_2$$CH_3$, J_{HH} = 7.5 Hz); 3.56 (2 H, s, *t*-Bu$_3$**L** CH_2CO); 3.70 (4 H, s, *t*-Bu$_3$**L** CH_2CO); 3.73 (2 H, septet, DIPEA C**H**(CH_3)$_2$, J_{HH} = 6.6 Hz); 4.08 (2 H, s, *t*-Bu$_3$**L** CH_2-py); 7.92 (1 H, dd, *t*-Bu$_3$**L** aryl, J_{HH} = 6.6 Hz, J_{HH} = 2.4 Hz); 8.08 (1 H, d, *t*-Bu$_3$**L** aryl, J_{HH} = 2.4 Hz); 8.36 (1 H, d, *t*-Bu$_3$**L** aryl, J_{HH} = 6.6 Hz). ESI-MS (*m*/*z*; found (calcd)) 666.1 (666.4) ($M+H^+$). Found: C, 57.16; H, 9.24; N, 9.70. Calc. for $C_{41}H_{74}N_6O_9$: C, 61.94; H, 9.38; N, 10.57%.

*General Procedure for the Synthesis of the Conjugates in the Form of t-Butyl Esters (***3a**−**3d***).* For preparation of about 300 mg of conjugate, the appropriate amount of methanolic solution of the dendrimer was weighed and evaporated on a rotary evaporator. The residue was dried in vacuum for 1 h and then dissolved in 2 mL of dry DMSO with HOBt (1.5 equiv per primary amino group of the dendrimer). The *t*-Bu$_3$**L**·DIPEA salt (1.5 equiv per primary amino group of the dendrimer) and TBTU (1.5 equiv per NH_2) were mixed and dissolved in dry acetonitrile (10 mL). The resulting solution was added dropwise (over period of 20 min) to a stirred solution of the dendrimer. The progress of the reaction was followed on RP-HPLC. After 30 min of stirring at RT, the reaction mixture was concentrated on a rotary evaporator. The residue was diluted with a MeOH/water mixture (1:1, v/v) to approximately 20 mL and filtered through a 0.22 μm syringe filter to the ultrafiltration cell. The solution was first concentrated in the cell to 10 mL and then continuously ultrafiltrated (solvent composition: 50% MeOH, 50% of 0.1 M aqueous NH_4OAc) until all low-molecular-weight compounds (i.e., the ligand, coupling agent, and DMSO) were removed (checked by RP-HPLC). This required approximately 150−200 mL of the solvent. The ultrafiltration was then continued with pure MeOH until at least 50 mL had run through. The obtained solution was then evaporated on a rotary evaporator; the residue was dissolved in 20 mL of benzene and then freeze-dried. The products were obtained as pale yellow solid foams with the yields 88−94%. δ_H (300 MHz, CD_3OD, 45 °C) 1.45−1.46 (s, −C(CH_3)$_3$); 1.47−1.48 (s, −C(CH_3)$_3$); 2.25−3.75 (overlapping CH_2 signals of **L** and the dendrimer); 3.96−4.03 (s, CH_2-py); 7.80−7.89 (m, arom.); 8.10−8.25 (m, arom.); 8.36−8.41 (m, arom.). MALDI-TOF-MS (only for G0-(*t*-Bu$_3$**L**)$_4$) (*m*/*z*; found (calcd)) 3109.4 (3108.0) ($M+H^+$).

*Cleavage of the t-Butyl Esters, General Procedure (***4a**−**4d***).* The conjugates obtained as *t*-butyl esters in the previous step (typically about 200 mg) were dissolved in neat TFA (ca. 10 mL) and stirred 24 h at RT. TFA was then removed on a rotary evaporator; the residue was dissolved in water (20 mL) and then neutralized with aqueous ammonia. The solution was transferred to the ultrafiltration cell, concentrated to 10 mL, and ultrafiltered continuously with 0.05 M aq ammonium acetate. After collecting ca. 100 mL of the filtrate, the solvent was exchanged for deionized water and the ultrafiltration was continued until another 100 mL of the filtrate was collected. The retained solution was then freeze−dried, and the products were obtained as pale yellow powders with the yields 76−84%. δ_H (300 MHz, D_2O, 60 °C) 2.40−3.80 (overlapping CH_2 signals of **L** and the dendrimer); 4.10−4.11 (s, CH_2-py); 7.72−7.82 (m, arom.); 8.30−8.43 (two overlapping m, arom.).

*Preparation of the Gd(III) Complexes, General Procedure (***5a**−**5d***).* The ligand−PAMAM conjugate (typically 100 mg) was dissolved in water (10 mL) and solid $GdCl_3$·$6H_2O$ (1.5 equiv relative to a number of the ligand molecules) was added. The pH was adjusted to 7 with 2 M NaOH. The mixture was stirred at RT for 24 h. Then, Na_2H_2EDTA (2 equiv relative to number of ligand molecules) was added and the pH again

Scheme 1. Synthesis of the Conjugates

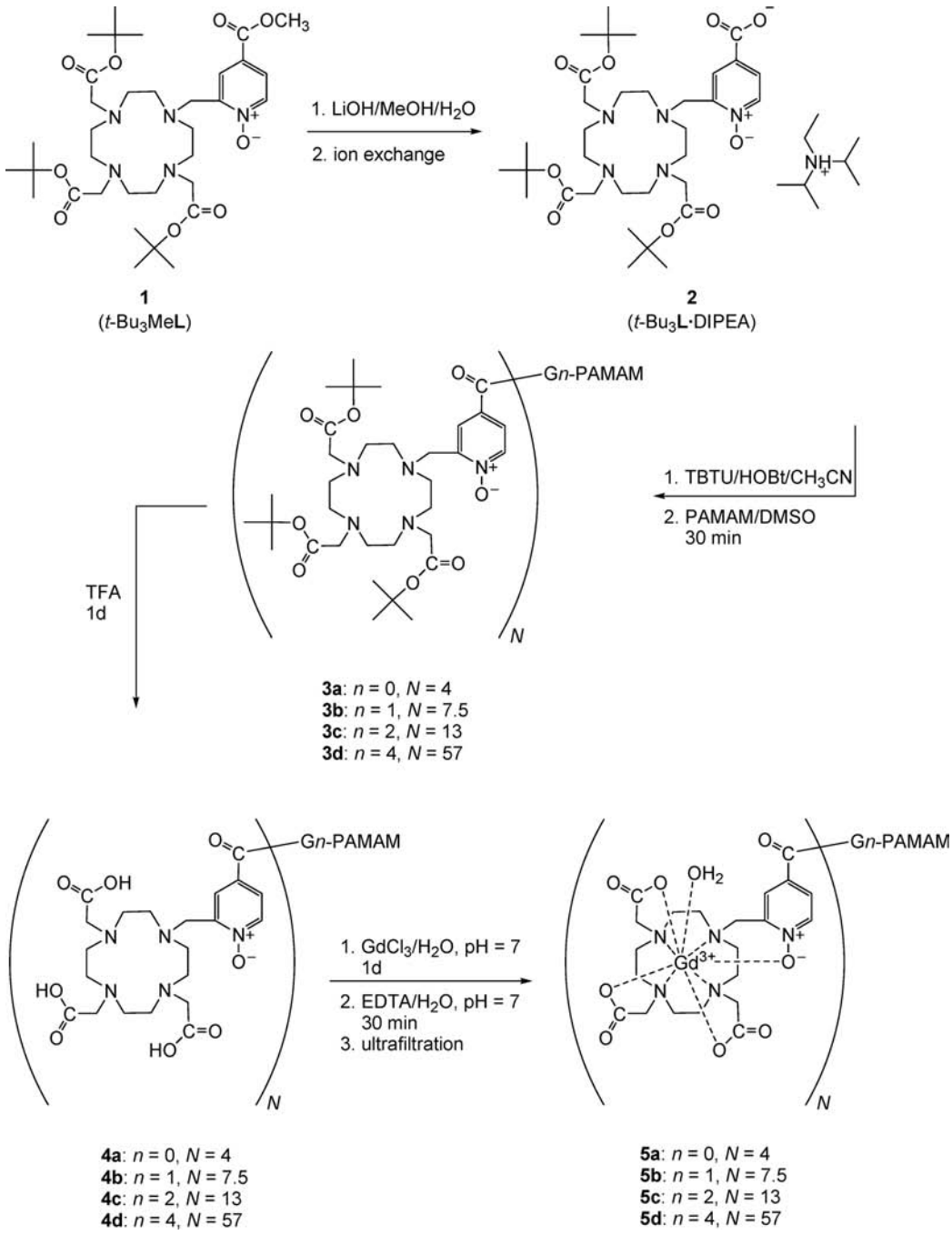

adjusted to 7 with NaOH. The xylenol orange test gave a negative reaction showing that the excess of Gd(III) ions was chelated by EDTA. The solution was then continuously ultrafiltered with deionized water until all low-molecular-weight compounds were removed (controlled by SEC). The solution was either used in further steps or freeze−dried to afford the pure Gd(III)-loaded conjugates as light yellowish powders. Complexes with other trivalent ions were obtained analogously.

RESULTS AND DISCUSSION

Synthesis. An attachment of DO3A-py$^{NO\text{-}C}$ to PAMAM dendrimers through an amide bond between the carboxylic group on the pyridine ring of DO3A-py$^{NO\text{-}C}$ and the primary amino groups of the dendrimer required a selective protection of the carboxylic groups in the acetate pendant arms of the DO3A moiety. Therefore, the previously described *t*-butyl methyl ester **1** (Scheme 1) (*45*) was used as starting material. The methyl ester function on the pyridine ring was selectively hydrolyzed with LiOH in a MeOH/H_2O mixture. According to RP-HPLC, the reaction was selective and fully completed in a few minutes. The presence of Li^+ ions complicated the NMR spectra of the reaction product due to formation of Li^+ complexes. Therefore, the Li^+ cation was exchanged for protonated DIPEA on an ion-exchange resin. The resulting DIPEA salt of *t*-Bu$_3$**L** could then be obtained as a dry, solid foam upon freeze-drying from benzene solution. The successful exchange for DIPEA was confirmed by ^{1}H NMR.

The coupling was accomplished using TBTU coupling agent and DMSO/CH_3CN solvent mixture and afforded conjugates in high yields and with high loadings. Conditions for the coupling were optimized using reversed-phase HPLC (Supporting Information Figure S1). With this technique, we were also

Table 1. Loadings of the Dendrimers with *t*-Bu$_3$L

generation of dendrimer	*N* (theoretical)	*N* (average)[a]	loading (%)[b]
0	4	4.2	104
1	8	7.5	94
2	16	13.0	81
4	64	57.0	89

[a] The average of the two values calculated from ratios of the integral intensities of aliphatic/aromatic and aliphatic/*t*-butyl regions in ^{1}H NMR spectra. [b] The loadings were calculated from intensities in the ^{1}H NMR spectra, assuming that the dendrimers were ideal (without defects). This is possibly the reason why the loading for G0 exceeds 100%. The accuracy of the loadings given is estimated to be ±5%.

able to detect impurities in the resulting conjugates (Supporting Information Figures S1 and S2), which have not commonly been mentioned in previous reports. Analysis of the impurities was possible only for the G0 conjugate; however, it revealed that these stem from the starting PAMAM dendrimers that are prone to various defects (Supporting Information Figure S7). Similarly, defective dendrimers were detected also with SEC, where dimers (two dendrimers fused together) could be seen in both the starting dendrimers and the conjugates (Supporting Information Figures S5 and S6). The loadings of the dendrimers with ligand molecules were determined from integral intensities in ^{1}H NMR spectra of the conjugates in the *t*-Bu ester form (see Table 1 and Supporting Information Figures S3 and S4). After cleavage of the *t*-Bu esters in neat TFA, the Gd(III) complexes of the conjugates were prepared. Each step of the synthesis was followed by purification with ultrafiltration. More detailed discussions of the synthetic protocol and characterization is described in the Supporting Information.

Relaxometry. One of the crucial parameters that affect the relaxivity of macromolecular contrast agents is the exchange rate of water molecules coordinated to the central Gd(III) ion. A slow water exchange has been stated as the major relaxivity-limiting factor in a number of conjugates (*11, 13, 16, 40*). This is particularly true for various amide derivatives of DOTA and DTPA, where the carboxyl groups coordinated to the metal ion were utilized for a linkage to other molecules through an amide bond. The change in the local coordination environment of the Gd(III) ion results in a decrease of the water exchange rate (*11, 13, 16, 24*−*27*). Thus, it is apparent that the point of attachment of the chelate must be sufficiently far from the coordination cage around the central ion in order not to interfere with the water exchange process. In a previous study, we have demonstrated that derivatization of the DO3A-py^{NO} (Chart 1) at position 4 of the pyridine ring with a carboxylic group (leading to the ligand DO3A-py$^{NO\text{-}C}$) had no significant effect on the water exchange rate in the Gd(III) complexes (*45*). Therefore, linking of DO3A-py$^{NO\text{-}C}$ to the PAMAM dendrimers by forming an amide to the carboxyl on the pyridine ring should similarly have no effect on the water exchange rate. To test this hypothesis, variable-temperature ^{17}O NMR transversal relaxation rates of a solution of the largest prepared conjugate, G4-[Gd(H$_2$O)(do3a-py$^{NO\text{-}C}$)]$_{57}$, were measured to assess the water exchange rate (*1, 11*). The data are shown in Figure 1 and compared to the data of the "monomer", [Gd(H$_2$O)(DO3A-py$^{NO\text{-}C}$)]$^-$ complex. Both sets give almost the same shape of the curve showing that there is no significant change in the water exchange rate of the chelate after the attachment to the dendrimer. The whole set of data for the conjugate, G4-[Gd(H$_2$O)(do3a-py$^{NO\text{-}C}$)]$_{57}$, including the temperature dependences of the ^{17}O transversal (Figure 1) and longitudinal (Supporting Information Figure S8) relaxation rates, ^{17}O chemical shifts (Supporting Information Figure S8), and ^{1}H NMRD profiles at 25 and 37 °C (Figure 2), was fitted according to the equations of the Solomon-Bloembergen-Morgan (SBM) theory of paramagnetic relaxation (for the set of equations, see Supporting Information). The water residence time ($\tau_M = 1/k_{ex}$) in the conjugate ($\tau_M = 55$ ns) as determined by this method is slightly longer than that found in the monomer ($\tau_M = 34$ ns) (*45*). However, the value is still short enough not to limit the relaxivity of the conjugates. As there was no significant change in the ^{17}O transversal relaxation rates going from the monomer to the largest conjugate, we did not perform the ^{17}O studies on the smaller conjugates.

As the water exchange in the Gd(III) complex of DO3A-py$^{NO\text{-}C}$ is fast regardless of its attachment to other molecules, the main parameter limiting the relaxivity is the rotational correlation time τ_R. Therefore, any increase of this parameter (i.e., slowing down of the molecular tumbling) should be reflected in a growth of the relaxivity. Figure 3 shows that the relaxivity of the conjugates is roughly linearly proportional to the dendrimer generation. This corresponds to the proportionality of the global rotational correlation time τ_g to the molecular volume (as given by the Debye-Stokes-Einstein equation), which is approximately doubled with each generation. The data are compared with those for the analogous negatively charged conjugates of DO3A-P$^{BnN\{SC\}}$ (Chart 2) that display similarly fast water exchange rates in the Gd(III) complexes (*15, 48*). In all cases, the conjugates of DO3A-py$^{NO\text{-}C}$ give significantly lower relaxivities compared to the conjugates of DO3A-P$^{BnN\{SC\}}$ of the same generation.

A simultaneous fitting of the variable-temperature ^{17}O NMR data and ^{1}H NMRD profiles for the conjugate G4-[Gd(H$_2$O)(do3a-py$^{NO\text{-}C}$)]$_{57}$ to the appropriate equations allowed us to investigate the relaxometric properties in more detail. The model comprises the Lipari-Szabo approach (*1*), which discriminates between the local (τ_l) and global (τ_g) rotational correlation times on the basis of a general order parameter S^2. For $S^2 = 0$, the local and global motions are completely independent of each other, while for $S^2 = 1$, both motions are totally correlated. It has been shown that the water molecule coordinated to the Gd(III) ion can rotate around the coordination bond. As a consequence, the τ_l values for ^{1}H nuclei are systematically lower by a factor of 0.65 than those for ^{17}O nuclei (*14, 49*). This internal motion of the water molecule is part of the local motion, and therefore, only values of τ_l are different for ^{1}H and ^{17}O. For the simultaneous fit of ^{1}H and ^{17}O data, we included this effect in our model (see Supporting Information). The number of parameters involved in the fit required fixing of some of them to the values previously determined for the monomer (number of inner-sphere water molecules $q = 1$; activation energy for the water exchange $\Delta H_M = 45.5$ kJ mol^{-1}; hyperfine coupling constant $A/\hbar = -3.75 \times 10^6$ rad s^{-1}) (*45*) or to generally accepted values (distances $r_{GdH} = 3.1$ Å and $r_{GdO} = 2.5$ Å, the closest approach of outer-sphere water molecules $A = 3.5$ Å) (*50*). The fitted parameters were the water residential lifetime τ_M, rotational correlation times τ_l and τ_g, the activation energies for rotational motions E_l and E_g, the order parameter S^2, and the parameters governing the electronic relaxation Δ^2 and τ_v. A reasonable agreement of the simultaneous fit with the longitudinal ^{17}O relaxation rates was obtained only when either the quadrupolar coupling constant $\chi(1 + \eta^{2/3})^{1/2}$ or the Gd···O$_w$ distance were allowed to vary. However, adjusting r_{GdO} led to unrealistically small values (~2.2 Å) that are not supported by any experimental evidence (*46*). Therefore, the constant $\chi(1 + \eta^{2/3})^{1/2}$ was allowed to vary, resulting in 11.1 ± 1.4 MHz. This value is somewhat larger than the recently reported value obtained from molecular dynamics simulations (8.7 MHz) (*51*), but smaller than the value obtained for the monomer (13.8 MHz) (*45*). For the conjugate G1-[Gd(H$_2$O)(do3a-py$^{NO\text{-}C}$)]$_{7.5}$, only the ^{1}H NMRD profiles were used in the fit, with adjustable parameters being τ_l, τ_g, S^2, Δ^2, and τ_v; other parameters were fixed at the values of the best fit for the conjugate G4-[Gd(do3a-py$^{NO\text{-}C}$)]$_{57}$. The most important

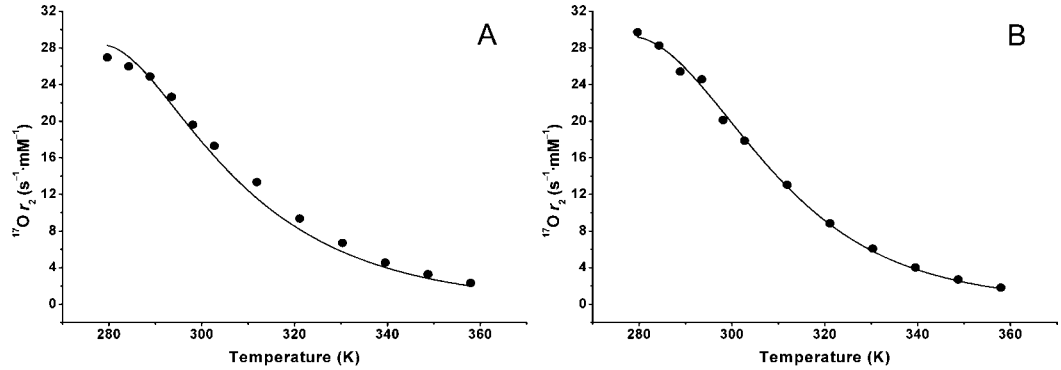

Figure 1. Temperature dependences of ^{17}O transversal relaxation rates of the macromolecular conjugate, G4-[Gd(H_2O)(do3a-py^{NO-C})]$_{57}$ (A), and the "monomeric" complex, [Gd(H_2O)(DO3A-py^{NO-C})]$^-$ (B, reproduced from ref *45*). The solid lines represent the results of the simultaneous least-squares fits.

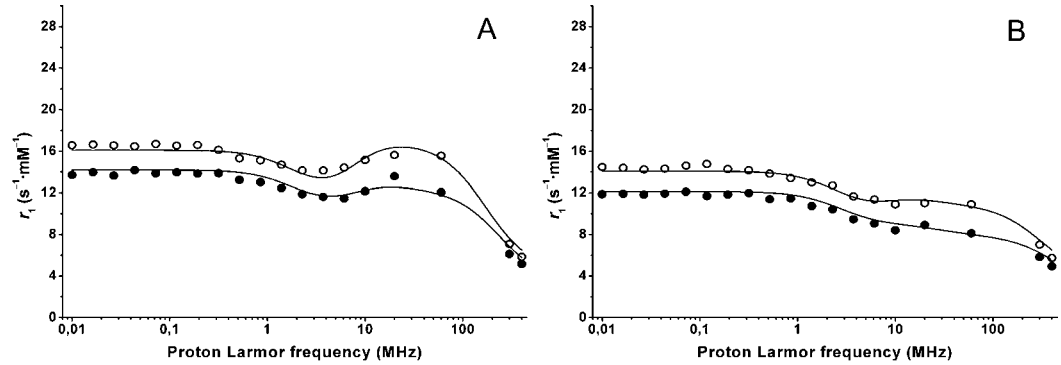

Figure 2. The ^1H NMRD profiles of G4-[Gd(H_2O)(do3a-py^{NO-C})]$_{57}$ (A) and G1-[Gd(H_2O)(do3a-py^{NO-C})]$_{7.5}$ (B) conjugates at 25 (empty circles) and 37 °C (filled circles). The solid lines represent the results of the simultaneous least-squares fits.

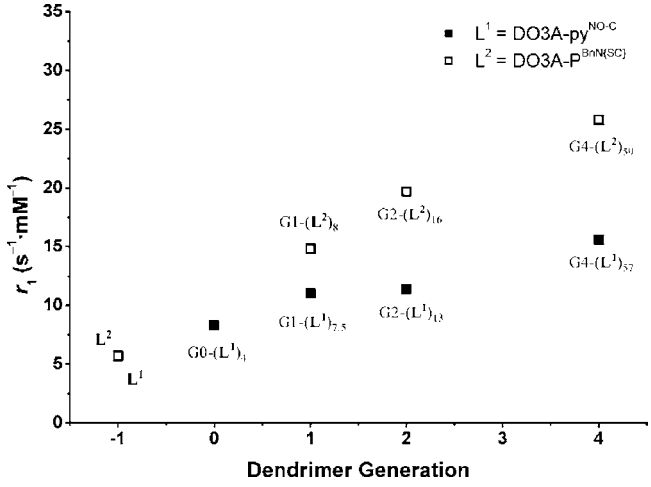

Figure 3. Dependence of relaxivity per mM Gd(III) (20 MHz, 25 °C) on the generation of the PAMAM dendrimers bearing electroneutral Gd(III) complexes of DO3A-py^{NO-C} (full squares) and negatively (1−)-charged Gd(III) complexes of DO3A-P$^{BnN\{SC\}}$ (open squares, data for ref *15a*.). The values at point −1 on the *x*-axis correspond to the "monomeric" chelates.

results of the fits are summarized in Table 2 and compared to similar conjugates and the corresponding "monomers" (for the full set of parameters, see Supporting Information).

From Table 2, one can deduce that the lower relaxivities in the conjugates of DO3A-py^{NO-C} are related to the shorter global rotational correlation times. The values of τ_g are approximately three times smaller than those for the corresponding conjugates of DO3A-P$^{BnN\{SC\}}$. By approximating the conjugates to spheres and using the Debye-Stokes-Einstein relation, this would correspond to a decrease in the radius by 30% going from the negatively charged conjugates of DO3A-P$^{BnN\{SC\}}$ to the uncharged conjugates of DO3A-py^{NO-C}. Changes in the radii of PAMAM dendrimers as a consequence of protonation/deprotonation of the terminal primary amines were reported in a number of simulation studies (*52*−*54*). The dendrimers were reported to adopt more expanded structures in the protonated state as a consequence of repulsive forces between the charges. This is analogous to the difference between the conjugates of DO3A-py^{NO-C} and DO3A-P$^{BnN\{SC\}}$, though the polarity of the charge in the Gd(III) chelates of DO3A-P$^{BnN\{SC\}}$ is opposite. However, recent analyses of NH_2-terminated PAMAM dendrimers by small-angle neutron scattering (SANS) (*55*, *56*) suggested that the size of the molecules is actually almost independent of the protonation state of the amino groups. The authors ascribe this fact to an enhanced counterion association inside the dendrimer molecule, which leads to shielding of the repulsive Coulombic forces between the charged terminal groups. The previously published simulation studies overestimated the changes in the size because they lacked proper models of the counterions (*57*). The role of counterions clearly cannot be disregarded when the properties of electroneutral and polyionic compounds are compared. One could argue that the SEC chromatograms (Supporting Information Figures S5 and S6) confirm the hypothesis that the charged (protonated) NH_2-terminated dendrimers are larger (give higher retention times) than the corresponding Gd(III)-loaded conjugates of DO3A-py^{NO-C}. However, the applied conditions (0.1 M sodium citrate pH = 2.77) are distinctively different from pure water, and the observed effect is most probably caused by citrate counterions traveling with the protonated dendrimers. Similar changes in retention times on SEC were observed after acetylation of the terminal amino groups (*58*). However, the retention times in SEC cannot be straightforwardly interpreted in terms of the molecular size when compounds with different chemical nature

Table 2. Relaxometric Parameters of Various Monomeric and Dendrimeric Gd(III) Chelates at 25 °C

compound	MW (kDa)	τ_R (ps)[a]	S^2	τ_M (ns)	r_1 (s^{-1} mM^{-1})[b]	ref
		Monomers				
$[Gd(H_2O)(DO3A\text{-}py^{NO\text{-}C})]^-$	0.65	93	-	34	4.5/5.7	*45*
$[Gd(H_2O)(DO3A\text{-}P^{ABn})]^-$	0.68	88	-	16	4.2/5.7	*48*
$[Gd(H_2O)(DO3A\text{-}AEM)]$[c]	0.64	180	-	294	4.8/5.8	*16*
		PAMAM Conjugates				
G1-$[Gd(H_2O)(do3a\text{-}py^{NO\text{-}C})]_{7.5}$	6.5	$\tau_1 = 124 \pm 8$ $\tau_g = 570 \pm 30$	0.35 ± 0.03	55[d]	8.9/11.0	this work
G4-$[Gd(H_2O)(do3a\text{-}py^{NO\text{-}C})]_{57}$	50.3	$\tau_1 = 138 \pm 4$ $\tau_g = 1040 \pm 100$	0.38 ± 0.03	55 ± 2	13.6/15.6	this work
G1-$[Gd(H_2O)(do3a\text{-}p^{BnN\{SC\}})]_8^{x-}$	7.2	$\tau_1 = 115$ $\tau_g = 1560$	0.25	48	10.1/14.8	*15*
G4-$[Gd(H_2O)(do3a\text{-}p^{BnN\{SC\}})]_{59}^{x-}$	57.0	$\tau_1 = 133$ $\tau_g = 3140$	0.29	68	18.6/25.8	*15*
G4-$[Gd(H_2O)(do3a\text{-}ma)]_{31}$	35	$\tau_1 = 140$ $\tau_g = 970$	0.33	294	12.8/13.2	*16*
Gadomer-17	17.5	$\tau_1 = 760$ $\tau_g = 3050$	0.50	1000	17.2/16.5	*13*

[a] The values of τ_1 refer to the reorientation of $Gd-H_{water}$ vector. [b] Relaxivity at 20 MHz and 37 °C/25 °C. [c] A monomer corresponding to the G4-$[Gd(H_2O)(do3a\text{-}ma)]_{31}$ conjugate. [d] The value determined for G4-$[Gd(H_2O)(do3a\text{-}py^{NO\text{-}C})]_{57}$ was used in the fit.

are compared. For instance, the conjugates of DO3A-$py^{NO\text{-}C}$ and DO3A-$P^{BnN\{SC\}}$ could not be compared at the same conditions and needed different buffers for elution (acidic and neutral, respectively).

In order to compare the conjugates of DO3A-$py^{NO\text{-}C}$ and DO3A-$P^{BnN\{SC\}}$ by an independent method, ^1H DOSY experiments (DOSY = diffusion-ordered spectroscopy) on the diamagnetic analogues G4-$[Y(H_2O)(DO3A\text{-}py^{NO\text{-}C})]_{57}$ and G4-$[Y(H_2O)(DO3A\text{-}P^{BnN\{SC\}})]_{59}^{x-}$ were performed. The counterions in the latter case were sodium(I) cations. The expected difference in the size of the macromolecules should be reflected in the values of the diffusion coefficient. Surprisingly, both compounds gave the same value $D^{298} = (57 \pm 5) \times 10^{-12}$ m^2 s^{-1}, which, using a spherical model, corresponds to a hydrodynamic radius of 3.5 nm (Supporting Information Figure S9). The actual difference in the size is therefore either much smaller than the expected 30%, or virtually nonexistent. The expansion of the macromolecule due to repulsion between the charged chelates therefore does not take place and cannot be the reason for the observed differences in τ_g in our case. An alternative explanation may be found in redistribution of the mass within the dendrimer due to counterions balancing the charge on the terminal groups. This phenomenon was observed in SANS data (*55, 56*) and molecular dynamics simulations (*57*) in NH_2-terminated PAMAM dendrimers. When the groups are electroneutral, a substantial back-folding of the branches into the interior of the dendrimer occurs resulting in a relatively even distribution of the mass throughout the molecule. On the other hand, the charged terminal groups accompanied by the counterions tend to create a rather dense outer shell, leaving the interior of the dendrimer hollow (*55, 57*). The moment of inertia for the rotational motion is likely to vary between the two cases and, thus, may be reflected in the values of τ_g. However, the structure of the free dendrimers is relatively open and allows such changes to take place, while the structure of the conjugates may be significantly altered due to the bulkiness of the attached chelates.

To explore the conjugates from this point of view, small-angle X-ray scattering (SAXS) measurements on samples of G4-$[Gd(H_2O)(DO3A\text{-}py^{NO\text{-}C})]_{57}$ and G4-$[Gd(H_2O)(DO3A\text{-}P^{BnN\{SC\}})]_{59}^{x-}$ in aqueous solutions at neutral pH were performed (Supporting Information Figure S10). A large part of the scattering intensity belongs to the chelates holding the relatively heavy Gd(III) ions, and therefore, the technique should be able to distinguish between a preferential placement of the chelates on the periphery and their distribution throughout the interior of the dendrimer. Both cases should give different values of the radii of gyration, R_G. The found values of R_G were 27.6 ± 0.3 Å for G4-$[Gd(H_2O)(DO3A\text{-}py^{NO\text{-}C})]_{57}$ and 29.4 ± 0.2 Å for G4-$[Gd(H_2O)(DO3A\text{-}P^{BnN\{SC\}})]_{59}^{x-}$. So, also in this case, the difference is too small to give supporting evidence for such structural changes (for more information about the SAXS data analysis, see Supporting Information). Nevertheless, the SAXS patterns of the charged conjugate display interparticle correlation peaks at values of the scattering vector <0.05 $Å^{-1}$ (Supporting Information Figure S10). This behavior provides evidence of strong interparticle repulsion forces caused by the charge; these forces are absent in the uncharged conjugate. One can anticipate that, if the charge can restrict the whole molecules from approaching each other, it must also be an important factor for the motion of the charged chelates within the conjugate.

The data listed in Table 2 should be handled with caution, as they were obtained by different authors using slightly different models in the fits. Also, the relatively simple separation of the local and global rotational motions by the Lipari-Szabo approach has limited credibility in the case of PAMAM dendrimers, as these allow many degrees of motion within their structures. There is a question regarding how, and to what extent, the rotation of the whole macromolecule, its segment, and individual chelates will be reflected in the values of τ_1 and τ_g. However, there is no doubt that lower relaxivities of the electroneutral PAMAM-based conjugates are related to the rotational motion. First, this phenomenon is common to all PAMAM-based conjugates bearing electroneutral Gd(III) complexes, namely, the conjugates of DO3A-$py^{NO\text{-}C}$ and of DOTA-monoamides (*16, 59*) (see G4-$[Gd(H_2O)(do3a\text{-}ma)]_{31}$ in Table 2). Second, the relaxivity rises when a substantially more rigid molecular scaffold is used instead of the PAMAM dendrimers, while the chelates are kept uncharged. This is demonstrated effectively on Gadomer-17, a molecule that consists of a lysine-based dendrimer bearing DOTA-monoamide Gd(III) chelates. The relaxivity of Gadomer-17 at 37 °C surpasses that of the G4-PAMAM-based electroneutral conjugates despite the lower molecular weight and the longer water residence time of the former (Table 2) (*13*).

On the basis of the results presented here, we can derive the following model of the PAMAM-based conjugates. A high loading of the dendrimer with Gd(III) chelates induces a steric crowding that is released by migration of some of the chelates inside the dendrimer, resulting in relatively uniformly distributed mass throughout the volume of the macromolecule. This arrangement applies to conjugates of both neutral and charged chelates. However, the charged chelates are accompanied by

their counterions, which also enter into the interior of the dendrimer and largely compensate long-distance charge-related effects. As a consequence, the conjugates with charged chelates do not exhibit any swelling effect compared with the electroneutral conjugates, and their sizes are similar. The situation is different at smaller distances where the Coulombic interactions become important. The motion of the charged chelates is limited due to specific temporal arrangements of other ions in their vicinity. Any positional change thus requires either overcoming an activation barrier or rearranging the surrounding ions. While the axial rotation around bonds connecting the chelates to the dendrimer is likely to be unaffected, the rotational motion of the larger segments (beyond the next branching point) will be slowed by multiple Coulombic interactions. On the contrary, the neutral chelates are not restrained in their motion and undergo all movements allowed by the dendrimeric scaffold. This includes the rotation and translation of the terminal atomic chains bearing the chelates as well as motions of larger segments of the dendrimeric structure. We suggest that it is mainly the motions of the larger segments that affect the values of τ_g and the relaxivity.

This model can explain also the peculiar dependence of relaxivity on pH for the PAMAM-based conjugates. The relaxivity of the charged conjugates was reported to increase with the protonation of the inner tertiary amines of the dendrimer (*14*, *15*). For example, for G4 dendrimer, this occurs in the pH-range 4−7 (*60*). The higher relaxivities at lower pH correlate with the higher determined values of τ_g and were ascribed to expansion of the dendrimeric structure as a consequence of the repulsive interactions between the protonated amines and to enhanced rigidity of the scaffold (*14*, *15*). If true, this mechanism would have to be effective also for the conjugates with electroneutral chelates. However, the relaxivity of G4-[Gd(H_2O)(DO3A-py^{NO-C})]$_{57}$ gave no response to pH in the range 1−7 (Supporting Information Figure S12). The increase of relaxivity for the charged conjugates is thus probably given by electrostatic interactions between the negatively charged chelates inside the dendrimer and the protonated tertiary amines. Being fixed in the molecular scaffold, the positive charges in this case lead to a more efficient immobilization of the negatively charged chelates and, hence, to increased values of τ_g and relaxivity. Obviously, the electroneutral chelates cannot be affected by this interaction, and therefore, they do not respond to pH.

In addition to the small values of τ_g, the local rotational motion characterized by the values of τ_l in conjugates G1-[Gd(H_2O)(do3a-py^{NO-C})]$_{7.5}$ (τ_l = 124 ns) and G4-[Gd(H_2O)(do3a-py^{NO-C})]$_{57}$ (τ_l = 138 ns) is also relatively fast and, therefore, significantly contributes to the overall loss of relaxivity. These values are similar to those obtained for the other PAMAM-based conjugates (Table 2), despite the fact that the attachment through the amide group on the pyridine ring should be rigid. This can be attributed to the significant flexibility of the linking bonds following this amide in the dendrimer moiety. Figure 4 depicts simulated ^{1}H NMRD profiles based on relaxometric parameters obtained for the G4-[Gd(H_2O)(do3a-py^{NO-C})]$_{57}$ conjugate by varying parameters τ_l, τ_g, and S^2 to values obtained for other conjugates. The dashed line demonstrates the expected increase of relaxivity if the global rotational motion was the same as in the negatively charged conjugate G4-[Gd(H_2O)(do3a-p$^{BnN\{SC\}}$)]$_{59}^{x-}$. In the dotted line, the values of τ_l, τ_g, and S^2 were fixed to those of Gadomer-17, a conjugate with substantially enhanced rigidity. In this case, the relaxivity at around 30 MHz is increased 2.4-fold relative to G4-[Gd(H_2O)(do3a-py^{NO-C})]$_{57}$. These results suggest that, with an appropriate design of the scaffold, high-relaxivity conjugates may be obtained.

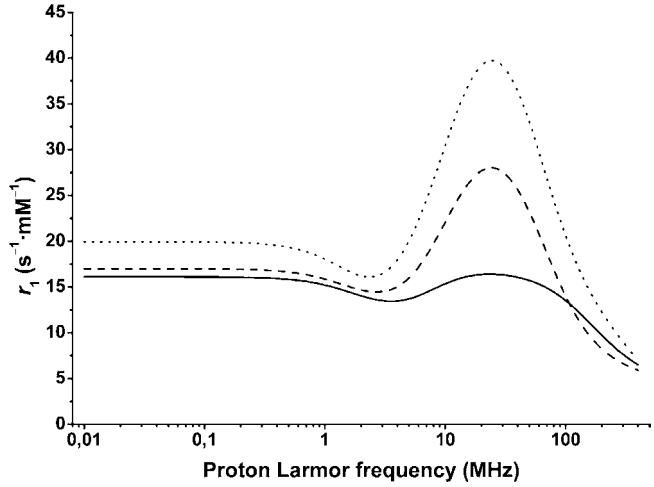

Figure 4. Simulation of ^{1}H NMRD profiles at 25 °C. Best fit of G4-[Gd(H_2O)(do3a-py^{NO-C})]$_{57}$ experimental data: τ_l = 138 ps, τ_g = 1040 ps, S^2 = 0.38 (solid line); τ_l = 138 ps, τ_g = 3050 ps, S^2 = 0.38 (dashed line); τ_l = 494 ps, τ_g = 3050 ps, S^2 = 0.50 (dotted line). The other parameters were the same as obtained for G4-[Gd(H_2O)(do3a-py^{NO-C})]$_{57}$.

The presented data show that the PAMAM dendrimers are not an appropriate scaffold for the binding of noncharged Gd(III) chelates if the main goal is to attain the maximal relaxivity. The flexibility of their structures leads to relatively fast global and local rotational motions of the conjugates that are detrimental to the efficiency. Therefore, other types of macromolecular scaffolds should be considered for this purpose. The macromolecular contrast agent Gadomer-17 is a nice example of such an uncharged system (*13*). A lysine-based dendrimer in this case provides a structure with sufficient rigidity, resulting in relatively high values of τ_l and τ_R (see Table 2). Consequently, the relaxivity of Gadomer-17 at 37 °C is considerably higher than the relaxivities of the G4-PAMAM-based uncharged conjugates, despite the lower molecular weight and the slower water exchange rate of the former. Another rigid system based on a polylysine dendrimer with an octasilsesquioxane core has been reported recently (*17*). Nonetheless, the commercial availability makes the PAMAM dendrimers still the first choice for the synthesis of new macromolecular contrast agents. The PAMAM conjugates with paramagnetic complexes are suitable for applications where a high number of gadolinium(III) ions per conjugate molecule and/or a well-defined molecular size is desired.

In Vivo Experiments. The electroneutral nature of the conjugates of DO3A-py^{NO-C} gives rise to concerns regarding whether the conjugates would be efficiently removed from the body through the renal system. We chose the conjugate G4-[Gd(H_2O)(do3a-py^{NO-C})]$_{57}$ for in vivo testing to determine the preferred route of excretion. Hyperintensity in rat kidney and urinary bladder was observed in all time points (10−90 min) with the maximum intensity of the signal at 60 min after contrast agent application (Supporting Information Figure S13); the signal difference at this time point was 63%. Surprisingly, no signal difference was noticed in the liver. Our results suggest that the modification of PAMAM dendrimers with Gd(III) chelates of DO3A-py^{NO-C} is compatible with the renal way of excretion.

CONCLUSIONS

We showed that the recently reported bifunctional ligand DO3A-py^{NO-C} can be efficiently coupled to other molecules through the carboxylic group at the pyridine ring through formation of an amide bond. The synthetic route for this

coupling was established. An improved design of the ligand ensures that the preferable fast water exchange observed for its Gd(III) complex is retained after the coupling. The combination of a noncharged chelate and a fast water exchange with a highly rigid spacer is unique. However, if flexible structures such as PAMAM dendrimers are used as the carrier molecules, the absence of electrostatic interactions between the attached chelates and surrounding ions endows the chelates with the motional freedom that is detrimental to the relaxivity of the conjugates. From a direct comparison of G4-PAMAM conjugates bearing uncharged and (1−)-charged Gd(III) chelates using several independent techniques, it can be concluded that it is the rotational motion of the large segments (dendrons) within the dendrimer that is responsible for the observed lower relaxivity of the electroneutral conjugates. Moreover, and contrary to the previous reports, the data suggest that the values of global rotational correlation times obtained from the fits of relaxometric data reflect mainly the motion of these large segments and not the motion of the whole conjugates. Such information may be useful in future developments of efficient electroneutral contrast agents.

ACKNOWLEDGMENT

Support from the Grant Agency of the Academy of Science of the Czech Republic (No. KAN201110651) and the Long-Term Research Plan of the Ministry of Education of the Czech Republic (No. MSM0021620857) are acknowledged. The work was carried out in the frame of COST D38 (MSMT OC 179) and the EU-supported NoE projects (6th FP) DiMI (No. LSHB-2005-512146) and EMIL (LSCH-2004-503569) and grant ENCITE, Seventh Framework Programme of EC, No. 201842. We thank Prof. Luce Vander Elst for the measurements of ^{1}H NMRD profiles, Prof. Jean-Marie Lehn for a support of and Dr. Lionel Allouche for the measurement of DOSY spectra, as well as Dr. Petr Jedelský for the MALDI-MS measurements. We also thank Dr. Daniel Jirák, Dr. Vít Herynek, and Dr. Milan Hájek for performing the MRI experiment. We acknowledge a help of Dr. Josef Pleštil in measurements and evaluation of SAXS data. M.P. is grateful for financial support through an early stage Marie Curie fellowship (MEST-CT-2004-7442). CFGCG acknowledges financial support from the Foundation of Science and Technology (FCT), Portugal (PTDC/QUI/70063/2006), and FEDER.

Supporting Information Available: Discussion on synthesis and characterization of the conjugates; RP-HPLC and SEC chromatograms and ^{1}H NMR spectra of conjugates in esterified form; MALDI-TOF MS spectra of HPLC-separated main product and main impurity in the G0-(*t*-Bu$_3$**L**)$_4$ conjugate; variable-temperature ^{17}O longitudinal relaxation rates and chemical shifts of conjugate G4-[Gd(do3a-py$^{NO\text{-}C}$)]$_{57}$; ^{1}H DOSY spectra of the G4-[Y(H_2O)(do3a-py$^{NO\text{-}C}$)]$_{57}$ and G4-[Y(H_2O)(DO3A-P$^{BnN\{SC\}}$)]$_{59}^{x-}$ conjugates; details and figures dealing with SAXS measurements; pH-dependence of relaxivity of G4-[Gd(do3a-py$^{NO\text{-}C}$)]$_{57}$; relaxometric parameters of G1-[Gd(do3a-py$^{NO\text{-}C}$)]$_{7.5}$ and G4-[Gd(do3a-py$^{NO\text{-}C}$)]$_{57}$; MRI scans of rat kidneys before and 60 min after the intravenous administration of the G4-[Gd(H_2O)(do3a-py$^{NO\text{-}C}$)]$_{57}$ conjugate; set of equations used for data fitting. This material is available free of charge via the Internet at http://pubs.acs.org.

LITERATURE CITED

(1) *The Chemistry of Contrast Agents in Medical Magnetic Resonance Imaging* (Merbach, A. E., and Tóth, É., Eds.) (2001) Wiley, Chichester.

(2) *Top. Curr. Chem.* (2002) Vol *221*, Springer Verlag, Heidelberg.

(3) Caravan, P., Ellison, J. J., McMurry, T. J., and Laufer, R. B. (1999) Gadolinium(III) chelates as MRI contrast agents: Structure, dynamics, and applications. *Chem. Rev. 99*, 2293–2352.

(4) Aime, S., Botta, M., and Terreno, E. (2005) Gd(III)-based contrast agents for MRI. *Adv. Inorg. Chem. 57*, 173–237.

(5) Hermann, P., Kotek, J., Kubíček, V., and Lukeš, I. (2008) Gadolinium(III) complexes as MRI contrast agents: ligand design and properties of the complexes. *Dalton Trans.* 3027–3047.

(6) Aime, S., Cabella, C., Colombatto, S., Crich, S. G., Gianolio, E., and Maggioni, F. (2002) Insights into the use of paramagnetic Gd(III) complexes in MR-molecular imaging investigations. *J. Magn. Reson. Imaging 16*, 394–406.

(7) Venditto, V. J., Regino, A. I. S., and Brechbiel, M. V. (2005) PAMAM dendrimer based macromolecules as improved contrast agents. *Mol. Pharmaceutics 2*, 302–311.

(8) Langereis, S., Dirksen, A, Hackeng, T. M., van Genderen, M. H. P., and Meijer, E. W. (2007) Dendrimers and magnetic resonance imaging. *New J. Chem. 31*, 1152–1160.

(9) Wiener, E. C., Konda, S., Shadron, A., Brechbiel, M., and Gansow, O. (1997) Targeting dendrimer-chelates to tumors and tumor cells expressing the high-affinity folate receptor. *Invest. Radiol. 32*, 748–754.

(10) Konda, S. D., Aref, M., Wang, S., Brechbiel, M., and Wiener, E. C. (2001) Specific targeting of folate-dendrimer MRI contrast agents to the high affinity folate receptor expressed in ovarian tumor xenografts. *Magn. Reson. Mater. Phys. Biol. Med. 12*, 104–113.

(11) Tóth, É., Pubanz, D., Vauthey, S., Helm, L., and Merbach, A. E. (1996) The role of water exchange in attaining maximum relaxivities for dendrimeric MRI contrast agents. *Chem.—Eur. J. 2*, 1607–1615.

(12) Ladd, D. L., Hollister, R., Peng, X., Wei, D., Wu, G., Delecki, D., Snow, R. A., Toner, J. L., Kellar, K., Eck, J., Desai, V. C., Raymond, G., Kinter, L. B., Desser, T. S., and Rubin, D. L. (1999) Polymeric gadolinium chelate magnetic resonance imaging contrast agents: Design, synthesis, and properties. *Bioconjugate Chem. 10*, 361–370.

(13) Nicolle, G. M., Tóth, É., Schmitt-Willich, H., Radüchel, B., and Merbach, A. E. (2002) The impact of rigidity and water exchange on the relaxivity of a dendritic MRI contrast agent. *Chem.—Eur. J. 8*, 1040–1048.

(14) Laus, S., Sour, A., Ruloff, R., Tóth, É., and Merbach, A. E. (2005) Rotational dynamics account for pH-dependent relaxivities of PAMAM dendrimeric, Gd-based potential MRI contrast agents. *Chem.—Eur. J. 11*, 3064–3076.

(15) (a) Rudovský, J., Botta, M., Hermann, P., Hardcastle, K. I., Lukeš, I., and Aime, S. (2006) PAMAM dendrimeric conjugates with a Gd-DOTA phosphinate derivative and their adducts with polyaminoacids: The interplay of global motion, internal rotation, and fast water exchange. *Bioconjugate Chem. 17*, 975–987. (b) Rudovský, J., Hermann, P., Botta, M., Aime, S., and Lukeš, I. (2005) Dendrimeric Gd(III) complex of a monophosphinated DOTA analogue: optimizing relaxivity by reducing internal motion. *Chem. Commun.* 2390–2392.

(16) Jaszberenyi, Z., Moriggi, L., Schmidt, P., Weidensteiner, C., Kneuer, R., Merbach, A. E., Helm, L., and Tóth, É. (2007) Physicochemical and MRI characterization of Gd^{3+}-loaded polyamidoamine and hyperbranched dendrimers. *J. Biol. Inorg. Chem. 12*, 406–420.

(17) Kaneshiro, T. L., Jeong, E.-K., Morrell, G., Parker, D. L., and Lu, Z.-R. (2008) Synthesis and evaluation of globular Gd-DOTA-monoamide conjugates with precisely controlled nanosizes for magnetic resonance angiography. *Biomacromolecules 9*, 2742–2748.

(18) Hüber, M. M., Staubli, A. B., Kustedjo, K., Gray, M. H. B., Shih, J., Fraser, S. E., Jacobs, R. E., and Meade, T. J. (1998) Fluorescently detectable magnetic resonance imaging agents. *Bioconjugate Chem. 9*, 242–249.

(19) Rebizak, R., Schaeferb, M., and Dellacheriea, É. (1999) Macromolecular contrast agents for magnetic resonance imaging. Influence of polymer content in ligand on the paramagnetic properties. *Eur. J. Pharm. Sci. 7*, 243–248.

(20) Corsi, D. M., Elst, L. V., Muller, R. N., van Bekkum, H., and Peters, J. A. (2001) Inulin as a carrier for contrast agents in magnetic resonance imaging. *Chem.—Eur. J. 7*, 64–71.

(21) Kotek, J., Lebdušková, P., Hermann, P., Elst, L. V., Muller, R. N., Geraldes, C. F. G. C, Maschmeyer, T., Lukeš, I., and Peters, J. A. (2003) Lanthanide(III) complexes of novel mixed carboxylic-phosphorus acid derivatives of diethylenetriamine. A step towards more efficient MRI contrast agents. *Chem.—Eur. J. 9*, 5899–5915.

(22) Ke, T., Feng, Y., Guo, J., Parker, D. L., and Lua, Z.-R. (2006) Biodegradable cystamine spacer facilitates the clearance of Gd(III) chelates in poly(glutamic acid) Gd-DO3A conjugates for contrast-enhanced MR imaging. *Magn. Reson. Imaging 24*, 931–940.

(23) Nicolle, G. M., Tóth, É., Esenwiener, K. P., Mäcke, H. R., and Merbach, A. E. (2002) From monomers to micelles: investigation of the parameters influencing proton relaxivity. *J. Biol. Inorg. Chem. 7*, 757–769.

(24) Tóth, É., van Uffelen, I., Helm, L., Merbach, A. E., Ladd, D., Briley-Saebo, K., and Kellar, K. E. (1998) Gadolinium-based linear polymer with temperature-independent proton relaxivities: a unique interplay between the water exchange and rotational contributions. *Magn. Reson. Chem. 36*, S125–S134.

(25) Tóth, É., Helm, L., Kellar, K. E., and Merbach, A. E. (1999) Gd(DTPA-bisamide)alkyl copolymers: A hint for the formation of MRI contrast agents with very high relaxivity. *Chem.—Eur. J. 5*, 1202–1211.

(26) Dunand, F. A., Tóth, É., Hollister, R., and Merbach, A. E. (2001) Lipari-Szabo approach as a toll for the analysis of macromolecular gadolinium(III)-based MRI contrast agents illustrated by the $[Gd(EGTA\text{-}BA\text{-}(CH_2)_{12})]_n^{n+}$ polymer. *J. Biol. Inorg. Chem. 6*, 247–255.

(27) Duarte, M. G., Gil, M. H., Peters, J. A., Colet, J. M., Elst, L. V., Muller, R. N., and Geraldes, C. F. G. C. (2001) Synthesis, characterization, and relaxivity of two linear Gd(DTPA)-polymer conjugates. *Bioconjugate Chem. 12*, 170–177.

(28) Duarte, M. G., Prata, M. I. M., Gil, M. H. M., and Geraldes, C. F. G. C. (2002) Macrocyclic and polymeric lanthanide chelates: from physico-chemical studies to biomedical applications. *J. Alloys Compnd. 344*, 4–8.

(29) Kobayashi, H., Sato, N., Kawamoto, S., Saga, T., Hiraga, A., Haque, T. L., Ishimori, T., Konishi, J., Togashi, K., and Brechbiel, M. W. (2001) Comparison of the macromolecular MR contrast agents with ethylenediamine-core versus ammonia-core generation-6 polyamidoamine dendrimer. *Bioconjugate Chem. 12*, 100–107.

(30) Kobayashi, H., Kawamoto, S., Jo, S.-K., Bryant, H. L., Jr., Brechbiel, M. W., and Star, R. A. (2001) Macromolecular MRI contrast agents with small dendrimers: Pharmacokinetic differences between sizes and cores. *Bioconjugate Chem. 14*, 388–394.

(31) Kobayashi, H., and Brechbiel, M. W. (2004) Dendrimer-based nanosized MRI contrast agents. *Curr. Pharm. Biotechnol. 5*, 539–549.

(32) Yordanov, A. T., Kobayashi, H., English, S. J., Reijnders, K., Milenic, D., Krishna, M. C., Mitchell, J. B., and Brechbiel, M. W. (2003) Gadolinium-labeled dendrimers as biometric nanoprobes to detect vascular permeability. *J. Mater. Chem. 13*, 1523–1525.

(33) Xu, R., Wang, Y., Wang, X., Jeong, E.-K., Parker, D. L., and Lu, Z.-R. (2007) In vivo evaluation of a PAMAM-cystamine-(Gd-DO3A) conjugate as a biodegradable macromolecular MRI contrast agent. *Exp. Biol. Med. 232*, 1081–1089.

(34) Kobayashi, H., Kawamoto, S., Star, R. A., Waldmann, T. A., Tagaya, Y., and Brechbiel, M. W. (2003) Micro-magnetic resonance lymphangiography in mice using a novel dendrimer-based magnetic resonance imaging contrast agent. *Cancer Res. 63*, 271–276.

(35) Swanson, S. D., Kukowska-Latallo, L. F., Patri, A. K., Chen, C., Ge, S., Cao, Z., Kotlyar, A., East, A. T., and Baker, J. R. (2008) Targeted gadolinium-loaded dendrimer nanoparticles for tumor-specific magnetic resonance contrast enhancement. *Int. J. Nanomed. 3*, 1–10.

(36) Boswell, C. A., Eck, P. K., Regino, C. A. S., Bernardo, M., Wong, K. J., Milenic, D. E., Choyke, P. L., and Brechbiel, M. W. (2008) Synthesis, characterization, and biological evaluation of integrin $\alpha_v\beta_3$-targeted PAMAM dendrimers. *Mol. Pharmaceutics 5*, 527–539.

(37) Zhu, W., Okollie, B., Bhujwalla, Z. M., and Artemov, D. (2008) PAMAM dendrimer-based contrast agents for MR imaging of Her- 2/*neu* receptors by a three-step pretargeting approach. *Magn. Reson. Med. 59*, 679–685.

(38) Lebdušková, P., Sour, A., Helm, L., Tóth, É., Kotek, J., Lukeš, I., and Merbach, A. E. (2006) Phosphinic derivative of DTPA conjugated to a G5 PAMAM dendrimer: an ^{17}O and ^{1}H relaxation study of its Gd(III) complex. *Dalton Trans.* 3399–3406.

(39) Wiener, E. C., Auteri, F. P., Chen, J. W., Brechbiel, M. W., Gansow, O. A., Schneider, D. S., Belford, R. L., Clarkson, R. B., and Lauterbur, P. C. (1996) Molecular dynamics of ion-chelate complexes attached to dendrimers. *J. Am. Chem. Soc. 118*, 7774–7782.

(40) Ali, M. M., Woods, M., Caravan, P., Opina, A. C. L., Spiller, M., Fettinger, J. C., and Sherry, A. D. (2008) Synthesis and relaxometric studies of a dendrimer-based pH-responsive MRI contrast agent. *Chem.—Eur. J. 14*, 7250–7258.

(41) Langereis, S., de Lussanet, Q. G., van Genderen, M. H. P., Backes, W. H., and Meijer, E. W. (2004) Multivalent contrast agents based on gadolinium-diethylenetriaminepentaacetic acid-terminated poly(propylene imine) dendrimers for magnetic resonance imaging. *Macromolecules 37*, 3084–3091.

(42) Langereis, S., de Lussanet, Q. G., van Genderen, M. H. P., Meijer, E. W., Beets-Tan, R. G. H., Griffioen, A. W., van Engelshoven, J. M. A., and Backes, W. H. (2006) Evaluation of Gd(III)-DTPA-terminated poly(propylene imine) dendrimers as contrast agents for MR imaging. *NMR Biomed. 19*, 133–141.

(43) Marckmann, P., Skov, L., Rossen, K., Dupont, A., Damholt, M. B., Heaf, J. G., and Thomsen, H. S. (2006) Nephrogenic systemic fibrosis: suspected causative role of gadodiamide used for contrast-enhanced magnetic resonance imaging. *J. Am. Soc. Nephrol. 17*, 2359–2362.

(44) Biacone, L., Geninatti Crich, S., Cantaluppi, V., Romanazzi, G. M., Russo, S., Scalabrino, E., Esposito, G., Figliolini, F., Beltramo, S., Perin, P. C., Segoloni, G. P., Aime, S., and Camussi, G. (2007) Magnetic resonance imaging of gadolinium-labeled pancreatic islets for experimental transplantation. *NMR Biomed. 20*, 40–48.

(45) Polášek, M., Šedinová, M., Kotek, J., Elst, L. V., Muller, R. N., Hermann, P., and Lukeš, I. (2009) Pyridine-*N*-oxide analogues of DOTA and their gadolinium(III) complexes endowed with a fast water exchange on the square-antiprismatic isomer. *Inorg. Chem. 48*, 455–465.

(46) Polášek, M., Kotek, J., Hermann, P., Císařová, I., Binnemans, K., and Lukeš, I. (2009) Lanthanide(III) complexes of pyridine-*N*-oxide analogues of DOTA in solution and in the solid state. A new kind of isomerism in complexes of DOTA-like ligands. *Inorg. Chem. 48*, 466–475.

(47) Bornais, J., and Brownstein, S. (1978) A low-temperature thermometer for ^{1}H, ^{19}F, and ^{13}C. *J. Magn. Reson. 29*, 207–211.

(48) Rudovský, J., Kotek, J., Hermann, P., Lukeš, I., Mainero, V., and Aime, S. (2005) Synthesis of a bifunctional monophosphinic acid DOTA analogue ligand and its lanthanide(III) complexes. A gadolinium(III) complex endowed with an optimal water exchange rate for MRI applications. *Org. Biomol. Chem. 3*, 112–117.

(49) Dunand, F. A., Borel, A., and Merbach, A. E. (2002) How does internal motion influence the relaxation of the water protons

in Ln^{III} DOTA-like complexes? *J. Am. Chem. Soc. 124*, 710–716.

(50) Caravan, P., Astashkin, A. V., and Raitsimring, A. M. (2003) The gadolinium(III)-water hydrogen distance in MRI contrast agents. *Inorg. Chem. 42*, 3972–3974.

(51) Yazyev, O. V., and Helm, L. (2008) Nuclear spin relaxation parameters of MRI contrast agents - insight from quantum mechanical calculations. *Eur. J. Inorg. Chem.* 201–211.

(52) Welch, P., and Muthukumar, M. (1998) Tuning the density profile of dendritic polyelectrolytes. *Macromolecules 31*, 5892–5897.

(53) Lee, I., Athey, B. D., Wetzel, A. W., Meixner, W., and Baker, J. R., Jr. (2002) Structural molecular dynamics studies on polyamidoamine dendrimers for a therapeutic application: Effects of pH and generation. *Macromolecules 35*, 4510–4520.

(54) Terao, T., and Nakayama, T. (2004) Molecular dynamics study of dendrimers: Structure and effective interaction. *Macromolecules 37*, 4686–4694.

(55) Chen, W.-R., Porcar, L., Liu, Y., Butler, P. D., and Magid, L. J. (2007) Small angle neutron scattering studies of the counterion effects on the molecular conformation and structure of charged G4 PAMAM dendrimers in aqueous solutions. *Macromolecules 40*, 5887–5898.

(56) Porcar, L., Liu, Y., Verduzco, R., Hong, K., Butler, P. D., Magid, L. J., Smith, G. S., and Chen, W.-R. (2008) Structural investigation of PAMAM dendrimers in aqueous solutions using small-angle neutron scattering: effect of generation. *J. Phys. Chem. B 112*, 14772–14778.

(57) Liu, Y., Bryantsev, V. S., Diallo, M. S., and Goddard, W. A. III. (2009) PAMAM dendrimers undergo pH responsive conformational changes without swelling. *J. Am. Chem. Soc. 131*, 2798–2799.

(58) Islam, M. T., Shi, X. Y., Balogh, L., and Baker, J. R., Jr. (2005) HPLC separation of different generations of poly(amidoamine) dendrimers modified with various terminal groups. *Anal. Chem. 77*, 2063–2070.

(59) Margerum, L. D., Campion, B. K., Koo, M., Shargill, N., Lai, J.-J., Marumoto, A., and Sontum, P. C. (1997) Gadolinium(III) DO3A macrocycles and polyethylene glycol coupled to dendrimers. Effect of molecular weight on physical and biological properties of macromolecular magnetic resonance imaging contrast agents. *J. Alloys Compnd. 249*, 185–190.

(60) Shi, X. Y., Lesniak, W., Islam, M. T., Muniz, M. C., Balogh, L. P., and Baker, J. R., Jr. (2006) Comprehensive characterization of surface-functionalized poly(amidoamine) dendrimers with acetamide, hydroxyl, and carboxyl groups. *Colloids Surf., A 272*, 139–150.

BC900288Q

PAMAM dendrimers conjugated with an uncharged gadolinium(III) chelate with a fast water exchange: the influence of chelate charge on rotational dynamics

Miloslav Polášek,[a] Petr Hermann,[a]* Joop A. Peters,[b] Carlos F. G. C. Geraldes[c] and Ivan Lukeš[a]

[a] *Department of Inorganic Chemistry, Faculty of Science, Universita Karlova (Charles University), Hlavova 2030, 128 40 Prague 2, Czech Republic. Tel: (+420)22195-1263. Fax: (+420)22195-1253. E-mail: petrh@natur.cuni.cz*

[b] *Biocatalysis and Organic Chemistry, Department of Biotechnology, Delft University of Technology, Julianalaan 136, 2628 BL Delft, The Netherlands.*

[c] *Department of Biochemistry, Faculty of Science and Technology, Center of Neurosciences and Cell Biology, University of Coimbra, 3001-401 Coimbra, Portugal.*

Synthesis and characterization of the conjugates

Figure S1. RP-HPLC chromatograms of reaction mixtures in preparation of the G0-conjugate with (bottom) and without (top) the use of excessive HOBt.

Figure S2. The RP-HPLC chromatograms of the prepared PAMAM dendrimer conjugates of various generations (G0, G1, G2, G4).

Figure S3. ^{1}H NMR spectra of conjugates G4-(*t*-Bu$_3$**L**)$_{57}$ and G2-(*t*-Bu$_3$**L**)$_{13}$.

Figure S4. ^{1}H NMR spectra of conjugates G1-(*t*-Bu$_3$**L**)$_{7.5}$ and G0-(*t*-Bu$_3$**L**)$_4$.

Figure S5. SEC chromatograms of the Gd(III) complexes of PAMAM-DO3A-py$^{NO\text{-}C}$ conjugates.

Figure S6. SEC chromatograms of the commercial PAMAM dendrimers (G0, G1, G2 and G4).

Figure S7. MALDI-TOF MS spectra of HPLC-separated main product and main impurity in the conjugate G0-(*t*-Bu$_3$**L**)$_4$.

Figure S8. Variable-temperature ^{17}O longitudinal relaxation rates and chemical shifts of H_2O in solution of conjugate G4-[Gd(do3a-py$^{NO\text{-}C}$)]$_{57}$.

Table S1. Set of parameters obtained in a multiparameter least square fit of ^{17}O NMR variable-temperature data and ^{1}H NMRD profiles for G1- and G4-conjugates

Figure S9. ^{1}H DOSY spectra of conjugates G4-[Y(H_2O)(do3a-py$^{NO\text{-}C}$)]$_{57}$ and G4-[Y(H_2O)(DO3A-P$^{BnN\{SC\}}$)]$_{59}^{59-}$.

SAXS data analysis

Figure S10. SAXS scattering curves at variable concentrations of the conjugates G4-[Gd(H_2O)(do3a-py$^{NO\text{-}C}$)]$_{57}$ and G4-[Gd(H_2O)(DO3A-P$^{BnN\{SC\}}$)]$_{59}^{x-}$ (sodium salt) at 25 °C and pH = 7.

Figure S11. Radii of gyration vs. the number of bonds contributing to the total chain length from the centre to the rim of the macromolecule.

Figure S12. ^{1}H relaxivity of conjugate G4-[Gd(H_2O)(do3a-py$^{NO\text{-}C}$)]$_{57}$ as a function of pH.

Figure S13. MRI scans of rat kidneys before and 60 min after the intravenous administration of G4-[Gd(H_2O)(do3a-py$^{NO\text{-}C}$)]$_{57}$ conjugate.

Equations. List of equations used for the fit of ^{1}H NMRD, ^{17}O T_2, ^{17}O T_1 and ^{17}O chemical shift data in Scientist format.

References

Synthesis and characterization of the conjugates

Coupling of *t*-Bu_3**L** to the PAMAM dendrimers was achieved by formation of an amide bond between the deprotected carboxylic group and the primary amines in PAMAM. In this way the local motion of DO3A moiety is minimized. The pyridine-*N*-oxide pendant arm is connected through two points to the Gd(III) chelates, which contributes to the rigidity of the system. Furthermore, the partial double-bond character of the amide bond provides additional rigidity. Altogether, it may be expected that this mode of attachment is considerably more rigid than attachments accomplished through benzyl-thiourea bridges (*1,2,3,4,5,6,7,8,9,10,11,12,13*) or through alkyl-chains.(*14,15,16*) Methods of peptide-coupling chemistry have been employed for the attachment of polydentate ligands to dendrimers and other similar substrates only marginally. Most of them rely on preactivation of the carboxylic acids to first afford an active ester, such as HOSu (*6,14,17,18*) or *p*-nitrophenol (*19*) ester, that is subsequently converted to the amide. Only a few examples have been described of couplings directly using EDC,(*20*) Py-BOP (*21*) or HBTU (*22*) as the coupling agents.

We have performed a fast HPLC-monitored screening of several coupling agents and methods using G0-dendrimer as the substrate (combinations: DCC + HOBt, EDC + HOBt, EDC + HOAt, TSTU and TBTU). TBTU gave the most satisfactory results regarding the yield and rate of the reaction. Due to the insolubility of *t*-Bu_3**L** in water and to avoid possible hydrolysis of the active ester intermediate, the coupling had to be performed in an organic solvent. The low solubility of the PAMAM dendrimers in most organic solvents limited the choice to DMSO. However, only a small amount of DMSO was necessary at the beginning of the reaction to ensure homogeneity of the solution, as the solubility of the dendrimer-conjugates in organic solvents increased with the progress of the reaction. Thus, the activation of the ligand was carried out in acetonitrile. The acetonitrile could easily be evaporated off, whereas the DMSO was conveniently removed by ultrafiltration. RP-HPLC chromatograms showed that the reaction was complete after 5 min. Maximum loading of the dendrimer with *t*-Bu_3**L** was achieved using 1.5 equiv. of *t*-Bu_3**L** and TBTU (per dendrimer primary amino group).

Guanidine side-products (*23*) were suppressed by addition of HOBt (see Figure S1). Some other impurities remained even after purification by ultrafiltration, showing that their molecular sizes are not significantly lower than that of the main product. Therefore, we assume that the minor peaks belong to the coupling products of defective dendrimer molecules. Various defects of PAMAM dendrimers, including missing branches and intramolecular loops, were reported in the literature for PAMAMs (*24,25*) or for the dendrimer core in Gadomer 17.(*26*) To test this hypothesis, we measured MALDI-TOF spectra of the product and of the main impurity found in G0-conjugate after their separation by RP-HPLC (Figure S7). The molecular peak of the main product matched the predicted mass of a perfect G0-dendrimer with four attached molecules of *t*-Bu_3**L** (calculated for $M+H^+$: 3108.0, found: 3109.4), whereas that of the side-product corresponded to a G0 dendrimer with one missing branch and three attached molecules of *t*-Bu_3**L** (calculated for $M+H^+$: 2346.5, found: 2346.1). Clearly, these impurities originate from defects present in the starting dendrimers. PAMAM dendrimers are mostly prepared by a divergent synthesis, which is prone to formation of various defects.(*24,25,27*) It is noteworthy that we could detect the impurities on reversed-phase HPLC thanks to the hydrophobic character of the conjugates in the *t*-butyl-ester form. Most of the previously reported conjugates were synthesized using the thiourea coupling without protection of the carboxylic groups and, thus, leading to highly polar species that were inseparable on RP-HPLC.

The impurities could be distinguished from the main product only for the smallest (i.e. G0 and G1) dendrimers. With higher generations, the differences between the retention times become smaller and only one broad peak is observed on HPLC (Figure S2). Unfortunately, attempts to characterize the conjugates of larger dendrimers (generation 1 and higher) by MALDI-TOF were unsuccessful. All low-molecular-weight compounds (including DMSO) were removed from the reaction mixtures by ultrafiltration in methanol.

The degree of substitution (loading) of the dendrimer surface with *t*-Bu$_3$**L** was determined from ^{1}H NMR spectra in CD_3OD at 45 °C. All exchangeable protons were assumed to be replaced with deuterium under these conditions (Figures S3–S4). The dendrimer loading *N* was calculated with

$$N = \frac{4 + 32 * \left(2^{G+1} - 1\right)}{H * R - 24},$$

where *G* is the generation of the dendrimer, *H* is the number of hydrogen atoms in one molecule of the ligand (i.e. 3 aromatic and 27 *t*-butyl protons) and *R* is the ratio of the integrals (aliphatic/aromatic or aliphatic/*t*-butyl). The loadings determined from aliphatic/aromatic and aliphatic/*t*-butyl signal ratios were generally in a good agreement with each other and the final loadings were calculated as averages of the two values (see Table 1). Therefore, the compositions of the conjugates could be determined with a higher accuracy before removal of *t*-butyl groups with TFA, assuming that the number of attached ligand molecules does not change during this deprotection. In all cases, the loadings were 80 – 100 %, showing that the coupling method is very efficient. One has to take into account that the numbers of the attached ligands were calculated for ideal dendrimers without any defects. This is the probable reason why, for the G0-conjugate, the loading exceeded 100 %. It can be deduced from the HPLC chromatograms that full loading was reached in G0-conjugate. In the other conjugates, full loadings were not reached probably due to bulkiness of the *t*-Bu$_3$**L** moieties.

The protective *t*-butyl groups were cleaved off quantitatively in neat TFA. The Gd(III) complexes were prepared with 50 % excess of gadolinium. The conditions for complexation were the same as for the DO3A-py$^{NO\text{-}C}$ monomer (24 h, RT, pH = 7).(*28*) The excess of gadolinium(III) was removed by chelation with EDTA followed by ultrafiltration. The complete removal of EDTA and of its Gd(III) complex was confirmed by SEC.

Size-exclusion chromatography was used to check the purity of the conjugates with respect to the molecular size. All low-molecular-weight compounds were efficiently removed by ultrafiltration. However, a small portion of conjugate with a higher molecular weight was observed in all cases except for the G0-conjugate, forming a “shoulder” with shorter retention time (Figure S5). This “shoulder” was found also in the PAMAM dendrimers used for the synthesis (Figure S6) and is likely due to a presence of “dimm

ers” (two dendrimer molecules fused together), which represent one type of structural deviations found in PAMAM dendrimers.(*24,25*) These impurities in the conjugates have not been mentioned previously by other authors, despite they were using the same commercial dendrimers for their syntheses.

Figure S1. RP-HPLC chromatograms of reaction mixtures of the preparation of the G0-conjugate with (bottom) and without (top) the use of excessive HOBt. Asterisks mark the peaks that were completely or partially suppressed by use of HOBt. G0-(*t*-Bu$_3$**L**)$_4$ is the main product; G0$_{3/4}$-(*t*-Bu$_3$**L**)$_3$ stands for the major impurity (identified by MALDI-TOF, see text). Gradient (A/B/C): from 20/40/40 to 50/40/10 in 15 min., 50/40/10 held for 5 min. Detection at 289 nm.

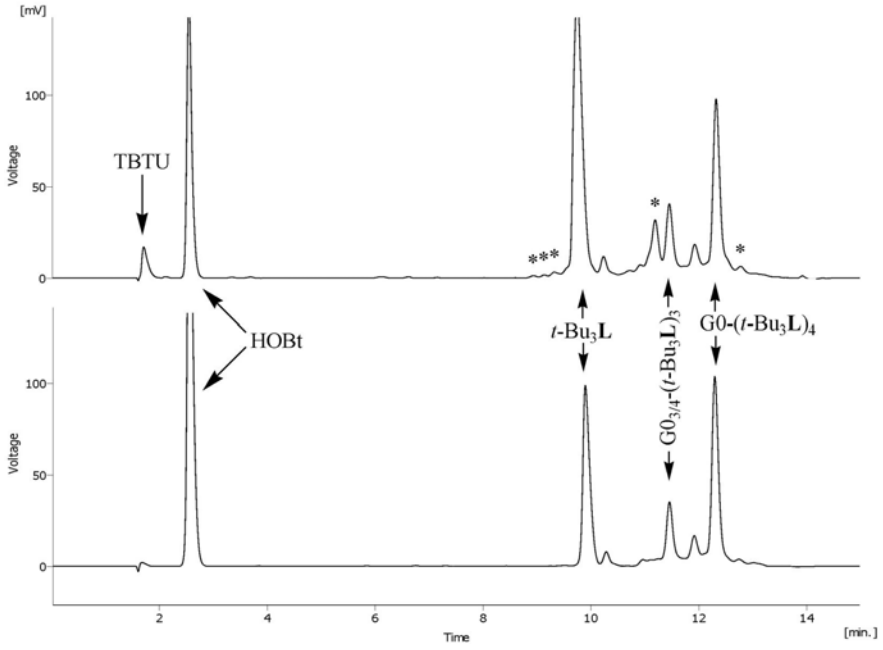

Figure S2. The RP-HPLC chromatograms of the prepared PAMAM dendrimer conjugates of various generations (G0, G1, G2, G4) after purification by ultrafiltration. Gradient (A/B/C): 20/40/40 to 50/40/10 in 15 min., 50/40/10 held for 5 min. Detection at 289 nm.

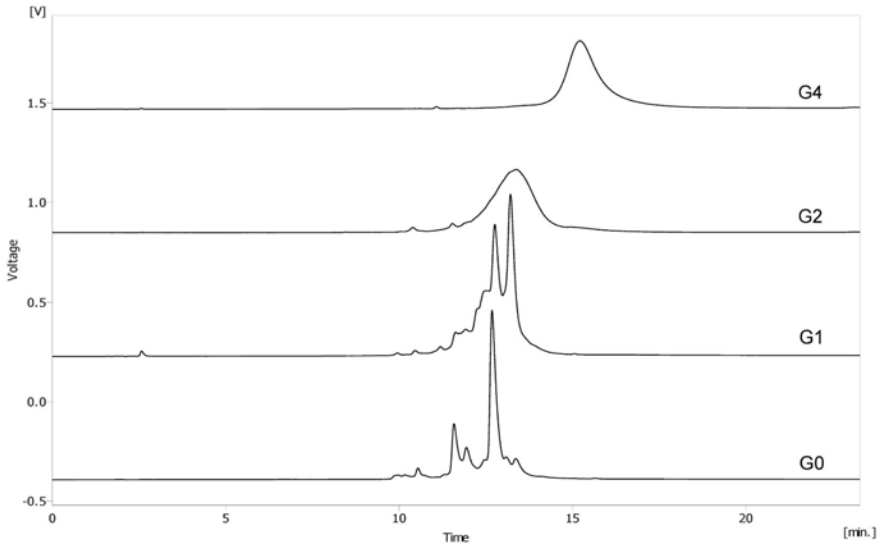

Figure S3. ^{1}H NMR spectra of conjugates G4-(*t*-Bu$_3$**L**)$_{57}$ and G2-(*t*-Bu$_3$**L**)$_{13}$ at 45 °C in CD_3OD. The asterisks denote (from left to right): residual O**H** and C**H**D$_2$ signals of the solvent and residual acetate C**H**$_3$.

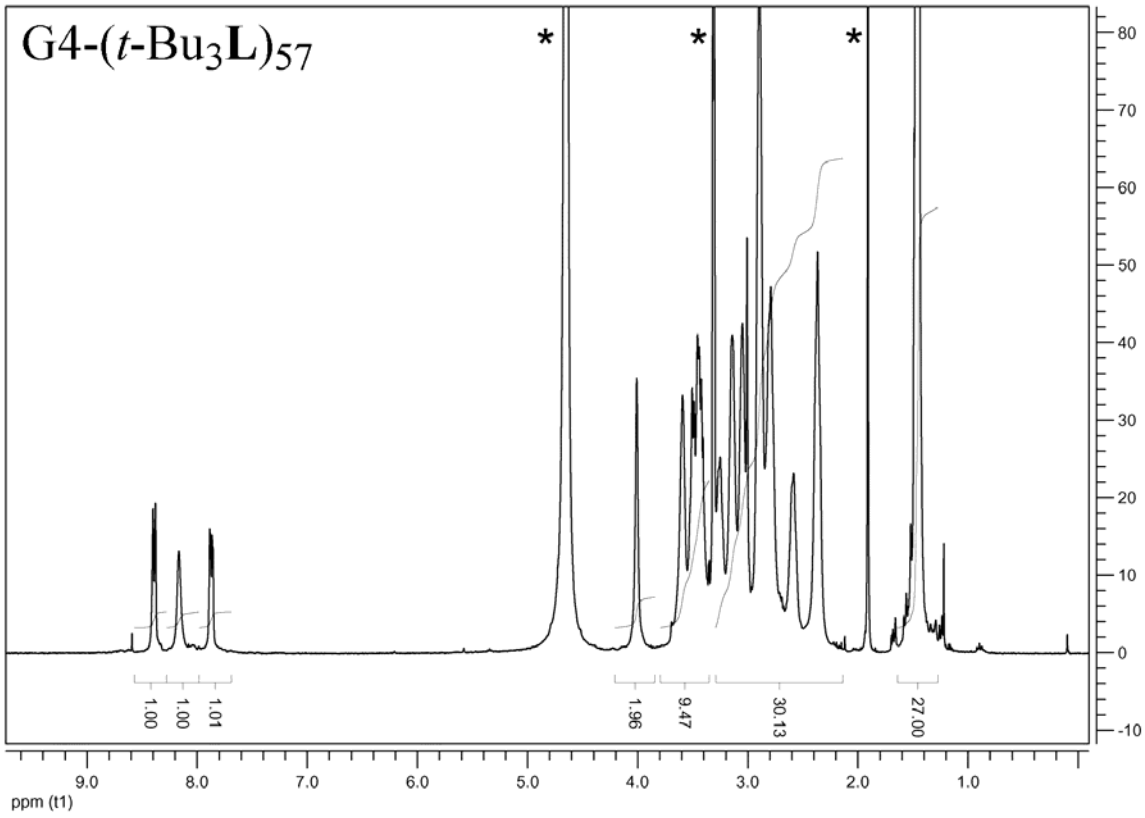

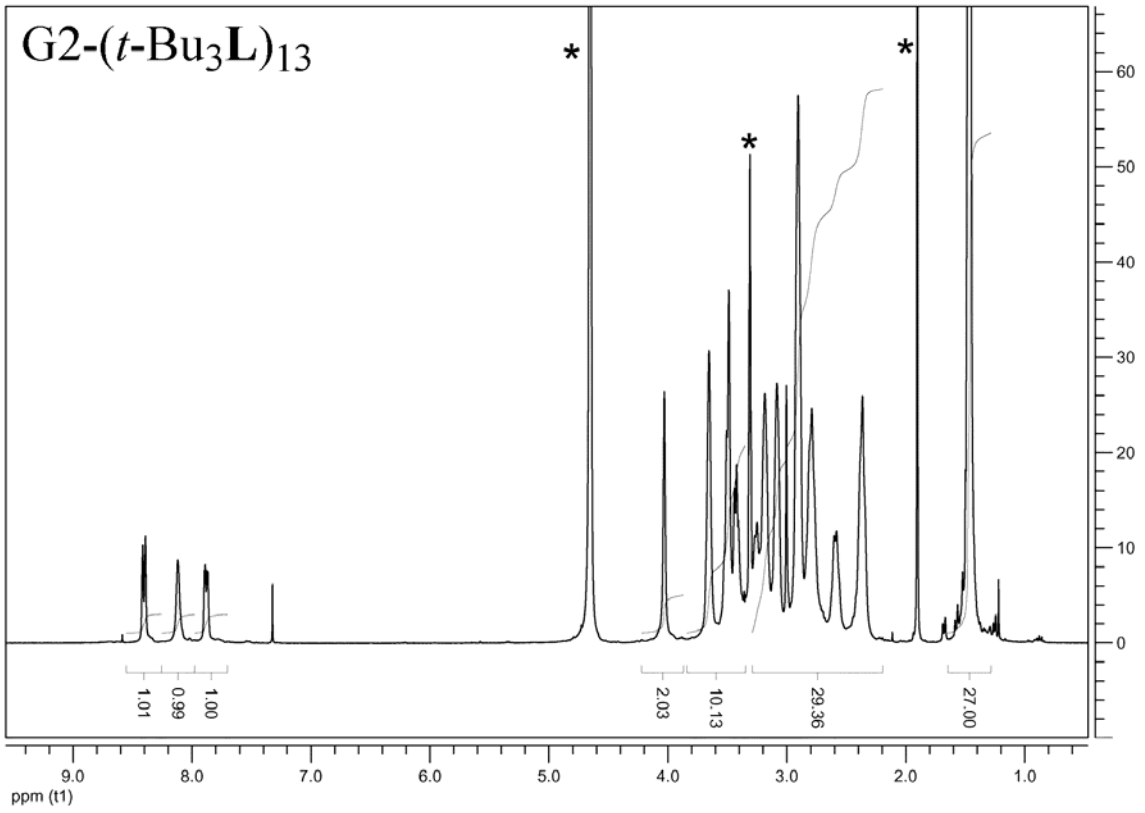

Figure S4. ^{1}H NMR spectra of conjugates G1-(*t*-Bu$_3$**L**)$_{7.5}$ and G0-(*t*-Bu$_3$**L**)$_4$ at 45 °C in CD_3OD. The asterisks denote (from left to right): residual O**H** and C**H**D$_2$ signals of the solvent and residual acetate C**H**$_3$.

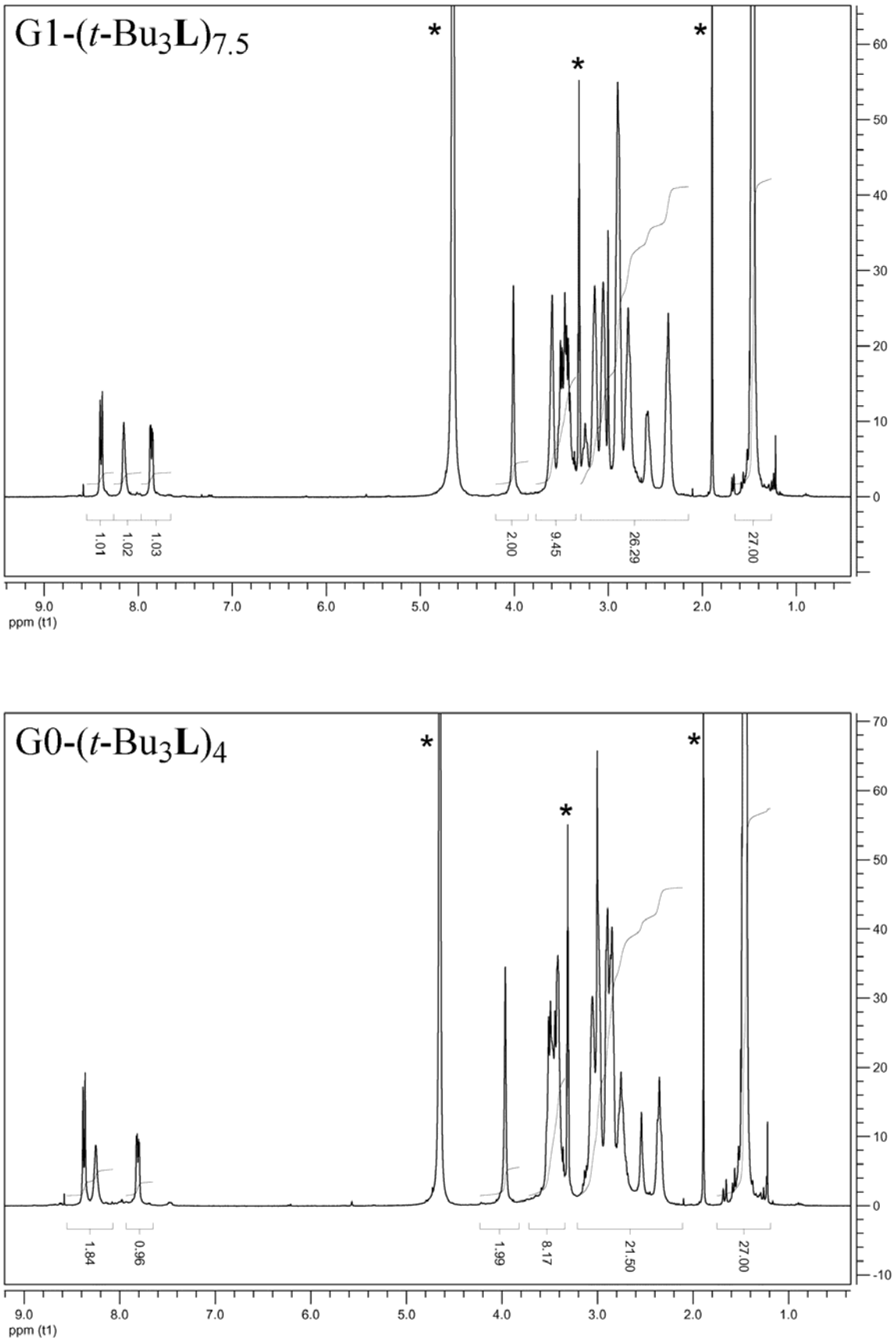

Figure S5. SEC chromatograms of the Gd(III) complexes of PAMAM-DO3A-py^{NO-C} conjugates in 0.1 M sodium citrate buffer (pH = 2.77, at 289 nm). The labels of the peaks indicate the generation of the PAMAM dendrimer (G0 – G4) and the average number of attached chelates. L-Gd stands for the "monomeric" $[Gd(H_2O)(do3a\text{-}py^{NO-C})]^-$ complex.

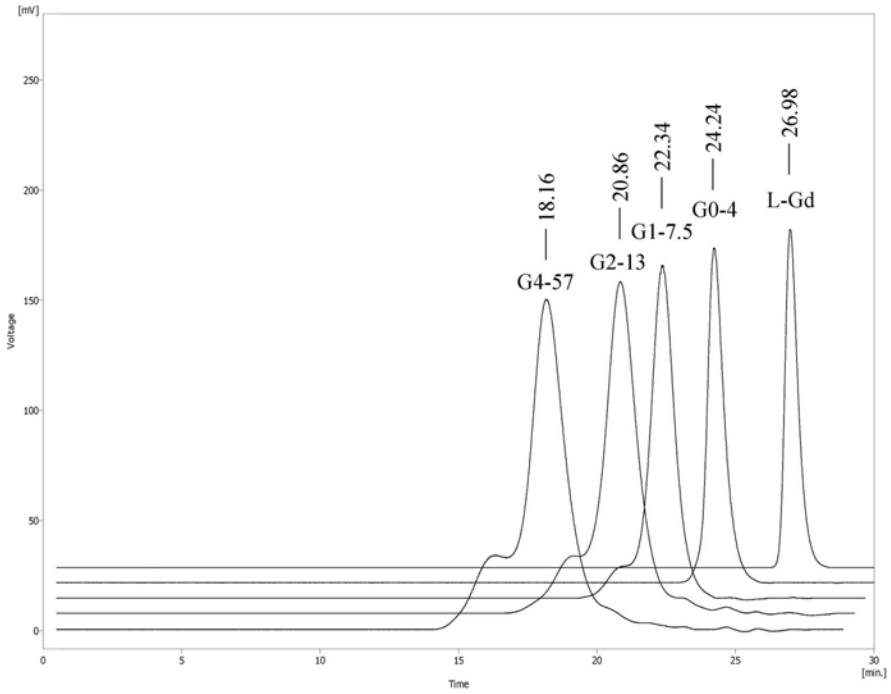

Figure S6. SEC chromatograms of the commercial PAMAM dendrimers (G0, G1, G2 and G4) used in the conjugation reactions (0.1 M sodium citrate buffer, pH = 2.77, refractive-index detection).

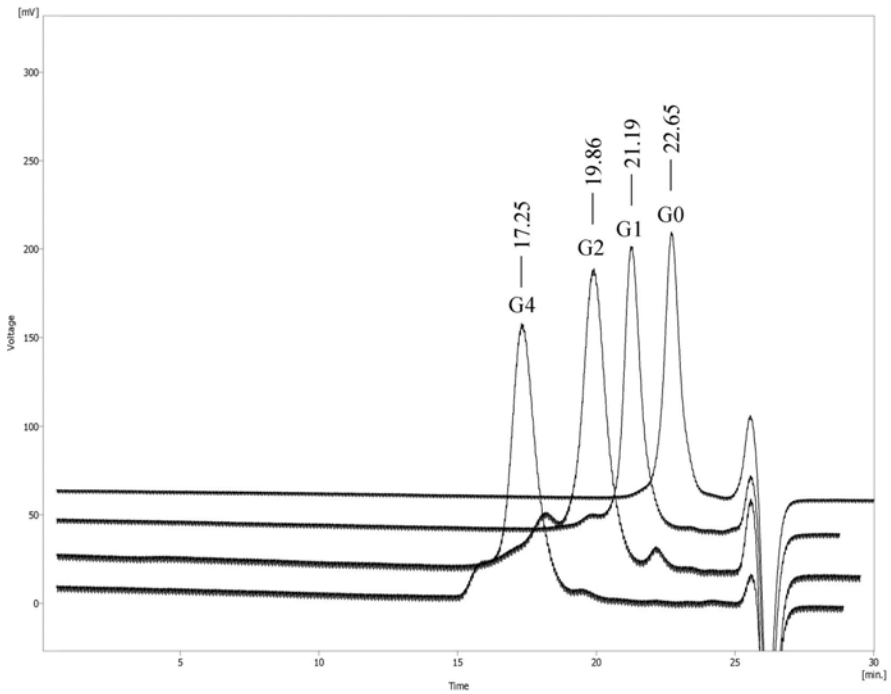

Figure S7. MALDI-TOF MS spectra of HPLC-separated main product (top) and main impurity (bottom) in the conjugate G0-(*t*-Bu$_3$**L**)$_4$. The patterns are due to loss of O-atoms from the *N*-oxides caused by ionization.

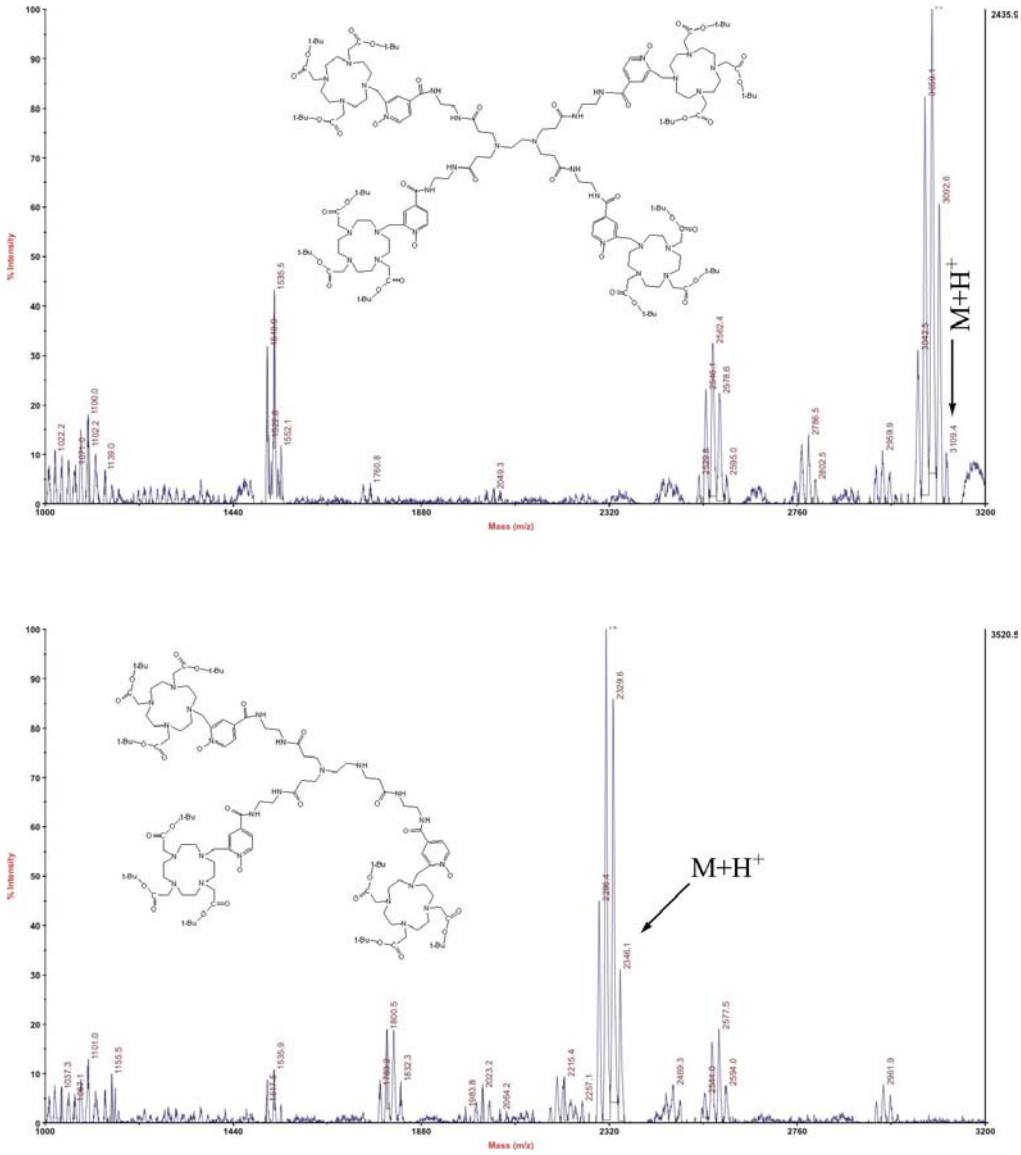

Figure S8. Variable-temperature ^{17}O longitudinal relaxation rates (left) and chemical shifts (right) of H_2O in solution of conjugate G4-[Gd(do3a-py$^{NO\text{-}C}$)]$_{57}$. The solid lines represent the results of a simultaneous least-square fit.

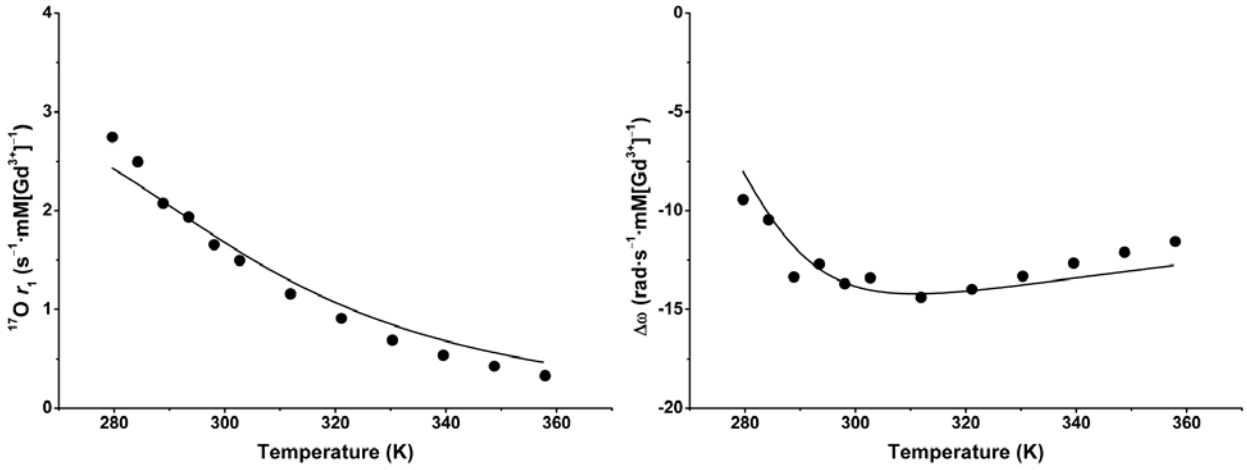

Table S1. Set of parameters obtained in a multiparameter least square fit of ^{17}O NMR variable-temperature data and ^{1}H NMRD profiles for G1- and G4-conjugates.

Parameter	G4-[Gd(do3a-py$^{NO\text{-}C}$)]$_{57}$	G1-[Gd(do3a-py$^{NO\text{-}C}$)]$_{7.5}$ [a]
$^{298}\tau_M$ / ns	55 ± 2	55 [b]
ΔH_M / kJ mol^{-1}	45.5	45.5
$^{298}\tau_v$ / ps	56 ± 1	49 ± 2
Δ^2 / 10^{19} s^{-2}	0.83 ± 0.02	1.05 ± 0.06
$^{298}\tau_g$ / ps	1040 ± 100	570 ± 30
$^{298}\tau_1$ / ps	138 ± 4[c]	124 ± 8[c]
E_{Rg} / kJ mol^{-1}	21.9 ± 2.7	21.9 [b]
E_{Rl} / kJ mol^{-1}	20.8 ± 1.1	20.8 [b]
S^2	0.38 ± 0.03	0.35 ± 0.03
$(A/\hbar)$ / 10^6 rad s^{-1}	–3.75	–3.75
r_{GdO} / Å	2.5	2.5
r_{GdH} / Å	3.1	3.1
A / Å	3.5	3.5
q	1	1
$\nu(1 + \eta^{2/3})^{1/2}$ / MHz	11.1 ± 1.4	11.1 [b]
C_{out}	0.02	0.02

The underlined values were fixed during the fit. [a]The fit was based only on ^{1}H NMRD profiles. [b]Values were fixed to those obtained for G4-[Gd(do3a-py$^{NO\text{-}C}$)]$_{57}$. [c]The values of τ_1 refer to the reorientation of Gd–H_{water} vector.

Figure S9. ^{1}H DOSY spectra of the conjugates G4-[Y(H_2O)(do3a-py$^{NO\text{-}C}$)]$_{57}$ and G4-[Y(H_2O)(do3a-P$^{BnN\{SC\}}$)]$_{59}^{x-}$ (sodium salt) at 25 °C and pH = 7.

G4-[Y(H_2O)(do3a-py$^{NO\text{-}C}$)]$_{57}$

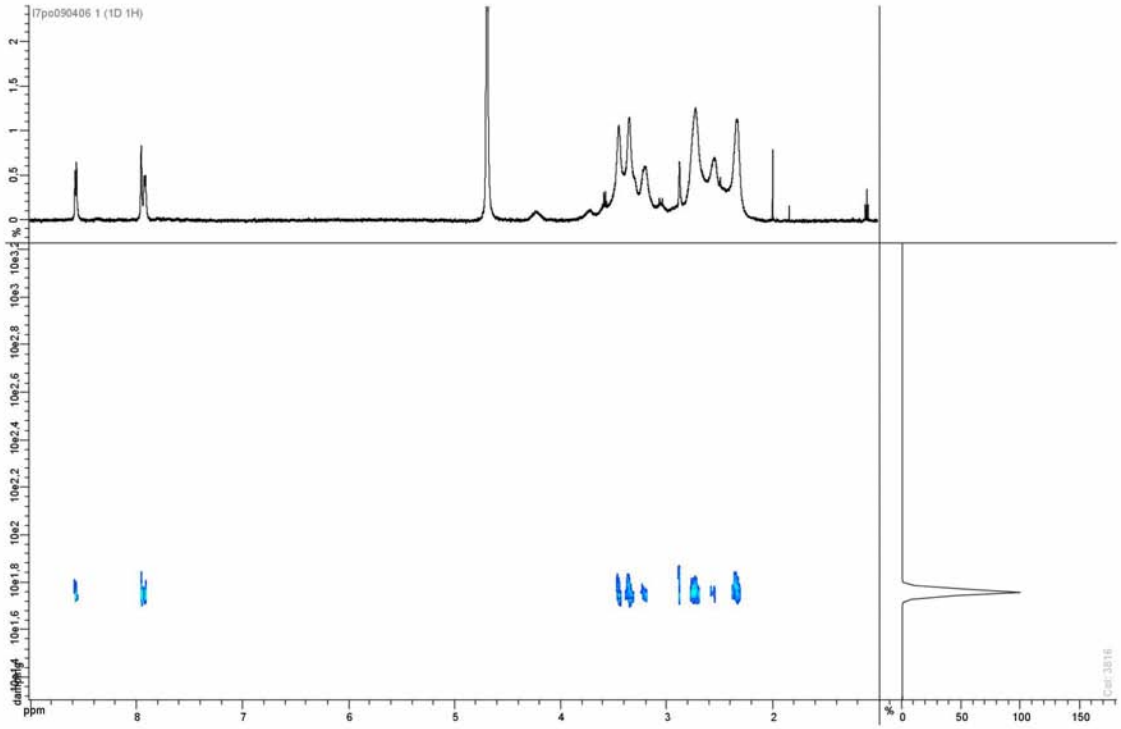

G4-[Y(H_2O)(DO3A-P$^{BnN\{SC\}}$)]$_{59}^{59-}$

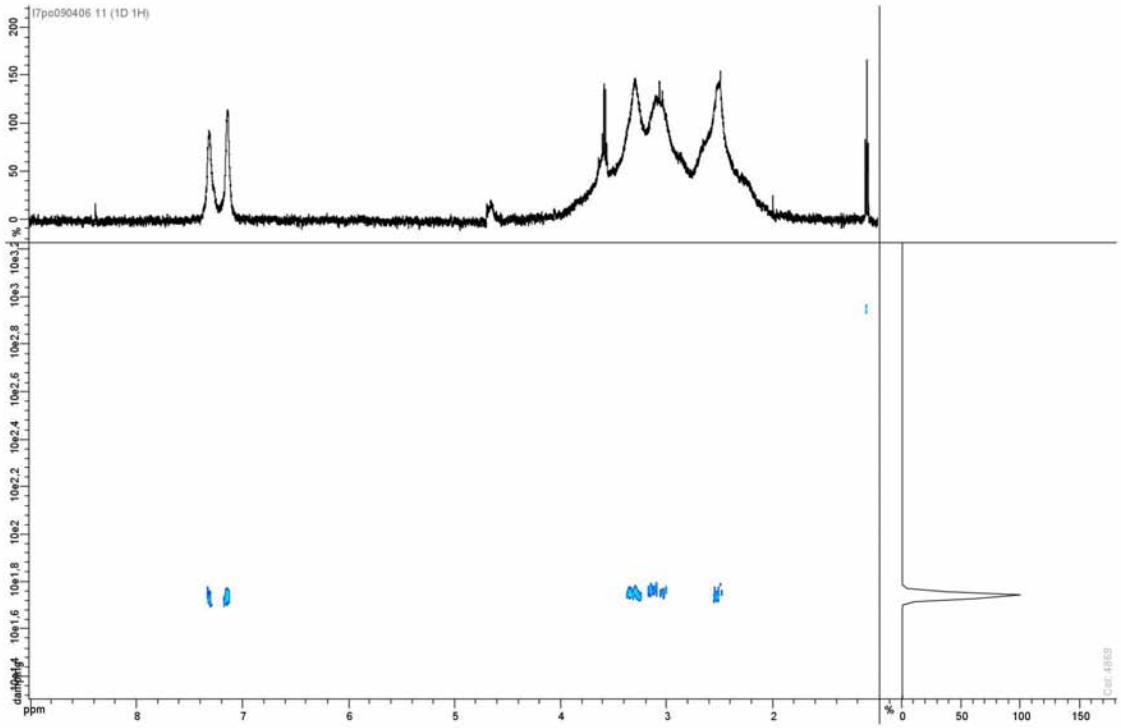

SAXS data analysis

Each compound was dissolved in distilled water and diluted to five different concentrations from 0.3 to 3 %. The SAXS data were measured for each solution and the scattering intensities normalized to the concentration (Figure S10). The scattering curves displayed the same shape for both compounds for the values of the scattering vector $q >$ 0.05 Å^{-1}. However, for $q < 0.05$ Å^{-1} the curves were concentration-dependent and the dependence was significantly larger for the charged compound G4-[Gd(H_2O)(do3a-$P^{BnN\{SC\}}$)]$_{59}^{x-}$ (sodium salt). This phenomenon is typical for strong repulsive inter-particle interaction; however, it does not imply an existence of any particular distance within the system. The size of the conjugates was determined from the scattering curves using Guinier's approximation, which led to the values of radii of gyration $R_g = 27.6 \pm 0.3$ Å for G4-[Gd(H_2O)(do3a-$py^{NO\text{-}C}$)]$_{57}$ and 29.4 ± 0.2 Å for G4-[Gd(H_2O)(do3a-$P^{BnN\{SC\}}$)]$_{59}^{x-}$ (sodium salt). The data affected by the inter-particle interference ($q \leq q_{max}$) were not included in the analysis. The Figure S11 shows the comparison of the radii of gyration determined by us with the data obtained from SANS measurements on NH_2-terminated PAMAM dendrimers at high pH.(*29*) The values of R_g were plotted against the number of bonds involved in the chains going from the centre to the rim of the macromolecule, so that the size of the chelates is taken into account. It is clear from the plot that both conjugates studied by us fit very well to the dependence. Therefore, it can be concluded that the size of the conjugates is not significantly altered by the charge of the attached metal chelates.

Figure S10. SAXS scattering data at variable concentrations of the conjugates G4-[Gd(H_2O)(do3a-$py^{NO\text{-}C}$)]$_{57}$ and G4-[Gd(H_2O)(do3a-$P^{BnN\{SC\}}$)]$_{59}^{x-}$ (sodium salt) at 25 °C and pH = 7.

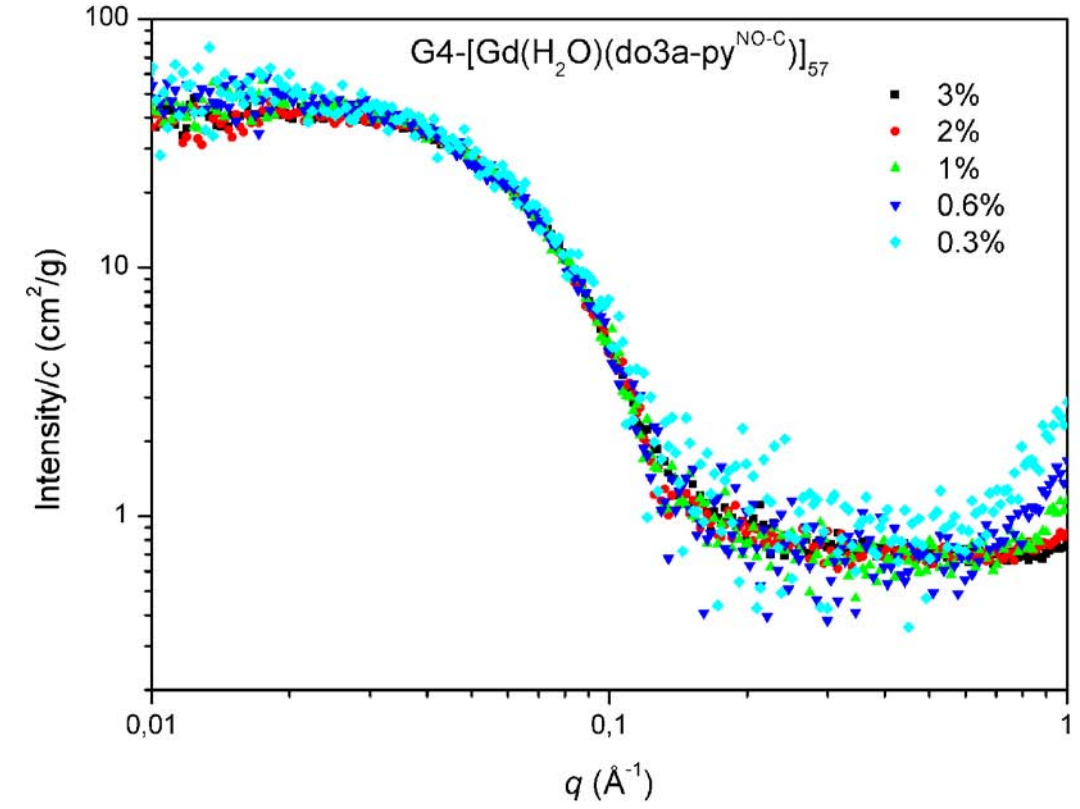

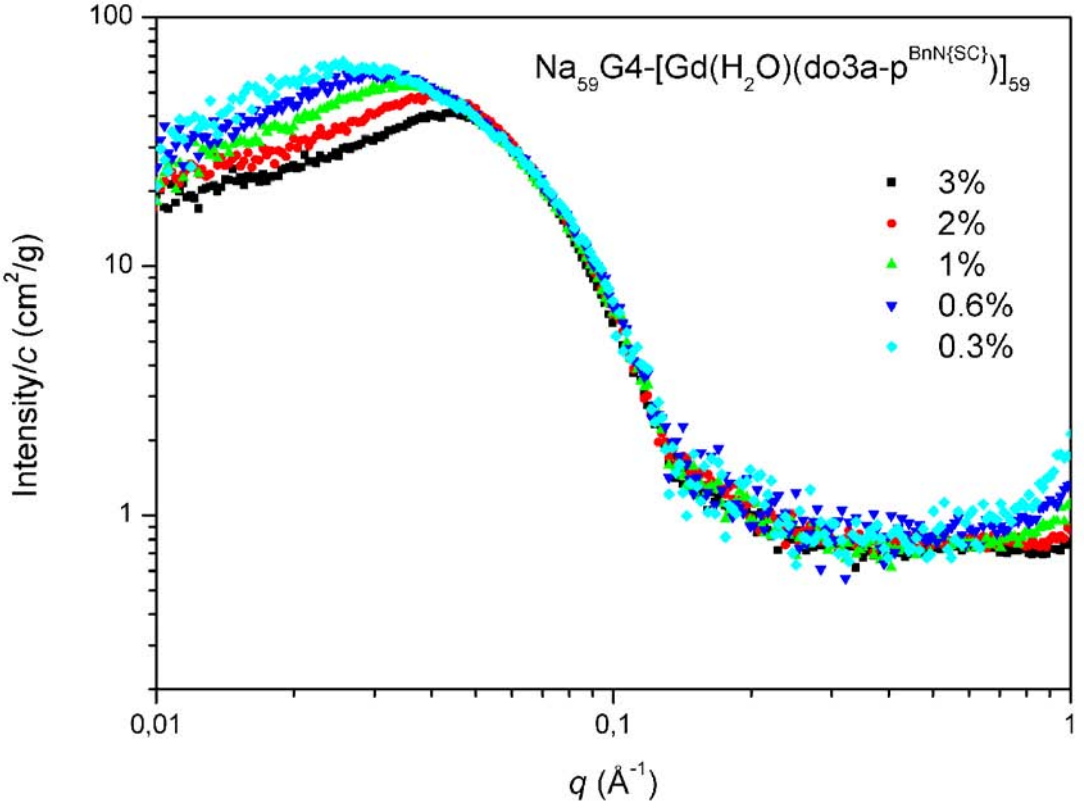

Figure S11. Radius of gyration vs. the number of bonds contributing to the total chain length from the centre to the rim of the macromolecule. Black squares: data for NH_2-terminated PAMAM dendrimers at high pH (no protonation) obtained from SANS (data taken from literature(*29*)).

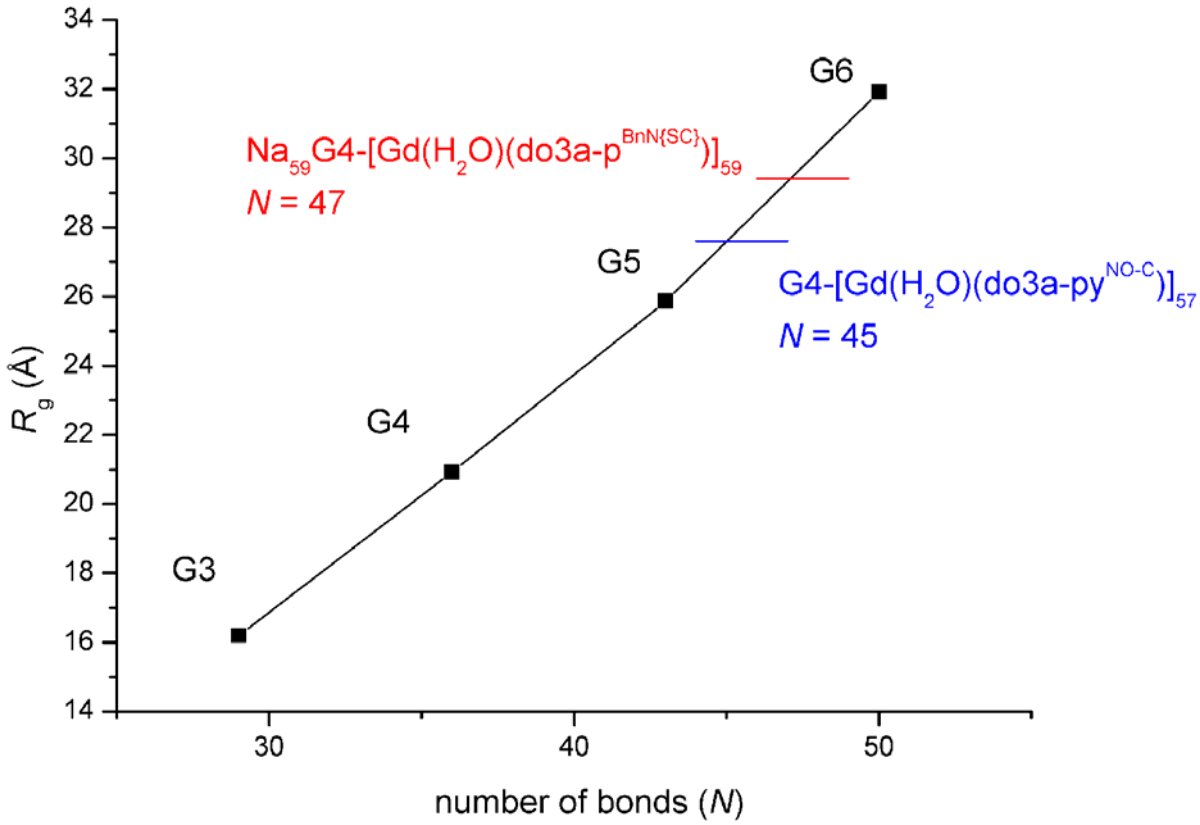

Figure S12. ^1H relaxivity of conjugate $G4\text{-}[Gd(H_2O)(do3a\text{-}py^{NO\text{-}C})]_{57}$ as a function of pH.

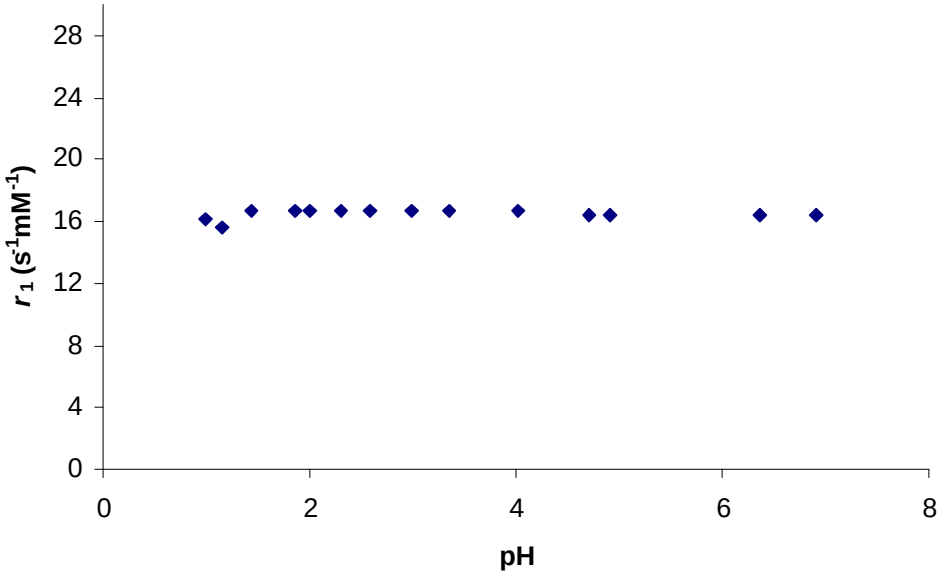

Figure S13. MRI scans of rat kidneys before (upper row) and 60 min after (lower row) intravenous administration of G4-[Gd(H_2O)(do3a-py^{NO-C})]$_{57}$ conjugate. From left to right: individual 2 mm thick slices. The arrow marks the highest image intensity enhancement in kidney.

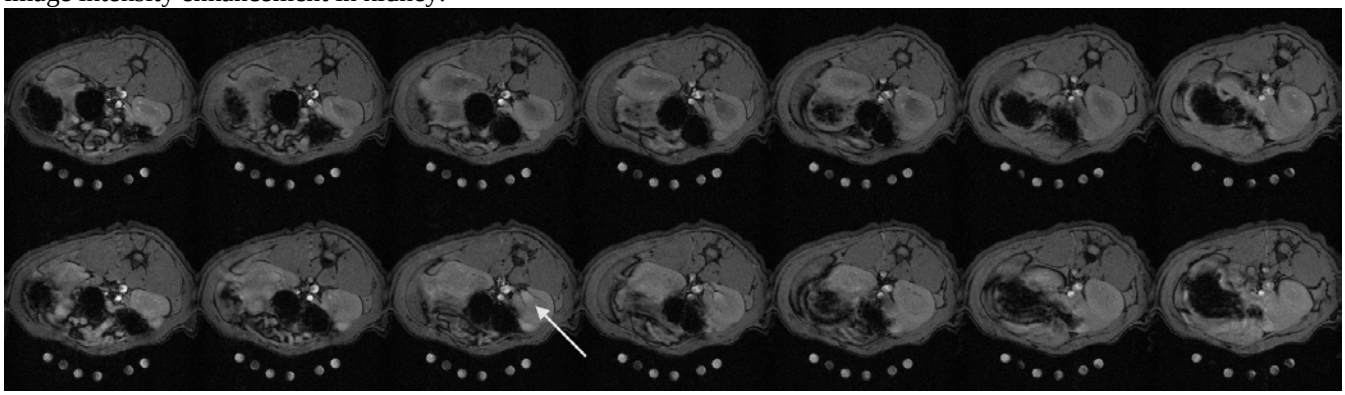

Equations.

// Fit of ^{1}H NMRD and ^{17}O T_1, T_2 and ω_r data - Lipari-Szabo
// Equation set prepared by Zuzana Kotková (Universita Karlova, Prague)

IndVars: T,B
DepVars:R1H,R2O,R1O,dwr,
Params: tv0,delta,Hm,tm0,Erl,Erg,tr0l,tr0g,acc,ro,rh,n,a,RLS,khi,Cout

// Parameters and variables used

// T - temperature at K
// B - used field at MHz
// R2O - 17O transversal relaxivity at ms-1mM-1
// R1O - 17O longitudinal relaxivity at ms-1mM-1
// dwr - 17O reduced radial frequency difference of bonded and free water at rads-1
// R1H - 1H longitudinal relaxivity at ms-1mM-1
// tv0 - correlation time for instantaneous distorsion of the metal coordination polyhedron at 298 K
// delta - D2 mean squared fluctuation of ZFS
// tm0 - water residence time at 298 K
// Erl - rotation free energy (local motion)
// Erg - rotation free energy (global motion)
// Hm - water exchange free energy
// tr0l - local rotation correlation time at 298 K
// tr0g - global rotation correlation time at 298 K
// acc - hyperfine Gd-O coupling constant A/hbar
// ro - Gd-O distance at m
// rh - Gh-H distance at m
// n - number of water molecules coordinated at Gd
// a - shortest distance from outer sphere to gadolinium - for os contribution
// RLS - degree of spatial restriction of the local motion
// D - diffusion coefficient at 298 K
// khi - term with quadrupolar coupling constant and asymmetry parameter = c*(1+(h^2)/3)^0.5
// Cout - outer sphere constant

// Physical constants implicitly used
// p - Ludolf´s number (p = 3.14159265)
// S - multiplicity of Gd (S = 3.5)
// Sz - spin z projection (Sz = 2*S*(S+1) = 31.5)
// univ - universal gas constant (R = 8.31441)
// mB - Bohr magneton (mB = 9.274E-24)
// m0 - vaccum magnetic susceptibility (m0 = 4pE-7)
// h - Planck constant (h = 6.626071E-34)
// hbar - reduced Planck constant (h/(2*p) = 1.0546E-34)
// NA - Avogadro constant (NA = 6.023E23)
// k - Boltzman constant (kB = 1.38066E-23)
// go - gyromagnetic ratio of 17O (go = -3.626E7)
// gh - gyromagnetic ratio of 1H (gh = 2.675E8)
// gs - electronic gyromagnetic ratio (gs = 1.75977E11)
// ws - Larmor frequency of the Gd3+ electron spin
// dg - deviation from th free electron gL value
// g - electron g-factor (g = 2.0023193043622)
// C1 = (1/25)*(4*S*(S+1)-3)
// C2 = (1/50)*(4*S*(S+1)-3)
// C3 = (1/3)*S*(S+1)
// C4 = (1/15)*go^2*g^2*mB^2*(m0/(4*p))^2*S*(S+1)
// C5 = (1/5)*(m0/(4*p))^2*(meff^4*mB^4)/(3*k)^2
// C6 = 2*S*(S+1)*mB/(3*k)
// C7 = (2/15)*go^2*g^2*mB^2*(m0/(4*p))^2*S*(S+1)
// C8 = ((3*p^2)/10)*((2I+3)/(I^2(2I-1)); I=5/2

// C9 = (2/15)*((gh^2*g^2*mB^2)*S*(S+1)*(m0/(4*p))^2
// C10 = (((32*NA*p)/405)*(m0/(4*p))^2)*hbar^2*gs^2*gh^2*S(S+1)

// Notes
// magnetic field is in Larmor frequencies

// ***Definitions of constants***
p=3.14159265
univ=8.31441
gs=1.75977E11
gh=2.675E8
go=-3.626E7
C1=2.4
C2=1.2
C3=5.25
C4=4.7604E-45
C5=3.4274E-59
C6=0.1657
C7=9.5209E-45
C8=0.9475
C9=5.181644E-43
C10=5.796E-19

// ***Definition of omegas; Lrmor frequencies of 1H (wh), 17O (wo) and electron (ws)***
wh=2*p*1E6*B
ws=2*p*1E6*B*(gs/gh)
wo=2*p*1E6*B*(go/gh)
// ***Eyring equations***
tm=((tm0^(-1)*T/298.15)*exp((Hm/univ)*((1/298.15)-(1/T))))^(-1)
trl=((tr0l^(-1))*exp((Erl/univ)*((1/298.15)-(1/T))))^(-1)
trg=((tr0g^(-1))*exp((Erg/univ)*((1/298.15)-(1/T))))^(-1)
tv=((tv0^(-1))*exp((Ev/univ)*((1/298.15)-(1/T))))^(-1)
// ***Electronic relaxation times T1e, T2e - Zero field splitting (ZFS) + spin rotation (SR) term***
T1e=(C1*delta*tv*((1/(1+ws^2*tv^2))+(4/(1+4*ws^2*tv^2)))+(dg/(9*trt)))^(-1)
T2e=(delta*tv*((5.26/(1+(0.372*ws^2*tv^2)))+(7.18/(1+(1.24*ws^2*tv^2)))) + dg/(9*trt))^(-1)
// Total correlation times (t - total, l - local, g - global, e - electronic)
trlH=trl*0.65
trt=(trl^(-1)+trg^(-1))^(-1)
trtH=(trlH^(-1)+trg^(-1))^(-1)
tc1l=(T1e^(-1)+trt^(-1)+tm^(-1))^(-1)
tc2l=(T2e^(-1)+trt^(-1)+tm^(-1))^(-1)
tc1lH=(T1e^(-1)+trtH^(-1)+tm^(-1))^(-1)
tc2lH=(T2e^(-1)+trtH^(-1)+tm^(-1))^(-1)
tc1g=(T1e^(-1)+trg^(-1)+tm^(-1))^(-1)
tc2g=(T2e^(-1)+trg^(-1)+tm^(-1))^(-1)
te1=(T1e^(-1)+tm^(-1))^(-1)
te2=(T2e^(-1)+tm^(-1))^(-1)
// ***R2 scalar - contact contribution for 17O (R2sO)***
R2sO=C3*acc^2*(te1+(te2/(1+ws^2*te2^2)))
// ***R2 dipolar - pseudocontact contribution for 17O - Lipari-Szabo***
d1O=(RLS*tc1g/(1+wo^2*tc1g^2))+((1-RLS)*tc1l/(1+wo^2*tc1l^2))
d2O=(RLS*tc2g/(1+ws^2*tc2g^2))+((1-RLS)*tc2l/(1+ws^2*tc2l^2))
// ***Total T2 relaxation time (T2mO)***
T2mO=(R2sO)^(-1)
// ***Radial frequency difference of bound and free water at rad/s (dwm)***
dwm=(C6/T)*acc*B
// ***Overall reduced T2 relaxation of 17O (R2O)***
num=(T2mO^(-2))+(T2mO*tm)^(-1)+dwm^2
denom=(tm^(-1)+T2mO^(-1))^2+dwm^2
fract=num/denom
pm=n*1E-3/55.55
T2r=ln(fract/tm)
R2O=pm*fract/tm

// Overall reduced T1 relaxation of 17O - Lipari-Szabo (R1O; consists of dipolar, R1dO, and quarupolar, R1qO, terms)
R1dO=(C7/(ro^6))*(3*d1O+7*d2O)
q1O=(RLS*trg/(1+wo^2*trg^2))+((1-RLS)*trt/(1+wo^2*trt^2))
q2O=(RLS*trg/(1+4*wo^2*trg^2))+((1-RLS)*trt/(1+4*wo^2*trt^2))
R1qO=C8*khi^2*(0.2*q1O+0.8*q2O)
T1mO=(R1dO+R1qO)^(-1)
R1O=pm/(T1mO+tm)
// ***Radial frequency difference of bond and free water - total reduced (dwr), contribution of os (dwos)***
dwos=Cout*dwm
dwr=pm*(dwm/((tm/T2mO+1)^2+(tm*dwm)^2)+dwos)
// ***R1 dipolar - pseudocontact contribution for 1H - Lipari-Szabo (R1dH)***
d1H=(RLS*tc1g/(1+wh^2*tc1g^2))+((1-RLS)*tc1l/(1+wh^2*tc1lH^2))
d2H=(RLS*tc2g/(1+ws^2*tc2g^2))+((1-RLS)*tc2l/(1+ws^2*tc2lH^2))
R1dH=(C9/(rh^6))*(3*d1H+7*d2H)
// ***Total inner sphere milimolar contribution to 1H relaxivity (R1Hin)***
T1mH=(R1dH)^(-1)
R1Hin=pm/(T1mH+tm)
// ***Calculus for difusion coefficient according to J.C.Hindman (D)***
B1=3.118150E-04
B2=5.062560E+03
B3=1.547920E+02
B4=1.629310E+03
D=(1E-4)/((B1*EXP(B2/T))+(B3*EXP(B4/T)))
// ***Outer sphere contribution to 1H relaxivity according to Freeds model (R1Hos); i - proton*** //***spins, s - Gd electron states)***
tau=a^2/D
z2i=(tau/T1e)+([0,1]*wh*tau)
z2s=(tau/T2e)+([0,1]*ws*tau)
os1=Re((1+0.25*(z2i^0.5))/(1+z2i^0.5+(4/9)*z2i+(1/9)*(z2i^1.5)))
os2=Re((1+0.25*(z2s^0.5))/(1+z2s^0.5+(4/9)*z2s+(1/9)*(z2s^1.5)))
R1Hos=(C10/(A*D))*(3*os1+7*os2)
// ***Overall R1 proton relaxivity (R1H)***
R1H=R1Hin+R1Hos
// **Estimation of parameters - combination of prof. Merbach DOTA parameters and estimation**
// **for second sphere**
n=1
delta=0.16E20
tm0=243E-9
Hm=49.8e3
tr0l=77E-12
tr0g=500e-12
Erl=40E3
Erg=20e3
tv0=11.1E-12
Ev=1000
acc=-3.7E6
ro=2.5E-10
rh=3.1E-10
n=1
a=3.5E-10
khi=7.58E6
Cout=0.1
dg=0.08
RLS=1

References

(1) Wiener, E. C., Konda, S., Shadron, A., Brechbiel, M. W., Gansow, O. (1997) Targeting dendrimer-chelates to tumors and tumor cells expressing the high-affinity folate receptor. *Invest. Radiol. 32*, 748–754.

(2) Konda, S. D., Aref, M., Wang, S., Brechbiel, M. W., Wiener, E. C. (2001) Specific targeting of folate–dendrimer MRI contrast agents to the high affinity folate receptor expressed in ovarian tumor xenografts. *Magn. Reson. Mater. Phys. Biol. Med. 12*, 104–113.

(3) Tóth, É., Pubanz, D., Vauthey, S., Helm, L., Merbach, A. E. (1996) The role of water exchange in attaining maximum relaxivities for dendrimeric MRI contrast agents. *Chem. Eur. J. 2*, 1607–1615.

(4) Laus, S., Sour, A., Ruloff, R., Tóth, É., Merbach, A. E. (2005) Rotational dynamics account for pH-dependent relaxivities of PAMAM dendrimeric, Gd-based potential MRI contrast agents. *Chem. Eur. J. 11*, 3064–3076.

(5) (*a*) Rudovský, J., Botta, M., Hermann, P. Hardcastle, K. I., Lukeš, I., Aime S.(2006) PAMAM dendrimeric conjugates with a Gd-DOTA phosphinate derivative and their adducts with polyaminoacids: The interplay of global motion, internal rotation, and fast water exchange. *Bioconjugate Chem. 17*, 975–987; (*b*) Rudovský, J., Hermann, P., Botta, M., Aime, S., Lukeš, I. (2005) Dendrimeric Gd(III) complex of a monophosphinated DOTA analogue: optimizing relaxivity by reducing internal motion. *Chem. Commun.* 2390–2392.

(6) Jaszberenyi, Z., Moriggi, L., Schmidt, P., Weidensteiner, C., Kneuer, R., Merbach, A. E., Helm, L., Tóth, É. (2007) Physicochemical and MRI characterization of Gd^{3+}-loaded polyamidoamine and hyperbranched dendrimers. *J. Biol. Inorg. Chem.* 12, 406–420.

(7) Kobayashi, H., Sato, N., Kawamoto, S., Saga, T., Hiraga, A., Haque, T. L., Ishimori, T., Konishi, J., Togashi, K., Brechbiel, M. W. (2001) Comparison of the macromolecular MR contrast agents with ethylenediamine-core versus ammonia-core generation-6 polyamidoamine dendrimer. *Bioconjugate Chem. 12*, 100– 107.

(8) Kobayashi, H., Brechbiel M. W. (2004) Dendrimer-based nanosized MRI contrast agents. *Curr. Pharm. Biotechnol. 5*, 539–549.

(9) Yordanov, A. T., Kobayashi, H., English, S. J., Reijnders, K., Milenic, D., Krishna, M. C., Mitchell, J. B., Brechbiel, M. W. (2003) Gadolinium-labeled dendrimers as biometric nanoprobes to detect vascular permeability. *J. Mater. Chem. 13*, 1523–1525.

(10) Kobayashi, H., Kawamoto, S., Star, R. A., Waldmann, T. A., Tagaya, Y., Brechbiel, M. W. (2003) Micro-magnetic resonance lymphangiography in mice using a novel dendrimer-based magnetic resonance imaging contrast agent. *Cancer Res. 63*, 271–276.

(11) Swanson, S. D., Kukowska-Latallo, L. F., Patri, A. K., Chen, C., Ge, S., Cao, Z., Kotlyar, A., East, A. T., Baker, J. R. (2008) Targeted gadolinium-loaded dendrimer nanoparticles for tumor-specifi c magnetic resonance contrast enhancement. *Int. J. Nanomed. 3*, 1–10.

(12) Wiener, E. C., Auteri, F. P., Chen, J. W., Brechbiel, M. W., Gansow, O. A., Schneider, D. S., Belford, R. L., Clarkson, R. B., Lauterbur, P. C. (1996) Molecular Dynamics of Ion-Chelate Complexes Attached to Dendrimers. *J. Am. Chem. Soc. 118*, 7774–7782.

(13) Ali, M. M., Woods, M., Caravan, P., Opina, A. C. L., Spiller, M., Fettinger, J. C., Sherry, A. D. (2008) Synthesis and relaxometric studies of a dendrimer-based pH-responsive MRI contrast agent. *Chem. Eur. J. 14*, 7250–7258.

(14) Ladd, D. L., Hollister, R., Peng, X., Wei, D., Wu,, G., Delecki, D., Snow, R. A., Toner, J. L., Kellar, K., Eck, J., Desai, V. C., Raymond, G., Kinter, L. B., Desser, T. S., Rubin, D. L. (1999) Polymeric gadolinium chelate magnetic resonance imaging contrast agents: Design, synthesis, and properties. *Bioconjugate Chem. 10*, 361–370.

(15) Langereis, S., de Lussanet, Q. G., van Genderen, M. H. P., Backes, W. H., Meijer, E. W. (2004) Multivalent contrast agents based on gadolinium-diethylenetriaminepentaacetic acid-terminated poly(propylene imine) dendrimers for magnetic resonance imaging. *Macromolecules 37*, 3084–3091.

(16) Langereis, S., de Lussanet, Q. G., van Genderen, M. H. P., Meijer, E. W., Beets-Tan, R. G. H., Griffioen, A. W., van Engelshoven, J. M. A., Backes, W. H. (2006) Evaluation of Gd(III)DTPA-terminated poly(propylene imine) dendrimers as contrast agents for MR imaging. *NMR Biomed. 19*, 133–141.

(17) Ke, T., Feng, Y., Guo, J., Parker, D. L., Lua, Z.-R. (2006) Biodegradable cystamine spacer facilitates the clearance of Gd(III) chelates in poly(glutamic acid) Gd-DO3A conjugates for contrast-enhanced MR imaging. *Magn. Reson. Imag. 24*, 931–940.

(18) Xu, H.; Regino, C. A. S.; Bernardo, M.; Koyama, Y.; Kobayashi, H.; Choyke, P. L.; Brechbiel, M. W. (2007) Toward improved syntheses of dendrimer-based magnetic resonance imaging contrast agents: New bifunctional diethylenetriaminepentaacetic acid ligands and nonaqueous conjugation chemistry. *J. Med. Chem. 50*, 3185–3193.

(19) Nicolle, G. M., Tóth, É., Schmitt-Willich, H., Radüchel, B., Merbach, A. E. (2002) The impact of rigidity and water exchange on the relaxivity of a dendritic MRI contrast agent. *Chem. Eur. J. 8*, 1040–1048.

(20) Rebizak, R., Schaeferb, M., Dellacheriea, É. (1999) Macromolecular contrast agents for magnetic resonance imaging. Influence of polymer content in ligand on the paramagnetic properties. *Eur. J. Pharm. Sci. 7*, 243–248.

(21) Wängler, C.; Wängler, B.; Eisenhut, M.; Haberkorn, U.; Mier, W. (2008) Improved syntheses and applicability of different DOTA building blocks for multiply derivatized scaffolds. *Bioorg. Med. Chem. 16*, 2606–2616.

(22) Kaneshiro, T. L., Jeong, E.-K., Morrell, G., Parker, D. L., Lu, Z.-R. (2008) Synthesis and evaluation of globular Gd-DOTA-monoamide conjugates with precisely controlled nanosizes for magnetic resonance angiography. *Biomacromolecules 9*, 2742–2748.

(23) Montalbetti, C. A. G. N.; Falque, V. (2005) Amide bond formation and peptide coupling. *Tetrahedron 61*, 10827–10852.

(24) Peterson, J.; V. Allikmaa, V.; Subbi, J.; Pehk, T.; Lopp, M. (2003) Structural deviations in poly(amidoamine) dendrimers: a MALDI-TOF MS analysis. *Eur. Polym. J. 39*, 33–42.

(25) Shi, X. Y.; Banyai, I.; Islam, M. T.; Lesniak, W.; Davis, D. Z.; Baker, J. R.; Balogh, L. P. (2005) Generational, skeletal and substitutional diversities in generation one poly(amidoamine) dendrimers. *Polymer 46*, 3022–3034.

(26) (*a*) Vetterlein, K.; Bergmann, U.; Büche, K.; Walker, M.; Hildebrand, M.; Lehmann, J.; Linscheid, M. W.; Scriba, G. K. E.; Hildebrand, M. (2007) Comprehensive profiling of the complex dendrimeric contrast agent Gadomer using a combined approach of CE, MS, and CE-MS. *Electrophoresis 28*, 3088–3099; (*b*) Vetterlein, K.; Büche, K.; Hildebrand, M.; Scriba, G. K. E.; Lehmann, J. (2006) Capillary electrophoresis for the characterization of the complex dendrimeric contrast agent Gadomer. *Electrophoresis 27*, 2400–2412.

(27) Esfand, R.; Tomalia, D. A. (2001) Poly(amidoamine) (PAMAM) dendrimers: from biomimicry to drug delivery and biomedical applications. *Drug Discovery Today 6*, 427–436.

(28) Polášek, M., Šedinová, M., Kotek, J., Elst, L. V., Muller, R. N., Hermann, P., Lukeš, I. (2009) Pyridine-*N*-oxide analogues of DOTA and their gadolinium(III) complexes endowed with a fast water exchange on the square-antiprismatic isomer. *Inorg. Chem. 48*, 455–465.

(29) Porcar, L., Liu, Y., Verduzco, R., Hong, K., Butler, P. D., Magid, L. J., Smith, G. S., Chen, W.-R. (2008) Structural Investigation of PAMAM Dendrimers in Aqueous Solutions Using Small-Angle Neutron Scattering: Effect of Generation. *J. Phys. Chem. B, 112*, 14772–14778.

Design, Synthesis, Characterization, and Biological Evaluation of Triazine Dendrimers Bearing Paclitaxel Using Ester and Ester/Disulfide Linkages

Jongdoo Lim,[†] Abdellatif Chouai,[†] Su-Tang Lo,[‡] Wei Liu,[‡] Xiankai Sun,[‡] and Eric E. Simanek*,[†]

Department of Chemistry, Texas A&M University, College Station, Texas 77843-3255, and Department of Radiology, University of Texas Southwestern Medical Center, Dallas, Texas 75390. Received July 22, 2009; Revised Manuscript Received September 14, 2009

The design, synthesis, characterization, and preliminary biological assessment of three dendrimers are reported. All three dendrimers, **1**−**3**, present twelve paclitaxel groups linked by acylation of the 2′-hydroxyl group. The linker for dendrimers **2** and **3** also includes a disulfide. Installation of the paclitaxel group relies on reacting twelve primary amines of a second generation triazine dendrimer, a scaffold available on kilogram scale, with a dichlorotriazine bearing the drug. This dichlorotriazine is available in four steps by (i) reacting paclitaxel with glutaric anhydride, (ii) activating with *N*-hydroxysuccinimide (NHS), (iii) treating the resulting ester with either 1,3-diaminopropane (for **1**) or cystamine (for **2** and **3**), and (iv), finally, reacting with cyanuric chloride. After reaction with the dendrimer, the resulting monochlorotriazine groups are reacted with 4-aminomethylpiperidine (AMP) and then a poly(ethylene glycol) (PEG) group of molecular weight 2 kDa. Two different PEG-NHS esters are employed that differ in lability. For **1** and **2**, the PEG incorporates an ester-linked succinic acid group. For **3**, the PEG incorporates an ether-linked acetic acid group. Both mass spectrometry and ^{1}H NMR spectroscopy prove valuable for determining the final ratios of dendrimer:paclitaxel:AMP:PEG. These values are typically 1:12:12:9. Cytotoxicity of these constructs using an MTT-based assay and PC-3 cells reveals IC_{50} values in the low nanomolar range with dithiothreitol and glutathione enhancing the toxicity of the disulfide-containing constructs **2** and **3**. Preliminary toxicology assessment of **1** suggests that it is well tolerated in vivo with preferential renal clearance. The elimination half-lives of all of the dendrimers appear shorter than predicted from the previous results. Tumor localization is observed for all the three dendrimers.

INTRODUCTION

The emerging field of polymeric therapeutics (*1*−*6*) captures attention with the prospect of improving the efficacy of conventional drugs by overcoming obstacles in their clinical use that might arise due to the drug's low solubility, high systemic toxicity, instability, low bioavailability, or rapid excretion. The architectures currently being explored represent an eclectic collection of linear polymers (*7, 8*), grafts (*9, 10*), stars (*11,12*), and other constructs (*13*) including dendrimers (*14*−*18*). Our interest in dendrimers stems from their globular shape and the opportunity to exploit multivalency. As monodisperse entities (or low dispersity mixtures), we hypothesize that the batch-to-batch behavior of these materials will be consistent; namely, reproducible pharmacodynamics and pharmacokinetics will be observed. Another inherent advantage of macromolecules is derived from their passive accumulation in solid tumors through the enhanced permeability and retention (EPR) effect (*19, 20*). In addition, some dendrimers display targeting ligands, biocompatible polymers, and reporting groups (*21*−*24*).

Triazine dendrimers have been our choice of scaffold due to their ease of synthesis. The differential reactivity of various amine nucleophiles with chlorotriazine derivatives allows us to prepare chemically diverse dendrimers at moderate to large scale (20 to 1000 g) with high purities (*23*−*30*). Here, the product of the kilogram-scale synthesis is intercepted with a drug-bearing dichlorotriazine (Scheme 1). This strategy—interception with a functional monomer—is of significance to us because the scope and limitations of this strategy have not been probed. The efforts reported serve as proof-of-concept for this potential: paclitaxel is elaborated successfully to a reactive dichlorotriazine and provides, on interception, a poly(monochlorotriazine) that is manipulated in two steps to yield the final pegylated target. We believe that this strategy will prove to be quite general.

We favor covalent attachment over noncovalent association of drugs. While the noncovalent encapsulation of hydrophobic drugs is straightforward, it is limited by drug loading and provides less control over release rates. As an alternative, covalent drug loading offers higher drug loading and a wealth of literature on biodegradable linkages including (i) acid-labile linkers for endosomal/lysosomal release including esters (*31, 32*), acetals (*33, 34*), and hydrazones (*35, 36*), (ii) reductively labile disulfide bonds (*37*) that can be cleaved by glutathione or other intracellular thiols, and (iii) enzymatically labile peptide linkers (*38*). Here, we attach paclitaxel with linkers that contain either an ester or an ester/disulfide pair.

Paclitaxel is a mitosis-inhibiting antitumor agent to treat patients with breast, ovarian, lung, head and neck cancers, and Kaposi's sarcoma (*39, 40*). The hydrophobic drug is, however, poorly water soluble (<0.1 μg/mL) and usually administered as Taxol with Cremophor EL or other cosolvent formulations that may cause severe allergic reactions in some patients (*41*). Solvent-free polymer-bound prodrugs have been pursued to improve the in vivo solubility, safety, and efficacy of the parent drug. Abraxane (*42, 43*) is an albumin-bound paclitaxel and approved for metastatic breast cancer with broad therapeutic interest. Xyotax (poliglumex) (*44*) is a poly(L-glutamic acid) paclitaxel conjugate and degradable to release paclitaxel or its derivatives from the polymer backbone by action of a lysosomal protease, cathepsin B, that is overexpressed in many tumors or

* To whom correspondence should be addressed. simanek@mail.chem.tamu.edu.

[†] Texas A&M University.

[‡] University of Texas Southwestern Medical Center.

10.1021/bc900324z CCC: $40.75 © 2009 American Chemical Society
Published on Web 10/30/2009

Scheme 1. General Strategy for Derivatization of Triazine Dendrimers by Interception with Functionalized Dichlorotriazine Monomers

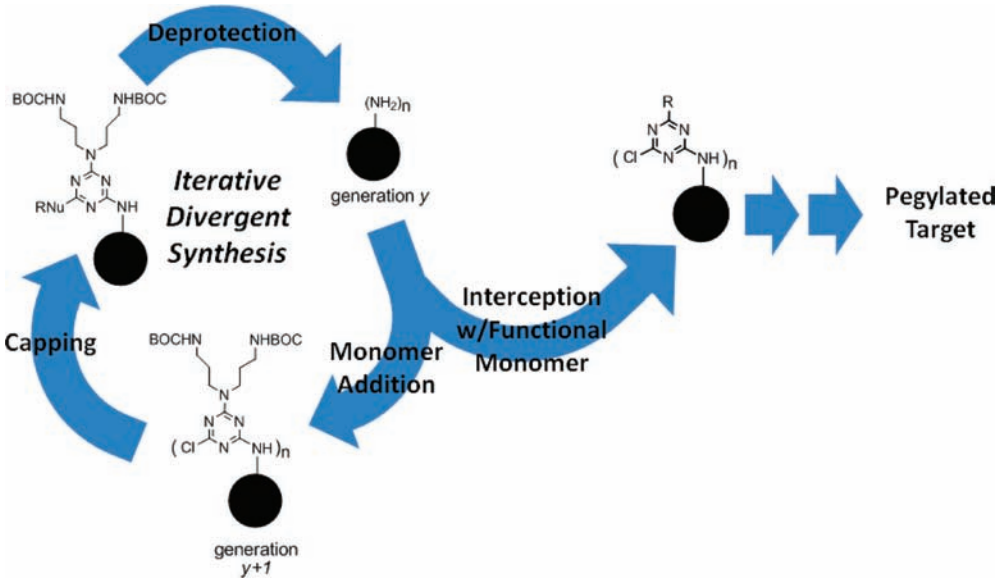

Chart 1. Dendrimers 1−3 with the Labile 2′-Ester and Disulfide Linkages[a]

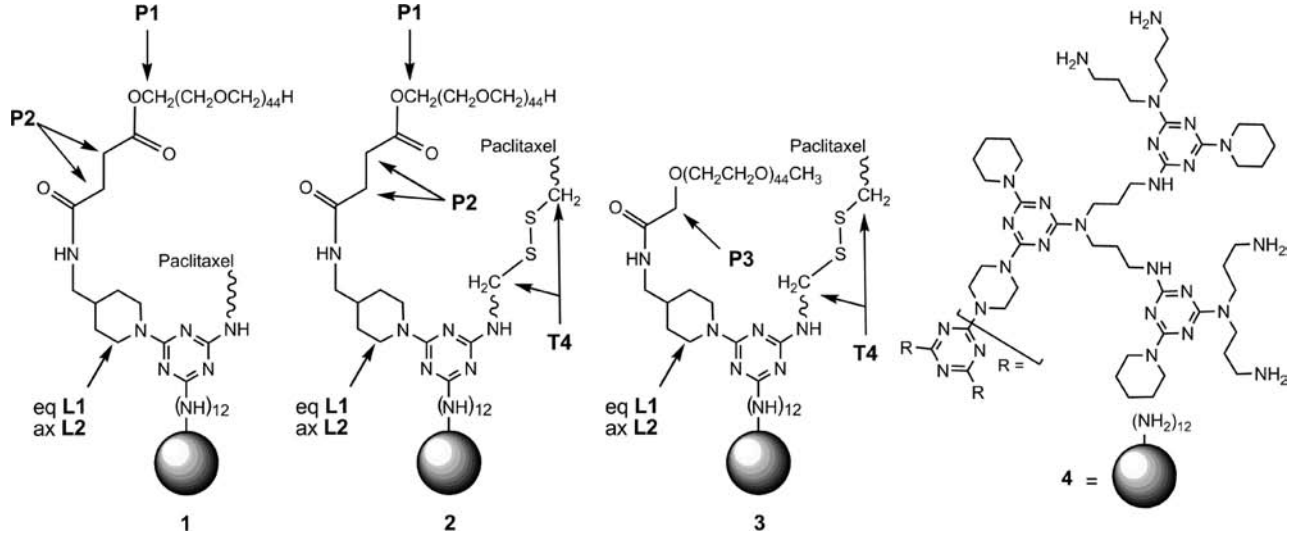

[a] The linkers for the PEG groups vary also. Additional atomic detail is available in Chart 2. The core of the dendrimer, **4**, is shown at the right. Labels refer to NMR spectra discussed later in the text.

high estrogenic environments. Xyotax has been studied in phase III trials and has shown prolonged survival for women with advanced lung cancer (*45*). Other prodrugs such as PEG-TXL (a poly(ethylene glycol) conjugate of paclitaxel) (*46*) and HPMA-TXL (a *N*-(2-hydroxypropyl)methacrylamide copolymer conjugate of paclitaxel) (*47*) have shown some success in early clinical trials. Other macromolecular and pro-drug constructs based on paclitaxel have been recently described (*48*−*55*).

The goal of this manuscript is to communicate the design, synthesis, characterization, and preliminary biological assessment of dendrimers **1**−**3** shown schematically in Chart 1. Such studies set the stage for evaluations of efficacy in animal models of disease. While all three dendrimers present twelve paclitaxel groups appended by acylation of the 2′-hydroxyl group, the nature of the linker and the composition of the PEGylation reagent vary. The linker for dendrimer **1** offers a single biolabile linkage, the 2′-ester. The linker for dendrimers **2** and **3** also includes a disulfide. While PEG is appended through an amide linker to the triazines, the PEG reagent used in **1** and **2** includes a succinic acid ester, while the PEG reagent for **3** has a linking ether group. Biological assessments are also reported.

EXPERIMENTAL SECTION

General Synthetic Procedures. Paclitaxel was purchased from AK Scientific, Inc., or CEC. The NHS-mPEGs were purchased from NOF Corporation. The intermediates, **4** (*28*, *29*) and **5** (*30*) were prepared as previously reported. All other chemicals were purchased from Aldrich and Acros and used without further purification. All solvents were ACS grade and used without further purification. Diafiltration purification was performed with Amicon stirred ultrafiltration cell equipment (model 8400, YM 10 membrane, Millipore Corp.) at 35 psi of N_2. Size exclusion chromatography (SEC) was carried out using a Waters Delta 600 system and a Waters 2414 refractive index detector. A Suprema 10 μm GPC analytical column (1000 Å, 8 × 300 mm) was used with 0.1 M $NaNO_3$ as the eluent and a flow rate of 1 mL/min. NMR spectra were recorded on an Inova 300 or 500 MHz spectrometer in $CDCl_3$ or $CDCl_3$/MeOH-d_4

Chart 2. Dichlorotriazines 5 and 6 Are Available in Four Steps in 60% and 49% Overall Yields, Respectively

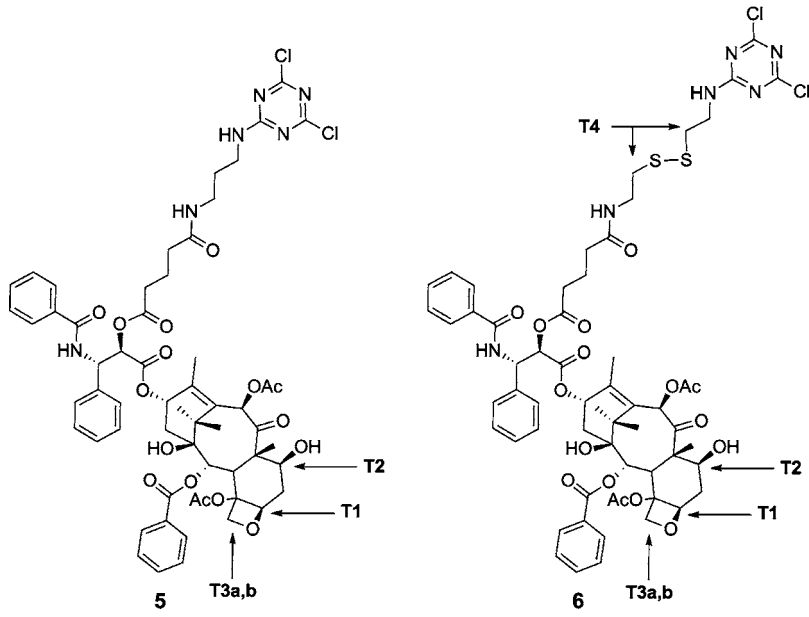

(10:1). All mass spectral analyses were carried out by the Laboratory for Biological Mass Spectrometry at Texas A&M.

Cytotoxicity. PC-3 cells (a human prostate cancer cell line) were cultured in T-medium (Invitrogen Corp., NY) at 37 °C in an atmosphere of 5% CO_2 and were passaged when reaching 75% confluence in a P100. T-Medium was supplemented with 5% FBS (Gemini Bio-Products, Woodland, CA) and 1× penicillin/streptomycin (Sigma, St. Louis, MO). The cells (2.5×10^3 cells/well in 50 μL T-medium) were plated in 96-well plates and incubated overnight for the treatment. A series of dilutions of **1**, **2**, and **3** at the paclitaxel concentration between 5 nM and 50 μM were prepared and added to the cells in the 96-well plates. For some studies, 10 μL of 10 mM of γ-L-glutamyl-L-cysteinyl-glycine (GSH, Sigma-Aldrich, St. Louis) or DL-dithiothreitol (DTT, Sigma-Aldrich, St. Louis) in PBS solution was added to each well, giving the final volume of 100 μL per well. Each treatment was duplicated in triplicates. After the three-day treatment, the cells were washed twice with 100 μL of prewarmed T-medium. After adding 100 μL of prewarmed T-medium to each well, 10 μL of the MTT reagent was added. The MTT assay was performed according to the described procedure in the cell proliferation colorimetric assay kit (Roche Diagnostics Corporation, IN). The absorbance of the formazan dye in each was measured on a SpectraMax M5 plate reader (Molecular Devices, Sunnyvale, CA). The IC_{50} data were calculated by GraphPad *Prism 5* (GraphPad Software, La Jolla, CA) and presented as the best-fit values and 95% confidence intervals. IC_{50} is the concentration of compound required to inhibit 50% of the cell growth compared to an untreated control.

Radiolabeling of 1, 2, and 3 with ^{125}I and Purification. IODO-GEN precoated iodination tubes (Pierce, Rockford, IL) were used for ^{125}I-radiolabeling of **1**, **2**, and **3** on Bolton-Hunter like groups attached at unreacted aminomethylpiperidine groups. IODO-GEN precoated tubes were rinsed with 1 mL of 10 mM PBS buffer (pH 7.5) before the labeling. To each IODO-GEN tube containing 15 nmol of dendrimer−taxol prodrug in 20 mM PBS was added ~600 μCi of Na^{125}I (2 μL of volume). The solution was kept at room temperature for 30 min with gentle swirling every 5 min. After radiolabeling reaction, the samples were further purified by using Millipore 10 k centrifugal filtration units. The reaction mixtures were loaded to the filter units and centrifuged at 14 000 rpm for 30 min to remove the free ^{125}I ion or other small molecular species. The products were then washed with 3 portions of 500 μL of 10 mM PBS. Radio-TLC or radio-HPLC was used to monitor the radiolabeling efficiency and determine the radiochemical purity of the three ^{125}I-labeled prodrugs.

Biodistribution Studies in SCID Mice Bearing PC-3 Xenografts. PC-3 cells were subcutaneously implanted into both front flanks ($2-2.5 \times 10^6$ of cells in 100 μL) of male SCID mice at 6−8 weeks of age. Tumors were allowed to grow for 3−4 weeks. Once the tumors reached the size of 50−500 mg, the mice were randomized into 3 groups ($n = 4$; 4 h, 24 h, and 48 h). Each mouse was intravenously injected with 100 μL of ^{125}I-radiolabed **1**, **2**, and **3** (~5 μCi/ mouse). Mice were sacrificed at 4 h, 24 h, and 48 h postinjection (p.i.). Organs of interest (blood, heart, lung, fat, liver, spleen, kidney, stomach, intestines, muscle, femur, thyroid, brain, and tumors) were harvested and weighed, and radioactivity was quantified by γ-counter. Standards were prepared, weighed, and counted along with the samples for %ID/g and %ID/organ calculation. Statistical analysis was performed using *Prism 5.0* (Graphpad, San Diego, CA).

RESULTS AND DISCUSSION

This section is subdivided into three parts, the design and synthesis of these targets, their chemical characterization, and a preliminary biological assessment in vitro and in vivo.

Design and Synthesis. The design criteria employed to arrive at **1**−**3** included (i) the choice of a broad spectrum drug that presents challenges in delivery; (ii) the use of a dendrimer platform that was available at large scale; (iii) the adoption of established strategies for drug conjugation that too were scalable; and (iv) the development of a route that could be generalized to other drugs and/or linkers. We met these criteria using paclitaxel as the drug and esterification of the 2′-hydroxyl group for linkage to the dendrimer. We favor covalent attachment of the drug because it increases drug loading from 1 or 2 molecules sequestered noncovalently to 12. This strategy should enable controlled release through ester hydrolysis and/or disulfide reduction. The routes employed could be scaled readily to yield multigram quantities of material (Scheme 2). The dendrimer, **4**, (in its BOC-protected form) has been prepared on kilogram scale (*28*). The two dichlorotriazines, **5** and **6**, are synthesized in four steps in 60% and 49% overall yields, respectively (Chart

Scheme 2. Synthesis of 1−3

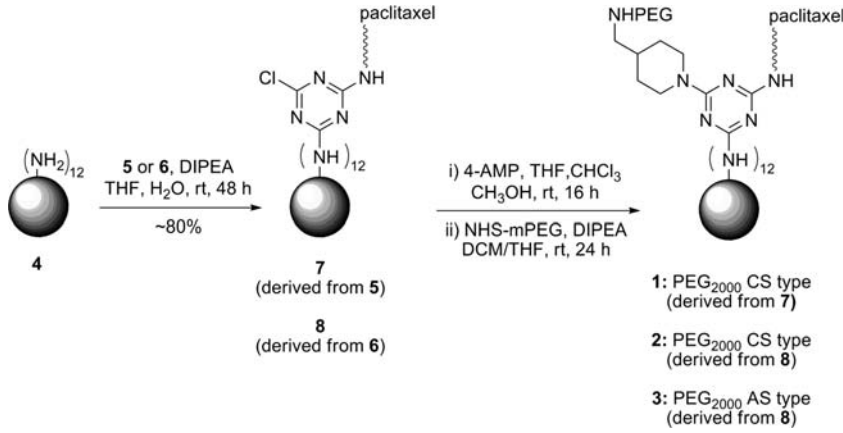

2). After paclitaxel is reacted with glutaric anhydride, the *N*-hydroxysuccinimide (NHS) ester is prepared as previously reported (*30*). Reaction of the ester with the excess amount of a diamine, either 1,3-diaminopropane or cystamine, gives free amine-terminated paclitaxel intermediates. Subsequently, these amines are reacted with cyanuric chloride using Hunig's base at 0 °C in THF for 1 h, to provide the desired dichlorotriazines, **5** and **6**. The generation three dendrimers, **7** and **8**, are respectively obtained from the reaction of **4** with either **5** or **6** using Hunig's base in THF/water for 48 h. Dendrimer **7** covalently carries twelve molecules of paclitaxel through ester linkage, while **8** carries the drug via both ester and disulfide linkages. The PEGylation of the amines of aminomethylpiperidine is accomplished using NHS-esters of PEG (2kDa) described as either CS type (succinate type; mPEG-O-$COCH_2CH_2CO$-NHS) or AS type (acetyl type; mPEG-O-CH_2CO-NHS). For the biodistribution study, radiolabeling groups are later incorporated by reacting an NHS-activated Bolton-Hunter reagent with the PEGylated dendrimers by taking advantage of unPEGylated aminomethylpiperidine groups.

Chemical Characterization. Synthesis and purification of dendrimers are followed by thin layer chromatography (TLC), ^1H and ^{13}C NMR, mass spectrometry, and gel permeation chromatography (GPC). MALDI-TOF MS showed all species presented appropriate molecular ions as $[M + H]^+$, $[M + Na]^+$, and/or $[M + K]^+$. Mass ions (*m*/*z*) of the poly(monochlorotriazine) dendrimers were observed at 16 657 for **7** (calculated mass: 16 567) and 17 481 for **8** (calculated mass: 17 503) (Supporting Information Figure S9). A ladder of peaks at lower mass region (~16 450) was found for **8** due to the fragmentation of the labile ester and disulfide bonds, most likely occurring during ionization.

PEGylated dendrimers **1**, **2**, and **3** were purified using ultrafiltration in deionized water over a week. GPC was used to analyze the PEGylated dendrimers using 0.1 M $NaNO_3$ (aq) as an eluent with a refractive index (RI) detector. As shown in the Supporting Information (Figure S10), the retention times of the analytes do not correspond to their molecular weights obtained from MALDI-TOF MS: **1** (10.1 min, 38.8 kDa), **2** (9.9 min, 36.6 kDa), and **3** (9.6 min, 33.9 kDa). We assume that either the hydrophobic interactions between the column matrix and the analyte affected the chromatography or that the increased hydrophobic nature promotes aggregation.

Figure 1 shows two regions of the ^1H NMR of PEGylated dendrimers that can be used to provide estimates of the degree of PEGylation. The peaks indicated derive from tethered paclitaxel (T1−T4; Chart 2), the linking aminomethylpiperidine group (L1,L2; Chart 1), and PEG (P1−P3; Chart 1). The Supporting Information includes complete NMR assignments of the spectra of these targets. The spectra are typified by resolved peaks of paclitaxel in the region of δ 4.8−8.2 ppm and a highly crowded upfield region populated by peaks from the PEG, paclitaxel, and dendrimer. The results provide support for our estimates of the degree of PEGylation derived from mass spectrometry (based on an average molecular mass of PEG of 2.3k Da as determined by MALDI-TOF MS). The theoretical integrations of paclitaxel protons (T1−T3) are in close agreement with experimental values. Discrepancy in the values of T4 are attributed to an inability to unambiguously integrate the signal. While we are inclined to believe that the reaction of AMP on the poly(monochlorotriazine) dendrimer proceeds almost quantitatively, ^1H NMR validates this belief; that is, the axial and equatorial protons of AMP appear in ratios that reflect almost a 1:1 correlation of drug to AMP. Accordingly, we infer that substoichiometric PEGylation derives from the conditions employed during PEGylation and is not due to a lack of amines installed during the AMP step. The overlapping signals of the ^1H NMR spectra make quantifying the degree of PEGylation inexact, but possible. The relatively close agreement of T-type and L-type signals leads us to assign overlap to these signals; that is, of the 2.64 protons expected for T3b and P1 of **1**, we assign 1.13 units of signal to T3b (an estimate based on T3a) leaving 1.51 units for P1. The result is that both P1 and P2 have 75% the expected area. We infer, accordingly, a ratio of 1:1:0.75 for paclitaxel/linker/PEG, which corresponds to 9 of the expected 12 chains. A similar ratio of 1:1:0.67 for paclitaxel/linker/PEG is seen for **2** corresponding to 8 PEG chains. The significant overlap between P3 and water in **3** allows us to place an upper limit on the degree of PEGylation: No more than 9 PEG appear attached. More likely, the number is closer to the estimate derived from mass spectrometry, 6 or 7. In summary, the targets are composed of 26 wt % drug and 9 PEG arms for **1**, 28 wt % drug and 8 PEG arms for **2**, and 30 wt % drug and 6.5 PEG arms for **3**, respectively (Table 1). Two Bolton-Hunter groups are incorporated into the PEGylated dendrimers for biodistribution study. The installation of the reporting groups was followed by ^1H NMR spectroscopy.

Biological Assessment. Cellular and in vivo toxicities of **1**−**3** were evaluated using an MTT assay. Briefly, the IC_{50} value reflects concentration required to inhibit 50% of cell growth compared with untreated control over a 72 h incubation (*56, 57*). In the assay, free paclitaxel administered as a DMSO solution showed an IC_{50} of 4.5 nM. The cytotoxicity of **1** was approximately 29 nM regardless of whether it was administered with or without 1 mM glutathione or 1 mM dithiothreitol. The toxicities of **2** and **3**, in contrast, increased from 74 nM without reductant to ~26 nM in the presence of 1 mM glutathione to ~13 nM in the presence of 1 mM dithiothreitol. While the similarities in toxicities between **2** and **3** are expected, we recognize a slight disparity between these values and that of **1**;

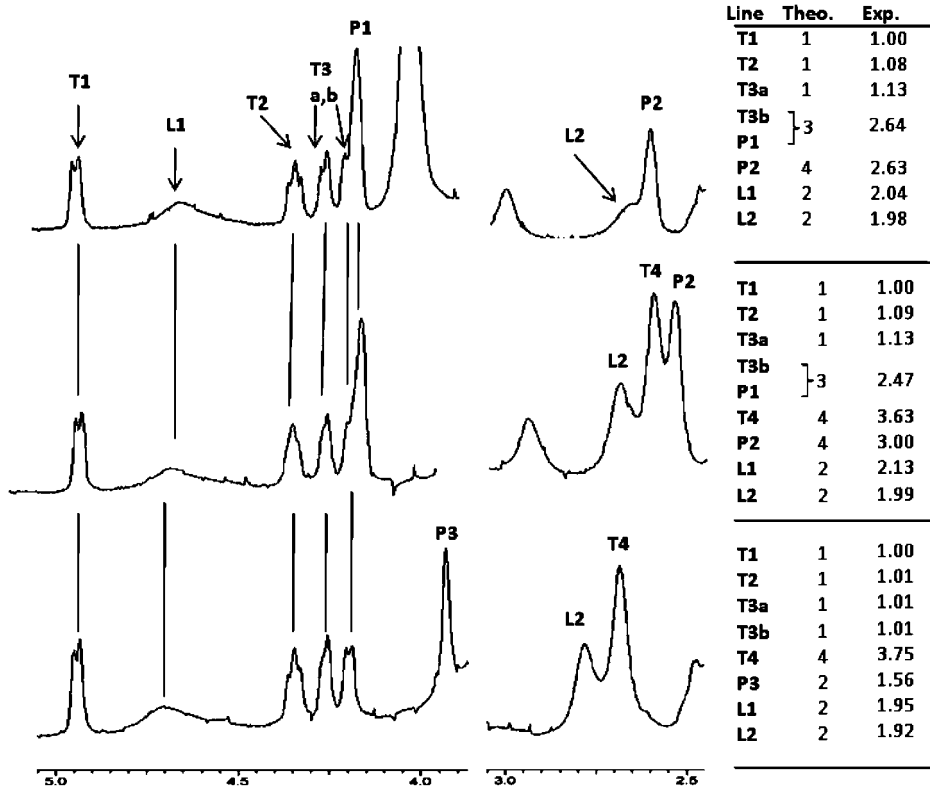

Line	Theo.	Exp.
T1	1	1.00
T2	1	1.08
T3a	1	1.13
T3b	3	2.64
P1		
P2	4	2.63
L1	2	2.04
L2	2	1.98
T1	1	1.00
T2	1	1.09
T3a	1	1.13
T3b	3	2.47
P1		
T4	4	3.63
P2	4	3.00
L1	2	2.13
L2	2	1.99
T1	1	1.00
T2	1	1.01
T3a	1	1.01
T3b	1	1.01
T4	4	3.75
P3	2	1.56
L1	2	1.95
L2	2	1.92

Figure 1. ^{1}H NMR of the PEGylated dendrimers, **1**, **2**, and **3** in $CDCl_3$/MeOH-d_4 (10:1).

Table 1. Chemical and Pharmacokinetic Summary of Dendrimers (1−3)

		paclitaxel		PEG (2 kDa)		half-lives (h)	
dendrimer	MW (kDa)	number	linker	number	linker	$t_{1/2\alpha}$	$t_{1/2\beta}$
1	38.8	12	ester	9	ester	0.4	15.3 ± 0.8
2	37.8	12	ester/disulfide	8	ester	0.4	19.3 ± 2.1
3	32.9	12	ester/disulfide	6.5	ether	0.4	19.6 ± 0.7

that is, we would have expected all three constructs to behave equally in the absence of reductant. The drug-free control dendrimer was not evaluated, as similar PEGylated architectures show no toxicity up to millimolar concentrations.

On the basis of the results of the cytotoxicity study, dendrimer **1** was examined in vivo as a prelude to more detailed efficacy evaluations. Five Balb/c mice were given three doses intravenously of 60 mg/kg on days 0, 4, and 8, a dose corresponding to three times the maximum tolerated dose of paclitaxel. None of the mice showed any adverse effects over the whole experimental period of three weeks based on visual inspection of the organs or measured levels of alanine transaminase or blood urea nitrogen levels as compared to a control group of 5 mice that were administered saline on the same days. We believe that the observed low systemic toxicity coupled with the hypothesized selective accumulation (and release) in a tumor may offer an opportunity for therapeutic relevance. The results of such studies will be reported in due course.

Biodistribution Studies in Tumor-Bearing Mice. In vivo pharmacokinetics of **1**, **2**, and **3** was evaluated in PC-3 bearing SCID mice. As shown in Table 1, the distribution half-lives ($t_{1/2\alpha}$) to other organs appeared almost same (0.4 h) in all three dendrimers. The elimination half-lives ($t_{1/2\beta}$) were significantly shorter than those predicted from the previous biodistribution results: **1** (15.3 h), **2**(19.3 h), **3** (19.6 h). The predicted elimination half-lives for these three dendrimers was ∼30 h. Previously, we examined the relationship of molecular weight and elimination half-life over different classes of PEGylated dendrimers including polyesters, polylysines, and polytriazines (*25*). The plot suggested, regardless of the dendrimer class, the elimination half-lives were closely related to the number of PEG chains and molecular weight. Dendrimers **1**, **2**, and **3** (6.5 to 9 PEG chains and 33 to 39 kDa) were predicted to have about 30 h of elimination half-life considering the previously observed trends (Supporting Information). The shorter elimination half-lives of **1**, **2**, and **3** suggest that drug loading can affect biodistribution times.

The smallest dendrimer, **3** (32.9 kDa), containing the fewest PEG arms (6.5) showed a similar or longer elimination half-life compared to **2** and **3.** At this time, we are not willing to attribute this to stability of the PEG attachment or the likelihood that **3** may aggregate into polymeric micelles due to increased hydrophobicity communicated by a more exposed core.

Tumor localization was observed for all three dendrimers. Our interest in these dendrimers as generic platforms for drug delivery led us to measure tumor-to-blood and tumor-to-muscle ratios. Dendrimer **2** showed the highest tumor-to-blood ratio (1.7 to 1) and the highest tumor-to-muscle ratio (23.8 to 1) at 48 h postinjection (Figure 2). The dendrimers accumulated in liver and spleen presumably due to the sequestration by the reticuloendothelial system (RES). Satisfyingly, the majority of the dendrimers were excreted through urine (35−55%ID), while less than 4%ID were found in the feces (Table 2). The trend of decreasing liver and spleen accumulation over time coupled with little fecal elimination suggests that these materials warrant additional investigation even in light of the relatively low tumor accumulation observed. This level of tumor accumulation is not

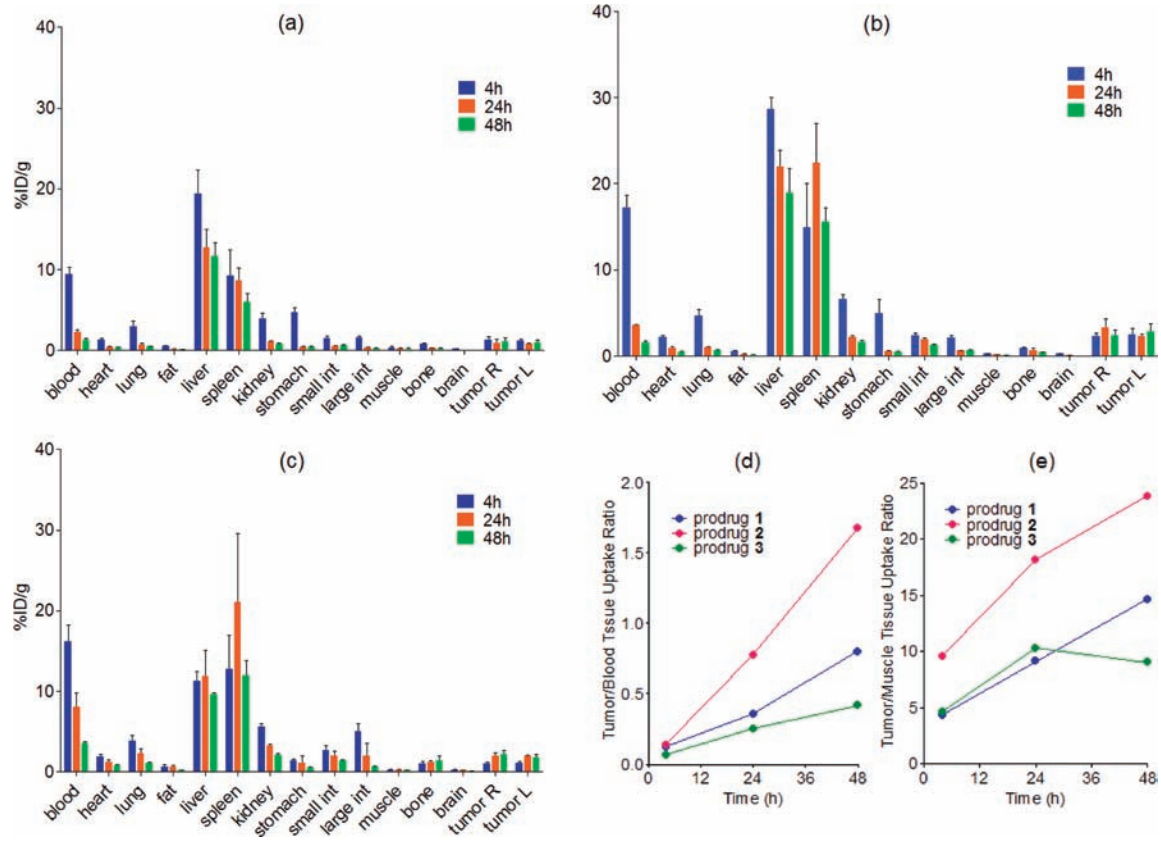

Figure 2. Biodistribution and tumor localization of the prodrugs (**1**−**3**) in SCID mice bearing PC-3 xenografts: (a) for **1**, (b) for **2**, and (c) for **3**; (d) and (e) showing tumor/blood and tumor/muscle uptake ratios at different time points, respectively.

Table 2. Cumulative Excretion Data of 1, 2, and 3 Found in the Urine and Feces

	%ID in urine			%ID in feces		
dendrimer	24 h	48 h	72 h	24 h	48 h	72 h
1	26.6	31.5	34.8	1.6	2.1	2.5
2	42.7	49.7	54.9	2.7	3.3	3.8
3	33.1	37.9	40.7	2.2	2.7	3.2

inconsistent with other macromolecular drug delivery constructs including poly(lysine) dendrimers decorated with camptothecin that have been described by Szoka and Fréchet (*58*). For comparison, and unlike Abraxane and Taxol formulations, tumor accumulation in mice appears rapid and sustained over time even with diminished levels in blood and organs. In contrast, both Taxol and Abraxane formulations show peak tumor levels within 2−3 h and drop significantly (∼3×) by 24 h (*59*). Separately, in rats both Taxol and Abraxane showed similar distributions in organs. Interesting, these distributions differ from those reported here. In addition, the primary route for elimination was fecal for Taxol and Abraxane constructs (*60*). This distinction should be taken with caution, as the reported constructs were evaluated by labeling the triazine dendrimer, whereas the preclinical studies involving Taxol and Abraxane reports rely on monitoring tritiated drug directly.

CONCLUSIONS

The three dendrimers (**1**, **2**, and **3**) provide compelling evidence that intercepting the iterative, divergent synthesis of triazine dendrimers with elaborate and reactive dichlorotriazines is an effective strategy for elaboration of these materials into candidate vehicles for drug delivery. The chemistry proceeds to yield pure material upon silica gel chromatography. Capping the resulting poly(monochlorotriazine) dendrimer with a diamine with differential reactivity followed by PEGylation provides materials whose composition is assignable, but are inherently more difficult to characterize due to heterogeneity within the PEG and incomplete reaction. The targets contain twelve molecules of paclitaxel (26−30 wt % drug) and six to nine PEG arms (43−54 wt % PEG). The targets described offer an entry point to probe hypotheses that range from the physical organic chemistry of drug release in vitro and in vivo, efficacy, to the impact the hydrolytically sensitive PEGs have on biodistribution. These constructs appear to be well tolerated in vivo at doses equal to 200% the maximum tolerated dose of paclitaxel. This low toxicity offers a variety of strategies for dosing. Tumor localization for the three dendrimers was observed at low levels, consistent with other formulations. The elimination half-lives were similar across all three constructs, but shorter than expected from previous studies. This observation suggests that drug may influence distribution times. Perhaps most interestingly, the distribution and route of elimination for these constructs appear to differ from those of current clinical interest, namely the free drug formulations of Taxol and Abraxane, although direct comparison is slightly more tenuous as our efforts track labeled dendrimer and not labeled drug. Further biological evaluation including in vivo efficacy study will be reported in due course.

ACKNOWLEDGMENT

We thank the National Institutes of Health (NIGMS R01 45650) and the Robert A. Welch Foundation (A 1430) for support.

Supporting Information Available: Experimental procedures, spectra, biodistribution data, and the plot of molecular

weight against elimination half-life. This material is available free of charge via the Internet at http://pubs.acs.org.

LITERATURE CITED

(1) Haag, R., and Kratz, F. (2006) Polymer therapeutics: Concepts and applications. *Angew. Chem., Int. Ed. 45*, 1198–1215.

(2) Esfand, R., and Tomalia, D. A. (2001) Poly(amidoamine) (PAMAM) dendrimers: from biomimicry to drug delivery and biomedical applications. *Drug Discovery Today 6*, 427–436.

(3) Duncan, R. (2003) The dawning era of polymer therapeutics. *Nat. Rev. Drug Discovery 2*, 347–360.

(4) Putnam, D. (2008) Drug delivery: the heart of the matter. *Nat. Mater. 7*, 836–837.

(5) Aulenta, F., Hayes, W., and Rannard, S. (2003) Dendrimers: a new class of nanoscopic containers and delivery devices. *Eur. Polym. J. 39*, 1741–1771.

(6) Nasongkla, N., Bey, E., Ren, J., Ai, H., Khemtong, C., Guthi, J. S., Chin, S.-F., Sherry, A. D., Boothman, D. A., and Gao, J. (2006) Multifunctional polymeric micelles as cancer-targeted, MRI-ultrasensitive drug delivery systems. *Nano Lett. 6*, 2427–2430.

(7) Lee, Y., Mo, H., Koo, H., Park, J.-Y., Cho, M. Y., Jin, G.-W., and Park, J.-S. (2007) Visualization of the degradation of a disulfide polymer, linear poly(ethylenimine sulfide), for gene delivery. *Bioconjugate Chem. 18*, 13–18.

(8) Luten, J., Nostrum, C. F. V., Smedt, S. C. D., and Hennink, W. E. (2008) Biodegradable polymers as non-viral carriers for plasmid DNA delivery. *J. Controlled Release 126*, 97–110.

(9) Germershaus, O., Merdan, T., Bakowsky, U., Behe, M., and Kissel, T. (2006) Trastuzumab-polyethylenimine-polyethylene glycol conjugates for targeting Her2-expressing tumors. *Bioconjugate Chem. 17*, 1190–1199.

(10) Dautzenberg, H., Zintchenko, A., Konak, C., Reschel, T., Subr, V., and Ulbrich, K. (2001) Polycationic graft copolymers as carriers for oligonucleotide delivery. Complexes of oligonucleotides with polycationic graft copolymers. *Langmuir 17*, 3096–3102.

(11) Wang, F., Bronich, T. K., Kabanov, A. V., Rauh, R. D., and Roovers, J. (2005) Synthesis and evaluation of a star amphiphilic block copolymer from poly(c-caprolactone) and poly(ethylene glycol) as a potential drug delivery carrier. *Bioconjugate Chem. 16*, 397–405.

(12) Fichter, K. M., Zhang, L., Kiick, K. L., and Reineke, T. M. (2008) Peptide-functionalized poly(ethylene glycol) star polymers: DNA delivery vehicles with multivalent molecular architecture. *Bioconjugate Chem. 19*, 76–88.

(13) Mammen, M., Choi, S. -K., and Whitesides, G. M. (1998) Polyvalent interactions in biological systems: Implications for design and use of multivalent ligands and inhibitors. *Angew. Chem., Int. Ed. 37*, 2754–2794.

(14) Fréchet, J. M. J., and Tomalia, D. A. (2001) *Dendrimers and Other Dendritic Polymers*, Wiley, Chichester.

(15) Boas, U., and Heegaard, P. M. H. (2004) Dendrimers in drug research. *Chem. Soc. Rev. 33*, 43–63.

(16) Cloninger, M. J. (2002) Biological applications of dendrimers. *Curr. Opin. Chem. Biol. 6*, 742–748.

(17) Gillies, E. R., Dy, E., Fréchet, J. M. J., and Szoka, F. C. (2005) Biological evaluation of polyester dendrimer: Poly(ethylene oxide) "bow-tie" hybrids with tunable molecular weight and architecture. *Mol. Pharmaceutics 2*, 129–138.

(18) Chen, H. T., Neerman, M. F., Parrish, A. R., and Simanek, E. E. (2004) Cytotoxicity, hemolysis, and acute in vivo toxicity of dendrimers based on melamine, candidate vehicles for drug delivery. *J. Am. Chem. Soc. 126*, 10044–10048.

(19) Matsumura, Y., and Maeda, H. (1986) A new concept for macromolecular therapeutics in cancer chemotherapy: mechanism of tumoritropic accumulation of proteins and the antitumor agent smancs. *Cancer Res. 6*, 6387–6392.

(20) Greish, K., Fang, J., Inutsuka, T., Nagamitsu, A., and Maeda, H. (2003) Macromolecular therapeutics: Advantages and prospects with special emphasis on solid tumour targeting. *Clin. Pharmacokinet. 42*, 1089–1105.

(21) Feng, X., Taton, D., Ibarboure, E., Chaikof, E. L., and Gnanou, Y. (2008) Janus-type dendrimer-like poly(ethylene oxide)s. *J. Am. Chem. Soc. 130*, 11662–11676.

(22) Goodwin, A. P., Lam, S. S., and Fréchet, J. M. J. (2007) Rapid, efficient synthesis of heterobifunctional biodegradable dendrimers. *J. Am. Chem. Soc. 129*, 6994–6995.

(23) Steffensen, M. B., and Simanek, E. E. (2004) Synthesis and manipulation of orthogonally protected dendrimers: building blocks for library synthesis. *Angew. Chem., Int. Ed. 43*, 5178–5180.

(24) Lim, J., and Simanek, E. E. (2005) Toward the next-generation drug delivery vehicle: Synthesis of a dendrimer with four orthogonally reactive groups. *Mol. Pharmaceutics 2*, 273–277.

(25) Lim, J., Guo, Y., Rostollan, C. L., Stanfield, J., Hsieh, J. -T., Sun, X., and Simanek, E. E. (2008) The role of the size and number of polyethylene glycol chains in the biodistribution and tumor localization of triazine dendrimers. *Mol. Pharmaceutics 5*, 540–547.

(26) Steffensen, M. B., and Simanek, E. E. (2003) Chemoselective building blocks for dendrimers from relative reactivity data. *Org. Lett. 5*, 2359–2361.

(27) Zhang, W., Tichy, S. E., Pérez, L. M., Maria, G., Lindahl, P. A., and Simanek, E. E. (2003) Evaluation of multivalent dendrimers based on melamine: kinetics of thiol-disulfide exchange depends on the structure of the dendrimer. *J. Am. Chem. Soc. 125*, 5086–5094.

(28) Chouai, A., and Simanek, E. E. (2008) Kilogram-scale synthesis of a second-generation dendrimer based on 1,3,5-triazine using green and industrially compatible methods with a single chromatographic step. *J. Org. Chem. 73*, 2357–2366.

(29) Hollink, E., and Simanek, E. E. (2006) A divergent route to diversity in macromolecules. *Org. Lett. 8*, 2293–2295.

(30) Lim, J., and Simanek, E. E. (2008) Synthesis of water-soluble dendrimers based on melamine bearing 16 paclitaxel groups. *Org. Lett. 10*, 201–204.

(31) Patri, A. K., Kukowska-Latallo, J. F., and Baker, J. R. J. (2005) Targeted drug delivery with dendrimers: Comparison of the release kinetics of covalently conjugated drug and non-covalent drug inclusion complex. *Adv. Drug Delivery Rev. 57*, 2203–2214.

(32) Safavy, A., Georg, G. I., Velde, D. V., Raisch, K. P., Safavy, K., Carpenter, M., Wang, W., Bonner, J. A., Khazaeli, M. B., and Buchsbaum, D. J. (2004) Site-specifically traced drug release and biodistribution of a paclitaxel-antibody conjugate toward improvement of the linker structure. *Bioconjugate Chem. 15*, 1264–1274.

(33) Gillies, E. R., Goodwin, A. P., and Fréchet, J. M. J. (2004) Acetals as pH-sensitive linkages for drug delivery. *Bioconjugate Chem. 15*, 1254–1263.

(34) Cui, W., Qi, M., Li, X., Huang, S., Zhou, S., and Weng, J. (2008) Electrospun fibers of acid-labile biodegradable polymers with acetal groups as potential drug carriers. *Int. J. Pharm. 361*, 47–55.

(35) Lee, C. C., Gillies, E. R., Fox, M. E., Guillaudeu, S. J., Fréchet, J. M. J., Dy, E. E., and Szoka, F. C. (2006) A single dose of doxorubicin-functionalized bow-tie dendrimer cures mice bearing C-26 colon carcinomas. *Proc. Natl. Acad. Sci. U.S.A. 103*, 16649–16654.

(36) Guan, H., McGuire, M. J., Li, S., and Brown, K. C. (2008) Peptide-targeted polyglutamic acid doxorubicin conjugates for the treatment of $\alpha_v\beta_6$-positive cancers. *Bioconjugate Chem. 19*, 1813–1821.

(37) El-Sayed, M. E. H., Hoffman, A. S., and Stayton, P. S. (2005) Rational design of composition and activity correlations for pH-responsive and glutathione-reactive polymer therapeutics. *J. Controlled Release 104*, 417–427.

(38) Satchi, R., Connors, T. A., and Duncan, R. (2001) PDEPT: Polymer directed enzyme prodrug therapy. I. HPMA copolymer-

cathepsin B and PK1 as a model combination. *Br. J. Cancer 85*, 1070–1076.
(39) Scripture, C. D., Figg, W. D., and Sparreboom, A. (2005) Paclitaxel chemotherapy: from empiricism to a mechanism-based formulation strategy. *Ther. Clin. Risk Manage. 1*, 107–114.
(40) Crown, J., O'Leary, M., and Ooi, W. S. (2004) Docetaxel and paclitaxel in the treatment of breast cancer: a review of clinical experience. *Oncologist 9*, 24–32.
(41) Singla, A. K., Garg, A., and Aggarwal, D. (2002) Paclitaxel and its formulations. *Int. J. Pharm. 235*, 179–192.
(42) Blum, J. L., Savin, M. A., Edelman, G., Pippen, J. E., Robert, N. J., Geister, B. V., Kirby, R. L., Clawson, A., and O'Shaughnessy, J. A. (2007) Phase II study of weekly albumin-bound paclitaxel for patients with metastatic breast cancer heavily pretreated with taxanes. *Clin. Breast Cancer 7*, 850–856.
(43) Hawkins, M. J., Soon-Shiong, P., and Desai, N. (2008) Protein nanoparticles as drug carriers in clinical medicine. *Adv. Drug Delivery Rev. 60*, 876–885.
(44) Bonomi, P. (2007) Paclitaxel poliglumex (PPX, CT-2103): macromolecular medicine for advanced non-small-cell lung cancer. *Expert Rev. Anticancer Ther. 7*, 415–422.
(45) Albain, K. S., Belani, C. P., Bonomi, P., O'Byrne, K. J., Schiller, J. H., and Socinski, M. (2006) PIONEER: a phase III randomized trial of paclitaxel poliglumex versus paclitaxel in chemotherapy-naive women with advanced-stage non-small-cell lung cancer and performance status of 2. *Clin. Lung Cancer 7*, 417–419.
(46) Beeram, M., Rowinsky, E. K., Hammond, L. A., Patnaik, A., Schwartz, G. H., de Bono, J. S., Forero, L., Forouzesh, B., Berg, K. E., Rubin, E. H., Beers, S., Killian, A., Kwiatek, J., McGuire, J., Spivey, L., and Takimoto, C. H. (2002) A phase I pharmacokinetic (PK) study of PEG-pacltiaxel in patients with advanced solid tumors. *Proc. Am. Soc. Clin. Oncol. 21*, 405.
(47) Meerum Terwogt, J. M., ten Bokkel Huinink, W. W., Schellens, J. H., Schot, M., Mandjes, I. A., Zurlo, M. G., Rocchetti, M., Rosing, H., Koopman, F. J., and Beijnen, J. H. (2001) Phase I clinical and pharmacokinetic study of PNU166945, a novel water-soluble polymer-conjugated prodrug of paclitaxel. *Anticancer Drugs 12*, 315–323.
(48) Khandare, J. J., Jayant, S., Singh, A., Chandna, P., Wang, Y., Vorsa, N., and Minko, T. (2006) Dendrimer versus linear conjugate: Influence of polymeric architecture on the delivery and anticancer effect of paclitaxel. *Bioconjugate Chem. 17*, 1464–1472.
(49) Gao, Y., Chen, L., Gu, W., Xi, Y., Lin, L., and Li, Y. (2008) Targeted nanoassembly loaded with docetaxel improves intracellular drug delivery and efficacy in murine breast cancer model. *Mol. Pharmaceutics 5*, 1044–1054.
(50) Vrudhula, V. M., MacMaster, J. F., Li, Z., Kerr, D. E., and Senter, P. D. (2002) Reductively activated disulfide prodrugs of paclitaxel. *Bioorg. Med. Chem. Lett. 12*, 3591–3594.
(51) Majoros, I. J., Myc, A., Thomas, T., Mehta, C. B., and Baker, J. R. (2006) PAMAM dendrimer-based multifunctional conjugate for cancer therapy: synthesis, characterization, and functionality. *Biomacromolecules 7*, 572–579.
(52) Papas, S., Akoumianaki, T., Kalogios, C., Hadjiarapolglou, L., Theodoropoulous, P. A., and Tsikaris, V. (2007) Synthesis and antitumor activity of peptide-paclitaxel conjugates. *J. Pept. Sci. 13*, 662–671.
(53) El Alaoui, A., Saha, N., Schmidt, F., Monneret, C., and Florent, J. -C. (2006) New Taxol (paclitaxel) prodrugs designed for ADEPT and PMT strategies in cancer chemotherapy. *Bioorg. Med. Chem. Lett. 14*, 5012–5019.
(54) Zou, Y., Fu, H., Ghosh, S., Farquhar, D., and Klostergaard, J. (2004) Antitumor activity of hydrophilic paclitaxel copolymer prodrug using locoregional delivery in human orthotopic non-small cell lung cancer xenograft models. *Clin. Cancer Res. 10*, 7382–7391.
(55) Guillemard, V., and Saragovi, H. U. (2001) Taxane-antibody conjugates afford potent cytotoxicity, enhanced solubility, and tumor target selectivity. *Cancer Res. 61*, 694–699.
(56) Concentrations reported for biological assessment are referenced to the dendrimer. Correction of these values for the concentration of paclitaxel requires multiplication by 12.
(57) FN: For **1**, 34 nM w/o (23−50 nM 95% confidence interval); 24 nM with 1 mM GSH (17−32 nM 95% confidence interval); 30 nM with 1 mM DTT (16−58 nM 95% confidence interval). For **2**, 74 nM w/o (45−121 nM 95% confidence interval); 28 nM with 1 mM GSH (21−37 nM 95% confidence interval); 16 nM with 1 mM DTT (11−24 nM 95% confidence interval). For **3**, 74 nM w/o (61−90 nM 95% confidence interval); 25 nM with 1 mM GSH (17−34 nM 95% confidence interval); 11 nM with 1 mM DTT (7−20 nM 95% confidence interval). For paclitaxel, 4.5 nM (2.9−7.0 nM 95% confidence interval).
(58) Fox, M. E., Guillaudeu, S., Fréchet, J. M. J., Jerger, K., Macaraeg, N., and Szoka, F. C. (2009) Synthesis and in vivo antitumor efficacy of PEGylated poly(L-lysine) dendrimer-camptothecin conjugates. *Mol. Pharmaceutics*, In press.
(59) Deasi, N., Trieu, V., Yao, Z., Louie, L., Ci, S., Yang, A., Tao, C., De, T., Beals, B., Dykes, D., Noker, P., Yao, R., Labao, E., Hawkins, M., and Soon-Shiong, P. (2006) Increased antitumor activity, intratumor paclitaxel concentrations, and endothelial cell transport of cremophor-free, albumin-bound paclitaxel, ABI-007, compared with cremophor-based paclitaxel. *Clin. Cancer Res. 12*, 1317–1324.
(60) Sparreboom, A., Scripture, C. D., Trieu, V., Williams, P. J., De, T., Yang, A., Beals, B., Figg, W. D., Hawkins, M., and Desai, N. (2005) Comparative preclinical and clinical pharmacokinetics of a cremophor-free, nanoparticle albumin-bound paclitaxel (ABI-007) and paclitaxel formulated in cremophore (Taxol). *Clin. Cancer Res. 11*, 4136–4143.

BC900324Z

Supporting Information For

Design, Synthesis, Characterization, and Biodistribution of Triazine Dendrimers Bearing Paclitaxel linked by Ester and Ester/Disulfide Linkages

Jongdoo Lim,[†] Abdellatif Chouai,[†] Su-Tang Lo,[‡] Wei Liu,[‡] Xiankai Sun,[‡] and Eric E. Simanek[†,]*

[†]Department of Chemistry, Texas A&M University, College Station, Texas 77843-3255, and

[‡]Department of Radiology, University of Texas Southwestern Medical Center, Dallas, Texas 75390

Table of Contents

page

Experimental Procedures.....S2

Spectra..... S6

Biodistribution Data …..... S35

The Plot of Molecular Weight against Elimination Half-Life…….…….. S42

MALDI-TOF Spectra of **7** and **8**..... S43

GPC Traces of the PEGylated Dendrimers..... S44

Experimental Procedures

G2-(Taxol-COO-CS-PEG)$_{12}$ (1). A solution of 4-aminomethylpiperidine (0.73 g, 6.38 mmol) in chloroform (10 mL) was added to a solution of **7** (1.47 g, 8.86*10^{-2} mmol) in chloroform (90 mL), THF (20 mL), and methanol (0.5 mL). The solution was stirred under nitrogen for 16 h at room temperature. The solution was washed two times with brine, dried over $MgSO_4$, filtered, and then the volume was reduced to 40 mL *in vacuo*. After addition of DIPEA (0.4 mL, 2.30 mmol) and a solution of NHS-mPEG (CS type, MW 2 kDa, 2.80 g, 1.40 mmol) in dichloromethane (10 mL), the reaction solution was stirred under nitrogen for 24 h at room temperature and concentrated *in vacuo*. The residue was dissolved in deionized water and filtered. The resulting solution was diafiltrated to remove low molecular weight impurities using Amicon stirred ultrafiltration cell equipment and a YM 10 membrane (MWCO: 10 kDa) in deionized water over a week. The purified solution was evaporated under vacuum to afford **1** (3.07 g, 89% over two steps) as a colorless solid. The product was analyzed by size exclusion chromatography. ^{1}H NMR (500 MHz, $CDCl_3$+MeOH-d_4) δ 8.08 (d, *J* = 7.5, 24H), 7.72 (d, *J* = 7.5, 24H), 7.57 (t, *J* = 7.3, 12H), 7.49-7.25 (m, 120H), 6.30 (s, 12H), 6.10 (br, 12H), 5.88 (br, 12H), 5.64 (d, *J* = 6.5, 12H), 5.38 (d, *J* = 2.5, 12H), 4.93 (br d, *J* = 8.0, 12H), 4.65 (br, 24H), 4.33 (br, 12H), 4.24 (br, 12H), 4.19 (br, 12H), 3.75 (br, 12H), 3.61 (br m, PEG C**H$_2$**C**H$_2$**O), 3.34 (s, PEG C**H$_3$**O), 3.65-3.00 (br m, 216H), 2.60-1.46 (br m, 438H), 1.14 (s, 36H), 1.10 (s, 36H), 1.04 (br, 24H); MS (MALDI-TOF) calcd for complete PEGylation 45100, found 38800 $(M+H)^+$.

G2-(Taxol-COO-SS-CS-PEG)$_{12}$ (2). A solution of 4-aminomethylpiperidine (0.22 g, 1.93 mmol) in chloroform (10 mL) was added to a solution of **8** (0.47 g, 2.68*10^{-2} mmol) in chloroform (90 mL), THF (10 mL), and methanol (0.5 mL). The solution was stirred under nitrogen for 16 h at room temperature. The solution was washed two times with brine, dried over $MgSO_4$, filtered, and then the volume was reduced to 30 mL *in vacuo*. After addition of DIPEA (0.4 mL, 2.30 mmol) and a solution of NHS-mPEG (CS type, MW 2 kDa, 0.9 g, 0.45 mmol) in dichloromethane (10 mL), the reaction solution was stirred under nitrogen for 24 h at room temperature and concentrated *in vacuo*. The residue was dissolved in deionized water and filtered. The resulting solution was diafiltrated to remove low molecular weight impurities using Amicon stirred ultrafiltration cell equipment and a YM 10 membrane (MWCO: 10 kDa) in deionized water over a week. The purified solution was evaporated under vacuum to afford **2** (0.80 g, 79% over two steps) as a colorless solid. The product was analyzed by size exclusion chromatography. ^{1}H NMR (500 MHz, $CDCl_3$+MeOH-d_4) δ 8.09 (d, *J* = 7.5, 24H),

7.72 (d, *J* = 7.0, 24H), 7.57 (t, *J* = 7.3, 12H), 7.49-7.27 (m, 120H), 6.29 (s, 12H), 6.13 (br, 12H), 5.91 (br, 12H), 5.65 (d, *J* = 5.0, 12H), 5.39 (br, 12H), 4.93 (br d, *J* = 8.5, 12H), 4.68 (br, 24H), 4.35 (br, 12H), 4.25-4.20 (br m, 24H), 3.75 (br, 12H), 3.80-3.30 (m, PEG), 3.65-3.00 (br m, 216H), 2.80-1.40 (br m, 462H), 1.16 (s, 36H), 1.11 (s, 36H), 1.03 (br, 24H); MS (MALDI-TOF) calcd for complete PEGylation 46000, found 36600 $(M+H)^+$.

G2-(Taxol-COO-SS-AS-PEG)$_{12}$ (3). Dendrimer **3** (0.64 g, 73% over two steps) was synthesized using NHS-mPEG (AS type, MW 2 kDa) as described above. ^{1}H NMR (500 MHz, $CDCl_3$+MeOH-d_4) δ 8.09 (d, *J* = 7.5, 24H), 7.73 (d, *J* = 7.5, 24H), 7.58 (t, *J* = 7.0, 12H), 7.50-7.25 (m, 120H), 6.31 (s, 12H), 6.13 (br, 12H), 5.91 (br, 12H), 5.65 (br, 12H), 5.39 (br, 12H), 4.94 (br d, *J* = 8.5, 12H), 4.70 (br, 24H), 4.35 (br, 12H), 4.26 (br, 12H), 4.20 (br, 12H), 3.75 (br, 12H), 3.80-3.30 (m, PEG), 3.65-3.00 (br m, 216H), 2.80-1.40 (br m, 462H), 1.16 (s, 36H), 1.12 (s, 36H), 1.08 (br, 24H); MS (MALDI-TOF) calcd for complete PEGylation 46000, found 33900 $(M+H)^+$.

Installation of Bolton-Hunter Group on the PEGylated Dendrimers (1, 2, and 3). The NHS-ester Bolton-Hunter reagent (SHPP, 2.4 eq. based on PEGylated dendrimer) was added to the solution of the PEGylated dendrimer and DIPEA (3 eq. based on PEGylated dendrimer) in DCM (2 mL). The solution was stirred under N_2 for 24 h at room temperature and concentrated *in vacuo*. The residue was dissolved in deionized water and filtered. The resulting solution was diafiltrated to remove low molecular weight impurities using Amicon stirred ultrafiltration cell equipment and a YM 10 membrane (MWCO: 10 kDa) in deionized water over 3 d. The purified solution was evaporated under vacuum to afford a colorless solid. The product was analyzed by size exclusion chromatography.

Taxol-COO-SS-Cl$_2$ (6). First, the paclitaxel NHS-ester was prepared as previously reported.[30] To prepare cystamine, cystamine dihydrochloride was dissolved in a minimal amount of water, adjusted to pH 12 with 0.5 M NaOH, and then extracted with dichloromethane. A solution of the paclitaxel NHS-ester (3.30 g, 3.10 mmol) in dichloromethane (20 mL) was slowly added to an ice-bath cooled solution of cystamine (2.90 g, 19.04 mmol) and triethylamine (1.50 mL, 10.75 mmol) in dichloromethane (110 mL). After reaction under nitrogen for 30 min at 0 ^{o}C, the solution was neutralized with 1 M HCl, washed three times with brine, dried over $MgSO_4$, and then evaporated *in vacuo* to give the paclitaxel-cystamine as a white solid. A solution of cyanuric chloride (0.60, 3.25 mmol) in THF (10 mL) was added to an ice-bath cooled solution of the prepared paclitaxel-cystamine and DIPEA (1.0 mL, 5.73 mmol) in THF (60 mL). The solution was stirred for 1 h at 0 ^{o}C and concentrated *in vacuo*. The residue

was dissolved in dichloromethane, washed three times with brine, dried over $MgSO_4$, and then evaporated. The crude product was purified by silica gel chromatography (ethyl acetate:hexanes =4:1; TLC R_f = 0.21) to give **6** as a white solid (2.40 g, 62%). ^{1}H NMR (300 MHz, $CDCl_3$+MeOH-d_4) δ 8.09 (d, *J* = 6.9, 2H), 7.73 (d, *J* = 6.9, 2H), 7.59 (t, *J* = 7.1 Hz, 1H), 7.50-7.27 (m, 10H), 6.31 (s, 1H), 6.13 (t, *J* = 8.4, 1H), 5.91 (d, *J* = 3.9, 1H), 5.66 (d, *J* = 7.2, 1H), 5.41 (d, *J* = 3.9, 1H), 4.95 (d, *J* = 8.1, 1H), 4.34 (dd, *J* = 10.8, 6.6, 1H), 4.27 (d, *J* = 8.4, 1H), 4.21 (d, *J* = 8.4, 1H), 3.77 (d, *J* = 7.2, 1H), 3.68 (t, *J* = 6.5 Hz, 2H), 3.44 (m, 2H), 2.83 (t, *J* = 6.6 Hz, 2H), 2.72 (t, *J* = 6.6 Hz, 2H), 2.55-2.42 (m, 3H), 2.38 (s, 3H), 2.31-2.03 (m, 7H), 1.96-1.80 (m, 6H), 1.65 (s, 3H), 1.16 (s, 3H), 1.12 (s, 3H); ^{13}C NMR (75 MHz, $CDCl_3$+MeOH-d_4) δ 203.9, 173.4, 172.5, 171.0, 169.9, 169.5, 168.9, 168.8, 166.5, 165.7, 141.6, 136.6, 133.7, 133.4, 133.2, 131.9, 130.0, 129.5, 128.9, 128.5, 127.2, 126.7, 84.5, 81.0, 77.9, 76.5, 75.6, 74.9, 74.1, 72.0, 71.4, 58.1, 53.0, 45.8, 43.2, 40.0, 38.1, 37.2, 36.7, 35.7, 35.2, 34.6, 32.6, 26.4, 22.4, 21.8, 20.7, 14.3, 9.5; MS (MALDI-TOF) calcd for $C_{59}H_{66}Cl_2N_6O_{16}S_2$ 1248.3354, found 1271.3062 $(M+Na)^+$.

G2-(Taxol-COO-Cl)$_{12}$ (7). A solution of **4** (245 mg, 8.29*10^{-2} mmol) in water (2 mL) and THF (3 mL) was slowly added to a solution of **5** (1.43 g, 1.22 mmol) and DIPEA (0.4 mL, 2.30 mmol) in THF (15 mL). The solution was stirred for 48 h at room temperature and evaporated under vacuum. The residue was dissolved in dichloromethane, washed with brine, dried over $MgSO_4$, filtered, and evaporated under vacuum. The crude product was purified by silica gel chromatography (washed with ethyl acetate:dichloromethane:methanol = 8:8:1 and eluted with dichloromethane:methanol = 8:1; TLC R_f = 0.50 with DCM:MeOH = 8:1) to give **7** (1.18 g, 86%) as a white solid. The excess or unreacted paclitaxel-dichlorotriazine was recovered from the purification and reused. ^{1}H NMR (500 MHz, $CDCl_3$+MeOH-d_4) δ 8.11 (d, *J* = 6.0, 24H), 7.73 (br, 24H), 7.59 (br, 12H), 7.50-7.30 (m, 120H), 6.32 (s, 12H), 6.15 (br, 12H), 5.92 (br, 12H), 5.67 (br, 12H), 5.41 (br, 12H), 4.96 (d, *J* = 7.0, 12H), 4.36 (br, 12H), 4.27 (br, 12H), 4.22 (br, 12H), 3.88-3.16 (br m, 192H), 2.50-1.50 (br m, 378H), 1.17 (s, 36H), 1.13 (s, 36H); ^{13}C NMR (75 MHz, $CDCl_3$+MeOH-d_4) δ 203.8, 173.2, 172.3 (two lines), 170.9, 169.8, 168.8, 168.7, 166.5, 165.2, 164.8, 164.5, 141.6, 136.6, 133.7, 133.4, 133.1, 131.8, 130.0, 129.4, 128.9, 128.4 (br two lines), 127.2, 126.7, 84.4, 81.0, 77.8, 76.4, 75.6, 74.9, 74.1, 71.9, 71.4, 58.1, 53.0, 45.7, 44.1, 43.2 (br), 37.9 (br), 37.4(br), 36.6, 35.7 (br), 35.2 (br), 34.8 (br), 34.6, 32.7, 29.2, 28.7, 27.5 (br), 26.4, 25.7, 24.8, 22.4, 21.9, 20.7, 20.6, 14.4, 9.6; MS (MALDI-TOF) calcd for $C_{837}H_{1008}Cl_{12}N_{144}O_{192}$ 16566.98, found 16657.53 $(M+Na)^+$.

G2-(Taxol-COO-SS-Cl)$_{12}$ (8). A solution of **4** (175 mg, 5.92*10^{-2} mmol) in water (2 mL) and THF (3 mL) was slowly added to a solution of **6** (1.10 g, 0.88 mmol) and DIPEA (0.4 mL, 2.30 mmol) in THF (15 mL). The solution was stirred for 48 h at room temperature and evaporated under vacuum. The residue was dissolved in dichloromethane, washed with brine, dried over $MgSO_4$, filtered, and evaporated under vacuum. The crude product was purified by silica gel chromatography (washed with ethyl acetate:dichloromethane:methanol = 10:10:1 and eluted with dichloromethane:methanol = 8:1; TLC R_f = 0.50 with DCM:MeOH = 8:1) to give **8** (0.84 g, 81%) as a white solid. The excess or unreacted paclitaxel-dichlorotriazine was recovered from the purification and reused. ^{1}H NMR (300 MHz, $CDCl_3$+MeOH-d_4) δ 8.09 (d, *J* = 8.7, 24H), 7.73 (d, *J* = 7.2, 24H), 7.59 (t, *J* = 7.4 Hz, 12H), 7.52-7.28 (m, 120H), 6.33 (s, 12H), 6.14 (*J* = 8.9 Hz, 12H), 5.91 (d, *J* = 3.9, 12H), 5.67 (d, *J* = 6.6, 12H), 5.41 (d, *J* = 3.6, 12H), 4.95 (d, *J* = 9.3, 12H), 4.36 (dd, *J* = 10.7, 7.4, 12H), 4.27 (d, *J* = 8.4, 12H), 4.21 (d, *J* = 8.4, 12H), 3.80-3.20 (br m, 192H), 2.82-2.70 (br m, 48H), 2.50-1.50 (br m, 354H), 1.17 (s, 36H), 1.13 (s, 36H); ^{13}C NMR (75 MHz, $CDCl_3$+MeOH-d_4) δ 203.8, 173.2, 172.4, 170.8, 169.8, 168.8, 168.7, 166.4, 165.2, 164.8, 164.5, 141.6, 136.6, 133.7, 133.4, 133.1, 131.8, 130.0, 129.4, 128.9, 128.4, 127.2, 126.7, 84.5, 81.0, 77.8, 76.4, 75.5, 74.8, 74.1, 71.9, 71.3, 58.0, 53.0, 45.8, 44.1, 43.1 (br), 39.8, 38.1, 37.1, 35.7, 35.2, 34.5, 32.6, 27.5 (br), 26.3, 25.6, 24.8, 22.4, 21.8, 20.6, 14.3, 9.5; MS (MALDI-TOF) calcd for $C_{849}H_{1032}Cl_{12}N_{144}O_{192}S_{24}$ 17502.50, found 17480.67 $(M+H)^+$.

Dendrimer **1**

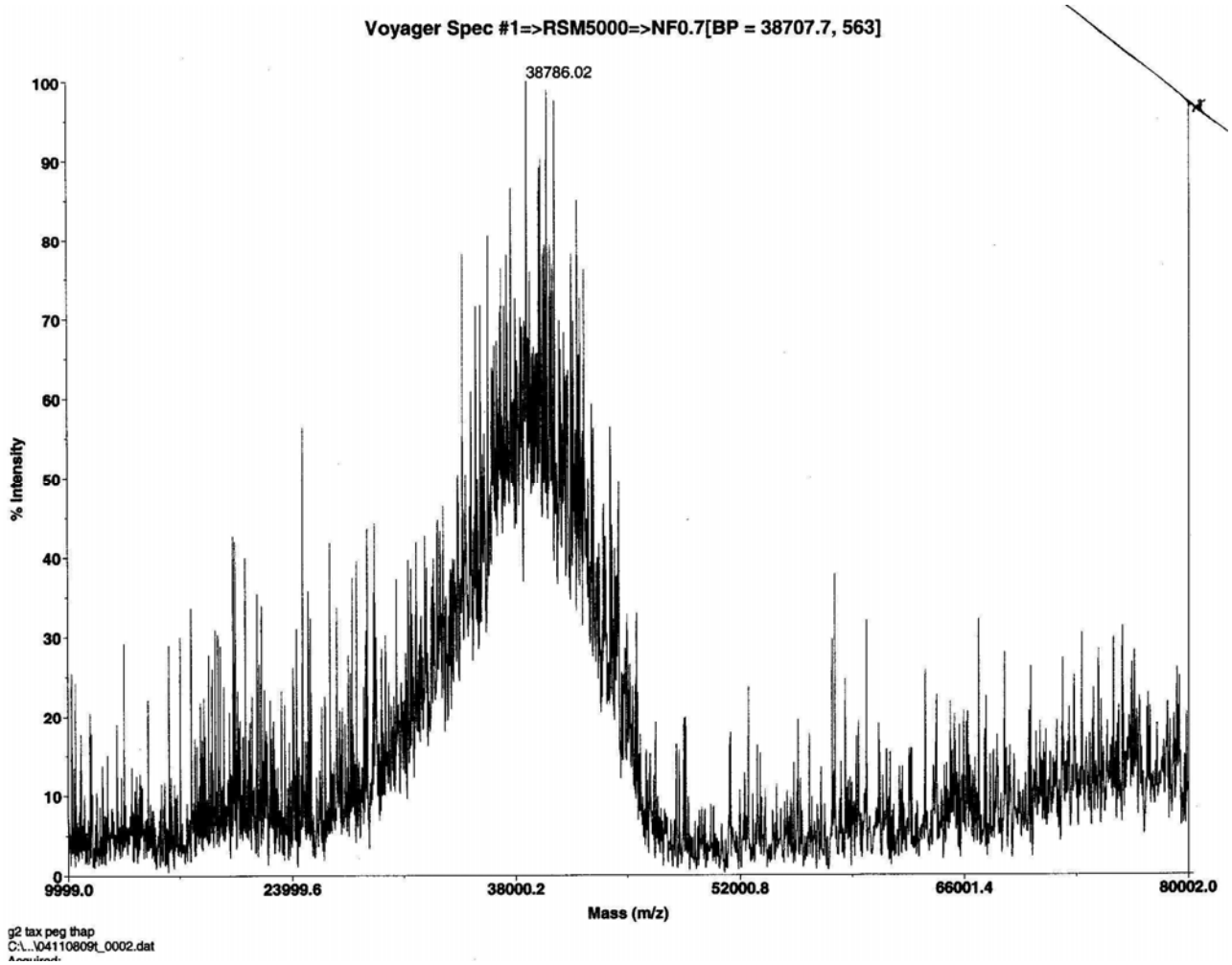
Voyager Spec #1=>RSM5000=>NF0.7[BP = 38707.7, 563]
38786.02
100
90
80
70
60
50
40
30
20
10
0
% Intensity
9999.0
23999.6
38000.2
52000.8
66001.4
80002.0
Mass (m/z)
g2 tax peg thap
C:\...\04110809t_0002.dat

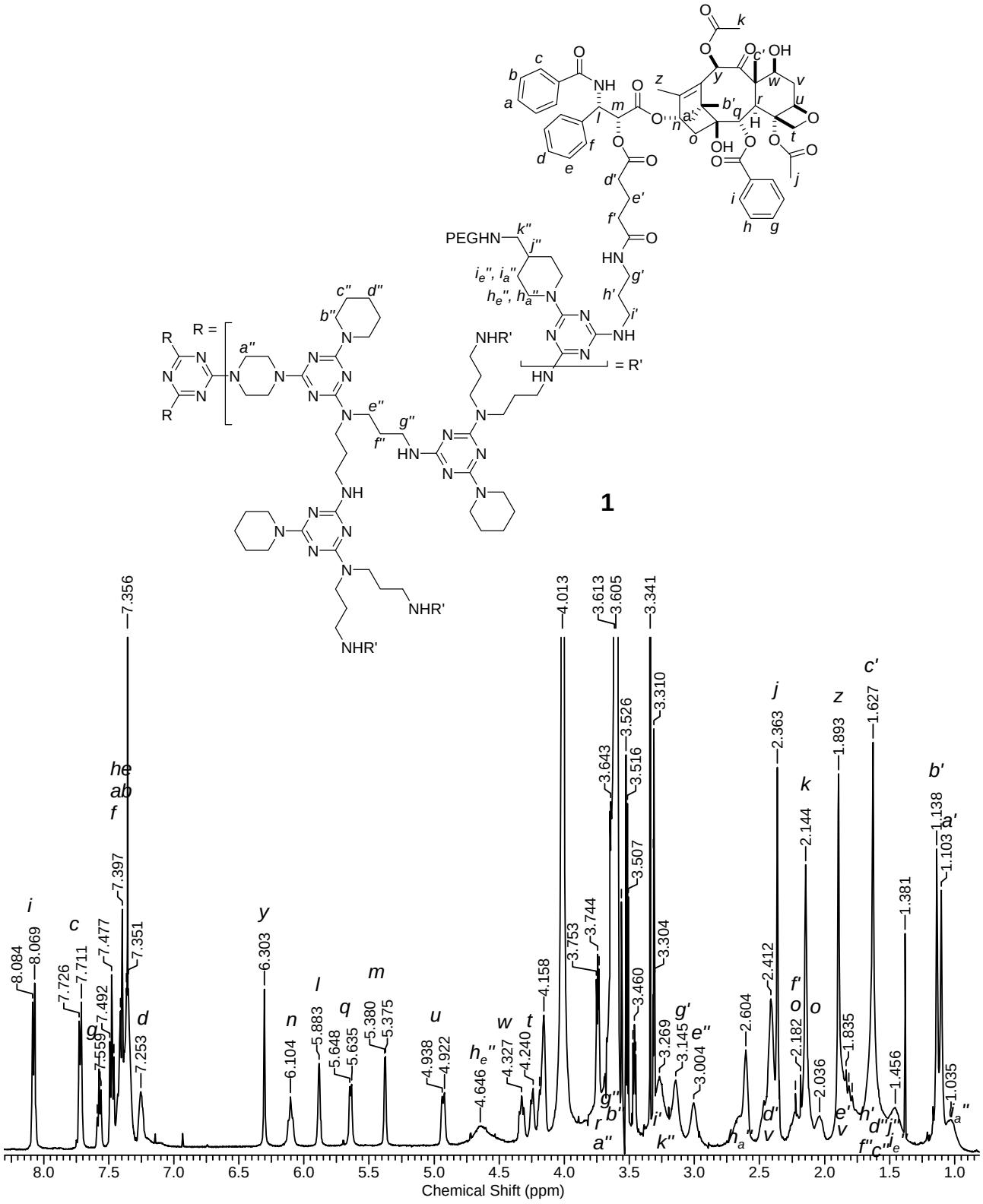
1
Chemical Shift (ppm)

Dendrimer **2**

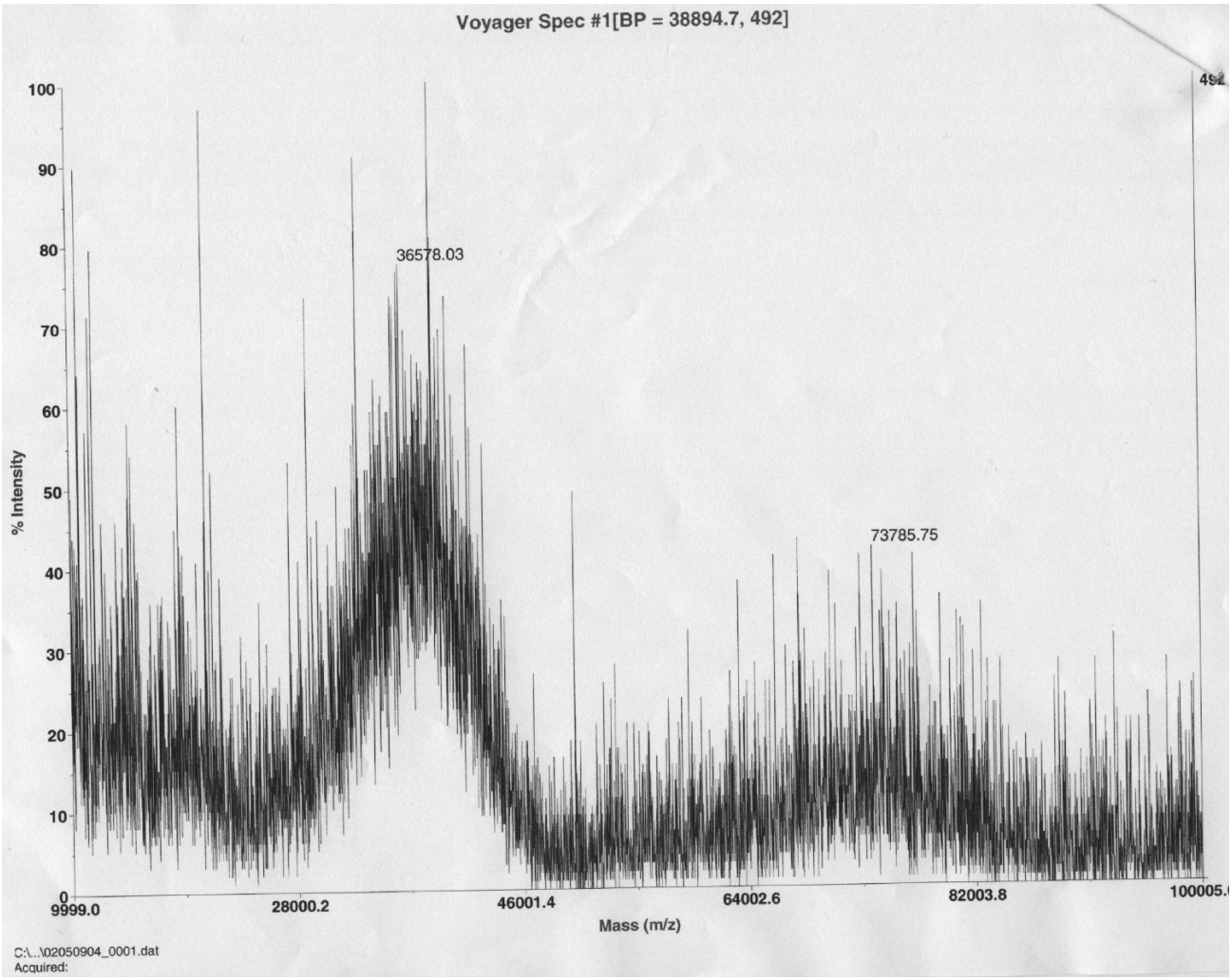
Voyager Spec #1[BP = 38894.7, 492]
% Intensity
Mass (m/z)
36578.03
73785.75
9999.0
28000.2
46001.4
64002.6
82003.8
C:\...\02050904_0001.dat
Acquired:

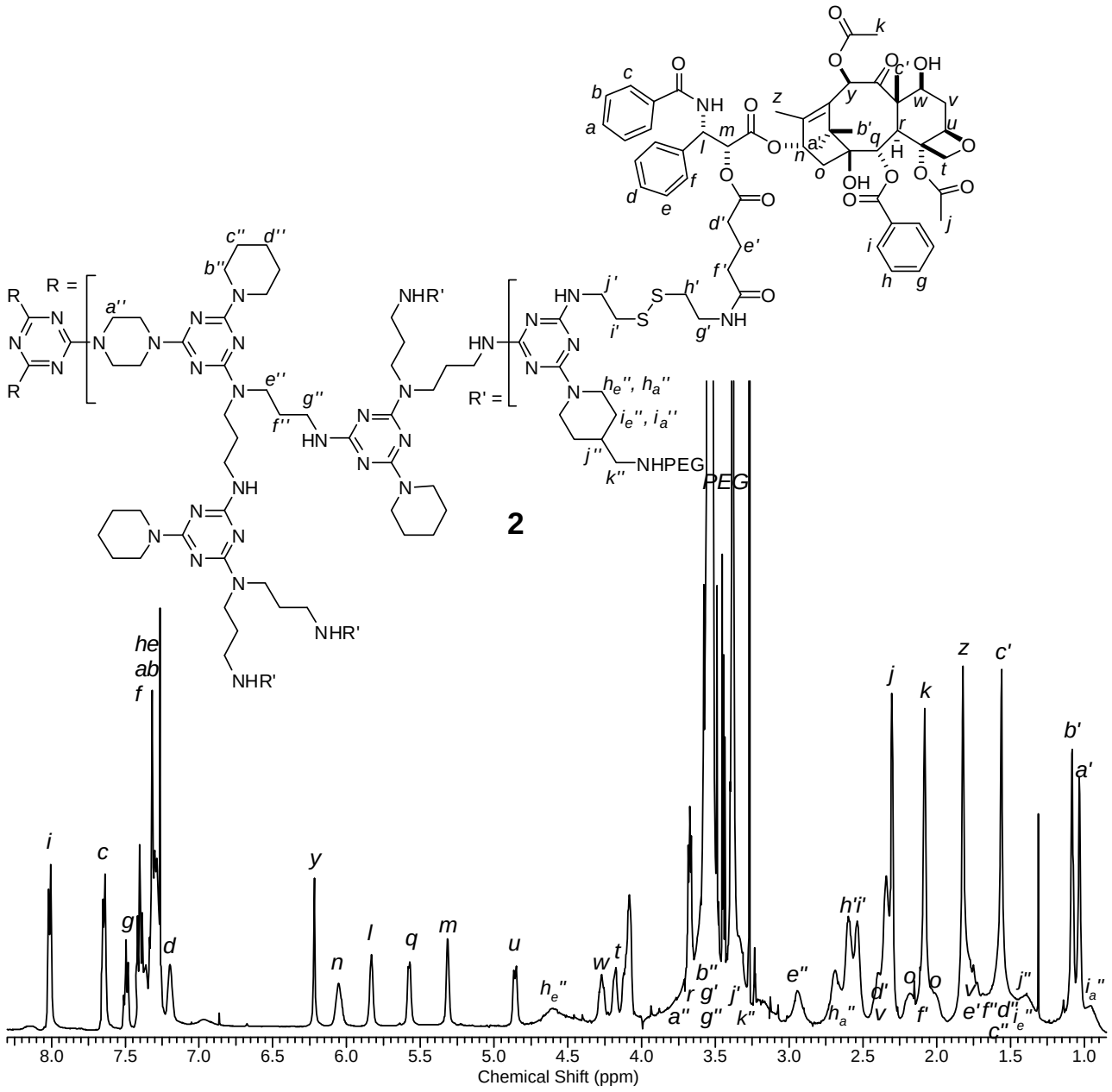
2
PEG
Chemical Shift (ppm)

Dendrimer **3**

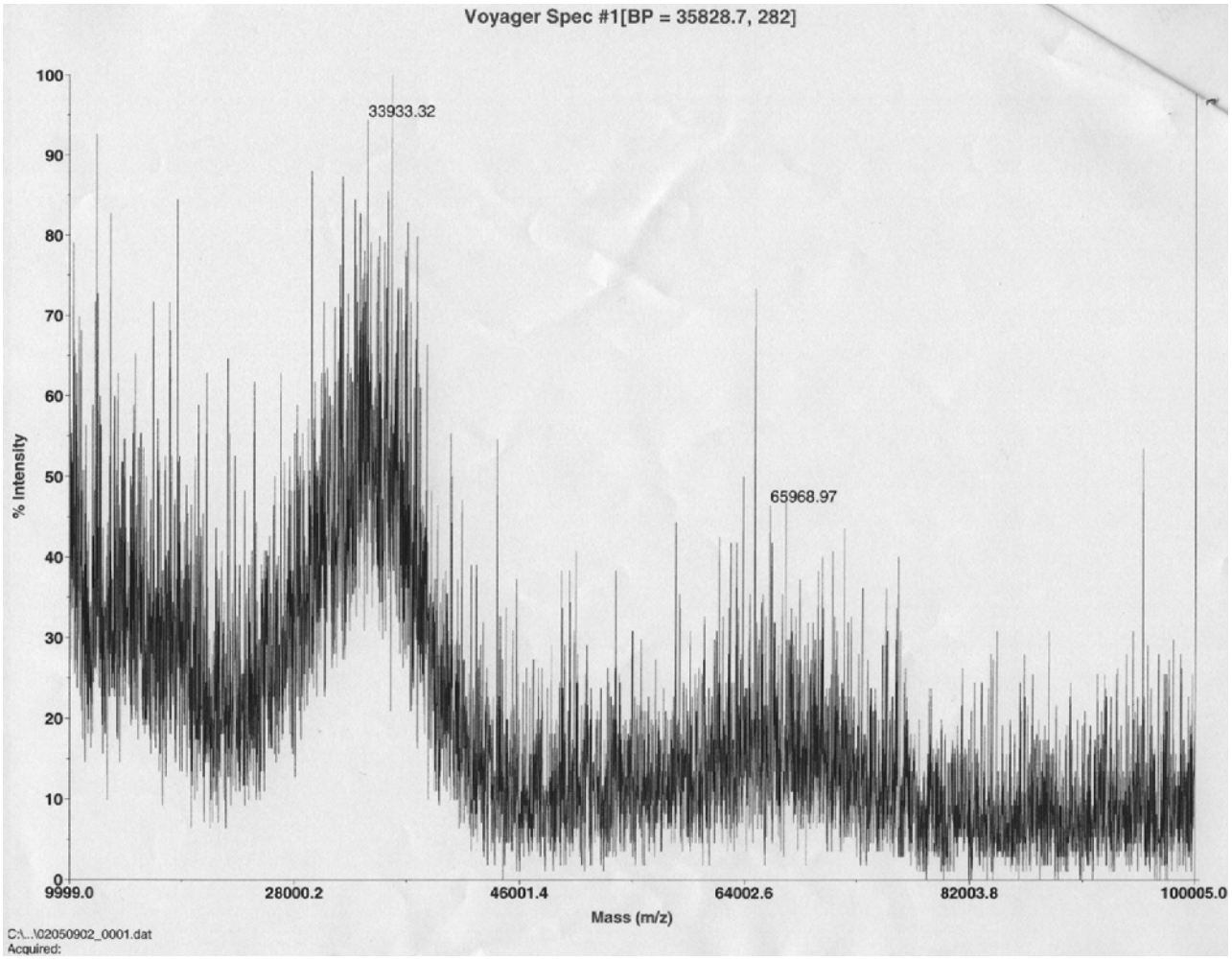
Voyager Spec #1[BP = 35828.7, 282]
33933.32
65968.97
% Intensity
100
90
80
70
60
50
40
30
20
10
0
9999.0
28000.2
46001.4
64002.6
82003.8
100005.0
Mass (m/z)
C:\...\02050902_0001.dat
Acquired:

Dendrimer **3**: See the spectrum of **2** for the peak assignment

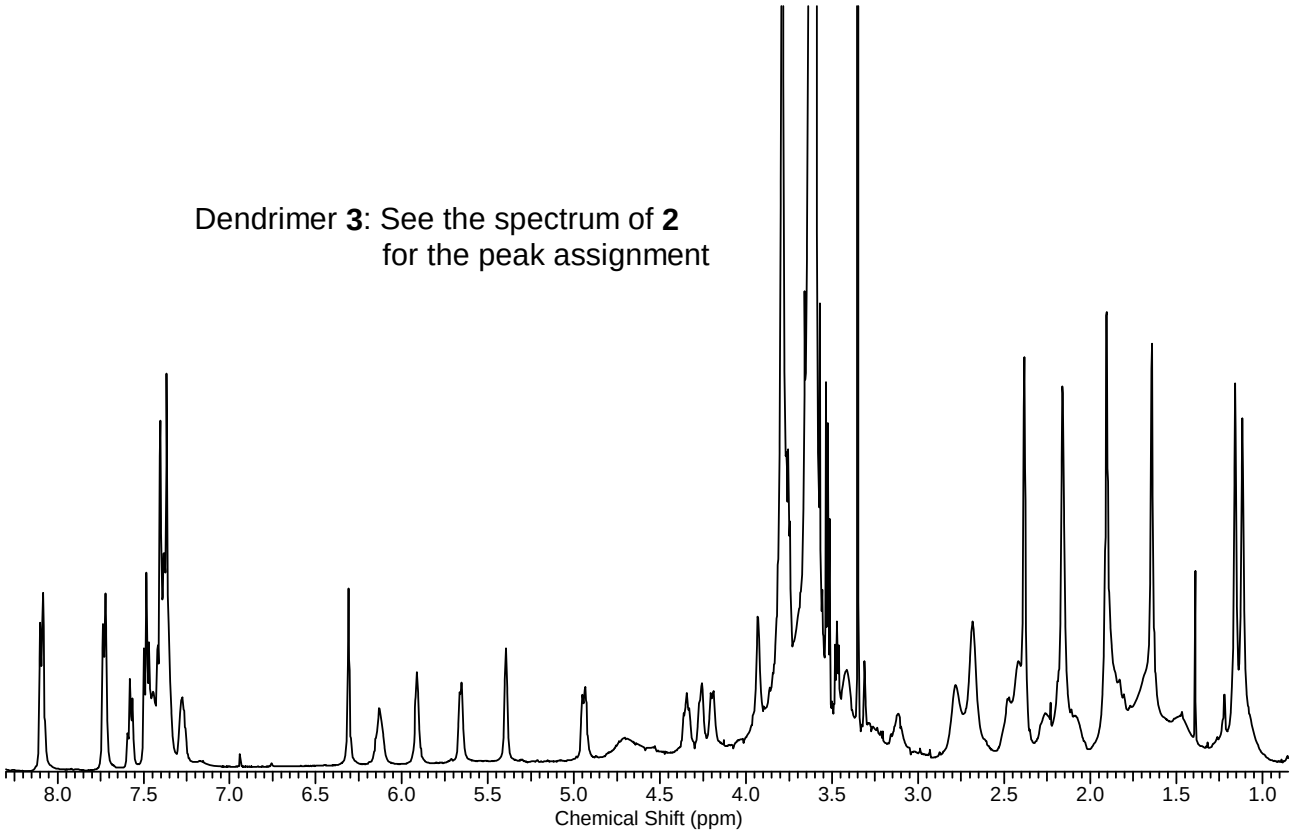

Installation of Bolton-Hunter Group on the PEGylated Dendrimers (1, 2, and 3)

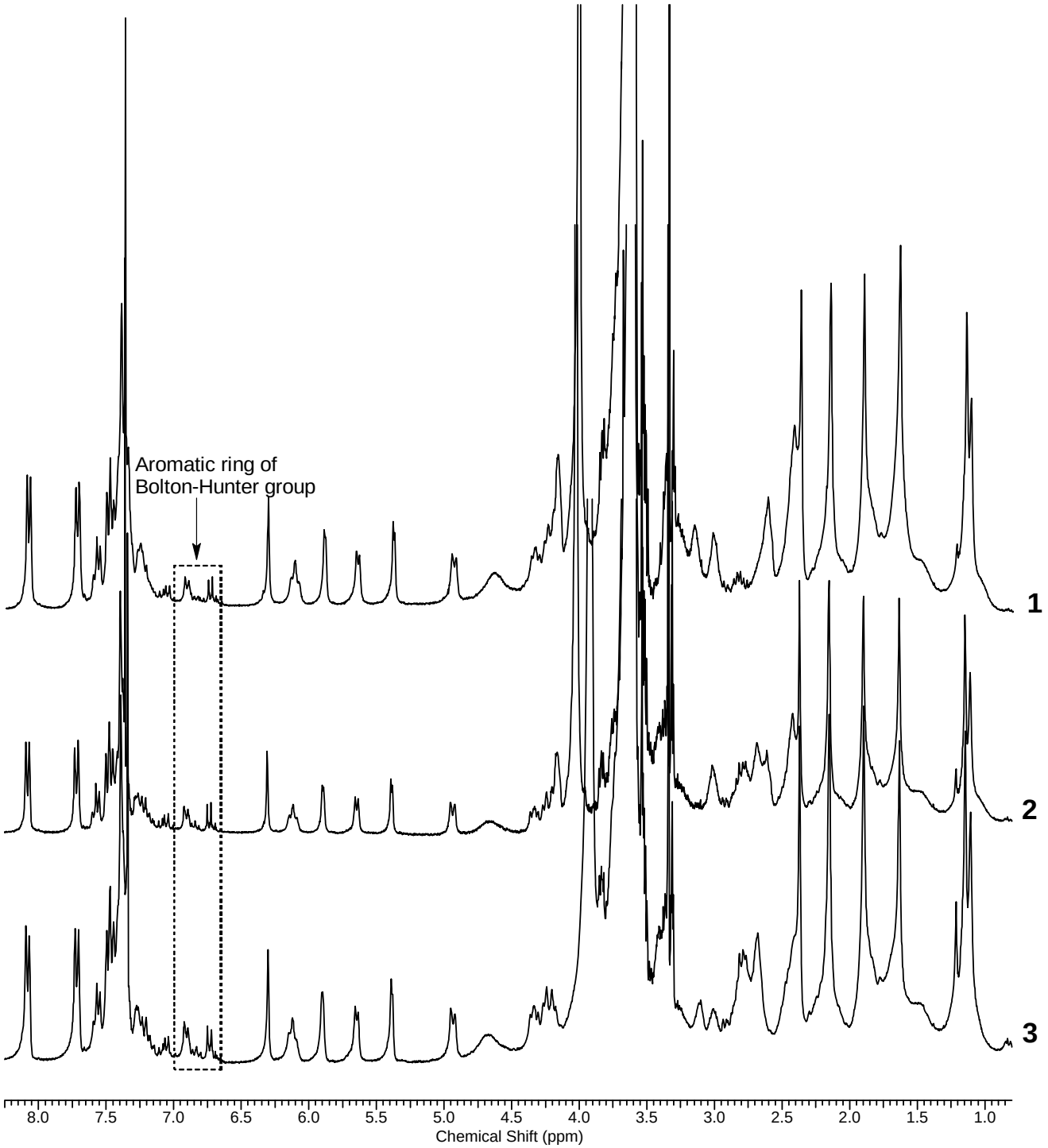

Compound **4** (Hollink, E., and Simanek, E. E. (2006) A divergent route to diversity in macromolecules. *Org. Lett*. *8*, 2293–2295)

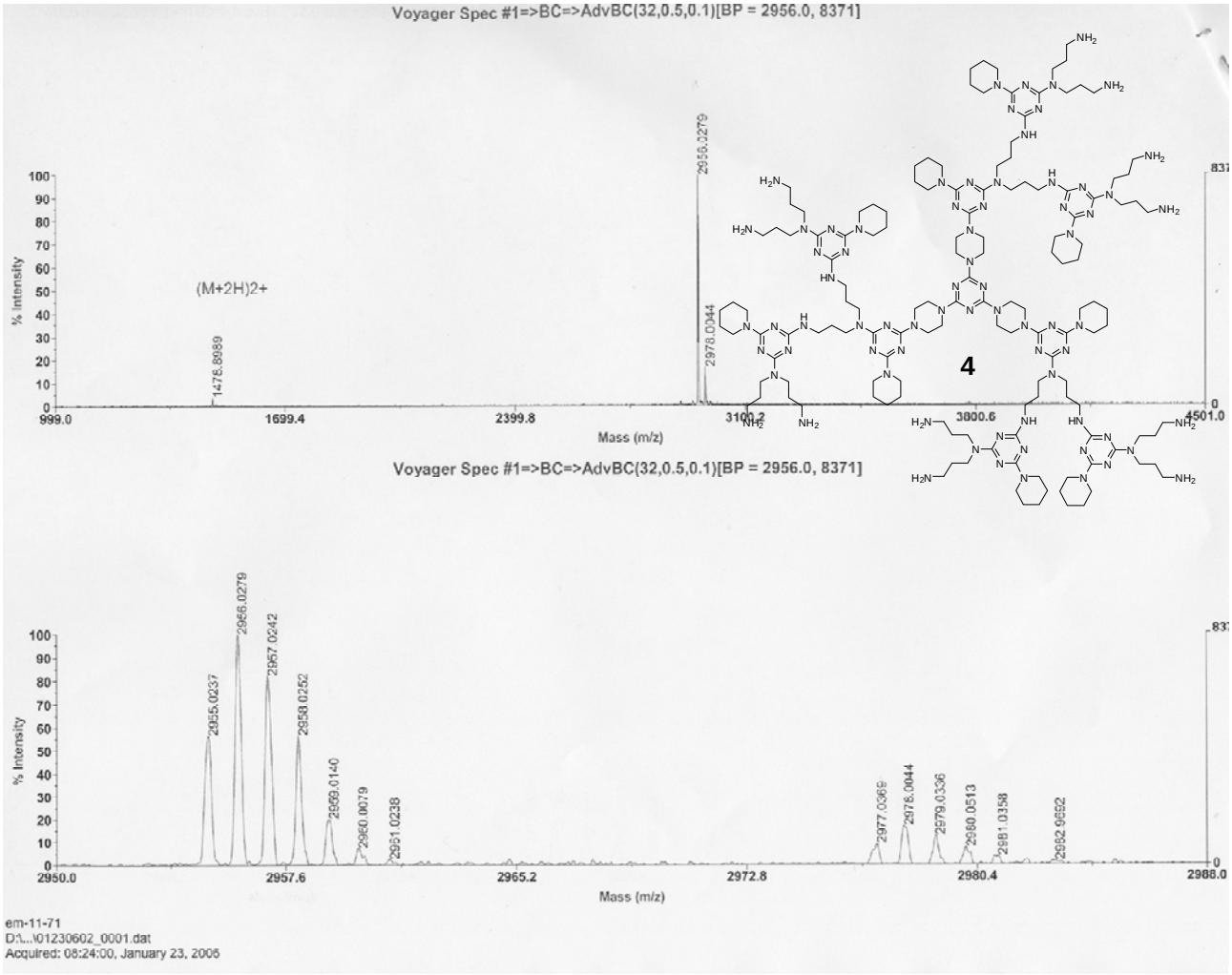

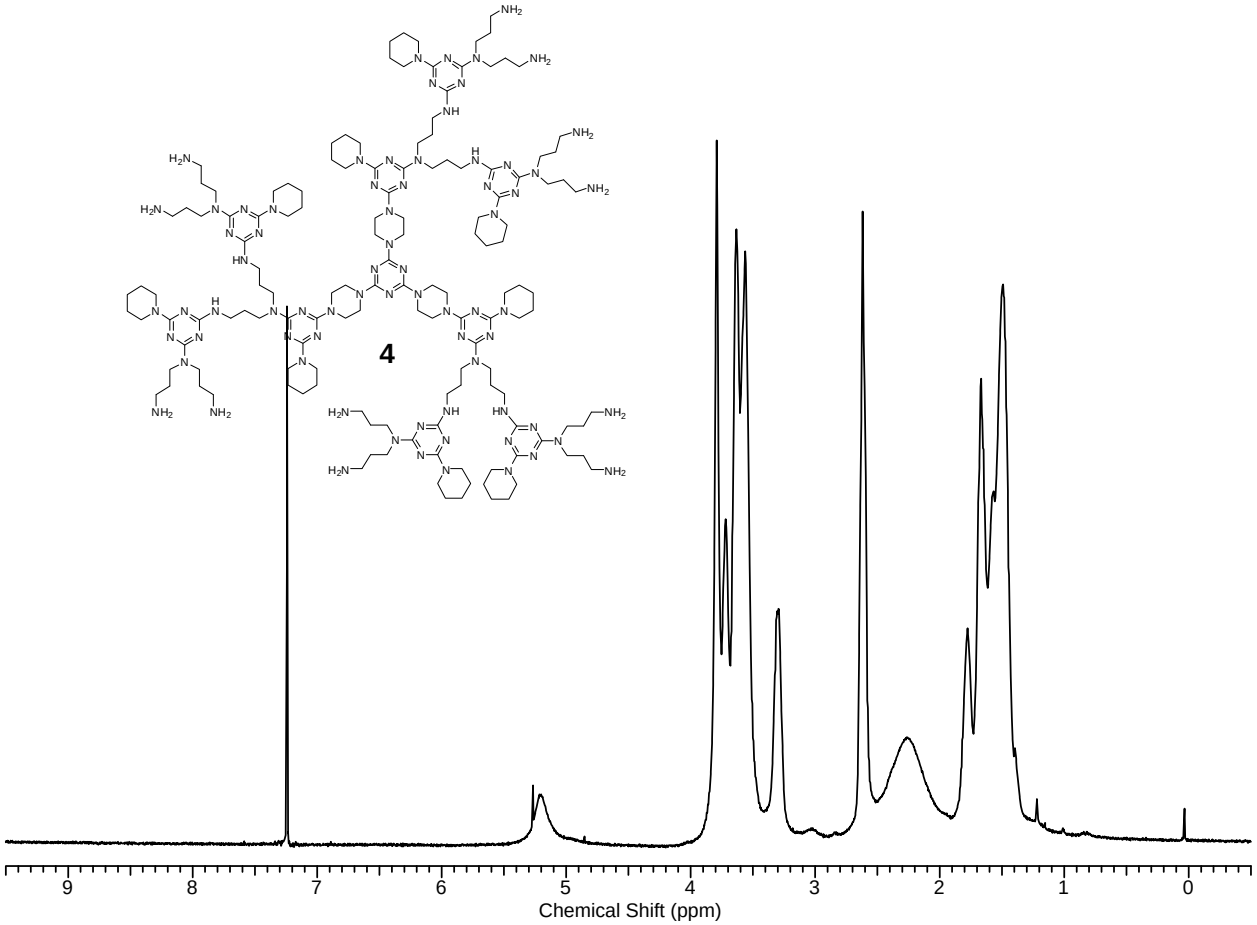

^{1}H NMR (300 MHz, $CDCl_3$ with trace CD_3OD) δ: 5.22 (br, 6H, N**H**), 3.68 (br, 24H, C**H**$_2$, piperazine), 3.60 (br, 12H, G1-C_5**H**$_{10}$N, α-H), 3.52 (br, 36H, G2-C_5**H**$_{10}$N, α-H, NC**H**$_2$), 3.45 (br, 24H, C**H**$_2$, NH_2-NC**H**$_2$), 3.19 (br, 12H, C**H**$_2$, C**H**$_2$NH-C_3N_3), 2.48 (br, 24H, C**H**$_2$$NH_2$), 1.69 (br, 12H, G1-$NCH_2$C**H**$_2$), 1.57 (br, 24H, G2-$NCH_2$C**H**$_2$), 1.48 (br, 18H, C_5**H**$_{10}$N, γ-H), 1.39 (br, 36H, C_5**H**$_{10}$N, β-H).

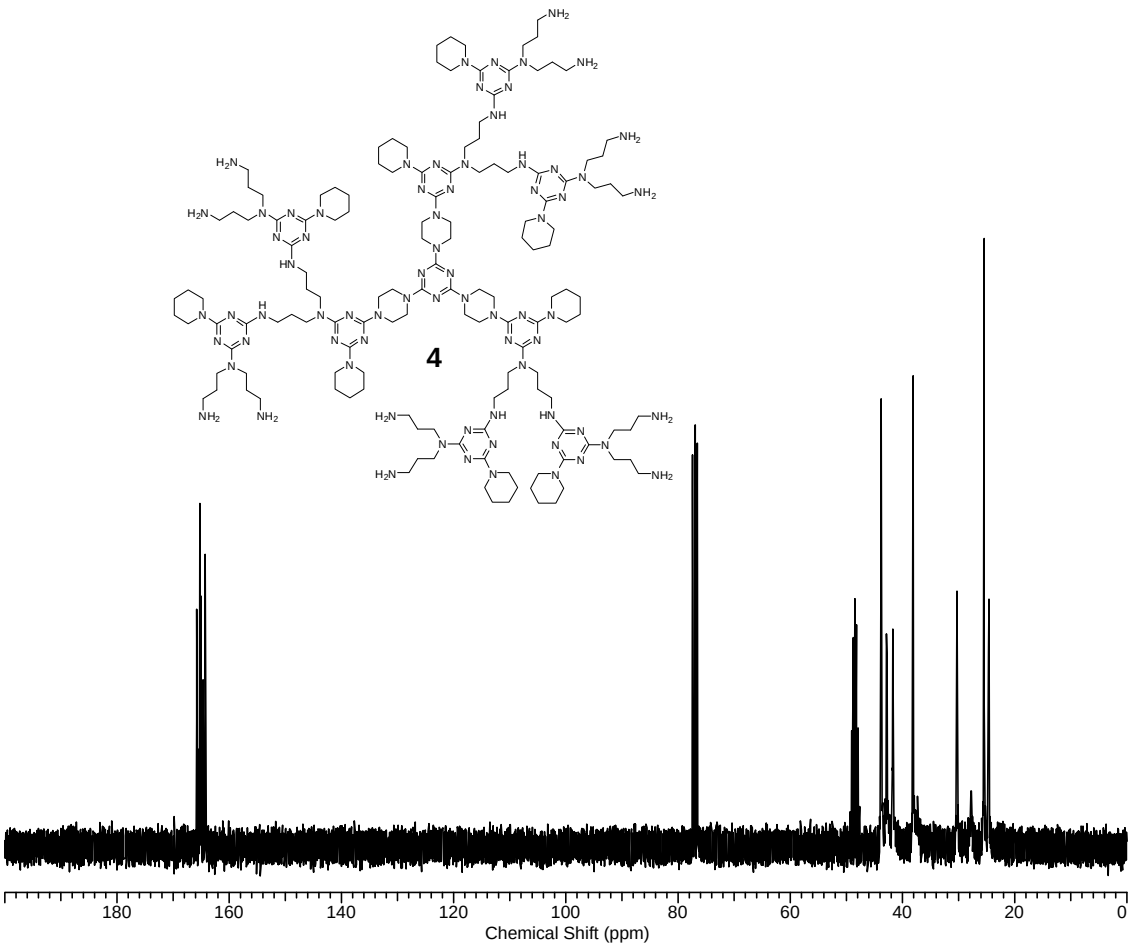

^{13}C NMR (75.5 MHz, $CDCl_3$ with trace CD_3OD) δ: 165.8 (s, C_3N_3), 165.4 (s, C_3N_3), 165.2 (s, C_3N_3), 165.1 (s, C_3N_3), 165.0 (s, C_3N_3), 164.6 (s, C_3N_3), 164.3 (s, C_3N_3), 43.8 (s, N**C**H_2), 42.8 (s, N**C**H_2), 41.7 (s, N**C**H_2), 38.1 (s, G2-**C**H_2NH_2), 37.3 (br, G1-**C**H_2NH-C_3N_3), 30.3 (s, G2-NCH_2**C**H_2), 27.7 (br, G1-NCH_2**C**H_2), 25.5 (**C**$_5H_{10}$N, β-C), 24.6 (**C**$_5H_{10}$N, γ-C).

Compound **5** (Lim, J., and Simanek, E. E. (2008) Synthesis of water-soluble dendrimers based on melamine bearing 16 paclitaxel groups. *Org. Lett. 10*, 201–204)

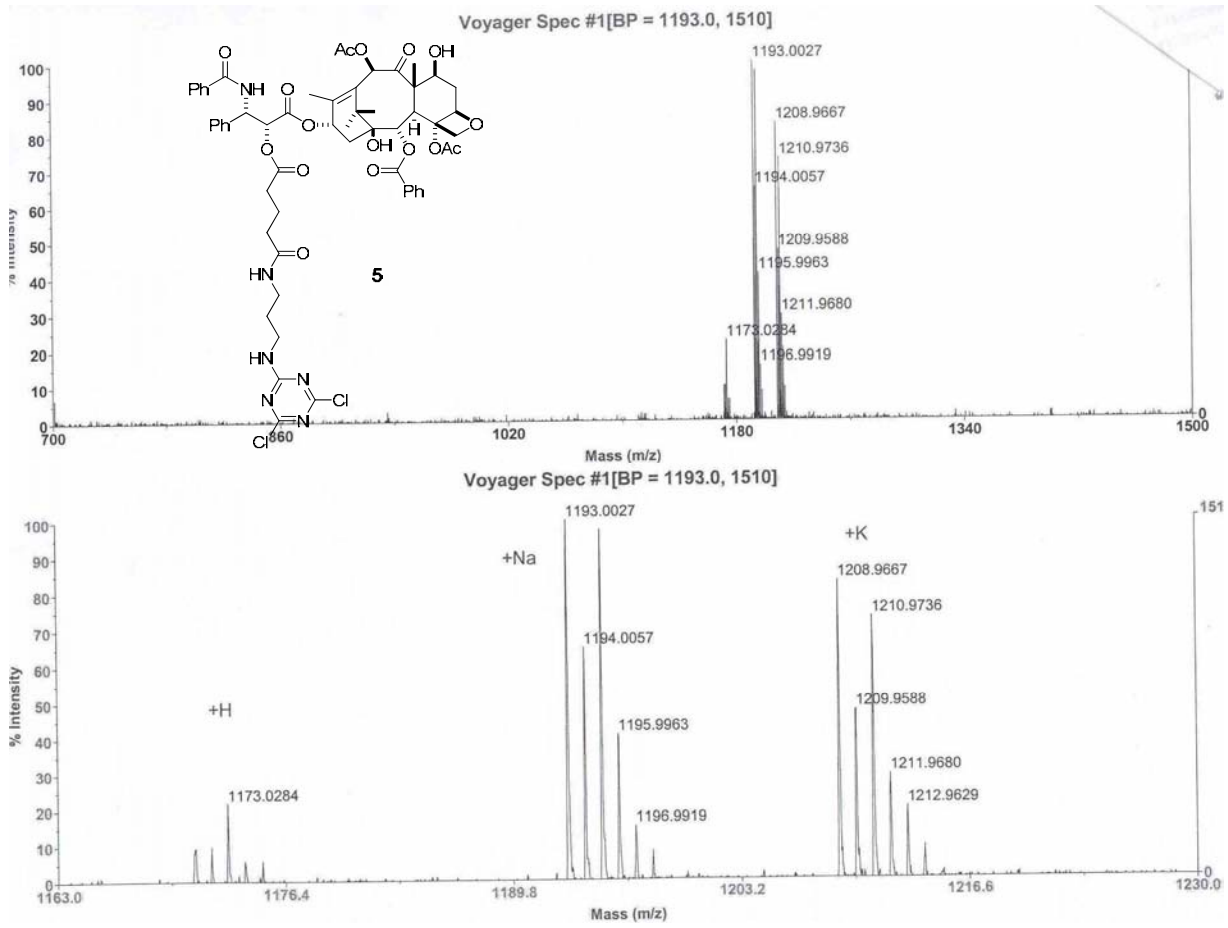

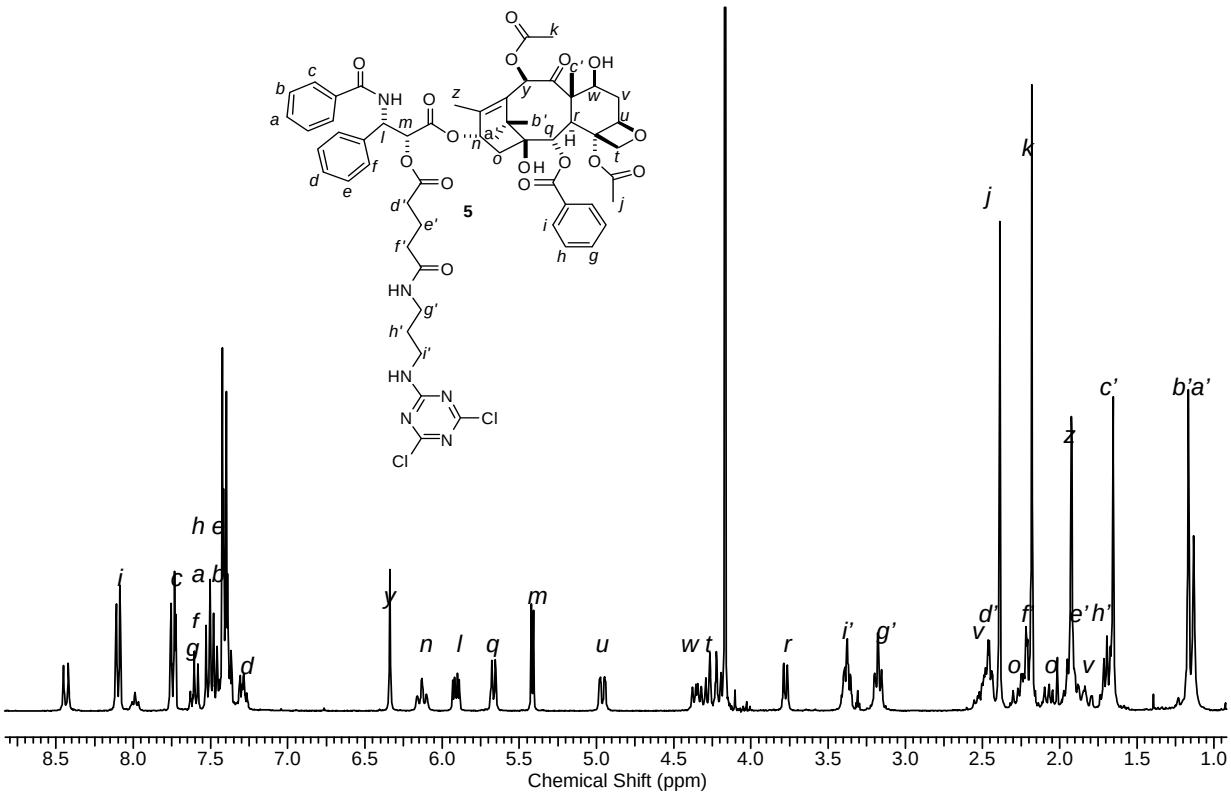
5
Chemical Shift (ppm)

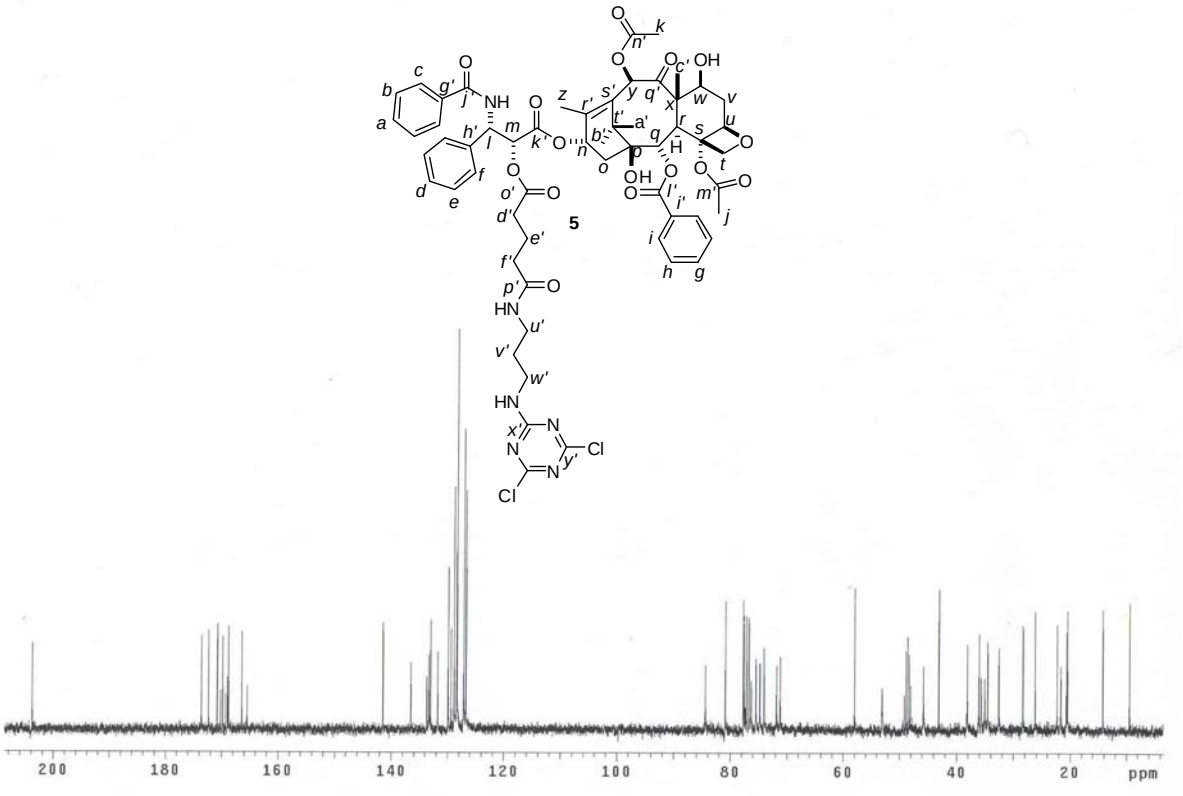
5
ppm

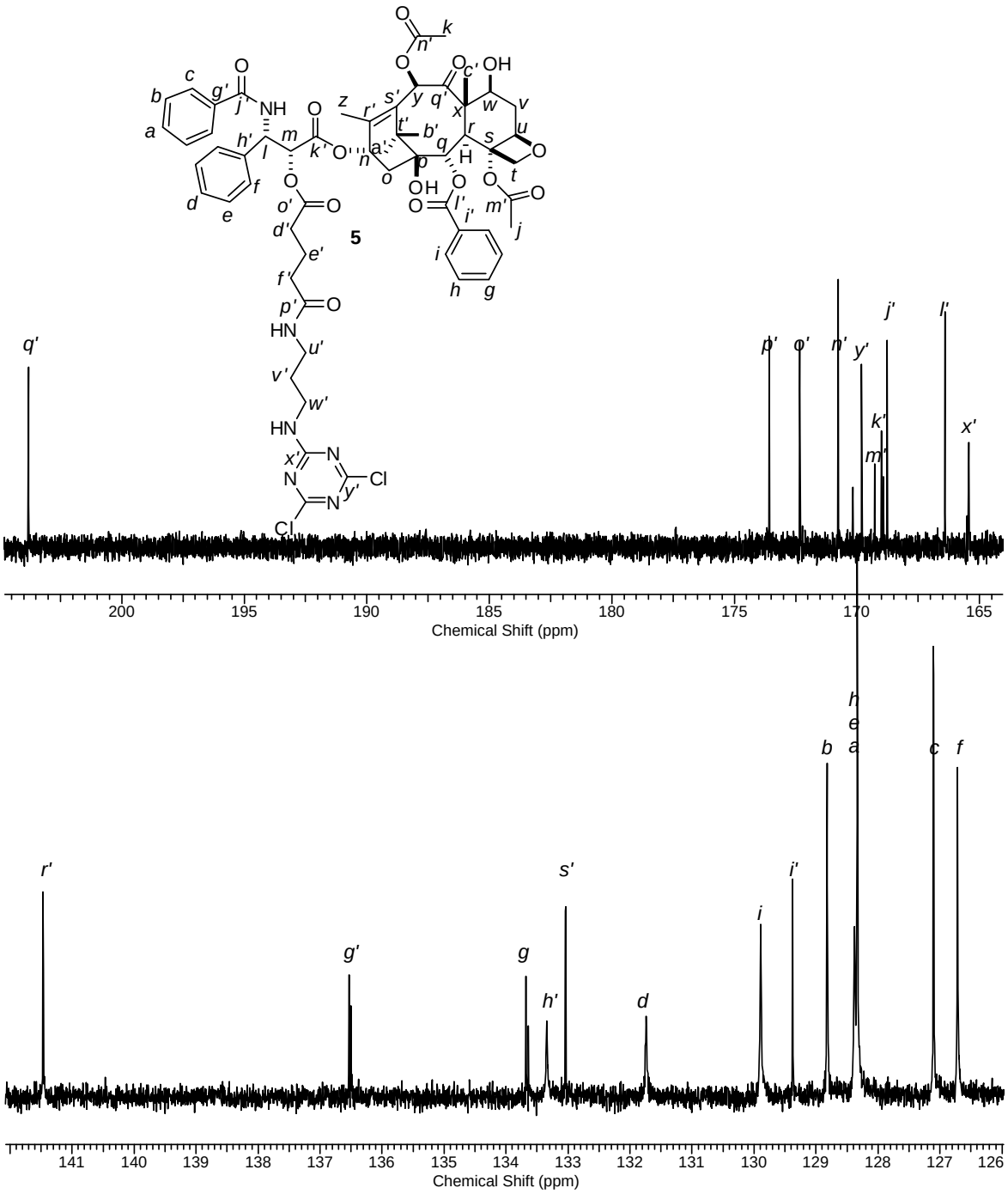

Comment: An additional line for the desymmetrized triazine is evident at 170 ppm.

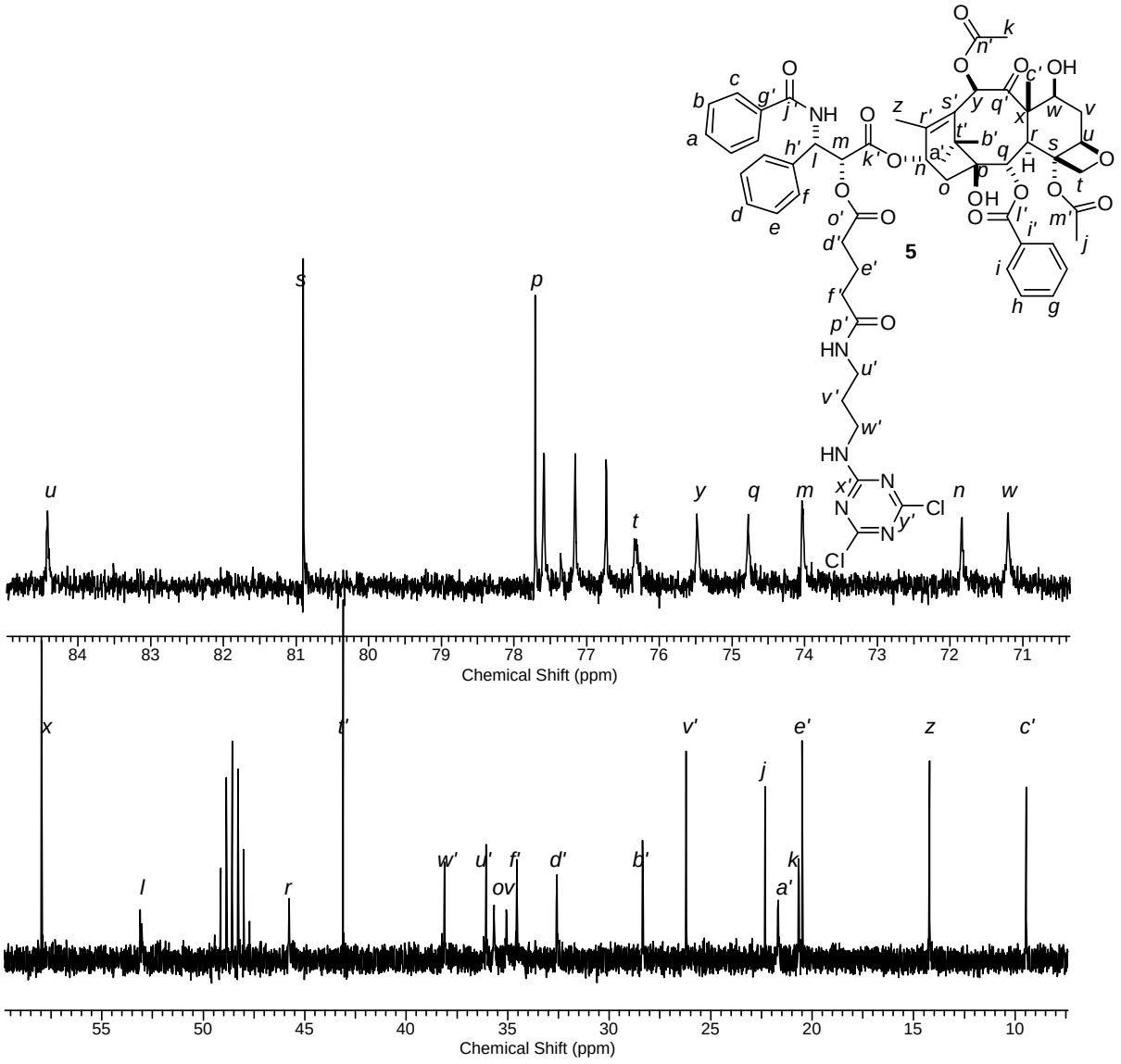
5
Chemical Shift (ppm)
Chemical Shift (ppm)

Compound **6**

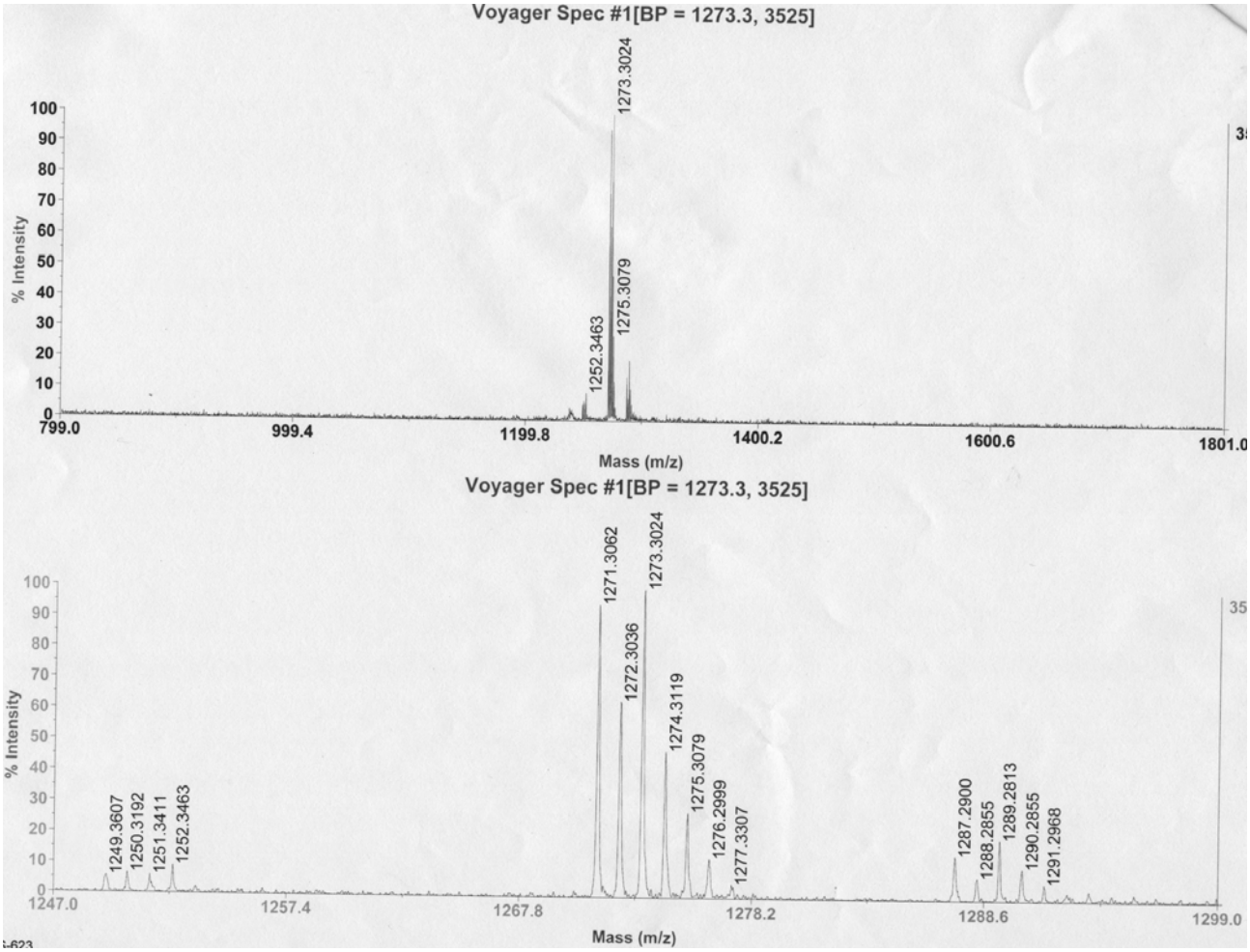
Voyager Spec #1[BP = 1273.3, 3525]
1273.3024
1252.3463
1275.3079
% Intensity
Mass (m/z)
Voyager Spec #1[BP = 1273.3, 3525]
1271.3062
1273.3024
1272.3036
1274.3119
1275.3079
1276.2999
1277.3307
1249.3607
1250.3192
1251.3411
1252.3463
1287.2900
1288.2855
1289.2813
1290.2855
1291.2968
% Intensity
Mass (m/z)

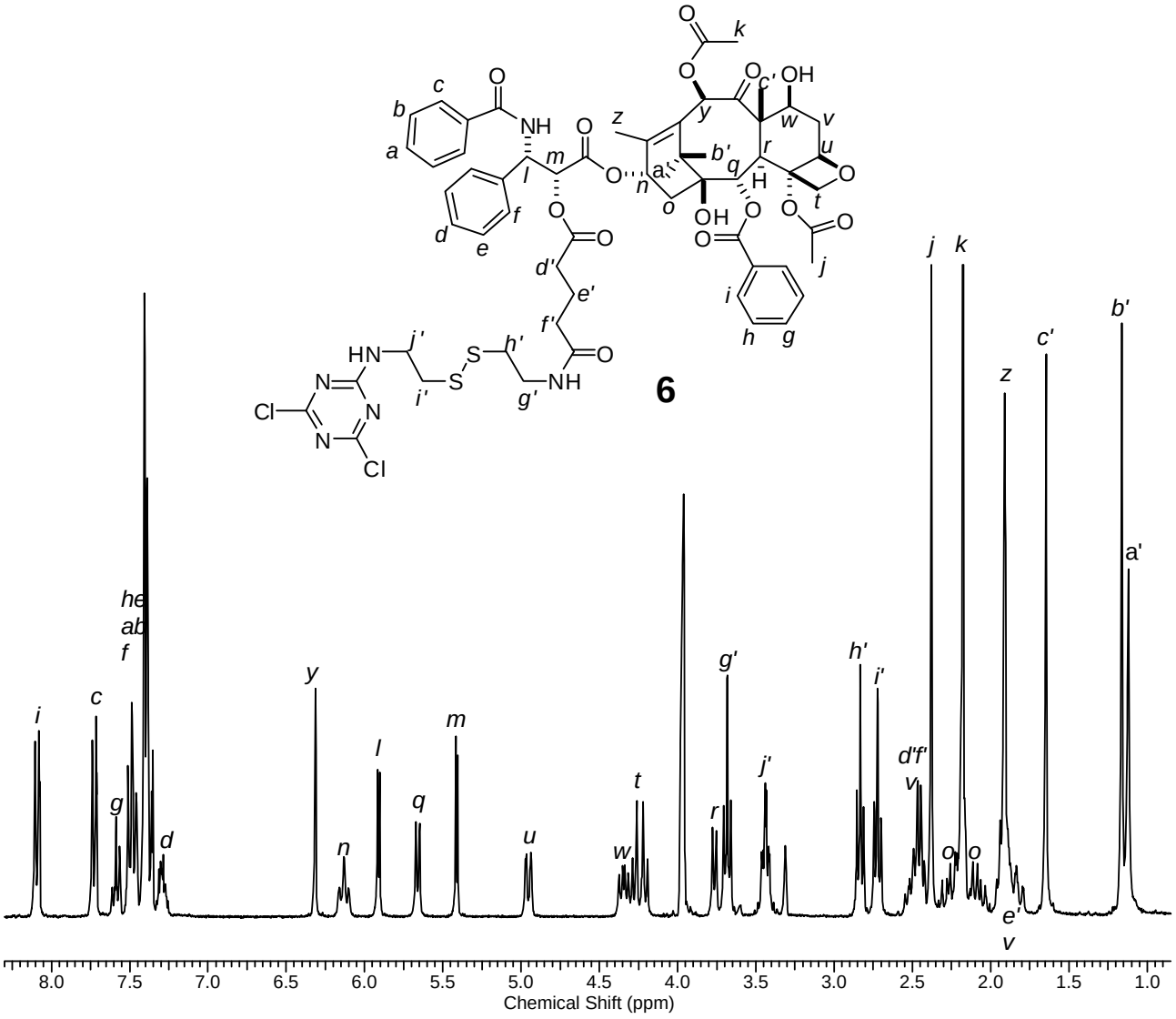
6
Chemical Shift (ppm)

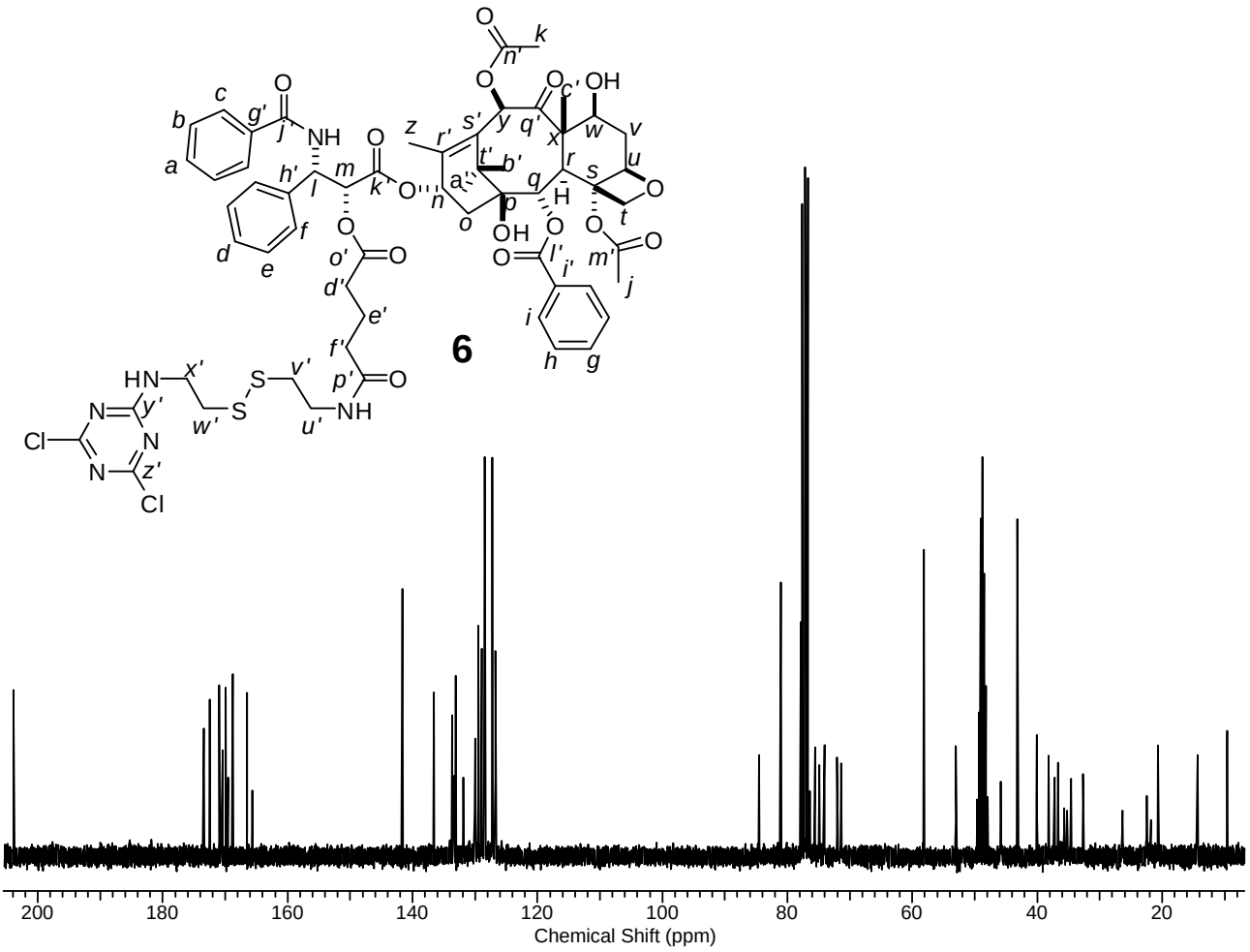
6
200
180
160
140
120
100
80
60
40
20
Chemical Shift (ppm)

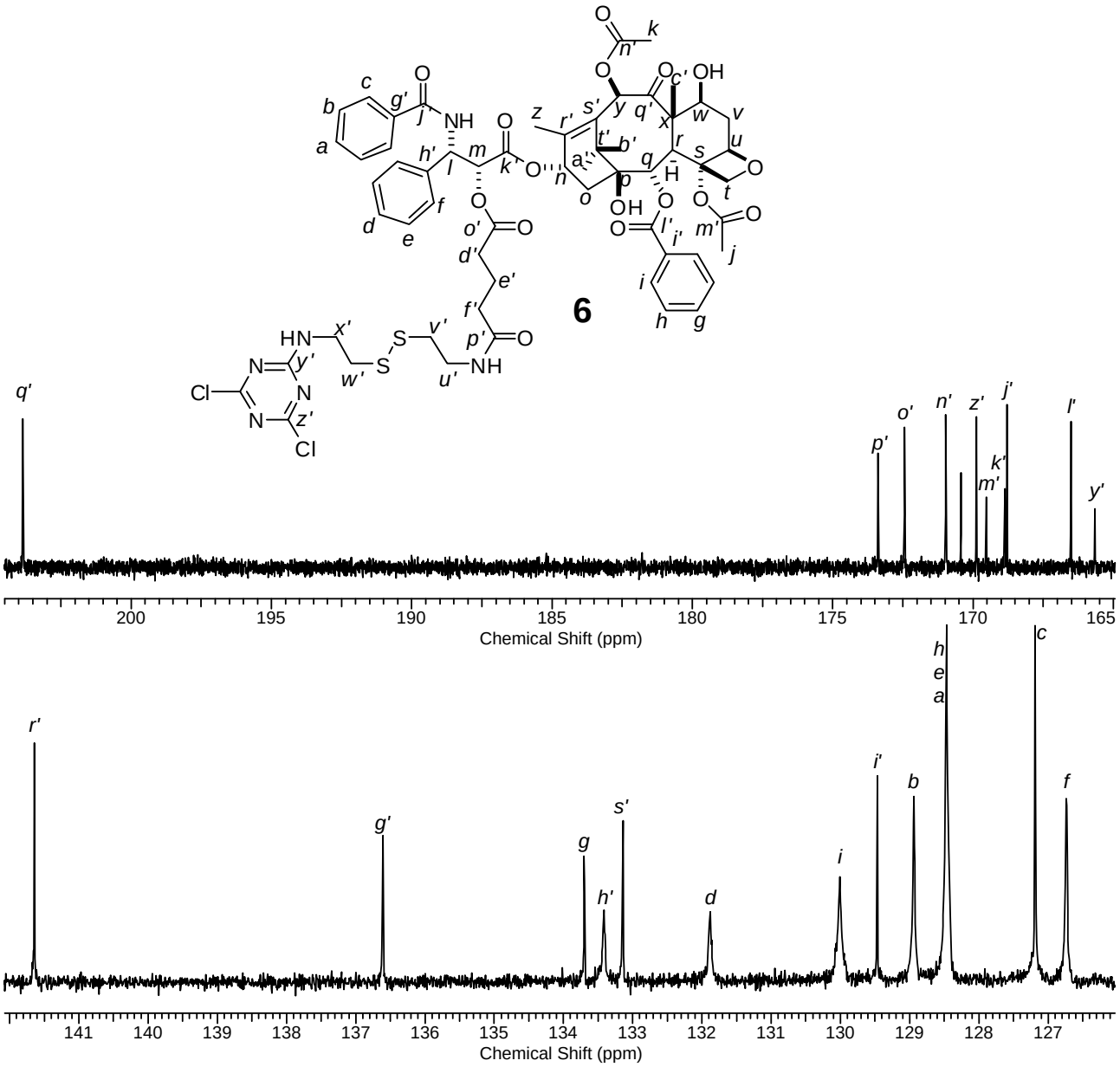
6
Chemical Shift (ppm)
Chemical Shift (ppm)

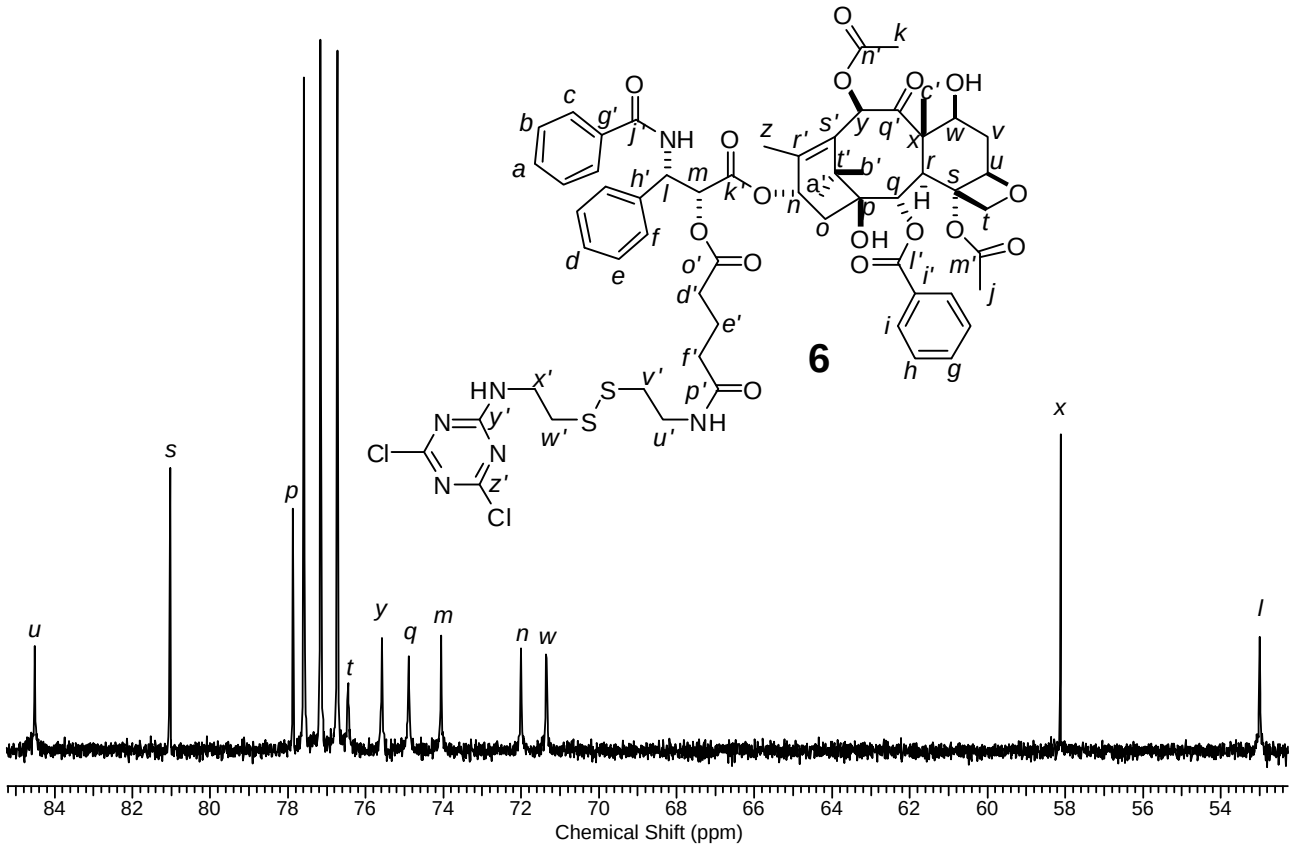
6
Chemical Shift (ppm)

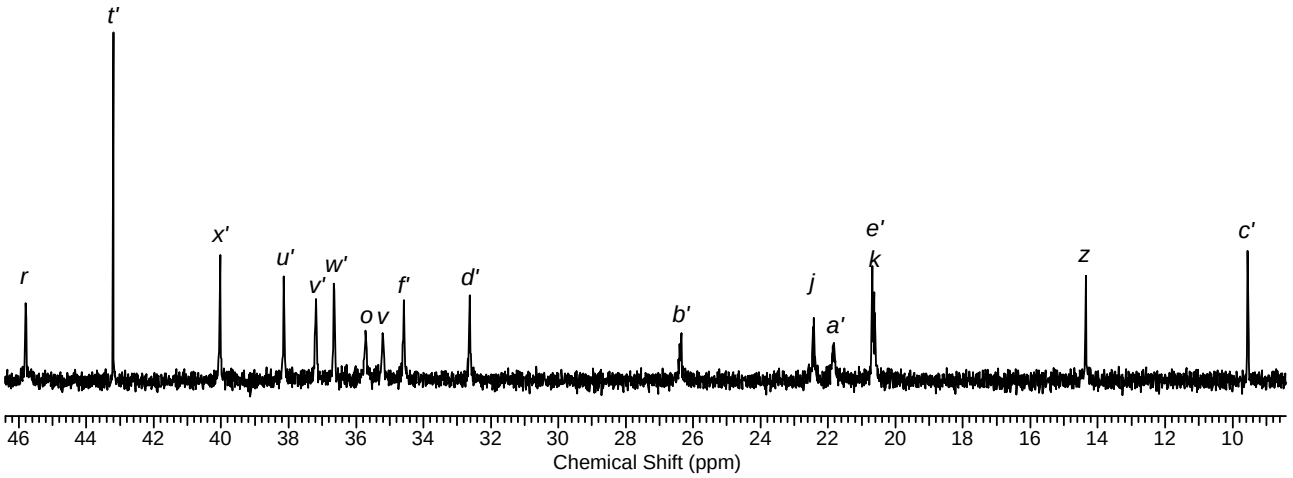
Chemical Shift (ppm)

Dendrimer **7**

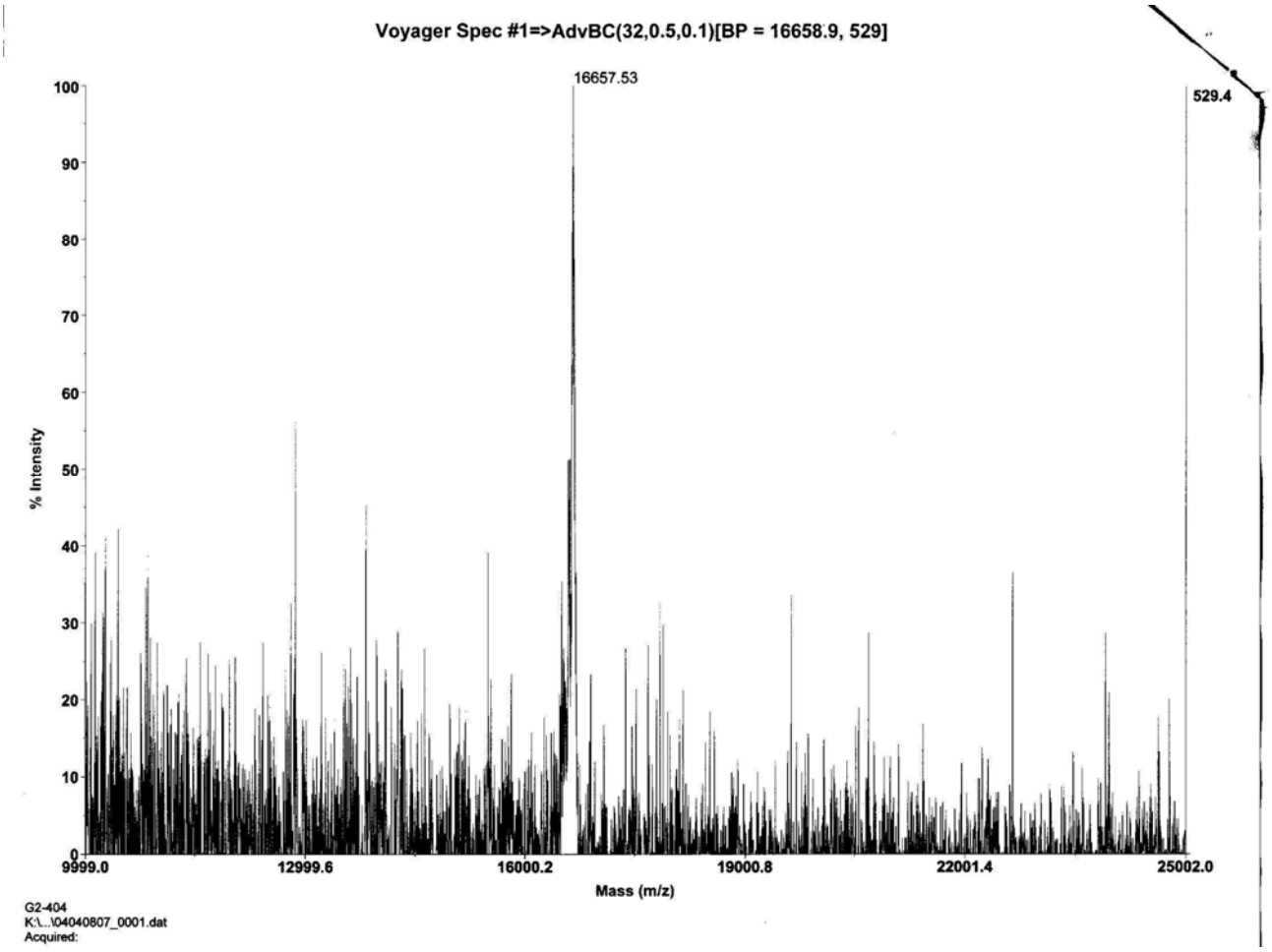
Voyager Spec #1=>AdvBC(32,0.5,0.1)[BP = 16658.9, 529]
16657.53
529.4
100
90
80
70
60
50
40
30
20
10
0
% Intensity
9999.0
12999.6
16000.2
19000.8
22001.4
25002.0
Mass (m/z)
G2-404
K:\...\04040807_0001.dat
Acquired:

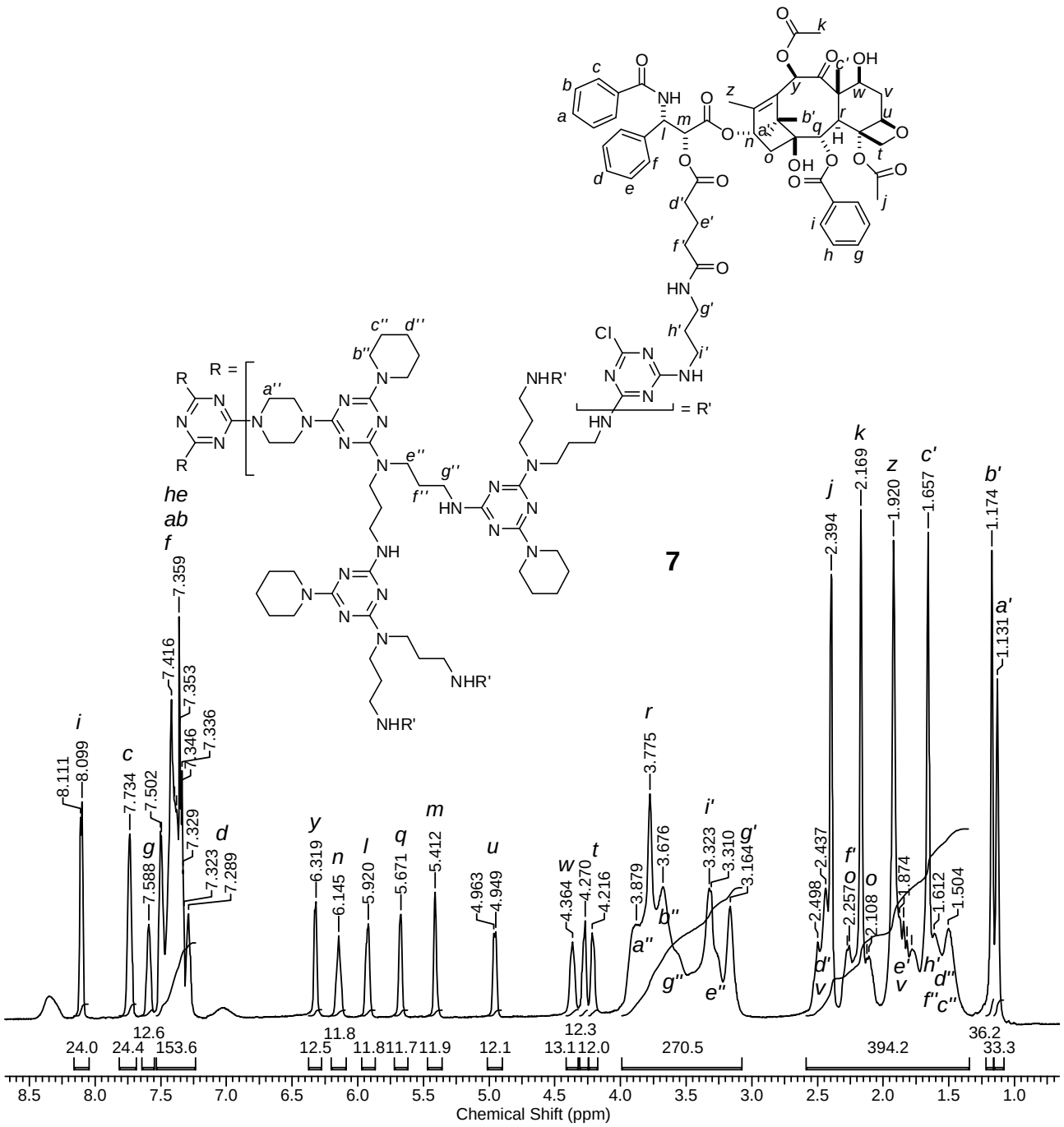
7
Chemical Shift (ppm)

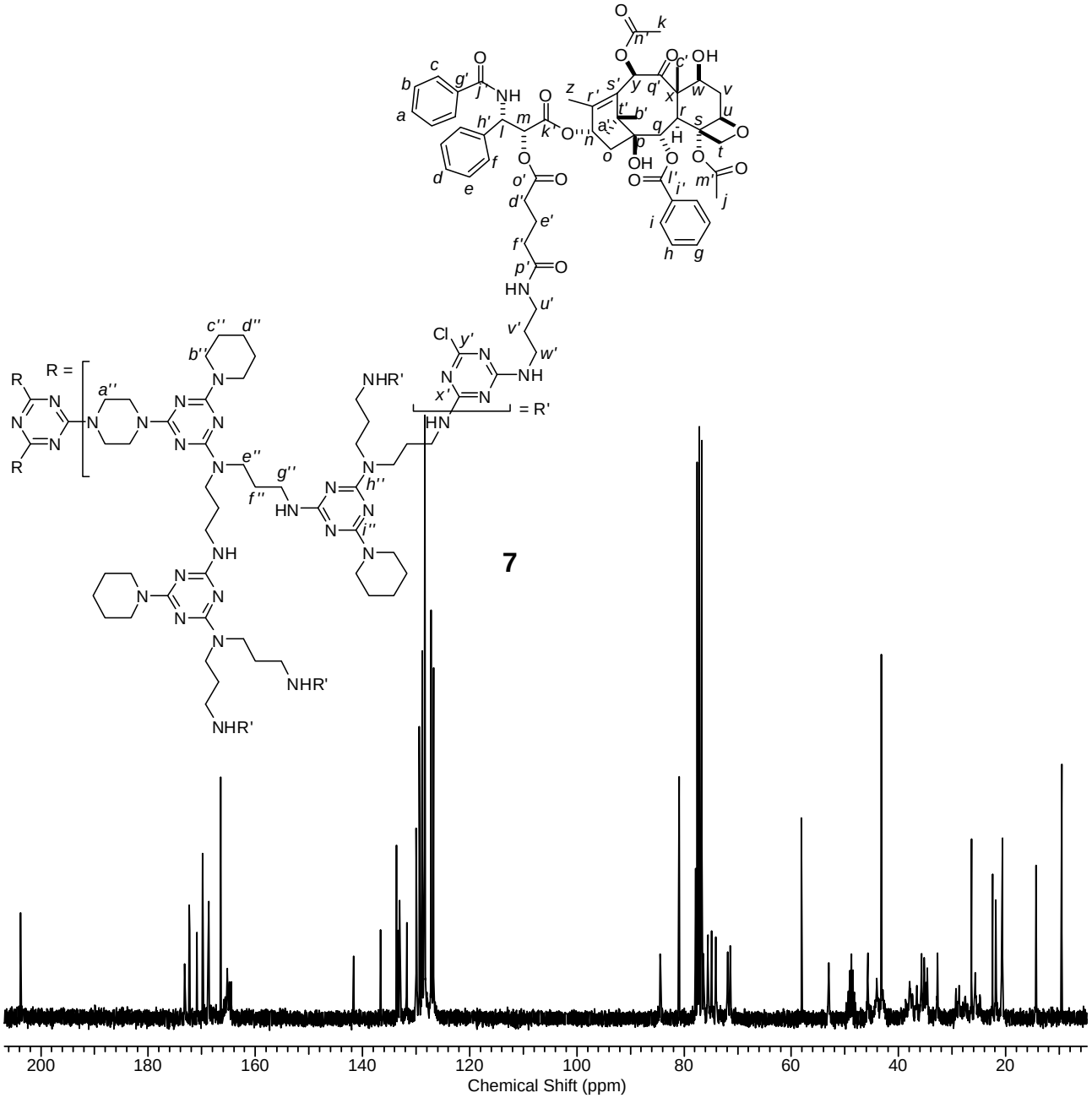
7
200
180
160
140
120
100
80
60
40
20
Chemical Shift (ppm)

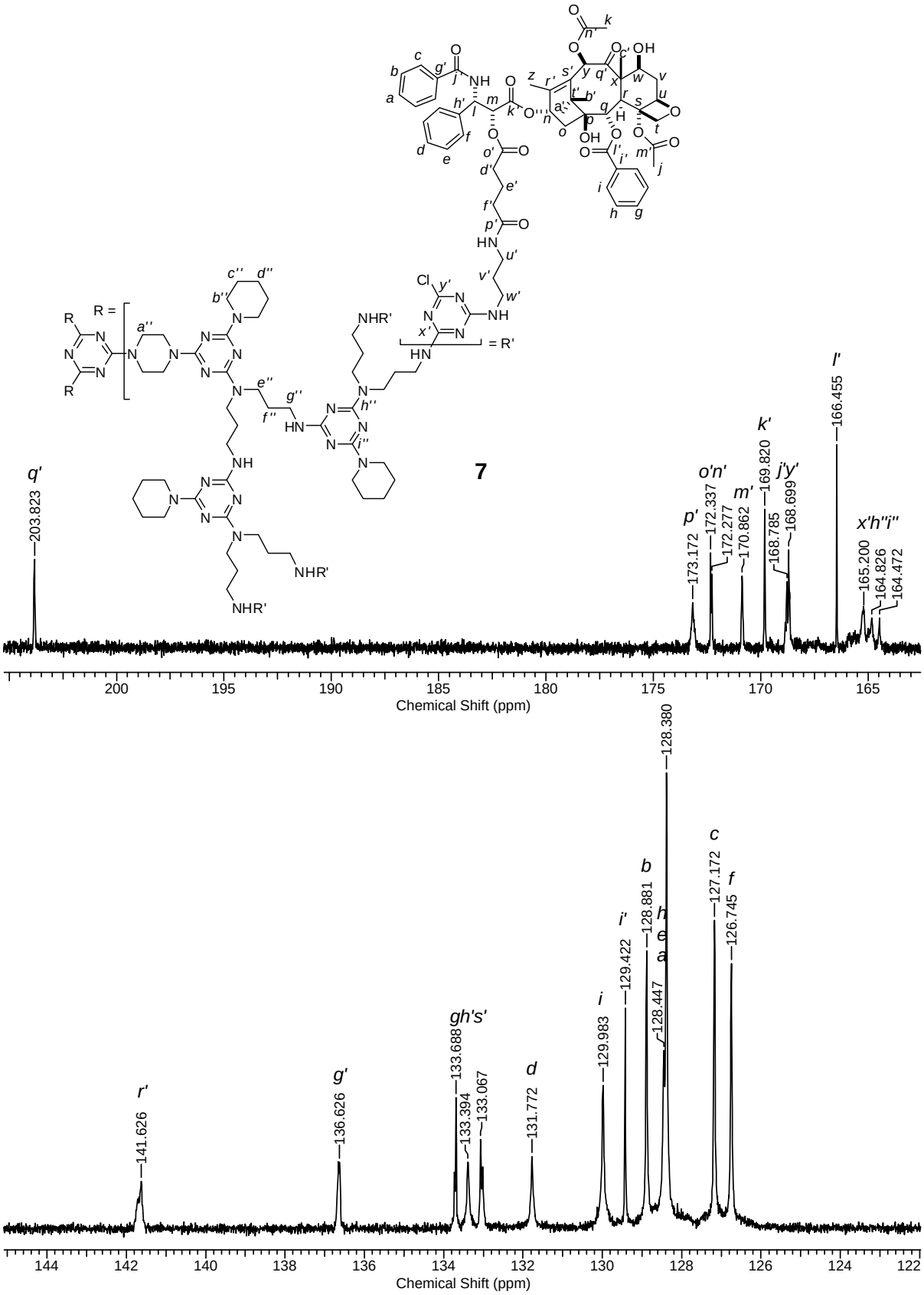
7
q'
203.823
p'
173.172
172.337
172.277
o'n'
170.862
m'
169.820
168.785
168.699
k'
j'y'
l'
166.455
x'h''i''
165.200
164.826
164.472
Chemical Shift (ppm)
r'
141.626
g'
136.626
gh's'
133.688
133.394
133.067
d
131.772
i
129.983
i'
129.422
b
128.881
h
e
a
128.447
128.380
c
127.172
f
126.745
Chemical Shift (ppm)

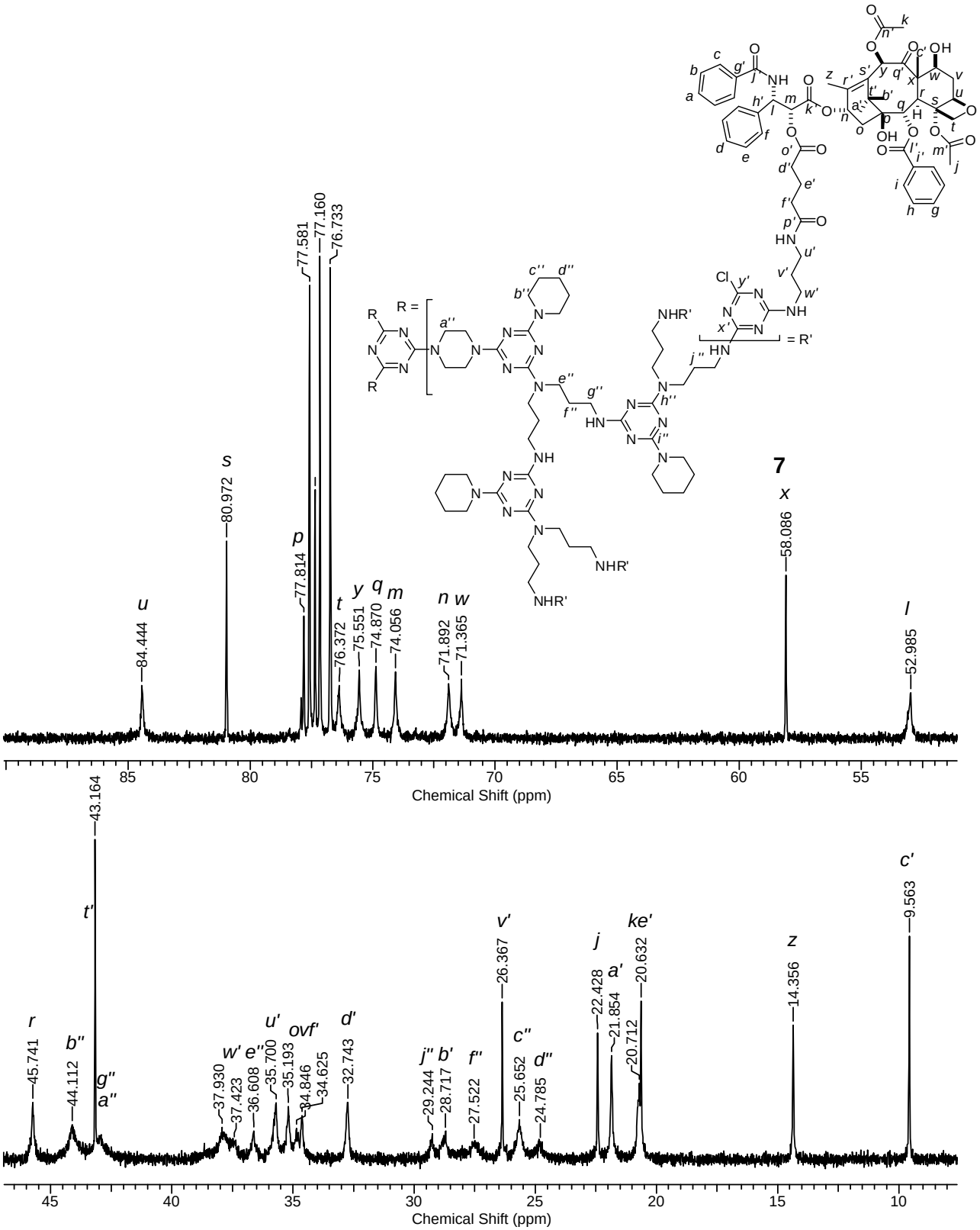
7
R =
= R'
NHR'
77.581
77.160
76.733
77.814
80.972
84.444
76.372
75.551
74.870
74.056
71.892
71.365
58.086
52.985
Chemical Shift (ppm)
43.164
45.741
44.112
37.930
37.423
36.608
35.700
35.193
34.846
34.625
32.743
29.244
28.717
27.522
26.367
25.652
24.785
22.428
21.854
20.712
20.632
14.356
9.563
Chemical Shift (ppm)

Dendrimer **8**

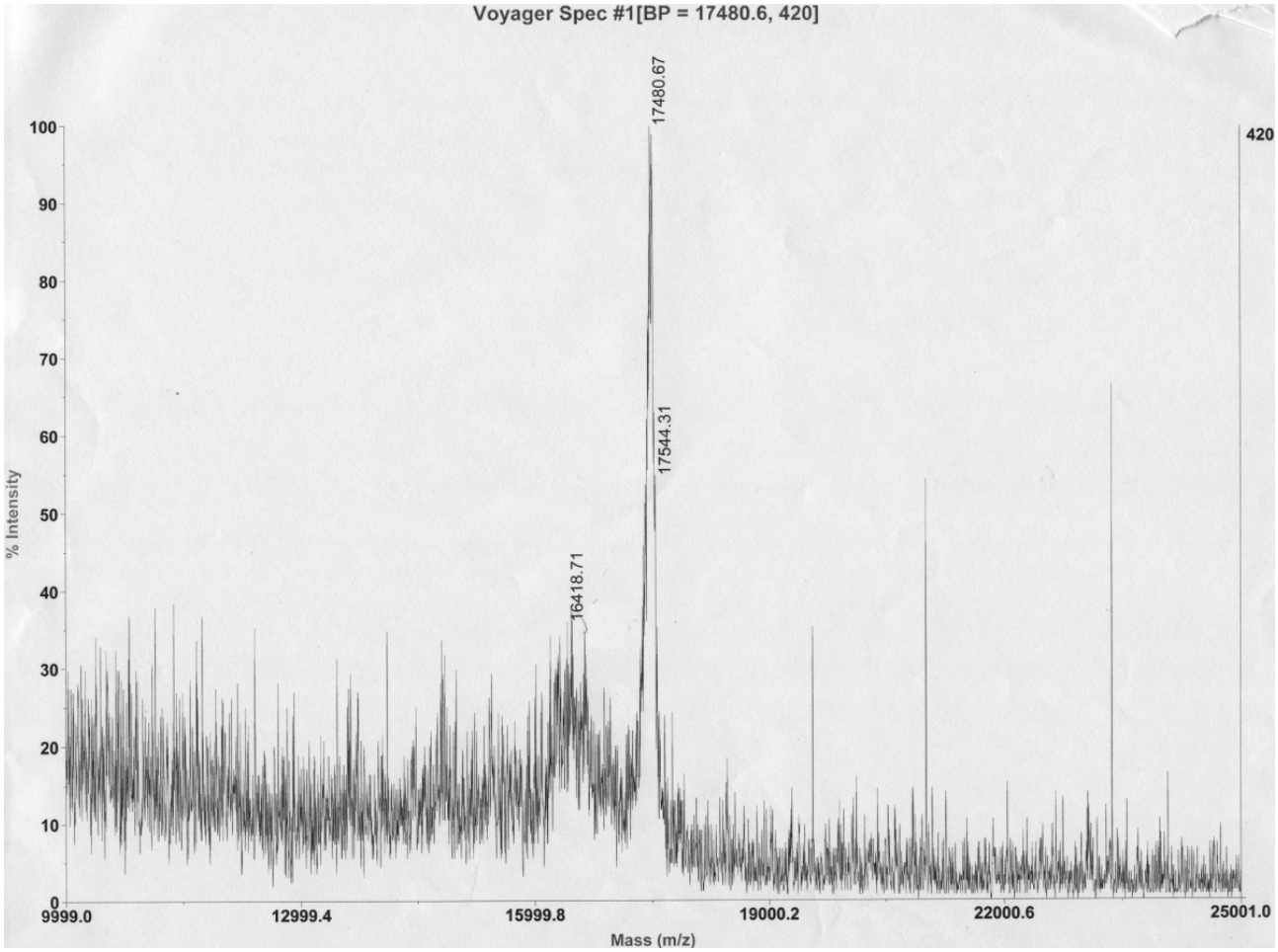
Voyager Spec #1[BP = 17480.6, 420]
17480.67
17544.31
16418.71
420
% Intensity
100
90
80
70
60
50
40
30
20
10
0
9999.0
12999.4
15999.8
19000.2
22000.6
25001.0
Mass (m/z)

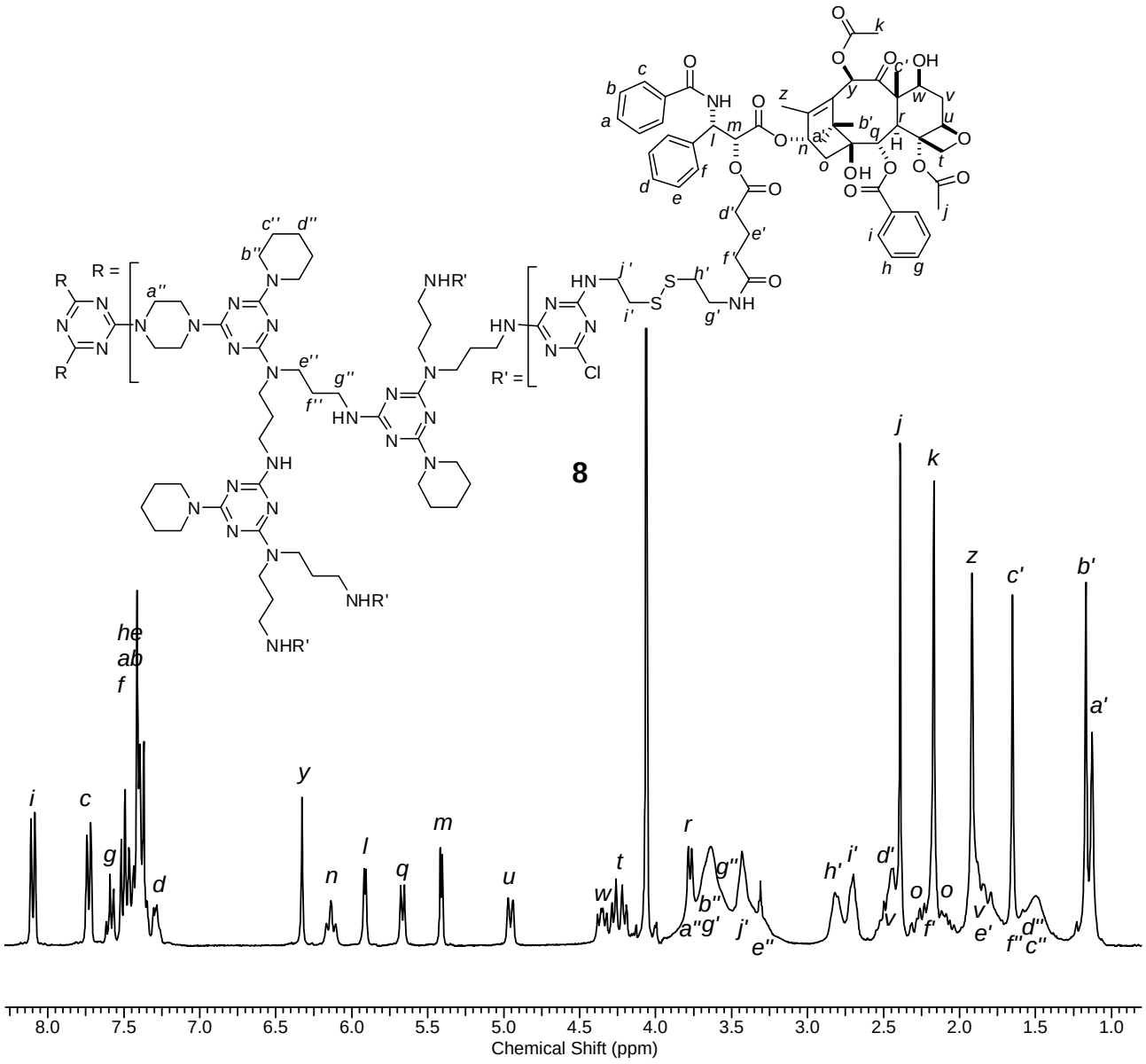
8
R =
R' =
NHR'
Cl
Chemical Shift (ppm)
8.0
7.5
7.0
6.5
6.0
5.5
5.0
4.5
4.0
3.5
3.0
2.5
2.0
1.5
1.0

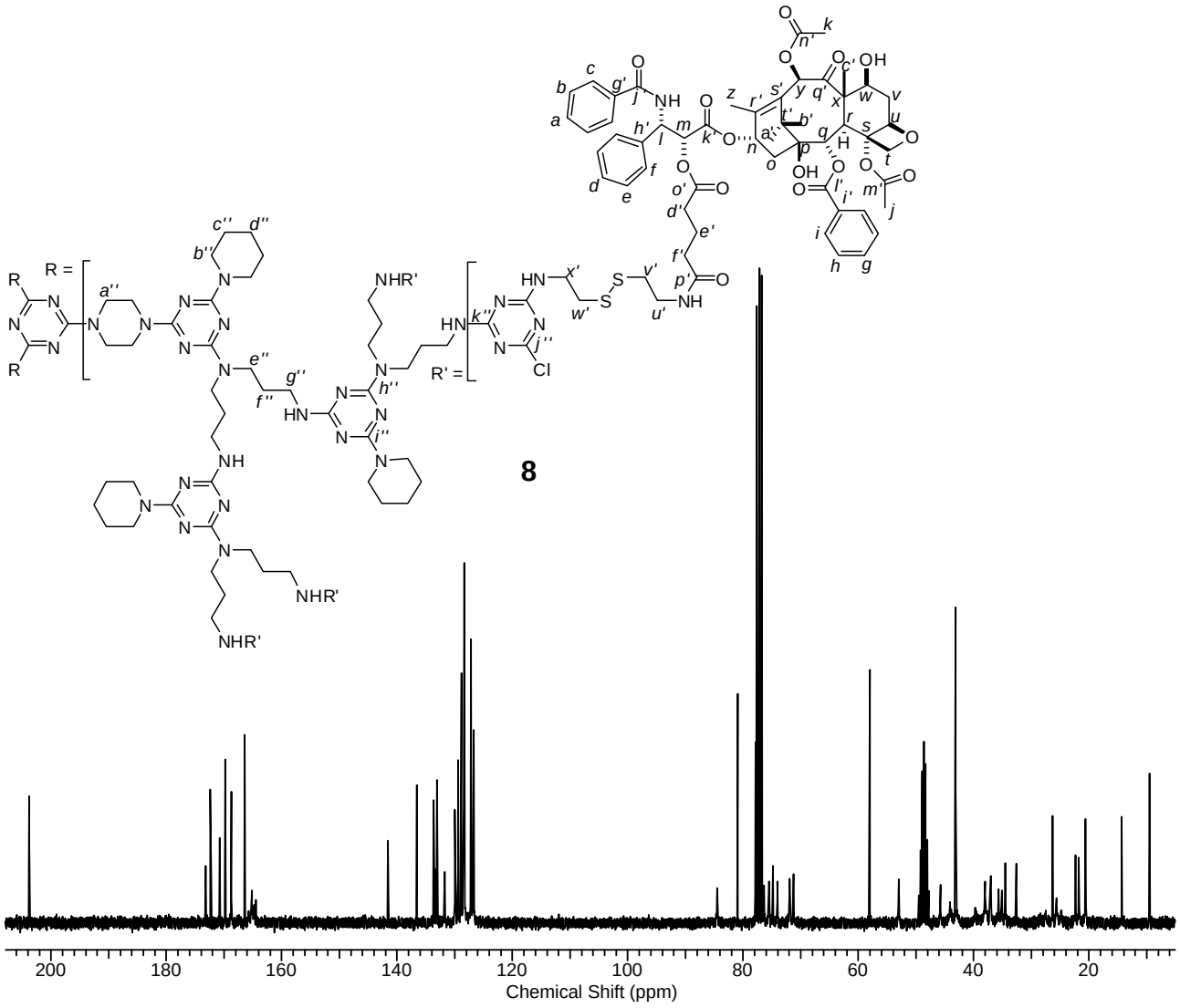
8
200
180
160
140
120
100
80
60
40
20
Chemical Shift (ppm)

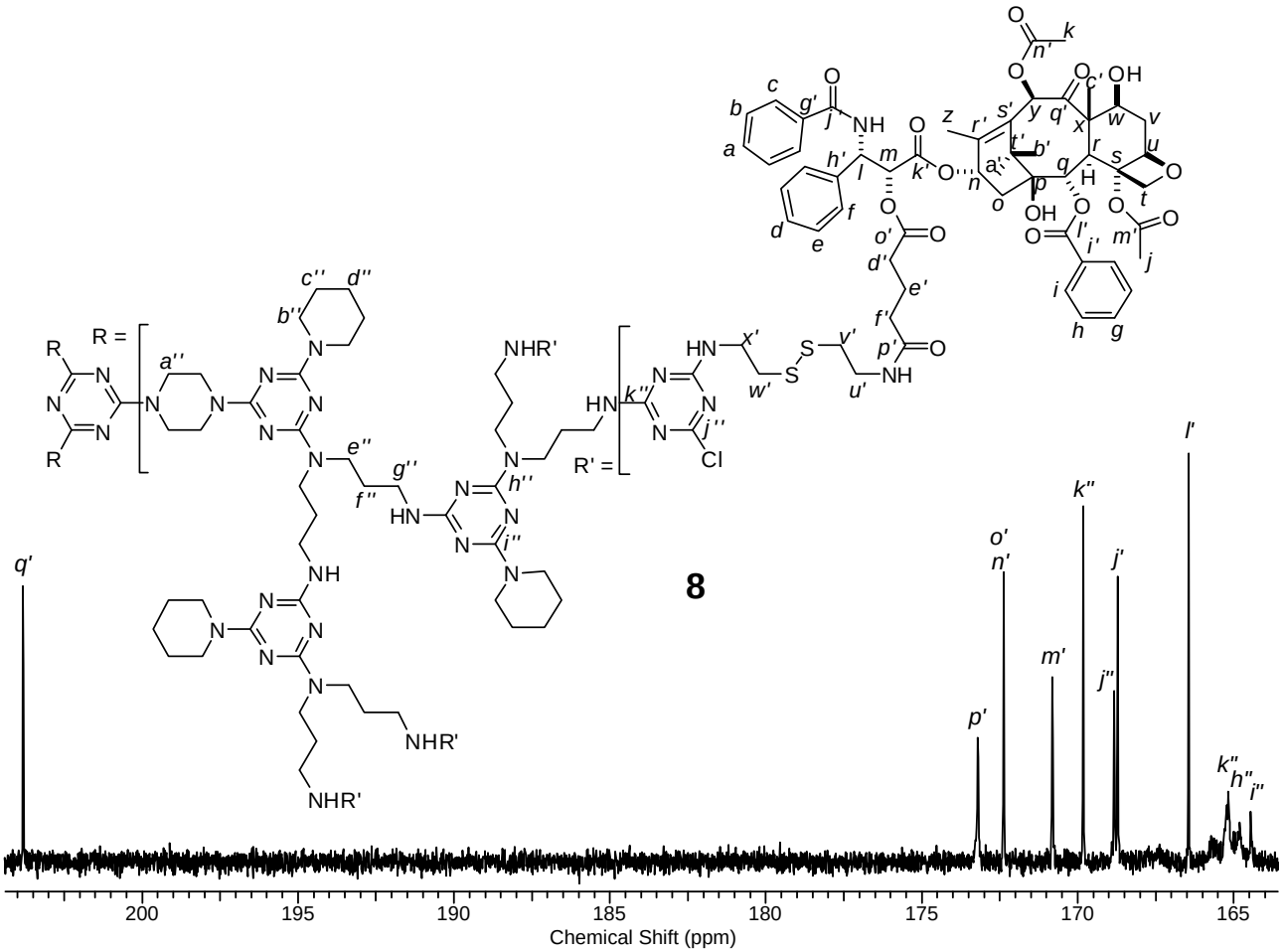
8
R =
R' =
NHR'
Cl
q'
p'
o'
n'
m'
k''
j'
j''
l'
k''
h''
i''
200
195
190
185
180
175
170
165
Chemical Shift (ppm)

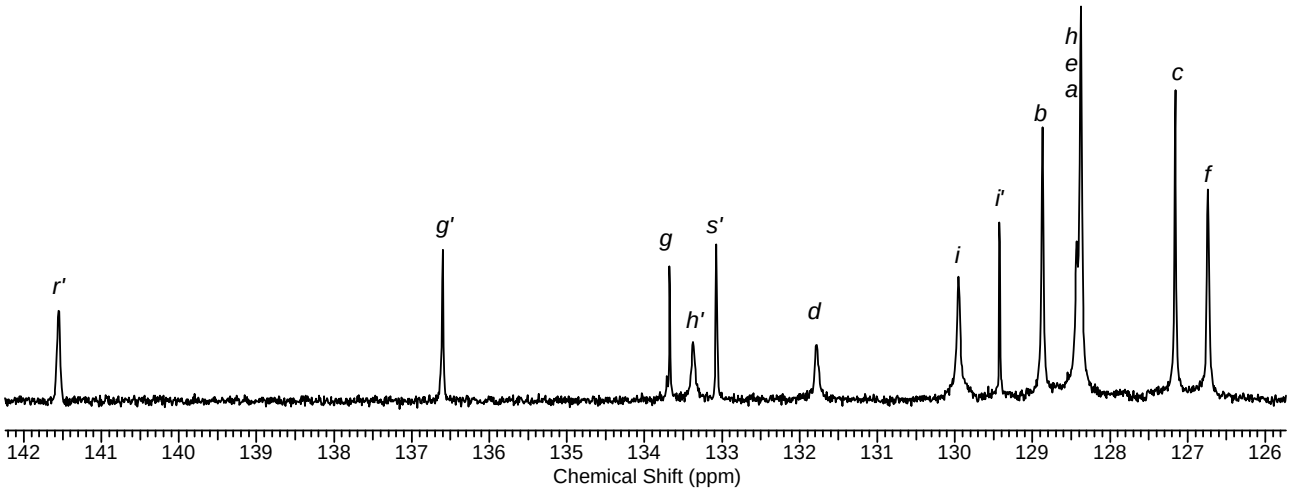
r'
g'
g
h'
s'
d
i
i'
b
h
e
a
c
f
142
141
140
139
138
137
136
135
134
133
132
131
130
129
128
127
126
Chemical Shift (ppm)

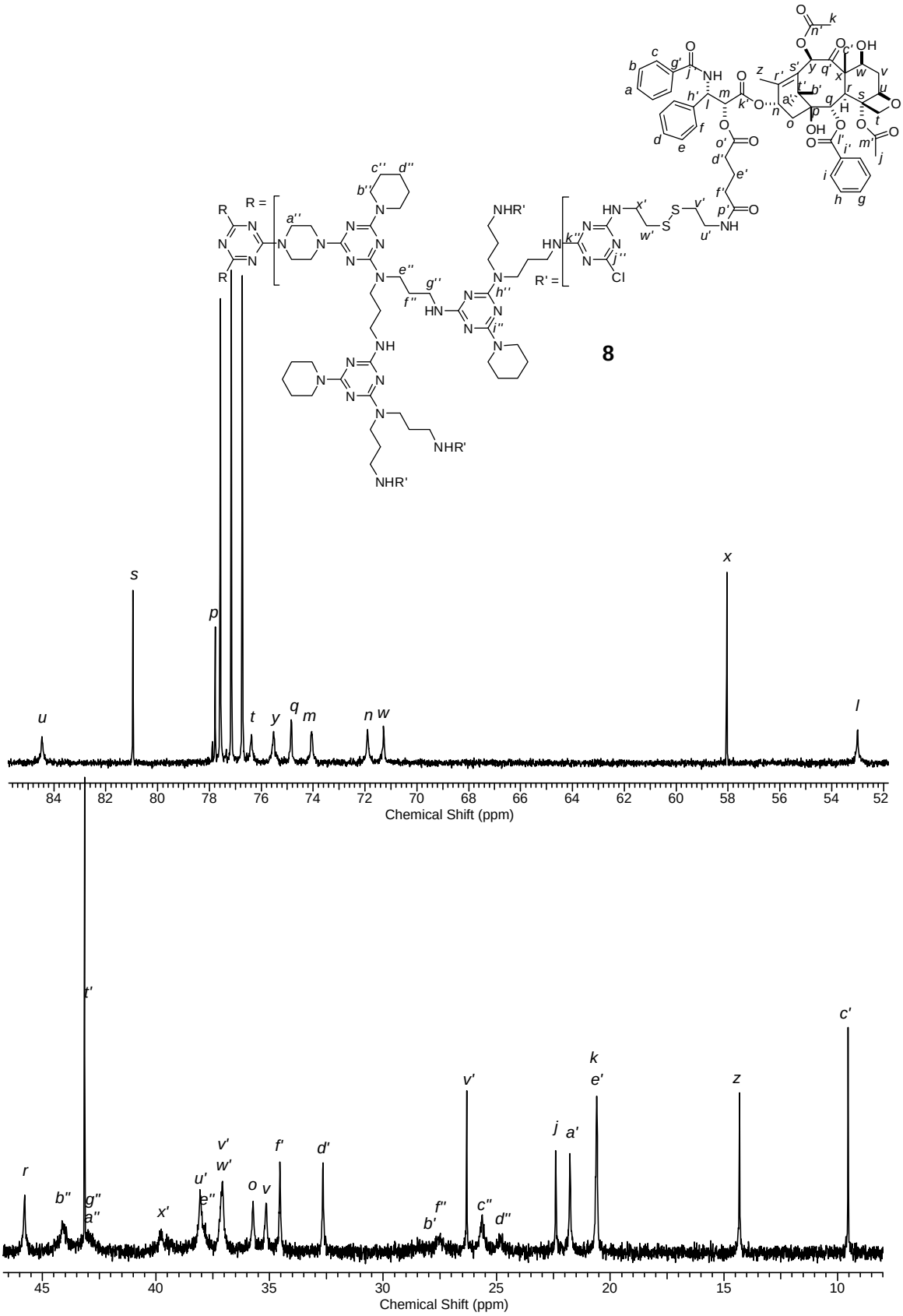
8
Chemical Shift (ppm)
Chemical Shift (ppm)

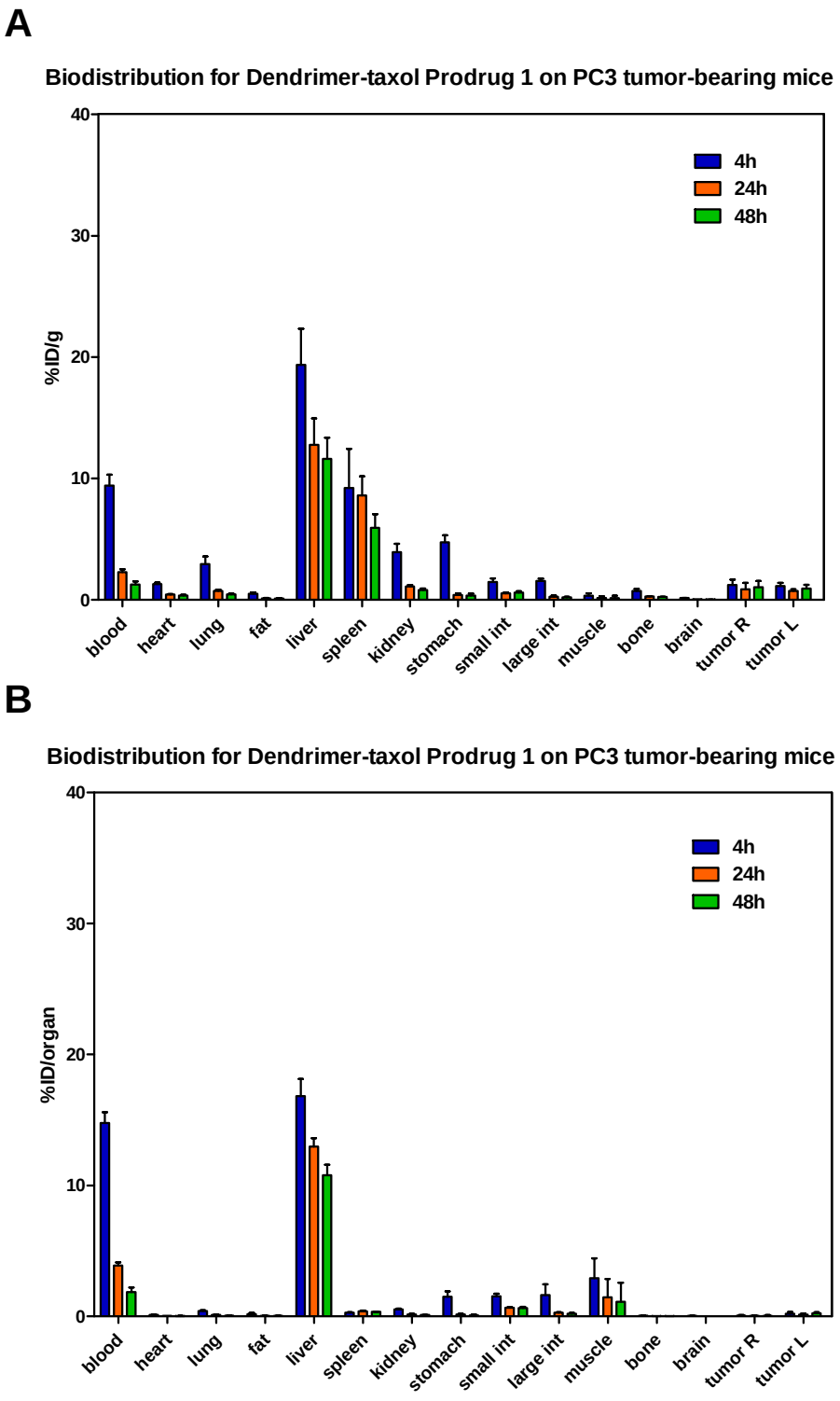

Figure S1. Biodistribution data for dendrimer-taxol prodrug **1** (n = 4). Data were presented as (A) %ID/g ± SD and (B) %ID/organ ± SD.

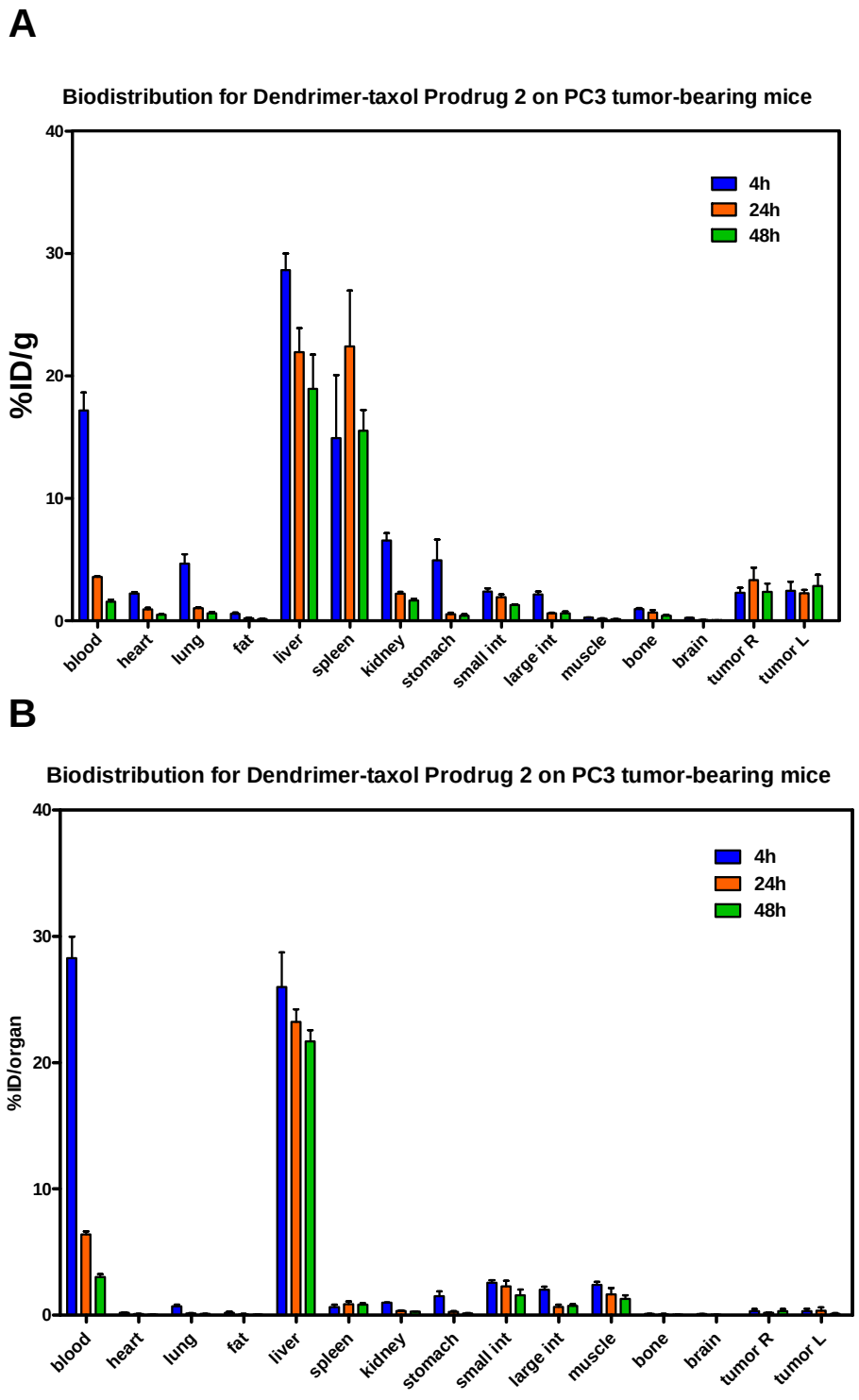

Figure S2. Biodistribution data for dendrimer-taxol prodrug **2** (n = 4). Data were presented as (A) %ID/g ± SD and (B) %ID/organ ± SD.

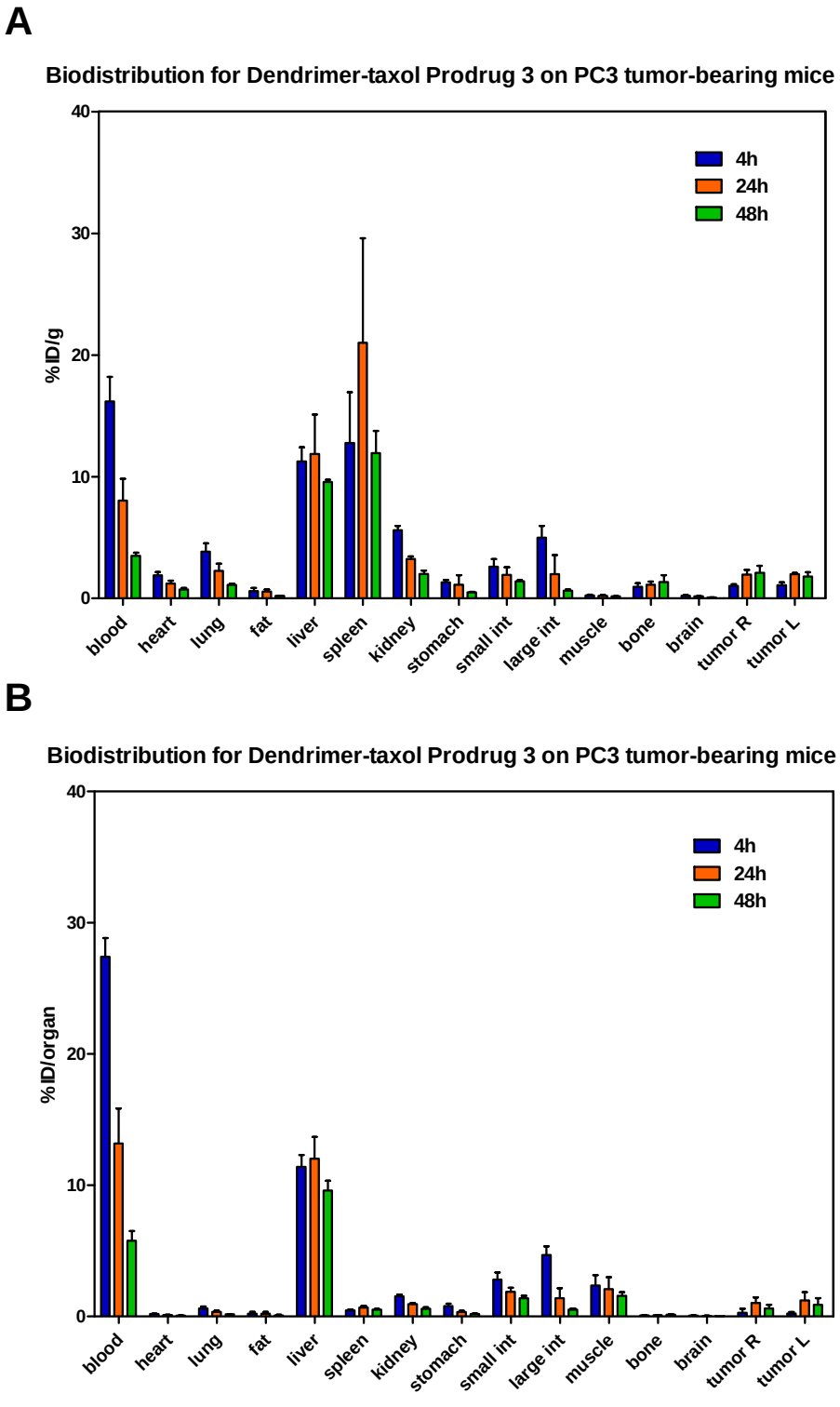

Figure S3. Biodistribution data for dendrimer-taxol prodrug **3** (n = 4). Data were presented as (A) %ID/g ± SD and (B) %ID/organ ± SD.

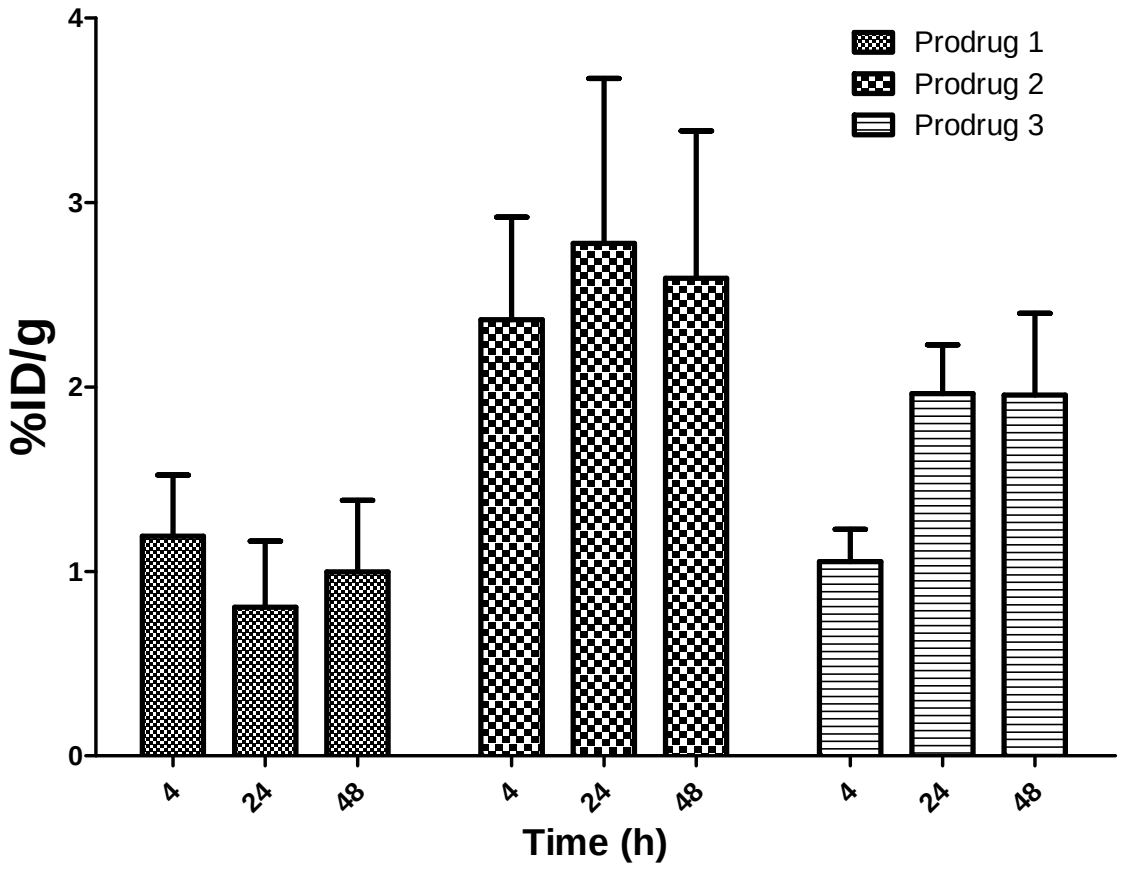

Figure S4. Tumor uptake (%ID/g) of prodrugs at 4, 24, and 48 h post-injection.

Table S1. Tumor-to-blood and tumor-to-muscle ratios of prodrugs at 4, 24, and 48h post-injection.

	4h			24h			48h		
Prodrug	**1**	**2**	**3**	**1**	**2**	**3**	**1**	**2**	**3**
Tumor/Blood	0.13	0.14	0.07	0.36	0.78	0.25	0.80	1.68	0.42
Tumor/Muscle	4.33	9.60	4.67	9.16	18.15	10.31	14.63	23.79	9.03

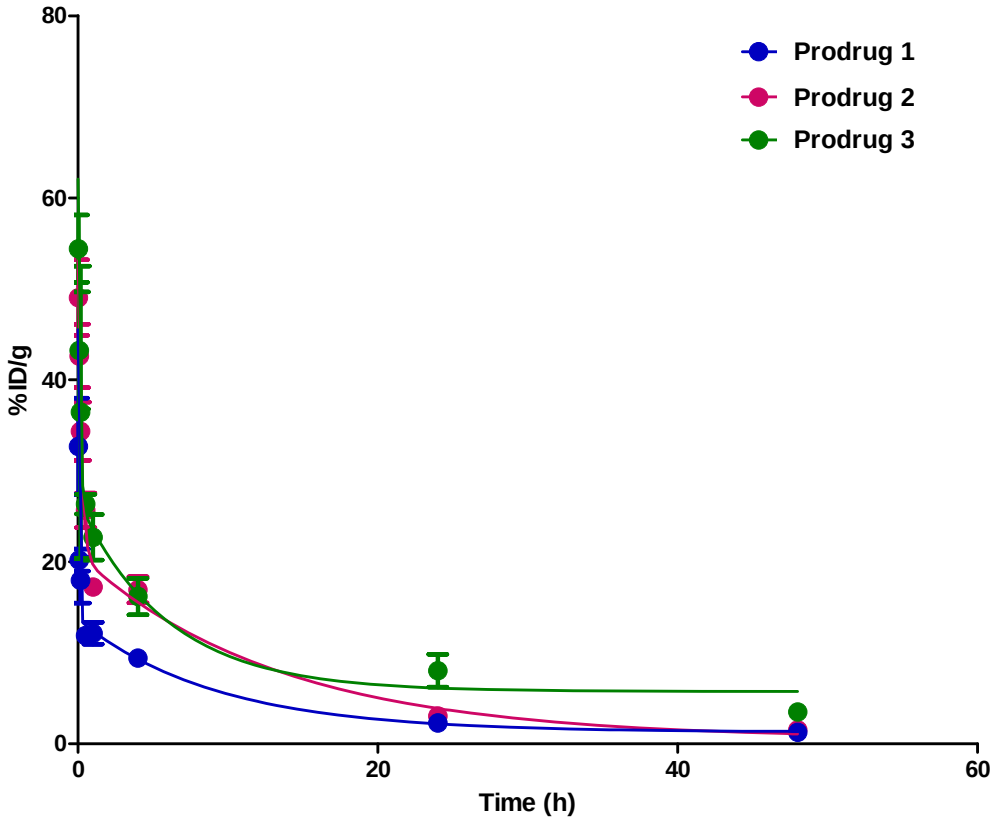

Figure S5. Time-activity curves of prodrugs in the blood.

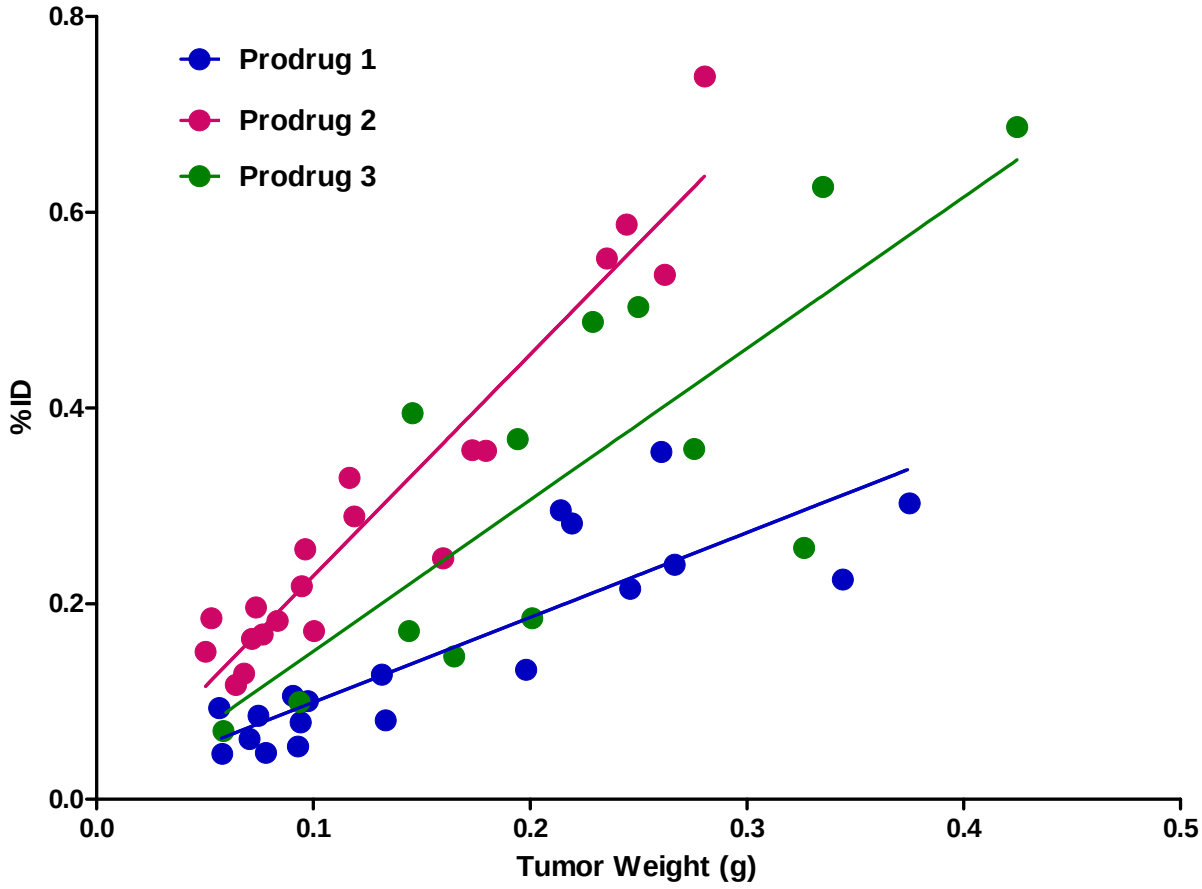

Figure S6. Tumor uptake (%ID/g) versus tumor size (0.05 – 0.5 g). R-square values of fitting line for **1**, **2**, and **3** are 0.7384, 0.9155, and 0.6351, respectively.

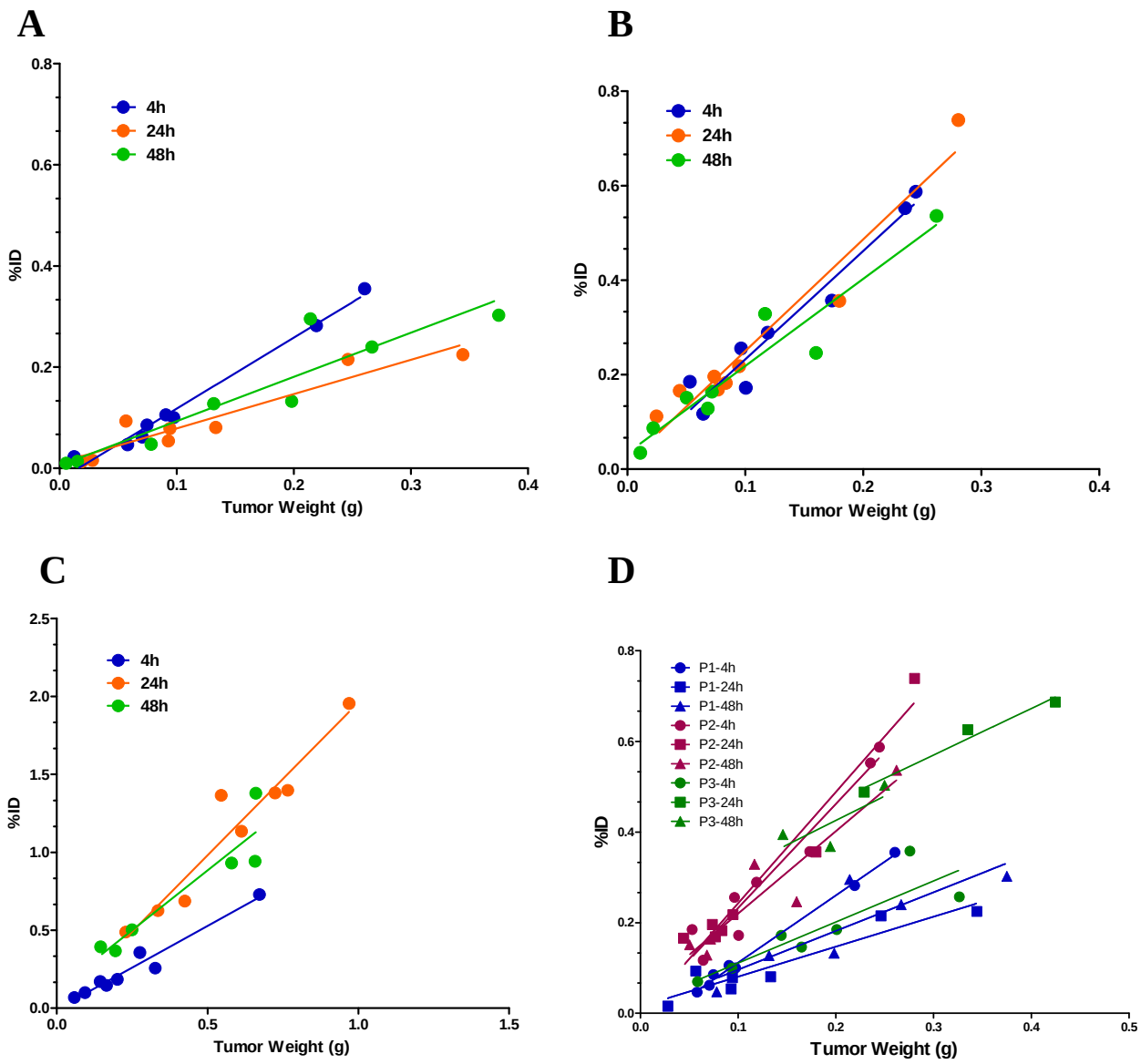

Figure S7. (A) Tumor uptake of **1** at different time points (data from three time points are significant different according to Prism analysis). (B) Tumor uptake of **2** at different time points (According to Prism analysis, data are not significant different). (C) Tumor uptake of **3** at different time points (data from three time points are significant different according to Prism analysis). (D) Combined tumor uptake data of three prodrugs.

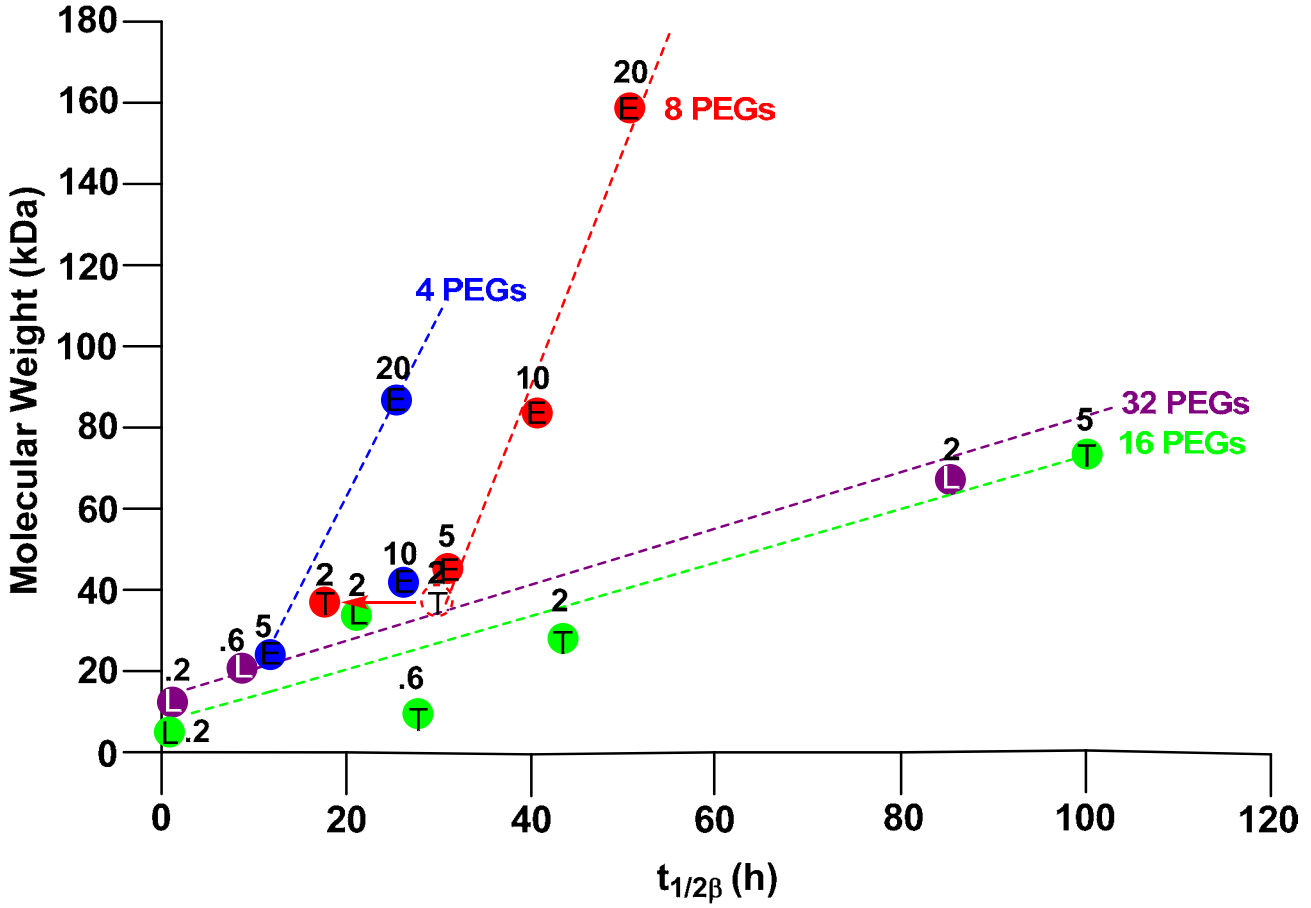

Figure S8. The plot of molecular weight against elimination half-life ($t_{1/2\beta}$). Dendrimers with 4 (blue), 8 (red), 16 (green), and 32 (violet) PEG chains are indicated and colored trend lines are added to guide the eye. The molecular weight of the PEG chains is indicated above each data point. The dendrimer class is indicated with a letter: E represents polyesters, L represents polylysine, T represents polytriazine. The dotted red circle with a letter T represents the predicted $t_{1/2\beta}$ for **1**, **2**, and **3**, while the red dot with a letter T shows the actual $t_{1/2\beta}$ of the dendrimers.

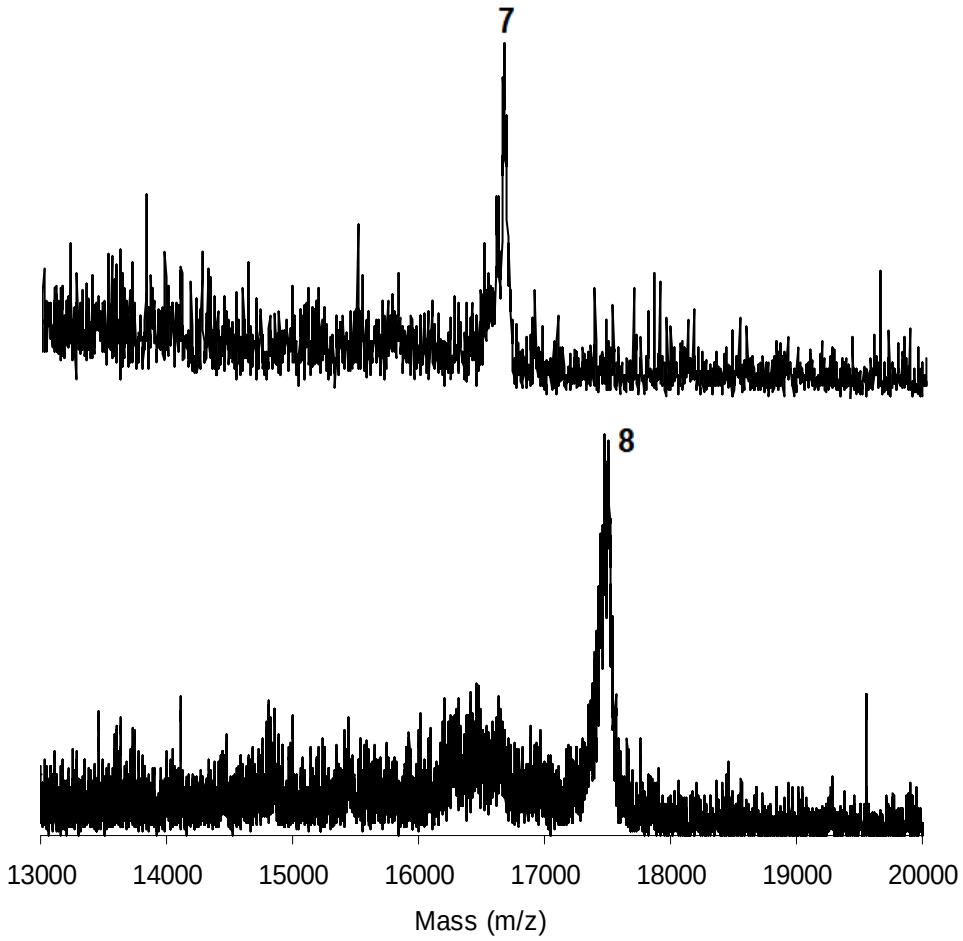

Figure S9. MALDI-TOF spectra of **7** and **8**.

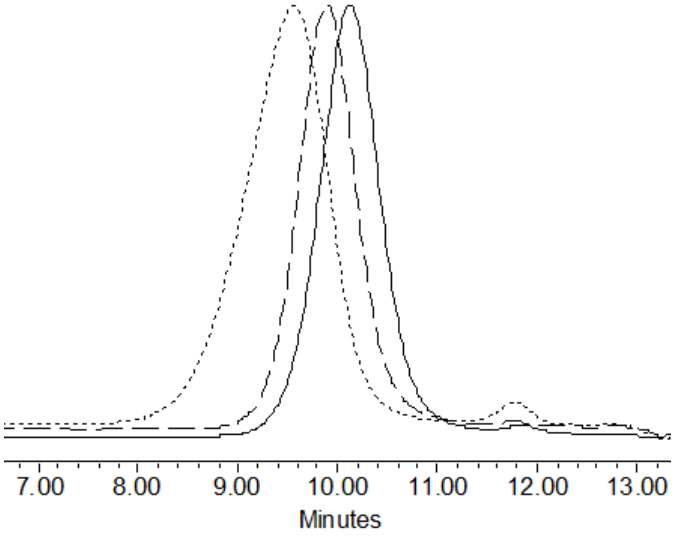

Figure S10. GPC traces of three PEGylated dendrimers: **1** (solid line), **2** (dashed line), and **3** (dotted line).

Effect of DOTA Position on Melanoma Targeting and Pharmacokinetic Properties of ^{111}In-Labeled Lactam Bridge-Cyclized α-Melanocyte Stimulating Hormone Peptide

Haixun Guo,[†] Jianquan Yang,[†] Fabio Gallazzi,[#] Eric R. Prossnitz,[‡,§] Larry A. Sklar,[†,‡,||] and Yubin Miao*[,†,‡,⊥]

College of Pharmacy, Cancer Research Treatment Center, Department of Cell Biology and Physiology, Department of Pathology, Department of Dermatology, University of New Mexico, Albuquerque, New Mexico 87131, and Department of Biochemistry, University of Missouri, Columbia, Missouri 65211. Received August 5, 2009; Revised Manuscript Received September 21, 2009

The purpose of this study was to examine the effect of DOTA (1,4,7,10-tetraazacyclododecane-1,4,7,10-tetraacetic acid) position on melanoma targeting and pharmacokinetics of radiolabeled lactam bridge-cyclized α-melanocyte stimulating hormone (α-MSH) peptide. Method: A novel lactam bridge-cyclized α-MSH peptide, Ac-GluGlu-CycMSH[DOTA] {Ac-Glu-Glu-c[Lys-Nle-Glu-His-DPhe-Arg-Trp-Gly-Arg-Pro-Val-Lys(DOTA)]}, was synthesized using standard 9-fluorenylmethyloxycarbonyl (Fmoc) chemistry. DOTA was directly attached to the α-amino group of Lys in the cyclic ring, while the N-terminus of the peptide was acetylated to generate Ac-GluGlu-CycMSH[DOTA]. The MC1 receptor binding affinity of Ac-GluGlu-CycMSH[DOTA] was determined in B16/F1 melanoma cells. Melanoma targeting and pharmacokinetic properties of Ac-GluGlu-CycMSH[DOTA]-^{111}In were determined in B16/F1 melanoma-bearing C57 mice and compared to that of ^{111}In-DOTA-Gly-Glu-c[Lys-Nle-Glu-His-DPhe-Arg-Trp-Gly-Arg-Pro-Val-Asp] (^{111}In-DOTA-GlyGlu-CycMSH; DOTA was coupled to the N-terminus of the peptide). Results: Ac-GluGlu-CycMSH[DOTA] displayed 0.6 nM MC1 receptor binding affinity in B16/F1 cells. Ac-GluGlu-CycMSH[DOTA]-^{111}In was readily prepared with greater than 95% radiolabeling yield. Ac-GluGlu-CycMSH[DOTA]-^{111}In exhibited high tumor uptake (11.42 ± 2.20% ID/g 2 h postinjection) and prolonged tumor retention (9.42 ± 2.41% ID/g 4 h postinjection) in B16/F1 melanoma-bearing C57 mice. The uptake values for nontarget organs were generally low (<1.3% ID/g) except for the kidneys 2, 4, and 24 h postinjection. Conclusions: DOTA position exhibited profound effect on melanoma targeting and pharmacokinetic properties of Ac-GluGlu-CycMSH[DOTA]-^{111}In, providing a new insight into the design of lactam bridge-cyclized peptide for melanoma imaging and therapy.

INTRODUCTION

Malignant melanoma is the most lethal form of skin cancer and the most commonly diagnosed malignancy among young adults with an increasing incidence in the United States. It is predicted that there will be 68 720 cases of malignant melanoma newly reported and 8650 fatalities in the year 2009 (*1*). Unfortunately, no curative treatment currently exists for metastatic melanoma due to its resistance to conventional chemotherapy and immunotherapy. It is highly desirable to develop novel effective diagnostic and therapeutic approaches to fulfill the desperate need in melanoma treatment. G protein-coupled melanocortin-1 (MC1) receptors are distinct molecular targets for developing peptide radiopharmaceuticals due to their overexpression on human and mouse melanoma cells (*2*−*6*). α-Melanocyte stimulating hormone (α-MSH) peptides can selectively target diagnostic and therapeutic radionuclides to MC1 receptors through specific peptide−receptor interaction for melanoma imaging and therapy (*7*−*19*).

Recently, we have reported a novel class of ^{111}In-labeled lactam bridge-cyclized α-MSH peptides as effective imaging probes for melanoma detection (*20, 21*). Unique lactam bridge-cyclization made the radiolabeled α-MSH peptides stable both *in vitro* and *in vivo*. Metal chelator DOTA was coupled to the N-terminus of the lactam bridge-cyclized α-MSH peptides for radiolabeling. ^{111}In-DOTA-GlyGlu-CycMSH exhibited high receptor-mediated melanoma uptake (10.40 ± 1.40% ID/g at 2 h postinjection) in B16/F1 melanoma-bearing C57 mice (*20*). Both primary melanoma and pulmonary melanoma metastases were clearly visualized by small animal SPECT/CT using ^{111}In-DOTA-GlyGlu-CycMSH as an imaging agent (*20, 21*), highlighting the potential applications of radiolabeled lactam bridge-cyclized α-MSH peptides as effective diagnostic and therapeutic agents for melanoma.

DOTA position (conjugation to N-terminus or toward C-terminus) of the radiolabeled linear α-MSH peptide has displayed a profound effect on melanoma and kidney uptakes of ^{111}In-labeled linear α-MSH peptide derivatives (*13*−*15*). For instance, DOTA was coupled to the N-terminus or toward C-terminus to generate ^{111}In-DOTA-MSHoct {^{111}In-DOTA-[β-Ala^3, Nle^4, Asp^5, D-Phe^7, Lys^{10}]-α-MSH$_{3-10}$} and ^{111}In-DOTA-NAPamide {[Nle^4, Asp^5, D-Phe^7, Lys^{11}(DOTA)-^{111}In]-α-MSH$_{4-11}$}, respectively. ^{111}In-DOTA-NAPamide exhibited 75% higher melanoma uptake and 63% less renal uptake than ^{111}In-MSHoct 4 h postinjection in B16/F1 melanoma-bearing C57 mice (*14*). In this report, we further examined the effect of

* Corresponding author. Yubin Miao, 2502 Marble NE, MSC09 5360, College of Pharmacy, University of New Mexico, Albuquerque, NM 87131-0001. Phone: (505) 925-4437; Fax: (505) 272-6749; E-mail: ymiao@salud.unm.edu.

[†] College of Pharmacy, University of New Mexico.

[‡] Cancer Research Treatment Center, University of New Mexico.

[§] Department of Cell Biology and Physiology, University of New Mexico.

[||] Department of Pathology, University of New Mexico.

[⊥] Department of Dermatology, University of New Mexico.

[#] University of Missouri.

10.1021/bc9003475 CCC: $40.75 © 2009 American Chemical Society
Published on Web 10/09/2009

DOTA position on the melanoma and renal uptakes of ^{111}In-labeled lactam bridge-cyclized α-MSH peptide. A novel DOTA-conjugated lactam bridge-cyclized α-MSH peptide, namely, Ac-GluGlu-CycMSH[DOTA] was synthesized using standard 9-fluorenylmethyloxycarbonyl (Fmoc) chemistry. DOTA was directly attached to the α-amino group of Lys (toward C-terminus) in the cyclic ring, while the N-terminus of the peptide was acetylated to generate Ac-GluGlu-CycMSH[DOTA]. The melanoma targeting and pharmacokinetic properties of Ac-GluGlu-CycMSH[DOTA]-^{111}In were determined in B16/F1 melanoma-bearing C57 mice. Meanwhile, the effect of L-lysine coinjection on the renal uptake of Ac-GluGlu-CycMSH[DOTA]-^{111}In was examined in B16/F1 melanoma-bearing C57 mice.

EXPERIMENTAL PROCEDURES

Chemicals and Reagents. Amino acid and resin were purchased from Advanced ChemTech Inc. (Louisville, KY) and Novabiochem (San Diego, CA). DOTA-tri-*t*-butyl ester was purchased from Macrocyclics Inc. (Richardson, TX). $^{111}InCl_3$ was purchased from Trace Life Sciences, Inc. (Dallas, TX). ^{125}I-Tyr^2-[Nle^4, D-Phe^7]-α-MSH {^{125}I-(Tyr^2)-NDP-MSH} was obtained from PerkinElmer, Inc. (Shelton, CT). All other chemicals used in this study were purchased from Thermo Fischer Scientific (Waltham, MA) and used without further purification. B16/F1 murine melanoma cells were obtained from American type Culture Collection (Manassas, VA).

Peptide Synthesis. Intermediate scaffold of Ac-Glu(OtBu)-Glu(OtBu)-Lys(Dde)-Nle-Glu(OtBu)-His(Trt)-DPhe-Arg(Pbf)-Trp(Boc)-Gly-Arg(Pbf)-Pro-Val was synthesized on Val-2-chlorotrityl chloride (Val-2ClTrt) resin using standard Fmoc chemistry by an Advanced ChemTech multiple-peptide synthesizer (Louisville, KY). A small aliquot of the scaffold material was cleaved and characterized by liquid chromatography−mass spectrometry (LC-MS) prior to further peptide synthesis and cyclization. The protecting group (Dde) of the Lys in the intermediate scaffold was removed by 2% hydrazine, and the branch moiety of the peptide was generated by coupling Fmoc-Lys(Dde) to the ε-amino group of the Lys in the intermediate scaffold manually. $(tBu)_3$DOTA was coupled to the α-amino group of Lys(Dde) in the peptide branch manually using standard Fmoc chemistry. The protecting group (Dde) of the Lys in peptide branch was removed by 2% hydrazine. After the removal of the (Dde) protecting group, the protected branched peptide was cleaved from the resin treating with 25% hexafluoroisopropanol (HFIP) and 5% triisopropylsilane (TIS) in dichloromethane (DCM) and characterized by LC-MS. Peptide cyclization between the acid moiety of Val and the ε-amino group of Lys in the peptide branch was achieved by overnight reaction in DMF in the presence of a mixture of 1 mM 1-hydroxybenzotriazole (HOBT), 2-(1*H*-benzotriazole-1-yl)-1,1,3,3-tetranethyluronium hexafluorophosphate (HBTU), and *N*,*N*-diisopropylethylamine (DIEA). The protecting groups were totally removed by treating with a mixture of trifluoroacetic acid (TFA), thioanisole, phenol, water, ethanedithiol, and triisopropylsilane (87.5:2.5:2.5:2.5:2.5:2.5) for 2 h at room temperature (25 °C). The peptide was precipitated and washed with ice-cold ether for four times, purified by reverse-phase−high performance liquid chromatography (RP-HPLC), and characterized by LC-MS.

***In Vitro* Competitive Binding Assay.** The IC_{50} value of Ac-GluGlu-CycMSH[DOTA] was determined by *in vitro* competitive binding assay according to the method described previously (*20*). B16/F1 cells were harvested and seeded into a 24-well cell culture plate (5×10^5 cells/well) and incubated at 37 °C overnight. After being washed once with binding medium [Dulbecco's Modified Eagle's Medium with 25 mM *N*-(2-hydroxyethyl)-piperazine-*N*′-(2-ethanesulfonic acid), 0.2% BSA, and 0.3 mM 1,10-phenathroline], the cells were incubated at 25 °C for 2 h with approximately 50 000 cpm of ^{125}I-(Tyr^2)-NDP-MSH in the presence of increasing concentrations (10^{-13} to 10^{-6} M) of Ac-GluGlu-CycMSH[DOTA] in 0.3 mL of binding medium. The reaction medium was aspirated after incubation. Cells were rinsed with 0.5 mL of ice-cold pH 7.4, 0.2% BSA/0.01 M PBS twice, and lysed in 0.5 mL of 1 N NaOH for 5 min. The activities associated with cells were measured in a Wallac 1480 automated gamma counter (PerkinElmer, NJ). The IC_{50} value of Ac-GluGlu-CycMSH[DOTA] was calculated by using *Prism* software (GraphPad Software, La Jolla, CA).

Complexation of the Peptide with ^{111}In. Ac-GluGlu-CycMSH[DOTA]-^{111}In was prepared using a 0.5 M NH_4OAc-buffered solution at pH 5.4. Briefly, 50 μL of $^{111}InCl_3$ (18.5−37.0 MBq in 0.05 M HCl), 10 μL of 1 mg/mL Ac-GluGlu-CycMSH[DOTA] aqueous solution, and 400 μL of 0.5 M NH_4OAc (pH 5.4) were added into a reaction vial and incubated at 75 °C for 45 min. After the incubation, 20 μL of 0.5% EDTA aqueous solution was added into the reaction vial to quench the reaction. The radiolabeled peptide was purified to single species by Waters RP-HPLC (Milford, MA) on a Grace Vadyc C-18 reverse-phase analytical column (Deerfield, IL) using the following gradient at a flow rate of 1 mL/min. The mobile phase consisted of solvent A (20 mM HCl aqueous solution) and solvent B (100% CH_3CN). The gradient was initiated and kept at 82:18 A/B for 3 min followed by a linear gradient of 82:18 A/B to 72:28 A/B over 20 min. Then, the gradient was changed from 72:28 A/B to 10:90 A/B over 3 min followed by an additional 5 min at 10:90 A/B. Thereafter, the gradient was changed from 10:90 A/B to 82:18 A/B over 3 min. Purified peptide sample was purged with N_2 gas for 20 min to remove the acetonitrile. The pH of final solution was adjusted to 7.4 with 0.1 N NaOH and normal saline for animal studies. Serum stability of Ac-GluGlu-CycMSH[DOTA]-^{111}In was determined according to the published procedure (*20*) by incubation in mouse serum at 37 °C for 24 h, and monitored for degradation by RP-HPLC.

Cellular Internalization and Efflux of Ac-GluGlu-CycMSH-[DOTA]-^{111}In. Cellular internalization and efflux of Ac-GluGlu-CycMSH[DOTA]-^{111}In were evaluated in B16/F1 cells as described by Miao et al. (*20*). After being washed once with binding medium, B16/F1 cells seeded in cell culture plates were incubated at 25 °C for 20, 40, 60, 90, and 120 min ($n = 3$) in the presence of approximately 160 000 counts per minute (cpm) of HPLC purified Ac-GluGlu-CycMSH[DOTA]-^{111}In. After incubation, the reaction medium was aspirated and cells were rinsed with 2×0.5 mL of ice-cold pH 7.4, 0.2% BSA/0.01 M PBS. Cellular internalization of Ac-GluGlu-CycMSH[DOTA]-^{111}In was assessed by washing the cells with acidic buffer [40 mM sodium acetate (pH 4.5) containing 0.9% NaCl and 0.2% BSA] to remove the membrane-bound radioactivity. The remaining internalized radioactivity was obtained by lysing the cells with 0.5 mL of 1 N NaOH for 5 min. Membrane-bound and internalized ^{111}In activities were counted in a gamma counter. Cellular efflux was determined by incubating B16/F1 cells with Ac-GluGlu-CycMSH[DOTA]-^{111}In for 2 h, removing non-specific-bound activity with 2×0.5 mL of ice-cold pH 7.4, 0.2% BSA/0.01 M PBS rinse, and monitoring radioactivity released into cell culture medium. At time points of 20, 40, 60, 90, and 120 min, the radioactivities on cell surfaces and in cells were separately collected and counted in a gamma counter.

Biodistribution Studies. All the animal studies were conducted in compliance with Institutional Animal Care and Use Committee approval. The biodistribution properties of Ac-GluGlu-CycMSH[DOTA]-^{111}In were determined in B16/F1 melanoma-bearing C57 female mice (Harlan, Indianapolis, IN).

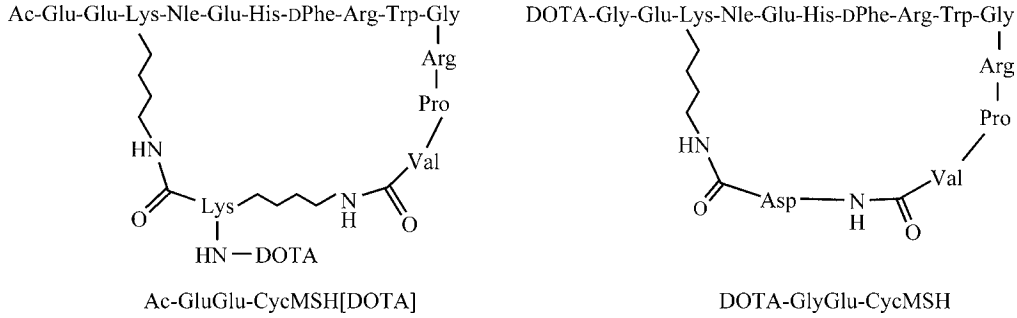

Figure 1. Schematic structures of Ac-GluGlu-CycMSH[DOTA] and DOTA-GlyGlu-CycMSH.

C57 mice were inoculated subcutaneously with 1×10^6 B16/F1 melanoma cells in the right flank for each mouse. After 10 days, when the weight of tumors reached approximately 0.2 g, 0.037 MBq of Ac-GluGlu-CycMSH[DOTA]-^{111}In was injected into each mouse through the tail vein. Groups of 5 mice were sacrificed at 0.5, 2, 4, and 24 h postinjection, and tumors and organs of interest were harvested, weighed, and counted. Blood values were taken as 6.5% of the whole-body weight. The specificity of the tumor uptake of Ac-GluGlu-CycMSH[DOTA]-^{111}In was determined by blocking the tumor uptake with the coinjection of 10 μg (6.07 nmol) of unlabeled NDP-MSH, a linear α-MSH peptide analogue with picomolar affinity for the MC1 receptor present on melanoma cells.

The effect of L-lysine coinjection on the renal uptake of Ac-GluGlu-CycMSH[DOTA]-^{111}In was examined in B16/F1 melanoma-bearing C57 as well. A group of 5 mice were injected with a mixture of 0.037 MBq of Ac-GluGlu-CycMSH[DOTA]-^{111}In and 15 mg of L-lysine. The mice were sacrificed at 2 h postinjection, and tumors and organs of interest were harvested, weighed, and counted. Blood values were taken as 6.5% of the whole body weight.

Imaging Melanoma with Ac-GluGlu-CycMSH[DOTA]-^{111}In. One B16/F1 melanoma-bearing C57 mouse was injected with 7.4 MBq of Ac-GluGlu-CycMSH[DOTA]-^{111}In via the tail vein. The mouse was anesthetized with 1.5% isoflurane for small animal SPECT/CT (Nano-SPECT/CT, Bioscan) imaging 2 h postinjection. The 9 min CT imaging was immediately followed by the SPECT imaging of whole body. The SPECT scans of 24 projections were acquired, and total acquisition time was 45 min. Reconstructed data from SPECT and CT were visualized and coregistered using InVivoScope (Bioscan, Washington, DC).

Urinary Metabolites of Ac-GluGlu-CycMSH[DOTA]-^{111}In. One hundred microliter of HPLC purified Ac-GluGlu-CycMSH[DOTA]-^{111}In (3.7 MBq) was injected into a B16/F1 melanoma-bearing C57 mouse through the tail vein. At 2 h after dose administration, the mouse was sacrificed and the urine was collected. The radioactive metabolites in the urine were analyzed by injecting aliquots of the urine into HPLC. A 20 min gradient of 18−28% acetonitrile/20 mM HCl was used for the urine analysis.

Statistical Methods. Statistical analysis was performed using the Student's *t* test for unpaired data to determine the significant differences between Ac-GluGlu-CycMSH[DOTA]-^{111}In with or without NDP-MSH coinjection and Ac-GluGlu-CycMSH[DOTA]-^{111}In with or without L-lysine coinjection described in biodistribution studies above. Differences at the 95% confidence level ($p < 0.05$) were considered significant.

RESULTS

To examine the effect of DOTA position on the melanoma and renal uptakes of ^{111}In-labeled lactam bridge-cyclized α-MSH peptide, a novel peptide of Ac-GluGlu-CycMSH[DOTA] was synthesized and purified by RP-HPLC. The identity of Ac-GluGlu-CycMSH[DOTA] was confirmed by electrospray ionization mass spectrometry (found MW 2220.5; calculated MW 2220.0). Ac-GluGlu-CycMSH[DOTA] displayed greater than 95% purity with 30% overall synthetic yield. The schematic structure of Ac-GluGlu-CycMSH[DOTA] is shown in Figure 1. Figure 2 illustrates the synthetic scheme of Ac-GluGlu-CycMSH[DOTA]. The competitive binding curve of Ac-GluGlu-CycMSH[DOTA] is presented in Figure 3. The IC_{50} value of Ac-GluGlu-CycMSH[DOTA] was 0.6 nM in B16/F1 melanoma cells.

The peptide was readily labeled with ^{111}In in 0.5 M ammonium acetate at pH 5.4 with greater than 95% radiolabeling yield. Ac-GluGlu-CycMSH[DOTA]-^{111}In was completely sepa-

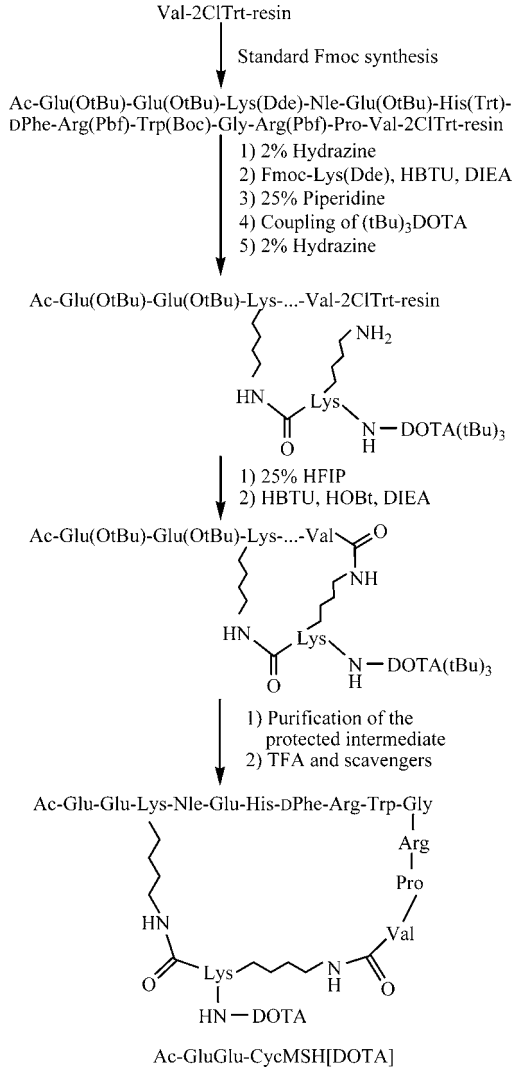

Figure 2. Synthetic scheme of Ac-GluGlu-CycMSH[DOTA].

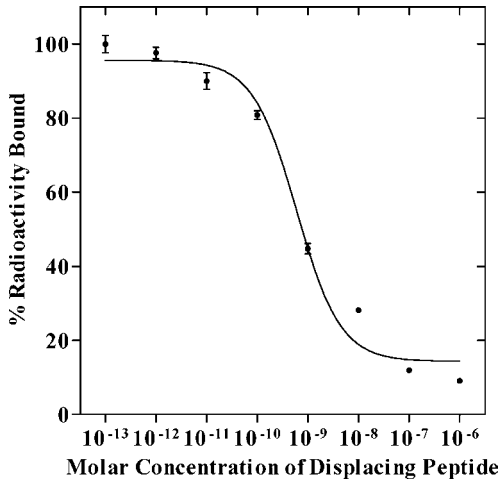

Figure 3. The competitive binding curve of Ac-GluGlu-CycMSH-[DOTA] in B16/F1 murine melanoma cells. The IC_{50} value of Ac-GluGlu-CycMSH[DOTA] was 0.6 nM.

rated from its excess nonlabeled peptide by RP-HPLC. The retention times of Ac-GluGlu-CycMSH[DOTA]-^{111}In and its nonlabeled peptide were 20.1 (Figure 4) and 15.5 min, respectively. The specific activity of Ac-GluGlu-CycMSH-[DOTA]-^{111}In was 7.41×10^8 MBq/g. Ac-GluGlu-CycMSH-[DOTA]-^{111}In showed greater than 98% radiochemical purity after the HPLC purification. Ac-GluGlu-CycMSH[DOTA]-^{111}In was stable in mouse serum at 37 °C. Only the Ac-GluGlu-CycMSH[DOTA]-^{111}In was detected by RP-HPLC after 24 h of incubation (Figure 4).

Cellular internalization and efflux of Ac-GluGlu-CycMSH-[DOTA]-^{111}In were evaluated in B16/F1 cells. Figure 5 illustrates cellular internalization and efflux of Ac-GluGlu-CycMSH[DOTA]-^{111}In. Ac-GluGlu-CycMSH[DOTA]-^{111}In exhibited rapid cellular internalization and extended cellular retention. There was 72.54 ± 3.10% of the cellular uptake of Ac-GluGlu-CycMSH[DOTA]-^{111}In activity internalized in the B16/F1 cells 40 min post-incubation. There was 81.12 ± 0.28% of the cellular uptake of Ac-GluGlu-CycMSH[DOTA]-^{111}In activity internalized in the cells after 2 h incubation. Cellular efflux results demonstrated that 68.60 ± 1.43% of the internalized Ac-GluGlu-CycMSH[DOTA]-^{111}In activity remained inside the cells 2 h after incubating cells in culture medium.

The melanoma targeting and pharmacokinetic properties of Ac-GluGlu-CycMSH[DOTA]-^{111}In were determined in B16/F1 melanoma-bearing C57 mice. The biodistribution results of Ac-GluGlu-CycMSH[DOTA]-^{111}In are shown in Table 1. Ac-GluGlu-CycMSH[DOTA]-^{111}In exhibited rapid and high melanoma uptake. The tumor uptake value was 12.11 ± 1.21% ID/g 0.5 h postinjection. There was 9.42 ± 2.41% ID/g of Ac-GluGlu-CycMSH[DOTA]-^{111}In activity remained in the tumors 4 h postinjection. The tumor uptake value of Ac-GluGlu-CycMSH[DOTA]-^{111}In gradually decreased to 3.64 ± 0.74% ID/g 24 h postinjection. In the blocking study, the tumor uptake value of Ac-GluGlu-CycMSH[DOTA]-^{111}In with 10 μg (6.07 nmol) of non-radiolabeled NDP-MSH co-injection were only 4.8% of the tumor uptake value without NDP-MSH co-injection at 2 h postinjection ($p < 0.05$), demonstrating that the tumor uptake was specific and receptor-mediated. Whole-body clearance of Ac-GluGlu-CycMSH[DOTA]-^{111}In was rapid, with approximately 78% of the injected radioactivity cleared through the urinary system by 2 h postinjection (Table 1). Normal organ uptakes of Ac-GluGlu-CycMSH[DOTA]-^{111}In were generally very low (<1.3% ID/g) except for the kidneys 2, 4, and 24 h postinjection. High tumor/blood and tumor/normal organ uptake

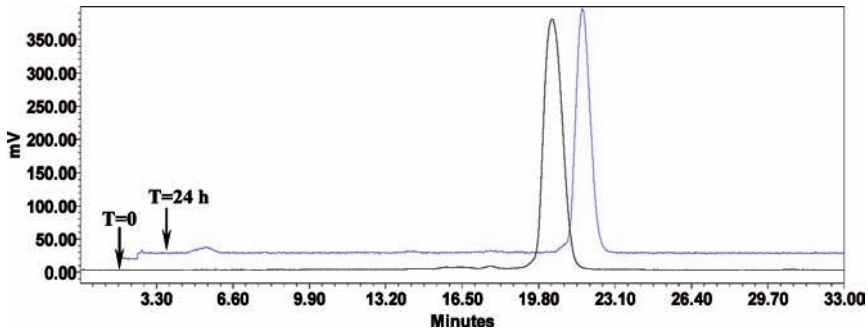

Figure 4. HPLC profile of radioactive Ac-GluGlu-CycMSH[DOTA]-^{111}In ($T = 0$) and mouse serum stability of Ac-GluGlu-CycMSH[DOTA]-^{111}In ($T = 24$ h) after 24 h incubation at 37 °C. The retention time of Ac-GluGlu-CycMSH[DOTA]-^{111}In was 20.1 min.

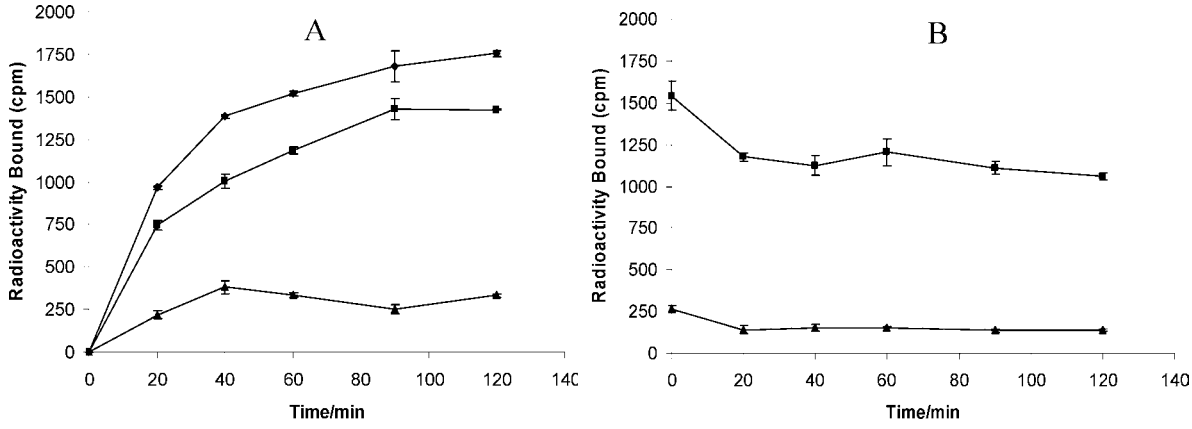

Figure 5. Cellular internalization (A) and efflux (B) of Ac-GluGlu-CycMSH[DOTA]-^{111}In in B16/F1 murine melanoma cells at 25 °C. Total bound radioactivity (◆), internalized activity (■), and cell membrane activity (▲) were presented as counts per minute (cpm).

Table 1. Biodistribution of Ac-GluGlu-CycMSH[DOTA]-^{111}In in B16/F1 Melanoma-Bearing C57 Mice[a]

tissues	0.5 h	2 h	2 h NDP blockade	2 h L-lysine coinjection	4 h	24 h
			Percent Injected Dose/Gram (%ID/g)			
tumor	12.11 ± 1.21	11.42 ± 2.20	0.49 ± 0.15[b]	11.86 ± 2.18	9.42 ± 2.41	3.64 ± 0.74
brain	0.14 ± 0.01	0.01 ± 0.01	0.04 ± 0.02	0.02 ± 0.01	0.03 ± 0.01	0.01 ± 0.00
blood	2.03 ± 0.32	0.21 ± 0.05	0.16 ± 0.13	0.32 ± 0.04[b]	0.16 ± 0.11	0.03 ± 0.02
heart	0.69 ± 0.17	0.13 ± 0.11	0.17 ± 0.13	0.38 ± 0.12[b]	0.26 ± 0.15	0.03 ± 0.03
lung	2.49 ± 0.25	0.64 ± 0.16	0.33 ± 0.05[b]	0.32 ± 0.04[b]	0.34 ± 0.10	0.07 ± 0.02
liver	1.85 ± 0.14	1.02 ± 0.18	0.62 ± 0.13[b]	0.58 ± 0.14[b]	1.28 ± 0.24	1.01 ± 0.28
spleen	0.79 ± 0.24	0.47 ± 0.05	0.48 ± 0.12	0.16 ± 0.14[b]	0.64 ± 0.36	0.27 ± 0.10
stomach	0.69 ± 0.09	0.32 ± 0.19	0.05 ± 0.02[b]	0.25 ± 0.06	0.18 ± 0.07	0.07 ± 0.04
kidneys	51.52 ± 6.17	60.48 ± 8.37	47.02 ± 13.14	18.35 ± 5.92[b]	67.21 ± 8.63	21.09 ± 6.59
muscle	0.37 ± 0.13	0.12 ± 0.02	0.36 ± 0.18	0.08 ± 0.10	0.04 ± 0.03	0.04 ± 0.02
pancreas	0.53 ± 0.08	0.12 ± 0.01	0.08 ± 0.01[b]	0.37 ± 0.29	0.07 ± 0.05	0.02 ± 0.02
bone	0.43 ± 0.22	0.41 ± 0.17	0.21 ± 0.14	0.35 ± 0.31	0.24 ± 0.14	0.05 ± 0.02
skin	1.75 ± 0.06	0.39 ± 0.03	0.25 ± 0.03[b]	0.46 ± 0.11	0.26 ± 0.15	0.18 ± 0.02
			Percent Injected Dose (%ID)			
intestines	0.78 ± 0.13	1.39 ± 0.87	0.63 ± 0.30	0.55 ± 0.09	0.44 ± 0.14	0.18 ± 0.07
urine	51.65 ± 5.38	77.59 ± 1.52	87.32 ± 2.53	90.77 ± 1.78	78.84 ± 2.34	90.82 ± 2.05
			Uptake Ratio of Tumor/Normal Organ			
tumor/blood	5.97	54.38	3.06	37.06	58.88	121.33
tumor/kidneys	0.24	0.19	0.01	0.65	0.14	0.17
tumor/lung	4.86	17.84	1.48	37.06	27.71	52.00
tumor/liver	6.55	11.20	0.79	20.45	7.36	3.60
tumor/muscle	32.73	95.17	1.36	148.25	235.50	91.00
tumor/skin	6.92	29.28	1.96	25.78	36.23	20.22

[a] The data were presented as percent injected dose/gram or as percent injected dose (mean ± SD, $n = 5$). [b] $p < 0.05$ significance comparison of Ac-GluGlu-CycMSH[DOTA]-^{111}In with or without peptide blockade, and with or without L-lysine co-injection 2 h postinjection.

ratios were demonstrated as early as 0.5 h postinjection (Table 1). The renal uptake of Ac-GluGlu-CycMSH[DOTA]-^{111}In was 51.52 ± 6.17% ID/g 0.5 h postinjection, reached its peak value of 67.21 ± 8.63% ID/g 4 h postinjection, and gradually decreased to 21.09 ± 6.59% ID/g 24 h postinjection. Co-injection of 15 mg of L-lysine reduced the kidney uptake value of Ac-GluGlu-CycMSH[DOTA]-^{111}In to 18.35 ± 5.92% ID/g (70% reduction) without affecting the tumor uptake value 2 h postinjection (Table 1).

One B16/F1 melanoma-bearing C57 mouse was injected with 7.4 MBq of Ac-GluGlu-CycMSH[DOTA]-^{111}In through the tail vein to visualize the tumors at 2 h after dose administration. The whole-body SPECT image of the mouse was fused with CT image. The whole-body SPECT/CT image is presented in Figure 6. Flank melanoma tumors were visualized clearly using Ac-GluGlu-CycMSH[DOTA]-^{111}In as an imaging probe 2 h postinjection. Ac-GluGlu-CycMSH[DOTA]-^{111}In exhibited high tumor to normal organ uptake ratios except for the kidney, which was coincident with the biodistribution results. In view of the substantial renal uptake value of Ac-GluGlu-CycMSH[DOTA]-^{111}In in the biodistribution results, the urinary metabolites of Ac-GluGlu-CycMSH[DOTA]-^{111}In were analyzed by RP-HPLC at 2 h postinjection. The HPLC elution profile of Ac-GluGlu-CycMSH[DOTA]-^{111}In is shown in Figure 7. Eighty-three percent of Ac-GluGlu-CycMSH[DOTA]-^{111}In was transformed to two more polar metabolites, and only 17% of Ac-GluGlu-CycMSH[DOTA]-^{111}In remained intact at 2 h postinjection.

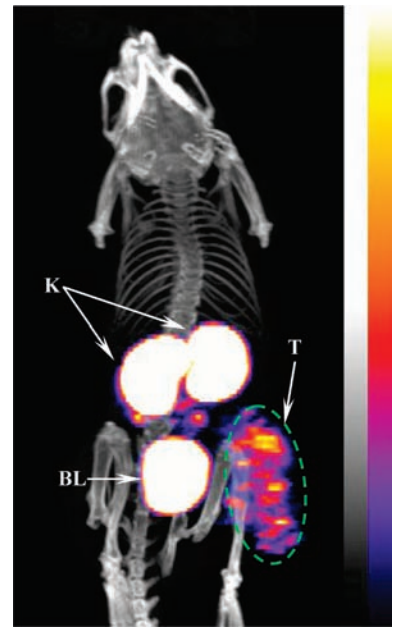

Figure 6. Whole-body image of Ac-GluGlu-CycMSH[DOTA]-^{111}In in B16/F1 flank melanoma-bearing C57 mice at 2 h postinjection. Tumor (T), kidneys (K), and bladder (BL) are highlighted with arrows on the image.

DISCUSSION

Both radiolabeled linear and cyclic α-MSH peptides have been reported to target the MC1 receptors for melanoma imaging and therapy (*4*−*22*). Cyclization of α-MSH peptides has been successfully used to improve the binding affinities and *in vivo* stability of peptides (*14*−*16*). In comparison with linear peptide, stabilization of secondary structures such as β-turns makes the cyclic peptide less flexible in conformation and better fit receptor binding pocket, enhancing the binding affinities of the cyclic peptides. Among the ^{111}In-labeled metal-cyclized, lactam bridge-cyclized and disulfide bridge-cyclized α-MSH peptides, ^{111}In-labeled metal-cyclized and lactam bridge-cyclized α-MSH peptides displayed higher melanoma uptake values and lower renal uptake values in B16/F1 melanoma-bearing C57 mice (*4*, *20*). We have recently developed a novel class of DOTA-conjugated lactam bridge-cyclized α-MSH peptides where the metal chelator DOTA was attached to the N-terminus of the peptide for radiolabeling. Both primary melanoma and pulmonary melanoma metastases were clearly imaged by small animal SPECT/CT using ^{111}In-DOTA-GlyGlu-CycMSH as an imaging probe (*20*, *21*).

Eberle and co-workers reported the profound effect of DOTA position on melanoma and kidney uptakes of ^{111}In-labeled linear

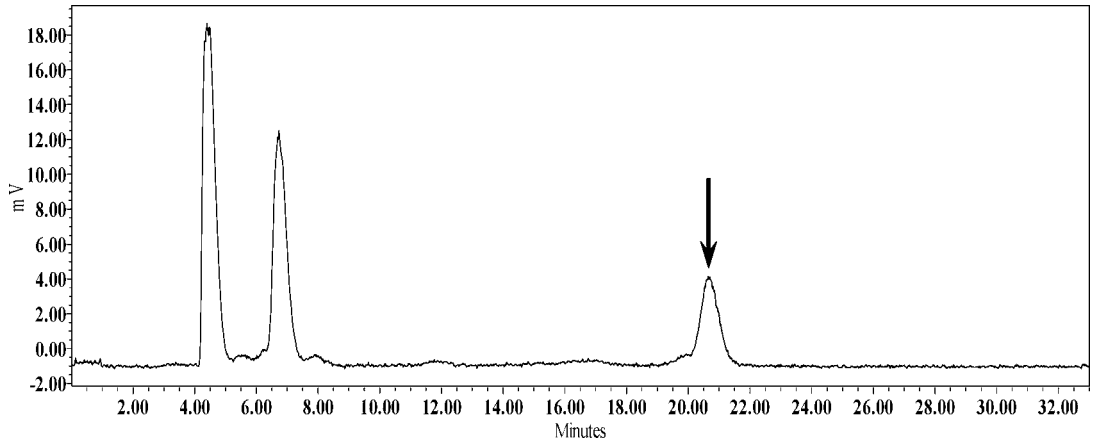

Figure 7. HPLC profile of radioactive urine sample of a B16/F1 melanoma-bearing C57 mouse at 2 h postinjection of Ac-GluGlu-CycMSH[DOTA]-^{111}In. The arrow indicates the retention time of the original compound of Ac-GluGlu-CycMSH[DOTA]-^{111}In prior to the tail vein injection.

α-MSH peptide derivatives (*14, 15*). Initially, DOTA was directly attached to the N-terminus of the peptide to yield ^{111}In-DOTA-MSH_{oct} {^{111}In-DOTA-[β-Ala^3, Nle^4, Asp^5, D-Phe^7, Lys^{10}]-α-MSH_{3-10}}, which exhibited 4.31 ± 0.30% ID/g tumor uptake 4 h postinjection in B16/F1 melanoma-bearing C57 mice (*14*). Thereafter, another ^{111}In-labeled linear α-MSH peptide derivative, namely, ^{111}In-DOTA-NAPamide {[Nle^4, Asp^5, D-Phe^7, Lys^{11}(DOTA)-^{111}In]-α-MSH_{4-11}} was developed by coupling DOTA to the ε-amino group of Lys in the C-terminus. Interestingly, coupling of DOTA toward the C-terminus of the linear peptide improved the tumor uptake and reduced renal uptake of ^{111}In-DOTA-NAPamide. At 4 h postinjection, ^{111}In-DOTA-NAPamide displayed 75% higher tumor uptake and 63% less renal uptake than ^{111}In-DOTA-MSH_{oct} (*14*), indicating that the DOTA position could dramatically affect the melanoma uptake and renal uptake of the radiolabeled α-MSH peptide. Hence, we examined the effect of DOTA position on the biodistribution properties of ^{111}In-labeled lactam bridge-cyclized α-MSH peptide in this study. DOTA was conjugated to the Lys in the cyclic ring, while the N-terminus of the peptide was acetylated to generate Ac-GluGlu-CycMSH[DOTA]. A Lys was used to connect DOTA (at α-amino group of the Lys) as well as to cyclize the peptide (through the epsilon amino group of the Lys). To eliminate the potential influence of the overall positive charge on the renal uptake of the radiolabeled α-MSH peptide, one more negatively charged Glu was introduced to replace the Gly at the N-terminus besides the acetylation of the N-terminus (Figure 1) to make the overall charge of Ac-GluGlu-CycMSH[DOTA] equal to that of DOTA-GlyGlu-CycMSH.

The structural change did not sacrifice the nanomolar binding affinity of Ac-GluGlu-CycMSH[DOTA] compared to DOTA-GlyGlu-CycMSH. Ac-GluGlu-CycMSH[DOTA] displayed 0.6 nM receptor binding affinity in B16/F1 cells, which was similar to that of DOTA-GlyGlu-CycMSH (0.8 nM). Ac-GluGlu-CycMSH[DOTA]-^{111}In exhibited rapid cellular internalization and extended cellular retention in B16/F1 cells (Figure 5), making Ac-GluGlu-CycMSH[DOTA]-^{111}In suitable for melanoma imaging. The shift of DOTA from the N-terminus toward the lactam bridge-cyclic ring did increase the melanoma uptake and retention. The tumor uptake values of Ac-GluGlu-CycMSH[DOTA]-^{111}In were 1.1, 1.3, and 1.5 times the tumor uptake values of ^{111}In-DOTA-GlyGlu-CycMSH 2, 4, and 24 h postinjection, respectively (*20*). Compared to the linear α-MSH peptide ^{111}In-DOTA-NAPamide, Ac-GluGlu-CycMSH[DOTA]-^{111}In exhibited 24.6% and 56.9% higher tumor uptake values 4 and 24 h postinjection, respectively. Flank melanoma tumors were clearly visualized by SPECT/CT using Ac-GluGlu-CycMSH[DOTA]-^{111}In as an imaging probe at 2 h postinjection (Figure 6). The SPECT imaging of tumors accurately matched the anatomical information from CT images. Ac-GluGlu-CycMSH[DOTA]-^{111}In displayed high tumor to normal organ uptake ratios except for the kidney. The high receptor-mediated tumor uptake and tumor to normal organ uptake ratios highlighted the potential of radiolabeled lactam bridge-cyclized α-MSH peptides as a novel class of peptide radiopharmaceuticals for melanoma imaging.

The liver uptake values of Ac-GluGlu-CycMSH[DOTA]-^{111}In were 3.8, 6.1, and 4.2 times the liver uptake values of ^{111}In-DOTA-GlyGlu-CycMSH 2, 4, and 24 h postinjection, respectively. The higher liver uptakes of Ac-GluGlu-CycMSH[DOTA]-^{111}In were likely due to its higher lipophilicity. Under the same HPLC gradient, Ac-GluGlu-CycMSH[DOTA]-^{111}In was washed out of the C18 analytical column later than ^{111}In-DOTA-GlyGlu-CycMSH. As shown in biodistribution results (Table 1) and SPECT/CT image (Figure 6), Ac-GluGlu-CycMSH[DOTA]-^{111}In was primarily excreted through the kidneys. Surprisingly, the renal uptake values of Ac-GluGlu-CycMSH[DOTA]-^{111}In were 4.6, 5.5, and 2.3 times the renal uptake values of ^{111}In-DOTA-GlyGlu-CycMSH 2, 4, and 24 h postinjection, respectively (*20*). The strategy of infusing basic amino acid such as lysine has been successfully employed to decrease the renal uptakes of radiolabeled metal-cyclized α-MSH peptides by shielding the electrostatic interaction between positively charged peptides and negatively charged surface of tubule cells (*5, 17, 22*). Therefore, 15 mg of L-lysine was co-injected with Ac-GluGlu-CycMSH[DOTA]-^{111}In to examine its effect in reducing the renal uptake of Ac-GluGlu-CycMSH[DOTA]-^{111}In. As we anticipated, co-injection of L-lysine dramatically reduced the renal uptake of Ac-GluGlu-CycMSH[DOTA]-^{111}In by 70% ($p < 0.05$) 2 h postinjection, demonstrating that the electrostatic interaction played a key role in the nonspecific renal uptake of Ac-GluGlu-CycMSH[DOTA]-^{111}In. The urine analysis showed that Ac-GluGlu-CycMSH[DOTA]-^{111}In was metabolized into two moieties that might be responsible for the activity retention in kidneys. Another way to decrease the renal uptake of the radiolabeled α-MSH peptide is to increase the overall negative charge of the peptide by introducing a negatively charged aspartic acid or glutamic acid into the peptide sequence. Introduction of a glutamic acid as a linker has successfully reduced the renal uptake values of ^{111}In-DOTA-GlyGlu-CycMSH by 44% compared to ^{111}In-DOTA-CycMSH {^{111}In-DOTA-c[Lys-Nle-Glu-His-DPhe-Arg-Trp-Gly-Arg-Pro-Val-Asp]} (*20*). Since we have demonstrated that shielding the electrostatic interaction dramatically reduced the renal uptake of Ac-GluGlu-CycMSH[DOTA]-^{111}In, it is likely that introducing a negatively charged amino acid between the DOTA and Lys in Ac-GluGlu-CycMSH[DOTA]-^{111}In will decrease the nonspecific renal uptake. Further decrease of the renal uptake will facilitate the

potential applications of radiolabeled lactam bridge-cyclized α-MSH peptides for melanoma imaging and therapy.

A potential application of this MC1 receptor-targeting peptide construct is to develop melanoma-specific dual-modality imaging agents. As demonstrated in this study and our previous work (*20*), no matter that the DOTA chelator was coupled to the N-terminus of ^{111}In-DOTA-GlyGlu-CycMSH or to the amino group of Lys in Ac-GluGlu-CycMSH[DOTA]-^{111}In, both ^{111}In-conjugates maintained high MC1 receptor binding affinities *in vitro* and *in vivo*. These results indicated that both amino groups at the N-terminus and at the Lys in the lactam bridge-cyclized peptide ring could be used to attach two different imaging tags for dual-modality imaging. For instance, both optical tag and radionuclide could be attached to the same lactam bridge-cyclized α-MSH peptide simultaneously to yield a dual-modality imaging peptide. The development of dual-modality imaging peptide would provide a robust imaging tool combining the advantages of both optical imaging and radioimaging for melanoma detection.

In conclusion, the shift of DOTA from the N-terminus toward the lactam bridge-cyclic ring increased the melanoma uptake and retention. DOTA position exhibited a profound effect on melanoma targeting and pharmacokinetic properties of Ac-GluGlu-CycMSH[DOTA]-^{111}In, providing new insight into the design of lactam bridge-cyclized peptide for melanoma imaging and therapy.

ACKNOWLEDGMENT

We thank Mr. Benjamin M. Gershman for his technical assistance. This work was supported in part by the Southwest Melanoma SPORE Developmental Research Program, the Stranahan Foundation, the Oxnard Foundation, the DOD grant W81XWH-09-1-0105 and the NIH grant NM-INBRE P20RR-016480. The image in this article was generated by the Keck-UNM Small Animal Imaging Resource established with funding from the W.M. Keck Foundation and the University of New Mexico Cancer Research and Treatment Center (NIH P30 CA118100).

LITERATURE CITED

(1) Jemal, A., Siegel, R., Ward, E., Hao, Y., Xu, J., and Thun, M. J. (2009) Cancer statistics, 2009. *CA. Cancer J. Clin. 59*, 225–249.

(2) Tatro, J. B., and Reichlin, S. (1987) Specific receptors for alpha-melanocyte-stimulating hormone are widely distributed in tissues of rodents. *Endocrinology 121*, 1900–1907.

(3) Siegrist, W., Solca, F., Stutz, S., Giuffre, L., Carrel, S., Girard, J., and Eberle, A. N. (1989) Characterization of receptors for alpha-melanocyte-stimulating hormone on human melanoma cells. *Cancer Res. 49*, 6352–6358.

(4) Chen, J., Cheng, Z., Hoffman, T. J., Jurisson, S. S., and Quinn, T. P. (2000) Melanoma-targeting properties of 99mTechnetium-labeled cyclic α-melanocyte-stimulating hormone peptide analogues. *Cancer Res. 60*, 5649–5658.

(5) Miao, Y., Owen, N. K., Whitener, D., Gallazzi, F., Hoffman, T. J., and Quinn, T. P. (2002) In vivo evaluation of 188Re-labeled alpha-melanocyte stimulating hormone peptide analogs for melanoma therapy. *Int. J. Cancer 101*, 480–487.

(6) Miao, Y., Whitener, D., Feng, W., Owen, N. K., Chen, J., and Quinn, T. P. (2003) Evaluation of the human melanoma targeting properties of radiolabeled alpha-melanocyte stimulating hormone peptide analogues. *Bioconjugate Chem. 14*, 1177–1184.

(7) Miao, Y., Owen, N. K., Fisher, D. R., Hoffman, T. J., and Quinn, T. P. (2005) Therapeutic efficacy of a ^{188}Re labeled α-melanocyte stimulating hormone peptide analogue in murine and human melanoma-bearing mouse models. *J. Nucl. Med. 46*, 121–129.

(8) Miao, Y., Benwell, K., and Quinn, T. P. (2007) ^{99m}Tc- and ^{111}In-labeled α-melanocyte-stimulating hormone peptides as imaging probes for primary and pulmonary metastatic melanoma detection. *J. Nucl. Med. 48*, 73–80.

(9) Miao, Y., Hylarides, M., Fisher, D. R., Shelton, T., Moore, H., Wester, D. W., Fritzberg, A. R., Winkelmann, C. T., Hoffman, T. J., and Quinn, T. P. (2005) Melanoma therapy via peptide-targeted α-radiation. *Clin. Cancer Res. 11*, 5616–5621.

(10) Miao, Y., Figueroa, S. D., Fisher, D. R., Moore, H. A., Testa, R. T., Hoffman, T. J., and Quinn, T. P. (2008) ^{203}Pb-labeled alpha-melanocyte stimulating hormone peptide as an imaging probe for melanoma detection. *J. Nucl. Med. 49*, 823–829.

(11) Miao, Y., Hoffman, T. J., and Quinn, T. P. (2005) Tumor targeting properties of ^{90}Y and ^{177}Lu labeled alpha-melanocyte stimulating hormone peptide analogues in a murine melanoma model. *Nucl. Med. Biol. 32*, 485–493.

(12) Miao, Y., Shelton, T., and Quinn, T. P. (2007) Therapeutic efficacy of a ^{177}Lu labeled DOTA conjugated α-melanocyte stimulating hormone peptide in a murine melanoma-bearing mouse model. *Cancer Biother. Radiopharm. 22*, 333–341.

(13) Froidevaux, S., Calame-Christe, M., Tanner, H., Sumanovski, L., and Eberle, A. N. (2002) A novel DOTA-α-melanocyte-stimulating hormone analog for metastatic melanoma diagnosis. *J. Nucl. Med. 43*, 1699–1706.

(14) Froidevaux, S., Calame-Christe, M., Schuhmacher, J., Tanner, H., Saffrich, R., Henze, M., and Eberle, A. N. (2004) A Gallium-labeled DOTA-α-melanocyte-stimulating hormone analog for PET imaging of melanoma metastases. *J. Nucl. Med. 45*, 116–123.

(15) Froidevaux, S., Calame-Christe, M., Tanner, H., and Eberle, A. N. (2005) Melanoma targeting with DOTA-alpha-melanocyte-stimulating hormone analogs: structural parameters affecting tumor uptake and kidney uptake. *J. Nucl. Med. 46*, 887–895.

(16) McQuade, P., Miao, Y., Yoo, J., Quinn, T. P., Welch, M. J., and Lewis, J. S. (2005) Imaging of melanoma using ^{64}Cu and 86Y-DOTA-ReCCMSH(Arg^{11}), a cyclized peptide analogue of α-MSH. *J. Med. Chem. 48*, 2985–2992.

(17) Wei, L., Butcher, C., Miao, Y., Gallazzi, F., Quinn, T. P., Welch, M. J., and Lewis, J. S. (2007) Synthesis and biological evaluation of Cu-64 labeled rhenium-cyclized α-MSH peptide analog using a cross-bridged cyclam chelator. *J. Nucl. Med. 48*, 64–72.

(18) Wei, L., Miao, Y., Gallazzi, F., Quinn, T. P., Welch, M. J., Vavere, A. L., and Lewis, J. S. (2007) Ga-68 labeled DOTA-rhenium cyclized α-MSH analog for imaging of malignant melanoma. *Nucl. Med. Biol. 34*, 945–953.

(19) Cheng, Z., Xiong, Z., Subbarayan, M., Chen, X., and Gambhir, S. S. (2007) ^{64}Cu-labeled alpha-melanocyte-stimulating hormone analog for MicroPET imaging of melanocortin 1 receptor expression. *Bioconjugate Chem. 18*, 765–772.

(20) Miao, Y., Gallazzi, F., Guo, H., and Quinn, T. P. (2008) ^{111}In-labeled lactam bridge-cyclized alpha-melanocyte stimulating hormone peptide analogues for melanoma imaging. *Bioconjugate Chem. 19*, 539–547.

(21) Guo, H., Shenoy, N., Gershman, B. M., Yang, J., Sklar, L. A., and Miao, Y. (2009) Metastatic melanoma imaging with an 111In-labeled lactam bridge-cyclized alpha-melanocyte stimulating hormone peptide. *Nucl. Med. Biol. 36*, 267–276.

(22) Miao, Y., Fisher, D. R., and Quinn, T. P. (2006) Reducing renal uptake of ^{90}Y and ^{177}Lu labeled alpha-melanocyte stimulating hormone peptide analogues. *Nucl. Med. Biol. 33*, 723–733.

BC9003475

Cationic Glyconanoparticles: Their Complexation with DNA, Cellular Uptake, and Transfection Efficiencies

Marya Ahmed,[†,‡] Zhicheng Deng,[†,‡] Shiyong Liu,[§] Robert Lafrenie,[||] Aseem Kumar,[‡] and Ravin Narain*[,†,‡]

Department of Chemical and Materials Engineering, University of Alberta, Edmonton, Alberta, T6G 2G6, Canada, Department of Chemistry and Biochemistry, Biomolecular Sciences Program, Laurentian University, 935, Ramsey Lake Road, Sudbury, Ontario, P3E 2C6, Canada, Department of Polymer Science and Engineering, University of Science and Technology of China, Hefei, Anhui, China, and Regional Cancer Program of the Hospital, 41 Ramsey Lake Road, Sudbury, Ontario, Canada. Received August 6, 2009; Revised Manuscript Received September 16, 2009

There is a need to synthesize new gene delivery vehicles that can deal with the problems of endosomal escape and nuclear entry. We propose cationic glycopolymer-stabilized gold nanoparticles as an effective gene delivery system. The cationic glyconanoparticles synthesized were revealed to be biocompatible and are resistant to aggregation in physiological conditions. The complexation of DNA to the cationic glyconanoparticles is determined by agarose gel electrophoresis. The localization of the DNA-glyconanoparticles inside the Hela cell line and their mechanism of uptake is studied by confocal microscopy. Finally, the efficacy of the glyconanoparticles as gene delivery vehicles *in vitro* is studied by their complexation with cyanine fluorescence protein encoded plasmid, and the transfection efficiency is found to be comparable to the commercially available control Lipofectamine 2000.

INTRODUCTION

Safety issues associated with viral gene delivery vehicles have led to the popularization of a variety of nonviral gene delivery vehicles, such as liposomes, cationic polymers, nanoparticles, and dendrimers (*1*−*10*). Another approach recommends the use of hybrid viral vehicles that are shown to produce high efficacy *in vitro*; however, the safety concerns associated with them cannot be ignored (*11*). In nonviral gene delivery vehicles, compared to those of lipoplex systems, polyplex-based ones can effectively promote vesicular escape and nuclear entry (*12, 13*). Polyethylenimine (PEI), despite its high toxicity, has been largely utilized as an effective gene delivery vehicle (*1*). Chitosan, a glucosamine-based polymer, is completely nontoxic and shows relatively low transfection efficiencies (*1*). The different chitosan modification approaches, including PEGylation and amination, have been reported to overcome the issues of gene delivery associated with these vectors (*1*). Reineke et al. has combined the high transfection abilities of PEI with low toxicity of chitosan, by synthesizing cationic glycopolymers of defined molecular weight, which show enhanced gene transfer ability with reduced toxicity (*14*). It has also been demonstrated that cationic polymer coated metallic nanoparticle-DNA complexes show enhanced gene transfer ability due to better DNA binding ability and increased stability in physiological conditions than their corresponding polyplexes (*15*−*17*). Although various macromolecule stabilized gold nanoparticles have been synthesized and their biological and chemical properties are reported (*18*−*22*), only a handful of papers discuss the *in vitro* uses of cationic gold nanoparticles as gene delivery systems (*7, 8, 17, 23, 24*). The use of gold nanoparticles as gene delivery vehicles is either facilitated by external forces or associated with significantly low transfection efficiencies, due to the possible entrapment of PEG-modified vehicles inside the endosomes (*7, 8*). Carbohydrate functionalized gold nanoparticles, also known as glyconanoparticles, are not only interesting due to their PEG-like biocompatibility, but are also found to be involved in cell-mediated interactions (*25*−*27*). The aforementioned strategies when combined can produce monodisperse, biocompatible, cationic glyconanoparticles as gene delivery vehicles that can enhance the cellular uptake by cell mediated interactions and lack the drawbacks of PEG stabilized vehicles, thus promoting higher transfection efficiencies (*3, 4, 28*). We have previously reported the comparison between transfection efficiencies of cationic glyconanoparticles of different core sizes (*29*). However, a complete study on the synthesis of cationic glyconanparticles prepared by UV radiation, their size control as a function of ligand concentrations and UV light intensity, and their mechanism of interactions with living cells has not yet been reported in detail (*29*).

Herein, we report a facile one-step synthesis of cationic glyconanoparticles as an effective gene delivery system. Well-defined cationic glycopolymers were first synthesized by the reversible addition−fragmentation chain transfer (RAFT) process and their cytotoxicity was determined. The cationic glyconanoparticles were then produced in one step using UV radiation (Scheme 1).

Photoirradiation process for the synthesis of unprotected gold nanoparticles, introduced by Scaiano et al., has been widely investigated (*30*−*32*). We have successfully synthesized the mixed monolayer stabilized gold nanoparticles using this technique (*31, 32*). The synthesis of cationic gold nanoparticles is achieved using the photoinitiator, Irgacure-2959, and the effect of concentration of glycopolymer and of the intensity of radiation on the size and polydispersity of nanoparticles is studied. The monodisperse cationic gold nanoparticles produced are further complexed with fluorescence-labeled oligonucleotides, and the confocal microscopy is performed to study the

* Corresponding author. narain@ualberta.ca or rnarain@laurentian.ca; Tel: +1 780 492 1736 or +1 705 675 1151 (2186); Fax: +1 780 492 2881 or +1 705 675 4844.

[†] University of Alberta.

[‡] Laurentian University.

[§] University of Science and Technology of China.

[||] Regional Cancer Program of the Hospital.

10.1021/bc900350c CCC: $40.75 © 2009 American Chemical Society
Published on Web 10/09/2009

Scheme 1. Synthesis of the Diblock Copolymer, Formation of Cationic Glyconanoparticles, and Their Complexation with DNA

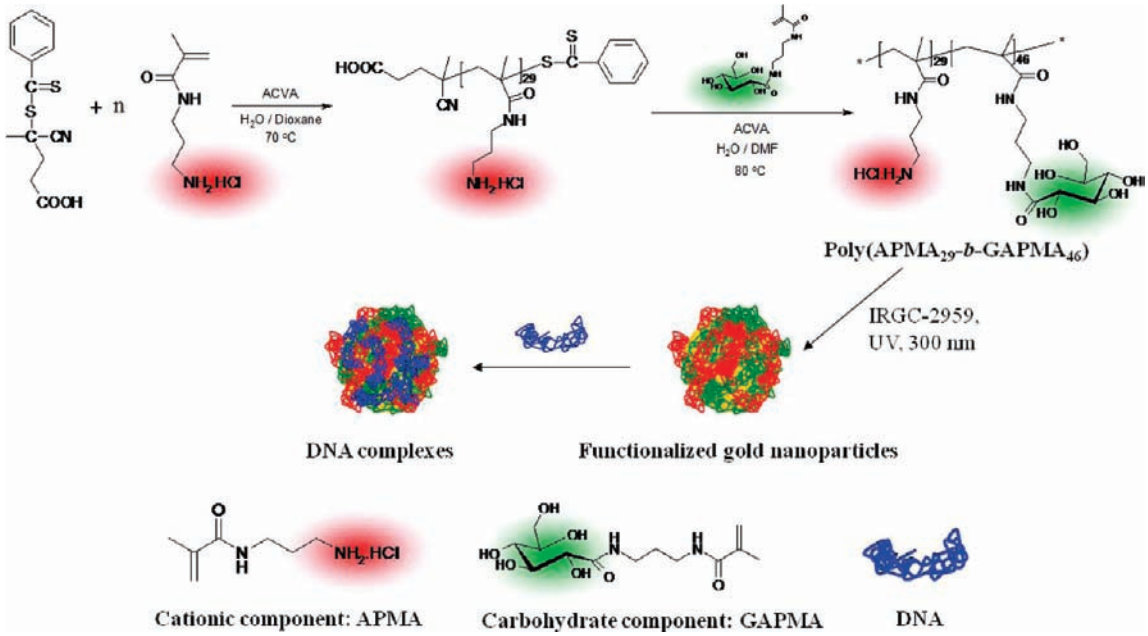

mechanism of uptake of novel gene carrier and their colocalization in human cells. The pECFP plasmid is complexed with the cationic gold nanoparticles, and agarose gel electrophoresis is performed to determine the net charge on the surface of nanoparticles−plasmid complex. Finally, the transfection efficiency of the carrier with net positive charge is demonstrated in Hela cells, and it is found that cationic glyconanoparticles exhibit high transfection efficiencies with significantly low toxicity.

MATERIALS AND METHODS

Materials. All chemicals were purchased from Sigma-Aldrich and were used without purification.

Methods. *Polymer Characterization.* ^{1}H NMR spectra of the monomers and polymers were recorded on a Varian 200 MHz instrument.

Molecular weight and molecular weight distributions were determined by a conventional Viscotek gel permeation chromatography (GPC) system using aqueous eluents, two Waters WAT011545 columns at room temperature, and a flow rate of 1.0 mL/min using a 0.5 M sodium acetate/0.5 M acetic acid buffer as eluent. p(APMA) was characterized based on six near-monodisperse PEO standards (M_p = 1010−101 200 g mol^{-1}). p(APMA-*b*-GAPMA) was characterized based on seven near-monodisperse Pullulan standards (M_w = 5900−404 000 g mol^{-1}).

Dynamic Light Scattering (DLS). Dynamic light scattering measurements were performed at room temperature using a Viscotek DLS instrument having a He−Ne laser at a wavelength of 632 nm and Pelltier temperature controller. p(APMA-*b*-GAPMA) stabilized gold nanoparticle solutions were filtered through Millipore membranes (0.45 μm pore size). The data were recorded with Omni Size Software.

UV−vis Spectroscopy. UV−vis absorption spectra (400−800 nm) were recorded on a Cary UV 100 spectrophotometer from the aqueous solutions of p(APMA-*b*-GAPMA) gold nanoparticles at room temperature.

Confocal Microscopy. The fluorescent images were obtained using Zeiss LSM 510 Meta confocal microscope with 63× objective. The wavelengths of excitation and emission used were 552 and 575 nm, respectively.

Plasmid Preparation and Purification. pECFP-N1, enhanced cyan fluorescent plasmid driven by cytomegalovirus (CMV) promoter, was transformed in super competent *E. coli* cells and was amplified in 30 μg/mL Kanmycin containing LB broth media at 37 °C overnight with 225 rpm. After sufficient bacterial growth, the cells were pelleted by centrifugation at 2000*g* and 20 °C for 5 min followed by plasmid extraction using QIAGEN mini plasmid purification kit as per vendor's protocol. Plasmid purity was assessed by UV spectrophotometry ($A_{260/280}$ > 1.75) and agarose gel electrophoresis.

Block Copolymerization of APMA with GAPMA. *Diblock Copolymerization of 3-Aminopropyl Methacrylamide Hydrochloride (APMA) with 3-Gluconamidopropyl Methacrylamide (GAPMA) via Reversible Addition−fragmentation Chain Transfer Process (RAFT).* APMA was first polymerized using 4-cyanopentanoic acid dithiobenzoate (CTP) as chain transfer agent (CTA) and 4,4′-azobis(4-cyanovaleric acid) (ACVA) as initiator according to the previous report (*37*). Detail protocol was as follows: in a 10 mL Schlenk flask, APMA (2 g, 11.2 mmol) was dissolved in double distilled water (4 mL) before the addition of 2 mL CTP (52 mg, 0. 186 mmol, target DP_n = 60) and ACVA (16 mg, 0.038 mmol) 1,4-dioxane stock solution. After degassing via three freeze−thaw cycles, the flask was placed in a preheated oil bath to initiate the polymerization at 70 °C. After 3 h 45 min, the polymerization was quenched at 50% conversion. Resulting polymer was precipitated in acetone, and the residual monomer was removed by washing with 2-propanol. Subsequently, poly (APMA) (M_n = 5200 g·mol^{-1}; M_w/M_n = 1.23) was used as macro chain transfer agent (Macro-CTA) to synthesize p(APMA-*b*-GAPMA) diblock copolymer. As the second monomer, GAPMA (0.95 g) was added to p(APMA) solution (0.5 g in 7.5 mL double distilled water) followed by the addition of 0.1 mL ACVA (7.5 mg) *N*,*N*-dimethylformamide (DMF) stock solution. After degassing via three freeze−thaw cycles, the flask was placed in a preheated oil bath for 20 h at 80 °C. The diblock copolymer p(APMA-*b*-GAPMA) was precipitated in acetone followed by washing with methanol.

Synthesis of Block Copolymer Coated Au Nanoparticles in the Presence of Irgacure-2959 (IRGC). p(APMA-*b*-GAPMA) coated gold nanoparticles were synthesized by photoirradiation using Irgacure-2959 (IRGC) as a

photoinitiator. The molar ratios of $HAuCl_4$, IRGC, and p(APMA-*b*-GAPMA) in deionized water were 1:3:0.01, 1:3:0.02, or 1:3:0.05. p(APMA-*b*-GAPMA) with molecular weights 19.9 kDa (2.5 mg), 25 kDa (3.3 mg), were used. In a typical synthesis, required amount of p(APMA-*b*-GAPMA) were dissolved in deionized water and solution was added to $HAuCl_4$ (0.50 mg/mL) solution in deionized water. The mixture was stirred using a magnetic stirrer at room temperature for 20 min. Irgacure-2959 (15.3 mM, 1 mL) was dissolved in the mixture of deionized water and MeOH (4:1, v/v). The initiator solution was then added to the $HAuCl_4$ and p(APMA-*b*-GAPMA) mixture was stirred for 20 min. The photoirradiation of the reaction mixture was carried out using sixteen, twelve, eight, and four 75 W UV lamps at wavelength a 300 nm in a Rayonet photoreactor (Southern N.E. Ultraviolet Co.) After 5 min, the reaction mixture was taken off the photoreactor and stirred at room temperature. The gold nanoparticles produced were centrifuged at 20 000 rpm for 2 h to remove the excess of polymer. The pellet was resuspended in deionized water.

Serum Assay. The cationic glycopolymer stabilized gold nanoparticles of size 6 nm were resuspended in deionized water, phosphate buffer saline, and 10% v/v human serum separately to achieve the final concentration of 2.5 μM in each solution. Then, the change in size of gold nanoparticles was measured by UV−vis spectroscopy in the wavelength range 400−700 nm and by dynamic light scattering instrument.

DNA Complexation. DNA complexation of gold nanoparticles was studied using agarose gel electrophoresis. The varying concentrations of gold nanoparticles (45, 89, 139, 196 μM) were complexed with 340 ng of pECFP-N1 plasmid and the complexes were loaded into 0.7% agarose gel. The gel was run for 1 h at 70 V, and the complexes were characterized after staining the gel with 0.5 μg/mL of ethidium bromide. The images were obtained on an ultraviolet transilluminator.

Confocal Microscopy. Hela cells were grown in Dulbecco's modified eagle medium, DMEM containing 10% fetal bovine serum, and 1% penicillin/streptomycin in a humidified atmosphere with 5% CO_2 at 37 °C. Upon 80% confluency, cells were trypsinized and neutralized with equal amounts of medium. The cells were then reseeded in a 6 well plate, in which each well contained sterile glass coverslips. The plate was incubated in humidified atmosphere at 37 °C, and upon 80% confluency, 1.3 mM nanoparticles complexed with 1.1 μM TAMARA dye labeled oligonucleotides containing medium were introduced in chambered cover glass. The other two wells served as controls, containing no treatment and 1.1 μM TAMARA labeled oligonucleotides in the medium, respectively. The cells were further incubated for 3 h at 37 °C. The growth medium was then removed, and cells were washed several times with phosphate buffer saline. The cells were fixed with 4% *p*-formaldehyde solution at room temperature for 5 min, followed by washing with Dulbecco's phosphate buffer saline (DPBS). The cover glass was then mounted on a microscopic glass slide and was studied under the microscope.

Mechanism of Uptake of Gold Nanoparticles by Human Cell Line. *Temperature Dependent Uptake of Gold Nanoparticles.* The energy dependent uptake of TAMARA labeled gold nanoparticles was studied using the same procedure as described before (*35*). In summary, the cells were seeded in 6 well plates, containing glass coverslips. The plate was incubated in humidified atmosphere at 37 °C for 24 h. The medium was removed and was replaced with 9.5 μM nanoparticles complexed with 1.1 μM TAMARA labeled oligonucleotides containing medium. The plate was then incubated for 3 h at 4 °C. The cells were then washed several times with DPBS and fixed with 4% *p*-formaldehyde. The coverslip was then finally washed with DPBS and was mounted on microscopic glass slide. The glass slide was studied under confocal microscope.

Clathrin Dependent Uptake of Gold Nanoparticles. Hela cells were seeded in 6 well plates as described above; upon 80% confluency, the cells were pretreated with 0.45 M sucrose containing medium for 30 min at 37 °C. The medium was removed and cells were washed several times with DPBS. The medium containing 9.5 μM nanoparticles complexed with 1.1 μM TAMARA labeled oligonucleotides was added and cell were further incubated for 3 h. The cells were washed with DPBS and fixed with *p*-formaldehyde. The coverslip was mounted on a microscopic glass slide to study under confocal microscope.

Transfection. Hela cells were maintained in Dulbecco's modified Eagles' medium, supplemented with 10% fetal bovine serum at 37 °C, in a humidified 5% CO_2 atmosphere, as described above. Before the experiment, 2000 Hela cells were seeded on a 96 well tissue culture plate and were allowed to adhere overnight. The test samples were prepared for each well by mixing 0.35 μg of CFP plasmid with varying amounts of cationic gold nanoparticles. The mixture was incubated for 15 min and was added to the cells; the plate was incubated for 6 h at 37 °C, in serum free medium. The cells were washed three times with DPBS and were allowed to grow for another 48 h in fresh culture medium supplemented with 10% FBS. The gene expression was evaluated using fluorescent microscopy. The presence of CFP protein was confirmed using the emission spectrum of cyanine fluorescence protein at 490 nm.

Toxicity Assays. *Toxicity Assay for Glycopolymer. 1. Preparation of Polymer Stock Solutions.* All polymers were dissolved into Dulbecco's phosphate buffer at the final concentration of 0.6 mM. The samples were autoclaved, and different volumes of prepared solution were added into different volumes of DMEM medium to obtain the final concentrations of 2, 4, and 6 μM concentration of polymer in the medium.

2. Cytotoxicity Test. Cytotoxicity was characterized using MTT assay. Hela cells were plated in 96 well plates at density of 15 000 cells/well in 100 μL of serum and antibiotic supplemented growth medium. Cells were incubated for 24 h at 37 °C and 5% CO_2, after which time the growth medium was replaced with DMEM medium containing different concentrations of polymers, prepared above (pAPMA) and p(APMA-*b*-GAPMA). The cells were further incubated for 24 h under the same conditions, after which 25 μL of MTT dye was added to each well and plate was incubated for 2 h. Next, 100 μL of MTT lysis solution was added to each well, and cells were incubated overnight. Absorbance was measured at 570 nm. Survival percentage was calculated by comparison to untreated cells (100% survival).

Toxicity Assay on Transfected Cells. Hela cells maintained at 80% confluency were seeded at 2000 cells/well in 96 well plate and were allowed to adhere overnight. The varying concentrations of gold nanoparticle−plasmid complex in serum free medium were added to each well, and each experiment was done in triplicate. After 6 h, the medium was changed to serum containing medium, and cells were allowed to grow for another 48 h. The cell viability was tested using MTT assay, as described above.

RESULTS AND DISCUSSION

The carbohydrate molecules present on the surface of cells are involved in a variety of biological functions, including cellular recognition, cell adhesion, and cell growth regulation. The polyvalent interactions between carbohydrate−carbohydrate molecules and carbohydrate−protein molecules on the surface of a pathogen lead to their uptake by a living cell (*25*−*27*). These specific carbohydrate based cellular interactions can be exploited to design novel carriers for the gene and drug delivery purposes. A variety of protein and peptide stabilized nanopar-

Table 1. Dynamic Light Scattering Data Showing the Size Control of Gold Nanoparticles as a Function of Ligand Concentration

entry	polymer conc. [M]	molar ratio Au:I:Polymer	intensity (W)	mass dist. size	PDI
1	2.2×10^{-4}	1:3:0.05	224	8.24	0.18
2	1.1×10^{-4}	1:3:0.02	224	14.85	0.21
3	5.1×10^{-5}	1:3:0.01	224	2.9	0.23
4	5.1×10^{-6}	1:3:0.005	224	3.7	0.13

ticles have been reported and their uptake by human cells is studied (*12, 17*). The studies have also shown that endosomal entrapment is also a major hindrance in the success of other gene delivery vehicles (*10*). The synthesis of cationic glyconanoparticles of 10 nm core diameter using cationic glycopolymer p($APMA_{31}$-*b*-$LAEMA_{32}$), has been previously reported (*29*); herein, we present a detailed study of the synthesis of cationic glycopolymer stabilized gold nanoparticles, using cationic glycopolymer p(APMA-*b*-GAPMA) of different molecular weights by photochemistry. The gold nanoparticles produced are stabilized with the diblock cationic glycopolymer p($APMA_{31}$-*b*-$GAPMA_{45}$) that serves a variety of purposes. The glycopolymer segment imparts the biocompatibility and mediates the cellular interactions with nanoparticles, while the cationic moiety provides the complexation of anionic macromolecules on the surfaces of nanoparticles. The synthesized cationic glycopolymer p(APMA-*b*-GAPMA) in this study has molar masses of 19.9 and 25.3 kDa with narrow molecular weight distributions ($M_w/M_n < 1.30$) (see Supporting Information Table S1 and Figure S1). In contrast to APMA homopolymer, cell viability studies revealed that the obtained sugar-containing diblock copolymer, p($APMA_{31}$-*b*-$GAPMA_{45}$), shows dramatically reduced toxicity at comparable polymer concentrations (see Supporting Information Figure S2). It is shown that toxicity of the block copolymer can be reduced up to 80%, as compared to that of PAPMA= APMA homopolymer. The cationic glycopolymers were subsequently used in the stabilization of gold nanoparticles. Monodisperse cationic glyconanoparticles were prepared *in situ* by the photoirradiation using Irgacure 2959 as photoinitiator. The photochemical approach for the synthesis of gold nanoparticles was first reported by Scaiano et al., and this method is extensively investigated in our group for both polymer and protein stabilized gold nanoparticles (*30*−*32*). The synthesized glyconanoparticles are stabilized by the primary amine pendant groups of the cationic glycopolymer, and therefore, they are expected to be more stable than thiol-stabilized gold nanoparticles due to the oxidative instability of the latter in physiological conditions (*33*). A recent study reports the physiochemical properties of gold nanoparticles stabilized by tertiary amines; however, detailed *in vitro* studies for this kind of nanoparticles are still to be investigated (*33*). The gold nanoparticles were synthesized using varying concentrations of polymer and UV radiation in an effort to achieve near-monodisperse cationic glyconanoparticles.

The results obtained by DLS indicated that the optimization of both parameters UV intensity and polymer concentration in solution are crucial to yield monodisperse nanoparticles of about 10 nm in diameter, as shown in Tables 1 and 2.

The gold nanoparticles produced were further analyzed by TEM and UV−vis spectroscopy to confirm the monodispersity of nanoparticles and to further support the DLS data obtained above (Figure 1; Supporting Information Figures S3, S4, S5). It can be seen that no shift in UV−vis spectrum was observed for the gold nanoparticles produced under different conditions, indicating that nanoparticles produced are of about the same size. TEM images obtained further confirmed the presence of nanoparticles of about 10 nm diameter.

The synthesis of gold nanoparticles was achieved with glycopolymers of molar masses of 19.9 and 25.3 kDa; however, no change in the size of nanoparticles as a function of molecular weight of polymer was observed, possibly due to the small difference in the molecular weight of the two polymers used (Supporting Information Table S3).

The cationic nanoparticles synthesized for *in vitro* gene delivery purposes not only are toxic, but also exhibit the aggregation tendency in biological fluids, due to the interaction of cationic moiety with serum proteins (*1*). Despite the drawbacks associated with PEGylated systems, the biocompatibility and stabilization of nanoparticles in biological fluid is usually obtained by the incorporation of a PEG layer (*1*). The cationic glyconanoparticles synthesized were studied for their stability in physiological conditions using DLS and UV−vis spectroscopy. The UV−vis spectrum shows that there is no shift in the spectrum of cationic glyconanoparticles, before and after their dispersion in saline solution and in serum indicating the stability of gold nanoparticles under physiological conditions. These results are in agreement with previously reported serum assay characterization of gold nanoparticles stabilized by cationic glycopolymer p(APMA-*b*-LAEMA), indicating that regardless of the type of glycopolymer moiety, it is the characteristic of cationic glyconanoparticles to maintain their dispersibility in physiological conditions (*29*). The quantitative results are then obtained by determining the size of gold nanoparticles before and after their dispersion in saline solution and in human serum by DLS, which show that there is no change in the size of gold nanoparticles before and after their dispersion in saline and in serum (Figure 1 and Supporting Information Table S4).

The study of uptake of cationic glyconanoparticles by Hela cells was performed using confocal microscopy. The TAMARA dye labeled oligonucleotides were complexed with slight excess of p($APMA_{31}$-*b*-$GAPMA_{45}$)-*f*-gold nanoparticles, to ensure the complete complexation of oligonucleotides and the complexes were incubated with Hela cells. The untreated Hela cells and TAMARA labeled oligonucleotides treated Hela cells were used as control (Figure 2).

It is apparent by confocal images that, although most of the nanoparticles seem to localize in the cytoplasm of the cells, few glyconanoparticles can be found entrapped in the endosomes (Figure 2, Supporting Information Figure S6). The presence of some of the nanoparticles in the endosomes of cells can be explained by the fact that the complexation of oligonucleotides with cationic glyconanoparticles is based upon electrostatic interactions. Although most oligos-modified-glyconanoparticles are positively charged due to slight excess of gold nanoparticles in the experiment, a few neutral complexes may form during the process, thus causing their entrapment in endosomes. The enhanced fluorescence images of oligonucleotide-labeled-glyconanoparticle incubated cells, compared to that of controls, confirm that the gene delivery vehicle successfully prevents oligonucleotides from degradation by cytosolic enzymes, even after 3 h of incubation inside the cell. The vesicular escape of

Table 2. Dynamic Light Scattering Data Showing the Effect of intensity of UV Radiation on the Size of Gold Nanoparticles

entry	polymer concentration [M]	Au:I:Polymer ratio	intensity (W)	UV time (min)	DLS size (nm)	DLS size distr.
4	5.1×10^{-6}	1:3:0.005	224	5	3.3	0.17
5	5.1×10^{-6}	1:3:0.005	168	5	4.56	0.10
6	5.1×10^{-6}	1:3:0.005	112	5	4.85	0.11
7	5.1×10^{-6}	1:3:0.005	56	15	4.73	0.10

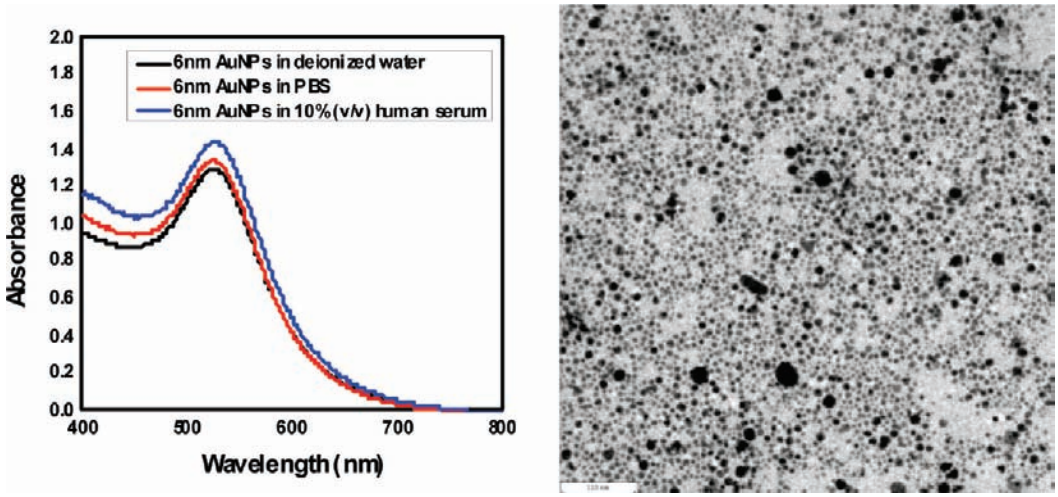

Figure 1. Dispersion of 2.5 μM gold nanoparticles in 10% v/v human serum. TEM micrograph (scale bar − 110 nm) of block copolymer p($APMA_{31}$-*b*-$GAPMA_{45}$) stabilized gold nanoparticles (entry-1).

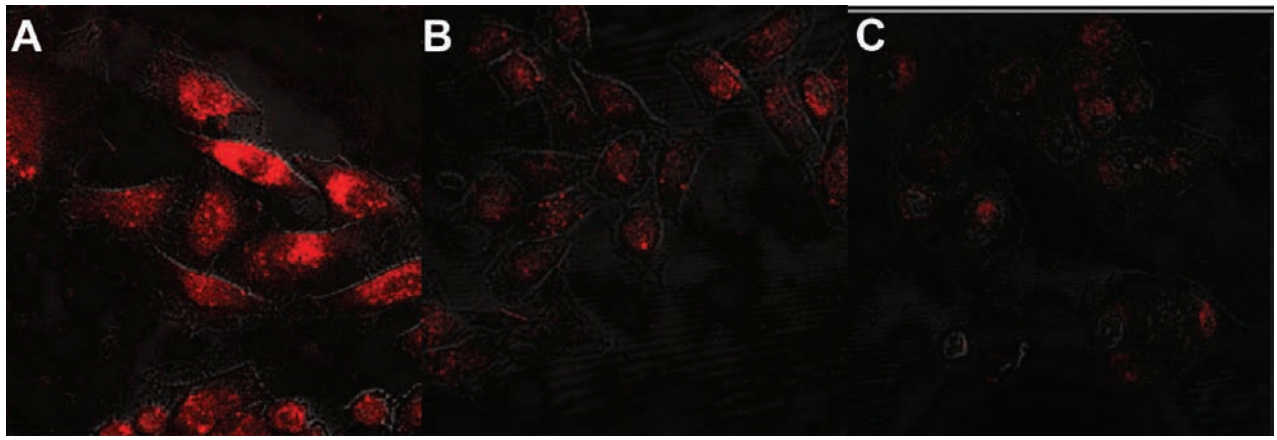

Figure 2. Confocal microscopy images of Hela cells labeled with (A) oligonucleotides complexed p($APMA_{31}$-*b*-$GAPMA_{45}$)-*f*-gold nanoparticles (entry-2), (B) oligonucleotides, and (C) no treatment.

gene delivery vehicle is apparent by the localization of glyconanoparticles inside the cytoplasm.

The mechanism of uptake of gene delivery carrier is a topic of interest to explore the possible routes adopted by the successful gene delivery vehicles. Funete et al. has compared the interaction of different carbohydrate monomers to the cell surface (*27*). It has been found that glucose modified glyconanoparticles are not endocytosed (*27*). The presence of cationic character, in combination with sugar residues, is expected to alter the mechanism of uptake of gold nanoparticles by cells (*1*). The mechanism of uptake of p($APMA_{31}$-*b*-$GAPMA_{45}$)-*f*-gold nanoparticles was studied in detail by exploiting energy dependent process of uptake by living cells and it was found that Hela cells at 4 °C show minimal or no uptake of synthesized nanoparticles, thus indicating that the uptake involves energy dependent processes. To further confirm that the lower uptake of nanoparticles observed at lower temperatures is not due to the physiological malfunctioning of the cells, as the presence of vacuoles in cells treated at lower temperatures is observed, the process was further investigated after the treatment of cells with hypertonic solution at 37 °C (*35*). The same fluorescently labeled gold nanoparticles were incubated with pretreated cells under the same conditions and the confocal images were obtained. The images show the minimum uptake of gold nanoparticles by Hela cell after the treatment with hypertonic medium compared to oligonucleotide-modified glyconanoparticle treated cells under normal conditions (Figure 3 and Supporting Information Figure S6).

The *z*-section images of cells taken from confocal microscope confirm that most of the nanoparticles though can associate themselves around the periphery of cells; they are not endocytosed (see Supporting Information Figure S7). Although a slight change in shape of some of the cells after treatment with hypertonic medium is seen, most of the cells maintain their physiological appearance. It is clear from the figure that cationic glyconanoparticles are capable of cellular interactions in the presence of endocytosis inhibitor, but they are not endocytosed. The cellular attachment of cationic glyconanoparticles can either be considered as a function of glycopolymer interactions to the glycoproteins of plasma membrane, or cationic segments of the nanoparticles can successfully mediate electrostatic interactions with anionic cell membrane. Thus, it can be concluded that the major route of uptake of nanoparticles is found to be receptor mediated endocytosis. It has been reported that uptake of polymer-DNA complexes by receptor mediated endocytosis leads to successful gene delivery (*1*). The major issue in this regard is the entrapment of gene delivery scaffold in the endocytic vesicles after their successful uptake (*1*). The localization of most of the nanoparticles in cytosol confirms that glyconanoparticles with net cationic character can successfully disrupt the endocytic vesicles, leading to the release of nanoparticles in the cytoplasm. This is one step forward toward the synthesis of gene delivery vehicles, where some recent works report the localization of vehicles inside the endosomes (*4, 36*).

The role of cationic glyconanoparticles as a novel gene delivery carrier was explored. The cyanine fluorescence protein-

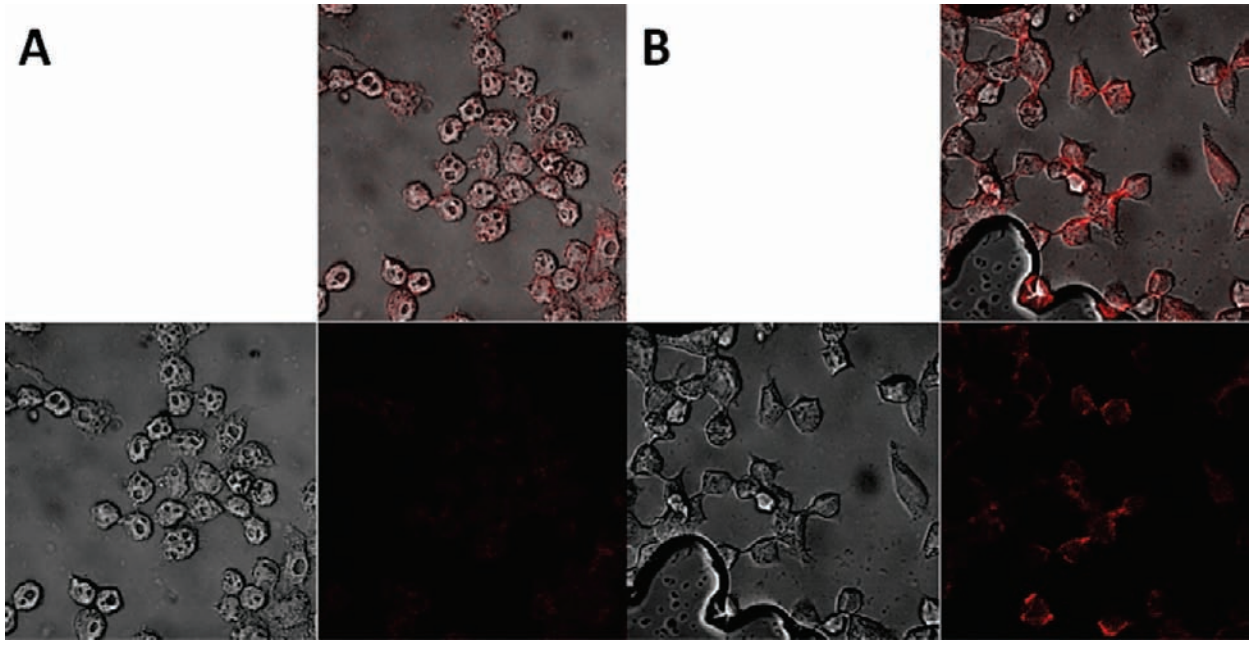

Figure 3. Confocal microscopy images of Hela cells incubated at (A) 4 °C, labeled with oligonucleotide-complexed gold nanoparticles stabilized with p($APMA_{31}$-*b*-$GAPMA_{45}$) (entry-2), (B) Hela cells pretreated with 0.45 M sucrose and incubated with oligonucleotide-complexed gold nanoparticles stabilized with p($APMA_{31}$-*b*-$GAPMA_{45}$) at 37 °C.

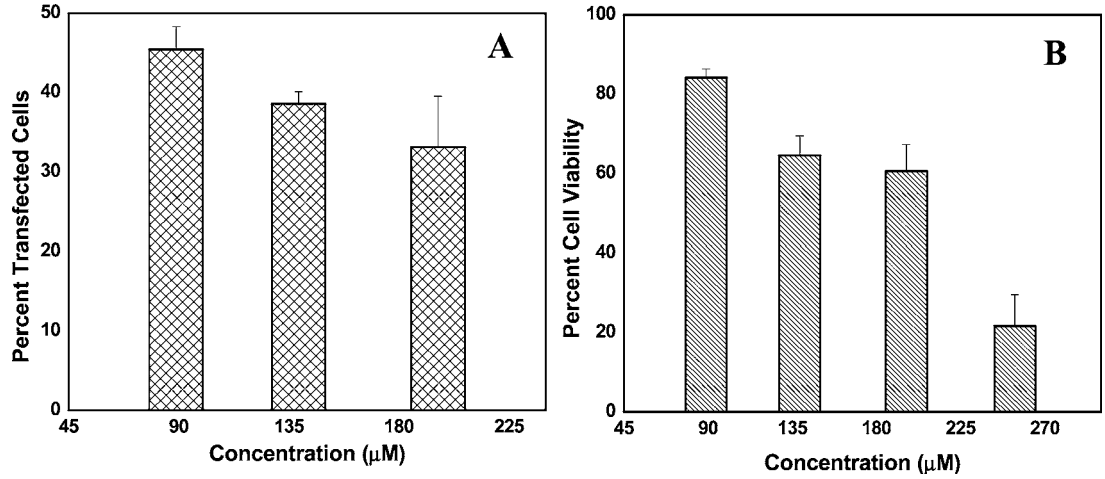

Figure 4. The gene transfection efficiencies and cell viability values of Hela cells upon treatment with cationic glyconanoparticle−plasmid complex. (A) Transfection efficiencies of p($APMA_{31}$-*b*-$GAPMA_{45}$)-*f*-gold nanoparticles in Hela cells upon their incubation with ECFP plasmid-nanoparticle complex at 37 °C. (B) Normalized viability of Hela cells transfected with glyconanoparticles−plasmid complex, determined by MTT assay (entry-1).

encoded DNA plasmid (pECFP-N1) was used to study the DNA complexation with the cationic glyconanoparticles by agarose gel electrophoresis. The plasmid is incubated with varying concentrations of p($APMA_{31}$-*b*-$GAPMA_{45}$)-*f*-gold nanoparticles, and it is found that the complete complexation of plasmid is obtained upon incubation with 89 μM gold nanoparticles (see Supporting Information Figures S8 and S9). The migration of complex was completely retarded upon incubation of the plasmid with 89 μM concentration of gold nanoparticles; it can be safely assumed that nanoparticle−plasmid complexes maintain their net cationic character, thus are able to mediate vesicular escape and are resistant to aggregation in physiological conditions.

Finally, the transfection experiments were performed to determine the efficacy of gold nanoparticles *in vitro*. The use of polyplex based nanomaterials for gene delivery purposes is a rapidly advancing field in gene therapy (*38*−*40*). Polymer stabilized metallic nanoparticles have also been employed for gene delivery purposes, and gold, due to its inert nature, is one of the most commonly used metals for this purpose (*41*). Sandhu et al. have reported the relatively high transfection efficiencies *in vitro* by using amphiphilic gold nanoparticles. However, the process was facilitated with chloroquine, and no cytotoxicity data were provided (*7*). Others describe significantly low transfection efficiencies of comparatively biocompatible gold nanoparticles based gene delivery scaffolds (*8*). Wang et al. have reported the transfection efficiency of cyclodextrin modified gold nanoparticles complexed with green fluorescence encoded protein (pEGFP) plasmid in MCF-7 cells. The gene delivery carrier is reported to be 100% cell viable at various N/P ratios; however, the maximum transfection efficiencies obtained are reported to be less than 10% (*8*). The study of transfection efficiencies of glyconanoparticles of different core sizes has shown that, regardless of the net negative charge on the surface of the complex, gold nanoparticles of 40 nm in core diameter show the highest gene transfection ability compared to the other

sizes of glyconanoparticles. The gold nanoparticles in the study were surface functionalized with cationic glycopolymer p(APMA$_{31}$-*b*-LAEMA$_{32}$) (*29*). Herein, we report the transfection efficiencies of biocompatible nanoparticles using cationic glycopolymer p(APMA$_{31}$-*b*-GAPMA$_{45}$). The transfection experiments were performed at various concentrations of gold nanoparticles, and the results indicated that transfection efficiencies were not significant compared to control (plasmid alone) when concentration of gold nanoparticles was less than 89 μM, possibly due to the net anionic character of the nanoparticles−plasmid complex, as determined by agarose gel electrophoresis. The significant transfection efficiencies (45−50%) with low toxicity values (∼85% cell viability) were observed upon the complexation of plasmid with 89 μM gold nanoparticles (Figure 4; see Supporting Information Figure S10).

The improved transfection efficiency of cationic glyconanoparticle−plasmid complexes in the absence of external force is attributed to the net cationic charge of the vehicle, thus leading to successful delivery of gene inside the cells. It should be noted that, despite possessing the same cationic component, the enhanced transfection efficiency of p(APMA-*b*-GAPMA) functionalized gold nanoparticles as compared to p(APMA-*b*-LAEMA) functionalized nanoparticles of the same sizes is attributed to higher glycopolymer component of the polymer (*29*). These results are in agreement with previous studies, which also show that the glycopolymer component of the carrier largely influences the transfection efficiencies (*14*).

As expected, further increase in the cationic character does not affect the transfection efficiency of the vehicle significantly, but does lead to significant toxicity to the cells, due to the presence of excess positive charge. These results are in agreement with the previous data where p(APMA-*b*-LAEMA)-*f*-gold nanoparticles of 10 nm core diameter are shown to exhibit the same behavior (*29*). The transfection efficiencies of novel gene delivery scaffolds were compared to that of commercially available control lipofectamine 2000. The previous experiments showed that lipofectamine can successfully transfect Hela cells and the transfection efficiency was found to be 55−60% with significant toxicity (20% cell viability). Although the transfection efficacy of glyconanoparticles was comparable to that of lipofectamine, the lower toxicity of glyconanoparticles was an obvious preference over the commercially available standard. Thus, the vehicle presents a desired compromise between two major issues: cell viability and transfection efficacy.

CONCLUSION

In short, we describe the facile synthesis of cationic glyconanoparticles using photochemistry. The size and polydispersity of gold nanoparticles were controlled by UV radiation and concentration of cationic glycopolymer. The near-monodisperse cationic glyconanoparticles produced were found to be resistant to aggregation in physiological conditions. The mechanism of uptake of this novel gene delivery vehicle was studied, and it was found that cationic nanoparticles produced undergo receptor mediated endocytosis following their vesicular escape, due to the net cationic character of the nanoparticles. Finally, the cationic nanoparticles were complexed with reported plasmid, and their transfection efficacy was determined. The results suggest that biocompatibility of nanoparticles and their easy uptake by cells followed by vesicular escape and nuclear entry, in the absence of external impulse, prove the successful fabrication of a novel type of gene delivery vehicle.

ACKNOWLEDGMENT

The author would like to thank Natural Sciences and Engineering Research Council of Canada for financial support of this research work.

Supporting Information Available: GPC and ^{1}H NMR data of block copolymer synthesis, toxicity results of the polymers, DLS data and agarose gel electrophoresis for the complexation of DNA to gold nanoparticles, confocal images of gold nanoparticles uptake by Hela cells, and transfection images. This material is available free of charge via the Internet at http://pubs.acs.org.

LITERATURE CITED

(1) Mintzer, A. M., and Simanek, E. E. (2009) Nonviral vectors for gene delivery. *Chem. Rev. 109*, 259–302.

(2) Srinivasachari, S., Liu, Y., Zhang, G., Prevette, L., and Reineke, M. T. (2006) Trehalose click polymers inhibit nanoparticle aggregation and promote pDNA delivery in serum. *J. Am. Chem. Soc. 128*, 8176–8184.

(3) Sharma, R., Lee, S.-J., Bettencourt, C. R., Xiao, C., Konieczny, F. S., and Won, Y.-Y. (2008) Effects of the incorporation of a hydrophobic middle block into a PEG-polycation diblock copolymer on the physicochemical and cell interaction properties of the polymer-DNA complexes. *Biomacromolecules 9*, 3294–3307.

(4) Pun, S. H., and Davis, E. M. (2002) Development of a nonviral gene delivery vehicle for systemic application. *Bioconjugate Chem. 13*, 630–639.

(5) Kostarelos, K., and Miller, D. A. (2005) Synthetic, self-assembly ABCD nanoparticles; a structural paradigm for viable synthetic non-viral vectors. *R. Soc. Chem.: Chem Soc. Rev. 34*, 970–994.

(6) Lomas, H., Massignani, M., Abdullah, A. K., Canton, I., Presti, L. C., MacNiel, S., Du, J., Blanazs, A., Madsen, J., Armes, P. S., Lewis, L. A., and Battaglia, G. (2008) Non-cytotoxic polymer vesicles for rapid and efficient intracellular delivery. *Faraday Discuss. 139*, 143–159.

(7) Snadhu, K. K., McIntosh, M. C., Simard, M. J., Smith, W. S., and Rotello, M. V. (2002) Gold nanoparticle-mediated transfection of mammalian cells. *Bioconjugate Chem. 13*, 3–6.

(8) Wang, H., Chen, Y., Li, X.-Y., and Liu, Y. (2007) Synthesis of Ooligo(ethylenediamino)-β-cyclodextrin modified gold nanoparticle as a DNA concentrator. *Mol. Pharmaceutics 4*, 189–198.

(9) Strand, P. S., Issa, M. M., Christensen, E. B., Varum, M. K., and Artursson, P. (2008) Tailoring of chitosans for gene delivery: novel self-branched glycosylated chitosan oligomers with improved functional properties. *Biomacromolecules 9*, 3268–3276.

(10) Gao, K., and Huang, L. (2008) Nonviral methods for siRNA delivery. *Mol. Pharmaceutics 6*, 651–658.

(11) Thompson, H. D. (2008) Adenovirus in a synthetic membrane wrapper: an example of hybrid vigor. *ACS Nano 2*, 821–826.

(12) Bergen, J. M., Recum, H. A., Goodman, T. T., Massey, P. A., and Pun, S. H. (2006) Gold nanoparticles as a versatile platform for optimizing physicochemical parameters for targeted drug delivery. *Macromol. Biosci. 6*, 506–516.

(13) Saul, M. J., Wang, H. C.-H., Ng, P. C., and Pun, S. H. (2008) Multilayer nanocomplexes of polymer and DNA exhibit enhanced gene delivery. *Adv. Mater. 20*, 19–25.

(14) Liu, Y., Wenning, L., Lynch, M., and Reineke, M. T. (2004) New poly(D-glucaramidoamine)s induce DNA nanoparticle formation and efficient gene delivery into mammalian cells. *J. Am. Chem. Soc. 126*, 7422–7423.

(15) Ghosh, S. P., Kim, C. K., Han, G., Forbes, S. N., and Rotello, M. V. (2008) Efficient gene delivery vectors by tuning the surface charge density of amino acid-functionalized gold nanoparticles. *ACS Nano 2*, 2213–2218.

(16) Li, P., Li, D., Zhang, L., Li, G., and Wang, E. (2008) Cationic lipid bilayer coated gold nanoparticles-mediated transfection of mammalian cells. *Biomaterials 29*, 3617–3624.

(17) Zhou, X., Zhang, X., Yu, X., Zha, X., Fu, Q., Liu, B., Wang, X., Chen, Y., Chen, Y., Shan, Y., Jin, Y., Wu, Y., Liu, J., Kong,

W., and Shen, J. (2008) The effect of conjugation to gold nanoparticles on the ability of low molecular weight chitosan to transfer DNA vaccine. *Biomaterials 29*, 111–117.

(18) Zheng, M., Li, Z., and Huang, X. (2004) Ethylene glycol monolayer protected nanoparticles: synthesis, characterization, and interactions with biological molecules. *Langmuir 20*, 4226–4235.

(19) Li, Z.-P., Wang, Y.-C., Liu, H.-C., and Li, Y.-K. (2005) Development of chemiluminescence detection of gold nanoparticles in biological conjugates for immunoassay. *Anal. Chim. Acta 551*, 85–91.

(20) Shimmin, G. R., Schoch, B. A., and Braun, V. P. (2004) Polymer size and concentration effects on the size of gold nanoparticles capped by polymeric thiols. *Langmuir 20*, 5613–5620.

(21) Guo, R., Zhang, L., Zhu, Z., and Jiang, X. (2008) Direct facile approach to the fabrication of chitosan-gold hybrid nanospheres. *Langmuir 24*, 3459–3464.

(22) Das, j., Huh, C.-H., Kwon, K., Park, S., Jon, S., Kim, K., and Yang, H. (2009) Comparison of the nonspecific binding of DNA-conjugated gold nanoparticles between polymeric and monomeric self-assembled monolayers. *Langmuir 25*, 235–241.

(23) Ganguli, M., Babu, V. J., and Maiti, S. (2004) Complex formation between cationically modified gold nanoparticles and DNA: an atomic force microscopic study. *Langmuir 20*, 5165–5170.

(24) Leroueil, R. P., Berry, A. S., Duthie, K., Han, G., Rotello, M. V., McNerny, Q. D., Baker, R. J., Orr, G. B., and Banaszak Holl, M. M. (2008) Wide varieties of cationic nanoparticles induce defects in supported lipid bilayers. *Nano Lett. 8*, 420–424.

(25) (a) De la Fuente, M. J., Barrientos, G. A., Rojas, C. T., Rojo, J., Canada, J., Fernandez, A., and Penades, S. (2001) Gold glyconanoparticles as water-soluble polyvalent models to study carbohydrate interactions. *Angew. Chem. 113*, 2318–2321.

(26) Barrientos, G. A., De la Fuente, M. J., Rojas, C. T., Fernandez, A., and Penades, S. (2003) Gold glyconanoparticles: synthetic polyvalent ligands mimicking glycocalyx-like surfaces as tools for glycobiological studies. *J. Chem. Eur. 9*, 1909–1921.

(27) Fuente, M. J., Alcantara, D., and Penades, S. (2007) Cell response to magnetic glyconanoparticles: does the carbohydrate matter? *IEE Trans. Nanobiosci. 6*, 275–281.

(28) Funete de la, M. J., and Berry, C. C. (2005) Tat peptide as an efficient molecule to translocate gold nanoparticles into the cell nucleus. *Bioconjugate Chem. 16*, 1176–1180.

(29) Ahmed, M., Deng, Z., and Narain, R. (2009) Study of transfection efficiencies of gold nanoparticles of different core sizes. *ACS Appl. Mater. Interfaces* ASAP.

(30) Mcgilvray, L. K., Decan, R. M., Wang, D., and Scaiano, C. J. (2006) Facile photochemical synthesis of unprotected aqueous gold nanoparticles. *J. Am. Chem. Soc. 128*, 15980–15981.

(31) Narain, R., Housni, A., Gody, G., Boullanger, P., Charreyre, M., and Delair, T. (2007) Preparation of biotinylated glycon-anoparticles via a photochemical process and study of their bioconjugation to streptavidin. *Langmuir 23*, 12835–12841.

(32) Housni, A., Ahmed, M., Liu, S., and Narain, R. (2008) Monodisperse Protein Stabilized Gold Nanoparticles via a Simple Photochemical Process. *J. Phys. Chem. C. 112*, 12282–12290.

(33) Miyamoto, D., Oishi, M., Kojima, K., Yoshimoto, K., and Nagasaki, Y. (2008) Completely dispersible PEGylated gold nanoparticles under physiological conditions: modification of gold nanoparticles with precisely controlled PEG-b-polyamine. *Langmuir 24*, 5010–5017.

(34) Wang, Z., Tan, B., Hussain, I., Schaeffer, N., Wyatt, F. M., Brust, M., and Cooper, I. A. (2007) Design of polymeric stabilizers for size-controlled synthesis of monodisperse gold nanoparticles in water. *Langmuir 23*, 885–895.

(35) Heuser, E. J., and Anderson, W. G. R. (1989) Hypertonic media inhibit receptor-mediated endocytosis by blocking clathrin-coated pit formation. *J. Cell Biol. 108*, 389–400.

(36) Yin, M., Ding, K., Gropeanu, A. R., Shen, J., Berger, R., Weil, T., and Mullen, K. (2008) Dendritic star polymers for efficient DNA binding and stimulus-dependent DNA release. *Biomacromolecules 9*, 3231–3238.

(37) Deng, Z., Bouchekif, H., Babooram, K., Housni, A., Choytun, N., and Narain, R. (2008) Facile synthesis of controlled-structure primary amine-based methacrylamide polymers via the reversible addition-fragmentation chain transfer process. *J. Polym. Sci., Part A: Polym. Chem. 46*, 4984–4996.

(38) Zhang, X., Sharma, K. K., Boeglin, M., Ogier, J., Mainard, D., Voegel, J.-C., Mely, V., and Benkirane-Jessel, N. (2008) Transfection ability and intracellular DNA pathway of nano-structured gene-delivery systems. *Nano Lett. 8*, 2432–2436.

(39) Meyer, M., Dohmen, C., Philipp, A., Kiener, D., Maiwald, G., Scheu, C., Ogris, M., and Wagner, M. (2009) Synthesis and biological evaluation of bioresponsive and endosomolytic siRNA-polymer conjugate. *Mol. Pharmaceutics 6*, 752–762.

(40) York, W. A., Zhang, Y., Holley, C. A., Guo, Y., Huang, F., and McCormick, L. C. (2009) Facile synthesis of multivalent folate-block copolymer conjugates via aqueous RAFT polymerization: targeted delivery of siRNA and subsequent gene supression. *Biomacromolecules 10*, 936–943.

(41) Koda, S., Inoue, Y., and Iwata, H. (2008) Gene transfection into adherent cells using electroporation on a dendrimer modified gold electrode. *Langmuir 24*, 13525–13531.

BC900350C

Supporting information for "Cationic Glyconanoparticles: Their Complexation with DNA, Cellular Uptake and Transfection Efficiencies "

Marya Ahmed[1,2], Zhicheng Deng[1,2], Shiyong Liu[3], Robert Lafrenie[4], Aseem Kumar[2], Ravin Narain[*1,2]

[1]*Department of Chemical and Materials Engineering, University of Alberta, Edmonton, AB, T6G 2G6, Canada*

[2]*Department of Chemistry and Biochemistry, Biomolecular Sciences Program, Laurentian University, 935, Ramsey Lake Rd, Sudbury, ON, Canada*

[3]*Department of Polymer Science and Engineering, University of Science and Technology of China, Hefei, Anhui, China*

[4]*Regional Cancer Program of the Hospital, 41 Ramsey Lake Road, Sudbury, ON, Canada.*

RECEIVED DATE (automatically inserted by publisher); rnarain@laurentian.ca or narain@ualberta.ca

Supporting Details:

Table S1. Summary of synthetic parameters for the RAFT copolymerization of APMA to GAPMA

Copolymer Type	Homopolymer[a]		Copolymer[b]	
	M_n	M_w/M_n	M_n	M_w/M_n
Poly($APMA_{45}$-*b*-$GAPMA_{54}$)	8,000	1.12	25,300	1.55
Poly($APMA_{31}$-*b*-$GAPMA_{45}$)	5,500	1.09	19,900	1.27

The evolution of the molecular weight with time for the polymerizations were studied with a conventional Viscotek GPC system using a 0.5 M sodium acetate / 0.5 M acetic acid buffer as eluent, two Waters WAT011545 columns at room temperature and a flow rate of 1.0 mL/min.

[a] Six near-monodisperse PEO standards (M_p = 1,010 - 101,200 g mol^{-1}) were used for calibration.

[b] Seven near-monodisperse Pullulan standards (M_w = 5,900 - 404,000 g mol^{-1}) were used for calibration.

The composition of the polymer p($APMA_{31}$-b-$GAPMA_{45}$) calculated by ^{1}H NMR

Table S2: A comparison of Intensity and Mass distribution of DLS showing the size control of gold nanoparticles as a function of UV intensity stabilized with p($APMA_{31}$-b-$GAPMA_{45}$) polymer.

Entry	Concentration of polymer	Intensity (watts)	UV time	% Area	Intensity Distribution Size (nm)	PDI	Mass Distribution Size	PDI
4	$5.1x10^{-6}$	224	5	91.5 8.5	18.1 3.31	0.25 0.17	2.9	0.17
5	$5.1x10^{-6}$	168	5	87.8 12.2	21.99 4.71	0.17 0.1	4.56	0.10
6	$5.1x10^{-6}$	112	5	60.6 39.4	27.04 5.04	0.14 0.11	4.85	0.11
7	$5.1x10^{-6}$	56	15	44.7 55.3	250.78 4.69	0.17 0.07	4.73	0.10

Table S3: Size control of gold nanoparticles as a function of UV intensity stabilized with p($APMA_{45}$-b-$GAPMA_{54}$) polymer.

Poly($APMA_{45}$-*b*-$GAPMA_{54}$) Molecular weight = 25,300 kDa, Mw/Mn = 1.55				**Mass Distribution**		**Intensity distribution**		
Entry	**Polymer Concentration**	**Au:I:Polymer**	**Intensity (Watts)**	**DLS Size (nm)**	**Size Distr.**	**% Area**	**DLS Size (nm)**	**Size Distr.**
8	$1.1x10^{-4}$	1:3:0.025	224	7.64	0.33	100	10.8	0.35
9	$1.1x10^{-4}$	1:3:0.025	168	10.23	0.20	100	11.59	0.21
10	$1.1x10^{-4}$	1:3:0.025	112	9.87	0.27	95.3	12.4	0.29
11	$5.1x10^{-6}$	1:3:0.005	224	2.9	0.17	8.2 91.8	15.5 2.9	0.23 0.17
12	$5.1x10^{-6}$	1:3:0.005	168	4.3	0.11	74.8 25.2	26.88 4.46	0.16 0.11
13	$5.1x10^{-6}$	1:3:0.005	112	4.5	0.07	48.1 51.9	120.5 4.58	0.13 0.07

Table S4. DLS mass distribution data showing the change in p($APMA_{31}$-*b*-$GAPMA_{45}$)-*f*-gold nanoparticles size upon the addition of human serum (entry-1)

Experimental Conditions	**% Area**	**Mass Distribution**	
		Size (nm)	**PDI**
AuNPs in deionized water	91.1	6.15	0.15
	8.9	19.15	0.22
AuNPs in PBS	99.5	6.58	0.07
	0.5	74.49	0.22
AuNPs in 10% v/v serum	99.4	6.0	0.07
	0.6	51.26	0.18

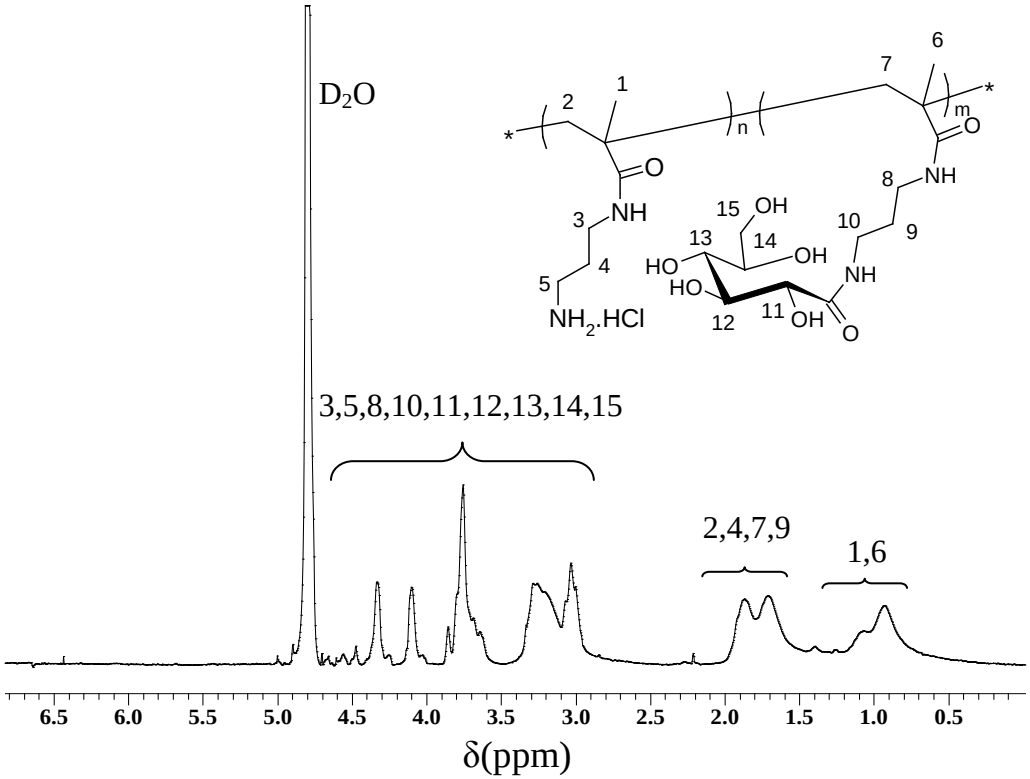

Figure S1. ^{1}H-NMR spectrum of poly ($APMA_{31}$-*b*-$GAPMA_{45}$) block copolymer.

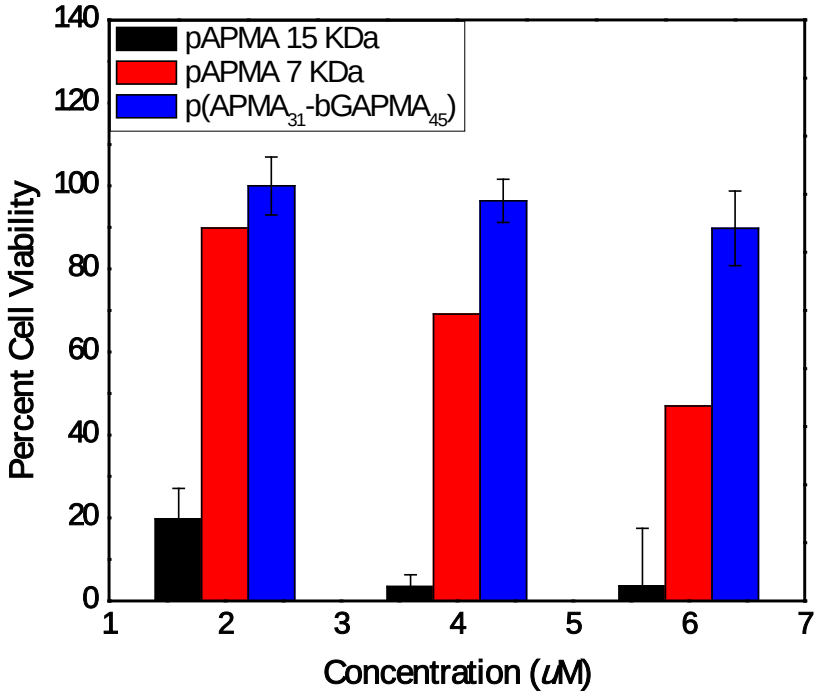

Figure S2. Comparison of % cell viability upon treatment with poly (APMA) of different molecular weights & glycopolymer poly ($APMA_{31}$-*b*-$GAPMA_{45}$).

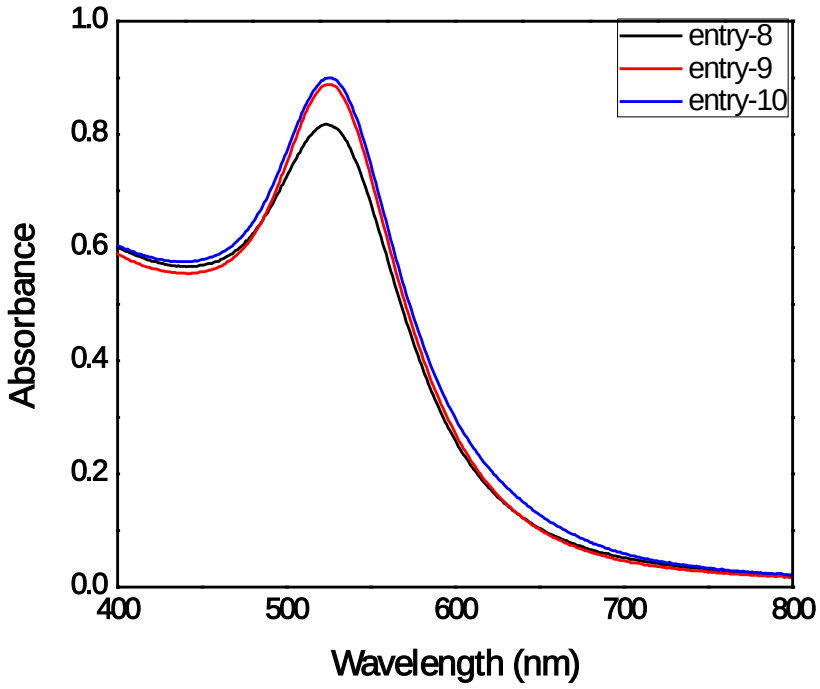

Figure S3: UV-Vis spectrum of gold nanoparticles synthesized with 0.11 mM concentration of p($APMA_{45}$-b-$GAPMA_{54}$), using 224, 168 and 112 W of UV intensity.

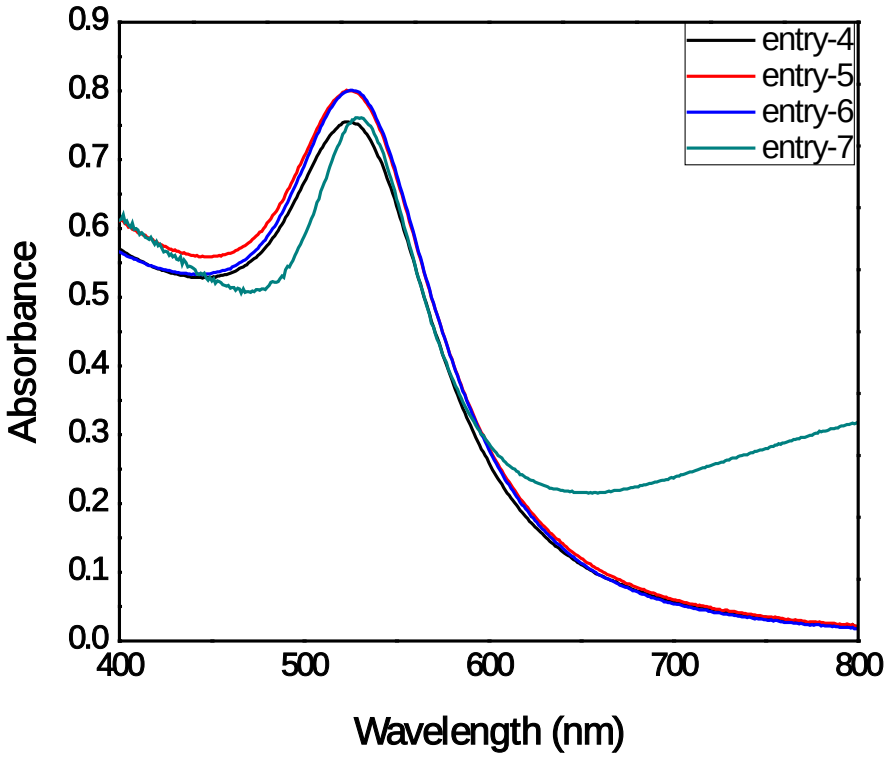

Figure S4: UV-visible spectrum of gold nanoparticles synthesized with 0.11 mM p($APMA_{31}$-b-$GAPMA_{45}$) using 224, 168 and 112 W of UV intensity.

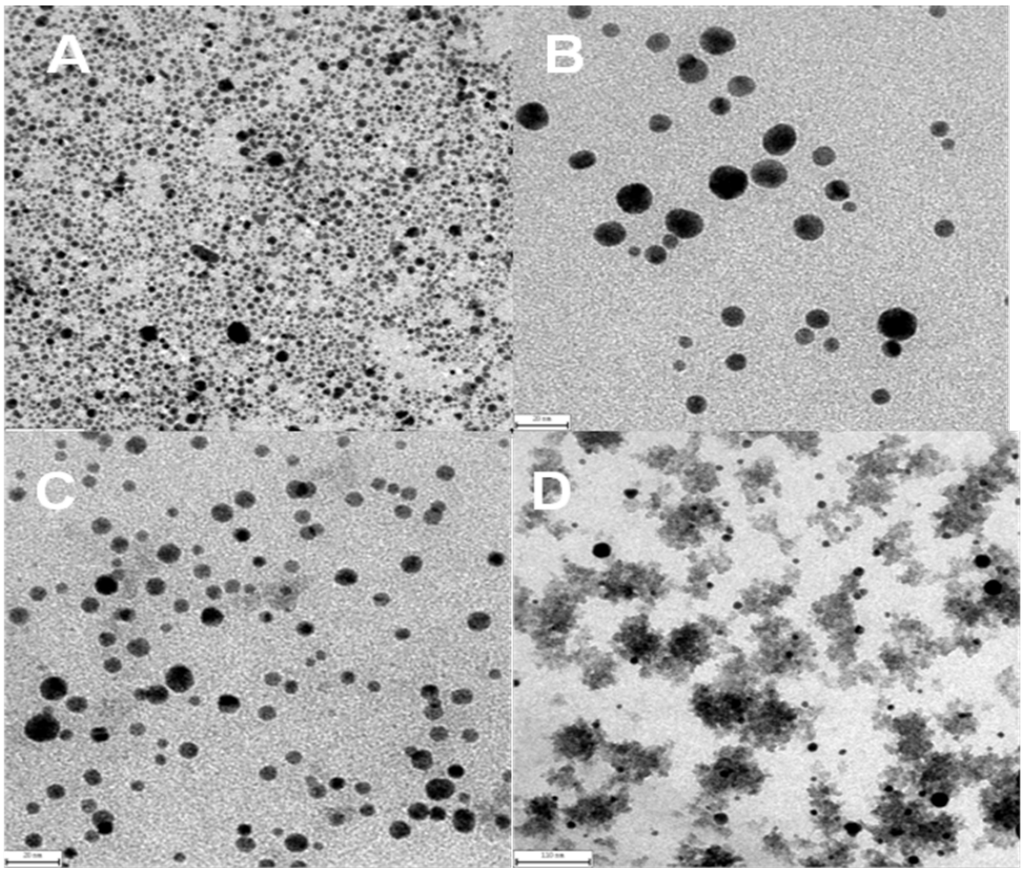

Figure S5: TEM micrographs show the size and monodispersity of gold nanoparticles synthesized by photochemical approach and stabilized by copolymer p($APMA_{31}$-*b*-$GAPMA_{45}$).

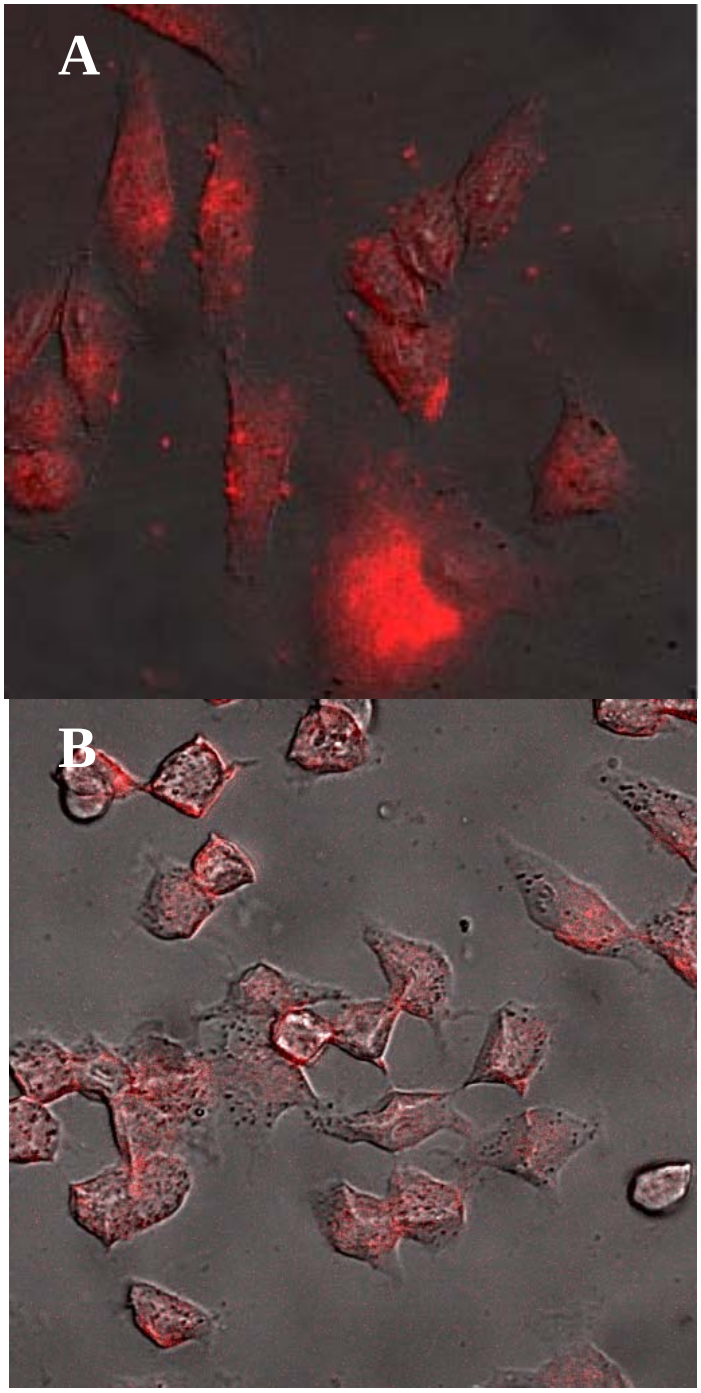

Figure S6. Confocal images of Hela cells incubated with p($APMA_{31}$-*b*-$GAPMA_{45}$)-*f*-gold nanoparticles A) at 37 ˚C. B) Sucrose treated at 37 ˚C. (entry-2)

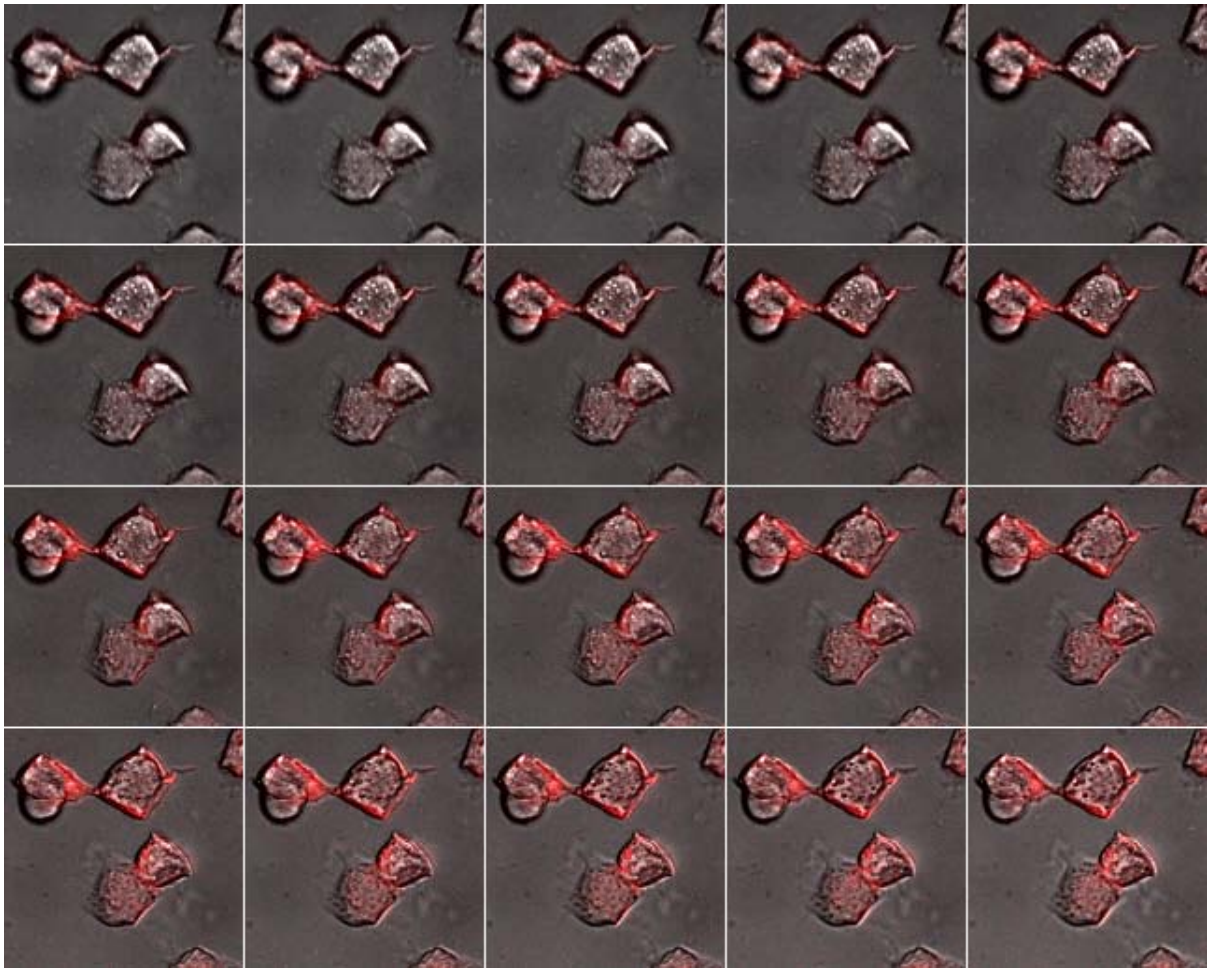

Figure S7. Confocal images of Hela cells incubated with p($APMA_{31}$-*b*-$GAPMA_{45}$) stabilized gold nanoparticles at 37 ˚C treated with sucrose, taken in stacks (entry-2).

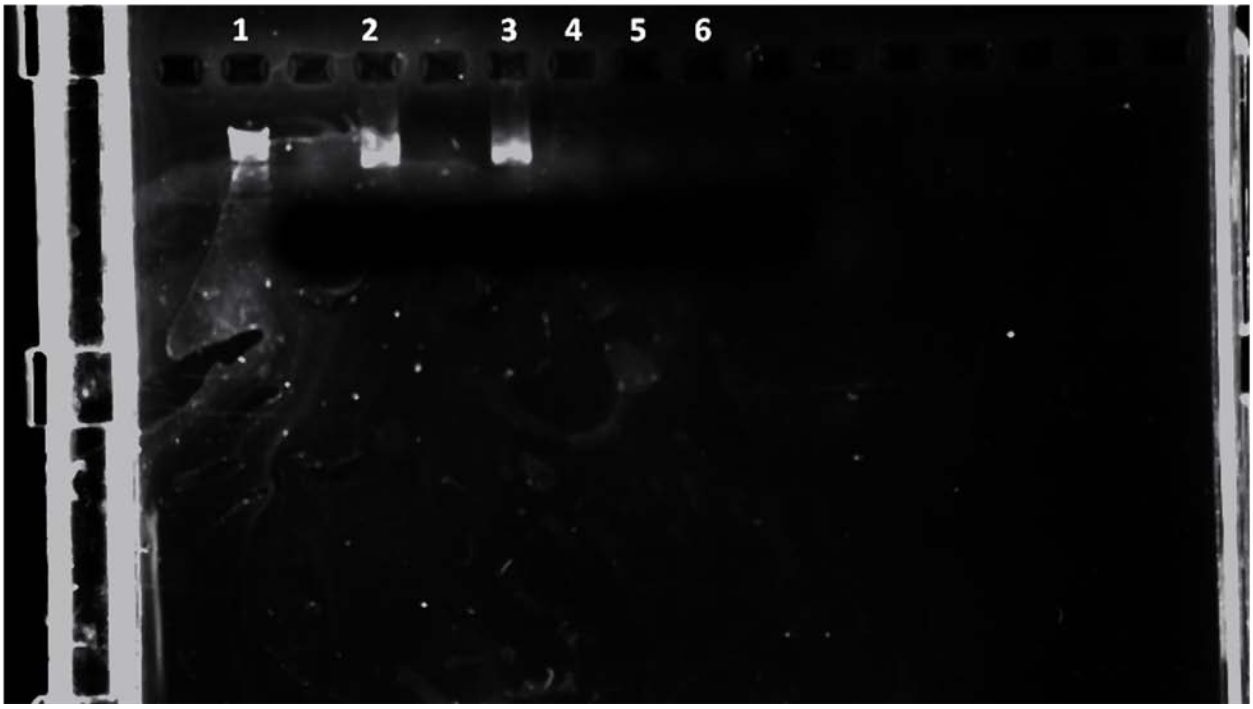

Figure S8: Agarose gel electrophoresis showing the complexation of CFP plasmid to gold nanoparticles stabilized with p($APMA_{31}$-*b*-$GAPMA_{45}$). (1.ladder, 2.CFP plasmid (340 ng), 3. CFP plasmid + 42 μM GNPs, 4. CFP plasmid + 89 μM GNPs, 5. CFP plasmid + 139 μM GNPs, 6. CFP plasmid + 254 μM GNPs.

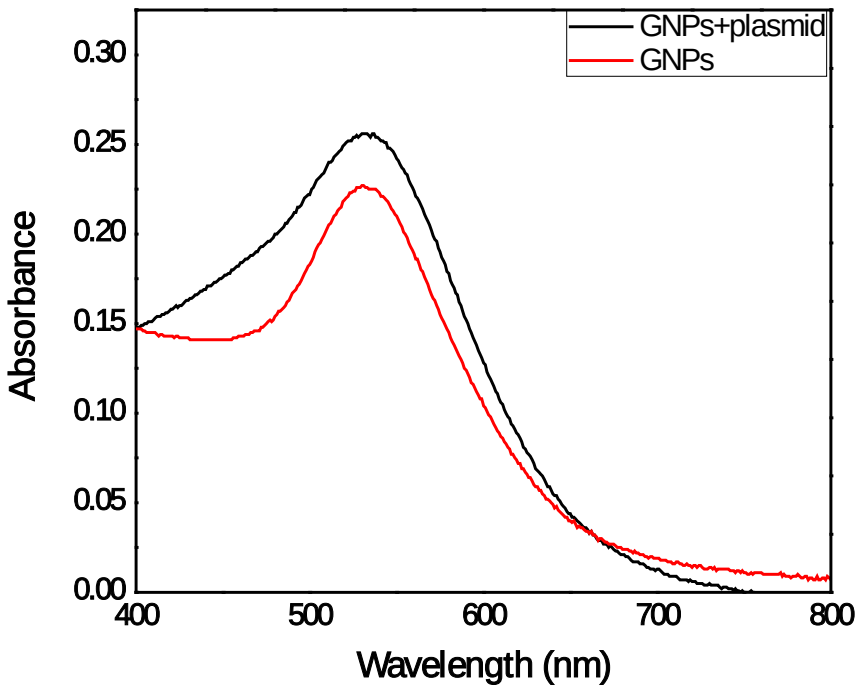

Figure S9: Characterization of p(APMA$_{31}$-*b*-GAPMA$_{45}$)-*f*-gold nanoparticles-plasmid complex using UV visible spectroscopy.

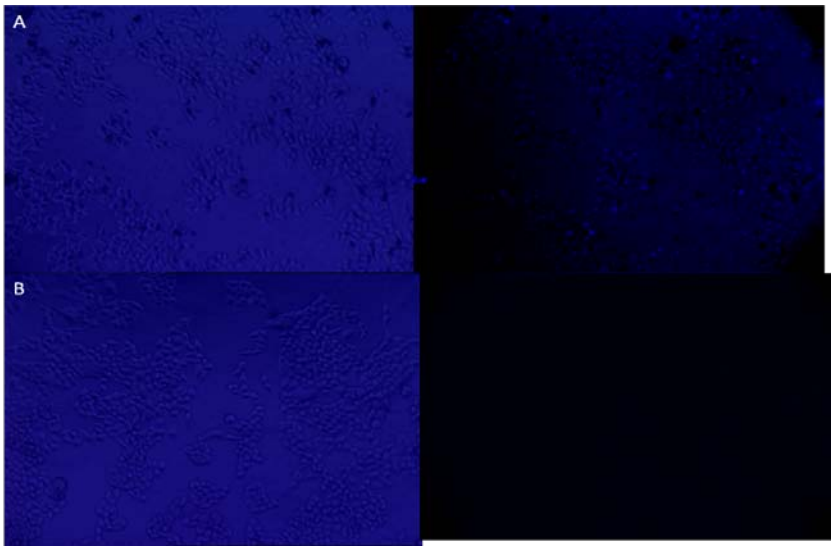

Figure S10: Transfection studies A) upon incubation of Hela cells with p($APMA_{31}$-*b*-$GAPMA_{45}$)-*f*- gold nanoparticles-pECFP plasmid complex(entry-1), B) upon incubation of Hela cells with pECFP plasmid only.

Dual-Modality Molecular Imaging Using Antibodies Labeled with Activatable Fluorescence and a Radionuclide for Specific and Quantitative Targeted Cancer Detection

Mikako Ogawa, Celeste A. S. Regino, Jurgen Seidel, Michael V. Green, Wenze Xi, Mark Williams, Nobuyuki Kosaka, Peter L. Choyke, and Hisataka Kobayashi*

Molecular Imaging Program, Center for Cancer Research, National Cancer Institute, National Institute of Health. Received August 13, 2009; Revised Manuscript Received September 21, 2009

Multimodality molecular imaging should have potential for compensating the disadvantages and enhancing the advantages of each modality. Nuclear imaging is superior to optical imaging in whole body imaging and in quantification due to good tissue penetration of γ rays. However, target specificity can be compromised by high background signal due to the always signal ON feature of nuclear probes. In contrast, optical imaging can be superior in target-specific imaging by employing target-specific signal activation systems, although it is not quantitative because of signal attenuation. In this study, to take advantage of the mutual cooperation of each modality, multimodality imaging was performed by a combination of quantitative radiolabeled probe and an activatable optical probe. The monoclonal antibodies, panitumumab (anti-HER1) and trastuzumab (anti-HER2), were labeled with ^{111}In and ICG and tested in both HER1 and HER2 tumor bearing mice by the cocktail injection of radiolabeled and optical probes and by the single injection of a dual-labeled probe. The optical and nuclear images were obtained over 6 days after the conjugates injection. The fluorescence activation properties of ICG labeled antibodies were also investigated by *in vitro* microscopy. *In vitro* microscopy demonstrated that there was no fluorescence signal with either panitumumab-ICG or trastuzumab-ICG, when the probes were bound to cell surface antigens but were not yet internalized. After the conjugates were internalized into the cells, both conjugates showed bright fluorescence signal only in the target cells. These results show that both conjugates work as activatable probes. In *in vivo* multimodality imaging by injection of a cocktail of radio-optical probes, only the target specific tumor was visualized by optical imaging. Meanwhile, the biodistribution profile of the injected antibody was provided by nuclear imaging. Similar results were obtained with radio and optical dual-labeled probes, and it is confirmed that pharmacokinetic properties did not affect the results above. Here, we could characterize the molecular targets by activatable optical probes and visualize the delivery of targeting molecules quantitatively by radioactive probes. Multimodality molecular imaging combining activatable optical and radioactive probes has great potential for simultaneous visualization, characterization, and measurement of biological processes.

INTRODUCTION

To date, *in vivo* molecular imaging techniques have made great progress due to improvements in imaging technology and the design of novel imaging probes. Several modalities are now utilized for molecular imaging, including nuclear imaging, optical imaging, MRI, and ultrasound (*1*−*3*). On the basis of the physical characteristics of the emitted signals and the signal detection systems, each modality has both advantages and disadvantages. As a result, multimodality imaging should have the potential for overcoming the disadvantages of a single modality by combining the advantages of more than one modality.

Both nuclear imaging and optical imaging have comparably high sensitivities; however, nuclear imaging is superior for quantification due to good tissue penetration of γ-rays and the ability to accurately measure count rate in tissue, which permits whole body quantitative imaging not only in small animals, but also in humans. However, it is impossible to control or "switch off" ionizing radiation *in vivo* because there are no bioavailable materials to quench γ-rays. Therefore, target specificity can be compromised by the high background signals originating from unbound or nonspecifically bound probes due to the "always on" feature of nuclear imaging probes, especially when slow-clearing probes including monoclonal antibodies are employed (*4*, *5*).

In contrast, optical imaging can be superior to nuclear imaging for target specificity because it can employ target-specific activatable systems. In these activatable systems, the fluorescent signal can be quenched by one of several mechanisms, and the quenched signal can subsequently be turned on in particular biological environments such as lowered pH. We and other groups have developed a number of target-specific activatable optical probes using several mechanisms, e.g., FRET-quenching, pH activation, self-quenching, and H-dimer formation (*6*−*13*). The fluorescent signals of these activatable probes are designed to be switched on only in the target cells or tissues. As a result, the background and nonspecific signal is dramatically reduced. However, optical imaging techniques are not quantitative, especially when the object is located deep to the skin because of significant signal attenuation in tissue. Near-infrared (NIR, emission spectra ∼700−850 nm) fluorescence is one of the potential solutions for overcoming this limitation, although the penetration of NIR is still lower than γ-rays (*14*−*16*). Among

* Corresponding author. Hisataka Kobayashi, M.D., Ph.D., Molecular Imaging Program, Center for Cancer Research, National Cancer Institute, NIH, Building 10, Room 1B40, MSC1088, Bethesda, MD 20892-1088. Phone: 301-451-4220; Fax: 301-402-3191; E-mail: kobayash@mail.nih.gov.

10.1021/bc900362k This article not subject to U.S. Copyright. Published 2009 by the American Chemical Society
Published on Web 10/19/2009

the NIR dyes, indocyanine green (ICG) is a fluorescence dye that has long been approved by the FDA for clinical use in retinal angiography and for intraoperative assessment of liver function (*17, 18*). However, ICG-conjugated antibodies were considered not useful for molecular imaging, because all ICG-conjugated antibodies examined in the literature yielded faint fluorescent signals and were not successful even in *in vitro* assays (*19, 20*). Recently, we demonstrated that ICG-conjugated monoclonal antibodies are able to target cells expressing the receptor, during *in vivo* molecular imaging (*21*). The fluorescent signal of an ICG-conjugated monoclonal antibody is quenched when the probe is unbound or located outside of the target cell; however, it activates when the probe is bound and internalized into the target cells. Therefore, an ICG-conjugated antibody can specifically visualize the target tumor with minimal background signal.

In this study, multimodality imaging was performed by the use of a radiolabeled antibody and a target cell-specific activatable NIR fluorescence-labeled antibody. We employed FDA-approved monoclonal antibodies, panitumumab (anti-HER1) and trastuzumab (anti-HER2), as internalizing targeting ligands. These antibodies were labeled with ^{111}In and ICG for radio-optical imaging and tested in both HER1 and HER2 tumor-bearing mice using an injection of a cocktail of radiolabeled and optical antibodies and by the single injection of a dual-labeled antibody.

MATERIALS AND METHODS

Reagents. Panitumumab, a human anti-HER1 antibody, was purchased from AMGEN Inc. (Thousand Oaks, CA). Trastuzumab, a humanized anti-HER-2 antibody, was purchased from Genentech Inc. (South San Francisco, CA). ICG-sulfo-OSu was purchased from Dojindo Molecular Technologies (Rockville, MD). 2-(4-Isothiocyanatobenzyl)-diethylenetriamine pentaacetic acid (*p*-SCN-BzDTPA) was purchased from Macrocyclics (Dallas, TX). Carrier-free $^{111}InCl_3$ was purchased from Perkin-Elmer Health Sciences, Inc. (North Billerica, MA). All other chemicals used were of reagent grade.

Cell Culture. The HER1 positive cell lines, A431 and MDA-MB468, were used for HER1 targeting studies with panitumumab conjugates. For HER2 targeting studies by trastuzumab conjugates, the *HER2* gene transfected NIH3T3 (3T3/HER2) cell line was used. The cell lines were grown in RPMI 1640 (Life Technologies, Gaithersburg, MD) containing 10% fetal bovine serum (Life Technologies), 0.03% L-glutamine, 100 units/mL penicillin, and 100 μg/mL streptomycin in 5% CO_2 at 37 °C.

Synthesis of ICG Conjugated Antibodies. Panitumumab or trastuzumab (1 mg, 6.8 nmol) was incubated with ICG-sulfo-OSu (68 nmol) in 0.1 M Na_2HPO_4 (pH 8.5) at room temperature for 30 min. Then, the mixture was purified with a Sephadex G25 column (PD-10; GE Healthcare, Piscataway, NJ). The concentration of ICG was measured by absorption with the UV−vis system to confirm the number of fluorophore molecules conjugated to each antibody molecule under conditions of 5% SDS and 2-mercapto ethanol (2-ME) which diminish intermolecular interaction among ICG molecules and between ICG and the antibody. The number of ICG per antibody was ∼4−5.

Radiolabeling of Antibodies. Panitumumab or trastuzumab was reacted with 15-fold molecular excess of *p*-SCN-Bz-DTPA at pH 8.5 in sodium hydrogen carbonate buffer for 1 h at 25 °C. The Bz-DTPA conjugated antibodies were purified by dialysis using 1×PBS on an Amicon Ultra-4 centrifugal device with Ultracel-30 (Millipore, Danvers, MA). Indium-111 chloride (3.5 μL of 295 MBq stock in 0.05 M HCl) is added to the Bn-DTPA antibody conjugate (100 μg) in 25 μL 0.15 M NH_4OAc pH ∼7 and incubated for 1 h at room temperature. EDTA (5 μL of 0.1 M) was then added to quench the reaction mixture. The radiolabeled antibody was then purified using a Sephadex G-25 column (PD-10; GE Healthcare) eluted with 1×PBS. The radiolabeled antibody fraction was collected and the specific activities of the radiolabeled antibodies were 211 and 210 MBq/mg for ^{111}In-panitumumab and ^{111}In-trastuzumab, respectively. Radiochemical purities were assessed by radio-ITLC and were 81% and 88% for the ^{111}In-panitumumab and ^{111}In-trastuzumab, respectively.

Dual-Labeling of Antibody with ICG and ^{111}In. Trastuzumab (1 mg, 6.8 nmol) was incubated with ICG-sulfo-OSu (13.6 nmol) in 0.1 M Na_2HPO_4 (pH 8.5) at room temperature for 30 min. Then, the mixture was purified as described above. The number of ICG per antibody was ∼1. Trastuzumab-ICG was then treated with 15-fold molecular excess of *p*-SCN-BzDTPA. The resulted ICG and BzDTPA conjugated trastuzumab was labeled with ^{111}In and purified in the same manner as above. The specific activity was 404 MBq/mg and the radiochemical purity was 89%.

Immunoreactivity of Radiolabeled Conjugates. Immunoreactivity of ^{111}In-panitumumab, ^{111}In-trastuzumab, or ^{111}In-trastuzumab-ICG was determined using a previously described method in cultured cell lines (*22, 23*). In brief, aliquots of the radiolabeled antibodies (2.6 ng) were incubated for 1 h at 4 °C with 2×10^6 A431 or 3T3/HER2 for panitumumab or trastuzumab conjugates, respectively. The cell binding fraction was collected by centrifuge, and the radioactivity levels of the cell and supernatant fractions were counted in a gamma counter. Nonspecific binding to the cells was determined by adding excess unlabeled antibody.

Investigation of Fluorescence Characteristics of ICG Conjugated Antibodies in Vitro. The fluorescence characteristics of ICG conjugated antibodies were investigated by treating the conjugates with 5% SDS and 2-ME to diminish the hydrophobic interactions and separate the IgG chains. The change in fluorescence intensity for each conjugate was investigated with an *in vivo* imaging system (Maestro, CRi Inc., Woburn, MA) using 710 to 760 nm excitation and 800 nm long-pass emission filters.

Fluorescence Microscopy Studies. 3T3/HER2 or A431 cells were plated on a cover glass-bottomed culture well and incubated for 16 h. Then, trastuzumab-ICG or panitumumab-ICG was added to the medium (10 μg/mL), and the cells were incubated for either 1 or 8 h. Cells were washed once with PBS, and fluorescence microscopy was performed using an Olympus BX61 microscope (Olympus America, Inc., Melville, NY) equipped with the following filters: excitation wavelength 672.5 to 747.5 nm, emission wavelength 765 to 855 nm. Transmitted light differential interference contrast images were also acquired.

Animal Tumor Model. All procedures were carried out in compliance with the Guide for the Care and Use of Laboratory Animal Resources (1996), National Research Council, and approved by the local Animal Care and Use Committee. A431 cells (HER1+, HER2−, 2×10^6 cells) were injected subcutaneously in the left dorsum of the female nude mice (National Cancer Institute Animal Production Facility, Frederick, MD), and 3T3/HER2 cells (HER1−, HER2+, 2×10^6 cells) were injected subcutaneously into the right dorsum. The experiments were performed at 10−17 days after cell injection. For dual-labeled antibody studies by ^{111}In-trastuzumab-ICG, the following cells, MDA-MB468 (HER1+, HER2−, 2×10^6 cells), A431 (HER1+, HER2−, 2×10^6 cells), and 3T3/HER2 (HER1−, HER2+, 2×10^6 cells), were injected subcutaneously into the left flank, right buttock, and right flank, respectively.

***In Vivo* Multimodal Imaging Studies by Fluorescent and Radioactive Antibodies.** A cocktail of panitumumab-ICG (50 μg) and ^{111}In-panitumumab (4.2 MBq/10 μg) or trastuzumab-

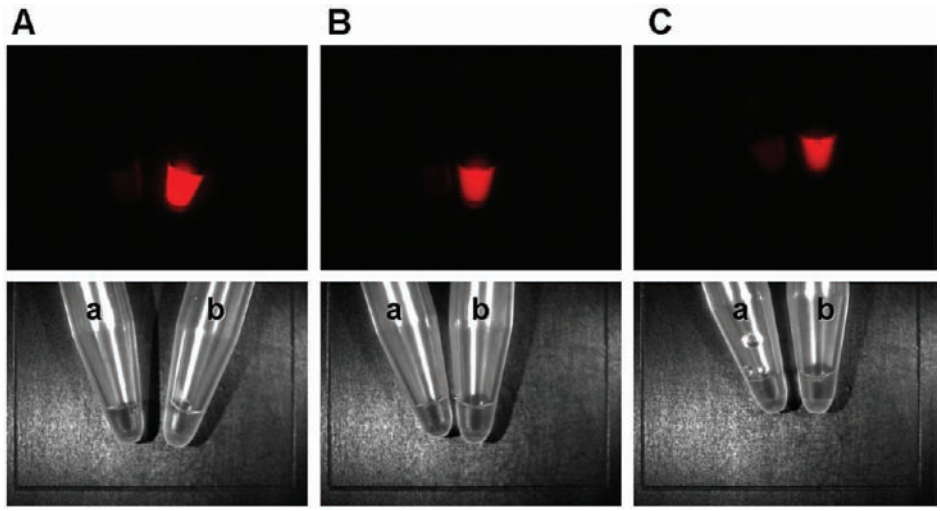

Figure 1. The fluorescence and white light images of antibody-ICG conjugates: (A) panitumumab-ICG, (B) trastuzumab-ICG, (C) BzDTPA-trastuzumab-ICG. (a) in PBS, (b) SDS and 2-ME added condition. In PBS, the conjugates have no fluorescence. Fluorescence is activated by SDS and 2-ME treatment.

ICG (50 μg) and ^{111}In-trastuzumab (4.2 MBq/10 μg) was injected intravenously into A431 and 3T3/HER2 tumor bearing mice ($n = 4$, each). The optical and nuclear images were obtained by Maestro (CRi Inc., Woburn, MA) and an in-house built flat panel gamma camera (Mobile Nuclear Imaging Camera, MONICA) imaging system, respectively, over 6 days after the injection.

For fluorescence imaging, a 710−760 nm band-pass filter was used for excitation and a long-pass filter over 700 nm was used for emission. The spectral fluorescence images consisting of autofluorescence spectra and the spectra from ICG were then unmixed based on their spectral patterns using commercial software (Maestro software, CRi, Inc., Woburn, MA). The regions of interest were placed on the ICG spectral images to measure the fluorescence intensities of the A431 and 3T3/HER2 tumors.

The scintigram of each mouse was obtained by 5 min scan with MONICA (see above) (*24*). Then, the images were processed using *Image-J* software (National Institutes of Health, Bethesda, MD, http://rsb.info.nih.gov/ij/). The regions of interest were placed on the scintigram, and the accumulated radioactivity was measured.

After the imaging on day 6, the mice were sacrificed with carbon dioxide and *ex vivo* images of the resected organs were obtained with both modalities as with the *in vivo* imaging. Then, the organs were weighed and counted in a gamma counter to calculate %ID/g. For histological validation, the dissected lesions were embedded in paraffin and stained with hematoxylin and eosin (H&E).

***In Vivo* Multimodal Imaging Studies with Dual-Labeled Antibodies.** To investigate the effect of pharmacokinetic properties on imaging by radio-optical labeled antibodies, ^{111}In-trastuzumab-ICG (3.8 MBq/60 μg) was injected intravenously into the three tumor bearing mice (A431 (HER1+), MDA-MB468 (HER1+), 3T3/HER2 (HER2+)). The optical and nuclear images were obtained over time and processed in the same manner as above.

RESULTS

Immunoreactivity of Radiolabeled Antibodies. The immumoreactivity values of the ^{111}In-panitumumab and ^{111}In-trastuzumab were 64% and 69%, respectively. The immunoreactivity of the dual-labeled probe, ^{111}In-trastuzumab-ICG, was 75%.

Fluorescence Quenching of ICG Conjugated Antibodies. The fluorescence quenching capacity was measured by treating the conjugates with SDS and 2-ME to dissociate the interactions between ICG molecules and between ICG and its antibody. The fluorescence intensity was very low before the SDS and 2-ME treatment (Figure 1). Intense fluorescence was detected after dissociation, and the quenching capacities were calculated at 17.4-, 19.1-, and 7.3-fold, for panitumumab-ICG, trastuzumab-ICG, and BzDTPA-trastuzumab-ICG, respectively.

***In Vitro* Fluorescence Microscopic Studies.** To investigate the fluorescence activation in the target cells, microscopy was performed. The results are summarized in Figure 2. Fluorescence was not observed for either panitumumab-ICG or trastuzumab-ICG after 0.5 h incubation, when the conjugates were still outside the cells and bound to cell surface receptors. After the conjugates were internalized into the cells after 8 h incubation, both conjugates showed bright fluorescence signal within the target cells. These results demonstrate that both panitumumab-ICG and trastuzumab-ICG are capable of activation; that is, the signal is switched on only within target cancer cells.

***In Vivo* Multimodality Imaging Studies.** The results of the cocktail injection of radiolabeled and fluorescently labeled probes are summarized in Figure 3 and Figure 4. With ^{111}In-panitumumab, radioactivity gradually accumulated in the target tumor (A431, HER1+), while the nontarget tumor (3T3/HER2) was not detected. ^{111}In-Trastuzumab showed both target-specific (3T3/HER2) and nonspecific (A431, HER1+) tumors. A high liver signal was observed in both antibodies. The biodistribution results were consistent with gamma scintigraphy (Figure 5). In contrast, fluorescent signal from both antibodies was activated beginning one day after the injection, although the background signal was detected just after the conjugate injections. Images of the dissected organs by both modalities confirmed these observations. That is, only the target specific tumors were visualized with optical imaging, while the biodistribution profile of the injected antibodies were provided by nuclear imaging.

To confirm that pharmacokinetic properties did not affect the results above, radio-optical dual-labeled trastuzumab was injected in mice bearing three tumors. The nuclear images showed A431 (HER1+) and liver uptake as well as 3T3/HER2 tumor uptake. MDA-MB468 (HER1+) tumor was not detected (Figure 3C). In contrast, fluorescent imaging only detected 3T3/HER2 tumor.

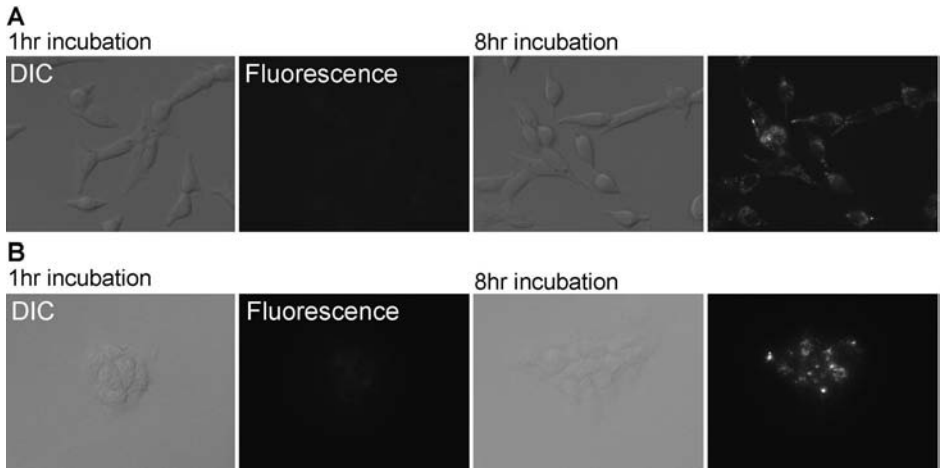

Figure 2. Fluorescence microscopy and differential interference contrast (DIC) images. A431 cells were incubated with panitumumab-ICG (A) and 3T3/HER2 cells were incubated with trastuzumab-ICG (B) for either 1 h or 8 h. The fluorescent signal was detected after internalization into the cells by 8 h incubation.

The H&E staining showed that the A431 tumor (HER1) had greater vascular density than 3T3/HER2 (HER2) tumor (Figure 3D).

DISCUSSION

Multimodality molecular imaging can provide molecular information *in vivo* using two more imaging technologies. Some investigators have already reported radio-optical labeling of probes and have succeeded in yielding nearly identical signals from both modalities despite differences in the physical characteristics of radiation and fluorescence signals (*25*−*30*). These imaging results reflect the biodistribution of the labeled probe because researchers generally have used "always on" optical probes, which yield signals similar to radionuclides. However, by acquiring different signals, i.e., "always on" and target-specific activatable probes ("conditionally on"), additional information could be obtained.

In this study, we showed that activatable fluorescence imaging was capable of cell-specific signal activation and thus highly specific imaging, while radioactive antibodies were more quantitative. The humanized antibodies, panitumumab (anti-HER1) and trastuzumab (anti-HER2), were selected as targeting moieties for molecular imaging in this study, because cancer-specific antigens are attractive "theragnostic" targets, and antibodies for these antigens are promising for seeing and treating cancers. Specific visualization of the target molecule is an important goal for accurate cancer characterization. At the same time, it is also important to visualize the delivery of targeted therapeutic molecules quantitatively for the effective treatment.

As expected, ICG-conjugated antibodies functioned as activatable optical probes emitting in the NIR and the baseline (non-internalized) fluorescence signal was vanishingly low *in vitro* (Figure 1). This was confirmed with microscopy of cultured cells as shown in Figure 2. When the probe is binding to the cell surface antigen (1 h of incubation), no fluorescence signal could be detected; however, when the conjugate was internalized (8 h of incubation), fluorescent signal was easily detectable. If the always on fluorescent probe was used for this investigation, the surface fluorescent signal can be clearly detected by 1 h incubation (Supporting Information Figure 1). Although the mechanism is still under investigation, we suggest that the strong negative charge due to the ICG's sulfonate groups might facilitate the interaction between the ICG and basic amino acid sequences on the IgG causing loss of fluorescence from ICG. By combination with the classic self-quenching system, ICG conjugated antibody might be able to produce high quenching capacities. In fact, the other NIR dye, cypate, which has a similar chemical structure to ICG with carboxylic acid groups instead of sulfonate groups, can label the peptides without the fluorescence quenching (*31, 32*).

Since sulfonate is a stronger acid than carboxylate, the negative charge effect should be weaker for cypate than ICG. Unlike other near-infrared dyes with carboxyl substitutes for sulfonate groups, free ICG is strongly incorporated with albumin probably for a similar reason. The lipophilicity might be another cause for fluorescence quenching by the hydrophobic interaction between dye molecule and hydrophobic amino acid sequences. However, DMSO did not affect the fluorescence dequenching of the ICG conjugated antibody (Supporting Information Figure 2) that suggests the minimal contribution of the hydrophobicity.

This unique feature of this ICG-conjugated antibody contributed to achieve fluorescence imaging with minimal background signal, when bound to the target and internalized into the living cells. In contrast, other researchers reported a few limited successes in the literature. Only weak fluorescence was observed, when ICG-conjugated antibodies were applied for *in vitro* assays using sliced tissue samples, although the fluorescence yield of the ICG-conjugates were slightly improved by changing the chemical linkage (*20*). Withrow et al. applied an ICG-conjugated antibody (cetuximab, anti-EGFR antibody) for imaging xenografted tumors in mice; however, they concluded that the sensitivity of this probe for cancer detection was low. This might be due to the smaller target numbers on the tumor cells or less efficient internalization process of the ICG-antibody conjugates than the cells, which we used in this study. Although their ICG-conjugated antibody appeared to be brighter than our quenched conjugate, a 7-fold larger amount of the ICG-conjugated antibody (350 μg) was injected into the mice; therefore, they might detect a fluorescence signal not only from tumor, but also from the background normal tissues, because a large amount of unbound probes remaining in the body could yield the fluorescence signal (*33*).

Then, we tested our multimodality imaging strategy by injecting radio-optically labeled antibody cocktails into the HER1+ and HER2+ tumor bearing mice. As expected, only the target-specific tumor was visualized by optical imaging (Figures 3 and 4). The observed background signal just after the ICG-conjugated antibodies injection might be due to the physiological excretion of noncovalently bound or catabolized ICG, which was dissociated from the antibody immediately after

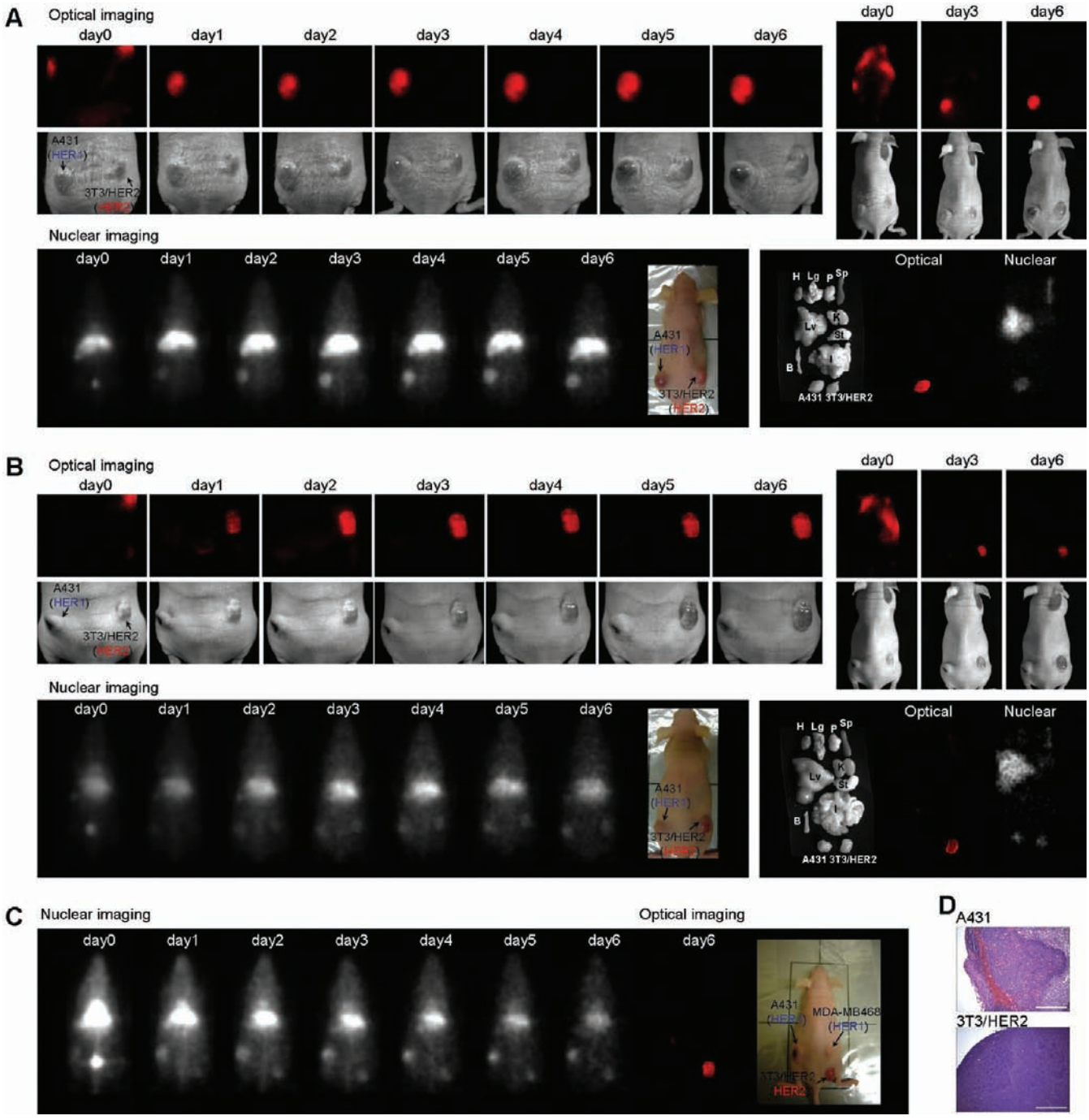

Figure 3. Multimodality imaging results after a cocktail injection of panitumumab-ICG and ^{111}In-panitumumab (A) or trastuzumab-ICG and ^{111}In-trastuzumab (B), and the results with dual-labeled probe, ^{111}In-trastuzumab-ICG (C). Only the target tumor was visualized by optical imaging; in contrast, antibody distribution could be determined by nuclear imaging. (D) HE staining of dissected tumors. The vascularity was higher in A431 tumor than 3T3/HER2 tumor. H, Heart; Lg, Lung; P, Pancreas; Sp, Spleen; Lv, Liver; K, Kidney; St, Stomach; B, Bone; I, Intestine.

the injection and complexed with albumin. The ICG-albumin complex is highly fluorescent, but it is rapidly eliminated from the body of normal subjects through the liver (*34*).

In contrast, radioactive signal could be detected from whole body (blood pool), the liver and the spleen as well as the target tumor. The nontarget tumor was also imaged in HER2 targeting studies. Since the vascularity of A431 tumor (HER1) was higher than 3T3/HER2 (HER2+) tumor (Figure 3D), the reason for the visualization of A431 tumor with ^{111}In-trastuzumab is thought to be its high blood supply and enhanced permeability and retention (EPR) effect (*35*, *36*). As indicated in Figure 5, a certain level of radioactivity remained in the blood especially for ^{111}In-trastuzumab even 6 days after the injection. The EPR effect depends only on the physical characteristics of the macromolecules injected and not on their binding characteristics, and thus, it often leads to nonspecific tumor uptake.

Thus, target-specific images were successfully obtained with activatable optical probes, while quantitative antibody biodistribution was provided by the "always on" radioactive probes. The difference between optical and nuclear imaging was not caused by differences in their pharmacokinetic properties, because the same results were obtained with the dual-labeled antibody (Figure 3C).

A limitation of optical imaging is difficulty in deep tissue detection. NIR fluorescence is one solution for this problem because of the better tissue penetration of NIR light in tissue

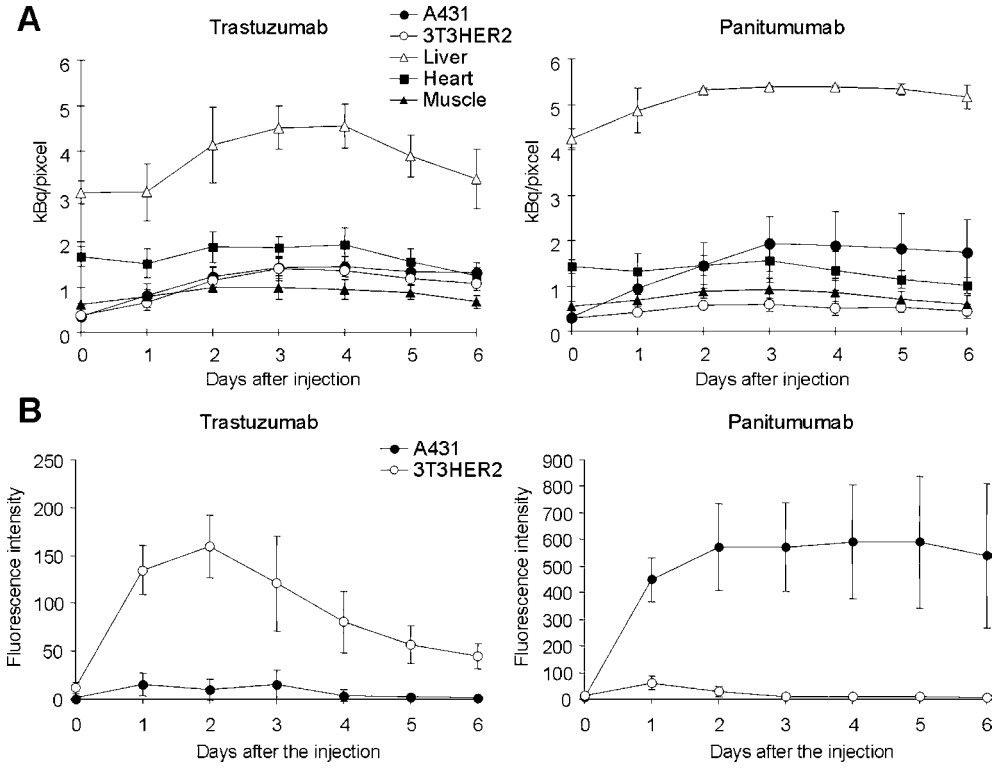

Figure 4. Time course of radioactivity (A) and fluorescence (B) intensities after the injection of a cocktail of panitumumab-ICG and ^{111}In-panitumumab or trastuzumab-ICG and ^{111}In-trastuzumab. High liver uptake was observed on radionuclide scans. The fluorescent signals were increased only in the target tumors, but the signal intensities of target and nontarget tumor were identical in ^{111}In-trastuzumab treated mice.

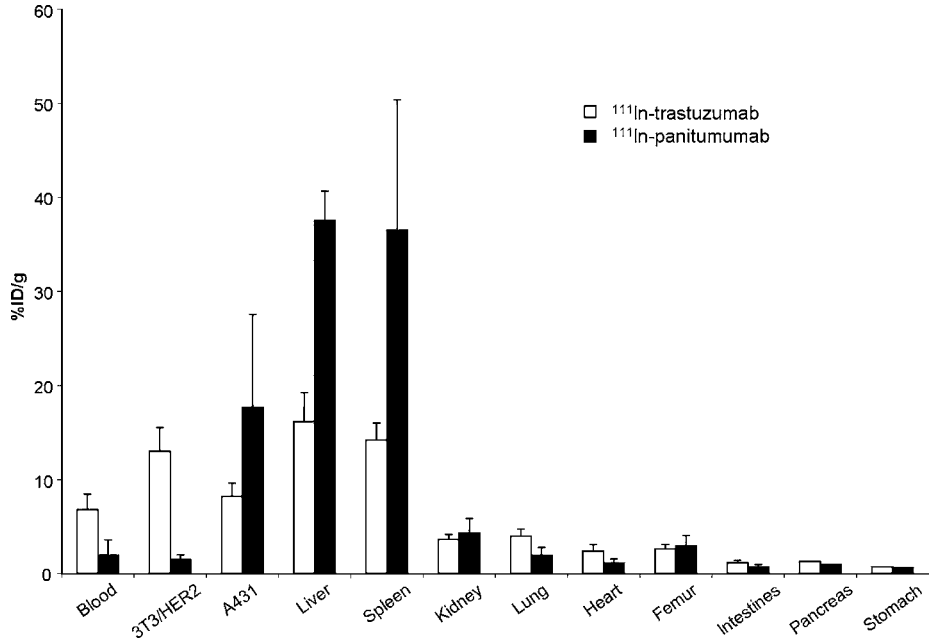

Figure 5. Biodistribution of ^{111}In-panitumumab and ^{111}In-trastuzumab immediately after obtaining 6 day images was shown. The biodistribution results were consistent with images obtained 6 days after injection taken with the MONICA dual camera system.

(*14*). Recently, diffuse optical tomography has improved the deep tissue sensitivity (*37*). This technique can visualize the target at ~50 mm depth volumetrically using NIR probes, and it might be applicable for human breast cancer imaging as well as small animal imaging. At the same time, optical imaging can make a significant contribution when it is utilized during endoscopy or surgery, because activatable optical probes can achieve fairly low background signals (*7, 8*). Thus, whole body imaging with radionuclides followed by optically guided surgery is a promising direction for multimodality imaging. Furthermore, optical imaging has the potential to add more functional information, for example, by using multicolor imaging or fluorescence lifetime imaging (*38*−*42*).

In conclusion, we characterized molecular targets with activatable optical probes, and visualized and quantified the delivery of targeted antibodies using radioactive labeling. Recently, the Molecular Imaging Center of Excellence stated that, "Molecular imaging is the visualization, characterization, and measurement of biological processes at the molecular and cellular levels in humans and other living systems" (*43*).

Multimodality molecular imaging, by combining activatable optical probes with radioactive probes, has great potential for achieving this definition.

ACKNOWLEDGMENT

This research was supported by the Intramural Research Program of the NIH, National Cancer Institute, Center for Cancer Research.

Supporting Information Available: Additional figures as described in the text. This material is available free of charge via the Internet at http://pubs.acs.org.

LITERATURE CITED

(1) Frangioni, J. V. (2008) New technologies for human cancer imaging. *J. Clin. Oncol. 26*, 4012–4021.
(2) Hoffman, J. M., and Gambhir, S. S. (2007) Molecular imaging: the vision and opportunity for radiology in the future. *Radiology 244*, 39–47.
(3) Weissleder, R., and Pittet, M. J. (2008) Imaging in the era of molecular oncology. *Nature 452*, 580–589.
(4) Wu, A. M. (2009) Antibodies and antimatter: the resurgence of immuno-PET. *J. Nucl. Med. 50*, 2–5.
(5) Wu, A. M., and Senter, P. D. (2005) Arming antibodies: prospects and challenges for immunoconjugates. *Nat. Biotechnol. 23*, 1137–1146.
(6) Bremer, C., Tung, C. H., and Weissleder, R. (2001) In vivo molecular target assessment of matrix metalloproteinase inhibition. *Nat. Med. 7*, 743–748.
(7) Hama, Y., Urano, Y., Koyama, Y., Gunn, A. J., Choyke, P. L., and Kobayashi, H. (2007) A self-quenched galactosamine-serum albumin-rhodamineX conjugate: a "smart" fluorescent molecular imaging probe synthesized with clinically applicable material for detecting peritoneal ovarian cancer metastases. *Clin. Cancer Res. 13*, 6335–6343.
(8) Hama, Y., Urano, Y., Koyama, Y., Kamiya, M., Bernardo, M., Paik, R. S., Shin, I. S., Paik, C. H., Choyke, P. L., and Kobayashi, H. (2007) A target cell-specific activatable fluorescence probe for in vivo molecular imaging of cancer based on a self-quenched avidin-rhodamine conjugate. *Cancer Res. 67*, 2791–2799.
(9) Kamiya, M., Kobayashi, H., Hama, Y., Koyama, Y., Bernardo, M., Nagano, T., Choyke, P. L., and Urano, Y. (2007) An enzymatically activated fluorescence probe for targeted tumor imaging. *J. Am. Chem. Soc. 129*, 3918–3929.
(10) Mahmood, U., Tung, C. H., Bogdanov, A., Jr., and Weissleder, R. (1999) Near-infrared optical imaging of protease activity for tumor detection. *Radiology 213*, 866–870.
(11) Ogawa, M., Kosaka, N., Longmire, M. R., Urano, Y., Choyke, P. L., and Kobayashi, H. (2009) Fluorophore-quencher based activatable targeted optical probes for detecting in vivo cancer metastases. *Mol. Pharm. 6*, 386–395.
(12) Ogawa, M., Regino, C. A., Choyke, P. L., and Kobayashi, H. (2009) In vivo target-specific activatable near-infrared optical labeling of humanized monoclonal antibodies. *Mol. Cancer. Ther. 8*, 232–239.
(13) Urano, Y., Asanuma, D., Hama, Y., Koyama, Y., Barrett, T., Kamiya, M., Nagano, T., Watanabe, T., Hasegawa, A., Choyke, P. L., and Kobayashi, H. (2009) Selective molecular imaging of viable cancer cells with pH-activatable fluorescence probes. *Nat. Med. 15*, 104–109.
(14) Frangioni, J. V. (2003) In vivo near-infrared fluorescence imaging. *Curr. Opin. Chem. Biol. 7*, 626–634.
(15) Sharma, R., Wendt, J. A., Rasmussen, J. C., Adams, K. E., Marshall, M. V., and Sevick-Muraca, E. M. (2008) New horizons for imaging lymphatic function. *Ann. N.Y. Acad. Sci. 1131*, 13–36.
(16) Weissleder, R. (2001) A clearer vision for in vivo imaging. *Nat. Biotechnol. 19*, 316–317.
(17) Dzurinko, V. L., Gurwood, A. S., and Price, J. R. (2004) Intravenous and indocyanine green angiography. *Optometry 75*, 743–755.
(18) Sakka, S. G. (2007) Assessing liver function. *Curr. Opin. Crit. Care 13*, 207–14.
(19) Muguruma, N., Ito, S., Hayashi, S., Taoka, S., Kakehashi, H., Ii, K., Shibamura, S., and Takesako, K. (1998) Antibodies labeled with fluorescence-agent excitable by infrared rays. *J. Gastroenterol. 33*, 467–471.
(20) Tadatsu, M., Ito, S., Muguruma, N., Kusaka, Y., Inayama, K., Bando, T., Tadatsu, Y., Okamoto, K., Ii, K., Nagao, Y., Sano, S., and Taue, H. (2003) A new infrared fluorescent-labeling agent and labeled antibody for diagnosing microcancers. *Bioorg. Med. Chem. 11*, 3289–3294.
(21) Ogawa, M., Kosaka, N., Choyke, P. L., and Kobayashi, H. (2009) In vivo molecular imaging of cancer with a quenching near-infrared fluorescent probe using conjugates of monoclonal antibodies and indocyanine green. *Cancer Res. 69*, 1268–1272.
(22) Barrett, T., Koyama, Y., Hama, Y., Ravizzini, G., Shin, I. S., Jang, B. S., Paik, C. H., Urano, Y., Choyke, P. L., and Kobayashi, H. (2007) In vivo diagnosis of epidermal growth factor receptor expression using molecular imaging with a cocktail of optically labeled monoclonal antibodies. *Clin. Cancer Res. 13*, 6639–6648.
(23) Kobayashi, H., Yoo, T. M., Kim, I. S., Kim, M. K., Le, N., Webber, K. O., Pastan, I., Paik, C. H., Eckelman, W. C., and Carrasquillo, J. A. (1996) L-lysine effectively blocks renal uptake of ^{125}I- or ^{99m}Tc-labeled anti-Tac disulfide-stabilized Fv fragment. *Cancer Res. 56*, 3788–3795.
(24) Xi, W., Seidel, J., Kakareka, J., Proffitt, J., Pohida, T., Majewski, S., Weisenberger, A. G., Green, M. V., Choyke, P. L. (2008) in *2008 World Molecular Imaging Congress abstract book* pp #0412.
(25) Cai, W., Chen, K., Li, Z. B., Gambhir, S. S., and Chen, X. (2007) Dual-function probe for PET and near-infrared fluorescence imaging of tumor vasculature. *J. Nucl. Med. 48*, 1862–1870.
(26) Culver, J., Akers, W., and Achilefu, S. (2008) Multimodality molecular imaging with combined optical and SPECT/PET modalities. *J. Nucl. Med. 49*, 169–172.
(27) Houston, J. P., Ke, S., Wang, W., Li, C., and Sevick-Muraca, E. M. (2005) Quality analysis of in vivo near-infrared fluorescence and conventional gamma images acquired using a dual-labeled tumor-targeting probe. *J. Biomed. Opt. 10*, 054010.
(28) Li, C., Wang, W., Wu, Q., Ke, S., Houston, J., Sevick-Muraca, E., Dong, L., Chow, D., Charnsangavej, C., and Gelovani, J. G. (2006) Dual optical and nuclear imaging in human melanoma xenografts using a single targeted imaging probe. *Nucl. Med. Biol. 33*, 349–358.
(29) Sampath, L., Kwon, S., Ke, S., Wang, W., Schiff, R., Mawad, M. E., and Sevick-Muraca, E. M. (2007) Dual-labeled trastuzumab-based imaging agent for the detection of human epidermal growth factor receptor 2 overexpression in breast cancer. *J. Nucl. Med. 48*, 1501–1510.
(30) Vera, D. R., Hall, D. J., Hoh, C. K., Gallant, P., McIntosh, L. M., and Mattrey, R. F. (2005) Cy5.5-DTPA-galactosyl-dextran: a fluorescent probe for in vivo measurement of receptor biochemistry. *Nucl. Med. Biol. 32*, 687–693.
(31) Achilefu, S., Bloch, S., Markiewicz, M. A., Zhong, T., Ye, Y., Dorshow, R. B., Chance, B., and Liang, K. (2005) Synergistic effects of light-emitting probes and peptides for targeting and monitoring integrin expression. *Proc. Natl. Acad. Sci. U.S.A. 102*, 7976–7981.
(32) Bloch, S., Xu, B., Ye, Y., Liang, K., Nikiforovich, G. V., and Achilefu, S. (2006) Targeting Beta-3 integrin using a linear hexapeptide labeled with a near-infrared fluorescent molecular probe. *Mol. Pharm. 3*, 539–549.
(33) Withrow, K. P., Gleysteen, J. P., Safavy, A., Skipper, J., Desmond, R. A., Zinn, K., and Rosenthal, E. L. (2007) Assessment of indocyanine green-labeled cetuximab to detect xenografted head and neck cancer cell lines. *Otolaryngol. Head Neck Surg. 137*, 729–734.

(34) Faybik, P., and Hetz, H. (2006) Plasma disappearance rate of indocyanine green in liver dysfunction. *Transplant Proc. 38*, 801–802.
(35) Baban, D. F., and Seymour, L. W. (1998) Control of tumour vascular permeability. *Adv. Drug Delivery Rev. 34*, 109–119.
(36) Torchilin, V. P. (2000) Drug targeting. *Eur. J. Pharm. Sci. 11* (2), S81−91.
(37) Ntziachristos, V., Ripoll, J., Wang, L. V., and Weissleder, R. (2005) Looking and listening to light: the evolution of whole-body photonic imaging. *Nat. Biotechnol. 23*, 313–320.
(38) Hosokawa, R., Kambara, N., Ohba, M., Mukai, T., Ogawa, M., Motomura, H., Kume, N., Saji, H., Kita, T., and Nohara, R. (2006) A catheter-based intravascular radiation detector of vulnerable plaques. *J. Nucl. Med. 47*, 863–867.
(39) Kobayashi, H., Hama, Y., Koyama, Y., Barrett, T., Regino, C. A., Urano, Y., and Choyke, P. L. (2007) Simultaneous multicolor imaging of five different lymphatic basins using quantum dots. *Nano Lett. 7*, 1711–1716.
(40) Kobayashi, H., Koyama, Y., Barrett, T., Hama, Y., Regino, C. A., Shin, I. S., Jang, B. S., Le, N., Paik, C. H., Choyke, P. L., and Urano, Y. (2007) Multimodal nanoprobes for radionuclide and five-color near-infrared optical lymphatic imaging. *ACS Nano 1*, 258–264.
(41) Kosaka, N., Ogawa, M., Longmire, M. R., Choyke, P. L., and Kobayashi, H. (2009) Multi-targeted multi-color in vivo optical imaging in a model of disseminated peritoneal ovarian cancer. *J. Biomed. Opt. 14*, 014023.
(42) Longmire, M., Kosaka, N., Ogawa, M., Choyke, P. L., and Kobayashi, H. (2009) Multicolor in vivo targeted imaging to guide real-time surgery of HER2-positive micrometastases in a two-tumor coincident model of ovarian cancer. *Cancer Sci. 100*, 1099–1104.
(43) Mankoff, D. A. (2007) A definition of molecular imaging. *J. Nucl. Med. 48*, 18N–21N.

BC900362K

A

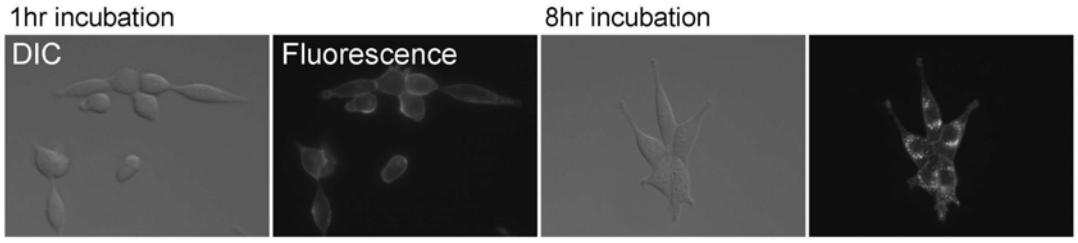

B

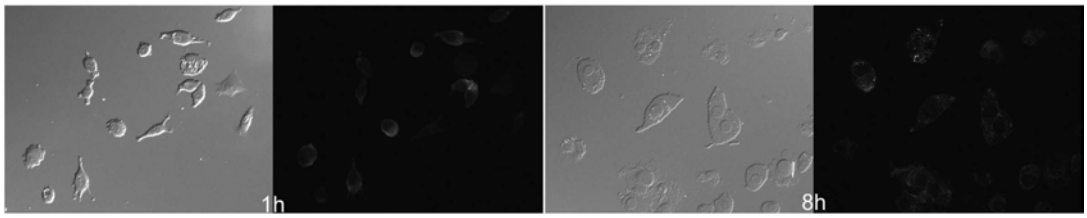

Supplemental figure 1. Always on conjugates show cell surface receptors

The always-ON fluorescence probe, trastuzumab-Rhodamine Green (A) and trastuzumab-Cy7 was incubated with 3T3/HER2 cells in the same manner as ICG conjugates. The surface fluorescence was detected after 1hr incubation, which shows the trastuzumab-Rhodamine Green and trastuzumab-Cy7 binding to the surface HER2 receptors. Many fluorescent dots were observed after the antibody internalization by 8hr incubation as well as the surface fluorescence with both conjugates.

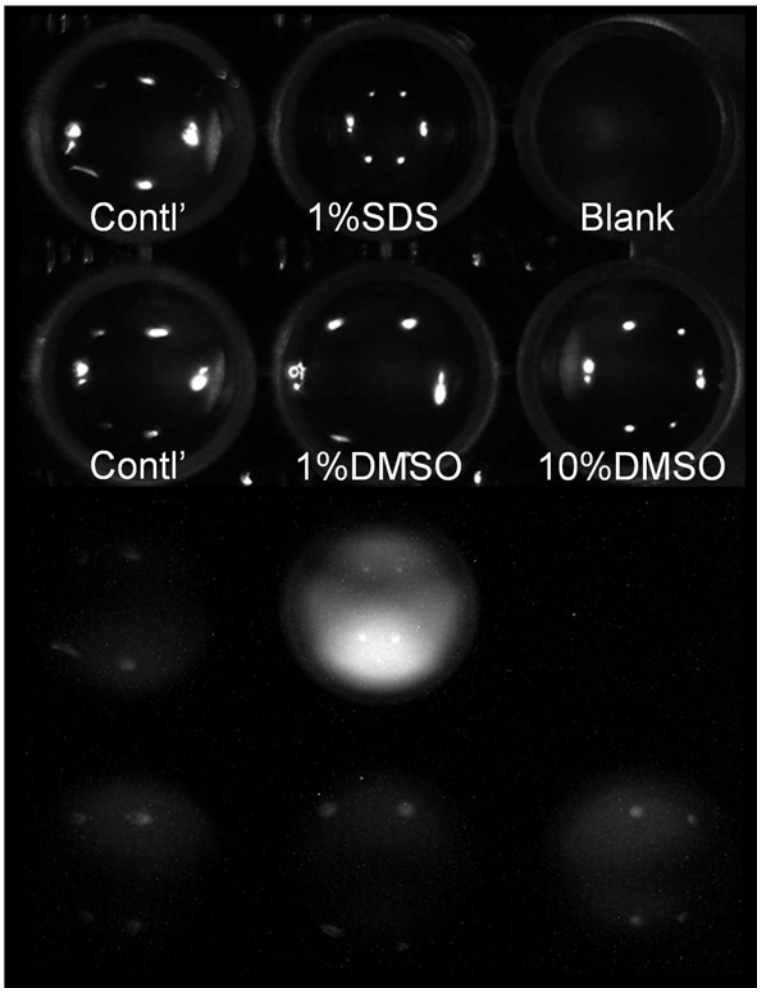

Supplemental figure 2. DMSO does not de-quench the quenched ICG-trastuzumab conjugate.

The de-quenching capacity of the quenched trastuzumab-ICG compared SDS with DMSO. DMSO does not efficiently de-quench the quenched trastuzumab-ICG as SDS does.

TECHNICAL NOTES

A Wortmannin−Cetuximab as a Double Drug

R. Adam Smith,[†] Hushan Yuan,[†] Ralph Weissleder,[†,‡] Lewis C. Cantley,[§] and Lee Josephson*[,†]

Center for Molecular Imaging Research, Massachusetts General Hospital and Harvard Medical School, 149 13th Street, Charlestown, Massachusetts 02129, Center for Systems Biology, Massachusetts General Hospital, Boston, Massachusetts 02114, and Department of Systems Biology, Harvard Medical School and Division of Signal Transduction, Beth Israel Deaconess Medical Center, 77 Avenue Louis Pasteur, Boston Massachusetts 02115. Received April 17, 2009; Revised Manuscript Received October 2, 2009

Double drugs are obtained when two pharmacologically active entities are covalently joined to improve potency. We conjugated the viridin Wm with a self-activating linkage to cetuximab and demonstrated the retention of immunoreactivity by the conjugate. Though cetuximab lacked a growth inhibitory activity against A549 cells, the Wm−cetuximab conjugate had an antiproliferative IC_{50} of 155 nM in vitro. The chemistry of attaching a self-releasing Wm to clinically approved antibodies is general and, in selected instances, may yield antibody-based double drugs with improved efficacy.

INTRODUCTION

Double drugs are obtained when two pharmacologically active entities are covalently joined to obtain a molecule with an improved potency that often results from a change in physical properties of one of the active entities (*1, 2*). The ability of modified viridins like wortmannin (Wm) to self-activate by generating the active species Wm offers a mechanism for the design of self-activating viridin double drugs, where X (Figure 1A) is a pharmacologically active entity. We have previously shown that when X is a 70 kDa dextran, a pharmacologically inactive carrier, the resulting self-activating viridin (SAV) prodrug has an improved antiproliferative activity compared to wortmannin (Wm) due to the slow release of active Wm over the 48 h incubation period of the in vitro antiproliferative assay (*3*). This slow release also occurs in vivo, evident by the nanomolar concentrations of active viridin generated by micromolar concentrations of circulating SAV prodrug (*4*). The SAV prodrug is anti-inflammatory in animal models of lung inflammation and arthritis (*5, 6*), as well as being cytostatic in the A549 xenograft model (*4*).

Cetuximab is a monoclonal antibody that binds to the epidermal growth factor receptor, ErbB1, and generates antitumor activity through several mechanisms, including an antagonism of growth stimulation by growth factors and immune mediated mechanisms such as antibody-dependent cellular cytotoxicity (ADCC) and complement-dependent cytolysis CDC (*7*−*9*). Consistent with a role for immune-mediated mechanisms in cetuximab's in vivo activity, cetuximab does not directly inhibit the proliferation of some cultured tumor cell lines, such as the A549 cell line used here (*10*−*12*).

We hypothesized that attaching wortmannin (Wm) to cetuximab using a self-activating linker employed with dextran-based SAV (compound **5a** of the current study) might yield a potentially general conjugation chemistry for the design monoclonal antibody based double drugs. A key pharmacokinetic property of blood half-life is comparable for the two materials, with human blood half-lives of 60−80 h for a 70 kDa dextran in humans (*13, 14*) and 112 h for cetuximab (*15*). Thus, it appeared that cetuximab, like a 70 kDa dextran, could serve as a reservoir of inactive Wm that slowly self-activated to yield the active species Wm, as we have shown on other occasions (*3, 4, 16*). We therefore hypothesized that cetuximab might serve as carrier for Wm, enhancing the antibody's antiproliferative activity and acting as a double drug.

EXPERIMENTAL METHODS

Reagents. Wortmannin (Wm) was a gift of the natural products branch of the National Cancer Institute. Fluorescein-labeled goat anti-human IgG (secondary antibody) was from Beckman Coulter. The NHS ester of 6-fluorescein-5-(and 6)-carboxamido-hexanoic acid (FAM) was from Molecular Probes.

Syntheses. The compounds employed are summarized in Figure 1. To obtain the self-activating Wm−cetuximab (**7a**), **2a** was synthesized and converted to the NHS ester of **2a** (*3*). To a solution of the NHS ester of **2a** (4 mg, 6 mmol) in DMSO (100 μL) was added 160 kDa monoclonal antibody cetuximab (3 mL, 10 mg/mL) in PBS. The solution was stirred and incubated at 37 °C for 1.5 h. The conjugate (**7a**) was purified with Sephadex G-50 in a 1 mM phosphate buffer at pH 7.0 followed by lyophilization. The number of moles of Wm per cetuximab were determined by its absorbance at 418 nm. Compound **7b** was prepared from **2b** in a similar fashion. The syntheses of **5a** and **5b**, which use a 70 kDa amino dextran carrier, have been described (*3*). The moles of Wm attached per mole of carrier were 4.5 (**7a**), 8.8 (**7b**), 7.8 (**5a**), and 13 (**5b**). To obtain the fluorescent compound **8**, cetuximab (1 mL,

* To whom correspondence should be addressed. Tel: (617) 726-6478. Fax: (617) 726-5708. E-mail: ljosephson@mgh.harvard.edu.

[†] Center for Molecular Imaging Research, Massachusetts General Hospital and Harvard Medical School.

[‡] Center for Systems Biology, Massachusetts General Hospital.

[§] Department of Systems Biology, Harvard Medical School and Division of Signal Transduction, Beth Israel Deaconess Medical Center.

10.1021/bc900176a CCC: $40.75 © 2009 American Chemical Society
Published on Web 11/02/2009

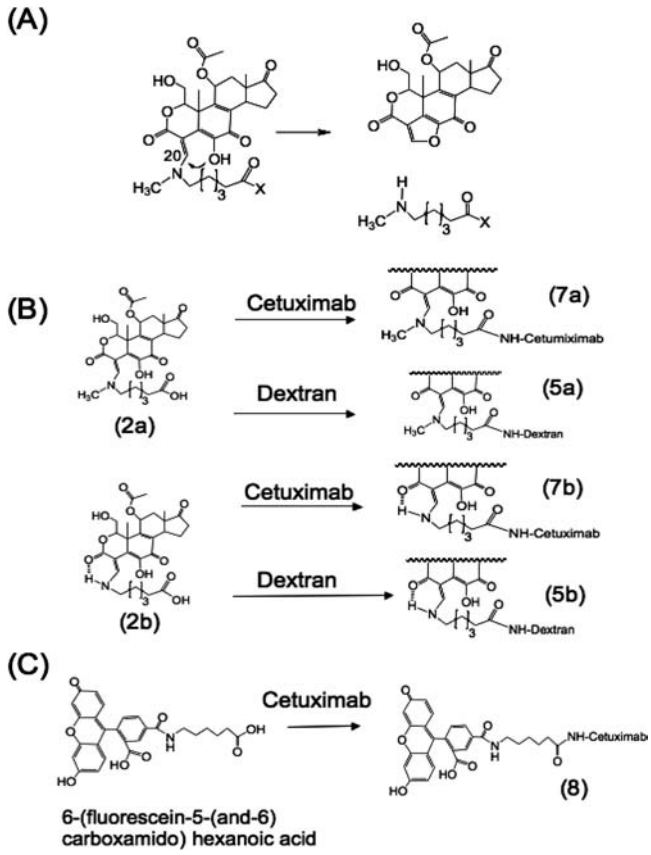

Figure 1. Self-activation of WmC20 derivatives and the compounds used. (A) Wm modified at C20 undergoes an intramolecular attack to yield Wm. The attack is independent of the group attached to the carboxyl group of the N(Me)hexanoic acid linker (*3*). (B) **2a** was converted to an NHS ester and reacted with the amines of cetuximab or amino-dextran (70 kDa) to yield **7a** or **5a**, respectively. Similar reactions were used with the Wm derivative **2b**, which features a secondary amine at C20, to yield **5b** or **7b**. "b type" WmC20 derivatives feature a hydrogen bond stabilization and do not self-activate to generate Wm. (C) An NHS ester of a fluorescein hexanoic acid was reacted with cetuximab to yield a fluorescent antibody **8**.

2 mg) was diluted with 1 M sodium bicarbonate buffer (pH 8.3, 100 μL). 3.91 μL of 5-FAM (10 mg/mL in DMSO) was added, and the mixture was stirred at room temperature for 1 h. The mixture was purified with PD10 column. Antibody concentration was determined by the BCA assay, while attached fluorescein was determined from its absorbance at 493 nm. There were 3.19 mol of fluorescein per mole of cetuximab.

Cellular Assays. All experiments used A549 cells (ATCC). Cells were maintained in F12−K medium, 10% fetal bovine serum, and 1% antibiotics of penicillin−streptomycin at 37 °C, 5% CO_2, and 95% humidity. To obtain antibody binding, cells were seeded at a density of 50 000 cells/well in 24-well culture plates and incubated overnight. Dilutions of antibodies in complete media (500 μL/well) were added. After incubation at 37 °C, cells were washed three times with HBSS, detached with trypsin, centrifuged (5 min at 200 × *g*), resuspended (200 μL cold HBSS), and analyzed by flow cytometry (FACSCalibur, Becton-Dickinson). Binding is expressed as the relative cellular fluorescence (RCF), which is the mean fluorescence intensity of treated cells divided by a similar value for untreated cells. To demonstrate immunoreactive cetuximab on the cell surface, cells were treated with cetuximab (37 °C, 10 nM, 1 h) and washed. Then, 500 μL of fresh media was added to each well, and the cells were incubated at 37 °C for 0, 1, 2, 3, 5, or 24 h. Cells were then detached by trypsinization, centrifuged, and resuspended in 100 μL FITC-labeled secondary antibody solution (50:1 dilution in HBSS). After 1 h incubation on ice, cells were washed three times with fresh HBSS and prepared for flow cytometry analysis as described above.

The amount of compound **8** bound per cell at saturation (10 nM) was determined as immunoreactive fluorescein using a fluorescein immunoassay (*17*). A sulforhodamine B (SRB) dye binding method was performed as an antiproliferative assay (*18*). Cells were allowed to proliferate for 48 h in the presence of increasing concentrations of drug as shown in Figure 3, where the drug concentration (*x*-axis) was plotted versus cell mass (*y*-axis). The IC_{50} is determined using a four-parameter equation (GraphPad *Prism* software) setting the maximum value as 100% and allowing the fit to generate a minimum nonzero cell mass value (the asymptote at high drug concentrations). On the basis of the reported doubling time of A549 of 22.9 h (http://dtp.nci.nih.gov/docs/misc/common_files/cell_list.html), complete growth inhibition would yield a cell mass of about 25% of control after the assay's 48 h incubation. The IC_{50}, therefore, is the midrange point for the change in cell mass (and not the point where cell mass is 50% of control). We term this an "antiproliferative assay" because it is run under conditions allowing cell proliferation, though no direct measurements of cell division were obtained.

RESULTS AND DISCUSSION

The self-activation the viridin Wm undergoes when modified at the C20 position by *N*-methyl hexanoic acid is shown in Figure 1A. An intramolecular attack of the C6 OH generates Wm, while the carboxyl group can be reacted with amines. WmC20 derivatives featuring a secondary amine at C20 (**2a**) and a tertiary amine at C20 (**2b**) were converted to NHS esters and attached to the amino groups of amino-dextran, to yield **5a** and **5b**, or to the amino groups of cetuximab to yield **7a** and **7b**. The compound designations shown in Figure 1B are from our previous communications, with new cetuximab-based compounds designated as **7a**, **7b**, and **8**. Thus, **2a**, **2b**, **5a**, and **5b** are the same as in our earlier publications, with the "a" designation referring to an N(Me) hexanoic acid, self-activating linker reacted with Wm's C20. The "b" designation refers to N(H)hexanoic acid based compounds, which do not self-activate due to an extra hydrogen bond stabilization shown in Figure 1B (*3, 16*).

We first characterized the binding of the fluorescein-labeled **8** to cells as shown in Figure 2A,B. Binding of **8** was determined as the relative cell fluorescence (RCF), that is the mean fluorescence intensity determined by FACS of cells incubated with **8** divided the mean fluorescence intensity of control cells. Preliminary experiments indicated that the binding of **8** to cells was rapid and independent of incubation times between 1 and 24 h. We then varied the concentration of **8** and determined a K_d of 0.40 nM as shown in Figure 2A. The amount of **8** bound per cell at a saturating concentration of 10 nM was determined by a fluorescein hapten immunoassay to be 56 400 ± 14 200 molecules per cell. Our estimate of the number of binding sites per cell was about 10-fold higher than Mukohara who used a FACS-based bead method (*12*), while we measured immunoreactive fluorescein from **8** after cell lysis.

To determine whether the attachment of Wm to cetuximab (as in **7a** and **7b**) resulted in a reduced immunoreactivity, a self-displacement assay (Figure 2C) was employed. We determined the immunoreactivity of the Wm-modified cetuximab **7a** by its ability to displace the binding of **8** (10 nM) from cells (Figure 2B). The similar decrease ($p > 0.05$ for all concentrations) in RCF produced by **7a** and cetuximab indicated the attachment of Wm to cetuximab, as occurred with **7a**, did not impair its immunoreactivity.

A surprising feature of the binding of **8** to A549 cells was lack of time dependence of this interaction, which suggested

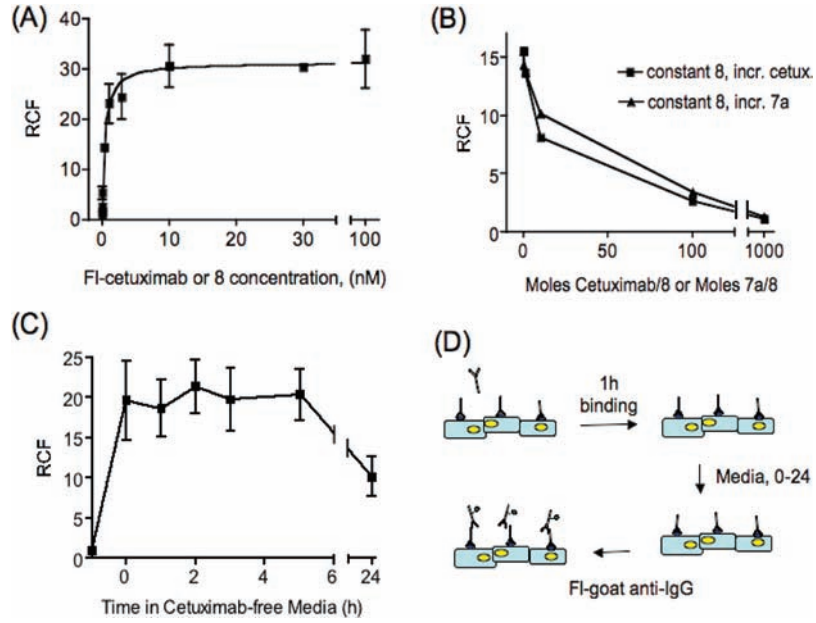

Figure 2. Binding of Fl-cetuximab (**8**) and Wm−cetuximab (**7a**) to cells. (A) Concentration dependence of the binding of Fl-cetuximab (**8**) to cells (K_d = 0.40 nM). (B) Immunoreactivity of **7a**. Cetuximab or **7a** blocked the binding of **8** to cells. Data indicating the retention of cetuximab on the cell surface are shown in (C) with the protocol summarized in (D). Cells were exposed to cetuximab for 1 h, washed, and incubated in media for varying amounts of time. Immunoreactive cetuximab on the cell surface was detected by a fluorescein-labeled goat anti-human IgG.

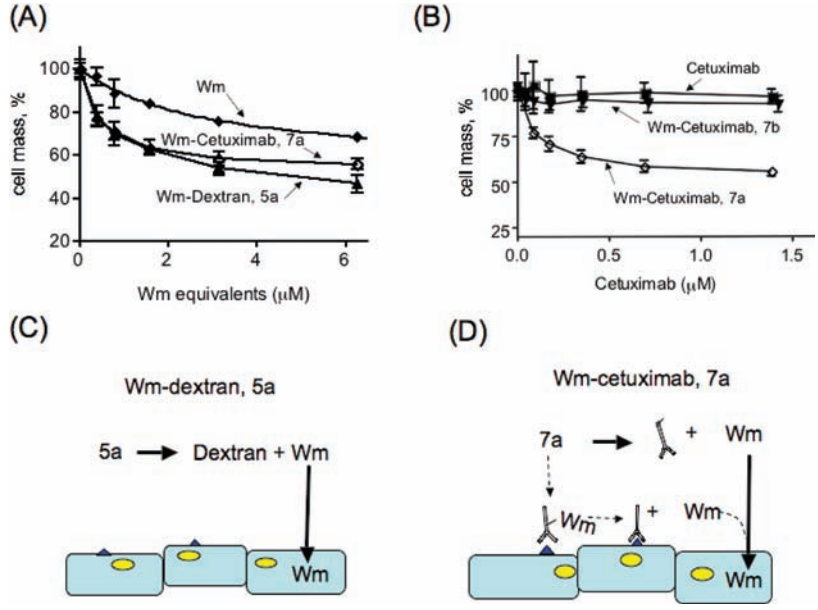

Figure 3. Increase in potency for the double drug, Wm−cetuximab. (A) Attaching Wm with a self-releasing linkage to either cetuximab or dextran increased its antiproliferative activity when data are plotted on a mole of Wm basis. (B) Attaching Wm with a self-releasing linker increases Wm potency when data were plotted on a cetuximab basis. (C) Schematic for the activity of Wm-dextran, **5a**. **5a** generates Wm outside of cells, which then enters cells. (D) Schematic for the behavior of Wm−cetuximab, **7a**. Like **5a**, **7a** releases Wm outside cells, which then enters cells. **7a** also bound cells and released Wm, but the major pathway (dark arrows) was Wm release into the bulk media, since the antiproliferative IC_{50} (Wm basis) was 700 nM **5a** and 690 nM for **7a**.

that **8** remained as a stable complex bound to its ErbB1 target receptor on the cell surface. To verify that this was in fact the case, we incubated cells with cetuximab (10 nM, 1 h), washed cells, and detected cell surface cetuximab by the addition of a fluorescein-labeled goat anti-human IgG. As shown in Figure 3C, the resulting RCF was essentially constant for 6 h and decreased to 50.6% of control at 24 h. A 50% decrease in cell fluorescence would be expected at 22.9 h based on the doubling time of A549 cells (see above). Thus, cetuximab appears not to be internalized by A549 cells.

We next assessed the antiproliferative activity of the Wm−cetuximab conjugates (**7a**, **7b**), with the dextran conjugates featuring the same linkages (**5a**, **5b**) serving as nonreceptor binding Wm controls. Representative curves for the decrease in cell mass as a function of concentration are shown in Figure 3A,B with IC_{50}s provided in Table 1. Cetuximab had no effect on the proliferation of A549 cells, consistent with the observations of others (*12*, *19*, *20*), though cetuximab has been shown to inhibit the growth of A549 xenografts (*10*, *11*), an effect that may reflect immune mediated killing, see above. On the basis of the similar IC_{50}s of **5a** and **7a** (Table 1), **5a** and **7a** release Wm into the media in a similar manner (Figure 3C,D). On the basis of the lack of internalization of cetuximab (Figure 2), **7a** was not internalized (Figure 3D).

Table 1. Antiproliferative Activity of Wortmannin−Cetuximab Conjugates[a]

compound	antiproliferative IC_{50} as cetuximab, (nM)	antiproliferative IC_{50} as Wm, (nM)
cetuximab	not detectable[b]	not detectable[b]
7a	155	700 ± 20
7b	>1000	>100 000
5a	not applicable	690 ± 20
5b	not applicable	>100 000
Wm	not applicable	11 400 ± 50

[a] Results from three assays on separate occasions are provided. [b] Depression of cell mass was too small for an accurate IC_{50} to be determined.

The antiproliferative activity of cetuximab was greatly enhanced by the attachment of Wm with a self-releasing linkage. That compound, **7a**, exhibited an IC_{50} of 153 nM on a per mole cetuximab basis (690 nM on a Wm basis at 4.5 Wm/per mole of cetuximab), while cetuximab lacked activity in this assay. This improvement in antiproliferative activity of **7a** relative to cetuximab was not due to an immune mediated binding of **7a**, since the IC_{50} of the self-activating dextran (**5a**) was 700 nM on a wortmannin basis, and not different from the IC_{50} of **7a** ($p > 0.05$). With both cetuximab and dextran carriers, the configuration at C20 was critical for activity, with nonreleasing C20 configurations of **5b** and **7b** showing no antiproliferative activity. The potency of Wm was greatly increased by its attachment to cetuximab with the self-releasing linkage. Wm has an IC_{50} of 11.4 μM against A549 cells, while **7a** had an IC_{50} of 690 nM on a per mole of Wm basis.

There are two conclusions from these studies. First, Wm could be attached to cetuximab at levels that did not affect its immunoreactivity but increased its antiproliferative activity. The experimental approach developed here, attachment of Wm followed by verification of immunoreactivity, could be employed to obtain slow Wm releasing, immunologically active, monoclonal antibodies. Second, the attachment of Wm to cetuximab increased the antiproliferative activity of both the antibody and Wm. This improvement occurred through the slow release of Wm into culture media, based on the similar antiproliferative IC_{50} of **5a** and **7a**.

Though we did not demonstrate the immune-mediated targeting of Wm to A549 cells in culture, this may still be possible in vivo with appropriate antibody/tumor combinations. The A549 line we employed is a Ras-driven tumor (*21, 22*), and the amount of Wm that must targeted to achieve a pharmacological effect might be considerably higher than for PI3 kinase driven tumors (see *refs* 23, 24). In addition, our Wm−cetuximab was not internalized by A549 cells, a fate common with cetuximab and other cell lines (*25*). Internalization of Wm−monoclonal antibodies and receptor recycling might lead to higher intracellular levels of Wm. Finally, a self-releasing Wm might be attached to a monoclonal antibody or protein with an immune-suppressive activity, which would then act as a pharmacologically active (but nontargeting) carrier for a slow Wm release. The slow release of Wm from **5a** is immune suppressive in animal models of lung inflammation and arthritis (*5, 6*). Wm is a potent antiangiogenic agent (*26*), offering a mechanism for immune suppression or inhibiting tumor growth without targeting.

From 1980 to 2005, some 206 monoclonal antibodies were studied in clinical trials with 12 being approved (*27*), offering a wide array of potential Wm−antibody double drugs. The conjugation of Wm with a self-activating linker to an approved monoclonal antibody offers a potential general chemistry for the design of double drugs, the pharmacological effectiveness of which will have to be evaluated for each antibody considered.

LITERATURE CITED

(1) Matsumoto, H., Hamawaki, T., Ota, H., Kimura, T., Goto, T., Sano, K., Hayashi, Y., and Kiso, Y. (2000) 'Double-Drugs'--a new class of prodrug form of an HIV protease inhibitor conjugated with a reverse transcriptase inhibitor by a spontaneously cleavable linker. *Bioorg. Med. Chem. Lett. 10*, 1227–31.

(2) Romeo, S., Parapini, S., Dell'Agli, M., Vaiana, N., Magrone, P., Galli, G., Sparatore, A., Taramelli, D., and Bosisio, E. (2008) Atovaquone-statine "double-drugs" with high antiplasmodial activity. *ChemMedChem 3*, 418–20.

(3) Blois, J., Yuan, H., Smith, A., Pacold, M. E., Weissleder, R., Cantley, L. C., and Josephson, L. (2008) Slow self-activation enhances the potency of viridin prodrugs. *J. Med. Chem. 51*, 4699–707.

(4) Smith, A., Blois, J., Yuan, H., Aikawa, E., Ellson, C., Figueiredo, J. L., Weissleder, R., Kohler, R., Yaffe, M. B., Cantley, L. C., and Josephson, L. (2009) The antiproliferative cytostatic effects of a self-activating viridin prodrug. *Mol. Cancer Ther. 8*, 1666–75.

(5) Cortez-Retamozo, V., Swirski, F. K., Waterman, P., Yuan, H., Figueiredo, J. L., Newton, A. P., Upadhyay, R., Vinegoni, C., Kohler, R., Blois, J., Smith, A., Nahrendorf, M., Josephson, L., Weissleder, R., and Pittet, M. J. (2008) Real-time assessment of inflammation and treatment response in a mouse model of allergic airway inflammation. *J. Clin. Invest. 118*, 4058–66.

(6) Stangenberg, L., Ellson, C., Cortez-Retamozo, V., Ortiz-Lopez, A., Yuan, H., Blois, J., Smith, R. A., Yaffe, M. B., Weissleder, R., Benoist, C., Mathis, D., Josephson, L., and Mahmood, U. (2009) Abrogation of antibody-induced arthritis in mice by a self-activating viridin prodrug and association with impaired neutrophil and endothelial cell function. *Arthritis Rheum. 60*, 2314–2324.

(7) Yan, L., Hsu, K., and Beckman, R. A. (2008) Antibody-based therapy for solid tumors. *Cancer J. 14*, 178–83.

(8) Kurai, J., Chikumi, H., Hashimoto, K., Yamaguchi, K., Yamasaki, A., Sako, T., Touge, H., Makino, H., Takata, M., Miyata, M., Nakamoto, M., Burioka, N., and Shimizu, E. (2007) Antibody-dependent cellular cytotoxicity mediated by cetuximab against lung cancer cell lines. *Clin. Cancer Res. 13*, 1552–61.

(9) Adams, G. P., and Weiner, L. M. (2005) Monoclonal antibody therapy of cancer. *Nat. Biotechnol. 23*, 1147–57.

(10) Steiner, P., Joynes, C., Bassi, R., Wang, S., Tonra, J. R., Hadari, Y. R., and Hicklin, D. J. (2007) Tumor growth inhibition with cetuximab and chemotherapy in non-small cell lung cancer xenografts expressing wild-type and mutated epidermal growth factor receptor. *Clin. Cancer Res. 13*, 1540–51.

(11) Wild, R., Fager, K., Flefleh, C., Kan, D., Inigo, I., Castaneda, S., Luo, F. R., Camuso, A., McGlinchey, K., and Rose, W. C. (2006) Cetuximab preclinical antitumor activity (monotherapy and combination based) is not predicted by relative total or activated epidermal growth factor receptor tumor expression levels. *Mol. Cancer Ther. 5*, 104–13.

(12) Mukohara, T., Engelman, J. A., Hanna, N. H., Yeap, B. Y., Kobayashi, S., Lindeman, N., Halmos, B., Pearlberg, J., Tsuchihashi, Z., Cantley, L. C., Tenen, D. G., Johnson, B. E., and Janne, P. A. (2005) Differential effects of gefitinib and cetuximab on non-small-cell lung cancers bearing epidermal growth factor receptor mutations. *J. Natl. Cancer Inst. 97*, 1185–94.

(13) Klotz, U., and Kroemer, H. (1987) Clinical pharmacokinetic considerations in the use of plasma expanders. *Clin. Pharmacokinet. 12*, 123–35.

(14) Terg, R., Miguez, C. D., Castro, L., Araldi, H., Dominguez, S., and Rubio, M. (1996) Pharmacokinetics of Dextran-70 in patients with cirrhosis and ascites undergoing therapeutic paracentesis. *J. Hepatol. 25*, 329–333.

(15) Imclone, and Squibb, B.-M. Erbitux Package Insert. Section 12.3 Pharmacokinetics.
(16) Yuan, H., Luo, J., Weissleder, R., Cantley, L., and Josephson, L. (2006) Wortmannin-C20 conjugates generate wortmannin. *J. Med. Chem. 49*, 740–7.
(17) Kelly, K. A., Reynolds, F., Weissleder, R., and Josephson, L. (2004) Fluorescein isothiocyanate-hapten immunoassay for determination of peptide-cell interactions. *Anal. Biochem. 330*, 181–5.
(18) Barnes, K. R., Blois, J., Smith, A., Yuan, H., Reynolds, F., Weissleder, R., Cantley, L. C., and Josephson, L. (2008) Fate of a bioactive fluorescent wortmannin derivative in cells. *Bioconjugate Chem. 19*, 130–7.
(19) Kimura, H., Sakai, K., Arao, T., Shimoyama, T., Tamura, T., and Nishio, K. (2007) Antibody-dependent cellular cytotoxicity of cetuximab against tumor cells with wild-type or mutant epidermal growth factor receptor. *Cancer Sci. 98*, 1275–80.
(20) Raben, D., Helfrich, B., Chan, D. C., Ciardiello, F., Zhao, L., Franklin, W., Baron, A. E., Zeng, C., Johnson, T. K., and Bunn, P. A., Jr. (2005) The effects of cetuximab alone and in combination with radiation and/or chemotherapy in lung cancer. *Clin. Cancer Res. 11*, 795–805.
(21) Aoyama, Y., Avruch, J., and Zhang, X. F. (2004) Nore1 inhibits tumor cell growth independent of Ras or the MST1/2 kinases. *Oncogene 23*, 3426–33.
(22) Omerovic, J., Hammond, D. E., Clague, M. J., and Prior, I. A. (2008) Ras isoform abundance and signalling in human cancer cell lines. *Oncogene 27*, 2754–62.
(23) Zhao, L., and Vogt, P. K. (2008) Class I PI3K in oncogenic cellular transformation. *Oncogene 27*, 5486–96.
(24) Engelman, J. A., Chen, L., Tan, X., Crosby, K., Guimaraes, A. R., Upadhyay, R., Maira, M., McNamara, K., Perera, S. A., Song, Y., Chirieac, L. R., Kaur, R., Lightbown, A., Simendinger, J., Li, T., Padera, R. F., Garcia-Echeverria, C., Weissleder, R., Mahmood, U., Cantley, L. C., and Wong, K. K. (2008) Effective use of PI3K and MEK inhibitors to treat mutant Kras G12D and PIK3CA H1047R murine lung cancers. *Nat. Med. 14*, 1351–6.
(25) Vincenzi, B., Schiavon, G., Silletta, M., Santini, D., and Tonini, G. (2008) The biological properties of cetuximab. *Crit. Rev. Oncol. Hematol. 68*, 93–106.
(26) Oikawa, T., and Shimamura, M. (1996) Potent inhibition of angiogenesis by wortmannin, a fungal metabolite. *Eur. J. Pharmacol. 318*, 93–6.
(27) Reichert, J. M., and Valge-Archer, V. E. (2007) Development trends for monoclonal antibody cancer therapeutics. *Nat. Rev. Drug Discovery 6*, 349–56.

BC900176A

Pyridinium Lipids with the Dodecaborate Cluster as Polar Headgroup: Synthesis, Characterization of the Physical−Chemical Behavior, and Toxicity in Cell Culture

Tanja Schaffran,*,† Alexander Burghardt,‡ Sabine Barnert,‡ Regine Peschka-Süss,‡ Rolf Schubert,‡ Mathias Winterhalter,§ and Detlef Gabel†

Department of Chemistry, University of Bremen, P.O. Box 330440, D-28357 Bremen, Institute of Pharmaceutical Sciences, Department of Pharmaceutical Technology and Biopharmacy, University of Freiburg, D-79104 Freiburg, and School of Science and Engineering, Jacobs University Bremen, P.O. Box 750561, D-28725 Bremen. Received April 6, 2009; Revised Manuscript Received September 10, 2009

We have prepared nine new dodecaborate cluster lipids with potential use in boron neutron capture therapy of tumors. This new generation of boron lipids is only singly negatively charged and consists of a pyridinium core with C_{12}, C_{14}, and C_{16} chains as lipid backbone, connected through the nitrogen atom via a butylene, pentylene, or ethyleneoxyethylene linker to the oxygen atom on the dodecaborate cluster as headgroup. The lipids were obtained by nucleophilic attack of 4-(bisalkylmethyl)pyridine on the tetrahydrofurane, the dioxane, and a newly prepared tetrahydropyrane derivative, respectively, of *closo*-dodecaborate. All of these boron lipids are able to form closed vesicles in addition to some bilayers in the pure state and in the presence of helper lipids. The thermotropic behavior was found to be increasingly complex and polymorphic with increasing alkyl chain length. Except for two lipids, all lipids have low *in vitro* toxicity, and longer alkyl chains lead to a significant decrease in toxicity. The choice of the linker plays no major role with respect to their ability to form liposomes and their thermotropic properties, but the toxicity is influenced by the linkers in the case of short alkyl chains.

INTRODUCTION

Therapy for patients with malignant neoplasms, especially high-grade gliomas, melanomas, and their metastatic manifestations, has been only marginally successful with conventional treatments such as surgery or chemotherapy (*1*−*3*). Boron neutron capture therapy (BNCT) is focused on the treatment of these types of cancer. The therapy is based on the nuclear reaction that occurs when boron-10 is irradiated with thermal neutrons followed by nuclear fission to high-energy α-particles and lithium-7 nuclei. These products only act in a short range (cell diameter), which offers a selective damaging of the cancer cells if the boron-10 is selectively accumulated in the tumor and not in the surrounding healthy tissue. For successful treatment, a high amount of boron is necessary (10^9 B atoms per cell, or 20−30 μg per gram of tumor).

Only two substances are in clinical trials, boronophenylalanine (BPA) and mercaptododecaborate (BSH), but they do not reach "ideal" boron concentration in the tumor (*2*) and are hence not optimal boron delivery agents.

In the past, many prospective boron agents have been synthesized, but most of them show disqualifying features (*4*). Low molecular weight boron-containing nucleosides and nucleotides have been prepared for targeting hyperproliferating malignant cells (*5*, *6*). Sugar derivatives are synthesized for cell uptake via specific transporters into cells with increased metabolism (*7*). Another strategy is to obtain boron-containing agents for which target receptors are present in the plasma membrane of the tumor cell, possibly followed by translocation into the cell (*4*). Porphyrin and phthalocyanine derivatives (*8*−*12*) are a part of this category; they often exhibit high toxicity, however. High molecular weight boronated agents, such as antibodies and their fragments, have been prepared that can recognize tumor-associated epitopes (*13*−*15*). Their rapid clearance by the reticuloendothelial system and the necessity to couple enough boron to an antibody molecule for successful therapy are, however, disadvantageous.

Liposomes are promising transport systems for boron agents, as they can carry a large amount of boron. In addition, targeting with tumor-seeking entities, e.g., folate (*16*), EGF (*17*), or transferrin (*18*), makes selective transfer possible. The encapsulation of low molecular weight boron agents into the inner liposomal core has been studied in a variety of experimental systems (*19, 20*). For effective delivery of boron, low encapsulation efficiency, leakage upon storage or in contact with serum and the effect of the liposome structure in the presence of charged boron clusters (*21*) are disadvantages. These problems can be avoided by incorporating boron-containing lipids directly into liposomal membranes.

The first dodecaborate ether lipid has been described by Lee et al. (*22*). The subsequently published dodecaborate lipids have BSH as the headgroup (*23, 24*). These lipids show similarly low toxicity to BSH. All these boron lipids are doubly negatively charged.

Recently, we published the first dodecaborate cluster lipids with only one negative charge (*25*). The chemical structure of these boron lipids are shown in Scheme 1.

The new boron lipids in this study also have a single negative charge. We used ring-opening reactions of different oxonium derivatives of the dodecaborate cluster with *p*-bisalkylmethylpyridine as nucleophile. This allows facile preparation and the possibility to vary the structure of the hydrophobic part of the lipid. Commonly, *N*-methyl-*p*-bisalkylmethylpyridinium is

* T.Schaffran@web.de. Phone +49 421 21863252, fax +49 421 21863259.

† Department of Chemistry, University of Bremen.

‡ Department of Pharmaceutical Technology and Biopharmacy, University of Freiburg.

§ School of Science and Engineering, Jacobs University Bremen.

10.1021/bc900147w CCC: $40.75 © 2009 American Chemical Society
Published on Web 10/19/2009

Scheme 1. Structures of the Boron Lipids: B-THF-14 and B-Dioxan-14 (left) (*25*) as well as B-6-14 and B-6-16 (right) (*24*)[a]

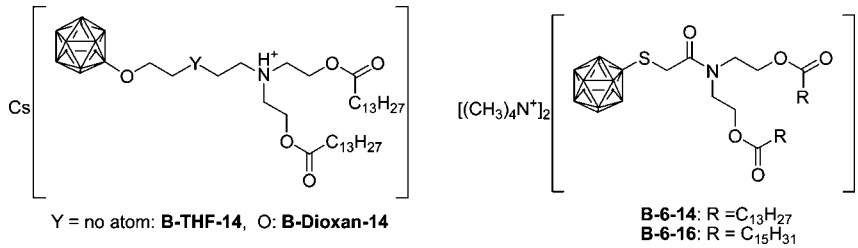

[a] In the icosahedral structures, each unsubstituted corner represents a B−H unit, and the substituted corner, a B atom. The cluster carries two negative charges which are omitted for clarity.

applied in lipoplexes (so-called SAINTs (synthetic amphiphiles for interdisciplinary nucleic acid therapy)) for gene therapy (*26*−*28*). We adapted this basic structure for the first time for boron lipids with potential use in BNCT.

EXPERIMENTAL PROCEDURES

General. A Bruker Esquire spectrometer was used for electrospray mass spectrometry. For boron-containing compounds, the peak with the highest intensity is given. To identify the charge of the compound isotope satellite peaks were used. NMR spectra were recorded on a Bruker DPX 200 spectrometer. IR spectra were collected on a BioRad FTS 155 using KBr pellet. Melting points were measured on a Büchi 512 melting point apparatus. Purity of the compounds was assessed by ESI mass spectrometry and ^{1}H-, ^{13}C-, and ^{11}B NMR spectroscopy, as it is known that the elemental analysis of dodecaborate containing compounds is not reliable (*29*, *30*).

Chemistry. *1-Tetramethylene-(3-oxa)-oxonium-closo-undecahydrododecaborate (−1), Tetrabutylammonium Salt (***1a***).* The convenient method recently described was used, in which closo-dodecaborate was reacted with hydrogen chloride in 1,4-dioxane in the presence of $NaBF_4$ (*31*).

*1-Tetramethyleneoxonium-closo-undecahydrododecaborate (−1), Tetrabutylammonium Salt (***1b***).* The same method as for **1a** was used, but replacing hydrogen chloride with *p*-toluenesulfonic acid (2 equiv) and tetrahydrofurane as solvent. The compound was identical to that described by Sivaev et al. (*32*).

*1-Pentamethyleneoxonium-closo-undecahydrododecaborate (−1), Tetrabutylammonium Salt (***1c***).* The same method as for **1b** was used, but the solvent was tetrahydropyrane instead of tetrahydrofurane. Yield 70%, mp 159 °C (lit. mp 159 °C (*33*). MS (ESI, acetonitrile, *m*/*z*) negative 227.1 [A$^-$], 695.6 [2 A$^-$ + N(n-$C_4H_9)_4^+$], 141.1 [$B_{12}H_{11}^-$]; positive 242.4 [N(n-$C_4H_9)_4^+$]. ^{1}H NMR (200 MHz, [D3] CD_3CN, 25 °C, TMS): δ = 1.32 (t, 12 H, −C*H*$_3$), 1.54 (m, 10 H, N$^+$−CH$_2$−CH$_2$−C*H*$_2$-, -O$^+$−CH$_2$−CH$_2$−C*H*$_2$-), 1.59 (m, 8 H, -N$^+$−CH$_2$−C*H*$_2$-), 1.64 (m, 8 H, -O$^+$−CH$_2$−C*H*$_2$-), 3.07 (m, 8 H, -N$^+$−C*H*$_2$-), 4.50 (t, 4 H, -O$^+$−C*H*$_2$-). ^{13}C NMR (200 MHz, [D3] CD_3CN, 25 °C, TMS): δ = 13.25, 19.76, 20.70, 23.74, 25.07, 58.76, 82.54. ^{11}B NMR (200 MHz, [D3] CD_3CN, 25 °C): −19.79 (1 B), −17.00 (10 B), 8.86 (1 B). IR (KBr): ν = 2962 (−C−H), 2873 (−C−H), 2492 (B−H), 1469 (−C−H), 1045 (−C−O−C−).

*4-(Bisdodecylmethyl)pyridine (***2a***), 4-(Bistetradecylmethyl)pyridine (***2b***), and 4-(Bishexadecylmethyl)pyridine (***2c***)* were synthesized as described by Meekel et al. *(34).*

General method for preparation of dodecaborate derivatives of SAINT lipids. **2** (0.42 g, 1 mmol) was suspended in 30 mL of dry acetonitrile and **1** (0.66 mmol) was added. The reaction mixture was refluxed for 4 days. The solvent was evaporated and the residue dissolved in methanol. After addition of cesium fluoride (0.15 g, 1 mmol) dissolved in methanol, a white precipitate as product was formed and filtered off. It was dried in oil pump vacuum.

4-(Bisdodecylmethyl)pyridinio-N-butoxy-undecahydro-closo-dodecaborate (−1), Cesium Salt (THF-SAINT-12). **2a** and **1b** were used. Yield 0.33 g (65%). MS (ESI, acetonitrile, *m*/*z*) negative 642.5 [A$^-$]; positive 132.8 [Cs$^+$]. ^{1}H NMR (200 MHz, [D6] DMSO, 25 °C, TMS): δ = 0.82 (t, 6H, −C*H*$_3$), 1.19 (m, 42 H, -(C*H*$_2$)$_{10}$CH$_3$, −O−CH$_2$−C*H*$_2$-), 1.62 (m, 6H, −C*H*$_2$−(C*H*$_2$)$_{10}$CH$_3$, −O−C*H*$_2$-), 1.91 (m, 2H, −C*H*$_2$−CH$_2$−N$^+$-), 2.86 (m, 1H, −C*H*-), 4.67 (m, 2H, −C*H*$_2$−N$^+$-), 7.93 (d, 2H, -C═C*H*-), 9.01 (d, 2H, -N$^+$═CH−). ^{13}C NMR (200 MHz, [D6] DMSO, 25 °C, TMS): δ = 14.84, 22.99, 27.56, 29.86, 30.79, 32.17, 35.65, 45.78, 60.25, 68.83, 127.39, 145.59, 166.68. ^{11}B NMR (200 MHz, [D6] DMSO, 25 °C): −23.28 (1 B), −17.24 (10 B), 6.62 (1 B). IR (KBr): ν = 2925 (−C−H), 2854 (−C−H), 2477 (−B−H), 1641 (-C═C−), 1468 (−C−H), 1159 (−C−N-), 1056 (−B−O−C-), 721 (═C−H).

4-(Bisdodecylmethyl)pyridinio-N-ethoxy-ethoxy-undecahydro-closo-dodecaborate (−1), Cesium Salt (Dioxan-SAINT-12). **2a** and **1a** were used. Yield 70%. MS (ESI, acetonitrile, *m*/*z*) negative 658.6 [A$^-$]; positive 132.9 [Cs$^+$]. ^{1}H NMR (200 MHz, [D6] DMSO, 25 °C, TMS): δ = 0.82 (t, 6H, −C*H*$_3$), 1.19 (m, 40H, -(C*H*$_2$)$_{10}$−CH$_3$), 1.61 (m, 4H, −C*H*$_2$−(CH$_2$)$_{10}$−CH$_3$), 2.86 (1 H, −C*H*-), 3.41 (m, 2H, B−O−C*H*$_2$-), 3.53 (m, 2H, −CH$_2$−C*H*$_2$−O−), 3.84 (m, 2H,−O−C*H*$_2$−CH$_2$−N$^+$-), 4.73 (m, 2H,-C*H*$_2$−N$^+$-), 7.92 (d, 2H, -C═C*H*-), 9.09 (d, 2H, -N$^+$═CH−). ^{13}C NMR (200 MHz, [D6] DMSO, 25 °C, TMS): δ = 13.96, 22.10, 26.70, 29.00, 31.28, 34.76, 44.90, 59.52, 67.27, 68.73, 72.63, 126.26, 143.35, 165.76. ^{11}B NMR (200 MHz, [D6] DMSO, 25 °C): −22.96 (1 B), −17.42 (10 B), 6.63 (1 B). IR (KBr): ν = 2919 (−C−H), 2852 (−C−H), 2478 (−B−H), 1643 (-C═C−), 1471 (−C−H), 1059 (−B−O−C-, −C−O−C-), 719 (═C−H).

4-(Bisdodecylmethyl)pyridinio-N-pentoxy-undecahydro-closo-dodecaborate (−1), Cesium Salt (Pyran-SAINT-12). **2a** and **1c** were used. Yield: 50%. MS (ESI, acetonitrile, *m*/*z*) negative 656.6 [A$^-$]; positive 132.8 [Cs$^+$]. ^{1}H NMR (200 MHz, [D6] DMSO, 25 °C, TMS): δ = 0.82 (t, 6H, −C*H*$_3$), 1.19−1.38 (m, 44H, -(C*H*$_2$)$_{10}$−CH$_3$, −O−CH$_2$−(C*H*$_2$)$_2$-), 1.61 (m, 6H, −C*H*$_2$−(CH$_2$)$_{10}$−CH$_3$, −C*H*$_2$−CH$_2$−N$^+$-), 1.89 (m, 2H, −O−C*H*$_2$-), 2.85 (m, 1H, −C*H*-), 4.53 (m, 2H, −CH$_2$−C*H*$_2$−N$^+$-), 7.97 (d, 2H, -C═C*H*-), 9.00 (d, 2H, -N$^+$═CH−). ^{13}C NMR (200 MHz, [D6] DMSO, 25 °C, TMS): δ = 14.10, 22.24, 26.76, 29.12, 30.61, 31.42, 34.87, 45.04, 60.03, 67.55, 126.88, 144.45, 166.04. ^{11}B NMR (200 MHz, [D6] DMSO, 25 °C): −22.99 (1 B), −17.42 (10 B), 6.60 (1 B). IR (KBr): ν = 3056 (═C−H), 2942 (−C−H), 2854 (−C−H), 2473 (−B−H), 1642 (-C═C−), 1468 (−C−H), 1160 (−C−N-), 1055 (−B−O−C-), 722 (═C−H).

4-(Bistetradecylmethyl)pyridinio-N-butoxy-undecahydro-closo-dodecaborate (−1), Cesium Salt (THF-SAINT-14). **2b** and **1b** were used. Yield 60%. MS (ESI, acetonitrile, *m*/*z*) negative 698.8 [A$^-$]; positive 132.9 [Cs$^+$]. ^{1}H NMR (200 MHz, [D6] DMSO, 25 °C, TMS): δ = 0.82 (t, 6H, −C*H*$_3$), 1.20 (m, 50 H, -(C*H*$_2$)$_{12}$CH$_3$, −O−CH$_2$−C*H*$_2$-), 1.61 (m, 6H, −C*H*$_2$−(CH$_2$)$_{12}$CH$_3$, −O−C*H*$_2$-), 1.91 (m, 2H, −C*H*$_2$−CH$_2$−N$^+$-), 2.86

(m, 1H, −C*H*-), 4.67 (m, 2H, −CH_2−N^+-), 7.93 (d, 2H, -C═C*H*-), 9.01 (d, 2H, -N^+═CH−). ^{13}C NMR (200 MHz, [D6] DMSO, 25 °C, TMS): δ = 13.93, 22.10, 26.65, 29.03, 29.93, 31.31, 34.73, 44.87, 59.30, 67.92, 126.46, 144.73, 165.76. ^{11}B NMR (200 MHz, [D6] DMSO, 25 °C): −22.52 (1 B), −17.86 − (−16.83) (10 B), 6.66 (1 B). IR (KBr): ν = 2924 (−C−H), 2854 (−C−H), 2477 (−B−H), 1642 (-C═C−), 1468 (−C−H), 1157 (−C−N-), 1056 (−B−O−C-), 721 (═C−H).

4-(Bistetradecylmethyl)pyridinio-N-ethoxy-ethoxy-undecahydro-closo-dodecaborate (−1), Cesium Salt (Dioxan-SAINT-14). **1a** and **2b** were used. Yield 60%. MS (ESI, acetonitrile, *m*/*z*) negative 714.8 [A^-]; positive 132.9 [Cs^+]. ^{1}H NMR (200 MHz, [D6] DMSO, 25 °C, TMS): δ = 0.82 (t, 6H, −CH_3), 1.2 (m, 48H, -(CH_2)$_{12}$−CH_3), 1.61 (m, 4H, −CH_2−(CH_2)$_{12}$−CH_3), 2.86 (1 H, −C*H*-), 3.40 (m, 2H, B−O−CH_2-), 3.54 (m, 2H, −CH_2−CH_2−O−), 3.84 (m, 2H,−O−CH_2−CH_2−N^+-), 4.73 (m, 2H,-CH_2−N^+-), 7.91 (d, 2H, -C═C*H*-), 9.10 (d, 2H, -N^+═CH−). ^{13}C NMR (200 MHz, [D6] DMSO, 25 °C, TMS): δ = 14.82, 22.99, 27.56, 29.9, 32.19, 35.59, 45.73, 60.41, 68.16, 69.65, 73.52, 127.15, 146.24, 166.62. ^{11}B NMR (200 MHz, [D6] DMSO, 25 °C): −22.67 (1 B), −17.65 − (−16.68) (10 B), 6.93 (1 B). IR (KBr): ν = 3059 (═C−H), 2924 (−C−H), 2853 (−C−H), 2473 (−B−H), 1643 (-C═C−), 1468 (−C−H), 1167 and 1109 (−C−N-), 1057 and 1027 (−B−O−C-, −C−O−C-), 722 (═C−H).

4-(Bistetradecylmethyl)pyridinio-N-pentoxy-undecahydro-closo-dodecaborate (−1), Cesium Salt (Pyran-SAINT-14). **1c** and **2b** were used. Yield 45%. MS (ESI, acetonitrile, *m*/*z*) negative 712.9 [A^-]; positive 132.8 [Cs^+]. ^{1}H NMR (200 MHz, [D6] DMSO, 25 °C, TMS): δ = 0.84 (t, 6H, −CH_3), 1.20−1.40 (m, 52H, -(CH_2)$_{12}$−CH_3, −O−CH_2−(CH_2)$_2$-), 1.63 (m, 6H, −CH_2−(CH_2)$_{12}$−CH_3, −CH_2−CH_2−N^+-), 1.91 (m, 2H, −O−CH_2-), 2.86 (m, 1H, −C*H*-), 4.55 (m, 2H, −CH_2−N^+-), 7.96 (d, 2H, -C═C*H*-), 9.02 (d, 2H, -N^+═CH−). ^{13}C NMR (200 MHz, [D6] DMSO, 25 °C, TMS): δ = 14.10, 22.24, 26.70, 29.15, 30.63, 31.45, 34.79, 44.98, 60.03, 67.55, 126.88, 144.45, 166.04. ^{11}B NMR (200 MHz, [D6] DMSO, 25 °C): −22.67 (1 B), −17.65 − (−16.68) (10 B), 6.93 (1 B). IR (KBr): ν = 3056 (═C−H), 2942 (−C−H), 2854 (−C−H), 2473 (−B−H), 1642 (-C═C−), 1468 (−C−H), 1160 (−C−N-), 1055 (−B−O−C-), 722 (═C−H).

4-(Bishexadecylmethyl)pyridinio-N-butoxy-undecahydro-closo-dodecaborate (−1), Cesium Salt (THF-SAINT-16). **2c** and **1b** were used. Yield 50%. MS (ESI, acetonitrile, *m*/*z*) negative 754.9 [A^-]; positive 132.8 [Cs^+]. ^{1}H NMR (200 MHz, [D6] DMSO, 25 °C, TMS): δ = 0.82 (t, 6H, −CH_3), 1.20 (m, 58H, -(CH_2)$_{14}$−CH_3, −O−CH_2−CH_2-), 1.62 (m, 6H, −CH_2−(CH_2)$_{14}$$CH_3$, −O−C$H_2$-), 1.92 (m, 2H, −C$H_2$−$CH_2$−$N^+$-), 2.86 (m, 1H, −C*H*-), 4.68 (m, 2H, −CH_2−N^+-), 7.92 (d, 2H, -C═C*H*-), 9.01 (d, 2H, -N^+═CH−). ^{13}C NMR (200 MHz, [D1] $CDCl_3$, 25 °C, TMS): δ = 13.98, 22.13, 26.65, 29.03, 30.72, 31.31, 34.73, 44.84, 59.35, 67.95, 126.46, 144.46, 149.34. ^{11}B NMR (200 MHz, [D6] DMSO, 25 °C): −19.82 (1 B), −17.00 (10 B), 7.13 (1 B). IR (KBr): ν = 2920 (−C−H), 2853 (−C−H), 2475 (−B−H), 1641 (-C═C−), 1468 (−C−H), 1160 (−C−N-), 1059 (−B−O−C-), 720 (═C−H).

4-(Bishexadecylmethyl)pyridinio-N-ethoxy-ethoxy-undecahydro-closo-dodecaborate (−1), Cesium Salt (Dioxan-SAINT-16). **1a** and **2c** were used. Yield. 60% MS (ESI, acetonitrile, *m*/*z*) negative 770.9 [A^-]; positive 132.9 [Cs^+]. ^{1}H NMR (200 MHz, [D6] DMSO, 25 °C, TMS): δ = 0.82 (t, 6H, −CH_3), 1.20 (m, 56H, -(CH_2)$_{14}$−CH_3), 1.61 (m, 4H, −CH_2−(CH_2)$_{14}$−CH_3), 2.86 (1 H, −C*H*-), 3.40 (m, 2H, B−O−CH_2-), 3.54 (m, 2H, −CH_2−CH_2−O−), 3.84 (m, 2H,−O−CH_2−CH_2−N^+-), 4.73 (m, 2H,-CH_2−N^+-), 7.91 (d, 2H, -C═C*H*-), 9.10 (d, 2H, -N^+═CH−). ^{13}C NMR (200 MHz, [D6] DMSO, 25 °C, TMS): δ = 13.93, 22.10, 26.65, 29.03, 30.66, 34.68, 44.81, 59.52, 67.30, 68.76, 72.66, 126.23, 145.38, 165.73. ^{11}B NMR (200 MHz, [D6] DMSO, 25 °C): −23.46 (1 B), −17.24 (10 B), 6.66 (1 B). IR (KBr): ν = 2922 (−C−H), 2853 (−C−H), 2476 (−B−H), 1642 (-C═C−), 1468 (−C−H), 1171 (−C−N-), 721 (═C−H).

4-(Bishexadecylmethyl)pyridinio-N-pentoxy-undecahydro-closo-dodecaborate (−1), Cesium Salt (Pyran-SAINT-16). **1c** and **2c** were used. Yield 40%. MS (ESI, acetonitrile, *m*/*z*) negative 769.8 [A^-]; positive 132.9 [Cs^+]. ^{1}H NMR (200 MHz, [D6] DMSO, 25 °C, TMS): δ = 0.85 (t, 6H, −CH_3), 1.22−1.41 (m, 60H, -(CH_2)$_{14}$−CH_3, −O−CH_2−(CH_2)$_2$-), 1.63 (m, 6H, −CH_2−(CH_2)$_{14}$−CH_3, −CH_2−CH_2−N^+-), 1.92 (m, 2H, −O−CH_2-), 2.85 (m, 1H, −C*H*-), 4.55 (m, 2H, −CH_2−CH_2−N^+-), 7.96 (d, 2H, -C═C*H*-), 8.99 (d, 2H, -N^+═CH−). ^{13}C NMR (200 MHz, [D6] DMSO, 25 °C, TMS): δ = 14.10, 22.24, 26.76, 29.12, 30.61, 31.42, 34.87, 45.04, 60.03, 67.55, 126.88, 144.45, 166.04. ^{11}B NMR (200 MHz, [D6] DMSO, 25 °C): −23.69 (1 B), −17.30 (10 B), 7.13 (1 B). IR (KBr): ν = 2923 (−C−H), 2853 (−C−H), 2475 (−B−H), 1641 (-C═C−), 1466 (−C−H), 1159 (−C−N-), 1056 (−B−O−C-), 722 (═C−H).

N-Methyl-4-(dihexydecylmethyl)pyridinium Iodide (Me-SAINT-16). The compound was synthesized according to Sudhölter et al. (1982) (*35*) and Meekel et al. (*34*).

Preparation of Liposomes. The boron-containing lipids were either used in pure form or mixed with equal molar amounts of DSPC and cholesterol plus 2 mol % DSPE-PEG_{2000}. The lipid, or lipid mixture, was dissolved in chloroform and dried to a thin lipid film in a round-bottom flask. The lipid film was hydrated and dispersed by vortexing in 10 mM HEPES[1]buffer saline, pH 7.4 (150 mM NaCl, 10 mM HEPES). The resulting suspension was frozen and thawed in 10 cycles followed by extrusion (21 times) through a polycarbonate membrane with a pore diameter of 100 nm (Avestin, Mannheim, Germany) at a temperature of 50 °C. Final lipid concentration was 10 mM. Lipid content was measured by the Stewart assay (*36*), using appropriate standard curves for the individual lipids and ICP-MS measurements.

Liposomes could not be prepared from Dioxan-SAINT-12; the suspension obtained after hydration of the lipid film yielded larger particles, which could not be extruded even after ultrasound treatment.

For DSC measurements, the pure lipids were dispersed from a lipid film (obtained as described above) by hydration with 10 mM Hepes 100 mM NaCl, pH 7.4, through ten freeze−thaw cycles, and stored at 4 °C prior to measurement.

Inductively Coupled Plasma Mass Spectrometry (ICP-MS). ICP-MS was used to quantify boron in liposome preparations. The analysis was carried out in a ThermoElectron Element 2 ICP-MS apparatus, by measuring the signal for the boron-11 nuclide. The samples were treated with concentrated nitric acid (HNO_3) in the first dilution step and further diluted with water to concentration ranges appropriate for the sensitivity of the apparatus. The water produced by a Milli-Q system was used. The boron concentrations were determined by a calibration curve obtained from samples with known boron content. Indium was added as internal standard.

Cryotransmission Electron Microscopy (cryo-TEM). A small amount (~1 μL) of the liposome suspension (final lipid

[1]Abbreviations: HEPES, 4-(2-hydroxyethyl)-1-piperazineethanesulfonic acid; BNCT, boron neutron capture therapy; DSPC, distearoylphosphatidylcholine; BSH, $Na_2B_{12}H_{11}SH$; DSC, differential scanning calorimetry; DPPC, dipalmitoylphosphatidylcholine; TEM, transmission electron microscopy; ATP, adenosine triphosphate; BPA, boronphenylalanine; EGF, epidermal growth factor; SAINT, *s*ynthetic *a*mphiphiles for *i*nterdisciplinary *n*ucleic acid *t*herapy; ESI, electrospray ionization; ICP-MS, inductively coupled plasma mass spectrometry; DSPE, distearoylphosphatidylethanolamine.

concentration 5 mM) was transferred to a polymer-coated copper grid and shock-frozen from 25 °C by injection into liquid ethane. The vitrified samples were examined in a Zeiss EM LEO 912Ω electron microscope, operating at an accelerating voltage of 80 keV in filtered bright field image mode at $\Delta E = 0$ eV. The stage temperature was kept below 108 K, and images were recorded at defocus settings between 1 and 3 μm. Images were recorded by a slow scan charge-coupled device (SSCCD) camera using the minimal dose focusing device. To assess the reproducibility of the results, several images were recorded in different areas of the specimen.

Differential Scanning Calorimetry Measurements. Differential scanning calorimetry (DSC) measurements were carried out on a VP-DSC microcalorimeter from Microcal (Northhampton, MA), using the pure boron lipid (final lipid concentration 10 mM). The samples were degassed under vacuum prior to the measurement. For the up- and down-scans, a scan rate of 60 °C/h and a filtering period of 2 s were used. From each scan, a buffer background scan was subtracted. For data analysis, the software package ORIGIN (Microcal) was used. The buffer system for this measurement was 10 mM HEPES with 100 mM sodium chloride, pH = 7.4.

Viability Assay. The cell viability was determined with the CellTiter-Glo assay (Promega GmbH, Mannheim, Germany), which is based on the quantification of ATP, which is in turn proportional to the number of metabolically active cells.

The cell line V79 (lung fibroblasts of Chinese hamster) was cultivated with Ham's F10 medium and 10% fetal calf serum at 37 °C and 5% CO_2. Cells (20 000 per well) were seeded into 48-well plates and grown for 24 h. Then, the cells were incubated with different concentrations of boron-containing liposomes (DSPC/cholesterol/boron lipid (1:1:1 molar ratio) plus 2 mol % DSPE-PEG_{2000}) for 24 h. Then, 300 μL CellTiter-Glo reagent was added, and the luminescence was measured after few minutes (Microlumat Plus LB 96, EG & Bertold, Bad Wildbad, Germany). The average of two wells was compared with the average of eight untreated samples ($n = 2$).

The IC_{50} values were obtained by fitting a sigmoidal curve with the following equation:

$$f = \frac{a}{[1 + \exp(-(x - IC_{50})/b)]}$$

in which f corresponds to the percentage survival of cells, a corresponds to the response without inhibition, x to the concentration of the tested substance, b to the slope of the response curve at $c = IC_{50}$, and IC_{50} to the concentration of the tested substance that provokes 50% reduction of cell viability.

RESULTS

Chemistry. In this study, nine different dodecaborate cluster lipids were synthesized. All of them carry only one negative net charge. Recently, we published (*25*) the first boron lipids with a net charge of −1, but with a completely different basic structure. The lipids prepared here carry a bisalkylmethyl group on the *p*-position of a pyridine, which is *N*-alkylated with a linker carrying the dodecaborate cluster as polar headgroup. The lipids differ both in the alkyl chain length of the tails and in the linkers. For the connection of the dodecaborate cluster with the lipid backbone nucleophilic ring-opening reactions of tetrahydrofurane (THF), dioxane and tetrahydropyrane (THP) derivatives of the cluster with the alkylpyridinium compound (**2a**,**b**,**c**) were used (Scheme 2).

Semioshkin et al. (*37*) recently reported reactions of oxonium derivatives (THF and dioxane) with amines (also pyridine), but under different conditions and not applied to boron lipids. For the first time, we accomplished a ring-opening reaction with

Scheme 2. Synthesis of the Boron Lipids via Ring-Opening Reactions between the Alkylpyridnium Compound (2a,b,c) and the THF, Dioxane, and THP Derivative of the Dodecaborate Cluster, Respectively

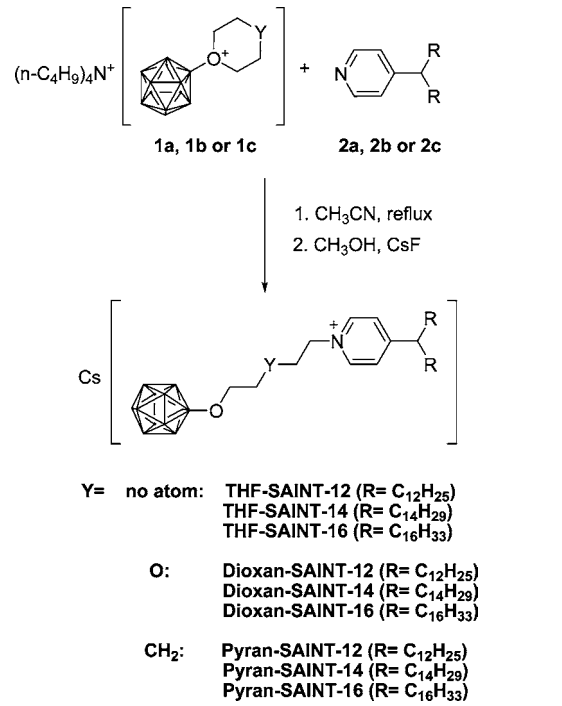

Scheme 3. Synthesis of the Tetrahydropyrane (THP) Derivative of the Dodecaborate Cluster

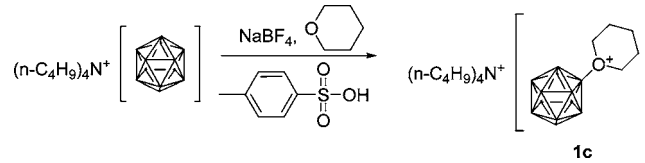

the THP derivative of the cluster. The THP derivative had first been published by Peymann et al. (*33*) and had been prepared by alkylation of hydroxyundecahydro-*closo*-dodecaborate with dibromopentane, which requires two synthesis steps from the dodecaborate cluster to the THP derivative. We developed a reaction procedure that leads to the THP derivative from the unsubstituted cluster in one step and in good yields (Scheme 3).

The dodecaborate cluster is suspended in tetrahydropyrane, and 2 equiv *p*-toluenesulfonic acid and 5 equiv $NaBF_4$ are added. The product is obtained with a yield of 70%.

The synthesis of the alkylpyridinium compounds followed the work of Meekel et al. (*34*). The ring-opening reactions are carried out with the THF, dioxane, or THP derivatives of the cluster and 1.5 equiv alkylpyridinium compound (**2a**,**b**,**c**) in acetonitrile. The reaction yields are 50−70% for the THF and dioxane derivatives and 40−50% for the THP derivative, slightly depending on the length of the alkyl chain of the pyridine unit.

Physical Characterization and Liposome Preparation. The lipid film hydration and extrusion method at 50 °C was used to prepare liposomes from pure boron lipid. The structures formed were investigated by cryo-TEM (Figure 1).

The shortest chains with 12 carbons produce a mixture of liposomes and some open structures. THF-SAINT-12 (Figure 1a) forms predominantly closed vesicles but also some thick bilayers. The closed structures are heterogeneous in size; some of them are smaller than 100 nm, which is the diameter of the extrusion membrane pores. Pyran-SAINT-12 (Figure 1f) is able

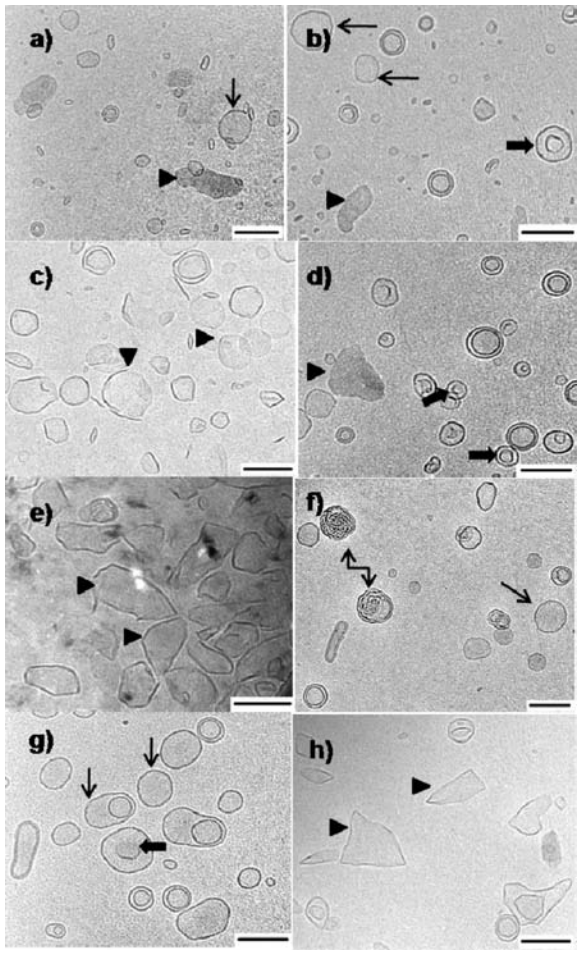

Figure 1. Cryo-TEM pictures from pure boron lipids: (a) THF-SAINT-12, (b) THF-SAINT-14, (c) THF-SAINT-16, (d) Dioxan-SAINT-14, (e) Dioxan-SAINT-16, (f) Pyran-SAINT-12, (g) Pyran-SAINT-14, (h) Pyran-SAINT-16. Scale bar 200 nm. Regular liposomes are indicated by ←, open structures by ▼, invaginated structures by thick arrows, and inverted structures by double-headed arrows.

to form liposomes, and inverted structures are observed. Closed structures are found in greatest abundance for all the three derivatives with 14-carbon chains. Only for THF-SAINT-14 and Dioxan-SAINT-14 are some bilayers observed. Interestingly, some of the liposomes show invagination. For the longer 16-carbon chains, the structures formed appear to be almost exclusively open. Several bilayers have edges bent upward, giving at first glance an impression of closed structures.

At the temperature of extrusion (50 °C) and preparation for cryo-TEM (25 °C), SAINT-16 derivatives are in the gel phase (see DSC data below), which is less favorable for the formation of liposomes. Extrusion at 65 °C and subsequent storage at 4 °C produces bilayer disks as well as closed liposomes (Figure 2a,b) in the case of THF-SAINT-16 and Dioxan-SAINT-16. This behavior is different from that of the lipid B-6−14, which forms very large bilayer sheets from liposomes below the phase transition temperature (*24*).

Interestingly, the choice of the spacer has no drastic influence on the morphology of the liposomes. Recently, we found drastic changes in the vesicle shape between the boron lipids B-THF-14 and B-Dioxan-14 (*25*) with change of the linker.

Cryo-TEM was employed also to visualize the structures formed when the boron-containing lipids had been mixed with helper lipids. For liposomal preparations, DSPC, cholesterol, and boron-containing lipid in the molar ratio of 1:1:1 plus 2 mol % DSPE-PEG_{2000} were used. THF-SAINT-12 (Figure 3a), THF-SAINT-14 (Figure 3b), and THF-SAINT-16 (Figure 3c) form liposomes in heterogeneous size. The liposome diameters differ from 100 nm, which is the pore size of the extrusion membrane, to 300 nm.

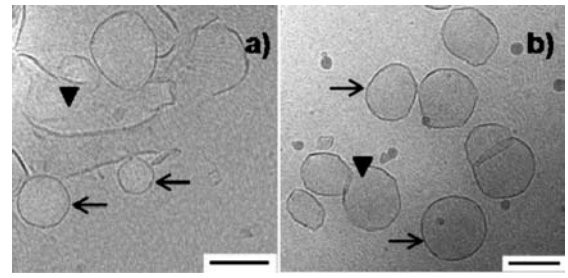

Figure 2. Samples from THF-SAINT-16 (a) and Dioxan-SAINT-16 (b) extruded at 65 °C and stored at 4 °C. Scale bar 200 nm. Regular liposomes are indicated by ←, open structures by ▼.

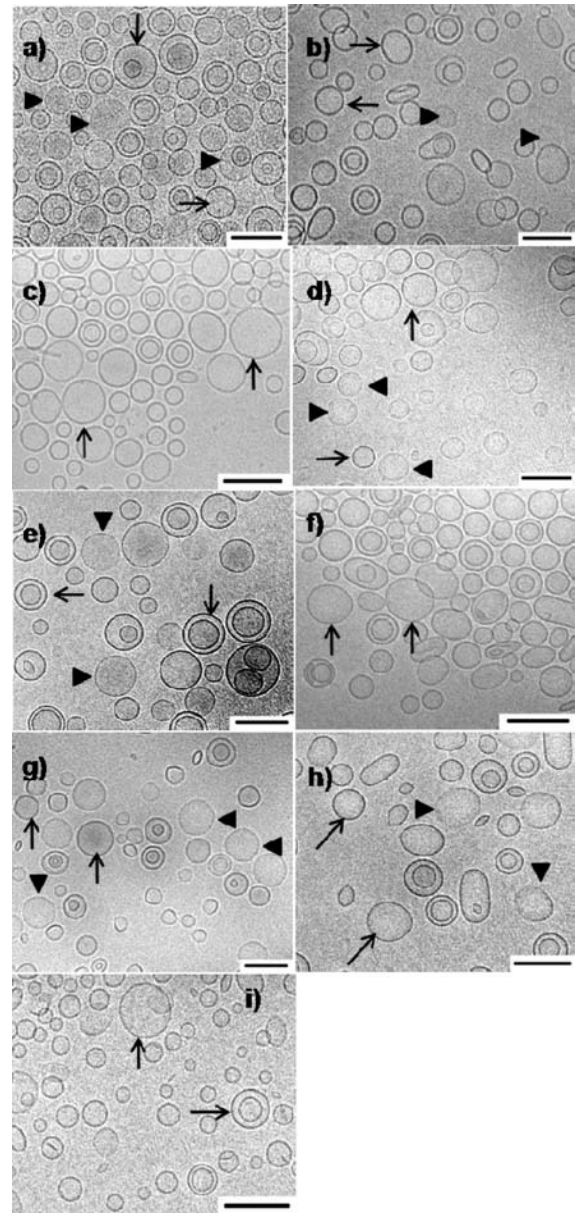

Figure 3. Cryo-TEM pictures of the liposomal preparations with helper lipids: DSPC/cholesterol/boron lipid (1:1:1) plus 2 mol % DSPE-PEG_{2000}: (a) THF-SAINT-12, (b) THF-SAINT-14, (c) THF-SAINT-16, (d) Dioxan-SAINT-12, (e) Dioxan-SAINT-14, (f) Dioxan-SAINT-16, (g) Pyran-SAINT-12, (h) Pyran-SAINT-14, (i) Pyran-SAINT-16. Scale bar 200 nm. Regular liposomes are indicated by ←, open structures by ▼.

For Dioxan-SAINT-12 (Figure 3d), Dioxan-SAINT-14 (Figure 3e), and Dioxan-SAINT-16 (Figure 3f), also liposomes can be observed in different sizes. By adding helper lipids, liposomal vesicles are also found for Pyran-SAINT-12 (Figure 3g), Pyran-SAINT-14 (Figure 3h), and Pyran-SAINT-16 (Figure 3i) with a size distribution. In general, the formation of liposomes is influenced by the chain length of the tails in the SAINTs. With mixtures containing the short-chain derivatives, an increased tendency to form open structures can be seen.

In the DSC measurements, no phase transition could be detected for any of the three SAINT-12 derivatives. This fact is, however, not surprising because Me-SAINT-12 (1-methyl-4-(bisdodecylmethyl)pyridinium chloride) has a phase transition at 0 °C (*34*), which is outside the range accessible by the DSC used.

The DSC profile of pure THF-SAINT-14 is shown in Figure 4a. From 4 to 20 °C, a broad peak with complex shape can be seen, which consists of two transitions at 13.8 and 16.8 °C. Both transitions change only insignificantly between the first and the second upscan. The two transitions might arise from the heterogeneity of the vesicle shapes and sizes (see Figure 1b). In the literature, it is known that small unilamellar vesicles (SUVs) give rise to a main transition different from that of multilamellar (MLVs) or large unilamellar vesicles (LUVs) (*38*). Interestingly, in the first upscan two further transitions at 33.0 and 66.5 °C can be observed, which disappear in the following upscans. Metastable subtransitions are described, e.g., for DPPC (dipalmitoylphosphatidylcholine) bilayers in gel phase (*39, 40*), which are reversible after storage at low temperatures for a few days. The transitions for THF-SAINT-14 are surprising in the liquid phase, and we have no evidence about the reversibility or explanation for structural changes in these phases. In cryo-TEM, no change in the vesicle shape was found after heating (pictures not shown here).

The temperature difference (approximately 4 °C) of the transition peaks between the up- and down-scans is remarkable; such strong hysteresis has only been described for the boron lipid B-THF-14 (*25*). Furthermore, it seems that the transitions in the downscan do not end at 4 °C and perhaps more transitions might follow. In contrast, Dioxan-SAINT-14 (Figure 4b) has a broad peak with a maximum at 12.3 °C. The broadness indicates that the liposome composition is heterogeneous, as can also be observed in cryo-TEM (see Figure 3d). The temperature difference (approximately 4 °C) of the transition peaks between the up- and down-scans is again remarkable. The transition does not end at 4 °C in the downscan. The DSC profile of Pyran-SAINT-14 (Figure 4c) shows a broad peak from 4 to 18 °C, similar to THF-SAINT-14. The maxima are located at 8.5 and 12.4 °C and are probably the main transitions. Meekel et al. (*34*) recorded a main transition of Me-SAINT-14 (1-Methyl-4-(ditetradecylmethyl)pyridinium chloride) at approximately 16 °C. We again attribute the two transitions to the heterogeneity of vesicle formation and size. No transitions in the downscan can be observed, which indicates that they are located outside of the temperature range in which the measurements were performed.

The DSC profile is more complex for all SAINT-16 derivatives (Figure 5). All of them show multiple transitions, which occur at similar temperatures; the transitions recur during all up- and down-scans. THF-SAINT-16 (Figure 5a) has a main transition at 56.0 °C. Sudhölter et al. (*35*) reported a main transition for Me-SAINT-16 (1-Methyl-4-(dihexadecylmethyl)pyridinium chloride) at 64 °C and we also detected it, although at 58 °C (data not shown here). THF-SAINT-16 passes through three further transitions at 24.9, 39.0, and 62.8 °C. A rich polymorphism in the DSC is known for N-methylated pyridinium cores depending on the counterion, with solid−solid

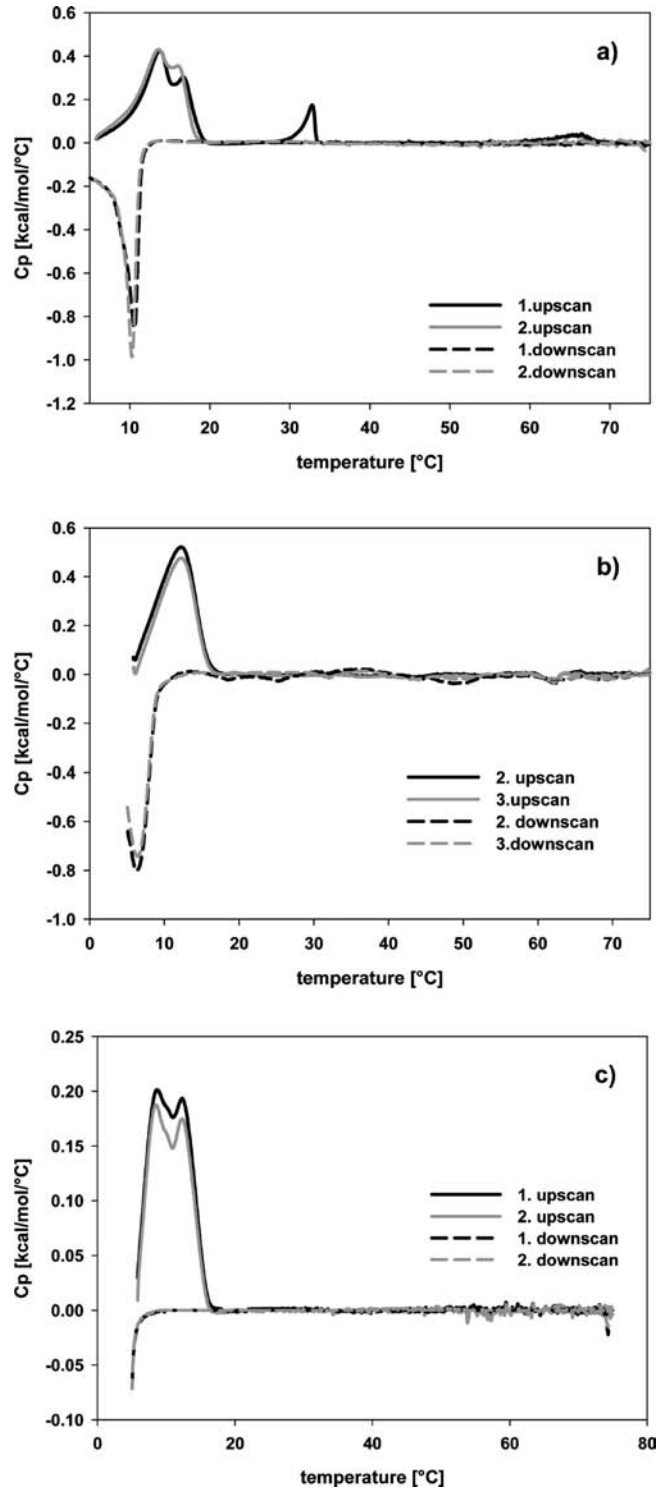

Figure 4. DSC of pure films of THF-SAINT-14 (a), Dioxan-SAINT-14 (b), and Pyran-SAINT-14 (c). Lipid concentration 5 mM.

transitions and transitions between smectic phases (*35*). Therefore, solid−solid and liquid−liquid transitions are not very special for this boronated pyridinium lipid.

A tilted smectic phase is described by Sudhölter et al. (*35*) for Me-SAINT-16 iodide. Molecular dynamics simulation would certainly be required for THF-SAINT-16 to answer precisely the question of lipid packing. In the downscan, only two transitions are visible. As can be seen in Figure 5b, Dioxan-SAINT-16 also has four transitions, which are located at 26.8, 39.9, 55.2, and 62.8 °C. Two solid−solid transitions can be noted, as well as a main transition at 55.2 °C and a liquid−liquid

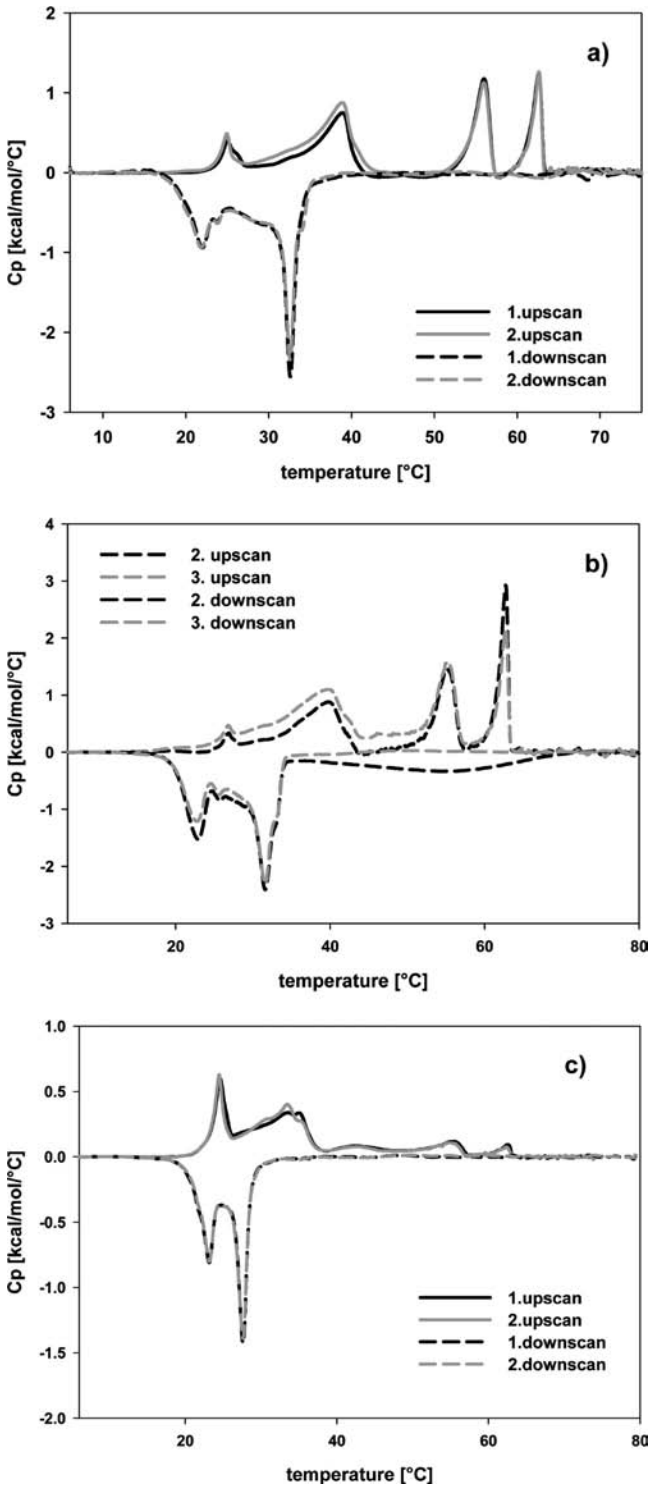

Figure 5. DSC of pure films of THF-SAINT-16 (a), Dioxan-SAINT-16 (b), and Pyran-SAINT-16 (c). Lipid concentration 10 mM.

transition at 62.8 °C, which is comparable to THF-SAINT-16. Again, only two peaks in the downscan can be observed. Pyran-SAINT-16 shows transitions in the same temperature region (24.4, 33.6, 55.1, and 62.4 °C) as THF-SAINT-16 and Dioxan-SAINT-16, but for Pyran-SAINT-16, the transitions at higher temperatures have very small enthalpies. We have no explanation for this, but it might be assumed that the transitions concern the same event of transitions as in THF-SAINT-16 and Dioxan-SAINT-16.

As summarized in Table 1, all investigated lipids have a low impact on cell viability except for Dioxan-SAINT-12 and Dioxan-SAINT-14 (Table 1). It seems that the choice of the linker influences the viability in the case of short alkyl chains. The dioxane linker leads to a higher toxic effect as compared to the THF or THP linker. This is contrary to the boron lipids B-THF-14 and B-Dioxan-14 where the introduction of an ether function in the hydrocarbon spacer leads to a decrease of toxicity (*25*).

Table 1. IC_{50} Values and Standard Deviations for All of the Tested Lipids[a]

name	log IC_{50} ± SD	IC_{50} [mM]
THF-SAINT-12	0.18 ± 0.02	1.5
THF-SAINT-14	0.51 ± 0.07	3.3
THF-SAINT-16	0.68 ± 0.01	4.8
Dioxan-SAINT-12	−0.56 ± 0.03	0.3
Dioxan-SAINT-14	−0.16 ± 0.14	0.7
Dioxan-SAINT-16	0.49 ± 0.02	3.0
Pyran-SAINT-12	0.27 ± 0.04	1.9
Pyran-SAINT-14	0.14 ± 0.02	1.4
Pyran-SAINT-16	0.54 ± 0.03	3.4

[a] For the determination of the cell viability, hamster V79 fibroblasts and the CellTiter-Glo assay were used.

The increasing alkyl chains lead to a significant decrease of toxicity in the case of THF-SAINT and Dioxan-SAINT lipids. This tendency is not well pronounced for the Pyran-SAINT lipids; however, the toxicity decreases by half from Pyran-SAINT-12 to Pyran-SAINT-16. Previously, we found a similar trend for the lipids B-6-14 and B-6-16 (*24*).

It seems that the linker influences the viability for longer alkyl chains less powerfully because the IC_{50} values are all in the same concentration range (4 mM ± 1.5 mM). Thus, for the SAINT-16 derivatives, the influence on cell viability depends only slightly on the nature of the linker, whereas this is not the case for shorter alkyl chains.

DISCUSSION

Synthesis of nine *closo*-dodecaborate cluster containing lipids was achieved. These SAINT derivatives are the first boron lipids with an alkylpyridinium core as lipid backbone. The lipids differ in their alkyl chain length and in the linker connecting the dodecaborate cluster with the lipid backbone. All of them are only singly negatively charged; thus, they are the second generation of boron lipids with a net charge of −1 (*25*). The net charge of liposomes influences the biological properties. The incorporation of negatively charged lipids into the liposomal membrane accelerates the opsonization and consequently the clearance of liposomes from the bloodstream (*41*). The decrease of lipid charge may, by reduced clearance, lead to longer retention times in the body in comparison to doubly negatively charged dodecaborate cluster lipids. Thus, dodecaborate cluster lipids with reduced net charge (up to a neutral molecule) might be desirable in regard to therapeutic efficacy.

The change in the negative net charge does not influence the toxicity of the dodecaborate cluster lipids against cells. Thus, the IC_{50} values of the SAINTs lie in the same concentrations range as B-6-14 (*24*). Studies of cell uptake are in progress for the SAINTs, B-Dioxan-14, B-6-14, and B-6-16, in order to investigate the influence of the different net charges in more detail.

Depending on the preparation temperature, the SAINT lipids are able to form closed liposomes in the absence of helper lipids and are stable after storing at 4 °C. The liposomes from pure boron lipid are able to transfer high amounts of boron to the tumor. Targeting with tumor-seeking entities probably allows selective accumulation.

Interestingly, the choice of the linker plays no major role with respect to liposome formation or thermotropic behavior. Recently, we reported about the lipids B-THF-14 and B-Dioxan-14 in which only the linker differs. For those lipids, the linker influences the vesicle formation as well as the DSC profile (*25*). The absence of the effect of the linker on toxicity observed here is very unexpected and makes it difficult to propose an optimal linker for further syntheses.

The length of the alkyl chains influences the properties of the lipids with regard to their thermotropic behavior, liposome formation in the absence and in the presence of helper lipids, and cell toxicity. Higher temperatures are necessary during the preparation of liposomes when the length of the chains increases. It must be pointed out that the helper and boron lipids should not differ significantly in their tail lengths. Therefore, DSPC, which is commonly used as helper lipid for *in vivo* experiments, is suitable for the SAINT-16 derivatives. Longer lipid tails lead to a decrease of toxicity and are consequently recommended for dodecaborate cluster lipids.

All SAINT lipids have been prepared as cesium salts. The purification of the lipids by precipitation from methanol could be achieved by addition of a solution of cesium fluoride in methanol; this is an elegant procedure and consequently recommended for synthesis strategies of boron lipids. In contrast to, e.g., the tetramethylammonium ion (which is toxic *in vivo*), the cesium ion does not carry a substantial toxicity on its own.

The new lipids, with the exception of Dioxan-SAINT-12 and Dioxan-SAINT-14, have low *in vitro* toxicity and hence might represent suitable boron carriers for BNCT. *In vivo* experiments on mice are in progress to proceed to the next stage toward successful treatment with BNCT.

ACKNOWLEDGMENT

The authors gratefully thank Dr. Uwe Schüßler for the ICP-MS measurements. We would also like to thank Lipoid GmbH for generous gifts of lipids. This work has been financially supported by the German Research Council DFG through a joint grant to DG, RS, and RPS.

Supporting Information Available: ^{1}H NMR, ^{13}C NMR, and ^{11}B NMR spectra; ESI mass spectra, and IR spectra of compounds **1c** and all SAINT lipids. This material is available free of charge via the Internet at http://pubs.acs.org.

LITERATURE CITED

(1) Barth, R. F. (2003) A critical assessment of boron neutron capture therapy: an overview. *J. Neurooncol. 62*, 1–5.

(2) Koryakin, S. N. (2006) Molecular-biological problems of drug design and mechanism of drug action. *Pharm. Chem. J. 40*, 583–587.

(3) Barth, R. F., Coderre, J. A., Vicente, M. G. H., and Blue, T. E. (2005) Boron neutron capture therapy of cancer: Current status and future prospects. *Clin. Cancer Res. 11*, 3987–4002.

(4) Hawthorne, M. F., and Lee, M. W. (2003) A critical assessment of boron target compounds for boron neutron capture therapy. *J. Neurooncol. 62*, 33–45.

(5) Schinanzi, R. F., and Prusoff, W. H. (1985) Synthesis of 5-(dihydroxyboryl)-2′-deoxyuridine and related boron-containing pyrimidines. *J. Org. Chem. 50*, 841–847.

(6) Yamamoto, Y., Seko, T., Nakamura, H., Nemoto, H., Hojo, H., Mukai, N., and Hashimoto, Y. (1992) Synthesis of carboranes containing nucleosides bases. Unexpectedly high cytostatic and cytocidal toxicity towards cancer cells. *J. Chem. Soc.: Chem. Commun. 2*, 157–18.

(7) Peymann, T., Preusse, D., and Gabel, D. (1997) Synthesis of S-glycosides of mercaptoundecahydro-closo-dodecaborate (2-). In *Advances in Neutron Capture Therapy, Volume II, Chemistry and Biology* (Larsson, B., Crawford, J., and Weinreich, R., Eds.) pp 35−37, Elsevier, Amsterdam.

(8) Bregadze, V. I., Sivaev, I. B., Gabel, D., and Wöhrle, D. (2001) Polyhedral boron derivatives of porphyrins and phthalocyanines. *J. Porphyrins Phthalocyanines 5*, 767–781.

(9) Vicente, M. G. H., Wickramasighe, A., Nurco, D. J., Wang, H. J. H., Nawrocky, M. M., Makar, M. S., and Miura, M. (2003) Synthesis, toxicity and biodistribution of two 5,15-di[3,5-(nidocarboranylmethyl)phenyl]porphyrin in EMT-6 tumor bearing mice. *Bioorg. Med. Chem. 11*, 3101–3108.

(10) Fronczek, F. R., and Vicente, M. G. H. (2005) Synthesis and cellular studies of an octa-anionic 5,10,15,20-tetra[3,5(nido-carboranylmethyl)phenyl]porphyrin (H_2OCP) for application in BNCT. *Bioorg. Med. Chem. 13*, 1633–1640.

(11) Hill, J. S., Kahl, S. B., Kaye, A. H., Stylli, S. S., Koo, M.-S., Gonzales, M. F., Vardaxis, N. J., and Johnson, C. I. (1992) Selective tumor uptake of boronated porphyrin in an animal model of cerebral glioma. *Proc. Natl. Acad. Sci. U.S.A. 89*, 1785–1789.

(12) Hill, J. S., Kahl, S. B., Stylli, S. S., Nakamura, Y., Koo, M.-S., and Kaye, A. H. (1995) Selective tumor kill of cerebral glioma by photodynamic therapy using a boronated porphyrin photosensitizer. *Proc. Natl. Acad. Sci. U.S.A. 92*, 12126–12130.

(13) Barth, R. F., Adams, D. M., Soloway, A. H., Alam, F., and Darby, M. V. (1994) Boronated starburst dendrimer-monoclonal antibody immunoconjugates: evaluation as a potential delivery system for neutron capture therapy. *Bioconjugate Chem. 5*, 58–66.

(14) Novick, S., Quastel, M. R., Marcus, S., Chipman, D., Shani, G., Barth, R. F., and Soloway, A. H. (2002) Linkage of boronated polylysine to glycoside moieties of polyclonal antibody; Boronated antibodies as potential delivery agents for neutron capture therapy. *Nucl. Med. Biol. 29*, 159–167.

(15) Wu, G., Barth, R. F., Yang, W., Chatterjee, M., Tjarks, W., Cielsielski, M. J., and Fenstermaker, R. A. (2004) Site-specific conjugation of boron containing dendrimers of anti-EGF receptor monoclonal antibody cetuximab (IMC-C225) and its evaluation as a potential delivery agent for neutron capture therapy. *Bioconjugate Chem. 15*, 185–194.

(16) Pan, X. Q., Wang, H., Shukla, S., Sekido, M., Adams, D. M., Tjarks, W., Barth, R. F., and Lee, R. J. (2002) Boron-containing folate receptor-targeted liposomes as potential delivery agents for neutron capture therapy. *Bioconjugate Chem. 13*, 435–442.

(17) Bohl-Kullberg, E., Bergstrand, N., Carlsson, J., Edwards, K., Johnsson, M., Sjöberg, S., and Gedda, L. (2002) Development of EGF-conjugated liposomes for targeted delivery or boronated DNA-binding agents. *Bioconjugate Chem. 13*, 737–743.

(18) Maruyama, K., Ishida, O., Kasaoka, S., Takizawa, T., Utoguchi, N., Shinohara, A., Chiba, M., Kobayashi, H., Eriguchi, M., and Yanagie, H. J. (2004) Intracellular targeting of sodium mercaptoundecahydrododecaborate (BSH) to solid tumors by transferrin-PEG liposomes, for boron neutron-capture therapy (BNCT). *J. Controlled Release 98*, 195–207.

(19) Mehta, S. C., Lai, J. C., and Lu, D. R. (1996) Liposomal formulations containing sodium mercaptoundecahydrododecaborate (BSH) for boron neutron capture therapy. *J. Microencapsul. 13*, 269–279.

(20) Feakes, D. A., Shelly, K., Knobler, C. B., and Hawthorne, M. F. (1994) $Na_3[B_{20}H_{17}NH_3]^-$ Synthesis and liposomal delivery to murine tumors. *Proc. Natl. Acad. Sci. U.S.A. 91*, 3029–3033.

(21) Gabel, D., Awad, D., Schaffran, T., Radovan, D., Daraban, D., Damian, L., Winterhalter, M., Karlsson, G., and Edwards, K. (2007) The anionic boron cluster ($B_{12}H_{11}SH$)2- as a means to trigger release of liposome contents. *ChemMedChem 2*, 51–53.

(22) Lee, J.-D., Ueno, M., Miyajima, Y., and Nakamura, H. (2007) Synthesis of boron cluster lipids: closo-dodecaborate as an alternative hydrophilic function of boronated liposomes for neutron capture therapy. *Org. Lett. 9*, 323–326.

(23) Nakamura, H., Lee, J.-D., Ueno, M., Miyajima, Y., and Ban, H. S. (2007) Synthesis of closo-dodecaboryl lipids and their liposomal formation for boron neutron capture therapy. *Nanobiotechnol. 3*, 135–145.

(24) Justus, E., Awad, D., Hohnholt, M., Schaffran, T., Edwards, K., Karlsson, G., Damian, L., and Gabel, D. (2007) Synthesis, liposomal preparation, and in vitro toxicity of two novel dodecaborate cluster lipids for boron neutron capture therapy. *Bioconjugate Chem. 18*, 1287–1293.

(25) Schaffran, T., Lissel, F., Samatanga, B., Karlsson, G., Burghardt, A., Edwards, K., Winterhalter, M., Peschka-Süss, R., Schubert, R., and Gabel, D. (2009) Dodecaborate cluster lipids with variable headgroups for boron neutron capture therapy: Synthesis, physical-chemical properties and toxicity. *J. Organomet. Chem. 694*, 1708–1712.

(26) Rejman, J., Wagenaar, A., Engberts, J. B. F. N., and Hoekstra, D. (2004) Characterization and transfection properties of lipoplexes stabilized with novel exchangeable polyethylene glycol-lipid conjugates. *Biochim. Biophys. Acta 1660*, 41–52.

(27) Van Zanten, J., Doornbos-van der Meer, B., Audouy, S., Kok, R. J., and de Leij, L. (2004) A nonviral carrier for targeted gene delivery to tumor cells. *Cancer Gene Ther. 11*, 156–164.

(28) Zuhorn, I. S., Bakowsky, U., Polushkin, E., Visser, W. H., Stuart, M. C. A., Engberts, J. B. F. N., and Hoekstra, D. (2005) Nonbilayer phase of lipoplex-membrane mixture determines endosomal escape of genetic cargo and transfection efficiency. *Mol. Ther. 11*, 801–810.

(29) Justus, E., Rischka, K., Wishart, J. F., Werner, K., and Gabel, D. (2008) Trialkylammonio-dodecaborates: Anions for ionic liquids with potassium, lithium and proton as cations. *Chem.—Eur. J. 14*, 1918–1923.

(30) King, G. T., and Miller, N. E. (1986) 1,12-Bis(hydroxymethyl)decahydrododecaborate(2-) and $B_{12}H_{10}(CH_2X)_2^{2-}$ and $B_{12}H_{10}(CH_2L)_2$ derivatives. *Inorg. Chem. 25*, 4309–4311.

(31) Sivaev, I. B., Kulikova, N. Y., Nizhnik, E. N., Vichuzhanin, M. V., Starikova, Z. A., Semioshkin, A. A., and Bregadze, V. I. (2008) Practical synthesis of 1,4-dioxane derivative of the closo-dodecaborate anion and its ring opening with acetylenic alkoxides. *J. Organomet. Chem. 693*, 519–525.

(32) Sivaev, I. B., Semioshkin, A. A., Brellochs, B., Sjöberg, S., and Bregatze, V. I. (2000) Synthesis of oxonium derivatives of the dodecahydro-closo-dodecaborate anion $[B_{12}H_{12}]2$-. Tetramethylene oxonium derivative of $[B_{12}H_{12}]2$- as a convenient precursor for the synthesis of functional compounds for boron nutron captre therapy. *Polyhedron 19*, 627–632.

(33) Peymann, T., Lork, E., and Gabel, D. (1996) Hydroxoundecahydro-closo-dodecaborate (2-) as a nucleophile. Preparation and structural characterization of O-acyl derivatives of Hydroxoundecahydro-closo-dodecaborate (2-). *Inorg. Chem. 35*, 1355–1360.

(34) Meekel, A. A. P., Wagenaar, A., Ŝmisterová, J., Kroeze, J. E., Haadsma, P., Bosgraaf, B., Stuart, M. C. A., Brisson, A., Ruiters, M. H. J., Hoekstra, D., and Engberts, J. B. F. N. (2000) Synthesis of pyridinium amphiphiles used for transfection and some characteristics of amphiphile/DNA complex formation. *Eur. J. Org. Chem.* 665–673.

(35) Sudhölter, E. J. R., Engberts, J. B. F. N., and de Jeu, W. H. (1982) Thermotropic liquid-crystalline behavior of some single- and double chained pyridinium amphiphiles. *J. Phys. Chem. 86*, 1908–1913.

(36) Stewart, J. C. (1980) Calorimetric determination of phospholipids with ammonium ferrothiocyanate. *Anal. Biochem. 104*, 10–14.

(37) Semioshkin, A., Nizhnik, E., Godovikov, I., Starikova, Z., and Bregadze, V. (2007) Reactions of oxonium derivatives of $[B_{12}H_{12}]2$- with amines: Synthesis and structure of novel B_{12}-based ammonium salts and amino acids. *J. Org. Chem. 692*, 4020–4028.

(38) Biltonen, R. L., and Lichtenberg, D. (1993) The use of differential scanning calorimetry as a tool to characterize liposome preparations. *Chem. Phys. Lipids 64*, 129–142.

(39) Chen, S. C., Sturtevant, J. M., and Gaffney, B. (1980) Scanning calorimetric evidence for a third phase transition in phosphatidylcholine bilayers. *Proc. Natl. Acad. Sci. U.S.A. 77*, 5060–5063.

(40) Finegold, L., and Singer, M. A. (1984) Phosphatidylcholine bilayers: Subtransitions in pure and in mixed lipids. *Chem. Phys. Lipids 35*, 291–297.

(41) Levchenko, T. S., Rammohan, R., Lukyanov, A. N., Whiteman, K. R., and Torchilin, V. P. (2002) Liposome clearance in mice: the effect of a separate and combined presence of surface charge and polymer coating. *Int. J. Pharm. 240*, 95–102.

BC900147W

Pyridinium lipids with the dodecaborate cluster as polar head group: Synthesis, physical-chemical and biological characterization

Tanja Schaffran, Alexander Burghardt, Regine Peschka-Süss, Rolf Schubert, Mathias Winterhalter, Detlef Gabel

Supplementary material

1H-NMR spectra of compounds **1c** and **all SAINT lipids**
13C-NMR spectra of compounds **1c** and **all SAINT lipids**
11B-NMR spectra of compounds **1c** and **all SAINT lipids**
ESI mass spectra of compounds **1c** and **all SAINT lipids**
IR spectra of compounds **1c** and **all SAINT lipids**

1-pentamethyleneoxonium-closo-undecahydrododecaborate (-1), tetrabutylammonium salt (1c).

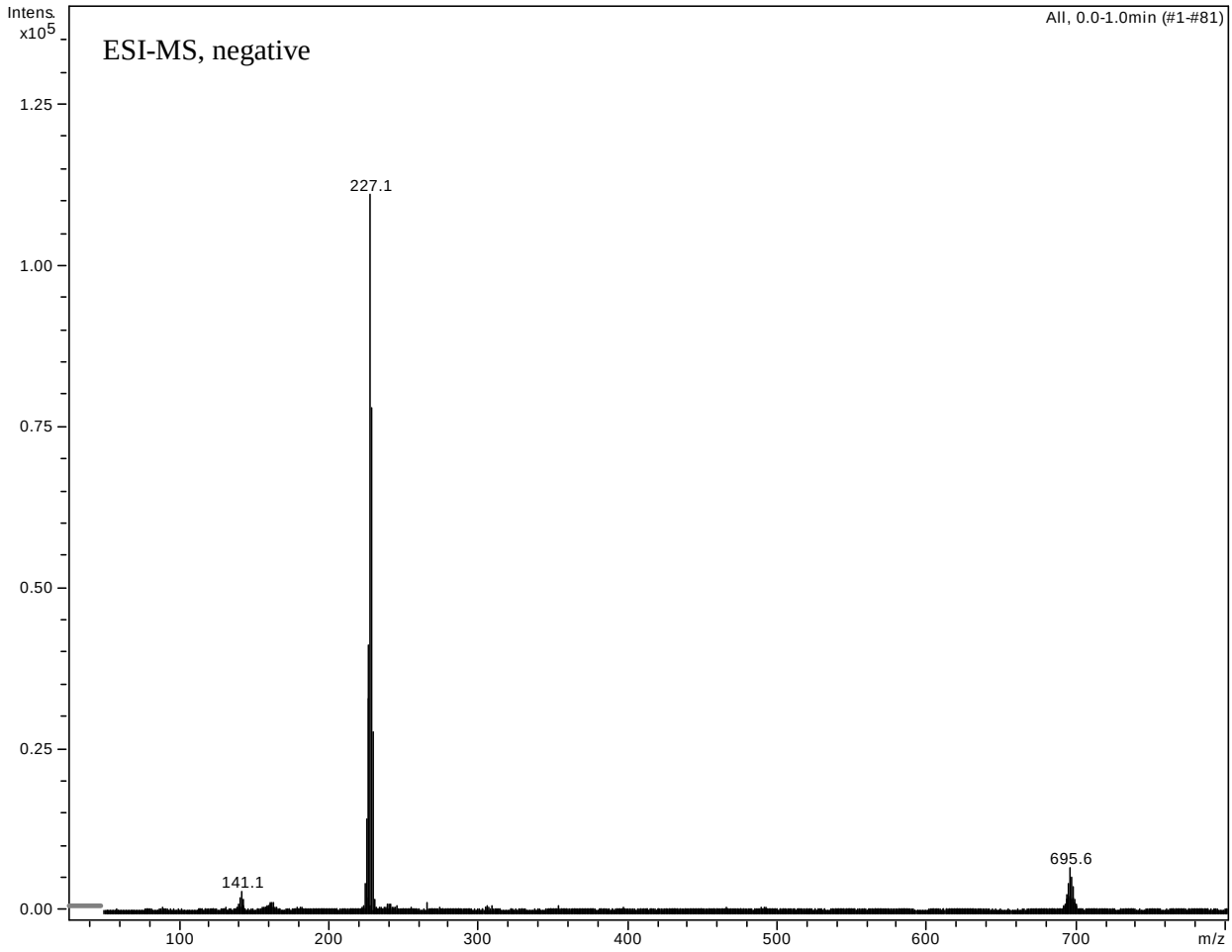

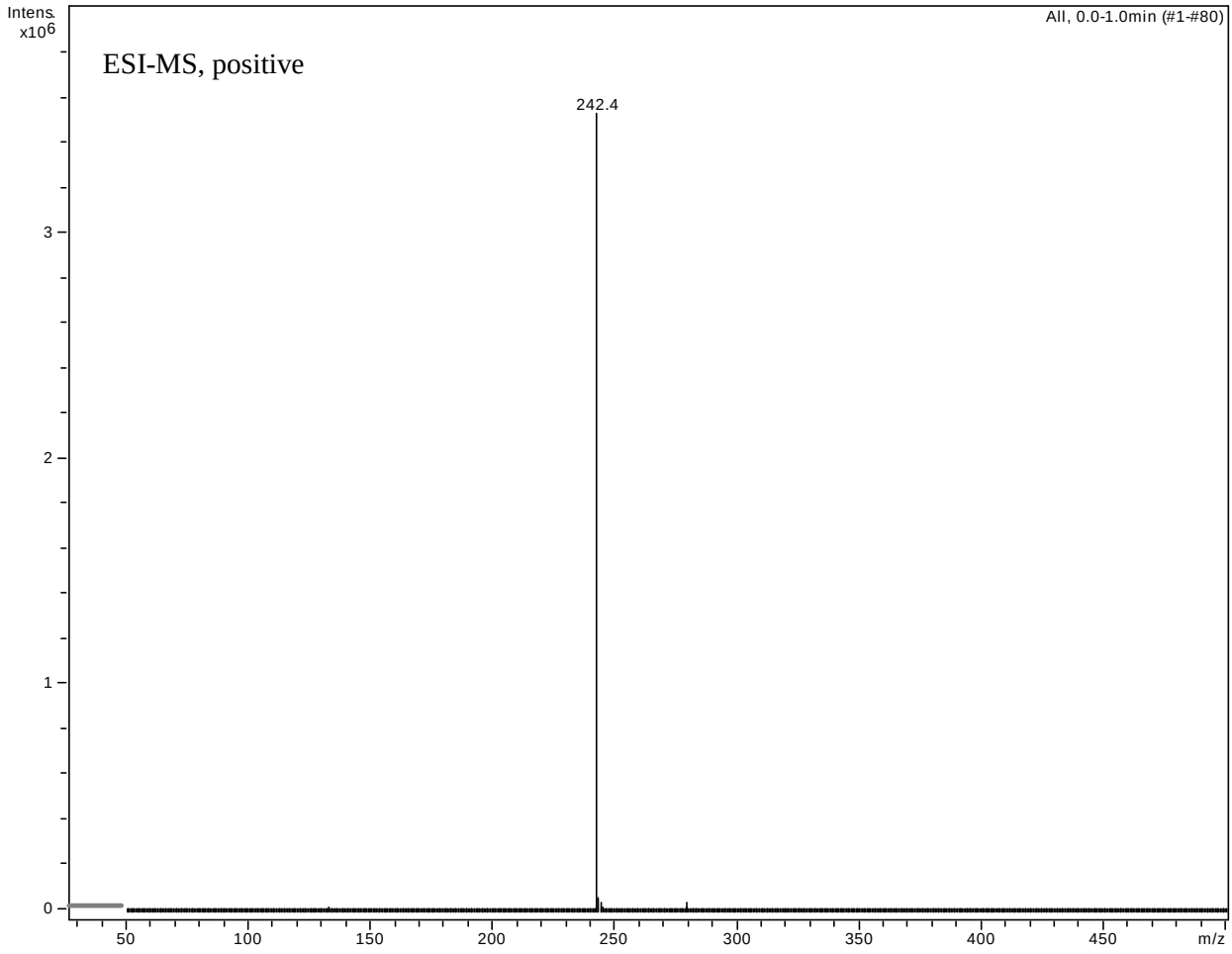
Intens.
x10^6
All, 0.0-1.0min (#1-#80)
ESI-MS, positive
242.4
3
2
1
0
50
100
150
200
250
300
350
400
450
m/z

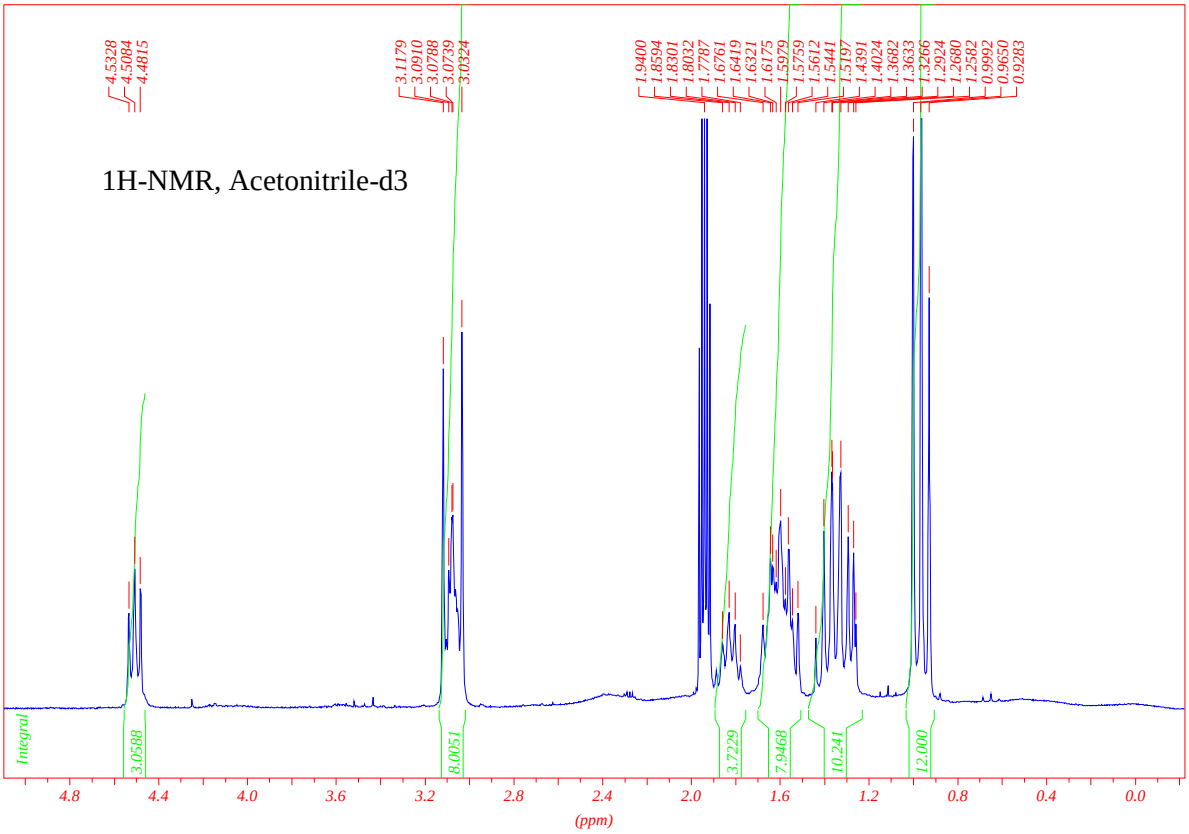
1H-NMR, Acetonitrile-d3
4.5328
4.5084
4.4815
3.1179
3.0910
3.0788
3.0739
3.0324
1.9400
1.8594
1.8301
1.8032
1.7787
1.6761
1.6419
1.6321
1.6175
1.5979
1.5759
1.5612
1.5441
1.5197
1.4391
1.4024
1.3682
1.3633
1.3266
1.2924
1.2680
1.2582
0.9992
0.9650
0.9283
Integral
3.0588
8.0051
3.7229
7.9468
10.241
12.000
4.8
4.4
4.0
3.6
3.2
2.8
2.4
2.0
1.6
1.2
0.8
0.4
0.0
(ppm)

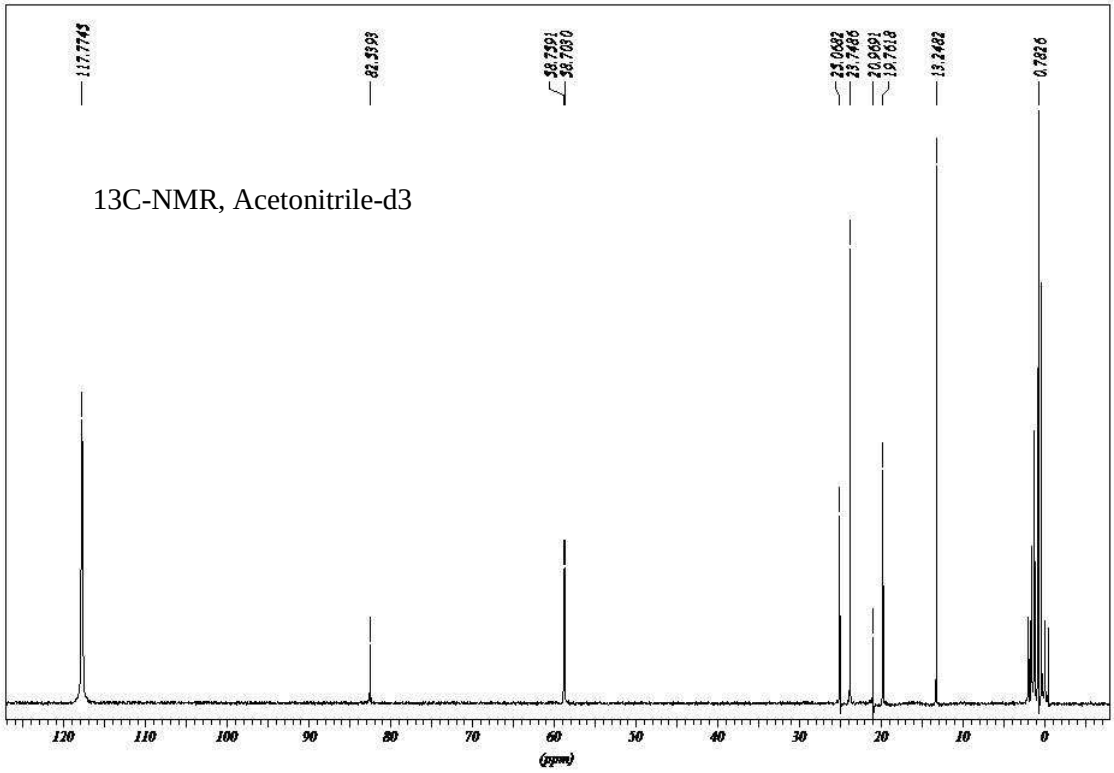
13C-NMR, Acetonitrile-d3
117.7745
82.5393
58.7391
58.7080
25.0682
25.7486
20.8691
19.7618
13.2482
0.7826
120
110
100
90
80
70
60
50
40
30
20
10
0
(ppm)

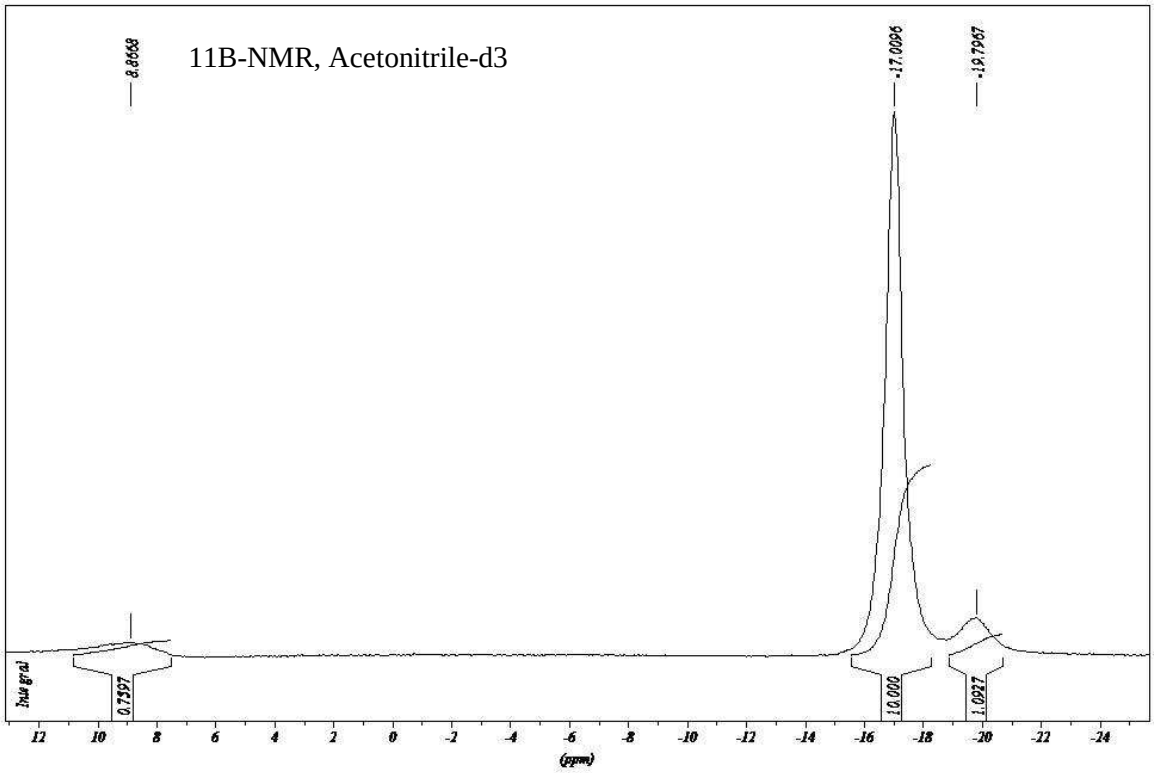
11B-NMR, Acetonitrile-d3
8.8668
-19.0967
0.7397
10.000
1.0927
(ppm)

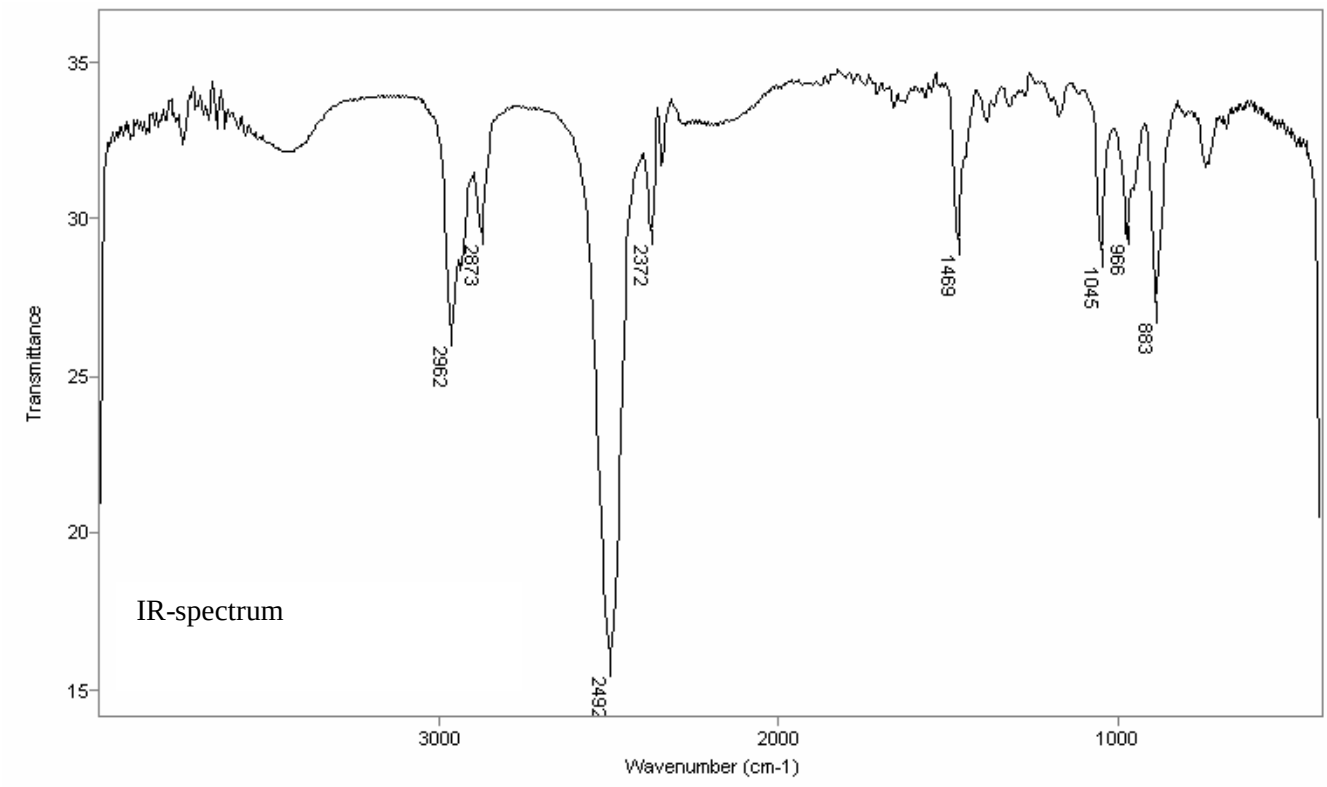
IR-spectrum
Transmittance
Wavenumber (cm-1)
2962
2873
2372
2492
1469
1045
966
883

4-(Bisdodecylmethyl)pyridinio-N-butoxy-undecahydro-closo-dodecaborate (-1), cesium salt (THF-SAINT-12).

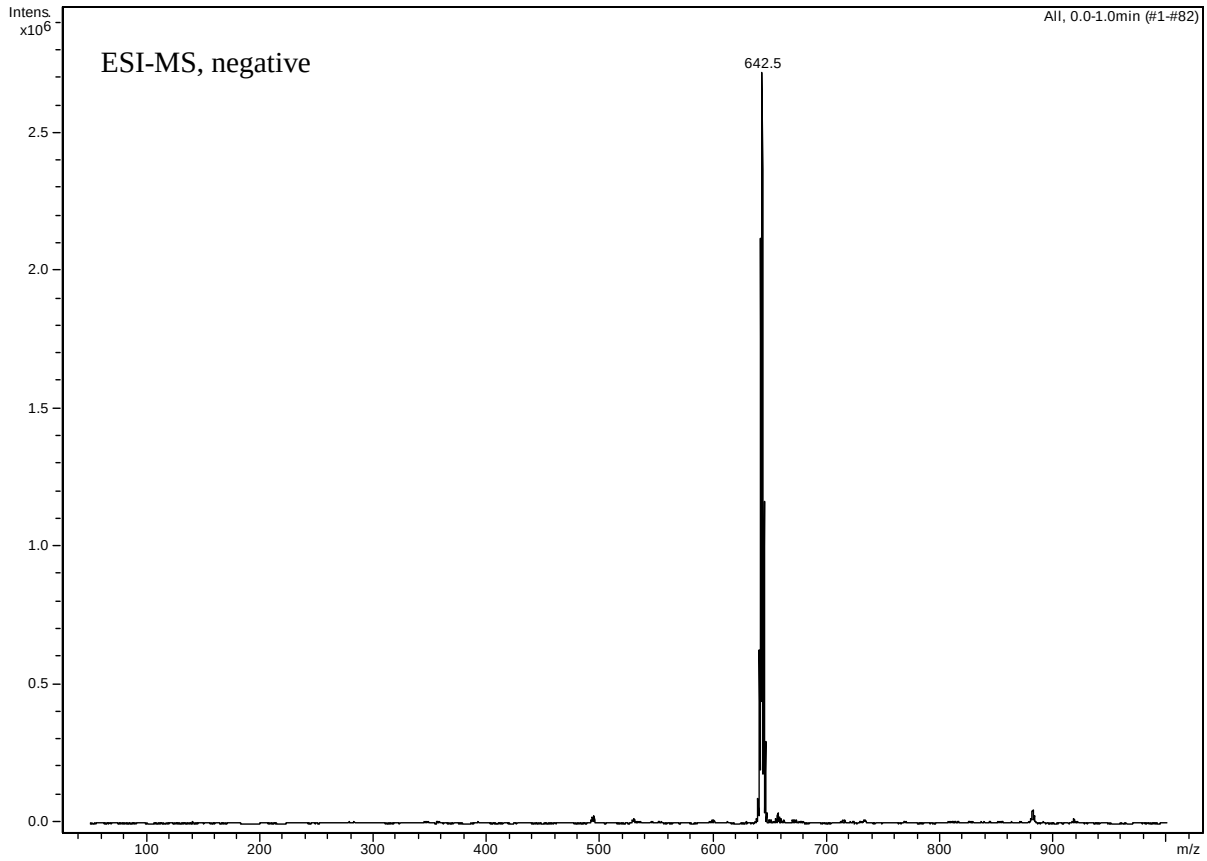

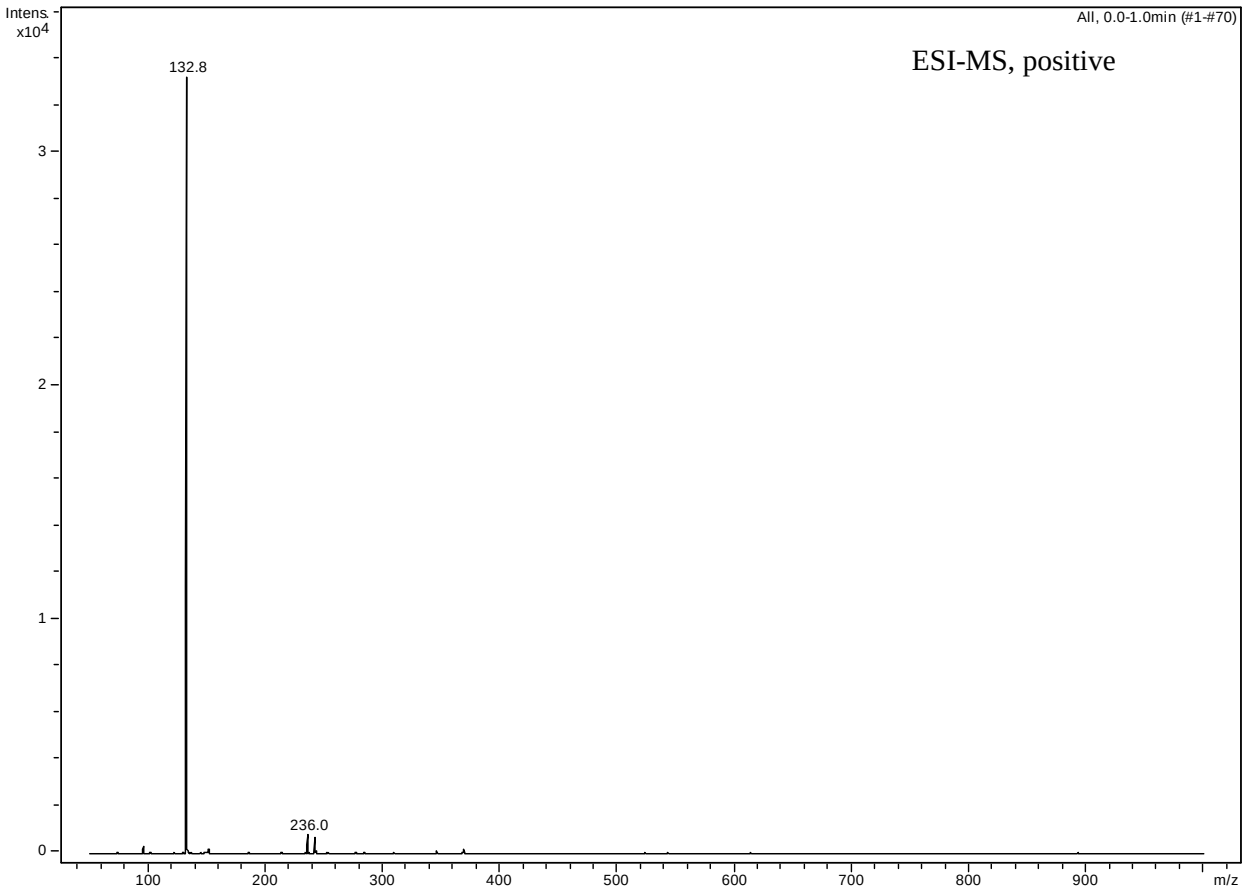
Intens.
x10^4
All, 0.0-1.0min (#1-#70)
ESI-MS, positive
132.8
236.0
m/z

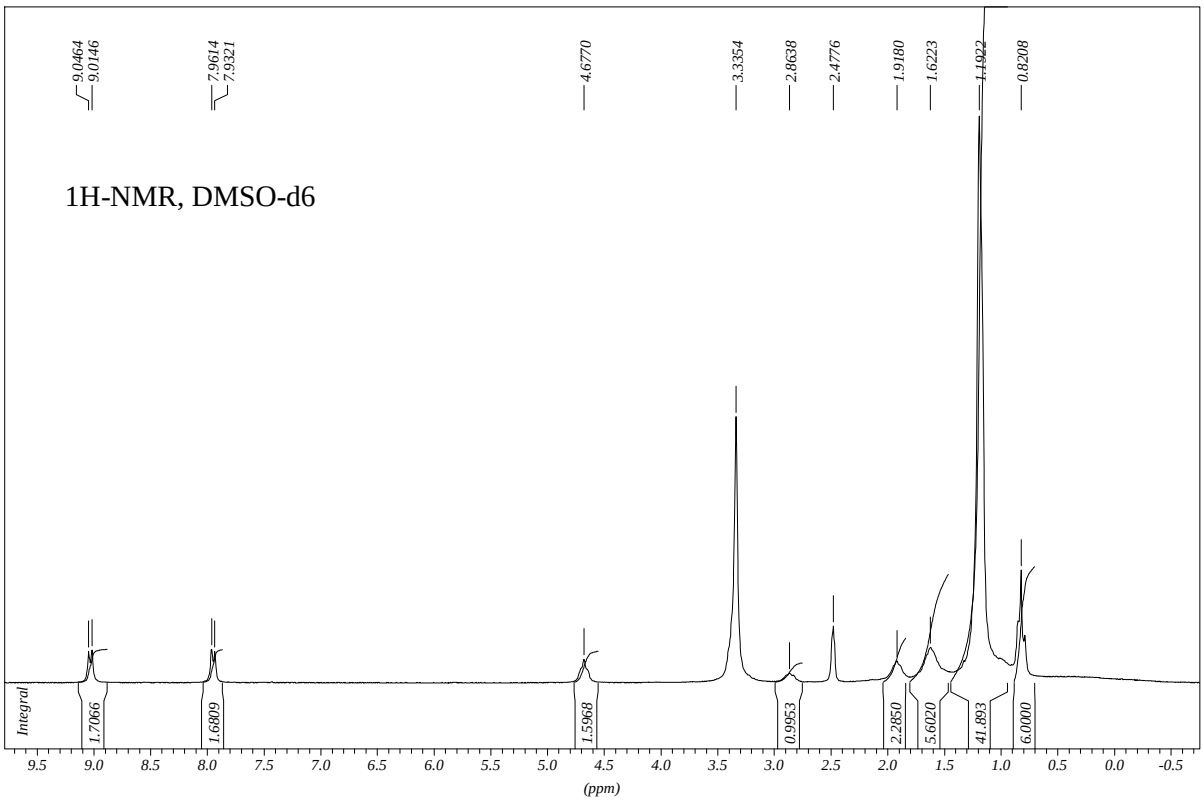
1H-NMR, DMSO-d6
9.0464
9.0146
7.9614
7.9321
4.6770
3.3354
2.8638
2.4776
1.9180
1.6223
1.1922
0.8208
Integral
1.7066
1.6809
1.5968
0.9953
2.2850
5.6020
41.893
6.0000
(ppm)

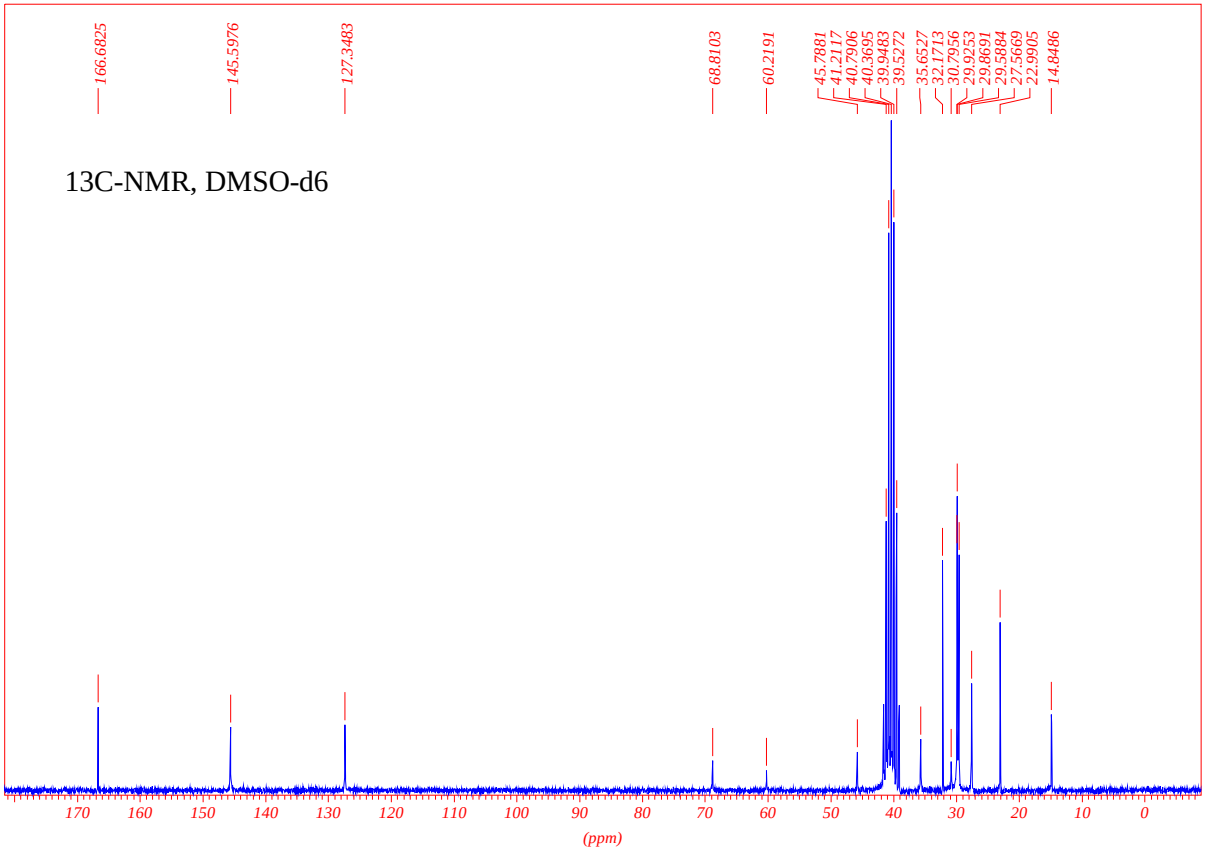
166.6825
145.5976
127.3483
68.8103
60.2191
45.7881
41.2117
40.7906
40.3695
39.9483
39.5272
35.6527
32.1713
30.7956
29.9253
29.8691
29.5884
27.5669
22.9905
14.8486
13C-NMR, DMSO-d6
170 160 150 140 130 120 110 100 90 80 70 60 50 40 30 20 10 0
(ppm)

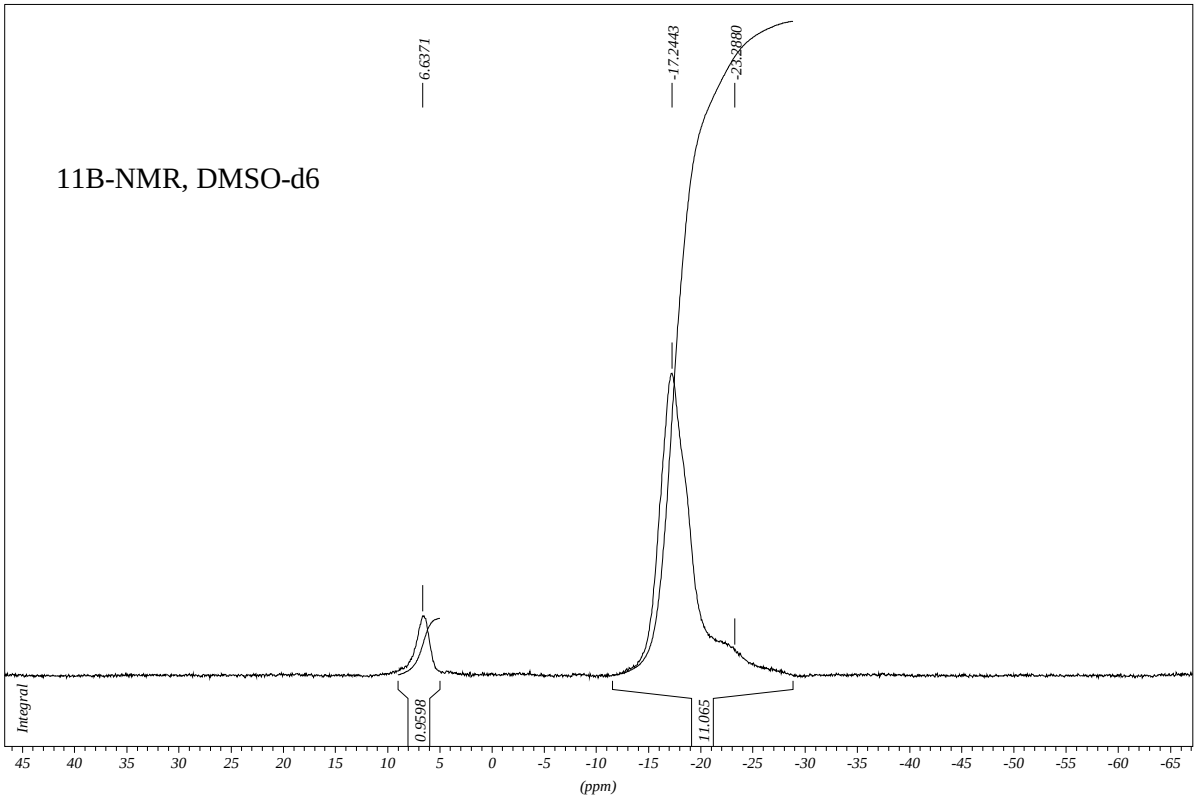
6.6371
-17.2443
-23.2880
11B-NMR, DMSO-d6
Integral
0.9598
11.065
45 40 35 30 25 20 15 10 5 0 -5 -10 -15 -20 -25 -30 -35 -40 -45 -50 -55 -60 -65
(ppm)

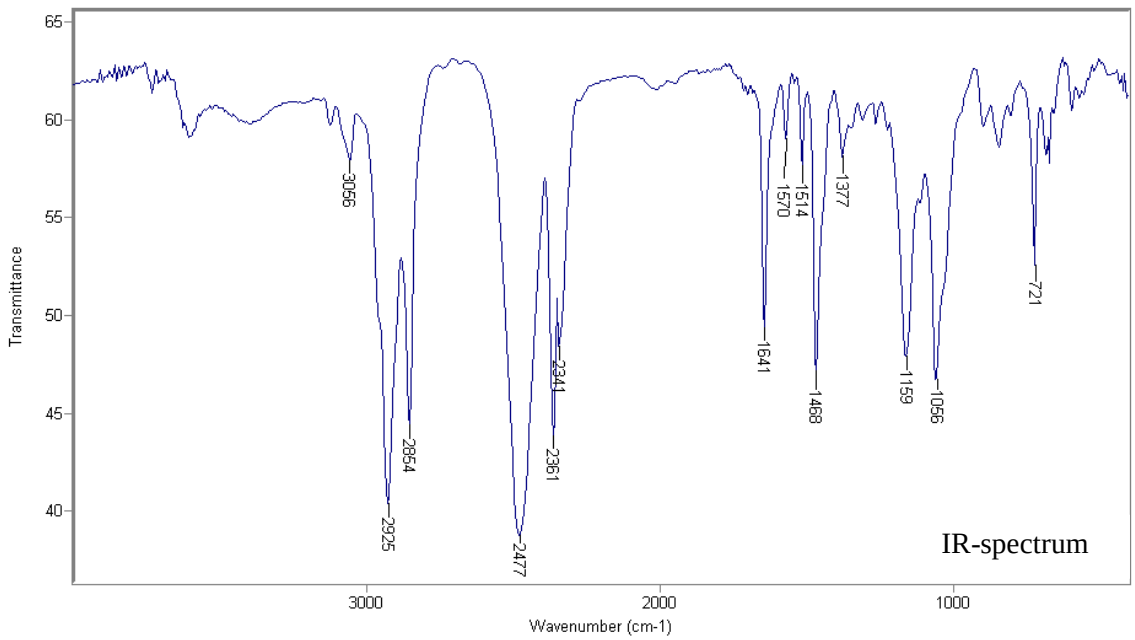

Transmittance / Wavenumber (cm-1)

File #1 : THF-SAINT 12

Bio-Rad FTS

Z-Zoom SCROLL

20.11.08 15:15 Res=8cm-1

4-(Bisdodecylmethyl)pyridinio-N-ethoxy-ethoxy-undecahydro-closo-dodecaborate (-1), cesium salt (Dioxan-SAINT-12).

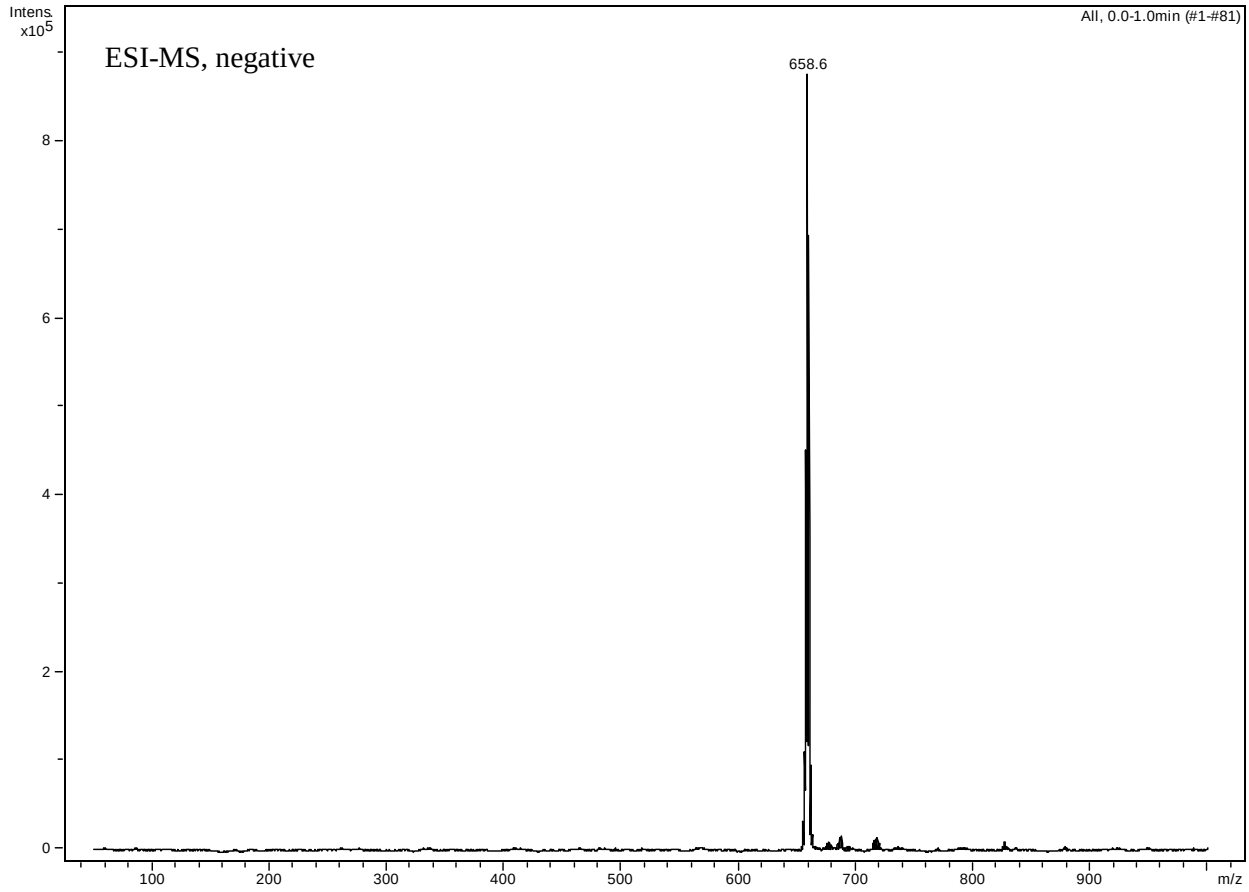

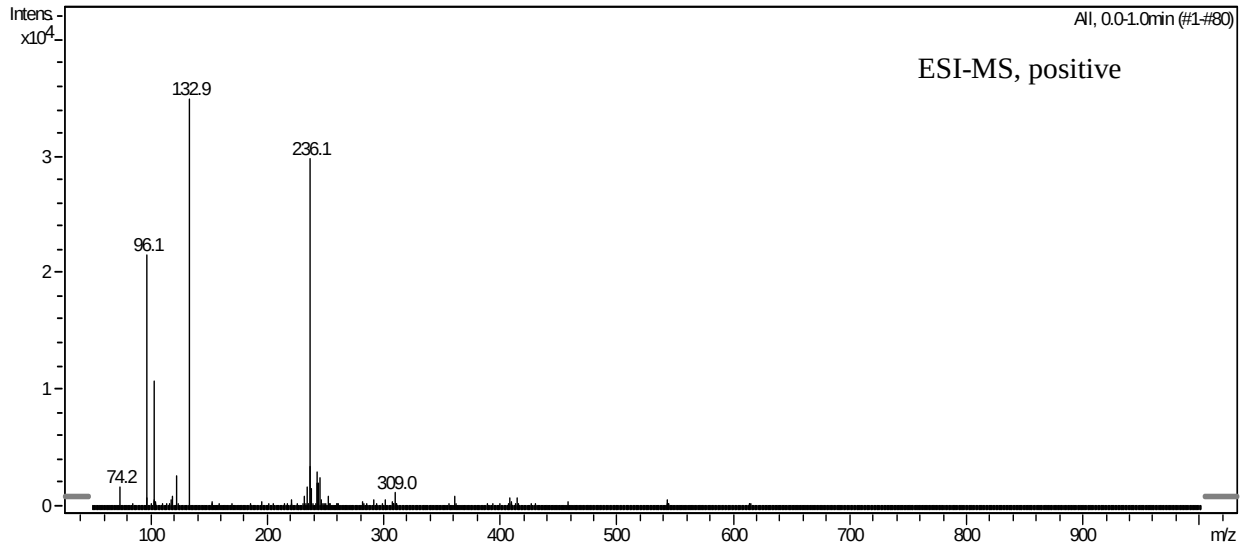

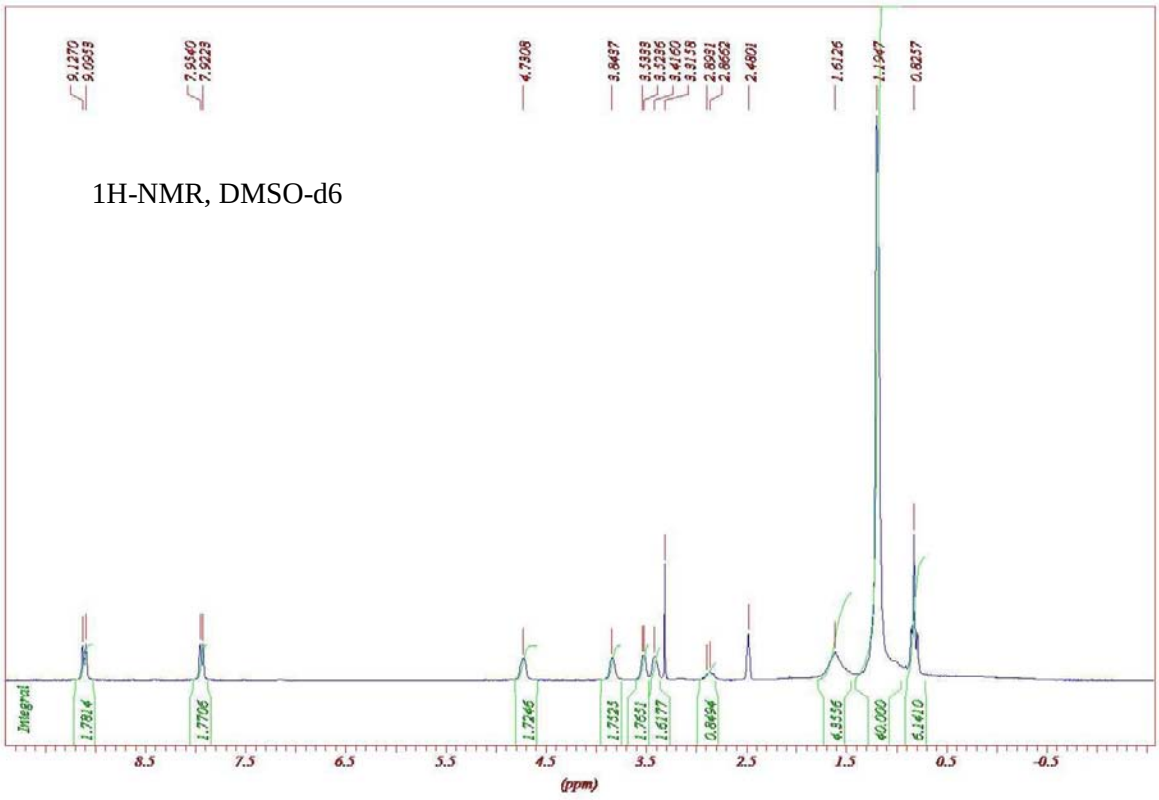

1H-NMR, DMSO-d6

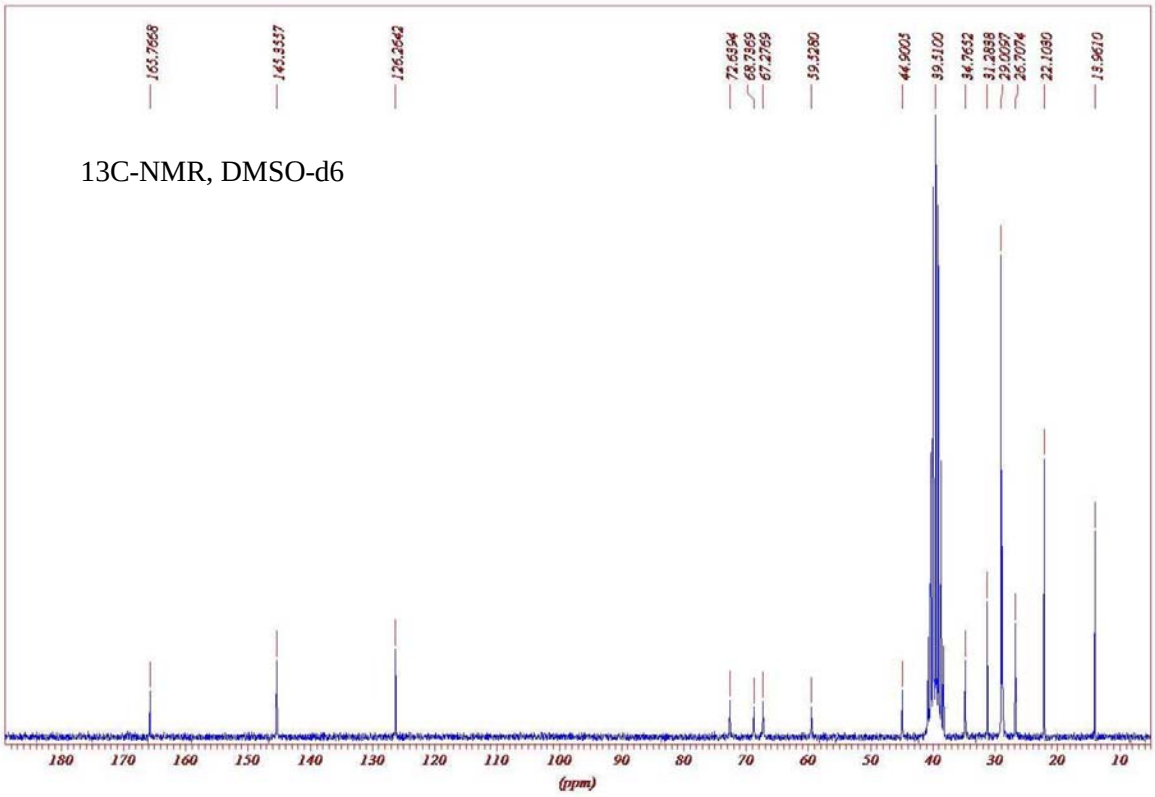

13C-NMR, DMSO-d6

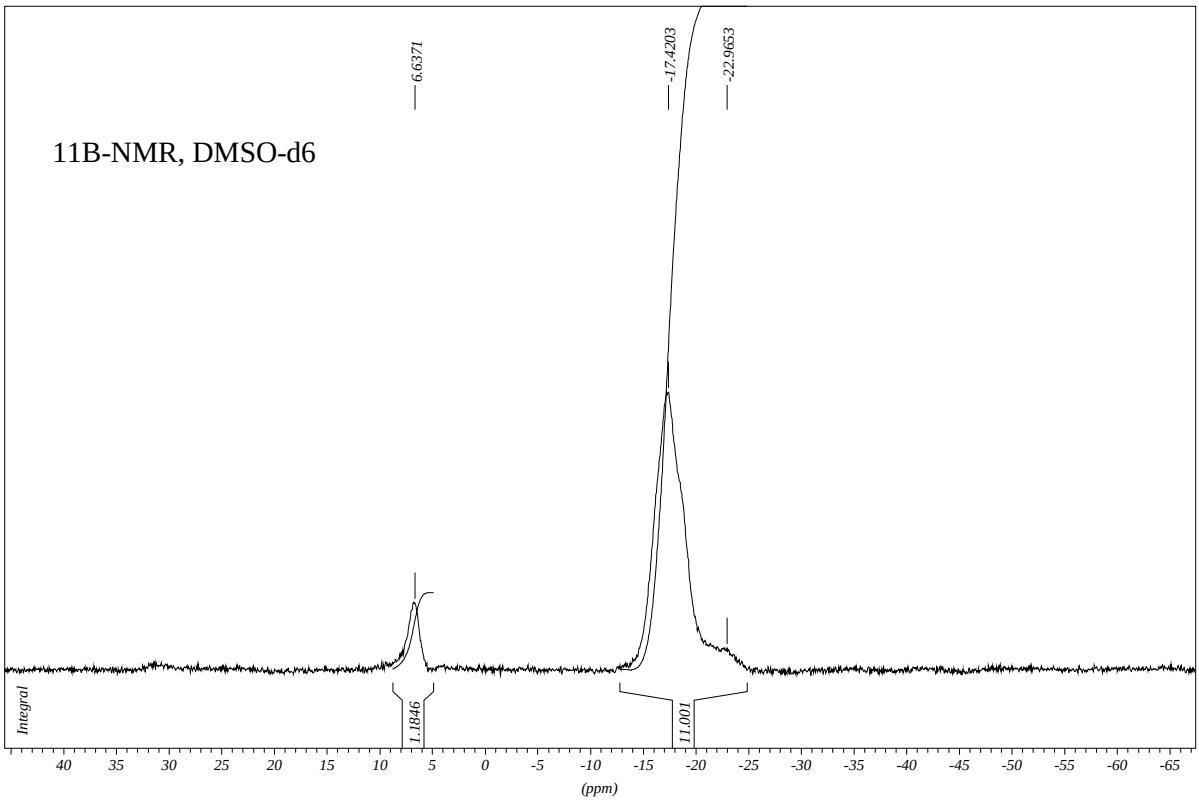

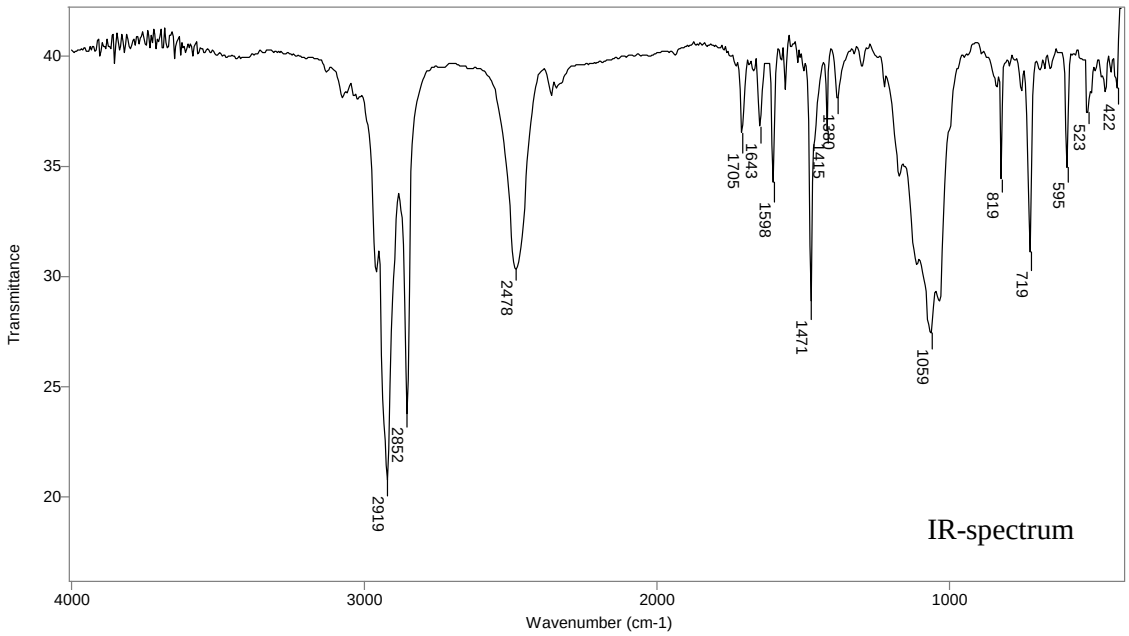

Transmittance / Wavenumber (cm-1)

File # 1 : DIOXANSAINT12

Bio-Rad FTS

X-Zoom SCROLL

05.01.09 17:04 Res=8cm-1

4-(Bisdodecylmethyl)pyridinio-N-pentoxy-undecahydro-closo-dodecaborate (-1), cesium salt (Pyran-SAINT-12).

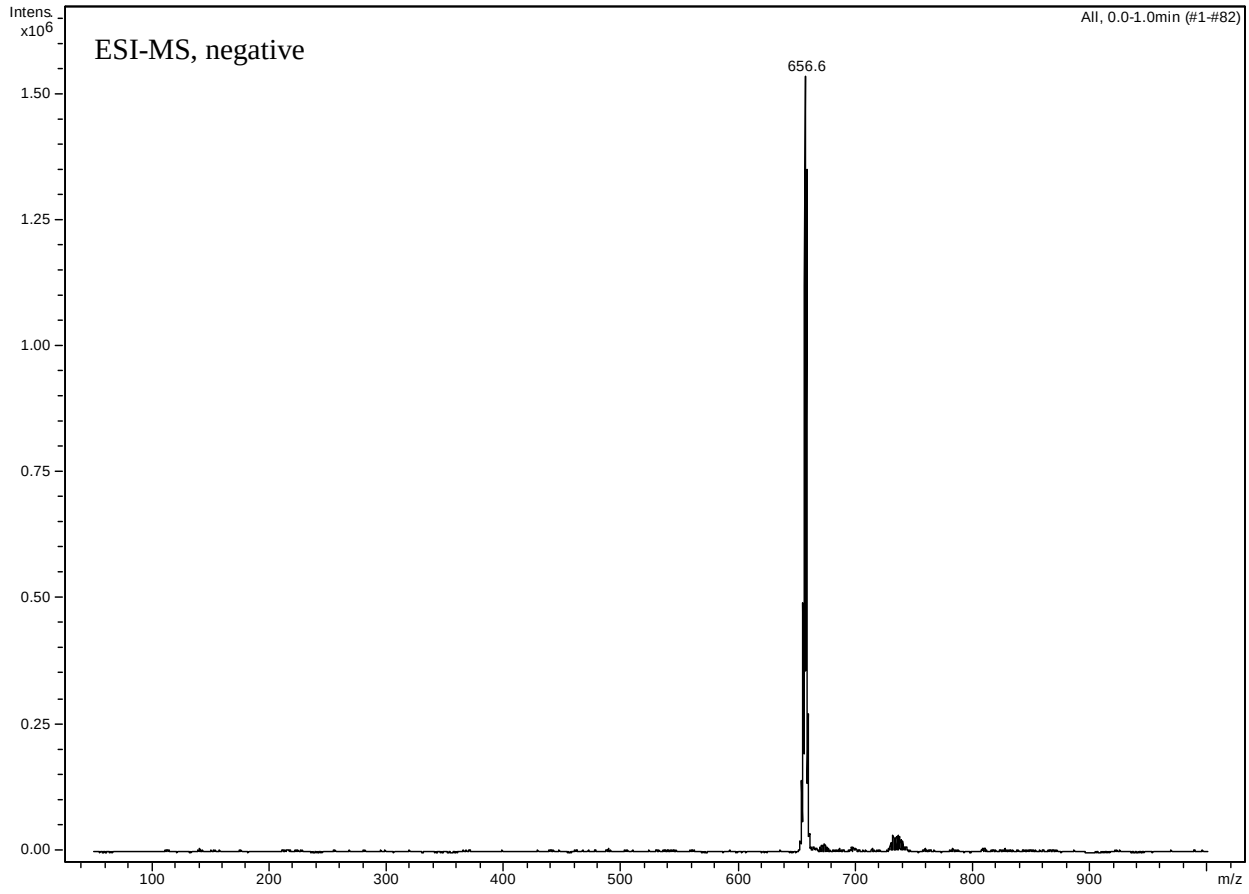

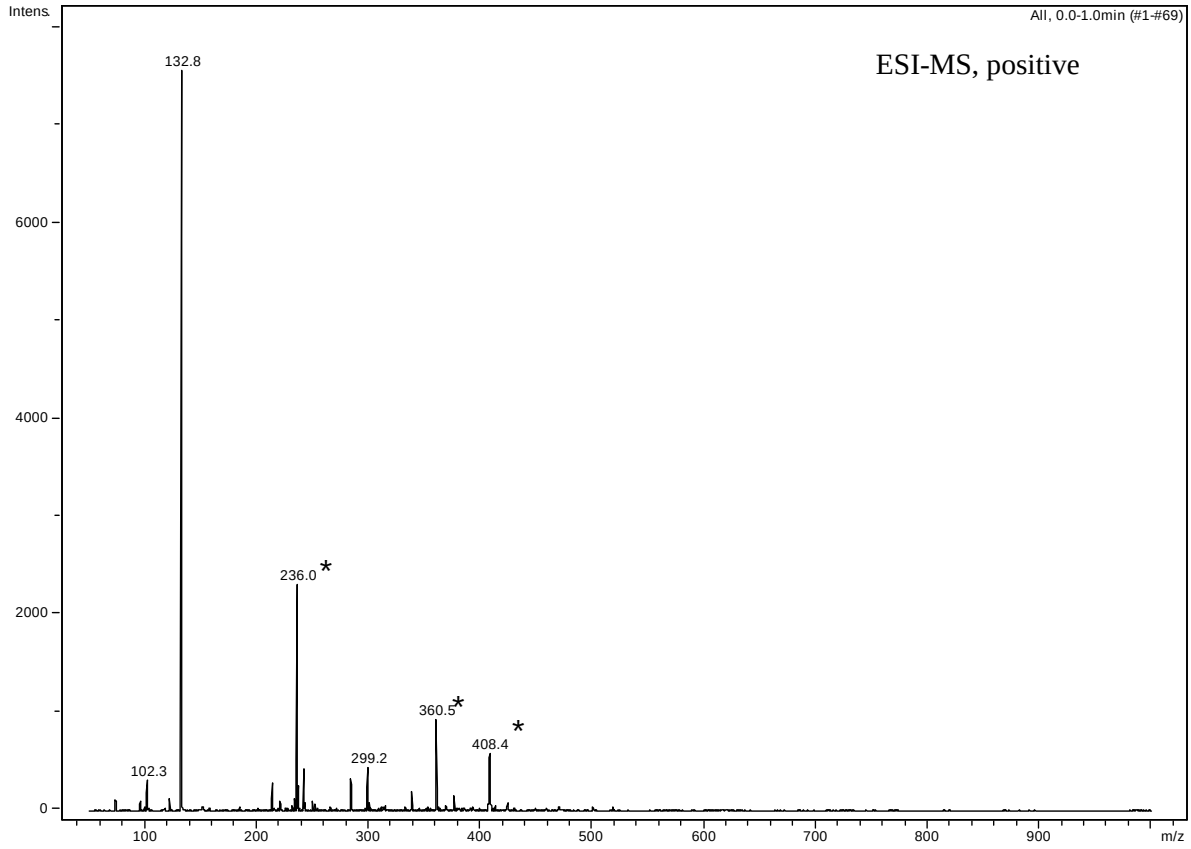

* Impurities in the MS machine.

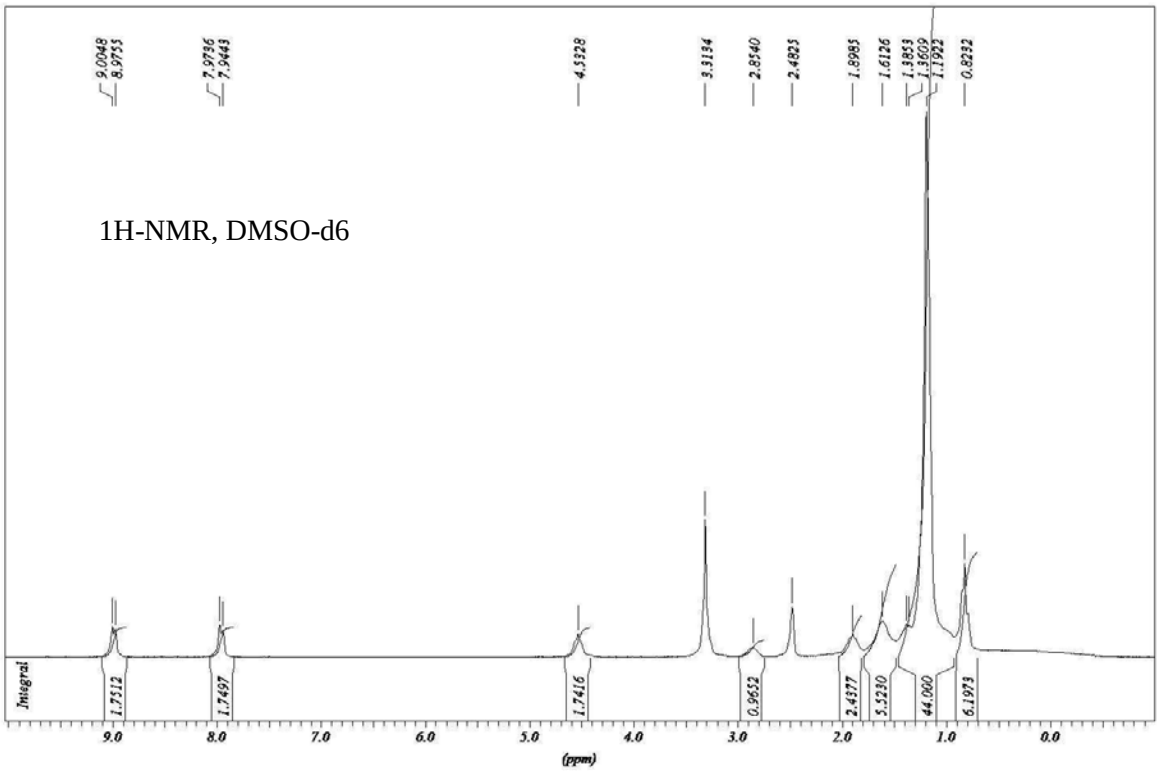

1H-NMR, DMSO-d6

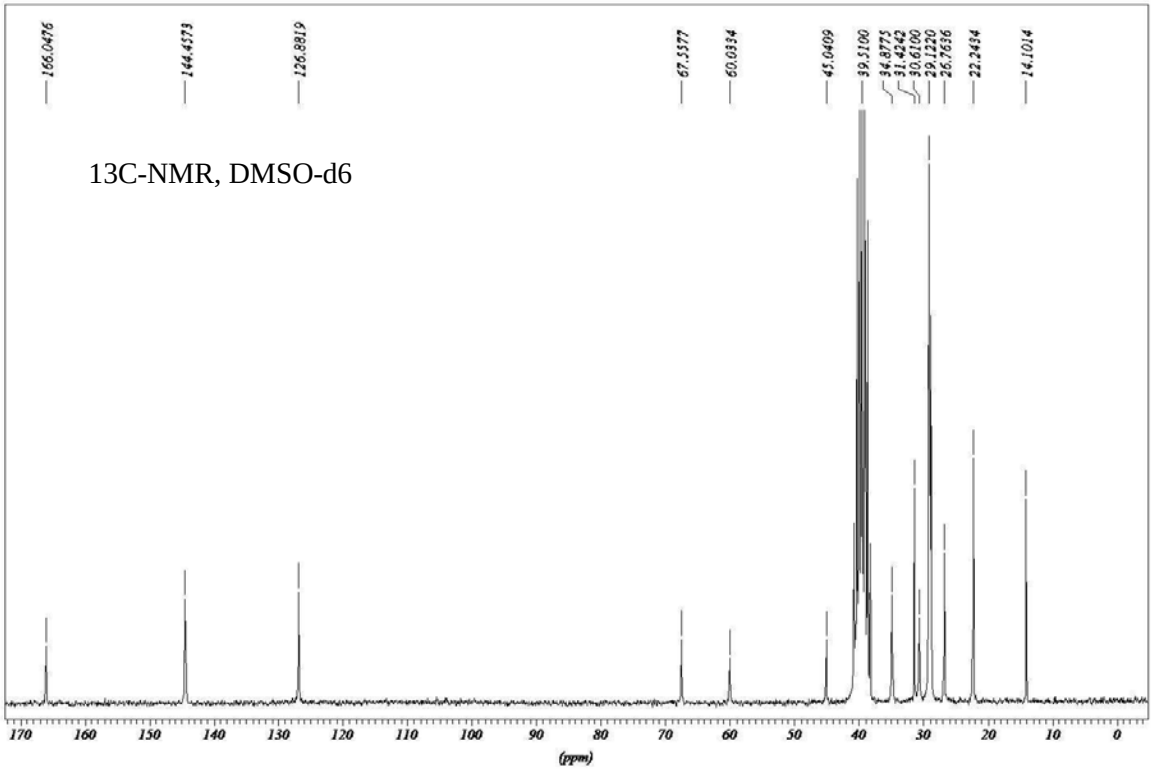

13C-NMR, DMSO-d6

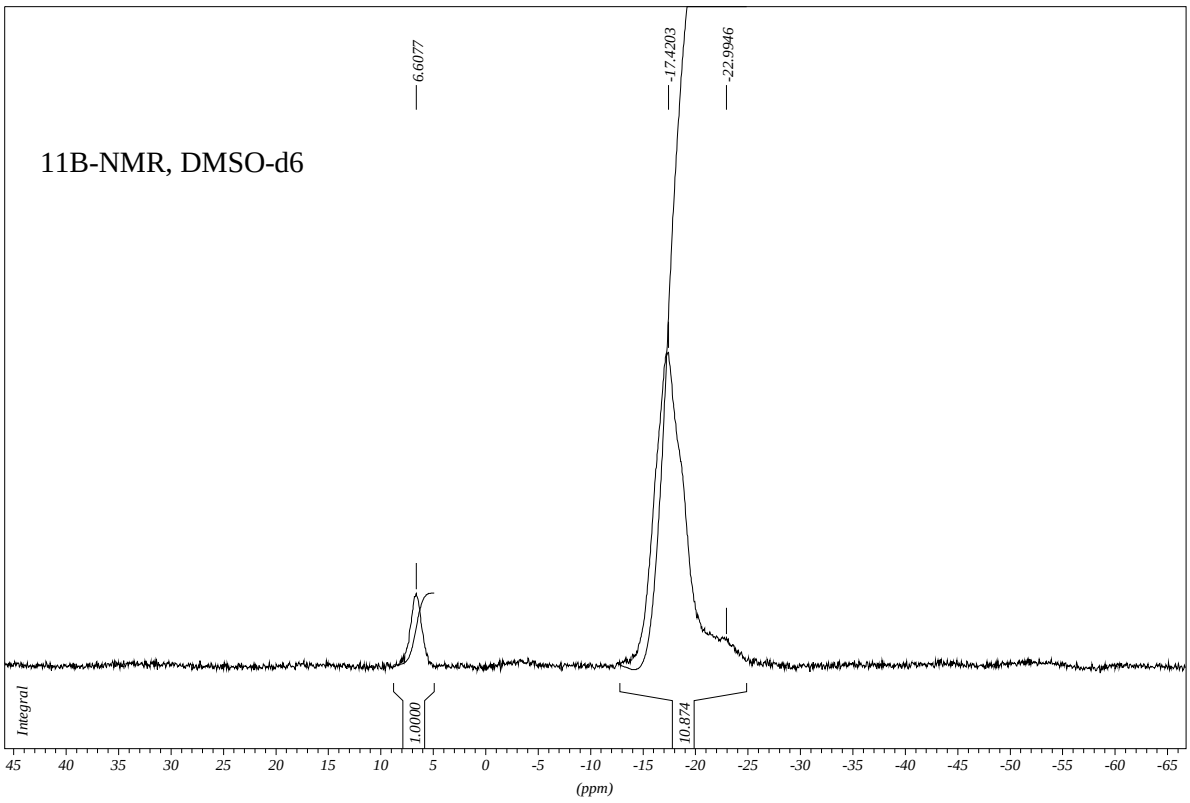

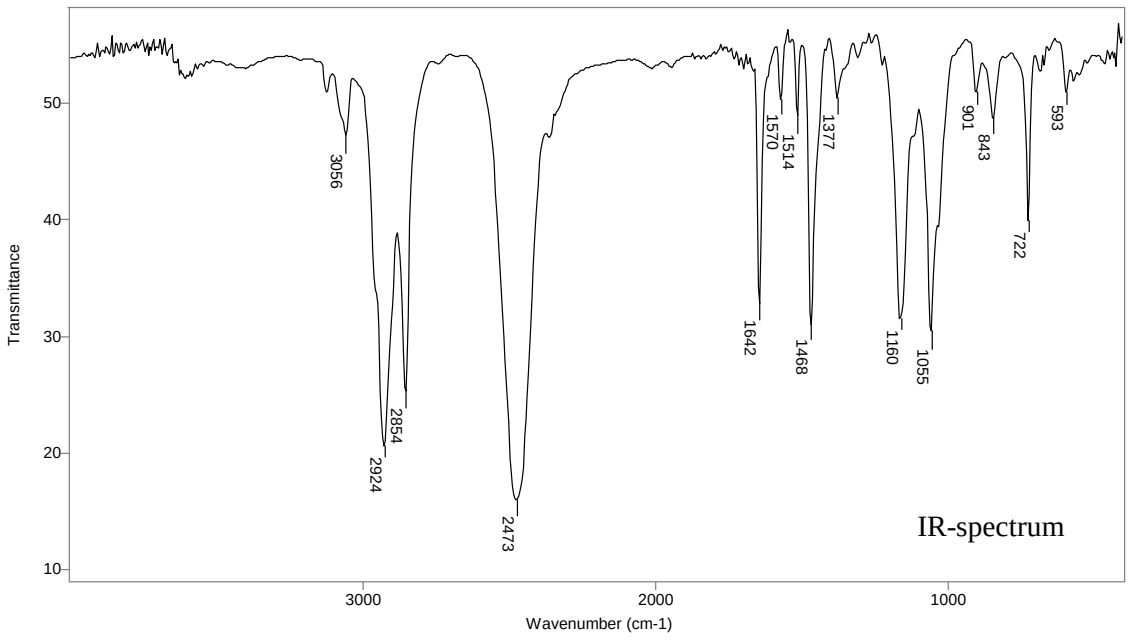

Transmittance / Wavenumber (cm-1)

File # 1 : THPSAINT12

Bio-Rad FTS

X-Zoom SCROLL

05.01.09 17:34 Res=8cm-1

4-(Bistetradecylmethyl)pyridinio-N-butoxy-undecahydro-closo-dodecaborate (-1), cesium salt (THF-SAINT-14).

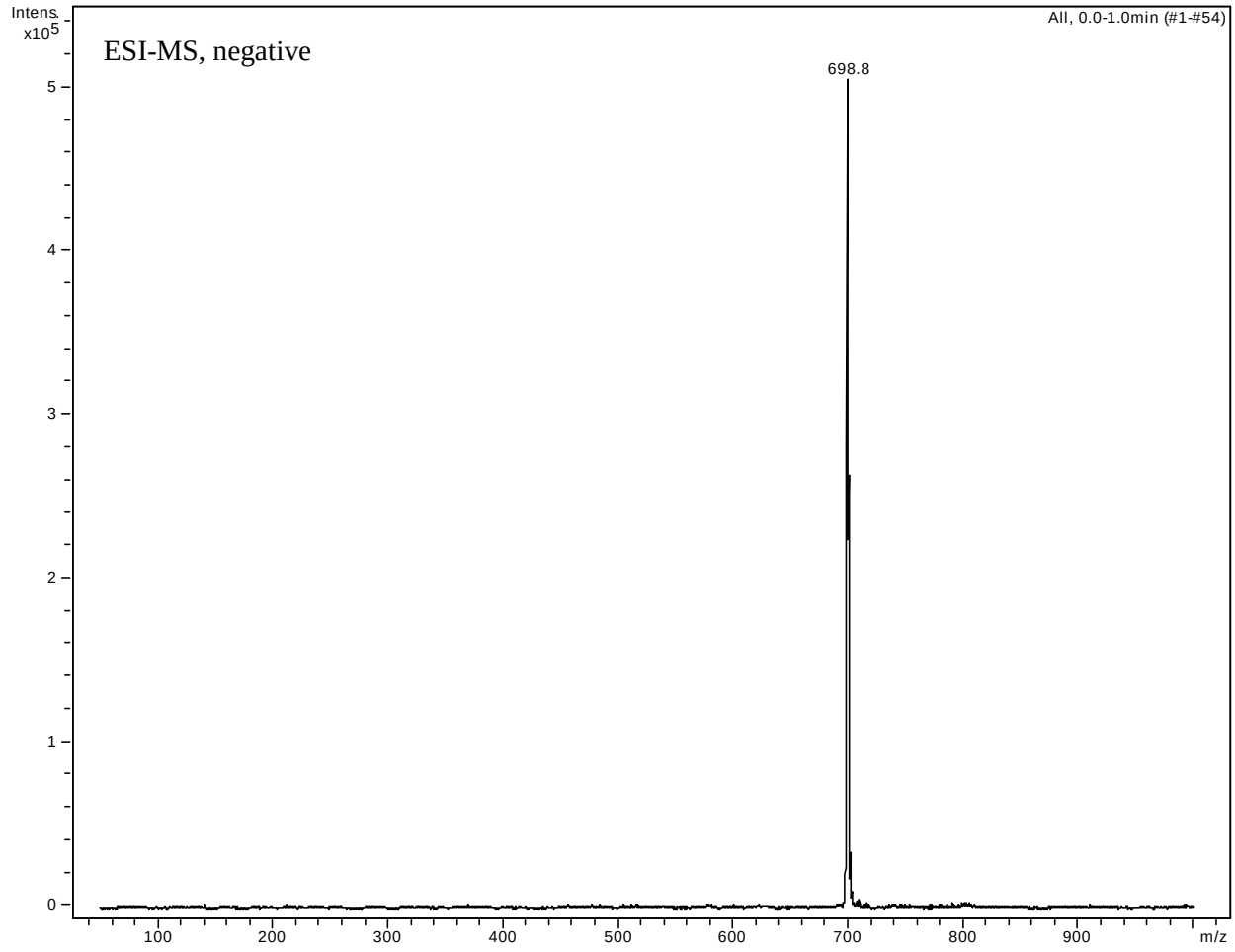

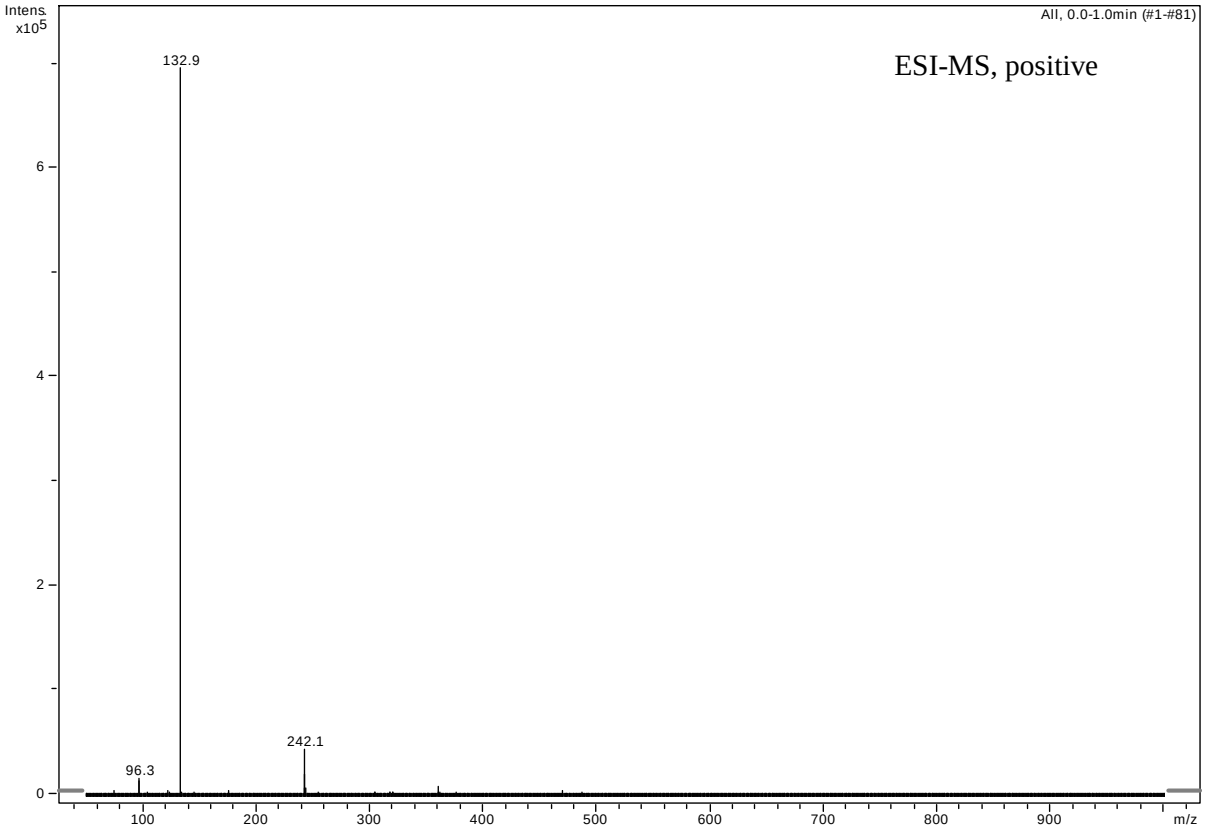
Intens.
x10^5
All, 0.0-1.0min (#1-#81)
ESI-MS, positive
132.9
242.1
96.3
m/z

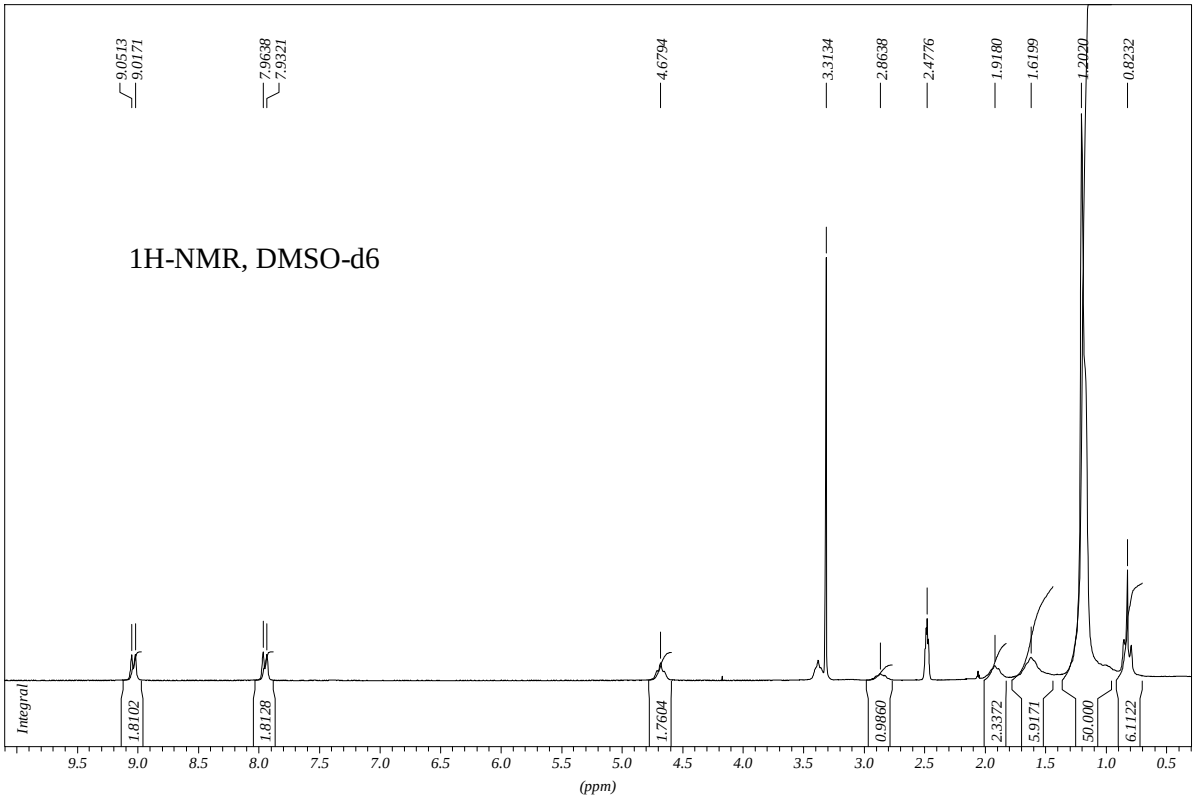
1H-NMR, DMSO-d6
9.0513
9.0171
7.9638
7.9321
4.6794
3.3134
2.8638
2.4776
1.9180
1.6199
1.2020
0.8232
Integral
1.8102
1.8128
1.7604
0.9860
2.3372
5.9171
50.000
6.1122
(ppm)

13C-NMR, DMSO-d6

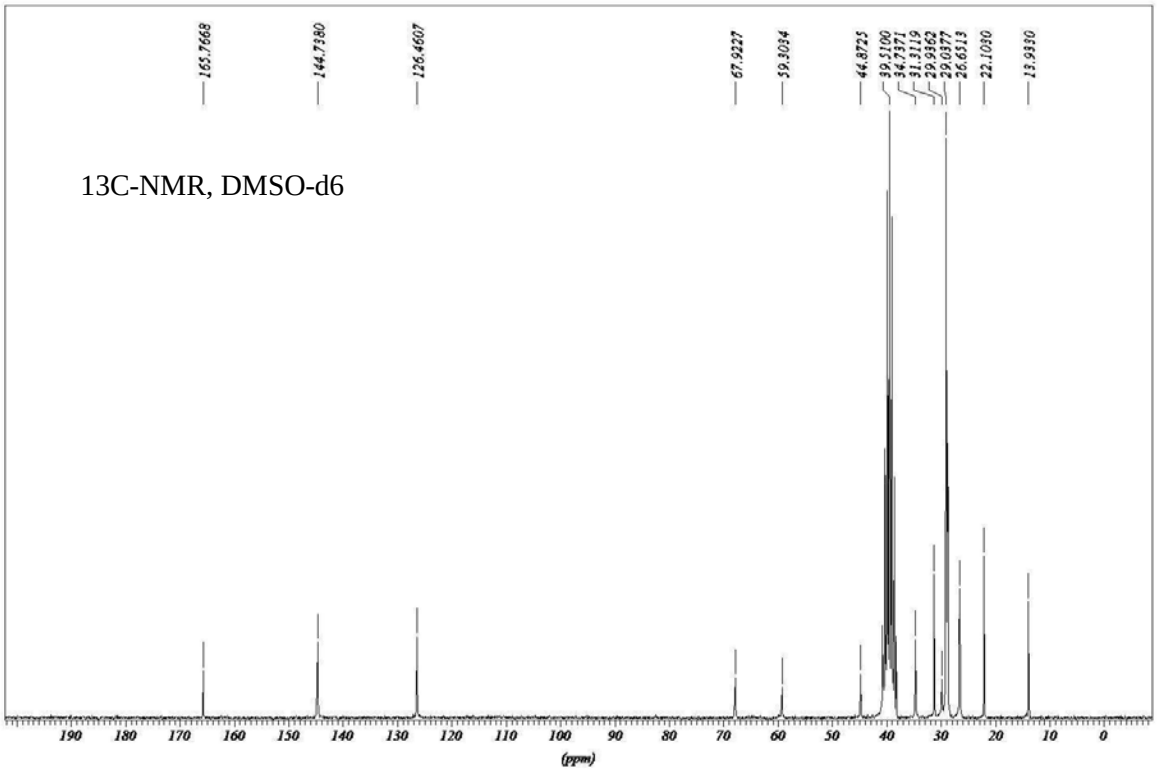

11B-NMR, DMSO-d6

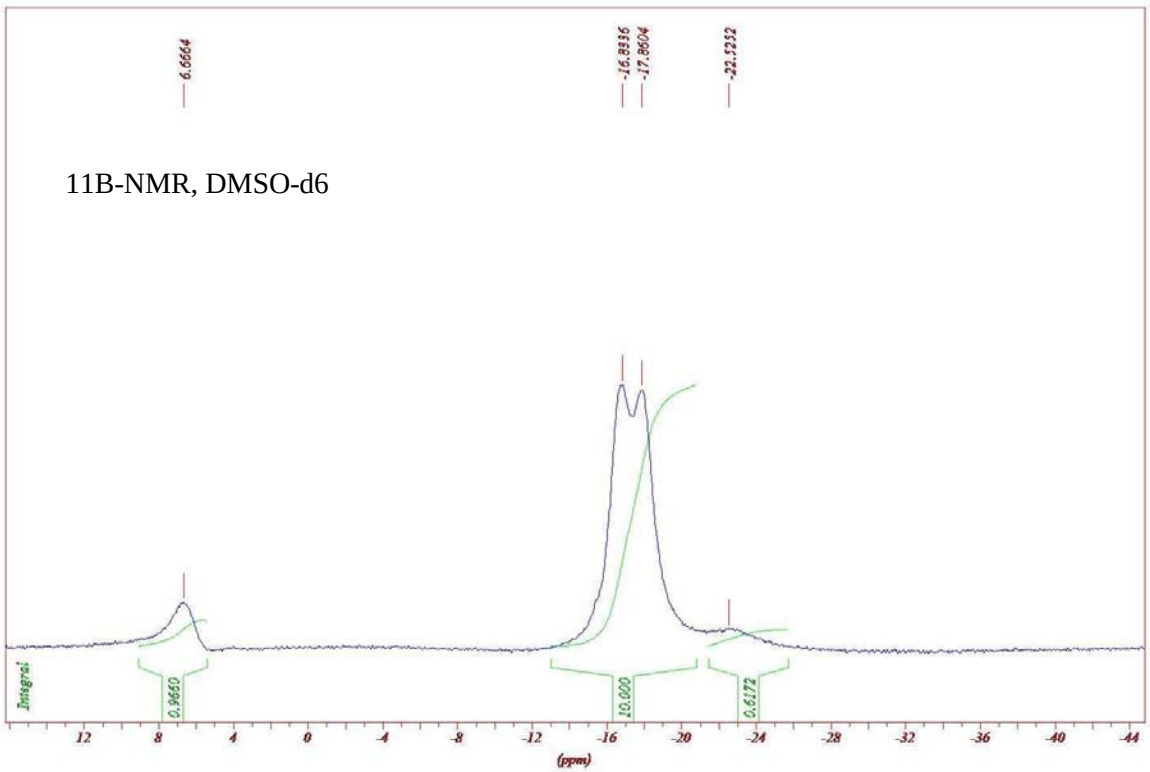

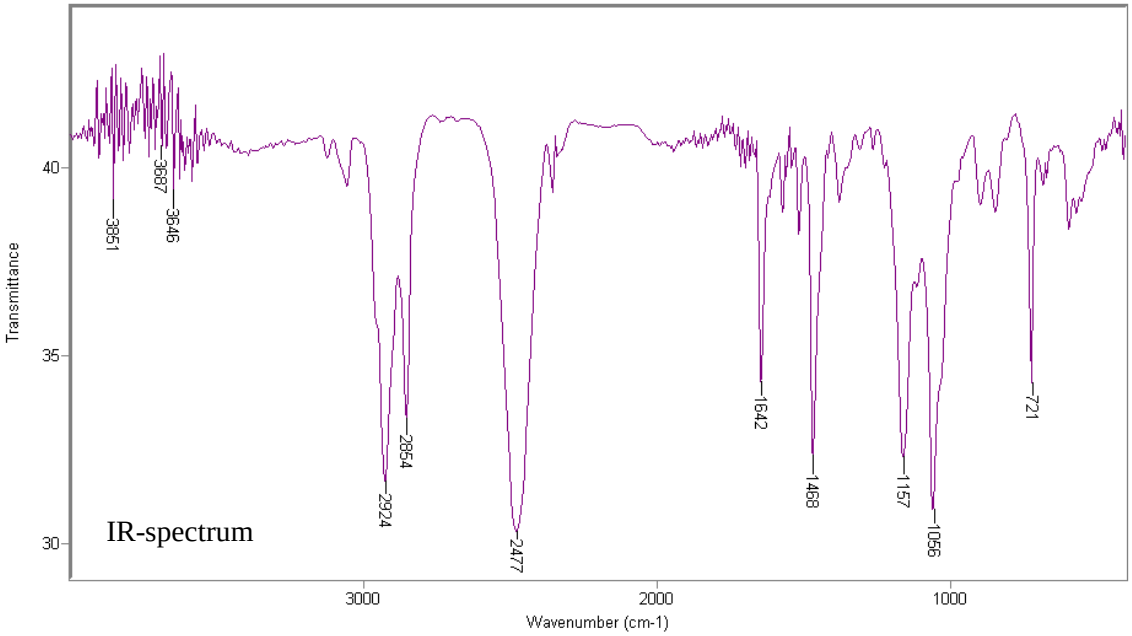

Transmittance / Wavenumber (cm-1)

File #1 : THF-SAINT 14

Bio-Rad FTS

Z-Zoom SCROLL

20.11.08 14:46 Res=8cm-1

4-(Bistetradecylmethyl)pyridinio-N-ethoxy-ethoxy-undecahydro-closo-dodecaborate (-1), cesium salt (Dioxan-SAINT-14).

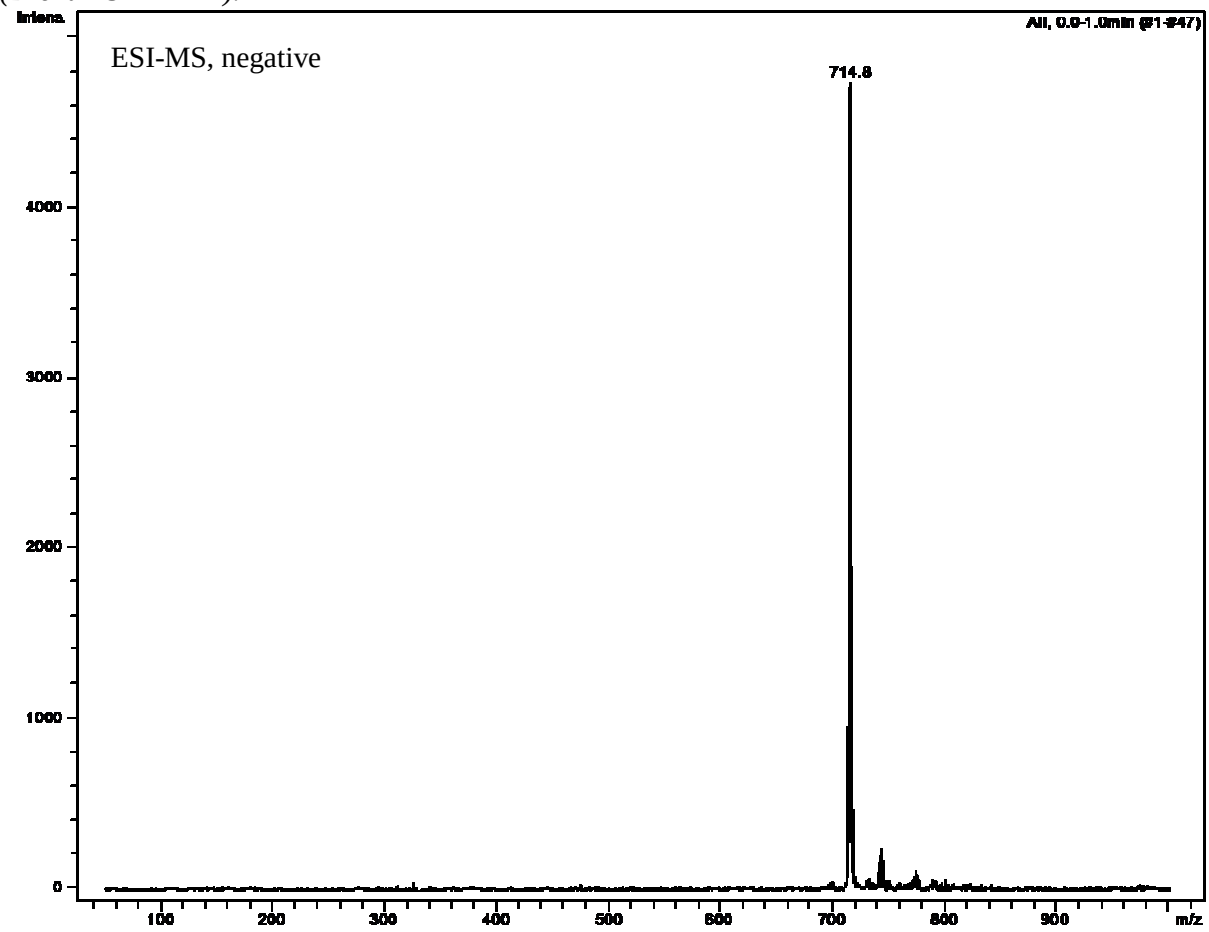

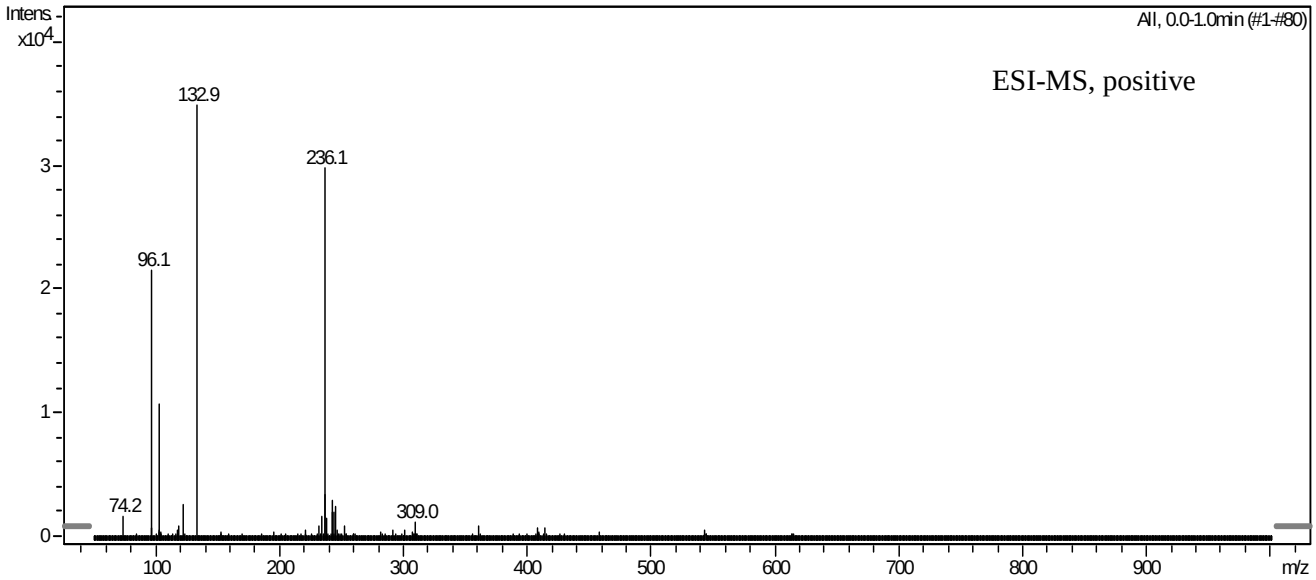

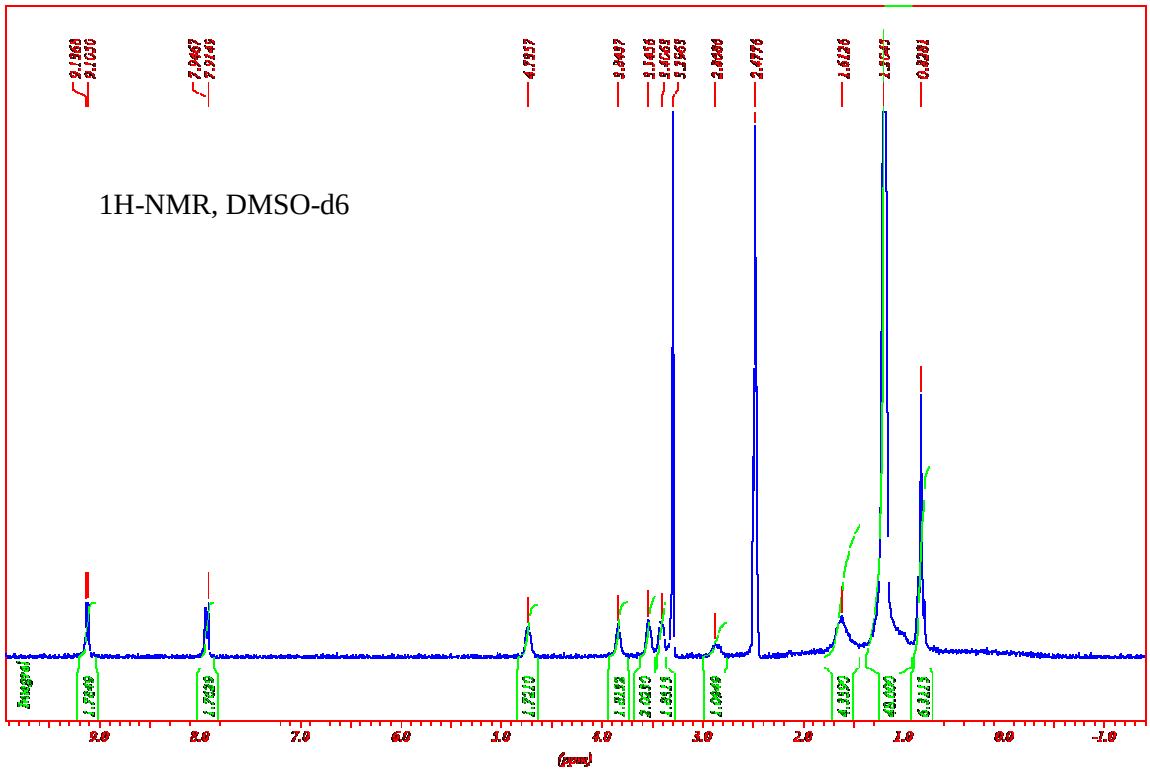
1H-NMR, DMSO-d6

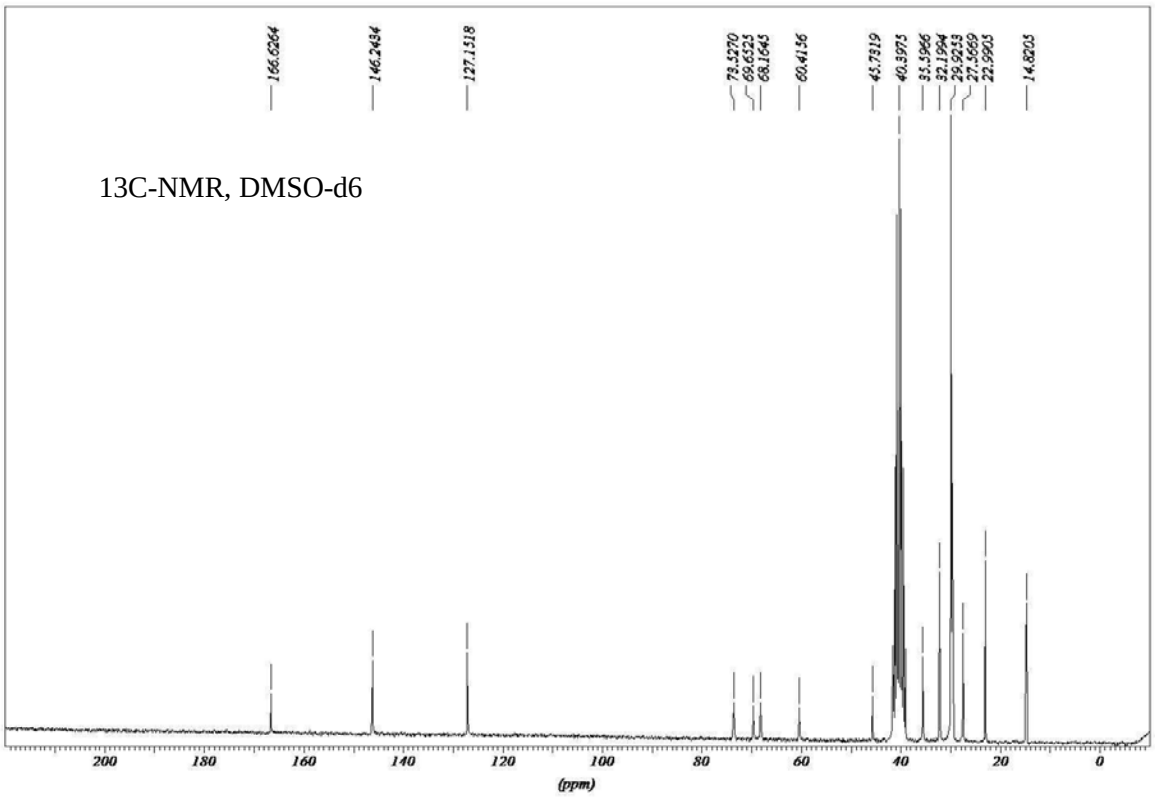
13C-NMR, DMSO-d6

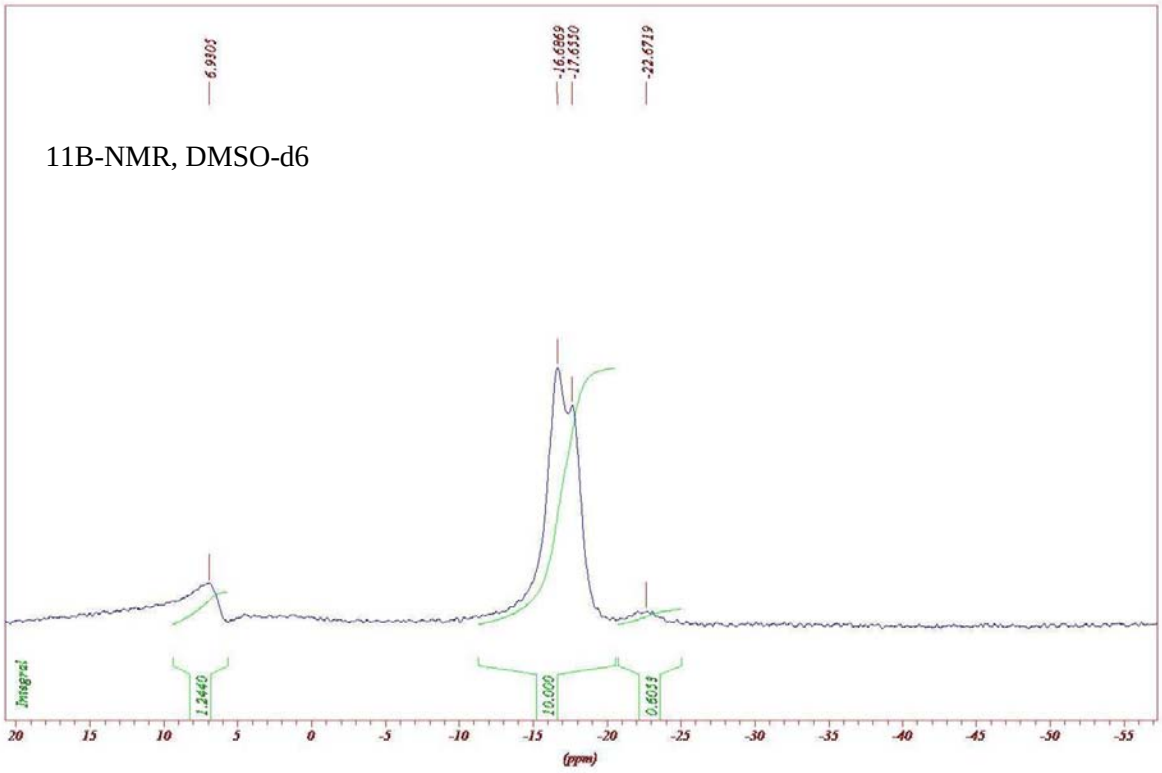

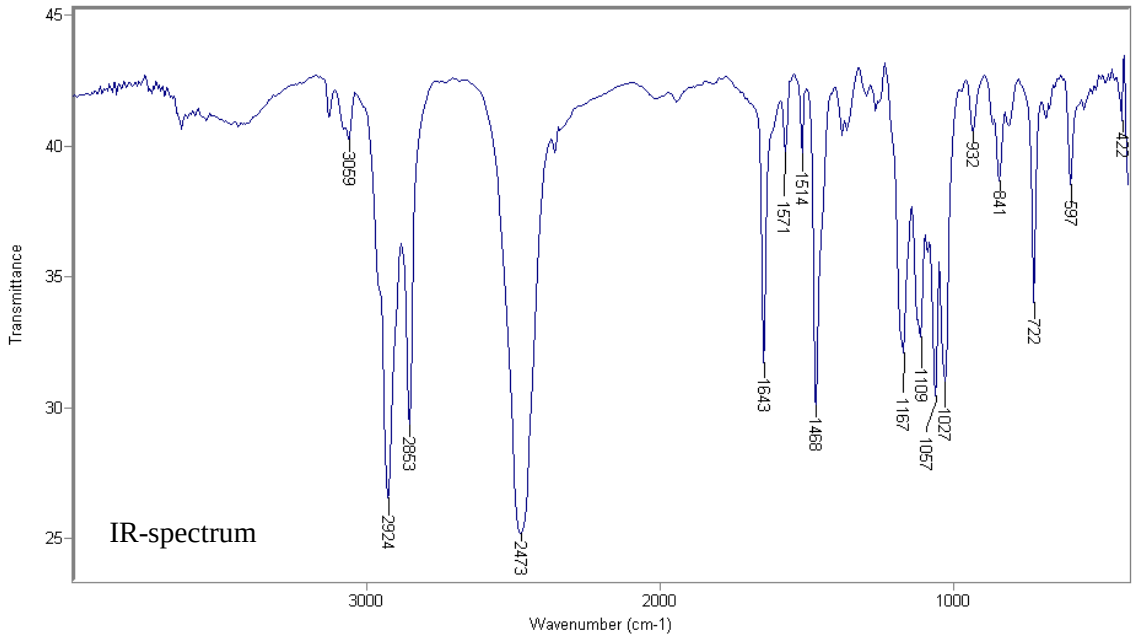

Transmittance / Wavenumber (cm-1)

File #1 : DIOXANE-SAINT 14

Bio-Rad FTS

Z-Zoom SCROLL

20.11.08 15:48 Res=8cm-1

4-(Bistetradecylmethyl)pyridinio-N-pentoxy-undecahydro-closo-dodecaborate (-1), cesium salt (Pyran-SAINT-14).

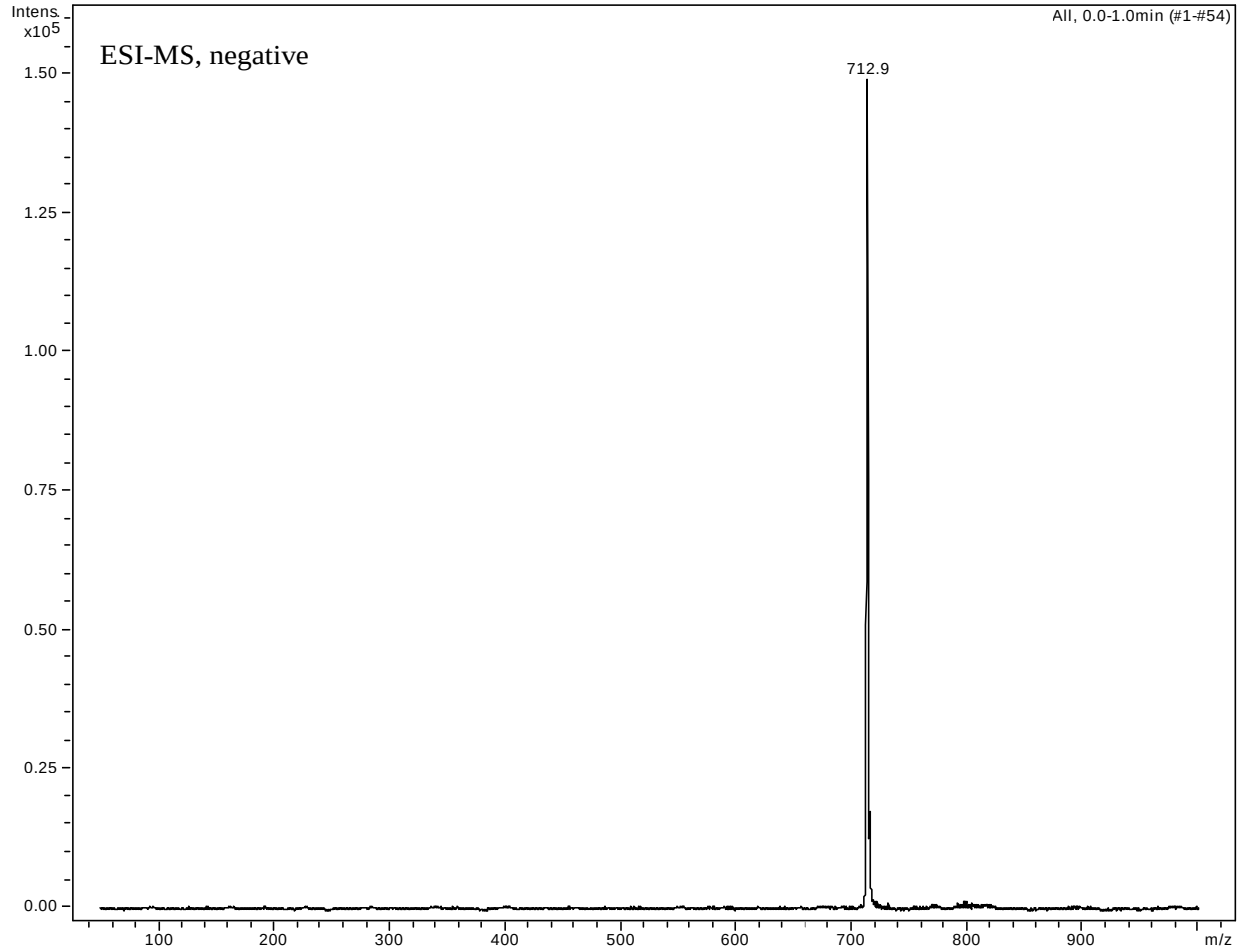

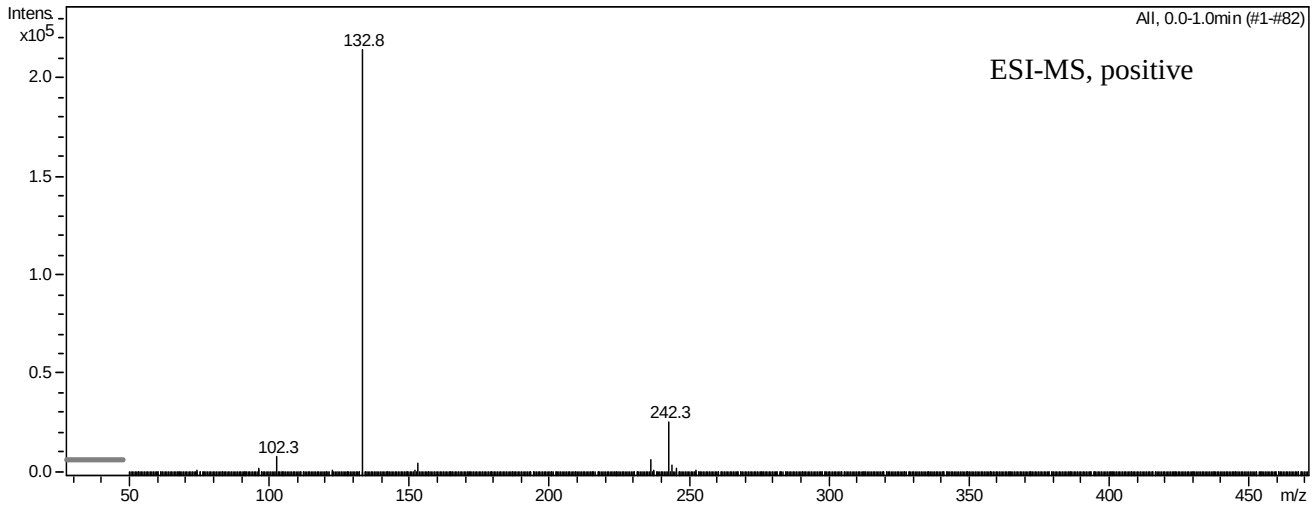

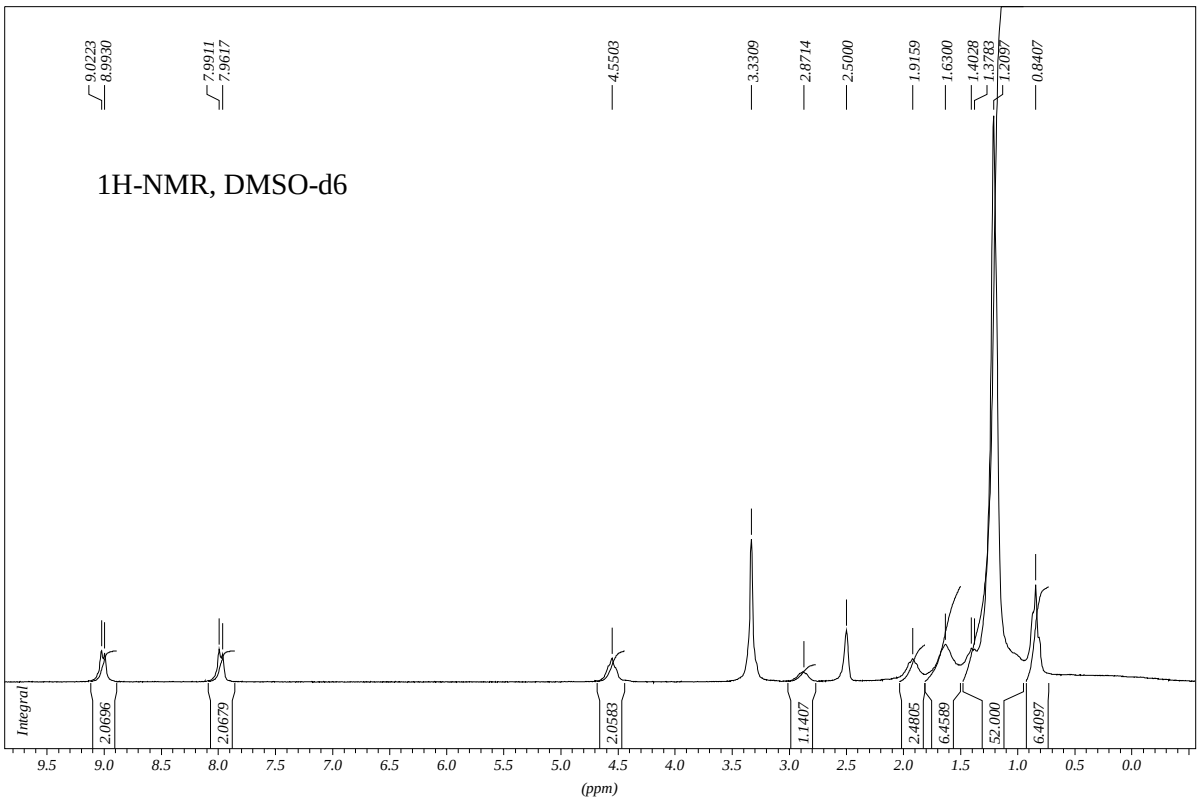
9.0223
8.9930
7.9911
7.9617
4.5503
3.3309
2.8714
2.5000
1.9159
1.6300
1.4028
1.3783
1.2097
0.8407
1H-NMR, DMSO-d6
Integral
2.0696
2.0679
2.0583
1.1407
2.4805
6.4589
52.000
6.4097
9.5 9.0 8.5 8.0 7.5 7.0 6.5 6.0 5.5 5.0 4.5 4.0 3.5 3.0 2.5 2.0 1.5 1.0 0.5 0.0
(ppm)

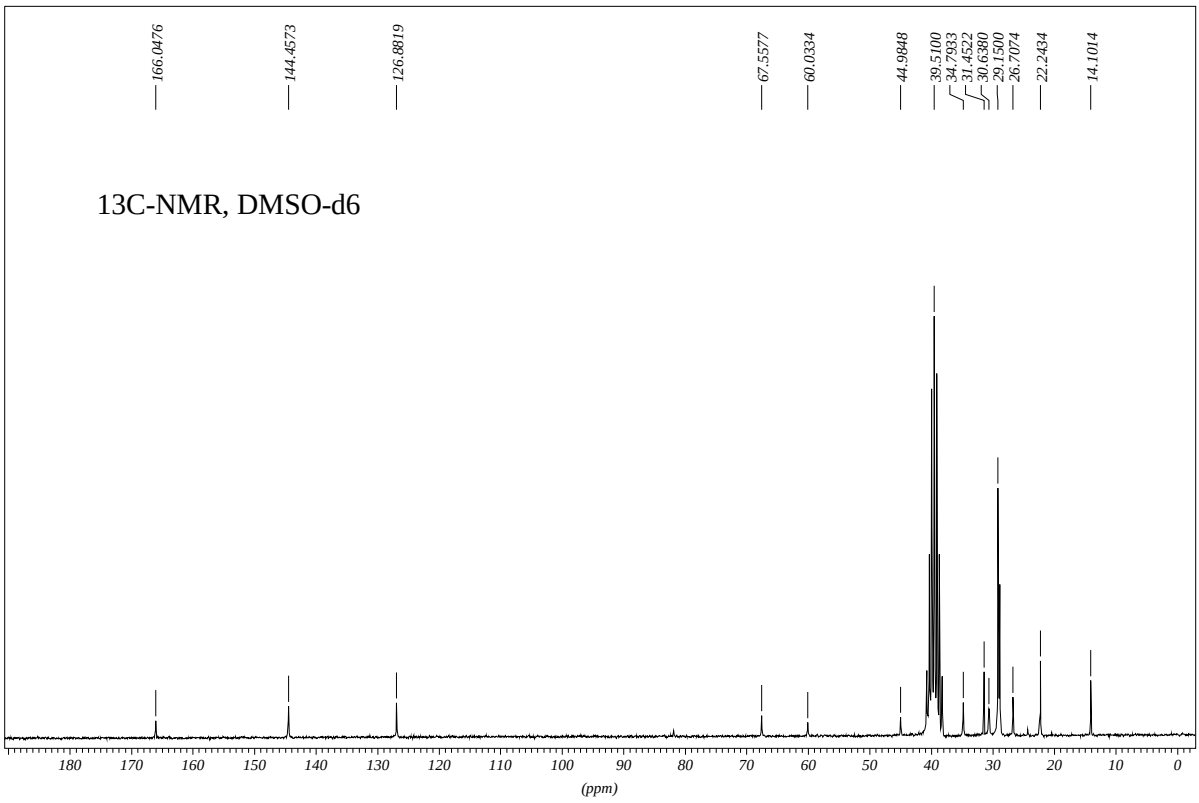
166.0476
144.4573
126.8819
67.5577
60.0334
44.9848
39.5100
34.7933
31.4522
30.6380
29.1500
26.7074
22.2434
14.1014
13C-NMR, DMSO-d6
180 170 160 150 140 130 120 110 100 90 80 70 60 50 40 30 20 10 0
(ppm)

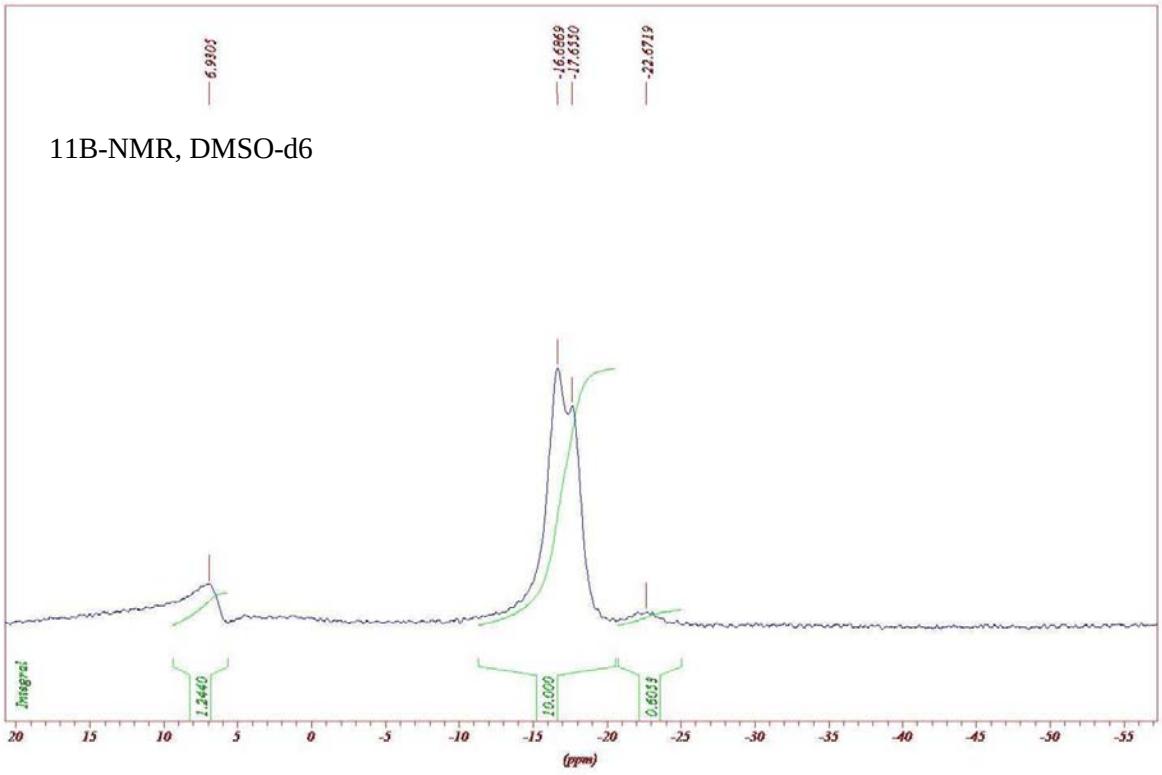
6.9303
-16.6869
-17.6550
-22.6719
11B-NMR, DMSO-d6
Integral
1.2440
10.000
0.6053
20 15 10 5 0 -5 -10 -15 -20 -25 -30 -35 -40 -45 -50 -55
(ppm)

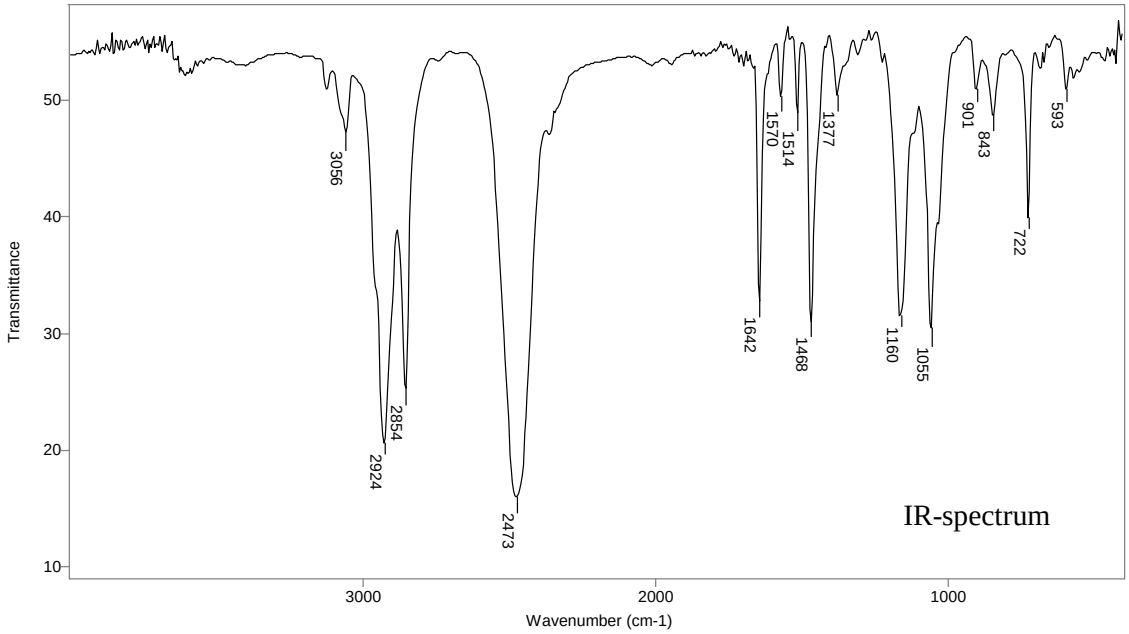

Transmittance / Wavenumber (cm-1)

X-Zoom SCROLL

File # 1 : THPSAINT12

05.01.09 17:34 Res=8cm-1

Bio-Rad FTS

4-(Bishexadecylmethyl)pyridinio-N-butoxy-undecahydro-closo-dodecaborate (-1), cesium salt (THF-SAINT-16).

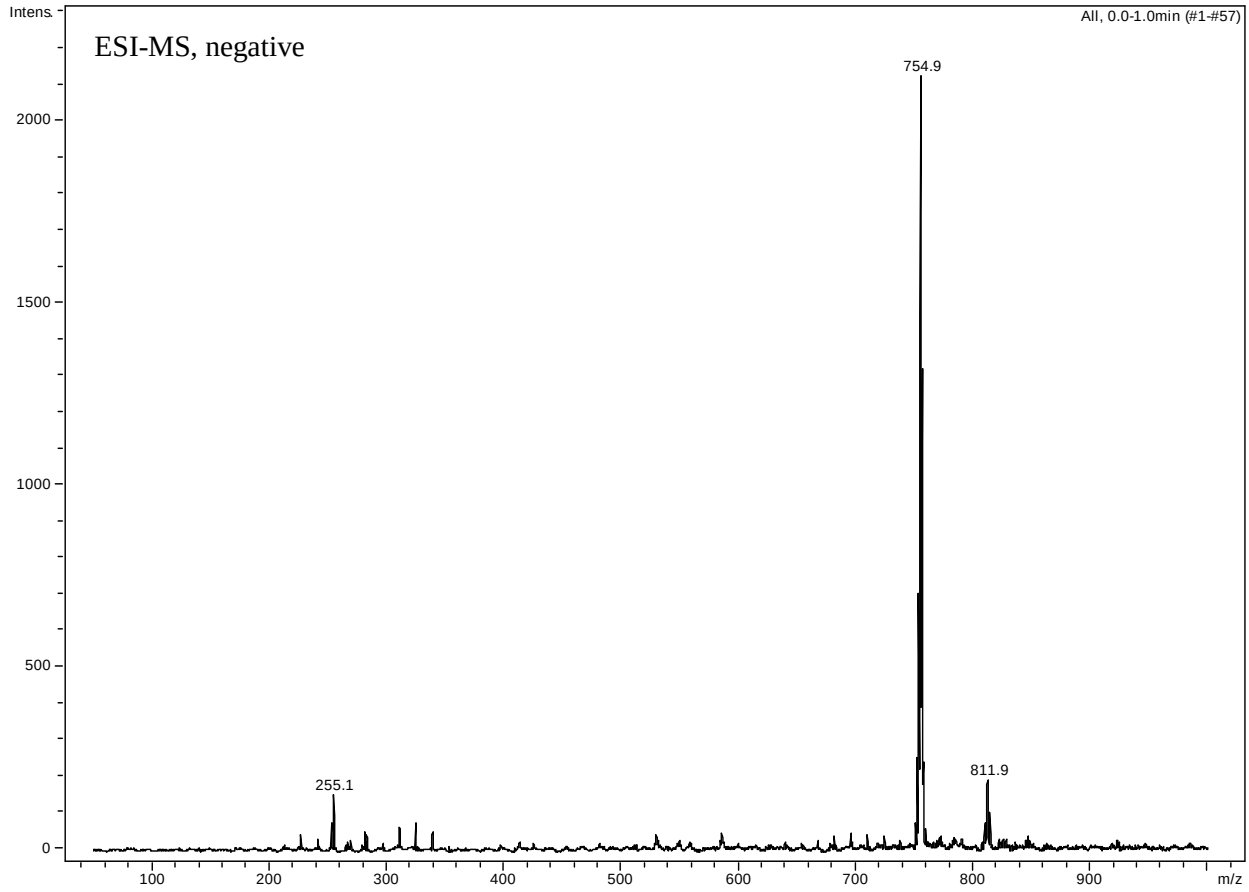

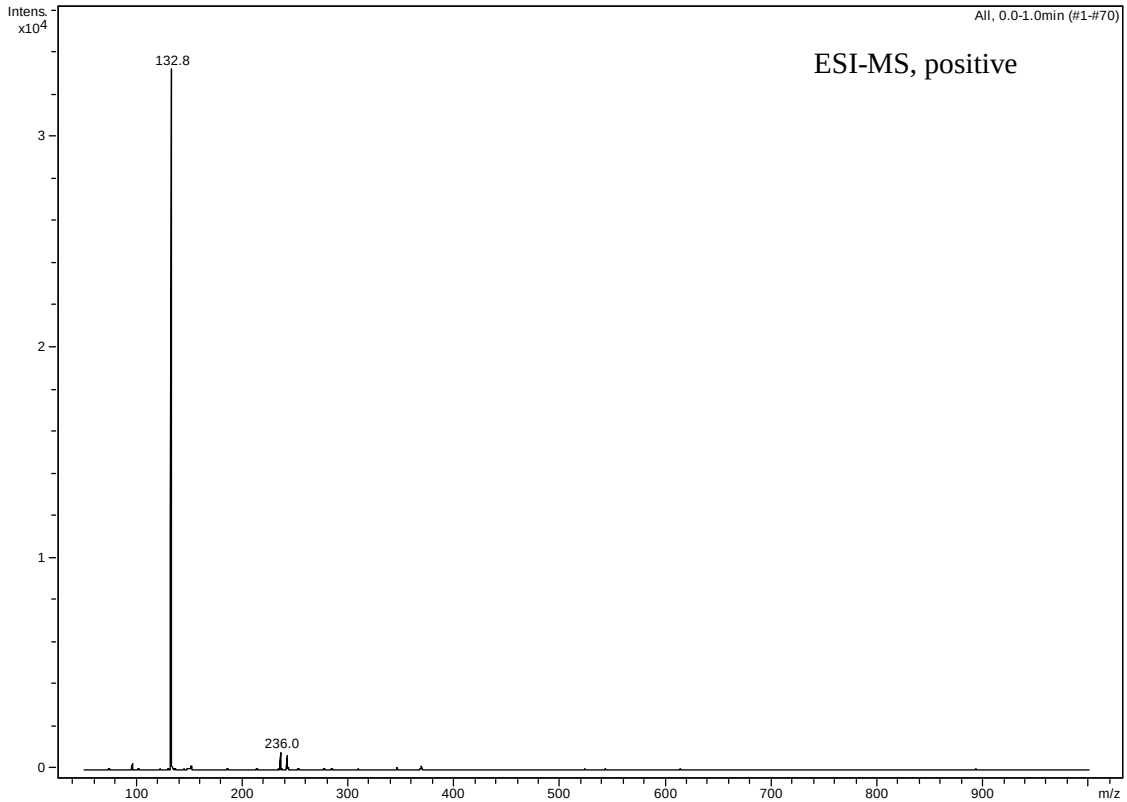

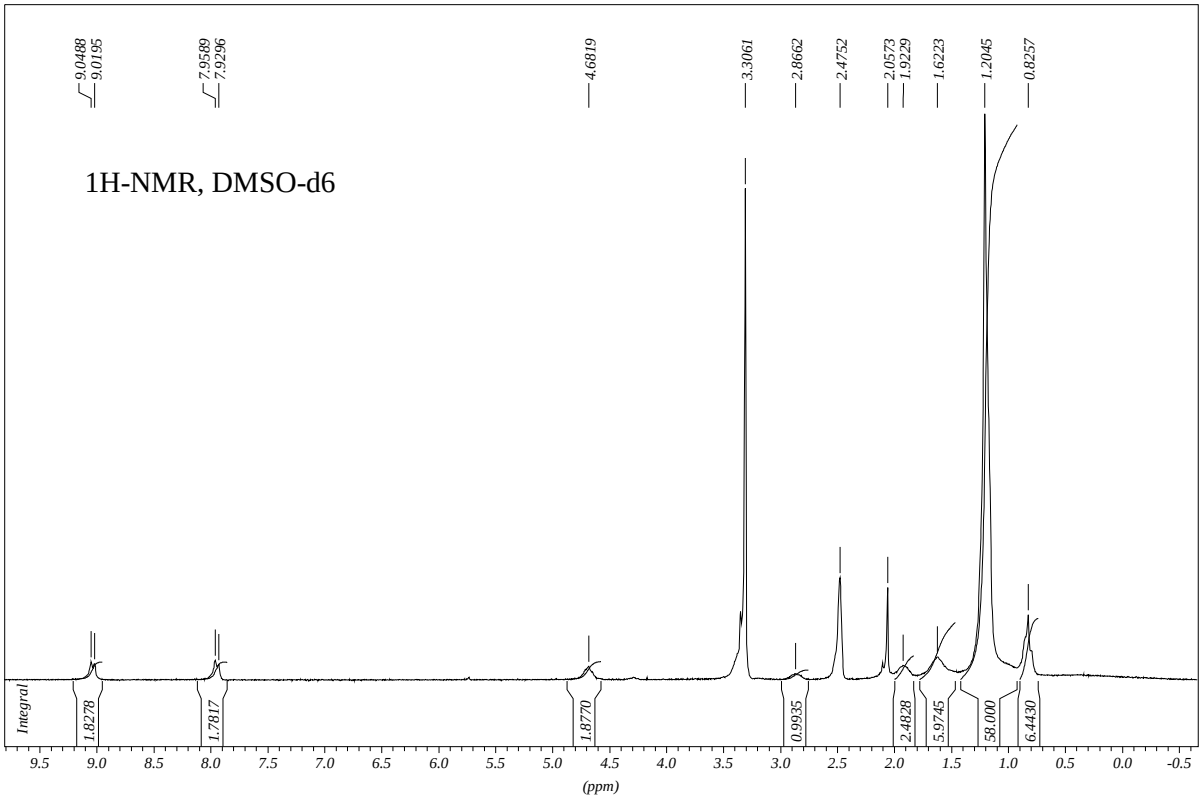
9.0488
9.0195
7.9589
7.9296
4.6819
3.3061
2.8662
2.4752
2.0573
1.9229
1.6223
1.2045
0.8257
1H-NMR, DMSO-d6
Integral
1.8278
1.7817
1.8770
0.9935
2.4828
5.9745
58.000
6.4430
9.5 9.0 8.5 8.0 7.5 7.0 6.5 6.0 5.5 5.0 4.5 4.0 3.5 3.0 2.5 2.0 1.5 1.0 0.5 0.0 -0.5
(ppm)

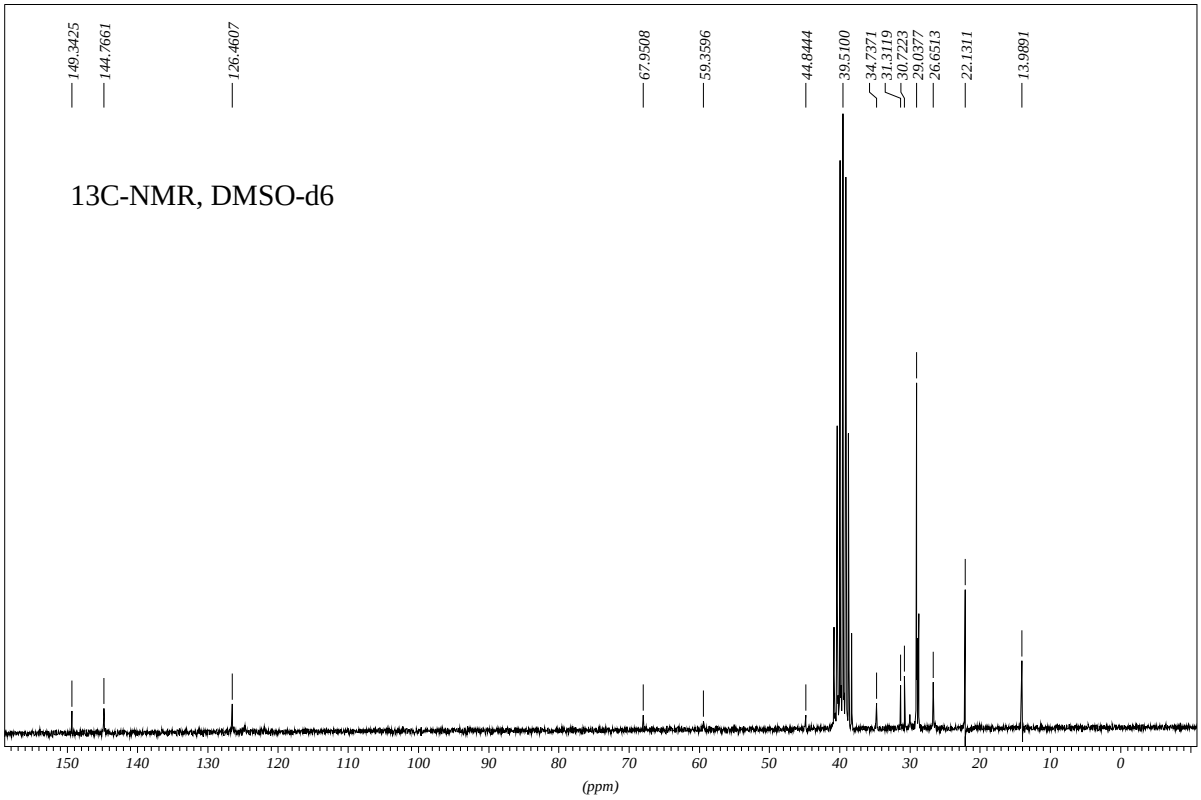
149.3425
144.7661
126.4607
67.9508
59.3596
44.8444
39.5100
34.7371
31.3119
30.7223
29.0377
26.6513
22.1311
13.9891
13C-NMR, DMSO-d6
150 140 130 120 110 100 90 80 70 60 50 40 30 20 10 0
(ppm)

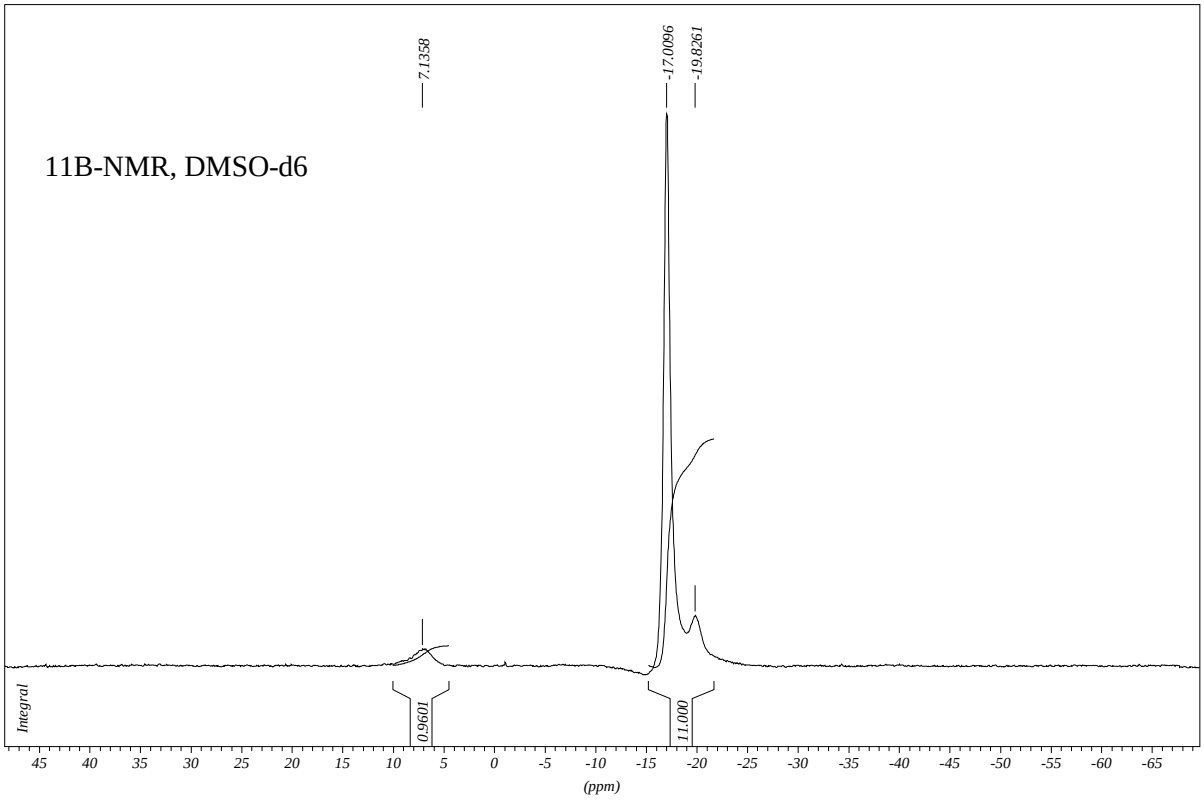
11B-NMR, DMSO-d6
7.1358
-17.9600
-19.8281
Integral
0.0960
1.0000
45 40 35 30 25 20 15 10 5 0 -5 -10 -15 -20 -25 -30 -35 -40 -45 -50 -55 -60 -65
(ppm)

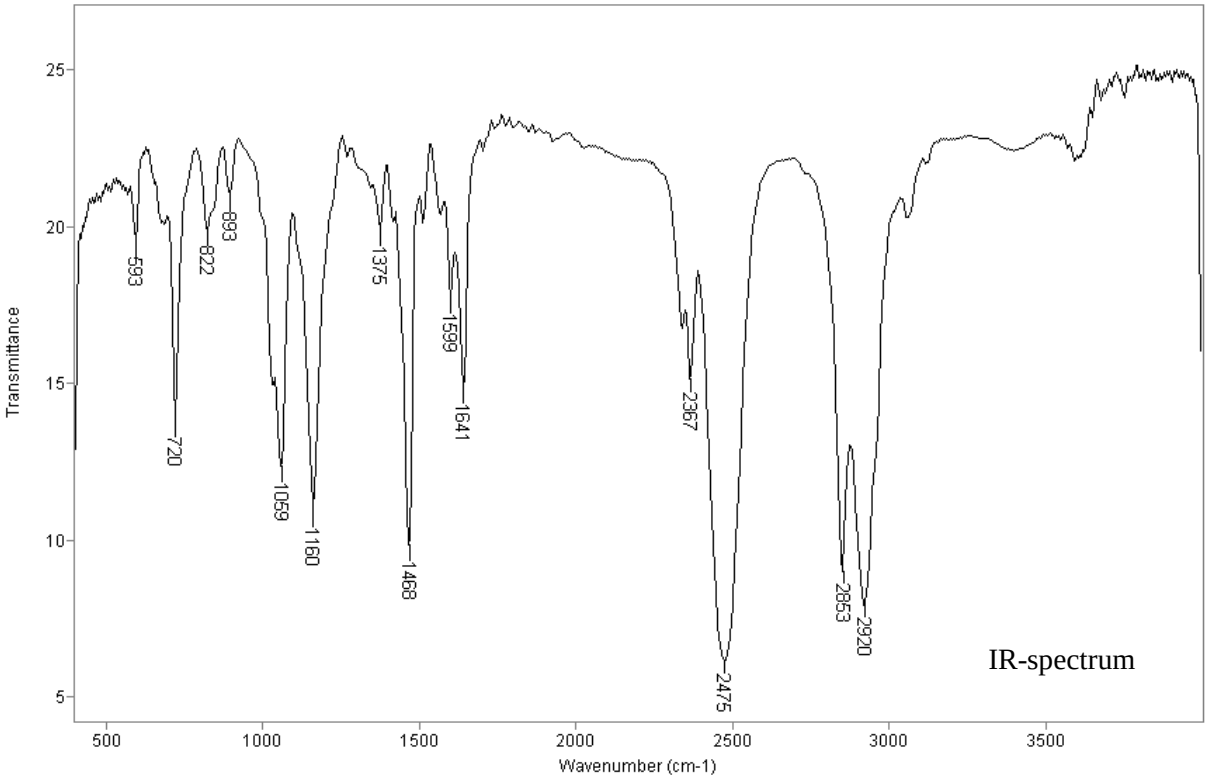
Transmittance
25
20
15
10
5
593
720
822
893
1059
1160
1375
1468
1599
1641
2367
2475
2853
2920
500 1000 1500 2000 2500 3000 3500
Wavenumber (cm-1)
IR-spectrum

4-(Bishexadecylmethyl)pyridinio-N-ethoxy-ethoxy-undecahydro-closo-dodecaborate (-1), cesium salt (Dioxan-SAINT-16).

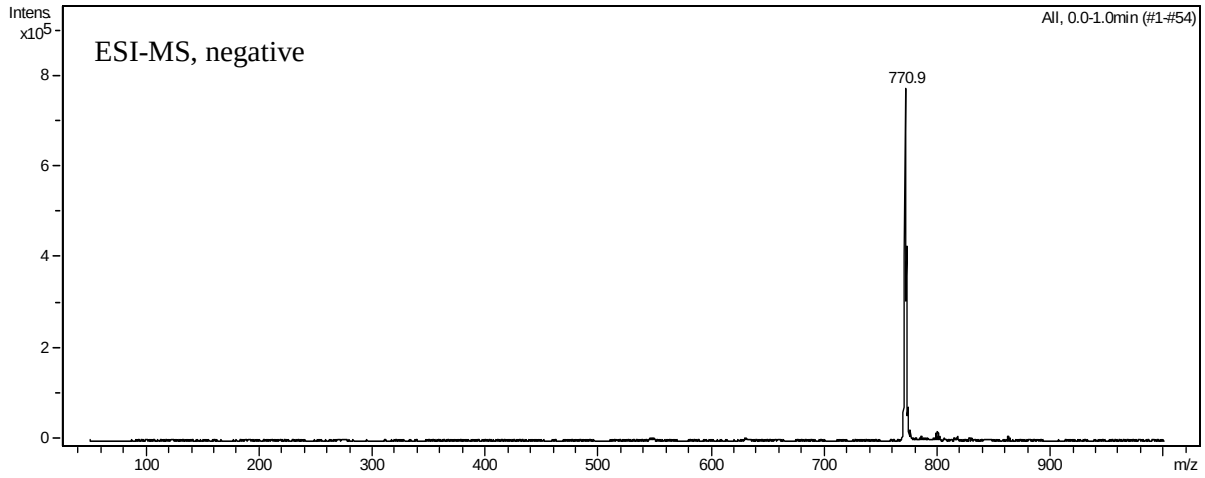

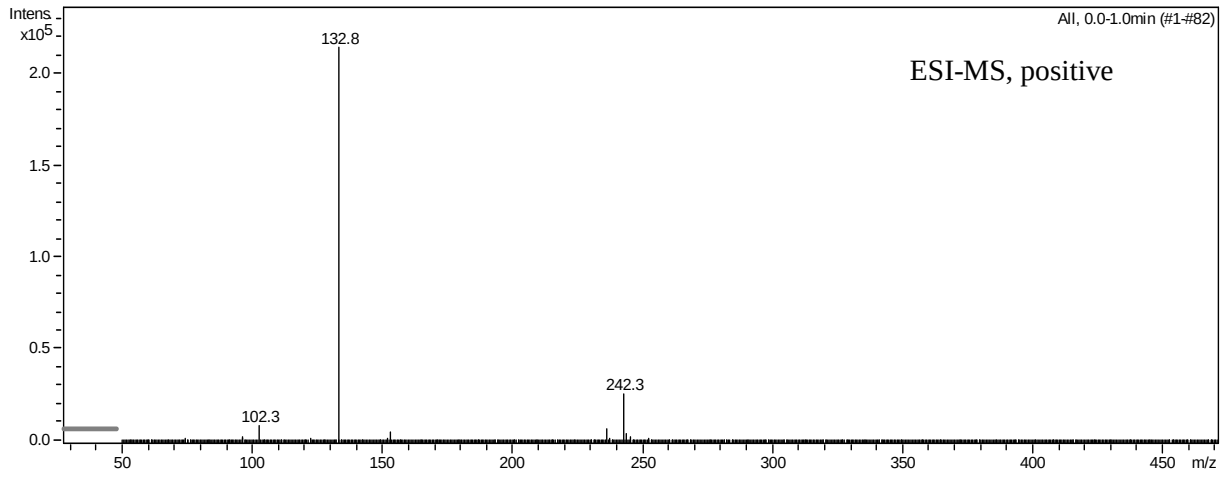

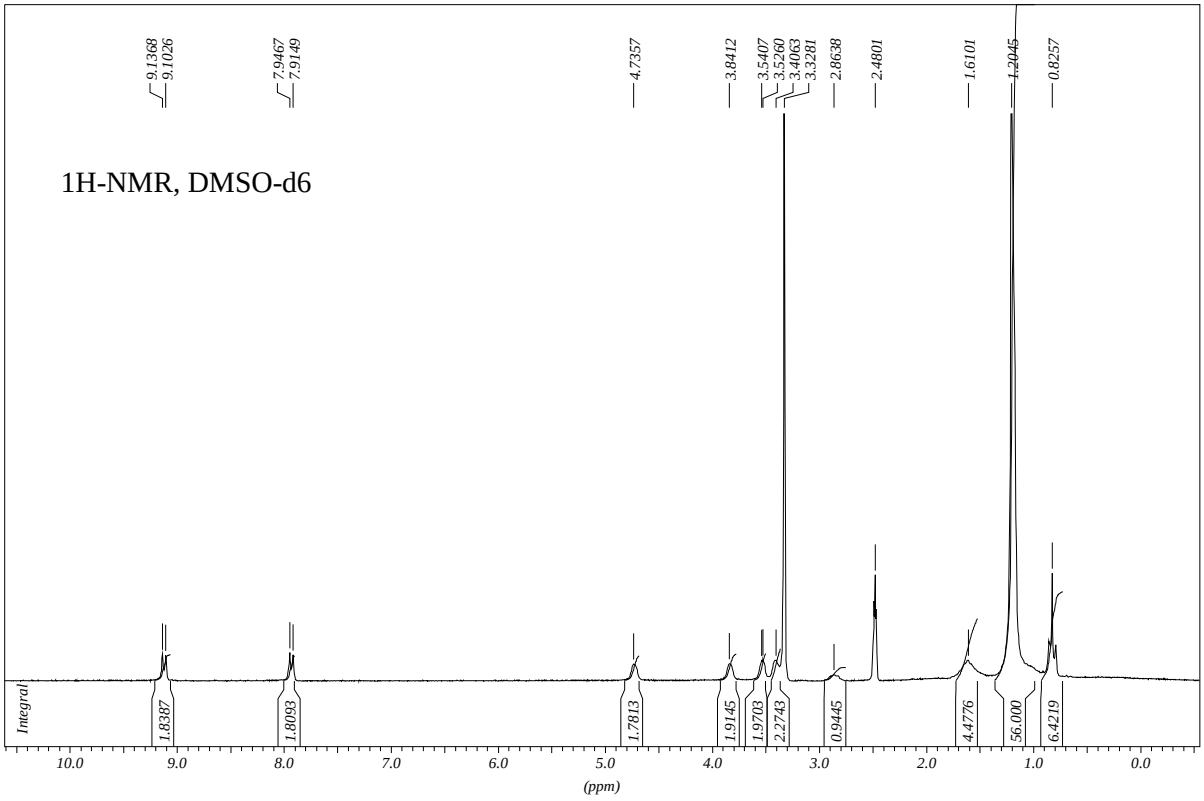
9.1368
9.1026
7.9467
7.9149
4.7357
3.8412
3.5407
3.5260
3.4063
3.3281
2.8638
2.4801
1.6101
1.2045
0.8257
1H-NMR, DMSO-d6
Integral
1.8387
1.8093
1.7813
1.9145
1.9703
2.2743
0.9445
4.4776
56.000
6.4219
10.0
9.0
8.0
7.0
6.0
5.0
4.0
3.0
2.0
1.0
0.0
(ppm)

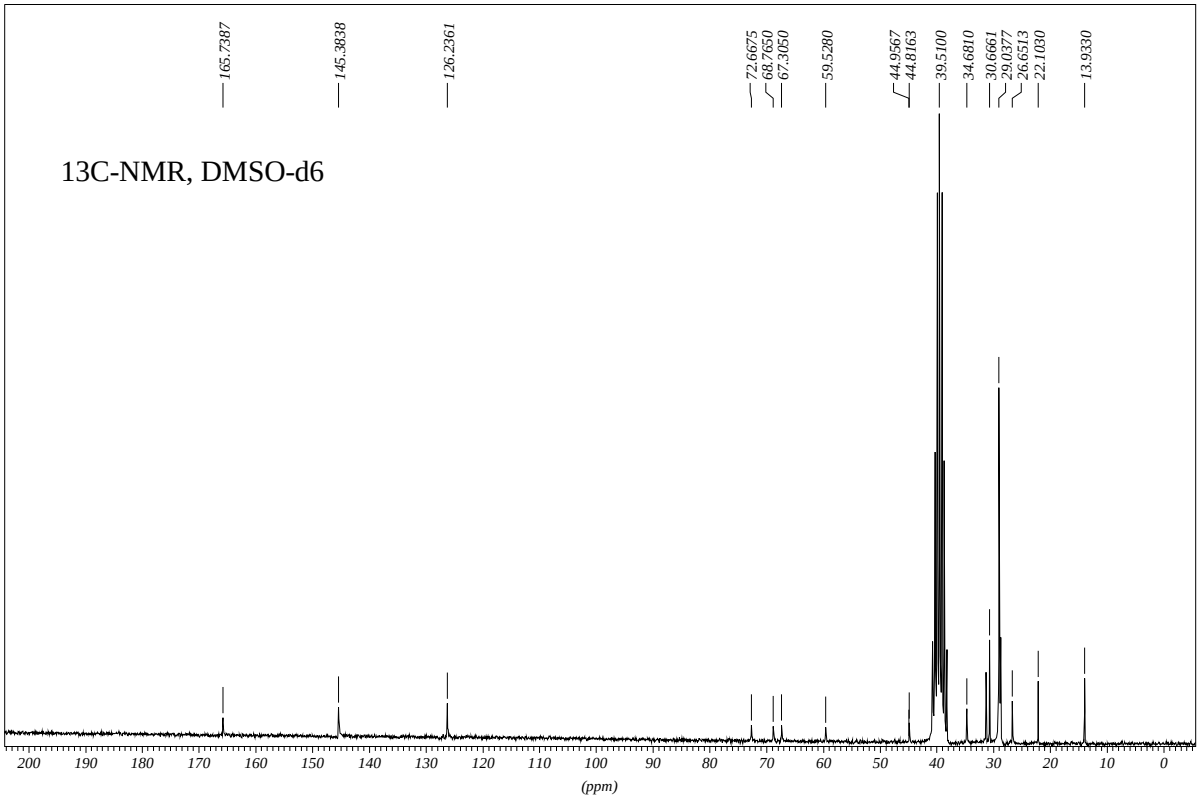
165.7387
145.3838
126.2361
72.6675
68.7650
67.3050
59.5280
44.9567
44.8163
39.5100
34.6810
30.6661
29.0377
26.6513
22.1030
13.9330
13C-NMR, DMSO-d6
200
190
180
170
160
150
140
130
120
110
100
90
80
70
60
50
40
30
20
10
0
(ppm)

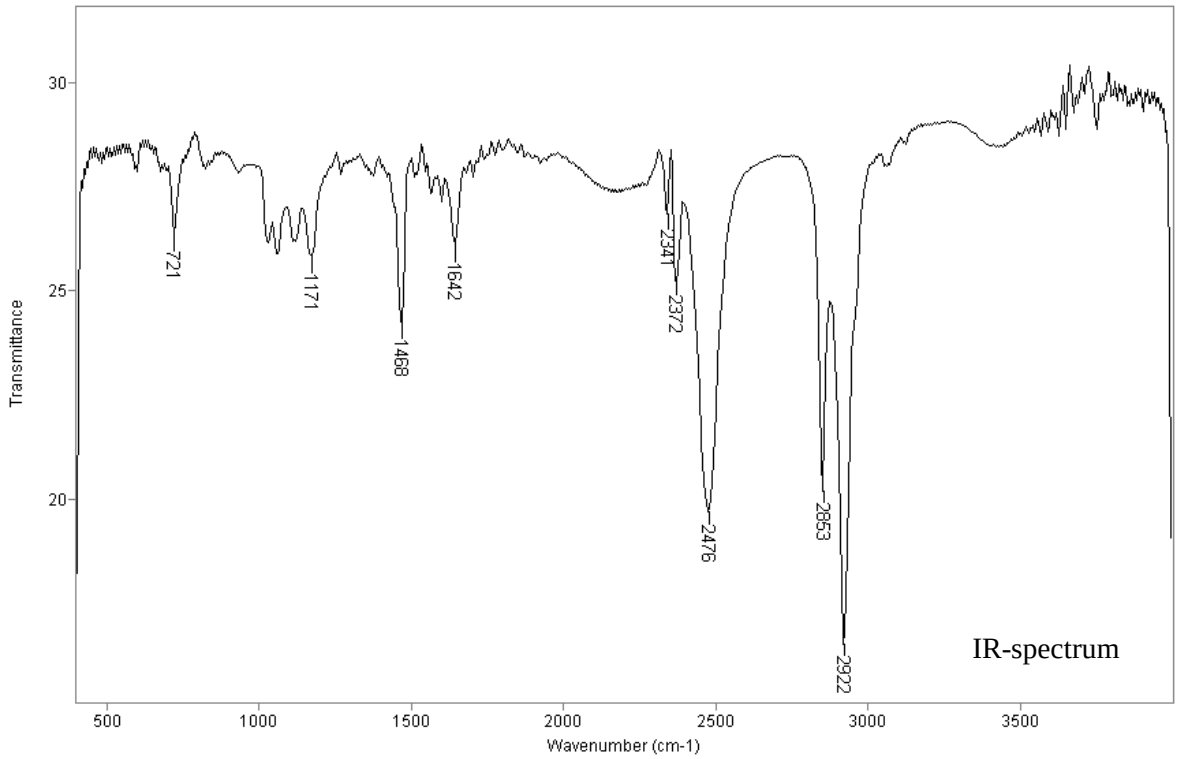
Transmittance
30
25
20
721
1171
1468
1642
2341
2372
2476
2853
2922
500
1000
1500
2000
2500
3000
3500
Wavenumber (cm-1)
IR-spectrum

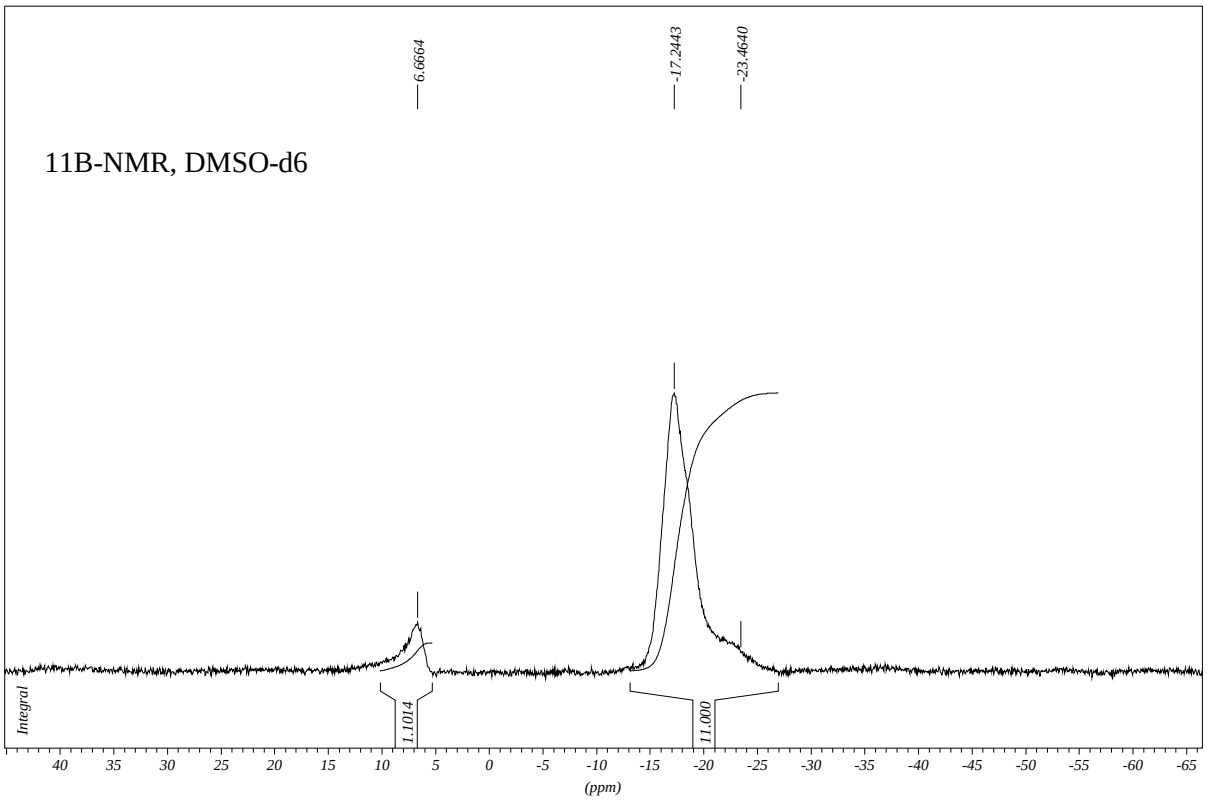
6.6664
-17.2443
-23.4640
11B-NMR, DMSO-d6
Integral
1.1014
11.000
40 35 30 25 20 15 10 5 0 -5 -10 -15 -20 -25 -30 -35 -40 -45 -50 -55 -60 -65
(ppm)

4-(Bishexadecylmethyl)pyridinio-N-pentoxy-undecahydro-closo-dodecaborate (-1), cesium salt (Pyran-SAINT-16).

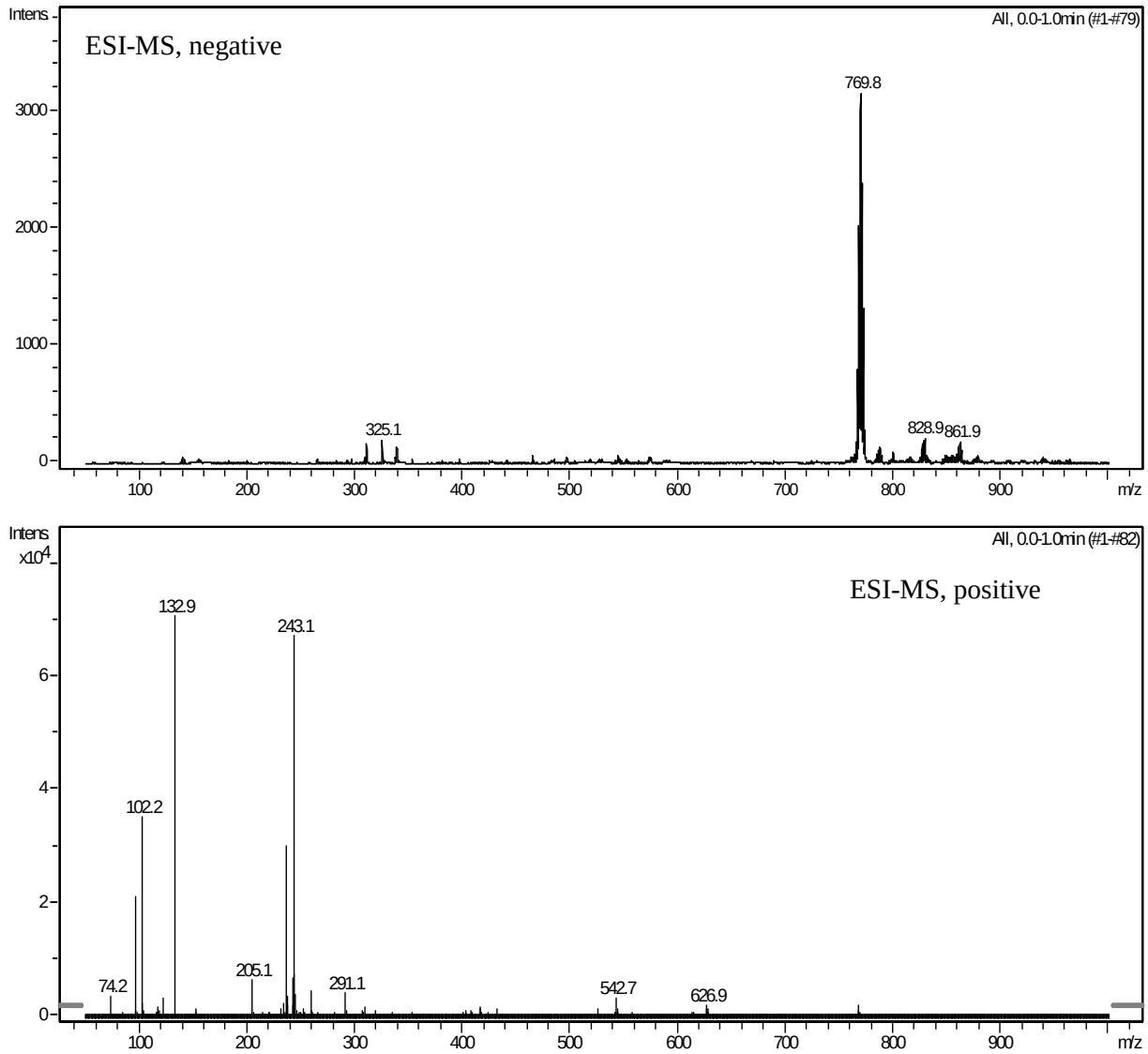

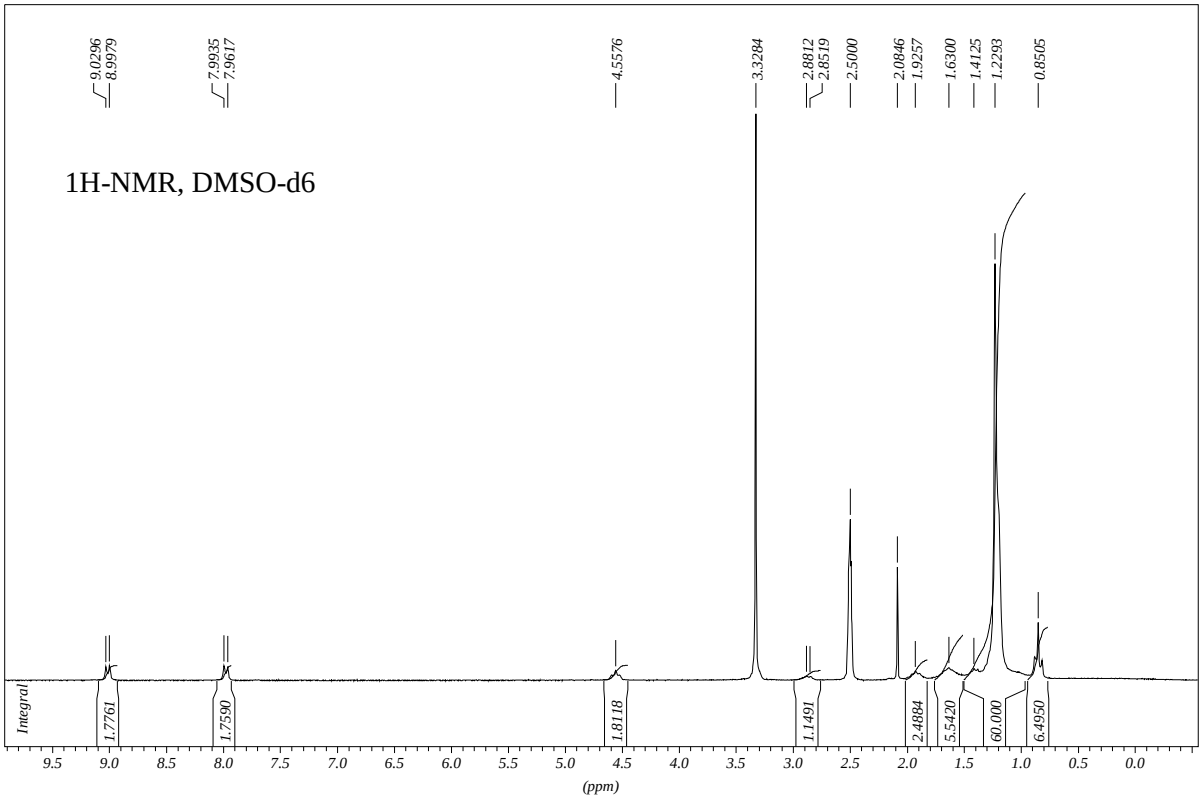
9.0296
8.9979
7.9935
7.9617
4.5576
3.3284
2.8812
2.8519
2.5000
2.0846
1.9257
1.6300
1.4125
1.2293
0.8505
1H-NMR, DMSO-d6
Integral
1.7761
1.7590
1.8118
1.1491
2.4884
5.5420
60.000
6.4950
9.5 9.0 8.5 8.0 7.5 7.0 6.5 6.0 5.5 5.0 4.5 4.0 3.5 3.0 2.5 2.0 1.5 1.0 0.5 0.0
(ppm)

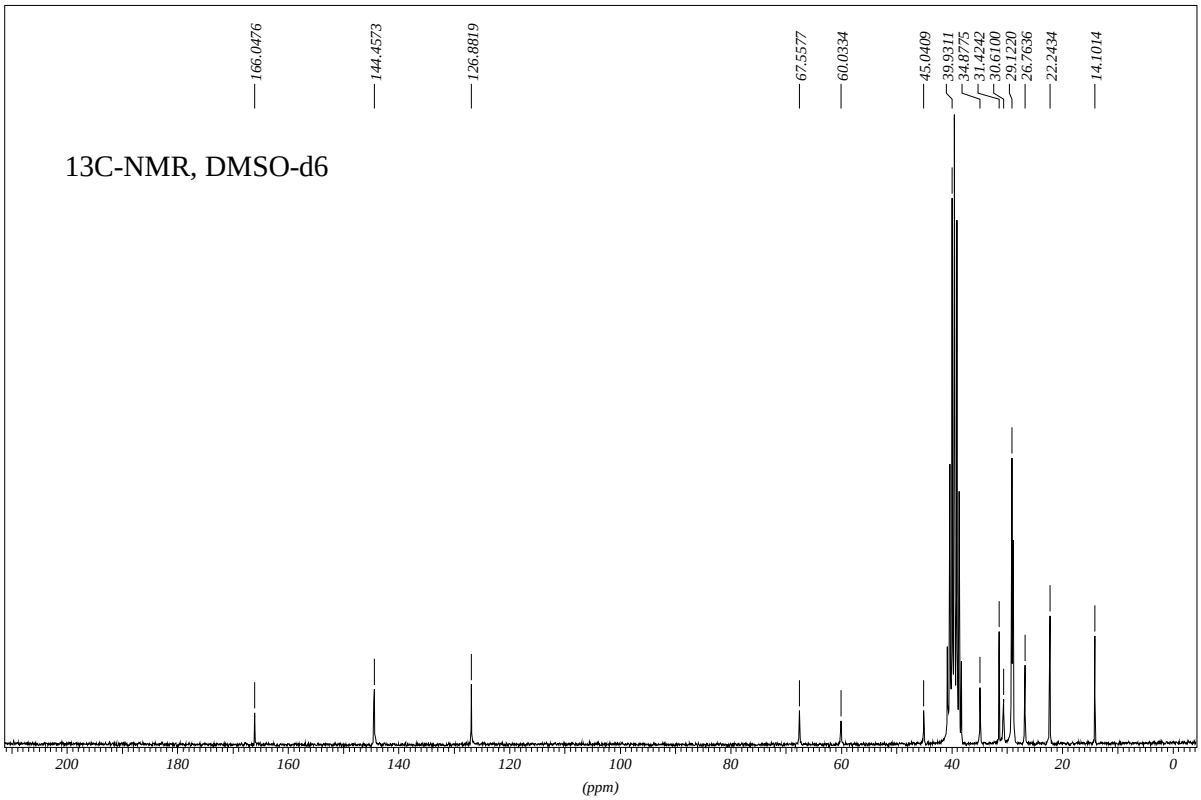
166.0476
144.4573
126.8819
67.5577
60.0334
45.0409
39.9311
34.8775
31.4242
30.6100
29.1220
26.7636
22.2434
14.1014
13C-NMR, DMSO-d6
200 180 160 140 120 100 80 60 40 20 0
(ppm)

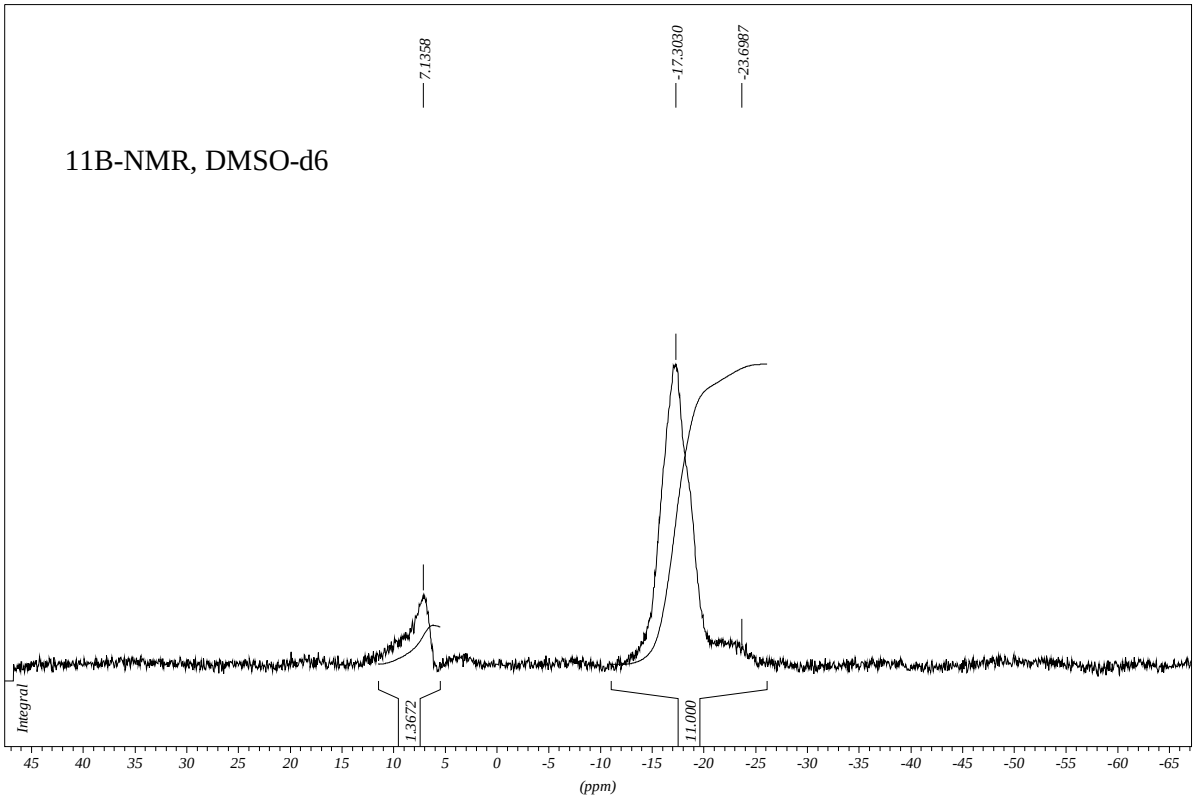
7.1358
-17.3030
-23.6987
11B-NMR, DMSO-d6
Integral
1.3672
11.000
45 40 35 30 25 20 15 10 5 0 -5 -10 -15 -20 -25 -30 -35 -40 -45 -50 -55 -60 -65
(ppm)

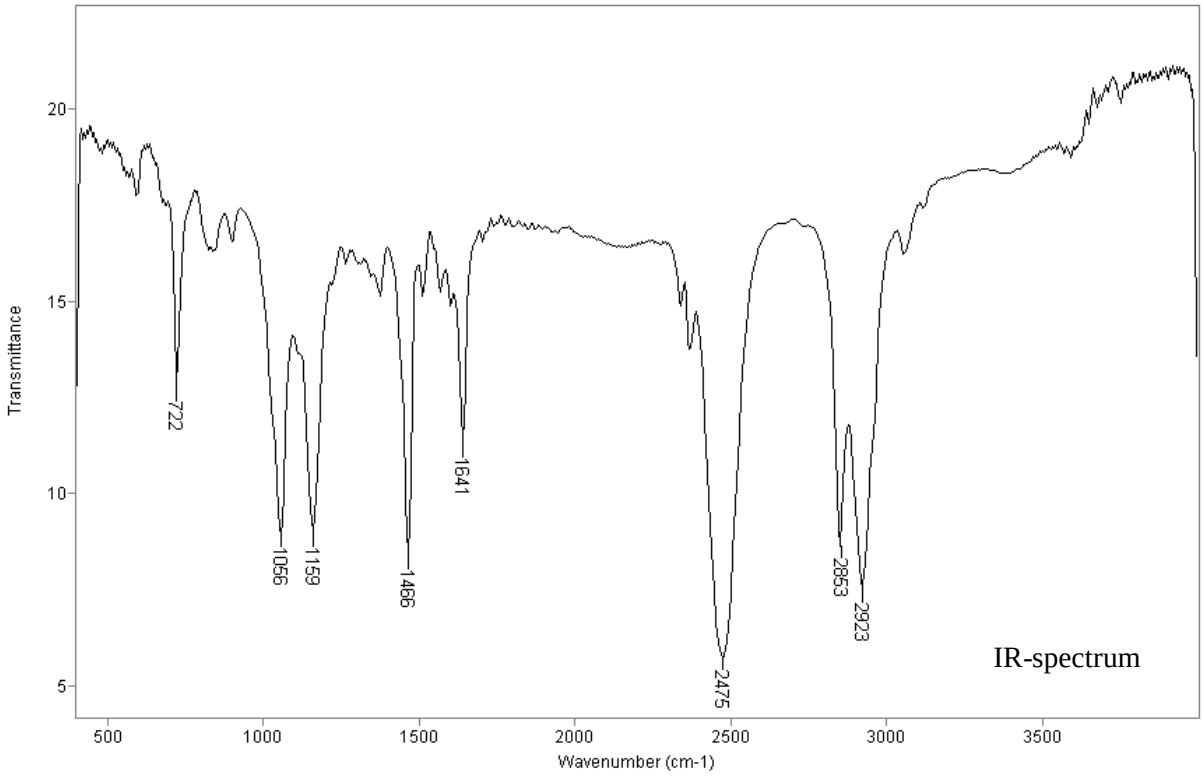
Transmittance
20
15
10
5
722
1056
1159
1466
1641
2475
2853
2923
500 1000 1500 2000 2500 3000 3500
Wavenumber (cm-1)
IR-spectrum

DECEMBER 2009
Volume 20, Number 12

© *Copyright 2009 by the American Chemical Society*

Bioconjugate Chemistry

REVIEWS

Radiolabeled Cyclic RGD Peptides as Integrin $\alpha_v\beta_3$-Targeted Radiotracers: Maximizing Binding Affinity via Bivalency

Shuang Liu*

School of Health Sciences, Purdue University, 550 Stadium Mall Drive, West Lafayette, Indiana 47907. Received April 13, 2009; Revised Manuscript Received July 7, 2009

Integrin $\alpha_v\beta_3$ plays a significant role in tumor angiogenesis and is a receptor for the extracellular matrix proteins with the exposed arginine-glycine-aspartic (RGD) tripeptide sequence. These include vitronectin, fibronectin, fibrinogen, lamin, collagen, Von Willibrand's factor, osteoponin, and adenovirus particles. Integrin $\alpha_v\beta_3$ is expressed at low levels on epithelial cells and mature endothelial cells, but it is overexpressed on the activated endothelial cells of tumor neovasculature and some tumor cells. The restricted expression of integrin $\alpha_v\beta_3$ during tumor growth, invasion, and metastasis presents an interesting molecular target for both early detection and treatment of rapidly growing solid tumors. Over the past decade, many radiolabeled linear and cyclic RGD peptide antagonists have been evaluated as integrin $\alpha_v\beta_3$-targeted radiotracers. Significant progress has been made on their use for imaging integrin $\alpha_v\beta_3$-positive tumors by SPECT or PET. Among the radiotracers evaluated in preclinical tumor-bearing models, [^{18}F]Galacto-RGD (2-[^{18}F]fluoropropanamide c(RGDfK(SAA); SAA = 7-amino-L-glyero-L-galacto-2,6-anhydro-7-deoxyheptanamide) and [^{18}F]-AH111585 are currently under clinical investigation for visualization of integrin $\alpha_v\beta_3$ expression in cancer patients. However, their low tumor uptake, high cost, and lack of preparative modules for routine radiosynthesis will limit their continued clinical application. Thus, there is a continuing need for more efficient integrin $\alpha_v\beta_3$-targeted radiotracers that are readily prepared from a kit formulation without further postlabeling purification. This article will focus on different approaches to maximize the targeting capability of cyclic RGD peptides and to improve the radiotracer excretion kinetics from noncancerous organs. Improvement of tumor uptake and tumor-to-background ratios is important for early detection of integrin $\alpha_v\beta_3$-positive tumors and/or noninvasive monitoring of therapeutic efficacy of antiangiogenic therapy.

INTRODUCTION

Cancer is the second leading cause of death worldwide. Although the exact cause of cancer remains unknown, most cancer patients will survive after surgery, radiation therapy, and chemotherapy or a combination thereof if it can be detected at an early stage. Thus, accurate early detection is highly desirable so that appropriate therapy can be given before the primary tumors become widely spread.

Tumors produce many angiogenic factors, which are able to activate endothelial cells in established blood vessels and induce endothelial proliferation, migration, and new vessel formation (angiogenesis) through a series of sequential but partially overlapping steps. Angiogenesis is a requirement for tumor growth and metastasis (*1*−*7*). Without the neovasculature to provide oxygen and nutrients, tumors cannot grow beyond 1−2

* Phone: 765-494-0236. Email: lius@pharmacy.purdue.edu.

10.1021/bc900167c CCC: $40.75 © 2009 American Chemical Society
Published on Web 08/31/2009

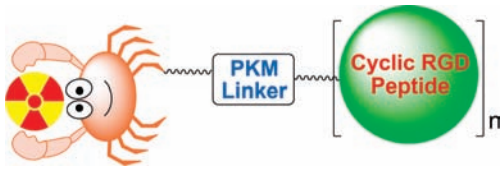

Figure 1. Schematic presentation of the radiotracer design. The targeting biomolecule is a multimeric cyclic RGD peptide. The PKM linker is used to modify radiotracer pharmacokinetics. For the metal-containing radiotracers, a multidentate BFC is often used to attach the metallic radionuclide to the targeting biomolecule. For ^{18}F-based radiotracers, an organic precursor or synthon is often needed to attach ^{18}F onto the multimeric cyclic RGD peptide.

mm in size. Once vascularized, the tumors begin to grow rapidly. The angiogenic process depends on vascular endothelial cell migration and invasion and is regulated by cell adhesion receptors. Integrins are such a family of proteins that facilitate the cellular adhesion to and the migration on extracellular matrix proteins in the intercellular spaces and basement membranes, and regulate cellular entry and withdraw from the cell cycle (*7*−*10*). Integrin $\alpha_v\beta_3$ serves as a receptor for extracellular matrix proteins with exposed arginine-glycine-aspartic (RGD) tripeptide sequence (*8*−*13*). These include vitronectin, fibronectin, fibrinogen, lamin, collagen, osteoponin, and adenovirus particles. Integrin $\alpha_v\beta_3$ is expressed at low levels on epithelial cells and mature endothelial cells; but it is highly expressed on activated endothelial cells in neovasculature of tumors, including osteosarcomas, neuroblastomas, glioblastomas, melanomas, lung carcinomas, and breast cancer (*14*−*16*). It has been demonstrated that integrin $\alpha_v\beta_3$ is overexpressed on both the endothelial cells and tumor cells in human breast cancer xenografts (*17*). The integrin $\alpha_v\beta_3$ expression correlates well with tumor progression and invasiveness of melanoma, glioma, ovarian, and breast cancers (*10*−*17*). The restricted expression of integrin $\alpha_v\beta_3$ during tumor growth, invasion, and metastasis present an interesting molecular target for diagnosis and treatment of the rapidly growing and metastatic tumors (*18*−*32*).

Over the past decade, many radiolabeled cyclic RGD peptides have been evaluated as radiotracers for imaging tumors by SPECT or PET (*33*−*68*). Several review articles have appeared covering the nuclear medicine applications of radiolabeled cyclic RGD peptide and nonpeptide antagonists as radiotracers for diagnosis and radiotherapy of integrin $\alpha_v\beta_3$-positive tumors (*17*−*29*). This article is not intended to be an exhaustive review of the current literature on radiolabeled RGD peptides and nuclear medicine applications. Instead, it will focus on different approaches to maximize their targeting capability and to improve the radiotracer excretion kinetics from noncancerous organs. Improvement of tumor uptake and tumor-to-background (T/B) ratios is important for both diagnostic and therapeutic radiotracers.

Radiotracer Design. Figure 1 shows a schematic illustration of an integrin $\alpha_v\beta_3$-targeted radiotracer. Cyclic RGD peptide serves as the targeting biomolecule to carry radionuclide to the integrin $\alpha_v\beta_3$ overexpressed on tumor cells and activated endothelial cells of tumor neovasculature. A multidentate bifunctional chelator (BFC) is used to attach the metallic radionuclide to the cyclic RGD peptide (*69*−*72*), whereas an organic precursor or synthon is often needed for the ^{18}F-labeling (*73*). The pharmacokinetic modifying linker (PKM) is used to improve the radiotracer excretion kinetics (*69*−*71*). For a new integrin $\alpha_v\beta_3$-targeted radiotracer to be successful, it must show clinical indications for high-incidence tumors (breast, lung, colorectal, prostate, and skin cancers). The radiotracer should have high tumor uptake and T/B ratios in a short period of time. To achieve this goal, the radiotracer should have a rapid blood clearance to minimize background radioactivity. Since most high-incidence tumors (breast, lung, and colorectal cancers) occur in the torso, renal excretion is necessary to avoid radioactivity accumulation in the gastrointestinal tract. The integrin $\alpha_v\beta_3$-targeted radiotracer should also be able to distinguish between benign and malignant tumors, to follow tumor growth and metastasis, and to predict therapeutic efficacy in integrin $\alpha_v\beta_3$-positive cancer patient. In addition, a kit formulation or preparative module is needed for routine preparation of the radiotracer in high yield and radiochemical purity at low cost.

Choice of Radionuclide. The choice of radionuclide depends largely on the clinical utility of radiotracer. For planar imaging and SPECT, more than 80% of radiotracers used in nuclear medicine departments are ^{99m}Tc compounds due to optimal nuclear properties of ^{99m}Tc and its easy availability at low cost (*69*−*72*). The 6 h half-life is long enough to allow radiopharmacists to carry out radiosynthesis and for physicians to collect clinically useful images. At the same time, it is short enough to permit administration of 20−30 mCi of ^{99m}Tc without imposing a significant radiation dose to the patient. The monochromatic 140 KeV photons are readily collimated to give high-quality images with high spatial resolution. The clinically most relevant radionuclides for PET include ^{18}F, ^{62}Cu, ^{64}Cu, and ^{68}Ga.

^{18}F is a cyclotron-produced isotope suitable for PET. It has a half-life of 110 min. For several years, ^{18}F-FDG (FDG = 2-fluoro-2-deoxyglucose) has been widely used as an imaging tool for diagnosis of cancers and brain and cardiovascular diseases. Despite its short half-life, the availability of preparative modules makes ^{18}F-labeled biomolecules much more accessible to researchers and clinicians in many clinical institutions.

^{62}Cu is a generator-produced radionuclide from the decay of ^{62}Zn. Its 9.7 min half-life allows repeated dosing without imposing a significant radiation burden to the patient. The commercially available ^{62}Zn−^{62}Cu generator has been successfully used in clinical trials (*74*−*77*). ^{64}Cu is another PET isotope useful for development of target-specific radiotracers. It has a half-life of 12.7 h and a β^+ emission (18%, E_{max} = 0.655 MeV). Despite poor nuclear properties, its long half-life makes it feasible to prepare, transport, and deliver the ^{64}Cu radiotracer for clinical applications. More importantly, recent breakthroughs in production of ^{64}Cu with high specific activity have made it more available to the small research institutions without on-site cyclotron facilities (*78*). ^{64}Cu is a viable alternative to ^{18}F for research programs that wish to incorporate high sensitivity and high spatial resolution of PET, but cannot afford to maintain the expensive radionuclide production infrastructure. Copper radionuclides and related radiochemistry have been reviewed by Blower et al. (*79*). Nuclear medicine applications of ^{64}Cu-labeled monoclonal antibodies and peptides have been reviewed by Anderson et al. (*75, 80*).

^{68}Ga is a generator-produced PET isotope with a half-life of 68 min. The ^{68}Ge−^{68}Ga generator can be used for more than a year, allowing PET studies without the on-site cyclotron. If the radiotracer is properly designed, ^{68}Ga could become as useful for PET as ^{99m}Tc for SPECT (*81, 82*). In support of this, the ^{68}Ga-labeled somatostatin analogues have been studied extensively for PET imaging of somatostatin-positive tumors in animal models and cancer patients (*83*−*91*). Gallium chemistry and related medical applications have been reviewed recently (*81, 82, 92*).

Bifunctional Chelators. The choice of BFC depends on the radionuclide. ^{18}F can be incorporated into the cyclic RGD peptide via a covalent bond without the need for BFC. In contrast, BFC is an important part of radiotracers containing a metallic radionuclide (*69*−*72, 92*). Among various BFCs (Figure 2), 6-hydazinonicotinic acid (HYNIC) is of great interest due to its high ^{99m}Tc-labeling efficiency (rapid radiolabeling and high

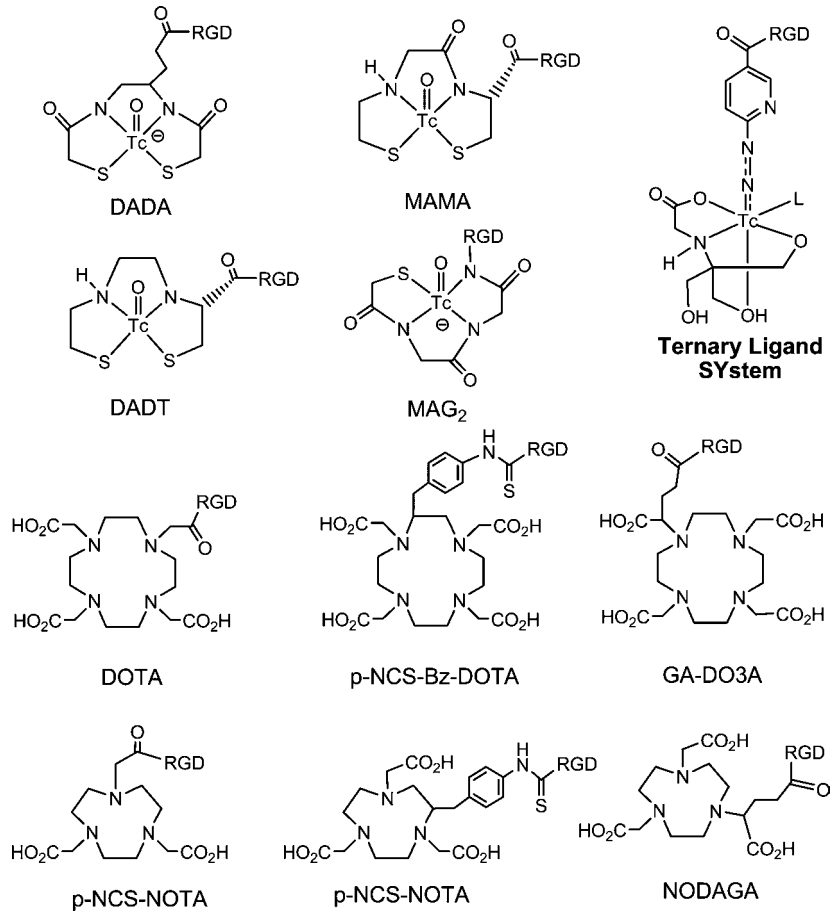

Figure 2. BFCs useful for radiolabeling of multimeric cyclic RGD peptides with ^{99m}Tc, ^{68}Ga, and ^{64}Cu. DADA (diamidodithiol), MAMA (monoaminemonoamidedithiol), MADT (diaminedithiol), MAG_2 (2-mecaptoacetylglycylglycyl), and HYNIC are particularly useful for ^{99m}Tc-labeling, while DOTA, NOTA, and their derivatives are excellent BFCs for chelation of ^{68}Ga and ^{64}Cu.

radiolabeling yield), the high solution stability of its ^{99m}Tc complexes, and the easy use of different coligands for modification of biodistribution characteristic of ^{99m}Tc-labeled small biomolecules (*93*). DOTA (1,4,7,10-tetraazacyclododecane-1,4,7,10-tetraacetic acid), NOTA (1,4,7-tritazacyclononane-1,4,7-triacetic acid), and their derivatives (Figure 2) have been used as BFCs for ^{68}Ga and ^{64}Cu-labeling of small biomolecules (*84*−*91*). NODAGA is particularly useful for ^{68}Ga- and ^{64}Cu-labeling due to high hydrophilicity and in vivo stability of its ^{68}Ga and ^{64}Cu chelates. It has been reported that NOTA derivatives have much higher ^{68}Ga and ^{64}Cu-labeling efficiency than their DOTA analogues (*94*−*98*). The fast and efficient radiolabeling is especially critical for ^{68}Ga and ^{62}Cu due to their short half-life ($t_{1/2}$ = 68 min for ^{68}Ga and 9.7 min for ^{62}Cu).

PKM Linkers. In general, high lipophilicity often leads to more hepatobiliary excretion and/or high protein binding, which will result in longer blood retention of radioactivity. Hepatobiliary excretion is detrimental for improvement of T/B ratio. Thus, an important aspect of radiotracer development is to improve T/B ratios by modifying pharmacokinetics of radiolabeled cyclic RGD peptides. For example, the negatively charged small peptide sequences or amino acids have been proposed as PKM linkers to reduce renal uptake and kidney retention of radiolabeled small biomolecules (*70, 71, 92*). The di(cysteic acid) linker has successfully been used to improve the blood clearance and minimize the liver and kidney activity of radiolabeled nonpeptide integrin $\alpha_v\beta_3$ receptor antagonists (*99*−*102*). The Asp_3 and Ser_3 tripeptide sequences were also used to modify excretion kinetics of the ^{99m}Tc-labeled cyclic RGD peptide (*39*). Harris et al. reported the use of a PEG_4 (15-amino-4,7,10,13-tetraoxapentadecanoic acid) linker to improve the tumor uptake and T/B ratios of the ^{99m}Tc-labeled nonpeptide integrin $\alpha_v\beta_3$ receptor antagonists (*99*−*102*). Kessler et al. reported the use of HEG (hexaethylene glycolic acid) as the PKM linker for the ^{18}F-labeled cyclic RGDfE dimers and tetramers (*40*−*42*). Using the HEG linker also increases the distance between the cyclic RGD motifs. Chen et al. also found that the introduction of the PEG (polyethylene glycolic acid) linker can improve the tumor uptake and excretion kinetics of ^{125}I- and ^{18}F-labeled c(RGDyK) and ^{64}Cu-labeled $E[c(RGDyK)]_2$ (*48, 49, 54, 103*).

Targeting Biomolecules. Figure 3 shows several examples of cyclic RGD peptides that have high affinity and selectivity for integrin $\alpha_v\beta_3$. Among the radiotracers evaluated in preclinical tumor-bearing models, [^{18}F]Galacto-RGD (Figure 3: 2-[^{18}F]fluoropropanamide c(RGDfK(SAA); SAA = 7-amino-L-glyero-L-galacto-2,6-anhydro-7-deoxyheptanamide) and [^{18}F]-AH111585, the core sequence of which was originally discovered from a phage display library (as ACDRGDCFCG), are currently under clinical investigation for visualization of integrin $\alpha_v\beta_3$ expression in cancer patients (*104*−*109*). The results from imaging studies in cancer patients show that there is sufficient integrin $\alpha_v\beta_3$ expression for PET imaging and the accumulation of radiolabeled RGD peptide radiotracer correlates well with the integrin $\alpha_v\beta_3$ expression levels in cancer patients (*108, 109*). However, their relatively low tumor uptake, high cost, and lack of preparative modules for routine radiosynthesis will limit their continued clinical applications. Several steps of manual radiosynthesis and postlabeling purification often cause significant radiation exposure to radiopharmacists. Of course, this problem can be solved by developing preparative modules for routine radiosynthesis, which will definitely lead to added cost for the

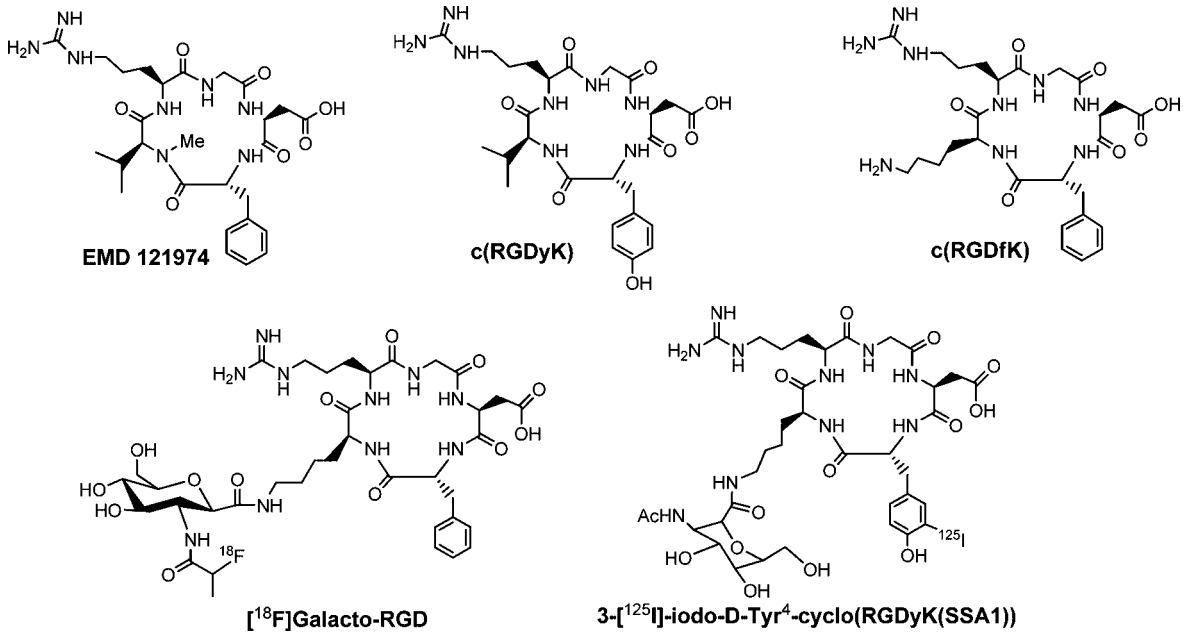

Figure 3. Chemdraw structures of cyclic RGD peptides useful as targeting biomolecules for the integrin $\alpha_v\beta_3$-targeted radiotracers. [^{18}F]Galacto-RGD (2-[^{18}F]fluoropropanamide c(RGDfK(SAA); SAA = 7-amino-L-glyero-L-galacto-2,6-anhydro-7-deoxyheptanamide) is currently under clinical investigation for visualization of integrin $\alpha_v\beta_3$ expression in cancer patients.

radiotracer. Thus, this is a continuing need for more efficient integrin $\alpha_v\beta_3$-specific radiotracers that are readily prepared from a kit formulation without further postlabeling chromatographic purification.

Maximizing Binding Affinity via Multimerization. *Cyclization to Improve Binding Affinity and Selectivity.* Many cyclic RGD peptides have been proposed as the integrin $\alpha_v\beta_3$ antagonists for treatment of cancer. It was found that incorporation of the RGD sequence into a cyclic pentapeptide framework (Figure 3) increases the binding affinity and selectivity for integrin $\alpha_v\beta_3$ over glycoprotein IIb/IIIa (*110*−*113*). After extensive structure−activity evaluations, it was concluded that the amino acid in position 5 has no significant impact on integrin $\alpha_v\beta_3$ binding affinity. The valine (V) residue in c(RGDfV) can be replaced by lysine (K) or glutamic acid (E) to afford c(RGDfK) and c(RGDfE), respectively, without changing the integrin $\alpha_v\beta_3$ binding affinity.

Cyclic RGD Dimers. To improve integrin $\alpha_v\beta_3$ binding affinity, multimeric RGD peptides, such as E[c(RGDfK)]$_2$, have been used to develop integrin $\alpha_v\beta_3$-targeted radiotracers. For example, Rajopadhye et al. were the first to use cyclic RGD dimers, such as E[c(RGDfK)]$_2$ (Figure 4), to develop diagnostic (^{99m}Tc) and therapeutic (^{90}Y and ^{64}Cu) radiotracers (*56, 57, 114, 115*). Recently, Chen et al. (*50, 51*) reported the ^{64}Cu- and ^{18}F-labeled E[c(RGDyK)]$_2$ (Figure 4) as PET radiotracers. Poethko et al. found that the RGDfE dimer [c(RGDfE)HEG]$_2$-K-Dpr-[^{18}F]FBOA (Figure 4) had much better targeting capability as evidenced by its higher integrin $\alpha_v\beta_3$ binding affinity and tumor uptake as compared to its monomeric analogue c(RGDfE)HEG-Dpr-[^{18}F]FBOA (*40*−*42*).

Cyclic RGD Tetramers and Octamers. Several groups have used the multimer concept to prepare cyclic RGD tetramers and octamers. For example, Boturyn et al. reported a series of cyclic RGDfK tetramers (*116*) and found that increasing the peptide multiplicity significantly enhanced the integrin $\alpha_v\beta_3$ binding affinity and internalization. Kessler et al. reported a cyclic RGDfE tetramer (Figure 5) that had better integrin $\alpha_v\beta_3$ binding affinity than its monomeric and dimeric analogues (*40*−*42*). Liu et al. reported the use of a cyclic RGDfK tetramer E[E-[c(RGDfK)]$_2$]$_2$ (Figure 5) for development of integrin $\alpha_v\beta_3$-targeted SPECT and PET radiotracers (*52, 64*−*68*). Chen et al. recently used ^{64}Cu- and ^{18}F-labeled cyclic RGD tetramer E[E[c(RGDxK)]$_2$]$_2$ and octamer E[E[E[c(RGDyK)]$_2$]$_2$]$_2$ for tumor imaging by PET (*52, 117*). Although the results from both in vitro assays and ex vivo biodistribution studies have demonstrated that radiolabeled (^{99m}Tc, ^{18}F, and ^{64}Cu) RGD tetramers and octamer have much better tumor targeting capability (higher integrin $\alpha_v\beta_3$ binding affinity and better radiotracer tumor uptake) than their dimeric analogues, it remains unclear whether the cyclic RGD motifs in E[E-[c(RGDxK)]$_2$]$_2$ (x = f and y) and E[E[E[c(RGDyK)]$_2$]$_2$]$_2$ are really multivalent in binding to integrin $\alpha_v\beta_3$. As the peptide multiplicity increases, the uptake of radiolabeled multimeric RGD peptides in the kidneys, liver, lungs, and spleen are also significantly increased. In addition, the cost for E[E[c(RGD-fK)]$_2$]$_2$ and E[E[E[c(RGDyK)]$_2$]$_2$]$_2$ is prohibitively high for development of integrin $\alpha_v\beta_3$-targeted radiotracers in the future. Thus, an alternate approach is needed to improve integrin $\alpha_v\beta_3$-targeting capability and minimize the radiotracer accumulation in noncancerous organs.

Maximizing Binding Affinity via Bivalency. *Factors Influencing Binding Affinity.* The success of E[c(RGDfK)]$_2$ as targeting biomolecules is very intriguing. Given the short distance (6 bonds excluding side-arms of K-residues) between two cyclic RGD motifs in E[c(RGDfK)]$_2$, it is unlikely that they would bind to two adjacent integrin $\alpha_v\beta_3$ sites simultaneously. However, the binding of one RGD motif to integrin $\alpha_v\beta_3$ will significantly increase the "local concentration" of a second RGD motif in the vicinity of integrin $\alpha_v\beta_3$ sites (Figure 6A). The "locally enhanced RGD concentration" may explain the higher tumor uptake of radiolabeled (^{99m}Tc, ^{111}In, ^{90}Y, ^{18}F, and ^{64}Cu) cyclic RGD dimers as compared to their monomeric analogues (*60*−*65*). To further improve the integrin $\alpha_v\beta_3$-targeting capability of cyclic RGD dimers, the distance between two cyclic RGD motifs must be increased so that they are to achieve simultaneous integrin $\alpha_v\beta_3$ binding (Figure 6B). The combination of "bivalency" and the "enriched local RGD concentration" is expected to result in higher integrin $\alpha_v\beta_3$ targeting capability of cyclic RGD dimers and better tumor uptake with longer tumor retention time for their corresponding radiotracers.

Improve Integrin $\alpha_v\beta_3$ Binding Affinity by Increasing Distance between Cyclic RGD Motifs. To demonstrate this

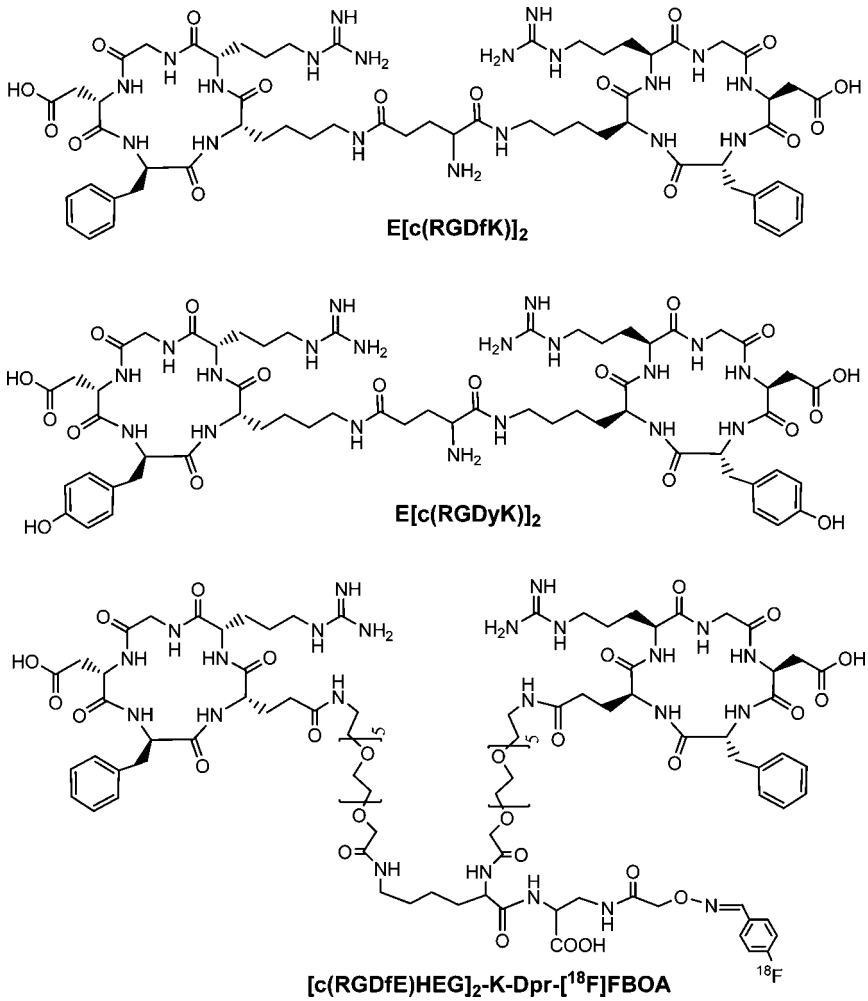

Figure 4. Cyclic RGD peptide dimers ($E[c(RGDfK)]_2$ and $E[c(RGDyK)]_2$) and $[c(RGDfE)HEG]_2$-K-Dpr-[^{18}F]FBOA.

concept, Shi et al. recently reported a series of cyclic RGD peptide dimers (Figure 7) containing triglycine (G_3) and PEG_4 linkers, which are used to increase the distance between two cyclic RGD motifs from 6 bonds in $E[c(RGDfK)]_2$ to 24 bonds in $3G_3$-dimer and 38 bonds in $3PEG_4$-dimer (*118, 119*). The integrin $\alpha_v\beta_3$ binding affinities (Table 1) against ^{125}I-echistatin bound to U87MG human glioma cells follow the order of HYNIC-tetramer ($IC_{50} = 7 \pm 2$ nM) > HYNIC-$2PEG_4$-dimer ($IC_{50} = 52 \pm 7$ nM) ~ HYNIC-$3PEG_4$-dimer ($IC_{50} = 60 \pm 4$ nM) ~ HYNIC-$3G_3$-dimer ($IC_{50} = 61 \pm 2$ nM) > HYNIC-PEG_4-dimer ($IC_{50} = 84 \pm 7$ nM) ~ HYNIC-dimer ($IC_{50} = 112 \pm 21$ nM) ≫ HYNIC-G_3-monomer ($IC_{50} = 358 \pm 8$ nM) > HYNIC-PEG_4-monomer ($IC_{50} = 452 \pm 11$ nM). These data indicate that the G_3 and PEG_4 linkers between two RGD motifs are responsible for the improved integrin $\alpha_v\beta_3$ affinity of HYNIC-$3G_3$-dimer and HYNIC-$3PEG_4$-dimer as compared to that of HYNIC-PEG_4-dimer. The higher binding affinity of HYNIC-tetramer is probably due to its two extra cyclic RGD motifs.

It is very important to note that the IC_{50} value depends largely on the radioligand (^{125}I-c(RGDyK) vs ^{125}I-echistatin) and tumor cell lines (U87MG vs MDA-MB-435) used in the competitive displacement assay. Caution should be taken when comparing the IC_{50} values of cyclic RGD peptides with those reported in the literature. Whenever possible, a "control compound", such as c(RGDfK) or c(RGDyK), should be used in each experiment.

Ternary ligand complexes [^{99m}Tc(HYNIC-$3PEG_4$-dimer)(tricine)(TPPTS)] (^{99m}Tc-$3PEG_4$-dimer) and [^{99m}Tc(HYNIC-$3G_3$-dimer)(tricine)(TPPTS)] (^{99m}Tc-$3G_3$-dimer) have been evaluated in the athymic nude mice bearing U87MG glioma and MDA-MB-435 breast tumor xenografts (*118, 119*). For comparison purposes, [^{99m}Tc(HYNIC-PEG_4-dimer)(tricine)(TPPTS)] (^{99m}Tc-PEG_4-dimer) and [^{99m}Tc(HYNIC-tetramer)(tricine)(TPPTS)] (^{99m}Tc-tetramer) were also evaluated in the same tumor-bearing animal model (*118, 119*). As expected, the breast tumor uptake of ^{99m}Tc-$3PEG_4$-dimer and ^{99m}Tc-$3G_3$-dimer was comparable to that of ^{99m}Tc-tetramer (Figure 8A), and was >2× higher than that of ^{99m}Tc-PEG_4-dimer (*118*). These data suggest that $3PEG_4$-dimer, $3G_3$-dimer, and tetramer are most likely "bivalent" (Figure 6B), whereas PEG_4-dimer is monodentate (Figure 6A). If PEG_4-dimer were bivalent, HYNIC-PEG_4-dimer would have shared similar integrin $\alpha_v\beta_3$ binding affinity with HYNIC-$3PEG_4$-dimer and HYNIC-$3G_3$-dimer while ^{99m}Tc-PEG_4-dimer would have had tumor uptake comparable to that of ^{99m}Tc-$3PEG_4$-dimer and ^{99m}Tc-$3G_3$-dimer. In addition, ^{99m}Tc-$3PEG_4$-dimer and ^{99m}Tc-$3G_3$-dimer had kidney and liver uptake that was half that for ^{99m}Tc-tetramer, probably because $3PEG_4$-dimer and $3G_3$-dimer have only two RGD motifs. Therefore, ^{99m}Tc-$3PEG_4$-dimer and ^{99m}Tc-$3G_3$-dimer have significant advantages over ^{99m}Tc-tetramer with respect to T/B ratios (*118, 119*).

Multimeric ≠ Multivalent. It is critical to note that multimeric RGD peptides are not necessarily multivalent. There are two factors (bivalency and enhanced local RGD concentration) contributing to high integrin $\alpha_v\beta_3$ binding affinity of multimeric RGD peptides. The concentration factor exists in all multimeric RGD peptides regardless of the linkers. The key for bivalency is the distance between two cyclic RGD motifs. For example, this distance in $3PEG_4$-dimer (38 bonds) and $3G_3$-dimer (26

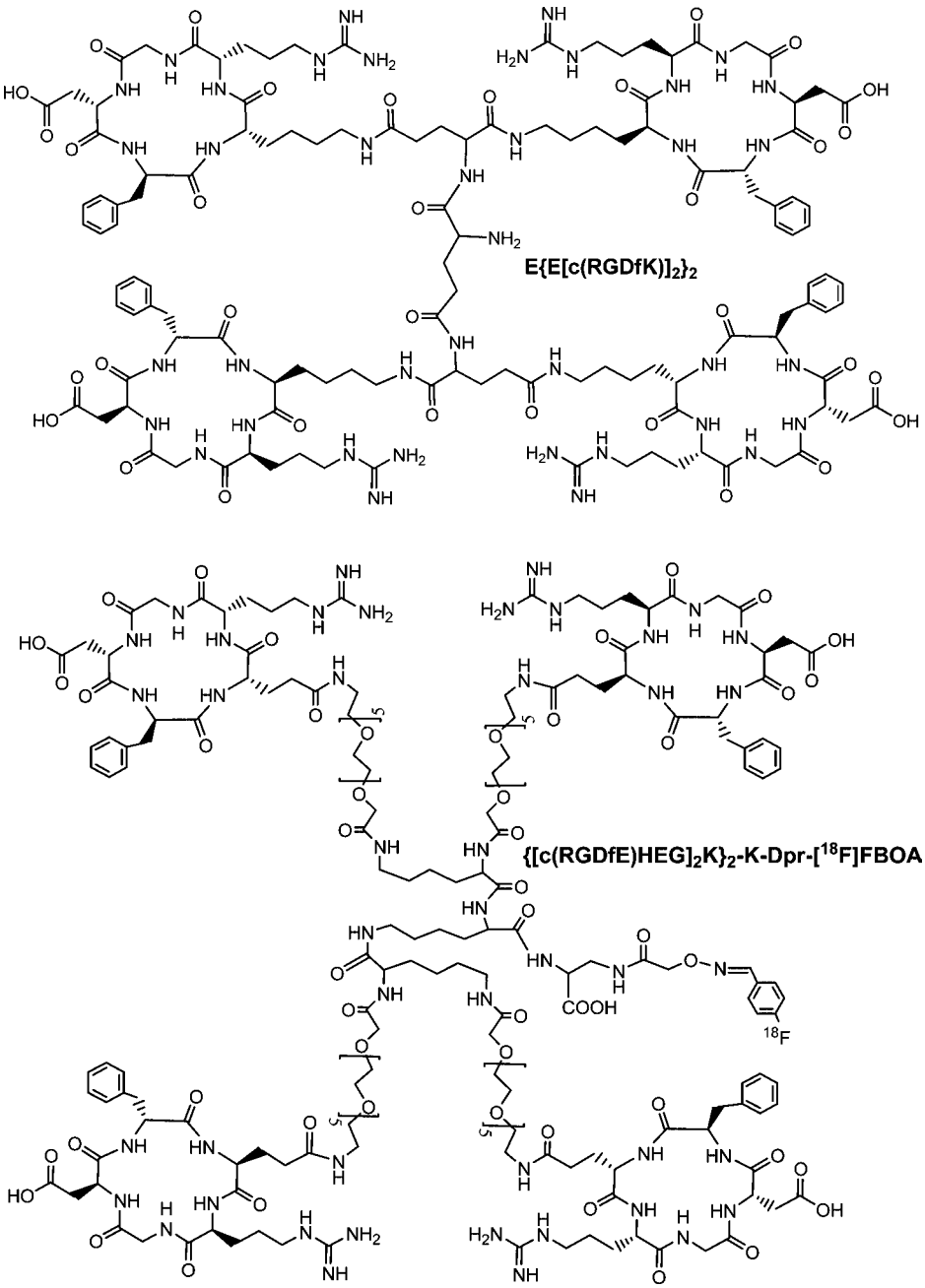

Figure 5. A cyclic RGDfK peptide tetramer, E{E[c(RGDfK)]$_2$}$_2$ and a ^{18}F-labeled cyclic RGDfE tetramer, {[c(RGDfE)HEG]$_2$K}$_2$-K-Dpr-[^{18}F]FBOA.

bonds) is long enough for them to achieve bivalency, which leads to the higher integrin $\alpha_v\beta_3$ binding affinity of HYNIC-3PEG$_4$-dimer and HYNIC-3G$_3$-dimer than that of HYNIC-PEG$_4$-dimer and the much higher breast tumor uptake (Figure 8A) for ^{99m}Tc-3PEG$_4$-dimer and ^{99m}Tc-3G$_3$-dimer as compared to that of ^{99m}Tc-PEG$_4$-dimer. In contrast, the concentration factor is responsible for the better binding affinity of HYNIC-tetramer than that of HYNIC-3PEG$_4$-dimer and HYNIC-3G$_3$-dimer. The fact that the breast tumor uptake of ^{99m}Tc-3PEG$_4$-dimer and ^{99m}Tc-3G$_3$-dimer is comparable to that of ^{99m}Tc-tetramer suggests that the contribution from the "concentration factor" might not be as significant as that from the "bivalency factor". In addition, the ability of a multimeric RGD peptide to achieve bivalency also depends on the integrin $\alpha_v\beta_3$ density. If the tumor integrin $\alpha_v\beta_3$ density is high, the distance between two neighboring integrin $\alpha_v\beta_3$ sites will be short, which makes it easier for the multimeric RGD peptide to achieve bivalency. If the integrin $\alpha_v\beta_3$ density is very low, the distance between two neighboring integrin $\alpha_v\beta_3$ sites will be long, and it might be more difficult for the same multimeric RGD peptide to achieve simultaneous integrin $\alpha_v\beta_3$ binding.

Relationship between Tumor Size and Radiotracer Tumor Uptake. The ability to quantify the integrin $\alpha_v\beta_3$ in vivo provides opportunities to select the patients more appropriately for antiangiogenic treatment and to monitor the therapeutic efficacy of integrin $\alpha_v\beta_3$-positive tumors (*120, 121*). The %ID tumor uptake reflects the total integrin $\alpha_v\beta_3$ level, while the %ID/g tumor uptake reflects the integrin $\alpha_v\beta_3$ density. Figure 8B shows the relationship between tumor size and tumor uptake (%ID and %ID/g) of ^{99m}Tc-3PEG$_4$-dimer. There was a linear relationship between tumor size and %ID tumor uptake with $R^2 = 0.9164$ (Figure 8B), suggesting that ^{99m}Tc-3PEG$_4$-dimer might be useful for monitoring tumor growth during antiangiogenic therapy (*118*). If the tumor uptake is expressed as %ID/g (Figure 8C), it seems that ^{99m}Tc-3PEG$_4$-dimer has a narrow window to achieve an optimal tumor uptake. When tumor size is small

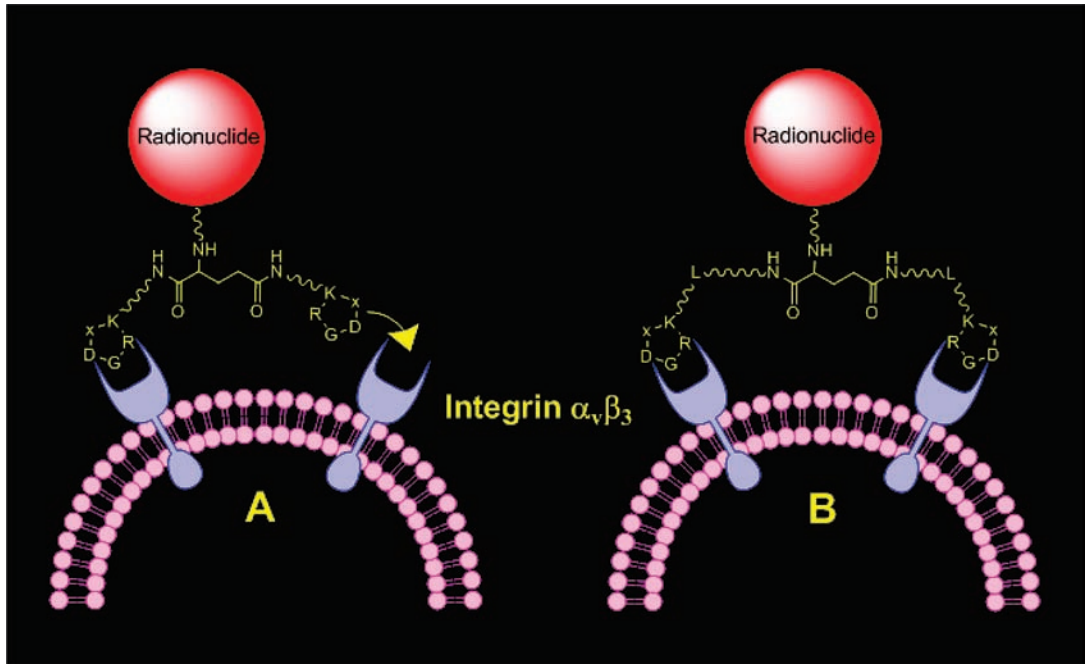

Figure 6. Schematic illustration of interactions between cyclic RGD peptide dimers and integrin $\alpha_v\beta_3$. (A) The distance between two RGD motifs is not long enough for simultaneous integrin $\alpha_v\beta_3$ binding. However, the RGD concentration is "locally enriched" in the vicinity of neighboring integrin $\alpha_v\beta_3$ once the first RGD motif is bound. (B) The distance between two RGD motifs is long due to the presence of two linkers (L). As a result, the cyclic RGD dimer is able to bind integrin $\alpha_v\beta_3$ in a "bivalent" fashion. In both cases, the end result would be higher integrin $\alpha_v\beta_3$ binding affinity for the multimeric cyclic RGD peptides.

(<0.05 g), there is little angiogenesis with low blood flow, and ^{99m}Tc-3PEG$_4$-dimer has low %ID/g tumor uptake. When the tumor size is 0.1 g−0.25 g, the microvessel density and integrin $\alpha_v\beta_3$ density are high. The %ID/g tumor uptake of ^{99m}Tc-3PEG$_4$-dimer is ~10%ID/g (Figure 8C). As tumors grow, the total integrin $\alpha_v\beta_3$ level is higher, and the %ID tumor uptake increases (Figure 8B). However, the microvessel density decreases due to maturity of blood vessels. The integrin $\alpha_v\beta_3$ density also decreases due to larger interstitial space (*122*). In addition, parts of the tumor may become necrotic, leading to the lower integrin $\alpha_v\beta_3$ density. As a result, larger tumors have lower %ID/g tumor uptake than smaller ones (Figure 8C).

Radiotracer Tumor Uptake and Tumor Cell Integrin $\alpha_v\beta_3$ Expression. Figure 9 compares the tumor uptake of ^{99m}Tc-3PEG$_4$-dimer and ^{99m}Tc-3G$_3$-dimer in athymic nude mice bearing U87MG glioma and HT29 colon cancer xenografts, and the integrin $\alpha_v\beta_3$ expression levels on U87MG glioma and HT29 cells. Both ^{99m}Tc-3PEG$_4$-dimer and ^{99m}Tc-3G$_3$-dimer have significantly higher uptake (%ID/g) in the glioma than HT29 tumors (Figure 9: top), which is supported by the presence of a higher level of integrin $\alpha_v\beta_3$ expression on U87MG glioma cells than those on HT29 cells (Figure 9: bottom). These data clearly show that the integrin $\alpha_v\beta_3$ level on tumor cells (U87MG > HT29) plays a significant role in the radiotracer tumor uptake. More fluorescent staining studies are needed to better quantify the contributions from the integrin $\alpha_v\beta_3$ expressed on the tumor cells and neovasculature in the tumor tissue.

^{64}Cu(DOTA-3PEG$_4$-dimer) and ^{64}Cu(DOTA-3G$_3$-dimer). Recently, Shi et al. (*123*) reported two cyclic RGD dimer conjugates: DOTA-3PEG$_4$-dimer and DOTA-3G$_3$-dimer (Figure 10). It was found that the integrin $\alpha_v\beta_3$ binding affinity (Table 1) follows the order of DOTA-tetramer ($IC_{50} = 10 \pm 2$ nM) > DOTA-3G$_3$-dimer ($IC_{50} = 74 \pm 3$ nM) ~ DOTA-3PEG$_4$-dimer ($IC_{50} = 62 \pm 6$, nM) > DOTA-dimer ($IC_{50} = 102 \pm 5$ nM) against ^{125}I-echistatin bound to U87MG glioma cells. Once again, bivalency is likely responsible for the higher integrin $\alpha_v\beta_3$ binding affinity of DOTA-3PEG$_4$-dimer and DOTA-3G$_3$-dimer than that of DOTA-dimer. This conclusion is completely consistent with the higher tumor uptake of ^{64}Cu(DOTA-3PEG$_4$-dimer) and ^{64}Cu(DOTA-3G$_3$-dimer) than that of ^{64}Cu(DOTA-dimer) (*123*). In contrast, the concentration factor is most likely responsible for higher integrin $\alpha_v\beta_3$ binding affinity of DOTA-tetramer than that of DOTA-3PEG$_4$-dimer and DOTA-3G$_3$-dimer, and the higher initial tumor uptake of ^{64}Cu(DOTA-tetramer) as compared to that of ^{64}Cu(DOTA-3PEG$_4$-dimer) and ^{64}Cu(DOTA-3G$_3$-dimer) (*123*). However, the uptake of ^{64}Cu-(DOTA-3PEG$_4$-dimer) in the liver and kidneys was significantly lower than that reported for ^{64}Cu(DOTA-tetramer) (*57*), due to the presence of four R-residues in E[E[c(RGDfK)]$_2$]$_2$ as compared to only two R-residues in ^{64}Cu(DOTA-3PEG$_4$-dimer) and ^{64}Cu(DOTA-3G$_3$-dimer) (*123*).

^{111}In(DOTA-3PEG$_4$-dimer) and ^{111}In(DOTA-3G$_3$-dimer). To explore the impact of radiometal chelates, ^{111}In(DOTA-3PEG$_4$-dimer) and ^{111}In(DOTA-3G$_3$-dimer) were evaluated in the same animal model (*124*). ^{111}In(DOTA-3PEG$_4$-dimer) and ^{111}In-(DOTA-3G$_3$-dimer) share the same DOTA chelator, have almost identical lipophilicity (log $P = -4.13 \pm 0.08$ and -4.20 ± 0.21, respectively), and show very similar metabolic stability (*124*). The tumor uptake of ^{111}In(DOTA-3G$_3$-dimer) is comparable to that of ^{111}In(DOTA-3PEG$_4$-dimer) (Figure 11A). Planar imaging studies showed that they both had very high tumor uptake with a long tumor retention and excellent tumor-to-background contrast (*124*). The activity accumulation in the chest and abdominal regions almost completely disappeared at 60 min p.i. The combination of the hydrophilic ^{111}In(DOTA) chelate with PEG$_4$/G$_3$ linkers is responsible for the low liver uptake for ^{111}In(DOTA-3PEG$_4$-dimer) and ^{111}In(DOTA-3G$_3$-dimer), leading to high tumor/liver ratios (Figure 11A). Both ^{111}In(DOTA-3PEG$_4$-dimer) and ^{111}In(DOTA-3G$_3$-dimer) also had low kidney and muscle uptake with very high tumor/kidney and tumor/muscle ratios (*124*). Their integrin $\alpha_v\beta_3$-specificity has been clearly demonstrated by the blocking experiment, in which ^{111}In(DOTA-3PEG$_4$-dimer) was used as the radiotracer and E[c(RGDfK)]$_2$ as the blocking agent (*124*). The RGD-specificity of ^{111}In-labeled cyclic RGD dimers was demonstrated by the higher integrin $\alpha_v\beta_3$ affinity of DOTA-3PEG$_4$-NS (IC_{50}

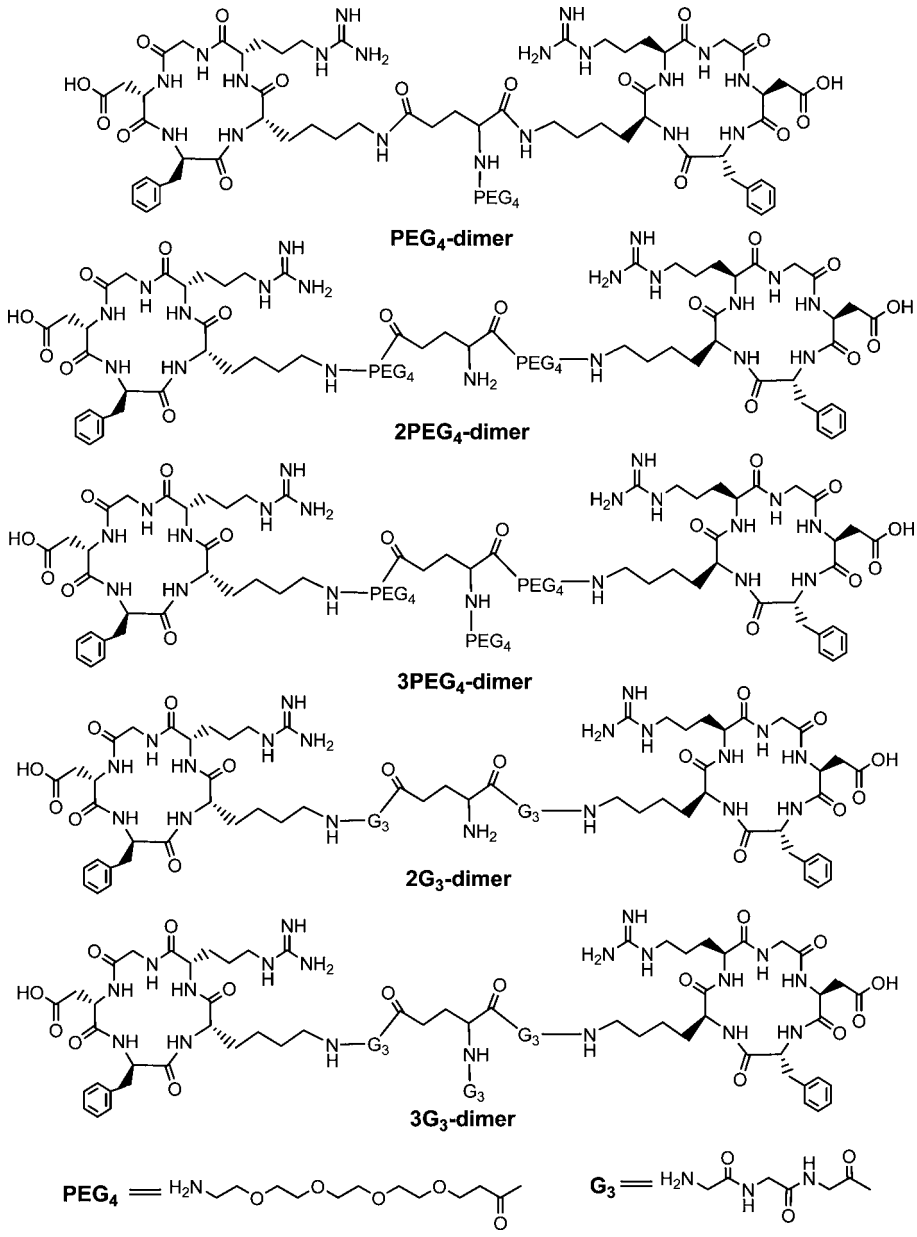

Figure 7. New cyclic RGD peptide dimers useful for the development of integrin $\alpha_v\beta_3$-targeted radiotracers. The PEG_4 and G_3 linkers are used to increase the distance between two RGD motifs and to improve radiotracer excretion kinetics from noncancerous organs.

Table 1. Integrin $\alpha_v\beta_3$ Binding Data for HYNIC-Conjugated Cyclic RGD Peptides against ^{125}I-Echistatin Bound to the Integrin $\alpha_v\beta_3$-Positive U87MG Human Glioma Cells

compound	radiotracer	IC_{50} (nM)
HYNIC-G_3-monomer	[^{99m}Tc(HYNIC-G_3-monomer)(tricine)(TPPTS)]	358 ± 8
HYNIC-PEG_4-monomer	[^{99m}Tc(HYNIC-PEG_4-monomer)(tricine)(TPPTS)]	452 ± 11
HYNIC-dimer	[^{99m}Tc(HYNIC-dimer)(tricine)(TPPTS)]	112 ± 21
HYNIC-PEG_4-dimer	[^{99m}Tc(HYNIC-PEG_4-dimer)(tricine)(TPPTS)]	84 ± 7
HYNIC-2G_3-dimer	[^{99m}Tc(HYNIC-2G_3-dimer)(tricine)(TPPTS)]	60 ± 4
HYNIC-2PEG_4-dimer	[^{99m}Tc(HYNIC-2PEG_4-dimer)(tricine)(TPPTS)]	52 ± 7
HYNIC-3G_3-dimer	[^{99m}Tc(HYNIC-3G_3-dimer)(tricine)(TPPTS)]	61 ± 2
HYNIC-3PEG_4-dimer	[^{99m}Tc(HYNIC-3PEG_4-dimer)(tricine)(TPPTS)]	62 ± 5
HYNIC-tetramer	[^{99m}Tc(HYNIC-tetramer)(tricine)(TPPTS)]	7 ± 2
DOTA-dimer	^{64}Cu(DOTA-dimer)/^{111}In(DOTA-dimer)	102 ± 5
DOTA-3G_3-dimer	^{64}Cu(DOTA-3G_3-dimer)/^{111}In(DOTA-3G_3-dimer)	74 ± 3
DOTA-3PEG_4-dimer	^{64}Cu(DOTA-3PEG_4-dimer)/^{111}In(DOTA-3PEG_4-dimer)	62 ± 6
DOTA-tetramer	^{64}Cu(DOTA-tetramer)/^{111}In(DOTA-tetramer)	10 ± 2
NOTA-dimer	^{68}Ga(NOTA-dimer)	100 ± 3
NOTA-2G_3-dimer	^{68}Ga(NOTA-2G_3-dimer)	66 ± 4
NOTA-3PEG_4-dimer	^{68}Ga(NOTA-2PEG_4-dimer)	54 ± 2

= 715 ± 45 nM; 3PEG_4-NS = PEG_4-E[PEG_4-(RGKfD)]$_2$, a scrambled nonsense peptide) than that of DOTA-3PEG_4-dimer (1.3 ± 0.3 nM), and the much better tumor uptake of ^{111}In(DOTA-3PEG_4-dimer) (10.06 ± 3.52%ID/g) than that of

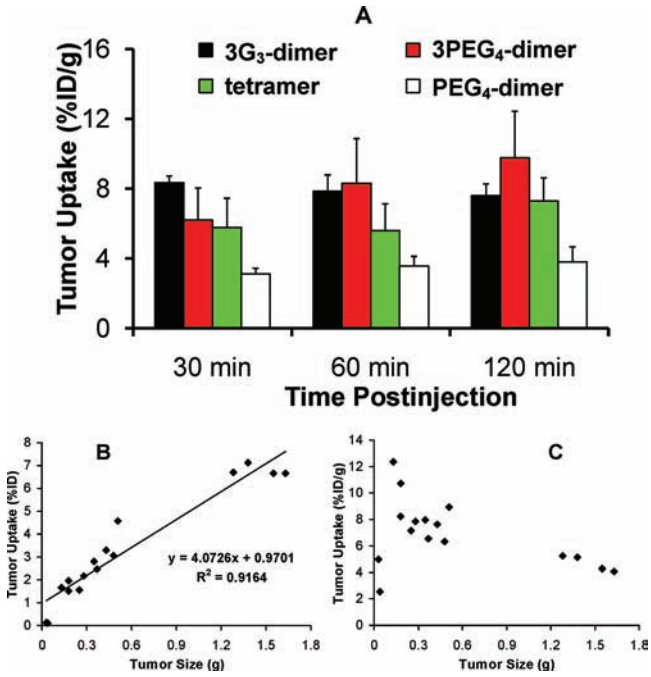

Figure 8. Top: direct comparison of the tumor uptake for ^{99m}Tc-PEG$_4$-dimer, ^{99m}Tc-3G$_3$-dimer, ^{99m}Tc-3PEG$_4$-dimer, and ^{99m}Tc-tetramer in athymic nude mice bearing MDA-MB-435 breast cancer xenografts (A). Bottom: the relationship between the tumor size and tumor uptake (B,C) of ^{99m}Tc-3PEG$_4$-dimer at 120 min p.i. in athymic nude mice bearing U87MG glioma xenografts. The linear relationship suggests that ^{99m}Tc-3PEG$_4$-dimer is for monitoring the tumor growth or shrinkage during antiangiogenic therapy.

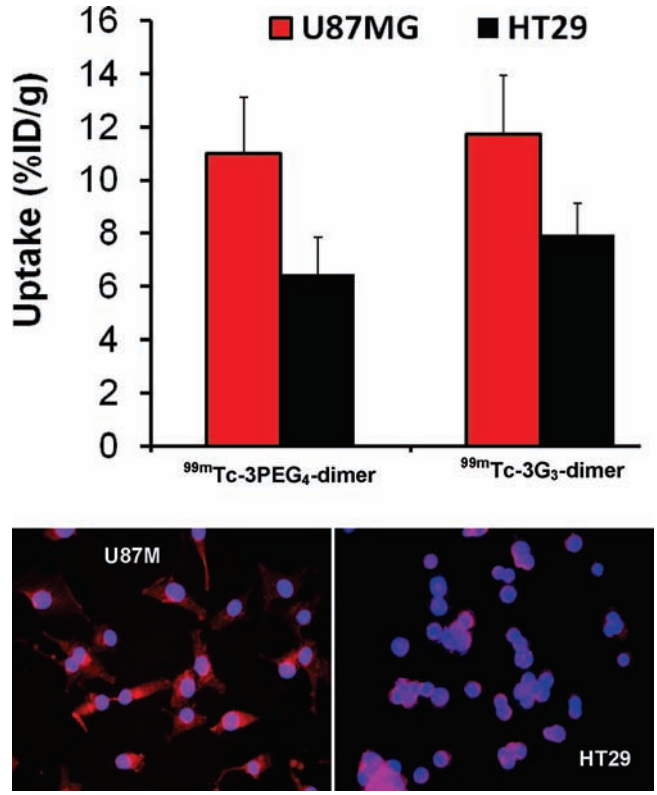

Figure 9. Top: Direct comparison of the tumor uptake for ^{99m}Tc-3PEG$_4$-dimer and ^{99m}Tc-3G$_3$-dimer in athymic nude mice bearing U87MG glioma and HT29 colon cancer xenografts. Bottom: Representative fluorescence microscopic images of U87MG glioma (left) and HT29 (right) tumor cells. The blue color indicates the presence cell nuclei (DAPI: 4′,6′-diamidino-2-phenylindole). The red color indicates the presence of integrin $\alpha_v\beta_3$ due to the binding of Alexa Fluor 488 conjugated mouse anti-human integrin $\alpha_v\beta_3$ monoclonal antibody LM609. These data show that the integrin $\alpha_v\beta_3$ level on tumor cells (U87MG > HT29) plays a significant role in the radiotracer tumor uptake.

^{111}In(DOTA-3PEG$_4$-NS) (0.30 ± 0.09%ID/g) in the same animal model. On the basis of the integrin $\alpha_v\beta_3$- and RGD-specificity of the ^{111}In-labeled cyclic RGD peptides, it has been suggested that their uptake in several normal organs (e.g., intestine, kidneys, liver, lungs, and spleen) might be also integrin $\alpha_v\beta_3$-mediated (*124*).

^{111}In(DOTA-3PEG$_4$-dimer) and ^{64}Cu(DOTA-3PEG$_4$-dimer) share the same DOTA-conjugate. In spite of their difference in radiometal, the tumor uptake ^{111}In(DOTA-3PEG$_4$-dimer) (10.89 ± 2.55 and 7.65 ± 3.17%ID/g at 30 and 240 min p.i., respectively) was close to that of ^{64}Cu(DOTA-3PEG$_4$-dimer) (8.23 ± 1.97 and 6.43 ± 1.22%ID/g at 30 and 240 min p.i., respectively). They also share similar uptake in normal organs. For example, the kidney uptake of ^{111}In(DOTA-3PEG$_4$-dimer) was 5.80 ± 0.95 and 2.78 ± 0.20%ID/g at 30 and 240 min p.i., respectively, and was comparable to that of ^{64}Cu(DOTA-3PEG$_4$-dimer) (6.59 ± 0.93%ID/g at 30 min p.i. and 2.81 ± 0.36% ID/g at 240 min p.i.). The liver uptake of ^{111}In(DOTA-3PEG$_4$-dimer) is 2.52 ± 0.57%ID/g at 30 min and 1.61 ± 0.06%ID/g at 240 min p.i., while ^{64}Cu(DOTA-3PEG$_4$-dimer) has liver uptake of 2.80 ± 0.35%ID/g at 30 min p.i. and 1.87 ± 0.51%ID/g at 240 min p.i. A similar conclusion can be made by comparing biodistribution properties of ^{64}Cu(DOTA-3G$_3$-dimer) and ^{111}In(DOTA-3G$_3$-dimer). These data suggest that the radiometal chelate (Figure 11B) has minimal impact on radiotracer tumor uptake and excretion kinetics.

^{68}Ga(NOTA-2PEG$_4$-dimer) and ^{68}Ga(NOTA-2G$_3$-dimer). We also prepared conjugates NOTA-2PEG$_4$-dimer and NOTA-2G$_3$-dimer (Figure 12: NOTA = 1,4,7-triaazacyclononane-1,4,7-tetracetic acid) and their ^{68}Ga complexes, ^{68}Ga(NOTA-2PEG$_4$-dimer), and ^{68}Ga(NOTA-2G$_3$-dimer) (*125*). The integrin $\alpha_v\beta_3$ binding affinity (Table 1) of NOTA-dimer (IC_{50} = 100 ± 3 nM), NOTA-2G$_3$-dimer (IC_{50} = 66 ± 4 nM), and NOTA-2PEG$_4$-dimer (IC_{50} = 54 ± 2 nM) were very close to those for DOTA-dimer (IC_{50} = 102 ± 5 nM), DOTA-3G$_3$-dimer (IC_{50} = 74 ± 3 nM), and DOTA-3PEG$_4$-dimer (IC_{50} = 62 ± 6 nM), respectively. These data further suggest that the G$_3$ and PEG$_4$ linkers between cyclic RGD motifs in dimeric RGD peptides make it possible for them to bind integrin $\alpha_v\beta_3$ in a bivalent fashion. The tumor uptake of ^{68}Ga(NOTA-2G$_3$-dimer) and ^{68}Ga(NOTA-2PEG$_4$-dimer) was much higher than that of ^{68}Ga(NOTA-dimer) in the same tumor-bearing animal model (*125*), suggesting that the addition of G$_3$ and PEG$_4$ linkers between two cyclic RGD motifs increases the radiotracer tumor uptake. In all cases, the tumors can be clearly visualized as early as 30 min p.i. with excellent contrast (Figure 12). It was also found that the tumor uptake of ^{68}Ga(NOTA-2PEG$_4$-dimer) in MDA-MB-435 breast tumor was significantly lower than that in U87MG glioma. Similar results were also obtained for ^{18}F-labeled 3PEG$_4$-dimer (*126*), which is consistent with that fact that the MDA-MB-435 breast tumors have lower integrin $\alpha_v\beta_3$ expression than U87MG glioma (*52*−*55*).

CONCLUSIONS

Over the past several years, many multimeric cyclic RGD peptides have been used to increase the integrin $\alpha_v\beta_3$-targeting capability. It was found that increasing the peptide multiplicity can significantly enhance their integrin $\alpha_v\beta_3$ binding affinity and improve the radiotracers tumor targeting ability. However, as peptide multiplicity increases, the uptake of radiolabeled multimeric RGD peptides is also significantly increased in normal organs. There is no significant advantage in using radiolabeled tetramers E{E[c(RGDxK)]$_2$}$_2$ (x = f and y) over their dimeric

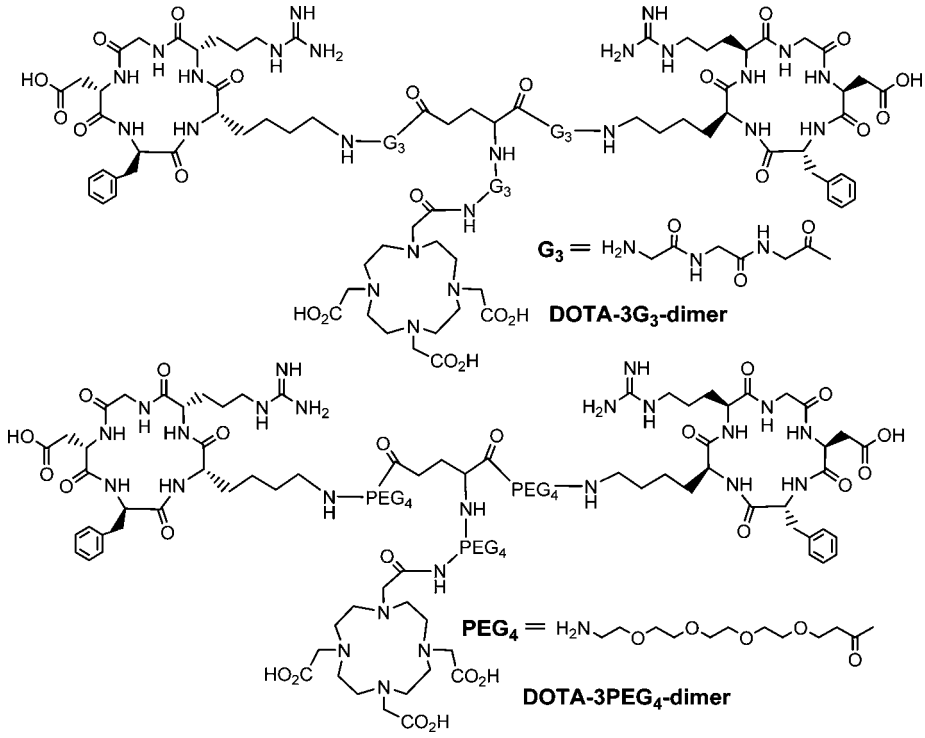

Figure 10. Structures of DOTA-3G_3-dimer and DOTA-3PEG_4-dimer.

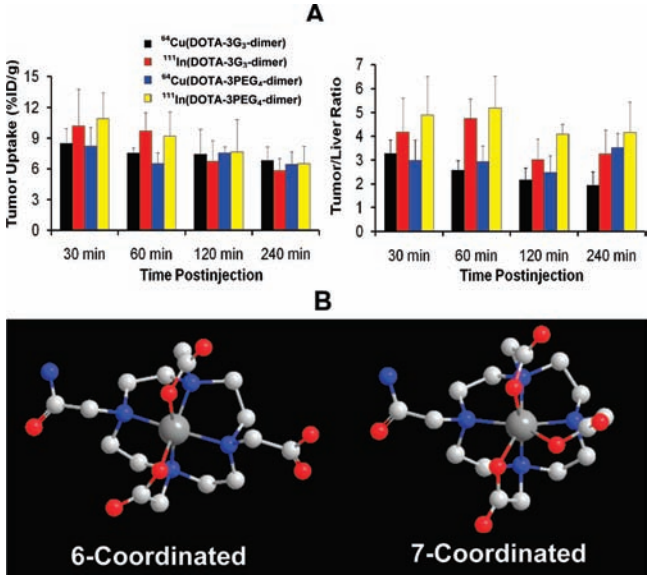

Figure 11. (A) Comparison of tumor uptake and tumor/liver ratios for ^{64}Cu(DOTA-3PEG_4-dimer), ^{64}Cu(DOTA-3G_3-dimer), ^{111}In(DOTA-3PEG_4-dimer), and ^{111}In(DOTA-3G_3-dimer) in athymic nude mice bearing U87MG human glioma xenografts. (B) Chem-3D presentation of ^{64}Cu(DOTA-monoamide) (6-coordinated) and ^{111}In(DOTA-monoamide) (7-coordinated).

analogues E[c(RGDxK)]$_2$ (x = f and y) with respect to T/B ratios. In addition, the cost for E{E[c(RGDxK)]$_2$}$_2$ (x = f and y), E{E[E[c(RGDyK)]$_2$]$_2$}$_2$ is too high for them to be useful for future radiotracer development.

Recent studies on cyclic RGD dimers suggest that two factors (bivalency and enhanced local RGD concentration) contribute to the high integrin $\alpha_v\beta_3$ binding affinity of multimeric cyclic RGD peptides (*118, 119, 123*−*126*). The concentration factor exists in all multimeric RGD peptides regardless of the linker length between two cyclic RGD motifs. To achieve bivalency, the distance between two RGD motifs must be long enough for them to bind the neighboring integrin $\alpha_v\beta_3$ sites simultaneously. Among the cyclic RGD peptides, 2PEG_4-dimer/3PEG_4-dimer and 2G_3-dimer/3G_3-dimer show most promising results with respect to the tumor uptake and T/B ratios of their radiotracers (^{99m}Tc, ^{111}In, ^{64}Cu, and ^{68}Ga). Thus, 2PEG_4-dimer/3PEG_4-dimer and 2G_3-dimer/3G_3-dimer are better integrin $\alpha_v\beta_3$-targeting biomolecules than the tetramer E{E[c(RGDfK)]$_2$}$_2$ with respect to their cost and the T/B ratios of their ^{99m}Tc, ^{111}In, ^{64}Cu, and ^{68}Ga radiotracers.

While current research efforts on the integrin $\alpha_v\beta_3$-targeted radiotracers have been focused on new cyclic RGD peptides, the formulation development for routine preparation of radiotracers is often neglected. It must be emphasized that it is common to use postlabeling chromatographic separation for improvement of radiotracer purity and specific activity for research purposes. In clinical settings, however, postlabeling purification is not practical. Regardless of the beauty of the science involved in the discovery of a new radiotracer, its success relies largely on the availability and capability to improve the quality of cancer patient's life. As a matter of fact, the main challenge for [^{18}F]Galacto-RGD and [^{18}F]-AH111585 to assume a widespread clinical utility is not their biological performance, but their clinical availability at reasonable cost. In this respect, the integrin $\alpha_v\beta_3$-targeted ^{99m}Tc radiotracers will offer significant advantages over their corresponding ^{18}F analogues because of the clinical availability of ^{99}Mo−^{99m}Tc generators, and the kit formulation for routine preparation of ^{99m}Tc radiotracers at low cost. However, both planar imaging and SPECT suffer a significant drawback with respect to quantification of the radiotracer "absolute" organ uptake, the speed of dynamic imaging, spatial resolution, and tissue attenuation.

The successful application of the ^{68}Ga-labeled somatostatin analogues for imaging tumors in cancer patients has clearly demonstrated that ^{68}Ga is an excellent alternative to ^{18}F. ^{68}Ga is available from an in-house commercially available ^{68}Ge/^{68}Ga generator (*127*−*129*), and its short half-life is best suited for the fast excretion kinetics of many ^{68}Ga-labeled small peptides. ^{64}Cu is another viable alternative to ^{18}F. The use of NOTA and its derivatives as BFCs allows the development of the kit

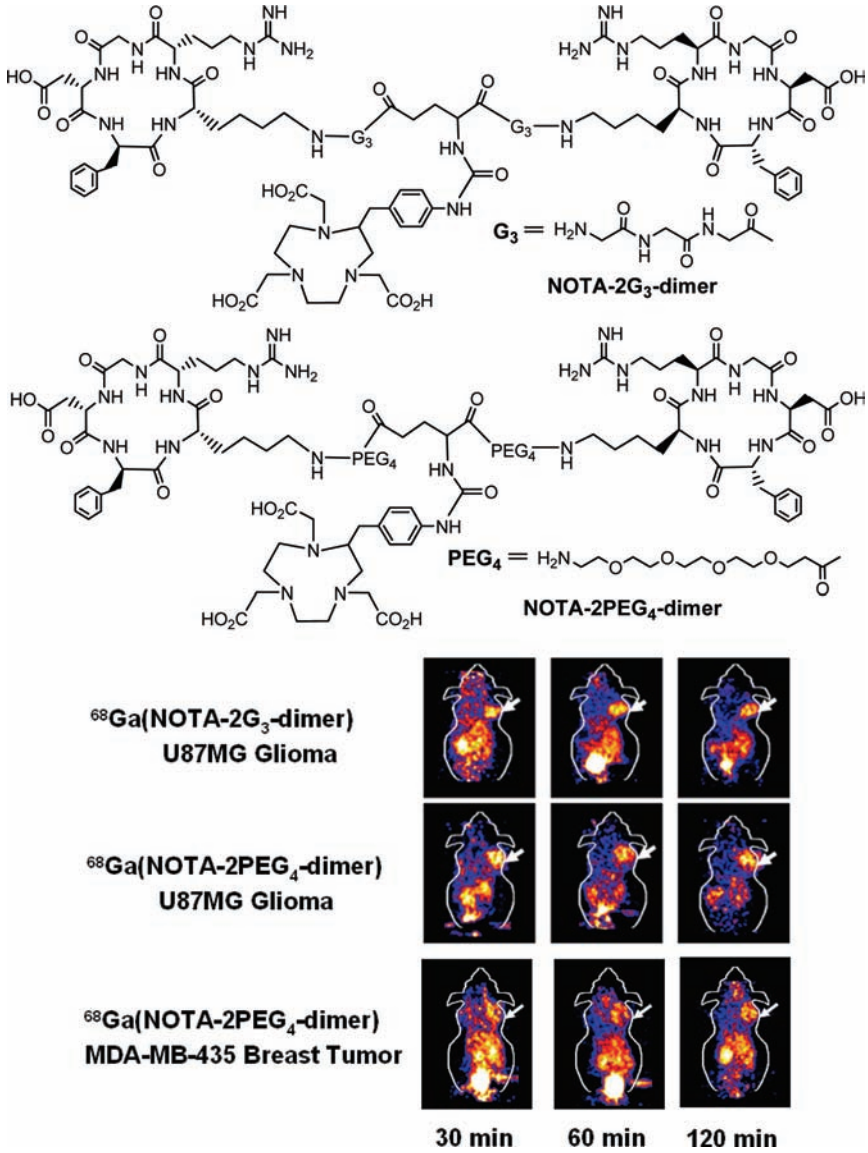

Figure 12. Top: Structures of NOTA-2G_3-dimer and NOTA-2PEG_4-dimer. Bottom: microPET images for ^{68}Ga(NOTA-2G_3-dimer) and ^{68}Ga(NOTA-2PEG_4-dimer). Arrows indicate the presence of tumors.

formulation for routine preparation of ^{68}Ga and ^{64}Cu radiotracers with high specific activity. In addition, ^{68}Ga(NOTA) and ^{64}Cu(NOTA) chelates have very high hydrophilicity, which is extremely important for improving the radiotracer clearance kinetics from noncancerous organs.

It is very important to note that integrin $\alpha_v\beta_3$ is also overexpressed on the activated endothelial cells during wound healing and postinfarct remodeling, in rheumatoid arthritis, and atherosclerotic plaque (*1*−*4, 130, 131*). The integrin $\alpha_v\beta_3$-targeted radiotracers have been proposed for imaging myocardial angiogenesis (*132*), inflammatory diseases (*133*), and hindlimb ischemia (*134*). Recent results showed that the ^{111}In-labeled nonpeptide integrin $\alpha_v\beta_3$ antagonist (RP748) was able to image the angiogenesis in the heart with myocardial infarction (*132*), and the radiotracer uptake in the infarct region was associated with the integrin $\alpha_v\beta_3$ expression level. The results reported by Pichler et al. suggest that [^{18}F]Galacto-RGD might be a powerful tool to distinguish between acute and chronic phases of T-cell mediated immune responses (*133*). Studies have also demonstrated the value of a ^{99m}Tc-labeled cyclic RGD monomer (NC100692) for imaging the integrin $\alpha_v\beta_3$ in rodent models of hindlimb ischemia (*134*). These promising results suggest that the newer and more effective integrin $\alpha_v\beta_3$-targeted radiotracers under development for tumor imaging might become valuable noninvasive markers of angiogenesis after ischemic injury, myocardial infarction, and inflammation. In addition, the combination of high tumor uptake, long tumor retention with favorable pharmacokinetics of ^{111}In(DOTA-3G_3-dimer) and ^{111}In(DOTA-3PEG_4-dimer) suggests that their corresponding ^{90}Y and ^{177}Lu analogues, M(DOTA-RGD) (M = ^{90}Y and ^{177}Lu; and RGD = 3G_3-dimer and 3PEG_4-dimer), might be useful for the treatment of integrin $\alpha_v\beta_3$-positive tumors.

ACKNOWLEDGMENT

The author would like to thank Dr. Xiaoyuan Chen at Stanford Medical School and Dr. Fan Wang at the Beijing University Medical Isotopes Research Center for their collaboration on the radiolabeled multimeric cyclic RGD peptides. This work is supported, in part, by Purdue University and research grants: R01 CA115883 A2 (S.L.) from the National Cancer Institute (NCI) and DE-FG02-08ER64684 from the Department of Energy.

LITERATURE CITED

(1) Folkman, J. (1995) Angiogenesis in cancer, vascular, rheumatoid and other disease. *Nat. Med. 1*, 27–31.

(2) Mousa, S. A. (1998) Mechanism of angiogenesis in vascular disorders: potential therapeutic targets. *Drugs of the Future 23*, 51–60.
(3) Carmeliet, P. (2000) Mechanisms of angiogenesis and arteriogenesis. *Nat. Med. 6*, 389–395.
(4) Meitar, D., Crawford, S. E., Rademaker, A. W., and Cohn, S. L. (1996) Tumor angiogenesis correlates with metastatic disease, N-myc-amplification, and poor outcome in human neuroblastoma. *J. Clin. Oncol. 14*, 405–414.
(5) Gasparini, G., Brooks, P. C., Biganzoli, E., Vermeulen, P. B., Bonoldi, E., Dirix, L. Y., Ranieri, G., Miceli, R., and Cheresh, D. A. (1998) Vascular integrin $\alpha_v\beta_3$: a new prognostic indicator in breast cancer. *Clin. Cancer Res. 4*, 2625–2634.
(6) Falcioni, R., Cimino, L., Gentileschi, M. P., D'Agnano, I., Zupi, G., Kennel, S. J., and Sacchi, A. (1994) Expression of beta 1, beta 3, beta 4, and beta 5 integrins by human lung carcinoma cells of different histotypes. *Exp. Cell Res. 210*, 113–122.
(7) Sengupta, S., Chattopadhyay, N., Mitra, A., Ray, S., Dasgupta, S., and Chatterjee, A. (2001) Role of $\alpha_v\beta_3$ integrin receptors in breast tumor. *J. Exp. Clin. Cancer Res. 20*, 585–590.
(8) Bögler, O., and Mikkelsen, T. (2003) Angiogenesis in Glioma: molecular mechanisms and roadblocks to translation. *Cancer J. 9*, 205–213.
(9) Folkman, J. (2002) Role of angiogenesis in tumor growth and metastasis. *Semin. Oncol. 29*, 15–18.
(10) Hwang, R., and Varner, J. V. (2004) The role of integrins in tumor angiogenesis. *Hematol. Oncol. Clin. North Am. 18*, 991–1006.
(11) Brooks, P. C., Clark, R. A. F., and Cheresh, D. A. (1994) Requirement of vascular integrin $\alpha_v\beta_3$ for angiogenesis. *Science 264*, 569–571.
(12) Friedlander, M., Brooks, P. C., Shaffer, R. W., Kincaid, C. M., Varner, J. A., and Cheresh, D. A. (1995) Definition of two angiogenic pathways by distinct α_v integrin. *Science 270*, 1500–1502.
(13) Horton, M. A. (1997) The $\alpha_v\beta_3$ integrin "vitronectin receptor". *Int. J. Biochem. Cell Biol. 29*, 721–725.
(14) Bello, L., Francolini, M., Marthyn, P., Zhang, J. P., Carroll, R. S., Nikas, D. C., Strasser, J. F., Villani, R., Cheresh, D. A., and Black, P. M. (2001) Alpha(v)beta3 and alpha(v)beta5 integrin expression in glioma periphery. *Neurosurgery 49*, 380–389.
(15) Albelda, S. M., Mette, S. A., Elder, D. E., Stewart, R. M., Damjanovich, L., Herlyn, M., and Buck, C. A. (1990) Integrin distribution in maliganant melanoma: association of the beta3 subunit with tumor progression. *Cancer Res. 50*, 6757–6764.
(16) Felding-Habermann, B., Mueller, B. M., Romerdahl, C. A., and Cheresh, D. A. (1992) Involvement of integrin alpha V gene expression in human melanoma tumorigenicity. *J. Clin. Invest. 89*, 2018–2022.
(17) Zitzmann, S., Ehemann, V., and Schwab, M. (2002) Arginine-glycine-aspartic acid (RGD)-peptide binds to both tumor and tumor endothelial cells in vivo. *Cancer Res. 62*, 5139–5143.
(18) Weber, W. A., Haubner, R., Vabuliene, E., Kuhnast, B., Webster, H. J., and Schwaiger, M. (2001) Tumor angiogenesis targeting using imaging agents. *Q. J. Nucl. Med. 45*, 179–182.
(19) Costouros, N. G., Diehn, F. E., and Libutti, S. K. (2002) Molecular imaging of tumor angiogenesis. *J. Cell Biol. Suppl. 39*, 72–78.
(20) van de Wiele, C., Oltenfreiter, R., De Winter, O., Signore, A., Slegers, G., and Dierckx, R. A. (2002) Tumor angiogenesis pathways: related clinical issues and implications for nuclear medicine imaging. *Eur. J. Nucl. Med. 29*, 699–709.
(21) Liu, S., and Edwards, D. S. (2002) Fundamentals of receptor-based diagnostic metalloradiopharmaceuticals. *Top. Curr. Chem. 222*, 259–278.
(22) Liu, S., Robinson, S. P., and Edwards, D. S. (2003) Integrin $\alpha_v\beta_3$ directed radiopharmaceuticals for tumor imaging. *Drugs of the Future 28*, 551–564.
(23) Haubner, R., and Wester, H. J. (2004) Radiolabeled tracers for imaging of tumor angiogenesis and evaluation of antiangiogenic therapies. *Curr. Pharm. Des. 10*, 1439–1455.
(24) D'Andrea, L. D., Del Gatto, A., Pedone, C., and Benedetti, E. (2006) Peptide-based molecules in angiogenesis. *Chem. Biol. Drug Des. 67*, 115–126.
(25) Chen, X. (2006) Multimodality imaging of tumor integrin $\alpha_v\beta_3$ expression. *Mini-Rev. Med. Chem. 6*, 227–234.
(26) Liu, S. (2006) Radiolabeled multimeric cyclic RGD peptides as integrin $\alpha_v\beta_3$-targeted radiotracers for tumor imaging. *Mol. Pharm. 3*, 472–487.
(27) Cai, W., and Chen, X. (2008) Multimodality molecular imaging of tumor angiogenesis. *J. Nucl. Med. 49*, 113S–128S.
(28) Cai, W., Niu, G., and Chen, X. (2008) Imaging of integrins as biomarkers for tumor angiogenesis. *Curr. Pharm. Des. 14*, 2943–2973.
(29) Chen, X. (2008) Advances in anatomic, functional, and molecular imaging of angiogenesis. *J. Nucl. Med. 49*, 511–514.
(30) Jin, H., and Varner, J. (2004) Integrins: roles in cancer development and as treatment targets. *Br. J. Cancer 90*, 561–565.
(31) Kumar, C. C. (2003) Integrin $\alpha_v\beta_3$ as a therapeutic target for blocking tumor-induced angiogenesis. *Curr. Drug Targets 4*, 123–131.
(32) Meyer, A., Aurenheimer, J., Modlinger, A., and Kessler, H. (2006) Targeting RGD recognizing integrins: drug development, biomaterial research, tumor imaging and targeting. *Curr. Pharm. Des. 12*, 2723–2747.
(33) Van Hagen, P. M., Breeman, W. A. P., Bernard, H. F., Schaar, M., Mooij, C. M., Srinivasan, A., Schmidt, M. A., Krenning, E. P., and de Jong, M. (2000) Evaluation of a radiolabeled cyclic DTPA-RGD analog for tumor imaging and radionuclide therapy. *Int. J. Cancer (Radiat. Oncol. Invest.) 90*, 186–198.
(34) Huabner, R., Wester, H. J., Senekowitsch-Schmidtke, R., Diefenbach, B., Kessler, H., Stöcklin, G., and Schwaiger, M. (1997) RGD-peptides for tumor targeting: biological evaluation of radioiodinated analogs and introduction of a novel glycosylated peptide with improved biokinetics. *J. Labelled Compd. Radiopharm. 40*, 383–385.
(35) Sivolapenko, G. B., Skarlos, D., Pectasides, D., Stathopoulou, E., Milonakis, A., Sirmalis, G., Stuttle, A., Courtenay-Luck, N. S., Konstantinides, K., and Epenetos, A. A. (1998) Imaging of metastatic melanoma utilizing a technetium-99m labeled RGD-containing synthetic peptide. *Eur. J. Nucl. Med. 25*, 1383–1389.
(36) Haubner, R., Wester, H. J., Weber, W. A., Mang, C., Ziegler, S. I., Goodman, S. L., Senekowitsch-Schmidtke, R., Kessler, H., and Schwaiger, M. (2001) Noninvasive imaging of $\alpha_v\beta_3$ integrin expression using ^{18}F-labeled RGD-containing glycopeptide and positron emission tomography. *Cancer Res. 61*, 1781–1785.
(37) Haubner, R., Wester, H. J., Reuning, U., Senekowitsch-Schmidtke, R., Diefenbach, B., Kessler, H., Stöcklin, G., and Schwaiger, M. (1999) Radiolabeled $\alpha_v\beta_3$ integrin antagonists: a new class of tracers for tumor imaging. *J. Nucl. Med. 40*, 1061–1071.
(38) Haubner, R., Wester, H. J., Burkhart, F., Senekowisch-Schmidtke, R., Weber, W., Goodman, S. L., Kessler, H., and Schwaiger, M. (2001) Glycolated RGD-containing peptides: tracer for tumor targeting and angiogenesis imaging with improved biokinetics. *J. Nucl. Med. 42*, 326–336.
(39) Haubner, R., Bruchertseifer, F., Bock, M., Kessler, H., Schwaiger, M., and Wester, H. J. (2004) Synthesis and biological evaluation of ^{99m}Tc-labeled cyclic RGD peptide for imaging the $\alpha_v\beta_3$ expression. *Nuklearmedizin 43*, 26–32.
(40) Thumshirn, G., Hersel, U., Goodman, S. L., and Kessler, H. (2003) Multimeric cyclic RGD peptides as potential tools for tumor targeting: solid-phase peptide synthesis and chemoselective oxime ligation. *Chem.—Eur. J. 9*, 2717–2725.
(41) Poethko, T., Schottelius, M., Thumshirn, G., Herz, M., Haubner, R., Henriksen, G., Kessler, H., Schwaiger, M., and Wester, H. J. (2004) Chemoselective pre-conjugate radiohalogenation of unprotected mono- and multimeric peptides via oxime formation. *Radiochim. Acta 92*, 317–327.
(42) Poethko, T., Schottelius, M., Thumshirn, G., Hersel, U., Herz, M., Henriksen, G., Kessler, H., Schwaiger, M., and Wester, H. J.

(2004) Two-step methodology for high yield routine radiohalogenation of peptides: ^{18}F-labeled RGD and octreotide analogs. *J. Nucl. Med. 45*, 892–902.

(43) Alves, S., Correia, J. D. G., Gano, L., Rold, T. L., Prasanphanich, A., Haubner, R., Rupprich, M., Alberto, R., Decristoforo, C., Santos, I., and Smith, C. J. (2007) In vitro and in vivo evaluation of a novel ^{99m}Tc(CO)$_3$-pyrazolyl conjugate of *cyclo*-(Arg-Gly-Asp-D-Tyr-Lys). *Bioconjugate Chem. 18*, 530–537.

(44) Fani, M., Psimadas, D., Zikos, C., Xanthopoulos, S., Loudos, G. K., Bouziotis, P., and Varvarigou, A. D. (2006) Comparative evaluation of linear and cyclic ^{99m}Tc-RGD peptides for targeting of integrins in tumor angiogenesis. *Anticancer Res. 26*, 431–434.

(45) Su, Z. F., Liu, G., Gupta, S., Zhu, Z., Rusckowski, M., and Hnatowich, D. J. (2002) In vitro and in vivo evaluation of a technetium-99m-labeled cyclic RGD peptide as specific marker of $\alpha_v\beta_3$ integrin for tumor imaging. *Bioconjugate Chem. 13*, 561–570.

(46) Decristoforo, C., Faintuch-Linkowski, B., Rey, A., von Guggenberg, E., Rupprich, M., Hernandez-Gonzales, I., Rodrigo, T., and Haubner, R. (2006) [^{99m}Tc]HYNIC-RGD for imaging integrin $\alpha_v\beta_3$ expression. *Nucl. Med. Biol. 33*, 945–952.

(47) Chen, X., Park, R., Tohme, M., Shahinian, A. H., Bading, J. R., and Conti, P. S. (2004) MicroPET and autoradiographic imaging of breast cancer α_v-integrin expression using ^{18}F- and ^{64}Cu-labeled RGD peptide. *Bioconjugate Chem. 15*, 41–49.

(48) Chen, X., Park, R., Shahinian, A. H., Tohme, M., Khankaldyyan, V., Bozorgzadeh, M. H., Bading, J. R., Moats, R., Laug, W. E., and Conti, P. S. (2004) ^{18}F-labeled RGD peptide: initial evaluation for imaging brain tumor angiogenesis. *Nucl. Med. Biol. 31*, 179–189.

(49) Chen, X., Park, R., Shahinian, A. H., Bading, J. R., and Conti, P. S. (2004) Pharmacokinetics and tumor retention of ^{125}I-labeled RGD peptide are improved by PEGylation. *Nucl. Med. Biol. 31*, 11–19.

(50) Chen, X., Liu, S., Hou, Y., Tohme, M., Park, R., Bading, J. R., and Conti, P. S. (2004) MicroPET imaging of breast cancer α_v-integrin expression with ^{64}Cu-labeled dimeric RGD peptides. *Mol. Imaging Biol. 6*, 350–359.

(51) Chen, X., Tohme, M., Park, R., Hou, Y., Bading, J. R., and Conti, P. S. (2004) MicroPET imaging of breast cancer α_v-integrin expression with ^{18}F-labeled dimeric RGD peptide. *Mol. Imaging 3*, 96–104.

(52) Wu, Y., Zhang, X., Xiong, Z., Cheng, Z., Fisher, D. R., Liu, S., Gambhir, S. S., and Chen, X. (2005) MicroPET imaging of glioma integrin $\alpha_v\beta_3$ expression using ^{64}Cu-labeled tetrameric RGD peptide. *J. Nucl. Med. 46*, 1707–1718.

(53) Zhang, X., Xiong, Z., Wu, Y., Cai, W., Tseng, J. R., Gambhir, S. S., and Chen, X. (2006) Quantitative PET imaging of tumor integrin $\alpha_v\beta_3$ expression with ^{18}F-FRGD2. *J. Nucl. Med. 47*, 113–121.

(54) Wu, Z., Li, Z., Chen, K., Cai, W., He, L., Chin, F. T., Li, F., and Chen, X. (2007) MicroPET of tumor integrin $\alpha_v\beta_3$ expression using ^{18}F-labeled PEGylated tetrameric RGD peptide (^{18}F-FPRGD4). *J. Nucl. Med. 48*, 1536–1544.

(55) Li, Z. B., Chen, K., and Chen, X. (2008) ^{68}Ga-labeled multimeric RGD peptides for microPET imaging of integrin $\alpha v\beta 3$ expression. *Eur. J. Nucl. Med. Mol. Imaging 35*, 1100–1108.

(56) Liu, S., Cheung, E., Rajopadhye, M., Ziegler, M. C., and Edwards, D. S. (2001) ^{90}Y- and ^{177}Lu-labeling of a DOTA-conjugated vitronectin receptor antagonist for tumor therapy. *Bioconjugate Chem. 12*, 559–568.

(57) Janssen, M., Oyen, W. J. G., Massuger, L. F. A. G., Frielink, C., Dijkgraaf, I., Edwards, D. S., Rajopadhye, M., Corsten, F. H. M., and Boerman, O. C. (2002) Comparison of a monomeric and dimeric radiolabeled RGD-peptide for tumor targeting. *Cancer Biother. Radiopharm. 17*, 641–646.

(58) Janssen, M., Oyen, W. J. G., Dijkgraaf, I., Massuger, L. F. A. G., Frielink, C., Edwards, D. S., Rajopadyhe, M., Boonstra, H., Corsten, F. H. M., and Boerman, O. C. (2002) Tumor targeting with radiolabeled $\alpha_v\beta_3$ integrin binding peptides in a nude mice model. *Cancer Res. 62*, 6146–6151.

(59) Janssen, M. L., Frielink, C., Dijkgraaf, I., Oyen, W. J., Edwards, D. S., Liu, S., Rajopadhye, M., Massuger, L. F., Corstens, F. H. M., and Boerman, O. C. (2004) Improved tumor targeting of radiolabeled RGD-peptides using rapid dose fractionation. *Cancer Biother. Radiopharm. 19*, 399–404.

(60) Liu, S., Hsieh, W. Y., Kim, Y. S., and Mohammed, S. I. (2005) Effect of coligands on biodistribution characteristics of ternary ligand ^{99m}Tc complexes of a HYNIC-conjugated cyclic RGDfK dimer. *Bioconjugate Chem. 16*, 1580–1588.

(61) Jia, B., Shi, J., Yang, Z., Xu, B., Liu, Z., Zhao, H., Liu, S., and Wang, F. (2006) ^{99m}Tc-labeled cyclic RGDfK dimer: initial evaluation for SPECT imaging of glioma integrin $\alpha_v\beta_3$ expression. *Bioconjugate Chem. 17*, 1069–1076.

(62) Liu, S., He, Z. J., Hsieh, W. Y., Kim, Y. S., and Jiang, Y. (2006) Impact of PKM linkers on biodistribution characteristics of the ^{99m}Tc-labeled cyclic RGDfK dimer. *Bioconjugate Chem. 17*, 1499–1507.

(63) Liu, S., Hsieh, W. Y., Jiang, Y., Kim, Y. S., Sreerama, S. G., Chen, X., Jia, B., and Wang, F. (2007) Evaluation of a ^{99m}Tc-labeled cyclic RGD tetramer for noninvasive imaging integrin $\alpha_v\beta_3$-positive breast cancer. *Bioconjugate Chem. 18*, 438–446.

(64) Dijkgraaf, I., Liu, S., Kruijtzer, J. A. W., Soede, A. C., Oyen, W. J. G., Liskamp, R. M. J., Corstens, F. H. M., and Boerman, O. C. (2007) Effect of linker variation on the in vitro and in vivo characteristics of an ^{111}In-labeled RGD peptide. *Nucl. Med. Biol. 34*, 29–35.

(65) Dijkgraaf, I., Kruijtzer, J. A. W., Liu, S., Soede, A., Oyen, W. J. G., Corstens, F. H. M., Liskamp, R. M. J., and Boerman, O. C. (2007) Improved targeting of the $\alpha_v\beta_3$ integrin by multimerization of RGD peptides. *Eur. J. Nucl. Med. Mol. Imaging 34*, 267–273.

(66) Liu, S., Kim, Y. S., Hsieh, W. Y., and Sreerama, S. G. (2008) Coligand effects on solution stability, biodistribution and metabolism of ^{99m}Tc-labeled cyclic RGDfK tetramer. *Nucl. Med. Biol. 35*, 111–121.

(67) Jia, B., Liu, Z., Shi, J., Yu, Z. L., Yang, Z., Zhao, H. Y., He, Z. J., Liu, S., and Wang, F. (2008) Linker effects on biological properties of ^{111}In-labeled DTPA conjugates of a cyclic RGDfK dimer. *Bioconjugate Chem. 19*, 201–210.

(68) Wang, J. J., Kim, Y. S., He, Z. J., and Liu, S. (2008) ^{99m}Tc-labeling of HYNIC-conjugated cyclic RGDfK dimer and tetramer using EDDA as coligand. *Bioconjugate Chem. 19*, 634–642.

(69) Liu, S., and Edwards, D. S. (1999) ^{99m}Tc-labeled small peptides as diagnostic radiopharmaceuticals. *Chem. Rev. 99*, 2235–2268.

(70) Liu, S. (2004) The role of coordination chemistry in development of target-specific radiopharmaceuticals. *Chem. Soc. Rev. 33*, 1–18.

(71) Liu, S., and Edwards, D. S. (2001) Bifunctional chelators for therapeutic lanthanide radiopharmaceuticals. *Bioconjugate Chem. 12*, 7–34.

(72) Jurisson, S. S., and Lydon, J. D. (1999) Potential technetium small molecule radiopharmaceuticals. *Chem. Rev. 99*, 2205–2218.

(73) Cai, W., Zhang, X., Wu, Y., and Chen, X. (2006) A thiol-reactive ^{18}F-labeling agent, N-[2-(4-^{18}F-fluorobenzamido)ethyl]maleimide, and synthesis of RGD peptide-based tracer for PET imaging of $\alpha v\beta 3$ integrin expression. *J. Nucl. Med. 47*, 1172–1180.

(74) Welch, M. J., and McCarthy, T. J. (2000) The potential role of generator-produced radiopharmaceuticals in clinical PET. *J. Nucl. Med. 41*, 315–317.

(75) Anderson, C. J., Green, M. A., and Yashi, Y. F. (2003) Chemistry of copper radionuclides and radiopharmaceutical products. In *Handbook of Radiopharmaceuticals: Radiochemistry and Applications* (Welch, M. J., and Redvanly, C. S., Ed.) pp 401−422, John Wiley & Sons, New York.

(76) Bormans, G., Janssen, A., Adriaens, P., Crombez, D., Witsenboer, A., Degoeij, J., Mortelmans, L., and Verbruggen, A. (1992) ^{62}Zn/^{62}Cu generator for the routine production of ^{62}Cu-PTSM. *Appl. Radiat. Isot. 43*, 1437–1441.

(77) Haynes, N. G., Lacy, J. L., Nayak, N., Martin, C. S., Dai, D., Mathias, C. J., and Green, M. A. (2000) Performance of a ^{62}Zn/^{62}Cu generator in clinical trials of PET perfusion agent ^{62}Cu-PTSM. *J. Nucl. Med. 41*, 309–314.

(78) Smith, S. V. (2004) Molecular imaging with copper-64. *J. Inorg. Biochem. 98*, 1874–1901.

(79) Blower, P. J., Lewis, J. S., and Zweit, J. (1996) Copper radionuclides and radiopharmaceuticals in nuclear medicine. *Nucl. Med. Biol. 23*, 957–980.

(80) Reichert, D. E., Lewis, J. S., and Anderson, C. J. (1999) Metal complexes as diagnostic tools. *Coord. Chem. Rev. 184*, 3–66.

(81) Maecke, H., Hofmann, M., and Haberkorn, U. (2005) ^{68}Ga-labeled peptides in tumor imaging. *J. Nucl. Med. 46*, 172S–178S.

(82) Heppeler, A., Froidevaux, S., Eberle, A. N., and Maecke, H. R. (2000) Receptor targeting for tumor localisation and therapy with radiopeptides. *Curr. Med. Chem. 7*, 971–994.

(83) Heppeler, A., Froidevaux, S., Mäcke, H. R., Jermann, E., Béhé, M., Powell, P., and Hennig, M. (1999) Radiometal-labelled macrocyclic chelator-derivatised somatostatin analogue with superb tumour targeting properties and potential for receptor-mediated internal radiotherapy. *Chem.—Eur. J. 5*, 1974–1981.

(84) Henze, M., Schuhmacher, J., Hipp, P., Kowalski, J., Becker, D. W., Doll, F., Mäcke, H. R., Hofmann, M., Debus, J., and Haberkorn, U. (2001) PET imaging of somatostatin receptors using [^{68}GA]DOTAD- Phe1-Tyr^3-octreotide: first results in patients with meningiomas. *J. Nucl. Med. 42*, 1053–1056.

(85) Froidevaux, S., Eberle, A. N., Christe, M., Sumanovski, L., Heppeler, A., Schmitt, J. S., Eisenwiener, K., Beglinger, C., and Mäcke, H. R. (2002) Neuroendocrine tumor targeting: study of novel galliumlabeled somatostatin radiopeptides in a rat pancreatic tumor model. *Int. J. Cancer 98*, 930–937.

(86) Hofmann, M., Maecke, H., Borner, A. R., Weckesser, E., Schoffski, P., Oei, M. L., Schumacher, J., Henze, M., Heppeler, A., Meyer, G. J., and Knapp, W. H. (2001) Biokinetics and imaging with the somatostatin receptor PET radioligand ^{68}Ga-DOTATOC: preliminary data. *Eur. J. Nucl. Med. 28*, 1751–1757.

(87) Kowalski, J., Henze, M., Schuhmacher, J., Macke, H. R., Hofmann, M., and Haberkorn, U. (2003) Evaluation of positron emission tomography imaging using ^{68}Ga-DOTA-D Phe(1)-Tyr(3)-octreotide in comparison to ^{111}In-DTPAOC SPECT. First results in patients with neuroendocrine tumors. *Mol. Imaging Biol. 5*, 42–48.

(88) Henze, M., Schuhmacher, J., Dimitrakopoulou-Strauss, A., Strauss, L. G., Macke, H. R., Eisenhut, M., and Haberkorn, U. (2004) Exceptional increase in somatostatin receptor expression in pancreatic neuroendocrine tumour, visualized with ^{68}Ga-DOTATOC PET. *Eur. J. Nucl. Med. Mol. Imaging 31*, 466.

(89) Koukouraki, S., Strauss, L. G., Georgoulias, V., Schuhmacher, J., Haberkorn, U., Karkavitsas, N., and Dimitrakopoulou-Strauss, A. (2006) Evaluation of the pharmacokinetics of ^{68}Ga-DOTATOC in patients with metastatic neuroendocrine tumours scheduled for ^{90}Y-DOTATOC therapy. *Eur. J. Nucl. Med. Mol. Imaging 33*, 460–466.

(90) Henze, M., Dimitrakopoulou-Strauss, A., Milker-Zabel, S., Schuhmacher, J., Strauss, L. G., Doll, J., et al. (2005) Characterization of (^{68}Ga)-DOTA-D-Phe1-Tyr3-octreotide (DOTATOC) kinetics in patients with meningiomas. *J. Nucl. Med. 46*, 763–769.

(91) Koukouraki, S., Strauss, L. G., Georgoulias, V., Eisenhut, M., Haberkorn, U., and Dimitrakopoulou-Strauss, A. (2006) Comparison of the pharmacokinetics of ^{68}Ga-DOTATOC and [^{18}F]FDG in patients with metastatic neuroendocrine tumours scheduled for ^{90}Y-DOTATOC therapy. *Eur. J. Nucl. Med. Mol. Imaging 33*, 1115–1122.

(92) Liu, S. (2008) Bifunctional coupling agents for target-specific delivery of metallic radionuclides. *Adv. Drug Delivery Rev. 60*, 1347–1370.

(93) Liu, S. (2005) HYNIC derivatives as bifunctional coupling agents for ^{99m}Tc-labeling of small biomolecules. *Top. Curr. Chem. 252*, 193–216.

(94) André, J., Maecke, H., Zehnder, M., Macko, L., and Akyel, K. (1998) 1,4,7-triazanonane-1-succinic acid-4,7-diacetic acid (NODASA): a new bifunctional chelator for radio gallium-labeling of biomolecules. *Chem. Commun. 12*, 1301–1302.

(95) Eisenwiener, K. P., Prata, M. I., Buschmann, I., Zhang, H. W., Santos, A. C., Wenger, S., Reubi, J. C., and Maecke, H. R. (2002) NODAGATOC, a new chelator-coupled somatostatin analogue labeled with [^{67}Ga/^{68}Ga] and [^{111}In] for SPECT, PET, and targeted therapeutic applications of somatostatin receptor ($hsst_2$) expressing tumors. *Bioconjugate Chem. 13*, 530–541.

(96) Eisenwiener, K. P., Powell, P., and Maecke, H. R. (2000) A convenient synthesis of novel bifunctional pro-chelators for coupling to bioactive peptides for radiometal labeling. *Bioorg. Med. Chem. Lett. 10*, 2133–2135.

(97) McQuade, P., Miao, Y., Yoo, J., Quinn, T. P., Welch, M. J., and Lewis, J. S. (2005) Imaging of melanoma using ^{64}Cu- and ^{86}Y-DOTA-ReCCMSH(Arg^{11}), a cyclized peptide analogue of α-MSH. *J. Med. Chem. 48*, 2985–2992.

(98) Prasanphanich, A. F., Nanda, P. K., Rold, T. L., Ma, L., Lewis, M. J., Garrison, J. C., Hoffman, T. J., Sieckman, G. L., Figueroa, S. D., and Smith, C. J. (2007) [^{64}Cu-NOTA-8-Aoc-BBN(7−14)NH_2] targeting vector for positron-emission tomography imaging of gastrin- releasing peptide receptor-expressing tissues. *Proc. Natl. Acad. Sci. U.S.A. 104*, 12462–12467.

(99) Harris, T. D., Kalogeropoulos, S., Nguyen, T., Liu, S., Bartis, J., Ellars, C. E., Edwards, D. S., Onthank, D., Yalamanchili, P., Robinson, S. P., Lazewatsky, J., Barrett, J. A., and Bozarth, J. (2003) Design, synthesis and evaluation of radiolabeled integrin $\alpha_v\beta_3$ receptor antagonists for tumor imaging and radiotherapy. *Cancer Biother. Radiopharm. 18*, 627–641.

(100) Onthank, D. C., Liu, S., Silva, P. J., Barrett, J. A., Harris, T. D., Robinson, S. P., and Edwards, D. S. (2004) ^{90}Y and ^{111}In complexes of A DOTA-conjugated integrin $\alpha_v\beta_3$ receptor antagonist: different but biologically equivalent. *Bioconjugate Chem. 15*, 235–241.

(101) Harris, T. D., Cheesman, E., Harris, A. R., Sachleben, R., Edwards, D. S., Liu, S., Bartis, J., Ellars, C., Onthank, D., Yalamanchili, P., Heminway, S., Silva, P., Robinson, S., Lazewatsky, J., Rajopadhye, M., and Barrett, J. A. (2007) Radiolabeled divalent peptidomimetic vitronectin receptor antagonists as potential tumor radiotherapeutic and imaging Agents. *Bioconjugate Chem. 18*, 1266–1279.

(102) Harris, T. D., Kalogeropoulos, S., Nguyen, T., Dwyer, G., Edwards, D. S., Liu, S., Bartis, J., Ellars, C., Onthank, D., Yalamanchili, P., Heminway, S., Robinson, S., Lazewatsky, J., and Barrett, J. (2006) Structure-activity relationships of ^{111}In- and ^{99m}Tc-labeled quinolin-4-one peptidomimetics as ligands for the vitronectin receptor: potential tumor imaging agents. *Bioconjugate Chem. 17*, 1294–1313.

(103) Chen, X., Sievers, E., Hou, Y., Park, R., Tohme, M., Bart, R., Bremner, R., Bading, J. R., and Conti, P. S. (2005) Integrin $\alpha_v\beta_3$-targeted imaging of lung cancer. *Neoplasia 7*, 271–279.

(104) Morrison, M. S., Ricketts, S. A., Barnett, J., Cuthbertson, A., Tessier, J., and Wedge, S. R. (2009) Use of a novel Arg-Gly-Asp radioligand, ^{18}F-AH111585, to determine changes in tumor vascularity after antitumor therapy. *J. Nucl. Med. 50*, 116–122.

(105) Kenny, L. M., Coombes, R. C., Oulie, I., Contractor, K. B., Miller, M., Spinks, T. J., McParland, B., Cohen, P. S., Hui, A., Palmieri, C., Osman, S., Glaser, M., Turton, D., Al-Nahhas, A., and Aboagye, E. O. (2008) Phase I trial of the positron-emitting Arg-Gly-Asp (RGD) peptide radioligand ^{18}F-AH111585 in breast cancer patients. *J. Nucl. Med. 49*, 879–886.

(106) Beer, A. J., Haubner, R., Goebel, M., Luderschmidt, S., Spilker, M. E., Wester, H. J., Weber, W. A., and Schwaiger, M. (2005) Biodistribution and pharmacokinetics of the $\alpha_v\beta_3$-selective tracer 18F-Galacto-RGD in cancer patients. *J. Nucl. Med. 46*, 1333–1341.

(107) Haubner, R., Weber, W. A., Beer, A. J., Vabulience, E., Reim, D., Sarbia, M., Becker, K. F., Goebel, M., Hein, R., Wester, H. J., Kessler, H., and Schwaiger, M. (2005) Noninvasive visualization of the activiated $\alpha_v\beta_3$ integrin in cancer patients by positron emission tomography and [^{18}F]Galacto-RGD. *PLOS Medicine 2 e70*, 244–252.

(108) Beer, A. J., Grosu, A. L., Carlsen, J., Kolk, A., Sarbia, M., Stangier, I., Watzlowik, P., Wester, H. J., Haubner, R., and Schwaiger, M. (2007) [^{18}F]Galacto-RGD positron emission tomography for imaging of $\alpha_v\beta_3$ expression on the neovasculature in patients with squamous cell carcinoma of the head and neck. *Clin. Cancer Res. 13*, 6610–6616.

(109) Beer, A. J., Niemeyer, M., Carlsen, J., Sarbia, M., Nahrig, J., Watzlowik, P., Wester, H. J., Harbeck, N., and Schwaiger, M. (2008) Patterns of alphavbeta3 expression in primary and metastatic human breast cancer as shown by ^{18}F-Galacto-RGD PET. *J. Nucl. Med. 49*, 255–259.

(110) Haubner, R., Finsinger, D., and Kessler, H. (1997) Stereoisomeric peptide libraries and peptidomimetics for designing selective inhibitors of the $\alpha_v\beta_3$ integrin for a new cancer therapy. *Angew. Chem., Int. Ed. Engl. 36*, 1375–1389.

(111) Haubner, R., Gratias, R., Diefenbach, B., Goodman, S. L., Jonczyk, A., and Kessler, H. (1996) Structural and functional aspect of RGD-containing cyclic pentapeptides as highly potent and selective integrin $\alpha_v\beta_3$ antagonists. *J. Am. Chem. Soc. 118*, 7461–7472.

(112) Aumailley, M., Gurrath, M., Müller, G., Calvete, J., Timpl, R., and Kessler, H. (1991) Arg-Gly-Asp constrained within cyclic pentapeptides strong and selective inhibitors of cell adhesion to vitronectin and laminin fragment P1. *FEBS Lett. 291*, 50–54.

(113) Gottschalk, K. E., and Kessler, H. (2002) The structures of integrins and integrin-ligand complexes: Implications for drug design and signal transduction. *Angew. Chem., Int. Ed. Engl. 41*, 3767–3774.

(114) Rajopadhye, M., Harris, A. R., Nguyen, H. M., Overoye, K. L., Bartis, J., Liu, S., Edwards, D. S., and Barrett, J. A. (2000) RP593, a ^{99m}Tc-labeled $\alpha_v\beta_3/\alpha_v\beta_5$ antagonist, rapidly detects spontaneous tumors in mice and dogs. 47th Annual Meeting of SNM, St. Louis, Missouri. *J. Nucl. Med. 41*, 34P.

(115) Liu, S., Edwards, D. S., Ziegler, M. C., Harris, A. R., Hemingway, S. J., and Barrett, J. A. (2001) ^{99m}Tc-Labeling of a hydrazinonicotinamide-conjugated vitronectin receptor antagonist useful for imaging tumor. *Bioconjugate Chem. 12*, 624–629.

(116) Boturyn, D., Coll, J. L., Garanger, E., Favrot, M. C., and Dumy, P. (2004) Template assembled cyclopeptides as multimeric system for integrin targeting and endocytosis. *J. Am. Chem. Soc. 126*, 5730–5739.

(117) Li, Z., Cai, W., Cao, Q., Chen, K., Wu, Z., and Chen, X. (2007) ^{64}Cu-Labeled tetrameric and octameric RGD peptides for small-animal PET of tumor $\alpha_v\beta_3$ integrin expression. *J. Nucl. Med. 48*, 1162–1171.

(118) Wang, L., Kim, Y. S., Shi, J., Zhai, S., Jia, B., Liu, Z., Zhao, H., Wang, F., Chen, X., and Liu, S. (2009) Improving tumor targeting capability and pharmacokinetics of ^{99m}Tc-labeled cyclic RGD dimers with PEG_4 linkers. *Mol. Pharm. 6*, 231–245.

(119) Shi, J., Wang, L., Kim, Y. S., Zhai, S., Liu, Z., Chen, X., and Liu, S. (2008) Improving tumor uptake and excretion kinetics of ^{99m}Tc-labeled cyclic arginine-glycine-aspartic (RGD) dimers with triglycine linkers. *J. Med. Chem. 51*, 7980–7990.

(120) Cai, W., Rao, J., Gambhir, S. S., and Chen, X. (2006) How molecular imaging is speeding up antiangiogenic drug development? *Mol. Cancer Ther. 5*, 2624–2633.

(121) Niu, G., and Chen, X. (2008) Has molecular and cellular imaging enhanced drug discovery and drug development? *Drugs in R&D 9*, 351–368.

(122) Jain, R. K. (1987) Transport of molecules in the tumor interstitium: a review. *Cancer Res. 47*, 3039–3051.

(123) Shi, J., Wang, L., Kim, Y. S., Zhai, S., Liu, Z., Chen, X., and Liu, S. (2009) Improving tumor uptake and pharmacokinetics of ^{64}Cu-labeled cyclic RGD dimers with triglycine and PEG_4 Linkers. *Bioconjugate Chem. 20*, 750–759.

(124) Shi, J., Kim, Y. S., Chakraborty, S., Zhou, Y., Wang, F., and Liu, S. Novel ^{111}In-labeled cyclic RGD peptide dimers: improving tumor uptake and pharmacokinetics with G_3 and PEG_4 Linkers. *Dalton Trans.* .

(125) Liu, Z., Niu, G., Shi, J., Liu, S. L., Wang, F., Liu, S., and Chen, X. (2009) ^{68}Ga-Labeled cyclic RGD dimers with Gly_3 and PEG_4 linkers: promising agents for tumor integrin $\alpha_v\beta_3$ PET imaging. *Eur. J. Nucl. Med. Mol. Imaging 36*, 947–957.

(126) Liu, Z., Liu, S., Wang, F., Liu, S., and Chen, X. (2009) Noninvasive imaging of tumor integrin expression using ^{18}F-labeled RGD dimer peptide with PEG_4 linkers. *Eur. J. Nucl. Med. Mol. Imaging* ASAP.

(127) Fani, M., Andre, J. P., and Maecke, H. R. (2008) ^{68}Ga-PET: a powerful generator-based alternative to cyclotron-based PET radiopharmaceuticals. *Contr. Media Mol. Imaging 3*, 53–63.

(128) Maecke, H. R., and Andre, J. P. (2007) ^{68}Ga-PET radiopharmacy: A generator-based alternative to ^{18}F-radiopharmacy. *Ernst Schering Res. Found. Workshop 62*, 215–242.

(129) Al-Nahhas, A., Win, Z., Szyszko, T., Singh, A., Khan, S., and Rubello, D. (2007) What can gallium-68 PET add to receptor and molecular imaging. *Eur. J. Nucl. Med. Mol. Imaging 34*, 1897–1901.

(130) Creamer, D., Allen, M., Sousa, A., Poston, R., and Barker, J. (1995) Altered vascular endothelium integrin expression in psoriasis. *Am. J. Pathol. 147*, 1661–1667.

(131) Waldeck, J., Häger, F., Höltke, C., Lanckohr, C., von Wallbrunn, A., Torsello, G., Heindel, W., Theilmeier, G., Schäfers, M., and Bremer, C. (2008) Fluorescent reflectance imaging of macrophage-rich atherosclerostic plaques using $\alpha_v\beta_3$ integrin-targeted fluorochrome. *J. Nucl. Med. 49*, 1845–1851.

(132) Meoli, D. F., Sadeghi, M. M., Krassilnikova, S., Bourke, B. N., Giordano, F. J., Dione, D. P., Su, H. L., Edwards, D. S., Liu, S., Harris, T. D., Madri, J. A., Zaret, B. L., and Sinusas, A. J. (2004) Noninvasive imaging of myocardial angiogenesis following experimental myocardial infarction. *J. Clin. Invest. 113*, 1684–1691.

(133) Pichler, B. J., Kneilling, M., Haubner, R., Braumüller, H., Schwaiger, M., Röcken, M., and Weber, W. A. (2005) Imaging of delayed-type hypersensitivity reaction by PET and ^{18}F-Galacto-RGD. *J. Nucl. Med. 46*, 184–189.

(134) Hua, J., Dobrucki, L. W., Sadeghi, M. M., Zhang, J., Bourke, B. N., Cavaliere, P., Song, J., Chow, C., Jahanshad, N., van Royen, N., Buschmann, I., Madri, J. A., Mendizabal, M., and Sinusas, A. (2005) Noninvasive imaging of angiogenesis with a ^{99m}Tc labeled peptide targeted at $\alpha_v\beta_3$ integrin after murine hindlimb ischemia. *Circulation 111*, 3255–3260.

BC900167C

ARTICLES

Heparin−Paclitaxel Conjugates as Drug Delivery System: Synthesis, Self-Assembly Property, Drug Release, and Antitumor Activity

Ying Wang,[†,‡,§] Dingcheng Xin,[†,‡] Kaijian Liu,[†,†] Mingqiang Zhu,[†] and Jiannan Xiang*[,†,‡,§]

Biomedical Engineering Center, College of Chemistry and Chemical Engineering, and State Key Laboratory of Chemo/Biosensing and Chemometrics, Hunan University, Changsha, 410082, China. Received September 5, 2008; Revised Manuscript Received November 5, 2009

We have synthesized a series of novel prodrugs consisting of amphiphilic heparin−paclitaxel conjugates. Each prodrug in the series consists of a succinylated-heparin carrier conjugated to paclitaxel via a single amino acid spacer, either valine, leucine, or phenylalanine (prodrug1, prodrug2, and prodrug3, respectively). Unlike physically encapsulated drugs, these prodrugs can self-assemble to form nanoparticles in aqueous solution while still maintaining structural integrity for loading parent drug due to the dual hydrophilic/hydrophobic nature of the carrier and drug compound. The structure of prodrugs has been characterized by ^{1}H NMR, FT-IR, and GPC. Their morphology has been investigated by SEM. Our results show that these self-assembled nanoparticles have a narrow size distribution (140−180 nm) and form an approximately spherical shape composed of a paclitaxel core and carrier shell. The anticoagulant activity of all the prodrugs is sharply decreased compared to that of heparin, as measured by activated partial thromboplastin time (aPTT), thereby reducing the risk of severe hemorrhagic complication during systemic administration. Furthermore, the prodrugs exhibit better *in vitro* cell inhibition for MCF-7 cells than free paclitaxel. Flow cytometric analyses (FCM) have shown that MCF-7 cells treated with prodrugs are arrested in the G_2/M phase of the cell cycle. Meanwhile, these three prodrugs each exhibit unique hydrolysis properties under various physiological or plasma conditions. In particular, prodrug2 with leucine spacer may result in favorable hydrolysis of the ester bond between the amino acid and paclitaxel under physiological conditions. In mice, prodrug2 shows a similar ovarian tumor growth inhibition as paclitaxel and induces no obvious body weight loss. Hence, the prepared nanoscale prodrugs are expected not only to render structural integrity to the parent drug, but also enhance targeting capacity to solid tumors.

INTRODUCTION

Paclitaxel has shown significant antineoplastic activity against various human cancers. However, when clinically used, solubility and toxicity are two major problems. Previous attempts in paclitaxel prodrug design have been focused on improving its water solubility and decreasing its toxicity (*1*). The prepared water-soluble prodrugs of paclitaxel are mainly ester derivatives and phosphate derivatives, among others (*2*−*6*). In recent years, the use of macromolecules for the targeted delivery of anticancer agents has generated considerable interest due to the enhanced permeability and retention (EPR) effect in tumor tissues (*7*−*11*). Meanwhile, the pharmaceutical activity of self-assembled nanoscale drug delivery systems has recently attracted considerable attention (*12*−*16*).

Nanoscale drug delivery systems can increase parent drug solubility as well as enable passive targeting to the solid tumor. Generally, nanoparticle systems, such as amphiphilic block copolymer micelles, for drug delivery self-assemble into a hydrophobic inner core and a hydrophilic outer shell. Various hydrophobic anticancer drugs can thus be physically entrapped within the core of the copolymers. However, copolymer micelles are often not stable enough to maintain structural integrity for loading the moderately hydrophobic drug. Additionally, nanoparticles with diameters greater than 200 nm are readily scavenged nonspecifically by monocytes and the reticuloendothelial system (*17*, *18*). On the basis of these considerations, we sought to design a new class of drug delivery systems by chemical method that retain structural integrity for the parent drug while offering many desirable properties in physiological conditions.

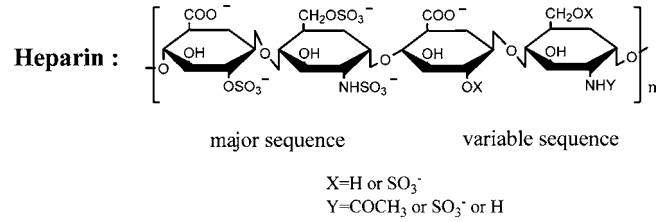

Figure 1. Structure of heparin.

Heparin is a biocompatible, biodegradable, and water-soluble natural polysaccharide with a complicated structure and is abundant in animal tissues (Figure 1). Heparin has attracted intense attention because it demonstrates a variety of biological activities including anticoagulant activity, inhibition of angiogenesis, tumor development, and proliferation of arterial smooth

* To whom correspondence should be addressed. Phone: 86-0731-8821740. Fax: 86-0731-8821740. E-mail: jnxiang@hnu.cn.
[†] Biomedical Engineering Center.
[‡] College of Chemistry and Chemical Engineering.
[§] University State Key Laboratory of Chemo/Biosensing and Chemometrics.

10.1021/bc8003809 © 2009 American Chemical Society
Published on Web 12/01/2009

Scheme 1. Designed Strategy of the Prodrug

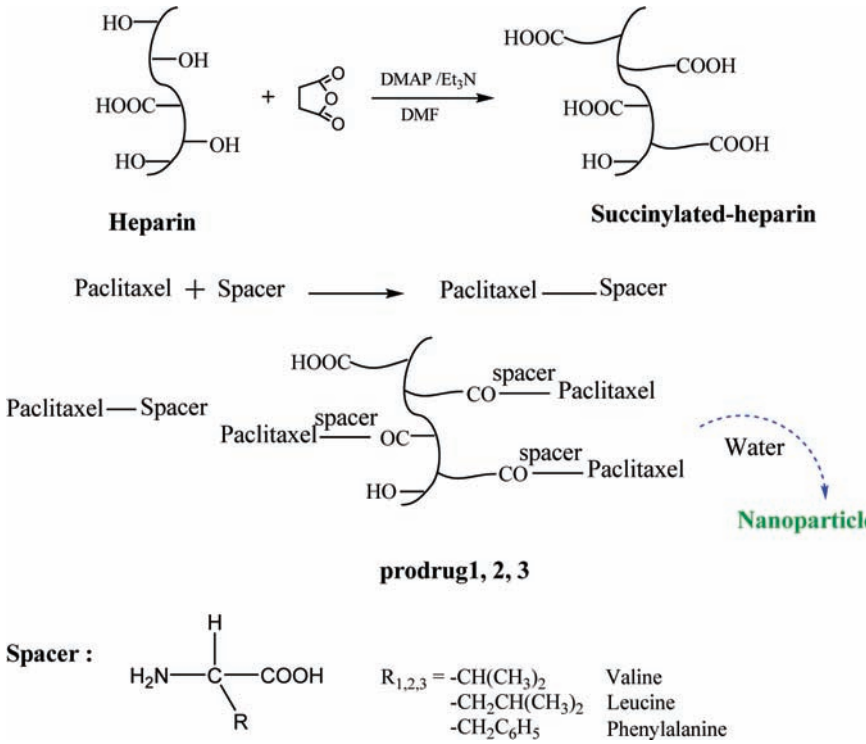

muscle cells (*19*, *20*). Meanwhile, chemically modified heparins are also known to effectively inhibit angiogenesis, metastasis, and tumor growth (*21*). It was reported that heparin derivatives with reduced anticoagulant activity have a great potential as antitumor drugs (*22*).

In this study, we conjugated a succinylated-heparin carrier to paclitaxel by inserting different amino acid as spacers, including valine, leucine, and phenylalanine (prodrug1, prodrug2, and prodrug3, respectively). Succinylated heparin was selected as a carrier in order to increase the drug loading capacity, in which the hydroxyl groups of heparin react with succinic anhydride under classical acylation conditions. Using this method, many more active carboxyl groups can be introduced to the carrier. The designed synthetic route of the prodrugs is in Scheme 1.

It has previously been reported that the particle size plays an important role in determining the biological response of the tissue to foreign biomaterials (*23*). Therefore, we investigated the behavior of the prepared prodrugs in aqueous solution and examined whether conjugation of paclitaxel to heparin by the different amino acid spacers would influence the physical properties and, consequently, the pharmacologic activity as compared with native paclitaxel. Finally, the *in vitro* cytotoxicity and *in vivo* antitumor effect of the prodrugs were evaluated against the MCF-7 human breast cell line and $SKOV_3$ human ovarian cell line compared with free pacitaxel.

EXPERIMENTAL SECTION

Materials. Heparin (sodium salt, from porcine intestinal mucosa, M_n = 12 kDa, 150 U/mg), *N*,*N*′-dimethylformamide (DMF), triethylamine, tributylamine, succinic anhydride, 4-dimethylaminopyridine (DMAP), 1-ethyl-3,3-dimethylaminopropyl carbodiimide hydrochloride (EDC), and *N*-hydroxysuccinimide (NHS) were purchased from Sinopharm Chemical Reagent Co. (Shanghai, China), and paclitaxel came from Tecano Science & Technology Co., Ltd. (Guangzhou, China). 3-(4,5-Dimethylthiazol-2-yl)-2,5-diphenyltetrazolium (MTT) was from Sigma. 732 cation-exchange resin, Sephadex G-25, and dialysis membrane (MWCO 3500) were purchased from Shanpu Co., Ltd. (Shanghai, China), Pharmacia (Piscataway, NJ), and Viskase Co., Inc. (Illinois, USA), respectively. 2′-Valyl-paclitaxel, 2′-leucyl-paclitaxel, and 2′-phenylalanyl-paclitaxel were prepared in our lab (*11*). All reagents were purified by distillation under nitrogen prior to use. Ultrapure water (Milli-Q, 18M·Ω) was used at all times in the experiment. The MCF-7 (breast carcinoma) cell line and $SKOV_3$ (human ovarian serous cystocarcinoma) cell line were kindly donated by the Institute of Life Science and Biotechnology in Hunan University.

Synthesis of Succinylated Heparin. Heparin sodium salt (0.25 g) dissolved in 20 mL of water was percolated through a 732 column (H^+ form, 100 mL) at 4 °C. The pH of the solution was adjusted to 6.0 by addition of tributylamine (2 mL). Excess tributylamine was eliminated by evaporating. The concentrated solution was diluted with water and lyophilized to yield tributylammonium salt (0.5 g). The tributylammonium salt (0.5 g) was dissolved in dry DMF (10 mL) and was then cooled down to 0 °C under a nitrogen atmosphere. Succinic anhydride (1.3 g, 13 mmol), triethylamine (1.31 g, 13 mmol), and DMAP (0.036 g, 0.3 mmol) were successively added, and the reaction was allowed to proceed at room temperature for 24 h under nitrogen. After cooling to 0 °C, cold ethanol (500 mL) was added. The precipitate was dissolved in water and passed through a 732 column (H^+ form, 200 mL) at 4 °C. Then, the product was purified by passing through a Sephadex G-25 column equilibrated in deionized water. The effluent was neutralized with 1 M NaOH and lyophilized as a white powder (0.20 g). ^{1}H NMR (D_2O): δ = 2.6 (−CH_2CH_2COOH, succinylated group). FT-IR (KBr): 1630 cm^{-1}, 1427 cm^{-1} (−COOH).

Synthesis of Succinylated-Heparin-Val-Paclitaxel (prodrug1). Succinylated heparin (0.20 g) was dissolved in dry DMF (20 mL) and maintained by gentle heating. 2′-Valyl-paclitaxel (48 mg, 0.05 mmol), EDC (19 mg, 0.1 mmol), and NHS (12 mg, 0.11 mmol) were successively added to the mixture, and the reaction was allowed to proceed at 35 °C for 24 h. After cooling to 0 °C, deionized water was gradually added and the solution was dialyzed against deionized water for 48 h in a

dialysis membrane. After lyophilization, prodrug1 (0.22 mg) was obtained as a white powder. Prodrug2 and prodrug3 were synthesized in a similar procedure as that of prodrug1. The ^{1}H NMR spectra showed the methyl group of valyl and leucyl at 0.92 ppm and 0.7 ppm in high field, respectively. In spite of the overlay of the benzene ring of paclitaxel in ^{1}H NMR, the δ-hydrogen of phenylalanyl was attributed to δ 7.2 ppm in low field. These results demonstrated that 2′-aminoacyl paclitaxel was successfully attached to succinylated heparin (see Supporting Information).

^{1}H NMR (D_2O: DMSO-d_6 = 1:2): δ = 0.7 ($-CH_3$, δ-Leu, prodrug2), 0.92 ($-CH_3$, γ-Val, prodrug1), 1.06 (17.16-CH_3, paclitaxel), 1.58 (19-CH_3, paclitaxel), 1.8 (18-CH_3, paclitaxel), 1.9−2.0 ($-NHCOCH_3$, succinylated heparin), 2.1 (C4-OAc, paclitaxel), 2.2 (C10-OAc, paclitaxel), 2.8 ($-CH_2CH_2-$CONH−, succinylated-heparin), 7.2 (δ-Phe, prodrug3), 7.4−8.1 (benzene ring, paclitaxel). FT-IR (KBr): 3068 cm^{-1} (−C−H−), 1533 cm^{-1}, 710 cm^{-1} (−C═C−).

Characterization of Prodrugs. The ^{1}H NMR spectra of the carrier and prodrugs were recorded on a Varian INOVA400 apparatus in D_2O and DMSO-d_6. The FT-IR spectra were determined by a FD-5DX infrared spectrum apparatus. In addition, the molecular weights of the prodrugs were determined using a 515 Waters GPC system equipped with a Waters Ultrahydrogel 250 column and Waters 410 refractive index detector. 0.1 mol/L NaCl was used as an elution solvent at a flow rate of 0.6 mL/ min, and the column temperature was maintained at 40 °C using poly(ethylene glycol) standards.

The mass of the succinylated group on the carrier was determined by quantitative analysis of ^{1}H NMR spectroscopy using pyridine as the internal standard, whose proton signal is δ 7.4, 7.9, and 8.4 ppm. The content of drug on the carrier was estimated by UV measurements based on a standard curve generated with known concentrations of paclitaxel in ethanol (λ = 228 nm) (*24*).

Size distributions and zeta potentials of prodrugs were measured at 25 °C using a Zetasizer Nano-Zs (Malvern Instruments, UK). The concentration of prodrugs in distilled water was kept constant at 0.3 mg/mL. SEM was used to observe the morphology of prodrugs in aqueous solution, which was performed on a JSM-6700F (JEOL, Japan). Prodrug was freeze−dried and mounted on a metal stub.

***In Vitro* Release of Paclitaxel from Prodrugs.** Prodrugs were dissolved in phosphate-buffered saline (0.01 M) at pH 5.0 and pH 7.4 or human plasma and mouse plasma (400 μL per mL of PBS 7.4, 0.01 M) at an equivalent paclitaxel concentration of 1 g/L. The solutions were incubated at 37 °C with gentle shaking. At selected time intervals, aliquots (500 μL) were removed and an equivalent PBS concentration was added to the solutions. The aliquots were extracted by chloroform, and the organic fraction was evaporated. At the same time, the residue was mixed with acetonitrile (1000 μL) and analyzed by HPLC.

The HPLC system consisted of a reverse-phase silica column (SepaxHP-C18, 4.6 × 250 mm, 5 μm, Sepax, USA), a mobile phase of acetonitrile, and 0.05% trifluoroacetic acid in water (60: 40) pumped (LC-20AT, Shimadzu) at a flow rate of 1.0 mL/ min. A 20 μL aliquot of sample was injected, and the column effluent was detected at 227 nm with a UV detector (SPD-20A, Shimadzu).

Anticoagulant Activity Assay. Anticoagulant activity of carrier and prodrugs, using heparin as the standard, was evaluated by measuring activated partial thromboplastin time (aPTT) using an Ellagic acid kit (Sun Biotech, China). The aPTT was recorded on a PRECIL C2000 Coagulometer. The aPTT was measured according to the manufacturer's procedure by using normal human plasma. Prodrugs and carrier (2.5 μg/mL, 25 μL) were added to 0.1 mL of citrated plasma, followed by adding 0.1 mL of aPTT reagent. This mixture was incubated at 37 °C for 2 min. Then, prewarmed $CaCl_2$ solution (0.1 mL, 0.025 mol/L) was added, and the time for fibrin clotting was recorded. The activity of heparin derivatives was calculated from the heparin standard curve (clotting time vs units/mg) (*25*).

***In Vitro* Cell Culture Cytotoxicity.** The cytotoxicity of the prodrugs and paclitaxel was determined using an MTT assay. MCF-7 cells were seeded at 100 000 cells/mL in a 96-well plate format in RPMI 1640 with 10% fetal bovine serum and 0.1% penicillin/streptomycin, at 37 °C, under a 5% CO_2 humidified atmosphere. After a 24 h incubation period, MCF-7 cells were subjected to various concentrations of prodrugs in 100 μL culture medium, and free paclitaxel was added as a DMSO stock solution (all performed at equivalent paclitaxel concentrations of 0.01, 0.1, 1, 10, and 100 μg/mL). Cells were then incubated at 37 °C for 48 h with each test material, and 20 μL of sterile MTT solution (0.5% w/v in PBS) was added to each well. After an additional 5 h incubation, the medium was removed and DMSO was added to dissolve the insoluble formazan dye which had formed. Cell viability was quantified by MTT dye absorption at 570 nm, which was recorded on a Microplate reader (Thermo Electron, China).

Flow Cytometric (FCM) Assay. Cell cycle analyses were performed on EPICS-XL flow cytometer (Beckman Coulter, USA) and data were analyzed by Mcycle software. MCF-7 cells were seeded on a 6-well plate and preincubated for 24 h, followed by coincubation with paclitaxel and prodrugs (an equivalent paclitaxel concentration of 100 μg/mL) for 6 h. The cells were then washed three times with PBS, detached by trypsinization, spun down by centrifugation, and dispersed again in PBS for FCM analysis.

***In Vivo* Antitumor Activity.** Athymic nude female nu/nu mice (7−8 weeks old) were injected with 200 μL of human ovarian serous cystocarcinoma cells ($SKOV_3$, 1×10^6) on the right flank. The tumors were allowed to grow for 10−12 days until their size reached between 9 and 25 mm^2. Mice were randomized into control and treatment groups (n = 4) and injected intraperitoneally with saline, free paclitaxel, or prodrug. The free paclitaxel was dissolved in DMSO and then diluted with saline. The paclitaxel and prodrugs (each at an equivalent dose of 30 mg/kg paclitaxel) were injected at seven day intervals. Tumor length (L), width (W) measurements, and body weight were recorded 2−3 times per week. Tumor weight was calculated according to the formula $(L) \times (W)^2/2$.

Statistical Analysis. Statistical analysis was performed to determine differences among the measured properties of each group. One-way analysis of variance was determined using a statistical program (*Statistical Package for the Social Sciences*, v 10.0, SPSS Inc., USA). To reject a null hypothesis, statistical significance was defined as $p < 0.05$. When there was statistical significance, multiple comparisons were determined using a least significant differences technique.

RESULTS AND DISCUSSION

In this study, we used succinylated heparin as a carrier, in which additional carboxyl groups were introduced to replace the hydroxyl groups of heparin via an O-acylation reaction. The aim of the design strategy was to increase the content of active groups linked with drug molecules and to investigate the behavior of prodrugs in aqueous solution. Amino acids are ideal linkers since, as bifunctional molecules, they provide both a reactive carboxyl group to conjugate with paclitaxel via an ester bond and an amino group that can be easily reacted with the carboxyl groups of the carrier via N-acylation reaction. Thus, we selected three amino acids—valine, leucine, and phenylalanine—as spacers, and synthesized 2′-aminoacyl paclitaxel. We first

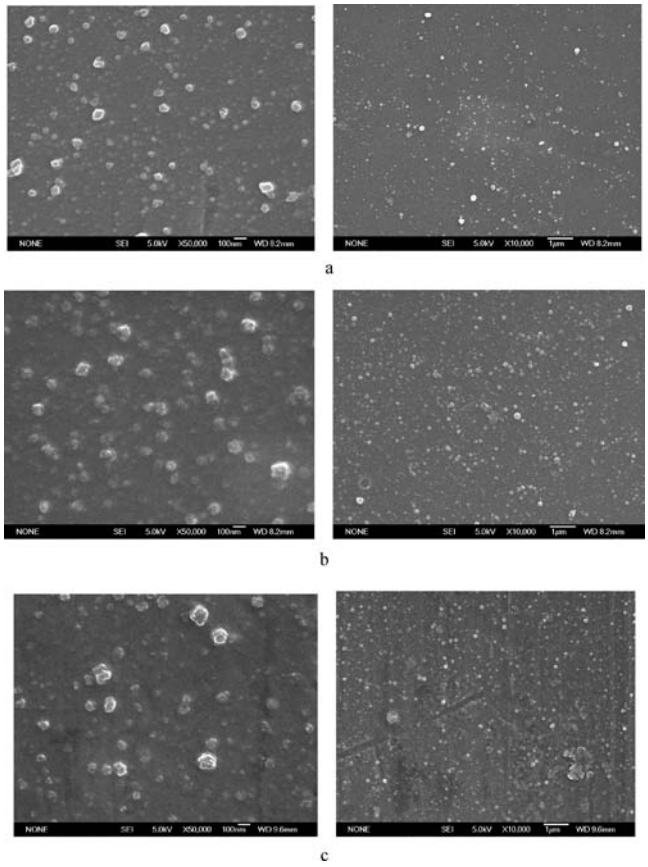

Figure 2. Scanning electron microscopy photographs of (a) prodrug1, ×50 000, ×10 000; (b) prodrug2, ×50 000, ×10 000; (c) prodrug3, ×50 000, ×10 000.

synthesized succinylated heparin using the classical O-acylation reaction conditions, and then 2′-aminocyl paclitaxel was introduced to the carrier in the presence of EDC and NHS, yielding amphiphilic heparin−paclitaxel conjugates as a type of novel prodrugs.

GPC measurement in aqueous phase showed the average molecular weight of succinylated heparin to be M_n ~12 957 with a polydispersity index (PDI) of about 1.8. However, the PDI of the prodrugs was significantly higher at 2.8−3.0, which may be due to the hydrophobicity of paclitaxel. Meanwhile, the weight percentages of succinyl groups and paclitaxel in the prodrugs were found to be about 8.5% and 35.4−39.1% using ^{1}H NMR and UV, respectively. During the experiment, the prodrugs self-assembled to form nanoparticles in aqueous solution, as supported by SEM and DLS (Figure 2 and Figure 3). The SEM micrograph of prodrugs showed an approximately spherical shape. The mean diameters of prodrug1, 2, and 3 measured by DLS were 141 ± 7, 171 ± 2, and 185 ± 2 nm, respectively, while the prodrugs had a zeta potential of approximately −21 to −31 mV (Table 1). The negative surface charge indicates that the hydrophobic paclitaxel species are buried within the carrier in aqueous solution while the carboxyl (COO^-) and sulfate (OSO_3^-) groups are exposed on the hydrophilic heparin shell. This further suggests that the prodrugs have formed a core/shell nanoparticle structure in aqueous solution.

Previously, Hashida and co-workers reported that the majority of fenestrates of the liver sinusoid have diameters smaller than 200 nm (*26*). Thus, large particles hardly reach the parenchymal cells of liver. It was also reported that smaller particles under 200 nm tend to selectively accumulate at tumor sites as a result of the EPR effect (*27*). Consequently, these prodrugs fall within the range required for passive tumor targeting.

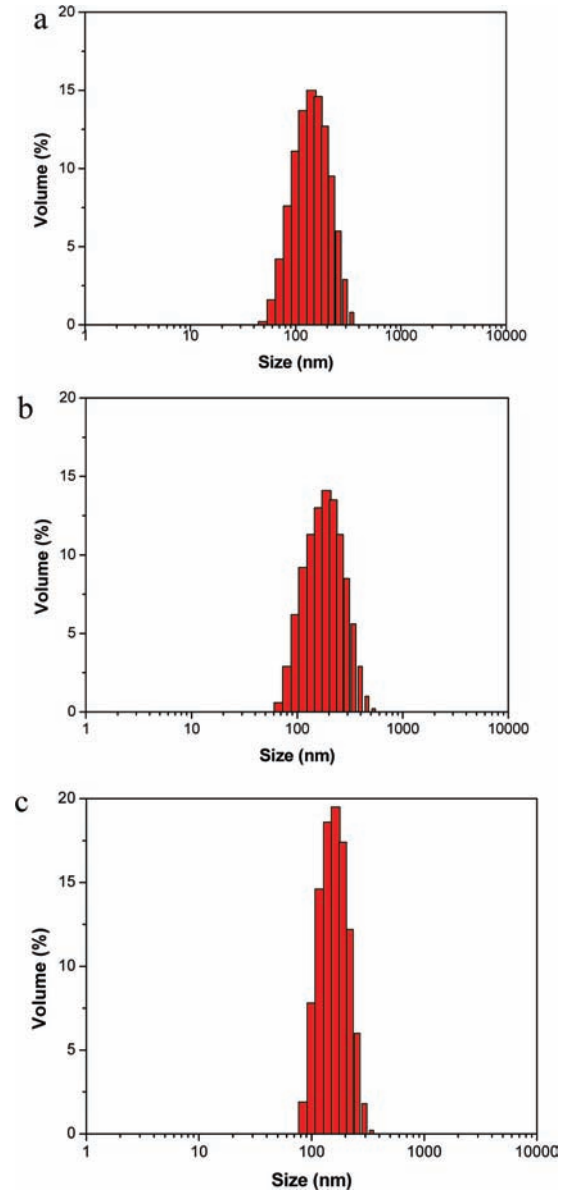

Figure 3. Size distribution of (a) prodrug1, (b) prodrug2, and (c) prodrug3 by DLS analysis in aqueous solution.

Table 1. Number Average Molecular Weights (M_n) and Polydispersity Indexes (PDI), as Determined by GPC, and Size, Polydispersity Index (PDI), and Zeta Potential of Prodrug as Determined by DLS

	GPC		DLS		
	M_n	PDI	particle size (nm)	PDI	zeta potential (mV)
succinylated heparin	12 957	1.8			
prodrug1	19 006	2.89	141 ± 7	0.14	−21.4 ± 4.59
prodrug2	19 287	2.81	171 ± 2	0.12	−22.1 ± 4.64
prodrug3	19 576	2.92	185 ± 2	0.21	−31.0 ± 8.35

These prodrugs were then subjected to chemical and plasma hydrolysis to test the paclitaxel release. The *in vitro* release time serves as a useful guide for formulation considerations and design of therapy protocols. Experiments performed under different conditions were reported in Figure 4. The hydrolysis rate of prodrugs was investigated by HPLC. As shown in Figure 4, a drug release half-life ($t_{1/2}$) of prodrug1 was similar with that of prodrug2 under physiological conditions. In the PBS, the amount of paclitaxel liberated from prodrugs increased as pH increased. Meanwhile, prodrug3 showed a much faster

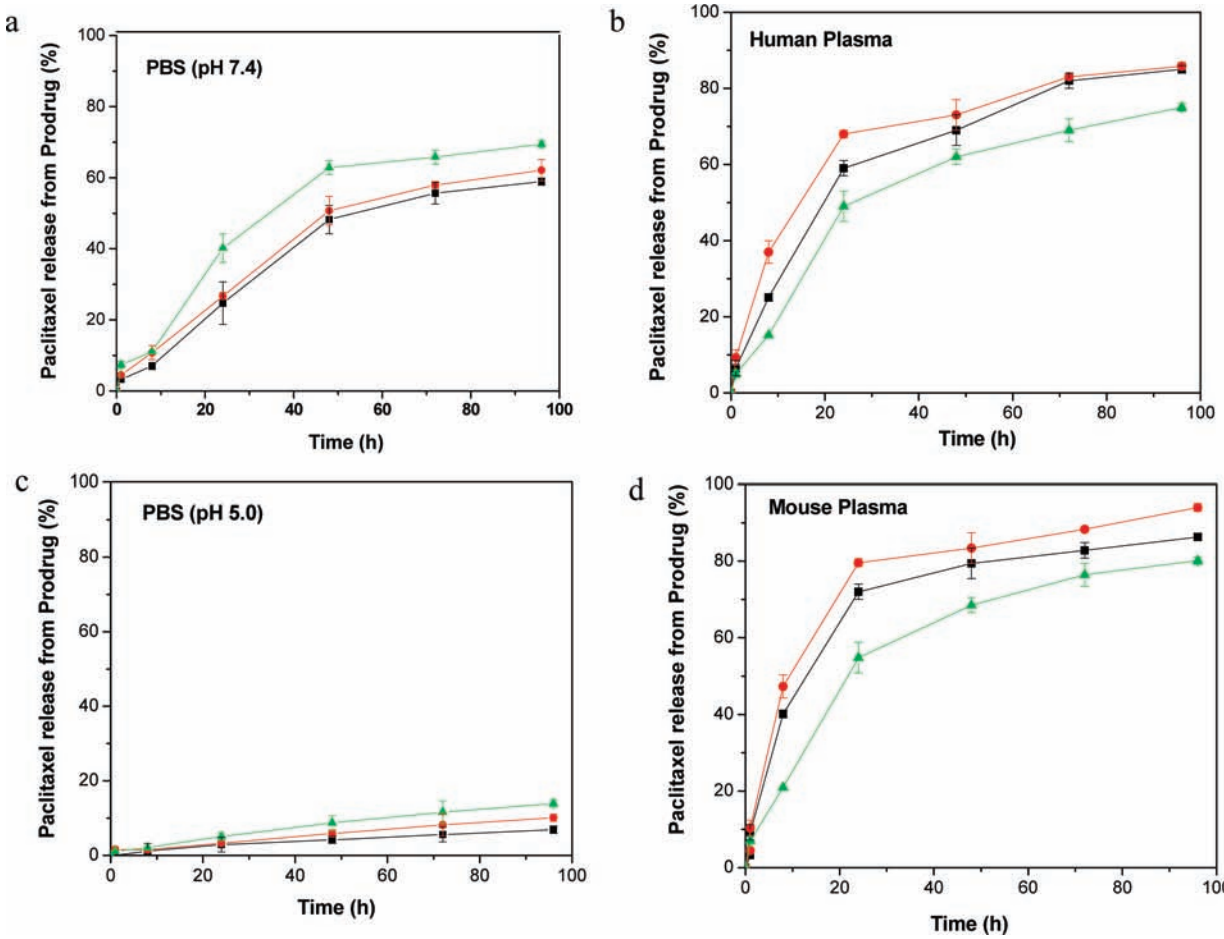

Figure 4. *In vitro* release profiles of paclitaxel from prodrug1 (black ■), prodrug2 (red ●), and prodrug3 (green ▲) under various conditions: (a) PBS in pH 7.4, (b) PBS in pH 5.0, (c) in human plasma, and (d) in mouse plasma. The data represent mean ± SD where $n = 3$.

release rate in PBS than that of any other prodrugs. Under physiological conditions, the amount of released paclitaxel was lower than that in plasma; more than 50% of paclitaxel was liberated from prodrugs under the plasma during 24 h. Additionally, the stability of prodrugs in mouse plasma was lower than that in human plasma.

Apparently, prodrug3 showed higher stability toward plasma compared with that of prodrug1 and prodrug2. This might be explained by steric hindrance from the phenylalanyl group, which might decrease the rate of release in enzymatic degradation. It has been reported that Leu derivatives are easily susceptible toward tritosomes using low-molecular-weight amino acid and dipeptide conjugates with paclitaxel (*28*). Hence, specific amino acids may result in favorable hydrolysis of the ester bond between the amino acid and paclitaxel when subject to changes in pH or upon entering the plasma. Therefore, prodrug2, which uses leucine as a spacer, can facilitate the release of pacitaxel from the carrier.

Although heparin has had a beneficial effect for cancer patients in some clinical trials, heparin therapy can be difficult to manage due to its anticoagulant potency and potential for inducing hemorrhagic complications. Therefore, we found it highly desirable to introduce chemical modification to the heparin moiety in order to reduce its anticoagulant activity. It was reported that chemically modified heparin derivatives with greatly reduced anticoagulant activity maintained nonanticoagulant effects, including antiadhesion, inhibition of angiogenesis, metastasis, and tumor growth (*29, 30*). The anticoagulant activities of succinylated heparin and prodrugs are shown in Table 2. The anticoagulant activities of succinylated heparin and prodrugs both decreased to some extent as compared to

Table 2. Loading Capacity, aPTT, IC_{50} of Carrier, Paclitaxel, and Prodrug by ^1H NMR, and Bioactivity Assays

	loading capacity (w/w %)	aPTT (U/mg)	IC_{50} (μg/mL)
succinylated heparin	8.5	109 ± 5	
paclitaxel			0.19
prodrug1	35.4	25 ± 6	0.10
prodrug2	37.8	54 ± 7	0.058
prodrug3	39.1	30 ± 4	0.06

that of heparin, but the activities of prodrugs decreased to a much greater extent. This might be attributed to the introduction of paclitaxel, which leads to a conformational change in heparin structure, resulting in decreased affinity to Antithrombin III and reduced effectiveness of the underlying anticoagulant mechanism (*31*). As a consequence, prodrugs with low anticoagulant activities could be safer and more effective drug delivery systems which decrease the high risk of excessive bleeding.

Cytotoxicity was studied by using an MTT assay to identify cells still active in respiration. Figure 5 summarizes the *in vitro* cytotoxicity results of prodrugs and paclitaxel in MCF-7 cell after 48 h. Prodrugs exhibited higher cytotoxicity than free paclitaxel. Specifically, IC_{50} values of prodrug2 and prodrug3 for MCF-7 were about 0.058 μg/mL and 0.06 μg/mL, respectively, which were about 3-fold lower than that of free paclitaxel (0.19 μg/mL). Prodrug2 therefore demonstrated significant anticancer activity. Although the hydrolysis rate of prodrug3 was slower than that of prodrug1 and prodrug2 in plasma, effective inhibition of MCF-7 for this prodrug was still observed.

Figure 6 shows the cell cycle profile of MCF-7 treated with paclitaxel and prodrugs. Since the cytotoxic activity of paclitaxel

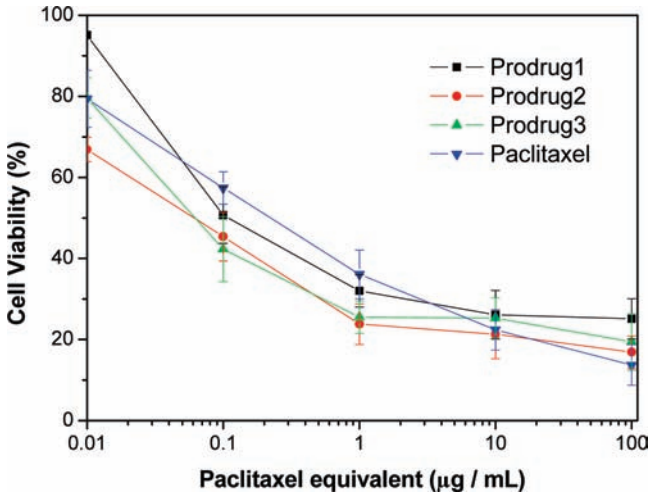

Figure 5. *In vitro* cytotoxicity of paclitaxel and prodrugs assessed using MCF-7 cells (MTT assay) after 48 h. The data represent mean ± SD where $n = 3$.

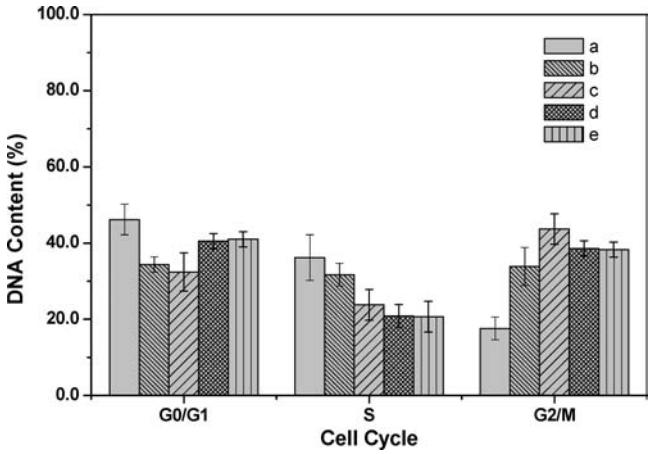

Figure 6. Flow cytometric analysis of the cell cycle profiles of MCF-7 cell treated with paclitaxel and Prodrugs for 6 h: (a) control cells, (b) paclitaxel, (c) prodrug1, (d) prodrug2, and (e) prodrug3. The data represent mean ± SD where $n = 3$.

is attributed to its stabilizing effect on microtubules necessary for spindle formation and cell division, paclitaxel has been shown to cause cell cycle arrest in the G_2/M phase and, ultimately, cell death through apoptotic mechanisms (*32*, *33*). As compared with control cells, the sharp peak observed for the G_0/G_1 phase was markedly attenuated and was observed instead of that for the G_2/M phase for cells treated with paclitaxel and prodrugs. Hence, paclitaxel progressively liberated from prodrugs can restrict MCF-7 cells in specific cell cycle stages.

We then evaluated the effectiveness of our prodrugs using an *in vivo* mouse model. The mice were treated with single i.p. injections of saline, free paclitaxel, and prodrugs at equivalent doses, and the tumor growth and body weight change were monitored daily as shown in Figure 7. The control group of mice showed a progressive increase in tumor growth for mean tumor volume up to day 32. The mice treated with free paclitaxel showed significant tumor growth inhibition compared with the control group. The treatment with prodrugs showed tumor growth inhibition to some extent. Although tumor growth inhibition induced by prodrugs was significant against the saline group ($p < 0.05$), it was not significantly different from that of free drug ($p > 0.05$). Free drug did, however, cause an obvious decrease in the body weight. In statistical summary (Table 3), the treatment induced by prodrugs indicated that body weight change was significantly different from that of free drug ($p <$ 0.05), and prodrug2 resulted in similar tumor growth inhibition to parent drug. These results implied that prodrugs induced less systemic toxicity; specifically, prodrug2 merited further investigation.

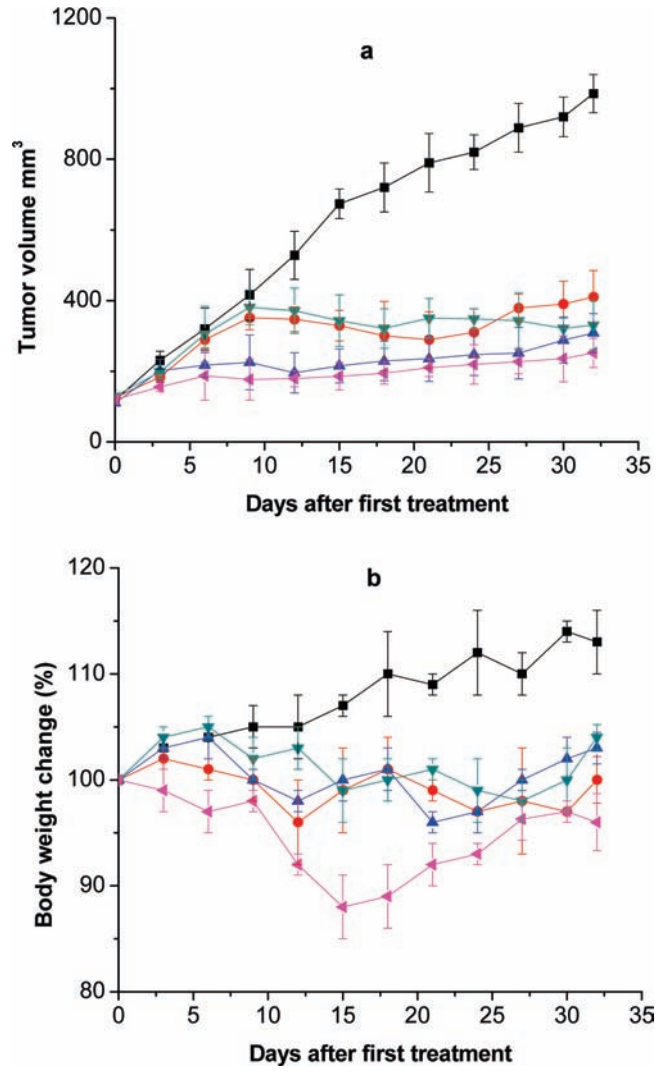

Figure 7. *In vivo* efficacy of Prodrugs and paclitaxel in nu/nu mice ($n = 4$) bearing $SKOV_3$ cells: (a) tumor growth; (b) body weight change. Mice were injected i.p. with 30 mg/kg paclitaxel equivalent dose: control (black), prodrug1 (red), prodrug2 (blue), prodrug3 (green), and paclitaxel (magenta).

Table 3. Antitumor Effect of Prodrugs after Intermittent Intravenous Administration in $SKOV_3$ Bearing Mice

treatment group	mean tumor volume (mm^3)[a] day 32	mean body weight change (%)[a] day 32 vs day 1
saline	986 ± 54	113 ± 3
prodrug1	410 ± 75[b]	100 ± 2.2[b,c]
prodrug2	308 ± 55[b]	103 ± 1.5[b,c]
prodrug3	330 ± 69[b]	104 ± 1.2[b,c]
paclitaxel	252 ± 41[b]	96 ± 2.7[b]

[a] Each value represents the mean ± SD of four mice. [b] Significant difference in comparison with the saline treated with controls ($p < 0.05$). [c] Significant difference in comparison with the paclitaxel-treated group ($p < 0.05$).

CONCLUSIONS

Distinctly different from physical encapsulation, a class of novel paclitaxel prodrugs was synthesized, one that can maintain the structural integrity of the loaded parent drug and self-assemble in aqueous solution. Meanwhile, the three prodrugs

we synthesized exhibited different hydrolysis properties under physiological conditions and plasma. In particular, prodrug2 showed favorable hydrolysis of the ester bond between the amino acid and paclitaxel. In order to increase the content of the drug, we use succinylated heparin with many more carboxyl groups as a carrier and different amino acids as a spacer between the carrier and paclitaxel. The nanoparticles self-assembled in aqueous solution, forming an approximately spherical shape composed of a paclitaxel core and carrier shell with diameter about 140−180 nm. Meanwhile, the results of our bioactivity and cytotoxicity assays showed that the prodrugs can be safe and effective as a novel drug delivery system. A cell cycle analysis studied by flow cytometry has shown that these prodrugs can block MCF-7 cells at the G2/M phase. In *in vivo* experiments, prodrug2 shows similar ovarian tumor growth inhibition to the parent drug while inducing no obvious body weight loss. Overall, our prepared prodrug2 offers promising potential for further clinical applications.

ACKNOWLEDGMENT

We thank Dr. Chunyi Tong from the Institute of Life Science and Biotechnology in Hunan University for his assistance with the experimental procedures during biomedical assays. Meanwhile, this work was supported by the Third Xiangya Hospital of Center South University. The authors are grateful for the financial support of 985 Foundation of Ministry of Education, the National High Technology Research and Development Program of China (grant no. 2007AA022006) and Department of Science and Technology Foundation of Hunan Province (grant no. 2009WK4005).

Supporting Information Available: Characterization of prodrugs, zeta potential of prodrugs, flow cytometry results, *in vivo* results, and experimental section. This material is available free of charge via the Internet at http://pubs.acs.org.

LITERATURE CITED

(1) Weiss, R. B., Donehower, R. C., Wiernik, P. H., Ohnuma, T., Gralla, R. J., Trump, D. L., Baker, J. R., Van-Echo, D. A., Von-Hoff, D. D., and Leyland-Jones, B. (1990) Hypersensitivity reactions from taxol. *J. Clin. Oncol. 8*, 1263–1268.

(2) Deutsch, H. M., Glinski, J. A., Hernandez, M., Haugwitz, R. D., Narayanan, V. L., Suffness, M., and Zalkow, L. H. (1989) Synthesis of congeners and prodrugs. 3. Water-soluble prodrugs of taxol with potent antitumor activity. *J. Med. Chem. 32*, 788–792.

(3) Mathew, A. E., Mejillano, M. R., Nath, J. P., Himes, R. H., and Stella, V. J. (1992) Synthesis and evaluation of some water-soluble prodrugs and derivatives of taxol with antitumor activity. *J. Med. Chem. 35*, 145–151.

(4) Zhao, Z., Kingston, D. G. I., and Crosswell, A. R. (1991) Modified taxols 6. Preparation of water-soluble prodrugs of taxol. *J. Nat. Prod. 54*, 1607–1611.

(5) Ueda, Y., Mikkilineni, A. B., Knipe, J. O., Rose, W. C., Casazza, A. M., and Vyas, D. M. (1993) Novel water soluble phosphate prodrugs of taxol possessing in vivo antitumor activity. *Bioorg. Med. Chem. Lett. 3*, 1761–1766.

(6) Nicolaou, K. C., Riemer, C., Kerr, M. A., Rideout, D. R., and Wrasidlo, W. W. (1993) Design, synthesis and biological activity of protaxols. *Nature 364*, 464–466.

(7) Veronese, F. M., Schiavon, O., Pasut, G., Mendichi, R., Andersson, L., Tsirk, A., Ford, J., Wu, G., Kneller, S., Davies, J., and Duncan, R. (2005) PEG-doxorubicin conjugates: influence of polymer structure on drug release, in vitro cytotoxicity, biodistribution, and antitumor activity. *Bioconjugate Chem. 16*, 775–784.

(8) Liang, H., Chen, S., Chen, M, Lee, P., Chen, C., and Sung, H. (2006) Paclitaxel-loaded poly(γ-glutamic acid)-poly(lactide) nanoparticles as a targeted drug delivery system against cultured HepG2 cells. *Bioconjugate Chem. 17*, 291–299.

(9) Sugahara, S., Kajiki, M., Kuriyama, H., and Kobayashi, T. (2007) Completed regression of xenografted human carcinomas by a paclitaxel-carboxymethyl dextran conjugate (AZ10992). *J. Controlled Release 117*, 40–50.

(10) De-Groot, F. M. H., Albrecht, C., Koekkoek, R., Beusker, P. H., and Scheeren, H. W. (2003) Cascade-release dendrimers" liberate all end groups upon a single triggering event in the dendritic core. *Angew. Chem., Int. Ed. 42*, 4490–4494.

(11) Wang, Y., Xin, D., Liu, K., and Xiang, J. (2009) Heparin-paclitaxel conjugates using mixed anhydride as intermediate: synthesis, influence of polymer structure on drug release, anticoagulant activity and in vitro efficiency. *Pharm. Res. 26*, 785–793.

(12) Shuai, X., Merdan, T., Schaper, A. K., Xi, F., and Kissel, T. (2004) Core-cross-linked polymeric micelles as paclitaxel carriers. *Bioconjugate Chem. 15*, 441–448.

(13) Li, S., Byrne, B., Welsh, J., and Palmer, A. F. (2007) Self-assembled poly(butadiene)-b-poly(ethylene oxide) polymersomes as paclitaxel carriers. *Biotechnol. Prog. 23*, 278–285.

(14) Lim, H. J., Nam, H. Y., Lee, B. H., Kim, D. J., Ko, J. Y., and Park, J. (2007) A novel technique for loading of paclitaxel-PLGA nanoparticles onto ePTFE vascular grafts. *Biotechnol. Prog. 23*, 693–697.

(15) You, J., Hu, F., Du, Y., and Yuan, H. (2007) Polymeric micelles with glycolipid-like structure and multiple hydrophobic domains for mediating molecular target delivery of paclitaxel. *Biomacromolecules 8*, 2450–2456.

(16) Sahoo, S. K., and Labhasetwar, V. (2005) Enhanced antiproliferative activity of transferring-conjugated paclitaxel-loaded nanoparticles is mediated via sustained intracellular drug retention. *Mol. Pharmacol. 5*, 373–383.

(17) Lee, Y., Park, S., Mok, H., and Park, T. G. (2008) Synthesis, characterization, antitumor activity of pluronic mimicking copolymer micelles conjugated with doxorubicin via acid-cleavable linkage. *Bioconjugate Chem. 19*, 525–531.

(18) Litzinger, D. C., Buiting, A. M., Rooijen, N., and Huang, L. (1994) Effect of liposomes size on the circulation time and intraorgan distribution of amphipathic poly(ethylene glycol)-containing liposomes. *Biochem. Biophys. Acta. 1190*, 99–107.

(19) Robert, J. L. (2003) Heparin: structure and activity. *J. Med. Chem. 46*, 2551–2563.

(20) Casu, B., Guerrini, M., Guglieri, S., Naggi, A., Perez, M., Torri, G., Cassinelli, G., Ribatti, D., Carminati, P., Giannini, G., Penco, S., Pisano, C., Belleri, M., Rusnati, M., and Presta, M. (2004) Undersulfated and glycol-split heparins endowed with antiangiogenic activity. *J. Med. Chem. 47*, 838–848.

(21) Lapierre, F., Holme, K., Lam, L., Tressler, R. J., Storm, N., Wee, J., Stack, R. J., Castellot, J., and Tyrrell, D. J. (1996) Chemical modifications of heparin that diminish its anticoagulant but preserve its heparanase-inhibitory, angiostatic, anti-tumor and anti-metastatic properties. *Glycobiology 6*, 355–366.

(22) Ito, S., Nakanishi, H., Hirai, T., Kato, T., Kodera, Y., Feng, Z., Kasai, Y., Ito, K., Akiyama, S., Nakao, A., and Tatematsu, M. (2002) Quantitative detection of CEA expressing free tumor cells in the peripheral blood of colorectal cancer patients during surgery with real-time RT-PCR on a lightcycler. *Cancer Lett. 183*, 195–203.

(23) Win, K. Y., and Feng, S. (2006) In Vitro and in Vivo studies on vitamin E TPGS-emulsified poly(D, L-lactic-co-glycolic acid) nanoparticles for paclitaxel formulation. *Biomaterials 27*, 2285–2291.

(24) Li, C., Yu, D., Newman, R. A., Cabral, F., Stephens, L. C., Hunter, N., Milas, L., and Wallace, S. (1998) Complete regression of well-established tumors using a novel water-soluble poly(l-Glutamic acid)-paclitaxel conjugate. *Cancer Res. 58*, 2404–2409.

(25) Wang, Y., Xin, D., Hu, J., Liu, K., and Xiang, J. (2009) Synthesis and characterization of ternary heparin conjugates by direct covalent bond strategy. *Bioorg. Med. Chem. Lett. 19*, 149–152.
(26) Hashida, M., Takemura, S., Nishikawa, M., and Takakura, Y. (1998) Targeted delivery of plasmid DNA complexed with galactosylated poly(L-lysine). *J. Controlled Release 53*, 301–310.
(27) Maeda, H., Sawa, T., and Konno, T. (2001) Mechanism of tumor-targeted delivery of macromolecular drugs, including EPR effect in solid tumor and clinical overview of the prototype polymeric drug SMANCS. *J. Controlled Release 74*, 47–61.
(28) Masquelier, M., Baurain, R., and Trouet, A. (1980) Amino acid and dipeptide derivatives of daunorubicin. 1. Synthesis, physicochemical properties, and lysosomal digestion. *J. Med. Chem. 23*, 1166–1170.
(29) Casu, B., and Naggi, A. (2003) Antiangiogenic heparin-derived heparan sulfate mimics. *Pure Appl. Chem. 75*, 157–166.
(30) Ono, K., Ishihara, M., Ishikawa, K., Ozeki1, Y., Deguchi, H., Sato, M., Hashimoto, H., Saito, Y., Yura, H., Kurita, A., and Maehara, T. (2002) Periodate-treated, non-anticoagulant heparin-carrying polystyrene (NAC-HCPS) affects angiogenesis and inhibits subcutaneous induced tumour growth and metastasis to the lung. *Br. J. Cancer 86*, 1803–1812.
(31) Yoshitomi, Y., Nakanishi, H., Kusano, Y., Munesue, S., Oguri, K., Tatematsu, M., Yamashina, I., and Okayama, M. (2004) Inhibition of experimental lung metastases of Lewis lung carcinoma cells by chemically modified heparin with reduced anticoagulant activity. *Cancer Lett. 207*, 165–174.
(32) Schiff, P. B., and Horwitz, S. B. (1980) Taxol stabilizes microtubules in mouse fibroblast cells. *Proc. Natl. Acad. Sci. U.S.A. 77*, 1561–1565.
(33) Jordan, M. A., Wendell, K., Gardiner, S., Derry, W. B., Copp, H., and Wilson, L. (1996) Mitotic block induced in Hela cells by low concentrations of paclitaxel (taxol) results in abnormal mitotic exit and apoptotic cell death. *Cancer Res. 56*, 816–825.

BC8003809

Transplatin-Conjugated Triplex-Forming Oligonucleotides Form Adducts with Both Strands of DNA

Meghan A. Campbell[†] and Paul S. Miller*

Department of Biochemistry and Molecular Biology, Johns Hopkins Bloomberg School of Public Health, 615 North Wolfe Street, Baltimore, Maryland 21205. Received January 8, 2009; Revised Manuscript Received November 5, 2009

Triplex-forming oligonucleotides (TFOs) can bind to polypurine·polypyrimidine tracts in DNA and, as a consequence, perturb the normal functioning of a targeted gene. The effectiveness of such antigene TFOs can potentially be enhanced by covalent attachment of the TFO to its DNA target. Here, we report that attachment of N-7-platinated guanine nucleosides to the 3′- and/or 5′-ends of oligopyrimidine TFOs enables these TFOs to form highly stable adducts with target DNA deoxyguanosines or deoxyadenosines that are adjacent to the TFO binding site. Such adduct formation stably anchors the TFO to its target. Depending on the sequences adjacent to the TFO binding site, adduct formation can occur on either strand of the DNA. Adduct formation by 3′,5′-bis-platinated TFOs can result in the formation of an interstrand cross-link between both strands of the DNA duplex. Formation of the adducts, which could be reversed by treatment with sodium cyanide, was dependent upon the ability of the TFO to bind to DNA and appeared to occur at a rate slower than that at which the TFO bound to the DNA duplex. The extent of adduct formation at 37 °C by platinated deoxyribo-TFOs diminished as the pH was increased from 6.5 to 7.4. In contrast, high levels (∼86%) of adduct formation by platinated 2′-*O*-methylribo-TFOs were observed at both pH 6.5 and pH 7.4. Platinated 2′-*O*-methylribo-TFOs were also shown to bind to plasmid DNA and inhibit transcription in vitro, and to inhibit plasmid replication in *E. coli* cells. These results suggest that platinum-conjugated TFOs may be good candidates for use as antigene agents.

INTRODUCTION

Over the past two decades, there has been considerable interest in developing oligonucleotides that can specifically inhibit gene expression. Two approaches that have received much attention are antisense oligonucleotides and siRNA. Both approaches target the RNA product of the expressed gene and ultimately result in destruction of this target. Because the RNA products are continuously produced when the gene is transcribed, the antisense oligonucleotide or siRNA must be present constantly in order to prevent their translation into protein.

An alternative approach that directly targets and inhibits gene expression utilizes triplex-forming oligonucleotides (TFOs). These oligonucleotides are designed to bind to double-stranded DNA at specific regions within the gene (*1*−*3*). As a consequence of this binding, transcription of the gene is inhibited or mutations are induced that result in aberrant expression of the gene. The potential advantages of the antigene strategy are the relatively few copies that need to be targeted and the possibility that targeting can permanently disable gene expression.

Triplex-forming oligonucleotides interact via the major groove by binding to polypurine tracts within the DNA target (*1*−*7*). Oligopurine TFOs utilize reverse-Hoogsteen hydrogen bonds to form A·A-G and G·G-C triads and are oriented antiparallel to the polypurine tract. Oligopyrimidine TFOs utilize Hoogsteen hydrogen bonds to form T·A-T and C^+·G-C triads and are oriented parallel to the polypurine tract. In this case, the N-3 of the cytosine of the C^+·G-C triad must be protonated in order to form a stable Hoogsteen interaction, and consequently, triplex stability diminishes with increasing pH.

Although TFOs can transiently block DNA transcription (*8*−*11*), inhibition of transcription can be enhanced considerably by linking the TFO covalently to the transcribed strand (*12*−*15*). Furthermore, covalent attachment of TFOs can provoke DNA repair leading to mutations in the targeted gene (*16*−*19*). For these reasons, efforts have been made to conjugate TFOs with functional groups that would enable the TFO to bind to its DNA target in an irreversible manner. Alkylating groups such as bromoacetamide (*20*, *21*) and chlorambucil (*22*, *23*) have been used successfully to covalently attach a TFO to DNA. In these cases alkylation occurs at the N-7 of a guanine adjacent to the TFO binding site. However, the alkylated guanine is prone to depurination, which would lead to a release of the TFO. TFOs have also been conjugated with derivatives of psoralen, a photoreactive molecule that intercalates into DNA and can form cyclobutane adducts with thymines upon irradiation with long wavelength UV light (*15*, *24*−*28*).

An alternative approach utilizes the ability of the cancer chemotherapeutic drug cisplatin to cross-link DNA. Cisplatin or *cis*-diamminedichloroplatinum(II) (*cis*-DDP) reacts primarily with the N-7 of purine bases to form a highly stable coordination complex (*29*−*31*). The primary target of cisplatin is guanine, and cisplatin can form both intrastrand and interstrand cross-links in DNA. Platinum compounds have been employed in several ways to cross-link TFOs to duplex DNA including tethering cisplatin to the 5′-end of a TFO (*32*, *33*), targeting an interruption in the polypurine tract with a transplatin-modified cytosine residue (*34*, *35*), and using transplatin monoadducts of guanine and cytosine to react within the Hoogsteen triad (*36*, *37*).

In the latter approach, a transplatin-modified dG, placed at the 5′-end of a TFO efficiently cross-linked to a guanine in the purine strand of the target DNA sequence. In contrast, a transplatin-modified dG placed at an internal position in the TFO was too destabilizing to allow efficient cross-linking. Cross-

* To whom correspondence should be addressed. Phone: 410-955-3489. Fax: 410-955-2926. E-mail: pmiller@jhsph.edu.

[†] Present address: Nucleic Acid Center, Institute of Physics and Chemistry, University of Southern Denmark, Campusvej 55, 5320 Odense M, Denmark.

10.1021/bc900008s © 2009 American Chemical Society
Published on Web 12/01/2009

Table 1. Platinated TFOs and Their Target DNA Duplex

Oligonucleotide[a]	Abr.	T_m °C[b]	Calc. mass	Obs. mass
d-GTTCTTCTTTTCCTTTCT	**1d**	51	5430.92	5431.64
d-TTCTTCTTTTCCTTTCTG	**2d**	46	5430.92	5433.50
d-GTTCTTCTTTTCCTTTCTG	**3d**	49	5759.97	5760.45
mr-TTCTTCTTTTCCTTTCTG	**2mr**	72	5971.32	5971.70
mr-GTTCTTCTTTTCCTTTCTG	**3mr**	71	6330.47	6332.39
d-(Pt-G)TTCTTCTTTTCCTTTCT	**t1d**	ND	5659.92	5656.13
d-TTCTTCTTTTCCTTTCT(Pt-G)	**t2d**	ND	5659.92	5658.37
d-(Pt-G)TTCTTCTTTTCCTTTCT(Pt-G)	**t3d**	ND	6218.07	6213.79
mr-TTCTTCTTTTCCTTTCT(Pt-G)	**t2mr**	ND	6200.42	6198.84
mr-(Pt-G)TTCTTCTTTTCCTTTCT(Pt-G)	**t3mr**	ND	6788.67	6785.19
d-CCG**AAGAAGAAAAGGAAAGA**GCC GGC**TTCTTCTTTTCCTTTCT**CGG-d	**4R** **4Y**	65[c]	7154.31 6926.07	7155.18 6926.12

[a] d, 2′-deoxyribo; mr, 2′-*O*-methylribo; C, 5-methylcytosine; Pt-G, N7-*trans*-diamminediaquaplatinum(II) derivative of guanine; and **bold**, TFO binding site. [b] Triplex melting temperatures were determined at pH 6.5 in triplex buffer containing 100 mM MOPS, 100 mM sodium acetate, and 2.5 mM magnesium acetate. ND, not determined. [c] Melting temperature of the target duplex at pH 6.5.

linking was found to be highly dependent upon pH, with virtually no cross-linking observed at pH 7.

In this article, we describe the binding and cross-linking properties of oligopyrimidine TFOs that have 5′-*trans*Pt-dG (Pt-TFO), 3′-*trans*Pt-dG (TFO-Pt), and bis-3′,5′-*trans*Pt-dG (Pt-TFO-Pt) modifications. We show that the platinum of a Pt-TFO can react with purines in either the purine or pyrimidine strand of a DNA target duplex and that it preferentially reacts with directly opposed G or A residues in the duplex. We also show that the platinum of a TFO-Pt, which can form adducts with purines in either strand of the duplex target, reacts more efficiently than the platinum of a Pt-TFO. Furthermore, the doubly modified TFO, Pt-TFO-Pt, can react with both strands of the duplex to form an interstrand cross-link. Finally, we show that TFO-Pt and Pt-TFO-Pt that consist of 2′-*O*-methylribonucleotides cross-link efficiently with their DNA target at physiological temperature and pH and can be used to disrupt *in vitro* transcription and prevent replication in *E. coli* of a plasmid containing a binding site for the TFO.

EXPERIMENTAL PROCEDURES

Protected 2′-deoxy- and 2′-*O*-methylribonucleoside-3′-*O*-bis(diisopropylamino)-β-cyanoethylphosphoramidites, and 2′-deoxy- and 2′-*O*-methylribonucleoside derivatized controlled pore glass supports (CPG) were purchased from Glen Research Inc. (Sterling, VA). 2′-*O*-Methylribo-5-methylcytosine phosphoramidite and 2′-*O*-methylribo-5-methyluridine derivatized CPG were purchased from ChemGenes Corp. (Ashland, MA). The base protecting groups were benzoyl (A and C) or isobutryl (G). 4,5-Dicyanoimidazole, 5-ethylthiotetrazole, Cap Mix A, Cap Mix B, and oxidizing solution were purchased from EMD Chemicals (Gibbstown, NJ). Phosphoramidite solutions were prepared using synthesis-grade acetonitrile that was dried and stored over calcium hydride. A platinum solution was prepared by incubating 5 mM *trans*-diamminedichloroplatinum(II) (*trans*-DDP) with 10 mM silver nitrate overnight at 37 °C. The resulting precipitate was pelleted by centrifugation, and the supernatant containing *trans*-diamminediaquaplatinum(II) dinitrate was stored in the dark at room temperature. MALDI-TOF mass spectrometry analysis was performed at the AB Mass Spectrometry/Proteomics Facility at The Johns Hopkins School of Medicine, with support from the National Center for Research Resources Shared Instrumentation, Grant 1S10-RR14702.

Synthesis of Oligonucleotides. The sequences of the oligonucleotides used in this article can be found in Table 1 and Figures 3−5 and 8. These oligonucleotides were synthesized on an ABI DNA synthesizer (model 3400), using phosphoramidite chemistry and standard automated procedures. The phosphoramidite solutions were made up to a concentration of 0.15 M, and 5-ethylthiotetrazole was used as the activating agent. Coupling times were 120 s for 2′-deoxyribonucleoside phosphoramidites and 360 s for 2′-*O*-methylribonucleoside phosphoramidites. The oligonucleotides were deprotected and removed from the solid support by incubating the CPG in a solution containing 300 μL of concentrated ammonium hydroxide and 100 μL of 95% ethanol for 3.5 h at 55 °C. The supernatant from this reaction was evaporated to dryness and the residue dissolved in 200 μL of 50% aqueous acetonitrile for storage at 4 °C. The crude oligonucleotides were purified by strong anion exchange HPLC on a Dionex DNAPac PA 100-4 250 mm column (Dionex Corp., Sunnyvale, CA), using a 30 min linear gradient of 0 to 0.5 M sodium chloride in a solution containing 100 mM Tris (pH 7.8) and 10% acetonitrile at a flow rate of 1.0 mL/min. The purified oligonucleotides were desalted on a C-18 Clarity Tube (Phenomenex, Inc., Torrance, CA). The concentration of purified oligomers was determined from their UV absorbance at 260 nm, using calculated extinction coefficients based on nearest neighbor approximations (*38*). The compositions of the oligonucleotides were confirmed by MALDI-TOF mass spectrometry, as shown in Table 1.

Preparation of *trans*-DDP Modified TFOs. The N7 position of the terminal guanines of the TFOs were platinated by dissolving the dried oligomer in an aqueous solution of 144 μM *trans*-diamminediaquaplatinum(II) dinitrate to give a final oligomer concentration of 0.2 nM. The solution was incubated at 37 °C for 2−3 h. The platinated TFOs were then purified by SAX-HPLC as described above, and their compositions were determined by MALDI-TOF mass spectrometry as shown in Table 1.

Thermal Denaturation Experiments. A solution of 1 μM **4RY** duplex and 1 μM TFO was prepared in triplex buffer (pH 6.5), which contained 100 mM MOPS, 100 mM sodium acetate, and 2.5 mM magnesium acetate. The solution was heated to 90 °C for 10 min, allowed to cool slowly to room temperature, and incubated overnight at 4 °C to anneal the triplex. The absorbance at 260 nm was monitored using a Cary 3E spectrophotometer as the solution was heated from 5 to 80 °C at a rate of 0.4 °C/min. The melting temperature was determined by plotting the first derivative of the absorbance versus temperature profile and is accurate to ±1 °C.

Determination of Binding of Platinum-Modified TFOs to DNA. The 5′-hydroxyl group of the pyrimidine strand of the target DNA duplex was labeled using polynucleotide kinase and γ-[^{32}P]-ATP at a specific activity of 10 Ci/mmol. The labeled strand was mixed with an equimolar amount of unlabeled complementary strand, and the solution was evaporated to dryness. The residue was dissolved in 100 μL of triplex buffer to a final duplex concentration of 1 μM. The solution was heated to 90 °C for 10 min and then slowly cooled to room temperature. Solutions containing 100 pmol of platinated TFO were evaporated to dryness, the residue dissolved in 10 μL of the labeled duplex solution, and the solution incubated overnight at 4 °C. A 2 μL aliquot of 50% glycerol was added to each sample, and the samples were electrophoresed on a 20% native polyacrylamide gel at 100 V and 4 °C in triplex buffer. The gel was imaged using a Fuji FLA-7000 phosphorimager.

Reaction of Platinum-Modified TFOs with DNA. One micromolar [^{32}P]-labeled duplex with a specific activity of 10 Ci/mmol was prepared as described above. Solutions containing 10−200 pmol of platinated TFO were evaporated to dryness and dissolved in 10 μL of the labeled duplex solution to a final concentration of 1−20 μM TFO. Each reaction mixture was incubated at 37 °C and quenched with 7 μL of formamide gel loading buffer. The samples were electrophoresed on a 20% denaturing polyacrylamide gel at 800 V. The gel was imaged by a Fuji FLA-7000 phosphorimager, and radioactivity in each band was quantitated using ImageGuage software.

Pt-TFO Cross-Link Reversal by Cyanide Treatment. Platinum-modified TFO (**t1d**, **t2d**, or **t3d**) was cross-linked to the target duplex using the procedure described above. The slower migrating band, which corresponds to the cross-linked product, was excised from the denaturing gel, and the gel slice was extracted by shaking in 20% acetonitrile solution containing 0.1 M ammonium acetate buffer (pH 6.25) for 48 h at 37 °C. The DNA was precipitated in 100% ethanol overnight at −20 °C and then centrifuged for 20 min at 4 °C. The pellet was resuspended in 70% ethanol and centrifuged for 10 min at 4 °C. The pellet was dried under vacuum and dissolved in either 20 μL of water or 20 μL of 200 mM sodium cyanide. Samples were incubated at 37 °C for 48 h and electrophoresed on a 20% denaturing polyacrylamide gel at 800 V. The gel was imaged by a Fuji FLA-7000 phosphorimager, and radioactivity in each band was quantitated using ImageGuage software.

TFO Binding Kinetics. Triplex formation results in a decrease in absorbance at 260 nm. This phenomenon has been employed previously to estimate the rate of third strand association (*39*, *40*). Separate solutions of 2 μM **t1d** and 2 μM **4RY** were prepared in triplex buffer (pH 6.5). The duplex solution (**4RY**) was annealed and stored overnight at 4 °C. Five hundred microliters of each solution was equilibrated at 37 °C, and the solutions were quickly, but thoroughly mixed in a 1 mL quartz cuvette to give a final concentration of 1 μM. The absorbance at 260 nm was immediately monitored using a Cary 3E spectrophotometer (1 data point/3 s) over the course of 20,000 s (5.56 h) at 37 °C. The k_{on} value was calculated using the Varian software supplied with the spectrophotometer using second order kinetics. The reported k_{on} value is an average of four independent experiments. The $t_{1/2}$ of binding was calculated using the equation $t_{1/2} = 1/(k_{on} \cdot [\text{duplex}]_0)$.

Construction of Plasmid p-GEM-TFO. Plasmid pGEM-3Z (Promega, Madison WI) was cut with *Eco*RI and *Hin*dIII, and the resulting linear DNA was purified by agarose gel electrophoresis. The *Hin*dIII restriction site is immediately adjacent to a T7 promoter sequence in the plasmid. One equivalent of the linearized DNA was ligated with 6 equivalents of duplex **5RY**, whose sequence is shown in Figure 8a, using T4 DNA ligase. The ligated DNA was then transformed into DH5α *E. coli* cells; the transformed cells were plated on LB agar plates supplemented with ampicilin, bromo-chloro-indolyl-galactopyranoside (X-gal), and isopropyl-β-D-thiogalactopyranoside (IPTG); and white colonies were selected. Individual colonies were grown in LB medium; plasmid DNA was isolated using a QIAprep Spin Miniprep kit (Qiagen Sciences); and the DNA was sequenced to confirm the presence of the **5RY** insert. The insert is oriented such that the **5Y** strand of the duplex is part of the plasmid strand that can be transcribed by T7 RNA polymerase.

Reaction of Platinum-Modified TFO t2mr with p-GEM-TFO. Solutions (10 μL) containing 500 ng of pGEM-TFO and 0 μM TFO, 10 μM nonplatinated TFO **2mr**, or 10 μM platinated TFO **t2mr** in buffer composed of 50 mM HEPES, 100 mM sodium chloride, and 5 mM magnesium chloride, pH 7.5, were incubated for 72 h at 37 °C. A 0.5 μL aliquot was removed from each reaction, and each aliquot was incubated in 9.5 μL of a solution containing 100 mM sodium chloride, 50 mM Tris-hydrochloride, 10 mM magnesium chloride, 1 mM dithiothreitol, pH 7.9, and 10 units of *Bgl*II for 2 h at 37 °C. A 5 μL aliquot of each digest was mixed with 5 μL of 20% glycerol loading buffer, and the solutions were electrophoresed on a 0.8% agarose gel containing Syber Green dye. The gel was scanned on a Fuji FLA-7000 imager.

Transcription of p-GEM-TFO DNA. pGEM-TFO treated with 0 μM TFO, 10 μM nonplatinated TFO **2mr**, or 10 μM platinated TFO **t2mr** as described above was incubated with *Hin*dIII for 2 h at 37 °C. Examination by agarose gel electrophoresis showed that all three plasmid preparations were completely linearized. Transcription was carried out using the Riboprobe System T-7 kit supplied by Promega. Each reaction contained between 1.5 to 11.6 ng of linearized plasmid DNA, 9.8 mM dithiothreitol, 40 units of RNasin inhibitor, 0.49 mM each of rATP/rCTP/rUTP, 11.8 μM rGTP, 50 μCi of α-^{32}-P-rGTP, and 19 units of T7 RNA polymerase in 20.4 μL of transcription buffer that consisted of 40 mM Tris-hydrochloride (pH 7.9), 10 mM sodium chloride, 6 mM magnesium chloride, 2 mM spermidine, and 0.05% Tween. The reactions were incubated for 1 h at 37 °C, passed through a Sephadex G-25 Micro-Spin column (GE Healthcare), and then electrophoresed on a 15% denaturing polyacrylamide gel at 800 V. The gel was phosphorimaged, the 42 nucleotide runoff products were quantified from the phosphorimage, and the amount of product was normalized to the amount of plasmid DNA used in the reaction.

Colony Formation by *E. coli* Transformed with p-GEM-TFO. Samples (150 pg each) of pGEM-TFO treated with 0 μM TFO, 10 μM nonplatinated TFO **2mr**, or 10 μM platinated TFO **t2mr** as described above were electroporated at 1.8 kV into electrocompetent DH5α *E. coli* cells in 40 μL of GYT medium that contained 1.25 mg/mL yeast extract, 2.5 mg/mL tryptone, and 10% glycerol. The cells were then immediately diluted with 1.0 mL of SOC medium that contained 20 mg/mL Bacto-tryptone, 5 mg/mL Bacto-yeast extract, 8.6 mM sodium chloride, and 2.5 mM potassium chloride, and then incubated with shaking at 37 °C for 1 h. The cells were then spread onto LB plates supplemented with ampicilin, and the plates were incubated overnight at 37 °C. Two separate experiments were carried out in triplicate, and the number of colonies formed was counted.

RESULTS AND DISCUSSION

Synthesis and Characterization of Platinated TFOs. Previous studies by Leng and co-workers had examined the ability of oligodeoxyribopyrimidine TFOs with a 5′-*trans*Pt-dG modification to form adducts with DNA (*36*, *37*). We have extended these studies to include oligodeoxyribopyrimidine and oligo-2′-*O*-methylribopyrimidine TFOs that contain 5′-, 3′-, and 5′,3′-*trans*Pt-dG modifications. The sequences of these TFOs and

the site targeted for triplex formation are shown in Table 1. The target duplex sequence (4RY) serves as a model for triplex formation with five cytosine residues within a 17 bp long polypurine tract and is similar to a previously studied purine target sequence found in the coding region of the polymerase gene of HIV-1 (*34*, *35*). Each of the TFOs consisted of either 2′-deoxyribonucleotides or 2′-*O*-methylribonucleotides and contained 5-methylcytosine (C) and 5-methyluracil (T) bases. One or both ends of the TFO contained guanine nucleosides that were platinated to give the monofunctional N-7 *trans*-$[Pt(NH_3)_2(G)(H_2O)]^+$ adduct. Platination of the TFOs was carried out by incubating the TFO in a solution containing *trans*-diamminediaquaplatinum(II) dinitrate at 37 °C. Under these conditions, platination occurs preferentially at the N-7 of the guanine of the TFO (*36*). Because addition of the platinum group adds a positive charge to the oligonucleotide, the platinated TFO can be separated from nonplatinated TFO by strong anion exchange HPLC (see Supporting Information, Figure S1). The compositions of the platinated TFOs were confirmed by MALDI-TOF mass spectrometry analysis (see Table 1). Additional peaks observed in the HPLC chromatograph (see Supporting Information, Figures S1 and S2) were isolated and identified by MALDI-TOF mass spectrometry as multiply platinated species. The overall yields of the purified and desalted Pt-TFOs were approximately 20−30%.

The TFOs were tested for their ability to bind to a DNA target sequence, **4RY**, by measuring the melting temperatures of the triplexes formed by the nonplatinated TFOs at pH 6.5, as shown in Table 1. The TFOs that consisted of deoxyribonucleotides, **1d**, **2d**, and **3d**, formed relatively stable triplexes whose third strands dissociated at approximately 50 °C, a temperature lower than the melting temperature of duplex **4RY**, 65 °C. We and others have shown previously that incorporation of 2′-*O*-methylribonucleotides can stabilize TFO binding (*40*−*45*). In accord with these findings, the TFOs containing 2′-*O*-methylribonucleotides, **2mr**, and **3mr**, formed triplexes that melted with a single transition at greater than 70 °C. Representative melting curves can be found in Supporting Information, Figure S3. Melting temperatures for the corresponding platinum modified TFOs were not determined because these TFOs were expected to form adducts with the DNA target. However, a previous study has shown that modification of a guanine at the end of a polypyrimidine TFO with a nonreactive platinum group resulted in a slight stabilization of a triplex formed by this TFO (*37*). Most likely this stabilization results from introduction of the positively charged platinum group. On the basis of this result, we expected that the platinated TFOs shown in Table 1 would form triplexes whose stabilities are comparable to those of the parent unmodified TFOs.

Adduct Formation between Platinated TFOs and DNA Duplexes. We examined the interactions of the platinated TFOs by electrophoretic mobility shift assays on native polyacrylamide gels. Each of the platinated deoxyribo-TFOs was incubated with DNA target duplex, **4RY**, at 4 °C, and the solution was then subjected to electrophoresis on a native polyacrylamide gel run at 4 °C to prevent dissociation of the triplex due to heating of the gel. As shown in Figure 1a, the mobility of **4RY** decreased in the presence of Pt-TFO, **t1d**, TFO-Pt, **t2d**, or Pt-TFO-Pt, **t3d**, a result consistent with triplex formation.

The platinated TFOs were then tested for their ability to form adducts with each strand of the target duplex. Increasing concentrations of the platinated TFOs were incubated at 37 °C with duplex **4RY** whose purine or pyrimidine strand was labeled with ^{32}P phosphate. The reaction mixtures were then subjected to electrophoresis on a denaturing polyacrylamide gel. As shown in Figure 1b, incubation of the target with Pt-TFO **t1d** resulted in 50% adduct formation with the purine strand, whereas only

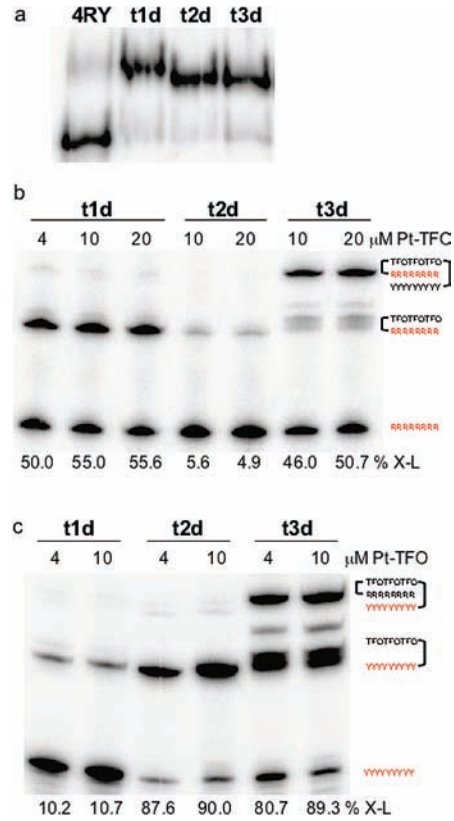

Figure 1. Interactions of platinated TFOs with DNA duplex **4RY**. (a) Solutions containing 10 μM platinated TFO and 1 μM duplex **4RY**, whose purine strand was labeled with ^{32}P-phosphate, were incubated at 4 °C in triplex buffer that contained 100 mM MOPS, pH 6.5, 100 mM sodium acetate, and 2.5 mM magnesium acetate, and were then subjected to electrophoresis on a 20% native polyacrylamide run at 4 °C and 100 V. (b) Solutions containing platinated TFO and 1 μM duplex **4RY**, whose purine strand was labeled with ^{32}P-phosphate (shown in red), were incubated at 37 °C for 48 h in triplex buffer and were then subjected to electrophoresis on a 20% denaturing polyacrylamide gel. Percent adduct formation is shown below the corresponding lane (% X-L). (c) Solutions containing platinated TFO and 1 μM duplex **4RY**, whose pyrimidine strand was labeled with ^{32}P-phosphate (shown in red), were incubated at 37 °C for 48 h in triplex buffer and were then subjected to electrophoresis on a 20% denaturing polyacrylamide gel. Percent adduct formation is shown below the corresponding lane (% X-L).

5% adduct formation was observed with TFO-Pt **t2d**. Approximately 50% adduct formation was observed when Pt-TFO-Pt **t3d** was incubated with purine strand-labeled **4RY**. In this case, however, the electrophoretic mobility of the adduct was significantly slower than that observed for the adducts formed by either **t1d** or **t2d**. This slower mobility suggested that **t3d** had formed adducts with both strands of the duplex. Reaction of Pt-TFO **t1d** with pyrimidine-labeled **4RY** resulted in approximately 10% adduct formation, as shown in Figure 1c, whereas approximately 90% adduct formation was observed with TFO-Pt **t2d**. A similar level of adduct formation was also observed with Pt-TFO-Pt **t3d**. As seen in Figure 1c, **t3d** formed two types of adducts, one whose mobility was similar to that of adducts formed by **t1d** and **t2d**, and a slower mobility adduct. This latter adduct, which represents approximately 35−40% of the total adduct formation, is most likely the TFO cross-linked to both strands of the duplex. It migrates more slowly on the denaturing gel because the three strands are linked together as indicated schematically in Figure 1c. These results show that adduct formation can occur when the *trans*Pt-dG is placed at either end of the TFO and that either strand of the duplex can be targeted. These results also suggest that cross-linking is strand

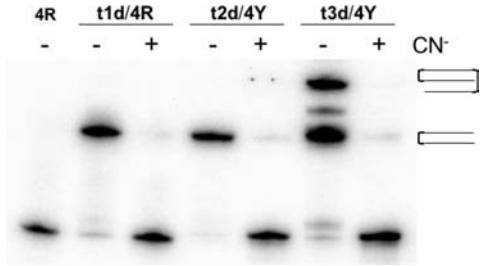

Figure 2. Reversal of platinated TFO adducts by treatment with cyanide. Adducts formed by reaction of the platinated TFOs with duplex **4RY** were isolated and treated with either water or 200 mM sodium cyanide. The reaction mixtures were then subjected to electrophoresis on a 20% denaturing polyacrylamide gel. The labeled strand of duplex **4RY** is indicated at the top of the gel.

specific and possibly sequence specific depending on the location, 5′ or 3′, of the platinated-G in the TFO.

It seemed likely that the *trans*Pt-dG group of the TFO platinates the guanine residues of **4RY** adjacent to the TFO binding site. It has been shown that cyanide is an extremely strong ligand for platinum and that adding cyanide to a Pt-G adduct will displace the platinum from guanine (*46*−*50*). The **t1d-4R**, **t2d-4Y**, and **t3d-4Y** adducts were isolated from the gel and were treated with 200 mM sodium cyanide. The products of these reactions were then analyzed on a denaturing gel. As shown in Figure 2, the mobilities of the treated adducts reverted to those of the labeled strand alone. This result is consistent with the formation of a platinum adduct between the platinated TFO and the labeled target strand.

In order to better understand the base preference of adduct formation, a series of duplexes were synthesized in which a set of two identical base pairs, which could serve as sites for platination, were placed at each end of the duplex. The sequences of the four duplexes containing the four possible combinations of the base pairs are shown in Figure 3a. The purine- or pyrimidine-rich strand of each duplex was labeled with ^{32}P, and the labeled duplexes were reacted with the platinated TFOs at 37 °C and the products analyzed by denaturing polyacrylamide gel electrophoresis (PAGE). The results are summarized in Figure 3b. As expected, significant adduct formation was observed with duplexes whose labeled strand contained guanine (**GY** or **GR**) or adenine (**AY** or **AR**) residues at the ends of the duplex. It is likely that adduct formation occurred as a result of platination of the N-7 of these bases. Very little adduct formation was observed when either cytosines or thymines were placed at the ends of the labeled strands, a result consistent with the known reactivity of these bases with platinum. We were surprised to find that adduct formation occurred equally well on either the pyrimidine or purine strand of the duplex when guanines or adenines were the target of platination. In a previous study of a 5′-*trans*Pt-dG modified TFO, no adduct formation with the pyrimidine strand was observed (*36*). However, in this case the pyrimidine strand of the target duplex contained only pyrimidines at the platination site.

The duplexes shown in Figure 3a contain two potential sites for platination: one base from the end of the triplex binding site (n-1) and two bases from the end of the triplex binding site (n-2). In order to better characterize the precise site of platination for each of the platinated TFOs, we employed another set of duplexes (shown in Figure 4a) that have a single G residue at either the n-1 or the n-2 position. The purine or pyrimidine strand of each duplex was 5′-end labeled with a ^{32}P phosphate group, and reactions were carried out with each of the platinated TFOs as described above. As shown in Figure 4b, a clear pattern of adduct formation emerged for each of the platinated TFOs.

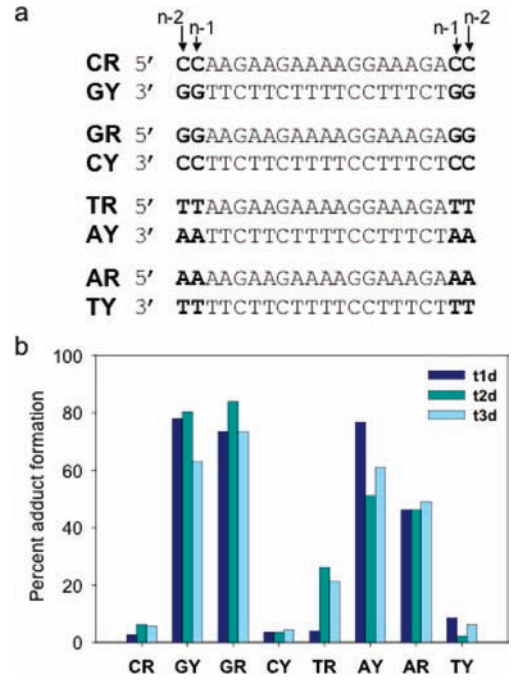

Figure 3. Adduct formation between platinated TFOs and DNA duplexes. (a) Sequences of the DNA duplexes. Bases shown in bold lie outside the TFO binding site. (b) Percent adduct formation between platinated TFOs **t1d** (dark blue), **t2d** (medium blue), or **t3d** (light blue) and the purine or pyrimidine strands of each of the DNA duplexes. Solutions containing 1 μM ^{32}P-labeled duplex and 2 μM platinated TFO were incubated in triplex buffer at 37 °C for 48 h and then analyzed by PAGE on a 20% denaturing gel. The amount of adduct formed was quantitated by phosphorimaging the gel.

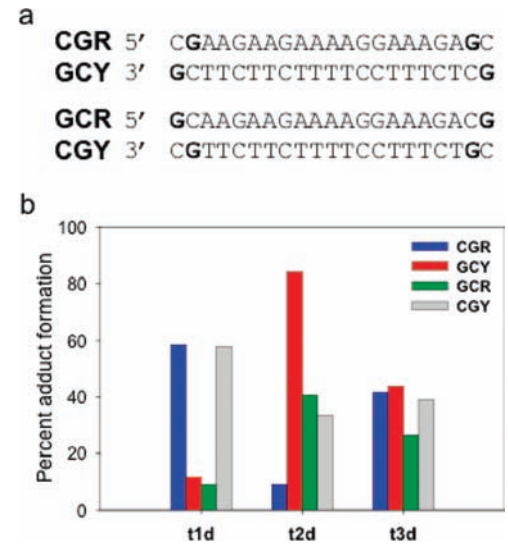

Figure 4. Adduct formation between platinated TFOs and DNA duplexes. (a) Sequences of DNA duplexes. Potential sites of platination are shown in bold. (b) Percent adduct formation between platinated TFOs **t1d**, **t2d**, or **t3d** and the purine or pyrimidine strands of the DNA duplexes. Solutions containing 1 μM ^{32}P-labeled duplex and 2 μM platinated TFO were incubated in triplex buffer at 37 °C for 48 h and then analyzed by PAGE on a 20% denaturing gel. The amount of cross-linking was quantitated by phosphorimaging the gel.

Preferential adduct formation by the Pt-TFO, **t1d**, was observed with duplexes that contained guanine at the n-1 position in either the purine or pyrimidine strand of the duplex. In contrast, adduct formation by the TFO-Pt, **t2d**, occurred to the greatest extent with the duplex whose pyrimidine strand contained a guanine at position n-2, and to lesser extents with the duplexes that

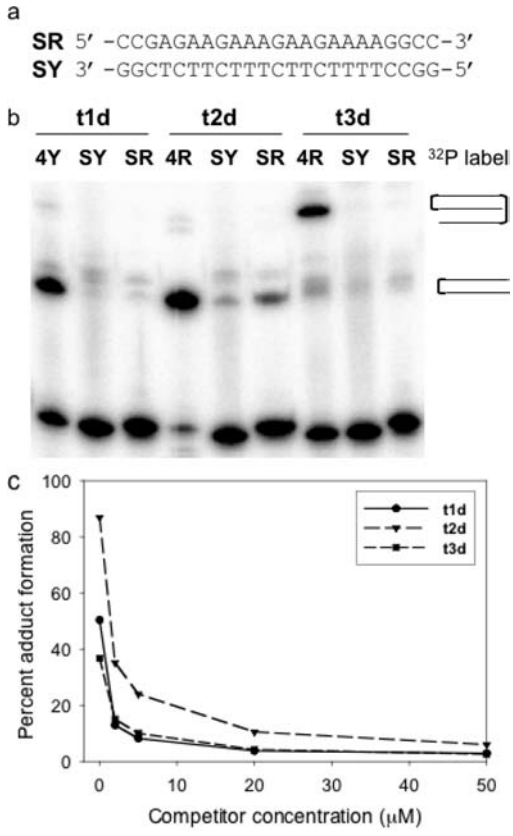

Figure 5. Sequence dependent interactions between platinated TFOs and DNA duplexes. (a) Sequence of the scrambled duplex, **SRY**. (b) Solutions containing 1 μM ^{32}P-labeled duplex **SRY** or 1 μM ^{32}P-labeled duplex **4RY** and 2 μM platinated TFO were incubated in triplex buffer at 37 °C for 48 h and then analyzed by PAGE on a 20% denaturing gel. (c) Solutions containing 1 μM ^{32}P-labeled duplex **4RY**, 2 μM platinated TFO, and increasing concentrations of competitor nonplatinated TFO were incubated in triplex buffer at 37 °C for 48 h and then analyzed by PAGE on a 20% denaturing gel. The percentage of adduct formed by each platinated TFO versus competitor concentration was determined.

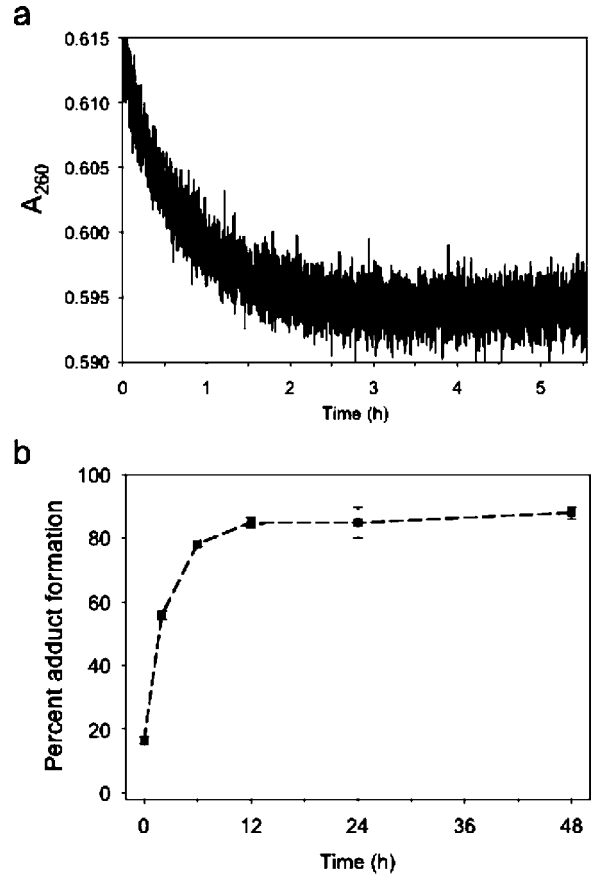

Figure 6. Kinetics of triplex adduct formation. (a) Equal volumes of solutions containing 1 μM TFO **1d** and DNA duplex **4RY** in triplex buffer were mixed, and the absorbance at 260 nm was recorded as a function of time at 37 °C. (b) Solutions containing 1 μM ^{32}P-labeled duplex **4RY** and 2 μM **t2d** were incubated in triplex buffer at 37 °C for various lengths of time and analyzed by PAGE on a 20% denaturing gel. The percent adduct formation was determined as a function of time.

contained an n-2 guanine in the purine strand or an n-1 guanine in the pyrimidine strand. As expected, the bis-platinated Pt-TFO-Pt, **t3d**, formed adducts equally well with the pyrimidine and purine strands of both duplexes.

The experiments described above show that platinated TFOs can form adducts with DNA duplexes that contain guanines or adenines adjacent to the TFO binding site in either strand of the duplex. These platinated TFOs retained approximately 60−90% of their initial activity after storage for 1.5 months in aqueous 50% acetonitrile at 4 °C. These results suggest that it should be possible to design stable platinated TFOs that can target a rather broad range of sequences in DNA.

Specificity of Adduct Formation. Experiments were carried out using a scrambled DNA duplex to ensure that adduct formation by the platinated TFOs was dependent upon the ability of the TFO to bind to its target. The sequence of this scrambled duplex, **SRY**, is shown in Figure 5a. It contains the same number of CG and TA base pairs as DNA duplex **4RY** (see Table 1) and has the same terminal sequences adjacent to the TFO binding site. Each of the platinated TFOs was incubated at 37 °C with duplex **SRY**, whose purine or pyrimidine strand was labeled with a 5′-^{32}P-phosphate group, and the products of the reaction were analyzed by denaturing PAGE. Control reactions were run using ^{32}P-labeled **4RY** as a target duplex. As shown in Figure 5b, the platinated TFOs formed adducts with either the purine or the pyrimidine strand of the **4RY**. In contrast, very little adduct formation with either the **SR** or the **SY** strand of the scrambled duplex was observed. In a second experiment, increasing concentrations of nonplatinated TFO were added to reaction mixtures containing the platinated TFOs and DNA duplex **4RY**. The amount of adduct formation was determined by denaturing PAGE. The results are summarized in Figure 5c. A significant decrease in adduct formation by each of the platinated TFOs was observed in the presence of an equimolar amount of competitor nonplatinated TFO (2 μM), and adduct formation was completely inhibited at higher competitor concentrations.

Taken together, the results described above demonstrate that adduct formation between the platinated TFOs and DNA duplex **4RY** is driven by the ability of the TFO to bind specifically to this target and not by nonsequence-specific platination of the DNA duplex. This behavior suggests that it should be possible to design platinated TFOs that can react with their designated DNA targets in a specific manner with little or no off-target effects.

Kinetics of TFO Binding and Adduct Formation. The kinetics of triplex formation were determined by observing the decrease in absorbance upon mixing TFO **1d** with DNA duplex **4RY** at 37 °C as shown in Figure 6a. The average rate constant, k_{on}, for the association of the TFO with the duplex is 654.51 s^{-1} M^{-1} as determined from four separate experiments. This translates to a half-life of triplex formation of 25.5 min. This value can be compared with those of Xodo, who found a k_{on} of 2557 M^{-1} s^{-1} for a 18-mer deoxy TFO that was assayed at 26.1

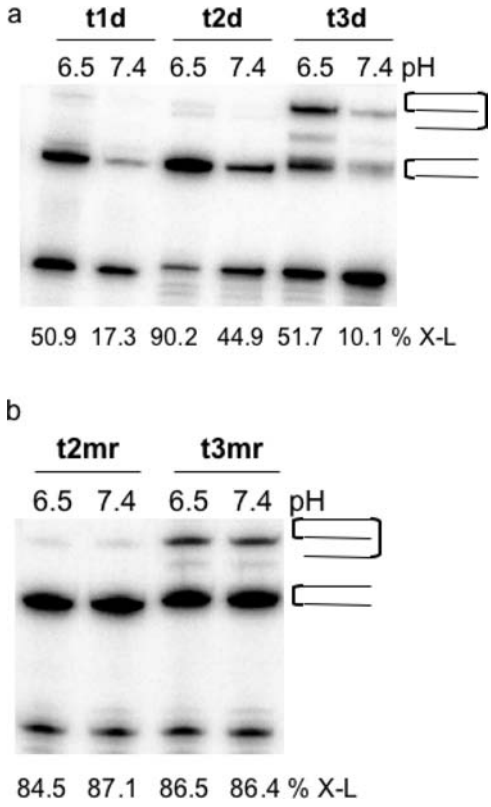

Figure 7. Effect of pH on adduct formation by platinated deoxyribo- and 2′-*O*-methylribo-TFOs. (a) Solutions containing 1 μM duplex **4RY** and 2 μM platinated deoxyribo-TFOs **t1d**, **t2d**, or **t3d** in pH 6.5 or pH 7.4 triplex buffer were incubated at 37 °C for 48 h and then subjected to 20% denaturing PAGE. (b) Solutions containing 1 μM duplex **4RY** and 2 μM platinated 2′-*O*-methylribo-TFOs **t2mr** or **t3mr** in pH 6.5 or 7.4 triplex buffer were incubated at 37 °C for 48 h and then subjected to 20% denaturing PAGE. The percent adduct formation as determined by phosphorimaging is shown below each lane. The purine strand of duplex **4RY** is labeled in each case.

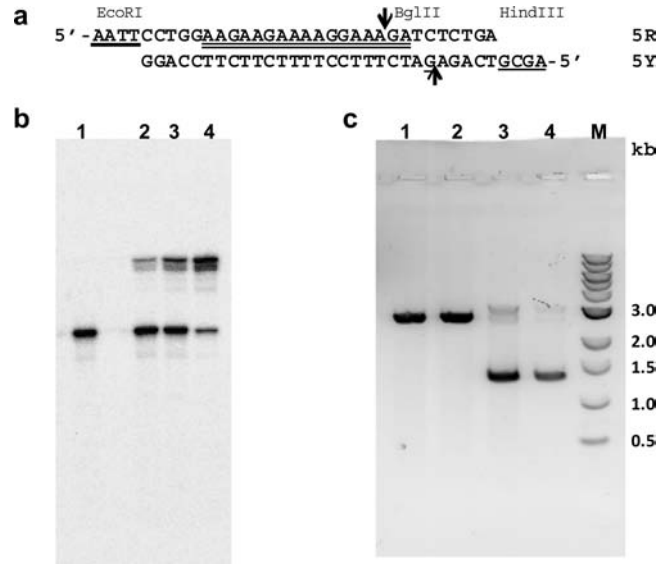

Figure 8. Interaction of platinated TFO with plasmid DNA. (a) Sequence of duplex insert **5RY**. The TFO binding site is indicated by the double underline; the guanine target for reaction with platinated TFO **t2mr** is underlined; *Eco*RI and *Hin*dIII complementary overhangs are indicated by heavy underlines; and the *Bgl*II restriction site is indicated by the arrows. (b) Reaction of 1 μM **5RY** with 0 μM (lane 1), 2 μM (lane 2), 4 μM (lane 3), or 10 μM **t2mr** in buffer containing 50 mM HEPES, 100 mM sodium chloride, and 5 mM magnesium chloride, pH 7.5, incubated at 37 °C for 24 h. The **5Y** strand was labeled with ^{32}P and the products of the reaction were analyzed on a 15% denaturing polyacrylamide gel. (c) Reaction of 500 ng of p-GEM-TFO with 0 μM TFO (lane 1), 10 μM **2mr** (lane 2), 10 μM **t2mr** (lane 3), or 0 μM TFO (lane 4) in buffer containing 50 mM HEPES, 100 mM sodium chloride, and 5 mM magnesium chloride, pH 7.5, incubated at 37 °C for 72 h. Following the reaction, the plasmids were digested with 10 units (lanes 1−3) or 0 units (lane 4) of *Bgl*II, and the digests were analyzed by electrophoresis on a 0.8% agarose gel. Lane M is a 1 kb DNA ladder.

°C (*39*), and Puri et al., observed a k_{on} value of approximately 600 M^{-1} s^{-1} for a 17-mer 2′-*O*-methylribo TFO at 25 °C (*40*).

The kinetics of adduct formation between the platinated TFO **t2d** and DNA duplex **4RY** were determined. In these experiments, 1 μM **4RY** was incubated with 2 μM platinated TFO, **t2d**, at 37 °C, and the extent of adduct formation at various times was assayed by denaturing PAGE. Figure 6b shows the averaged results from three independent experiments. The platinated TFO achieves maximal adduct formation after 10−12 h, and the $t_{1/2}$ of adduct formation is approximately 3 h. This result suggests that adduct formation occurs at a rate significantly slower than that at which the TFO binds to its target. It appears then that platination is the rate limiting step in adduct formation. These observations are consistent with the specificity of adduct formation described above and further support the idea that TFO binding precedes platination of the DNA target.

Effect of pH on Adduct Formation. The experiments described above were carried out at pH 6.5, a pH that favors protonation of the 5-methylcytosines in the TFO and thus enhances the stability of the triplex. A 2−5-fold decrease in adduct formation was observed when the reactions were carried out at pH 7.4 (see Figure 7a). As demonstrated in Table 1, triplex stability can be increased significantly by replacing deoxyribonucleotides in the TFO with 2′-*O*-methylribonucleotides. This change significantly increases the amount of adduct formation as shown in Figure 7b. The 3′-platinated mr-TFO, **t2mr**, and 3′,5′-bis-platinated mr-TFO, **t3mr**, both give extensive adduct formation with duplex **4RY** at both pH 6.5 and pH 7.4. These results suggest that platinated 2′-*O*-methyribo-TFOs could be designed that would function effectively under physiological conditions.

Interactions with Plasmid DNA. The interaction of 3′-platinated mr-TFO **t2mr** with a purine tract in the supercoiled form of plasmid p-GEM-TFO was studied. This plasmid was constructed by inserting duplex **5RY**, whose sequence is shown in Figure 8a, into the *Eco*RI and *Hin*dIII restriction sites of the polylinker region of p-GEM-3Z. Duplex **5RY**, whose purine tract is identical in sequence to that of duplex **4RY**, contains a unique *Bgl*II restriction site that is not otherwise found in p-GEM-3Z. The underlined guanine located 10 nucleotides from the 5′-end of **5Y** serves as a target site for platination by TFO **t2mr**.

Binding experiments were carried out at pH 7.5 and 37 °C to measure the extent of adduct formation between **t2mr** and duplex **5RY**, whose pyrimidine-rich strand was labeled with ^{32}P. As shown in Figure 8b, addition of increasing concentrations of **t2mr** resulted in the formation of a new product whose mobility on a denaturing polyacrylamide gel was consistent with formation of an adduct between **t2mr** and strand **5Y** of the duplex. Quantification of the phosphorimage of the gel showed that 79% of the duplex was converted to adduct after incubation with 10 μM **t2mr** for 24 h. The cross-linked duplex was not hydrolyzed when treated with *Bgl*II (data not shown). This result demonstrates that triplex and adduct formation by **t2mr** obstructs the recognition site of the restriction enzyme.

Plasmid p-GEM-TFO was incubated with 10 μM **t2mr** or 10 μM nonplatinated TFO **2mr** at 37 °C. The plasmid DNA was then treated with *Bgl*II, and the resulting digests were

analyzed by agarose gel electrophoresis. As shown in Figure 8c, supercoiled plasmid alone (lane 1) or supercoiled plasmid that had been incubated with **2mr** (lane 2) was completely converted by *Bgl*II to linear DNA. In contrast, 84% of the plasmid that had been incubated with **t2mr** was resistant to digestion by *Bgl*II and remained in the supercoiled form (lane 3). These results show that platinated TFO **t2mr** can bind to and react with the **5RY** insert in the supercoiled plasmid under essentially physiological conditions.

The site on the plasmid into which duplex **5RY** was inserted is flanked by promoter sequences for T-7 and Sp6 RNA polymerases. The insert is oriented such that the strand containing the **5Y** sequence would be used as a template for transcription by T-7 RNA polymerase. Run-off transcription experiments were carried out to determine if transcription is inhibited when **t2mr** is bound to the plasmid. Plasmid that had been incubated with **t2mr** as described above was linearized by digestion with *Bgl*II. The linearized plasmid was then transcribed using T-7 RNA polymerase, and the amount of runoff transcript, which is 42 nucleotides in length, was compared to that obtained from untreated p-GEM-TFO or plasmid treated with **2mr**. The nonplatinated TFO, **2mr**, inhibited transcription approximately 25%, whereas transcription was inhibited approximately 95% by the platinated TFO, **t2mr**.

In addition to inhibiting transcription, the platinated TFO would also be expected to interfere with plasmid replication. To test this, **2mr**- or **t2mr**-treated p-GEM-TFO, which contains an ampicilin resistance gene, was electroporated into wild type DH5α *E. coli* cells, and the electroporated cells were spread on LB agar plates that contained ampicilin. The number of colonies formed by cells electroporated with **2mr** was reduced 67% relative to cells electroporated with untreated pGEM-TFO. An even greater amount of inhibition of colony formation, 84%, was observed for the cells electroporated with **t2mr**-treated p-GEM-TFO.

Taken together, the experiments described above suggest that the platinated 2′-*O*-methylribo-TFO can bind effectively to supercoiled DNA and that such binding is able to interfere with transcription and replication of plasmid DNA. Experiments are currently in progress to determine if platinated TFOs of this type can be used to inhibit gene expression in mammalian cells.

ACKNOWLEDGMENT

This research was supported by a grant from the National Institutes of Health, GM 057140 (to P.S.M.). We thank Ms. Lynn Periera for carrying out the transcription experiments; the laboratory of Dr. Michael Matunis for providing electrocompetent DH5α cells; and Ms. Erica Hlavin for advice on transforming *E. coli* cells.

Supporting Information Available: SAX HPLC chromatograms of **t2d** (Figure S1), **t3d** (Figure S2), and representative thermal denaturation curves (Figure S3). This material is available free of charge via the Internet at http://pubs.acs.org.

LITERATURE CITED

(1) Chan, P. P., and Glazer, P. M. (1997) Triplex DNA: fundamentals, advances, and potential applications for gene therapy. *J. Mol. Med. 75*, 267–282.
(2) Knauert, M. P., and Glazer, P. M. (2001) Triplex forming oligonucleotides: sequence-specific tools for gene targeting. *Hum. Mol. Genet. 10*, 2243–2251.
(3) Vasquez, K. M., and Glazer, P. M. (2002) Triplex-forming oligonucleotides: principles and applications. *Q. Rev. Biophys. 35*, 89–107.
(4) Thuong, N. T., and Helene, C. (1993) Sequence-specific recognition and modification of double-helical DNA by oligonucleotides. *Angew. Chem., Int. Ed. Engl. 32*, 666–690.
(5) Radhakrishnan, I., and Patel, D. J. (1994) DNA triplexes: solution structures, hydration sites, energetics, interactions, and function. *Biochemistry 33*, 11405–11416.
(6) Frank-Kamenetskii, M. D., and Mirkin, S. M. (1995) Triplex DNA structures. *Annu. Rev. Biochem. 64*, 65–95.
(7) Fox, K. R. (2000) Targeting DNA with triplexes. *Curr. Med. Chem. 7*, 17–37.
(8) Alunni-Fabbroni, M., Manfioletti, G., Manzini, G., and Xodo, L. E. (1994) Inhibition of T7 RNA polymerase transcription by phosphate and phosphorothioate triplex-forming oligonucleotides targeted to a R.Y site downstream from the promoter. *Eur. J. Biochem. 226*, 831–839.
(9) Hacia, J. G., Dervan, P. B., and Wold, B. J. (1994) Inhibition of Klenow fragment DNA polymerase on double-helical templates by oligonucleotide-directed triple-helix formation. *Biochemistry 33*, 6192–6200.
(10) Giovannangeli, C., Perrouault, L., Escude, C., Gryaznov, S., and Helene, C. (1996) Efficient inhibition of transcription elongation in vitro by oligonucleotide phosphoramidates targeted to proviral HIV DNA. *J. Mol. Biol. 261*, 386–398.
(11) Giovannangeli, C., and Helene, C. (2000) Triplex-forming molecules for modulation of DNA information processing. *Curr. Opin. Mol. Ther. 2*, 288–296.
(12) Degols, G., Clarenc, J. P., Lebleu, B., and Leonetti, J. P. (1994) Reversible inhibition of gene expression by a psoralen functionalized triple helix forming oligonucleotide in intact cells. *J. Biol. Chem. 269*, 16933–16937.
(13) Ebbinghaus, S. W., Fortinberry, H., and Gamper, H. B., Jr. (1999) Inhibition of transcription elongation in the HER-2/neu coding sequence by triplex-directed covalent modification of the template strand. *Biochemistry 38*, 619–628.
(14) Intody, Z., Perkins, B. D., Wilson, J. H., and Wensel, T. G. (2000) Blocking transcription of the human rhodopsin gene by triplex-mediated DNA photocrosslinking. *Nucleic Acids Res. 28*, 4283–4290.
(15) Besch, R., Marschall, C., Schuh, T., Giovannangeli, C., Kammerbauer, C., and Degitz, K. (2004) Triple helix-mediated inhibition of gene expression is increased by PUVA. *J. Invest. Dermatol. 122*, 1114–1120.
(16) Wang, G., Levy, D. D., Seidman, M. M., and Glazer, P. M. (1995) Targeted mutagenesis in mammalian cells mediated by intracellular triple helix formation. *Mol. Cell. Biol. 15*, 1759–1768.
(17) Wang, G., Seidman, M. M., and Glazer, P. M. (1996) Mutagenesis in mammalian cells induced by triple helix formation and transcription-coupled repair. *Science 271*, 802–805.
(18) Vasquez, K. M., Narayanan, L., and Glazer, P. M. (2000) Specific mutations induced by triplex-forming oligonucleotides in mice. *Science 290*, 530–533.
(19) Faruqi, A. F., Datta, H. J., Carroll, D., Seidman, M. M., and Glazer, P. M. (2000) Triple-helix formation induces recombination in mammalian cells via a nucleotide excision repair-dependent pathway. *Mol. Cell. Biol. 20*, 990–1000.
(20) Grant, K. B., and Dervan, P. B. (1996) Sequence-specific alkylation and cleavage of DNA mediated by purine motif triple helix formation. *Biochemistry 35*, 12313–12319.
(21) Taylor, M. J., and Dervan, P. B. (1997) Kinetic analysis of sequence-specific alkylation of DNA by pyrimidine oligodeoxyribonucleotide-directed triple-helix formation. *Bioconjugate Chem. 8*, 354–364.
(22) Kutyavin, I. V., Gamper, H. B., Gall, A. A., and Meyer, R. B. (1993) Efficient, specific interstrand cross-linking of double-stranded DNA by a chlorambucil-modified triplex-forming oligonucleotide. *J. Am. Chem. Soc. 115*, 9303–9304.
(23) Reed, M. W., Lukhtanov, E. A., Gorn, V., Kutyavin, I. V., Gall, A. A., Wald, A., and Meyer, R. B. (1998) Synthesis and reactivity of aryl nitrogen mustard-oligodeoxyribonucleotide conjugates. *Bioconjugate Chem. 9*, 64–71.

(24) Takasugi, M., Guendouz, A., Chassignol, M., Decout, J. L., Lhomme, J., Thuong, N. T., and Helene, C. (1991) Sequence-specific photo-induced cross-linking of the two strands of double-helical DNA by a psoralen covalently linked to a triple helix-forming oligonucleotide. *Proc. Natl. Acad. Sci. U.S.A. 88*, 5602–5606.

(25) Giovannangeli, C., Thuong, N. T., and Helene, C. (1992) Oligodeoxynucleotide-directed photo-induced cross-linking of HIV proviral DNA via triple-helix formation. *Nucleic Acids Res. 20*, 4275–4281.

(26) Havre, P. A., Gunther, E. J., Gasparro, F. P., and Glazer, P. M. (1993) Targeted mutagenesis of DNA using triple helix-forming oligonucleotides linked to psoralen. *Proc. Natl. Acad. Sci. U.S.A. 90*, 7879–7883.

(27) Guieysse, A. L., Praseuth, D., Giovannangeli, C., Asseline, U., and Helene, C. (2000) Psoralen adducts induced by triplex-forming oligonucleotides are refractory to repair in HeLa cells. *J. Mol. Biol. 296*, 373–383.

(28) Ping, Y. H., and Rana, T. M. (2005) Mechanism of site-specific psoralen photoadducts formation in triplex DNA directed by psoralen-conjugated oligonucleotides. *Biochemistry 44*, 2501–2509.

(29) Connors, T. A., and Roberts, J. J. (1974) *Platinum Coordination Complexes in Cancer Chemotherapy*, Springer-Verlag, Berlin.

(30) Lippert, B. (2000) Multiplicity of metal ion binding patterns to nucleobases. *Coord. Chem. Rev. 200*, 487–516.

(31) Cohen, S. M., and Lippard, S. J. (2001) Cisplatin: from DNA damage to cancer chemotherapy. *Prog. Nucleic Acid Res. Mol. Biol. 67*, 93–130.

(32) Sharma, S. K., and McLaughlin, L. W. (2002) Cross-linking of a DNA conjugate tethering a cis-bifunctional platinated complex to a target DNA duplex. *J. Am. Chem. Soc. 124*, 9658–9659.

(33) Sharma, S. K., and McLaughlin, L. W. (2004) Triplex mediated delivery of a platinum complex to a specific DNA target site. *J. Inorg. Biochem. 98*, 1570–1577.

(34) Campbell, M. A., Mason, T. M., and Miller, P. S. (2007) Interactions of platinum(II)-derivatized triplex-forming oligonucleotides with DNA. *Can. J. Chem. 85*, 241–248.

(35) Campbell, M. A., and Miller, P. S. (2009) Cross-linking to an interrupted polypurine sequence with a platinum-modified triplex-forming oligonucleotide. *J. Biol. Inorg. Chem. 14*, 873–881.

(36) Colombier, C., Lippert, B., and Leng, M. (1996) Interstrand cross-linking reaction in triplexes containing a monofunctional transplatin-adduct. *Nucleic Acids Res. 24*, 4519–4524.

(37) Bernal-Mendez, E., Sun, J.-s., Gonzalez-Vilchez, F., and Leng, M. (1998) Reactivity of transplatin-modified oligonucleotides in triple-helical DNA complexes. *New J. Chem. 22*, 1479–1483.

(38) Puglisi, J. D., and Tinoco, I., Jr. (1989) Absorbance melting curves of RNA. *Methods Enzymol. 180*, 304–325.

(39) Xodo, L. E. (1995) Kinetic analysis of triple-helix formation by pyrimidine oligodeoxynucleotides and duplex DNA. *Eur. J. Biochem. 228*, 918–926.

(40) Puri, N., Majumdar, A., Cuenoud, B., Miller, P. S., and Seidman, M. M. (2004) Importance of clustered 2′-O-(2-aminoethyl) residues for the gene targeting activity of triple helix-forming oligonucleotides. *Biochemistry 43*, 1343–1351.

(41) Shimizu, M., Konishi, A., Shimada, Y., Inoue, H., and Ohtsuka, E. (1992) Oligo(2′-O-methyl)ribonucleotides. Effective probes for duplex DNA. *FEBS Lett. 302*, 155–158.

(42) Shimizu, M., Koizumi, T., Inoue, H., and Ohtsuka, E. (1994) Effects of 5-methyl substitution in 2′-O-methyloligo-(pyrimidine)nucleotides on triple-helix formation. *Bioorg. Med. Chem. Lett. 4*, 1029–1032.

(43) Wang, S., and Kool, E. T. (1995) Relative stabilities of triple helices composed of combinations of DNA, RNA and 2′-O-methyl-RNA backbones: chimeric circular oligonucleotides as probes. *Nucleic Acids Res. 23*, 1157–1164.

(44) Wang, S., and Kool, E. T. (1995) Origins of the large differences in stability of DNA and RNA helices: C-5 methyl and 2′-hydroxyl effects. *Biochemistry 34*, 4125–4132.

(45) Ushijima, K., Ishibashi, T., Yamakawa, H., Tsukahara, S., Takai, K., Maruyama, T., and Takaku, H. (1999) Inhibition of restriction endonuclease cleavage by triple helix formation with RNA and 2′-O-methyl RNA oligonucleotides containing 8-oxo-adenosine in place of cytidine. *Biochemistry 38*, 6570–6575.

(46) Cassidy, R. A., Puri, N., and Miller, P. S. (2003) Effect of DNA target sequence on triplex formation by oligo-2′-deoxy- and 2′-O-methylribonucleotides. *Nucleic Acids Res. 31*, 4099–4108.

(47) Lippard, S. J., Ushay, H. M., Merkel, C. M., and Poirier, M. C. (1983) Use of antibodies to probe the stereochemistry of antitumor platinum drug binding to deoxyribonucleic acid. *Biochemistry 22*, 5165–5168.

(48) Raudaschl-Sieber, G., and Lippert, B. (1985) Reaction of cyanide with Pt-nucleobase complexes: preparative, spectroscopic, and structural studies. Unexpected stability of Pt-thymine and Pt-uracil complexes. *Inorg. Chem. 24*, 2426–2432.

(49) Anin, M. F., and Leng, M. (1990) Distortions induced in double-stranded oligonucleotides by the binding of cis- or trans-diammine-dichloroplatinum(II) to the d(GTG) sequence. *Nucleic Acids Res. 18*, 4395–4400.

(50) Blommaert, F. A., and Saris, C. P. (1995) Detection of platinum-DNA adducts by 32P-postlabelling. *Nucleic Acids Res. 23*, 1300–1306.

BC900008S

Supplementary Information for

TRANSPLATIN-CONJUGATED TRIPLEX-FORMING OLIGONUCLEOTIDES FORM ADDUCTS WITH BOTH STRANDS OF DNA

Meghan A. Campbell and Paul S. Miller

Department of Biochemistry and Molecular Biology

Johns Hopkins Bloomberg School of Public Health

615 North Wolfe Street

Baltimore, MD 21205

Contents:

Figure S1 - Purification of **t2d** by SAX HPLC

Figure S2 - Purification of **t3d** by SAX HPLC

Figure S3 - Melting curves of triplexes formed by deoxyribo- and 2'-O-methylribo-TFOs

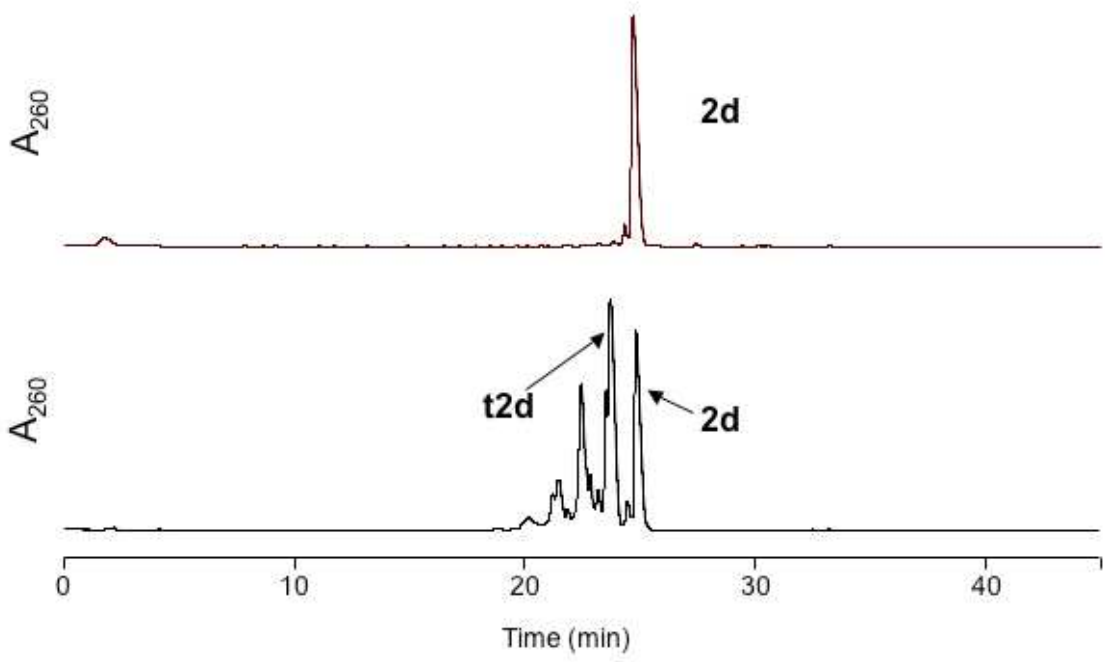

Figure S1 *Purification of **t2d** by SAX HPLC.* TFO **2d** was incubated with 72 μM *trans*-diamminediaquaplatinum(II) dinitrate for 3h at 37°C. The upper chromatogram shows **2d** before platination and the lower chromatogram shows platination reaction mixture. The peak labeled **t2d** was isolated, desalted, and analyzed by MALDI-TOF mass spectrometry. The SAX HPLC column was eluted with a 30 min linear gradient of 0 to 0.5 M NaCl in solution containing 0.1 M Tris, pH 7.8 and 10% acetonitrile at a flow rate of 1.0 mL/min.

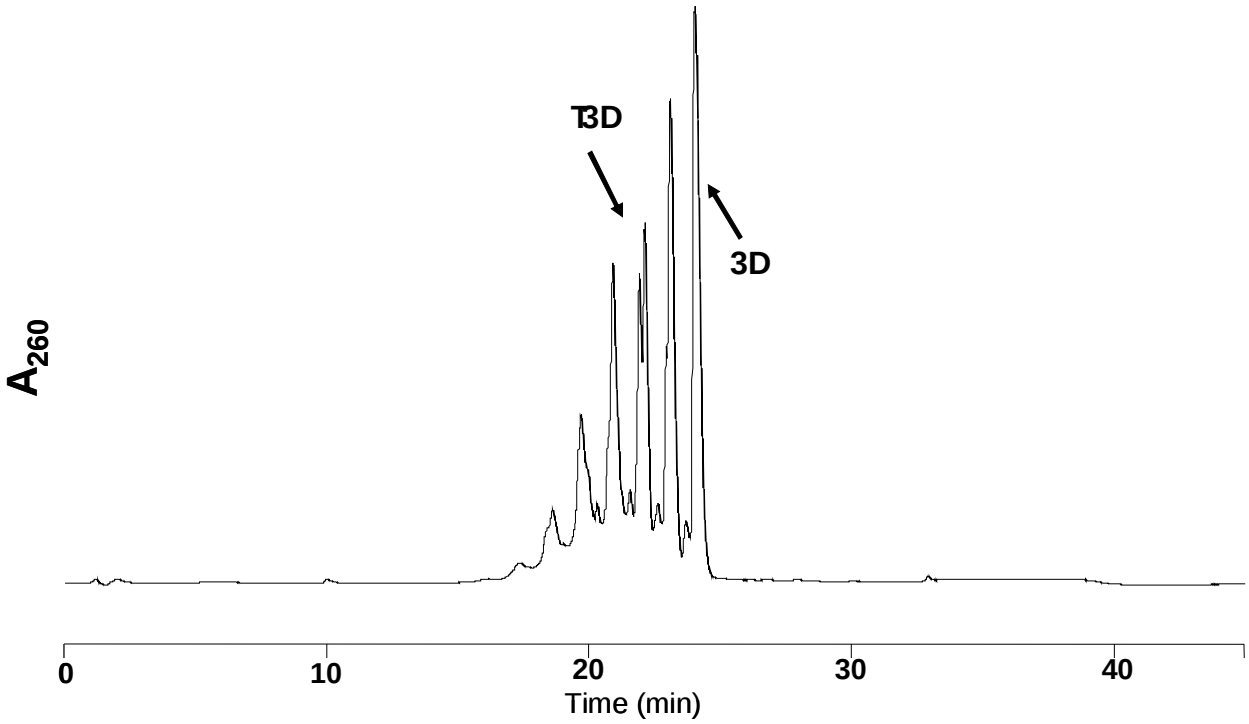

Figure S2 *Purification of **t3d** by SAX HPLC.* TFO **3d** was incubated with 144 μM *trans*-diamminediaquaplatinum(II) dinitrate for 2h at 37°C. The peak labeled **t3d** was isolated, desalted, and analyzed by MALDI-TOF mass spectrometry. The SAX HPLC column was eluted with a 30 min linear gradient of 0 to 0.5 M NaCl in solution containing 0.1 M Tris, pH 7.8 and 10% acetonitrile at a flow rate of 1.0 mL/min

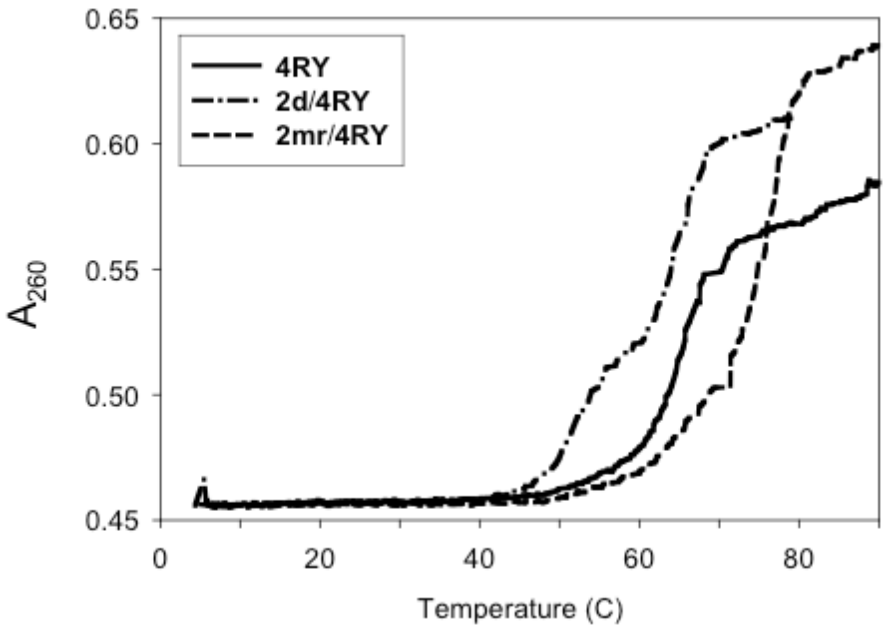

Figure S3 *Melting curves of triplexes formed by deoxyribo- and 2'-O-methylribo-TFOs.* Absorbance versus temperature profiles were recorded for solutions containing 1 μM deoxyribo-TFO **2d** and 1 μM **4RY**, 1 μM 2'-*O*-methylribo-TFO **2mr** and 1 μM **4RY**, or 1 μM **4RY** alone in pH6.5 triplex buffer. In the case of the **2d**/**4RY** triplex, the first transition corresponds to dissociation of the TFO from the triplex and the second transition corresponds to dissociation of duplex **4RY**. The single transition observed for triplex **2mr**/**4RY** indicates that all three strands dissociate simultaneously at a temperature above the melting temperature of the duplex **4RY**.

Efficient Gene Delivery with Osmotically Active and Hyperbranched Poly(ester amine)s

Rohidas B. Arote,[†,§] Eun-Sun Lee,[‡] Hu-Lin Jiang,[‡] You-Kyoung Kim,[†] Yun-Jaie Choi,[†] Myung-Haing Cho,*[,‡] and Chong-Su Cho*[,†]

Department of Agricultural Biotechnology and Research Institute for Agriculture and Life Sciences, Seoul National University, Seoul 151-921, and College of Veterinary Medicine, Seoul National University, Seoul, 151-742, South Korea. Received April 22, 2009; Revised Manuscript Received October 22, 2009

Degradable and hyperbranched poly (ester amine)s (PEAs) were successfully synthesized by Michael addition reaction between hydrophilic glycerol triacrylate (GTA) and low-molecular-weight polyethylenimine (LMW-PEI) and evaluated as nonviral gene carriers. PEAs effectively condensed DNA with particle sizes below 200 nm and suitable surface charges (15−45 mV), suitable for intracellular delivery. PEAs degraded in a controlled fashion showing half-lives of more than 12 days and were essentially nontoxic in three different cell lines. Elevated transfection levels by luciferase assay revealed the superiority of PEAs over PEI 25K and Lipofectamine. PEAs synthesized using 1:4 mol ratio of GTA to PEI [GTA/PEI-1.2(1:4)] showed highest transfection efficiency in HepG2 cells. PEAs showed significant gene expression *in vitro* as well as *in vivo* through aerosol administration. Reduction in packed cell volume (PCV) of cells when treated with polyplexes supported the hyperosmotic effect of PEAs. Effect of bafilomycin A1 on transfection efficiency of PEAs on 293T cells indicated its endosomal buffering capacity. High transfection efficiency was attributed to the synergism from hyperosmotic glycerol backbone in the PEAs and endosomal buffering capacity of PEI amine groups. Therefore, this convergence of osmotically active biodegradable PEAs suggests their potential as a safe and efficient gene delivery vector.

INTRODUCTION

The human genome project has substantially increased our knowledge about molecular mechanisms of cancer during the past decade, thus opening up new possibilities for cancer gene therapy. Gene therapy is one of the most challenging and promising therapies of inherited and acquired diseases. However, the lack of safety and efficient gene carriers limits the success of gene therapy. Viral vectors are more potent gene delivery vehicles because of their specific machinery to enter the cell and to deliver the nucleic acid into the cell and into the nucleus (*1, 2*). However, severe immune responses, limited insert size, and insertional mutagenesis risk limits their use as a successful gene delivery vehicle. Polymeric vectors have remarkable advantages as gene delivery vectors which make them a promising alternative to most efficient recombinant viruses (*3*−*6*). Polyethylenimine (PEI) is one of the successful and widely used gene delivery polymers which have become the gold standard of nonviral gene delivery because of its proton sponge effect (*7, 8*). However, several groups have reported that PEI is cytotoxic in many cell lines. Moreover, higher molecular weight reveals higher toxicity and high transfection efficiency compared with low-molecular-weight PEI (LMW-PEI) (*9, 10*).

Several natural and synthetic biodegradable polymers such as polyesters (*11, 12*), linear poly(ester amine)s (*13, 14*), polypeptides (*15*), PEA networks (*16*), and cyclodextrins (*17*) are among the most preferable materials for the preparation of nonviral vectors in terms of their long-term safety and biocompatibility. Our group developed various biodegradable polymeric gene carriers using LMW-PEI and various cross-linkers such as poly(ethylene glycol) diacrylate (PEGDA) (*18*), polycaprolactone diacrylate (PCLDA) (*19*), poloxamer diacrylate (GDM) (*20*), and glycerol dimethacylate (*21*) to reduce cytotoxicity and increase transfection efficiency. Various strategies to enhance transfection efficiencies and reduce cytotoxicity and polyplex stability are being explored. One approach is the generation of biodegradable polymers by cross-linking LMW-PEI having low cytotoxicity with various cross-linkers so as to produce high-molecular-weight polycations with high transfection efficiency and reduced cytotoxicity.

It is noteworthy that successful carriers possess sufficient DNA binding ability, effective polyplex uptake by cells, subsequent release into cytoplasm, trafficking of polyplex to nucleus, and immediate dissociation of the polyplex. On the basis of the reports by Zauner et al., polyplex uptake and its subsequent release from endosomal environment to the cytoplasm have been considered as one of the rate-limiting steps for successful delivery of gene (*22*). In correlation with the above assumptions, our approaches to enhance transfection efficiency, reduce cytotoxicity, and increase cellular uptake are designed on the synthesis of biodegradable poly(ester amine) (PEA) containing LMW-PEI and hydrophilic glycerol triacrylate (GTA) as a cross-linker. PEAs based on GTA and LMW-PEI will facilitate cellular uptake by exerting a hyperosmotic effect owing to the presence of a glycerol backbone while PEI residues will enhance the endosomal release by the "proton sponge effect".

MATERIALS AND METHODS

Materials. Branched PEI (1.2 and 25 kDa), glycerol triacrylate (GTA) (MW: 254 Da), and anhydrous methanol were purchased from Sigma (St. Louis, MO, USA) and were used as received. Cell Titer 96 AQueous One Solution Reagent for cell viability, luciferase reporter 1000 assay system for *in vitro*

* Correspondence authors. C. S. Cho, Tel: +82-2-880-4636, Fax: +82-2-875-2494, E-mail: chocs@plaza.snu.ac.kr; M. H. Cho, Tel: +82-2-880-1276, Fax: +82-2-873-1268, E-mail: mchotox@snu.ac.kr.

[†] Department of Agricultural Biotechnology.

[‡] Research Institute for Agriculture and Life Sciences.

[§] College of Veterinary Medicine.

10.1021/bc900184k © 2009 American Chemical Society
Published on Web 11/24/2009

Table 1. Characteristics of Synthesized PEAs

code	mol. wt. of reactants		feed ratio GTA/PEI	PEI mol[a] %	yield of copolymer %	molecular weight[b] (Da)
	PEI	GTA				
GTA/PEI-1.2 (1:1)	1200	254	1:1	52.18	25.06	4190
GTA/PEI-1.2 (1:2)	1200	254	1:2	65.35	29.45	5880
GTA/PEI-1.2 (1:4)	1200	254	1:4	74.24	40.42	5480

[a] Determined by ^{1}H NMR. [b] Determined by GPC-MALLS.

transfection and pGL3-control vector with SV-40 promoter, and enhancer encoding firefly (*Photonus pyralis*) luciferase were obtained from Promega (Medison, WI, USA). Plasmid pEGFP-N_2, which has the early promoter of CMV and enhanced green fluorescence protein (EGFP) gene, was obtained from Clontech (Palo Alto, CA, USA). The plasmid was amplified with a competent *E. coli* strain JM109.

Synthesis of PEAs. PEAs were successfully synthesized following modified Michael addition reaction as reported previously (*19*). Briefly, GTA and LMW-PEI (M_n: 1.2 kDa) were separately dissolved in anhydrous methanol, and GTA solution was slowly added to PEI solution at three different GTA/PEI stoichiometric ratios (Table 1). The reaction mixtures were heated at 60 °C with constant stirring for 24 h. Subsequently, the reaction mixtures were dialyzed at 4 °C for 24 h using Spectra/Por membrane (molecular mass cutoff 3.5 kDa; Spectrum Medical Industries, Inc., California) against distilled water. Finally, the polymers were lyophilized and stored at 0 °C.

Characterizations of PEAs. ^{1}H NMR samples were prepared by dissolving polymers in $CDCl_3$ at a concentration of 10 mg/mL. NMR spectra were recorded using Avance 500 spectrometer (Bruker, Germany). Absolute molecular weights of the polymers were measured by gel permeation chromatography coupled with multiangle laser light scattering (GPC-MALLS) using Sodex OHpack SB-803 HQ (Phenomenox, USA) column (column temperature at 25 °C; flow rate 0.5 mL/min). Ammonium acetate (0.5M, pH 5.5) was used as a mobile phase (*19*).

Degradation of PEAs. The extent of polymer degradation was estimated by measuring the reduction in molecular weight of PEAs. Polymers dissolved in PBS (0.1 g/mL) were incubated in a shaking incubator (37 °C; 100 rpm) and sampled at various time intervals. Subsequently, the lyophilized samples were subjected to GPC for molecular weight determination.

Complexation Study. Polymer/pDNA complexation was carried out in sterilized distilled water by gently mixing DNA (pGL3 control; 0.1 μg) with polymer solutions (10 μL) at various N/P ratios to mitigate the possibilities of mechanical damage of DNA. The complexes were incubated at room temperature for 30 min, and a 12 μL volume including loading dye mixture was loaded on 0.8% agarose gel containing ethidium bromide (0.1 μg/mL). The gel was run with tris-acetate buffer at 100 V for 40 min. The gel image was captured under UV illumination.

Protection and Release Assay of DNA. Protection and release of DNA in complexes were measured using electrophoresis, according to the method in our previous reports (*19*).

Particle Size and Zeta Potential Measurement. Particle sizes and zeta potentials of polymer/DNA complexes (prepared in water at various N/P ratios) were measured using dynamic light scattering spectrophotometer (DLS) (ELS8000, Otsuka Electronics, Osaka, Japan), with 90 and 20° scattering angles, respectively. Polymer/DNA complexes were prepared in water from N/P ratios 1 to 30.

Transmission Electron Microscopy (TEM). The morphology of PEA/DNA complexes was observed using energy filtered TEM (EF-TEM) (JEM 1010, JEOL, Japan).TEM specimens were prepared by placing a drop of PEA/DNA complexes on a copper grid and stained with 1% uranyl acetate solution for 5 s. The specimens were allowed to dry further for 10 min and were then examined under the microscope.

Cell Lines and Cell Culture. Human cervix epithelial carcinoma cells (HeLa), human hepatoblastoma cells (HepG2), and human kidney transformed cells (293T) were maintained in a DMEM culture medium supplemented with 10% heat-inactivated FBS, penicillin/streptomycin. Cells were grown under standard conditions, in a 37 °C humidified incubator containing 5% CO_2.

Cell Viability Assay *in Vitro*. Cell viability of PEAs was investigated by Cell Titer 96 Aqueous One Solution Cell Proliferation Kit (Promega). Cells seeded in 96 well plate at an initial density of 1×10^4 (HeLa and 293T) or 2×10^4 (HepG2) cells/well in 0.2 mL growth medium were incubated for 18−20 h to reach 80% confluency prior to the addition of PEAs. Growth medium was replaced by fresh serum-free media containing PEA solutions at various concentrations (5, 10, 20, and 40 μg/mL), and the cell viability study was carried out by the method reported in our previous reports (*19*).

***In Vitro* Cell Transfection.** All assays were conducted in 24 well plates. One milliliter of HeLa, 293T and HepG2 cell cultures (for HeLa and 293T, 1×10^5 cells/mL; and for HepG2, 2×10^5) was grown to ∼70−80% confluency under standard incubation conditions. The media in the wells were replaced with either serum-free media or 10% serum-containing media supplemented with 1 μg of polymer/pGL3 complexes of various N/P ratios, and incubated at 37 °C for 6 h. Subsequently, serum-free media were replaced with fresh media containing serum and incubated for additional 24 h under standard incubation conditions. The luciferase assay was carried out per manufacturer's protocol (Promega). Relative light units (RLU) were measured with chemiluminometer (Autolumat, LB953, EG&G Berthold, Germany). The obtained RLUs were normalized with respect to protein concentration in the cell extract determined using BCA protein assay kit.

Flow Cytometry and Confocal Microscopy Study. The transfection efficiency was also verified by flow cytometric measurement using EGFP reporter gene. 293T cells after being transfected with PEA/pEGFP-N_2 were washed with PBS and trypsinized. Transfection efficiency was evaluated by scoring the percentage of cells expressing green fluorescence protein using a FACS Calibur System from Becton-Dickinson (San Joes, CA). The experiments were performed in triplicate and 20 000 cells were counted in each experiment (*21*).

293T cells were plated on collagen-coated glass coverslips in 24 well plates (5×10^4 cells/well) and were grown to ∼60−70% confluency. The media were then replaced with serum-free media containing PEA/pEGFP-N_2 (1 μg) complexes (N/P ratio 30). After 6 h of incubation, serum-free media were changed with fresh media containing serum and incubated for additional 18 h. Cells were washed twice with PBS and immobilized by adding 200 μL of 2% glutaraldehyde solution. The coverslips were washed with PBS and enclosed in glycerol, and finally, the cells were visualized by confocal laser scanning microscopy (CLSM) (Micro Systems LSM 410, Carl Zeiss, Germany) equipped with a 488 nm argon/krypton laser. Fluorescence emission was collected using a 515 nm/30 nm

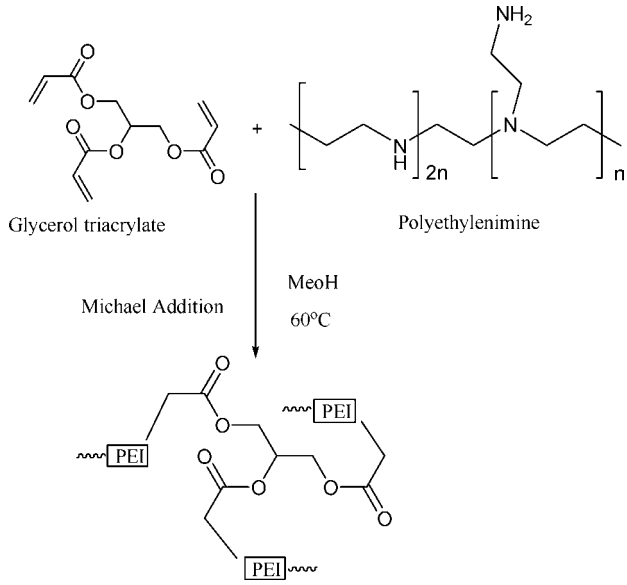

Figure 1. Synthesis scheme of PEAs. GTA linker reacts with primary and secondary amines of PEI resulting in formation of ester bonds.

bandpass filter. Cells treated with only PBS or polymers were taken as controls.

Packed Cell Volume Measurement. Trypsinized 293T cells were centrifuged and resuspended in DMEM supplemented with 10% FBS. To monitor the effect of glycerol content (wt %) in PEAs on packed cell volume (PCV), different concentrations of PEAs and/or PEA/DNA complexes were then added to the cell suspensions. For each set, 1 mL of cell suspension was transferred to a mini-PCV tube (TPP, Trasadingen, Switzerland) and centrifuged for 1 min at 5000 rpm. The volume of the packed cells in the graduated capillary was reported as the % PCV and compared with the experiments done under the identical conditions using different concentrations of glycerol instead of PEA/DNA complexes as control.

Effect of Bafilomycin A_1. 293 T cells seeded in 12 well plates (2×10^5 cells/well) were incubated for 18 to 20 h to reach 80% confluency. The cells were incubated for 10 min before transfection, with endosome proton pump inhibitor, bafilomycin A1 (a specific inhibitor of vacuolar type H^+-ATPase). The cells were then subjected to *in vitro* luciferase assay as described above. The cells without treatment with bafilomycin A1 were taken as control.

***In Vivo* Transfection.** Aerosol administration in mice was carried out to determine the *in vivo* transfection ability of PEAs. Thirteen-week-old female BALB/c mice, maintained at 23 ± 2 °C and relative humidity of 50 ± 20%, were placed in nose-only exposure chamber (NOEC; Dusturbo, Seoul, Korea) and exposed to aerosol administration. Aerosol was prepared using 1 mg of pEGFP-N_2 plasmid DNA, and transfection ability of PEAs was evaluated according to a method previously reported (*19*).

RESULTS AND DISCUSSION

Synthesis and Characterization of PEAs. In general, PEAs are formed from nucleophilic addition of amines to acrylates under normal conditions. The main objective of this study is to rationally design, characterize, and evaluate a novel class of potentially safe, biodegradable, and hyperbranched polymers with poly(ester amine) backbone based on hydrophilic glycerol triacrylate and LMW-PEI. Hyperbranched PEAs were obtained using LMW-PEI (M_n: 1200 Da) as amine nucleophile and glycerol triacrylate (GTA) as a cross-linker at different stoichiometric ratios in anhydrous methanol through Michael addition reaction (Figure 1). The absence of water during synthesis should prevent hydrolysis of sensitive ester linkages. Triacrylate linker reacts with PEI by Michael addition reaction to either primary or secondary amines, generating ester-based

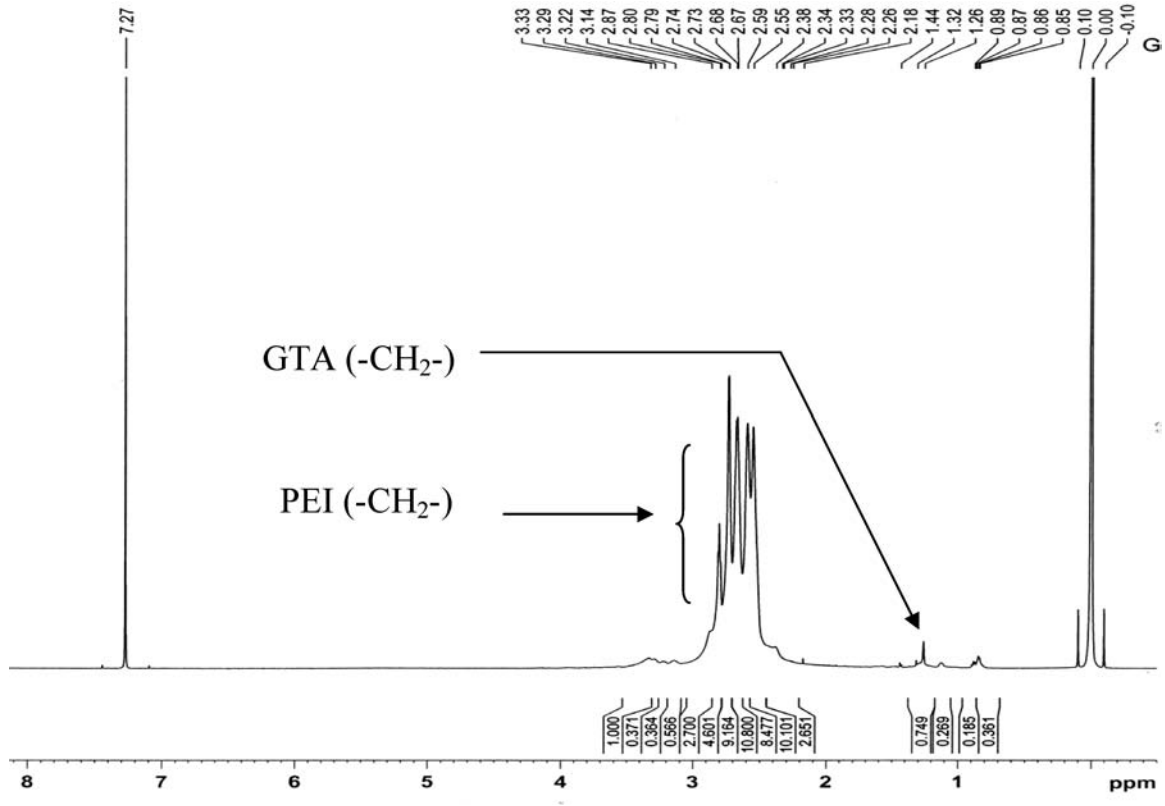

Figure 2. Representative ^{1}H NMR spectrum of PEA [GTA/PEI-1.2(1:4)] in $CDCl_3$.

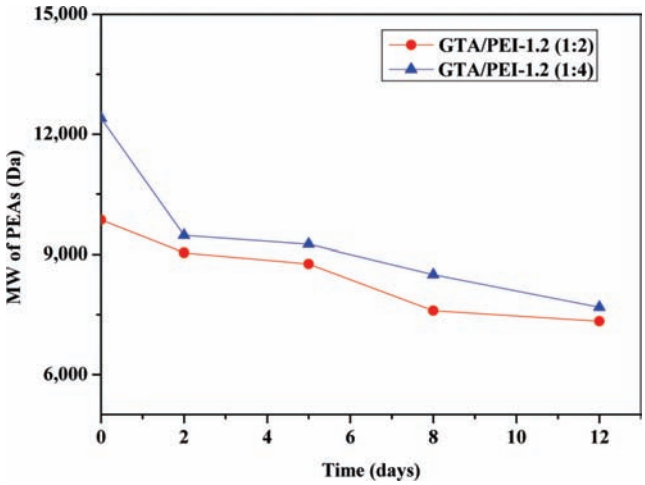

Figure 3. Degradation pattern of PEAs.

polymers. An excess of cross-linker resulted in gelation and originated highly cross-linked polymers insoluble in aqueous media. Unlike the reaction condition mentioned in our earlier previous work, the reaction was carried out at slightly elevated temperature (60 °C) to increase the cross-linking and thereby the molecular weight of final polymer (*19*, *21*). The characteristics of synthesized PEAs at different GTA/PEI stoichiometric ratios are summarized in Table 1. Unlike the reports by Langer group, no significant difference in the MW of PEAs was observed through variation in stoichiometric ratio of GTA to LMW PEI (*13*). The compositions of synthesized PEAs were confirmed through ^{1}H NMR spectroscopy (Figure 2). The signals at δ 1.3 ppm are related to GTA protons, which are highlighted by arrows. The signals of PEI protons were found in the range δ 2.2−3.0 ppm. The ratios of integrals of GTA protons to PEI protons and molecular weight are shown in Table 1.

Unlike our previous reports, the composition of PEAs was found to match those of the stoichiometric feed ratios of the reactants (*21*). Cross-linking of these small polycations using potentially degradable linkages was conceived as a way of increasing molecular weight and thus enhanced DNA binding capacity and polyplex stability while maintaining their nontoxic nature and high transfection efficiency. One feature that has to be fulfilled by the compacting domains is high DNA binding affinity and, moreover, the ability to form stable DNA complexes. As DNA binding activity of polyplexes is strongly influenced by charge density and molecular weight (*23*), the biophysical characterization provided preliminary information about the original structures. It has been shown from the reports of Lynn et al. that DNA condensation, transfection efficiency, and cytotoxicity are significantly affected by the molecular weight of the carrier. In addition, monomer structure, choice of solvent, and reaction temperature affects the average molecular weight of polymer which lies in the range 2000−50 000 Da (*8*, *24*). GPC-MALLS measurements were performed to characterize PEAs, and it was found that maximum molecular weights were observed at equivalent stoichiometric ratios as reported by Langer group and our previous reports (*14*, *19*). The average molecular weights of synthesized PEAs were found not to vary widely (4190 to 5480 Da), with polydispersity indices close to 2 indicating the difficulty in controlling cross-linking by simple change in reactant feed ratio (Table 1). To determine the degradability, PEAs were subjected to aqueous degradation environment incubated at 37 °C and aliquots were removed at appropriate time points. The degradation was calculated by measuring the reduction in the molecular weight. Figure 3 shows the degradation profile of PEAs as a function of time. The results showed that PEAs degraded slowly and

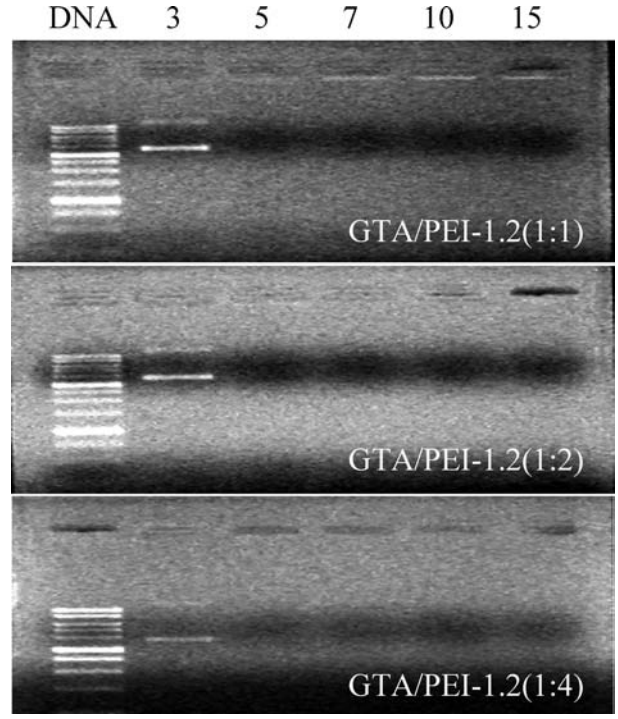

Figure 4. Agarose gel electrophoresis of PEA/DNA (pGL3-control) complexes at various N/P ratios: (a) GTA/PEI-1.2 (1:1), (b) GTA/PEI-1.2 (1:2), and (c) GTA/PEI-1.2 (1:4). 0.1 μg pDNA was used to prepare complexes with PEAs.

the half-life of degradation was approximately more than 12 days. Absence of cytotoxicity is one of the significant features for *in vivo* application of any polymeric gene carriers. Generally, cytotoxicity arises from accumulation of nondegraded and nondischarged polymers in the cell (*16*). The ester bonds in PEAs are susceptible to hydrolysis at physiological conditions to form the respective diol linker and amino acid, thereby generating low-molecular-weight nontoxic byproduct.

PEA/DNA Polyplex Characteristics. One feature that has to be fulfilled by the compacting domains is high DNA binding affinity and, moreover, the ability to form stable DNA complexes. The ability of polymers to complex with plasmid DNA (pGL3) was demonstrated using agarose gel electrophoresis. The band of pGL3-control was retarded as the amount of PEAs increased. As shown in Figure 4, all PEAs have a great capacity to condense DNA effectively where pGL3-control was completely retarded at N/P ratio 5. In contrast, the pDNA band was completely moved. N/P ratio 5 at which all PEAs showed complete DNA binding was considered in future characterization.

Effective DNA condensation by polycation and polyplex stability are important requirements for DNA stability against degradation by nucleases (*25*). PEA efficacy to protect DNA from attack of DNase-I was confirmed by agarose gel electrophoresis. PEAs were able to guard DNA as compared with naked DNA, which was completely degraded by DNase-I (data not shown).

Successful transfection efficiency of gene carrier depends on its ability to condense negatively charged DNA into nanosized particles with positive charges so as to enter into the cell. The size and surface charge of PEA/DNA complexes were measured using dynamic light scattering as shown in Figure 5. It was found that all three PEAs effectively condensed DNA into nanosized, positively charged polymer/DNA complexes. Lower amounts of polymer tended to give larger nanoparticles owing to the aggregation. An increase in PEA/DNA charge ratio produced smaller-sized nanoparticles. All three PEAs showed

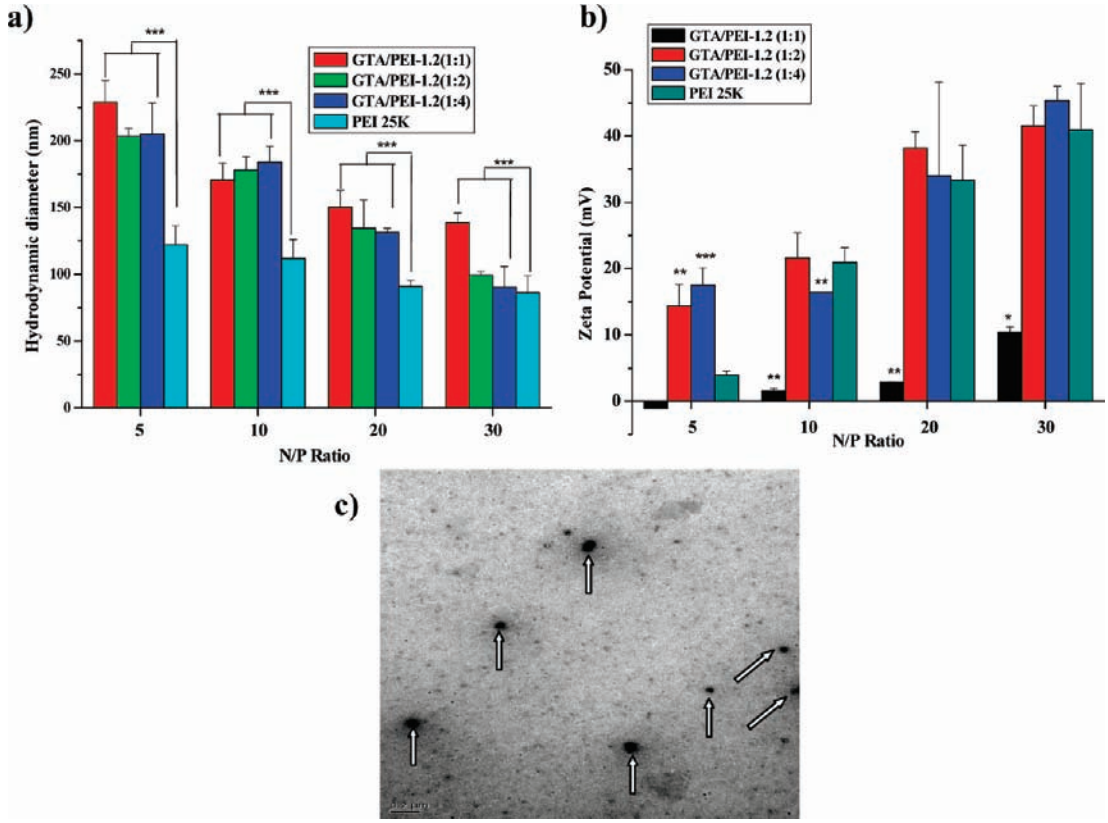

Figure 5. Biophysical properties of PEA/DNA complexes at various N/P ratios: (a) particle size measurement of PEA/DNA complexes, (b) zeta potential measurement of PEA/DNA complexes, and (c) EF-TEM images of GTA/PEI-1.2(1:4)/DNA complexes at N/P ratio 30 ($n = 3$). (*$p < 0.1$; **$p < 0.05$; ***$p < 0.01$, two-tailed Student's *t*-test).

polyplex sizes below 200 nm which are suitable for intracellular delivery. In all three PEA cases, the polyplexes had positive surface charges in the range 15−45 mV. An increase in the charge ratio from 5 to 30 increased the surface charge of the polyplexes from 15 to 45 mV as shown in Figure 5b. In correlation with our previous findings, the particle size and zeta potential results of PEA/DNA polyplexes typically match the DNA condensation pattern where DNA was initially condensed into larger particles upon addition of cationic PEAs through a charge neutralization mechanism (*19, 21*). The particle sizes and zeta potential measurements indicated that polymer/DNA complexes were cationic with effective diameter below 200 nm and surface charges cationic enough for attachment to anionic cell surfaces. These features suggest that PEA/DNA particles are cationic enough for association with negatively charged cell membranes and subsequent endocytosis.

For efficient endocytosis and transfection, the polyplexes must be small, compact, and spherical. The morphology of PEA/DNA polyplexes was observed by EF-TEM. Figure 5c shows morphology of GTA/PEI-1.2(1:4) at N/P ratio 30. The GTA/PEI-1.2(1:4)/pDNA polyplexes reveal the formation of spherical nanoparticles with an average diameter smaller than that obtained in particle size measurement.

Cell Cytotoxicity. Cell compatibility studies were performed by incubating PEA solutions in different concentrations on cells and assessing the metabolic activity by MTS-based cell viability method after 24 h. PEAs prepared from hydrophilic glycerol triacrylate and LMW-PEI have remarkably low cytotoxicity in all three cell lines compared with highly cytotoxic PEI 25K. As depicted in Figure 6, all PEAs showed reduced cytotoxicity with concentrations as high as 60 μg/mL. In contrast, PEI 25K showed significant cytotoxicity reflected by the fact that less than 40% of the cells were viable when the concentration of PEI 25K was higher than 20 μg/mL. Among the many attempts to reduce the cytotoxicity of the gene carrier, the introduction of biodegradable linkage, i.e., ester linkage, has been the prominent method until today (*11*−*14*, *18*−*21*). Reduced cytotoxicity of PEAs is undoubtedly a significant advantage of the degradable ester linkage over nondegradable PEI 25K. It also appears that the reduced cytotoxicity may be correlated with PEA degradation. The increased cell viability is undoubtedly due to the nontoxic building blocks and biodegradation products appearing from the ester backbone of PEAs. It is noteworthy that cytotoxicity of PEAs is cell-line dependent and free polymers are usually more toxic to cells and tissues, while the cytotoxicity is reduced when polymers are complexed with DNA (*10, 26*). As shown in Figure 6, interestingly all PEAs revealed at least 70% cell viability in all three cell lines at concentration as high as 60 μg/mL. In contrast, in case of nondegradable PEI, it aggregates on cell surface, thereby impairing important membrane functions (*10*), and reduces cell viability. MTS assay results clearly indicated the significant cell viability of PEAs, and thereby, it is potential as a safe gene carrier.

***In Vitro* Transfection by Luciferase Assay.** The ability of PEAs based on GTA and LMW-PEI to deliver DNA into cells was determined by performing luciferase reporter gene transfections. Figure 7 shows the transfection efficiency of PEAs in HeLa, HepG2, and 293T cells. *In vitro* luciferase activity of PEAs was assessed in triplicate using 1 μg of pGL3 complexed with PEAs at various N/P ratios from 5 to 30. After 48 h gene expression time, lysates of transfected cells were assessed for luciferase activity by measuring the relative light units (RLUs) normalized by total protein content. All PEAs showed increase in reporter gene expression owing to effective DNA binding ability thereby forming nanosized polyplexes. Interestingly, all PEAs were able to mediate higher levels of gene expression despite lower levels of molecular weight. Consistent with our

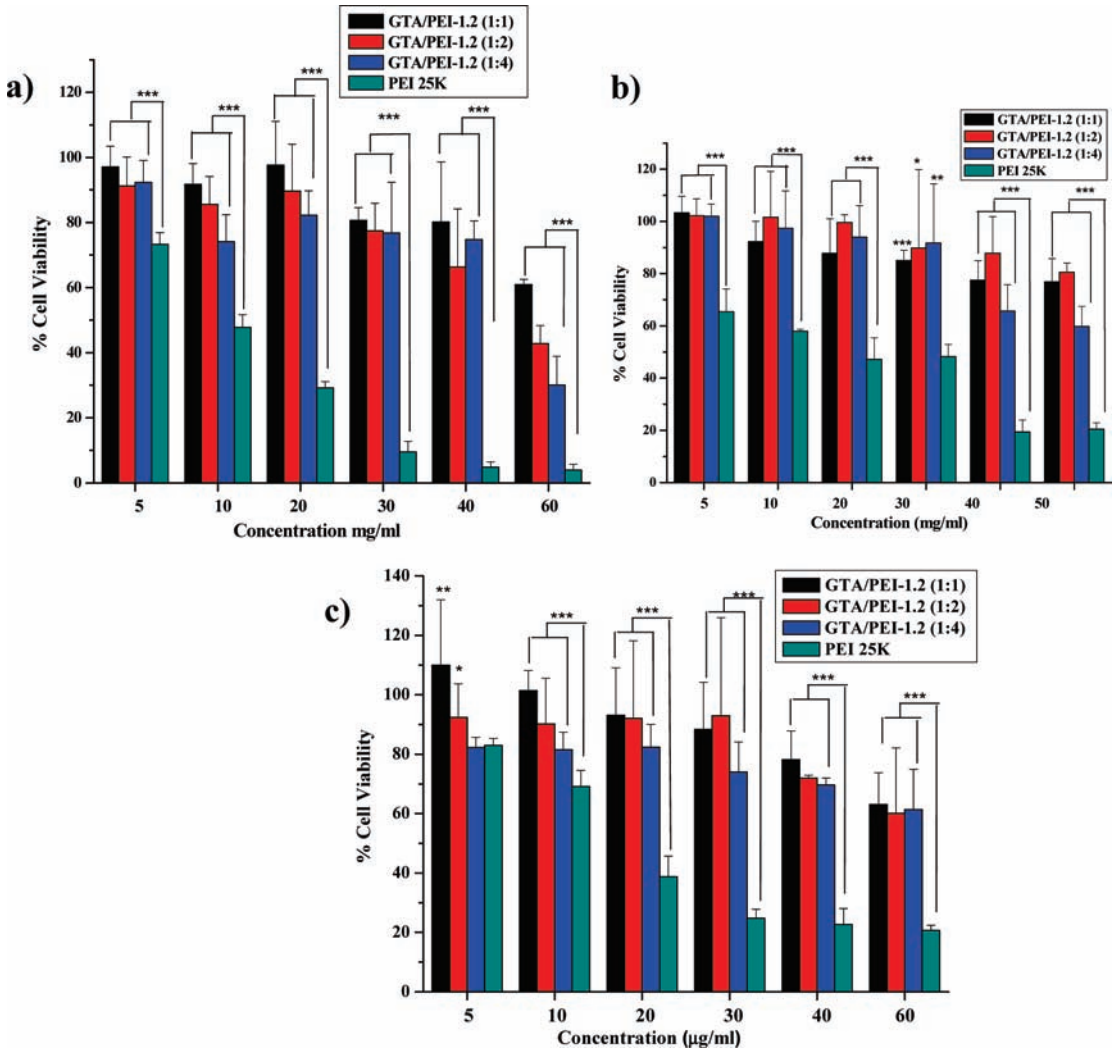

Figure 6. Cytotoxicity of PEAs at various concentrations in different cell lines: (a) HeLa, (b) HepG2, and (c) 293T cells (*$p < 0.1$; ** $p < 0.05$; ***$p < 0.001$, two-tailed Student's *t*-test) ($n = 3$, error bar represents standard deviation).

previous work (*21*), PEAs composed of GTA and LMW-PEI also revealed higher gene expression levels owing to the presence of biodegradable ester linkage, thereby reducing the cytotoxicity. It was noteworthy that GTA/PEI-1.2(1:4) showed 30−35-fold higher transfection levels compared with "golden standard" PEI 25K at N/P ratio of 30 in all three cell lines. Reporter gene expressions in HeLa and 293T cells remained at rather similar levels in the case of all three PEAs probably due to a smaller difference in the molecular weights, as transfection efficiency of PEAs was shown to be dependent on molecular weight, in correlation with the reports by our group and Mikos group (*9, 19, 21*). As expected from our previous results, transfection results of GTA/PEI-1.2 copolymers followed a somewhat similar pattern where the introduction of an ester bond with hydrophobic/hydrophilic balance boosted the gene-carrying activity on one hand and reduced cytotoxicity on other hand, which is also in agreement with reports by Anderson et al. (*19, 27*). Unlike our previous reports, the extent of hydrophobicity in GTA/PEI-1.2 copolymers is higher than GDM/PEI-1.2 owing to the absence of a free hydroxyl group (*21*). Even though PEI 25K is a highly transfection efficient polymer used in gene delivery, its transfection was decreased with increasing charge ratio owing to its cytotoxicity. As depicted in Figure 7, it was found that the transfection efficiency of PEAs in HepG2 cells was in the order GTA/PEI-1.2(1:1) < GTA/PEI-1.2(1:2) < GTA/PEI-1.2(1:4).

Figure 7d shows the transfection efficiency of PEA/pDNA complexes with and without serum in HeLa cells at N/P ratio of 30. A normal difference was found between the transfection abilities of PEAs in the absence and presence of serum. Polyplexes prepared from PEAs and pDNA were stable and showed a quite similar transfection profile in the presence and absence of 10% serum owing to the hydrophilic property of glycerol moieties in PEA backbone, which correlates with our previous reports (*21*). This also matches the hypothesis reported by Kabanov et al. where complexes formed by P123-*g*-PEI (2K) and DNA in the presence of free polaxamer reveals stability in a variety of conditions especially in the presence of serum (*28*). All three PEAs showed a little decrease in the gene expression level when tested in the presence of serum compared with serum-free transfection. On the other hand, PEI 25K showed a significant reduction in the transfection level when tested in the presence of serum.

Confocal Microscopy and Flow Cytometry. The transfection ability of PEAs was also checked using GFP gene by CLSM and flow cytometry. Figure 8a shows the GFP reporter gene expression shown by PEAs using confocal microscopy in A549 cells. Optimized charge ratios (N/P ratio 30) of PEA/pDNA complexes (checked by Luciferase assay) were used for confocal experiments. Polyplexes containing PEA/pEGFP-N_2 transfection complexes transfected into A549 cells and revealed interesting

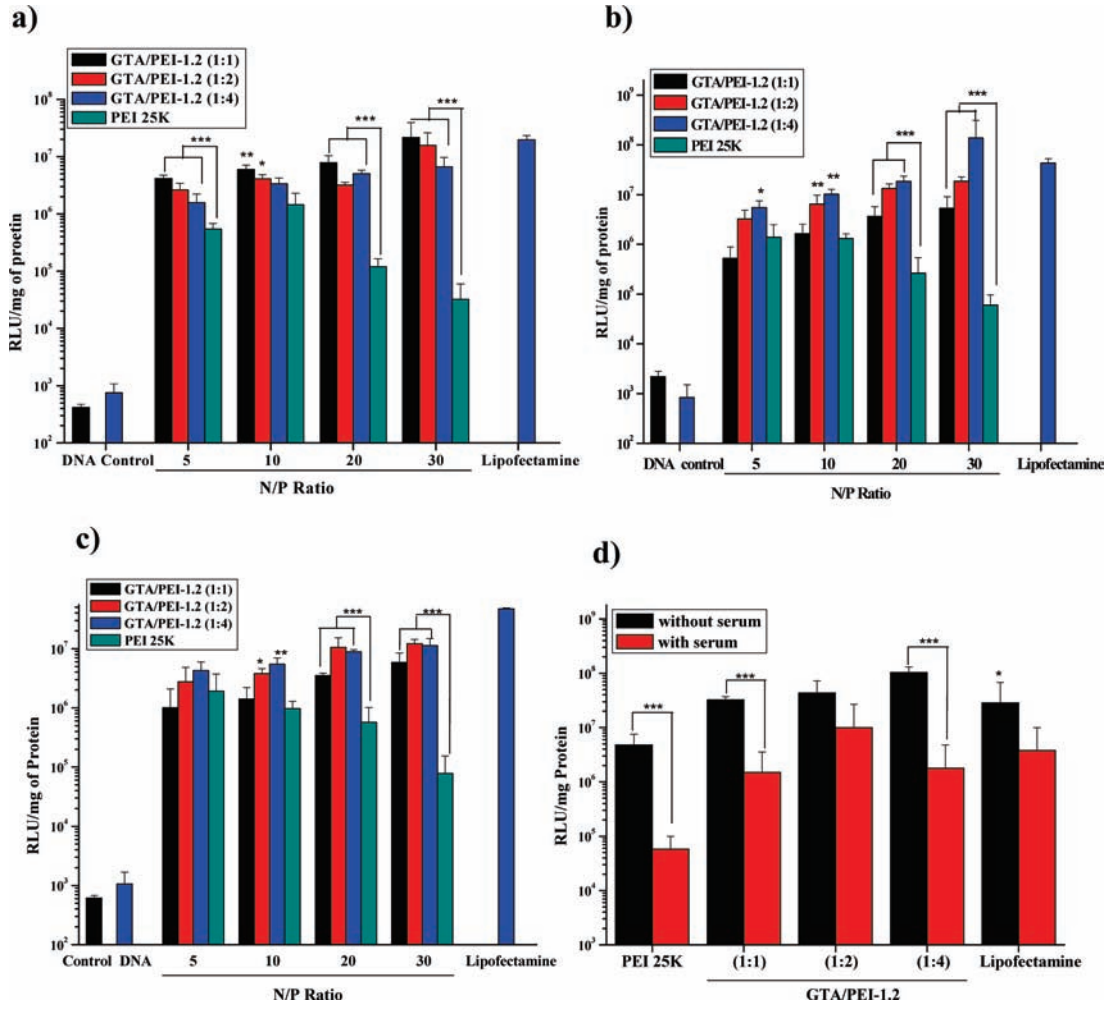

Figure 7. Luciferase activity of PEA/pGL3-control at various N/P ratios in three different cell lines: (a) HeLa, (b) HepG2, (c) 293T, and (d) with and without serum on HeLa cells (*$p < 0.1$; **$p < 0.05$; ***$p < 0.01$, two-tailed Student's *t*-test) ($n = 3$, error bar represents standard deviation).

fluorescence compared with PEI 25K in correlation with luciferase assay results.

The transfection efficiency of PEAs using pEGFP-N_2 was also monitored by flow cytometry. Flow cytometry studies in 293T cells revealed a significantly high level of transfection as shown in Figure 8b. With increasing N/P ratio, the maximum in transfection efficiency shifted to polyplexes made with GTA/PEI-1.2(1:4) at N/P ratio of 30. The mean fluorescence intensity of pEGFP-N_2 positive cells can serve as the average expression of GFP per cell. In contrast, PEI 25K showed optimum transfection at N/P ratio of 10 and further decreased up to 30 owing to its cytotoxicity. This significant increase in transfection efficiency of PEAs is undoubtedly the advantage of ester linkage which on one hand increases the momentum of transfection efficiency and on the other hand reduces the cell cytotoxicity. The above results of transfection level as a measure of luciferase and GFP expression clearly indicate the excellence of PEAs over PEI 25K as a potential gene carrier.

Effect of Bafilomycin A1. To elucidate the mechanism of transfection efficiency of PEAs, we analyzed the effect of bafilomycin A1, an endosome proton pump inhibitor (*29*) on the transfection efficiency of PEA in 293T cells. Reporter gene expression shown by PEAs was reduced by more than 20−25-fold when transfected in the presence of 200 nM bafilomycin A1, compared to the experiments without inhibition of endosomal acidification as shown in Figure 9a. The decrease in reporter gene expression levels shown by PEAs in the presence of bafilomycin A1 is undoubtedly the advantage of the presence of PEI moieties in the PEA backbone which acidifies these endosomal vesicles, thereby allowing the influx of water and swelling and bursting the endosome. Thus, PEAs with significant bursting capacity in the lysosomal pH range show a much higher transfection capability. The evidence of the reduction in transfection efficiency of PEAs in the presence of bafilomycin A1 strongly suggests the involvement of the proton sponge effect in PEI-mediated transfection.

Estimation of Hyperosmolarity of PEAs. Nevertheless, it has not been shown yet whether the presence of glycerol moiety in the PEA backbone has any effect on increased cell cellular uptake and thereby increased transfection efficiency. To elucidate the mechanism of increased transfection efficiency of PEA through increased cellular uptake, we analyzed the reduction in packed cell volume in 293T cells when treated with PEA/pDNA polyplexes. To determine the impact of the osmotic effect of polyplexes containing PEAs, 293T cells were suspended in DMEM with 10% FBS and GTA/PEI-1.2(1:4)/pGL3 complexes with varying glycerol content (3, 4, and 5 wt %) in the polymer backbone and the same protocol followed as reported by us previously (*21*). As shown in Figure 9b, GTA/PEI-1.2(1:4)/pGL3 complexes with increasing glycerol content (viz. 3, 4, and 5 wt %) reduced PCV by 18%, 17%, and 27%, respectively. The differences in the osmolarity of different glycerol solutions and polymer/DNA polyplexes are also shown in Table 2. Pure glycerol was used as a control in the same amounts of

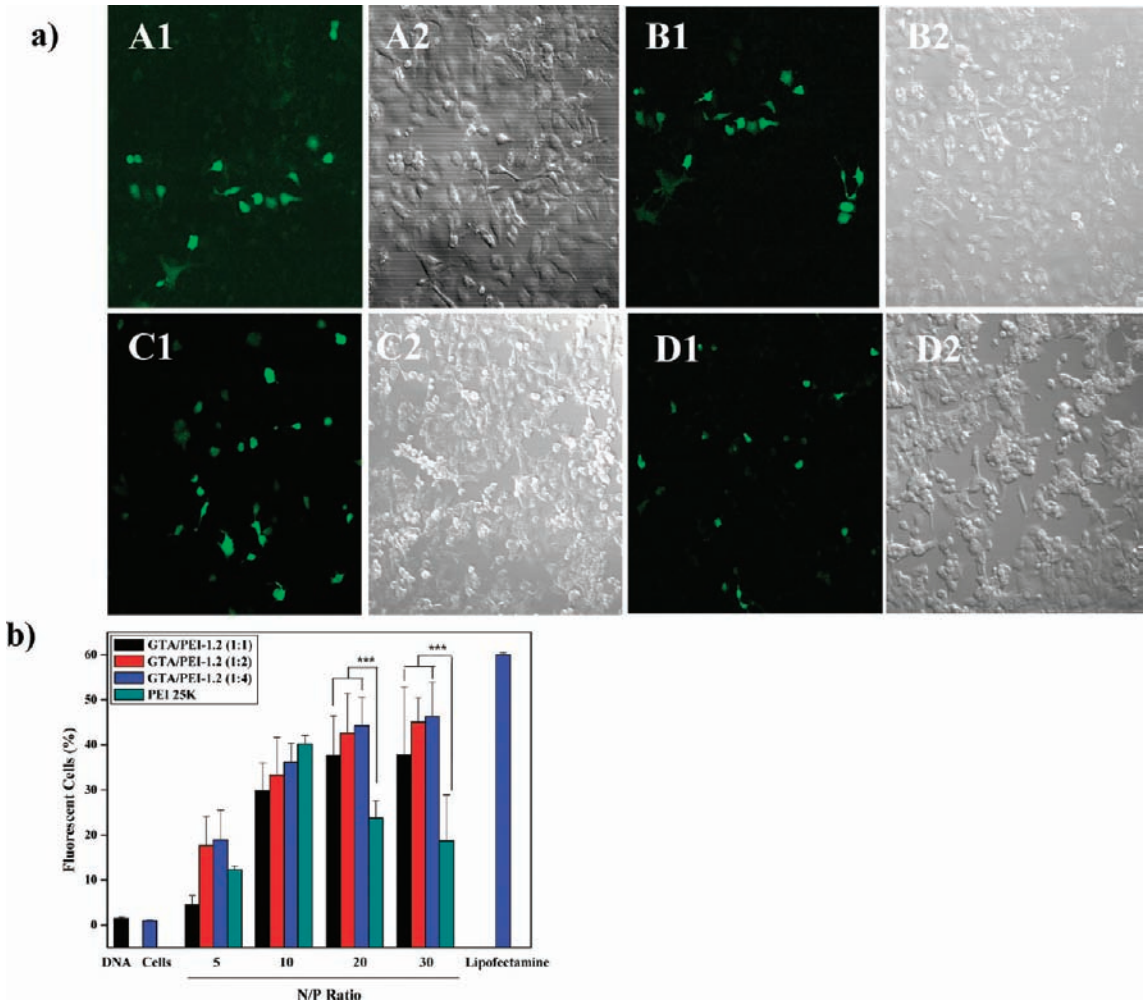

Figure 8. (a) GFP expressed in the A549 cell line transfected with PEA/pEGFP-N_2 complexes at N/P ratio of 30. A1, B1, C1, and D1 represent the fluorescent images of the pEGFP-N_2 reporter gene complexed with GTA/PEI-1.2(1:1), GTA/PEI-1.2(1:2), GTA/PEI-1.2(1:4), and PEI 25K, respectively. Phase contrast images are also shown along with fluorescent images, respectively (A2 to D2). (b) pEGFP-N_2 expressed in 293T cells transfected with PEA/DNA (pEGFP-N_2) complexes at various N/P ratios and analyzed by flow cytometry (*$p < 0.1$; **$p < 0.05$; ***$p < 0.01$, two-tailed Student's *t*-test) ($n = 3$, error bar represents standard deviation).

concentration (3, 4, and 5 wt %) and revealed 20%, 20%, and 38% reduction in PCV, respectively, whereas almost a 50% decrease in cell volume was observed as a result of exposure to 10 wt % glycerol in DMEM.

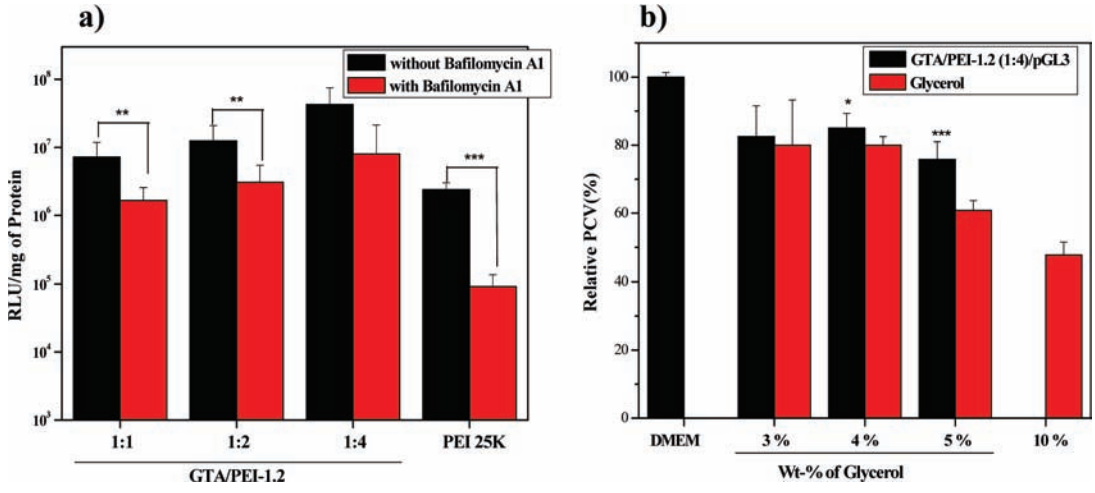

Figure 9. (a) Effect of bafilomycin A1, an inhibitor of vacuolar type H^+-ATPase, on pGL_3 expression with PEAs at N/P ratio of 30 in serum-free transfection medium determined by luciferase assay. (b) Effect of high osmolarity of GTA/PEI-1.2(1:4)/pGL3 complexes and glycerol concentration on cell volume. The approximate volume of 293T cells was determined using mini-PCV tubes following exposure to the conditions indicated for 5 min. As a control, the cells were suspended for 5 min in DMEM prior to the PCV determination. Each bar represents the average of three independent experiments (*$p < 0.1$; **$p < 0.05$; ***$p < 0.01$, two-tailed Student's *t*-test) ($n = 3$, error bar represents standard deviation).

Table 2. Osmolarity Measurement of Various Solutions and Complexes

		osmolarity [mOsm]
DMEM + 10% FBS		354 ± 3
Glycerol	3%	751 ± 4
	4%	914 ± 3
	5%	1102 ± 3
GTA/PEI-1.2(1:4)/DNA complexes	3% glycerol (wt %)	601 ± 2
	4% glycerol (wt %)	649 ± 2
	5% glycerol (wt %)	759 ± 7

Grosjean et al. reported the significant decrease in cellular volume and thereby an increase in transient reporter gene expression in nonsynchronized CHO cells after post-transfection shocks (*30*). In addition, the synergistic effect of glycerol and poly(L-lysine) (PLL) was able to lyse human erythrocytes as well as internal vesicles (microsomes) of H225 cells more efficiently than either glycerol and PLL alone as per the reports of Zauner et al. It was found that vesicular membranes became susceptible to PLL-mediated disruption owing to glycerol labilization, thereby releasing the vesicular content into the cytoplasm. However, unlike calcium phosphate mediated transfection, post-transfection osmotic shocks with glycerol barely increased gene transfer activity in transferrin-PLL mediated gene delivery stating the need for synergism between glycerol and polyplexes during transfection (*22*). Hyperosmotic glycerol generally causes shrinkage of cells and thus increases cellular uptake; however, a reduction in transfection efficiency was observed owing to increased cytotoxicity by using glycerol concentration higher than 15% according to the reports of Wilson et al. (*31*). In the case of polyplexes formed from PEA, the reduction in PCV can be explained by the evidence that the glycerol backbone in PEAs exerted osmotic pressure on the cell membrane, which in turn labilizes the vesicular membrane and facilitates cellular uptake by improving membrane permeability.

pEGFP-N_2 Expression after Aerosol Administration. Encouraging *in vitro* results of PEA-mediated gene delivery, especially reduced cytotoxicity, increased cellular uptake, and significant transfection efficiency, prompted us to investigate its *in vivo* gene delivery potential by aerosol administration. One would expect that the presence of glycerol backbone and PEI moieties in PEAs boosts the delivery of nucleic acid *in vivo* after aerosol administration. PEA [GTA/PEI-1.2(1:4)] showing optimum transfection efficiency *in vitro* was selected for aerosol administration in mice. pEGFP-N_2 expression in the lungs after aerosol administration is shown in Figure 10. Although some groups (*32*, *33*) reported the superior efficacy of simple positively charged polyplexes with linear PEI 22 K by aerosol administration, the application of such polyplexes remains restricted because of severe toxicity in the pulmonary region (*34*). In addition, according to the reports of Koshkina

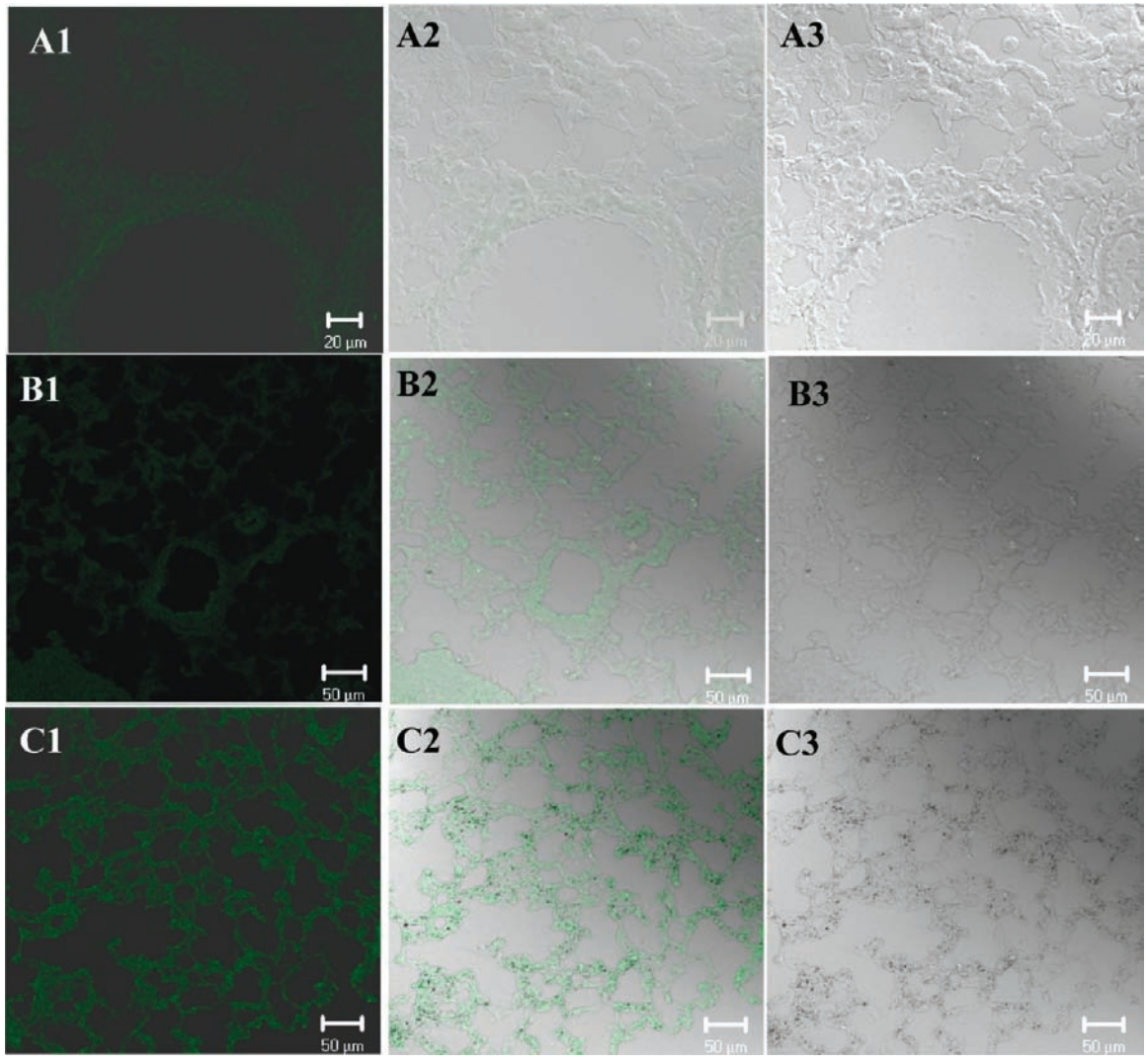

Figure 10. *In vivo* pEGFP-N_2 expression analysis after aerosol administration to lungs. A1, B1, and C1 are the fluorescent images of control, PEI 25K, and GTA/PEI-1.2(1:4), respectively. A2, B2, and C2 are the merged images of control, PEI 25K, and GTA/PEI-1.2(1:4), respectively. A3, B3, and C3 are phase contrast images of control, PEI 25K, and GTA/PEI-1.2(1:4), respectively ($n = 3$, error bar represents standard deviation).

et al., even though both aerosol and intravenous (i.v.) routes deliver gene to lung, aerosol administration is more promising and advantageous, because it results in substantial deposition of DNA and its extended retention in the pulmonary region (*35*). GTA/PEI-1.2(1:4)/pEGFP-N_2 showed promising GFP fluorescence compared to PEI 25K after aerosol administration as shown in Figure 10. This increased GFP expression level shown by GTA/PEI undoubtedly evidences its ability as a potential gene carrier *in vitro* and *in vivo*. Because of the large surface area of the pulmonary region, alveolar cells are much more eligible to internalize PEA/pEGFP-N_2 polyplexes, resulting in elevated levels of transfection efficiency. On the contrary, smaller levels of gene expression shown by PEI 25K may be supported by its low uptake into the lung and its non-biodegradability, which leads to cytotoxicity.

Despite development of various successful cationic polymers by our group which showed remarkable transfection efficiency both *in vitro* and *in vivo*, the superior efficacy of the present polymeric system and an earlier one (GDM/PEI-1.2 copolymers) over others is the hyperosmotic effect that it exerts because of the presence of glycerol moieties in the PEA backbone. This present polymer system exhibits a higher gene expression level presumably due to the synergistic effect of endosomal buffering capacity (resulting from PEI amine groups) and the hyperosmotic effect (resulting from glycerol backbone).

CONCLUSIONS

The approach described in this paper represents an easy and efficient method to obtain a fairly stable vector system with hyperbranched, degradable, and osmotically active PEAs. These PEAs were successfully synthesized by the Michael addition reaction between GTA and LMW-PEI and exhibited remarkable biophysical properties such as polyplex size below 200 nm and surface charge in the range 15−45 mV suitable for intracellular gene delivery carrier. The presence of ester linkage indicated the controlled hydrolytic degradation of PEAs with a half-life of more than 12 days and was essentially nontoxic in all three cell lines (HeLa, HepG2, and 293T cells) at higher doses as compared with PEI 25K. Furthermore, PEAs exhibited higher levels of transfection efficiencies *in vitro* and *in vivo* compared with the "gold standard" PEI 25 K and Lipofectamine as a commercial control. The higher transfection levels of PEAs over PEI could be attributed to the synergism arising from the hyperosmotic effect from glycerol backbone and the "proton sponge effect" from PEI residues. Currently, we are conducting more comprehensive studies such as structure−activity relationships of this vector system with regard to the cellular uptake, reduction in cytotoxicity, and increased transfection efficiency.

ACKNOWLEDGMENT

This research work was supported by National Research Laboratory of Korean Science and Engineering Foundation by the Korean Government (MEST) (ROA-2008-000-20024-0). National Instrumentation Center for Environmental Management (NICEM) is acknowledged for providing analytical facilities. R. A. was supported by Korea Research Foundation.

LITERATURE CITED

(1) Robbis, P. D., Tahara, T., and Ghivizzani, T. (1998) Viral vectors for gene therapy. *Trends Biotechnol. 16*, 35–40.
(2) Kay, M. A., Glorioso, J. C., and Naldini, L. (2001) Viral vectors for gene therapy: the art of turning infectious agents into vehicles of therapeutics. *Nat. Med. 7* (1), 33–40.
(3) Wolfert, M. A., Schacht, E. H., Toncheva, V., Ulbrich, K., Nazarova, O., and Seymour, L. W. (1996) Characterization of vectors for gene therapy formed by self-assembly of DNA with synthetic block co-polymers. *Hum. Gene Ther. 7* (17), 2123–2133.
(4) Luo, D., and Saltzman, W. M. (2000) Synthetic DNA delivery systems. *Nat. Biotechnol. 18*, 33–37.
(5) Wagner, E., Ogris, M., and Zauner, W. (1998) Polylysine-based transfection systems utilizing receptor-mediated delivery. *Adv. Drug Delivery Rev. 30* (1−3), 97–113.
(6) Vijayanathan, V., Thomas, T., and Thomas, T. J. (2002) DNA nanoparticles and development of DNA delivery vehicles for gene therapy. *Biochemistry 41* (48), 14085–14094.
(7) Godbey, W. T., Wu, K. K., and Mikos, A. G. (1999) Poly(ethylenimine) and its role in gene delivery. *J. Controlled Release 60*, 149–160.
(8) Boussif, O., Lenzoualc'h, F., Zanta, M. A., Mergny, M. D., Scherman, D., Demeneix, B., and Behr, J. P. (1995) A versatile vector for gene and oligonucleotide transfer into cells in culture and in vivo: polyethylenimine. *Proc. Natl. Acad. Sci. U.S.A. 92*, 7297–7301.
(9) Godbey, W. T., Wu, K. K., and Mikos, A. G. (1999) Size matters: molecular weight affects the efficiency of poly(ethylenimine) as a gene delivery vehicle. *J. Biomed. Mater. Res. 45*, 268–275.
(10) Fischer, D., Bieber, T., Li, Y., Elsasser, H. P., and Kissel, T. (1999) A novel non-viral vector for DNA delivery based on low molecular weight, branched polyethylenimine: effect of molecular weight on transfection efficiency and cytotoxicity. *Pharm. Res. 16*, 1273–7129.
(11) Lim, Y. B., Kim, C. H., Kim, K., Kim, S. W., and Park, J. S. (2000) Development of safe gene delivery system using biodegradable polymer, poly[α-(4-aminobutyl)-L-glycolic acid. *J. Am. Chem. Soc. 122*, 6524–6525.
(12) Lim, Y. B., Han, S. O., Kong, H. U., Lee, Y., Park, J. S., Jeong, B., and Kim, S. W. (2000) Biodegradable polyester, poly[alpha-(4-aminobutyl)-L-glycolic acid], as a non-toxic gene carrier. *Pharm. Res. 17* (7), 811–816.
(13) Lynn, D. M., and Langer, R. (2000) Degradable poly (β-amino esters): synthesis, characterization and self assembly with plasmid DNA. *J. Am. Chem. Soc. 122*, 10761–10768.
(14) Anderson, D. G., Akinc, A., Hossain, N., and Langer, R. (2005) Structure/property studies of polymeric gene delivery using a library of poly (β-amino esters). *Mol. Ther. 11* (3), 426–434.
(15) Oupicky, D., Parker, A. L., and Seymour, L. W. (2002) Laterally stabilized complexes of DNA with linear reducible polycations: strategy of triggering intracellular activation of DNA delivery vectors. *J. Am. Chem. Soc. 124* (1), 8–9.
(16) Lim, Y. B., Kim, S. M., Suh, H., and Park, J. S. (2002) Biodegradable, endosome disruptive, and cationic network-type polymer as a highly efficient and nontoxic gene delivery carrier. *Bioconjugate Chem. 13*, 952–957.
(17) Pun, S. H., and Davis, M. K. (2002) Development of nonviral gene delivery vehicle for systemic application. *Bioconjugate Chem. 13*, 630–639.
(18) Park, M. R., Han, K. O., Cho, M. H., Nah, J. W., Choi, Y. J., and Cho, C. S. (2005) Degradable polyethylenimine-alt-poly(ethylene glycol) copolymers as novel gene carriers. *J. Controlled Release 105*, 367–380.
(19) Arote, R., Kim, T. H., Kim, Y. K., Hwang, S. K., Jiang, H. L., Song, H. H., Nah, J. W., Cho, M. H., and Cho, C. S. (2007) A biodegradable poly(ester amine) based on polycaprolactone and polyethylenimine as a gene carrier. *Biomaterials 28* (4), 735–744.
(20) Kim, T. H., Cook, S. E., Arote, R. B., Cho, M. H., Nah, J. W., Choi, Y. J., and Cho, C. S. (2007) A degradable hyperbranched poly(ester amine) based on poloxamer diacrylate and polyethylenimine as a gene carrier. *Macromol. Biosci. 7* (5), 611–619.
(21) Arote, R. B., Hwang, S. K., Yoo, M. K., Jere, D., Jiang, H. L., Kim, Y. K., Choi, Y. J., Nah, J. W., Cho, M. H., and Cho, C. S. (2008) Biodegradable poly(ester amine) based on glycerol dimethacrylate and polyethylenimine as a gene carrier. *J. Gene. Med. 10* (11), 1223–1235.

(22) Zauner, W., Kichler, A., Schmidt, W., Mechtler, K., and Wagner, E. (1997) Glycerol and polylysine synergize in their ability to rupture vesicular membranes: a mechanism for increased transferrin-polylysine-mediated gene transfer. *Exp. Cell. Res. 232* (1), 137–145.

(23) Plank, C., Tang, M. X., Wolfe, A. R., and Szoka, F. C., Jr. (1999) Branched cationic peptides for gene delivery: role of type and number of cationic residues in formation and in vitro activity of DNA polyplexes. *Hum. Gene Ther. 10* (2), 319–332.

(24) Lynn, D. M., Anderson, D. G., Putnam, D., and Langer, R. (2001) Accelerated discovery of synthetic transfection vectors: parallel synthesis and screening of a degradable polymer library. *J. Am. Chem. Soc. 123* (33), 8155–8156.

(25) Kunath, K., von Harpe, A., Fischer, D., Petersen, H., Bickel, U., Voigt, K., and Kissel, T. (2003) Low-molecular-weight polyethylenimine as a non-viral vector for DNA delivery: comparison of physicochemical properties, transfection efficiency and in vivo distribution with high-molecular-weight polyethylenimine. *J. Controlled Release 89* (1), 113–125.

(26) Dubruel, P., Dekie, L., Christiaens, B., Vanloo, B., Rosseneu, M., Van De Kerckhove, J., Mannisto, M., Urtti, A., and Schacht, E. (2003) Poly-l-glutamic acid derivatives as multifunctional vectors for gene delivery. Part B. Biological evaluation. *Biomacromolecules 4* (5), 1177–1183.

(27) Anderson, D. G., Lynn, D. M., and Langer, R. (2003) Semiautomated synthesis and screening of a large library of degradable cationic polymers for gene delivery. *Angew. Chem., Int. Ed. Engl. 42* (27), 3153–3158.

(28) Gebhart, C. L., and Kabanov, A. V. (2001) Evaluation of polyplexes as gene transfer agents. *J. Controlled Release 73* (2−3), 401–416.

(29) Boussif, O., Lezoualc'h, F., Zanta, M. A., Mergny, M. D., Scherman, D., Demeneix, B., and Behr, J. P. (1995) A versatile vector for gene and oligonucleotide transfer into cells in culture and in vivo: polyethylenimine. *Proc. Natl. Acad. Sci. U.S.A. 92* (16), 7297–7301.

(30) Grosjean, F., Bertschinger, M., Hacker, D. L., and Wurm, F. M. (2006) Multiple glycerol shocks increase the calcium phosphate transfection of non-synchronized CHO cells. *Biotechnol. Lett. 28*, 1827–1833.

(31) Wilson, S. P., and Smith, L. A. (1997) Addition of glycerol during DNA exposure enhances calcium phosphate transfection. *Anal. Biochem. 246*, 148–150.

(32) Goula, D., Becker, N., Lemkine, G. F., Normandie, P., Rodrigues, J., Mantero, S., Levi, G., and Demeneix, B. A. (2000) Rapid crossing of the pulmonary endothelial barrier by polyethylenimine/DNA complexes. *Gene Ther. 7* (6), 499–504.

(33) Zou, S. M., Erbacher, P., Remy, J. S., and Behr, J. P. (2000) Systemic linear polyethylenimine (L-PEI)-mediated gene delivery in the mouse. *J. Gene Med. 2* (2), 128–134.

(34) Chollet, P., Favrot, M. C., Hurbin, A., and Coll, J. L. (2002) Side-effects of a systemic injection of linear polyethylenimine-DNA complexes. *J. Gene Med. 4* (1), 84–91.

(35) Koshkina, N. V., Agoulnik, I. Y., Melton, S. L., Densmore, C. L., and Knight, V. (2003) Biodistribution and pharmacokinetics of aerosol and intravenously administered DNA-polyethyleneimine complexes: optimization of pulmonary delivery and retention. *Mol. Ther. 8* (2), 249–254.

BC900184K

Detection of Bioactive Small Molecules by Fluorescent Resonance Energy Transfer (FRET) in RNA−Protein Conjugates

Tamaki Endoh,*[,†,‡] Ryo Shintani,[‡] Masayasu Mie,[§] Eiry Kobatake,[§] Takashi Ohtsuki,[‡] and Masahiko Sisido[‡]

Frontier Institute for Biomolecular Engineering Research (FIBER), Konan University, 7-1-20 Minatojimaminamimachi, Chuo-ku, Kobe 650-0047, Japan, Department of Bioscience and Biotechnology, Okayama University, 3-1-1 Tsushimanaka, Okayama 700-8530, Japan, and Department of Biological Information, Tokyo Tech., 4259 Nagatsuta, Midori-ku, Yokohama 226-8501, Japan. Received May 15, 2009; Revised Manuscript Received November 3, 2009

Bioactive small molecules such as metabolites and drugs play important roles in regulating biological functions. A technique for visualizing such small molecules is very useful to understand their molecular mechanisms. In this study, an RNA−protein conjugate, which consists of an RRE-RNA sensor protein (EYFP-Rev-ECFP) and an altered RRE-RNA, was constructed to detect bioactive small molecules by fluorescent resonance energy transfer (FRET). We designed a theophylline-aptamer-inserted RRE-RNA (Theo-RRE) to detect theophylline as a model target molecule. Theo-RRE formed an RNA−protein conjugate with EYFP-Rev-ECFP in the presence of theophylline. As a result, theophylline was specifically detected down to 10 μM by the FRET increase in distinction from theophylline analogue, caffeine, in cell lysates.

INTRODUCTION

There are a wide variety of functional small metabolites inside cells. They modulate biological functions by working as extracellular and intracellular messengers for signal transduction through complex metabolism networks (*1, 2*). In addition, small analogous molecules of such metabolites can be molecular-targeted drugs, agonists or antagonists, for regulating cellular functions or treating metabolic disorders (*3*). To investigate intracellular functions of those bioactive small molecules, metabolites, and drugs, it is important to directly detect them inside cells.

In previous works, many molecular probes have been constructed to visualize intracellular signal transductions and their messenger molecules by using GFP-based fluorescent proteins (*4*−*6*). They are promising tools for understanding biomolecular events in living cells. However, it is difficult to accommodate functionally unidentified molecules because proteins or domains that are functionally related to the target molecules have been utilized as sensor moieties in their systems. Therefore, it is desirable to construct a biosensor system, which is flexibly applicable to many types of biomolecules.

Some specific RNA sequences and structures have the ability to recognize biomolecules, such as proteins and peptides, with strong affinity. Many kinds of RNA−protein and RNA−peptide interactions have been discovered from natural RNA sequences (*7*−*11*). In addition, systematic evolution of ligands by exponential enrichment (SELEX) technology has been applied to *in vitro* selection of artificial combinative RNA sequences, known as RNA-aptamers, from random sequence libraries (*12, 13*). RNA-aptamers targeting not only natural proteins and peptides but also organic small molecules and nonnatural drugs have been discovered by the SELEX technology (*13*−*15*). Since many of the RNA-aptamers induce conformational changes in response to target binding, they can be utilized as biosensor moieties, if the conformational changes will be detected by an obvious output signal (*16*−*20*).

Previously, we constructed a protein probe containing a Rev-peptide inserted between EYFP and ECFP (EYFP-Rev-ECFP; YRG0C-11ad) (*21*) for detecting a rev response element RNA (RRE-RNA) by the increase of a FRET signal. The interaction between the RRE-RNA and the Rev-peptide is one of the most well characterized interactions between natural RNA and peptides, originating from the HIV-1 virus (*7*). The YRG0C-11ad indicated a conformational change in response to RRE-RNA binding and increased its FRET signal both *in vitro* and *in vivo* (*21, 22*). In this study, YRG0C-11ad and RRE-RNA were utilized as basal units to form an RNA−protein conjugate for visualizing target small molecules. Theophylline-aptamer is an *in vitro* selected aptamer that binds to a small bronchodilator theophylline (*23, 24*) and is widely utilized to construct theophylline-triggered RNA switches (*18, 25*−*30*). Here, the theophylline-aptamer was inserted into the RRE-RNA (Theo-RRE). Theo-RRE specifically binds theophylline and induces a conformational change, which results in the reconstruction of the RRE-RNA structure. Then, the YRG0C-11ad binds to the reconstructed Theo-RRE to form the RNA−protein conjugate and increases its FRET signal as an output signal (Figure 1). The detection system schemed in Figure 1 was confirmed in a HeLa cell lysate expressing YRG0C-11ad.

MATERIALS AND METHODS

Preparation of RNAs. RNAs used in this study (Table 1) were transcribed by T7 RNA polymerase from DNA templates, which were prepared by primer extension (*31*). The crude transcripts were purified in a 12% denaturing polyacrylamide gel. The sense primer containing the T7 promoter was 5′-GGCTAATACGACTCACTATAGG-3′. Antisense primers annealed with the sense primer were as follows: RRE-RNA, 5′-GGGCCTGTACCGTCAGCTTGCGCTGCGC-CCAGACCCTATAGTGAGTCGTATTAGCC-3′; Theo-RRE, 5′-CTGCGCCCAGCTGCCAAGGGCCTTTCGGCTGGTATCTG-TACCGTCAGATCCTATAGTGAGTCGTATTAGCC-3′; Theo-

* Corresponding author. Frontier Institute for Biomolecular Engineering Research (FIBER), Konan University, 4-1-20, Minatojimaminamimachi, Chuo-ku, Kobe 650-0047, Japan. Tel: +81-78-303-1314. Fax: +81-78-303-1495. E-mail: t-endoh@center.konan-u.ac.jp.

† Konan University.

‡ Okayama University.

§ Tokyo Tech.

10.1021/bc9002184 © 2009 American Chemical Society
Published on Web 11/24/2009

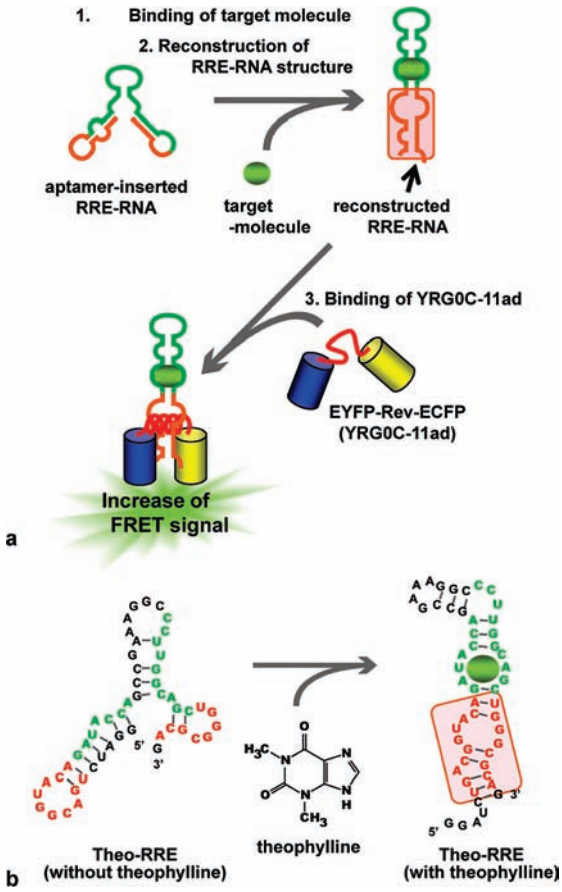

Figure 1. (a) Principle of detection system for small molecules by RNA−protein conjugates. Aptamer-inserted RRE-RNA captures a target small molecule (*1*). The RRE-RNA structure is reconstructed by the RNA conformational change (*2*). Protein probe, YRG0C-11ad, binds to the reconstructed RRE-RNA and increases the FRET signal (*3*). (b) Sequence and expected conformational change of Theo-RRE before (left) and after (right) theophylline binding. RNA structure without theophylline was estimated by GENETYX (Genetyx Corporation). RNA sequences essential for the binding of theophylline (green) or YRG0C-11ad (orange) are indicated as bold characters.

RRE(ex), 5′-TTGGCTGCGCCCAGCTGCCAAGGGCCTTT-CGGCTGGTATCTGTACCGTCAGATCCTATAGTGAGT-CGTATTAGCC-3′; and Theo-RRE(mut), 5′-CTGCGCCCAGC-TGCCAAGGGCCTTTCGGCTGGTATCTGTAACGTCAGA-TCCTATAGTGAGTCGTATTAGCC-3′.

Preparation of Cell Lysate. HeLa cells stably expressing the YRG0C-11ad fluorescent protein were cultured as described (*21*). Cells were trypsinized and suspended in buffer (10 mM HEPES, 100 mM KCl, 1 mM $MgCl_2$, 0.5 mM EDTA, and 10% glycerol, pH 7.5). They were lysed by sonication for 7 min and filtered through a 0.45 μm Ultrafree-MC filter (Amicon) following centrifugation at 3,500*g* for 3 min. The amount of total protein in the lysate was measured by Bio-Rad Protein Assay (Bio-Rad).

Gel Mobility Shift Assay. Interaction between RNA and the YRG0C-11ad was evaluated by nondenaturing polyacrylamide gel electrophoresis as described before (*21*). Briefly, the cell lysate (total protein amount of 0.7 μg) was mixed with RNA, RRE-RNA, or Theo-RRE, and the ligand, theophylline or caffeine, in 16 μL of reaction buffer (50 mM Tris-HCl and 1 mM $MgCl_2$, pH 7.5). After 30 min of incubation at 37 °C followed by 30 min of incubation at 25 °C, the mixture was resolved on a 12% nondenaturing polyacrylamide gel. The YRG0C-11ad mobility shift patterns were imaged by a fluorescence image scanner (FMBIO III; Hitachi) using a 488 nm excitation laser and a 555 nm emission filter.

FRET Measurement. Varied concentrations of the RNA and the ligand were mixed with the cell lysate (total protein amount of 4.4 μg for the fluorescence spectrum and 3.5 μg for the multiwell assay) in 100 μL of reaction buffer. The fluorescence spectrum of the mixture was recorded on a fluorescence spectrometer (FluoroMax-2; ISA). For the multiwell assay, samples were mixed in a 96-well black plate (Sumilon), and FRET signals were evaluated by a fluorescence microplate reader (FLUOstar OPTIMA; BMG). The fluorescence signal was obtained using a 427 ± 5 nm filter for excitation, 480 ± 5 nm for ECFP emission, and 530 ± 5 nm for EYFP emission. For both assays, FRET signals of the mixtures were measured after 30 min of incubation at 37 °C followed by 30 min of incubation at 25 °C.

Evaluation of the Dissociation Constant. The increases of FRET signals under different RNA concentrations were evaluated from the ratios of fluorescence intensities (530 nm/480 nm), with respect to the ratio in the absence of the RNA. Concentration of the YRG0C-11ad in the cell lysate or values of the dissociation constant were calculated from the FRET increase by using Origin8 software (Origin Lab). The theoretical formula fitted to the FRET increase is expressed as follows (*32*):

$$\text{FRET increase} = 1 + \Delta(\text{FRET increase}) \times \frac{\text{Kd} + [\text{protein}] + [\text{RNA}] - \sqrt{(\text{Kd} + [\text{protein}] + [\text{RNA}])^2 - 4[\text{protein}][\text{RNA}]}}{2[\text{protein}]}$$

RESULTS AND DISCUSSION

Formation of RNA−Protein Conjugates and FRET Increase in the Presence of Theophylline. Figure 2a shows a fluorescence image of a nondenaturing polyacrylamide gel which visualizes mobility shift patterns of YRG0C-11ad. In the lanes in which the lysate was mixed with the ligands without RNA, YRG0C-11ad did not migrate into the gel and stayed on thresholds (lanes 1−3). In contrast, strong bands were observed at lower shift positions, when the lysate was mixed with wild type RRE-RNA, regardless of ligand addition (lanes 4−6). These results agreed with our previous result (*21*) and indicate that the ligands did not affect YRG0C-11ad mobility. In the case of Theo-RRE, although a small amount of shifted band was observed without the ligand (lane 7), the band intensity increased by the addition of theophylline even at 250 μM (lanes 8−10). The addition of caffeine by 1 mM did not affect the band intensity even if a slight increase was observed at 2 mM (lanes 11−13). These results indicate that the formation of the RNA−protein (Theo-RRE/YRG0C-11ad) conjugate was enhanced specifically in the presence of theophylline.

Then, fluorescence spectra were measured to confirm whether the FRET signal was increased by the addition of theophylline through the formation of the Theo-RRE/YRG0C-11ad conjugate (Figure 2b). The addition of Theo-RRE at 20 nM without the ligand decreased ECFP intensity and increased EYFP intensity compared to the lysate only. In addition, however, the additional theophylline at 2 mM induced further ECFP decrease and EYFP increase, while caffeine did not affect the spectrum. Fluorescence intensity ratios (523 nm/473 nm) calculated from the spectra (Figure 2c) indicated that either without Theo-RRE or with RRE-RNA, the addition of the ligands did not affect the FRET signal as well as the gel mobility shift assay. From the results, it was revealed that the FRET increase was caused by the formation of the Theo-RRE/YRG0C-11ad conjugate and specifically enhanced by the addition of theophylline.

Characterization of Theo-RRE Variants. Since the FRET signal was moderately increased by an addition of Theo-RRE without ligand, sequence variants of Theo-RRE (Table 1 and Figure 3a) were designed to prevent a self-interaction between

Table 1. RNA Variants, Sequences, and Dissociation Constants Calculated from FRET Increase

RNA	sequence	dissociation constant (nM)	
		without theophylline	with 4 mM theophylline
RRE-RNA (36-mer)	5′-GGGUCUGGGCGCAGCGCAAGCUGACG GUACAGGCCC-3′	0.19 ± 0.07	
Theo-RRE (51-mer)	5′-GGAUCUGACGGUACAGAUACCAGCCG AAAGGCCCUUGGCAGCUGGGCGCAG-3′	36.04 ± 5.22	2.53 ± 0.34
Theo-RRE(ex) (55-mer)	5′-GGAUCUGACGGUACAGAUACCAGCCG AAAGGCCCUUGGCAGCUGGGCGCAGCCAA-3′	18.63 ± 2.67	0.14 ± 0.20
Theo-RRE(mut) (51-mer)	5′-GGAUCUGACGUUACAGAUACCAGCCG AAAGGCCCUUGGCAGCUGGGCGCAG-3′	N.D.	140.0 ± 44.0

Theo-RRE and the YRG0C-11ad in the absence of theophylline. Theo-RRE(ex) was designed to form 4 additional basepairs at the 3′-end, not to easily open the stem. Theo-RRE(mut) was designed to depresses an interaction between the RRE-RNA and the Rev-peptide by a G11U mutation at the bulge region, which is important for the interaction (*33*).

First, the wild type RRE-RNA was added to the lysate, and the FRET increase was evaluated by a fluorescence microplate reader. From the FRET increase under different RRE-RNA concentrations, the concentration of the YRG0C-11ad at the experimental conditions (3.5 μg of total lysate protein in 100 μL of reaction buffer) was estimated at 5.96 nM (see Supporting Information, Figure 1). Then, the value of the concentration of YRG0C-11ad was fixed to the calculated result, 5.96 nM, and dissociation constants between Theo-RRE variants and YRG0C-11ad in the presence (4 mM) or absence of theophylline were calculated from the FRET increase under different Theo-RRE concentrations (Table 1 and Figure 3b). In the presence of 4 mM theophylline, the variants were supposed to completely bind to theophylline and reconstruct the RRE-RNA structure. As a result, in the presence of 4 mM theophylline, all of the Theo-RRE variants indicated smaller dissociation constants than those in the absence of 4 mM theophylline. In the case of Theo-RRE(mut), the self-interaction between YRG0C-11ad and RNA was successfully repressed, and the dissociation constant could not be calculated in the absence of theophylline. However, Theo-RRE(ex) had no effect on repressing the self-interaction, rather it indicated a smaller dissociation constant than Theo-RRE. Longer basepairs were possibly required to repress the self-interaction because Theo-RRE(ex) already contained a stem loop of similar length at the 5′-end, which might be as effective as the 3′-end stem loop.

Homogeneous Detection of Theophylline in Cell Lysate. Theo-RRE(mut) (150 nM) was mixed with the cell lysate, and relative FRET increases were evaluated under different concentrations of theophylline or caffeine (Figure 4). The FRET increase was dependent on theophylline concentration and was not affected by caffeine. The result indicates that theophylline could be specifically detected down to 10 μM by the Theo-RRE/YRG0C-11ad conjugate. Although a more sensitive theophylline biosensor has performed using other detection systems (*18*, *26*), our system worked in a composite and homogeneous solution of the cell lysate without any modification of RNA or protein. When Theo-RRE was mixed with the cell

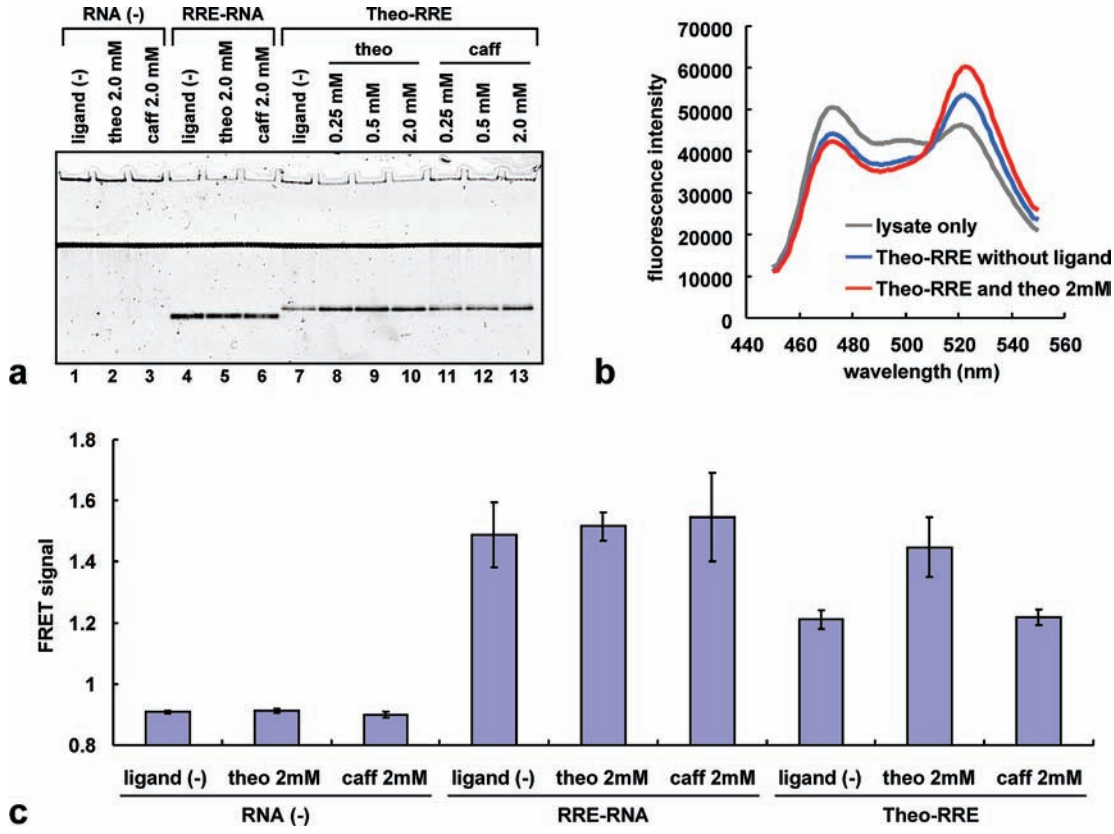

Figure 2. (a) Gel mobility shift assay. Wild type RRE-RNA or Theo-RRE was added to the cell lysate at 20 nM. Additional theophylline (theo) or caffeine (caff) was added at different concentrations (0.25, 0.5, or 2.0 mM). (b) Fluorescence spectra of the cell lysate. The mixture was excited at 425 nm, and spectra were measured from 450 to 550 nm. (c) FRET signals calculated from fluorescence spectra (523 nm/473 nm). Values are average with standard deviation ($n = 3$).

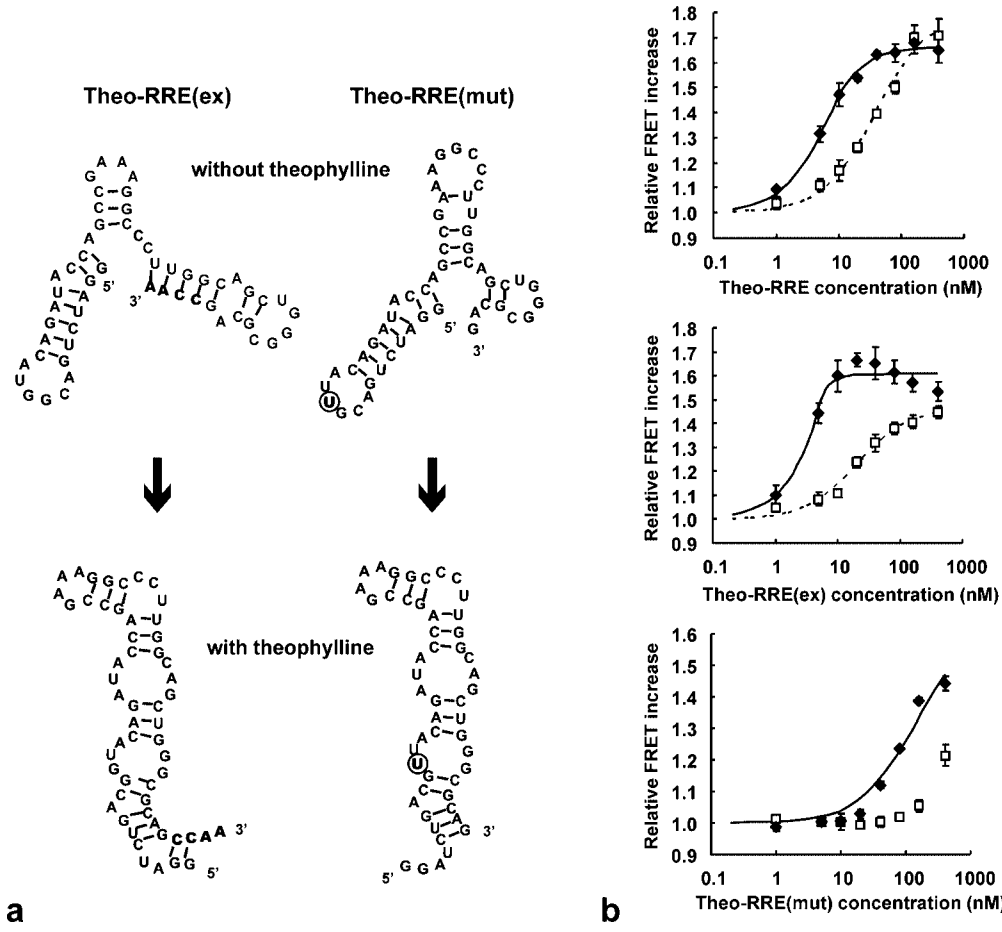

Figure 3. (a) Sequences and expected conformational changes of Theo-RRE variants. RNA structure without theophylline was estimated by GENETYX. Extended bases were indicated as bold characters in Theo-RRE(ex), and the mutated base in Theo-RRE(mut) was indicated as an encircled bold character. (b) FRET increase under different concentrations of Theo-RRE variants in the presence (♦) or absence (□) of theophylline (4 mM). The dashed line and solid line represent fitting curves calculated by Origin 8. Values are average with standard deviation ($n = 3$).

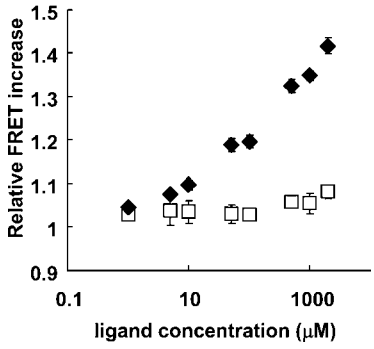

Figure 4. Homogeneous detection of theophylline by FRET increase caused by the formation of the Theo-RRE(mut)/YRG0C-11ad conjugate. Varied concentrations of theophylline (♦) or caffeine (□) were mixed with the cell lysate (3.5 μg of total protein) and Theo-RRE(mut) (150 nM). Values are average with standard deviation ($n = 3$).

lysate at 20 nM, FRET increase was also observed down to 10 μM, even though the error bars were larger than that of Theo-RRE(mut) (see Supporting Information, Figure 2).

CONCLUSIONS

The RNA−protein conjugate sensor consists of a pair of unmodified RNA (Theo-RRE) and fluorescent protein (YRG0C-11ad) and specifically detected a small bioactive molecule, theophylline, by FRET increase. They worked in a composite and homogeneous solution of the cell lysate and enabled theophylline detection down to 10 μM. It would be one of the useful bioimaging techniques because Theo-RRE and the YRG0C-11ad can be stably and continuously produced in living cells by transfecting DNA vectors (*22*). In addition, since the Rev-peptide inserted in YRG0C-11ad functions as a cell penetrating peptide (*34, 35*), it might be practical if the purified YRG0C-11ad could be introduced into significant cells, such as neuronal and embryonic cells.

High throughput metabolome analyses or drug screenings are expected to identify valuable molecules that contribute to interesting bioactivities, such as embryogenesis and particular diseases (*36, 37*), and an intracellular detection system of such molecules would be desirable. The RNA−protein conjugate demonstrated in this study has a unique property, compared with those of other GFP-based FRET sensors, in that the RNA functions as a recognition unit for target molecules, while the fluorescent protein functions as a signaling unit. Artificially selected RNAs, aptamers, have an ability to recognize many types of biomolecules, and its selection method has been well established. Therefore, the RNA−protein conjugate sensor would be flexibly applicable for other small molecules by using other aptamers or selecting RNAs, which specifically interact with YRG0C-11ad in the presence of target molecules (*38, 39*).

Supporting Information Available: Relative FRET increase depending on RRE-RNA concentration (Figure 1) and homogeneous detection of theophylline using Theo-RRE (Figure 2). This material is available free of charge via the Internet at http://pubs.acs.org.

LITERATURE CITED

(1) Minghetti, P. P., and Norman, A. W. (1988) 1,25(OH)2-vitamin D3 receptors: gene regulation and genetic circuitry. *FASEB J. 2*, 3043–3053.

(2) Mishra, J., and Bhalla, U. S. (2002) Simulations of inositol phosphate metabolism and its interaction with InsP(3)-mediated calcium release. *Biophys. J. 83*, 1298–1316.

(3) Nagpal, S., Na, S., and Rathnachalam, R. (2005) Noncalcemic actions of vitamin D receptor ligands. *Endocr. Rev. 26*, 662–687.

(4) Griekspoor, A., Zwart, W., Neefjes, J., and Michalides, R. (2007) Visualizing the action of steroid hormone receptors in living cells. *Nucl. Recept. Signaling 5*, e003.

(5) Miyawaki, A., Llopis, J., Heim, R., McCaffery, J. M., Adams, J. A., Ikura, M., and Tsien, R. Y. (1997) Fluorescent indicators for Ca^{2+} based on green fluorescent proteins and calmodulin. *Nature 388*, 882–887.

(6) Vincent, P., Gervasi, N., and Zhang, J. (2008) Real-time monitoring of cyclic nucleotide signaling in neurons using genetically encoded FRET probes. *Brain Cell Biol. 36*, 3–17.

(7) Battiste, J. L., Mao, H., Rao, N. S., Tan, R., Muhandiram, D. R., Kay, L. E., Frankel, A. D., and Williamson, J. R. (1996) Alpha helix-RNA major groove recognition in an HIV-1 rev peptide-RRE RNA complex. *Science 273*, 1547–1551.

(8) Lee, A. L., Volkman, B. F., Robertson, S. A., Rudner, D. Z., Barbash, D. A., Cline, T. W., Kanaar, R., Rio, D. C., and Wemmer, D. E. (1997) Chemical shift mapping of the RNA-binding interface of the multiple-RBD protein sex-lethal. *Biochemistry 36*, 14306–14317.

(9) Nagai, K., Oubridge, C., Jessen, T. H., Li, J., and Evans, P. R. (1990) Crystal structure of the RNA-binding domain of the U1 small nuclear ribonucleoprotein A. *Nature 348*, 515–520.

(10) Puglisi, J. D., Chen, L., Blanchard, S., and Frankel, A. D. (1995) Solution structure of a bovine immunodeficiency virus Tat-TAR peptide-RNA complex. *Science 270*, 1200–1203.

(11) Scharpf, M., Sticht, H., Schweimer, K., Boehm, M., Hoffmann, S., and Rosch, P. (2000) Antitermination in bacteriophage lambda. The structure of the N36 peptide-boxB RNA complex. *Eur. J. Biochem. 267*, 2397–2408.

(12) Tuerk, C., and Gold, L. (1990) Systematic evolution of ligands by exponential enrichment: RNA ligands to bacteriophage T4 DNA polymerase. *Science 249*, 505–510.

(13) Stoltenburg, R., Reinemann, C., and Strehlitz, B. (2007) SELEX: A (r)evolutionary method to generate high-affinity nucleic acid ligands. *Biomol. Eng. 24*, 381–403.

(14) Romero-López, C., Díaz-González, R., and Berzal-Herranz, A. (2007) RNA selection and evolution *in vitro*: powerful techniques for the analysis and identification of new molecular tools. *Biotechnol. Biotechnol. EQ. 21*, 272–282.

(15) Wilson, D. S., and Szostak, J. W. (1999) In vitro selection of functional nucleic acids. *Annu. Rev. Biochem. 68*, 611–647.

(16) Mairal, T., Ozalp, V. C., Lozano Sanchez, P., Mir, M., Katakis, I., and O'Sullivan, C. K. (2008) Aptamers: molecular tools for analytical applications. *Anal. Bioanal. Chem. 390*, 989–1007.

(17) Navani, N. K., and Li, Y. (2006) Nucleic acid aptamers and enzymes as sensors. *Curr. Opin. Chem. Biol. 10*, 272–281.

(18) Ferapontova, E. E., Olsen, E. M., and Gothelf, K. V. (2008) An RNA aptamer-based electrochemical biosensor for detection of theophylline in serum. *J. Am. Chem. Soc. 130*, 4256–4258.

(19) Liu, J., Lee, J. H., and Lu, Y. (2007) Quantum dot encoding of aptamer-linked nanostructures for one-pot simultaneous detection of multiple analytes. *Anal. Chem. 79*, 4120–4125.

(20) Nutiu, R., and Li, Y. (2003) Structure-switching signaling aptamers. *J. Am. Chem. Soc. 125*, 4771–4778.

(21) Endoh, T., Funabashi, H., Mie, M., and Kobatake, E. (2005) Method for detection of specific nucleic acids by recombinant protein with fluorescent resonance energy transfer. *Anal. Chem. 77*, 4308–4314.

(22) Endoh, T., Mie, M., and Kobatake, E. (2008) Direct detection of RNA transcription by FRET imaging using fluorescent protein probe. *J. Biotechnol. 133*, 413–417.

(23) Jenison, R. D., Gill, S. C., Pardi, A., and Polisky, B. (1994) High-resolution molecular discrimination by RNA. *Science 263*, 1425–1429.

(24) Zimmermann, G. R., Wick, C. L., Shields, T. P., Jenison, R. D., and Pardi, A. (2000) Molecular interactions and metal binding in the theophylline-binding core of an RNA aptamer. *RNA 6*, 659–667.

(25) Ogawa, A., and Maeda, M. (2008) An artificial aptazyme-based riboswitch and its cascading system in *E. coli*. *ChemBioChem 9*, 206–209.

(26) Sekella, P. T., Rueda, D., and Walter, N. G. (2002) A biosensor for theophylline based on fluorescence detection of ligand-induced hammerhead ribozyme cleavage. *RNA 8*, 1242–1252.

(27) Amontov, S., and Jaschke, A. (2006) Controlling the rate of organic reactions: rational design of allosteric Diels-Alderase ribozymes. *Nucleic Acids Res. 34*, 5032–5038.

(28) Bayer, T. S., and Smolke, C. D. (2005) Programmable ligand-controlled riboregulators of eukaryotic gene expression. *Nat. Biotechnol. 23*, 337–343.

(29) Kim, D. S., Gusti, V., Dery, K. J., and Gaur, R. K. (2008) Ligand-induced sequestering of branchpoint sequence allows conditional control of splicing. *BMC Mol. Biol. 9*, 23.

(30) An, C. I., Trinh, V. B., and Yokobayashi, Y. (2006) Artificial control of gene expression in mammalian cells by modulating RNA interference through aptamer-small molecule interaction. *RNA 12*, 710–716.

(31) Ohtsuki, T., Manabe, T., and Sisido, M. (2005) Multiple incorporation of non-natural amino acids into a single protein using tRNAs with non-standard structures. *FEBS Lett. 579*, 6769–6774.

(32) Luedtke, N. W., and Tor, Y. (2000) A novel solid-phase assembly for identifying potent and selective RNA ligands. *Angew. Chem., Int. Ed. 39*, 1788–1790.

(33) Kjems, J., Calnan, B. J., Frankel, A. D., and Sharp, P. A. (1992) Specific binding of a basic peptide from HIV-1 Rev. *EMBO J. 11*, 1119–1129.

(34) Suzuki, T., Futaki, S., Niwa, M., Tanaka, S., Ueda, K., and Sugiura, Y. (2002) Possible existence of common internalization mechanisms among arginine-rich peptides. *J. Biol. Chem. 277*, 2437–2443.

(35) Kameyama, S., Okada, R., Kikuchi, T., Omura, T., Nakase, I., Takeuchi, T., Sugiura, Y., and Futaki, S. (2006) Distribution of immunoglobulin Fab fragment conjugated with HIV-1 REV peptide following intravenous administration in rats. *Mol. Pharmaceutics 3*, 174–180.

(36) Desbordes, S. C., Placantonakis, D. G., Ciro, A., Socci, N. D., Lee, G., Djaballah, H., and Studer, L. (2008) High-throughput screening assay for the identification of compounds regulating self-renewal and differentiation in human embryonic stem cells. *Cell Stem Cell 2*, 602–612.

(37) Cezar, G. G., Quam, J. A., Smith, A. M., Rosa, G. J., Piekarczyk, M. S., Brown, J. F., Gage, F. H., and Muotri, A. R. (2007) Identification of small molecules from human embryonic stem cells using metabolomics. *Stem Cells Dev. 16*, 869–882.

(38) Seetharaman, S., Zivarts, M., Sudarsan, N., and Breaker, R. R. (2001) Immobilized RNA switches for the analysis of complex chemical and biological mixtures. *Nat. Biotechnol. 19*, 336–341.

(39) Stojanovic, M. N., and Kolpashchikov, D. M. (2004) Modular aptameric sensors. *J. Am. Chem. Soc. 126*, 9266–9270.

BC9002184

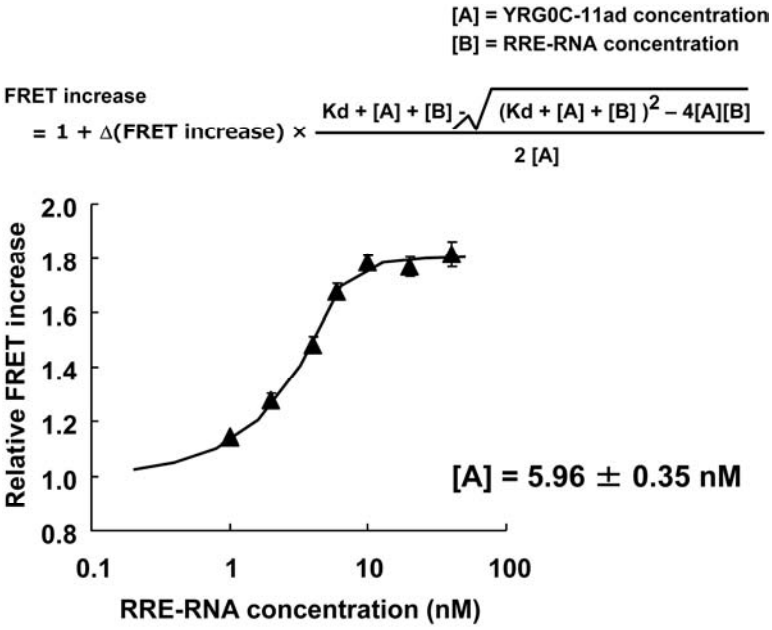

Supplementary Figure 1

Varied concentrations of the wild type RRE-RNA were mixed with the cell lysate (3.5 μg total proteins in 100 μL reaction buffer), and FRET signals were evaluated by using fluorescence microplate reader. The concentration of the YRG0C-11ad ([A]) in the cell lysate was calculated by fitting the above formula to the relative FRET increase under the different concentrations of the RRE-RNA. Values were average with standard deviation (n = 3).

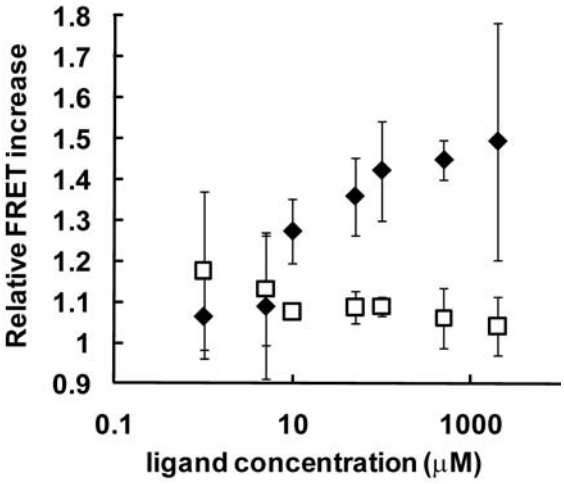

Supplementary Figure 2

Homogeneous detection of theophylline by FRET increase caused by the formation of theo-RRE/YRG0C-11ad conjugate. Varied concentrations of theophylline (filled diamond) or caffeine (open square) was mixed with the cell lysate (3.5 μg total proteins) and Theo-RRE (20 nM). Values were average with standard deviation (n =3).

Tamoxifen−Poly(ethylene glycol)−Thiol Gold Nanoparticle Conjugates: Enhanced Potency and Selective Delivery for Breast Cancer Treatment

Erik C. Dreaden,[†] Sandra C. Mwakwari,[‡] Quaovi H. Sodji,[‡] Adegboyega K. Oyelere,*[,‡] and Mostafa A. El-Sayed*[,†]

Department of Chemistry and Biochemistry, Georgia Institute of Technology, 901 Atlantic Drive NW, Atlanta, Georgia 30332-0400. Received May 20, 2009; Revised Manuscript Received September 4, 2009

The breast cancer treatment drug tamoxifen has been widely administered for more than three decades. This small molecule competes with 17β-estradiol for binding to estrogen receptor, a hormone receptor upregulated in a majority of breast cancers, subsequently initiating programmed cell death. We have synthesized a thiol-PEGylated tamoxifen derivative that can be used to selectively target and deliver plasmonic gold nanoparticles to estrogen receptor positive breast cancer cells with up to 2.7-fold enhanced drug potency in vitro. Optical microscopy/spectroscopy, time-dependent dose−response data, and estrogen competition studies indicate that augmented activity is due to increased rates of intracellular tamoxifen transport by nanoparticle endocytosis, rather than by passive diffusion of the free drug. Both ligand- and receptor-dependent intracellular delivery of gold nanoparticles suggest that plasma membrane localized estrogen receptor alpha may facilitate selective uptake and retention of this and other therapeutic nanoparticle conjugates. Combined targeting selectivity and enhanced potency provides opportunities for both multimodal endocrine treatment strategies and adjunctive laser photothermal therapy.

INTRODUCTION

Binding of the steroidal hormone 17β-estradiol (E_2) to estrogen receptor (ER)[1] is a process essential to normal cell proliferation and differentiation in women. E_2 binding induces a conformational change in ER, which allows it to recruit cofactors necessary for the transcription of various genes commonly upregulated in malignant cells (*1*) (e.g., transforming growth factor alpha (*2*), *c-myc* (*3*), and cathepsin D (*4*)). Accordingly, hormone receptors such as ER or progesterone receptor are overexpressed in 75−80% of all breast cancers (*5*). Antiestrogen compounds, such as the small molecule breast cancer treatment drug tamoxifen (TAM) compete with E_2 for binding to ER, conformationally preventing adoption of associated transcription cofactors and subsequently initiating programmed cell death (*6*−*9*).

Diagnostic and therapeutic applications of functionalized nanoparticles are highly attractive due to the inherently multivalent nature of their surfaces (*10*−*14*). Like divalent antibodies, the binding affinity of a nanoparticle conjugate is enhanced proportional to the density of its binding sites. Receptor-mediated therapeutic response (i.e., potency) is similarly increased as a function of local ligand concentration and in cases where intracellular drug transport relies on passive diffusion, uptake of nanoparticle conjugates can greatly increase delivery rates (*15, 16*). Enhanced permeability and retention (EPR) of nanosized drug conjugates can also lead to augmented and preferential accumulation at tumor sites in vivo (*17, 18*). Due to their biocompatibility (*19, 20*), stability (*21*), and potential use in photothermal laser treatments (*18, 22*−*26*), gold nanoparticles are excellent candidates for such ligand−receptor targeting strategies of cancer treatment.

Selective targeting and delivery of gold nanoparticles functionalized with ligands of cell surface receptors overexpressed by malignant cells has been well documented. Huang et al. have shown that oral cancer cells upregulating human epidermal growth factor receptor (EGFR, HER1, ErbB1) can be selectively labeled and photothermally destroyed by gold nanospheres and nanorods targeted with IgG antibodies (*24, 27*). ScFv fragments of anti-EGFR have also been used to selectively target and accumulate gold nanoparticles at tumor sites in vivo (*28*). Folate receptor has been employed to selectively deliver gold nanospheres to malignant cells in vitro (*29*), while Wei and co-workers have similarly demonstrated selective uptake and photothermal therapy of cancer cells using gold nanorods functionalized with a thiol−poly(ethylene glycol) (PEG−SH) folate derivative (*25, 30*).

Like several members of the hormone receptor family, ER isoforms are located both intracellularly and on the cell membrane (*31*−*33*). Gold nanoparticle analogs of the commercial pharmaceutical tamoxifen could therefore act not only as selective targeting agents but also as increasingly potent endocrine treatments for malignancies that overexpress ER (e.g., breast cancer). To this aim, a PEG−SH−tamoxifen derivative was synthesized for subsequent gold nanoparticle (AuNP) conjugation (Scheme 1). A biocompatible (*18, 34*) PEG−SH linker was employed (i) to enable covalent attachment to the AuNP surface (Au−S 126 kJ·mol^{-1}) (*35, 36*), (ii) to minimize opsonin binding and reticulo-endothelial system uptake (*37*), (iii) to suppress nonspecific cell binding/uptake (*38*) and protein adsorption (*18, 21*), and (iv) to afford stability (*21*) over a wide range of temperature, ionic strength, and pH.

Our results have shown enhanced potency and selective intracellular delivery of tamoxifen-targeted gold nanoparticles to ER(+) breast cancer cells in vitro. Particle uptake was observed in both a receptor- and ligand-dependent fashion with up to 2.7-fold enhanced drug potency versus the free drug. Both

* Authors to whom correspondence should be addressed. M.A.E.: e-mail melsayed@gatech.edu, tel 404 894 0292, fax 404 894 6078. A.K.O.: e-mail aoyelere@gatech.edu, tel 404 894 4047, fax 404 894 7452.

[†] Laser Dynamics Laboratory.

[‡] Parker H. Petit Institute for Bioengineering & Biosciences.

[1] Abbreviations: ER, estrogen receptor; E_2, 17β-estradiol; TAM, tamoxifen; EPR, enhanced permeability and retention; PEG, poly(ethylene glycol); EGFR, epidermal growth factor receptor; PEG−SH, thiol−poly(ethylene glycol); AuNP, gold nanoparticle; TAM−PEG−SH, thiol−poly(ethylene glycol)−tamoxifen; DPBS, Dulbecco's phosphate-buffered saline.

10.1021/bc9002212 © 2009 American Chemical Society
Published on Web 11/17/2009

Scheme 1. Synthesis of Thiol−PEGylated Tamoxifen (TAM−PEG−SH) (a) and Covalent Attachment to 25 nm Gold Nanoparticles (AuNPs) (b)

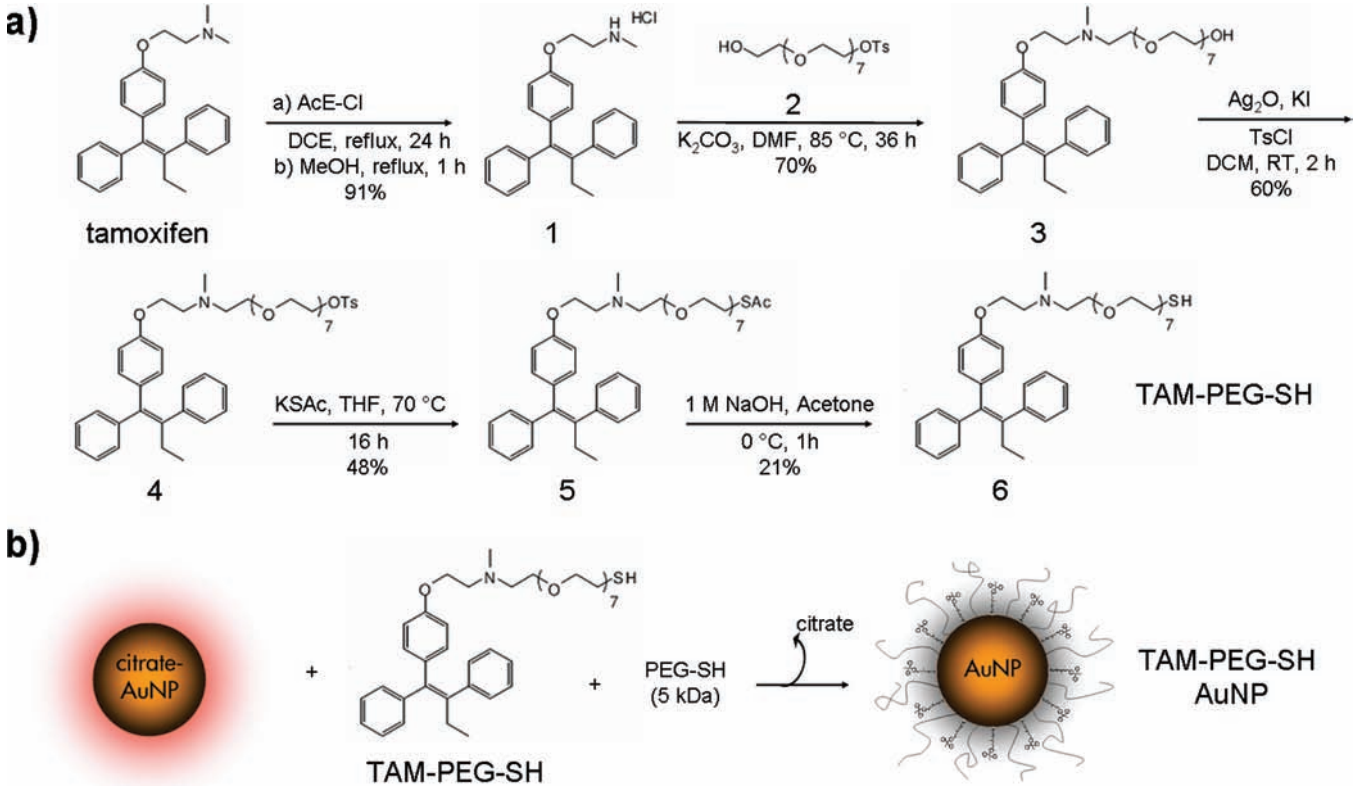

delivery and therapeutic response were shown to be suppressed by estrogen competition. Optical microscopy/spectroscopy and cell viability indicate that augmented growth inhibition versus the free drug can be attributed to increased rates of intracellular TAM transport by cellular uptake of the nanoparticle conjugate. Receptor- and ligand-dependent nanoparticle delivery suggests that the plasma membrane localized estrogen receptor alpha may facilitate selective particle uptake and presents future opportunities for coadministration of laser photothermal therapy (*18*, *22*−*26*).

EXPERIMENTAL PROCEDURES

Synthesis of Thiol−PEGylated Tamoxifen (TAM−PEG−SH). Octa(ethylene glycol) (OEG), tamoxifen, and all chemicals used in the synthesis were purchased from Sigma Aldrich. Anhydrous solvents and other reagents were purchased and used without further purification. Analtech silica gel plates (60 F_{254}) were used for analytical TLC, and Analtech preparative TLC plates (UV 254, 2000 μm) were used for purification. UV light was used to examine the spots. Silica gel (200−400 mesh) was used in column chromatography. NMR spectra were recorded on a Varian-Gemini 400 magnetic resonance spectrometer. ^{1}H and ^{13}C NMR spectra (Figures S1−8, Supporting Information) were recorded in parts per million (ppm) relative to the peaks of $CDCl_3$ (7.24 and 77.0 ppm, respectively). Mass spectra were recorded at the Georgia Institute of Technology mass spectrometry facility in Atlanta, GA.

*Synthesis of N-Desmethyl Tamoxifen (**1**).* The synthetic procedure was adapted from Olofson et al. (*39*). Briefly, tamoxifen (0.53 g, 1.43 mmol) was dissolved in anhydrous CH_2Cl_2 (15 mL) at 0 °C followed by addition of α-chloroethyl chloroformate (0.17 mL, 1.49 mmol). After 15 min at 0 °C, the reaction was refluxed for 24 h. The solvent was evaporated off to obtain a yellowish oil, to which methanol (10 mL) was added, and the mixture was refluxed for approximately 3 h. The solvent was evaporated off, and purification was performed by gel filtration using CH_2Cl_2, then 10:1 CH_2Cl_2/CH_3OH to obtain 0.52 g (91%) of *N*-desmethyl tamoxifen, **1**. ^{1}H NMR (DMSO, 400 MHz) δ 0.89 (3H, t, J = 7.2 Hz), 2.43 (2H, q, J = 14.8, 7.6 Hz), 2.56 (3H, s), 3.12 (2H, t, J = 4.0 Hz), 4.08 (2H, t, J = 4.8 Hz), 6.57 (2H, d, J = 8.8 Hz), 6.76 (2H, d, J = 8.8 Hz), 7.03−7.31 (10H, m), 9.56 (1H, br); HRMS [FAB, mnba] $(C_{25}H_{27}NO)^+$ calcd, 358.2171; found, 358.2198.

*Synthesis of Tosyl Octa(ethylene glycol) (**2**).* The synthetic procedure was adapted from Bouzide and Sauvé (*40*). Briefly, octa(ethylene glycol) (0.50 g, 1.35 mmol) was dissolved in anhydrous CH_2Cl_2 (7 mL) at 0 °C, followed by addition of freshly prepared Ag_2O (0.47 g, 2.02 mmol), KI (0.09 g, 0.50 mmol), and then TsCl (0.26 g, 1.35 mmol). The reaction mixture was left to stir at 0 °C under argon for 30 min, after which TLC deemed the reaction complete. Ag_2O was filtered off over a pad of Celite cake, washing with 12:1 CH_2Cl_2/CH_3OH. The filtrate was concentrated and purified on a silica column using 3:2 then gradually 1:4 CH_2Cl_2/acetone to yield the title compound as a colorless oil (0.55 g, 78%). ^{1}H NMR ($CDCl_3$, 400 MHz) δ 2.44 (3H, s), 2.81 (1H, br), 3.58−3.70 (30H, m), 4.15 (2H, t, J = 4.8 Hz), 7.35 (2H, d, J = 8.4 Hz), 7.80 (2H, d, J = 8.4 Hz); HRMS [ESI] $(C_{23}H_{40}O_{11}S + H)^+$ calcd, 525.2364; found, 525.2377.

*Synthesis of Tamoxifen−OEG−OH (**3**).* *N*-Desmethyl tamoxifen (**1**) (0.27 g, 0.68 mmol) and tosyl octa(ethylene glycol) (**2**) (0.54 g, 1.05 mmol) were dissolved in anhydrous DMF (10 mL), followed by addition of K_2CO_3 (0.95 g, 6.85 mmol), and stirred under argon at ∼85 °C for 24 h. DMF was evaporated off. Ethyl acetate was added to the residue, and the resulting suspension was filtered to remove excess K_2CO_3. Solvent was evaporated from the filtrate, and the crude was purified by preparatory TLC using 12:1:0.1 CH_2Cl_2/CH_3OH/NH_4OH to obtain 0.342 g (70%) of compound **3** as an oil. ^{1}H NMR ($CDCl_3$, 400 MHz) δ 0.90 (3H, t, J = 7.2 Hz), 1.85 (1H, br), 2.31 (3H, s), 2.44 (2H, q, J = 14.0, 7.2 Hz), 2.64 (2H, t, J = 6.0 Hz), 2.76 (2H, t, J = 6.0

Hz), 3.53−3.72 (30H, m), 3.91 (2H, t, $J = 6.4$ Hz), 6.54 (2H, m), 6.76 (2H, m), 7.10−7.40 (10H, m); ^{13}C NMR ($CDCl_3$, 100 MHz) δ 13.8, 29.2, 43.3, 50.7, 56.6, 57.2, 61.7, 65.6, 69.1, 70.3, 70.5, 70.6, 70.7, 70.8, 73.0, 113.6, 126.2, 126.7, 128.0, 128.3, 129.7, 129.9, 132.1, 135.8, 138.4, 141.5, 142.6, 144.0, 156.8; HRMS [ESI] $(C_{41}H_{59}NO_9 + H)^+$ calcd, 710.4262; found, 710.4253.

Synthesis of Tamoxifen−OEG−Tosylate (4). Tamoxifen−OEG−OH (**3**) (0.33 g, 0.46 mmol) was dissolved in anhydrous CH_2Cl_2 (10 mL) at 0 °C, followed by addition of Ag_2O (0.16 g, 0.69 mmol), KI (0.03 g, 0.18 mmol), and then TsCl (0.096 g, 0.5 mmol). Stirring was continued for 2 h at 0 °C, then at room temperature overnight. Ag_2O was filtered off through a pad of Celite cake, washing with ethyl acetate. Purification was performed on a silica column, eluting with 12:1 CH_2Cl_2/CH_3OH yielding the title compound as oil (0.24 g, 60%). ^{1}H NMR ($CDCl_3$, 400 MHz) δ 0.91 (3H, t, $J = 7.2$ Hz), 2.31−2.46 (8H, m), 2.71 (2H, br), 2.83 (2H, br), 3.57−3.70 (28H, m), 3.95 (2H, br), 4.15 (2H, t, $J = 4.4$ Hz), 6.53 (2H, d, $J = 8.4$ Hz), 6.76 (2H, d, $J = 8.8$ Hz), 7.10−7.34 (12H, m), 7.80 (2H, d, $J = 8.4$ Hz); LRMS [ESI] $(C_{48}H_{65}NO_{11}S + H)^+$ calcd, 864.1; found, 864.5.

Synthesis of Tamoxifen−OEG−SAc (5). KSAc (0.079 g, 0.69 mmol) was added to tamoxifen−OEG−tosylate (**4**) (0.12 g, 0.14 mmol) dissolved in anhydrous THF and refluxed under argon at ∼75 °C for 16 h. TLC analysis indicated a substantial consumption of the starting material. THF was evaporated off, and the crude product was dissolved in ethyl acetate. Decolorizing carbon was added and then filtered. Solvent was evaporated from the filtrate and the crude was purified by preparatory TLC using 12:1 CH_2Cl_2/CH_3OH to obtain 50 mg (48%) of **5** as reddish oil. ^{1}H NMR ($CDCl_3$, 400 MHz) δ 1.03 (3H, t, $J = 7.2$ Hz), 2.45 (3H, s), 2.47 (3H, s), 2.56 (2H, q, $J = 15.2$, 7.6 Hz), 2.80 (2H, t, $J = 6.0$ Hz), 2.91 (2H, t, $J = 5.6$ Hz), 3.21 (2H, t, $J = 6.0$ Hz), 3.70−3.80 (28H, m), 4.05 (2H, t, $J = 6.0$ Hz), 6.66 (2H, d, $J = 8.0$ Hz), 6.88 (2H, d, $J = 8.0$ Hz), 7.22−7.46 (10H, m); HRMS [ESI] $(C_{43}H_{61}NO_9S + H)^+$ calcd, 768.4139; found, 768.4118.

Synthesis of Thiol−PEGylated Tamoxifen (6). Tamoxifen−OEG−SAc (**5**) (0.05 g, 0.065 mmol) was dissolved in acetone (1.5 mL) at 0 °C, followed by addition of 1 M NaOH (1.5 mL), and stirring continued at 0 °C for 7 h. The reaction mixture was quenched with water (20 mL) and then extracted with 20% CH_3OH in CH_2Cl_2 (4 × 15 mL). The organic layers were combined, dried under sodium sulfate, evaporated, and purified on preparatory TLC using 11:1 CH_2Cl_2/CH_3OH to give 10 mg (21%) of the title compound as reddish semisolid. ^{1}H NMR ($CDCl_3$, 400 MHz) δ 0.90 (3H, t, $J = 7.2$ Hz), 2.32 (3H, s), 2.44 (2H, q, $J = 8.0$,7.6 Hz), 2.65 (2H, t, $J = 6.0$ Hz), 2.76 (2H, t, $J = 6.4$ Hz), 2.85 (2H, t, $J = 6.8$ Hz), 3.53−3.72 (28H, m), 3.91 (2H, t, $J = 6.0$ Hz), 6.52 (2H, d, $J = 8.8$ Hz), 6.74 (2H, d, $J = 8.8$ Hz), 7.08−7.32 (10H, m);^{13}C NMR ($CDCl_3$, 100 MHz) δ 13.5, 28.9, 29.6, 38.3, 43.3, 56.4, 57.0, 65.6, 69.2, 69.6, 70.3, 70.4, 70.5, 70.6, 113.3, 125.9, 126.4, 127.8, 128.0, 129.4, 129.6, 131.8, 135.4, 138.1, 141.2, 142.3, 143.7, 156.6; HRMS [ESI] $(C_{41}H_{59}NO_8S]^+$ calcd, 725.3961; found, 725.4011.

Gold Nanoparticle Synthesis and TAM−PEG−SH Conjugation. Gold nanoparticles (25 nm dia) were synthesized by Turkevich reduction of chloroauric acid (*41*). Briefly, 20 mL of 3.5 mg/mL aqueous sodium citrate was added to 200 mL of 1.0 mM aqueous $HAuCl_4$ under reflux, with stirring. The solution was refluxed for 15 min, then removed from the heat and stirred for an additional 30 min. Excess sodium citrate was removed from the crude AuNP solution by centrifugation (13 000 × *g*).

TAM−PEG−SH (5 mg) was solubilized in 100 μL of ethanol and diluted to 0.5 mM in deionized water. PEG−SH (0.5 mM, 5 kDa, Lysan Bio) was solubilized in deioninized water, and PEG−SH or a 1:1 ratio TAM−PEG−SH and PEG−SH were added at a (1.4×10^4)-fold molar excess to a concentrated solution of citrate-capped AuNPs followed by overnight sonication. Particle concentration was estimated using the molar extinction coefficient for 23 nm citrate-capped gold nanospheres determined by Orendorff and Murphy (*42*) (1.3×10^9 M^{-1} cm^{-1}). TAM−PEG−SH−AuNP conjugates were dispersed in DMEM growth media without L-glutamine and phenol red supplemented with 10% v/v heat-inactivated fetal bovine serum, penicillin (100 U/mL), streptomycin (100 μg/mL), 4.5 g/L glucose, and 4.5 g/L sodium pyruvate to final *ligand* concentrations of 0.1, 0.5, 1, 2, 5, 10, and 20 μM and used immediately.

Gold Nanoparticle and Bioconjugate Characterization. Gold nanoparticles were analyzed by diffraction-contrast transmission electron microscopy (TEM, JEOL 100CX II) and UV−vis absorption spectroscopy (Ocean Optics, HR4000CG-UV-NIR). Absorption of TAM−PEG−SH at 280 nm was used to quantify the number of bound TAM−PEG−SH ligands per nanoparticle. An aqueous solution of gold nanospheres was incubated with a (1.4×10^4)-fold molar excess of both TAM−PEG−SH and PEG−SH overnight with sonication. Nanoparticle conjugates were removed from solution by centrifugation (45 min, 13 000 × *g*), and the observed change in UV absorption (280 nm) before and after nanoparticle conjugation was used to approximate the number of bound ligands. No contribution to absorption by PEG−SH was observed at these wavelengths, and it was assumed to occupy the majority of the remaining surface sites.

Zeta potential of the gold nanoparticles and conjugates was measured using a NanoZS Zetasizer particle analyzer (Malvern) equipped with a 633 nm laser.

Cell Culture and Nanoparticle Incubation. ERα(−) MDA-MB-231 and ERα(+) MCF-7 breast cancer cells (human adenocarcinoma, ATCC) or ERα(+) human squamous cell carcinoma (*43*−*45*) (HSC-3) cells were cultured to 10^5 cells/cm^2 in DMEM growth media without L-glutamine and phenol red supplemented with 10% v/v heat-inactivated fetal bovine serum, penicillin (100 U/mL), streptomycin (100 μg/mL), 4.5 g/L glucose, and 4.5 g/L sodium pyruvate at 37 °C in a 5% CO_2 humidified atmosphere. Growth media was removed from the cell cultures and replaced with identical media containing gold nanoparticle conjugates heated to 37 °C at time = 0 h.

Cell Viability Assay. Following incubation, growth media containing gold nanoparticle conjugates was removed, and cells were rinsed twice in sterile Dulbecco's phosphate-buffered saline (DPBS). Mitochondrial dehydrogenase activity was assessed by 3-(4,5-dimethylthiazol-2-yl)-2,5-diphenyltetrazolium bromide (MTT) or 2,3-bis-(2-methoxy-4-nitro-5-sulfophenyl)-2*H*-tetrazolium-5-carboxanilide (XTT) spectrophotometric assay (Sigma TOX1, TOX2) following the manufacturer's instructions. The assay was performed using a SpectraMax Plus 384 microplate reader and statistical analysis was performed by *t* test.

Selected-Area Absorption Microspectrometry and Dark-Field Scattering Microscopy. Collagen-coated growth substrates were prepared by immersion of 18 mm diameter glass coverslips in ethanol, followed by 30 min UV sterilization. Coverslips were immersed in a 0.22 μm filtered 0.04 mg/mL collagen (Roche) solution, prepared by solubilization in 5 mL of 1% v/v aqueous acetic acid and dilution in 250 mL of sterile DPBS, for 6 h at 37 °C in a 5% CO_2 humidified atmosphere. The coated substrates were rinsed in sterile DPBS and placed in 12-well plates immediately prior to cell passage. Following incubation with gold nanoparticle conjugates, substrates were twice rinsed in sterile DPBS buffer, and cells were fixed in cold 4% wt/wt paraformaldehyde in DPBS buffer for 15 min.

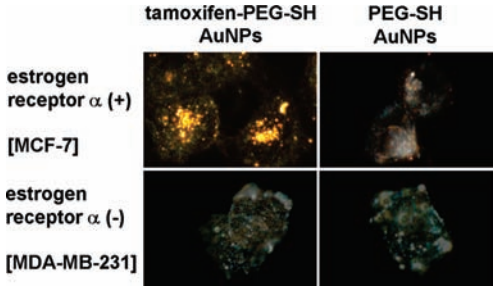

Figure 1. Dark-field scattering microscopy showing ligand- and receptor-dependent intracellular targeting of breast cancer cells by gold nanoparticle conjugates. Representative dark-field scattering images of ERα(+) [MCF-7, top] and ERα(−) [MDA-MB-231, bottom] human adenocarcinoma cells incubated for 24 h with 1 μM TAM−PEG−SH−AuNP (left) and PEG−SH−AuNP (right) conjugates (ca. 1.2 × 10^4 TAM−PEG−SH per AuNP).

Coverslips were coated in glycerol, then mounted and sealed onto glass slides.

Dark-field microscopy was performed using an inverted objective Olympus IX70 microscope fitted with a dark-field condenser (U-DCW), 100×/1.35 oil iris objective (UPLANAPO), tungsten lamp, and Nikon D200 digital SLR camera. Optical extinction spectra were obtained in a transmission configuration using a SEE110 absorption microspectrometer fitted with a pinhole aperture, fiber optic-coupled CCD array detector, 50× objective, and tungsten lamp. Periodic oscillations observed in some spectra are the result of interference between adjacent surfaces of the glass slides.

RESULTS AND DISCUSSION

The crude AuNP colloid (ca. 3 nM) was found by TEM to be predominantly comprised of 25 nm gold spheres exhibiting an extinction maximum at 530 nm (Figure S9, Supporting Information). Based on the change in UV absorption (280 nm) of TAM solutions following nanoparticle conjugation and removal, we estimate 12 000 TAM−PEG−SH ligands per particle, 41% of the maximum theoretical surface coverage for a 25 nm diameter Au(111) surface. A change in zeta potential from −38.4 to −5.79 mV was also observed following TAM−PEG−SH functionalization. To preserve aqueous stability, TAM−PEG−SH−AuNPs were not centrifuged prior to in vitro experiments, leaving 13% of free drug in solution. For comparison with the free drug, concentrations for the nanoparticle conjugate are reported as total effective ligand concentration (i.e., TAM−PEG−SH) throughout.

Dark-field scattering microscopy was performed to assess intracellular nanoparticle uptake. Figure 1 illustrates representative images of ERα(+) [MCF-7, top] and ERα(−) [MDA-MB-231, bottom] breast cancer cells incubated for 24 h with 1 μM TAM−PEG−SH−AuNPs and PEG−SH−AuNPs. ERα(+) breast cancer cells displayed a high degree of intracellular and perinuclear localization of TAM−PEG−SH−AuNPs, while ER(−) breast cancer cells showed no such labeling. These findings are consistent with both reported expression levels and cellular localization (*46*) of ERα in MCF-7 (*47*−*49*) and MDA-MB-231 (*48*, *50*) cell lines. As anticipated (*38*), AuNPs labeled only with PEG−SH exhibited no apparent cellular labeling or uptake for either ERα(+) or ERα(−) breast cancer cells. Uptake of TAM−PEG−SH−AuNPs by ERα(+) breast cells was observed to be time-dependent, with marginal cell surface labeling at 2−6 h and a high degree of perinuclear and cytoplasmic localization at 24 h (Figure S10, Supporting Information). To further demonstrate ER expression-dependent targeting, ERα(+) human squamous [HSC-3] oral cancer cells were incubated for 24 h in the presence of 1 μM TAM−PEG−SH−AuNPs and PEG−SH−AuNPs. Dark-field scattering images from HSC-3 cells show selective uptake of the TAM−PEG−SH−AuNPs in a manner similar to that obtained from MCF-7 breast cancer cells (Figure S11, Supporting Information). Selected-area optical extinction spectra obtained from the ERα(+) and ERα(−) breast cells exhibited AuNP surface plasmon extinction exclusively from perinuclear regions of ERα(+) cells incubated with TAM−PEG−SH−AuNPs (s/n ≈ 10) (Figure S12, Supporting Information). Extinction from PEG−SH−AuNPs was not observed from either cell line.

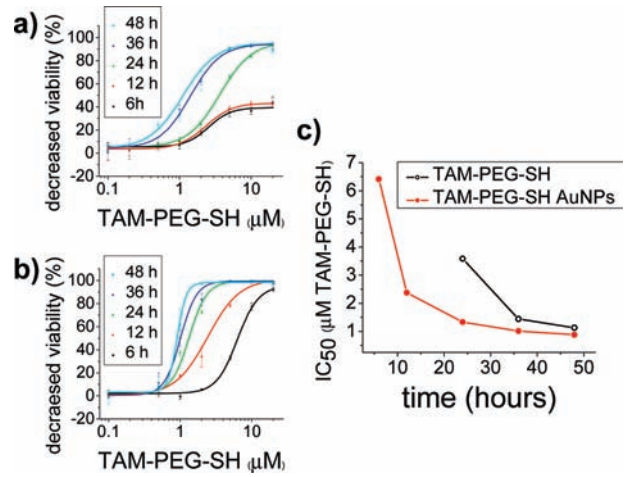

Figure 2. Time-dependent dose−response curves for cell viability of estrogen receptor alpha positive [MCF-7] breast cancer cells incubated with equivalent concentrations of TAM−PEG−SH as a free drug (a) and as a gold nanoparticle conjugate (b). Time-dependent IC_{50} (50% inhibitory concentration) values (c) show 1.3−2.7-times enhanced potency from the nanoparticle conjugate versus the free drug. Error bars represent standard deviation: 3.6, 1.4, 1.1 μM TAM−PEG−SH IC_{50} (24, 36, 48 h, respectively) versus 6.4, 2.4, 1.3, 1.0, 0.88 μM TAM−PEG−SH−AuNP IC_{50} (6, 12, 24, 36, 48 h, respectively).

Figures 2a,b illustrates time-dependent dose−response curves for cell viability of ERα(+) MCF-7 breast cancer cells incubated with equivalent concentrations of TAM−PEG−SH as the free drug and the nanoparticle conjugate, respectively. A comparison of the time-dependent IC_{50} (50% inhibitory concentration) values obtained for the free drug and its AuNP conjugate indicate 1.3−2.7-fold enhanced potency (Figure 2c) for TAM−PEG−SH−AuNPs. While IC_{50} values for TAM−PEG−SH alone are comparable to or better than those previously reported for MCF-7 breast cancer cells treated with both tamoxifen (*43*) and its active metabolite (*51*), a much more dramatic improvement is observed upon nanoparticle ligation, in contrast to the free drug, with significant growth inhibition observed for TAM−PEG−SH−AuNPs at both 6 and 12 h incubation (6.4 and 2.4 μM IC_{50}, respectively). In accordance with previous studies (*19*), no cytotoxic effects were observed in MCF-7 cells treated with PEG−SH−AuNPs at the highest concentrations and incubation times used in the present study ($P > 0.75$). Moreover, cytotoxic effects were not observed in ERα(−) MDA-MB-231 breast cancer cells incubated with TAM−PEG−SH alone, PEG−SH−AuNPs, or TAM−PEG−SH−AuNPs at the highest concentrations and incubation times used in the present study ($P > 0.28$, 0.33, and 0.11, respectively). Although differences in sensitivity to and rates of particle or drug uptake and metabolism for ERα(+) and ERα(−) cell lines may contribute to variation in apparent cytotoxicity, the observed ligand dependency correlates well with levels of cellular ER expression, particularly under the conditions of extended incubation time and excess concentration used. In addition, cell viability following incubation with TAM−PEG−SH−AuNPs in the absence of free drug was found to be statistically indistinguishable in difference from that

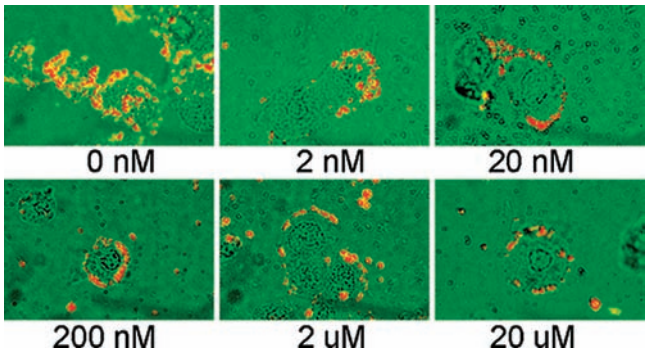

Figure 3. Representative dark-field scattering (red) and bright-field transmission (green) image overlays of TAM−PEG−SH−AuNP competitive binding following 24 h incubation with 17β-estradiol. ERα(+) breast cancer cells [MCF-7] were incubated overnight with increasing concentrations of estrogen, followed by 24 h incubation with 10 μM tamoxifen−gold nanoparticle conjugates.

observed in its presence. Here, AuNPs functionalized with TAM−PEG−SH equivalent to that present at the 24 h IC_{50} of the conjugate in the presence of free drug subsequently exhibited 57% ± 14% cell viability ($P > 0.6$). The lack of significant growth inhibition by the free drug at short incubation times, together with an observed decrease in the disparity between IC_{50} values of the free drug and the AuNP conjugate over time, and the apparent ligand-dependent response indicate increased rates of TAM−PEG−SH transport by the AuNP conjugate.

Although our results with the HSC-3 cell line, an ERα(+) oral cancer cell line, further attested to the role of ERα in nanoparticle uptake, it is however conceivable that particle lipophilicity could also contribute to differences in cellular uptake and cytotoxicity. In light of this possibility, blocking experiments were performed using ERα's endogenous ligand 17β-estradiol (estrogen) to further confirm receptor-dependent targeting and therapeutic response. ERα(+) MCF-7 breast cells were incubated overnight with increasing concentrations of estrogen, followed by 24 h incubation with 10 μM TAM−PEG−SH−AuNPs. Image overlays from bright-field transmission and dark-field scattering microscopy of these cells (Figure 3) indicate near complete suppression of TAM−PEG−SH−AuNP intracellular localization at estrogen concentrations as low as 20 nM. Decreased cell surface labeling was also observed with increasing estrogen concentration. Such competitive effects are in agreement with previous reports indicating 1−2 orders of magnitude greater ERα binding affinity for 17β-estradiol versus TAM (*52*). Cell viability experiments with ERα(+) breast cells incubated for 24 h with 10 μM TAM−PEG−SH−AuNPs and previously blocked overnight with equimolar concentrations of estrogen were also performed (Figure 4). As in previous studies with the free drug (*8*), the cytotoxic activity of TAM-labeled AuNPs was near completely suppressed following pre-exposure of the cells to estrogen ($P > 0.87$), while they retained optimal potency in the absence of estrogen ($P < 0.0001$). These findings correlate ERα binding with both TAM−PEG−SH−AuNP intracellular localization and subsequent cell death.

The ERα expression-dependent uptake observed here also suggests that the cell membrane-associated receptor may facilitate intracellular nanoparticle transport. Indeed, plasma membrane localized ERα is well documented, as is its recognition of both antibody epitopes for the nuclear receptor and 17β-estradiol in mammalian cells (*31, 33*). The functions of membrane ERα beyond classical gene transcription and more recently membrane-initiated signaling are however less understood (*53*). Comprehensive studies by Levin and co-workers indicate intracellular transport and caveolar localization of ERα in the plasma membrane of MCF-7 cells in vitro (via caveolin-1

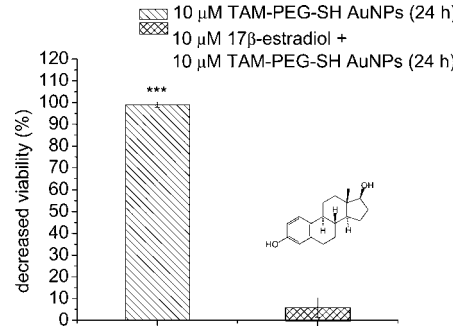

Figure 4. Suppression of TAM−PEG−SH−AuNP activity by estrogen competition in ERα(+) breast cancer cells. Growth inhibition of MCF-7 cells incubated for 24 h with 10 μM TAM−PEG−SH−AuNPs when previously untreated (left) and treated overnight with 10 μM 17β-estradiol (right).

and -2 association) (*49*). In order to determine whether plasma membrane localized ERα could contribute to receptor-mediated endocytosis of TAM−PEG−SH−AuNP conjugates, cytotoxicity was examined under conditions of negligible endocytotic activity. MCF-7 cell viability was shown to increase by 87% ± 2% following incubation with 20 μM TAM−PEG−SH−AuNPs for 6 h at 4 °C versus 37 °C ($P < 0.04$), indicating that endocytosis, in addition to ERα binding and intracellular particle delivery, is required for therapeutic response from tamoxifen-labeled AuNP conjugates.

CONCLUSIONS

In summary, tamoxifen−gold nanoparticle conjugates were shown to selectively target estrogen receptor alpha in human breast cancer cells with up to 2.7-times enhanced potency in vitro. Optical microscopy and spectroscopy indicate a high degree of perinuclear and cytoplasmic localization of the targeted particles, while neither localization nor cytotoxic effects were observed from the untargeted nanoparticles. Time-dependent dose−response studies show that augmented potency results from increased rates of drug transport by nanoparticle uptake versus passive diffusion of the free drug. Receptor-selective and estrogen-competitive cytotoxicity and uptake of the nanoparticle conjugates indicates no additive effects associated with the gold particles themselves and suggests that plasma membrane-localized ERα may facilitate selective endocytotic transport of these and other therapeutic nanoparticle conjugates. Increased potency and selective intracellular delivery of tamoxifen−gold nanoparticle conjugates provides opportunities for further enhancement by cofunctionalization or adjunctive laser photothermal therapy.

ACKNOWLEDGMENT

The authors wish to acknowledge generous support from Merck, the National Cancer Institute (CCNE Award U54CA119338), the U.S. Deptartment of Energy (Grant No. DE-FG02-97 ER14799), the Center for Nanostructured Materials Technology under the 21st Century Frontier R&D Programs of the Korean Ministry of Education, Science, and Technology (Grant No. 08K1501-01910), the Georgia Institute of Technology, and the Blanchard Foundation. Cell subculture by Omar Dellanoy-Bruno, electron microscopy by Steven W. Hayden, and the facilities of the Center for Nanostructure Fabrication and Characterization (CNCF) are also acknowledged.

Supporting Information Available: ^{13}C and ^{1}H NMR spectra, TEM and UV−vis analysis, time-dependent uptake images, oral cancer cell targeting images, selected-area microspectrometry, imaging and spectroscopy of conjugate stabil-

ity, and estrogen competition images. This material is available free of charge via the Internet at http://pubs.acs.org.

LITERATURE CITED

(1) Obrero, M., Yu, D. V., and Shapiro, D. J. (2002) Estrogen receptor-dependent and estrogen receptor-independent pathways for tamoxifen and 4-hydroxytamoxifen-induced programmed cell death. *J. Biol. Chem. 277*, 45695–45703.

(2) Bates, S. E., Davidson, N. E., Valverius, E. M., Freter, C. E., Dickson, R. B., Tam, J. P., Kudlow, J. E., Lippman, M. E., and Salomon, D. S. (1988) Expression of transforming growth factor-alpha and its messenger ribonucleic-acid in human-breast cancer - its regulation by estrogen and its possible functional-significance. *Mol. Endocrinol. 2*, 543–555.

(3) Dubik, D., Dembinski, T. C., and Shiu, R. P. C. (1987) Stimulation of c-myc oncogene expression associated with estrogen-induced proliferation of human-breast cancer-cells. *Cancer Res. 47*, 6517–6521.

(4) Krishnan, V., Wang, X. H., and Safe, S. (1994) Estrogen receptor-SP1 complexes mediate estrogen-induced cathepsin-D gene-expression in MCF-7 human breast-cancer cells. *J. Biol. Chem. 269*, 15912–15917.

(5) Cleator, S., Heller, W., and Coombes, R. C. (2007) Triple-negative breast cancer: Therapeutic options. *Lancet Oncol. 8*, 235–244.

(6) Jordan, V. C. (2007) Chemoprevention of breast cancer with selective oestrogen-receptor modulators. *Nat. Rev. Cancer 7*, 46–53.

(7) Shiau, A. K., Barstad, D., Loria, P. M., Cheng, L., Kushner, P. J., Agard, D. A., and Greene, G. L. (1998) The structural basis of estrogen receptor/coactivator recognition and the antagonism of this interaction by tamoxifen. *Cell 95*, 927–937.

(8) Coezy, E., Borgna, J.-L., and Rochefort, H. (1982) Tamoxifen and metabolites in MCF7 cells: Correlation between binding to estrogen receptor and inhibition of cell growth. *Cancer Res. 42*, 317–323.

(9) Jordan, V. C. (2003) Tamoxifen: A most unlikely pioneering medicine. *Nat. Rev. Drug Discovery 2*, 205–213.

(10) Weissleder, R., Kelly, K., Sun, E. Y., Shtatland, T., and Josephson, L. (2005) Cell-specific targeting of nanoparticles by multivalent attachment of small molecules. *Nat. Biotechnol. 23*, 1418–1423.

(11) Montet, X., Funovics, M., Montet-Abou, K., Weissleder, R., and Josephson, L. (2006) Multivalent effects of RGD peptides obtained by nanoparticle display. *J. Med. Chem. 49*, 6087–6093.

(12) Gestwicki, J. E., Cairo, C. W., Strong, L. E., Oetjen, K. A., and Kiessling, L. L. (2002) Influencing receptor-ligand binding mechanisms with multivalent ligand architecture. *J. Am. Chem. Soc. 124*, 14922–14933.

(13) Goodman, C. M., and Rotello, V. M. (2004) Biomacromolecule surface recognition using nanoparticles. *Mini-Rev. Org. Chem. 1*, 103–114.

(14) Gibson, J. D., Khanal, B. P., and Zubarev, E. R. (2007) Paclitaxel-functionalized gold nanoparticles. *J. Am. Chem. Soc. 129*, 11653–11661.

(15) Cho, K., Wang, X., Nie, S., Chen, Z., and Shin, D. M. (2008) Therapeutic nanoparticles for drug delivery in cancer. *Clin. Cancer Res. 14*, 1310–1316.

(16) Chawla, J. S., and Amiji, M. M. (2002) Biodegradable poly([var epsilon]-caprolactone) nanoparticles for tumor-targeted delivery of tamoxifen. *Int. J. Pharm. 249*, 127–138.

(17) Maeda, H. (2001) The enhanced permeability and retention (EPR) effect in tumor vasculature: The key role of tumor-selective macromolecular drug targeting. *Adv. Enzyme Regul. 41*, 189–207.

(18) von Maltzahn, G., Park, J.-H., Agrawal, A., Bandaru, N. K., Das, S. K., Sailor, M. J., and Bhatia, S. N. (2009) Computationally guided photothermal tumor therapy using long-circulating gold nanorod antennas. *Cancer Res. 69*, 3892–3900.

(19) Connor, E. E., Mwamuka, J., Gole, A., Murphy, C. J., and Wyatt, M. D. (2005) Gold nanoparticles are taken up by human cells but do not cause acute cytotoxicity. *Small 1*, 325–327.

(20) Khan, J. A., Pillai, B., Das, T. K., Singh, Y., and Maiti, S. (2007) Molecular effects of uptake of gold nanoparticles in HeLa cells. *ChemBioChem 8*, 1237–1240.

(21) Zhang, F., Skoda, M. W. A., Jacobs, R. M. J., Zorn, S., Martin, R. A., Martin, C. M., Clark, G. F., Goerigk, G., and Schreiber, F. (2007) Gold nanoparticles decorated with oligo(ethylene glycol) thiols: Protein resistance and colloidal stability. *J. Phys. Chem. A 111*, 12229–12237.

(22) Dickerson, E. B., Dreaden, E. C., Huang, X., El-Sayed, I. H., Chu, H., Pushpanketh, S., McDonald, J. F., and El-Sayed, M. A. (2008) Gold nanorod assisted near-infrared plasmonic photothermal therapy (PPTT) of squamous cell carcinoma in mice. *Cancer Lett. 269*, 57–66.

(23) O'Neal, D. P., Hirsch, L. R., Halas, N. J., Payne, J. D., and West, J. L. (2004) Photothermal tumor ablation in mice using near infrared absorbing nanoshells. *Cancer Lett. 209*, 171–176.

(24) Huang, X., El-Sayed, I. H., and El-Sayed, M. A. (2006) Cancer cell imaging and photothermal therapy in the near-infrared region by using gold nanorods. *J. Am. Chem. Soc. 128*, 2115–2120.

(25) Huff, T. B., Tong, L., Zhao, Y., Hansen, M. N., Cheng, J. X., and Wei, A. (2007) Hyperthermic effects of gold nanorods on tumor cells. *Nanomedicine 2*, 125–132.

(26) Hirsch, L. R., Stafford, R. J., Bankson, J. A., Sershen, S. R., Rivera, B., Price, R. E., Hazle, J. D., Halas, N. J., and West, J. L. (2003) Nanoshell-mediated near-infrared thermal therapy of tumors under magnetic resonance guidance. *Proc. Natl. Acad. Sci. U.S.A. 100*, 13549–13554.

(27) El-Sayed, I. H., X., H., and El-Sayed, M. A. (2006) Selective laser photo-thermal therapy of epithelial carcinoma using anti-EGFR antibody conjugated gold nanoparticles. *Cancer Lett. 239*, 129–135.

(28) Qian, X. M., Peng, X. H., Ansari, D. O., Yin-Goen, Q., Chen, G. Z., Shin, D. M., Yang, L., Young, A. N., Wang, M. D., and Nie, S. M. (2008) In vivo tumor targeting and spectroscopic detection with surface-enhanced Raman nanoparticle tags. *Nat. Biotechnol. 26*, 83–90.

(29) Dixit, V., Van den Bossche, J., Sherman, D. M., Thompson, D. H., and Andres, R. P. (2006) Synthesis and grafting of thioctic acid-PEG-folate conjugates onto Au nanoparticles for selective targeting of folate receptor-positive tumor cells. *Bioconjugate Chem. 17*, 603–609.

(30) Tong, L., Zhao, Y., Huff, T. B., Hansen, M. N., Wei, A., and Cheng, J. X. (2007) Gold nanorods mediate tumor cell death by compromising membrane integrity. *Adv. Mater. 19*, 3136–3141.

(31) Levin, E. R. (2005) Integration of the extranuclear and nuclear actions of estrogen. *Mol. Endocrinol. 19*, 1951–1959.

(32) Campbell, C. H., Bulayeva, N., Brown, D. B., Gametchu, B., and Watson, C. S. (2002) Regulation of the membrane estrogen receptor-alpha: Role of cell density, serum, cell passage number, and estradiol. *FASEB J. 16*, 1917–1927.

(33) Zivadinovic, D., Gametchu, B., and Watson, C. S. (2005) Membrane estrogen receptor-alpha levels in MCF-7 breast cancer cells predict cAMP and proliferation responses. *Breast Cancer Res. 7*, R101–R112.

(34) Niidome, T., Yamagata, M., Okamoto, Y., Akiyama, Y., Takahashi, H., Kawano, T., Katayama, Y., and Niidome, Y. (2006) PEG-modified gold nanorods with a stealth character for in vivo applications. *J. Controlled Release 114*, 343–347.

(35) Jang, S. S., Jang, Y. H., Kim, Y.-H., Goddard, W. A., Flood, A. H., Laursen, B. W., Tseng, H.-R., Stoddart, J. F., Jeppesen, J. O., Choi, J. W., Steuerman, D. W., DeIonno, E., and Heath, J. R. (2005) Structures and properties of self-assembled monolayers of bistable [2]rotaxanes on Au (111) surfaces from molecular dynamics simulations validated with experiment. *J. Am. Chem. Soc. 127*, 1563–1575.

(36) Lavrich, D. J., Wetterer, S. M., Bernasek, S. L., and Scoles, G. (1998) Physisorption and chemisorption of alkanethiols and alkyl sulfides on Au(111). *J. Phys. Chem. B 102*, 3456–3465.

(37) Gref, R., Domb, A., Quellec, P., Blunk, T., Muller, R. H., Verbavatz, J. M., and Langer, R. (1995) The controlled intravenous delivery of drugs using PEG-coated sterically stabilized nanospheres. *Adv. Drug Delivery Rev. 16*, 215–233.

(38) Nativo, P., Prior, I. A., and Brust, M. (2008) Uptake and intracellular fate of surface-modified gold nanoparticles. *ACS Nano 2*, 1639–1644.

(39) Olofson, R. A., Martz, J. T., Senet, J. P., Piteau, M., and Malfroot, T. (1984) A new reagent for the selective, high-yield N-dealkylation of tertiary-amines - improved syntheses of naltrexone and nalbuphine. *J. Org. Chem. 49*, 2081–2082.

(40) Bouzide, A., and Sauve, G. (2002) Silver(I) oxide mediated highly selective monotosylation of symmetrical diols. Application to the synthesis of polysubstituted cyclic ethers. *Org. Lett. 4*, 2329–2332.

(41) Turkevich, J., Stevenson, P. C., and Hillier, J. (1951) A study of the nucleation and growth processes in the synthesis of colloidal gold. *Discuss. Faraday Soc.* 55–75.

(42) Orendorff, C. J., and Murphy, C. J. (2006) Quantitation of metal content in the silver-assisted growth of gold nanorods. *J. Phys. Chem. B 110*, 3990–3994.

(43) Guthrie, N., Gapor, A., Chambers, A. F., and Carroll, K. K. (1997) Inhibition of proliferation of estrogen receptor-negative MDA-MB-435 and -positive MCF-7 human breast cancer cells by palm oil tocotrienols and tamoxifen, alone and in combination. *J. Nutr. 127*, 544S–548S.

(44) Jordan, V. C. (2007) New insights into the metabolism of tamoxifen and its role in the treatment and prevention of breast cancer. *Steroids 72*, 829–842.

(45) Nozoe, T., Oyama, T., Takenoyama, M., Hanagiri, T., Sugio, K., and Yasumoto, K. (2007) Significance of immunohistochemical expression of estrogen receptors alpha and beta in squamous cell carcinoma of the esophagus. *Clin. Cancer Res. 13*, 4046–4050.

(46) Htun, H., Holth, L. T., Walker, D., Davie, J. R., and Hager, G. L. (1999) Direct visualization of the human estrogen receptor alpha reveals a role for ligand in the nuclear distribution of the receptor. *Mol. Biol. Cell 10*, 471–486.

(47) Brooks, S. C., Locke, E. R., and Soule, H. D. (1973) Estrogen receptor in a human cell line (MCF-7) from breast carcinoma. *J. Biol. Chem. 248*, 6251–6253.

(48) Horwitz, K. B., Zava, D. T., Thilagar, A. K., Jensen, E. M., and McGuire, W. L. (1978) Steroid receptor analyses of nine human breast cancer cell lines. *Cancer Res. 38*, 2434–2437.

(49) Razandi, M., Oh, P., Pedram, A., Schnitzer, J., and Levin, E. R. (2002) ERs associate with and regulate the production of caveolin: Implications for signaling and cellular actions. *Mol. Endocrinol. 16*, 100–115.

(50) Chen, X. M., Danes, C., Lowe, M., Herliczek, T. W., and Keyomarsi, K. (2000) Activation of the estrogen-signaling pathway by p21(WAF1/CIP1) in estrogen receptor-negative breast cancer cells. *J. Natl. Cancer Inst. 92*, 1403–1413.

(51) Seeger, H., Diesing, D., Gückel, B., Wallwiener, D., Mueck, A. O., and Huober, J. (2003) Effect of tamoxifen and 2-methoxyestradiol alone and in combination on human breast cancer cell proliferation. *J. Steroid Biochem. Mol. Biol. 84*, 255–257.

(52) Rich, R. L., Hoth, L. R., Geoghegan, K. F., Brown, T. A., LeMotte, P. K., Simons, S. P., Hensley, P., and Myszka, D. G. (2002) Kinetic analysis of estrogen receptor/ligand interactions. *Proc. Natl. Acad. Sci. U.S.A. 99*, 8562–8567.

(53) Qing, L., Pallas, D. C., Surks, H. K., Baur, W. E., Mendelsohn, M. E., and Karas, R. H. (2004) Striatin assembles a membrane signaling complex necessary for rapid, nongenomic activation of endothelial NO synthase by estrogen receptor alpha. *Proc. Natl. Acad. Sci. U.S.A. 101*, 17126–17131.

BC9002212

Tamoxifen-PEG-Thiol Gold Nanoparticle Conjugates: Enhanced Potency and Selective Delivery for Breast Cancer Treatment

Erik C. Dreaden[†], Sandra C. Mwakwari[‡], Quaovi H. Sodji[‡], Adegboyega K. Oyelere*[,‡], and Mostafa A. El-Sayed*[,†]

Department of Chemistry and Biochemistry, Georgia Institute of Technology, 901 Atlantic Drive NW, Atlanta, GA 30332-0400.

Supporting Information

CONTENTS

S1: ^{1}H NMR of **1** ---------- pg. 2

S2: ^{1}H NMR of **2** ---------- pg. 2

S3: ^{1}H NMR of **3** ---------- pg. 3

S4: ^{13}C NMR of **3** ---------- pg. 3

S5: ^{1}H NMR of **4** ---------- pg. 4

S6: ^{1}H NMR of **5** ---------- pg. 4

S7: ^{1}H NMR of **6** ---------- pg. 5

S8: ^{13}C NMR of **6** ---------- pg. 5

S9: TEM and optical extinction of AuNPs used in tamoxifen-targeting experiments ---------- pg. 6

S10: Dark-field scattering images of time- and ERα expression- dependent intracellular delivery of TAM-PEG-SH AuNPs ---------- pg. 6

S11: Dark-field scattering images of ligand-dependent TAM-PEG-SH AuNP targeting selectivity with oral cancer cells ---------- pg. 7

S12: Optical imaging/spectroscopy of receptor- and ligand- dependent perinuclear localization of TAM-PEG-SH AuNPs ---------- pg. 7

S13: Dark-field scattering images of TAM-PEG-SH AuNP competitive binding with estrogen ---------- pg. 8

S14: Images of various TAM-PEG-SH AuNP conjugate solutions showing aqueous stability prior to and following centrifugation ---------- pg. 8

S15: Extinction spectra of various TAM-PEG-SH AuNP conjugate solutions showing aqueous stability prior to and following centrifugation ---------- pg. 9

* Authors to whom correspondence should be addressed: (Prof. Mostafa A. El-Sayed) Email: melsayed@gatech.edu. Tel: 404 894 0292. Fax: 404 894 6078. (Prof. Adegboyega K. Oyelere) Email: aoyelere@gatech.edu Tel: 404 894 4047 Fax: 404 894 7452.

† Laser Dynamics Laboratory

‡ Parker H. Petit Institute for Bioengineering & Biosciences

¶ Abbreviations: estrogen receptor (ER), 17β-estradiol (E2), tamoxifen (TAM), enhanced permeability and retention (EPR), polyethylene glycol (PEG), epidermal growth factor receptor (EGFR), thiol-polyethylene glycol (PEG-SH), gold nanoparticle (AuNP), thiol-polyethylene glocol tamoxifen (TAM-PEG-SH), Dulbecco's phosphate buffered saline (DPBS).

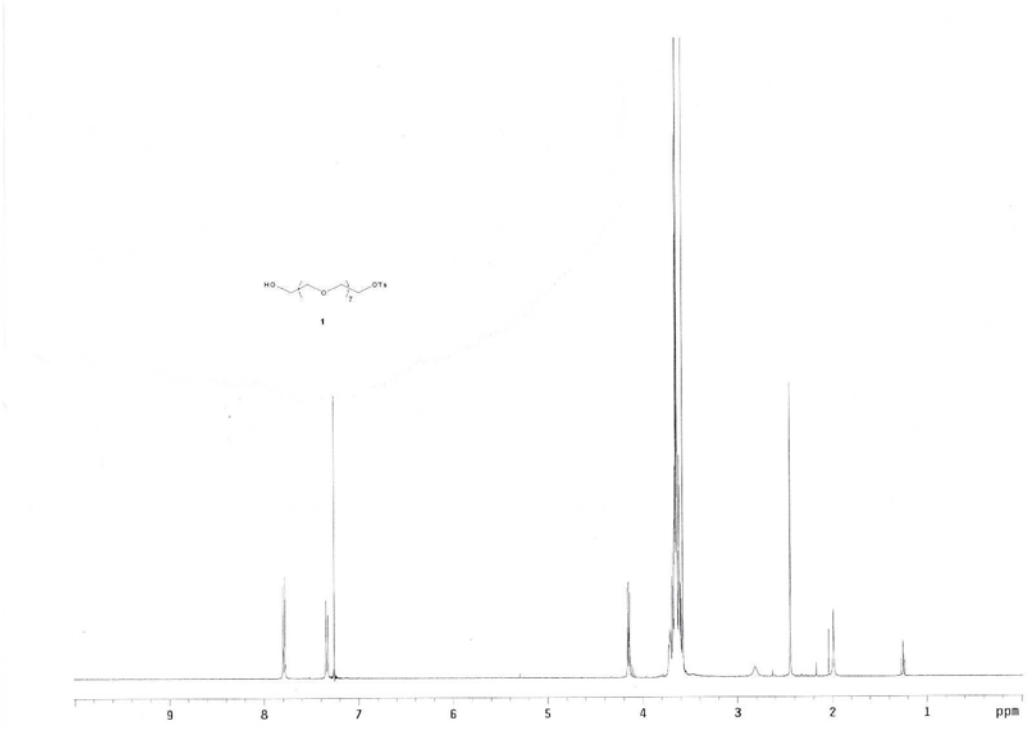

Figure S1. ^{1}H NMR of **1**.

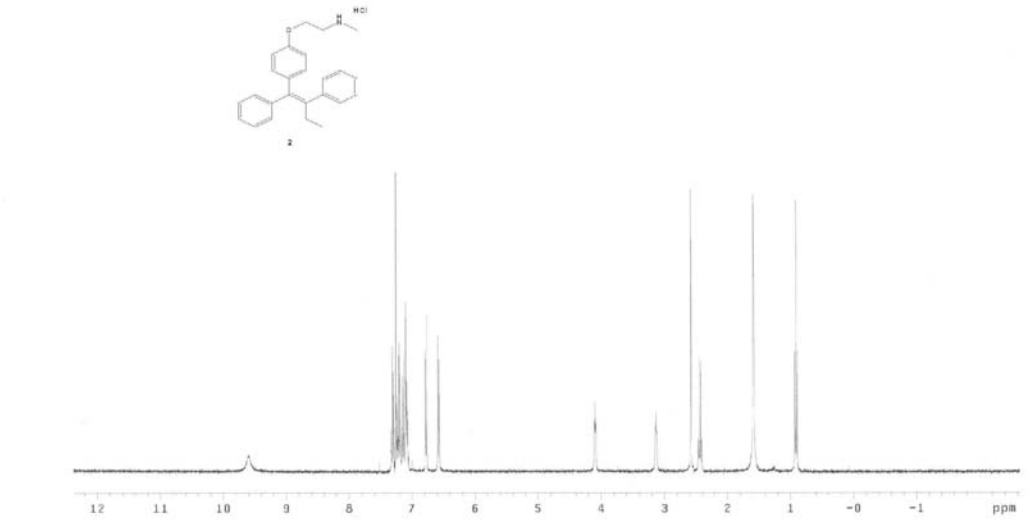

Figure S2. ^{1}H NMR of **2**.

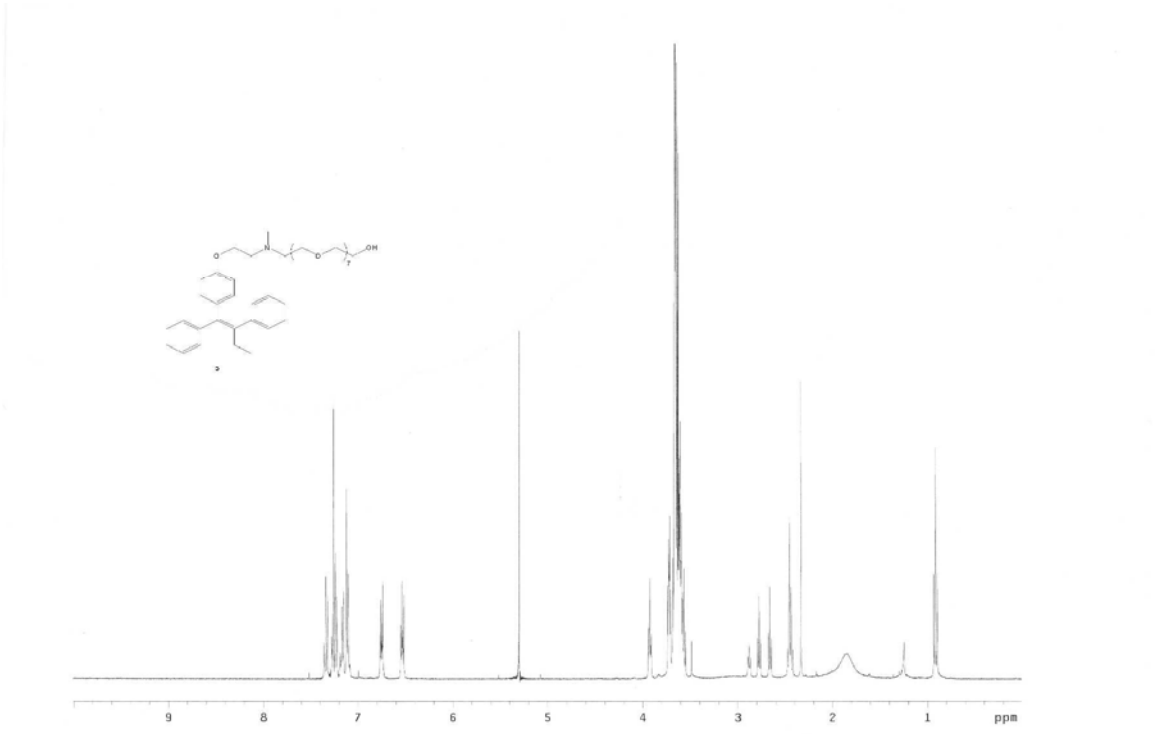

Figure S3. ^{1}H NMR of **3**.

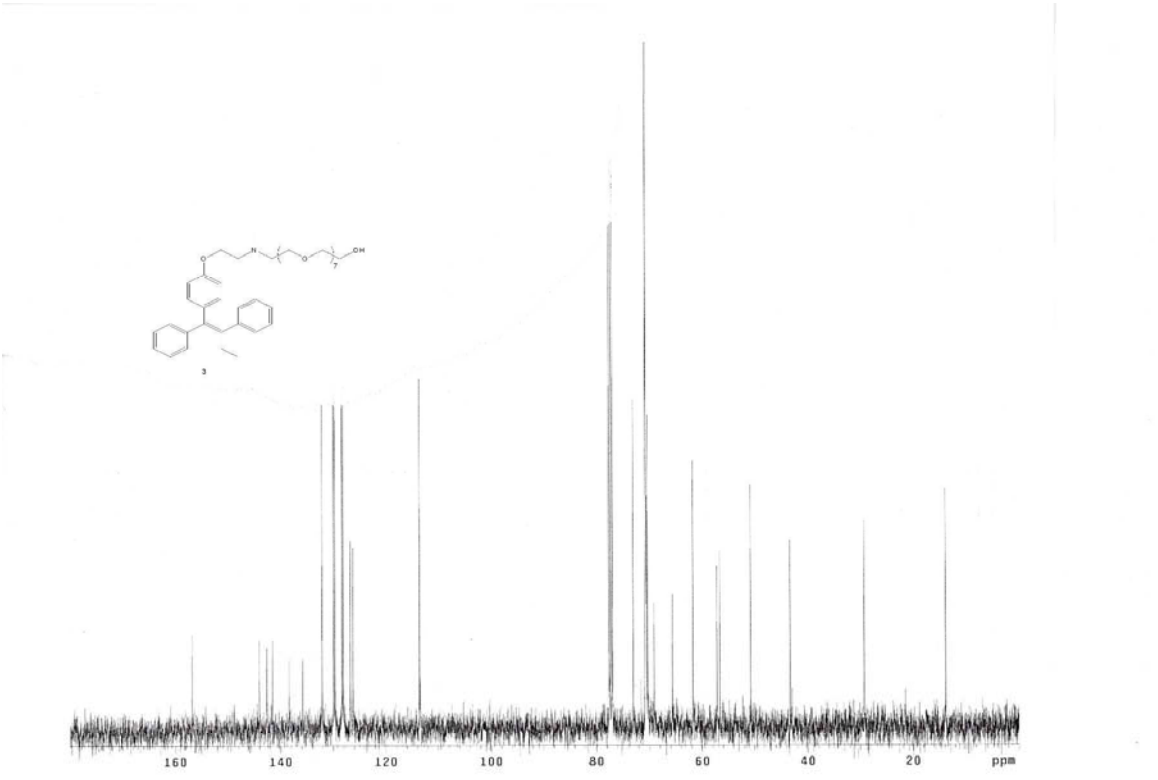

Figure S4. ^{13}C NMR of **3**.

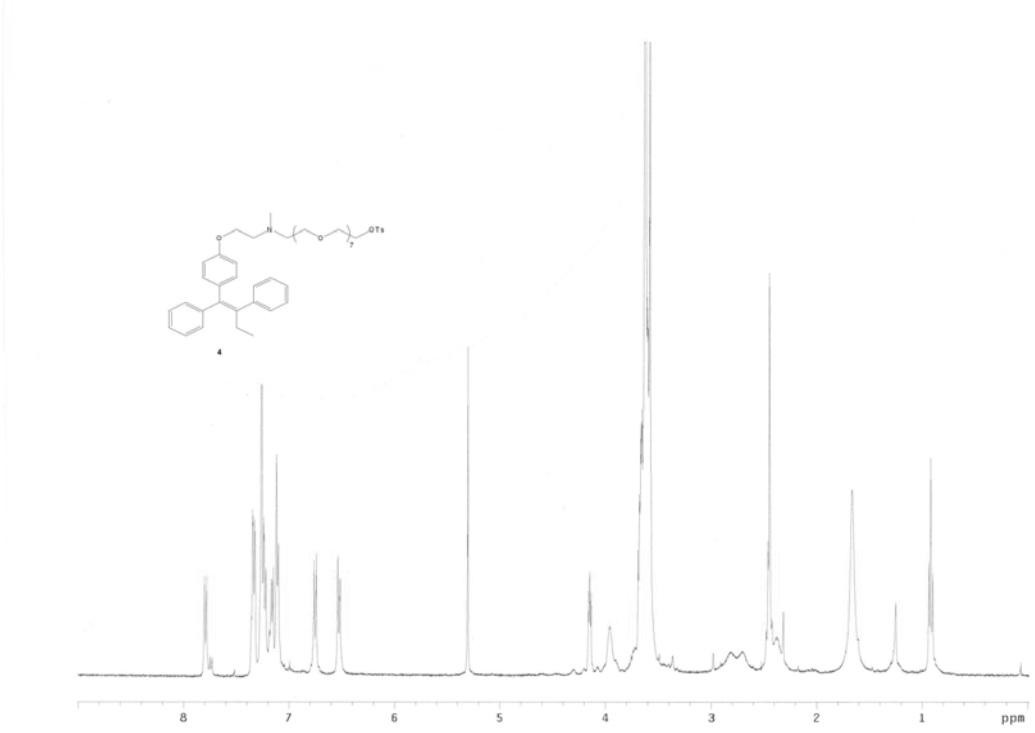

Figure S5. ^{1}H NMR of **4**.

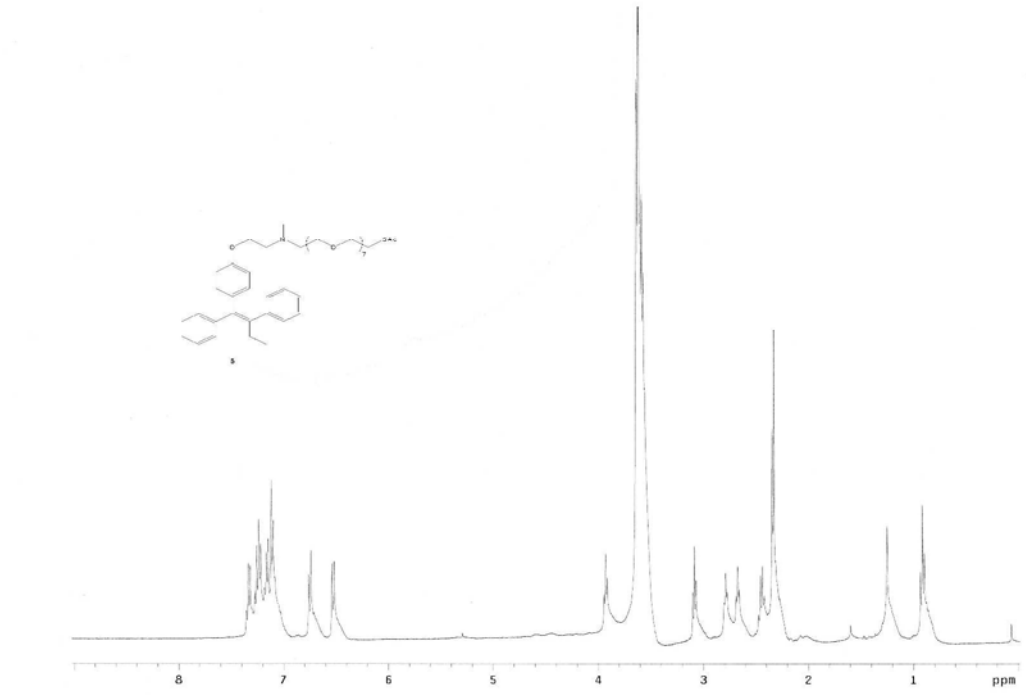

Figure S6. ^{1}H NMR of **5**.

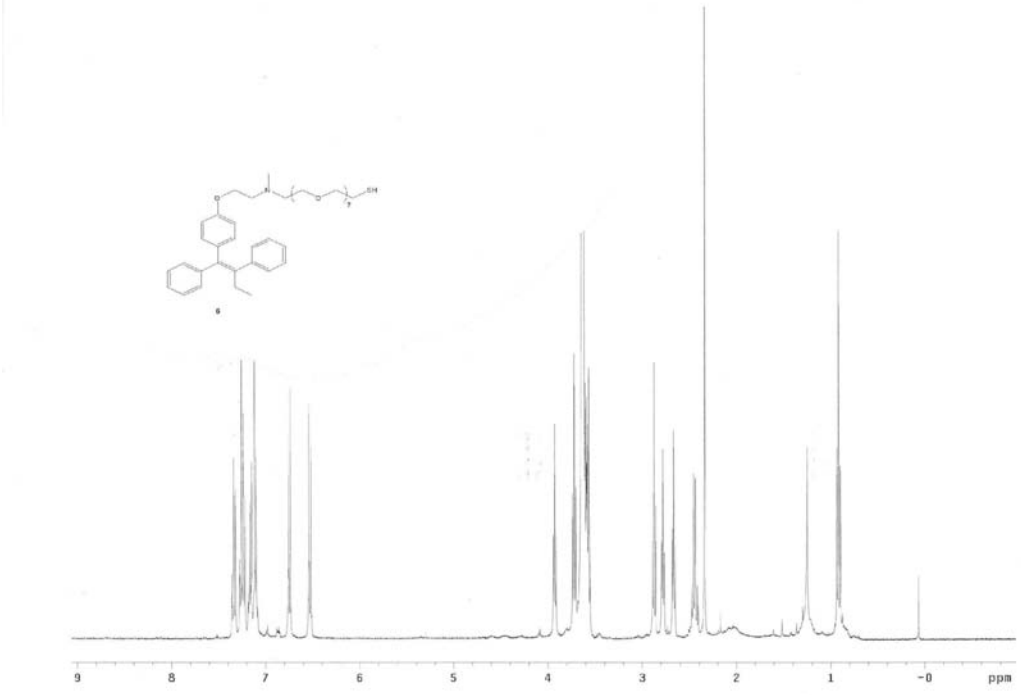

Figure S7. ^{1}H NMR of **6**.

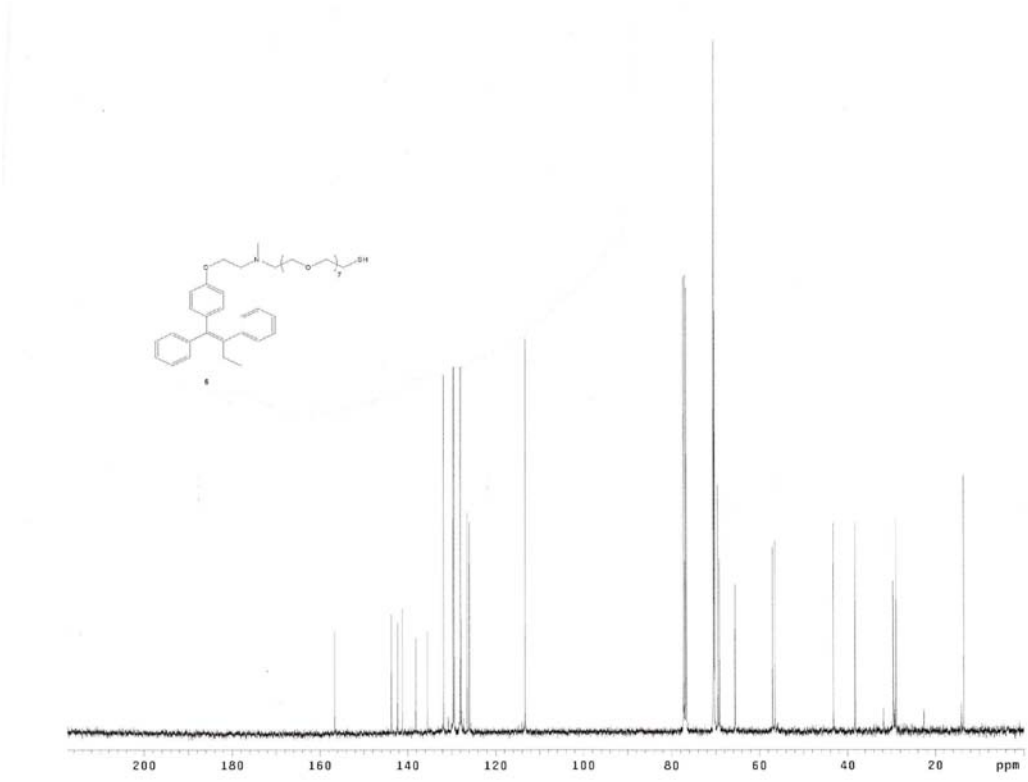

Figure S8. ^{13}C NMR of **6**.

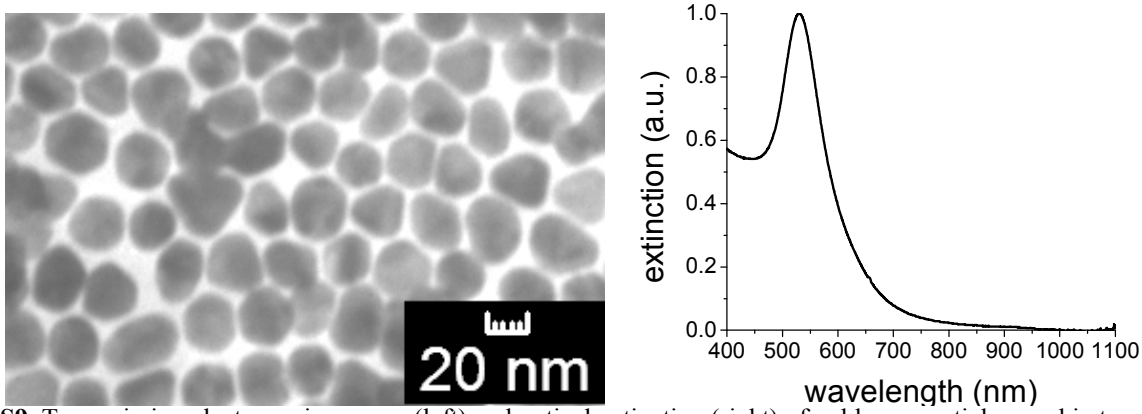

Figure S9. Transmission electron microscopy (left) and optical extinction (right) of gold nanoparticles used in tamoxifen-targeting experiments.

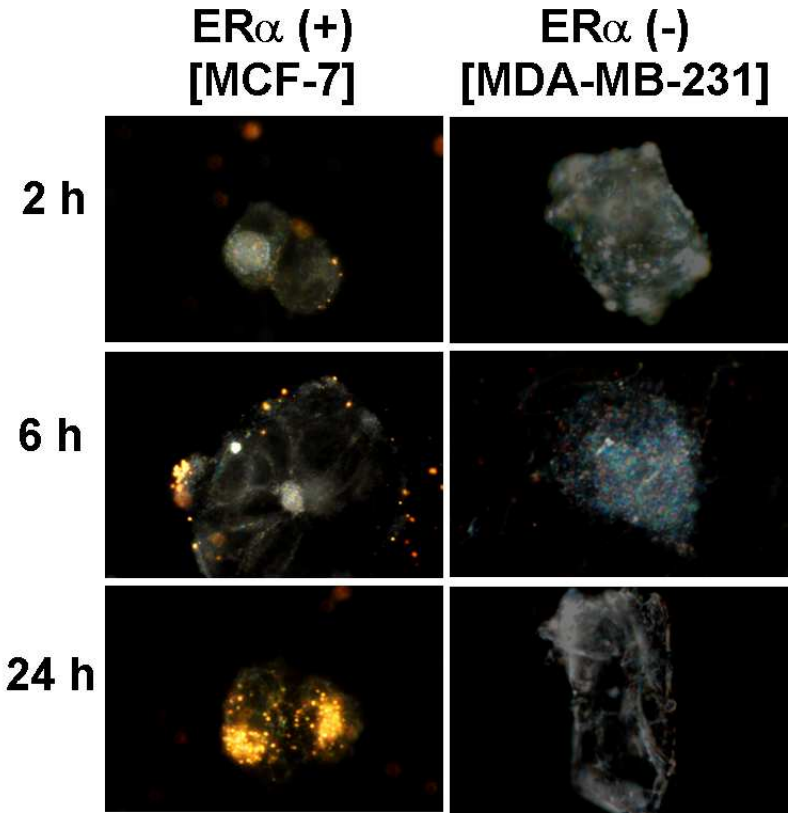

Figure S10. Dark-field scattering images of time- and ERα expression- dependent intracellular delivery of TAM-PEG-SH AuNPs (1 μM) to ERα(+) (MCF-7, left) and ERα(-) (MDA-MB-231, right) breast cancer cells.

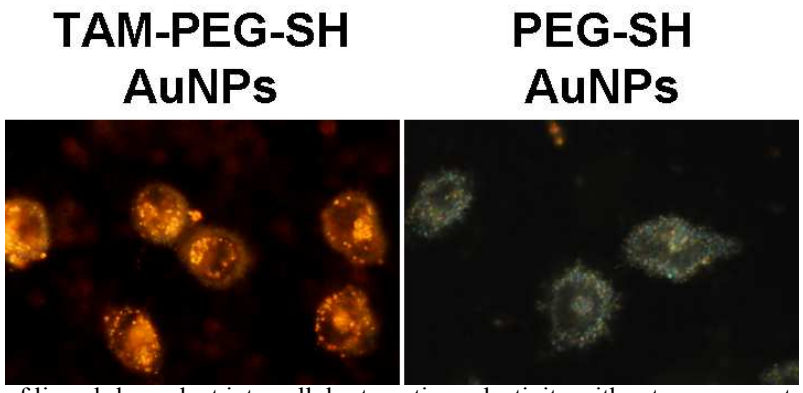

Figure S11. Comparison of ligand-dependent intracellular targeting selectivity with estrogen receptor positive oral cancer cells. Representative dark-field scattering images of human squamous cell carcinoma (HSC-3) cells incubated for 24 h with 1 μM TAM-PEG-SH AuNPs (left) and PEG-SH AuNPs (right).

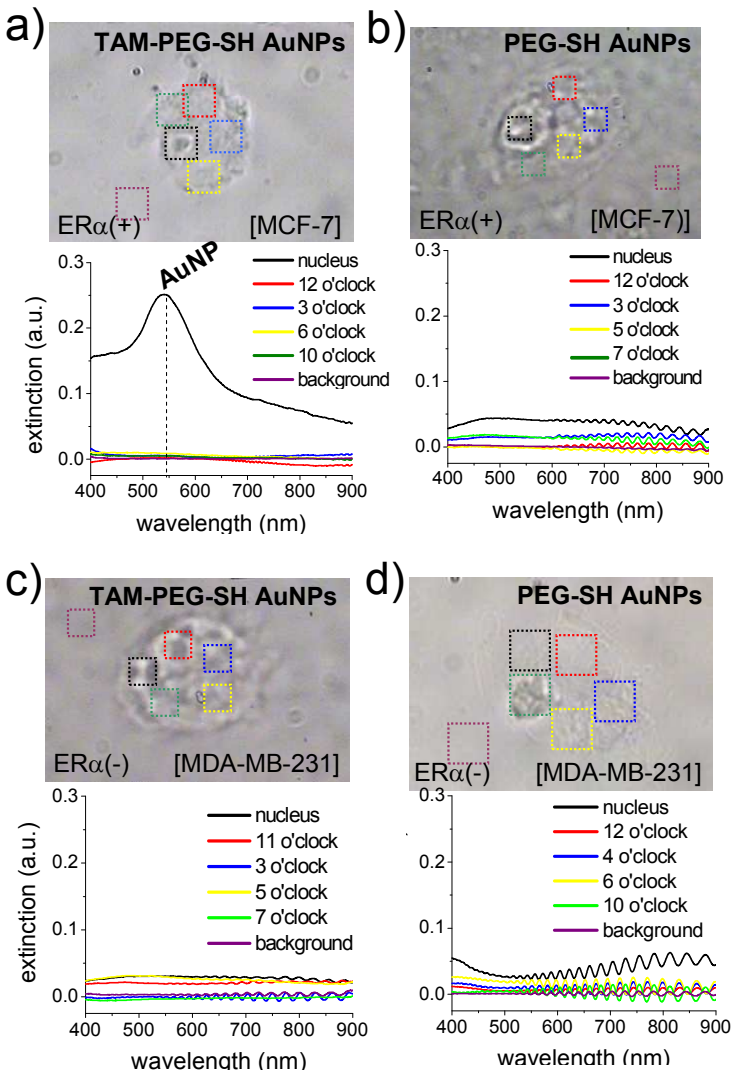

Figure S12. Optical imaging and spectroscopy showing receptor- and ligand- dependent perinuclear localization of tamoxifen-gold nanoparticle conjugates in breast cancer cells (s/n~10). Representative microscopic images and selected-area optical extinction spectra obtained from ERα(+) MCF-7 breast cancer cells incubated for 24 h with 1 μM TAM-PEG-SH AuNPs (a) and unfunctionalized (PEG-SH) AuNPs (b), as well as ERα(-) MDA-MB-231 breast cancer cells incubated for 24 h with 1 μM TAM-PEG-SH AuNPs (c) and unfunctionalized (PEG-SH) AuNPs (d).

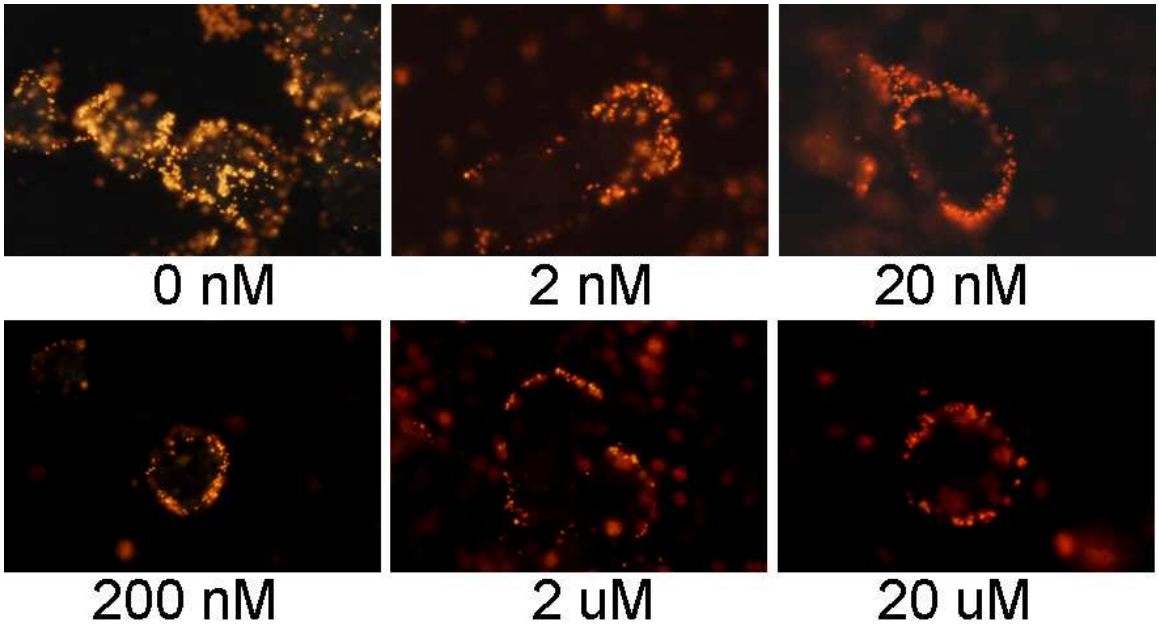

Figure S13. Representative dark-field scattering images of TAM-PEG-SH AuNP competitive binding following overnight incubation with estrogen. ERα(+) breast cancer cells [MCF-7] were incubated overnight with increasing concentrations of 17β-estradiol, followed by 24 h incubation with 10 μM TAM-PEG-SH AuNPs.

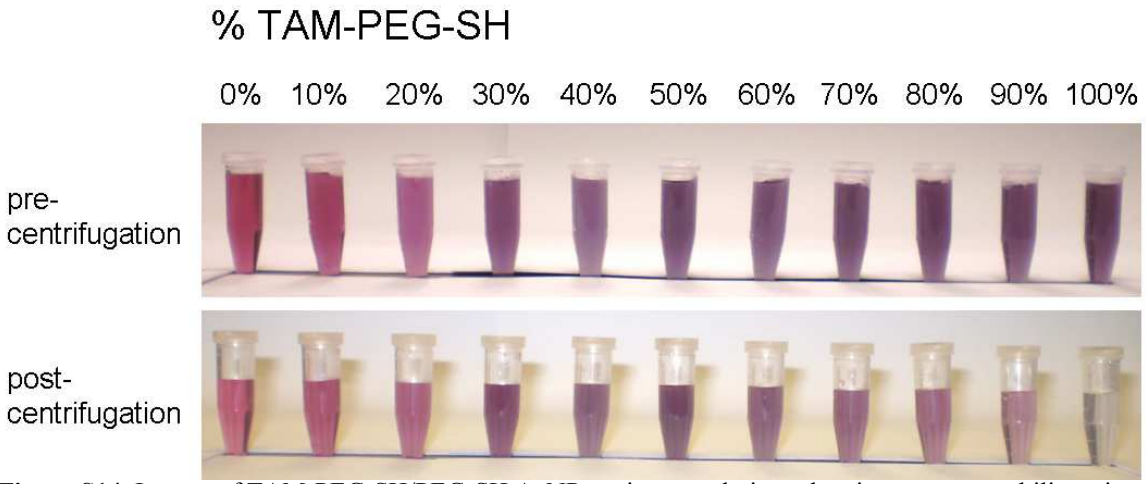

Figure S14. Images of TAM-PEG-SH/PEG-SH AuNP conjugate solutions showing aqueous stability prior to and following centrifugation. Note an increase in the characteristic blue color associated with particle aggregation and a decrease in concentration of stable particles following centrifugation as a function of increasing TAM-PEG-SH functionalization.

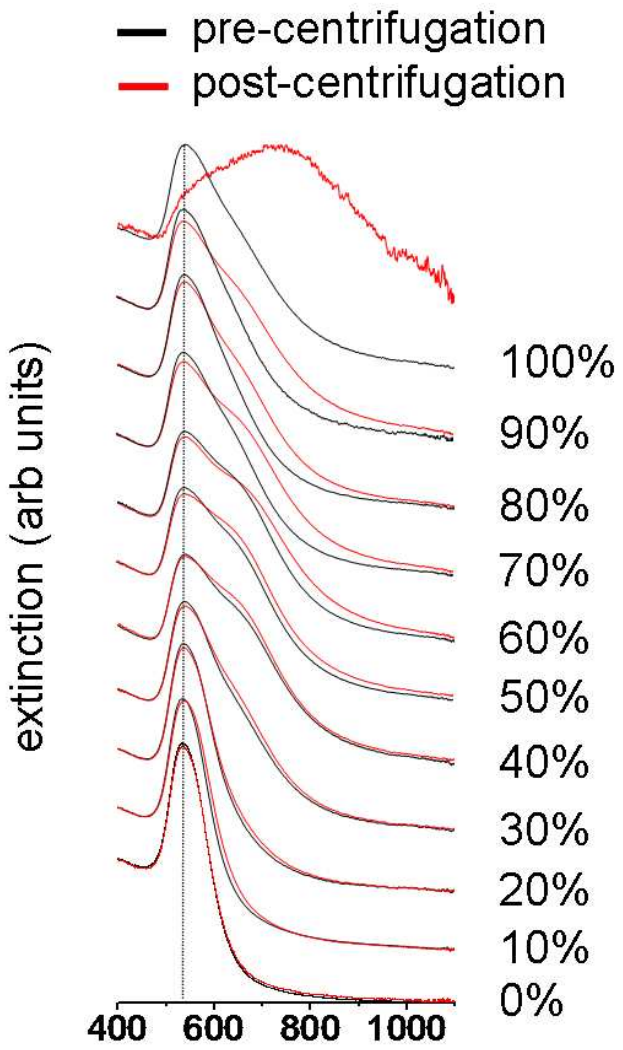

Figure S15. Extinction spectra of TAM-PEG-SH/PEG-SH AuNP conjugate solutions showing aqueous stability prior to and following centrifugation. Note an increase in red-shifted aggregate extinction following centrifugation as a function of increasing TAM-PEG-SH functionalization.

Direct One-Step ^{18}F-Labeling of Peptides via Nucleophilic Aromatic Substitution

Jessica Becaud,[†] Linjing Mu,[†] Mylène Karramkam,[†] Pius A. Schubiger,[†] Simon M. Ametamey,*[,†] Keith Graham,[‡] Timo Stellfeld,[‡] Lutz Lehmann,[‡] Sandra Borkowski,[‡] Dietmar Berndorff,[‡] Ludger Dinkelborg,[‡] Ananth Srinivasan,*[,‡] René Smits,[§] and Beate Koksch[§]

Center for Radiopharmaceutical Science of ETH, PSI and USZ, Department of Chemistry and Applied Biosciences, ETH Zurich, CH-8093 Zurich, Switzerland, Bayer Schering Pharma AG, Global Drug Discovery, D-13342 Berlin, Germany, Department of Chemistry and Biochemistry - Organic Chemistry, FU Berlin, Takustraβe 3, D-14195 Berlin, Germany. Received June 3, 2009; Revised Manuscript Received October 30, 2009

Methods for the radiolabeling molecules of interest with [^{18}F]-fluoride need to be rapid, convenient, and efficient. Numerous [^{18}F]-labeled prosthetic groups, e.g., *N*-succinimidyl 4 [^{18}F]-fluorobenzoate ([^{18}F]-SFB), 4-azidophenacyl-[^{18}F]-fluoride ([^{18}F]-APF), and 1-(3-(2-[^{18}F]fluoropyridin-3-yloxy)propyl)pyrrole-2,5-dione ([^{18}F]-FpyMe), for conjugating to biomolecules have been developed. As the synthesis of these prosthetic groups usually requires multistep procedures, there is still a need for direct methods for the nucleophilic [^{18}F]-fluorination of biomolecules. We report here on the development of a procedure based on the trimethylammonium (TMA) leaving group attached to an aromatic ring and activated with different electron-withdrawing groups (EWGs). A series of model compounds containing different electron-withdrawing substituents, a trimethylammonium leaving group, and carboxylic functionality for subsequent coupling to peptides were designed and synthesized. The optimal model compound, 2-cyano-4-(methoxycarbonyl)-*N*,*N*,*N*-trimethylbenzenaminium trifluoromethanesulfonate, was converted to carboxylic acid and coupled to peptides. The results of the one-step [^{18}F]-fluorination of tetrapeptides and bombesin peptides show that the direct ^{18}F-labeling of peptides is feasible under mild conditions and in good radiochemical yields.

INTRODUCTION

Positron emission tomography (PET) is of particular interest in diagnostic nuclear medicine as it can track positron emitting probes in a repetitive and noninvasive manner (*1, 2*). ^{18}F is considered an ideal PET isotope because it has the best imaging characteristics due to the low positron energy (0.64 MeV). In addition, the 110 min half-life of ^{18}F is sufficiently long to permit complex or multistep organic syntheses, commercial distribution to other imaging centers, and extended *in vivo* investigations.

In general, large biomolecules such as peptides or oligonucleotides are not readily amenable to direct fluorination with no-carrier-added (nca) ^{18}F-fluoride. As a result, ^{18}F has been incorporated into many biologically active molecules such as peptides (*3*−*6*), proteins (*7, 8*), and oligonucleotides (*9, 10*) via indirect methods using as building blocks so-called prosthetic groups. These prosthetic groups serve to enhance the efficiency and site-specificity of labeling. The first report on protein labeling with ^{18}F-fluoride was published by Mueller-Platz et al. (*11*) who tagged urokinase with ^{18}F-acetate. Herman et al. (*12*) successfully labeled human serum albumin (HSA) protein using two pentafluorophenyl derivatives as prosthetic groups. The well-known ^{18}F-SFB (*13, 14*) has been employed by several research groups to label bioactive molecules. Besides the aforementioned ^{18}F labeling synthons, a large number of other ^{18}F-labeled prosthetic groups have been investigated (*12, 15, 16*) and prominent routes for their conjugation to macromolecules have been mainly via ^{18}F-fluoroalkylation (*16, 17*), ^{18}F-fluoroacylation (*18, 19*), ^{18}F-fluoroamidation (*20, 21*), thiol-coupling (*22, 23*), or photochemical conjugation (*8, 24*). Among the above-mentioned methods, nucleophilic aromatic fluorination with nca ^{18}F-fluoride has been well-established. The ^{18}F-for-$^{+}$N(CH$_3$)$_3$ substitution was first reported more than two decades ago, and a large variety of ^{18}F-labeled aromatic radiopharmaceuticals have been reported (*25*). A disadvantage, however, of the established methods is the fact that the synthetic methods entail multistep syntheses and the ^{18}F label is incorporated very early in the synthesis sequence. In order to circumvent this shortcoming, research groups are focusing on new synthetic strategies that avoid the use of prosthetic groups. Recent studies have demonstrated the feasibility of labeling organoboron and organosilicon bioconjugates with ^{18}F in a single step (*26*−*28*). The one-step process can easily be automated for routine production. The aim of this work was to develop a direct one-step method for the nca fluorine-18 labeling of peptides.

EXPERIMENTAL PROCEDURES

General. All chemicals unless otherwise stated were purchased from Sigma-Aldrich or Merck and used without further purification. Fmoc-amino acids were purchased from IRIS Biotech except Fmoc-statine and FA01010, which were purchased from NeoMPS (now Polypeptide). The solvents were of HPLC quality. Peptide syntheses were carried out using Rink amide resin (0.68 mmol/g) following the standard Fmoc strategy (*29*). All amino acid residues were, if not further specified, L-amino acid residues. FA01010 denotes (4*R*,5*S*)-4-amino-5-methylheptanoic acid, statine (Sta) (3*S*,4*S*)-4-amino-3-hydroxy-6-methylheptanoic acid, and Ava 5-aminopentanoic acid. High-

* Corresponding author. Center for Radiopharmaceutical Science of ETH, PSI and USZ, ETH Hönggerberg D-CHAB IPW HCI H427, Wolfgang-Pauli-Strasse 10, CH-8093 Zurich, Switzerland. Tel.: +41 44 633 74 63; fax: +41 44 633 13 67. E-mail address: simon.ametamey@pharma.ethz.ch (S. Ametamey).

[†] ETH Zurich.

[‡] Bayer Schering Pharma AG.

[§] FU Berlin.

10.1021/bc900240z © 2009 American Chemical Society
Published on Web 11/18/2009

performance liquid chromatography (HPLC) analyses were performed using either a Altech Econsphere C18 RP column (53 × 7 mm, 3 μm) or an ACE C18 column (50 × 4.6 mm, 3 μm) under the indicated conditions. Analytical HPLC chromatograms were obtained using an Agilent 1100 system with *Gina* software, equipped with UV multiwavelength and Raytest Gabi Star detectors. Semipreparative HPLC purifications were carried out using a semipreparative ACE C18 column (250 × 10 mm, 5 μm) under the indicated conditions. Semipreparative HPLC system used was a Merck-Hitachi L6200A system equipped with Knauer variable wavelength detector and Eberline radiation detector.

TMA-Based Peptides Syntheses. *Peptide Synthesis (General Procedure).* The resin-bound Fmoc peptide was treated with 20% piperidine in DMF (v/v) for 5 min. This step was repeated with a reaction time of 20 min, and thereafter, the resin was washed with DMF (2×), CH_2Cl_2 (2×), and DMF (2×). A solution of Fmoc-Xaa-OH (Xaa = amino acid, 4 equiv), HBTU (*O*-(benzotriazol-1-yl)-*N*,*N*,*N*′,*N*′-tetramethyluronium hexafluorophosphate, 4 equiv), HOBT (1-hydroxybenzotriazole, 4 equiv), DIPEA (*N*,*N*′-di-iso-propylethylamine, 8 equiv) in DMF was added to the resin-bound free amine peptide and shaken for 90 min at room temperature. This step was repeated with a reaction time of 60 min, and the resin was washed with DMF (2×), CH_2Cl_2 (2×), and DMF (2×). The two steps of Fmoc-deprotection and amino acid addition were then repeated until the final elongation of the desired peptide was achieved. The peptides were typically prepared starting with 147 mg (0.1 mmol) of the resin. The amounts of reagents and building blocks in all subsequent reactions were calculated on the basis of this amount.

*Procedure for the Synthesis of (4-Trimethylammonium-3-cyanobenzoyl)-Functionalized Peptides Trifluoroacetate Salts (Precursor Compounds **6a**−**11a**).* Representative procedure: *N*-methylmorpholine (NMM, 22 μL, 0.2 mmol) was added to a solution of 2-cyano-4-carboxylphenyl)trimethylammonium triflate salt (71 mg, 0.2 mmol) and 4-(4,6-dimethoxy-1,3,5-triazin-2-yl)-4-methylmorpholinium tetrafluoroborate (66 mg, 0.2 mmol) in DMF (2 mL). The mixture was added to the resin-bound, side-chain-protected, Fmoc-deprotected peptide (0.1 mmol, based on the initial resin loading), which was prepared by following the general procedures described above. The reaction mixture was shaken intensively for 4 h. The resin was then filtered and washed with DMF (3 × 4 mL) and CH_2Cl_2 (3 × 4 mL). The coupling step was repeated. Thereafter, the resin was treated with a mixture of trifluoroacetic acid, distilled water, phenol, and triisopropylsilane (85/5/5/5, 1.5 mL) for 3 h. The mixture was added to ice-cold methyl *tert*-butyl ether, and the precipitate was separated by centrifugation. Water was added to the pellet, and the supernatant was lyophilized. The residue was purified by preparative RP-18 HPLC-MS with a gradient of 5−30% acetonitrile in 20 min and 0.1% trifluoroacetic acid as cosolvent. The desired fraction was collected and lypophilized, and the product was analyzed by HPLC-MS.

3-Cyano-4-trimethylammonium-benzoyl-Val-βAla-Arg-Gly-NH_2-trifluoroacetate salt (tetrapeptide **6a**, 17 mg, 24%): *m*/*z* M^+ calcd 587.3; found 587.4.

3-Cyano-4-trimethylammonium-benzoyl-Val-βAla-Phe-Gly-NH_2-trifluoroacetate salt (tetrapeptide **7a**, 25 mg, 36%): *m*/*z* M^+ calcd 578.3; found 578.6.

3-Cyano-4-trimethylammonium-benzoyl-Val-βAla-Lys-Gly-NH_2-trifluoroacetate salt (tetrapeptide **8a**, 19.5 mg, 29%): *m*/*z* M^+ calcd 559.3; found 559.1.

3-Cyano-4-trimethylammonium-benzoyl-Val-βAla-Met-Gly-NH_2-trifluoroacetate salt (tetrapeptide **9a**, 19 mg, 28%): *m*/*z* M^+ calcd 562.3; found 562.5.

3-Cyano-4-trimethylammonium-benzoyl-Ava-Gln-Trp-Ala-Val-Gly-His-FA01010-Leu-NH_2-trifluoroacetate salt (**10a**, 0.03 mmol scale, 15 mg, 37%): *m*/*z* M^+ calcd 1235.7; found 1235.8.

3-Cyano-4-trimethylammonium-benzoyl-Arg-Ava-Gln-Trp-Ala-Val-NMeGly-His-Sta-Leu-NH_2-trifluoroacetate salt (**11a**, 10 mg, 7%): *m*/*z* $[M+H]^{2+}/2$ calcd 711.4; found 711.9.

*Syntheses of Fluorinated TMA-Based Peptides (Reference Compounds **6b**−**11b**).* Representative procedure: A solution of 3-cyano-4-fluorobenzoic acid (66 mg, 4 equiv), HBTU (*O*-(benzotriazol-1-yl)-*N*,*N*,*N*′,*N*′-tetramethyluronium hexafluorophosphate, 151 mg, 4 equiv), HOBT (1-hydroxybenzotriazole, 61 mg, 4 equiv), and DIPEA (*N*,*N*′-di-iso-propylethylamine, 70 μL, 4 equiv) in DMF (2 mL) was added to the resin-bound, side-chain-protected peptide (0.1 mmol, based on the initial resin loading), which was prepared by following the general procedures described above. The reaction mixture was shaken intensively for 4 h. The resin was then filtered and washed with DMF (3 × 4 mL) and CH_2Cl_2 (3 × 4 mL). Thereafter, the resin was treated with a mixture of trifluoroacetic acid, distilled water, phenol, and triisopropylsilane (85/5/5/5, 1.5 mL) for 3 h. The mixture was added to ice-cold methyl *tert*-butyl ether, and the precipitate was separated by centrifugation. Water was added to the pellet, and the supernatant was lyophilized. The residue was purified by preparative RP-18 HPLC-MS with a gradient of 5−50% acetonitrile in 20 min and 0.1% trifluoroacetic acid as cosolvent. The desired fraction was collected and lypophilized, and the product was analyzed by HPLC-MS.

3-Cyano-4-fluorobenzoyl-Val-βAla-Arg-Gly-NH_2 (tetrapeptide **6b**, 32 mg, 58%): *m*/*z* $[M+H]^+$ calcd 548.3; found 548.0.

3-Cyano-4-fluorobenzoyl-Val-βAla-Phe-Gly-NH_2 (tetrapeptide **7b**, 18 mg, 33%): *m*/*z* $[M+H]^+$ calcd 539.2; found 539.1.

3-Cyano-4-fluorobenzoyl-Val-βAla-Lys-Gly-NH_2 (tetrapeptide **8b**, 16.5 mg, 32%): *m*/*z* $[M+H]^+$ calcd 520.3; found 520.1.

3-Cyano-4-fluorobenzoyl-Val-βAla-Met-Gly-NH_2 (tetrapeptide **9b**, 17 mg, 33%): *m*/*z* $[M+H]^+$ calcd 523.2; found 523.0.

3-Cyano-4-fluorobenzoyl-Ava-Gln-Trp-Ala-Val-Gly-His-FA01010-Leu-NH_2 (**10b**, 0.03 mmol scale, 9 mg, 25%): *m*/*z* $[M+H]^+$ calcd 1196.6; found 1196.7.

3-Cyano-4-fluorobenzoyl-Arg-Ava-Gln-Trp-Ala-Val-NMeGly-His-Sta-Leu-NH_2 (**11b**, 0.03 mmol scale, 6.5 mg, 16%): *m*/*z* $[M+2H]^{2+}/2$ calcd 692.9; found 692.4.

^{18}F-Radiolabeling of TMA-Based Model Compounds and Peptides. *General.* No-carrier-added [^{18}F] fluoride was produced via the ^{18}O (p,n) ^{18}F nuclear reaction by irradiation of enriched [^{18}O] water. ^{18}F-fluoride was trapped on an anion-exchange resin cartridge (Sep-Pak QMA light, Waters). The cartridge was eluted with a solution of Kryptofix (5 mg), potassium carbonate (1 mg), or Cs_2CO_3 (2.4 mg) in water (500 μL) and MeCN (1 mL). The solvent was removed by azeotropic drying at 110 °C under vacuum for 10 min with a stream of nitrogen. Anhydrous MeCN (1 mL) was added and evaporated. This step of adding acetonitrile (1 mL) was repeated two more times. The tested precursor was dissolved in DMSO and added to the dry K[^{18}F]F/$K_{2.2.2.}$ or Cs[^{18}F]F/$K_{2.2.2}$ complex. The reaction mixture was then heated at 50−70 °C for 5−15 min. An aliquot was taken from the reaction mixture and analyzed by analytical HPLC. The ^{18}F-labeled product was confirmed by coinjection with the nonradioactive reference compound on the same analytical HPLC using either ACE C18 column (50 × 4.6 mm, 3 μm) or Altech Econsphere C18 RP column (53 × 7 mm, 3 μm). Elute conditions with ACE C18 column: 10 mM K_2HPO_4 in water (solvent A), 10 mM K_2HPO_4 in water/acetonitrile 3/7 (solvent B); 0 min, 5% B; 0−7.00 min, 5→95% B; 7.00−7.10 min, 95→100% B; 7.10−8.80 min, 100% B; 8.80−9.00 min, 100→5% B. The flow rate was 2 mL/min. Elute conditions with Altech Econsphere C18 RP column: 0.1% aq TFA (solvent A), 0.1% TFA in acetonitrile/water 9/1 (solvent B); 0 min, 5% B;

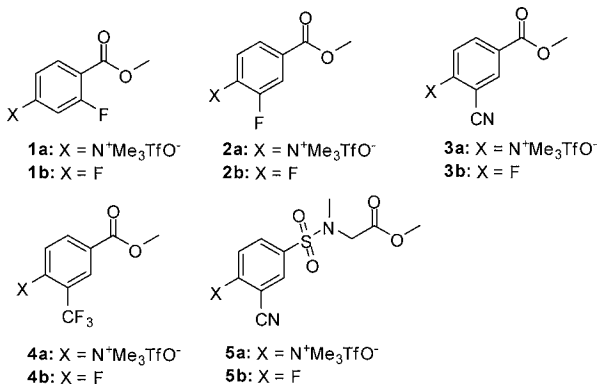

Figure 1. Structures of synthesized TMA-based model precursor compounds **1a**−**5a** and their corresponding fluorinated compounds **1b**−**5b.**

0−7 min, 5→95% B; 7.00−7.10 min, 95→100% B; 7.10−8.80 min, 100% B; 8.80−9.00 min, 100→5% B; flow rate: 2 mL/min.

^{18}F-Radiolabeling of TMA-Based Model Compounds. TMA-based bifunctional model precursor compounds (**1a**−**5a**, Figure 1) were synthesized and characterized (see Supporting Information). Their corresponding reference compounds (**1b**−**5b**) are, in most cases, commercially available. Typical experimental conditions for the ^{18}F-radiolabeling of precursor compounds **3a** and **5a** are described below.

Methyl-3-cyano-4-[^{18}F]fluorobenzoate (**[^{18}F]3b**). Compound **3a** (4.2 mg) in anhydrous DMSO (300 μL) was added to a reaction vial containing dry K[^{18}F]F/$K_{2.2.2}$ complex (6.57 GBq). After heating at 50 °C for 15 min, an aliquot was taken for HPLC analysis (ACE C18 column), and more than 90% ^{18}F-incorporation was obtained. The reaction mixture was diluted with water (1.5 mL), and this solution (3.86 GBq) was injected onto an ACE semipreparative HPLC column (0.1% TFA in water (solvent A), 0.1% TFA in acetonitrile/water 9/1 (solvent B), isocratic 30% B, flow rate: 4 mL/min). The decay-corrected radiochemical yield of the isolated product (2.89 GBq) was around 77% and radiochemical purity was greater than 99%. Specific activity was 95 GBq/μmol at the end of the synthesis.

Methyl 2-(3-cyano-4-[^{18}F]fluoro-*N*-methyl-phenyl-sulfonamido)acetate (**[^{18}F]5b**). A solution of compound **5a** (1 mg) in anhydrous DMSO (100 μL) was added to a reaction vial containing dry K[^{18}F]F/$K_{2.2.2}$ complex. After heating at 70 °C for 5 min, an aliquot of the reaction mixture was taken for HPLC analysis (ACE C18 column). The ^{18}F-incorporation was 80%.

^{18}F-Radiolabeling of TMA-Based Peptides. ^{18}F-labeling of the TMA-based peptides (Figure 2) was performed under similar reaction conditions as described above.

3-Cyano-4-[^{18}F]fluorobenzoyl-Val-βAla-Arg-Gly-NH_2 (**[^{18}F]6b**). A solution of compound **6a** (2 mg) in anhydrous DMSO (300 μL) was added to a reaction vial containing dry K[^{18}F]F/$K_{2.2.2}$ complex. After heating the reaction mixture at 50 °C for 15 min, the crude reaction mixture was analyzed using an Altech Econsphere C18 RP column (53 × 7 mm, 3 μm) with the following elute: 0.1% aq TFA (solvent A), 0.1% TFA in acetonitrile/water 9/1 (solvent B); 0 min, 5% B; 0−7 min, 5→95% B; 7.00−7.10 min, 95→100% B; 7.10−8.80 min, 100% B; 8.80−9.00 min, 100→5% B; flow rate: 3 mL/min.). The ^{18}F-incorporation determined by HPLC was 92%.

The similar procedure described for **[^{18}F]6b** was used for the preparation of 3-cyano-4-[^{18}F]fluorobenzoyl-Val-βAla-Phe-Gly-NH_2 (**[^{18}F]7b**) and 3-cyano-4-[^{18}F]fluorobenzoyl-Val-βAla-Lys-Gly-NH_2 (**[^{18}F]8b**), and resulted in 80% and 25% ^{18}F-incorporation, respectively.

3-Cyano-4-[^{18}F]fluorobenzoyl-Val-βAla-Met-Gly-NH_2 (**[^{18}F]9b**). A solution of compound **9a** (2 mg) in anhydrous DMSO (300 μL) was added to a reaction vial containing dry K[^{18}F]F/$K_{2.2.2}$ complex. After heating at 90 °C for 15 min, the crude reaction mixture was analyzed under the same analytical HPLC conditions as described for **[^{18}F]6b**. The ^{18}F-incorporation determined by HPLC was 89%. The reaction mixture was diluted with water and injected onto an ACE semipreparative HPLC column (0.1% TFA in water (solvent A), B: 0.1% TFA in acetonitrile/water 9/1 (solvent B), isocratic, 35% B, flow rate: 4 mL/min) and the product was collected. The decay-corrected radiochemical yield of the isolated product was around 57% and radiochemical purity was greater than 99%. Specific activity was 74 GBq/μmol at the end of the synthesis.

3-Cyano-4-[^{18}F]fluorobenzoyl-Ava-Gln-Trp-Ala-Val-Gly-His-FA01010-Leu-NH_2 (**[^{18}F]10b**). A solution of compound **10a** (2 mg) in DMSO (150 μL) was added to a reaction vial containing dry Cs[^{18}F]F/$K_{2.2.2}$ complex. The reaction vessel was sealed and heated at 70 °C for 15 min. Analysis of an aliquot of the crude reaction mixture afforded an ^{18}F-incorporation of 77% with ACE C18 column. Thereafter, the reaction mixture was transferred to a vial containing water (4 mL) and then injected onto a semipreparative ACE column (0.1% aq TFA (solvent A); 0.1% TFA in acetonitrile/water 9/1 (solvent B), gradient 0−5 min, 30% B, flow rate 2 mL/min; 5−15 min, 30→70% B, flow rate: 3 mL/min). The desired ^{18}F-labeled product was collected (253 MBq, 20% d.c.), and the specific activity was around 75 GBq/μmol at the end of the synthesis.

3-Cyano-4-[^{18}F]fluorobenzoyl-Arg-Ava-Gln-Trp-Ala-Val-NMeGly-His-Sta-Leu-NH_2 (**[^{18}F]11b**). A solution of compound **11a** (2 mg) in DMSO (150 μL) was added to a reaction vial containing dry C_S[^{18}F]F/$K_{2.2.2}$ complex. The reaction vessel was sealed and heated at 70 °C for 15 min. An aliquot was taken from the crude reaction mixture and analyzed by HPLC (ACE C18 column); the ^{18}F-incorporation was 74%. The reaction mixture was then transferred to a vial containing water (4 mL). This product was purified using a semipreparative HPLC column (ACE C18, 0.1% aq TFA (solvent A); 0.1% TFA in acetonitrile/water 9/1 (solvent B), 0−5 min, 29% B; 5−25 min, 29→34% B, flow rate: 3 mL/min). The desired ^{18}F-labeled product was collected (150 MBq, 21% d.c.), and the specific activity obtained was 73 GBq/μmol at the end of the synthesis.

***In Vitro* Binding Affinity Assay.** The receptor affinities of two bombesin (BBN) analogues **10b** and **11b** were determined in quadruplicate in a scintillation proximity assay (SPA) using cellular membranes transfected with human bombesin 2 receptors (gastrin-releasing peptide receptors) from PerkinElmer (RBHBS2M). The membranes and agglutinin-coupled SPA beads type A (PVT PEI Treated Wheatgerm, Amersham Bioscience) were mixed in assay buffer (50 mM Tris/HCl pH 7.2; 5 mM $MgCl_2$; 1 mM EGTA, protease inhibitor (Roche Diagnostics GmbH; 1 tablet/50 mL) and 0.3% polyethylenemine) to give final concentrations of approximately 20 μg/mL protein and 8 mg/mL PVT-SPA beads. The ligand [^{125}I]-Tyr^4-bombesin (PerkinElmer; specific activity: 81.4 TBq/mmol) was diluted to 0.2 nM in assay buffer. The test compounds were dissolved in DMSO to give 1 mM stock solutions. They were further diluted in assay buffer to 2 pM to 300 nM. Unspecific binding was determined by an excess of 10 000 nM Tyr^4-bombesin (Sigma).

The assay was then performed as follows: First, 10 μL of compound solution to be tested for binding was placed in white 384 well plates (Lumitrac 200, Greiner). Next, 20 μL GRPR/PVT-SPA bead mixture and 20 μL of the ligand solution were added. After 120 min incubation at room temperature, another 50 μL of assay buffer was added; the plate was sealed and centrifuged for 10 min at 520 × *g* at room temperature. Signals were measured in a TopCount (Perkin-Elmer) for 1 min integration time per well. Unspecific binding determined by an

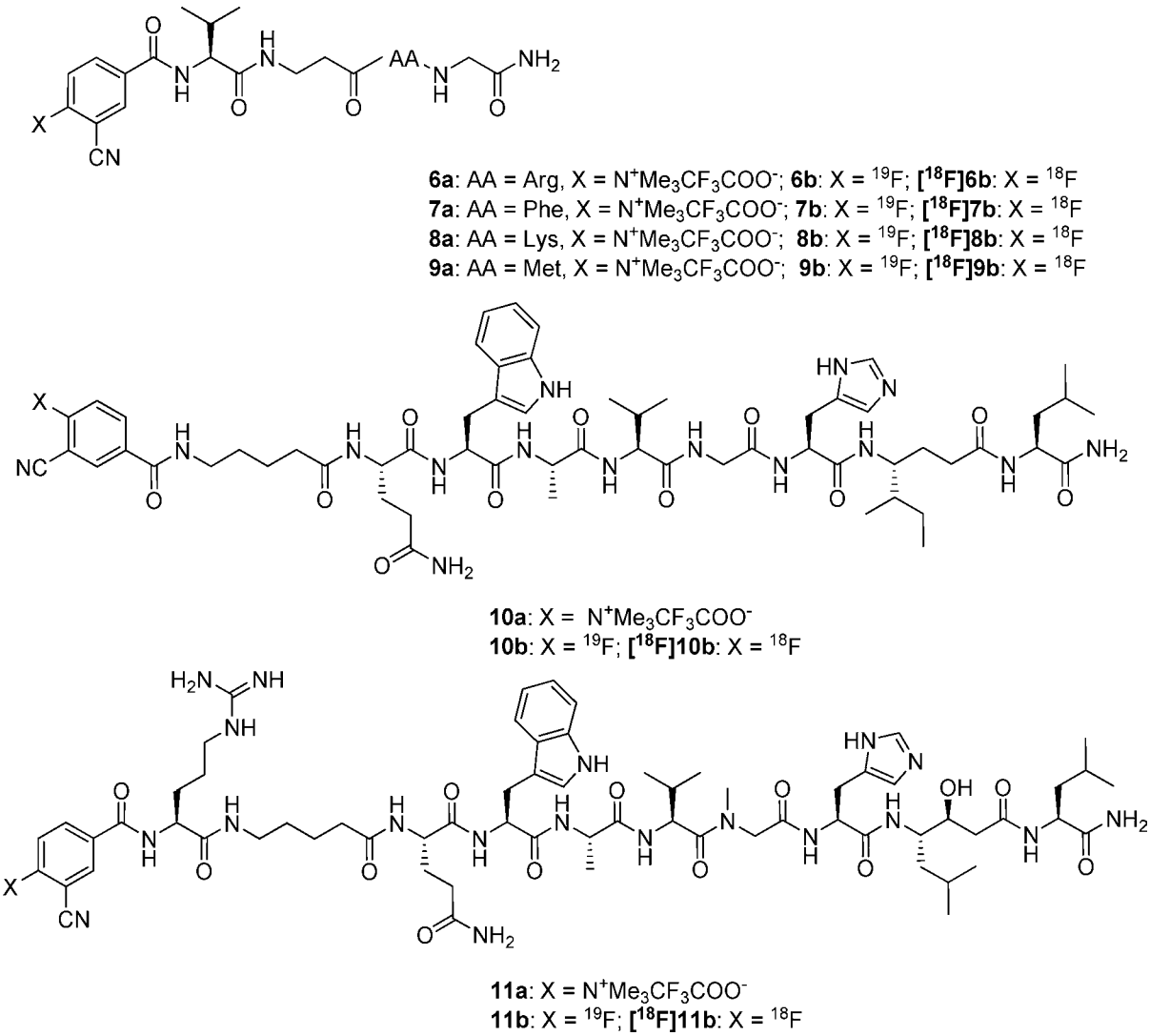

Figure 2. Structures of TMA-based peptides.

excess of Tyr^4-bombesin was subtracted from total binding to yield the specific binding at each concentration. The IC_{50} and K_i values were calculated by nonlinear regression using *GraFit 5* data analysis software (Erithacus Software Ltd.).

Plasma Stability Studies. The stability of the radiolabeled compound **[^{18}F]10b** and **[^{18}F]11b** was investigated in mouse plasma at different time points (from 0 to 90 min) at 37 °C. Phosphate-buffered saline (PBS) was used as a control. After incubation, plasma proteins were precipitated with acetonitrile followed by centrifugation (10 min, 13 000 rpm) at 4 °C. The PBS controls were diluted with the same volume of acetonitrile. The supernatants and PBS controls were analyzed by HPLC (Column Ecosphere C18, 53 × 7 mm, 3 mm, flow rate: 1.8 mL/min). The percentage of intact compound was determined at different incubation times.

RESULTS AND DISCUSSION

Syntheses and ^{18}F-Labeling of TMA-Based Model Compounds. Precursor compounds **1a**−**5a** were obtained in two steps with moderate to good yields (Supporting Information). In most cases, the displacement of fluoride with dimethylamine was carried out via nucleophilic aromatic substitution under basic conditions. The quarternization of dimethylamine intermediate with methyl triflate was performed under normal or increased pressure (1−10 bar). The crude products were purified by reversed-phase column chromatography. All the corresponding reference compounds **1b**−**5b** are commercially available except **3b**. Compound **3b** was obtained in two steps starting from commercially available 2-fluoro-5-formylbenzonitrile, which was converted to the corresponding acid by classical oxidation method followed by acid esterification.

Since nucleophilic aromatic substitutions of ^{18}F-for-$^{+}$N(CH$_3$)$_3$ typically require high temperatures (>100 °C) which are not suitable for radiolabeling of peptides, electron withdrawing groups such as −CF$_3$, −CN, and −F and a carbonyl functionality have been introduced to the aromatic ring in order to increase the reactivity of the trimethylammonium leaving group. To demonstrate the feasibility of direct ^{18}F-labeling of peptides, a series of trimethylammonium-based model compounds **1a**−**5a** (Figure 1) bearing electron-withdrawing groups (−CN, −CF$_3$, −F) were tested. The carbonyl functionality has the added attraction that, via conversion to the corresponding acid, these trimethylammonium building blocks can be coupled to peptides. There are only a few publications on nucleophilic aromatic substitution of a TMA group by ^{18}F-fluoride ion in aromatic compounds containing two or more substitutents besides the trimethylammonium moiety (*30*, *31*). The radiosynthetic route is depicted in Scheme 1, and the radiolabeling results are shown in Table 1.

From the results shown in Table 1, high ^{18}F-incorporation was obtained with all the model compounds under mild radiolabeling conditions. The radiolabeling efficiency was not

Scheme 1. General Radiosynthetic Pathway to TMA-Based Model Compounds (1a−5a)

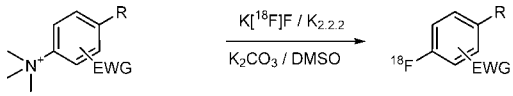

1a: EWG = 3-F, R = 4-$COCH_3$; **2a**: EWG = 2-F, R = 4-$COCH_3$;
3a: EWG = 2-CN, R = 4-$COCH_3$; **4a**: EWG =2-CF_3, R = 4-$COCH_3$;
5a: EWG = 2-CN, R = 4-$SO_2N(CH_3)CH_2COOCH_3$

Table 1. ^{18}F-Radiolabeling of TMA-Based Model Compounds[a]

entry	compd.	precursor amount	temp (°C)	reaction time	conversion(%)
1	**1a**	1 mg	70	15 min	79 ± 7 (n = 3)
2	**2a**	1 mg	50	15 min	82 ± 4 (n = 3)
3	**3a**	4 mg	50	15 min	89 ± 4 (n = 3)
4	**3a**	2 mg	50	15 min	83 ± 15 (n = 2)
5	**3a**	1 mg	50	15 min	80 ± 2 (n = 2)
6	**4a**	2 mg	50	15 min	79 ± 10 (n = 2)
7	**5a**	1 mg	50	5 min	65 ± 4 (n = 3)
8	**5a**	1 mg	70	5 min	80 ± 4 (n = 2)

[a] ^{18}F-labeling was carried out in DMSO with K_2CO_3 as the base. Conversion was determined from radio-HPLC chromatogram representing the percentage of radioactivity area of product related to the total radioactivity area.

dramatically influenced by the amount of precursor (Table 1, entries 3−5). However, by increasing the reaction temperature from 50 to 70 °C, the ^{18}F-incorporation of compound **[^{18}F]5b** increased from 65% to 80% (Table 1, entries 7 and 8). Although no detailed study on the influence of reaction time was performed, it seems that 5 min reaction time is sufficient for a good conversion. The combined effect of the electron-withdrawing group and the carbonyl/sulfonyl on the phenyl ring facilitated an easy ^{18}F-for-$^{+}N(CH_3)_3$ substitution. This would explain why no decomposition of the ammonium precursors and the formation of volatile methyl [^{18}F]fluoride were observed with precursor compounds **1a**−**5a** under the indicated radiolabeling conditions (Table 1) compared to published results (*32*). Furthermore, no ^{18}F−^{19}F isotopic exchange was observed for compounds **[^{18}F]1b** and **[^{18}F]2b** under the mild radiolabeling conditions (50 and 70 °C). The large polarity difference between the TMA-precursor and fluorinated product allowed an easy semi-HPLC separation of the ^{18}F-labeled products from their corresponding precursors. For example, the radiochemical purity of compound **[^{18}F]3b** was greater than 99% after semi-HPLC purification, and the specific activity obtained was around 95 GBq/μmol at the end of the synthesis. Among the model compounds studied, compound **[^{18}F]3b** with the cyano-activating group gave the best radiochemical yield of 77%.

Syntheses and ^{18}F-Labeling of TMA-Based Peptides. On the basis of the radiolabeling results of model compounds **1a**−**5a**, compound **3a** was converted to its corresponding acid 4-carboxy-2-cyano-*N*,*N*,*N*-trimethylbenzenaminium trifluoromethanesulfonate (Supporting Information) for coupling to target peptides using standard solid-phase peptide synthesis protocols (*29*). For TMA-based tetrapeptides, amino acids such as Arg, Phe, Lys, and Met were introduced in order to study their influence on ^{18}F-labeling efficiency. Two bombesin analogues were synthesized with modifications of the amino acid sequence of BBN(7−14)-NH_2. Non-natural amino acid such as FA01010 or Sta were incorporated into the bombesin peptide sequence for increasing its metabolic stability; Ava or Arg-βAla was used as a linker for attaching the aryltrimethylammonium building block and the N-terminal bombesin peptide. The corresponding standard references were synthesized by the conjugation of 3-cyano-4-fluorobenzoic acid with the same peptides applying similar protocols used for the syntheses of the precursors.

Table 2. ^{18}F-Radiolabeling of TMA-Based Peptides[a]

entry	compd.	temp (°C)	base	reaction time	conversion (%)
1	**6a**	50	K_2CO_3	15 min	92 (n = 1)
2	**7a**	50	K_2CO_3	15 min	80 (n = 1)
3	**8a**	90	K_2CO_3	15 min	0 (n = 2)
4	**8a**	90	Cs_2CO_3	15 min	24 ± 8 (n = 3)
5	**9a**	50	K_2CO_3	15 min	19 ± 4 (n = 3)
6	**9a**	90	K_2CO_3	15 min	89 ± 3 (n = 3)
7	**10a**	70	Cs_2CO_3	15 min	70 ± 7 (n = 3)
8	**11a**	70	Cs_2CO_3	15 min	51 ± 5 (n = 2)

[a] ^{18}F-labeling was carried out in DMSO (200−300 μL) with 2 mg of precursor. Conversion was determined from radio-HPLC chromatogram representing the percentage of radioactivity area of product related to the total radioactivity area.

The direct one-step ^{18}F-labeling was applied to four tetrapeptides (Table 2, entries 1−6) differing only in one amino acid in the peptide sequence. Using similar radiolabeling conditions as applied to the model compounds, tetrapeptides **6a** and **7a** gave ^{18}F-incorporation of 92% and 80%, respectively. In the case of the lysine-containing tetrapeptide **8a** (entry 3), there was no product formation when potassium carbonate was used as the base; however, a moderate ^{18}F-incorporation (24%) was achieved with cesium carbonate as the base at 90 °C. The low ^{18}F-incorporation might be due to the presence of free amino functionality. Nevertheless, the improvement is remarkable. With the methionine-containing tetrapeptide **9a**, the temperature effect for the ^{18}F-incorporation is worth mentioning. The ^{18}F-incorporation was only 19% after 15 min at 50 °C; however, by increasing the temperature to 90 °C, a dramatic increase of ^{18}F-incorporation (89%) was achieved (Table 2, entries 5 and 6). Because these results were encouraging, this one-step ^{18}F-labeling approach was applied to two bombesin peptides **10a** and **11a**. As shown in Table 2, more than 70% ^{18}F-incorporation was found for **[^{18}F]10b** when an aliquot was directly removed from the reaction mixture and analyzed by HPLC. A typical radio-HPLC profile of compound **[^{18}F]10b** is shown in Figure 3. Only two radioactive peaks were observed from the analytical HPLC chromatogram of the reaction mixture. Apart from free ^{18}F-fluoride and the desired ^{18}F-labeled compound (retention time = 7.2 min), no other radioactive compound was observed. After adding HPLC eluent to the reaction vial and purifying the mixture by semi-HPLC, around 20% (decay-corrected) radiochemical yield of the final product was obtained. The relatively large difference between isolated radiochemical yield and ^{18}F-incorporation of compound **[^{18}F]10b** (20% vs 70%) is due to the fact that Cs[^{18}F]F/$K_{2.2.2}$ complex can be absorbed on the surface of the reaction vial (*33*). This absorbed ^{18}F-fluoride activity is, however, not taken into account when an aliquot of the reaction mixture is taken for analysis. The radiochemical purity was 99% and specific activity was around 79 GBq/μmol at the end of synthesis.

With respect to the stereochemistry of the peptides, similar peptides have been labeled under basic conditions (pH 8−10) and even at higher or elevated temperatures (75−100 °C), and no racemization of the peptides was observed (*34*−*36*). Because our radiolabeling conditions (pH < 8, temp 50−70 °C) are even milder than those previously reported, we do not expect that racemization will occur with any of the peptides reported in this manuscript.

***In Vitro* Binding Affinity Assay.** The *in vitro* binding affinity of the fluorinated bombesin peptides **10b** and **11b** to the gastrin-releasing peptide receptor were assessed via a competitive displacement assay using [^{125}I]-Tyr^4-bombesin as the radioligand. Both peptides demonstrated high binding affinity to the gastrin-releasing peptide receptor with IC_{50} values of 9.20 nM and 2.71 nM (Figure 4). The K_D value of the radioligand I-125-Tyr^4-bombesin was determined in former assays to be ap-

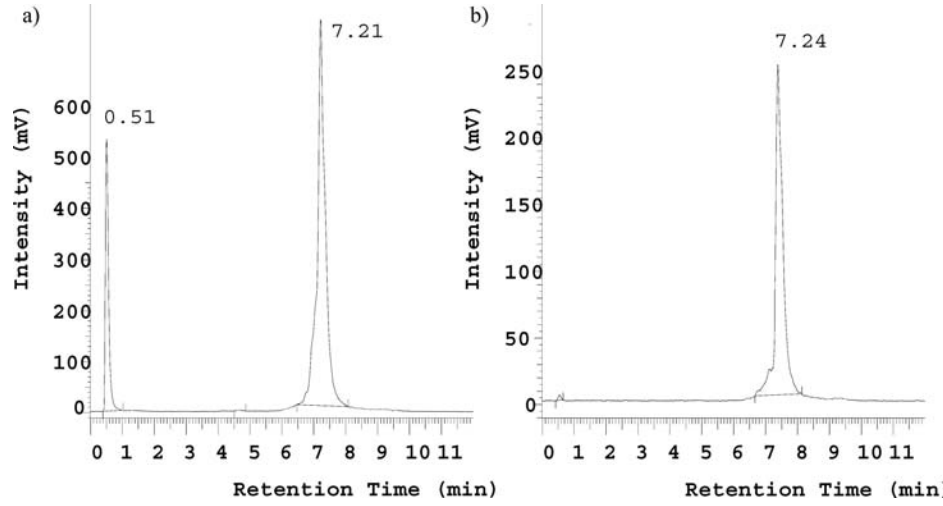

Figure 3. Radio-HPLC profiles of 3-cyano-4-[^{18}F]fluorobenzoyl-Ava-Gln-Trp-Ala-Val-Gly-His-FA01010-Leu-NH_2 (**[^{18}F]10b**): (a) reaction mixture; (b) purified compound.

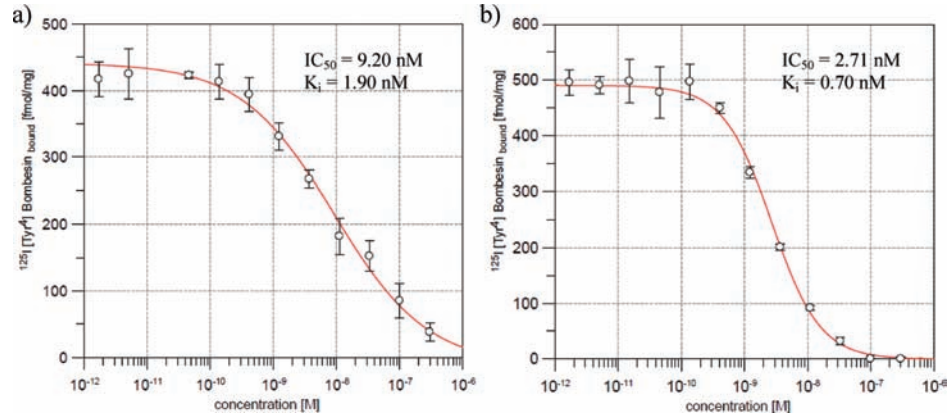

Figure 4. Competitive binding of (a) 3-cyano-4-fluorobenzoyl-Ava-Gln-Trp-Ala-Val-Gly-His-FA01010-Leu-NH_2 (**10b**) and (b) 3-cyano-4-fluorobenzoyl-Arg-Ava-Gln-Trp-Ala-Val-NMeGly-His-Sta-Leu-NH_2 (**11b**) versus [^{125}I]-Tyr^4-bombesin on human bombesin 2 receptor membranes in a scintillation proximity assay.

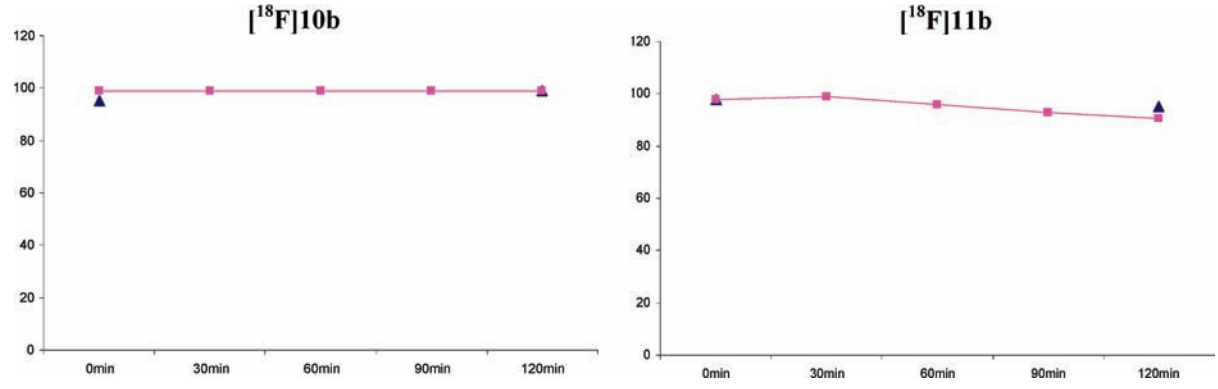

Figure 5. Radiochemical stability studies of **[^{18}F]10b** and **[^{18}F]11b** at 37 °C. ▲, with PBS; ■, with mouse plasma.

proximately 0.06 nM. Therefore, the normalized binding affinities represented excellent K_i values of 1.90 nM and 0.70 nM for **10b** and **11b**, respectively (Figure 4). For comparison, human GRP serving as a positive control showed a K_i of 5−10 nM, whereas Neuromedin B serving as a negative control had a K_i of >500 nM (see Supporting Information).

Plasma Stability Studies. Plasma stability was evaluated for both bombesin peptides **[^{18}F]10b** and **[^{18}F]11b** in mouse plasma at time points of 0, 30, 60, 90, and 120 min at 37 °C, with PBS as control. As indicated in Figure 5, **[^{18}F]10b** showed excellent plasma stability over the tested time period. **[^{18}F]11b**, however, was slightly degraded to ^{18}F-fluoride, but is stable enough to allow for *in vivo* studies. There are no significant differences between plasma results and PBS findings of compounds **[^{18}F]10b** and **[^{18}F]11b.**

CONCLUSION

In conclusion, a series of trimethylammonium-based model compounds containing different electron-withdrawing substituents, a trimethylammonium (TMA) leaving group, and a linker

for coupling to peptides were designed and synthesized. The appropriate model compounds were converted to their corresponding carboxylic acids and coupled to model tetrapeptides containing different amino acids and bombesin peptides. High ^{18}F-incorporation was obtained with all the model compounds under mild radiolabeling conditions. The results of the one-step [^{18}F]-fluorination of the tetrapeptides and bombesin peptides show that the direct ^{18}F-labeling of peptides is feasible under mild conditions and in good radiochemical yields. This method might not be applicable in all cases. However, in our hands, we were able to achieve a 24% radiochemical yield of one of the peptides bearing a free amino group in lysine. Peptides containing histidine, tryptophan, and arginine amino acids are also amenable to fluorine-18 labeling using this direct approach. Under normal circumstances, these amino acids would require protection with appropriate protecting groups. We are currently working on more peptides which contain cysteine and tyrosine amino acids. In conclusion, this work demonstrates that a rational approach to peptide design can be useful for the direct ^{18}F labeling of peptides and other large biomolecules.

ACKNOWLEDGMENT

We gratefully acknowledge Katrin Dinse, Peter Friese, Selahattin Ede, Marion Zerna, Jörg Pioch, Ingo Horn, René Zernicke and Cindy Fischer for technical support. Dr. Detlev Suelzle for fruitful discussions and computational chemistry.

Supporting Information Available: Analytical data for compounds **1a**−**5a** and experimental parts. This material is available free of charge via the Internet at http://pubs.acs.org.

LITERATURE CITED

(1) Kilbourn, M. R., and Welch, M. J. (1986) 18F-labeled receptor based radiopharmaceuticals. *Appl. Radiat. Isot. 37*, 677–683.

(2) McGuire, A. H., Dehdashti, F., Siegel, B. A., Lyss, A. P., Brodack, J. W., Mathias, C. J., Mintun, M. A., Katzenellenbogen, J. A., and Welch, M. J. (1991) Positron tomographic assessment of 16-α-[^{18}F]-fluoro-17-β-estradiol uptake in metastatic breast carcinoma. *J. Nucl. Med. 32*, 1526–1531.

(3) Vaidyanathan, G., and Zalutsky, M. R. (1997) Fluorine-18-labeled [Nle^4, D-Phe^7]-α-MSH, an α-melanocyte stimulating hormone analogue. *Nucl. Med. Biol. 24*, 171–178.

(4) Vaidyanathan, G., and Zalutsky, M. R. (1995) 18F-Labeled chemotactic peptides - a potential approach for the PET imaging of bacterial-infection. *Nucl. Med. Biol. 22*, 759–764.

(5) Guhlke, S., Wester, H. J., Bruns, C., and Stoecklin, G. (1994) (2-[^{18}F]Fluoropropionyl-(D)phe^1)-octreotide, a potential radiopharmaceutical for quantitative somatostatin receptor imaging with PET - synthesis, radiolabeling, in-vitro validation and biodistribution in mice. *Nucl. Med. Biol. 21*, 819–825.

(6) Moody, T. W., Leyton, J., Unsworth, E., John, C., Lang, L. X., and Eckelman, W. C. (1998) (Arg15, Arg21)VIP: Evaluation of biological activity and localization to breast cancer tumors. *Peptides 19*, 585–592.

(7) Vaidyanathan, G., Bigner, D. D., and Zalutsky, M. R. (1992) Fluorine-18-labeled monoclonal antibody fragments - a potential approach for combining radioimmunoscintigraphy and positron emission tomography. *J. Nucl. Med. 33*, 1535–1541.

(8) Wester, H. J., Hamacher, K., and Stoecklin, G. (1996) A comparative study of n.c.a. fluorine-18 labeling of proteins via acylation and photochemical conjugation. *Nucl. Med. Biol. 23*, 365–372.

(9) Dolle, F., Hinnen, F., Vaufrey, F., Tavitian, B., and Crouzel, C. (1997) A general method for labeling oligodeoxynucleotides with 18F for in vivo PET imaging. *J. Labelled Compd. Radiopharm. 39*, 319–330.

(10) Kuhnast, B., Dolle, F., Terrazzino, S., Rousseau, B., Loc'h, C., Vaufrey, F., Hinnen, F., Doignon, I., Pillon, F., David, C., Crouzel, C., and Tavitian, B. (2000) General method to label antisense oligonucleotides with radioactive halogens for pharmacological and imaging studies. *Bioconjugate Chem. 11*, 627–636.

(11) Mueller-Platz, C. M., Kloster, G., Legler, G., and Stoecklin, G. (1982) 18F-Fluoroacetate - an agent for introducing no-carrier-added fluorine-18 into urokinase without loss of biological activity. *J. Labelled Compd. Radiopharm. 19*, 1645–1646.

(12) Herman, L. W., Fischman, A. J., Tompkins, R. G., Hanson, R. N., Byon, C., Strauss, H. W., and Elmaleh, D. R. (1994) The use of pentafluorophenyl derivatives for the 18F labeling of proteins. *Nucl. Med. Biol. 21*, 1005–1010.

(13) Lang, L. X., and Eckelman, W. C. (1994) One-step synthesis of 18F labeled [^{18}F] N-succinimidyl 4-(fluoromethyl)benzoate for protein labeling. *Appl. Radiat. Isot. 45*, 1155–1163.

(14) Lang, L., and Eckelman, W. C. (1997) Labeling proteins at high specific activity using N-succinimidyl 4-[^{18}F](fluoromethyl) benzoate. *Appl. Radiat. Isot. 48*, 169–173.

(15) Okarvi, S. M. (2001) Recent progress in fluorine-18 labelled peptide radiopharmaceuticals. *Eur. J. Nucl. Med. 28*, 929–938.

(16) Kilbourn, M. R., Dence, C. S., Welch, M. J., and Mathias, C. J. (1987) Fluorine-18 labeling of proteins. *J. Nucl. Med. 28*, 462–470.

(17) Block, D., Coenen, H. H., and Stoecklin, G. (1988) N.c.a. 18F-Fluoroalkylation of H-Acidic Compounds. *J. Labelled Compd. Radiopharm. 25*, 201–216.

(18) Block, D., Coenen, H. H., and Stoecklin, G. (1988) N.c.a. 18F-fluoroacylation via fluorocarboxylic acid-esters. *J. Labelled Compd. Radiopharm. 25*, 185–200.

(19) Jacobson, K. A., Furlano, D. C., and Kirk, K. L. (1988) A prosthetic group for the rapid introduction of fluorine into peptides and functionalized drugs. *J. Fluorine Chem. 39*, 339–347.

(20) Shai, Y., Kirk, K. L., Channing, M. A., Dunn, B. B., Lesniak, M. A., Eastman, R. C., Finn, R. D., Roth, J., and Jacobson, K. A. (1989) 18F-Labeled insulin - a prosthetic group methodology for incorporation of a positron emitter into peptides and proteins. *Biochemistry 28*, 4801–4806.

(21) Jelinski, M., Hamacher, K., and Coenen, H. H. (2002) C-Terminal 18F-fluoroethylamidation exemplified on [Gly-OH9] oxytocin. *J. Labelled Compd. Radiopharm. 45*, 217–229.

(22) Shiue, C. J., Wolf, A. P., and Hainfeld, J. F. (1988) 18F labeled N-(p-(18F)fluorophenyl)maleimide and its derivatives for labelling monoclonal antibodies with 18F. *J. Labelled Compd. Radiopharm. 26*, 287–289.

(23) Toyokuni, T., Walsh, J. C., Dominguez, A., Phelps, M. E., Barrio, J. R., Gambhir, S. S., and Satyamurthy, N. (2003) Synthesis of a new heterobifunctional linker, N-[4-(Aminooxy-)butyl]maleimide, for facile access to a thiol-reactive 18F-labeling agent. *Bioconjugate Chem. 14*, 1253–1259.

(24) Wester, H. J., Hamacher, K., Guhlke, S., and Stoecklin, G. (1994) Simple and fast 18F-labeling of proteins by coupling with photogenerated [^{18}F]-arylnitrene. *J. Nucl. Med. 35*, P73–P73.

(25) Coenen, H. H. (2007) in *PET chemistry - the driving force in molecular imaging* (Schubiger, P. A. L., L., and Friebe, M., Eds.) Springer-Verlag, Berlin.

(26) Ting, R., Adam, M. J., Ruth, T. J., and Perrin, D. M. (2005) Arylfluoroborates and alkylfluorosilicates as potential PET imaging agents: High-yielding aqueous biomolecular 18F-labeling. *J. Am. Chem. Soc. 127*, 13094–13095.

(27) Mu, L. J., Hoehne, A., Schubiger, R. A., Ametamey, S. M., Graham, K., Cyr, J. E., Dinkelborg, L., Stellfeld, T., Srinivasan, A., Voigtmann, U., and Klar, U. (2008) Silicon-based building blocks for one-step 18F-radiolabeling of peptides for PET imaging. *Angew. Chem., Int. Ed. 47*, 4922–4925.

(28) Schirrmacher, R., Bradtmoller, G., Schirrmacher, E., Thews, O., Tillmanns, J., Siessmeier, T., Buchholz, H. G., Bartenstein, P., Waengler, B., Niemeyer, C. M., and Jurkschat, K. (2006) F-18-labeling of peptides by means of an organosilicon-based fluoride acceptor. *Angew. Chem., Int. Ed. 45*, 6047–6050.

(29) Fields, G. B., and Noble, R. L. (1990) Solid-phase peptide-synthesis utilizing 9-fluorenylmethoxycarbonyl amino-acids. *Int. J. Pept. Protein Res. 35*, 161–214.

(30) Oya, S., Choi, S. R., Coenen, H., and Kung, H. F. (2002) New PET imaging agent for the serotonin transporter: [^{18}F]ACF (2-[(2-amino-4-chloro-5-fluorophenyl)thiol-N, N-dimethyl-benzenmethanamine). *J. Med. Chem. 45*, 4716–4723.

(31) Li, Z. Z., Ding, Y. S., Gifford, A., Fowler, J. S., and Gatley, J. S. (2003) Synthesis of structurally identical fluorine-18 and iodine isotope labeling compounds for comparative imaging. *Bioconjugate Chem. 14*, 287–294.

(32) Gail, R., and Coenen, H. H. (1994) A one-step preparation of the n.c.a. ^{18}F labeled synthons - 4-fluorobromobenzene and 4-fluoroiodobenzene. *Appl. Radiat. Isot. 45*, 105–111.

(33) Hoehne, A., Mu, L., Honer, M., Schubiger, P. A., Ametamey, S. M., Graham, K., Stellfeld, T., Borkowski, S., Berndorff, D., Klar, U., Voigtmann, U., Cyr, J. E., Friebe, M., Dinkelborg, L., and Srinivasan, A. (2008) Synthesis, F-18-labeling, and in vitro and in vivo studies of bombesin peptides modified with silicon-based building blocks. *Bioconjugate Chem 19*, 1871–1879.

(34) Boswell, C. A., Regino, C. A. S., Baidoo, K. E., Wong, K. J., Bumb, A., Xu, H., Milenic, D. E., Kelley, J. A., Lai, C. C., and Brechbiel, M. W. (2008) Synthesis of a cross-bridged cyclam derivative for peptide conjugation and Cu-64 radiolabeling. *Bioconjugate Chem. 19*, 1476–1484.

(35) Van Domselaar, G. H., Okarvi, S. M., Fanta, M., Suresh, M. R., and Wishart, D. S. (2000) Synthesis and 99(m)Tc-labelling of bz-MAG3-triprolinyl-peptides, their radiochemical evaluation and in vitro receptor-binding. *J. Labelled Compd. Radiopharm. 43*, 1193–1204.

(36) Smith, C. J., Sieckman, G. L., Owen, N. K., Hayes, D. L., Mazuru, D. G., Kannan, R., Volkert, W. A., and Hoffman, T. J. (2003) Radiochemical investigations of gastrin-releasing peptide receptor-specific [Tc-99m(X)(CO)(3)-Dpr-Ser-Ser-Ser-Gln-Trp-Ala-Val-Gly-His-Leu-Met-(NH2)] in PC-3, tumor-bearing, rodent models: Syntheses, radiolabeling, and in vitro/in vivo studies where Dpr=2,3-diaminopropionic acid and X = H2O or P(CH2OH)(3). *Cancer Res. 63*, 4082–4088.

BC900240Z

Direct one-step ^{18}F-labeling of peptides via nucleophilic aromatic substitution

Jessica Becaud[a], Linjing Mu[a], Mylène Karramkam[a], Pius A. Schubiger[a], Simon M. Ametamey*[a], Keith Graham[b], Timo Stellfeld[b], Lutz Lehmann[b], Sandra Borkowski[b], Dietmar Berndorff[b], Ludger Dinkelborg[b], Ananth Srinivasan[b]*, René Smits[c], Beate Koksch[c]

[a] *Center for Radiopharmaceutical Science of ETH, PSI and USZ, Department of Chemistry and Applied Biosciences, ETH Zurich, CH-8093 Zurich, Switzerland*

[b] *Bayer Schering Pharma AG, Global Drug Discovery, D-13342 Berlin, Germany*

[c] *Department of Chemistry and Biochemistry-Organic Chemistry, FU Berlin, Takustraße 3, D-14195 Berlin, Germany.*

** Corresponding author. Center for Radiopharmaceutical Science of ETH, PSI and USZ, ETH Hönggerberg D-CHAB IPW HCI H427, Wolfgang-Pauli-Strasse 10, CH-8093 Zurich, Switzerland, Tel.: +41 44 633 74 63; fax: +41 44 633 13 67. E-mail address: simon.ametamey@pharma.ethz.ch (S. Ametamey).*

Supporting Information

General. All chemicals unless otherwise stated were purchased from Sigma-Aldrich or Merck and used without further purification. Analytical thin–layer chromatography (TLC) was performed on silica gel, NH_2 or RP-18 (60 F_{254}) plates (0.25 mm) precoated with a fluorescent indicator. Preparative thin-layer chromatography (preparative TLC) was performed on silica gel (60 F_{254}) plates (0.5 mm with concentrating zone) precoated

with a fluorescent indicator. Bruker Avance 300 and 400 were used for NMR measurements. ^{1}H-NMR, ^{13}C-NMR spectra were recorded as δ values relative to the solvent signal. Coupling constants are reported in Hertz. The multiplicity is defined by s (singlet), d (doublet), t (triplet), sept (septet), br (broad), m (multiplet).

Preparation of TMA-based model compounds

3-Fluoro-4-(methoxycarbonyl)-*N*,*N*,*N*-trimethylbenzenaminium trifluoromethanesulfonate (1a)

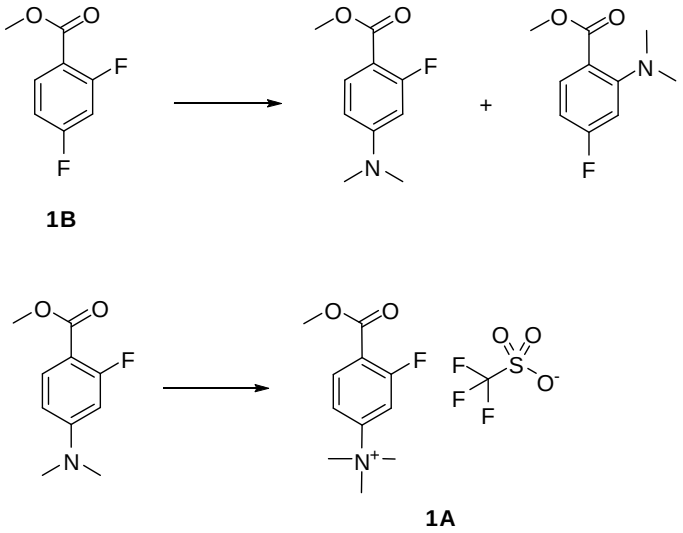

Scheme 1: Synthetic route for compound **1a**

To an autoclaved vessel was added methyl 2,4-difluorobenzoate (40 g, 225 mmol) in DMSO (600 ml) followed by dimethylamine hydrochloride (22.3 g, 270 mmol) and potassium carbonate (65.4 g, 473 mmol). The suspension was stirred for 5 hours at 55°C under a pressure of 0.5 bar. The reaction mixture was concentrated and the residue was

dissolved in dichloromethane and washed with water, brine, dried over Na_2SO_4 and concentrated *in vacuo*. The crude residue was subjected to silica chromatography (Hexane:EtOAc, 20:1 to 8:1) to give the methyl 4-(dimethylamino)-2-fluorobenzoate (25.2 g, 57%) and a by-product identified to be methyl 2-(dimethylamino)-4-fluorobenzoate (13.9 g, 31%).

Methyl 4-(dimethylamino)-2-fluorobenzoate

^{1}H NMR (400 MHz, $CDCl_3$) δ ppm 3.01 (s, 6 H), 3.86 (s, 3 H), 6.29 (dd, *J*=14.9, 2.5 Hz, 1 H, H-3), 6.41 (dd, *J*=8.9, 2.5 Hz, 1 H, H-5), 7.80 (t, *J*=8.9 Hz, 1 H, H-6)

^{13}C NMR (75 MHz, $CDCl_3$) δ ppm 40.1, 51.7, 98.8, 105.1, 107.1, 133.4, 154.8, 163.9 (d, *J* = 256.7 Hz), 165.3

ESI-MS: m/z 198 $[M+H]^+$

Methyl 2-(dimethylamino)-4-fluorobenzoate

^{1}H NMR (400 MHz, $CDCl_3$) δ ppm 2.87 (s, 6 H, NCH_3), 3.89 (s, 3 H, OCH_3), 6.52 (ddd, *J*=8.6, 7.6, 2.3 Hz, 1 H, H-5), 6.62 (dd, *J*=12.0, 2.3 Hz, 1 H, H-3), 7.70 (dd, *J*=8.6, 6.9 Hz, 1 H, H-6)

^{13}C NMR (75 MHz, $CDCl_3$) δ ppm 43.5, 52.1, 103.5, 105.5, 116.2, 134.1, 154.4, 165.4 (d, *J* = 250.7 Hz) 167.9

ESI-MS: m/z 198 $[M+H]^+$

To a solution of methyl 4-(dimethylamino)-2-fluorobenzoate (2.5 g, 13 mmol) in anhydrous dichloromethane (50 ml) was added methyl trifluoromethanesulfonate (20.5 g, 125 mmol) dropwise under a nitrogen atmosphere. The reaction mixture was refluxed for 2 days. The reaction mixture was concentrated and diethylether was added slowly. The product precipitates and the solvent was decanted. The solid was washed with

diethylether and purified by (C-18) RP-column chromatography (acetonitrile/water-gradient 1:99 to 80:20). The desired product **1a** was obtained in 78% yield (3.5 g).

^{1}H NMR (300 MHz, D_2O) δ ppm 3.59 (s, 9 H), 3.87 (s, 3 H), 7.69 (dd, *J*=8.7, 2.6 Hz, 1 H, H-5), 7.78 (dd, *J*=11.8, 2.6 Hz, 1 H, H-3), 8.10 (dd, *J*=8.7, 8.1 Hz, 1 H, H-6)

^{13}C NMR (75 MHz, D_2O) δ ppm 53.1, 57.0, 110.4, 116.2, 120.1, 133.9, 150.6, 161.6 (d, *J* = 261.5 Hz), 164.9

ESI-MS: m/z 212 $[M]^+$

2-Fluoro-4-(methoxycarbonyl)-*N*,*N*,*N*-trimethylbenzenaminium trifluoromethane-sulfonate (2a)

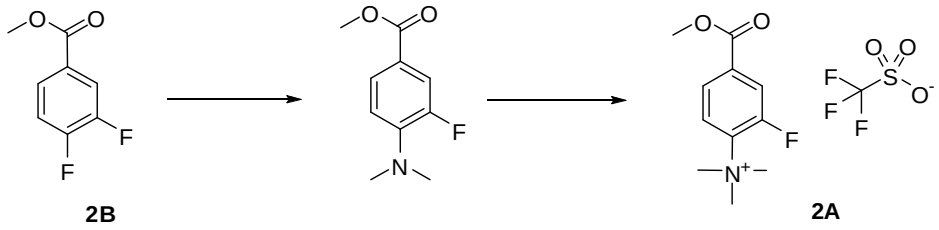

Scheme 2: Synthetic route for compound **2a**

To an autoclaved vessel was added methyl 3,4-difluorobenzoate (4 g, 23 mmol) in DMSO (60 ml) followed by dimethylamine hydrochloride (2.2 g, 27 mmol) and potassium carbonate (6.5 g, 47 mmol). The suspension was stirred for 5 h at 55°C under a pressure of 0.5 bar. The reaction mixture was concentrated and the residue was dissolved in dichloromethane (100 ml) and washed with water (2 x 50 ml), brine, dried over Na_2SO_4 and concentrated *in vacuo* to give methyl 4-(dimethylamino)-3-fluorobenzoate (3.9 g, 88%) which was used without further purification.

^{1}H NMR (600 MHz, $CDCl_3$) δ ppm 2.98 (d, *J*=1.5 Hz, 6 H), 3.87 (s, 3 H), 6.78 (t, *J*=8.6 Hz, 1 H), 7.64 (dd, *J*=14.7, 2.0 Hz, 1 H), 7.71 (dd, *J*=8.6, 2.0 Hz, 1 H)

ESI-MS: m/z 197 $[M]^+$

To a stirred solution of methyl 4-(dimethylamino)-3-fluorobenzoate (3.9 g, 20 mmol) in anhydrous dichloromethane (70 ml) was added methyl trifluoromethanesulfonate (32.8 g, 603 mmol) dropwise under nitrogen atmosphere. The reaction mixture was stirred for 2.5 days at RT and diethylether was added slowly. The product precipitates and the solvent was decanted. The solid was washed with diethylether and purified by (C-18) RP-column chromatography (acetonitrile/water-gradient 1:99 to 80:20). The desired product **2a** was obtained in 71% yield (5.1 g).

^{1}H NMR (300 MHz, D_2O) δ ppm 3.73 (s, 9 H), 3.93 (s, 3 H), 7.80 - 8.13 (m, 3 H)

^{13}C NMR (75 MHz, D_2O) δ ppm 53.2, 56.5, 120.0, 122.3, 126.6, 134.3, 136.1, 154.6 (d, *J* = 253.1 Hz), 166.2

ESI-MS: m/z 212 $[M]^+$

2-cyano-4-(methoxycarbonyl)-*N*,*N*,*N*-trimethylbenzenaminium trifluoromethanesulfonate (3a)

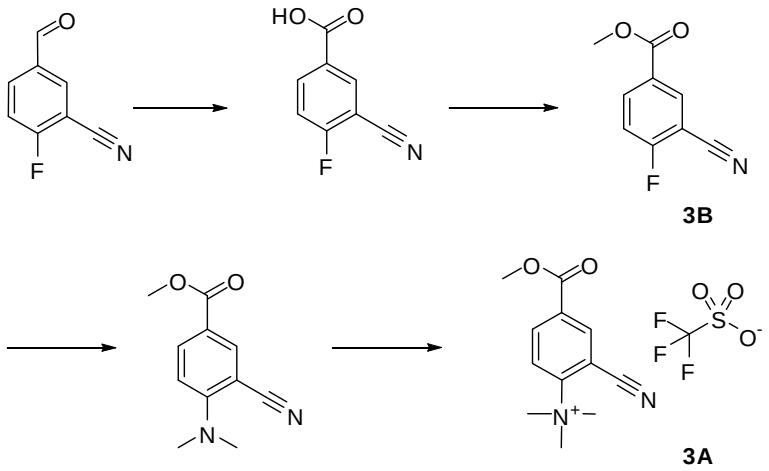

Scheme 3: Synthetic route for compound **3a** and **3b**

To an ice-cooled solution of 2-fluoro-5-formylbenzonitrile (20 g, 130 mmol) in tert-butanol (840 ml) and deionized water (200 ml) was added 2-methyl-2-butene (73 ml, 680 mmol), NaCl (54.4 g, 480 mmol) and Na_2HPO_4 (47.9 g, 307 mmol). The reaction mixture was stirred for 16 h at RT. The suspension was diluted with water and acidified to pH 3.5 with 1 M HCl. The solution was extracted twice with a mixture of dichloromethane and isopropanol (10:1). The combined organic phases were dried over sodium sulphate and concentrated. The solid residue was dissolved in sodium hydrogen carbonate solution and washed three times with diethylether. The aqueous phase was acidified to pH 3.5 with HCl (1 M) and the resulting precipitate was collected by filtration. The solid was dissolved in methanol, dried over Na_2SO_4, filtered and concentrated *in vacuo*. The resulting solid was washed with hexane and dried *in vacuo* at 35°C to give the 3-cyano-4-fluorobenzoic acid (20.2 g, 94%) which was used without further purification.

^{1}H NMR (300 MHz, MeOD) δ ppm 7.19 - 7.57 (m, 1 H), 8.23 - 8.44 (m, 2 H)

ESI-MS: m/z 164 $[M-H]^+$

Synthesis of methyl 3-cyano-4-fluorobenzoate (**3b**)

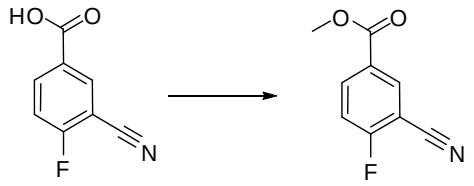

3B

To an ice-cooled suspension of 3-cyano-4-fluorobenzoic acid (24.6 g, 145 mmol) in methanol (250 ml) was added acetyl chloride (64 ml, 894 mmol) dropwise. The reaction mixture was stirred for 15 h. The reaction mixture was filtered and concentrated. The residue was dissolved in dichloromethane (300 ml) and washed with saturated $NaHCO_3$ solution (2 x 300 ml). The organic phase was dried over Na_2SO_4, filtered and concentrated to give the methyl 3-cyano-4-fluorobenzoate (24,6g, 92%) which was used without further purification.

^{1}H NMR (300 MHz, $CDCl_3$) δ = 3.96 (s, 3 H), 7.31 (t, *J*=8.6 Hz, 1 H), 8.19 - 8.40 (m, 2 H) ppm.

^{13}C NMR (63 MHz, $CDCl_3$) δ ppm 52.9, 112.2, 116.8, 117.1, 135.6, 136.5, 136.6, 164.3, 165.6 (d, *J*=218.3)

ESI-MS: m/z 180 $[M+H]^+$

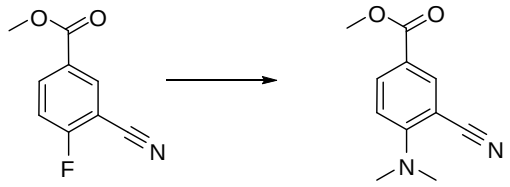

To a stirred solution of methyl 3-cyano-4-fluorobenzoate (19.5 g, 109 mmol) in DMSO (195 ml) was added dimethylamine hydrochloride (10.8 g, 131 mmol) followed by

potassium carbonate (31.6 g, 229 mmol). The reaction mixture was stirred at room temperature overnight and concentrated. The residue was dissolved in dichloromethane (200 ml) and washed with water (2 x 100 ml), brine, dried over Na_2SO_4 and concentrated *in vacuo* to give the methyl 3-cyano-4-(dimethylamino)benzoate in quantitative yield and was used without further purification in the next step.

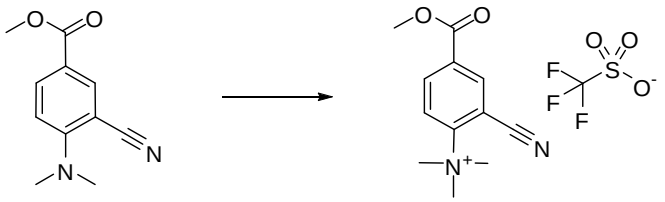

3A

To a stirred solution of methyl 3-cyano-4-(dimethylamino)benzoate (23.5 g, 115 mmol) in anhydrous dichloromethane (120 ml) was added methyl trifluoromethanesulfonate (100 g, 603 mmol) dropwise. The reaction was stirred at RT for 16 h and tert-butylmethylether (120 ml) was added slowly. The suspension was filtered and the collected solid was washed with tert-butylmethylether. The crude product was purified by (C-18) RP-column chromatography (acetonitrile/water-gradient 1:99 to 80:20) to afford product **3a** (14.8 g) in 63% yield.

^{1}H NMR (400 MHz, D_2O) δ ppm 3.87 (s, 9 H), 3.93 (s, 3 H), 8.15 (d, *J*=9.1 Hz, 1 H), 8.44 (dd, *J*=9.1, 2.1 Hz, 1 H), 8.67 (d, *J*=2.1 Hz, 1 H)

^{13}C NMR (101MHz, D_2O): δ ppm 53.6, 57.3, 105.9, 116.0, 122.9, 132.8, 136.4, 139.1, 148.7, 165.4

ESI-MS: m/z 219 $[M]^+$

4-carboxy-2-cyano-*N*,*N*,*N*-trimethylbenzenaminium trifluoromethanesulfonate

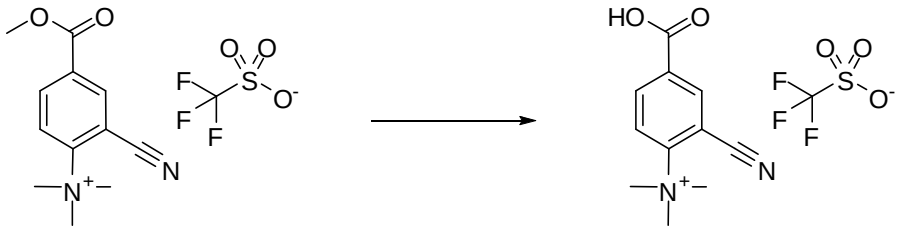

A solution of **3a** (5.4 g, 15 mmol) in water (127 ml) and TFA (127 ml) was heated at 120°C for 48 h. The reaction mixture was concentrated *in vacuo*, the light green oil was treated with diethylether to result a suspension. This solid was collected by filtration, washed with diethylether and dried *in vacuo* to give 4-carboxy-2-cyano-*N*,*N*,*N*-trimethylbenzenaminium trifluoromethanesulfonate (4.6 g, 89%)

^{1}H NMR (300 MHz, DMSO) δ ppm 3.85 (s, 9 H), 8.23 - 8.35 (m, 1 H), 8.39 - 8.49 (m, 1 H), 8.58 (d, *J*=2.07 Hz, 1 H)

^{13}C-NMR (101 MHz, D_2O) δ ppm 57.3, 105.7, 116.1, 122.7, 133.8, 136.5, 139.2, 148.5, 166.8

ESI-MS: m/z 205 $[M]^+$

4-(methoxycarbonyl)-*N*,*N*,*N*-trimethyl-2-(trifluoromethyl)benzenaminium trifluoro-methanesulfonate (4a)

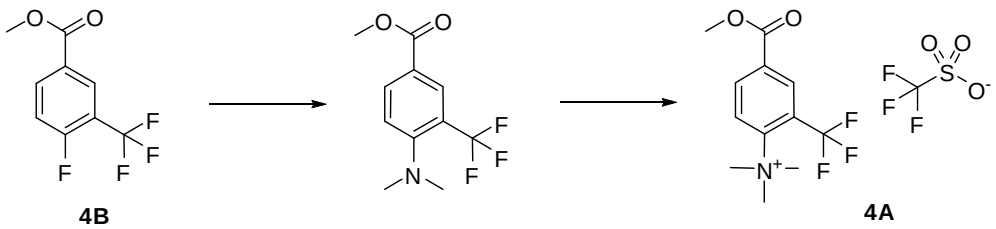

Scheme 4: Synthetic route for compound **4a**

To a solution of methyl 4-fluoro-3-(trifluoromethyl)benzoate (45.5 g, 200 mmol) in DMSO (500 ml) under nitrogen atmosphere was added dimethylamine hydrochloride (20.0 g, 250 mmol) followed by potassium carbonate (59.5 g, 430 mmol). The reaction mixture was stirred at 60°C for 8 h in an autoclave and then concentrated with high vacuum rotation evaporator at 65°C. The residue was dissolved in dichloromethane (200 ml) and washed with water (2 x 100 ml), brine, dried over Na_2SO_4 and concentrated. The oily crude product was purified by column chromatography (Hexane: EtOAc; 9:1) to give methyl 4-(dimethylamino)-3-(trifluoromethyl)benzoate (12.3 g, 45%).

^{1}H NMR (300 MHz, $CDCl_3$) δ ppm 2.94 (s, 6 H, NCH_3), 3.94 (s, 3 H, OCH_3), 7.15 (d, *J*=8.8 Hz, 1 H, H-6), 8.07 (dd, *J*=8.8, 2.1 Hz, 1 H, H-5), 8.31 (d, *J*=2.1 Hz, 1 H, H-3)

^{13}C-NMR (125 MHz, $CDCl_3$) δ ppm 44.4, 52.2, 110.5, 119.9, 124.3 (q, *J*=272 Hz), 130.6, 133.6, 135.0, 156.0, 166.2

ESI-MS: m/z 248 $[M+H]^+$

To a stirred solution of methyl 4-(dimethylamino)-3-(trifluoromethyl)benzoate (22.4 g, 91 mmol) in anhydrous dichloromethane (400 ml) under a nitrogen atmosphere was added dropwise methyl trifluoromethanesulfonate (150.2 g, 603 mmol). The reaction was stirred at RT for 60 h. To the reaction mixture was added diethylether slowly which led to the precipitate. After filtration, the residue was purified by using a LiChroPrep RP18 column (H2O 100% to H2O:acetonitrile 3:1). Starting material (8.8 g, 39%) and 4-

(methoxycarbonyl)-*N*,*N*,*N*-trimethyl-2-(trifluoromethyl) benzenaminium trifluoro-methanesulfonate (11.8 g, 32%) was isolated.

^{1}H NMR (400 MHz, D_2O) δ ppm 3.86 (s, 9 H, NCH_3), 3.97 (s, 3 H, OCH_3), 8.28 (d, *J*=9.0 Hz, 1 H, H-6), 8.44 (dd, *J*=9.0, 2.1 Hz, 1 H, H-5), 8.65 (d, *J*=2.1 Hz, 1 H, H-3)

^{13}C NMR (100 MHz, D_2O) δ ppm 55.9, 61.6, 120.6, 123.7, 125.7 (d, *J*=232 Hz), 126.7, 135.0, 137.9, 149.5, 168.4

ESI-MS: m/z 262 $[M]^+$

2-cyano-4-(*N*-(2-methoxy-2-oxoethyl)-*N*-methylsulfamoyl)-*N*,*N*,*N*-trimethylbenzenaminium trifluoromethanesulfonate (5a)

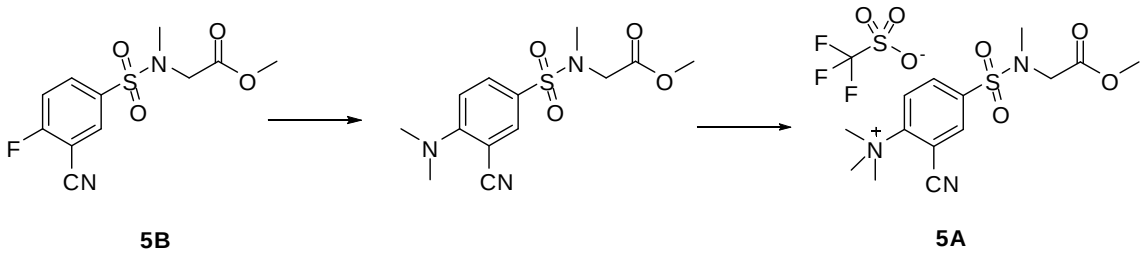

Scheme 5: Synthetic route for compound **5a**

To a stirred solution of methyl 2-(3-cyano-4-fluoro-*N*-methylphenyl-sulfonamido)acetate (5.7 g, 20 mmol) in DMSO (60 ml) were added dimethylamine hydrochloride (2.0 g, 24.7 mmol) and potassium carbonate (6.0 g, 43 mmol). The reaction mixture was stirred over night and then concentrated under high vacuum at 60°C. The residue was diluted with dichloromethane and washed twice with water. The combined aqueous phases were extracted with dichloromethane. The combined dichloromethane phases were washed with diluted sodium hydrogen carbonate solution, dried over sodium sulphate and

concentrated. The oily crude product methyl 2-(3-cyano-4-(dimethylamino)-*N*-methylphenylsulfonamido) acetate was obtained in 95% yield (5.9 g, 20 mmol) and was used directly in the next step without further purification.

To a stirred solution of methyl 2-(3-cyano-4-(dimethylamino)-*N*-methylphenylsulfonamido)acetate (3.9 g, 13 mmol) in dichloromethane (50 ml) was added methyl trifluoromethanesulfonate (20.5 g, 125 mmol) dropwise. The reaction mixture was refluxed for 2 days then cooled to room temperature. Diethylether was added. The desired compound precipitated and the solvent was decanted off. The crude product was purified by (C-18) RP-column chromatography (acetonitrile/water - gradient 1:99 to 80:20). The desired compound **5a** was obtained in 43 % yield (2.6 g, 5 mmol).

^{1}H NMR (400 MHz, D_2O) δ ppm 3.03 (s, 3 H), 3.75 (s, 3 H), 4.00(S, 9H), 4.29 (S, 2H), 8.37 (d, *J*=9.1 Hz, 1 H), 8.44 (dd, *J*=9.1, 2.2 Hz, 1 H), 8.73 (d, *J*=2.2 Hz, 1 H)

^{13}C NMR (100 MHz, D_2O) δ ppm 35.5, 50.9, 52.9, 57.3, 106.8, 115.3, 123.7, 134.3, 136.8, 140.6, 148.7, 171.1

ESI-MS: 326 (M^+ , 100).

^{18}F-labeling of TMA-based model compounds

Methyl-2-fluoro-4-[^{18}F]fluorobenzoate (**[^{18}F]1b**). ^{18}F-fluoride (839 MBq) was azeotropically dried in the presence of Kryptofix $K_{2.2.2}$ (5 mg in 1 ml MeCN) and potassium carbonate (1.0 mg in 0.5 ml water) by heating under nitrogen at 105°C for 30 min. During this time 2 × 1 ml MeCN were added and evaporated. After drying, a solution of compound **1a (**1 mg) in DMSO (100 μl) was added. The reaction vessel was

sealed and heated at 70°C for 15 min to effect labeling. The crude reaction mixture was analyzed using an analytical HPLC (ACE C18 column (50 × 4.6 mm, 3 μm)), the incorporation yield was 79%. The ^{18}F labeled product was confirmed by co-injection with the ^{19}F cold standard on the same column.

Methyl-3-fluoro-4-[^{18}F]fluorobenzoate (**[^{18}F]2b**). ^{18}F-fluoride (751 MBq) was azeotropically dried in the presence of Kryptofix $K_{2.2.2}$ (5 mg in 1 ml acetonitrile) and potassium carbonate (1 mg in 0.5 ml water) by heating under nitrogen at 105°C for 30 min. During this time 2 × 1 ml MeCN were added and evaporated. After drying, a solution of compound **2a** (1 mg) in DMSO (100 μL) was added. The reaction vessel was sealed and heated at 50°C for 15 min to effect labeling. The crude reaction mixture was analyzed using an analytical HPLC (ACE C18 column (50 × 4.6 mm, 3 μm)), the incorporation yield was 82%.

Methyl-3-trifluoromethyl-4-[^{18}F]flurobenzoate (**[^{18}F]4b**). ^{18}F-fluoride (73 MBq) was azeotropically dried in the presence of Kryptofix $K_{2.2.2}$ (5 mg in 1.5 ml MeCN) and potassium carbonate (1 mg in 0.5 ml water) by heating under nitrogen at 105°C for 30 min. During this time 2 × 1 ml MeCN were added and evaporated. After drying, a solution of methyl 3-trifluoromethyl-4-trimethylammoniumbenzoate triflate salt (2 mg) in DMSO (300 μL) was added. The reaction vessel was sealed and heated at 50°C for 15 min to effect labeling. The crude reaction mixture was analyzed using an analytical HPLC (ACE C18 column), the incorporation yield was 79%. The ^{18}F labeled product was confirmed by co-injection with the ^{19}F cold standard on the same HPLC column.

In vitro binding affinity assay

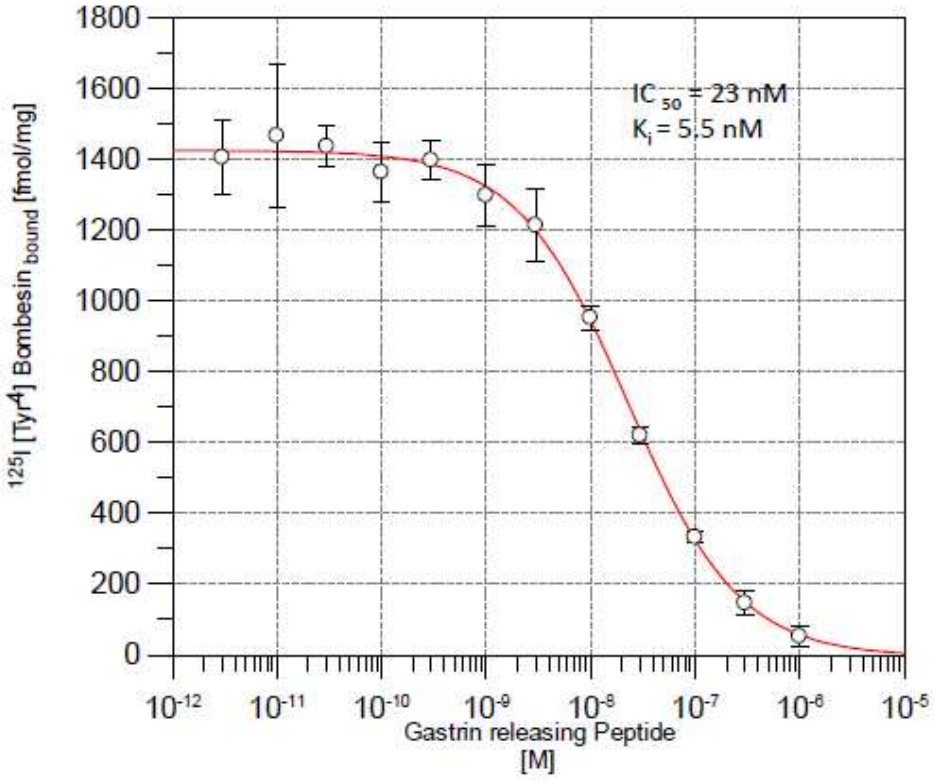

Figure 1. Competitive binding of human GPR versus [^{125}I]-Tyr^4-bombesin on human bombesin 2 receptor membranes in a scintillation proximity assay (Positive control).

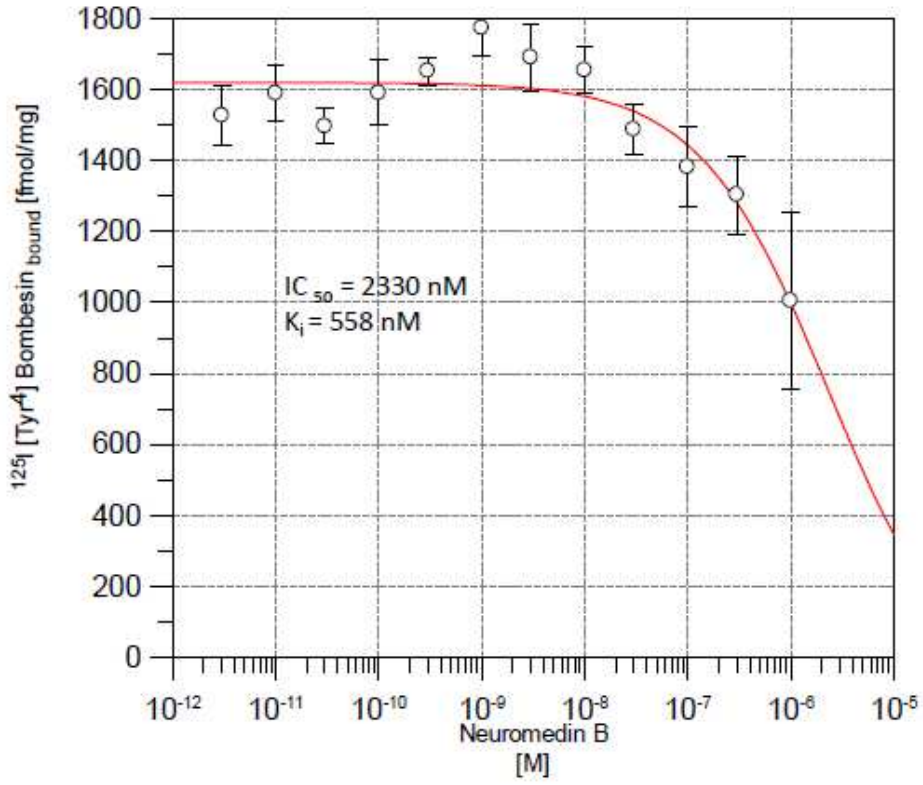

Figure 2. Competitive binding of Neuromedin B versus [^{125}I]-Tyr^4-bombesin on human bombesin 2 receptor membranes in a scintillation proximity assay (Negative control).

Snail1 Down-Regulation using Small Interfering RNA Complexes Delivered through Collagen Scaffolds

Rosa Viñas-Castells,[†,‡] Carolyn Holladay,[†] Andrea di Luca,[†] Victor Manuel Díaz,[‡,§] and Abhay Pandit*[,†]

Network of Excellence for Functional Biomaterials, National University of Ireland, Galway, Ireland, Programa de Recerca en Cancer, IMIM-Hospital del Mar, Barcelona, Spain, and Departament de Ciències Experimentals i de la Salut, Universitat Pompeu Fabra, Barcelona, Spain. Received June 10, 2009; Revised Manuscript Received October 16, 2009

Control of gene expression via small interfering RNA has enormous potential for the treatment of a variety of diseases, including cancer and Huntington's disease. However, before any therapies can be developed, effective techniques for controlled delivery of these molecules must be devised. In this proof-of-concept study, small interfering RNA was complexed with a polymer and loaded into a biomaterial scaffold. The scaffold was introduced primarily to control the release of the complexes, and the polymer was introduced to improve the transfection efficiency. An optimal dose and complexation ratio were selected, at which more than 50% down-regulation of the target gene Snail1 was observed in two-dimensional culture. Delayed release of the complexes was observed, and significant sustained down-regulation of Snail1 was seen in a three-dimensional scaffold system after 7 days. Thus, the use of the scaffold altered the transfection profile significantly, demonstrating the feasibility of a collagen scaffold as a controlled release system for delivery of small interfering RNA−dendrimer complexes.

INTRODUCTION

Cancer manifests through six basic alterations in cell behavior that lead to malignant growth: self-sufficient growth signaling, insensitivity to growth-inhibitory signals, evasion of apoptosis, unlimited reproduction, sustained angiogenesis, and metastasis (*1*). In epithelial tumor progression, metastasis can occur when loosely attached cancerous cells detach and migrate via the bloodstream to other tissues and organs.

E-cadherin (EC), which is localized in the adherens junctions between epithelial cells, has been found to be down-regulated in epithelial tumors that undergo a process termed "epithelial to mesenchymal transition" (EMT). Decreasing EC levels damage the adherens junctions, and therefore low EC is hypothesized to be among the factors promoting metastasis. The transcription factor Snail1 represses EC production (*2, 3*). Therefore, elevated levels of Snail1 decrease the strength of adherens junctions and thus increase tumor metastasis (*4*). Down-regulation of Snail1 is thus hypothesized to decrease metastasis of epithelial tumors.

RNA interference is a technique used in gene therapy to down-regulate expression of targeted genes. Short (21−23 nucleotides), double-stranded RNA sequences are incorporated into a RNA-induced silencing complex (RISC) and then can bind complementary mRNA strands. The bound mRNA is degraded, thus preventing translation of the gene in question (*5, 6*). However, to be effective, the small interfering RNA (siRNA) must reach the RISC and selectively bind the targeted sequence. Thus, the siRNA must be internalized by the targeted cell type, escape the endosome or lysosome, avoid incorrect intracellular routing, and still be bioactive when it reaches the RISC (*7*). Many of the challenges cited here are similar to those encountered for plasmid gene delivery (*8*).

siRNA is not biologically stable, and even *in vitro*, chemical modification of the sequence or complexation with a carrier system is required to prevent rapid degradation. While chemical modifications can increase the half-life of the siRNA, they do not significantly increase internalization. Thus, carrier systems are an appealing alternative. Both *in vitro* and *in vivo* delivery of siRNA using cationic liposomes and polymers has been described (*7*). Many of these systems are theoretically suitable for conjugation to targeting molecules that can guide them to the targeted tissues or cell types. These carriers may also have the potential to improve endosomal escape and intracellular routing (*9*).

Early transfection studies using the polyamidoamine (PAMAM) dendrimeric system indicated that PAMAM could be effectively complexed with a variety of forms of nucleic acids, and that increased complexation could be achieved by modifying the chemistry of the interaction (*10*). However, later studies focused on modified PAMAM dendrimers (*11−13*). In many of these studies, a partially degraded version, SuperFect (dPAMAM), has been shown to be among the most effective transfection reagents on the market (*10−20*). These compounds have been used both *in vitro* and *in vivo* with significant success (*10, 11, 18, 21, 22*).

Biomaterials have also been described as gene transfer agents, both for plasmids and for siRNA. Atelocollagen, in particular, has been found to be an effective complexing agent for siRNA (*23*). Atelocollagen−siRNA complexes were found to be efficiently internalized and resistant to nucleases that would ordinarily destroy exogenous nucleic acids (*24*). Furthermore, treatment with these atelocollagen−siRNA complexes resulted in effective down-regulation of targeted genes both *in vitro* and *in vivo* (*24, 25*).

The relative success of dendrimer−siRNA complexes in protecting siRNA, increasing its level of internalization, and assisting its endosomal escape make these agents promising vectors. However, it is well-known that the time scale of siRNA transfection can be problematic; for greater than 90% inhibition of a target gene, biologically active siRNA must be able to act for longer than three times the half-life of the protein in question

* To whom correspondence should be addressed. Phone: +353 91 492758. E-mail: abhay.pandit@nuigalway.ie.
[†] National University of Ireland.
[‡] IMIM-Hospital del Mar.
[§] Universitat Pompeu Fabra.

10.1021/bc900241w © 2009 American Chemical Society
Published on Web 11/16/2009

Table 1. Details of Anti-Snail1 siRNA Sequences

versions of anti-Sna1 siRNA	sequence
1	UGACCUCGCUGUCCGAUGAUU (sense)
	5′-PUCAUCGGACAGCGAGGUCAUU (antisense)
2	GAUCUUCAACUGCAAAUAUUU (sense)
	5′-PAUAUUUGCAGUUGAAGAUCUU (antisense)
3	CAAACCCACUCGGAUGUGAUU (sense)
	5′-PUCACAUCCGAGUGGGUUUGUU (antisense)
4	GCCGGAAGCCCAACUAUAGUU (sense)
	5′-PCUAUAGUUGGGCUUCCGGCUU (antisense)

(*7*). Thus, a combination of dendrimer−siRNA complexes with an atelocollagen scaffold is proposed. It is hypothesized that combining the high transfection efficiency of the dendrimer and the slow release mechanism from the collagen will allow efficient, longer-term gene down-regulation.

Optimization of dendrimer−siRNA complexation was required prior to any transfection experiments. Characterization of the chemical interactions between the two components, followed by basic internalization experiments was used to choose the formulations tested for transfection ability. Basic transfection experiments were then used to determine the optimal complex formulation for use in the final set of experiments. The final experiments test the hypothesis that the combination of dendrimer−siRNA complexes with an atelocollagen scaffold can be used to control the release rate of the complexes and the time course of siRNA-mediated protein down-regulation.

EXPERIMENTAL PROCEDURES

Anti-Snail1 siRNA. Anti-Snail1 siRNA was purchased from Dharmacon (Chicago, IL). The siRNA was specific to the Snail1 homologue 1 (*Drosophila*), ID20613 for mouse (SNAI1) ON-TARGET*plus* SMART*pool*. It was supplied as a pool of four sequences (Table 1). The dPAMAM (SuperFect) used to complex siRNA for delivery was purchased from Qiagen (Germany).

Preparation of Complexes. Control siRNA (siGLO anti-cyclophilin B siRNA ON-TARGET*plus* control siRNA, Dharmacon, Chicago, IL) was combined with dPAMAM at a variety of amine to phosphate (N/P) ratios. The dPAMAM concentration was approximately 2.8 mM amine groups (2.8 nmol/μL). Thus, 1 μg of siRNA combined with 1 μL of dPAMAM yielded complexes at an N/P ratio of 1:1. The siRNAs were supplied lyophilized and were resuspended in an RNase-free buffer (20 mM KCl, 6 mM *N*-2-hydroxyethylpiperazine-*N*′-2-ethanesulfonic acid (HEPES) at pH 7.5 and 0.2 mM $MgCl_2$) at a concentration of 20 μM. Appropriate volumes of dPAMAM solution were combined with the siRNA solution in sterile TE buffer. The siRNA-containing solutions were kept on ice to minimize siRNA degradation.

Confirmation of Complexation. Complexation was confirmed using two methods. For dye exclusion studies, complexes prepared at N/P ratios of 1−10 were loaded into a polyacrylamide gel. The gel was run at 150 V for approximately 1 h, then removed from the electrophoresis apparatus and stained with SYBRGold nucleic acid gel stain (Invitrogen, Paisley, U.K.) for 45 min. The gel was imaged at 254 nm in a transilluminator (Universal Hood II, Bio-Rad, Hercules, CA). For the TEM studies, complexes were prepared at varying N/P ratios then imaged with a Hitachi H-7500 transmission electron microscope (Tokyo, Japan).

Cell Culture. NIH3T3 fibroblast cells were used for all cell culture experiments since they are well-characterized and readily available. Furthermore, they constitutively express high levels of Snail1, which is a good model to use to revert or reduce EMT. Twenty-four hours before siRNA was delivered, 2×10^5 NIH3T3 cells were plated in 6 well plates. After 24 h incubation, which was necessary to allow cells to attach and start proliferating, the cells were washed with phosphate-buffered saline (PBS) and fluorescently tagged control siRNA complexes were delivered at N/P ratios of 1−10 and at doses of 50, 75, 100, and 200 nM. The transfected plates were then returned to the incubator and left for 24 h.

Internalization Studies. The internalization studies included fluorescent microscopy and fluorescence-activated cell sorting (FACS) analysis. In the samples intended for microscopy, the transfected cells were washed, fixed, and stained with 4′,6-diamidino-2-phenylindole (DAPI). Images were taken with DAPI and rhodamine filter sets and superimposed over phase contrast images.

For FACS analysis, cells were washed twice with PBS, trypsinized, centrifuged, washed again, and resuspended in media. The resuspended cells were analyzed with a FACScalibur (Becton Dickinson, Franklin Lakes, NJ) equipped with CellQuest software, V3.3. The threshold was selected based on unmodified NIH3T3 cells (control).

Cytotoxicity Studies. The cytotoxicity of the complexes was evaluated by measuring the metabolic activity of transfected wells. The metabolic activity was assessed with the AlamarBlue (AB) assay (Invitrogen, U.K.). Briefly, 24 h after transfection, cells were washed with PBS, a dilution of 1:10 of AB in PBS was added to the wells, and the plate was returned to the 37 °C incubator for 3 h. The AB solution was then transferred into a 96 well plate, and the fluorescence was read at 590 nm.

Semiquantitative Reverse Transcription Polymerase Chain Reaction (RT-PCR). Initial transfection experiments indicated that a single delivery of siRNA complexes, while allowing high levels of internalization, did not measurably decrease protein expression levels. Thus double delivery of the complexes was used in the transfection experiments. The transfection protocol used was similar to that described earlier, except that 24 h after the first transfection, the same dose and N/P ratio of siRNA complexes was added and the cells were left a further 24 h. In this case, the control condition was control siRNA complexed at an N/P of 8. It was also delivered twice.

Analysis of mRNA levels was carried out by RT-PCR using 0.25 μg of total RNA per sample. RNA was extracted using PureLink Micro-to-Midi total RNA purification system (Invitrogen, Carlsbad, CA) and quantified using a Nanodrop system (ND-1000 spectrophotometer with the analysis software V3.3.0).

PCR analysis was performed using SuperScript OneStep RT-PCR kit with Platinum Taq (Invitrogen, Carlsbad, CA) and using oligonucleotides corresponding to the sequence +104/+125 and +290/+31 in order to analyze the RNA levels of Snail1 in the cells. The following oligonucleotides were used for the analysis of Snail1: 5′-GGCGGATCCACCATGCCGCGCTCCTTCCTG-3′ for forward transcription and 5′-CAAGATATCCGCCTC-CGGAGCA-3′ for reverse transcription. The endogenous housekeeping gene HPRT (hypoxanthine-guanine phosphoribosyl transferase) was used to normalize the RNA quantifications, using the oligonucleotides 5′-GGCCAGACTTTGTTGGATTTG-3′ for forward transcription and 5′-TGCGCTCATCTTAG-GCTTTGT-3′ for reverse transcription. All primers were obtained from Invitrogen (UK) and the thermocycler was from Biometra (T-Gradient Thermoblock, Göttingen, Germany).

Western Blotting. Analysis of protein expression levels was conducted using Western blotting. Twenty-four hours after the second delivery of siRNA, the cells were washed with PBS and lysed using 150 μL of total lysis buffer (20 mM HEPES, pH 7.8, 25% glycerol, 420 mM NaCl, 1% Triton X-100, 1.5 mM $MgCl_2$, 0.2 mM EDTA, and protease inhibitors). The lysate was scraped from the plate, placed in a centrifuge tube and agitated at 4 °C for 10 min. The tubes were centrifuged to precipitate insoluble particles. Total protein quantity was estimated using a standard kit (Bio-Rad Laboratories, Hercules, CA). Bovine serum albumin was used as a standard. Snail1 protein levels were measured via Western blotting. Annexin II was used as

loading control. Anti-Snail1 antibody was monoclonal (*26*), and antiannexin II was rabbit polyclonal (*27*).

Scaffold Preparation. One milligram cross-linked atelocollagen scaffolds were prepared as described by Holladay et al. (*28*). Briefly, 333 μL of 3 mg/mL atelocollagen solution was lyophilized, then cross-linked with 1-ethyl-3-(3-dimethylaminopropyl) (EDC) and *N*-hydroxylsuccinimide (NHS) at an EDC−NHS−collagen carboxyl group ratio of 5:5:1. The scaffolds were then washed thoroughly and freeze-dried again. siRNA−dPAMAM complexes (200 nM) in a total volume of 30 μL were loaded into the dry 1 mg scaffolds.

Elution Studies. Release of the siRNA−dPAMAM complexes was evaluated using the fluorescence from the control siRNA, which is labeled with rhodamine. Briefly, complexes were prepared at N/P = 8 then loaded onto the cross-linked scaffolds in a black 96 well plate. The loaded scaffolds were incubated for 2 h at room temperature to allow the complexes to associate with the scaffold. After this time, cell culture media containing 10% FBS was added to each scaffold. The scaffolds were removed from the media and placed in fresh media. At each time point, this process was repeated. At the end of the experiment, the siRNA content of the solutions was quantified by measuring the fluorescence with a Varioskan Flash spectral scanning multimode reader (Thermo Scientific, Vantaa, Finland) and the cumulative release of siRNA−dPAMAM complexes from the scaffold was calculated.

Scaffold-Based Transfection. siRNA−dPAMAM complexes (200 nM) in a total volume of 30 μL were loaded into dry 1 mg scaffolds. The loaded scaffolds were incubated at room temperature for 2 h to allow the complexes to associate with the collagen. NIH3T3 cells (7×10^4) were added to the scaffolds after this incubation. After 24 h, the scaffolds were transferred to a new plate to ensure that all of the cells were attached to the scaffold and not to the plate. New media was added to the scaffolds in the new plate, and the media was changed every 2 days until the end of the experiment.

At given time points (24 h, 48 h, and 7 days), the scaffolds were removed from the wells, placed in centrifuge tubes, and centrifuged for 5 min at 3000 rpm, and the supernatant was discarded. The scaffolds were stored at −20 °C. When the samples from all of the experiments were ready, the tubes were thawed, and 25 μL of 2× Laemmli sample buffer was added to each sample. The samples were vortexed for 5 min, then boiled for 5 min at 100 °C. Western blotting, as previously described, was then carried out. Quantification was performed with densitometry using annexin II levels as a normalizing control.

Statistics. Graphical results are expressed as mean ± standard deviation. Where applicable, statistical significance was assessed using the analysis of variance (ANOVA). *P* values of <0.05 were considered significant. The minimum sample size (*n*) was 3.

RESULTS

Basic confirmation of siRNA−dPAMAM complexation was performed by dye exclusion of SYBRGold nucleic acid stain. Figure 1 shows an acrylamide gel with a variety of N/P ratios, and uncomplexed siRNA as a control. With increasing N/P ratio, the degree of complexation increases as evidenced by the decreasing intensity of the bands. Complexation was further confirmed with TEM, as shown in Figure 2. The particles formed at N/P = 4 had an average diameter of approximately 100 ± 25 nm, while the particles prepared at N/P = 8 were much smaller, with an average diameter of 25 ± 12 nm.

Having observed complex formation, it was necessary to determine that the complexes were internalized. Thus, control siRNA with a fluorescent tag was complexed at a variety of N/P ratios and added to cell culture media. The cells were

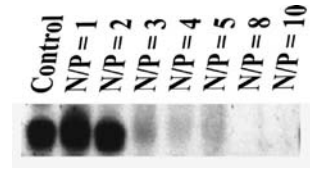

Figure 1. siRNA complexation as a function of N/P ratio. As the degree of complexation increases, the binding of SYBRGold stain to the siRNA becomes more inhibited. Thus, the SYBRGold is able to bind completely in the control band, and it is only at a N/P ratio of 3 that visually clear inhibition of binding occurs.

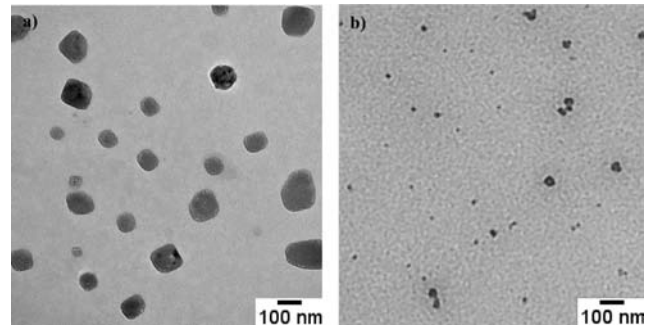

Figure 2. Representative transmission electron micrographs (TEM) of siRNA−dendrimer complexes. Complexes prepared at (a) N/P = 4 and (b) N/P = 8 demonstrate the effect of N/P ratio on the size of the complexes. At N/P = 4, the size of the complexes were significantly larger than at N/P = 8. The average particle diameters were, respectively, 100 ± 25 nm and 25 ± 12 nm.

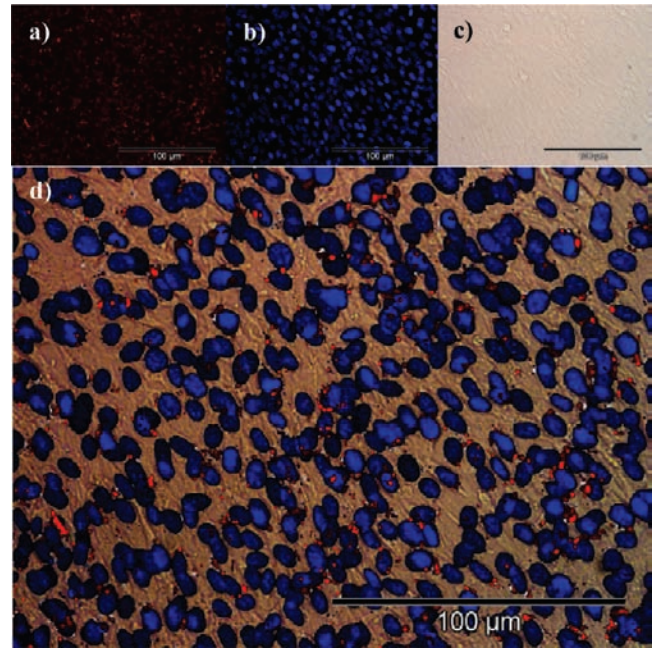

Figure 3. Micrograph showing uptake of DY-547 tagged siRNA by NIH3T3 cells. The siRNA dose used in this experiment was 200 nM at an N/P of 8. The control siRNA used in this experiment (siGLO cyclophilin B control siRNA, Dharmacon) fluoresces in the Cy3/rhodamine range. The siRNA appears to mostly localize to the nuclei (stained blue with DAPI). The two fluorescence images are superimposed over a phase-contrast image of the same area.

washed to remove unbound complexes, and analyzed by fluorescence microscopy 48 h after exposure to complexes. Figure 3 shows red complexes inside the vast majority of cell, indicating relatively high internalization levels. Figure 4 consists of FACS output graphs showing fluorescence vs side scatter from control cells and cells transfected with 100 and 200 nM

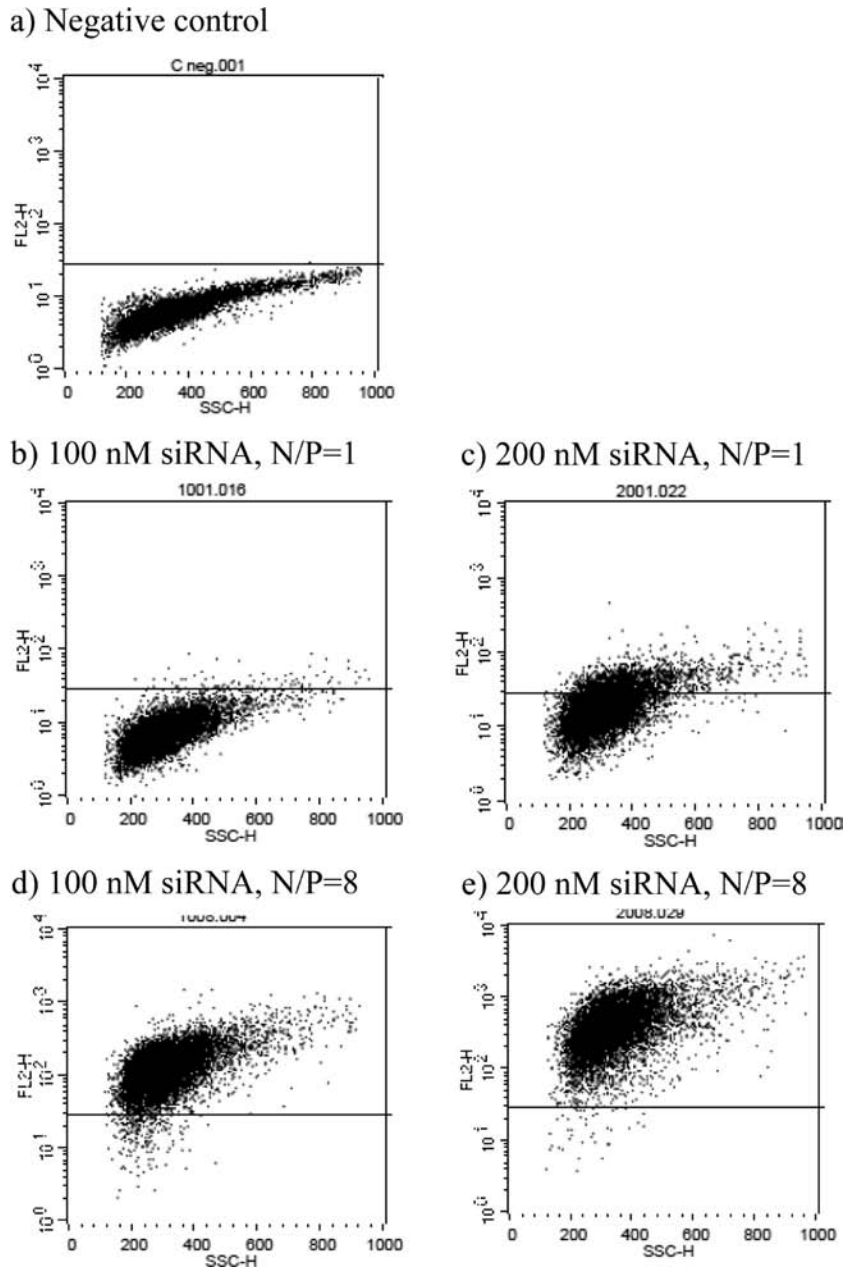

Figure 4. FACS output after transfection of siGLO control siRNA into NIH3T3 cells. The control sample had no fluorescent signal above the line, whereas with increasing N/P ratio and dose, the fluorescent signal of the cells was significantly increased implying internalization of labeled siRNA.

siRNA doses at two different N/P ratios. The distribution of fluorescence with respect to side scatter shifts slightly upward after exposure to siRNA at N/P = 1. Exposure of cells to siRNA complexed at N/P = 8 shifted the distribution almost entirely outside of the range of the control cells. The 200 nM dose had a more significant effect than the 100 nM dose at both N/P = 1 and N/P = 8. Because the lower N/P ratios were found to be less effectively internalized, only N/P ratios of 4−8 were tested in subsequent studies.

Cytotoxicity was evaluated by comparing the metabolic activity of NIH3T3 cells after exposure to 100 and 200 nM doses at N/P = 4−8 as shown in Figure 5. No significant differences were observed between the two doses, nor was any dependency on N/P ratio observed. In fact, no difference between any group and the control samples was found to be statistically significant. Because no effect on cell viability could be observed, it was concluded that the complexes demonstrated negligible cytotoxicity.

The effects of Snail1 transfection were evaluated at the mRNA level, as well as the protein expression level. Figure 6 shows representative semiquantitative RT-PCR bands of cells transfected with 200 nM anti-Snail1 siRNA and N/P ratios of 6−8. These bands are compared with cells transfected with control siRNA (200 nM, N/P = 8). The only band that qualitatively showed a major change in Snail1 level was a dose of 200 nM at N/P = 8. Figure 7 shows representative protein expression levels (Western blot) at 100 and 200 nM doses and an N/P ratio of 4−8. No significant differences were observed after densitometry analysis of the bands treated with 100 nM of anti-Snail1 siRNA, but the 200 nM dose was found to significantly decrease Snail1 production at N/P = 5−8.

The optimal formulation for anti-Snail1 siRNA−dPAMAM complexes was thus selected as a dose of 200 nM and N/P = 8 for NIH3T3 cells. Significant down-regulation was observed at both the mRNA and protein level with this formulation. The

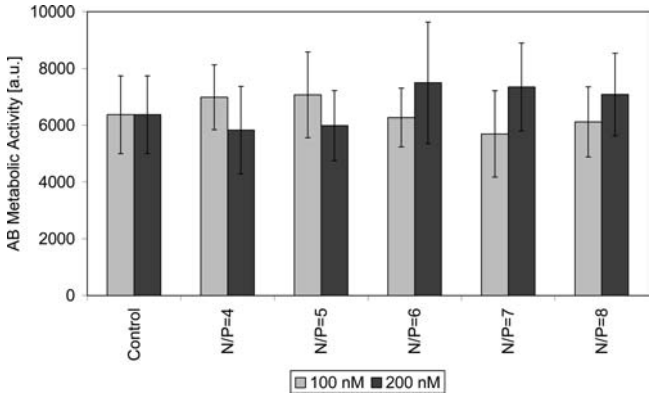

Figure 5. Metabolic activity as a function of siRNA dose and N/P ratio. No significant differences were observed between the control (no siRNA added) and 100 and 200 nM doses nor varying charge ratios, indicating negligible cytotoxicity (ANOVA, $p < 0.05$, $n = 5$).

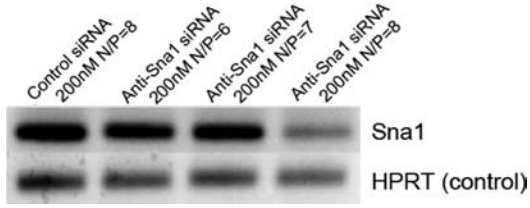

Figure 6. Down-regulation of Snail1 mRNA levels as a function of dose and N/P ratio. Twenty-four hours in advance, 2×10^5 NIH3T3 cells were seeded in a 6 well plate. siRNA complexed with dPAMAM was delivered twice (24 and 48 h after seeding), at a variety of charge ratios, and mRNA levels were evaluated with RT-PCR 72 h after seeding. HPRT was used to normalize the data. Three N/P ratios were compared with control (anticyclophilin B) siRNA.

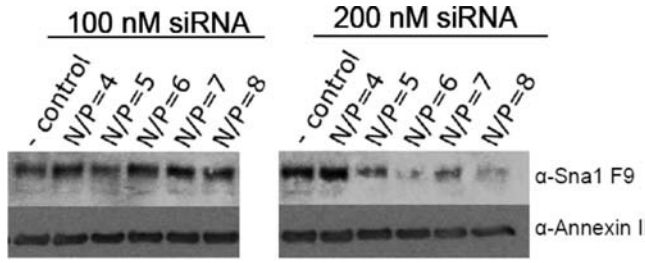

Figure 7. Protein expression as a function of siRNA dose and N/P ratio. Twenty-four hours in advance, 2×10^5 NIH3T3 cells were seeded in a 6 well plate. siRNA complexed with dPAMAM was delivered twice (24 and 48 h after seeding), at a variety of charge ratios, and protein levels were evaluated by Western blot 72 h after seeding. α-Annexin II was used to normalize the data, and the control condition was cells transfected with anti-cyclophilin B siRNA. No significant differences were observed at a dose of 100 nM, but at 200 nM, above a N/P of 5, significant down-regulation was observed (ANOVA, $p < 0.05$, $n = 3$).

final section of this study was thus performed using the optimized complexes.

The controlled release of siRNA−dPAMAM complexes from a collagen matrix is shown in Figure 8. The encapsulation of the siRNA was observed to be relatively high at time 0 (98%) but a significant amount of complex was released in the following 3 h. After 2 days, the release of complexes slowed significantly to a rate of approximately 10 ng siRNA/day.

The ability of a complex-loaded scaffold to control protein expression in a time-dependent manner was evaluated by measuring Snail1 levels from NIH3T3 cells seeded on collagen scaffolds loaded with anti-Snail1 siRNA−dPAMAM complexes. Figure 9a shows representative Western Blot

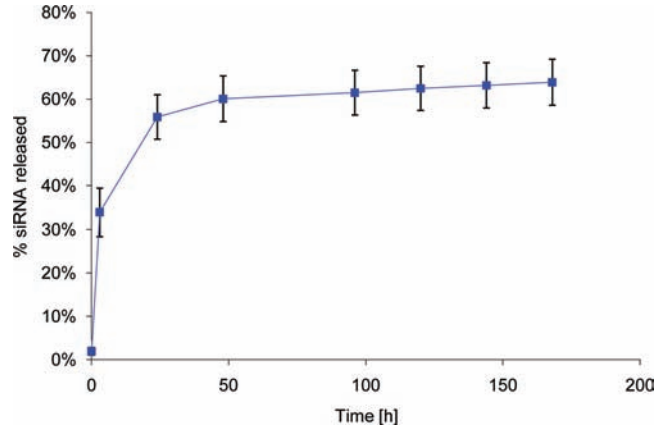

Figure 8. Cumulative percent release of siRNA−dPAMAM complexes from cross-linked collagen scaffolds over time. While only approximately 2% of the complexes were removed at time 0, indicating a 98% encapsulation efficiency, almost 35% were released within the first 3 h. After 7 days, approximately 35% of the siRNA complexes originally loaded into the scaffold were still retained with the matrix. Slow release of the complexes was still observed at this point, but only approximately 10 ng of siRNA was eluted per day, translating to a dose of approximately 50 nM.

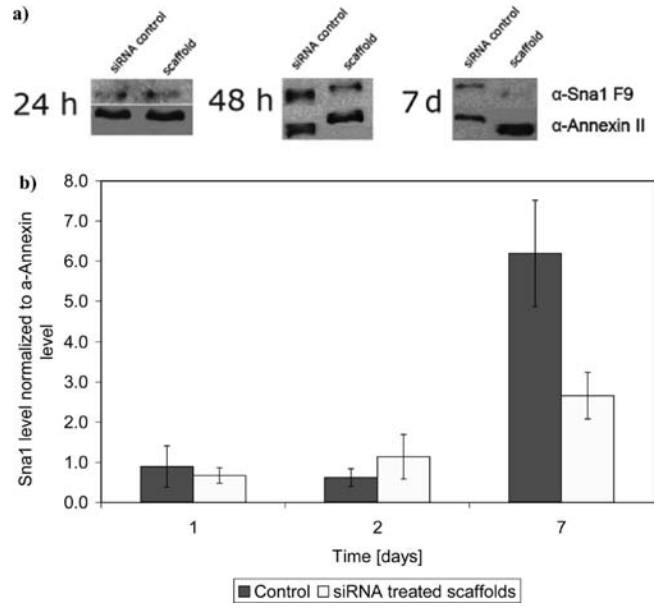

Figure 9. Protein expression from fibroblasts grown on anti-Snail1 siRNA loaded scaffolds as a function of time. Anti-Snail1 siRNA was loaded onto collagen scaffolds at a dose of 200 nM and an N/P of 8. Western blotting was used to evaluate the protein levels. Panel a shows a representative sample of the Western blot. α-Annexin II was used to normalize the results. Densitometry quantification (panel b) reveals significant down-regulation only after 7 days. (ANOVA, $p < 0.01$, $n = 3$). Thus while adherent cells showed significant down-regulation of Snail1 after 2 days, the scaffold reservoir system delays the effect of the siRNA until 7 days after cells were seeded onto the scaffold.

bands for cells grown on scaffolds containing the siRNA control (anti-cyclophilin B) compared with cells grown on scaffolds loaded with anti-Snail1 siRNA (both at concentration of 200 nM, N/P = 8). Figure 9b shows the densitometry quantification of all samples and controls, normalized to annexin II levels. Thus significant down-regulation of Snail1 levels was not observed until 7 days after cells were seeded onto the siRNA complex loaded scaffolds. This is in marked contrast to the earlier studies on siRNA transfected into

adherent cells where significant effects were observed only 48 h after transfection.

DISCUSSION

While it has been established that complexation of dendrimers to siRNA is possible (*7*), the optimal ratios and doses remain undefined. For plasmids, it has been observed that different cell types have different optimal N/P ratios and doses. Thus, characterization and optimization of complexes are necessary initial steps. Dye exclusion is an effective technique for estimating the quality of complexation, as most nuclear stains cannot access tightly bound nucleic acids (*29*). The bands shown in Figure 1 give a qualitative measure of complexation, which is confirmed by the TEM micrographs in Figure 2. The average diameter of the complexes was observed to vary inversely with N/P ratio, implying higher levels of interaction at higher N/P ratios. This correlates with observations in plasmid−dPAMAM interactions (*10, 14, 28*).

The cell membrane provides a major barrier for nonviral transfection, whether with siRNA or plasmids. Thus, complexes that are capable of crossing that barrier are much more likely to be able to affect gene expression. Figure 4 shows the increase in fluorescence of cells as an indirect measure of the amount of internalized fluorescent siRNA, while Figure 3 is an image of siRNA control complexes inside a select group of cells. The micrograph in Figure 3 was taken 48 h after transfection, the same point at which significant levels of Snail1 down-regulation were observed in Figures 6 and 7. Thus it would appear that the siRNA complexes internalized within 48 h were biologically active.

The efficiency of dPAMAM-mediated plasmid DNA transfection has been measured in other studies as approximately 17% in HeLa cells (*30*), 15% in CHO cells, and 18% in HEK 293 cells (*31*). No measurements of siRNA transfection efficiency are available. This may be because silencing is not necessarily complete, and therefore quantification of the number of siRNA transfected cells is very difficult. Comparison of relative protein levels is the most practical method of quantifying transfection; however this method does not provide insight into the mechanics of siRNA transfection. While almost 100% of the cells in Figure 4e have greatly increased fluorescence indicating internalization of fluorescent complexes, it is not valid to assume that internalized siRNA affects gene expression in all of these cells. The first barrier to transfection is the cell membrane, but it is not the only barrier. Depending on the internalization mechanism, lysosomal escape and cytoplasmic transport can pose major problems as well. Detailed analysis of internalization pathways involved in nonviral gene delivery has been conducted (*8, 9, 32−34*), but without similar analysis with siRNA complexes, it is difficult to be sure that the same barriers exist. However, the siRNA complexes measured in this study were observed to be approximately the same size as the plasmid complexes measured by Holladay et al., and thus it seems likely that the internalization mechanisms and pathways are similar.

Cytotoxicity is often cited as a downfall of cationic DNA complexation agents (i.e., polyethylene imine (PEI), poly(L-lysine) (PLL), (diethylamino)ethyl (DEAE)-dextran) (*35*). Dendrimers are considered less cytotoxic than some alternatives, (*10,12,13*) but this may be a function of the cell types and transfection protocols used (*36*). This study found no significant differences between control samples and test samples, indicating negligible cytotoxicity. This may be because the dose was not high enough to cause significant damage, but no "cytotoxic" control was used to compare. Regardless, the lack of change in metabolic activity indicates that changes in gene expression are more likely to be as a result of siRNA transfection than cytotoxicity from complexes. Furthermore, while the control condition in the cytotoxicity study had no siRNA added, the controls used in subsequent experiments were cells transfected with control siRNA, namely, anti-cyclophilin B siRNA, which should not have affected Snail1 gene expression but would control for any effects of the transfection procedure including cytotoxicity.

The down-regulation of Snail1 expression, as quantified at the mRNA and protein level in Figures 6 and 7 respectively, demonstrate the effects of anti-Snail1 siRNA transfection. Forty-eight hours after the initial transfection is evidently a sufficient interval over which to evaluate the siRNA transfection of adherent cells because significant down-regulation in mRNA and protein expression was observed. The discrepancy between the mRNA and Western blot results highlights the importance of measuring protein levels and not solely mRNA. While mRNA levels may correlate in some cases to protein expression levels, protein expression is dependent on a number of other factors, including post-transcriptional modifications to the mRNA and degradation rates of the proteins (*37−39*).

Combining siRNA−dPAMAM complexes with a collagen scaffold was hypothesized to extend the duration of action of the siRNA. It has been previously demonstrated that plasmid−dPAMAM complexes can be encapsulated in collagen scaffolds to change the release and transfection profiles (*28*). In that study, the peak transfection level from the scaffolds was (in some cases) decreased as compared with the transfected adherent cells, but the period of transfection was extended for up to three weeks. While the current study looked at a more limited time period, similar observations were made. The release profile (Figure 8) showed that the scaffold was capable of acting as a reservoir. The transfection profile was also affected because the two-dimensional transfection study (Figure 7) showed significant down-regulation after 48 h, but in the scaffold study, significant down-regulation was not observed until after 7 days (Figure 9).

Atelocollagen has been investigated in conjunction with siRNA delivery in a number of studies, both *in vitro* and *in vivo* (*23−25, 40*). However, while atelocollagen is generally described as a complexing agent, Minakuchi et al. observed that a solution of atelocollagen−siRNA complexes solidified when injected *in vivo* (*24*). Thus, an atelocollagen−siRNA complex system may be considered relatively similar to the system described in this paper. In studies with a luciferase reporter gene, approximately 60% inhibition (compared with a nonsense siRNA control) was observed *in vitro* (*23, 24*).

In this study, greater than 55% inhibition of Snail1 level was observed at day 2 when siRNA−dPAMAM complexes were delivered directly to a monolayer of cells. A similar level of inhibition was observed at day 7 when the complexes were delivered through scaffolds. Without an *in vivo* study, it is unclear whether the level of inhibition is therapeutically significant, but the *in vitro* results are comparable to the studies using atelocollagen as a complexing agent.

The delay in Snail1 down-regulation may be partly due to changes in the protocol and not solely the siRNA transfection. In the two-dimensional transfection study, cells were seeded and allowed to adhere for 24 h before siRNA complexes were introduced. In the scaffold study, the siRNA complexes were allowed to bind to the scaffold, then cells were added directly to the loaded scaffold. Thus the cells were not allowed to adhere prior to transfection. A similar protocol was used in the plasmid−dPAMAM complex study by Holladay et al., but transfection was observed in that study after 48 h, (*28*) whereas no effects on gene expression were observed until 7 days in this study.

Snail1 is involved in the initial stages of detachment and migration of tumor cells into other tissues (*4*). As shown in

Figure 9, the levels of Snail1 expressed in the control cells at 24 and 48 h after seeding were relatively low, but this level greatly increased at the 7 day time point. This might be partly due to the increase in the total cell number and partly due to up-regulation of genes that promote migration of the fibroblasts throughout the scaffold. The scaffold in this case is a collagen matrix, which may actually stimulate migration of fibroblasts. To have significant down-regulation, high expression levels might be required. Alternatively, the siRNA may be bound more tightly to the collagen matrix than the plasmid−dPAMAM complexes were, and thus longer incubation times were required for internalization.

Because the only Snail1 down-regulation in the scaffold study was observed after 7 days, measurement of Snail1 levels over longer growth periods needs to be investigated. If the scaffold is capable of suppressing Snail1 expression for 3 weeks (as in the plasmid scaffold transfection study by Holladay et al.) but has no effects for the first 7 days, the system may not be ideal for epithelial cancer treatment. While long-term delivery of siRNA would possibly allow long-term down-regulation of the Snail1, thereby decreasing the level of metastasis, there would be no major therapeutic benefit to delaying siRNA delivery. However, *in vivo* studies with the system are required to determine the *in vivo* transfection profile and efficacy before any hypothesis can be put forward regarding the overall therapeutic potential of this system.

Thus, complexation between siRNA and dPAMAM was confirmed with SYBRGold dye exclusion and TEM. Confocal microscopy and FACS demonstrated that NIH3T3 cells readily internalized fluorescently tagged siRNA complexed with dPAMAM. Negligible cytotoxicity was observed with 100 or 200 nM siRNA complex doses and with varying N/P ratios. Snail1 gene expression was down-regulated at mRNA level and protein expression level when anti-Snail1 siRNA was complexed with dPAMAM and transfected into adherent NIH3T3 cells. Finally, it was observed that siRNA complexes were slowly released from a collagen scaffold and down-regulation of protein expression was delayed by up to 7 days.

ACKNOWLEDGMENT

This project was supported by the Irish Research Council for Science Engineering and Technology (IRCSET) funded by the National Development Plan and a grant awarded by the Ministerio de Ciencia y Tecnología (SAF2006-00339) to Antonio García de Herreros. Partial support from Instituto Carlos III (RD06/0020/0040) and from the Generalitat de Catalunya (2005SGR00970) is also appreciated. V.M.D. was a recipient of a Juan de la Cierva contract. Thanks to Dr. Antonio García de Herreros for his input in this project. Additional acknowledgement is due to Dr. Oliver Carroll for editorial assistance.

LITERATURE CITED

(1) Hanahan, D., and Weinberg, R. A. (2000) The hallmarks of cancer. *Cell 100*, 57–70.
(2) Batlle, E., Sancho, E., Franci, C., Dominguez, D., Monfar, M., Baulida, J., and Garcia de Herreros, A. (2000) The transcription factor Snail is a repressor of E-cadherin gene expression in epithelial tumour cells. *Nat. Cell Biol. 2*, 84–89.
(3) Ikenouchi, J., Matsuda, M., Furuse, M., and Tsukita, S. (2003) Regulation of tight junctions during the epithelium-mesenchyme transition: Direct repression of the gene expression of claudins/occludin by Snail. *J. Cell Sci. 116*, 1959–1967.
(4) Peinado, H., Olmeda, D., and Cano, A. (2007) Snail, Zeb and bHLH factors in tumour progression: An alliance against the epithelial phenotype? *Nat. Rev. Cancer 7*, 415–428.
(5) Caplen, N. J., Fleenor, J., Fire, A., and Morgan, R. A. (2000) dsRNA-mediated gene silencing in cultured *Drosophila* cells: A tissue culture model for the analysis of RNA interference. *Gene 252*, 95–105.
(6) Fire, A. (1999) RNA-triggered gene silencing. *Trends Genet. 15*, 358–363.
(7) Akhtar, S., and Benter, I. F. (2007) Nonviral delivery of synthetic siRNAs in vivo. *J. Clin. Invest. 117*, 3623–3632.
(8) Lechardeur, D., and Lukacs, G. L. (2002) Intracellular barriers to non-viral gene transfer. *Curr. Gene Ther. 2*, 183–194.
(9) Kodama, K., Katayama, Y., Shoji, Y., and Nakashima, H. (2006) The features and shortcomings for gene delivery of current non-viral carriers. *Curr. Med. Chem. 13*, 2155–2161.
(10) Bielinska, A. U., Chen, C. L., Johnson, J., and Baker, J. R. (1999) DNA complexing with polyamidoamine dendrimers: Implications for transfection. *Bioconjugate Chem. 10*, 843–850.
(11) Tang, M. X., Redemann, C. T., and Szoka, F. C. (1996) In vitro gene delivery by degraded polyamidoamine dendrimers. *Bioconjugate Chem. 7*, 703–714.
(12) Dennig, J. (2003) Gene transfer in eukaryotic cells using activated dendrimers, in *Dendrimers V: Functional and Hyperbranched Building Blocks, Photophysical Properties, Applications in Materials and Life Sciences* pp 227−236, Springer-Verlag, Berlin.
(13) Dennig, J., and Duncan, E. (2002) Gene transfer into eukaryotic cells using activated polyamidoamine dendrimers. *Rev. Mol. Biotechnol. 90*, 339–347.
(14) Kukowska-Latallo, J. F., Bielinska, A. U., Johnson, J., Spindler, R., Tomalia, D. A., and Baker, J. R. (1996) Efficient transfer of genetic material into mammalian cells using Starburst polyamidoamine dendrimers. *Proc. Natl. Acad. Sci. U.S A. 93*, 4897–4902.
(15) Haensler, J., and Szoka, F. C. (1993) Polyamidoamine cascade polymers mediate efficient transfection of cells in culture. *Bioconjugate Chem. 4*, 372–379.
(16) Su, C. J., Liu, Y. C., Chen, H. L., Li, Y. C., Lin, H. K., Liu, W. L., and Hsu, C. S. (2007) Two-dimensional densely packed DNA nanostructure derived from DNA complexation with a low-generation poly(amidoamine) dendrimer. *Langmuir 23*, 975–978.
(17) Kukowskalatallo, J., Johnson, J., Bielinska, A., Tomalia, D., Spindler, R., and Baker, J. (1995) Efficient transfer and expression of genetic material in eukaryotic cells using starburst(Tm) dendrimer conjugates. *FASEB J. 9*, A409–A409.
(18) Kukowska-Latallo, J. F., Raczka, E., Quintana, A., Chen, C., Rymaszewski, M., and Baker, J. R., Jr. (2000) Intravascular and endobronchial DNA delivery to murine lung tissue using a novel, nonviral vector. *Hum. Gene Ther. 11*, 1385–1395.
(19) Tomalia, D. A. (1995) Dendrimer molecules. *Sci. Am. 272*, 62–66.
(20) Kiefer, K., Clement, J., Garidel, P., and Peschka-Suss, R. (2004) Transfection efficiency and cytotoxicity of nonviral gene transfer reagents in human smooth muscle and endothelial cells. *Pharm. Res. 21*, 1009–1017.
(21) Gupta, U., Agashe, H. B., Asthana, A., and Jain, N. K. (2006) A review of in vitro-in vivo investigations on dendrimers: the novel nanoscopic drug carriers. *Nanomedicine 2*, 66–73.
(22) Smith, D. K. (2008) Dendrimers and the double helix - From DNA binding towards gene therapy. *Curr. Top. Med. Chem. 8*, 1187–1203.
(23) Hanai, K.; Takeshita, F.; Honma, K.; Nagahara, S.; Maeda, M.; Minakuchi, Y.; Sano, A.; Ochiya, T. (2006) Atelocollagen-mediated systemic DDS for nucleic acid medicines, in Oligonucleotide Therapeutics (Tuschl, T., and Rossi, J., Eds.), Blackwell, Boston, MA, pp 9−17.
(24) Minakuchi, Y., Takeshita, F., Kosaka, N., Sasaki, H., Yamamoto, Y., Kouno, M., Honma, K., Nagahara, S., Hanai, K., Sano, A., Kato, T., Terada, M., and Ochiya, T. (2004) Atelocollagen-mediated synthetic small interfering RNA delivery for effective gene silencing in vitro and in vivo. *Nucleic Acids Res. 32*, e109.
(25) Kinouchi, N., Ohsawa, Y., Ishimaru, N., Ohuchi, H., Sunada, Y., Hayashi, Y., Tanimoto, Y., Moriyama, K., and Noji, S. (2008) Atelocollagen-mediated local and systemic applications of myo-

statin-targeting siRNA increase skeletal muscle mass. *Gene Ther. 15*, 1126–1130.

(26) Franci, C., Takkunen, M., Dave, N., Alameda, F., Gomez, S., Rodriguez, R., Escriva, M., Montserrat-Sentis, B., Baro, T., Garrido, M., Bonilla, F., Virtanen, I., and Garcia de Herreros, A. (2006) Expression of Snail protein in tumor-stroma interface. *Oncogene 25*, 5134–5144.

(27) Aguilar, S., Corominas, J. M., Malats, N., Pereira, J. A., Dufresne, M., Real, F. X., and Navarro, P. (2004) Tissue plasminogen activator in murine exocrine pancreas cancer: Selective expression in ductal tumors and contribution to cancer progression. *Am. J. Pathol. 165*, 1129–1139.

(28) Holladay, C., Keeney, M., Greiser, U., Murphy, M., O'Brien, T., and Pandit, A. (2009) A matrix reservoir for improved control of non-viral gene delivery. *J. Controlled Release 136*, 220–225.

(29) Shcharbin, D., Pedziwiatr, E., and Bryszewska, M. (2009) How to study dendriplexes I: Characterization. *J. Controlled Release 135*, 186–197.

(30) Georgiou, T. K., Vamvakaki, M., Phylactou, L. A., and Patrickios, C. S. (2005) Synthesis, characterization, and evaluation as transfection reagents of double-hydrophilic star copolymers; effect of star architecture. *Biomacromolecules 6*, 2990–2997.

(31) Manunta, M., Tan, P. H., Sagoo, P., Kashefi, K., and George, A. J. T. (2004) Gene delivery by dendrimers operates via a cholesterol dependent pathway. *Nucleic Acids Res. 32*, 2730–2739.

(32) Roth, C. M., and Sundaram, S. (2004) Engineering synthetic vectors for improved DNA delivery: Insights from intracellular pathways. *Annu. Rev. Biomed. Eng. 6*, 397–426.

(33) Ruponen, M., Honkakoski, P., Rönkkö, S., Pelkonen, J., Tammi, M., and Urtti, A. (2003) Extracellular and intracellular barriers in non-viral gene delivery. *J. Controlled Release 93*, 213–217.

(34) Lechardeur, D., Verkman, A. S., and Lukacs, G. L. (2005) Intracellular routing of plasmid DNA during non-viral gene transfer. *Adv. Drug Delivery Rev. 57*, 755–767.

(35) Dufes, C., Uchegbu, I. F., and Schatzlein, A. G. (2005) Dendrimers in gene delivery. *Adv. Drug Delivery Rev. 57*, 2177–2202.

(36) Uchida, E., Mizuguchi, H., Ishii-Watabe, A., and Hayakawa, T. (2002) Comparison of the efficiency and safety of non-viral vector-mediated gene transfer into a wide range of human cells. *Biol. Pharm. Bull. 25*, 891–897.

(37) Greenbaum, D., Colangelo, C., Williams, K., and Gerstein, M. (2003) Comparing protein abundance and mRNA expression levels on a genomic scale. *Genome Biol. 4*, 117.

(38) Greenbaum, D., Jansen, R., and Gerstein, M. (2002) Analysis of mRNA expression and protein abundance data: an approach for the comparison of the enrichment of features in the cellular population of proteins and transcripts. *Bioinformatics 18*, 585–596.

(39) Greenbaum, D., Luscombe, N. M., Jansen, R., Qian, J., and Gerstein, M. (2001) Interrelating different types of genomic data, from proteome to secretome: 'Oming in on function. *Genome Res. 11*, 1463–1468.

(40) Takeshita, F., and Ochiya, T. (2006) Therapeutic potential of RNA interference against cancer. *Cancer Sci. 97*, 689–696.

BC900241W

Bisphosphonate Adaptors for Specific Protein Binding on Zirconium Phosphonate-based Microarrays

Mathieu Cinier,[†] Marc Petit,[‡] Monique N. Williams,[§] Roxane M. Fabre,[§] Frédéric Pecorari,[†] Daniel R. Talham,[§] Bruno Bujoli,[‡,*] and Charles Tellier[†,*]

Laboratoire de Biotechnologie, Biocatalyse et Biorégulation, UFR Sciences et Techniques, Université de Nantes, CNRS, UMR 6204, 2, rue de la Houssinière, BP 92208, 44322 NANTES Cedex 3, France, Chimie Et Interdisciplinarité: Synthèse Analyse Modélisation (CEISAM), Université de Nantes, CNRS, UMR 6230, 2 Rue de la Houssinière, BP92208, 44322 Nantes Cedex 03, France, and Department of Chemistry, University of Florida, Gainesville, Florida 32611-7200. Received June 16, 2009; Revised Manuscript Received September 29, 2009

Two bisphosphonate adaptors were designed to immobilize histidine-tagged proteins onto glass substrates coated with a zirconium phosphonate monolayer, allowing efficient and oriented immobilization of capture proteins, affitins directed to lysozyme, on a microarray format. These bifunctional adaptors contain two phosphonic acid anchors at one extremity and either one nitrilotriacetic acid (NTA) or two NTA groups at the other. The phosphonate groups provide a stable bond to the zirconium interface by multipoint attachment and allow high density of surface coverage of the linkers as revealed by X-ray photoelectron spectroscopy (XPS). Reversible high-density capture of histidine-tagged proteins is shown by real-time surface plasmon resonance enhanced ellipsometry and in a microarray format using fluorescence detection of AlexaFluor 647-labeled target protein. The detection sensitivity of the microarray for the target protein was below 1 nM, despite the monolayer arrangement of the probes, due to very low background staining, which allows high fluorescent signal-to-noise ratio. The performance of these Ni-NTA-modified zirconium phosphonate coated slides compared favorably to other types of microarray substrates, including slides with a nitrocellulose-based matrix, epoxide slides, and epoxide slides functionalized with Ni-NTA groups. This immobilization strategy has a large potential to fix any histidine-tagged proteins on zirconium or titanium ion surfaces.

INTRODUCTION

Proteins play a key role in cellular mechanisms, but most of their functions remain unknown (*1*). Proteomics, which is the study of protein function, expression, and localization on a cellular-wide scale, needs more high-throughput analysis tools to achieve this goal. By analogy to work in genomics with DNA microarrays (*2, 3*), protein capture microarrays have been used successfully to identify differentially expressed biomarker proteins (*4*−*8*). However, it is still an emerging technology, which needs selective methods for surface immobilization (*1, 9*) and alternative strategies to antibodies for use as capture agents in protein microarrays (*10, 11*).

A significant challenge for protein microarrays is attachment on the chip surface. Immobilization of the protein by nonspecific adsorption is often associated with problems such as a high background signal and significant loss of the protein probes during stringent washes (*12*). Furthermore, random orientations of the immobilized proteins affect their activities, which decrease the sensivity of detection (*13, 14*). Therefore, specific protein attachment through covalent coupling (*15*−*22*) or affinity interaction (*23*−*27*) is considered to be a better strategy (*13*). In the present work and in other studies (*28*−*31*), specific orientation of capture proteins is achieved by affinity interaction between a histidine-tag protein and a transition metal chelated to a nitrilotriacetic acid (NTA) moiety. Ni-NTA resins (*32*−*34*) are routinely used for the purification of oligo-histidine-tagged proteins, which can be easily prepared by genetic fusion of an oligohistidine tag to the C- or N-terminus. Despite the moderate affinity ($K_d \approx 1-10\ \mu M$) (*35*−*37*) and stability of individual Ni-NTA/oligohistidine complexes, this strategy has been successfully used in a microarray format for the immobilization of about 6000 histidine-tag-labeled yeast proteins, of which more than 80% were shown to retain their biological activity after immobilization (*38*). However, most NTA surfaces used for the design of protein microarrays are obtained by spreading a functionalized polymer matrix on a glass surface, leading to inhomogeneous surface coatings without rigorous control of the NTA density.

In previous work on DNA microarrays, our laboratories described a new ultraflat support with which the biological probes are bound to a monolayer-coated surface through an "inorganic" linkage, in contrast to existing systems based on the covalent attachment of the DNA probes via covalent organic bonds. We demonstrated the spontaneous linkage of oligonucleotide probes, phosphorylated at their 5′ end, onto a zirconium phosphonate modified surface (*39*). More recently, we demonstrated that the phosphate/zirconium bond is strong enough for dsDNA attachment and for studying DNA/protein interactions (*40*). The zirconium−phosphonate linkage has been shown to be very robust between pH 1 and pH 10 and stable to displacement by competing bases (*39*). On the other hand, unmodified proteins are poorly adsorbed on such zirconium phosphonate surfaces and oligo-histidine-tagged proteins do not provide specific binding on these surfaces.

In order to provide specific anchoring of oligo-histidine-tagged proteins to the zirconium phosphonate surface, we

* To whom correspondence should be addressed. E-mail addresses: charles.tellier@univ-nantes.fr; bruno.bujoli@univ-nantes.fr

[†] Laboratoire de Biotechnologie, Biocatalyse et Biorégulation, Université de Nantes.

[‡] Chimie Et Interdisciplinarité: Synthèse Analyse Modélisation, Université de Nantes.

[§] University of Florida.

10.1021/bc9002597 © 2009 American Chemical Society
Published on Web 11/23/2009

designed a bifunctional adaptor containing a multivalent phosphonic acid anchor at one extremity and a NTA group at the other. The phosphonate groups provide a stable bond to the zirconium interface by multipoint attachment. This affinity tag strategy provides a uniform orientation of proteins on the surface and high-density coverage without the need to perform complicated chemistry on the protein targets or on the solid support. Stable binding of the bifunctional adaptor is demonstrated, allowing reversible capture of histidine-tagged proteins. This technology is applied to a new class of small and stable capture proteins, the affitins (*41, 42*), which are shown to keep their binding properties when immobilized on the zirconium phosphonate surface and to exhibit a high signal-to-noise ratio relative to arrays prepared from other NTA-functionalized supports.

EXPERIMENTAL PROCEDURES

Materials. Glass slides were purchased from Gold Seal Products (cat no. 3013, 3×1 in.^{2}, thickness 0.93−1.05 mm). Reagents were of analytical grade and used as received from commercial sources, unless indicated otherwise. Hydrophobic glass slides were made using octadecyltrichlorosilane (OTS) following a method by Sagiv (*43*). The zirconium octadecylphosphonate Langmuir−Blodgett monolayers were prepared on the hydrophobic slides as described previously (*44, 45*). Nexterion Slides E were obtained from Schott. FASTslide coated with nitrocellulose were obtained from Whatman/Schleicher & Schuell. *N*α,*N*α-bis(carboxymethyl)-L-lysine hydrate and lyzozyme were purchased from Sigma Aldrich.

Synthesis of the Mono-NTA and Bis-NTA Bisphosphonate Adaptors. The synthesis of the monovalent and multivalent linkers is outlined in Scheme 1; the details are given in Supporting Information.

Protein Expression and Purification. H4 and B3 are recombinant proteins derived from Sac7d from *Sulfolobus acidocaldarius* and evolved by ribosome display to bind lysozyme (*41, 42*). H4 was overexpressed in a recombinant *Escherichia coli* BL21 strain carrying the corresponding plasmid. The culture was grown in Luria−Bertoni medium containing ampicillin (50 μg/mL) at 37 °C until an OD600 of 0.8−1. Induction using isopropyl-1-β-D-thio-1-galactopyranoside (IPTG) (0.5 mM) was continued overnight. The protein was purified on nickel−nitrilotriacetic acid (Ni-NTA) columns according to the manufacturer's recommendations (Qiagen, Courtaboeuf, France), eluting with a TBS 250 buffer (20 mM TrisHCl, pH 7.4, 150 mM NaCl, 250 mM imidazole). The protein concentration was measured using a Nanodrop 1000 spectrophotometer (Thermoscientific). The same procedure was applied to B3.

Microoarray Spotting and Incubation Conditions. To prepare the LB Ni-NTA substrate, the zirconium phosphonate modified slides were incubated overnight with a 1 mM mono-NTA (**13**) or bis-NTA (**18**) adaptor aqueous solution. For the Nexterion Slide E Ni-NTA substrate, Nexterion Slides E were incubated overnight with a 3 mM solution of *N*α,*N*α-bis(carboxymethyl)-L-lysine hydrate in PBS (12 mM phosphate, pH 8.3, 150 mM NaCl). Slides were washed 3 times with ultrapure water and then incubated for 1 h with a 100 mmol L^{-1} $NiCl_2$ aqueous solution. The slides were washed again 3 times with ultrapure water and dried by centrifugation (1500 rpm, 1 min).

The slides were then spotted with a microcaster TM 8-pin system (Whatman/Schleicher & Schuell). The spotted slides were placed overnight in an incubation chamber at 4 °C and 75% humidity. To passivate the unspotted areas, slides were treated after spotting with a solution of 0.3% α-casein (Sigma) in a TBS (Tris-buffered saline) solution of TrisHCl (20 mM) and NaCl (150 mM) at pH 7.4. Incubation was performed by applying an Alexa 647-labeled lysozyme solution (1 μM in TBS−0.3% α-casein) to the substrate for 1 h at room temperature. Microarrays were washed 3 times with TBS−0.05% Tween 20 for 5 min, then once with TBS and ultrapure water. Finally, the slides were spun dry centrifuging at 1500 rpm for 1 min. All washes and incubations were performed in small staining jars at room temperature on an oscillating shaker.

Microarray Analysis. All microarrays were scanned on a Scanarray Gx apparatus (Perkin-Elmer) with a laser power and gain value of 60. Suitable excitation wavelength and emission filter were used to detect Alexa 647: 650 nm (excitation), 665 nm (emission). The location of each analyte spot on the array was outlined using the mapping software Genepix (Axon laboratories, Palo Alto, CA).

X-ray Photoelectron Spectroscopy (XPS). XPS was performed using a UHV XPS/ESCA PHI 5100 system. Survey scans and multiplex scans (Zr 3d, P 2p, N 1s, Ni 2p3) were taken with an Al Kα X-ray source (using a power setting of 300 W and a takeoff angle of 45° with respect to the surface). Survey scans were taken for all samples with a pass energy of 89.4 eV and multiplex scans were taken with a pass energy of 22.36 eV. The peak areas were determined using commercial XPS analysis software with Shirley background subtraction. Elemental ratios reported in the text are averages of at least three experiments.

Slides for XPS analysis containing the NTA linkers were prepared using a Whatman Fast-Frame slide plate and a two-pad incubation chamber. One pad of the zirconium phosphonate modified slide was immersed in 1 mL of 1 mM biphosphonate adapter, while the other pad was immersed in 1 mL of nanopure water as an experimental control. The slide was kept at 4 °C overnight, rinsed with water, and then deposited in a solution of 100 mM $NiCl_2$ for 1 h. Finally, the slide was then rinsed with nanopure water and spin-dried in air for analysis.

Surface Plasmon Resonance (SPR) Spectroscopy. Surface plasmon resonance enhanced ellipsometry measurements were performed on a commercial EP^3−SW imaging system (Nanofilm Surface Analysis, Germany). The ellipsometer employed a frequency-doubled Nd:YAG laser (adjustable power up to 20 mW) at 532 nm. Linearly p-polarized light was directed through a 60° equilateral SF10 prism coupled to a gold-coated SF10 slide via diiodomethane index matching oil in the Kretschmann configuration. The angle of incidence was kept at 64° for all kinetics experiments because this condition provided the highest sensitivity. Curve fitting of the kinetics data used the AnalysR software from Nanofilm, using a 1:1 Langmuir binding model.

SPR slides were prepared by rendering the gold-coated slides hydrophobic with octadecylmercaptan before transferring the zirconium phosphonate layer. The slides were then immersed overnight in 1 mM aqueous solutions of either the mono-NTA linker or the bis-NTA linker, followed by rinsing with ultrapure water and drying under a stream of nitrogen. The NTA-modified slides were placed in the SPR flow cell and treated with a 100 mM solution of nickel chloride. Protein binding onto the Ni-NTA surface was carried out by injecting 5 μM protein solutions in TBS. The surface was regenerated using 250 mM imidazole in TBS buffer.

RESULTS AND DISCUSSION

Design of the Anchoring Linker. In previous studies, we showed that oligonucleotides and dsDNA can be immobilized on zirconium phosphonate surfaces and that phosphate-terminated oligonucleotides are selectively adsorbed over those without terminal phosphates (*39, 40*). It was also shown that dsDNA phosphorylated at both ends binds better to the zirconium surface than monophosphorylated DNA.

Based on these results, in order to make the zirconated phosphonate film suitable for oligohistidine-tagged protein

Scheme 1. Synthesis of the Mono-NTA and Bis-NTA Bisphosphonate Adaptors

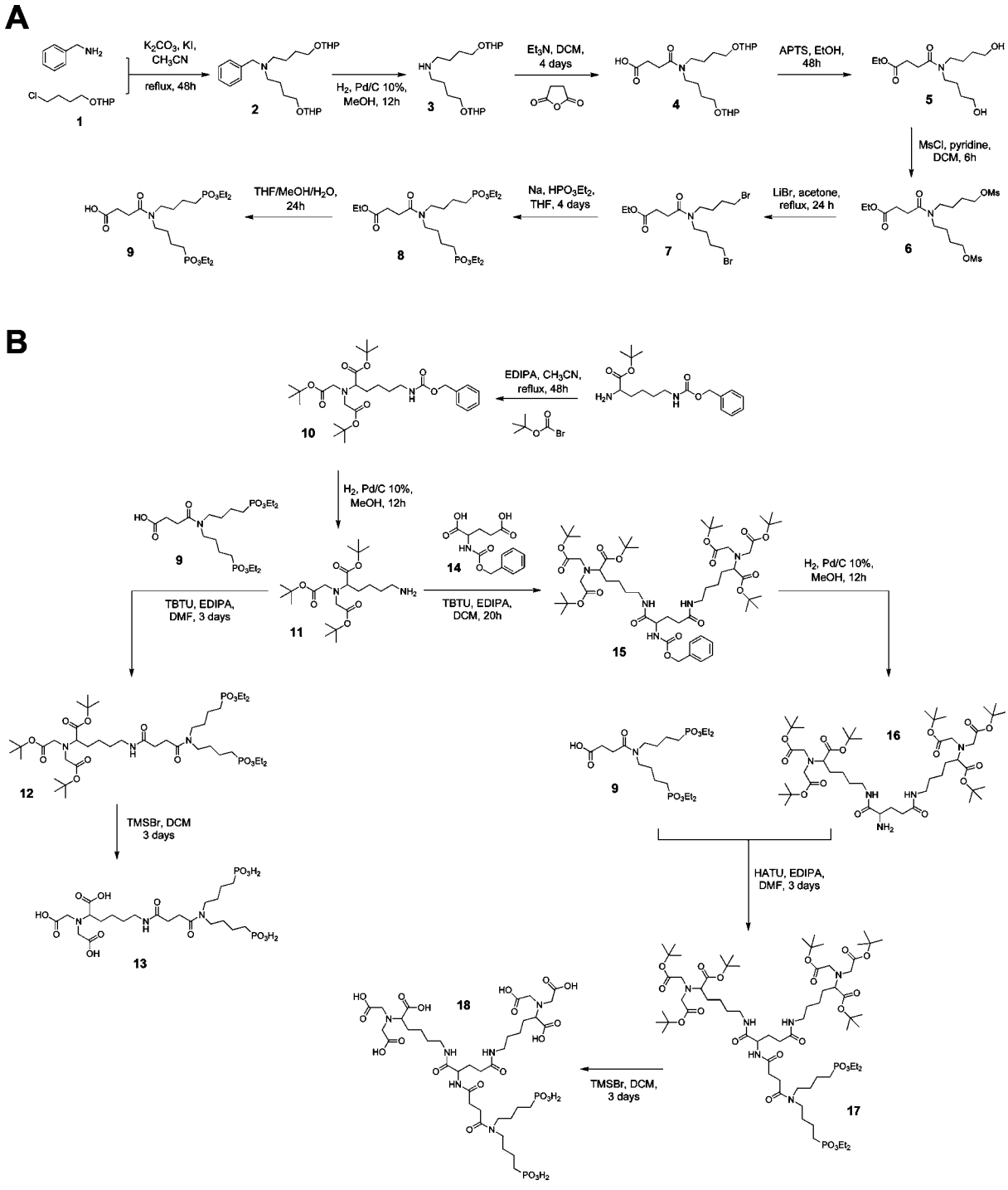

immobilization, surface modification with either mono-NTA or bis-NTA end groups was performed using adaptors **13** and **18**, respectively, which contained a similar scaffold bearing two phosphonic acid functions for binding to the zirconated surface (Scheme 1A,B). These two adaptors were synthesized in around 15 steps in good yield. First benzylamine was alkylated twice using compound **1** synthesized by reacting 4-chloro-1-butanol with 3,4-dihydro-2*H*-pyran to yield compound **2**. After hydrogenolysis, compound **3** was reacted with succinimide to produce the acid compound **4**. Reaction with *p*-toluene sulfonic acid in ethanol resulted in the esterification of the carboxylic acid function and removal of the THP protective groups. The two alcohol groups were then activated (mesylate) and substituted by bromine atoms, which were subsequently replaced by diethyl phosphonate groups using sodium salt of diethylphosphite to yield compound **8**. Finally, saponification of the ester function led to compound **9,** which was then coupled to the mono-NTA or bis-NTA precursors **11** and **16**, respectively, as described in Scheme 1B, to obtain the two expected bisphosphonate mono- and bis-NTA adaptors **13** and **18**. Compounds **11** and **16** were derived from L-lysine, as previously reported by Lata et al. (*46*).

Similar adaptors with only one phosphonic acid moiety were found to bind poorly to the zirconated surface and were inadequate for the present application.

Zr/phosphonate Surfaces and Linker Anchoring. Zirconium phosphonate modified surfaces are generated by adsorbing Zr^{4+} ions to surface phosphonate or phosphate groups. An active metal layer results when the phosphorylated groups are closely organized into a monolayer so that the Zr^{4+} ions bind to the surface groups to form a layer while retaining some coordination

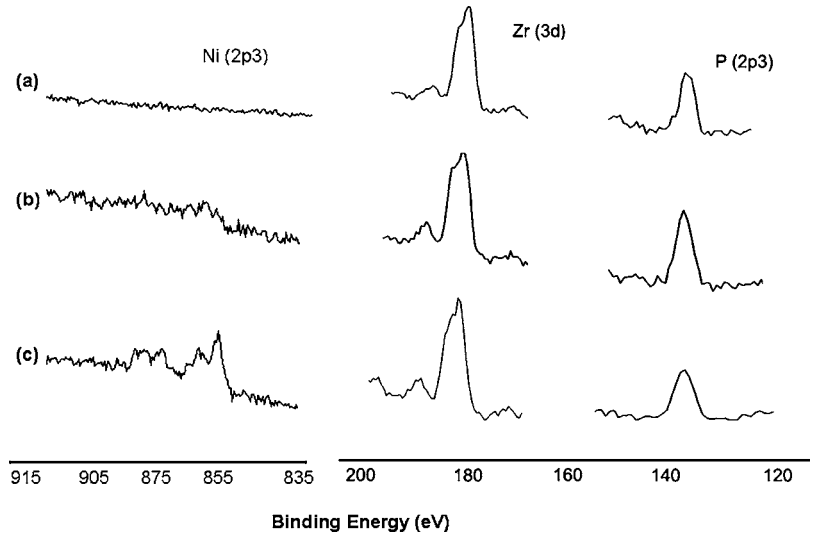

Figure 1. Peaks of Ni(2p3), Zr(3d), and P(2p3) obtained from XPS analysis for (a) zirconium phosphonate monolayer surface, (b) mono-NTA modified surface, and (c) bis-NTA modified surface. No Ni(2p3) is seen on the bare zirconium phosphonate surface.

sites that are free of the surface phosphate or phosphonate ligands. The starting phosphorylated surfaces can be prepared in different ways, including covalent attachment of the phosphorylated groups to silica (*47*−*54*) or gold (*49, 50, 53, 55, 56*) and by Langmuir−Blodgett deposition of an organophosphonic acid (*44, 45, 57*−*60*). We have long utilized LB methods to prepare the zirconium phosphonate monolayers because the surface films formed in this way are of high quality, stable, and highly reproducible, and the surface chemistry can be applied to nearly any substrate material, permitting application of a wide range of surface analytical techniques on the same surface (*61*) Modification of the zirconium phosphonate surface was thus investigated by incubating the substrate in a 1 mM aqueous solution of the desired bisphosphonate adaptor (**13** or **18**), the binding of which was then monitored by XPS. XPS is a powerful surface analytical technique, which provides qualitative and quantitative information about the elements on a surface, and was recently shown to be an efficient, label-free method for studying DNA surface coverage on zirconium phosphonate surfaces (*62, 63*). The P/Zr ratio of 1.1 for the naked zirconated phosphonate monolayer indicates that it is almost fully reticulated by the zirconium ions (*44*). Upon reaction with adaptor **13**, a significant increase of this ratio was observed (P/Zr = 1.4), which confirms binding of the bisphosphonate on the surface (Figure 1). Knowing the surface density of the zirconium ions within the monolayer, 4.2×10^{14} atoms/cm^2 (*44*), the mono-NTA adaptor coverage can be estimated at 6.3×10^{13} molecules/cm^2, which corresponds to one NTA moiety every 1.58 nm^2. With the bis-NTA adaptor (**18**), a P/Zr ratio of 1.18 was determined, which indicates half the surface coverage observed for the mono-NTA molecule. However, because this adaptor presents two NTAs per molecule, the NTA density on the surface is roughly similar to that obtained with the mono-NTA adaptor.

Nickel complexation to the NTA end groups was then performed to make them capable of covalent binding to histidine-tagged proteins. In Figure 1, XPS spectra of mono-NTA and bis-NTA coated slides are compared with the bare zirconium phosphonate surface, after exposure to Ni^{2+}. Binding to the NTA-coated slides is evident, with more Ni^{2+} complexed to the bis-NTA coated slide.

Protein Immobilization. The octadecylphosphonic acid (OPDA)-Zr surfaces modified with mono-NTA and bis-NTA end groups were used to study the specificity and reversibility of their interaction with histidine-tagged proteins as well as the proteins' activity when immobilized. For this purpose, monomeric proteins (affitins) with a single N-terminal oligohistidine tag were used. These affitins were derived from the Sac7d scaffold and selected by ribosome display to selectively recognize lysozyme (*41, 42*). Binding of the H4 affitin on the zirconium phosphonate monolayer functionalized with nickel-loaded NTA groups was first studied using SPR (Figure 2). As a control experiment, low and totally reversible binding of the protein was observed in the absence of nickel complexation to the NTA group (Figure 2a). In the case of both adaptors **13** and **18**, the surface exhibits a high and specific binding of the histidine-tagged-affitin (Figure 2b,c). A higher phase shift amplitude was observed for the binding of the affitin to the mono-NTA adaptor ($\Delta\Delta\psi \approx 0.22°$) than for the bis-NTA ($\Delta\Delta\psi \approx 0.17°$), reflecting a higher amount of bound protein using the mono-NTA adaptor. This result can be correlated to the higher surface coverage with this adaptor. However, a significant dissociation of the affitin was observed with the mono-NTA linker upon prolonged washing (~1 h) (Figure 2b), while washing out of the protein was reduced in the case of the bis-NTA linker (Figure 2c). This observation reflects the intrinsically low affinity of mono-NTA toward a polyhistidine sequence ($K_d \approx 10^{-5}$ to 10^{-6} M), which can be improved when bis-NTA functional groups are used (*29*). After washing, the amount of the proteins retained on the surface was similar for both adaptors. The specificity of the interaction is confirmed by the full reversibility of binding upon injection of a high concentration of imidazole (Figure 3). The protein loading followed by imidazole washing cycle can be repeated without a decrease in binding amplitude, as shown in Figure 3 for two cycles.

Microarray Experiments. Having shown that both linkers **13** and **18** can be efficiently immobilized on the zirconium phosphonate surface, making it suitable for histidine-tagged protein immobilization, the next step was to verify that the immobilized proteins are still functional and capable of binding lysozyme. Affitin immobilization on a microarray format was carried out according to Scheme 2. The nickel-loaded NTA functionalized slides were spotted with affitin at fixed concentrations prior to a blocking step with α-casein, which due to its high phosphate content provides efficient saturation of the nonspotted areas, hindering nonspecific protein binding (*40*). The activity of the immobilized affitin was investigated upon incubation of the surface with AlexaFluor 647 labeled lysozyme overnight. To verify that immobilization of the affitin proceeds via the expected Ni-NTA/histidine-tag interaction, the same

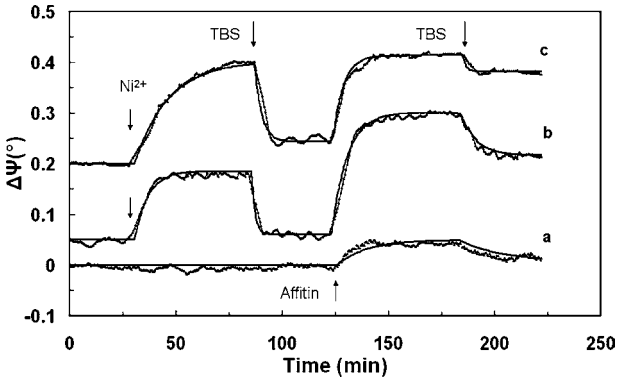

Figure 2. Affitin immobilization on the zirconium phosphonate surface functionalized with mono- and bis-NTA, probed in real time by surface plasmon resonance enhanced ellipsometry (SPREE). Kinetic adsorption curves of affitin on (a) mono-NTA without nickel, (b) mono-NTA with nickel, or (c) bis-NTA with nickel. Experimental data (dotted line) were fitted (solid line) using a 1:1 Langmuir binding model for each step. Curves b and c were shifted by 0.05° and 0.2°, respectively.

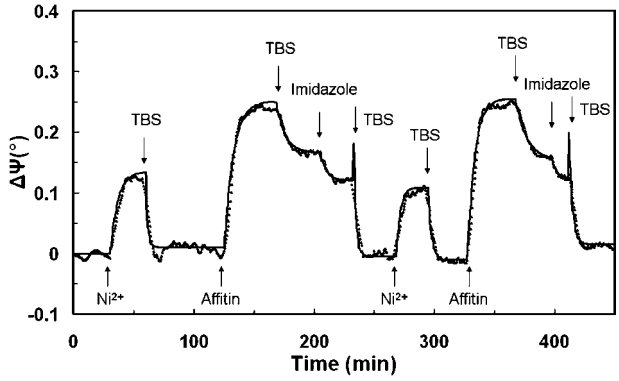

Figure 3. Sensorgram for the interaction of affitin with a mono-NTA functionalized surface that shows binding of Ni^{2+}, adsorption and desorption of affitin, and regeneration of the surface by 250 mM imidazole. This procedure was then repeated to show the reproducibility of the surface. Experimental data (dotted line) were fitted (solid line) using a 1:1 Langmuir binding model for each step.

experiment was performed on the naked zirconium octadecylphosphonate surface. To avoid interslide variation, each slide had only half of its surface functionalized with Ni-NTA groups, and incubation chambers with two compartments were used. As an additional control, the affitins were spotted under two different conditions, one in a 25 mM imidazole-containing buffer to reduce nonspecific bonding to the Ni-NTA surface and the second in a 250 mM imidazole containing buffer to prevent histidine-tagged protein binding by competition (Figure 4). A negative control experiment was also performed with an affitin that does not bind lysozyme. At low imidazole concentration, only spots present on the surface functionalized with the Ni-NTA groups gave high signal intensities, which indicated that affitins were still functional after immobilization. As expected, a high concentration of imidazole (250 mM) prevented affitin binding on the Ni-NTA surface and subsequent lysozyme capture. Interestingly, a very low background value was observed in the absence of affitin, confirming the low nonspecific interaction of lysozyme with the surface when saturated with α-casein. However, nonspecific binding of the affitin on the naked zirconated surface was not completely avoided by α-casein saturation since a low intensity signal was detected in that control.

Different spotting concentrations of the affitins were explored, incubating at a fixed concentration of the lysozyme target. An increase in signal intensity was detected, with no saturation of the lysozyme capture, using affitin concentrations of 1.25−10 μM (Figure 5), confirming the high density of Ni-NTA groups available on the surface of the slides. Both bisphosphonates **13** and **18** led to similar fluorescence intensities at a given affitin concentration, in agreement with SPR data, which had shown that the amount of bound protein after washing is similar with the two linkers. However, the spot shape remains better defined on the bis-NTA modified surface. On the mono-NTA functionalized surface, the spot shape was irregular if affitin was spotted at high concentration, likely as a result of significant dissociation occurring during the washing steps. In the case of the bis-NTA functionalized surface, stronger binding of the histidine tag by a bivalent interaction strongly reduces this effect (Figure 5).

The sensitivity of the microarrays was explored by spotting with a constant affitin concentration and incubating with decreasing concentrations of AlexaFluor 647-labeled lysozyme, using the same slide divided into several independent incubation areas. For this experiment, two affitins differing in their affinity for lysozyme were chosen (H4, $K_d = 5 \times 10^{-9}$ M, and B3, $K_d = 2.9 \times 10^{-7}$ M) (see Supporting Information). For the H4 affitin, the observed limit of detection was below 1 nM (Figure 6). As expected, the slide spotted with B3 affitin, which has a lower affinity for lysozyme, exhibited a detection limit around 0.1 μM, with low sensitivity even at high lysozyme concentration, likely because the weakly associating B3 lysozyme is lost during the washing process.

Comparison with Other Microarray Surfaces. The performance of our Ni-NTA-modified zirconium phosphonate surface was evaluated relative to other types of microarray substrates, including slides coated with a nitrocellulose-based matrix (FAST slides, Schleicher & Schuell), epoxide slides (Nexterion, Schott), and epoxide slides functionalized with Ni-NTA groups using *N*α,*N*α-bis(carboxymethyl)-L-lysine hydrate. All slides were spotted with the same affitin concentrations and incubated with a fixed concentration of the labeled lysozyme. The resulting fluorescence intensities are reported in Figure 7.

Scheme 2. Description of the Different Steps Employed To Test Affitin Activity on a Microarray Platform

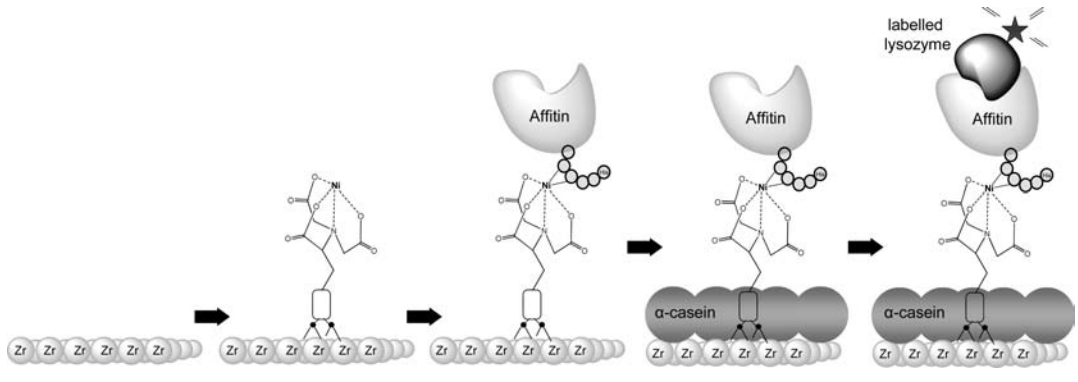

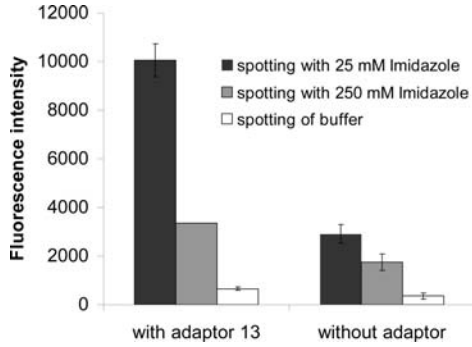

Figure 4. Detection of lysozyme captured by affitin spotted at 1 μM on a Ni-NTA-modified zirconium phosphonate microarray: white bar, buffer spotted only; light gray bar, affitin spotted with 250 mM imidazole; dark gray bar, affitin spotted with 25 mM imidazole. Fluorescence intensities were measured at 90% laser power and 50% photomultiplier gain.

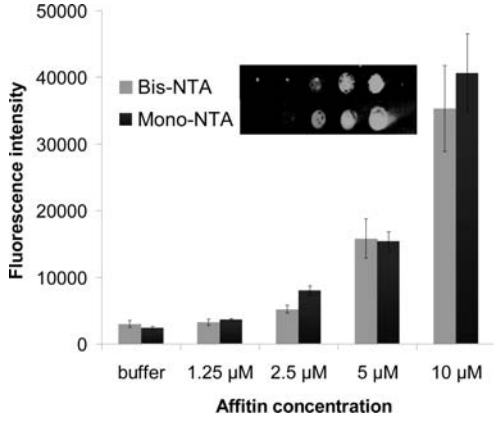

Figure 5. Fluorescence intensity versus concentration of spotted affitin on zirconium phosphonate slides functionalized with mono-Ni-NTA (dark gray) and bis-Ni-NTA (light gray) groups. Fluorescence data values correspond to the mean and the ecart type range for three replicates within one slide (inset) image obtained at 60% laser power and 60% photomultiplier gain.

Slides coated with nitrocellulose membrane gave the highest fluorescence signal, making it necessary to use a lower laser power in this case to avoid excessive background. However, even at lower laser power, the background signal is still high, resulting in a low signal-to-noise ratio (S/N = 1.5). It is known that this polymeric material with defined microporosity binds large amounts of protein in a noncovalent and nonspecific way (*13*). The poor signal-to-noise ratio could be related to the nature of the affitin, which is very small, and possibly easily washed out during the incubation process.

Slides modified with a chemical reactive group, such as an epoxide, provide a covalent yet random immobilization of the proteins via reaction with amino groups present on the protein surface. At the highest concentration of spotted protein (10 μM), the fluorescence intensity using the epoxide E slide is about 50% lower than that obtained using the zirconium phosphonate slides functionalized with Ni-NTA. Somewhat surprisingly, when the epoxide E slides were functionalized with Ni-NTA groups using *N*α,*N*α-bis(carboxymethyl)-L-lysine hydrate, the observed fluorescence intensities were comparable to those obtained for the unmodified E slides. Although modifying the epoxide slides with Ni-NTA groups should provide an oriented immobilization of the affitins, similar to the Ni-NTA-functionalized zirconium phosphonate surface, the observed fluorescence intensity was lower throughout the 1.25−10 μM spotting concentration range. A possible reason might be that the

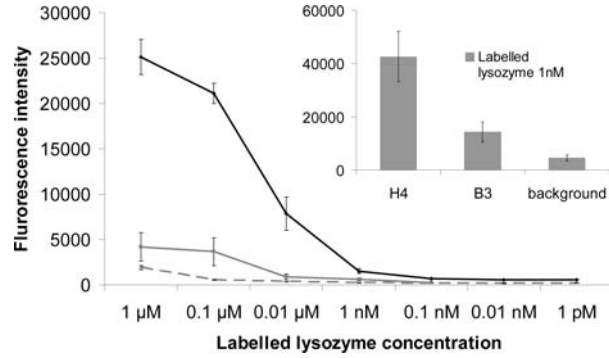

Figure 6. Fluorescence intensity versus concentration of AlexaFluor 647-labeled lysozyme in the incubation solution. Affitins H4 (black line) and B3 (gray line) were spotted (5 μM) on a mono-Ni-NTA-functionalized ODPA/Zr surface. The gray dotted line corresponds to spotting of buffer.

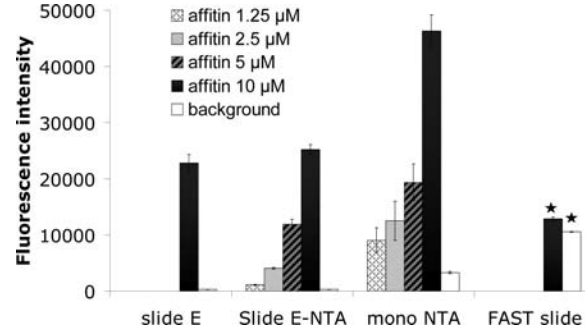

Figure 7. Compared performances for lysozyme capture of H4 affitin immobilized on different substrates: slide E, epoxide surface from Nexterion; slide E-NTA, Ni-NTA functionalized epoxide surface; mono-NTA, mono Ni-NTA functionalized ODPA/Zr surface; FAST slide. The ∗ indicates the fluorescence intensities were measured at lower laser power (30) and gain value (40) with the FAST slide.

zirconium phosphonate surface provides a higher density of NTA groups compared with the epoxide surface. Alternatively, the long spacer separating the NTA group from the phosphonic acid groups attached to the zirconium phosphonate surface may provide better accessibility to the proteins.

CONCLUSION

In this paper, we demonstrate that a zirconium phosphonate modified surface can be efficiently functionalized with metal NTA groups in order to specifically bind histidine-tagged proteins in an oriented way. The NTA linkers bind the zirconated surface via a bis-phosphonic acid functional group with high avidity for the surface. These results further extend to the protein microarray field the applications of mixed organic/inorganic zirconium phosphonate surfaces, on which simple and irreversible modifications can be introduced without the need for chemical activation steps. By use of these bifunctional adaptors, a high density of accessible NTA groups was obtained, allowing high efficiency of protein binding. Proteins immobilized in this way retain their ability to capture protein target with high sensitivity, and the modified zirconium phosphonate surfaces were shown to compete favorably with commercially available substrates designed for protein microarrays. Finally, we also show that the affitin scaffold (*41, 42*) can be used as a capture agent on different types of microarray slides. The small size of this scaffold (66 aa), which has been evaluated as an alternative to antibodies, allows a high density of spotting and consequently a high level of specific activity of the surfaces.

ACKNOWLEDGMENT

This work was partially supported by grants (Nos. 04.04.025 and 2008.34.0010) from the Délégation Générale à l'Armement (DGA). M.C. was supported by a grant from the DGA. Partial support for this work was provided by the US National Science Foundation through Grant Number CHE-0514437 (D.R.T.).

Supporting Information Available: Detailed description of the synthesis, purification, and spectroscopic characterization of the mono- and bis-NTA bisphosphonate adaptors (**13** and **18**) and determination of the affitin dissociation constants by SPR measurement. This material is available free of charge via the Internet at http://pubs.acs.org.

LITERATURE CITED

(1) Kusnezow, W., and Hoheisel, J. D. (2002) Antibody microarrays: Promises and problems. *Biotechniques 33*, 14–23.

(2) DeRisi, J. L., Iyer, V. R., and Brown, P. O. (1997) Exploring the metabolic and genetic control of gene expression on a genomic scale. *Science 278*, 680–686.

(3) Schena, M., Shalon, D., Davis, R. W., and Brown, P. O. (1995) Quantitative monitoring of gene expression patterns with a complementary DNA microarray. *Science 270*, 467–470.

(4) Knezevic, V., Leethanakul, C., Bichsel, V. E., Worth, J. M., Prabhu, V. V., Gutkind, J. S., Liotta, L. A., Munson, P. J., Petricoin, E. F., and Krizman, D. B. (2001) Proteomic profiling of the cancer microenvironment by antibody arrays. *Proteomics 1*, 1271–1278.

(5) Li, B., Jiang, L. X., Song, Q. F., Yang, J. X., Chen, Z. L., Guo, Z. B., Zhou, D. S., Du, Z. M., Song, Y. J., Wang, J., Wang, H. X., Yu, S. Y., Wang, J., and Yang, R. F. (2005) Protein microarray for profiling antibody responses to *Yersinia pestis* live vaccine. *Infect. Immun. 73*, 3734–3739.

(6) Miller, J. C., Zhou, H. P., Kwekel, J., Cavallo, R., Burke, J., Butler, E. B., Teh, B. S., and Haab, B. B. (2003) Antibody microarray profiling of human prostate cancer sera: Antibody screening and identification of potential biomarkers. *Proteomics 3*, 56–63.

(7) Sreekumar, A., Nyati, M. K., Varambally, S., Barrette, T. R., Ghosh, D., Lawrence, T. S., and Chinnaiyan, A. M. (2001) Profiling of cancer cells using protein microarrays: Discovery of novel radiation-regulated proteins. *Cancer Res. 61*, 7585–7593.

(8) Steller, S., Angenendt, P., Cahill, D. J., Heuberger, S., Lehrach, H., and Kreutzberger, J. (2005) Bacterial protein microarrays for identification of new potential diagnostic markers for *Neisseria meningitidis* infections. *Proteomics 5*, 2048–2055.

(9) Steinhauer, C., Ressine, A., Marko-Varga, G., Laurell, T., Borrebaeck, C. A. K., and Wingren, C. (2005) Biocompatibility of surfaces for antibody microarrays: Design of macroporous silicon substrates. *Anal. Biochem. 341*, 204–213.

(10) Brody, E. N., and Gold, L. (2000) Aptamers as therapeutic and diagnostic agents. *J. Biotechnol. 74*, 5–13.

(11) Nygren, P. A., and Skerra, A. (2004) Binding proteins from alternative scaffolds. *J. Immunol. Methods 290*, 3–28.

(12) Zhu, H., and Snyder, M. (2003) Protein chip technology. *Curr. Opin. Chem. Biol. 7*, 55–63.

(13) Peluso, P., Wilson, D. S., Do, D., Tran, H., Venkatasubbaiah, M., Quincy, D., Heidecker, B., Poindexter, K., Tolani, N., Phelan, M., Witte, K., Jung, L. S., Wagner, P., and Nock, S. (2003) Optimizing antibody immobilization strategies for the construction of protein microarrays. *Anal. Biochem. 312*, 113–124.

(14) Vijayendran, R. A., and Leckband, D. E. (2001) A quantitative assessment of heterogeneity for surface-immobilized proteins. *Anal. Chem. 73*, 471–480.

(15) Angenendt, P., Glokler, J., Sobek, J., Lehrach, H., and Cahill, D. J. (2003) Next generation of protein microarray support materials: Evaluation for protein and antibody microarray applications. *J. Chromatogr. A 1009*, 97–104.

(16) Grazu, V., Abian, O., Mateo, C., Batista-Viera, F., Fernandez-Lafuente, R., and Guisan, J. M. (2003) Novel bifunctional epoxy/thiol-reactive support to immobilize thiol containing proteins by the epoxy chemistry. *Biomacromolecules 4*, 1495–1501.

(17) Kusnezow, W., Jacob, A., Walijew, A., Diehl, F., and Hoheisel, J. D. (2003) Antibody microarrays: An evaluation of production parameters. *Proteomics 3*, 254–264.

(18) Li, Y. W., and Reichert, W. M. (2003) Adapting cDNA microarray format to cytokine detection protein arrays. *Langmuir 19*, 1557–1566.

(19) MacBeath, G., and Schreiber, S. L. (2000) Printing proteins as microarrays for high-throughput function determination. *Science 289*, 1760–1763.

(20) Mateo, C., Torres, R., Fernandez-Lorente, G., Ortiz, C., Fuentes, M., Hidalgo, A., Lopez-Gallego, F., Abian, O., Palomo, J. M., Betancor, L., Pessela, B. C. C., Guisan, J. M., and Fernandez-Lafuente, R. (2003) Epoxy-amino groups: A new tool for improved immobilization of proteins by the epoxy method. *Biomacromolecules 4*, 772–777.

(21) Patel, N., Davies, M. C., Hartshorne, M., Heaton, R. J., Roberts, C. J., Tendler, S. J. B., and Williams, P. M. (1997) Immobilization of protein molecules onto homogeneous and mixed carboxylate-terminated self-assembled monolayers. *Langmuir 13*, 6485–6490.

(22) Viitala, T., Vikholm, I., and Peltonen, J. (2000) Protein immobilization to a partially cross-linked organic monolayer. *Langmuir 16*, 4953–4961.

(23) Bieri, C., Ernst, O. P., Heyse, S., Hofmann, K. P., and Vogel, H. (1999) Micropatterned immobilization of a G protein-coupled receptor and direct detection of G protein activation. *Nat. Biotechnol. 17*, 1105–1108.

(24) Hodneland, C. D., Lee, Y. S., Min, D. H., and Mrksich, M. (2002) Selective immobilization of proteins to self-assembled monolayers presenting active site-directed capture ligands. *Proc. Natl. Acad. Sci. U.S.A. 99*, 5048–5052.

(25) Kwon, Y., Han, Z. Z., Karatan, E., Mrksich, M., and Kay, B. K. (2004) Antibody arrays prepared by cutinase-mediated immobilization on self-assembled monolayers. *Anal. Chem. 76*, 5713–5720.

(26) Pavlickova, P., Lensen, N. M., Paul, H., Schaeferling, M., Giammasi, C., Kruschina, M., Du, W. D., Theisen, M., Ibba, M., Ortigao, F., and Kambhampati, D. (2002) Antibody detection in human serum using a versatile protein chip platform constructed by applying nanoscale self-assembled architectures on gold. *J. Proteome Res. 1*, 227–231.

(27) Wacker, R., Schroder, H., and Niemeyer, C. M. (2004) Performance of antibody microarrays fabricated by either DNA-directed immobilization, direct spotting, or streptavidin-biotin attachment: a comparative study. *Anal. Biochem. 330*, 281–287.

(28) Chen, H. M., Wang, W. C., and Chen, S. H. (2004) A metal-chelating piezoelectric sensor chip for direct detection and oriented immobilization of polyHis-tagged proteins. *Biotechnol. Prog. 20*, 1237–1244.

(29) Lata, S., and Piehler, J. (2005) Stable and functional immobilization of histidine-tagged proteins via multivalent chelator headgroups on a molecular poly(ethylene glycol) brush. *Anal. Chem. 77*, 1096–1105.

(30) Lee, J. K., Kim, Y. G., Chi, Y. S., Yun, W. S., and Choi, I. S. (2004) Grafting nitrilotriacetic groups onto carboxylic acid-terminated self-assembled monolayers on gold surfaces for immobilization of histidine-tagged proteins. *J. Phys. Chem. B 108*, 7665–7673.

(31) Schmid, E. L., Keller, T. A., Dienes, Z., and Vogel, H. (1997) Reversible oriented surface immobilization of functional proteins on oxide surfaces. *Anal. Chem. 69*, 1979–1985.

(32) Chaga, G. S. (2001) Twenty-five years of immobilized metal ion affinity chromatography: Past, present and future. *J. Biochem. Biophys. Methods 49*, 313–334.

(33) Porath, J. (1988) IMAC-immobilized metal ion affinity based chromatography. *Trends Anal. Chem. 7*, 254–259.

(34) Porath, J., and Olin, B. (1983) Immobilized metal ion affinity adsorption and immobilized metal ion affinity chromatography of biomaterials: Serum protein affinities for gel-immobilized iron and nickel ions. *Biochemistry 22*, 1621–1630.
(35) Dorn, I. T., Neumaier, K. R., and Tampe, R. (1998) Molecular recognition of histidine-tagged molecules by metal-chelating lipids monitored by fluorescence energy transfer and correlation spectroscopy. *J. Am. Chem. Soc. 120*, 2753–2763.
(36) Guignet, E. G., Hovius, R., and Vogel, H. (2004) Reversible site-selective labeling of membrane proteins in live cells. *Nat. Biotechnol. 22*, 440–444.
(37) Kapanidis, A. N., Ebright, Y. W., and Ebright, R. H. (2001) Site-specific incorporation of fluorescent probes into protein: Hexahistidine-tag-mediated fluorescent labeling with (Ni^{2+}: Nitrilotriacetic acid)$_n$−fluorochrome conjugates. *J. Am. Chem. Soc. 123*, 12123–12125.
(38) Zhu, H., Bilgin, M., Bangham, R., Hall, D., Casamayor, A., Bertone, P., Lan, N., Jansen, R., Bidlingmaier, S., Houfek, T., Mitchell, T., Miller, P., Dean, R. A., Gerstein, M., and Snyder, M. (2001) Global analysis of protein activities using proteome chips. *Science 293*, 2101–2105.
(39) Nonglaton, G., Benitez, I. O., Guisle, I., Pipelier, M., Leger, J., Dubreuil, D., Tellier, C., Talham, D. R., and Bujoli, B. (2004) New approach to oligonucleotide microarrays using zirconium phosphonate-modified surfaces. *J. Am. Chem. Soc. 126*, 1497–1502.
(40) Monot, J., Petit, M., Lane, S. M., Guisle, I., Leger, J., Tellier, C., Talham, D. R., and Bujoli, B. (2008) Towards zirconium phosphonate-based microarrays for probing DNA−protein interactions: Critical influence of the location of the probe anchoring groups. *J. Am. Chem. Soc. 130*, 6243–6251.
(41) Krehenbrink, M., Chami, M., Guilvout, I., Alzari, P. M., Pecorari, F., and Pugsley, A. P. (2008) Artificial binding proteins (affitins) as probes for conformational changes in secretin PulD. *J. Mol. Biol. 383*, 1058–1068.
(42) Mouratou, B., Schaeffer, F., Guilvout, I., Tello-Manigne, D., Pugsley, A. P., Alzari, P. M., and Pecorari, F. (2007) Remodeling a DNA-binding protein as a specific in vivo inhibitor of bacterial secretin PulD. *Proc. Natl. Acad. Sci. U.S.A. 104*, 17983–17988.
(43) Maoz, R., and Sagiv, J. (1984) On the formation and structure of self-assembling monolayers. 1. A comparative ATR-wetability study of Langmuir-Blodgett and adsorbed films on flat substrates and glass microbeads. *J. Colloid Interface Sci. 100*, 465–496.
(44) Byrd, H., Pike, J. K., and Talham, D. R. (1993) Inorganic monolayers formed at an organic template: A Langmuir−Blodgett route to monolayer and multilayer films of zirconium octadecylphosphonate. *Chem. Mater. 5*, 709–715.
(45) Byrd, H., Pike, J. K., and Talham, D. R. (1994) Extended-lattice Langmuir−Blodgett films: Manganese octadecylphosphonate Langmuir−Blodgett films are structural and magnetic analogs of solid-state manganese phosphonates. *J. Am. Chem. Soc. 116*, 7903–7904.
(46) Lata, S., Reichel, A., Brock, R., Tampe, R., and Piehler, J. (2005) High-affinity adaptors for switchable recognition of histidine-tagged proteins. *J. Am. Chem. Soc. 127*, 10205–10215.
(47) Horne, J. C., and Blanchard, G. J. (1996) Dynamics within a single molecular layer. Aggregation, relaxation, and the absence of motion. *J. Am. Chem. Soc. 118*, 12788–12795.
(48) Horne, J. C., Huang, Y., Liu, G. Y., and Blanchard, G. J. (1999) Correspondence between layer morphology and intralayer excitation transport dynamics in zirconium-phosphonate monolayers. *J. Am. Chem. Soc. 121*, 4419–4426.
(49) Katz, H. E., Schilling, M. L., Chidsey, C. E. D., Putvinski, T. M., and Hutton, R. S. (1991) Quaterthiophenediphosphonic acid (QDP): A rigid, electron-rich building block for zirconium-based multilayers. *Chem. Mater. 3*, 699–703.
(50) Lee, H., Kepley, L. J., Hong, H. G., Akhter, S., and Mallouk, T. E. (1988) Adsorption of ordered zirconium phosphonate multilayer films on silicon and gold surfaces. *J. Phys. Chem. 92*, 2597–2601.
(51) Lee, H., Kepley, L. J., Hong, H. G., and Mallouk, T. E. (1988) Inorganic analogs of Langmuir−Blodgett films: Adsorption of ordered zirconium 1,10-decanebisphosphonate multilayers on silicon surfaces. *J. Am. Chem. Soc. 110*, 618–620.
(52) Neff, G. A., Helfrich, M. R., Clifton, M. C., and Page, C. J. (2000) Layer-by-layer growth of acentric multilayers of Zr and azobenzene bis(phosphonate): Structure, composition, and second-order nonlinear optical properties. *Chem. Mater. 12*, 2363–2371.
(53) Putvinski, T. M., Schilling, M. L., Katz, H. E., Chidsey, C. E. D., Mujsce, A. M., and Emerson, A. B. (1990) Self-assembly of organic multilayers with polar order using zirconium phosphate bonding between layers. *Langmuir 6*, 1567–1571.
(54) Snover, J. L., Byrd, H., Suponeva, E. P., Vicenzi, E., and Thompson, M. E. (1996) Growth and characterization of photoactive and electroactive zirconium bisphosphonate multilayer films. *Chem. Mater. 8*, 1490–1499.
(55) Byrd, H., Suponeva, E. P., Bocarsly, A. B., and Thompson, M. E. (1996) Photocurrent generation in metal bisphosphonate multilayer thin films. *Nature 380*, 610–612.
(56) Katz, H. E., and Schilling, M. L. (1993) Electrical properties of multilayers based on zirconium phosphate/phosphonate bonds. *Chem. Mater. 5*, 1162–1166.
(57) Benitez, I. O., Bujoli, B., Camus, L. J., Lee, C. M., Odobel, F., and Talham, D. R. (2002) Monolayers as models for supported catalysts: Zirconium phosphonate films containing manganese(III) porphyrins. *J. Am. Chem. Soc. 124*, 4363–4370.
(58) Nixon, C. N., Le Claire, K., Odobel, F., Bujoli, B., and Talham, D. R. (1999) Palladium porphyrin containing zirconium phosphonate Langmuir−Blodgett films. *Chem. Mater. 11*, 965–976.
(59) Petruska, M. A., Fanucci, G. E., and Talham, D. R. (1998) Organic/inorganic Langmuir−Blodgett films based on metal phosphonates: Preparation and characterization of phenoxy- and biphenoxy-substituted zirconium phosphonate films. *Chem. Mater. 10*, 177–189.
(60) Wu, A. P., and Talham, D. R. (2000) Photoisomerization of azobenzene chromophores in organic/inorganic zirconium phosphonate thin films prepared using a combined Langmuir−Blodgett and self-assembled monolayer deposition. *Langmuir 16*, 7449–7456.
(61) Bujoli, B., Lane, S. M., Nonglaton, G., Pipelier, M., Leger, J., Talham, D. R., and Tellier, C. (2005) Metal phosphonates applied to biotechnologies: a novel approach to oligonucleotide microarrays. *Chemistry 11*, 1980–1988.
(62) Lane, S. M., Monot, J., Petit, M., Bujoli, B., and Talham, D. R. (2007) XPS investigation of DNA binding to zirconium-phosphonate surfaces. *Colloids Surf., B 58*, 34–38.
(63) Lane, S. M., Monot, J., Petit, M., Tellier, C., Bujoli, B., and Talham, D. R. (2008) Poly(dG) spacers lead to increased surface coverage of DNA probes: An XPS study of oligonucleotide binding to zirconium phosphonate modified surfaces. *Langmuir 24*, 7394–7399.

BC9002597

Supporting Information for:

Bisphosphonate Adaptors for Specific Protein Binding on Zirconium Phosphonate-based Microarrays

Mathieu Cinier,[1] Marc Petit,[2] Monique N. Williams,[3] Roxane M. Fabre,[3] Frédéric Pecorari,[1] Daniel R. Talham,[3] Bruno Bujoli,[2]* and Charles Tellier [1]*

Contribution from :

Université de Nantes, CNRS, UMR 6204, Laboratoire de Biotechnologie, Biocatalyse et Biorégulation, UFR Sciences et Techniques, 2, rue de la Houssinière, BP 92208, 44322 NANTES Cedex 3, France

Université de Nantes, CNRS, UMR 6230, Chimie Et Interdisciplinarité : Synthèse Analyse Modélisation (CEISAM), 2 Rue de la Houssinière , BP92208, 44322 Nantes Cedex 03, France

Department of Chemistry, University of Florida, Gainesville, Florida, 32611-7200, USA,

E-mail: charles.tellier@univ-nantes.fr; bruno.bujoli@univ-nantes.fr

* Authors to whom correspondence should be addressed.
[1] Laboratoire de Biotechnologie, Biocatalyse et Biorégulation.
[2] Chimie Et Interdisciplinarité : Synthèse Analyse Modélisation
[3] University of Florida

Supporting Information

Phosphonated Adaptors for Specific Protein Anchoring on Zirconium Phosphonate-based Microarrays

Contents

1) Synthesis of the phosphorylated mono-NTA (13) and bis-NTA linker (18)
Experimental procedure for the synthesis of coumponds **1** to **18**.
^{1}H, ^{13}C NMR spectra for **1** to **18**

GENERAL:

All experiments were done under argon atmosphere. THF was distilled from sodium/benzophenone and dichloromethane from CaH_2. DMF was purchased from Aldrich as extra dry grade. Other solvents and reagents were purchased from Aldrich and used without further purification. All NMR spectra were recorded on a AC-300 or AC-400 Bruker spectrometer. Chemical shifts were reported in ppm using the residual solvent signal of $CDCl_3$ (^{1}H spectra: 7.28 ppm: ^{13}C spectra: 77.23 ppm) or D_2O (^{1}H spectra: 4.78 ppm). In reporting spectral data, the following abbreviations were used: s = singlet, d = doublet, t = triplet, q = quadruplet, m = multiplet, dd = doublet of doublet, dt = doublet of triplet. Constants (*J*) are given in Hertz (Hz). Low resolution (MS) mass spectra were taken under ESI mode on a LCQAdvantage (Thermo) micromass instrument or under CI mode on a DSQ-II (Thermo) micromass instrument with ammonia as reagent gas. All mass data and are reported in *m/z* units. Flash chromatographies were performed using Kieselgel-60 silica gel (230-400 mesh, Merck). Thin layer (TLC) analyses were done with Merck silica gel F-254 aluminum-backed plates.

Compound 1

To a stirred solution of 4-chlorobutanol (21.6 g, 198 mmol) and 3, 4-dihydro-2H-pyran (16.7 g, 198 mmol) in CH_2Cl_2 (900 mL), PTSA (catalytic) was added at room temperature. The mixture was stirred during 20 h, then washed with a saturated $NaHCO_3$ solution, dried over $MgSO_4$, filtered and evaporated under reduced pressure. The residue was purified by flash chromatography (EP/AcOEt, 95/5) to give **1** (29.36 g, 152.4 mmol, 77%). **^{1}H NMR (300 MHz, $CDCl_3$) δ:** 1.46-1.60 (m, 4H); 1.62-1.80 (m, 4H); 1.81-1.94 (m, 2H, -

$C\underline{H}_2CH_2Cl$); 3.40 (dt, *J* = 9.7, 6 Hz, 1H, -$C\underline{H}_2O$-); 3.44-3.52 (m, 1H, -$C\underline{H}_2O$-); 3.56 (t, *J* = 6.5 Hz, 2H, -$C\underline{H}_2Cl$); 3.75 (dt, *J* = 9.7, 6 Hz, 1H, -$C\underline{H}_2O$-); 3.79-3.87 (m, 1H, -$C\underline{H}_2O$-); 4.46 (t, *J* = 2.2, 1H, -OC<u>H</u>O-). **^{13}C NMR (100.6 MHz, $CDCl_3$) δ:** 19.56 (-$CHCH_2\underline{C}H_2$-); 25.40 (-$CH(CH_2)_2\underline{C}H_2$-); 27.07 ($Cl(CH_2)_2\underline{C}H_2$-); 29.60 ($ClCH_2\underline{C}H_2$-); 30.70 (-$CH\underline{C}H_2$-); 44.92 (-$\underline{C}H_2Cl$); 62.30 (-$\underline{C}H_2O$-, THP); 66.55 (-$\underline{C}H_2O$-); 98.80 (-O<u>C</u>HO-).

Compound 2

To a stirred solution of benzylamine (6.22 g, 58.12 mmol) and O-tetrahydropyranyl-4-chlorobutanol (**1**) (28 g, 145.31 mmol) in CH_3CN (150 mL), K_2CO_3 (20 g, 145.31 mmol) and KI (1.7 g, 11.62 mmol) were added at room temperature. The reaction mixture was refluxed for 48 h under argon atmosphere. The reaction mixture was cooled to room temperature, and the insoluble material was filtered off and the filtrate was concentrated under reduced pressure. The residue was purified by flash chromatography (EP/AcOEt, 100/0 to 30/70) to give **2** (15.1g, 36 mmol, 62%) as a colourless oil. **^{1}H NMR (300 MHz, $CDCl_3$) δ:** 1.54-1.90 (m, 20H); 2.43 (dd, *J* = 6.6 and 7.3Hz, 4H, -$NC\underline{H}_2$-); 3.35 (m, 2H, -$OC\underline{H}_2$-); 3.47 (m, 2H, -$OC\underline{H}_2$-, THP); 3.54 (s, 2H, $PhC\underline{H}_2$-); 3.70 (m, 2H, -$OC\underline{H}_2$-); 3.84 (m, 2H, -$OC\underline{H}_2$-, THP); 4.54 (dd, J = 2.7 and 4.4Hz, 2H, -OC<u>H</u>O-); 7.15-7.35 (m, 5H, aromatic). **^{13}C NMR (100.6 MHz, $CDCl_3$) δ:** 19.6 (-$CHCH_2\underline{C}H_2$-); 23.8 (-$NCH_2\underline{C}H_2$-); 25.5 (-$CH(CH_2)_2\underline{C}H_2$-); 27.6 ($NH(CH_2)_2\underline{C}H_2$-); 30.7 (-$CH\underline{C}H_2$-); 53.5 (-$N\underline{C}H_2$-); 58.6 (-$\underline{C}H_2O$-, THP); 62.3 ($Ph\underline{C}H_2$-); 67.5 (-$\underline{C}H_2O$-); 98.8 (-O<u>C</u>HO-); 126.6 (CAr); 128.1 (CAr); 128.8 (CAr); 140.2 (CAr).

Compound 3

To a stirred solution of **2** (12 g, 28.59 mmol) in methanol (60 mL), 10% Pd/C (1.2 g) was added and argon was bubbled in the resulting mixture. The flask was then evacuated and flushed with hydrogen. The reaction mixture was vigorously stirred under hydrogen overnight, and then filtered through a celite pad. The celite was washed with methanol and the solvent was concentrated *in vacuo* to yield **3** quantitatively. **^{1}H NMR (300 MHz, $CDCl_3$) δ:** 1.39-1.89 (20H); 2.65 (m, 4H, -$NC\underline{H}_2$-); 2.77 (s, 1H, -N<u>H</u>-); 3.38 (m, 2H, -$OC\underline{H}_2$-); 3.48 (m, 2H, -$OC\underline{H}_2$-, THP); 3.73 (m, 2H, -$OC\underline{H}_2$-), 3.83 (m, 2H, -$OC\underline{H}_2$-, THP); 4.55 (m, 2H, -OC<u>H</u>O-). **^{13}C NMR (100.6 MHz, $CDCl_3$) δ:** 19.61 (-$CHCH_2\underline{C}H_2$-); 25.42 (-$CH(CH_2)_2\underline{C}H_2$-); 26.47 ($NHCH_2\underline{C}H_2$-); 27.49 ($NH(CH_2)_2\underline{C}H_2$-); 30.71 (-$CH\underline{C}H_2$-); 49.44 (-$N\underline{C}H_2$-); 62.32 (-$\underline{C}H_2O$-, THP); 67.32 (-$\underline{C}H_2O$-); 98.84 (-O<u>C</u>HO-). **MS** (CI, $C_{18}H_{35}NO_4$): 330.2 $[MH]^+$.

Compound 4

To a stirred solution of **3** (9.92 g, 30.13 mmol) in CH_2Cl_2 (50 mL), Et_3N (7.62 g, 75.33 mmol, 10.5 mL) and succinimide (4.52 g, 45.20 mmol) were added sequentially at room temperature. The reaction mixture was stirred for 4 days and then poured into water. The organic layer was washed with water (4 times). The aqueous layers were separated, acidified at pH = 2 with HCl and washed with CH_2Cl_2. Then, the organic layers were collected, dried over $MgSO_4$, filtered and evaporated under reduced pressure. Product **4** was obtained (11.87 g, 27.64 mmol, 92%) and used without further purification. **^{1}H NMR (300 MHz, $CDCl_3$) δ:** 1.39-1.78 (20H); 2.61 (s, 4H, -CO($C\underline{H}_2$)$_2$CO-); 3.21-3.47 (m, 8H, -OC$\underline{H}_2$- and –NC$\underline{H}_2$-); 3.63-3.82 (m, 4H, -OC$\underline{H}_2$-); 4.49 (m, 2H, -OC$\underline{H}$O-). **^{13}C NMR (100.6 MHz, $CDCl_3$) δ:** 19.75 (-CHCH$_2\underline{C}$H$_2$-); 24.53 (-CH(CH$_2$)$_2\underline{C}$H2-); 25.42, 25.82; 26.90; 27.12; 27.98; 30.12 (-$\underline{C}$H$_2$CO-); 30.73 (-CH$\underline{C}$H$_2$-); 46.20 (-$\underline{C}$H$_2$N-); 47.96 (-$\underline{C}$H$_2$N-); 62.42 (-$\underline{C}$H$_2$O-, THP); 62.61 (-$\underline{C}$H$_2$O-, THP); 66.87 (-$\underline{C}$H$_2$O-); 67.17 (-$\underline{C}$H$_2$O-); 98.94 (-O$\underline{C}$HO-); 99.10 (-O$\underline{C}$HO-); 171.97 (-N$\underline{C}$O-); 175.69 (-$\underline{C}$O$_2$H). **MS** (MALDI, ESI, $C_{22}H_{39}NO_7$): 429.9 $[MH]^+$, 452.2 $[MNa]^+$.

Compound 5

To a stirred solution of **4** (5 g, 11.63 mmol) in EtOH (250 mL) PTSA (5.5 g, 29 mmol) was added at room temperature. The reaction mixture was stirred for 48 h and then partially concentrated under reduced pressure. The reaction mixture was poured into CH_2Cl_2 and washed with a saturated $NaHCO_3$ aqueous solution. The aqueous layer was extracted with CH_2Cl_2 (3 times). The organic layers were collected, dried over $MgSO_4$, filtered and concentrated *in vacuo*. Product **5** was obtained (2.56 g, 8.85 mmol, 75%) and used without further purification. **^{1}H NMR (300 MHz, $CDCl_3$) δ:** 1.25 (t, *J* = 7.1Hz, 3H); 1.48-1.75 (m, 8H, -CH$_2$($C\underline{H}_2$)$_2$CH$_2$-); 2.58-2.68 (m, 4H, -COC$\underline{H}_2$C$\underline{H}_2$CO-); 3.33 (m, 4H, -C$\underline{H}_2$N-); 3.66 (m, 4H, -C$\underline{H}_2$OH); 4.12 (q, *J* = 7.15 Hz, 2H, CH$_3$C$\underline{H}_2$O-). **^{13}C NMR (100.6 MHz, $CDCl_3$) δ:** 14.04 ($\underline{C}$H$_3$CH$_2$O-); 24.03; 25.30; 27.78; 29.37; 29.47; 29.54; 45.71 (-$\underline{C}$H$_2$N-); 47.71 (-$\underline{C}$H$_2$N-); 60.52 (CH$_3\underline{C}$H$_2$O-); 61.77 (-CH$_2\underline{C}$H$_2$O-); 61.82 (-CH$_2\underline{C}$H$_2$O-); 171.08 (-$\underline{C}$ON-); 173.27 (-$\underline{C}$O$_2$Et). **MS** (CI, $C_{14}H_{27}NO_5$): 290.2 $[MH]^+$.

Compound 6

Under argon atmosphere, pyridine (1.18 g, 15 mmol, 1.21 mL) was added to a stirred solution of **5** (0.88 g, 3 mmol) in dry CH_2Cl_2 (20 mL). The reaction mixture was cooled with an ice bath and methanesulfonyl chloride (2.16 g, 15 mmol, 1.46 mL) was added. The reaction was stirred at room temperature for 6 h. The reaction mixture was then diluted with ether, washed with cold 10% aqueous HCl, cold 10% aqueous NaOH, water and brine. The

organic layer was dried over $MgSO_4$, filtered and evaporated *in vacuo*. Product **6** was obtained (1.34 g, 3 mmol, 100%) and used without further purification. **^{1}H NMR (300 MHz, $CDCl_3$) δ:** 1.25 (t, 3H, *J* = 7.14Hz, $C\underline{H}_3CH_2O$-); 1.49-1.85 (m, 8H, $-NCH_2(C\underline{H}_2)_2CH_2$-); 2.56-2.68 (m, 4H, $-CO(C\underline{H}_2)_2CO$-); 3.00 (s, 3H, $C\underline{H}_3S$-); 3.02 (s, 3H, $C\underline{H}_3S$-); 3.26-3.41 (m, 4H, $-NC\underline{H}_2$-); 4.12 (q, 2H, *J* = 7.14Hz, $CH_3C\underline{H}_2O$-); 4.21-4.29 (m, 4H, $-CH_2C\underline{H}_2S$-). **^{13}C NMR (100.6 MHz, $CDCl_3$) δ:** 14.17 ($\underline{C}H_3CH_2O$-); 23.85; 25.17; 26.62; 27.98 ($-OCOCH_2\underline{C}H_2CO$-); 29.52 ($-OCO\underline{C}H_2CH_2CO$-); 37.49 ($\underline{C}H_3S$-); 45.19 ($-\underline{C}H_2N$-); 47.20 ($-\underline{C}H_2N$-); 60.48 ($CH_3\underline{C}H_2O$-); 68.99 ($-\underline{C}H_2OS$-); 69.64 ($-\underline{C}H_2OS$-); 171.11 ($-\underline{C}ON$-); 173.00 ($-\underline{C}O_2Et$). **MS** (MALDI, ESI, $C_{16}H_{31}NO_9S_2$): 446 $[MH]^+$**,** 468 $[MNa]^+$.

Compound 7

To a stirred solution of **6** (1.34 g, 3 mmol) in acetone (60 mL), LiBr (2.6 g, 30 mmol) was added at room temperature. The reaction mixture was refluxed for 24 h under argon atmosphere. The solvent was removed under reduced pressure and the reaction mixture was diluted with CH_2Cl_2. The organic layer was washed with water (3 times), dried over $MgSO_4$, filtered and concentrated under reduced pressure. Product **7** was obtained (1.08 g, 2.6 mmol, 87%) and used without further purification. **^{1}H NMR (300 MHz, $CDCl_3$) δ:** 1.25 (t, 3H, *J* = 7.14Hz, $C\underline{H}_3CH_2O$-); 1.50-1.96 (m, 8H, $-NCH_2(C\underline{H}_2)_2CH_2$-); 2.56-2.71 (m, 4H, $-CO(C\underline{H}_2)_2CO$-); 3.33 (m, 4H, $-NC\underline{H}_2$-); 3.43 (m, 4H, $-C\underline{H}_2Br$); 4.13 (q, 2H, *J* = 7.14Hz, $CH_3C\underline{H}_2O$-). **^{13}C NMR (100.6 MHz, $CDCl_3$) δ:** 14.11 ($\underline{C}H_3CH_2O$-); 26.22; 27.33; 27.81 ($-COCH_2\underline{C}H_2CON$-); 29.34 ($-CO\underline{C}H_2CH_2CON$-); 29.67; 29.85; 32.75 ($-\underline{C}H_2Br$); 33.39 ($-\underline{C}H_2Br$); 44.79 ($-N\underline{C}H_2$-); 46.75 ($-N\underline{C}H_2$-); 60.47 ($CH_3\underline{C}H_2O$-); 170.87 ($-\underline{C}ON$-); 173.03 ($-\underline{C}O_2Et$). **MS** (MALDI, ESI, $C_{14}H_{25}Br_2NO_3$): 416 $[MH]^+$, 438 $[MNa]^+$.

Compound 8

Under argon atmosphere, diethylphosphite (1.11 g, 8.1 mmol, 0.8 mL) was added to a stirred suspension of metallic sodium (0.19 g, 8.1 mmol) in dry THF (30 mL). The reaction mixture was stirred at room temperature until all sodium had reacted. Then, a solution of **7** (1.08 g, 2.6 mmol) in dry THF was added via a canula and salt formation occurred rapidly in the reaction mixture. The reaction mixture was stirred for 4 days and then poured into ethyl acetate. The organic layer was washed with a NH_4Cl saturated solution and then brine. The aqueous layer was extracted 3 times with CH_2Cl_2. The organic layers were combined, dried over $MgSO_4$, filtered, and concentrated *in vacuo*. The residue was separated by flash chromatography (EP/AcOEt, 100/0 to 0/100 and next AcOEt/MeOH, 90/10 to 70/30) to give

8 (1.16 g, 2.19 mmol, 81%) as a colourless oil. **^{1}H NMR (300 MHz, $CDCl_3$) δ:** 1.25 (t, 3H, *J* = 7.14, $C\underline{H}_3CH_2OCO$-); 1.31 (t, 6H, *J* = 7.05, $C\underline{H}_3CH_2OPO$-); 1.32 (t, 6H, *J* = 7.05, $C\underline{H}_3CH_2OPO$-); 1.82-2.24 (m, 12H, -$PO(C\underline{H}_2)_3CH_2$-); 2.53-2.69 (m, 4H, -$CO(C\underline{H}_2)_2CO$-); 3.21-3.35 (m, 4H, -$CONC\underline{H}_2$-); 4.01-4.17 (m, 10H, $CH_3C\underline{H}_2OCO$- and $CH_3C\underline{H}_2OPO$-). **^{13}C NMR (100.6 MHz, $CDCl_3$) δ:** 14.09 ($\underline{C}H_3CH_2OCO$-); 16.35 ($\underline{C}H_3CH_2OP$-); 16.41 ($\underline{C}H_3CH_2OP$-); 19.92 (-$\underline{C}H_2CH_2P$-); 24.29; 24.41; 26.16; 26.29; 27.78 (-$OCOCH_2\underline{C}H_2CON$-); 28.35; 28.56; 29.32 (-$OCOCH_2\underline{C}H_2CON$-); 29.55; 29.75; 45.47 (-$\underline{C}H_2N$-); 47.36 (-$\underline{C}H_2N$-); 60.44 ($CH_3\underline{C}H_2OCO$-); 61.46 ($CH_3\underline{C}H_2OP$-); 170.70 (-$OCOCH_2CH_2\underline{C}ON$-); 173.07 (-$O\underline{C}OCH_2CH_2CON$-). **MS** (MALDI, ESI, $C_{20}H_{41}NO_9P_2$): 502.1 $[MH]^+$, 524.1 $[MNa]^+$.

Compound 9

To a stirred solution of **8** (1.16 g, 2.19 mmol) in a THF/MeOH/H_2O (3/1/1) mixture, LiOH (0.13 g, 5.47 mmol) was added. The reaction mixture was stirred for 24 h and then acidified with a 0.2 M HCl aqueous solution. The aqueous layer was extracted 4 times with CH_2Cl_2. The organic layers were combined, dried over $MgSO_4$, filtered and concentrated *in vacuo*. Product **9** was obtained (1.11 g, 2.21 mmol, 100%) and used without further purification. **^{1}H NMR (300 MHz, $CDCl_3$) δ:** 1.32 (m, 12H, $C\underline{H}_3CH_2OP$-); 1.47-1.83 (m, 12H, -$NCH_2(C\underline{H}_2)_3P$-); 2.58-2.72 (m, 4H, -$CO(C\underline{H}_2)_2CO$-); 3.27 (m, 2H, -$NC\underline{H}_2$-); 3.38 (m, 2H, -$NC\underline{H}_2$-); 4.01-4.18 (m, 8H, $CH_3C\underline{H}_2OP$-). **^{13}C NMR (100.6 MHz, $CDCl_3$) δ:** 16.33 ($\underline{C}H_3CH_2OP$-); 16.39 ($\underline{C}H_3CH_2OP$-); 19.70 (-$\underline{C}H_2CH_2P$-); 19.98 (-$\underline{C}H_2CH_2P$-); 24.45; 26.30; 28.18; 28.30; 28.52; 29.58; 29.77; 29.98; 45.30 (-$\underline{C}H_2N$-); 47.53 (-$\underline{C}H_2N$-); 61.34 ($CH_3\underline{C}H_2OP$-); 61.69 ($CH_3\underline{C}H_2OP$-); 171.76 (-$OCOCH_2CH_2\underline{C}ON$-); 174.33 (-$O\underline{C}OCH_2CH_2CON$-). **MS** (MALDI, ESI, $C_{20}H_{41}NO_9P_2$): 502 $[MH]^+$, 524.1 $[MNa]^+$.

Compound 10

tert-Butyl bromoacetate (12.52 g, 64.20 mmol, 9.47 mL) and EDIAP (6.63 g, 51.36 mmol, 8.48 mL) were added to a solution of N^{ε}-benzyloxycarbonyl-L-Lysine *tert*-butyl ester (4.32 g, 12.84 mmol) in CH_3CN (40 mL). The reaction mixture was purged with argon and then refluxed for 48 h. The volatiles were evaporated *in vacuo*. The residue was purified by flash chromatography (EP/AcOEt, 100/0 to 80/20) to give **10** as a colourless oil (6.24 g, 11.05 mmol, 86%). **^{1}H NMR (300 MHz, $CDCl_3$) δ:** 1.44 (s, 18H, $((C\underline{H}_3)_3COCOCH_2)_2N$-); 1.47 (s, 9H, $(C\underline{H}_3)_3COCOCH$-); 1.49 (m, 4H, -$NHCH_2(C\underline{H}_2)_2$-); 1.59 (m, 2H, -$NH(CH_2)_3C\underline{H}_2$-); 3.20 (m, 2H, -$NHC\underline{H}_2$-); 3.31 (t, 1H, *J* = 7.1 Hz, -$NC\underline{H}$-); 3.46 (dd, 4H, *J* = 4.9 Hz and *J* = 17.2 Hz,

(($CH_3)_3COCOC\underline{H}_2)_2N$-); 5.07 (s, 2H, ($C_6H_5)C\underline{H}_2O$-); 7.33 (m, 5H, aromatic). **^{13}C NMR (100.6 MHz, $CDCl_3$) δ:** 23.02 (-$\underline{C}H_2(CH_2)_2NH$-); 28.11 ($\underline{C}H_3$-); 29.24 (-$\underline{C}H_2(CH_2)_3NH$-); 30.13 (-$\underline{C}H_2CH_2NH$-); 40.83 (-$\underline{C}H_2NH$-); 53.92 (($CH_3)_3COCO\underline{C}H_2)_2N$-); 65.10 (-N(CH2)$_4\underline{C}H$-); 66.45 (Ar$\underline{C}H_2CO$-); 80.71 (($CH_3)_3\underline{C}OCOCH_2)_2N$-); 81.11 (($CH_3)_3\underline{C}OCOCH$-); 127.94 (Ar); 128.43 (Ar); 136.79 (Ar); 156.48 (Ar$CH_2\underline{C}O$-)); 170.74 (($CH_3)_3CO\underline{C}OCH_2)_2N$-); 172.32 (($CH_3)_3CO\underline{C}OCH$-). **MS** (MALDI, ESI, $C_{30}H_{48}N_2O_8$): 565 $[MH]^+$.

Compound 11

After dissolution of **10** (11 g, 19.47 mmol) in methanol (50 mL), 10% Pd/C (300 mg) was added and the resulting mixture was purged with argon. The flask was evacuated and flushed with hydrogen. The reaction mixture was vigorously stirred under hydrogen overnight, and then filtered through a celite pad. The celite was washed with methanol and the solvent was concentrated *in vacuo*. The residue was purified by flash chromatography (EP/AcOEt, 80/20 to 50/50 and next CH_2Cl_2/MeOH, 90/10) to give **11** as a colourless oil (5.78 g, 13.43 mmol, 70%). **^{1}H NMR (300 MHz, $CDCl_3$) δ:** 1.44 (s, 18H, (($C\underline{H}_3)_3COCOCH_2)_2N$-); 1.47 (s, 9H, ($C\underline{H}_3)_3COCOCH$-); 1.51 (m, 4H, $NH_2CH_2(C\underline{H}_2)_2$-); 1.62 (m, 2H, $NH_2(CH_2)_3C\underline{H}_2$-); 2.69 (t, 2H, J = 7.1 Hz, $NH_2C\underline{H}_2$-); 3.31 (t, 1H, -NC$\underline{H}$-); 3.47 (dd, 4H, J = 5.1 Hz and J = 17.2 Hz, (($CH_3)_3COCOC\underline{H}_2)_2N$-). **^{13}C NMR (100.6 MHz, $CDCl_3$) δ:** 23.16 ($NH_2(CH_2)_2\underline{C}H_2$-); 28.17 (($\underline{C}H_3)_3COCOCH_2)_2N$-); 28.25 (($\underline{C}H_3)_3COCOCH$-); 30.40 (-$\underline{C}H_2(CH_2)_3NH_2$); 32.48 (-$\underline{C}H_2CH_2NH_2$); 41.74 (-$\underline{C}H_2NH_2$) 54.03 (($CH_3)_3COCO\underline{C}H_2)_2N$-); 77.19 (($CH_3)_3COCO\underline{C}H$-); 80.68 (($CH_3)_3\underline{C}OCOCH_2)_2N$-); 80.99 (($CH_3)_3\underline{C}OCOCH$-); 170.74 (($CH_3)_3CO\underline{C}OCH_2)_2N$-); 172.32 (($CH_3)_3CO\underline{C}OCH$-). **MS** (MALDI, ESI, $C_{22}H_{42}N_2O_6$): 431 $[MH]^+$.

Compound 12

To a stirred solution of **9** (0.45 g, 1.16 mmol) in extra dry DMF (5 mL), TBTU (0.55 g, 1.73 mmol) and EDIAP (0.31 g, 2.43 mmol, 0.4 mL) were added. The reaction mixture was purged with argon and stirred for 30 min. Then, a solution of **11** (0.6 g, 1.39 mmol) in DMF (10 mL) was added via a canula. The reaction mixture was stirred under argon atmosphere for 48 h. DMF was evaporated under reduced pressure and the reaction mixture was diluted in CH_2Cl_2. The organic layer was washed with water (3 times), dried over $MgSO_4$, filtered and evaporated under reduced pressure. The residue was purified by flash chromatography (CH_2Cl_2/MeOH, 100/0 to 90/10) to give **12** (0.42 g, 0.46 mmol, 40%). **^{1}H NMR (300 MHz, $CDCl_3$) δ:** 1.28-1.34 (m, 12H, $C\underline{H}_3CH_2OP$-); 1.43 (s, 18H, (($C\underline{H}_3)_3COCOCH_2)_2N$-)); 1.45 (s,

9H, ($C\underline{H}_3$)$_3$COCOCH-); 1.49-1.82 (m, 18H); 2.46-2.66 (m, 4H, -CO($C\underline{H}_2$)$_2$CO-); 3.14-3.33 (m, 7H, -$C\underline{H}_2$N-, (CH_3)$_3$COCO$C\underline{H}$- and –$C\underline{H}_2$NHCO-); 3.44 (dd, 4H, *J* = 5.4 and 17.1 Hz, ((CH_3)$_3$COCO$C\underline{H}_2$)$_2$N-)); 3.98-4.17 (m, 8H, $CH_3C\underline{H}_2$OP-); 6.25 (t, 1H, *J* = 4.8 Hz, -N$\underline{H}$-). **^{13}C NMR (100.6 MHz, $CDCl_3$) δ:** 16.46; 16.54; 20.02; 23.15; 24.46; 26.28; 26.34; 28.13; 28.21; 28.45; 28.64; 28.80; 29.64; 29.84; 30.07; 31.48; 39.34; 45.56; 47.50; 53.82; 61.42; 61.52; 61.62; 65.03; 80.72; 170.72; 171.46; 172.31; 172.39. **MS** (MALDI, ESI, $C_{42}H_{81}N_3O_{14}P_2$): 914.4 $[MH]^+$.

Compound (13)

To a stirred solution of **12** (0.42 g, 0.46 mmol) in dry CH_2Cl_2 (5 mL), bromotrimethylsilane (0.85 g, 5.56 mmol, 0.73 mL) was added. The reaction mixture was stirred at room temperature for 4 days and volatiles were evaporated *in vacuo*. The reaction mixture was diluted with water and washed with CH_2Cl_2 (3 times). The aqueous layer was evaporated under reduced pressure to give **13** (quantitative) as a hygroscopic white solid. **^{1}H NMR (400 MHz, D_2O) δ:** 1.45-2.09 (m, 18H); 2.54 (t, 2H, *J* = 6.7 Hz, -CO($C\underline{H}_2$)$_2$CO-); 2.74 (t, 2H, *J* = 6.7 Hz, -CO($C\underline{H}_2$)$_2$CO-); 3.22 (m, 2H, –$C\underline{H}_2$NHCO-); 3.37(m, 3H, -$C\underline{H}_2$N- and (CH_3)$_3$COCO$C\underline{H}$-); 3.43 (t, 2H, *J* = 7.4 Hz, -$C\underline{H}_2$N-); 4.16 (s, 4H, ((CH_3)$_3$COCO$C\underline{H}_2$)$_2$N-)). **MS** (MALDI, ESI, $C_{22}H_{41}N_3O_{14}P_2$): 633.2 [M].

Compound (15)

To a stirred solution of **11** (1 g, 2.32 mmol) in dry CH_2Cl_2 (50 mL), was added **14** (0.28 g, 1 mmol), TBTU (0.93 g, 2.9 mmol) and EDIAP (0.4 g, 3.5 mmol, 0.57 mL). The slurry solution obtained was purged with argon and stirred for 20 h at room temperature. The reaction mixture was washed with water (3 times), 0.5 M HCl (1 time) and 0.5 M NaOH (1 time). The organic layer was dried over $MgSO_4$, filtered, and evaporated *in vacuo*. The residue was separated by flash chromatography (EP/AcOEt, 80/20 to 30/70) to give **15** (1.06 g, 0.96 mmol, 96%). **^{1}H NMR (300 MHz, $CDCl_3$) δ:** 1.43 (s, 36H, (($C\underline{H}_3$)$_3$COCOCH_2-); 1.45 (s, 18H, ($C\underline{H}_3$)$_3$COCOCH-); 1.47-1.65 (m, 12H, -NCH($C\underline{H}_2$)$_3$-); 1.96-2.04 (m, 2H, -NHCH$CH_2C\underline{H}_2$-); 2.22-2.30 (m, 2H, -NHCH$C\underline{H}_2$-); 3.14-3.30 (m, 6H, -N$C\underline{H}$(CH_2)$_3C\underline{H}_2$NH-); 3.46 (m, 8H, ((CH_3)$_3$COCO$C\underline{H}_2$)$_2$N-); 4.17 (m, 1H, -NHC$\underline{H}$-); 5.03 (s, 2H, (C_6H_5)$C\underline{H}_2$-); 6.40 (m, 1H, (C_6H_5)CH_2OCON$\underline{H}$-); 6.53 (m, 1H, (-OCONHCHCON$\underline{H}$-); 6.90 (m, 1H, -NHCH(CH_2)$_2$CON$\underline{H}$-); 7.28 (m, 5H, aromatic). **^{13}C NMR (100.6 MHz, $CDCl_3$) δ:** 22.81 (-CONH(CH_2)$_2\underline{C}H_2$-); 23.07 (-CONH(CH_2)$_2\underline{C}H_2$-); 28.12 (($\underline{C}H_3$)$_3$COCOCH_2)$_2$N-); 28.21 (($\underline{C}H_3$)$_3$COCOCH-); 28.78; 29.25; 29.67; 30.03; 32.43 (-NHCO$\underline{C}$HC$H_2\underline{C}H_2$CO-); 38.61 (-

$\underline{C}H_2NH$-); 39.36 (-$\underline{C}H_2NH$-); 53.73 (($CH_3)_3COCO\underline{C}H_2)_2N$-); 53.98 (($CH_3)_3COCO\underline{C}H_2)_2N$-); 54.44 (-NHCO$\underline{C}H(CH_2)_2CO$-); 64.76 (-N(CH2)$_4\underline{C}H$-); 64.89 (-N(CH2)$_4\underline{C}H$-); 66.75 (Ar$\underline{C}H_2CO$-); 80.84 (-$CO_2\underline{C}(CH_3)_3$); 81.11 (($CH_3)_3\underline{C}OCOCH$-); 81.19 (($CH_3)_3\underline{C}OCOCH$-); 127.98 (CAr); 128.45 (CAr); 136.2 (CAr); 170.70; 170.75; 171.29; 172.30; 172.38; 172.98. **MS** (MALDI, ESI, $C_{57}H_{95}N_5O_{16}$): 1107 $[MH]^+$

Compound (16)

Upon dissolving **15** (1.06 g, 0.96 mmol) in methanol (20 mL), 10% Pd/C (70 mg) was added and the resulting mixture was purged with argon. The flask was evacuated and flushed with hydrogen. The reaction mixture was vigorously stirred under hydrogen overnight, and then filtered through a pad of celite. The celite was washed with methanol and the solvent was concentrated *in vacuo*. The product **16** obtained (0.92 g, 0.95 mmol, 100%) was used without further purification. **^{1}H NMR (300 MHz, $CDCl_3$) δ:** 1.43 (s, 36H, (($C\underline{H}_3)_3COCOCH_2$-); 1.45 (s, 18H, ($C\underline{H}_3)_3COCOCH$-); 1.47-1.65 (m, 12H, -NCH($C\underline{H}_2)_3$-); 2.00-2.10 (m, 2H, -NHCHC$\underline{H}_2$-); 2.37-2.44 (m, 2H, -NHCHC$H_2C\underline{H}_2$-); 3.20-3.30 (m, 6H, -NC$\underline{H}(CH_2)_3C\underline{H}_2NH$-); 3.36-3.50 (m, 8H, (($CH_3)_3COCOC\underline{H}_2)_2N$-); 3.56 (m, 1H, -NHC$\underline{H}$-); 6.88 (m, 1H, $NH_2CH(CH_2)_2CON\underline{H}$-); 7.68 (m, 1H, $NH_2CHCON\underline{H}$-). **^{13}C NMR (100.6 MHz, $CDCl_3$) δ:** 23.02 (-CONH$(CH_2)_2\underline{C}H_2$-); 23.30 (-CONH$(CH_2)_2\underline{C}H_2$-); 28.12 (($\underline{C}H_3)_3COCOCH_2)_2N$-); 28.20 (($\underline{C}H_3)_3COCOCH$-); 28.56; 29.11; 29.91; 30.25; 31.28; 33.02; 38.94 (-$\underline{C}H_2NH$-); 39.27 (-$\underline{C}H_2NH$-); 53.74 (($CH_3)_3COCO\underline{C}H_2)_2N$-); 53.88 (($CH_3)_3COCO\underline{C}H_2)_2N$-); 54.41 (-NHCO$\underline{C}H(CH_2)_2CO$-); 64.93 (-N(CH2)$_4\underline{C}H$-); 65.07 (-N(CH2)$_4\underline{C}H$-); 80.69 (($CH_3)_3\underline{C}OCOCH$-); 80.78 (($CH_3)_3\underline{C}OCOCH$-); 81.11 (($CH_3)_3\underline{C}OCOCH$-); 170.68; 170.78; 172.34; 172.97; 174.76. **MS** (MALDI, ESI, $C_{49}H_{89}N_5O_{14}$): 973 $[MH]^+$

Compound (17)

To a stirred solution of **9** (0.12 g, 0.30 mmol) in extradry DMF (5 mL) was added HATU (0.175 g, 0.46 mmol) and EDIAP (0.083 g, 0.64 mmol, 0.107 mL). The reaction mixture was purged with argon and stirred at room temperature for 30 min. Then, a solution of **16** (0.3 g, 0.3 mmol) in DMF (10 mL) was added by canulation. The reaction mixture was stirred under argon atmosphere for 48 h. DMF was evaporated under reduce pressure and the reaction mixture was diluted in CH_2Cl_2. The organic layer was washed with water and the aqueous layer was extracted 3 times with CH_2Cl_2. The organic layers were combined, dried over $MgSO_4$, filtered and evaporated under reduce pressure. The residue was separated by flash chromatography (CH_2Cl_2/MeOH, 99/1 to 95/5) to give **17** (0.38 g, 0.26 mmol, 85%). **^{1}H**

NMR (300 MHz, $CDCl_3$) δ: 1.25 (dt, 12H, *J* = 3.9 and 7.2 Hz, -$POCH_2C\underline{H}_3$); 1.37 (s, 36H, $(C\underline{H}_3)_3COCOCH_2$-); 1.38 (s, 18H, $(C\underline{H}_3)_3COCOCH$-); 1.42-1.82 (m, 22H); 1.87-2.75 (m, 10H); 3.01-3.28 (m, 10H); 3.30-3.45 (m, 8H, $(CH_3)_3COCOC\underline{H}_2$-); 3.92-4.11 (m, 8H, -$POC\underline{H}_2CH_3$); 4.29 (m, 1H, -NHC<u>H</u>-); 6.72 (t, 1H, *J* = 5.1 Hz, -N<u>H</u>-); 7.33 (t, 1H, *J* = 5.1Hz, -N<u>H</u>-); 7.54 (d, 1H, *J* = 7.5 Hz; -N<u>H</u>CH-).

Compound (18)

To a stirred solution of **17** (0.15 g, 0.10 mmol) in dry CH_2Cl_2 (15 mL) was added bromotrimethylsilane (0.315 g, 2.06 mmol, 0.27 mL). The reaction mixture was stirred at room temperature for 4 days and MeOH was added. The solution was stirred for 30 min and volatiles were evaporated *in vacuo*. The reaction mixture was diluted with water and washed with CH_2Cl_2 (3 times). The aqueous layer was evaporated under reduce pressure to give **18** quantitatively. **^{1}H NMR (300 MHz, D_2O) δ:** 1.30-2.03(m, 24H, -CH_2-) ; 2.29 (m, 2H); 2.53 (m, 2H); 2.72 (m,2H); 3.17 (m, 4H); 3.27-3.40 (m, 5H); 4.00-4.27 (m, 10H). **MS** (MALDI, ESI, $C_{37}H_{64}N_6O_{22}P_2$): 1005.2 $[MH]^-$

2) Lysozyme affinity determination of affitins H4 and B3

Surface plasmon resonance (SPR) was measured using a BIAcore 3000 instrument (BIAcore, Uppsala Sweden). All measurements were performed at a flow rate of 60 μL/min. A solution of lysozyme at 4 μg/mL in sodium acetate buffer (10 mM, pH= 5.5) was used for the target immobilization on CM5 chip and lysozyme was immobilized at 250 RU. Kinetics was realized for B3 (A) with concentrations of 2000, 1000, 500, 166, 55, 18, 6, 2, 0.69 nM. For H4 (B), concentrations used were 500, 166, 55, 18, 6, 2, 0.69, 0.23 and 0 nM. Association and dissociation times were 3 and 10 min respectively. The kinetic data of the interaction were evaluated with a global fit using Langmuir model (Bioevaluation software 4.1). For each affitin a representative set of fitted curves are shown below.

$$\frac{dR}{dt} = ka \,.\, C \,.\, (Rmax - R) - kd \,.\, R$$

A) B3

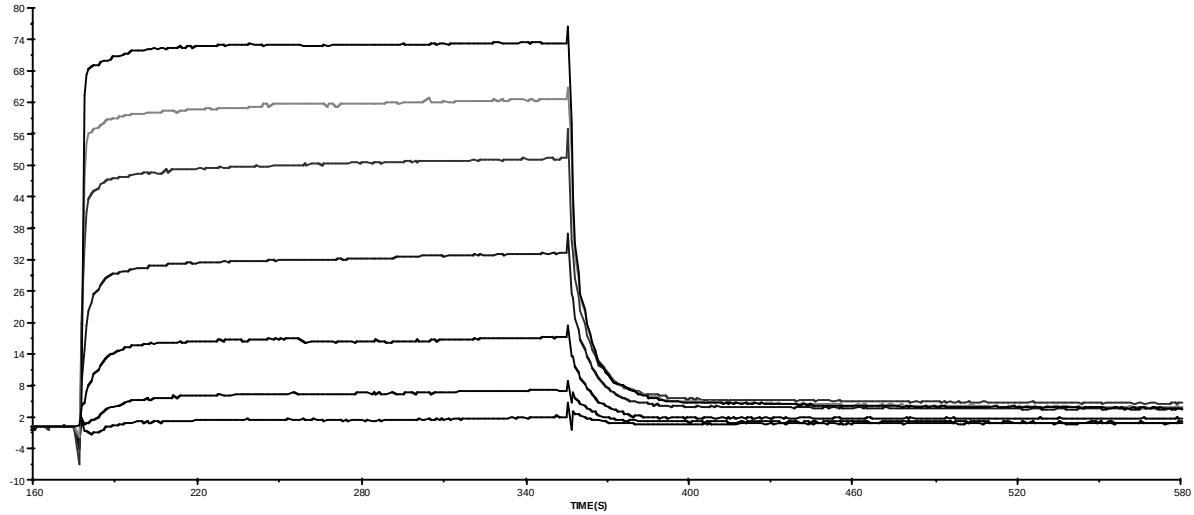

K_D = 286 nM; k_{on} = 4.38 x 10^5 $M^{-1}s^{-1}$; k_{off} = 0.125 s^{-1}

B) H4

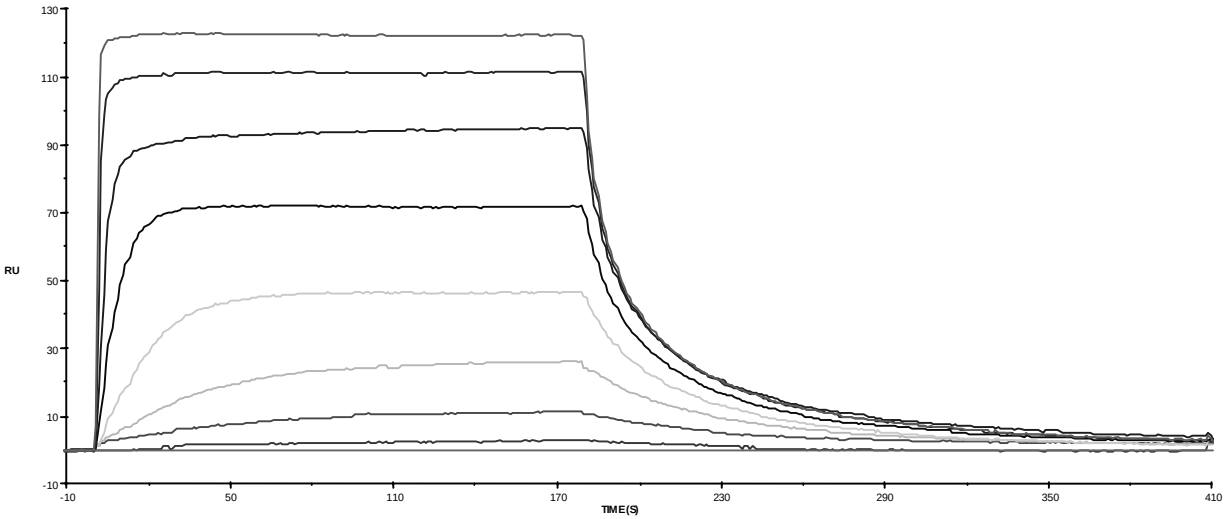

K_D = 4.6 nM; k_{on} = 2.53 x 10^6 $M^{-1}s^{-1}$; k_{off} = 0.029 s^{-1}

Alignment of Gold Clusters on DNA via a DNA-Recognizing Zinc Finger-Metallothionein Fusion Protein

Shinya Ariyasu,[†] Akira Onoda,[‡] Ryota Sakamoto,[†] and Takeshi Yamamura*[,†]

Department of Chemistry, Faculty of Science, Tokyo University of Science, Kagurazaka 1-3, Shinjuku-ku, Tokyo, 162-8601, Japan, and Department of Applied Graduate School of Engineering, Osaka University, Yamadaoka 2-1, Suita, Osaka. Received June 20, 2009; Revised Manuscript Received September 18, 2009

The complementary recognition of base pairs (bp) is the major strategy in the "DNA lithography" of gold (Au) clusters or nanoparticles, where single-stranded DNAs sulfurized at their termini are generally used to bind Au clusters or nanoparticles. In this report, we discuss a new material that can be used to locate Au clusters on the desired positions of DNA. For this purpose, we combined a two-domain zinc finger (ZF) and the analogue of α domain of rat's liver metallothionein (MT) to utilize the DNA-recognizing ability of ZF motifs and the heavy-metal binding ability of MTs, and prepared an artificial fusion protein, ZFZF-MTα (**1**). Titration experiments monitored by absorption and circular dichroism spectroscopies, as well as an electrophoretic mobility shift assay and quantification using 5,5′-dithiobis(2-nitrobenzoic acid), clarified that (1) the ZF domain traps two divalent metal ions to fold in a ZF structure with $M(Cys)_2(His)_2$ (M = Co, Zn, and Cd) coordination units, (2) the MT domain traps metal ions to form clusters (Cd^{2+} particularly forms a $Cd_4(Cys)_9$ cluster) without interfering with the folding of the ZF domain, and (3) **1** recognizes the 5′-GGGGGG-3′ (G_6) bp sequence in the presence of Zn^{2+} based on the amino acid sequence encoded in the ZF domain. The titration of $Au_{11}(PPh_3)_8Cl_3$ (Au11) into the solution of **1** in the presence of Zn^{2+} revealed that the MT domain strongly binds the Au11 cluster with a 1:1 ratio, and a Au_{11}-containing conjugate, ZF(Zn)ZF(Zn)-MTα(Au_{11}) was obtained. Transmission electron microscopy (TEM), energy-dispersive X-ray spectroscopy, and X-ray photoelectron spectroscopy showed that this conjugate maintains an Au_{11} core in the form of $Au_{11}(PPh_3)_4(S\text{-}Cys)_6$ without disturbing the folding nature of the ZF domain. ZF(Zn)ZF(Zn)-MTα(Au_{11}) recognizes the bp sequence G_6 with $K_{d1} = 450$ nM, while simultaneously forming a dimer on the DNA with $K_{d2} = 200$ nM. TEM experiments showed that the conjugates form parallelograms or triangles (defective parallelograms) on a double crossover (dx) DNA, according to the positions of G_6 encoded in the dx DNA.

INTRODUCTION

The alignment of inorganic large clusters and nanoparticles (nps) on the "desired points" of double-stranded (ds) DNA[1]is one of the gateways for "DNA lithography" (*1*), which has the potential to provide new electronic and optical devices based on the nanoscale patterning of mesoscale compounds. In order to approach this problem, complementary interaction between two single-stranded (ss) DNAs is generally used, where the terminus of an ssDNA is thiolated to SH to bind Au clusters (*2*).

In this study, we developed a new method for positioning Au clusters at will on DNA; that is, we coupled the DNA-recognizing ability of a zinc finger (ZF) (*3, 4*) motif with the heavy-metal binding ability of a metallothionein (MT) (*5*). We prepared a new artificial fusion protein ZFMT (comprising ZF and MT domains) as the linker that mediates the positioning of Au clusters at the desired points of DNA.

ZFs are DNA-binding motifs that rank with the leucine-zipper (*6*) and helix−loop−helix motifs (*7*) in DNA recognition ability. ZFs are classified into $[Zn(Cys)_4]^{2-}$ (*8*), $[Zn_2(Cys)_6]^{2-}$ (*9*), and $Zn(Cys)_2(His)_2$ (*10*) from the viewpoint of Zn coordination geometry. Among these ZFs, we focused our attention on the $Zn(Cys)_2(His)_2$ type, because this ZF is the smallest of the ZFs (its consensus sequence is written as [Tyr/Phe]-X-Cys-$X_{2\text{-}4}$-Cys-X_3-Phe-X_5-Leu-X_2-His-$X_{2\text{-}4}$-His, comprising only 25−30 amino acid residues) and folds into a compact $\beta\beta\alpha$ structure in the presence of Zn^{2+}. $Zn(Cys)_2(His)_2$-type ZFs strongly and accurately recognize the specific positions of dsDNA when they are connected in tandem repeat structures (*11*); therefore, this type is more versatile (*12*) than the other types of ZFs and DNA-binding motifs. However, the most important point is that the $Zn(Cys)_2(His)_2$-type ZF is easy to handle. It is easily prepared by solid-phase synthesis and elongated by the native chemical

* Corresponding author. Takeshi Yamamura, Faculty of Science, Tokyo University of Science, Kagurazaka 1-3, Shinjuku-ku, Tokyo, 162-8601, Japan. E-mail: tyamamur@rs.kagu.tus.ac.jp, Telephone: +81352288251, Fax: +81352288251.

[†] Tokyo University of Science.

[‡] Osaka University.

[1]Abbreviations: dsDNA, double-stranded DNA; ssDNA, single-stranded DNA; ZF, zinc finger; MT, metallothionein; NCL, native chemical ligation; Au11, $Au_{11}(PPh_3)_8Cl_3$; dxDNA, double crossover DNA; G_6, 5′-GGGGGG-3′; Fmoc, fluorenylmethoxycarbonyl; *t*-Bu, *tert*-butyl; PyBOP, benzotriazole-1-yl-oxy-tris-pyrolidino-phosphonium hexafluorophosphate; HOBt, hydroxybenzotriazole; CD, circular dichroism; LMCT, ligand−metal charge transfer; DTNB, 5,5′-dithiobis(2-nitrobenzoic acid); EMSA, electrophoretic mobility shift assay; GPC, gel permeation chromatography; SDS, sodium dodecyl sulfate; PAGE, polyacrylamido gel electrophoresis; TEM, transmission electron microscopy; EDS, energy-dispersive X-ray spectroscopy; XPS, X-ray photoelectron spectroscopy; DCC, dicyclohexylcarbodiimide; TFA, trifluoroacetic acid; EDT, 1,2-ethanedithiol; TIS, triisopropylsilane; AcOH, acetic acid; TFE, trifluoroethanol; MPAEt, ethyl 3-mercaptopropionate; DIEA, diisopropylethylamine; DCM, dichloromethane; MeOH, methanol; NMP, *N*-methyl-2-pyrolidinone; DMF, *N,N*-dimethylformamide; MeCN, acetnitrile (MeCN); MALDI-TOF, matrix-assisted laser desorption ionization-time-of-flight; CHCA, α-cyano-4-hydroxycinnamic acid; Boc, *tert*-butyloxycarbonyl; EDTA, ethylenediaminetetraacetic acid.

10.1021/bc9002713 © 2009 American Chemical Society
Published on Web 11/25/2009

Figure 1. Positioning of an Au cluster on dsDNA using ZF(Zn)ZF(Zn)-MTα(Au_{11}).

ligation (NCL) method. Furthermore, the amino acid sequence is easily designed for the recognition of DNA based on the code tables reported by Pabo (*10*), Choo (*13*), and Sera (*14*).

On the other hand, MTs are ubiquitous, small, and Cys-rich proteins that strongly bind heavy metal ions such as zinc (Zn^{2+}), copper (Cu^{2+}), cadmium (Cd^{2+}), and silver (Ag^{+}) ions (*15, 16*) to reduce the ionic concentrations to physiological or nontoxic levels (*17*). MTs not only trap these metal ions as $M_x(Cys)_y$ clusters (*18*), but also react with Au^{+} to form nanoparticles (*19*). Recently (*20*), we succeeded in demonstrating that $Au_{11}(PPh_3)_8Cl_3$ cluster (Au11), a small cluster with discrete electronic states (*21*), reacts with a MT-like peptide MTα (**2**),[2]composed of N-terminus α domain of rat's liver MTII and Cys-Gly to form 1:1 conjugate, where Cys-Gly is a junction assumed for introducing new peptide moieties by NCL (*22*).

In this study, we synthesized a novel fusion protein ZFZF-MTα (**1**) (Figures 1 and 2) composed of a two-domain $Zn(Cys)_2(His)_2$-type ZF, ZFZF (**3**), and **2** by applying the NCL method. In our previous study, we also constructed a fusion protein comprising a two-domain ZF and **2**. Unfortunately, the ZF domain did not bind to the specific positions of DNA; therefore, we designed and synthesized a new protein in this study. **1** showed binding affinities to heavy metal ions, such as Co^{2+}, Zn^{2+}, and Cd^{2+}, as well as Au11. Titration experiments monitored by UV−vis and CD spectroscopies showed that each domain of **1** independently coordinated to Zn^{2+} and Au11 without losing the original folding structures of the ZF and MTα. The fusion protein **1** containing two Zn^{2+} ions in the ZF domain and a Au11 cluster in the MTα domain, ZF(Zn)ZF(Zn)-MTα(Au_{11}) (**9**), realized the alignment of Au clusters on ds and double crossover (dx)DNAs based on the information encoded in the DNA sequences.

RESULTS

Sequence Design and Synthesis. 3 was designed to recognize 5′-GGGGGG-3′ (G_6) and its complementary bp (Figure 2) based on the amino acid sequence of zif268 (*23*); therefore, each ZF of **1** has a set of four key amino acid residues—Arg, Asp, His, and Arg—at the −1, 2, 3, and 6 positions, respectively, counting from the starting point of the α-helix. The two ZFs are connected to each other via the canonical linker Thr-Gly-Glu-Lys-Pro. The C-terminus of **3** contains the N-terminal part of the canonical linker Thr-Gly-Gly to stabilize the C-terminus of the finger part. It is assumed that the extra Gly gives sufficient flexibility to this part in cooperation with the adjacent amino acid residue, Gly; thus, steric hindrance between **2** and **3** is avoided.

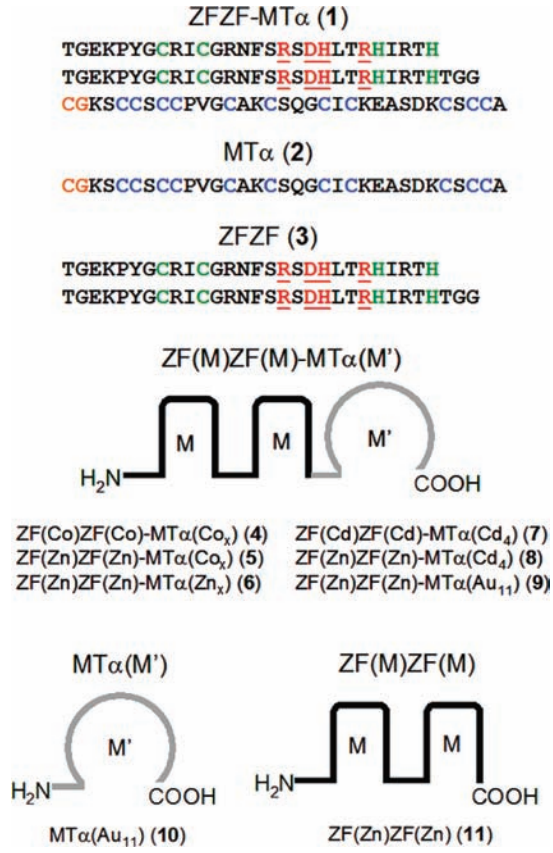

Figure 2. Schematic drawings of the peptides **1**, **2**, and **3** and the inorganic bioconjugates investigated in this study **4**, **5**, **6**, **7**, **8**, **9**, **10**, and **11**. The amino acid sequences are written according to the IUPAC-IUB JCBN nomenclature. The DNA-recognizing and metal-binding residues of the ZF domain are shown by the underlined red and green characters, respectively, whereas the metal-binding residues of the MT domain are shown by the blue characters. The orange characters denote the residues for NCL.

The syntheses of **2** and **3** were carried out by a standard solid-phase method with Fmoc/*t*-Bu chemistry, and the C-terminus of **3** was thioesterificated using 25 equiv of PyBOP and HOBt (*24*) to obtain **3-COSR**. This reaction was completed within 24 h in spite of the length of ca. 60 residues. The synthesis of **1** by the NCL method from **3-COSR** and **2** was completed within 24 h.

Metal Coordination and Folding of ZFZF-MTα. The complexation of artificial or consensus ZF proteins was confirmed by Co^{2+} titration monitored by UV−vis spectrometry (*25*). In order to discuss whether or not the ZF and MTα domains of **1** independently folded into the ZF and MTα structures without interfering, titration experiments on **1** were carried out in the presence of Co^{2+}. The results are shown in Figure 3. In the first stage of the Co^{2+} titration (0−1 equiv) into **1**, we observed a rapid increase in the basal absorption for the whole wavelength region of 600−750 nm; the intensities of the three peaks at 525, 655, and 725 nm prominently increased with the amount of Co^{2+}. In the second stage of the titration (Co^{2+} 1−2 equiv), the intensities of the peaks at 525 and 725 nm decreased with an increase in the amount of Co^{2+},

[2]Numbering and abbreviations of the compounds (collected in Figure 2). Two types of abbreviations are adopted: first, the apo-proteins and their metallo compounds are numbered with bold Arabic numerals **1**, **2**, ---, and **11**; second, supplementary abbreviations are also introduced to help chemical understanding for the compounds. For example, ZFZF-MTα (**1**) denotes the apo-fusion protein composed of ZFZF and MTα, where ZFZF denotes the two-domain ZF. **2** and **3** denote apo-MTα and apo ZFZF, respectively. The metal ions coordination to ZF and MTα domains is shown in the parentheses adjacent to domains. The abbreviations and numberings are as follows: ZF(Co)ZF(Co)-MTα(Co_x) (**4**), ZF(Zn)ZF(Zn)-MTα(Co_x) (**5**), ZF(Zn)ZF(Zn)-MTα(Zn_x) (**6**), ZF(Cd)ZF(Cd)-MTα(Cd_4) (**7**), ZF(Zn)ZF(Zn)-MTα(Cd_4) (**8**), and ZF(Zn)ZF(Zn)-MTα(Au_{11}) (**9**), MTα(Au_{11}) (**10**), and ZF(Zn)ZF(Zn) (**11**). The dsDNAs having one, two, and zero ZF-recognizing regions are abbreviated as **ds1**, **ds2**, and **ds3**, respectively (see Figure 5 for the base sequences). The dxDNA having four ZF-recognizing regions is abbreviated **dx1** (see Figure 13 for the base sequences).

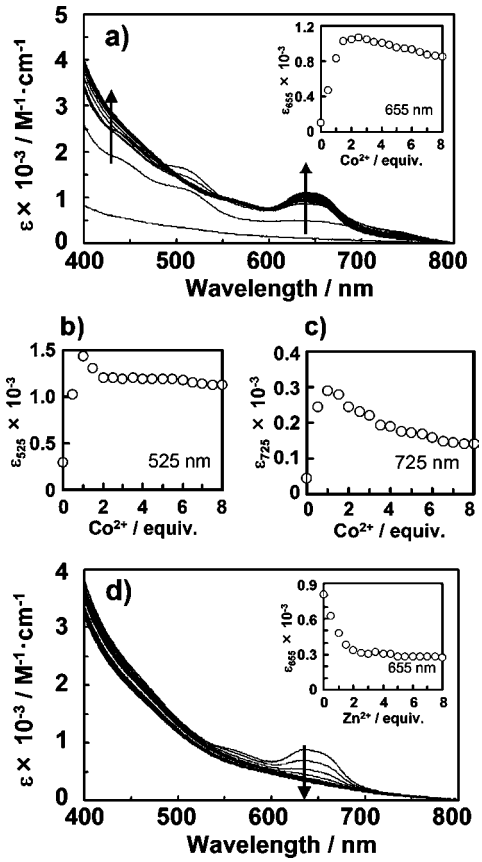

Figure 3. The results of Co^{2+} (2 mM) titration to a solution (10 mM Tris−HCl) containing **1** (50 μM) monitored by UV−vis spectroscopy (a). The titration curves monitored at 655, 525, and 725 nm are shown in the insets of (a), (b), and (c), respectively. The result of Zn^{2+} (2 mM) titration to a solution (10 mM Tris−HCl) containing **4** (50 μM) (d). The inset shows the titration curve monitored at 655 nm.

whereas the intensity of the peak at 655 nm gradually increased. Finally, in the third stage (Co^{2+} > 2 equiv), the intensity of the peak at 655 nm decreased; however, the degree of decrease in the 725 nm peak was larger than that in the 655 nm peak. Among the three absorption peaks, the peak at 725 nm was assigned to the d−d transition arising from $[Co(Cys)_4]^{2-}$ coordination, according to Michael (*25*); on the other hand, the peak at 655 nm was assigned to the d−d transition arising from $Co(Cys)_2(His)_2$ coordination. The feature of the increase in the basal absorption observed at 400−800 nm was similar to that observed in the titration process of Co^{2+} to **2**, which forms a Co_xCys_y cluster (Supporting Information). This means that Co^{2+} is incompletely distributed in either the MTα or ZF domains of **1** at the initial stage of Co^{2+} titration; however, as titration proceeds, it begins to form the cobalt finger with the ZF domain, as well as a $Co_x(Cys)_y$ cluster with the MTα domain (Figure 3a) to form ZF(Co)ZF(Co)-MTα(Co_x) (**4**).

The reverse titration of Zn^{2+} with the solution of **4** was then carried out in the presence of a sufficient amount of Co^{2+} in order to verify the superiority of Zn^{2+} in ZF domain. As expected, the intensity of the peak at 645 nm decreased with an increase in the amount of Zn^{2+}, which means that the Co^{2+} ions trapped in the ZF domain of **4** were substituted with Zn^{2+} as titration proceeded (Figure 3d). The titration curve (inset of Figure 3d) shows that each of the ZFs of **4** bind 1 equiv of Zn^{2+}, which is similar to a wild-type ZF, whereas the Co^{2+} ions trapped in the MTα domain of **4** are not substituted with Zn^{2+}. Consequently, the reverse titration generates ZF(Zn)ZF(Zn)-MTα(Co_x) (**5**) at the final stage.

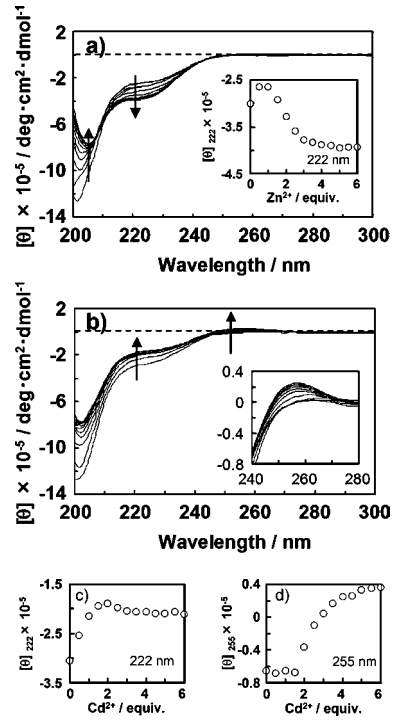

Figure 4. Results of Zn^{2+} and Cd^{2+} titrations for **1** monitored by CD spectroscopy: (a) **1** + Zn^{2+}, the inset shows the titration curve observed at 222 nm; (b) **1** + Cd^{2+}; (c) the titration curve observed at 220 nm; and (d) 255 nm. 500 μM aqueous solutions of Zn^{2+} or Cd^{2+} was added dropwise to 10 mM of Tris-HCl solution containing 12.5 μM of **1**.

The folding nature of **1** was investigated in the presence of Zn^{2+} and Cd^{2+} using CD spectroscopy. As shown in Figure 4, the intensity of the negative CD peak at 205 nm decreased with an increase in the amount of Zn^{2+} added to **1** (Figure 4a), whereas that of the peak at 222 nm increased. The addition of Zn^{2+} caused almost no change at the ligand−metal charge transfer (LMCT) region (~255 nm) of the MTα domain. The spectral change, particularly at 222 nm, was similar to that shown by wild-type ZF upon addition of Zn^{2+} (*26*). In conjunction with the above-mentioned results of reverse titration with Zn^{2+}, this result means that Zn^{2+} preferentially reacts with the ZF domain of **1** so as to fold into $\beta\beta\alpha$ structures; however, Zn^{2+} does not clearly affect the folding of the MTα domain; therefore, ZF(Zn)ZF(Zn)-MTα(Zn_x) (**6**) is finally formed. On the other hand, the addition of Cd^{2+} to **1** weakens the intensities of the negative CD peaks at 210 and 222 nm, whereas it slightly strengthens the intensity of the positive peak at 255 nm (Figure 4b). The feature of the spectral change at 255 nm is similar to that shown by a wild-type MTα upon addition of Cd^{2+} (*27*); however, the peak intensity is about 1/7 of the Cd_4Cys_{11} cluster of the α domain of wild-type MTα. The titration curves observed at 222 and 255 nm indicated that 2 equiv of Cd^{2+} coordinated to the ZF domain at the first stage. Then, it began to coordinate to the MTα domain. From the amount of Cd^{2+} used for the completion of the reaction, the species formed at the final stage was estimated to be ZF(Cd)ZF(Cd)-MTα(Cd_4) (**7**) that contains two Cd^{2+} in the ZF domain and a Cd_4Cys_y cluster in the MTα domain. The reverse titration with Zn^{2+} indicated that two Cd^{2+} ions in the ZF domain of **7** were substituted with Zn^{2+} ions at the final stage to form ZF(Zn)-ZF(Zn)-MTα(Cd_4) (**8**). On the other hand, Cd^{2+} titration into **6** indicated the formation of **8** (Supporting Information). A quantification experiment using 5,5′-dithiobis(2-nitrobenzoic acid) (DTNB) revealed that about three of the twelve Cys residues remained free from the coordination to Zn^{2+} and Cd^{2+}. Considering the results, the species obtained in the final stage

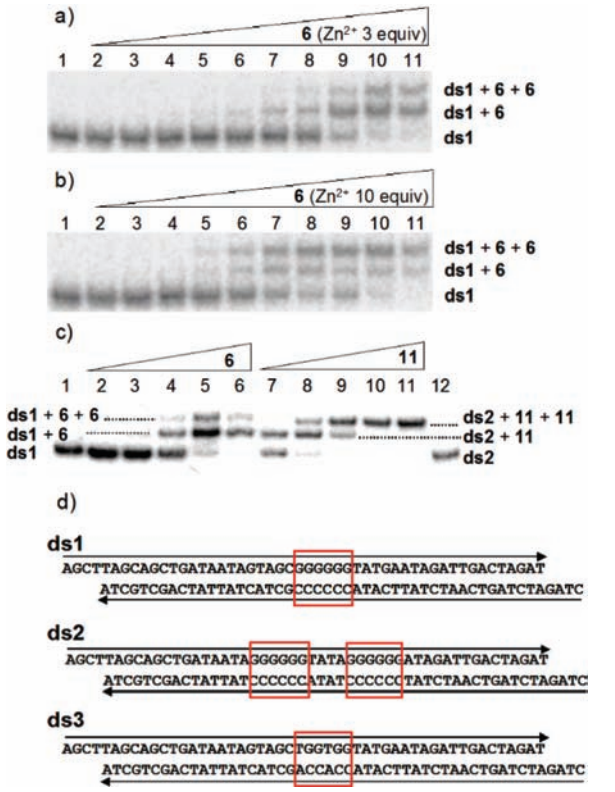

Figure 5. EMSA for **6** (^{32}P labeled DNA was used). (a) **6** (3 equiv of Zn^{2+}) + **ds1**. (b) **6** (10 equiv of Zn^{2+}) + **ds1**. The concentration of **6** increases from left to right in lanes 1−11 (0, 2.9, 5.9, 11.7, 23.4, 46.4, 93.8, 187.5, 375, 750, and 1500 nM). (c) Lanes 2−6, **6** (10 equiv of Zn^{2+}) + **ds1**; lanes 7−11, **11** (10 equiv of Zn^{2+})+ **ds2**. The concentration of **6** or **11** increases from left to right in the lanes. Each loading mixture contained 10 mM Tris-HCl (pH 8), 33.3 mM NaCl, 5% glycerol, 0.005% NP-40, 1 mM dithiothreitol, poly-(dI-dC) (10 ng/μL), and ^{32}P-end-labeled DNA fragments (ca. 500 cpm). (d) The base sequences of the DNAs, **ds1**, **ds2**, and **ds3**, used in this study (lower). The ZF-recognizing bp are surrounded by red squares.

comprised a Cd_4Cys_9 cluster in the MTα domain. This is an interesting observation, considering that the α domain of rat's liver MTII and a natural-occurring MT-ZF fusion protein SmtA (*28*) form Cd_4Cys_{11} and $Cd_4Cys_9(His)_2$ clusters, respectively.

Consequently, it can be said that both the ZF and MTα domains of **1** conserve their original metal-coordination and folding natures. The ZF domain favors Zn^{2+}, whereas the MTα domain favors Cd^{2+}; however, they are not independent of each other in the initial stage of the metal ion insertion in spite of their independence in coordination and folding. It was impossible to separate the two species in which either the ZF or MTα domain is metal-free. The nucleophilicities of these two parts for Zn^{2+} and Cd^{2+}seem to be close to each other in the initial stage of metal insertion.

DNA Binding Ability of ZF(Zn)ZF(Zn)-MTα(Zn_x). The DNA binding ability of **6** was determined by an electrophoretic mobility shift assay (EMSA) in the presence of different amounts of Zn^{2+} using **ds1** (Figure 5), which had the ZF-recognizing region G_6. The EMSA results observed in the presence of 3 and 10 equiv of Zn^{2+} are shown in Figure 5a,b, respectively; the figures clearly show the binding of **6** to **ds1**. A control experiment using a DNA, **ds3**, with noncognate 5′-TGGTGG-3′ instead of G_6, clarified that **6** does not bind **ds3**. These figures demonstrate that **ds1** yields two shift bands suggestive of the binding of two proteins of **6**. The intensity ratio of these two shift bands changed with the amount of Zn^{2+}, with an increase in the amount of Zn^{2+} leading to an increase in the relative amount of the higher molecular band. As **ds1** yielded only one shift band for simple Zn-bound **3**, ZF(Zn)-ZF(Zn) (**11**), the appearance of the second band was induced by the formation of Zn_xCys_y cluster in the MTα domain of **6** (see Supporting Information). Considering that the mobility of the second band observed in **6** + **ds1** (Figure 5c, lanes 2−6) almost agreed with that of the second band in **11** + **ds2** (Figure 5c, lanes 7−11), where **ds2** (Figure 2) was a new dsDNA having two G_6 sequences 5′-GGGGGGTATAGGGGGG-3′, the species of the second band in Figure 5a,b was estimated to be a dimer of **6**.

Figure 6. Schematic drawing of the formation of a **6** dimer on **ds1**.

$$2(\text{monomer}) \rightleftarrows \underset{1-\gamma}{\text{dimer}}_{0.5\gamma} \qquad [\text{monomer}] = (1-\gamma)[\text{monomer}]_{tot}, \quad [\text{dimer}] = 0.5\gamma[\text{monomer}]_{tot}$$

$$\text{monomer} + \textbf{ds1} \overset{K_{d1}}{\rightleftarrows} \text{monomer-}\textbf{ds1}$$

$$\text{dimer} + \textbf{ds1} \overset{K_{d2}}{\rightleftarrows} \text{dimer-}\textbf{ds1}$$

$$K_{d1} = \frac{[\text{monomer}][\textbf{ds1}]}{[\text{monomer-}\textbf{ds1}]} \qquad [\text{monomer-}\textbf{ds1}] = \frac{(1-\gamma)[\textbf{ds1}][\text{monomer}]_{tot}}{K_{d1}}$$

$$K_{d2} = \frac{[\text{dimer}][\textbf{ds1}]}{[\text{dimer-}\textbf{ds1}]} \qquad [\text{dimer-}\textbf{ds1}] = \frac{\gamma[\textbf{ds1}][\text{monomer}]_{tot}}{2K_{d2}}$$

Figure 7. Equations for the dimerization of **6**. K_{d1} and K_{d2} denote the dissociation constants of the monomeric and dimeric **6**, respectively, from **ds1**. γ denotes the degree of the association of **6** to a dimeric **6**.

On the other hand, gel permeation chromatography (GPC) and SDS-PAGE experiments carried out under anaerobic conditions (details in Supporting Information) showed that simple **2** increases in size upon the addition of Zn^{2+} or Cd^{2+}. Consequently, dimerization of **6** will be mediated by Zn^{2+} (Figure 6).

Assuming the formation of the **6** dimer mediated by Zn^{2+}, the dissociation constants of the monomer and the dimer, K_{d1} and K_{d2}, respectively, from **ds1** were determined by simulating the results of the EMSA experiments based on the formula shown in Figure 7.

The system gives $K_{d1} = 150$ nM and $K_{d2} = 150$ nM in the presence of 3 equiv of Zn^{2+}, whereas it gives $K_{d1} = 100$ nM and $K_{d2} = 60$ nM in the presence of 10 equiv of Zn^{2+}. These values are larger than that observed for **11** ($K_d = 7.5$ nM). This can be attributed to the steric hindrance between the large-sized MTα domain containing the Zn_xCys_y cluster and dsDNA. On the other hand, the decrease in the second dissociation constant, K_{d2}, in the presence of higher amounts of Zn^{2+} indicates that the second recognition process, which is promoted by Zn^{2+} via dimer formation, may contain nonspecific recognition of the second ZF by dsDNA.

Complexation of ZF(Zn)ZF(Zn)-MTα(Zn_x) with Au11. Next, the complexation of **6** with Au11 was investigated. Experiments were carried out in the presence of 3 equiv of Zn^{2+} to conserve the folding of the ZF domain of **6** referring to the results mentioned above. Figure 8 shows the results of the titration of Au11 into **6** (monitored by CD spectroscopy). The negative peak enhancement observed at 222 nm upon

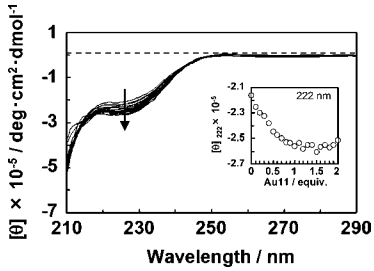

Figure 8. CD spectral change observed for Au11 titration into **6**. The titration curve observed at 222 nm is shown in the inset. A 50 μM MeOH solution of Au11 was added dropwise to 10 mM of Tris-HCl solution containing 12.5 μM of **6** (3 equiv of Zn^{2+}).

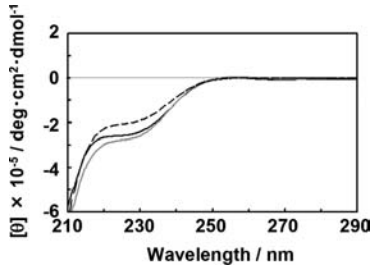

Figure 9. Additivity observed in the CD spectra of **9** systems: the CD spectra of **6** (black dashed line) and **9** (black solid line), and the sum of **6** + Au11 calculated by adding the CD spectra of **10** and **11** (gray solid line).

addition of Au11 is similar to that of our previous results for the complexation between **2** and Au11, MTα(Au_{11}) (**10**) (*20*). The titration curve at 222 nm shows that **6** reacts with an equimolar amount of Au11, which indicates that **6** forms a 1:1 complex with Au11, ZF(Zn)ZF(Zn)-MTα(Au_{11}) (**9**). As will be mentioned later, **9** conserves the number of Au atoms in the process of the reaction with Au11. The CD spectrum of **9** (the black solid line in Figure 9) almost overlaps the sum of the CD spectra of **11** and **10** (the gray solid line in Figure 9). These results indicate that **9** conserves the $\beta\beta\alpha$ folding of the ZF domains of **9** after being coupled with Au11.

Au Core of ZF(Zn)ZF(Zn)-MTα(Au_{11}). We used transmission electron microscopy (TEM) to estimate the number of Au atoms in the Au cluster of **9**. The TEM image is shown in Figure 10a. From the cluster size distribution shown in Figure 10b, we can obtain 0.9 $\pm$ 0.2 nm as the average particle size, which is close to that reported for Au11 (average 0.8 $\pm$ 0.2 nm) (*29*). Furthermore, energy-dispersive X-ray spectroscopy (EDS) measurements on the black regions of this image showed that the regions contained Au, P, S, and Zn (Figure 10c). Therefore, the TEM results strongly indicated that the number of Au atoms in the Au cluster was conserved at 11 under the complexation conditions adopted here. The Au-binding state of **9** was analyzed by X-ray photoelectron spectroscopy (XPS) (Figure 11), which gave peaks attributable to Au 4f at 87.8 ($4f_{5/2}$) and 84.0 ($4f_{7/2}$) eV. These values agreed well with those we previously observed for **10** (87.7 and 84.1 eV) (*20*). In our previous paper, we simulated the XPS spectrum by $Au_{11}(PPh_3)_4(S\text{-}Cys)_6$, based on the quantification results for the amounts of S and P. According to our previous assignment, the results obtained here indicate that **9** contains the Au cluster as $Au_{11}(PPh_3)_4(S\text{-}Cys)_6$ and that six CysSH are free from coordination.

DNA-Binding Ability of ZF(Zn)ZF(Zn)-MTα(Au_{11}). In order to clarify whether or not the ZF domains of **9** had an affinity for **ds1**, EMSA experiments on **9** were carried out in the presence of 3 equiv of Zn^{2+}. As is shown in Figure 12, **9** yielded two shift bands. Considering the molecular weight of the two shift bands, which correspond to those observed for **6**

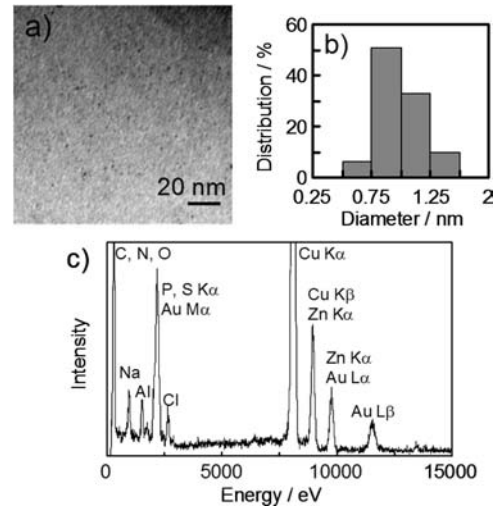

Figure 10. Results of TEM-EDS analyses for **9** (accelerating voltage, 200 kV; bright-field mode; resolution of scale bar, 20 nm). (a) TEM image of **9**. (b) Core size distribution of the Au clusters in **9**. (c) EDS analyses for **9** (the EDS peaks of Cu and Al originate from the Cu grid and sample holder, respectively).

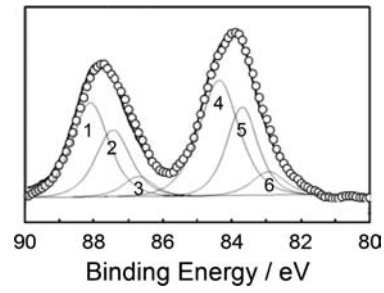

Figure 11. XPS spectrum of **9** observed at the Au 4f region (Mg Kα, $h\nu$ = 1253.6 eV). The observed spectrum is shown by the black circles. The deconvolution results are shown by the gray lines. The resolved spectra are shown by the black lines. The peak numbers 1−6 indicate Au−S $4f_{5/2}$, Au−P $4f_{5/2}$, internal Au $4f_{5/2}$, Au−S $4f_{7/2}$, Au−P $4f_{7/2}$, and internal Au $4f_{7/2}$, respectively.

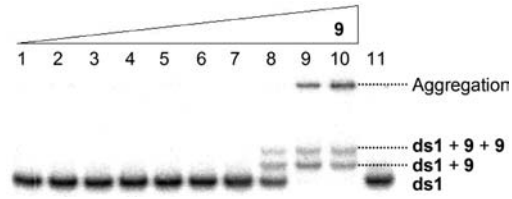

Figure 12. EMSA of **9** + **ds1** (^{32}P labeled DNAs were used). The concentration of **9** was increased from left to right in lanes 1−11 (0, 3.9, 7.8, 15.6, 31.3, 62.5, 125, 250, 500, 1000, and 2000 nM). Each loading mixture contained 10 mM Tris-HCl (pH 8), 33.3 mM NaCl, 5% glycerol, 0.005% NP-40, 1 mM dithiothreitol, poly-(dI-dC) (10 ng/μL), and ^{32}P-end-labeled DNA fragments (ca. 500 cpm).

(Figure 5c), as well as the results of the Au11 titration experiment monitored by CD spectroscopy, which showed 1:1 complexation between **6** and Au11, the lower molecular weight band of Figure 12 is assigned to **ds1** + **9**, whereas the higher molecular weight band is assigned to **ds1** + **9** + **9**. The dissociation constants (K_{d1} = 450 nM, K_{d2} = 200 nM) were estimated by simulating the intensity of each band according to the formula in Figure 7. These dissociation constants were 2−3 times higher than those of the cases observed for **9** probably because of an increase in molecular size and rigidity due to the existence of **10**. **9** also specifically recognized the sextet G_6 site

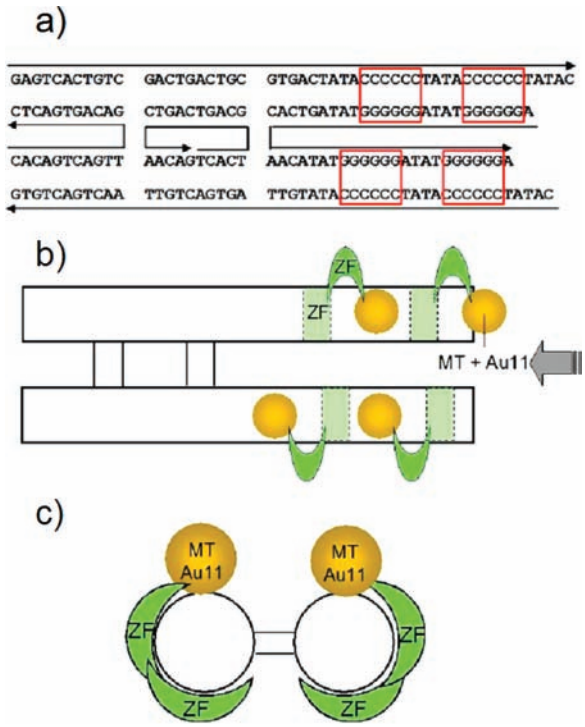

Figure 13. DNA or nucleotide sequence and design of **dx1**. DNA or nucleotide sequence of **dx1** (a). Schematic images of the position of **9** on **dx1** from the (b) top view and (c) side view.

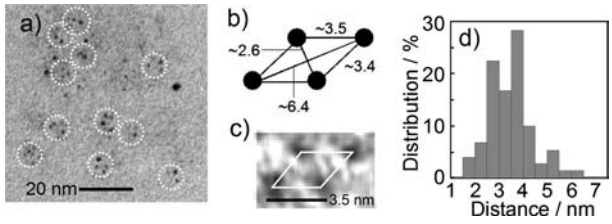

Figure 14. TEM observation of the Au cluster alignment used by **9** + **dx1** (accelerating voltage, 200 kV; bright-field mode; resolution of scale bar, 20 nm). (a) TEM observation of the mixture of **9** and **dx1**. (b) Expected interparticle distances of Au clusters on **dx1**. (c) Expanded TEM image of the typical parallelogram comprising four Au_{11}. (d) The interparticle distance distribution in **9** + **dx1**.

in dsDNA, because it did not bind to **ds3** without this sextet (Supporting Information).

Alignment of Multiple Au_{11} Clusters on dxDNA via ZF(Zn)ZF(Zn)-MTα(Au_{11}). A double-crossover dxDNA, **dx1**, with four G_6 sequences as the ZF-recognizing units, was designed and synthesized according to the dxDNA by Seeman et al. (*30*) and the idealized alignment of **9** on the dxDNA template was estimated using the reported X-ray structure (or cystral structure) of ZF-dsDNA (*31*) (see Figure 13). dxDNA is composed of five ssDNAs, in which two dsDNAs are doubly cross-linked. Because of these cross-linkings, dxDNAs are thought to be more rigid than simple dsDNAs. The four G_6 sequences were aligned to form a parallelogram that crossed over the gap between the two dsDNA of **dx1**. The two recognition sequences in each arm are located ~3.5 nm, namely, 10 bps = one turn, apart from each other, directed virtually toward the plane made of the two dsDNA. At the same time, the sequences on different arms form shorter (~2.6 nm) and longer (~6.4 nm) diagonals (Figure 14b). A TEM image of the mixture of **9** and **dx1** is shown in Figure 14a, in which we observe a 14% four-particle alignment, 35% three-particle alignment, and 51% two-particle alignment. The distances between the nearest-neighbor spots seen in this figure are shown in Figure 14d as a frequency map, which demonstrates the existence of two maxima at ~2.7 and ~3.7 nm. These values agree with those of the designed distances for the recognition sequences mentioned above. A typical parallelogram observed in the expanded TEM image is shown in Figure 14c with the theoretical one. These results show that the fusion protein can align an Au_{11} cluster on **dx1**, as expected.

DISCUSSION

Au clusters show attractive electronic properties, such as Coulomb blockade, which are applicable for nanodevices such as a single electron transistor (*32*, *33*), and quantum cell automata, which originate from the quantum size effect. Au clusters synthesized by chemical processes based on a bottom-up strategy are suitable for large-scale preparation; however, it is difficult to construct Au clusters in the complex patterns desired for nano electronics. Many groups have used DNA as programmable templates for the patterning of Au clusters, in which the complementary recognition of bps is the main strategy for "DNA lithography". They generally sulfurize the termini of ssDNAs to bind Au clusters and introduce the ssDNA conjugates to the other complementary ssDNAs to form dsDNAs. This method may be limited to simple DNAs because ssDNAs cannot hold rigid structures as templates; therefore, it is impossible to design complex DNA architectures. On the other hand, the insertion of an Au-attached ssDNA to a dsDNA, which yields a triplex DNA (*34*), distorts the duplex structures of the target dsDNA and changes the helical phase.

This report proposed a new method that utilizes the sequence information of bps via the interaction between a dsDNA and a DNA-recognizing motif, ZF, to align Au clusters on the desired points of the dsDNA. The ZF method, in principle, can escape the limit of the complementary ssDNA method mentioned above. However, it also has a limit. The DNA recognition depends on the binding constants. The ZF domain adopted in this study is short and requires only a sextet of bps to fix an Au cluster on dsDNA; therefore, the binding constant is small. In practice, the observed ratio of the desired alignment of four Au_{11} particles on the dxDNA (**dx1**) is not high (only 15%). This result may be attributed to three points: (i) the existence of Au_{11}-bound MTα domain increases ~10^2 times the dissociation constants K_ds (from ~nM to ~10^2 nM) as we showed in control experiments using **11**. (ii) In this study, we could not mix an excess amount of **9** with **dx1** to avoid the disappearance of the parallelogram alignment of Au_{11} into the crowd of free **9**. (iii) The four ZF-binding regions in **dx1** may be too close to each other to maintain the stable formation of dsDNA. It should be noted that ZF slightly bends dsDNA (*31*), which weakens the subsequent binding of the second, third, and fourth ZFs. These problems may be solved by optimizing the interaction between DNA and ZF, as well as ZF and MTα.

EXPERIMENTAL PROCEDURES

Materials. Reagents for peptide syntheses, such as Fmoc-protected amino acids, Fmoc-Ala Wang resin, H-Gly-2Cl-Trt resin, dicyclohexylcarbodiimide (DCC), benzotriazole-1-yl-oxy-tris-pyrolidino-phosphonium hexafluorophosphate (PyBOP), hydroxybenzotriazole (HOBt), piperidine, trifluoroacetic acid (TFA), 1,2-ethanedithiol (EDT), triisopropylsilane (TIS), acetic acid (AcOH), trifluoroethanol (TFE), ethyl 3-mercaptopropionate (MPAEt), diisopropylethylamine (DIEA), guanidine hydrochloride, benzyl mercaptan, and thiophenol were purchased from Peptide Institute, Inc., Tokyo Chemical Industry, and Novabiochem. Metal source reagents, such as zinc sulfate heptahydrate, cobalt(II) sulfate heptahydrate, copper(I) iodide, and cadmium chloride were purchased from Kanto Kagaku Reagent Division. Solvents for peptide syntheses and HPLC, such as dichlo-

romethane (DCM), methanol (MeOH), *N*-methyl-2-pyrolidinone (NMP), *N*,*N*-dimethylformamide (DMF), diethyl ether, distilled water, and acetnitrile (MeCN) were purchased from Kanto Kagaku Reagent Division. 5,5′-Dithiobis(2-nitrobenzoic acid) (DTNB) for the quantification of SH groups was purchased from Nacalai tesque. The matrix reagents for matrix-assisted laser desorption ionization−time-of-flight (MALDI-TOF) mass spectrometry measurements, such as α-cyano-4-hydroxy-cinnamic acid (CHCA), were purchased from Aldrich.

Synthesis. 2 (*20*) and **3** were synthesized by the standard solid-phase method. The Fmoc/*t*-Bu chemistry in NMP was adopted using DCC and HOBt as the coupling reagents. H-Gly-2Cl-Trt resin and Fmoc-Ala Wang resin were used for the syntheses of **2** and **3**, respectively. The coupling reactions were carried out with a peptide synthesizer (Applied Biosystems model 433A). DCM and MeOH were used for washing the resins. **3-COSR** was synthesized by the modified method of Futaki et al. (*24*) Namely, ZF(side chain protected)-2Cl-Trt resin was treated with 2% $(Boc)_2O$/NMP for 1 h at room temperature to protect the NH_2 group of the N-terminus; then, it was treated with DCM/AcOH/TFE = 8:1:1 for 2 h at room temperature to remove the Boc-ZF(side chain protected)−OH. The obtained peptide solution was concentrated and reacted with a solution containing 25 equiv of PyBOP, HOBt, and DIEA, as well as 50 equiv of MPAEt, for 24 h at room temperature in an Ar atmosphere to obtain Boc-ZF(side chain protected)-MPAEt (**Boc-3-COSR**). The solution was dried in vacuo, redissolved into DCM, washed with water five times, and dried in vacuo. Finally, the deprotection of **Boc-3-COSR** was carried out with TFA/EDT/H_2O/TIS = 95:5:2.5:2.5 for 4 h at room temperature. The solution was concentrated in vacuo, diluted with diethyl ether, and centrifuged to obtain crude solids. Mass analysis: Calcd for $[\mathbf{2}]^+$, m/z = 3268.2; observed, m/z = 3268.4. Calcd for $[\mathbf{3}]^+$, m/z = 6790.3; observed, m/z = 6790.0. Calcd for $[\mathbf{3\text{-}COSR}]^+$, m/z = 6910.8; observed, m/z = 6910.9.

The fusion peptide **1** was synthesized by the NCL method. This reaction was carried out by mixing **3-COSR** and **2** with a 1:1 molar ratio in a 0.1 M sodium phosphate buffer (pH 8.0) solution containing 6 M guanidine hydrochloride, 4% (v/v) thiophenol, and 4% (v/v) benzyl mercaptan for 24 h at room temperature in Ar atmosphere. After reaction completion, the solution was washed five times with diethyl ether, deionized using a Sep-Pak 3 cm^3 + C18 column, and purified on a reverse-phase HPLC column. The solutions were lyophilized to white powders. Mass analysis: Calcd for $[\mathbf{1}]^+$, m/z = 10046.6; observed, m/z = 10046.6.

Au11 was prepared according to the method by Bartlett et al. (*21*, *35*), and characterized by UV−vis spectroscopy (λ_{max}: 420 nm) and TEM (core size distributions: 0.8 ± 0.2 nm).

dx1 and **dx2** were constructed according to the method of Fu et al. (*30*) from the component ssDNAs (the DNA sequences are shown in the Supporting Information) purchased from Nihon Gene Research Laboratories and used without further purification. Ten micromolar ssDNA solutions, each containing 40 mM of Tris buffer, 20 mM of acetic acid, 2 mM of ethylenediaminetetraacetic acid (EDTA), and 12.5 mM of magnesium acetate, were mixed and set at 95 °C, then annealed to room temperature for over 12 h. The obtained dxDNA solutions were dialyzed by distilled water to remove EDTA, which forms a chelate complex with Zn^{2+}, prior to use for EMSA and TEM measurements.

Analysis and Physicochemical Measurements. A process analysis was carried out with a Shimadzu LC-6AD HPLC system and a Shiseido CAPCELLPAK C18 UG120 (4.6 × 250 mm). Crude peptides were purified on a reverse-phase HPLC column (Senshu Docosil-B C22 column 30 × 50 mm) with MeCN and water as an eluent (gradient containing 0.1% TFA). A Shimadzu LC-10 HPLC system and a Shodex Asahipak GF-310HQ (7.6 × 300 mm) were used for gel permeation chromatography (GPC). UV−vis measurements were performed with a Shimadzu UV-2450 spectrophotometer. Circular dichroism (CD) spectra were recorded on a Jasco J-725 spectrophotometer. The MALDI-TOF mass spectra were recorded on a PerSpective Biosystems Voyager Liner RD VDA-500 system with CHCA as the matrix. All of the samples used in the Ellman test, **1**, **2**, and **3**, were prepared in an N_2 atmosphere in a glovebox (P_{O2} < 0.1 ppm; dew point < −87 °C).

Electrophoretic Mobility Shift Assay. Before EMSA experiments, the unincorporated ^{32}P label and EDTA were carefully removed by gel filtration equilibrated in deionized water, followed by dialysis against water. Each reaction mixture contained 10 mM Tris-HCl (pH 8), 50 mM NaCl, 5% glycerol, 0.005% NP-40, 1 mM dithiothreitol, ^{32}P-end-labeled substrate DNA fragments (ca. 500 cpm), and a selected concentration of zinc finger peptides. The experiments were performed in the presence of a competitor DNA, poly(dI-dC) (10 ng/μL). The binding of the ZF and DNAs was completed by incubating at 25 °C for 3 h. Gels were pre-electrophoresed for at least 30 min at a constant voltage. The DNA-bound proteins and free probe were electrophoretically separated on a 15% polyacrylamide gel with 0.5× Tris-Borate running buffer at 230 V. The gels were vacuum-dried and visualized by autoradiography using an FLA-2000 (FUJI FILM). The bands were quantified with the MacBAS (FUJI FILM) software.

Fluorescent-labeled (IRD700) oligo nucleotides were purchased from LI-COR, and used for fluorescent EMSA, which was performed according to the procedures used in ^{32}P-labeled experiments. The gels were visualized by an ODYSSEY infrared imaging system (LI-COR).

ACKNOWLEDGMENT

We gratefully acknowledge Fumiaki Uchiumi and Hidetaka Torigoe for access to ^{32}P-EMSA and IRD EMSA experiments, respectively. This work was supported by Grants-in Aid for Scientific Research 16651051 and 18350034 from the Ministry of Education, Culture, Sports, Science, and Technology (MEXT) of the Japanese Government.

Supporting Information Available: Results of Co^{2+} titration on **2**, results of Zn^{2+} and Cd^{2+} titrations into holo-**1**, EMSA of **11** + **ds1**, EMSA of **9** + **ds3**, GPC trace for **2** + Cd^{2+}, nonreduced SDS-PAGE experiments for **2** + Zn^{2+} or Cd^{2+}, DNA sequences of **dx2**, and EMSA of **9** + **dx2**. This material is available free of charge via the Internet at http://pubs.acs.org.

LITERATURE CITED

(1) Storhoff, J. J., and Mirkin, C. A. (1999) Programmed materials synthesis with DNA. *Chem. Rev. 99*, 1849–1862.
(2) Aldaye, F. A., and Sleiman, H. F. (2007) Dynamic DNA templates for discrete gold nanoparticle assemblies: control of geometry, modularity, write/erase and structural switching. *J. Am. Chem. Soc. 129*, 4130–4131.
(3) Millar, J., McLachlan, A. D., and Klug, A. (1985) Repetitive zinc-binding domains in the protein transcription factor IIIA fron *Xenopus* oocytes. *EMBO J. 4*, 1609–1614.
(4) Berg, J. M. (1986) Potential metal-binding domains in nucleic acid binding proteins. *Science 232*, 485–487.
(5) Chan, J., Huang, Z., Merrifield, M. E., Salgado, M. T., and Stillman, M. J. (2002) Studies of metal binding reactions in metallothioneins by spectroscopic, molecular biology, and molecular modeling techniques. *Coord. Chem. Rev. 233*−*234*, 319–339.
(6) Park, C., Campbell, J. L., and Goddard, W. A. (1996) Can the monomer of the leucine zipper proteins recognize the dimer

binding site without dimerization? *J. Am. Chem. Soc. 118*, 4235–4239.
(7) Bishop, P., Ghosh, I., Jones, C., and Chmielewski, J. (1995) Basic-helix-loop-helix region of Tal: evaluation of structure and DNA affinity. *J. Am. Chem. Soc. 117*, 8283–8284.
(8) Spuches, A. M., and Wilcox, D. E. (2008) Monomethylarsenite competes with Zn^{2+} for binding sites in the glucocorticoid receptor. *J. Am. Chem. Soc. 130*, 8148–8149.
(9) Marmorstein, R., Carey, M., Ptashne, M., and Hariison, S. C. (1992) DNA recognition by GAL4: structure of a protein-DNA complex. *Nature 356*, 408–414.
(10) Pabo, C. O., Peisach, E., and Grant, R. A. (2001) Design and selection of novel Cys_2His_2 zinc finger proteins. *Annu. Rev. Biochem. 70*, 313–340.
(11) Jantz, D., Amann, B. T., Gregory, J., Gatto, J., and Berg, J. M. (2004) The design of functional DNA-binding proteins based on zinc finger domains. *Chem. Rev. 104*, 789–799.
(12) Mandell, J. G., and Barbas, C. F. (2006) Zinc finger tools: custom DNA-binding domains for transcription factors and nucleases. *Nucleic Acids Res. 34*, W516–W523.
(13) Choo, Y., and Klug, A.1994 Selection of DNA binding sites for zinc fingers using rationally randomized DNA reveals coded interactions. *Proc. Natl. Acad. Sci. U.S.A. 91*, 11168–11172.
(14) Sera, T., and Uranga, C. (2002) Rational design of artificial zinc-finger proteins using a nondegenerate recognition code table. *Biochemistry 41*, 7074–7081.
(15) Stillman, M. J., Cai, W., and Zelazowski, A. J. (1987) Cadmium Binding to metallothioneins. *J. Biol. Chem. 262*, 4538–4548.
(16) Stillman, M. J., Presta, A., Gui, Z., and Jiang, D.-T. (1994) Spectroscopic studies of copper, silver and gold-metallothioneins. *Metal Based Drugs 1*, 375–394.
(17) Kägi, J. H. R., and Schäffer, A. (1988) Biochemistry of metallothionein. *Biochemistry 27*, 8409–8515.
(18) Robbins, A. H., McRee, D. E., Williamson, M., Collett, S. A., Xuong, N. H., Furey, W. F., Wang, B. C., and Stout, C. D. (1991) Refined crystal structure of Cd, Zn metallothionein at 2.0 A resolution. *J. Mol. Biol. 221*, 1269–1293.
(19) Mercogliano, C. P., and DeRosier, D. J. (2006) Gold nanocluster formation using metallothionein: mass spectrometry and electron microscopy. *J. Mol. Biol. 355*, 211–223.
(20) Ariyasu, S., Onoda, A., Sakamoto, R., and Yamamura, T. (2009) Conjugation of Au11 cluster with Cys-rich peptides containing the α-domain of metallothionein. *Dalton Trans.* 3742–3747.
(21) Bartiett, P. A., Bauer, B., and Singer, S. J. (1978) Synthesis of water-soluble undecagold cluster compounds of potential importance in electron microscopic and other studies of biological systems. *J. Am. Chem. Soc. 100*, 5085–5089.
(22) Dawson, P. E., and Kent, S. B. H. (2000) Synthesis of native proteins by chemical ligation. *Annu. Rev. Biochem. 69*, 923–960.
(23) Pavletich, N. P., and Pabo, C. O. (1991) Zinc finger-DNA recognition: crystal structure of a Zif268-DNA complex at 2.1 Å. *Science 252*, 809–817.
(24) Futaki, S., Sogawa, K., Maruyama, J., Asahara, T., Niwa, M., and Hojo, H. (1997) Preparation of peptide thioesters using fmoc-solid-phase peptide synthesis and its application to the construction of a template-asssembled synthetic protein (TASP). *Tetrahedron Lett. 38*, 6237–6240.
(25) Michael, S. F., Kilfoil, V. J., Schmidt, M. H., Amann, B. T., and Berg, J. M. (1992) Metal binding and folding properties of a minimalist Cys_2His_2 zinc finger peptide. *Proc. Natl. Acad. Sci. U.S.A. 89*, 4796–4800.
(26) Frankel, A. D., Berg, J. M., and Pabo, C. O. (1987) Metal-dependent folding of a single zinc finger from transcription factor IIIA. *Proc. Natl. Acad. Sci. U.S.A. 84*, 4841–4845.
(27) Hasler, D. W., Jensen, L. T., Zerbe, O., Winge, D. R., and Vašák, M. (2000) Effect of two conserved prolines of human growth inhibitory factor (metallothionein-3) on its biological activity and structure fluctuation: comparison with a mutant protein. *Biochemistry 39*, 14567–14575.
(28) Blindauer, C. A., Harrison, M. D., Parkinson, J. A., Robinson, A. K., Cavet, J. S., Robbinson, N. J., and Sadler, P. J. (2001) A metallothionein containing a zinc finger within a four-metal cluster protects a bacterium from zinc toxicity. *Proc. Natl. Acad. Sci. U.S.A. 98*, 9593–9598.
(29) Woehrle, G. H., and Hutchison, J. E. (2005) Thiol-functionalized undecagold clusters by ligand exchange: synthesis, mechanism, and properties. *Inorg. Chem. 44*, 6149–6158.
(30) Fu, T., and Seeman, N. C. (1993) DNA double-crossover molecules. *Biochemistry 32*, 3211–3220.
(31) Kim, C. A., and Berg, J. M. (1996) A 2.2 Å resolution crystal structure of a designed zinc finger protein bound to DNA. *Nat. Struct. Biol. 3*, 940–945.
(32) Chi, L. F., Hartig, M., Drechsler, T., Schwaack, T., Seidel, C., Fuchs, H., and Schmid, G. (1998) Single-electron tunneling in Au_{55} cluster monolayers. *Appl. Phys. A: Mater. Sci. Proc. 66*, S187–S190.
(33) Schmid, G., and Liu, Y. (2001) Quasi one-dimensional arrangements of $Au_{55}(PPh_3)_{12}Cl_6$ clusters and their electrical properties at room temperature. *Nano Lett. 1*, 405–407.
(34) Lytton-Jean, A. K. R., Han, M. S., and Mirkin, C. A. (2007) Microarray detection of duplex and triplex DNA binders with DNA-modified gold nanoparticles. *Anal. Chem. 79*, 6037–6041.
(35) Woehrle, G. H., Warner, M. G., and Hutchison, J. E. (2002) Ligand exchange reactions yield subnanometer, thiol-stabilized gold particles with defined optical transitions. *J. Phys. Chem. B 106*, 9979–9981.

BC9002713

Supporting Information

Alignment of Gold Clusters on DNA via DNA-recognizing Zinc Finger–Metallothionein Fusion Protein

*Shinya Ariyasu, Akira Onoda, Ryota Sakamoto, and Takeshi Yamamura**

Faculty of Science, Tokyo University of Science, Kagurazaka 1-3, Shinjuku-ku, Tokyo,

162-8601, Japan

tyamamur@rs.kagu.tus.ac.jp

1. Co^{2+} titration on MTα monitored by UV-vis spectroscopy.

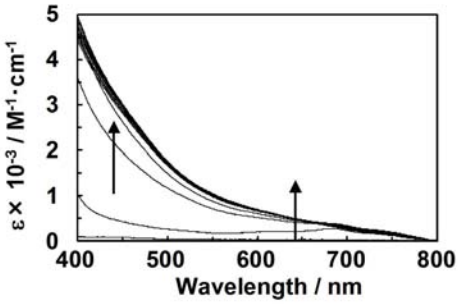

Fig. S1. Results of Co^{2+} titration on **2** monitored by UV-vis spectroscopy. A 2 mM aqueous solution of Co^{2+} was added dropwise to a 10 mM of Tris-HCl solution containing 50 μM of **2**.

As shown here, the spectral change of MTα (**2)** upon Co^{2+} titration is similar to that of ZFZF-MTα (**1)** (manuscript). In the first stage of Co^{2+} titration (0~1 equiv) to **2**, we observe a rapid increase of the absorption in all wavelength regions, suggesting that this absorption originates from the formation of a Co cluster Co_xCys_y in **2**. This result suggests that the increase of the basal absorption observed in the Co^{2+} titration into **1** (manuscript) originates

from the formation of Co_xCys_y at MT domain.

2. Zn^{2+} and Cd^{2+} titrations into holo-ZFZF-MTα monitored by CD spectroscopy

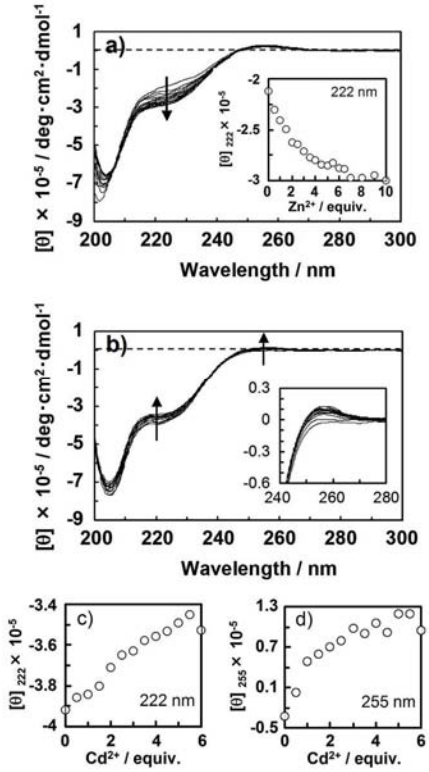

Fig. S2. Results of Zn^{2+} and Cd^{2+} titrations into holo-**1** monitored by CD spectroscopy: (a) **7** + Zn^{2+}, the inset shows the titration curve observed at 222 nm, (b) **6** + Cd^{2+}, (c) and (d) the titration curves observed at 220 nm and (d) 255 nm, respectively. Aqueous solutions containing 500 μM of Zn^{2+} or Cd^{2+} were added dropwise to 10 mM of Tris-HCl solution containing 12.5 μM of holo-**1**.

The negative peak observed at 222 nm in Zn^{2+} titration into ZF(Cd)ZF(Cd)-MTα(Cd_4) (**7**) (Fig. S2a) originates from the ββα folding of the ZF domain. This spectral change is similar to that of Zn^{2+} titration for **1**; however, the titration requires more of Zn^{2+} than the case of simple Zn^{2+} titration into apo protein to finish the spectral change. This is probably because the Cd^{2+} ion already added to the solution prior to Zn^{2+} titration interrupts the insertion of Zn^{2+} to the ZF domain. The positive peak at 255 nm, which is conserved through Zn^{2+} titration, originates from Cd_4Cys_y at the MT domain.

On the other hand, in the case of Cd^{2+} titration into ZF(Zn)ZF(Zn)-MTα(Zn_x) (**7**) (Fig. S2b), the negative peak observed at 222 nm decreases, whereas the positive peak at 255 nm increases.

This spectral change is similar to that of the formation of Cd_xCys_4 at the MT domain of **1** (manuscript). The spectral change is moderate in comparison with that of the apo protein. This difference was also speculated that excess Zn^{2+} already contained before Cd^{2+} titration interrupted the exchange to Cd^{2+} at the MT domain.

3. EMSA of ZF(Zn)ZF(Zn) + ds1

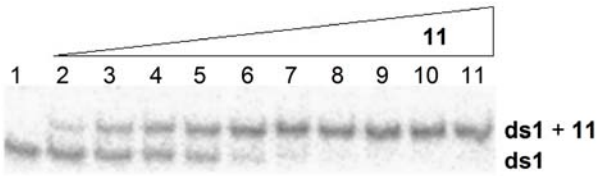

Fig. S3. EMSA of **11** + **ds1** (^{32}P labeled DNA were used). Concentration of **11** increases from left to right (lane 1~11; 0, 1.5, 2.9, 5.9, 11.7, 23.4, 46.4, 93.8, 187.5, 375, 750 nM). Each mixture loaded contains 10 mM Tris-HCl (pH 8), 33.3 mM NaCl, 5% glycerol, 0.005% NP-40, 1 mM DTT, poly-(dI-dC) (10 ng/μl), and ^{32}P-end labeled DNA fragment (ca 500 cpm).

As shown here, ZF(Zn)ZF(Zn) (**11**) affords only one shift band originating from DNA-ZF differently from the case of ZF(Zn)ZF(Zn)-MTα(Zn_x) (**6**), which shows the existence of two DNA-ZF spices. Furthermore, the dissociation constant K_d calculated from radioactive intensities of Fig. S3 is estimated to be 7.5 nM, which is 1/10 of the case for **6**.

4. EMSA of ZF(Zn)ZF(Zn)-MTα(Zn_x) + ds3

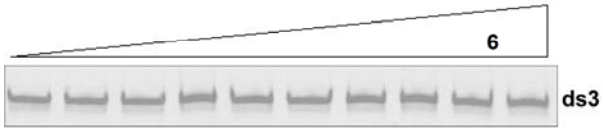

Fig. S4. EMSA of **6** + **ds3** (IRD700 labeled DNA were used). Concentration of **6** increases from left to right (lane 1~11; 0, 2.9, 5.9, 11.7, 23.4, 46.4, 93.8, 187.5, 375, 750, 1500 nM). Each mixture loaded contains 10 mM Tris-HCl (pH 8), 33.3 mM NaCl, 5% glycerol, 0.005% NP-40, 1 mM DTT, poly-(dI-dC) (10 ng/μl), and IRD700-end labeled DNA fragment (ca 0.1 μM).

ds3 has 5'-GGGGGG-3' instead of 5'-TGGTGG-3'. As is shown here, **6** do not show affinity to **ds3**. This result shows that **6** does not undergo non-specific binding to DNA.

5. GPC trace and nonreduced SDS-PAGE for MTα.

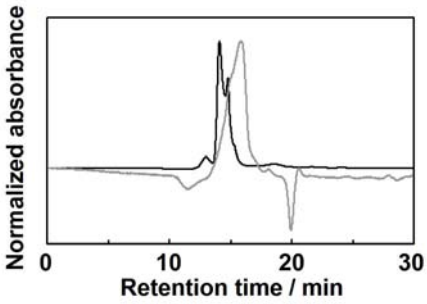

Fig. S5. GPC trace for **2** + Cd^{2+}. 10 μl injections of 100 μM **2**/0.1% TFA/H_2O solution and 100 μM **2** + Cd^{2+}/H_2O solution are shown by gray and black lines, respectively. 50 % MeOH/H_2O was used as the eluent. Flow rate was controlled at 0.5 ml/min. The negative peak at 20 min originates from the solvent at sample injection.

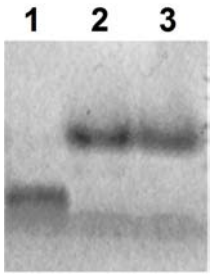

Fig. S6. Nonreduced SDS-PAGE experiments for **2** + Zn^{2+} or Cd^{2+}. Lanes 1, 2, and 3 show the bands for **2**, **2** + Zn^{2+}, and **2** + Cd^{2+}, respectively. Each concentration of **2** was controlled at 80 μM.

This GPC result indicates that the addition of Cd^{2+} to MTα (**2**) induces the increase of molecular size. This is supported by the result of nonreduced SDS-PAGE of **2** (Fig. S6). The addition of Zn^{2+} or Cd^{2+} to **2** causes the band of **2** shift to a higher side. This result suggests that the size of **2** increases with the addition of metal ions. Considering the results of Figs. S5

and 6, those observed in the Fig. 5C of the manuscript suggest that the dimerization of **6** originates from the MT domains through binding of Zn^{2+}.

6. Alignment of multiple Au_{11} clusters on dxDNA via ZF(Zn)ZF(Zn)-MTα(Au_{11}).

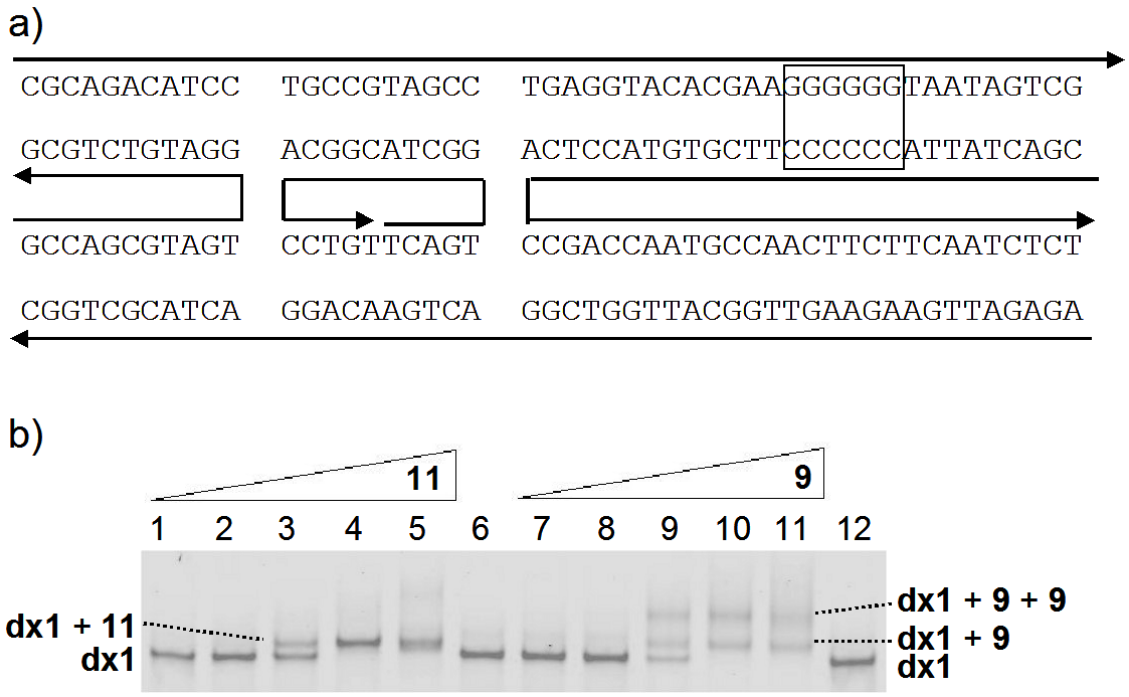

Fig. S7. a) Nucleic-acid base sequences of **dx2**. ZF-recognizing sequence is shown with black square. b) EMSA of **6** + **dx2** (IRD700 labeled DNA were used). lanes 1~5: **11** + **dx2**、lanes 7~11: **9** + **dx2**. Concentrations of **11** and **9** increase from left to right in the lanes. Each loading mixture contains 10 mM Tris-HCl (pH 8), 33.3 mM NaCl, 5% glycerol, 0.005% NP-40, 1 mM DTT, poly-(dI-dC) (10 ng/μl), and ^{32}P-end labeled substrate DNA fragment (ca 500 cpm). IRD700-end labeled substrate DNA fragment (ca 0.1 μM).

As is shown here, both peptides have affinity to dxDNA, although dxDNA is sterically crowded more than dsDNA.

New Strategy for the Extension of the Serum Half-Life of Antibody Fragments

Sabrina Trüssel,[†] Christoph Dumelin,[‡] Katharina Frey,[†] Alessandra Villa,[‡] Fabian Buller,[†] and Dario Neri*[,†]

Department of Chemistry and Applied Biosciences, Institute of Pharmaceutical Sciences, and Philochem AG, ETH Zurich, Wolfgang-Pauli-Str. 10, CH-8093 Zurich, Switzerland. Received June 26, 2009; Revised Manuscript Received September 9, 2009

Antibody fragments can recognize their cognate antigen with high affinity and can be produced at high yields, but generally display rapid blood clearance profiles. For pharmaceutical applications, the serum half-life of antibody fragments is often extended by chemical modification with polymers or by genetic fusion to albumin or albumin-binding polypeptides. Here, we report that the site-specific chemical modification of a C-terminal cysteine residue in scFv antibody fragments with a small organic molecule capable of high-affinity binding to serum albumin substantially extends serum half-life in rodents. The strategy was implemented using the antibody fragment F8, specific to the alternatively spliced EDA domain of fibronectin, a tumor-associated antigen. The unmodified and chemically modified scFv-F8 antibody fragments were studied by biodistribution analysis in tumor-bearing mice, exhibiting a dramatic increase in tumor uptake for the albumin-binding antibody derivative. The data presented in this paper indicate that the chemical modification of the antibody fragment with the 2-(3-maleimidopropanamido)-6-(4-(4-iodophenyl)butanamido)hexanoate albumin-binding moiety may represent a general strategy for the extension of the serum half-life of antibody fragments and for the improvement of their *in vivo* targeting performance.

INTRODUCTION

Monoclonal antibodies represent the fastest growing class of pharmaceutical biotechnology (*1*). While intact IgG immunoglobulins often represent the format of choice for pharmaceutical applications, antibody derivatives (*2, 3*), antibody fragments (*4*), and globular protein mutants capable of specific binding to cognate antigens (*5*−*7*) are increasingly being considered for the implementation of diagnostic and therapeutic biomedical strategies, in view of their potency and of considerations related to the manufacturing process.

Antibody fragments and small globular proteins are typically cleared very rapidly from circulation via the renal route shortly after intravenous administration (*8*−*12*). While short serum half-life values may be desirable for certain pharmaceutical applications (e.g., radionuclide-based imaging, clearance of toxic drugs, transient interference with the function of a target protein *in vivo*), in many cases a long circulation time in the blood is desirable in order to ensure antibody function *in vivo* over an extended period of time and reduce the number of administrations. For this reason, a number of strategies for the extension of serum half-lives of antibody fragments have been considered and implemented at the clinical or preclinical level. They include antibody modification with polymers (such as PEG[1] or polysialic acid) (*13*−*16*), as well as fusion of the antibody molecule with albumin (*17, 18*) or with albumin-binding polypeptides (*19*−*21*). Interestingly, a recent comparative analysis of the tumor targeting properties of the monoclonal antibody Herceptin has revealed that a variant of the antibody Fab fragment format fused to an albumin-binding peptide yielded a more homogeneous *in vivo* targeting of tumor cells, compared to the unmodified Fab or IgG format (*22*).

We have recently described a novel, general approach for the extension of serum half-lives of small organic molecules, based on their chemical modification with a portable 6-(4-(4-iodophenyl)butanamido)hexanoate moiety, which mediates a stable noncovalent interaction with serum albumin in mouse, monkey, and man. The K_d values for the interaction between Albu-fluorescein and human serum albumin were 108 nM range at 25 °C and 330 nM range at 37 °C, respectively (*23*). In that study, we could show that the serum half-life of two commonly used contrast agents for biomedical imaging (fluorescein and gadolinium-DTPA) could be dramatically extended by chemical modification with the portable albumin-binding moiety. In principle, a similar strategy could be considered for the improvement of pharmacokinetic properties of globular proteins, including recombinant antibody fragments.

In this paper, we describe the experimental implementation of a site-specific modification of recombinant antibodies with 2-(3-maleimidopropanamido)-6-(4-(4-iodophenyl)butanamido) hexanoate ("Albu" tag), with the aim of prolonging circulatory half-lives and improving pharmaceutical properties. We used for these studies the F8 antibody, which binds with high affinity and specificity to the alternatively spliced EDA domain of fibronectin, a marker of tumor angiogenesis (*3, 24*−*27*). The F8 antibody was originally isolated from a human antibody library and was shown to efficiently localize to the tumor neovasculature *in vivo* following intravenous administration. At the beginning of this study, F8 was available in recombinant scFv (*28*), SIP (*27, 29, 30*), and IgG format and had been shown to stain a variety of different tumors in mouse, while being negative in most mouse and rodent tissues, with an exception

* Corresponding author. Prof. Dr. Dario Neri, Department of Chemistry and Applied Biosciences, Institute of Pharmaceutical Sciences, ETH Zurich, Wolfgang-Pauli-Str.10, CH-8093 Zurich, Switzerland. Tel: +41-44-6337401; Fax: +41-44-6331358; e-mail: neri@pharma.ethz.ch.

[†] Institute of Pharmaceutical Sciences.

[‡] Philochem AG.

[1] Abbreviations: PEG, poly(ethylene glycol); aa, amino acid; HSA, human serum albumin; EDA, extra-domain A of fibronectin; 11A12, recombinant preparation of an EDA-containing human fibronectin fragment; CHO, Chinese hamster ovary; EDB, extra-domain B of fibronectin.

10.1021/bc9002772 CCC: $40.75 © 2009 American Chemical Society
Published on Web 11/16/2009

made for the endometrium in the proliferative phase and some vessels in the ovaries (*26, 27*).

ScFv-F8 was cloned and expressed in mammalian cells in scFv format with a C-terminal cysteine residue and with either a 14-aa linker between VH and VL (leading to the formation of both monomer and noncovalent homodimer) or with a 5-aa linker (driving the preferential formation of a diabody structure) (*27, 31, 32*). ScFv-F8-Cys with the 5-aa linker and carrying a site-specific chemical modification with the Albu tag exhibited the best *in vivo* tumor targeting profiles, with percent injected doses per gram of tissue (%ID/g) in the tumor of >20% at 24 h, which persisted for several days. The data presented in this paper indicate that the chemical modification of the antibody fragments with albumin-binding moieties may represent a general strategy for the extension of the serum half-life of antibody fragments and for the improvement of their *in vivo* targeting performance.

EXPERIMENTAL PROCEDURES

All chemicals were purchased from Sigma-Aldrich unless specified.

Synthesis of the Albu Tag. To a solution of 10 μmol of 4-(-*p*-iodophenyl)butanoic acid in 50 μL of dimethyl sulfoxide (DMSO), 8 μmol of *N*-(3-dimethylaminopropyl)-*N*′-ethylcarbodiimide hydrochloride (EDC-HCl) and 10 μmol of *N*-hydroxysuccinimide (NHS) were added and the reaction mixture was stirred for 3 h at 30 °C. After addition of 20 μmol of Fmoc-Lys−OH-HCl (Bachem) and 43 μmol of triethylamine (TEA) in 100 μL of DMSO, the reaction was stirred overnight at 30 °C. Removal of the Fmoc-protection group was performed by addition of 30 μL of 5 M KOH and stirring for 2 h at 30 °C. The reaction was purified by HPLC (Waters 2795 Alliance HT with 2487 dual-wavelength absorbance detector, Waters XTerra Prep RP_{18} column (5 μM, 10 × 150 mm), buffers 0.1% trifluoroacetic acid and acetonitrile), the desired fractions with the obtained intermediate 6-(4-(4-iodophenyl)butanamido)hexanoate were collected and solvents and buffer were removed under vacuum. The synthesis of the maleimide derivative was performed as follows: 27 μmol of maleimidopropionic acid, 30 μmol of EDC-HCl, and 30 μmol of NHS in 600 μL of dry DMF were stirred for 3 h at 30 °C. The reaction mixture was added to 32 μmol of the previously obtained 6-(4-(4-iodophenyl)butanamido)hexanoate dissolved in 650 μL of 200 mM phosphate buffer, pH 7. After stirring for 2 h at room temperature and quenching of excess reagents by addition of HCl, HPLC purification was performed. The resulting product 2-(3-maleimidopropanamido)-6-(4-(4-iodophenyl)butanamido)hexanoate ("Albu" tag) was collected and dried under vacuum.

6-(4-(4-Iodophenyl)butanamido)hexanoate. ESI-MS (*m*/*z*): 418.9 [M + H^+], calcd.: 418.1. ^{1}H NMR (D_2O, TFA): 7.31 (d, 8.1 Hz, 2H), 6.66 (d, 8.3 Hz, 2H), 3.88 (t, 6.4 Hz, 1H), 2.93 (t, 6.5 Hz, 2H), 2.27 (t, 7.6 Hz, 2H), 1.97 (t, 7.4 Hz, 2H), 1.86−1.68 (m, 2H), 1.65−1.54 (m, 2H), 1.36−1.18 (m, 4H). 2-(3-maleimidopropanamido)-6-(4-(4-iodophenyl)butanamido) hexanoate. ESI-MS (*m*/*z*): 569.8 [M + H^+], calcd.: 569.1.

Affinity Resins of HSA and 11A12. Human serum albumin (HSA) and the antigen 11A12, a recombinant preparation of an EDA-containing human fibronectin fragment (*27*), were conjugated to sepharose beads as follows: 300 mg of CNBr-sepharose (GE-Healthcare) beads were resuspended in cold 1 mM HCl resulting in 1 mL resin after swelling. The resin was washed several times with cold 1 mM HCl (200 mL/g resin) and 100 mM $NaHCO_3$, 500 mM NaCl, pH 8.2 (coupling buffer, 20 mL/g resin), followed by addition of HSA (5−10 mg/mL resin) or 11A12 (5 mg/mL resin), respectively, dissolved in coupling buffer. After incubation overnight at 4 °C, the resin was washed again several times with coupling buffer (5 column volumes) and excessive reactive groups on the beads were quenched by addition of 100 mM Tris/HCl, pH 8.9. After blocking for 2 h at room temperature, the beads were washed repeatedly with alternating buffers (100 mM HOAc/NaAc, 500 mM NaCl, pH 4, and 100 mM Tris/HCl, 500 mM NaCl, pH 8). The resin was washed with PBS, redissolved in PBS containing 0.1% sodium azide, and stored at 4 °C.

Cloning, Expression, and Purification of scFv-F8 with a C-Terminal Cysteine Residue. ScFv-F8(14aa) as well as scFv-F8(5aa) were amplified and the residues Gly-Gly-Cys introduced at the C-terminal using the primers (5′-CCAAGCTTGTCGAC-CATGGGCTGGAGC-3′ and 5′-GGCCAAGGGACCAAGGTG-G A A A T C A A A G G C G G A T G T T A A T G A G C G G C-CGCAAAAGGAAAA-3′). After digestion with the restriction enzymes *Hind*III and *Not*I and Ligation into a *Hind*III/*Not*I double-digested vector pcDNA3.1, the ligation product was electroporated into electrocompetent *E. coli* TG1, sequenced, and used for transfection of CHO-S cells (Gibco/Invitrogen, Basel, Switzerland) with Amaxa Nucleofactor (Lonza, Vervier, Belgium) following the manufacturer's protocol. The transfected cells were grown in RPMI media supplemented with 10% FBS (fetal bovine serum) and selected using 500 μg/mL of Geneticin (G418, Calbiochem, San Diego, CA, USA). After cell-sorting by FACS (BD FACSAria, Becton Dickinson, Basel, Switzerland; equipped with FACSDiva Software) (*33*), monoclonals were grown in RPMI supplemented with 10% FBS. The best expressing monoclonal culture was determined by ELISA, brought into suspension, and cultured in PowerCHO-2 CD (Lonza, Vervier, Belgium) supplemented with 8 mM glutamine and HT supplement (Gibco/Invitrogen, Basel, Switzerland). The recombinant scFv were purified from supernatant using 11A12-affinity resin. After elution with 100 mM glycine, pH 3, the purified scFv were dialyzed against PBS overnight at 4 °C and characterized by SDS-PAGE, size-exclusion chromatography using a Superdex 75 HR 10/30 column (GE Healthcare), surface plasmon resonance (BIAcore 3000 system, GE Healthcare) studies, and LC-ESI-MS measurements. LC-ESI-MS: scFv-F8(5aa)-Cys (deconvoluted) m 25006, calcd. 25004; scFv-F8(14aa)-Cys (deconvoluted) m 25549, calcd. 25548 (Supporting Information Figure 1).

Conjugation of the Albu Tag to the scFv. The conjugation was performed by reducing 500 μL of 18 μM of scFv-F8-Cys with 1 mM final concentration of Tris(2-carboxyethyl)phosphine hydrochloride (TCEP-HCl, Thermo Scientific) for 20 min at room temperature followed by addition of 100-fold molar excess of the Albu tag. The reaction was stirred overnight at 4 °C, and the turnover of the conjugation was confirmed by LC-ESI-MS. The purification was performed as follows: the reaction mixture was loaded on an 11A12-affinity resin and incubated for 30 min at room temperature. The resin was then washed with PBS (10× the column volume), the bound antibody conjugate eluted with 100 mM glycine, pH 3, and dialyzed twice 2 h against PBS at 4 °C. In order to completely remove eventually nonconjugated antibody and confirm the ability of the antibody conjugate to bind to HSA, the purification was repeated on an HSA-affinity resin. Each step of the purifications was monitored by SDS-PAGE, and the final antibody conjugate was characterized by LC-ESI-MS, SDS-PAGE, and size exclusion chromatography using a Superdex 75 HR 10/30 column (Amersham Biosciences). The binding of the antibody−conjugate to the antigen 11A12 was confirmed by ELISA and surface plasmon resonance (BIAcore 3000 system, GE Healthcare) studies using a low-density coated chip. LC-ESI-MS scFv-F8(5aa)-Albu (deconvoluted) m 25574.0, calcd. 25574.2; scFv-F8(14aa)-Albu (deconvoluted) m 26122.0, calcd. 26117.7.

Analysis by Mass Spectrometry. Low molecular weight compounds: all molecules synthesized were characterized by

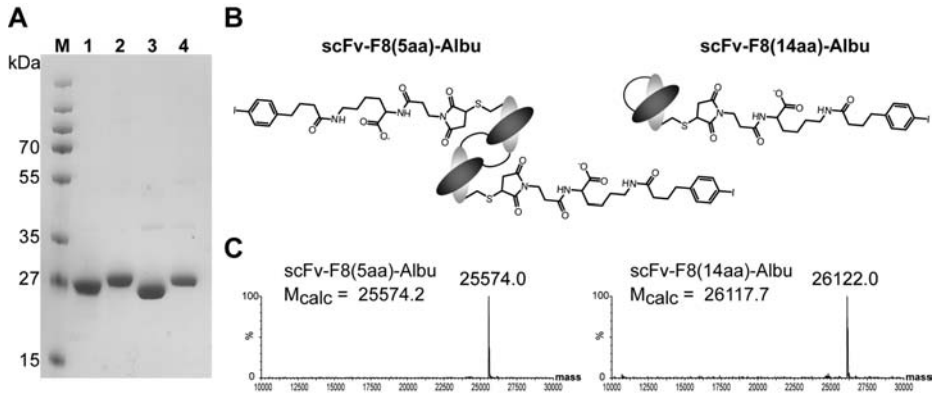

Figure 1. (A) Nonreducing SDS-PAGE analysis documenting the conjugation of the antibodies to the Albu tag. M: molecular weight marker. Lane 1, reduced scFv-F8(5aa)-Cys; lane 2, reduced scFv-F8(14aa)-Cys; lane 3, purified scFv-F8(5aa)-Albu; lane 4, purified scFv-F8(14aa)-Albu (B) schematic representation of the antibody formats scFv-F8(5aa)-Albu and scFv-F8(14aa)-Albu (C) LC-ESI-MS characterization of the antibody conjugates scFv-F8(5aa)-Albu and scFv-F8(14aa)-Albu after deconvolution of the spectra.

mass spectrometry on a Micromass Quattro API instrument. The antibodies and antibody conjugates were analyzed by LC-ESI-MS on a Micromass Quattro API instrument using a XBridge BEH300 C_4 column (3.5 μM, 2.1× 50 mm) running a gradient from 20% to 80% acetronitrile in 0.1% formic acid.

The digestion and MALDI-TOF/TOF analysis were performed as follows: both scFv-F8-Albu conjugates as well as the nonmodified scFv-F8-Cys were diluted to a concentration of ~140 nM in 500 μL of digestion buffer (50 mM Tris/HCl, 1 mM $CaCl_2$, pH 8), followed by addition of 8 nmol of sequencing grade modified trypsin (Promega, Madison, WI, USA). After digestion overnight at 37 °C in a thermomixer (Eppendorf, Hamburg, Germany) at 1000 rpm, purification and concentration of the tryptic peptides were performed using C_{18} microcolumns (Omix Pipette Tips C18, Varian, Lake Forest, CA, USA) according to the manufacturer's protocol with elution in 90% acetonitrile, 0.1% TFA. MALDI-TOF-TOF mass spectrometric analyses were carried out with a 4800 Proteomics Analyzer (Applied Biosystems, Foster City, CA, USA). Spectra were processed and analyzed by the Global Protein Server Workstation (Applied Biosystems).

Cell Line and Tumor Mouse Model. The tumor cell line used was F9 murine teratocarcinoma (CRL-1720, ATCC). The cell line was maintained in DMEM, supplemented with 10% fetal bovine serum (FBS) and antibiotic−antimycotic solution in flasks coated with 0.1% gelatin. F9 tumor-bearing mice were obtained by s.c. injection of 3×10^7 million F9 murine teratocarcinoma cells into the left flank of 10- to 12-week-old female 129SvPas mice (Charles Rivers Laboratories, Sulzfeld, Germany). For biodistribution, F9-tumors were allowed to grow for 8−10 days to a size of typically 100−200 mm^3.

Biodistribution Experiments. The *in vivo* targeting performances of scFv-F8-Cys and the corresponding conjugates scFv-F8-Albu were evaluated by quantitative biodistribution analysis as previously described (*34*). Briefly, purified antibody and antibody conjugate preparation were radiolabeled using ^{125}I and Chloramine T solution (0.25 μg Chloramine T per 1 μg protein) followed by purification on a PD-10 column (GE Healthcare) and injected into the tail vein of immunocompetent 129SvPas mice bearing s.c. implanted F9 murine teratocarcinoma (~30 μg per mouse). Mice were sacrificed 3, 24, 48, and 72 h after injection (4−5 mice per group). Organs were weighed and radioactivity was counted with a PackardCobra γ counter. Radioactivity content of representative organs was expressed as the percentage of the injected dose per gram of tissue (%ID/g). The immunoreactivity of the radiolabeled antibodies and antibody conjugates was confirmed by radioimmunoassay (*34*), using 11A12 as antigen and measuring the bound radioactivity. Further the binding capacity of the radiolabeled antibody conjugates toward HSA was also confirmed on a HSA-affinity resin. Prior to the radiolabeling, the monomeric fraction of scFv-F8(14aa)-Cys as well as scFv-F8(14aa)-Albu was separated and collected using size-exclusion chromatography (Superdex 75 HR 10/30 column, GE Healthcare).

Microautoradiography. Mice were sacrificed 24 h after the i.v. injection of radiolabeled scFv-F8(5aa)-Albu and tumors and organs were embedded and frozen in OCT medium (MICROM). Sections of 10 μm were cut, fixed with 4% *p*-formaldehyde in PBS, followed by washing with PBS and deionized water, and dried. The sections were then coated with NBT KODAK autoradiography emulsion, dried, and stored at 4 °C in the dark for ~9 weeks. The autoradiography emulsions were developed (Kodak Developer D-19) for 4 min and fixed (Kodak Eastman Fixer) for 5 min. Finally, slides were rinsed with deionized water and counterstained with hematoxylin (Sigma).

BIAcore Studies. BIAcore sensograms were recorded on a BIAcore 3000 instrument (GE Healthcare) using CM5 microsensor chips coated with recombinant 11A12 fibronectin fragment, as previously described (*27*).

RESULTS

Design, Production, and Characterization of Albumin-Binding Antibody Derivatives. ScFv-F8-Cys was cloned and expressed in CHO cells, appending the Gly-Gly-Cys tag (GGC) at the C-terminus of the molecule (*35*) and omitting any peptidic tag for immunodetection (see also Experimental Procedures). Two different variants of the scFv-F8-Cys antibody were used: one with a 14-aa linker (GGGGSGGGGSGGGG) and one with a 5-aa linker (GSGGS) between VH and VL domains. Both antibody fragments could be produced with high yields (25−30 mg/L in roller bottles) in nonoptimized conditions and purified to homogeneity by affinity chromatography (Figure 1A). As expected, the antibody with the 5aa linker yielded a stable noncovalent homodimer when analyzed by gel filtration (data not shown) corresponding to a diabody structure (Figure 1B) (*27*, *31*, *32*). By contrast, the antibody fragment with the 14aa linker yielded a mixture of monomer and noncovalent homodimer, from which the monomeric fraction could be quantitatively recovered by preparative gel filtration (Figure 1B). Both antibody preparations could be chemically modified with the Albu tag, yielding the corresponding albumin-binding antibody derivatives (scFv-F8(5aa)-Albu and scFv-F8(14aa)-Albu; Figure 1B), which displayed the expected theoretical mass in LC-ESI-MS analysis (Figure 1C). Maldi-TOF/TOF analysis after tryptic digestion confirmed the site-specific chemical

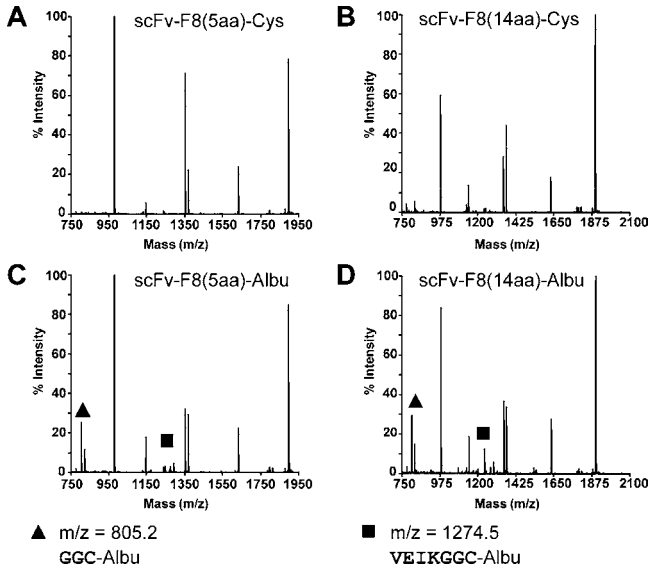

Figure 2. Mass spectra of tryptic peptides of (A,B) scFv-F8-Cys and (C,D) modified scFv-F8-Albu. (C,D) The spectra of the modified scFv-F8-Albu show two peaks not present in the nonmodified scFv-F8-Cys with the *m*/*z* of 805.2 (▲) corresponding to the modified peptide GGC-Albu and with the *m*/*z* of 1274.5 (■) corresponding to the larger modified peptide VEIKGGC-Albu of the C-terminus.

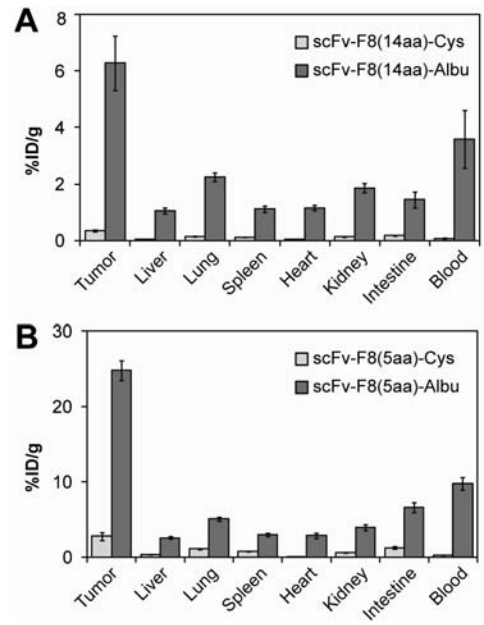

Figure 3. Biodistribution studies of radioiodinated scFv-F8-Cys antibodies and scFv-F8-Albu antibody derivatives 24 h after i.v. injection into F9 tumor bearing 129SvPas mice. Mean targeting results are expressed as %ID/g ± standard error (A) scFv-F8(14aa)-Cys and scFv-F8(14aa)-Albu (B) scFv-F8(5aa)-Cys and scFv-F8(5aa)-Albu.

modification of the antibody derivatives (Figure 2). In the spectra of the chemically modified albumin-binding antibody derivatives (scFv-F8(5aa)-Albu and scFv-F8(14aa)-Albu), two newly emerging peaks were identified, which corresponded to the C-terminal peptides modified with the Albu tag (Figure 2C,D). As expected, scFv-F8-Cys preparations displayed identical performance in BIAcore analysis in the presence or in the absence of chemical modification with the Albu tag (Supporting Information Figure 2).

Tumor Targeting Properties of Albumin-Binding Antibody Derivatives. The tumor targeting properties of scFv-F8(5aa)-Albu and scFv-F8(14aa)-Albu were investigated by quantitative biodistribution analysis in mice bearing F9 tumors, following antibody radioiodination, using conventional organ counting (*9, 27, 30, 34*). After radioiodination, full retention of immunoreactivity and of albumin-binding activity for the conjugates was confirmed by affinity chromatography (see Experimental Procedures). In a first *in vivo* experiment, biodistribution results (expressed as percent injected dose per gram of tissue; %ID/g) for scFv-F8(14aa) and scFv-F8(5aa) were studied 24 h post injection, in the presence or the absence of the Albu tag (Figure 3). In line with previous reports for scFv fragments devoid of a C-terminal cysteine residue, the homodimeric scFv-F8(5aa)-Cys antibody displayed a greater tumor uptake (2.8%ID/g) compared to the monomeric scFv-F8(14aa)-Cys antibody (0.4%ID/g). In both cases, the antibody exhibited a preferential accumulation at the tumor site (Figure 3). As expected, the chemical modification of the recombinant antibodies with the albumin-binding moiety resulted in a dramatic increase of antibody uptake at the tumor site (6.3% ID/g for scFv-F8(14aa)-Albu, and 24.8%ID/g for scFv-F8(5aa)-Albu), as a result of a slower blood clearance profile (3.6% ID/g for scFv-F8(14aa)-Albu, and 9.8%ID/g for scFv-F8(5aa)-Albu).

In order to study in more detail the pharmacokinetic properties of the antibody derivative which displayed the highest tumor uptake (scFv-F8(5aa)-Albu), we performed a new series of biodistribution studies in F9 tumor bearing mice, sacrificing the animals at 3, 24, 48, and 72 h. Figure 4 presents the biodistribution results, expressed as %ID/g and as tumor/organ ratios. In Figure 4A,B, the uncorrected data are presented, while in Figure 4C,D, a correction for the increase of tumor mass during the experimental protocol was applied. Indeed, F9 tumors have a doubling time of approximately 1−2 days (*34*), with the result that the antibody dose in the tumor mass gets "diluted" while the neoplastic mass increases in size. The maximal antibody uptake in the tumor was observed at 48 h (25%ID/g and 64%ID/g in the absence or presence of the correction for tumor growth, respectively; Figure 4A,C), but in general, we observed an excellent antibody retention at the tumor site, in line with previous preclinical and clinical studies obtained with antibodies specific to the extradomain B (EDB) of fibronectin (*30, 36−39*). From the data of Figure 4A, blood clearance can be fitted with a single exponential, corresponding to a half-life of 1000 min. By contrast, unmodified scFv fragments typically exhibit a monoexponential clearance profile, with half-lives of approximately 20−30 min (*30, 34*). As a consequence of antibody clearance from blood and tissues, tumor/organ ratios were found to continuously increase through the whole duration of the biodistribution experiment (Figure 4B,D). As expected, the radiolabeled antibody was found to preferentially localize at tumor neovascular sites (*27*), as evidenced by *ex vivo* microautoradiographic analysis (Figure 5).

DISCUSSION

In this article, we have shown that the site-specific modification of the tumor-targeting recombinant antibody F8 with a small organic chemical moiety, conferring high-affinity binding to albumin, resulted in an ∼10-fold increase in antibody tumor uptake and in an ∼35-fold reduction of blood clearance rate. When correcting for tumor growth during the biodistribution studies, tumor uptake values >60% ID/g could be observed at optimal time points (48 h), with excellent tumor/organ ratios (Figure 3).

The observation that antibody uptake in the tumor grows as a consequence of a corresponding increase of serum half-life is in line with the results of previous biodistribution studies, in which the targeting properties of antibodies in different formats (e.g., scFv, mini-antibody, IgG) were compared (*30, 37, 38, 40, 41*). Similarly, chemical modification of antibody fragments with PEG or polysialic acid polymers has previously been shown to

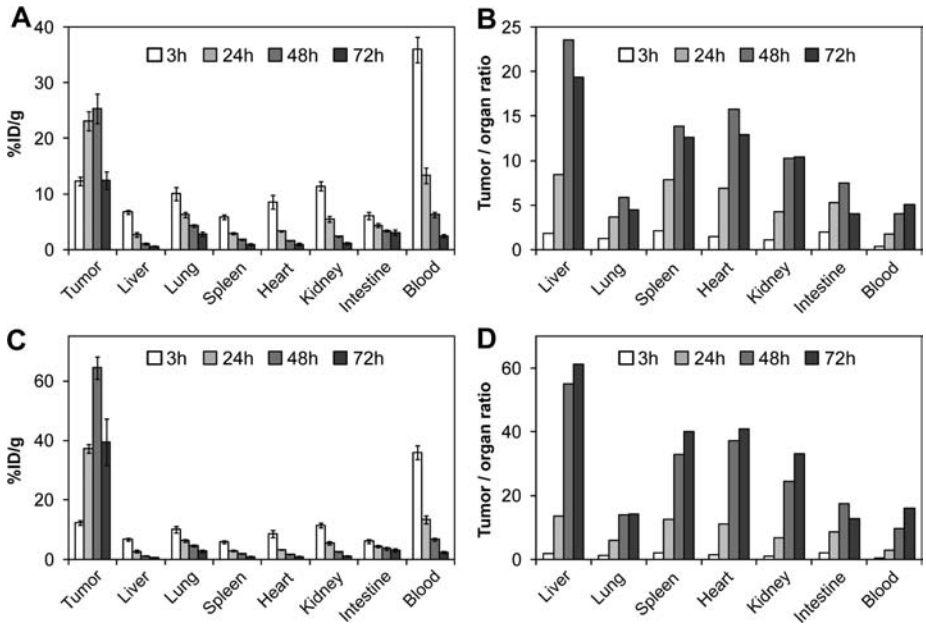

Figure 4. Biodistribution studies of radioiodinated scFv-F8(5aa)-Albu 3, 24, 48, and 72 h after i.v. injection into F9 tumor bearing 129SvPas mice. Results are depicted as follows: (A) %ID/g of all four time points and (B) the tumor to organ ratio. In addition, panels (C) and (D) present biodistribution data results corrected for the tumor volume increase, during the time period between injection and sacrifice of the mice.

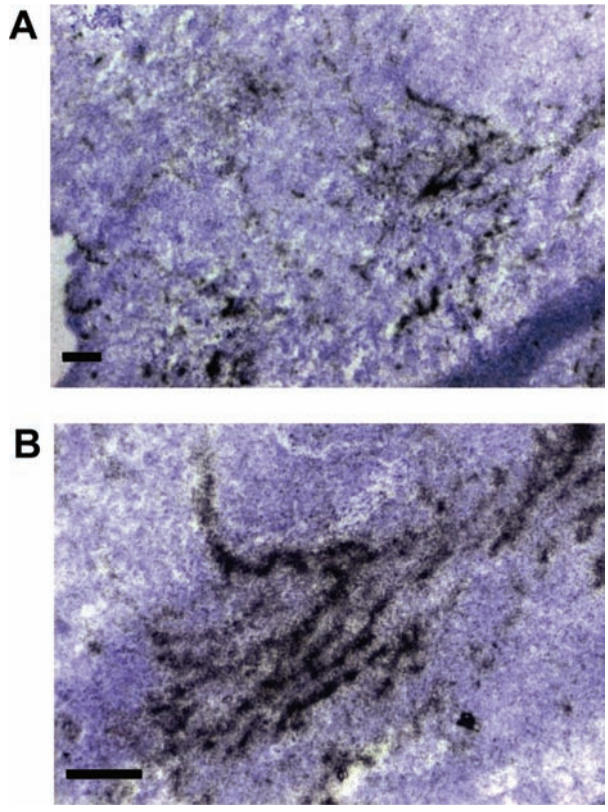

Figure 5. Microautoradiography of a 10-μm-thick F9 tumor section, obtained 24 h after i.v. injection of ^{125}I-scFv-F8(5aa)-Albu. (A,B) Scale bar = 100 μm.

considerably extend serum half-lives and tumor uptake values (*13*−*15*). However, Albu-tagging technology as described in this article may have the potential advantage of yielding a single molecular species in mass spectrometric analysis (Figure 1), thus facilitating batch-to-batch comparison, while polymer-based modification strategies typically exhibit a distribution of molecular weights.

In the past, we had performed C-terminal tagging of scFv fragments with cysteine residues, using *E. coli* and *P. pastoris* expression systems (*35, 42*). In our hands, the CHO-cell based expression strategy described in this article appears to be particularly suited for pharmaceutical development programs, in view of the good expression yields, excellent product homogeneity, and absence of proteolytic degradation of the C-terminal tail. Monomeric and noncovalent homodimeric preparations of scFv-F8 can be quantitatively separated and recovered (*31, 43, 44*) by gel filtration or by ion exchange chromatography, with no detectable subsequent interconversion, if the antibodies are stored at micromolar concentrations (or higher) in physiological solution at neutral pH and room temperature, over a period of several weeks. The site-specific and stoichiometric modification of recombinant antibody fragments described in this article for Albu tags may be adapted in order to accommodate other conjugation strategies (e.g., drugs with cleavable linkers, photosensitizers) (*45*−*48*).

ACKNOWLEDGMENT

Financial support from the ETH Zürich (ETHIRA Grant), the Swiss National Science Foundation (grant # 3100A0-105919/1), the Swiss Cancer League (Robert-Wenner-Award), the SWISSBRIDGE-Stammbach Foundation and European Union Projects IMMUNO-PDT (grant # LSHC-CT-2006-037489), DIANA (grant # LSHB-CT-2006-037681), and ADAMANT (HEALT-F2-2008-201342) is gratefully acknowledged. Furthermore, we would like to thank Dr. Christoph Schliemann and Dr. Christoph Rösli for their technical help.

Supporting Information Available: Additional figures as described in the text. This material is available free of charge via the Internet at http://pubs.acs.org.

LITERATURE CITED

(1) Walsh, G. (2005) Biopharmaceuticals: recent approvals and likely directions. *Trends Biotechnol. 23*, 553–8.
(2) Schrama, D., Reisfeld, R. A., and Becker, J. C. (2006) Antibody targeted drugs as cancer therapeutics. *Nat. Rev. Drug Discovery 5*, 147–59.

(3) Neri, D., and Bicknell, R. (2005) Tumour vascular targeting. *Nat. Rev. Cancer 5*, 436–46.
(4) Holliger, P., and Hoogenboom, H. (1998) Antibodies come back from the brink. *Nat. Biotechnol. 16*, 1015–6.
(5) Binz, H. K., Amstutz, P., and Pluckthun, A. (2005) Engineering novel binding proteins from nonimmunoglobulin domains. *Nat. Biotechnol. 23*, 1257–68.
(6) Skerra, A. (2007) Alternative non-antibody scaffolds for molecular recognition. *Curr. Opin. Biotechnol. 18*, 295–304.
(7) Orlova, A., Magnusson, M., Eriksson, T. L., Nilsson, M., Larsson, B., Hoiden-Guthenberg, I., Widstrom, C., Carlsson, J., Tolmachev, V., Stahl, S., and Nilsson, F. Y. (2006) Tumor imaging using a picomolar affinity HER2 binding affibody molecule. *Cancer Res. 66*, 4339–48.
(8) Begent, R. H., Verhaar, M. J., Chester, K. A., Casey, J. L., Green, A. J., Napier, M. P., Hope-Stone, L. D., Cushen, N., Keep, P. A., Johnson, C. J., Hawkins, R. E., Hilson, A. J., and Robson, L. (1996) Clinical evidence of efficient tumor targeting based on single-chain Fv antibody selected from a combinatorial library. *Nat. Med. 2*, 979–84.
(9) Viti, F., Tarli, L., Giovannoni, L., Zardi, L., and Neri, D. (1999) Increased binding affinity and valence of recombinant antibody fragments lead to improved targeting of tumoral angiogenesis. *Cancer Res. 59*, 347–52.
(10) Adams, G. P., Schier, R., McCall, A. M., Crawford, R. S., Wolf, E. J., Weiner, L. M., and Marks, J. D. (1998) Prolonged in vivo tumour retention of a human diabody targeting the extracellular domain of human HER2/neu. *Br. J. Cancer 77*, 1405–12.
(11) Orlova, A., Tolmachev, V., Pehrson, R., Lindborg, M., Tran, T., Sandstrom, M., Nilsson, F. Y., Wennborg, A., Abrahmsen, L., and Feldwisch, J. (2007) Synthetic affibody molecules: a novel class of affinity ligands for molecular imaging of HER2-expressing malignant tumors. *Cancer Res. 67*, 2178–86.
(12) Gebauer, M., and Skerra, A. (2009) Engineered protein scaffolds as next-generation antibody therapeutics. *Curr. Opin. Chem. Biol*.
(13) Pedley, R. B., Boden, J. A., Boden, R., Begent, R. H., Turner, A., Haines, A. M., and King, D. J. (1994) The potential for enhanced tumour localisation by poly(ethylene glycol) modification of anti-CEA antibody. *Br. J. Cancer 70*, 1126–30.
(14) Chapman, A. P., Antoniw, P., Spitali, M., West, S., Stephens, S., and King, D. J. (1999) Therapeutic antibody fragments with prolonged in vivo half-lives. *Nat. Biotechnol. 17*, 780–3.
(15) Constantinou, A., Epenetos, A. A., Hreczuk-Hirst, D., Jain, S., Wright, M., Chester, K. A., and Deonarain, M. P. (2009) Site-specific polysialylation of an antitumor single-chain Fv fragment. *Bioconjugate Chem. 20*, 924–931.
(16) Dinesen, L., and Travis, S. (2007) Targeting nanomedicines in the treatment of Crohn's disease: focus on certolizumab pegol (CDP870). *Int. J. Nanomed. 2*, 39–47.
(17) Dou, W. F., Lei, J. Y., Zhang, L. F., Xu, Z. H., Chen, Y., and Jin, J. (2008) Expression, purification, and characterization of recombinant human serum albumin fusion protein with two human glucagon-like peptide-1 mutants in *Pichia pastoris*. *Protein Expression Purif. 61*, 45–9.
(18) Smith, B. J., Popplewell, A., Athwal, D., Chapman, A. P., Heywood, S., West, S. M., Carrington, B., Nesbitt, A., Lawson, A. D., Antoniw, P., Eddelston, A., and Suitters, A. (2001) Prolonged in vivo residence times of antibody fragments associated with albumin. *Bioconjugate Chem. 12*, 750–6.
(19) Dennis, M. S., Zhang, M., Meng, Y. G., Kadkhodayan, M., Kirchhofer, D., Combs, D., and Damico, L. A. (2002) Albumin binding as a general strategy for improving the pharmacokinetics of proteins. *J. Biol. Chem. 277*, 35035–43.
(20) Cortez-Retamozo, V., Lauwereys, M., Hassanzadeh Gh, G., Gobert, M., Conrath, K., Muyldermans, S., De Baetselier, P., and Revets, H. (2002) Efficient tumor targeting by single-domain antibody fragments of camels. *Int. J. Cancer 98*, 456–62.
(21) Tolmachev, V., Wallberg, H., Andersson, K., Wennborg, A., Lundqvist, H., and Orlova, A. (2009) The influence of Bz-DOTA and CHX-A″-DTPA on the biodistribution of ABD-fused anti-HER2 Affibody molecules: implications for (114m)In-mediated targeting therapy. *Eur. J. Nucl. Med. Mol. Imaging*.
(22) Dennis, M. S., Jin, H., Dugger, D., Yang, R., McFarland, L., Ogasawara, A., Williams, S., Cole, M. J., Ross, S., and Schwall, R. (2007) Imaging tumors with an albumin-binding Fab, a novel tumor-targeting agent. *Cancer Res. 67*, 254–61.
(23) Dumelin, C. E., Trussel, S., Buller, F., Trachsel, E., Bootz, F., Zhang, Y., Mannocci, L., Beck, S. C., Drumea-Mirancea, M., Seeliger, M. W., Baltes, C., Muggler, T., Kranz, F., Rudin, M., Melkko, S., Scheuermann, J., and Neri, D. (2008) A portable albumin binder from a DNA-encoded chemical library. *Angew. Chem., Int. Ed. Engl. 47*, 3196–201.
(24) Muro, A. F., Caputi, M., Pariyarath, R., Pagani, F., Buratti, E., and Baralle, F. E. (1999) Regulation of fibronectin EDA exon alternative splicing: possible role of RNA secondary structure for enhancer display. *Mol. Cell Biol. 19*, 2657–71.
(25) Kaspar, M., Zardi, L., and Neri, D. (2006) Fibronectin as target for tumor therapy. *Int. J. Cancer 118*, 1331–9.
(26) Rybak, J. N., Roesli, C., Kaspar, M., Villa, A., and Neri, D. (2007) The extra-domain A of fibronectin is a vascular marker of solid tumors and metastases. *Cancer Res. 67*, 10948–57.
(27) Villa, A., Trachsel, E., Kaspar, M., Schliemann, C., Sommavilla, R., Rybak, J. N., Rosli, C., Borsi, L., and Neri, D. (2008) A high-affinity human monoclonal antibody specific to the alternatively spliced EDA domain of fibronectin efficiently targets tumor neo-vasculature in vivo. *Int. J. Cancer 122*, 2405–13.
(28) Huston, J. S., Levinson, D., Mudgett-Hunter, M., Tai, M. S., Novotny, J., Margolies, M. N., Ridge, R. J., Bruccoleri, R. E., Haber, E., Crea, R., et al. (1988) Protein engineering of antibody binding sites: recovery of specific activity in an anti-digoxin single-chain Fv analogue produced in *Escherichia coli*. *Proc. Natl. Acad. Sci. U.S.A. 85*, 5879–83.
(29) Li, E., Pedraza, A., Bestagno, M., Mancardi, S., Sanchez, R., and Burrone, O. (1997) Mammalian cell expression of dimeric small immune proteins (SIP). *Protein Eng. 10*, 731–6.
(30) Borsi, L., Balza, E., Bestagno, M., Castellani, P., Carnemolla, B., Biro, A., Leprini, A., Sepulveda, J., Burrone, O., Neri, D., and Zardi, L. (2002) Selective targeting of tumoral vasculature: comparison of different formats of an antibody (L19) to the ED-B domain of fibronectin. *Int. J. Cancer 102*, 75–85.
(31) Holliger, P., Prospero, T., and Winter, G. (1993) "Diabodies": small bivalent and bispecific antibody fragments. *Proc. Natl. Acad. Sci. U.S.A. 90*, 6444–8.
(32) Dolezal, O., Pearce, L. A., Lawrence, L. J., McCoy, A. J., Hudson, P. J., and Kortt, A. A. (2000) ScFv multimers of the anti-neuraminidase antibody NC10: shortening of the linker in single-chain Fv fragment assembled in V(L) to V(H) orientation drives the formation of dimers, trimers, tetramers and higher molecular mass multimers. *Protein Eng. 13*, 565–74.
(33) Zuberbuhler, K., Palumbo, A., Bacci, C., Giovannoni, L., Sommavilla, R., Kaspar, M., Trachsel, E., and Neri, D. (2009) A general method for the selection of high-level scFv and IgG antibody expression by stably transfected mammalian cells. *Protein Eng. Des. Sel. 22*, 169–74.
(34) Tarli, L., Balza, E., Viti, F., Borsi, L., Castellani, P., Berndorff, D., Dinkelborg, L., Neri, D., and Zardi, L. (1999) A high-affinity human antibody that targets tumoral blood vessels. *Blood 94*, 192–8.
(35) Berndorff, D., Borkowski, S., Moosmayer, D., Viti, F., Muller-Tiemann, B., Sieger, S., Friebe, M., Hilger, C. S., Zardi, L., Neri, D., and Dinkelborg, L. M. (2006) Imaging of tumor angiogenesis using 99mTc-labeled human recombinant anti-ED-B fibronectin antibody fragments. *J. Nucl. Med. 47*, 1707–16.
(36) Santimaria, M., Moscatelli, G., Viale, G. L., Giovannoni, L., Neri, G., Viti, F., Leprini, A., Borsi, L., Castellani, P., Zardi, L., Neri, D., and Riva, P. (2003) Immunoscintigraphic detection of the ED-B domain of fibronectin, a marker of angiogenesis, in patients with cancer. *Clin. Cancer Res. 9*, 571–9.
(37) Berndorff, D., Borkowski, S., Sieger, S., Rother, A., Friebe, M., Viti, F., Hilger, C. S., Cyr, J. E., and Dinkelborg, L. M.

(2005) Radioimmunotherapy of solid tumors by targeting extra domain B fibronectin: identification of the best-suited radioimmunoconjugate. *Clin. Cancer Res. 11*, 7053s–7063s.

(38) Tijink, B. M., Neri, D., Leemans, C. R., Budde, M., Dinkelborg, L. M., Stigter-van Walsum, M., Zardi, L., and van Dongen, G. A. (2006) Radioimmunotherapy of head and neck cancer xenografts using 131I-labeled antibody L19-SIP for selective targeting of tumor vasculature. *J. Nucl. Med. 47*, 1127–35.

(39) Sauer, S., Erba, P. A., Petrini, M., Menrad, A., Giovannoni, L., Grana, C., Hirsch, B., Zardi, L., Paganelli, G., Mariani, G., Neri, D., Durkop, H., and Menssen, H. D. (2009) Expression of the oncofetal ED-B-containing fibronectin isoform in hematologic tumors enables ED-B-targeted 131I-L19SIP radioimmunotherapy in Hodgkin lymphoma patients. *Blood 113*, 2265–74.

(40) Sundaresan, G., Yazaki, P. J., Shively, J. E., Finn, R. D., Larson, S. M., Raubitschek, A. A., Williams, L. E., Chatziioannou, A. F., Gambhir, S. S., and Wu, A. M. (2003) 124I-labeled engineered anti-CEA minibodies and diabodies allow high-contrast, antigen-specific small-animal PET imaging of xenografts in athymic mice. *J. Nucl. Med. 44*, 1962–9.

(41) Adams, G. P., Schier, R., Marshall, K., Wolf, E. J., McCall, A. M., Marks, J. D., and Weiner, L. M. (1998) Increased affinity leads to improved selective tumor delivery of single-chain Fv antibodies. *Cancer Res. 58*, 485–90.

(42) Bhadra, U., Pal-Bhadra, M., and Birchler, J. A. (1999) Role of the male specific lethal (msl) genes in modifying the effects of sex chromosomal dosage in Drosophila. *Genetics 152*, 249–68.

(43) Atwell, J. L., Breheney, K. A., Lawrence, L. J., McCoy, A. J., Kortt, A. A., and Hudson, P. J. (1999) scFv multimers of the anti-neuraminidase antibody NC10: length of the linker between VH and VL domains dictates precisely the transition between diabodies and triabodies. *Protein Eng. 12*, 597–604.

(44) Griffiths, A. D., Malmqvist, M., Marks, J. D., Bye, J. M., Embleton, M. J., McCafferty, J., Baier, M., Holliger, K. P., Gorick, B. D., Hughes-Jones, N. C., et al. (1993) Human anti-self antibodies with high specificity from phage display libraries. *EMBO J. 12*, 725–34.

(45) Carter, P. J., and Senter, P. D. (2008) Antibody-drug conjugates for cancer therapy. *Cancer J. 14*, 154–69.

(46) Fabbrini, M., Trachsel, E., Soldani, P., Bindi, S., Alessi, P., Bracci, L., Kosmehl, H., Zardi, L., Neri, D., and Neri, P. (2006) Selective occlusion of tumor blood vessels by targeted delivery of an antibody-photosensitizer conjugate. *Int. J. Cancer 118*, 1805–13.

(47) Bhatti, M., Yahioglu, G., Milgrom, L. R., Garcia-Maya, M., Chester, K. A., and Deonarain, M. P. (2008) Targeted photodynamic therapy with multiply-loaded recombinant antibody fragments. *Int. J. Cancer 122*, 1155–63.

(48) Birchler, M., Viti, F., Zardi, L., Spiess, B., and Neri, D. (1999) Selective targeting and photocoagulation of ocular angiogenesis mediated by a phage-derived human antibody fragment. *Nat. Biotechnol. 17*, 984–8.

BC9002772

“A new strategy for the extension of the serum half-life of antibody fragments”

Sabrina Trüssel[‡], Christoph Dumelin[§], Katharina Frey[‡], Alessandra Villa[§], Fabian Buller[‡], Dario Neri[‡*]

Supporting Figure 1

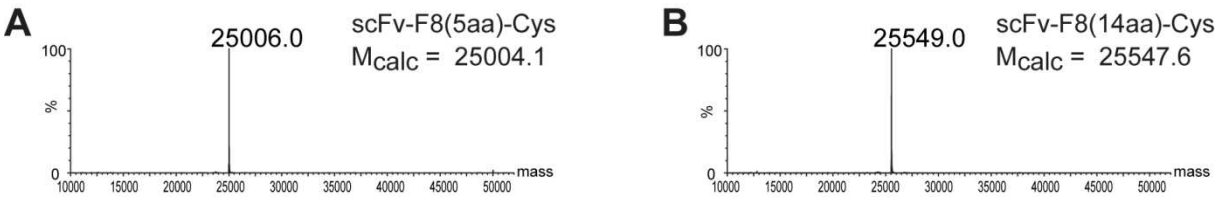

LC-ESI-MS characterization of the scFv-F8-Cys antibody fragments with (A) 5aa linker and (B) 14aa linker after deconvolution of the spectra.

Supporting Figure 2

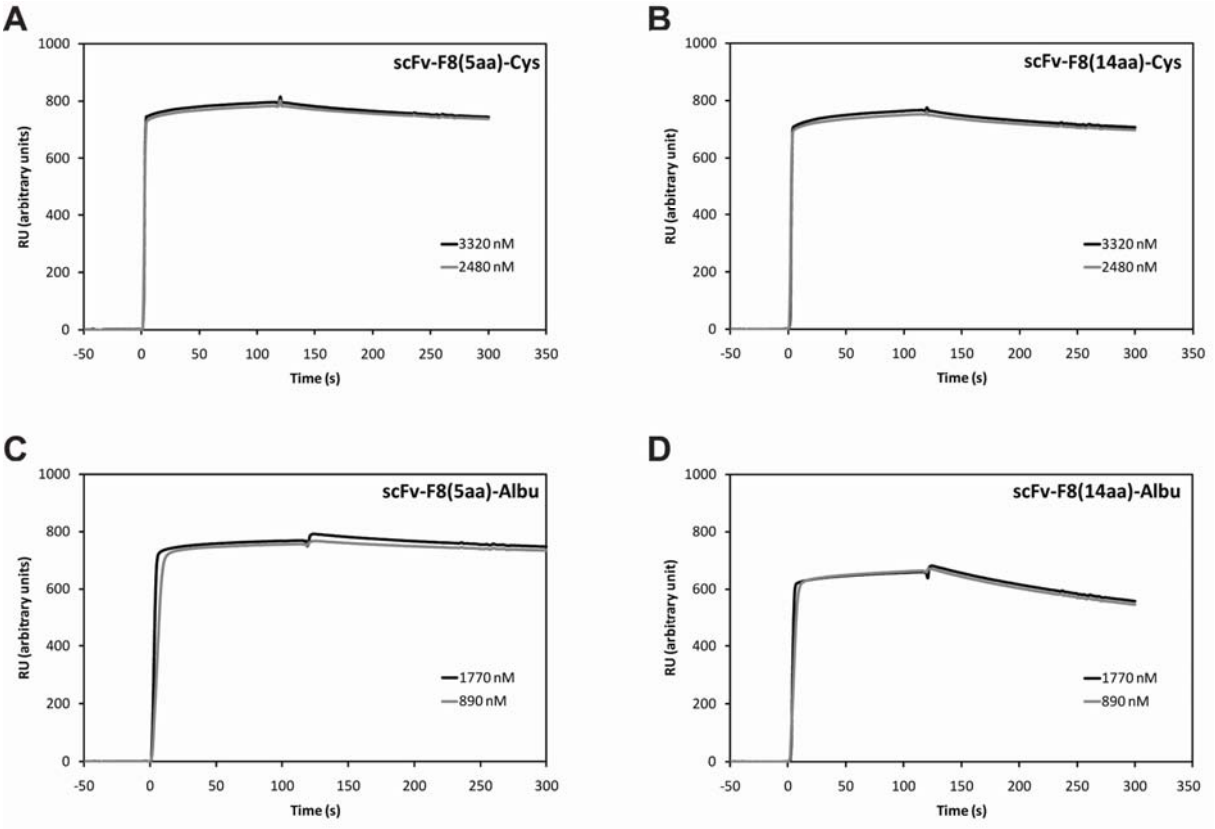

BIAcore analysis of the binding of scFv-F8 in the presence or absence of the Albu tag to the antigen 11A12. Binding plots of homodimeric scFv-F8(5aa)-Cys and scFv-F8(5aa)-Albu are depicted in panel (A) and (C), respectively; binding plots of scFv-F8(14aa)-Cys and scFv-F8(14aa)-Albu are reported in panel (B) and (D), respectively.

Impact of Molecular Weight in Four-Branched Star Vectors with Narrow Molecular Weight Distribution on Gene Delivery Efficiency

Yasushi Nemoto,[†,‡,§] Alexey Borovkov,[†,‡] Yue-Min Zhou,[†,||] Yoshiaki Takewa,[||] Eisuke Tatsumi,[||] and Yasuhide Nakayama*[,†,‡]

Department of Bioengineering and Department of Artificial Organs, Advanced Medical Engineering Center, National Cardiovascular Center Research Institute, Division of Molecular Chemistry, Graduate School of Engineering, Hokkaido University, and Development Department, Chemical Products Development Department, Bridgestone Company. Received June 29, 2009; Revised Manuscript Received September 20, 2009

A series of star-shaped cationic polymers, termed star vectors (SVs), has been developed as effective nonviral gene delivery carriers. In this study, we separated SVs into several fractions having different molecular weights with very narrow molecular weight distributions in order to examine in detail the influence of the molecular weight of the SVs on the gene transfection efficiency. As a model compound for several types of SVs, 4-branched poly(*N*,*N*-dimethylaminopropyl acrylamide) having a molecular weight (M_n) of approximately 35 kDa and polydispersity of 1.6 was prepared by iniferter-based radical polymerization. The SVs were separated using size-exclusion chromatography to obtain seven fractions having M_n ranging from 27 kDa to 73 kDa with polydispersity ranging from 1.1 to 1.2. All the fractionated SVs have similar pH of 10.2−10.4 and were able to interact with and condense luciferase-encoding plasmid deoxyribonucleic acid (DNA) to yield SV/DNA polyplexes. A water-soluble tetrazolium-1 (WST) assay showed that all SVs had minimal cellular cytotoxicity under an N/P charge ratio of 10. The critical micellar concentration decreased with an increase in the M_n of the fractionated SVs; however, the particle size of the polyplexes, exclusion activity of ethidium bromide, and ζ-potential of the polyplexes increased. An in vitro evaluation using COS-1 cells at an N/P ratio of 10 showed that transfection activity increased almost linearly with M_n. The highest transfection activity was obtained for SVs with the highest M_n (73 kDa), which was over 7 times that for the SVs with the lowest M_n (27 kDa), the nonfractionated original SV, or PEI standard. The transfection efficiency was more correlated with the amphiphilicity or hydrophobicity of the SVs and the surface potential and condensate density of the polyplexes than with the particle size.

INTRODUCTION

Almost all synthetic cationic polymers can spontaneously condense polyanionic deoxyribonucleic acid (DNA) to form electrostatic complexes, termed polyplexes, which is a requirement for gene transfer in most cell lines (*1*−*4*). The gene transfection efficiency of these cationic polymers strongly depends on their structural, chemical, and physical properties. Molecular weight is one of the greatest influences on gene transfection efficiency. This influence has been evaluated by many researchers; it was found that the gene transfection efficiency, in general, was high for cationic polymers having high molecular weight (*5*−*12*). Godbey et al. reported that linear polyethylenimine (PEI) having a molecular weight of 1.8 kDa or less showed no gene transfection activity; however, PEI having a molecular weight higher than 1.8 kDa showed gene transfection activity, which peaked at a molecular weight of 70 kDa (*13*). On the other hand, Park et al. reported that there was no difference between the gene transfection efficiencies of linear PEI having molecular weights of 50 kDa and 200 kDa (*14*). Hennink et al. reported that poly(*N*,*N*-dimethylaminoethyl methacrylate) (PDMAEMA) having a molecular weight of 60 kDa or less did not exhibit gene transfection activity; however, PDMAEMA having a molecular weight of 309 kDa and more exhibited gene transfection activity (*15*). A similar molecular weight dependency was observed in a higher molecular weight region. Recently, the influence of molecular weight on PDMAEMA-mediated DNA delivery was investigated by Long et al. (*16*). Extremely high molecular weight PDMAEMA showed high transfection activity among five molecular weights ranging from 43 to 915 kDa. However, the polymers examined, unfortunately, had very wide molecular weight distribution. In our previous study, 4-branched poly(*N*,*N*-dimethylaminopropyl acrylamide) (PDMAPAAm) had molecular weights of approximately 10, 20, and 50 kDa and polydispersity of approximately 1.4, which were prepared by living radical polymerization (*17*). Although detailed examination was not performed, the luciferase expression increased with the molecular weight.

The objective of our study was to elucidate structure−transfection relationships in polycation-mediated plasmid DNA delivery. To improve the efficiency of gene transfection, several types of star-shaped polymers were attempted (*17*−*21*). We recently designed a novel nonviral vector, i.e., a star vector (SV), which is a star-shaped and cation-based polymer (*22*) or its cross-linked complex (*23*). The SVs have been shown to be effective in inducing gene expression from plasmid DNA (pDNA) and gene silencing from siRNA or shRNA in vitro and in vivo (*24*). In addition, in combination with ligands such as C45D18 peptide (*25*), which promotes nuclear trafficking, or an integrin-binding

* To whom correspondence should be addressed. Yasuhide Nakayama, Department of Bioengineering, Advanced Medical Engineering Center, National Cardiovascular Center Research Institute, Osaka, 565-8565, Japan. Tel: +81-6-6833-5004 (ex.2624); Fax: +81-6-6872-8090; E-mail: nakayama@ri.ncvc.go.jp.

† Department of Bioengineering, National Cardiovascular Center Research Institute.

‡ Hokkaido University.

§ Bridgestone Company.

|| Department of Artificial Organs, National Cardiovascular Center Research Institute.

10.1021/bc900283h CCC: $40.75 © 2009 American Chemical Society
Published on Web 11/09/2009

RGD peptide (*26*), DNA can be selectively delivered to macrophages or endothelial cells.

In this study, we investigated the influence of molecular weight with narrow molecular weight distribution in polycation on the transfection activity. In general, synthetic polymers have a range of molecular weights, even if they are synthesized by living radical polymerization. In other words, these polymers are a mixture of molecules having different molecular weights. Therefore, molecular weight distribution is an important factor for characterizing polymers. Unfortunately, the distribution, including polydispersity, has not been described in most reports in the field of gene delivery. In the evaluation of transfection activity, use of uniform polymers is considered ideal. Therefore, we attempted to separate the SV into seven fractions having different molecular weights with narrow molecular weight distributions in order to examine the effect of molecular weight of the SV in terms of gene transfection efficiency. Previously, we designed a series of branched cationic polymers, linear and 3-, 4-, or 6-branched SVs, prepared to have the same molecular weights of about 18 kDa. The relative gene expression efficiency increased in the degree of branching that may affect the cationic charge density. On the other hand, iniferters for preparation of 6-branched SVs were very hard to treat because of their lower solubility in polymerization solvents. Therefore, as a model compound, in this study, we selected 4-branched SV. Physicochemical properties including pH and the critical micellar concentration of the fractionated SVs, particle size, exclusion efficiency of ethidium bromide, and ζ-potential of SV/DNA polyplexes were measured to determine the reason for the molecular-weight-dependent gene-transfection efficiency change.

EXPERIMENTAL SECTION

Materials. 1,2,4,5-Tetrakis(*N,N*-diethyldithiocarbamylmethyl)benzene (iniferter) was synthesized according to our previously reported method (*17*). DMAPAAm purchased from Tokyo Kasei Co. (Tokyo, Japan) was used after distillation. Other solvents and chemical reagents, all of which were of special reagent grade, were purchased from Kanto Chemical Co. (Tokyo, Japan) or Aldrich (Milwaukee, WI) and were used without further purification. pGL3 control vector (5266 bp, Promega Inc., Tokyo, Japan) encoding luciferase was used as luciferase reporter plasmid DNA; it was amplified in competent *Escherichia coli* (Promega Inc.) cells and purified using Maxiprep according to a protocol of QIAGEN (Tokyo, Japan). ExGen 500 (linear 22 kDa PEI) was obtained from Cosmo Bio Co., Ltd. (Tokyo, Japan).

Synthesis and Fractionation Separation of SV. Iniferter (45.6 mg, 63 mmol) was dissolved in approximately 20 mL of toluene. DMAPAAm (7.88 g, 50.5 mmol) was added to the solution. The total volume of the mixture was increased to 50 mL with toluene. The final concentrations of the iniferter and monomer were 5.0 mM and 1.0 M, respectively. The mixture was poured into a hard-glass cubic cell (40 mm $\times$ 40 mm; glass thickness of 3 mm) and bubbled with N_2 gas (G1 grade, 99.9999% purity or more, Japan Fine Products Co., Kanagawa, Japan) at a flow rate of 2 L/min for 10 min. The solution was irradiated for 30 min with ultraviolet (UV) light (light intensity of 2.5 mW/cm^2) using a 300 W xenon lamp (MAX-301, Asahi Spectra Co., Ltd., Tokyo, Japan). The light intensity was adjusted to 2.5 mW/cm^2 using a photometer (UIT-150 with UVD-405 detector, Ushio, Tokyo). The reaction mixture was concentrated to approximately 10 mL using a rotary evaporator and poured into 1 L of diethyl ether to obtain a polymeric precipitate. The diethyl ether solution supernatant was removed by decantation. Reprecipitation was carried out six times in a chloroform/diethyl ether system. The final precipitate was dried under vacuum and dissolved in an adequate quantity of H_2O. The resultant aqueous solution was filtered with a disposable syringe filter unit having a pore size of 0.22 μm (Mixed Cellulose Ester, Toyo Roshi Ltd., Tokyo, Japan) and freeze−dried for 72 h using a vacuum pump (GCD136X, ULVAC, Tokyo) and freeze−dryer (FUD 2200, EYELA, Tokyo) to yield the SV. The molecular weight of the SV was determined by gel permeation chromatography (GPC) analysis as 35 kDa (polydispersity; 1.6). ^{1}H NMR measurements (300 MHz, in chloroform-d_1) were δ 1.5−1.7, 1.8−2.0, 2.1−2.2, 2.2−2.4, 3.0−3.2, and 7.4−7.8.

The fractionation separation of SVs was performed by GPC (LC-9101, Japan Analytical Industry Co., Ltd. Tokyo, Japan) with a styrene−divinylbenzene gel column (JAIGEL-2H-40, JAIGEL-3H-40, 40 mm $\times$ 600 mm) and chloroform mobile phase with 50 mM triethylamine. The flow rate of the mobile phase was adjusted to 10 mL/min.

General Procedures. UV/visible (VIS) absorption spectra were recorded using a spectrophotometer (U-1800, Hitachi, Tokyo). GPC of *N,N*-dimethylformamide with 30 mM lithium bromide for molecular weight measurements was carried out with a high-performance liquid chromatography system (LC-10Avp, Shimadzu, Kyoto, Japan) and columns (Asahipack GF-710HQ and Asahipack GF-510HQ, Shodex, Tokyo, Japan) that were calibrated for molecular weight with narrow weight distribution poly(ethylene glycol) standards. The mean diameter was determined by static light scattering (SLS) on a Zeta Sizer Nano-ZS system (Sysmex, Kobe, Japan).

Critical Micellar Concentration. The critical micellar concentration of the SV was determined by dye (1,6-diphenyl-1,3,5-hexatriene) solubilization into a water assay. SVs were dissolved into deionized water and adjusted to aqueous solutions having concentrations of 0.08, 0.10, 1.25, 2.50, 5.00, 10.0, 25.0, 50.0, and 100 mg/mL. Ten microliters of the 1,6-diphenyl-1,3,5-hexatriene solution, prepared by dissolving 2.2 mg of 1,6-diphenyl-1,3,5-hexatriene into 25 mL of methanol with sonication in the dark for 10 min, was added to 1 mL of the SV solutions and incubated at room temperature in a dark condition for 6 h. A reference solution mixture was prepared by adding 10 μL of the 1,6-diphenyl-1,3,5-hexatriene solution to 1 mL of deionized water. UV absorption spectra of these solution mixtures were measured at 365 nm using a UV/vis spectrophotometer. The absorption at 365 nm was plotted against the concentration of the SV, and the crossing point of extrapolated straight lines for the low-concentration region and high-concentration region was defined as a critical micellar concentration of the SV.

Preparation of Polyplexes. SVs were dissolved in a saline solution at a concentration of 0.24 μg/μL. 60 μL aliquots of the SV solution were mixed with 90 μL of Tris-HCl buffered saline solution (pH 7.4) containing plasmid DNA (pGL3-control) at a concentration of 3.33×10^{-2} μg/μL at room temperature. The solutions (total volume of 150 μL, plasmid concentration of 20 μg/mL) were mixed using a pipet to obtain polyplexes at a charge (N/P) ratio of 10.

Mean diameters of the polyplexes in a saline solution were obtained by dynamic light scattering (DLS) using an ELS-8000 system (Otsuka Co., Osaka, Japan) equipped with a 10 mW He−Ne laser by cumurant analysis in multimodal. Since data of the diameters were reproducible ($n = 4$, SD < 10%), only the average values have been described.

The ζ-potentials of the polyplexes in water solution were measured by employing a ζ-potential meter in the Zeta Sizer Nano-ZS system (Sysmex) at 25 °C. The concentration was set at 1/10 of the transfection concentration at an N/P ratio of 10.

Ethidium Bromide Exclusion Assay. DNA condensation was evaluated by the fluorescence of the polyplex solution upon addition of ethidium bromide solution. 90 μL of DNA (con-

centration of 33.3 μg/mL in 10 mM Tris-HCL buffer with 1 mM EDTA) was placed into each well of a 96-well microplate after 60 μL of 0.26, 0.51, 1.02, 1.28, or 2.56 μg/μL of aqueous SV solutions was placed so that the N/P ratio was from 0.25 to 10.0. A 37.5 μL quantity of aqueous ethidium bromide solution (20 μg/mL) was added to each well. After 10 min incubation, the fluorescence strength was measured by a Luminous CT-9000D fluorescence microplate reader (Dia-Iatron, Tokyo, Japan) with an excitation wavelength at 560 nm and emission wavelength at 620 nm. Results are given as relative fluorescence where 1.0 is fluorescence of the DNA solution without the SV and 0.0 is the remaining fluorescence of the non-intercalating ethidium bromide.

Cell Lines. COS-1 African green monkey kidney cells were purchased from Riken Cell Bank (Tsukuba, Japan). COS-1 cells were maintained in Dulbecco's modified Eagle's medium (DMEM; Gibco, Invitrogen Corp., Carlsbad, CA) with 10% fetal calf serum (FCS; Hyclone Laboratories Inc., Logan, UT), 200 units/mL penicillin (ICN Biomedicals Inc., Aurora, OH), and 200 mg/mL streptomycin (ICN Biomedicals Inc.) in a 5% CO_2 atmosphere at 37 °C.

In Vitro Transfection Assays. COS-1 cells were seeded at a density of 6×10^4 cells/well in a 24-well plate in medium containing 10% FCS and grown to reach 70−80% confluence prior to transfection for 24 h. Transfections were performed with 0.5 μg of plasmid DNA (pGL3-control) and 2.4 μg of SVs in 24-well dishes containing 0.2 mL of OPTI-MEM I (Gibco) for COS-1. After 3 h incubation, the cells were washed once with phosphate-buffered saline (PBS) (−) and cultured in 1 mL of appropriate medium for an additional 48 h. The medium was removed, and the cells were washed twice with PBS (−), lysed with 0.2 mL of cell lysis buffer (Promega, Madison, WI), and mixed by vortexing. The lysate was centrifuged at 15 000 rpm for 1 min at 4 °C, and 5 μL of the supernatant was analyzed for luciferase activity using a Luminous CT-9000D (Dia-Iatron, Tokyo, Japan) luminometer. The relative light unit (RLU)/s values were converted into the amount of luciferase (pg) using a standard luciferase curve, which was obtained by diluting recombinant luciferase (Promega) in lysis buffer. The protein concentrations of the cell lysates were measured by performing a Bio-Rad protein assay (Bio-Rad, Hercules, CA) with bovine serum albumin as a standard. The final amount of luciferase was determined as the amount of expressed luciferase (mole quantity) standardized to the total protein content of the cell lysate. Data are given as mean ± standard deviation (SD) of the mean ($n = 5$).

Cell Viability Assays. Cytotoxicity was assessed by performing a cell viability assay using the water-soluble tetrazolium (WST)-8 method (Dojindo, Kumamoto, Japan). The COS-1 cells were seeded 24 h prior to treatment in 96-well plates at 5000 cells/well. The cells were treated under the same conditions as those used for the luciferase assay; 6.2 μL of the transfection mixture, containing 0.124 μg of pDNA and 0.6 μg of the SV, was added to each well. The cells were treated under the appropriate conditions for 3 h, washed once with PBS, and cultured in 50 μL of DMEM (Gibco) containing 10% fetal calf serum for an additional 24 h. To each well, 10 μL of WST-8 reagent (5 mmol/L) was added. After 2 h incubation at 37 °C, the absorbance at 450 nm was determined using a Bio-Rad microplate reader (model 680). Data are given as mean ± SD ($n = 5$).

RESULTS

Fractionation Separation and Characterization of the SV. An SV having a molecular weight of 35 kDa and relatively wide polydispersity of 1.6 was prepared by the iniferter-based radical polymerization of a cationic monomer, DMAPAAm, from a 4-functional iniferter, 1,2,4,5-tetrakis(*N*,*N*-diethyldithiocarbamylmethyl)benzene (*17*). The chemical structure of the SV is shown in Figure 1. The SV was loaded with size exclusion chromatography to separate seven elution fractions with different molecular weights. GPC of each fraction showed that SVs having molecular weights of approximately 27, 32, 37, 42, 48, 56, and 73 kDa with narrow polydispersity of less than 1.2 were obtained (Table 1). Overlaid gel permeation chromatograms for all SV samples are shown in Figure 2. The molecular weight determined by GPC correlated well with the molecular weight calculated from the molecular diameter determined by SLS analysis (Table 1).

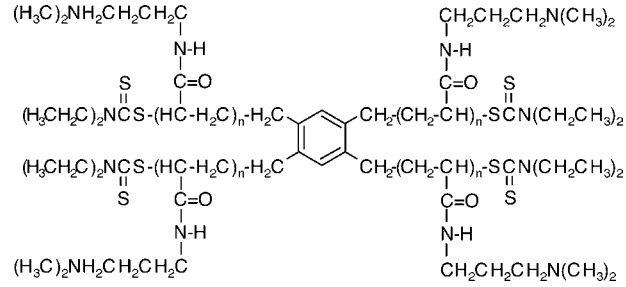

Figure 1. Chemical structure of 4-branched cationic star vector (SV).

Table 1. Molecular Weights of the Fractionated SVs

sample	M_n (kDa)[a]	M_w/M_n[a]	molecular diameter (nm)[b]	pH
crude	35	1.6	-	10.2
fraction 1	73	1.2	6.4	10.4
fraction 2	56	1.2	5.5	10.4
fraction 3	48	1.1	5.1	10.3
fraction 4	42	1.1	4.6	10.4
fraction 5	37	1.1	4.0	10.2
fraction 6	32	1.2	3.7	-
fraction 7	27	1.2	3.3	-

[a] Determined by GPC (PEO standard). [b] Determined by SLS.

SVs composed only of DMAPAAm units are strong cationic polymers originating from *N*,*N*-dimethylaminopropyl functional groups at the terminal of the polymer side chains, which are considered to be hydrophilic chemical compounds. All the SVs before and after fractionation had similar pH of 10.2−10.4. On the other hand, polymer main chains are considered to be hydrophobic; therefore, SVs having high molecular weights are considered to be amphiphilic compounds. Therefore, with an increasing concentration of the SVs, it is considered that the

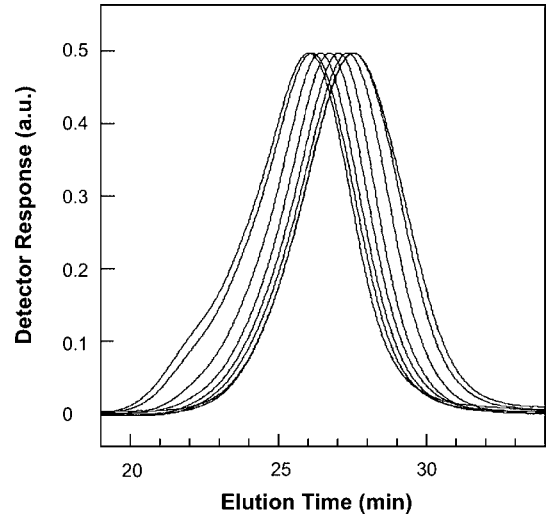

Figure 2. Overlaid GPC chromatograms of the fractionated SVs.

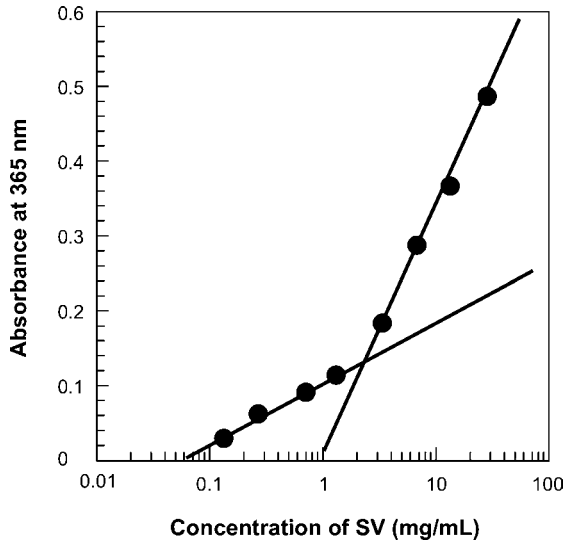

Figure 3. Behavior of the relationship between a concentration of the fractionated SV having molecular weight of 42 kDa and polydispersity of 1.1 and absorbance of an aqueous solution of the SV and 1,6-diphenyl-1,3,5-hexatriene. The critical micellar concentration of the SV having molecular weight of 42 kDa was determined to be 2.2 mg/mL, which was the cross point of two extrapolated straight lines in the low concentration region and high concentration region.

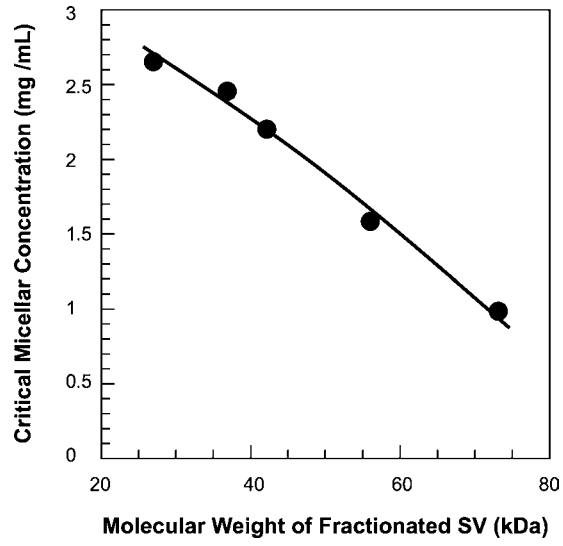

Figure 4. The relationship between the critical micellar concentration and molecular weight of the fractionated SVs.

SVs can usually form multimolecular micelles or micellar aggregates. 1,6-Diphenyl-1,3,5-hexatriene having λ_{max} of 365 nm is a hydrophobic compound, of which the water solution has no UV absorption at 365 nm. Figure 3 shows the typical relationship between the concentration of an SV having a molecular weight of 42 kDa and absorbance of the aqueous mixture of the SV and 1,6-diphenyl-1,3,5-hexatriene. As expected, with the formation of micelles with SVs, 1,6-diphenyl-1,3,5-hexatriene was partitioned into the micelles as hydrophobic cores and this resulted in the increase in the absorbance of an aqueous solution of SVs at 365 nm. The critical micellar concentration of the SV was determined to be 2.2 mg/mL, which was the crossing point of extrapolated straight lines for the low-concentration region and high-concentration region. The critical micellar concentrations of other SVs were determined using the same procedure. Figure 4 shows the relationship between the critical micellar concentration and molecular weight of the SVs.

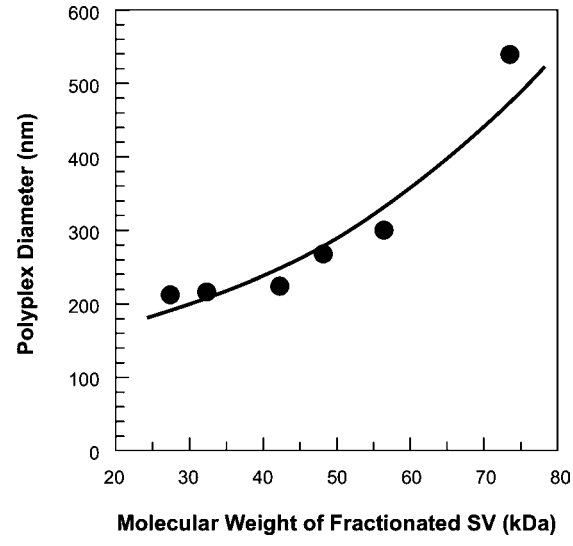

Figure 5. Mean diameters of the polyplexes prepared from the fractionated SVs and pDNA after 10 min.

The hydrophobicity increased with an increase in the molecular weight of the SVs.

Characterization of Polyplexes. Approximately 10 min after mixing a Tris-HCl-buffered solution of pDNA (pGL3-control) and a saline solution of the fractionated SVs at a charge (N/P) ratio of 10, an increase in the scattering intensity in the DLS measurements was clearly observed, indicating the formation of DNA polyplexes as observed previously in the original SVs. The mean diameters of the polyplexes after 10 min are shown in Figure 5. An SV with lower molecular weight produced a polyplex with smaller diameter, whereas the particle size was the largest for the polyplexes formed from the SV having the highest molecular weight (73 kDa).

ζ-Potentials of the polyplexes were measured after dilution of the polyplex solutions, prepared at an N/P ratio of 10, with saline solution to 1/10 of the cell transfection concentration. Moderate positive ζ-potentials over 20 mV were observed for all polyplexes irrespective of the molecular weight of the SVs (Figure 6). The ζ-potential increased with the molecular weight of the SVs. The polyplexes for the SV with the highest molecular weight had the highest surface positive charge.

The pDNA condensation potential of the polyplexes was evaluated using an ethidium bromide exclusion assay. Ethidium bromide produces strong fluorescence when intercalating with pDNA but very weak fluorescence in its free form. If pDNA is condensed by SVs and stabilized polyplex particles formed, then ethidium bromide molecules cannot intercalate with DNA. As shown in Figure 7, a significant exclusion of ethidium bromide was observed at an N/P ratio of more than 4 for polyplexes prepared from three SVs with different molecular weights. The polyplexes formed from SVs with higher molecular weight had higher exclusion activity, indicating higher condensate density of the polyplexes.

In Vitro Transfection Efficiency and Cell Cytotoxicity. The transfection efficiencies of SVs before and after fractionation were evaluated in COS-1 cells at an N/P ratio of 10. The highest transfection activity was obtained for SVs with the highest molecular weight (73 kDa), which was more than 7 times that for SVs with the lowest molecular weight (27 kDa), the nonfractionated original SV, or PEI (ExGen 500), which is one of the major commercially available typical polymeric vectors used as a positive control (Figure 8).

The in vitro cytotoxicity of polyplexes was studied as a function of the molecular weight of SVs using the WST assay. All the polyplexes prepared from SVs with different molecular

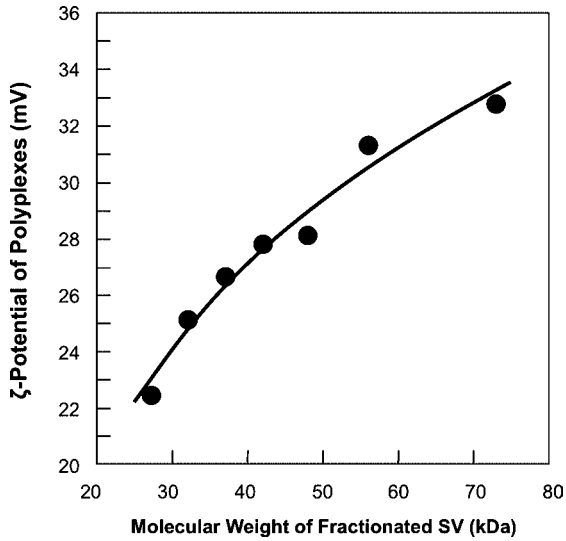

Figure 6. Relationship between ζ-potentials of the polyplexes and molecular weight of the fractionated SVs in the polyplexes. The polyplexes were prepared in N/P ratio of 10. The ζ-potentials were measured after dilution of the polyplex solutions with saline solution to 1/10. The resultant diluted solution corresponded to the cell transfection concentration.

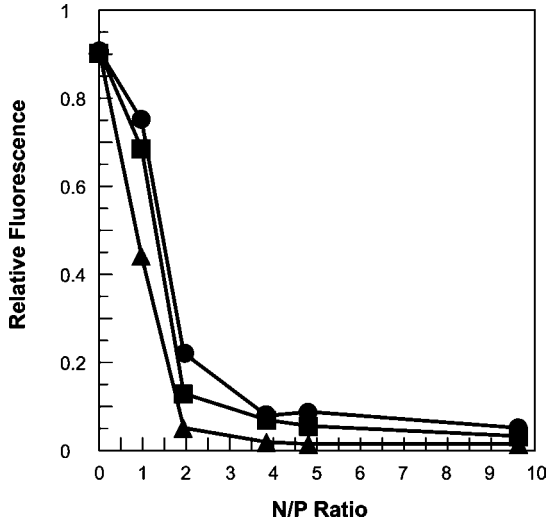

Figure 7. Condensation potential of the fractionated SVs as determined by ethidium bromide exclusion assay. Molecular weights are 37 kDa (•), 56 kDa (□), and 73 kDa (▲).

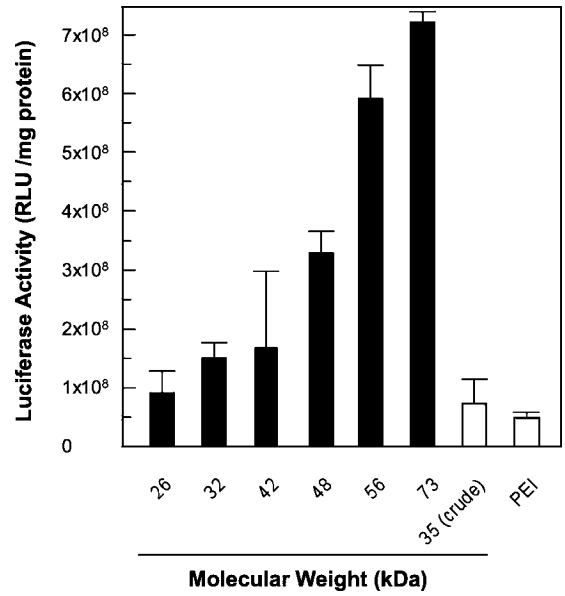

Figure 8. The transfection efficiency of polyplexes prepared by mixing DNA (pGL3-control) and the fractionated SVs at N/P ratio of 10 or linear PEI (ExGen 500) at the charge ratio of 5 in the COS-1 cell line.

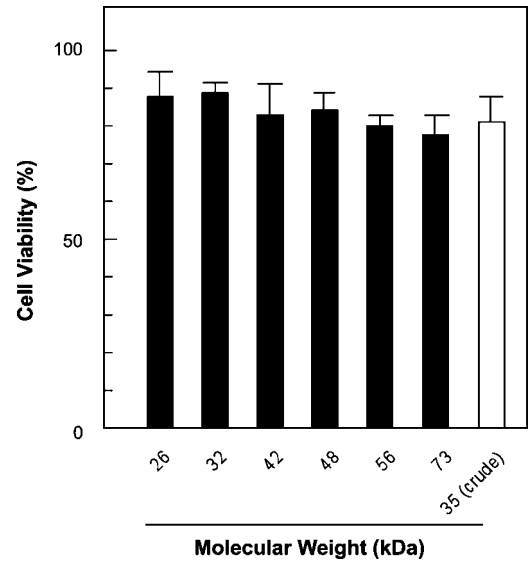

Figure 9. Cytotoxicity of polyplexes prepared by mixing DNA (pGL3-control) and the fractionated SVs at N/P ratio of 10 in COS-1 cell line. Cell viability was determined by the WST assay.

weights had permissible cell viability (Figure 9). Although the molecular weight of the cationic polymers was confirmed as the main parameter affecting their interaction with the cell membrane and consequently cell damage, SVs with molecular weights of less than 73 kDa are considered to have no significant cytotoxicity.

DISCUSSION

This study demonstrated that the molecular weight with narrow molecular weight distribution in SVs was found to have a dramatic influence on transfection activity, and luciferase reporter gene expression increased with the molecular weight. In our previous report, the molecular weight dependent transfection activity change in SVs having molecular weights ranging from approximately 10 kDa to 50 kDa with wider polydispersity of approximately 1.4 than this study was also observed at different N/P ratio of 5, which is half of this study (*17*). It was said that in 4-branched SVs the higher molecular weight resulted in the higher transfection activity in the molecular weights ranging from approximately 10 kDa to 73 kDa. On the other hand, interestingly, it was clearly indicated that narrowing of the molecular weight distribution induced high transfection activity. In the similar molecular weight of approximately 30−35 kDa, the transfection activity of the fractionated SV was two times larger than that of the crude one. The mixture of the different molecular weights may avoid uniform formation of polyplexes, which may induce less transfection activity. The narrow molecular weight distribution may be important in achieving a high efficiency as well as a high molecular weight. We are planning the investigation of effect of the molecular weight distribution, where the effect of combination of different molecular weight fractions will be also evaluated. These results will be reported in the near future.

The physicochemical properties of SVs or polyplexes are factors that control the polyplex-mediated DNA delivery (*27, 28*).

In this study, with an increase in the molecular weight of SVs, the amphiphilicity or hydrophobicity of SVs, determined by critical micellar concentration measurements, decreased (Figure 4); however, the particle size of polyplexes, determined by DLS measurements (Figure 5), surface potential of polyplexes, determined by ζ-potential measurements (Figure 6), and condensate density of polyplexes, determined by an ethidium bromide exclusion assay (Figure 7), increased. On the other hand, it is considered that DNA expression due to the polyplex was observed owing to five sequential steps: (1) attachment of the polyplex onto the cell surface, (2) internalization of the polyplexes into the cell, (3) endosomal escape of the polyplex, (4) DNA release from the polyplex, and (5) internalization of DNA into the nucleus. However, despite our better understanding of nonviral gene delivery, there are many unanswered questions relating to its fundamental mechanisms. Since the cell surface has a negative charge owing to the existence of glycoproteins on the cellular membrane, positively charged polyplexes can easily attach onto the cell surface by electrostatic interaction, similar to the case of polyplex formation from negatively charged DNA and a positively charged SV. Therefore, for more positively charged polyplexes, which form from SVs having higher molecular weights (Figure 6), attachment of polyplexes onto the cell surface is enhanced, which might be advantageous for the aforementioned first step.

On the other hand, polyplexes formed from SVs having lower molecular weight had smaller particle size (Figure 5). In general, it was found that transfection efficiency was low for large particles owing to the difficulty internalizing the polyplexes into cells (*29, 30*). Hennink et al. reported that PDMAEMA-induced polyplexes with large particle size (0.5−1.0 μm) have a lower transfection efficiency than those with small particle size (0.15−0.20 μm) (*30*). Therefore, the polyplexes formed from SVs with a higher molecular weight might be at a disadvantage in penetrating the cell membrane owing to their steric factor, which may be correlated by the aforementioned second step. However, the higher molecular weight of an SV induces higher transfection efficiency. This suggests that the polyplex size is less important to the overall transfection efficiency in this system. This was also observed in PDMAEMA-mediated DNA delivery (*16*).

SVs with higher molecular weight had higher amphiphilic ability on the basis of increasing hydrophobicity (Figure 4). Therefore, polyplexes formed from SVs having high molecular weights had high amphiphilic ability, i.e., they could fuse to the cell membrane or endosome membrane (*31, 32*), which may correlate with the aforementioned second and third steps. On the contrary, the hydrophobic character of SVs might induce rigidity of the polyplexes. Indeed, it was seen from the condensate density measurements that the polyplexes formed from SVs having higher molecular weights were more rigid (Figure 7). These are advantages for the prevention of DNase degradation but disadvantages for the intracellular DNA decondensation correlating with the aforementioned fourth step, which may induce low transfection efficiency owing to the difficulty of the DNA releasing from the polyplexes.

In summary, we used 4-branched SV consisting of *N*,*N*-dimethylaminopropyl acrylamide monomer units as a model polymer. The highest transfection activity was obtained for the SV with the highest molecular weight (73 kDa) and was more than 7 times that for the SV with the lowest molecular weight (27 kDa) or the nonfractionated original SV. The transfection efficiency correlated more with the amphiphilicity or hydrophobicity of the SV and the surface potential and condensate density of the polyplexes than with particle size. It was very difficult to clearly explain the relationship between the transfection activity and the physicochemical properties of SVs or the polyplexes. However, SV with the highest molecular weight could be easily extracted by separation using size-exclusion chromatography. In the comparison with the fractionated SVs with narrow molecular weight distribution, a small difference of molecular weight induced great difference of the physicochemical properties and the transfection efficiency. It is considered that the optimal molecular weight is different for each polymeric vector species because the vectors show different physicochemical properties. Therefore, precise and reliable evaluation of the transfection activity needs to be performed using polymeric vectors with narrow molecular weight distribution. The fractionation will be useful for enhancement of the efficiency of gene transfection induced also by other cationic polymers.

ACKNOWLEDGMENT

We would like to express our thanks to Ayaka Ishikawa for technical assistance.

LITERATURE CITED

(1) Mintzer, M. A., and Simanek, E. E. (2009) Nonviral vectors for gene delivery. *Chem. Rev. 109*, 259–302.
(2) Wong, S. Y., Pelet, J. M., and Putnam, D. (2007) Polymer systems for gene delivery: past, present, and future. *Prog. Polym. Sci. 32*, 799–837.
(3) Jeong, J. H., Kim, S. W., and Park, T. G. (2007) Molecular design of functional polymers for gene therapy. *Prog. Polym. Sci. 32*, 1239–1274.
(4) Prevette, L. E., Kodger, T. E., Reineke, T. M., and Lynch, M. L. (2007) Deciphering the role of hydrogen bonding in enhancing pDNA-polycation interactions. *Langmuir 23*, 9773–9784.
(5) Banerjee, P., Reichardt, W., Weissleder, R., and Bogdanov, A, Jr. (2004) Novel hyperbranched dendron for gene transfer in vitro and in vivo. *Bioconjugate Chem. 15*, 960–968.
(6) Fischer, D., Bieber, T., Li, Y., Elsasser, H. P., and Kissel, T. (1999) A novel non-viral vector for DNA delivery based on low molecular weight, branched polyethylenimine: effect of molecular weight on transfection efficiency and cytotoxicity. *Pharm. Res. 16*, 1273–1279.
(7) Bieber, T., and Elsasser, H. P. (2001) Preparation of a low molecular weight polyethylenimine for efficient cell transfection. *Biotechniques 30*, 74–81.
(8) Tomas, M., Ge, Q., Lu, J. J., Chen, J., and Klibanov, A. M. (2005) Cross-linked small polyethylenimines: while still nontoxic, deliver DNA efficiently to mammalian cells in vitro and in vivo. *Pharm. Res. 22*, 373–380.
(9) Gosselin, M. A., Guo, W., and Lee, R. J. (2001) Efficient gene transfer using reversibly cross-linked low molecular weight polyethylenimine. *Bioconjugate Chem. 12*, 989–994.
(10) Tang, M. X., and Szoka, F. C. (1997) The influence of polymer structure on the interactions of cationic polymers with DNA and morphology of the resulting complexes. *Gene Ther. 4*, 823–832.
(11) Kurowska-Latallo, J. F., Bielinska, A. U., Johnson, J., Spindler, R., Tomalia, D. A., and Baker, J. R., Jr. (1996) Efficient transfer of genetic material into mammalian cells using Starburst polyamidoamine dendrimers. *Proc. Natl. Acad. Sci. U.S.A. 93*, 4897–4902.
(12) Wightman, L., Kircheis, R., Rossler, V., Carotta, S., Ruzicka, R., Kursa, M., and Wagner, E. (2001) Different behavior of branched and linear polyethylenimine for gene delivery in vitro and in vivo. *J. Gene Med. 3*, 362–372.
(13) Godbey, W. T., Wu, K. K., and Mikos, A. G. (1999) Size matters: molecular weight affects the efficiency of poly(ethylenimine) as a gene delivery vehicle. *J. Biomed. Mater. Res. 45*, 268–275.
(14) Jeong, J. H., Song, S. H., Lim, D. W., Lee, H., and Park, T. G. (2001) DNA transfection using linear poly(ethylenimine) prepared by controlled acid hydrolysis of poly(2-ethyl-2-oxazoline). *J. Controlled Release 73*, 391–399.

(15) Wetering, P., Cherng, J. Y., Talsma, H., Crommelin, D. J., and Hennik, W. E. (1998) 2-(Dimethylamino)ethyl methacrylate based (co)polymers as gene transfer agents. *J. Controlled Release 53*, 145–153.

(16) Layman, J. M., Ramiez, S. M., Green, M. D., and Long, T. E. (2009) Influence of polycation molecular weight on poly(2-dimethylaminoethyl methacrylate)-mediated DNA delivery in vitro. *Biomacromolecules 10*, 1244–1252.

(17) Nakayama, Y., Kakei, C., Ishikawa, A., Zhou, Y. M., Nemoto, Y., and Uchida, K. (2007) Synthesis and in vitro evaluation of novel star-shaped block copolymers (blocked star vectors) for efficient gene delivery. *Bioconjugate Chem.* , 2037–2044.

(18) Xu, F. J., Zhang, Z. X., Ping, Y., Li, J., Kang, E. T., and Neoh, K. G. (2009) Star-shaped cationic polymers by atom transfer radical polymerization from beta-cyclodextrin cores for nonviral gene delivery. *Biomacromolecules 10*, 285–293.

(19) He, E., Yeu, C. Y., Simeon, F., Zhou, L. H., Too, H. P., Tam, K. C. (2009) Polyplex formation between four-arm poly(ethylene oxide)-b-poly(2-(dimethylamino)ethyl methacrylate) and plasmid DNA in gene delivery. *J. Biomed. Mater. Res. 91*, 708−718.

(20) Fichter, K. M., Zhang, L., Kiick, K. L., and Reineke, T. M. (2008) Peptide-functionalized poly(ethylene glycol) star polymers: DNA delivery vehicles with multivalent molecular architecture. *Bioconjugate Chem. 19*, 76–88.

(21) Yang, C., Li, H., Goh, S. H., and Li, J. (2007) Cationic star polymers consisting of alfa-cyclodextrin core and oligoethylenimine arms as nonviral gene delivery vectors. *Biomaterials 28*, 3245–3254.

(22) Nakayama, Y., Masuda, T., Nagaishi, M., Hayashi, M., Ohira, M., and Harada-Shiba, M. (2005) High performance gene delivery polymeric vector: nano-structured cationic star polymers (star vectors). *Curr. Drug. Delivery 2*, 53–57.

(23) Nemoto, Y., Zhou, Y. M., Tatsumi, E., and Nakayama, Y. (2008) Photoinduced cross-linking of star vector for improvement of gene transfer efficiency. *Bioconjugate Chem. 19*, 2513–2519.

(24) Mori, T., Ishikawa, A., Nemoto, Y., Kambe, N., Sakamoto, M., and Nakayama, Y. (2009) Development of a novel nonviral gene silencing system that is effective both in vitro and in vivo by using a star-shaped block copolymer (star vector). *Bioconjugate Chem. 20*, 1262–1269.

(25) Mizoguchi, I., Ooe, Y., Hoshino, S., Shimura, M., Kasahara, T., Kano, S., Ohta, T., Takaku, F., and Nakayama, Y. (2005) Improved gene expression in resting macrophages using an oligopeptide derived from Vpr of human immunodeficiency virus type-1. *Biochem. Biophys. Res. Commun. 338*, 1499–1506.

(26) Ishikawa, A., Zhou, Y. M., Kambe, N., and Nakayama, Y. (2008) Enhancement of star vector-based gene delivery to endothelial cells by addition of RGD-peptide. *Bioconjugate Chem. 19*, 558–561.

(27) Takaku, Y., Nishikawa, M., Yamashita, F., and Hashida, M. (2002) Influence of physicochemical properties on pharmacokinetics of non-viral vectors for gene delivery. *J. Drug Targeting 10*, 99–104.

(28) Wakabayashi, D., Nishiyama, N., Itaka, K., Miyata, K., Yamasaki, Y., Harada, A., Koyama, H., Nagasaki, Y., and Kataoka, K. (2004) Polyion complex micelles of pDNA with acetal-poly(ethylene glycol)-poly(2-(dimethylamino)ethyl methacrylate)block copolymer as the gene carrier system: physicochemical properties of micelles relevant to gene transfection efficacy. *Biomacromolecules 5*, 2128–2136.

(29) Zhao, X., Pan, F., Zhan, Z., Grant, C., Ma, Y., Armes, S. P., Tang, Y., Lewis, A. L., Waigh, T., and Lu, J. R. (2007) Nanostructure of polyplexes formed between cationic diblock copolymers and antisense oligodeoxynucleotide and its influence on cell transfection. *Biomacromolecules 8*, 3493–3502.

(30) Wetering, P., Moret, E. E., Schuurmans-Nieuwenbroek, N. M., Steenbergen, M. J., and Hennik, W. E. (1999) Structure-activity relationships of water-soluble cationic methacrylate/methacrylamide polymers for nonviral gene delivery. *Bioconjugate Chem. 10*, 589–597.

(31) Shrma, R., Lee, L. S., Betterncourt, R. C., Xiao, C., Konieczny, S. F., and won, Y. Y. (2008) Effects of the incorporation of a hydrophobic middle block into a PEG-polycation diblock copolymer on the physicochemical and cell interaction properties of the polymer-DNA complexes. *Biomacromolecules 9*, 3294–3307.

(32) Wong, S. Y., Sood, N., and Putnam, D. (2009) Combinatorial evaluation of cations, pH-sensitive and hydrophobic moieties for polymeric vector design. *Mol. Ther. 17*, 480–490.

BC900283H

Engineering Phage Materials with Desired Peptide Display: Rational Design Sustained through Natural Selection

Anna Merzlyak[†] and Seung-Wuk Lee*

UCSF and UC Berkeley Joint Graduate Group in Bioengineering, Berkeley, California 94720, Physical Biosciences Division, Lawrence Berkeley National Laboratory, Berkeley, California 94720, Department of Bioengineering, University of California, Berkeley, California 94720, and Berkeley Nanoscience and Nanoengineering Institute, Berkeley, California 94720. Received July 8, 2009; Revised Manuscript Received August 24, 2009

Genetic engineering of phage provides novel opportunities to build various nanomaterials by displaying functional peptide motifs on its surface coat protein. However, any genetic modifications of phage coat proteins must be able to accommodate their many biological roles in the phage replication process. To express functional but inherently unfavorable peptide motifs on major coat protein pVIII, we devised a novel genetic conjugation method to circumvent bacterial biological censorship. Constraining the designed peptides among the degenerate flanking residues, we obtained a pVIII library of phage that retained the desired sequences yet could navigate through the phage replication process due to the naturally selected flanking residues. Further, we systematically analyzed the biochemical and size-related compensation mechanisms of the pVIII expressed peptides by constructing four chemically diverse (His, Trp, Glu, Lys) partial library series. Described genetic conjugation methodology can serve to improve the design of engineered phage and allow further exploitation of these particles as functional nanobiomaterials for various applications.

INTRODUCTION

Monodisperse nanofibers with a uniform programmable surface that are able to store information and be reproduced in mass quantities can serve a multitude of biological and material needs. Filamentous bacteriophage (phage) are bacterial viruses 880 nm long and 6.6 nm in diameter (*1, 2*). Through genetic engineering, phage have been shown to be extremely versatile in peptide presentation on both their major coat protein, pVIII, and minor coat proteins, pIII and pIX (*1*−*7*). Additionally, the monodispersity of their shape and chemical character, derived from clonal replication, allows them to self-assemble into directionally organized liquid crystalline structures. Previously, these phage have demonstrated an ability to be formed into one-dimensional ordered fibers, two-dimensional films, and three-dimensional materials (*4, 6, 8*−*10*).

The potential to control both structural organization and chemical function of materials at the nanoscale level makes genetically engineered phage very appealing candidates for use as material building blocks. The surface of the filamentous phage is represented by 2700 copies of its major coat protein, pVIII, which packs around the phage DNA to make a tight and cylindrical shell (*11*). The acidic N-termini of pVIII form a dense periodic display spaced at 2.7 nm (*1, 12*). The final five residues of pVIII have been determined to be structurally unconstrained and exposed to the solvent (*11*), therefore presenting an optimal target for engineering, manipulation, and substrate interaction.

A tremendous amount of research has gone into studying the structural characteristics and biological interactions of pVIII through the phage and *Escherichia coli* (*E. coli*) life cycle (*13*−*23*). Numerous peptide libraries have been developed for use as information mining tools in a high-throughput evolutionary screening method called phage display (*1, 2*). Additionally, research efforts have gone into finding out how to improve the diversity of the amino acid libraries presented by the phage, thereby potentially improving the quality of binding information between the peptide and its target (*24*−*26*). More recently, functionalized bacteriophage and virus capsids have become an attractive tool for material synthesis (*27, 28*). The "landscape" peptide presentation on the major coat protein of the filamentous phage has been utilized to template inorganic crystals for energy and memory storage devices (*4, 6, 9, 10*) and make stimulus-responsive materials (*29*). The phage has also been exploited for medical applications, such as targeted drug (*30*), gene (*31*), and imaging agent (*32*) delivery, as well as a tissue engineering material (*33*).

To further exploit and push the limits of the phage particle versatility, it is important to understand the intricate biological processes that occur before pVIII proteins can be successfully packaged into a viable phage. If a very low copy number vector such as fd-tet is utilized (*24*), the stress on the replication process is reduced, and an engineered octapeptide pVIII library has a capability of forming 10^9 various phage particles (*1*). The utilization of a phagemid cloning system also allows a much greater versatility of expressed proteins in terms of both size and chemical characteristic, albeit on a much lower percentage of phage proteins (*2*). Even though the phagemid system offers greater flexibility, limitations still exist. A recent study showed that both the charge of the expressed peptide as well as its size influence the number of fused peptides that could be displayed on the phage particle (*34*). The potential complexity of the libraries drops when using a higher copy vector or when expressing the desired peptide on every protein of the phage (*25*). However, as the yield of propagated phage and the density of expressed peptides become much more important for material synthesis applications these attributes should play an important role in choosing both the phage type and the expression system.

Whether the certain insert sequence will be expressed or not depends strongly on its fitness for the processes encountered

* Corresponding author. Seung-Wuk Lee. University of California, Berkeley, CA 94720. Phone: 510-486-4628, Fax: (510) 486-6488, E-mail: leesw@berkeley.edu.

[†] UCSF and UC Berkeley Joint Graduate Group in Bioengineering, Berkeley and Lawrence Berkeley National Laboratory.

10.1021/bc900303f CCC: $40.75 © 2009 American Chemical Society
Published on Web 10/20/2009

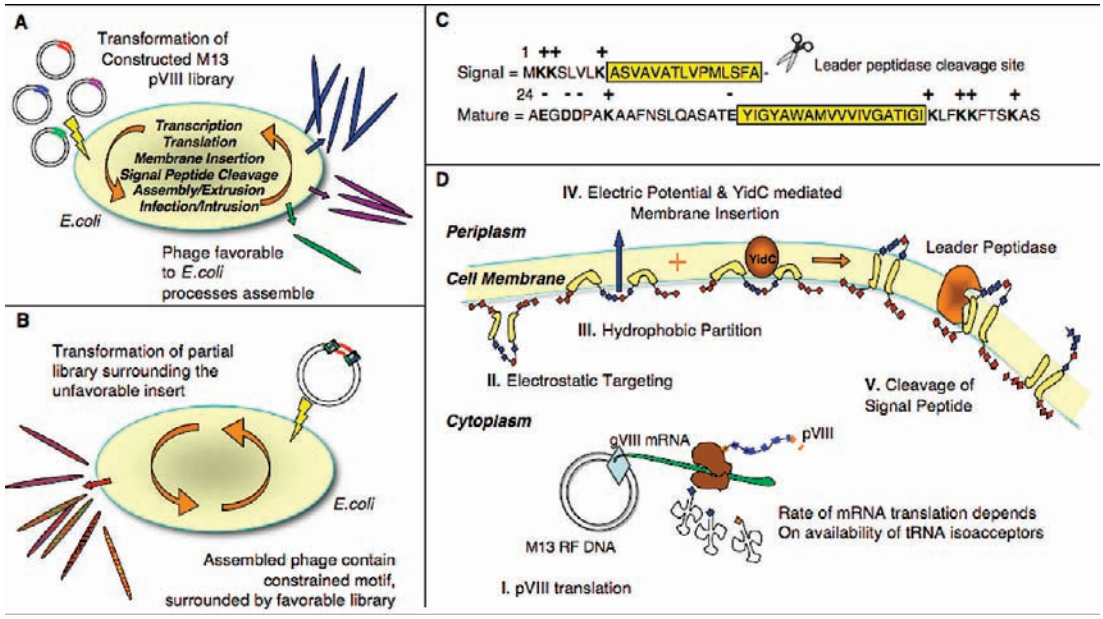

Figure 1. pVIII major coat protein, and its biological role in M13 phage replication in *E. coli*. (A) Schematic representation of pVIII library construction. (B) Schematic representation of partially constrained pVIII libraries. (C) Signal and mature peptide sequences of pVIII protein, with hydrophobic portions marked by yellow rectangles, and a marked leader peptidase cleavage site. (D) More detailed diagram of translation, membrane insertion, and procoat cleavage processes most instrumental in biocensoring the pVIII insert expression. (In part adapted from ref *51*).

by pVIII during its lifecycle, including (1) transcription, (2) translation, (3) membrane insertion, (4) signal peptide cleavage, (5) assembly and extrusion, and finally (6) infection and intrusion (*23*, *35*); see Figure 1. If the interactions of the engineered pVIII are favorable within this context, its genetic sequence will be more stable, and more phage will be produced during amplification. If the insert sequence makes pVIII interactions less biologically favorable, it will be more likely to mutate and/or produce fewer phage particles. Here, we describe a novel partially constrained library method to add peptide motifs to every copy of pVIII protein. We show how this approach was used to display an Arg-Gly-Asp (RGD) integrin-binding peptide on every copy of pVIII protein to promote cell interaction, which we developed for phage-based novel tissue engineering materials. Additionally, we show how this method can be useful for presenting other functionally designed groups on the major coat protein of the phage. Finally, we quantitatively analyze how the characteristics of the inserts and their constrained sequences affect their expression on a phage particle.

EXPERIMENTAL PROCEDURES

Reagents. Phusion high-fidelity DNA polymerase was purchased from Finnzymes (Espoo, Finland). *Pst*I, *Bam*HI, and *Dpn*I restriction endonucleases, T4 DNA ligase, and dNTP 10 mM solution mix were from New England Biolabs (Ipswich, MA). QuikChange Site-Directed Mutagenesis Kit was from Stratagene (La Jolla, CA). DNA purification was performed with the help of QIAquick PCR Purification and Gel Extraction Kits, and QIAprep Spin Miniprep Kit all from QIAGEN, Inc. (Valencia, CA).

Bacterial and Phage Strains. M13KE single-stranded phage that was used as a base for the library and insert construction was purchased from New England Biolabs. XL10-Gold Ultracompetent Cells (F′ *lacI*^{q}*Z*Δ*M15*) from Stratagene were used to transform the ligated DNA products. XL1-Blue Competent Cells (F′ *lacI*^{q}*Z*Δ*M15*) from Stratagene were used for phage amplification.

Inverse PCR Method for M13 Phage Cloning. To present peptide motifs on every copy of M13 major coat protein, an inverse polymerase chain reaction (PCR) cloning method was adapted (*36*). The insert was positioned between the first and fifth amino acids of the wild-type pVIII, replacing wild-type M13KE residues 2−4 (Ala-**Glu-Gly-Asp**-Asp to Ala-(**Insert**)-Asp). All primers were ordered from IDT DNA technologies (Coralville, IA). To allow for recircularization of the vector following the PCR, a *Pst*I restriction site was created upstream of the insert location using a QuikChange Site-Directed Mutagenesis Kit by changing position 1372 of M13KE vector from T to A (CTGCAG), as previously described (*1*). The resulting DNA was verified by picking blue plaques resulting from phage transformation, isolating the DNA using common biological methods (*37*), and sequencing at the University of California, Berkeley DNA sequencing facility (Berkeley, CA).

For the inverse PCR reaction, the forward primer was designed to include a *Pst*I restriction site followed by an insert sequence and a segment complementary to the gVIII 3′−5′ strand. The reverse primer, designed to make the M13 plasmid linear, also included the *Pst*I restriction site and was fully complementary to the gVIII 5′−3′ region. To incorporate the gene sequences, PCR was performed using Phusion high-fidelity DNA polymerase, the two primers, and an M13 vector with an engineered *Pst*I restriction site as the template. The obtained product was purified on an agarose gel, eluted with spin column purification, digested with *Pst*I enzyme, and recircularized with an overnight ligation at 16 °C with T4 DNA ligase (*37*). The ligated DNA vector was transformed into XL10-Gold Ultracompetent bacteria cells, and the resulting phage verified via DNA sequencing.

Partial Library Cloning Method. All the libraries were cloned into the M13 vector by following the above scheme. For the partial libraries, the primers were designed to constrain a region of interest (i.e., RGD) and to allow degeneracy within the flanking codons (i.e., XXXRGDXX). As in previous phage libraries, a 32 codon degeneracy was used (X = NNK, N = A/T/C/G, K = G/T) to reduce the bias among presented amino acids (AAs) and eliminate two of the three potential stop codons (*1*, *2*). For a fully unconstrained library, degeneracy was allowed at all of the 8 positions. See Table 1 for primer and corresponding library sequences. To reduce the advantage of

Table 1. Primer Sequences for Phages and Phage Libraries[a]

name	sequence	primer[b]
wild-type	AEGDDP	
unconstrained	AX^c*(X)*$_7$DP...	5′ATATATCTGCAG*NK (NNK)*$_7$GATCCCGCAAAAGCGG CCTTTAATCCC3′
RGD	AX^c*XX***RGD***XX*DP	5′...CTGCAG*NK (NNK)*$_2$ **CGTGGTGAC***(NNK)*$_2$...3′
WHWQ	A***GWHWQGGG***DP	5′...CTGCAG***GC TGG CAT TGG CAG GGC GGC GGC***...3′
WHWQ-2X	AX^c**WHWQ***X***GG**DP	5′...CTGCAG *NK* **TGG CAT TGG CAG** *NNK* **GGC GGC**...3′
WHWQ-3X	AX^c**WHWQ**XX**G**DP	5′...CTGCAG *NK* **TGG CAT TGG CAG** *(NNK)*$_2$**GGC**...3′
WHWQ-4X	AX^c*X***WHWQ***XX*DP	5′...CTGCAG *NK NNK* **TGG CAT TGG CAG** *(NNK)*$_2$...3′
	AX^c**WHWQ***XXX*DP	5′...CTGCAG *NK* **TGG CAT TGG CAG** *(NNK)*$_3$...3′
1E[d]	AX^c*XX***E***XXXX*DP	5′...CTGCAG *NK (NNK)*$_2$**GAA** *(NNK)*$_4$...3′
2E	AX^c*XX***EE***XXX*DP	5′...CTGCAG *NK (NNK)*$_2$**GAAGAG** *(NNK)*$_3$...3′
3E	AX^c*X***EEE***XXX*DP	5′...CTGCAG *NK NNK* **GAAGAGGAA** *(NNK)*$_3$...3′
4E	AX^c*X***EEEE***XX*DP	5′...CTGCAG *NK NNK* **(GAAGAG)**$_2$*(NNK)*$_2$...3′
5E	AX^c***EEEEE***XXDP	5′...CTGCAG *NK* **(GAAGAG)**$_2$ **GAA** *(NNK)*$_2$...3′
6E	AX^c***EEEEEE***XDP	5′...CTGCAG *NK* **(GAAGAG)**$_3$*NNK* ...3′
p8-rev1376		5′ CCTCTGCAGCGAAAGACAGCATCGG 3′

[a] X's refer to degenerate residues, **Bold** to constrained, and *Italics* to the insert portion. [b] Full primer sequence shown only for the first listed; for the rest, only the *Pst*I restriction site and the insert portion are included. [c] X^c refers to residues coded for by a GNK codon (i.e., A,D,E,G,V). [d] Glu libraries shown as representative; same pattern applied for Lys library (AAA AAG codons); for His (CAT) and W (TGG) libraries, only one type of codon was used.

wild-type or fast-amplifying phage, the cells were allowed to recover for only 30 min after transformation (*38*). To analyze the library sequence space, the cells were plated in agarose top, and phage-formed plaques after an overnight incubation at 37 °C were picked and their DNA sequenced.

Library Quantification and Analysis. *Number of Transformants.* Using 2 μL of each ligation reaction, 50 μL of XL-10 Gold Ultracompetent cells were transformed via heat shock following the manufacturer's recommendations. The cells were recovered in 1 mL LB at 37 °C incubator with shaking for 30 min. Aliquots of 150 and 450 μL of cells were then plated in agarose top on LB plates with IPTG/Xgal (*37*). The number of transformants was quantified for each of the engineered libraries by calculating an average quantity of plaque forming units.

Amino Acid Diversity. Ten sequences were obtained for each library producing plaques (*37*), except for the 3H library where only seven plaques could be obtained with retained 3H sequence. The frequency and number distributions were determined on the basis of the amino acid (AA) side-chain characteristic (i.e., aromatic, negative, and positive), both in the degenerate positions and in the insert as a whole. Observed frequency of occurrence (*F*) was calculated via the following formula: $F =$ (# of type of AA)/(total # AAs in sequences evaluated) $\times$ 100%, with type of AA = Aromatic (Trp, Tyr, Phe), Negative (Asp, Glu), or Positive (Arg, Lys). Expected frequency (E.F.) was calculated on basis of the number of codons corresponding to each AA residue as used in a 32 codon library, and grouped by the type of AA.

RESULTS

Fabrication of Partially Constrained pVIII Library with Desired Peptides. We fabricated a partially constrained pVIII library with desired peptides for construction of engineering materials. The initial purpose for engineering the pVIII protein of M13 phage was to decorate it with cell signaling motifs, so it could serve as a novel material for tissue regeneration scaffolds (*33*). As the target cell type was of neural origin, the signaling motifs chosen were IKVAV and RGD, which are peptide groups taken from laminin and fibronectin and previously shown to have a positive effect on neural progenitor cell attachment and differentiation (*39, 40*). Initial cloning attempts were to display an AS**IKVAV** and a GG**RGD**-SP peptide immediately at the N-terminus of pVIII, thereby maintaining the signaling motifs within their naturally occurring flanking sequences (*41, 42*). After the original attempt failed, the insert sequences were modified to shift the ASIKVAV to start at position three of the mature pVIII (i.e., AE-*AS***IKVAV**DP), and GRGDS was shortened and moved to start after the first Ala residue (i.e., A*G**RGD**S*DP). Both were redesigned to contain a positive and a negative residue, making the overall charge of pVIII N-terminus -1. The described measures should have theoretically allowed for the expression of the insert (*3*). However, both of the constructed bacteriophage showed a strong tendency for deletions and single nucleotide mutations, which resulted in amino acid substitutions. In nine out of ten sequences obtained, the ASIKVAV insert had a K6N mutation (AE*ASINVAV*), and only one preserved the desired IKVAV sequence with an A3D mutation (AE*DS**IKVAV***).

A GRGDS peptide addition on pVIII resulted in a phage that made very small plaques, initially indicating a greatly reduced fitness of the phage (*3, 15, 16, 24*). Furthermore, when the phage was amplified and titrated following standard microbiological procedures (*37*), the resulting phage all had G2D, R3X (i.e., A*D***RGD***S*DP or A*GXGDS*DP, with X = residue from a single base mutation, i.e., Pro, Leu, Gly, His) or deletion mutations. Even when a DRGDS phage was amplified, the resulting population again showed consistent instability at the Arg position, often mutating it to a neutral residue. From these initial cloning attempts, it was seen that the preference for the phage expression was not to have a positive residue in the N-terminus insert location, unless stabilized by at least two negative charges. However, even with two negative residues the shorter DRGDS peptide continued to remain unstable.

A partial 8mer library was utilized to display the unfavorable RGD peptide, which allowed the unconstrained library residues to be controlled and chosen by the *E. coli* host (see Figure 1). In this manner, only the favorable full inserts would be displayed and contain both the designed constrained motif as well as a flanking amino acid library chosen by the natural selection pressures of the *E. coli* cellular mechanisms. Cloning the RGD sequence with the partial library method as described above resulted in formation of phage particles that upon sequencing were found to retain the RGD sequence (see Table 2). From the resulting RGD library, the most physiologically relevant flanking amino acids GRGDT (for a full sequence of A*DS*-**GRGDT***E*DP) were chosen to resemble a fibronectin integrin binding domain GRGDS (*43*). The stability of both the IKVAV- and RGD-modified phages was verified by mass amplification (*33*). Furthermore, they were found to have specific interaction with cells and were used to build tissue engineering scaffolds that could control cell behavior in two and three dimensions (*33*).

Table 2. RGD Constrained Library Sequences

Sequence #	pVIII N-terminus Sequence										Insert charge	Insert mol wt
1[a]	A	*G*	*V*	*I*	***R***	***G***	***D***	*G*	*D*	DP	-1	769.82
2	A	*G*	*A*	*S*	***R***	***G***	***D***	*D*	*G*	DP	-1	715.69
3	A	*G*	*T*	*A*	***R***	***G***	***D***	*G*	*E*	DP	-1	743.75
4	A	*E*	*T*	*I*	***R***	***G***	***D***	*G*	*G*	DP	-1	785.82
5	A	*G*	*G*	*G*	***R***	***G***	***D***	*E*	*D*	DP	-2	743.69
6[b]	A	*D*	*S*	*G*	***R***	***G***	***D***	*T*	*E*	DP	-2	817.78
7	A	*D*	*V*	*G*	***R***	***G***	***D***	*I*	*A*	DP	-1	783.86
8	A	*A*	*E*	*V*	***R***	***G***	***D***	*I*	*E*	DP	-2	869.96
9	A	*D*	*V*	*G*	***R***	***G***	***D***	*D*	*A*	DP	-2	785.79
10	A	*D*	*V*	*M*	***R***	***G***	***D***	*S*	*G*	DP	-1	817.88
11	A	*E*	*N*	*V*	***R***	***G***	***D***	*A*	*N*	DP	-1	855.9
12	A	*A*	*E*	*A*	***R***	***G***	***D***	*H*	*S*	DP	-1	823.85

[a] The insert is shown in *italics,* constrained sequences are marked in **bold** and outlined, positive residues marked in red and the negative in blue. [b] The sequence of a phage chosen to serve as a part of a tissue-engineering scaffold (*33*).

Table 3. WHWQ Constrained Library Sequences

Sequence #	pVIII WHWQ Sequences										Insert charge	Insert mol wt
1[a]	A	*E*	*E*	***W***	***H***	***W***	***Q***	*E*	*G*	DP	-3	1082.11
2	A	*D*	*E*	***W***	***H***	***W***	***Q***	*D*	*G*	DP	-3	1054.05
3	A	*E*	*D*	***W***	***H***	***W***	***Q***	*D*	*G*	DP	-3	1054.05
4	A	*D*	*D*	***W***	***H***	***W***	***Q***	*E*	*G*	DP	-3	1054.05
5	A	*E*	*E*	***W***	***H***	***W***	***Q***	*E*	*G*	DP	-3	1082.11
6	A	*D*	*D*	***W***	***H***	***W***	***Q***	*D*	*G*	DP	-3	1040.02
7	A	*E*	***W***	***H***	***W***	***Q***	*E*	*G*	*D*	DP	-3	1068.08
8	A	*D*	***W***	***H***	***W***	***Q***	*D*	*G*	*D*	DP	-3	1040.02
9	A	*D*	***W***	***H***	***W***	***Q***	*D*	*S*	*E*	DP	-3	1084.08
10	A	*D*	***W***	***H***	***W***	***Q***	*E*	*D*	*A*	DP	-3	1068.09
11	A	*D*	*E*	***W***	***H***	***W***	***Q***	*Y*	*D*	DP	-3	1160.18
12	A	*E*	*D*	***W***	***H***	***W***	***Q***	*I*	*E*	DP	-3	1124.19
13	A	*D*	*E*	***W***	***H***	***W***	***Q***	*E*	*S*	DP	-3	1098.11
14	A	*E*	*E*	***W***	***H***	***W***	***Q***	*E*	*S*	DP	-3	1112.14
15	A	*D*	*T*	***W***	***H***	***W***	***Q***	*E*	*E*	DP	-3	1112.14
16	A	*E*	*A*	***W***	***H***	***W***	***Q***	*E*	*E*	DP	-3	1096.15
17	A	*E*	*D*	***W***	***H***	***W***	***Q***	*Q*	*E*	DP	-3	1139.17
18	A	*D*	*D*	***W***	***H***	***W***	***Q***	*N*	*D*	DP	-3	1097.08
19	A	*E*	*D*	***W***	***H***	***W***	***Q***	*Q*	*N*	DP	-2	1124.16
20	A	*D*	*D*	***W***	***H***	***W***	***Q***	*S*	*T*	DP	-2	1056.07

[a] The insert is shown in *italics,* constrained sequences are marked in **bold** and outlined, positive residues marked in red and the negative in blue.

To further verify the utility of the partial library method to express unfavorable short peptide groups on every copy of the major coat protein, we attempted to express a WHWQ sequence found previously in our lab as a trinitrotoluene (TNT) binding peptide (*44*). A fully defined WHWQ insert and four different WHWQ libraries were attempted (see Table 1). The fully constrained WHWQ insert (A*G****WHWQ****GGG*DP) resulted in no plaque forming phage. The transformation of a library with two unconstrained positions (A*XX****WHWQ****XGG*DP) resulted in several plaques, but all were either wild-type mutants or original template phage. Finally, libraries constructed with degeneracy at three (A*XXX****WHWQ****XG*DP) and four positions (A*XXX****WHWQ****XXX*DP or A*XX****WHWQ****XX*DP) resulted in phages that were able to retain the desired WHWQ sequences (see Table 3). Within the resulting sequences, there was a very strong tendency of the unconstrained residues to be negative. From 20 of the phage that were sequenced and found to display the WHWQ motif, 18 had 3 negative residues in the unconstrained space and 2 had 2 negative residues. These 2 phage were from the A*XX****WHWQ****XX*DP library, and both had the negative charges preceding the constrained WHWQ motif.

Limitation and Compensation Trends in Partially Constrained pVIII Libraries. To explore whether there was any compensation between the constrained and unconstrained sequence space of the insert and elucidate any potential trends, several partially constrained library series were designed. One to six amino acids of the 8mer inserts were defined in the middle of the pVIII libraries as His, Lys, Trp, or Glu, leaving the rest as degenerate (see Table 1). The purpose was to systematically test the constraints of insert expression for amino acids with side groups of diverse chemical characteristics and potential functionalities. Histidine, a very functionally interesting residue, has a nearly physiological pK_a of 6.0, and is therefore very sensitive to its surroundings. However, in a more basic *E. coli* environment (*45*) it is most often found in a neutral confirmation. Lysine (pK_a = 10.53) is consistently positive in *E. coli* and has a modifiable amine group, whereas glutamic acid is negative (pK_a = 4.25) and similarly has a chemically modifiable carboxyl group. Tryptophan is uncharged, but it is the largest (mol wt = 186.21 g/mol) hydrophobic amino acid that is both aromatic and polar by nature, lending itself to a variety of binding interactions.

Effect of pVIII Constrained Sequence on Library Size. The size of the libraries, as measured by the quantity of plaque-forming phage after library transformation, was seen to strongly depend on the sequences constrained within the 8mer library inserts (Figure 2). The most apparent trend was that for all libraries the number of plaque forming phage produced within the library declined as the number of repeating residues increased. For the H-libraries, 1H and 2H constraints produced

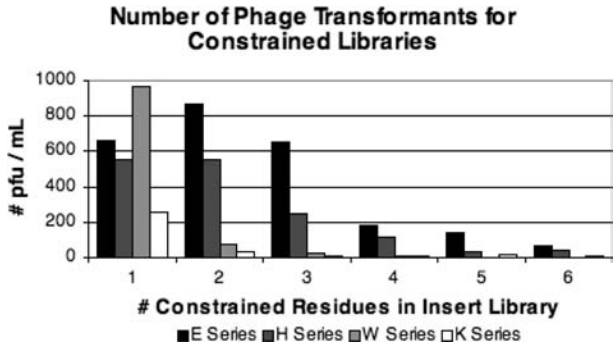

Figure 2. Partial library size dependence on the constrained peptide. Average number of plaque forming units (pfu) is shown in relation to the number of constrained residues in each of the constructed libraries.

an equal population of transformants at 550 pfu/mL and the 3H library population was reduced by half to 240 pfu/mL. The 4H library produced 120 pfu/mL, but did not result in any phage containing four His residues. Instead, the phage sequence always either had a deletion, wild-type revertant mutations, or original template background. Even though the 5H and 6H libraries produced some plaques, they were similar in quality to the 4H library. The W-libraries had the most dramatic change where the 1W seemed a very favorable constraint producing 970 pfu/mL, but the drop to the 2W library population was more than 10 times to 70 pfu/mL, and 3W was again reduced by another half to 30 pfu/mL. The 4W libraries produced less than 10 pfu/mL and had no 4W sequences. The 5W and 6W libraries produced no plaques at all. Within the K-series, only 1K (at ~260 pfu/mL) contained the constrained Lys residue. The 2K−6K libraries produced a population of plaques, but each was either a deletion or wild-type mutant, or original template DNA background. The E-constrained phage showed high numbers of pfu/mL in the 1−3E libraries (650−870 pfu/mL), with the 2E library being the best producer. The 4E library showed a marked decline (180 pfu/mL), and even though it did contain some deletion and revertant mutants, there was still a population of phage expressing the constrained 4E sequences. The 5E (140 pfu/mL) and 6E (70 pfu/mL) libraries produced a fairly large population of plaque-forming phage compared to other high repeating libraries. However, among the obtained sequences, there were no phage that expressed five or six Glu repeats. Instead, these libraries had a high number of deletion mutants, often displaying one to four Glu residues.

Dependence of Partial Library Diversity on the Constrained Sequence. In the constructed partial libraries, the unconstrained library amino acids were seen to partially compensate for the constrained amino acids in both chemical character and size, in order to preserve the overall favorability of insert display. The residues were grouped and characterized by their side-chain functionality rather than by individual presence. The positive groups, Lys and Arg, as well as the hydrophobic groups Trp, Tyr, and Phe, were previously described to aide in anchoring the pVIII protein in the cell membrane (*46, 47*). The negative residues (Asp and Glu) are thought to assist in the electrophoretic dependent insertion of pVIII across the *E. coli* membrane and serve as its hydrophilic anchors (*22, 47*). This diversity analysis was done on the whole 8mer inserts including the constrained sequences, as well as on only the degenerate parts of the inserts, that exclude the constrained sequences (see Figure 3). These distributions were compared to an 8mer pVIII library population constructed in a similar fashion, as well as expected frequencies of these amino acids as based on the 32 codon representation (NNK codon library). As observed in previously constructed libraries, the frequency of expression of negative Asp and Glu residues were greatly overrepresented in the fully unconstrained library, whereas both the aromatic and the positive residues were underrepresented in relation to the theoretically expected frequencies (*3, 25*). However, as more constraints were imposed on the insert space some trends were seen to emerge. The most pronounced effect was the direct relationship between the number of charged residues and the aromatic residues. The constriction of aromatic amino acids showed a dramatic influence on the increase of negatively charged residues within the library portions of these phage pVIII proteins (10% increase for 1W, 41% increase for 2W, and 62% increase for 3W libraries in relation to fully unconstrained). Inversely, while the expressed frequency of aromatic residues did not increase for 1E and 2E libraries, it more than tripled, in relation to the library expression, to 14% for 3E and 15% for 4E library. It is also noteworthy that, whereas the number of aromatic residues is underrepresented in the fully unconstrained and most of the constrained libraries, it exceeds the expected rate of representation (9%) by 50−60% in the 3E and 4E libraries. Additionally, the 1K library had the third largest expression rate of aromatic residues, exactly matching the expected frequency at 9%.

Since the more constrained libraries have a lower quantity of unconstrained residues, a similar number of residues of a certain type will inherently result in a higher frequency of expression. Therefore, to better interpret the behavior of the full pVIII protein, it is useful to also evaluate the average number of residues seen in the whole 8mer insert (see Figure 4) compared to both the fully unconstrained library and the wildtype residues replaced by library insertion (A**EGD**DP). With this approach, even though less dramatic, the same trends as seen with the frequency of expression can be observed. While the number of negative residues is ~1.7 per insert for the fully unconstrained library, there is a significant increase in negative residues for the 2W and 3W as related to the library (2.5 and 3.1, respectively). Due to the overall low rate of expression of aromatic residues within unconstrained library portions of the phage, there was a large variance within each population. Therefore, besides the constrained aromatic libraries there were no statistically significant changes in the expression of aromatic residues as compared to the library. However, there was an upward trend of aromatic residue expression in the negatively constrained 3E and 4E libraries (0.6 residue/insert) in relation to the library.

When analyzing the expression of positive residues, it was seen that a maximum of one positive residue was expressed in any of the insert libraries, whether it was a constrained Lys residue or positive residues appearing in the unconstrained sections of other libraries. The constrained library had significantly higher expression of positive residues than any other library. Even though all of the negatively constrained libraries had an increased expression of positive residues, the only one that was significantly higher than the fully unconstrained library was the 2E constrained phage library. In fact, the 2E phage library expressed a significantly higher number of positive residues than all the other phage libraries with the exception of the other Glu libraries. Furthermore, in all of the inserts displaying a positive group, at least two negative residues were present.

A direct compensation mechanism seemed to occur for the constrained 1K library. It expressed an average charge of −1.5 (2.5 negative residues and 1 positive residues per insert), the same as the unconstrained library with an average charge of −1.54 (1.74 negative residues and 0.2 positive residues per insert) (Figure 3). The aromatic Trp constrained libraries expressed positive residues but at a lower rate than the unconstrained library. On the other hand, as mentioned above the Lys constrained library showed a relatively high rate of

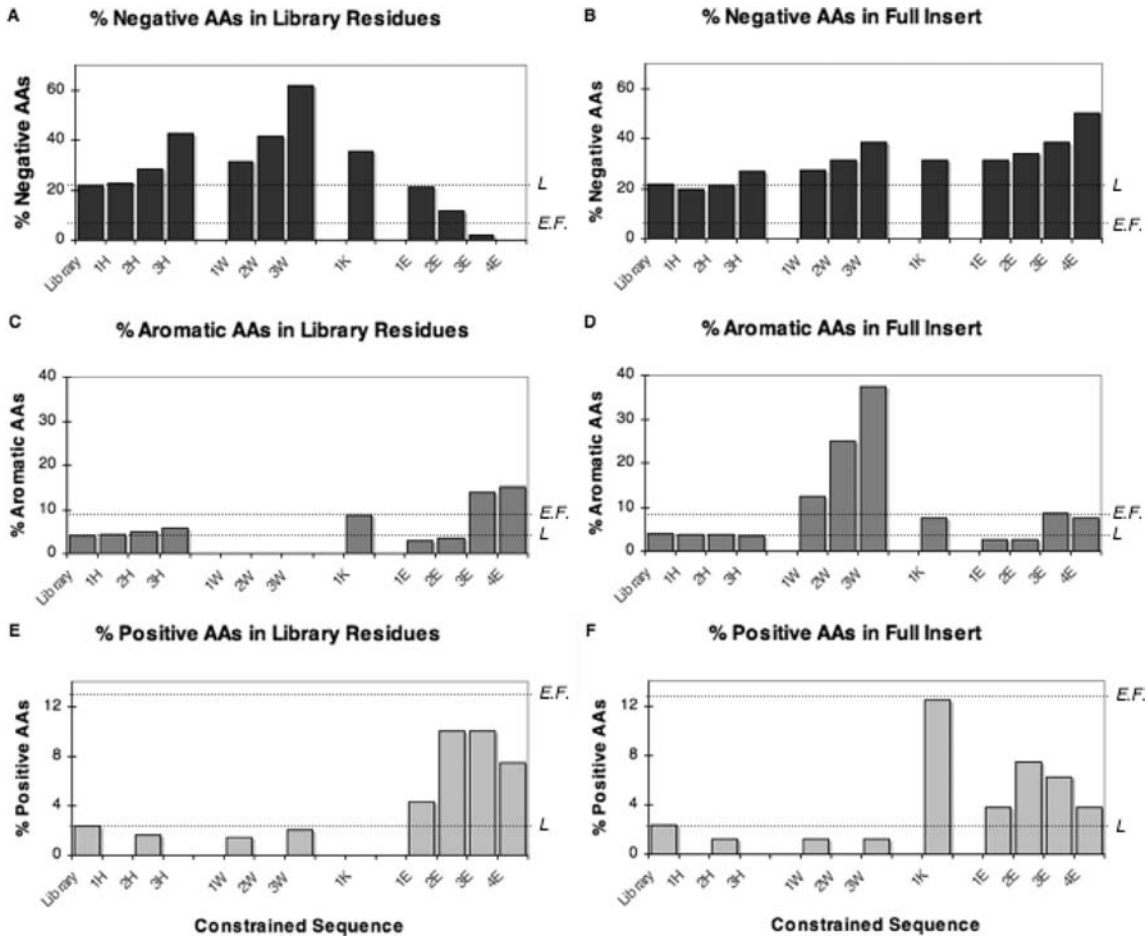

Figure 3. Frequency distribution of functional groups in expressed partial library inserts. The observed frequency of AAs with (A,B) negative, (C,D) aromatic, and (E,F) positive side chain groups is shown for both (A,C,E) the unconstrained library populations only, as well as for (B,D,F) the full 8mer insert containing both the unconstrained and the constrained sequences. Comparison lines are indicated at frequency of differently functional AAs seen in the fully unconstrained 8mer library (marked by L), and the expected frequency (marked by E.F.) as based on number of AA codons in a 32 codon library.

aromatic residue expression. When the whole insert was analyzed, the library had 0.6 aromatic residues/insert, which is similar to 3E and 4E constrained libraries.

Furthermore, with the exception of 1E, 2E, and 3E none of the constrained libraries showed any of the residues of same functionality within their unconstrained regions (i.e., Trp libraries expressed no additional aromatic residues). For the Glu libraries, the unconstrained space for 1E had the same frequency of expression for negative residues as the fully unconstrained library. The 2E library had 50% of that rate, 3E only 10%, whereas the 4E library expressed no extra negative residues within its unconstrained sequences (see Figures 3 and 4).

The His constrained libraries showed no significant variation of the aromatic residues from the fully unconstrained libraries or among each other. There was a slightly lower representation of positive residues in the His libraries, which could be attributed to the His pK_a of 6.0 having the potential to act as a slightly positive residue depending on its surroundings. The number of negative residues in the full 8mer insert did not differ significantly from the library, or each other, matching the fully unconstrained library for 1H and 2H library and then rising slightly by ~25% for the 3H library (Figure 4).

Correlation between Charge and Size on the pVIII Inserts. The size of the pVIII inserts, quantified by their molecular weights, was found to have a significant inverse relationship with their charges, indicating that larger inserts tended to be more negatively charged. The size−charge correlation was assessed independently for each of the library series and is depicted here by a linear regression and characterized by the correlation coefficient r, population size n, and the significance value p for a two-tailed t-value, with $t = r\sqrt{[(n-2)/(1-r^2)]}$. The correlation strength varied among different libraries. It was moderately weak for the fully unconstrained library ($r = -0.43$, $n = 53$, $p < 0.01$) and the E-series ($r = -0.40$, $n = 40$, $p < 0.02$), moderately strong for both H-series ($r = -0.59$, $n = 27$, $p < 0.01$) and W-series ($r = -0.60$, $n = 30$, $p < 0.001$), and very strong for the K-series ($r = -0.86$, $n = 10$, $p < 0.01$) (see Figure 5C). Regardless of the linear strength of this relationship, it was found to be statistically significant for all libraries considered. Additionally, all of the 8mer libraries expressed on pVIII seemed to have a preferred size and charge range (Figure 5A,B). The majority of inserts expressed and subsequently sequenced from all the libraries had a molecular weight between 700 and 1000, and had a net charge of −1 to −3 charges. Within that space, there was a visible shift toward both greater size and greater charge preference from unconstrained (average: −1.5, 810 Da) to constrained libraries (average: −2.3, 890 Da).

DISCUSSION

M13 bacteriophage can serve as a versatile and multifunctional material building block due to the ease of its genetic manipulation and its monodisperse filamentous shape. The coat proteins of this phage may be modified with rationally designed

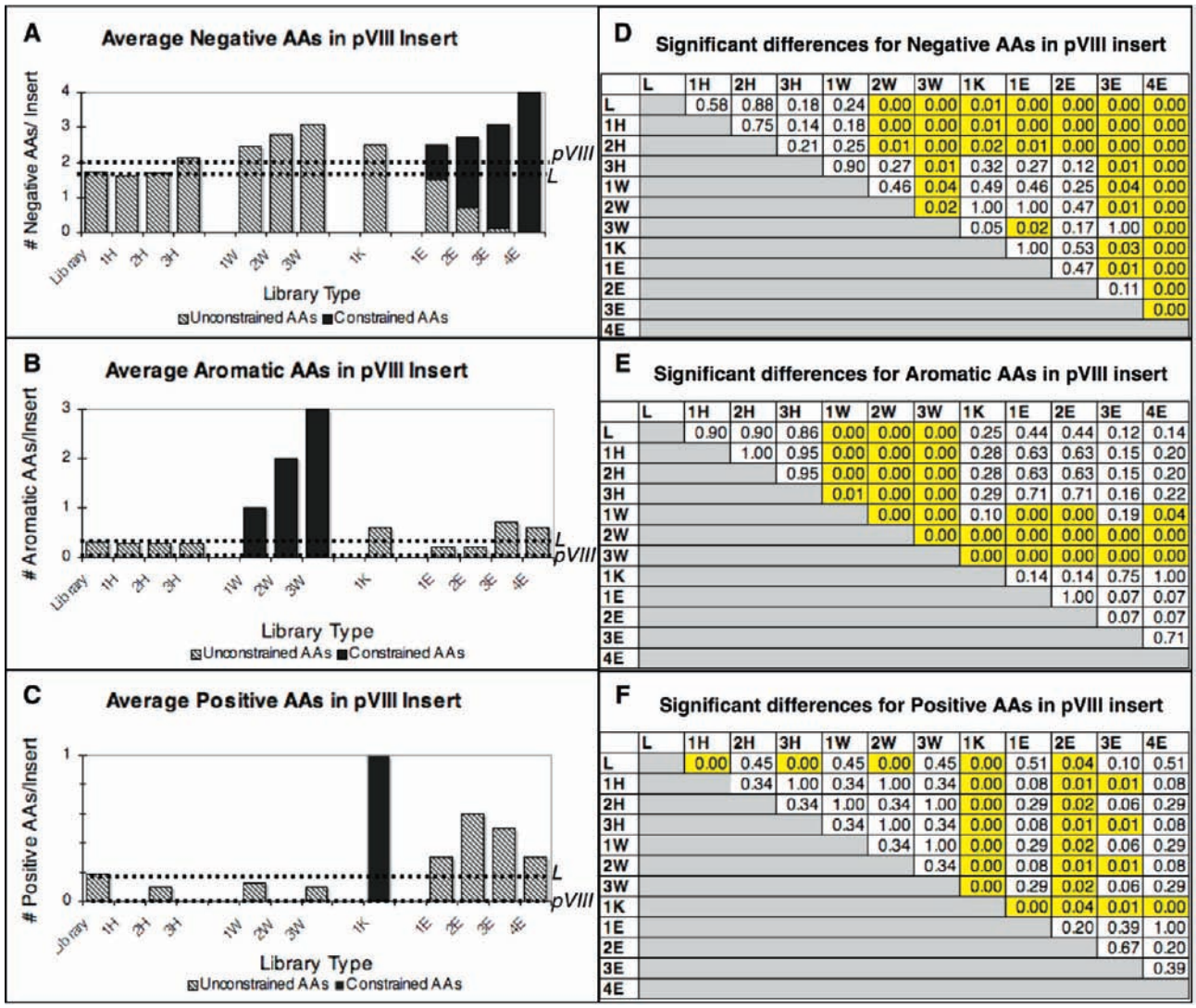

D Significant differences for Negative AAs in pVIII insert

	L	1H	2H	3H	1W	2W	3W	1K	1E	2E	3E	4E
L		0.58	0.88	0.18	0.24	0.00	0.00	0.01	0.00	0.00	0.00	0.00
1H			0.75	0.14	0.18	0.00	0.00	0.01	0.00	0.00	0.00	0.00
2H				0.21	0.25	0.01	0.00	0.02	0.01	0.00	0.00	0.00
3H					0.90	0.27	0.01	0.32	0.27	0.12	0.01	0.00
1W						0.46	0.04	0.49	0.46	0.25	0.04	0.00
2W							0.02	1.00	1.00	0.47	0.01	0.00
3W								0.05	0.02	0.17	1.00	0.00
1K									1.00	0.53	0.03	0.00
1E										0.47	0.01	0.00
2E											0.11	0.00
3E												0.00
4E												

E Significant differences for Aromatic AAs in pVIII insert

	L	1H	2H	3H	1W	2W	3W	1K	1E	2E	3E	4E
L		0.90	0.90	0.86	0.00	0.00	0.00	0.25	0.44	0.44	0.12	0.14
1H			1.00	0.95	0.00	0.00	0.00	0.28	0.63	0.63	0.15	0.20
2H				0.95	0.00	0.00	0.00	0.28	0.63	0.63	0.15	0.20
3H					0.01	0.00	0.00	0.29	0.71	0.71	0.16	0.22
1W						0.00	0.00	0.10	0.00	0.00	0.19	0.04
2W							0.00	0.00	0.00	0.00	0.00	0.00
3W								0.00	0.00	0.00	0.00	0.00
1K									0.14	0.14	0.75	1.00
1E										1.00	0.07	0.07
2E											0.07	0.07
3E												0.71
4E												

F Significant differences for Positive AAs in pVIII insert

	L	1H	2H	3H	1W	2W	3W	1K	1E	2E	3E	4E
L		0.00	0.45	0.00	0.45	0.00	0.45	0.00	0.51	0.04	0.10	0.51
1H			0.34	1.00	0.34	1.00	0.34	0.00	0.08	0.01	0.01	0.08
2H				0.34	1.00	0.34	1.00	0.00	0.29	0.02	0.06	0.29
3H					0.34	1.00	0.34	0.00	0.08	0.01	0.01	0.08
1W						0.34	1.00	0.00	0.29	0.02	0.06	0.29
2W							0.34	0.00	0.08	0.01	0.01	0.08
3W								0.00	0.29	0.02	0.06	0.29
1K									0.00	0.04	0.01	0.00
1E										0.20	0.39	1.00
2E											0.67	0.20
3E												0.39
4E												

Figure 4. Average number of functional groups in expressed partial library inserts. Average number of AAs with (A) negative, (B) aromatic, and (C) positive side chain groups is shown for the constructed libraries. A contribution to the total number of groups is shown from both the unconstrained and constrained residues within the insert. Comparison lines are indicated for fully unconstrained library (marked L) and for the replaced wild-type pVIII residues at positions 2−4 (A**EGD**DP) (marked pVIII). Significant differences in expression (indicated by yellow shading) among the libraries are indicated in (D−F), with *p*-values shown as obtained from a Student's *t* test.

short peptides, or endowed with peptide libraries to find specific binding information via a phage display directed evolution screening method (*2, 48, 49*). We have previously demonstrated the use of such genetically engineered phage for a tissue engineering scaffold application (*33*). As specific phage interaction with the cells was the main goal, a rational design approach was chosen to display well-known RGD and IKVAV cell signaling motifs (*39*−*41*). Additionally, a peptide expression on every copy of pVIII was preferred over a more sparse phagemid system display (*2, 34*), in order to obtain a high density of the signaling motifs ($\sim 1.5 \times 10^{13}$ epitopes/cm^2) (*33*). Surfaces displaying such a high density of peptide motifs have been shown to promote a stronger cellular response ranging from attachment to differentiation (*39, 40*).

Whereas the sequence of the wild-type pVIII protein has naturally evolved to be a good fit for all of the biological interactions and processes involved in phage replication, any engineered protein additions or modifications have to pass through this imposed censorship prior to expression (see Figure 1). PVIII is a product of M13 phage gene gVIII and begins its existence through transcription and translation by the *E. coli* cell machinery. PVIII is a very high copy number protein, with 0.5 to 5 million units being transcribed and translated every cell division cycle, and 2700 units are needed to package every virus before it is able to leave the cell (*19, 50*). The full protein, called procoat, is 73 amino acids in length, and contains a signal and mature peptide regions (Figure 1C). Positive Lys charges at both its amino and carboxy ends target the procoat molecule to the phospholipid membrane by electrostatic attraction (*51*) (Figure 1D). Once at the membrane, the hydrophobic segments located in the signal and mature portions of the procoat protein partition into the lipid bilayer. YidC transporter protein and electrophoretic potential are responsible for inserting the connecting loop into the periplasm (*22, 23, 52, 53*). Leader peptidase is a protein that is responsible for releasing the signal peptide sequences from many bacterial transmembrane proteins. The cleavage site utilized by the peptidase is dictated by the sequence of the substrate protein, its position in relation to the membrane interface, and the quality of fit to the peptidase (*54*−*56*). The pVIII procoat is one of the proteins cleaved by the leader peptidase, releasing the N-terminus of the mature peptide (*16, 17, 54*). After a sufficient concentration of the pVIII protein has been processed and collected in the *E. coli* inner membrane, the pVIII units pack around the extruding phage DNA strand (*23*). The phage extrusion process is orchestrated by pI and pXI phage proteins and an *E. coli* protein threoxin.

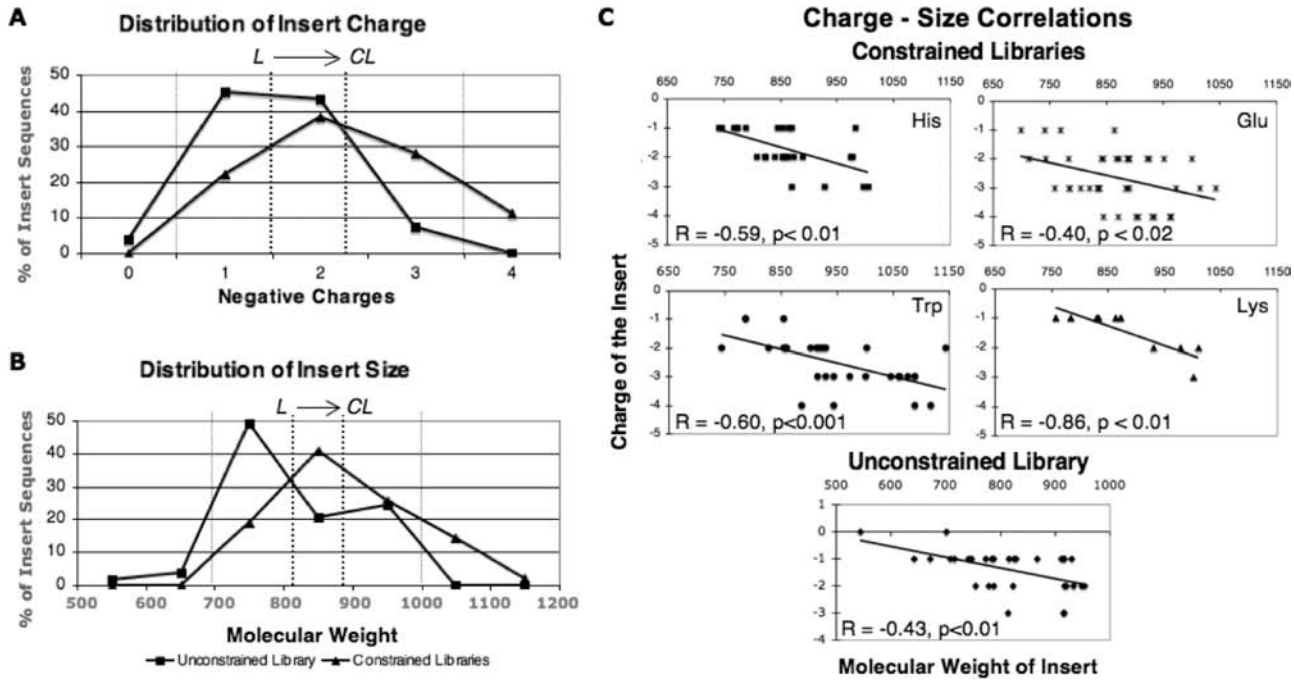

Figure 5. The charge and size of the expressed pVIII library inserts. (A) Charge and (B) molecular weight distributions of the pVIII unconstrained library (■) were compared to the partially constrained insert libraries (▲). The light dashed lines indicate the preferred size and charge for both libraries, whereas the dark dashed lines show a shift of average charge and average size from the unconstrained library (marked by *L*) to the partially constrained libraries (marked by *CL*). (C) An inverse relationship of insert charge to insert size is represented by a linear regression for all of the constructed libraries. The correlation coefficient *R*, and the statistical significance value *p*, is indicated for each of the libraries.

As the phage leaves the cell, it moves through a complex formed by the three above-mentioned proteins from the inner membrane, as well as through a multimeric pore formed by the pIV phage proteins in the outer membrane (*14*). The extrusion is propelled by the packing of the pVIII molecules around the phage DNA (*57*) and by the energy derived from the ATP hydrolysis and proton motive force (*58*). The phage reenters the cell via infection, which depends on the binding event between the pIII minor phage coat protein to the F-pili of the cell and pVIII interaction with both the TolQRA and pIII proteins (*13*). If the infection is successful, the phage DNA is unpackaged and injected into the cell, restarting the process over again.

To find the full insert sequence that would be expressed on pVIII protein, yet contain the desired RGD motif, we used a partially constrained library approach described above (see Figure 1). Although similarly constrained libraries are often used in phage display approaches to improve the binding of the identified short motif sequences (*59, 60*), in our application it was utilized as a means to display the initially unfavorable RGD peptide by allowing the unconstrained library residues to be controlled and chosen by the *E. coli* host. In this manner, the full inserts that were expressed contained both the designed constrained motif and a library chosen through evolutionary selection processes by the *E. coli* cellular mechanisms. This biologically chosen favorability of the insert would then allow for resulting phage particles to preserve their sequence during large-scale amplifications, which could then be used to build structured phage materials.

As seen in previous studies investigating pVIII peptide libraries, when attempting to express IKVAV and RGD cell signaling peptides, or later, Lys constrained libraries on M13 pVIII protein, we succeeded only when the overall charge of the insert was lower than or equal to −1 (*3*). Whereas Lys residues are expressed easily by the bacteria at the signal peptide end as well as the C-terminus of pVIII (Figure 1), their apparent lack in the periplasmic loop, which later becomes the N-terminus of the mature pVIII is well-documented (*22, 25, 34*). This distribution of positive charges on pVIII can be explained by their function within the phage replication process. As explained above, the presence of positive residues on either end of the procoat protein is needed for the electrostatic binding and anchoring of the protein to the phospohlipid membrane interface of bacteria, and then later to the phage DNA. Their lack in the periplasmic loop can be attributed to the electrophoretic gradient across the bacterial cell membrane that drives the negatively charged portions of the protein across and keeps the positively charged portions in the cytoplasm (*22, 45, 47, 61*).

Further application of the partial library method allowed us to express a TNT binding peptide WHWQ on pVIII (*44*). With expression on all 2700 copies, the WHWQ M13 phage has a very high avidity, likely improving its utilization as a sensor material (*44*). The bulky aromatic peptide motif could only be displayed when surrounded by two to three negative residues, corresponding to an observed increased display of negative residues in the aromatic Trp constrained libraries. The under-representation of aromatic residues at the N-terminus portion of M13 pVIII and other mature peptides of bacterial proteins has previously been observed (*25, 55, 56*). Potentially, this trend can be attributed to the "anti-snorkeling" properties of the aromatic residues located just outside of the membrane interface. Anti-snorkeling refers to the tendency of the aromatic residues to bury their side groups in the membrane interface region, facing the aromatic portion toward the hydrophobic lipid chains and the polar groups toward the negative phospholipid layer (*46, 47, 61*−*63*).

In the wild-type pVIII, the leader peptidase cleavage site is framed by a transmembrane segment of the signal peptide and the acidic periplasmic loop. A hydrophobic Phe residue at position −2 is likely buried in the membrane, while three negatively charged hydrophilic residues at positions +2, +4, and +5 serve as a hydrophilic anchor of the periplasmic loop, propelling it out of the membrane and away from the negatively charged membrane phospholipid groups (Figure 1C). These

opposing forces expose the leader peptidase cleavage site in the periplasm, allowing the leader peptidase to cleave the signal peptide and release the mature pVIII protein. The increase of negatively charged residues observed in the unconstrained spaces of the library inserts carrying large aromatic segments (WHWQ, 2W, and 3W) could be necessary to counteract the affinity of such constrained sequences toward the interface region. Thus, it is possible that only the proteins where the cleavage site was sufficiently exposed in the periplasm were cleaved and could be further processed into viable phage. The reverse trend was seen for the very negatively constrained libraries (3E and 4E) where the frequency of aromatic residues was 50−60% higher than expected. This could explain the opposite side of this phenomenon, where the aromatic residues served to counteract the tendency of very hydrophilic Glu amino acids to pull the signal peptide out of the membrane, therefore shifting the position of the cleavage site and making it less accessible for processing (*54*).

Protein translation was another process that was seen to impose strong limitations on the allowed insert sequences. In our library engineering efforts, none of the four designed series were able to display five or six long amino acid repeats, and only the 4E library was successful in producing phage with four repeating consecutive residues. This observation can be attributed to a previously shown dependence of protein translation accuracy and library residue expression on tRNA isoacceptor population in the *E. coli* host (*50, 64*). The repetitive use of amino acids combined with the high copy number of the pVIII protein resulted in draining the pool of the available corresponding tRNA isoacceptors. The necessary recharging of the isoacceptors could have slowed the translation process to a rate that was too slow to keep up with the demand of pVIII proteins necessary to package and extrude the accumulated single-stranded phage DNA, thus causing the host cell death (*50, 64*−*66*). The more repetitive pVIII phage inserts that were incorporated, translated, and packaged had mutations containing a large number of deletions (data not shown), which is common in long stretches of repeating residues (*67*). Even though the 4E phage still occasionally showed deletions and mutations, it was the only kind that could sustain a four amino acid repeat. This was likely due to the large number of Glu isoacceptors in *E. coli* cells (*50*) and to the favorable negative charge at pVIII N-terminus location.

The inverse charge−size relationship seen within the libraries might be attributed to the increased number of negatively charged groups expressed in the large aromatic group containing inserts. However, this relationship is seen even when the inserts are not aromatic and is most pronounced when the constrained insert is carrying a positively charged residue. The size of the insert presented at the N-terminus of pVIII protein is thought to be partially limited by both the size and the properties of the phage extrusion channel formed by pIV proteins (*12, 35*), measuring 6-9 nm in diameter (*18*). The exact structure of pIV protein has not yet been solved, and the exact mechanism of phage extrusion is unknown. However, a strong homology has been identified between the phage extrusion mechanism and type II secretion proteins, which control macromolecule export from bacterial outer membranes (*19, 68*). Many of the type II secretion proteins, including phage pIV protein, have highly conserved C-terminal domains, composed of strongly amphipathic β-sheet structures. These structures anchor the pore in the membrane with the hydrophobic residues and face the charged residues toward the center of the pore to make a large aqueous channel (*20, 69*). Additionally, it has been shown that transport through these channels depends on both ATP hydrolysis and the proton motive force (*58*). Thus, in our system, the greater hydrophilicity of the phage surface is favorable to reduce the hydration necessary for hydrophobic molecules when traveling through a hydrophilic pore (*70*), and the negative charge is favorable to help the phage molecule move down the proton motive force gradient.

In summary, we have described a novel partially constrained library cloning method that allows for the expression of short functional peptide motifs on all of the phage major coat proteins. Our cloning method works through adaptation of the flanking library residues by host induced natural selection, to make the full protein favorable for phage replication. Furthermore, we analyzed the ability of such 8mer insert partial library systems to display positive, negative, and hydrophobic groups, as well as the relationship between the insert charge and its size. Such host−pathogen interaction analysis could be combined with a recently developed virus protein association assay to further our knowledge of general phage biology, and potentially identify novel targets for antibacterial drug development (*71*).

The utilization of such a library engineering approach would be useful in any application where a short functional peptide motif is known, and the current phage display methodology might not provide superior information (*72, 73*). This approach allows not only to express a desired functional group on every copy of the major coat protein of the phage, but also to identify the phage particles that can preserve their sequence during large-scale amplification. Thus, it would be beneficial in a variety of materials applications where density and uniformity of peptide display are favored, including crystal templation (*10, 27, 28*), cell differentiation (*39, 40*), and sensor platforms (*44*). Overall, the utilization of the novel partial library method to express desired peptide groups on all of the major coat proteins of the M13 bacteriophage can serve to further exploit it as a functional nanobiomaterial.

ACKNOWLEDGMENT

This work was supported by the Hellman Family Faculty Fund (SWL), start-up funds from the Nanoscience and Nanotechnology Institute at the University of California, Berkeley (SWL), the Laboratory Directed Research and Development fund from the Lawrence Berkeley National Laboratory, and the Graduate Student Fellowship from the National Science Foundation (AM). We thank Drs. Irina Merzlyak and Justyn Jaworski for help in editing this manuscript.

LITERATURE CITED

(1) Petrenko, V. A., Smith, G. P., Gong, X., and Quinn, T. (1996) A library of organic landscapes on filamentous phage. *Protein Eng. 9*, 797–801.
(2) Smith, G. P., and Petrenko, V. A. (1997) Phage display. *Chem. Rev. 97*, 391–410.
(3) Iannolo, G., Minenkova, O., Petruzzelli, R., and Cesareni, G. (1995) Modifying filamentous phage capsid: limits in the size of the major capsid protein. *J. Mol. Biol. 248*, 835–44.
(4) Lee, S. W., Mao, C. B., Flynn, C. E., and Belcher, A. M. (2002) Ordering of quantum dots using genetically engineered viruses. *Science 296*, 892–895.
(5) Huang, Y., Chiang, C. Y., Lee, S. K., Gao, Y., Hu, E. L., De Yoreo, J., and Belcher, A. M. (2005) Programmable assembly of nanoarchitectures using genetically engineered viruses. *Nano Lett. 5*, 1429–1434.
(6) Merzlyak, A., and Lee, S. W. (2006) Phage as templates for hybrid materials and mediators for nanomaterial synthesis. *Curr. Opin. Chem. Biol. 10*, 246–252.
(7) Petrenko, V. A., Smith, G. P., Mazooji, M. M., and Quinn, T. (2002) alpha-helically constrained phage display library. *Protein Eng. 15*, 943–950.
(8) Dogic, Z., and Fraden, S. (2006) Ordered phases of filamentous viruses. *Curr. Opin. Colloid Interface Sci. 11*, 47–55.

(9) Lee, S. W., Wood, B. M., and Belcher, A. M. (2003) Chiral smectic C structures of virus-based films. *Langmuir 19*, 1592–1598.
(10) Nam, K. T., Kim, D. W., Yoo, P. J., Chiang, C. Y., Meethong, N., Hammond, P. T., Chiang, Y. M., and Belcher, A. M. (2006) Virus-enabled synthesis and assembly of nanowires for lithium ion battery electrodes. *Science 312*, 885–888.
(11) Wang, Y. A., Yu, X., Overman, S., Tsuboi, M., Thomas, G. J., and Egelman, E. H. (2006) The structure of a filamentous bacteriophage. *J. Mol. Biol. 361*, 209–215.
(12) Makowski, L. (1993) Structural constraints on the display of foreign peptides on filamentous bacteriophages. *Gene 128*, 5–11.
(13) Click, E. M., and Webster, R. E. (1998) The TolQRA proteins are required for membrane insertion of the major capsid protein of the filamentous phage f1 during infection. *J. Bacteriol. 180*, 1723–8.
(14) Feng, J. N., Model, P., and Russel, M. (1999) A trans-envelope protein complex needed for filamentous phage assembly and export. *Mol. Microbiol. 34*, 745–755.
(15) Hohn, B., Lechner, H., and Marvin, D. A. (1971) Filamentous bacterial viruses 0.1. DNA synthesis during early stages of infection with Fd. *J. Mol. Biol. 56*, 143.
(16) Kuhn, A., and Wickner, W. (1985) Isolation of mutants in M13 coat protein that affect its synthesis, processing, and assembly into phage. *J. Biol. Chem. 260*, 15907–13.
(17) Malik, P., Tarry, T. D., Gowda, L. R., Langara, A., Petukhov, S. A., Symmons, M. F., Welsh, L. C., Marvin, D. A., and Perham, R. N. (1996) Role of capsid structure and membrane protein processing in determining the size and copy number of peptides displayed on the major coat protein of filamentous bacteriophage. *J. Mol. Biol. 260*, 9–21.
(18) Opalka, N., Beckmann, R., Boisset, N., Simon, M. N., Russel, M., and Darst, S. A. (2003) Structure of the filamentous phage pIV multimer by cryo-electron microscopy. *J. Mol. Biol. 325*, 461–470.
(19) Russel, M., Linderoth, N. A., and Sali, A. (1997) Filamentous phage assembly: Variation on a protein export theme. *Gene 192*, 23–32.
(20) Marvin, D. A., Welsh, L. C., Symmons, M. F., Scott, W. R., and Straus, S. K. (2006) Molecular structure of fd (f1, M13) filamentous bacteriophage refined with respect to X-ray fibre diffraction and solid-state NMR data supports specific models of phage assembly at the bacterial membrane. *J. Mol. Biol. 355*, 294–309.
(21) Samuelson, J. C., Jiang, F. L., Yi, L., Chen, M. Y., de Gier, J. W., Kuhn, A., and Dalbey, R. E. (2001) Function of YidC for the insertion of M13 Procoat protein in Escherichia coli - Translocation of mutants that show differences in their membrane potential dependence and Sec requirement. *J. Biol. Chem. 276*, 34847–34852.
(22) Schuenemann, T. A., Delgado-Nixon, V. M., and Dalbey, R. E. (1999) Direct evidence that the proton motive force inhibits membrane translocation of positively charged residues within membrane proteins. *J. Biol. Chem. 274*, 6855–6864.
(23) Stopar, D., Spruijt, R. B., Wolfs, C. J., and Hemminga, M. A. (2003) Protein-lipid interactions of bacteriophage M13 major coat protein. *Biochim. Biophys. Acta 1611*, 5–15.
(24) Smith, G. P. (1988) Filamentous phage assembly - morphogenetically defective-mutants that do not kill the host. *Virology 167*, 156–165.
(25) Kuzmicheva, G. A., Jayanna, P. K., Sorokulova, I. B., and Petrenko, V. A. (2009) Diversity and censoring of landscape phage libraries. *Protein Eng., Des. Sel. 22*, 9–18.
(26) Rodi, D. J., Soares, A. S., and Makowski, L. (2002) Quantitative assessment of peptide sequence diversity in M13 combinatorial peptide phage display libraries. *J. Mol. Biol. 322*, 1039–52.
(27) Yamashita, I. (2008) Biosupramolecules for nano-devices: biomineralization of nanoparticles and their applications. *J. Mater. Chem. 18*, 3813–3820.
(28) Uchida, M., Klem, M. T., Allen, M., Suci, P., Flenniken, M., Gillitzer, E., Varpness, Z., Liepold, L. O., Young, M., and Douglas, T. (2007) Biological containers: Protein cages as multifunctional nanoplatforms. *Adv. Mater. 19*, 1025–1042.
(29) Bermudez, H., and Hathorne, A. P. (2008) Incorporating stimulus-responsive character into filamentous virus assemblies. *Faraday Discuss. 139*, 327–35, discussion 399−417, 419−20.
(30) Krag, D. N., Shukla, G. S., Shen, G. P., Pero, S., Ashikaga, T., Fuller, S., Weaver, D. L., Burdette-Radoux, S., and Thomas, C. (2006) Selection of tumor-binding ligands in cancer patients with phage display libraries. *Cancer Res. 66*, 8925–8925.
(31) Hajitou, A., Trepel, M., Lilley, C. E., Soghomonyan, S., Alauddin, M. M., Marini, F. C., Restel, B. H., Ozawa, M. G., Moya, C. A., Rangel, R., Sun, Y., Zaoui, K., Schmidt, M., von Kalle, C., Weitzman, M. D., Gelovani, J. G., Pasqualini, R., and Arap, W. (2006) A hybrid vector for ligand-directed tumor targeting and molecular imaging. *Cell 125*, 385–398.
(32) Frenkel, D., and Solomon, B. (2002) Filamentous phage as vector-mediated antibody delivery to the brain. *Proc. Natl. Acad. Sci. U.S.A. 99*, 5675–9.
(33) Merzlyak, A., Indrakanti, S., and Lee, S. W. (2009) Genetically engineered nanofiber-like viruses for tissue regenerating materials. *Nano Lett. 9*, 846–52.
(34) Imai, S., Mukai, Y., Takeda, T., Abe, Y., Nagano, K., Kamada, H., Nakagawa, S., Tsunoda, S., and Tsutsumi, Y. (2008) Effect of protein properties on display efficiency using the M13 phage display system. *Pharmazie 63*, 760–764.
(35) Rodi, D. J., Mandova, S., Makowski, L. (2005) Filamentous Bacteriophage Structure and Biology, in *Phage Display in Biotechnology and Drug Discovery* (Sidhu, S. S., Ed.) p 748, CRC Press Taylor & Francis Group, Boca Raton, FL.
(36) Chen, G., and Courey, A. J. (1999) Generation of epitope-tagged proteins by inverse PCR mutagenesis. *BioTechniques 26*, 814–816.
(37) Sambrook, J., and Russell, D. W. (2001) *Molecular Cloning: A Laboratory Manual*, 3rd ed., CSHL Press.
(38) Noren, K. A., and Noren, C. J. (2001) Construction of high-complexity combinatorial phage display peptide libraries. *Methods 23*, 169–78.
(39) Schense, J. C., Bloch, J., Aebischer, P., and Hubbell, J. A. (2000) Enzymatic incorporation of bioactive peptides into fibrin matrices enhances neurite extension. *Nat. Biotechnol. 18*, 415–9.
(40) Silva, G. A., Czeisler, C., Niece, K. L., Beniash, E., Harrington, D. A., Kessler, J. A., and Stupp, S. I. (2004) Selective differentiation of neural progenitor cells by high-epitope density nanofibers. *Science 303*, 1352–5.
(41) Pierschbacher, M. D., and Ruoslahti, E. (1984) Cell attachment activity of fibronectin can be duplicated by small synthetic fragments of the molecule. *Nature 309*, 30–3.
(42) Sephel, G. C., Tashiro, K. I., Sasaki, M., Greatorex, D., Martin, G. R., Yamada, Y., and Kleinman, H. K. (1989) Laminin A chain synthetic peptide which supports neurite outgrowth. *Biochem. Biophys. Res. Commun. 162*, 821–9.
(43) Ruoslahti, E. (1996) RGD and other recognition sequences for integrins. *Annu. Rev. Cell Dev. Biol. 12*, 697–715.
(44) Jaworski, J. W., Raorane, D., Huh, J. H., Majumdar, A., and Lee, S. W. (2008) Evolutionary screening of biomimetic coatings for selective detection of explosives. *Langmuir 24*, 4938–43.
(45) Zilberstein, D., Agmon, V., Schuldiner, S., and Padan, E. (1984) Escherichia coli intracellular pH, membrane potential, and cell growth. *J. Bacteriol. 158*, 246–52.
(46) Adamian, L., Nanda, V., DeGrado, W. F., and Liang, J. (2005) Empirical lipid propensities of amino acid residues in multispan alpha helical membrane proteins. *Proteins 59*, 496–509.
(47) Stopar, D., Spruijt, R. B., and Hemminga, M. A. (2006) Anchoring mechanisms of membrane-associated M13 major coat protein. *Chem. Phys. Lipids 141*, 83–93.
(48) Whaley, S. R., English, D. S., Hu, E. L., Barbara, P. F., and Belcher, A. M. (2000) Selection of peptides with semiconductor

binding specificity for directed nanocrystal assembly. *Nature 405*, 665–668.
(49) Lee, S. K., Yun, D. S., and Belcher, A. M. (2006) Cobalt ion mediated self-assembly of genetically engineered bacteriophage for biomimetic Co-Pt hybrid material. *Biomacromolecules 7*, 14–7.
(50) Rodi, D. J., and Makowski, L. (1997) In *Proceedings of the 22nd Tanaguchi International Symposium*, p 155.
(51) Kuhn, A., Wickner, W., and Kreil, G. (1986) The cytoplasmic carboxy terminus of M13 procoat is required for the membrane insertion of its central domain. *Nature 322*, 335–9.
(52) Russel, M. (1993) Protein-protein interactions during filamentous phage assembly. *J. Mol. Biol. 231*, 689–697.
(53) Samuelson, J. C., Chen, M. Y., Jiang, F. L., Moller, I., Wiedmann, M., Kuhn, A., Phillips, G. J., and Dalbey, R. E. (2000) YidC mediates membrane protein insertion in bacteria. *Nature 406*, 637–641.
(54) Jain, R. G., Rusch, S. L., and Kendall, D. A. (1994) Signal peptide cleavage regions. Functional limits on length and topological implications. *J. Biol. Chem. 269*, 16305–10.
(55) Choo, K. H., Tong, J. C., and Ranganathan, S. (2008) Modeling Escherichia coli signal peptidase complex with bound substrate: determinants in the mature peptide influencing signal peptide cleavage. *BMC Bioinf. 9* (Suppl. 1), S15.
(56) Choo, K. H., and Ranganathan, S. (2008) Flanking signal and mature peptide residues influence signal peptide cleavage. *BMC Bioinf. 9* (Suppl. 12), S15.
(57) Papavoine, C. H. M., Christiaans, B. E. C., Folmer, R. H. A., Konings, R. N. H., and Hilbers, C. W. (1998) Solution structure of the M13 major coat protein in detergent micelles: A basis for a model of phage assembly involving specific residues. *J. Mol. Biol. 282*, 401–419.
(58) Feng, J. N., Russel, M., and Model, P. (1997) A permeabilized cell system that assembles filamentous bacteriophage. *Proc. Natl. Acad. Sci. U.S.A. 94*, 4068–73.
(59) Brissette, R., and Goldstein, N. I. (2007) The use of phage display peptide libraries for basic and translational research, In *Methods in Molecular Biology* (Fisher, P., Ed.) pp 203−213, Humana Press, Inc., Totowa, NJ.
(60) Li, R., Hoess, R. H., Bennett, J. S., and DeGrado, W. F. (2003) Use of phage display to probe the evolution of binding specificity and affinity in integrins. *Protein Eng. 16*, 65–72.
(61) von Heijne, G. (1994) Membrane proteins: from sequence to structure. *Annu. Rev. Biophys. Biomol. Struct. 23*, 167–92.
(62) Liang, J., Adamian, L., and Jackups, R., Jr. (2005) The membrane-water interface region of membrane proteins: structural bias and the anti-snorkeling effect. *Trends Biochem. Sci. 30*, 355–7.
(63) Braun, P., and von Heijne, G. (1999) The aromatic residues Trp and Phe have different effects on the positioning of a transmembrane helix in the microsomal membrane. *Biochemistry 38*, 9778–82.
(64) Elf, J., Nilsson, D., Tenson, T., and Ehrenberg, M. (2003) Selective charging of tRNA isoacceptors explains patterns of codon usage. *Science 300*, 1718–22.
(65) Pratt, D., Tzagoloff, H., and Erdahl, W. S. (1966) Conditional lethal mutants of the small filamentous coliphage M13. I. Isolation, complementation, cell killing, time of cistron action. *Virology 30*, 397–410.
(66) Hohn, B., Schutz, H. V., and Marvin, D. A. (1971) Filamentous bacterial viruses 0.2. killing of bacteria by abortive infection with Fd. *J. Mol. Biol. 56*, 155.
(67) Vilette, D., Ehrlich, S. D., and Michel, B. (1995) Transcription-induced deletions in Escherichia coli plasmids. *Mol. Microbiol. 17*, 493–504.
(68) Genin, S., and Boucher, C. A. (1994) A superfamily of proteins involved in different secretion pathways in gram-negative bacteria: modular structure and specificity of the N-terminal domain. *Mol. Gen. Genet. 243*, 112–8.
(69) Nikaido, H. (2003) Molecular basis of bacterial outer membrane permeability revisited. *Microbiol. Mol. Biol. Rev. 67*, 593–656.
(70) Nikaido, H. (1992) Porins and specific channels of bacterial outer membranes. *Mol. Microbiol. 6*, 435–42.
(71) Zlotnick, A., Lee, A., Bourne, C. R., Johnson, J. M., Domanico, P. L., and Stray, S. J. (2007) In vitro screening for molecules that affect virus capsid assembly (and other protein association reactions). *Nat. Protocols 2*, 490–498.
(72) Brammer, L. A., Bolduc, B., Kass, J. L., Felice, K. M., Noren, C. J., and Hall, M. F. (2008) A target-unrelated peptide in an M13 phage display library traced to an advantageous mutation in the gene II ribosome-binding site. *Anal. Biochem. 373*, 88–98.
(73) Kolb, G., and Boiziau, C. (2005) Selection by phage display of peptides targeting the HIV-1 TAR element. *RNA Biol. 2*, 28–33.

BC900303F

Cellular Uptake Mechanism of Molecular Umbrella

Dongtao Ge,[†] Dewang Wu,[†] Zuyong Wang,[†] Wei Shi,*[,†,‡] Ting Wu,[§] Aifeng Zhang,[†] Shimin Hong,[†] Jun Wang,[†] Ye Zhang,[§] and Lei Ren*[,†,‡]

Department of Biomaterials/Biomedical Engineering Research Center, College of Materials, State Key Laboratory for Physical Chemistry of Solid Surfaces, and Department of Preclinical Medicine, Medical College, Xiamen University, Xiamen 361005, China. Received July 11, 2009; Revised Manuscript Received September 23, 2009

Molecular umbrella provided a promising avenue for the design of the intracellular delivery of hydrophilic therapeutic agents. However, the limited understanding of its cellular uptake would be a roadblock to its effective application. Herein, we investigate the ability and mechanism of cellular entry of a fluorescently labeled diwalled molecular umbrella, which was synthesized from cholic acid, spermine, and 5-carboxyfluorescein, into Hela cells, with the extent of uptake analyzed by confocal fluorescence microscopy and flow cytometry. It is found that the as-synthesized diwalled molecular umbrella can greatly facilitate cellular uptake of hydrophilic agent, 5-carboxyfluorescein. *In vitro* experiments with diffuse marker, endocytic marker, and inhibitors suggested that several distinct uptake pathways (e.g., passive diffuse, clathrin-mediated endocytosis, and caveolae/lipid-raft-dependent endocytosis) are involved in the internalization of diwalled molecular umbrella. These results, together with its low toxicity and good biocompatibility, thus demonstrate the suitability of molecular umbrella for application as vectors in drug delivery systems.

INTRODUCTION

Cellular internalization of hydrophilic therapeutic agents such as anticancer drugs, proteins, and nucleic acids is still a challenge because the strongly hydrophobic interior of the plasma membrane inhibits the entry of these molecules (*1, 2*). Therefore, intracellular delivery of these pharmaceuticals relies on delivery systems that allow improved transport across the cell membrane.

A novel drug delivery vector, molecular umbrella, devised by Regen's group (*3*) in 1996, has been extensively studied for its potential to transport across the cell membrane. The classical molecular umbrella was composed of two facially amphiphilic units (i.e., rigid units having a hydrophobic and a hydrophilic face) and a central scaffold bearing a bioactive agent (*3, 4*). When the hydrophilic agent that attached to a molecular umbrella is immersed in an aqueous environment, an exposed conformation is favored such that intramolecular hydrophobic interactions are maximized and the external face of each wall is hydrated. In contrast, in a hydrophobic environment such as a lipid bilayer, the umbrella is closed on the compound in a shielded conformation so that the hydrophilic faces of the sterols now interact with the compound while the hydrophobic faces interact with the lipid tails (*3*−*5*). So far, many biologically active agents, such as glutathione (*6*), antisense oligonucleotides (*7*), and ATP (*8*), have been reported to be bound to the molecular umbrellas, and these agents were transported across the synthetic phospholipid bilayers by passive diffusion under the assistance of molecular umbrella. Recently, an important question for molecular umbrellas as drug carriers, i.e., whether molecular umbrellas are capable of crossing the plasma membrane of living cells, was sought by Mehiri et al. (*9*). Using confocal microscopy, they found that fluorescently labeled molecular umbrellas could enter live Hela cells and the distributions of molecular umbrellas were throughout the cytoplasm and the nucleus. This finding raises the possibility that molecular umbrellas could be used as drug vectors of intracellular delivery.

In order to design a new drug delivery system of a molecular umbrella for intracellular delivery more rationally, it is important to understand its cellular uptake mechanism. In general, the main routes into a cell are endocytosis, active transport, facilitated diffusion, and passive diffusion (*10*). Since molecular umbrella has the ability to cross liposomal membranes by passive diffusion and the cell membrane consists of phosolipid bilayer and proteins, Mehiri et al. suggested that passive diffusion should be a pathway in cellular uptake of molecular umbrella (*9*). However, whether there are other mechanisms that are contributing to the cellular entry of molecular umbrella is still unknown. This limited understanding of cellular uptake of the molecular umbrella has been a roadblock to its effective application.

In this paper, we synthesized a fluorescently labeled diwall molecular umbrella, and evaluated the ability and mechanism of molecular umbrellas across the cell membrane. We chose cholic acid as the amphiphilic wall and spermidine as the central scaffold. The diwall molecular umbrella (N_1,N_3-dicholeamidospermidine) was prepared by coupling two cholic acid molecules on the spermidine. Followed by conjunction of N_1,N_3-dicholeamidospermidine and 5-carboxyfluorescein (5-cf), 5-cf labeled molecular umbrella (5-cf-mu) was obtained. The cytotoxicity of 5-cf-mu toward Hela cells was described by MTT assays. The internalization of 5-cf-mu was tracked by confocal fluorescence microscopy (CLSM) and flow cytometry analysis (FACS). *In vitro* colocation and endocytosis inhibition experiments were further used to evaluate the cellular uptake of 5-cf-mu in Hela cells.

EXPERIMENTAL DETAILS

Materials and Methods. Cholic acid, spermidine, and diisopropylethylamine were purchased from Acros Organic

* Corresponding authors. W. Shi and L. Ren, Department of Biomaterials/Biomedical Engineering Research Center, College of Materials, Xiamen University, Xiamen 361005, China. Tel.: +865922188502 (W. Shi); +865922188530 (L. Ren). Fax: +865922185299. E-mail: shiwei@xmu.edu.cn (W. Shi); renlei@xmu.edu.cn (L. Ren).

[†] College of Materials.

[‡] State Key Laboratory for Physical Chemistry of Solid Surfaces.

[§] Medical College.

10.1021/bc9003074 © 2009 American Chemical Society
Published on Web 11/17/2009

(USA). *N*,*N*-Dicyclohexylcarbodiimide (DCC), *N*-hydroxysuccinimide (NHS), sodium azide (NaN_3), 5-carboxyfluorescein (5-cf), 2′-(4-hydroxyphenyl)-5-(4-methyl-1-piperazinyl)-2,5′-bi-1*H*-benzimidazole (Hoechst 33258), 3-hydroxy-1,2,3-benzotriazin-4(3*H*)-one (HOObt), Nocodazole (Noc), and chlorpromazine hydrochloride (CpZ) were obtained from Sigma-Aldrich (USA). Carboxyfluorescein diacetate succinimidyl ester (CFSE), Alexa Fluor 546-transferrin, Alexa Fluor 594-Ctx B reagent, and LysoTracker Red were purchased from Molecular Probe (USA). Trypsin and 3-(4,5-dimethylthiazol-2-yl)-2,5-diphenyltetrazolium bromide (MTT) were obtained from Amresco Inc. (America). Penicillin and streptomycin were purchased from Bio Basic Inc. (Canada). Fetal bovine serum (FBS) was purchased from Sangon (China). 2-deoxy-D-glucose (2-DG) and β-cyclodextrin (β-CD) were obtained from ABCR GmbH & Co. KG (Germany) and Tokyo Kasei Kogyo Co. (Japan), respectively. Hela cells were obtained from Committee on Type Culture Collection of Chinese Academy of Sciences (CTCCCAS, China). Dulbecco's Modified Eagle's Medium (DMEM) was purchased from Invitrogen Corporation (USA). All materials used were of analytical grade and used without further purification. The glassware was thoroughly cleaned and rinsed with deionized water.

HSGF 254 silica gel (150−200 μm thickness; Yantai Jiangyou Silica Gel Development Co., Shandong, China) was used for the preparative thin-layer chromatography (TLC); column chromatography employed 200−300 mesh silica gels (Sinopharm Chemical Reagent Co., Shanghai, China). Detection on TLC was made by a combination of sulfuric acid 10% in water, I_2, and UV (254 and 365 nm). Melt points were recorded on an X-4 Microscopic Melting Point Apparatus (Beijing Tech Instrument Co., China). Infrared spectrum was recorded on an Avatar 360 Fourier transform infrared spectrometer (Nicolet, USA). ^{1}H NMR was recorded on a Bruker AV-400 NMR spectrometer (Bruker, German); chemical shifts were reported in parts per million (ppm, δ). The electron spray ionization mass spectrometry (ESI-MS) was carried out on a 3200 Q TRAP instrument (Applied Biosystems, USA).

Synthesis of 5-cf Labeled Molecular Umbrella. *NHS Ester of Cholic Acid.* To a solution of cholic acid (409 mg, 1 mmol) in dry tetrahydrofuran (8 mL) and dry acetonitrile (2 mL), NHS (127 mg, 1.1 mmol) was added. To the resulting homogeneous solution, DCC (206 mg, 1 mmol) in dry tetrahydrofuran (2 mL) was added dropwise at 10−15 °C. The mixture was stirred at 25 °C for 12 h and the precipitated *N*,*N*′-dicyclohexylurea was removed by filtration. The solvent was removed under reduced pressure, and the residue was extracted with ethyl acetate (3 × 20 mL). The extract was washed successively with aqueous $NaHCO_3$ and water. The extract was then dried over Na_2SO_4, and ethyl acetate was removed under reduced pressure to get crude solid. The dried white solid was purified by column chromatography [silica, ethyl acetate/methanol (50/1, v/v)] to give the NHS ester of cholic acid as a white powder (283 mg, 60%) having R_f 0.26 [silica, ethyl acetate/methanol (50/1, v/v)] and mp 118−119 °C (lit. (*11*) mp 119−120 °C); IR ν_{max} (KBr)/cm^{-1} 3420, 1816, 1785, 1738; ^{1}H NMR ($CDCl_3$) δ 0.64 (s, 3 H, 18-H), 0.83 (s, 3 H, 19-H), 0.96 (d, 3 H, 21-H), 1.00−2.00 (m, 22 H, steroidal H), 2.20 (m, 2 H, 23-H), 2.78 (s, 4 H), 3.40 (m, 1 H, 3-H), 3.79 (m, 1 H, 7-H), 3.92 (m, 1 H, 12-H); ESI-MS for $[C_{28}H_{43}NO_7+Na]^+$ calcd 528.6, found 528.5 (100%).

N_1,N_3-Dicholeamidospermidine. The NHS ester of cholic acid (202 mg, 0.4 mmol) was dissolved in 5 mL anhydrous *N*,*N*′-dimethlformamide (DMF), and the resulting solution was added dropwise at room temperature to 1 mL of anhydrous DMF, which contained 29 mg (0.2 mmol) of spermidine and 100 μL (0.6 mmol) diisopropylethylamine. The resulting homogeneous solution was stirred for 4 h at room temperature, and the reaction mixture was poured into 50 mL of saturated aqueous solution of $NaHCO_3$. The precipitate was collected through centrifugation and purified by column chromatography [silica, $CHCl_3$/CH_3OH/NH_4OH, 65/25/4, v/v/v] to afford 113 mg (60%) of N_1,N_3-dicholeamidospermidine having R_f 0.63 [silica, $CHCl_3$/CH_3OH/NH_4OH, 65/25/4, v/v/v] and mp 163−165 °C; ^{1}H NMR (CD_3OD) δ 0.67 (s, 6 H), 0.88 (s, 6 H), 0.99 (d, 6 H), 1.1−2.0 (m, 50 H), 2.23 (m, 4 H), 2.98 (m, 4H), 3.17 (m, 2 H), 3.25 (m, 4 H), 3.76 (br s, 2 H), 3.92 (br s, 2 H); ESI-MS for $[C_{55}H_{95}O_8N_3+H]^+$ calcd 926.7, found 926.3 (100%).

5-cf Labeled Molecular Umbrella. To a solution of 5-cf (94 mg, 0.25 mmol) and HOObt (41 mg, 0.25 mmol) in 5 mL of anhydrous DMF, 52 mg (0.25 mmol) of DCC was added. The homogeneous solution was stirred at room temperature for 24 h in dark. The precipitated dicyclohexylurea was removed by filtration, and the filtrate was concentrated under reduced pressure. The resulting yellow solid was dried under reduced pressure to give the triazinyl ester (166 mg).

To a stirred solution of N_1,N_3-dicholeamidospermidine (102 mg, 0.11 mmol) and the triazinyl ester (55 mg, 0.11 mmol) in 1.0 mL of anhydrous DMF, 62 μL (0.44 mmol) of triethylamine was added. The mixture was then stirred at room temperature for 48 h in dark. The solvent was removed under reduced pressure at 45 °C. The crude product was washed with water, then dissolved in little methanol and purified by preparative TLC [silica, $CHCl_3$/CH_3OH/NH_4OH, 20/10/3 (v/v/v)] to give 35 mg (25%) of 5-cf labeled molecular umbrella (5-cf-mu) having R_f 0.36 [silica, $CHCl_3$/CH_3OH/NH_4OH, 20/10/3 (v/v/v)] and ^{1}H NMR (CD_3OD) δ 8.03 (m, 1 H), 7.83 (m, 1 H), 7.34 (d, 1 H), 6.73 (s, 2 H), 6.65 (s, 2 H), 6.59 (m, 2 H), 3.98 (m, 2 H), 3.82 (s, 2 H), 3.4−3.7 (m, 8 H), 3.17 (m, 2 H), 2.2 (m, 4 H), 1.1−2.0 (m, 62 H), 0.74 (s, 6 H). ESI-MS for $[C_{76}H_{105}N_3O_{14}+Na]^+$ calcd 1306.7, found 1306.6 (100%).

Cells and Cell Cultures. Hela cells were cultured as exponentially growing subconfluent monolayers on 100 mm plates in DMEM supplemented with 10% (v/v) FBS, penicillin (100 units/mL), and streptomycin (100 μg/mL) in a humidified incubator containing 5% CO_2 atmosphere.

MTT Cell Viability Assays. The MTT assay was used to determine the toxicity of 5-cf-mu toward Hela cells. Hela cells were seeded in 96-well plate at a density of 1×10^4 cells/well and cultured in DMEM supplemented with 10% FBS and 1% penicillin−streptomycin at 37 °C. The cells were allowed to adhere to the well bottom upon overnight incubation. After that, the medium was removed and the cells were incubated with the 5-cf-mu at concentration of 25, 50, 100, and 200 μM, respectively. At the designated time (24 h), the supernatant of each well was removed and the cells were washed twice by PBS. Twenty microliters of MTT solution (5 mg/mL in PBS) and 100 μL medium were then introduced. After 4 h incubation, the formed precipitates were solubilized by 100 μL dimethyl sulfoxide (DMSO). Absorbance intensity was then measured by the microplate reader (model 680, Bio-RAD, USA) at 490 nm with a reference wavelength of 620 nm. Cell viability was expressed by the following equation:

$$\text{cell availability (\%)} = \frac{\text{Abs}_{\text{sample}}}{\text{Abs}_{\text{control}}} \times 100\% \qquad (1)$$

The results are given as relative value to the negative control in percent, whereas the negative control is set to be 100% viable.

Flow Cytometry. To analyze the internalization of fluorochrome-labeled molecular umbrellas by FACS, exponentially growing Hela cells were dissociated with 0.25% trypsin. 6×10^5 cells were plated and cultured overnight on 60 mm dishes. The culture medium was discarded, and the cells were washed with PBS (pH 7.2). Then, PBS was discarded, and the cell

monolayers were incubated with different concentrations of 5-cf-mu for 1 h at 37 °C to analyze dose−response of 5-cf-mu uptake. To examine the effects of time, the cells were incubated with 10 μM of 5-cf-mu at different incubation times.

To investigate the cellular uptake mechanism of 5-cf-mu, the incubations of Hela cells were carried out as follows: (1) Cells were kept at 4 °C for 1 h, instead of the regular 37 °C condition. (2) For the ATP-depletion studies, the cells were preincubated in PBS supplemented with NaN_3 (50 mM) and 2-DG (0.5%) for 1 h at 37 °C. (3) For cholesterol depletion assay, the cells were pretreated with β-CD (10 μM) in PBS for 1 h at 37 °C. (4) The inhibition of clathrin- and caveolae/lipid raft-mediated endocytosis were carried out by preincubating cells with CpZ (30 μM) and Noc (10 μM) in PBS for 1 h at 37 °C. Once treatments were complete, 5-cf-mu (10 μM) was added and cells were incubated for another 1 h. The cells were then resuspended in ice-cold PBS buffer solution, and the fluorescent cells with 5-cf-mu were then measured from 2×10^4 cells by using an EPICS XL flow cytometer (Beckman Coulter, USA) in the FL1 channel. Data analysis was performed with EPICS XL flow cytometer software, and the cellular uptake of 5-cf-mu was expressed by the following equation:

$$\text{cellular uptake (\%)} = \frac{\text{CFD}_i}{\text{CFD}_{37}} \times 100\% \qquad (2)$$

where, CFD_i and CFD_{37} represent the mean value of cell fluorescence distribution for each incubation condition and the normal condition (37 °C), respectively.

Confocal Laser Scanning Microscope. To investigate the colocalization of 5-cf-mu and LysoTracker Red, 5-cf-mu (10 μM) was added and incubated with Hela cells (5×10^5) in a 30 mm cell culture coverslip for 1 h. After washing away the extracellular 5-cf-mu with PBS, cells were then treated with LysoTracker Red for 15 min for lysosome staining. For investigation of endocytosis, Hela cells (5×10^5/30 mm cell culture coverslip) were incubated with 5-cf-mu (10 μM) in a serum-free medium, together with CFSE (10 μM), Alexa Fluor 546-transferrin (50 μg/mL), and Alexa Fluor 594-Ctx B (10 μg/mL) for 5 h at 37 °C, respectively. Extracellularly bound 5-cf-mu was removed by washing three times with PBS.

After fixing with paraformaldehyde (4% in PBS) for 30 min and subsequently washing twice with PBS, the stained cells were finally observed with CLSM (Fluoview FV1000, Olympus, Japan) equipped with a Plan-Apochromat 60 × 0.7 NA lens (λ_{ex}, 488 nm, and λ_{em}, 520 nm, for 5-cf-mu; λ_{ex}, 577 nm, and λ_{em}, 590 nm, for LysoTracker Red; λ_{ex}, 488 nm, and λ_{em}, 530 nm, for CFSE; λ_{ex}, 556 nm, and λ_{em}, 573 nm, for Alexa Fluor 546; λ_{ex}, 590 nm, and λ_{em}, 617 nm, for Alexa Fluor 594). Images were captured by multitracking to avoid bleedthrough between the fluorophores and further processed and analyzed with Olympus CLSM software.

RESULTS AND DISCUSSION

Design and Synthesis of 5-cf Labeled Molecular Umbrella. Molecular umbrellas are synthesized from materials that are potentially biocompatible. Generally, cholic acid and spermidine are selected as amphiphilic wall and central scaffold, respectively (*12, 13*). Cholic acid, a major component of bile acids, has a sterol nucleus that presents a hydroxylated, hydrophilic face and also a face that is all-hydrocarbon and lipophilic. Spermidine, which is also found in mammalian cells, has terminal amino groups that can be used for wall attachment, and a secondary amino group can serve as a handle to bind a cargo. Their structures were shown in Scheme 1.

Here, we focus on the diwalled molecular umbrella, which has amphiphilic walls for effective shielding. Cholic acid was

Scheme 1. Structures of Cholic Acid and Spermidine

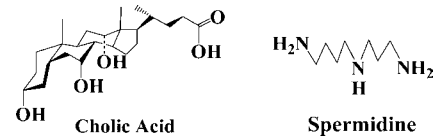

Scheme 2. Synthetic Route to 5-cf Labeled Molecular Umbrella

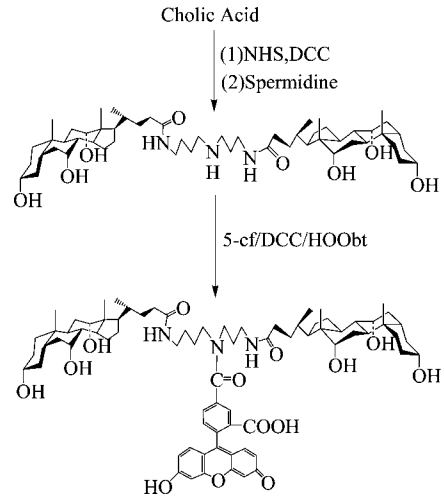

first activated with NHS to afford the corresponding NHS ester of cholic acid and then coupled to both terminal amino groups of spermidine to give the diwalled molecular umbrella. 5-cf with high hydrophilicity was selected as a fluorescent label because it was difficult to transport across the biological membrane and because its green fluorescence could be easily detected (*14*). The carboxyl group of 5-cf was preactivated with DCC/HOObt and then coupled to the secondary amino group of spermidine on the molecular umbrella. The synthetic route of 5-cf labeled molecular umbrella was shown in Scheme 2.

Cytotoxicity of 5-cf-mu. To verify that molecular umbrellas could be used for drug delivery vectors, it is important to gain information about its toxicity toward the cells. Here, the cytotoxicity of 5-cf-mu was evaluated in Hela cells by the MTT assay.

The viability of Hela cells after 24 and 48 h treatment with 5-cf-mu at concentrations ranging from 50 to 200 μM was illustrated in Figure 1. 5-cf-mu exhibited low toxicity to Hela cells at concentrations as high as 200 μM following 24 h incubation. Although the concentration of 5-cf-mu from 50 to 200 μM exhibited some inhibition to cells after 48 h incubation, 5-cf-mu showed no toxicity to Hela cells at 25 μM even after 48 h. The MTT assay results thus indicated that the molecular umbrella was a good biocompatible vector.

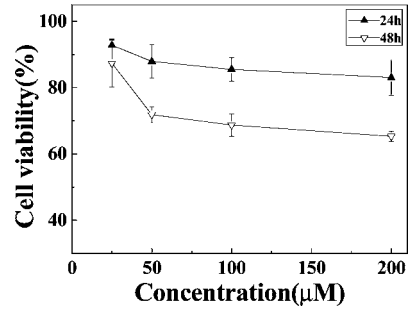

Figure 1. Cytotoxicity of 5-cf-mu toward Hela cells. The cell viability following 24 and 48 h exposure of Hela cells to 5-cf-mu was quantified by the colorimetric MTT assay. All samples were tested in triplicate, and results are given as the average values ± standard.

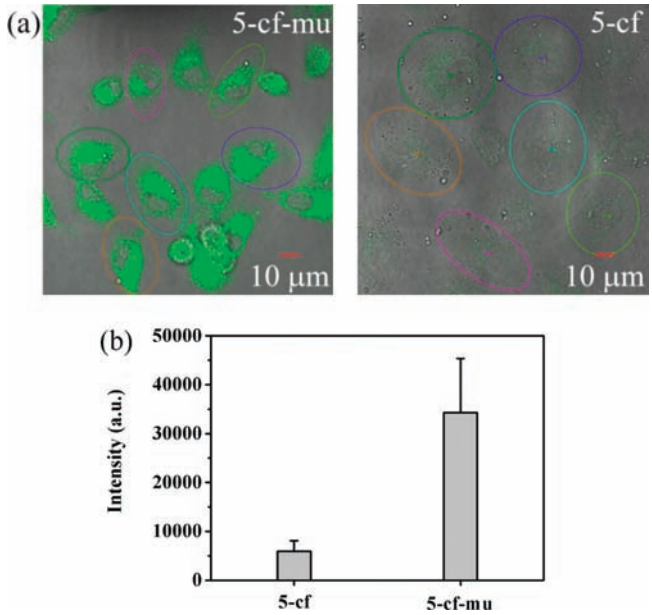

Figure 2. (a) CLSM images for 5-cf-mu (10 μM) and 5-cf (10 μM) treated Hela cells. (b) The average fluorescence intensity of cells in (a) ($n = 6$).

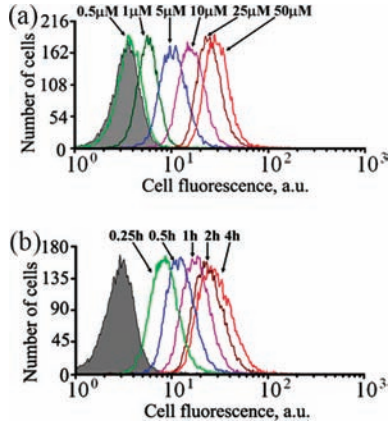

Figure 3. (a) Concentration dependence by FACS analysis. Cells were exposed to 5-cf-mu at the corresponding concentration for 60 min. (b) Incubation dependence by FACS analysis. Cells were exposed to 5-cf-mu (10 μM) for corresponding hours.

Cellular Uptake of 5-cf-mu. Molecular umbrellas may function as novel carriers for hydrophilic therapeutic agents which need transportation into living cells. Previously, many studies demonstrated that molecular umbrellas could transport these molecules across lipid bilayers (*3*−*8, 15, 16*). Herein, we investigated the membrane-penetrating ability of diwalled molecular umbrella into living cells. 5-cf was set as the fluorescently label molecule facilitating the detection of molecular umbrella entering into cells. As shown in Figure 2a, 5-cf-mu (green) was demonstrated to enter into Hela cells by tomography of CLSM as lots of green dots distributed in the cytoplasm district. Note that 5-cf only entered into cells slightly. For quantitative analysis of internalization of 5-cf-mu and 5-cf, cells within the visual field were selected randomly and presented as the ellipse. The average cell fluorescence intensity of 5-cf-mu was about 4.8-fold higher than that of 5-cf (Figure 2b), indicating that molecular umbrellas can greatly facilitate cellular uptake of 5-cf. Moreover, the fluorescence information within cells with different depths indicated that most 5-cf-mu was distributed in the middle of Hela cells (data not shown).

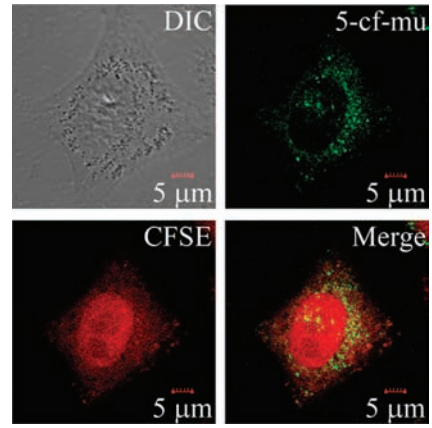

Figure 4. Colocalization (yellow dots) with carboxyfluorescein diacetate succinimidyl esters (CFSE, red) with 5-cf-mu (green) in Hela cells.

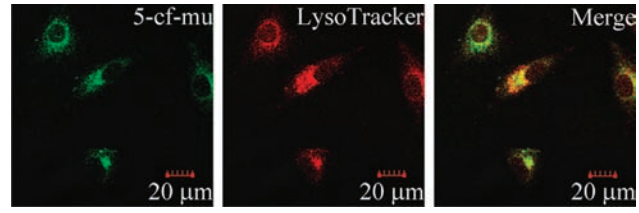

Figure 5. Colocalization of 5-cf-mu (green) and lysosome tracker (red) in Hela cells. Overlay of the two fluorescent layers results in yellow fluorescent emission wherever overlap is complete.

The entrance of 5-cf-mu into cells was further confirmed by FACS. As shown in Figure 3, the cell fluorescence increased gradually along with the concentration and incubation time, respectively. It is thus suggested that the cellular uptake of 5-cf-mu has the characteristics of both concentration- and incubation time-dependence.

Internalization Pathways of 5-cf-mu. Different entry mechanisms may be preferred depending on the application, as the mode of entry affects cell-type specificity, the rate of internalization, and the fate of the compound once inside the cell. In order to design molecular umbrella-based drug delivery systems more rationally, it is important to understand the physiological processing of molecular umbrellas.

Despite molecular umbrellas having been used as carriers of peptides, nucleotides, and oligonucleotides (*7, 15, 16*), the mechanism of transduction responsible for the entry of molecular umbrellas into cells is still poorly understood. In a pioneering work, Mehiri et al. (*9*) ascribed the cellular uptake of exogenously added molecular umbrellas to a diffusion pathway. One of the limitations of this hypothesis is based on the fact that the treatment of NaN_3 and 2-deoxyglucose (to deplete ATP production) causes no significant reduction of molecular umbrella cellular uptake. However, some studies indicated that ATP depletion might specifically impair macropinocytosis process (*17*−*19*), but not the whole endocytic pathway, which is indeed subdivided into four categories: (1) clathrin-mediated endocytosis, (2) caveolae/lipid raft-mediated endocytosis, (3) macropinocytosis, and (4) phagocytosis (*20*). Interestingly, Mehiri et al. (*9*) also found no cellular uptake of molecular umbrellas at 4 °C, which is consistent with the endocytic pathway. Hence, one question might arise regarding whether the transport of molecular umbrellas across cell membranes could be due to the combination of diffusion and endocytosis. In the work reported herein, we sought to answer this question.

To obtain direct visual evidence of the internalization diffusion pathway described by Mehiri et al. (*9*), we first cocultured 5-cf-mu with CFSE, which is a well-known marker

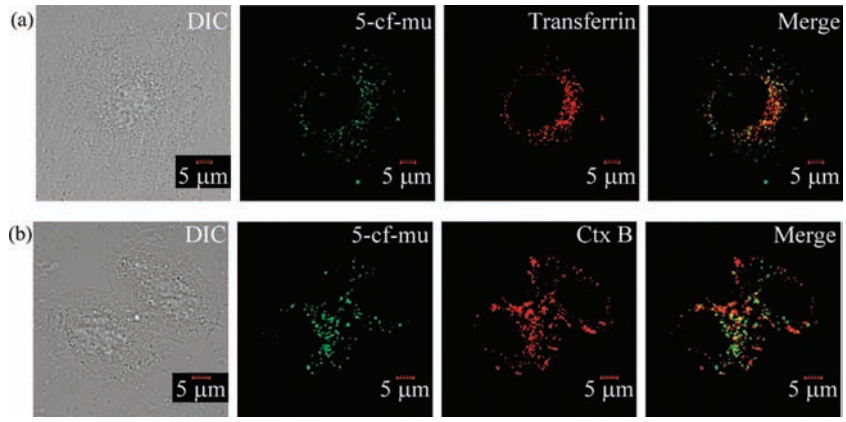

Figure 6. Colocalization of 5-cf-mu with Alexa Fluor 546-labeled transferrin (a) and Alexa Fluor 546-labeled Ctx B (b) in Hela cells, respectively. The emissions for 5-cf and Alexa Fluor 546 are green and red, respectively. Overlay of the two fluorescent layers results in yellow fluorescent emission wherever overlap is complete.

for diffusion (*21, 22*). It is indicated from Figure 4 that 5-cf-mu (green) was partly colocalized with CFSE (red) presenting as yellow dots. Note that CFSE is distributed as a dispersion within both cytoplasm and nucleus, while the distribution of 5-cf-mu was an association between diffuse and puncta. The former is generally considered to be an indication of cellular entry via passive diffusion, while the latter implies that 5-cf-mu might enter Hela cells by a fundamentally different pathway, most probably via endocytosis. It is noteworthy that the distribution of 5-cf-mu is not all the same as that of persulfated molecular umbrellas synthesized by Mehiri et al. (*9*), indicating that the framework of molecular umbrellas might affect their internalization pathway. The above finding inspires us to further investigate the internalization pathways of 5-cf-mu.

Taking into account the fact that the cell membrane comprises not only lipid bilayers but also a lot of specific districts and proteins which might offer the cell membrane the active transport ability via endocytosis for carrying materials into cells, it is reasonable to suppose that molecular umbrellas could undergo endocytosis. To test this hypothesis, we determined whether 5-cf-mu internalized by the cells is indeed in endosomal compartments. LysoTracker Red was used to track endosomes in the cells because it has been extensively shown to partition to acidic compartments within a cell, e.g., lysosomes and endosomes (*23*). The CLSM analysis indicated part of 5-cf-mu (green) in the endosome (red), presented as dots (Figure 5). The FACS analysis further demonstrated that the uptake of 5-cf-mu was considerably inhibited at 4 °C compared to 37 °C (Supporting Information). On this basis, we posit that endocytosis is one of internalization pathways for cellular uptake of 5-cf-mu.

To further explore subcategories of endocytosis, we respectively performed colocalization experiments by using Alexa Fluor 594-labeled transferrin (a positive marker of clathrin-mediated endocytosis) and Alexa Fluor 594-labeled Ctx B (a marker for caveolae/lipid-raft-mediated endocytosis) on Hela cells. It is observed from CLSM images (Figure 6a) that a part of 5-cf-mu (green) colocalized with Alexa Fluor 594-labeled transferrin (red) presented as yellow dots. On the other hand, 5-cf-mu (green) had much colocalization with Alexa Fluor 594-labeled Ctx B (red), presented as yellow dots (Figure 6b).

We also examined the effects of the endocytosis inhibitors on the uptake of 5-cf-mu into the cells by using four different types of chemical inhibitors: (1) NaN_3/2-DG, which is a ATP-depleting agent, for macropinocytosis (*17*−*19*), (2) β-CD, which is a cholesterol-depleting agent, for caveolae/lipid raft-mediated endocytosis pathway (*17, 20, 24*), (3) Noc, which can disrupt the intracellular vesicles transport along microtubule, for caveolae/lipid raft-mediated endocytosis pathway (*25*), (4) CpZ, which can interact with clathrin, for clathrin-mediated endocytosis pathway (*20, 26*). It is demonstrated from Figure 7 that the cellular uptake of 5-cf-mu was not inhibited by pretreating cells with NaN_3/2-DG. This is consistent with Mehiri's result (*9*). In contrast, it is observed that the cellular uptake level of 5-cf-mu from CpZ, β-CD, and Noc pretreated cells dramatically plunged to 72.11%, 26.59%, and 50.29%, respectively. With these results taken together, our experimental data thus suggested that the following uptake pathways are involved in the cell uptake of 5-cf-mu: (1) passive diffuse; (2) clathrin-mediated endocytosis; (3) caveolae/lipid-raft-dependent endocytosis.

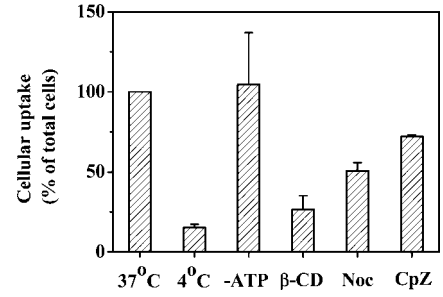

Figure 7. Cellular uptake mechanism of 5-cf-mu as measured by FACS. The inhibitory effect of 4 °C, NaN_3/2-DG, β-CD, or CpZ on the cellular uptake of 5-cf-mu, compared to normal cellular uptake efficiency (37 °C). Means ± SD are indicated ($n = 3$).

CONCLUSIONS

A diwalled molecular umbrella bearing 5-cf as a fluorescent label was synthesized. The molecular umbrella was prepared through coupling of cholic acid to both terminal amino groups of spermidine with the DCC and NHS. Further attachment of 5-cf to the remaining secondary amine on the molecular umbrella was performed with DCC and HOObt to obtain 5-cf-mu. Little toxicity was detected even after 24 h incubation at a high concentration of 5-cf-mu by MTT assay. Confocal microscopy showed that molecular umbrellas were able to transport high hydrophilic agent 5-cf across biological membrane of Hela cells. FACS results indicated that the uptake of 5-cf-mu depends on incubated time and concentration. By analyzing the mechanism of transmembrane movement, we reason that 5-cf-mu transported across the cell membrane in an association pathway between diffusion and endocytosis. All of these results indicate that the molecular umbrella is highly feasible as a smart intracellular delivery carrier for hydrophilic molecules, molecular probes, and therapeutic drugs.

ACKNOWLEDGMENT

We are extremely grateful to the National Nature Science Foundation of China (No. 30670559, 30870648, 30870617), the National Basic Research Program of China (973 Program) (2007CB935603), and the Program for New Century Excellent Talents in Fujian Province University for supporting this research.

Supporting Information Available: ^{1}H NMR, ESI-MS, and IR spectra of 5-cf-mu, and FACS analysis of inhibited factors on the cellular uptake of 5-cf-mu. This material is available free of charge via the Internet at http://pubs.acs.org.

LITERATURE CITED

(1) Alper, J. (2002) Drug delivery-breaching the membrane. *Science 296*, 838–839.
(2) Mehiri, M., Chen, W. H., Janout, V., and Regen, S. L. (2009) Molecular umbrella transport: exceptions to the classic size/lipophilicity rule. *J. Am. Chem. Soc. 131*, 1338–1339.
(3) Janout, V., Lanier, M., and Regen, S. L. (1996) Molecular umbrellas. *J. Am. Chem. Soc. 118*, 1573–1574.
(4) Janout, V., Jing, B. W., and Regen, S. L. (2002) Molecular umbrellas-assisted transport of thiolated AMP and ATP across phospholipid bilayers. *Bioconjuate Chem. 13*, 351–356.
(5) Janout, V., and Regen, S. L. (2009) Bioconjugate-based molecular umbrellas. *Bioconjugate Chem. 20*, 183–192.
(6) Janout, V., Zhang, L. H., Staina, I. V., DiGiorgio, C., and Regen, S. L. (2001) Molecular umbrella-assisted transport of glutathione across a phospholipid membrane. *J. Am. Chem. Soc. 123*, 5401–5406.
(7) Janout, V., Jing, B. W., and Regen, S. L. (2005) Molecular umbrella-assisted transport of an oligonucleotide across cholesterol-rich phospholipid bilayers. *J. Am. Chem. Soc. 127*, 15862–15870.
(8) Janout, V., Jing, B. W., Staina, I. V., and Regen, S. L. (2003) Selective transport of ATP across a phospholipid bilayer by a molecular umbrella. *J. Am. Chem. Soc. 125*, 4436–4437.
(9) Mehiri, M., Jing, B. W., Ringhoff, D., Janout, V., Cassimeris, L., and Regen, S. L. (2008) Cellular entry and nuclear targeting by a highly anionic molecular umbrella. *Bioconjugate Chem. 19*, 1510–1513.
(10) Puckett, C. A., and Barton, J. K. (2008) Mechanism of cellular uptake of a ruthenium polypyridyl complex. *Biochemistry 47*, 11711–11716.
(11) Okahata, Y., Ando, R., and Kunitakb, T. (1979) Catalytic hydrolysis of p-nitrophenyl esters in the presence of representative ammonium aggregates-Specific activation of a cholesteryl nucleophile bound to a dialkylammonium bilayer membrane. *Bull. Chem. Soc. Jpn. 52*, 3647–3653.
(12) Shawaphun, S., Janout, V., and Regen, S. L. (1999) Chemical evidence for transbilayer movement of molecular umbrellas. *J. Am. Chem. Soc. 121*, 5860–5864.
(13) Debart, F., Abes, S., Deglane, G., Moulton, H. M., Clair, P., Gait, M. J., Vasseur, J. J., and Lebleu, B. (2007) Chemical modifications to improve the cellular uptake of oligonucleotides. *Curr. Top. Med. Chem. 7*, 727–737.
(14) Onoue, S., Liu, B. S., Nemoto, Y., Hirose, M., and Yajima, T. (2006) Chemical synthesis and application of C-terminally 5-carboxyfluorescein-labelled thymopentin as a fluorescent probe for thymopoietin receptor. *Anal. Sci. 22*, 1531–1535.
(15) Janout, V., and Regen, S. L. (2005) A needle-and-thread approach to bilayer transport: permeation of a molecular umbrella-oligonucleotide conjugate across a phospholipid membrane. *J. Am. Chem. Soc. 127*, 22–23.
(16) Jing, B. W., Janout, V., and Regen, S. L. (2003) Fully detachable molecular umbrellas as peptide delivery agents. *Bioconjugate Chem. 14*, 1191–1196.
(17) Khalil, I. A., Kogure, K., Akita, H., and Harashima, H. (2006) Uptake pathways and subsequent intracellular trafficking in nonviral gene delivery. *Pharmacol. Rev. 58*, 32–45.
(18) Vazquez, E., Ferrer-Miralles, N., and Villaverde, A. (2008) Peptide-assisted traffic engineering for nonviral gene therapy. *Drug Discovery Today 13*, 1067–1074.
(19) Hewlett, L. J., Prescott, A. R., and Watts, C. (1994) The coated pit and macropinocytic pathways serve distinct endosome populations. *J. Cell Biol. 124*, 689–703.
(20) Wang, Z. Y., Zhao, Y., Ren, L., Jin, L. H., Sun, L. P., Yin, P., zhang, Y. F., and Zhang, Q. Q. (2008) Novel gelatin-siloxane nanoparticles decorated by Tat peptide as vectors for gene therapy. *Nanotechnology 19*, 445103.
(21) Sun, L., Zhu, C. J., Tan, P., and Wong, M. C. (2004) Endothelial progenitor cells' 'homing' specificity to brain tumors. *Gene Ther. 11*, 811–818.
(22) Muranski, P., Chmielowski, B., and Ignatowicz, L. (2000) Mature CD^{4+} T cells perceive a positively selecting class II MHC/peptide complex in the periphery. *J. Immunol. 164*, 3087–3094.
(23) Huynh, K. K., Eskelinen, E. L., Scott, C. C., Malevanets, A., Saftig, P., and Grinstein, S. (2007) LAMP proteins are required for fusion of lysosomes with phagosomes. *EMBO J. 26*, 313–324.
(24) Wang, Y., Li, D., Fan, H., Tian, L. J., Zhong, Y. C., Zhang, Y., Zhang, Y. M., Yuan, L., Jin, C. N., Yin, C. H., and Ma, D. L. (2006) Cellular uptake of exogenous human PDCD5 protein. *J. Biol. Chem. 281*, 24803–24817.
(25) Malorni, W., Giammarioli, A. M., Garofalo, T., and Sorice, M. (2007) Dynamics of lipid raft components during lymphocyte apoptosis: the paradigmatic role of GD3. *Apoptosis 12*, 941–949.
(26) Richard, J. P., Melikov, K., Brooks, H., Prevot, P., Lebleu, B., and Chernomordik, L. V. (2005) Cellular uptake of unconjugated TAT peptide involves clathrin-dependent endocytosis and heparan sulfate receptors. *J. Biol. Chem. 280*, 15300–15306.

BC9003074

Cellular Uptake Mechanism of Molecular Umbrella

Dongtao Ge,[†] Dewang Wu,[†] Zuyong Wang,[†] Wei Shi,*[,†,‡] Ting Wu,[§] Cunfeng Song,[†] Shimin Hong,[†] Jun Wang,[†] Ye Zhang,[§] and Lei Ren*[,†,‡]

[†] Department of Biomaterials/Biomedical Engineering Research Center, College of Materials, Xiamen University, Xiamen 361005, China,
[‡] State Key Laboratory for Physical Chemistry of Solid Surfaces, Xiamen University, Xiamen 361005, China
[§] Department of Preclinical Medicine, Medical College, Xiamen University, Xiamen 361005, China

Email: shiwei@xmu.edu.cn; renlei@xmu.edu.cn

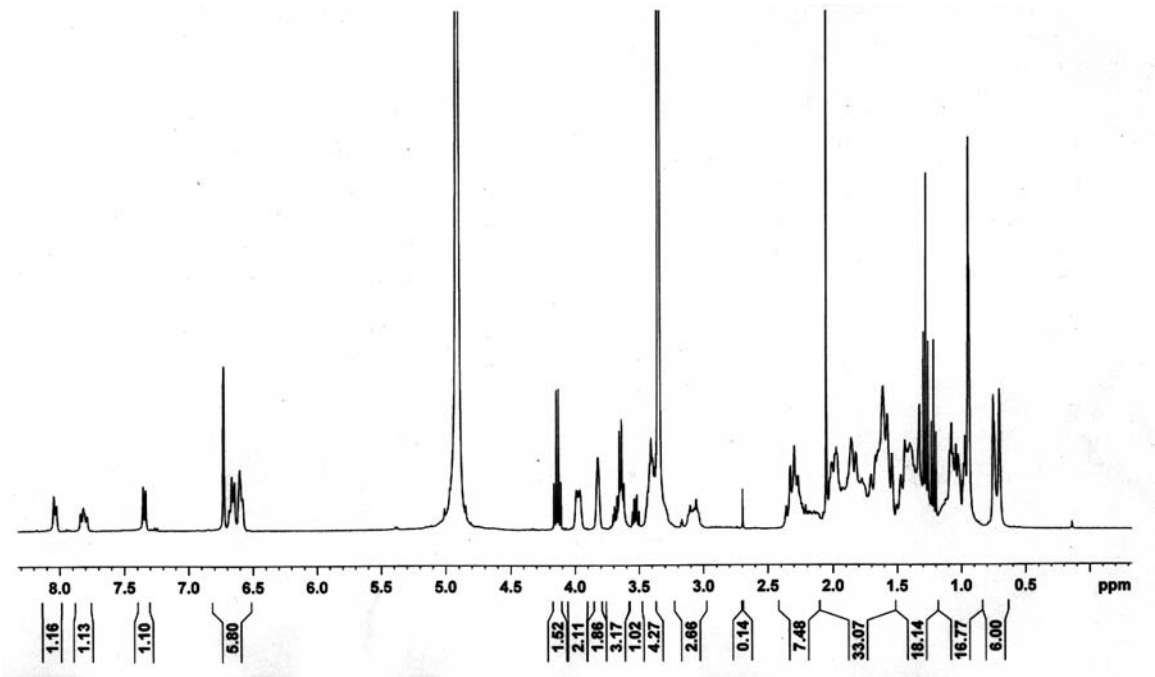

Figure S1. The NMR spectrum of 5-cf-mu

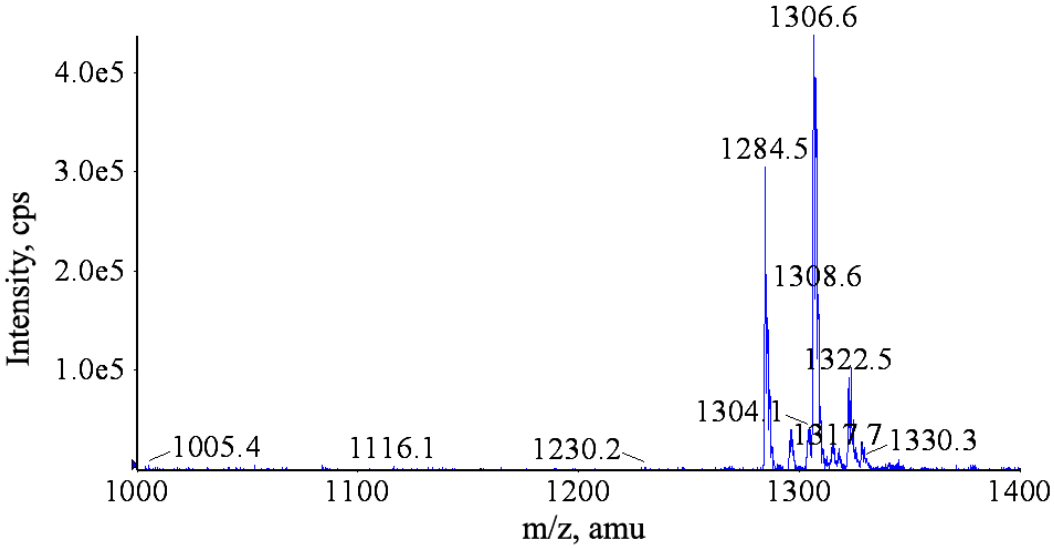

Figure S2. The ESI-MS spectrum of 5-cf-mu

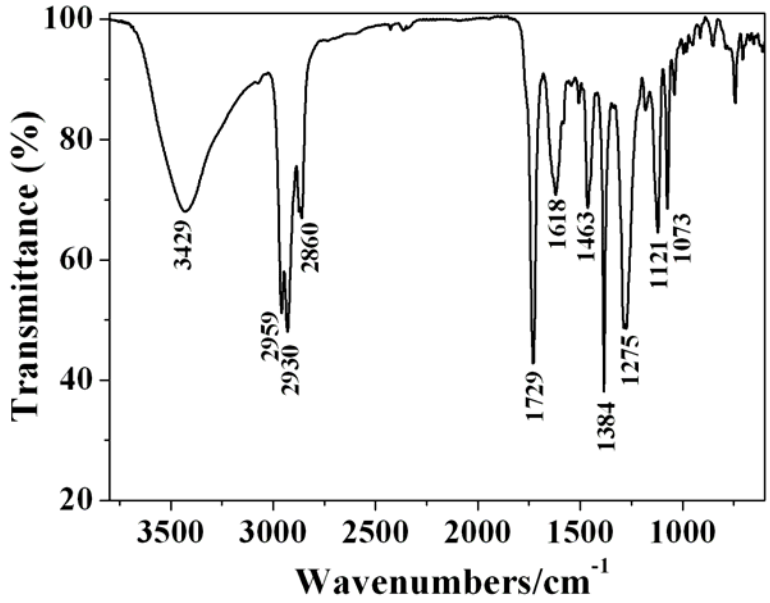

Figure S3. The IR spectrum of 5-cf-mu

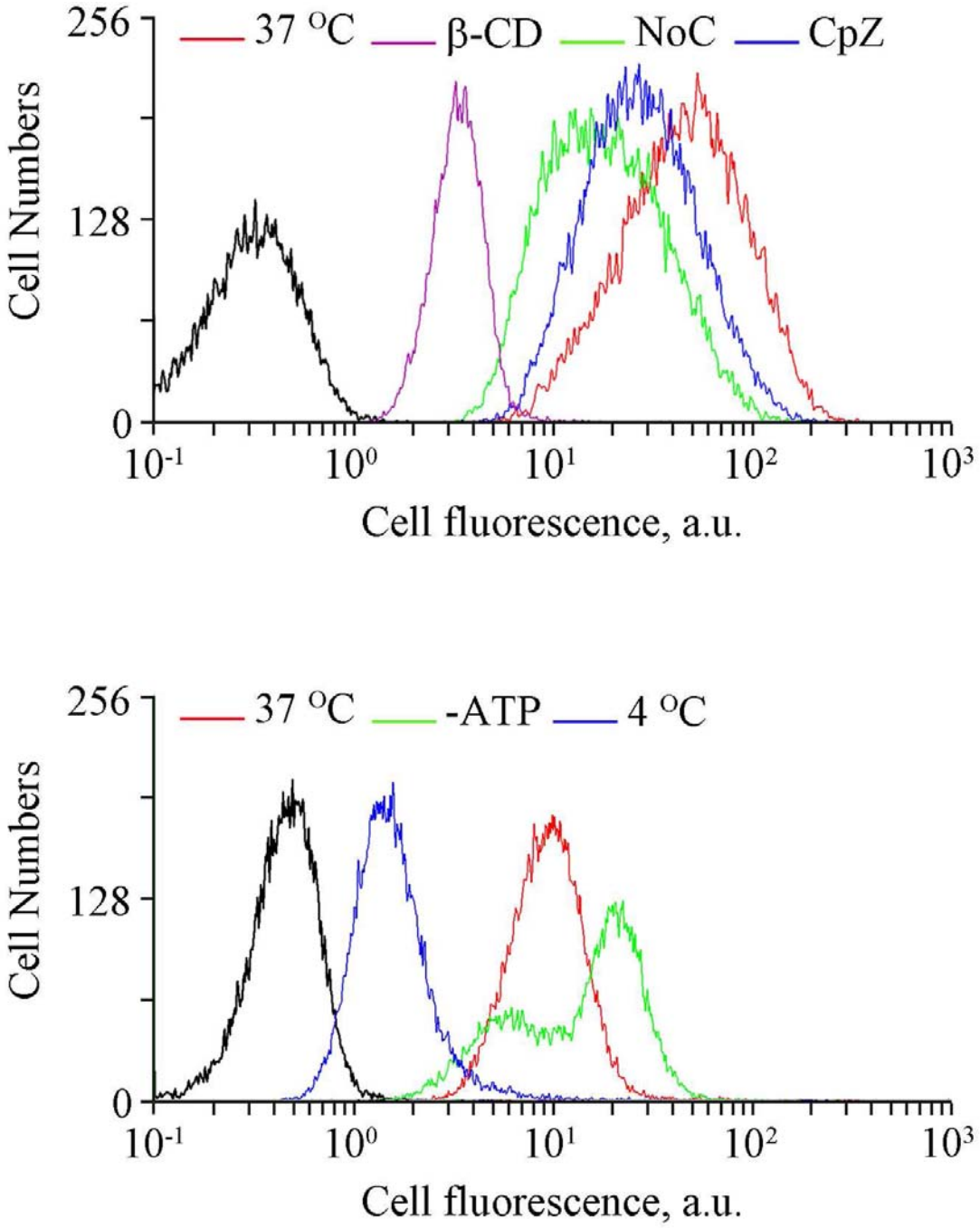

Figure S4. FACS analysis of inhibited factors on the cellular uptake of 5-cf-mu

Poly(β-aminoester)s with Pendant Primary Amines for Efficient Gene Delivery

Min Liu, Jun Chen, Ya-Nan Xue, Wen-Ming Liu, Ren-Xi Zhuo, and Shi-Wen Huang*

Key Laboratory of Biomedical Polymers of Ministry of Education, Department of Chemistry, Wuhan University, Wuhan 430072, P. R. China. Received July 16, 2009; Revised Manuscript Received November 2, 2009

Three hydrolytically degradable poly(β-aminoester)s containing ester bonds in the main chain and primary amines in the side chain, synthesized by Michael polyaddition, were applied to deliver foreign DNA into cells *in vitro*. These linear polycations can condense DNA into small-sized particles with positive surface charge at high N/P ratios. Their high buffer capacity at pH 5−7 facilitated the escape of DNA from the endosome and resulted in efficient gene expression. Under the optimal conditions, poly(β-aminoester)s with a pendant aminoethyl group (**1a**) showed higher transfection efficiencies than branched poly(ethylenimine) (PEI) 25KDa in 293T cells. The effect of side chain structure of the poly(β-aminoester) on transfection efficiency has been investigated, which indicated that the poly(β-aminoester) containing the pendant aminoethyl group was the most efficient carrier for both of 293T cells and COS-7 cells. The combination of hydrolytical degradation, high buffer capacity, relatively low cytotoxicity, and high transfection efficiency suggested that this kind of poly(β-aminoester)s are novel promising nonviral gene carriers.

INTRODUCTION

The safe and efficient delivery of DNA remains a great challenge in the application of gene delivery (*1*−*3*). Nonviral vectors are less efficient than viral vectors; however, nonviral vectors have certain advantages, including ease of production, safety of use, large DNA binding capacity, and low immunogenicity and toxicity (*4, 5*). A wide variety of cationic polymers have been developed for gene delivery, such as poly(L-lysine) (PLL) (*6, 7*), poly(ethylenimine) (PEI) (*8*−*11*), poly(amidoamine) dendrimer (*12*−*14*), etc. These cationic polymers can condense DNA into nanosized particles with positive surface charge; as a result, the polymers can facilitate cellular uptake and protect DNA from nuclease degradation to improve transfection efficiencies (*15*).

Cationic polymers have been widely applied in both *in vitro* and *in vivo* gene delivery (*16*). However, many of the current polymeric gene delivery vectors are nondegradable under physiological conditions. Recent efforts in designing new nonviral gene carriers have partly focused on the introduction of hydrolyzable linkage into the polymer main chains in order to improve biodegradability and decrease toxicity (*17*−*20*). Typically, these polymers contain both an amino group, interacting with polyanionic DNA via electrostatic interaction, and a degradable region, such as a hydrolyzable linkage. The important examples include poly(4-hydroxy-L-proline ester) (*21,22*), cationic polyphosphoester (*23, 24*), poly(β-aminoester)s (*25*−*27*), etc. These hydrolytically degradable polycations are significantly less toxic than branched PEI 25KDa and possess high transfecion efficiencies.

Poly(β-aminoester)s are promising and efficient gene delivery vectors (*25*−*27*), which were first synthesized by Langer et al. They reported a library of more than 2000 poly(β-aminoester)s with a variety of pendant groups including hydroxyl, tertiary amine, etc. About 2% of these polycations showed equal or higher transfection efficiencies than PEI in COS-7 cells. Among the current poly(β-aminoester)s as gene carriers, we have not found poly(β-aminoester)s with pendant primary amines applied in gene delivery. It was expected that the introduction of primary amine into the side chain of poly(β-aminoester)s would enhance the ability to condense DNA and improve biodegradabilty. We have previously described the synthesis and hydrolytical degradation of poly(β-aminoester)s with a tertiary amine in the main chain and a primary amine in the side chain via Michael polyaddition of N-Boc protected diamine to butanediol diacrylate, followed by removing Boc-protective groups under anhydrous acidic conditions (*28*). We report here the ability of poly(β-aminoester)s with pendant primary amines to condense DNA and efficiently deliver foreign DNA into cells.

EXPERIMENTAL PROCEDURES

Materials. Poly(β-aminoester)s (polymers **1a**−**1c**) were synthesized as previously described (*28*), branched PEI 25KDa and 3-[4,5-dimethylthiazol-2-yl]-2,5-diphenyltetrazoplium bromide (MTT) were obtained from Sigma-Aldrich and used directly. Dulbecco's modified Eagle's medium (DMEM), L-glutamine, streptomycin, and penicillin were purchased from Gibco BRL (Grand Island, NY), and fetal bovine serum was purchased from domestic suppliers and used directly. Other reagents and solvents were of analytical grade obtained from domestic suppliers and used directly. 293T and COS-7 cells were purchased from China Center for Type Culture Collection (CCTCC) (Wuhan University) and cultured in DMEM supplemented with 4 mmol L^{-1} L-glutamine, 10% fetal bovine serum (FBS), and antibiotics (100 U/mL penicillin and 100 μg/mL streptomycin) at 37 °C in a humidified air atmosphere containing 5% CO_2.

Plasmid DNA. pGL-3 was used as the luciferase reporter gene and transformed in *E. coli* JM109. pEGFP-C1 was used as the green fluorescent protein gene and transformed in *E. coli* DH5α. Both plasmids were amplified in Luria-Bertani (LB) medium at 37 °C for 12−16 h at 250 rpm. They were purified by a QIAfilter plasmid Giga kit according to the manufacturer's protocol. The quantity and quality of plasmid DNA were analyzed by spectrophotometric analysis at 260 and 280 nm and by electrophoresis in

* To whom correspondence should be addressed. Fax: 86-27-68755317. E-mail: swhuang@whu.edu.cn.

10.1021/bc900317m © 2009 American Chemical Society
Published on Web 11/25/2009

0.7% (w/v) agarose gel. The purified plasmid was dissolved in Tris-EDTA (TE) buffer and stored at −20 °C.

Buffer Capacity. The buffer capacity of polymers **1a**−**1c** was determined by acid−base titration as described previously (*28*,*29*). Briefly, polymers **1a**−**1c** were separately dissolved in 10 mL of 150 mmol L^{-1} sodium chloride aqueous solution. The concentration of primary amine in each sample solution was 5 mmol L^{-1}. After the solution was titrated to pH 10 with 0.1 mol L^{-1} sodium hydroxide solution, the solution was titrated to pH 2 with 0.1 mol L^{-1} hydrochloride solution. The pH values were recorded with a Microprocessor pH meter.

***In Vitro* Cytotoxicity Assay.** MTT assay was used to measure the cytotoxicity of polycations against 293T and COS-7 cells. 293T and COS-7 cells were separately seeded into 96-well plates at a density of 6000 cells/well in 100 μL of complete DMEM. When cells achieved 50−60% confluence after 24 h of incubation, 100 μL of polymer solution in DMEM at different concentrations was added to each well and incubated for further 24 h. Then, 20 μL of MTT solution (5 mg/mL in PBS) was added to each well except for the background wells and incubated for further 4 h. The medium was removed, and 150 μL of DMSO was added. The absorbance was measured at 570 nm using a microplate reader (BIO-RAD, Model 550, USA). The percent relative viability in reference to control wells containing complete DMEM without the added polymer was calculated by the following equation (A is absorbance at 570 nm; A_0 is the absorbance of the solution containing cells and complete DMEM without MTT and polymer): relative cell viability (%) = $100 \times (A_{test} - A_0)/(A_{control} - A_0)$.

Formation of Polymer/DNA Complexes. All of the polymer/DNA complexes were prepared fresh before use. Appropriate amounts of polymer solution (in 150 mmol L^{-1} NaCl) were added to the DNA solution in equal volume to achieve desired N/P ratios, then complexes were mixed by vortexing for 5 s and incubated for 30 min at room temperature.

Agarose Gel Retardation Assay. Complexes for this assay were prepared at N/P ratios of 0.5:1, 1:1, 2:1, 5:1, 10:1, 15:1, and 20:1. Various amounts of polymer solution in 150 mmol L^{-1} NaCl were rapidly mixed with 100 ng of pEGFP-C1 in equal volume of 150 mmol L^{-1} NaCl solution, then vortexed for 5 s, and incubated at room temperature for 30 min. Gel electrophoresis was carried out in TAE buffer in 0.7% (w/v) agarose gel containing GelRed at 80 V for 80 min. The gel was visualized by a Vilber Lourmat imaging system (France).

Particle Size and Zeta Potential Measurements. The particle size and zeta potential of polymer/DNA complexes were measured by Nano-ZS (MALVERN Instr.) at 25 °C. The polymer/DNA complexes at various N/P ratios were prepared by adding appropriate volumes of polymer solution (in 150 mmol L^{-1} NaCl) to 1 μg of pEGFP-Cl in equal volume, followed by vortexing for 5 s and incubating at room temperature for 30 min, and then the solution was diluted to 1 mL with 150 mmol L^{-1} NaCl for particle size measurement or pure water for zeta potential measurement.

SEM Imaging of Complexes. Freshly prepared aqueous solutions of polymer/DNA complexes were examined by scanning electron microscopy (SEM, FEI Quanta 200). The complexes at an N/P ratio of 30 were prepared by adding appropriate volumes of polymer solution to 1 μg of pEGFP-C1 in equal volume, followed by vortexing for 5 s and incubating for 30 min at room temperature. Afterward, a drop of solution was dropped onto a glass slide and stored in a desiccator overnight.

***In Vitro* Transfection.** Transfection experiments were carried out in 293T and COS-7 cells. 293T cells were seeded into 24-well plate at a density of 8×10^4/well with 1 mL of complete DMEM containing 10% FBS under 5% CO_2 at 37 °C. The cells were incubated for 24 h to 60% confluence prior to transfection. For the transfection experiment, the media were replaced with fresh DMEM without serum, and then, 100 μL of polycation/pGL-3 or polycation/pEGFP-C1 complexes containing 1 μg of DNA at various N/P ratios prepared as described above were added to each well. Afterward, the cells were incubated for 4 h, followed by replacement of the media with complete DMEM, and the cells were incubated for further 48 h.

Scheme 1. Chemical Structures of Poly(β-aminoester)s with Pendant Primary Amines (1a−1c)

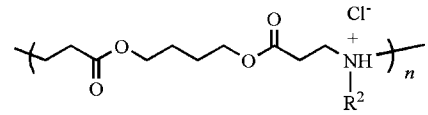

1a R^2=$CH_2CH_2NH_3^+Cl^-$

1b R^2=$CH_2CH_2CH_2CH_2NH_3^+Cl^-$

1c R^2=$CH_2CH_2CH_2CH_2CH_2CH_2NH_3^+Cl^-$

For luciferase expression, after 48 h of transfection with polymer/pGL-3 complexes, DMEM was replaced with 200 μL of cell lysis buffer and freezed−thawed twice. The lysate was centrifuged at 12000 rpm for 3 min, 20 μL of supernatant was mixed with 100 μL of the luciferase assay substrate (Promega), and light emission was measured with a Lumat 9507 luminometer (Berthold, Germany) for 10 s. The relative light units (RLU/mg protein) were normalized against the total protein concentration in the cell extracts, which was determined using a BCA assay kit (Pierce).

For green fluorescent protein (GFP) expression, after 48 h of transfection with polymer/pEGFP-C1 complexes at an N/P of 30, the cells expressing GFP were observed by a reverse fluorescent microscope (IX 70, Olympus, Japan).

To evaluate the effect of serum on gene delivery, we used DMEM containing 10% FBS for transfection of cells with polymer/pGL-3 or polymer/pEGFP-C1 complexes. For transfection in the presence of serum, when the cells achieved 60% confluence, the media were replaced with fresh DMEM containing 10% FBS, and then, complexes at various N/P ratios were added to each well. The other procedure was the same as that described above.

In the case of the transfection of COS 7 cells, cells were seeded into 24-well plates at a density of 5×10^4/well. The other procedure was similar to that of 293T cells.

RESULTS AND DISCUSSION

Characterization of Poly(β-aminoester)s with Pendant Primary Amines (1a−1c). The preparation and characterization of poly(β-aminoester)s (**1a**−**1c**) were reported in our previous work (*28*). The chemical structures of **1a**−**1c** are shown in Scheme 1. The molecular weight and polydispersity of polymers **1a**−**1c** were determined by size exclusion chromatography combined with multiangle laser light scattering. The weight average molecular weights (M_w) of **1a**−**1c** were 1.01×10^4, 8.34×10^3, and 6.68×10^3 with the polydispersity index ranging from 1.20−1.40, respectively.

The degradation kinetics of ester bonds in the main chains of **1a**−**1c**, measured with ^{1}H NMR, demonstrated that the degradation rate of **1b** is the fastest among **1a**, **1b**, and **1c**. The half-lives for ester degradation in **1a**−**1c** in phosphate buffer at pH 7.4 were approximately 144, 48, and 72 h, respectively (*28*). The degradation rate differences among **1a**−**1c** should be attributed to the length of side chains because the main chains of polymers **1a**−**1c** are same.

Buffer Capacity of the Polymer. According to the "proton sponge hypothesis" proposed by Behr et al. (*29*), the buffer

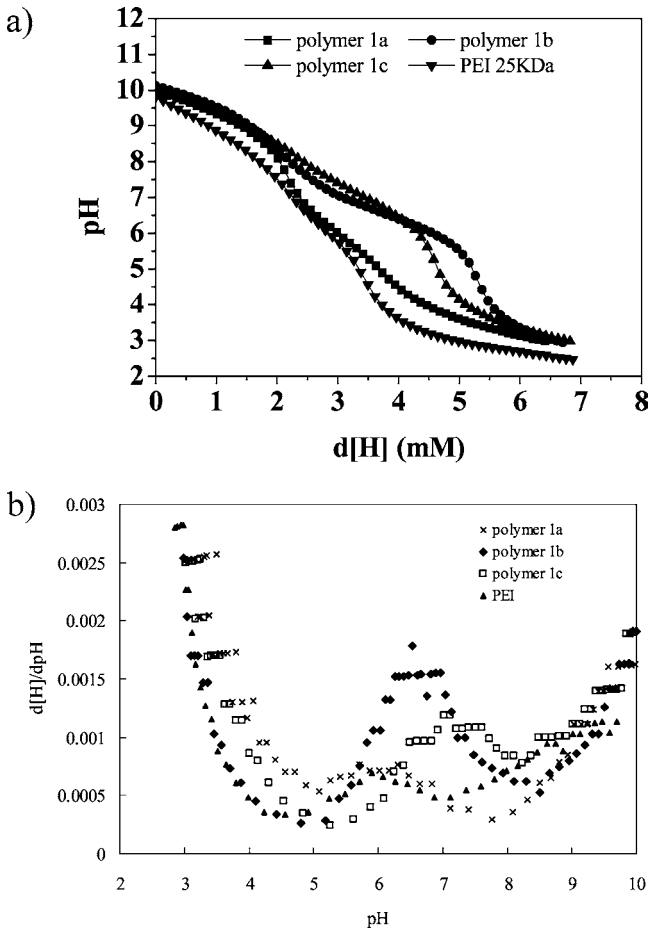

Figure 1. (a) Acid−base titration of polymers **1a**−**1c** in 150 mmol L^{-1} NaCl aqueous solution. Titration curves were obtained by titrating solutions of polymers **1a**−**1c** in 10 mL of 150 mmol L^{-1} NaCl aqueous solution from pH 10 to 3. Branched PEI 25KDa was used as a control. (b) Buffer capacities (d[H]/dpH) of polymers **1a**−**1c** and PEI 25 KDa in solution as a function of pH. Buffer capacities were calculated from potentiometric titration curves according to ref *30*.

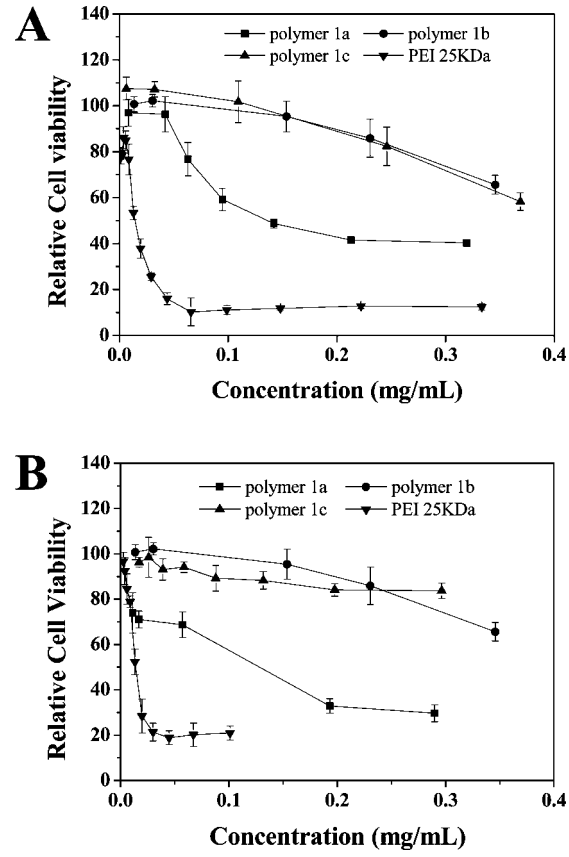

Figure 2. *In vitro* cytotoxicity of polymers **1a**−**1c** against 293T (A) and COS-7 (B) cells. Branched PEI 25KDa was used as a control.

capacity of the polycation at low pH values of 5−7 may play an important role in nonviral gene delivery, which can facilitate the escape of polycation/DNA complexes from endosomes. The buffer capacity of PEI and **1a**−**1c** was determined by acid−base titration. The titration curves are shown in Figure 1a. Buffer capacity (p[H]/dpH) was calculated from acid−base titration data according to ref *30*, which are shown in Figure 1b. We found that the buffer capacity of polymer **1a**−**1c** and PEI 25 KDa changes as a function of the pH values. At pH from 8 to 10, all of polymers **1a**−**1c** and PEI possess high buffer capacity, and there are no significant differences among polymers **1a**−**1c** and PEI. At pH values from 5 to 6, significant differences can be found. The buffer capacity of polymer **1a** was comparable to that of PEI, which was relatively lower than that of polymer **1b**. In contrast, the buffer capacity of polymer **1c** was significantly lower than those of polymers **1a**−**b** and PEI. The high buffer capacity of polycations at pH 5−7 will be beneficial in facilitating endosomal escape of polycation/DNA complexes and improving transfection efficiencies.

Cytotoxicity Assay. *In vitro* cytotoxicity is an important parameter for polycations in gene delivery. The efficacy of a gene carrier is influenced by its toxicity. In this study, the MTT assay, a colorimetric test based on the ability of mitochondrial reductase enzymes in viable cells to reduce MTT to a purple formazan, was carried out to evaluate the cytotoxicity of polymers **1a**−**1c** against 293T and COS-7 cells. Branched PEI 25KDa was used as a control. The results are shown in Figure 2. The cytotoxicity of all polymers was found to be concentration dependent, namely, the cell viability decreased with increasing polymer concentration. Branched PEI 25KDa showed high cytotoxicity against both 293T and COS-7 cells, which was in accordance with the results we observed previously (*12*). Figure 2A shows the cytotoxicity of polymers **1a**−**1c** against 293T cells. The cytotoxicity of polymers **1a**−**1c** was much lower than that of branched PEI 25KDa. In addition, the cytotoxicity of polymers **1b** and **1c** was almost same. The viability of 293T cells incubated with the solution of polymers **1b** and **1c** was about 60% at a concentration of 0.4 mg/mL, while the viability of 293T cells with polymer **1a** was about 50% at 0.4 mg/mL, which was a little lower than that of polymers **1b** and **1c**. Figure 2B shows the cytotoxicity of polymers **1a**−**1c** against COS-7 cells. The viability of COS-7 cells incubated in the solution of polymers **1a**−**1c** at a concentration of 0.4 mg/mL was about 30%, 70%, 90%, respectively. For COS-7 cells, polymers **1b** and **1c** were also less toxic than polymer **1a**, whose toxicity was similar to that in the case of 293T cells.

The cytotoxicity of cationic polymers is possibly caused by the aggregation of polymers on the cell surface via the electrostatic interaction between positively charged polymers and negatively charged sites on the cell, which induces cell membrane damage and leads to cell death (*31*, *32*). Many factors, including molecular weight, charge density (the ratio of amine numbers to polymer molecular weight), type of amines, chemical structures, biodegradation etc., affect the cytotoxicity of polycations. Generally, polycations with high molecular weight and high density of primary/or secondary amine show high cytotoxicity. In addition, the introduction of a biodegradable unit into the polycations reduces their cytotoxicity. In our previous work, we have demonstrated that the degradation rates of **1b** and **1c** are much faster than that of **1a** (*28*). We can conclude that the combination of relatively high molecular

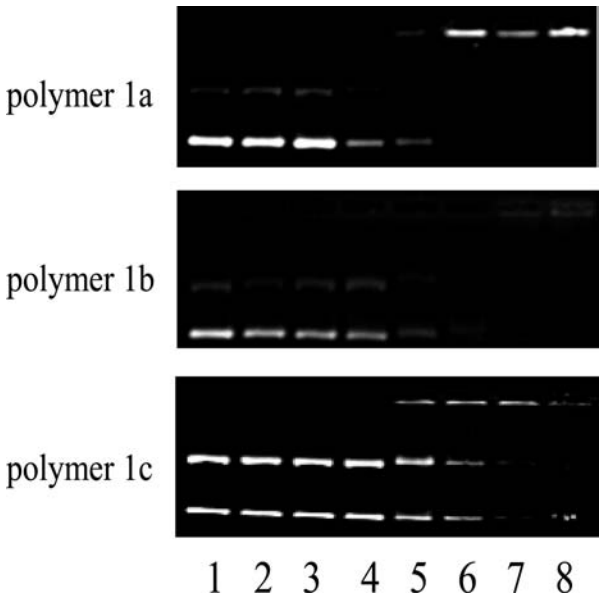

Figure 3. Agarose gel electrophoresis retardation assay of polymer/DNA complexes at various N/P ratios. Lane 1, naked DNA; lane 2−8, N/P ratios of 0.5/1, 1/1, 2/1, 5/1, 10/1, 15/1, 20/1, respectively.

weight, charge density, and slower degradation of **1a** results in the highest cytotoxicity among **1a**, **1b**, and **1c**.

DNA Condensation and Characterization. The ability of polycations to condense DNA into nanoparticles is important for gene delivery. To facilitate efficient gene expression, cationic polymers should strongly condense DNA to protect the DNA against digestion by enzymes, which can improve the transfection efficiency. The interaction of polymers **1a**−**1c** with the pEGFP-C1 plasmid was characterized by the gel retardation assay, particle size and zeta potential measurement, and SEM observation.

Agarose gel retardation assays were performed to study the condensation ability of polymers **1a**−**1c**. As shown in Figure 3, in the case of **1a**, DNA was entirely retained in the wells at the N/P ratio above 5. In contrast, **1b** and **1c** completely retarded the migration of DNA in the gel at N/P ratios above 10 and 20, respectively. The ability to bind and condense DNA followed the order of **1a** > **1b** > **1c**. Polycations with high molecular weight and high charge density often show strong DNA binding ability at low N/P ratios. In this work, the order of DNA binding ability is consistent with that of the molecular weight and charge density of **1a**−**1c**.

The complexation of positively charged polycation and negatively charged plasmid DNA via electrostatic interaction between amino groups and phosphate groups usually results in the formation of small-sized particles. The physical properties of the formed complexes particles, such as sizes and zeta potentials, have great impact on transfection efficiency. Complexes with positive charge and small size are beneficial for cellular uptake and intracellular trafficking. The average sizes of **1a**−**1c**/pEGFP-C1 complex particles at various N/P ratios were measured using dynamic light scattering. As shown in Figure 4, the average diameters of polymer/DNA complexes are dependent on both the chemical structure of polycations and N/P ratios. The average diameters of **1b** and **1c**/DNA complexes at N/P ratios ranging from 10 to 60 are between 400 and 500 nm. N/P ratios had no significant effects on the sizes of **1b** and **1c**/DNA complexes. In the case of **1a**, the average diameters varied between 120 and 480 nm, which decreased with the increase of N/P ratios. In comparison to **1b** and **1c**, the relatively high molecular weight and charge density of **1a** resulted in the formation of polycation/DNA complexes with smaller sizes,

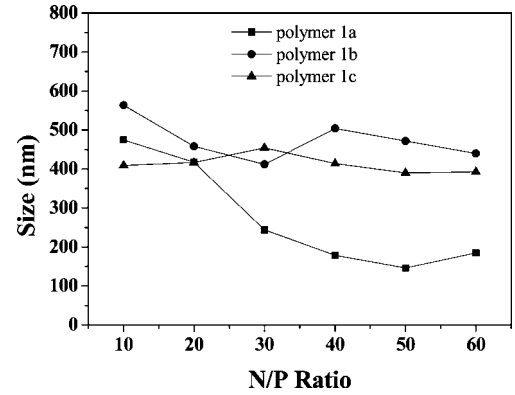

Figure 4. Particle sizes of polymer/DNA complexes at N/P ratios ranging from 10 to 60 in 150 mmol L^{-1} NaCl aqueous solution.

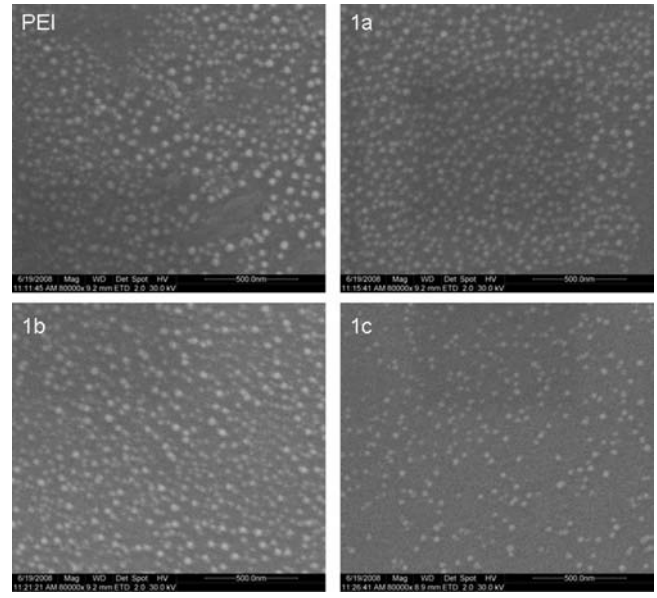

Figure 5. Scanning electron microscopy (SEM, FEI Quanta 200) of polymers **1a**−**1c**/pEGFP-C1 complexes at an N/P of 30, while the branched PEI 25KDa/pEGFP-C1 complex was at an optimal N/P of 10.

which is consistent with the DNA binding ability measured by the agarose gel assay.

The size and shape of **1a**−**1c**/pEGFP-C1 complexes at an N/P ratio of 30 were observed by SEM. PEI/pEGFP-C1 complexes at an N/P of 10, which is optimal for *in vitro* transfection, were measured as a reference. The results are shown in Figure 5. In the cases of all polycations we used in this work including PEI and **1a**−**1c**, the complexes of polycation/DNA were observed to be nanosized and uniform spherical particles. The diameters of PEI/DNA complexes at an N/P ratio of 10 ranged from 30 to 50 nm, whereas those of **1a**−**1c**/DNA complexes at an N/P ratio of 30 ranged from 20 to 40 nm. There was no significant difference in **1a**−**1c**/DNA complexes, which was greatly different from that measured by dynamic light scattering in solution. Similar results have been observed in our previous work (*10*) in the cases of PEI/DNA and cross-linked PEI 800/DNA complexes measured with TEM. The results demonstrated that the weak ability of **1b** and **1c** to bind DNA induced the formation of loose polycation/DNA complexes in solution with relatively large sizes and that the strong ability of **1a** and PEI to bind DNA resulted in the formation of compact complexes with small sizes. In comparison to compact complexes of PEI and **1a**/DNA, the loose complexes of **1b** and **1c**/DNA were easier to collapse to be small-sized particles under

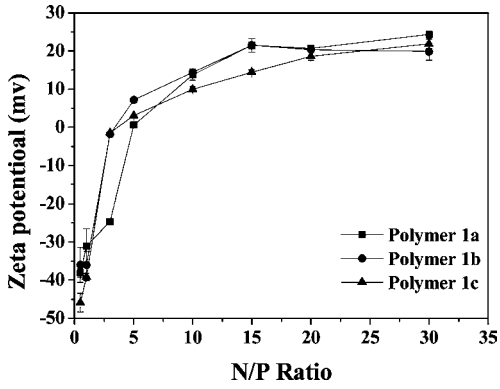

Figure 6. Zeta potentials of polymer/DNA complexes at N/P ratios ranging from 0.5 to 30 in 150 mmol L^{-1} NaCl aqueous solution.

vacuum conditions for SEM measurements. As a result, no obvious difference in the morphologies and diameters of **1a**−**1c** and PEI/DNA complexes was observed by SEM.

Positive surface charge of polycation/DNA complexes can facilitate the nonspecific attachment of complex nanoparticles to the negatively charged cellular membranes and the uptake of polycation/DNA complexes by cells. The zeta potentials of polycation/DNA complexes were measured to assess their surface charge. As shown in Figure 6, at the same N/P ratios, **1a**−**1c**/DNA complexes possessed similar surface charge. At N/P ratios below 5, the zeta potentials of all the complexes are negative, indicating incomplete complexation. With the increase of the N/P ratio, the zeta potential rapidly increased and reached a plateau of about 22 mV, which is a little lower than that of PEI/DNA complexes. The N/P ratios for the plateau zeta potentials of **1a**−**1c** were 15, 15, and 20, respectively. The N/P ratio for the plateau zeta potentials of **1c** is higher than those of **1a** and **1b**, also indicating the weak ability of **1c** to condense DNA. In comparison to PEI/DNA complexes, the moderate surface charges of **1a**−**1c**/DNA complexes are expected to be suitable for reaching a better balance between cellular uptake and cytotoxicity.

***In Vitro* Transfection.** *In vitro* transfection was conducted on 293T and COS-7 cells to evaluate the ability of the polycations **1a**−**1c** to deliver foreign DNA into cells. Branched PEI 25KDa at the optimal N/P ratio of 10 was used as a positive control, and pGL-3 plasmid, expressing luciferase, was used as the report gene.

As shown in Figure 7A, the transfection results revealed that polymer **1a** showed excellent transfection efficiency in 293T cells at the tested N/P ratios from 10 to 60, which was comparable or higher than that of branched PEI 25KDa at the optimal N/P ratio of 10. Luciferase expression (RLU/mg protein) was related to the N/P ratio. Optimized luciferase expression (RLU/mg protein) in 293T cells with **1a**/pGL-3 complexes was 2.27×10^9, which was a little higher than that with PEI/pGL-3 complexes (2.09×10^9). In contrast, **1b** and **1c** showed very low luciferase expression in 293T cells at N/P ratios of 10 and 20, respectively. Although the transfection efficiencies gradually increased with the increase of N/P ratios, they were still lower than that of PEI. The low transfection efficiencies of **1b** and **1c** should be related to the combinational factors including the low DNA binding ability of **1b** and **1c**, the relatively large sizes (about 400−500 nm) of **1b** and **1c**/pGL-3 complexes at the tested N/P from 10 to 60, and rapid hydrolytical degradation of **1b** and **1c** under physiological conditions as described in our previous work (*28*). The degradation of **1b** and **1c** at pH 7.4 is much faster than that of **1a**, especially at the early stage within 24 h. The rapid degradation of **1b** and **1c** is considered to be unsuitable to prevent the incorporated DNA from degradation before entering the cell nucleus.

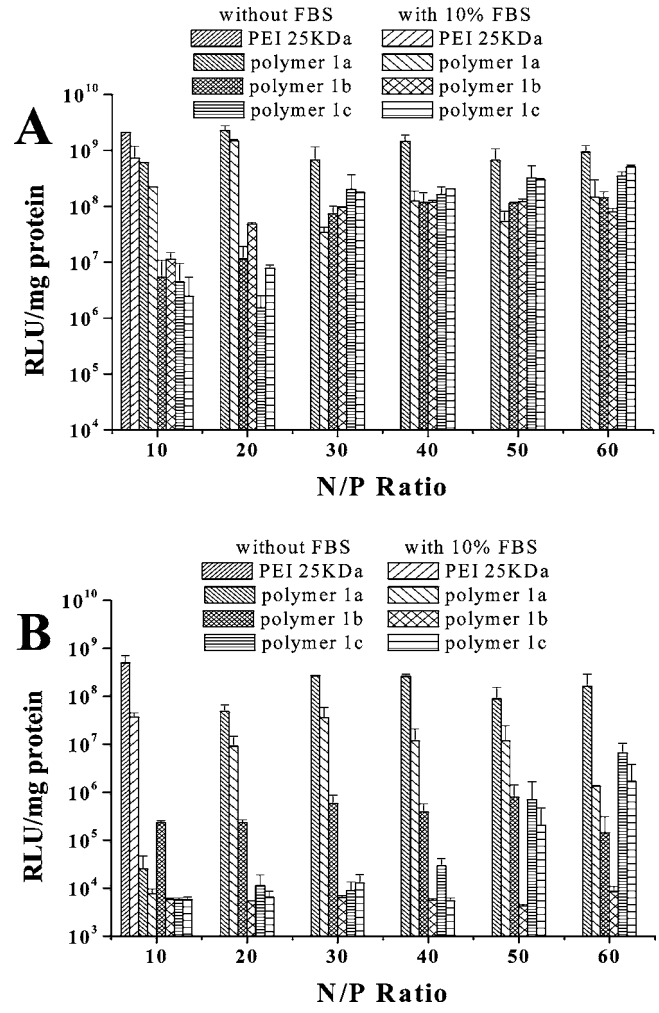

Figure 7. Transfection efficiencies of polymers **1a**−**1c**/pGL-3 complexes in 293T (A) and COS-7 cells (B). Branched PEI 25KDa was used as a positive control.

Similarly, COS-7 cells were transfected with **1a**−**1c** and PEI/pGL-3 complexes. The results shown in Figure 7B indicated that **1a** was the most efficient carrier among **1a**, **1b**, and **1c**. The highest luciferase expression in COS-7 cells with **1a**/pGL-3 complexes at optimized N/P ratios of 30 and 40 was comparable to that of PEI/pGL-3 complexes at an N/P of 10. The effects of N/P ratios on the luciferase expression level in COS-7 cells are similar to that in 293T cells.

Serum protein can hinder cellular uptake and promote aggregation, which often reduces the transfection efficiency (*33*). Transfection experiments were then performed with 293T and COS-7 cells in the presence of 10% FBS. As shown in Figure 7A and B, 10% of serum inhibited luciferase expression in 293T and COS-7 cells with each polycation tested in this work including PEI and **1a**−**1c**. The results illustrated that luciferase expression in 293T cells only slightly decreased, while serum significantly decreased luciferase expression in COS-7 cells at various N/P ratios. However, we also found that luciferase expression with polymer **1a** only slightly decreased both in 293T and COS-7 cells at various N/P ratios, which indicated that **1a**/DNA complexes are less serum-sensitive for *in vitro* transfection.

pGFP Transfection. *In vitro* transfection with **1a**/pEGFP-C1 complexes at an N/P of 30 was then conducted on 293T and COS-7 cells to directly visualize the transfected cells expressing green fluorescent protein (GFP). Branched PEI 25KDa was used as a control. The transfected cells which express GFP were observed by a reverse fluorescent microscope.

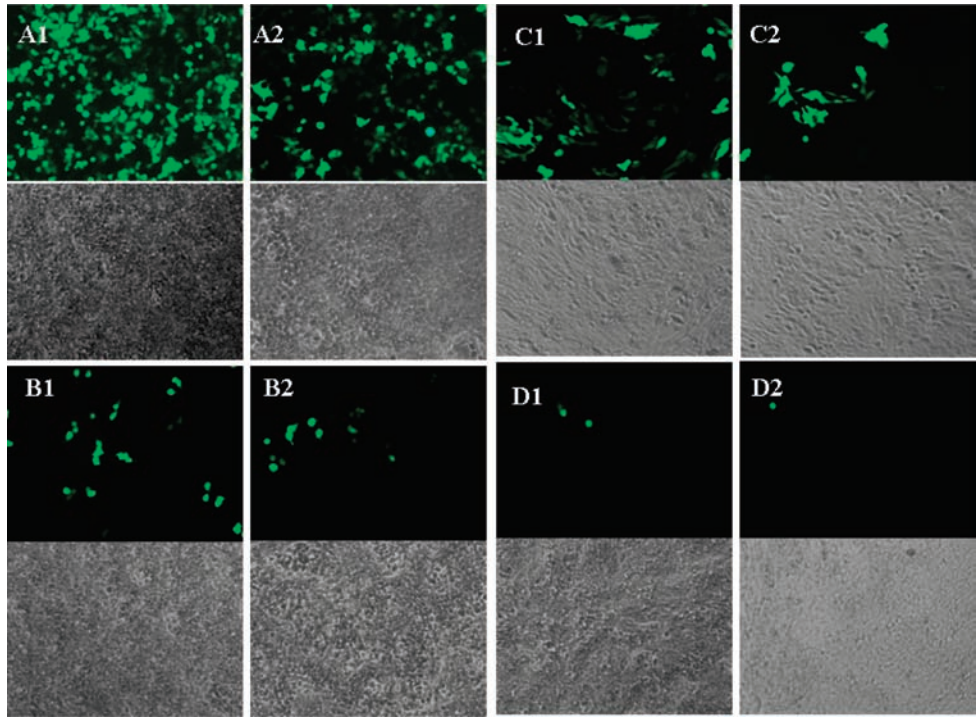

Figure 8. Fluorescent microscope images of 293T cells (A,B) and COS-7 cells (C,D) transfected with **1a**/pEGFP-C1 complexes at an N/P of 30 and branched PEI 25KDa/pEGFP-C1 complexes at an optimal N/P ratio of 10. A1 (PEI), A2 (**1a**), C1 (PEI), and C2 (**1a**) show the transfection without serum, while B1 (PEI), B2 (**1a**), D1 (PEI), and D2 (**1a**) show the transfection in the presence of 10% FBS. Transfected cells were observed by a reverse fluorescent microscope (IX 70, Olympus, Japan; 400×).

The results shown in Figure 8A1 and A2 indicates that the percentage of GFP-expressed 293T cells transfected with **1a**/pEGFP-C1 complexes at an N/P ratio of 30 is only slightly lower than that with PEI/pEGFP-C1 complexes.

Figure 8B1 and B2 shows that the percentage of GFP-expressed 293T cells transfected with PEI and **1a**/pEGFP-C1 complexes in the presence of 10% FBS obviously decreased, which indicated that the serum greatly inhibited the transfection efficiency of PEI and **1a**. In Figure 8C and D, we found a similar trend in the effect of serum on the transfection of COS-7 cells with PEI and **1a**/pEGFP-C1 complexes. In addition, GFP expression in COS-7 transfected with PEI and **1a**/pEGFP-C1 complexes is lower than that in 293T cells, which implied that both PEI and **1a** were cell-dependent for *in vitro* transfection.

CONCLUSIONS

In summary, novel hydrolytically degradable poly(β-aminoester)s with pendant primary amine were evaluated for gene delivery including buffer capacity, cytotoxicity, DNA binding ability, charaterization of polyplexes, and *in vitro* transfection. We have demonstrated that poly(β-aminoester)s with a pendant aminoethyl group (**1a**) show slightly higher gene delivery efficiencies than PEI 25 KDa under optimal conditions, while the IC_{50} of **1a** is 1 order of magnitude higher than that of PEI 25 KDa. The results revealed the potentials of novel hydrolytically degradable polycations in gene delivery and will provide valuable insight into the design of highly efficient and less toxic polycationic gene carriers.

ACKNOWLEDGMENT

This work was financially supported by National Natural Science Foundation of China (20674058 and 20874076), National Basic Research Program of China (2005CB623903 and 2009CB930300), and Ministry of Education of China (Program for New Century Excellent Talents in University).

LITERATURE CITED

(1) Li, S., and Huang, L. (2000) Nonviral gene therapy: promises and challenges. *Gene Ther. 7*, 31–34.

(2) Yu, B., Zhao, X. B., Lee, L. J., and Lee, R. J. (2009) Targeted delivery systems for oligonucleotide therapeutics. *AAPS J. 11*, 195–203.

(3) Colella, P., Cotugno, G., and Auricchio, A. (2009) Ocular gene therapy: current progress and future prospects. *Trends Mol. Med. 15*, 23–31.

(4) Seow, Y., and Wood, M. J. (2009) Biological gene delivery vehicles: beyond viral vectors. *Mol. Ther. 17*, 767–777.

(5) Mintzer, M. A., and Simanek, E. E. (2009) Nonviral vectors for gene delivery. *Chem. Rev. 109*, 259–302.

(6) Zauner, W., Ogris, M., and Wagner, E. (1998) Polylysine-based transfection systems utilizing receptor-mediated delivery. *Adv. Drug Delivery Rev. 30*, 97–113.

(7) Ward, C. M., Pechar, M., Oupicky, D., Ulbrich, K., and Seymour, L. W. (2002) Modification of pLL/DNA complexes with a multivalent hydrophilic polymer permits folate-mediated targeting in vitro and prolonged plasma circulation in vivo. *J. Gene Med. 4*, 536–547.

(8) Neu, M., Fischer, D., and Kissel, T. (2005) Recent advances in rational gene transfer vector design based on poly(ethyleneimine) and its derivatives. *J. Gene Med. 7*, 992–1009.

(9) Godbey, W. T., Wu, K. K., and Mikos, A. G. (1999) Poly(ethylenimine) and its role in gene delivery. *J. Controlled Release 60*, 149–160.

(10) Peng, Q., Zhong, Z. L., and Zhuo, R. X. (2008) Disulfide cross-linked polyethylenimines (PEI) prepared via thiolation of low molecular weight PEI as highly efficient gene vectors. *Bioconjugate Chem. 19*, 499–506.

(11) Jiang, H. L., Arote, R., Jere, D., Kim, Y. K., Cho, M. H., and Cho, C. S. (2008) Degradable polyethylenimines as gene carriers. *Mater. Sci. Technol. 24*, 1118–1126.

(12) Zhang, X. Q., Wang, X. L., Huang, S. W., Zhuo, R. X., Liu, Z. L., Mao, H. Q., and Leong, K. W. (2005) In vitro gene delivery

using poly(amidoamine) dendrimers with a trimesyl core. *Biomacromolecules 6*, 341–350.
(13) Wang, Y. M., Kong, W. L., Song, Y., Duan, Y. J., Wang, L. Y., Steinhoff, G., Kong, D. L., and Yu, Y, T. (2009) Polyamidoamine dendrimers with a modified pentaerythritol core having high efficiency and low cytotoxicity as gene carriers. *Biomacromolecules 10*, 617–622.
(14) Parekh, H. S. (2007) The advance of dendrimers: A versatile targeting platform for gene/drug delivery. *Curr. Pharm. Des. 13*, 2837–2850.
(15) Pack, D. W., Hoffman, A. S., Pun, S., and Stayton, P. S. (2005) Design and development of polymers for gene delivery. *Nat. Rev. Drug Discovery 4*, 581–593.
(16) Rao, N. M., and Gopal, V. (2006) Cationic lipids for gene delivery in vitro and in vivo. *Expert Opin Ther. Pat. 16*, 825–844.
(17) Luten, J., van Nostruin, C. F., De Smedt, S. C., and Hennink, W. E. (2008) Biodegradable polymers as non-viral carriers for plasmid DNA delivery. *J. Controlled Release 126*, 97–110.
(18) Arote, R., Kim, T. H., Kim, Y. K., Kim, Y. K., Hwang, S. K., Jiang, H. L., Song, H. H., Nah, J. W., Cho, M. H., and Cho, C. S. (2007) A biodegradable poly(ester amine) based on polycaprolactone and polyethylenimine as a gene carrier. *Biomaterials 28*, 735–744.
(19) Akinc, A., Lynn, D. M., Anderson, D. G., and Langer, R. (2003) Parallel synthesis and biophysical characterization of a degradable polymer library for gene delivery. *J. Am. Chem. Soc. 125*, 5316–5323.
(20) Lynn, D. M., Anderson, D. G., Putnam, D., and Langer, R. (2001) Accelerated discovery of synthetic transfection vectors: Parallel synthesis and screening of degradable polymer library. *J. Am. Chem. Soc. 123*, 8155–8156.
(21) Li, Z. H., and Huang, L. (2004) Sustained delivery and expression of plasmid DNA based on biodegradable polyester, poly(D,L-lactide-co-4-hydroxy-L-proline). *J. Controlled Release 98*, 437–446.
(22) Putnam, D., and Langer, R. (1999) Poly(4-hydroxy-L-proline ester): Low-temperature polycondensation and plasmid DNA complexation. *Macromolecules 32*, 3658–3662.
(23) Wang, J., Mao, H. Q., and Leong, K. W. (2001) A novel biodegradable gene carrier based on polyphosphoester. *J. Am. Chem. Soc. 123*, 9480–9481.
(24) Wang, J., Huang, S. W., Zhang, P. C., Mao, H. Q., and Leong, K. W. (2003) Effect of side-chain structures on gene transfer efficiency of biodegradable cationic polyphosphoesters. *Int. J. Pharm. 265*, 75–84.
(25) Lynn, D. M., and Langer, R. (2000) Degradable poly(beta-amino esters): Synthesis, characterization, and self-assembly with plasmid DNA. *J. Am. Chem. Soc. 122*, 10761–10768.
(26) Zugates, G. T., Anderson, D. G., Little, S. R., Lawhorn, I. E. B., and Langer, R. (2006) Synthesis of poly(beta-amino ester)s with thiol-reactive side chains for DNA delivery. *J. Am. Chem. Soc. 128*, 12726–12734.
(27) Akinc, A., Anderson, D. G., Lynn, D. M., and Langer, R. (2003) Synthesis of poly(beta-amino ester)s optimized for highly effective gene delivery. *Bioconjugate Chem. 14*, 979–988.
(28) Chen, J., Huang, S. W., Liu, M., and Zhuo, R. X. (2007) Synthesis and degradation of poly(beta-aminoester) with pendant primary amine. *Polymer 48*, 675–681.
(29) Benns, J. M., Choi, J. S., Mahato, R. I., Park, J. S., and Kim, S. W. (2000) pH-sensitive cationic polymer gene delivery vehicle: N-Ac-poly(L-histidine)-graft-poly(L-lysine) comb shaped polymer. *Bioconjugate Chem. 11*, 637–645.
(30) von Harpe, A., Petersen, H., Li, Y. X., and Kissel, T. (2000) Characterization of commercially available and synthesized polyethylenimines for gene delivery. *J. Controlled Release 69*, 309–322.
(31) Kunath, K., Harpe, A. V., Fischer, D., Petersen, H., Bickel, U., Voigt, K., and Thomas, K. (2003) Low-molecular-weight polyethylenimine as a non-viral vector for DNA delivery: comparison of physicochemical properties, transfection efficiency and in vivo distribution with high-molecular-weight polyethylenimine. *J. Controlled Release 89*, 113–125.
(32) Choksakulnimitr, S., Masuda, S., Tokuda, H., Takakura, Y., and Hashida, M. (1995) In vitro cytotoxicity of macromolecules in different cell culture systems. *J. Controlled Release 34*, 233–241.
(33) Dash, P. R., Read, M. L., Barrett, L. B., Wolfert, M. A., and Seymoura, L. W. (1999) Factors affecting blood clearance and in vivo distribution of polyelectrolyte complexes for gene delivery. *Gene Ther. 6*, 643–650.

BC900317M

Molecular Tension-Indexed Bioluminescent Probe for Determining Protein−Protein Interactions

Sung Bae Kim,[†] Moritoshi Sato,[‡] and Hiroaki Tao[†,*]

Research Institute for Environmental Management Technology, National Institute of Advanced Industrial Science and Technology (AIST), 16-1 Onogawa, Tsukuba 305-8569, Japan, Graduate School of Arts and Sciences, The University of Tokyo, 3-8-1 Komaba, Meguro-ku, Tokyo 153-8902, Japan. Received July 28, 2009; Revised Manuscript Received October 25, 2009

This study demonstrates a unique, nontranscriptional assay system based on molecular tension of a luciferase artificially appended by protein−protein binding. We hypothesized that an artificially appended molecular tension to a full-length luciferase may diversify the enzymatic activity through a modification of the active site. For the basic probe design, a full-length luciferase was sandwiched between two component proteins of interest. The length of flexible linkers between the components was minimized to exert an efficient molecular tension to the sandwiched luciferase. When N- and C-terminal ends of *Renilla* luciferase 8 were flanked by the ligand-binding domain of human estrogen receptor α (ER LBD) and SH2 domain of Src, named ERS, this simple probe was surprisingly sensitive to estrogens. The luminescence spectra by ERS were largely enhanced by an addition of 4-hydroxytamoxifen (OHT), 17β-estradiol, and genistein. The detection limit of ERS reached 1 nM OHT. Quantum yield (QY) and Michaelis−Menten constant of ERS were found to be 6.3% and 94.3 μM, respectively. The enzymatic activities of ERS are also governed by different types of coelenterazine (CTZ) variants. The two hydroxy groups in CTZ are critical for the enzymatic activities of ERS. This study is the first example that an artificially appended molecular tension to a full-length luciferase can be taken as an optical signature upon molecular imaging. This study also provides new insight into the construction of a new lineage of bioluminescent probes for estimating protein−protein interactions.

INTRODUCTION

Recent revolutionary advances in enzyme manipulation technologies now allow researchers to carry out quantitative examination of molecular dynamics and cell signaling in living subjects (*1*).

Luciferases are nearly ideal reporters for bioanalysis and molecular imaging: (i) The assays are potentially very simple, sensitive, and do not require an external light source or cofactors. (ii) The assay time is usually less than one min, which enables a high throughput analysis. (iii) The assay is cheap, nonhazardous, and broadly applicable to living organisms.

To date, various luciferases have been engineered for determining protein−protein interactions: (i) Bioluminescence resonance energy transfer (BRET) is a potential technique for determining protein−protein interactions on the basis of energy transfer between bioluminescent donor and acceptor proteins (*2*) (*3*) (*4*). (ii) Two-hybrid assay allows a simple determination of protein−protein interactions in living mammalian cells and animals (*5*). (ii) Protein-fragment complementation assay (PCA) is another strategy for determining protein−protein interactions in cell lines, where monomeric luciferases are split into two fragments with resulting temporally inactive portions (*6*) (*7*) (*8*) (*9*) (*10*). The luciferase activity is reconstituted only upon protein−protein interactions. (iii) Recently, a circular permutation (CP) of a dissected luciferase was utilized to determine protein−protein interactions. Original N- and C-terminals of a luciferase are directly linked with a flexible linker, whereas new N- and C-terminals are created in the middle of the luciferase sequence, and modified with proteins of interest (*11*) (*12*). This manipulation exerts a conditional reconstitution of the luciferase activity in response to ligand-activated protein−protein interactions.

Many of the previous studies dissect the luciferases into two fragments for a temporal loss and conditional recovery of luciferase activities. However, this methodology inevitably invades the intrinsic enzymatic property of the luciferase and recovers merely 0.5−5% of the original luciferase activity (*13*) (*14*). The poor absolute luminescence intensities are especially problematic upon application to living animals. Furthermore, the luciferase-dissection strategy requires a sophisticated probe design and a tedious optimization step for deciding a suitable splitting site for the luciferase. These procedures consequently consume time and resources. In our review examinations, many of the previous dissection sites in luciferases are frequently inadequate in other protein−protein interaction cases (*15*).

To address such drawbacks of the conventional methods, we have investigated a simple but efficient bioluminescent probe for determining protein−protein interactions. We initially hypothesized that a luciferase activity may vary according to the molecular tension artificially appended to the full-length luciferase. *Renilla* luciferase 8 (RLuc8) was selected to examine the probability. N- and C-terminal ends of full-length RLuc8 were fused with the ligand-binding domain of the human estrogen receptor (ER LBD)[1] and the Src homology domain 2 of *v*-Src (SH2), respectively. Upon ligand activation, Tyr537 in ER LBD is phosphorylated, and consequently recognized by the adjacent SH2 domain. The ligand-activated ER LBD–SH2 binding appends a molecular tension to the sandwiched full-length RLuc8. The consequent variation in the luciferase activity was surprisingly large enough to be indexed as an optical signature. This probe was named ERS from the consecutive component initials, that is, ER LBD-RLuc8-SH2.

* Corresponding author: hiro-tao@aist.go.jp.
[†] AIST.
[‡] The University of Tokyo.

10.1021/bc900330w CCC: $40.75 © 2009 American Chemical Society
Published on Web 11/25/2009

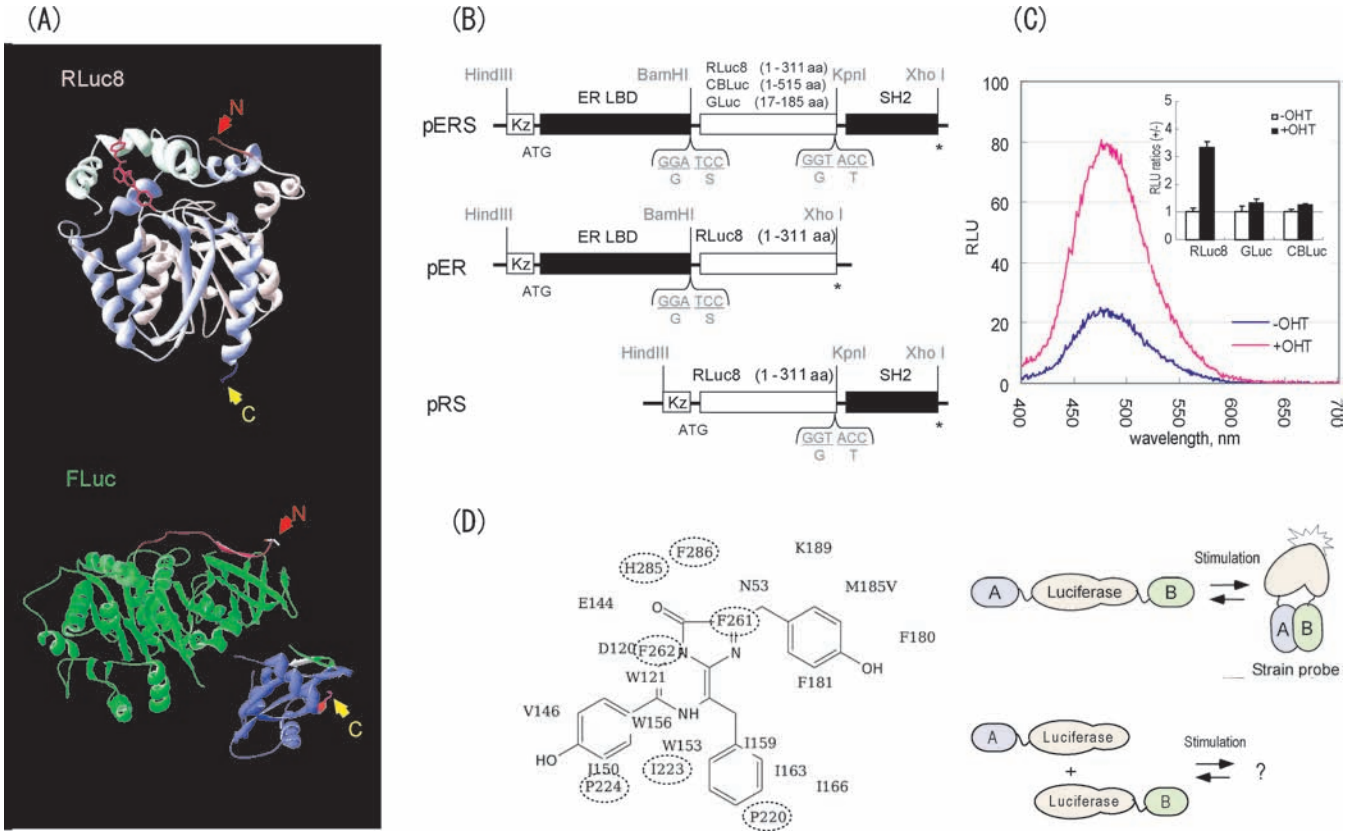

Figure 1. (A) Crystal structure of *Renilla* luciferase 8 (RLuc8; pdb 2PSJ) and firefly luciferase (FLuc). Red and yellow arrows indicate N- and C-terminal ends, respectively. The red chemical in RLuc8 shows coelenterazine (CTZ). The rectangular active site embraces CTZ. An external molecular tension may distort this rectangular frame. (B) Schematic structures of cDNA constructs. Abbrevations: ER LBD, ligand binding domain of human estrogen receptor; RLuc8, *Renilla* luciferase 8; CBLuc, click beetle luciferase red; GLuc, *Gaussia* luciferase; SH2, SH2 domain of Src; Kz, kozak sequence. (C) Variance in the bioluminescence emission spectra before and after addition of 1 μM 4-hydroxytamoxifen (OHT), obtained by a spectrophotometer (F-7000, Hitachi). Inset shows the relative luminescence intensities before and after addition of 1 μM OHT, obtained by a luminometer (Berthold). ER LBD-RLuc8-SH2 (ERS) showed a considerable enhancement in the bioluminescence in response to OHT, whereas ER LBD-GLuc-SH2 (EGS) and ER LBD-CBLuc-SH2 (ECS) did not enhance the luminescence intensities. (D) The chemical structure shows coelenterazine (CTZ) interacting with the active site of RLuc8 (left: a modification of a reference (*18*)). Dotted circles highlight amino acids close to the C-terminal end of RLuc8. An illustration of the working mechanism of ERS in response to a ligand (right). A ligand activates an interaction between proteins A and B, which consequently transforms the sandwiched luciferase. This transformation is not valid in *ER+RS* combination.

The sensitivity and selectivity of ERS to various ligands are initially demonstrated with respect to the sensorial properties. The spectral properties of ERS according to various coelenterazine (CTZ) derivatives are also discussed. Quantum yields (QYs), turnover rates, and Michaelis−Menten constants (K_M) of ERS are reported. Finally, we propose the molecular mechanism of ERS upon sensing estrogens based on a series of control studies.

[1]Abbreviations: ER LBD, the ligand-binding domain of the human estrogen receptor (305−550 AA); SH2, the Src homology domain 2 of a proto-oncogene tyrosine-protein kinase, *v*-Src; ERS, a bioluminescent probe custom-made and named from the consecutive component initials, that is, ER LBD-RLuc8-SH2; *p*Cold I vector, A Coldshock expression vector (Takara) for *E. coli*; *p*Ers, a custom-made plasmid encoding ERS (ER LBD-RLuc8-SH2); *p*Ecs, a custom-made plasmid encoding ECS (ER LBD-CBLuc-SH2); *p*Egs, a custom-made plasmid encoding EGS (ER LBD-GLuc-SH2); *p*Er, a custom-made plasmid encoding *ER* (ER LBD-RLuc8); *p*Rs, a custom-made plasmid encoding *RS* (RLuc8-SH2); COS-7, a mammalian culture cell line derived from African green monkey kidney fibroblast; OHT, a known antagonist of estrogen receptors called 4-hydroxytamoxifen; CTZ, a native luciferin for various luciferases derived from marine animals called coelenterazine; CTZ *hcp*, a synthetic derivative of coelenterazine carrying hydrogen (*h*) at C2 and cyclopentyl (*cp*) group at C8 position; CTZ *cp*, a synthetic derivative of coelenterazine carrying a cyclopentyl (*cp*) group at C8 position; CTZ *fcp*, a synthetic derivative of coelenterazine carrying fluorine (*f*) at C2 and cyclopentyl (*cp*) group at C8 position; CTZ *ip*, a synthetic derivative of coelenterazine carrying iodine (*i*) at C2 and 2-propionyl (*p*) group at C8 position; E_2, an agonist of estrogen receptors called 17β-estradiol; CTZ *400A*, a synthetic derivative of coelenterazine carrying no side chains at C2, C6, and C8 positions, also called DeepBlueC.

EXPERIMENTAL PROCEDURES

Construction of Plasmids. As a template for polymerase chain reaction (PCR), cDNAs encoding the following luciferases were obtained from the corresponding providers: *Renilla* luciferase 8 (RLuc8) was kindly presented by Professor Gambhir (Stanford University); click beetle luciferase red (CBLuc) was purchased from Promega; and *Gaussia* luciferase (GLuc) from Nanolight. cDNAs encoding the human estrogen receptor (hER) and full-length *v*-Src were presented by Professor Umezawa (Tokyo University).

The cDNAs encoding ER LBD and SH2 domain of *v*-Src were generated by PCR using corresponding primers to introduce unique restriction sites, *Hind*III/ *BamH*I and *Kpn*I/ *Xho*I, respectively. Both ends of cDNAs encoding RLuc8, CBLuc, and GLuc were also modified by PCR to introduce specific restriction sites, *BamH*I and *Kpn*I. The cDNA blocks were ligated to make a series of chimera constructs as shown in Figure 1 and subcloned into a mammalian expression vector *p*cDNA 3.1(+) vector (Invitrogen).

A plasmid for *Escherichia coli* expression was constructed as follows: The cDNA encoding ERS was modified by PCR to

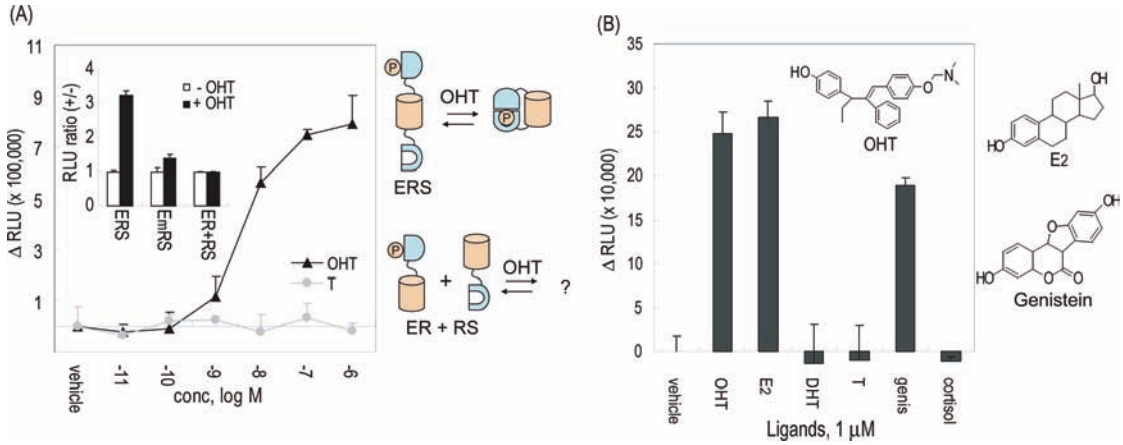

Figure 2. (A) Dose−response curves of ER LBD-RLuc8-SH2 (ERS) in response to steroid hormones. The luminescence intensity reflects the enzymatic activity of transformed RLuc8 in ERS in response to varying concentrations of OHT. Inset shows ligand sensitivity of a series of control probes. E_mRS shows a point-mutated form of ERS at Tyr537, while *ER+RS* means coexistence of the two truncated forms of ERS, that is, *ER* and *RS*. Values were measured in triplicate. The working mechanism of ERS and *ER+RS* was illustrated in the middle column. (B) Ligand selectivity of ERS. The luminescence intensities were compared after activation of ERS with various ligands. Abbrevations: 4-hydroxytamoxifen (OHT), 17β-estradiol (E_2), 5α-dihydrotestosterone (DHT), testosterone (T), genistein (genis).

introduce unique restriction sites, *Sac*I/ *Xho*I, at the 5′- and 3′-ends. The chimera DNA restricted by *Sac*I and *Xho*I was subcloned into the *E. coli* Coldshock expression vector *p*Cold I vector (Takara).

The sequences of the cDNAs were confirmed with a BigDye Terminators v1.1 cycle sequencing kit and a genetic sequencer (ABI PRISM 310 Genetic Analyzer, Applied Biosystems). The consequent plasmids were named *p*Ers, *p*Ecs, *p*Egs, *p*Er, and *p*Rs according to the consecutive component initials. The corresponding probes after expression were named ERS, ECS, EGS, *ER*, and *RS*. The *p*Cold I vector for expressing ERS was named *p*Cold-Ers.

Bioluminescence Spectra of COS-7 Cells Carrying *p*Ers. Variance in the bioluminescence spectra from mammalian COS-7 cells carrying *p*Ers was examined in the presence or absence of 4-hydroxytamoxifen (OHT) (Figure 1C).

For the present experiment, COS-7 cells were cultured in a Dulbecco's modified Eagle's medium (DMEM) supplemented with 10% fetal bovine serum (FBS; Gibco) and 1% penicillin/streptomycin (P/S; Gibco) at 37 °C in 5% CO_2. The cells were seeded in 12-well culture plates, transiently transfected with 2 μg of *p*Ers per well using a transfection reagent, TransIT-LT1 (Mirus), and incubated for 16 h at 37 °C in 5% CO_2 before experiments.

The cells on the 12-well plates were stimulated for 20 min with vehicle (0.1% DMSO) or 1 μM 4-hydroxytamoxifen (OHT). The cells were washed once with phosphate buffered saline (PBS; pH 7.4, 0.01 M), and lysed with a lysis buffer (Promega). The lysates were transferred into a quartz cuvette for monitoring the spectral variance with a spectrophotometer (F-7000, Hitachi) in the presence of coelenterazine native (CTZ).

Ligand Sensitivity of COS-7 Cells Carrying *p*Ers, *p*Ecs, or *p*Egs. Relative ligand sensitivities among ERS, ECS, and EGS were examined in the presence or absence of OHT (Figure 1C Inset).

COS-7 cells carrying *p*Ers, *p*Ecs, or *p*Egs were stimulated with vehicle (0.1% dimethyl sulfoxide (DMSO)) or OHT for 20 min, washed once with PBS, and finally lysed with a lysis buffer for 15 min. The cell lysates were transferred to test tubes, and the subsequent bioluminescence intensities were determined with a luminometer (MiniLumat LB9506; Berthold) in the presence of coelenterazine (CTZ).

The brief procedure for the normalization of bioluminescence was as follows: The RLuc luminescence intensities were expressed as a ratio of relative luminescence unit (RLU), that is, RLU (+)/RLU (−), where RLU (+) and RLU (−) are the luminescence intensities with 1 μg of cell lysate after the cells were incubated with and without a ligand, respectively; the RLU is an amplified value of photon counts generated from the luminometer (arbitrary unit).

Sensorial Properties of ERS to Varying Concentrations of Ligands. Sensorial properties of ERS to ligands were estimated with different concentrations of ligands (Figure 2A). COS-7 cells were transfected with *p*Ers as described in Figure 1C.

The cells cultured on 24-well plates were stimulated with vehicle (0.1% DMSO) or varying concentrations of OHT or testosterone (T) for 20 min. The cells were washed once with PBS and lysed. Ligand-activated ER LBD–SH2 interactions were estimated on the basis of the bioluminescence variance using a spectrophotometer (F-7000, Hitachi). The ΔRLU was calculated as shown in a previous study (*16*): the bioluminescence intensities developed by varying concentrations of a ligand were subtracted by the bioluminescence intensities developed by vehicle (0.1% DMSO). Values were measured in triplicate.

A series of control studies was parallely conducted with COS-7 cells carrying *p*Ers, *p*E_mRS, or both *p*Er and *p*Rs (Figure 2A Inset). The cells were stimulated with vehicle (0.1% DMSO) or 1 μM OHT for 20 min. The subsequent luminescence variances were determined with a luminometer (MiniLumat LB9506; Berthold).

Substrate Dependence of OHT-Activated ERS. Contribution of coelenterazine derivatives to the enzymatic activities of ERS was examined on the basis of the bioluminescence spectra (Figure 3A). COS-7 cells transfected with *p*Ers were cultured on 24-well plates. The cells were stimulated with 1 μM OHT for 20 min, washed once with PBS, and lysed. The lysates were transferred into a quartz cuvette for monitoring the spectral variance with a spectrophotometer (F-7000, Hitachi) in the presence of coelenterazine native (CTZ), coelenterazine *hcp* (CTZ *hcp*), coelenterazine *cp* (CTZ *cp*), coelenterazine *fcp* (CTZ *fcp*), or coelenterazine *ip* (CTZ *ip*). Values were measured in duplicate.

Enzymatic Properties of ERS in the Presence or Absence of OHT. ERS was affinity-column purified for determining quantum yields (QYs) and turnover rates according to ligand stimulations and variation of CTZ derivatives (Table 1).

*p*Cold-Ers was transformed into BL21 (DE3) *p*LysS competent cells (Novagen). The seed culture of the bacterial strain carrying *p*Cold-Ers was initially grown in 10 mL of Luria−Bertani

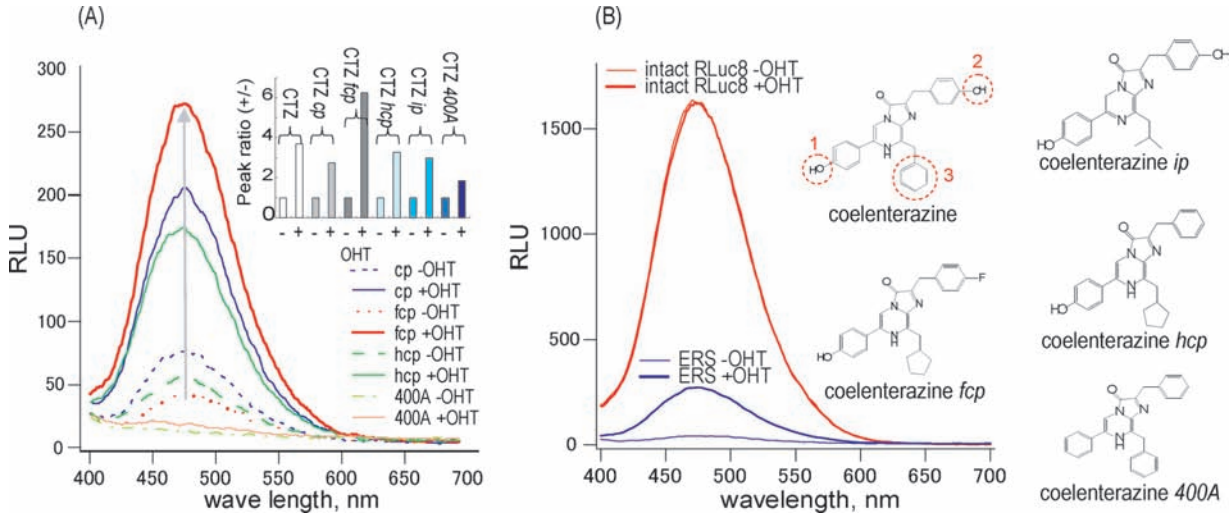

Figure 3. (A) Bioluminescence emission spectra before and after stimulation of 1 μM 4-hydroxytamoxifein (OHT). The spectra generated by ER LBD-RLuc8-SH2 (ERS) were recorded using a spectrophotometer (F-7000, Hitachi). The gray arrow shows the spectrum variance before and after supplementation of 1 μM OHT. Inset shows the peak heights of the spectra before and after addition of 1 μM OHT. Maximal bioluminescence intensities were obtained in the presence of native coelenterazine (CTZ), while coelenterazine fcp (CTZ *fcp*) exhibited the largest signal-to-background ratios. Values were averaged after duplicate determination. The marks "+" and "−" show the presence or absence of 1 μM OHT. (B) Comparison of the bioluminescence emission spectra of ERS and net *Renilla* luciferase 8 (RLuc8) alone before and after stimulation of 1 μM OHT. All of the luminescence spectra were recorded in the presence of CTZ *fcp*. Intact RLuc8 alone was insensitive to OHT, that is, the spectra are almost superimposed (red lines), whereas ERS varied with the luminescence spectra in response to OHT (black lines). The dotted circles show critical side chains of CTZ for interacting with ERS. Dotted circles *1*, *2*, and *3* highlight (i) the *p*-OH of the phenol attached at C6 of native CTZ, (ii) the *p*-OH group on the benzyl substituent at C2 of native CTZ, and (iii) the benzyl group attached at C8 of native CTZ, respectively.

Table 1. Bioluminescence Activity Variance of ER LBD-RLuc8-SH2 (ERS) According to Ligands and Substrates[a]

probe	substrate[b]	stimulator	quantum yield (%)	K_M[c] (μM)	turnover rate (photons/s/mol)
RLuc8	CTZ	-	6.9 ±0.1[f]	1.6 ± 0.2 [f]	$4.3 \pm 0.2 \times 10^{22}$
ERS	CTZ	-	6.3 ± 1.1	94.3 ± 37.1	$6.1 \pm 0.5 \times 10^{19}$
	CTZ	vehicle [d]	5.6 ± 0.9	-	-
	CTZ	OHT [e]	5.0 ± 0.7	-	-
	CTZ	E_2 [e]	5.0 ± 0.6	-	-
	CTZ *cp*	-	1.3 ± 0.1	-	-
	CTZ *fcp*	-	1.8 ± 0.2	-	-
	CTZ *hcp*	-	1.9 ± 0.2	-	-
	CTZ *ip*	-	1.3 ± 0.1	-	-
	CTZ *400A*	-	1.4 ± 0.0	-	-
	CTZ *f*	-	1.7 ± 0.2	-	-
	CTZ *i*	-	1.5 ± 0.2	-	-

[a] Values were measured in quadruplicate, and standard errors of the mean are given. As the internal standards, quantum yields (QYs) of RLuc and RLuc8 were parallelly estimated with our instrument (Mithras LB940; Berthold). [b] CTZ indicates coelenterazine dissolved in a phosphate buffered saline (PBS; 0.01 M, pH 7.4). [c] K_M means Michaelis−Menten constant. [d] Vehicle represents 0.1% dimethyl sulfoxide (DMSO). [e] OHT and E_2 were dissolved in 0.1% DMSO to make 1 μM (final concentration). [f] Values are from the literature (*21*).

(LB) broth supplemented with ampicillin (0.14 mM) at 37 °C for 16 h. The seed culture was transferred into 400 mL of LB broth in a flask, extensively incubated in a cooled incubator (Taitac) at 15 °C for 24 h after addition of isopropyl β-D-1-thiogalactopyranoside (IPTG; a final concentration of 1 mM). The cells harvested by centrifugation at 5000 *g* were dissolved in 10 mL of Tris-HCl (20 mM, pH 7.6) and crushed with a tip sonicator for cell homogenation. His-tag-fused ERS in the homogenate was purified with a TALON metal affinity resin (Clontech). The eluted ERS solution was dialyzed overnight at 4 °C against phosphate buffered saline (PBS; 0.01 M, pH 7.4). Concentration of the purified ERS was determined using a Bradford reagent (Bio-Rad).

In the presence of an excess level of enzymes, quantum yields (QYs) are defined by N_{tot}/S_{tot}, where N_{tot} and S_{tot} mean the total amounts of emitted photons and consumed substrate, respectively (*17*). If a luciferase level is excess compared to luciferins ($E \gg S$), all of the luciferins should be consumed. In this case, the initial level of luciferin is equivalent to the total consumed luciferin.

For measurements of quantum yields (QYs), ERS was first mock-stimulated or stimulated with vehicle (0.1% DMSO), 1 μM OHT (final concentration), or 1 μM 17β-estradiol (E_2; final concentration). A quantity of 60 μL of ERS (24 pmol) was set on each well of a 96-well plate, which was then loaded in a microplate reader (Mithras LB940; Berthold). At the same time, the injector of the microplate reader was filled with CTZ solution dissolved in 0.01 M PBS (pH 7.4). Immediately after automatic injection of 10 μL of CTZ (0.59 pmol) into each well, the total light emission was integrated until the reaction approached completion (ca. 10 min) at room temperature (22.5 °C).

QYs according to CTZ variants were estimated as follows: 10 μL of CTZ or its derivatives (0.59 pmol per well) was set in each well of the 96-well plate, while the ERS solution was loaded in the injector. After automatic injection of 30 μL of the ERS solution (12 pmol per well) to each well, the total light emission was integrated until the reaction approached completion (ca. 10 min). As internal standards, QYs of RLuc and RLuc8 were estimated in the same instrumental setup for fidelity.

Turnover rate is defined by v_{max}/E_{tot}, where v_{max} and E_{tot} are the maximal reaction rate and the total enzyme amount applied. For the measurement, 40 μL of native CTZ (ranging from 1.2 to 0.075 nmol) was set in each well of a 96-well plate, while PBS-buffered ERS solution was loaded in the injector before

the experiments. After automatic injection of 10 μL of ERS (1 pmol) to each well, the kinetics were immediately recorded every 0.05 s. The initial rates were plotted against the CTZ concentrations applied. The kinetic data were processed using a kinetic curve fitting software GraFit6 (Erithacus Software).

RESULTS

Correlation between Molecular Tension and Bioluminescence Intensity of RLuc8. For an initial evaluation of molecular tension−bioluminescence correlation, a series of luciferases were sandwiched between ER LBD and Src SH2 domain (Figure 1). The examined luciferases include a full-length *Renilla* luciferase 8 (RLuc8; 36 kDa), *Gaussia* luciferase (GLuc; 20 kDa), and click beetle luciferase red (CBLuc; 60 kDa).

Bioluminescence spectra of ERS largely varied before and after supplementation of 4-hydroxytamoxifen (OHT). The peak height (λ_{max}: 486 nm) was surprisingly 3.5 times enhanced by a stimulation of 1 μM OHT. In contrast, both EGS and ECS did not exhibit a considerable variance in the luminescence intensities in the same experimental setup.

The results are interpreted as follows: (i) According to the crystal structural analysis on RLuc8, the active site of RLuc8 consists of amino acids ranging from Asn53 to Phe286 (*18*). A ligand-activated ER LBD−SH2 binding should append a tension to the active site of the sandwiched RLuc8 (Figure 1D). (ii) Molecular structural comparison of ERS with EGS and ECS reveals that globular RLuc8 is appropriate to receive molecular tension, and thus advantageous for determining protein−protein interactions compared to other luciferases.

Verification of Phosphorylation of ER LBD and the Subsequent ER LBD−SH2 Binding. It was previously demonstrated with a Western blot analysis that Tyr537 of ER LBD is phosphorylated by an addition of E_2 and recognized by the SH2 domain of *v*-Src (*9*) (*19*) (*20*). Additionally, we verified the ligand-activated ER LBD−SH2 binding with a point mutant of ERS at Tyr537 to phenylalanine (Y537F), named E_mRS (Figure 2A Inset). E_mRS exhibited a largely diminished signal-to-background (*S*/*B*) ratio (ca. 1.7 times) compared to intact ERS.

As another control study, ERS was split into *ER* and *RS* for exerting a tension-free experimental setup, where *ER* and *RS* mean ER LBD-linked RLuc8 and RLuc8-linked SH2 (Figure 2A Inset), respectively. COS-7 cells carrying both *ER* and *RS* exhibited no variance in the luminescence intensities in response to 1 μM OHT, whereas ERS efficiently enhanced the bioluminescence intensities in response to the same stimulation.

These results in Figure 2A Inset demonstrate that (i) a ER LBD−SH2 binding appends a molecular tension to the sandwiched RLuc8, resulting in an enhancement of the enzymatic activity; (ii) the ER LBD−SH2 binding occurs through a ligand-activated conformation change and phosphorylation of Tyr537 of ER LBD; and (iii) the luminescence intensities enhanced by ER LBD−SH2 binding can be taken as a measure of the estrogenicity of ligands.

Ligand Sensitivity and Selectivity of ERS. Ligand sensitivity and selectivity of ERS were estimated in varying concentrations and types of ligands (Figure 2A,B).

First, COS-7 cells carrying ERS were stimulated with varying concentrations of OHT or testosterone (T) for 20 min, and the consequent elevation of bioluminescence intensities was determined with a luminometer (Minilumat LB9507; Berthold). The luminescence intensities were quickly enhanced from 1 nM OHT and reached a plateau at 1 μM OHT. Fifty percent effective concentration (EC_{50}) appeared at 6 nM OHT.

In addition, we estimated the ligand selectivity of ERS in the presence of various steroids and chemicals. COS-7 cells carrying ERS were stimulated for 20 min with vehicle (0.1% DMSO) or 1 μM of E_2, OHT, 5α-dihydrotestosterone (DHT), testosterone (T), genistein, or cortisol. The consequent bioluminescence intensites by ligands were subtracted by those from COS-7 cells stimulated with vehicle (0.1% DMSO).

The results show that E_2 elevates the bioluminescence intensities, which are almost equivalent with OHT, while genistein called a phytoestrogen also exhibited significant luminescence intensities under the same conditions. On the other hand, the other steroids such as DHT, T, and cortisol did not exhibit any considerable activity for ER LBD−SH2 binding.

Genistein is one of several known isoflavones to interact with animal and human ER, that is, phytoestrogen or dietary estrogens. E_2 is a natural, steroidal agonist of ER, whereas OHT is known as the synthetic antagonist. The luminescence intensities by ligands decreased in the following order: $E_2 \geq$ OHT > genistein $\gg$ DHT = T = cortisol.

The results represent that (i) the estrogenicities of E_2, OHT, and genistein are efficiently converted by ERS to bioluminescence intensities through an intramolecular ER LBD−SH2 binding and (ii) ERS exerts ligand selectivity.

Substrate Specificity of ERS. We fabricated a bioluminescent probe, where an intramolecular ER LBD−SH2 binding appends a molecular tension to the active site of RLuc8. Thus, we speculated that this transformation of the active site may influence substrate specificity. On the basis of this consideration, we examined the substrate specificity of ERS in the presence or absence of OHT (Figure 3). According to the results, the native coelenterazine, CTZ, was superior to other derivatives in the absolute bioluminescence intensities, whereas CTZ *fcp* was beneficial in the *S*/*B* ratio. The absolute luminescence intensities in the presence of native CTZ were ca. four times stronger than those in the presence of the other CTZ derivatives. The peak ratio before and after supplementation of OHT was as large as six in the presence of CTZ *fcp* (Figure 3A Inset). The distinctive luminescence intensities of native CTZ compared to other derivatives corresponded to the results in Table 1.

Enzymatic Properties of ERS. To examine the enzymatic properties of ERS, the quantum yields (QYs), Michaelis−Menten constant (K_M), and turnover rates were estimated by altering the ligands and CTZ variants (Table 1). The measurements were conducted using a luminescence microplate reader (Mithras LB940; Berthold) equipped with an automatic injector.

QY, K_M, and turnover rate of column-purified ERS were 6.3 $\pm$ 1.1%, 94.3 $\pm$ 37.1 μM, and 6.05 $\pm$ 0.51 $\times$ 10^{19} photons/s/mol, respectively. This QY of ERS is approximately equivalent to a previous calculation, that is, 6.9 $\pm$ 0.1%, with intact RLuc8 (*21*). On the other hand, the present K_M value of ERS is 58 times higher than a reference evaluation, that is, 1.6 $\pm$ 0.2 μM with native RLuc8. The turnover rate of ERS is 705 times slower than a previous calculation with intact RLuc8 (Table 1) (*22*). These comparisons demonstrate that enzymatic properties of RLuc8 except the QY are largely impaired by modification with ER LBD (28 kDa) and SH2 (12 kDa).

QYs were similarly estimated after stimulation of vehicle-, OHT-, or E_2-stimulated ERS (Table 1). QYs were found to be invariant by stimulation of the ligands. It is because E_2 or OHT may alter the conformation of ER LBD in the purified ERS. However, ER LBD in purified ERS is not phosporylated because of the deficiency of endogenous protein kinases. This is additional evidence of phosphorylation-mediated ER LBD−SH2 binding.

In addition, QYs of ERS were determined in the presence of a different kind of coelenterazine (CTZ) variant (Table 1). The results exhibited that ERS with native CTZ exhibited approximately four times higher QYs than the other CTZ derivatives, implicating substrate selectivity of ERS to native CTZ. This substrate preference was not significant in a previous study with intact RLuc8 (*21*).

Considering that the chemical backbone of CTZ is similar to that of the variants, the side chains of CTZ should play a critical role in the substrate selectivity of ERS. The basic structure of CTZ is called imidazo[1,2-*a*]pyrazin-3(7*H*)-one. CTZ *400A* is deficient in both (i) the *p*-OH group of the phenol attached at C6 of native CTZ and (ii) the *p*-OH group on the benzyl substituent at C2 of native CTZ. The importance of these functional groups in CTZ was proven with the poorest luminescence intensity and *S*/*B* ratio in the presence of CTZ *400A* as shown in Figure 3A. CTZ *cp* lacks the benzyl group attached at C8 of native CTZ. In practice, CTZ *cp* showed a diminished luminescence intensity and *S*/*B* ratio compared to native CTZ.

Taken together, the present structural comparison between native CTZ and its variants revealed that three side chains are critical for the substrate activity: (i) the *p*-OH of the phenol attached at C6 of CTZ, (ii) the benzyl group attached at C8 of CTZ, and (iii) the *p*-OH group on the benzyl substituent at C2 of CTZ. Their contributions to enzymatic reactions of ERS were significant in this decreasing order: (i) > (ii) > (iii).

DISCUSSION

Molecular Mechanism of the Present Molecular Distortion-Indexed Probe. The phosphorylation of estrogen receptor (ER) at Tyr537 is recognized by the Src homology domain 2 of υ-Src (SH2), known as a nongenomic pathway of ER (*19*) (*20*). We previously demonstrated that both 17β-estradiol (E_2) and 4-hydroxytamoxifen (OHT) phosphorylate Tyr537 of ER LBD using both our custom-made probes and Western blot analysis (*9*). In the present study, when RLuc8 is sandwiched between ER LBD and SH2 with a tight, minimal linker, the enzymatic activity surprisingly depended on the estrogenicity of the stimulators (Figures 1 and 2). Our control studies using both E_mRS and *ER+RS* revealed that this activity variance is mediated by ligand-activated ER LBD−SH2 binding and the subsequent molecular distortion of the active site of RLuc8.

Thus, the molecular mechanism may be explained as follows: (i) A specific ligand phosphorylates ER LBD at Tyr537; (ii) the phosphorylation is recognized by SH2, initiating ER LBD−SH2 binding; (iii) this binding should append a molecular tension to the sandwiched, globular RLuc8. In practice, Asn53, His285, and Phe286 in the active site of RLuc8 are in proximity of N- or C-terminal end of RLuc8 (1−311 AA) (*18*); and consequently, (iv) the molecular tension artificially appended by ER LBD–SH2 binding should vary the enzymatic activities.

In contrast to RLuc8, beetle luciferases such as FLuc consist of two main domains linked with a long flexible hinge (*23*) (Figure 1A). The flexible hinge should relieve the molecular tension appended by ER LBD–SH2 binding. This relaxation of molecular tensions in CBLuc results in poor variance in the bioluminescence intensities of ECS by ligand activations. EGS carrying a full-length GLuc also enhanced little bioluminescence in response to OHT (Figure 1C). The sandwiched GLuc in EGS is the smallest luciferase among those discovered, which may sterically relieve the molecular tension to GLuc.

Interpretation of Enzymatic Properties of ERS. According to a previous measurement, quantum yield (QY) and turnover rate of native *Renilla* luciferase 8 (RLuc8) are ca. 6.9 ± 0.1% and (4.4 ± 0.2) × 10^{22} photons/s/mol enzyme (*21*). This QY approximately corresponds with our calculation with ERS, whereas the literature turnover rate of intact RLuc8 is 7.1 × 10^2 times higher than that of ERS. A fundamental difference between native RLuc8 and ERS is the modification of RLuc8 with ER LBD (28 kDa) and SH2 (12 kDa). Considering that some amino acid membering the active sites are close to the N- and C-terminals of RLuc8 (*18*), the modification of RLuc8 with ER LBD and SH2 is considered to influence the turnover rate rather than QY. In addition, both ER LBD and SH2 inside ERS were prepared by genetic truncation from a full-length ER and Src. The hydrophobic cross sections may have been exposed to the cytosol and would have been easy to impair, aggregate, or decompose.

QYs before and after stimulation of purified ERS with 1 μM OHT or E_2 were almost invariant (Table 1). These results are interpreted as follows: It is known that both OHT- and E_2-bound ER LBDs expose the hydrophobic site to the cytosol and recruit phosphorylation (*24*) (*25*). However, the present *in vitro* system with purified ERS lacks tyrosine kinases. Ligand-activated ER LBD cannot be phosphorylated and thus are not recognized by SH2. This is indirect evidence that ER LBD−SH2 binding occurs via phosphorylation of ER LBD. The other control studies in Figure 2A using E_mRS ("m" abbreviates the mutation in Tyr537) and *ER+RS* and literature comprising a Western blot analysis (*9*) (*19*) (*20*) also support this view.

Determination of Protein Phosphorylation with ERS. Phosphorylation-mediated protein−protein interactions prevail among intracellular signal transduction pathways in mammalian cells (*26*) (*27*). The phosphorylation of Tyr537 is a prerequisite for pivotal actions of ER including (i) estrogen-dependent hyperphosphorylation of the serine residues, (ii) dimerization, (iii) nuclear retention, and (iv) DNA binding (*20*). In particular, a number of effects of estrogens such as kinase activation in the cytosol are so rapid that they cannot be related to direct gene expression. These actions are known as nongenomic actions and mediated through phosphorylation of membrane-associated ERs (*28*). The phosphorylation is conducted by cytoplasmic Src (*19*) (*20*) and thus can be an index of nongenomic actions of ER mediated by Src. On the basis of this knowledge, ERS was designed as a molecular distortion-indexed bioluminescent probe, in which ER LBD−SH2 binding was fabricated to evoke a molecular tension to the sandwiched RLuc8.

Conventional approaches to determine protein phosphorylation heavily depend on the Western blot analysis. However, by using such a conventional method, it is impossible to trace the ligand-activated, rapid dynamics of intracellular protein−protein interactions. The present study represents a competent methodology for tracing ligand-activated protein−protein interactions via molecular distortion.

Sensorial Properties of ERS. Cell-based assays may be categorized into (i) genetic, transcriptional, and (ii) nontranscriptional assays. A genetic, transcriptional assay such as a reporter gene assay requires a long ligand stimulation time until the reporter protein is sufficiently accumulated. In contrast, the present method is characterized as a nontranscriptional assay using an intramolecular transformation of a luciferase. ERS is expressed earlier and localized in adequate intracellular compartments of interest. The luminescence intensity is ready to be developed once the cell is stimulated by a signal. The present data acquisition time, 20 min, is largely shortened in comparison with those of the reporter gene and protein-splicing schemes, which require from 2 to 24 h (*29*). Thus, the present method is applicable to a high-throughput analysis of the activities of bioactive small molecules, which activate temporal, short-term molecular events.

The detection limits of precedent nontranscriptional assays such as FRET-based and single-chain probes to E_2 ranged from 0.1 nM to 10 nM (*9*) (*30*) (*31*). Considering that the detection limit of ERS to OHT is close to 0.1 nM, the present scheme is competent for a sensitive determination of estrogen activities.

Taken together, we have demonstrated a unique, nontranscriptional assay system based on the molecular tension of a luciferase appended by ER LBD−SH2 binding. Full-length RLuc8 was sandwiched between ER LBD and Src SH2 for constructing an integrated molecule-format probe. The working mechanism is supposed as follows: (i) estrogens first activate a phosphorylation of Tyr537 of ER LBD and subsequent intramolecular interaction between ER LBD and Src SH2. (ii) This

binding triggers a distortion of the active site of full-length RLuc8. (iii) This molecular tension results in an enhancement of the luciferase activity. Modification of RLuc8 with ER LBD and Src SH2 interestingly decrease the turnover rate rather than the QY. ERS exhibited substrate selectivity to native CTZ, and was as sensitive as 1 nM OHT. The present strategy for determining phosphorylation and the consequent molecular distortion may be utilized in evaluating a broad range of ligand-mediated protein−protein interactions. Future studies should be directed for investigating an optimal combination of luciferases and a pair of interacting proteins, where distortion of the active site of luciferases may exert significant color changes and sensitive intensity variances.

LITERATURE CITED

(1) Weissleder, R., and Ntziachristos, V. (2003) Shedding light onto live molecular targets. *Nat. Med. 9*, 123–128.

(2) Hoshino, H., Nakajima, Y., and Ohmiya, Y. (2007) Luciferase-YFP fusion tag with enhanced emission for single-cell luminescence imaging. *Nat. Methods 4*, 637–639.

(3) Gammon, S. T., Villalobos, V. M., Roshal, M., Samrakandi, M., and Piwnica-Worms, D. (2009) Rational design of novel red-shifted BRET pairs: Platforms for real-time single-chain protease biosensors. *Biotechnol. Prog. 25*, 559–569.

(4) De, A., Ray, P., Loening, A. M., and Gambhir, S. S. (2009) BRET3: a red-shifted bioluminescence resonance energy transfer (BRET)-based integrated platform for imaging protein-protein interactions from single live cells and living animals. *FASEB J. 23*, 2702–2709.

(5) Pichler, A., Prior, J. L., Luker, G. D., and Piwnica-Worms, D. (2008) Generation of a highly inducible Gal4-->Fluc universal reporter mouse for in vivo bioluminescence imaging. *Proc. Natl. Acad. Sci. U.S.A. 105*, 15932–15937.

(6) Tarassov, K., Messier, V., Landry, C. R., Radinovic, S., Serna Molina, M. M., Shames, I., Malitskaya, Y., Vogel, J., Bussey, H., and Michnick, S. W. (2008) An in vivo map of the yeast protein interactome. *Science 320*, 1465–1470.

(7) Luker, K. E., Smith, M. C., Luker, G. D., Gammon, S. T., Piwnica-Worms, H., and Piwnica-Worms, D. (2004) Kinetics of regulated protein-protein interactions revealed with firefly luciferase complementation imaging in cells and living animals. *Proc. Natl. Acad. Sci. U.S.A. 101*, 12288–12293.

(8) Kim, S. B., Awais, M., Sato, M., Umezawa, Y., and Tao, H. (2007) Integrated molecule-format bioluminescent probe for visualizing androgenicity of ligands based on the intramolecular association of androgen receptor with its recognition peptide. *Anal. Chem. 79*, 1874–1880.

(9) Kim, S. B., Umezawa, Y., Kanno, K. A., and Tao, H. (2008) An integrated-molecule-format multicolor probe for monitoring multiple activities of a bioactive small molecule. *ACS Chem. Biol. 3*, 359–372.

(10) Stefan, E., Aquin, S., Berger, N., Landry, C. R., Nyfeler, B., Bouvier, M., and Michnick, S. W. (2007) Quantification of dynamic protein complexes using Renilla luciferase fragment complementation applied to protein kinase A activities in vivo. *Proc. Natl. Acad. Sci. U.S.A. 104*, 16916–16921.

(11) Kim, S. B., Sato, M., and Tao, H. (2008) Circularly permutated bioluminescent probes for illuminating ligand-activated protein dynamics. *Bioconjugate Chem. 19*, 2480–2486.

(12) Kim, S. B., Sato, M., and Tao, H. (2009) Genetically encoded bioluminescent indicators for stress hormones. *Anal. Chem. 81*, 3760–3768.

(13) Paulmurugan, R., and Gambhir, S. S. (2005) Firefly luciferase enzyme fragment complementation for imaging in cells and living animals. *Anal. Chem. 77*, 1295–1302.

(14) Kim, S. B., Otani, Y., Umezawa, Y., and Tao, H. (2007) Bioluminescent indicator for determining protein−protein interactions using intramolecular complementation of split click beetle luciferase. *Anal. Chem. 79*, 4820–4826.

(15) Kim, S. B., Sato, M., and Tao, H. (2009) Split Gaussia luciferase-based bioluminescence template for tracing protein dynamics in living cells. *Anal. Chem. 81*, 67–74.

(16) Awais, M., Sato, M., Lee, X. F., and Umezawa, Y. (2006) A fluorescent indicator to visualize activities of the androgen receptor ligands in single living cells. *Angew. Chem., Int. Ed. 45*, 2707–2712.

(17) Seliger, H. H., and Mc, E. W. (1960) Spectral emission and quantum yield of firefly bioluminescence. *Arch. Biochem. Biophys. 88*, 136–141.

(18) Loening, A. M., Wu, A. M., and Gambhir, S. S. (2007) Red-shifted Renilla reniformis luciferase variants for imaging in living subjects. *Nat. Methods 4*, 641–643.

(19) Arnold, S. F., Vorojeikina, D. P., and Notides, A. C. (1995) Phosphorylation of tyrosine 537 on the human estrogen receptor is required for binding to an estrogen response element. *J. Biol. Chem. 270*, 30205–30212.

(20) Migliaccio, A., Castoria, G., Di Domenico, M., De Falco, A., Bilancio, A., and Auricchio, F. (2002) Src is an initial target of sex steroid hormone action. *Ann. N.Y. Acad. Sci. 963*, 185–190.

(21) Loening, A. M., Fenn, T. D., Wu, A. M., and Gambhir, S. S. (2006) Consensus guided mutagenesis of Renilla luciferase yields enhanced stability and light output. *Protein Eng. Des. Sel. 19*, 391–400.

(22) Loening, A. M. (2006) Technologies for imaging with bioluminescently labeled probes. Doctor thesis, Stanford.

(23) Nakatsu, T., Ichiyama, S., Hiratake, J., Saldanha, A., Kobashi, N., Sakata, K., and Kato, H. (2006) Structural basis for the spectral difference in luciferase bioluminescence. *Nature 440*, 372–376.

(24) Zeng, J., Li, W., Zhao, Y., Liu, G., Tang, Y., and Jiang, H. (2008) Insights into ligand selectivity in estrogen receptor isoforms: molecular dynamics simulations and binding free energy calculations. *J Phys. Chem. B 112*, 2719–2726.

(25) Dubbink, H. J., Hersmus, R., Verma, C. S., van der Korput, H. A., Berrevoets, C. A., van Tol, J., Ziel-van der Made, A. C., Brinkmann, A. O., Pike, A. C., and Trapman, J. (2004) Distinct recognition modes of FXXLF and LXXLL motifs by the androgen receptor. *Mol. Endocrinol. 18*, 2132–2150.

(26) Liu, B. A., Jablonowski, K., Raina, M., Arce, M., Pawson, T., and Nash, P. D. (2006) The human and mouse complement of SH2 domain proteins-establishing the boundaries of phosphotyrosine signaling. *Mol. Cell 22*, 851–868.

(27) Lee, S. J., Sekimoto, T., Yamashita, E., Nagoshi, E., Nakagawa, A., Imamoto, N., Yoshimura, M., Sakai, H., Chong, K. T., Tsukihara, T., and Yoneda, Y. (2003) The structure of importin-β bound to SREBP-2: nuclear import of a transcription factor. *Science 302*, 1571–1575.

(28) Bjornstrom, L., and Sjoberg, M. (2005) Mechanisms of estrogen receptor signaling: convergence of genomic and nongenomic actions on target genes. *Mol. Endocrinol. 19*, 833–842.

(29) Kim, S. B., Ozawa, T., Watanabe, S., and Umezawa, Y. (2004) High-throughput sensing and noninvasive imaging of protein nuclear transport by using reconstitution of split Renilla luciferase. *Proc. Natl. Acad. Sci. U.S.A. 101*, 11542–11547.

(30) Awais, M., Sato, M., Sasaki, K., and Umezawa, Y. (2004) A genetically encoded fluorescent indicator capable of discriminating estrogen agonists from antagonists in living cells. *Anal. Chem. 76*, 2181–2186.

(31) Paulmurugan, R., and Gambhir, S. S. (2006) An intramolecular folding sensor for imaging estrogen receptor-ligand interactions. *Proc. Natl. Acad. Sci. U.S.A. 103*, 15883–15888.

BC900330W

Polymeric Phosphorylcholine−Camptothecin Conjugates Prepared by Controlled Free Radical Polymerization and Click Chemistry

Xiangji Chen, Samantha McRae, Sangram Parelkar, and Todd Emrick*

Polymer Science & Engineering Department, 120 Governors Drive, University of Massachusetts, Amherst, Massachusetts 01003.
Received July 31, 2009; Revised Manuscript Received October 9, 2009

Novel polymer−drug conjugates, consisting of zwitterionic poly(methacryloyloxyethyl phosphorylcholine) (polyMPC) as the polymer component, and camptothecin (CPT) as the drug, were prepared by two methods. In one case, CPT was transformed by acylation into a functional initiator for copper catalyzed atom transfer radical polymerization (ATRP), and polyMPC was grown from this therapeutic initiator. In the other case, a one-pot ATRP-"click" conjugation strategy was employed to synthesize novel polyMPC structures containing multiple copies of the drug pendant to the zwitterionic polymer chain. The latter method allows polyMPC-*graft*-CPT conjugates to be prepared with a high weight percent drug loading (up to 14% CPT) with excellent solubility in pure water (>250 mg/mL). The linkage chemistry chosen between the polyMPC backbone and the pendant drugs proved critically important for assuring drug release within a time frame reasonable to consider these structures as a platform for injectable cancer therapeutics. Liberation of the drug from the polymer backbone was monitored by high-performance liquid chromatography, using size-exclusion and reverse-phase columns, and the toxicity of the polymer−drug conjugates was examined in cell culture against breast (MCF7), ovarian (OVCAR-3), and colorectal (COLO 205) cancer cell lines.

INTRODUCTION

Small molecule antitumor agents used clinically often display poor pharmacokinetics, undesired toxicity and side effects, and poor water solubility that presents delivery difficulties. Numerous chemotherapeutic drugs used today have a relatively low therapeutic index, or therapeutic ratio, described as the lethal dose divided by the therapeutic dose (LD_{50}/ED_{50}). In essence, therapeutic benefits are offset by detrimental side effects. Conjugation of chemotherapeutics to water-soluble polymers can greatly enhance their aqueous solubility and ease of administration, and further reduce side effects toward improving therapeutic efficacy by altering pharmacokinetics. The underlying *in vivo* characteristics of polymer drugs that lead to their beneficial effects are described by the enhanced permeation and retention (EPR) effect (*1*), which provides for a passive and selective uptake of the polymer-bound drugs into tumor tissue, and retention in that tissue due to a characteristic poor lymphatic drainage.

Effective polymer therapeutics requires the use of biocompatible polymers with high water solubility and biocompatibility. Poly(ethylene glycol) (PEG) has been conjugated to numerous therapeutic protein and peptide drugs to enhance their therapeutic efficacy, such as erythropoeiten (EPO) and granulocyte-colony stimulating factor (G-CSF), and interferon (IFN). PEGylation increases the apparent size of the proteins and peptides (thereby reducing the rate of renal clearance), shields them from proteolytic enzymes, and improves their pharmacokinetic profile (*2*). Advantages stemming from PEGylation have led to the development of new and improved medicines, such as the PEGylated proteins PEG-Intron (PEGylated Interferon α-2b) and Pegasys (PEGylated Interferon α-2a) for the treatment of Hepatitis C (*3*). PEGylation also offers opportunities to improve small molecule drug delivery, needed for example in chemotherapy. Prominent among PEGylated cancer drug candidates is camptothecin, for which PEGylated versions show modestly enhanced circulation time and reduced side effects (*4*). PEGylated camptothecin, described by Enzon, Inc., as Prothecan, consists of a 40 000 g/mol PEG chain with camptothecin at each chain end, connected by ester linkages at the C-20-OH position of the drug (*5*). The chemotherapeutic agent doxorubicin (DOX) has also been improved by PEGylation, including, for example, by linear PEG conjugation (*6*), as well as through elegant architectures such as "bow-tie" dendrimers (*7*), with the resulting DOX-polymer therapeutic displaying increased water solubility, decreased toxicity, and enhanced specificity due to the action of the EPR effect.

Phosphorylcholine-containing polymers, such as poly(methacryloyloxyethyl phosphorylcholine) (polyMPC), are among the most biocompatible polymers known. PolyMPC has been used extensively in bulk materials and as coatings, for contact lenses and blood-contacting devices, for which a high level of biocompatibility and resistance to protein adsorption is required (*8*−*14*). As polyMPC has a decidedly lower commercial availability than functional PEG-based derivatives (even the MPC monomer is not readily available), its use in conjugation chemistry toward polymer therapeutics has been limited to only a few recent examples. However, polyMPC shows excellent promise in injectable therapeutics, having been conjugated recently to therapeutic proteins, such as EPO and G-CSF, using end-functional derivatives prepared by atom transfer radical polymerization (ATRP) (*15*). Such structures were shown to possess in vivo pharmacokinetic profiles superior to PEGylated proteins (*16*).

Living free radical polymerization techniques, such as ATRP (*17*−*20*) and reversible addition−fragmentation chain transfer (RAFT) (*21, 22*), enable the preparation of well-defined polyMPC−drug conjugates with diverse architectures that cannot be achieved by conventional PEGylation. In particular, through covalent grafting to polyMPC copolymers, a very high drug loading can be envisaged, whereas PEGylation chemistry restricts covalent drug attachment to the polymer chain end(s). It should be noted that physical encapsulation of drugs using

* tsemrick@mail.pse.umass.edu.

10.1021/bc900339x CCC: $40.75 © 2009 American Chemical Society
Published on Web 11/09/2009

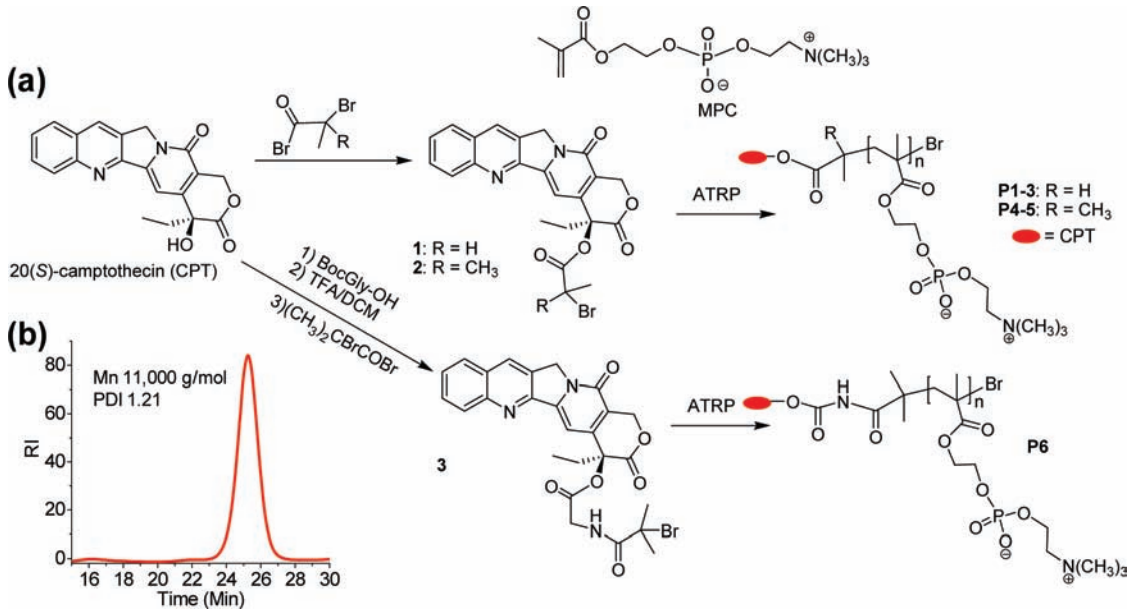

Figure 1. (a) Synthesis of ATRP initiators **1**, **2**, and **3**, and CPT-terminated polyMPC structures; (b) aqueous GPC trace of CPT terminated polyMPC P2.

polyMPC-based micelles has been reported, in which self-assembly of polyMPC copolymers gives micelles that sequester drugs in the hydrophobic core (*20, 21, 23*−*25*). For example, cholesterol-polyMPC amphiphiles were synthesized and tested as a novel drug delivery system, incorporating adriamycin (ADR) in the micelle core (*26*). These micelles released ADR in a manner that was controlled by polyMPC molecular weight and drug concentration.

Here, we describe the preparation of polyMPC copolymers tailored for Cu(I)-catalyzed Huisgen 1,3-cycloaddition of azides and alkynes, a type of "click" chemistry that has recently permeated small molecule (*27*−*29*), dendrimer (*30*), and polymer synthesis (*31, 32*). The efficiency and regioselectivity of the azide−alkyne click reaction, combined with its tolerance toward a diverse range of functionality, has enabled the preparation of novel, complex materials (*33, 34*). Well-defined functional materials have also been synthesized by combining Cu(I)-catalyzed ATRP with click chemistry, such as star-shaped polystyrene (*35*) and glycopolymers (*36*). Here, we exploit the advantages of click chemistry for bioconjugation and polymer therapeutics, providing a robust triazole cycloadduct, good tolerance to aqueous conditions and functionality present on CPT, and the high yields that enable the generation of such materials in appreciable quantities.

The natural alkaloid 20(*S*)-camptothecin (CPT) was first isolated from the Chinese tree *Camptotheca acuminate* in the 1960s (*37*). CPT shows potent anticancer activity over a broad range of cancer cells (*38, 39*), but has poor water solubility (2.5 μg/mL) and high toxicity that has limited its clinical use. The more water-soluble CPT derivatives, Topotecan and Irinotecan, were approved in 1997 by the U.S. Food and Drug Administration (FDA) to treat some forms of ovarian and colon cancers. However, like CPT, the efficacy of these derivatives is compromised by opening of the E-ring lactone, giving the corresponding carboxylate at physiological pH (*40, 41*). Binding of the carboxylate to serum albumin contributes to the observed toxic side effects. In order to help solubilize CPT, its conjugation to water-soluble polymers has been explored, especially by acylation at the 20-OH position; this carries an added benefit of stabilizing the ring-closed (lactone) form of the drug (*42*). Water-soluble polymers such as poly(ethylene glycol) (PEG) (*5, 43*), poly-*N*-(2-hydroxypropyl)methacrylamide (HPMA) (*44, 45*), poly(L-glutamic acid) (PG) (*46*−*48*), cyclodextrin-based polymers (*49, 50*), and PEG-grafted polyesters (*32*) have been used to conjugate CPT; these polymer−CPT conjugates show increased in vivo efficacy, over CPT itself, to varying degrees.

Our aim is to apply click chemistry methodology to CPT conjugation on the polyMPC backbone, using an acylated and azide-modified form of CPT that gives polyMPC−CPT conjugates with high drug loading and potential for future integration into CPT-based injectable cancer therapeutics. To first demonstrate the compatibility of CPT with ATRP conditions, we functionalized CPT with propionyl bromide and isobutyryl bromide, giving CPT-ATRP initiators for polymerization of MPC (Figure 1). This approach gives CPT−polyMPC conjugates (i.e., having one drug per chain). With that demonstration in hand, we sought to prepare polyMPC copolymers in which CPT is integrated into the structure as pendant groups (Figure 2). The latter strategy permits control over drug loading, by altering the average number of CPTs on the polymer backbone through variation of the feed ratio of the protected alkyne monomer. Different drug release rates were achieved by incorporating different linkers between CPT and the polyMPC backbone. Finally, cell culture experiments were performed to test the activity of the conjugates in vitro with a variety of cancer cell lines.

RESULTS AND DISCUSSION

Synthesis of CPT-Terminated polyMPC. CPT-ATRP initiators **1** and **2** were synthesized as shown in Figure 1. The 20-OH group of CPT was acylated with 2-bromopropionyl bromide and 2-bromoisobutyryl bromide in the presence of *N*,*N*′-diisopropylethylamine (DIPEA) and 4-*N*,*N*-(dimethylamino)pyridine (DMAP) in CH_2Cl_2. A typical reaction mixture was stirred at 0 °C for 1 h, then at room temperature for 1 h, to give compounds **1** or **2** in ∼75−85% yield, respectively. In addition to CPT initiators **1** and **2**, glycine-linked initiator **3** was prepared by reacting BocGly-OH with CPT in the presence of *N*-(3-dimethylaminopropyl)-*N*′-ethylcarbodiimide hydrochloride (EDC). Boc-removal with trifluoroacetic acid (TFA), and reaction of the liberated amine with 2-bromoisobutyryl bromide, generated **3** in 62% yield.

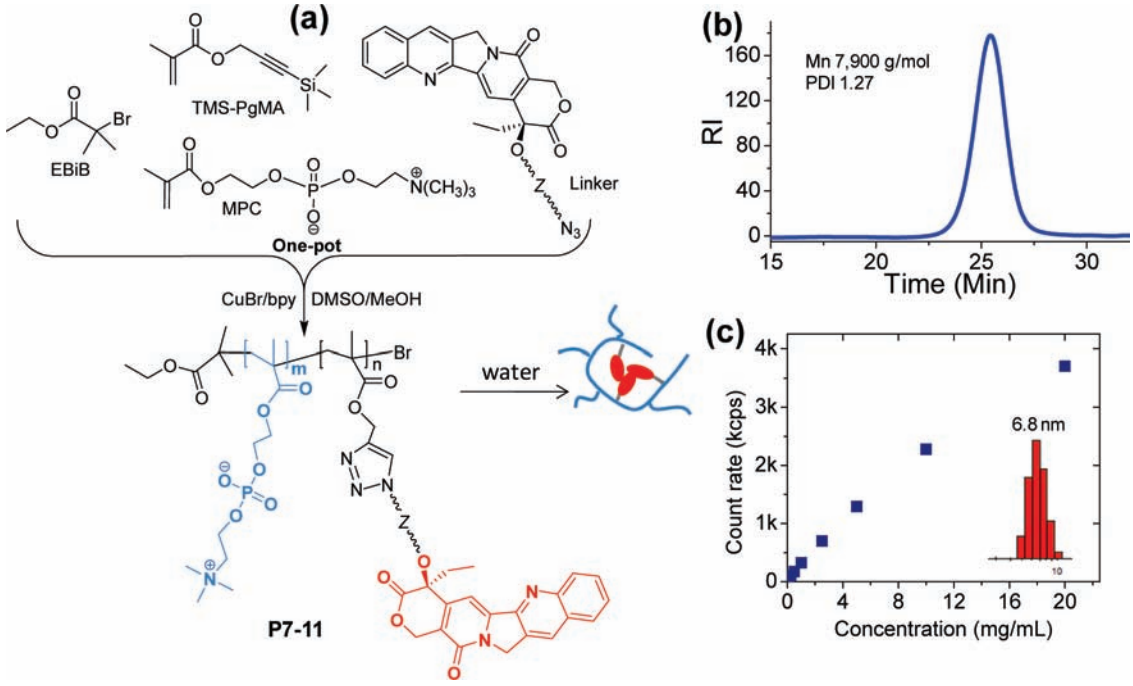

Figure 2. (a) One-pot synthesis of polyMPC-*graft*-CPT copolymers; (b) aqueous GPC trace of copolymer P11; (c) light scattering intensity vs concentration of P11 (inset is polymer diameter distribution).

Table 1. CPT-Terminated polyMPC Prepared from CPT-Based Initiators[a]

polymer	initiator	N_{MPC}	target M_n (kDa)	conversion	M_n (kDa)	PDI	diameter (nm)
P1	**1**	20	6.0	93%	6.5	1.21	5.0
P2	**1**	34	10	86%	11	1.21	6.6
P3	**1**	70	21	91%	17	1.40	7.9
P4	**2**	20	6.0	95%	6.2	1.23	5.0
P5	**2**	34	10	62%	9.3	1.23	5.5
P6	**3**	30	9.0	80%	11	1.34	6.7

[a] N_{MPC}, targeted number of MPC monomer units per polymer chain; diameter, solution size as determined by dynamic light scattering (DLS).

Polymerizations of MPC using these CPT-ATRP initiators were performed with a Cu(I)Br/bipyridine catalyst/ligand system in DMSO−MeOH mixtures at room temperature. Monomer conversion was monitored by ^{1}H NMR spectroscopy, integrating the vinyl protons of MPC against the methyl and methylene protons of the polymer backbone, using signals at 5.6 ppm (monomer CH_2═C), 6.1 ppm (monomer CH_2═C), 1.4−2.1 ppm (polymer CH_2), and 0.5−1.2 ppm (polymer CH_3). The CPT−polyMPC conjugates were isolated by precipitation in tetrahydrofuran (THF), and purified over a short column of silica gel to remove residual copper. The DMSO−MeOH mixture was chosen to provide solution homogeneity throughout the course of the reaction (the initiators are soluble in DMSO and the polymer in MeOH). Good initiator solubility is critically important for enabling clean polymerization kinetics to give polymer products with low PDI values. Characteristic of a controlled polymerization, the CPT-terminated polyMPC structures obtained displayed narrow PDI values (∼1.2, as seen in Figure 1) over a range of molecular weights from 6 to 17 kDa (Table 1), and number-average molecular weights (M_n) in agreement with monomer-to-initiator ratios (as judged by aqueous gel permeation chromatography (GPC) against PEO calibration standards). Initiators **1** and **2** gave higher initiation efficiency than **3**, which required longer reaction times (48 h) and gave higher-than-targeted molecular weights and PDI (>1.3). This observation is consistent with literature reports on ester vs amide-containing ATRP initiators (*51, 52*).

CPT-terminated polyMPC structures are highly water soluble, as the hydrophilic polymeric zwitterionic structure easily solubilizes the hydrophobic CPT end-group. Preliminary dynamic light scattering (DLS) results suggest that dilute solutions of CPT-terminated polyMPC do not exhibit significant aggregation (i.e., are essentially molecularly dissolved), with estimated solution diameters of 8 nm or less (Table 1). ^{1}H NMR analysis of CPT-polyMPC in CD_3OD showed broad and weak aromatic CPT signals, in the range 7−9 ppm (Supporting Information-Figure S1). Poor local solvation of the hydrophobic CPT component of the conjugate is likely responsible for this broadening, which precludes a reliable molecular weight estimation by NMR spectroscopic end-group analysis. TEM experiments were also performed on the CPT-polyMPC polymers, providing visualization of small discrete structures of ∼13 nm diameter.

PolyMPC-*graft*-CPT Copolymer Synthesis. With confirmation that CPT can be used effectively in conjunction with ATRP conditions, and considering our prior work that demonstrated the amenability of CPT to click chemistry (*32*), we prepared polyMPC-*graft*-CPT conjugates by combining these synthetic methodologies. For this, we chose copolymerization of MPC with trimethylsilyl (TMS)-protected propargyl methacrylate (TMS-PgMA), prepared from 3-TMS-propargyl alcohol and methacryloyl chloride (*36*). However, this method proved unsatisfactory, as the ethyl 2-bromoisobutyrate initiated ATRP copolymerization of MPC and TMS-PgMA gave copolymers with high PDI (nearly 2), and often multimodal elution peaks by GPC. Moreover, ^{1}H NMR spectroscopy of these copolymers indicated a loss of the TMS protecting groups, likely the result of copper(I) acetylide formation during polymerization. Similar TMS deprotection and copper(I) acetylide formation has been observed by others in polar organic solvents as well (*53*). This undesired side reaction promotes interchain coupling or even light cross-linking, and control experiments showed that the TMS protecting group was lost completely when TMS-PgMA was stirred in solution under typical ATRP conditions.

Considering the role of copper(I) acetylide as an intermediate in the Cu(I)-catalyzed Huisgen azide−alkyne click cycloaddition, we attempted to perform the ATRP and click reactions

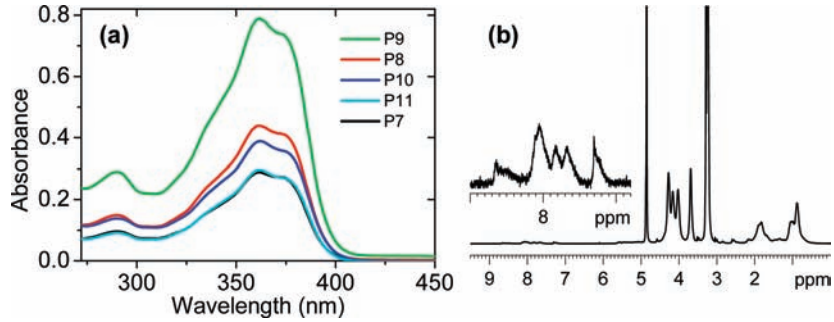

Figure 3. (a) UV/vis absorbance of the polyMPC-*graft*-CPT copolymers at 1 mg/mL in 1:1 DMSO/MeOH solution; (b) ^{1}H NMR spectrum of P7 in CD_3OD.

Table 2. PolyMPC-*graft*-CPT Copolymers Prepared by One-Pot Procedure[a]

polymer	N_{CPT}	CPT-*Z*-N_3	target CPT wt %	monomer conversion	M_n (kDa)	PDI	diamter (nm)	UV Cal. CPT wt %	M_n' (kDa)	PDI′
P7	1.4	**6**	5%	94%	5.2	1.27	5.3	5.1%	6.8	1.17
P8	3	**6**	10%	96%	5.5	1.25	5.5	7.7%	7.5	1.16
P9	5	**6**	15%	>98%	5.1	1.36	5.7	13.8%	7.5	1.17
P10	3	**7**	8.5%	>98%	13	1.31	9.3	7.0%	15	1.18
P11	3	**8**	8.5%	>98%	7.0	1.26	6.8	5.1%	9.0	1.16

[a] N_{CPT}, number of CPT groups per polymer chain; CPT-*Z*-N_3, CPT azide compounds varying linker, *Z*; Conversion, average conversion of both monomers; M_n' = number-average molecular weight of polymer after CPT cleavage from the polymer; PDI′ = PDI of polymer after CPT is cleaved from polymer by hydrolysis.

simultaneously, by introduction of CPT-azide at the outset of the polymerization. This one-pot ATRP/click reaction, shown in Figure 2a, used reaction conditions similar to those we employed to prepare the CPT-terminated polyMPC conjugates. Monomer conversion was monitored by ^{1}H NMR spectroscopy, and cycloaddition was followed by disappearance of the CPT-azide N═N═N stretching signal at ~2100 cm^{-1} in the FTIR spectrum. The polyMPC-*graft*-CPT conjugates prepared in this fashion were purified by precipitation into THF, followed by passage over a short plug of silica gel in mixed solvents.

The polyMPC-*graft*-CPT copolymers were characterized by aqueous GPC as shown in Figure 2 and NMR spectroscopy as shown in Figure 3. The PDI values of the copolymers obtained by this one-pot procedure were slightly higher than the CPT-terminated polyMPC conjugates, in the range 1.25−1.36. A homogeneous distribution of CPT functionality throughout the polymer molecular weight distribution was confirmed by overlaying the UV and RI traces obtained from GPC characterization (Supporting Information Figure S3). Aqueous solution sizes of these structures were also characterized using dynamic light scattering (DLS), showing the copolymers as largely nonaggregated, in which the hydrophilic polymers can be expected to form a corona around a collapsed core of hydrophobic CPT groups. Up to 20 mg/mL, the highest concentration tested, the graft copolymers showed a narrow diameter distribution of less than 10 nm, as shown in Figure 2c.

We found that CPT loading levels on the polyMPC backbone could be varied easily by adjusting the MPC/TMS-PgMA/CPT ratio, as exemplified by the samples listed in Table 2, containing different levels of CPT loading. Importantly, PDI control was achieved at CPT loadings up to 14 wt % (compare this to SN-38-PEG 4-arm stars containing 3.7 wt % CPT (*54*)), and the aqueous solubility of this highly drug-loaded polyMPC structure was excellent (>250 mg/mL, or >35 mg/mL of CPT). The lactone form of CPT alone has a solubility of 2.5 μg/mL; thus, the polyMPC framework provides orders-of-magnitude greater solubility. Aqueous solutions of these conjugates exhibit viscosities that qualitatively resemble pure water, a notable difference from PEGylated drugs that often exhibit an undesirably high solution viscosity. The strongly hydrated zwitterionic moiety affects a wide variety of properties, from solubility to sliding friction (*55*), making these structures appealing for many biological applications including cancer drug delivery.

The GPC-estimated molecular weight values of these polyMPC-*graft*-CPT copolymers (calibrated against linear PEO standards) were lower than expected theoretically, suggesting a possible effect of intramolecular collapse of the hydrophobic pendant CPT groups in aqueous solution, perturbing solution size relative to PEO standards. Interestingly, when the grafted CPT groups were cleaved from the polyMPC-*graft*-CPT copolymers, using 1 N NaOH solution, the GPC-estimated molecular weights were actually seen to increase (Table 2). This observation can be rationalized by the homogeneous hydrophilicity of the CPT-liberated polyMPC product relative to the grafted structure containing CPT-hydrophobes.

^{1}H NMR spectroscopic analysis of the polyMPC-*graft*-CPT copolymers in CD_3OD again presented difficulties in quantifying CPT incorporation, showing only weak aromatic CPT signals in the 7−9 ppm range (Figure 3). This chemical shift region overlaps with the expected proton resonance from the triazole generated by click cycloaddition. Light scattering performed on the polyMPC−CPT copolymers indicated the presence of structures with diameters less than 10 nm (Table 2). As seen in CPT-terminated structures, the characteristic CPT protons in the graft copolymer conjugates broaden significantly in the ^{1}H NMR spectra. However, the intensity of the CPT resonances was seen to change as a function of NMR solvent; signals for CPT and MPC protons were best visualized in a 1:1 DMSO-d_6/CD_3OD mixture. Moreover, UV−vis spectroscopy proved useful for estimating CPT loading. Recording the UV absorbance of the CPT-loaded polymer at 370 nm (Figure 3a) allowed for a calculation of weight percent CPT in the polymer, using known concentrations of the CPT-azide compounds and their molar extinction coefficients. The CPT loading for each sample is given in Table 2 as CPT weight percent. As expected, the relative absorbance at 370 nm from CPT increased with increasing amount of CPT incorporated, with experimental values corresponding reasonably well with that expected for the number of CPT grafts per chain.

The polyMPC-*graft*-CPT copolymers with different linkers between CPT and the polymer backbone, as depicted in Scheme 1, were synthesized to investigate drug release associated with

Scheme 1

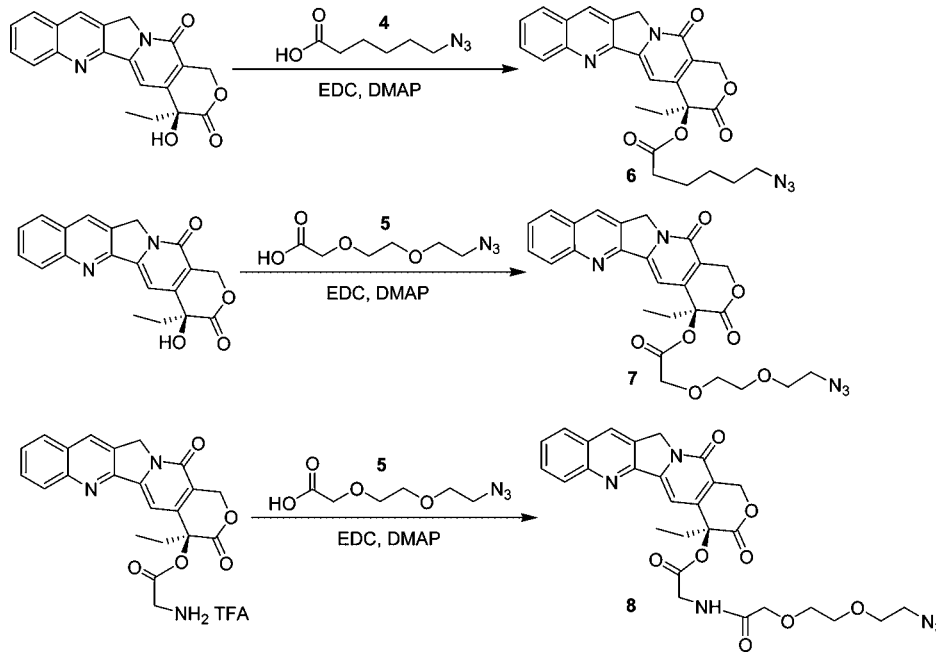

ester linkages of variable hydrophilicity. For example, to contrast the case of the hydrophobic 6-azidohexanoic acid linker (*32*), 2-[2-(2-azidoethoxy)ethoxy]acetic acid was synthesized. This was done by oxidation of 2-[2-(2-chloroethoxy)ethoxy]ethanol to the corresponding carboxylic acid using Jones reagent at room temperature, followed by displacement of the chloride with NaN_3 at 80 °C, to give azide **5** in 53% overall yield. The presence of the azide group was confirmed by its characteristic infrared spectral signal at ∼2100 cm^{-1}, and the α-azido methylene ($\underline{C}H_2N_3$) resonance at 50.6 ppm in the ^{13}C NMR spectrum. CPT azide compounds were obtained by acylation of CPT with linkers **4** and **5** in the presence of EDC and DMAP. Fortunately, we found the linkers to have little-to-no effect on the polymerization and cycloaddition reactions, as indicated by the relatively low PDI values, and theoretical-to-experimental agreement in the drug loadings. Thus, this one-pot click/ATRP procedure provides an easy one-step process to introduce the very hydrophobic camptothecin into hydrophilic, biocompatible MPC polymers with good control over drug loading. We expect that various synthetic camptothecin derivatives will also be amenable to such grafting chemistry.

While a one-pot simultaneous Cu(I)-catalyzed ATRP and "click" was reported for propargyl methacrylate and different organic azide compounds, including 1-octyl azide, methoxytriethylene glycol azide, and 2′-azidoethyl-α-mannopyranoside (*56*), the TMS-protected alkyne has not, to our knowledge, been used in such click cycloadditions without prior deprotection. The facile deprotection, and rapid ensuing click reaction, allows the polymerization and click-conjugation to proceed cleanly in one pot, without complications associated with conventional free radical polymerization in the presence of an alkyne.

Drug Release from polyMPC−CPT Conjugates. In vitro drug release studies were performed on polyMPC−CPT conjugates to gauge their relative release rates and potential utility in delivery applications. To begin, CPT-terminated polyMPC materials were incubated in PBS at various buffered pH values (5.5, 7.4, and 9.1) to measure the CPT hydrolysis half-lives from the polymer backbone. Polymers prepared from CPT initiator **1** (containing one methyl group) showed very slow CPT release (at $t = 30$ days, no drug release was seen at pH 5.5, and only 5% at pH 7.4). However, in human plasma, which contains enzymes that can accelerate ester cleavage, 50% of the drug was released in 10 days. Interestingly, no CPT release was detected from the polymer prepared from CPT initiator **2** (containing two methyl groups), pointing to the importance of the local steric environment around the ester linkage. Placing a glycine linkage between the polymer and CPT did little to accelerate ester bond cleavage and drug release.

For the polyMPC-*graft*-CPT copolymer conjugates, the choice of backbone-to-drug linkage led to significant changes in ester cleavage and drug release. The 6-azidohexanoic acid linker was first chosen for CPT conjugation, giving copolymers **P7**−**9**. These structures exhibited very little hydrolysis over four days incubation under several different aqueous conditions, suggesting that this hydrophobic linker forms conjugates that are possibly too stable for effective in vivo use. To expedite ester hydrolysis, the more hydrophilic linker 2-[2-(2-azidoethoxy)-ethoxy]acetic acid was used to prepare copolymers **P10** and **P11**. Results obtained from hydrolysis studies in different media are given in Figure 5 and Table 3. For example, SEC-HPLC traces of **P10** incubated in cell culture medium are shown in Figure 4a, where the polymer−drug conjugate elutes at 9.4 min and the free CPT elutes at 16.9 min. Over the course of 96 h, the conjugate peak intensity diminishes, while the CPT peak intensity increases, as expected when CPT is released from the polymer backbone. Reverse-phase HPLC analysis of the copolymers after incubation is shown in Figure 4b, confirming CPT release. Copolymers **P10** and **P11**, despite their rather long half-lives of 210−220 h in PBS (pH 7.4), showed much faster release profiles than the CPT-terminated polyMPC structures and polyMPC-*graft*-CPT copolymers containing the 6-azidohexanoic acid linker. Copolymers **P10** and **P11** showed progressively shorter half-lives in mouse serum (∼80 h), cell culture medium (∼40 h), and human plasma (8−9 h). The combined hydrophilicity and substituent effects of the linker accelerate ester cleavage and thus drug release.

Cell Culture Assays Using polyMPC−CPT Conjugates. HPLC characterization of CPT liberation from polyMPC-*graft*-CPT conjugates confirmed the importance of tailored linker chemistry and was informative for in vitro cell culture evaluation of conjugate toxicity against various cell lines. Taking **P10** and **P11** as examples, both containing **5** as linkers, one as an ester (*7*) and the other as a glycine form (*8*), a much faster CPT release profile was seen in human plasma relative to PBS.

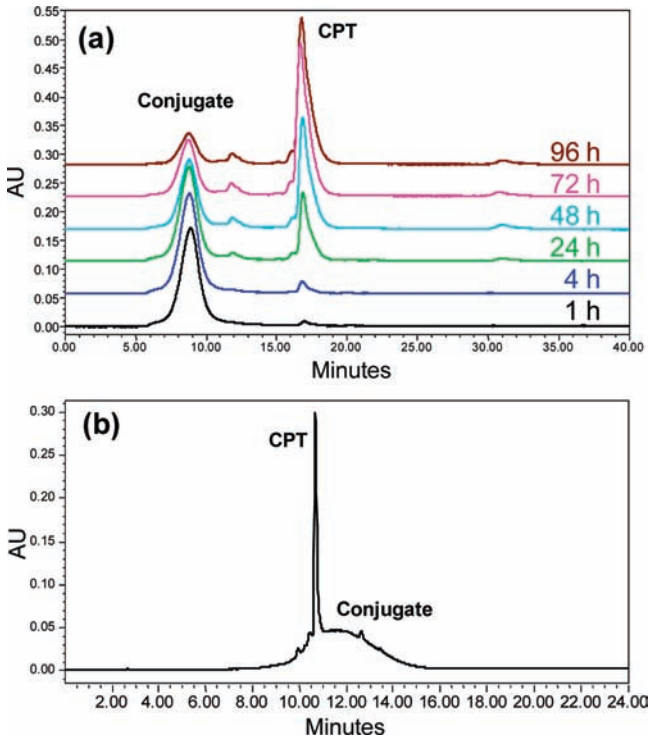

Figure 4. (a) SEC-HPLC traces of **P10** incubated with cell culture medium at 37 °C for different times; (b) reverse-phase HPLC trace of **P10** incubated with PBS at pH 7.4 for 72 h, with a sharp peak for free CPT, and a broad conjugate peak.

However, these CPT hydrolysis half-lives are slower than those reported for PEGylated-SN38 conjugates (*54*), suggesting an expected longer in vivo circulation time.

The anticancer activity of these polyMPC-*graft*-CPT structures (**P10** and **P11**) was tested against different cancer cell lines, including human breast (MCF7), ovarian (OVCAR-3), and colon (COLO 205) adenocarcinoma cells. This was done by incubating CPT-equivalent concentrations of **P10** and **P11** with these cell lines for 72 h, followed by cell viability measurements using a luminescence plate reader (see Experimental Section). Control experiments included a DMSO solution of CPT and polyMPC itself in sterile distilled water. Dose−response curves showed that both **P10** and **P11** were potent against the cancer cell lines tested, and importantly, the cytotoxicity was through the CPT only, since polyMPC by itself was, as expected, nontoxic (Figure 6). Table 4 shows that both **P10** and **P11** induced cytotoxicity at IC_{50} values higher than native CPT, an expected result of the gradual liberation of CPT from the polymer chain over time. From Table 4, it can also be seen that the colon cancer cells were the most sensitive to these novel CPT-polyMPC conjugates of the three cell lines tested (IC_{50} **P10** 3.9 and **P11** 2.3 μM). The comparable IC_{50} values for conjugates **P10** and **P11** originate from their similar hydrolysis rates. The tunable hydrolysis rate, using these and other linkers, will be of benefit for controlling drug release in vivo, and the very high solubility and drug weight percent loading possible in these polyMPC conjugate systems will allow for future in vivo evaluation of very high drug loadings, at any of a range of polyMPC molecular weights, with an objective of maximizing drug efficacy and minimizing toxicity.

EXPERIMENTAL SECTION

Materials. Sodium azide, 4-*N*,*N*-(dimethylamino)pyridine (DMAP), *N*,*N*′-diisopropylethylamine (DIPEA), triethylamine (TEA), *N*-(3-dimethylaminopropyl)-*N*′-ethylcarbodiimide hydrochloride (EDC), 2-bromopropionyl bromide, 2-bromoisobutyryl bromide, copper(I) bromide, 2,2′-bipyridine (bpy), 6-bromohexanoic acid, 2-[2-(2-chloroethoxy)ethoxy]ethanol, ethyl 2-bromoisobutyrate, 3-(trimethylsilyl)propargyl alcohol, methacryloyl chloride, mouse serum, and human plasma were purchased from Aldrich. 20(*S*)-Camptothecin (CPT) was purchased from Acros. Chromium trioxide was purchased from Alfa Aesar. TFA was purchased from Fisher Scientific. Boc-Gly-OH was purchased from Advanced ChemTech. MPC monomer was synthesized on the basis of literature methods (*57*). Dichloromethane (DCM) was distilled over CaH_2. All other materials were used without additional purification. The human colon (COLO 205), ovarian (OVCAR-3), and breast (MCF7) adenocarcinoma cells were purchased from American Type Culture Collection (ATCC), and RPMI 1640 and MEM cell culture media were purchased from Invitrogen and Mediatech, respectively. Fetal bovine serum (FBS) was purchased from Atlanta Biologicals and bovine insulin from Aldrich. Cell viability was measured using CellTiter-Glo luminescent cell viability assays (Promega).

Instrumentation. NMR spectra were recorded on Bruker DPX300 spectrometer ($\omega_{13C} = 0.25\ \omega_{1H}$). High-resolution mass spectral (HRMS) data were obtained on a JEOL JMS700 MStation. UV/vis absorbance measurements were taken on a Perkin-Elmer Lambda 25 UV/vis spectrometer. IR data were recorded on a Perkin-Elmer Spectrum One FT-IR spectrometer equipped with a universal ATR sampling accessory. Dynamic light scattering was performed on the Malvern Zetasizer Nano-ZS, and transmission electron microscopy (TEM) was performed on JEOL 2000 FX MARK II 200 keV transmission electron microscope. Molecular weights and polydispersity indices (PDIs) were estimated by gel permeation chromatography (GPC) in sodium nitrate (0.1 M with 0.02 wt % of NaN_3) aqueous solution, calibrated against poly(ethylene oxide) standards, operating at 1.0 mL/min with an HP Series 1050 Pump, HP 1047A refractive index detector, and three Waters Ultrahydrogel linear columns (300 × 7.8 mm). The HPLC consisted of the Waters Alliance system with a 2996 photodiode array detector. A size-exclusion Shodex KW-803 column was used, eluting with 10% ethanol in PBS buffer (pH 7.4) at a flow rate of 1 mL/min, on a reverse-phase C18 column (250 × 4.6 mm) with a gradient of 5−95% of acetonitrile in 0.05% TFA.

Synthesis of CPT-polyMPC Homopolymer. *Synthesis of Initiator **1**.* CPT (600 mg, 1.72 mmol) and DIPEA (445 mg, 3.45 mmol) were suspended in 30 mL of dry DCM. After adding DMAP (440 mg, 3.45 mmol), the suspension was cooled to 0 °C. 2-Bromopropionyl bromide (745 mg, 3.45 mmol) in 20 mL of dry DCM was added to the suspension dropwise. The reaction mixture was stirred at 0 °C for 1 h, then at room temperature for 1 h. After washing with 1 N HCl (50 mL × 3), 1% $NaHCO_3$ (50 mL × 3), and brine (50 mL × 1), the organic phase was dried over $MgSO_4$, filtered, and concentrated by rotary evaporation, giving the crude product. This was crystallized in MeOH/CH_2Cl_2 (95:5) to give compound **1** (650 mg, 78% yield) as a light yellow solid. ^{1}H NMR ($CDCl_3$, 300 MHz): δ 8.44 (s 1H), 8.29 (d, J = 8.7 Hz, 1H), 7.97 (d, J = 8.1 Hz, 1H), 7.86 (t, J = 7.5 Hz, 1H), 7.70 (t, J = 7.2 Hz, 1H), 7.52 (s 1H), 5.73 (d, J = 17.4 Hz, 1H), 5.43 (d, J = 17.4 Hz, 1H). 5.32 (s 2H), 4.62 (q, J = 6.9 Hz, 1H), 2.16−2.41 (m, 2H), 1.86 (d, J = 6.9 Hz, 3H), 1.03 (t, J = 7.5 Hz, 3H). ^{13}C NMR ($CDCl_3$, 75 MHz): δ 169.0, 167.1, 157.3, 152.2, 148.8, 146.4, 145.0, 131.2, 130.7, 129.8, 128.4, 128.1(2C), 120.2, 96.2, 76.9, 67.2, 50.0, 38.7, 31.8, 21.1, 7.6. HRMS-FAB (m/z): $[M+H]^+$ calculated for $C_{23}H_{20}BrN_2O_5$: 483.0556, found: 483.0587.

*Synthesis of Initiator **2**.* CPT (300 mg, 0.86 mmol) and DIPEA (222 mg, 1.72 mmol) and DMAP (210 mg, 1.72 mmol) were stirred in 20 mL of dry DCM at 0 °C. 2-Bromoisobutyryl bromide (594 mg, 2.58 mmol) in 10 mL of dry DCM was added

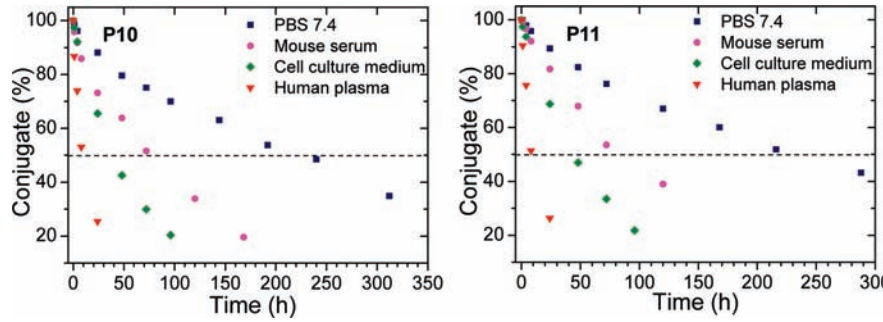

Figure 5. PolyMPC−CPT conjugate (**P10** and **P11**) degradation data over time in different media at 37 °C.

Table 3. Half-Lives ($T_{1/2}$) of polyMPC-*graft*-CPT Copolymers with Hydrophilic Linkers in Different Media

medium		PBS 7.4	mouse serum	cell culture medium	human plasma
$T_{1/2}$	**P10**	212 h	80 h	43 h	8.4 h
	P11	220 h	76 h	37 h	9.0 h

to the suspension dropwise. The reaction mixture was stirred at 0 °C for 1 h, then room temperature for 1 h. After washing with 1 N HCl (40 mL × 3), 1% $NaHCO_3$ (40 mL × 3), and brine (40 mL × 1), the organic phase was dried over $MgSO_4$. The solvent was removed under reduced pressure to give a crude product, which was crystallized from MeOH/CH_2Cl_2 (95:5) to give compound **2** (300 mg, 89% yield) as a light yellow solid. ^{1}H NMR ($CDCl_3$, 300 MHz): δ 8.40 (s, 1H), 8.24 (d, J = 8.3 Hz, 1H), 7.95 (d, J = 7.9 Hz, 1H), 7.84 (t, J = 7.1 Hz, 1H), 7.67 (t, J = 7.5 Hz, 1H), 7.45 (s, 1H), 5.74 (d, J = 17.0 Hz, 1H), 5.44 (d, J = 17.0 Hz, 1H), 5.30 (s, 2H), 2.15−2.41 (m, 2H), 2.12 (s, 3H), 1.95 (s, 3H), 1.65 (t, J = 7.5 Hz, 3H). ^{13}C NMR ($CDCl_3$, 75 MHz): δ 170.3, 167.0, 157.4, 152.4, 149.0, 146.5, 145.5, 131.0, 130.5, 130.0, 128.4, 128.2, 128.1, 128.0, 120.0, 96.0, 76.8, 67.1, 54.7, 50.0, 31.7, 30.5, 30.4, 7.7. HRMS-FAB (m/z): $[M+H]^+$ calculated for $C_{24}H_{22}O_5N_2Br$: 497.0712, found: 497.0669.

Synthesis of Initiator ***3.*** CPT (1.0 g, 2.87 mmol) and Boc-protected glycine (1.0 g, 5.7 mmol) were added into 50 mL of dry DCM. After the suspension was cooled to 0 °C, DMAP (0.70 g, 5.74 mmol) and EDC·HCl (1.1 g, 5.7 mmol) were added to the suspension. The reaction mixture was stirred at 0 °C for 20 min, then at room temperature for 1 h. After washing with 1 N HCl (100 mL × 3), 1% $NaHCO_3$ (100 mL × 3), and brine (100 mL × 1), the organic phase was dried over $MgSO_4$, filtered, and concentrated by rotary evaporation to give CPT-Gly-Boc (1.23 g, 86% yield), which was used in the next step without further purification. ^{1}H NMR ($CDCl_3$, 300 MHz): δ 8.42 (s, 1H), 8.26 (d, J = 7.6 Hz, 1H), 7.96 (d, J = 7.5 Hz, 1H), 7.86 (t, J = 7.5 Hz, 1H), 7.69 (t, J = 7.5 Hz, 1H), 7.30 (s, 1H), 5.71 (d, J = 17.5 Hz, 1H), 5.42 (d, J = 17.5 Hz, 1H), 5.31 (s, 2H), 4.99 (b, 1H), 4.14 (m, 2H), 2.13−2.38 (m, 2H), 1.42 (s, 9H), 1.00 (t, J = 6.9 Hz, 3H). To a solution of compound CPT-Gly-Boc (1.3 g, 2.57 mmol) in 30 mL of DCM was added 4 mL of TFA. The reaction mixture was stirred at room temperature for 1 h, and the solvent was removed under vacuum. The product was precipitated in ethyl ether, filtered, and dried under vacuum to give compound CPT-Gly (1.2 g, 90% yield). ^{1}H NMR (DMSO, 300 MHz): δ 8.74 (s, 1H), 8.37 (b, 3H), 8.16 (d, J = 8.2 Hz, 2H), 7.89 (t, J = 7.6 Hz, 1H), 7.74 (t, J = 7.6 Hz, 1H), 7.30 (s, 1H), 5.56 (s, 2H), 5.34 (s, 2H), 4.36 (d, J = 18.0 Hz, 1H), 4.11 (d, J = 18.0 Hz, 1H), 2.19 (m, 2H), 0.96 (t, J = 7.4 Hz, 3H). ^{13}C NMR (DMSO, 75 MHz): δ 167.4, 167.3, 156.9, 152.8, 148.3, 146.5, 145.1, 132.2, 131.0, 130.3, 129.2, 129.1 128.5 128.3, 119.35, 96.0, 77.9, 66.8, 50.7, 40.2, 30.6, 8.0. HRMS-FAB (m/z): $[M+H]^+$ calculated for $C_{22}H_{20}O_5N_3$: 406.1403, found: 406.1401.

To a solution of compound CPT-Gly (280 mg, 0,69 mmol) and DIPEA (267 mg, 2.07 mmol) in 10 mL DCM was added dropwise 2-bromoisobutyryl bromide (318 mg, 1.38 mmol) in 5 mL of DCM at −20 °C. The reaction mixture was stirred at −20 °C for 20 min and then room temperature for 2 h. After washing with 1 N HCl (30 mL × 3), 1% $NaHCO_3$ (30 mL × 3), and brine (30 mL × 1), the organic phase was dried over $MgSO_4$. After removing the $MgSO_4$ by filtration, evaporation of the solvent under reduced pressure gave the crude product as a yellow solid, which was crystallized from MeOH/CH_2Cl_2 (95:5) to give initiator **3** (135 mg, 35% yield) as light yellow solid. ^{1}H NMR ($CDCl_3$, 300 MHz): δ 8.42 (s, 1H), 8.25 (d, J = 8.6 Hz, 1H), 7.90 (d, J = 8.1 Hz, 1H), 7.86 (t, J = 7.5 Hz, 1H), 7.69 (t, J = 7.5 Hz, 1H), 7.15 (s, 1H), 5.72 (d, J = 17.3 Hz, 1H), 5.42 (d, J = 17.3 Hz, 1H), 5.30 (s, 2H), 4.20−4.40 (m, 2H), 2.13−2.39 (m, 2H), 1.97 (s, 3H), 1.92 (s, 3H), 1.01 (t, J = 7.4 Hz, 3H). ^{13}C NMR ($CDCl_3$, 75 MHz): δ 172.2, 168.7, 167.1, 157.3, 152.2, 148.9, 146.6, 145.2, 131.2, 130.8, 129.7, 128.4, 128.2, 128.1, 120.1, 96.0, 87.2, 77.2, 67.2, 61.6, 50.0, 42.1, 32.4, 32.3, 31.9, 7.6. HRMS-FAB (m/z): $[M+H]^+$ calculated for $C_{26}H_{24}O_6N_3Br$: 554.0927, found: 554.0927.

General Procedure for ATRP of MPC from CPT-Initiators. CPT-initiator (29.0 mg, 0.06 mmol) was charged into a 10 mL two-neck round-bottom flask and three cycles of vacuum−nitrogen were employed. Nitrogen gas bubbled DMSO (1.5 mL) was injected with a syringe. After the initiator was dissolved completely, CuBr (8.6 mg, 0.06 mmol) and bipyridine (18.7 mg, 0.12 mmol) were added quickly under nitrogen atmosphere. Different amount of MPC dissolved in MeOH (0.5 mL) was then added to the mixture. The reaction mixture was subjected to four freeze−pump−thaw cycles, then stirred at room temperature, and the polymerization conversion was monitored by NMR. The polymerization was stopped by precipitating the reaction mixture into THF (100 mL), and the crude product was isolated by filtration. The polymer was purified by column chromatography on silica gel, eluting with MeOH−DCM mixtures. The polymers were characterized using ^{1}H NMR and aqueous GPC.

Synthesis of polyMPC-*graft*-CPT Copolymers. *Synthesis of Compound* ***5.*** Chromium trioxide (25.0 g, 164 mmol) was dissolved in 300 mL of 1.5 M H_2SO_4, and the solution was cooled to 0 °C. 2-[2-(2-Chloroethoxy)ethoxy]ethanol (8.3 g, 49 mmol) in 150 mL acetone was added dropwise, and the reaction mixture was stirred at room temperature for 6 h. Acetone was removed by evaporation under vacuum, and the aqueous phase was extracted with DCM (3 × 100 mL). After the combined organic phase was dried over $MgSO_4$, the 2-[2-(2-chloroethoxy)-ethoxy]acetic acid (6.3 g, 70% yield) was obtained by removing the solvent by rotary evaporation. IR: (cm^{-1}) 1734 (C═O). ^{1}H NMR ($CDCl_3$, 300 MHz): δ 10.49 (b, 1H), 4.23 (s, 2H), 3.80 (t, J = 5.8 Hz, 4H), 3.74 (t, J = 5.7 Hz, 2H), 3.66 (t, J = 5.8 Hz, 2H). ^{13}C NMR ($CDCl_3$, 75 MHz): δ 174.4, 71.4, 71.1, 70.4, 68.5, 42.6.

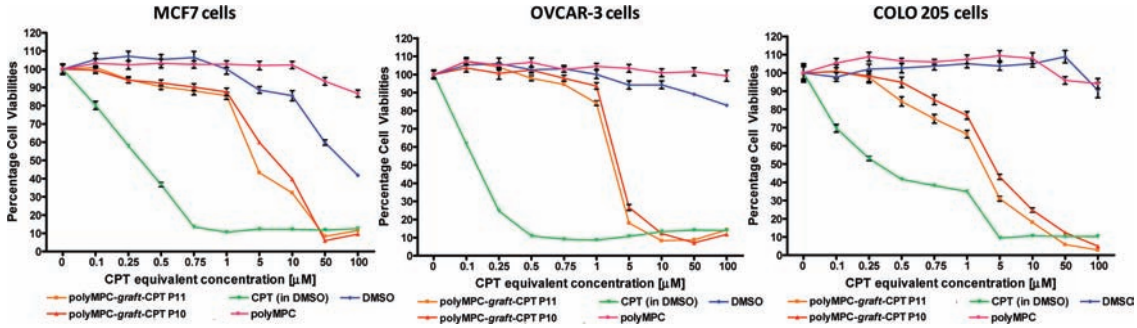

Figure 6. In vitro cytotoxicity of polyMPC-*graft*-CPT conjugates in cell culture of human breast (MCF7), ovarian (OVCAR-3), and colon (COLO 205) adenocarcinoma cells.

Table 4. IC_{50} Values (μM) of polyMPC-*graft*-CPT Copolymers Across Various Cancer Cell Lines

cell type	**P10**	**P11**	CPT
MCF7	6.7	4.6	0.29
OVCAR-3	3.3	2.5	0.13
COLO 205	3.9	2.3	0.32

2-[2-(2-Chloroethoxy)ethoxy]acetic acid (6.3 g, 34 mmol) and NaN_3 (9.00 g, 138 mmol) were dissolved in 20 mL of water. The reaction mixture was stirred with heating at 80 °C for 48 h. After cooling to room temperature, the reaction mixture was acidified with HCl solution and extracted with DCM (4 × 50 mL). The combined organic phase was dried over $MgSO_4$. Filtration and extraction by rotary evaporation gave compound **5** as a clear oil (5.0 g, 77% yield). IR: (cm^{-1}) 2097 (N═N═N). ^1H NMR ($CDCl_3$, 300 MHz): δ 10.80 (b, 1H), 4.22 (s, 2H), 3.79 (t, J = 5.7 Hz, 2H), 3.69−3.74 (m, 4H), 3.43 (t, J = 5.3 Hz, 2H). ^{13}C NMR ($CDCl_3$, 75 MHz): δ 174.7, 71.2, 70.5, 70.1, 68.4, 50.6. HRMS-FAB (*m*/*z*): $[M+H]^+$ calculated for $C_6H_{12}O_4N_3$: 190.0828, found: 190.0816.

Synthesis of Compound ***6.*** Compound **4** was synthesized according to a literature procedure (*32*). 6-Bromohexanoic acid (5 g, 25.6 mmol) was stirred with sodium azide (8.40 g, 129 mmol) in 50 mL of DMSO at room temperature to afford compound **4**, 6-azidohexanoic acid. Esterification of compound **4** with CPT using EDC/DMAP catalysis in DCM gave compound **6**. IR: (cm^{-1}) 2094 (N_3). ^1H NMR ($CDCl_3$, 300 MHz): δ 8.43 (s, 1H), 8.24 (d, J = 8.3 Hz, 1H), 7.97 (d, J = 8.0 Hz, 1H), 7.87 (t, J = 7.0 Hz, 1H), 7.70 (t, J = 7.1 Hz, 1H), 7.23 (s, 1H), 5.71 (d, J = 17.6 Hz, 1H), 5.43 (d, J = 17.6 Hz, 1H), 5.31 (s, 2H), 3.25 (t, J = 6.8 Hz, 2H), 2.45−2.63 (m, 2H), 2.11−2.37 (m, 2H), 1.71 (qp, J = 7.6 Hz, 2H), 1.63 (m, 2H), 1.42 (m, 2H), 1.00 (t, J = 7.3 Hz, 3H).

Synthesis of Compound ***7.*** A solution of compound **5** (327 mg, 1.72 mmol) and EDC hydrochloride (330 mg, 1.72 mmol) in 20 mL DCM was stirred at 0 °C. CPT (300 mg, 0.86 mmol) and DMAP (210 mg, 1.72 mmol) were added. The reaction was stirred at room temperature until the suspension became visibly homogeneous. After washing with 1 N HCl (50 mL × 3), 1% $NaHCO_3$ (50 mL × 3), and brine (50 mL × 1), the organic phase was dried over $MgSO_4$. Filtration and concentration by rotary evaporation gave a yellow solid, which was recrystallized from MeOH/CH_2Cl_2 (95:5) to give pure compound **7** (389 mg, 87% yield) as a light yellow solid. IR: (cm^{-1}) 2104 (N═N═N). ^1H NMR ($CDCl_3$, 300 MHz): δ 8.43 (s, 1H), 8.24 (d, J = 8.0 Hz, 1H), 7.97 (d, J = 8.0 Hz, 1H), 7.87 (t, J = 7.5 Hz, 1H), 7.70 (t, J = 7.5 Hz, 1H), 7.23 (s, 1H), 5.73 (d, J = 17.4 Hz, 1H), 5.44 (d, J = 17.4 Hz, 1H), 5.31 (s, 2H), 4.39 (d, J = 5.0 Hz, 2H), 3.77 (t, J = 5.5 Hz, 2H), 3.66−3.70 (m, 4H), 3.40 (t, J = 5.1 Hz, 2H), 2.13−2.39 (m, 2H), 1.00 (t, J = 7.4 Hz, 3H). ^{13}C NMR ($CDCl_3$, 75 MHz): δ 169.7, 167.3, 157.3, 152.2, 148.9, 146.4, 145.4, 131.2, 130.7, 129.6, 128.4, 128.2, 128.2, 128.1, 120.3, 95.9, 76.4, 71.1, 70.6, 70.0, 68.2, 67.2, 50.6, 50.0, 31.8, 7.6. HRMS-FAB (*m*/*z*): $[M+H]^+$ calculated for $C_{26}H_{26}O_7N_5$: 520.1832, found: 520.1821.

Synthesis of Compound ***8.*** A solution of compound **5** (304 mg, 1.60 mmol) and EDC hydrochloride (461 mg, 2.40 mmol) in 20 mL DCM was stirred at 0 °C. CPT-Gly TFA salt (415 mg, 0.80 mmol) and DMAP (293 mg, 2.40 mmol) were added. The mixture was stirred at room temperature for 5 h, then washed with 1 N HCl (30 mL × 3), 1% $NaHCO_3$ (30 mL × 3), and brine (30 mL × 1). The organic phase was dried over $MgSO_4$, filtered, and concentrated by rotary evaporation to give the crude product, which was recrystallized from MeOH to give pure compound **8** (374 mg, 81% yield). IR: (cm^{-1}) 2113 (N═N═N). ^1H NMR ($CDCl_3$, 300 MHz): δ 8.41 (s, 1H), 8.26 (d, J = 8.5 Hz, 1H), 7.95 (d, J = 7.7 Hz, 1H), 7.85 (t, J = 7.0 Hz, 1H), 7.68 (t, J = 7.7 Hz, 1H), 7.37 (t, J = 5.3 Hz, 1H), 7.27 (s, 1H), 5.71 (d, J = 17.2 Hz, 1H), 5.43 (d, J = 17.2 Hz, 1H), 5.29 (s, 2H), 4.46−4.54 (dd, J_1 = 18.6 Hz, J_2 = 6.5 Hz, 1H), 4.18−4.26 (dd, J_1 = 18.6 Hz, J_2 = 4.7 Hz, 1H), 4.02 (q, J = 8.2 Hz, 1H), 3.66−3.70 (m, 2H), 3.62 (t, J = 5.0 Hz, 4H), 3.34 (t, J = 4.9 Hz, 2H), 2.14−2.40 (m, 2H), 1.00 (t, J = 7.5 Hz, 3H). ^{13}C NMR ($CDCl_3$, 75 MHz): δ 170.3, 169.0, 167.1, 157.3, 152.2, 148.9, 146.6, 145.3, 131.2, 130.7, 129.8, 128.4, 128.2 (2C overlap), 182.1, 120.2, 96.0, 76.9, 71.1, 70.3, 70.2, 70.0, 67.2, 50.6, 50.0, 40.4, 31.9, 7.6. HRMS-FAB (*m*/*z*): $[M+H]^+$ calculated for $C_{28}H_{29}N_6O_8$: 577.2047, found: 577.2021.

Synthesis of TMS-PgMA. The TMS-protected alkyne monomer was synthesized according to a literature method (*36*). 3-(Trimethylsilyl)propargyl alcohol (2.00 g, 15.6 mmol) and triethylamine (2 g, 20.3 mmol) in 20 mL of dry ethyl ether was cooled to −20 °C. A solution of methacryloyl chloride (2 g, 18.7 mmol) in 10 mL of dry ethyl ether was added dropwise over 30 min. The reaction mixture was stirred for 30 min at −20 °C, then overnight at room temperature. The precipitate was removed by filtration, and the solvent was removed by rotary evaporation. The crude product was further purified on silica column chromatography eluting with hexane−ethyl ether (100:1) to give the pure TMS-PgMA monomer as colorless oil (4.0 g, 58% yield). IR: (cm^{-1}) 2961 (C−H), 1723 (C═O), 1638 (C═C). ^1H NMR ($CDCl_3$, 300 MHz): δ 6.16 (m, 1H), 5.61 (m, 1H), 4.75 (s, 2H), 1.95 (m, 3H), 0.18 (s, 9H). ^{13}C NMR ($CDCl_3$, 75 MHz): δ 166.6, 135.7, 126.4, 99.1, 91.9, 53.0, 18.3, 0.3. HRMS-FAB (*m*/*z*): $[M]^+$ calculated for $C_{10}H_{16}O_2Si$: 196.0920, found: 196.0891.

General Procedure for One-Pot ATRP and Click Cycloaddition. CPT azide was charged into a 10 mL two-neck round-bottom flask and three cycles of vacuum-nitrogen were employed. Degassed DMSO (2 mL) was injected with a syringe. After the CPT azide was dissolved completely, a solution of ethyl 2-bromoisobutyrate (11.7 mg. 0.06 mmol), MPC and alkyne monomer in 0.7 mL MeOH was injected. CuBr (17 mg, 0.12 mmol) and bipyridine (37.4 mg, 0.24 mmol) were added quickly under nitrogen atmosphere. The reaction mixture was then subjected to four freeze−pump−thaw cycles. The reaction

mixture was stirred at room temperature for 20 h, and monomer conversion was monitored by ^{1}H NMR spectroscopy. The polymerization was stopped by precipitating the reaction mixture into THF (100 mL), and the crude product was isolated by filtration. The crude product was further purified by column chromatography on silica gel, eluting with MeOH−DCM mixtures, to give the polyMPC-*graft*-CPT copolymers as light yellow solid. The polymers were characterized by NMR spectroscopy and aqueous GPC.

TEM. TEM images were obtained using a JEOL 2000FX transmission electron microscope operating at an acceleration voltage of 200 kV. The samples were prepared by dropping 2 μL of polymer solution onto the carbon-coated copper grid. After the samples were dried, 1 wt % phosphotungstenic acid solution (PTA) was used for staining.

DLS Measurements. DLS was performed on a Malvern Zetasizer Nano-ZS (4 mW He−Ne laser, 633 nm) with a detector set to collect backscattered light at a 173° angle. The light scattering intensity was recorded with fixed measurement position and attenuator for different concentrations. The size measurements were performed at polymer concentration of 1 mg/mL, and optimum position and automatic attenuation were selected to generate the optimum correlation curve. Samples was dissolved in water and filtered through a 0.45 μm filter membrane before the measurement. Each measurement was performed at 25 °C by equilibrating the samples for 10 min.

Calibration of CPT Loading in Polymer. Compounds **6**, **7**, and **8** were dissolved in DMSO−MeOH (1:1) at a concentration of 0.01 mg/mL, and copolymers (**P7**−**P11**) were also dissolved in DMSO−MeOH (1:1) at a concentration of 0.1 mg/mL. The CPT loading in each polymer was calculated on the basis of UV absorbance values at 370 nm and known concentration of its corresponding CPT azide compound.

CPT Release Measurements. The CPT containing polymers were dissolved in different media at a concentration of 3 mg/mL. The mixtures were incubated at 37 °C, and aliquots (100 μL) were taken at different time points. Twenty microliter aliquots of the sample from PBS and cell culture media were analyzed by SEC-HPLC. The samples taken from mouse serum and human plasma were mixed with 200 uL of PBS and filtered through a 0.45 μm filter membrane; 60 μL of the filtrate was analyzed on SEC-HPLC. The stability profile was generated by plotting the percentage of remaining CPT on the polymer over a time course. The percentage was calculated on the basis of peak area of UV absorbance at 370 nm. The sample was also analyzed by RP-HPLC, and the integrity of the released CPT (i.e., ring-opened or ring-closed form) was based on the retention times.

Cell Culture. The OVCAR-3 and COLO 205 cancer cells were cultured in RPMI-1640 medium supplemented with 10% fetal bovine serum (FBS) or 20% FBS and 0.01 mg/mL bovine insulin, while MCF7 cells were cultured in MEM medium supplemented with 10% FBS and 0.01 mg/mL bovine insulin. All cells were grown in 5% CO_2 incubators at 37 °C. For in vitro cytotoxicity assays, cells were seeded into 96 well plates, and after reaching about 40% cell density were incubated for 72−96 h with varying camptothecin equivalent concentrations of polymer drug conjugates, as well as polymer control samples (i.e., no attached drug). Cell viability post-treatment was measured using CellTiter-Glo luminescent cell viability assays (Promega) as per manufacturer's instructions on a FLUOstar OPTIMA plate reader (BMG LABTECH). The percentage camptothecin mediated toxicity was calculated with respect to untreated cells and graphed to give dose−response curves. IC_{50} values for each treatment were then calculated using the GraphPad *Prism4* statistical analysis software.

ACKNOWLEDGMENT

The authors acknowledge the financial support of the National Science Foundation Materials Research Science & Engineering Center (MRSEC) on Polymers, the Nanoscale Science & Engineering Center (NSEC, DMI-0531171) at the University of Massachusetts Amherst, and the Center for Excellence in Apoptosis Research of the Pioneer Valley Life Sciences Institute.

Supporting Information Available: NMR spectra of polyMPC-camptothecin conjugates, and GPC traces of polyMPC-*graft*-CPT. This material is available free of charge via the Internet at http://pubs.acs.org.

LITERATURE CITED

(1) Maeda, H., Wu, J., Sawa, T., Matsumura, Y., and Hori, K. (2000) Tumor vascular permeability and the EPR effect in macromolecular therapeutics: a review. *J. Controlled Release 65*, 271–284.

(2) Harris, J. M., and Chess, R. B. (2003) Effect of pegylation on pharmaceuticals. *Nat. Rev. Drug Discovery 2*, 214–221.

(3) Veronese, F. M., and Pasut, G. (2005) PEGylation, successful approach to drug delivery. *Drug Discovery Today 10*, 1451–1458.

(4) Rowinsky, E. K., Rizzo, J., Ochoa, L., Takimoto, C. H., Forouzesh, B., Schwartz, G., Hammond, L. A., Patnaik, A., Kwiatek, J., Goetz, A., Denis, L., McGuire, J., and Tolcher, A. W. (2003) A phase I and pharmacokinetic study of pegylated camptothecin as a 1-h infusion every 3 weeks in patients with advanced solid malignancies. *J. Clin. Oncol. 21*, 148–157.

(5) Greenwald, R. B., Pendri, A., Conover, C. D., Lee, C., Choe, Y. H., Gilbert, C., Martinez, A., Xia, J., Wu, D. C., and Hsue, M. (1998) Camptothecin-20-PEG ester transport forms: the effect of spacer groups on antitumor activity. *Bioorg. Med. Chem. 6*, 551–562.

(6) Rodrigues, P. C. A., Beyer, U., Schumacher, P., Roth, T., Fiebig, H. H., Unger, C., Messori, L., Orioli, P., Paper, D. H., Mulhaupt, R., and Kratz, F. (1999) Acid-sensitive polyethylene glycol conjugates of doxorubicin: Preparation, in vitro efficacy and intracellular distribution. *Bioorg. Med. Chem. 7*, 2517–2524.

(7) Lee, C. C., Gillies, E. R., Fox, M. E., Guillaudeu, S. J., Frechet, J. M. J., Dy, E. E., and Szoka, F. C. (2006) A single dose of doxorubicin-functionalized bow-tie dendrimer cures mice bearing C-26 colon carcinomas. *Proc. Natl. Acad. Sci. U.S.A. 103*, 16649–16654.

(8) Ishihara, K., and Iwasaki, Y. (1998) Reduced protein adsorption on novel phospholipid polymers. *J. Biomater. Appl. 13*, 111–127.

(9) Ishihara, K., Nomura, H., Mihara, T., Kurita, K., Iwasaki, Y., and Nakabayashi, N. (1998) Why do phospholipid polymers reduce protein adsorption? *J. Biomed. Mater. Res. 39*, 323–330.

(10) Ishihara, K. (2000) New polymeric biomaterials: Phospholipid polymers with a biocompatible surface. *Front. Med. Biol. Eng. 10*, 83–95.

(11) Lewis, A. L. (2000) Phosphorylcholine-based polymers and their use in the prevention of biofouling. *Colloid Surf., B 18*, 261–275.

(12) Nakabayashi, N., and Williams, D. F. (2003) Preparation of non-thrombogenic materials using 2-methacryloyloxyethyl phosphorylcholine. *Biomaterials 24*, 2431–2435.

(13) Iwasaki, Y., and Ishihara, K. (2005) Phosphorylcholine-containing polymers for biomedical applications. *Anal. Bioanal. Chem. 381*, 534–546.

(14) Ishihara, K., and Takai, M. (2009) Bioinspired interface for nanobiodevices based on phospholipid polymer chemistry. *J. R. Soc. Interface 6*, S279–S291.

(15) Samanta, D., McRae, S., Cooper, B., Hu, Y. X., and Emrick, T. (2008) End-functionalized phosphorylcholine methacrylates and their use in protein conjugation. *Biomacromolecules 9*, 2891–2897.

(16) Lewis, A., Tang, Y. Q., Brocchini, S., Choi, J. W., and Godwin, A. (2008) Poly(2-methacryloyloxyethyl phosphorylcholine) for protein conjugation. *Bioconjugate Chem. 19*, 2144–2155.

(17) Lobb, E. J., Ma, I., Billingham, N. C., Armes, S. P., and Lewis, A. L. (2001) Facile synthesis of well-defined, biocompatible phosphorylcholine-based methacrylate copolymers via atom transfer radical polymerization at 20 °C. *J. Am. Chem. Soc. 123*, 7913–7914.

(18) Ma, I. Y., Lobb, E. J., Billingham, N. C., Armes, S. P., Lewis, A. L., Lloyd, A. W., and Salvage, J. (2002) Synthesis of biocompatible polymers. 1. Homopolymerization of 2-methacryloyloxyethyl phosphorylcholine via ATRP in protic solvents: An optimization study. *Macromolecules 35*, 9306–9314.

(19) Ma, Y. H., Tang, Y. Q., Billingham, N. C., Armes, S. P., Lewis, A. L., Lloyd, A. W., and Salvage, J. P. (2003) Well-defined biocompatible block copolymers via atom transfer radical polymerization of 2-methacryloyloxyethyl phosphorylcholine in protic media. *Macromolecules 36*, 3475–3484.

(20) Licciardi, M., Tang, Y., Billingham, N. C., and Armes, S. P. (2005) Synthesis of novel folic acid-functionalized biocompatible block copolymers by atom transfer radical polymerization for gene delivery and encapsulation of hydrophobic drugs. *Biomacromolecules 6*, 1085–1096.

(21) Yusa, S. I., Fukuda, K., Yamamoto, T., Ishihara, K., and Morishima, Y. (2005) Synthesis of well-defined amphiphilic block copolymers having phospholipid polymer sequences as a novel blocompatible polymer micelle reagent. *Biomacromolecules 6*, 663–670.

(22) Yu, B., Lowe, A. B., and Ishihara, K. (2009) RAFT synthesis and stimulus-induced self-assembly in water of copolymers based on the blocompatible monomer 2-(methacryloyloxy)ethyl phosphorylcholine. *Biomacromolecules 10*, 950–958.

(23) Konno, T., Watanabe, J., and Ishihara, K. (2003) Enhanced solubility of paclitaxel using water-soluble and biocompatible 2-methacryloyloxyethyl phosphorylcholine polymers. *J. Biomed. Mater. Res., Part A 65A*, 209–214.

(24) Wada, M., Jinno, H., Ueda, M., Ikeda, T., Kitajima, M., Konno, T., Watanabe, J., and Ishihara, K. (2007) Efficacy of an MPC-BMA co-polymer as a nanotransporter for paclitaxel. *Anticancer Res. 27*, 1431–1435.

(25) Du, J. Z., Tang, Y. P., Lewis, A. L., and Armes, S. P. (2005) pH-sensitive vesicles based on a biocompatible zwitterionic diblock copolymer. *J. Am. Chem. Soc. 127*, 17982–17983.

(26) Xu, J. P., Ji, J., Chen, W. D., and Shen, J. C. (2005) Novel biomimetic polymersomes as polymer therapeutics for drug delivery. *J. Controlled Release 107*, 502–512.

(27) Kolb, H. C., Finn, M. G., and Sharpless, K. B. (2001) Click chemistry: Diverse chemical function from a few good reactions. *Angew. Chem., Int. Ed. 40*, 2004–2021.

(28) Rostovtsev, V. V., Green, L. G., Fokin, V. V., and Sharpless, K. B. (2002) A stepwise Huisgen cycloaddition process: Copper(I)-catalyzed regioselective "ligation" of azides and terminal alkynes. *Angew. Chem., Int. Ed. 41*, 2596–2599.

(29) Tornoe, C. W., Christensen, C., and Meldal, M. (2002) Peptidotriazoles on solid phase: [1,2,3]-triazoles by regiospecific copper(I)-catalyzed 1,3-dipolar cycloadditions of terminal alkynes to azides. *J. Org. Chem. 67*, 3057–3064.

(30) Wu, P., Feldman, A. K., Nugent, A. K., Hawker, C. J., Scheel, A., Voit, B., Pyun, J., Frechet, J. M. J., Sharpless, K. B., and Fokin, V. V. (2004) Efficiency and fidelity in a click-chemistry route to triazole dendrimers by the copper(I)-catalyzed ligation of azides and alkynes. *Angew. Chem., Int. Ed. 43*, 3928–3932.

(31) Helms, B., Mynar, J. L., Hawker, C. J., and Frechet, J. M. J. (2004) Dendronized linear polymers via "click chemistry. *J. Am. Chem. Soc. 126*, 15020–15021.

(32) Parrish, B., and Emrick, T. (2007) Soluble camptothecin derivatives prepared by click cycloaddition chemistry on functional aliphatic polyesters. *Bioconjugate Chem. 18*, 263–267.

(33) Binder, W. H., and Sachsenhofer, R. (2007) 'Click' chemistry in polymer and materials science. *Macromol. Rapid Commun. 28*, 15–54.

(34) Meldal, M., and Tornoe, C. W. (2008) Cu-catalyzed azide-alkyne cycloaddition. *Chem. Rev. 108*, 2952–3015.

(35) Gao, H. F., and Matyjaszewski, K. (2006) Synthesis of star polymers by a combination of ATRP and the "click" coupling method. *Macromolecules 39*, 4960–4965.

(36) Ladmiral, V., Mantovani, G., Clarkson, G. J., Cauet, S., Irwin, J. L., and Haddleton, D. M. (2006) Synthesis of neoglycopolymers by a combination of "click chemistry" and living radical polymerization. *J. Am. Chem. Soc. 128*, 4823–4830.

(37) Wall, M. E., Wani, M. C., Cook, C. E., Palmer, K. H., McPhail, A. T., and Sim, G. A. (1966) Plant antitumor agents. I. The isolation and structure of camptothecin, a novel alkaloidal leukemia and tumor inhibitor from *Camptotheca acuminata*. *J. Am. Chem. Soc. 88*, 3888–3890.

(38) Slichenmyer, W. J., Rowinsky, E. K., Donehower, R. C., and Kaufmann, S. H. (1993) The current status of camptothecin analogues as antitumor agents. *J. Natl. Cancer Inst. 85*, 271–291.

(39) Muggia, F. M., Dimery, I., and Arbuck, S. G. (1996) In *Conference on the Camptothecins - From Discovery to the Patient* (Pantazis, P., Giovanella, B. C., and Rothenberg, M. L., Eds.) pp 213−223, New York Academy Sciences, Bethesda, MD.

(40) Herben, V. M. M., Huinink, W., and Beijnen, J. H. (1996) Clinical pharmacokinetics of topotecan. *Clin. Pharmacokinet. 31*, 85–102.

(41) Mathijssen, R. H. J., van Alphen, R. J., Verweij, J., Loos, W. J., Nooter, K., Stoter, G., and Sparreboom, A. (2001) Clinical pharmacokinetics and metabolism of irinotecan (CPT-11). *Clin. Cancer Res. 7*, 2182–2194.

(42) Zhao, H., Lee, C., Sai, P. K., Choe, Y. H., Boro, M., Pendri, A., Guan, S. Y., and Greenwald, R. B. (2000) 20-O-acylcamptothecin derivatives: Evidence for lactone stabilization. *J. Org. Chem. 65*, 4601–4606.

(43) Greenwald, R. B., Pendri, A., Conover, C., Gilbert, C., Yang, R., and Xia, J. (1996) Drug delivery systems 0.2. Camptothecin 20-O-poly(ethylene glycol)ester transport forms. *J. Med. Chem. 39*, 1938–1940.

(44) Zamai, M., vandeVen, M., Farao, M., Gratton, E., Ghiglieri, A., Castelli, M. G., Fontana, E., d'Argy, R., Fiorino, A., Pesenti, E., Suarato, A., and Caiolfa, V. R. (2003) Camptothecin poly[N-(2-hydroxypropyl) methacrylamide] copolymers in antitopoisomerase-1 tumor therapy: Intratumor release and antitumor efficacy. *Mol. Cancer Ther. 2*, 29–40.

(45) Caiolfa, V. R., Zamai, M., Fiorino, A., Frigerio, E., Pellizzoni, C., d'Argy, R., Ghiglieri, A., Castelli, M. G., Farao, M., Pesenti, E., Gigli, M., Angelucci, F., and Suarato, A. (2000) Polymer-bound camptothecin: initial biodistribution and antitumour activity studies. *J. Controlled Release 65*, 105–119.

(46) Singer, J. W., Bhatt, R., Tulinsky, J., Buhler, K. R., Heasley, E., Klein, P., and de Vries, P. (2001) Water-soluble poly-(L-glutamic acid)-Gly-camptothecin conjugates enhance camptothecin stability and efficacy in vivo. *J. Controlled Release 74*, 243–247.

(47) Zou, Y. Y., Wu, Q. P., Tansey, W., Chow, D., Hung, M. C., Vej, C. C., Wallace, S., and Li, C. (2001) Effectiveness of water soluble poly(L-glutamic acid)camptothecin conjugate against resistant human lung cancer xenografted in nude mice. *Int. J. Oncol. 18*, 331–336.

(48) Bhatt, R. L., de Vries, P., Tulinsky, J., Bellamy, G., Baker, B., Singer, J. W., and Klein, P. (2003) Synthesis and in vivo antitumor activity of poly(L-glutamic acid) conjugates of 20(S)-camptothecin. *J. Med. Chem. 46*, 190–193.

(49) Cheng, J. J., Khin, K. T., Jensen, G. S., Liu, A. J., and Davis, M. E. (2003) Synthesis of linear, beta-cyclodextrin-based polymers and their camptothecin conjugates. *Bioconjugate Chem. 14*, 1007–1017.

(50) Cheng, J., Khin, K. T., and Davis, M. E. (2004) Antitumor activity of beta-cyclodextrin polymer - Camptothecin conjugates. *Mol. Pharmacol. 1*, 183–193.
(51) Li, Y. T., Tang, Y. Q., Narain, R., Lewis, A. L., and Armes, S. P. (2005) Biomimetic stimulus-responsive star diblock gelators. *Langmuir 21*, 9946–9954.
(52) Adams, D. J., and Young, I. (2008) Oligopeptide-based amide functional initiators for ATRP. *J. Polym. Sci., Polym. Chem. 46*, 6082–6090.
(53) Ito, H., Arimoto, K., Sensui, H., and Hosomi, A. (1997) Direct alkynyl group transfer from silicon to copper: New preparation method of alkynylcopper (I) reagents. *Tetrahedron Lett. 38*, 3977–3980.
(54) Zhao, H., Rubio, B., Sapra, P., Wu, D. C., Reddy, P., Sai, P., Martinez, A., Gao, Y., Lozanguiez, Y., Longley, C., Greenberger, L. M., and Horak, I. D. (2008) Novel prodrugs of SN38 using multiarm poly(ethylene glycol) linkers. *Bioconjugate Chem. 19*, 849–859.
(55) Chen, M., Briscoe, W. H., Armes, S. P., and Klein, J. (2009) Lubrication at physiological pressures by polyzwitterionic brushes. *Science 323*, 1698–1701.
(56) Geng, J., Lindqvist, J., Mantovani, G., and Haddleton, D. M. (2008) Simultaneous copper(I)-catalyzed azide-alkyne cycloaddition (CuAAC) and living radical polymerization. *Angew. Chem., Int. Ed. 47*, 4180–4183.
(57) Ishihara, K., Ueda, T., and Nakabayashi, N. (1990) Preparation of phospholipid polymers and their properties as polymer hydrogel membranes. *Polym. J. 22*, 355–360.

BC900339X

Polymeric phosphorylcholine-camptothecin conjugates prepared by controlled free radical polymerization and click chemistry

Xiangji Chen, Samantha McRae, Sangram Parelkar, and Todd Emrick[*]

Polymer Science & Engineering Department, 120 Governors Drive

University of Massachusetts, Amherst, Massachusetts 01003

Supporting Information

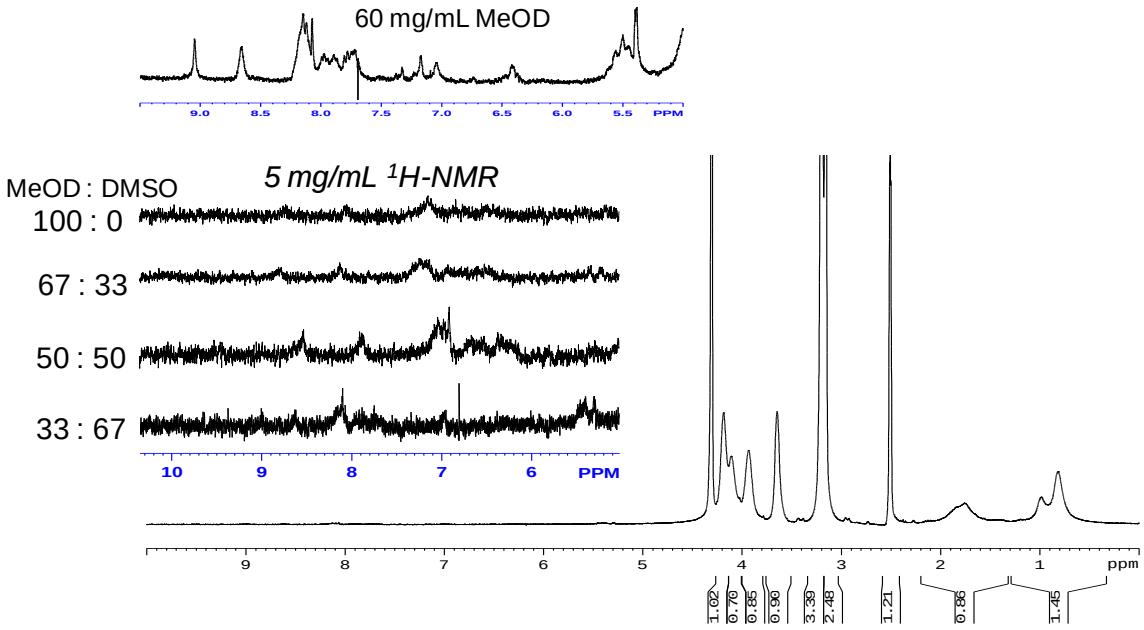

Figure S1. ^{1}H NMR spectra of CPT-polyMPC in CD_3OD.

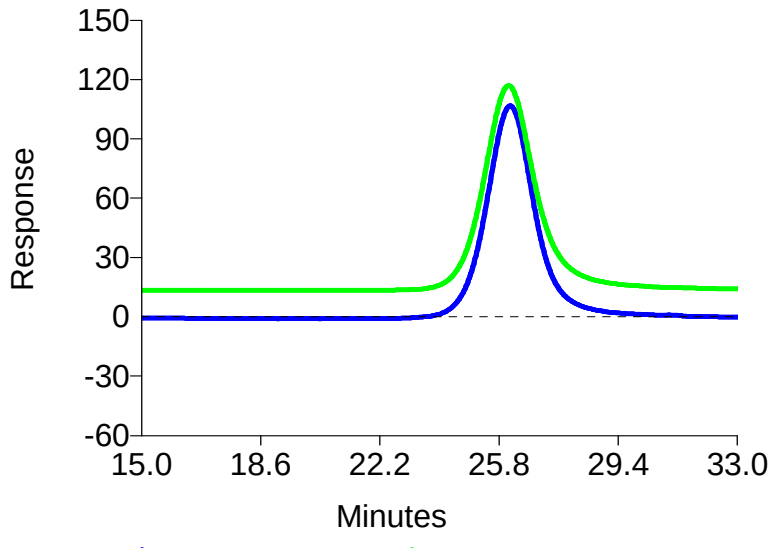

Figure S2. Aqueous GPC traces of pMPC-*graft*-CPT (**P9**) with UV and IR channels.

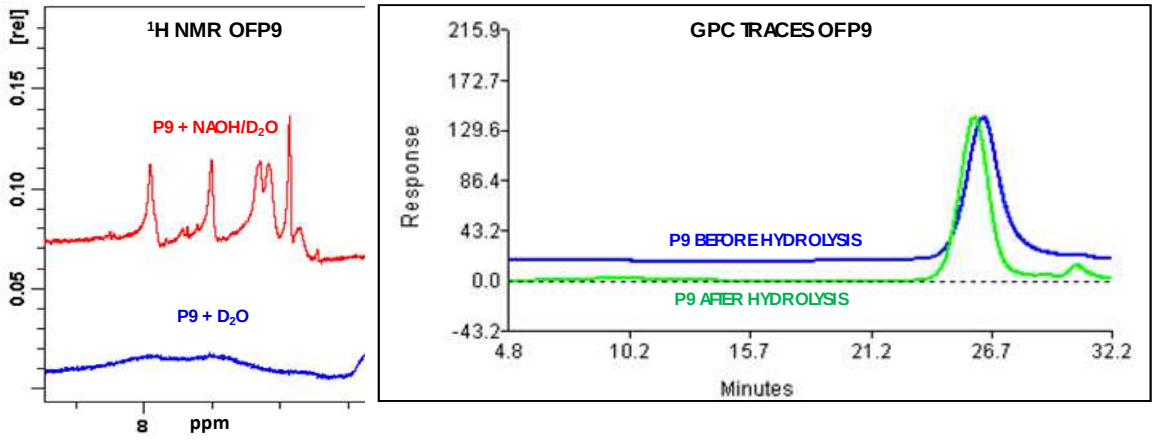

Figure S3. ^{1}H NMR spectra and GPC traces of CP3 in D_2O before and after the CPTs were cleaved from polymer.

An Engineered Knottin Peptide Labeled with ^{18}F for PET Imaging of Integrin Expression

Zheng Miao,[†,‡,§] Gang Ren,[†,‡,§] Hongguang Liu,[†,‡,§] Richard H. Kimura,[†,‡,||] Lei Jiang,[†,‡,§] Jennifer R. Cochran,[†,‡,||] Sanjiv Sam Gambhir,[†,‡,§,||] and Zhen Cheng*[,†,‡,§]

Molecular Imaging Program at Stanford (MIPS), Bio-X Program, and Departments of Radiology and Bioengineering, Stanford University, Stanford California, 94305. Received August 12, 2009; Revised Manuscript Received September 30, 2009

Knottins are small constrained polypeptides that share a common disulfide-bonded framework and a triple-stranded β-sheet fold. Previously, directed evolution of the *Ecballium elaterium* trypsin inhibitor (EETI-II) knottin led to the identification of a mutant that bound to tumor-specific $\alpha_v\beta_3$ and $\alpha_v\beta_5$ integrin receptors with low nanomolar affinity. The objective of this study was to prepare and evaluate a radiofluorinated version of this knottin (termed 2.5D) for microPET imaging of integrin positive tumors in living subjects. Knottin peptide 2.5D was prepared by solid-phase synthesis and folded *in vitro*, and its free N-terminal amine was reacted with *N*-succinimidyl-4-$^{18/19}$F-fluorobenzoate ($^{18/19}$F-SFB) to produce the fluorinated peptide $^{18/19}$F-FB-2.5D. The binding affinities of unlabeled knottin peptide 2.5D and ^{19}F-FB-2.5D to U87MG glioblastoma cells were measured by competition binding assay using ^{125}I-labeled echistatin. It was found that unlabeled 2.5D and ^{19}F-FB-2.5D competed with ^{125}I-echistatin for binding to cell surface integrins with IC_{50} values of 20.3 ± 7.3 and 13.2 ± 5.4 nM, respectively. Radiosynthesis of ^{18}F-FB-2.5D resulted in a product with high specific activity (ca. 100 GBq/μmol). Next, biodistribution and positron emission tomography (PET) imaging studies were performed to evaluate the *in vivo* behavior of ^{18}F-FB-2.5D. Approximately 3.7 MBq ^{18}F-FB-2.5D was injected into U87MG tumor-bearing mice via the tail vein. Biodistribution studies demonstrated that ^{18}F-FB-2.5D had moderate tumor uptake at 0.5 h post injection, and coinjection of a large excess of the unlabeled peptidomimetic c(RGDyK) as a blocking agent significantly reduced tumor uptake (1.90 ± 1.15 vs 0.57 ± 0.14%ID/g, 70% inhibition, $P < 0.05$). *In vivo* microPET imaging showed that ^{18}F-FB-2.5D rapidly accumulated in the tumor and quickly cleared from the blood through the kidneys, allowing excellent tumor-to-normal tissue contrast to be obtained. Collectively, ^{18}F-FB-2.5D allows integrin-specific PET imaging of U87MG tumors with good contrast and further demonstrates that knottins are excellent peptide scaffolds for development of PET probes with potential for clinical translation.

INTRODUCTION

Recent advancement in *in vitro* display technologies (phage, bacterial, yeast, ribosome, and mRNA) and rational protein engineering has resulted in many novel peptide scaffolds that bind to a variety of molecular targets (*1*−*5*). Following the discovery of these new affinity ligands came their adaptation for use in cancer imaging applications (*6*, *7*). These small polypeptides can easily be produced by chemical approaches such as solid-phase peptide synthesis or generated recombinantly using the tools of molecular biology. Moreover, the small size of these polypeptides generally leads to fast tumor targeting and relatively short *in vivo* half-life compared with monoclonal antibodies. Collectively, these properties bode well for nuclear imaging applications with potential for clinical translation.

Cystine knot proteins (also known as knottins) are small constrained polypeptides that share a common disulfide-bonded framework and a triple-stranded β-sheet fold (Figure 1A) (*8*). Indeed, the scaffold's core structure is very rigid. In general, this class of polypeptides is relatively stable in various physical, chemical, and biological environments. Individual family members share little sequence homology except the core cysteine residues. Knottin family members possess one or more surface-exposed loops that tolerate much sequence diversity. These looped regions are responsible for a range of biological activities (*9*, *10*). However, in most cases, their natural functions remain unknown.

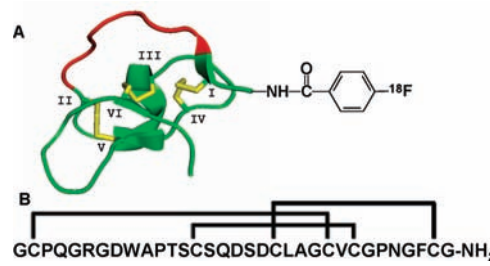

Figure 1. Schematic and sequence of engineered knottin peptides. (A) Cartoon representation of knottin peptide scaffold. The imaging label ^{18}F-FB was site-specifically conjugated to the N terminal amino group. (B) Amino acid sequence integrin-binding knottin peptide 2.5D with disulfide bonds between Cys1-Cys4, Cys2-Cy5, and Cys3-Cys6.

Previously, the *Ecballium elaterium* trypsin inhibitor II (EETI-II), a knottin from the squash family of protease inhibitors, was used as a scaffold for directed evolution studies (*11*). An Arg-Gly-Asp (RGD) integrin binding motif was grafted into a surface-exposed loop, where yeast surface display combined FACS led to the identification of peptides including 2.5D that bound integrin receptors ($\alpha_v\beta_3$, $\alpha_v\beta_5$, and $\alpha_5\beta_1$) with low

* Correspondence should be sent to: Zhen Cheng, Ph.D, Molecular Imaging Program at Stanford, Department of Radiology and Bio-X Program, 1201 Welch Road, Lucas Expansion, P020A, Stanford University, Stanford, CA 94305, 650-723-7866 (V), 650-736-7925(Fax), E-mail: zcheng@stanford.edu.

† MIPS.

‡ Bio-X Program.

§ Department of Radiology.

|| Department of Bioengineering.

10.1021/bc900361g CCC: $40.75 © 2009 American Chemical Society
Published on Web 11/12/2009

nanomolar affinities (Figure 1). Near infrared-dye Cy5.5- and ^{64}Cu-DOTA-conjugated knottin peptides were then synthesized and evaluated in mouse xenograft models (*12*). Biodistribution and micropositron emission tomography (microPET) imaging studies revealed that these engineered knottin peptides performed well *in vivo* and show promise as a new class imaging agent. These peptides demonstrated rapid and high tumor accumulation, fast clearance from blood and normal organs, and low uptake in the kidney and liver (*12*).

^{18}F is the most commonly used PET[a] radionuclide and has almost ideal physical properties ($t_{1/2}$: 110 min, emits $\beta+$ particles at E_{max} = 635 keV and E_{ave} = 250 keV, 97% abundant) for PET imaging. In this study, to further evaluate the clinical translation ability of engineered knottins, peptide 2.5D was site-specifically labeled with ^{18}F by conjugation with the radiofluorination synthon, *N*-succinimidyl-4-^{18}F-fluorobenzoate (^{18}F-SFB), through the peptide N-terminus amine (Figure 1). ^{18}F-FB-2.5D was then evaluated in nude mice bearing subcutaneous U87MG xenografts characterized by high levels of integrin expression (*13*).

EXPERIMENTAL PROCEDURES

General. SFB was obtained from ABX GmbH (Radeberg, Germany). All 9-fluorenylmethyloxycarbonyl (Fmoc) protected amino acids were purchased from Novabiochem/EMD Chemicals Inc. (La Jolla, CA) or CS Bio (Menlo Park, CA). ^{125}I-labeled echistatin and c(RGDyK) were purchased from GE Healthcare Life Sciences (Piscataway, NJ), and Peptides International (Louisville, KY), respectively. Phosphate buffered saline (PBS) was from Gibco/Invitrogen (Carlsbad, CA). Echistatin and *N*,*N*′-diisopropylethylamine (DIPEA) were purchased from Sigma-Aldrich Chemical Co. (St. Louis, MO). All other chemicals were purchased from Thermo Fisher Scientific (Fair Lawn, NJ) unless otherwise specified. The U87MG human glioblastoma cell line was obtained from American Type Culture Collection (Manassas, VA). Nude mice (nu/nu, female 5−6 weeks old) were purchased from Charles River Laboratory (Wilmington, MA). A CRC-15R PET dose calibrator (Capintec Inc., Ramsey, NJ) was used for all radioactivity measurements. Reverse-phase high-performance liquid chromatography (RP-HPLC) was performed on a Dionex Summit HPLC system (Dionex Corporation, Sunnyvale, CA) equipped with a 170U 4-Channel UV−vis absorbance detector and radioactivity detector (Carroll & Ramsey Associates, model 105S, Berkeley, CA). UV detection wavelengths were 218, 254, and 280 nm for all the experiments. Both semipreparative (Vydac, Hesperia, CA. 218TP510-C18, 10 mm × 250 mm) and analytical (Dionex, Sunnyvale, CA. Acclaim120 C18, 4.6 mm × 250 mm) RP-HPLC columns were used. The mobile phase was solvent A, 0.1% trifluoroacetic acid (TFA)/H_2O, and solvent B, 0.1%TFA/acetonitrile. Matrix-assisted laser desorption/ionization time-of-flight mass spectrometry (MALDI-TOF-MS) were performed on a Perseptive Voyager-DE RP Biospectrometry instrument (Framingham, MA) by the Stanford Protein and Nucleic Acid Biotechnology Facility (Stanford, CA).

Chemistry and Radiochemistry. Peptide 2.5D was synthesized on a CS Bio CS336 instrument (Menlo Park, CA) using Fmoc-based solid-phase peptide synthesis method. Briefly, Rink amide resin was swollen in *N*,*N*-dimethylformamide (DMF) for 30 min. Fmoc groups were removed with 20% piperidine in DMF. Aliquots of amino acids (1 mmol) were activated in a solution containing 1 mmol of hydroxybenzotriazole (HOBt) and 0.5 M diisopropylcarbodiimide (DIC) in DMF. Following synthesis, side-chain deprotection and resin cleavage was achieved by addition of a 94:2.5:2.5:1 (v/v) mixture of trifluoroacetic acid (TFA)/trimethylsilane/ethanedithiol/water for 2 h at room temperature. The crude product was precipitated with cold anhydrous diethyl ether and purified by a preparative or semipreparative RP-HPLC using a Varian Prostar instrument and Vydac C_{18} columns. Peptide purity was analyzed by analytical-scale RP-HPLC using a Vydac C_{18} column.

Folding reactions were performed by incubating the linear peptide with 2.5 mM reduced glutathione and 20% dimethyl sulfoxide (DMSO) in 0.1 M ammonium bicarbonate, pH 9, with gentle rocking. The final oxidized product was purified by RP-HPLC as described above; the folded knottin peptide exhibited a distinct chromatographic profile that allowed it to be separated from unfolded and misfolded isomers (*11*). Following purification, folded peptide 2.5D was lyophilized and stored at room temperature until use. Purified peptide was dissolved in water, and concentration was determined by amino acid analysis (Molecular Structure Facility, Davis, CA). Peptide purity and molecular mass were determined by analytical-scale RP-HPLC and MALDI-TOF-MS or ESI-MS.

Nonradioactive ^{19}F-FB-2.5D, a reference standard, was prepared by reaction of knottin peptide 2.5D with SFB. Briefly, 0.15 μmol of knottin peptide 2.5D (0.5 mg in 400 μL of DMSO) was mixed with 1.5 μmol of SFB (0.36 mg in 100 μL of DMSO) and 30 μL of DIPEA and reacted for 1 h at 60 °C. The resulting conjugate ^{19}F-FB-2.5D was then purified by RP-HPLC on a semipreparative C_{18} column using a gradient system of 0.1% trifluoroacetic acid in acetonitrile (solvent B) and 0.1% trifluoroacetic acid in water (solvent A). The flow rate was 3 mL/min, with the mobile phase starting from 90% solvent A and 10% solvent B (0−3 min) to 35% solvent A and 65% solvent B at 33 min. Fractions containing the product were collected and lyophilized. The identity of ^{19}F-FB-2.5D was confirmed by MALDI-TOF-MS.

^{18}F-SFB was prepared on the basis of a previously reported procedure (*14*). The specific activity of ^{18}F-SFB was 200−250 GBq/μmol at the end of synthesis (EOS), as estimated by radio-HPLC. Radiolabeling agent ^{18}F-SFB in 100 μL of DMSO was added to knottin peptide 2.5D (100 μg, in 100 μL of DMSO) and 10 μL of DIPEA and reacted for 1 h at 60 °C. After adding 50 μL of TFA to quench the reaction, the mixture was purified with semipreparative HPLC, using the same elution gradient as for the cold ^{19}F-FB-2.5D purification. The eluted fractions containing the ^{18}F-FB-2.5D were then collected, combined, and dried using a rotary evaporator. The radiolabeled peptide was reconstituted in PBS (0.01 M, pH 7.4) and passed through a 0.22 μm Millipore filter into a sterile vial for cell culture and animal experiments.

Octanol/Water Partition Coefficient. To determine the hydrophilicity of ^{18}F-FB-2.5D, approximately 370 kBq of the probe in 500 μL of PBS (0.01 M, pH 7.4) was added to 500 μL of octanol in a microcentrifuge tube. The resulting biphasic system was mixed vigorously for 0.5 h and left at room temperature for another 0.5 h. The two phases were then separated by centrifugation at 3000 *g* for 5 min (model 5415R Eppendorf microcentrifuge; Brinkman, Westbury, NY). An aliquot of 100 μL was removed from each layer and analyzed in a γ-counter (model 1470; PerkinElmer). The partition coefficient (log *P*) was then calculated as a ratio of counts in the octanol fraction to the counts in the water fraction. The experiment was repeated three times.

Cell Culture. U87MG cells were cultured in DMEM containing high glucose (Gibco, Carlsbad, CA), which was supplemented with 10% fetal bovine serum (FBS) and 1% penicillin−streptomycin. The cells were expanded in tissue culture dishes and kept in a humidified atmosphere of 5% CO_2 at 37 °C. The media was changed every other day. A confluent

[a]Abbreviations: PET, positron emission tomography; HPLC, high-performance liquid chromatography; pi, postinjection.

monolayer was detached with 0.5% Trypsin−EDTA and 0.01 M PBS (pH 7.4) and dissociated into a single-cell suspension for further cell culture and assays.

U87MG Cell Binding Assay. This assay was performed as previously described (*11, 12*). Briefly, 2×10^5 U87MG cells were incubated with 0.06 nM ^{125}I-labeled echistatin and varying concentrations of compounds (echistatin, knottin 2.5D, ^{19}F-FB-2.5D) in integrin binding buffer [IBB, 25 mM Tris pH 7.4, 150 mM NaCl, 2 mM $CaCl_2$, 1 mM $MgCl_2$, 1 mM $MnCl_2$, and 0.1% bovine serum albumin (BSA)] at room temperature for 3 h. The cell-bound radioactivity remaining after washing was determined by gamma-counting. IC_{50} values, the concentration of competitor required to inhibit 50% of the radioligand binding, were determined by nonlinear regression analysis using Kaleidagraph (Synergy Software, Reading, PA), and are presented as the average of three experiments performed.

Animal Biodistribution Studies. All animal studies were carried out in compliance with federal and local institutional rules for the conduct of animal experimentation. Approximately 10×10^6 cultured U87MG cells were suspended in PBS and subcutaneously implanted in the left shoulders of nude mice. Tumors were allowed to grow to a size of 0.5 cm (2−3 weeks) before imaging experiments. For biodistribution studies, mice bearing U87MG xenografts ($n = 3$ for each group) were injected with approximately 740 KBq (20 μCi) of ^{18}F-FB-2.5D with or without 330 μg of unlabeled c(RGDyK) via the tail vein and sacrificed at 0.5 h post injection (p.i.). Tumor and normal tissues of interest were removed and weighed, and their radioactivity was measured in a gamma counter. The radioactivity uptake in the tumor and normal tissues was expressed as a percentage of the injected radioactive dose per gram of tissue (% ID/g).

MicroPET Imaging. Mice bearing U87MG xenografts were injected with approximately 4.44 MBq (120 μCi) of ^{18}F-FB-2.5D with or without 330 μg of c(RGDyK) via the tail vein and PET imaging was performed using a microPET R4 rodent model scanner (Siemens Medical Solutions USA, Inc., Knoxville, TN). At 0.5 and 1 h p.i., mice were anesthetized with isoflurane (5% for induction and 2% for maintenance in 100% O_2). With the help of a laser beam attached to the scanner, mice were placed in the prone position and near the center of the field of view of the scanner, and 3 min static scans were obtained. For dynamic scanning, approximately 3.7MBq (100 μCi) of ^{18}F-FB-2.5D was injected into U87MG tumor-bearing mice via the tail vein, and a 35 min duration dynamic scan (10×1 min, 10×2 min, 1×5 min; total of 21 frames) was started approximately 2.5 min after injection of the probe. Images were reconstructed by a two-dimensional ordered subsets expectation maximization (OSEM) algorithm. No background correction was performed. Region of interests (ROIs; 5 pixels for coronal and transaxial slices) were drawn over the tumor on decay-corrected whole-body coronal images. The maximum counts per pixel per minute were obtained from the ROIs and were converted to counts per milliliter per minute using a calibration constant. ROIs were then converted to counts per gram per minute based on the assumption of a tissue density of 1 g/mL, and image ROI-derived %ID/g values were determined by dividing counts per gram per minute by injected dose. No attenuation correction was performed.

Statistical Method. Statistical analysis was performed using the Student's *t*-test for unpaired data. A 95% confidence level was chosen to determine the significance between groups, with $P < 0.05$ being designated as significantly different.

RESULTS

Chemistry and Radiochemistry. Knottin peptide 2.5D was synthesized in two steps. First, the linear peptide was prepared by conventional solid-phase peptide synthesis and purified by RP-HPLC. Next, the peptide was oxidatively folded using a mixture of glutathione and DMSO, and the final oxidized product was purified by semipreparative reversed-phase HPLC (*11*).The folded peptide was obtained in ~10% yield with >95% purity. Reaction of SFB with the N-terminal amine of knottin peptide 2.5D generated ^{19}F-FB-2.5D, a nonradioactive species, as a reference compound for cell binding affinity studies. For all knottin peptides prepared above, the measured molecular weights were consistent with the expected masses: 2.5D linear peptide, $m/z = 3249.6$ Da for $[M+H]^+$ (calculated $[M+H]^+ = 3249.6$ Da); 2.5D folded peptide, $m/z = 3243.8$ Da for $[M+H]^+$ (calculated $[M+H]^+ = 3243.6$ Da); ^{19}F-FB-2.5D, $m/z = 3365.7$ Da for $[M+H]^+$ (calculated $[M+H]^+ = 3365.7$ Da).

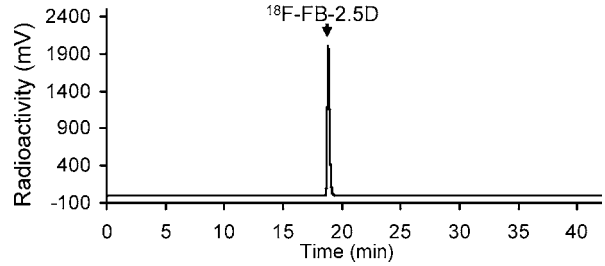

Figure 2. HPLC radiochromatogram of purified ^{18}F-FB-2.5D.

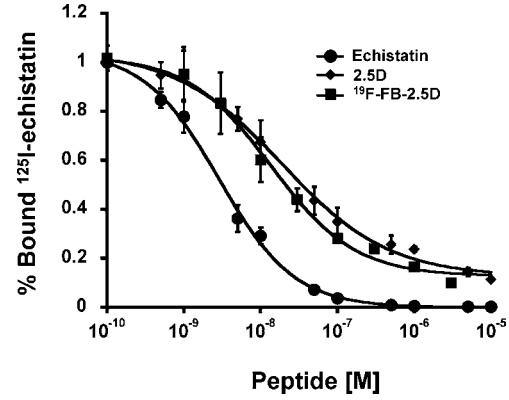

Figure 3. Inhibition of ^{125}I-echistatin binding to integrin receptors on U87MG cells by 2.5D, ^{19}F-FB-2.5D, and echistatin [$IC_{50} = 20.3 \pm 7.3$ (♦), 13.2 ± 5.4 (■) and 3.7 ± 1.1 (•) nM, respectively). Results are expressed as the percentage of ^{125}I-echistatin binding and are the mean of triplicate measurements ± SD.

Similarly, ^{18}F-FB-2.5D was synthesized by coupling knottin peptide 2.5D with radiosynton ^{18}F-SFB. Radiolabeled ^{18}F-FB-2.5D, which had a retention time of 20.2 min, was easy to differentiate by RP-HPLC compared to unlabeled knottin peptide 2.5D, which had a retention time of 16.9 min. Radiosynthesis and purification of ^{18}F-FB-2.5D was completed in approximately 3 h, which is important for experimental use due to the short half-life of ^{18}F. The maximum overall radiochemical yield with decay correction was 28.3% at EOS. The radiochemical purity of the labeled peptide was over 95% as verified by analytic HPLC analysis (Figure 2). An octanol/water distribution study performed on ^{18}F-FB-2.5D showed good hydrophilicity with a partition coefficient number (log *P*) of −1.68.

U87MG Cell Binding Assay. The relative binding affinities of 2.5D and ^{19}F-FB-2.5D to cell surface integrin receptors were determined through a competition binding assay with ^{125}I-echistatin. Echistatin, a snake venom protein that binds to $\alpha_v\beta_3$ integrin with $K_D \sim 0.3$ nM, was also used as the positive control (*15*). Both knottin peptides inhibited the binding of ^{125}I-echistatin to integrin-expressing U87MG cells in a concentration-dependent manner (Figure 3). The mean ± standard deviation IC_{50} values of 2.5D, ^{19}F-FB-2.5D, and echistatin were 20.3 ± 7.3

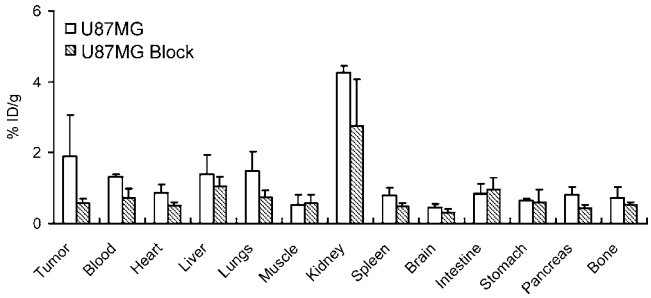

Figure 4. Biodistribution data for ^{18}F-FB-2.5D in nude mice bearing subcutaneous U87MG human tumor xenografts. Data are expressed as the percentage administered activity (injected dose) per gram of tissue (%ID/g) after intravenous injection of 370 kBq (10 μCi) ^{18}F-FB-2.5D at 0.5 h p.i. with or without coinjection of 330 μg of c(RGDyK) (n = 3 for each group). Significant inhibition of U87MG tumor uptake (P < 0.05) was observed upon co-injection of this blocking agent.

nM, 13.2 ± 5.4 nM, and 3.7 ± 1.1 nM, respectively. These studies indicate that conjugation of fluorobenzoic acid moiety to the N-terminus of knottin peptide 2.5D does not reduce its integrin binding affinity.

Biodistribution Studies. The *in vivo* biodistribution of ^{18}F-FB-2.5D was next performed in mice bearing U87MG human glioblastoma xenografts 0.5 h p.i. (Figure 4). Radiolabeled ^{18}F-FB-2.5D displayed moderate accumulation in U87MG tumors (1.90 ± 1.15%ID/g at 0.5 h p.i.). Kidney and liver uptake were 4.24 ± 0.19 and 1.38 ± 0.55%ID/g, respectively. Lower levels of radioactivity were observed in blood (1.32 ± 0.07%ID/g) and the most other organs. To measure integrin specificity, ^{18}F-FB-2.5D was coinjected with an excess (330 μg) of the unlabeled c(RGDyK) to block integrin binding sites. Co-injection of c(RGDyK) specifically reduced the tumor uptake of ^{18}F-FB-2.5D to 0.57 ± 0.14%ID/g (70% inhibition, P < 0.05), without changing the distribution of the probe in most normal tissues studied.

MicroPET Imaging. The *in vivo* tumor targeting profile of ^{18}F-FB-2.5D was further investigated in U87MG tumor-bearing nude mice by dynamic microPET scanning over a 35 min time period. As shown in Figure 5A, ^{18}F-FB-2.5D rapidly accumulated in the tumor and reached a maximum of 3.5%ID/g at 5 min p.i. and gradually decreased to 1.73%ID/g over the duration of the 35 min scan. The scan revealed relatively low radioactivity in the muscle. Lung uptake was high at early time points and rapidly washed out to 1.09%ID/g at 35 min p.i. Rapid blood clearance of the probe was determined by ROI analysis of the heart. At 35 min p.i., radioactivity in the blood was approximately 9.2% of the amount observed at 3 min p.i. (Figure 5B). High kidney uptake was observed at early time points (for example, 51.8%ID/g at 4 min p.i.), but this activity rapidly cleared out and dropped to 6.2%ID/g at 35 min p.i. ^{18}F-FB-2.5D displayed relatively low liver uptake, in agreement with previous data on knottin peptides (*12*). Collectively, these data indicate that ^{18}F-FB-2.5D was mainly cleared through the renal system.

Representative decay-corrected coronal (top) and transaxial (bottom) microPET images of nude mice bearing U87MG tumors on their left shoulder at 0.5 and 1 h after tail vein injection of 4.44 MBq (120 μCi) of ^{18}F-FB-2.5D are shown in Figure 6. The U87MG tumor was clearly delineated with good tumor to contralateral background contrast at 0.5 and 1 h p.i. (left and right images in Figure 6). Moreover, coinjection of an excess of c(RGDyK) peptide reduced the tumor uptake of ^{18}F-FB-2.5D, resulting in lower tumor to background contrast at 0.5 h (middle images in Figure 6). Finally, relatively high activities were observed in the bladder and gallbladder. Quantitative analyses were performed on microPET images (Figure 7). Tumor uptake values were determined to be 2.60 ± 0.72%ID/g at 0.5 h p.i., and decreased to 1.46 ± 0.35%ID/g at 1 h p.i. Co-injection of c(RGDyK) significantly blocked uptake of the radiotracer in the tumor to 0.61 ± 0.14%ID/g (P < 0.05) at 0.5 h p.i., which agreed well with biodistribution results.

DISCUSSION

Novel nonimmunogenic scaffold-based polypeptides have drawn a lot of attention for the development of molecular imaging probes because of easy synthesis, site-specific labeling, stable structure, and high versatility targeting various cancer biomarkers. In our recent work, an antihuman epidermal growth factor receptor type 2 (HER2) Affibody molecule, engineered from one IgG binding domain of protein A and ~1/20 size of an antibody, was site-specifically labeled with ^{18}F. The resulting probe demonstrated great potential for PET imaging of the expression of HER2 in the clinic (*16*). HER2 Affibody molecules have also been labeled with many other radioisotopes and organic dyes for preclinical and clinical imaging (*17*−*19*). These progressions in scaffold protein based molecular probe development have motivated us to explore other scaffold protein as molecular platforms targeting different biomarkers.

The cystine knot miniprotein family represents a unique peptide scaffold of ~3 kDa with three interwoven disulfide bridges. Engineered knottin peptides, such as the integrin-binding peptide 2.5D, have been identified, and their potential for *in vivo* integrin molecular imaging has recently been evaluated as a ^{64}Cu-labeled PET tracer (*12*). Preliminary evaluation of ^{64}Cu-labeled knottin peptides showed excellent tumor imaging properties in living mice. To facilitate the translation of knottin peptides as clinical imaging agents, we next tested an ^{18}F-labeled version of knottin peptide 2.5D in tumor-bearing mouse models in this research. With these studies, we wanted to determine whether there are any advantages and disadvantages of using knottin scaffolds as imaging agents, as well as to further enrich our understanding of the *in vivo* behavior of knottin peptides when they are coupled with different radionuclides.

In this research, ^{18}F-SFB was used as a prosthetic group for site-specifically labeling knottin 2.5D (Figure 1). Methods to couple ^{18}F-SFB have been well-established in our program (*14*). The nonradioactive version, ^{19}F-FB-2.5D, competes with ^{125}I-echistatin for binding cell surface integrins with an IC_{50} of 13.2 ± 5.4 nM, which is similar to that of the unmodified knottin peptide 2.5D (20.3 ± 7.3 nM). These data suggest that the N-terminal amine of the knottin peptide tolerates modification, and further *in vivo* evaluation of its radioactive counterpart confirmed this finding. Radiofluorination of 2.5D was efficiently achieved through site-specific conjugation of the radiosynthon, ^{18}F-SFB, with the N-terminal amino group under mild conditions (60 °C, 1 h). ^{18}F-FB-2.5D was prepared in a reasonable yield (final yield, 28.3%) and high specific activity (~100 GBq/μmol) at EOS, which boded well for clinical applications.

Considering the short physical half-life of ^{18}F as well as short biological blood half-life of the knottin peptide, our biodistribution and imaging data of ^{18}F-FB-2.5D were acquired in a relatively short time frame (up to 1 h p.i.). Consistent with our expectation, we observed good tumor uptake resulting in good image quality. These data are attributable to the peptide's tumor targeting ability and rapid clearance from normal tissues (Figure 4). As early as 0.5 h p.i., probe uptake in the tumor was 1.90 ± 1.15%ID/g. Liver uptake remained low at around 1.4 ± 0.5%ID/g at 0.5 h, which was similar compared with its ^{64}Cu labeled knottin counterpart (2.3 ± 0.8%ID/g) (*12*). Overall, microPET imaging data correlated well with the data derived from biodistribution studies. The U87MG tumor is clearly delineated from normal tissue at both 0.5 and 1 h p.i..

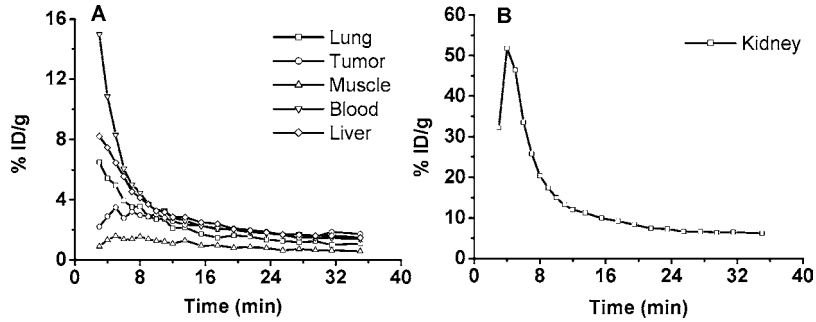

Figure 5. Time activity curves of major organs derived from a microPET dynamic scan of a mouse bearing U87MG tumors, after intravenous injection of ~3.7MBq (~100 μCi) ^{18}F-FB-2.5D.

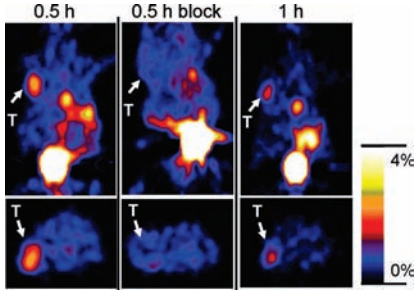

Figure 6. Decay corrected coronal (top) and transaxial (bottom) microPET images of nude mice bearing U87MG tumors (unit: %ID/g). Images were acquired 0.5 and 1 h after tail vein injection of 4.44 MBq (120 μCi) of ^{18}F-FB-2.5D with or without coinjection of 330 μg of c(RGDyK) ($n = 3$ for each group). Arrows indicate the location of tumors (T). Gallbladder and bladder can also be clearly seen.

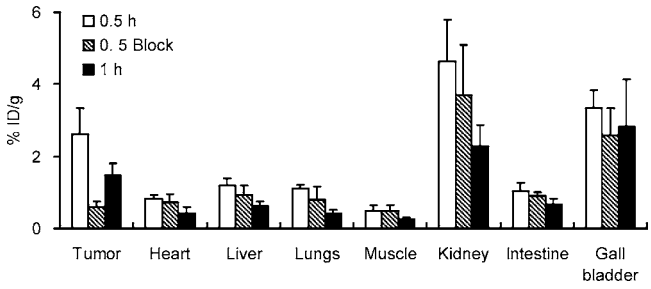

Figure 7. PET imaging quantification of intravenously injected ^{18}F-FB-2.5D measured by using ROI analysis of static small-animal PET data sets in nude mice bearing U87MG tumors ($n = 3$).

Quantification of microPET images showed that 56% of the activity remained in the tumor 1 h p.i., compared to the 0.5 h time point. Dynamic PET scans showed that the majority of ^{18}F-FB-2.5D was quickly cleared through renal system, and the blood radioactivity concentration dropped dramatically in the first 35 min p.i. These pharmacokinetic properties suggest translational potential.

Integrin $\alpha_v\beta_3$ expression *in vivo* has extensively been imaged by small, backbone cyclized peptidomimetics [c(RGDyK), c(RGDfK), etc.] (*20*−*24*). ^{18}F-FB labeled c(RGDyK) [abbreviated as FB-RGD] was reported to moderately target U87MG tumors *in vivo* (ca. 3 and 2.5%ID/g uptake at 0.5 and 1 h, respectively) (*21*). ^{18}F-FB-2.5D demonstrated lower liver uptake (1.5%ID/g at 0.5 h p.i.) compared to ^{18}F-FB-RGD (ca. 2.5 and 1%ID/g at 0.5). However, ^{18}F-FB-2.5D has lower tumor uptake (ca. 2% ID/g at 0.5 h p.i.), and the kidney uptake is slightly higher than ^{18}F-FB-RGD (4.5 vs 3.5%ID/g at 0.5 h p.i.). The findings presented here are different from our previous experience. In our recent report, ^{64}Cu labeled DOTA-2.5D did show significant advantages over ^{64}Cu-DOTA-c(RGDyK) (*12*). This difference indicates that various labeling methods impact *in vivo* performance of knottins. Moreover, it suggests that further optimization of ^{18}F-FB-2.5D may lead to a radiofluorinated knottin probe with improved properties. It was reported that PEGylation enhanced the tumor uptake and prolonged the retention of ^{18}F labeled c(RGDyK) (ca. 5%ID/g at 0.5 h and 2.5%ID/g at 2 h p.i.), while the liver uptake remained the same (ca. 2.6%ID/g at 0.5 h) (*24*). Similar strategies could be adapted to improve the tumor uptake and retention of ^{18}F-labeled knottins and increase the tumor-to-liver ratios.

As an important target for cancer therapy, $\alpha_v\beta_3$ integrin is highly overexpressed on tumor cells and the tumor neovasculature of many cancer including melanoma and glioblastoma (*13, 25, 26*). An optimized ^{18}F labeled 2.5D probe could be used for diagnosis of $\alpha_v\beta_3$-positive tumors, at both primary and metastatic sites. ^{18}F-labeled 2.5D could also be used for stratification of patients, detection of cancer recurrence, and monitoring therapeutic efficacy of integrin-targeted drugs. In conclusion, radiolabeled knottin peptide ^{18}F-FB-2.5D allows integrin-specific PET imaging of U87MG tumors with good contrast and is mainly cleared from the body through the renal system. Knottins are excellent peptide scaffolds for the development of PET probes for clinical translation.

ACKNOWLEDGMENT

This work was supported, in part, by Department of Radiology, Stanford University (ZC), National Cancer Institute (NCI) In Vivo Cellular Molecular Imaging Center (ICMIC) grant P50 CA114747 (SSG), NCI Small Animal Imaging Resource Program (SAIRP) grant R24 CA93862, NCI 5R01 CA119053 (ZC), NCI 5K01 CA104706 (JRC), and the Edward Mallinckrodt Jr. Foundation (JRC). The Stanford University cyclotron team, particularly Fred Chin, is acknowledged for radionuclide production.

LITERATURE CITED

(1) Rothe, A., Hosse, R. J., and Power, B. E. (2006) In vitro display technologies reveal novel biopharmaceutics. *FASEB J. 20*, 1599–1610.

(2) Hosse, R. J., Rothe, A., and Power, B. E. (2006) A new generation of protein display scaffolds for molecular recognition. *Protein Sci. 15*, 14–27.

(3) Uchiyama, F., Tanaka, Y., Minari, Y., and Tokui, N. (2005) Designing scaffolds of peptides for phage display libraries. *J. Biosci. Bioeng. 99*, 448–456.

(4) Nygren, P. A., and Skerra, A. (2004) Binding proteins from alternative scaffolds. *J. Immunol. Methods 290*, 3–28.

(5) Binz, H. K., Amstutz, P., and Pluckthun, A. (2005) Engineering novel binding proteins from nonimmunoglobulin domains. *Nat. Biotechnol. 23*, 1257–1268.

(6) Orlova, A., Feldwisch, J., Abrahmsén, L., and Tolmachev, V. (2007) Update: affibody molecules for molecular imaging and therapy for cancer. *Cancer Biother. Radiopharm. 22*, 573–584.

(7) Ladner, R. C. (1999) Polypeptides from phage display: A superior source of in vivo imaging agents. *Q. J. Nucl. Med. 43*, 119–124.
(8) Pallaghy, P. K., Nielsen, K. J., Craik, D. J., and Norton, R. S. (1994) A common structural motif incorporating a cystine knot and a triple-stranded beta-sheet in toxic and inhibitory polypeptides. *Protein Sci. 3* 1833–1839.
(9) Chiche, L., Heitz, A., Gelly, J. C., Gracy, J., Chau, P. T., Ha, P. T., Hernandez, J. F., and Le-Nguyen, D. (2004) Squash inhibitors: from structural motifs to macrocyclic knottins. *Curr. Protein Pept. Sci. 5*, 341–349.
(10) Craik, D. J., Daly, N. L., and Waine, C. (2001) The cystine knot motif in toxins and implications for drug design. *Toxicon 39*, 43–60.
(11) Kimura, R. H., Levin, A. M., Cochran, F. V., and Cochran, J. R. (2009) Engineered cystine knot peptides that bind alphavbeta3, alphavbeta5, and alpha5beta1 integrins with low-nanomolar affinity. *Proteins 77*, 359–369.
(12) Kimura, R. H., Cheng, Z., Gambhir, S. S., and Cochran, J. R. (2009) Engineered knottin peptides: a new class of agents for imaging integrin expression in living subjects. *Cancer Res. 69*, 2435–2442.
(13) Zako, T., Nagata, H., Terada, N., Utsumi, A., Sakono, M., Yohda, M., Ueda, H., Soga, K., and Maeda, M. (2009) Cyclic RGD peptide-labeled upconversion nanophosphors for tumor cell-targeted imaging. *Biochem. Biophys. Res. Commun. 381,* 54–58.
(14) Cheng, Z., Zhang, L., Graves, E., Xiong, Z., Dandekar, M., Chen, X., and Gambhir, S. S. (2007) Small-animal PET of melanocortin 1 receptor expression using a ^{18}F-labeled alpha-melanocyte-stimulating hormone analog. *J. Nucl. Med. 48*, 987–994.
(15) Kumar, C. C., Nie, H., Rogers, C. P., Malkowski, M., Maxwell, E., Catino, J. J., and Armstrong, L. (1997) Biochemical characterization of the binding of echistatin to integrin alphavbeta3 receptor. *J. Pharmacol. Exp. Ther. 283*, 843–853.
(16) Cheng, Z., Padilla, De Jesus, O., Namavari, M., De A., Levi, J., Webster, J. M., Zhang, R., Lee, B., Syud, F. A., and Gambhir, S. S. (2008) Small-animal PET imaging of human epidermal growth factor receptor type 2 expression with site-specific ^{18}F-labeled protein scaffold molecules. *J. Nucl. Med. 49*, 804–813.
(17) Lee, S. B., Hassan, M., Fisher, R., Chertov, O., Chernomordik, V., Kramer-Marek, G., Gandjbakhche, A., and Capala, J. (2008) Affibody molecules for in vivo characterization of HER2-positive tumors by near-infrared imaging. *Clin. Cancer Res. 14*, 3840–3849.
(18) Baum, R., Orlova, A., Tolmachev, V., and Feldwisch, J. (2006) Receptor PET/CT and SPECT using an Affibody molecule for targeting and molecular imaging of HER2-positive cancer in animal xenografts and human breast cancer patients [abstract]. *J. Nucl. Med. 47* (suppl), 108P.
(19) Engfeldt, T., Orlova, A., Tran, T., Bruskin, A., Widström, C., Karlström, A. E., and Tolmachev, V. (2007) Imaging of HER2-expressing tumours using a synthetic Affibody molecule containing the ^{99m}Tc-chelating mercaptoacetyl-glycyl-glycyl-glycyl (MAG3) sequence. *Eur. J. Nucl. Med. Mol. Imaging 34*, 722–733.
(20) Cheng, Z., Wu, Y., Xiong, Z., Gambhir, S. S., and Chen, X. (2005) Near-infrared fluorescent RGD peptides for optical imaging of integrin $\alpha_v\beta_3$ expression in living mice. *Bioconjugate Chem. 16*, 1433–1441.
(21) Chen, X., Park, R., Shahinian, A. H., Tohmea, M., Khankaldyyanb, V., Bozorgzadeha, M. H., Badinga, J. R., Moatsb, R., Laugb, W. E., and Contia, R. S. (2004) ^{18}F-labeled RGD peptide: initial evaluation for imaging brain tumor angiogenesis. *Nucl. Med. Biol. 31*, 179–189.
(22) Zhang, X., Xiong, Z., Wu, Y., Cai, W., Tseng, J. R., Gambhir, S. S., and Chen, X. (2006) Quantitative PET imaging of tumor integrin $\alpha v\beta 3$ expression with [^{18}F]FRGD$_2$. *J. Nucl. Med. 47*, 113–121.
(23) Cai, W., Gambhir, S. S., and Chen, X. (2005) Multimodality tumor imaging targeting integrin alpha(v)beta(3). *BioTechniques 39*, S6–S17.
(24) Chen, X., Park, R., Khankaldyyan, V., Tohme, M., Bading, J. R., Laug, W. E., and Conti, P. S. (2004) MicroPET Imaging of Brain Tumor Angiogenesis with ^{18}F-Labeled PEGylated RGD Peptide. *Eur. J. Nucl. Med. Mol. Imaging 31*, 1081–1089.
(25) Putnam, A. J., Schulz, V. V., Freiter, E. M., Bill, H. M., and Miranti, C. K. (2009) Src, PKCalpha, and PKCdelta are required for alphavbeta3 integrin-mediated metastatic melanoma invasion. *Cell Commun. Signal 7*, 10.
(26) Skuli, N., Monferran, S., Delmas, C., Favre, G., Bonnet, J., Toulas, C., and Cohen-Jonathan Moyal, E. (2009) Alphavbeta3/alphavbeta5 integrins-FAK-RhoB: a novel pathway for hypoxia regulation in glioblastoma. *Cancer Res. 69*, 3308–3316.

BC900361G

Targeting Glioma Cells in Vitro with Ascorbate-Conjugated Pharmaceutical Nanocarriers

Stefano Salmaso,*[,†,‡] Juan S. Pappalardo,[†] Rupa R. Sawant,[†] Tiziana Musacchio,[†] Karen Rockwell,[†] Paolo Caliceti,[‡] and Vladimir P. Torchilin[†]

Department of Pharmaceutical Sciences and Center for Pharmaceutical Biotechnology and Nanomedicine, Northeastern University, Boston, Massachusetts 02115, and Department of Pharmaceutical Sciences, University of Padova, via F. Marzolo 5, 35131 Padova, Italy. Received August 19, 2009; Revised Manuscript Received October 16, 2009

6-Ascorbate-PEG-1,2-distearoyl-*sn*-glycero-3-phosphoethanolamine (6-ascorbate-PEG-PE) was synthesized according to a two-step procedure: (1) activation of ascorbic acid with bromine, and (2) synthesis of 6-ascorbate-PEG-PE by reacting 1,2-distearoyl-*sn*-glycero-3-phosphoethanolamine-*N*-[amino (poly(ethylene glycol))-2000] with an excess of 6-Br-ascorbic acid. The 6-ascorbate-PEG-PE was recovered by precipitation in diethyl ether and purified by gel permeation chromatography. The analysis of the product by ^{1}H NMR and UV−vis spectroscopy confirmed the identity of the conjugate. Liposomes and PEG-PE-based lipid-core micelles were prepared by thin film hydration technique incorporating 6-ascorbate-PEG-PE as targeting moiety. The targeting properties of the ascorbate-decorated nanosystems were tested by fluorescence-activated cell sorting (FACS) analysis and fluorescent microscopy on a panel of tumor cell lines preliminary selected for their ability to express the SVCT2 ascorbate transporter. Cell lines had been selected on the basis of the immunological properties assessed by FACS, which showed that two glioma cell lines, C6 and F98, and fibroblasts NIH/3T3 express plasma membrane-associated SVCT2 transporter for reduced ascorbic acid. Ascorbate-decorated pharmaceutical nanocarriers were endowed with selective targeting properties toward the SVCT2 transporter expressed in glioma cell models. This study shows that SVCT2 transporter for ascorbic acid expressed both in peculiar epithelial cells of the choroid plexus responsible for the filtering of vitamin C into the central nervous system (CNS) and, in some brain tumor cell lines, can be conceivably exploited as a potential target for delivery of drug-loaded pharmaceutical nanocarriers to the brain.

INTRODUCTION

In the past decades, a great deal of research has focused on targeting the central nervous system for therapeutic and diagnostic purposes. The goal appeared to be extremely challenging due to the physiological architecture of the biological barriers, namely, the blood−brain barrier (BBB) and the blood−cerebrospinal fluid (CSF) barrier, which have poor permeability and allow for only restricted access to selected molecules. Such barriers limit the permeation to the brain compartment, protecting the nervous systems from toxic compounds, metabolites, viruses, and bacteria. By virtue of these physiologic barriers, most of the targeting strategies for drug delivery to the brain have shown limited efficiency.

Central nervous system penetration is favored for molecules having low molecular weight and adequate hydrophilic/hydrophobic balance (*1*). Besides unspecific permeation, endothelial cells of the brain capillaries, which constitute the BBB, are provided with selective transport systems for specific nutrients and endogenous biomolecules. Thus, they are responsible for the transport of glucose; neutral, acidic, and basic amino acids; alanine and taurine; some monocarboxylic acids; amines; neuromediators, such as choline; some vitamins; nucleosides; and the peptide transport system for small neurotropic peptides (*2, 3*).

A limited district of the BBB, namely, the epithelium of the choroid plexus (CP), is considered to be responsible for the maintenance of central nervous system (CNS) homeostasis of few micronutrients, namely, vitamin C and riboflavin (*4*). It has been found that, in some neurons, ascorbic acid concentration can reach up to 200-fold higher than that measured in the bloodstream (*5*). Specific physiological mechanisms are operating in order to transfer ascorbic acid from the blood, where its concentration is ∼50 μM, into the cerebrospinal fluid where the concentration is maintained at 200 μM (*6*). Within the CNS, ascorbic acid plays a pivotal role as a cofactor in a number of different enzymatic activities relating to the neurotransmitters processing and as an antioxidant allowing for neuroprotection.

According to H. Tsukaguchi, the reduced form of ascorbic acid is taken up by a mechanism that involves the sodium-dependent-vitamin C transporters SVCT2, whose RNA was detected in the choroid plexus epithelium (*7*). SVCT2 transporter was found to be expressed by neuroepithelial cells of the choroid plexus and the retinal pigmented epithelium mostly. Despite other mechanisms having been proposed raising options for ascorbic acid penetration mechanism into the brain as the oxidized form, the SVCT2-mediated pathway seems the most likely one, since the oxidized form of vitamin C is undetectable in the blood at physiological conditions and unstable in water (*8*). Besides, the evidence that ascorbic acid reaches the cerebrospinal fluid through the route of CP and then slowly penetrates the brain substance from the CSF was demonstrated by the intravenous injection of [^{14}C] ascorbic acid (*9*). How specifically ascorbic acid exits CSF to permeate the brain is still to be investigated, and no extensive data are available in literature so far.

* Corresponding author. Stefano Salmaso, Department of Pharmaceutical Sciences, University of Padua, Via F. Marzolo, 5, 35131 Padova, Italy, phone +39 049 8271602, Fax +39 049 8275366, e-mail: stefano.salmaso@unipd.it.

† Northeastern University.

‡ University of Padova.

10.1021/bc900369d © 2009 American Chemical Society
Published on Web 11/23/2009

Few in vitro cell models are available for evaluating the mechanism of ascorbic acid uptake mediated by the SVCT2 translocator. SVCT2 transporter expression and function in primary cell culture of astrocytes (*10, 11*) and in monolayers obtained from the porcine choroid epithelial cells have been investigated (*12*−*14*). Many studies concerning SVCT function and targeting for drug delivery have been carried out by using cloned *Xenopus* oocytes, which were induced to express the desired plasma membrane associated vitamin C translocator (*7, 15, 16*).

Only a limited number of studies are available in the literature on the exploitation of ascorbic acid SVCT transporter as a biological target mediating the brain delivery of therapeutic or diagnostic molecules. Small molecular weight prodrugs were synthesized according to adequate chemical strategies combining ascorbic acid with CNS active molecules and underwent investigation for brain therapeutic activity. It was shown that ascorbic acid endowed such prodrugs with efficient binding features to epithelial-associated SVCT2 translocator (*17*). Despite the fact that such prodrugs were not found to cross the BBB, they were effective in releasing the drug in the vicinity of the site of action and promote the diffusion through the brain barrier. These results outline the potential of ascorbic acid transporter as a new mediator for drug delivery by using drug-loaded systems, which bind the CP epithelium and possibly either translocate through it or release the drug payload that, by virtue of its hydrophilic/hydrophobic balance, can permeate into the brain.

So far, the literature is lacking in macromolecular systems aimed at brain targeting, which take advantage of the SVCT2 transporter features, namely, molecular selectivity and physiological disposition. In order to set up a new in vitro cellular model to exploit for brain delivery studies, immunological characterization of a panel of immortalized cell lines was carried out to assess which of them express the SVCT2 transporter. The potential of pharmaceutical nanocarriers, namely, liposomes and lipid-core polymeric micelles, to target such cells via the SVCT transporter was investigated after the nanocarriers were decorated with ascorbate by modifying the 1,2-distearoyl-*sn*-glycero-3-phosphoethanolamine-PEG_{2kDa}-NH_2 with ascorbic acid.

MATERIALS AND METHODS

Cell lines, mouse fibroblast NIH/3T3 and melanoma B16−F10, human glioblastoma LN-18 and neuroblastoma SK-N-AS, rat glioma C6 and F98, were purchased from the American Type Culture Collection (Manassas, VA). All cell culture media, RPMI, heat-inactivated fetal bovine serum (FBS), and penicillin/streptomycin stock solutions were purchased from Cellgro (Herndon, VA).

LAB-TEK 4-well cell culture chambers were purchased from Nunc (Rochester, NY). Goat polyclonal antibody anti-SVCT2 transporter (G-19) and donkey antigoat IgG-FITC were purchased from Santa Cruz Biotechnology, Inc. (Santa Cruz Biotechnology, CA). Goat antimouse IgG antibody was from ICN Biomedical (Aurora, OH).

Egg phosphatidylcholine (PC), cholesterol, 1,2-distearoyl-*sn*-glycero-3-phosphoethanolamine-*N*-[methoxy (poly(ethylene glycol))-2000] ($mPEG_{2kDa}$-PE), 1,2-distearoyl-*sn*-glycero-3-phosphoethanolamine-N-[amino(poly(ethylene glycol))2000] (PE-PEG_{2kDa}-amine) and 1,2-dioleoyl-*sn*-glycero-3-phosphoethanolamine-*N*-(lissamine rhodamine B sulfonyl) (Rh-PE) were obtained from Avanti Polar Lipids, Inc. (Alabaster, AL). Bovine serum albumin and all other chemicals and buffer solution components were from Sigma (St. Louis, MO) and were of analytical grade. Sephadex G25 superfine medium was from GE Healthcare Bio-Sciences Corp. (Piscataway, NJ, USA).

Synthesis of 6-Bromodeoxy-ascorbic Acid. The preparation of the 6-bromo derivative of ascorbic acid was performed according to the published procedure (*18*) with some modifications. Two grams of ascorbic acid (11.35 mmol) was added to 2.7 mL of 33% w/v hydrobromic acid in glacial acetic acid (17.18 mmol). The suspension was stirred overnight at room temperature. Afterward, hydrobromic and acetic acid were removed by nitrogen flux and rotary evaporation. Five milliliters of deionized water was added to the syrup, and the mixture was stirred at 60 °C for 30 min. After reduction of the volume by rotary evaporation, the residue was extracted 6 times with 5 mL of ethylacetate, and traces of water were removed by sodium sulfate treatment. The organic solvent was removed under reduced pressure, and the resulting solid product was dissolved in 3 mL of acetonitrile warmed to 70 °C. The solution was cooled to 4 °C to allow crystallization. The white crystals were redissolved and recrystallized according to the same procedure. The final product was recovered by filtration and dried under the vacuum overnight.

6-Bromodeoxy-ascorbic acid dissolved in DMSO-d_6 was analyzed by ^{1}H NMR and ^{13}C NMR using a Varian 500 MHz spectrometer. ^{1}H NMR: δ 3.36 (dd, 1H, J = 10.06, δ 7.14 Hz, BrCC*H*H), δ 3.60 (dd, 1H, J = 10.06, 6.56 Hz, BrCCH*H*), δ 3.96 (t, 1H, J = 6.67 Hz, BrCH2C*H*OH), δ 4.83 (broad s, 1H, OCH), δ 5.63 (broad s, 5.63, 1H, BrCH2CHO*H*), δ 8.42 (s, 1H, OCOCOHCO*H*), δ 11.66 (s, 1H, OCOCO*H*COH). ^{13}C NMR: δ 34.6 (BrC), 68.2 (BrC*C*), 75.2 (OCH), 152.3 (OC-*C*OH), 118.1 (OCCOH═*C*OH), 170.3 (OC═O). Mass spectroscopy analysis was carried out by MALDI-TOF using 2,5-dihydroxybenzoic acid as a matrix. The negative ion was found to have 237.05 *m*/*z*.

Synthesis of 6-Ascorbate-PEG-PE. Into a 25 mL round-bottomed flask, 2.8 mL of a 25 mg/mL solution of PE-PEG_{2kDa}-amine in chloroform was added (25 μmol, 70 mg). The solvent was removed by rotary evaporation, and the solid residue was dissolved in 2 mL of DMF. Then, 60 mg of 6-bromodeoxy-ascorbic acid (250 μmol) and 35 μL of triethylamine (250 μmol) were added. The solution was stirred overnight under argon in the dark. The mixture was precipitated by dropwise addition to cold diethyl ether under stirring. The crude precipitate was washed several times with diethyl ether, and the solid was dried under vacuum. The dry powder was dissolved in 2 mL of deionized water, and the derivative was purified by size exclusion chromatography using a column prepacked with Sephadex G25 superfine medium eluted with milli-Q water. Fractions positive both to UV analysis and iodine test were pooled together and lyophilized. Yield was 40 mg (57%).

In order to assess the PEG/ascorbate molar ratio in the conjugate, iodine test for PEG (*19*), UV spectroscopic analysis for ascorbate (*20*), and Snyder colorimetric test for the residual PEG unconjugated amino groups (*21*) were carried out on a weighed amount of the purified derivative. 6-Ascorbate-PEG-PE dissolved in $CDCl_3$ underwent ^{1}H NMR spectroscopic analysis. ^{1}H NMR: δ 3.73 (d, 1H, OC*H*CHOHCH$_2$ of ascorbate), δ 3.642 (s, ∼180 H, −[OCH$_2$CH$_2$]$_n$− of PEG), δ 2.308 (m, 4H, OCOC*H*$_2$ of phospholipid stearate), 1.249 (m, 56 H, −[CH$_2$]$_n$− of phospholipid stearate).

Preparation and Characterization of Liposomes and Micelles. Rhodamine-labeled targeted liposomes were prepared by thin film hydration technique. A lipid film was obtained by removing organic solvent from the chloroform solution of 6-ascorbic acid-PEG-PE, egg PC, cholesterol, and Rh-PE in 3/60/30/0.25 molar ratio. The lipid film was suspended in RPMI, pH 7.4, containing 300 μM Tris(2-carboxyethyl)phosphine (TCEP) at a total lipid concentration of 0.435 mg/mL and sonicated in a bath sonicator for 10 min, followed by 11 passages through a mini-extruder equipped with 200 nm pore size polycarbonate filter (Avanti Polar Lipids). Untargeted

liposomes were prepared according to the same procedure using $mPEG_{2kDa}$-PE instead of 6-ascorbic acid-PEG-PE.

Rhodamine-labeled targeted micelles were prepared by dissolving 6-ascorbic acid-PEG-PE in chloroform. To that solution, 1 mol % of Rh-PE was added. The organic solvent was then removed by rotary evaporation, and the film was rehydrated at a final concentration of 1 mg/mL in RPMI containing TCEP 300 μM. Untargeted micelles were prepared using $mPEG_{2kDa}$-PE according to the same procedure.

The micelle and liposome sizes and size distributions were measured by dynamic light scattering (DLS) using a Zeta Plus instrument (Brookhaven Instrument Corporation, Holtsville, NY). The sample suspensions were analyzed after the appropriate dilution required for DLS. For each sample, size distribution measurements were performed six cycles per run.

The zeta-potential of liposome and micelle formulations was measured by a Zeta phase Analysis Light scattering (PALS) with an ultrasensitive Zeta Potential Analyzer instrument (Brookhaven Instruments, Holtsville, NY). The micelle and liposome suspensions were diluted properly with a 1 M KCl solution. All zeta-potential measurements were performed in triplicate.

Assessment of SVCT2-Expressing Cell Lines by Flow Cytometry. In order to select immortalized cell lines, which express SVCT2 transporter on plasma membrane, cells (NIH/3T3, B16−F10, LN-18, SK-N-AS, C6, and F98) were grown in RPMI with 10% FBS in 10 cm tissue culture plates for 72 h. Medium was removed; cells were washed with RPMI and detached by prechilling incubation for 15 min and pipetting. Cells were recovered by centrifugation at 1500 rpm, and 1 million cells were resuspended in 50 μL of PBS containing 3% FBS. Three microliters of a 200 μg/mL goat polyclonal anti SVCT2 transporter (G-19) or goat antimouse IgG antibody was added to each sample and incubated in the dark in an ice-cold bath for 30 min. Cells were then washed once with 1 mL of PBS containing 3% FBS, recovered by centrifugation, resuspended in 50 μL of the same medium, and treated with 3 μL of 200 μg/mL donkey antigoat IgG-FITC for 30 min in the dark in the ice bath. After washing with PBS containing 3% FBS, samples were fixed with 2% paraformaldehyde in PBS and analyzed by FACS (10 000 cells in average count) using BD FACSCalibur flow cytometer and BD CellQuest Pro software (Beckton Dickinson Biosciences, San Jose, CA). Cells were live-gated upon acquisition using forward versus side scatter to exclude debris and dead cells.

Ascorbate-Mediated Targeting of Pharmaceutical Nanocariers. *FACS Analysis.* In order to assess the cell-targeting capacity of ascorbate-conjugated nanocarriers, SVCT2-expressing cells incubated with liposomal or micellar formulations were subjected to the FACS analysis. SVCT2-expressing cells (C6, F98) were grown in 10 cm cell culture plates for 48 h.

Cells were washed with serum-free medium, detached by prechilling incubation and repetitive pipetting, recovered by centrifugation, and 1 million cells were resuspended in serum-free medium containing fluorescently labeled either targeted or untargeted nanocarriers prepared as described. Samples were incubated at 37 °C in the dark with gentle shaking for 90 min. Afterward, the cell samples were recovered by centrifugation, washed twice with PBS, and gated using forward versus side scatter to exclude debris and dead cells and analyzed (10 000 cells in average count) using BD FACSCalibur flow cytometer and BD CellQuest Pro software.

Epi-Fluorescence Microscopy. C6 and F98 cells were investigated using the fluorescence microscopy after incubation with fluorescently labeled targeted liposomes and micelles or untargeted nanocarriers as a reference. After the initial passage in tissue culture flasks, cells were grown in four-well tissue culture detachable LAB-TEK chambers, at a concentration of 5×10^5 cells per well in RPMI with 10% FBS. After 24 h, the chambers were washed twice with RPMI and then incubated at 37 °C with 0.5 mL of liposome or micelle formulations prepared as described in RPMI. After 1 h incubation, the medium was removed, and the plates were washed with medium three times. Samples were further incubated for 10 min at 37 °C with complete medium containing 0.5 μg/mL of Hoechst 33342 and washed twice with complete medium. Individual slides were covered with coverslips. Cells were observed immediately on a Nikon Eclipse E400 fluorescence microscope equipped with appropriate filters for bright light, Rhodamine and Hoechst detection, and a Nikon N60 camera.

For competition studies with ascorbic acid, cells grown on LAB-TEK chambers were washed twice with RPMI and incubated at 37 °C with 0.5 mL of 200 μM ascorbic acid in RPMI for 30 min followed by incubation for an additional 1 h with 6-ascorbate-PEG-PE-containing liposomes (0.464 mg/mL of total lipids). Samples were then washed three times with PBS and mounted with the fluormount medium. Cells were observed immediately by fluorescence microscopy as described, and the fluorescence intensity associated with the cells was quantified by image analysis software (*ImageJ*).

Scheme 1

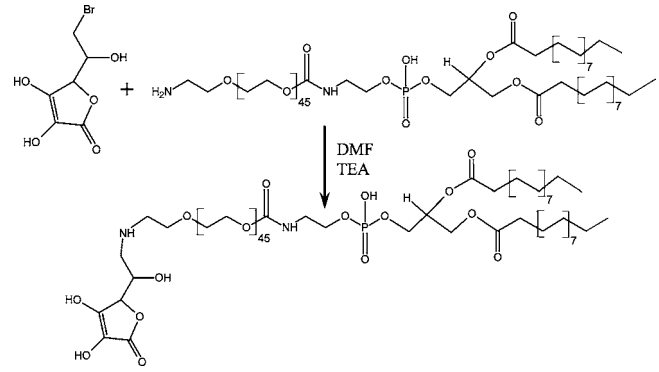

RESULTS

Synthesis and Characterization of 6-Ascorbate-PEG-PE and Ascorbate-Conjugated Nanocarriers. The preparation of the 6-ascorbate-PEG-PE was carried out by a two-step procedure: (1) activation of ascorbic acid with bromine; (2) synthesis of 6-ascorbate-PEG-PE by PE-PEG_{2kDa}-amine reaction with excess of 6-Br-ascorbic acid. The procedure adopted to synthesize the 6-bromodeoxy ascorbic acid allowed, after the crystallization, a 40.5% yield. The ^{1}H NMR spectroscopic analysis showed that hydroxyl groups of ascorbate in positions 2, 3, and 5 are unmodified as confirmed by the corresponding signals at δ 8.42, 11.66, and 5.63, respectively. Mass spectrometry analysis of 6-bromo-ascorbic acid showed a signal at 237.05 *m*/*z*, which has been attributed to the monodeprotonated ion $[6\text{-bromoscorbate-H}^+]^{-1}$.

The reaction of the commercially available PE-PEG_{2kDa}-amine with a 20-fold molar excess of 6-bromo-ascorbate (Scheme 1) allowed for obtaining 6-ascorbate-PEG-PE in 12 h as determined by the disappearance of the primary PEG amino group by ninhydrin assay. The conjugation was carried out in anhydrous conditions in order to avoid water deactivation of the 6-bromo-ascorbate.

The crude product was precipitated in ether and dissolved in water to allow the formation of the micelles. The conjugate was purified by size exclusion chromatography from the unreacted 6-bromo-ascorbate yielding 70% product recovery. UV−vis, iodine, and Snyder colorimetric tests were carried out on a 1

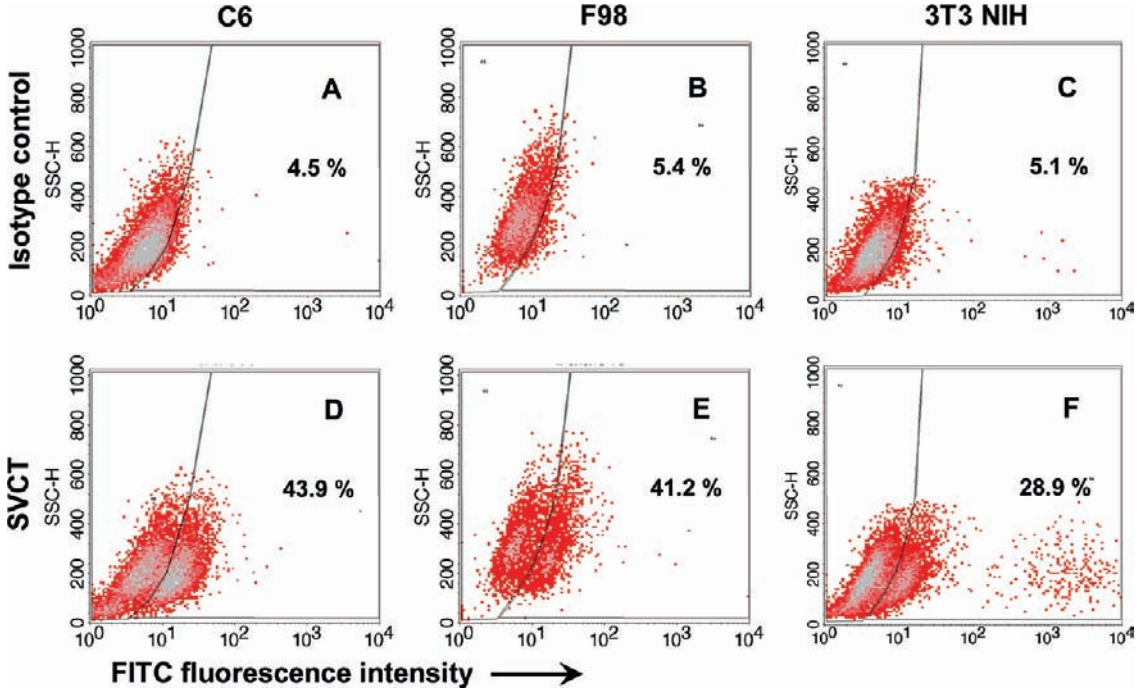

Figure 1. Characterization of SVCT2 expression in different cells. Cells were treated and analyzed by flow cytometry to evaluate expression of SVCT2 transporter. (A,D) C6 cells; (B,E) F98 cells; (C,F) NIH/3T3 cells. Above: cells treated with isotype control. Below: cells treated with goat polyclonal antibody anti SVCT2 transporter.

mg/mL water solution of 6-ascorbate-PEG-PE in order to assess ascorbate, PEG, and free amino groups, respectively. According to the tests, the conjugation yield was 98.9%, i.e., practically complete conjugation of the amino-terminating PEG-phospholipid to ascorbate was achieved by the procedure reported. The chemical identity of the conjugate was confirmed by ^{1}H NMR spectroscopy that showed typical signals of phospholipids at δ 2.308 and 1.249, PEG at δ 3.642, and ascorbate at δ 3.73.

The newly synthesized ascorbate-conjugated moiety was incorporated into liposomes or lipid-core PEG-PE micelles. As shown by the dynamic light scattering analysis, the lipid film rehydration techniques and extrusion yielded liposomal formulations of a similar size: 175.1 ± 21.2 nm and 181.9 ± 24.9 nm for untargeted and targeted liposomes, respectively. Micelle size was found to be 13.65 ± 5.1 nm and 21.3 ± 2.4 nm for $mPEG_{2kDa}$-PE and 6-ascorbate-PEG_{2kDa}-PE micelles, respectively. A slight increase in the micelle size can be ascribed to the additional presence of ascorbate moieties in the outer surface of the micelles.

Zeta-potential analysis of the lipid-based nanosystems showed that the presence of the ascorbate on their surface enhances their negative character due to the dissociation of the acid. PEGylated liposomes and PEG-PE-based micelles had zeta-potential of −12.8 ± 3.2 mV and −13.2 ± 2.3 mV, respectively, while ascorbate-conjugated liposomes and micelles showed a slight increase in the negative surface charge with zeta-potentials of −16.4 ± 4.2 mV and −19.2 ± 7.3 mV, respectively. Liposome and micelle sizes and zeta-potentials were unaffected by the presence of the reducing agent TCEP.

Selection of SVCT2-Expressing Cell Lines. In order to select a proper cell model suitable for further targeting studies, a panel of immortalized cell lines was tested to identify those expressing SVCT2 translocator on the plasma membrane by using saturating amounts of specific antibodies against the extracellular domain of SVCT2 protein. SK-N-AS (human neuroblastoma), LN18 (human glioblastoma), C6 and F18 (rat gliomas), NIH 3T3 (mouse fibroblasts), and B16−F10 (mouse melanoma) cells were investigated.

Cell lines were grown in an appropriate medium and detached by prechilling incubation and pipeting to prevent surface proteins from being proteolitically degraded by trypsin treatment, which is commonly used to recover cells from culture plastic surfaces. Detached cells were first incubated with goat polyclonal IgG anti SVCT2 transporter, which has selectivity for the detection of SVCT2 of mouse, rat, and human origin as stated by the provider. After washing, cells were incubated with donkey FITC-labeled antigoat antibody as a secondary antibody, and the degree of binding was determined by FACS analysis. Isotype control was performed by incubating cells with goat antimouse IgG in order to detect nonspecific antibody binding on the cell membrane.

As shown in Figure 1, 43.9%, 41.1%, and 28.9% of C6, F98, and NIH/3T3 cells stained positive for the SVCT2 expression, respectively (panels D, E and F), while nonspecific immunostaining with the isotype control was about 5% only (panels A, B, and C, respectively).

When the FACS analysis was carried out with murine LN18, SK-N-AS, and B16F10 cell lines treated with the monoclonal anti SVCT2 transporter, only a nonspecific weak immunoreactivity was detected, and the cell-associated fluorescence increase accounted for about 5% regardless of cell incubation with goat polyclonal IgG anti SVCT2 transporter or goat antimouse IgG antibody. The FACS experiments demonstrated that such cell lines do not express constitutionally the plasma membrane SVCT2 transporter.

Nanocarrier Targeting Studies. *FACS Analysis.* The ability of ascorbate-conjugated nanocarriers to selectively target SVCT2 transporter-expressing cells was evaluated using FACS analysis after an hour and a half incubation with liposomes or micelles. Ascorbate-free PEGylated liposomes or $mPEG_{2kDa}$-PE micelles were used as control. Two different cell lines of rat origin, C6 and F98 glioma cell lines, both expressing SVCT2 transporter, were incubated with liposomes containing 3% of 6-ascorbate-PEG-PE or with 6-ascorbate-PEG-PE micelles fluorescently labeled with Rh-PE.

As depicted in Figure 2, FACS analysis showed that ascorbate conjugation increases C6 cells targeting by 23.2% and 10.1%

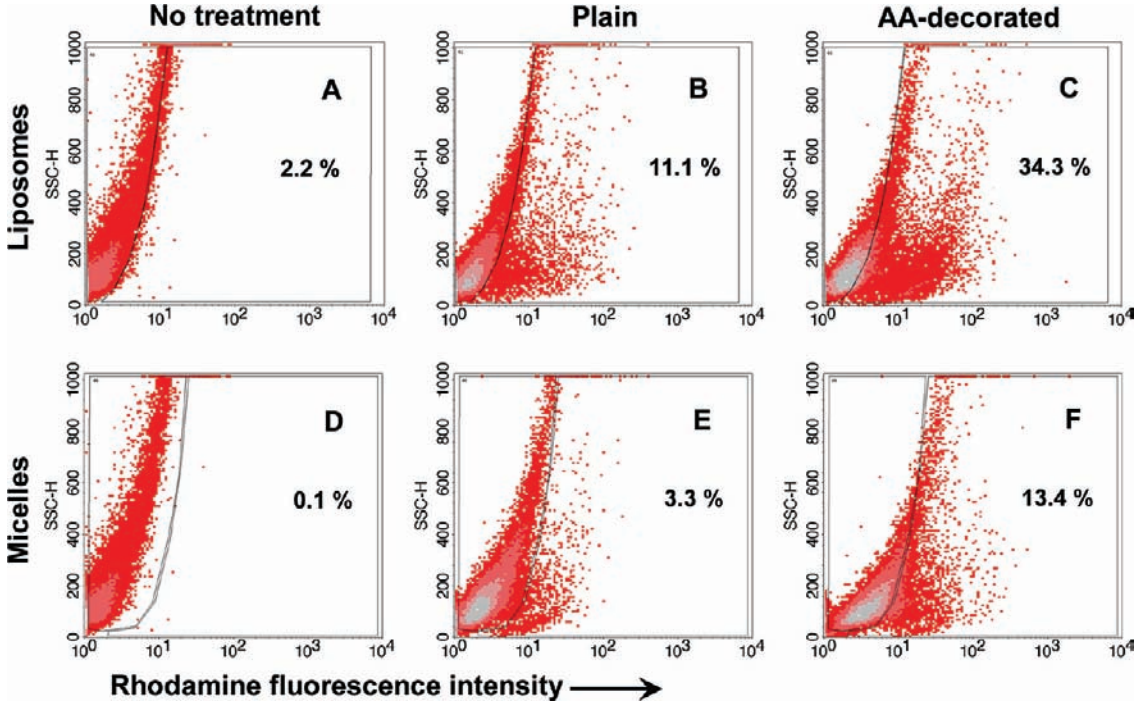

Figure 2. FACS analysis of rat C6 cells untreated (A,D), and after 1.5 h treatment with rhodamine-labeled PEG-liposomes (B), ascorbate-PEG-liposomes (C), $mPEG_{2kDa}$-PE micelles (E), and ascorbate-PEG-PE micelles (F).

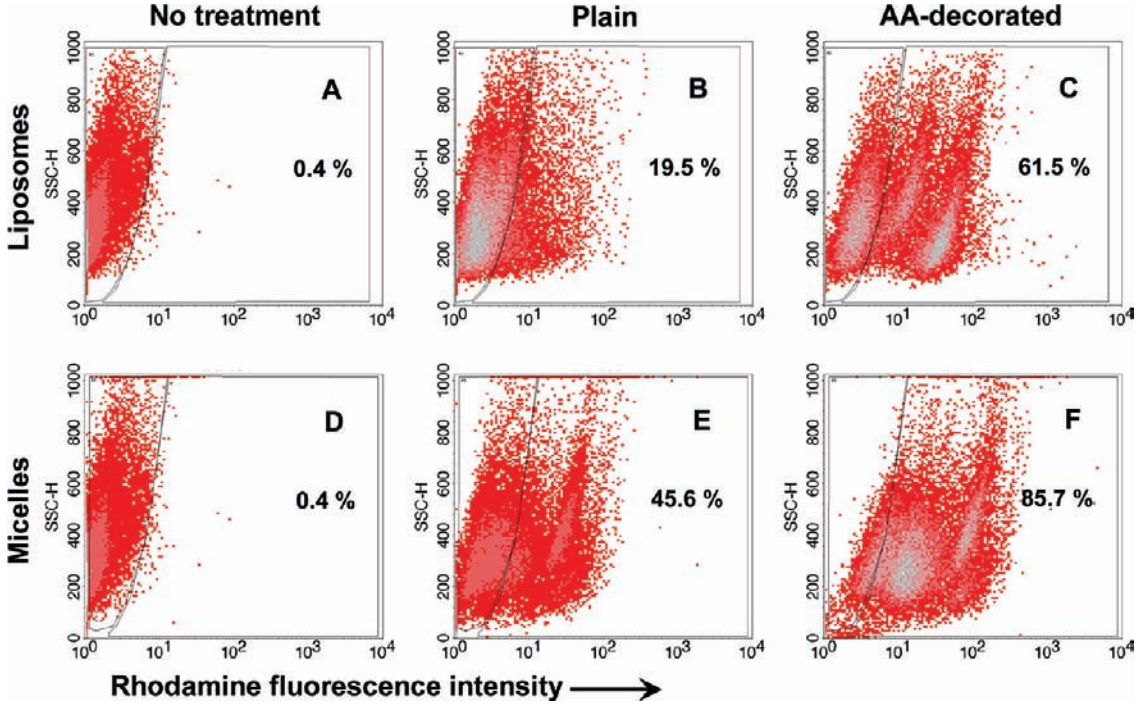

Figure 3. FACS analysis of rat F98 cells untreated (A,D), and after 1.5 h treatment with rhodamine-labeled PEG-liposomes (B), ascorbate-PEG-liposomes (C), $mPEG_{2kDa}$-PE micelles (E), and ascorbate-PEG-PE micelles (F).

when targeted liposomes and micelles were employed, respectively (pannels C and F), compared to ascorbate-free PEG-liposomes and $mPEG_{2kDa}$-PE micelles controls. Nonspecific cell targeting was shown to account for about 9% and 3% fluorescence increase for PEGylated liposomes and $mPEG_{2kDa}$-PE micelles (panels B and E, respectively) with respect to untreated cell samples (panels A and D, respectively). Cells were analyzed as a whole without gating (data not shown).

Figure 3 reports the results obtained by FACS analysis to evaluate the targeting efficiency of ascorbate-conjugated nanocarriers toward F98 glioma cell line. F98 cells fluorescence increase was remarkably higher compared to C6 cells when cell samples were treated with ascorbate-decorated liposomes (C) and micelles (F), 42% and 40.1%, respectively. A stronger nonspecific cell-associated fluorescence was also found on the F98 cell line for nontargeted liposome and micelles, 19.1% and 45.2%, respectively (B and E), compared to the C6 cell line, which could be explained by the higher nonspecific uptake activity of these cells.

Epifluorescence Microscopy. To additionally evaluate whether the ascorbate can be employed as a targeting moiety to deliver pharmaceutical nanocarriers to SVCT transporter-expressing

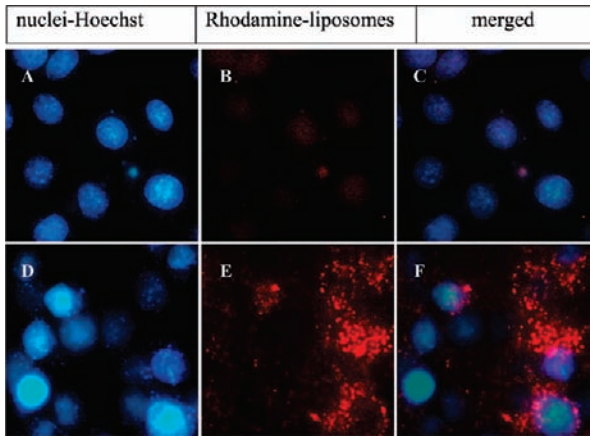

Figure 4. Epifluorescent microscopic examination of C6 cell line treated with fluorescently labeled PEG-liposomes (A,B,C) and ascorbate-PEG-liposomes (D,E,F). Cell images were acquired in a blue channel for nuclei detection after staining with Hoechst 33342 (panels A and D) and red channel for Rh-PE-labeled liposome detection (panels B and E). Panels C and F are the superimpositions of the two channels. Images were taken at 100× magnification.

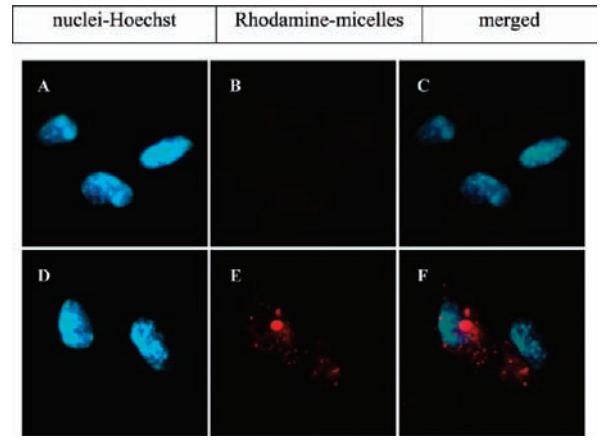

Figure 5. Epifluorescent microscopic examination of C6 cell line treated with fluorescently labeled PEG-PE micelles (A,B,C) and ascorbate-PEG-PE micelles (D,E,F). Cell images were acquired in a blue channel for nuclei detection after labeling with Hoechst 33342 (panels A and E) and red channel for rhodamine-labeled micelles detection (panels B and E). Panels C and F are the superimpositions of the two channels. Images were taken at 100× magnification.

cells, C6 cells were also investigated using fluorescence microscopy after the incubation with fluorescently labeled liposomes and micelles. Nuclei were stained by Hoechst 33342 treatment (Figure 4, blue fluorescence on panels A and D). The epifluorescence micrographs obtained clearly support ascorbate-PEG-liposome targeting to the investigated glioma cells. In fact, strongly fluorescent red spots associated with the cells were clearly visible (panel E in Figure 4 shows the red fluorescence of targeted liposomes; panel F shows superimposition of blue and red fluorescence). On the contrary, the treatment with nontargeted PEGylated liposomes did not result in any defined fluorescent spots associated to the glioma cells, indicating the lack of targeting toward this cell line (panel B in Figure 4 shows undetectable red fluorescence of PEG-liposomes; panel C shows superimposition of blue and red fluorescence). It is important to note here that PEGylated liposomes are commonly recognized for their stealth properties, which reduce the interaction with biological surfaces.

The ascorbate-mediated targeting was investigated also after the treatment of C6 cells with rhodamine-labeled micelles as shown in Figure 5. Panels A and D report nuclei staining by the Hoechst treatment. Panels B and E report red fluorescence of cells treated with untargeted micelles and ascorbate-PEG-PE micelles, respectively, while panels C and F are the superimpositions of the two channels. Cells treated with ascorbate-conjugated micelles showed small punctuate red fluorescent spots (panels E and F), which might be due to aggregation of micelles and uptake of the aggregates by C6 glioma cells.

Competition studies were performed with epifluorescence microscopy by C6 cells preincubation with free ascorbic acid followed by the treatment with rhodamine-labeled ascorbate-PEG-liposomes. The presence of ascorbic acid in the medium dramatically reduced the cell-associated fluorescence as depicted in Figure 6 (panel B) compared to cell samples treated with targeted liposomes only (Figure 6, panel A). The preincubation of cell samples with ascorbic acid followed by the treatment with ascorbate-PEG-liposomes reduced the cell-associated fluorescence induced by targeted nanosystems by 7-fold as determined by the image analysis (Figure 7).

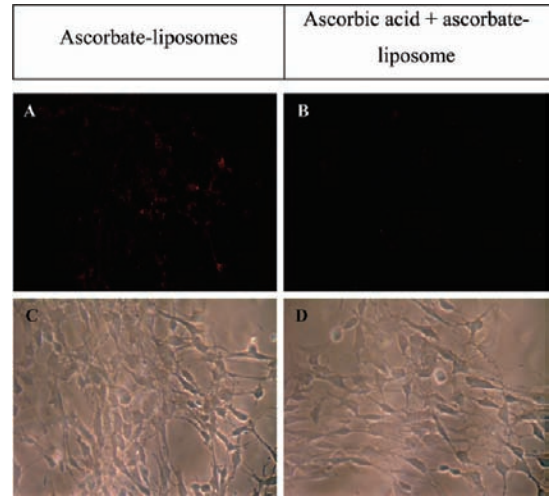

Figure 6. Epifluorescent microscopic examination of C6 cells treated with fluorescently labeled ascorbate-PEG-liposomes without (A) and with (B) ascorbic acid preincubation. Images were acquired in a red channel for rhodamine detection. Panels C and D show the bright light acquisition of the same samples. Images were taken at 40× magnification.

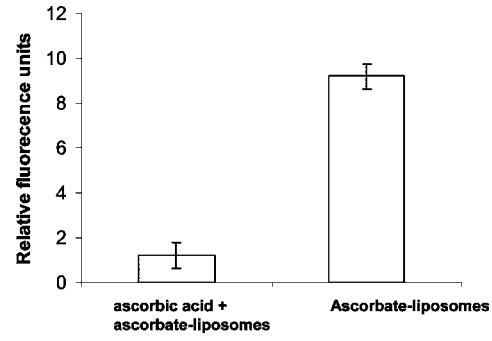

Figure 7. Relative fluorescence intensity associated with C6 cells after treatment with rhodamine-labeled ascorbate-PEG-liposomes with or without preincubation with free ascorbic acid.

DISCUSSION

In the present study, we have investigated the targeting capacity of ascorbic acid moiety to confer selectivity to pharmaceutical nanocarriers. A new in vitro cellular model was set up to evaluate the targeting activity of ascorbate-conjugated nanocarriers.

Ascorbic acid was activated as a bromo derivative, and the chemical identity of the intermediate was confirmed by ^{1}H NMR

and mass spectroscopy. Activation at the carbon in position 6 of ascorbic acid was chosen according to reported data which showed the biological activity and the selective binding capacity of the 6-deoxy-ascorbic acid derivatives toward the SVCT2 transporter (*22*). Activated 6-bromodeoxy-ascorbic acid was reacted in anhydrous condition with the primary amino group of commercially available PE-PEG_{2kDa}-amine by using excess of the 6-bromo-ascorbic acid. At the end, the excess of reactive ascorbic acid was removed by precipitation of the reaction mixture in diethyl ether and size exclusion chromatography that allowed for obtaining a product with high purity. The identity of the conjugated product was investigated by ^{1}H NMR and UV spectroscopy and colorimetric tests for assessing ascorbate and PEG in the conjugate. The tests confirmed high conjugation yield and 1/1 ascorbic acid/PEG-PE molar ratio. In order to maintain the conjugated ascorbic acid in the reduced form, which binds selectively SVCT transporter, buffered solutions were kept in the dark and in the presence of TCEP as reducing agent, which allowed the regeneration of traces of oxidized ascorbate eventually formed during the conjugation and purification processes (*20*).

The targeting moiety was incorporated into pharmaceutical nanocarriers, such as liposomes and polymeric lipid-core micelles, by the thin film rehydration method that allowed for obtaining liposomes and micelles with defined dimensions and surface properties. As assessed by photocorrelation spectroscopy, targeted and untargeted liposomes had diameters of about 180 nm and negative zeta potential, which was expectedly increased by the presence of ascorbic acid. Micelle dimensions were found to be in a close range (15−20 nm) regardless of the presence of ascorbate on the surface. Slight increase of the negative zeta-potential was found for ascorbate micelles similar to liposomes.

In order to set up a cell model to evaluate the targeting performance of ascorbate-decorated nanocarriers, a panel of diverse immortalized cell lines underwent investigation for the expression of SVCT2 transporter by immunostaining and flow cytometry analysis. Keeping in mind the future use of this approach for brain-targeted delivery, we have chosen for investigation a panel of cell lines related to the brain glia (LN-18, SK-N-AS, C6, and F98) as well as cells with potential involvement in processing of ascorbic acid (NIH/3T3 and B16−F10) (*23, 24*). Cells were treated with a goat polyclonal anti SVCT2 trasporter antibody recognizing an extracellular epitope of the protein. Among the cells scanned, two rat glioma cells, C6 and F98, were shown to express plasma membrane-associated SVCT2 transporter. NIH/3T3 cells also gave positive test results. This cell-line phenotypic characterization technique is new with respect to many SVCT transporter expression studies reported in the literature, which were aimed at assessing solely the presence of RNA encoding for such protein, rather than its disposition on the cell surface (*25*).

The partial positivity of the cellular population to the immunological characterization, which results in only partial shift of the cells in Figure 1, can be explained by variation of the ascorbate transporter expression throughout the cell cycle. In light of such immunologic results, it is conceivable that C6 and F98 glioma cells represent a good cancer cell model to analyze a possible use of the SVCT2 transporter for specific targeting of pharmaceutical nanocarriers. Such a model can be complementary to reported primary cell culture (*13, 26*) and SVCT2-transfected *Xenopus* oocytes models (*22*) for investigation of drug delivery systems intended to target SVCT2-expressing cells. Besides, such a study introduces the perspective that the SVCT2 transporter can be a good ligand to target the brain through the choroid plexus, where it is selectively expressed, and allow drug delivery systems to reach SVCT2-expressing tumor cells.

On the basis of the results originating from the immunological characterization, we have studied the targeting capacity of ascorbate-conjugated liposomes and micelles toward C6 and F98 glioma cells. Flow cytometry analysis of C6 and F98 cells treated with targeted liposomes and micelles labeled with Rh-PE showed that both nanosystems bind with the target cells much better than nontargeted ascorbate-free nanocarriers used as controls. FACS analysis displayed that untargeted liposomes and micelles associate to a different extent with C6 and F98 cell lines. Nonspecific cell uptake of untargeted liposomes was lower with both cell lines, C6 and F98 (panels B in Figure 2 and 3, respectively), testifying to better "stealth" properties of PEGylated liposomes compared to micelles. Instead, nonspecific cell uptake of $mPEG_{2kDa}$-PE based micelles is detectable with C6 cells (Figure 2, panel E) but more remarkable in the case of F98 cells (Figure 3, panel E). The different behavior may be ascribed to the diverse physical stability of the two nanosystems. This can allow for membrane fusion of micelles rather than liposomes within the same cell line. On the other hand, the different surface properties of the two cell lines investigated may affect the biological behavior of a given nanosystem. However, the unspecific uptake does not prevail over the effect of ascorbate-mediated cell targeting for both nanosystems.

The capacity of ascorbate-conjugated liposomes and micelles to selectively interact with SVCT2-expressing cells was also investigated with glioma C6 cells by fluorescence microscopy. It was found that the cell-associated liposomes (the quantity of cell-associated rhodamine fluorescence) were clearly visible already after 1 h contact with targeted liposomes (Figure 4). Well-defined red spots were found to be coupled to the cells; they may be deposited either on the outer side of the plasma membrane or inside the cytosol undergoing intracellular trafficking. The increase in cell-associated fluorescence observed for ascorbate liposomes compared to nontargeted liposomes may be explained by the ascorbate-mediated cellular uptake. Samples treated with nontargeted liposomes do not show red fluorescence (Figure 4, panels B and C). Similar patterns were observed when C6 cells were imaged by fluorescence microscopy after the treatment with ascorbate-targeted and nontargeted PEG-PE micelles (Figure 5). These results clearly demonstrate targeting selectivity of the ascorbate-conjugated nanocarriers toward these cells.

In order to confirm the specific addressing of SVCT transporter by ascorbate-conjugated nanocarriers, we have performed the competition study in the presence of an excess of free ascorbic acid. Preincubation of tumor cells with free ascorbic acid strongly reduced the ascorbate−liposome cellular association confirming that the nanosystems selectively target the ascorbate cell membrane transporter.

Nanosystems that target solely the ascorbic acid transporter can potentially reach and accumulate in the brain due to local expression of SVCT2, which is limited to choroid plexus epithelial cells, some neurons, tanycytes, astrocites, and the arachnoid membrane (*7*). The conjugation of the ascorbate moiety to nanocarriers via the carbon in position 6 was shown to preserve its binding recognition for SVCT2 transporter and avoid binding to the glucose (GLUT) transporters, which are targeted by the oxidized ascorbic acid. Furthermore, the eventually oxidized form of conjugated 6-deoxyascorbate cannot bind the GLUT transporters, which are spread over the whole body (*22*). The targeting of the glucose transporter by ascorbate-conjugated pharmaceutical nanocarriers was unlikely, since the cells were treated with the medium containing 2 g/L of glucose that competes with the oxidized ascorbate if any of its trace is present. According to these considerations, ascorbate moiety can be considered as a potential site-selective targeting agent for brain delivery.

As reported in the literature, great efforts have focused on targeting the brain with nanosystems having adequate dimension,

morphology, and surface properties. Systemically administered polymeric nanoparticles were shown to be filtered through fenestrated capillaries of the CP and were rapidly transported into the CSF by absorptive transcytosis (*27*). Reported nanosystems showed promising performance, which could be ascribed to the tiny dimensions and decoration with a proper BBB transporting vector. Some peculiar features make such colloidal systems potential tools for brain drug delivery and support new perspectives that the CP can be exploited as a physiologic gateway to reach the brain. With this in mind, adequate nanosystems can be designed, which filter off the capillaries and bind to SVCT2 transporters of the choroid ependymal cells (*12*). At this site, they can either release their payload, which can diffuse into the brain, or undergo transcytosis allowing for further delivery toward the brain.

This study has also highlighted that ascorbic acid can be employed as a targeting agent to promote the disposition of drug-loaded nanosystems to neoplastic tissues (namely, the gliomas). Our data may facilitate the potential therapeutic use of ascorbate-conjugated nanosystems for the treatment of some brain-associated diseases.

ACKNOWLEDGMENT

This research was based in part on a concept suggested by Anthony Manganaro.

LITERATURE CITED

(1) Pardridge, W. M. (1988) Recent advances in blood brain-barrier transport. *Annu. Rev. Pharmacol. Toxicol. 28*, 25–39.

(2) Pardridge, W. M. (1995) Transport of small molecules through the blood-brain barrier: biology and methodology. *Adv. Drug Delivery Rev. 15*, 5–36.

(3) Bergley, D. J. (1996) The blood-brain barrier: principles for targeting peptides and drugs to the central nervous system. *J. Pharm. Pharmacol. 48*, 136–146.

(4) Spector, R. (2000) Drug transport in the mammalian central nervous system: multiple complex systems. A critical analysis and commentary. *Pharmacology 60*, 58–73.

(5) Rice, M. E. (2000) Ascorbate regulation and its neuroprotective role in brain. *Trends Neurosci. 23*, 209–216.

(6) Reiber, H., Ruff, M., and Uhr, M. (1993) Ascorbate concentration in human cerebrospinal fluid (CSF) and serum. Intrathecal accumulation and CSF flow rate. *Clin. Chim. Acta 217*, 163–173.

(7) Tsukaguchi, H., Tokui, T., Mackenzie, B., Berger, U. V., Chen, X. Z., Wang, Y., Brubaker, R. F., and Hediger, M. A. (1999) A family of mammalian Na+-dependent L-ascorbic acid transporters. *Nature 399*, 70–75.

(8) Cioffi, N., Losito, I., Terzano, R., and Zambonin, C. G. (2000) An electrospray ionization ion trap mass spectrometric (ESI-MS-MSn) study of dehydroascorbic acid hydrolysis at neutral pH. *Analyst 125*, 2244–2248.

(9) Hammarstrom, L. (1966) Autoradiographic studies on the distribution of 14C-labelled ascorbic acid and dehydroascorbic acid. *Acta Physiol. Scand. 70*, 1–79.

(10) Korcok, J., Yan, R., Siushansian, R., Dixon, S. J., and Wilson, J. X. (2000) Sodium-ascorbate cotransport controls intracellular ascorbate concentration in primary astrocyte cultures expressing the SVCT2 transporter. *Brain Res. 881*, 144–151.

(11) Siushansian, R., Tao, L., Dixon, S. J., and Wilson, J. X. (1997) Cerebral astrocytes transport ascorbic acid and dehydroascorbic acid through distinct mechanisms regulated by cyclic AMP. *J. Neurochem. 68*, 2378–2385.

(12) Angelow, S., Zeni, P., and Galla, H. J. (2004) Usefulness and limitation of primary cultured porcine choroid plexus epithelial cells as an in vitro model to study drug transport at the blood-CSF barrier. *Adv. Drug Delivery Rev. 56*, 1859–1873.

(13) Angelow, S., Haselbach, M., and Galla, H. J. (2003) Functional characterisation of the active ascorbic acid transport into cerebrospinal fluid using primary cultured choroid plexus cells. *Brain Res. 988*, 105–113.

(14) Hakvoort, A., Haselbach, M., and Galla, H. J. (1998) Active transport properties of porcine choroid plexus cells in culture. *Brain Res. 795*, 247–256.

(15) Daruwala, R., Song, J., Koh, W. S., Rumsey, S. C., and Levine, M. (1999) Cloning and functional characterization of the human sodium-dependent vitamin C transporters hSVCT1 and hSVCT2. *FEBS Lett. 460*, 480–484.

(16) Rajan, D. P., Huang, W., Dutta, B., Devoe, L. D., Leibach, F. H., Ganapathy, V., and Prasad, P. D. (1999) Human placental sodium-dependent vitamin C transporter (SVCT2): molecular cloning and transport function. *Biochem. Biophys. Res. Commun. 262*, 762–768.

(17) Dalpiaz, A., Pavan, B., Vertuani, S., Vitali, F., Scaglianti, M., Bortolotti, F., Biondi, C., Scatturin, A., Tanganelli, S., Ferraro, L., Marzola, G., Prasad, P., and Manfredini, S. (2005) Ascorbic and 6-Br-ascorbic acid conjugates as a tool to increase the therapeutic effects of potentially central active drugs. *Eur. J. Pharm. Sci. 24*, 259–269.

(18) Kiss, J., Berg, K. P., Dirsherl, A., Oberhansli, W. E., and Arnold, W. (1980) Synthese und eigenschaften von 6-desoxy-6-halogen-derivaten der L-ascorbinsäure. *Helv. Chim. Acta 63*, 1728–1739.

(19) Sims, G. E. C., and Snape, T. J. (1980) A method for the estimation of polyethylene glycol in plasma protein fractions. *Anal. Biochem. 107*, 60–63.

(20) Karlsen, A., Blomhoff, R., and Gundersen, T. E. (2005) High-throughput analysis of Vitamin C in human plasma with the use of HPLC with monolithic column and UV-detection. *J. Chromatogr., B 824*, 132–138.

(21) Snyder, S. L., and Sobocinsky, P. Z. (1975) An improved 2,4,6-trinitroben-nesulphonic acid method for the determination of amines. *Anal. Biochem. 64*, 284–288.

(22) Corpe, C. P., Lee, J. H., Kwon, O., Eck, P., Narayanan, J., Kirk, K. L., and Levine, M. (2005) 6-bromo-6-deoxy-L-ascorbic acid: an ascorbate analog specific for Na-dependent vitamin C transporter but not glucose transporter pathways. *J. Biol. Chem. 280*, 5211–5220.

(23) Welch, R. W., Wang, Y., Jr., Park, J. B., Kirk, K. L., and Levine, M. (1995) Accumulation of vitamin C (ascorbate) and its oxidized metabolite dehydroascorbic acid occurs by separate mechanisms. *J. Biol. Chem. 270*, 12584–12592.

(24) Godoy, A., Ormazabal, V., Moraga-Cid, G., Zúñiga, F. A., Sotomayor, P., Barra, V., Vasquez, O., Montecinos, V., Mardones, L., Guzmán, C., Villagrán, M., Aguayo, L. G., Oñate, S. A., Reyes, A. M., Cárcamo, J. G., Rivas, C. I., and Vera, J. C. (2007) Mechanistic insights and functional determinants of the transport cycle of the ascorbic acid transporter SVCT2. Activation by sodium and absolute dependence on bivalent cations. *J. Biol. Chem. 282*, 615–624.

(25) Manfredini, S., Pavan, B., Vertuani, S., Scaglianti, M., Compagnone, D., Biondi, C., Scatturin, A., Tanganelli, S., Ferraro, L., Prasad, P. D., and Dalpiaz, A. (2002) Design, synthesis and activity of ascorbic acid prodrugs of nipecotic, kynurenic and diclophenamic acids, liable to increase neurotropic activity. *J. Med. Chem. 45*, 559–562.

(26) Del Monte, M. A., and Maumenee, I. H. (1981) In vitro culture of human retinal pigment epithelium for biochemical and metabolic study. *Vision Res. 21*, 137–142.

(27) Lua, W., Zhangb, Y., Tanc, Y. Z., Hua, K. L., Jianga, X. G., and Fu, S. K. (2005) Cationic albumin-conjugated pegylated nanoparticles as novel drug carrier for brain delivery. *J. Controlled Release 107*, 428–448.

BC900369D

Gallium-67-Labeled Lactam Bridge-Cyclized α-Melanocyte Stimulating Hormone Peptide for Primary and Metastatic Melanoma Imaging

Haixun Guo,[†] Jianquan Yang,[†] Nalini Shenoy,[†] and Yubin Miao*[,†,‡,§]

College of Pharmacy, Cancer Research Treatment Center, and Department of Dermatology, University of New Mexico, Albuquerque, New Mexico 87131. Received September 28, 2009; Revised Manuscript Received October 19, 2009

The purpose of this study was to examine the melanoma imaging properties of a novel ^{67}Ga-labeled lactam bridge-cyclized α-melanocyte stimulating hormone (α-MSH) peptide. A lactam bridge-cyclized α-MSH peptide, DOTA-GlyGlu-CycMSH {DOTA-Gly-Glu-c[Lys-Nle-Glu-His-DPhe-Arg-Trp-Gly-Arg-Pro-Val-Asp]}, was synthesized and radiolabeled with ^{67}Ga. The melanoma targeting and pharmacokinetic properties of ^{67}Ga-DOTA-GlyGlu-CycMSH were determined in B16/F1 flank primary melanoma-bearing and B16/F10 pulmonary metastatic melanoma-bearing C57 mice. Flank primary melanoma and pulmonary metastatic melanoma imaging were performed by small animal single photon emission computed tomography (SPECT)/CT using ^{67}Ga-DOTA-GlyGlu-CycMSH as an imaging probe. ^{67}Ga-DOTA-GlyGlu-CycMSH was readily prepared with greater than 95% radiolabeling yield. ^{67}Ga-DOTA-GlyGlu-CycMSH exhibited substantial tumor uptake (12.93 ± 1.63%ID/g at 2 h postinjection) and prolonged tumor retention (5.02 ± 1.35%ID/g at 24 h postinjection) in B16/F1 melanoma-bearing C57 mice. The uptake values for nontarget organs were generally low (<0.30%ID/g) except for the kidneys at 2, 4, and 24 h postinjection. ^{67}Ga-DOTA-GlyGlu-CycMSH exhibited significantly ($p < 0.05$) higher uptakes (1.44 ± 0.75%ID/g at 2 h postinjection and 1.49 ± 0.69%ID/g at 4 h postinjection) in metastatic melanoma-bearing lung than those in normal lung (0.15 ± 0.10%ID/g and 0.17 ± 0.11%ID/g at 2 and 4 h postinjection, respectively). Both flank primary B16/F1 melanoma and B16/F10 pulmonary melanoma metastases were clearly visualized by SPECT/CT using ^{67}Ga-DOTA-GlyGlu-CycMSH as an imaging probe 2 h postinjection. ^{67}Ga-DOTA-GlyGlu-CycMSH exhibited favorable melanoma targeting and imaging properties, highlighting its potential as an effective imaging probe for early detection of primary and metastatic melanoma.

INTRODUCTION

G protein-coupled melanocortin-1 (MC1) receptors are distinct molecular targets for developing melanoma-specific peptide radiopharmaceuticals due to their overexpression on human and mouse melanoma cells (*1*−*5*). α-Melanocyte stimulating hormone (α-MSH) peptides can specifically target the MC1 receptors with diagnostic and therapeutic radionuclides through specific peptide−receptor interaction for melanoma imaging and therapy (*6*−*18*). Recently, we have reported a novel class of ^{111}In-labeled lactam bridge-cyclized α-MSH peptides as effective imaging probes for melanoma detection (*19, 20*). Unique lactam bridge cyclization made the radiolabeled peptides stable both *in vitro* and *in vivo*. Both primary melanoma and pulmonary melanoma metastases were clearly visualized by small animal SPECT/CT using ^{111}In-DOTA-GlyGlu-CycMSH {^{111}In-1,4,7,10-tetraazacyclododecane-1,4,7,10-tetraacetic acid-c[Lys-Nle-Glu-His-DPhe-Arg-Trp-Gly-Arg-Pro-Val-Asp]} as an imaging agent (*19, 20*), highlighting the potential applications of radiolabeled lactam bridge-cyclized α-MSH peptides as effective diagnostic and therapeutic agents for melanoma.

Gallium-67 and Gallium-68 are suitable SPECT and positron emission tomography (PET) radiometals with desirable radiophysical properties (*21, 22*). Gallium-67 has a half-life of 78.3 h and decays with three γ-emissions at 93 keV (38% abundance), 185 keV (24% abundance), and 300 keV (16% abundance) that are suitable for SPECT imaging (*23, 24*). Moreover, ^{67}Ga is also a potential therapeutic radiometal due to its emissions of Auger and conversion electrons (*25*). Gallium-67 is a cyclotron-produced radionuclide (^{68}Zn(p, 2n)^{67}Ga) and is commercially available. The relatively long half-life of ^{67}Ga (78.3 h) makes it feasible to ship to the hospital or research institution after the production at the cyclotron site. Gallium-68 is an attractive radionuclide for PET imaging due to its 89% positron emission (maximum energy of 1.92 MeV). Gallium-68 has a half-life of 68 min and can be easily obtained via an in-house commercial ^{68}Ge−^{68}Ga generator, making the production of ^{68}Ga independent of an onsite dedicated cyclotron (*26*). The 68-min half-life of ^{68}Ga allows the generator elution every 3−4 h, which is ideal for several clinical studies in patients in one day. The half-life of the parent ^{68}Ge is 260.8 days, which makes the shelf life of a ^{68}Ge/^{68}Ga generator greater than one year. Importantly, ^{67}Ga and ^{68}Ga can be easily conjugated by the DOTA-peptides, which makes the kit formulation possible and facilitates the clinical use of gallium radiopharmaceuticals for SPECT and PET imaging.

Our laboratory has been interested in developing radiometal-labeled lactam bridge-cyclized α-MSH peptides for melanoma SPECT imaging. Hence, we prepared ^{67}Ga-DOTA-GlyGlu-CycMSH and examined its melanoma imaging properties in primary and pulmonary metastatic melanoma models to determine whether it could be used as an effective SPECT agent for both primary and metastatic melanoma detection in this study. The biodistribution and melanoma imaging properties of ^{67}Ga-DOTA-GlyGlu-CycMSH were determined in B16/F1 flank primary melanoma-bearing C57 mice and B16/F10 pulmonary metastatic melanoma-bearing C57 mice. The effect of L-lysine

* Yubin Miao, 2502 Marble NE, MSC09 5360, College of Pharmacy, University of New Mexico, Albuquerque, NM 87131, USA. Phone: (505) 925-4437; Fax: (505) 272-6749; E-mail: ymiao@salud.unm.edu.
[†] College of Pharmacy.
[‡] Cancer Research Treatment Center.
[§] Department of Dermatology.

10.1021/bc900428x © 2009 American Chemical Society
Published on Web 11/17/2009

coinjection in reducing the renal uptake of ^{67}Ga-DOTA-GlyGlu-CycMSH was examined in B16/F1 melanoma-bearing C57 mice.

MATERIALS AND METHODS

Chemicals and Reagents. Amino acids and resin were purchased from Advanced ChemTech Inc. (Louisville, KY) and Novabiochem (San Diego, CA). DOTA-tri-*t*-butyl ester was purchased from Macrocyclics Inc. (Richardson, TX). $^{67}GaCl_3$ was purchased from MDS Nordion, Inc. (Vancouver, Canada). All other chemicals used in this study were purchased from Thermo Fischer Scientific (Waltham, MA) and used without further purification. B16/F1 and B16/F10 murine melanoma cells were obtained from American Type Culture Collection (Manassas, VA).

Complexation of the Peptide with ^{67}Ga. DOTA-GlyGlu-CycMSH was synthesized as described previously (*19*) and identified by mass spectrometry. DOTA-GlyGlu-CycMSH was radiolabeled with ^{67}Ga using a 0.5 M NH_4OAc-buffered solution at pH 3.5. Briefly, 10 μL of $^{67}GaCl_3$ (18.5−37.0 MBq in 0.05 M HCl), 10 μL of 1 mg/mL DOTA-GlyGlu-CycMSH aqueous solution and 100 μL of 0.5 M NH_4OAc (pH 3.5) were added into a reaction vial and incubated at 90 °C for 20 min. After the incubation, 10 μL of 0.5% EDTA aqueous solution was added into the reaction vial to quench the reaction. The radiolabeled peptide was purified to single species by Waters RP-HPLC (Milford, MA) on a Grace Vadyc C-18 reverse-phase analytical column (Deerfield, IL) using the following gradient at a flow rate of 1 mL/min. The mobile phase consisted of solvent A (20 mM HCl aqueous solution) and solvent B (100% CH_3CN). The gradient was initiated and kept at 84:16 A/B for 3 min followed by a linear gradient of 84:16 A/B to 74:26 A/B over 20 min. Then, the gradient was changed from 74:26 A/B to 10:90 A/B over 3 min followed by an additional 5 min at 10:90 A/B. Thereafter, the gradient was changed from 10:90 A/B to 84:16 A/B over 3 min. The purified ^{67}Ga-peptide sample was purged with N_2 gas for 20 min to remove the acetonitrile. The pH of final solution was adjusted to 7.4 with 0.1 N NaOH and normal saline for cell work and animal studies. Serum stability of ^{67}Ga-DOTA-GlyGlu-CycMSH was determined by incubation in mouse serum at 37 °C according to the published procedure (*19*) for 24 h, and monitored for degradation by RP-HPLC.

Cellular Internalization and Efflux of ^{67}Ga-DOTA-GlyGlu-CycMSH. Cellular internalization and efflux of ^{67}Ga-DOTA-GlyGlu-CycMSH were evaluated in B16/F1 melanoma cells. After being washed once with binding medium, B16/F1 cells in cell culture plates were incubated at 25 °C for 20, 40, 60, 90, and 120 min ($n = 3$) in the presence of approximately 200 000 counts per minute (cpm) of HPLC-purified ^{67}Ga-DOTA-GlyGlu-CycMSH. After incubation, the reaction medium was aspirated and the cells were rinsed with 2 × 0.5 mL of ice-cold pH 7.4, 0.2% BSA/0.01 M PBS. Cellular internalization of ^{67}Ga-DOTA-GlyGlu-CycMSH was assessed by washing the cells with acidic buffer [40 mM sodium acetate (pH 4.5) containing 0.9% NaCl and 0.2% BSA] to remove the membrane-bound radioactivity. The remaining internalized radioactivity was obtained by lysing the cells with 0.5 mL of 1 N NaOH for 5 min. Membrane-bound and internalized ^{67}Ga activities were counted in a γ-counter. Cellular efflux of ^{67}Ga-DOTA-GlyGlu-CycMSH was determined by incubating B16/F1 cells with ^{67}Ga-DOTA-GlyGlu-CycMSH for 2 h at 25 °C, removing nonspecific-bound activity with 2 × 0.5 mL of ice-cold pH 7.4, 0.2% BSA/0.01 M PBS rinse, and monitoring radioactivity released into cell culture medium. At time points of 20, 40, 60, 90, and 120 min, the radioactivities on the cell surface and in the cells were separately collected and counted in a Wallac 1480 automated γ-counter (PerkinElmer, NJ).

B16/F1 Flank Primary and B16/F10 Pulmonary Metastatic Melanoma Models. B16/F1 flank primary melanoma and B16/F10 pulmonary metastatic melanoma models were generated to evaluate the biodistribution properties of ^{67}Ga-DOTA-GlyGlu-CycMSH. B16/F1 or B16/F10 melanoma cells were cultured in RPMI 1640 medium (Invitrogen Corporation, Grand Island, NY) containing $NaHCO_3$ (2 g/L), which was supplemented with 10% heat-inactivated fetal calf serum, 2 mmol/L L-glutamine, and 48 mg of gentamicin. B16/F1 flank primary melanoma tumors were generated by subcutaneously inoculating 1×10^6 B16/F1 cells/mouse in the right flank of the C57 mice (Harlan, Indianapolis, IN). The tumors reached approximately 0.2 g 10−12 days after the cell implantation. Pulmonary metastatic melanoma tumors were generated via injecting 2×10^5 B16/F10 cells/mouse into the C57 mice through the tail vein. The metastatic melanoma-bearing mice were used for biodistribution studies 16 days after cell injection.

Biodistribution Studies. All the animal studies were conducted in compliance with Institutional Animal Care and Use Committee approval. The biodistribution properties of ^{67}Ga-DOTA-GlyGlu-CycMSH were determined in B16/F1 flank melanoma-bearing C57 mice. Each mouse was injected with 0.037 MBq of ^{67}Ga-DOTA-GlyGlu-CycMSH through the tail vein. Groups of 5 mice were sacrificed at 0.5, 2, 4, and 24 h postinjection; and tumors and organs of interest were harvested, weighed, and counted. Blood values were taken as 6.5% of the whole-body weight. The results were expressed as percent injected dose/gram (%ID/g) and as percent injected dose (%ID). The specificity of the tumor uptake of ^{67}Ga-DOTA-GlyGlu-CycMSH was determined by blocking the tumor uptake with the coinjection of 10 μg of non-radiolabeled DOTA-GlyGlu-CycMSH. The biodistribution of ^{67}Ga-DOTA-GlyGlu-CycMSH in B16/F10 pulmonary metastatic melanoma-bearing C57 mice was determined and compared with that in normal C57 mice at 2 and 4 h postinjection.

Effect of L-Lysine Co-Injection on the Renal Uptake of ^{67}Ga-DOTA-GlyGlu-CycMSH. L-Lysine coinjection is effective in decreasing the renal uptakes of radiolabeled α-MSH peptides. Hence, the effect of L-lysine coinjection on the renal uptake of ^{67}Ga-DOTA-GlyGlu-CycMSH was examined in B16/F1 melanoma-bearing C57 mice. A group of 5 mice were injected with a mixture of 0.037 MBq of ^{67}Ga-DOTA-GlyGlu-CycMSH and 15 mg of L-lysine. The mice were sacrificed at 2 h postinjection, and tumors and kidneys were harvested, weighed, and counted in a γ-counter.

Imaging Melanoma with ^{67}Ga-DOTA-GlyGlu-CycMSH. The melanoma imaging properties of ^{67}Ga-DOTA-GlyGlu-CycMSH were examined in B16/F1 primary melanoma-bearing and B16/F10 pulmonary metastatic melanoma-bearing C57 mice. Two B16/F1 flank melanoma-bearing C57 mice were injected with 7.1 MBq of ^{67}Ga-DOTA-GlyGlu-CycMSH with or without 30 μg of non-radiolabeled DOTA-GlyGlu-CycMSH via the tail vein to demonstrate the specificity of the melanoma uptake. The mice were anesthetized with 1.5% isoflurane for small animal SPECT/CT (Nano-SPECT/CT, Bioscan) imaging 2 h postinjection. The 9 min CT imaging was immediately followed by the SPECT imaging of whole body. The SPECT scans of 24 projections were acquired, and total acquisition time was 60 min. Reconstructed data from SPECT and CT were visualized and coregistered using InVivoScope (Bioscan, Washington, DC).

A B16/F10 pulmonary metastatic melanoma-bearing mouse was used for ^{67}Ga-DOTA-GlyGlu-CycMSH SPECT/CT imaging to determine whether the melanoma metastases developed in the early stage (13 days after the cell injection) could be detected. The mouse was injected with 4.6 MBq of ^{67}Ga-DOTA-GlyGlu-CycMSH via the tail vein. The mouse was anesthetized

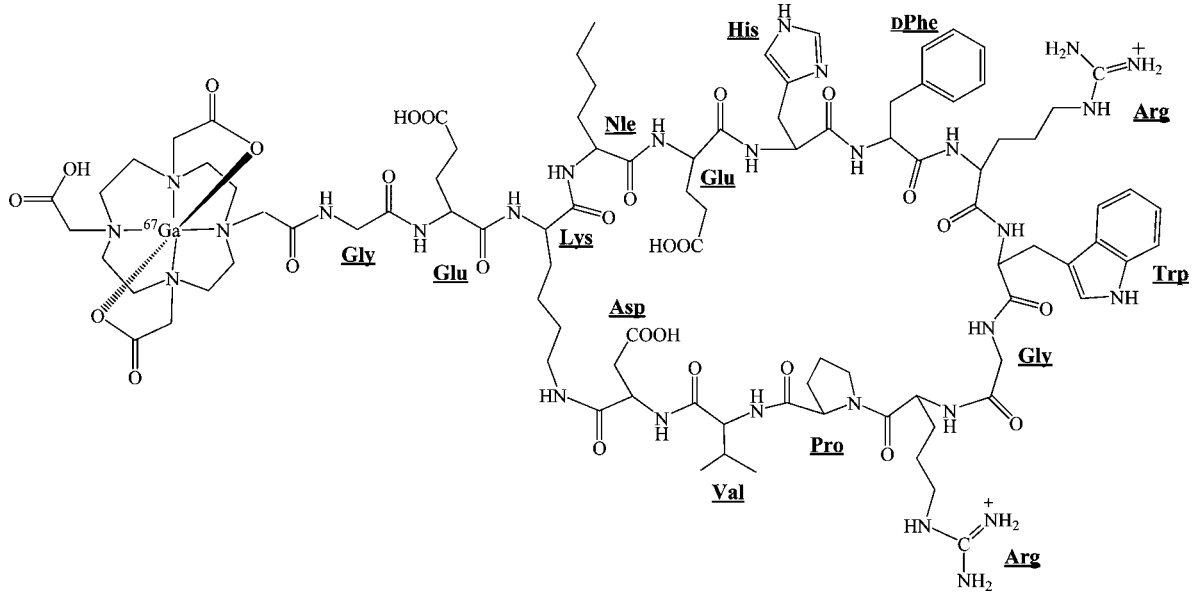

Figure 1. Structure of ^{67}Ga-DOTA-GlyGlu-CycMSH.

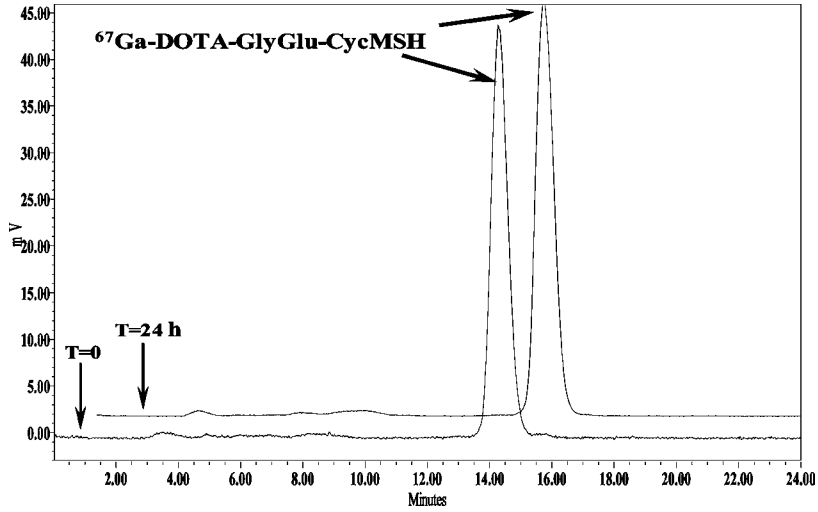

Figure 2. HPLC profile of radioactive ^{67}Ga-DOTA-GlyGlu-CycMSH ($T = 0$) and mouse serum stability of ^{67}Ga-DOTA-GlyGlu-CycMSH ($T =$ 24 h) after 24 h incubation at 37 °C. The retention time of ^{67}Ga-DOTA-GlyGlu-CycMSH was 14.4 min.

with 1.5% isoflurane for small animal SPECT/CT (NanoSPECT/CT, Bioscan) imaging 2 h postinjection. The 9 min CT imaging was immediately followed by the SPECT imaging of whole body. Reconstructed data from SPECT and CT were visualized and coregistered using InVivoScope (Bioscan, Washington, DC).

Statistical Methods. Statistical analysis was performed using the Student's *t* test for unpaired data to determine the significant differences between ^{67}Ga-DOTA-GlyGlu-CycMSH with or without non-radiolabeled DOTA-GlyGlu-CycMSH coinjection, between the bodistribution of ^{67}Ga-DOTA-GlyGlu-CycMSH in pulmonary metastatic melanoma-bearing mice and normal mice, and between ^{67}Ga-DOTA-GlyGlu-CycMSH with or without L-lysine coinjection. Differences at the 95% confidence level ($p < 0.05$) were considered significant.

RESULTS

DOTA-GlyGlu-CycMSH was synthesized, purified by RP-HPLC, and characterized by electrospray ionization mass spectrometry. DOTA-GlyGlu-CycMSH displayed greater than 95% purity with 30% overall synthetic yield. The peptide was labeled with ^{67}Ga using a 0.5 M NH_4OAc-buffered solution at pH 3.5. The radiolabeling yield was greater than 95%. Figure 1 illustrates the schematic structure of ^{67}Ga-DOTA-GlyGlu-CycMSH. ^{67}Ga-DOTA-GlyGlu-CycMSH was completely separated from its excess nonlabeled peptide by RP-HPLC. The retention times of ^{67}Ga-DOTA-GlyGlu-CycMSH and its nonlabeled peptide were 14.4 and 15.9 min, respectively. ^{67}Ga-DOTA-GlyGlu-CycMSH was stable in mouse serum at 37 °C. Only ^{67}Ga-DOTA-GlyGlu-CycMSH was detected by RP-HPLC after 24 h of incubation (Figure 2).

Cellular internalization and efflux of ^{67}Ga-DOTA-GlyGlu-CycMSH were evaluated in B16/F1 cells. Figure 3 illustrates cellular internalization and efflux of ^{67}Ga-DOTA-GlyGlu-CycMSH. ^{67}Ga-DOTA-GlyGlu-CycMSH exhibited rapid cellular internalization and extended cellular retention. There was 53.82 ± 3.96% of the cellular uptake of ^{67}Ga-DOTA-GlyGlu-CycMSH activity internalized in the B16/F1 cells 20 min post incubation. There was 69.91 ± 3.33% of the cellular uptake of ^{67}Ga-DOTA-GlyGlu-CycMSH activity internalized in the cells after 90 min incubation. Cellular efflux results demonstrated that 79.77 ± 9.49% of the internalized ^{67}Ga-DOTA-GlyGlu-CycMSH activity remained inside the cells 2 h after incubating cells in culture medium.

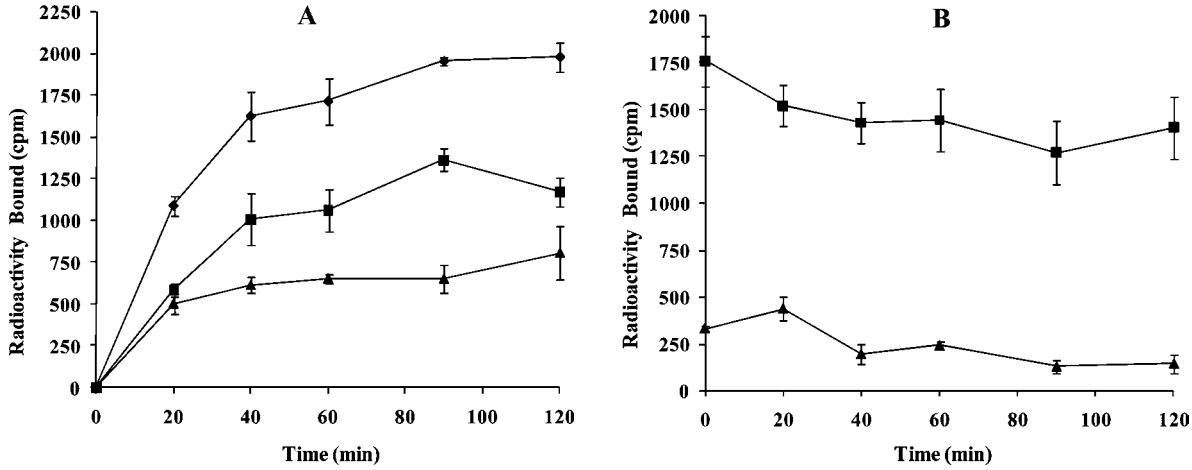

Figure 3. Cellular internalization (A) and efflux (B) of ^{67}Ga-DOTA-GlyGlu-CycMSH in B16/F1 melanoma cells at 25 °C. Total bound radioactivity (◆), internalized activity (■), and cell membrane activity (▲) were presented as counts per minute (cpm).

Table 1. Biodistribution of ^{67}Ga-DOTA-GlyGlu-CycMSH in B16/F1 Flank Primary Melanoma-Bearing C57 Mice[a]

tissue	0.5 h	2 h	2 h peptide blockade	4 h	24 h
			Percent Injected Dose/Gram (%ID/g)		
tumor	8.59 ± 1.37	12.93 ± 1.63	0.37 ± 0.02[b]	8.12 ± 0.60	5.02 ± 1.35
brain	0.10 ± 0.03	0.01 ± 0.01	0.01 ± 0.00	0.01 ± 0.00	0.01 ± 0.00
blood	1.22 ± 0.59	0.05 ± 0.04	0.24 ± 0.02[b]	0.17 ± 0.13	0.15 ± 0.11
heart	0.29 ± 0.10	0.04 ± 0.04	0.04 ± 0.01	0.05 ± 0.02	0.14 ± 0.13
lung	1.44 ± 0.47	0.02 ± 0.02	0.04 ± 0.03	0.11 ± 0.09	0.10 ± 0.06
liver	0.69 ± 0.27	0.23 ± 0.01	0.29 ± 0.04	0.25 ± 0.07	0.24 ± 0.08
spleen	0.41 ± 0.22	0.09 ± 0.08	0.07 ± 0.03	0.06 ± 0.04	0.22 ± 0.07
stomach	1.30 ± 0.36	0.08 ± 0.07	0.06 ± 0.05	0.08 ± 0.07	0.07 ± 0.04
kidneys	23.94 ± 7.15	27.55 ± 7.87	22.75 ± 4.32	22.6 ± 4.03	20.92 ± 5.77
muscle	0.46 ± 0.28	0.04 ± 0.02	0.09 ± 0.06	0.04 ± 0.01	0.09 ± 0.08
pancreas	0.47 ± 0.07	0.10 ± 0.08	0.09 ± 0.01	0.07 ± 0.05	0.11 ± 0.07
bone	0.61 ± 0.29	0.10 ± 0.01	0.18 ± 0.03	0.10 ± 0.02	0.21 ± 0.20
skin	1.62 ± 0.54	0.25 ± 0.03	0.04 ± 0.00[b]	0.20 ± 0.15	0.07 ± 0.06
			Percent Injected Dose (%ID)		
intestine	2.76 ± 1.34	0.37 ± 0.23	0.74 ± 0.10	0.35 ± 0.16	0.20 ± 0.01
urine	77.33 ± 0.74	81.90 ± 2.42	92.00 ± 1.50	86.59 ± 1.73	88.56 ± 6.78
			Tumor to Normal Tissue Uptake Ratio		
tumor/blood	7.04	258.59	1.54	47.76	33.47
tumor/kidney	0.36	0.46	0.02	0.36	0.24
tumor/lung	5.97	646.48	9.25	73.82	50.20
tumor/liver	12.45	56.21	1.28	32.48	20.92
tumor/muscle	18.67	323.24	4.11	203.00	55.78
tumor/skin	5.30	51.72	9.25	40.60	71.71

[a] The data were presented as percent injected dose/gram or as percent injected dose (mean ± SD, $n = 5$). [b] $p < 0.05$, significance comparison between ^{67}Ga-DOTA-GlyGlu-CycMSH with or without peptide blockade at 2 h postinjection.

The pharmacokinetics and tumor targeting properties of ^{67}Ga-DOTA-GlyGlu-CycMSH were determined in B16/F1 flank primary melanoma-bearing and B16/F10 pulmonary metastatic melanoma-bearing C57 mice. The biodistribution results of ^{67}Ga-DOTA-GlyGlu-CycMSH are shown in Tables 1 and 2. ^{67}Ga-DOTA-GlyGlu-CycMSH exhibited rapid and substantial tumor uptake. The tumor uptake value of ^{67}Ga-DOTA-GlyGlu-CycMSH was 8.59 ± 1.37%ID/g at 0.5 h postinjection. ^{67}Ga-DOTA-GlyGlu-CycMSH reached its peak tumor uptake value of 12.93 ± 1.63%ID/g at 2 h postinjection. There was 8.12 ± 0.60%ID/g of the ^{67}Ga-DOTA-GlyGlu-CycMSH activity remaining in the tumors at 4 h postinjection. The tumor uptake value of ^{67}Ga-DOTA-GlyGlu-CycMSH decreased to 5.02 ± 1.35%ID/g at 24 h postinjection. In the blocking study, the tumor uptake value of ^{67}Ga-DOTA-GlyGlu-CycMSH with 10 μg of non-radiolabeled DOTA-GlyGlu-CycMSH coinjection were only 2.9% of the tumor uptake value without non-radiolabeled DOTA-GlyGlu-CycMSH co-injection at 2 h postinjection ($p < 0.05$), demonstrating that the tumor uptake was specific and receptor-mediated. Whole-body clearance of ^{67}Ga-DOTA-GlyGlu-CycMSH was rapid, with approximately 82% of the injected radioactivity cleared through the urinary system by 2 h postinjection (Table 1). Normal organ uptakes of ^{67}Ga-DOTA-GlyGlu-CycMSH were generally very low (<0.30%ID/g) except for the kidneys at 2, 4, and 24 h postinjection. The renal uptake values of ^{67}Ga-DOTA-GlyGlu-CycMSH were 23.94 ± 7.15, 27.55 ± 7.87, 22.60 ± 4.03 and 20.92 ± 5.77%ID/g at 0.5, 2, 4, and 24 h postinjection. High tumor/blood and tumor/normal organ uptake ratios were demonstrated as early as 0.5 h postinjection except for the tumor/kidney ratio (Table 1). Co-injection of 15 mg of L-lysine reduced the kidney uptake value of ^{67}Ga-DOTA-GlyGlu-CycMSH to 8.32 ± 5.18%ID/g (69.8% reduction) without affecting the tumor uptake at 2 h postinjection (Figure 4).

The biodistribution results of ^{67}Ga-DOTA-GlyGlu-CycMSH in B16/F10 pulmonary metastatic melanoma-bearing C57 mice

Table 2. Biodistribution of ^{67}Ga-DOTA-GlyGlu-CycMSH in B16/F10 Pulmonary Metastatic Melanoma-Bearing (Lung Mets) and Normal C57 Mice (Normal)[a]

	2 h		4 h	
Tissue	Lung Mets	Normal	Lung Mets	Normal
	Percent injected dose/gram (%ID/g)			
Brain	0.03 ± 0.02	0.01 ± 0.01	0.01 ± 0.01	0.02 ± 0.02
Blood	0.21 ± 0.15	0.13 ± 0.07	0.06 ± 0.04[b]	0.19 ± 0.11
Heart	0.02 ± 0.02[b]	0.09 ± 0.06	0.12 ± 0.08	0.24 ± 0.07
Lung	1.44 ± 0.75[b]	0.15 ± 0.10	1.49 ± 0.69[b]	0.17 ± 0.11
Liver	0.42 ± 0.01[b]	0.46 ± 0.03	0.47 ± 0.10	0.55 ± 0.14
Spleen	0.41 ± 0.07	0.33 ± 0.08	0.14 ± 0.11	0.04 ± 0.04
Stomach	0.19 ± 0.03	0.21 ± 0.02	0.18 ± 0.13	0.28 ± 0.12
Kidneys	29.67 ± 6.55	37.20 ± 2.16	28.75 ± 4.30	31.98 ± 5.35
Muscle	0.07 ± 0.01	0.10 ± 0.05	0.17 ± 0.11[b]	0.05 ± 0.02
Pancreas	0.16 ± 0.09	0.15 ± 0.07	0.18 ± 0.09	0.20 ± 0.07
Bone	0.16 ± 0.09	0.12 ± 0.08	0.44 ± 0.09	0.42 ± 0.16
Skin	0.57 ± 0.19	0.50 ± 0.09	0.33 ± 0.12	0.46 ± 0.15
	Percent injected dose (%ID)			
Intestines	0.52 ± 0.18	1.32 ± 0.73	1.13 ± 0.11	2.00 ± 0.81
Urine	90.55 ± 0.38	85.76 ± 3.76	88.12 ± 1.12	88.17 ± 1.22

[a] The data were presented as percent injected dose/gram or as percent injected dose (mean ± SD, $n = 5$). [b] $p < 0.05$, significance comparison between ^{67}Ga-DOTA-GlyGlu-CycMSH in pulmonary metastatic melanoma-bearing and normal C57 mice.

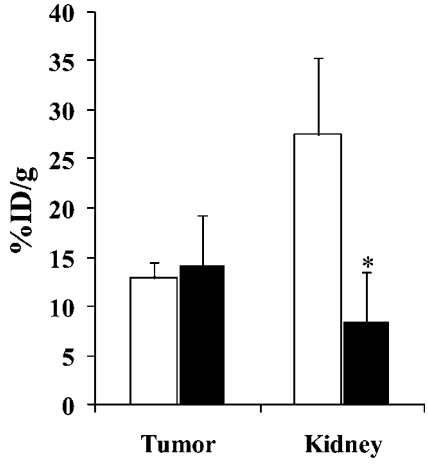

Figure 4. Effect of L-lysine co-injection on the renal uptake of ^{67}Ga-DOTA-GlyGlu-CycMSH at 2 h postinjection. Black and white columns represented the tumor and kidney uptakes of ^{67}Ga-DOTA-GlyGlu-CycMSH with or without L-lysine coinjection, respectively. L-Lysine coinjection significantly (*$p < 0.05$) reduced the renal uptake of ^{67}Ga-DOTA-GlyGlu-CycMSH by 69.8% at 2 h postinjection without affecting the tumor uptake.

at 2 and 4 h postinjection are presented in Table 2 and compared with those in normal C57 mice. ^{67}Ga-DOTA-GlyGlu-CycMSH exhibited significantly ($p < 0.05$) higher uptake value in metastatic melanoma-bearing lung than that in normal lung. The uptake values of ^{67}Ga-DOTA-GlyGlu-CycMSH radioactivity in the metastatic melanoma-bearing and normal lungs were 1.44 ± 0.75 and 0.15 ± 0.10%ID/g, 1.49 ± 0.69 and 0.17 ± 0.11%ID/g at 2 and 4 h postinjection, respectively. The ^{67}Ga-DOTA-GlyGlu-CycMSH displayed higher lung/normal organ uptake ratios in pulmonary metastatic melanoma-bearing mice than those in normal mice (Table 2). Similar rapid whole-body clearance of ^{67}Ga-DOTA-GlyGlu-CycMSH exhibited in both B16/F10 pulmonary metastatic melanoma-bearing C57 mice and normal C57 mice (Table 2).

Two B16/F1 flank primary melanoma-bearing C57 mice were injected with ^{67}Ga-DOTA-GlyGlu-CycMSH with or without nonradioactive DOTA-GlyGlu-CycMSH to visualize the tumors and determine the specificity of the tumor uptake

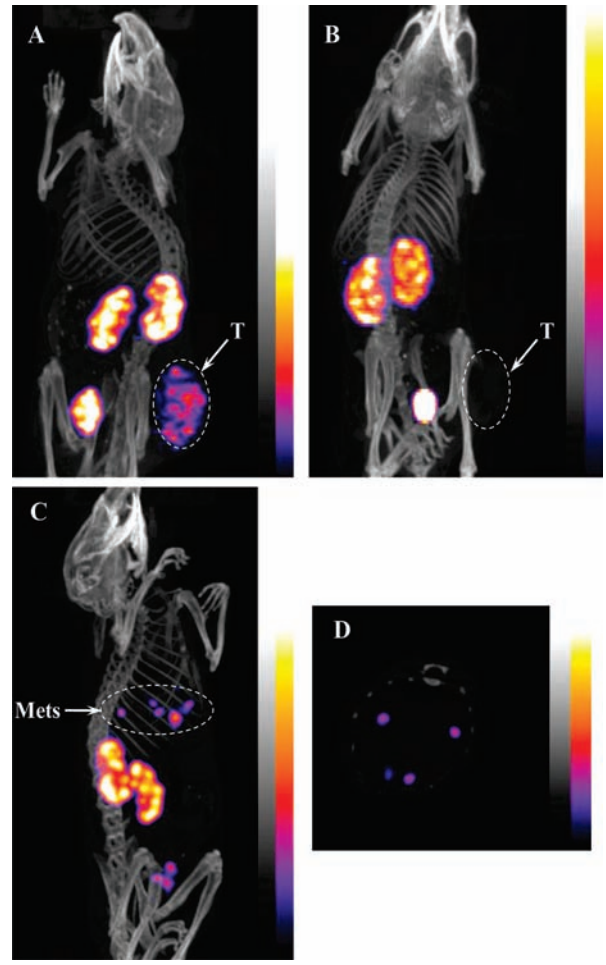

Figure 5. Whole-body images of ^{67}Ga-DOTA-GlyGlu-CycMSH in B16/F1 flank melanoma-bearing C57 mice with or without peptide blockade (A and B) at 2 h postinjection; whole-body (C) and transversal (D) images of ^{67}Ga-DOTA-GlyGlu-CycMSH in a B16/F10 pulmonary metastatic melanoma-bearing C57 mouse at 2 h postinjection. Flank melanoma (T) and pulmonary melanoma metastases (Mets) were highlighted with arrows on the images.

at 2 h after dose administration. The whole-body SPECT/CT images of the mice are presented in Figure 5A and B. The flank melanoma tumors were clearly visualized by SPECT/CT using ^{67}Ga-DOTA-GlyGlu-CycMSH as an imaging probe. ^{67}Ga-DOTA-GlyGlu-CycMSH exhibited high tumor to normal organ uptake ratios except for the kidney, which were coincident with the biodistribution results. Accumulation of the ^{67}Ga-DOTA-GlyGlu-CycMSH activity in the bladder demonstrated the major urinary clearance. Co-injection of nonradioactive DOTA-GlyGlu-CycMSH blocked the melanoma uptake (Figure 5B), demonstrating that the melanoma uptake of ^{67}Ga-DOTA-GlyGlu-CycMSH was specific and MC1 receptor-mediated. A B16/F10 pulmonary melanoma-bearing C57 mouse was injected with ^{67}Ga-DOTA-GlyGlu-CycMSH via the tail vein to image melanoma metastases early developed in the lung (13 days after the cell injection). The whole-body and transverse images are presented in Figure 5C and D. The pulmonary metastatic melanoma foci were clearly visualized in both whole-body and transversal images by SPECT/CT using ^{67}Ga-DOTA-GlyGlu-CycMSH as an imaging probe.

DISCUSSION

Gallium-67 and gallium-68 are attractive radiometals in nuclear medicine due to their suitable imaging properties for

SPECT and PET. Compared to ^{68}Ga, ^{67}Ga has longer half-life and is thus a better radionuclide to use for examining the melanoma targeting property of the radioactive gallium-labeled lactam bridge-cyclized α-MSH peptide *in vivo*. In this study, we selected ^{67}Ga to radiolabel the novel lactam bridge-cyclized DOTA-GlyGlu-CycMSH peptide to evaluate its potential for primary and metastatic melanoma detection. DOTA-GlyGlu-CycMSH was readily labeled with ^{67}Ga in greater than 95% radiolabeling yield. The metal chelator DOTA formed a stable complex with ^{67}Ga. ^{67}Ga-DOTA-GlyGlu-CycMSH was stable in serum at 37 °C for 24 h (Figure 2). ^{67}Ga-DOTA-GlyGlu-CycMSH exhibited substantial melanoma uptake and prolonged melanoma retention in B16/F1 melanoma-bearing C57 mice (Table 1). ^{67}Ga-DOTA-GlyGlu-CycMSH showed higher melanoma uptake values than those of ^{111}In-DOTA-GlyGlu-CycMSH (*19*). The tumor uptake values of ^{67}Ga-DOTA-GlyGlu-CycMSH were 1.24, 1.10, and 2.12 times the tumor uptake values of ^{111}In-DOTA-GlyGlu-CycMSH at 2, 4, and 24 h postinjection. In 2004, Froidevaux et al. (*13*) reported a ^{67}Ga-labeled linear α-MSH peptide (^{67}Ga-DOTA-NAPamide) for melanoma targeting. The tumor uptake values of ^{67}Ga-DOTA-NAPamide were 9.43 ± 1.06 and 3.10 ± 0.36%ID/g at 4 and 24 h postinjection in the B16/F1 flank melanoma-bearing C57 mice (*13*). ^{67}Ga-DOTA-GlyGlu-CycMSH exhibited a 14% lower tumor uptake value than ^{67}Ga-DOTA-NAPamide at 4 h postinjection. However, the tumor uptake value of ^{67}Ga-DOTA-GlyGlu-CycMSH was 1.62 times the tumor uptake value of ^{67}Ga-DOTA-NAPamide at 24 h postinjection. The renal uptake values of ^{67}Ga-DOTA-GlyGlu-CycMSH were 5.68 and 10.25 times the renal uptake values of ^{67}Ga-DOTA-NAPamide at 4 and 24 h postinjection. Recently, it has been reported that different pathways may play roles in the mechanism of the renal uptakes of radiolabeled peptides besides the electrostatic interaction between the peptides and tubule cells (*27, 28*). For instance, the use of colchicines (preventing endocytosis in tubular cells) decreased the renal uptake up to 25% in a rat model (*28*). The transmembrane glycoprotein megalin is involved in the renal uptakes of radiolabeled somatostatin analogues (*29*). Since the extracellular domains of megalin can accommodate a variety of ligands, megalin may be involved in the renal uptakes of other radiolabeled peptides. L-Lysine coinjection decreased the renal uptake value by 69.8% at 2 h postinjection (Figure 4), demonstrating that the electrostatic interaction between the peptide and tubular cells was a key factor for the renal uptake of ^{67}Ga-DOTA-GlyGlu-CycMSH. Reduction of the nonspecific renal uptake of ^{67}Ga-DOTA-GlyGlu-CycMSH by L-lysine coinjection in this study was consistent with the published results on radiolabeled metal-cyclized α-MSH peptides (*4*). Although more studies need to be conducted in the future, it is likely that other mechanisms besides the electrostatic interaction are involved in the renal uptake of ^{67}Ga-DOTA-GlyGlu-CycMSH as well.

Despite the clinical use of [^{18}F]FDG in melanoma staging and melanoma metastases identification, [^{18}F]FDG is not a melanoma-specific imaging agent and is also not effective in imaging small melanoma metastases (<5 mm) and melanomas that have primary energy sources other than glucose (*30*−*32*). Radiolabeled lactam bridge-cyclized α-MSH peptides are melanoma-specific and can be employed to noninvasively confirm the identity of a tumor as melanoma. As shown in Figure 5, the flank primary melanoma lesions were clearly visualized by SPECT/CT using ^{67}Ga-DOTA-GlyGlu-CycMSH as an imaging probe. Importantly, the melanoma uptake of ^{67}Ga-DOTA-GlyGlu-CycMSH was blocked by 30 μg of nonradioactive DOTA-GlyGlu-CycMSH, demonstrating the melanoma uptake of ^{67}Ga-DOTA-GlyGlu-CycMSH was specific and MC1 receptor-mediated. ^{67}Ga-DOTA-GlyGlu-CycMSH may have its greatest utilization when combined with a therapeutic radiometal-labeled DOTA-GlyGlu-CycMSH. Since the DOTA can form stable complexes with a variety of therapeutic radiometals (i.e., ^{177}Lu, ^{90}Y, and ^{212}Pb), the same DOTA-conjugated lactam bridge-cyclized α-MSH peptide can be radiolabeled with diagnostic and therapeutic radionuclides to yield matched-pair diagnostic and therapeutic peptides. The radiolabeled diagnostic peptide can be used to not only detect melanoma lesions, but also identify the expression levels of the MC1 receptors in different melanoma lesions. The important information on the expression of the MC1 receptors will provide the physicians critical guidance for selecting the right melanoma patients for MC1 receptor-targeted radionuclide therapy. The patient-specific dosimetry determined by the diagnostic peptide will guide the physicians to select safe and effective doses of the therapeutic peptide for the melanoma patients. Moreover, the follow-up imaging using the radiolabeled diagnostic peptide can monitor the response of melanoma to the treatment and provide the physicians the evidence for choosing more efficacious and safer therapeutic peptide doses to the melanoma patients for further treatment.

High mortality of malignant melanoma is tightly associated with the occurrence of metastatic melanoma due to its aggressiveness and resistance to current chemotherapy and immunotherapy regimens. Over the past several years, both radiolabeled linear and cyclic α-MSH peptides have been investigated to target the MC1 receptors for the detection of melanoma metastases (*7, 12, 13, 20*) by tissue autoradiograph and small animal SPECT/CT. Initially, linear ^{111}In-DOTA-MSH$_{oct}$ and ^{67}Ga-DOTA-NAPamide were reported to be able to identify both melanotic and amelanotic melanoma metastases in lung by tissue autoradiograph (*12, 13*). In 2007,^{99m}Tc- and ^{111}In-labeled metal-cyclized DOTA-Re(Arg^{11})CCMSH were reported to be successful in visualizing well-developed B16/F10 pulmonary melanoma metastases (24 days after the cell injection) in euthanized melanoma-bearing mice by small animal SPECT/CT (*7*), demonstrating the potential of using radiolabeled α-MSH peptides for noninvasive melanoma metastases imaging. Recently, we reported the successful utilization of ^{111}In-labeled lactam bridge-cyclized DOTA-GlyGlu-CycMSH in detecting B16/F10 relatively early developed pulmonary metastases (17 and 20 days after the cell injection) in live melanoma-bearing mice by Nano-SPECT/CT (*20*). Both individual metastatic melanoma foci (17 days after the cell injection) and bigger lesions (20 days after the cell injection) developed in the lung were clearly visualized with ^{111}In-DOTA-GlyGlu-CycMSH (*20*), demonstrating the feasibility of using ^{111}In-DOTA-GlyGlu-CycMSH as an imaging probe to monitor tumor response to therapy. Despite the fact that ^{111}In-DOTA-GlyGlu-CycMSH was superior to [^{18}F]FDG in detecting pulmonary melanoma metastases reported in our previous publication (*20*), it was not determined whether the metastatic melanoma foci in the even earlier stage of development (<17 days) could be detected by Nano-SPECT/CT using radiolabeled DOTA-GlyGlu-CycMSH as an imaging probe. It seemed to us that it would be possible to detect the metastatic melanoma foci in the even earlier stage of development (<17 days) based on the fact that the spatial resolution of Nano-SPECT with multiple-pinhole collimator was approximately 0.8 mm for a Jaszczak phantom filled with ^{111}In aqueous solution. It was reported that pulmonary metastatic melanoma deposits were initially detectable by small animal CT approximately 15−18 days post tail vein injection of 0.2 million of B16/F10 melanoma cells (*33*). Hence, we selected 13 days after the cell injection (0.2 million B16/F10 cells) as an early development time point of

pulmonary melanoma metastases to evaluate the imaging property of ^{67}Ga-DOTA-GlyGlu-CycMSH in this study. As shown in Figure 5C and D, individual pulmonary metastatic melanoma foci were clearly visualized by SPECT/CT using ^{67}Ga-DOTA-GlyGlu-CycMSH as an imaging probe 2 h postinjection. Compared to the metastatic melanoma images we reported previously (*20*), the images of melanoma metastases reported in this study were even more striking since the pulmonary melanoma metastases were developed only 13 days after the cell injection. The remarkable images of melanoma metastases presented in this study demonstrated the feasibility of using ^{67}Ga-DOTA-GlyGlu-CycMSH as an effective imaging probe for early detection of metastatic melanoma.

In conclusion, ^{67}Ga-DOTA-GlyGlu-CycMSH exhibited favorable primary and metastatic melanoma targeting and imaging properties, highlighting its potential as an effective imaging probe for early detection of primary and metastatic melanoma.

ACKNOWLEDGMENT

We appreciate Dr. Fabio Gallazzi and Mr. Benjamin M. Gershman for their technical assistance. This work was supported in part by the Southwest Melanoma SPORE Developmental Research Program, the Oxnard Foundation, the DOD grant W81XWH-09-1-0105 and the NIH grant NM-INBRE P20RR016480. The image in this article was generated by the Keck-UNM Small Animal Imaging Resource established with funding from the W.M. Keck Foundation and the University of New Mexico Cancer Research and Treatment Center (NIH P30 CA118100).

LITERATURE CITED

(1) Tatro, J. B., and Reichlin, S. (1987) Specific receptors for alpha-melanocyte-stimulating hormone are widely distributed in tissues of rodents. *Endocrinology 121*, 1900–1907.

(2) Siegrist, W., Solca, F., Stutz, S., Giuffre, L., Carrel, S., Girard, J., and Eberle, A. N. (1989) Characterization of receptors for alpha-melanocyte-stimulating hormone on human melanoma cells. *Cancer Res. 49*, 6352–6358.

(3) Chen, J., Cheng, Z., Hoffman, T. J., Jurisson, S. S., and Quinn, T. P. (2000) Melanoma-targeting properties of ^{99m}Technetium-labeled cyclic α-melanocyte-stimulating hormone peptide analogues. *Cancer Res. 60*, 5649–5658.

(4) Miao, Y., Owen, N. K., Whitener, D., Gallazzi, F., Hoffman, T. J., and Quinn, T. P. (2002) In vivo evaluation of ^{188}Re-labeled alpha-melanocyte stimulating hormone peptide analogs for melanoma therapy. *Int. J. Cancer 101*, 480–487.

(5) Miao, Y., Whitener, D., Feng, W., Owen, N. K., Chen, J., and Quinn, T. P. (2003) Evaluation of the human melanoma targeting properties of radiolabeled alpha-melanocyte stimulating hormone peptide analogues. *Bioconjugate Chem. 14*, 1177–1184.

(6) Miao, Y., Owen, N. K., Fisher, D. R., Hoffman, T. J., and Quinn, T. P. (2005) Therapeutic efficacy of a ^{188}Re labeled α-melanocyte stimulating hormone peptide analogue in murine and human melanoma-bearing mouse models. *J. Nucl. Med. 46*, 121–129.

(7) Miao, Y., Benwell, K., and Quinn, T. P. (2007) ^{99m}Tc- and ^{111}In-labeled α-melanocyte-stimulating hormone peptides as imaging probes for primary and pulmonary metastatic melanoma detection. *J. Nucl. Med. 48*, 73–80.

(8) Miao, Y., Hylarides, M., Fisher, D. R., Shelton, T., Moore, H. A., Wester, D. W., Fritzberg, A. R., Winkelmann, C. T., Hoffman, T. J., and Quinn, T. P. (2005) Melanoma therapy via peptide-targeted α-radiation. *Clin. Cancer Res. 11*, 5616–5621.

(9) Miao, Y., Figueroa, S. D., Fisher, D. R., Moore, H. A., Testa, R. F., Hoffman, T. J., and Quinn, T. P. (2008) ^{203}Pb-labeled alpha-melanocyte stimulating hormone peptide as an imaging probe for melanoma detection. *J. Nucl. Med. 49*, 823–829.

(10) Miao, Y., Hoffman, T. J., and Quinn, T. P. (2005) Tumor targeting properties of ^{90}Y and ^{177}Lu labeled alpha-melanocyte stimulating hormone peptide analogues in a murine melanoma model. *Nucl. Med. Biol. 32*, 485–493.

(11) Miao, Y., Shelton, T., and Quinn, T. P. (2007) Therapeutic efficacy of a ^{177}Lu labeled DOTA conjugated α-melanocyte stimulating hormone peptide in a murine melanoma-bearing mouse model. *Cancer Biother. Radiopharm. 22*, 333–341.

(12) Froidevaux, S., Calame-Christe, M., Tanner, H., Sumanovski, L., and Eberle, A. N. (2002) A novel DOTA-α-melanocyte-stimulating hormone analog for metastatic melanoma diagnosis. *J. Nucl. Med. 43*, 1699–1706.

(13) Froidevaux, S., Calame-Christe, M., Schuhmacher, J., Tanner, H., Saffrich, R., Henze, M., and Eberle, A. N. (2004) A Gallium-labeled DOTA-α-melanocyte-stimulating hormone analog for PET imaging of melanoma metastases. *J. Nucl. Med. 45*, 116–123.

(14) Froidevaux, S., Calame-Christe, M., Tanner, H., and Eberle, A. N. (2005) Melanoma targeting with DOTA-alpha-melanocyte-stimulating hormone analogs: structural parameters affecting tumor uptake and kidney uptake. *J. Nucl. Med. 46*, 887–895.

(15) McQuade, P., Miao, Y., Yoo, J., Quinn, T. P., Welch, M. J., and Lewis, J. S. (2005) Imaging of melanoma using ^{64}Cu and ^{86}Y-DOTA-ReCCMSH(Arg^{11}), a cyclized peptide analogue of α-MSH. *J. Med. Chem. 48*, 2985–2992.

(16) Wei, L., Butcher, C., Miao, Y., Gallazzi, F., Quinn, T. P., Welch, M. J., and Lewis, J. S. (2007) Synthesis and biological evaluation of Cu-64 labeled rhenium-cyclized α-MSH peptide analog using a cross-bridged cyclam chelator. *J. Nucl. Med. 48*, 64–72.

(17) Wei, L., Miao, Y., Gallazzi, F., Quinn, T. P., Welch, M. J., Vavere, A. L., and Lewis, J. S. (2007) Ga-68 labeled DOTA-rhenium cyclized α-MSH analog for imaging of malignant melanoma. *Nucl. Med. Biol. 34*, 945–953.

(18) Cheng, Z., Xiong, Z., Subbarayan, M., Chen, X., and Gambhir, S. S. (2007) ^{64}Cu-labeled alpha-melanocyte-stimulating hormone analog for MicroPET imaging of melanocortin 1 receptor expression. *Bioconjugate Chem. 18*, 765–772.

(19) Miao, Y., Gallazzi, F., Guo, H., and Quinn, T. P. (2008) ^{111}In-labeled lactam bridge-cyclized alpha-melanocyte stimulating hormone peptide analogues for melanoma imaging. *Bioconjugate Chem. 19*, 539–547.

(20) Guo, H., Shenoy, N., Gershman, B. M., Yang, J., Sklar, L. A., and Miao, Y. (2009) Metastatic melanoma imaging with an ^{111}In-labeled lactam bridge-cyclized alpha-melanocyte stimulating hormone peptide. *Nucl. Med. Biol. 36*, 267–276.

(21) Green, M. A., and Welch, M. J. (1989) Gallium radiopharmaceutical chemistry. *Int. J. Rad. Appl. Instrum. B 16*, 435–448.

(22) Anderson, C. J., and Welch, M. J. (1999) Radiometal-labeled agents (non-technetium) for diagnostic imaging. *Chem. Rev. 99*, 2219–2234.

(23) Eisenwiener, K., Prata, M. I., Buschmann, I., Zhang, H. W., Santos, A. C., Wenger, S., Reubi, J. C., and Mäcke, H. R. (2002) NODAGATOC, a new chelator-coupled somatostatin analogue labeled with [$^{67/68}$Ga] and [^{111}In] for SPECT, PET, and targeted therapeutic applications of somatostatin receptor (hsst2) expression tumors. *Bioconjugate Chem. 13*, 530–541.

(24) Zhernosekov, K., Aschoff, P., Filosofov, D., Jahn, M., Jennewein, M., Adrian, H. J., Bihl, H., and Rösch, F. (2005) Visualisation of a somatostatin receptor-expressing tumor with ^{67}Ga-DOTATOC SPECT. *Eur. J. Nucl. Med. Mol. Imaging 32*, 1129.

(25) Mariani, G., Bodei, L., Adelstein, S. J., and Kassis, A. I. (2000) Emerging roles for radiometabolic therapy of tumors based on auger electron emission. *J. Nucl. Med. 41*, 1519–1521.

(26) Maecke, H. R., Hofmann, M., and Haberkorn, U. (2005) ^{68}Ga-labeled peptides in tumor imaging. *J. Nucl. Med. 46*, 172S–178S.

(27) Béhé, M., Kluge, G., Becker, W., Gotthardt, M., and Behr, T. M. (2005) Use of polyglutamic acids to reduce uptake of

radiometal-labeled minigastrin in the kidneys. *J. Nucl. Med. 46*, 1012–1015.
(28) Rolleman, E. J., Krenning, E. P., Van Gameren, A., Bernard, B. F., and De Jong, M. (2004) Uptake of [^{111}In-DTPA^{0}]octreotide in the rat kidney is inhibited by colchicine and not by fructose. *J. Nucl. Med. 45*, 709–713.
(29) De Jong, M., Barone, R., Krenning, E. P., Bernard, B. F., Melis, M., Vissor, T., Gekle, M., Willnow, T. E., Walrand, S., Jamar, F., and Pauwels, S. (2005) Megalin is essential for renal proximal tubule reabsorption of ^{111}In-DTPA-Octreotide. *J. Nucl. Med. 46*, 1696–1700.
(30) Alonso, O., Martínez, M., Delgado, L., De León, A., De Boni, D., Lago, G., Garcés, M., Fontes, F., Espasandín, J., and Priario, J. (2003) Staging of regional lymph nodes in melanoma patients by means of ^{99m}Tc-MIBI scintigraphy. *J. Nucl. Med. 44*, 1561–1565.
(31) Nabi, H. A., and Zubeldia, J. M. (2002) Clinical application of ^{18}F-FDG in oncology. *J. Nucl. Med. Technol. 30*, 3–9.
(32) Dimitrakopoulou-Strauss, A., Strauss, L. G., and Burger, C. (2001) Quantitative PET studies in pretreated melanoma patients: A comparison of 6-[^{18}F]fluoro-L-DOPA with ^{18}F-FDG and ^{15}O-water using compartment and non-compartment analysis. *J. Nucl. Med. 42*, 248–256.
(33) Winkelmann, C. T., Figueroa, S. D., Rold, T. L., and Volkert, W. A. (2006) Microimaging characterization of a B16-F10 melanoma metastasis mouse model. *Mol. Imaging 5*, 105–114.

BC900428X

Photo-Click Immobilization of Carbohydrates on Polymeric Surfaces—A Quick Method to Functionalize Surfaces for Biomolecular Recognition Studies

Oscar Norberg,[†] Lingquan Deng,[†] Mingdi Yan,*[,‡] and Olof Ramström*[,†,‡]

Department of Chemistry, KTH - Royal Institute of Technology, Teknikringen 30, S-10044, Stockholm, Sweden, and Department of Chemistry, Portland State University, P.O. Box 751, Portland, Oregon 97207-0751. Received August 10, 2009; Revised Manuscript Received October 10, 2009

Methods to rapidly functionalize specific polymeric surfaces with alkynes, which can subsequently be linked to azide-containing carbohydrates, are presented. The methods comprise two main concepts: azide photoligation and Cu-catalyzed azide−alkyne cycloaddition. 2-Azidoethyl-functionalized α-D-mannopyranoside was synthesized and covalently attached to alkyne-functionalized polymeric surfaces using the techniques. The protein recognition properties of the carbohydrate-presenting surfaces were evaluated using quartz crystal microbalance biosensor instrumentation.

INTRODUCTION

Carbohydrates play highly diverse roles in biology. In polymeric form, they act as an energy source as well as a cell form stabilizer. In mono- and oligomeric forms, they build up DNA/RNA and function in the glycosylation process to increase protein diversity and stability. Carbohydrates also exist in high concentrations in the cell membrane where they have key functions as recognition markers, e.g., in cell−cell communication, cell adhesion and development, fertilization, immune response, signal transduction, and viral/bacterial infections (*1*−*4*). Considering the vast amount of data obtained from DNA and protein microarrays to date, it is desirable to apply the same methods to carbohydrates. Unfortunately, the analyses of these interactions are associated with several difficulties, which have made glycobiology a demanding area of research. The most important difference between carbohydrates and other biomolecules, like DNA and proteins, is that the biosynthesis of carbohydrates is not performed by replication of a template, but rather by a complex pathway of glycosyltransferases and glycosidases in several compartments of the cell, which severely complicates the *in vivo* amplification and purification of complex oligosaccharides. Further, the complex structure and reactivity aggravates the *in vitro* synthesis and quantification, creating a bottleneck that has delayed the development of high-throughput analysis methods, like microarrays, in glycobiology. Finally, since glycans in biology are presented in a specific direction, attached at the reducing end, the manufacturing of glycan arrays requires highly selective methods of immobilization (*1, 5, 6*). Despite, or perhaps due to, the difficulties in glycobiology, several promising examples of glycoarrays have appeared to date (*7*−*11*).

Herein, we present a 1-/2-step method to quickly functionalize specific polymeric surfaces with alkynes using a photoligation technique based on perfluorophenylazide (PFPA). The alkyne surfaces can subsequently be linked to azide-containing biomolecules like carbohydrates using Cu-catalyzed azide−alkyne cycloaddition (CuAAC, click chemistry) (*12, 13*). Both azides and alkynes are rare in biological systems and have been shown to be highly inert under biological conditions (*14*). CuAAC has received a lot of attention since its discovery, especially within glycobiology where several examples of carbohydrate arrays utilizing CuAAC have been published (*15*−*21*).

EXPERIMENTAL PROCEDURES

General. All commercially available starting materials were of reagent grade and used as received. Lectins were purchased from Sigma-Aldrich and Vector Laboratories. QCM crystals were purchased from Attana AB. ^{1}H, ^{13}C, and ^{19}F NMR data were recorded on a Bruker Avance 400 instrument at 400 MHz (^{1}H) or a Bruker DMX 500 instrument at 500 MHz (^{1}H), 125 (^{13}C), or 470 MHz (^{19}F). Chemical shifts are reported as δ values (ppm) with $CDCl_3$ (^{1}H: $\delta = 7.26$, ^{13}C = 77.16), DMSO-d_6 (^{1}H: $\delta = 2.50$, ^{13}C = 39.52), or D_2O (^{1}H: $\delta = 4.79$) as internal standard. *J* values are given in Hz. ^{1}H peak assignments were made by first-order analysis of the spectra supported by standard ^{1}H−^{1}H correlation spectroscopy (COSY). Thin layer chromatography (TLC) was performed on precoated Cromatofolios AL Silica gel 60 F_{254} plates (Merck). Flash column chromatography was performed on silica gel 60, 0.040−0.063 mm (SDS). All experiments containing penta-/tetrafluorophenylazide groups were conducted in the absence of light with all reaction flasks covered with aluminum foil to prevent decomposition.

2-(2-(2-(Prop-2-ynyloxy)ethoxy)ethoxy)ethanol (2). Triethylene glycol (22.3 mL, 167 mmol) was added to a flask containing ground potassium hydroxide (3.7 g, 61.7 mmol). The mixture was stirred at 40 °C for 30 min after which propargyl bromide (6 mL, 55.7 mmol) was added. The mixture was then stirred at 60 °C for 3 h. The mixture was then diluted with water (50 mL) and acidified to pH 1 with 1 M hydrochloric acid (∼80 mL). The resulting mixture was extracted with EtOAc (3 × 100 mL) and the extract was washed with brine (2 × 100 mL). The organic phase was dried (Na_2SO_4) and the solvent evaporated under reduced pressure giving a yellow oil (6.3 g). The crude product was purified by flash column chromatography using solvent system hexanes/EtOAc (1:1 v/v) giving **2** as a colorless oil (3.76 g, 36%).

^{1}H NMR (500 MHz, $CDCl_3$): δ 4.21 (d, 2 H, $J = 2.2$ Hz, CHCC*H*$_2$O), 3.74−3.66 (m, 11 H, OC*H*$_2$ and O*H*) 3.61 (t, 2 H,

* ramstrom@kth.se, Tel: +46 8 7909615, Fax: +46 8 7912333; yanm@pdx.edu, Tel: +1 503 725-5756, Fax: +1 503 725-9525.
[†] KTH - Royal Institute of Technology.
[‡] Portland State University.

10.1021/bc9003519 CCC: $40.75 © 2009 American Chemical Society
Published on Web 11/04/2009

J = 4.6 Hz, CH_2OH), 2.43 (t, 1 H, J = 2.4 Hz, C*H*CCH$_2$). ^{13}C NMR (125 MHz, $CDCl_3$): δ 79.68, 74.72, 72.60, 70.76, 70.51, 70.47, 69.20, 61.89, 58.54.

2-(2-(2-(Prop-2-ynyloxy)ethoxy)ethoxy)ethyl 4-methylbenzenesulfonate (3). 2-(2-(2-(Prop-2-ynyloxy)ethoxy)ethoxy)ethanol (**2**) (1.639 g, 8.7 mmol) was dissolved in DCM (10 mL). Tosyl chloride (1.826 g, 9.6 mmol) was added, and the mixture was cooled to 0 °C on an ice bath. KOH (1.95 g, 34.8 mmol) was added slowly, and the mixture was stirred vigorously for 2 h. The mixture was then poured on ice water and extracted with DCM (3 × 50 mL). The combined organic phase was washed with brine, dried over $MgSO_4$, and evaporated under reduced pressure to give **3** as white crystals in quantitative yield (2.977 g).

^{1}H NMR (500 MHz, $CDCl_3$): δ 7.80 (d, 2 H, J = 8.2 Hz, ArH), 7.34 (d, 2 H, J = 8.2 Hz, ArH), 4.19 (d, 2 H, 2.2 Hz, CHCCH_2O), 4.16 (t, 2 H, J = 4.7 Hz, CH_2OTs), 3.70−3.67 (m, 4 H, OCH_2), 3.65−3.63 (m, 2 H, OCH_2), 3.59 (s, 4 H, OCH_2), 2.45 (s, 3 H, ArCH_3), 2.43 (t, 1 H, J = 2.3 Hz, C*H*CCH$_2$). ^{13}C NMR (125 MHz, $CDCl_3$): δ 144.93, 133.18, 129.97, 128.14, 79.77, 74.68, 70.90, 70.72, 70.59, 69.37, 69.24, 68.85, 58.55, 21.79.

3-(2-(2-(2-Azidoethoxy)ethoxy)ethoxy)prop-1-yne (4). 2-(2-(2-(Prop-2-ynyloxy)ethoxy)ethoxy)ethyl 4-methylbenzenesulfonate (**3**) (2.515 g, 7.34 mmol) was dissolved in DMF (20 mL). Then, NaN_3 (525 mg, 8.08 mmol) and tetrabutyl ammonium iodide (TBAI) (271 mg, 0.734 mmol) was added, and the mixture was stirred vigorously at 45 °C overnight. The resulting mixture was diluted with EtOAc and washed with saturated $NaHCO_3$ (aq). The water phase was extracted twice with EtOAc, and the combined organic phase was washed with water and brine and dried over $MgSO_4$. Evaporation under reduced pressure yielded 1.705 g of crude product, which was purified by flash column chromatography using solvent system hexanes/EtOAc (1:1, v/v) yielding **4** (1.055 g, 67%).

^{1}H NMR (500 MHz, $CDCl_3$): δ 4.21 (d, 2 H, J = 2.4 Hz, CHCCH_2O), 3.72−3.67 (m, 10 H, OCH_2), 3.39 (t, 2 H, J = 5.1 Hz, CH_2N$_3$), 2.43 (t, 1 H, J = 2.4 Hz, C*H*CCH$_2$). ^{13}C NMR (125 MHz, $CDCl_3$): δ 79.65, 74.51, 70.71, 70.69, 70.52, 70.07, 69.13, 58.42, 50.71.

2-(2-(2-(Prop-2-ynyloxy)ethoxy)ethoxy)ethanamine (5). 3-(2-(2-(2-Azidoethoxy)ethoxy)ethoxy)prop-1-yne (**4**) (1.055 g, 4.95 mmol) was dissolved in dry THF (25 mL). PPh_3 (1.427 g, 5.44 mmol) was added, and the mixture was stirred at r.t. for 2.5 h. The temperature was then raised to 30 °C, and the mixture was stirred overnight. Water (0.2 mL) was added, and the mixture was stirred at 30 °C for 25 h, after which the solvent was evaporated under reduced pressure. The crude product was dissolved in EtOAc and extracted four times with 1 M HCl (aq). The combined water phase was then basified with ground NaOH to basic pH and extracted four times with EtOAc. The combined organic phase was dried over $MgSO_4$ and evaporated under reduced pressure to give the crude product, which was purified by flash column chromatography using solvent system hexanes/EtOAc (1:1, v/v) yielding **5** (648 mg, 70%).

^{1}H NMR (500 MHz, D_2O): δ 4.26 (s, 2 H, OCH_2CCH), 3.77−3.76 (m, 2 H, OCH_2), 3.73−3.68 (m, 6 H, OCH_2), 3.58 (t, 2 H, J = 5.4 Hz, CH_2NH$_2$). ^{13}C NMR (125 MHz, D_2O): δ 78.86 (t, J = 7.4 Hz, OCH$_2$*C*CH), 75.72 (t, J = 38 Hz, OCH$_2$C*C*H), 71.99, 69.60, 69.41, 69.31, 68.67, 57.87, 39.80.

Methyl 4-Azido-2,3,5,6-tetrafluorobenzoate (7). Methyl pentafluorobenzoate (2 mL, 13.55 mmol) was dissolved in a 2:1 (v/v) mixture of acetone and water (30 mL). Sodium azide (1.15 g, 17.6 mmol) was added to the flask and the mixture was refluxed at 90 °C for 2 h. The mixture was subsequently cooled to r.t., diluted with water (60 mL), and extracted with diethyl ether (3 × 60 mL). The extract was dried (Na_2SO_4) and the solvent evaporated under reduced pressure, yielding **7** as white crystals (3.4 g, quant.).

^{1}H NMR (400 MHz, $CDCl_3$): δ 3.97 (s, 3 H, COCH_3). ^{19}F NMR (470 MHz, $CDCl_3$): δ −138.6 (m, 2 F), −150.9 (m, 2 F).^{13}C NMR (125 MHz, $CDCl_3$): δ 159.98, 146.59−144.35 (m, J_{C-F} = 260 Hz), 141.69−139.50 (m, J_{C-F} = 250 Hz), 123.53, 107.77, 53.42.

4-Azido-2,3,5,6-tetrafluorobenzoic Acid (8). Methyl 4-azido-2,3,5,6-tetrafluorobenzoate (**7**) (3.86 g, 15.49 mmol) was dissolved in MeOH (14.6 mL), aqueous sodium hydroxide solution (20%, w/w; 1.5 mL) and water (3.1 mL). The mixture was then stirred at r.t. for 2.5 h, acidified with 1 M aqueous hydrochloric acid and extracted with DCM (3 × 60 mL). The solvent was evaporated under reduced pressure, yielding **8** (3.4 g, 84.4%).

^{13}C NMR (125 MHz, DMSO-d_6): δ 160.09 (s), 145.40−143.06 (m, J_{C-F} = 250 Hz), 141.32−139.02 (m, J_{C-F} = 250 Hz), 122.70 (m), 108.41 (m).

2,5-Dioxopyrrolidin-1-yl 4-azido-2,3,5,6-tetrafluorobenzoate (9). 4-Azido-2,3,5,6-tetrafluorobenzoic acid (**8**) (933 mg, 3.97 mmol), *N*-hydroxysuccinimide (502 mg, 4.36 mmol), and EDAC (836 mg, 4.36 mmol) were dissolved in DCM (15 mL) and stirred at 35 °C for 22 h. Additional EDAC (433 mg, 2.26 mmol) was then added, and the mixture was stirred at 35 °C for another 3 h. The resulting mixture was diluted with water and extracted twice with DCM. The combined organic phase was washed with water, dried over $MgSO_4$, and evaporated under reduced pressure to give **9** as white crystals (1.244 g, 94%).

^{1}H NMR (500 MHz, $CDCl_3$): δ 2.91 (s, 4 H, COCH_2CH_2). ^{13}C NMR (125 MHz, $CDCl_3$): δ 168.47, 155.31, 147.72−145.30 (m, J_{C-F} = 260 Hz), 141.82−139.52 (m, J_{C-F} = 250 Hz), 126.49, 102.13, 25.75.

4-Azido-2,3,5,6-tetrafluoro-*N*-(2-(2-(2-(prop-2-ynyl-oxy)-ethoxy)ethoxy)ethyl)benzamide (10). 2-(2-(2-(Prop-2-ynyl-oxy)ethoxy)ethoxy)ethanamine (**5**) (402 mg, 2.15 mmol) and 2,5-dioxopyrrolidin-1-yl 4-azido-2,3,5,6-tetrafluorobenzoate (**9**) (713 mg, 2.15 mmol) were dissolved in MeCN (6 mL) and stirred at r.t. overnight. A white precipitate was formed, and the mixture was filtered through a glass filter and washed with MeCN. The filtrate was evaporated under reduced pressure and the crude product purified by flash column chromatography using solvent system hexanes/EtOAc (1:1, v/v) yielding product **10** (605 mg, 70%).

^{1}H NMR (500 MHz, $CDCl_3$): δ 6.90 (s, 1 H, NH), 4.11 (d, 2 H, J = 2.4 Hz, CHCCH_2O), 3.69−3.64 (m, 12 H, OCH_2CH_2), 2.41 (t, 1 H, J = 2.4 Hz, C*H*CCH$_2$). ^{13}C NMR (125 MHz, $CDCl_3$): δ 157.92, 145.32−143.11 (m, J_{C-F} = 250 Hz), 141.67−139.48 (m, J_{C-F} = 250 Hz), 121.79, 111.98, 79.44, 74.74, 70.64, 70.40, 70.35, 69.54, 69.16, 58.45, 40.20. Anal. $C_{16}H_{16}F_4N_4O_4$ calcd. C 47.53, H 3.99, N 13.86; found C 47.60, H 4.10, N 13.79.

1-(2-Azidoethyl)-2,3,4,6-tetra-*O*-acetyl-α-D-mannopyranoside (12). A solution of 2-azidoethanol (424 mg, 4.88 mmol) in DCM (20 mL) was added to α-D-mannose pentaacetate (1.586 g, 4.06 mmol). The mixture was stirred at 0 °C and $BF_3 \cdot Et_2O$ (2.04 mL, 16.25 mmol) was added slowly. After 1 h, the mixture was allowed to reach r.t., and after 18 h added to ice water (20 mL). The resulting mixture was extracted with DCM (2 × 20 mL), and the combined organic phase was washed with ice water, saturated $NaHCO_3$ (aq), and ice water. The organic phase was dried over Na_2SO_4 and the solvent evaporated under reduced pressure, yielding product **12** (1.411 g, 83%).

^{1}H NMR (500 MHz, $CDCl_3$): δ 5.34 (dd, 1 H, J = 3.5 and 9.8 Hz, H-3), 5.28 (d, 1 H, J = 10.1 Hz, H-4), 5.25 (dd, 1 H, J = 1.9 and 3.5 Hz, H-2), 4.85 (d, 1 H, J = 1.9 Hz, H-1), 4.26 (dd, 1 H, J = 5.4 and 12.3 Hz, H-6), 4.10 (dd, 1 H, J = 2.2 and

12.3 Hz, H-6′), 4.02 (ddd, 1 H, J = 2.5, 5.4, and 9.8 Hz, H-5), 3.85 (ddd, 1 H, J = 3.8, 6.9, and 10.7 Hz, CH_2CH$_2$N$_3$), 3.65 (ddd, 1 H, J = 3.9, 6.2, and 10.3 Hz, CH_2CH$_2$N$_3$), 3.47 (ddd, 1 H, J = 3.5, 6.9, and 13.2 Hz, CH_2N$_3$), 3.42 (ddd, 1 H, J = 3.8, 6.0, and 13.2 Hz, CH_2N$_3$), 2.14 (s, 3 H, Ac), 2.08 (s, 3 H, Ac), 2.03 (s, 3 H, Ac), 1.97 (s, 3 H, Ac). ^{13}C NMR (125 MHz, CDCl$_3$): δ 170.74, 170.13, 169.93, 169.88, 97.88, 69.53, 69.00, 68.98, 67.18, 66.14, 62.59, 50.49, 21.00, 20.87, 20.83, 20.78.

Compound 13. 1-(2-Azidoethyl)-2,3,4,6-tetra-*O*-acetyl-α-D-mannopyranoside (**12**) (203 mg, 0.486 mmol), 2-(2-(2-(prop-2-ynyloxy)ethoxy)ethoxy)ethyl 4-methyl-benzenesulfonate (**3**) (200 mg, 0.5837 mmol), CuI (4.6 mg, 0.024 mmol), and DIPEA (8.5 μL, 0.049 mmol) were dissolved in MeCN (15 mL) and stirred at r.t. for 28 h. Additional CuI (5 mg) was subsequently added, and the mixture was stirred at r.t. for 20 h. The resulting mixture was evaporated under reduced pressure, and the crude product was purified by flash column chromatography using solvent system DCM/MeCN (1:1, v/v) yielding product **13** (279 mg, 76%).

^{1}H NMR (500 MHz, DMSO-d_6): δ 8.09 (s, 1 H, triazol-H), 7.78 (d, 2 H, J = 8.3 Hz, Ar−H), 7.47 (d, 2 H, J = 8.3 Hz, Ar−H), 5.08−5.04 (m, 2 H, H-2 and H-4), 5.01 (dd, 1 H, J = 3.4 and 10.2, H-3), 4.90 (s, 1 H, H-1), 4.67−4.58 (m, 2 H, OCH_2CH$_2$N-triazol), 4.52 (s, 2 H, OCH_2C-triazol), 4.11 (t, 2 H, J = 4.4 Hz, OCH_2), 4.07 (dd, 1 H, J = 5.0 and 12.3 Hz, H-6), 4.02−3.89 (m, 3 H, H-7 and OCH$_2$CH_2N-triazol), 3.57 (t, 2 H, J = 4.4 Hz, OCH_2), 3.54−3.51 (m, 3 H, H-5 and OCH_2), 3.50−3.48 (m, 2 H, OCH_2), 3.44 (s, 4 H, OCH_2), 2.41 (s, 3 H, Ar−CH_3), 2.09 (s, 3 H, Ac), 2.01 (s, 3 H, Ac), 2.00 (s, 3 H, Ac), 1.92 (s, 3 H, Ac). ^{13}C NMR (125 MHz, DMSO-d_6): δ 169.99, 169.55, 169.54, 169.40, 144.89, 143.98, 132.41, 130.12, 127.61, 124.29, 96.33, 69.97, 69.68, 69.67, 69.65, 68.87, 68.57, 68.48, 67.92, 67.88, 65.71, 65.09, 63.46, 61.65, 48.94, 21.07, 20.55, 20.48, 20.39, 20.37. $[\alpha]^{20}_D$ +27.0 (*c* 0.673).

Compound 14. Compound **13** (279 mg, 0.368 mmol) and NaN_3 (29 mg, 0.441 mmol) were dissolved in DMF (25 mL) and stirred at 65 °C for 20 h. The solvent was then evaporated under reduced pressure yielding a crude product, which was dissolved in a small amount of DCM/MeCN (1:1, v/v) and passed through a short silica column yielding product **14** (221 mg, 95%).

^{1}H NMR (500 MHz, DMSO-d_6): δ 8.09 (s, 1 H, triazol-H), 5.08−5.04 (m, 2 H, H-2 and H-4), 5.00 (dd, 1 H, J = 3.3 and 10.2 Hz, H-3), 4.90 (d, 1 H, J = 1.3 Hz, H-1), 4.67−4.58 (m, 2 H, OCH_2CH$_2$N-triazol), 4.53 (s, 2 H, OCH_2C-triazol), 4.06 (dd, 1 H, J = 5.0 and 12.3 Hz, H-6), 4.01−3.89 (m, 3 H, H-7 and OCH$_2$CH_2N-triazol), 3.59 (t, 2 H, J = 4.9 Hz, OCH_2), 3.56−3.51 (m, 9 H, H-5 and OCH_2), 3.38 (t, 2 H, J = 4.9 Hz, OCH_2), 2.09 (s, 3 H, Ac), 2.02 (s, 3 H, Ac), 2.00 (s, 3 H, Ac), 1.92 (s, 3 H, Ac). ^{13}C NMR (125 MHz, DMSO-d_6): δ 170.00, 169.56, 169.53, 169.41, 144.00, 124.28, 96.33, 69.80, 69.73, 69.67, 69.23, 68.91, 68.57, 68.48, 67.91, 65.72, 65.09, 63.47, 61.64, 49.98, 48.94, 20.55, 20.49, 20.39, 20.38. MS (ESI$^+$): [M+Na]$^+$ *m/z* calcd for $C_{25}H_{38}N_6O_{13}$, 653.24; found 653.27. $[\alpha]^{20}_D$ +30.6 (*c* 0.727).

Compound 15. Compound **14** (399 mg, 0.632 mmol) was dissolved in MeOH (15 mL) under nitrogen atmosphere. NaOMe (17 mg, 0.316 mmol) in MeOH (1 mL) was added, and the mixture was stirred at r.t. for 2 h. The resulting mixture was neutralized with Amberlyst 15 and filtered. Pd/C (10%, 67 mg, 0.0632 mmol) was added, and the reaction vessel was subjected to H_2-atmosphere (1 atm) for 5 h at r.t. The mixture was subsequently filtered through Celite, and the filtrate evaporated under reduced pressure to yield compound **15** (204 mg, 74%).

^{1}H NMR (500 MHz, D$_2$O): δ 8.13 (s, 1 H, triazol-H), 4.82 (d, 1 H, J = 1.4 Hz, H-1), 4.73−4.70 (m, 4 H, CH_2N-triazol + CH_2C-triazol), 4.14 (ddd, 1 H, J = 11.0, 7.0, 4.1 Hz, CH_2CH$_2$N-triazol), 3.96 (dt, 1 H, J = 9.1, 4.3 Hz, CH_2CH$_2$NNC), 3.88 (dd, 1 H, J = 3.2, 1.7 Hz, H-2), 3.77−3.59 (m, 15 H), 3.07 (ddd, 1 H, J = 9.4, 5.8, 2.2 Hz), 2.94 (t, 1 H, J = 5.3 Hz, CH_2NH$_2$). ^{13}C NMR (125 MHz, D$_2$O) δ 143.91, 125.59, 99.56, 72.79, 70.39, 70.22, 69.85, 69.58, 69.48, 69.35, 68.89, 66.35, 65.48, 62.97, 60.64, 50.08, 39.57. MS (ESI$^+$): [M+H]$^+$ *m/z* calc for $C_{17}H_{32}N_4O_9$, 437.23; found 437.27.

Compound 16. 2,5-Dioxopyrrolidin-1-yl 4-azido-2,3,5,6-tetra-fluorobenzoate (**9**) (178 mg, 0.537 mmol) and compound **15** (195 mg, 0.448 mmol) were dissolved in 10 mL of DMF and stirred at r.t. for 22 h. The solvent was then evaporated under reduced pressure to give 289 mg of crude product which was purified by flash column chromatography with solvent system DCM/MeOH (6:1, v/v) yielding product **16** (201 mg, 69%).

^{1}H NMR (500 MHz, D$_2$O): δ 8.10 (s, 1 H, triazol-H), 4.80 (d, 1 H, J = 1.6 Hz, H-1), 4.71−4.67 (m, 4 H, CH_2NNC + CH_2CNC), 4.12 (ddd, 1 H J = 11.0, 7.0, and 4.0 Hz, CH_2CH$_2$NNC), 3.97−3.91 (m, 1H, CH_2CH$_2$NNC), 3.87 (dd, 1 H J = 3.2 and 1.7 Hz, H-2), 3.76−3.57 (m, 17 H), 3.07 (ddd, 1 H, J = 9.5, 5.7, and 2.2 Hz). ^{13}C NMR (125 MHz, D$_2$O): δ 160.66, 144.60−142.39 (dm, J = 250 Hz), 143.97, 141.44−139.30 (dm, J = 252 Hz), 125.46, 122.51−122.26 (m), 110.12 (t, J = 19.1 Hz), 99.57, 72.79, 70.40, 69.86, 69.65, 69.55, 69.49, 68.96, 68.46, 66.36, 65.47, 63.01, 60.64, 50.06, 39.72. MS (ESI$^+$): [M+Na]$^+$ *m/z* calcd for $C_{24}H_{31}F_4N_7O_{10}$, 653.21; found 653.27. Anal. $C_{24}H_{31}F_4N_7O_{10}$ calcd. C 44.11, H 4.78, N 15.00; found C 44.07, H 4.77, N 14.92. $[\alpha]^{20}_D$ +21.4 (*c* 0.58).

1-(2-Azidoethyl)-α-D-mannopyranoside (17). 1-(2-Azidoethyl)-2,3,4,6-tetra-*O*-acetyl-α-D-mannopyranoside (**12**) (66 mg, 0.158 mmol) was dissolved in 30 mL of MeOH. Then sodium methoxide (25.5 mg, 0.474 mmol) was added and the reaction mixture was stirred at r.t. until TLC indicated full conversion. Then, Amberlyst 15 was added until pH reached ∼7. The Amberlyst was then filtered off and the solvent was evaporated under reduced pressure, giving the pure product **17** (37 mg, 95%).

^{1}H NMR (500 MHz, D$_2$O): δ 4.93 (d, 1 H J = 1.6 Hz, H-1), 3.99 (dd, 1 H, J = 1.6 and 3.5 Hz, H-2), 3.93 (ddd, 1 H, J = 3.4, 7.0, and 10.8 Hz, CH_2CH$_2$N$_3$), 3.91 (dd, 1 H, J = 1.3 and 12.3 Hz, H-6), 3.85 (dd, 1 H, J = 3.5 and 9.1 Hz, H-3), 3.77 (dd, 1 H, J = 5.7 and 12.0 Hz, H-6′), 3.73 (ddd, 1 H, J = 3.2, 6.3, and 11.0 Hz, CH_2CH$_2$N$_3$), 3.70−3.65 (m, 2 H, H-4 and H-5), 3.56 (ddd, 1 H, J = 3.1, 6.9, and 13.6, CH_2N$_3$), 3.50 (ddd, 1 H, J = 3.2, 6.4 and 13.6, CH_2N$_3$).^{13}C NMR (125 MHz, D$_2$O): δ 99.80, 72.88, 70.37, 69.92, 66.67, 66.29, 60.90, 50.19.

General Surface Modification (cf. Figure 1). All QCM experiments were performed on gold-plated 10 MHz quartz crystals (Attana), either coated with poly(ethylene glycol) by a previously reported method (*22*) or purchased precoated with polystyrene. The photoreaction step was performed at 240−400 nm at a measured intensity of 13.3−13.5 mW/cm^2 with a LC8 equipped Hg−Xe UV-lamp from Hamamatsu Photonics. The fabricated crystals were mounted in a flowthrough QCM system (Attana 100).

Method A - 1-Step Functionalization. The precoated QCM crystal was immersed in a methanol solution of **16** (2.0 mM) for 5 min, after which it was dried under a stream of N_2 for 5 min, and irradiated for 5 min with UV light. The crystal was then rinsed with methanol in a supersonic bath for 5 min, dried under N_2, and placed in the QCM flowthrough system.

Method B - 2-Step Functionalization. The precoated QCM crystal was immersed in a methanol solution of **10** (2.0 mM) for 5 min, after which it was dried under a stream of N_2 for 5 min, and irradiated for 5 min with UV light. The crystal was then rinsed with methanol in a supersonic bath for 5 min and dried under N_2. The crystal was then immersed in a solution of

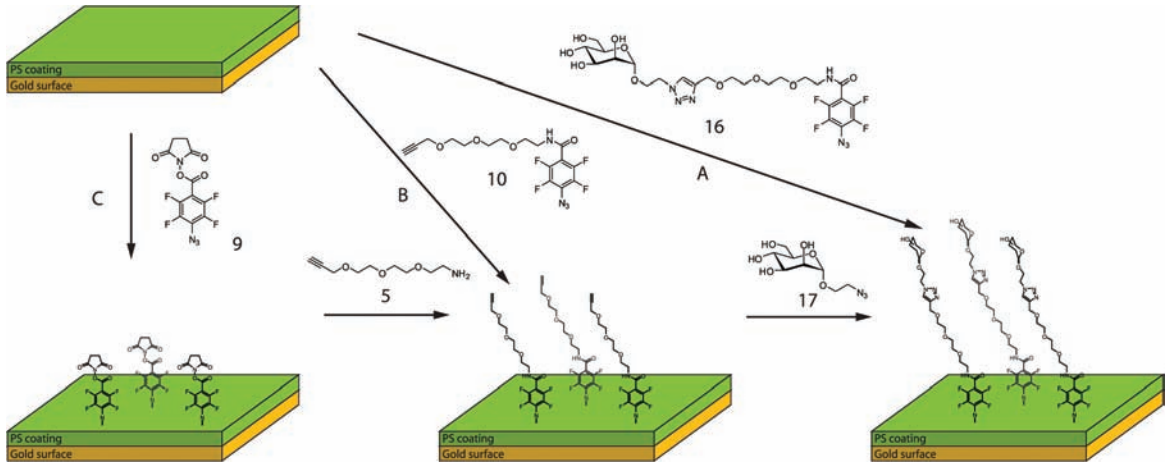

Figure 1. Developed methods for carbohydrate functionalization on polystyrene (PS) surfaces. Method A consists of one step in which a carbohydrate-functionalized PFPA is covalently bound to the polystyrene surface using UV-irradiation. In method B, the surface is primarily functionalized with alkynes and subsequently connected to carbohydrate-azides via Click chemistry. Method C consists of three steps in which a NHS-activated PFPA-ester is immobilized using UV irradiation. Then, compound **5** is attached to the surface, by the formation of a stable amide bond, creating an alkyne-functionalized surface (equivalent to method B), which is subsequently bound to carbohydrate-azides using Click chemistry.

water:acetonitrile (1:1, v/v) containing **17** (19.2 mM), CuI (0.96 mM), and DIPEA (9.7 mM) for 10 h. The crystal was then rinsed, first with acetonitrile/methanol, and then with acetonitrile/water (1:1, v/v) in a supersonic bath for 5 min. The crystal was then dried under N_2 and placed in the QCM flowthrough system.

Method C - 3-Step Functionalization. The precoated QCM crystal was immersed in an ethanol solution of **9** (5.0 mM) for 5 min after which it was dried under a stream of N_2 for 5 min and irradiated for 5 min with UV light. The crystal was then immersed in an acetonitrile solution of **5** (50 mM) for 8 h after which it was rinsed with methanol in a supersonic bath for 5 min. The crystal was then dried under N_2 for 5 min and subsequently immersed in a solution of water/acetonitrile (1:1, v/v) containing **17** (19.2 mM), CuI (0.96 mM), and DIPEA (9.7 mM) for 10 h. The crystal was then rinsed, first with acetonitrile/methanol, and then with acetonitrile/water (1:1, v/v) in a supersonic bath for 5 min. The crystal was then dried under N_2 and placed in the QCM flowthrough system.

General Surface Analysis. A continuous flow of running buffer (PBS 10 mM, pH 7.4, 25−50 μL/min) was used throughout the experiments, and samples of Concanavalin A (Con A) and peanut agglutinin (PNA) were prepared in the same buffer (sample injection volume: 50 μL). The crystals were washed/equilibrated with buffer solution prior to manipulations/measurements. After the crystal was equilibrated in the flowthrough system, it was subjected to several injections of BSA (1 mg/mL), low pH buffer (pH 1.5), and BSA (1 mg/mL) to fully block any nonfunctionalized surface. Binding to the surface was monitored by frequency logging with Attester 1.1 (Attana) and adsorption/desorption to the surface recorded as the resulting frequency shifts. Solutions (0.2 mg/mL) of Con A (1.92 μM) or PNA (1.82 μM) were then injected on the system, where the resulting shift in frequency corresponds to the binding to the surface. Bound lectin was released from the surface between measurements by several successive injections of low pH buffer (PBS 10 mM, pH 1.5). The procedure was then repeated several times for each lectin to determine the surface stability over time.

RESULTS AND DISCUSSION

Perfluorophenylazides (PFPAs) have been shown to be efficient reagents in photolabeling using UV light. Unlike other aryl azides, which quickly decompose upon radiation, PFPA forms a less reactive nitrene intermediate, which inserts into C−H bonds with moderate to high efficiency (*23*−*25*). We have previously reported the use of PFPA in the immobilization of carbohydrates to poly(ethylene glycol) surfaces for quartz crystal microbalance (QCM) and microarray studies (*22*, *26*). In the present approach, the versatility of the system is further improved by introducing the Cu-catalyzed azide−alkyne cycloaddition (click chemistry) step. This enables the use of more readily available carbohydrate-azides in the manufacturing of the surfaces.

To demonstrate the concept of the method, three experimental procedures of immobilizing the carbohydrates were designed, all of which resulted in very similar final surfaces (Figure 1). This experimental design also enabled the evaluation and analysis of the efficiency of the different steps, i.e., the photoligation and the CuAAC reaction. The simplest method (A) consists of a single photoligation step in which a carbohydrate-derivatized photoprobe (α-D-mannopyranose derivative **16** in the example) is immobilized on the surface by UV irradiation. In method B, an alkyne-functionalized PFPA (**10**) is primarily coupled to the surface by UV irradiation. The alkyne surface is then coupled to a 2-azidoethyl functionalized carbohydrate species (**17**) using CuAAC. In method C, the alkyne surface is produced in two steps. First, the polymeric surface is functionalized with an NHS-activated PFPA-ester (**9**) (*24*, *25*), and the resulting surface is subsequently submerged in an acetonitrile solution of an alkyne-functionalized amine linker (**5**), forming a stable amide bond with the surface. The alkyne surface is then subjected to the same procedure as the last step in method B.

All three methods result in carbohydrate-functionalized surfaces of the same type. Methods B and C, however, generate stable alkyne-functionalized intermediate surfaces, which in a one-step highly chemoselective reaction can be linked to azide-containing molecules, in this case, carbohydrates. The photoligation step, in the presence of surface C−H bonds, results in stable amine bonds, which makes hydrocarbon-based polymers a suitable substrate. This expands the end use of this method to a large extent, considering the extensive use of polymeric analysis equipment in life sciences. In this study, we have evaluated the methods on poly(ethylene glycol) (PEG) and polystyrene (PS) surfaces with successful results in both cases.

All compounds used were synthesized according to Schemes 1 and 2. The NHS-activation of compound **8** was essential for the synthesis of compounds **10** and **16**. The reaction between compound **10** and compounds **12** and **17**, to form structure **16**,

Scheme 1[a]

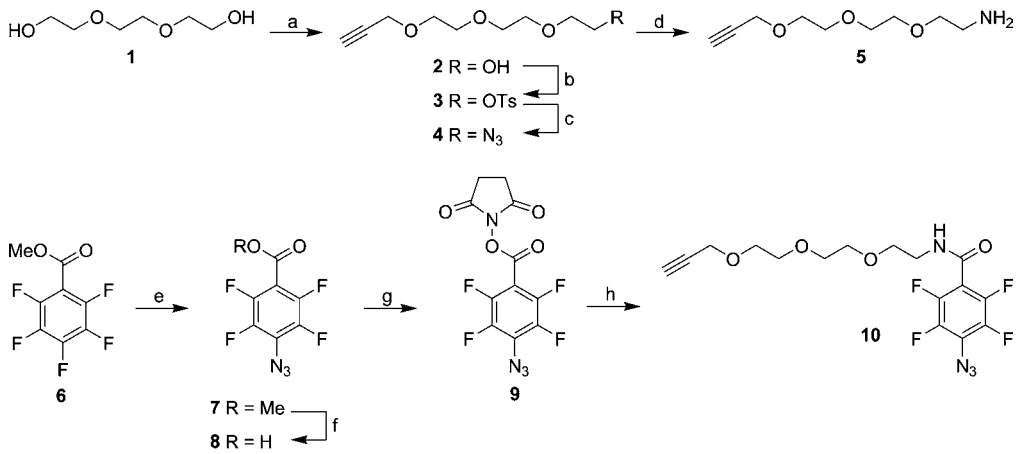

[a] (a) KOH, propargyl bromide, 60 °C, 3 h (36%); (b) TsCl, KOH, 0 °C, 2 h (quant.); (c) NaN_3, TBAI, DMF, 45 °C, overnight (67%); (d) (i) PPh_3, THF, 30 °C, 19 h, (ii) H_2O, 30 °C, 25 h (70%); (e) NaN_3, Acetone/H_2O (2:1), 90 °C, 2 h (quant.); (f) NaOH aq (20% w/w):MeOH (1:18), rt, 5 h (97%); (g) NHS, EDAC, 35 °C, 25 h (94%); (h) **5**, MeCN, rt, overnight (70%).

Scheme 2[a]

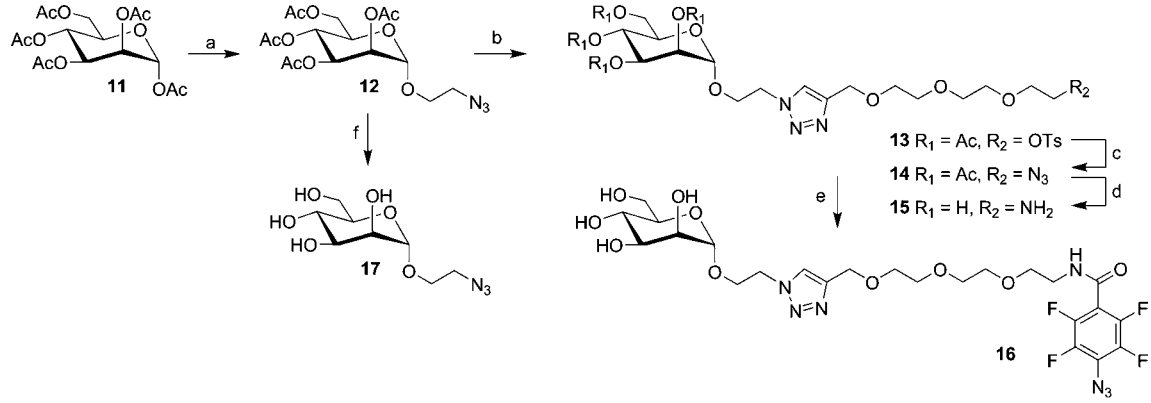

[a] (a) 2-azidoethanol, $BF_3 \cdot (Et_2O)_2$, DCM, 0 °C, 18 h (83%); (b) **3**, CuI, DIPEA, MeCN, rt, 48 h (76%); (c) NaN_3, DMF, 65 °C, 20 h (95%); (d) (i) NaOMe, MeOH, rt, 5 h, (ii) 10 mol % Pd(C) under H_2, 6 h (74%); (e) **9**, MeCN, rt, overnight (69%); (f) NaOMe, MeOH, rt, 2 h (quant.).

resulted in complex mixtures due to the higher reactivity of the aryl azide group compared to the carbohydrate azide moiety. This reactivity difference necessitated the chosen route to compound **16**. Compound **10** was also found to undergo self-cycloaddition in concentrated form, but proved stable in dilute solution at low temperature.

During initial studies, different catalytic systems for the cycloaddition reaction were examined, including $CuSO_4 \cdot 5H_2O$ + sodium ascorbate in water and water/*t*-butanol (1:1, v/v), $Cu(OAc)_2$ in water, and CuI + DIPEA in water/acetonitrile (1:1, v/v). The CuI system was, however, found to be the most appropriate for the surfaces used. Experiments were also performed for method B without the copper catalyst, in which the concentration of compound **17** was increased from 19.2 mM to 300 mM. Preliminary results indicated similar efficiencies of the thermal cycloaddition reaction but required longer reaction times (>19 h) and heating to 40 °C. This could, however, be a useful approach if copper needs to be avoided during immobilization.

The biorecognition properties of the surfaces were subsequently analyzed by injections of the lectins Con A (primarily specific for α-D-mannopyranose units) and PNA (primarily specific for β-D-galactopyranose units) in the flowthrough QCM system. The QCM technique allows for real-time monitoring of the association and dissociation of the lectins and provides an easy way to assess the stability of the immobilization over several injections.

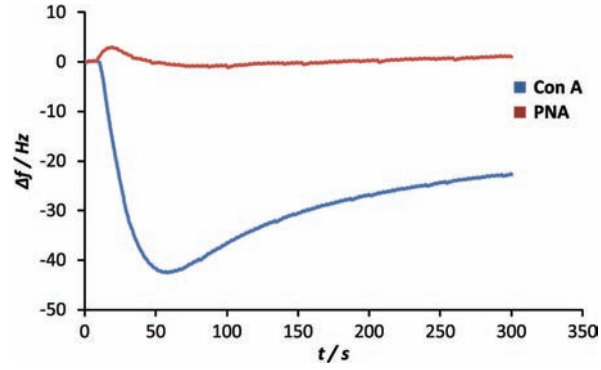

Figure 2. General binding curve of Con A and PNA to mannose-functionalized surface.

The binding study was performed by measuring the decrease in frequency upon lectin injection. Typical binding curves for the two lectins are presented in Figure 2. As can be seen for the α-D-mannopyranose-specific lectin Con A, the frequency drops immediately upon injection as a consequence of the association of the lectin to the surface. As the injection plug comes to an end, dissociation takes place where the lectin is washed away from the surface. In comparison, PNA shows no binding in agreement with the specificities for this protein.

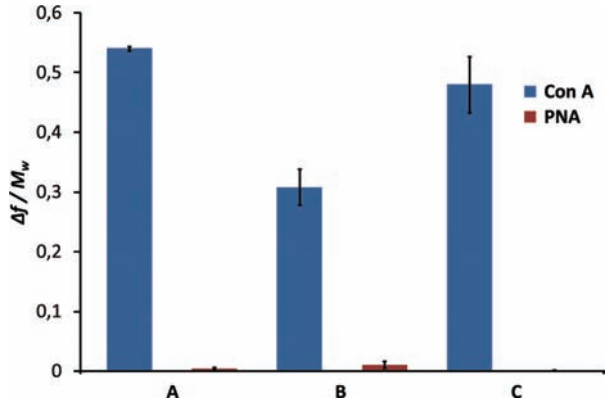

Figure 3. Binding results for the three different methods (normalized for the molecular weight of the lectins).

The resulting binding analyses for all three methods are presented in Figure 3, where the maximum decrease in frequency corresponds to the binding of the lectins at the conditions used. As can be seen, method A produces the highest and most consistent binding of Con A, with negligible nonspecific binding of PNA to the surfaces. This observation is reasonable, since method A is the simplest approach with only one photoligation step and is also most likely to produce the most carbohydrate-dense surface. On the other hand, both methods B and C show high specific binding of Con A with good consistency, although the capacity differs slightly between the methods. These results confirm the generality of the different methods to produce surfaces of similar quality. Method C requires roughly 8 h longer preparation time than method B, but in return produces surfaces which stabilize faster in the QCM system than surfaces produced by method B (cf. Figure 4). This indicates that surfaces produced by method C have lower thickness and are more uniform, which is most likely due to the increased potential cross-linking of compound **10** compared to compound **9** in the photoligation step. This also explains the slightly lower capacity of method B, where more alkyne moieties are likely buried, resulting in lower surface density of alkynes in method B than in method C. Method B further deviates from method A and C in the regeneration step, where it results in considerably larger responses to the change in pH, similar to the 3D pH-responsive dynamic polymer surfaces previously reported (*27*). The response times for all methods are, however, generally good, although surfaces produced by method A or C respond much faster than surfaces produced by method B, a desirable feature in real-time monitoring instrumentations. This supports the theory that methods A and C produce more ordered surfaces than method B.

CONCLUSIONS

Fast and straightforward methods to regio- and chemoselective functionalization of polymeric surfaces with carbohydrate structures have been developed and evaluated. The methods make use of the highly efficient PFPA-photoligation technique, combined with the CuAAC chemistry. The surfaces were evaluated using a QCM instrumentation, allowing for real-time analysis of the association/dissociation effects of unlabeled proteins. High specificities and capacities were recorded for all surfaces. All methods can be used for a variety of polymeric substrates, and methods B and C can furthermore be easily expanded with more azide-functionalized carbohydrates, as well as other structures. These features make the developed technology highly versatile, and show the potential for other applications.

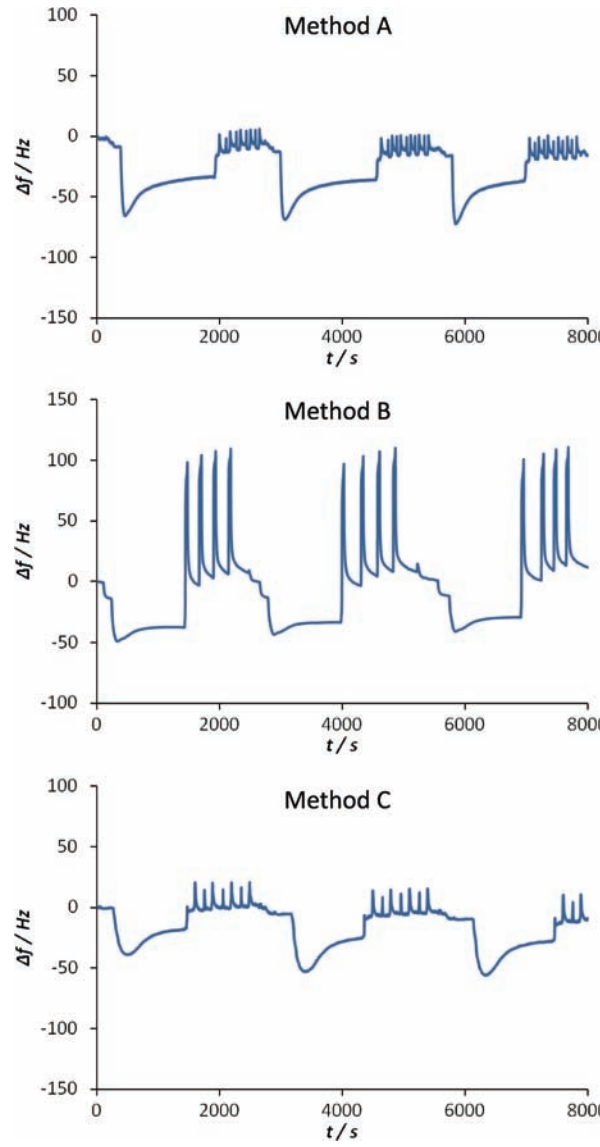

Figure 4. General frequency response curves for the three different methods. Con A was injected at 400 s, 3000 s, and 5900 s. The positive frequency peaks between lectin injections correspond to regeneration by release buffer solution. The average Con A binding values are presented in Figure 3.

ACKNOWLEDGMENT

This study was supported in part by the Swedish Research Council, the Royal Institute of Technology, the National Institutes of General Medical Science (NIGMS) under NIH Award Numbers R01GM080295 and 2R15GM066279, ARL-ONAMI Center for Nanoarchitectures for Enhanced Performance, and the European Commission (MRTN-CT-19561). L.D. thanks the China Scholarship Council for a special scholarship award.

LITERATURE CITED

(1) Varki, A. (2009) *Essentials of glycobiology*, Cold Spring Harbor Laboratory Press, Cold Spring Harbor, NY.
(2) Hirabayashi, J. (2003) Oligosaccharide microarrays for glycomics. *Trends Biotechnol. 21*, 141–143.

(3) Feizi, T., and Chai, W. (2004) Innovation: Oligosaccharide microarrays to decipher the glyco code. *Nat. Rev. Mol. Cell Biol. 5*, 582–588.

(4) Shin, I., Park, S., and Lee, M.-r. (2005) Carbohydrate microarrays: An advanced technology for functional studies of glycans. *Chem.—Eur. J. 11*, 2894–2901.

(5) Love, K. R., and Seeberger, P. H. (2002) Carbohydrate arrays as tools for glycomics. *Angew. Chem., Int. Ed. 41*, 3583–3586.

(6) Dube, D. H., and Bertozzi, C. R. (2005) Glycans in cancer and inflammation - potential for therapeutics and diagnostics. *Nat. Rev. Drug Discovery 4*, 477–488.

(7) Horlacher, T., and Seeberger, P. H. (2008) Carbohydrate arrays as tools for research and diagnostics. *Chem. Soc. Rev. 37*, 1414–1422.

(8) Laurent, N., Voglmeir, J., and Flitsch, S. L. (2008) Glycoarrays-tools for determining protein-carbohydrate interactions and glycoenzyme specificity. *Chem. Commun.* 4400–4412.

(9) Park, S., Lee, M.-R., and Shin, I. (2008) Carbohydrate microarrays as powerful tools in studies of carbohydrate-mediated biological processes. *Chem. Commun.* 4389–4399.

(10) Bernardes, G. J. L., Castagner, B., and Seeberger, P. H. (2009) Combined approaches to the synthesis and study of glycoproteins. *ACS Chem. Biol.* posted ASAP.

(11) Wu, C.-Y., Liang, P.-H., and Wong, C.-H. (2009) New development of glycan arrays. *Org. Biomol. Chem. 7*, 2247–2254.

(12) Rostovtsev, V. V., Green, L. G., Fokin, V. V., and Sharpless, K. B. (2002) A stepwise Huisgen cycloaddition process: copper(I)-catalyzed regioselective "ligation" of azides and terminal alkynes. *Angew. Chem., Int. Ed. 41*, 2596–2599.

(13) Tornoe, C. W., Christensen, C., and Meldal, M. (2002) Peptidotriazoles on solid phase: [1,2,3]-triazoles by regiospecific copper(iI)-catalyzed 1,3-dipolar cycloadditions of terminal alkynes to azides. *J. Org. Chem. 67*, 3057–3064.

(14) Wang, Q., Chan, T. R., Hilgraf, R., Fokin, V. V., Sharpless, K. B., and Finn, M. G. (2003) Bioconjugation by copper(I)-catalyzed azide-alkyne [3 + 2] cycloaddition. *J. Am. Chem. Soc. 125*, 3192–3193.

(15) Hanson, S. R., Greenberg, W.A., and Wong, C.-H. (2007) Probing glycans with the copper(I)-catalyzed [3 + 2] azide-alkyne cycloaddition. *QSAR Comb. Sci. 26*, 1243–1252.

(16) Fazio, F., Bryan, M. C., Blixt, O., Paulson, J. C., and Wong, C.-H. (2002) Synthesis of sugar arrays in microtiter plate. *J. Am. Chem. Soc. 124*, 14397–14402.

(17) Bryan, M. C., Fazio, F., Lee, H.-K., Huang, C.-Y., Chang, A., Best, M. D., Calarese, D. A., Blixt, O., Paulson, J. C., Burton, D., Wilson, I. A., and Wong, C.-H. (2004) Covalent display of oligosaccharide arrays in microtiter plates. *J. Am. Chem. Soc. 126*, 8640–8641.

(18) Wu, P., Malkoch, M., Hunt, J. N., Vestberg, R., Kaltgrad, E., Finn, M. G., Fokin, V. V., Sharpless, K. B., and Hawker, C. J. (2005) Multivalent, bifunctional dendrimers prepared by click chemistry. *Chem. Commun.* 5775–5777.

(19) Sun, X.-L., Stabler, C. L., Cazalis, C. S., and Chaikof, E. L. (2006) Carbohydrate and protein immobilization onto solid surfaces by sequential Diels-Alder and azide-alkyne cycloadditions. *Bioconjugate Chem. 17*, 52–57.

(20) Zhang, Y., Luo, S., Tang, Y., Yu, L., Hou, K.-Y., Cheng, J.-P., Zeng, X., and Wang, P. G. (2006) Carbohydrate-protein interactions by "clicked" carbohydrate self-assembled monolayers. *Anal. Chem. 78*, 2001–2008.

(21) Michel, O., and Ravoo, B. J. (2008) Carbohydrate microarrays by microcontact "click" chemistry. *Langmuir 24*, 12116–12118.

(22) Pei, Y., Yu, H., Pei, Z., Theurer, M., Ammer, C., Andre, S., Gabius, H.-J., Yan, M., and Ramström, O. (2007) Photoderivatized polymer thin films at quartz crystal microbalance surfaces: sensors for carbohydrate-protein interactions. *Anal. Chem. 79*, 6897–6902.

(23) Keana, J. F. W., and Cai, S. X. (1990) New reagents for photoaffinity labeling: synthesis and photolysis of functionalized perfluorophenyl azides. *J. Org. Chem. 55*, 3640–7.

(24) Yan, M., Cai, S. X., Wybourne, M. N., and Keana, J. F. W. (1993) Photochemical functionalization of polymer surfaces and the production of biomolecule-carrying micrometer-scale structures by deep-UV lithography using 4-substituted perfluorophenyl azides. *J. Am. Chem. Soc. 115*, 814–816.

(25) Yan, M., Cai, S. X., Wybourne, M. N., and Keana, J. F. W. (1994) *N*-Hydroxysuccinimide ester functionalized perfluorophenyl azides as novel photoactive heterobifunctional crosslinking reagents. the covalent immobilization of biomolecules to polymer surfaces. *Bioconjugate Chem. 5*, 151–157.

(26) Pei, Z., Yu, H., Theurer, M., Walden, A., Nilsson, P., Yan, M., and Ramström, O. (2007) Photogenerated carbohydrate microarrays. *ChemBioChem 8*, 166–168.

(27) Dunér, G., Anderson, H., Myrskog, A., Hedlund, M., Aastrup, T., and Ramström, O. (2008) Surface-confined photopolymerization of pH-responsive acrylamide/acrylate brushes on polymer thin films. *Langmuir 24*, 7559–7564.

BC9003519

Polyfluorophore Excimers and Exciplexes as FRET Donors in DNA

Yin Nah Teo and Eric T. Kool*

Department of Chemistry, Stanford University, Stanford, California 94305. Received September 5, 2009; Revised Manuscript Received October 15, 2009

We describe studies aimed at testing whether oligomeric exciplex and excimer fluorophores conjugated to DNA have the potential to act as donors for energy transfer by the Förster mechanism. Oligodeoxyfluorosides (ODFs) are composed of stacked, electronically interacting fluorophores replacing the bases on a DNA scaffold. The monomer chromophores in the twenty tetramer-length ODFs studied here include pyrene (Y), benzopyrene (B), perylene (E), dimethylaminostilbene (D), and a nonfluorescent spacer (S); these are conjugated in varied combinations at the 3′ end of a 14mer DNA probe sequence. In the absence of an acceptor chromophore, many of the ODF-DNAs show broad, unstructured long-wavelength emission peaks characteristic of excimer and exciplex excited states, similar to what has been observed for unconjugated ODFs. Although such delocalized excited states have been widely studied, we know of no prior report of their use in FRET. We tested the ability of the twenty ODFs to donate energy to Cy5 and TAMRA dyes conjugated to a complementary strand of DNA, with these acceptors oriented either at the near or far end of the ODF-conjugated probes. Results showed that a number of the ODF fluorophores exhibited relatively efficient energy transfer characteristic of the Förster mechanism, as judged by drops in donor emission quantum yield and fluorescence lifetime, accompanied by increases in intensity of acceptor emission bands. Excimer/exciplex bands in the donors were selectively quenched while shorter-wavelength monomer emission stayed relatively constant, consistent with the notion that the delocalized excited states, rather than individual fluorophores, are the donors. Interestingly, only specific sequences of ODFs were able to act as donors, while others did not, even though their emission wavelengths were similar. The new FRET donors possess large Stokes shifts, which can be beneficial for multiple applications. In addition, all ODFs can be excited at a single wavelength; thus, ODFs may be candidates as "universal FRET donors", thus allowing multicolor FRET of multiple species to be carried out with one excitation.

INTRODUCTION

Multichromophoric systems have displayed tremendous utility in numerous applications, giving some useful advantages over their monomeric counterparts. Applications in light harvesting, material science, electronic, photonic, and sensor devices have inspired the design of systems like conjugated polymers (*1*−*3*), dendrimers (*4*, *5*), photonic wires (*6*, *7*), and functionalized polypeptides (*8*). In recent years, the deoxyribose backbone of DNA has also been harnessed as a scaffold for the design of new multichromophoric systems. Oligodeoxyfluorosides (ODFs), an example of the latter, are a novel system of fluorophores built on the deoxyribose backbone. Aromatic fluorophores such as pyrene, perylene, and benzopyrene are attached to consecutive anomeric positions of the deoxyribose backbone (*9*, *10*). This backbone provides a rigid structure that brings the aromatic fluorophores into close proximity, allowing π-stacking interactions and various forms of photophysical interactions to occur (*11*, *12*).

Other systems of functionalizing the DNA scaffold with multiple chromophores have been developed recently. Häner and co-workers assembled a series of phenanthrenes and pyrenes as non-nucleosidic base surrogates (*13*, *14*). These aromatic compounds interact favorably through stacking interactions. In work by Wagenknecht, clusters of aromatic chromophores covalently attached to uridine were also shown to form a helical π-array along the major groove of the DNA duplex (*15*, *16*). Strongly enhanced emission from clusters of stacked pyrene-labeled uridines was observed. Nonfluorescent methyl red and napthyl red dyes had been incorporated as base substitutes and assembled as clusters into duplex DNA (*17*, *18*). Bipyridyl and biphenyl moieties were employed by Leumann as base substitutes for C-nucleosides to synthesize a zipper-like interstrand stacking motif of DNA (*19*). Excimer formation has also been observed by Inouye in alkynyl C-nucleosides with pyrene, perylene, and anthracene as base substitutes (*20*). Besides DNA, multilabeling of other nucleic acids architectures, RNA (*21*, *22*) and LNA (*23*), was also carried out. Noncovalent assembly of chromophores on the DNA structure had been explored with cyanine dyes in the minor groove (*24*, *25*).

A number of laboratories have also explored multichromophore FRET (Förster resonance energy transfer) interactions in DNA using traditional monomeric fluorescent dyes (*26*, *27*). In addition, multifluorophore systems based on conjugated polymers have also been employed as FRET donors (*28*, *29*). FRET is widely employed in biological and biophysical studies because of the well-known distance dependence of the nonradiative energy transfer (*30*, *31*). This allows quantitative information about the association of biomolecules and their relative distance and orientation on length scales beyond what other methods can provide. Because of this broad utility, the addition of new classes of chromophores that can undergo FRET can positively affect the types of experiments that can be carried out.

Here, we report studies in employing the multichromophore excimer and exciplex interactions of the stacked chromophores of ODFs to test a set of possible FRET donors that can be excited at a single wavelength. To the best of our knowledge, the use of excimers and exciplexes as FRET donors has not been explored. In this report, twenty different ODFs were

* To whom correspondence should be addressed: Department of Chemistry, Stanford University, Stanford, CA 94305. Phone: (650) 724-4741. Fax (650): 725-0259. E-mail: kool@stanford.edu.

10.1021/bc9003926 CCC: $40.75 © 2009 American Chemical Society
Published on Web 11/16/2009

attached to DNA sequences as potential donors, and common acceptor dyes TAMRA and Cy5 were placed on complementary DNA strands at either proximal or distal ends. Upon hybridization, Förster energy transfer was observed between several ODF donors and Cy5 or TAMRA acceptors. Since multiple ODFs can be excited at a single wavelength, this might ultimately lead to their use as "universal" FRET donors.

EXPERIMENTAL SECTION

Fluoroside Phosphoramidites Syntheses E, Y, D, S, B. Syntheses of the monomer 1′-α-2′-deoxyriboside 5′-dimethoxytrityl-3′-phosphoramidite derivatives of pyrene (Y), perylene (E), benzopyrene (B), and dimethylaminostilbene (D) were carried out as previously described (*9*, *10*, *32*). The abasic tetrahydrofuran spacer S was obtained commercially (dSpacer CE phosphoramidite from Glen Research Corporation).

Synthesis of ODF-Labeled Oligodeoxynucleotides. Oligodeoxynucleotides were synthesized on an Applied Biosystems 394 DNA/RNA synthesizer on a 1 μmol scale and possessed a 3′-phosphate group. Coupling employed standard β-cyanoethyl phosphoramidite chemistry, but with extended coupling time (900 s) for fluoroside phosphoramidites. ODFs were synthesized directly on the CPG beads, and the DNA sequence was then built on its 5′ end. All oligomers were deprotected using the Ultramild deprotection method with potassium carbonate solution (25 °C, 8 h), then purified by reverse-phase HPLC. The recovered material was quantified by absorbance at 260 nm with molar extinction coefficients determined by the nearest-neighbor method. Molar extinction coefficients for ODFs were estimated by adding the measured value of the molar extinction coefficient of the fluoroside (at 260 nm) to the calculated value for the natural DNA fragments. ODF-labeled oligomers were characterized by MALDI-TOF mass spectrometry (data are given in the Supporting Information, Table S1). TAMRA-CPG, TAMRA-dT, and Cy5 phosphoramidites were purchased from Glen Research Corporation. Phosphoramidites were attached to either the 3′- or 5′-end of the complementary DNA sequence using manufacturer's methods. Purification was achieved using reverse-phase HPLC.

Optical Methods. Steady-state absorption measurements were carried out on a Varian Cary 100 UV−visible spectrophotometer. Steady-state fluorescence measurements were carried out at 2 μM concentration (each strand) on a on a HORIBA Jobin Yvon Fluorolog-3 fluorescence spectrometer (2 nm slit width) equipped with Lauda Brinkmann RM6 temperature controller at 25 °C. Samples were buffered at pH 7.0 with 100 mM NaCl, 10 mM $MgCl_2$, and 10 mM Na·PIPES. Buffers were not deoxygenated. The excitation wavelength for ODF-labeled strands was 330 nm. To prevent aggregation and reabsorption of light during quantum yield measurements, samples were diluted to solutions with absorption of less than 0.1 at wavelengths longer than λ_{ex}. 9,10-Diphenylanthracene (Φ = 0.90) (*33*) in cyclohexane was used as the reference for quantum yield calculations. Quantum yields were calculated using the following equation (*34*)

$$\frac{\Phi}{\Phi_R} = \frac{n^2}{n_R^2} \times \frac{A_R}{A} \times \frac{\int F}{\int F_R}$$

where Φ and Φ_R are the quantum yields of the unknown and reference compounds respectively. n and n_R are the refractive indices of water and cyclohexane, respectively. A and A_R denote the absorbances at 330 nm for the unknown and reference samples and $\int F$ and $\int F_R$ are the integrals of fluorescence emission intensities of the unknown and the reference samples, respectively.

Fluorescence lifetime measurements were carried out on a PTI EasyLife instrument using 325 nm LED for excitation of all ODFs. A bandpass filter with transmittance from 400−510 nm was used to ensure that only emission from the donor ODF was monitored. Fitting and analysis was performed using *Felix32* software. The goodness of fit was evaluated based on χ^2 values and the randomness of the residuals. The instrument response function (IRF) was measured using a 2% Ludox scattering solution (Sigma Aldrich, MO). To prevent aggregation and reabsorption of light, samples were diluted to absorption at λ_{max} of less than 0.05.

Table 1. Sequences of DNA Probes in This Study

strand ID	sequence[a]
P1 - P20	5′-TCC ACA GAA ACA TA - XXXX-3′
C5′	3′- AGG TGT CTT TGT AT - Cy5 -5′
T5′	3′- AGG TGT CTT TGT AT - TAMRA -5′
C3′	3′- Cy5 - AGG TGT CTT TGT AT -5′
T3′	3′- TAM - AGG TGT CTT TGT AT -5′

[a] XXXX denotes the sequence of ODF (listed in Table 2).

Analysis of Energy Transfer. The efficiency of FRET, E_{FRET}, was calculated from the sensitized emission of the acceptors using eq 1 (*35*, *36*)

$$E_{FRET} = \left(\frac{I_{AD}}{I_A} - 1\right)\frac{\varepsilon_A}{\varepsilon_D} \quad (1)$$

where I_{AD} and I_A are the fluorescence emission intensities of the acceptor in the presence and absence of donor, respectively. ε_A and ε_D are the molar extinction coefficients of the acceptor and donor, respectively, at the excitation wavelength. The excitation wavelength was 330 nm for all experiments. TAMRA emission was monitored at its emission maxima at 580 nm, while Cy5 emission was monitored at its emission maxima at 662 nm. Where only a diminished donor emission signal was observed, and the acceptor emission remained the same or decreased, quenching was likely due to contact quenching. This quenching efficiency was calculated using eq 2

$$Q_{eff} = 1 - \frac{I_{DA}}{I_D} \quad (2)$$

where I_{DA} and I_D are the integrated emission intensities of the donor in the presence and absence of the acceptor, TAMRA, respectively. The efficiency of FRET computed from lifetime measurements, EL_{FRET}, was determined using eq 3 (*35*).

$$EL_{FRET} = 1 - \frac{\langle\tau_D\rangle}{\langle\tau_D^0\rangle} \quad (3)$$

where $\langle\tau\rangle = (\sum_i \alpha_i\tau_i)/(\sum_i \alpha_i)$ and $\langle\tau_D\rangle$ and $\langle\tau_D^0\rangle$ are the amplitude-averaged donor lifetimes in the presence and absence of the acceptor, respectively.

RESULTS

A representative set of 20 tetrameric sequences of ODFs was chosen from a larger random library for this study; for hybridization experiments, they were appended to the 3′-terminus of a 14-mer probe DNA sequence (Table 1). The ODF labels were synthesized from five monomeric 2′-deoxyfluorosides where the base-replacement fluorophore was a benzopyrene (B), pyrene (Y), perylene (E), or dimethylaminostilbene (D), or an abasic spacer-tetrahydrofuran moiety (S) (see Figure 1A). The α-glycosidic anomers, which like β-anomers can stack with one another in a DNA context (*11*), were used for synthetic convenience in this study. ODFs were assembled using automated DNA synthesis chemistry from phosphoramidite derivatives of the monomeric fluorosides. Note that sequences of ODFs are listed in 5′ to 3′ order in analogy to DNA.

Fluorescence Properties of ODFs. Absorption and emission spectra of the twenty ODF labels conjugated to single-stranded

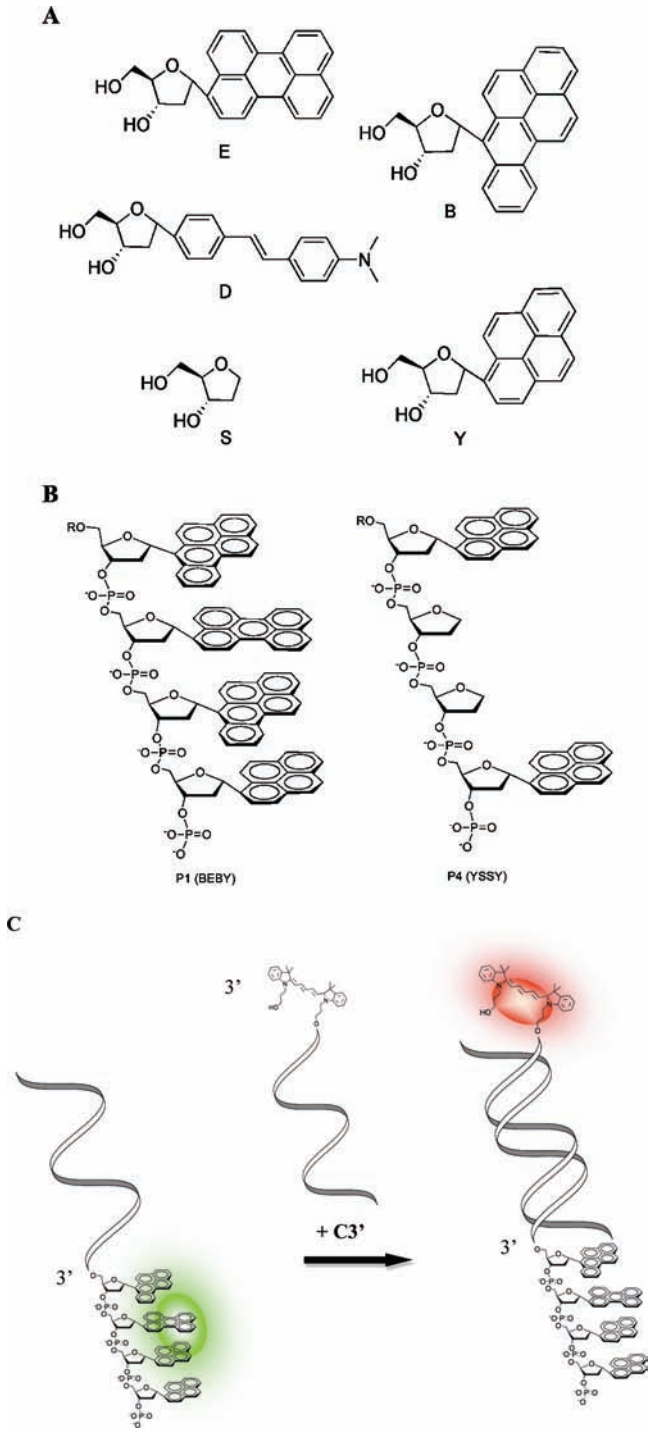

Figure 1. Structures in this study. (A) Monomeric 2′-deoxyfluorosides B, E, Y, D, and S. (B) Structures of two representative ODFs (BEBY and YSSY) that were studied as DNA conjugates. These were attached to the 3′ end of a DNA probe sequence (R). (C) An example of a hybridization experiment: hybridization of BEYY-labeled probe (P2) with an acceptor-labeled complement (C3′).

DNA were measured in pH 7.0 hybridization buffer containing 100 mM Na^+ and 10 mM Mg^{2+} (see Experimental Procedures). The primary absorption and emission bands are given in Table 2, and emission spectra are shown in Supporting Information. Quantum yields for fluorescence were measured in the same buffer (Table 2). Emission spectra of the ODF labels were in nearly all cases quite different from the combined monomer emissions, which were reported previously (*37*). Most cases showed broad bands between 450 and 600 nm, consistent with excited-state dimer (exciplex and excimer) states. The maxima of these bands varied from 460 to 530 nm, and some cases showed multiple maxima (as many as three) in this range. In general, the twenty DNA-conjugated ODFs were efficient fluorophores, with quantum yields for emission as high as 42% (Table 2). The quantum yields varied with chromophore composition and sequence; for an example of the latter, SSYY (Φ_{FL} = 19%) and YSSY (Φ_{FL} = 2.5%) have the same composition but substantially different fluorescence quantum yields.

ODFs as Donors in Förster Energy Transfer. To test the possibility of Förster energy transfer between ODFs and common acceptor dyes, we hybridized the 3′-ODF-conjugated probes with their DNA complements carrying Cy5 or TAMRA dye (Figure 1). To test the effect of distance between the putative donors and acceptors, we prepared dye-conjugates in which Cy5 or TAMRA was located at either the 5′ end of the ODF complement (proximal to the ODF) or at the 3′ end (distal to the ODF). Since the probes were 14 nt in length, the difference in distance at proximal and distal locations was approximately 56 Å based on a 3.4 Å rise per base pair of B-DNA. This distance was calculated from the middle of each ODF donor dye to either Cy5 or TAMRA. Hybridization and fluorescence experiments were performed using DNA strand concentrations of 2 μM each, and 10 mM PIPES buffer with 100 mM NaCl, 10 mM $MgCl_2$, at a temperature of 25 °C. An example is shown in Figure 1C.

The sequences of the ODFs in this initial, labeled DNA probe set were chosen essentially at random from an earlier study of quenching behavior (*38*) (see sequences in Table 2) with some additional cases included on the basis of early observations in this study. To initially screen the photophysical interactions of each ODF with the Cy5 and TAMRA acceptors, we measured the emission spectra of the duplexes containing both ODF putative donors and the acceptor dyes. In addition, we measured the emission spectra of the acceptor dyes (conjugated to their DNAs) alone and the ODF donor strands alone, again using this same excitation wavelength (330 nm; chosen for efficient excitation of the aromatic monomers in the ODFs). At this wavelength, the absorbances of TAMRA or Cy5-conjugated strands are minimal.

As a control for the effects of the acceptor dyes on ODF quenching, we also measured the effects of hybridizing the ODF DNAs to unlabeled DNA complement, D1 (see Supporting Information). The effects of hybridization to D1 varied from a small enhancement of fluorescence to a small degree of quenching, and several of the ODFs displayed no change. Thus, in the majority of cases, the quenching effects observed in the hybridization experiments came entirely (or nearly so) from the presence of the acceptor fluorophore on the complement DNA strand.

Exciplexes as FRET Donors. Emission data from selected experiments are shown in Figures 2 (TAMRA) and 3 (Cy5); see Supporting Information for spectra from all cases. Upon hybridization, the long-wavelength emission band between 460 and 510 nm of the donor ODF was diminished in all cases, compared to the emission before hybridization. In addition, a significant enhancement of fluorescence intensity at 590 nm was observed when the ODF strands were hybridized to T3′. This corresponded to the sensitized emission of TAMRA upon hybridization. Since TAMRA cannot be significantly excited at 330 nm, the enhanced emission was likely due to energy transfer from the ODF donor, upon its excitation. Since there is significant overlap of the emission spectra of ODFs and the absorbance spectra of TAMRA, and both ODF and TAMRA are about 14 DNA bases apart (~56 Å), the energy transfer was tentatively characterized as a long-range weak dipole−dipole interaction, or Förster resonance energy transfer (FRET).

Table 2. Sequences and Photophysical Data for 20 Composition- and Sequence-Varied ODFs Appended to the 3′ End of the DNA Probe Sequences P1−P20[a,b]

strand ID	ODF sequence (5′→3′)				λ_{abs}, max (nm)	λ_{em}, max (nm)	Φ_D (fluor)	E_{FRET} T3′	Q_{eff} T5′	E_{FRET} C3′	E_{FRET} C5′
P1	B	E	B	Y	258, 347, 401, 450	492	0.194	0.244	0.595	n.a.	0.125
P2	B	E	Y	Y	264, 344, 402, 452	487	0.266	0.037	0.325	0.056	0.105
P3	S	S	Y	Y	263, 331, 347	488	0.187	0.048	0.480	1.449	1.065
P4	Y	S	S	Y	264, 332, 350	378, 395, 490	0.025	0.045	0.315	0.463	0.646
P5	Y	H	H	Y	267, 333, 349	375, 395, 490	0.044	0.051	0.500	1.374	1.261
P6	B	Y	S	S	261, 349, 403	375, 395, 416, 470	0.205	0.075	0.689	0.129	0.503
P7	E	Y	S	S	257, 346, 451	461, 490	0.421	0.752	0.502	n.a.	0.053
P8	E	Y	E	Y	257, 349, 452	375, 465, 493	0.124	0.054	0.725	0.018	n.a.
P9	E	Y	Y	E	256, 347, 451	464, 490	0.130	0.037	0.487	0.004	n.a.
P10	E	E	Y	Y	257, 347, 451	490	0.141	0.001	0.384	n.a.	n.a.
P11	Y	Y	E	E	254, 349, 441	462, 489	0.110	0.017	0.663	n.a.	n.a.
P12	E	S	E	Y	256, 347, 451	375, 395, 494, 530	0.148	0.028	0.401	n.a.	0.038
P13	B	S	B	D	258, 361, 401	375, 492	0.044	0.070	0.536	n.a.	n.a.
P14	E	Y	B	E	257, 347, 401, 451	465, 493	0.092	0.037	0.615	n.a.	n.a.
P15	E	D	S	S	257, 355, 450	461, 490	0.161	0.057	0.739	n.a.	n.a.
P16	E	S	Y	D	257, 346, 349, 451	460,488	0.191	0.014	0.630	n.a.	0.056
P17	D	S	E	Y	257, 343, 349, 451	375, 463, 490	0.303	0.038	0.435	n.a.	n.a.
P18	E	S	B	S	258, 402, 451	470, 500	0.219	0.159	0.712	n.a.	n.a.
P19	S	E	S	E	254, 449	449, 477	0.182	0.034	0.329	n.a.	n.a.
P20	E	E	D	E	254, 355, 449	374, 454, 478	0.062	0.077	0.038	n.a.	n.a.

[a] T3′ is 3′-conjugated TAMRA on the complementary strand; T5′ is 5′-conjugated TAMRA. C3′ is 3′-conjugated Cy5; C5′ is 5′-conjugated Cy5. B is benzopyrene deoxyriboside; D is dimethylaminostilbene deoxyriboside; E is perylene deoxyriboside; Y is pyrene deoxyriboside, and S is an abasic spacer. [b] E_{FRET} values were calculated using eq 1. n.a. indicates no FRET observed. Q_{eff} is quenching efficiency, given for T5′, where no significant FRET was observed.

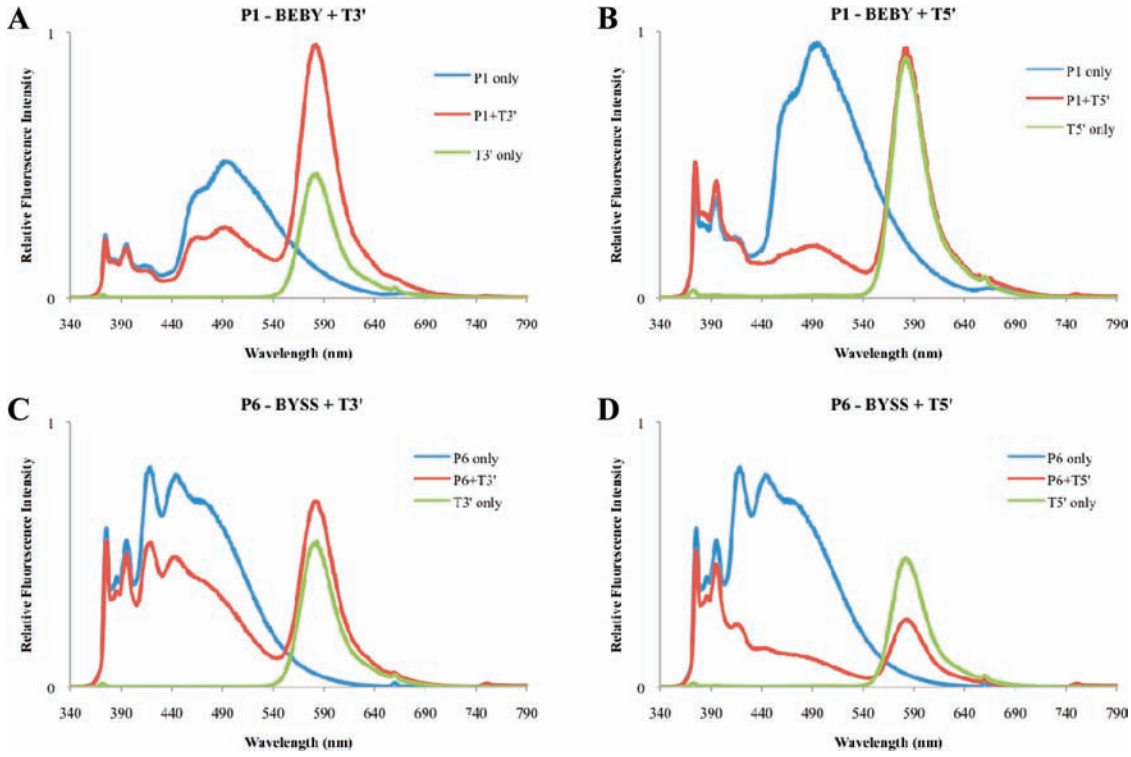

Figure 2. Representative evidence for FRET between ODF fluorophores and TAMRA in a DNA duplex (see full data in Supporting Information). Fluorescence emission spectra (excitation 330 nm) are shown for hybridization of P1 and P6 with T3′ and T5′ (red lines) and individual emission spectra of P1, P6 (blue), T3′, and T5′ (green). Note spectral changes characteristic of FRET for the distal-substituted TAMRA (A,C).

The sensitized enhancement of the acceptor emission can be used to determine the efficiency of FRET (E_{FRET}, see Experimental Procedures). As shown in Table 2, the ODF sequence EYSS displayed the highest apparent efficiency of FRET to T3′ at 0.752, followed by BEBY (0.244) and ESBS (0.159). The other ODF sequences had relatively low E_{FRET}, showing weak or borderline FRET behavior, possibly due to low quantum yields, weak dipoles, or unfavorable dipolar orientation.

Contact Quenching in Proximally Labeled ODF Strands. When the 3′ ODF-labeled strands were hybridized to 5′ TAMRA-labeled complement or 5′ Cy5-labeled complement, the ODF dyes were at a proximal distance to the acceptor fluorophores. Contact quenching can come into play when the two fluorophores are within close distance of each other (*39*). As observed from our experimental data, quenching of more than 30% was observed in 19 out of 20 ODF-labeled strands when hybridized to T5′. Only one strand, P20 (EEDE), experienced little (4%) quenching upon hybridization (see Supporting Information for complete emission spectra). Quenching efficiency, Q_{eff}, for each pair was determined (see Experimental Procedures) and is shown in Table 2. Q_{eff} values ranged from 0.038 to 0.739. The TAMRA emission band was also

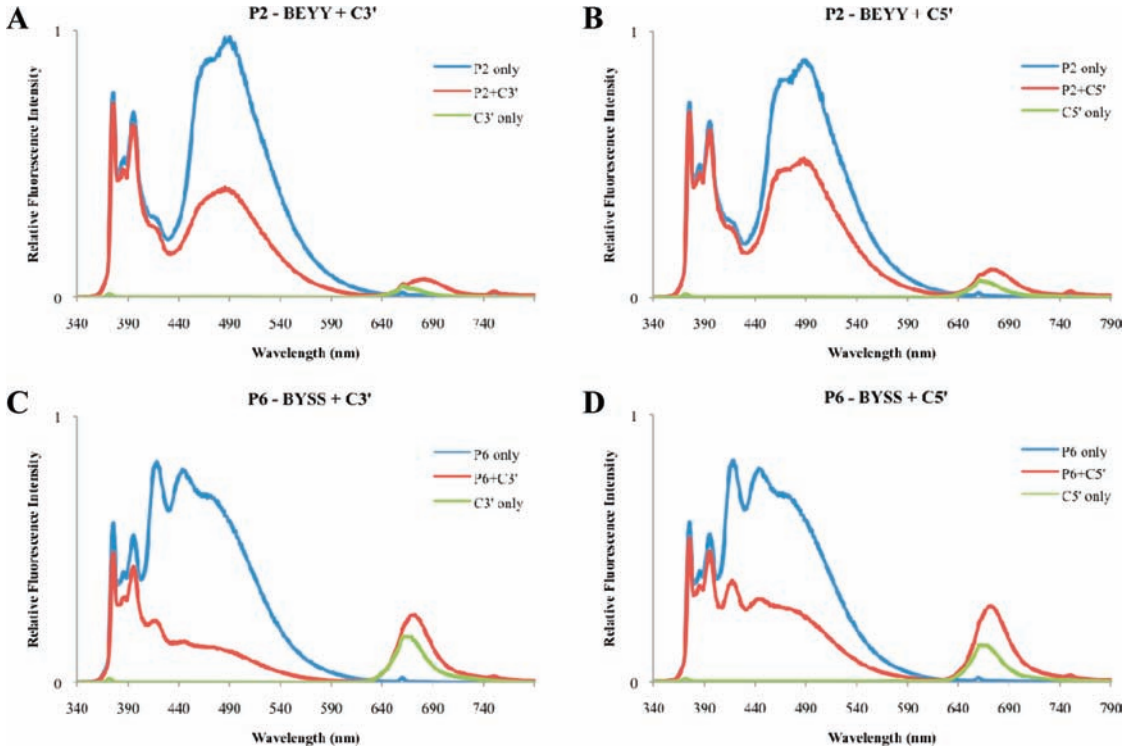

Figure 3. Evidence for FRET between ODF donors and a Cy5 acceptor in duplex DNA. Fluorescence emission spectra are shown for hybridization of ODF conjugates P2 and P6 with C3′ and C5′ (red lines) (λ_{ex} = 330 nm) and individual emission spectra of P2, P6, C3′, and C5′ (λ_{ex} = 330 nm) (blue and green lines). Note quenching of excimer and exciplex bands (440−560 nm) concomitant with enhancement of Cy5 emission at ∼670 nm.

quenched in most cases, or experienced no change in emission intensity. Because quenching in these cases was not coupled to an associated increase in TAMRA emission, we assigned these cases to simple contact quenching and not to FRET. Additional evidence for contact quenching was obtained for one case (sequence P6; BYSS) by measurement of the lifetime of the acceptor (data not shown). Results showed a decrease in lifetime of the TAMRA acceptor fluorophore upon hybridization with donor ODF-labeled strand at the direct excitation wavelength of TAMRA.

Hybridization with Cy5-Labeled Complements. Hybridization between ODF-labeled strands and their Cy5-labeled complements, C3′ and C5′, also resulted in the sensitized emission of the acceptor Cy5 coupled with a decrease in donor emission in some of the strands. Selected examples are given in Figure 3. The emission intensity of the hybrid at 660 nm was enhanced compared to the emission profile of the acceptor dye strand alone in 7 out of the 20 strands tested with distal cyanine dye (C3′), consistent with FRET behavior. Interestingly, hybridization of ODF-labeled strands with proximal C5′ also resulted in the enhancement of acceptor emission in 9 cases, which was distinct from the results with TAMRA, where quenching dominated. The remaining cases with Cy5 exhibited quenching of both the donor emission and acceptor emission upon hybridization, most probably due to the phenomenon of contact quenching.

Excimers as FRET Donors. The above examples document FRET behavior in exciplexes, which have inherent dipoles. To test if similar effects were observed in excimers (which in some cases do not have dipoles in the excited state; see Discussion), the pyrene excimer was used and three different ODF variants were synthesized. Two pyrene nucleosides were placed adjacent to each other in SSYY (P3), producing the highest efficiency of excimer formation. The efficiency of excimer formation was tested by placing spacer groups (S) between the pyrenes in YSSY (P4) or two dihydrothymidine nucleosides (H) between the pyrenes in YHHY (P5). Dihydrothymidine was shown in a previous study to possess excited-state "insulating" effects in oligodeoxyfluorosides (*40*).

The data for hybridization with TAMRA-containing strands are shown in Figure 4; results showed little if any evidence for FRET, displaying only a decrease in donor emission intensity, typical of contact quenching. In marked contrast, hybridization of the pyrene excimer-emitting ODFs to DNAs containing Cy5 (either proximal or distal, Figure 5) yielded significant decreases in donor emission intensity and strong increases in the acceptor emission intensity, providing evidence for efficient FRET. Detailed emission spectra are shown in the Supporting Information. The most efficient FRET occurred in the case of adjacent pyrenes or pyrenes with dihydrothymidine monomers in between, while the addition of spacers lowered the efficiency substantially.

Time-Resolved Measurements. To seek additional evidence for a putative FRET energy transfer mechanism from donor ODF fluorophores to acceptor TAMRA or Cy5, we measured donor emission lifetimes in the absence and presence of the acceptor dye. For the Förster mechanism, one expects a decrease in lifetime of the ODF donor in the presence of the acceptor. If this occurred, this would provide further evidence for FRET with these unusual donors, in addition to the above steady-state spectral observations. Time-resolved fluorescence decay profiles were measured for selected ODF dyes upon hybridization with TAMRA- and Cy5-labeled complement strands. Emission filter sets were selected to ensure that only the lifetime of the donor ODF was measured. Lifetime measurements were determined before and after the addition of the complement and results are shown in Table S2 (Supporting Information).

The results showed that ODF labels (P1−P8) that experienced sensitized acceptor emission and decreased donor emission as described above also experienced shortened donor emission lifetimes. Hybridization with the acceptor-containing strands lowered excited-state lifetimes by 8−27%, with one exception (P5 + C5′). Combined with data from the steady-state studies, this provides further evidence for the occurrence of FRET

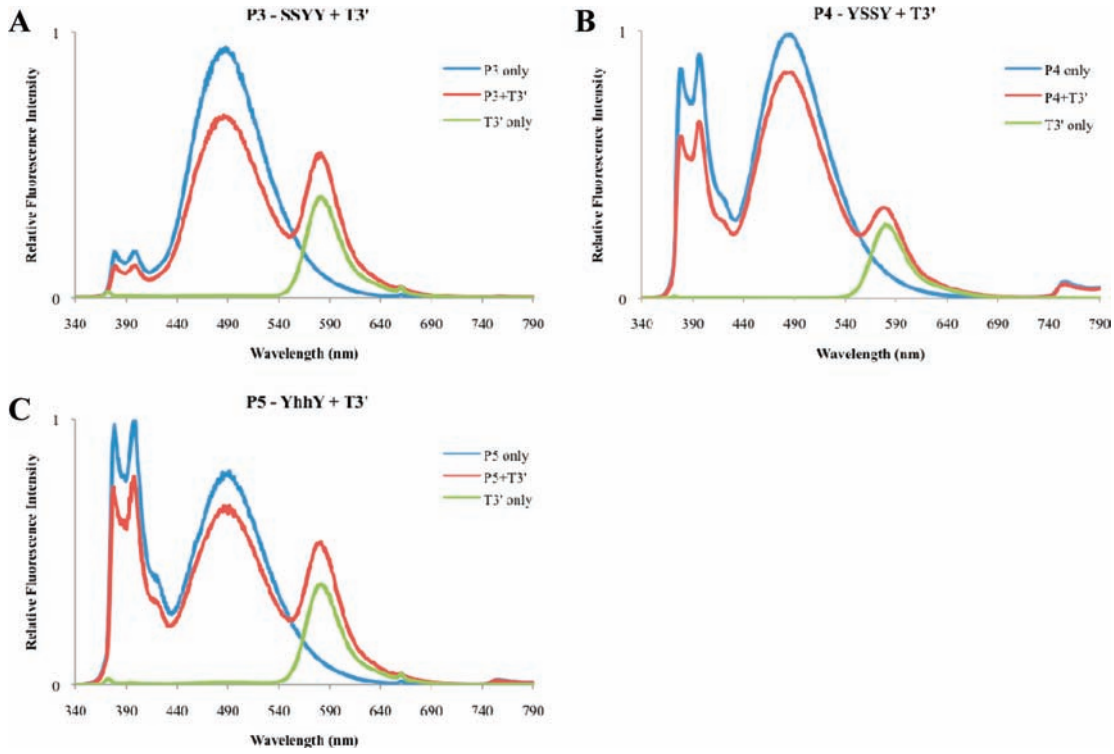

Figure 4. Testing possible FRET donation from pyrene excimers to TAMRA. Fluorescence emission spectra upon hybridization of (A) P3; (B) P4; and (C) P5 with T3′, respectively (red lines) (λ_{ex} = 330 nm) and individual emission spectra of P3, P4, P5, and T3′ (λ_{ex} = 330 nm).

between ODFs and acceptor TAMRA and Cy5 dyes. It is worth noting that the E_{FRET} and EL_{FRET} values calculated from the two methods were not especially well correlated; the most extreme examples are the P5 cases, where two dihydrothymine bases are placed between excimer-forming pyrenes in the ODF donor. We hypothesize that poor correlations for this ODF are due to a delay in formation of the excimer state by the intervening bases (see below). In addition, differences between efficiency values measured from different FRET methods can result from the presence of more than one species in the excited state, which results in lifetimes that vary from single exponential decay, and also by factors such as cross-talk in emission detection and bleedthrough in excitation (*41*).

Determination of Förster Distance, R_0. To further characterize ODFs as FRET donors we measured the Förster distance, R_0, with TAMRA and Cy5. Förster distance, R_0, determined using eq 4, is the distance between the donor and acceptor when the FRET efficiency is 50%. The orientation factor, κ^2, in the determination R_0 can be approximated to 2/3 if both donors and acceptors sample random orientations during the excited state lifetime, and an estimation of $\kappa^2 = 1/3$ is used for cases when either the FRET donor or acceptor experiences static orientation (*36, 42*). Although the orientations of ODFs are not known to certainty, evidence suggests they are stacked with the adjacent DNA, which suggests the use of $\kappa^2 = 1/3$. Nevertheless, we calculated R_0 between each ODF-labeled strand and its complement T3′ strand, using either $\kappa^2 = 1/3$ or $\kappa^2 = 2/3$; these are shown in Table 3 for comparison. R_0 values ranged from 25.3 Å (P4, YSSY) to 42.6 Å (P7, EYSS), and varying the value of κ^2 led to a ~10% difference in the value of R_0. The R_0 values calculated for P1−P20 and T3′ are typical of values of commonly used FRET dye pairs such as dansyl and FITC (33−41 Å) or pyrene and perylene (36 Å) (*43*).

$$R_0(\text{cm}) = [(8.79 \times 10^{-25})\kappa^2\eta^{-4}Q_D J(\lambda)]^{1/6} \quad (4)$$

where κ^2 is the orientation factor, η is the refractive index of water (1.33), Q_D is the quantum yield of the donor, and $J(\lambda)$ is the spectral overlap integral between the emission spectrum of the donor and absorption spectrum of the acceptor. The spectral overlap $J(\lambda)$ is calculated with eq 5

$$J_{DA} = \int_0^\infty F_D(\lambda)\varepsilon_A(\lambda)\lambda^4 \, d\lambda \quad (5)$$

where F_D is the normalized donor emission and ε_A is the molar extinction coefficient of the acceptor.

Upon the determination of R_0, the actual distance between the donor (ODF) and acceptor (TAMRA) of FRET, R_{DA}, can be determined by eq 6. Using both E_{FRET} and EL_{FRET}, R_{DA} was calculated and shown in Table 3. The ODF fluorophore in P1−P20 and TAMRA in T3′ were 14 base pairs apart. On the basis of canonical B-DNA structure, the distance between them approximated from the center of a tetrameric ODF to the TAMRA dye stacked on the end of the double strand was approximately 56.1 Å. As shown in Table 3, the calculated values of R when using $\kappa^2 = 2/3$ and E_{FRET} were within 25% of this approximated distance, except for three cases (P7, P10, and P16), where the calculated distance was considerably longer, reflecting very poor FRET efficiency. Interestingly, calculations of R_{DA} using $\kappa^2 = 1/3$ provided closer approximations to the theoretical distance of 56.1 Å, giving smaller average deviation per strand. This is, however, an approximation and deviations can occur due to the flexible tether of TAMRA on T3′ and the varied distance of the excited donor of each ODF.

$$E = \frac{R_0^6}{R_0^6 + R_{DA}^6} \quad (6)$$

where E is the energy transfer efficiency, using either E_{FRET} or EL_{FRET}.

DISCUSSION

Taking both the steady-state and time-resolved spectroscopy data together, our results establish that both exciplex and excimer ODFs can act as FRET donors to the common acceptor

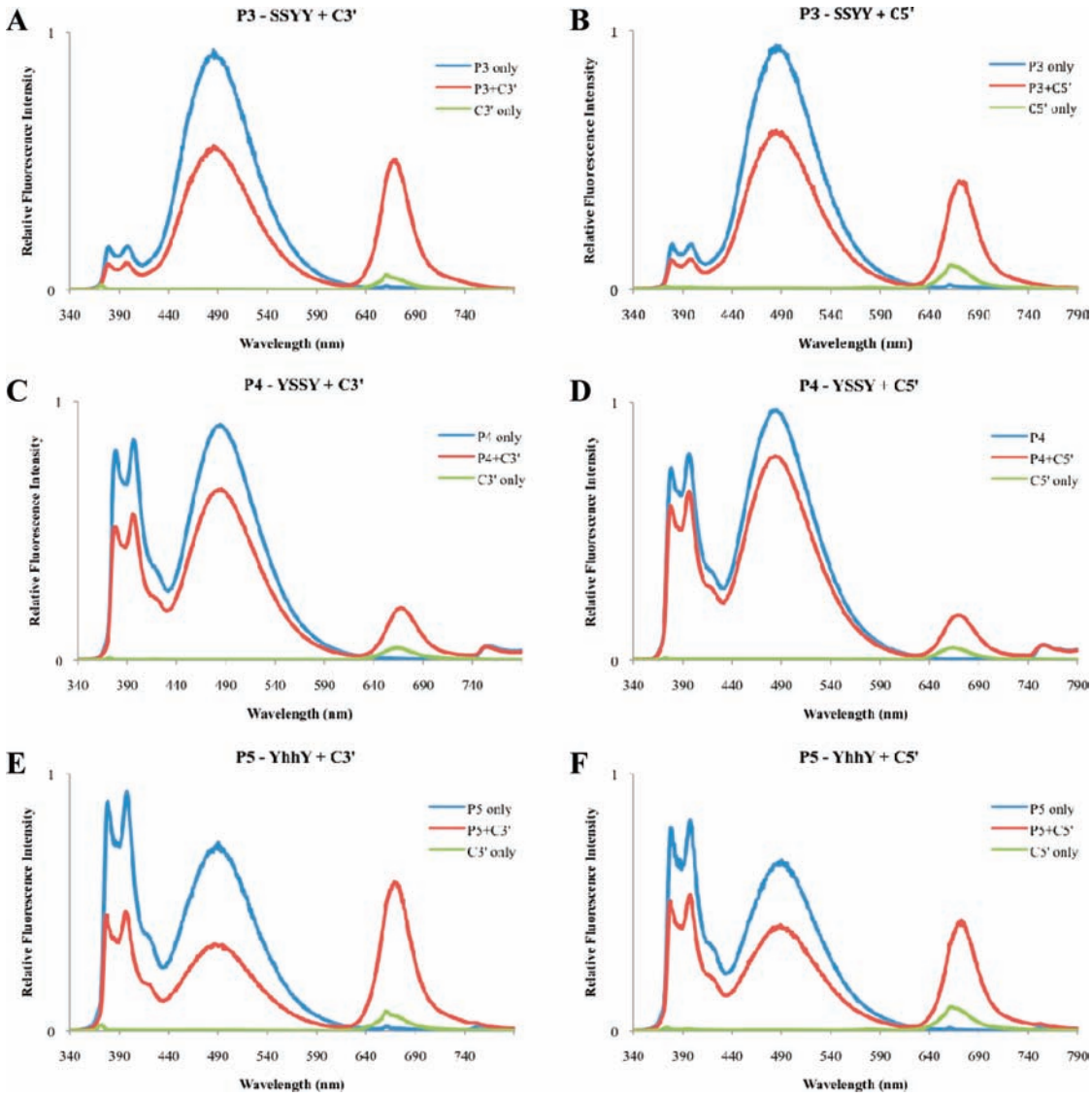

Figure 5. Evidence for strong FRET donation from pyrene excimers to Cy5 acceptor in DNA. Fluorescence emission spectra upon hybridization of P3, P4, and P5 with C3′ and C5′, respectively (red lines) (λ_{ex} = 330 nm) and individual emission spectra of P3, P4, P5, C3′, and C5′ (blue and green lines) (λ_{ex} = 330 nm).

Table 3. Calculated R_0 Values and R_{DA} Values for ODF Donors[a]

strand ID	R_0/Å (κ^2 = 2/3)	R_0/Å (κ^2 = 1/3)	R_{DA}/Å (κ^2 = 2/3; E_{FRET})	R_{DA}/Å (κ^2 = 1/3; E_{FRET})	R_{DA}/Å (κ^2 = 2/3; EL_{FRET})	R_{DA}/Å (κ^2 = 1/3; EL_{FRET})
P1	39.4	35.1	47.6	42.4	46.5	41.4
P2	38.5	34.3	66.2	59.0	52.0	46.3
P3	37.9	33.8	62.4	55.6	46.0	41.0
P4	25.3	22.5	42.1	37.5	36.2	32.3
P5	27.8	24.8	45.2	40.3	23.2	20.7
P6	33.7	30.0	51.1	45.6	39.8	35.5
P7	42.6	38.0	35.4	31.6	57.4	51.2
P8	37.5	33.4	60.4	53.8	48.8	43.5
P9	38.1	34.0	65.6	58.4	n.d.	n.d.
P10	38.3	34.2	118.5	105.6	n.d.	n.d.
P11	34.3	30.5	67.3	59.9	n.d.	n.d.
P12	36.2	32.2	65.4	58.2	n.d.	n.d.
P13	28.8	25.6	44.3	39.4	n.d.	n.d.
P14	34.5	30.8	59.4	52.9	n.d.	n.d.
P15	34.3	30.6	54.8	48.9	n.d.	n.d.
P16	38.2	34.0	77.7	69.2	n.d.	n.d.
P17	40.0	35.7	68.5	61.0	n.d.	n.d.
P18	39.1	34.8	51.6	46.0	n.d.	n.d.
P19	37.2	33.1	64.8	57.7	n.d.	n.d.
P20	29.4	26.2	44.5	39.6	n.d.	n.d.

[a] Note that only a subset of cases exhibit efficient FRET (Table 2). n.d. = not determined. R_0 = R value calculated from drop in donor emission; R_{0A} = value calculated from changes in both donor and acceptor.

fluorophores TAMRA and Cy5. To the best of our knowledge, neither of these delocalized excited-state species has been reported as a FRET donor before. Excimers and exciplexes are unusual as fluorophores in the sense that the excited state is delocalized over two adjacent chromophores. For exciplexes, where the two chromophores are different, this has the important consequence of creating an excited-state dipole that is expected to have a strong component perpendicular to the plane of the stacked chromophores. If (as expected) (*11*) they are stacked with the neighboring DNA, the dipole then has a strong directional component parallel to the helix axis. This is quite different from other DNA-stacked dyes (such as 2-aminopurine), where the chief dipole lies in the plane of the chromophore. Excimers are yet more unusual because the two chromophores are identical. In the absence of DNA, a pyrene excimer has no net excited-state dipole due to symmetry (*44*). As a result, it should not be able to participate in Förster energy transfer. However, by placing pyrenes in DNA the symmetry is broken, and our data establish that a net dipole clearly exists in the present structural context, since FRET from pyrene excimer donors appears to be among the most efficient cases observed here.

All of the ODF fluorophores studied here have emission bands between 440 and 540 nm. Most of them likely have substantial or dominant components of excimer and exciplex that account for this long-wavelength emission, since the monomers B, D, Y, and S do not emit above 430 nm. However, perylene (E) monomer emits at 440−470 nm, and a few of the perylene-containing ODF donors here are likely to emit as a mixture of perylene monomer and excimer or exciplex states. In those cases, we cannot rule out FRET from the perylene monomer state rather than (or in addition to) the delocalized states. However, some of the strongest FRET donors here are unambiguous. For example, P6 (BYSS) emits strongly at 450−550 nm, far red-shifted from the monomer emissions of B or Y and strongly indicative of an exciplex. In the presence of a Cy5 acceptor, this emission drops by 60−80% in intensity, while the Cy5 acceptor emission increases by 25% to >100% (depending on acceptor distance). Likewise, the sequence P3 (SSYY) is an excimer donor, emitting strongly at 440−560 nm. In the presence of Cy5, the donor band is quenched by 25−30%, and the acceptor increases its emission intensity by strong factors of 5−10-fold. Exciplex and excimer FRET cases are also supported by the time-resolved data (Supporting Information Table S2). Interestingly, monomer emission bands of pyrene are also quenched in these excimer donor cases. Since the pyrene monomer emission does not overlap with the absorbance of Cy5 (with a nearly 100 nm gap separating them), it is unlikely that pyrene monomers contribute directly to the FRET donor properties of these cases. It seems possible that this quenching instead reflects the dynamic equilibrium between excimer and monomer excited states.

Of the two acceptor dyes examined here, a distal TAMRA (T3′) was able to act as a more universal acceptor dye for FRET, which may be due to its greater spectral overlap of ODF donor emissions with TAMRA absorption. Thus, weak to moderate FRET occurred from all 20 of the ODF labels to the distal T3′ label. The most efficient donors for TAMRA were the exciplex ODF sequences BEBY and EYSS, which showed relatively large spectral changes in donor and acceptor emission (Figure 2 and Supporting Information). At too close proximity, when P1−20 were hybridized near TAMRA (T5′), this resulted in mutual quenching of the ODF emission and its own emission.

Cy5 was also shown here to be an acceptor dye for FRET with ODF donors, and indeed showed highest efficiency with some examples. FRET was observed in 7 and 9 cases of hybridization of P1−20 with C3′ and C5′, respectively. It is interesting to note that, in these cases, the hybridization of ODF to a proximal Cy5 acceptor did not result in mutual quenching. The most efficient donors for the Cy5 acceptor were found to be the pyrene excimer cases SSYY and YHHY, which showed strong spectral changes due to FRET (Figure 5). This occurred despite the non-optimal spectral overlap of the donor excimer emission (440−590 nm) with the Cy5 absorption band (band 548−689 nm; maximum at 646 nm). The results are consistent with a strong dipole in the ODF excimer and efficient dipolar interaction with Cy5.

Interestingly, although the emission bands of the present donor ODFs were mostly around the same range of wavelengths, FRET efficiencies varied considerably. One possible reason is that quantum yields vary to a substantial extent among ODF donors. Quantum yields of the donors affect the Förster distance, R_0, directly, and thus plays a role in E_{FRET}. The varying excited-state lifetimes of the donors could also affect the ability of the ODFs to sample favorable orientations and allow efficient FRET to occur. Thus, ODF donors with longer lifetimes typically displayed higher FRET efficiencies. In addition, the dipole strength and orientation of the excimers and exciplexes in the various ODFs may vary significantly, resulting in different degrees of FRET efficiency.

As mentioned above, the lifetimes measurements for these unusual multichromophore FRET donors can be complicated by two factors that may not be seen in some common single-chromophore donors: namely, the presence of multiple excited-state species, and the competing kinetics of delayed formation of an excited state. The former can complicate evaluation of decay kinetics by presenting more than one overlapping decay curve. The latter can result when excimer- or exciplex-forming species are separated physically. For example, the P5 + C5′ case, where two H residues separate two pyrenes, shows clear steady-state evidence of FRET (Figure 5F) but no shortening of lifetime (Supporting Information Table S2). We suggest that in this case the kinetics most likely reflect the added time required for structural reorganization of the chromophores during the long pyrene monomer excited state, until the favored conformation for excimer interaction can be reached. As a result of such effects, we consider the steady-state spectral changes (see Figures 2−5, Table 2) to be the most convincing measurement of FRET behavior for multichromophore ODF donors, and interpret the decrease in lifetimes as being consistent with, but not necessarily diagnostic of, FRET. More detailed time-resolved studies would be useful in investigating these phenomena.

The uncertainty of the orientation dipole factor (κ^2) in R_0 calculations is a known problem in the literature (*45*, *46*). In our study, we used two estimations of κ^2: a value of 1/3 (typically used when one member of the FRET pair is in a static orientation), and the value 2/3, assuming both donor and acceptor sample random orientations during the excited state. In our experiments, the former assumption yielded a better approximation to the theoretical distance between donor ODF and acceptor TAMRA. This would be consistent with the notion that either ODF donor chromophores or TAMRA and Cy5 acceptor dyes were stacked at the end of the DNA with relatively fixed orientation. Previous studies have shown that aromatic hydrocarbons such as those in these ODFs stack with DNA with high affinity (*11*) and absorption spectra support the notion that the neighboring aromatic chromophores are stacked with one another in the ground state as well (*37*). NMR studies showed that a significant population of Cy5 dyes can stack onto the end of a DNA duplex (*47*) while some remain freely mobile as shown in single molecule experiments and simulations (*48*).

Not only is the observance of FRET from excimer and exciplex dyes of theoretical interest, but the ODFs also offer some potential advantages in practical use. Relative to common donors used with

TAMRA and Cy5, the ODFs offer high quantum yields and a fixed orientation in the DNA. In addition, ODFs are directly incorporated into DNA using automated solid-phase synthesis, unlike some common dyes that require postsynthetic labeling. The ODFs are composed of combinations of a small set of monomers; for example, optimal donor ODFs for TAMRA and Cy5 are composed of only two fluorescent monomers (Y and E) along with a commercially available spacer (S).

In addition to the above, perhaps the most distinctive aspect of the current multichromophoric dyes as FRET donors is their unusual spectral characteristics. Since all the ODFs studied can be excited simultaneously at one wavelength (330 nm was used here), the ODFs can function as FRET donors potentially to a wide variety of acceptors using a simple filter set. Further experiments will be needed to confirm this. In addition, the ODFs have unusually large Stokes shifts (144−149 nm in the present cases), thus providing a large spectral separation between exciting light and emission. These properties can simplify experimental setups involving simultaneous analysis of multiple species. Thus, these multichromophore labels present substantial potential for development and application in biomolecular analysis and imaging.

ACKNOWLEDGMENT

We thank the U.S. National Institutes of Health (Grant GM067201) for support. Y.N.T. acknowledges an A*STAR NSS scholarship.

Supporting Information Available: Mass spectrometric data for ODF-containing oligonucleotides; fluorescence lifetimes measurements; emission spectra from hybridization experiments of all ODF-DNA duplexes with 5′-TAMRA, 5′-Cy5, 3′-TAMRA, and 3′-Cy5-labeled complementary strands; as well as the natural complementary strand. This material is available free of charge via the Internet at http://pubs.acs.org.

LITERATURE CITED

(1) Hoeben, F. J., Jonkheijm, P., Meijer, E. W., and Schenning, A. P. (2005) About supramolecular assemblies of pi-conjugated systems. *Chem. Rev. 105*, 1491–1546.
(2) Bazan, G. C. (2007) Novel organic materials through control of multichromophore interactions. *J. Org. Chem. 72*, 8615–8635.
(3) Ho, H. A., Najari, A., and Leclerc, M. (2008) Optical detection of DNA and proteins with cationic polythiophenes. *Acc. Chem. Res. 41*, 168–178.
(4) Gensch, T., Hofkens, J., Heirmann, A., Tsuda, K., Verheijen, W., Vosch, T., Christ, T., Basche, T., Mullen, K., and De Schryver, F. C. (1999) Fluorescence detection from single dendrimers with multiple chromophores. *Angew. Chem., Int. Ed. Engl. 38*, 3752–3756.
(5) De Schryver, F. C., Vosch, T., Cotlet, M., Van der Auweraer, M., Mullen, K., and Hofkens, J. (2005) Energy dissipation in multichromophoric single dendrimers. *Acc. Chem. Res. 38*, 514–522.
(6) Tinnefeld, P., Heilemann, M., and Sauer, M. (2005) Design of molecular photonic wires based on multistep electronic excitation transfer. *ChemPhysChem 6*, 217–222.
(7) Lewis, F. D. (2005) DNA molecular photonics. *Photochem. Photobiol. 81*, 65–72.
(8) Hossain, M. A., Mihara, H., and Ueno, A. (2003) Novel peptides bearing pyrene and coumarin units with or without beta-cyclodextrin in their side chains exhibit intramolecular fluorescence resonance energy transfer. *J. Am. Chem. Soc. 125*, 11178–11179.
(9) Ren, R. X. F., Chaudhuri, N. C., Paris, P. L., Rumney, S., and Kool, E. T. (1996) Naphthalene, phenanthrene, and pyrene as DNA base analogues: synthesis, structure, and fluorescence in DNA. *J. Am. Chem. Soc. 118*, 7671–7678.
(10) Gao, J., Strassler, C., Tahmassebi, D., and Kool, E. T. (2002) Libraries of composite polyfluors built from fluorescent deoxyribosides. *J. Am. Chem. Soc. 124*, 11590–11591.
(11) Cuppoletti, A., Cho, Y., Park, J. S., Strassler, C., and Kool, E. T. (2005) Oligomeric fluorescent labels for DNA. *Bioconjugate Chem. 16*, 528–534.
(12) Teo, Y. N., Wilson, J. N., and Kool, E. T. (2009) Polyfluorophores on a DNA backbone: a multicolor set of labels excited at one wavelength. *J. Am. Chem. Soc. 131*, 3923–3933.
(13) Malinovskii, V. L., Samain, F., and Haner, R. (2007) Helical arrangement of interstrand stacked pyrenes in a DNA framework. *Angew. Chem., Int. Ed. Engl. 46*, 4464–4467.
(14) Trkulja, I., and Haner, R. (2007) Triple-helix mediated excimer and exciplex formation. *Bioconjugate Chem. 18*, 289–292.
(15) Wagenknecht, H. A. (2008) Fluorescent DNA base modifications and substitutes: multiple fluorophore labeling and the DETEQ concept. *Ann. N.Y. Acad. Sci. 1130*, 122.
(16) Mayer-Enthart, E., and Wagenknecht, H. A. (2006) Structure-sensitive and self-assembled helical pyrene array based on DNA architecture. *Angew. Chem., Int. Ed. Engl. 45*, 3372–3375.
(17) Kashida, H, A. H. K. M. (2004) Alternating hetero H aggregation of different dyes by interstrand stacking from two DNA-dye conjugates. *Angew. Chem., Int. Ed. Engl. 43*, 6522.
(18) Kashida, H., Tanaka, M., Baba, S., Sakamoto, T., Kawai, G., Asanuma, H., and Komiyama, M. (2006) Covalent incorporation of methyl red dyes into double-stranded DNA for their ordered clustering. *Chemistry 12*, 777–784.
(19) Brotschi, C., Mathis, G., and Leumann, C. J. (2005) Bipyridyl- and biphenyl-DNA: a recognition motif based on interstrand aromatic stacking. *Chemistry 11*, 1911.
(20) Chiba, J., Takeshima, S., Mishima, K., Maeda, H., Nanai, Y., Mizuno, K., and Inouye, M. (2007) Artificial DNAs based on alkynyl C-nucleosides as a superior scaffold for homo- and heteroexcimer emissions. *Chem. Eur. J. 13*, 8124–8130.
(21) Nakamura, M., Shimomura, Y., Ohtoshi, Y., Sasa, K., Hayashi, H., Nakano, H., and Yamana, K. (2007) Pyrene aromatic arrays on RNA duplexes as helical templates. *Org. Biomol. Chem. 5*, 1945–1951.
(22) Nakamura, M., Murakami, Y., Sasa, K., Hayashi, H., and Yamana, K. (2008) Pyrene-zipper array assembled via RNA duplex formation. *J. Am. Chem. Soc. 130*, 6904.
(23) Hrdlicka, P. J., Babu, B. R., Sorensen, M. D., Harrit, N., and Wengel, J. (2005) Multilabeled pyrene-functionalized 2′-amino-LNA probes for nucleic acid detection in homogeneous fluorescence assays. *J. Am. Chem. Soc. 127*, 13293–13299.
(24) Hannah, K. C., and Armitage, B. A. (2004) DNA-templated assembly of helical cyanine dye aggregates: a supramolecular chain polymerization. *Acc. Chem. Res. 37*, 845–853.
(25) Benvin, A. L., Creeger, Y., Fisher, G. W., Ballou, B., Waggoner, A. S., and Armitage, B. A. (2007) Fluorescent DNA nanotags: supramolecular fluorescent labels based on intercalating dye arrays assembled on nanostructured DNA templates. *J. Am. Chem. Soc. 129*, 2025–2034.
(26) Sanchez-Mosteiro, G., vanDijk, E. M. H. P., Hernando, J., Heilemann, M., Tinnefeld, P., Sauer, M., Koberlin, F., Patting, M., Wahl, M., Erdmann, R., vanHulst, N. F., and Garcia-Parajo, M. F. (2006) DNA-based molecular wires: multiple emission pathways of individual constructs. *J. Phys. Chem. B 110*, 26349–26353.
(27) Tong, A. K., Li, Z., Jones, G. S., Russo, J. J., and Ju, J. (2001) Combinatorial fluorescence energy transfer tags for multiplex biological assays. *Nat. Biotechnol. 19*, 756–759.
(28) Li, H. P., and Bazan, G. C. (2009) Conjugated oligoelectrolyte/ssDNA aggregates: self-assembled multicomponent chromophores for protein discrimination. *Adv. Mater. 21*, 964+.
(29) Wang, S., Gaylord, B. S., and Bazan, G. C. (2004) Fluorescein provides a resonance gate for FRET from conjugated polymers to DNA intercalated dyes. *J. Am. Chem. Soc. 126*, 5446–5451.
(30) Clegg, R. M. (1992) Fluorescence resonance energy transfer and nucleic acids. *Methods Enzymol. 211*, 353–388.
(31) Stryer, L. (1978) Fluorescence energy transfer as a spectroscopic ruler. *Annu. Rev. Biochem. 47*, 819–846.

(32) Gao, J., Watanabe, S., and Kool, E. T. (2004) Modified DNA analogues that sense light exposure with color changes. *J. Am. Chem. Soc. 126*, 12748–12749.

(33) Hamai, S., and Hirayama, F. (1983) Actinometric determination of absolute fluorescence quantum yields. *J. Phys. Chem. 87*, 83–89.

(34) Williams, A. T. R., Winfield, S. A., and Miller, J. N. (1983) Relative fluorescence quantum yields using a computer-controlled luminescence spectrometer. *Analyst 108*, 1067–1071.

(35) Valeur, B. (2002) *Molecular Fluorescence: principles and applications*, 1st ed., Wiley-VCH, Weinheim.

(36) Selvin, P. R. (1995) Fluorescence resonance energy transfer. *Methods Enzymol. 246*, 300–334.

(37) Wilson, J. N., Gao, J., and Kool, E. T. (2007) Oligodeoxyfluorosides: strong sequence dependence of fluorescence emission. *Tetrahedron 63*, 3427–3433.

(38) Teo, Y. N., Wilson, J. N., and Kool, E. T. (2009) Polyfluorophore labels on DNA: dramatic sequence dependence of quenching. *Chem.—Eur. J.* (Online early access) Sep 24 2009, DOI: 10.1002/chem.200901607.

(39) Marras, S. A., Kramer, F. R., and Tyagi, S. (2002) Efficiencies of fluorescence resonance energy transfer and contact-mediated quenching in oligonucleotide probes. *Nucleic Acids Res. 30*, e122.

(40) Wilson, J. N., Cho, Y., Tan, S., Cuppoletti, A., and Kool, E. T. (2008) Quenching of fluorescent nucleobases by neighboring DNA: the "insulator" concept. *ChemBioChem 9*, 279–285.

(41) Berney, C., and Danuser, G. (2003) FRET or no FRET: a quantitative comparison. *Biophys. J. 84*, 3992–4010.

(42) Neubauer, H., Gaiko, N., Berger, S., Schaffer, J., Eggeling, C., Tuma, J., Verdier, L., Seidel, C. A., Griesinger, C., and Volkmer, A. (2007) Orientational and dynamical heterogeneity of rhodamine 6G terminally attached to a DNA helix revealed by NMR and single-molecule fluorescence spectroscopy. *J. Am. Chem. Soc. 129*, 12746–12755.

(43) Lakowicz, J. R. (2006) *Principles of Fluorescence Spectroscopy*, 3rd ed., Springer, New York.

(44) Tavares, M. A. F. (1970) Excited molecular complexes of aromatic hydrocarbons. *Trans. Faraday Soc. 66*, 2431–&.

(45) Dale, R. E., Eisinger, J., and Blumberg, W. E. (1979) Orientational freedom of molecular probes - orientation factor in intramolecular energy-transfer. *Biophys. J. 26*, 161–193.

(46) Munoz-Losa, A., Curutchet, C., Krueger, B. P., Hartsell, L. R., and Mennucci, B. (2009) Fretting about FRET: failure of the ideal dipole approximation. *Biophys. J. 96*, 4779–4788.

(47) Iqbal, A., Wang, L., Thompson, K. C., Lilley, D. M., and Norman, D. G. (2008) The structure of cyanine 5 terminally attached to double-stranded DNA: implications for FRET studies. *Biochemistry 47*, 7857–7862.

(48) Iqbal, A., Arslan, S., Okumus, B., Wilson, T. J., Giraud, G., Norman, D. G., Ha, T., and Lilley, D. M. (2008) Orientation dependence in fluorescent energy transfer between Cy3 and Cy5 terminally attached to double-stranded nucleic acids. *Proc. Natl. Acad. Sci. U.S.A. 105*, 11176–11181.

BC9003926

SUPPORTING INFORMATION

Polyfluorophore Excimers and Exciplexes as FRET Donors in DNA

Yin Nah Teo, Eric T. Kool*

Department of Chemistry, Stanford University, Stanford, CA 94305

*to whom correspondence should be addressed: kool@stanford.edu

CONTENTS:

Table S1. MALDI-TOF characterization of ODF-labeled oligonucleotides ..... p. 2

Table S2. Fluorescence lifetime measurements and EL_{FRET} values of ODF donor–conjugated DNAs and hybridized donor and acceptor strands. ..…… p. 3

Figure S1. Fluorescence emission spectra for hybridization of P1-P20 with T3', T5', C3' and C5'……..… p. 4

Figure S2. Fluorescence emission spectra for hybridization of P2, P3, P5, P8, P13 and P19 with unlabeled complementary strand, D1..……..… p. 24

Table S1: MALDI-TOF mass spectrometric data for the 20 ODF-labeled oligonucleotides P1-P20.

Strand ID	ODF Seq (5'-3')				Calc.	Found
P1	B	E	B	Y	5975.0	5978.24
P2	B	E	Y	Y	5925.0	5931.41
P3	S	S	Y	Y	5425.6	5432.57
P4	Y	S	S	Y	5425.6	5432.92
P5	Y	H	H	Y	5677.9	5716.00
P6	B	Y	S	S	5475.7	5470.80
P7	E	Y	S	S	5475.7	5478.69
P8	E	Y	E	Y	5926.2	5926.00
P9	E	Y	Y	E	5926.2	5943.99
P10	E	E	Y	Y	5926.2	5929.34
P11	Y	Y	E	E	5926.2	5926.96
P12	E	S	E	Y	5725.0	5731.33
P13	B	S	B	D	5746.0	5743.70
P14	E	Y	B	E	5975.0	5976.93
P15	E	D	S	S	5496.0	5500.12
P16	E	S	Y	D	5696.0	5700.76
P17	D	S	E	Y	5696.0	5687.47
P18	E	S	B	S	5525.0	5532.18
P19	S	E	S	E	5525.0	5529.49
P20	E	E	D	E	5996.0	6021.87

Table S2. Fluorescence lifetime measurements and EL_{FRET} values of ODF donor–conjugated DNAs and hybridized donor and acceptor strands. Lifetimes were obtained upon fitting with either a single or double exponential decay function. EL_{FRET} values (FRET efficiency measured by changes in lifetimes) were determined using eq. 3 (see Experimental Section).

Strands	χ^2	α_1	τ_1 (ns)	α_2	τ_2(ns)	$<\tau>$ (ns)	EL_{FRET}
P1	1.57	0.26	4.21 (±0.39)	0.34	20.37 (±0.37)	13.27	
P1+T3'	1.36	0.28	2.74 (±0.36)	0.28	16.76 (±0.42)	9.69	0.269
P1+C5'	1.35	0.17	2.90 (±0.29)	0.20	15.80 (±0.66)	10.01	0.245
P2	1.26	0.51	5.06 (±0.01)	0.07	33.47 (±0.15)	8.57	
P2+T3'	0.96	0.61	4.74 (±0.01)	0.16	17.60 (±0.03)	7.37	0.141
P2+C5'	0.96	0.36	4.13 (±0.02)	0.16	15.70 (±0.09)	7.66	0.107
P3	1.00	0.37	46.71 (±1.51)	0.24	12.80 (±0.68)	33.59	
P3+T3'	0.93	0.42	34.61 (±0.62)	0.20	6.69 (±0.55)	25.54	0.240
P4	1.09	0.61	38.03 (±0.76)	n.a.[a]	n.a.[a]	23.02	
P4+T3'	1.08	0.57	36.49 (±0.20)	n.a.[a]	n.a.[a]	20.62	0.104
P5	1.46	0.97	96.67 (±0.86)	n.a.[a]	n.a.[a]	94.06	
P5+T3'	1.04	0.49	48.67 (±0.72)	n.a.[a]	n.a.[a]	23.84	0.747
P5+C5'	1.34	0.79	102.00 (±1.35)	n.a.[a]	n.a.[a]	80.63	0.143
P6	1.21	0.33	8.02 (±0.01)	0.29	28.86 (±0.01)	17.71	
P6+T3'	1.28	0.29	4.46 (±0.01)	0.24	23.20 (±0.01)	12.98	0.267
P6+C3'	1.08	0.22	5.39 (±0.25)	0.33	23.59 (±0.41)	16.36	0.076
P7	1.43	0.51	7.21 (±0.001)	0.19	2.25 (±0.002)	5.85	
P7+T3'	1.44	0.51	7.10 (±0.07)	0.33	1.79 (±0.18)	5.01	0.143
P8	1.03	0.71	6.25 (±0.39)	0.07	23.92 (±4.74)	7.83	
P8+T3'	0.92	0.52	4.61 (±0.003)	0.20	11.50 (±0.01)	6.50	0.170

[a] A single exponential was used to fit the fluorescence decay profile in these cases.

Figure S1. Fluorescence emission spectra for hybridization of P1-P20 with T3', T5', C3' or C5'. Conditions: 10 mM Na·PIPES, 100 mM NaCl, 10 mM $MgCl_2$, pH 7.0, 25°C, 2 μM of P1-P20 with 1.0 molar equivalents of T3', T5', C3' or C5'.

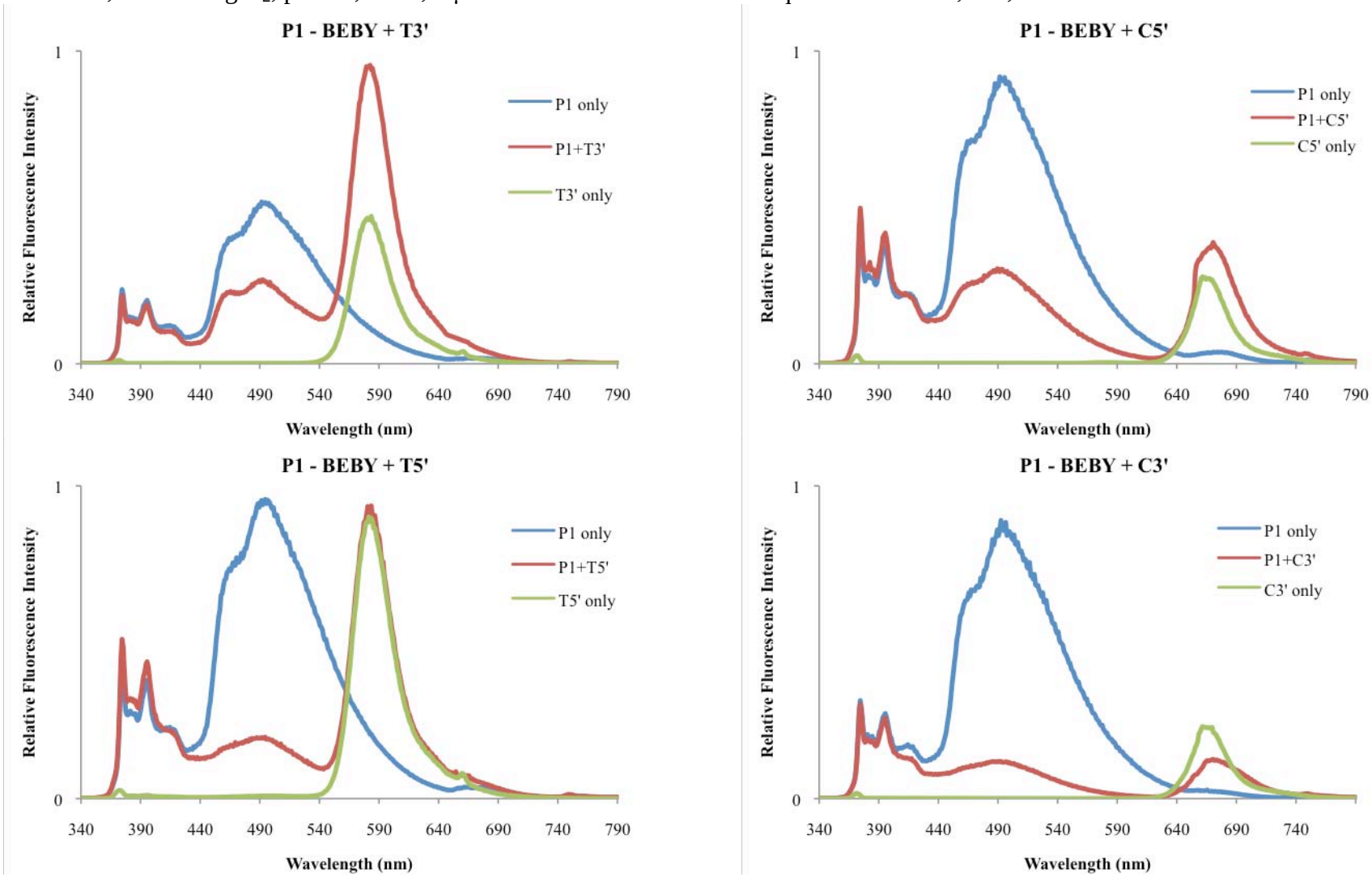

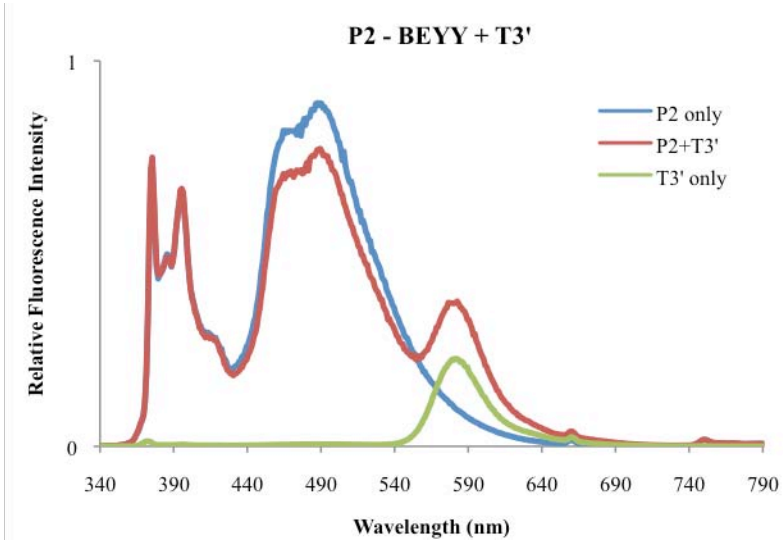
P2 - BEYY + T3'
Relative Fluorescence Intensity
1
0
340 390 440 490 540 590 640 690 740 790
Wavelength (nm)
P2 only
P2+T3'
T3' only

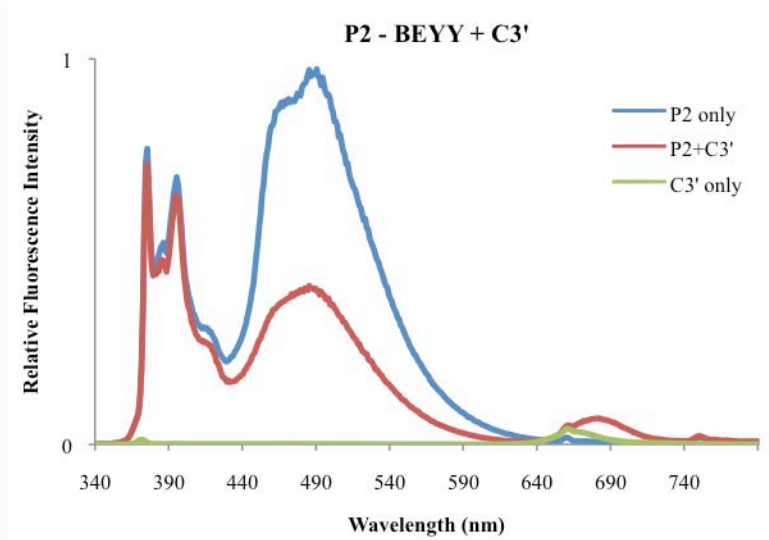
P2 - BEYY + C3'
Relative Fluorescence Intensity
1
0
340 390 440 490 540 590 640 690 740
Wavelength (nm)
P2 only
P2+C3'
C3' only

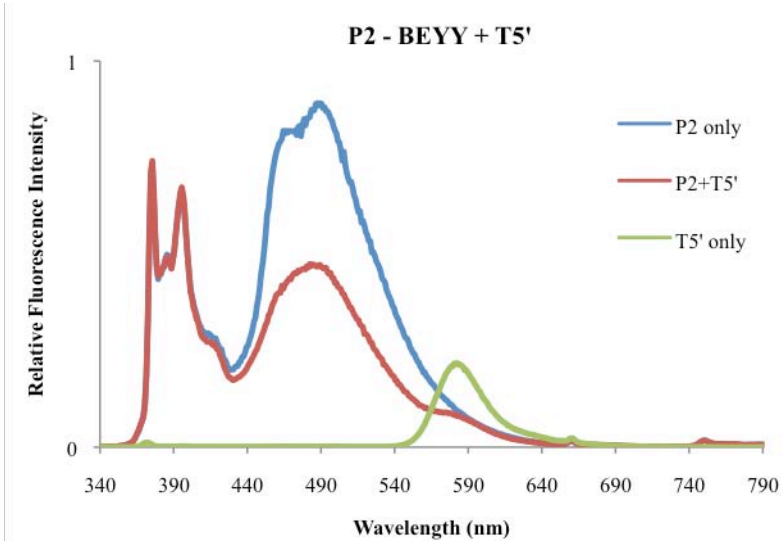
P2 - BEYY + T5'
Relative Fluorescence Intensity
1
0
340 390 440 490 540 590 640 690 740 790
Wavelength (nm)
P2 only
P2+T5'
T5' only

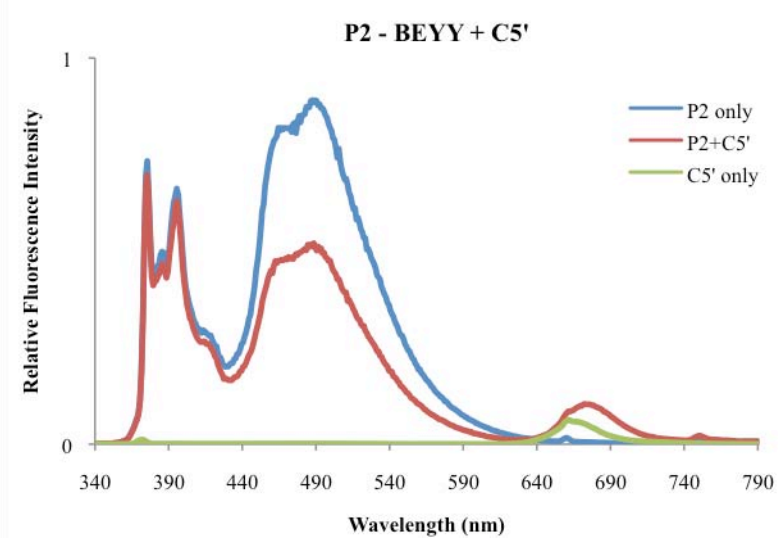
P2 - BEYY + C5'
Relative Fluorescence Intensity
1
0
340 390 440 490 540 590 640 690 740 790
Wavelength (nm)
P2 only
P2+C5'
C5' only

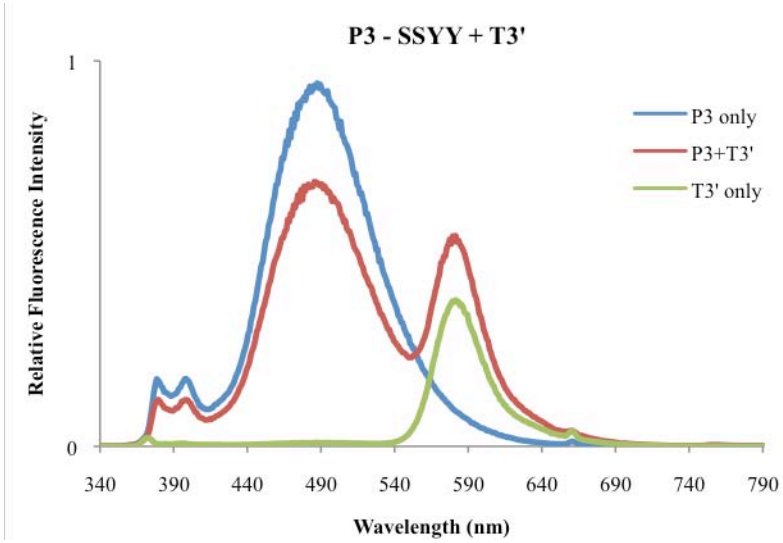
P3 - SSYY + T3'
Relative Fluorescence Intensity
1
0
340 390 440 490 540 590 640 690 740 790
Wavelength (nm)
P3 only
P3+T3'
T3' only

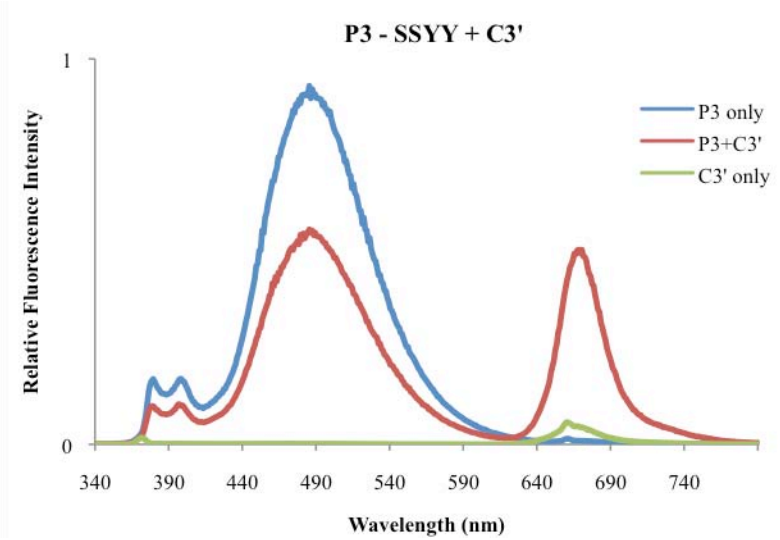
P3 - SSYY + C3'
Relative Fluorescence Intensity
1
0
340 390 440 490 540 590 640 690 740
Wavelength (nm)
P3 only
P3+C3'
C3' only

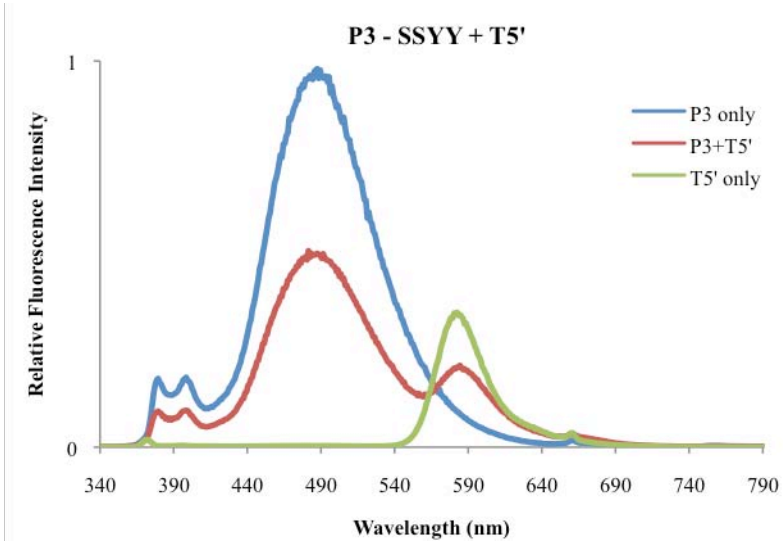
P3 - SSYY + T5'
Relative Fluorescence Intensity
1
0
340 390 440 490 540 590 640 690 740 790
Wavelength (nm)
P3 only
P3+T5'
T5' only

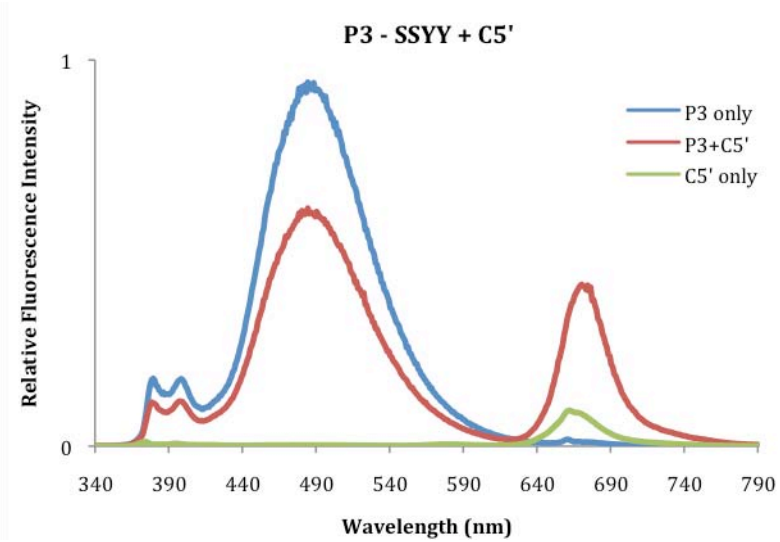
P3 - SSYY + C5'
Relative Fluorescence Intensity
1
0
340 390 440 490 540 590 640 690 740 790
Wavelength (nm)
P3 only
P3+C5'
C5' only

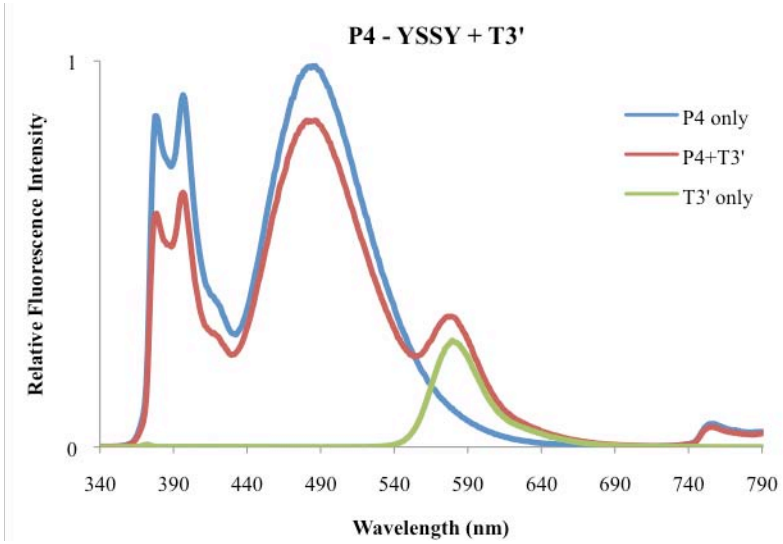
P4 - YSSY + T3'
Relative Fluorescence Intensity
1
0
340
390
440
490
540
590
640
690
740
790
Wavelength (nm)
P4 only
P4+T3'
T3' only

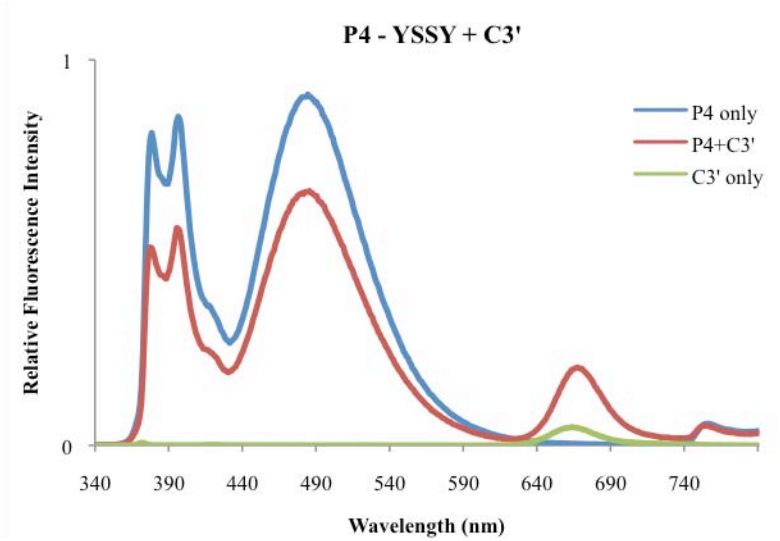
P4 - YSSY + C3'
Relative Fluorescence Intensity
1
0
340
390
440
490
540
590
640
690
740
Wavelength (nm)
P4 only
P4+C3'
C3' only

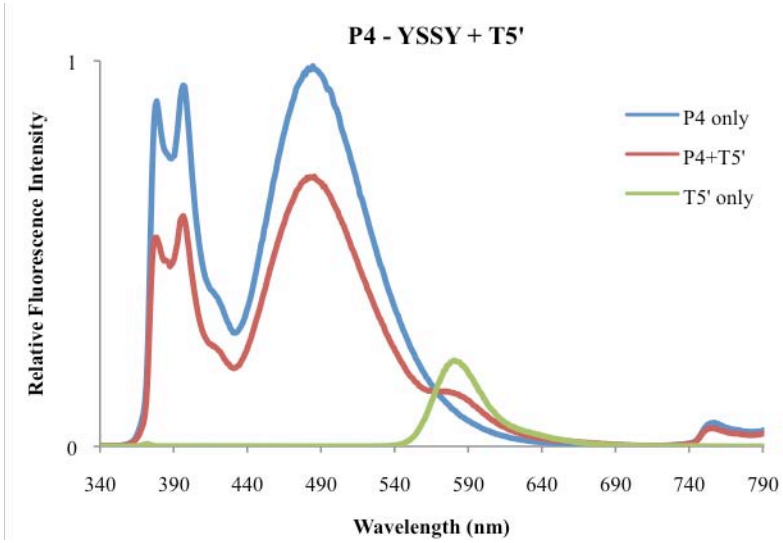
P4 - YSSY + T5'
Relative Fluorescence Intensity
1
0
340
390
440
490
540
590
640
690
740
790
Wavelength (nm)
P4 only
P4+T5'
T5' only

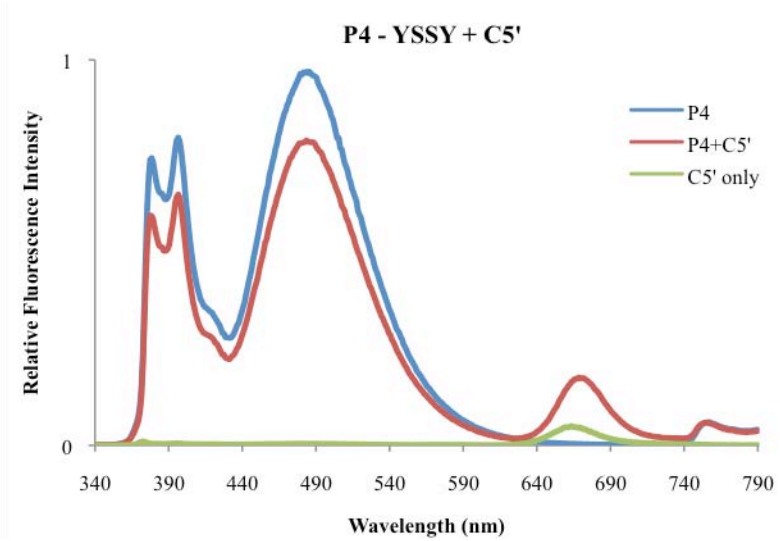
P4 - YSSY + C5'
Relative Fluorescence Intensity
1
0
340
390
440
490
540
590
640
690
740
790
Wavelength (nm)
P4
P4+C5'
C5' only

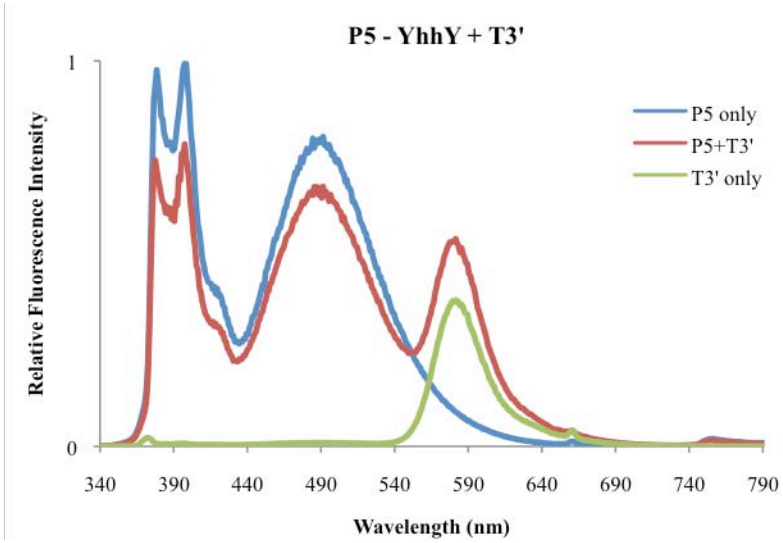
P5 - YhhY + T3'
Relative Fluorescence Intensity
1
0
340 390 440 490 540 590 640 690 740 790
Wavelength (nm)
P5 only
P5+T3'
T3' only

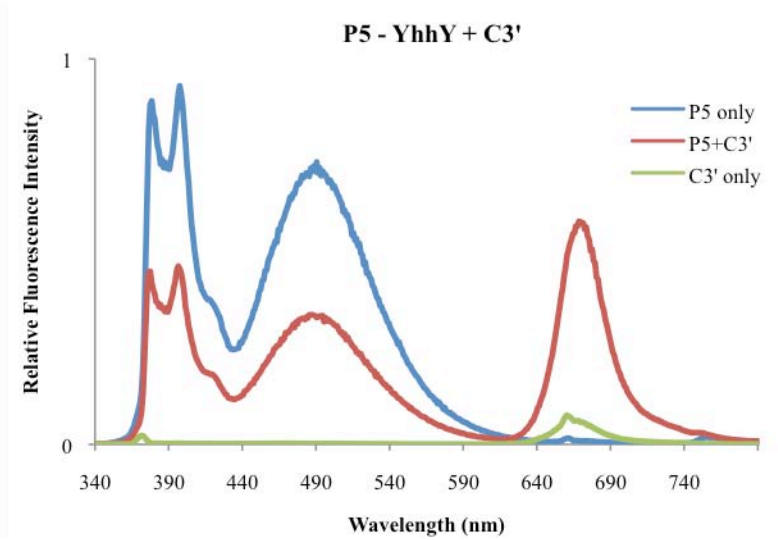
P5 - YhhY + C3'
Relative Fluorescence Intensity
1
0
340 390 440 490 540 590 640 690 740
Wavelength (nm)
P5 only
P5+C3'
C3' only

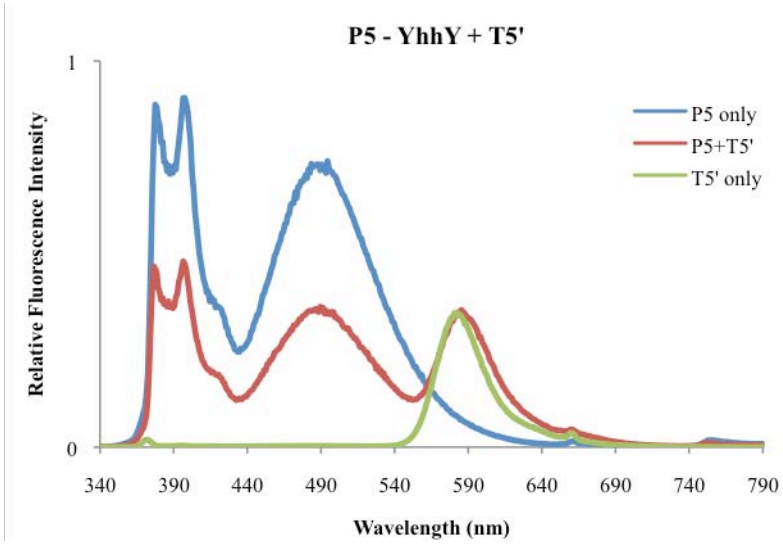
P5 - YhhY + T5'
Relative Fluorescence Intensity
1
0
340 390 440 490 540 590 640 690 740 790
Wavelength (nm)
P5 only
P5+T5'
T5' only

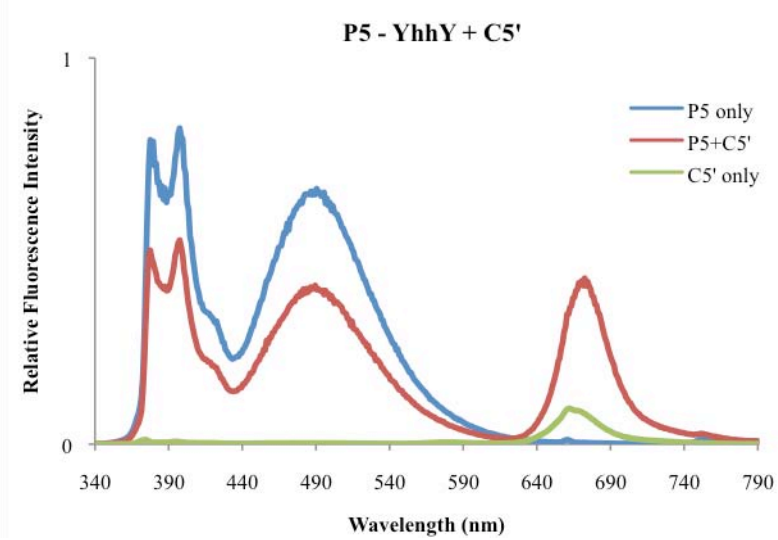
P5 - YhhY + C5'
Relative Fluorescence Intensity
1
0
340 390 440 490 540 590 640 690 740 790
Wavelength (nm)
P5 only
P5+C5'
C5' only

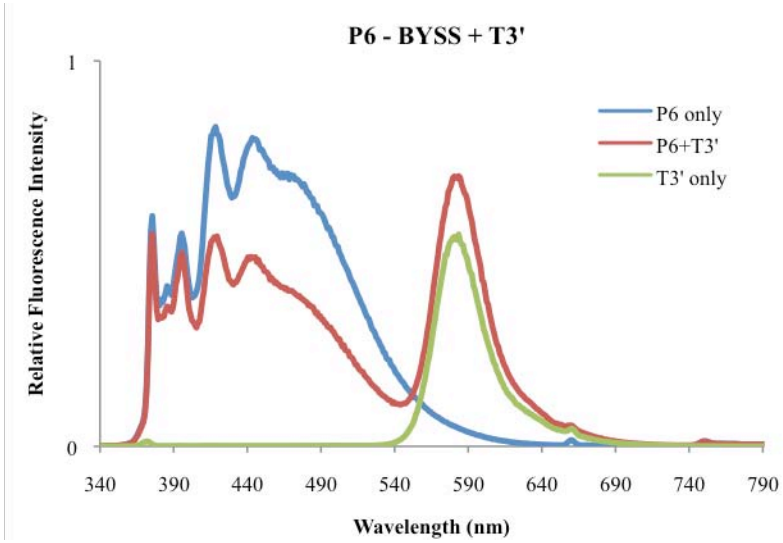
P6 - BYSS + T3'
Relative Fluorescence Intensity
1
0
340
390
440
490
540
590
640
690
740
790
Wavelength (nm)
P6 only
P6+T3'
T3' only

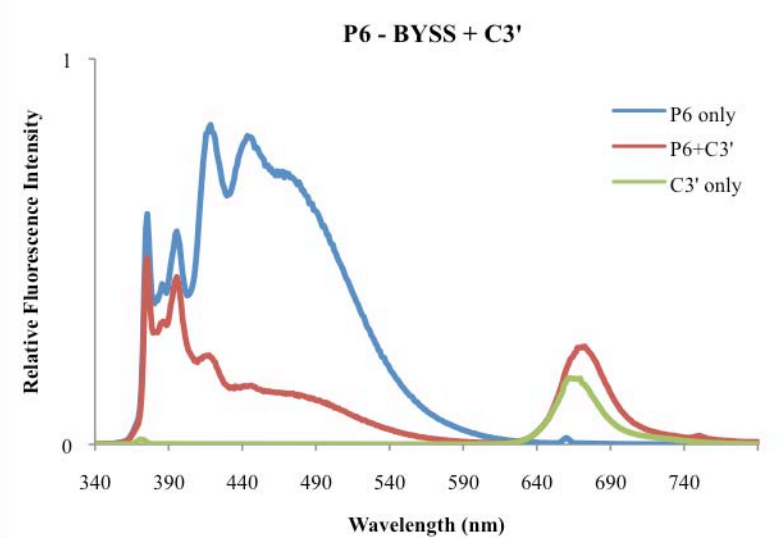
P6 - BYSS + C3'
Relative Fluorescence Intensity
1
0
340
390
440
490
540
590
640
690
740
Wavelength (nm)
P6 only
P6+C3'
C3' only

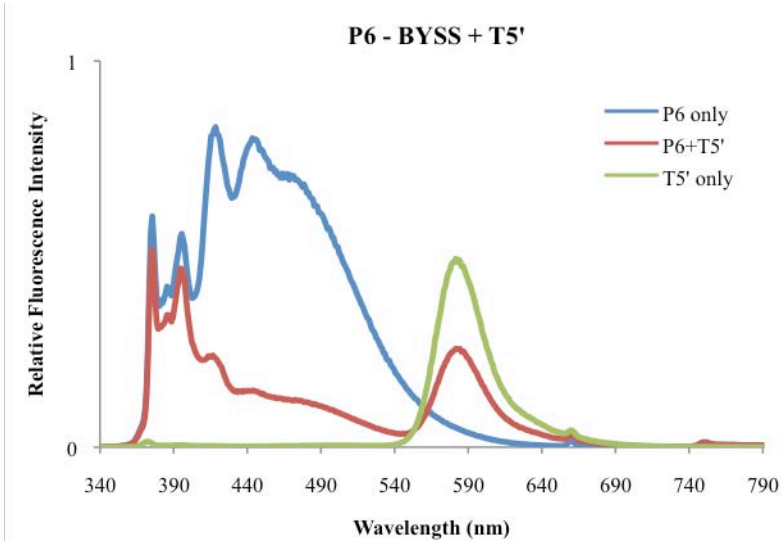
P6 - BYSS + T5'
Relative Fluorescence Intensity
1
0
340
390
440
490
540
590
640
690
740
790
Wavelength (nm)
P6 only
P6+T5'
T5' only

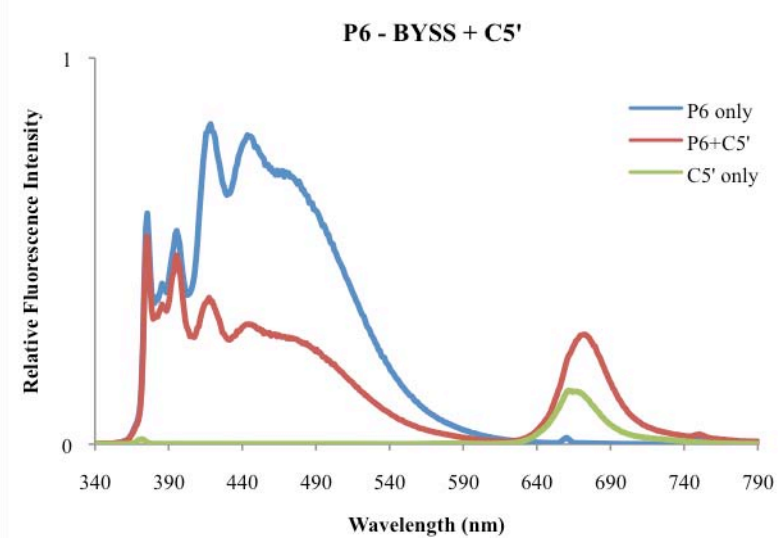
P6 - BYSS + C5'
Relative Fluorescence Intensity
1
0
340
390
440
490
540
590
640
690
740
790
Wavelength (nm)
P6 only
P6+C5'
C5' only

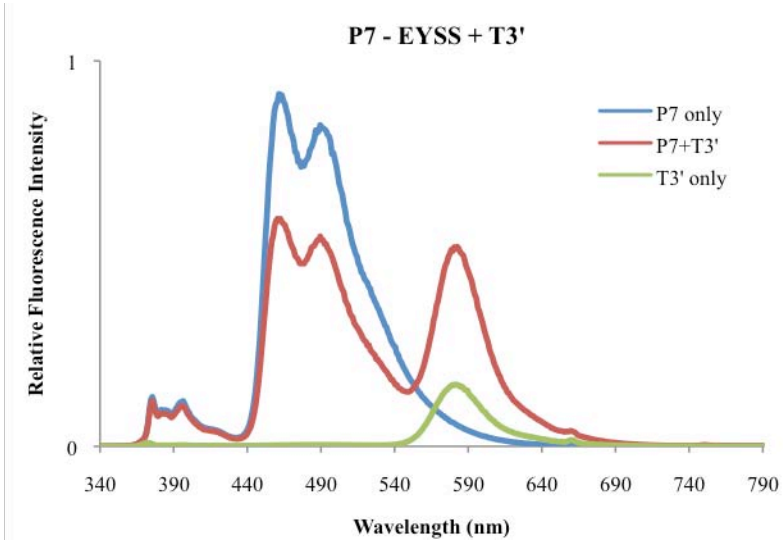
P7 - EYSS + T3'
Relative Fluorescence Intensity
1
0
340 390 440 490 540 590 640 690 740 790
Wavelength (nm)
P7 only
P7+T3'
T3' only

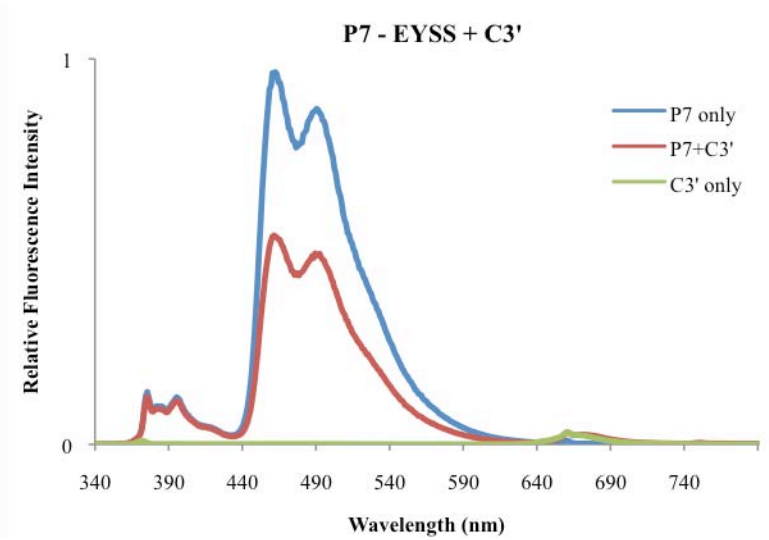
P7 - EYSS + C3'
Relative Fluorescence Intensity
1
0
340 390 440 490 540 590 640 690 740
Wavelength (nm)
P7 only
P7+C3'
C3' only

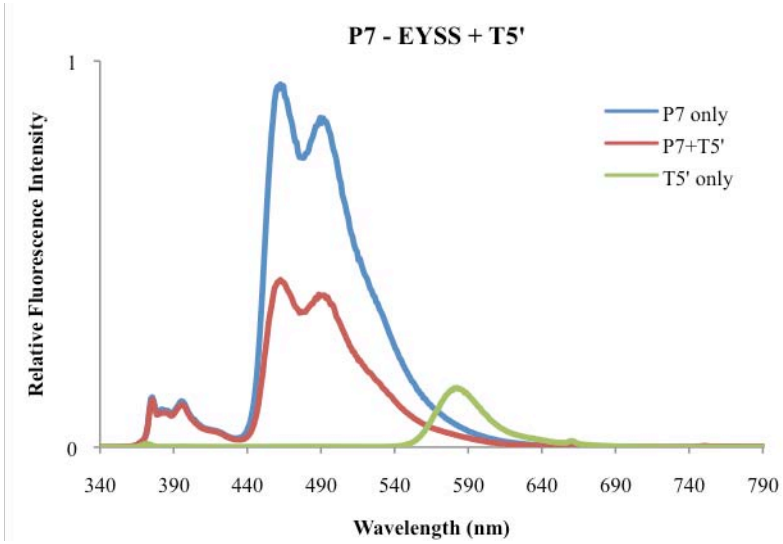
P7 - EYSS + T5'
Relative Fluorescence Intensity
1
0
340 390 440 490 540 590 640 690 740 790
Wavelength (nm)
P7 only
P7+T5'
T5' only

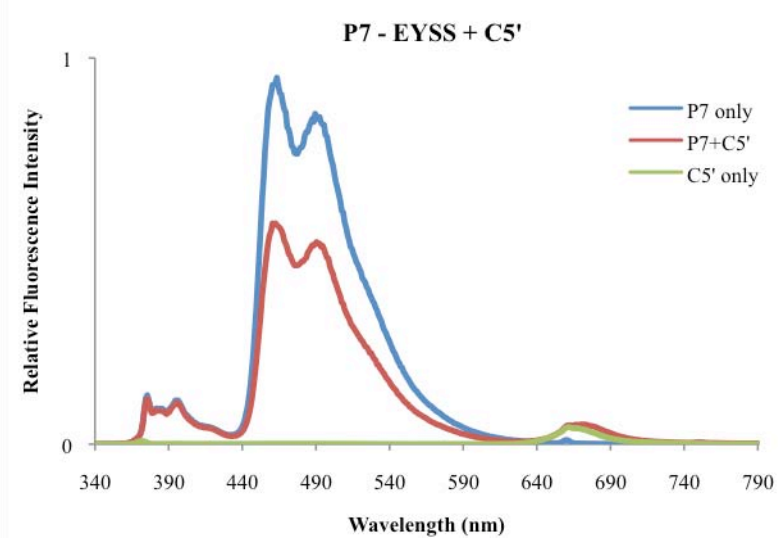
P7 - EYSS + C5'
Relative Fluorescence Intensity
1
0
340 390 440 490 540 590 640 690 740 790
Wavelength (nm)
P7 only
P7+C5'
C5' only

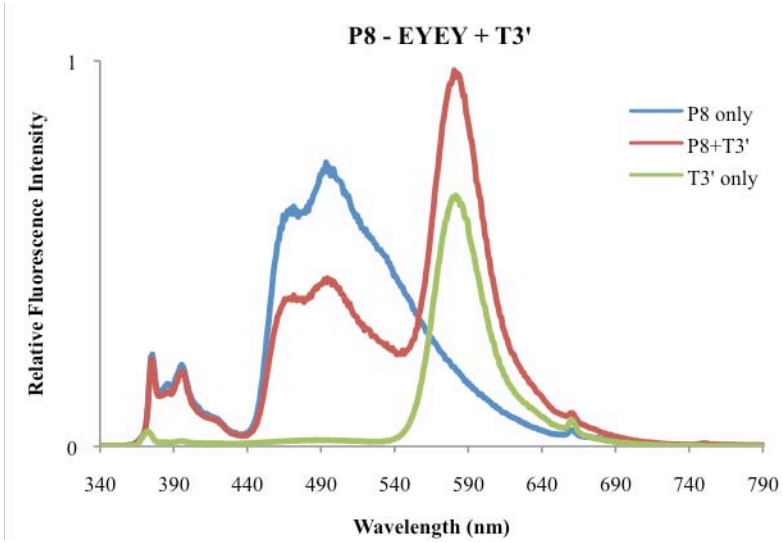
P8 - EYEY + T3'
Relative Fluorescence Intensity
1
0
340 390 440 490 540 590 640 690 740 790
Wavelength (nm)
P8 only
P8+T3'
T3' only

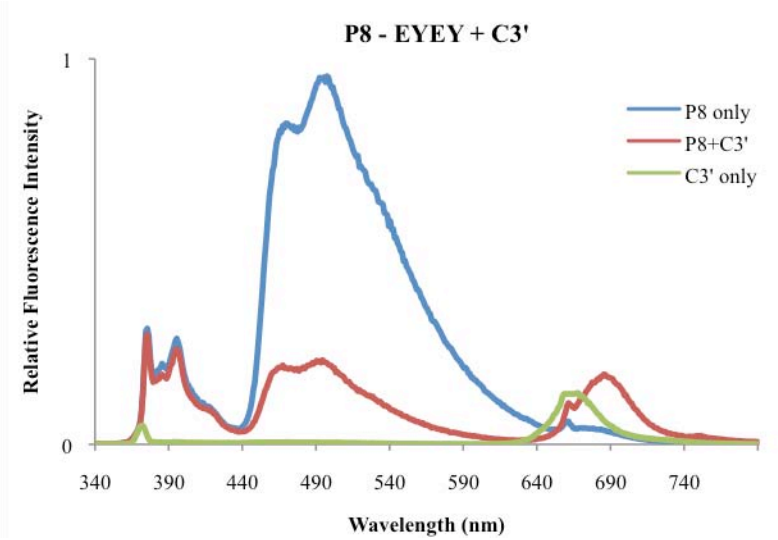
P8 - EYEY + C3'
Relative Fluorescence Intensity
1
0
340 390 440 490 540 590 640 690 740
Wavelength (nm)
P8 only
P8+C3'
C3' only

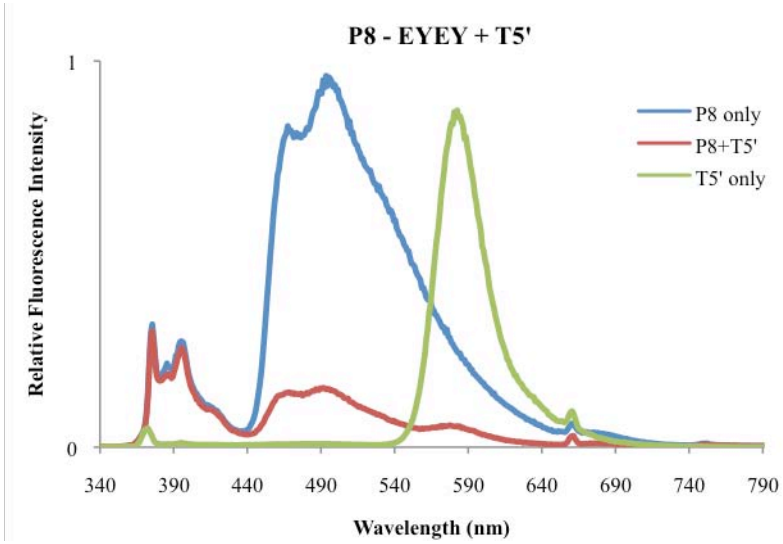
P8 - EYEY + T5'
Relative Fluorescence Intensity
1
0
340 390 440 490 540 590 640 690 740 790
Wavelength (nm)
P8 only
P8+T5'
T5' only

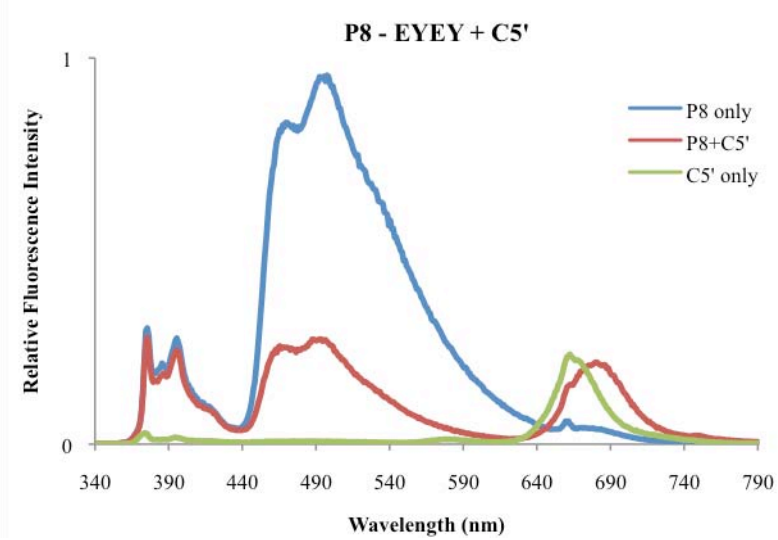
P8 - EYEY + C5'
Relative Fluorescence Intensity
1
0
340 390 440 490 540 590 640 690 740 790
Wavelength (nm)
P8 only
P8+C5'
C5' only

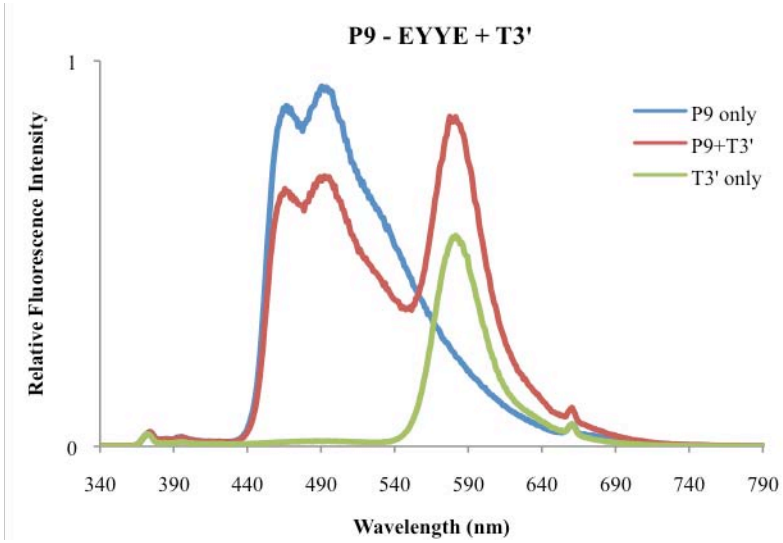
P9 - EYYE + T3'
Relative Fluorescence Intensity
1
0
340 390 440 490 540 590 640 690 740 790
Wavelength (nm)
P9 only
P9+T3'
T3' only

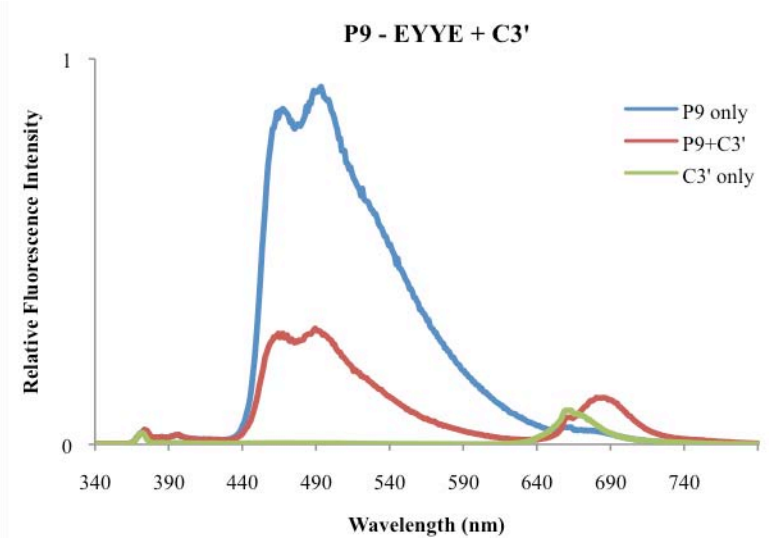
P9 - EYYE + C3'
Relative Fluorescence Intensity
1
0
340 390 440 490 540 590 640 690 740
Wavelength (nm)
P9 only
P9+C3'
C3' only

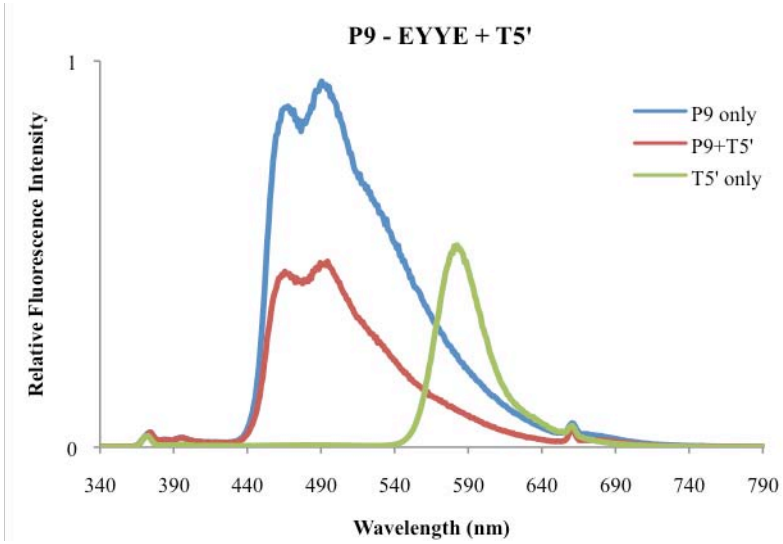
P9 - EYYE + T5'
Relative Fluorescence Intensity
1
0
340 390 440 490 540 590 640 690 740 790
Wavelength (nm)
P9 only
P9+T5'
T5' only

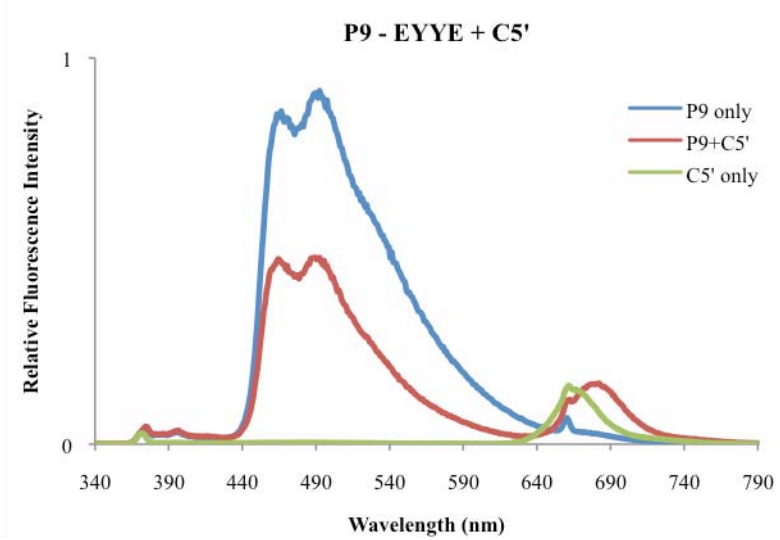
P9 - EYYE + C5'
Relative Fluorescence Intensity
1
0
340 390 440 490 540 590 640 690 740 790
Wavelength (nm)
P9 only
P9+C5'
C5' only

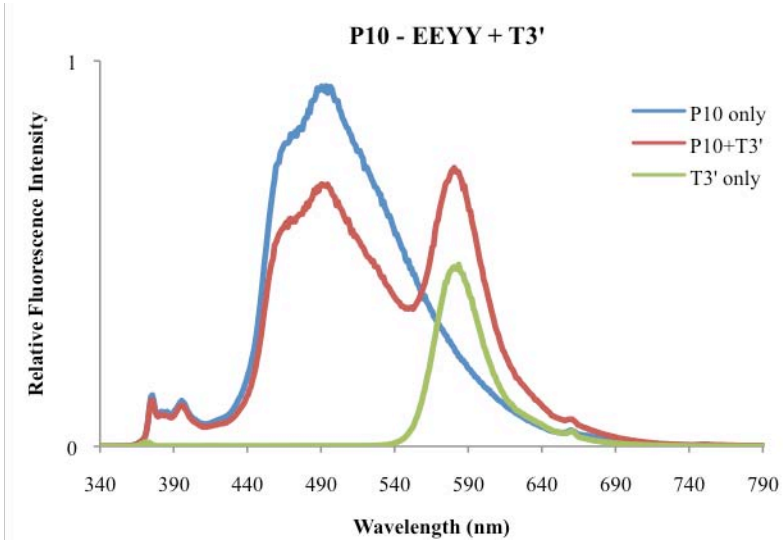
P10 - EEYY + T3'
Relative Fluorescence Intensity
1
0
340 390 440 490 540 590 640 690 740 790
Wavelength (nm)
P10 only
P10+T3'
T3' only

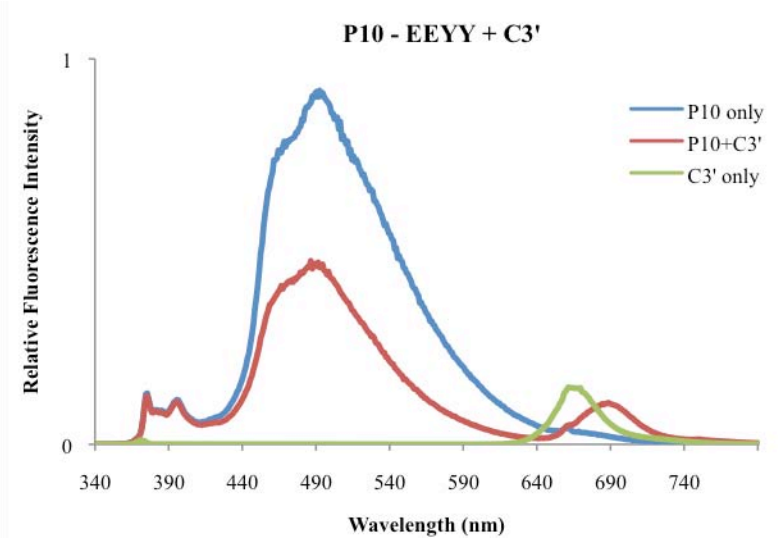
P10 - EEYY + C3'
Relative Fluorescence Intensity
1
0
340 390 440 490 540 590 640 690 740
Wavelength (nm)
P10 only
P10+C3'
C3' only

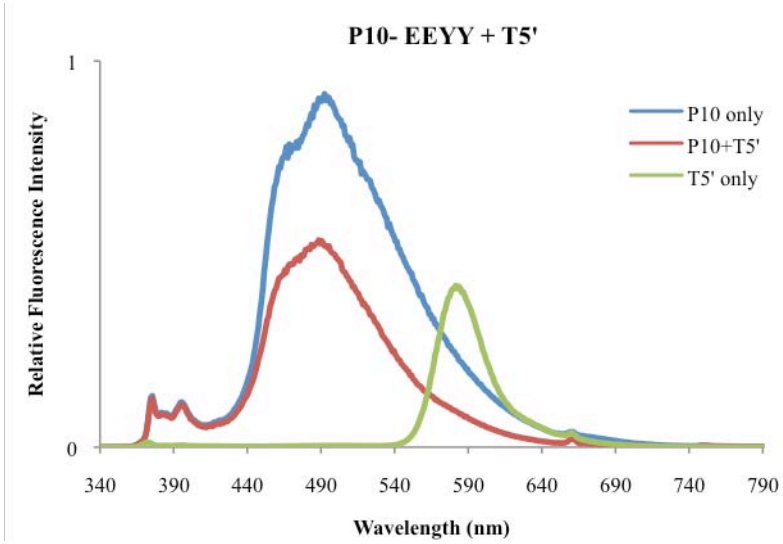
P10- EEYY + T5'
Relative Fluorescence Intensity
1
0
340 390 440 490 540 590 640 690 740 790
Wavelength (nm)
P10 only
P10+T5'
T5' only

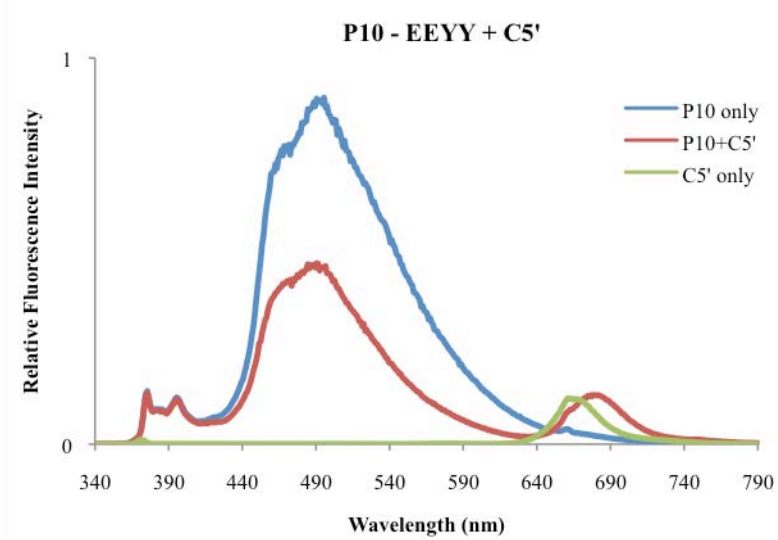
P10 - EEYY + C5'
Relative Fluorescence Intensity
1
0
340 390 440 490 540 590 640 690 740 790
Wavelength (nm)
P10 only
P10+C5'
C5' only

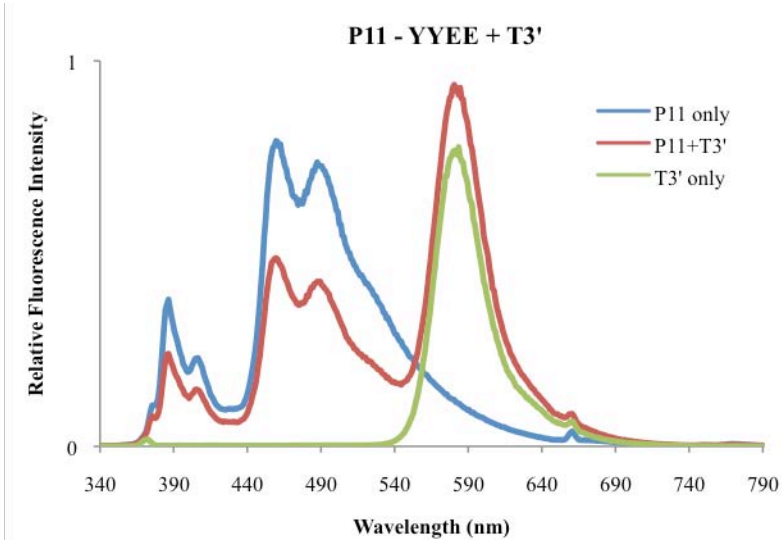
P11 - YYEE + T3'
Relative Fluorescence Intensity
1
0
340 390 440 490 540 590 640 690 740 790
Wavelength (nm)
P11 only
P11+T3'
T3' only

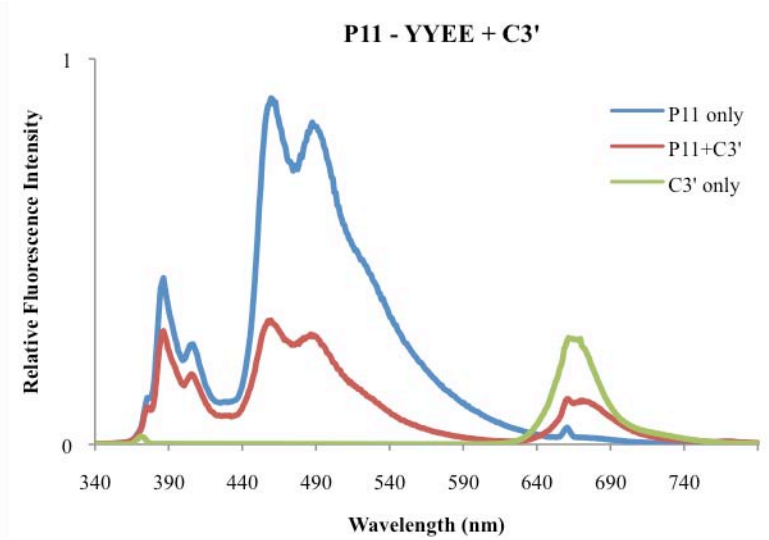
P11 - YYEE + C3'
Relative Fluorescence Intensity
1
0
340 390 440 490 540 590 640 690 740
Wavelength (nm)
P11 only
P11+C3'
C3' only

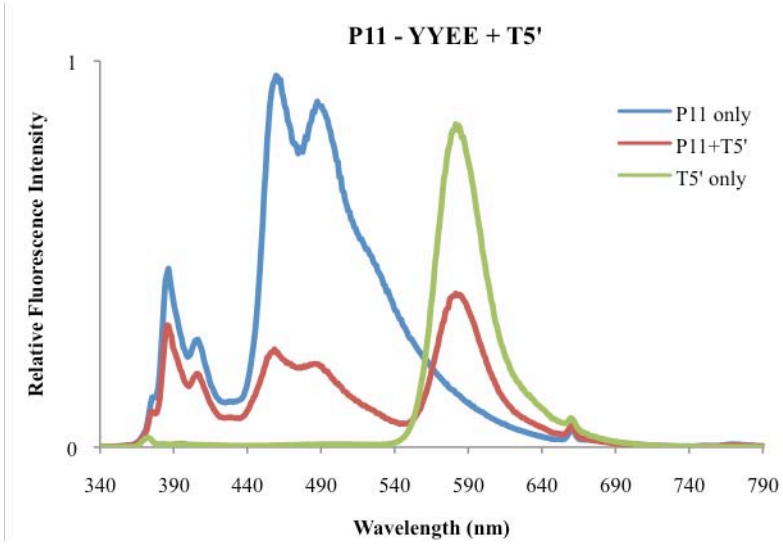
P11 - YYEE + T5'
Relative Fluorescence Intensity
1
0
340 390 440 490 540 590 640 690 740 790
Wavelength (nm)
P11 only
P11+T5'
T5' only

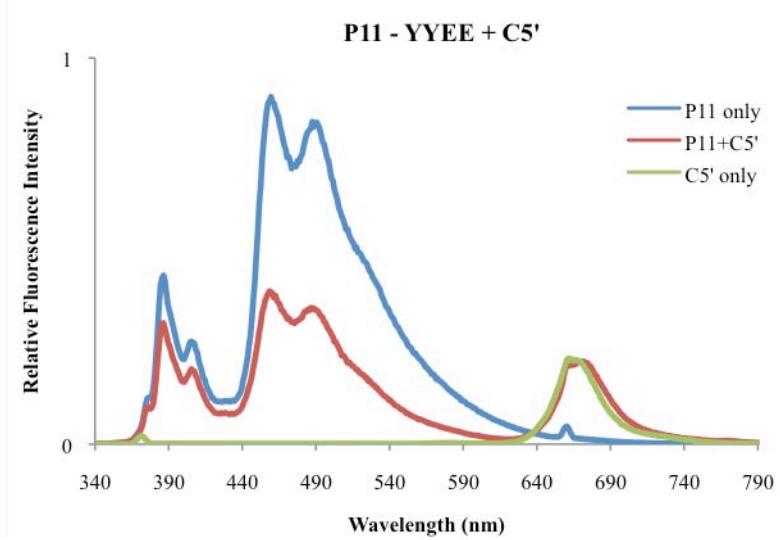
P11 - YYEE + C5'
Relative Fluorescence Intensity
1
0
340 390 440 490 540 590 640 690 740 790
Wavelength (nm)
P11 only
P11+C5'
C5' only

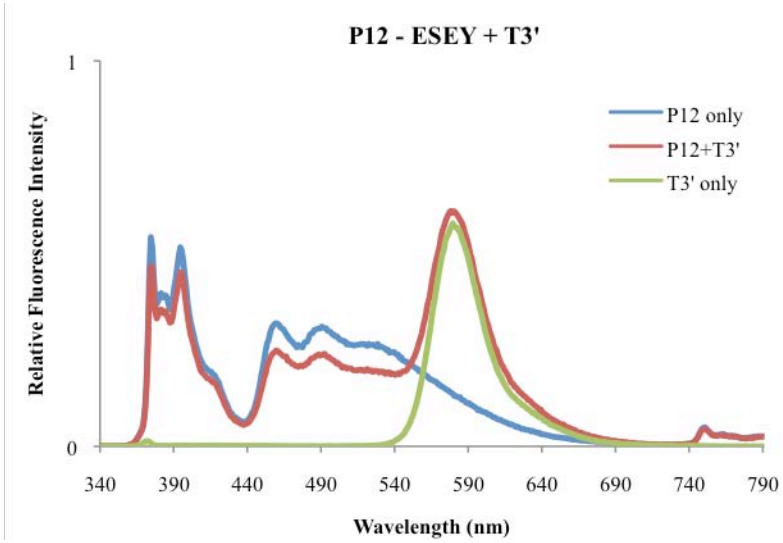
P12 - ESEY + T3'
Relative Fluorescence Intensity
1
0
340 390 440 490 540 590 640 690 740 790
Wavelength (nm)
P12 only
P12+T3'
T3' only

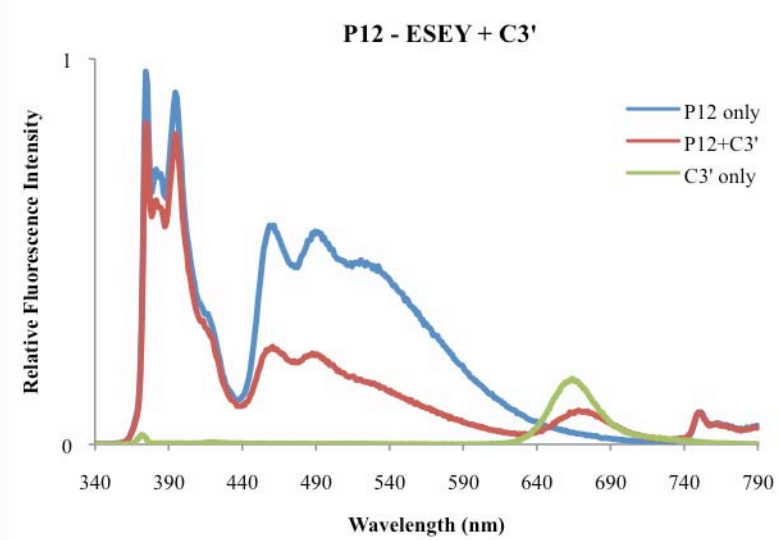
P12 - ESEY + C3'
Relative Fluorescence Intensity
1
0
340 390 440 490 540 590 640 690 740 790
Wavelength (nm)
P12 only
P12+C3'
C3' only

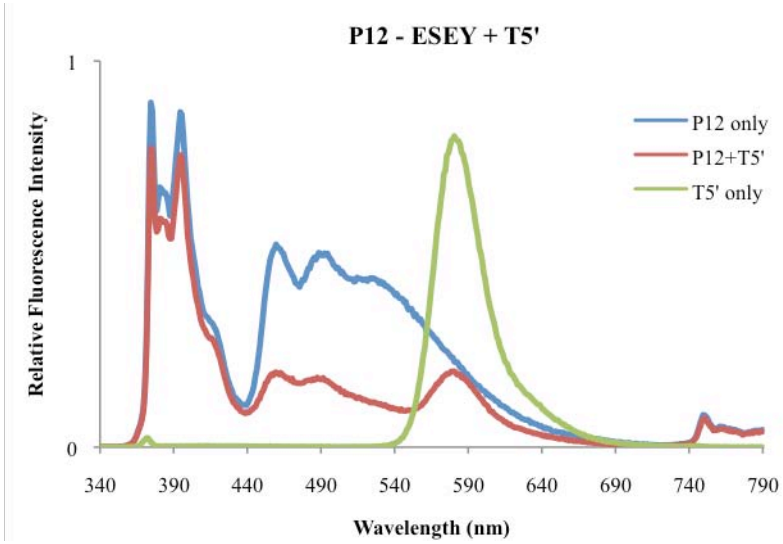
P12 - ESEY + T5'
Relative Fluorescence Intensity
1
0
340 390 440 490 540 590 640 690 740 790
Wavelength (nm)
P12 only
P12+T5'
T5' only

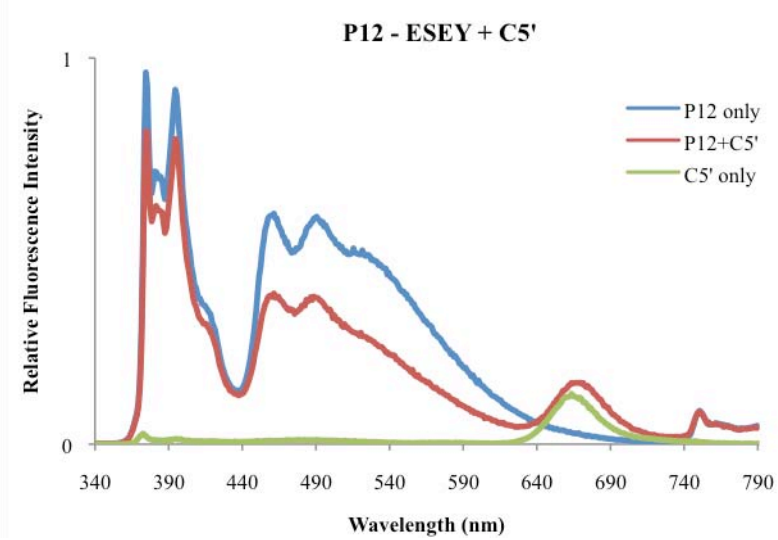
P12 - ESEY + C5'
Relative Fluorescence Intensity
1
0
340 390 440 490 540 590 640 690 740 790
Wavelength (nm)
P12 only
P12+C5'
C5' only

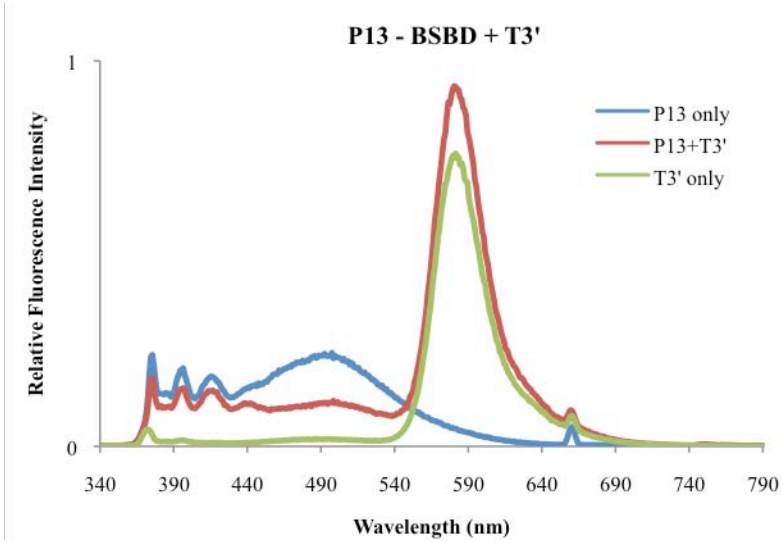
P13 - BSBD + T3'
Relative Fluorescence Intensity
1
0
340
390
440
490
540
590
640
690
740
790
Wavelength (nm)
P13 only
P13+T3'
T3' only

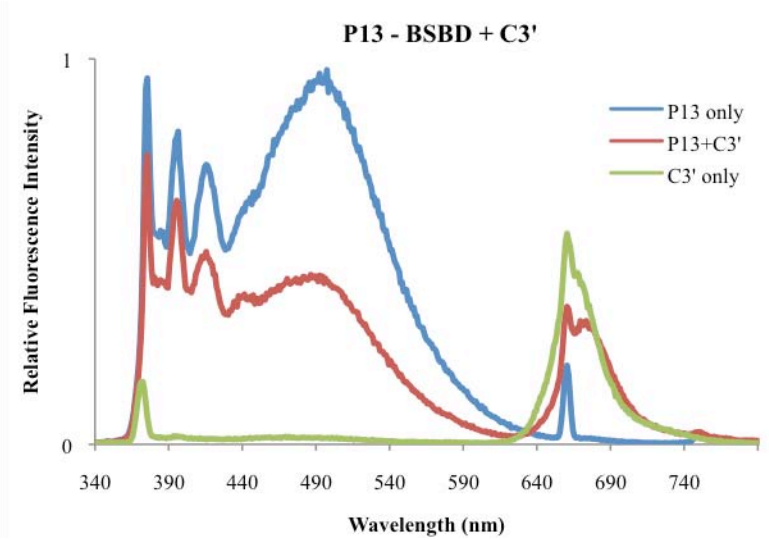
P13 - BSBD + C3'
Relative Fluorescence Intensity
1
0
340
390
440
490
540
590
640
690
740
Wavelength (nm)
P13 only
P13+C3'
C3' only

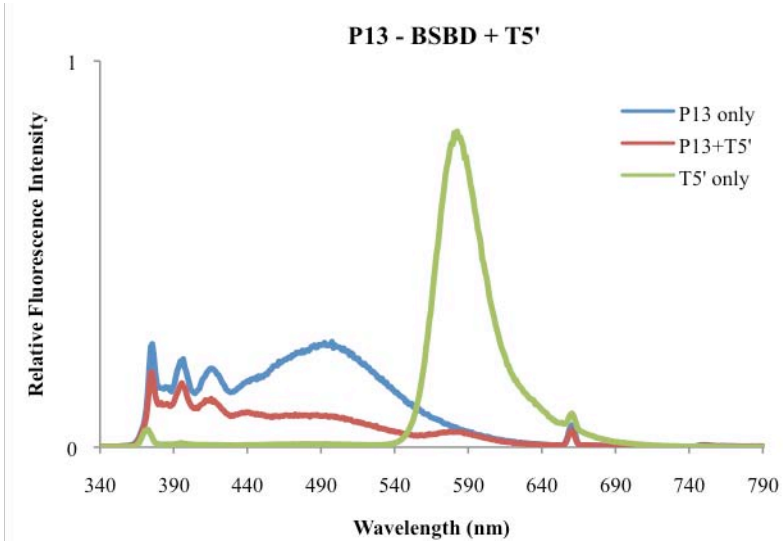
P13 - BSBD + T5'
Relative Fluorescence Intensity
1
0
340
390
440
490
540
590
640
690
740
790
Wavelength (nm)
P13 only
P13+T5'
T5' only

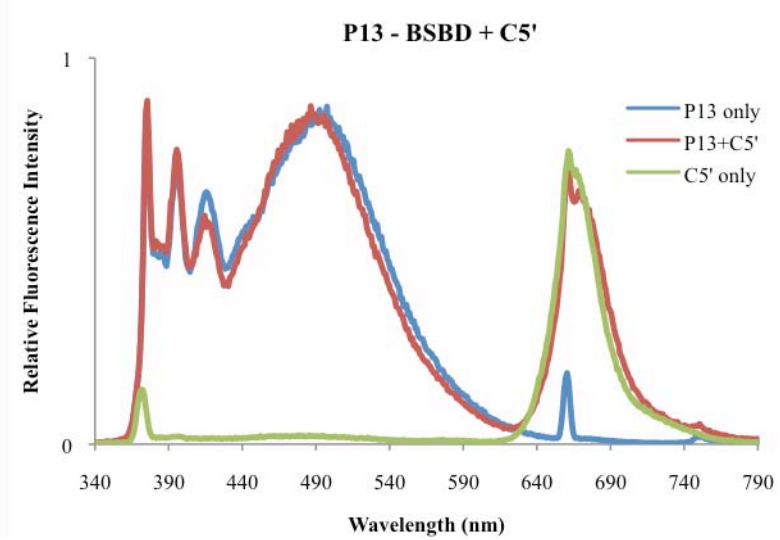
P13 - BSBD + C5'
Relative Fluorescence Intensity
1
0
340
390
440
490
540
590
640
690
740
790
Wavelength (nm)
P13 only
P13+C5'
C5' only

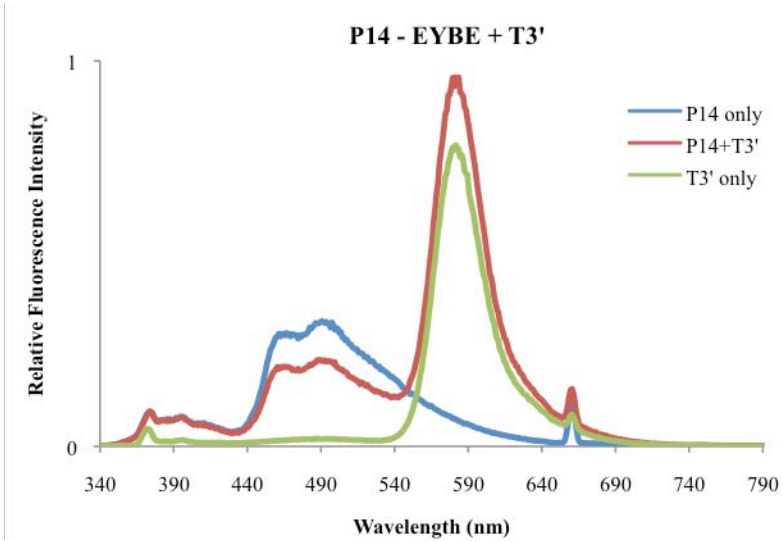
P14 - EYBE + T3'
Relative Fluorescence Intensity
1
0
340 390 440 490 540 590 640 690 740 790
Wavelength (nm)
P14 only
P14+T3'
T3' only

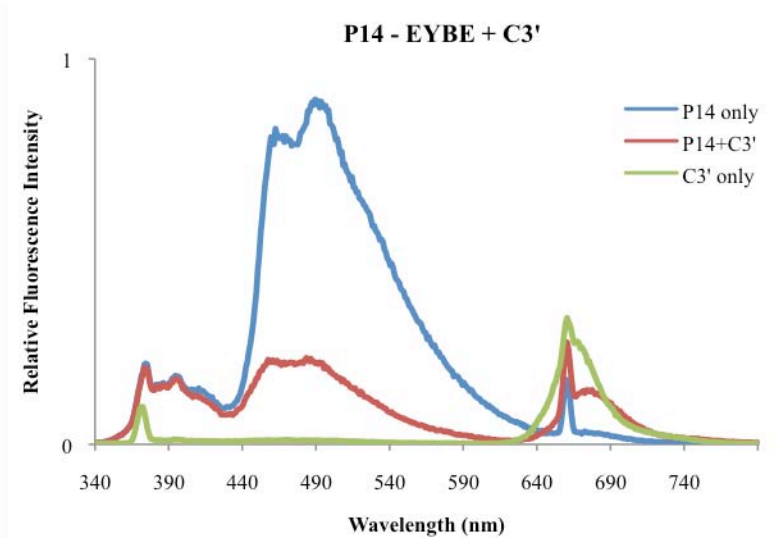
P14 - EYBE + C3'
Relative Fluorescence Intensity
1
0
340 390 440 490 540 590 640 690 740
Wavelength (nm)
P14 only
P14+C3'
C3' only

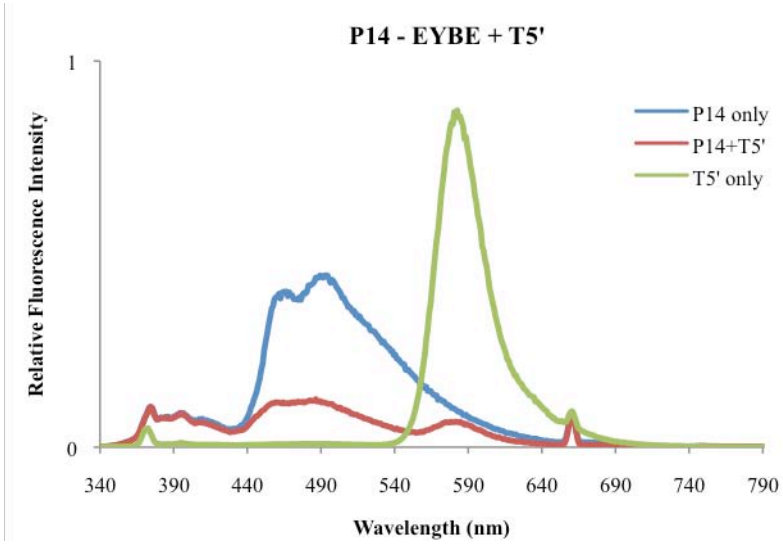
P14 - EYBE + T5'
Relative Fluorescence Intensity
1
0
340 390 440 490 540 590 640 690 740 790
Wavelength (nm)
P14 only
P14+T5'
T5' only

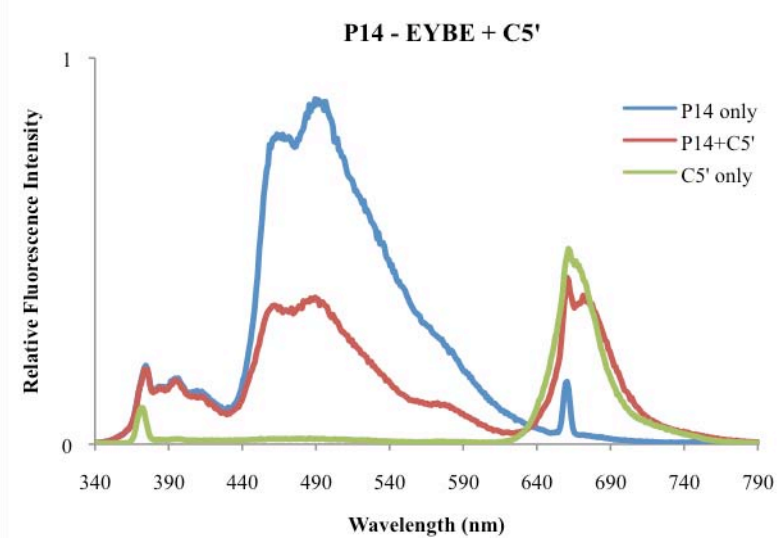
P14 - EYBE + C5'
Relative Fluorescence Intensity
1
0
340 390 440 490 540 590 640 690 740 790
Wavelength (nm)
P14 only
P14+C5'
C5' only

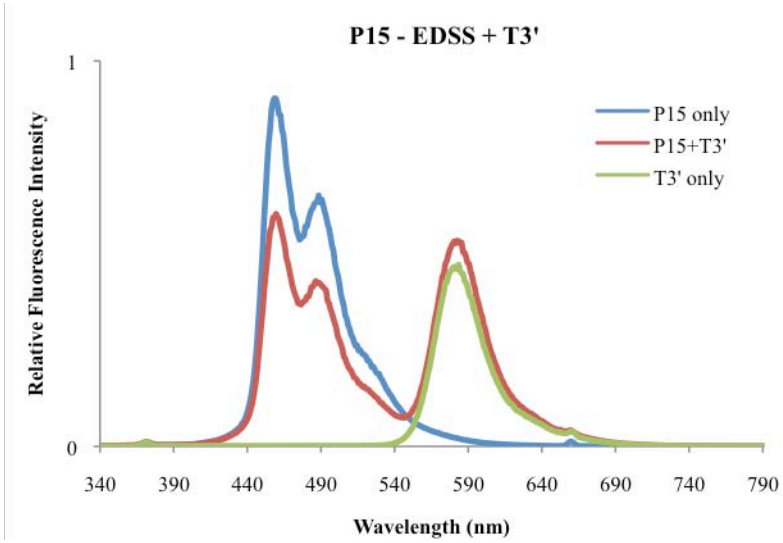
P15 - EDSS + T3'
Relative Fluorescence Intensity
1
0
340
390
440
490
540
590
640
690
740
790
Wavelength (nm)
P15 only
P15+T3'
T3' only

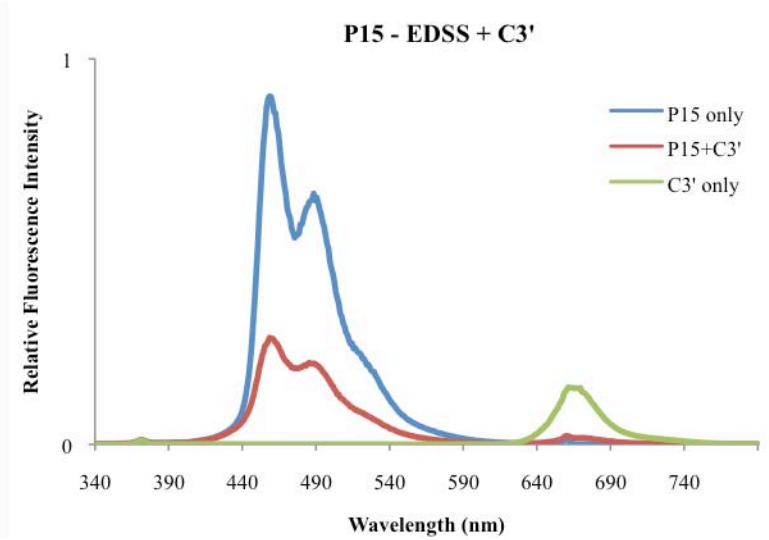
P15 - EDSS + C3'
Relative Fluorescence Intensity
1
0
340
390
440
490
540
590
640
690
740
Wavelength (nm)
P15 only
P15+C3'
C3' only

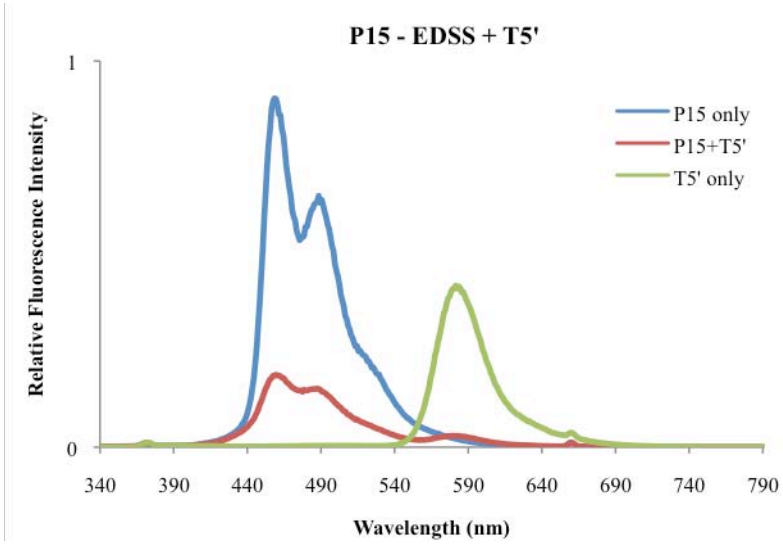
P15 - EDSS + T5'
Relative Fluorescence Intensity
1
0
340
390
440
490
540
590
640
690
740
790
Wavelength (nm)
P15 only
P15+T5'
T5' only

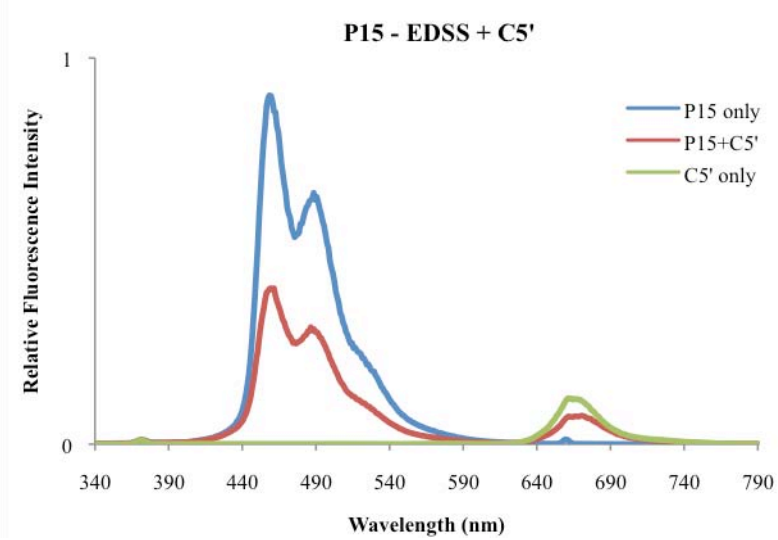
P15 - EDSS + C5'
Relative Fluorescence Intensity
1
0
340
390
440
490
540
590
640
690
740
790
Wavelength (nm)
P15 only
P15+C5'
C5' only

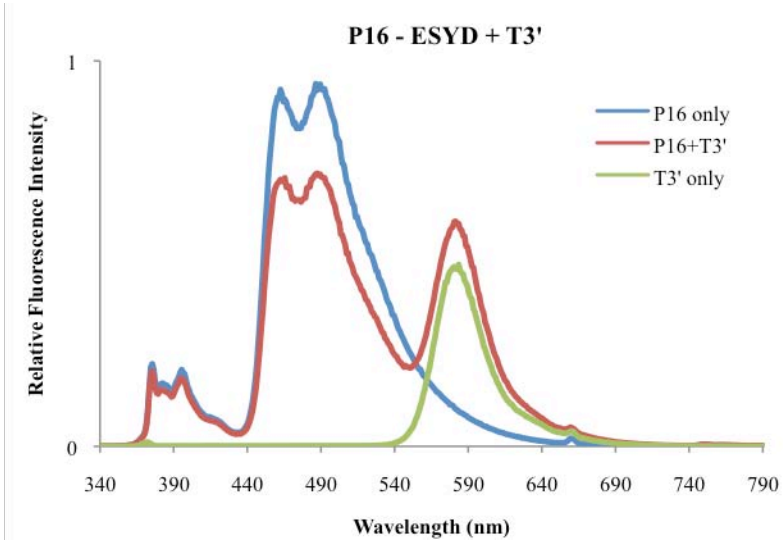
P16 - ESYD + T3'
Relative Fluorescence Intensity
1
0
340 390 440 490 540 590 640 690 740 790
Wavelength (nm)
P16 only
P16+T3'
T3' only

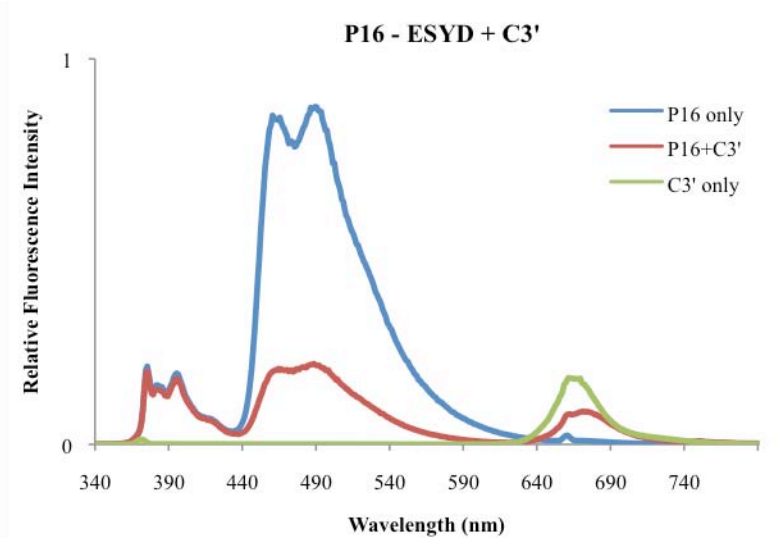
P16 - ESYD + C3'
Relative Fluorescence Intensity
1
0
340 390 440 490 540 590 640 690 740
Wavelength (nm)
P16 only
P16+C3'
C3' only

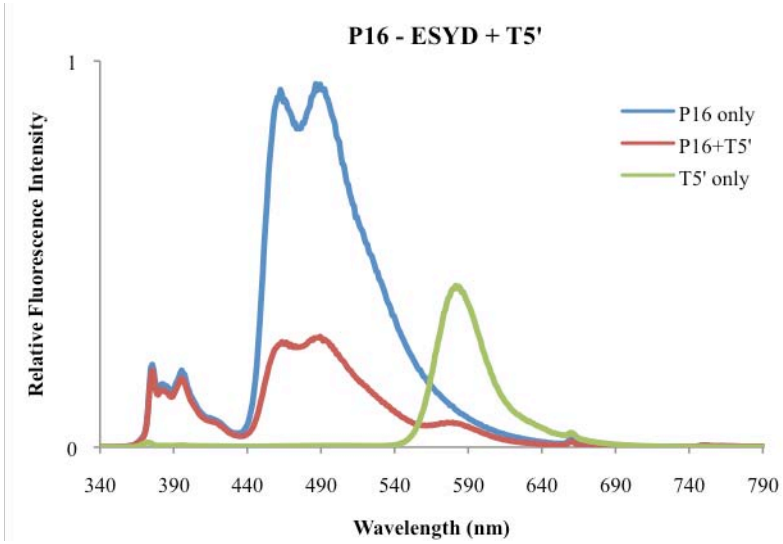
P16 - ESYD + T5'
Relative Fluorescence Intensity
1
0
340 390 440 490 540 590 640 690 740 790
Wavelength (nm)
P16 only
P16+T5'
T5' only

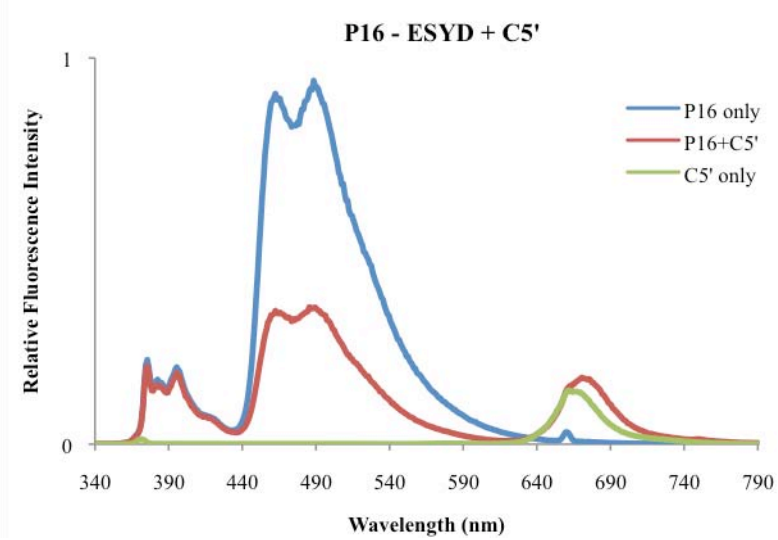
P16 - ESYD + C5'
Relative Fluorescence Intensity
1
0
340 390 440 490 540 590 640 690 740 790
Wavelength (nm)
P16 only
P16+C5'
C5' only

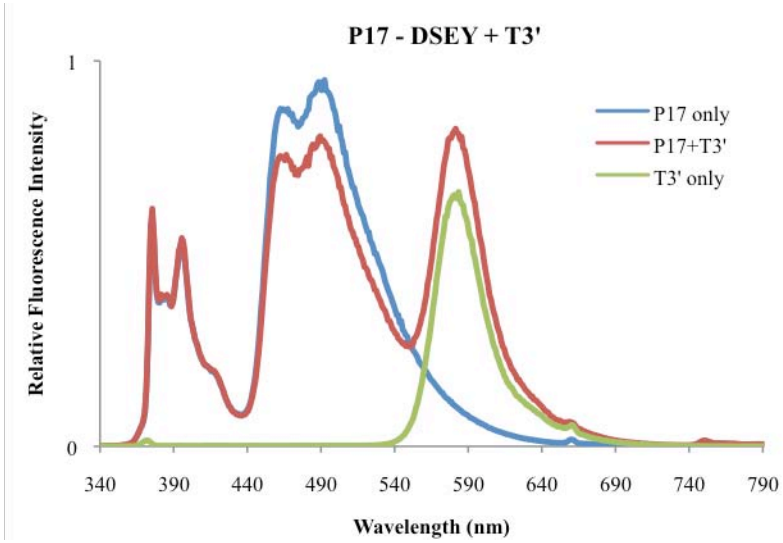
P17 - DSEY + T3'
Relative Fluorescence Intensity
1
0
340 390 440 490 540 590 640 690 740 790
Wavelength (nm)
P17 only
P17+T3'
T3' only

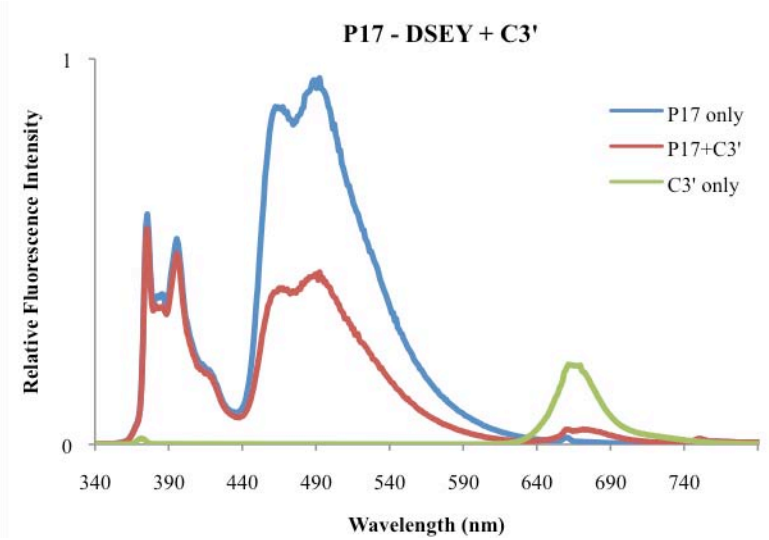
P17 - DSEY + C3'
Relative Fluorescence Intensity
1
0
340 390 440 490 540 590 640 690 740
Wavelength (nm)
P17 only
P17+C3'
C3' only

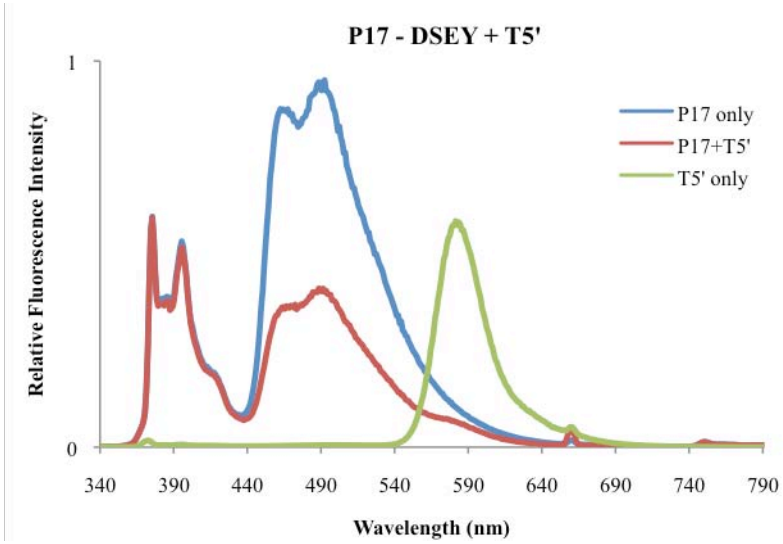
P17 - DSEY + T5'
Relative Fluorescence Intensity
1
0
340 390 440 490 540 590 640 690 740 790
Wavelength (nm)
P17 only
P17+T5'
T5' only

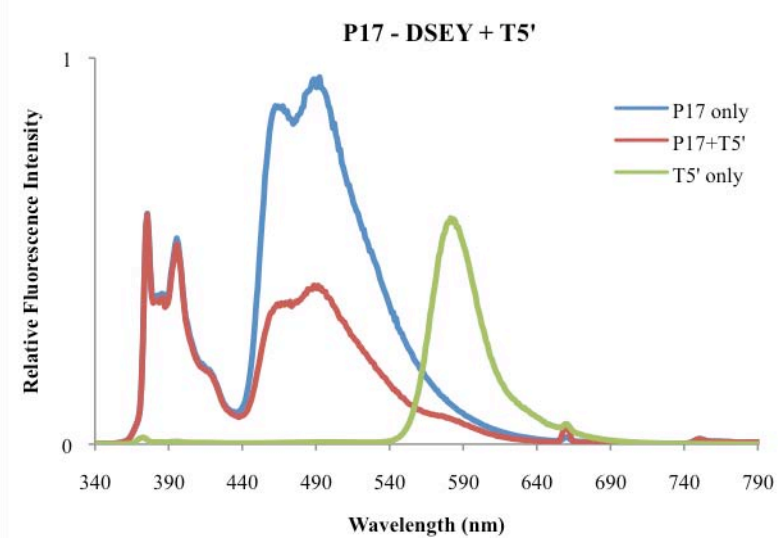
P17 - DSEY + T5'
Relative Fluorescence Intensity
1
0
340 390 440 490 540 590 640 690 740 790
Wavelength (nm)
P17 only
P17+T5'
T5' only

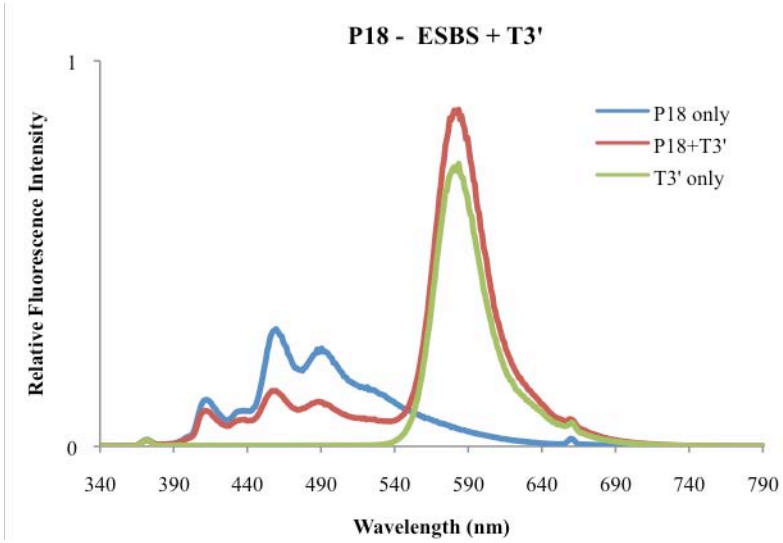
P18 - ESBS + T3'
Relative Fluorescence Intensity
1
0
340 390 440 490 540 590 640 690 740 790
Wavelength (nm)
P18 only
P18+T3'
T3' only

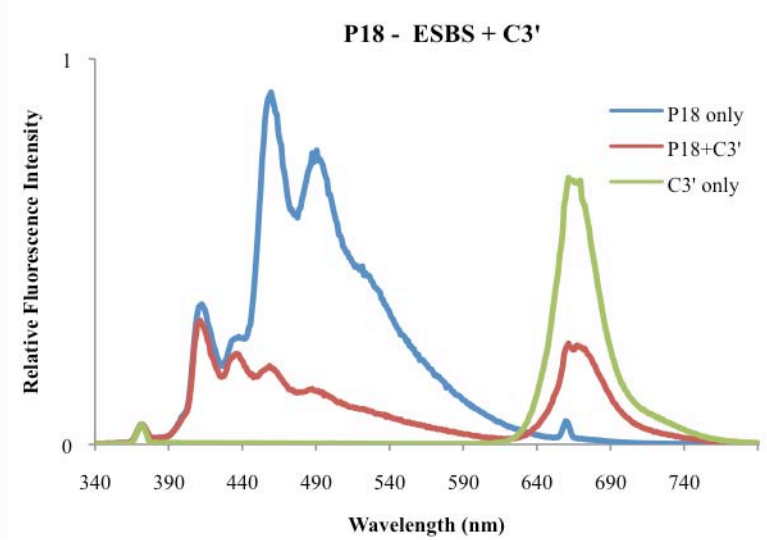
P18 - ESBS + C3'
Relative Fluorescence Intensity
1
0
340 390 440 490 540 590 640 690 740
Wavelength (nm)
P18 only
P18+C3'
C3' only

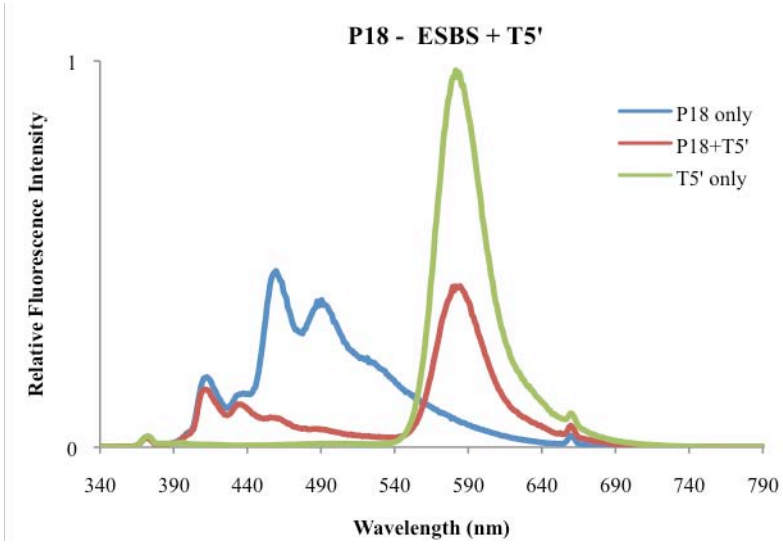
P18 - ESBS + T5'
Relative Fluorescence Intensity
1
0
340 390 440 490 540 590 640 690 740 790
Wavelength (nm)
P18 only
P18+T5'
T5' only

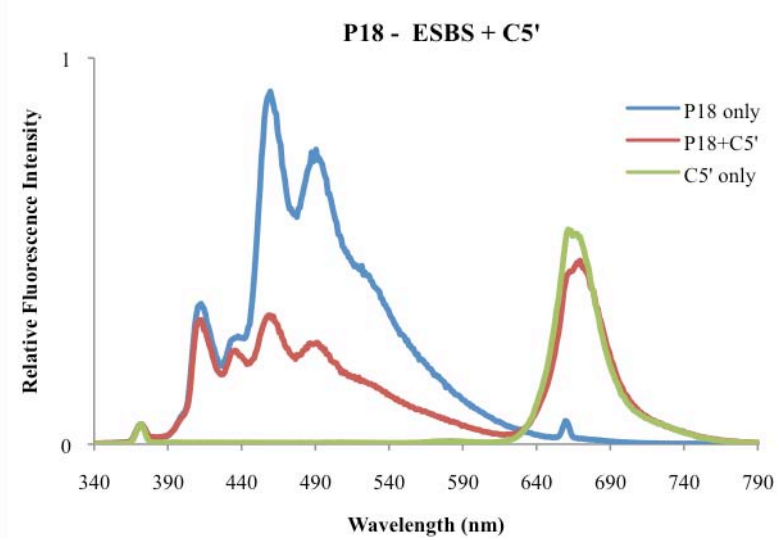
P18 - ESBS + C5'
Relative Fluorescence Intensity
1
0
340 390 440 490 540 590 640 690 740 790
Wavelength (nm)
P18 only
P18+C5'
C5' only

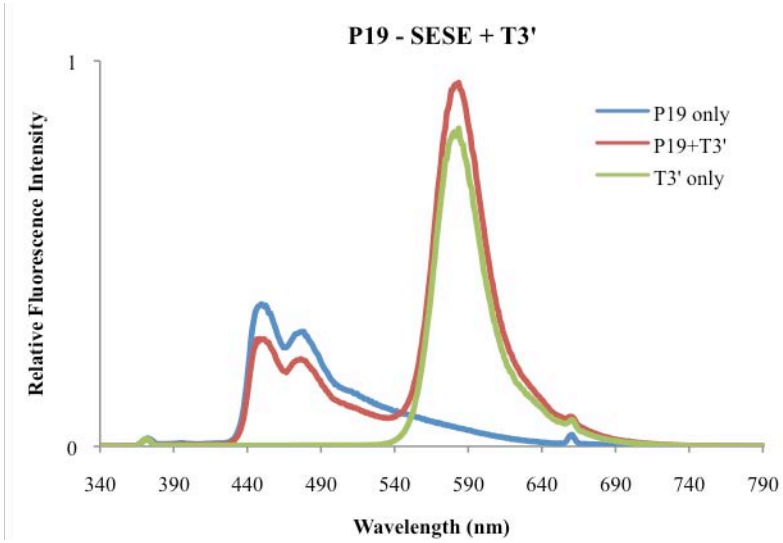
P19 - SESE + T3'
Relative Fluorescence Intensity
1
0
340 390 440 490 540 590 640 690 740 790
Wavelength (nm)
P19 only
P19+T3'
T3' only

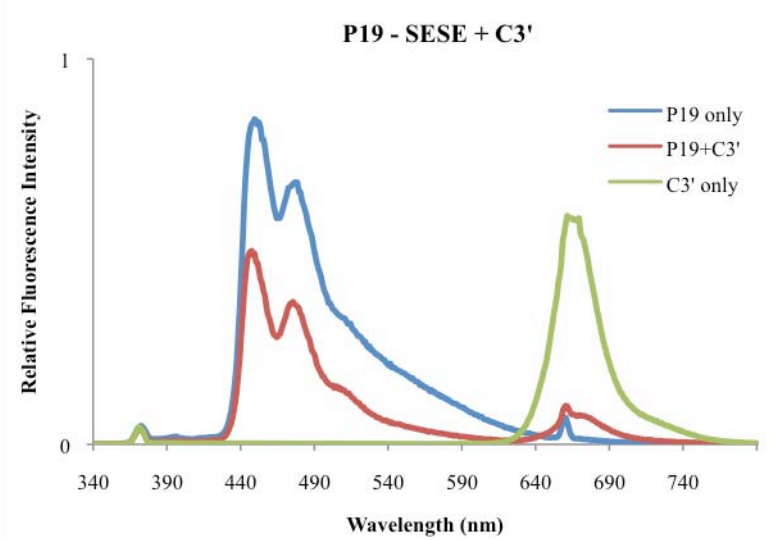
P19 - SESE + C3'
Relative Fluorescence Intensity
1
0
340 390 440 490 540 590 640 690 740
Wavelength (nm)
P19 only
P19+C3'
C3' only

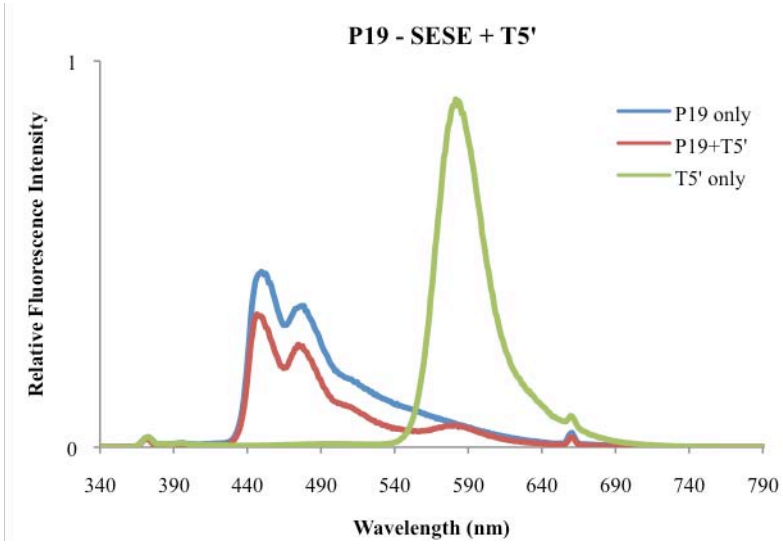
P19 - SESE + T5'
Relative Fluorescence Intensity
1
0
340 390 440 490 540 590 640 690 740 790
Wavelength (nm)
P19 only
P19+T5'
T5' only

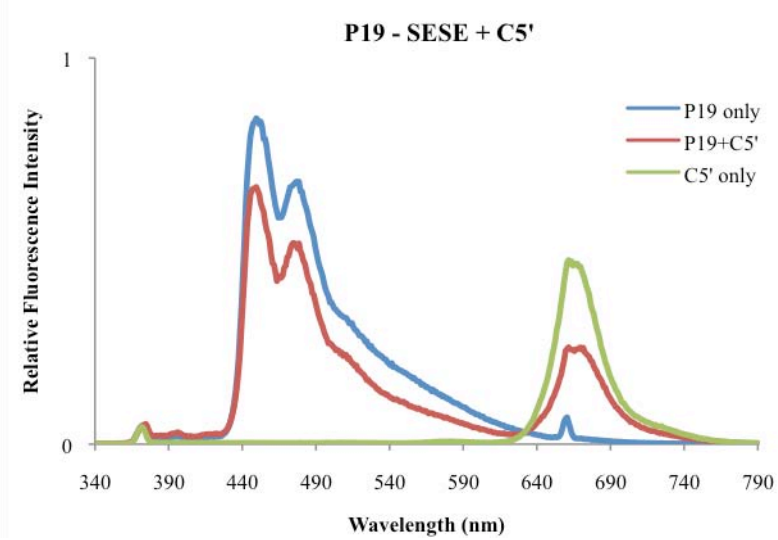
P19 - SESE + C5'
Relative Fluorescence Intensity
1
0
340 390 440 490 540 590 640 690 740 790
Wavelength (nm)
P19 only
P19+C5'
C5' only

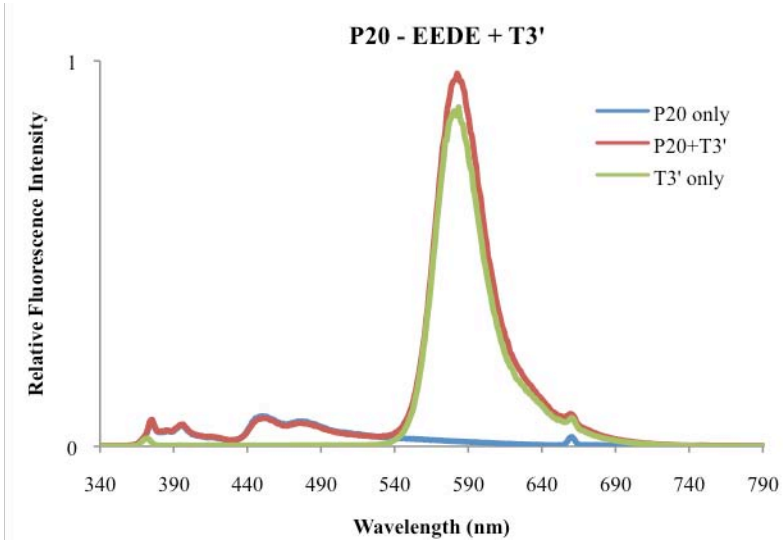
P20 - EEDE + T3'
Relative Fluorescence Intensity
1
0
340
390
440
490
540
590
640
690
740
790
Wavelength (nm)
P20 only
P20+T3'
T3' only

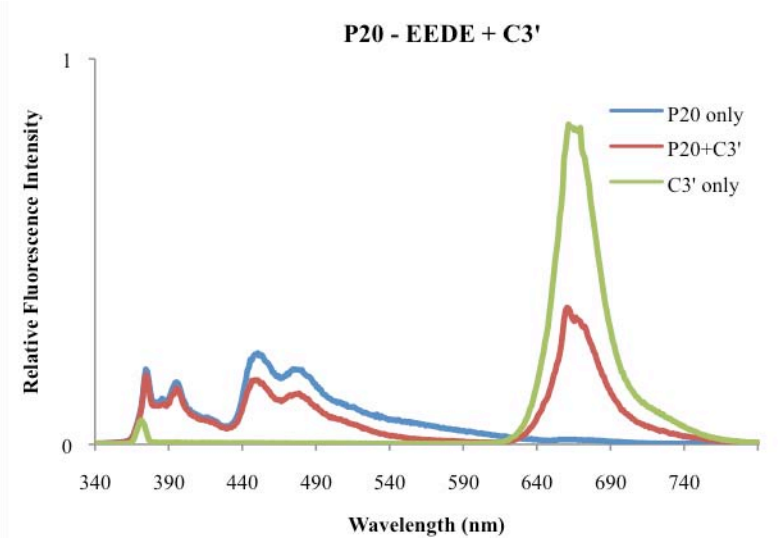
P20 - EEDE + C3'
Relative Fluorescence Intensity
1
0
340
390
440
490
540
590
640
690
740
Wavelength (nm)
P20 only
P20+C3'
C3' only

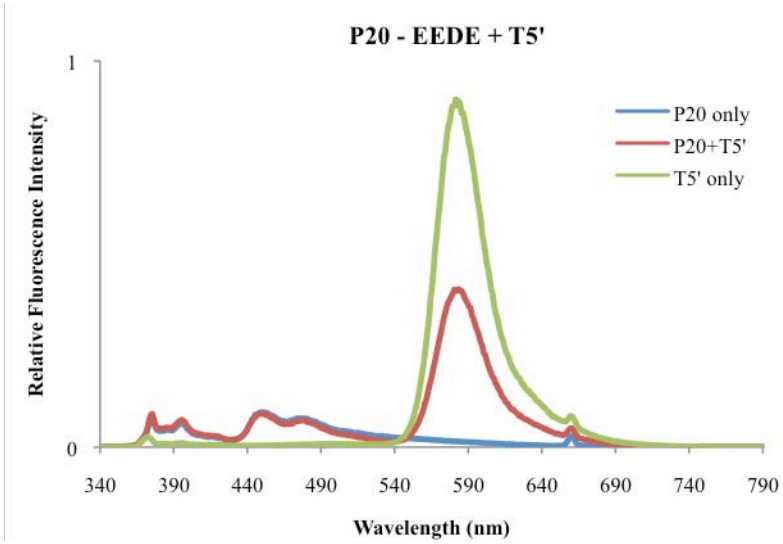
P20 - EEDE + T5'
Relative Fluorescence Intensity
1
0
340
390
440
490
540
590
640
690
740
790
Wavelength (nm)
P20 only
P20+T5'
T5' only

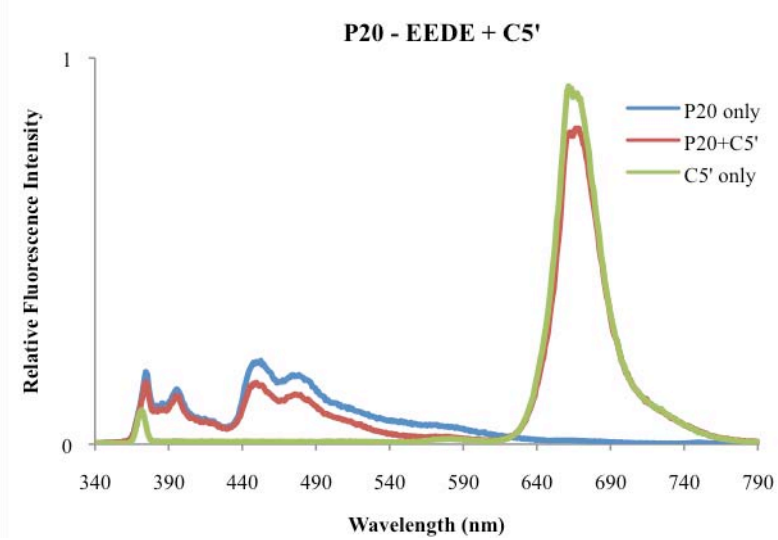
P20 - EEDE + C5'
Relative Fluorescence Intensity
1
0
340
390
440
490
540
590
640
690
740
790
Wavelength (nm)
P20 only
P20+C5'
C5' only

Figure S2. Fluorescence emission spectra for hybridization of P2, P3, P5, P8, P13 and P19 with unlabeled DNA complementary strand, D1 (5'- TAT GTT TCT GTG GA – 3'). Conditions: 10 mM Na·PIPES, 100 mM NaCl, 10 mM $MgCl_2$, pH 7.0, 25°C, 2 μM of P1-P20 with 2.0 molar equivalents of D1. Please refer to attached in press paper (Teo, Wilson, Kool Chem. Eur. J. 2009, in press) for hybridization data of other strands with D1.

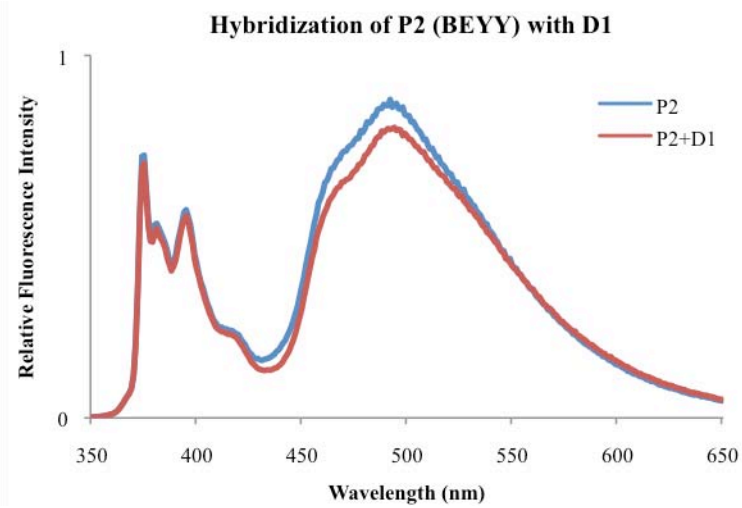

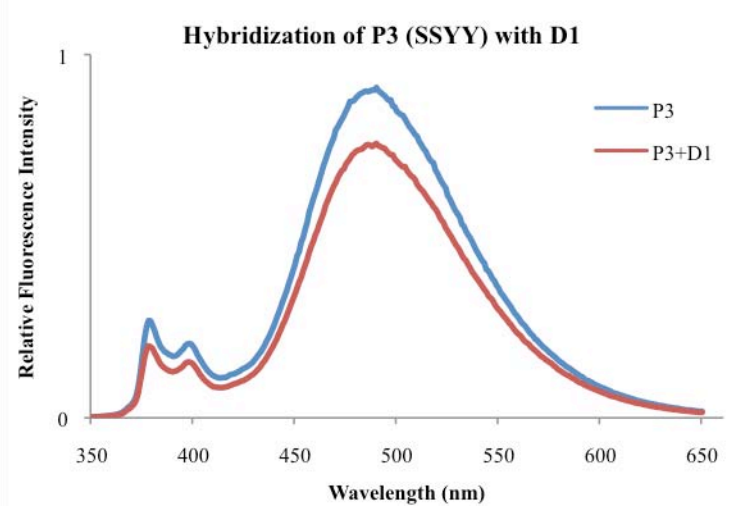

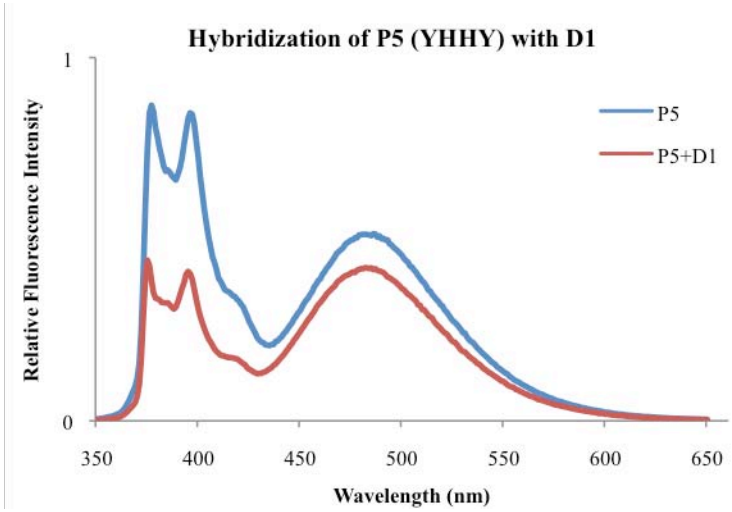
Hybridization of P5 (YHHY) with D1
Relative Fluorescence Intensity
1
0
350
400
450
500
550
600
650
Wavelength (nm)
P5
P5+D1

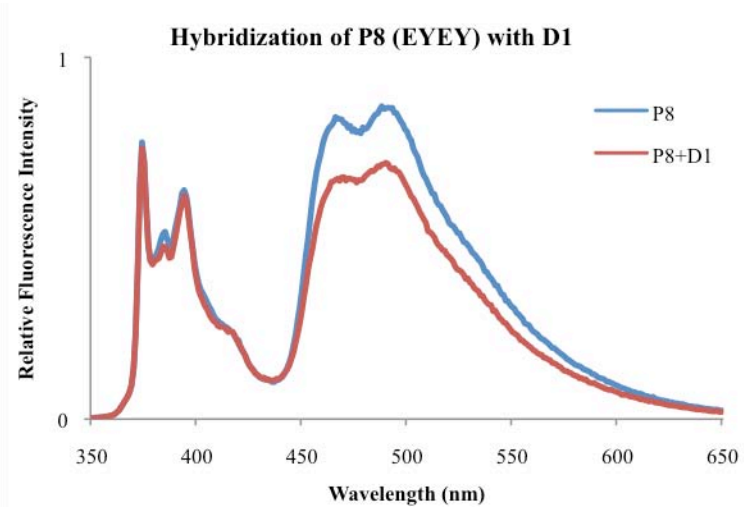
Hybridization of P8 (EYEY) with D1
Relative Fluorescence Intensity
1
0
350
400
450
500
550
600
650
Wavelength (nm)
P8
P8+D1

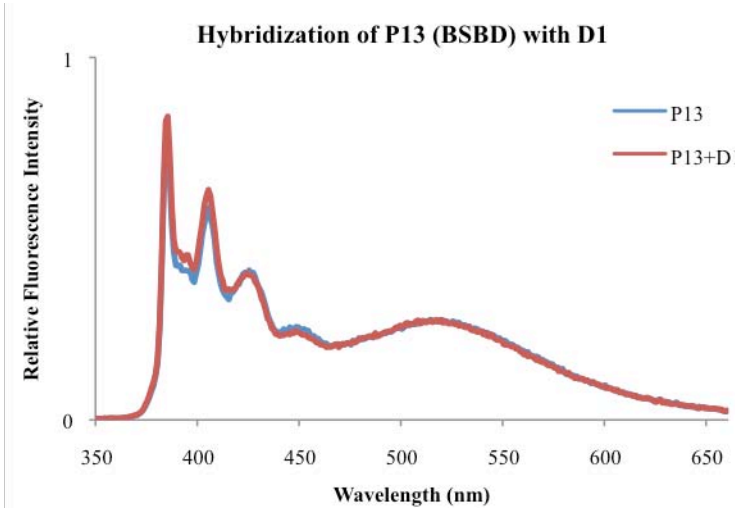
Hybridization of P13 (BSBD) with D1
Relative Fluorescence Intensity
1
0
350
400
450
500
550
600
650
Wavelength (nm)
P13
P13+D1

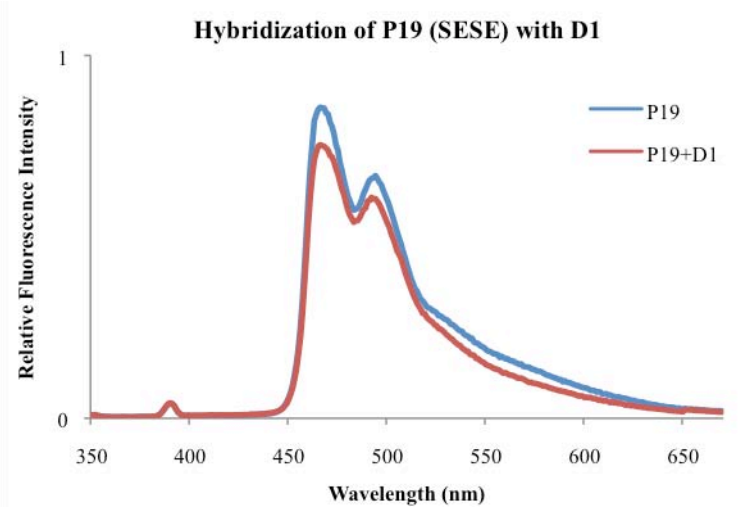
Hybridization of P19 (SESE) with D1
Relative Fluorescence Intensity
1
0
350
400
450
500
550
600
650
Wavelength (nm)
P19
P19+D1

TECHNICAL NOTES

PEGylation of a Maltose Biosensor Promotes Enhanced Signal Response When Immobilized in a Silica Sol−Gel

Andrew M. Dattelbaum,[‡] Gary A. Baker,[§] John M. Fox,[†] Srinivas Iyer,[‡] and Jonathan D. Dattelbaum*,[†]

Department of Chemistry, University of Richmond, Gottwald Center for the Sciences, 28 Westhampton Way, Richmond, Virginia 23173, Center for Integrated Nanotechnologies, Los Alamos National Lab, Los Alamos, New Mexico 87545, and Chemical Sciences Division, Oak Ridge National Lab, Oak Ridge, Tennessee 37831. Received August 3, 2009; Revised Manuscript Received October 23, 2009

A robust method to immobilize a maltose biosensor is described using an engineered maltose periplasmic binding protein (PBP) covalently coupled to NBDamide, an environmentally sensitive fluorophore. A mesoporous silica sol−gel derived from diglycerylsilane (DGS) was constructed to embed the maltose biosensor, and the ligand reporting fluorescence properties were measured. When sequestered in the DGS-derived silica matrix, the biosensor retained maltose-dependent fluorescence sensing capability with micromolar affinity, which is consistent with the protein free in solution. The MBP-NBD conjugate was further modified by covalent conjugation with poly(ethylene glycol)-5000 (PEG) to promote the retention of water molecules around the protein and to reduce possible steric effects between the silica matrix and protein. Bioconjugation with PEG molecules does not significantly affect the signaling response of the protein in solution. When immobilized in the DGS polymer, a consistent increase in fluorescence intensity was observed as compared to the protein not functionalized with PEG. To our knowledge, this report presents the first successful method to embed a PBP biosensor in a polymerized matrix and retain signaling response using an environmentally sensitive probe. The immobilization method presented here should be easily adaptable to all conformation-dependent biosensors.

INTRODUCTION

The construction of protein biosensors for the detection of analytical targets requires high ligand specificity and selectivity, combined with a robust delivery strategy (e.g., *refs* 1, 2). The first two criteria are determined by the polypeptide utilized in the biosensing scheme, whereas a reliable way to mobilize the sensor out of the lab requires a deliberate, empirical approach that ideally leads to operational and storage stability (*3*). One protein superfamily studied for the design of fluorescent protein biosensors is the periplasmic binding proteins [1](PBPs), which facilitate the collection of nutrients from the surrounding environment for use in bacterial metabolism (*4*). A diverse set of PBPs has been characterized with binding capabilities to a variety of ligands including metals, sugars, amino acids, and anions (*5*−*7*). PBPs share a conserved structural organization whereby a single polypeptide chain folds into two easily identifiable domains separated by a hinge region where binding to cognate ligand may occur (*8*). Upon ligand binding, the protein domains undergo large bending or rotational motions around the hinge region. As a result of these well-documented conformational changes, many spectroscopic and electrochemical techniques provide a measurable signal output to report on ligand binding.

Two factors have inhibited the advancement of promoting the design of PBP biosensors. First, because large conformational changes are required for signal transduction, it has been difficult to construct a system using these potential biosensors embedded in a polymeric matrix which typically prevents conformational flexibility. Second, the majority of PBP biosensors are designed using environmentally sensitive probes covalently attached to single cysteine residues (*5*). Because all measurements and associated calculations are optimized in an aqueous solution, transfer of the system to an altered environment (e.g., different polarity medium) may have a significant impact on signal output, response, and stability. In this report, we tested a silica gel polymer derived from diglycerylsilane (DGS) as a carrier for a maltose biosensor. Sugar alcohol- and polyol-modified silanes, such as DGS, have been extensively used for the gentle encapsulation of biomolecules because these materials condense at neutral pH while releasing benign glycerol molecules (*9*−*11*). We also examined the effect of covalent attachment of poly(ethylene glycol) (PEG) on maltose-dependent fluorescence intensity changes upon encapsulation in the sol−gel; this polymer conjugation is intended to increase the hydration of the protein, as well as prevent interactions between the protein and silica matrix walls. To our knowledge, this report presents the first successful method to embed a PBP biosensor in a polymerized matrix and retain signaling response using an

* To whom correspondence should be addressed: jdattelb@richmond.edu.

[†] Gottwald Center for the Sciences.

[‡] Los Alamos National Lab.

[§] Oak Ridge National Lab.

[1]Abbreviations: PBP, bacterial periplasmic binding proteins; MBP, *Escherichia coli* maltose binding protein; NBD, *N*,*N*′-dimethyl-*N*-(iodoacetyl)-*N*′-(7-nitrobenz-2-oxa-1,3-diazol-4-yl)ethylenediamine; DGS, diglycerylsilane; PEG, poly(ethylene glycol) 5000-NHS ester; MALDI-TOF, matrix assisted laser desorption/ionization−time-of-flight; MS, mass spectrometry.

10.1021/bc900341s © 2009 American Chemical Society
Published on Web 11/24/2009

environmentally sensitive probe. The immobilization method presented here is general and should be easily adaptable to other conformation-dependent biosensors.

EXPERIMENTAL SECTION

Construction of the Maltose Biosensor. Purification of *E. coli* MBP D95C was performed as previously described using Ni-NTA affinity chromatography (*12*). Covalent attachment of a thiol-reactive NBDamide (Anaspec, Inc., San Jose, CA) was performed either at room temperature for 4 h or overnight at 4 °C in the dark with a 3-fold molar excess of dye. Unbound probe was removed using PD-10 gel filtration chromatography followed by dialysis against 5 mM phosphate buffer, pH 7.0. Typically, PEGylation was then performed by combining an 8-fold molar excess of NHS-PEG-5000 (Nanocs, Inc.) to MBP D95C for 12 h at room temperature. The mixture was then filtered through a 10 kDa microcentrifuge column (Microcon) to remove unreacted PEG; no further attempt was made to separate PEGylated protein from the unmodified protein. Dynamic light scattering (Zetasizer Nano, Malvern Instruments) was used to measure the hydrodynamic radii of the protein before and after PEGylation. Mass spectrometry was performed on a 4800 Plus (ABI, Framingham, MA) MALDI-TOF mass spectrometer.

DGS was synthesized following previously reported procedures (*13, 14*). In a typical silica gel preparation, ~150 mg of DGS was partially dissolved in deionized water (>18.0 MΩ cm) and sonicated for 30 min at 10−15 °C. The resulting solution was filtered through a 0.45 μm polycarbonate filter to remove any undissolved particulates of DGS and then mixed in a 96 well plate with an equal volume of labeled protein in 5 mM phosphate buffer (pH 7). The resulting monoliths measure 7 mm × 6 mm (height × width). The plate was covered with parafilm, and samples were allowed to gel at 4 °C for at least 5 days before performing maltose binding assays. Sensors were stable and operationally viable for at least 2 months stored at 4 °C.

Steady-State Fluorescence. Fluorescence measurements were performed at room temperature using a Varian Cary Eclipse spectrofluorometer equipped with a plate reader and thin film polarizers set to the magic angle (0° excitation and 54.7° emission). Protein conjugate samples were excited at 480 nm and were titrated with increasing amounts of maltose to achieve signal saturation. Fluorescence intensity at the emission maximum was plotted against maltose concentration to determine the apparent binding constant of the protein conjugate as previously described (*15*). Data analysis was performed using the nonlinear curve fitting procedures in the *Origin 7.0* software.

RESULTS AND DISCUSSION

The maltose-dependent fluorescence response of a MBP-D95C mutant labeled with IANBDamide (NBD) has been characterized previously (*12*). This bioconjugate sensing system is one of the few PBP biosensors where the mechanism of ligand-dependent fluorescence change is understood to result from a specific hydrogen bond interaction between the NBD and the hydroxyl group on Tyr171. Upon binding maltose, the hinge-bending motion of MBP removes this contact resulting in an increase in NBD emission. For device applications, immobilization of these types of proteins in a solid matrix is preferred. However, many encapsulating systems, like silica, dehydrate over time causing proteins to denature. Functionalization of MBP with a poly(ethylene glycol) (PEG) polymer may improve the protein's ability to maintain proper conformation in a solid matrix, as PEG is known to be heavily hydrated by water (*16*). In addition, the steric bulk of the PEG moieties should reduce protein−matrix sidewall interactions, which can disrupt protein function (*17*).

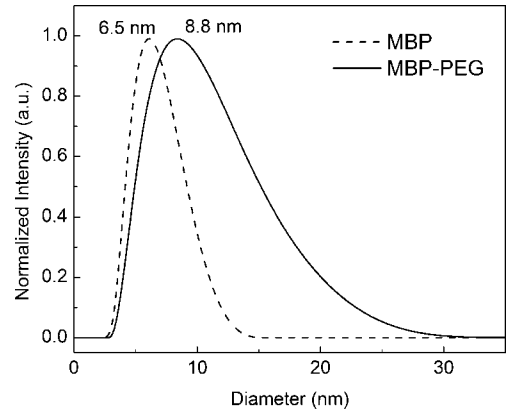

Figure 1. Representative dynamic light scattering data for MBP D95C before (6.5 nm) and after (8.8 nm) the reaction with an 8-fold molar excess of amine-reactive PEG-5000.

Prior to encapsulation, we investigated the addition of an amine-reactive PEG-5000 moiety to lysine residues of the maltose biosensor. Because PEG is spectroscopically inactive, we used dynamic light scattering to measure the increase in molecular volume upon reaction with PEG and MALDI-TOF MS to further characterize the PEGylated biomolecules. Before the PEGylation reaction, the ensemble of proteins in the MBP solution showed a narrow light scattering curve with an average diameter of 6.5 nm, as seen in Figure 1, which is consistent with previous determinations of the hydrodynamic radius for similar MBP monomeric proteins in solution (*18*). Following the labeling of amino groups with 8 mol equiv of PEG, the mean distribution broadened significantly and shifted to an average diameter near 8.8 nm (Figure 1). While there is a clear increase in the hydrodynamic diameter for the PEGylated-MBP which represents a correlation to the increase in size of the protein−PEG conjugate, it is difficult to quantitatively determine the average number of PEG molecules attached to each protein (*19*). A distribution of the number of PEG units covalently attached to the protein is observed, and additional experimentation with changes to the PEG and protein concentration had little effect on the resulting scattering data providing consistent evidence for the addition of PEG molecules to the protein. To further investigate what PEGylated species were present following conjugation, MALDI-TOF MS was used. Prior to PEGylation, a singly charged MBP parent ion was observed around 42 kDa. After PEGylation, three new peaks were observed at ~46 kDa, 52 kDa, and 56 kDa as expected for MBP plus one, two, or three PEG molecules, respectively (see Supporting Information), along with the parent MBP ion at ~42 kDa. While MALDI of intact proteins is not accurately quantitative, these spectra provide a reasonable estimate of the level of PEGylation in our samples. Taken together, the DLS and MALDI-TOF data demonstrate that MBP was labeled with a distribution of PEG groups.

Following PEGylation, we tested the protein samples for any quantitative differences in maltose sensing ability in solution compared to the non-PEGylated protein sensor. The fluorescence response of NBD-labeled MBP with and without PEG showed no significant differences in phosphate buffered solution with respect to reporting on maltose concentration (Figure 2). A 4.5-fold increase in fluorescence was measured for both systems, and the dissociation constant for maltose of the PEGylated protein conjugate was determined to be 5 μM (Figure 2, inset). PEGylation of the protein does not produce a noticeable lag in response time in solution, where signal equilibrium is reached within the mixing time. Also, the dissociation constant measured

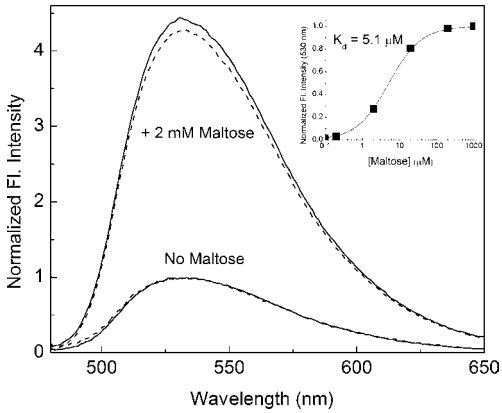

Figure 2. Fluorescence emission spectra of MBP D95C-NBD with (solid lines) and without (dashed lines) the attachment of PEG in the presence and absence of maltose. (inset) Titration of PEGylated protein with maltose in solution yields a dissociation constant of 5 μM.

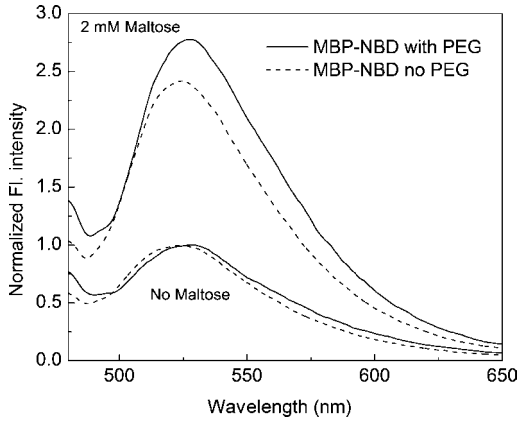

Figure 3. Fluorescense spectra of a maltose biosensor embedded in DGS before (dashed) and after (solid) conjugation with PEG. Spectra were normalized to the signal measured for the unbound protein immobilized in DGS. Samples were prehydrated with phosphate buffer, pD 7.0, and measurement was performed in a 96 well plate.

for the PEGylated protein is consistent with the value found previously for the maltose sensor in the absence of PEG, providing further support that the PEG molecules conjugated to the MBP sensor do not produce a significant effect on the binding characteristics of the protein (*12*).

The fluorescently tagged MBP with and without PEG conjugation was encapsulated into DGS-derived sol−gel slabs or cast as thin films in 96 well plates. Several spectral differences were observed between unmodified and PEGylated protein upon encapsulation into the DGS polymer and titration with maltose. The fluorescence intensity of the starting material was checked prior to addition of ligand to ensure consistency of the experimental data collected. Following immobilization in the DGS-derived sol−gels, the PEGylated sensor demonstrated a 2.8-fold increase in fluorescence intensity upon saturation with maltose, while the protein without PEG showed a smaller 2.4-fold change in emission intensity (Figure 3). In general, we observed a ∼10% increase in fluorescence from PEG-functionalized MBP compared to unfunctionalized MBP upon encapsulation and exposure to maltose. Additionally, we observed a 5 nm red shift of the NBD emission maximum in the PEGylated MBP, which suggests that the probe molecule may be experiencing an increased level of polarity in its microenvironment compared to the protein free in solution (*20*). While a difference in signal intensity is observed between the two protein conjugates trapped in DGS-derived sol−gel films, titration with

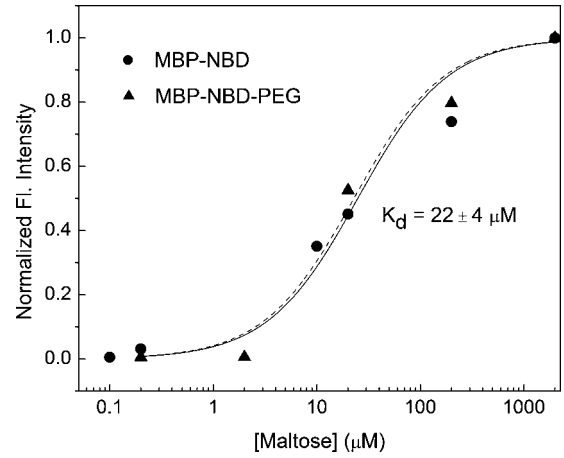

Figure 4. Representative maltose titration data for the constructed biosensor in DGS with (triangle) and without (circle) the covalent attachment of PRG-5000. The data were fit to a single binding isotherm and the K_d was calculated to be approximately 22 μM for maltose for both sensors.

increasing concentrations of maltose (0 to 2 mM) yielded similar dissociation constants (∼22 μM) as shown in Figure 4.

There have been few reports in the literature describing the successful interface of PBP-based fluorescent biosensors on surfaces for the construction of immobilized biosensors. Cass and colleagues reported the first successful surface immobilization of a PBP biosensor using a glutamine binding protein translational fusion with a C-terminal hydrophobic polypeptide (*21*). Using thermophilic PBPs, deLormier et al. were able to covalently attach glucose and ribose sensing proteins to the bottom of well plates via masked cysteine residues (*22*). However, both of these methods required further engineering of the protein biosensor, and because emission is provided from a single layer of protein molecules, there is a reduced level of signal intensity which may lower the sensitivity of the sensor. There are examples in the literature of protein immobilization entrapment in silica-based polymers with retention of ligand binding and fluorescence signaling (*20, 23*); however, these systems typically do not require the magnitude of the conformational flexibility needed for ligand binding in PBPs.

We tested the ability of an MBP sensor to respond to maltose when encapsulated in a DGS-derived silica matrix. The ideal matrix needs to allow easy diffusion of ligand to the protein, as well as allowing for the conformational transition between open and closed states of MBP, which is required for proper signal transduction of the binding event. Typical matrices used to embed proteins include polyvinyl alcohol, carboxydextran, and polyethylenimine. All of these polymers have been tried and found to greatly reduce or eliminate the ligand-dependent fluorescence response of PBP-based biosensors (unpublished observations). DGS, however, forms a silica gel that has not previously been used with PBP sensing systems and has several benefits including condensation at neutral pH and optical transparency. The DGS matrix was shown to be effective at allowing an observable signaling response to maltose. Although there was a considerable lag in response time compared to solution (∼20 min for 50% signal intensity), there is no difference in time response between PEGylated and non-PEG protein in DGS, suggesting that the time required for signaling is most likely due to diffusion of maltose into the DGS matrix. Retention of protein flexibility upon entrapment is clearly adequate for maintenance of equilibrium binding affinity, despite the slowed dynamics upon entrapment within the biogels. This trend is consistent with earlier observations showing arrested nanosecond rotational reorientation dynamics for intact poly-

clonal antidansyl antibodies sequestered within sol−gel-derived biogels accompanied by minimal losses in the equilibrium binding constant describing antibody association with its target hapten (*24*). Covalent conjugation with PEG may have increased the stability of MBP by keeping it better hydrated even after immobilization within the silica gel, as well as minimizing denaturing steric effects. We believe that the beneficial effects of PEGylation will be even more significant for PBP biosensors where the signaling response is not as well-characterized as the MBP system studied here. In summary, the covalent attachment of PEG chains to residues on protein surfaces, followed by mild immobilization procedures based upon bioconjugate entrapment within sol−gels formed from biofriendly precursors such as DGS, may prove to be a generic approach to designing robust, portable fluorescent protein biosensor platforms and forms the subject of future research in our group.

ACKNOWLEDGMENT

JDD thanks Research Corporation for contributing funding to this work. This work was performed, in part, at the Center for Integrated Nanotechnologies (CINT), a U.S. Department of Energy, Office of Basic Energy Sciences user facility. Los Alamos National Laboratory, an affirmative action equal opportunity employer, is operated by Los Alamos National Security, LLC, for the National Nuclear Security Administration of the U.S. Department of Energy under contract DE-AC52-06NA25396.

Supporting Information Available: Additional figure as described in the text. This material is available free of charge via the Internet at http://pubs.acs.org.

LITERATURE CITED

(1) Dattelbaum, J. D. (2009) Genetically engineered proteins as recognition receptors, In *Recognition receptors in biosensors* (Zourob, M., Ed.) Springer, New York.
(2) Hosse, R. J., Rothe, A., and Power, B. E. (2006) A new generation of protein display scaffolds for molecular recognition. *Protein Sci. 15*, 14–27.
(3) D'Souza, S. F. (2001) Immobilization and stabilization of biomaterials for biosensor applications. *Appl. Biochem. Biotechnol. 96*, 225–238.
(4) Higgins, C. F. (1992) Abc transporters: From microorganisms to man. *Annu. Rev. Cell Biol. 8*, 67–113.
(5) deLorimier, R. M., Smith, J. J., Dwyer, M. A., Looger, L. L., Sali, K. M., Paavola, C. D., Rizk, S. S., Sadigov, S., Conrad, D. W., Loew, L., and Hellinga, H. W. (2002) Construction of a fluorescent biosensor family. *Protein Sci. 11*, 2655–2675.
(6) Moschou, E. A., Bachas, L. G., Daunert, S., and Deo, S. K. (2006) Binding proteins: Unraveling their analytical potential. *Anal. Chem. 78*, 6693–6700.
(7) Dwyer, M. A., and Hellinga, H. W. (2004) Periplasmic binding proteins: A versatile superfamily for protein engineering. *Curr. Opin. Struct. Biol. 14*, 495–504.
(8) Quiocho, F. A. (2002) Paradigms for protein-ligand interactions. *ACS Symp. Ser. 827*, 216–230.
(9) Besanger, T. R., Chen, Y., Deisingh, A. K., Hodgson, R., Jin, W., Mayer, S., Brook, M. A., and Brennan, J. D. (2003) Screening of inhibitors using enzymes entrapped in sol-gel -derived materials. *Anal. Chem. 75*, 2382–2391.
(10) Avnir, D., Coradin, T., O., L., and Livage, J. (2006) Recent bio-applications of sol-gel materials. *J. Mater. Chem. 16*, 1013–1030.
(11) Brennan, J. D. (2007) Biofriendly sol-gel processing for the entrapment of solution and membrane-bound proteins: Toward novel solid-phase assays for high-throughput screening. *Acc. Chem. Res. 40*, 827–835.
(12) Dattelbaum, J. D., Looger, L. L., Benson, D. E., Sali, K. M., Thompson, R. B., and Hellinga, H. W. (2005) Analysis of allosteric signal transduction mechanisms in an engineered fluorescent maltose biosensor. *Protein Sci. 14*, 284–291.
(13) Satishkumar, B. C., Doorn, S. K., Baker, G. A., and Dattelbaum, A. M. (2008) Fluorescent single walled carbon nanotube/silica composite materials. *ACS Nano 2*, 2283–2290.
(14) Brook, M. A., Chen, Y., Guo, K., Zhang, Z., and Brennan, J. D. (2004) Sugar-modified silanes: Precursors for silica monoliths. *J. Mater. Chem. 14*, 1469–1479.
(15) Dattelbaum, J. D., and Lakowicz, J. R. (2001) Optical determination of glutamine using a genetically engineered protein. *Anal. Biochem. 291*, 89–95.
(16) Oesterhelt, F., Rief, M., and Gaub, H. E. (1999) Single molecule force spectroscopy by afm indicates helical structure of poly(ethylene-glycol) in water. *New J. Phys. 1*, 6.16.11.
(17) Bailon, P., and Won, C.-Y. (2009) Peg-modified biopharmaceuticals. *Expert Opin. Drug Delivery 6*, 1–16.
(18) Shilton, B. H., Flocco, M. M., Nilsson, M., and Mowbray, S. L. (1996) Conformational changes of three periplasmic receptors for bacterial chemotaxis and transport: The maltose-, glucose/galactose- and ribose-binding proteins. *J. Mol. Biol. 264*, 350–363.
(19) Kusterle, M., Jevsevar, S., and Porekar, V. G. (2008) Size of pegylated protein conjugates studied by various methods. *Acta Chim. Slov. 55*, 594–601.
(20) Brennan, J. D., Flora, K. K., Bendiak, G. N., Baker, G. A., Kane, M. A., Pandey, S., and Bright, F. V. (2000) Probing the origins of spectroscopic responses to analyte-induced conformational changes in fluorescently-labeled cod iii parvalbumin. *J. Phys. Chem. B 194*, 10100–10110.
(21) Wada, A., Mie, M., Aizawa, M., Lahoud, P., Cass, A. E., and Kobatake, E. (2003) Design and construction of glutamine binding proteins with a self-adhering capability to unmodified hydrophobic surfaces as reagentless fluorescence sensing devices. *Inorg. Chem. 125*, 16228–16234.
(22) deLorimier, R. M., Tian, Y., and Hellinga, H. W. (2006) Binding and signaling of surface-immobilized reagentless fluorescent biosensors derived from periplasmic binding proteins. *Protein Sci. 15*, 1936–1944.
(23) Flora, K. K., and Brennan, J. D. (1998) Fluorometric detection of Ca^{2+} based on an induced change in the conformation of sol-gel entrapped parvalbumin. *Anal. Chem. 70*, 4505–4513.
(24) Doody, M. A., Baker, G. A., Pandey, S., and Bright, F. V. (2000) Affinity and mobility of polyclonal anti-dansyl antibodies sequestered within sol-gel-derived biogels. *Chem. Mater. 12*, 1142–1147.

BC900341S

Supplementary figure 1.

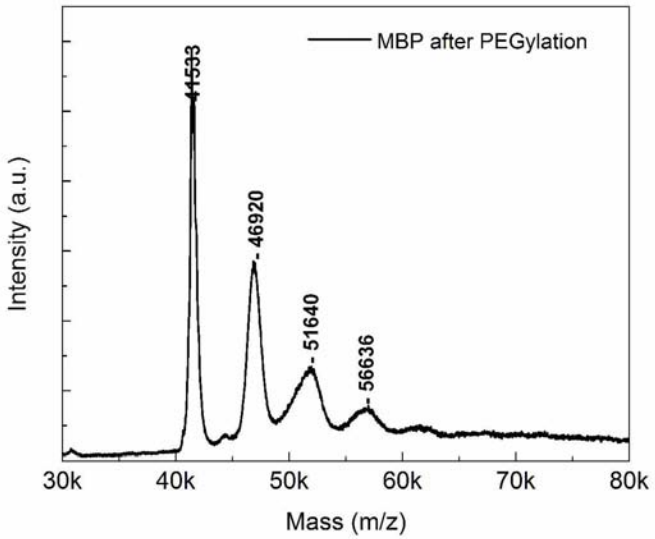

205x268mm (600 x 600 DPI)